JOURNAL OF AGRICULTURAL AND FOOD CHEMISTRY

Article

pubs.acs.org/JAFC

Microbial Synthesis of Myrcene by Metabolically Engineered *Escherichia coli*

Eun-Mi Kim,[†] Jin-Hee Eom,[†,‡] Youngsoon Um,[†,∥] Yunje Kim,[†] and Han Min Woo*[,†,§,∥]

[†]Clean Energy Research Center, Korea Institute of Science and Technology, Hwarang-ro 14-gil 5, Seongbuk-gu, Seoul 136-791, Republic of Korea

[‡]Department of Chemistry, and [§]Green School (Graduate School of Energy and Environment), Korea University, 145 Anam-ro, Seongbuk-gu, Seoul 136-701, Republic of Korea

[∥]Department of Clean Energy and Chemical Engineering, Korea University of Science and Technology, 217 Gajeong-ro, Yuseong-gu, Daejeon 305-350, Republic of Korea

ABSTRACT: Myrcene, a monoterpene (C_{10}), has gathered attention as a starting material for high-value compounds, such as geraniol/linalool and (−)-menthol. Metabolic engineering has been successfully applied to produce monoterpenes, such as pinene and limonene, at high levels in microbial hosts. However, microbial synthesis of myrcene has not yet been reported. Thus, we metabolically engineered *Escherichia coli* for production of myrcene by introducing a heterologous mevalonate pathway and overexpressing tailoring enzymes, such as geranyl diphosphate synthase (GPPS) and myrcene synthase (MS). Although MSs have broad ranges of functionality for producing various monoterpenes, our engineered *E. coli* strains harboring MS from *Quercus ilex* L. produced only myrcene (1.67 ± 0.029 mg/L). Subsequent engineering resulted in higher production of myrcene by optimizing the levels of GPPS in amino-acid-enriched (EZ-rich) defined medium, where glycerol as a carbon source was used. The production level of myrcene (58.19 ± 12.13 mg/L) was enhanced by 34-fold using *in situ* two-phase extraction to eliminate cellular toxicity and the evaporation of myrcene.

KEYWORDS: *mevalonate pathway, metabolic engineering, monoterpene, myrcene*

INTRODUCTION

Monoterpenes [C_{10} terpenes, consisting of two isoprene (C_5) units] are an important and large class of natural products that are widely used in the cosmetic and pharmaceutical industries.[1,2] Either the mevalonate (MVA) pathway[3] in eukaryotes and some bacteria or the methylerythritol phosphate (MEP) pathway[4] in plastids, bacteria, protozoa, and algae can produce isopentenyl diphosphate (IPP) and dimethylallyl disphosphate (DMAPP). These are catalyzed by prenyltransferase to form geranyl diphosphate (GPP, a precursor to monoterpene), which is further converted to monoterpene by various monoterpene synthases. Over 1000 naturally occurring monoterpenes (C_{10}; acylic-, mono-, and bicyclic monoterpene isomers) have been identified among the volatile organic compounds found in the resins of many woody plants, notably in citrus plants.[5]

Among the monoterpenes, myrcene (β-myrcene, the only naturally occurring isomer) has been considered as a starting material for complex compounds, including heteroatom-linked chemicals (nerol/geraniol/linalool) and carbon-rearranged chemicals [(−)-menthol], which can be used as commercial olefinic scents.[1] Myrcene synthase (MS) encoded by cDNA from flowers,[6] grand fir,[7] holm oak,[8] and labiatae leaves[9] was isolated and functionally characterized. Although myrcene can be extracted from essential oils or derived from β-pinene by pyrolysis, economic large-scale production has not yet been commercialized because of the high volatility of the substance and the inefficiency of the harvesting technology. Thus, development of engineered microbial platforms for large-scale industrial production is needed to provide myrcene from sugars.[10,11]

Metabolic engineering of microorganisms has enabled production of monoterpenes, such as α/β-pinene,[12−14] limonene,[15,16] and sabinene.[17] The monoterpenes were biosynthesized in *Escherichia coli* by introducing a heterologous MVA pathway for re-directing carbon flux from acetyl-coA to IPP/DMAPP and in a yeast by engineering the native MVA pathway. However, the levels of monoterpenes are lower than the levels of sesquiterpene[18,19] (C_{15}) or diterpene[20] (C_{20}) from the same microbial hosts, suggesting that geranyl pyrophosphate synthase (GPPS) and monoterpene synthase are still bottlenecks to high-level productions. It is also important that monoterpenes, including myrcene, are toxic to microbial hosts (minimum inhibitory concentrations: myrcene, 2.12 mM; β-pinene, 1.45 mM; and limonene, 0.44 mM, for yeast).[12,15,21,22]

Here, we report metabolic engineering of *E. coli* for the production of myrcene using heterologous expression of the MVA pathway and engineering at prenyl phosphate nodes with overexpression of GPPS and MS. In addition, the toxicity of myrcene was investigated and relieved in *E. coli* using *in situ* two-phase extraction. Further biological engineering to optimize high-cell-density fermentation will be the next challenge for achieving high-level myrcene production for industrial applications.

MATERIALS AND METHODS

Construction of Plasmids and Strains. *E. coli* DH5α (RBC Bioscience, Songnam, South Korea) was used as a host for cloning.

Received: March 4, 2015
Revised: April 23, 2015
Accepted: April 24, 2015
Published: April 24, 2015

ACS Publications © 2015 American Chemical Society

DOI: 10.1021/acs.jafc.5b01334
J. Agric. Food Chem. 2015, 63, 4606−4612

Table 1. Bacteria Strains and Plasmids Used in This Study

strain or plasmid	relevant characteristics	reference
	Strains	
E. coli HIT-DH5α	F⁻(80d *lac*Z M15) (*lac*ZYA-*arg*F) U169 *hsd*R17($r^- m^+$) *rec*A1 *end*A1 *rel*A1 *deo*R96	RBC Bioscience
E. coli DH1	F- endA1 recA1 gyrA96 thi-1 glnV44 relA1 hsdR17(rK-mK+) λ-	CGSC
myrcene producing *E. coli* DH1	DH1, co-transformation of MevT-MBI plasmid and myrcene production plasmid	this work
	Plasmids	
pBbA5c-RFP	p15A, Cm^r, P_{lacUV5}, *rfp*	21
pBbE1a-RFP	ColE1, Amp^r, P_{trc}, *rfp*	21
pBbA5c-MevT(co)-MBIS(co)	p15A, Cm^r, P_{lacUV5}, MVA pathway genes	22
pM1	p15A, Cm^r, P_{lacUV5}, pBbA5c-MevT(co)-MBI(co)	this work
pM2	p15A, Cm^r, P_{lacUV5}, pBbA5c-MevT(co)-MBI(co)-tGPPS2(co.Ag)	this work
pM3	p15A, Cm^r, P_{lacUV5}, P_{trc}, pBbA5c-MevT(co)-T1-MBI(co)	this work
pM4	p15A, Cm^r, P_{lacUV5}, P_{trc}, pBbA5c-MevT(co)-T1-MBI(co)-tGPPS2(co.Ag)	this work
pM(Ag)	ColE1, Amp^r, P_{trc}, tMS from *A. grandis*, pBbE1a-tMS(co.Ag)	this work
pM(Pf)	ColE1, Amp^r, P_{trc}, tMS from *P. frutescens*, pBbE1a-tMS(co.Pf)	this work
pM(Qi)	ColE1, Amp^r, P_{trc}, tMS from *Q. ilex* L., pBbE1a-tMS(co.Qi)	this work
pGM(Ag)	ColE1, Amp^r, P_{trc}, tGPPS2 and tMS from *A. grandis*, pBbE1a-tGPPS2(co.Ag)-tMS(co.Ag)	this work
pGM(Pf)	ColE1, Amp^r, P_{trc}, tGPPS2 from *A. grandis* and tMS from *P. fruntescens*, pBbE1a-tGPPS2(co.Ag)-tMS(co.Pf)	this work
pGM(Qi)	ColE1, Amp^r, P_{trc}, tGPPS2 from *A. grandis* and tMS from *Q. ilex* L., pBbE1a-tGPPS2(co.Ag)-tMS(co.Qi)	this work

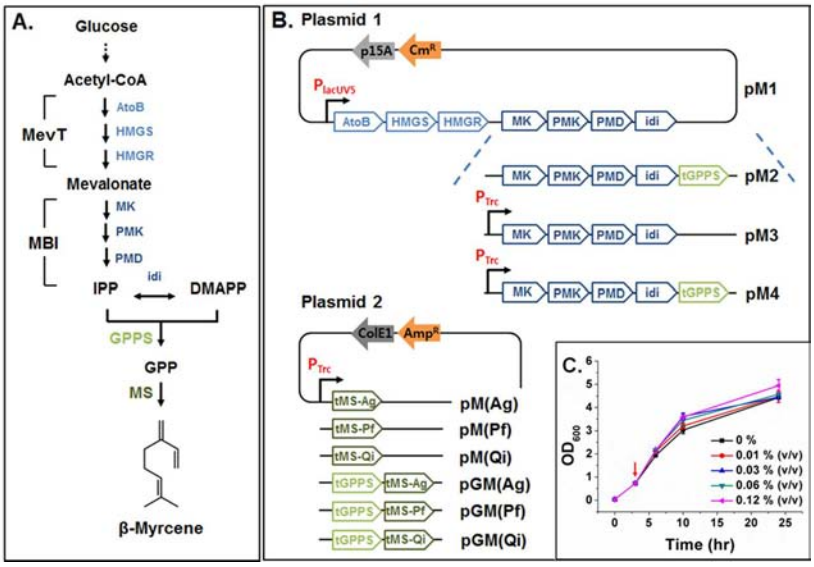

Figure 1. Scheme of myrcene production in engineered *E. coli* and the cellular toxicity of myrcene. (A) Construction of the myrcene biosynthetic pathway in *E. coli*. The heterologous MVA pathway in *E. coli* consists of six enzymes for conversion from acetyl-CoA to IPP. To convert IPP to myrcene, GPPS and MS were expressed. Abbreviations of the corresponding genes to the MVA pathway were described in the Materials and Methods. (B) Plasmid construction for metabolic engineering of *E. coli* for myrcene production. A two-plasmid system was used. Plasmid 1 contains genes corresponding to the MVA pathway or MVA pathway with truncated AgGPPS2 on a medium copy number vector and medium strength promoter. Plasmid 2 harbors genes encoding for tMS or tGPPS2-MS on a high copy number vector and strong promoter. Three different kinds of MSs were introduced. (C) Cellular toxicity test of myrcene to *E. coli*. Growth of *E. coli* under various concentrations of myrcene [0, 0.01, 0.03, 0.06, and 0.12% (v/v)] was tested. The arrow indicates the myrcene addition to the culture medium at OD_{600} of 1.

All plasmids and strains used in this study are listed in Table 1. All plasmids were prepared from the BglBrick expression plasmid library using the BglBrick standard cloning method.[23,24]

For construction of the heterologous MVA pathway in *E. coli*, the top portion (MevT) of the MVA pathway (Figure 1A) contains three genes needed for the conversion of acetyl-CoA to MVA.[18] These are the genes encoding for acetyl-CoA thiolase (AtoB from *E. coli*), 3-hydroxyl-3-methyl-glutaryl-coA synthase, and reductase (HMGS and HMGR from *Saccharomyces cerevisiae*). The bottom portion (MBI) of the MVA pathway contains four genes for the conversion of MVA to IPP and DMAPP.[25] These are the genes encoding mevalonate kinase (MK from *S. cerevisiae*), phosphomevalonate kinase (PMK from *S. cerevisiae*), mevalonate diphosphate decarboxylase (PMD from *S. cerevisiae*), and isopentenyl diphosphate isomerase (Idi from *E. coli*). For construction of the MVA pathway plasmids (plasmid 1 in Figure 1B), the gene encoding for farnesyl disphodphate synthase from *E. coli* (*ispA*) was removed from pBbA5c-MevT(co)-MBIS(co, ispA)[25] using polymerase chain reaction (PCR) amplification of MevT(co)-MBI(co) (forward primer, 5′-ATT GAA TTC AAA AGA TCT AAA GGA GGC C-3′; reverse primer, 5′-TAT CTC GAG TTT GGA TCC TTA TTT AAG CTG GGT AAA TGC AG-3′, where underlines describe restriction enzyme sites), which was inserted into the pBbA5c plasmid. This resulted in a pM1 plasmid (Table 1). An additional pTrc promoter was inserted into a pM1, to construct a single operon of MevT and MBI, resulting in a pM3 plasmid. The DNA sequences were confirmed by DNA sequencing.

To convert IPP/DMAPP to myrcene, a myrcene production plasmid containing genes encoding for MS and GPPS was constructed. The

DOI: 10.1021/acs.jafc.5b01334
J. Agric. Food Chem. 2015, 63, 4606−4612

N-terminal plastid-targeting sequence of MSs and GPPS2 was truncated, and four codon-optimized genes (three MSs and one GPPS2) were synthesized (GenScript, Inc., Piscataway, NJ). Using the SignalP 4.1 server, amino acid sequences for signal peptide cleavage were predicted as followings: MS(Ag), 1−62; MS(Pf), 1−57; MS(Qi), 1−56; and GPPS2(Ag), 1−84, in the amino acid sequence. The genes encoding for MS were cloned in a pBbE1a, resulting in pM(Ag), pM(Pf), and pM(Qi). Subsequently, the gene encoding for GPPS2 was cloned into MevT-MBI plasmids (pM1 and pM3), resulting in pM2 and pM4. In addition, the *GPPS2* gene was cloned into the myrcene production plasmids, yielding the series pGM(Ag), pGM(Pf), and pGM(Qi). The gene accession numbers of MSs and GPPS2 are MS(Ag) from *Abies grandis* (AAB71084), MS(Pf) from *Perilla frutescens* (AAF76186), MS(Qi) from *Quercus ilex* L. (CAC41012), and GPPS2 from *A. grandis* (AF513112).

For myrcene production, the MevT-MBI plasmids and the myrcene production plasmids were combinatorially co-transformed into a *E. coli* DH1 strain, yielding different myrcene production strains.

Growth Conditions for Myrcene Toxicity Test. *E. coli* DH1 was used as a host for the myrcene toxicity test and was cultured in an amino-acid-enriched (EZ-rich) defined medium (Teknova, Hollister, CA) in an Erlenmeyer flask (250 mL) at 37 °C and 200 rpm. When cell densities reached an OD_{600} of 0.8−1.0, different concentrations of myrcene [0, 0.01, 0.03, 0.06, 0.12% (v/v)] were added for the myrcene toxicity test in the absence of dodecane overlay. Then, cells were cultivated at 30 °C and 200 rpm for optical density (OD) measurements.

Growth Conditions for Myrcene Production. *E. coli* DH1 was used as a host for myrcene production and was pre-cultured in Luria−Bertani (LB) medium. Myrcene production strains were grown in the three different media: LB medium, EZ-rich defined medium (Teknova, Hollister, CA), or M9-MOPS medium [M9 salt, 75 mM 3-(*N*-morpholino)propanesulfonic acid (MOPS), 2 mM $MgSO_4$, 0.01 mM $CaCl_2$, 1 mg/L thiamine·HCl, and 2.78 mg/L $FeSO_4$ at pH 7]. The micronutrients provided were 3 nM ammonium molybdate, 0.4 μM boric acid, 30 nM cobalt chloride, 23 nM cupric sulfate, 80 nM manganese chloride, and 10 nM zinc sulfate. These were supplemented with either 1% glucose or 1% glycerol. Chloramphenicol (Cm) and ampicillin (Amp) were provided for plasmid maintenance at final concentrations of 30 and 100 μg/mL, respectively.

Pre-cultured production strains were added to inoculate the media (1:100 dilution). For the cultivation in M9-MOPS medium, cells were adapted to M9-MOPS medium. The cultures (50 mL) were grown in an Erlenmeyer flask (250 mL) at 37 °C and 200 rpm. When cell densities reached at OD_{600} of 0.8−1.0, 100 μM isopropyl-β-D-1-thiogalactopyranoside (IPTG) was added for induction and 20% (v/v) dodecane overlay was added for *in situ* extraction. Cells were cultivated at 30 °C and 200 rpm for production of myrcene. Samples were collected from the dodecane layer at 24, 48, and 72 h for quantification of myrcene.

Myrcene Analysis and Quantification. After the centrifugation (4400*g* for 10 min), the dodecane layers were collected. The collected samples (20 μL) were diluted with ethyl acetate (980 μL) containing 5 μg/mL (−)-*trans*-caryophyllene as an internal standard. To quantify myrcene, the diluted samples were analyzed using gas chromatography−mass spectrometry [GC−MS, Aglilent 6890N series GC/TOF-MS (LECO), under these conditions: injector temperature, 250 °C; flow rate, 1.2 mL/min; split ratio, 2:1; oven initially at 60 °C for 5 min, followed by 4 °C/min, and increase to 240 °C; carrier gas, He; and HP-Ultra2 column (25 m long, 0.2 mm diameter, and 0.11 μm film thick)]. Myrcene (CAS Registry Number 123-35-3) was used as an authentic standard for quantitative analysis, and the concentrations were normalized using an internal standard. All chemicals used in this study were purchased from Sigma-Aldrich.

RESULTS AND DISCUSSION

Development of the *E. coli* Strain for Myrcene Production. For microbial production of myrcene, a two-plasmid system was employed to modulate the MVA pathway and terpene biosynthesis as previously studied.[18,26] The first plasmid, MevT-MBI (plasmid 1 in Figure 1B), consisted of seven genes of the heterologous MVA pathway (see the Materials and Methods). As shown by the authors of the previous studies,[15,18,26] balanced gene expression was crucial for high-level production of terpenes. Because a pBbA5c vector containing a medium copy origin and a medium strength promoter has worked for production of various terpenes, including mono- and sesquiterpenes,[12,18,27] we also chose the pBbA5c vector for the expression of MVA pathway genes. In combination with the MevT-MBI plasmid, we chose the pBbE1a vector (the second plasmid), which has a high copy origin and a strong pTrc promoter. Thus, MS was overexpressed in the pBbE1a vector (plasmid 2 in Figure 1B) to achieve myrcene production based on the "push and pull strategy" of metabolic engineering. Also, this two-plasmid system allowed screening for more efficient MS versions, from diverse candidates.

Another important strategy for myrcene production is providing sufficient intermediates. Biosynthesis of monoterpene in an engineered *E. coli* was previously limited because of insufficient GPP and the low activity of monoterpene synthase.[12,14] Combinational expression of tGPPS2 from *A. grandis* and pinene synthase Pt30 from *Pinus taeda* increased α-pinene production significantly up to 5.44 mg/L in a shaking flask and 0.95 g/L in fed-batch fermentation.[14] Thus, we used tGPPS2 from *A. grandis*, specific geranyl diphosphate synthase, which has been shown to achieve high production results in monoterpene synthesis.[12,15] Truncated AgGPPS2 was expressed in different plasmids to optimize gene expressions in (1) MevT-MBI plasmids (pM2/pM4), (2) myrcene production plasmids (pGM), and (3) both plasmids. AgGPPS2 expressions from different gene expression platforms could produce different levels of GPP, which are used as a substrate for MS. Also, higher levels of GPP might inhibit the activity of monoterpene synthase.[28] Therefore, optimal gene expression of GPP is to be examined for higher production of myrcene, and we constructed the Ec-pM1/pGM, Ec-pM2/pM, and Ec-pM2/pGM strains.

The last strategy for the development of the production strain was balancing gene expression in the MVA pathway. As shown previously using targeted proteomics, low expression of MK and PMK was identified as potential bottlenecks to sesquiterpene production.[26] To overcome low expression, a strong pTrc promoter was inserted to increase gene expressions in the bottom portion of MVA, resulting in high production of bisabolene[25] and limonene.[15] Thus, we employed this strategy, yielding Ec-pM3/pGM, Ec-pM4/pM, and Ec-pM4/pGM strains.

Monoterpene, including pinene and limonene, has been shown to exhibit microbial toxicity because of phase toxicity caused by extraction during cell−solvent contact and molecular level of toxicity.[13,21,22,29] To alleviate monoterpene toxicity, two-phase extraction fermentation was widely applied to restore the growth to the level of the control. Interestingly, myrcene showed relatively low toxicity to microbial cells. The minimum inhibitory concentration (MIC, the amount of terpene for 50% reduction in growth) of myrcene for *S. cerevisiae* is 2.12 mM (288 mg/L), higher compared to other monoterpenes (limonene, MIC of 0.4 mM; β-pinene, MIC of 1.45 mM).[21] Thus, we determined the myrcene toxicity in *E. coli* by adding different amounts of myrcene up to 0.12% (v/v) in the absence of dodecane when the cells reached an OD_{600} of 1 (Figure 1C). As a result, *E. coli* spiked with myrcene showed almost no growth inhibition. However, because myrcene has very low solubility (0.043 mM) and high volatility, we applied *in situ* extraction of myrcene from cell cultures using dodecane overlay.

Selection of Myrcene Synthases for Myrcene-Specific Production. Monoterpene synthases are capable of producing a

DOI: 10.1021/acs.jafc.5b01334
J. Agric. Food Chem. 2015, 63, 4606−4612

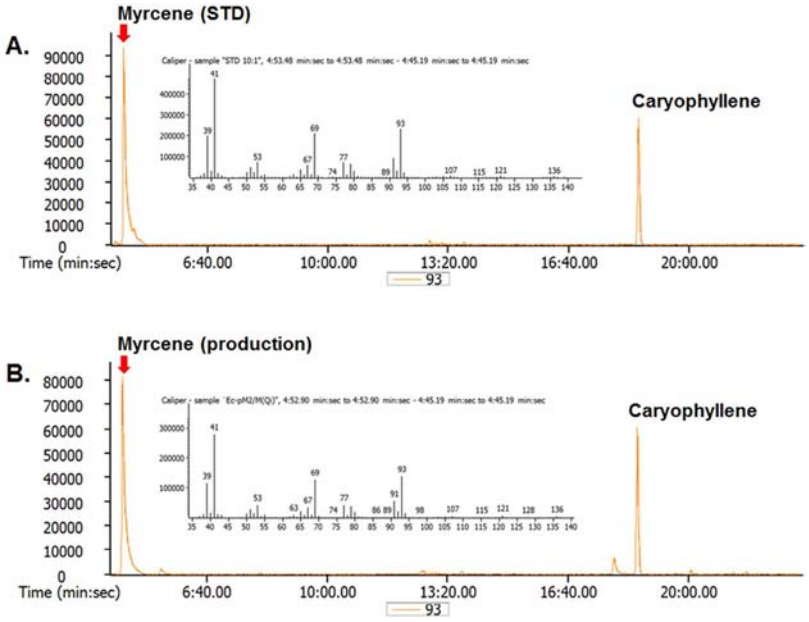

Figure 2. GC−MS analysis of dodecane fractions from the engineered *E. coli* strains: (A) standard myrcene and (B) myrcene produced by a production strain [Ec-pM2/pM(Qi)]. Caryophyllene was used as the internal standard.

variety of monoterpenes from GPP. Monoterpene synthase catalyzes divalent metal ion-dependent ionization and isomerization of GPP to enzyme-bound linalyl diphosphate, which further converts to various monoterpenes.[7] After isomerization and cyclic steps of the α-terpinyl cation, monocylic [(−)-limonene] and bicyclic [(−)-α/β-pinene and β-phellandrene] products were synthesized, whereas deprotonation of the carbocatation leads to an acyclic product (myrcene). Thus, it is important to express a myrcene-specific synthase in *E. coli* to achieve microbial synthesis of myrcene.

From the literature of identified and characterized MSs, we selected three promising MSs (from *A. grandis*,[7] *P. frutescens*,[9] and *Q. ilex* L.[8]). Using a two-plasmid system, we cloned each MS encoding gene, yielding pM(Ag), pM(Pf), and pM(Qi), respectively. Subsequently, each plasmid was co-transformed with the MevT-MBI plasmid in *E. coli* DH1. Thus, we constructed three production strains: Ec-pM1/pM(Ag), Ec-pM1/pM(Pf), and Ec-pM1/pM(Qi). None of these strains produced myrcene (data not shown). To express heterologous GPPS in *E. coli*, truncated AgGPPS2 was cloned into three MS-containing plasmids. As a result, Ec-pM2/pM(Ag), Ec-pM2/pM(Pf), and Ec-pM2/pM(Qi) were constructed. LB medium with 1% glucose was used for the production test. Only strains harboring MS(Qi) produced amounts of myrcene detectable by GC−MS (Figure 2A, 1.67 ± 0.029 mg/L myrcene was produced; limit of detection of 0.030 mg/L). As reported previously,[8] we also confirmed that MS(Qi)-expressing *E. coli* produced only myrcene and other side products were not detected. Therefore, we further engineered the *E. coli* strain harboring the MS(Qi)-encoding gene [Ec-pM2/pM(Qi)] to enhance myrcene production.

Microbial Synthesis of Myrcene. Metabolic engineering of the *E. coli* strain harboring the MS(Qi)-encoding gene was applied to increase myrcene production. On the basis of the "push and pull" strategy, we decided to overexpress AgGPPS2 in addition to MS. The Ec-pM2/pM(Qi), Ec-pM1/pGM(Qi), and Ec-pM2/pGM(Qi) strains were cultivated in LB medium with 1% glucose (Figure 3A). Over the production times (24, 48, and 72 h), the three strains produced low levels of myrcene (less than 2 mg/L). Thus, we changed the medium to the EZ-rich defined and M9-MOPS media with 1% glucose. The growth profiles were similar, regardless of the media and strains, resulting in the fact that the pattern of the myrcene concentration (mg/L) is almost identical to that of specific production of myrcene (mg/L/OD_{600}). Higher levels of myrcene (over 15 mg/L) were produced using the M9-MOPS medium compared to production when using the LB or EZ-rich media (Figure 3). Although each expression of AgGPPS2 in the three production strains was not quantitatively analyzed, different gene expressions of AgGPPS2 could be tested for the optimization based on the combination of the number of plasmid copies and the promoter strength of the BglBrick vectors.[24] Thus, we expected that the relative levels of AgGPPS2 expression would differ in Ec-pM2/pM(Qi), Ec-pM1/pGM(Qi), and Ec-pM2/pGM(Qi) and that the levels of expression would be low, intermediate, and high, respectively. Interestingly, Ec-pM1/pGM(Qi) showed the highest level of myrcene (15.08 ± 0.63 mg/L) with 1% glucose, which is a 3-fold increase from the lowest level of production. This result suggests that the Ec-pM1/pGM(Qi) strain, with the intermediate level of AgGPPS2, is optimal for myrcene production.

As a third approach, balancing the gene expression of the top and bottom portions by dividing two-different operons [Ec-pM3/pGM(Qi), pM4/pM(Qi), and Ec-pM4/pGM(Qi)] did not enhance myrcene production (5−8 mg/L). This could be due to poor GPPS and MS activity in converting IPP/DMAPP to myrcene; however, molecular analysis of MS has not yet been extensively studied.

Besides glucose, glycerol was used as a renewable carbon source, a byproduct of the biodiesel synthesis.[30,31] Because glycerol is a more reduced carbon source than glucose, it could enhance the production of myrcene in the NADPH-consuming MVA pathway. Thus, the Ec-pM2/pM(Qi), Ec-pM1/pGM(Qi), and Ec-pM2/pGM(Qi) strains were cultivated with 1% glycerol in either EZ-rich or M9-MOPS medium (panels A and B of Figure 4). As a result, the Ec-pM2/pM(Qi) strain in EZ-rich medium showed the highest level of myrcene production (58.19 ± 12.13 mg/L) from 1% glycerol, which is a 34-fold increase,

DOI: 10.1021/acs.jafc.5b01334
J. Agric. Food Chem. 2015, 63, 4606−4612

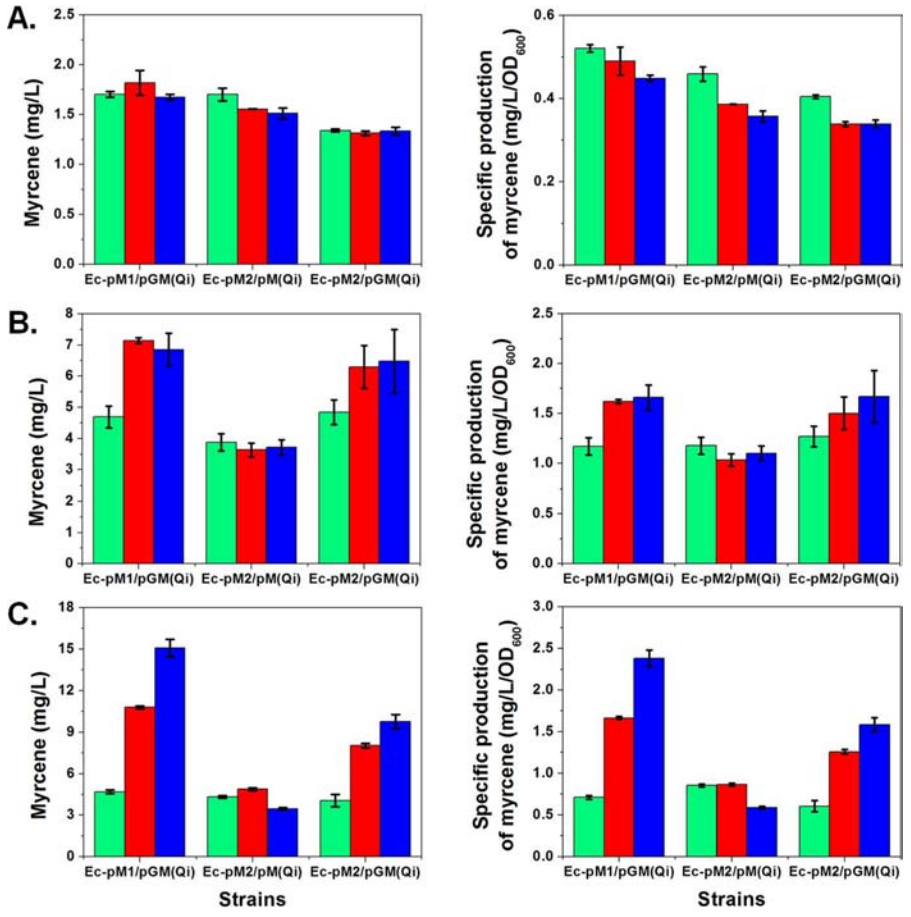

Figure 3. Myrcene production from 1% glucose using engineered *E. coli*: (A) LB, (B) EZ-rich, and (C) M9-MOPS media (green bar, 24 h; red bar, 48 h; and blue bar, 72 h). Myrcene concentrations (mg/L) and specific production of myrcene (mg/L/OD_{600}) were shown in the left and right panels, respectively. All data are the mean ± standard deviation (SD) from triplicate cultures.

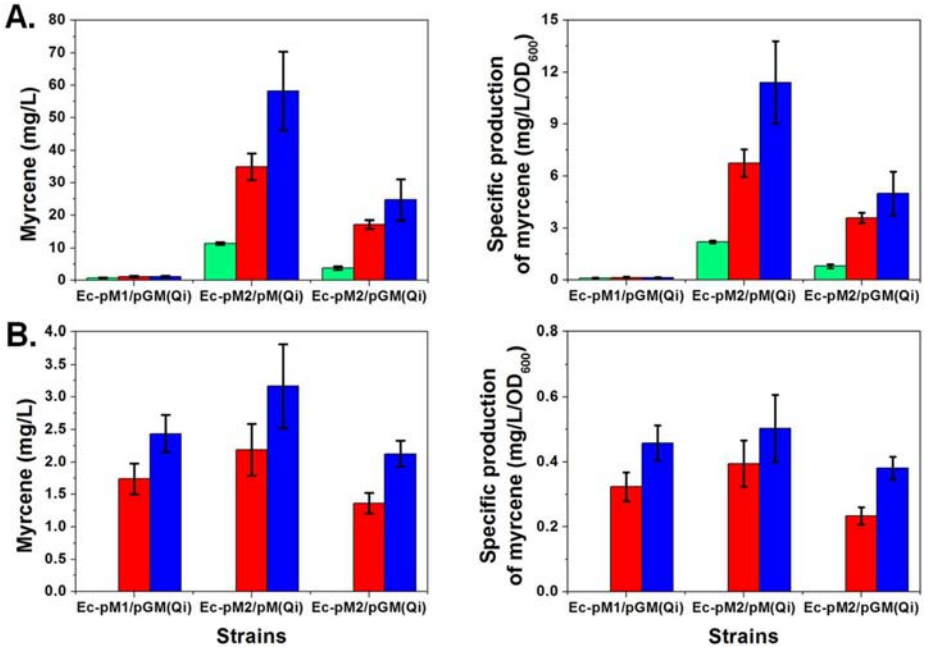

Figure 4. Myrcene production from 1% glycerol using engineered *E. coli*: (A) EZ-rich and (B) M9-MOPS media (green bar, 24 h; red bar, 48 h; and blue bar, 72 h). Myrcene concentrations (mg/L) and specific production of myrcene (mg/L/OD_{600}) were shown in the left and right panels, respectively. All data are the mean ± SD from triplicate cultures.

DOI: 10.1021/acs.jafc.5b01334
J. Agric. Food Chem. 2015, 63, 4606−4612

compared to production by the same strain in LB medium with 1% glucose.

Unlike for myrcene production from glucose, a relatively low expression of AgGPPS2 was preferred in *E. coli* for production of myrcene from glycerol. Therefore, the combinatorial expressions of GPPS and MS must be regarded as a critical task for myrcene production in *E. coli*. Targeted proteomic analysis[18,26] could be informative to understand the quantitatively correlation with GPPS/MS expressions and myrcene production depending upon the carbon sources (glucose and glycerol). Nonetheless, the level of myrcene production (58.19 ± 12.13 mg/L) from our engineered strain showed the highest production level published thus far. Further protein engineering of AgGPPS2 and MS based on directed evolution through random mutagenesis or protein structures could be necessary for enhancing activities of GPPS and MS and improving myrcene production.

***In Situ* Extraction of Volatile Myrcene from *E. coli*.** Because of high volatility of myrcene, *in situ* extraction of myrcene from cell cultures was conducted using dodecane overlay.[12,15,18] The dodecane layer can be used as an efficient product sink. Without the dodecane overlay, we observed the complete loss of the myrcene product from the Ec-pM2/pM(Qi) strain using 1% glycerol (Figure 5A). From this result, we

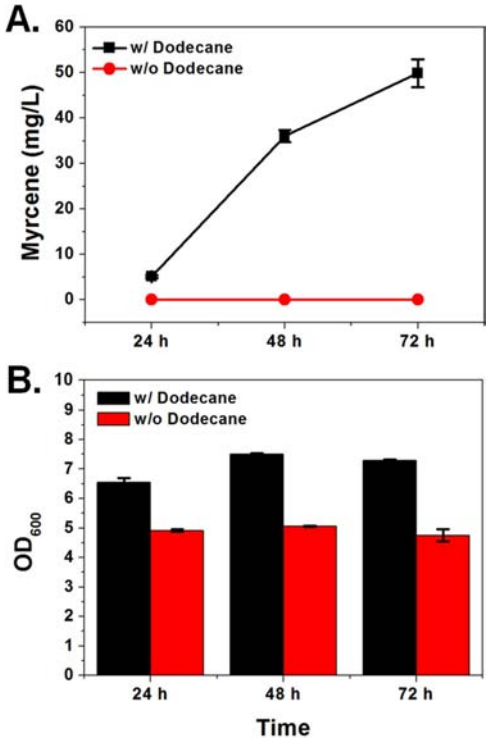

Figure 5. *In situ* extraction of myrcene using a dodecane overlay. (A) Concentration of myrcene produced by the Ec-pM2/M(Qi) strain from 1% glycerol in the EZ-rich medium either with (black square) or without (red circle) dodecane over the culture medium. (B) Cell growth of the Ec-pM2/M(Qi) strain either with (black bar) or without (red bar) dodecane over the culture. OD_{600} was measured at 24, 48, and 72 h. Error bars present the SD from triplicate cultures.

confirmed that myrcene rapidly evaporates after microbial synthesis. The cellular growth was also inhibited (Figure 5B), although the level of microbial synthesis of myrcene in *E. coli* was far less than exogenous myrcene tested for cellular toxicity in this study. This could be due to molecular level toxicity of intracellular myrcene. Therefore, a two-phase culture system with *in situ* extraction using dodecane is needed to eliminate cellular toxicity and the evaporation of myrcene.

For the first time, we have demonstrated metabolic engineering of *E. coli* for the production of myrcene. Combinatorial gene expression of tGPPS2(Ag) and tMS(Qi) was a key success for myrcene production in *E. coli* harboring the heterologous MVA pathway. For enhanced production, system biology could be applied to understand the cellular metabolism of the myrcene-producing *E. coli* to identify bottlenecks. Furthermore, bioprocess engineering is needed to achieve commercially relevant product concentrations and space-time yields of myrcene from engineered *E. coli*.

AUTHOR INFORMATION

Corresponding Author

*Telephone: +82-2-958-5249. Fax: +82-2-958-5209. E-mail: hmwoo@kist.re.kr.

Funding

This work was financially supported by the Research and Development (R&D) Convergence Program of the National Research Council of Science and Technology (NST) of the Republic of Korea and the Korea Institute of Science and Technology (KIST, 2E25402) and the Korea Carbon Capture and Sequestration (CCS) R&D Center (KCRC) Grant 2014M1A8A1049277, funded by the Korean Government [Ministry of Science, Information and Communications Technology (ICT) and Future Planning].

Notes

The authors declare no competing financial interest.

REFERENCES

(1) Behr, A.; Johnen, L. Myrcene as a natural base chemical in sustainable chemistry: A critical review. *ChemSusChem* **2009**, *2*, 1072−1095.

(2) Davis, E. M.; Ringer, K. L.; McConkey, M. E.; Croteau, R. Monoterpene metabolism. Cloning, expression, and characterization of menthone reductases from peppermint. *Plant Physiol.* **2005**, *137*, 873−881.

(3) Bloch, K.; Chaykin, S.; Phillips, A. H.; De Waard, A. Mevalonic acid pyrophosphate and isopentenylpyrophosphate. *J. Biol. Chem.* **1959**, *234*, 2595−2604.

(4) Fellermeier, M.; Raschke, M.; Sagner, S.; Wungsintaweekul, J.; Schuhr, C. A.; Hecht, S.; Kis, K.; Radykewicz, T.; Adam, P.; Rohdich, F.; Eisenreich, W.; Bacher, A.; Arigoni, D.; Zenk, M. H. Studies on the nonmevalonate pathway of terpene biosynthesis. The role of 2*C*-methyl-D-erythritol 2,4-cyclodiphosphate in plants. *Eur. J. Biochem.* **2001**, *268*, 6302−6310.

(5) Marmulla, R.; Harder, J. Microbial monoterpene transformations—A review. *Front. Microbiol.* **2014**, *5*, 346.

(6) Aros, D.; Gonzalez, V.; Allemann, R. K.; Muller, C. T.; Rosati, C.; Rogers, H. J. Volatile emissions of scented *Alstroemeria* genotypes are dominated by terpenes, and a myrcene synthase gene is highly expressed in scented *Alstroemeria* flowers. *J. Exp. Bot.* **2012**, *63*, 2739−2752.

(7) Bohlmann, J.; Steele, C. L.; Croteau, R. Monoterpene synthases from grand fir (*Abies grandis*). cDNA isolation, characterization, and functional expression of myrcene synthase, (−)-(4*S*)-limonene synthase, and (−)-(1*S*,5*S*)-pinene synthase. *J. Biol. Chem.* **1997**, *272*, 21784−21792.

(8) Fischbach, R. J.; Zimmer, W.; Schnitzler, J. P. Isolation and functional analysis of a cDNA encoding a myrcene synthase from holm oak (*Quercus ilex* L.). *Eur. J. Biochem.* **2001**, *268*, 5633−5638.

(9) Hosoi, M.; Ito, M.; Yagura, T.; Adams, R. P.; Honda, G. cDNA isolation and functional expression of myrcene synthase from *Perilla frutescens*. *Biol. Pharm. Bull.* **2004**, *27*, 1979−1985.

DOI: 10.1021/acs.jafc.5b01334
J. Agric. Food Chem. 2015, 63, 4606−4612

(10) Reiling, K. K.; Yoshikuni, Y.; Martin, V. J.; Newman, J.; Bohlmann, J.; Keasling, J. D. Mono and diterpene production in *Escherichia coli*. *Biotechnol. Bioeng.* **2004**, *87*, 200−212.
(11) Kirby, J.; Keasling, J. D. Metabolic engineering of microorganisms for isoprenoid production. *Nat. Prod. Rep.* **2008**, *25*, 656−661.
(12) Sarria, S.; Wong, B.; Garcia Martin, H.; Keasling, J. D.; Peralta-Yahya, P. Microbial synthesis of pinene. *ACS Synth. Biol.* **2014**, *3*, 466−475.
(13) Kang, M. K.; Eom, J. H.; Kim, Y.; Um, Y.; Woo, H. M. Biosynthesis of pinene from glucose using metabolically-engineered *Corynebacterium glutamicum*. *Biotechnol. Lett.* **2014**, *36*, 2069−2077.
(14) Yang, J.; Nie, Q.; Ren, M.; Feng, H.; Jiang, X.; Zheng, Y.; Liu, M.; Zhang, H.; Xian, M. Metabolic engineering of *Escherichia coli* for the biosynthesis of α-pinene. *Biotechnol. Biofuels* **2013**, *6*, 60.
(15) Alonso-Gutierrez, J.; Chan, R.; Batth, T. S.; Adams, P. D.; Keasling, J. D.; Petzold, C. J.; Lee, T. S. Metabolic engineering of *Escherichia coli* for limonene and perillyl alcohol production. *Metab. Eng.* **2013**, *19*, 33−41.
(16) Willrodt, C.; David, C.; Cornelissen, S.; Buhler, B.; Julsing, M. K.; Schmid, A. Engineering the productivity of recombinant *Escherichia coli* for limonene formation from glycerol in minimal media. *Biotechnol. J.* **2014**, *9*, 1000−1012.
(17) Zhang, H.; Liu, Q.; Cao, Y.; Feng, X.; Zheng, Y.; Zou, H.; Liu, H.; Yang, J.; Xian, M. Microbial production of sabinene—A new terpene-based precursor of advanced biofuel. *Microb. Cell Fact.* **2014**, *13*, 20.
(18) Woo, H. M.; Murray, G. W.; Batth, T. S.; Prasad, N.; Adams, P. D.; Keasling, J. D.; Petzold, C. J.; Lee, T. S. Application of targeted proteomics and biological parts assembly in *E. coli* to optimize the biosynthesis of an anti-malarial drug precursor, amorpha-4,11-diene. *Chem. Eng. Sci.* **2013**, *103*, 21−28.
(19) Paddon, C. J.; Westfall, P. J.; Pitera, D. J.; Benjamin, K.; Fisher, K.; McPhee, D.; Leavell, M. D.; Tai, A.; Main, A.; Eng, D.; Polichuk, D. R.; Teoh, K. H.; Reed, D. W.; Treynor, T.; Lenihan, J.; Fleck, M.; Bajad, S.; Dang, G.; Dengrove, D.; Diola, D.; Dorin, G.; Ellens, K. W.; Fickes, S.; Galazzo, J.; Gaucher, S. P.; Geistlinger, T.; Henry, R.; Hepp, M.; Horning, T.; Iqbal, T.; Jiang, H.; Kizer, L.; Lieu, B.; Melis, D.; Moss, N.; Regentin, R.; Secrest, S.; Tsuruta, H.; Vazquez, R.; Westblade, L. F.; Xu, L.; Yu, M.; Zhang, Y.; Zhao, L.; Lievense, J.; Covello, P. S.; Keasling, J. D.; Reiling, K. K.; Renninger, N. S.; Newman, J. D. High-level semi-synthetic production of the potent antimalarial artemisinin. *Nature* **2013**, *496*, 528−532.
(20) Ajikumar, P. K.; Xiao, W. H.; Tyo, K. E.; Wang, Y.; Simeon, F.; Leonard, E.; Mucha, O.; Phon, T. H.; Pfeifer, B.; Stephanopoulos, G. Isoprenoid pathway optimization for Taxol precursor overproduction in *Escherichia coli*. *Science* **2010**, *330*, 70−74.
(21) Brennan, T. C.; Turner, C. D.; Krömer, J. O.; Nielsen, L. K. Alleviating monoterpene toxicity using a two-phase extractive fermentation for the bioproduction of jet fuel mixtures in *Saccharomyces cerevisiae*. *Biotechnol. Bioeng.* **2012**, *109*, 2513−2522.
(22) Dunlop, M. J.; Dossani, Z. Y.; Szmidt, H. L.; Chu, H. C.; Lee, T. S.; Keasling, J. D.; Hadi, M. Z.; Mukhopadhyay, A. Engineering microbial biofuel tolerance and export using efflux pumps. *Mol. Syst. Biol.* **2011**, *7*, 487.
(23) Anderson, J. C.; Dueber, J. E.; Leguia, M.; Wu, G. C.; Goler, J. A.; Arkin, A. P.; Keasling, J. D. BglBricks: A flexible standard for biological part assembly. *J. Biol. Eng.* **2010**, *4*, 1.
(24) Lee, T. S.; Krupa, R. A.; Zhang, F.; Hajimorad, M.; Holtz, W. J.; Prasad, N.; Lee, S. K.; Keasling, J. D. BglBrick vectors and datasheets: A synthetic biology platform for gene expression. *J. Biol. Eng.* **2011**, *5*, 12.
(25) Peralta-Yahya, P. P.; Ouellet, M.; Chan, R.; Mukhopadhyay, A.; Keasling, J. D.; Lee, T. S. Identification and microbial production of a terpene-based advanced biofuel. *Nat. Commun.* **2011**, *2*, 483.
(26) Redding-Johanson, A. M.; Batth, T. S.; Chan, R.; Krupa, R.; Szmidt, H. L.; Adams, P. D.; Keasling, J. D.; Lee, T. S.; Mukhopadhyay, A.; Petzold, C. J. Targeted proteomics for metabolic pathway optimization: Application to terpene production. *Metab. Eng.* **2011**, *13*, 194−203.
(27) Alonso-Gutierrez, J.; Kim, E. M.; Batth, T. S.; Cho, N.; Hu, Q.; Chan, L. J.; Petzold, C. J.; Hillson, N. J.; Adams, P. D.; Keasling, J. D.; Garcia Martin, H.; Lee, T. S. Principal component analysis of proteomics (PCAP) as a tool to direct metabolic engineering. *Metab. Eng.* **2014**, *28C*, 123−133.
(28) Phillips, M. A.; Savage, T. J.; Croteau, R. Monoterpene synthases of loblolly pine (*Pinus taeda*) produce pinene isomers and enantiomers. *Arch. Biochem. Biophys.* **1999**, *372*, 197−204.
(29) Sikkema, J.; Weber, F. J.; Heipieper, H. J.; Debont, J. A. M. Cellular toxicity of lipophilic compounds—Mechanisms, implications, and adaptations. *Biocatal. Biotransform.* **1994**, *10*, 113−122.
(30) da Silva, G. P.; Mack, M.; Contiero, J. Glycerol: a promising and abundant carbon source for industrial microbiology. *Biotechnol. Adv.* **2009**, *27*, 30−39.
(31) Yang, F.; Hanna, M. A.; Sun, R. Value-added uses for crude glycerol—A byproduct of biodiesel production. *Biotechnol. Biofuels* **2012**, *5*, 13.

DOI: 10.1021/acs.jafc.5b01334
J. Agric. Food Chem. 2015, 63, 4606−4612

JOURNAL OF AGRICULTURAL AND FOOD CHEMISTRY

Article

pubs.acs.org/JAFC

Dehydrogenative Polymerization of Coniferyl Alcohol in Artificial Polysaccharides Matrices: Effects of Xylan on the Polymerization

Qiang Li,[†] Keiichi Koda,[‡] Arata Yoshinaga,[§] Keiji Takabe,[§] Masatsugu Shimomura,[⊥] Yuji Hirai,[⊥] Yutaka Tamai,[‡] and Yasumitsu Uraki*[,‡]

[†]Graduate School of Agriculture and [‡]Research Faculty of Agriculture,Hokkaido University, Kita-ku, Sapporo 060-8589, Japan

[§]Graduate School of Agriculture, Kyoto University, Sakyo-ku, Kyoto 606-8502, Japan

[⊥]Faculty of Photonic Science, Chitose Institute of Science and Technology, 758-65 Bibi, Chitose 066-8655, Japan

Supporting Information

ABSTRACT: To elucidate the influence of wood polysaccharide components on lignin formation in vitro, models for polysaccharide matrix in wood secondary cell wall were fabricated from two types of bacterial cellulosic films, flat film (FBC) and honeycomb-patterned film (HPBC), as basic frameworks by depositing xylan onto the films. An endwise type of dehydrogenative polymerization, "Zutropfverfahren", of coniferyl alcohol was attempted in the films with/without xylan. The resultant dehydrogenation polymer (DHP) was generated inside and outside xylan-deposited films, whereas DHP was deposited only outside the films without xylan. The amount of the generated DHP in the xylan-deposited films was larger than that in the films without xylan. The frequency of 8-*O*-4′ interunitary linkage in DHP was also increased by the xylan deposition. These results suggest that xylan acts as a scaffold for DHP deposition in polysaccharides matrix and as a structure regulator for the formation of the 8-*O*-4′ linkage. In addition, mechanical properties, i.e., tensile strength and modulus of elasticity (MOE), of both cellulosic films were found to be augmented by the deposition of xylan and DHP. Especially, DHP deposition remarkably enhanced MOE. Such effects of xylan on DHP formation and augmentation of mechanical strength were clearly observed for HPBC, revealing that HPBC is a promising framework model to investigate wood cell wall formation in vitro.

KEYWORDS: *honeycomb-patterned bacterial cellulose film, xylan, dehydrogenation polymer, 8-O-4′ linkage, mechanical property*

INTRODUCTION

Lignin is one of the three major components in wood secondary cell wall and has a complex structure due to a variety of interunitary linkages resulting from radical coupling of monolignols initiated by hydrogen abstraction with oxidase and/or peroxidase.[1] A main interunitary linkage is 8-*O*-4′ bonding. Its frequency in native lignin is much greater than that of dehydrogenation polymer (DHP) as an artificial lignin, even though DHP is prepared by the endwise polymerization method "Zutropfverfahren," which yields DHP richer in 8-*O*-4′ bonding than the bulk polymerization does.[2−5] The radical coupling of monolignols in a living tree, namely lignification, always occurs in the polysaccharides matrix composed of cellulose and hemicelluloses,[6,7] whereas DHP is normally prepared in an aqueous medium. Thus, it is plausible to suppose that the polysaccharides play a significant role in the lignin formation.[8−10] In fact, the frequency of 8-*O*-4′ linkages in DHP was increased by adding polysaccharides, such as pectin,[11−14] extracted hemicellulose,[13] and cyclodextrin,[15] to the reaction media. However, such effects of polysaccharides addition on lignification in solid media are still unclear.

Xylan, as a major hemicellulose, accounts for 15−30% of wood components in hardwood and for 5−10% in softwood,[16] and its influence on lignification is in debate. When xylan is fully deposited in S1 and S2 layers of phloem fibers in *Mallotus japonicus*, lignin deposition is spatially associated with xylan location.[17] In addition, Reis and Vian[18] reported that xylan acted as a "host structure" for the regulation of lignin structure. Salmén and Burgert[8] reported that highly substituted xylan was closely associated with lignin with less condensed structure in hardwood. The 8-*O*-4′ frequency of DHP was increased by the presence of xylan.[19] Thus, xylan is assumed to contribute to lignin deposition in cell wall and steric regulation of lignin polymerization.

On the other hand, Donaldson and Knox[20] reported that xylan was not closely related to the degree of lignification in radiata pine. In *Eucalyptus globulus*, a xylan-bonded lignin fraction had fewer 8-*O*-4′ linkages than other hemicellulose-bonded lignin.[21,22] In spruce, the lignin−xylan fraction was also rich in condensed structure (fewer 8-*O*-4′ linkages) in comparison with the lignin−glucomannan fraction.[23,24] There were, thus, opposite findings and hypotheses in the previous reports. The first objective in this investigation was to elucidate the effects of xylan on lignin formation in vitro, using solid models for wood polysaccharide matrix.

Wood has excellent mechanical strength. Of course, this characteristic is mainly attributed to a crystalline material, cellulose.[25−27] However, the contribution of other components, hemicellulose and lignin, to the mechanical strength of wood cell wall is also unclear. Our second objective was to clarify the

Received: December 24, 2014
Revised: March 13, 2015
Accepted: March 16, 2015
Published: March 16, 2015

ACS Publications © 2015 American Chemical Society

DOI: 10.1021/acs.jafc.5b01070
J. Agric. Food Chem. 2015, 63, 4613−4620

influence of such components on the mechanical properties of cellulose.

To achieve the objectives, we prepared models for polysaccharide matrices from bacterial cellulose (BC) secreted by *Gluconacetobacter xylinus* as a basic framework. The bacterium produces pellicles in Hestrin−Schramm (HS) liquid media.[28] The pellicle produced for a short time can be used as a thin film. However, most cellulose fibrils of the film are not exposed outside, indicating low response of cellulose filaments to guest molecules or external stimuli. To overcome the problem, we fabricated honeycomb-patterned bacterial cellulose film (HPBC), in addition to flat bacterial cellulose film (FBC), as a BC pellicle. Most fibrils of HPBC are assumed to be exposed to the outer circumstance, and thus, they would have high accessibility to external guests. Its hexagonal alignment mimicked the cross-section of native wood cell wall arrangement. Therefore, we consider HPBC as a better model framework than FBC to investigate the effect of xylan on lignification and the contribution of xylan and DHP to the mechanical property of cellulose.

MATERIALS AND METHODS

Fabrication of HPBC and FBC. HPBC was prepared by our method reported previously.[29,30] Briefly, a precultured *G. xylinus* (ATCC53582) was cultured on a template of concave honeycomb-patterned agarose film containing the nutrients of HS medium. After 48 h incubation, HPBC was obtained by dissolving the agarose film with hot, distilled water at 70 °C.

FBC as a normal BC pellicle was prepared by culture of the bacterium in HS medium for 12 h. Both HPBC and FBC were soaked in 1 M aqueous sodium hydroxide at 65 °C for 1 h and then washed by distilled water repeatedly until the pH of the washings became 7. Afterward, the films were air-dried and kept in a refrigerator until use.

Xylan Adsorption Analysis. Beech xylan was purchased from Sigma-Aldrich (Steinheim, Germany), and used as received. Xylan was subjected to acid hydrolysis bythe Klason method for measuring its lignin content, and neutral sugar compositions in the filtrate by this method were analyzed.[31] Uronic acid content of xylan was determined according to the method reported by Blumenkranz and Asboe-Hansen,[32] using a calibration line.[33]

A sheet of cellulosic film (2.5 mg of FBC and 0.8 mg of HPBC with 90 mm in diameter) was immersed in 10 mL of aqueous xylan solution at different concentrations of 0.1−1.0 mg/mL for 1 d at room temperature and then washed with 1 mL of distilled water. After the adsorption, the residual xylan solutions were subjected to HPLC to measure the xylan concentration. The column used was a 300 × 7.5 mm i.d., Shodex Asahipak GF 7 M HQ, with a 50 mm × 7.5 mm i.d. guard column of the same material (Showa Denko K.K., Tokyo, Japan). Column oven temperature was set at 40 °C, and Milli-Q water as an eluent and a Corona detector (ESA Bioscience Inc., Chelmsford, MA) were used. The xylan concentration was calculated from the total area of the xylan peak using a calibration line. The adsorption of xylan was expressed as the following equation

$$W = \frac{10(C_0 - C_1)}{M}$$

where W (g/g of cellulose) is the adsorption of xylan on a BC film, 10 (mL) is the volume of xylan solution, C_0 (mg/mL) is xylan concentration before adsorption, C_1 (mg/mL) is xylan concentration after adsorption, and M (mg) is the weight of a BC film.

The cellulosic films, which were soaked in xylan solution at 1 mg/mL, washed once with 1 mL of distilled water, and air-dried, were subjected to the following experiment.

Dehydrogenative Polymerization of Coniferyl Alcohol with Enzyme in the Presence of Cellulosic Films. Coniferyl alcohol was synthesized according to the procedure reported previously.[34] For its polymerization with enzyme (horseradish peroxidase), the following three solutions were prepared.[4] Solution I: 100 mg of coniferyl alcohol was dissolved in 2 mL of acetone and then mixed with 48 mL of phosphate buffer saline (PBS) solution (pH 6.1, 0.01 M phosphate containing 0.8 w/v% of NaCl and 0.02 w/v% of KCl). Solution II: 5 mg of horseradish peroxidase (100 units/mg) (Wako Pure Chemicals, Osaka, Japan) was dissolved in 50 mL of PBS solution. Solution III: 0.25 mL of hydrogen peroxide (30 wt % in aqueous solution, 14.6 mmol) was mixed with 50 mL of PBS solution. Both HPBC and FBC with/without adsorption of xylan were immersed in solution II, and solutions I and III were injected dropwise into solution II separately from two syringes each using a YSP-101 syringe pump (YMC Keyboard Chemistry, Kyoto, Japan) at a flow rate of 5 mL/h for 10 h, and then the mixture was kept for a further 16 h. The resultant films were picked up and immersed in distilled water two times for 5 min each and then air-dried.

The remaining DHP not deposited on the film but suspended in the buffer solution was collected by centrifugation (2000*g*, 10 min) and washed two times with distilled water and then lyophilized. The collected DHP was used as a lignin standard for the acetyl bromide method.

The morphologies of the obtained films were observed under a VK-9500 violet-laser color 3D profile microscope (Keyence, Osaka, Japan) or a JSM-6301F field emission scanning electron microscope (FE-SEM) (JEOL Ltd., Tokyo, Japan) operated at an accelerating voltage of 5 kV. The samples for SEM observation were coated with gold−palladium by cathodic spreading with an E101 ion sputter (Hitachi, Tokyo, Japan).

Lignin Bromination and SEM−EDXA Analysis. DHP on the cellulosic films was brominated with bromine vapor in a sealed desiccator. The cellulosic films and bromine (5 mL, 99% purity) in a Petri dish were separately placed in the desiccator and kept for 1 d at room temperature after being tightly sealed in the desiccator with a glass cap. The brominated films were placed in air for half a day and then embedded in epoxy resin. After polymerizing in an oven (35 °C for 1 d, followed by 45 °C for 1 d, and then 65 °C for 3 d), the resins were trimmed with a RM2255 microtome (Leica Biosystems, Nussloch, Germany) to obtain the cross sections of films. The location of bromine on the cross sections of films was analyzed on a S-800 FE-SEM (Hitachi, Tokyo, Japan) equipped with an EMAX-2000 energy dispersive X-ray analyzer (EDXA) (Horiba, Tokyo, Japan) after specimens were coated with carbon under a VC-100 carbon coater (Vacuum-Device Ltd., Ibaraki, Japan). SEM analysis was completed at an accelerating voltage of 10 kV. The EDXA images were represented as an inversion mode of black and white using Microsoft Powerpoint 2007 software.

Immunofluorescence Labeling. Immunofluorescence labeling of xylan was preformed according to the method of Kim et al.[35] Two kinds of primary antibodies, LM 10 and LM 11 (PlantProbes, Leeds, UK), were used to label xylan. A secondary antibody, goat anti-rat IgG Alexa Fluor 568 (Invitrogen, Carlsbad, CA), was used to recognize the primary antibodies. As control experiments, the specimens were incubated with the secondary antibody only. Micrographs of immunolabeling specimens were taken with a BX50 fluorescence microscope (Olympus, Tokyo, Japan) equipped with a Semrock TxRed-4040C filter set (Opto-Line Inc., Tokyo, Japan).

Characterization of DHP. All specimens were washed with 5 mL of 90% 1,4-dioxane aqueous solution (aq dioxane) once, and dried in vacuo at 50 °C. DHP contents in DHP-deposited cellulosic films before and after washing were determined by the acetyl bromide method.[36] The absorptivity of acetylated DHP at 280 nm was found to be 19.9 L/g cm, which was obtained by using the DHP not deposited on the film but recovered from the suspension by centrifugation, as mentioned above.

Alkaline nitrobenzene oxidation for the specimens washed with aq dioxane was conducted according to the method reported by Chen.[37] Reaction products (vanillin and vanillic acid) were determined by a GC-2010 gas chromatograph (Shimadzu, Kyoto, Japan) under the following conditions: detector, FID; column, InertCap 1701 (30 m, 0.25 mm i.d., 0.25 μm film thickness) (GL Science, Tokyo, Japan); split ratio, 5.0; carrier gas, He (110 mL/min); injector temperature,

DOI: 10.1021/acs.jafc.5b01070
J. Agric. Food Chem. 2015, 63, 4613−4620

250 °C; detector temperature, 280 °C; column temperature program, 150 °C (5 min), 5 °C/min to 230 °C (1 min), 10 °C/min to 250 °C (10 min). All experiments described above were performed in duplicate, and the average value was shown as a result.

Mechanical Test. Films were gently pressed under a 300 g load for 10 min, and then cut into 1−2 mm in width and 5 mm in length. The cut specimens were allowed to stand at 50% relative humidity and 22 °C for 1 d and subjected to tensile testing under ambient conditions. Tensile strength, modulus of elasticity (MOE), and elongation were measured on a specially designed testing apparatus reported previously.[38] Film thickness was measured for at least five different positions under the aforementioned 3D profile microscope. The mechanical test was carried out for at least 20 specimens cut from four different films.

RESULTS AND DISCUSSION

Deposition of Xylan onto HPBC and FBC. Beech xylan used in this study contained 1.3% of lignin as Klason lignin. The lignin-free part of this xylan was found to give 86.0% xylose, 1.2% galactose, 0.5% mannose, 0.5% glucose, and 11.8% glucuronic acid.

Adsorption isotherms of the xylan on HPBC and FBC are shown in Figure 1. The adsorption of xylan on HPBC was much higher than that on FBC at any concentration. This result indicated that HPBC had a larger accessible area to xylan than FBC did. The reason may be attributed to the difference in cellulose fibrils: most cellulose fibrils in HPBC are exposed outward (facing air and solvent), whereas most of the fibrils in FBC face inside the pellicle and only the fibrils at the surface are exposed outward. Thereby, xylan could easily interact with most of the cellulose microfibrils in HPBC as compared with those in FBC. We thus considered that HPBC was a suitable platform for the evaluation of the interaction between cellulose microfibrils and guest molecules.

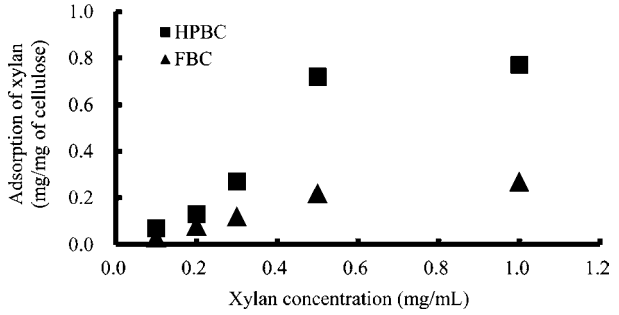

Figure 1. Adsorption isotherms of xylan on HPBC and FBC films.

Dehydrogenative Polymerization of Coniferyl Alcohol in the Presence of Cellulosic Films with/without Xylan. The endwise polymerization of coniferyl alcohol[4] was attempted in the presence of cellulosic films to obtain DHP-deposited cellulosic films. Surface images of the resultant films are shown in Figure 2. Before DHP deposition, no white region was observed for HPBC and FBC, respectively (Figure 2A,B). After DHP deposition, white regions were observed on the surfaces of all HPBC and FBC, respectively (Figure 2C−F). The number of white regions in xylan-deposited FBC (Xyl−FBC) (Figure 2F) was much larger than that in FBC without xylan (Figure 2D). It was presumed that white regions of HPBC and FBC were deposited DHP. To prove this assumption, bromination of the specimens was conducted in order to stain and visualize DHP with bromine. The bromine distribution on the surface of the films was observed under a

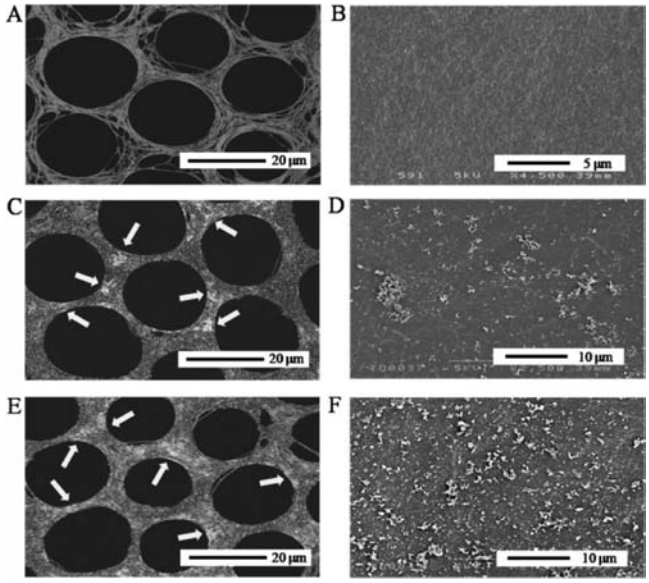

Figure 2. 3D microscopic images of the HPBC series (A, C, and E) and SEM images of the FBC series (B, D, and F). A and B are intact cellulosic films. C and D are images of both cellulosic films after DHP preparation. E and F are images of xylan-deposited films after DHP preparation. White arrows show the "white region" in HPBC.

SEM-EDXA.[39] Figure 3 shows the SEM-EDXA images of Figure 2 at high magnification. The location of bromine dots in parts a3, b3, c3, and d3 of Figure 3 was consistent with the location of white regions in parts A3, B3, C3, and D3 of Figure 3, respectively. Consequently, DHP deposition on the surface of cellulosic films was confirmed by a combined analysis of bromination and SEM-EDXA. Afterward, films were identified as follows: DHP-deposited HPBC and FBC (DHP−HPBC and DHP−FBC, respectively) and DHP-deposited Xyl−HPBC and Xyl−FBC (DHP−Xyl−HPBC and DHP−Xyl−FBC, respectively).

Effects of Xylan on DHP Formation. To further investigate the DHP location inside the films, the Br-stained films were embedded into epoxy resins, and then the specimens were trimmed and microtomed after polymerizing the resins. Figure 4 shows the microtomed positions for HPBC and FBC series. Two cross sections from the first and the second micotome cutlines were analyzed under SEM-EDXA. Figure 5 shows the SEM-EDXA images of the cross sections of DHP-deposited cellulosic films at the first cutline (line 1) (Figure 4). In Figure 5a3 of DHP−FBC without xylan, Br dots (or DHP) were observed only at the outside of the film, but not in the inside. However, when xylan was adsorbed on FBC (DHP−Xyl−FBC), DHP was located on both sides of the film (Figure 5b3). Identical results (Figure S1, Supporting Information) were obtained from the cross sections at the second cutline (line 2) (Figure 4). From these images, we anticipated that xylan induced DHP formation into the inside of the FBC films.

To confirm this assumption, xylan distribution in the films was observed by a combination of immunolabeling and fluorescent microscopy. LM 10 can recognize low-substituted and/or unsubstituted xylan, while LM 11 can recognize not only low-substituted and/or unsubstituted xylan but also arabinoxylan.[40] Both antibodies have been widely used for immunolabeling xylan in both hardwood and softwood, for instance, birch,[40] poplar,[41] pine,[20] and cedar.[35] The control specimens (with the secondary antibody only) omitting

DOI: 10.1021/acs.jafc.5b01070
J. Agric. Food Chem. 2015, 63, 4613−4620

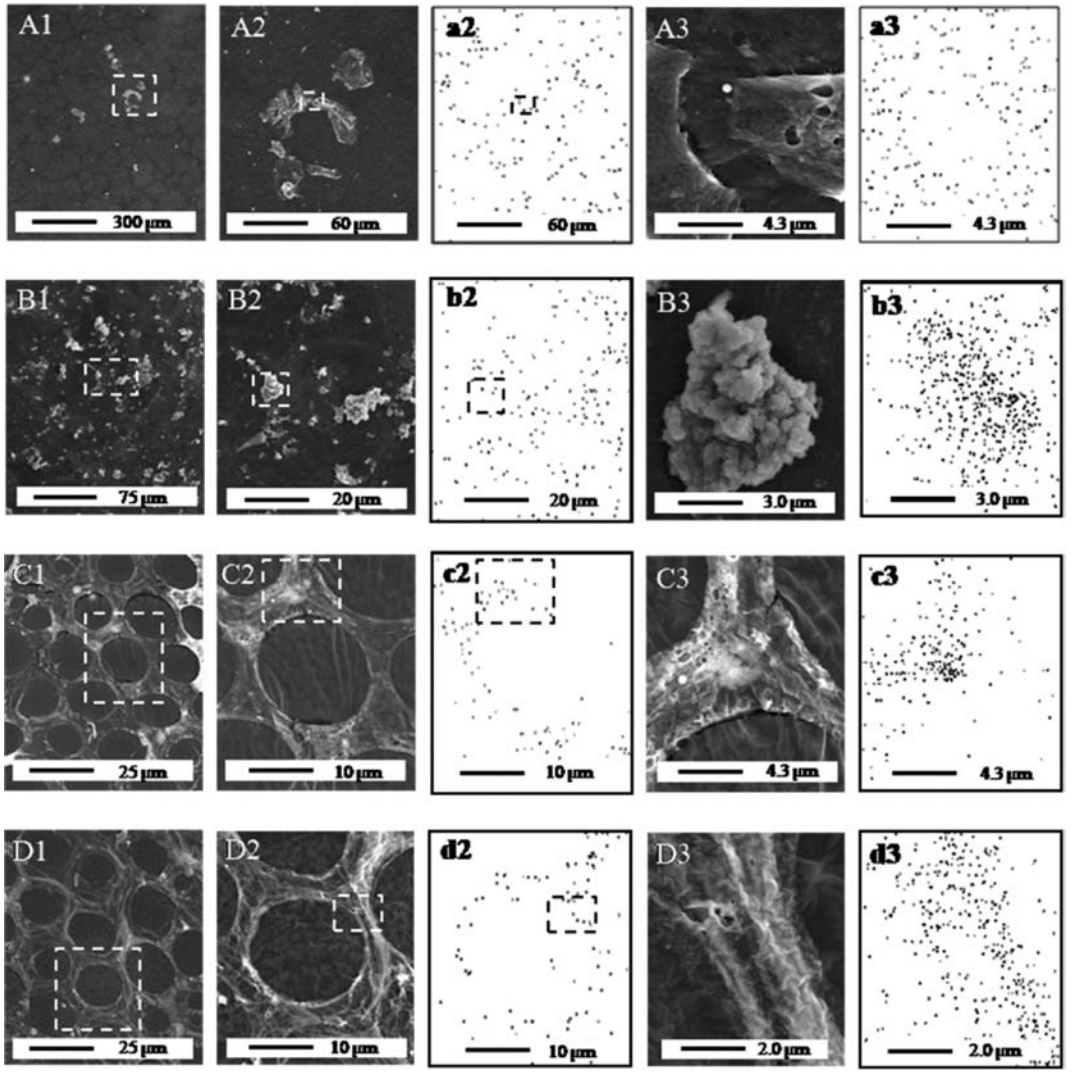

Figure 3. SEM-EDXA images of the surface of DHP-deposited FBC and HPBC films. A series, FBC after DHP preparation without xylan; B series, xylan-deposited FBC after DHP preparation; C series, HPBC after DHP preparation without xylan; and D series, xylan-deposited HPBC after DHP preparation. The magnification is shown by the bar below each panel. The area in the dotted square was magnified under SEM and is shown in the photo for which the numerical label is increased by one (e.g., A1 to A2). The lower case letters, a, b, c, and d, are Br-mapping images by EDXA for the corresponding images labeled with upper case letters.

incubation of primary antibodies (LM 10 and LM 11) did not show obvious fluorescence, including self-fluorescence of lignin (Figure 6A1−D1), whereas the other test specimens clearly indicated red fluorescence, which revealed the existence of xylan. In Figure 6A2, and A3, xylan distributes in the whole inside of Xyl−FBC. In addition, the xylan distribution was also confirmed in the whole inside of DHP−Xyl−FBC (Figure 6B2,B3). From Figures 5b3 and 6B2,B3, DHP existed with xylan. These phenomena suggest the following DHP formation in the matrix; xylan first penetrates into the cellulosic film. Coniferyl alcohol attaches to the xylan-deposited film, and then it migrates inside the film because of its high affinity for xylan.[33] Finally, the coniferyl alcohol is polymerized with peroxidase to form DHP in the polysaccharide matrix.

In the case of HPBC, Br dots or DHP were observed (Figure 5c3,d3). The density of dots was increased by the xylan adsorption. In addition, xylan deposition inside the film was confirmed in Figure 6D2,D3. These observations suggest that coniferyl alcohol can easily penetrate inside HPBC because most bundles or fibrils composed of several microfibrils in HPBC are exposed outward. By xylan deposition, migration of coniferyl alcohol was accelerated. Consequently, more DHP was observed in Figure 5d3 than in Figure 5c3.

Effects of Xylan on Lignin Content and Frequency of 8-*O*-4′ Linkage. To further examine the effects of xylan on DHP formation quantitatively, DHP content in the films and the frequency of interunitary linkage in DHP were estimated by the acetyl bromide method and alkaline nitrobenzene oxidation, respectively.

Parts A and B of Figure 7 show DHP contents in the cellulosic films based on the total weight of DHP-deposited films and the initial weight of cellulose before and after washing with aq dioxane, respectively. The DHP contents of FBC and HPBC, based on the initial weight of cellulose, were increased by the xylan adsorption on cellulosic films in both parts A and B of Figure 7. This result also suggests that xylan enhances the amount of DHP deposition in the films and contradicts the previous findings,[13,14] where hemicelluloses (pectin, pectic acid, and dilute alkali-extracted hemicellulose) did not affect the

DOI: 10.1021/acs.jafc.5b01070
J. Agric. Food Chem. 2015, 63, 4613−4620

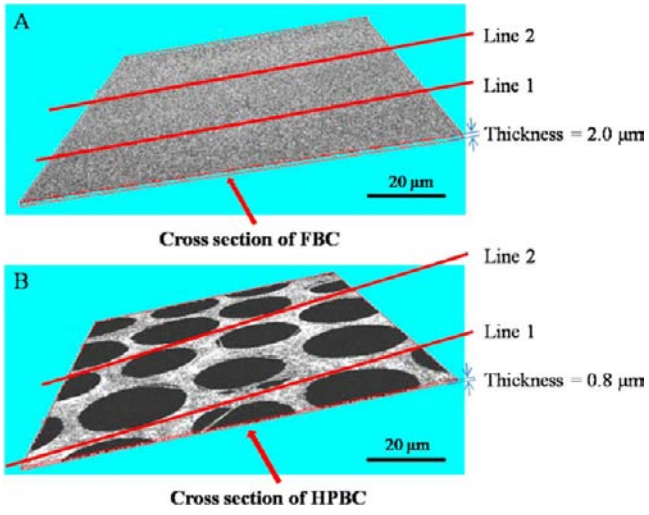

Figure 4. Cutting positions for SEM-EDXA observation at the cross section of (A) FBC and (B) HPBC. Images were taken under the violet-laser color 3D profile microscope.

DHP formation in both solid and liquid media. Consequently, xylan affected DHP formation as a scaffold.

DHP content was remarkably decreased by washing with aq dioxane. However, a significant amount of DHP remained in the films, for HPBC in particular (Figure 7B). The remained DHP fraction was tightly associated with the polysaccharide matrix, suggesting that this aq-dioxane-unwashable DHP fraction might be a lignin−carbohydrate complex.

The DHP-deposited films, after washing with aq dioxane, were then subjected to nitrobenzene oxidation. The oxidation products, vanillin and vanillic acid, are generated from the noncondensed structure of lignin, and therefore, the yield of the oxidation products is one of the measures to estimate the frequency of aryl ether interunitary linkages in lignin, mainly the 8-*O*-4′ linkage.[37]

The yield of the oxidation products from DHP prepared in liquid media (without cellulosic films) was increased by the addition of xylan into the buffered media, as shown in Figure 8. Similarly, the yield from DHP formed in the HPBC and FBC films was increased by the xylan adsorption. These results

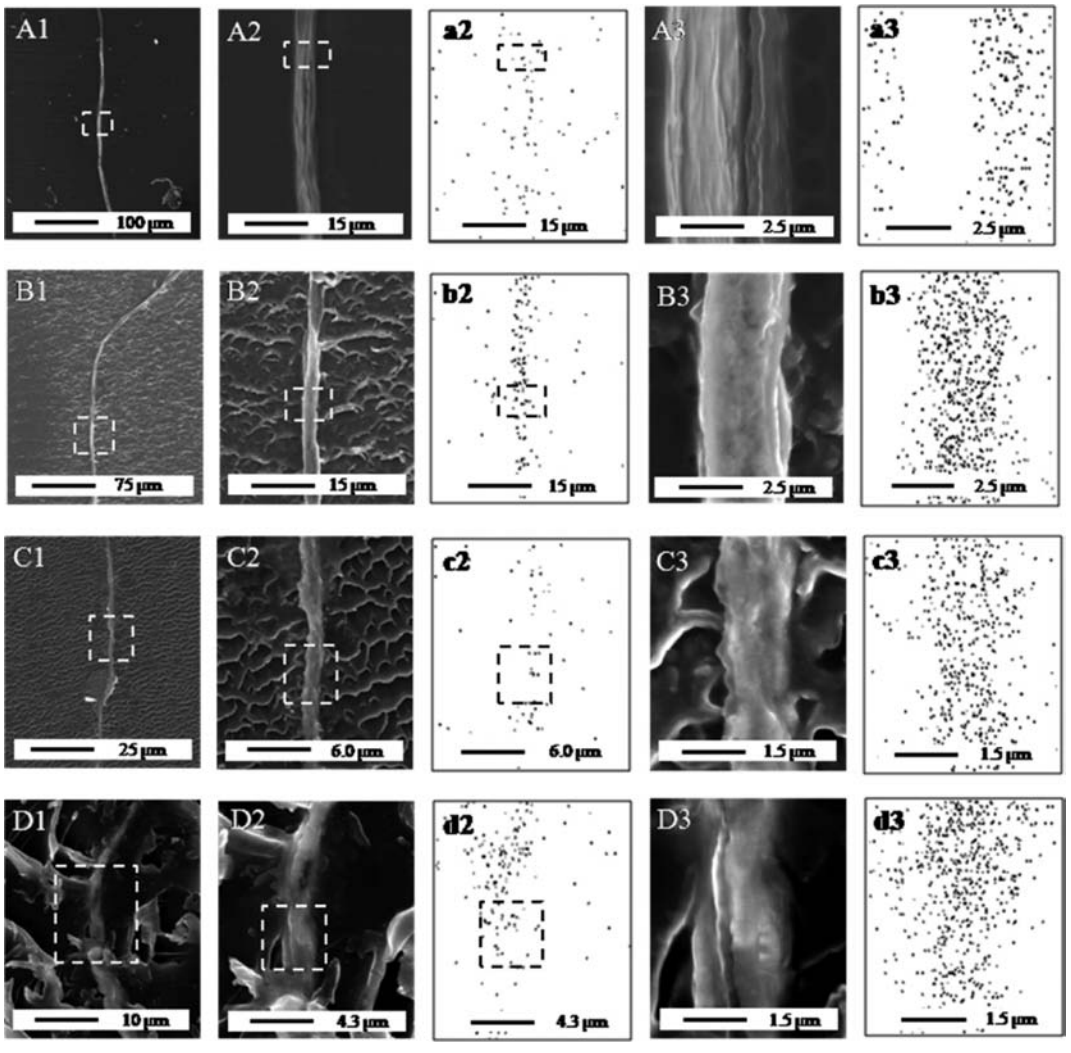

Figure 5. SEM-EDXA images of DHP-deposited FBC and HPBC films at the cross section from the first cutline. A series, FBC after DHP preparation without xylan; B series, xylan-deposited FBC after DHP preparation; C series, HPBC after DHP preparation without xylan; D series, xylan-deposited HPBC after DHP preparation. The magnification is shown by the bar below each panel. The area in the dotted square was magnified under SEM and is shown in the photo for which the numerical label is increased by one (e.g., A1 to A2). The lower case letters, a, b, c, and d, are Br-mapping images by EDXA for the corresponding images labeled with upper case letters.

DOI: 10.1021/acs.jafc.5b01070
J. Agric. Food Chem. 2015, 63, 4613−4620

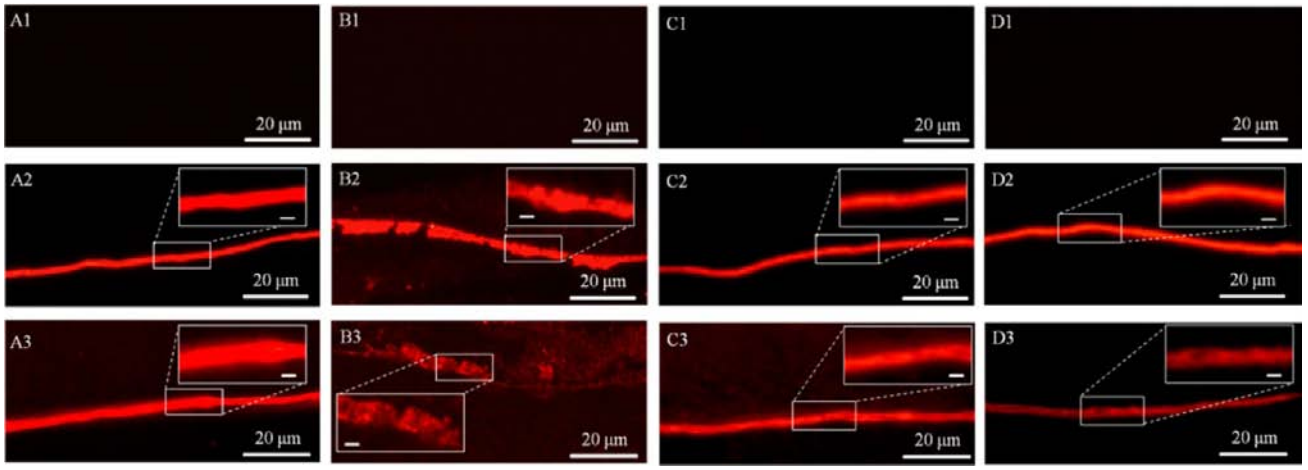

Figure 6. Immunofluoresence labeling of xylan in the cross sections of the xylan−FBC series (A1−A3), DHP−xylan−FBC series (B1−B3), xylan−HPBC series (C1−C3), and DHP−xylan−HPBC series (D1−D3). A1−D1, controls without primary antibodies labeling; A2−D2, immunolabeling with LM 10; A3−D3, immunolabeling with LM 11. Bars in magnified images are 2 μm.

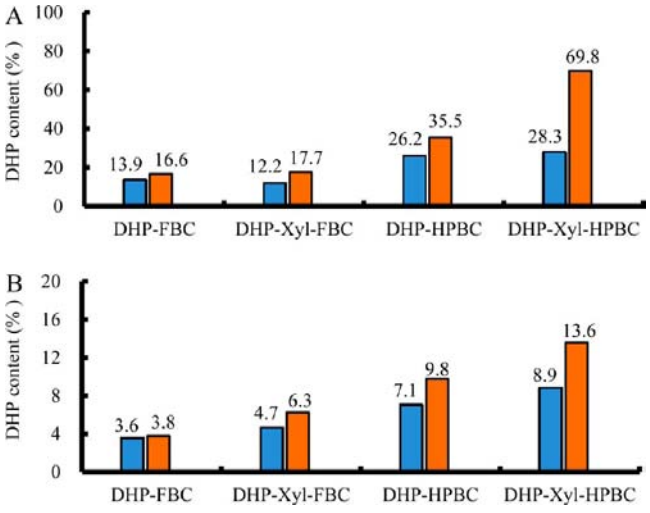

Figure 7. DHP content in the cellulosic films (A) before and (B) after washing with 90% 1,4-dioxane solution: blue, based on the total weight of DHP-deposited films; orange, based on the initial weight of cellulose.

suggested that xylan enhanced the frequency of the aryl ether linkage in DHP, probably resulting in the predominant formation of the 8-*O*-4′ linkage. This observation is consistent with the findings by Barakat et al.,[19] where the higher the concentration of arabinoxylan added to the DHP reactant, the higher the yield of thioacidolysis products obtained. Therefore, we conclude that xylan can act not only as a scaffold for lignin deposition but also as a structure regulator of lignin, especially formation of the aryl ether linkage.

Figures 7 and 8 also demonstrated the difference of the two cellulosic models in the deposition of DHP. A larger amount of DHP was deposited on/in the HPBC film, but a lower frequency of the 8-*O*-4′ linkage was formed than on the FBC film. It is supposed that HPBC is a promising model for the adsorption of wood components on cellulose, while FBC gives a good framework to increase the frequency of the 8-*O*-4′ linkage in DHP in artificial polysaccharide matrix. Our next target is to elucidate the effect of glucomannan on the cell wall formation using the similar models of polysaccharides matrices.

Effects of Xylan and DHP on the Mechanical Properties of Cellulosic Films. In general, hemicellulose and lignin influence the mechanical properties of wood cell wall or cellulosic framework.[8,25,42] To confirm these hypotheses, the

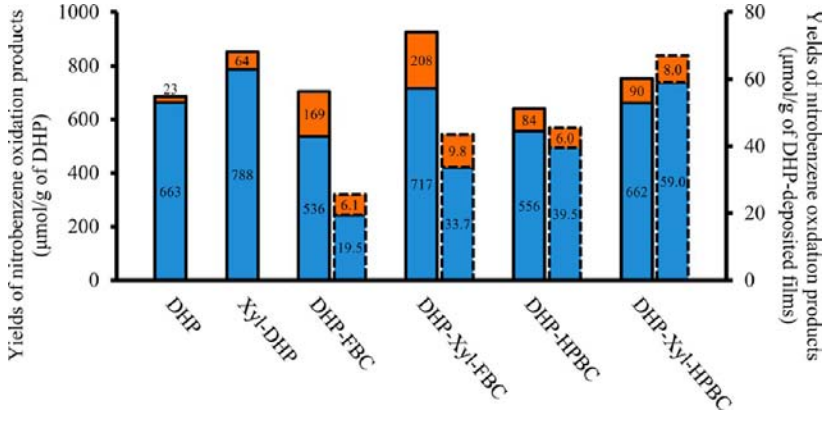

Figure 8. Yields of nitrobenzene oxidation products (vanillin and vanillic acid) from DHP deposited on cellulosic films after washing with 90% 1,4-dioxane solution: Blue, vanillin; orange, vanillic acid; columns with profiles of solid lines, based on the weight of DHP (left axis); columns with profiles of dashed lines, based on the total weight of DHP-deposited films (right axis).

DOI: 10.1021/acs.jafc.5b01070
J. Agric. Food Chem. 2015, 63, 4613−4620

Table 1. Mechanical Properties of BC Films after Xylan and DHP Deposition

	tensile strength (MPa)	MOE[a] (MPa)	elongation (%)	film thickness (μrn)
FBC	55.1 ± 22.9	574 ± 215	8.5 ± 2.4	2.0 ± 0.6
Xyl−FBC	72.7 ± 26.4	1058 ± 359	8.3 ± 4.4	2.0 ± 0.4
DHP−FBC	71.6 ± 22.7	965 ± 233	8.6 ± 2.8	2.1 ± 0.3
DHP−Xyl−FBC	90.4 ± 26.6	1434 ± 331	8.6 ± 3.4	1.9 ± 0.4
HPBC	19.4 ± 6.9	278 ± 100	6.3 ± 1.4	0.77 ± 0.03
Xyl−HPBC	23.6 ± 5.7	352 ± 110	6.9 ± 3.2	0.79 ± 0.05
DHP−HPBC	31.9 ± 9.2	486 ± 128	7.1 ± 3.1	0.76 ± 0.06
DHP−Xyl−HPBC	36.6 ± 14.3	833 ± 256	6.4 ± 3.8	0.77 ± 0.05

[a]Modulus of elasticity.

mechanical properties, tensile strength, and modulus of elasticity (MOE) were measured for the specimens prepared in this study. Table 1 summarizes the mechanical properties of cellulosic films after deposition of xylan and/or DHP. The tensile strength and MOE of HPBC were smaller than those of FBC, which was attributed to the lower density of HPBC (0.17 mg/mm^3) than that of FBC (0.36 mg/mm^3). The amount of cellulose in HPBC is much smaller than that in FBC with same thickness. The smaller amount of cellulose in HPBC caused the weaker mechanical strength.[38]

The tensile strength of FBC and HPBC was increased 1.6 and 1.9 times, respectively, by xylan deposition followed by DHP deposition. MOE of FBC and HPBC was augmented 2.4 and 3.0 times, respectively, by the deposition of xylan and DHP. Thus, both materials strengthen the cellulosic films. If the increment between tensile strength and MOE was compared, the MOE increment was larger than that of tensile strength upon the deposition of both xylan and DHP on FBC and HPBC, especially DHP deposition on HPBC. It seems that DHP gives cellulose more rigidity.

In addition, the increments of tensile strength and MOE were clearly observed for HPBC. Therefore, we suppose that HPBC is a better model for the investigation of the mechanical effect of wood components than FBC.

■ ASSOCIATED CONTENT

Supporting Information

Supplemental SEM-EDXA images of the DHP-deposited FBC and HPBC films at the cross section from the second cutline. The Supporting Information is available free of charge on the ACS Publications website at DOI: 10.1021/acs.jafc.5b01070.

■ AUTHOR INFORMATION

Corresponding Author

*Tel and Fax: +81-11-706-2817. E-mail: uraki@for.agr.hokudai.ac.jp.

Funding

This research work was financially supported by JSPS KAKENHI [Grant-in-Aid for Scientific Research (A), Grant No. 2625202204].

Notes

The authors declare no competing financial interest.

■ ACKNOWLEDGMENTS

The authors thank Dr. Yuzo Sano and Hiromi Shibui from the Laboratory of Woody Plant Biology, Hokkaido University, for their kind help with embedding cellulose films with epoxy resin. Gratitude also goes to Toshiaki Ito, Masanori Yasui, and Manabu Nagao at the Laboratory of Electron Microscopy, Hokkaido University, for their kind help and discussion about microtome cutting and SEM-EDXA analysis.

■ ABBREVIATIONS USED

PDMS, polydimethylsiloxane; DHP, dehydrogenation polymer; BC, bacterial cellulose; HPBC, honeycomb-patterned bacterial cellulose film; FBC, flat bacterial cellulose film; DHP−FBC, DHP-deposited FBC; DHP−Xyl−FBC, DHP- and xylan-deposited FBC; DHP−HPBC, DHP-deposited HPBC; DHP−Xyl−HPBC, DHP- and xylan-deposited HPBC; MOE, modulus of elasticity

■ REFERENCES

(1) Higuchi, T. Biosynthesis of lignin. In *Biosynthesis and Biodegradation of Wood Components*. Higuchi, T., Ed.; Academic Press: Orlando, FL, 1985; pp 141−160.

(2) Sarkanen, K. V. Precursors and their polymerization. In *Lignins: Occurrence, Formation, Structure and Reactions*; Sarkanen, K. V., Ludwig, G. H., Eds.; John Wiley & Sons, Inc.: New York, 1971; pp 95−163.

(3) Jacquet, G.; Pollet, B.; Lapierre, C.; Francesch, C.; Rolando, C.; Faix, O. Thioacidolysis of enzymatic dehydrogenation polymers from *p*-hydroxylphenyl, guaiacyl, and syringyl precursors. *Holzforschung* **1997**, *51*, 349−354.

(4) Cathala, B.; Saake, B.; Faix, O.; Monties, B. Evaluation of the reproducibility of the synthesis of dehydrogenation polymer models of lignin. *Polym. Degrad. Stab.* **1998**, *59*, 65−69.

(5) Cathala, B.; Aguié-Béghin, V.; Douillard, R.; Monties, B. Properties of model compounds of lignin (dehydrogenation polymers = DHPs) at the air/water interface. *Polym. Degrad. Stab.* **1998**, *59*, 77−80.

(6) Northcote, D. H. Chemistry of the plant cell wall. *Annu. Rev. Plant Physiol.* **1972**, *23*, 113−132.

(7) Boerjan, W.; Ralph, J.; Baucher, M. Lignin biosynthesis. *Annu. Rev. Plant Physiol.* **2003**, *54*, 519−546.

(8) Salmén, L.; Burgert, I. Cell wall features with regard to mechanical performance. A review COST Action E35 2004−2008: Wood machining− micromechanics and fracture. *Holzforschung* **2009**, *63*, 121−129.

(9) Houtman, C. J.; Atalla, R. H. Cellulose−lignin interactions. *Plant Physiol.* **1995**, *107*, 977−984.

(10) Atalla, R. H. Cellulose and hemicelluloses: Patterns for the assembly of lignin. In *Lignin and Lignan Biosynthesis*; ACS Symposium Series *697*; Lewis, N. G., Sarkanen, S., Eds.; American Chemical Society: Washington, DC, 1996; pp 172−179.

(11) Terashima, N.; Atalla, R. H.; Ralph, S. A.; Landucci, L. L.; Lapierre, C.; Monties, B. New preparations of lignin polymer models under conditions that approximate cell wall lignifications II. Structure characterization of the models by thioacidolysis. *Holzforschung* **1996**, *50*, 9−14.

(12) Terashima, N.; Atalla, R. H.; Ralph, S. A.; Landucci, L. L.; Lapierre, C.; Monties, B. New preparations of lignin polymer models under conditions that approximate cell wall lignifications I. Synthesis

DOI: 10.1021/acs.jafc.5b01070
J. Agric. Food Chem. 2015, 63, 4613−4620

of novel lignin polymer models and their structural characterization by ^{13}C NMR. *Holzforschung* **1995**, *49*, 521−527.
(13) Higuchi, T.; Ogino, K.; Tanahashi, M. Effect of polysaccharides on dehydropolymerization of coniferyl alcohol. *Wood Res.* **1971**, *51*, 1−11.
(14) Touzel, J.-P.; Chabbert, B.; Monties, B.; Debeire, P.; Cathala, B. Synthesis and characterization of dehydrogenation polymers in *Gluconacetobacter xylinus* cellulose and cellulose/pectin composite. *J. Agric. Food Chem.* **2003**, *51*, 981−986.
(15) Nakamura, R.; Matsushita, Y.; Umemoto, K.; Usuki, A.; Fukushima, K. Enzymatic polymerization of coniferyl alcohol in the presence of cyclodextrins. *Biomacromolecules* **2006**, *7*, 1929−1934.
(16) Sjöström, E. Wood polysaccharides. In *Wood Chemistry: Fundamental and Applications*. Academic Press: San Diego, CA, 1993; pp 51−69.
(17) Nakagawa, K.; Yoshinaga, A.; Takabe, K. Xylan deposition and lignification in the multi-layered cell walls of phloem fibres in *Mallotus japonicus* (Euphorbiaceae). *Tree Physiol.* **2014**, *34*, 1018−1029.
(18) Reis, D.; Vian, B. Helicoidal pattern in secondary cell walls and possible role of xylans in their construction. *C. R. Biol.* **2004**, *327*, 785−790.
(19) Barakat, A.; Chabbert, B.; Cathala, B. Effect of reaction media concentration on the solubility and the chemical structure of lignin model compounds. *Phytochemistry* **2007**, *68*, 2118−2125.
(20) Donaldson, L. A.; Knox, J. P. Localization of cell wall polysaccharides in normal and compression wood of radiata pine: Relationships with lignification and microfibril orientation. *Plant Physiol.* **2012**, *158*, 642−653.
(21) Miyagawa, Y.; Takemoto, O.; Takano, T.; Kamitakahara, H.; Nakatsubo, F. Fractionation and characterization of lignin−carbohydrate complexes (LCCs) of *Eucalyptus globulus* in residues left after MWL isolation. Part I: Analyses of hemicellulose−lignin fraction (HC−L). *Holzforschung* **2012**, *66*, 459−465.
(22) Miyagawa, Y.; Kamitakahara, H.; Takano, T. Fractionation and characterization of lignin−carbohydrate complexes (LCCs) of *Eucalyptus globulus* in residues left after MWL isolation. Part II: Analyses of xylan−lignin fraction (X−L). *Holzforschung* **2013**, *67*, 629−642.
(23) Lawoko, M.; Henriksson, G.; Gellerstedt, G. Structural differences between the lignin−carbohydrate complexes present in wood and in chemical pulps. *Biomacromolecules* **2005**, *6*, 3467−3473.
(24) Du, X.; Pérez-Boada, M.; Fernández, C.; Rencort, J.; C. del Río, J.; Jiménez-Barbero, J.; Li, J.; Gutiérrez, A.; Martínez, A. T. Analysis of lignin−carbohydrate and lignin−lignin linkages after hydrolase treatment of xylan−lignin, glucomannan−lignin and glucan−lignin complexes from spruce wood. *Planta* **2014**, *239*, 1079−1090.
(25) Salmén, L. Micromechanical understanding of the cell-wall structure. *C. R. Biol.* **2004**, *327*, 873−880.
(26) Burgert, I. Exploring the micromechanical design of plant cell walls. *Am. J. Bot.* **2006**, *93*, 1391−1401.
(27) Gibson, L. J. The hierarchical structure and mechanics of plant materials. *J. R. Soc. Interface* **2012**, *9*, 2749−2766.
(28) Hestrin, S.; Schramm, M. Synthesis of cellulose by *Acetobacter xylinum* II. Preparation of freeze-dried cells capable of polymerizing glucose to cellulose. *Biochem. J.* **1954**, *58*, 345−352.
(29) Uraki, Y.; Tamai, Y.; Hirai, T.; Koda, K.; Yabu, H.; Shimomura, M. Fabrication of honeycomb-patterned cellulose material that mimics wood cell wall formation processes. *Mater. Sci. Eng., C* **2011**, *31*, 1201−1208.
(30) Uraki, Y.; Nemoto, J.; Otsuka, H.; Tamai, Y.; Sugiyama, J.; Kishimoto, T.; Ubukata, M.; Yabu, H.; Tanaka, M.; Shimomura, M. Honeycomb-like architecture produced by living bacteria, *Gluconacetobacter xylinus*. *Carbohydr. Polym.* **2007**, *69*, 1−6.
(31) Winarni, I.; Oikawa, C.; Yamada, T.; Igarashi, K.; Koda, K.; Uraki, Y. Improvement of enzymatic saccharification of unbleached cedar pulp with amphipathic lignin derivatives. *BioResources* **2013**, *8*, 2195−2208.
(32) Blumenkrantz, N.; Asboe-Hansen, G. New method for quantitative determination of uronic acids. *Anal. Biochem.* **1973**, *54*, 484−489.
(33) Uraki, Y.; Nakamura, A.; Kishimoto, T.; Ubukata, M. Interaction of hemicelluloses with monolignols. *J. Wood Chem. Technol.* **2007**, *27*, 9−21.
(34) Quideau, S.; Ralph, J. Facile large-scale synthesis of coniferyl, sinapyl, and ρ-coumaryl alcohol. *J. Agric. Food Chem.* **1992**, *40*, 1108−1110.
(35) Kim, J. S.; Awano, T.; Yoshinaga, A.; Takabe, K. Immunolocalization and structural variations of xylan in differentiating earlywood tracheid cell walls of *Cryptomeria japonica*. *Planta* **2010**, *232*, 817−824.
(36) Hatfield, R. D.; Grabber, J.; Ralph, J.; Brei, K. Using the acetyl bromide assay to determine lignin concentrations in herbaceous plants: Some cautionary notes. *J. Agric. Food Chem.* **1999**, *47*, 628−632.
(37) Chen, C.-L. Nitrobenzene and cupric oxide oxidations. In *Methods in Lignin Chemistry*; Lin, S. Y., Dence, C. W., Eds.; Springer-Verlag: New York, 1992; pp 301−321.
(38) Uraki, Y.; Matsumoto, C.; Hirai, T.; Tamai, Y.; Enoki, M.; Hiroshi, Y.; Tanaka, M.; Shimomura, M. Mechanical effect of acetic acid lignin adsorption on honeycomb-patterned cellulosic films. *J. Wood Chem. Technol.* **2010**, *30*, 348−359.
(39) Saka, S.; Thomas, R. J.; Gratzl, J. S. Lignin distribution: Determination by energy-dispersive analysis of X rays. *Tappi* **1978**, *61*, 73−76.
(40) McCartney, L.; Marcus, S. E.; Knox, J. P. Monoclonal antibodies to plant cell wall xylans and arabinoxylans. *J. Histochem. Cytochem.* **2005**, *53*, 543−546.
(41) Kaneda, M.; Rensing, K.; Samuels, L. Secondary cell wall deposition in developing secondary xylem of poplar. *J. Integr. Plant Biol.* **2010**, *52*, 234−243.
(42) Terashima, N.; Kitano, K.; Kojima, M.; Yoshida, M.; Yamamoto, H.; Westermark, U. Nanostructural assembly of cellulose, hemicellulose, and lignin in the middle layer of secondary wall of ginkgo tracheid. *J. Wood Sci.* **2009**, *55*, 409−416.

DOI: 10.1021/acs.jafc.5b01070
J. Agric. Food Chem. 2015, 63, 4613−4620

JOURNAL OF AGRICULTURAL AND FOOD CHEMISTRY

Article

pubs.acs.org/JAFC

Significant Enrichment of Polyunsaturated Fatty Acids (PUFAs) in the Lipids Extracted by Supercritical CO_2 from the Livers of Australian Rock Lobsters (*Jasus edwardsii*)

Trung T. Nguyen,[†,‡,§] Wei Zhang,*[,†,‡] Andrew R. Barber,[†,‡] Peng Su,[†,‡] and Shan He[†,‡]

[†]Centre for Marine Bioproducts Development and [‡]Department of Medical Biotechnology, School of Medicine, Flinders University, Adelaide, South Australia 5042, Australia

[§]Food Science and Technology Department, Agricultural and Natural Resources Faculty, An Giang University, Long Xuyen, Vietnam

ABSTRACT: Australian rock lobster (*Jasus edwardsii*) liver contains approximately 24.3% (w/w) lipids, which can contain a high amount of polyunsaturated fatty acids (PUFAs). However, this material has been found to be contaminated with arsenic (240 mg/kg) and cadmium (8 mg/kg). The high level of contaminants in the raw material and the large amount of PUFAs in the lipids prove a significant challenge in the extraction of high-quality lipids from this byproduct by conventional methods. Supercritical carbon dioxide (SC-CO_2) extraction is a highly promising technology for lipid extraction with advantages including low contamination and low oxidation. The technique was optimized to achieve nearly 94% extraction of lipids relative to conventional Soxhlet extraction in Australian rock lobster liver at conditions of 35 MPa and 50 °C for 4 h. The extracted lipids are significantly enriched in PUFAs at 31.3% of total lipids, 4 times higher than those in the lipids recovered by Soxhlet extraction (7.8%). Specifically, the concentrations of docosahexaenoic acid (DHA) and eicosapentaenoic acid (EPA) in SC-CO_2 extraction are 7 times higher than those obtained by Soxhlet extraction. Moreover, very small amounts of toxic heavy metals such as lead (Pb), arsenic (As), mercury (Hg), and cadmium (Cd) were detected in the SC-CO_2-extracted lipids, 0.5−27 times lower than those in the Soxhlet-extracted lipids, which are 40−200 times lower than the regulatory limit maximum values. The low levels of contaminants and the high proportion of PUFAs (dominated by DHA and EPA) found in the SC-CO_2-extracted lipids from Australian rock lobster liver suggest that the material could potentially be used as a valuable source of essential fatty acids for human consumption.

KEYWORDS: *Australian rock lobster (Jasus ewardsii), rock lobster liver, supercritical CO_2 extraction, ω-3 fatty acids, heavy metal*

INTRODUCTION

Polyunsaturated fatty acids (PUFAs) have been extensively reported in the literature as being beneficial to human health.[1−3] In particular, omega-3 (ω-3) or highly unsaturated fatty acids (HUFAs) are believed to play an important role in the prevention of certain health problems such as diabetes, allergies, and some types of cancers, as well as having antithrombotic, antiarrhythmic, and anti-inflammatory effects.[4] Fishery processing byproducts have been recognized as an important potential source of ω-3 fatty acids, which could be used in the production of ω-3-rich lipids. According to a previous investigation by Tsvetnenko et al.,[5] one major source of PUFAs in the Australian rock lobster (*Panulirus cygnus*) is the hepatopancreas (liver), but this inedible part is usually removed during processing and discarded. Australia is the largest producer and exporter of rock lobster in the world.[5] More than 10000 tons of rock lobster processing wastes including heads, shells, and livers are produced each year, in which the lobster liver accounts for 2−5%. However, only about 25% of these materials are utilized for manufactured products and almost entirely for low commercial value items, such as animal feed, aquafeed, and biofertilizer; the other 75% of the materials are often disposed of as waste with a cost to the processor of up to $150/ton.[6] As a result of the cost and environmental burdens, the Australian lobster processing industry is examining how to utilize these processing coproducts, especially the rock lobster liver, as a valuable potential resource for the production of ω-3-rich lipids.

In recent years, processing coproducts from different types of fish including tuna,[7] herring,[8] salmon,[9] walleye pollock,[10] and shrimp[11] have been extensively studied for lipid extraction; however, very little work has been done on rock lobster liver. It is also important to improve the current extraction procedure of marine coproducts to produce lipids with a high concentration of PUFAs and low contaminants of heavy metals.

Currently, there are several available technologies for the extraction of lipids and pigments from crustacean processing coproducts. The most common technology is solvent extraction.[3,11,12] The solvent selection, a decisive factor in the quality of the extracted lipids, is crucial. Lipids are generally soluble in nonpolar solvents that have been traditionally used for lipid extraction.[13] Several organic solvents including acetone, ethyl acetate, hexane, isopropanol, methanol, methyl ethyl ketone, and ethanol are used in the food industry, whereas others such as dicloromethane, dimethyl sulfoxide, and chloroform cannot be used due to their toxicity.[14] There is, however, increasing public awareness of the health, environ-

Received: December 8, 2014
Revised: April 8, 2015
Accepted: April 23, 2015
Published: April 23, 2015

ACS Publications © 2015 American Chemical Society

DOI: 10.1021/jf5059396
J. Agric. Food Chem. 2015, 63, 4621−4628

mental, and safety hazards related to the use of organic solvents for lipid extraction and the possible solvent contamination of the final lipid products. These issues have stimulated the interest in developing alternative extraction methods.[15] As such, supercritical fluid extraction (SFE) has become an important technology for extracting high-quality lipids[16−19] from fishery processing coproducts[20−22] and is also performed as an effective separation technique in the production of nutraceutical supplements and functional foods.[23,24] SFE can be employed at moderate temperature and provides an oxygen-free medium in reducing lipid oxidation during the extraction process. In addition, it allows for the selective extraction of low-polar lipid compounds, avoiding the coextraction polar impurities such as some organic derivatives with heavy metals.[25] Supercritical carbon dioxide (SC-CO_2) extraction is the common SFE technology because this technique is able to extract the heat-sensitive, easily oxidized compounds such as PUFAs and omega-3[17−19,21,22,26] without any contaminated residues in the products. Moreover, CO_2 is a generally recognized as safe (GRAS) solvent type, which is relatively cheap and easy to separate from the solid matrix and extracts.[3,13,23] The excellent extraction performance of the SC-CO_2 extraction is a result of the low viscosity of SC-CO_2, high diffusivity, and high solubility. In contrast, conventional extraction processes such as Soxhlet extraction produce dilute extracts and contain materials that are easily oxidized. Furthermore, the subsequent steps of solvent separations can lead to the degradation of the target products. Several authors have used SC-CO_2 successfully to extract lipids and carotenoids from vegetable[27−30] and animal matrices.[20,30−32] Recent studies have used the SC-CO_2 extraction of lipids and astaxanthin from crustacean processing waste such as shrimp byproducts.[33−36] To our knowledge, no work has been done on the SC-CO_2 extraction of lipids from rock lobster liver. Therefore, the PUFAs proportion and heavy metal contamination, which are major concerns for potential consumers of rock lobster lipids extracted by SC-CO_2 and Soxhlet, have not yet been investigated. The objectives of this study were to optimize the SC-CO_2 extraction of lipids from Australian rock lobster liver, with the aims of obtaining the lipids with enriched PUFAs, comparing them with the lipids extracted from conventional processing methods, and evaluating the PUFA profiles and heavy metal content of the extracted lipids for potential health benefits and to confirm that they meet food safety standards.

MATERIALS AND METHODS

Materials. Fresh livers of Australian rock lobsters were provided by Ferguson Lobster Co. in South Australia. Food grade carbon dioxide (CO_2) gas used for SFE was supplied by CoreGas, South Australia.

Methods. *Proximate Analysis of Lobster Liver.* According to the AOAC (2006) methods, moisture was determined by oven-drying at 105 °C (AOAC 950.46) until a constant weight was obtained, whereas ash content was quantified by incineration in a muffle furnace at 600 °C (AOAC 920.153). Lipid content was determined by using the Soxhlet extraction method (AOAC 991.36), and protein content was determined according to the micro-Kjeldahl method (AOAC 928.08).

Preparation of Rock Lobster Liver for Extraction. One kilogram of fresh lobster liver was held frozen (Thermo Scientific, TSE series -86C Ultra Low Temperature freezer) at −80 °C for 8 h. The frozen lobster liver was transferred to a plastic box with a large surface before it was freeze-dried at −85 °C and 15 mTorr for 48 h by a benchtop freeze-dryer (Virtis model BT6KEL 301804). The freeze-dried lobster liver was collected and stored in the freezer at −80 °C for 1 week before it was used for the lipid extraction.

Supercritical CO_2 Extraction of Lipids from Rock Lobster Liver. Extractions were carried out by using the laboratory supercritical CO_2 extraction system (Applied Separation model Spe-ed SFE-2 7071) equipped with 100 and 1000 mL extraction vessels. The 100 mL extraction vessel was packed with around 10 g of freeze-dried lobster liver for each batch of extraction, and the void volumes at two ends of the extraction vessel were completed with washed sand and glass wool layers. A 20 min static time was used for making a good contact between the sample and the supercritical solvent before the needle valve was opened to release the extracted lipid. For extraction, CO_2 at supercritical state was continuously drained through the extraction vessel, and the extracted lipid was collected in a preweighed dark glass bottle. The CO_2 mass flow rate was maintained at around 0.434 kg/h, and the time for extraction was 240 min. The extraction temperatures of the oven, valve, and vessel were set at 50, 60, and 50 °C, respectively, whereas the extraction pressures were adjusted to 25, 30, and 35 MPa as experimental design. The lipid-collecting bottle was weighed every hour to calculate lipid recovery. Extractions at every condition were carried out in three replicates.

Soxhlet Extraction of Lipids from Rock Lobster Liver. Soxhlet extraction of lipids from rock lobster liver was carried out at the National Measurement Institute (NMI) of Australia. Ten grams of freeze-dried rock lobster liver was homogenized thoroughly before it was placed in a Soxhlet thimble. The thimble containing the sample was then placed in a hot extraction beaker while 90 mL of diethyl ether was added and locked into the hot extraction unit. Extraction was carried out using a preprogramed period of approximately 4 h with a temperature of 40 °C. The amount of crude lipids obtained by this method was 2.43 g/10 g of the freeze-dried lobster liver.

Fatty Acid Analysis. The fatty acid composition of the lipids extracted by SFE and Soxhlet was analyzed at NMI.

Extracted fats were converted into fatty acids methyl esters (FAME), separated, and then measured on a Hewlett-Packard 6890 gas chromatograph equipped with a 50 cm capillary column (0.32 mm i.d.; SGE, Victoria, Australia) coated with 70% (w/w) cyanopropyl polysilphenylene-siloxane (BPX-70) (0.25 μm film thickness), which was fitted with a flame ionization detector. Helium was the carrier gas (flow rate = 60 mL/min). and the split ratio was 20:1. The injector temperature was set at 250 °C and the detector temperature at 300 °C. The initial oven temperature was 140 °C and programmed to rise to 220 °C at 5 °C/min and then held for up to 3 min. FAMEs were identified on the basis of the retention time of standards obtained from Nucheck Prep Inc. (Elysian, MN, USA) using Chemstation software. An external standard of 463 from NuCheck Prep Inc. was analyzed and used for calibration.

Heavy Metals and Inorganic Arsenic Analysis. The content of heavy metals and inorganic arsenic was determined using the standard methods VL247 ver. 9.1[37] and NT 2.56[38] described by NMI of Australia.

RESULTS AND DISCUSSION

Composition of Australian Rock Lobster Liver. *Chemical Composition.* The chemical composition of

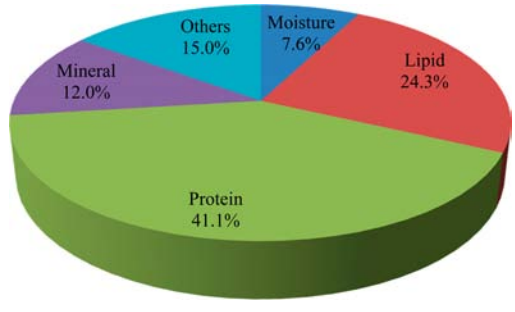

Figure 1. Chemical composition of freeze-dried Australian rock lobster liver (*Jasus ewardsii*).

DOI: 10.1021/jf5059396
J. Agric. Food Chem. 2015, 63, 4621−4628

Table 1. Heavy Metal Contents[a] in Liver of Australian Rock Lobster (on a Dry Weight Basis), Regulatory Limits, and WHO/FAO Recommendation

trace element	Australian rock lobster liver (mg/kg)	regulatory limits (mg/kg)	WHO/FAO recommendation
antimony	0.028		
arsenic (inorganic form)	0.67	2.0	
arsenic (organic and inorganic forms)	240		
cadmium	8.7	2.0	
copper	1000		10–12 mg/day
lead	0.024	0.5	
mercury	0.28	0.5	
selenium	16.0		46–61 μg/day
tin	<0.01	250	
zinc	170		35–45 mg/day

[a]These analyses were carried out by National Measurement Institute of Australia, following its established standard measurement procedures.

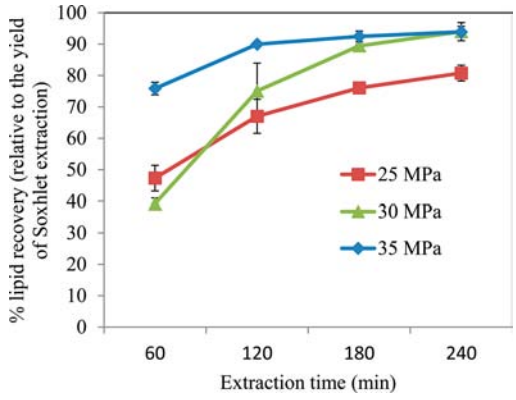

Figure 2. Lipid recovery extracted by SC-CO_2 at different pressures over extraction time.

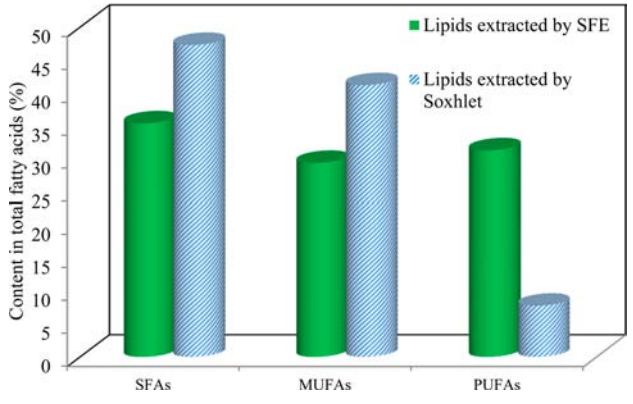

Figure 3. Differences in fatty acid composition of the lipids extracted by SC-CO_2 and Soxhlet method.

Australian rock lobster liver was analyzed. As shown in Figure 1, the two major components of the Australian rock lobster livers obtained in this study are protein (41.1% by dry weight) and lipids (24.3% by dry weight). The lipid content obtained in this study is higher than the 19.4% lipid content reported in the study by Tsvetnenko et al.[5] This could be caused by different species of lobster being used in the experiments or by

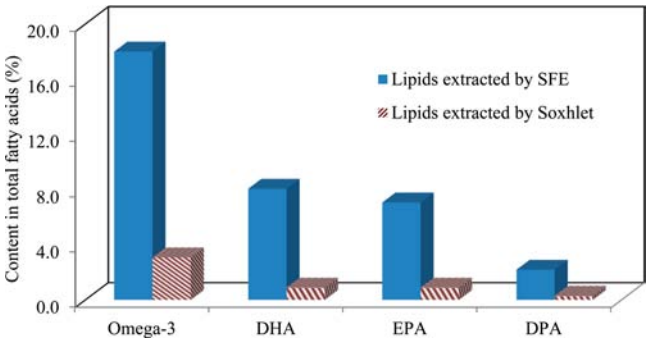

Figure 4. Contents of omega-3 in the lipids extracted by SC-CO_2 and Soxhlet method.

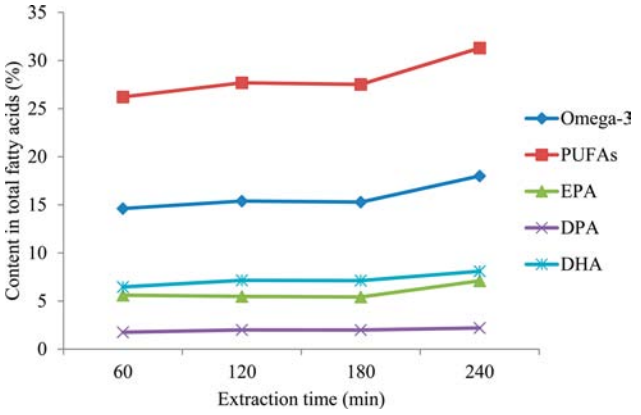

Figure 5. Evolution of PUFAs, omega-3 fatty acids, DHA, EPA, and DPA over the extraction time.

Table 2. Heavy Metal Contents[a] in the Lipids Extracted by SC-CO_2 (50 °C, 35 MPa, 4 h, CO_2 Flow Rate = 0.434 kg/h) and Soxhlet (40 °C, 4 h) as well as Regulatory Limits

trace element	lipids extracted by SC-CO_2 (mg/kg)	lipids extracted by Soxhlet (mg/kg)	regulatory limits (mg/kg)
antimony	<0.01	<0.01	
arsenic (inorganic form)	0.05	0.22	2.0
arsenic (organic and inorganic forms)	2.2	31	
cadmium	<0.01	0.27	2.0
copper	13	150	
lead	0.012	0.022	0.5
mercury	<0.01	0.012	0.5
selenium	0.25	2.6	
tin	0.19	<0.01	250
zinc	12	18	

[a]These analyses were carried out by National Measurement Institute of Australia, following its established standard measurement procedures.

environmental or other factors. Compared with the lipid content of menhaden, which is an Atlantic fish caught primarily for production of fish oil and meal (9.13%), the lipid content in rock lobster liver was nearly 3 times higher. Moreover, Tsvetnenko et al.[5] also reported that the lipids recovered from rock lobster cephalothorax were rich in PUFAs, of which HUFAs accounted for 50.8%. The results indicated that Australian rock lobster liver, a relatively readily available lobster

DOI: 10.1021/jf5059396
J. Agric. Food Chem. 2015, 63, 4621–4628

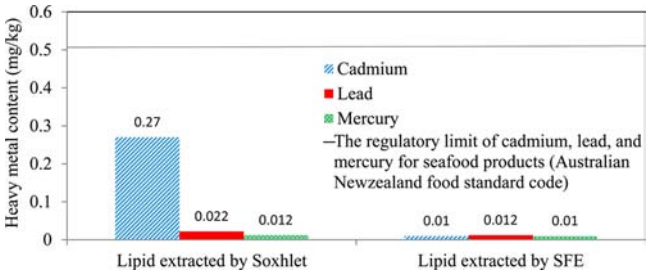

Figure 6. Contents of cadmium, lead, and mercury in the lipids extracted by SC-CO_2 and Soxhlet methods.

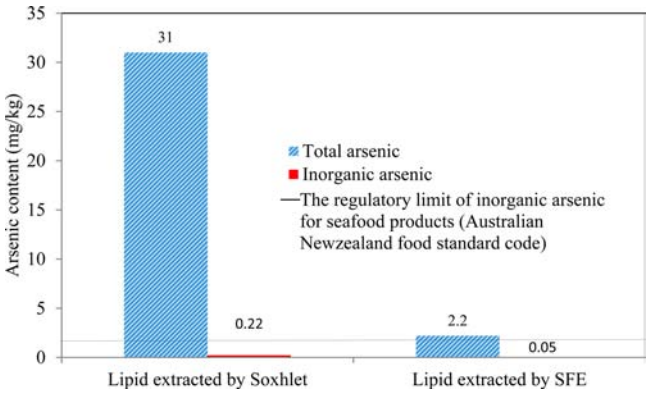

Figure 7. Contents of total and inorganic arsenic in the lipids extracted by SC-CO_2 and Soxhlet methods.

processing byproduct, could be a valuable but inexpensive resource for the extraction of ω-3-rich lipids.

Heavy Metal Composition. The concentration of heavy metals found in Australian rock lobster liver is shown in Table 1. Copper was detected in very high amounts of approximately 1000 mg/kg. This value for copper is several times higher than 151 mg/kg in veal liver, which in turn is regarded as a very high copper content food.[39] Consuming just 10−15 g of rock lobster liver could meet the daily requirement for copper suggested by the WHO/FAO. Copper is an essential mineral required for bone and connective tissue production and for coding specific enzymes that possess the function of eliminating free radicals. A deficiency in copper can lead to osteoporosis, joint pain, and lowered immunity because copper is essential for the absorption of iron.[40] Apart from having a rich copper content, Australian rock lobster liver also has high contents of zinc (170 mg/kg) and selenium (16 mg/kg), which are beneficial for human health.[39] Whereas zinc is good for skin care, healing of wounds, prostate disorders, colds, weight loss, appetite loss, pregnancy, diarrhea, respiratory infections, and malaria,[41] selenium is one of the most effective mineral antioxidants because it actually prevents the formation of new free radicals by participating in various cellular reactions that lower the peroxide concentration in the cellular body.[42] Therefore, Australian rock lobster liver could be an excellent dietary source of zinc and selenium for human demands.

However, four other elements including lead (Pb), cadmium (Cd), arsenic (As), and mercury (Hg) that are generally considered to be hazardous to human health at low to medium concentrations[43] have also been found in Australian rock lobster liver. The amounts of Pb and Hg were just half of the regulatory limit (0.5 mg/kg) of seafood products, but the total As and Cd were quite high, at contents of 240 and 8.7 mg/kg,

Table 3. Fatty Acid Composition[a] of the Lipids Extracted from Liver of South Australian Rock Lobster Using SC-CO_2 (50 °C, 35 MPa, 4 h, CO_2 Flow Rate = 0.434 kg/h) and Soxhlet (40 °C, 4 h)

fatty acid		lipids extracted by SC-CO_2 (%)	lipids extracted by Soxhlet (%)
saturated fatty acids (SFAs)		35.4	47.3
C4:0	butyric	<0.1	<0.1
C6:0	caproic	<0.1	0.3
C8:0	caprylic	<0.1	<0.1
C10:0	capric	<0.1	<0.1
C12:0	lauric	<0.1	0.1
C14:0	myristic	4.3	5.7
C15:0	pentadecanoic	1.9	2.2
C16:0	palmitic	16.7	22.5
C17:0	margaric	2.0	2.6
C18:0	stearic	8.1	10.6
C20:0	arachidic	1.4	1.9
C22:0	behenric	0.7	0.9
C24:0	lignoceric	0.1	0.3
monounsaturated fatty acids (MUFAs)		29.4	41.2
C14:1	myristoleic	<0.1	<0.1
C16:1	palmitoleic	5.5	7.6
C17:1	heptadecenoic	0.3	0.3
C18:1	oleic	20.5	28.4
C20:1	eicosenic	2.3	3.4
C22:1	docosenoic	0.5	0.8
C24:1	nervonic	0.4	0.7
polyunsaturated fatty acids (PUFAs)		31.3	7.8
C18:2ω-6	linoleic	1.8	1.8
C18:3ω-6	γ-linolenic	<0.1	<0.1
C18:3ω-3	α-linolenic	0.5	0.2
C20:2ω-6	eicosadienoic	1.0	0.9
C20:3ω-6	eicosatrienoic	0.2	<0.1
C20:3ω-3	eicosatrienoic	0.2	0.8
C20:4ω-6	arachidonic	8.0	1.2
C20:5ω-3	eicosapentaenoic (EPA)	7.1	0.9
C22:2ω-6	docosadienoic	0.3	0.4
omega 3	fatty acids (ω-3)	18.0	3.1
omega 6	fatty acids (ω-6)	13.3	4.7
C22:4ω-6	docosatetraenoic	2.0	0.4
C22:5ω-3	docosapentaenoic (DPA)	2.2	0.3
C22:6ω-3	docosahexaenoic (DHA)	8.1	0.9
total mono trans fatty acids		0.6	0.5
total poly trans fatty acids		3.2	3.2
P:M:S ratio		0.9:0.8:1	0.2:0.9:1

[a]These analyses were carried out by National Measurement Institute of Australia, following its established standard measurement procedures.

respectively (Table 1). The high contamination of these toxic heavy metals could be caused by a large amount of As and its derivatives present in seawater due to natural processes[44] and pollution as many species of fish and shellfish can bioaccumulate As and toxic heavy metals.[45] Despite contamination with high levels of As, the vast majority of As and its derivatives in Australian rock lobster liver are in organic forms, which are harmless,[45] and its limit is not specified in the food code. By contrast, soluble inorganic arsenic compounds, which

DOI: 10.1021/jf5059396
J. Agric. Food Chem. 2015, 63, 4621−4628

are highly toxic,[46] are present in very small amounts of about 0.67 mg/kg compared with the regulatory limit of 2 mg/kg. However, the content of Cd in rock lobster liver is 4 times higher than the maximum value recommended for seafood according to our study. This high Cd content should be brought into account when rock lobster liver is directly consumed or utilized as a raw material for food. As a result of this, rock lobster liver is usually removed during lobster processing to avoid cross-contamination of toxic heavy metals. An advanced technology is required to ensure the extracted lipids have significantly reduced contaminants.

Optimization of SC-CO_2 Extraction of Lipids from Rock Lobster Liver. SC-CO_2 extraction has been applied to several materials to investigate extraction yield. A number of processing parameters including pressure, temperature, CO_2 rate, and extraction time have been reported to have significant influence on lipid recovery, with extraction pressure and temperature being the most important factors. Several optimum conditions have been suggested for SC-CO_2 extraction of lipids from different materials, but these conditions could be changed depending upon the nature of the materials being treated. In the literature, the suggested pressure usually ranges from 20 to 40 MPa and the temperature varies from 40 to 60 °C. In the present work, extractions of lipids from Australian rock lobster liver were carried out with pressures from 25 to 35 MPa for 1−4 h at 50 °C and the CO_2 flow rate of 0.434 kg/h in order to find the efficient condition for lipid extraction from this material. Although the SC-CO_2 extraction can be carried out at the mild temperature for better prevention of lipid oxidation, the results from initial studies carried out at the same temperature as the Soxhlet extraction (40 °C) indicated that lipid recovery was very low (only 32.17% after 2 h of extraction). Therefore, a slightly higher extraction temperature of 50 °C was chosen to minimize negative effects on the PUFA profile but to achieve a high enough lipid recovery (>90%).

As shown in Figure 2, the extraction curves obtained in this study fit well with the empirical model suggested by Kandiah and Spiro,[47] with an assumption that two diffusion stages, which are based on the amount of lipids accessible to the supercritical CO_2, could control the process. At the early stage, the content of most accessible lipids is high and, thus, the extraction rate is high. As can be seen in Figure 2, the initial extraction rate, or the lipid recovery, increases significantly with applied pressure. When the extraction pressure rose from 25 to 35 MPa, the lipid recovery increased significantly by about 30% (from 47.30 to 75.86%) during the first 2 h of extraction. Up to 90% of the lipids in rock lobster liver relative to the Soxhlet extraction could be recovered in this stage once the pressure of 35 MPa was applied, but for the extraction pressure of 30 and 25 MPa these values were just 75 and 67%, respectively. This result indicates that the internal mass transfer is negligible and the process is controlled by the lipid solubility in SC-CO_2. Because both solvent density and capacity increase with pressure, a rise in pressure leads to an increase in the lipid solubility of the solvent. However, at the second stage, the remaining lipids, which are less accessible to the solvent, were extracted much more slowly because of the considerably higher internal mass transfer resistance.[21] This can be clearly observed in Figure 2 when only around 4, 13, and 19% of the lipids were recovered during the last 2 h of extraction with pressures of 35, 30, and 25 MPa, respectively. The results indicate that using high pressure for SC-CO_2 extraction of lipids from rock lobster liver can shorten the extraction time because the extraction rate increases with pressure.

Although the amount of recovered lipids can be increased with an extended extraction time at all observed pressures, the maximum value of lipid recovery was found at 4 h of extraction. The lipid recovery for 4 h of extraction at 35 and 30 MPa was approximately 94.0%, whereas this value for 25 MPa was reduced to 80.76%. The result, that lipid recovery increased with higher extraction pressure, is in agreement with the previous investigation by Sahena et al.[48] Therefore, SC-CO_2 extraction of lipids from rock lobster liver using high pressure not only shortened the extraction time but also improved the extraction yield.

It is also observed in Figure 2 that the appropriate time for extraction is significantly different among the extraction pressures. Although 4 h of extraction seems to be an appropriate time for the pressure of 30 MPa, this time is clearly not suitable for 35 MPa. This is because the lipid recovery for the pressure of 35 MPa at 2 and 4 h was not significantly different (nearly 90.0 and 94.0%). The prolonged extraction time could lead to a considerable increase in processing costs, and in the case of extraction at 35 MPa, 2 h of extraction is clearly more economical than others. In the overall consideration of extraction yield, extraction time, and PUFA content, the SC-CO_2 extraction at 35 MPa and 50 °C for 2 h of extraction was chosen as the efficient condition for lipid extraction from freeze-dried rock lobster liver.

Significant Improvement in Nutritional Profile of the SC-CO_2-Extracted Lipid. *PUFA-Rich Lipid Extracted by SC-CO_2 Extraction.* Lipid extraction with SC-CO_2 has been suggested as a promising alternative for producing lipids with a high amount of PUFAs. CO_2 at supercritical condition possesses superior mass transfer characteristics, and this technique involves the use of a nonoxidant atmosphere and mild temperature, which could prevent the oxidation of PUFAs. In current research, the lipids extracted from Australian lobster liver by SC-CO_2 extraction and Soxhlet were analyzed, and their fatty acid profiles were compared. It can be observed in Figure 3 that there are significant differences in the fatty acid composition of the two extracted lipid mixtures. Whereas the majority of total fatty acids in the Soxhlet-extracted lipids are saturated fatty acids (SFAs) and monounsaturated fatty acids (MUFAs), its PUFAs are very low, at only around 7.8%. In contrast, the SC-CO_2-extracted lipids have a very high proportion of PUFAs (31.3%), which is greater than the level of MUFAs (29.4%) and equivalent to SFAs. Notably, the level of PUFAs in the SC-CO_2-extracted lipids is 4 times higher than that in the Soxhlet-extracted lipids and considerably higher compared to 22.6% of PUFAs in the previous work of Tsvetnenko et al.,[5] who extracted lipids from rock lobster (*Panulirus cygnus*) cephalothorax using a mixture of methanol/chloroform solvent that was then evaporated under vacuum. This result is also supported by the study of Cheung et al.,[49] who compared the fatty acid composition of lipids extracted from brown seaweed by SC-CO_2 and Soxhlet. Their work also showed that the lipid oxidation of PUFAs had been minimized under low oxidizing conditions used in SC-CO_2 extraction and, therefore, the obtained lipids contained higher PUFAs.

Apart from significantly enriching PUFAs, the SC-CO_2-extracted lipids also have a significantly higher proportion of ω-3 fatty acids, which account for 18% of total fatty acids, 6 times higher compared with the 3.1% of ω-3 fatty acids found in the lipids recovered by the Soxhlet method (Figure 4). This result

DOI: 10.1021/jf5059396
J. Agric. Food Chem. 2015, 63, 4621−4628

is similar to the study of Cheung et al.,[49] who discovered that ω-3 fatty acid levels in the SC-CO_2-extracted lipids from brown seaweed were significantly higher than those in the Soxhlet-extracted lipids and concluded that ω-3 fatty acids were extracted more effectively with SC-CO_2 extraction than with the Soxhlet. More specifically, ω-3 HUFAs such as DHA, EPA, and DPA, which have biochemical activities that may be useful in the prevention and treatment of several disorders and diseases including coronary heart disease, rheumatoid arthritis, asthma, cancers, diabetes, and others,[50] were the most dominant PUFAs of the lipids extracted by SC-CO_2 extraction. These ω-3 HUFA concentrations were 7 times higher than those in the Soxhlet-extracted lipids, and they comprised >95% of the total ω-3 fatty acids in the SC-CO_2-extracted lipids. The maintenance of a high amount of PUFAs in the composition of the extracted lipids with the vast majority of these being ω-3 HUFAs provides a significant advantage for the SC-CO_2 extraction technique for extracting ω-3 rich lipids from the liver of Australian rock lobster.

The investigation on the evolution of PUFAs and ω-3 fatty acids of the SC-CO_2-extracted lipids over the extraction time (Figure 5) indicated that these fatty acid contents are relatively constant in the first 3 h and slightly increase in the fourth hour. The extraction time does not have a significant impact on the fatty acid profile.

Significantly Lower Toxic Heavy Metals in the SC-CO_2 Extracted Lipids. More than 50 different arsenic species have been found in marine environments, and arsenic derivatives, such as arsenobetaine, being the main species and water-soluble form, have been detected in fish.[51] Therefore, seafood is considered as a major dietary source for arsenic exposure.[46] In our current work, the heavy metal content of the extracted lipids have been especially taken into account because some toxic heavy metals were detected over the regulatory limit in the raw materials used for extracting the lipids. This becomes more necessary because a considerable amount (4.3−10.5 ppm) of arsenolipids, which are nonpolar lipids bound with As, have been found in 10 different fish lipids.[52] Table 2 shows the concentration of heavy metals detected in the lipids extracted by the SC-CO_2 extraction and by the Soxhlet. The lipids extracted by both methods contain very small amounts of heavy metals compared with the raw materials and the regulatory limits, whereas their beneficial elements such as Zn and Se are still quite high. The content of these heavy metals in the extracted lipids changed significantly from 0.5 to 870 times depending on the method used for the lipid extraction and the types of trace elements. The low contamination of heavy metals in the extracted lipids is a result of these methods utilizing nonpolar solvents for extraction, which usually solubilize mainly the nonpolar compounds and leave behind the polar compounds.

However, this work has been specifically focused on an investigation of toxic heavy metals because contamination with these compounds can render the material unusable due to potential risks of excessive ingestion, which may lead to a decline in mental, cognitive, and physical health. As shown in Figures 6 and 7, there are significant differences in the amounts of toxic heavy metals in the lipids extracted by SC-CO_2 and Soxhlet techniques. The contents of all toxic heavy metals in the SC-CO_2-extracted lipids were considerably lower than those in the Soxhlet-extracted lipid. Whereas the concentration of Pb in the SC-CO_2-extracted lipids was just half of that in the Soxhlet-extracted lipids (0.022 mg/kg), the content of inorganic arsenic in the former was 4 times lower compared with the amount of 0.22 mg/kg in the latter. Notably, the content of Cd in the SC-CO_2-extracted lipids (<0.01 mg/kg) was 27 times lower than that in the Soxhlet-extracted lipids, whereas the concentration of total arsenic was nearly 15 times lower (2.2 mg/kg compared with 31 mg/kg). This trend is strongly supported by the recent investigations by Rubio-Rodríguez et al.[25] Their results indicate that SC-CO_2 extraction is an effective technology for extracting fish lipids with greatly reduced contamination with toxic heavy metals.

Lipid Profiles. Table 3 illustrates the fatty acid composition of the lipids extracted by SC-CO_2 (50 °C, 35 MPa, 0.434 kg/h) and by Soxhlet from Australian rock lobster liver. It needs to be highlighted that there are significant differences in the fatty acid compositions of the lipids extracted by these two methods. Whereas the highest proportion in the Soxhlet-extracted lipids was SFAs (47.3%) followed by MUFAs (41.2%) and PUFAs (7.8%), these contents in the SC-CO_2-extracted lipids were 35.4% of SFAs, 29.4% of MUFAs, and 31.1% of PUFAs, respectively. The former was rich in SFAs and MUFAs but very poor in PUFAs, whereas the latter has very high amounts of PUFAs dominated by ω-3 (18%) and ω-6 (13.3%). The differences in fatty acid profiles of these two lipids could be explained by differences in conditions used for extracting the lipids. Whereas the Soxhlet method employed organic solvents such as diethyl ether for extraction in this study, the SC-CO_2 extraction used CO_2 at supercritical condition that has high diffusion and very low surface tension compared to liquid solvents.[53] These novel properties could be a favorable condition for PUFA extraction. This point, that the yield of omega-3 fatty acids extracted by SC-CO_2 extraction at higher pressure (31.0 and 37.9 MPa) was significantly higher than that in the Soxhlet, was confirmed by Cheung et al.[49]However, both lipids have diversified fatty acids in which oleic is the most dominant in their composition (20.5% for SC-CO_2-extracted lipids and 28.4% for Soxhlet-extracted lipids). Palmitic is abundant in SFAs (16.7% for SC-CO_2-extracted lipids and 22.5% for Soxhlet-extracted lipids), whereas DHA, EPA, and arachidonic are three main fatty acids in PUFAs, accounting for up to 75%.

AUTHOR INFORMATION

Corresponding Author

*(W.Z.) Phone: +61-8-7221-8557. Fax: +61-8-7221-8555. E-mail: wei.zhang@flinders.edu.au.

Funding

We acknowledge funding support from the Premier's Research and Industry Fund of the South Australian government and Ferguson Lobster Co., Ltd.

Notes

The authors declare no competing financial interest.

ACKNOWLEDGMENTS

We acknowledge Flinders University, the Centre for Marine Bioproducts Development, and the National Measurement Institute for technical support.

ABBREVIATION USED

AOAC, Association of Official Analytical Chemists; WHO, World Health Organization; FAO, Food and Agriculture Organization

DOI: 10.1021/jf5059396
J. Agric. Food Chem. 2015, 63, 4621−4628

REFERENCES

(1) Sampath, H.; Ntambi, J. M. Polyunsaturated fatty acids and regulation of gene expression. In *Fatty Acids in Food and Their Health Implications*, 3rd ed.; Chow, C. K., Ed.; CRC Press: Boca Raton, FL, USA, 2007; Vol. 32, pp 727−739.

(2) FAO. . Fat and fatty acids in human nutrition: report of an expert consultation. *FAO Food Nutr. Pap.* **2010**, 1−166.

(3) Sahena, F.; Zaidul, I. S. M.; Jinap, S.; Saari, N.; Jahurul, H. A.; Abbas, K. A.; Norulaini, N. A. PUFAS in fish: extraction, fractionation, importance in health. *Compr. Rev. Food Sci. Food Saf.* **2009**, *8*, 59−74.

(4) Morales, R.; Munío, M. d. M.; Gálvez, P. P.; Guadix, A.; Guadix, E. M. Lipids from marine sources. In *Utilization of Fish Waste*, 1st ed.; Gálvez, R. P., Bergé, J.-P., Eds.; CRC Press: New York, 2013; pp 154−192.

(5) Tsvetnenko, E.; Kailis, S.; Evans, L.; Longmore, R. Fatty acid composition of lipids from the contents of rock lobster (*Panulirus cygnus*) cephalothorax. *J. Am. Oil Chem. Soc.* **1996**, *73*, 2559−2561.

(6) Knuckey, I. Utilisation of seafood processing waste − challenges and opportunites. In *Australian New Zealand Soils Conference*; University of Sydney: Australia, 2004; pp 1−7.

(7) Chantachum, S.; Benjakul, S.; Sriwirat, N. Seperation and quality of fish oil from precooked and non-precooked tuna head. *Food Chem.* **2000**, *69*, 289−294.

(8) Aidos, I.; Van-der-Padt, A.; Boom, R. M.; Luten, J. B. Seasonal changes in crude and lipid composition of herring fillet, by-products and respective produced oils. *J. Agric. Food Chem.* **2002**, *50*, 4589−4599.

(9) Wu, T. H.; Bechtel, P. J. Salmon by-product storage and oil extraction. *Food Chem.* **2008**, *111*, 868−871.

(10) Wu, T. H.; Bechtel, P. J. Quality of crude oil extracted from agigin walleye pollock (*Theragra chalcogramma*) by-products. *J. Am. Oil Chem. Soc.* **2009**, *86*, 903−908.

(11) Sachindra, N. M.; Bhaskar, N.; Mahendrakar, N. S. Recovery of carotenoids from shrimp waste in organic solvents. *Waste Manage.* **2006**, *26*, 1092−1098.

(12) Meyers, S. P.; Bligh, D. Characterization of astaxanthin pigment from heat processed crawfish waste. *J. Agric. Food Chem.* **1981**, *9*, 509−512.

(13) Mercadante, A. Z. Analysis of carotenoids. In *Food Colorants: Chemical and Functionality*; Socaciu, C., Ed.; CRC Presss: Boca Raton, FL, USA, 2008; pp 447−472.

(14) FDA. Listing of food additives status; http://.fda.gov/Food/FoodIngredientsPackaging/FoodAdditives/FoodAdditivesListings/ucm091048.htm (accessed Sept 26, 2014).

(15) Delgado-Vargas, F.; Paredes-López, O. Carotenoids. In *Natural Colorants for Food and Nutraceutical Uses*; Delgado-Vargas, F., Paredes-López, O., Eds.; CRC Press: Boca Raton, FL, USA, 2002; pp 113−157.

(16) Walker, T. H.; Cochran, H. D.; Hulbert, G. J. Supercritical carbon dioxide extraction of lipids from *Pythium irregulare*. *J. Am. Oil Chem. Soc.* **1999**, *76*, 595−602.

(17) Cheng, Y.-J.; Shieh, C.-J.; Wang, Y.-C.; Lai, S.-M.; Chang, C.-M. J. Supercritical carbon dioxide extraction of omega-3 oil compounds from *Ficus awkeotsang* Makino achenes. *Sep. Purif. Technol.* **2012**, *98*, 62−68.

(18) Andrich, G.; Nesti, U.; Venturi, F.; Zinnai, A.; Fiorentini, R. Supercritical fluid extraction of bioactive lipids from the microalga *Nannochloropsis* sp. *Eur. J. Lipid Sci. Technol.* **2005**, *107*, 381−386.

(19) Follegatti-Romero, L. A.; Piantino, C. R.; Grimaldi, R.; Cabral, F. A. Supercritical CO_2 extraction of omega-3 rich oil from Sacha inchi (*Plukenetie volubilis* L.) seeds. *J. Supercrit. Fluids* **2009**, *49*, 323−329.

(20) Letisse, M.; Rozieres, M.; Hiol, A.; Sergent, M.; Comeau, L. Enrichment of of EPA and DHA from sardine by supercritical fluid extraction without organic modifier: optimization of extraction conditions. *J. Supercrit. Fluids* **2006**, *38*, 27−36.

(21) Rubio-Rodríguez, N.; Diego, S. M. d.; Beltrán, S.; Jaime, I. Supercritical fluid extraction of the omega-3 rich oil contained in hake (*Merluccius capensis-Merluccius paradoxus*) by-products: study of the influence of process parameters on the extraction yield and oil quality. *J. Supercrit. Fluids* **2008**, *47*, 215−226.

(22) Amiguet, V. T.; Kramp, K. L.; Mao, J.; McRae, C.; Coulah, A.; Kimpe, L. E.; Blais, J. M.; Arnason, J. T. Supercritical carbon dioxide extraction of polyunsaturated fatty acids from Northern shrimp (*Pandalus borealis* Kreyer) processing by-products. *Food Chem.* **2012**, *130*, 853−858.

(23) Reverchon, E.; De Marco, I. Supercritical fluid extraction and fractionation of natural matter. *J. Supercrit. Fluids* **2006**, *38*, 146−166.

(24) Parajó, J. C.; Domínguez, H.; Moure, A.; Diáz-Reinoso, B. Obtaining antioxidants by supercritical fluid extraction applied. In *Extracting Bioactive Compounds for Food Products: Theory and Applications*, Meireles, M. A. A., Ed.; CRC Press: Boca Raton, FL, USA, 2008; pp 288−315.

(25) Rubio-Rodríguez, N.; Diego, S. M. d.; Beltrán, S.; Jaime, I.; Sanz, M. T.; Rovira, J. Supercritical fluid extraction of fish oil from fish by-products: a comparision with other extraction methods. *J. Food Eng.* **2012**, *109*, 238−248.

(26) López-Cervantes, J.; Sánchez-Machado, D. I.; Rosas-Rodríguez, J. A. Analysis of free amino acids in fermented shrimp waste by high-performance liquid chromatography. *J. Chromatogr., A* **2006**, *1105*, 106−110.

(27) Filho, G. L.; De Rosso, V. V.; Meireles, M. A. A.; Rosa, P. T. V.; Oliveira, A. L.; Mercadante, A. Z.; Cabral, F. A. Supercritical CO_2 extraction of carotenoids from pitanga fruits (*Eugenia uniflora* L.). *J. Supercrit. Fluids* **2008**, *46*, 33−39.

(28) Mendes, R. L.; Fernandes, H. I.; Coelho, J. P.; Reis, E. C.; Cabral, J. M.; Novais, J. M.; Palavra, A. F. Supercritical CO_2 extraction of carotenoids and other lipids from *Chlorella vulgaris*. *Food Chem.* **1995**, *53*, 99−103.

(29) Silva, G. F.; Gamarra, F. M. C.; Oliveira, A. L.; Cabral, F. A. Extraction of bixin from annatto seeds using supercritical carbon dioxide. *Braz. J. Chem. Eng.* **2008**, *25*, 419−426.

(30) Hardardottir, I.; Kinsella, J. E. Extraction of lipids and cholesterol from fish muscle with supercritical fluid. *J. Food Sci.* **1988**, *53*, 1656−1661.

(31) Tanaka, Y.; Ohkubo, T. Extraction of lipids from salmon roes with supercritical carbon dioxide. *J. Oleo Sci.* **2003**, *52*, 295−301.

(32) Froning, G. W.; Wheling, R. L.; Cuppett, S. L.; Pierce, M. M.; Niemann, L.; Seikman, D. K. Extraction of cholesterol and other lipids from dried egg yolk using supercritical carbon dioxide. *J. Food Sci.* **1990**, *55*, 95−98.

(33) Charest, D. J.; Balaban, M. O.; Marshall, M. A.; Cornell, J. A. Astaxanthin extraction from crawfish shells by supercritical CO_2 with ethanol as cosolvent. *J. Aquat. Food Prod. Technol.* **2001**, *3*, 81−96.

(34) Kamaguchi, K.; Murakami, M.; Nakano, H.; Konosu, S.; Kokura, T.; Yamamoto, H.; Kosaka, M.; Hata, K. Supercritical carbon dioxide extraction of oils from Antarctic krill. *J. Agric. Food Chem.* **1986**, *34*, 904−907.

(35) Lopez, M.; Arce, L.; Garrido, J.; Rios, A.; Valcarcel, M. Selective extraction of astaxanthin from crustaceans by use of supercritical carbon dioxide. *Talanta* **2004**, *64*, 726−731.

(36) Felix-Valenzuela, L.; Higuera-Ciapara, I.; Goycoolea, F. M.; Arguelles-Monal, W. Supercritical CO_2/ethanol extraction of astaxanthin from blue crab (*Callinectes sapidus*) shell waste. *J. Food Process Eng.* **2001**, *24*, 101−112.

(37) NMI. *Trace Elements in Food and Biota*; National Measurement Institute of Australia: Sydney, Australia, 2013; Vol. VL247_Ver. 9.1.

(38) NMI. *Inorganic Arsenic in Selected Food and Biota*; National Measurement Institute of Australia: Sydney, Australia, 2013; Vol. NT 2.56.

(39) WHO; FAO; IAEA. *Essential Trace Elements: Copper*; World Health Organization: Geneva, Switzerland, 1996; pp 123−139.

(40) Ness, H. A. Top 10 foods highest in copper; http://www.healthaliciousness.com/articles/high-copper-foods.php (accessed Oct 27, 2014).

(41) Deshpande, J. D.; Joshi, M. M.; Giri, P. A. Zinc: the trace element of major importance in human nutrition and health. *Int. J. Med. Sci. Public Health* **2013**, *2*, 1−6.

DOI: 10.1021/jf5059396
J. Agric. Food Chem. 2015, 63, 4621−4628

(42) Chan, S.; Gerson, B.; Subramaniam, S. The role of copper, molybdenum, selenum, and zinc in nutrition and health. *Clin. Lab. Med.* **1998**, *18*, 673−685.
(43) Davidowski, L.; Grosser, Z.; Thompson, L. *The Determination of Metals in Dietary Supplements*; PerkinElmer: Shelton, CT, USA, 2009; pp 1−4.
(44) Smedley, P. L.; Kinniberg, D. G. Review of the source, behaviour and distribution of arsenic in natural waters. *Appl. Geochem.* **2002**, *17*, 517−568.
(45) NSW Food Authority *Inorganic Arsenic in Seaweed and Certain Fish*; NSW Food Authority: Newington, NSW, Australia, 2010; pp 1−7.
(46) Hedegaard, R. V.; Hansen, M.; Larsen, E. H.; Sloth, J. J. *Selective Determination of Inorganic Arsenic in Food and Feed by Microwave-Assisted Extraction and Solid Phase Extraction*; National Food Institute: Kongens Lyngby, Denmark, 2005; p 1.
(47) Kandiah, M.; Spiro, M. Extraction of ginger rhizome: kinetic studies with supercritical carbon dioxide. *Int. J. Food Sci. Technol.* **1990**, *25*, 328−338.
(48) Sahena, F.; Zaidul, I. S. M.; Jinap, S.; Jahurul, M. H. A.; Khatib, A.; Norulaini, N. A. N. Extraction of fish oil from the skin of Indian mackerel using supercritical fluids. *J. Food Eng.* **2010**, *99*, 63−69.
(49) Cheung, P. C. K.; Leung, A. Y. H.; Ang, P. O. Comparison of supercritical carbon dioxide and Soxhlet extraction of lipids from brown seaweed, *Sargassum hemiphyllum* (Turn.). *J. Agric. Food Chem.* **1998**, *46*, 4228−4232.
(50) Pamela, M. Fish oil: nutrition. *Pharm. J.* **2001**, *265*, 720−724.
(51) Ackley, K.; Bhymer, C.; Sutton, K.; Caruso, J. Speciation of arsenic in fish tissue using microwave-assisted extraction followed by HPLC-ICP-MS. *J. Anal. At. Spectrom.* **1999**, *14*, 845−850.
(52) Schemeisser, E.; Goessler, W.; Kienzl, N.; Francesconi, K. A. Direct measurement of lipid-soluble arsenic species in biological samples with HPLC-ICP-MS. *Analyst* **2005**, *130*, 948−955.
(53) Karale Chandrakant, K.; Dere Pravin, J.; Hondre Bharat, S.; Sachin, K.; Kote Amol, P. An overview on supercritical fluid extraction for herbal drugs. *Pharmacologyonline* **2011**, *2*, 575−596.

DOI: 10.1021/jf5059396
J. Agric. Food Chem. 2015, 63, 4621−4628

JOURNAL OF AGRICULTURAL AND FOOD CHEMISTRY

Article

pubs.acs.org/JAFC

Isomerization of Cholecalciferol through Energy Transfer as a Protective Mechanism Against Flavin-Sensitized Photooxidation

Regina S. Scurachio,[†] Willy G. Santos,[†] Eduardo S. P. do Nascimento,[†] Leif H. Skibsted,*[,‡] and Daniel R. Cardoso*[,†]

[†]Instituto de Química de São Carlos, Universidade de São Paulo, Avenida Trabalhador São Carlense 400, CP 780, 13560-470 São Carlos, Brazil

[‡]Food Chemistry, Department of Food Science, University of Copenhagen, Rolighedsvej 30, DK-1958 Frederiksberg C, Denmark

ABSTRACT: Cholecalciferol, vitamin D_3, was found to isomerize to 5,6-*trans*-vitamin-D_3 with a quantum yield of 0.15 ± 0.01 in air-saturated 7/3 *tert*-butyl alcohol/water (v/v) at 25 °C, increasing to 0.32 ± 0.02 in the absence of oxygen, through quenching of triplet excited state flavin mononucleotide, FMN, rather than becoming oxidized. The quenching was found by laser flash photolysis to have a rate constant of 1.4×10^8 L mol^{-1} s^{-1} in 7/3 *tert*-butyl alcohol/water (v/v) at 25 °C, assigned to energy transfer from ^{3}FMN* to form a reactive vit.D_3 diradical. vit.D_3 forms a 1/1 precomplex with FMN by hydrophobic stacking with $\Delta H° = -36 \pm 7$ kJ mol^{-1} and $\Delta S° = -4 \pm 3$ J mol^{-1} K^{-1}, as shown by single photon counting fluorescence spectroscopy and steady-state fluorescence spectroscopy. Both ground-state precomplex formation and excited-state energy transfer seem important for vit.D_3 protection against flavin-sensitized photooxidation of nutrients in food and biological systems.

KEYWORDS: *vitamin D, riboflavin, photochemistry, 5,6-trans-vitamin D*

INTRODUCTION

Vitamins have varying reactivity depending on their biological functions. For some vitamins, the reactivity is modulated in provitamins with better stability, and the vitamin function depends on an activation step. The lipophilic vitamin D provides examples such as 7-dehydrocholesterol, which is found as a pro-vitamin D in food of animal origin, and ergosterol, which is found as pro-vitamin D in food from the plant kingdom.[1,2] The activation step involves for both provitamins a photochemical reaction to form cholecalciferol, vit.D_3, or ergocalciferol, vit.D_2, respectively, as occurring in human skin upon exposure to UV-B sunlight.[1−3] Among the water-soluble vitamins, vitamin B_2 is also photoactive, since riboflavin, the form of vitamin B_2 normally in foods, and the biological forms of vitamin B_2, flavin mononucleotide (FMN) and flavin adenine dinucleotide (FAD), are potent photosensitizers, inducing oxidative damage in food and skin, including degradation of the isoalloxazine ring common for these flavins.[4,5]

Vitamin B_2 and vitamin D_2 or D_3 (Figure 1) or their pro-vitamin forms will interact upon light exposure when the two types of vitamins are present together. Milk and dairy products provides such examples where the lipophilic vitamin D forms are found in the lipid phase of the emulsions, while vitamin B_2 is water-soluble.[2] Human skin provides another example, since both of the different vitamin B_2 forms, including flavoproteins located at the plasma membrane, and pro-vitamin D_2 or D_3 are present in the skin and become exposed to light.[6,7] Riboflavin is known to initiate photodegradation of important nutrients in dairy products upon light exposure in reactions normally assigned to oxidation.[5] A more detailed understanding of the interaction between light-activated forms of the flavins and the vitamin D homologues is, however, not available at present. Such knowledge at the mechanistic level would be important both in relation to improvement of the stability of food exposure to light and also in relation to skin health.[5−7]

Vitamin B_2 and vitamin D apparently have opposite effects on skin health upon light exposure, since riboflavin induces oxidative damage and radical formation with increased cancer risk, while the different forms of vitamin D apparently protect against light damage to the skin.[8−10] Most importantly, exposure of biological systems containing both vitamin B_2 and vitamin D to visible light and UV-A light will activate only the flavin vitamin forms due to the spectral characteristic of the two types of vitamins, and the activated flavin may react with vitamin D. We have accordingly undertaken photophysical studies using visible and UV-A light for activation of flavins and studied the interaction with vitamin D; the results of these investigations should be valuable for both protection of the nutritive value of foods and for nutritional advice for better skin health.

MATERIALS AND METHODS

Chemicals. Cholecalciferol (vitamin D_3), flavin mononucleotide (FMN), $LiClO_4$ salt, and deuterated methanol (CD_3OD) were purchased from Sigma-Aldrich (Steinheim, Germany). Acetonitrile HPLC grade was purchased from Mallinckrodt (Phillipsburg, NJ). *tert*-Butanl alcohol (99.5%) and Tween-20 (pure) were purchased from Acros Organics (Geel, Belgium). Water was purified (18 MΩ cm) by means of a Milli-Q purification system from Millipore (Billerica, MA).

Steady-State Fluorescence Spectroscopy. Fluorescence measurements were carried out using a Hitachi F-7000 fluorescence spectrometer (Hitachi High-Tech, Tokyo, Japan). The samples were excited in 1.0 cm × 1.0 cm fluorescence cuvettes from Hellma (Mulheim, Germany) at 440 nm. Emission spectra were recorded using

Received: December 11, 2014
Revised: April 15, 2015
Accepted: April 20, 2015
Published: April 20, 2015

ACS Publications © 2015 American Chemical Society

DOI: 10.1021/jf505958c
J. Agric. Food Chem. 2015, 63, 4629−4637

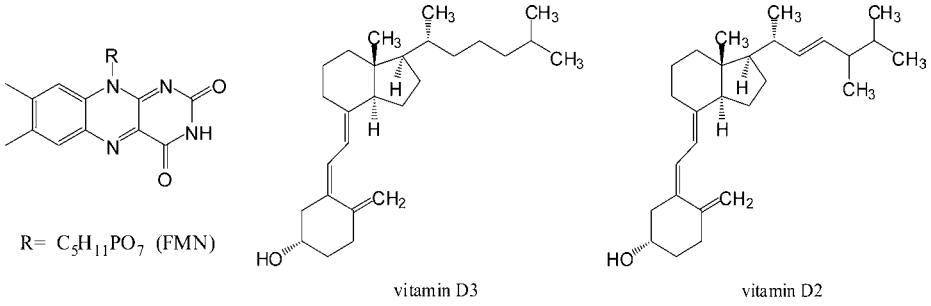

Figure 1. Chemical structures for FMN, vitamin D_3, and vitamin D_2.

a 2.0 nm band pass for the excitation monochromator and a 4.0 nm band pass for the emission monochromator. The recorded spectra were corrected for instrument response. The fluorescence was measured at 25.0 ± 0.2 °C in 7/3 *tert*-butyl alcohol/water solution (v/v).

Time-Resolved Fluorescence Spectroscopy. Time-resolved fluorescence were measured by time-correlated single-photon counting using a picosecond spectrometer equipped with Glan-Laser polarizers (Newport, Irvine, CA), a Peltier-cooled PMTMCP from Hamamatsu, Model R3809U-50 (Hamamatsu, Japan), as the photon detector, and Tennelec-Oxford (Oxford, Abingdon, U.K.) counting electronics. The light pulse was provided by frequency-doubling the 200 fs laser pulse of a Mira 900 Ti-sapphire laser pumped by a Verdi 5 W coherent laser (Santa Clara, CA), and the pulse frequency was reduced to 800 kHz using a Conoptics pulse picker. The fluorescence decays were taken at the magic angle (λ_{exc} 400 nm) and analyzed by a reconvolution procedure with instrument response function (irf) with exponential decay models, and the goodness of the fit was evaluated by the statistical parameter χ^2. The fluorescence was measured at 25.0 ± 0.2 °C in 7/3 *tert*-butyl alcohol/water solution (v/v).

Laser Flash Photolysis. Laser flash photolysis experiments were carried out with an LFP-112 nanosecond laser flash photolysis spectrometer from Luzchem (Ottawa, Canada) using the third harmonic (355 nm) of a pulsed Q-switched Nd:YAG laser (BrilliantB, LesUlis, France) attenuated to 10 mJ cm^{-2} as the excitation source with pulse duration 8 ns. Appropriate UV cutoff filters were used to minimize the sample degradation by the monitoring light. The signal from the monochromator/photomultiplier detection system was captured by a Tektronix TDS 2012 digitizer (Beaverton, OR). The laser system and the digitizer were connected to a personal computer via a general purpose instrumentation bus (GPIB) and serial interfaces controlling all the experimental parameters and providing suitable processing and data storage capabilities. Each kinetic trace was averaged 16 times, and observed rate constants were determined by parameter fitting with MatLab R2013 to exponential decay functions (Mathworks Inc., Natick, MA). All measurements were made with fresh 7/3 *tert*-butyl alcohol/water (v/v) solutions or Tween-20 micelle (0.1 mol l^{-1}) thermostated at 25.0 ± 0.5 °C and purged with high-purity N_2 for at least 30 min before the experiment.

Steady-State Photolysis. A 7/3 *tert*-butyl alcohol/water (v/v) solution containing 1.0×10^{-4} mol L^{-1} of FMN and 1.0×10^{-3} mol L^{-1} of vitamin D_3 was exposed to 440 nm monochromatic light generated by a mercury lamp (HBO 200 w/4 short arc, Osram, Augsburg, Germany) accommodated with a focusing quartz lens, a water-filled heat filter, and an Oriel narrow-band interference filter (center wavelength, 440 nm; Oriel Corp., Irvine, CA). The intensity of light, $q^0_{n,p}$, was measured by ferrioxalate actinometry[11] and had an average value of 2.53×10^{-8} einstein min^{-1}. The absorbance measurements were carried out employing a Hitachi U-3501 (Hitachi-Hitech, Japan) spectrophotometer.

Cyclic Voltammetry. Cyclic voltammetry of vit.D_3 (1.0×10^{-3} mol L^{-1}) dissolved in nitrogen-purged acetonitrile containing $LiClO_4$ (0.5 M) was carried out using a PAR 264A potentiostat (Princeton Applied Research, Princeton, NJ) equipped with glassy carbon as the working electrode, a platinum wire as the auxiliary electrode, and an Ag/AgCl reference electrode. The scan rate was 100 mV s^{-1}, and the electrochemical cell was thermostated at 25.0 ± 0.2 °C.

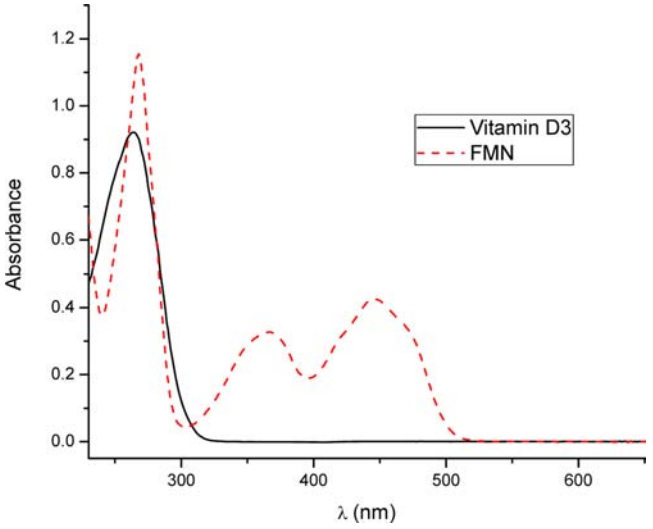

Figure 2. UV−vis absorption spectra for solutions of flavin mononucleotide and vitamin D_3 (both 1.0×10^{-4} mol L^{-1}) in 7/3 *tert*-butyl alcohol/water (v/v) at 25 °C.

LC-DAD-SPE. The irradiated sample of FMN (1×10^{-4} mol L^{-1}) and vit.D (1×10^{-4} mol L^{-1}) was analyzed by LC-DAD (Shimadzu Prominence 20A system, Shimadzu Co., Kyoto, Japan). Chromatographic separation was carried out on an Agilent Extend C18 reverse phase column (2.1 mm × 150 mm × 50 μm). The injection volume was 100 μL. The chromatographic separation was performed at a flow rate of 0.25 mL min^{-1} in isocratic mode consisting of 15% of solvent B in solvent A (A, 80/20 ACN/H_2O (v/v); B, MeOH). The peaks of interest were detected using the UV response at 265 nm. After the chromatographic separation, peaks of interest were trapped on Hysphere C18 cartridges from Spark-Holland using a Prospek-II automatized SPE system (Spark-Holland, Emmen, Holland) attached to the LC-DAD instrument; the target peaks from 10 chromatographic runs were sequentially trapped on the SPE cartridge to ensure enough quantity for the NMR analysis. Solvents used were nondeuterated. A makeup flow of eluent A was added to the postcolumn eluate in a ratio of 10/1 in order to improve the retention. After the trapping process, the cartridges were dried with high-purity nitrogen to remove residual solvents. Pure deuterated methanol was used to flush the peak from the SPE cartridge directly into the sample vial for posterior NMR analysis.

Nuclear Magnetic Resonance Spectroscopy. ^1H NMR experiments were performed using a Bruker Avance-III 600 MHz NMR spectrometer equipped with a ^1H {^{13}C, ^{15}N} triple-resonance inverse cryoprobe (TCI).

The one-dimensional ^1H NMR experiment was based on the 1D version of the NOESY sequence, using double presaturation suppression (methanol and water) during the relaxation delay (4 s). The spectrum was acquired using 16k data points in a 9578.54 Hz spectral width, giving an acquisition time of 3.42 s. Processing was performed using exponential multiplication, applying a line broadening factor of 0.5 Hz.

DOI: 10.1021/jf505958c
J. Agric. Food Chem. 2015, 63, 4629−4637

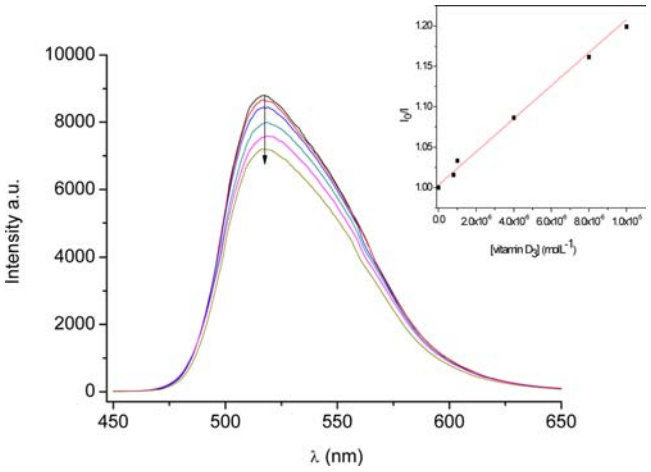

Figure 3. Fluorescence emission spectra at 25 °C of 1.0×10^{-4} mol L^{-1} flavin mononucleotide (in 7/3 *tert*-butyl alcohol/water (v/v)) for increasing concentrations of vit.D_3, from 8.0×10^{-7} to 8.0×10^{-6} mol L^{-1}. Inset: Stern–Volmer plot (see eq 1). λ_{exc} 440 nm and λ_{emis} 520 nm.

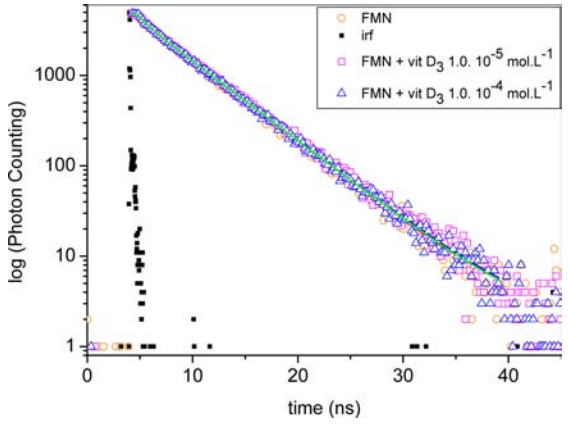

Figure 4. Fluorescence lifetime measurements at 25 °C by time-resolved single-photon counting for 1.0×10^{-5} mol L^{-1} flavin mononucleotide, in the absence or presence of 1.0×10^{-5} or 1.0×10^{-4} mol L^{-1} vitamin D_3 in 7/3 *tert*-butyl alcohol/water (v/v). irf denotes the instrument response function.

High-Resolution Accurate Mass Spectrometry. Direct infusion high-resolution accurate ESI-MS spectra of reaction products were obtained on an LTQ-Orbitrap Thermo Fisher Scientific mass spectrometry system (Bremen, Germany) operating in the positive ion detection mode. General conditions: heater temperature, 50 °C' sheath gas flow rate, 5 au; spray voltage, 3.7 kV; capillary temperature, 275 °C; flow rate, 5 μL/min.

RESULTS AND DISCUSSION

The biologically active forms of vitamin B_2, i.e. flavin mononucleotide (FMN) and flavin adenine dinucleotide (FAD), may be present in human skin together with a form of vitamin D, cholecalciferol (vit.D_3) or ergocalciferol (vit.D_2), and certain vitamin D precursors.[3,5] FMN and FAD absorb visible light, in contrast to vit.D, as is seen from Figure 1 for FMN and vit.D_3. Vitamin D precursors as well as vit.D absorb only UV-B light, which, however, initiates their conversion. Exposure to sunlight with its UV-B component is important for the vit.D status of humans, due to these photoconversions and to other sterol photoreactions.[6] In contrast, FAD and FMN form excited states

Table 1. Second-Order Rate Constants of Singlet-State–Excited-State Riboflavin Quenching, ^1k_q, by Vitamin D_3 at Different Temperatures

temp (°C)	^1k_q (10^{12} L mol^{-1} s^{-1})
15	3.6
25	3.5
35	3.4
45	3.3

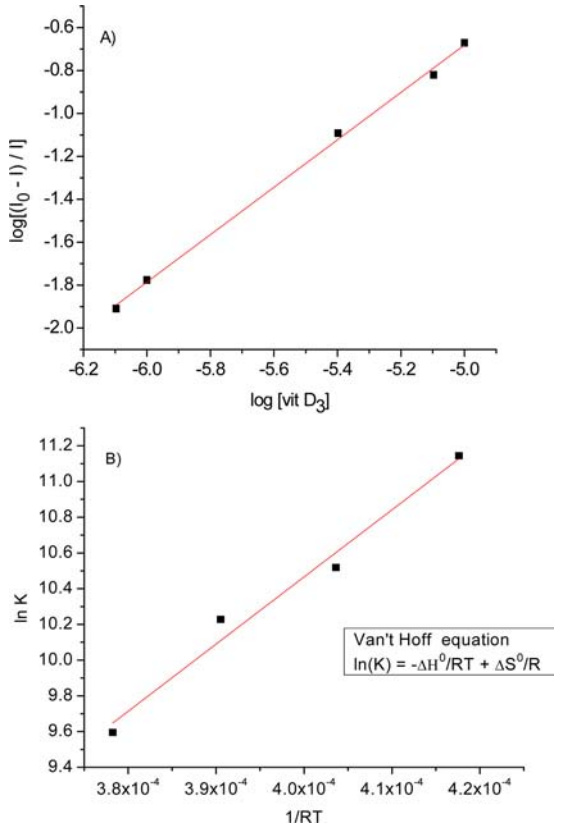

Figure 5. (A) Quenching of singlet excited state flavin mononucleotide fluorescence by vit.D_3 at 25 °C in 7/3 *tert*-butyl alcohol/water (v/v), plotted according to eq 2 for static quenching. (B) van't Hoff plot of the data extracted from (A) for varying temperatures (15, 25, 35, and 45 °C).

Table 2. Association Constants (K_a) and Numbers of Binding Quenchers (n) for Formation of the vit.D_3–FMN Ground-State Precomplex at Different Temperatures in 7/3 *tert*-Butyl Alcohol/Water (v/v)

T (°C)	K_a (10^4 L mol^{-1})	n
15	6.9 ± 0.1	1.10 ± 0.02
25	3.7 ± 0.2	0.75 ± 0.01
35	3.4 ± 0.2	1.04 ± 0.03
45	1.5 ± 0.2	0.96 ± 0.02

by absorption of visible light, with the risk of inducing oxidative damage to the skin.[12] The clear spectral separation between FMN/FAD and vit.D_3, as seen from Figure 2, gave inspiration to a novel approach for a photophysical investigation of a possible protective effect of vit.D_3 against vit.B_2 induced pathological conditions in human skin upon exposure to sunlight. No complications from spectral interference from vit.D_3 was to be expected, as seen from Figure 2, upon excitation of FMN with 355 nm or with 440 nm monochromatic light, the wavelengths

DOI: 10.1021/jf505958c
J. Agric. Food Chem. 2015, 63, 4629–4637

used for the time-resolved photophysical investigation of the triplet states of riboflavin and of the excited singlet state of riboflavin, respectively, and their interaction with vit.D_3.

Exposure of FMN to 440 nm monochromatic light resulted in intense fluorescence, which for 7/3 *tert*-butyl alcohol/water (v/v) as solventwas centered at 540 nm with a lifetime of 4.8 ns for 25 °C[13] (see Figures 3 and 4). The fluorescence intensity decreased in the presence of increasing concentrations of vit.D_3 without affecting the fluorescence lifetime, as probed by time-resolved single photon counting fluorescence spectroscopy with 355 nm light excitation for experiments with a FMN concentration of 1.0×10^{-5} mol L^{-1} and a vit.D_3 concentration of 1.0×10^{-5} or 1.0×10^{-4} mol L^{-1}. The quenching of FMN fluorescence intensity by vit.D_3 was analyzed in accord with the Stern−Volmer equation for vit.D_3, ranging from 8.0×10^{-7} to 1.0×10^{-6} mol L^{-1}:

$$\frac{I_0}{I} = 1 + k_q \times \tau \times [\text{vit.D}_3] \quad (1)$$

where I_0 is the fluorescence intensity at 525 nm in the absence of vit.D_3, I is the fluorescence emission intensity for increasing concentrations of vit.D_3, τ is the natural lifetime of the FMN singlet excited state, determined to have a value of 4.8 ns (see Figure 4, confirming previous findings),[13] and k_q is the specific rate constant for singlet excited state quenching (see insert in Figure 3). The experimentally obtained Stern−Volmer constants for different temperatures (15, 25, 35, and 45 °C) are collected in Table 1. The high values observed for the second-order rate constant, which were above the diffusion limit, indicate static quenching involving formation of a FMN−vit.D_3 ground-state precursor complex. An increase in temperature from 15 to 45 °C

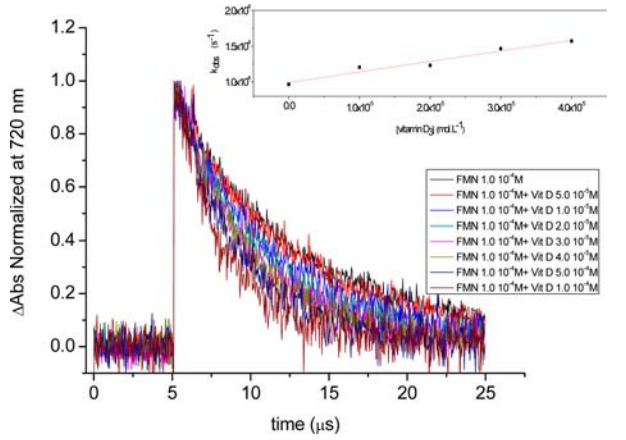

Figure 6. Kinetic traces for triplet excited state flavin mononucleotide decay monitored at 720 nm following 8 ns laser pulses of 10 mJ cm^2 at 355 nm for increasing concentrations of vitamin D_3 in N_2-saturated 7/3 *tert*-butyl alcohol/water (v/v) at 25 °C. Inset: k_{obs} from exponential fitting of absorption decay (720 nm) versus vit.D_3 concentration.

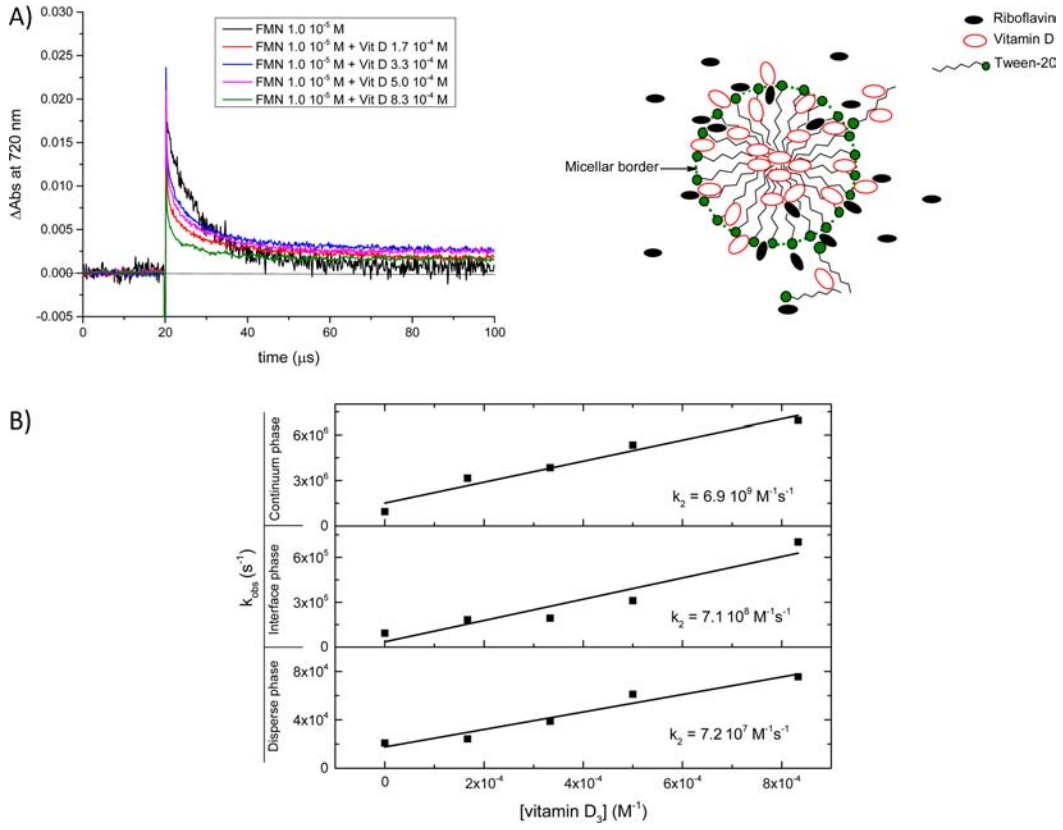

Figure 7. (A) Kinetic traces for triplet excited state flavin mononucleotide decay monitored at 720 nm following 8 ns laser pulses of 10 mJ cm^2 at 355 nm for increasing concentrations of vitamin D_3 in N_2-saturated aqueous Tween-20 micelles at 25 °C (right panel) and graphical illustration of the microdomains for triplet excited state flavin mononucleotide in aqueous Tween-20 micellar solution. (B) k_{obs} from triple-exponential fitting of absorption decay (720 nm) versus vit.D_3 concentration for the reaction at different microdomains (continuous phase, micelle interface, and hydrophobic core of the micellar aggregates).

DOI: 10.1021/jf505958c
J. Agric. Food Chem. 2015, 63, 4629−4637

reduces the observed quenching rate constant, indicating formation of the ground-state precursor complex to be an exothermic process. Formation of a ground-state complex was further investigated by analyzing FMN fluorescence emission decay curves in the presence of increasing concentrations of vit.D_3 (Figure 4). The normalized time decay curves for the FMN singlet excited emission did not change for increasing concentrations of vit.D_3, confirming the formation of the ground-state precursor complex and static quenching.

The formation of this precursor complex may be represented by the reaction

$$n \text{ vit.D}_3 + \text{FMN} \overset{K_a}{\rightleftharpoons} [\text{vit.D}_3]_n - \text{FMN} \quad (2)$$

The number of quenchers binding (n) to the fluorophore FMN was calculated according to

$$\log[(I_0 - I)I] = \log K_a + (n \log[\text{vit.D}_3]) \quad (3)$$

where K_a is the equilibrium constant for the reaction of eq 2. The experimental values determined for K_a and n for four different temperatures were obtained by fitting eq 3 to the data plotted in Figure 5A and are collected in Table 2. The thermodynamic parameters for the ground-state complex formation were found to have values of $\Delta H° = -36 \pm 7$ kJ mol^{-1} and $\Delta S° = -3.9 \pm 3.0$ J mol^{-1} K^{-1} according to the van't Hoff equation for a 1/1 stoichiometry (see Figure 5). The binding of FMN to vit.D_3 is suggested to be due to a hydrophobic interaction, which often is an exothermic process, as is the present case. The small change in entropy for binding of FMN to vit.D_3 seems to indicate little solvent involvement. The isoalloxazine ring of FMN is hydrophobic and has the possibility of binding to hydrophobic parts of vitamin D_3 through $\pi-\pi$ stacking.[14] The observed FMN fluorescence quenching by vit.D_3 indicates interaction between these two vitamins when they are in their ground states, due to hydrophobic interaction.

As a consequence of an efficient intersystem crossing in singlet excited FMN (and riboflavin and FAD) to their lowest-energy triplet states, these vit.B_2 forms become strongly reactive upon light exposure, as in skin or in dairy products.[15] vit.D_3 is a possible reactant for ^{3}FMN in the skin, and the reaction between ^{3}FMN and vit.D_3 was studied using transient absorption spectroscopy following laser flash photolysis. The triplet−triplet absorption of ^{3}FMN around 720 nm[13,16] was used to monitor the decay of the reactive ^{3}FMN in the presence of increasing concentrations of vit.D_3 (see Figure 6). ^{3}FMN was found to decay mono-exponentially for 7/3 *tert*-butyl alcohol/water (v/v) as solvent according to

$$\Delta A_t = \Delta A_{t=0} \exp^{-k_{obs}t} \quad (4)$$

and k_{obs} was determined for increasing vit.D_3 concentration. As may be seen from the inset in Figure 6, k_{obs} showed a linear dependence on vit.D_3 concentration:

$$k_{obs} = k_0 + k_2[\text{vit.D}_3] \quad (5)$$

where k_0 is the rate constant for the triplet-state self-decay and k_2 is the second-order rate constant for the triplet-state deactivation by vit.D_3. The value of $k_2 = 1.4 \times 10^8$ L mol^{-1} s^{-1} at 25 °C (7/3 *tert*-butyl alcohol/water (v/v)) was calculated by linear regression (Figure 6) together with $k_0 = 5.0 \times 10^4$ s^{-1} corresponding to a natural triplet-FMN lifetime of 13 μs at 25 °C, in agreement with previous findings.[16] However, in aqueous Tween-20 micelles, as a probe for specific microdomain reactivity of ^{3}FMN toward vit.D_3 that is preferentially located

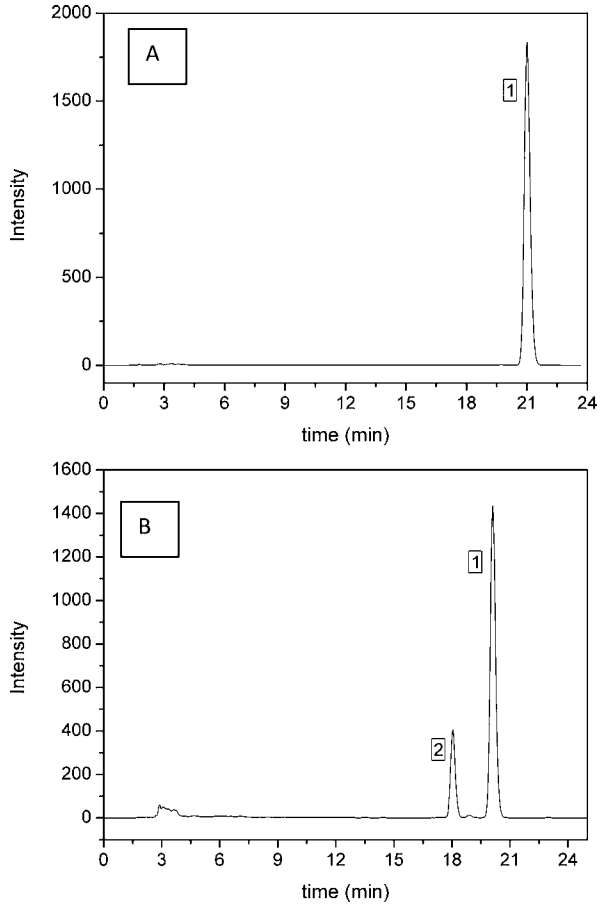

Figure 8. LC-DAD-SPE chromatograms monitored at 265 nm of flavin mononulceotide/vit.D_3 solution in 7/3 *tert*-butyl alcohol/water (v/v) prior to light exposure (A) and following 120 min of exposure to 440 nm monochromatic light (B).

inside the hydrophobic core of the micellar aggregates, ^{3}FMN was found to shown a triple-exponential decay curve (experimental goodness of fit $\chi^2 = 1.05$) according to

$$\Delta A_t = \Delta A_{1,t=0} \exp^{-k_{1,obs}t} + \Delta A_{2,t=0} \exp^{-k_{2,obs}t} + \Delta A_{3,t=0} \exp^{-k_{3,obs}t} \quad (6)$$

From fitting of eq 6 to the experimental data in Figure 7A, the k_{obs} values for each microdomain were determined for increasing concentrations of vit.D_3 together with the estimated percentage distributions of ^{3}FMN in the three observed microdomains (average of 89.4% in the continuous phase, 9.6% at the interface, and 1% at the disperse phase in the presence of 0.83 mM vit.D_3), as extracted from the pre-exponential term of eq 6. Figure 7B shows the linear dependence of k_{obs} for each microdomain with increasing concentrations of vit.D_3, yielding the second-order rate constant for the triplet-state deactivation by vit.D_3 in the three different environments: $k_2 = 6.9 \times 10^9$ L mol^{-1} s^{-1} for the reaction at the continuous phase, $k_2 = 7.1 \times 10^8$ L mol^{-1} s^{-1} for the reaction at the micelle interface, and $k_2 = 7.2 \times 10^7$ L mol^{-1} s^{-1} for the reaction inside the hydrophobic core of the micellar aggregates. The right panel of Figure 7A illustrates the three different microdomains for deactivating ^{3}FMN by vit.D_3 in aqueous Tween-20 micelles. The kinetic results in aqueous Tween-20 micelles provide strong evidence that ^{3}FMN may be deactivated by vit.D_3 at the interface of the cell membrane or inside the plasma membrane when ^{3}FMN is present as a

DOI: 10.1021/jf505958c
J. Agric. Food Chem. 2015, 63, 4629−4637

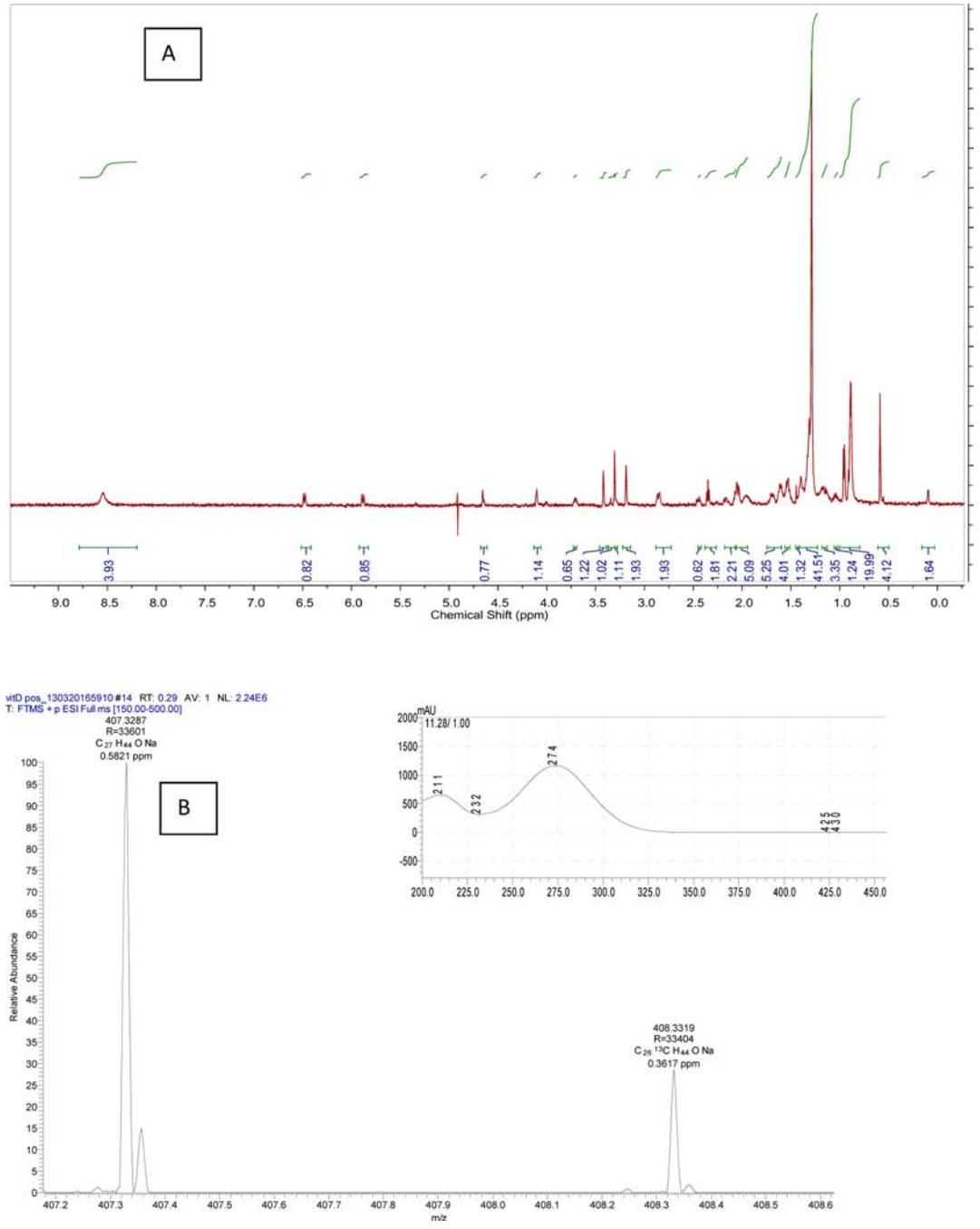

Figure 9. Spectroscopic characterization of photoproduct from exposure of flavin mononucleotide/vit.D3 solution in 7/3 *tert*-butyl alcohol/water (v/v) for 120 min with 440 nm monochromatic light: (A) ^{1}H NMR spectrum of photoproduct from isolated peak 2 of chromatogram B of Figure 6; (B) ESI-MS high-resolution accurate mass spectrum of photoproduct from peak 2 of chromatogram B in Figure 6. Inset in (B): UV−vis absorption spectrum of photoproduct.

flavoprotein, as in NAD(P)H oxidase and NAD(P)H quinone oxidoreductase.

The photochemical reaction quantum yield (Φ) for vit.D_3 disappearance provides a more practical measurement of the efficiency with which the reaction between the two vitamins occurs upon visible UV-A light exposure occurs and may be determined from eq 7 for 440 nm light exposure:

$$\Phi = \frac{\text{molecules}_{\text{reacted}}}{\text{photons}_{\text{absorbed}}} = \frac{V([\text{vit.D3}]_{\text{dark}} - [\text{vit.D3}]_{\text{irradiated}})}{q^0_{\text{n,p}}(I - 10^{-A_\lambda})} \quad (7)$$

in which the ratio between the number of molecules of vit.D_3 reacted and the number of photons absorbed by vit.B_2 was calculated from the results of HPLC analysis of vit.D_3 exposed to and protected against light in a solution together with FMN and from chemical actinometry. $q^0_{\text{n,p}}$ is the light intensity for the 440 nm monochromatic light used for exposure, and A_λ is the absorbance at 440 nm of the 7/3 *tert*-butyl alcohol/water (v/v) solution with vit.D_3 and FMN. Φ for disappearance of vit.D_3 in the photoreaction sensitized by FMN was found to have a value of 0.15 ± 0.01 in air-saturated 7/3 *tert*-butyl alcohol/water (v/v) for a concentration of 1.0×10^{-3} mol L^{-1} for vit.D_3 and 1.0×10^{-4} mol L^{-1} for FMN. For anaerobic conditions, a value of

DOI: 10.1021/jf505958c
J. Agric. Food Chem. 2015, 63, 4629−4637

0.32 ± 0.01 was found; both values are means of three independent determinations at 25 °C.

The photoprocess of vit.D_3 considered relates to the triplet state of FMN as a photosensitizer, ^{3}FMN*, and not to the singlet state, ^{1}FMN*, since the lifetime of ^{3}FMN* decreases in the presence of vit.D_3 in contrast to the lifetime of ^{1}FMN*, as is seen from Figures 6 and 7 and Figure 5, respectively. The photochemical reaction occurs accordingly as a sequence:

$$\text{FMN} + h\nu \rightarrow {}^1\text{FMN}^* \quad (8)$$

$$^1\text{FMN}^* \rightarrow {}^3\text{FMN}^* \quad (9)$$

$$^3\text{FMN}^* + \text{vit.D}_3 \rightarrow \text{FMN} + \text{photoproduct} \quad (10)$$

in which initial excitation of FMN to form the excited singlet state is followed by an efficient intersystem crossing (ISC) conversion to the reactive triplet state. ^{3}FMN* is reacting with vit.D_3 to form a photoproduct, which was identified by high-resolution accurate ESI-MS and LC-SPE-NMR to be 5,6-*trans*-vit.D_3. The FMN/vit.D_3 solution was exposed to 440 nm monochromatic light for 2 h. Prior to and following irradiation, the solution was analyzed by LC-SPE; the chromatograms obtained are shown in Figure 8. In chromatogram A shown in Figure 8, the peak 1 eluting at 20 min refers to standard vit.D_3. In chromatogram B shown in Figure 8, peak 2 eluting at 18 min refers to the photoproduct formed. Peak 2 was isolated by LC-SPE and further analyzed by ^{1}H NMR and ESI-MS. The electrospray high-resolution accurate mass spectrum, recorded in the positive ion mode, showed a peak related to the photoproduct with a pseudomolecular ion at m/z 407.3287 with a error of 0.6 ppm and the expected isotopic pattern calculated for $C_{27}H_{44}ONa$ and assigned to a sodium adduct of an isomer of vit.D_3 (see Figure 9).

With the purpose of obtaining more information about the identity of the photoproduct, the isolated photoproduct was analyzed by ^{1}H NMR. The ^{1}H NMR spectrum obtained is shown in Figure 9A. The spectrum displays signals in the region 0−7 ppm. On the basis of the chemical shifts reported in Table 3, in comparison with literature values for vit.D_3 isomers, it was concluded that the photoproduct was the isomer 5,6-*trans*-vit.D_3.[17] The UV−vis absorption spectrum of the isolated photoproduct (Figure 9B) with a maximum absorption at 274 nm matches that of the 5,6-*trans*-vit.D_3 isomer.[17,18]

Riboflavin and its biologically active forms, FMN and FAD, are known to be strong oxidants in their triplet excited state with $E^{\ominus}$ = +1.7 V[5]. This very reactive triplet state is formed by an efficient intersystem crossing from the initially populated singlet excited state as the result of light absorption. For vit.D_3, FMN was found to form a 1/1 precursor complex in the ground state, resulting in static quenching, as was previously observed for cholesterol and ergosterol and assigned to hydrophobic $\pi-\pi$ stacking.[13] The singlet excited state of FMN was found to be too short-lived for any bimolecular reactions to occur, with a lifetime of 4.8 ns. The reaction of light-activated FMN was accordingly assigned to the triplet state and found to have a second-order rate constant of 1.4×10^8 L mol^{-1} s^{-1} for 7/3 *tert*-butyl alcohol/water (v/v) as solvent or of 6.9×10^9 L mol^{-1} s^{-1} at the continuous phase, 7.1×10^8 L mol^{-1} s^{-1} at the micelle interface, and 7.2×10^7 L mol^{-1} s^{-1} at the hydrophobic core of the micellar aggregates.[13] This is faster than the ^{3}FMN* reaction with most lipids, including cholesterol, but comparable with the ^{3}FMN* reaction with ergosterol with a rate constant of 6.2×10^8 L mol^{-1} s^{-1}.[13] The most important observation for the ^{3}FMN* reaction with vit.D_3 is, however, that ^{3}FMN* does not oxidize vit.D_3. Other lipophilic substrates and uric acid have been found to be oxidized by flavin triplet states.[13,19] An estimate of the redox potential for vit.D_3 was obtained by cyclic voltammetry (see Figure 10), and with a value of +1.5 V, oxidation of vit.D_3 by ^{3}FMN* was shown to be possible with +1.7 V for triplet FMN. However, isomerization dominates completely and no oxidation products of vit.D_3 were detected. Isomerization of vit.D_3, to yield 5,6-*trans*-vit.D_3 requires rotation around the conjugated double bonds in vit.D_3 and would be facilitated in a diradical triplet state of vit.D_3. The formation of the diradical form of vit.D_3 followed by rotation and recombination to a vit.D_3/5,6-*trans*-vit.D_3 mixture apparently competes efficiently with electron transfer from vit.D_3 to ^{3}FMN*:

$$^3\text{FMN}^* + \text{vit.D}_3 \rightarrow \text{FMN} + {}^3\text{vit.D}_3\text{-diradical} \quad (11)$$

$$^3\text{FMN}^* + \text{vit.D}_3 \rightarrow {}^2\text{FMN}^{\bullet-} + {}^2\text{vit.D}_3{}^{\bullet+} \quad (12)$$

An energy transfer mechanism involving the ^{3}vit.D_3 diradical is outlined in Scheme 1A for photosensitized isomerization of vit.D_3. The triplet energy of vit.D_3 has been estimated to be around 200 kJ mol^{-1}, while the energy of the triplet 5,6-*trans*-vit.D_3 is

Table 3. Chemical Shifts for Hydrogen in the ^{1}H NMR Spectrum of Product of Cholecalciferol Reaction with Light-Activated Flavin Mononucleotide in 7/3 *tert*-Butyl Alcohol/Water (v/v) (See Figure 7A) in Comparison with Chemical Shifts in the Spectrum of 5,6-*trans*-vit.D_3 from the Literature[17,18,20]

assignment	δ (measd)	δ (lit.)
H-6	6.43	6.50
H-7	5.85	5.84
H-19Z	4.97	4.95
H-19E	4.63	4.65
H-3α	3.90	3.86
H-4α	2.85	2.84
H-9β	2.85	2.84
H-1β	2.42	2.44
H-4β	2.31	2.31
H-1α	2.19	2.17
H-2α	1.91	1.94
H-2β	1.55	1.58
CH_3-21	0.91	0.92

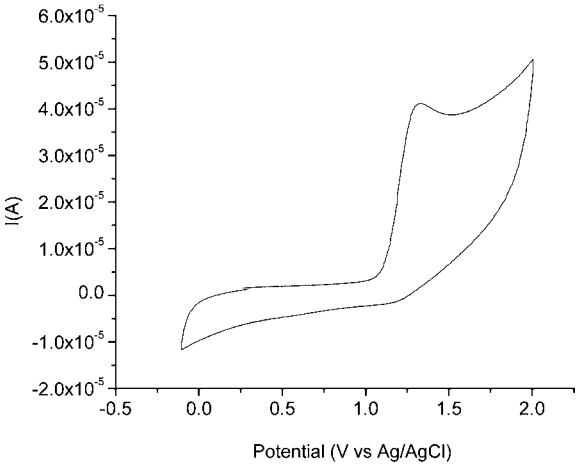

Figure 10. Cyclic voltammetry of vitamin D_3 (1×10^{-3} mol L^{-1}) in acetonitrile solution containing 50 mM of $LiClO_4$ at 25 °C.

DOI: 10.1021/jf505958c
J. Agric. Food Chem. 2015, 63, 4629−4637

Scheme 1. Proposed Reaction Mechanism for Vitamin D_3 Isomerization through Charge Transfer Exchange of Electrons (Energy Transfer) From Triplet-State Flavin Mononucleotide Yielding 5,6-*trans*-Vitamin D_3

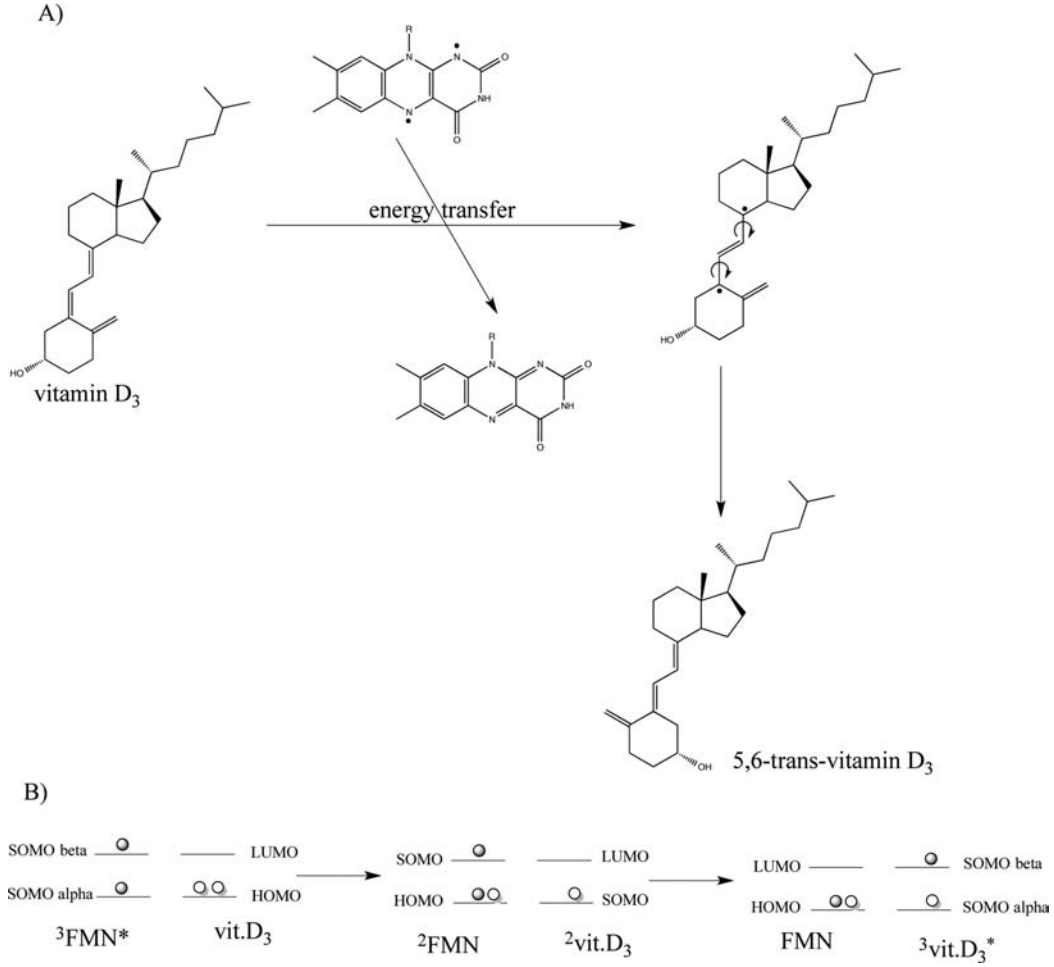

lower with a value of around 170 kJ mol^{-1}, both comparable to that of ^{3}FMN*.[20] The observed quenching constant of $k_2 = 1.4 \times 10^8$ L mol^{-1} s^{-1} may thus be assigned to the reaction of eq 11, with the electron transfer reaction of eq 12 being significantly slower.

An energy transfer mechanism rather than electron transfer could be explained by a stepwise charge transfer exchange of electrons where vit.D_3 donates an electron to the lowest energy SOMO orbital of ^{3}FMN* with formation of a radical ion pair [$^2FMN^{\bullet -}\cdots{}^2vit.D_3^{\bullet +}$] followed by electron transfer from the SOMO orbital of the $^2FMN^{\bullet -}$ to the LUMO orbital of $^2vit.D_3^{\bullet +}$ of the radical ion pair (see Scheme 1B). For FMN this exchange will deactivate ^{3}FMN* to form ground-state FMN, while for vit.D_3 a triplet diradical is formed in order to conserve spin. The ^{3}vit.D_3 may rotate as shown in Scheme 1A around the 5,6- and 7,8-bonds to form an equilibrium mixture prior to deactivation. Notably, this mechanism entails that the trans product formed may re-form the vit.D_3 also in a photochemical process. 5,6-*trans*-vit.D_3 still has biological effects in relation to calcium biomineralization.[7]

The competition between deactivation of ^{3}FMN* by $^3O_2$ and vit.D_3 depends on the second-order rate constants 9.8×10^8 L mol^{-1} s^{-1} for oxygen and 1.4×10^8 L mol^{-1} s^{-1} for vit.D_3 in the reaction of eq 11 and the actual concentrations of quenchers to yield the relative deactivation by vit.D_3 to yield 5,6-*trans*-vit.D_3:

$$\text{relative } {}^3\text{FM}^* \text{ deactivation by vit.D}_3 = \frac{k_{\text{vit.D3}}[\text{vit.D}_3]}{k_{\text{vit.D3}}[\text{vit.D}_3] + k_{\text{O2}}[\text{O}_2]} \quad (13)$$

The relative deactivation by vit.D_3 corresponds accordingly, using $[O_2] = 3 \times 10^{-4}$ mol L^{-1}, the value for water, also for the mixed solvent and $[\text{vit.D}_3] = 1 \times 10^{-3}$ mol L^{-1}, to a fraction of 0.32, which should be compared to the ratio between the quantum yields in the presence and in the absence of oxygen, which is seen to have an approximate value of 0.5. This is an acceptable agreement, and in the absence of electron transfer, this explains the surprising protective effect of oxygen against isomerization. Ground-state oxygen will form singlet oxygen, $^1O_2$, but the reaction of $^1O_2$ with vit.D_3 apparently is too slow to result in oxidation under the present conditions, and $^1O_2$ may deactivate thermally or react with FMN.[21]

Vitamin D_3 was found to be an efficient quencher of the triplet excited state of FMN, one of the biologically active forms of riboflavin, vitamin B_2. Triplet flavins such as FMN are strong oxidants, which ae known to be harmful for skin and eyes under light exposure and deplete nutrients in milk during retail display.[4,21] A number of otherwise biologically important nutrients are known to deactivate these photosensitizers derived from vitamin B_2 in food and tissue exposed to light.[5] Our findings are important in the respect that we have shown that vit.D_3 isomerizes rather than being oxidized as the result of this

DOI: 10.1021/jf505958c
J. Agric. Food Chem. 2015, 63, 4629−4637

quenching reaction. The isomerization leads to a photostationary state, and vit.D_3 is still active as a vitamin in this mixture and may re-form vit.D_3 from the isomerized 5,6-*trans*-vit.D_3 photochemically. These observations may add a new perspective to the role of vit.D_3 accumulated in the skin as a protector against light-induced oxidative damage and radical formation from flavins acting as photosensitizers.

AUTHOR INFORMATION

Corresponding Authors

*L.H.S.: e-mail, ls@food.ku.dk, tel, +45 35 33 32 21.

*D.R.C.: e-mail, drcardoso@iqsc.usp.br; tel, +55 16 33 73 99 76.

Funding

This research is part of the bilateral Brazilian/Danish Food Science Research Program "BEAM-Bread and Meat for the Future" supported by the FAPESP (Grant 2011/51555-7 and EMU 2009/54040) and by the Danish Research Council for Strategic Research (Grant 11-116064). D.R.C. thanks the Brazilian National Research Council-CNPq for financial support (305385/2009-7 and 142145/2012-2).

Notes

The authors declare no competing financial interest.

ACKNOWLEDGMENTS

Prof. Marcelo H. Gehlen (IQSC-USP) is acknowledged for the time-resolved single photon counting measurements (FAPESP 2011/18215-8).

REFERENCES

(1) Tsiaras, W. G.; Weinstock, M. A. Factors Influencing Vitamin D Status. *Acta Derm. Venereol.* **2011**, *91*, 115−124.

(2) Gorman, A. A.; Hamblett, I.; Rodgers, M. A. J. Ergosterol (Provitamin D_2) Triplet State: An Efficient Sensitiser of Singlet Oxygen, O_2, Formation. *Photochem. Photobiol.* **1987**, *45*, 215−221.

(3) Norman, A. W. Sunlight, Season, Skin Pigmentation, Vitamin D, and 25-hydroxyvitamin D: Integral Components of the Vitamin D Endocrine System. *Am. J. Clin. Nutr.* **1998**, *67*, 1108−1110.

(4) Li, T.; King, J. M.; Min, D. B. Quenching Mechanisms and Kinetics of Carotenoids in Riboflavin Photosensitized Singlet Oxygen Oxidation of Vitamin D2. *J. Food Biochem.* **2000**, *24*, 477−492.

(5) Cardoso, D. R.; Libardi, S. H.; Skibsted, L. H. Riboflavin as a Photosensitizer. Effects on human health and food quality. *Food Funct.* **2012**, *3*, 487−502.

(6) Wacker, M.; Holick, M. F. Sunlight and Vitamin D a Global Perspective for Health. *Derm.-Endocrinol.* **2013**, *5*, 51−108.

(7) Wondrak, G. T.; Jacobson, M. K.; Jacobson, E. L. Endogenous UVA-photosensitizers: mediators of skin photodamage and novel targets for skin photoprotection. *Photochem. Photobiol.* **2006**, *5*, 215−237.

(8) Moan, J.; Porojnicu, A. C.; Dahlback, A.; Setlow, R. B. Addressing the Health Benefits and Risk, Involving Vitamin D or Skin Cancer, of Increased Sun Exposure. *Proc. Natl. Acad. Sci. U. S. A.* **2008**, *105*, 668−673.

(9) Garland, C. F.; Gorham, E. D.; Mohr, S. B.; Garland, F. C. Vitamin D for Cancer Prevention: Global Perspective. *Ann. Epidemiol.* **2009**, *19*, 468−483.

(10) Bikle, D. D. Protective Actions of Vitamin D in UVB Induced Skin Cancer. *Photochem. Photobiol. Sci.* **2012**, *11*, 1808−1816.

(11) Harchard, C. G.; Parker, C. A. A New Sensitive Chemical Actinometer II. Potassium Ferrioxalate as a Standard Chemical Actinometer. *Proc. R. Soc. London, Ser. A* **1956**, *235*, 518−536.

(12) Haywood, R.; Andrady, C.; Kassouf, N.; Sheppard, N. Intensity-dependent Direct Solar Radiation- and UVA-induced Radical Damage to Human Skin and DNA, Lipids, and Proteins. *Photochem. Photobiol.* **2011**, *87*, 117−130.

(13) Cardoso, D. R.; Scurachio, R. S.; Santos, W. G.; Homem-de-Mello, P.; Skibsted, L. H. Riboflavin-Photosensitized Oxidation Is Enhanced by Conjugation in Unsaturated Lipids. *J. Agric. Food Chem.* **2013**, *61*, 2268−2275.

(14) Kamat, B. P.; Seetharamappa, J.; Melwanki, M. B. Spectroscopic Studies on the interaction of riboflavin with bovine serum albumin. *Indian J. Biochem. Biophys.* **2004**, *41*, 173−178.

(15) Heelis, P. F. The Photophysical and Photochemical Properties of Flavins (Isoalloxazines). *Chem. Soc. Rev.* **1982**, *11*, 15−39.

(16) Cardoso, D. R.; Franco, D. W.; Olsen, K.; Andersen, M. L.; Skibsted, L. H. Reactivity of Bovine Whey Proteins, Peptides and Amino Acids Toward Triplet Riboflavin as Studied by Laser Flash Photolysis. *J. Agric. Food Chem.* **2004**, *52*, 6602−6606.

(17) Okamura, W. H.; Hammond, M. L.; Rego, A.; Norman, A. W.; Wing, R. M. Studies on Vitamin D (Calciferol) and its Analogues 12. Structural and Synthetic Studies of 5,6-Dihydrovitamin D3 and the Stereoisomers of 10,19-Dihydrovitamin D3 Including Dihydrotachysterol. *J. Org. Chem.* **1977**, *42*, 2284−2291.

(18) Yamada, S.; Nakayama, K.; Takayama, H. Studies of Vitamin D Oxidation. 3. Dye-sensitized Photooxidation of Vitamin D and Chemical Behavior of Vitamin D 6,19-Epidioxides. *J. Org. Chem.* **1983**, *48*, 3477−3483.

(19) Clausen, M. R.; Huvaere, K.; Skibsted, L. H.; Stagsted, J. Characterization of Peroxides Formed by Riboflavin and Light Exposure of Milk. Detection of Urate Hydroperoxide as a Novel Oxidation Product. *J. Agric. Food Chem.* **2010**, *58*, 481−487.

(20) Gielen, J. W. J.; Koolstra, R. B.; Jacobs, H. J. C.; Havinga, E. Triplet-sensitized Interconversion and Photooxidation of Vitamin D and trans-Vitamin D. *J. Royal Netherl. Chem. Soc.* **1980**, *99*, 306−311.

(21) Jung, M. Y.; Oh, Y. S.; Kim, D. K.; Min, D. B. Photoinduced Generation of 2,3-butanedione from Riboflavin. *J. Agric. Food Chem.* **2007**, *55*, 170−174.

DOI: 10.1021/jf505958c
J. Agric. Food Chem. 2015, 63, 4629−4637

JOURNAL OF AGRICULTURAL AND FOOD CHEMISTRY

Article

pubs.acs.org/JAFC

Linking Soil, Water, and Honey Composition To Assess the Geographical Origin of Argentinean Honey by Multielemental and Isotopic Analyses

María V. Baroni,[†] Natalia S. Podio,[†] Raúl G. Badini,[‡] Marcela Inga,[‡] Héctor A. Ostera,[§] Mariana Cagnoni,[§] Eduardo A. Gautier,[⊥] Pilar Peral García,[Δ] Jurian Hoogewerff,[#] and Daniel A. Wunderlin*[,†]

[†]ICYTAC, Instituto de Ciencia y Tecnología de Alimentos Córdoba, CONICET and ISIDSA−Facultad de Ciencias Químicas, Universidad Nacional de Córdoba, Ciudad Universitaria, 5000 Córdoba, Argentina

[‡]Ministerio de Ciencia y Tecnología Provincia de Córdoba−CEPROCOR, Santa María de Punilla, Córdoba, Argentina

[§]Facultad de Ciencias Exactas y Naturales−INGEIS, Universidad de Buenos Aires−CONICET, Ciudad Universitaria, Buenos Aires, Argentina

[⊥]Comisión Nacional de Energía Atómica, Gerencia Química, Centro Atómico Constituyentes, San Martín, Buenos Aires, Argentina

[Δ]Facultad de Ciencias Veterinarias−IGEVET, Universidad Nacional de La Plata−CONICET, Ciudad Universitaria, La Plata, Argentina

[#]Department of Chemistry, University of Otago, P.O. Box 56, Dunedin 9054, New Zealand

Supporting Information

ABSTRACT: The objective of this research was to investigate the development of a reliable fingerprint from elemental and isotopic signatures of Argentinean honey to assess its geographical provenance. Honey, soil, and water from three regions (Córdoba, Buenos Aires, and Entre Ríos) were collected. The multielemental composition was determined by ICP-MS. $\delta^{13}C$ was measured by isotopic ratio mass spectrometry, whereas the $^{87}Sr/^{86}Sr$ ratio was determined using thermal ionization mass spectrometry. The data were analyzed by chemometrics looking for the association between the elements, stable isotopes, and honey samples from the three studied areas. Honey samples were differentiated by classification trees and discriminant analysis using a combination of eight key variables (Rb, K/Rb, B, U, $^{87}Sr/^{86}Sr$, Na, La, and Zn) presenting differences among the studied regions. The application of canonical correlation analysis and generalized procrustes analysis showed 91.5% consensus between soil, water, and honey samples, in addition to clear differences between studied areas. To the authors' knowledge, this is the first report demonstrating the correspondence between soil, water, and honey samples using different statistical methods, showing that elemental and isotopic honey compositions are related to soil and water characteristics of the site of origin.

KEYWORDS: *honey, trace elements, isotopic composition, geographical origin, authenticity, traceability, fingerprint*

INTRODUCTION

In these past years, authenticity and traceability of foodstuffs became a major requirement for consumers and producers worldwide. Food products have been linked to a specific geographical origin; however, such links have disappeared over time mostly because of the globalization of the food industry[1] Food is becoming more regulated, with the increase in global trade and free markets. That is why there is an increased need for developing new methods and techniques to discriminate different food origins, sources, or farming systems.[2]

Honey is a high value-added product, which is of high interest for assessing its authenticity (both geographical origin and floral sources). Additionally, the detection of disallowed substances, such as syrups or sugars, contributes to honey authenticity and safety.[3,4] According to the European legislation (Council Directive 2001/110), the country where the honey was collected has to be declared. Honey with geographical and botanical origins declared are differently valued and, for that reason, subjected to frauds, leading to doubtful labeling.[3]

Honey chemical composition is generally associated with its botanical origin and, to a lesser degree, with the geographical area where it was collected, because environment (soil and climate) determine the melliferous flora.[5,6] For botanical origin classification, conventional methods (physical characteristics, chemical composition, pollen analysis, and sensory parameters) are mainly used.[3,7−10]

The multielemental content of food reflects the type of soil and environment conditions.[11−13] Honey contains between 0.04 and 0.2% (w/w) of trace elements. The soil composition of the origin, determined by geochemical and geological features (i.e., regional geology and climatic changes), affects the composition and concentration of metals in honey.[14,15] The botanical origin (nectar, pollen, and floral type of honey plants) are also responsible for the metal content of honey.[14,16] Furthermore, trace element contents in honey could also serve as indicators of environmental pollution.

Received: December 11, 2014
Revised: April 21, 2015
Accepted: April 23, 2015
Published: April 23, 2015

ACS Publications © 2015 American Chemical Society

DOI: 10.1021/jf5060112
J. Agric. Food Chem. 2015, 63, 4638−4645

On the other hand, the analysis of stable isotopes has gained importance in the determination of the geographic origin of food. Stable isotope measurements were first introduced within the European wine industry to ensure authenticity and to detect adulteration using carbon, oxygen, and hydrogen, mostly, but also strontium.[17] These measurements have been extended to many other foods (e.g., milk, meat, honey, juices, spirits, and flavors).[9,11−13,18,19] Small but significantly different ratios of stable isotopes can be correlated with the botanical−metabolic and/or geographical−geological origin of a product. Isotope ratios may add to the element fingerprint information on the plant type and the geographical−geological origin.[20]

Even though there are many studies focusing on the elemental profile of honey,[6,21−23] or on stable isotopes,[9,19,24] there are few that combine both parameters.[9] In addition, there are also few studies that consider the association with soil and water from places where honey is made.[19] Furthermore, there has been little research on the determination of both the content of elements and stable isotopes in Argentinean honey.[14,21,25] In this paper, for the first time, we present the results of the determination of 33 elements and carbon and strontium isotopes in Argentinean honey from three different regions (Buenos Aires, Córdoba, and Entre Ríos). Additionally, we were interested in demonstrating the link between honey, soil, and water by applying different chemometric tools. To our knowledge, this is the first approach in Argentina on the combined use of Sr and C isotope ratios and multielement analysis of soil, water, and honey to assess the geographical origin.

MATERIALS AND METHODS

Reagents and Materials. Ultrapure water (<5 μg L^{-1} total organic content) was obtained from an Arium 61316-RO purification system combined with an Arium 611 UV (Sartorius, Germany). The certified ICP-MS multielement Merck VI CertiPUR standard solution was obtained from Merck Química Argentina (Buenos Aires, Argentina). Nitric acid (63.7%), sub-boiling grade, was prepared from analytical grade acid (Merck Química Argentina) using a distiller (Figmay sub-boiling distiller, Córdoba, Argentina).

The purity of nitric acid was verified by ICP-MS. Filters (0.45 μm, HAWG04756) were obtained from Millipore (São Paulo, Brazil). Trace element certified reference material (CRM) wheat flour 1567a was obtained from the National Institute of Standards and Technology (Gaithersburg, MD, USA). The best estimate values for constituent elements in CRM 1567a are detailed in the accompanying certificate of analysis provided by the manufacturer. Ion exchange chromatography Sr Spec resin was obtained from Eichrom Technologies (USA). Strontium isotopic standard (NBS SRM 987) was employed to determine mass discrimination during the isotopic analyses by thermal ionization mass spectrometry (TIMS). All other analytical grade reagents were used.

Sampling. Soil, water, and honey samples were collected from selected producing areas from three provinces of Argentina: Buenos Aires, Córdoba, and Entre Ríos. These provinces are the most important honey-producing areas in Argentina (Figure 1). The sampling area in Buenos Aires is located between 37°25′ and 37°38′ S and between 59°10′ and 59°14′ W; the Córdoba sampling area is located between 30°30′ and 31°08′ S and between 63°34′ and 64°08′ W; and the Entre Ríos sampling area is located between 32°49′ and 32°53′ S and between 58°32′and 58°34′ W. The altitude varies from 460 m above sea level in Córdoba to 240 m above sea level in Buenos Aires to 30 m above sea level in Entre Ríos. Soil, water, and honey samples were collected from different beekeepers during three harvests (2007, 2008, and 2009): seven in Córdoba, five in Buenos Aires, and six in Entre Ríos. Soil and water samples were collected and processed according to the method of Baroni et al.[11] A total of 79 honey samples were collected: 27 samples were collected in Buenos Aires, 25 in Córdoba, and 27 in Entre Ríos. Five hundred grams of honey was collected in plastic recipients, transported to the laboratory within 48 h, and stored at 4−8 °C until analysis.

Figure 1. Map of the three regions where honey samples were collected.

Elemental Analyses. Five hundred milligrams of honey sample was mineralized with 8 mL of concentrated nitric acid using a microwave oven (Anton Paar Multiwave 3000, Vienna, Austria) following methods described by Podio et al.[13] CRM 1567a was processed and measured in the same way used for honey. Values obtained for the latter were between 85 and 105% of certified values.

Thirty-one elements were quantified in honey samples: Al, B, Ba, Ca, Cd, Ce, Co, Cs, Cu, Eu, Ga, K, La, Li, Lu, Mg, Mn, Mo, Na, Nd, Ni, Pb, Rb, Se, Sm, Sr, Tl, U, V, Yb, and Zn. The analysis was carried out by quadrupole inductively coupled plasma mass spectrometry (QICP-MS) for all elements except sodium as stated in Baroni et al.[11]

Stable Isotope Analysis. *Carbon Isotope Analysis.* Carbon isotope ratios were determined on whole honey and protein fraction. Protein isolation and purification were done according to AOAC Official Method 998.12 (repetitive washing procedure), using tungstic acid, sodium salt, and sulfuric acid. Both honey and protein samples were placed in quartz tubes, with added copper oxide. Tubes were prepared for combustion by evacuation on a vacuum line and sealed with a torch. Combustion was performed at 550 °C over 8 h, after which the tubes were allowed to cool at room temperature inside the oven. Following combustion the tubes were cracked open to extract pure CO_2 on the vacuum line using a cryogenic trap to retain water and non-CO_2 gases. The purified CO_2 was collected with a liquid nitrogen trap in a glass collection tube. The purified CO_2 was measured in a Multiport Dual Inlet IRMS (Finnigan MAT Delta S), using CO_2 gas as reference.

The isotope ratios were normalized using laboratory working standards, calibrated with international standards supplied by the International Atomic Energy Agency (NBS 22, NBS18). The $^{13}C/^{12}C$ ratios are expressed in the delta notation, $\delta^{13}C$ as the deviation per mil (‰) from the Vienna Pee Dee Belemnite (V-PDB) standard. The uncertainty of carbon isotope determinations was ±0.2‰.

Strontium Isotope Analysis. Bulk samples were processed by dry ashing technique in a muffle furnace. More than 100 g of sample was placed in porcelain crucibles and heated at 550−600 °C. The furnace was programmed to ramp up to the ashing temperature over a period of 8 h. Complete ashing was ensured by maintaining this temperature for 10 h. Residues were treated with concentrated HNO_3 on a hot plate and then transferred again to the muffle until white ashes appeared. The residues were dissolved in HNO_3, and subsequently Sr was separated by ion chromatography on a Sr-specific resin (Sr-spec). Sample manipulation was carried out in a clean environment (Class 100 laboratory). To prevent contamination, all laboratory-ware was soaked in 50% (v/v) nitric acid for at least 24 h, rinsed several times with ultrapure water, and dried in a Class 100 laminar flow exhaust hood.

DOI: 10.1021/jf5060112
J. Agric. Food Chem. 2015, 63, 4638−4645

Table 1. Means and Standard Deviations of Measured Elements (Micrograms per Kilogram) and Isotopic Ratios Corresponding to Honey According to Region of Origin and the Contribution of Two Spoons of Ingested Honey to DDA of Nutritional Elements[a]

variable	Buenos Aires	Córdoba	Entre Ríos	contribution to DDA (%)
Li	163 ± 112a	174 ± 183a	495 ± 159b	
B	(84 ± 18) × 10^3c	(39 ± 15) × 10^3a	(66 ± 16) × 10^3b	
Na	(12 ± 52) × 10^3a	(16 ± 11) × 10^3a	(46 ± 20) × 10^3b	0.1
Mg	(177 ± 174) × 10^3a	(359 ± 209) × 10^3b	(496 ± 238) × 10^3c	2.1
Al	(4.63 ± 4.67) × 10^3a	(10.93 ± 8.12) × 10^3a	(22 ± 35) × 10^3b	
K	(339 ± 105) × 10^3a	(1041 ± 528) × 10^3b	(1575 ± 760) × 10^3c	2.1
Ca	(698 ± 542) × 10^3a	(862 ± 453) × 10^3a	(1298 ± 1009) × 10^3b	5.4
V	1431 ± 1287a	1798 ± 1450a	1038 ± 747a	
Mn	(2.05 ± 1.08) × 10^3a	(9.88 ± 4.33) × 10^3b	(21.78 ± 16.88) × 10^3c	12
Co	28 ± 22a	40 ± 19a	67 ± 42b	
Ni	847 ± 1786a	617 ± 1647a	955 ± 862a	
Cu	1290 ± 480a	1202 ± 607a	5863 ± 3629b	3.97
Zn	(12.16 ± 21.89) × 10^3a	(12.72 ± 8.73) × 10^3a	(30.76 ± 21.88) × 10^3b	5.25
Ga	12 ± 13a	25 ± 16b	17 ± 9a	
Se	392 ± 302a	642 ± 287b	431 ± 251a	
Rb	(3.95 ± 2.19 × 10^3a)	(1.75 ± 0.73 × 10^3a)	(31.62 ± 8.32 × 10^3b)	
Sr	1760 ± 1099a	3883 ± 1479b	5292 ± 2337c	
Mo	28 ± 30a	57 ± 31a	112 ± 79b	
Cs	113 ± 145a	84 ± 140a	134 ± 192a	
Ba	0.87 ± 0.83a	6.71 ± 6.41b	5.97 ± 10.58b	
La	6.70 ± 20.93a	<LOD	116 ± 197b	
Ce	3.47 ± 7.72a	20.50 ± 33.87a	39.02 ± 55.37b	
Nd	3.65 ± 4.43a	4.63 ± 5.41a	12.55 ± 7.84b	
Sm	6.39 ± 5.34b	6.30 ± 4.04b	2.73 ± 2.30a	
Eu	0.54 ± 0.69a	0.66 ± 0.80a	1.40 ± 0.64b	
Yb	1.08 ± 1.53a	2.70 ± 2.11a	1.58 ± 1.01b	
Lu	0.20 ± 0.24a	0.21 ± 0.18a	4.78 ± 4.92b	
Tl	<LOD	<LOQ	<LOD	
Pb	21 ± 51a	209 ± 512a	191 ± 714a	
U	1.70 ± 2.99a	3.25 ± 2.56a	22.46 ± 19.95b	
K/Rb	120 ± 78a	617 ± 234b	48 ± 16a	
Ca/Sr	430 ± 182b	232 ± 113a	245 ± 83a	
$^{87}Sr/^{86}Sr$	0.7125 ± 0.0015a	0.7172 ± 0.0023c	0.7160 ± 0.0024b	
$\delta^{13}C$ (‰) bulk	−25.7 ± 1a	−24.1 ± 2.4b	−25.7 ± 0.4a	
$\delta^{13}C$ (‰) protein	−26.1 ± 0.3a	−24.7 ± 0.7b	−26.1 ± 0.5a	

[a]<LOD, below limit of detection; <LOQ, below limit of quantification; IDL (μg kg^{-1}), La (1.0) Tl (0.5); IQL (μg kg^{-1}), Tl (1.67). Different letters in the same row indicate significant differences ($p < 0.05$).

Strontium isotope ratios were measured following the method described by Baroni et al.[11]

Soil and Water Analysis. The methodology and the results of soil and water samples in the regions under study were published by Baroni et al.[11]

Statistical Analysis. Data were analyzed using the statistical package Statistica 8.0 from StatSoft Inc. (2007) and the Infostat software package.[26]

Analysis of Variance. Results were analyzed by ANOVA, and significant differences between mean values were determined by DGC test ($p < 0.05$).

Classification Tree Analysis (C&RT). Classification trees are used to predict membership of cases or objects in the classes of a categorical dependent variable from their measurements on one or more predictor variables. These methods consist of algorithms based on rule induction, which is a way of partitioning the data space into different class subspaces. Basically, the data set is recursively split into smaller subsets, where each subset contains objects belonging to as few categories as possible. A test set, containing objects not used in the training and also with known class memberships, serves to test the performance of the classifier.[27] The training set contains 75% of total honey samples. The subsets were selected randomly for each class separately. A leave-one-object out cross-validation procedure was adopted to optimize models constructed. The efficiency of the model was used to characterize quality of model prediction, which is the total percentage of a correctly classified test sample.

Discriminant Analysis (DA). DA was performed in stepwise mode to discriminate honey samples according to their geographical origin. Most significant variables were selected according to the F value. A cross-validation test was used to evaluate the robustness of the classification model.

Generalized Procrustes Analysis (GPA). GPA is a useful statistical method to evaluate the correspondence between different data from the same object. In this case, we evaluate correspondence of elemental and isotopic data from soil, water, and honey from each geographical origin.[11]

Canonical Correlation Analysis (CCA). CCA was used to find relationships between concentrations of elements and isotopes in soil, water, and honey. This analysis allows us to investigate the relationship of two sets of variables, honey versus soil and honey versus water.

RESULTS AND DISCUSSION

Multielement Contents. Table 1 shows mean values and standard deviations of element data for honey samples from the

DOI: 10.1021/jf5060112
J. Agric. Food Chem. 2015, 63, 4638−4645

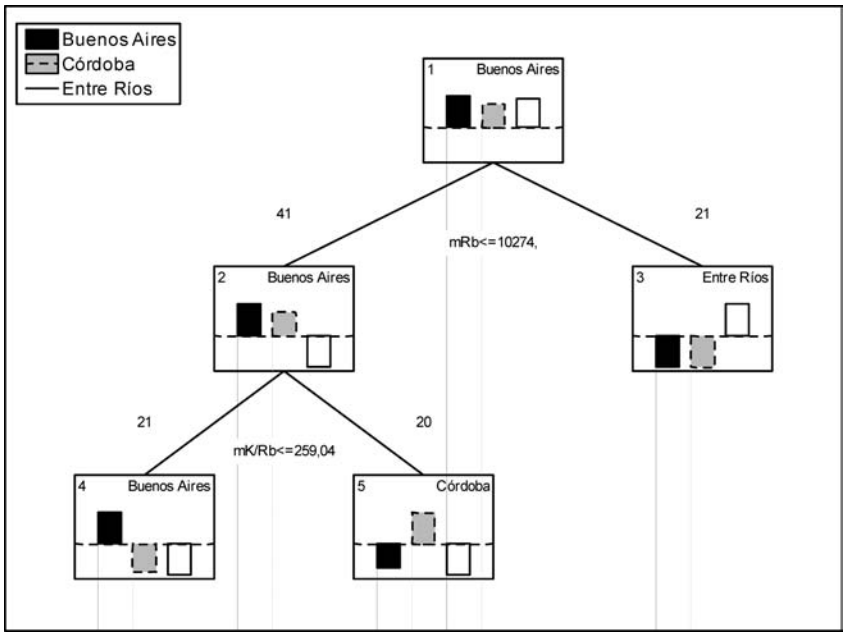

Figure 2. Classification tree of honey samples according to their type using the classification tree method.

three studied regions. Furthermore, K/Rb and Ca/Sr ratios were included. The K/Rb ratio can greatly differ among various types of rocks and soils.[28] On the other hand, the Ca/Sr ratio has been used as a chemical tracer in geochemistry, hydrogeochemistry, and bioavailability studies.[29]

Tl was the only element analyzed that fell below the detection level in honey. In line with most previous studies,[21−23,27] potassium (K) was the most abundant element in studied honey, followed by Ca, Mg, and Na. B, Al, Mn, Zn, Rb, and Ba were present in intermediate concentrations (Table 1). The other analyzed elements were below 1 ppm.

We observed some differences between the geographical origins despite honey samples being multifloral in majority causing certain variability in the elemental composition. Twenty-five elements were significantly different at least in one region ($p < 0.05$), demonstrating that honeys from different regions have a characteristic elemental profile. Five variables (B, Mg, K, Mn, and Sr) were significantly different among the three studied regions. Conversely, V, Ni, Yb, and Pb did not show significant differences between the three studied areas. Ba presented lowest values in Buenos Aires, whereas Córdoba and Entre Ríos had similar higher values. Additionally, Li, Na, Al, Ca, Co, Cu, Zn, Rb, Mo, Ce, Nd, Eu, Yb, and Lu presented highest values in honey from Entre Ríos, whereas Buenos Aires and Córdoba presented similar lower values. Conversely, Sm presented lower values in Entre Ríos and similar higher values in Córdoba and Buenos Aires.

The ratios Ca/Sr and K/Rb also showed variations. Ca/Sr was higher in Buenos Aires and had similar lower values in Córdoba and Entre Ríos, whereas K/Rb was higher in Córdoba and presented lower values in Buenos Aires and Entre Ríos.

The contents of nutritionally important elements were calculated in a daily intake of 42.8g of honey (two spoons) and compared to their daily dose allowance (DDA) in the human body, taken from Seiler et al.[30] The ingestion of two spoons of honey represents between 0.1 and 12% of the DDA (Table 1).[31]

Apart from mineral nutrients, the analysis of the elemental composition of honey may also give information about environmental pollution. The contents of trace elements in the Argentinean honey were comparable with the contents in honey from uncontaminated areas.[22,23,27] This emphasizes the good quality of Argentinean honey, especially with regard to the contents of toxic trace elements, such as Cd, Pb, and U. All of the honey samples presented a concentration of heavy metals below maximum levels for food set by Commission Regulation (EC) No. 1881/2006 (EC, 2006) amended by EC 629/2008 (EC, 2008).[32] With respect to cadmiun content, samples from Córdoba showed the highest values (600 ppb), even though these values are below the maximum levels set. From previous studies, it can be noted that industry, mining, automobile exhaust gases, etc., may be responsible for cadmium contamination in honey.[33]

Carbon Isotopes. The carbon isotopes in plants and resulting products are mainly influenced by metabolism (carbon fixation), which is why the $\delta^{13}C$ values can be used to detect honey adulterated with C4 plant sugars, such as high fructose corn syrup (HFCS).[6,30,31] On the other hand, carbon isotopes are related to humidity and temperature (climate) and can be useful for food geographical origin assignment.[34]

On the basis of $\delta^{13}C$ values obtained, samples of this study were derived from C3 plants and have not been adulterated, at least with respect to C4 plant addition (corn or cane) (Table 11).[35,36] In previous studies[11,13] we found differences in meat and wheat $\delta^{13}C$ values from the same geographical origin, so we expected to find similar differences in honey samples. Córdoba showed the highest $\delta^{13}C$ value, whereas Buenos Aires and Entre Ríos had similar lower values. The difference between the highest (Córdoba) and lowest (Buenos Aires and Entre Ríos) $\delta^{13}C$ mean values is 1.6‰. $\delta^{13}C$ values of honey increase with increasing temperatures, increasing amount of sun exposure, and decreasing humidity.[19] As noted for wheat,[13] the highest $\delta^{13}C$ values from Córdoba honey samples could be related to an evaporation effect due to its warm and dry growing conditions with respect to Buenos Aires and Entre Ríos. This is so because the cultivation area of Córdoba is located close to a semiarid region. The difference between the climate in Córdoba and Buenos Aires−Entre Ríos is sufficient to influence the $\delta^{13}C$

DOI: 10.1021/jf5060112
J. Agric. Food Chem. 2015, 63, 4638−4645

values of the honey and make this parameter useful to discriminate the geographic origin of food.[19] However, one has to bear in mind that there is variability also within each sampling area. Observed variations could be explained by different temperature ranges at harvest times of each honey, leading to different $\delta^{13}C$ values.

Strontium Isotopes. The strontium isotope composition of plants, and the animals that eat them, is related to the $^{87}Sr/^{86}Sr$ signature of the bioavailable strontium derived from water and soil (bedrock). Once a $^{87}Sr/^{86}Sr$ database of one crop has been constructed, it can be applicable to new crops from the same geographical origin. For example, it has been reported that $^{87}Sr/^{86}Sr$ values of water could be used to estimate the geographic origin of honey and wheat.[37] Therefore, the Sr isotope ratio inherits the geological character of a production area.[38]

We found statistically significant differences for $^{87}Sr/^{86}Sr$ between honeys from Córdoba, Entre Ríos, and Buenos Aires. Cordoba had the highest values, followed by Entre Ríos and Buenos Aires. Similar results were found in our previous studies for meat and wheat from the same geographical origin.[11,13] This shows the importance of including strontium isotopes in the determination of the geographical origin of foods.

Honey Geographical Classification. Analyzing only one isotopic element gives us an incomplete view regarding the interpretation of the origin of food in general and honey in particular. A multielement evaluation is essential to enhance the reliability of origin classification of food. To get greater origin resolution, the first choice will be to use multivariate statistical methods. In this case, classification trees and lineal discriminant analysis were applied.

Classification and regression tree (C&RT) analysis is a nonparametric methodology that segments populations into subgroups of increasing group homogeneity. The results are formed into a tree structure (decision tree), according logical rules "if–then". C&RT selects those variables that are most important for predicting classification without concern for the possible relationships between variables.[27]

Variables selected by C&RT as most important were Rb and K/Rb, which have 100 and 95% prediction power, respectively. The content of Rb allows discriminating Entre Ríos honey from the others, whereas K/Rb content separated Buenos Aires honey from Córdoba honey samples (Figure 2). The results are shown in Table 2. In the training set none of the samples were misclassified, whereas in the test set two samples of Buenos Aires were misclassified (13.4%).

Linear Discriminant Analysis. Eight of 35 original variables were pointed out by stepwise discriminant analysis as the most important for geographical discrimination, Rb being the most significant variable, followed by K/Rb, B, U, $^{87}Sr/^{86}Sr$, Na, La, and Zn. With these eight elements and isotopes, 98.7% of samples were classified correctly according to its origin. Two different independent discriminant functions were obtained by linear combination of these variables. The combination of the two canonical variables explained 100% of variability (Figure 3A). As shown in Figure 3, Rb was the most important variable in root 1, separating Entre Ríos samples from Buenos Aires and Córdoba; meanwhile, B and K/Rb improved the discrimination between Córdoba and Buenos Aires in root 2.

Rb, Na, Zn, and La presented higher values in Entre Ríos and lower values in Buenos Aires and Córdoba (Figure 3D). Additionally, $^{87}Sr/^{86}Sr$ shows higher values in Córdoba, intermediate values in Entre Ríos, and lowest values in Buenos Aires (Figure 3C). The K/Rb ratio shows the highest values in Córdoba and lower values in Entre Ríos and Buenos Aires (Table 1). Finally, B is capable of differentiating the three honey origins (Figure 3B).

Table 2. Classification Tree Analysis: Recognition and Prediction Ability[a]

		Córdoba	Entre Ríos	Buenos Aires	total correct classification (%)
training set $N = 62$	Córdoba ($N = 19$)		0	0	
	Entre Ríos (N=21)	0		0	
	Buenos Aires ($N = 22$)	0	0		
% correctly classified		100	100	100	**100**
test set $N = 17$	Córdoba ($N = 6$)		0	0	
	Entre Ríos ($N = 6$)	0		0	
	Buenos Aires ($N = 5$)	2	0		
% correctly classified		60	100	100	**86.6**

[a]Number of samples in the training and test set and efficiency (in percentage) of the model.

Elements and isotopes selected by discriminant and classification tree analysis were also pointed out in previous studies as capable of differentiating diverse food matrices from the same Argentinean regions. For example, wheat samples from Córdoba, Buenos Aires, and Entre Ríos were classified by K/Rb, Na, $^{87}Sr/^{86}Sr$, and Zn;[13] meat samples from the same provinces were characterized by $\delta^{13}C$, Rb, $\delta^{15}N$, Ca/Sr, and $^{87}Sr/^{86}Sr$.[11] Furthermore, wine samples from different Argentinean regions were classified by B, Na, Zn, and $^{87}Sr/^{86}Sr$.[12] It is worth noting that $^{87}Sr/^{86}Sr$ is not capable of discriminating wine variety, but it is always associated with geographical origin. Voerkelius et al.[37] noted that $^{87}Sr/^{86}Sr$ serves as an indicator of geographical origin; in fact, they found a good correlation between honey strontium isotopes values and surface water values.

Furthermore, in various papers honey was also discriminated by the same elements. Chua et al.[23] found that Na, between other elements, was capable of discriminating the geographical origin of honey. Pisani et al.[39] showed that some geological and geochemical features appeared to affect honey chemistry composition, Na being one of the most important. Pellerano et al.[14] also classified Argentinean honey but from other locations using La and Zn as the most important elements.

Correlation between Soil, Water, and Honey Chemical Composition. Taking into account the previous background where it is known that metals in honey derived from soil and to some extent also from nectar and pollen, we were interested in evaluating the correlation between geographical origin (soil and water) and honey.[38−41] Characterization (elemental profile and isotopes ratios) of soil and water from the three regions of origin has been previously published (see the Supporting Information).[11]

GPA was applied to evaluate the correspondence between the elemental profile and isotopes ratios of honey, soil, and water. One hundred percent of the variability between samples could be explained by first and second principal axes (Figure 4). Furthermore, multielement and isotope concentrations from

DOI: 10.1021/jf5060112
J. Agric. Food Chem. 2015, 63, 4638−4645

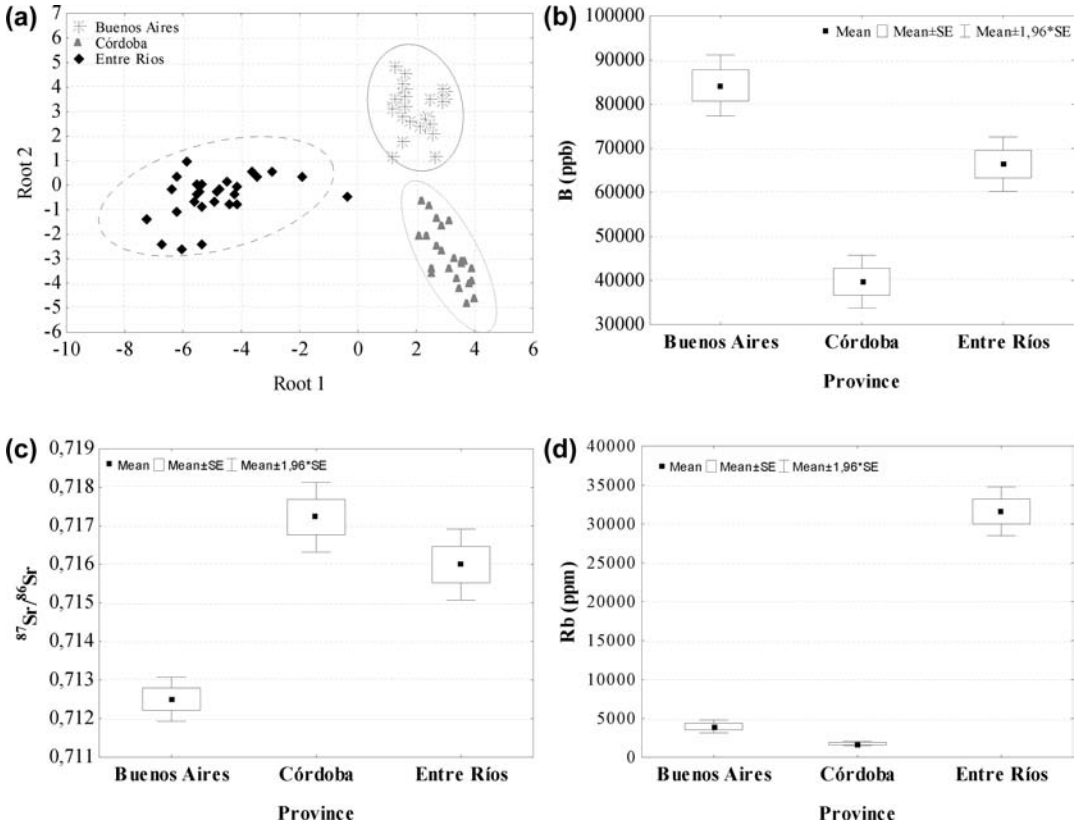

Figure 3. Discriminant analysis (canonical roots) and some selected parameters differentiating honey.

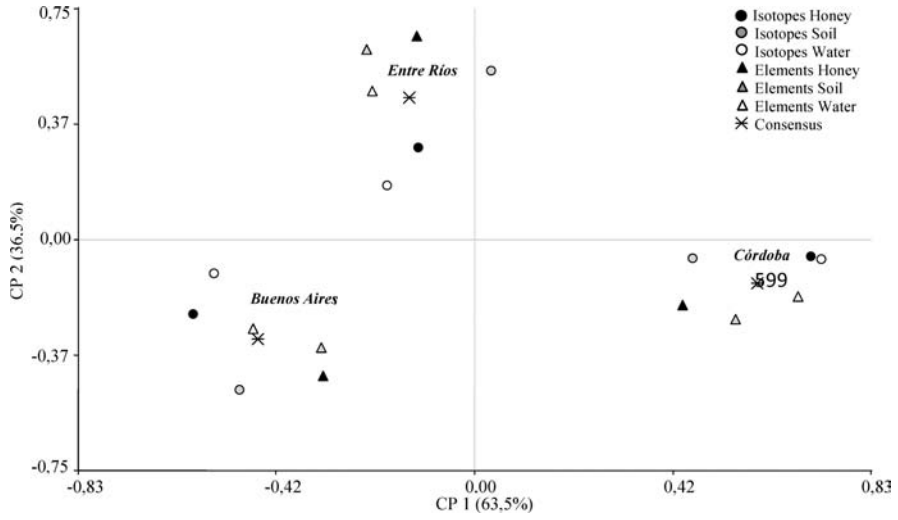

Figure 4. Consensus space from Generalized Procrustes analysis: plot in the plane defined by the first two dimensions.

soil, water, and honey samples allow discrimination of the three geographical origins. Honey chemical data have a significant consensus (91.5%) with those obtained from soil and water, as three data sets project the different geographical origins in the same way onto the plane defined by its first and second principal axes. GPA results show evidence on the correspondence between the three studied matrices.

Finally, we applied CCA to assess the correspondence between soil, water, and honey composition. The first CCA showed significant correlation (r^2 = 0.99732; p < 0.001) between soil and honey data sets. Contents of Co, Ni, Sr, and K/Rb in soil as well as Mn and Rb in honey were pointed out as the variables that mainly contribute to the correlation between soil and honey. The CCA between water and honey data sets also showed a significant correlation (r^2 = 0.9899; p < 0.001). Ca, B, and Ca/Sr contents in water as well as Rb and Mg contents in honey were the variables that mainly contribute to the correlation between water and honey. Therefore, both GPA and CCA coincide, showing the influence of environment (soil and water) on honey composition.

In this work, geographical discrimination of honey through a suitable multivariate statistical analysis was accomplished because differences between elemental concentrations and isotope ratios were found. Linear discriminant analysis enabled

DOI: 10.1021/jf5060112
J. Agric. Food Chem. 2015, 63, 4638−4645

correct classification of honey samples from different Argentinean regions when the isotopic ratio $^{87}Sr/^{86}Sr$ as well as elements such as Rb, La, U, B, Na, Zn, and the K/Rb ratio were considered. Moreover, we were able to demonstrate correspondence between soil, water, and honey samples by appropriate statistical methods, such as Generalized Procrustes analysis and canonical correlations.

■ ASSOCIATED CONTENT

Supporting Information

Table showing element and isotope concentrations in soil and water samples from studied regions. The Supporting Information is available free of charge on the ACS Publications website at DOI: 10.1021/jf5060112.

■ AUTHOR INFORMATION

Corresponding Author

*(D.A.W.) Phone: +54 351 433 3193/94. E-mail: dwunder@fcq.unc.edu.ar.

Funding

This work was mainly supported by European TRACE Integrated Project (VI FP, Contract 006942); additional funding from SECyT National University of Córdoba is acknowledged.

Notes

The authors declare no competing financial interest.

■ ACKNOWLEDGMENTS

N.S.P. is a fellow colleague from CONICET (National Research Council, Argentina).

■ REFERENCES

(1) Drivelos, S. A.; Georgiou, C. A. Multi-element and multi-isotoperatio analysis to determine the geographical origin of foods in the European Union. *TrAC, Trends Anal. Chem.* **2012**, *40*, 38−51.

(2) Oulhote; Le Bot, B.; Deguen, S.; Glorennec, P. Using and interpreting isotope data for source identification. *TrAC, Trends Anal. Chem.* **2011**, *30*, 302−312.

(3) De la Guardia, M.; Gonzalvez, A. Food protected designation of origin. Methodologies and applications. In *Comprenhesive Analytical Methods*; Barceló, D., Ed.; Elsevier: Amsterdam, The Netherlands, 2013; Vol. 60, pp 511−530.

(4) Rogers, K. M.; Sim, M.; Stewart, S.; Phillips, A.; Cooper, J.; Douance, C.; Pyne, R.; Rogers, P. Investigating C4 sugar contamination of manuka honey and other New Zealand honey varieties using carbon isotopes. *J. Agric. Food Chem.* **2014**, *62*, 2605−2614.

(5) Rashed, M. N.; Soltan, M. E. Major and trace elements in different types of Egyptian mono-floral and non-floral bee honeys. *J. Food Compos. Anal.* **2004**, *17*, 725−735.

(6) Chen, H.; Fan, C.; Chang, Q.; Pang, G.; Hu, X.; Lu, M.; Wang, W. Chemometric determination of the botanical origin for Chinese honeys on the basis of mineral elements determined by ICP-MS. *J. Agric. Food Chem.* **2014**, *62*, 2443−2448.

(7) Schievano, E.; Morelato, E.; Facchin, C.; Mammi, S. Characterization of markers of botanical origin and other compounds extracted from unifloral honeys. *J. Agric. Food Chem.* **2013**, *61*, 1747−1755.

(8) Roshan, A.-R.; Gad, H. A.; El-Ahmady, S. E.; Khanbash, M. S.; Abou-Shoer, M. I.; Al-Azizi, M. M. Authentication of monofloral Yemeni sidr honey using ultraviolet spectroscopy and chemometric analysis. *J. Agric. Food Chem.* **2013**, *61*, 7722−7729.

(9) Kropf, U.; Golob, T.; Necemer, E.; Kump, P.; Korosec, M.; Bertoncelj, J.; Ogrinc, N. Carbon and nitrogen natural stable isotopes in Slovene honey: adulteration and botanical and geographical aspects. *J. Agric. Food Chem.* **2010**, *58*, 12794−12803.

(10) Zieliński, L.; Deja, S.; Jasicka-Misiak, I.; Kafarski, P. Chemometrics as a tool of origin determination of Polish monofloral and multifloral honeys. *J. Agric. Food Chem.* **2014**, *62*, 2973−2981.

(11) Baroni, M. V.; Podio, N. S.; Badini, R. G.; Inga, M.; Ostera, H. A.; Cagnoni, M.; Gallegos, E.; Gautier, E.; Peral-García, P.; Hoogewerff, J.; Wunderlin, D. A. How much do soil and water contribute to the composition of meat? A case study: meat from three areas of Argentina. *J. Agric. Food Chem.* **2011**, *59*, 11117−11128.

(12) Di Paola-Naranjo, R. D.; Baroni, M. V.; Podio, N. S.; Rubinstein, H. R.; Fabani, M. P.; Badini, R. G.; Inga, M.; Ostera, H. A.; Cagnoni, M.; Gallegos, E.; Gautier, E.; Peral-García, P.; Hoogewerff, J.; Wunderlin, D. A. Fingerprints for main varieties of Argentinean wines: terroir differentiation by inorganic, organic, and stable isotopic analyses coupled to chemometrics. *J. Agric. Food Chem.* **2011**, *59*, 7854−7865.

(13) Podio, N. S.; Baroni, M. V.; Badini, R. G.; Inga, M.; Ostera, H. A.; Cagnoni, M.; Gallegos, E.; Gautier, E.; Peral-García, P.; Hoogewerff, J.; Wunderlin, D. A. Elemental and isotopic fingerprint of Argentinean wheat. Matching soil, water, and crop composition to differentiate provenance. *J. Agric. Food Chem.* **2013**, *61*, 3763−3773.

(14) Pellerano, R. G.; Uñates, M. A.; Cantarelli, M. A.; Camiña, J. M.; Marchevsky, E. J. Analysis of trace elements in multifloral Argentine honeys and their classification according to provenance. *Food Chem.* **2012**, *134*, 578−582.

(15) Rizelion, V. M.; Gonzaga, L. V.; Campelo Borges, G. S.; Maltez, E. F.; Oliveira Costa, A. C.; Fett, R. Fast determination of cations in honey by capillary electrophoresis: a possible method for geographic origin discrimination. *Talanta* **2012**, *99*, 450−456.

(16) Bilandzic, N.; Dokic, M.; Sedak, M.; Kolanovic, B. S.; Varenina, I.; Koncurat, A.; Rudan, N. Determination of trace elements in Croatian floral honey originating from different regions. *Food Chem.* **2011**, *128*, 1160−1164.

(17) Almeida, M.; Vasconcelos, M. T. Does the winemaking process influence the wine $^{87}Sr/^{86}Sr$? A case study. *Food Chem.* **2004**, *85*, 7−12.

(18) Rossmann, A. Determination of stable isotope ratios in food analysis. *Food Rev. Int.* **2001**, *17*, 347−381.

(19) Schellenberg, A.; Chmielus, S.; Schlicht, C.; Camin, F.; Perini, M.; Bontempo, L.; Heinrich, K.; Kelly, S. D.; Rossmann, A.; Thomas, F.; Jamin, E.; Horacek, M. Multielement stable isotope ratios (H, C, N, S) of honey from different European regions. *Food Chem.* **2010**, *121*, 770−777.

(20) Camin, F.; Larcher, R.; Nicolini, G.; Bontempo, L.; Bertoldi, D.; Perini, M.; Schlicht, C.; Schellenberg, A.; Thomas, F.; Heinrich, K.; Voerkelius, S.; Horacek, M.; Ueckermann, H.; Froeschl, H.; Wimmer, B.; Heiss, G.; Baxter, M.; Rossmann, A.; Hoogewerff, J. Isotopic and elemental data for tracing the origin of European olive oils. *J. Agric. Food Chem.* **2010**, *58*, 570−577.

(21) Baroni, M. V.; Arrua, C.; Nores, M. L.; Fayé, P.; Díaz, M. P.; Chiabrando, G. A.; Wunderlin, D. A. Composition of honey from Córdoba (Argentina): assessment of north/south provenance by chemometrics. *Food Chem.* **2009**, *114*, 727−733.

(22) Batista, B. L.; da Silva, L. R. S.; Rocha, B. A.; Rodrigues, J. L.; Berretta-Silva, A. A.; Bonates, T. O.; Gomes, V. S. D.; Barbosa, R. M.; Barbosa, F. Multi-element determination in Brazilian honey samples by inductively coupled plasma mass spectrometry and estimation of geographic origin with data mining techniques. *Food Res. Int.* **2012**, *49*, 209−215.

(23) Chua, L. S.; Abdul-Rahaman, N. L.; Sarmidi, M. R.; Aziz, R. Multi-elemental composition and physical properties of honey samples from Malaysia. *Food Chem.* **2012**, *135*, 880−887.

(24) Chesson, L. A.; Tipple, B. J.; Erkkila, B. R.; Cerling, T. E.; Ehleringer, J. R. B-HIVE: Beeswax hydrogen isotopes as validation of environment. Part I: Bulk honey and honeycomb stable isotope analysis. *Food Chem.* **2011**, *125*, 576−581.

(25) Domínguez, M. A.; Gonçalves Dias Diniz, P. H.; Di Nezio, M. S.; Ugulino de Araújo, M. C.; Centurión, M. E. Geographical origin classification of Argentinean honeys using a digital image-based flow-batch system. *Microchem. J.* **2014**, *112*, 104−108.

DOI: 10.1021/jf5060112
J. Agric. Food Chem. 2015, 63, 4638−4645

(26) Di Rienzo, J. A.; Casanoves, F.; Balzarini, M. G.; Gonzalez, L.; Tablada, M.; Robledo, C. W. *Infostat Versión*; Grupo InfoStat, FCA, Universidad Nacional de Córdoba: Córdoba, Argentina, 2010.
(27) Chudzinka, M.; Baralkiewwicz, D. Application of ICP-MS method of determination of 15 elements in honey with chemometric approach for the verification of their authenticity. *Food Chem. Toxicol.* **2011**, *49*, 2741−2749.
(28) Peltola, P.; Brun, C.; Mats, A.; Tomilina, O. High K/Rb ratios in stream waters − exploring plant litter decay, ground water and lithology as potential controlling mechanisms. *Chem. Geol.* **2008**, *257*, 92−100.
(29) Pett-Ridge, J. C.; Derry, L. A.; Barrows, J. K. Ca/Sr and $^{87}Sr/^{86}Sr$ ratios as tracers of Ca and Sr cycling in the Rio Icacos watershed, Luquillo Mountains, Puerto Rico. *Chem. Geol.* **2009**, *267*, 32−45.
(30) Seiler, H. G., Sigel, A., Sigel, H., Eds. *Handbook on Metals in Clinical and Analytical Chemistry*; CRC Press: Boca Raton, FL, USA, 1994; 0-8247-9094-4, pp 1−11.
(31) Almeida-Silva, M.; Canha, N.; Galinha, C.; Dung, H. M.; Freitas, M. C.; Sitoe, T. Trace elements in wild and orchard honeys. *Appl. Radiat. Isot.* **2011**, *69*, 1592−1595.
(32) Council directive 2001/110/EC of Dec 20, 2001 relating to honey. *Off. J. Eur. Communities* **2002**, *10*, 47−52.
(33) Erbilir, F.; Erdogrul, O. Determination of heavy metals in honey in Kahramanmaras City, Turkey. *Environ. Monit. Assess.* **2005**, *109*, 181−187.
(34) Peck, W. H.; Tubman, S. C. Changing carbon isotope ratio of atmospheric carbon dioxide: implications for food authentication. *J. Agric. Food Chem.* **2010**, *58*, 2364−2367.
(35) Padovan, G. J.; De, D.; Rodrigues, L. P.; Marchini, J. S. Detection of adulteration of commercial honey samples by the $^{13}C/^{12}C$ isotopic ratio. *Food Chem.* **2003**, *82*, 633−636.
(36) Simsek, A.; Bilsel, M.; Goren, A. C. $^{13}C/^{12}C$ pattern of honey from Turkey and determination of adulteration in commercially available honey samples using EA-IRMS. *Food Chem.* **2012**, *130*, 1115−1121.
(37) Voerkelius, S.; Lorenz, G. D.; Rummel, S.; Quétel, C. R.; Heiss, G.; Baxter, M.; Brach-Papa, C.; Deters-Itzelsberger, P.; Hoelzl, S.; Hoogewerff, J.; Ponzevera, E.; Van Bocxstaele, M.; Uneckermann, H. Strontium isotopic signatures of natural mineral waters, the reference to a simple geological map and its potential for authentication of food. *Food Chem.* **2010**, *118*, 933−940.
(38) Ariyama, K.; Shinozaki, M.; Kawasaki, A. Determination of the geographic origin of rice by chemometrics with strontium and lead isotope ratios and multielement concentrations. *J. Agric. Food Chem.* **2012**, *60*, 1628−1634.
(39) Pisani, A.; Protano, G.; Riccobono, F. Minor and trace elements in different honey types produced in Siena County (Italy). *Food Chem.* **2008**, *107*, 1553−1560.
(40) Stankovska, E.; Stafilov, T.; Sajn, R. Monitoring of trace elements in honey from the Republic of Macedonia by atomic absorption spectrometry. *Environ. Monit. Assess.* **2008**, *142*, 117−126.
(41) Hernández, O. M.; Fraga, J. M. G.; Jiménez, A. I.; Jiménez, F.; Arias, J. J. Characterization of honey from the Canary Islands: determination of the mineral content by atomic absorption spectrophotometry. *Food Chem.* **2005**, *93*, 449−458.

DOI: 10.1021/jf5060112
J. Agric. Food Chem. 2015, 63, 4638−4645

JOURNAL OF AGRICULTURAL AND FOOD CHEMISTRY

Article

pubs.acs.org/JAFC

Effects of Granule Size of Cross-Linked and Hydroxypropylated Sweet Potato Starches on Their Physicochemical Properties

Jianwei Zhao,[†,‡] Zhenghong Chen,[§] Zhengyu Jin,[‡] Piet Buwalda,[§] Harry Gruppen,[†] and Henk A. Schols*[,†]

[†]Laboratory of Food Chemistry, Wageningen University, Post Office Box 17, 6700 AA Wageningen, Netherlands

[‡]School of Food Science and Technology, Jiangnan University, Wuxi, Jiangsu 214122, People's Republic of China

[§]AVEBE Food Innovation Centre, 9640 AA Veendam, Netherlands

ABSTRACT: Sweet potato starch was modified by cross-linking, hydroxypropylation, and combined cross-linking and hydroxypropylation, and the starches were subsequently sieved to obtain differently sized granule fractions. The effects of granule size of native and modified sweet potato starch fractions and all fractions were investigated with respect to their physicochemical properties. The large-size granule fraction (27−30 μm) showed a 16−20% higher chemical phosphorylation and a 4−7% higher hydroxypropylation than the small-size granule fraction (14−16 μm). The large-size granule fractions of native and modified sweet potato starches showed lower transition temperatures (0.7−3.1 °C for peak temperature of gelatinization) and lower enthalpy changes (0.6−1.9 J/g) during gelatinization than the small-size granule fractions, making the sweet potato starch different from cereal starches. The large-size granule fraction of native starch showed a higher paste viscosity (78−244 cP) than the corresponding small-size granule fraction. In addition, cross-linking and hydroxypropylation affected the paste viscosity of the large-size granule fraction significantly more than that of the small-size granule fraction when compared to the corresponding parental starch fractions. The large-size granule fraction of native and dual-modified starches showed a lower syneresis after freeze−thaw treatments than the small-size granule fractions. The difference in swelling power between large- and small-size granule fractions was not significant. In general, the large-size granule fraction of sweet potato starch was more susceptible for cross-linking and hydroxypropylation and the physicochemical properties were changed to a higher extent compared to the corresponding small-size granule fraction.

KEYWORDS: *cross-linking, hydroxypropylation, physicochemical property, paste viscosity, syneresis*

INTRODUCTION

Starch is one of the main ingredients used in the food industry. Starch is often modified to overcome shortcomings of native starches, such as cooking loss and syneresis of frozen food. Cross-linking and hydroxypropylation are two important types of modification. Cross-linking reinforces the molecule structure of granular starch by covalent bonds between starch chains, thereby improving the stability of starch under acid, heat, and shear force conditions.[1] Hydroxypropylation allows starch to have good clarity, higher viscosity, reduced syneresis, and improved freeze−thaw stability.[2] Cross-linking of starch is often combined with other modifications, such as hydroxypropylation, to obtain even better functional properties.[3]

Sweet potato (*Ipomoea batatas* Lam.) is one of the most important economic species of tropical root and tuber crops, which can grow in great abundance on marginal soils.[4] Isolated sweet potato starch is widely used as a food ingredient for noodles, bakery foods, snack foods, and confectionery products.[5] To overcome limitations of native sweet potato starch, chemical modifications have been performed to extend the range of food applications. Cross-linking reduced the swelling power and apparent viscosity and increased the gelatinization temperature, enthalpy, storage modulus, loss modulus, and complex viscosity of sweet potato starch.[6] Hydroxypropylation increased the swelling power, freeze−thaw stability, and flow behavior index and decreased the transition temperature and enthalpy of gelatinization, consistency index, apparent viscosity, and complex viscosity of sweet potato starch.[7] It has also been reported that the processability and quality of dried and cooked sweet potato starch noodles made from the small-size granule fraction were significantly better than those made from the parental starch preparation and much better than those made from the large-size granule fraction.[8,9] In addition, it was reported that the small-size granule fractions of acetylated yellow pea, cow pea, and chick pea starch exhibited larger swelling volumes and higher peak viscosities compared to the corresponding large-size fractions.[10] Until now, the improved functional properties of small-sized sweet potato granules have not been explained. In addition, the effect of granule size on the functional properties of hydroxypropylated sweet potato starch and the effect of granule size of dual-modified sweet potato starch have not been investigated thus far.

In this study, sweet potato starch was modified with cross-linking and/or hydroxypropylation, and the granules were sieved to obtain the large- and small-size granule fractions. All fractions were investigated for their physicochemical properties. The effects of starch granule size on the starch properties of the various modified starches are discussed.

Received: January 5, 2015
Revised: April 20, 2015
Accepted: April 23, 2015
Published: April 23, 2015

ACS Publications © 2015 American Chemical Society

DOI: 10.1021/jf506349w
J. Agric. Food Chem. 2015, 63, 4646−4654

MATERIALS AND METHODS

Starch Samples. Native sweet potato starch (NT-SPS, SuShu2) having a amylose content of 19.3% (w/w, dry basis), was isolated as described previously.[5] The modified starches were prepared at the AVEBE Research and Development facilities (Veendam, Netherlands). All of the modifications were conducted in aqueous suspensions of the granular starches. The cross-linked sweet potato starch (CL-SPS) was obtained by adding 0.002 mol of trimetaphosphate/mol of glucose to the starch suspension. A 39% (w/w) suspension of starch (1 kg) was prepared with tap water, and 0.70 mol of Na_2SO_4 was dissolved in this suspension at room temperature. The pH of the suspension was adjusted to 10.5 with dropwise 4.4% (w/w) NaOH. Subsequently, 0.002 mol of sodium trimetaphosphate (STMP) was added for reaction of 6 h at 35 °C, and then the suspension was neutralized to pH 5.5 with H_2SO_4 (10 N) and dewatered over a Büchner funnel. The product was washed with tap water (1:5) and dried at 40 °C in an oven.

The hydroxypropylated sweet potato starch (HP-SPS) was obtained by adding 0.2 mol of propylene oxide/mol of glucose residues. A 39% (w/w) suspension of starch (1 kg) was prepared with tap water, and 0.70 mol of Na_2SO_4 was dissolved in this suspension at room temperature. The pH of the suspension was adjusted to 10.5 with dropwise 4.4% (w/w) NaOH. A total of 0.2 mol of propylene oxide was added with a dropping funnel to the closed vessel. After 24 h of reaction at 35 °C, the suspension was neutralized to pH 5.5 with 10 N H_2SO_4 and dewatered over a Büchner funnel. The filter cake was washed with tap water (1:5). The starch was dried in an oven at 40 °C.

The cross-linked and hydroxypropylated sweet potato starches (CLHP-SPS) were first cross-linked and subsequently hydroxypropylated.

Starches were fractionated by sieving on an analytical sieve shaker (20 μm sieve, model AS200 digit, Retsch, Haan, Germany) at a vibrational amplitude of 1 mm and rinsing with tap water. When the rinsing water was clear and no starch granules could be detected visually, the sieving was stopped. The large-size granule fraction (>20 μm) and the small-size granule fraction (<20 μm) of the starches were collected, allowed to precipitate overnight, and collected after decanting. The starch was dried at 40 °C overnight before analysis.

Particle Size Distribution of Starches. Particle size distribution of starch granules was measured with a laser diffraction system (Mastersizer 2000, Malvern Instruments, Worcestershire, U.K.) equipped with a small volume sample dispersion unit (Hydro 2000SM). Starch granules were dispersed in Millipore water in a sampler by stirring at 1500 rpm. The particle size was evaluated as volume-weighted mean diameter (μm). Results given are the average values of three measurements.

Level of Starch Modification. The phosphorus and hydroxypropyl group contents of native and modified sweet potato starches were determined using spectrophotometric methods, and these values were used to calculate the degree substitution (DS) of chemical phosphorylation and molar substitution (MS) of hydroxypropylation.[11]

Thermal Properties of Starch Samples. Thermal properties were measured using a differential scanning calorimeter (DSC 7, PerkinElmer, Walthan, MA) equipped with a thermal analysis data station and a cooling system following the method by Gunaratne and Corke,[12] with some modifications. Starch (3 mg, dry weight basis) was directly weighed into an aluminum differential scanning calorimeter (DSC) pan. Distilled water (7 μL) was added to the starch with a micropipette. After mixing, the pan was hermetically sealed and allowed to stand for at least 1 h at room temperature to obtain an even distribution of water with the sample. The scanning temperature included a gradient from 20 to 100 °C at the rate of 10 °C/min. An empty pan was used as a reference for all measurements. The parameters onset temperature (T_o), peak temperature (T_p), conclusion temperature (T_c), and enthalpy change during gelatinization (ΔH) were calculated using the Pyris software provided by the manufacturer. The reported results are an average of three measurements.

Paste Properties of Starch Samples. The pasting properties of starches were measured using a rapid visco analyzer (RVA-4, Newport Scientific, Warriewood, New South Wales, Australia). The starch slurry (7%, w/v, in distilled water, dry weight basis, 27 g of total slurry) was prepared in a RVA canister. A paddle was placed into the canister, and the blade was vigorously stirred through the sample up and down to avoid lump formation. Next, the canister was inserted into the instrument for measurement. The sample was equilibrated at 50 °C for 1 min, heated to 95 °C in 7.5 min, held at 95 °C for 5 min, cooled to 50 °C in 7.5 min, and held at 50 °C for 2 min.

Swelling Power of Starch Samples. The swelling power of starches was measured as described before,[5,13] with some modifications. Starch was weighed (0.1−0.2 g, dry weight basis) into a 15 mL polypropylene tube, and 12 mL of distilled water was added, followed by mixing. The tubes were equilibrated at 25 °C for 5 min and subsequently heated for 30 min in a water bath at a given temperature (55−95 °C range) with shaking to avoid lump formation. The sample was cooled to 25 °C and centrifuged (1000*g* at 25 °C for 15 min). The supernatant was removed by pipetting, and the swollen starch sediment was weighed. The swelling power was the ratio in weight of the swelled starch sediment to the initial weight of dry starch.[14] Results used for calculation were means of triplicate measurements.

Freeze−Thaw Stability of Starch Samples. Freeze−thaw stability was determined as syneresis as described before.[15] In short, starch was suspended (6%, w/w, dry weight basis, 5 g of slurry) in distilled water in a 10 mL screw-capped tube. The tubes were tightly capped and heated in a 95 °C water bath for 30 min with agitation by inverting the tubes 5 times at 3 min intervals during the first 15 min of heating. These tubes were cooled and stored at 4 °C for 24 h before being subjected to 7 freeze−thaw cycles. The tubes were centrifuged (1500*g* at 25 °C for 15 min) to remove the excluded water. During each cycle, the tubes were put into a freezer at −20 °C for 22 h and thawed at 30 °C in a water bath for 1.5 h. After centrifugation (1500*g* at 25 °C for 15 min), the water eliminated from the gel was weighed. The syneresis was expressed as the proportion of the weight of the separated water to the total weight of the initial paste. Duplicated tests were used for each cycle.

Refrigerated Storage Stability of Starch Samples. Syneresis of starch gel without freeze−thaw treatment was measured by storing the gel at 4 °C. Starch pastes were prepared as described above. The tubes were stored in a refrigerator at 4 °C for several days. With a 1 day interval, the excluded water was measured after centrifugation (1000*g* at 25 °C for 20 min). The weight difference of the gel before and after 4 °C storage was measured as water loss. The syneresis was calculated as the weight percentage of water loss based on the parental starch paste weight.

Statistical Analysis. The statistical analysis was performed using SAS 9.2 for Windows (SAS Institute, Cary, NC). The analysis of variance was conducted using Tukey's range test using honestly significant difference (HSD) values at a 0.05 significance.

RESULTS AND DISCUSSION

Particle Size Distribution of Starch Granules. The native, cross-linked, hydroxypropylated, and dual-modified sweet potato starches were sieved with a 20 μm sieve to obtain two fractions consisting of the large-size (>20 μm) and small-size (<20 μm) granules. The particle size distributions of native and cross-linked sweet potato starch and the corresponding sieved fractions (<20 and >20 μm) are shown in Figure 1. Before sieving, the particle diameter of native sweet potato starch granules is in the range of 5−70 μm, with an average diameter of 19.7 μm. This result is in agreement with previous research.[16,17] After sieving, the particle diameters of the large- and small-size granule fractions are in the range of 11−70 μm (67.5%, w/w) and 5−40 μm (32.5%, w/w) with average diameters of 27.6 and 14.5 μm, respectively.

After the modifications (cross-linking, hydroxypropylation, and cross-linking combined with hydroxypropylation), the

DOI: 10.1021/jf506349w
J. Agric. Food Chem. 2015, 63, 4646−4654

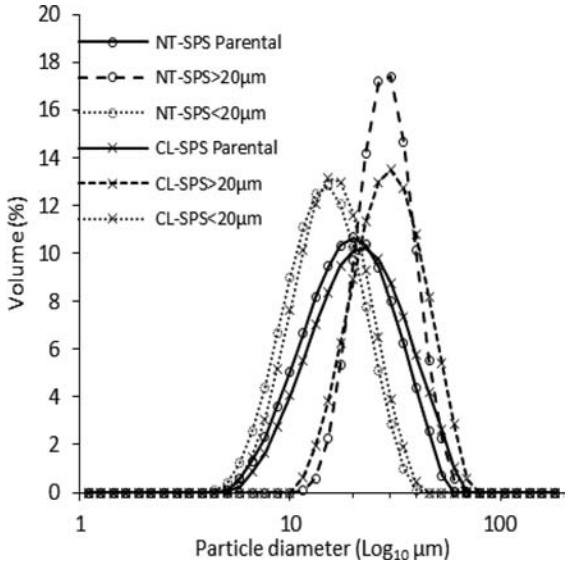

Figure 1. Granule diameter distribution of native (NT-SPS) and cross-linked sweet potato starch (CL-SPS) before and after sieving over a 20 μm sieve using a laser diffraction system in water. Parental, unfractionated starch; >20 μm, large-size granule fraction; and <20 μm, small-size granule fraction.

average diameters of starch granules increased slightly compared to the corresponding native starch granules, as visualized by the granule diameter distribution of cross-linked starch compared to the native starch (Figure 1). The probable reason is that the cross-linking and/or the hydroxypropylation reaction slightly enhance the water absorptivity. Hence, the granule diameter was slightly enlarged.

Level of Starch Modification. The contents of phosphorus and hydroxypropyl groups in the starches are shown in Table 1. The natural phosphorus in sweet potato starch is almost exclusively present as phosphorus monoester.[18] The phosphorus content of the large-size granule fraction of the native sweet potato starch was lower than that of the small-size granule fraction. These findings are in agreement with those found for native potato starch.[19] This can be explained by the lower amylopectin content in large-size granules[20] and the fact that phosphorus is primarily present in the amylopectin part of native starch.[21] It should be noted that the phosphorus content of the parental starch was always slightly higher than those found for both size fractions, for which a possible reason is that traces of residual inorganic phosphorus as present in the parental starch are removed in the additional washing procedure of wet sieving.

When comparing the phosphorus contents of modified starches and native starch (Table 1), it is seen that cross-linking increased the phosphorus content of the non-sieved starches at around 50%. Subsequent hydroxypropylation decreased the phosphorus content at around 20%, because of the alkaline condition of hydroxypropylation and the consequent saponification of phosphate esters. When combining the two treatments of cross-linking and hydroxypropylation, the integral effect resulted in a phosphorus increase of 35% compared to the native starch.

To estimate the effect of chemical phosphorylation, the change in the phosphorus content (ΔP, %, w/w) of the modified starch was compared to the phosphorus level of the native starch (Table 1). The degree of substitution (DS) was calculated on the basis of this value. After modification, the large-size granule fraction still had a lower phosphorus content than the small-size granule fraction. Nevertheless, it was seen that the increment in the phosphorus content (ΔP, %) of the large-size granule fraction (>20 μm) was around 20% higher than that found for the small-size granule fraction (<20 μm). The results indicate that the large-size granule fraction is more susceptible to the cross-linking agent than the small-size granule fraction. Because it has been reported that the reaction of starch with trimetaphosphate is rather slow[22] and surface effects on the reaction are not significant, our findings suggests that the level of cross-linking is not determined by a surface reaction only and that, e.g., the more loosen packing of larger granules might play a role.[23]

For the hydroxypropylated starch, the hydroxypropyl content of the large-size granular fraction was about 5% higher than that of the small-size granule fraction (Table 1), indicating that there was a slight difference of hydroxypropylation reactivity for the different size granules. Next to the mentioned effect of a loose packing of large starch granules, the higher amylose

Table 1. Phosphorus and Hydroxypropyl Levels of Native and Modified Sweet Potato Starches before and after Sieving[a]

		phosphorus			hydroxypropyl	
starch	fraction	P (%, db)	ΔP (%, w/w)	DS (×10^{-4})	HP (%, db)	MS
NT-SPS	parental	0.0197 ± 0.0008	0.0000	0.00	0.00 ± 0.00	0.000
NT-SPS	>20 μm	0.0147 ± 0.0000	0.0000	0.00	0.00 ± 0.00	0.000
NT-SPS	<20 μm	0.0174 ± 0.0000	0.0000	0.00	0.00 ± 0.00	0.000
CL-SPS	parental	0.0296 ± 0.0001	0.0099	5.18	−0.02 ± 0.03	0.000
CL-SPS	>20 μm	0.0265 ± 0.0001	0.0118	6.19	−0.03 ± 0.00	0.000
CL-SPS	<20 μm	0.0276 ± 0.0001	0.0101	5.28	−0.04 ± 0.01	0.000
HP-SPS	parental	0.0154 ± 0.0001	−0.0043	0.00	5.85 ± 0.36	0.176
HP-SPS	>20 μm	0.0126 ± 0.0001	−0.0021	0.00	5.67 ± 0.01	0.171
HP-SPS	<20 μm	0.0150 ± 0.0000	−0.0024	0.00	5.46 ± 0.05	0.164
CLHP-SPS	parental	0.0265 ± 0.0011	0.0068	3.55	5.06 ± 0.09	0.151
CLHP-SPS	>20 μm	0.0231 ± 0.0001	0.0084	4.38	5.16 ± 0.02	0.154
CLHP-SPS	<20 μm	0.0244 ± 0.0000	0.0070	3.66	4.84 ± 0.05	0.144

[a]NT, native; CL, cross-linked; HP, hydroxypropylated; CLHP, cross-linked and hydroxypropylated; SPS, sweet potato starch; >20 μm, oversize granules of 20 μm sieve; <20 μm, undersize granules of 20 μm sieve; P, phosphorus percentage based on weight; ΔP, phosphorus content change on weight percentage of modified starches compared to that of corresponding native starch; db, dry basis; DS, degree of chemical substitution; and MS, molar substitution. Values are means of duplicate determinations and standard deviation.

DOI: 10.1021/jf506349w
J. Agric. Food Chem. 2015, 63, 4646−4654

Table 2. Differential Scanning Calorimetry Temperatures and Enthalpy of Native and Modified Sweet Potato Starches[a]

starch[b]	fraction[c]	T_o (°C)[d]	T_p (°C)[d]	T_c (°C)[d]	ΔH (J/g)[e]
NT-SPS	parental	60.06 ± 0.75 dc	76.78 ± 0.25 b	84.14 ± 0.23 b	16.57 ± 0.38 ab
NT-SPS	>20 μm	61.76 ± 0.58 abc	76.94 ± 0.34 b	85.38 ± 0.18 ab	14.33 ± 0.68 de
NT-SPS	<20 μm	58.90 ± 0.44 d	79.17 ± 0.38 a	86.28 ± 0.88 a	16.28 ± 0.83 abc
CL-SPS	parental	62.13 ± 0.23 ab	77.78 ± 0.09 b	84.67 ± 0.20 ab	17.31 ± 0.56 a
CL-SPS	>20 μm	62.84 ± 0.42 a	77.45 ± 0.25 b	86.41 ± 1.04 a	14.74 ± 0.75 bcde
CL-SPS	<20 μm	61.10 ± 0.86 bc	78.11 ± 0.82 ab	86.20 ± 0.23 a	16.09 ± 0.77 abcd
HP-SPS	parental	50.98 ± 0.38 f	63.45 ± 0.25 d	75.15 ± 0.82 cd	12.81 ± 0.68 e
HP-SPS	>20 μm	52.44 ± 0.32 ef	61.25 ± 0.69 e	74.35 ± 0.93 d	8.42 ± 0.77 f
HP-SPS	<20 μm	52.47 ± 0.79 ef	62.78 ± 0.35 d	76.61 ± 0.48 c	9.22 ± 0.48 f
CLHP-SPS	parental	53.28 ± 0.83 e	65.97 ± 0.67 c	75.62 ± 0.35 cd	14.37 ± 0.77 cde
CLHP-SPS	>20 μm	52.29 ± 0.70 ef	63.22 ± 0.42 d	75.75 ± 0.75 cd	9.04 ± 0.79 f
CLHP-SPS	<20 μm	53.02 ± 0.18 e	66.39 ± 0.38 c	75.92 ± 0.86 cd	9.66 ± 0.40 f

[a]Values are means of triplicate determination ± standard deviation. Means with the same letter are not significantly different. [b]NT, native; CL, cross-linked; HP, hydroxypropylated; CLHP, cross-linked and hydroxypropylated; and SPS, sweet potato starch. [c]Parental, not sieved; >20 μm, oversize granules of 20 μm sieve; and <20 μm, undersize granules of 20 μm sieve. [d]T_o, T_p, and T_c are the onset, peak, and conclusion temperatures of gelatinization, respectively. [e]ΔH is the enthalpy of gelatinization.

content of the large-size fraction,[8] which might be more susceptible to hydroxypropylation than amylopectin,[23] could explain these increased levels. In contrast, for potato, maize, and wheat starch, it has been reported that there were no evident differences in hydroxypropylation between the large- and small-size granule fractions.[24] This may be due to the difference of starch biosynthesis, the granule architecture, and possibly the amylose content. Overall, the large-size granule fraction of sweet potato starch is more efficiently cross-linked and hydroxypropylated than the small-size granule fraction, indicating that the reactions are influenced by the packing density of the starch granules.

Effect of Modification on Thermal Properties. The thermal transition properties of starch are commonly measured using a DSC and expressed as the onset temperature (T_o), peak temperature (T_p), conclusion temperature (T_c), and enthalpy change (ΔH) of gelatinization.[3] The transition temperatures and their range ($T_c - T_o$) give a measure of crystallite quality (double helix length), and the enthalpy change (ΔH) gives an overall measure of crystallinity (quantity and quality) and is an indicator of the loss of molecular order within the granule on gelatinization. The results of thermal properties for the native starch and modified large- and small-size granule fractions are presented in Table 2. It is found that the cross-linking reaction slightly increased in most cases the transition temperatures (~1 °C) and enthalpy (~0.7 J/g) of starch gelatinization, which can be explained by the formation of additional covalent bonds during cross-linking, tightening the starch granule structure.[2,25]

Hydroxypropylation significantly decreased the transition temperature by 13−16 °C and enthalpy of starch gelatinization by 4−7 J/g compared to native starch, probably as a result of disruption of part of the double helices present within the amorphous regions of the starch granules by the hydroxypropylation.[7] The results of DSC suggest that both cross-linking and hydroxypropylation affect the thermal behavior of starch, but the hydroxypropylation has the strongest effect in dually modified starch.

Effect of Starch Granule Size on Thermal Properties. The parental starch showed higher enthalpy change (relatively higher 1.8−59.0%) of gelatinization compared to its sieved size fractions (Table 2). The significant difference of enthalpy may indicate that sieving with washing has an effect on the starch granules, where minor quantities of phosphorus and other minerals may have been lost during sieving. Furthermore, the large-size granules showed a lower enthalpy change than small-size granules, indicating that large-size granules have less crystallinity than small-size granules, which also explains the higher levels of modification found for large-size granules compared to small-size granule fractions (Table 1). This tendency is different for native wheat and potato starch, of which the large-size granule fraction showed a lower temperature and higher enthalpy of gelatinization than the small-size granule fractions.[26,27] The probable reason is the differences in the amylose content (amylose in sweet potato starch, 19.3%;[5] potato starch, 19.4−27.0%;[26] and wheat starch, 27.8%[28]) and contents of amylose−lipid complexes in starches (lipids in sweet potato starch, 0.4%;[5] potato starch, 0.19%[24]).

The large-size granule fraction of cross-linked starch showed only a slightly lower peak temperature and enthalpy when compared to the small-size granule fraction. In general, cross-linking increased the transition temperatures and enthalpy of the large-size granule fraction more than the small-size granule fraction, and the transition temperature and enthalpy of the large-granule fraction remained close to the values found for the small-size granule fraction.

For hydroxypropylated starch, the modification significantly decreased the peak temperature and enthalpy of gelatinization. The large-size granule fraction showed a significantly lower transition peak temperature than the small-size granule fraction. In fact, all of the large-size granule fractions showed a lower transition peak temperature than the small-size fractions, indicating a less crystalline structure in the large-size granules. The significantly lower transition peak temperatures of the hydroxypropylated starches indicate that hydroxypropylation further decreased the crystallite quality to come to the same level of crystallinity for both large- and small-size granule fractions maintained equally for both the large- and small-size granule fractions. All of the large-size granule fractions showed a lower transition peak temperature than the small-size fractions, suggesting the less crystallite structure in the large-size granules. The significantly lower transition peak temperatures of the hydroxypropylated starches indicate that hydroxypropylation decreased the crystallite quality similarly for both the large- and small-size granule fractions.

Dual-modified granules showed a similar tendency of the transition temperature and enthalpy of gelatinization to the

DOI: 10.1021/jf506349w
J. Agric. Food Chem. 2015, 63, 4646−4654

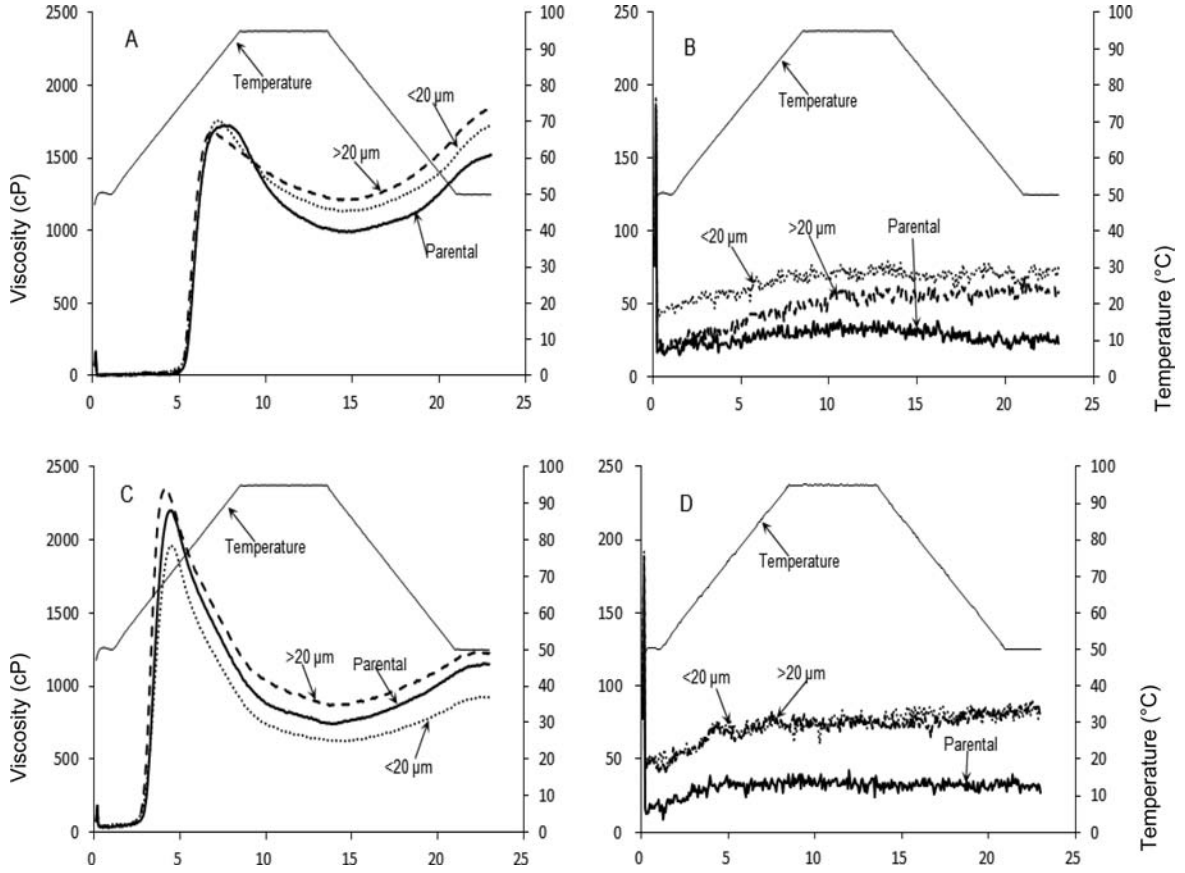

Figure 2. RVA profiles of (A) native, (B) cross-linked, (C) hydroxypropylated, and (D) dual-modified (cross-linking combined with hydroxypropylation) sweet potato starch at a concentration of 7% in water before and after sieving of 20 μm. Parental, unfractionated starch; >20 μm, large-size granule fraction; and <20 μm, small-size granule fraction.

hydroxypropyl-modified granules. This indicated that the change of the transition temperature and enthalpy of gelatinization after dual modification predominantly resulted mainly from the hydroxypropylation.

Pasting Properties of Starches. The pasting curves of native sweet potato starch showed a high peak viscosity and rapid shear thinning at high temperatures (Figure 2A). The peak viscosity of the large-size granule fraction is slightly lower than that of the small-size granule fraction, probably because of the lower phosphorus and lower amylopectin content of the large-size granule fraction (Table 1). The viscosity of the parental starch was lower than that of the large- and small-size granule fractions, which was also found for potato starch.[29] This may be due to an optimal packing of small and large granules in the parental starch paste, resulting in a lower viscosity.

The pasting curve of cross-linked starches expressed a low but stable viscosity (20−80 cP) and no obvious pasting peak (Figure 2B). The large-size granule fraction had the higher degree of cross-linking than the small-size granule fraction, resulting in even a lower pasting viscosity. This indicates that the viscosity of starch paste is sensitive to the degree of cross-linking.

As expected, it was found that the hydroxypropylation increased the peak viscosity and decreased the trough and final viscosity of starch pasting (Figure 2C). The introduction of hydroxypropyl groups increased the hydrophilicity of starch molecules, resulting in swelling to a greater extent, creating a high peak viscosity.[3,12] The large-size granule fraction showed a higher viscosity than the small-size granule fraction, probably because of the slightly higher level of hydroxypropylation. The parental hydroxypropylated starch showed a viscosity profile just between the profiles of the large- and small-size granule fractions.

The dual-modified starches showed similar profiles to the cross-linked starch with very low viscosities (Figure 2D). This indicated that the effect of cross-linking on the viscosity was more predominant than that of hydroxypropylation. Furthermore, no difference in viscosity was found between the large- and small-size granule fractions. This may be due to the combination of counteracting effects of cross-linking and hydroxypropylation on viscosity.

Swelling Power of Starches. The swelling power of the large- and small-size granule fractions of starches was measured in water at various temperatures. The results showed that the swelling power of native and modified sweet potato starches decreased in the order: hydroxypropylated > native > dual-modified > cross-linked starches (Figure 3).

The small-size granule fractions of hydroxypropylated sweet potato starch showed a slightly higher swelling power than the large-size granule fraction and parental starch fraction, indicating that the higher amylopectin content in the small-size granule fraction increases the swelling power more than the hydroxypropylation. The swelling power of the parental hydroxypropylated starch was lower than that of sieved starch fractions. Swelling power indicates the extent of water absorption and volume expansion of the starch granules. The volume includes the starch granule itself and the interspace between swollen granules. It is probable that the volume of

DOI: 10.1021/jf506349w
J. Agric. Food Chem. 2015, 63, 4646−4654

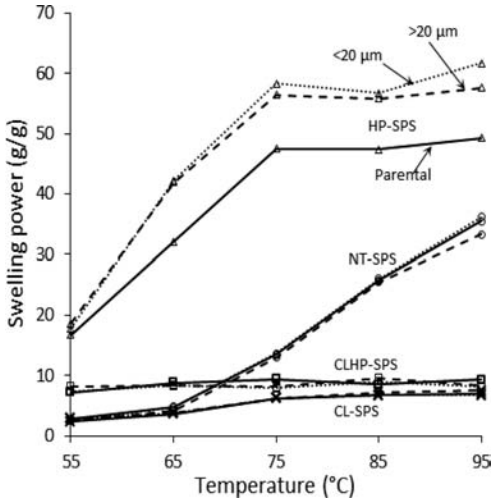

Figure 3. Swelling power of native (NT-SPS), cross-linked (CL-SPS), hydroxypropylated (HP-SPS), and dual-modified (cross-linked and hydroxypropylated, CLHP-SPS) sweet potato starches at various temperatures. Parental, unfractionated starch; >20 μm, large-size granule fraction; and <20 μm, small-size granule fraction.

interspace between granules affects the swelling power. Parental starch has a heterogeneous size of starch granules, where small granules may fill in the interspace between large granules, leading to a relatively small total volume and small total weight increase compared to the same dry weight of more uniform starch granules.

The cross-linked as well as the dual-modified starch showed a lower swelling power than the native starch. There was not a significant difference in swelling power between the large- and small-size granule fractions of cross-linked starch.

The swelling tendency of sweet potato starch in different granule size fractions is different from that reported for wheat starch, in which the small-size fraction had the lowest swelling power. Most likely, this can be explained by the high level of amylose−lipid complexes present in the small-size fraction of wheat starch.[30]

Effects of Starch Modification on the Refrigeration and Freeze−Thaw Properties. Low-temperature storage stability involves the sensitivity of starch to retrogradate when cooling and stored, in which the process may result in syneresis of the starch gel, resulting in excluded water from the gel. In our experiment, we used 6% starch pastes heated at 95 °C, before subjecting the gel to the storage conditions. As a consequence of the swelling power of the parental and modified

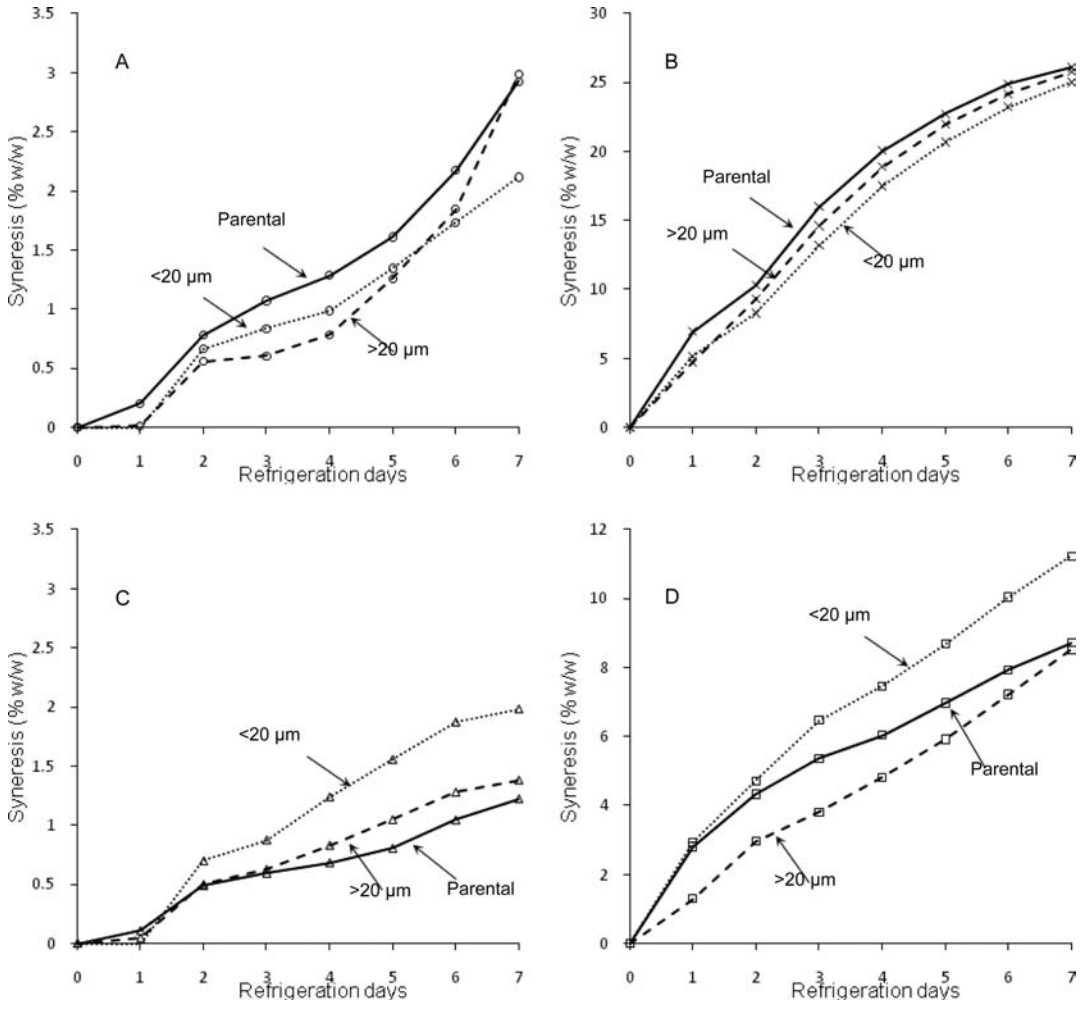

Figure 4. Refrigerator storage stability of different granule size fractions of (A) native, (B) cross-linked, (C) hydroxypropylated, and (D) dual-modified (cross-linking combined with hydroxypropylation) sweet potato starch. Parental, unfractionated starch; >20 μm, large-size granule fraction; and <20 μm, small-size granule fraction.

DOI: 10.1021/jf506349w
J. Agric. Food Chem. 2015, 63, 4646−4654

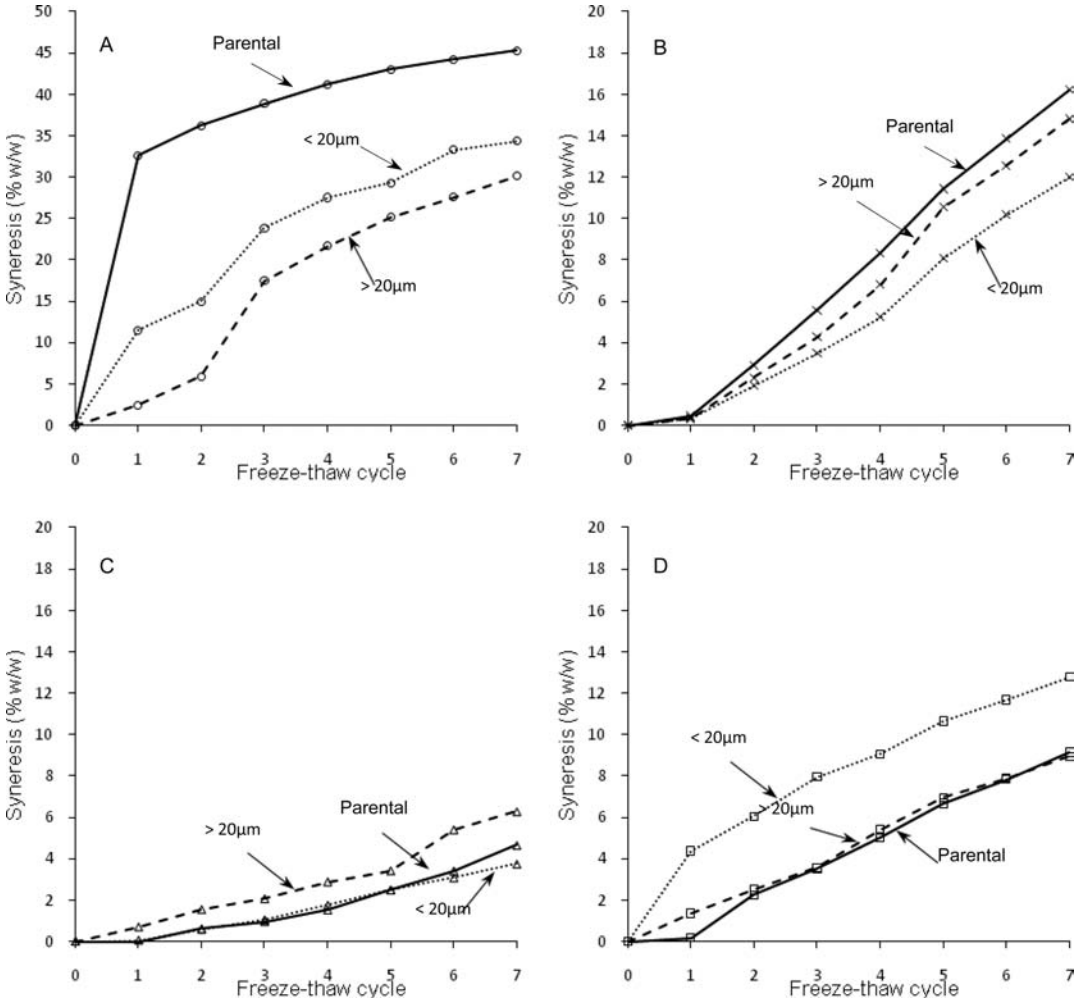

Figure 5. Freeze−thaw stability of different granule size fractions of (A) native, (B) cross-linked, (C) hydroxypropylated, and (D) dual-modified (cross-linking combined with hydroxypropylation) sweet potato starches. Parental, unfractionated starch; >20 μm, large-size granule fraction; and <20 μm, small-size granule fraction.

starches (Figure 3), the gelatinized parental starch granules will fill the available volume of water rather completely, while the cross-linked starch will be far from a close packing because of the lower swelling power. Hydroxypropylation of the starch will not influence the packing enormously, although the hydroxypropyl groups will prevent a rapid interaction between the molecules, preventing the retrogradation process.[31] Storage under refrigerator conditions at 4 °C lead to some syneresis for the parental starch (Figure 4A), while there is significantly more water expulsed from the cross-linked starch (Figure 4B). Because the retrogradation is a concentration-dependent process, the close packing of the parental starch molecules will not change dramatically, leading to a minor release of water only. In contrast, the cross-linked starch, having a considerably higher starch concentration within swollen granules, will retrogradate rather easily, and syneresis is significant (Figure 4B; up to 26%). Hydroxypropylation leads to less syneresis of the singly modified starch (Figure 4C) compared to the parental starch and corrects the enormous water exclusion of the cross-linked starch to a great extent for the dual-modified starch (Figure 4D). This effect has been described before for corn and amaranth starches.[31]

When considering the freeze−thaw effect, the syneresis observed for the various starches is quite different (panels A−D of Figure 5). Under these conditions, the parental starch shows the highest syneresis of all starches, followed by the cross-linked starch, while hydroxypropylation stabilized the starch gel during the freeze−thawing process significantly. During the freezing step, ice crystals will be formed progressively and the remaining starch phase will gradually enrich in starch. A higher starch concentration persists throughout the freeze−thaw process until the melting is complete. The retrogradation will be enhanced during freezing and thawing stages. Because of the high effective starch concentration, considerable retrogradation happened during the thawing process, resulting in the syneresis behavior, as seen in Figure 5A. Cross-linked starch is affected less by the freezing process. Although the enrichment of starch in the starch phase is expected to be roughly similar to the native starch, the cross-links clearly offer some protection against syneresis (compare panels A and B of Figure 5). The effect of hydroxypropyl substitution is clear, in both native and cross-linked starches. Obviously, the hydroxypropyl groups are quite effective in suppressing retrogradation during the freezing and thawing stages (panel A versus panel C of Figure 5 and panel B versus panel D of Figure 5).

Effects of Granule Size on the Refrigeration and Freeze−Thaw Properties. Obviously, the same considerations on the effective concentration of the starch gels are valid

DOI: 10.1021/jf506349w
J. Agric. Food Chem. 2015, 63, 4646−4654

Table 3. Effects of the Granular Size on the Sweet Potato Starch Physical Properties[a]

starch	NT-SPS	HP-SPS	CL-SPS	CLHP-SPS
granules showing higher viscosity	>20 μm	>20 μm	<20 μm	no difference
difference at the trough of the viscosity curve (cP)	78	244	14	0
relative difference (%)	7	39	30	0
granules showing better freeze−thaw stability	>20 μm	<20 μm	<20 μm	>20 μm
difference at cycle 4	5.8	1.1	2.4	3.7
relative difference (%)	27	64	28	69
granules showing better cold storage stability	>20 μm	>20 μm	<20 μm	>20 μm
difference at 4 days (%)	0.2	0.4	1.4	2.7
relative difference (%)	25	50	8	36

[a]Relative difference is the relative percentage of difference of property between large- and small-granule fractions to the average of property between large- and small-granule fractions. NT, native; CL, cross-linked; HP, hydroxypropylated; CLHP, cross-linked and hydroxypropylated; and SPS, sweet potato starch.

when looking at the effect of the granule size toward the cold storage and freeze−thaw stability in the gels. Other parameters influencing gel properties of starches and which may be different for the different size fractions are the phosphorus content of the parental size fraction and the levels of cross-linking and hydroxypropylation (Table 1). As reported before, the amylose content of small-sized (19.2%) and large-sized (19.7%) fractions are slightly different.[20] The cold storage and freeze−thaw stability of the starch gels from the size fraction can be seen in Figures 4 and 5, respectively. Both the large-size and small-size starch fractions showed a better stability compared to the parental starch. The lower syneresis for the large-size granules during the freeze−thawing process when compared to the small-size fractions has also been seen before[8] but cannot easily be explained because a higher amylose content and a lower phosphorus content are found for these larger granules (Table 1). As expected from these same starch parameters, the stability during cold storage of the large granules is lower than that found for the small-size granule at the end of 7 cycles. However, this is not the case for earlier cycles (Figure 4A), and this observation cannot be explained. The better stability for the dual-modified large-size fraction (Figures 4D and 5D) seemed to be a consequence of the higher hydroxypropylated content, which counteracts the lower degree of cross-linking. For cross-linked starches, the better stability of the small granules (Figures 4B and 5B) can be governed by the lower level of cross-linking compared to large granules. The higher hydroxypropyl content of large-size granules of hydroxypropylated (Table 1) starch does only explain the better refrigeration stability (Figure 4C) but not its poorer freeze−thaw stability (Figure 5C).

A summary of starch granule size, type of starch modification, and physicochemical characteristics is given in Table 3. As discussed above and as seen from this table, the functional differences between different size populations are quite diverse, making it rather difficult to assign them to specific structural characteristics. In general, it can be stated that large-sized granules are more sensitive to modification reactions than small granules, but no generic prediction can be made for specific benefits for a given application.

AUTHOR INFORMATION

Corresponding Author

*Telephone: +31-317-482239. E-mail: henk.schols@wur.nl.

Funding

This work was supported by the Royal Netherlands Academy of Arts and Sciences (KNAW, Grant 08CDP019), the International Science and Technology Cooperation Program (Grant 2007DFA31120, China), and the AVEBE Food Innovation Centre.

Notes

The authors declare no competing financial interest.

REFERENCES

(1) Mason, W. R. Starch use in foods. In *Starch: Chemistry and Technology*, 3rd ed.; BeMiller, J., Whistler, R., Eds.; Academic Press: Burlington, MA, 2009; pp 745−795.

(2) Gunaratne, A.; Corke, H. Effect of hydroxypropylation and alkaline treatment in hydroxypropylation on some structural and physicochemical properties of heat-moisture treated wheat, potato and waxy maize starches. *Carbohydr. Polym.* **2007**, *68*, 305−313.

(3) Singh, J.; Kaur, L.; McCarthy, O. J. Factors influencing the physico-chemical, morphological, thermal and rheological properties of some chemically modified starches for food applications—A review. *Food Hydrocolloids* **2007**, *21*, 1−22.

(4) Lebot, V. *Tropical Root and Tuber Crops: Cassava, Sweet Potato, Yams and Aroids*; CAB International: Wallingford, U.K., 2009.

(5) Chen, Z.; Schols, H. A.; Voragen, A. G. J. Physicochemical properties of starches obtained from three varieties of Chinese sweet potatoes. *J. Food Sci.* **2003**, *68*, 431−437.

(6) Kim, B. Y.; Yoo, B. Effects of cross-linking on the rheological and thermal properties of sweet potato starch. *Starch-Starke* **2010**, *62*, 577−583.

(7) Lee, H. L.; Yoo, B. Effect of hydroxypropylation on physical and rheological properties of sweet potato starch. *Lwt-Food Science and Technology* **2011**, *44*, 765−770.

(8) Chen, Z.; Schols, H. A.; Voragen, A. G. J. Starch granule size strongly determines starch noodle processing and noodle quality. *J. Food Sci.* **2003**, *68*, 1584−1589.

(9) Peng, M.; Gao, M.; Abdel-Aal, E. S. M.; Hucl, P.; Chibbar, R. N. Separation and characterization of A- and B-type starch granules in wheat endosperm. *Cereal Chem.* **1999**, *76*, 375−379.

(10) Huang, J. R.; Schols, H. A.; Jin, Z. Y.; Sulmann, E.; Voragen, A. G. J. Characterization of differently sized granule fractions of yellow pea, cowpea and chickpea starches after modification with acetic anhydride and vinyl acetate. *Carbohydr. Polym.* **2007**, *67*, 11−20.

(11) Zhao, J.; Schols, H. A.; Chen, Z.; Jin, Z.; Buwalda, P.; Gruppen, H. Substituent distribution within cross-linked and hydroxypropylated sweet potato starch and potato starch. *Food Chem.* **2012**, *133*, 1333−1340.

(12) Gunaratne, A.; Corke, H. Functional properties of hydroxypropylated, cross-linked, and hydroxypropylated cross-linked tuber and root starches. *Cereal Chem.* **2007**, *84*, 30−37.

(13) Collado, L. S.; Corke, H. Heat-moisture treatment effects on sweetpotato starches differing in amylose content. *Food Chem.* **1999**, *65*, 339−346.

(14) Lee, H. L.; Yoo, B. Dynamic rheological and thermal properties of acetylated sweet potato starch. *Starch-Starke* **2009**, *61*, 407−413.

DOI: 10.1021/jf506349w
J. Agric. Food Chem. 2015, 63, 4646−4654

(15) Yeh, A. I.; Yeh, S. L. Some characteristics of hydroxypropylated and cross-linked rice starch. *Cereal Chem.* **1993**, *70*, 596−601.
(16) Noda, T.; Takigawa, S.; Matsuura-Endo, C.; Suzuki, T.; Hashimoto, N.; Kottearachchi, N. S.; Yamauchi, H.; Zaidul, I. S. M. Factors affecting the digestibility of raw and gelatinized potato starches. *Food Chem.* **2008**, *110*, 465−470.
(17) Srichuwong, S.; Sunarti, T. C.; Mishima, T.; Isono, N.; Hisamatsu, M. Starches from different botanical sources I: Contribution of amylopectin fine structure to thermal properties and enzyme digestibility. *Carbohydr. Polym.* **2005**, *60*, 529−538.
(18) Lim, S. T.; Kasemsuwan, T.; Jane, J. L. Characterization of phosphorus in starch by ^{31}P-nuclear magnetic-resonance spectroscopy. *Cereal Chem.* **1994**, *71*, 488−493.
(19) Jane, J. L.; Shen, J. J. Internal structure of the potato starch granule revealed by chemical gelatinization. *Carbohydr. Res.* **1993**, *247*, 279−290.
(20) Chen, Z.; Schols, H. A.; Voragen, A. G. J. Differently sized granules from acetylated potato and sweet potato starches differ in the acetyl substitution pattern of their amylose populations. *Carbohydr. Polym.* **2004**, *56*, 219−226.
(21) Jane, J.; Kasemsuwan, T.; Chen, J. F.; Juliano, B. O. Phosphorus in rice and other starches. *Cereal Foods World* **1996**, *41*, 827−832.
(22) Hirsch, J. B.; Kokini, J. L. Understanding the mechanism of cross-linking agents (POCl3, STMP, and EPI) through swelling behavior and pasting properties of cross-linked waxy maize starches. *Cereal Chem.* **2002**, *79*, 102−107.
(23) Kavitha, R.; BeMiller, J. N. Characterization of hydroxypropylated potato starch. *Carbohydr. Polym.* **1998**, *37*, 115−121.
(24) Stapley, J. A.; BeMiller, J. N. Hydroxypropylated starch: Granule subpopulation reactivity. *Cereal Chem.* **2003**, *80*, 550−552.
(25) Kaur, L.; Singh, J.; Singh, N. Effect of cross-linking on some properties of potato (*Solanum tuberosum* L.) starches. *J. Sci. Food Agric.* **2006**, *86*, 1945−1954.
(26) Singh, N.; Kaur, L. Morphological, thermal, rheological and retrogradation properties of potato starch fractions varying in granule size. *J. Sci. Food Agric.* **2004**, *84*, 1241−1252.
(27) Chiotelli, E.; Le Meste, M. Effect of small and large wheat starch granules on thermomechanical behavior of starch. *Cereal Chem.* **2002**, *79*, 286−293.
(28) Schirmer, M.; Hochstotter, A.; Jekle, M.; Arendt, E.; Becker, T. Physicochemical and morphological characterization of different starches with variable amylose/amylopectin ratio. *Food Hydrocolloids* **2013**, *32*, 52−63.
(29) Fortuna, T.; Januszewska, R.; Juszczak, L.; Kielski, A.; Palasinski, M. The influence of starch pore characteristics on pasting behaviour. *Int. J. Food Sci. Technol.* **2000**, *35*, 285−291.
(30) Van Hung, P.; Morita, N. Physicochemical properties of hydroxypropylated and cross-linked starches from A-type and B-type wheat starch granules. *Carbohydr. Polym.* **2005**, *59*, 239−246.
(31) Pal, J.; Singhal, R. S.; Kulkarni, P. R. Physicochemical properties of hydroxypropyl derivative from corn and amaranth starch. *Carbohydr. Polym.* **2002**, *48*, 49−53.

DOI: 10.1021/jf506349w
J. Agric. Food Chem. 2015, 63, 4646−4654

JOURNAL OF AGRICULTURAL AND FOOD CHEMISTRY

Article

pubs.acs.org/JAFC

Inhibition of Palm Oil Oxidation by Zeolite Nanocrystals

Kok-Hou Tan,[†,∥] Hussein Awala,[‡,∥] Rino R. Mukti,[§] Ka-Lun Wong,[⊥] Baptiste Rigaud,[‡] Tau Chuan Ling,[#] Hristiyan A. Aleksandrov,[Δ] Iskra Z. Koleva,[Δ] Georgi N. Vayssilov,[Δ] Svetlana Mintova,*[,‡] and Eng-Poh Ng*[,†]

[†]School of Chemical Sciences, Universiti Sains Malaysia, Penang, Malaysia

[‡]Laboratoire Catalyse & Spectrochimie, CNRS-ENSICAEN, Université de Caen, Caen, France

[§]Division of Inorganic and Physical Chemistry, Institut Teknologi Bandung, Bandung, Indonesia

[⊥]National Institute of Education, Nanyang Technological University, Singapore

[#]Institute of Biological Sciences, Faculty of Science, University of Malaya, Kuala Lumpur, Malaysia

[Δ]Faculty of Chemistry and Pharmacy, University of Sofia, Sofia, Bulgaria

Supporting Information

ABSTRACT: The efficiency of zeolite X nanocrystals (FAU-type framework structure) containing different extra-framework cations (Li^+, Na^+, K^+, and Ca^{2+}) in slowing the thermal oxidation of palm oil is reported. The oxidation study of palm oil is conducted in the presence of zeolite nanocrystals (0.5 wt %) at 150 °C. Several characterization techniques such as visual analysis, colorimetry, rheometry, total acid number (TAN), FT-IR spectroscopy, ^{1}H NMR spectroscopy, and Karl Fischer analyses are applied to follow the oxidative evolution of the oil. It was found that zeolite nanocrystals decelerate the oxidation of palm oil through stabilization of hydroperoxides, which are the primary oxidation product, and concurrently via adsorption of the secondary oxidation products (alcohols, aldehydes, ketones, carboxylic acids, and esters). In addition to the experimental results, periodic density functional theory (DFT) calculations are performed to elucidate further the oxidation process of the palm oil in the presence of zeolite nanocrystals. The DFT calculations show that the metal complexes formed with peroxides are more stable than the complexes with alkenes with the same ions. The peroxides captured in the zeolite X nanocrystals consequently decelerate further oxidation toward formation of acids. Unlike the monovalent alkali metal cations in the zeolite X nanocrystals (K^+, Na^+, and Li^+), Ca^{2+} reduced the acidity of the oil by neutralizing the acidic carboxylate compounds to $COO^-(Ca^{2+})_{1/2}$ species.

KEYWORDS: *palm oil, oxidation, inhibition, zeolite nanocrystals, extra-framework cations*

INTRODUCTION

The overwhelming palm oil global production (30% of global vegetable oil output) and trade volume (60% of global exports) are due to its cheaper production cost and nontoxic nature. Palm oil has been utilized as a base oil in formulating lubricants due to its favorable viscosity−temperature characteristics, high flash point, and compatibility with mineral oil and additive molecules.[1,2] However, the low thermal and oxidative stabilities, poor low-temperature fluidity, and hydrolytic instability limit the use of palm oil as a long-life cooking oil for deep-frying culinary purposes. Previous studies have reported that heated cooking oils may pose health risks to consumers due to the generation of oil oxidation products.[3−5] Although natural antioxidants can improve the oxidation stability of vegetable oil, their performances are usually heavily rely on the oil composition, heating temperature, and presence of other additives.[6] Thus, thermally stable, low-cost, and environmentally safe antioxidant additives are desired to replace the traditional antioxidants in inhibiting oil oxidation, particularly in the food industry.

Zeolites are aluminosilicate microporous solids with well-defined pores and cages, which are commonly used as heterogeneous catalysts, ion exchangers, and adsorbents. In our previous investigation, zeolite nanocrystals (NCs) were used as selective adsorbents for oil purification.[7−9] This was based on the fact that zeolite molecular sieves with electrostatic charged frameworks tend to adsorb and trap polar compounds (e.g., moisture contaminant and carbonyl oxidized products) in the pores of zeolites without interacting with the nonpolar oil molecules. As a result, the oxidized mineral oil after purification can be recycled and reused with longer service lifetimes. Recently, the use of zeolite NCs as an ecofriendly antioxidant additive was also reported.[10,11] Zeolite NCs with different framework type structures (LTL, EMT, and FAU) were found to possess distinctive antioxidation behavior in palm oil during oxidation at high temperature (180 °C) for a long period of time (40 days).[10,11] It was shown that the delay of oxidation progress is the result of free radical inactivation, C═C bond stabilization, and also adsorption of polar primary (hydroperoxides) and secondary (carboxylic acids) oxidation products, which are greatly dependent on the hydrophilicity, pore openings, and framework type of the zeolites.

Received: January 22, 2015
Revised: March 14, 2015
Accepted: April 21, 2015
Published: April 21, 2015

ACS Publications © 2015 American Chemical Society

DOI: 10.1021/acs.jafc.5b00380
J. Agric. Food Chem. 2015, 63, 4655−4663

Contrary to the well-understood mechanism of chemical reactions contributed by protonated forms of zeolites (Brönsted acids), the chemical properties in cation-exchanged zeolites remain the subject of intense study. The extra-framework cations are compensating the negatively charged framework of zeolites, and they are reactive and readily interact with a variety of guest molecules.[12,13] This is due to the van der Waals and Coulombic interactions between the extra-framework cations and guest molecules. The charge, polarizability, deformation ability, and influence of non-framework cations on the homogeneity of the framework electric field will eventually affect the sorption and stabilization of diffused species because these cations are capable of generating strong local electrical fields. Thus, attracting the negative centers of polar molecules and polarizing or deforming the polarizable molecules through static electric induction was observed.[14,15]

Synthetic high alumina-containing zeolites (FAU, LTA) having alkali and alkaline earth metals as extra-framework cations have been extensively studied and mainly used as selective adsorbents and for separation of oxygen from air. However, the effect of these cation-exchanged zeolites in oil oxidation has not been investigated. On the other hand, it has been shown that nanosized zeolites prepared via a template-free synthesis method do not cause toxicity under cell viability and cell life cycle studies (evaluation of living or dead cells due to toxins was reported).[16] Hence, these zeolites prepared from template-free precursor suspensions can be considered as additives in palm oil. Furthermore, nanosized zeolites can be incorporated in membranes or deposited as thin films on culinary tools for deep-frying, apart from being added directly into the cooking oil.

Herein, we report the influence of extra-framework cations in nanosized FAU type zeolite (X type) on the oxidation process of palm oil. Nanosized zeolite X samples with four different types of extra-framework cations (Li^+, Na^+, K^+, and Ca^{2+}) are prepared and added as additives during the thermal oxidation of palm oil. The oil oxidative evolution is then characterized and followed by various analytical methods. In addition, periodic DFT calculations are performed to clarify the effect of extra-framework cations on the chemical interactions and binding energy during host−guest interactions.

EXPERIMENTAL PROCEDURES

Synthesis and Ion Exchange of Zeolite Nanocrystals. The sodium form of zeolite X (Na-X) nanocrystals (ca. 20 nm) was synthesized without organic template.[17] The Li-, K-, and Ca-X NCs were prepared through ion exchange method. Typically, 1.50 g of zeolite powder was stirred in 100 mL of nitrate solution of the targeted metal cations (0.50 mol/L) at 60 °C for 6 h. The process was repeated five times by separating supernatant from the mother liquid, redispersing in metal nitrate solution, and carrying on with aforementioned ion exchange process to ensure that the highest possible ion exchange was achieved. The samples after ion exchange were washed thoroughly (pH 7.5) prior to freeze-drying.

Oxidation of Palm Oil. Zeolite nanocrystals (0.250 g, equivalent to 0.5 wt %) were activated at 180 °C overnight prior to addition into 50.00 g of palm oil. The oxidation process was carried out at 150 °C under continuous stirring (300 rpm) and reflux; the oil samples were periodically collected after 100, 200, 300, and 400 h. The zeolite NCs were recovered from the oils via centrifugation (25000 rpm, 2 h). For comparison, a similar amount of palm oil (50.00 g) without zeolite NCs was also oxidized at the same oxidation conditions and denoted as a reference sample (reference).

Characterization. The X-ray diffraction (XRD) patterns of zeolite samples were recorded using a PANalytical X'Pert PRO XRD diffractometer. The morphology of the as-synthesized and ion-exchanged zeolite NCs was evaluated by field emission scanning electron microscope (FE-SEM) using a Leo Supra 50VP with an accelerating voltage of 30 kV. The porosity of the samples was determined by nitrogen sorption with a Micromeritics ASAP 2010 instrument. The chemical composition of all zeolite samples was measured by induced couple plasma using an Agilent 720 series ICP-OES spectrometer. The IR spectra of zeolites were recorded using a PerkinElmer 3000 FTIR spectrophotometer. The thermal stability of the zeolites was measured using a Mettler TGA SDTA851 instrument with a heating rate of 10 °C/min under nitrogen flow.

Evaluation of the Oxidation Degree of Palm Oil. Visual analysis of oil samples was carried out by following their color change after 100, 200, 300, and 400 h of oxidation at 150 °C. Colorimetric measurements of oil samples were performed using a Shimadzu UV 3000 spectrophotometer at 530 nm; fresh palm oil was used as a reference. Two measurements were made for each oil sample, and no difference was observed. Qualitative information for the formation of carbonyl compounds, hydroperoxides, and moisture in the oil samples was obtained by recording the IR spectra. The IR measurements (50 scans, 4 cm^{-1}) were performed on 0.5 mL of oil introduced in a ZnSe liquid cell (1 mm spacer).

The rheological behavior of the oils was investigated by a Malvern Kinexus rheometer. The analysis was performed twice for each sample, and the average values were used for plotting the results. The amount of moisture and organic compounds adsorbed by the zeolite nanocrystals was measured by a Mettler TGA SDTA851 instrument with a heating rate of 10 °C/min under air flow.

The water content in oil was measured using a volumetric Karl Fischer titrator. The Karl Fischer titration system (Metrohm) was charged with Hydranal Composite-2 reactant (Riedel-de Häan) and Hydranal Solvent CM (Riedel-de Häan). All samples were analyzed twice to obtain average values by direct injection without preliminary treatment.

The potassium hydroxide (KOH) titrimetric method was applied to determine the total acid number (TAN) of the oil samples. Typically, 0.200 g of oil was mixed with 2.000 g of a mixture containing water/isopropanol/toluene with a molar ratio equal to 1:30:20, followed by the addition of 3 drops of phenolphthalein indicator. The resulting solution was titrated with 0.01 mol/L ethanolic KOH solution until a color change was observed. The results were recorded, and the TAN was calculated as milligrams of KOH per gram of oil using the equation

$$\text{TAN (mg KOH/g oil)} = \frac{V \times M \times M_r}{m} \quad (1)$$

where V is the volume (mL) and M is the molarity (mol/L) of the ethanolic KOH solution, M_r is the molar mass of KOH (g/mol), and m is the mass (g) of the oil sample. Two titrations of each oil sample were performed.

^{1}H NMR analyses were performed using a Bruker AVIII spectrometer operating at a frequency of 500 MHz with the following acquisition parameters: pulse sequence, zg30; acquisition time, 3.17 s; relaxation delay, 5 s; pulse width, 30° for 512 scans. Prior to analysis, the oil samples were dissolved in deuterated chloroform ($CDCl_3$) (mass ratio of zeolite/ $CDCl_3$ = 1:3); tetramethylsilane (TMS) was used as an internal standard.

DFT Modeling of the Interaction of Absorbates with Metal Ions in Zeolite Nanocrystals. Periodic density functional theory (DFT) calculations were performed with the PW91 exchange-correlation functional[18] using a Vienna ab initio simulation package (VASP).[19,20] Ultrasoft pseudopotentials were used as implemented in the VASP package.[21,22] Due to the large unit cell of the zeolites, the Brillouin zone was sampled using only the Γ point.[23] The valence wave functions were expanded in a plane-wave basis with a cutoff energy of 400 eV.

The unit cell of the cubic FAU type zeolite was optimized using a pure silica structure with dimensions $a = b = c = 24.345$ Å.[24] During the geometry optimization, all of the zeolite atoms and the adsorbate species were allowed to relax until the force on each atom was <2 ×

DOI: 10.1021/acs.jafc.5b00380
J. Agric. Food Chem. 2015, 63, 4655−4663

10^{-4} eV/pm. The binding energy (BE) of the adsorbates hydroperoxides (C_2H_5OOH and HOOH) and alkenes including ethene (C_2H_4) and *cis*-butene (C_4H_8) per ligand was determined as

$$\mathrm{BE\ [adsorbate/Zeo]} = (E[\mathrm{adsorbate/Zeo}] - E[\mathrm{Zeo}] - E[\mathrm{adsorbate}])$$

where E[adsorbate/Zeo] is the energy of the zeolite together with the adsorbed molecule in the optimized geometry; E[Zeo] and E[adsorbate] are the energies of the pure zeolite and pure adsorbate molecule in the gas phase, respectively. With the above definition, the negative values of BE imply favorable interactions.

RESULTS AND DISCUSSION

Ion-Exchanged Zeolite Nanocrystals. The degree of crystallinity and phase purity of FAU zeolite NCs are characterized by XRD. The XRD patterns of all zeolite samples show that the peaks' intensity remains intact and no phase transformation occurs, revealing that the degree of crystallinity and phase purity do not change after ion exchange (see the Supporting Information, Figure S1). Besides, the FE-SEM analyses reveal that the size and morphology of zeolite NCs remain stable after ion exchange. All of the crystals have a narrow particle size distribution and diameter of 20−40 nm (Figure 1).

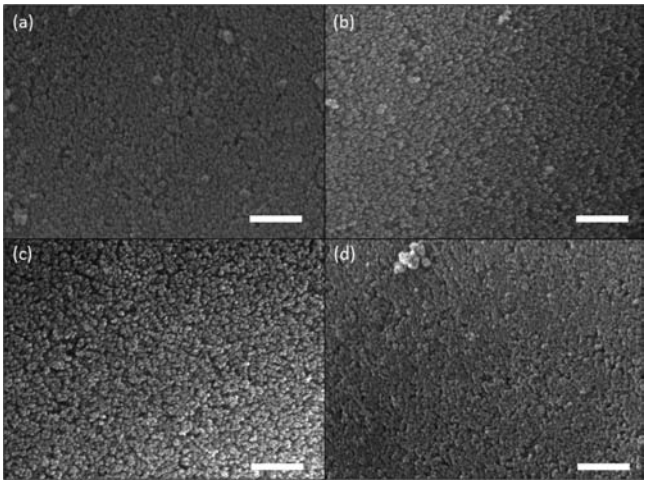

Figure 1. SEM images of (a) Li-X, (b) Na-X, (c) K-X, and (d) Ca-X zeolite nanocrystals. Scale bar = 500 nm.

The schematic structure of zeolite X and the potential positions (I, I′, II, II′, III, and III′) to be occupied by its charge compensating cations are shown in Figure S2, and the results from the chemical analysis of zeolite NCs exchanged with alkali metal and alkali earth metal cations are also listed (Table S1). As can be seen, zeolite X with the FAU framework topology contains pores with a size of 0.74 nm and supercages made up of sodalite cage connected via double 6-rings. The zeolite X nanocrystals have a Si/Al ratio of ca. 1.3. After five cycles of ion exchange at 60 °C, the Li-X, K-X, and Ca-X zeolites are successfully prepared while keeping the same Si/Al ratio. In all cases, not 100% exchange of Na^+ is attained (Table S1). The highest degree of exchange of Na-X is achieved for Ca^{2+} (88%), followed by K^+ (86%) and Li^+ (74%). Their different ionic radiuses of univalent and divalent cations explain the various degrees of ion exchange of Na^+ in zeolite X.[25] On the other hand, Li-X has the lowest degree of ion exchange, which can be due to its high hydration energy, high mobility, and low occupancy of certain sites.[26−28]

The porosity of zeolite nanocrystals after ion exchange was probed by N_2 sorption analysis. All samples exhibit type I isotherm at low P/P_0, which is characteristic for microporous materials (Figure 2). A high adsorption uptake at $P/P_0 > 0.8$ is

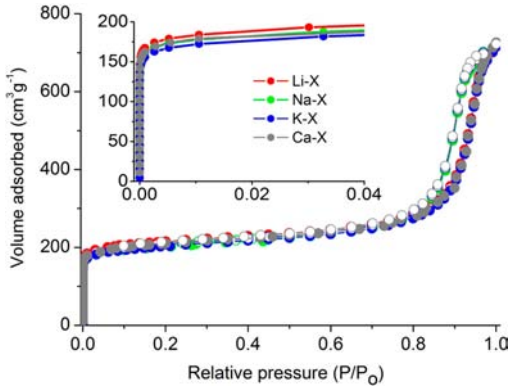

Figure 2. Nitrogen adsorption (solid symbols) and desorption (open symbols) isotherms of zeolites Li-X, Na-X, K-X, and Ca-X.

due to the textural mesoporosity resulting from the close packing of zeolite NCs. From the N_2 sorption isotherms, it can be seen that the N_2 uptake at low P/P_0 is inversely proportional to the size of cations (Table S1; inset of Figure 2). As a result, Li-X zeolite exhibits the highest BET surface area and pore volumes (both V_{micro} and V_{meso}), whereas the K-X zeolite containing the larger cation K^+ (1.33 Å) gives the lowest porosity (Tables S1 and S2). Ca^{2+} (0.99 Å) is almost similar to Na^+ (0.97 Å) in size, but Ca^{2+} is a divalent ion and the amount of Ca^{2+} in the Ca-X zeolite is lower. As a result, a slightly increased surface area and pore volume are measured for the Ca-X zeolite. Thus, the results from nitrogen sorption are in agreement with the chemical analysis data, demonstrating that the porosity is slightly affected by the size and number of cations introduced into zeolite X via ion exchange.

Characterization of Palm Oil Oxidation. *Color Change and Colorimetry Analysis of Palm Oil.* Color change is a simple indication of oil degradation. Basically, the reference oil containing no zeolites shows faster color change where the oil color progressively turns from yellow to amber, dark brown, and finally black color as the severity of the oxidation conditions was increased with time (photograph not shown here). The reference oil sample also has a strong smell resulting from volatile organic acids or carbonyl compounds, showing that the oil is degraded. The appearance of oil samples containing zeolite NCs (Na-, Li-, K-, and Ca-X) as a function of oxidation time is shown in Figure 3. As can be seen, the oils oxidized with zeolites have brighter color, highly basic K-X displaying the brightest color even after 400 h of oxidation. The color change was also found to follow the polarizability/basicity of the cations present in zeolite X: $Li^+ < Na^+ < Ca^{2+} < K^+$.

The oxidative deterioration of palm oil is always associated with a darkening effect. Some organic substances are responsible for the development of color in oil during autoxidation. For example, the oxidation of carotene, which naturally exists in palm oil, can cause increasing red and yellow colors in vegetable oils.[29] Apart from carotene, high molecular weight compounds are also accountable for the color change of palm cooking oil.[6]

The color change was also characterized quantitatively using colorimetry at wavelength λ = 530 nm, where the signal at this

DOI: 10.1021/acs.jafc.5b00380
J. Agric. Food Chem. 2015, 63, 4655−4663

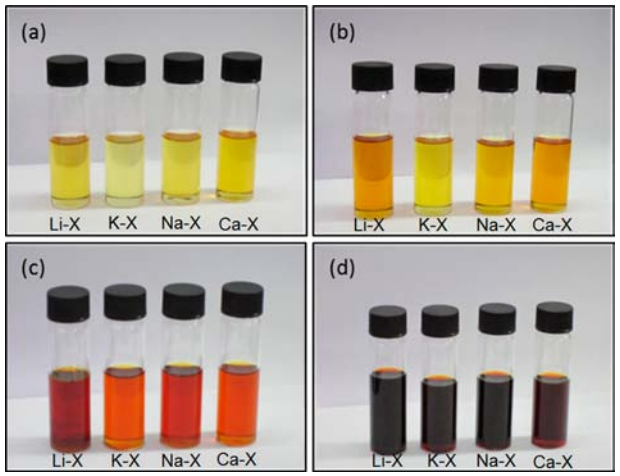

Figure 3. Color change of palm oil with increasing oxidation time: (a) 100 h; (b) 200 h; (c) 300 h; (d) 400 h.

wavelength is strongly influenced by the degree of oil deterioration.[30]

As observed by visual analysis, the reference oil evidenced a fast increment in light absorption, and the absorbance value increased tremendously from 3.49 (at 200 h) to 47.11 (at 400 h) (Figure 4). The addition of zeolite NCs to the palm oil

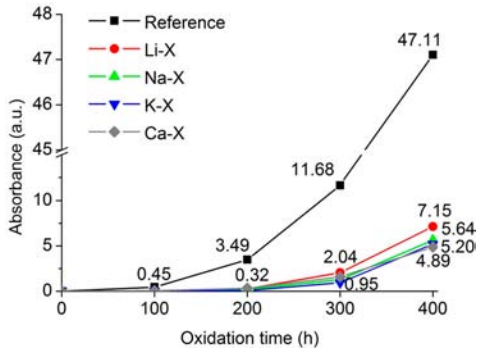

Figure 4. Colorimetric evaluation of palm oil samples oxidized with and without zeolites Li-X, K-X, Na-X, and Ca-X.

lowered significantly the level of oil darkness. As shown, the control of absorbance values is highly dependent on the polarizability/basicity of the non-framework cations. Particularly, the oil samples oxidized with highly basic Ca-X and K-X zeolite NCs exhibit much slower increment in absorbance intensity before 300 h, where only about 0.95 of light absorbance was recorded. After 400 h of oxidation, the palm oil with Ca-X zeolite has the lowest absorbance value of 4.89, whereas the palm oil containing K-X has an absorbance value of 5.20. On the other hand, less basic Li-X and Na-X were less effective in controlling oil darkening; absorbance values of 7.15 and 5.64 were measured, respectively, after 400 h of oxidation.

Viscosity and Acidity Changes of Palm Oil. Rheometry was used to determine the fluidity of the palm oil samples as a function of oxidation time (Figure 5). At the beginning, the fresh oil had a viscosity value as low as 72 cSt. With increasing oxidation time, each oil sample experienced different extents of viscosity elevation. The rate of oil thickening was significantly reduced when zeolite X NCs were added. For instance, the viscosity of palm oil with K-X NCs increased slowly to 912 cSt after 400 h of oxidation, which was 5 times lower than that of

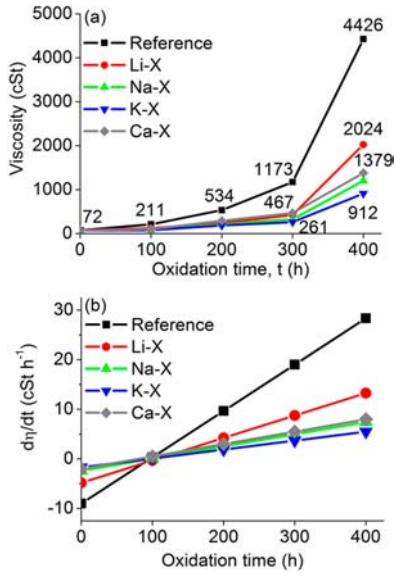

Figure 5. (a) Viscosity of palm oil samples with or without zeolites Li-X, K-X, Na-X, and Ca-X with oxidation time and (b) plot of $d\eta/dt$ versus time showing the increasing rate of viscosity of the oil samples.

the oxidized reference oil (4426 cSt). The rate of viscosity change with time was also calculated on the basis of the slope of the original function ($d\eta/dt$), where this derivative enables the correlation of cation properties with oil viscosity at any instant (Figure 5b). The results show that the control of oil viscosity in the presence of zeolite NCs is dependent on the cations' charge density and polarizability. For example, larger extra-framework cations with low charge density such as K^+ (0.101 e/Å^3) and Na^+ (0.268 e/Å^3) have better performance in resisting the change in viscosity of palm oil than Li^+ (0.779 e/Å^3) and Ca^{2+} (0.505 e/Å^3).[31] Thus, the results show that the oil oxidized with zeolite K-X has the lowest viscosity due to the presence of a low concentration of polymeric oxidized compounds.

Furthermore, oil viscosity and oil darkening are also related to oil acidity because the presence of polar acidic groups (oxidized products) tends to enhance the polarity of oil molecules, thus attracting the organic compounds and resulting in bulkier molecules. Typically, the acidic compounds are mainly alcohols, aldehydes, lactones, and carboxylic acids. These oxidation products, which contain acidic protons, are formed as a result of scission reactions of unsaturated fatty acid chains during oxidative chain reaction.[32] The acidity of oil was evaluated on the basis of total acid number (TAN) measurements of the oil samples. As expected, the trend of oil acidity is somewhat similar to the trend of viscosity of oil, where the reference oil shows fast increment in the TAN value, that is, a TAN of 46.83 mg KOH/g oil was recorded after 400 h (Figure 6a). In contrast, the oils with zeolite NCs exhibit a slow rise in acidity. The acidity of the oils containing zeolite NCs is approximately 4 times lower than that of reference oil. The derivative measurement of the instantaneous changes in the TAN value of oil samples was also performed, and the plot is shown in Figure 6b. It can be clearly seen that the oils oxidized with highly basic zeolite K-X have the lowest rate of TAN value change, indicating that K-X is the most effective in controlling oil deterioration, whereas the basic divalent cation in sample Ca-X has comparable performance to sample Na-X in halting oil oxidation, followed by Li-X. Thus, the similarity of trend in the TAN plot to those of colorimetry and rheometry provides

DOI: 10.1021/acs.jafc.5b00380
J. Agric. Food Chem. 2015, 63, 4655−4663

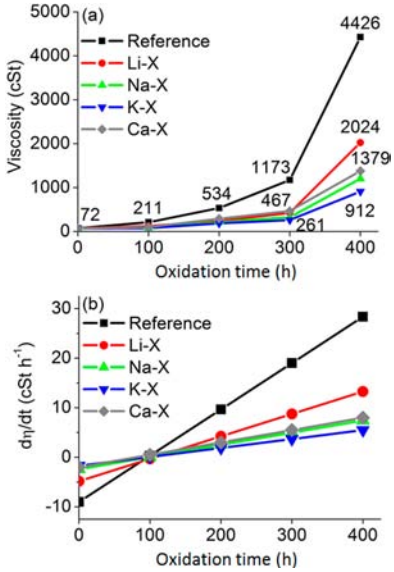

Figure 6. (a) Development of TAN and (b) differential function of TAN of palm oil samples with or without zeolites Li-X, K-X, Na-X, and Ca-X with oxidation time. (b, inset) magnification of the plot is shown.

strong proof of the existence of a relationship between oil composition, the rate of oil darkening, and the total acidic compounds produced, which is consistent with our previous finding.[10]

Oil Oxidation Followed by FTIR and ^{1}H NMR Spectroscopy. FTIR spectroscopy was further applied to study the development of carbonyl-oxidized products in the oil (vibrations in the range 1900−1400 cm^{-1}). Mainly, four signals are slowly developed at 1784, 1743, 1703, and 1655 cm^{-1} during the oxidation process of oil, which correspond to lactones, esters, carboxylic acids, and water, respectively (inset of Figure 7). The reference sample (oil without zeolite)

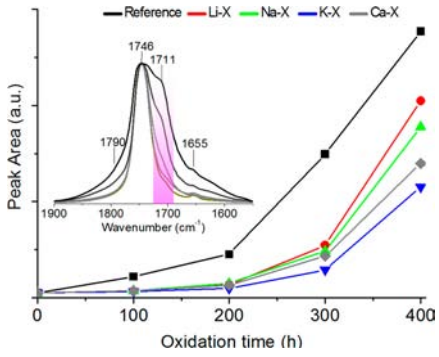

Figure 7. Development of integrated IR peak area (1690−1725 cm^{-1}) corresponding to the carboxylic acids formed during the oxidation of palm oil with and without zeolites Li-X, K-X, Na-X, and Ca-X. (Inset) FTIR spectra of reference oil in the range of 1550−1900 cm^{-1}. The pink area indicates the region used for integration of peak area.

experiences fast peak broadening and significant baseline offset at 1680−1740 cm^{-1} during the oxidation process (inset of Figure 7). Integration of the peak area (1690−1725 cm^{-1}) is used to provide a comprehensive view of the quantitative evolution of carboxylic acids along the oxidation for 400 h (Figure 7). The result reveals a sharp increase in peak area in the reference oil, especially after 200 h of oxidation, indicating the fast development of carbonyl-oxidized compounds in the palm oil. The addition of zeolite NCs slows oxidation, and the broadening of the IR peak at 1700−1800 cm^{-1} indicates deceleration of carboxylic acids in the oil. The effect of extra-framework cations in halting oil oxidation is followed; the changes in the integrated peak area at 1700−1720 cm^{-1} show the dependency of carboxylic acid generation on the types of extra-framework cations in the zeolite nanocrystals. As can be seen, the production rate of carboxylic acid is directly proportional to the polarizability of the alkali metal cations (Figure 7). This is evidenced by the steeper slope of the curves obtained from the integrated peak area for oil samples treated with Li-X than those with K-X and Ca-X. Among all oil samples, the one containing K-X has the least steep slope, suggesting that the oxidative inhibition of the zeolite improves with increasing basicity.

Additionally, the formation of hydroxyl compounds in the oil under oxidation is estimated using the FTIR data. The absorption bands of alcohols (ca. 3615 cm^{-1}), water (ca. 3534 cm^{-1}), and hydroperoxides (ca. 3468 cm^{-1}) are overlapping; thus, only an indication for the overall development of these compounds in the oil samples is observed (Figure S3). The IR results reveal that the zeolite NCs are controlling the rate of formation of hydroxyl compounds in comparison to the oil free of zeolite (reference) during the oxidation process. The formation rate of hydroxyl compounds in the palm oil with Li-X is higher than those of Na-X, K-X, and Ca-X oil samples, indicating that Ca-X and K-X are able to hinder the formation of hydroxyl compounds.

Water is an undesirable oxidized byproduct because it catalyzes oil oxidation and promotes acid formation. Hence, the water content in the oil samples is evaluated using the area of the IR peaks in the region 3500−3350 cm^{-1}. As can be seen, the peaks areas in this region increase with oxidation time, which is a clear indication for the increase of water content during the oxidation process (Figure S3). Nevertheless, this region is not sensitive and accurate to determine the water content in oil media due to the disrupted O−H (alcohols, carboxylic acids, and hydroperoxides) stretching vibration modes.[33] Therefore, the moisture content was quantitatively measured with the Karl Fischer titration method.

The initial water content in the fresh palm oil is 826 ppm, which is <0.1% of the mass of cooking oil—a desired level of water content according to the Palm Oil Refiners Association of Malaysia (PORAM) specification (Figure 8).[34] As can be seen, in the reference oil the water content during the oxidation process is increasing quickly. This can be explained by the high oxidation rate of the oil, where water is produced as a

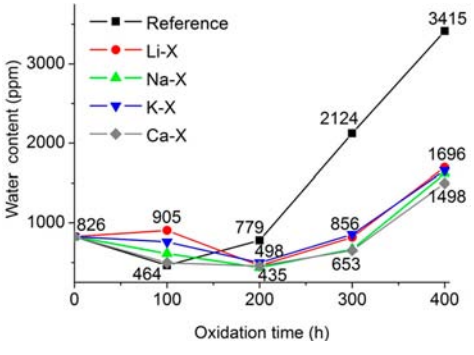

Figure 8. Change in water content of oxidized palm oil samples with and without zeolites Li-X, K-X, Na-X, and Ca-X with oxidation time.

DOI: 10.1021/acs.jafc.5b00380
J. Agric. Food Chem. 2015, 63, 4655−4663

degradation byproduct via condensation. On the contrary, the oil samples containing zeolite NCs overall have a lower water content than the reference oil during the oxidation period. The moisture content in palm cooking oil is dropped during the first 200 h, which might be due to the adsorption of water in the zeolites. Since then, the quantity of water slowly increases, depending on the type of counterions of zeolite X. The lowest water content after 400 h is detected in the oil with Ca-X (1498 ppm), whereas the oil with Li-X has the highest level of moisture (1696 ppm). These changes in water content can be explained by the effect of controlled thermal oxidation process. The better the zeolite in reducing the rate of oxidation, the slower the generation of water, and hence the lower amount of water is present in the oil.

Furthermore, a detailed study on the formation of carbonyl compounds including carboxylic acid (>9.6 ppm) and aldehydes (9.3−9.6 ppm) using ^{1}H NMR spectroscopy is performed. It is demonstrated that the cations with lower polarizability/lower basicity are acting less effectively in slowing the formation of the acidic components in the palm oil (Figure 9). For instance, the formation of aldehydes and carboxylic

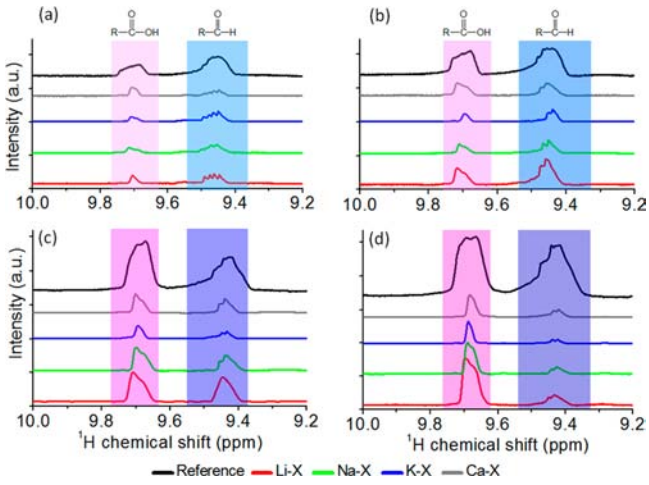

Figure 9. ^{1}H NMR spectra of palm oil samples oxidized with and without zeolites Li-X, K-X, Na-X, and Ca-X for (a) 100 h, (b) 200 h, (c) 300 h, and (d) 400 h.

acids in the palm oil oxidized in the presence of Li-X is faster than the oil containing more basic cations. Among all samples, the palm oil containing K^+ with high cation polarizability has the least increment in both aldehyde and carboxylic contents, followed by the divalent Ca-X in halting oil oxidation possess.

The different colors in oil samples can be due to the presence of high-molecular-weight polymeric oxidized compounds via intensive light absorption and scattering effect. In addition, different contents of β-carotene will also lead to different colors in oxidized oil samples as well. Hence, ^{1}H NMR spectroscopy was used to detect the presence of β-carotene in oil samples after 300 h of oxidation (Figure S4). These oil samples were selected because they exhibited colors significantly different from their counterparts. The ^{1}H NMR spectra show the characteristics peaks of β-carotene at 6.77 ppm arising from protons 11/11′ (6.76 ppm) and protons 15/15′ (6.74 ppm). In addition, protons 7/7′ (6.24 ppm) together with protons 10/10′ (6.23 ppm) show an overlapping signal at 6.24 ppm. The protons 8/8′ are found at 6.19 ppm.[35] It can be seen that the peak intensity of carotene in the oils oxidized with zeolite NCs is almost identical to that of reference oil, indicating that the oxidation rate of carotene is not affected by the presence of zeolite NCs. Thus, taking this fact into consideration, the change of oil color is mainly due to the oxidation products.

Besides, the content of hydroperoxides in the palm oils is also followed by ^{1}H NMR spectroscopy; the signal at ca. 8.80 ppm corresponds to hydroperoxide group (RO−OH).[36] It can be seen that no peak is observed in the reference oil throughout the oxidation process, showing that the hydroperoxides (primary oxidized products) are very unstable and they are directly converted into carboxylic acids, aldehydes, etc. (secondary oxidized products) (Figure S5). As a result, the oxidation rate and acidity of the palm oil increases. In contrast, a broad peak at 8.8 ppm is observed in all oils samples containing zeolite NCs during the first 200 h, indicating their stabilization in the zeolite NCs (Figure S6). Thus, fewer secondary oxidized products (e.g., carboxylic acids and aldehydes) and lower TAN values are observed in these samples. Among four basic exchanged cations, the Ca^{2+} with the highest polarizability contributes most significantly to the stabilizing of hydroperoxides, followed by K^+, Na^+, and Li^+. The broad peak at 8.8 ppm, however, completely disappears after 300 h, and the oxidation rate increases as shown by colorimetry, TAN, rheometry, and IR spectroscopic studies. This can be explained by competitive adsorption of primary and secondary oxidation products. The mechanism of oxidative inhibition of palm oil by zeolite NCs will be discussed further under Characterization of Zeolite Nanocrystals after Oil Oxidation.

Characterization of Zeolite Nanocrystals after Oil Oxidation. The zeolite nanocrystals used during oil oxidation were separated from the oil and washed before being subjected to characterization. Figure S7 shows the IR spectra of zeolite samples before and after use in oil oxidation. It can be seen that fresh Na-X has several peaks at 1006, 752, 670, 566, and 459 cm^{-1} characteristic for the framework structure of zeolite X, and the peaks at 3410 and 1647 cm^{-1} are due to adsorbed water. After oil oxidation, the IR bands of zeolite NCs remain unchanged, indicating that the framework structure of all zeolite samples does not change after 400 h of oxidation. In addition, several peaks are observed at 2921, 2857, 1462, and 1363 cm^{-1}, which are attributed to the adsorption of organic molecules by the zeolite NCs. Furthermore, the hydroxyl band at 3410 cm^{-1} is broadened and slightly shifted to 3405 cm^{-1}, revealing that the zeolites adsorb also hydrocarbons containing hydroxyl groups such as alcohols and hydroperoxides. For zeolite NCs with monovalent cations, a signal at 1745 cm^{-1} that corresponds to esters is overlapping with the signal of 1650 cm^{-1} (OH bending). Thus, the IR results conclude that the oxidative inhibition in oil by monovalent cation exchanged zeolite is not due to oxidation products removal action because no carboxylic acids are adsorbed (no peak is found at 1715 cm^{-1}). On the other hand, the zeolite Ca-X containing divalent cations exhibits a strong peak at 1599 cm^{-1}, which corresponds to the COO^- species.

All zeolites used during the oxidation of palm oil are studied by TG/dTG analysis. Basically, all samples display two steps of weight losses. The zeolites adsorb almost similar amounts of water (5.0%), which is desorbed at 160 °C (Figure S8a). However, the amount of organic compounds adsorbed and their desorption temperature vary depending on the type of zeolite nanocrystals. Li-X with the largest surface area and pore volume adsorbs the highest amount of organic compounds (35.0%) followed by Na-X (28.0%) and K-X (23.0%). The

DOI: 10.1021/acs.jafc.5b00380
J. Agric. Food Chem. 2015, 63, 4655−4663

temperature of desorption identifies the species adsorbed and also provides information on the strength of interaction between that compound and the countercations of zeolite. The dTG curve of Li-X exhibits two signals at 275 and 338 °C (Figure S8b), whereas only one signal around 301−310 °C for samples Na-X and K-X is observed (Figure S8b). As seen, the desorption temperature for K-X is slightly lower than that of Na-X, indicating that K-X has weaker interaction with the organic compounds due to its lower charge density. On the other hand, divalent cations in sample Ca-X adsorb about 30% of organic compounds, which is almost similar to Na-X. Three signals at 275, 387, and 433 °C for sample Ca-X are observed, showing that the Ca^{2+} has higher affinity to organic species than monovalent cations.

Modeling of the Interaction of Peroxide and Alkene Complexes with Metal Ions in Zeolite Nanocrystals. Countercations in the zeolites can interact with C═C bonds and hydroperoxides during the oil oxidation process. Therefore, we consider adsorption of simplified hydroperoxides (e.g., HOOH and C_2H_5OOH) and alkenes (e.g., ethene and *cis*-butene) on the M-X zeolites (M = Li, Na, K, Ca). The calculations show that the countercations introduced in zeolite X more preferably interact with the hydroperoxides than with the alkenes. As shown in Table S3, the binding energy of peroxides (from −50 to −109 kJ/mol) with the metal cations is much higher than that of the binding energy of alkenes (from −17 to −69 kJ/mol), which clearly indicates that the extra-framework cations of zeolite X tend to stabilize peroxides. This result is in good agreement with the ^{1}H NMR spectroscopy data, where a large concentration of hydroperoxides is detected in the oil containing zeolite NCs during the first 200 h of oxidation and, thus, the decomposition rate of hydroperoxide is decelerated due to the stabilization of hydroperoxides by the extra-framework cations (Figure S6). On the other hand, basic countercations have a lower tendency to interact with the alkenes as indicated by their lower binding energy (from −17 to −69 kJ/mol). An attempt to investigate the effect of the addition of methyl and ethyl groups in the alkene molecules on the binding energy is made. The DFT calculations reveal that the insertion of alkyl groups in the alkene chain has an insignificant effect (<5 kJ/mol) on their binding energy toward monovalent cations (Li^+, Na^+, and K^+). This effect, nevertheless, is larger for the divalent Ca^{2+}, where the binding energy of *cis*-butene (−69 kJ/mol) is larger than the binding energy of ethane (−54 kJ/mol). The same trend is also valid for the interaction of the peroxides with Ca-X zeolite, and a strong binding with HOOH (−94 kJ/mol) and C_2H_5OOH (−109 kJ/mol) is calculated.

The periodic DFT calculations show that the interaction of the peroxide with the metal ions is stronger than the interaction of the alkenes with the same ions. This rationalizes the experimental results that M-X zeolites slow the thermal oxidation of palm oil, because the formed peroxides are mostly captured from the metal cations in the zeolites and consequently decelerate further oxidation toward acidic organic compounds such as aldehydes and carboxylic acids. On the basis of the DFT calculations one can conclude that the Ca-X zeolite is the best candidate for hindering the oxidation of palm oil, whereas Li-X, Na-X, and K-X are equally plausible (binding energies for these three cations toward peroxides are somewhat similar). The latter finding is not completely in accordance with the conclusion drawn from the experimental part where K-X shows the best results followed by Ca-X, Na-X, and Li-X. On the other hand, some of the experiments conducted in this work (e.g., colorimetric evaluation, water content analysis, and TAN) show minor differences between the Li^+, Na^+, K^+, and Ca^{2+} cations, which may be difficult to be distinguished by the DFT calculations because oil oxidation is a complex process.

Proposed Mechanisms of Oxidative Inhibition of Palm Oil in the Presence of Zeolite Nanocrystals. The influence of extra-framework alkali metal and alkali earth metal cations on hindering oil oxidation is demonstrated. On the basis of the experimental results and DFT calculations shown in the previous sections, a mechanism of inhibiting oil oxidation by zeolite nanoparticles is proposed. At high temperature, the initiation step starts where unsaturated hydrocarbons are oxidized by air, and hydroperoxides are formed as primary oxidation products (eq 2). The hydroperoxides are very unstable according to ^{1}H NMR spectroscopy (no peak at 8.8 ppm corresponding to hydroperoxides is detected, Figure S6). The hydroperoxides tend to decompose into radicals (water is produced as a byproduct) and react to form more stable compounds (propagation step) (eqs 3a−5). In addition, the reactive radicals also have a high tendency to attack unsaturated C═C bonds of triglycerides. This affects the breaking of C═C bonds, yielding secondary acidic oxidized products (e.g., aldehydes, lactones, and carboxylic acids) as presented in eq 6. The oxidation and propagation continue until the polymerization processes occur (eqs 7 and 8).

$$\text{initiation step: } RH + O_2 \rightarrow ROOH \tag{2}$$

$$\text{propagation: } ROOH \rightarrow RO^{\bullet} + HO^{\bullet} \tag{3a}$$

$$ROOH \xrightarrow{\text{slow}} RO^{\bullet} + HO^{\bullet} \tag{3b}$$

$$2ROOH \rightarrow ROO^{\bullet} + RO^{\bullet} + H_2O \tag{4a}$$

$$2ROOH \xrightarrow{\text{slow}} ROO^{\bullet} + RO^{\bullet} + H_2O \tag{4b}$$

$$ROO^{\bullet} + R'H \rightarrow R'OO^{\bullet} + RH \tag{5}$$

$$\text{cleavage and oxidation: } >C{=}C< + ROO^{\bullet} \rightarrow >C{=}O + >C{=}O + R^{\bullet} \tag{6}$$

$$\text{polymerization: } R^{\bullet} + R'^{\bullet} \rightarrow R - R' \text{(high molecular weight compounds)} \tag{7}$$

$$\text{and termination: } ROO^{\bullet} + R^{\bullet} \rightarrow ROOR \tag{8}$$

When the zeolite NCs containing different alkali metal cations are added during oil oxidation, the oxidation process pathway is altered, and the oxidation rate is slowed. Initially, the hydrocarbons are oxidized to hydroperoxides. In the presence of zeolites, the hydroperoxides are stabilized by the extra-framework cations and, thus, the decomposition rate of the hydroperoxides is decelerated (eqs 3a and 4a). This process is confirmed by the ^{1}H NMR spectroscopy results and supported by the periodic DFT calculations. The palm oild with zeolite NCs have large amountd of hydroperoxides as proven by the presence of a broad signal at 8.8 ppm in the ^{1}H NMR spectra. As a result, this reaction becomes a limitation step to inhibit the oxidation reaction. Thus, a slow oxidation process of the palm oil is observed during the first 200 h by colorimetry, rheometry, TAN, and IR spectroscopy analyses (Figures 4−7). Among the exchanged cations, the divalent Ca^{2+} with the highest ion

DOI: 10.1021/acs.jafc.5b00380
J. Agric. Food Chem. 2015, 63, 4655−4663

polarizability stabilizes the peroxides better than the monovalent K^+, Na^+, and Li^+ cations.

The stabilizing effect by extra-framework cations, however, becomes weaker and the ^1H NMR signal at 8.8 ppm completely disappears after 300 h (Figure S6). Hence, oil oxidation and polymerization increase after 300 h. At this stage, the zeolites are also behaving as oxidative inhibitors by adsorbing oxidation products such as alcohols, hydroperoxides, esters, and water. Unlike monovalent alkali metal cation exchanged zeolites, the alkaline earth Ca-X also reduced the acidity of the oil by neutralizing the acidic carboxylate compounds to $COO^-(Ca^{2+})_{1/2}$ species as proven by IR spectroscopy (Figure S7) and DFT simulations (Figure 10; Table S3).

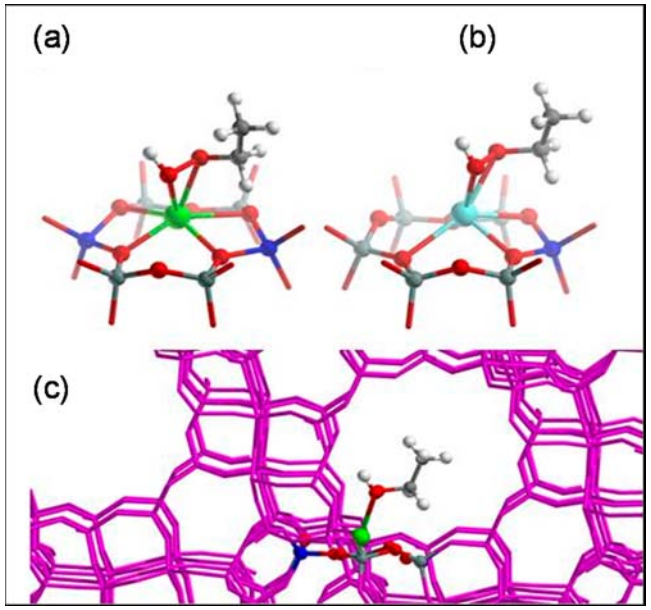

Figure 10. Optimized structures in periodic models. Local structures of selected complexes: (a) $Ca^{2+}(CH_3CH_2OOH)$; (b) $Na^+(CH_3CH_2OOH)$. (c) Location of the complexes in the cavity of the FAU type structure, represented by $Ca^{2+}(CH_3CH_2OOH)$. Color coding: red, O; gray, Si; blue, Al; white, H; green, Ca; light blue, Na.

Conclusions. This work reveals the effect of extra-framework cations in zeolite X nanocrystals on the oxidation of palm oil. The results show that the antioxidation behavior of zeolite nanocrystals depends on basicity, charge density, and polarizability of the countercations of the zeolites. Li-X zeolite nanocrystals with the lowest cation polarizability are found to have the lowest oxidative inhibition activity, whereas the highly basic and highly polarized K-X zeolite nanocrystals are the best candidates to hinder oil oxidation. The effect of zeolite nanocrystals on oil oxidation is found to be different for mono- and divalent cations containing materials. According to ^1H NMR spectroscopy and periodic DFT calculation, all counterions, especially Ca^{2+} with bidentate property, are able to stabilize the hydroperoxides, which are the primary oxidation products and, hence, the decomposition rate of hydroperoxides and the propagation step are decelerated. Furthermore, the adsorption is also another mechanism in halting oil degradation by removing harmful compounds such as esters, alcohols, water, and hydroperoxides as revealed by IR spectroscopy. For Ca-X zeolite nanocrystals, the bidentate capability of Ca^{2+} leads to neutralization of the acidic carboxylate compounds that reduces the acidity of the oil and further decelerates the oil oxidation process.

■ ASSOCIATED CONTENT

Supporting Information

X-ray diffraction patterns of zeolite samples; FTIR spectra of oil samples; ^1H NMR spectra of palm oil (6.0−7.2 ppm and 8.5−9.3 ppm) oxidized at 150 °C; ^1H NMR spectra of the palm oil oxidized in the presence of zeolites; FTIR spectra of zeolite samples; TGA and dTG of zeolite nanocrystals after 400 h of oxidation. The Supporting Information is available free of charge on the ACS Publications website at DOI: http://pubs.acs.org/doi/abs/10.1021/acs.jafc.5b00380.

■ AUTHOR INFORMATION

Corresponding Authors

*(S.M.) E-mail: mintova@ensicaen.fr.
*(E.-P.N.) E-mail: epng@usm.my.

Author Contributions

‖K.-H.T. and H.A. contributed equally to this work as first authors.

Funding

We acknowledge Bio-Asia Program and FRGS (203/PKIMIA/6711362) research grants for financial support. K.-H.T. also thanks the MyBrain and USM fellowship for the scholarship provided.

Notes

The authors declare no competing financial interest.

■ REFERENCES

(1) Carter, C.; Finley, W.; Fry, J.; Jackson, D.; Willis, L. Palm oil markets and future supply. *Eur. J. Lipid Sci. Technol.* **2007**, *109*, 307−314.

(2) Sharma, B. K.; Adhvaryu, A.; Liu, Z.; Erhan, S. Z. Chemical modification of vegetable oils for lubricant applications. *J. Am. Oil Chem. Soc.* **2006**, *83*, 129−136.

(3) Takeoka, G. R.; Full, G. H.; Dao, L. T. Effect of heating on the characteristics and chemical composition of selected frying oils and fats. *J. Agric. Food Chem.* **1997**, *45*, 3244−3249.

(4) Billek, G. Health aspects of thermoxidized oils and fats. *Eur. J. Lipid Sci. Technol.* **2000**, *102*, 587−593.

(5) Ebong, P. E.; Owu, D. U.; Isong, E. U. Influence of palm oil (*Elaesis guineensis*) on health. *Plant Foods Hum. Nutr.* **1999**, *53*, 209−222.

(6) Fox, N. J.; Stachowiak, G. W. Vegetable oil-based lubricants − a review of oxidation. *Tribol. Int.* **2007**, *40*, 1035−1046.

(7) Ng, E.-P.; Delmotte, L.; Mintova, S. Selective capture of water using microporous adsorbents to increase the lifetime of lubricants. *ChemSusChem* **2009**, *2*, 255−260.

(8) Majano, G.; Ng, E.-P.; Mintova, S. Inhibition of lubricant degradation by nanoporous materials. *Stud. Surf. Sci. Catal.* **2008**, *174*, 569−572.

(9) Ng, E.-P.; Mintova, S. Nanoporous materials as high selective water sorbents in lubricants. In *Topics in Chemistry and Material Science: Advanced Micro- and Mesoporous Materials*; Hadjiivanov, K., Valtchev, V., Mintova, S., Vayssilov, G., Eds.; Heron Press Science Series: Bulgaria, 2008; Vol. 1, pp 322−329.

(10) Tan, K.-H.; Ng, E.-P.; Awala, H.; Mukti, R. R.; Wong, K.-L.; Yeong, S.-K.; Mintova, S. Halting oxidation of palm oil with eco-friendly zeolites. In *Topics in Chemistry and Material Science: Advanced Micro- and Mesoporous Materials*; Hadjiivanov, K., Valtchev, V., Mintova, S., Vayssilov, G., Eds.; Heron Press Science Series: Bulgaria, 2014; Vol. 7, pp 102−108.

DOI: 10.1021/acs.jafc.5b00380
J. Agric. Food Chem. 2015, 63, 4655−4663

(11) Majano, G.; Ng, E.-P.; Lakiss, L.; Mintova, S. Nanosized molecular sieves utilized as an environmentally friendly alternative to antioxidants for lubricant oils. *Green Chem.* **2011**, *13*, 2435−2440.
(12) Mikosch, H.; Uzunova, E. L.; Nikolov, G. S. Interaction of molecular nitrogen and oxygen with extraframework cations in zeolites with double six-membered rings of oxygen-bridged silicon and aluminum atoms: a DFT study. *J. Phys. Chem. B* **2005**, *109*, 11119−11125.
(13) Sethia, G.; Somani, R. S.; Bajaj, H. C. Adsorption of carbon monoxide, methane and nitrogen on alkaline earth metal ion exchanged zeolite-X: structure, cation position and adsorption relationship. *RSC Adv.* **2015**, *5*, 12773−12781.
(14) Cozens, F. L.; Cano, M. L.; García, H.; Schepp, N. P. Alkali metal cation control of oxidation reactions of radicals in zeolites. *J. Am. Chem. Soc.* **1998**, *120*, 5667−5673.
(15) Xu, R.; Pang, W.; Yu, J.; Huo, Q.; Chen, J. *Chemistry of Zeolites and Related Porous Materials: Synthesis and Structure*; Wiley: Singapore, 2007; 354 pp.
(16) Laurent, S.; Ng, E.-P.; Thirifays, C.; Lakiss, L.; Goupil, G.-M.; Mintova, S.; Burtea, C.; Oveisi, E.; Hébert, C.; de Vries, M.; Motazacker, M. M.; Rezaee, F.; Mahmoudi, M. Corona protein composition and cytotoxicity evaluation of ultra-small zeolites synthesized from template free precursor suspensions. *Toxicol. Res.* **2013**, *2*, 270−279.
(17) Awala, H.; Gilson, J.-P.; Retoux, R.; Boullay, P.; Goupil, J.-M.; Valtchev, V.; Mintova, S. Template-free nanosized faujasite type zeolites. *Nat. Mater.* **2015**, *14*, 447−451.
(18) Perdew, J. P.; Wang, Y. Accurate and simple analytic representation of the electron-gas correlation energy. *Phys. Rev. B: Condens. Matter Mater. Phys.* **1992**, *45*, 13244−13249.
(19) Kresse, G.; Hafner, J. Ab initio molecular-dynamics simulation of the liquid-metal amorphous-semiconductor transition in germanium. *Phys. Rev. B: Condens. Matter Mater. Phys.* **1994**, *49*, 14251−14269.
(20) Kresse, G.; Furthmüller, J. Efficiency of ab-initio total energy calculations for metals and semiconductors using a plane-wave basis set. *Comput. Mater. Sci.* **1996**, *6*, 15−50.
(21) Vanderbilt, D. Soft self-consistent pseudopotentials in a generalized eigenvalue formalism. *Phys. Rev. B: Condens. Matter Mater. Phys.* **1990**, *41*, 7892−7895.
(22) Kresse, G.; Hafner, J. Norm-conserving and ultrasoft pseudopotentials for first-row and transition elements. *J. Phys.: Condens. Matter* **1994**, *6*, 8245−8257.
(23) Jeanvoine, Y.; Ángyán, J. G.; Kresse, G.; Hafner, J. Brønsted acid sites in HSAPO-34 and chabazite: an ab initio structural study. *J. Phys. Chem. B* **1998**, *102*, 5573−5580.
(24) *Database of Zeolite Structures*; http://www.iza-structure.org/databases/ (accessed Nov 8, 2014).
(25) Yang, Y.; Burke, N.; Zhang, J.; Huang, S.; Lim, S.; Zhu, Y. Influence of charge compensating cations on propane adsorption in X zeolites: experimental measurement and mathematical modeling. *RSC Adv.* **2014**, *4*, 7279−7287.
(26) Sherry, H. S. *Handbook of Zeolite Science and Technology*; Dekker: New York, 2003; pp 1007−1061.
(27) Feuerstein, M.; Accardi, R. J.; Lobo, R. F. Adsorption of nitrogen and oxygen in the zeolites Li-A and Li-X investigated by ^{6}Li and ^{7}Li MAS NMR spectroscopy. *J. Phys. Chem. B* **2000**, *104*, 10282−10287.
(28) Zhu, J.; Mosey, N.; Woo, T.; Huang, Y. Study of the adsorption of toluene in zeolite LiNa−Y by solid-state NMR spectroscopy. *J. Phys. Chem. C* **2007**, *111*, 13427−13436.
(29) Golumbic, C. Antioxidants and autoxidation of fats. XIV. The isolation of new antioxidants. *J. Am. Chem. Soc.* **1942**, *64*, 2337−2340.
(30) Engelsen, S. B. Explorative spectrometric evaluations of frying oil deterioration. *J. Am. Oil Chem. Soc.* **1997**, *74*, 1495−1508.
(31) *CRC Handbook of Chemistry and Physics*; http://www.hbcpnetbase.com (accessed Nov 8, 2014).
(32) Schaich, K. M. Lipid oxidation: theoretical aspects. In *Bailey's Industrial Oil and Fat Products*; Shahidi, F., Ed.; Wiley: Hoboken, NJ, USA, 2005; Vol. 1, pp 269−357.
(33) Ng, E.-P.; Mintova, S. Quantitative determination of moisture in lubricating oils by FT-IR spectroscopy combined with solvent extraction approach. *Microchem. J.* **2011**, *98*, 177−185.
(34) *PORAM Standard Specifications for Processed Palm Oil*; http://poram.org.my/contracts/poram-standard-specifications-for-processed-palm-oil/ (accessed Nov 8, 2014).
(35) Holtin, K.; Albert, K. Chapter 4: The use of NMR detection of LC in carotenoid analysis. In *Carotenoids: Physical, Chemical, and Biological Functions and Properties*; Landrum, J. T., Ed.; CRC Press: Boca Raton, FL, USA, 2009; pp 61−74.
(36) Turovskij, N. A.; Berestneva, Y. V.; Raksha, E. V.; Zubritskij, M. Y.; Grebenyuk, S. A. NMR study of the complex formation between *tert*-butyl hydroperoxide and tetraalkylammonium bromides. *Monatsh. Chem.* **2014**, *145*, 1443−1448.

DOI: 10.1021/acs.jafc.5b00380
J. Agric. Food Chem. 2015, 63, 4655−4663

JOURNAL OF AGRICULTURAL AND FOOD CHEMISTRY

Article

pubs.acs.org/JAFC

Influence of Grape Composition on Red Wine Ester Profile: Comparison between Cabernet Sauvignon and Shiraz Cultivars from Australian Warm Climate

Guillaume Antalick,*[,†] Katja Šuklje,[†] John W. Blackman,[†,‡] Campbell Meeks,[†] Alain Deloire,[†] and Leigh M. Schmidtke[†,‡]

[†]National Wine and Grape Industry Centre and [‡]School of Agricultural and Wine Sciences, Charles Sturt University, Locked Bag 588, Wagga Wagga, NSW 2678, Australia

ABSTRACT: The relationship between grape composition and subsequent red wine ester profile was examined. Cabernet Sauvignon and Shiraz, from the same Australian very warm climate vineyard, were harvested at two different stages of maturity and triplicate wines were vinified. Grape analyses focused on nitrogen and lipid composition by measuring 18 amino acids by HPLC-FLD, 3 polyunsaturated fatty acids, and 6 C6-compounds derived from lipid degradation by GC-MS. Twenty esters and four higher alcohols were analyzed in wines by HS-SPME-GC-MS. Concentrations of the ethyl esters of branched acids were significantly affected by grape maturity, but the variations were inconsistent between cultivars. Small relative variations were observed between wines for ethyl esters of fatty acids, whereas higher alcohol acetates displayed the most obvious differences with concentrations ranging from 1.5- to 26-fold higher in Shiraz than in Cabernet Sauvignon wines regardless of the grape maturity. Grape analyses revealed the variations of wine ester composition might be related to specific grape juice nitrogen composition and lipid metabolism. To the authors' knowledge the present study is the first to investigate varietal differences in the ester profiles of Shiraz and Cabernet Sauvignon wines made with grapes harvested at different maturity stages.

KEYWORDS: *yeast metabolism, nitrogen, lipids, grape berry maturity*

INTRODUCTION

Wine aromatic composition is one of the primary attributes assessed by the wine consumer and is an integral component of the overall wine tasting experience. Wine aromatic compounds are classified within three different groups according to their origin: varietal (primary), fermentative (secondary), and derived from aging (tertiary). Although the tertiary component is primarily important in aged wines, the varietal and fermentative components are crucial for wine aroma quality regardless of wine age.[1] Fermentative aromas are mainly derived from yeast activity and are considered as the wine-like aromatic base common to all wines.[1] The varietal component, which is derived from grape aroma and aromatic precursors, imparts specific aromas depending on the cultivars and vineyard characteristics. Within wine categories produced by a similar winemaking process, varietal aromas are considered to contribute to the unique characters.[2] Therefore, the varietal component regulated by the environment and cultural practices appears to be more related to the concept of wine aromatic typicality[2] than the fermentative component.

Several key markers of varietal aroma have been identified in white cultivars such as Muscat, Sauvignon blanc, and Gewürstraminer.[1] In contrast, the understanding of red wine aroma is less advanced, possibly because of the higher level of complexity of such a medium. A limited number of key varietal markers associated with herbaceous[3] and peppery aromas[4] have been identified in red wines. Conversely, the origin of fruity aroma in red wines is still poorly understood despite the evidence of the existence of fruity attributes (red and black berry) typical of red wines.[5] Several studies have emphasized the potential role of some grape-derived compounds such as C13-norisoprenoids and furanones in the perception of fruity aromas specific to red wines.[6−8] However, the contribution of these markers in red wine aroma seems to be indirect through complex perceptive interactions.[7,8]

Other authors have recently highlighted the potential role of esters in the fruity attributes typical of red wines via similar complex interactions.[7−9] Most wine esters are enzymatically synthesized by yeast during alcoholic fermentation[10] and can also be modulated by the lactic acid bacteria (LAB) during malolactic fermentation (MLF).[11,12] However, the possibility of fermentation-derived volatiles, such as esters, playing an important role in varietal differentiation of wines has not been studied extensively. The subsequent opportunity to utilize these esters as "varietal markers" is therefore novel and contradicts paradigms that have been previously assigned to varietal and fermentative aroma and the understanding of wine aroma perception. A lack of knowledge of "key" aromatic compounds responsible for typical fruity aromas of red wines does not necessarily mean that they do not exist.[9] Conversely, esters are known to significantly contribute to aromas of red and black berry fruits generally used as attributes to describe the specific aromas of red wines.[13] Furthermore, it has been shown that esters such as isoamyl acetate contribute

Received: February 23, 2015
Revised: April 16, 2015
Accepted: April 23, 2015
Published: April 23, 2015

ACS Publications © 2015 American Chemical Society

DOI: 10.1021/acs.jafc.5b00966
J. Agric. Food Chem. 2015, 63, 4664−4672

significantly to the varietal aromas of Pinotage[14] and Tempranillo.[15]

Although it is accepted that grape berry parameters such as nitrogen status[16] influence the final wine ester profile, the association between grape and wine ester compositions is poorly understood and requires investigation. This study examined the relationship between grape composition and red wine ester profiles by comparing Cabernet Sauvignon and Shiraz at two different stages of maturity, from a warm to very warm and irrigated region of Australia (Riverina, New South Wales). Distinct cultivars were utilized to contrast the ester profiles between varieties.

MATERIALS AND METHODS

Experimental Vineyard and Harvesting. Grapes were sourced from two adjacent commercial vineyard plots, Shiraz and Cabernet Sauvignon, located within the same larger vineyard in Griffith (Riverina, New South Wales, Australia) (34′17′′00 S; 146′02′′00 E). This vine-growing region is classified as very warm according to the Huglin index[17,18] (HI > 3000). Both cultivars were own-rooted, drip irrigated, and trellised to double cordon with an open sprawling canopy and mechanically pruned. The nitrogen management throughout the season was similar for both cultivars and consisted of fertigating 20 kg of nitrogen per hectare per season via small additions from budburst to veraison. The average crop yields of both plots were approximately 15−20 tons per hectare. Both cultivars were harvested sequentially, at two different dates using the evolution of berry sugar accumulation as indicator in conjunction with °Brix.[19] The first harvest for both cultivars occurred at approximately 21 °Brix and was designated as fresh fruit (FF). The second harvest, designated as mature fruit (MF), occurred at 23 °Brix for both cultivars. At each harvest date, 60 kg of grapes per replicate was randomly harvested across the vineyards with an addition of 40 mg/kg of potassium metabisulfite prior to transport to the Charles Sturt University (CSU)/National Wine and Grape Industry Centre (NWGIC) experimental winery. On arrival, a 100 berry subsample from each replicate was collected and immediately frozen at −20 °C for further analyses.

Winemaking. All replicates were kept separate during the winemaking process. Grapes were destemmed, crushed, and transferred into 100 L stainless steel vats for fermentation. The acidity of each must replicate was adjusted to approximately pH 3.6 using tartaric acid. Fermentation was performed by EC1118 yeast (*Saccharomyces cerevisiae*) and carried out at 25−26 °C with the use of cool rooms. All ferments had identical nutritional supplements, consisting of an addition of 0.3 g/L GoFerm 24 h after yeast inoculation and 0.1 g/L diammonium phosphate (DAP) and 0.25 g/L Fermaid A after a 6 °Brix decrease. This corresponded to total additions of 57 and 15 mg N/L of ammonium and free amino nitrogen, respectively. Malolactic fermentation was carried out using a co-inoculation procedure, with Enoferm alpha LAB (*Oenococcus oeni*) added 2 days post yeast inoculation. Ferments were pressed to 1 bar pressure using a small basket press when the residual sugar decreased to <0.5 g/L. The wine temperature was then maintained at 22 °C until the malic acid concentration decreased to <0.05g/L. The wine was then racked off the gross lees into variable-capacity tanks to prevent ullage and 80 ppm of SO_2 added to achieve levels of 25−30 ppm of free SO_2. Tanks were then moved to a −4 °C cool room for 3 weeks to achieve cold stabilization and racked a further two times during this period for clarification. Heat stability was tested and SO_2 concentrations were adjusted to approximately 30 ppm of free SO_2 to achieve 0.5−0.8 molecular SO_2.Wines were bottled using a four-head filler with CO_2 utilized to prevent oxidation. Bottles were also filled with CO_2 prior to filling and then capped with a Stelvin screwcap.

General Analyses of Grape Maturity, Yeast Available Nitrogen, and Wine Composition. Grape juice samples collected after crushing were analyzed for basic maturity and fermentation parameters. Total soluble solids (TSS), expressed as °Brix, were analyzed with a portable density meter (Anton Paar DMA 35N, Graz, Austria). Titratable acidity (TA) and pH were determined by sodium hydroxide titration to the end point pH 8.2 with an automatic titrator (Metrohm Fully Automated 59 Place Titrando System, Metrohm AG, Herisau, Switzerland). Ammonium, α-amino acids, and acetic acid were determined using commercially available enzymatic tests purposely designed and deployed on an Arena discrete analyzer (ThermoFisher). Yeast assimilable nitrogen (YAN) was calculated from ammonium and free amino nitrogen (FAN) measurements according to a previously published method.[20] Ethanol was measured with an Anton Paar Alcolyser DMA 4500 density meter. Sugar to ethanol conversion rate was calculated as the ratio of potential wine alcohol according to TSS measurements and ethanol level measured in wines.

Ester and Higher Alcohol Analysis in Wines. All of the esters, except ethyl leucate, ethyl acetate, and ethyl phenylacetate, were quantified using a mix of isotopically labeled esters as previously described[21] by employing CDN isotopes (Pointe-Claire, Canada). The final solution used to spike the samples was composed of 20 mg/L [$^2H_5$]-ethyl butyrate, 20 mg/L [$^2H_5$]-ethyl hexanoate, [$^2H_{15}$]-ethyl octanoate, 4 mg/L [$^2H_{23}$]-ethyl decanoate, and 5 mg/L [$^2H_5$]-ethyl cinnamate. Twenty microliters of internal standard mix solution was added to an exact 10 mL volume of wine. A 5 mL sample aliquot was placed into a 20 mL SPME vial previously filled with 3 g of NaCl and diluted with 5 mL of deionized water. The samples were immediately capped and analyzed by HS-SPME-GC-MS as described previously by Antalick et al.[21] with a PDMS-CAR-DVB fiber (Supelco, Bellefonte, PA, USA). Fibers were desorbed into an Agilent 7890 gas chromatograph fitted with a DB-WAXetr capillary column (60 m, 0.25 mm, 0.25 μm film thickness, J&W Scientific, Folsom, CA, USA) using a Gerstel MPX autosampler with a Peltier tray cooler at 4 °C. The GC was coupled to a 5975C mass spectrometer (Agilent Technologies) operating in electron ionization mode using selected ion monitoring (SIM) and scan modes simultaneously. All of the esters, except ethyl leucate, ethyl acetate, and ethyl phenylacetate, were quantified using SIM mode as described elsewhere.[21] *trans*-2-Hexenyl and *cis*-3-hexenyl acetates were quantified with ions 100 and 82, respectively. Ethyl leucate and ethyl phenylacetate were semiquantitatively analyzed in SIM with ions 87 and 91, respectively. Ethyl acetate and the higher alcohols (propanol, isoamyl alcohol, isobutanol, and phenylethanol) were semiquantitatively measured in scan mode using total ion chromatogram (TIC). Relative concentrations were calculated using [$^2H_5$]-ethyl butyrate for ethyl acetate, propanol, isobutanol, and isoamyl alcohol, [$^2H_5$]-ethyl hexanoate for *trans*-2-hexenyl acetate, *cis*-3-hexenyl acetate, and ethyl leucate, and [$^2H_5$]-ethyl cinnamate for ethyl phenylacetate and phenylethanol.

C6-Compounds Analysis in Grapes. Hexanol, hexanal, *E*-2-hexenol, *E*-2-hexenal, *Z*-3-hexenol, and *Z*-3-hexenal were analyzed in grapes using a method adapted from Loscos et al.[22] Grapes were deseeded in the presence of liquid nitrogen and homogenized with a ball mill TissueLyser (Quiagen, Retsch, Shenzhen, China) for 30 s at 20 Hz. Approximately 500 mg of grape berry powder was weighed into the SPME vial in the presence of liquid nitrogen. Two milliliters of acidic buffer containing 5g/L of tartaric acid and 2 g/L of ascorbic acid with pH adjusted to 3.0 was added to the frozen grape berry powder. Samples were spiked with 15 μL of internal standard containing octan-2-ol and [$^2H_{12}$]-hexanal at concentrations of 68 and 46.5 mg/L, respectively, and 0.5 g of sodium chloride was added to the vial. Vials were randomly positioned on a tray cooler set at 4 °C prior to analysis to limit the influence of sample order on the results due to lipoxygenase activity. Samples were analyzed by HS-SPME-GC-MS with a PDMS-CAR-DVB fiber (Supelco). Fibers were desorbed at 250 °C in splitless mode for 1 min into an Agilent 7890 gas chromatograph fitted with a DB-WAXetr capillary column (60 m, 0.25 mm, 0.25 μm film thickness, J&W Scientific) using a Gerstel MPX autosampler with a Peltier tray cooler at 4 °C. The oven temperature was programmed at 40 °C for 5 min, then raised to 220 °C at 3 °C/min, and then held at that temperature for 30 min. The GC was coupled to a 5975C mass spectrometer (Agilent Technologies) operating in electron ionization mode using SIM and scan modes simultaneously. Quantifying ions

DOI: 10.1021/acs.jafc.5b00966
J. Agric. Food Chem. 2015, 63, 4664−4672

Table 1. Grapes, Juice, and Wine Analytical Parameters[a,b,c]

	Cabff	Cabmf	Shff	Shmf
harvest date:	March 6, 2013	March 22, 2013	Feb 20, 2013	March 6, 2013
grapes				
berry fresh mass (g)	0.81 ± 0.04b	0.79 ± 0.05b	1.11 ± 0.1a	1.04 ± 0.04a
fresh juice				
TSS (°Brix)	20.9 ± 0.5b	22.7 ± 0.3a	21.1 ± 0.1b	23.0 ± 0.2a
pH	3.55 ± 0.01c	3.69 ± 0.04b	3.63 ± 0.04b	3.98 ± 0.03a
TA (g/L)	4.7 ± 0.15a	4.4 ± 0.15ab	4.2 ± 0.09b	3.1 ± 0.06c
FAN (mg/L as N)	73 ± 2c	85 ± 3b	99 ± 5a	104 ± 2a
ammonium (mg/L as N)	115 ± 1a	90 ± 3b	45 ± 2c	37 ± 2d
YAN (mg/L as N)	175 ± 2a	159 ± 1b	136 ± 6c	135 ± 3c
FAN:Am	0.63 ± 0.01d	0.94 ± 0.06c	2.18 ± 0.05b	2.84 ± 0.08a
wine				
pH	3.60 ± 0.01b	3.71 ± 0.01a	3.60 ± 0.01b	3.74 ± 0.01a
TA (g/L)	5.8 ± 0.0a	5.9 ± 0.2a	5.8 ± 0.0a	5.8 ± 0.0a
ethanol (v/v)	10.7 ± 0.2c	11.6 ± 0.3b	11.5 ± 0.1b	12.4 ± 0.0a
acetic acid (g/L)	0.29 ± 0.02b	0.27 ± 0.02b	0.36 ± 0.02a	0.21 ± 0.01c
sugar:ethanol (%)	88.7 ± 2.8bc	86.3 ± 1.5c	93.3 ± 0.6a	91.0 ± 1.0b

[a]Cabff, Cabernet Sauvignon fresh fruit; Cabmf, Cabernet Sauvignon mature fruit; Shff, Shiraz fresh fruit; Shmf, Shiraz mature fruit. [b]One-way ANOVA was used to compare data. Means followed by different letters in a row are significant at $p \leq 0.05$ (Fischer's LSD). All quoted uncertainty is the standard deviation of three replicates per treatment. [c]TSS, total soluble solids; TA, titratable acidity; FAN, free amino nitrogen; YAN, yeast assimilable nitrogen; sugar:ethanol, sugar to ethanol conversion rate; FAN:Am, ratio of free amino nitrogen (mg/L as N) to ammonium concentration (mg/L as N).

chosen for the internal standards were 45 for octan-2-ol and 92 for [$^2H_{12}$]-hexanal. C6-compounds were measured in SIM mode in a semiquantitative way using peak to area ratios and octan-2-ol and [$^2H_{12}$]-hexanal as internal standards for alcohols and for aldehydes, respectively. Compound identity was confirmed by checking the mass spectra in scan mode performed simultaneously to SIM mode and comparing the retention times with those available in the literature. Quantifying ions chosen were 56 for hexanal and hexanol, 83 for *E*-2-hexenal and *Z*-3-hexenal, 57 for *E*-2-hexenol, and 67 for *Z*-3-hexenol.

Lipid Analysis in Grapes. Oleic, linoleic, and linolenic acids were analyzed by semiquantification according to a method adapted from Roufet et al.[23] A 1 g sample of frozen grape powder prepared as previously described was weighed into a 20 mL glass vial and immediately extracted to limit lipid oxidation. Semiquantitative analysis was performed by adding 1 mL of 1 g/L decanoic acid solution as internal standard to samples immediately prior to extraction. The amount of decanoic acid added was approximately 10000 times higher than the initial concentration of this compound present in grape berry samples. Therefore, the initial concentration of decanoic acid present in grapes did not interfere with lipid quantification. Lipid extraction was performed three times for 5 min by stirring in 10 mL, followed by two 5 mL mixtures of chloroform/methanol (2:1). The chloroform phases were collected and pooled. Lipids were thereafter methylated to be analyzed by GC-MS, stirring the chloroform phase with 5 mL of a 3% methanolic solution of HCl for 1 h. The organic phase was washed twice with deionized water and collected for drying over ammonium sulfate. Organic extracts were concentrated to 2 mL by evaporation under low pressure before being injected in GC-MS. A 1 μL sample volume of extract was injected at 250 °C in split mode (ratio 10:1) into the same chromatograph and column as previously described. The oven temperature was programmed at 40 °C, then immediately raised to 220 °C at 8 °C/min, and then held at that temperature for 57.5 min. The mass spectrometer was operating in electron ionization mode using SIM and scan modes simultaneously. Methyl esters of lipids were analyzed in SIM mode in a semiquantitative manner using peak to area ratios and decanoic acid as an internal standard. Quantifying ions chosen were 74 for methyl decanoate, 55 for methyl oleate, 67 for methyl linoleate, and 79 for methyl linolenate. The identity of compounds was confirmed by checking the mass spectra in scan mode performed simultaneously to SIM mode and comparing the retention times with the retention indices available in the literature. Qualification ions were used in SIM mode to avoid any integration mistake (87 for methyl decanoate, 264 for methyl oleate, 294 for methyl linolenate, and 292 for methyl linolenate).

Amino Acid Analysis in Grapes. The extraction protocol for amino acids from frozen grape berry powder was adopted from a previously published method.[24] Grape berry powder sample weight was reduced from 2.5 (±0.1) to 0.1 (±0.0005) g. To maintain the ratio of grape powder/extraction medium 1:1 (w/v),[25] 100 μL of a water/methanol mixture (20:80) was added to the samples. The samples were then vigorously vortexed (MS 3 basic, IKA, Selangor, Malaysia) for 1 min and sonicated at room temperature for 15 min to complete the extraction. Samples were then centrifuged for 10 min at 12000g, and the supernatant was collected and placed in a new Eppendorf tube for the derivatization process as described elsewhere.[25] Briefly, grape extracts were diluted 1:20 (v/v) with 0.25 M borate buffer (pH 8.5). The amino groups were derivatized with 9-fluoroenyl-ethyl chloroformate, and an internal standard of 13.1 mg/L L-hydroxyproline was used. Amino acids were analyzed by high-performance liquid chromatography (HPLC) using a Waters 600 controller (Milford, MA, USA) connected to an autosampler (Waters 717 plus). Separation of amino acids was achieved with a reverse phase column (Thermo 5 μm ODS hypersil, Waltham, MA, USA) and quantification with a fluorescence detector (Waters 2475). The column temperature was increased to 45 °C to separate γ-aminobutyric acid and proline. Quantification was performed as previously reported.[24]

Statistical Analysis. One-way and two-way analyses of variance (ANOVA) for the variables cultivar and harvest date were performed on the chemical data using Statistica, version 12 (StatSoft, Tulsa, OK, USA), and the means were separated using Stats-Fisher's LSD test (different letters account for significant differences at $p \leq 0.05$).

RESULTS AND DISCUSSION

Description of Grape Juice Parameters. In the present study both cultivars were harvested at very similar TSS contents (Table 1); therefore, it is unlikely that differences observed in wine ester profile between cultivars for a given maturity stage originated from yeast sugar metabolism. The FF harvest was performed at approximately 21 °Brix, whereas grapes were harvested at around 23 °Brix for the MF harvest (Table 1).

DOI: 10.1021/acs.jafc.5b00966
J. Agric. Food Chem. 2015, 63, 4664−4672

Table 2. Mean Concentrations of Esters for Each Group of Wines[a]

	concentration[b] (μg/L)				*p* value[c]		
compound	Cabff	Cabmf	Shff	Shmf	cultivar	harvest stage	cultivar × harvest stage
ethyl esters of straight-chain fatty acids							
ethyl propionate	157 ± 5.5a	147 ± 9.3a	151 ± 9.5a	143 ± 8.8a	0.283	0.108	0.824
ethyl butyrate	119 ± 3.7bc	109 ± 5.6c	120 ± 3b	133 ± 8.2a	**0.004**	0.604	**0.008**
ethyl hexanoate	508 ± 18a	434 ± 15b	522 ± 2.2a	549 ± 22a	**<0.001**	**0.035**	**<0.001**
ethyl octanoate	510 ± 30a	451 ± 24b	522 ± 4.3a	571 ± 45a	**0.005**	0.776	**0.012**
ethyl decanoate	124 ± 12ab	105 ± 5.5b	135 ± 12a	138 ± 17a	**0.016**	0.319	0.171
ethyl dodecanoate	15.5 ± 2.6ab	11.9 ± 1.7b	19.5 ± 2.1a	18.5 ± 2.6a	**0.004**	0.125	0.367
higher alcohol acetates							
propyl acetate	31.5 ± 1.3ab	31.8 ± 1.1ab	28.8 ± 2.3b	33.9 ± 1.6a	0.763	**0.018**	**0.033**
isobutyl acetate	18.1 ± 2.1d	21.4 ± 0.99c	34.9 ± 1.4a	28.9 ± 2.6b	**<0.001**	0.261	**0.003**
isoamyl acetate	473 ± 49c	596 ± 39b	1389 ± 34a	1294 ± 123a	**<0.001**	0.737	**0.039**
hexyl acetate	5.6 ± 0.5b	4.9 ± 0.2b	48.2 ± 1.7a	46.4 ± 0.04a	**<0.001**	**0.049**	0.305
trans-2-hexenyl acetate	0.27 ± 0.02b	0.24 ± 0.03b	0.91 ± 0.06a	0.87 ± 0.09a	**<0.001**	0.283	0.834
cis-3-hexenyl acetate	0.021 ± 0.03c	0.013 ± 0.02d	0.47 ± 0.03a	0.31 ± 0.03b	**<0.001**	**<0.001**	**<0.001**
phenylethyl acetate	54 ± 7.5d	71.5 ± 6c	95 ± 10.6b	119 ± 7.8a	**<0.001**	**0.002**	0.508
ethyl esters of branched acid							
ethyl isobutyrate	30 ± 2.7b	43.5 ± 7.3a	54.7 ± 3.6a	34.4 ± 2.6b	**0.017**	**0.023**	**<0.001**
ethyl 2-methylbutyrate	10 ± 0.5b	14.2 ± 1.6a	10.8 ± 0.3b	7.6 ± 0.4c	**<0.001**	0.318	**<0.001**
ethyl isovalerate	11.8 ± 0.5b	16.6 ± 2.1a	14.8 ± 0.37a	10.2 ± 0.5c	**0.037**	0.884	**<0.001**
ethyl leucate[d]	0.008 ± 0.001b	0.010 ± 0.001a	0.009 ± 0a	0.006 ± 0.001c	0.068	0.392	**0.002**
ethyl phenylacetate[d]	1.06 ± 0.19a	1.32 ± 0.08a	0.73 ± 0.06b	0.6 ± 0.04c	**<0.001**	0.356	**0.015**
miscellaneous compounds							
ethyl cinnamate	2.23 ± 0.5a	2.36 ± 0.39a	1.31 ± 0.25b	1.31 ± 0.2b	**0.001**	0.768	0.768
ethyl acetate[d]	2.2 ± 0.1a	2.3 ± 0.1a	2.2 ± 0.1a	2.2 ± 0.2a	0.477	0.404	0.124
propanol[d]	0.45 ± 0.02a	0.47 ± 0.15a	0.34 ± 0.02b	0.44 ± 0.05a	**0.004**	**0.004**	**0.037**
isobutanol[d]	0.13 ± 0.04a	0.16 ± 0.05a	0.16 ± 0.05a	0.14 ± 0.03a	0.889	0.854	0.289
isoamyl alcohol[d]	21.7 ± 1.1b	25.5 ± 1.2a	22.9 ± 0.18b	22.3 ± 1.4b	0.133	**0.031**	**0.007**
phenylethanol[d]	189 ± 29.6a	209 ± 21.3a	138 ± 6.7b	146 ± 10.4b	**<0.001**	0.227	0.559

[a]Cabff, Cabernet Sauvignon fresh fruit; Cabmf, Cabernet Sauvignon mature fruit; Shff, Shiraz fresh fruit; Shmf, Shiraz mature fruit. [b]Two-way ANOVA was used to compare data. Means expressed in μg/L followed by different letters in a row are significant at $p \leq 0.05$ (Fischer's LSD). All quoted uncertainty is the standard deviation of three replicates of one treatment. [c]Significance of two-way ANOVA for cultivar, harvest date, and interaction cultivar × harvest date. Bold numbers indicate significant differences. [d]Compound measured by semiquantification; relative peak areas (compound:internal standard areas ratio) were used to calculate means and standard deviation.

However, the relationship between potential variations in esters during ripening and yeast sugar metabolism is difficult to establish. Yeast ester metabolism depends not only on yeast sugar metabolism,[11] and the relationship between grape berry sugar accumulation and aromatic maturity is complicated, often indirect, and compound specific.[26]

Higher pH and lower TA values were measured for MF stage compared to FF and for Shiraz compared to Cabernet Sauvignon juice (Table 1), but these differences were reduced before fermentation by the addition of tartaric acid. Consequently, TA concentrations were similar in all of the wines, whereas wine pH values were similar between cultivars, remaining higher in the MF stage in comparison to FF (Table 1).

The general nitrogen composition significantly differed between cultivars and, to a lesser extent, maturity stages. Cabernet Sauvignon grapes exhibited higher values of YAN than Shiraz mainly due to higher concentrations of ammonium regardless of nutrient addition (Table 1). In contrast, Shiraz grape juices showed higher concentrations of free amino nitrogen (FAN). Therefore, FAN:ammonium ratios were 3–3.5-fold higher in Shiraz than Cabernet Sauvignon grape juices (Table 1). These values decreased from 1.8- to 2.1-fold higher in Shiraz than Cabernet Sauvignon when the nutrient additions were taken into consideration. The comparison of relative grape juice nitrogen composition between Shiraz and Cabernet Sauvignon has not been previously reported in the literature. In addition, ammonium concentrations significantly decreased during ripening for both varieties, whereas FAN increased over maturation only in Cabernet Sauvignon (Table 1). The decrease of ammonium and the lack of consistency for increasing FAN over grape ripening have both been extensively reported in the literature.[16]

Varietal and Maturity Effect on Esters Concentrations. Quantified esters were grouped according to their origin into three groups: ethyl esters of fatty acids (EEFAs), ethyl esters of branched acids (EEBAs), and higher alcohol acetates (HAAs) (Table 2). A two-way ANOVA was used to assess the effect of cultivar, maturity (harvest date), and cultivar × maturity interactions on esters and amino acid variations. Interestingly, 80% of esters measured in this study were influenced by a varietal effect, whereas only 30% were influenced by grape maturity (Table 2). Similar results were found for most of the amino acids (Table 3).

Ethyl Esters of Fatty Acids. Overall, similar ranges of EEFA concentrations were measured in Cabernet Sauvignon and Shiraz wines (Table 2). However, some variations in EEFAs were observed between wines, and interestingly they were more related to variety than maturity (Table 2). Indeed, five of six EEFAs were influenced by cultivar, whereas only ethyl

DOI: 10.1021/acs.jafc.5b00966
J. Agric. Food Chem. 2015, 63, 4664–4672

Table 3. Mean Concentrations of Amino Acids with Their Standard Deviations[a]

	concentration[b] (μg/g of berry)				p value[c]		
compound	Cabff	Cabmf	Shff	Shmf	cultivar	harvest stage	cultivar × harvest stage
yeast-preferred amino acids							
aspartic acid	18.7 ± 0.9b	14.7 ± 3.2c	25.1 ± 2.9a	18.9 ± 0.4b	**0.003**	**0.004**	0.409
glutamic acid[d]	0.022 ± 0.001bc	0.013 ± 0.002c	0.034 ± 0.02a	0.027 ± 0.004b	**<0.001**	**<0.001**	0.183
asparagine	2.7 ± 0.4bc	1.7 ± 0.5c	3.6 ± 0.9ab	4.7 ± 0.9a	**0.002**	0.969	**0.030**
glutamine	58 ± 12.6bc	86.9 ± 14.7a	51.3 ± 2.6c	66.7 ± 8.7b	0.059	**0.007**	0.304
serine	44.0 ± 3.3b	43.6 ± 4.0b	43.9 ± 1.7b	52.4 ± 3.9a	0.055	0.068	**0.047**
alanine	42.5 ± 6.3b	43.9 ± 4.6b	52.6 ± 7.8ab	56.1 ± 4.9a	**0.012**	0.493	0.773
arginine	371 ± 38b	336 ± 73b	806 ± 47a	925 ± 121a	**<0.001**	0.373	0.119
branched amino acids							
valine	31.8 ± 4.1b	42.5 ± 5.3a	28.2 ± 0.9b	39.7 ± 3.0a	0.172	**<0.001**	0.844
isoleucine	13.4 ± 1.6b	22.4 ± 2.6a	11.9 ± 1.9b	20.5 ± 4.9a	0.353	**<0.001**	0.902
leucine	25.8 ± 3.3b	33.6 ± 2.7a	23.8 ± 1.7b	36.0 ± 4.1a	0.914	**<0.001**	0.255
phenylalanine	12.3 ± 0.7a	7.8 ± 0.6c	9.8 ± 1.0b	10.4 ± 2.2ab	0.967	**0.030**	**0.008**
other amino acids							
proline	2710 ± 414b	3498 ± 118a	318 ± 13d	556 ± 89c	**<0.001**	**0.004**	0.062
hystidine	3.5 ± 0.4b	4.1 ± 0.2a	2.9 ± 0.2c	3.4 ± 0.7bc	**0.028**	0.052	0.849
glycine	28.8 ± 4.5a	29.8 ± 5.8a	7.6 ± 0.5b	6.8 ± 3.1b	**<0.001**	0.946	0.699
threonine	37.4 ± 2.7b	39.5 ± 7.2b	58.4 ± 3.0a	61.5 ± 6.2a	**<0.001**	0.405	0.867
γ-aminobutyric acid	108 ± 9.5c	114 ± 10.2bc	122 ± 3.0b	155 ± 29a	**0.0187**	0.065	0.175
methionine	11.5 ± 1.6b	18.4 ± 5.2a	3.5 ± 0.2d	5.5 ± 0.9c	**<0.001**	**0.024**	0.161
lysine	5.3 ± 0.5b	5.7 ± 0.5a	9.2 ± 0.9a	11.1 ± 3.2a	**0.003**	0.327	0.533

[a]Cabff, Cabernet Sauvignon fresh fruit; Cabmf, Cabernet Sauvignon mature fruit; Shff, Shiraz fresh fruit; Shmf, Shiraz mature fruit. [b]Two-way ANOVA was used to compare data. Means expressed in μg/g of berry weight followed by different letters in a row are significant at $p \leq 0.05$ (Fischer's LSD). All quoted uncertainty is the standard deviation of three replicates of one treatment. [c]Significance of two-way ANOVA for cultivar, harvest date, and interaction cultivar × harvest date. Bold numbers indicate significant differences. [d]Compound measured by semiquantification, relative peak area (compound:internal standard areas ratio) were used to calculate means and standard deviation.

hexanoate varied according to maturity (Table 2). Similar results have been recently reported in Australian Riesling;[26] however, the differences in EEFA concentrations between Cabernet Sauvignon and Shiraz wines were significant only for the MF stage (Table 2). EEFA concentrations decreased in Cabernet Sauvignon wines during maturation, particularly for ethyl hexanoate and octanoate. These two esters were subject to interactions between cultivar and harvest stage effect (Table 2). On the other hand, EEFA concentrations in Shiraz wines were steady over maturation (Table 2). Increases of EEFAs concentrations during grape ripening have been recently reported in Australian Cabernet Sauvignon.[27] The contrast observed between the different studies suggests that the link between grape composition and yeast EEFA metabolism is complex. EEFAs are generally synthesized by yeast during alcoholic fermentation, and their levels in wines seem to largely depend on winemaking conditions such as fermentation temperature, aeration, skin contact, and yeast strain.[11,28] In the present study these type of parameters (temperature, yeast strain, time of skin contact, punching down frequency) were standardized by the winemaking protocol. In parallel, the nitrogen composition of grape juice seems to influence EEFA synthesis to a lesser extent,[29] and the relative variations observed for this group of esters were the smallest of all the wine volatiles analyzed in this study (Table 2).

Ethyl Esters of Branched Acids. EEBA variations were largely driven by interactions between grape maturity and the choice of the cultivar (Table 2). In the present study Cabernet Sauvignon and Shiraz displayed opposite trends during grape maturation (Table 2). Although grape maturation favored higher concentrations of EEBAs in Cabernet Sauvignon, it significantly reduced EEBA concentrations in Shiraz wines (Table 2). At FF stage the concentrations of ethyl isobutyrate, isovalerate, and leucate were higher in Shiraz wines, whereas the concentrations of these esters and ethyl 2-methylbutyrate were higher in Cabernet Sauvignon wines at MF stage (Table 2). These variations were particularly evident for ethyl isobutyrate, with concentrations of 30 and 54.7 μg/L in Shiraz and Cabernet Sauvignon, respectively, at FF stage, representing a 1.8 factor difference.

EEBAs are primarily synthesized during wine aging by esterification between branched acids and ethanol.[28,30] However, a small proportion is also biosynthesized by yeast during alcoholic fermentation through branched amino acid metabolism.[31] Consequently, branched amino acid juice composition significantly affects EEBA concentrations and their corresponding acids found in wines. In the present study the concentrations of branched amino acids measured in grapes were predominantly influenced by maturity without specific varietal effect (Table 3). The similar concentrations of branched amino acids measured in Cabernet Sauvignon and Shiraz grapes increased with grape maturity. The variations measured during ripening in Cabernet Sauvignon grapes may be linked to the increase of EEBA concentrations observed in the corresponding wines. Prior observations support the trend of increased EEBAs during grape maturation in Cabernet Sauvignon.[27] On the other hand, the decreases of EEBA concentrations with grape maturity observed in Shiraz wines (Table 2) did not reflect the variations of branched amino acids contents in the corresponding grape berries (Table 3). In that case, EEBA variations could be potentially linked to yeast redox metabolism as suggested by previous studies.[28,31] This hypothesis is supported by the similar variations observed in Shiraz wines for acetic acid and the highest variations measured

DOI: 10.1021/acs.jafc.5b00966
J. Agric. Food Chem. 2015, 63, 4664−4672

for ethyl isobutyrate (Tables 1 and 3). Acetic acid production during alcoholic fermentation is known to depend on yeast redox metabolism,[32] and it has been recently suggested that isobutyric acid could also be a specific marker of yeast redox metabolism.[28,33] However, such speculations will need to be studied in the future using appropriate investigations.

Interestingly, ethyl phenylacetate, ethyl cinnamate, and 2-phenylethanol concentrations were significantly higher in Cabernet Sauvignon wines irrespective of the grape maturity stage (Table 2). Weldegergis et al.[34] reported that Cabernet Sauvignon wines exhibited significantly higher concentrations in 2-phenylethanol than Shiraz wines. Other authors suggested that benzene derivatives could be considered as markers of ripe Cabernet Sauvignon grapes.[35] Ethyl phenylacetate, cinnamate, and 2-phenylethanol are derived from phenyalanine metabolism, originating from yeast, grapes, and yeast and grapes, respectively.[28,35] In the present study, no trend between these compounds in wines and the phenylalanine concentrations of the corresponding grapes are evident (Table 3). The variations measured in wines for ethyl phenylacetate, cinnamate, and 2-phenylethanol might therefore reflect differences of phenylalanine metabolism between Cabernet Sauvignon and Shiraz varieties.

Higher Alcohol Acetates. The most important varietal effect in regard to the relative variations of ester concentrations was observed for HAAs. Conversely, maturity levels exhibited a lower effect on this group of esters (Table 2). Shiraz wines, irrespective of maturity stage, displayed significantly higher concentrations of all HAAs except propyl acetate in comparison to Cabernet Sauvignon wines (Table 2). Two groups of HAAs were influenced by measured parameters: acetates of higher alcohols from yeast nitrogen and sugar metabolism and C6-acetates from grape lipid degradation. Isobutyl, isoamyl, and 2-phenylethyl acetates, classified in the first group, were at concentrations from 1.5- to 3-fold higher in Shiraz compared to Cabernet Sauvignon wines (Table 2). These esters were also influenced by harvest date; however, the effect was ester specific. In Shiraz wines 2-phenylethyl acetate concentration increased with maturity, whereas concentrations of isoamyl and isobutyl acetates decreased slightly. On the other hand, the concentrations of these acetates increased with grape maturity in Cabernet Sauvignon wines. These results are supported by previous observations made in Cabernet Sauvignon wines,[27] whereas there is no previous reported information with regard to Shiraz. Furthermore, important varietal differences were also noted for C6-acetates as hexyl, *cis*-3-hexenyl, and *trans*-2-hexenyl acetates. Concentrations of hexyl and *cis*-3-hexenyl acetates were 9- and 22-fold higher, respectively, in Shiraz than in Cabernet Sauvignon wines. Such quantitative differences in acetate esters, particularly for isoamyl and hexyl acetates, may alter the aromatic profile of red wines.[9]

Investigations on the Origin of Varietal Differences in Higher Alcohol Acetate Composition. Higher alcohol acetates were the group of esters most influenced by variety. Only propyl acetate exhibited variations between harvest dates and cultivars that were well correlated to the variation of the corresponding higher alcohol (Table 2). Other acetates derived from amino acid metabolism, such as isobutyl, isoamyl, and 2-phenylethyl acetate, were quantified at significantly higher concentrations in Shiraz than in Cabernet Sauvignon wines (Table 2). Unlike propyl acetate, no specific relationship could be established between the levels of higher alcohols (isobutanol, isoamyl alcohol, 2-phenylethanol) and the corresponding acetates measured in wines (Table 2). Higher alcohol acetates are mainly synthesized during alcoholic fermentation by yeast from acetyl-CoA and higher alcohols through alcohol acetyltransferase activities.[11] Even though higher alcohol availability strongly influences HAA production, the limiting factor for their synthesis is the expression of alcohol acetyltransferase activities.[11] Oxygen, lipids, and nitrogen are the main nutrients found in must, which are known to particularly regulate alcohol acetyltransferase.[11] It could be reasonably expected that oxygen levels in the grape musts prior to fermentation were similar for all wines due to the standardization of the winemaking protocol. Moreover, unsaturated fatty acids, known to repress alcohol acetyltransferase expression, were higher in Shiraz grapes, whereas Shiraz wines exhibited higher concentrations of HAAs (Figure 1; Table 2). This contrast indicates that it is unlikely that cultivar differences observed for HAAs between Shiraz and Cabernet Sauvignon wines originated from alcohol acetyltransferase repression due to lipid concentrations. The influence of grape lipids on HAA production in Shiraz wines by boosting cellular growth and general yeast metabolism[36,37] cannot, however, be fully excluded.

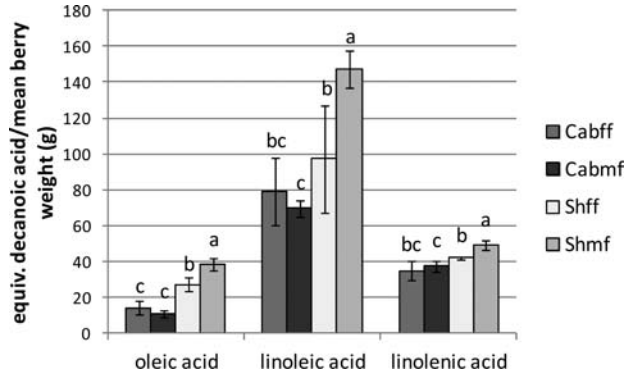

Figure 1. Mean ± SD of unsaturated fatty acids in grape berries expressed as decanoic acid equivalent per gram of berry weight. One-way ANOVA was used to compare data. Different letters above bars indicate significance at $p \leq 0.05$ (Fischer's LSD). All quoted uncertainty is the standard deviation of three replicates per treatment. Cabff, Cabernet Sauvignon fresh fruit; Cabmf, Cabernet Sauvignon mature fruit; Shff, Shiraz fresh fruit; Shmf, Shiraz mature fruit.

Yeast assimilable nitrogen (YAN) is the most common analytical parameter used to assess grape juice nitrogen status. In general, higher YAN concentration favors higher HAA production.[38,39] Must YAN levels could be considered as low to moderate[16] for both cultivars, with slightly higher values in Cabernet Sauvignon compared to Shiraz (Table 1). Consequently, no direct link between YAN and HAA production could be established in the present study. However, YAN composition differed greatly between both varieties with a higher ratio FAN:ammonium measured in Shiraz musts regardless of nutrient addition. This is due to higher FAN and lower ammonium concentrations in Shiraz compared to Cabernet Sauvignon (Table 1).

On the other hand, some of the amino acids assimilable by yeast that contribute to FAN have been classified as "preferred" in regard to their importance for yeast metabolism.[40] Interestingly, Shiraz grapes consistently possessed higher concentrations of "preferred" amino acids than Cabernet Sauvignon (Table 3). High amino nitrogen media may

DOI: 10.1021/acs.jafc.5b00966
J. Agric. Food Chem. 2015, 63, 4664−4672

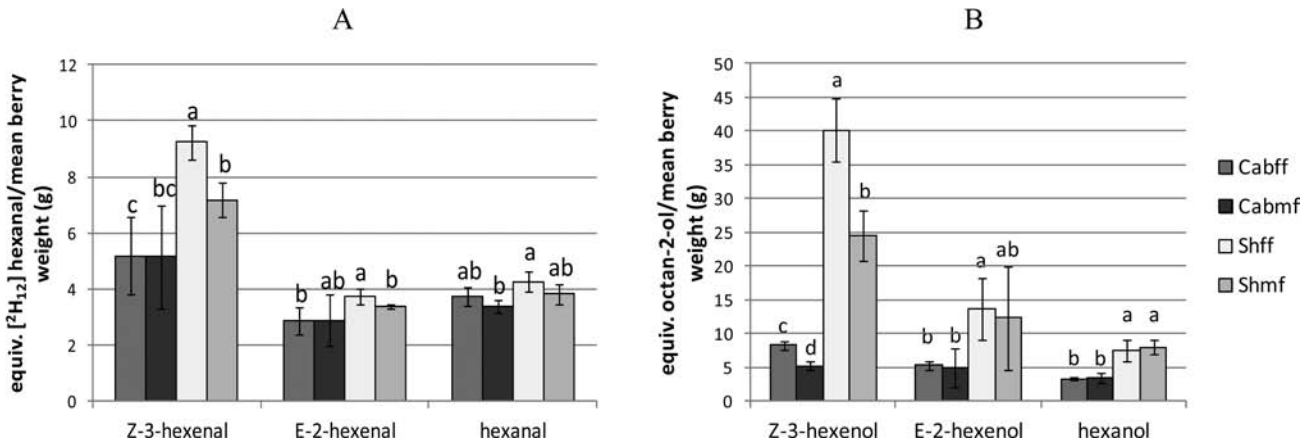

Figure 2. Mean ± SD of C6-aldehydes (A) and C6-alcohols (B) in grape berries expressed as equivalent [$^2H_{12}$]-hexanal and octan-2-ol per gram of berry weight. One-way ANOVA was used to compare data. Different letters above bars indicate significance at $p \leq 0.05$ (Fischer's LSD). All quoted uncertainty is the standard deviation of three replicates per treatment. Cabff, Cabernet Sauvignon fresh fruit; Cabmf, Cabernet Sauvignon mature fruit; Shff, Shiraz fresh fruit; Shmf, Shiraz mature fruit.

stimulate alcohol acetyltransferase expression and, consequently, HAA synthesis by yeast.[41] Furthermore, alcohol acetyltransferase expression has been reported to be particularly important during the early stage of the fermentation.[42] Amino acid uptake by yeast is also known to be maximal during the early phase of alcoholic fermentation as ethanol inhibits their transfer from the external medium into yeast cell.[43] In parallel, ammonium is the first source of nitrogen assimilated by yeast.[16] Therefore, a low ratio of FAN:ammonium in must may down-regulate yeast metabolic activity due to the lower assimilation of amino acids during the early stages of alcoholic fermentation.[43] A relationship between grape nitrogen composition and the varietal differences for HAAs in wines is suggested. Higher levels of FAN and FAN:ammonium ratio found in Shiraz grapes may influence the yeast metabolism that favors alcohol acetyltransferase expression and consequently HAA synthesis. Some cultivars rich in amino nitrogen such as Pinotage are known to exhibit specific esters profile with high concentrations of HAAs.[14] Sugar to ethanol conversion rates were also higher in Shiraz (Table 1). Glycolytic enzymes involved in the conversion of sugar to ethanol are known to be especially influenced by FAN:ammonium balance.[43] This helps explain the differences in HAAs between varieties found in this study and suggests an important relationship between grape nitrogen composition and yeast metabolism regardless of the nitrogen supplementation in the winery. Further studies linking grape nitrogen composition and HAA production by yeast at microbiological and transcriptomic levels are therefore warranted. The influence of other grape metabolites on yeast ester metabolism also requires further investigation.

The varietal differences between Shiraz and Cabernet Sauvignon were the most important for C6-acetates. These esters are derived from the acetylation of C6-alcohols originating from lipid oxidation in grape berries throughout ripening and during crushing.[35,44] Surprisingly, in the present study Shiraz grapes exhibited much higher concentrations of C6-alcohols and C6-aldehydes, particularly *Z*-3-hexenol and *Z*-3-hexenal, than Cabernet Sauvignon (Figure2). Therefore, in this case the stimulation of acetate synthesis in Shiraz wines due to nitrogen composition was accentuated by a higher synthesis of C6-compounds in Shiraz grapes. Interestingly, the levels of linoleic and linolenic acid, from which C6-aldehydes and alcohols are derived, were similar at FF stage between Shiraz and Cabernet Sauvignon grapes (Figure 1), whereas C6-compound contents were significantly higher in Shiraz compared to Cabernet Sauvignon grapes (Figure 2). This result suggests that in the vineyards studied, some enzymes involved in the lipoxygenase pathway may have been more active in Shiraz in comparison to Cabernet Sauvignon, at least for the early stage of grape maturation. For the MF stage, unsaturated fatty acids were measured at higher levels in Shiraz compared to Cabernet Sauvignon grapes (Figure 1), causing the origin of varietal differences of C6-compounds in grapes to be less clear. Further studies that investigate potential differences in the lipoxygenase pathway between Shiraz and Cabernet Sauvignon would be of interest.

This study has demonstrated that red wine ester profiles could be strongly influenced by grape composition and, in particular, grape nitrogen and lipid metabolism. New perspectives for a more detailed investigation to determine the impact of nitrogen and lipid interactions on yeast ester metabolism have been proposed. The present study is the first to investigate varietal differences in ester profiles of Shiraz and Cabernet Sauvignon wines made with grapes harvested from commercial vineyards at different maturity stages. This work was performed in a very warm climatic region of Australia on irrigated vines. Consequently, the variations in ester profiles between Shiraz and Cabernet Sauvignon wines observed in this study may reflect varietal differences in grape composition arising from different responses to abiotic factors and potential stress or constraints (temperature, heat waves, water constraint pre- and post-veraison, and light quality and quantity at the canopy and fruit zone levels) as it has been recently reported in Sauvignon blanc wines.[45] Further investigations will be needed to determine if the varietal differences observed in this study were specific to the site chosen or if they can be extrapolated to a wider scale.

AUTHOR INFORMATION

Corresponding Author

*(G.A.) E-mail: gantalick@csu.edu.au.

Funding

We thank Australia's grape growers and winemakers for their financial support through their investment body the Australian

DOI: 10.1021/acs.jafc.5b00966
J. Agric. Food Chem. 2015, 63, 4664−4672

Grape and Wine Authority (AGWA) and the Australian federal government.

Notes

The authors declare no competing financial interest.

■ ACKNOWLEDGMENTS

We thank Jason Capello (Department of Primary Industry, NSW) for his technical support as well as Beelbangera grape growers who provided grapes.

■ REFERENCES

(1) Ribéreau-Gayon, P.; Glories, Y.; Maujean, A.; Dubourdieu, D. *Handbook of Enology. The Chemistry of Wine: Stabilisation and Treatments*; Wiley: Chichester, UK, 2000; Vol. 2.

(2) Darriet, P.; Nikolantanaki, M.; Schüttler, A.; Rauhut, D.; Pons, A.; Stamatopoulos, P. From compounds to sensory perception. What affects complexity and uniqueness of wine aroma? *Proceedings of the 15th Australian Wine Industry Technical Conference*, Sydney, Australia, AWITC; Beames K., Robinson E., Godden P., Johnson D., Eds.; 2013; pp 63−67.

(3) Allen, M. S.; Lacey, M. J.; Harris, R. L. N.; Brown, W. V. Contribution of methoxypyrazines to Sauvignon blanc wine aroma. *Am. J. Enol. Vitic.* **1991**, *42*, 109−112.

(4) Wood, C.; Siebert, T. E.; Parker, M.; Capone, D. L.; Gordon, M. E.; Pollnitz, A. P.; Eggers, M.; Meier, M.; Vössing, T.; Widder, S.; Krammer, G.; Sefton, M. A.; Herderich, M. J. From wine to pepper: rotundone, an obscure sesquiterpene, is a potent spicy aroma compound. *J. Agric. Food Chem.* **2008**, *56*, 3738−3744.

(5) Pineau, B.; Barbe, J. C.; Van Leeuwen, C.; Dubourdieu, D. Examples of perceptive interactions involved in specific "red-and-black-berry" aromas in red wines. *J. Agric. Food Chem.* **2009**, *57*, 3702−3708.

(6) Kotseridis, Y.; Baumes, R. Identification of impact odorants in Bordeaux red grape juice, in the commercial yeast used for its fermentation, and in produced wine. *J. Agric. Food Chem.* **2000**, *48*, 400−406.

(7) Escudero, A.; Campo, E.; Farina, L.; Cacho, J.; Ferreira, V. Analytical characterization of the aroma of five premium red wines. Insights into the role of odor families and the concept of fruitiness of wines. *J. Agric. Food Chem.* **2007**, *55*, 4501−4510.

(8) Pineau, B.; Barbe, J. C.; Van Leeuwen, C.; Dubourdieu, D. Which impact for β-damascenone on red wines aroma? *J. Agric. Food Chem.* **2007**, *55*, 4103−4108.

(9) Lytra, G.; Tempere, S.; de Revel, G.; Barbe, J. C. Impact of perceptive interactions on red wines fruity aroma. *J. Agric. Food Chem.* **2012**, *60*, 12260−12269.

(10) Bertrand, A. Volatiles from grape must fermentation. In *Flavour of Distilled Beverages Origin and Development*; Pigott, J. R., Horwood, E., Eds.; Wiley: Chichester, UK, 1983; pp 93−109.

(11) Sumby, K. M.; Grbin, P. R.; Jiranek, V. Microbial modulation of aromatic esters in wine: current knowledge and future prospects. *Food Chem.* **2010**, *121*, 1−16.

(12) Antalick, G.; Perello, M. C.; de Revel, G. Characterization of fruity aroma modifications in red wines during malolactic fermentation. *J. Agric. Food Chem.* **2012**, *60*, 12371−12383.

(13) Rowe, D. J.; Tangel, B. Aroma chemicals for the sweet field. *Perfum. Flavor.* **1999**, *24*, 36−41.

(14) Marais, J. Literature overview on Pinotage research; http://www.wineland.co.za/technical/literature-overview-of-pinotage-research, 2014.

(15) Hernández-Orte, P.; Cacho, J. F.; Ferreira, V. Relationship between varietal amino acid profile of grapes and wine aromatic composition. Experiments with model solution and chemiometric study. *J. Agric. Food Chem.* **2002**, *50*, 2891−2899.

(16) Bell, S. J.; Henschke, P. A. Implications of nitrogen nutrition for grapes, fermentation and wine. *Aust. J. Grape Wine Res.* **2005**, *11*, 242−295.

(17) Huglin, P. Nouveau mode d'évaluation des possibilites héliothermiques d'un milieu viticole. In *Proceedings of the Symposium International sur l'ecologie de la Vigne*; Ministère de l'Agriculture et de l'Industrie Alimentaire, Contança, 1978; pp 89−98.

(18) Tonietto, J.; Carbonneau, A. A multicriteria climatic classification system for grape-growing regions worldwide. *Agric. For. Meterol.* **2004**, *124*, 81−97.

(19) Deloire, A. Physiological indicator to predict harvest date and wine style. *Proceedings of the 15th Australian Wine Industry Technical Conference*, Sydney, Australia, AWITC; Beames K., Robinson E., Godden P., Johnson D., Eds.; 2013; pp 47−50.

(20) Iland, P., Bruer, N., Edwards, G., Caloghiris, S., Wilkes, E., Eds. *Chemical Analysis of Grapes and Wine: Techniques and Concepts*, 2nd ed.; Adelaide, Australia, 2004.

(21) Antalick, G.; Perello, M. C.; de Revel, G. Development, validation and application of a specific method for the quantitative determination of wine esters by headspace-solid-phase micro-extraction-gas chromatography-mass spectrometry. *Food Chem.* **2010**, *121*, 1236−1245.

(22) Loscos, N.; Hernández-Orte, P.; Cacho, J. F.; Ferreira, V. Comparison of the suitability of different hydrolytic strategies to predict aroma potential of different grape varieties. *J. Agric. Food Chem.* **2009**, *57*, 2468−2480.

(23) Roufet, M.; Bayonove, C. L.; Cordonnier, R. E. Etude de la composition lipidique du raisin, *Vitis vinifera* L.: evolution au cours de la maturation et localisation dans la baie. *Vitis* **1987**, *26*, 85−97.

(24) Gika, H. G.; Theodoridis, G. A.; Vrhovsek, U.; Mattivi, F. Quantitative profiling of polar primary metabolites using hydrophilic interaction ultrahigh performance liquid chromatography−tandem mass spectrometry. *J. Chromatogr., A* **2012**, *1259*, 121−127.

(25) Hynes, P.; Sheumack, D.; Greig, L.; Kibby, J.; Redmond, J. Application of automated amino acid analysis using 9-fluoroenylmethyl chloroformate. *J. Chromatogr., A* **1991**, *588*, 107−114.

(26) Boss, P. K.; Böttcher, C.; Davies, C. Various influences of harvest date and fruit sugar content on different wine flavour and aroma compounds. *Am. J. Enol. Vitic.* **2014**, *65*, 341−353.

(27) Bindon, K.; Varela, C.; Kennedy, J.; Holt, H.; Herderich, M. Relationships between harvest time and wine composition in *Vitis vinifera* L. cv. Cabernet Sauvignon 1. Grape and wine chemistry. *Food Chem.* **2013**, *138*, 1696−1705.

(28) Antalick, G.; Perello, M.-C.; de Revel, G. Esters in wines: new insight through the establishment of a database of French wines. *Am. J. Enol. Vitic.* **2014**, *65*, 293−304.

(29) Smit, A. Y. *The Impact of Nutrients on Aroma and Flavour Production during Wine Fermentation*. Ph.D. thesis, Stellenbosch University, 2013.

(30) Diaz-Maroto, M. C.; Schneider, R.; Baumes, R. Formation pathways of ethyl esters of branched short-chain fatty acids during wine aging. *J. Agric. Food Chem.* **2005**, *53*, 3503−3509.

(31) Hazelwood, L. A.; Daran, J. M.; Van Maris, A. J. A.; Pronk, J. T.; Dickinson, J. R. The Ehrlich pathway for fusel alcohol production: a century of research on *Saccharomyces cerevisiae* metabolism. *Appl. Environ. Microbiol.* **2008**, *74*, 2259−2266.

(32) Bely, M.; Rinaldi, A.; Dubourdieu, D. Influence of assimilable nitrogen on volatile acidity production by *Saccharomyces cerevisiae* during high sugar fermentation. *J. Biosci. Bioeng.* **2003**, *96*, 507−512.

(33) Renault, P.; Miot-Certier, C.; Marullo, P.; Hernández-Orte, P.; Lagarrigue, L.; Lonvaud-Funel, A.; Bely, M. Genetic characterization and phenotypic variability in *Torulaspora delbrueckii* species: potential applications in the wine industry. *Int. J. Food Microbiol.* **2009**, *134*, 201−210.

(34) Weldegergis, B. T.; de Villiers, A.; Crouch, A. M. Chemometric investigation of the volatile content of young South African wines. *Food Chem.* **2011**, *128*, 1100−1109.

(35) Kalua, C. M.; Boss, P. K. Comparison of major volatile compounds from Riesling and Cabernet Sauvignon grapes (*Vitis vinifera* L.) from fruitset to harvest. *Aust. J. Grape Wine Res.* **2010**, *16*, 337−348.

DOI: 10.1021/acs.jafc.5b00966
J. Agric. Food Chem. 2015, 63, 4664−4672

(36) Mauricio, J. C.; Moreno, J.; Zea, L.; Ortega, J. M.; Medina, M. The effects of grape must fermentation conditions on volatile alcohols and esters formed by *Saccharomyces cerevisiae*. *J. Sci. Food Agric.* **1997**, *75*, 155−160.
(37) Varela, C.; Torrea, D.; Schmidt, S. A.; Ancin-Azpilicueta, C.; Henscke, P. A. Effect of oxygen and lipid supplementation on the volatile composition of chemically defined medium and Chardonnay wine fermented with *Saccharomyces cerevisiae*. *Food Chem.* **2012**, *135*, 2863−2871.
(38) Ugliano, M.; Travis, B.; Francis, I. L.; Henschke, P. A. Volatile composition and sensory properties of Shiraz wines as affected by nitrogen supplementation and yeast species: rationalizing nitrogen modulation of wine aroma. *J. Agric. Food Chem.* **2010**, *58*, 12417−12425.
(39) Torrea, D.; Varela, C.; Ugliano, M.; Ancin-Azpilicueta, C.; Francis, I. L.; Henschke, P. A. Comparison of inorganic and organic nitrogen supplementation of grape juice − effect on volatile composition and aroma profile of a Chardonnay wine fermented with *Saccharomyces cerevisiae* yeast. *Food Chem.* **2011**, *127*, 1072−1083.
(40) Ljungdahl, P. O.; Daignan-Fornier, B. Regulation of amino acid, nucleotide, and phosphate metabolism in *Saccharomyces cerevisiae*. *Genetics* **2012**, *190*, 885−929.
(41) Fujiwara, D.; Kobayashi, O.; Yoshimoto, H.; Harashima, S.; Tamai, Y. Molecular mechanism of the multiple regulation of the *Saccharomyces cerevisiae ATF1* gene encoding alcohol acetyltransferase. *Yeast* **1999**, *15*, 1183−1197.
(42) Mauricio, J. C.; Moreno, J. J.; Valero, E. M.; Zea, L.; Medina, M.; Ortega, J. M. Ester formation and specific activities of in vitro alcohol acetyltransferase and esterase by *Saccharomyces cerevisiae* during grape must fermentation. *J. Agric. Food Chem.* **1993**, *41*, 2086−2091.
(43) O'Kennedy, K.; Reid, G. Yeast nutrient management in winemaking. *Aust. N.Z. Grapegrowers Winemakers* **2008**, *537*, 92−100.
(44) Dennis, E. G.; Keyzers, R. A.; Kalua, C. M.; Maffei, S. M.; Nicholson, E. L.; Boss, P. K. Grape contribution to wine aroma: production of hexyl acetate, octyl acetate and benzyl acetate during yeast fermentation is dependent upon precursors in the must. *J. Agric. Food Chem.* **2012**, *60*, 2638−2646.
(45) Šuklje, K.; Antalick, G.; Coetzee, Z.; Schmidtke, L. M.; Baša Česnik, H.; Brandt, J.; du Toit, W. J.; Lisjak, K.; Deloire, A. Effect of leaf removal and ultraviolet radiation on the composition and sensory perception of *Vitis vinifera* L. cv. Sauvignon blanc wine. *Aust. J. Grape Wine Res.* **2014**, *20*, 223−233.

DOI: 10.1021/acs.jafc.5b00966
J. Agric. Food Chem. 2015, 63, 4664−4672

JOURNAL OF AGRICULTURAL AND FOOD CHEMISTRY

Article

pubs.acs.org/JAFC

Mechanism of Nonpolar Model Substances to Inhibit Primary Gushing Induced by Hydrophobin HFBI

Zahra Shokribousjein,*[,†] David Riveros Galan,[†] Patricia Losada-Pérez,[‡,§] Patrick Wagner,[‡,§] Jeroen Lammertyn,[∥] Iulia Arghir,[∥] Asefeh Golreihan,[⊥] Hubert Verachtert,[†] Ahmet Alper Aydın,[#,¶] Marc De Maeyer,[▽] Jean Titze,[○] Vladimír Ilberg,[#] and Guy Derdelinckx[†]

[†]KU Leuven, Department of Microbial and Molecular Systems (M2S), and Leuven Food Science and Nutrition Research Centre (LFoRCe-MaltBeerSci), Kasteelpark Arenberg 20, Heverlee, Belgium

[‡]Institute for Materials Research IMO, Hasselt University, Wetenschapspark 1, B-3590, Diepenbeek, Belgium

[§]Soft Matter and Biophysics Section, Departement of Physics and Astronomy, KU Leuven, Celestijnenlaan 200D bus 2416, B-3001, Leuven, Belgium

[∥]KU Leuven, Department of Biosystems, Division of Mechatronics, Biostatistics and Sensors, Willem de Croylaan 42, Heverlee, Belgium

[⊥]KU Leuven, Department of Earth and Environmental Science, Division of Geology, Celestijnenlaan 200e - box 2410, 3001 Leuven, Belgium

[#]University of Applied Sciences Weihenstephan-Triesdorf, Faculty of Gardening and Food Technology, Am Staudengarten 11, 85350 Freising, Germany

[¶]Chemical Engineering Department, Faculty of Chemical and Metallurgical Engineering, Istanbul Technical University, 34469 Maslak, Istanbul, Turkey

[▽]KU Leuven, Department of Chemistry, Division of Chemistry, section: Molecular and Structural Biology, Laboratory for Biomolecular Modelling and BioMacS, Heverlee, Belgium

[○]Döhler GmbH, Riedstraße 7-9, 64295 Darmstadt, Germany

Supporting Information

ABSTRACT: In this work, the interactions of a well-studied hydrophobin with different types of nonpolar model substances and their impact on primary gushing is evaluated. The nature, length, and degree of saturation of nonpolar molecules are key parameters defining the gushing ability or inhibition. When mixed with hydrophobins, the nonpolar molecule-hydrophobin assembly acts as a less gushing or no gushing system. This effect can be explained in the framework of a competition effect between non-polar systems and CO_2 to interact with the hydrophobic patch of the hydrophobin. Interactions of these molecules with hydrophobins are promoted as a result of the similar size of the nonpolar molecules with the hydrophobic patch of the protein, at the expense of the formation of nanobubbles with CO_2. In order to prove the presence of interactions and to unravel the mechanisms behind them, a complete set of experimental techniques was used. Surface sensitive techniques clearly show the presence of the interactions, whose nature is not covalent nor hydrogen bonding according to infrared spectroscopy results. Interactions were also reflected by particle size analysis in which mixtures of particles displayed larger size than their pure component counterparts. Upon mixing with nonpolar molecules, the gushing ability of the protein is significantly disrupted.

KEYWORDS: *self-assembly, hydrocarbons, hydrophobins, gushing, quartz crystal microbalance with dissipation, surface plasmon resonance, infrared spectroscopy, particle size analysis*

1. INTRODUCTION

Hydrophobins are globular surface active proteins produced by filamentous fungi, with a molecular weight of between 7 and 15 kDa and a diameter of 2−3 nm.[1,2] They are not toxic to humans when ingested upon consumption of mushrooms nor cytotoxic or immunogenic.[3] The ability of class II hydrophobins to form self-assemblies results in the possibility to function as nucleation sites for gaseous molecules like CO_2. This occurs in carbonated beverages and causes primary gushing, an important problem in the brewing industry, which is economically disastrous.[4−6] Much research was devoted to explain the basic mechanism of gushing.[7−9] A coherent mechanism was described by Deckers et al.[10,11] They explained that hydrophobins stabilize CO_2 gas bubbles by their hydrophobic patches and form nanobubbles. The formed nanobubbles agglomerate at the gas−liquid interface as nanoparticles surrounded by hydrophobins. On opening the bottle, the pressure drops and the particles grow and explode. This explosion provides the

Received: March 6, 2015
Revised: April 9, 2015
Accepted: April 19, 2015
Published: April 19, 2015

ACS Publications © 2015 American Chemical Society

DOI: 10.1021/acs.jafc.5b01170
J. Agric. Food Chem. 2015, 63, 4673−4682

required energy for the simultaneous formation of more nucleation sites, bubble growth and instantaneous gushing.

Several methods to prevent and to solve gushing have been proposed. For example, the addition of proteolytic enzymes or adsorbents like charcoal or activated alumina during the beer filtration step and the addition of a mixture of different calcium-enriched silicates.[5,12−14] The addition of hop components like free linalool (50 μg/L) and humulones (5 mg/L) to the beer was one of the gushing decreasing methods.[15] The amount of total linalool (free and cell wall bound which will be used by yeast) in beer is 500 μg/L and humulones is 5−20 mg/L, which are high amounts but not free to decrease gushing.[16−18] Membrane filtration of beer (0.1 μm pore size) and the addition of unsaturated fatty acids have also been claimed to decrease gushing.[15,19] Among the curative methods of gushing, one study on hop oils demonstrated that the hydrophobic characteristic of hop oils leads to their accumulation on hydrophobic−hydrophilic interfaces. This would result in nonstable nuclei by making gaps between the molecules of gushing promoting surfactants, therefore reducing the gushing tendency.[15]

Hydrophobins are not the only molecules with gushing ability. In a study by Christian et al.[19] on the gushing provoking tendency of hydrocarbons, they found a relation between structure (either carbon chain length or degree of saturation/unsaturation) and gushing potential of fatty acids. By increasing the carbon length of fatty acids from C_{10} to C_{16}, overfoaming increased, due to the fact that a specific hydrophobic interaction is needed to initiate gushing. Unsaturated fatty acids were not gushing inducers and even suppressed gushing by saturated molecules.

In order to characterize class II hydrophobins, the interaction of these molecules with solid surfaces was studied. Several works reported on the immobilization of hydrophobins on hydrophobic surfaces such as polytetrafluoroethylene (PTFE), poly(lactide-*co*-glycolide) (PLGA), graphite, and silicon surfaces.[20−25] The interaction of hydrophobins with hydrophilic surfaces (glass) was investigated by Qin et al.[26,27] Simulation studies showed that hydrophobins interact with silicon and graphite surfaces through their hydrophobic patch.[24,25] The hydrophobic patch of class II hydrophobin HFBI includes 13 amino acids. Using molecular dynamics simulations mentioned six aliphatic residues of HFBI interacting with the graphite surface including three leucines (Leu12, Leu26, and Leu68), one isoleucine (Ile27), one alanine (Ala66), and one valine (Val62).[24]

Despite the experimental research efforts carried out with a view to prevent gushing, the mechanisms behind gushing inhibitors are not completely understood. This work aims to shed light on this topic by studying the interactions between hydrophobins and nonpolar model substances with differing nature, length, and degree of saturation and how these interactions may influence the inhibition of gushing. To this end, we have used robust characterization techniques. To the best of our knowledge, no systematic studies on the interaction of hydrophobins with nonpolar substances have been published yet.

2. MATERIALS AND METHODS

2.1. Extraction and Purification of Hydrophobins. Hydrophobin HFBI from *Trichoderma reesei* MUCL 44908 was extracted from the mycelium and purified using the method reported by Deckers et al.[6] The molecular mass of purified protein was estimated by means of matrix-assisted laser desorption ionization time-of-flight (MALDI-TOF) mass spectrometry (with an Ultraflex II instrument in linear mode and α-cyano-4-hydroxy cinnamic acid matrix (Brüker Daltonics GmbH)). Fractions containing 7.5 kDa molecular weight peptides were proved to be HFBI by N-terminal amino acid sequence by automated Edman degradation on a capillary protein sequencer (Procise 491cLC, Applied Biosystems). HFBI solutions were dried by lyophilizing and dissolved in distilled water or pure ethanol. The concentration of HFBI was measured with NanoDrop ND-1000 spectrophotometer (Nanodrop Technologies, Wilmington, DE, USA).

2.2. Gushing Measurement. The gushing potential was evaluated for nonpolar model substances such as alkanes, alkenes, and fatty acids and for class II hydrophobin HFBI. In this study, saturated hydrocarbons C_nH_{2n+2} with n ranging from 6 to 28, unsaturated hydrocarbons 1-C_nH_{2n} with n ranging from 7 to 20, and fatty acids were evaluated regarding their effect on gushing. Gushing amounts of sparkling water caused by all these substances were determined according to the modified Carlsberg test (MCT).[28] To ensure comparable results on the gushing potential of hydrocarbons, an identical number of the molecules (5×10^{-5} M) was used. Solid alkanes were dissolved in 1 mL of hot ethanol (purity: 99.9%, temperature: 60 °C) prior to gushing analysis. All gushing experiments were carried out at least five times. Statistical analysis of the data was carried out by IBM SPSS Statistics 22. The normality distribution test and difference of variances were analyzed and used to discuss the gushing results.

2.3. Optical Microscopy. Microscopy analysis was carried out for hydrophobin HFBI, for two model non-polar systems, oleic acid and *n*-hexadecane, and for mixtures of the protein with each of the two nonpolar molecules. Freeze-dried HFBI obtained by RP-HPLC was dissolved to a concentration of 0.15 mg/mL in 1 mL of ethanol. Afterward, the protein sample (20 μL) was spread on a clean microscopic glass slide and dried overnight at room temperature in a closed environment to avoid contamination with small dust particles. Oleic acid (20 μL) and *n*-hexadecane (20 μL) samples were prepared following the same procedure and spread over the microscope slides. The mixtures of HFBI (0.15 mg/mL) with *n*-hexadecane (3.5 μL) and with oleic acid (5 μL) were prepared in a glass tube containing ethanol and mixed for 1 h prior to exposure and drying on a glass slide. Measurements were carried out on an optical microscope (Leica DM LP Leica Microsystems Wetzlar GmbH) using transmitted, reflected, and polarized light (90°).

2.4. Attenuated Total Reflection Fourier Transform Infrared Spectroscopy (ATR/FTIR spectrometry). Attenuated total reflection Fourier transform infrared spectroscopy (ATR/FTIR) is a label-free, nondestructive spectroscopic technique with large analytical potential to study protein crystallization studies, surface properties on protein behavior, and protein structure and function.[29] The principle behind ATR/FTIR consists of directing infrared light (an infrared beam) at an interface between the sample and a ATR crystal, an IR transparent material with a high refractive index. The angle of incidence of the beam is greater than the critical angle, and so total internal reflection takes place. At the surface, a standing wave of light radiation is formed, called the evanescent way, attenuating the exiting IR beam leaving the crystal. The penetration depth of the evanescent wave depends on its IR wavelength and angle of incidence and the refractive indices of ATR crystal and the sample. In this work, we used ATR-FTIR to explore the type of intermolecular interactions present when HFBI interacts with nonpolar model systems.

ATR/FTIR spectroscopy was performed for HFBI, oleic acid, and for the mixture of both compounds. Freeze-dried purified HFBI from RP-HPLC was dissolved to a concentration of 4 mg/mL in ethanol, while the mixture of HFBI with oleic acid (1 mL ethanol containing 0.15 mg/mL HFBI and 5 μL oleic acid) was prepared and stirred for 5 min prior to each measurement. For the current measurements, a Tensor 27 FT-IR spectrometer (Bruker Optik GmbH, 2006) equipped with a mid-infrared source (MIR) (2.5−25 μm) and a mercury−telluride detector (MCT) were used. This system was operated with OPUS (Bruker Optik GmbH) software (version 6.5). The ATR accessory was a three reflection ZnSe/Diamond μATR (6 mm in

DOI: 10.1021/acs.jafc.5b01170
J. Agric. Food Chem. 2015, 63, 4673−4682

Table 1. Gushing Amount by Saturated/Unsaturated Hydrocarbons and Their Impact on Gushing Induced by Hydrophobin HFBI[a]

		overfoaming (g/L)		overfoaming (g/L) in presence of HFBI (0.15 mg/mL)		
saturated hydrocarbons	amount (μL /μg)	mean	STDV	mean	STDV	t test[b]
n-hexane (n-C_6H_{14})	1.4 μL	0	0	159	4	−112[b]
n-nonane (n-C_9H_{20})	2.3 μL	0	0	143	7	−70[b]
n-decane (n-$C_{10}H_{22}$)	2.3 μL	0	0	0	0	−483[b]
n-tetradecane (n-$C_{14}H_{30}$)	3.5 μL	0	0	0	0	−483[b]
n-hexadecane (n-$C_{16}H_{34}$)	3.5 μL	0	0	0	0	−483[b]
n-heptadecane (n-$C_{17}H_{36}$)	3.5 μg	0	0	0	0	−483[b]
n-octadecane (n-$C_{18}H_{38}$)	7.0 μg	0	0	46	5	−142[b]
n-eicosane (n-$C_{20}H_{42}$)	7.0 μg	247	3.5	348	15	−20[b]
n-docosane (n-$C_{22}H_{46}$)	7.0 μg	315	3.1	252	12	−24[b]
n-tetracosane (n-$C_{24}H_{50}$)	7.0 μg	403	13	641	19	28[b]
n-octacosane (n-$C_{28}H_{58}$)	7.0 μg	404	24	659	16	37[b]
hydrophobin (HFBI)	150 μg			386	5	
		overfoaming (g/L)		overfoaming (g/L) in presence of HFBI (0.15 mg/mL)		
unsaturated hydrocarbons	amount (μL/μg)	mean	STDV	mean	STDV	t test
1-heptene (1-C_7H_{14})	1.4 μL	0	0	211	14	−16[b]
1-nonene (1-C_9H_{18})	2.3 μL	0	0	199	17	−16[b]
1-decene (1-$C_{10}H_{20}$)	2.3 μL	0	0	0	0	−59[b]
1-tetradecene (1-$C_{14}H_{28}$)	3.5 μL	0	0	0	0	−59[b]
1-hexadecene (1-$C_{16}H_{32}$)	3.5 μL	0	0	0	0	−59[b]
1-octadecene (1-$C_{18}H_{36}$)	7.0 μg	0	0	63	7	−42[b]
1-eicosene (1-$C_{20}H_{40}$)	7.0 μg	0	0	165	15	−21[b]
hydrophobin (HFBI)	150 μg			358	38	
		overfoaming (g/L)		overfoaming (g/L) in presence of HFBI (0.15 mg/mL)		
fatty acids	amount (μL/μg)	mean	STDV	mean	STDV	t test
octanoic acid ($C_8H_{16}O_2$)	1.6 μL	0	0	405	8	−5[b]
decanoic acid ($C_{10}H_{20}O_2$)	2.5 μg	0	0	477	23	ns
palmitic acid ($C_{16}H_{32}O_2$)	5 μg	351	4.2	523	53	2.4[b]
oleic acid ($C_{18}H_{34}O_2$)	5 μL	0	0	0	0	−53[b]
linolenic acid ($C_{18}H_{32}O_2$)	5 μL	0	0	0	0	−53[b]
behenic acid ($C_{22}H_{44}O_2$)	5 μL	462	53	549	17	7.5[b]
hydrophobin (HFBI)	150 μg			**462**	19	

[a]The standard deviations are mentioned after each measurement. The numbers of repeats were at least five times. [b]$p < 0.05$; ns = not significant.

diameter) with refractive indices of 2.4 and a path length of 13.08 μm. One-hundred coadded scans were taken at a resolution of 4 cm^{-1} (data points were collected every 2 cm^{-1} due to the software interpolation). For each measurement, 50 μL of the sample under study was placed over the crystal. The ATR accessory was carefully cleaned between measurements using distilled water and dried with a soft nonabrasive tissue. Each sample was measured at least five times at room temperature (22 ± 1 °C).

2.5. Quartz Crystal Microbalance with Dissipative Monitoring Measurements (QCM-D). Quartz crystal microbalance with dissipation monitoring (QCM-D) is an acoustic surface-sensitive technique that provides information on the mass and the viscoelastic properties of adsorbed layers by measuring the changes of resonance frequency Δf and dissipation ΔD.[30−32] QCM-D was used for monitoring in real-time the frequency and dissipation changes, Δf and ΔD, upon binding of n-hexadecane onto a HFBI monolayer. Gold-coated quartz sensors were first ultrasonicated for 15 min in Milli-Q water, cleaned with 98% iso-propanol solution at 70 °C for 15 min, UV-ozone treated with a Digital PSD series UV-ozone system from Novascan for 5 min, and then rinsed with Milli-Q water and dried with N_2 prior to placement in the QCM-D measurement modules. All measurements were performed in a Q-sense E4 instrument (Biolin Scientific, Sweden) with a flow rate of 50 μL/min at 20 °C. After a baseline in water was established, protein solutions with a concentration of 0.15 mg/mL in water were added. After a protein monolayer was formed, n-hexadecane (pure) was introduced at the same flow rate. All the changes were monitored at different overtones (from third to seventh).

2.6. Fiber Optic Surface Plasmon Resonance (FO-SPR). FO-SPR was used, together with QCM-D, to monitor the interactions and binding between HFBI and n-hexadecane. The FO-SPR sensor platform consists of a tungsten halogen light source (HL-2000, Ocean optics, USA), an UV−vis spectrophotometer (USB4000, Ocean Optics, USA), an interchangeable FO-SPR probe inserted in a SMA (SubMiniature version A) connector (Avantes, USA) and mounted in a bifurcated optical fiber (FO) (Ocean optics, USA), a modified T1 thermocycler (Biometra, Germany) to accurately control the rack temperature containing the samples in the PCR tubes (200 μL, Eppendorf, Belgium), and an automated computer-controlled robotic arm programmed using the ColiDrive software (Colinbus, Belgium). The white light is guided from the tungsten halogen lamp through the bifurcated FO toward the sensor's SPR sensitive gold area and afterward is reflected back to the UV−vis spectrophotometer. Depending on the refractive index of the medium in which the fiber is submerged, the spectral resonance SPR-dip occurs at a certain wavelength. Any binding event at the gold surface will trigger a shift in the signal response. The SPR wavelength shifts are plotted as a function of time and allow the monitoring of molecular interaction

DOI: 10.1021/acs.jafc.5b01170
J. Agric. Food Chem. 2015, 63, 4673−4682

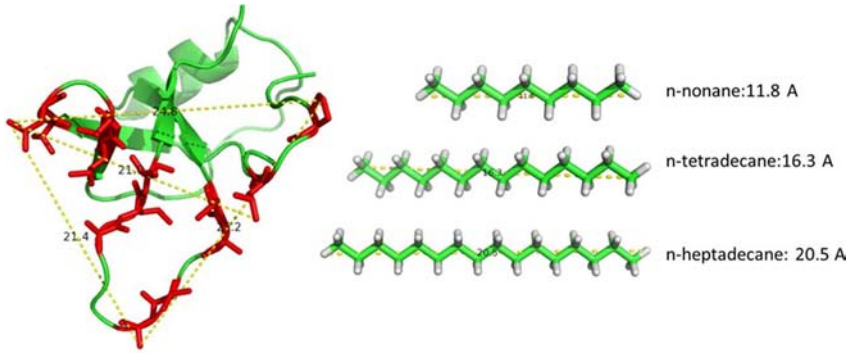

Figure 1. Comparing the length of hydrophobic patch of hydrophobin HFBI (21.4 Å × 25.2 Å × 21.0 Å × 24.8 Å) with *n*-nonane (11.8 Å; decreases gushing by HFBI) and *n*-tetradecane (16.3 Å) and *n*-heptadecane (20.5 Å; suppress gushing by HFBI completely).

phenomena in real time. A detailed description of the FO-SPR setup is given in refs 33 and 34. The interchangeable FO-SPR sensors were manufactured by cutting a 400 μm diameter TEQS multimode fiber (Thorlabs, Germany) to a length of 3.6 cm. A SPR-sensitive zone of 0.6 cm was constructed at one side of the fiber tip by removing the jacket and the polymer cladding in acetone. The fibers were then cleaned in a 30:70 (v/v) solution of hydrogen peroxide and concentrated sulfuric acid (99.8%), subsequently rinsed in distilled water and methanol, and finally dried with nitrogen gas. Next, the fibers were coated with a 50 nm gold layer using a magnetron sputtering device (Quorum Q150T ES, UK) as described in ref 35. The existing interactions between HFBI and *n*-hexadecane are relatively difficult to investigate, due to the typically small molecular structure of the alkane (0.3 kDa) compared to the protein (7.5 kDa). In this context, two approaches were tested in order to assess the weak responses between the two molecules. In the first protocol, the freshly prepared sensors were first dipped in a solution of HFBI (0.15 mg/mL in ethanol) for 10 min and then immersed in pure and diluted (3.5 μL/mL in ethanol) *n*-hexadecane for 20 min, respectively. In the second protocol, the FO-SPR probes were incubated overnight in pure *n*-hexadecane at room temperature and used the next day to detect HFBI (10 min). The experiments were repeated five times for each protocol.

2.7. Particle Size Analysis. Particle size distribution was studied for mixtures of HFBI (4 mg/mL) with a gushing inhibitor, *n*-hexadecane (3.5 μL/mL) in ethanol, and with a noninhibitor, *n*-docosane (5 mg/mL) in hot ethanol (60 °C). In the case of *n*-docosane, hot ethanol was used to dissolve this material completely, and the temperature remained 60 °C during the measurement. The reason for selecting these molecules was to see how a gushing inducer and a nongushing inducer molecule can affect overfoaming of the hydrophobin. Measurements were carried out by a Microtrac Nanotrac Ultra instrument (Particle Metrix GmbH, Meerbusch, Germany) which measures diameters between 0.8 to 6500 nm. Statistical analysis of the data was carried out by IBM SPSS Statistics 22. The normality distribution test and difference of variances were analyzed and used to discuss the results. Descriptive analysis was carried out using an independent samples *t* test for normally distributed data and one way ANOVA for not normally distributed data.

3. RESULTS AND DISCUSSION

3.1. Gushing Reference Measurements. The statistical analysis was carried out by normalizing the obtained data for all systems using the Shapiro−Wilk method. All data displayed normal distributions, thus the independent samples *t* test method was carried out for calculating the variance differences. The gushing potential of the saturated and unsaturated linear hydrocarbons and fatty acids as well as their effect on the gushing amount of sparkling water by hydrophobin HFBI is shown in Table 1. As can be observed, unsaturated hydrocarbons do not induce gushing irrespective of their chain length, while saturated hydrocarbons with $n > 18$ are gushing inducers with increasing gushing potential upon increasing alkyl chain length. As for saturated fatty acids, those with $n > 16$ induce gushing, whereas neither unsaturated oleic acid nor linolenic acid induced gushing. When mixed with HFBI, all analyzed alkanes and alkenes significantly decreased gushing. In turn, mixtures with fatty acids exhibited diverse behavior. Decanoic acid was the only one not to change the gushing by HFBI ($t = 1.209$, $d_f = 8$, $P > 0.05$), while octanoic acid slightly decreased gushing as compared with HFBI. Palmitic and behenic acids significantly increased gushing by HFBI, while oleic and linolenic acids completely inhibited gushing (see Table 1).

The above-exposed results indicate that the carbon chain length and the degree of saturation affect significantly the gushing and gushing inhibition potential of pure substances and of mixtures with hydrophobins, respectively. For pure nonpolar molecules, a critical carbon chain length is required to promote a hydrophobic interaction with CO_2 molecules in order to form the nanostructures needed for gushing: the longer the carbon chain, the stronger the interaction and thus the gushing amount is larger. Shorter carbon chains cannot provide a stable nucleus for CO_2 bubbles and gushing does not occur. In turn, the introduction of double bounds as in the case of oleic and linoleic acids inhibits and weakens the interactions with CO_2 preventing gushing. *Cis* forms of unsaturated bonds are nonlinear, in contrast to *trans* forms and cannot form suitable assemblies. Therefore, *cis*-forms of unsaturated bonds in either fatty acids or alkenes are not gushing inducers. Apart from the configuration of the chains, alkenes with the double bonds between the first and second carbon were tested to investigate whether being unsaturated, regardless of *cis* or *trans* forms, has an influence on the gushing ability. Indeed, comparing *n*-$C_{20}H_{42}$ with 1-$C_{20}H_{40}$ shows that unsaturation is the cause of loss of the gushing potential irrespective of the *cis*/*trans* form.

As regards mixtures with hydrophobin HFBI, both linear saturated and unsaturated hydrocarbons containing 10 to 17 carbons (saturated) and 10 to 16 carbons (unsaturated) were strong gushing suppressors. Among the fatty acids, only oleic and linolenic acids inhibit gushing. These results can be rationalized as follows. The hydrophobic patch of hydrophobins is responsible for the formation of nanobubbles during gushing: the size of this patch turns out to be very similar to the dimensions of the nonpolar molecules that act as gushing inhibitors, as shown in Figure 1. It seems that the similar lengths of hydrocarbon chains are able to interact perfectly with

DOI: 10.1021/acs.jafc.5b01170
J. Agric. Food Chem. 2015, 63, 4673−4682

the hydrophobic patch of hydrophobins and inhibit their further interaction with CO_2. Therefore, gushing is thoroughly inhibited.

3.2. Optical Microscopy of HFBI and Oleic Acid Mixtures. The microscopy images with reflected light of hydrophobin, oleic acid, and their mixture are shown in Figure 2. Though not shown, the results of mixtures of HFBI with *n*-hexadecane are analogous to those with oleic acid. Neither oleic acid nor the mixture of this fatty acid with HFBI induced gushing. The microscopy analysis shows the large changes of HFBI in the presence of gushing suppressive molecules. The crystal structures formed by HFBI molecules disappear when oleic acid is present. These changes may be attributed to the chemical interaction of hydrophobins with the nonpolar molecules that cover the hydrophobic patch of these proteins. Additional experimental techniques used in order to understand the mechanisms behind the observed structural changes will be described in the following.

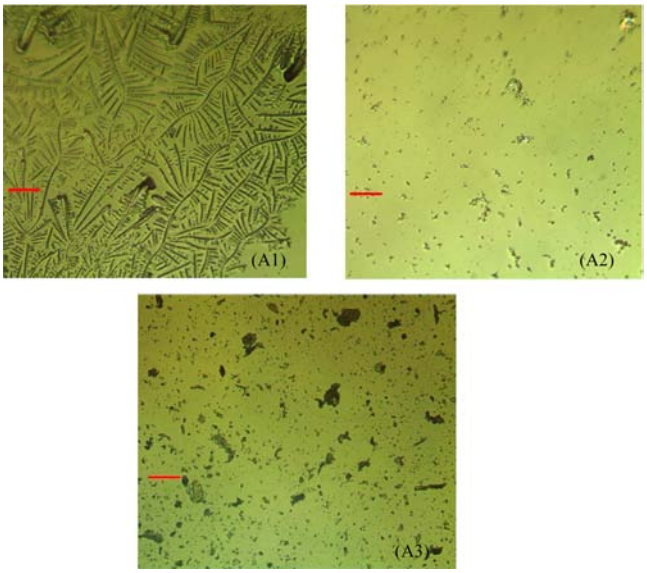

Figure 2. Microscopic image of (A1) crystals formed by HFBI (0.15 mg/mL) in ethanol, (A2) oleic acid (5 μL/mL) in ethanol, and (A3) a mixture of HFBI with oleic acid. All samples were dried on a glass slide at room temperature in an isolated environment. All images are taken by reflected light, and the red scale bars indicate 20 μm. The same preparations for all samples were carried out.

3.3. ATR/FTIR Spectrometry of HFBI and Oleic Acid Mixtures. Figure 3a shows the absorbance spectra for HFBI, oleic acid, and their mixture measured with the μATR (ZnSe/Diamond) crystal. The spectral group frequencies provided in this text were obtained from a practical source written by Coates.[36] In the spectral region between 1900 and 2300 cm^{-1}, there are no absorbance peaks, except of diamond (2300−1900 cm^{-1}), and therefore, this region is shown as a break in the wavenumber axis. In the case of any new covalent bonding, a new spectrum will appear in the MIR absorbance spectra, and it can be identified by referring to the IR range of electromagnetic spectra which have already been published, see for instance ref 36. The spectrum of the mixture of HFBI with oleic acid significantly resembles the spectrum of the individual compounds, indicating that no new covalent bonds are formed by mixing fatty acid with HFBI. Oleic acid exhibits extremely strong hydrogen bonding through its carboxylic group; we focused on detecting hydrogen bonds built. Considering the structure of HFBI, hydrogen bonding is possible between the carboxylic group of oleic acid and the N−H groups in the hydrophobic patch of HFBI, some of which are shown in Figure 3b. An important characteristic of hydrogen bonds is the shifting of peaks to lower frequencies,[37] since they can form a stable dimeric structure. Apart from that, hydrogen bonding produces significant band broadening. However, in these experiments none of these changes are detected.

3.4. Adsorption of HFBI and Alkanes to Gold Crystals Using QCM-D. The frequency and dissipation shifts, Δf and ΔD, upon adsorption and formation of a HFBI monolayer and subsequent binding of *n*-hexadecane are shown in Figure 4. Δf is related to the adsorbed mass of the film, and ΔD accounts for the dissipated energy reflecting the viscoelastic properties of the layer. The rinsing of hydrophobins results in a small increased frequency which is removed to avoid complexity in the graph. Upon adsorption of the protein, Δf decreases rapidly and ΔD slightly increases, indicating the fast physical adsorption and slower formation of a protein layer onto the QCM-D sensors. The small gap in the graph is due to washing off the weakly bound hydrophobins from the gold surface using distilled water. The obtained responses in $\Delta f \sim -25$ Hz and $\Delta D \sim 3 \times 10^{-6}$ reveal the formation of a thin and rigid hydrophobin layer, in agreement with previous experimental works.[38] After a baseline was reached indicating the formation of a stable protein layer, pure *n*-hexadecane was added. The interaction of *n*-hexadecane with the protein layer is reflected by a slight decrease in $\Delta f \sim -4$ Hz and somewhat larger increase in $\Delta D \sim 5 \times 10^{-6}$. These responses can be translated into non-polar molecule mass adsorption onto the protein layer by virtue of the direct relation between frequency shift Δf and mass change Δm introduced by Sauerbrey.[30] This reflects that *n*-hexadecane is immobilized on the gold surface covered with HFBI.

3.5. Adsorption of HFBI and Alkanes to Gold Coated FO-SPR Sensors. The obtained results with the wavelength values at which the SPR-dip occurs plotted as a function of time are represented in Figure 5, where binding events are reflected in a shift of the wavelength. In a first approach, the FO-SPR probes were immersed in HFBI for 10 min and afterward dipped in pure and diluted (3.5 μL/mL in ethanol) *n*-hexadecane, respectively (see Figure 5A). The attachment of HFBI onto the gold-coated fiber surface resulted in an average shift of 1 ± 0.5 nm. Since hydrophobins have both hydrophilic and hydrophobic patches, they are physically adsorbed onto the gold coated fiber surface (positively charged) through their negatively charged area located in the hydrophilic patch (see green part in Figure 1) as reported by Zampieri et al.[39] Afterward, the FO-SPR probes were immersed in pure and diluted *n*-hexadecane, respectively, for 20 min. Alkanes most likely bind to the hydrophobic patch of HFBI, since this hydrophobin interacts with hydrophobic surfaces via its hydrophobic patch. In both cases, the interaction of HFBI with *n*-hexadecane was not detectable. The results showed that when *n*-hexadecane was diluted in ethanol, attached hydrophobins started to be rinsed from the fiber surface (Figure 5A, red curve). Therefore, a second approach was evaluated. An alkane self-assembling monolayer (SAM) was created by incubating the FO-SPR probes overnight in a pure *n*-hexadecane solution. Next, the SAM functionalized FOs and the normal FOs were immersed in HFBI for 10 min (see Figure 5B). As can be observed in the sensogram in Figure 5B, the binding of HFBI onto the alkane-SAM functionalized FO was

DOI: 10.1021/acs.jafc.5b01170
J. Agric. Food Chem. 2015, 63, 4673−4682

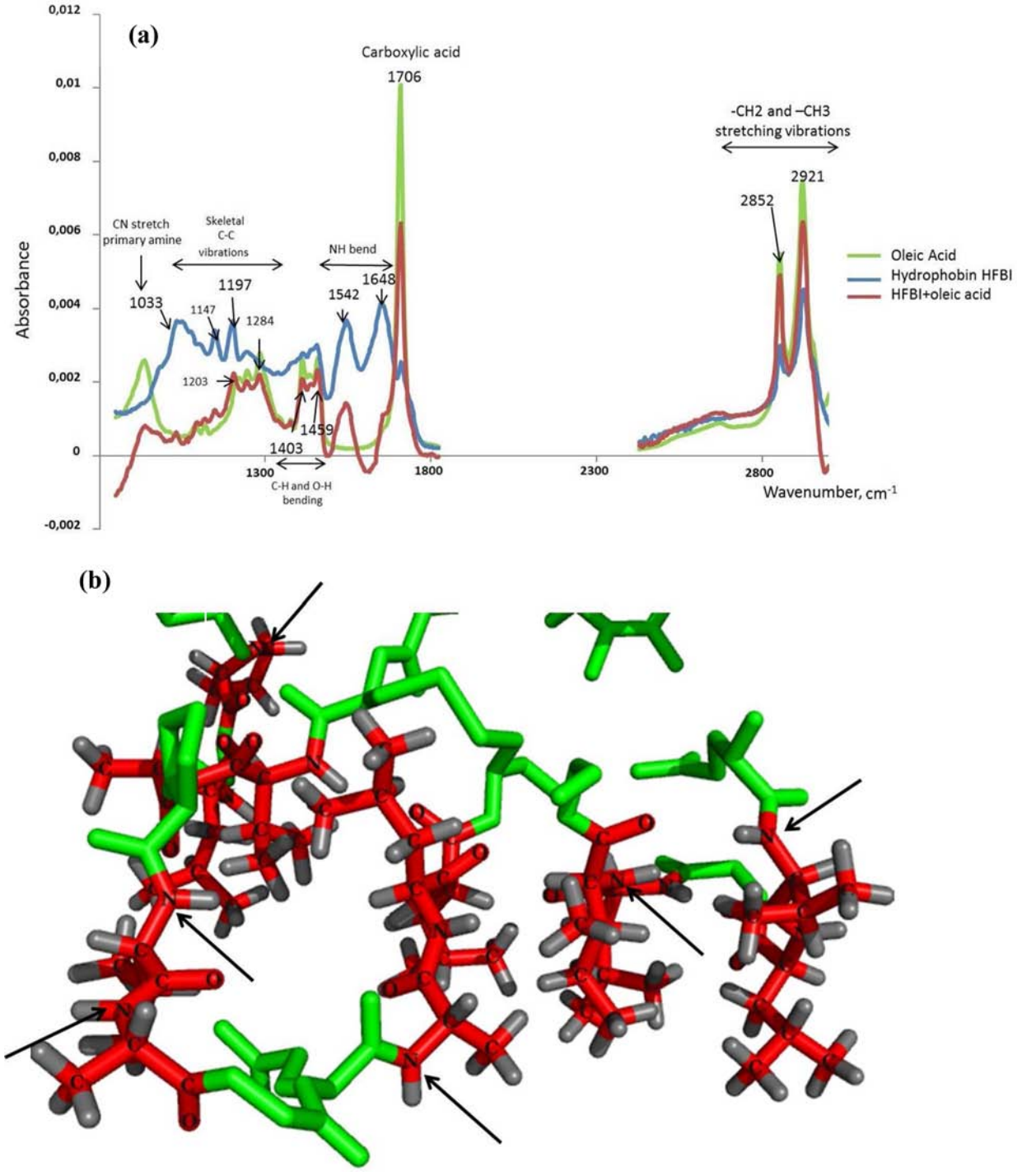

Figure 3. (a) Mid-IR absorption spectra of oleic acid, HFBI, and their mixture measured with μATR accessory. (b) The arrows show some possible positions in the hydrophobic patch of HFBI for hydrogen binding with carboxylic group of oleic acid.

twice the size (2.5 ± 0.5 nm) compared to the first approach. These results are in agreement with the ones obtained from QCM-D, showing that there is an effective interaction between alkanes and hydrophobins.

3.6. Particle Size Distribution. Particle size distributions were measured in order to obtain stronger evidence of the interaction of hydrophobin HFBI with gushing suppressive molecules. This method was used not only to compare the particle sizes of individual compounds but also to analyze the changes of particle sizes during the time.

The particle size distribution of HFBI, nonpolar molecules (*n*-hexadecane and *n*-docosane), and their mixtures were all evaluated in ethanol, and the results are presented in Figure 6. As a first step, the particle sizes of pure *n*-hexadecane and *n*-docosane were measured, and afterward, these nonpolar molecules were mixed separately with HFBI, and the particle size distributions were compared with the individual molecules. The results are shown in Figure 6a and b, respectively. In the ethanol solution of HFBI, particles of HFBI with a similar size to that of the monomeric form of HFBI (1−2 nm) are observed (graphs blue, Figure 6a and b), while after mixing

DOI: 10.1021/acs.jafc.5b01170
J. Agric. Food Chem. 2015, 63, 4673−4682

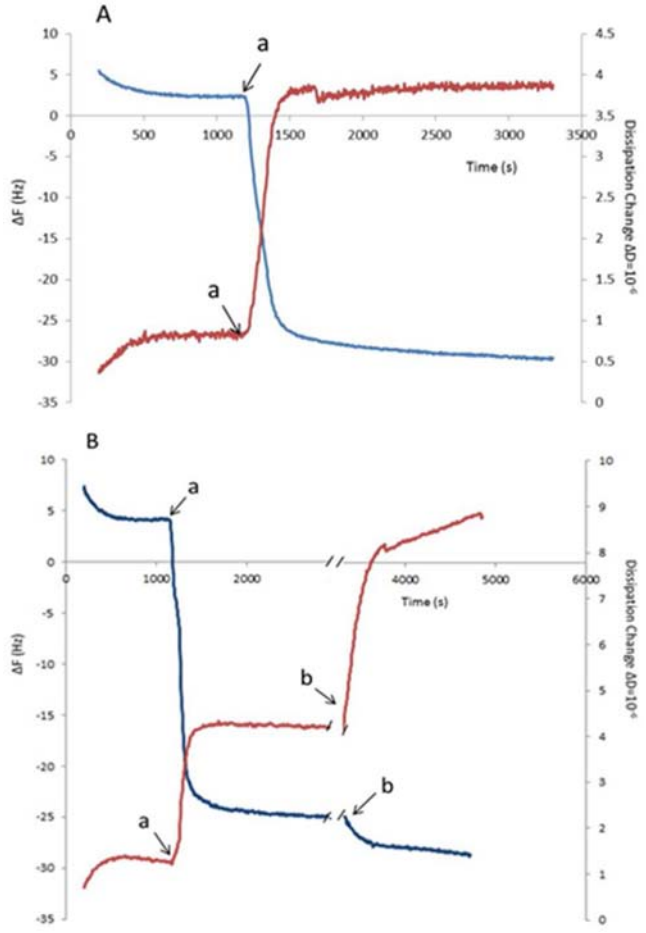

Figure 4. QCM-D data of (A) adsorption of HFBI to the bare gold crystal and (B) adsorption of *n*-hexadecane to gold crystal covered with HFBI. The break in graph B is due to rinsing of weakly bounded HFBI to the gold surface with distilled water. Frequency changes are shown in blue, and dissipation changes are in red. In both graphs, part a corresponds to HFBI injection, and part b in graph B resembles *n*-hexadecane (pure) injection. The experiment was repeated five times.

with nonpolar molecules they are such small sizes that they are no longer detected (graphs yellow, Figure 6a and b). This indicates that by mixing HFBI proteins with nonpolar molecules, these molecules attach to HFBI monomers and form larger particles. Therefore, the 1−2 nm monomers are not observed in the mixture. These large particles had a diameter of 1 μm for the mixture of HFBI with *n*-hexadecane (graph yellow, Figure 6a) and 0.9 μm with *n*-docosane (graph yellow, Figure 6b). The large values of standard deviation STDV in both graphs (Figure 6a and b) can be explained by the quick formation of big particles during the time of the experiment.

The results were validated by analyzing the changes of particle sizes after mixing HFBI with nonpolar molecules during the time and are shown in Figure 6c,d,e. The particle size distribution of HFBI was compared during the time to figure out if the molecules of this protein tend to self-assemble. The results are illustrated in Figure 6c, and multimerization of HFBI molecules is clearly observed after 4, 6, and 8 min of measurement. Afterward, the evaluation of particle sizes in the mixture of HFBI and nonpolar molecules was carried out during the time. As illustrated in Figure 6d, the formation of bigger particles in the mixture of HFBI with *n*-hexadecane was clearly observed among 1, 8, and 9 min after mixing. After mixing HFBI with *n*-docosane, the formation of larger particles was evident among 3, 4, and 5 min after mixing (Figure 6e).

Statistical analysis was carried out for the normal distribution test of data. The variance analyses for particle sizes with normal distribution was carried out with the independent samples *t* test method, and for the data with non-normal distribution, one-way ANOVA was used. The descriptive data analysis is shown in the Supporting Information. In order to reduce the number of data in the table, only the particles with significant differences are shown.

Four different statistical analyses carried out with a view to show whether the particle size distributions of HFBI with nonpolar molecules is significantly different from the individual molecules. The results from this analysis are shown as A, B, C, and D in the Supporting Information. The A and B statistical analyses evaluate whether the particles of HFBI and *n*-hexadecane are significantly different from the particles in their mixture, respectively. The C and D statistical analysis are analogous to A and B but with *n*-docosane. These data clearly show that there are significant differences between the particle sizes when HFBI was mixed with *n*-hexadecane and *n*-docosane. This aggregation is probably due to the presence of a hydrophobic patch at the surface of HFBI which attracts nonpolar molecules.

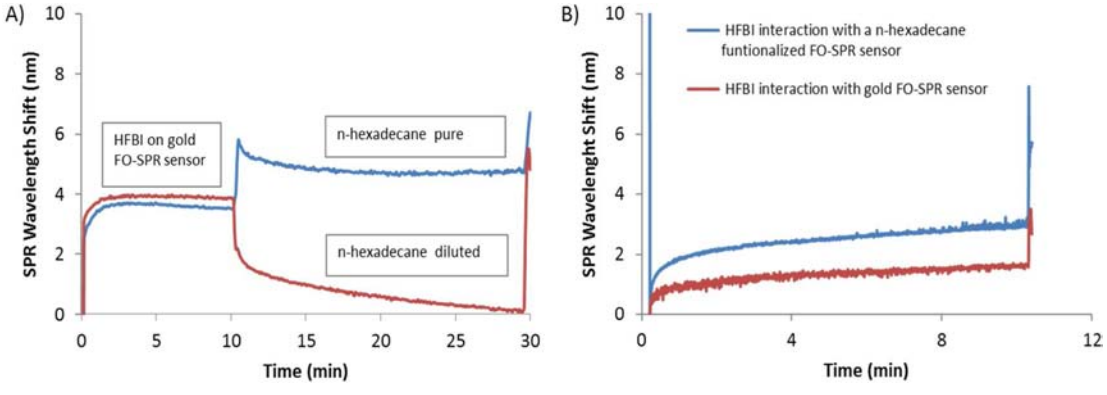

Figure 5. Interaction of HFBI with *n*-hexadecane. (A) FO-SPR sensorgram representing the immobilization of HFBI (0.15 mg/mL in ethanol, 10 min) on the FO-SPR sensor surface and the subsequent immersion of the fires in pure (blue) and diluted (red, 3.5 μL/mL in ethanol) *n*-hexadecane, respectively, for 20 min. (B) FO-SPR sensorgram representing the physical absorption of HFBI (0.15 mg/mL in ethanol, 10 min) on a FO-SPR probe (red) and on a FO-SPR probe functionalized overnight in pure *n*-hexadecane (blue). Number of repeats for these experiments was 5.

DOI: 10.1021/acs.jafc.5b01170
J. Agric. Food Chem. 2015, 63, 4673−4682

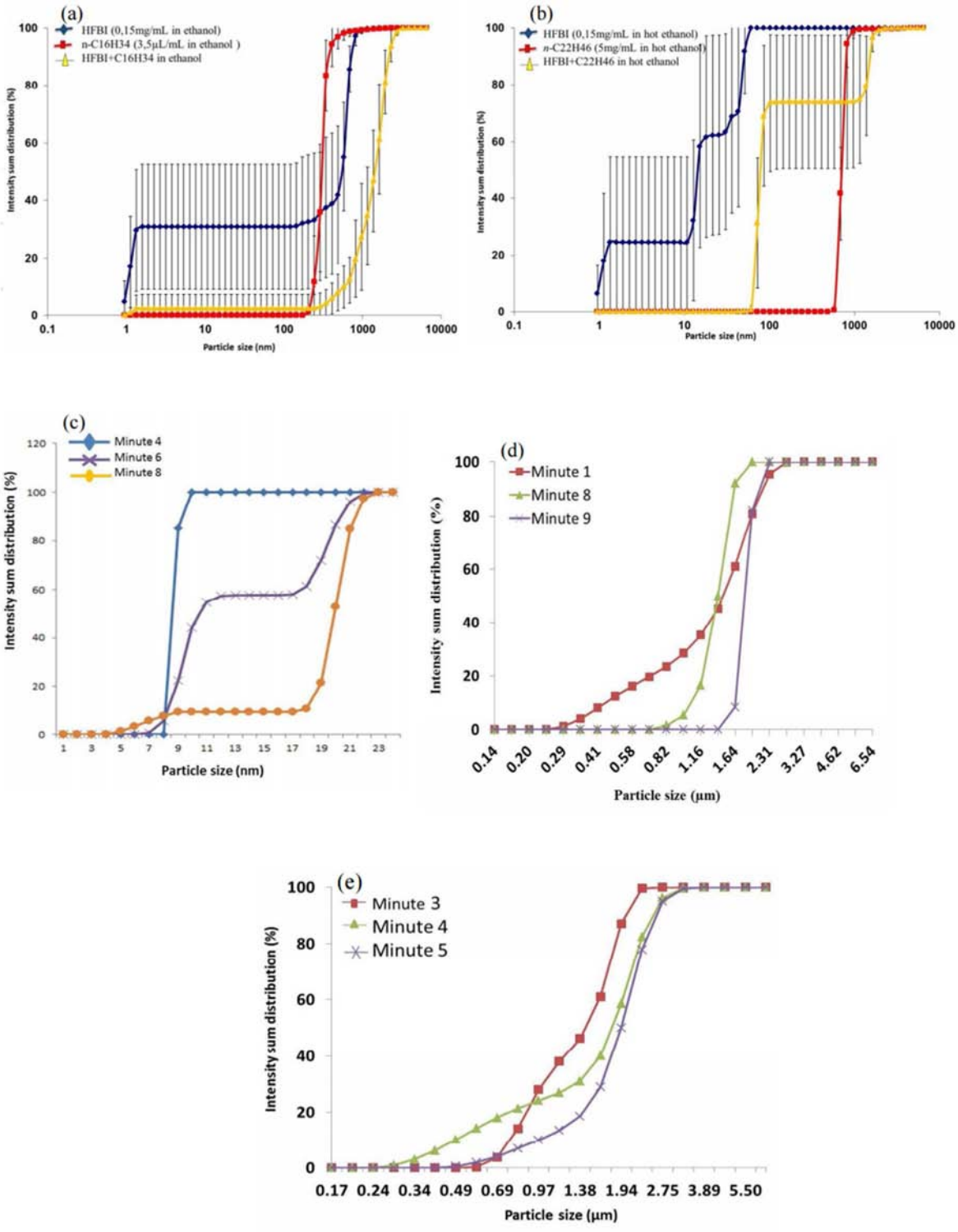

Figure 6. Particle size distribution of (a) hydrophobin HFBI (blue graph), *n*-hexadecane (red graph), and the mixture of HFBI and *n*-hexadecane (yellow graph). (b) Hydrophobin HFBI (blue graph), *n*-docosane (red graph), and the mixture of HFBI and *n*-docosane (yellow graph). Comparison of the particle size distribution over time for (c) hydrophobin HFBI, (d) the mixture of HFBI and *n*-hexadecane in ethanol, and (e) the mixture of HFBI and *n*-docosane in hot ethanol. All results are obtained from 10 runs, five repeats. The standard deviation bars are indicated in all graphs.

In summary, gushing ability reference measurements have provided valuable information on the gushing ability or inhibition of hydrophobin HFBI, nonpolar model systems, and mixtures of them. These measurements show that for pure non-polar molecules, the gushing ability depends strongly of the carbon chain length and the degree of saturation. The longer the carbon chain, the larger the gushing amount. Unsaturation in turn inhibits and weakens the interactions with CO_2 irrespective of the *cis/trans* form. These results are in agreement with the ones reported by Christian et al.[40] As for

DOI: 10.1021/acs.jafc.5b01170
J. Agric. Food Chem. 2015, 63, 4673−4682

mixtures of HFBI with non-polar molecules, the combination acts as the assembly acts as a less gushing or no gushing system. This effect takes place within a specific range of carbon chain length range (C = 10 to 17) and can be explained in the framework of a competition effect between non-polar systems and CO_2 to interact with the hydrophobic patch of the hydrophobin. Interactions of these molecules with hydrophobins are promoted as a result of the similar size of the nonpolar molecules with the hydrophobic patch of the protein, at the expense of the formation of nanobubbles with CO_2. Shorter carbon chain lengths than the above-mentioned range do not form a strong hydrophobic interaction with these patches, and therefore gushing is only decreased. Longer hydrocarbon lengths interact with CO_2 molecules and induce gushing themselves. Thus, their effect on the gushing by HFBI is not detectable.

Complementary measurements of mixtures with HFBI and model non-polar systems by a complete set of characterization techniques support the above statements. Optical microscopy shows dramatic structural changes of HFBI in the presence of oleic acid, while ATR/FTIR results do not indicate the presence of either covalent or hydrogen bonds between HFBI and this system. In turn, both QCM-D and SPR show that there is an effective interaction between *n*-hexadecane and hydrophobins, judging from the increase in the frequency (mass) and wavelength shift responses, respectively. To our knowledge, this is the first study where both QCM-D and SPR are used to monitor hydrophobins and nonpolar molecules interactions. Particle size analysis reveals that particles of HFBI and nonpolar molecules aggregate and form larger particles. On the basis of the obtained results, we believe that the hydrophobic patch in HFBI, which is responsible for the interaction of HFBI with CO_2 molecules, is capped by the interaction of HFBI molecules with nonpolar molecules. Thus, the stable nanobubbles which typically arise by HFBI and CO_2 interactions are not formed, and gushing does not occur. The information provided in this work will be useful both from a fundamental and an applied point of view, helping the understading of the molecular characteristics involved in gushing prevention and application of this knowledge in food beverage companies in general and breweries in particular to provide alternative preventive and curative solutions for overfoaming.

■ ASSOCIATED CONTENT

Supporting Information

Descriptive particle size analysis using independent samples *t* test and one-way ANOVA for hydrophobin HBFI, *n*-hexadecane, *n*-docosane, and mixtures of hydrophobin and nonpolar components.. The Supporting Information is available free of charge on the ACS Publications website at DOI: 10.1021/acs.jafc.5b01170.

■ AUTHOR INFORMATION

Corresponding Author

*E-mail: zahrashokri@gmail.com.

Notes

The authors declare no competing financial interest.

■ ACKNOWLEDGMENTS

We are grateful for financial support from KUL-University Foundation-Hydrophobin grant by the Duvel-Moortgat, Orval, and Chimay breweries and Cargill Malting. We thank laboratory of Food Microbiology and Food Technology for the use of equipment.

■ ABBREVIATIONS USED

ATR/FTIR spectrometry, attenuated total reflection Fourier transform infrared spectroscopy; QCM-D, quartz crystal microbalance with dissipative monitoring measurements; FO-SPR, fiber-optic surface plasmon resonance; SAM, self-assembling monolayer

■ REFERENCES

(1) Linder, M. B.; Szilvay, G. R.; Nakari-Setälä, T.; Penttila, M. E. Hydrophobins: the protein-amphiphiles of filamentous fungi. *FEMS Microbiol. Rev.* **2005**, *29*, 877−896.

(2) Linder, M. B. Hydrophobins: proteins that self-assemble at interfaces. *Curr. Opin. Colloid Interface Sci.* **2009**, *14*, 356−363.

(3) Scholtmeijer, K.; Wessels, J. G. H.; Wösten, H. A. B. Fungal hydrophobins in medical and technical applications. *Appl. Microbiol. Biotechnol.* **2001**, *56*, 1−8.

(4) Sarlin, T.; Vilpola, A.; Kotaviita, E.; Olkku, J.; Haikara, A. *Fungal hydrophobins in the barley-to-beer chain. J. Inst. Brew.* **2007**, *113*, 147−153.

(5) Evans, D. E.; Bamforth, C. W. Beer foam: achieving a suitable head. *Handbook of Alcoholic Beverages Series, Beer, A Quality Perspective*; Bamforth, C. W., Russell, I., Stewart, G., Eds.; Elsevier Ltd.: 2009, Chapter 6, pp 1−60.

(6) Deckers, S. M.; Lorgouilloux, Y.; Gebruers, K.; Baggerman, G. A.; Michiels, C.; Verachtert, H.; Neven, H.; Derdelinckx, G.; Delcour, J. A.; Martens, J. Dynamic light scattering (DLS) as a tool to detect CO_2-hydrophobin structures and study the primary gushing potential of beer. *J. Am. Soc. Brew. Chem.* **2011**, *69*, 144−149.

(7) Draeger, M. Physikalische Überlegungen zum Thema Gushing. *Brauwelt* **1996**, *136*, 259−264.

(8) Fischer, S. Blasenbildung von in Flüssigkeiten gelösten Gasen. Ph.D. Dissertation. TU München, 2001.

(9) Sahu, K. K.; Hazama, Y.; Ishihara, K. N. *Gushing in canned beer: the effect of ultrasonic vibration. J. Colloid Interface Sci.* **2006**, *302*, 356−362.

(10) Deckers, S. M.; Gebruers, K.; Baggerman, G.; Lorgouilloux, Y.; Delcour, J. A.; Michiels, C.; Derdelinckx, G.; Martens, J.; Neven, H. CO2-hydrophobin structures acting as nanobombs in beer. *Brewing Science* **2010**, *63*, 54−61.

(11) Deckers, S.; Venken, T.; Khalesi, M.; Gebruers, K.; Baggerman, G.; Lorgouilloux, Y.; Shokribousjein, Z.; Ilberg, V.; Schönberger, C.; Titze, J.; Verachtert, H.; Michiels, C.; Neven, H.; Delcour, J.; Martens, J.; Derdelinckx, G.; De Maeyer, M. Combined Modeling and Biophysical Characterisation of CO2 Interaction with Class II Hydrophobins: New Insight into the Mechanism Underpinning Primary Gushing. *J. Am. Soc. Brew. Chem.* **2012**, *70*, 249−256.

(12) Aastrup, S.; Legind-Hansen, P.; Nielsen, H. Enzymatic reduction of gushing tendencies in beer. *Brauwelt International* **1996**, Volume *II*, 136−138.

(13) Sarlin, T.; Nakari-Setälä, T.; Linder, M.; Penttilä, M.; Haikara, A. *Fungal hydrophobins as predictors of the gushing activity of malt. J. Inst. Brew.* **2005**, *111* (2), 105−111.

(14) Besier, A.; Müller, V.; Fröhlich, J.; Pätz, R. Reduce over-foaming−Method for the treatment of the phenomenon gushing in beer and malt beverages. *Brewing and Beverage Industry International* **2013**, *2*, 46−49.

(15) Hanke, S.; Kern, M.; Herrmann, M.; Back, W.; Becker, T.; Krottenthaler, M. Suppression of gushing by Hop constituents. *Brewing Science* **2009**, *62*, 181−186.

(16) Briggs, D. E.; Boulton, C. A.; Brookes, P. A.; Stevens, R. *Brewing Science and Practice*; CRC Press: Boca Raton, FL, 2010.

(17) Hanke, S.; Seidl, J.; Back, W. Bedeutung und Einfluss von Hopfenaromastoffen. *Weihenstephaner* **2008**, *76*, 121−123.

DOI: 10.1021/acs.jafc.5b01170
J. Agric. Food Chem. 2015, 63, 4673−4682

(18) Hanke, S. Untersuchungen zum Einfluss der Hopfungstechnologie auf die Geschmacksstabilität und Harmonie untergäriger Biere. Ph.D. dissertation. Freising, Technische Universität München, Wissenschaftszentrum Weihenstephan für Ernährung, Landnutzung und Umwelt, 2009.
(19) Christian, M.; Ilberg, V.; Aydin, A. A.; Titze, J.; Friess, A.; Jacob, F.; Parlar, H. New gushing mechanism proposed by applying particle size analysis and several surfactants. *Brewing Science* **2009**, *62*, 100−107.
(20) Askolin, S.; Linder, M.; Scholtmeijer, K.; Tenkanen, M.; Penttila, M.; de Vocht, M. L.; Wösten, H. A. B. Interaction and Comparison of a Class I Hydrophobin from Schizophyllum commune and Class II Hydrophobins from Trichoderma reesei. *Biomacromolecules* **2006**, *7*, 1295−1301.
(21) De Stefano, L.; Rea, I.; De Tommasi, E.; Rendina, I.; Rotiroti, L.; Giocondo, M.; Longobardi, S.; Armenante, A.; Giardina, P. *Bioactive modification of silicon surface using self-assembled hydrophobins from Pleurotus ostreatus. Eur. Phys. J. E: Soft Matter Biol. Phys.* **2009**, *30*, 181−185.
(22) Hou, S.; Li, X.; Li, X.; Feng, X. Coating of hydrophobins on three-dimensional electrospun poly(lactic-co-glycolic acid) scaffolds for cell adhesion. *Biofabrication* **2009**, *1*, 1−7.
(23) Hou, S.; Li, X.; Li, X.; Feng, X.; Wang, R.; Wang, C.; Yu, L.; Qiao, M. Q. Surface modification using a novel type A hydrophobin HGFI. *Anal. Bioanal. Chem.* **2009**, *394*, 783−789.
(24) Mereghetti, P.; Wade, R. C. Diffusion of hydrophobin proteins in solution and interactions with a graphite surface. *BMC Biophys.* **2011**, 4−9.
(25) Moldovan, C.; Thompson, D. Molecular dynamics of the "hydrophobic patch" that immobilizes hydrophobin protein HFBII on silicon. *J. Mol. Model.* **2010**, *1*, 9−9.
(26) Qin, M.; Hou, S.; Wang, L.; Feng, X.; Wang, R.; Yang, Y.; Wang, C.; Yu, L.; Shao, B.; Qiao, M. Two methods for glass surface modification and their application in protein immobilization. *Colloids Surf., B* **2007**, *60*, 243−249.
(27) Qin, M.; Wang, L. K.; Feng, X.; Yang, Y.; Wang, R.; Wang, C.; Yu, L.; Shao, B.; Qiao, M. Bioactive surface modification of mica and poly(dimethylsiloxane) with hydrophobins for protein immobilization. *Langmuir* **2007**, *23*, 4465−71.
(28) Garbe, L. A.; Nagel, R.; Rauschmann, M.; Lamers, M.; Ehmer, A.; Tressl, R. *Correlation of deoxynivalenol, hydrophobins and gushing*; European Brewery Convention Congress: Venice, 2007.
(29) Glassford, S. E.; Byrne, B.; Kazarian, S. G. Recent applications of ATR FTIR spectroscopy and imaging to proteins. *Biochim. Biophys. Acta, Proteins Proteomics* **2013**, *1834*, 2849−2858.
(30) Sauerbrey, Günter. Verwendung von Schwingquarzen zur Wägung dünner Schichten und zur Mikrowägung. *Eur. Phys. J. A* **1959**, *155*, 206−222.
(31) Höök, F.; Rodahl, M.; Kasemo, B.; Brzezinski, P. Structural changes in hemoglobin during adsorption to solid surfaces: Effects of pH, ionic strength, and ligand binding. *Proc. Natl. Acad. Sci. U. S. A.* **1998**, *95*, 12271−12276.
(32) Losada-Pérez, P.; Jiménez-Monroy, K.; van Grinsven, B.; Leys, J.; Janssens, S. D.; Peeters, M.; Glorieux, C.; Thoen, J.; Haenen, K.; De Ceuninck, W.; Wagner, P. Phase transitions in lipid vesicles detected by a complementary set of methods: heat-transfer measurements, adiabatic scanning calorimetry, and dissipation-mode quartz crystal microbalance. *Phys. Status Solidi A* **2014**, *211*, 1377−1388.
(33) Pollet, J.; Delport, F.; Janssen, K. P. F.; Jans, K.; Maes, G.; Pfeiffer, H.; Wevers, M.; Lammertyn, J. Fiber optic SPR biosensing of DNA hybridization and DNA-protein interactions. *Biosens. Bioelectron.* **2009**, *25*, 864−869.
(34) Pollet, J.; Delport, F.; Janssen, K. P. F.; Tran, D. T.; Wouters, J.; Verbiest, T.; Lammertyn, J. Fast and accurate peanut allergen detection with nanobead enhanced optical fiber SPR biosensor. *Talanta* **2011**, *83*, 1436−1441.
(35) Knez, K.; Janssen, K.; Pollet, J.; Spasic, D.; Lammertyn, J. Fiber optic high-resolution genetic screening using gold-labeled gene probes. *Small* **2012**, *8*, 868−872.
(36) Coates, J. Interpretation of Infrared Spectra, A Practical Approach. *Encyclopedia of Analytical Chemistry*; Meyers, R. A., Ed.; John Wiley & Sons Ltd., Chichester, 2000; pp 10815−10837.
(37) Barth, A. Infrared spectroscopy of proteins. *Biochim. Biophys. Acta, Bioenerg.* **2007**, *1767*, 1073−1101.
(38) Linder, M.; Szilvay, G. R.; Nakari-Setälä, T.; Söderlund, H.; Penttilä, M. Surface adhesion of fusion proteins containing the hydrophobins HFBI and HFBII from Trichoderma reesei. *Protein Sci.* **2002**, *11*, 2257−2266.
(39) Zampieri, F.; Wösten, H. A. B.; Scholtmeijer, K. Creating Surface Properties Using a Palette of Hydrophobins. *Materials* **2010**, *3*, 4607−4625.
(40) Christian, M.; Titze, J.; Ilberg, V. Chemical Structure of Model Substances Related to Their Gushing-inducing and -suppressing Activity. *J. Am. Soc. Brew. Chem.* **2011**, *69*, 170−179.

DOI: 10.1021/acs.jafc.5b01170
J. Agric. Food Chem. 2015, 63, 4673−4682

JOURNAL OF AGRICULTURAL AND FOOD CHEMISTRY

Article

pubs.acs.org/JAFC

Electrophoretic Behavior in Relation to the Structural Integrity of Codfish Parvalbumin upon Heat Treatment

Harmen H. J. de Jongh,*[,†] Marta de los Reyes Jimenez,[†] Joseph L. Baumert,[§] Steve L. Taylor,[§] and Stef J. Koppelman[§]

[†]TI Food and Nutrition, P.O. Box 557, 6700 AN, Wageningen, The Netherlands

[§]Food Allergy Research and Resource Program, Food Science and Technology, University of Nebraska—Lincoln, Lincoln, Nebraska 68583, United States

ABSTRACT: This work evaluates the impact of heat processing of parvalbumin, a major fish allergen, on the consequences for quantitative analysis of this protein embedded in different matrices during heating (either isolated, in an aqueous extract, or in whole fillets) to assess potential health risks. It is shown that oligomerization of parvalbumin does occur, but only upon heat treatment above 80 °C. This coincides with the ability of the isolated protein to refold up to this temperature in a fully reversible way, as demonstrated by circular dichroism analysis. In autoclaved samples a disintegration of the protein structure is observed. The situation becomes different when parvalbumin is embedded in a matrix with other constituents, as in fish extracts or whole fillets. The electrophoretic analysis of parvalbumin (SDS-PAGE and immunoblotting) is largely determined by complexation with other proteins resulting in insoluble materials caused by the partial unfolding of the parvalbumin at elevated temperatures. This effect is more strongly observed for cod fish extract, compared to whole cod fillets, as in the latter situation the integrity of the tissue hampers this interprotein complexation. Moreover, it is shown by ELISA analysis of heat-treated samples that using blotting procedures where disintegration of complexes may be promoted, restoring some of the IgG-binding propensity, may provide false outcomes. It was concluded that antibody binding to parvalbumin is dominated by the potential to form heat-induced complexes with other proteins. The possibly less-soluble or extractable character of these complexes may provide confusing information regarding potential health risks of fish and fish protein-containing food composites when such heat-treated samples are analyzed by immunochemical assays.

KEYWORDS: *parvalbumin, Western blot, heat processing, allergen, protein structure*

INTRODUCTION

Fish plays an important role in human nutrition as a source for proteins, polyunsaturated fatty acids, vitamins A and D, and iron and calcium.[1] However, fish is also one of the most frequent causes of food allergy.[2] The rising consumption of fish contributes to the prevalence of fish allergy. Fish-allergic individuals are counselled to follow a strict fish-avoidance diet to prevent reactions. The increasing availability of fish-derived ingredients, including as a powdered constituent in complex food products, raises concerns for fish-allergic consumers. Prevalence rates of fish allergy range from 0.2 to 2.3% of the population, reaching up to 8% among fish-processing workers.[1−3] Individuals allergic to ingestion or inhalation of or even skin contact with fish proteins subjected to cooking or other processing may exhibit IgE-mediated type I responses including symptoms such as urticaria, dermatitis, angioedema, diarrhea, asthma, or anaphylactic reactions.[3]

Parvalbumin (PV) is considered to be a pan-allergen for fish-allergic patients. Parvalbumins from many different fish species commonly consumed in western Europe share similar biochemical and immunochemical characteristics[4,5] and are reported to cross-react with each other and with parvalbumins in frog meat[6] or in tropical fish species consumed in Asian−Pacific countries.[7] Recently it was shown that parvalbumin cross-reactivity is related to the molecular origin of this major allergen.[8]

Parvalbumins are proteins conserved in lower vertebrates and are abundant in white muscle. Parvalbumins are found in fast-twitch skeletal muscles of higher vertebrates, as well as in a variety of nonmuscle tissues, including testes, endocrine glands, skin, and specific neurons,[9] and are involved in muscle contraction, calcium buffering, and signal transduction between cellular compartments.[10−13] For cod it is estimated that 0.15−0.63% of fish muscle tissue (wet weight) consists of parvalbumin.[14] They are typically 10−12 kDa, acidic (pI = 4.0−5.2), and structurally characterized by the presence of three typical helix−loop−helix domains, of which two are capable of binding divalent cations, such as Ca^{+}. The third domain forms a cap that covers the hydrophobic surface of the pair of functional domains.[15,16] On the basis of the amino acid sequences, two distinct phylogenetic lineages of parvalbumins, named α and β, have been identified.[17] The β lineage is reported to be especially allergenic,[3] and its IgE binding has been shown to be strongly calcium-dependent.[18]

Heat treatment is an important food preparation and preservation procedure. It is required to ensure microbial safety or to obtain desirable organoleptic attributes, improving the appearance, texture, flavor, and taste of products.[16]

Received: December 11, 2014
Revised: April 16, 2015
Accepted: April 16, 2015
Published: April 16, 2015

ACS Publications © 2015 American Chemical Society

DOI: 10.1021/jf505990h
J. Agric. Food Chem. 2015, 63, 4683−4689

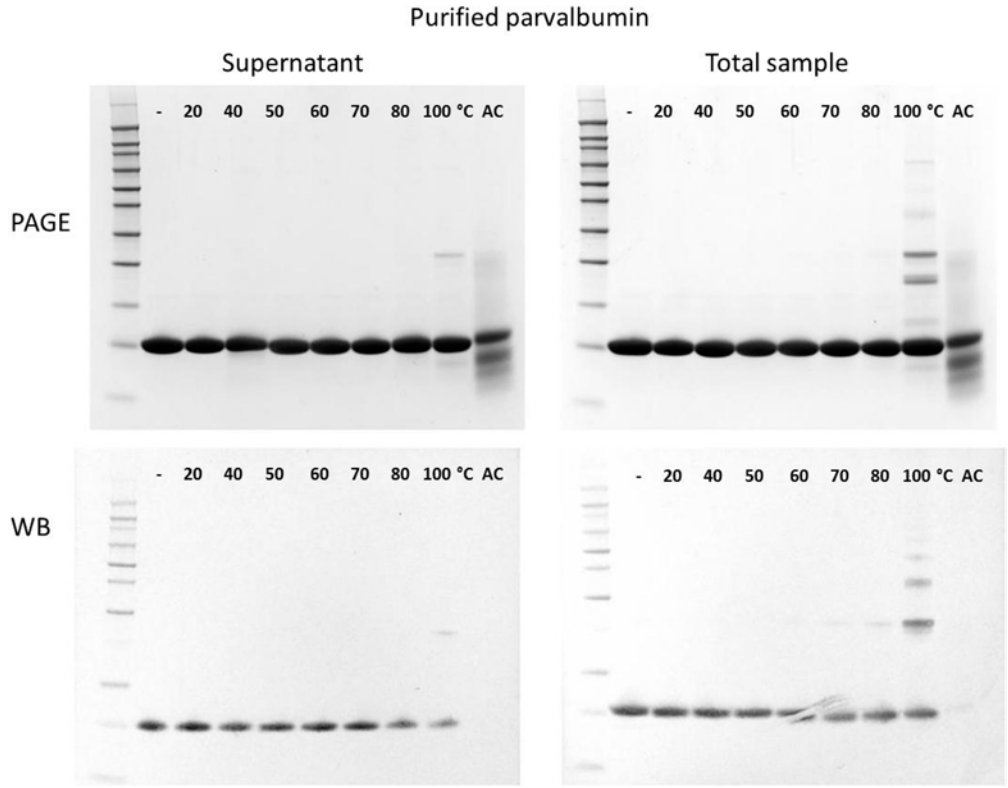

Figure 1. Heating of purified cod parvalbumin: (top panels) SDS-PAGE analysis with protein stain; (bottom panels) immunoblotting with anti-parvalbumin antiserum; (left panels) supernatant; (right panels) total sample. In all lanes 10 μg of total protein was applied. The incubation temperatures (2 h) are indicated.

Parvalbumins are renowned for their strong resistance against heat treatment, associated with the high reversibility in their denaturation in the presence of calcium[19] and other denaturing conditions.[20] The heat stability of parvalbumin provides a major source of risk for fish-allergic consumers.[21] It was recently reported that heat treatment of cod parvalbumin at high temperatures alters the structure of the protein, losing partially its secondary structure and initiating aggregation[22] and thereby affecting antibody reactivity.[8] The thermal stability of parvalbumins is different among isotypes, as has been studied in carp[23] and red stingray,[24] where some isoforms formed aggregates during heat processing.

Allergenicity is described by two key parameters: the potency to sensitize an (atopic) individual and the IgE binding essential to elicit an allergic reaction once an individual is sensitized. Therefore, fish processing may affect structural epitopes responsible for IgE binding to parvalbumin.[25] Boiling and cooking of fish can also lead to the formation of molecular aggregates and thereby enhancement of IgE reactivity as shown for tuna, salmon, cod, flounder, and whiff,[26,27] despite the observation that the allergenicity to certain proteins in tuna and salmon was reduced by heat processing.[28,29] Also, other IgE-binding proteins have been identified in Baltic[30,19] and Atlantic cod.[31,32] Some of these proteins were also recognized by monoclonal parvalbumin antibodies,[19,30−32] associated with dimers or oligomers.[31] It has been suggested that IgE binding to multimers is stronger than to monomeric parvalbumin.[33] The occurrence of monomeric and oligomeric parvalbumin has also been demonstrated in different fish extracts.[8] A direct link between their presence and their IgE-binding potential has not been reported.

The aim of this work is to evaluate the impact of heat processing of PV on structural motifs in relation to the matrix in which PV is embedded (isolated, in an aqueous extract, or in whole fillets). In particular, the heat-induced effects on the PV aggregation state were evaluated by electrophoresis and immunoblotting. Circular dichroism analysis was applied to assess the reversibility of structural motifs in the proteins.

MATERIALS AND METHODS

Materials. Atlantic cod (*Gadus morhua*) was purchased as frozen fillets produced by Albert Heijn (Zaandam, The Netherlands). The fillets were stored at −20 °C until further use. Three types of parvalbumin batches were prepared: sliced pieces of cod fillet, cod fillet protein extract, and purified parvalbumin.

Cod fillet samples were prepared as ∼5 g pieces. Cod fillet protein extracts were from defrosted 20 g portions of cod muscle as described elsewhere.[34] The thawed fillet was homogenized in 60 mL of deionized water and 6.4 mL of 1 M Tris-HCl (pH 9) using an Ultra Turrax blender (IKA, Staufen, Germany). Thereafter the pH was maintained around pH 8 using 1 M NaOH. The slurry was stirred for 2 h on ice and then centrifuged for 30 min at 1800*g* at 4 °C. The supernatant was collected and stored in the freezer. Purified parvalbumin was obtained as described earlier by Koppelman and co-workers.[35]

Heating of Protein Samples. Aliquots of purified parvalbumin, cod fillet protein extracts, and pieces of cod fillet were heated at 20, 40, 50, 60, 70, 80, or 100 °C for 2 h in a water bath. This incubation time was selected to be sufficiently long to avoid uncertainties in warming of the samples and to represent processing-relevant times. For cod fillet pieces, the heating time was extended by 5 min, as a control experiment showed that this time was needed to obtain the set temperature at the interior of the pieces. Alternatively, samples were heated in an autoclave for 2 h at 120 °C. After the heating step, the samples were cooled to room temperature. After centrifugation (3612*g* in a table-top centrifuge at 4 °C for 30 min) of the extracts and

DOI: 10.1021/jf505990h
J. Agric. Food Chem. 2015, 63, 4683−4689

purified parvalbumin, a sample was collected from the supernatant (20 μL). The remaining mass (30 μL) was kept separately and referred to as total sample. The volume ratio for the supernatant was kept at two-fifths of the sample volume to be sure that the supernatant did not contain any pelleted material. As a consequence, the total sample contains the pelleted material and part of the supernatant. Both samples, supernatant and total sample, were immediately mixed with Laemmli buffer (1:1 v/v).

Protein Concentration Determination. Protein concentrations were determined using the Bradford assay kit (Sigma-Aldrich, USA). Bovine serum albumin standards (Sigma-Aldrich, USA) were used, and the absorbance was determined at 595 nm using a UV−vis spectrophotometer (PerkinElmer, USA) in a quartz cell with a path length of 1 cm. It is assumed that in the assay also pelleted protein becomes accessible for Coomassie binding.

SDS-PAGE Analysis. Protein profiles for pure PV, raw extracts, and cod fillet extracts were obtained using sodium dodecyl sulfate−polyacrylamide gel electrophoresis (SDS-PAGE). Fish proteins already diluted in Laemmli sample buffer containing 2-mercaptoethanol were heated for 10 min at 70 °C, loaded on a 12% Bis-Tris gel, and subjected to SDS-PAGE using the XCell Surelock Min-Cell (Invitrogen, USA) at 200 V. Novex Sharp Prestained Protein standards (Novex, USA) were used to estimate the molecular weights of individual proteins. Proteins were visualized by SimplyBlue SafeStain (Invitrogen, USA).

Immunoblotting. PV and fish protein extracts were separated using SDS-PAGE as described above and then transferred to an activated PVDF membrane (Invitrogen, USA) using the XCell II Blot Module (Invitrogen, USA) for 1 h at 30 V. After blocking with 5% (w/v) skim milk in TBST for 1 h at 4 °C, membranes were incubated overnight with the primary polyclonal rabbit anti-parvalbumin antibody,[14] diluted 1:2500 in the blocking buffer. Membranes were subsequently washed in TBST (diluted Tris-buffered saline) and incubated with the secondary goat anti-rabbit IgG antibody (Thermo Fisher Scientific) for 1 h. The protein−antigen interaction was visualized using DAB substrate (Roche, Germany). The staining reaction was stopped after 10 min with TBST.

ELISA for Parvalbumin. A sandwich enzyme-linked immunosorbent assay (ELISA) based on affinity-purified polyclonal antibodies (IgG) raised against purified cod parvalbumin was used with all samples.[14] Purified cod parvalbumin was used as standard. First, a wide dilution range using 5-fold serial dilutions was tested to determine the dilution that resulted in a half-maximal signal. Subsequently, a narrow dilution range (serial dilution of 2-fold) around this dilution was tested. Then, five dilutions in this area were tested in triplicate. Calibration curves were fitted using a four-parameter logistic function and had a correlation coefficient (R^2) of at least 0.998. Results are expressed in micrograms of parvalbumin per milliliter in undiluted sample.

Circular Dichroism (CD). The different samples, heated for 2 h at indicated temperatures at a concentration of 2 mg/mL, were diluted to 0.2 mg/mL with deionized water (pH 6.8) and transferred to a quartz cuvette with a 1 mm optical path. Far-UV CD spectra were recorded on a Jasco J-715 spectropolarimeter in the spectral range from 190 to 260 nm with a resolution of 0.2 nm, a bandwidth of 2 nm, a scan speed of 100 nm/min, and an instrumental response time of 0.125 s. The instrument was equipped with a computer-controlled Peltier element to set the temperature or apply temperature ramps between 20 and 95 (±0.1) °C. Sixteen spectra were accumulated and averaged. The spectrum of a protein-free sample was subtracted. Alternatively, the ellipticity at 222 nm was monitored during applied heating and cooling ramps of 1 °C/min.

RESULTS AND DISCUSSION

Electrophoretic Analysis of Heat Processed Purified Parvalbumin. Figure 1 shows that purified parvalbumin in aqueous buffer without heat treatment runs on an SDS-PAGE gel (upper panels) as a single band at approximately 12 kDa, as reported previously.[36] Heating the sample and subsequent centrifugation and analysis using gel electrophoresis under reducing conditions shows that parvalbumin can be found in both the supernatant and total sample. With heat treatments of up to 80 °C even for prolonged incubation for 2 h, no traces of multimeric protein were observed on the SDS-PAGE gel. Incubation at 100 °C leads to a small (estimated as <1%) contribution of dimeric protein in the supernatant. The total sample under this condition contains a more significant contribution (~5%) of aggregated proteins, as judged from

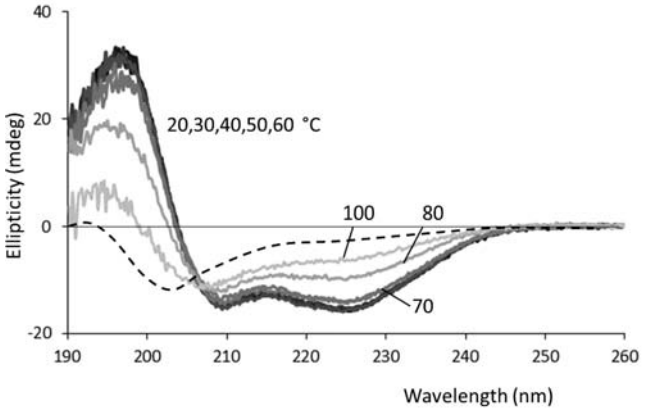

Figure 2. Far-UV CD spectra of 0.2 mg/mL purified parvalbumin samples recorded at 20 °C, pretreated for 2 h at a concentration of 2 mg/mL at indicated temperatures. The dashed line represents the redrawn spectrum of the autoclaved sample (2 h at 120 °C) where the intensity was multiplied by a factor of 5.

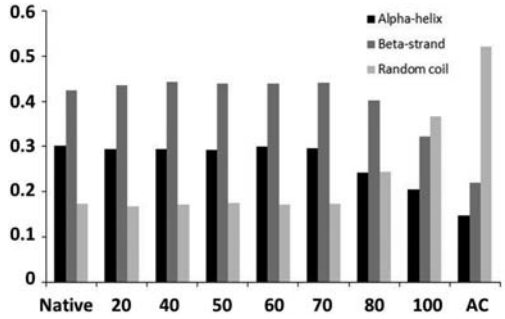

Figure 3. Secondary structure analysis of the spectra shown in Figure 2 using a nonlinear regression fitting procedure with reference spectra as described under Materials and Methods. The α-helix contributions are represented by the black bars, β-strands by the dark gray bars, and nonstructured contributions by the light gray bars.

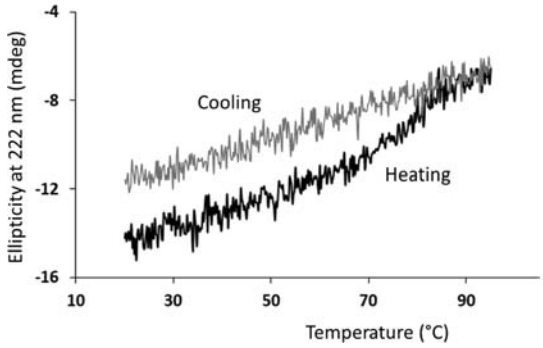

Figure 4. Temperature scans of 0.2 mg/mL purified parvalbumin with a heating and cooling rate of 1 °C/min. The ellipticity is monitored at 222 nm.

DOI: 10.1021/jf505990h
J. Agric. Food Chem. 2015, 63, 4683−4689

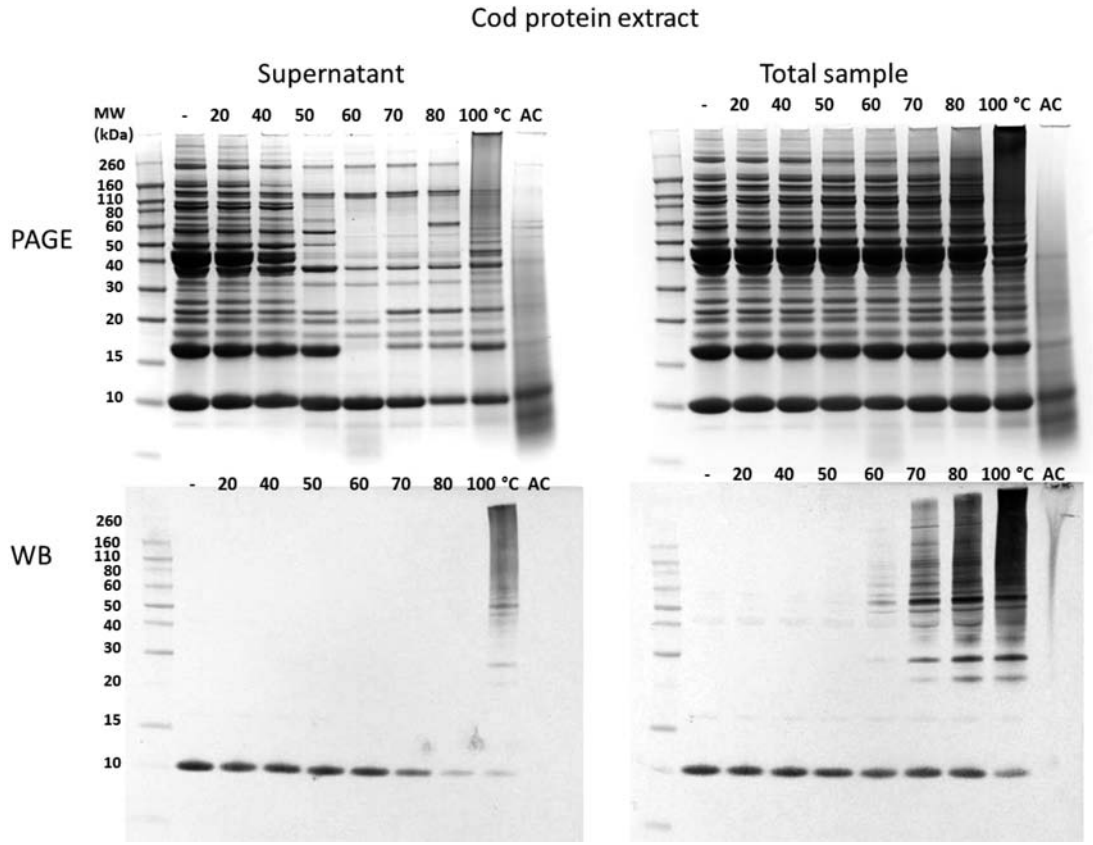

Figure 5. Heating of cod protein extract: (top panels) SDS-PAGE analysis with protein stain; (bottom panels) immunoblotting with anti-parvalbumin antiserum; (left panels) supernatant; (right panels) total sample. In all lanes 10 μg of total protein was applied. The incubation temperatures (2 h) are indicated.

visual inspection of the gel. Monomeric proteins are the predominant fraction, but dimers, trimers, and other aggregates up to hexamers can be distinguished under both nonreducing and reducing conditions with a predominance of the apparent dimeric and trimeric forms. Cod parvalbumin oligomers have been previously reported.[31] Analysis of the autoclaved sample showed that degradation of the protein had occurred into smaller (<12 kDa) peptide fragments in both the supernatant and the total sample. It is likely that the observed degradation products arise from the supernatant contribution to the total sample rather than its insoluble components.

The polyclonal rabbit anti-parvalbumin serum recognizes parvalbumin including all of the oligomeric structures observed in the 100 °C-treated samples as shown by the immunoblot analysis (lower panels in Figure 1). Interestingly, the intensity of staining on the blot decreases progressively with heat treatment (compare with upper panels), especially at temperatures above 80 °C. This effect appears to be stronger for the supernatant compared to the total sample. Moreover, the autoclaved sample does not show any significant IgG binding, except for a very faint band in the total sample.

Heat-Induced Conformational Changes of Parvalbumin. Parvalbumin is rather temperature-resistant, especially due to its refolding propensity.[19] To evaluate this in more detail, the secondary structure of the protein was studied as a function of temperature using CD. Figure 2 shows the CD spectra of samples that were heat-treated at different temperatures for 2 h and subsequently cooled to 20 °C. Typically, the spectra show three extremes, at 198, 208, and 222 nm, indicative for highly structured proteins, as described before.[33] The shape of the spectra deviated from that of the native material only when the sample was heated above 80 °C. Despite the similar protein concentration, the autoclaved sample (dashed line in Figure 2, which is a redrawn spectrum where the intensity was amplified 5 times to allow comparison with the other spectra) showed a low intensity, likely to be caused by disintegration of the protein in smaller fragments as illustrated in Figure 1. This degradation will lower the number of chiral peptide bonds detected with CD. When analysis of these spectra was conducted using a shape-analysis curve-fitting procedure, it was observed that the native protein bears a high secondary structure content with approximately 30% α-helix and 42% β-strands (Figure 3). The proportion of these two secondary structure contributions remains constant up to 70 °C and decreases gradually at higher incubation temperatures to about half their proportions for the autoclaved sample, illustrating the occurrence of some irreversible conformational change. When the temperature profile is shown at an ellipticity of 222 nm during heating from 20 to 95 °C (Figure 4), the secondary structure was in fact gradually reduced already at low temperatures, with a small cooperative unfolding starting between 70 and 80 °C, in line with previous results.[37] Moreover, no cooperative refolding step was observed upon subsequent cooling, and the secondary structure gradually increased again, as evidenced by the increase in absolute ellipticity (Figure 4). The difference at 20 °C prior to heating and after cooling reflects the irreversible unfolding as illustrated in Figure 2. By taking spectra at intervals of 10 °C during heating and cooling and subsequent analysis for the secondary structure content, this gradual unfolding−refolding was evident

DOI: 10.1021/jf505990h
J. Agric. Food Chem. 2015, 63, 4683−4689

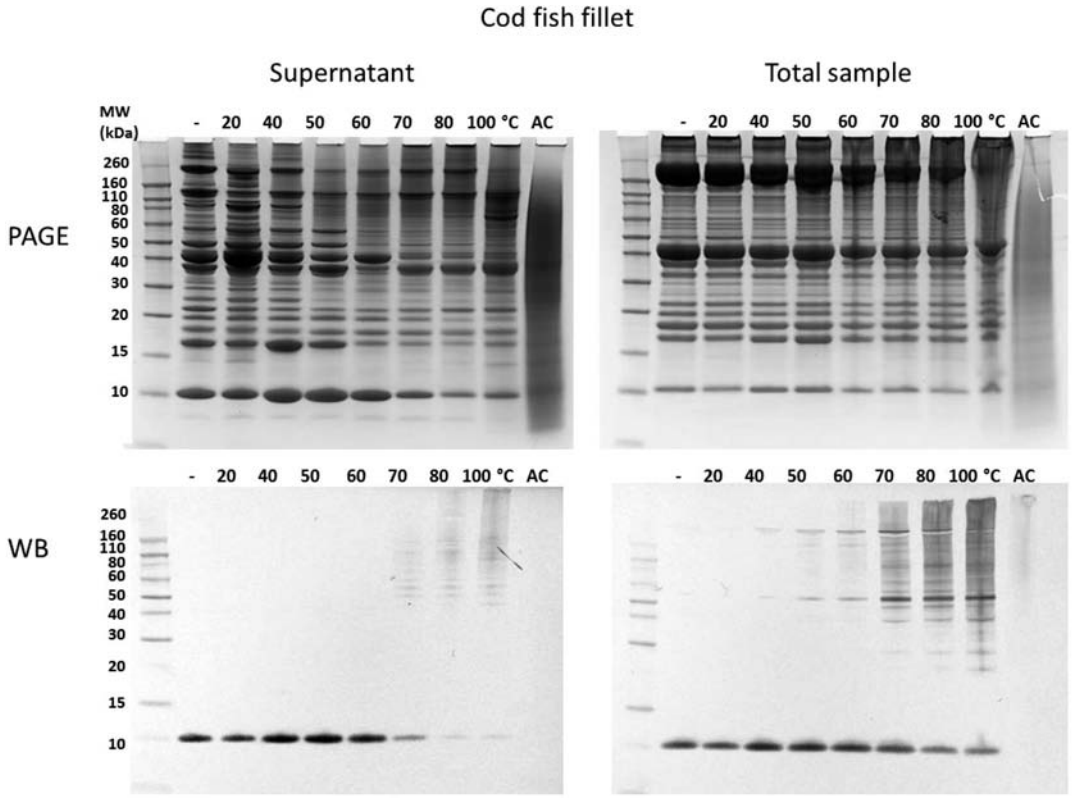

Figure 6. Heating of whole cod fillet: (top panels) SDS-PAGE analysis with protein stain; (bottom panels) immunoblotting with anti-parvalbumin antiserum; (left panels) supernatant; (right panels) total sample. In all lanes 10 μg of total protein was applied. The incubation temperatures (2 h) are indicated.

Table 1. Content of Parvalbumin Extracted from Whole Cod Fillet Incubated for 2 h at Different Temperatures As Detected by IgE Binding in an ELISA Assay

	parvalbumin content in extract (μg/mL)
not heated	388.2
heated at 50 °C	275.4
heated at 80 °C	45.3
heated at 100 °C	29.0
autoclaved (120 °C)	0.5

(results not shown). The spectrum of parvalbumin at 95 °C (not shown) shows a much more profound degree of unfolding (up to about 65% random coil) that partly refolds during cooling. At this point, it cannot be concluded whether this partial refolding reflects an ensemble-averaged behavior of unfolded and fully refolded contributions or whether all denatured proteins refold to a non-native state containing a less defined secondary structure.

At this point it is unclear whether the observed irreversible conformational changes above 80 °C can be held entirely responsible for the diminished staining intensity on the immunoblot. Although the correlation between the structural integrity and the immunoblot band intensity is striking, a more extensive and detailed analysis would be required to determine if these two observations were linked or coincidental. The absence of IgG binding with the autoclaved sample is remarkable and can be partially linked to the degradation of the protein into smaller fragments (Figure 1) with more limited IgG-binding potential. Alternatively, as Figure 1 still shows a significant population of protein in the autoclaved sample that runs with an apparent molecular mass as the native protein, and in view of the presence of a far-UV CD spectrum, it can also be concluded that irreversible unfolding of the protein beyond a certain level of the native protein results in a strongly diminished IgG binding.

Electrophoretic Behavior of Heated Parvalbumin Embedded in Matrices. Figures 5 and 6 show the electrophoretic analysis of parvalbumin heated either in an extract or embedded in a whole fillet and incubated for 2 h at temperatures ranging from 20 to 100 °C. Samples not subjected to heat reatment (lanes next to the marker ane) and those treated in the autoclave (AC) (2 h at 120 °C) (right lanes) are also included. With the cod fish protein extract (Figure 5), a large number of distinctive bands are observed from the nonheated sample with dominant bands, next to that of parvalbumin, at around 16, 36, and 40 kDa. The vast majority of these proteins, with the exception of parvalbumin, lose their solubility when incubated at temperatures above 50 °C. Parvalbumin is very heat resistant and remains soluble at high temperatures, as similarly observed for the pure protein (see Figure 2). Also, proteins can be observed at higher molecular weights in the total sample at elevated temperatures, but there are no indications for extensive aggregation phenomena, because no material can be observed at the top of the (stacking) gel shown in Figure 5. As observed for purified parvalbumin, the autoclave treatment resulted in degradation of the proteins and no apparent aggregation of the material. Immunoblot analysis of these samples shows that the IgG is specific for parvalbumin and does not show any significant cross-sensitivity for other extracted fish proteins. In the supernatant, a pattern similar to that of the pure parvalbumin

DOI: 10.1021/jf505990h
J. Agric. Food Chem. 2015, 63, 4683−4689

is observed where at higher temperatures the relative staining intensity to protein bands on the blot is reduced. Analysis of the total sample suggests that the heat treatment resulted in a complexation of parvalbumin with other fish muscle proteins. For example, bands at approximate molecular weights of 20, 40, and 60 kDa were observed (Figure 5) at heat treatments of 60 °C and above. Identification of these other proteins, however, is currently unresolved.

When parvalbumin is heated in the matrix of whole cod fish fillet (Figure 6), the extensive complexation of parvalbumin with other fish muscle proteins is not as evident as observed for the fish extract (compare with Figure 5). Such complexation could be hampered by the spatial organization of proteins within the tissue, providing a stable network that becomes disrupted in the extraction process. Less extensive complexation was observed after heating of the whole cod fish fillet where only two main contributions were observed at 40 and 200 kDa in addition to monomeric parvalbumin.

ELISA Analysis. Table 1 presents the analysis of the parvalbumin content using the IgG ELISA in the whole cod fish fillet when heated for prolonged times (2 h) at various temperatures. At 50 °C, IgG binding was reduced by 29%, whereas IgG binding was reduced by 93% when heated at 100 °C. The reduced reactivity in ELISA at moderate incubation temperatures (50 and 80 °C) is not in line with the staining intensities observed in the immunoblotting of these samples (Figure 6). Most likely this is related to the blotting procedure where the proteins are exposed to SDS, an unfolding agent, and mercaptoethanol, a reducing agent. The protein-dissociative conditions in the immunoblot analysis might promote the recognition by IgG. Clearly, autoclave treatment caused the complete loss of IgG binding in the ELISA, as similarly observed for the immunoblot analysis. Recent work showed that heating purified parvalbumin (i.e., in the absence of a matrix) for 20 min at 100 °C had no significant influence on IgG binding as assessed by ELISA, whereas the same heat treatment of whole cod fillet reduced the reactivity to only 14% (results not shown[34]). This suggests that the matrix plays an important role in the stability of immunogenicity of parvalbumin. Our observation that autoclave treatment of cod fish fillet strongly reduced the IgG reactivity of parvalbumin is in line with the observation that canned salmon was less reactive then nonheated salmon in an oral food challenge in fish-allergic patients,[38] although at this stage we cannot be sure that the same mechanism plays a role.

Concluding Remarks. This work shows that the matrix affects the aggregation behavior of parvalbumin upon heating. Less aggregation was observed with parvalbumin embedded in whole cod fillets, where the tissue orientation of the protein likely hampers protein complexation and aggregation. Dimerization or oligomerization of parvalbumin does occur, but only to a limited extent and does not interfere substantially with a quantitative analysis of the allergenic potential of a heat-treated material. Sampling conditions, like storage time and incubation buffers, may affect the aggregation process of parvalbumin and, thereby, the degree of oligomerization.

Heat treatment as such, and especially the structural refolding propensity of the protein, is thus only partially responsible for the loss of IgG reactivity. Antibody binding to parvalbumin is dominated by the potential of the protein to form heat-induced insoluble complexes with itself and other proteins, and immunoblot analysis of such heat-treated samples may provide confusing information regarding the potential health risks of heat-processed fish and fish-containing composite foods. Especially when parvalbumin enters the food chain as fish extract as in fish meal, a thorough immunochemical analysis is essential.

AUTHOR INFORMATION

Corresponding Author

*(H.H.J.d.J.) E-mail: dejongh@tifn.nl.

Notes

The authors declare no competing financial interest.

REFERENCES

(1) Failler, P. *Future Prospects for Fish and Fishery Products. Fish Consumption in the European Union in 2015 and 2030*; FAO Fisheries Circular 972/4; Food and Agriculture Organization of the United Nations: Rome, Italy, 2007.

(2) Sicherer, S. H. Epidemiology of food allergy. *J. Allergy Clin. Immunol.* **2011**, *127*, 594−602.

(3) Sharp, M. F.; Lopata, A. L. Fish allergy: in review. *Clin. Rev. Allergy Immunol.* **2014**, *46*, 258−271.

(4) Taylor, S. L.; Hefle, S. L.; Bindslev-Jensen, C.; et al. Factors affecting the determination of threshold doses for allergenic foods: how much is too much? *J. Allergy Clin. Immunol.* **2002**, *109*, 24−30.

(5) Van Do, T.; Elsayed, S.; Florvaag, E.; Hordvik, I.; Endresen, C. Allergy to fish parvalbumins: studies on the cross-reactivity of allergens from 9 commonly consumed fish. *J. Allergy Clin. Immunol.* **2005**, *116*, 1314−1320.

(6) Hilger, C.; Thill, L.; Grigioni, F.; Lehners, C.; Falagiani, P.; Ferrara, A.; Romano, C.; Stevens, W.; Hentges, F. IgE antibodies of fish allergic patients cross-react with frog parvalbumin. *Allergy* **2004**, *59*, 653−660.

(7) Lim, D. L.; Neo, K. H.; Yi, F. C.; Chua, K. Y.; Goh, D. L.; Shek, L. P.; Giam, Y. C.; van Bever, H. P.; Lee, B. W. Parvalbumin − the major tropical fish allergen. *Pediatr. Allergy Immunol.* **2008**, *19*, 399−407.

(8) Saptarshi, S. R.; Sharp, M. F.; Kamath, S. D.; Lopata, A. L. Antibody reactivity to the major fish allergen parvalbumin is determined by isoforms and impact of thermal processing. *Food Chem.* **2014**, *148*, 321−328.

(9) Lehky, P.; Blum, H. E.; Stein, E. A.; Fischer, E. H. Isolation and characterization of parvalbumins from the skeletal muscle of higher vertebrates. *J. Biol. Chem.* **1974**, *249*, 4332−4334.

(10) Holmes, K. C. Muscle proteins: their actions and interactions. *Curr. Opin. Struct. Biol.* **1996**, *6*, 781−789.

(11) Skelton, N. J.; Kordel, J.; Akke, M.; Forsen, S.; Chazin, W. J. Signal-transduction versus buffering activity in Ca^{2+}-binding proteins. *Nat. Struct. Biol.* **1994**, *1*, 239−245.

(12) Kranz, J. K.; Flynn, P. F.; Fuentes, E. J.; Wand, A. J. Dissection of the pathway of molecular recognition by calmodulin. *Biochemistry* **2002**, *41*, 2599−2608.

(13) Arif, S. H. A Ca^{2+}-binding protein with numerous roles and uses: parvalbumin in molecular biology and physiology. *BioEssays* **2009**, *31*, 410−421.

(14) Koppelman, S. J.; Nordlee, J. A.; Lee, P. W.; Happe, R. P.; et al. Parvalbumin in fish skin-derived gelatin: is there a risk for fish allergic consumers? *Food Addit. Contam., Part A* **2012**, *29*, 1347−1355.

(15) Swain, A. L.; Kretsinger, R. H.; Amma, E. L. Restrained least squares refinement of native (calcium) and cadmium-substituted carp parvalbumin using X-ray crystallographic data at 1.6 resolution. *J. Biol. Chem.* **1989**, *264*, 16620−16628.

(16) Moraes, A. H.; Ackerbauer, D.; Kostadinova, M.; Bublin, M.; Ferreira, F.; Almeida, F. C. L.; Breiteneder, H.; Valente, A. P. ^{1}H, ^{13}C and ^{15}N resonance assignments and second structure information of Gad m 1: a β-parvalbumin allergen from Atlantic cod (*Gadus morhua*). *Biomol. NMR Assignments* **2012**, *7*, 133−136.

(17) Goldmann, M.; Pechere, J.-F. The evolution of muscular parvalbumins investigated by the maximum parsimony method. *J. Mol. Evol.* **1977**, *9*, 131−158.

DOI: 10.1021/jf505990h
J. Agric. Food Chem. 2015, 63, 4683−4689

(18) Dory, D.; Chopin, C.; Aimone-Gastin, I.; Gueant, J. L.; Guerin, L.; Sainte-Laudy, J.; Moneret-Vautrin, D. A.; Fleurence, J. Recognition of an extensive range of IgE-reactive proteins in cod extract. *Allergy* **1998**, *53*, 42−50.
(19) Bugajska-Chretter, A.; Grote, M.; Vangelista, L.; Valent, P.; Sperr, W.; Rumpold, H.; Pastore, A.; Reichelst, R.; Valenta, R.; Spitzauer, S. Purification, biochemical, and immunological characterization of a major food allergen: different immunoglobulin E recognition of the apo- and calcium-bound forms of carp parvalbumin. *Gut* **2000**, *44*, 661−669.
(20) Bugajska-Schretter, A.; Elfman, L.; Fuchs, T.; Kapiotis, S.; Rumpold, H.; Valenta, R.; Spitzauer, S. Parvalbumin, a cross-reactive fish allergen, contains IgE-binding epitopes sensitive to periodate treatment and Ca^{2+} depletion. *J. Allergy Clin. Immunol.* **1998**, *101*, 67−74.
(21) Arif, S. H.; Jabben, M.; Hasnain, A. Biochemical characterization and thermostable capacity of parvalbumins: the major fish-food allergens. *J. Food Biochem.* **2007**, *31*, 121−137.
(22) Somkuti, J.; Bublin, M.; Breiteneder, H.; Smeller, L. Pressure−temperature stability, Ca^{2+} binding, and pressure−temperature phase diagram of cod parvalbumin: Gad m1. *Biochemistry* **2012**, *51*, 5903−5911.
(23) Liu, G.-M.; Wang, N.; Cai, Q.-F.; Li, T.; Sun, L. C.; Sua, W. J.; Caoa, M.-J. Purification and characterization of parvalbumins from silver carp (*Hypophthalmichthy molitrix*). *J. Sci. Food Agric.* **2010**, *90*, 1034−1040.
(24) Qiu-Feng, C.; Guang-Ming, L.; Teng, L.; Kemji, H.; Xi-Chang, W.; Wen-Jin, S.; Min-Jie, C. Purification and characterization of parvalbumins, the major allergens in red stingray (*Dasyatis akajei*). *J. Agric. Food Chem.* **2010**, *58*, 12964−12969.
(25) Thomas, K.; Herouet-Guicheney, C.; Ladics, G.; Bannon, G.; Cockburn, A.; Crevel, R.; Fitzpatrick, J.; Mills, C.; Privalle, L.; Vieths, S. Evaluating the effect of food processing on the potential human allergenicity of novel proteins: international workshop report. *Food Chem. Toxicol.* **2007**, *45*, 1116−1122.
(26) Griesmeier, U.; Bublin, M.; Radauer, C.; Vazquez-Cortes, S.; Ma, Y.; Fernandez-Rivas, M.; Breiteneder, H. Physicochemical properties and thermal stability of Lep w 1, the major allergen of whiff. *Mol. Nutr. Food Res.* **2010**, *54*, 861−869.
(27) Bernhisel-Broadbent, J.; Scanlon, S. M.; Sampson, H. A. Fish hypersensitivity 1. In vitro and oral challenge results in fish-allergic patients. *J. Allergy Clin. Immunol.* **1992**, *89*, 730−737.
(28) Bernhisel-Broadbent, J.; Strause, D.; Sampson, H. A. Fish hypersensitivity. II. Clinical relevance of altered fish allergenicity caused by various preparation methods. *J. Allergy Clin. Immunol.* **1992**, *90*, 622−629.
(29) Chatterjee, U.; Mondal, G.; Chakraborti, P.; Patra, H. K.; Chatterjeem, B. P. Changes in the allergenicity during different preparations of pomfret, hilsa, bhetki and mackerel fish as illustrated by enzyme-linked immunosorbent assay and immunoblotting. *Int. Arch. Allergy Immunol.* **2006**, *141*, 1−10.
(30) Galland, A. V.; Dory, D.; Pons, L.; Chopin, C.; Rabesona, H.; Gueant, J. L.; Fleurence, J. Purification of a 41-kDa cod-allergenic protein. *J. Chromatogr., Biomed. Appl.* **1998**, *706*, 63−71.
(31) Das Dores, S.; Chopin, C.; Villaume, C.; Fleurence, J.; Gueant, J. L. A new oligomeric parvalbumin allergen of Atlantic cod (Gad mI) encoded by a gene distinct from that of Gad cI. *Allergy* **2002**, *57*, 79−83.
(32) Sletten, G.; Van Do, T.; Lindvik, H.; Egaas, E.; Florvaag, E. Effect of industrial processing on the immunogenicity of commonly ingested fish species. *Int. Arch. Allergy Immunol.* **2010**, *151*, 223−236.
(33) de Jongh, H. H. J.; Robles, C. L.; Timmerman, E.; Nordlee, J. A.; Lee, P.-W.; Baumert, J. L.; Hamilton, R. G.; Taylor, S. L.; Koppelman, S. J. Digestibility and IgE-binding of glycosylated codfish parvalbumin. *BioMed Res. Int.* **2013**, article ID 756789, 10 pages.10.1155/2013/756789
(34) Koppelman, S. J.; Reyes Jiménez, M.; Timmerman, E.; Lee, P.-W.; Nordlee, J. A.; Baumert, J. L.; Taylor, S. L.; de Jongh, H. H. J. *Reactivity of codfish parvalbumin in immune-assays; heating plays an indirect role*, unpublished results.
(35) Koppelman, S. J.; Romijn, R. A.; de Jongh, H. H. J.; Nordlee, J. A.; Piersma, S.; Hessing, M.; Taylor, S. L. Purification of parvalbumin from carp: a protocol that avoids heat-treatment. *J. Food Sci.* **2010**, *75*, 49−56.
(36) Elsayed, S.; Aas, K. Isolation of purified allergen (cod) by isoelectric focussing. *Int. Arch. Allergy Immunol.* **1971**, *40*, 428−438.
(37) de Jongh, H. H. J.; Taylor, S. L.; Koppelman, S. J. Controlling the aggregation propensity and thus digestibility of allergens by Maillardation as illustrated for cod fish parvalbumin. *J. Biosci. Bioeng.* **2011**, *111*, 204−211.
(38) Bernhisel-Broadbent, J.; Strause, D.; Sampson, H. A. Fish hypersensitivity. II: Clinical relevance of altered fish allergenicity caused by various preparation methods. *J. Allergy Clin. Immunol.* **1992**, *90*, 622−629.

DOI: 10.1021/jf505990h
J. Agric. Food Chem. 2015, 63, 4683−4689

JOURNAL OF AGRICULTURAL AND FOOD CHEMISTRY

Article

pubs.acs.org/JAFC

Application of ^{1}H NMR Profiling To Assess Seed Metabolomic Diversity. A Case Study on a Soybean Era Population

George G. Harrigan,*[,†] Kirsten Skogerson,*[,†] Susan MacIsaac,[§] Anna Bickel,[†] Tim Perez,[†] and Xin Li[†]

[†]Monsanto Company, 800 North Lindbergh Boulevard, St. Louis, Missouri 63167, United States

[§]150 North Research Campus Drive, Kannapolis, North Carolina 28081, United States

Supporting Information

ABSTRACT: ^{1}H NMR spectroscopy offers advantages in metabolite quantitation and platform robustness when applied in food metabolomics studies. This paper provides a ^{1}H NMR-based assessment of seed metabolomic diversity in conventional and glyphosate-resistant genetically modified (GM) soybean from a genetic lineage representing ∼35 years of breeding and differing yield potential. ^{1}H NMR profiling of harvested seed allowed quantitation of 27 metabolites, including free amino acids, sugars, and organic acids, as well as choline, *O*-acetylcholine, dimethylamine, trigonelline, and *p*-cresol. Data were analyzed by canonical discriminant analysis (CDA) and principal variance component analysis (PVCA). Results demonstrated that ^{1}H NMR spectroscopy was effective in highlighting variation in metabolite levels in the genetically diverse sample set presented. The results also confirmed that metabolite variability is influenced by selective breeding and environment, but not genetic modification. Therefore, metabolite variability is an integral part of crop improvement that has occurred for decades and is associated with a history of safe use.

KEYWORDS: *soybean (Glycine max), NMR, metabolomics, canonical discriminant analysis, principal variance component analysis*

INTRODUCTION

Soybean (*Glycine max* L.) is a global food and feed commodity, utilized primarily as a source of protein and oil. It also contains bioactive metabolites such as isoflavones, which are associated with health benefits.[1,2] Globally, breeding programs are committed to developing new varieties with improved agronomic characteristics[3,4] and nutritional profiles.[5] The steady rise in yield potential observed in newer varieties over the past few decades[6−8] has been driven by the need to maintain sustainable production of this important crop to meet the demands of a growing population. Studies have shown that selective breeding as well as differences in crop genetics and environment can affect soybean composition.[8−11] In general, levels of protein and oil, the major value components of soybean, are inversely correlated to each other and vary depending on yield potential, genotype, and environment.[5,12,13] Levels of other soybean components such as isoflavones as well as antinutrients such as certain oligosaccharides are similarly variable. A better understanding of the relationships between agronomic performance and levels of key crop nutrients and metabolites will be of value as improvements to soybean yield potential continue apace.

Metabolomics may be an effective tool in evaluating agronomic and nutritional performance.[2,14−19] In recent mass spectrometry (MS)-based metabolomics studies, it has been demonstrated that soybean cultivars can be differentiated on the basis of metabolite profiles.[1] Nuclear magnetic resonance (NMR) spectroscopy has several benefits as a metabolite profiling technique including ease of sample preparation, high sample throughput, identification of a broad range of chemical compounds in a single experiment, and generation of quantitative data. ^{1}H NMR techniques have been broadly applied in the metabolomics community for biomedical, food, and plant research,[2,15,17−21] including applications to soybean. The objectives of the study described here were to characterize metabolomic variability in soybean seed through application of ^{1}H NMR and applied multivariate statistics and to interpret results in the context of selective breeding and the history of safe consumption of soybean. ^{1}H NMR profiles of nine soybean varieties sharing a genetic lineage representing ∼35 years of breeding (commercial launch years 1972−2008) and increasing yield potential were therefore generated. The selected varieties included four older conventional lines (commercial launch years 1972−1996), two newer conventional lines (1997−2008), and three glyphosate-tolerant genetically modified (GM) lines (1999−2008) that were grown concurrently at two replicated field sites in the United States during the 2011 growing season.

The ^{1}H NMR analysis utilized standard one-dimensional profiling techniques, and a total of 27 metabolites were quantified. Analysis of the metabolite data set included canonical discriminant analysis (CDA), a multivariate approach that finds linear combinations of the quantitative variables that can provide maximal separation between classes or groups. Principal variance component analysis (PVCA) was pursued to assess interrelationships between the seed metabolites as well as the impacts of location and pedigree (variety) on variation in metabolite levels.

Received: February 26, 2015
Revised: April 23, 2015
Accepted: April 24, 2015
Published: May 5, 2015

ACS Publications © 2015 American Chemical Society

DOI: 10.1021/acs.jafc.5b01069
J. Agric. Food Chem. 2015, 63, 4690−4697

MATERIALS AND METHODS

Biological Material. Nine soybean varieties representing a genetic lineage from Williams (1972) to A3555 (2008) were grown concurrently at two sites in Illinois [Jerseyville (ILJE) and Jacksonville (ILJA)] during the 2011 season. Varieties included six conventional and three glyphosate-tolerant (GM) lines. Variety launch year and grouping based on genetic similarity (see the Supporting Information) are listed in Table 1. Starting seeds were planted in a randomized complete block design with six replicates. Soybean plants were treated with maintenance pesticides as necessary throughout the growing season at both sites. The three glyphosate-tolerant varieties were not treated with glyphosate. Seed was harvested at maturity and homogenized by grinding with dry ice to a fine powder, lyophilized, and stored in a freezer set to maintain −20 °C prior to analysis. Two samples (one replicate of AG3705 at ILJA and one replicate of CX375 at ILJE) were lost at harvest.

Table 1. Launch Year and Average Yield of Each Variety

variety	launch year	yield at ILJA[a]	yield at ILJE[a]
Williams	1972	66.5	65.3
A3127	1979	68.2	61.0
CX366	1986	71.9	66.6
CX375	1996	71.8	66.3
A3469	1997	80.3	73.5
AG3701	1999	72.8	71.1
AG3705	2006	80.6	77.2
A3555	2008	85.9	74.2
AG3803	2008	78.8	76.4

[a]Bushels/acre. ILJA represents the Jacksonville, IL, site, and ILJE represents the Jerseyville, IL, site.

Comprehensive compositional and MS-based metabolomics assessments of these study samples have been presented in Harrigan et al.[11] and Kusano et al.,[22] respectively. Genetic characterization of all varieties using the Illumina Infinium platform was also presented in Kusano et al.;[22] a summary of thaose data has been incorporated into Supporting Information Figure 1.

Sample Extraction and NMR Analysis. Ground, lyophilized grain samples (50 mg) were suspended in 1.8 mL of 80% MeOH and sonicated for 15 min at room temperature. Following sonication the sample was centrifuged and supernatant collected. The pellet was re-extracted twice as above. Pooled supernatants were dried and resuspended in 1 mL of NMR buffer (100 mM sodium phosphate, pD 7.4, with 0.5 mM 4,4-dimethyl-4-silapentane-1-sulfonic acid (DSS) chemical shift standard). Samples were filtered prior to loading into NMR tubes (700 μL) due to the presence of insoluble material.

All NMR data were collected on a Bruker AVANCE III spectrometer (600.13 MHz) at 298 K with a Bruker 5 mm TCI CryoProbe. One-dimensional ^{1}H NMR spectra were acquired using a standard Bruker noesypr1d pulse sequence. Each spectrum consisted of 128 scans of 65563 data points with a spectral width of 7.2 kHz, an acquisition time of 4.55 s, and a recycle delay of 1 s per scan. Data collection parameters were based on those used by Chenomx to generate the standard spectra in the library to ensure best possible results for the quantitative fitting of the spectra. Exponential line broadening of 0.3 Hz was applied before Fourier transformation. Spectra were phase corrected manually and referenced to DSS (methyl singlet chemical shift of 0.00 ppm). Processed spectra were uploaded into the Chenomx NMR Suite for metabolite identification and quantitation using the 600 MHz library (version 7.7). The Chenomx software algorithms reconstruct each sample spectrum from a linear sum of the individual standard spectra in the library, and quantitation is based on the concentration of the DSS methyl singlet reference. Spectra were also binned (0.02 and 0.01 ppm bin size) from 0.0 to 10.0 ppm with selected regions excluded to remove variations from residual solvents: δ 3.33−3.36 (residual MeOH), δ −0.04 to 0.04, δ 0.58−0.67, δ 1.75−1.80, δ 2.88−2.93 (DSS), δ 4.68−4.88 (H_2O). Additional regions where spectral alignment was poor were also removed prior to binning the data (δ 6.51−6.8, δ 7.07−7.095, δ 7.2−7.31, δ 7.52−7.60, δ 7.78−7.9, δ 8.09−8.30). Binned data were normalized to the spectrum area excluding the regions that were removed to account for solvent peaks and alignment shifts. These binned data (files S1 and S2) are available as Supporting Information. Chemical shifts of metabolites identified and quantified from ^{1}H NMR spectra of soybean extracts are available in Table 2.

Table 2. Chemical Shifts of Metabolites Identified and Quantified from ^{1}H NMR Spectra of Soybean Extracts

metabolite	^{1}H chemical shift (multiplicity)[a]
2-oxoglutarate	2.43 (t), 2.99 (t)
4-aminobutyrate	1.89 (m), 2.28 (t), 3.0 (t)
acetate	1.90 (s)
alanine	1.47 (d), 3.78 (q)
arginine	1.64 (m), 1.72 (m), 1.89 (m), 1.92 (m), 3.23 (t), 3.76 (t)
asparagine	2.85 (dd), 2.94 (dd), 3.99 (q)
aspartate	2.67 (dd), 2.80 (dd), 3.89 (dd)
choline	3.19 (s), 3.51 (m), 4.06 (m)
citrate	2.53 (d), 2.67 (d)
dimethylamine	2.72 (s)
formate	8.44 (s)
fumarate	6.51 (s)
galactose	3.48 (dd), 3.64 (dd), 3.69 (m), 3.71 (m), 3.73 (m), 3.74 (m), 3.77 (m), 3.80 (dd), 3.84 (dd), 3.92 (d), 3.98 (d), 4.07 (t), 4.57 (d), 5.25 (d)
glucose	3.22 (dd), 3.40(m), 3.46 (m), 3.48 (t), 3.53 (dd), 3.70 (t), 3.72 (dd), 3.76 (dd), 3.82 (m), 3.84 (m), 3.89 (dd), 4.63 (d), 5.22 (d)
glutamate	2.04 (m), 2.12 (m), 2.32 (m), 2.36 (m), 3.75 (dd)
isoleucine	0.93 (t), 1.00 (d), 1.25 (m), 1.46 (m), 1.97 (m), 3.66 (d)
lactate	1.32 (d), 4.11 (q)
leucine	0.95 (m), 1.67 (m), 1.70 (m), 1.73 (m), 3.73 (m)
malate	2.35 (q), 2.66 (dd), 4.29 (d)
O-acetylcholine	2.14 (s), 3.22 (s), 3.72 (m), 4.54 (m)
p-cresol	2.22 (s), 6.84 (m), 7.14 (m)
succinate	2.39 (s)
sucrose	3.46 (t), 3.55 (dd), 3.68 (s), 3.75 (t), 3.79 (m), 3.82 (m), 3.83 (m), 3.88 (m), 4.04 (t), 4.21 (t), 5.40 (d)
threonine	1.32 (d), 3.58 (d), 4.25 (m)
trigonelline	4.42 (s), 8.07 (t), 8.82 (dd), 9.11 (s)
tryptophan	7.18 (m), 7.27 (m), 7.31 (s), 7.53 (d), 7.72 (d)
valine	0.98 (d), 1.03 (d), 2.26 (m), 3.6 (d)

[a]^{1}H chemical shifts used for metabolite identification and quantification were determined at pD 7.4 in 100 mM sodium phosphate buffer and expressed as relative values to that of DSS at 0 ppm. Letters in parentheses denote the peak multiplicities: s, singlet; d, doublet; t, triplet; dd, doublet of doublets; q, quartet; and m, multiplet.

Univariate Statistical Analysis. Means, standard errors, and ranges were calculated in SAS 9.4 (SAS Institute Inc.) (Table 3). Values were combined across both sites. Pearson correlation coefficients were also determined between the 27 metabolites and yield.

Canonical Discriminant Analysis. CDA is a dimension-reduction technique related to principal component analysis and canonical correlation. CDA finds linear combinations of the quantitative variables that provide maximal separation between classes or groups. Given a classification variable and several quantitative variables, the CANDISC procedure in SAS derives *canonical variables*, linear combinations of the quantitative variables that summarize between-class variation in much the same way that principal components summarize total variation.

Principal Variance Component Analysis. The procedure and rationale for applying PVCA to crop compositional data are similar to

DOI: 10.1021/acs.jafc.5b01069
J. Agric. Food Chem. 2015, 63, 4690−4697

Table 3. Least-Squares Means of Metabolites Assessed across Both Sites

	Williams	A3127	CX366	CX375	A3469	AG3701	AG3705	A3555	AG3803
metabolite[a]	1972	1979	1986	1996	1997	1999	2006	2008	2008
2-oxoglutarate	6.26	6.00	6.28	6.50	8.08	7.42	6.73	7.10	6.48
4-aminobutyrate	9.57	10.90	10.24	10.09	10.67	9.45	9.79	11.05	9.90
acetate	33.01	40.73	41.89	38.86	38.21	41.48	42.61	27.73	38.92
alanine	7.18	10.18	9.38	7.66	8.94	7.95	7.33	10.47	9.41
arginine	21.51	23.29	25.43	23.56	25.00	22.74	22.02	33.14	23.81
asparagine	9.51	10.40	10.90	10.75	9.16	10.01	8.75	11.22	8.24
aspartate	46.49	46.40	44.14	50.39	43.72	56.67	52.39	48.56	42.79
choline	96.97	102.09	93.35	100.43	95.44	102.11	88.87	86.53	94.14
citrate	583.34	618.18	609.53	635.69	555.20	585.56	554.94	567.81	622.98
dimethylamine	66.99	102.29	94.50	91.47	80.85	86.35	90.41	69.82	83.39
formate	4.02	4.37	4.61	4.17	4.08	4.35	4.70	3.63	3.93
fumarate	2.56	2.36	2.45	2.48	3.42	2.82	2.63	4.34	3.14
galactose	19.42	20.70	20.78	19.99	20.82	21.54	19.48	22.79	24.28
glucose	22.73	21.27	23.09	22.61	23.82	24.63	23.85	27.81	28.72
glutamate	58.69	65.70	63.76	59.49	53.60	53.40	59.03	53.71	47.99
isoleucine	8.03	8.75	8.50	7.77	8.15	7.49	7.17	10.48	8.54
lactate	5.23	5.54	5.45	4.88	5.19	5.17	5.06	5.37	5.19
leucine	14.16	15.46	14.49	13.76	11.62	12.89	11.94	15.26	14.07
malate	116.78	113.06	123.83	111.11	176.29	155.28	119.64	179.45	152.08
O-acetylcholine	9.60	11.96	12.12	12.43	8.69	7.69	9.19	9.65	10.33
succinate	5.36	5.23	5.18	4.76	4.98	4.65	5.46	5.19	5.93
sucrose	4052.38	3393.53	4156.46	3851.73	4364.50	4512.91	4266.23	3945.86	4613.51
threonine	7.36	8.19	7.98	7.74	7.92	7.77	7.89	8.54	8.28
trigonelline	16.53	18.30	19.41	15.99	16.03	18.37	16.15	13.74	12.43
tryptophan	24.76	22.98	22.14	23.71	27.73	22.44	17.74	26.02	23.70
valine	8.26	9.60	9.06	8.79	9.40	9.46	8.42	10.83	9.32
p-cresol	17.78	23.17	21.11	21.36	22.66	25.26	20.27	22.44	16.12
seed weight[b]	14.72	12.02	13.56	13.36	12.23	12.66	14.55	13.95	14.89
yield[c]	65.87	64.58	69.26	69.30	76.87	71.95	78.73	80.05	77.57

[a]Micrograms per 50 mg DW. [b]Grams per 100 seed. [c]Bushel/acre. Least-squares means were based on a total of 12 biological replicates, six from the Jacksonville (ILJA) site and six from the Jerseyville (ILJE) site (n = 12), with an exception for AG3705 (n = 11), where one replicate was lost at harvest at ILJA, and for CX375 (n = 11), where one replicate was lost during harvest at ILJE.

those described in detail in Harrigan et al.[11] Essentially, the first step of the PVCA procedure is to normalize the responses, if necessary. In this study the responses were all approximately normally distributed. The second step is to check for linear dependencies in the data. This can be done by computing the correlation matrix of variables and then computing the rank of that matrix. If the rank is less than the number of variables, then some variables must be dropped from the analysis. The third step is to apply PCA to the correlation matrix. Li et al.[23] continued development of the original PVCA procedure with the principal components, but we added an intermediate step, factor analysis, to assist with results interpretation. Factor analysis with varimax rotation is a method of deriving new linear combinations of variables with information derived from PCA that assist in deciding the appropriate number of factors needed to capture sufficient variability. The final step is to apply variance components analysis to each of the derived factor variables (F^1, F^2, ..., F^j). An ANOVA model is applied, and all of the sources of variation of interest to the researcher are modeled with random effects. In our application of PVCA,[1,11] the principal components and factor scores are strongly correlated with individual compositional analytes if the absolute value of the linear correlation between the derived variable and the analyte exceeds 0.707, with the interpretation that at least 50% of the variation in the analyte can be explained by its linear relationship with the new variable. Absolute correlations between 0.5 and 0.707 can be described as moderately correlated, with the amount of variation in the analyte that can be explained by the factor ranging between 25 and 50%. PVCA was conducted in SAS 9.4 (SAS Institute Inc.).

RESULTS AND DISCUSSION

Selective plant breeding has contributed to an increase in soybean yield over time, as reflected in the varieties assessed in this study (Table 1). The genotypic diversity found in these soybean varieties (see the Supporting Information) allowed an opportunity to evaluate metabolite variability associated with decades of selective breeding and yield differences. ^{1}H NMR spectroscopy was assessed as a profiling technique due to the robustness of the platform and its quantitation capabilities, although it typically detects many fewer metabolites than mass spectrometry-based methods. In this study ^{1}H NMR profiling allowed quantitation of 27 metabolites, which included free amino acids (alanine, arginine, asparagine, aspartate, glutamate, isoleucine, leucine, threonine, tryptophan, valine, 4-amino-butyrate), sugars (galactose, glucose, and sucrose), organic acids (2-oxoglutarate, acetate, citrate, formate, fumarate, lactate, malate, and succinate), choline, *O*-acetylcholine, dimethyl-amine, trigonelline, and *p*-cresol (Table 2). Least-squares means combined across both sites are presented in Table 3. Corresponding ranges and standard errors are included in the Supporting Information. Portions of each spectrum remained unassigned due to the available metabolites in the Chenomx library and spectral overlap. Metabolite coverage could be improved for these soybean samples through the addition of soybean-specific metabolites to the Chenomx library.

DOI: 10.1021/acs.jafc.5b01069
J. Agric. Food Chem. 2015, 63, 4690−4697

Statistical analysis of the data set focused on two key methods. The first method is CDA to determine if linear combinations of the quantitative variables exist that can be used to discriminate between the nine varieties. The second method is PVCA to estimate the percentage of the total variability in the data set attributed to each major source of variability.

Canonical Discriminant Analysis. CDA is a dimension-reduction technique related to principal component analysis and canonical correlation. CDA finds linear combinations of the quantitative variables that provide maximal separation between classes or groups. When applied here, the first three canonical factors (Can 1, Can 2, and Can 3) accounted for 87% of the variation in the data (Supporting Information Table 1). These factors proved effective in providing discrete clustering of the nine different varieties, as shown in Figure 1 and Supporting Information Figure 2. The older varieties were discriminated from the newer varieties, with the exception of AG3705.

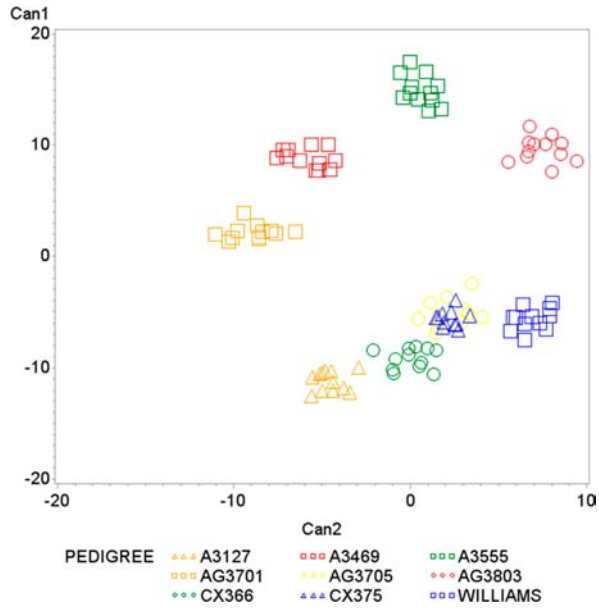

Figure 1. Canonical discriminant analysis of metabolite data for all nine varieties. On canonical 1 axis, the four older varieties (A3127, CX375, CX366, and Williams) can be distinguished from four of newer varieties (A3469, A3555, AG3701, and AG3803). AG3705 clustered with the older varieties and was shown (see text) to have some metabolic features similar to these.

Notably, Can 1 proved highly effective in discriminating between the older varieties and, with the exception of AG3705, the newer varieties. Can 1 was strongly correlated with malate (r = 0.93), fumarate (r = 0.92), glucose (r = 0.86), and glutamate (r = −0.88) (Supporting Information Table 2). The least-squares mean values (combined site) for these metabolites could, at least in part, also differentiate the varieties. For example, mean malate values for the older varieties and AG3705 ranged from 111.11 to 123.83 μg/50 mg DW in contrast to 155.28−179.45 μg/50 mg DW for the newer varieties (excluding AG3705). Corresponding values (older varieties plus AG3705 versus newer varieties excluding AG3705) for the other metabolites were as follows: fumarate, 2.36−2.56 versus 2.63−4.34 μg/50 mg DW; glucose, 21.27−23.09 versus 23.82−28.72 μg/50 mg DW; and glutamate, 58.69−65.70 versus 47.99−59.03 μg/50 mg DW. Other metabolites such as galactose (r = 0.72), trigonelline (r = −0.75), and formate (r = −0.75) also correlated well with Can 1. Varieties contained within either of the two main clusters discriminated by Can 1 showed separation along the Can 2 axis (Figure 1). Can 2 was most highly correlated with *p*-cresol (r = −0.82).

Principal Variance Component Analysis. PVCA included the variables yield and seed size in addition to the metabolite data. It was applied here to investigate the interrelationships among metabolite components as well as the impact of location and pedigree on variability in the levels of these metabolites. A total of eight factors described >80% of the variance in the study (Supporting Information Table 3). Factors F^1−F^5 are discussed in more detail below. The correlation matrix of components listed by factor, as determined by the varimax rotation, can be found in Supporting Information Table 4. Next, analysis of variance with only random effects was used to estimate the variance within each factor from the following sources: location, pedigree (i.e., variety), block (location) (i.e., biological replicate within location), and residual error (Figure 2). Percent of total variability shows that residual accounted for 42.3%; pedigree, 37.8%; unexplained, 17.3%; location, 1.7%; and block (location), 0.9% (Figure 3).

Factor F^1: Free Amino Acids (Alanine, Arginine, 4-Aminobutyrate, Asparagine, Isoleucine, Leucine, and Valine) and an Organic Acid (Fumarate). The first factor, F^1, explained 24.4% of the total variation in the metabolomics study (Figure 2 and Table 4). It was strongly correlated with three free amino acids (arginine, isoleucine, and valine) and moderately correlated with four free amino acids (alanine, 4-aminobutyrate, asparagine, and leucine) as well as the organic acid fumarate. Analysis of variance showed that the largest source of variance in F^1 was pedigree followed by residual error. Figure 4 contains box plots to display the variation of values in F^1 according to pedigree.

These results from PVCA were consistent with those from CDA. For example, in the CDA analysis all amino acids listed above, with the exception of leucine, had correlations with Can 3 of r > 0.6, whereas fumarate, as noted earlier, correlated very strongly with Can 1 (r = 0.92). In other words, metabolites shown by PVCA to be highly variable according to pedigree were also observed to contribute to separation in the CDA plots showing that results from both multivariate approaches were broadly consistent with each other. Variety A3555, which had the highest score for factor F^1 in the PVCA (see Figure 4), also had (or shared) the highest combined-site mean values for alanine, arginine, 4-aminobutyrate, asparagine, isoleucine, leucine, valine, and fumarate. This newer conventional line may therefore be a major contributor to the metabolite variation observed in these data.

Factor F^2: Sugars (Galactose and Glucose), Organic Acids (Lactate and Fumarate), and Free Amino Acids (Alanine and Threonine). The second factor, F^2, explained 16.6% of the total variation in the metabolomics study (Supporting Information Table 5). It was strongly correlated with two sugars (galactose and glucose), two organic acids (lactate and succinate), and the free amino acid threonine. It was moderately correlated with the free amino acid alanine. The largest source of variance in F^2 was residual error. Supporting Information Figure 3 contains box plots that display the variation of values in F^2 according to pedigree. F^2 also had the most notable contribution to variance from location.

DOI: 10.1021/acs.jafc.5b01069
J. Agric. Food Chem. 2015, 63, 4690−4697

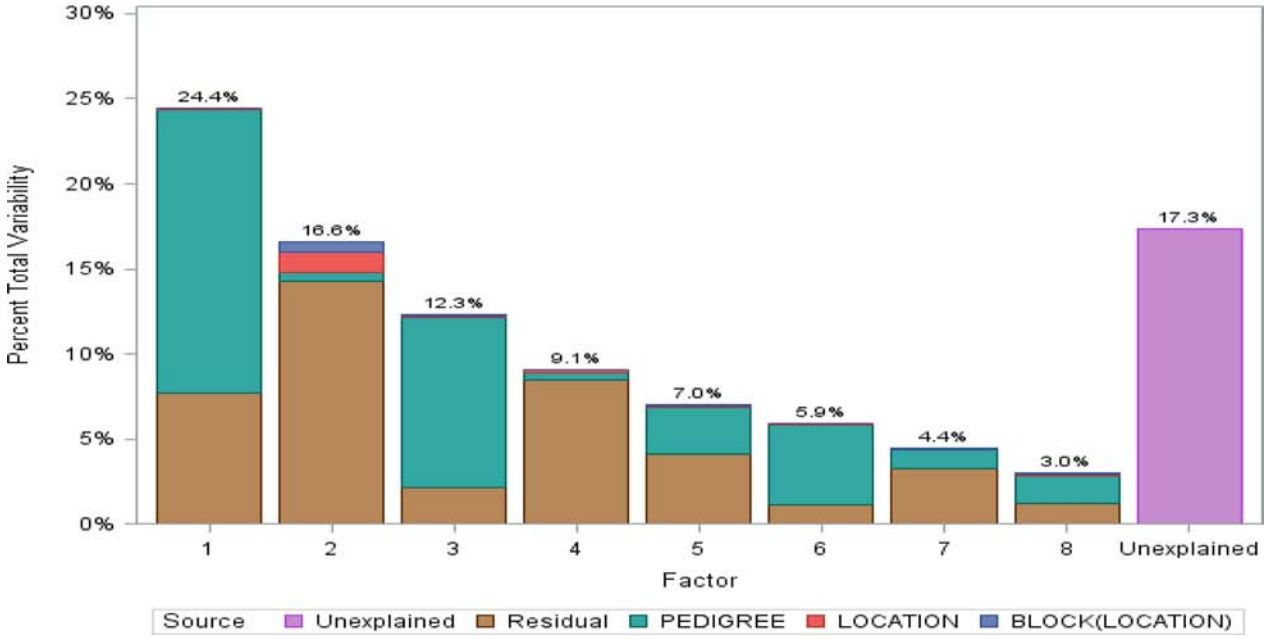

Figure 2. Proportions of variance explained by variance components for each factor.

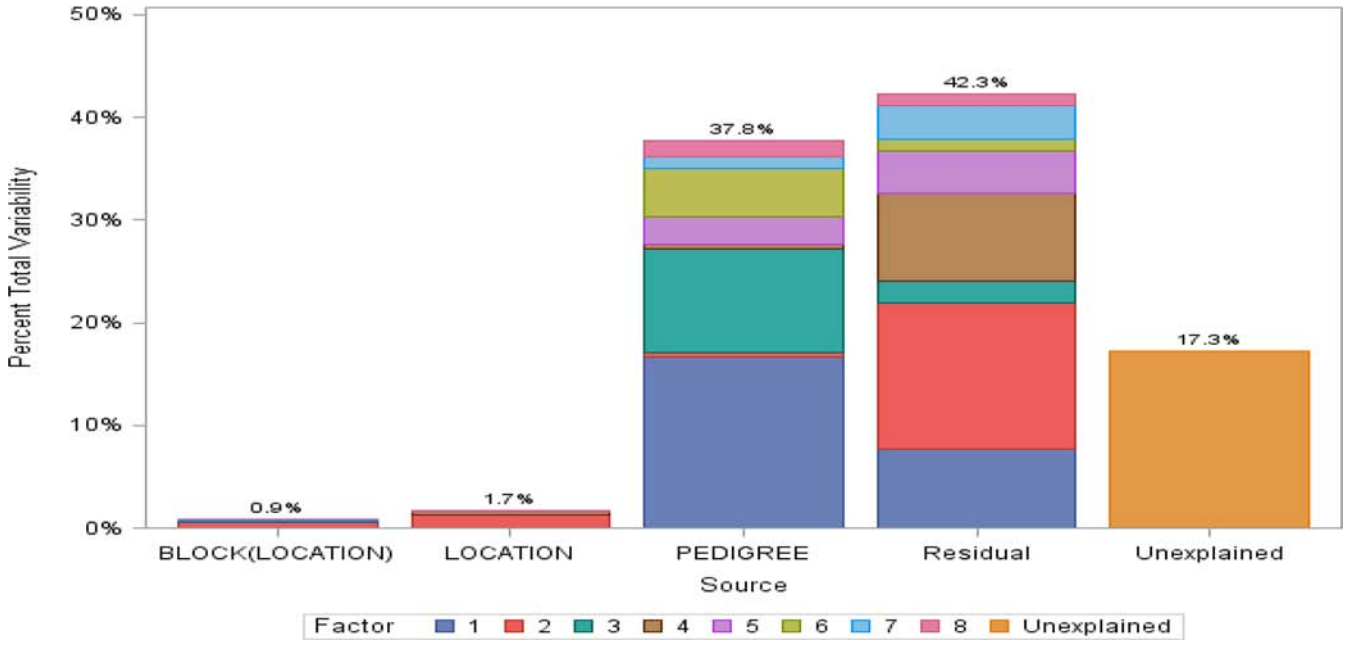

Figure 3. Proportions of variance explained by each factor.

Table 4. Summary of Factor 1 Sources of Variation (24.4%)

source of variance	fraction of variance due to source	PVC contribution
pedigree	68.33	16.67
residual error	31.50	7.69
location	0.18	0.04
block (location)	0.00	0.00

Factor F^3: Yield, Sucrose, Organic Acids (Malate and Fumarate), Glutamate, and *O*-Acetylcholine. The third factor, F^3, explained 12.35% of the total variation in the study (Table 5). It was strongly correlated with malate and glutamate and moderately correlated with yield, sucrose, fumarate, and *O*-acetylcholine. The largest source of variance in F^3 was pedigree. Figure 5 contains box plots to display the variation of values in F^3 according to pedigree. Figure 6 shows the contribution of pedigree to variation in each metabolite associated with F^3.

Figure 5 reveals that the five newer higher yielding soybean varieties have F^3 scores above the zero reference line, whereas the four older lower-yielding lines have negative scores. This is broadly consistent with results from the CDA where Can 1 also discriminated (with the exception of AG3705) the older and newer varieties. Malate, glutamate, and fumarate all correlated highly with Can 1 in that analysis. Sucrose and *O*-acetylcholine had lower correlations with Can 1 (r = 0.51 and −0.55, respectively) with the exception of A3555, 4.27−4.61 mg/50 mg DW (A3555 value = 3.95) versus 3.39−4.16 mg/50 mg DW for the older varieties. Sucrose has been reported to

DOI: 10.1021/acs.jafc.5b01069
J. Agric. Food Chem. 2015, 63, 4690−4697

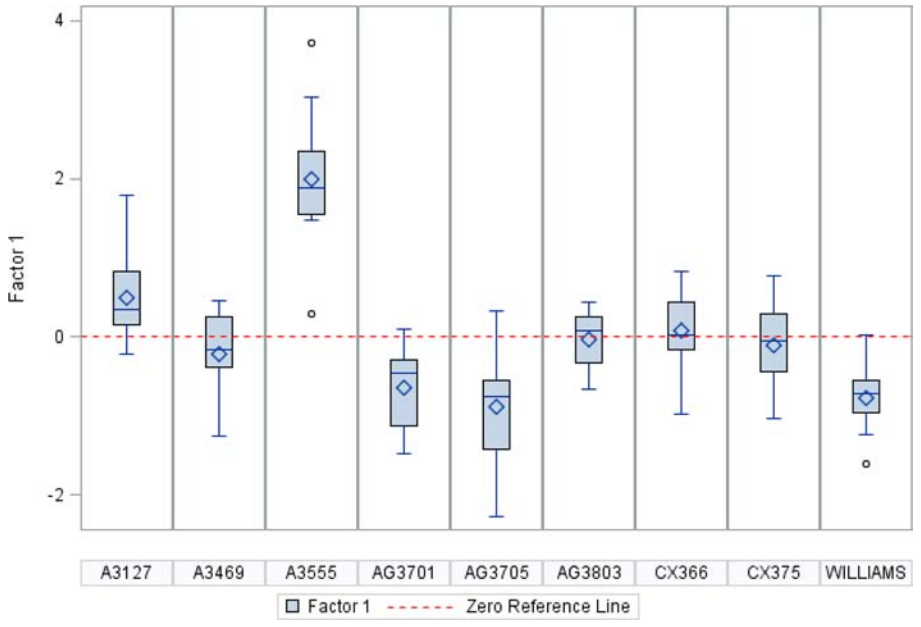

Figure 4. Factor F^1 by pedigree. This factor was highly associated with pedigree (variety). Plotting factor 1 for each pedigree allows a visual representation of how varieties vary in levels of metabolites associated with this factor.

Table 5. Summary of Factor 3 Sources of Variation (12.35%)

source of variance	fraction of variance due to source	PVC contribution
pedigree	81.19	10.03
residual error	17.28	2.13
block (location)	1.07	0.13
location	0.46	0.06

correlate positively with yield,[24] and NMR profiling results are also consistent with those observed in a targeted analysis of the same sample set reported here.[11] Correlation coefficients for individual metabolites and yield (including individual scatter plots) are presented in the Supporting Information; as described there, fumarate, malate, glutamate, and *O*-acetylcholine had some of the highest correlations relative to that of the other metabolites.

Factor F^4: Acetate, Formate, and Dimethylamine. The fourth factor, F^4, explained 9.1% of the total variation in the study (Supporting Information Table 6). It was strongly correlated with acetate, formate, and dimethylamine. The largest source of variance in F^4 was residual error. Supplementary Figure 4 contains box plots to display the variation of values in F^4 according to pedigree. Although variance in F^4 due to pedigree was relatively low, a wide range

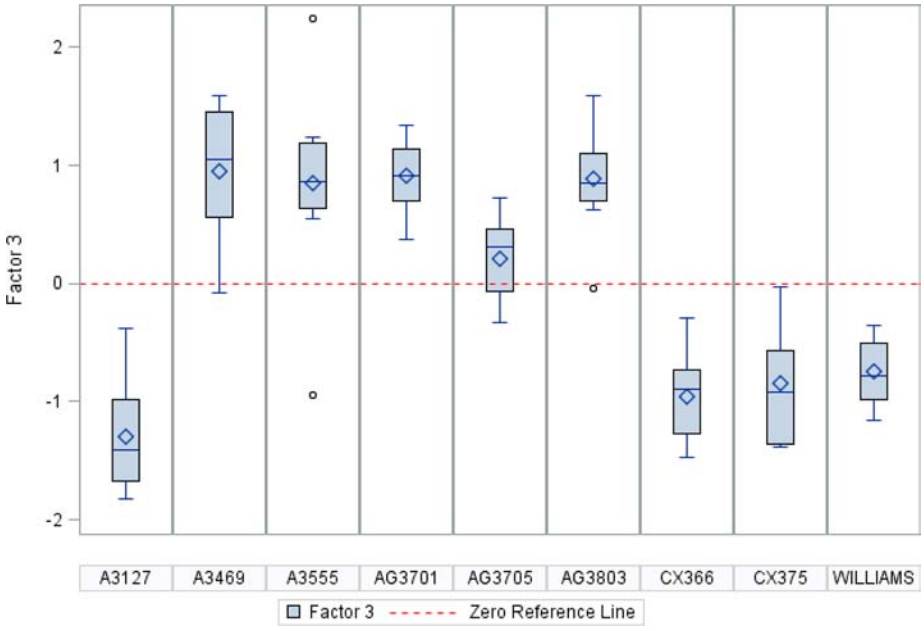

Figure 5. Factor F^3 by pedigree. This factor was highly associated with pedigree (variety). Plotting factor 3 for each pedigree shows that the four older varieties (A3127, CX375, CX366, and Williams) can be distinguished from the newer varieties (A3469, A3555, AG3701, AG3705, and AG3803).

DOI: 10.1021/acs.jafc.5b01069
J. Agric. Food Chem. 2015, 63, 4690−4697

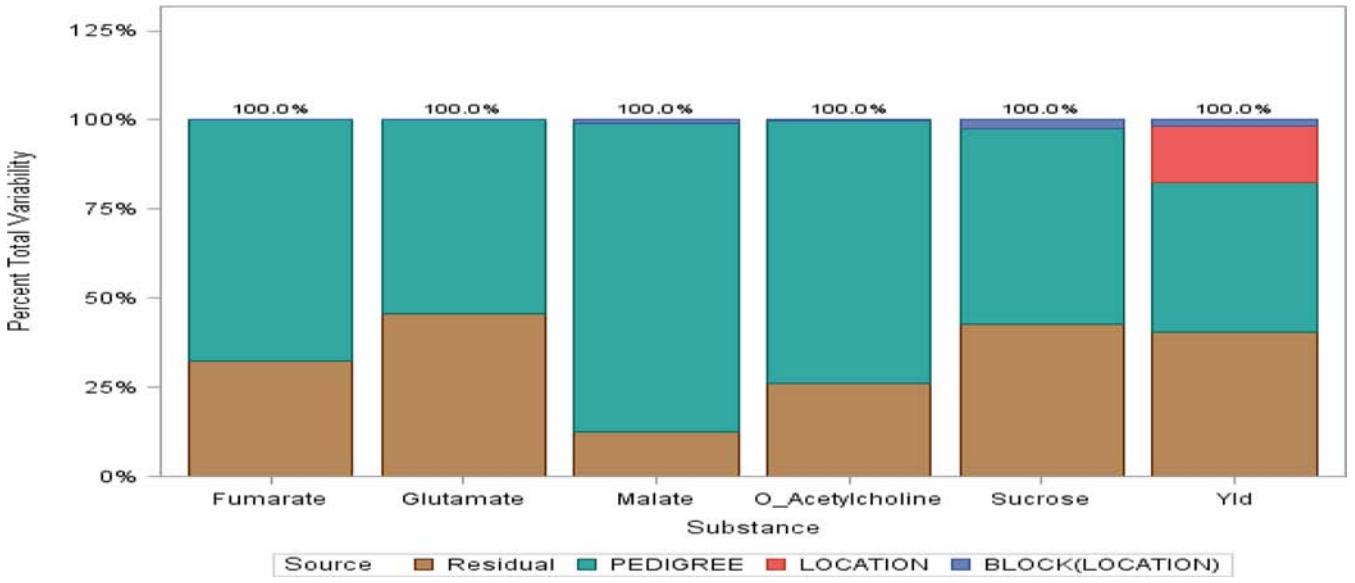

Figure 6. Pedigree effect accounts for notable proportion of variation for those components that strongly correlated with factor F^3. For yield, a location effect also contributed to variation.

of values for these metabolites was observed. This variation did not show a trend with launch era; in fact, the combined-site mean values, as well as the F^4 score, for the oldest variety (Williams, 1972) and one of the newest (A3555, 2008) are most similar.

Factor F^5: Aspartate, Asparagine, Oxoglutarate, and *p*-Cresol. The fifth factor, F^5, explained 7.0% of the total variation in the study (Supporting Information Table 7). It was strongly correlated with aspartate and moderately correlated with asparagine, oxoglutarate, and *p*-cresol. The largest sources of variance in F^5 were residual error and pedigree. Supporting Information Figure 5 contains box plots to display the variation of values in F^5 according to pedigree.

Of these metabolites, the CDA analysis indicated *p*-cresol had the highest correlation with any of the canonical scores (Can 2, $r = -0.82$). Aspartate and oxoglutarate also had negative correlations with Can 2 ($r = -0.62$ and -0.60, respectively). It was noted earlier that Can 2 was effective in within-group separation of the two major clusters discriminated by CDA. For example, the Can 2 scores groups for the newer varieties can be ordered as AG3701 < A3469 < A3555 < AG3803. The difference between AG3701 and AG3803 is reflected both in the F^5 scores and in the individual metabolite combined-site mean values. For example, the mean value for *p*-cresol in AG3701 is 25.26 μg/50 mg DW and in AG3803 is 16.12 μg/50 mg DW. Corresponding values for aspartate are 56.673 and 42.79 μg/50 mg DW, respectively. The wide range appears to be driven predominantly by AG3701, which has the highest *p*-cresol and aspartate values in the entire data set. Otherwise, the within-group variation for these metabolites is very similar for the older and newer varieties.

A better understanding of the relationships between agronomic performance and levels of key crop nutrients and metabolites in soybean seed will be of value as improvements to yield potential continue apace. This study provided a quantitative comparison of seed metabolite profiles from a soybean lineage representing decades of breeding and differing yield potential. The application of ^{1}H NMR spectroscopy and multivariate statistics generated data that could differentiate soybean cultivars based on metabolite profiles. Notably CDA could distinguish older lower yielding from newer higher yielding varieties, which implies the potential for associating metabolite changes with improved soybean yield and quality. PVCA indicated the major source of metabolite variability in the study was associated with variety (pedigree), but location was a notable source of variation for some components. Several metabolites were grouped in the same factor as yield, which suggests those metabolites are correlated with yield potential. This was consistent with the CDA analysis that showed some metabolites were associated with the newer higher yielding varieties as well as correlation analyses of the individual 27 metabolites and yield (Supporting Information). Overall, these analyses suggest that certain metabolite pathways may be linked to yield potential. Other metabolites were less associated with yield potential but were still highly variable when assessed across the entire data set. This would indicate that some pathways are incidental to yield gain but can be expected to vary depending on genetic background and growing location.

The study confirms that crop genetics and breeding for crop improvements can have a notable influence on metabolite variability; some metabolites may be associated with gains in yield potential, and others more incidental to germplasm improvement and/or differences in growing location. In addition, the transgenic and conventional lines were not uniquely distinguishable from each other, which is consistent with numerous publications (e.g., ref 22) and supports the position that genetic modification is not a meaningful contributor to metabolite variability. In summary, metabolite variability is associated with a history of safe use and possibly essential for crop improvement.

■ ASSOCIATED CONTENT

Supporting Information

Additional figures and tables as described in the text. The Supporting Information is available free of charge on the ACS Publications website at DOI: 10.1021/acs.jafc.5b01069.

DOI: 10.1021/acs.jafc.5b01069
J. Agric. Food Chem. 2015, 63, 4690−4697

AUTHOR INFORMATION

Corresponding Authors

*(G.G.H.) Phone: (314) 694-7432. E-mial: george.g.harrigan@monsanto.com.

*(K.S.) Phone: (636) 737-6071. E-mail: kirsten.skogerson@monsanto.com.

Notes

The authors declare the following competing financial interest(s): The authors are employed in the agricultural biotechnology business.

ACKNOWLEDGMENTS

We are very grateful for the agronomic support provided by Matt Culler of Monsanto. The excellent logistical support provided by James McCarter and his sample management team was also critical to the success of this experiment.

REFERENCES

(1) Lin, H.; Rao, J.; Shi, J.; Hu, C.; Cheng, F.; Wilson, Z. A.; Zhang, D.; Quan, S. Seed metabolomic study revelas significant metabolite variations and correlations among different soybean cultivars. *J. Integr. Plant Biol.* **2014**, *56*, 826−836.

(2) Caligiani, A.; Palla, G.; Maietti, A.; Cirlini, M. B. ^{1}H NMR fingerprinting of soybean extracts, with emphasis on identification and quantification of isoflavones. *Nutrients* **2010**, *2*, 280−289.

(3) Mikel, M. A.; Diers, B. W.; Randall, L. N.; Smith, H. H. Genetic diversity and agronomic improvement of North American soybean germplasm. *Crop Sci.* **2010**, *50*, 1219−1229.

(4) Thompson, J. A.; Randall, L. N. Utilization of diverse germplasm for soybean yield improvement. *Crop Sci.* **1998**, *38*, 1362−1368.

(5) Clemente, T. E.; Cahoon, E. B. Soybean oil: genetic approaches for modification of functionality and total content. *Plant Physiol.* **2009**, *151*, 1030−1040.

(6) Jin, J.; Liu, X.; Wang, G.; Mi, L.; Shen, Z.; Chen, X.; Herbert, S. J. Agronomic and physiological contributions to the yield improvement of soybean cultivars released from 1950 to 2006 in Northeast China. *Field Crop Res.* **2010**, *115*, 116−123.

(7) Koester, R. P.; Skoneczka, J. A.; Cary, T. R.; Diers, B. W.; Ainsworth, E. A. Historical gains in soybean (*Glycine max* Merr.) seed yield are driven by linear increases in light interception, energy conversion, and partitioning efficiencies. *J. Exp. Bot.* **2014**, *65*, 3311.

(8) Specht, J. E.; Hume, D. J.; Kumudini, S. V. Soybean yield potential − a genetic and physiological perspective. *Crop Sci.* **1999**, *39*, 1560−1570.

(9) Rotundo, J. L.; Westgate, M. E. Meta-analysis of environmental effects on soybean seed composition. *Field Crop Res.* **2009**, *110*, 147−156.

(10) Harrigan, G. G.; Lundry, D.; Drury, S.; Berman, K.; Riordan, S. G.; Nemeth, M. A.; Ridley, W. P.; Glenn, K. C. Natural variation in crop composition and the impact of transgenesis. *Nat. Biotechnol.* **2010**, *28*, 402−404.

(11) Harrigan, G. G.; Culler, A.; Culler, M.; Breeze, M.; Berman, K.; Halls, S.; Harrison, J. Investigation of biochemical diversity in a soybean lineage representing 35 years of breeding. *J. Agric. Food Chem.* **2013**, *61*, 10807−10815.

(12) Morrison, M. J.; Voldeng, H. D.; Cober, E. R. Agronomic changes from 58 years of genetic improvement of short-season soybean cultivars in Canada. *Agron. J.* **2000**, *92*, 780−784.

(13) Morrison, M. J.; Cober, E. R.; Saleem, M. F.; McLaughlin, N. B.; Frégeau-Reid, J.; Ma, B. L.; Yan, W.; Woodrow, L. Changes in isoflavone concentration with 58 years of genetic improvement of short-season soybean cultivars in Canada. *Crop Sci.* **2008**, *48*, 2201−2208.

(14) Cheng, J.; Yuan, C.; Grahamn, T. L. Potential defense-related prenylated isoflavones in lactofen-induced soybean. *Phytochemistry* **2011**, *72*, 875−881.

(15) Jiao, Z.; Si, X.; Zhang, Z.; Li, G.; Cai, Z. Compositional study of different soybean (*Glycine max* L.) varieties by ^{1}H NMR spectroscopy, chromatographic and spectrometric techniques. *Food Chem.* **2012**, *135*, 285−291.

(16) Kusano, M.; Saito, K. Role of metabolomics in crop improvement. *J. Plant Biochem. Biotechnol.* **2012**, *21* (Suppl. 1), S24−S31.

(17) Silvente, S.; Sobolev, A. P.; Lara, M. Metabolite adjustments in drought tolerant and sensitive soybean genotypes in response to water stress. *PLoS One* **2012**, *7*, 1−11.

(18) Valdes, A.; Simo, C.; Ibanez, V.; Garcia-Cana, V. Foodomics strategies for the analysis of transgenic food. *TrAC, Trends Anal. Chem.* **2013**, *52*, 2−15.

(19) Hohmann, M.; Christoph, N.; Wachter, H.; Holzgrabe, U. ^{1}H NMR profiling as an approach to differentiate conventionally and organically grown tomatoes. *J. Agric. Food Chem.* **2014**, *62*, 8530−8540.

(20) Mannina, L.; D'Imperio, M.; Capitani, D.; Rezzi, S.; Guillou, C.; Mavromoustakos, T.; Vilchez, M. D. M.; Fernandez, A.; Thomas, F.; Aparicio, R. ^{1}H NMR-based protocol for detection of adulteration of refined olive oil with refined hazelnut oil. *J. Agric. Food Chem.* **2009**, *57*, 11550−11556.

(21) Neumuller, K. G.; Carvalho de Souza, A.; Van Rijn, J.; Appeldoorn, M. M.; Streekstra, H.; Schols, H. A.; Gruppen, H. Fast and robust method to determine phenoyl and acetyl esters of polysaccharides by quantitative ^{1}H NMR. *J. Agric. Food Chem.* **2013**, *61*, 6282−6287.

(22) Kusano, M.; Baxter, I.; Fukushima, A.; Oikawa, A.; Okazaki, Y.; Nakabayashi, R.; Bouvrette, D. J.; Achard, F.; Jakubowski, A. R.; Ballam, J. M.; Phillips, J. R.; Culler, A. H.; Saito, K.; Harrigan, G. G. Assessing metabolomic and chemical diversity of a soybean lineage representing 35 years of breeding. *Metabolomics* **2015**, *11*, 261−270.

(23) Li, J.; Bushel, P. R.; Chu, T.-M.; Wolfinger, R. D. Principal variance components analysis: estimating batch effects in microarray gene expression data. In *Batch Effect and Experiemental Noise in Microarray Studies: Sources and Solutions*; Wiley: West Sussex, UK, 2009; pp 141−154.

(24) Wilcox, J. R.; Shibles, R. M. Interrelationships among seed quality attributes in soybean. *Crop Sci.* **2001**, *41*, 11−12.

DOI: 10.1021/acs.jafc.5b01069
J. Agric. Food Chem. 2015, 63, 4690−4697

JOURNAL OF AGRICULTURAL AND FOOD CHEMISTRY

Review

pubs.acs.org/JAFC

Micro- and Nanoparticles by Electrospray: Advances and Applications in Foods

José A. Tapia-Hernández,[†] Patricia I. Torres-Chávez,[†] Benjamín Ramírez-Wong,[†] Agustín Rascón-Chu,[‡] Maribel Plascencia-Jatomea,[†] Carlos G. Barreras-Urbina,[†] Norma A. Rangel-Vázquez,[§] and Francisco Rodríguez-Félix*[,†]

[†]Department of Food Research and Graduate Program (DIPA), University of Sonora, Hermosillo, Sonora, Mexico

[‡]Laboratory of Biopolymers, Research Center for Food and Development, CIAD, A. C., 83000 Hermosillo, Sonora, Mexico

[§]Department of Metalmechanical, Aguascalientes Institute of Technological, Aguascalientes, Aguascalientes, Mexico

ABSTRACT: Micro- and nanotechnology are tools being used strongly in the area of food technology. The electrospray technique is booming because of its importance in developing micro- and nanoparticles containing an active ingredient as bioactive compounds, enhancing molecules of flavors, odors, and packaging coatings, and developing polymers that are obtained from food (proteins, carbohydrates), as chitosan, alginate, gelatin, agar, starch, or gluten. The electrospray technique compared to conventional techniques such as nanoprecipitation, emulsion−diffusion, double-emulsification, and layer by layer provides greater advantages to develop micro- and nanoparticles because it is simple, low cost, uses a low amount of solvents, and products are obtained in one step. This technique could also be applied in the agrifood sector for the preparation of controlled and/or prolonged release systems of fertilizer or agrochemicals, for which more research must be conducted.

KEYWORDS: *nanotechnology, electrospray, microparticles, nanoparticles, foods*

1. INTRODUCTION

Nowadays, food technologists are looking at alternatives to help improve food production for human consumption.[1,2] Among those technologies applied are micro- and nanotechnology[3] used in food microbiology for coatings or bacterial-free packaging,[4] micro- and nanoparticles for encapsulating products derived from food, e.g., bioactive compounds,[5] encapsulation of biological molecules (proteins and carbohydrates),[6,7] production of emulsions,[8] and the current boom for controlled and prolonged release fertilizers for agricultural use.[9]

The electrospray technique or electrohydrodynamic atomization is one of the tools that is included as a novel method for application in the field of micro- and nanotechnology of foods.[10] This technique is based on the production of spheres from a polymer solution, by applying a high electric field and thereby obtaining an encapsulation of different foodstuffs.[11]

Applying this technique in foods facilitates the production of products with endless applications, besides being more friendly for the environment and humans; however, few studies have been realized in the area of food. The aim of this paper is to present the advances and applications of the electrospray technique in the food technology area, showing their advantages and disadvantages.

2. ELECTROSPRAY TECHNIQUE

Electrospray is a variant of the method of electrospinning, which began to be used in medicine with the aim to encapsulate drugs.[12,13] Vonnegut and Neubauer (1952) were pioneers applying voltage to produce micrometer-sized spherical particles for application as sprays.[14] Today this technology is extending to other areas where it is booming in food technology, because it is simple and uses low-cost equipment.[15]

According to the way of collecting the droplets, there are two variants of the electrospray technique: electrospray in plates[16] and electrospray in solution.[17]

(1) Electrospray in plates consists of collecting charged droplets in a grounded plate, and collection can be of two forms. The first one, charged droplet, is deposited individually or can be deposited as an agglomerate of droplets on the plate (Figure 1).[18]

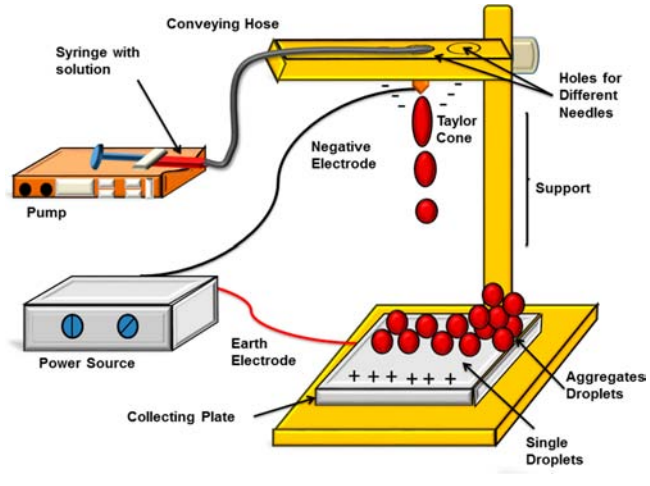

Figure 1. Method of electrospray in plates.

Received: March 19, 2015
Revised: April 22, 2015
Accepted: May 4, 2015
Published: May 4, 2015

ACS Publications © 2015 American Chemical Society

DOI: 10.1021/acs.jafc.5b01403
J. Agric. Food Chem. 2015, 63, 4699−4707

(2) Electrospray in solution is based on collection of charged droplets in a cross-linking solution into a precipitate glass to facilitate the formation of micro- and nanospheres. The most studied and used in this method as a cross-linking agent is calcium chloride ($CaCl_2$) (Figure 2).[17]

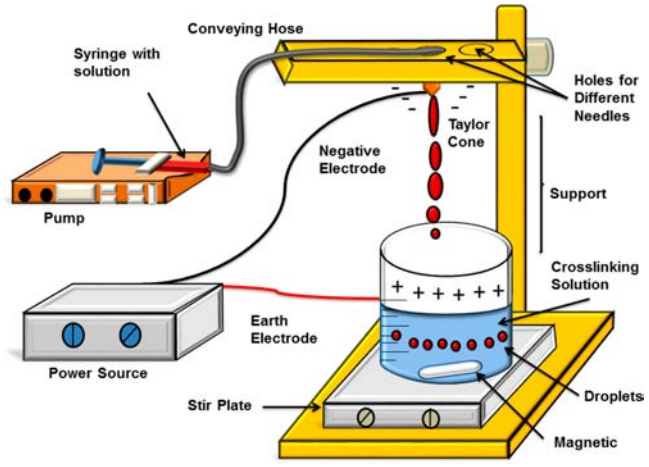

Figure 2. Method of electrospray in solution.

The principle of the electrospray is based on the ability of an electric field to deform the interface of the droplet and get droplets in the range of a micrometer or nanometer depending on the parameters to control.[19] This principle was grounded in the theory of charged droplets which establishes that if an electric field is applied to a droplet, the electric charge generates an electrostatic force into the droplet, known as the coulomb force, which competes with the force of cohesion in the droplet.[20] When the coulomb force applied is capable of overcoming the cohesive force of the droplet, that manifests in the release of the surface tension and formation of nanodroplets (Figure 3). A limit, named the Rayleigh limit L_R, exists to

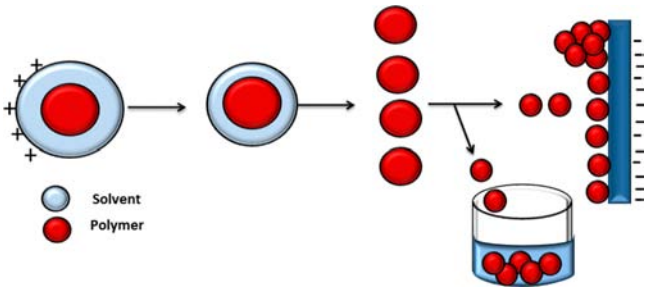

Figure 3. Mechanism of droplets formation during the electrospraying.

determine the rupture of the droplet. This limit is when the surface tension of the drop is overcome by the electrostatic force. Equation 1 represents the Rayleigh limit.[6]

$$L_R = q(64\pi^2\varepsilon\gamma R^3)$$

$$q = 8\pi\sqrt{\varepsilon_0\gamma R^3} \quad (1)$$

where q is charge on the droplet surface, ε is permittivity of the surrounding medium, γ is surface tension of the fluid, and R is radius of the droplet.

Although the electrospray technique is simple, it has to take into account the control variables to obtain desirable polymer particles in particle size and size distribution. These variables involve system parameters such as flow rate of the solution, applied electric potential, collector distance, viscosity of solution, conductivity, surface tension, molecular weight, and concentration of polymer (Table 1).[21]

2.1. System Parameters. Flow rate (Q): knowing this parameter of the method allows prediction of the behavior that the material will have in determining particle size. Chan et al.'s (2010) elaboration of microspheres of poly methylsilsesquioxane (PMSQ) was used as a model material for the microsphere shell encapsulating a core of liquid perfluorohexane (PFH) with a particle size from 310 to 1000 nm.[22] Second, Ghayempour et al. (2013) fabricated micronanoparticles of sodium alginate cross-linked with calcium chloride for the encapsulation of essential oils of particle size from 80 nm to 900 μm.[23] These two works determined how the flow rate affects the particle size obtaining the following results:

(1) At a high flow rate, it can lead to the formation of large size particles. This phenomenon occurs because the rate of the jet and the polymer concentration that drips from the needle are higher; therefore, the solvent does not volatilize completely.

(2) A low flow rate and increasing the electrical conductivity can lead to smaller particles, to 80 nm, since the rate of the jet is smaller, resulting in greater volatilization of the solvent.

Electric potential (Ø): this parameter represents the driving force of importance in the electrospray process, because it affects the size and form of the droplets. A potential of sufficient electric charge can overcome the surface tension of polymer solution to produce micro- and nanoparticles.[24]

Moghadam et al. (2010) applied the electrospray method to investigate the effect of the voltage (0−9 kV).[25] In this study, Moghadam prepared nanospheres of sodium alginate cross-linked with calcium chloride and observed that the range from 4.5 to 6.5 kV was changing the effect drip to jet mode, favoring the production of droplets, and came to the conclusion that higher voltage (9 kV) produces micrometric particles (400 μm). Hartman et al. (2000), Fanzheng et al. (2009), and Nguyen et al. (2014) agreed in their results confirming that higher voltage (15 kV) produces greater stability of the jet cone (Taylor cone) and the diameter of particles of 3.4 μm for Fanzheng and 10 μm for Hartman, but this voltage should not exceed 15 kV because creates an instability of the jet cone.[21,26,27]

Collector distance (L): to control particles formed and uniformity, it must take into account the effective evaporation of the solvent, and this will depend on the collector distance and the evaporation rate of solvent.[28] A fast evaporation rate can cause the inclusion of porous holes even up to reaching the final particle fragmentation and is undesirable for the formation of high quality droplets. On the other hand, if evaporation is slow, the form that these particles adopt is more spherical, since there is more time for the solvent to evaporate and a solvent-free polymer to form.[29]

Other studies show that if the distance of the collector is very small, it will not be possible to evaporate the solvent, and therefore the particle will be more unstable, and the size particle will be great. However, if the distance of the collector is considerable (15−20 cm), it may be easier for volatilization of the solvent and fission of the polymeric particle. However, there are no studies that relate a high jet rate and a long collector distance (15−20 cm) with particle size, as the case of research of Ghayempour et al. (2013) and Nedovic et al. (2001) reported that with a high jet rate and shorter distance (4−8

DOI: 10.1021/acs.jafc.5b01403
J. Agric. Food Chem. 2015, 63, 4699−4707

Table 1. Effect of System Parameters of Electrospray Technique on Size Particle

system parameters	characteristic: increases parameter	characteristic: decreases parameter	reference
electric potential	Range optimum 10−20 kV, 15 kV ideal. At greater voltage there is instability of Taylor cone	There is no formation of Taylor cone	Wang et al.,[24] Moghadam et al.,[25] Hartman et al.[26]
flow rate	There are larger particles, by higher concentration solution and less volatilization of solvent	Ideal to form micro- and nanoparticles	Fanzheng et al.[21]
collector distance	Allows more volatilization of the solvent and generates smaller particles	It increases the electrical conductivity and generates smaller particles, but at low electrical conductivity generates larger particles	Jun et al.,[28] Nedović et al.[30]
viscosity	At higher concentration of the polymer, the viscosity is increased and larger particles are obtained	Increasing the voltage and the flow rate, the viscosity decreases and smaller particles are obtained	Moghadam et al.[25] Moghadam et al.[31]
electrical conductivity	Favors obtaining small particles, but at higher electrical conductivity and higher flow rate, there are larger particles	Does not allow path of the electric charge; therefore, larger particles are obtained	Khan et al.[32]
surface tension	Larger particles are obtained	There is fission of droplets, and particles of smaller size are obtained	Khan et al.[32]

Table 2. Compared of Conventional Methods for Obtaining Micro- and Nanoparticles against the Electrospray Technique

method	advantages	disadvantages
conventional: nanoprecipitation, emulsion-diffusion, double-emulsification, polymer-coated, layer by layer	• Applies to versatile materials • Load wide range of organic or biological molecules • Particles can be used in controlled release system	• Requires several step • High molecular weight polymers are not used • Several solvents are used • Uses one or several surfactants • Have to modify the method for obtained nanometric particles • Generates more residue
Electrospray	• Uses one step • High molecular weight polymers can be used • Nanoparticles are obtained • Low cost • Uses fewer solvents • Does not use surfactant • Generates little residue	• Small amount of particles is obtained • In some cases uses a cross-linking agent

cm) smaller particles are obtained.[23,30] Nedovic et al. prepared nanocapsules of sodium alginate con yeast (*Saccharomyces uvarum*) and obtained particle sizes from 250 μm.[30]

In the meantime, viscosity is an important parameter to obtain particles with a desired diameter and is closely related to the concentration (C) of polymer and the flow rate (Q). Holding constant the concentration, viscosity tend to be the same for obtaining similar sized particles, but if these parameters increase the voltage in a growing range, the diameter of the particles will tend to decrease.[31] Moghadam et al. (2010) studied the relationship of concentration and viscosity in the electrospray technique, and they proved that if the concentration is increased in the range of 10−30 g L^{-1} of sodium alginate an increase flow rate, the viscosity will tend to decrease, being more evident at the concentration of 30 g L^{-1}; conversely, at a concentration of 10 g L^{-1}, there is little variation in viscosity.[25]

The electrical conductivity is another parameter that like the viscosity is influenced by flow velocity and electric potential. It is defined as the ability that a material has to let the electric charge pass, in this case, a polymeric material. In an investigation carried by Khan et al. (2012), a relationship between conductivity and flow rate was predicted, obtaining as result that the increase of conductivity resulted in a decrease of the surface tension and particle size of sunflower oil down 20 μm; however, if the flow rate and electrical conductivity increase, the particle size increases.[32]

The reduction of particle size in range of micro- or nanometric is a parameter that is influenced by the other parameters of the system. Reducing the particle size provides greater surface area; therefore, it allows greater bioavailability of micro- and nanocapsules for biomedical and food application.[33] The importance of particle size was first explained in the medicine area and could be applied in food technology, and is described in eq 2 of Noyes-Whitney (1897):[34]

$$\frac{dm}{dt} = \frac{DA}{h}(C_s - C_b) \quad (2)$$

where (dm/dt) = dissolution rate, A = surface area of the drug exposed to the dissolution medium, D = the diffusion coefficient of the drug, h = the thickness of the boundary layer of the dissolving drug, C_s = saturation concentration (solubility), and C_b = drug concentration in the medium at time t.

If the above-described parameters in function particle size help to obtain favorable particles, it is evident that it must take

DOI: 10.1021/acs.jafc.5b01403
J. Agric. Food Chem. 2015, 63, 4699−4707

into account other aspects involving the nature of the polymer such as molecular weight, interactions, and chemical composition. If it not known how the raw material behaves, the results will not be desirable.

3. ADVANTAGES AND DISADVANTAGES OF ELECTROSPRAY TECHNIQUE

There are currently several techniques both in basic science and in industry for the development of micro- and nanoparticles with different applications. Techniques that stand out for preparation of nanoparticles based mainly on polymers include: nanoprecipitation, emulsion−diffusion,[35] double-emulsification, emulsion−coacervation, polymer-coating, and layer by layer (Table 2).

3.1. Nanoprecipitation Method. The nanoprecipitation method is based on the synthesis of nanocapsules from a phase named solvent (organic) and a phase named nonsolvent (aqueous).[36] In the organic phase, there is a solution or several solutions which include the polymer (synthetic or natural), active substance, oil, and surfactant (oil−water), and the aqueous phase is a nonsolvent or mixture of nonsolvents.[37] The procedure is to include the organic phase in the aqueous phase forming a colloidal suspension, by manipulating conditions such as flow and agitation of the aqueous phase velocity, and obtaining particle smaller size (<100 nm).[38]

3.2. Emulsion−Diffusion Method. Unlike the nanoprecipitation method, the emulsion−diffusion method has three phases: organic, aqueous, and diffusion, allowing the encapsulation of hydrophilic and lipophilic active substances.[39] The method is based on achieving emulsification with organic and aqueous phases by stirring of polymer, surfactant, and a saturated solution; after the solution is subjected to diffusion, the solvent leaves and the active compound enters and nanocapsules smaller than 200 nm form.[40]

3.3. Double-Emulsification Method. Double-emulsification is obtained from a system composed of several emulsifications and is classified as emulsification oil−water−oil (O−W−O) and emulsification water−oil−water (W−O−W). The method is performed in two steps using two surfactants: first a hydrophobic surfactant used to stabilize the interface internal layer W−O, and another that stabilizes the interface of the outer layer of W−O−W.[41] The correct choice of surfactant is essential to shape the film and barrier at the interface of the internal layer, as well as a steric stabilizer in the interface of the outer layer.[42] For the preparation of the nanocapsules by this method, the first emulsion is obtained by ultrasound and surfactant W−O; the second emulsion is also obtained by ultrasound, and dispersion nanocapsules are stabilized by stabilizing agent; finally the solvents are removed by vacuum evaporation. The particle size obtained is in the range 150−200 nm.[43]

3.4. Emulsion−Coacervation Method. The emulsion−coacervation method has been used to develop nanocapsules natural and synthetic polymers. The procedure involves an O−W emulsion with an organic phase (oil, active substance, and solvent for the active substance, if is necessary) and an aqueous phase (water, polymer, stabilizing agent) by mechanical stirring; then the process is given coacervation with electrolytes.[44] This method uses the emulsion as a template phase and phase coacervation to cause precipitation of the polymer and a film to form on the template for the nanocapsules. Finally a cross-linking agent is added to strengthen the nanocapsules.[45]

3.5. Polymer-Coating Method. The method of polymer coating consists of depositing a thin layer of polymer on the surface of the formed nanocapsules. This method is very versatile since it does not provide a unique methodology; it can be applied depending on the conditions in which the particles are obtained. One way is to provide the layer of polymer during the preparation of the nanocapsules, and the other way is to apply the coat of polymer at the end of the formation of the nanocapsule from other conventional methods as nanoprecipitation or double-emulsification.[46]

3.6. Layer by Layer Method. The layer by layer method is based on assembling a series of polymer layers to form nanospheres, where each of these layers is from different materials and therefore a different chemical nature.[47] This method requires a colloidal template on which a layer of polymer is adsorbed by incubation in the solution of polymer, subsequent washes or the decrease in solubility of the polymer, and adding dropwise an immiscible solvent.[48] This procedure is then repeated with a second polymer and multiple layers of polymer are deposited sequentially, one after another.[49]

All these techniques have great advantages as they are applicable to versatile materials, such as the possibility to load and stabilize a wide range of organic or biological molecules, and particles can be released in a controlled manner (by diffusion through the polymer matrix, swelling followed by broadcast, or in response to the local environment).[50−52] The disadvantages of these methods are that they need more than one step for synthesis, using various solvents and surfactants; they are therefore expensive and their residues can harm the environment, they need to be modified to obtain nanometer-sized particle, and it is difficult to obtain particles with polymers of high molecular weight. Table 2 shows that the technique of electrospray, apart from sharing benefits with other methods, nowadays is considered one of the best options to obtain particles, showing few downsides in its application.

4. FIELD APPLICATION IN FOOD

The electrospray technique began to be used in medicine for the purposes of encapsulating drugs that deliver greater bioavailability from its prolonged and/or controlled release. A study by Lee et al. (2010) describes the synthesis of particles of drug coated with poly(lactic-*co*-glycolic acid) by the electrospray method. They showed that the studied system can reach almost 100% efficiency of encapsulation of drugs with proper adjustment of the method, through the variation of the concentration of PLGA and the electrical conductivity of solutions sprayed, obtaining particle sizes from 165 nm to 1.2 μm.[53]

Recently the use of the electrospray expanded beyond food technology, being a novel technique that is booming. In this area, the electrospray technique can be used for three purposes: primarily as an application in the area of inedible food being used to develop intelligent packaging that can resist the entry of a pathogen and cause putrefaction of food;[54] the second one is to apply the use of nanostructures as food ingredients, i.e., to produce particles encapsulating compounds or foodstuffs;[55] and the third application is to use polymeric materials from food to encapsulate any compound or active substance.[56]

4.1. Application Packaging and Containers for Food. The application of nanotechnology to obtain nanospheres has a great impact on many aspects of food and agricultural systems, from the development of new materials of food packaging to the systems of nanorelease, including the analytical control of

DOI: 10.1021/acs.jafc.5b01403
J. Agric. Food Chem. 2015, 63, 4699−4707

the food chain.[57] There are investigations where they review the incorporation of nanoparticles to containers containing preservatives, which are released when food starts to deteriorate, thus prolonging the shelf life and increasing their bioavailability.[58]

Devices are also used in plastic packaging named biosensors that offer the potential for the detection of pathogens and their toxins in real time and provide food security. Polydiacetylene (PDA) is an ideal selection to use as a sensor due to its unique optical properties. PDA molecules can form thin films or vesicles that change from blue to deep red in response to different stimuli, such as temperature, pH, and the presence of biological molecules.[59]

4.2. Encapsulation of Compounds for Use in Food. The nanospheres in the food industry are important for the incorporation of substances or compounds that can be used to encapsulate phytonutrients, prebiotics,[60] bioactive compounds,[61] antioxidants, or some flavor enhancers.[62]

There are studies demonstrating the application of the electrospray technique to encapsulate bioactive compounds. Jung et al. (2013) showed that it can be used to generate stable antimicrobial nanoparticles continuously from natural plant products ethanol extracts.[63] Eltayeb et al. (2013) encapsulated active compounds in a lipid polymeric membrane by the electrospray method, and the parameters used were an electric potential of 13−15 kV and a flow rate in the range of 10−15 μL min^{-1}; obtained particles were between 10 and 100 nm in diameter and encapsulation efficiency and performance were 69.5% and 69%, respectively.[5]

Bocanegra et al. (2005) developed an emulsion W−O of cocoa with aqueous solutions by the electrospray method, which proved to be an effective method for encapsulating ingredients based on aqueous foods such as flavors, flavorings, enzymes, salts, minerals, and vitamins in the micrometer range with a relatively high monodispersity and controllable geometry.[64]

Food oils are other substances that can encapsulated for use in the food, pharmaceutical, and cosmetic industries. Curcume oil has antibacterial, antifungal, antioxidant, and repellent properties of insects but is unstable and volatile. For this reason is encapsulated from a membrane of chitosan and alginate, forming nanometer-size polymer particles.[65]

4.3. Capsules of Polymeric Materials from Food. Micro- and nanoparticles of polymeric materials from food are particles with diameters of 100 nm or less and which have the characteristic of being biodegradable and can be made by the electrospray technique. These polymers are already used heavily in the pharmaceuticals industry, where they serve as the basis for systems of administration of drugs and other compounds. It has been shown that particles can also serve as carriers of antimicrobial components; for example, the nanoparticles of materials from food containing nisin exhibit much more activity against *Escherichia coli* O157: H7 than particles without nisin.[66] The most commonly used polymers are starch, cellulose, chitosan, alginate, gelatin, and gluten and wheat gliadins.

Chitosan is a polymer obtained from chitin widely used to develop micro- and nanocapsules.[67,68] The chitin can be found in marine animals as in the shell of shrimp and some terrestrial origin insects. Some studies have shown that chitosan is widely used and that it serves as a basis to produce particles and encapsulating compounds.[69] Xu et al. (2013) used the coaxial electrospray method to prepare and characterize nanoparticles of folate−chitosan−gemcitabine, obtaining nanoparticles from 200 to 300 nm with activity against pancreatic cancer, and concluding that it is simple to develop nanocomposites of chitosan by this method.[70]

Starch is a natural, renewable, and biodegradable polymer obtained from a variety of vegetables, formed from simpler compounds (amylose and amylopectin).[71] Starch has been widely used to develop micro- and nanoparticles for drug delivery and other natural compounds. Atyabi et al. (2006) studied the effect of cross-linked starch microspheres with epichlorohydrin, controlling the parameters such as morphology, size and release of the drug, type and duration of the cross-linking. Atyaba reported that a concentration 4% epichlorohydrin, 14 h of cross-linking, and 3% of the drug produced spherical particles in the range 425−500 μm.[72] Tan et al. (2009) reported the production of nanoscale, monodisperse, and controlled size of nanospheres of starch acetate.[73] Santander-Ortega et al. (2010) developed nanoparticles from 2 derived from starch (propyl-starch: ps-1 and ps-1.45) for encapsulating flufenamic acid, testosterone, and caffeine as transdermal release systems and obtained particles of 180.3 nm for ps-1 and 185.5 nm for ps-1.45.[74]

Alginate is a polysaccharide that is obtained from the cell walls of marine algae. This polysaccharide is used to develop micro- and nanoparticles for encapsulating substances. It can be used individually or with other materials to form composites.[75] Bhowmik et al. (2006) prepared nanocapsules of alginate loaded with testosterone for application as a prolonged release system and obtained particles of 34.5 nm.[76] Rastogi et al. (2007) prepared sodium alginate microparticles as a carrier hydrophilic for encapsulating isoniazid.[77] Results indicated that the size of the microspheres increased with increasing concentration of the polymer, the cross-linking agent, and the cross-linking time; an encapsulation efficiency of 40−91% was obtained.[77] Shadab et al. (2011) prepared alginate microparticles encapsulating acyclovir to prolong the gastric residence time. Results showed a particle size of 70.6 μm, and an encapsulation efficiency in the range of 51−80%.[78] Tabbei et al. (2012) in their research studied the effect of viscosity, non-Newtonian effects, and thixotropic of alginate solution prepared by the electrospray method.[79]

Gelatin and agar−agar are polymeric substances (polysaccharides) with a complex structure and are colorless and contain amino acids. Gelatin is obtained from collagen found in connective tissue of animals,[80,81] whereas agar−agar is obtained from plants.[82] Doi et al. (2012) developed biodegradable nanospheres of gelatin with a reduction of size distribution for the transport of DNA plasmids into cells.[83] Cursio et al. (2013) prepared biodegradable gelatin nanospheres to evaluate the effect of pH on the release of drugs.[84] Kanmani et al. (2014) reported the development of antimicrobial biopolymer films from extracts of grapefruit for packaging, as an alternative to the synthesis of films for packaging.[85]

Other material from food used to create nanocapsules is wheat gluten. In many countries mainly from the European Union, this material is considered as a byproduct for many processes where wheat is not used as food, for instance, to develop biofuels as well as having viscoelastic capacity.[86] Gluten is a polymer network formed mainly by two proteins (the gliadins and glutenins) attached to the starch granules within the endosperm of the wheat grain. Liao et al. (2012) developed nanocapsules of wheat gluten deaminated with succinic acid for the encapsulation of fish oil with particles of 527 nm.[87]

DOI: 10.1021/acs.jafc.5b01403
J. Agric. Food Chem. 2015, 63, 4699−4707

More recently gliadins, a wheat gluten protein, has been used to develop nanospheres as drug delivery systems.[88,89] Ezpeleta et al. (1996) developed nanoparticles of gliadin for the controlled release of retinoic acid.[90] Gulfam et al. (2012) used an electrospray system in plates to develop nanocomposites of gliadins and gliadin-gelatin for encapsulation and release of anticancer drugs (cyclophosphamide).[91] Results of this study showed that breast cancer cells in culture with 7% gliadin nanoparticles loaded with cyclophosphamide during 24 h suffered apoptosis, and it was concluded that the nanoparticles on gliadin can be a powerful tool for the encapsulation and controlled release of drugs against cancer.[91]

4.4. Other Applications in Food. In the chocolate industry, one of the oldest industries in the world, the electrospray technique has been used to improve the quality of products based on this food. Gorty et al. (2011) applied this technique in chocolate as a new method through which a thin coat and uniformity of chocolate can be obtained.[92] Electrospray helps in the reduction of losses and therefore reduces costs. The objective of this study was to determine the effect of various ingredients of chocolate on the viscosity, yield, and electrical resistance, in turn, determine the effect of these parameters on the quality of the chocolate, which was studied by measuring the size of the droplet and the percentage of covered area.[92]

Edible films and coatings are another application that can be used for food preservation, such as the waxes on fruits to avoid moisture loss and create a bright surface for aesthetic purposes.[93] A film is different from a coating; the film may form a material independently to control the exchange of oxygen, carbon dioxide, and ethylene involved in the process of respiration, and in addition, to prevent the loss of moisture; a coating on the food provides sterility to the surface of the food and helps avoid the loss of important components. Polysaccharides, proteins, and lipids are examples of materials to develop coatings and edible films.[93]

Du et al. (2008) evaluated the storage and antimicrobial activity of edible films of apples containing carvacrol to avoid contamination by *E. coli* O157: H7.[94] Ravishankar et al. (2009) developed edible films of apple containing an extracted antimicrobial plant that inactivated foodborne pathogens in meat and poultry products.[95] Morsy et al. (2014) incorporated essential oils and pullulan nanoparticles in films in order to control food-borne pathogens in meat and poultry products.[96] Kurt et al. (2014) characterized a new edible biodegradable film made of glucomannan and evaluated the rheological properties of the solution.[97] Khazaei et al. (2014) prepared and characterized an edible film from seed gum basil (*Ocimum basilicum L.*) and glycerol as plasticizer and obtained favorable results.[98] Table 3 shows different materials that can be used in the electrospray technique, with potential applications in the food area.

5. FUTURE PERSPECTIVES

The electrospray technique can be applied to produce a wide range of materials at the micro- and nanoscale, which have already been produced by conventional techniques such as nanoprecipitation, emulsion−diffusion, double-emulsification, polymer-coating, and layer by layer. In addition, the use of this new technique produces important advantages; for example, as it is simple, low-cost, does not use various solvents (aqueous and organic), does not use surfactants, and is produced in a single step.

Table 3. Food Applications Where Electrospray Technique May Be Used

material	aplication food	reference
pullulan−corn starch	food packaging	Yan et al.[99]
pullulan−sodium alginate	food packaging	Xiao et al.[100]
cellulose−alginate films	food packaging	Sirviö et al.[101]
chitosan	capsule preparation	Massotti et al.[102]
alginate	capsule preparation	Paques et al.[103]
calcium alginate	capsule preparation	Liu et al.[104]
hyme essential oil and apple skin polyphenols	edible films	Espitia et al.[105]
gelatin-chitosan composite	edible films	Jridi et al.[106]
fish gelatin−chitosan blend edible films	edible films	Fakhreddin et al.[107]
mucilage films containing thyme essential oil	encapsulation of essential oil	Jouki et al.[108]
electrosprayed zein prolamine and omega-3 fatty acid	stabilization of compounds	Torres-Giner et al.[109]

Furthermore, the electrospray technique can be applied to the agrifood sector to develop micro- and nanoparticles of controlled release and prolonged fertilizer.[110] There are studies that show the importance of research in this sector since the demand to make the best fertilizer is a very broad challenge. Currently conventional fertilizer application cause losses to the atmosphere by evaporation, leaching, and denitrification, causing great economic losses and environmental pollution.

6. CONCLUSIONS

The electrospray technique is considered one of the best options for developing micro- and nanospheres above conventional techniques of nanoprecipitation, double-emulsification, and layer by layer, among others. This technique has been applied in the pharmaceutical industry, but today is being applied in the food industry and is seeing great advantages in the encapsulation of bioactive compounds, aromatic enhancers, and manufacturing smart packaging, edible films, and coatings in food. This technique could also be applied in the agrifood sector for the preparation of controlled and/or prolonged release systems of fertilizer or agrochemicals, for which more research must be done.

AUTHOR INFORMATION

Corresponding Author

*E-mail: rodriguez_felix_fco@hotmail.com.

Funding

The authors greatly appreciate the economic support of the CONACYT through the project of basic science 178436, and the University of Sonora. José Agustín Tapia Hernández is thankful to CONACYT for the granted scholarship.

Notes

The authors declare no competing financial interest.

REFERENCES

(1) Caba, K.; Peña, C.; Ciannamea, E.; Stefani, P.; Mondragon, I.; Ruseckaite, R. Characterization of Soybean Protein Concentrate Stearic Acid/Palmitic Acid Blend Edible Films. *J. Appl. Polym. Sci.* **2012**, *124*, 1796−1807.

(2) Bakhshi, P. K.; Nangrejo, M. R.; Stride, E.; Edirisinghe, M. Application of Electrohydrodynamic Technology for Folic Acid Encapsulation. *Food Bioprocess. Technol.* **2013**, *6*, 1837−1846.

DOI: 10.1021/acs.jafc.5b01403
J. Agric. Food Chem. 2015, 63, 4699−4707

(3) Villacrez, J. L.; Carriazo, J. G.; Osorio, C. Microencapsulation of Andes Berry (*Rubus glaucus Benth.*) Aqueous Extract by Spray Drying. *Food Bioprocess. Technol.* **2014**, *7*, 1445−1456.
(4) Hazeri, N.; Tavanai, H.; Moradi, A. R. Production and properties of electrosprayed sericin nanopowder. *Sci. Technol. Adv. Mater.* **2012**, *13*, 1−7.
(5) Eltayeb, M.; Bakhshi, P.; Stride, E.; Edirisinghe, M. Preparation of solid lipid nanoparticles containing active compound by electrohydrodynamic spraying. *Food Res. Int.* **2013**, *53*, 88−95.
(6) Xie, J.; Kuang, L.; Phua, Y.; Hua, J.; Wang, C.-H. Electrohydrodynamic atomization for biodegradable polymeric particle production. *J. Colloid Interface Sci.* **2006**, *302*, 103−112.
(7) Xie, J.; Wang, C.-W. Electrospraying, a Reproducible Method for Production of Polymeric Microspheres for Biomedical Applications Biotechnology and Bioengineering. *Polymers.* **2007**, *97*, 1278−1290.
(8) Khan, M. K. I.; Maan, A. A.; Schutyser, M.; Schroën, K.; Boom, R. Electrospraying of water in oil emulsions for thin film coating. *J. Food Eng.* **2013**, *119*, 776−780.
(9) Hussain, Md. R.; Devi, R. R.; Maji, T. K. Controlled release of urea from chitosan microspheres prepared by emulsification and cross-linking method. *Iran Polym. J.* **2012**, *21*, 473−479.
(10) Jaworek, A. Electrospray droplet sources for thin film deposition. *J. Mater. Sci.* **2007**, *42*, 266−297.
(11) Gaskell, S. Electrospray: Principles and Practice. *J. Mass Spectrom.* **1997**, *32*, 677−688.
(12) Ikeuchi, M.; Tane, R.; Ikuta, K. Electrospray deposition and direct patterning of polylactic acid nanofibrous microcapsules for tissue engineering. *Biomed. Microdevices* **2012**, *14*, 35−43.
(13) Qingxing, X.; Hao, Q.; Zhenyuan, Y.; Jinsong, H.; Daniel, W. P.; Chi-Hwa, W. Coaxial electrohydrodynamic atomization process for production of polymeric composite microspheres. *Chem. Eng. Sci.* **2013**, *104*, 330−346.
(14) Vonnegut, B.; Neubauer, R. L. Production of monodisperse liquid particles by electrical atomization. *J. Colloid Sci.* **1952**, *7*, 616−622.
(15) Yadav, J. B.; Joo, O.-S. Electrospray deposited Pt for films hydrogen evolution reaction: effect of solvent solution. *Appl. Surf. Sci.* **2013**, *265*, 222−225.
(16) Hwang, W.; Xin, G.; Cho, M.; Cho, S. M.; Chae, H. Electrospray deposition of polymer thin films for organic light-emitting diodes. *Nanoscale Res. Lett.* **2012**, *7*, 52.
(17) Suksamran, T.; Ngawhirunpat, T.; Rojanarata, T.; Sajomsang, W.; Pitaksuteepong, T.; Opanasopit, P. Methylated N-(4-N,N-dimethylaminocinnamyl) chitosan-coated electrospray OVA-loaded microparticles for oral vaccination. *Int. J. Pharm.* **2013**, *448*, 19−27.
(18) Suhendi, A.; Nandiyanto, A. B.; Munir, M. M.; Ogi, T.; Okuyama, K. Preparation of agglomeration-free spherical hollow silica particles using an electrospray method with colloidal templatin G. *Mater. Lett.* **2013**, *106*, 432−435.
(19) Jaworek, A.; Sobczyk, A. T. Electrospraying route to nanotechnology: An Overview. *J. Electrostat.* **2008**, *66*, 197−219.
(20) Bock, N.; Woodruff, M. A.; Hutmacher, D. W.; Dargaville, T. R. Electrospraying, a Reproducible Method for Production of Polymeric Microspheres for Biomedical Applications. *Polymers* **2011**, *3*, 131−149.
(21) Fanzheng, M.; Yi, J.; Zhihui, S.; Yizi, Y.; Yanyan, L. Electrohydrodynamic Liquid Atomization of Biodegradable Polymer Microparticles: Effect of Electrohydrodynamic Liquid Atomization Variables on Microparticles. *J. Appl. Polym. Sci.* **2009**, *113*, 526−534.
(22) Chan, M.-W.; Stride, E.; Edirisinghe, M. Controlling the thickness of hollow polymeric microspheres prepared by electrohydrodynamic atomization. *J. R. Soc. Interface* **2010**, *7* (Suppl 4), S451−S460.
(23) Ghayempour, S.; Mortazavi, S. M. Fabrication of micro-nanocapsules by a new electrospraying method using coaxial jets and examination of effective parameters on their productions. *J. Electrostat.* **2013**, *71*, 717−727.
(24) Wang, K.; Stark, J. P. Voltage effects on the nanoelectrospray characteristics in fully voltage-controlled atomisation of gold nanocolloids. *Anal. Chim. Acta* **2010**, *679*, 81−84.
(25) Moghadam, H.; Samimi, M.; Samimi, A.; Khorram, M. Electrospray Modeling of Highly Viscous and Non-Newtonian Liquids. *J. Appl. Polym. Sci.* **2010**, *118*, 1288−1296.
(26) Hartman, R. P. A.; Brunner, D. J.; Camelot, D. M. A.; Marijnissen, J. C. M.; Scarlett, B. Jet break-up in electrohydrodynamic atomization in the cone-jet mode. *J. Aerosol Sci.* **2000**, *31*, 65−69.
(27) Nguyen, T. K.; Nguyen, V. D.; Seong, B.; Hoang, N.; Park, P.; Byun, D. Control and improvement of jet stability by monitoring liquid meniscus in electrospray and electrohydrodynamic jet. *J. Aerosol Sci.* **2014**, *71*, 29−39.
(28) Jun, Y.; Liang, K.; Jingwei, X.; Jinsong, H.; Chi-Hwa, W. Characterization of electrospraying process for polymeric particle fabrication. *J. Aerosol Sci.* **2008**, *39*, 987−1002.
(29) Chul, H. P.; Jonghwi, L. Electrosprayed polymer particles: Effect of the solvent properties. *J. Appl. Polym. Sci.* **2009**, *114*, 430−437.
(30) Nedović, V.; Obradović, B.; Leskošek-Čukalović, I.; Trifunović, O.; Pešić, R.; Bugarski, B. Electrostatic generation of alginate microbeads loaded with brewing yeast. *Process Biochem.* **2001**, *37*, 17−22.
(31) Moghadam, H.; Samimi, M.; Samimi, A.; Khorram, M. Electrospray of high viscous liquids for producing mono-sized spherical alginate beads. *Particuology* **2008**, *6*, 271−275.
(32) Khan, M. K. I.; Schutyser, M.; Schroën, K.; Boom, R. The potential of electrospraying for hydrophobic films coating on food. *J. Food Eng.* **2012**, *108*, 410−416.
(33) Kawabata, Y.; Wada, K.; Nakatani, M.; Yamada, S.; Onoue, S. Formulation design for poorly water-soluble drugs based on biopharmaceutics classification system: Basic approaches and practical applications. *Int. J. Pharm.* **2011**, *420*, 1−10.
(34) Noyes, A. A.; Whitney, W. R. The rate of solution of solid substances in their own solutions. *J. Am. Chem. Soc.* **1897**, *19*, 930−934.
(35) Galindo-Rodríguez, S.; Allémamm, E.; Fessi, H.; Doelker, E. Physicochemical Parameters Associated with Nanoparticle Formation in the Salting-out, Emulsification-Diffusion, and nanoprecipitation Methods. *Pharm. Res.* **2004**, *21*, 1428−1439.
(36) Simchua, W.; Narkkong, N. A.; Baimark, Y. Silk Fibroin Nanospheres for Controlled Gentamicin Sulfate Delivery. *Res. J. Nanoscie. Nanotechnol.* **2011**, *1*, 34−41.
(37) Chidambaram, M.; Krishnasamy, K. Modifications to the Conventional Nanoprecipitation Technique: an Approach to Fabricate Narrow Sized Polymeric Nanoparticles. *Adv. Pharm. Bull.* **2014**, *4*, 205−208.
(38) Chorny, M.; Fishbein, I.; Danenberg, H.; Golomb, G. Lipophilic drug loaded nanospheres prepared by nanoprecipitation: effect of formulation variables on size, drug recovery and release kinetics. *J. Controlled Release* **2002**, *83*, 389−400.
(39) Zambrano-Zaragoza, M. L.; Mercado-Silva, E.; Gutierrez-Cortez, E. Optimization of nanocapsules preparation by the emulsion-diffusion method for food applications. *LWT - Food Sci. Technol.* **2011**, *44*, 1362−1368.
(40) Moinard-Chécot, D.; Chevalier, Y.; Briançon, S.; Beney, L.; Fesprsi, H. Mechanism of nanocapsules formation by the emulsion−diffusion process. *J. Colloid Interface Sci.* **2008**, *317*, 458−468.
(41) Kim, S. H.; Kim, B. Controlled formation of double-emulsion drops in sudden expansion channels. *J. Colloid Interface Sci.* **2014**, *415*, 26−31.
(42) Khoee, S.; Yaghoobian, M. An investigation into the role of surfactants in controlling particle size of polymeric nanocapsules containing penicillin-G in double emulsion. *Eur. J. Med. Chem.* **2009**, *44*, 2392−2399.
(43) Lee, S. S.; Abbaspourrad, A.; Kim, S. H. Nonspherical double emulsions with multiple distinct cores enveloped by ultrathin shells. *ACS Appl. Mater. Interfaces.* **2014**, *6*, 1294−1300.
(44) Lertsutthiwong, P.; Noomun, K.; Jongaroonngamsang, N.; Rojsitthisak, P.; Nimmannit, U. Preparation of alginate nanocapsules containing turmeric oil. *Carbohydr. Polym.* **2008**, *74*, 209−2014.
(45) Mora-Huertas, C. E.; Fessi, H.; Elaissari, A. Polymer-based nanocapsules for drug delivery. *Int. J. Pharm.* **2010**, *385*, 113−142.

DOI: 10.1021/acs.jafc.5b01403
J. Agric. Food Chem. 2015, 63, 4699−4707

(46) Prego, C.; Fabre, M.; Torres, D.; Alonso, M. J. Efficacy and mechanism of action of chitosan nanocapsules for oral peptide delivery. *Pharm. Res.* **2006**, *23*, 549−556.
(47) Grigoriev, D.; Miller, R. Mono- and multilayer covered drops as carriers. *Colloid Interface Sci.* **2009**, *14*, 48−59.
(48) Radtchenko, I. L.; Sukhorukov, G. B.; Möhwald, H. Incorporation of macromolecules into polyelectrolyte micro-and nanocapsules via surface controlled precipitation on colloidal particle. *Colloids Surf.* **2002**, *202*, 127−133.
(49) Li, W.; Xu, D.; Hu, Y.; Cai, K.; Lin, Y. Surface modification of titanium substrates with silver nanoparticles embedded sulfhydrylated chitosan/gelatin polyelectrolyte multilayer films for antibacterial application. *J. Mater. Sci. Mater. Med.* **2014**, *25*, 1435−1448.
(50) Zambaux, M. F.; Bonneaux, F.; Gref, R.; Dellacherie, E.; Vigneron, C. Preparation and characterization of protein C-loaded PLA nanoparticles. *J. Controlled Release* **1999**, *60*, 179−188.
(51) Ferreira, S. A.; Pereira, P.; Sampaio, P.; Coutinho, P. J. G.; Gama, F. M. Supramolecular assembled nanogel made of mannan. *J. Colloid Interface Sci.* **2011**, *361*, 97−108.
(52) Lee, S. H.; Heng, D.; Ng, W. K.; Chan, H.; Tan, R. B. H. Nano spray drying: a novel method for preparing protein nanoparticles for protein therapy. *Int. J. Pharm.* **2011**, *403*, 192−200.
(53) Lee, Y.-H.; Mei, M.; Bai, M.-Y.; Zhao, S.; Chen, D.-R. Release profile characteristics of biodegradable-polymer-coated drug particles fabricated by dual-capillary electrospray. *J. Controlled Release* **2010**, *145*, 58−65.
(54) Guillaume, C.; Pinte, J.; Gontard, N.; Gastaldi, E. Wheat gluten-coated papers for bio-based food packaging: Structure, surface and transfer properties. *Food Res. Int.* **2010**, *1*, 1395.
(55) Pan, K.; Zhong, Q.; Baek, S. J. Enhanced dispersibility and bioactivity of curcumin by encapsulation in casein nanocapsules. *J. Agric. Food. Chem.* **2013**, *61*, 6036−6043.
(56) Musyanovych, A.; Landfester, K. Polymer Micro- and Nanocapsules as Biological Carriers with Multifunctional Properties. *Macromol. Biosci.* **2014**, *14*, 458−477.
(57) Granda, V. M.; Valdés, G. A. C.; García, C. J. A.; Díaz-García, M. E. Analytical nanotechnology for food analysis. *Microchim. Acta* **2009**, *166*, 1−19.
(58) Shrivastava, S.; Dash, D. Nanotechnology in Food Sector and Agriculture. *Proc. Nat. Acad. Sci. India Sect. B: Biol. Sci.* **2012**, *82*, 29−35.
(59) Santos, P. A.; Ferreira, S. A.; Mendes, S. L.; Andrade, N.; Araujo, S. M.; Fernandes, C. A. Polydiacetylene as a Biosensor: Fundamentals and Applications in the Food Industry. *Food Bioprocess. Technol.* **2010**, *3*, 172−181.
(60) Shewan, H. M.; Stokes, J. R. Review of techniques to manufacture micro-hydrogel particles for the food industry and their applications. *J. Food Eng.* **2013**, *119*, 781−792.
(61) López-Rubio, A.; Lagaron, J. M. Whey protein capsules obtained through electrospraying for the encapsulation of bioactives. *Innovative Food Sci. Emerg. Technol.* **2012**, *13*, 200−206.
(62) Li, W.; Li, L.; Wang, Q.; Pan, Y.; Wang, T.; Wang, H.; Song, R.; Deng, H. Antibacterial activity of nanofibrous mats coated with lysozyme-layered silicate composites via electrospraying. *Carbohydr. Polym.* **2014**, *99*, 218−225.
(63) Jung, J. H.; Lee, J. E.; Bae, G.-N. Use of electrosprayed Sophora flavescens natural-product nanoparticles for antimicrobial air filtration. *J. Aerosol Sci.* **2013**, *57*, 185−193.
(64) Bocanegra, R.; Gaonkar, A. G.; Barrero, A.; Loscertales, I. G.; Pechack, D.; Marquez, M. Production of Cocoa Butter Microcapsules Using an Electrospray Process. *J. Food Sci.* **2005**, *70*, 492−497.
(65) Lertsutthiwong, P.; Rojsitthisak, P. Chitosan-alginate nanocapsules for encapsulation of turmeric oil. *Pharmazie* **2011**, *66*, 911−915.
(66) Pray, L.; Yaktn, A. *Nanotechnology in Food Products: Workshop Summary*; The National Academies Press: Washington, D.C., 2009; Chapter 2, pp 55−57.
(67) Arya, N.; Chakraborty, S.; Dube, N.; Katti, D. S. Electrospraying: a facile technique for synthesis of chitosan-based micro/nanospheres for drug delivery applications. *J. Biomed. Mater. Res. B Appl. Biomater.* **2009**, *88*, 17−31.
(68) Zhang, S.; Kawakami, K. One-step preparation of chitosan solid nanoparticles by electrospray deposition. *Int. J. Pharm.* **2010**, *397*, 211−217.
(69) Piras, A. M.; Maisetta, G.; Sandreschi, S.; Esin, S.; Gazzarri, M.; Batoni, G.; Chiellini, F. Preparation, physical-chemical and biological characterization of chitosan nanoparticles loaded with lysozyme. *Int. J. Biol. Macromol.* **2014**, *67*, 124−131.
(70) Xu, S.; Xu, Q.; Zhou, J.; Wang, J.; Zhang, N.; Zhang, L. Preparation and characterization of folate-chitosan-gemcitabine core-shell nanoparticles for potential tumor-targeted drug delivery. *J. Nanosci. Nanotechnol.* **2013**, *13*, 129−138.
(71) Le Corre, D.; Bras, J.; Dufresne, A. Starch nanoparticles: a review. *Biomacromolecules* **2010**, *11*, 1139−1153.
(72) Atyabi, F.; Manoochehri, S.; Mohamad, S. H.; Dinarvand, R. Cross-linked starch microspheres: effect of cross-linking condition on the microsphere characteristics. *Arch. Pharm. Res.* **2006**, *29*, 1179−1186.
(73) Tan, Y.; Xu, K.; Li, L.; Liu, C.; Song, C.; Wang, P. Fabrication of size-controlled starch-based nanospheres by nanoprecipitation. *ACS Appl. Mater. Interfaces* **2009**, *1*, 956−959.
(74) Santander-Ortega, M. J.; Stauner, T.; Loretz, B.; Ortega-Vinuesa, J. L.; Bastos-González, D.; Wenz, G.; Schaefer, U. F.; Lehr, C. M. Nanoparticles made from novel starch derivatives for transdermal drug delivery. *J. Controlled Release* **2010**, *141*, 85−92.
(75) Chávarri, M.; Marañón, I.; Ares, R.; Ibáñez, F. C.; Marzo, F.; Villarán, M. C. Microencapsulation of a probiotic and prebiotic in alginate-chitosan capsules improves survival in simulated gastro-intestinal conditions. *Int. J. Food Microbiol.* **2010**, *142*, 185−189.
(76) Bhowmik, B. B.; S a, B.; Mukherjee, A. Preparation and in vitro characterization of slow release testosterone nanocapsules in alginates. *Acta Pharm.* **2006**, *56*, 417−429.
(77) Rastogi, R.; Sultana, Y.; Aqil, M.; Ali, A.; Kumar, S.; Chuttani, K.; Mishra, A. K. Alginate microspheres of isoniazid for oral sustained drug delivery. *Int. J. Pharm.* **2007**, *334*, 71−77.
(78) Shadab; Ahuja, A.; Khar, R. K.; Baboota, S.; Chuttani, K.; Mishra, A. K.; Ali, J. Gastroretentive drug delivery system of acyclovir-loaded alginate mucoadhesive microspheres: formulation and evaluation. *Drug Delivery* **2011**, *18*, 255−64.
(79) Tabeei, A.; Samimi, A.; Khorram, M.; Moghadam, H. Study pulsating electrospray of non-Newtonian and thixotropic sodium alginate solution. *J. Electrostat.* **2012**, *70*, 77−82.
(80) Ofokansi, K.; Winter, G.; Fricker, G.; Coester, C. Matrix-loaded biodegradable gelatin nanoparticles as new approach to improve drug loading and delivery. *Eur. J. Pharm. Biopharm.* **2010**, *76*, 1−9.
(81) Chen, L.; Siemiarczuk, A.; Hai, H.; Chen, Y.; Huang, G.; Zhang, J. Development of biocompatible and proton-resistant quantum dots assembled on gelatin nanospheres. *Langmuir* **2014**, *30*, 1893−1899.
(82) Rhim, J. W.; Wang, L. F.; Lee, Y.; Hong, S. I. Preparation and characterization of bio-nanocomposite films of agar and silver nanoparticles: laser ablation method. *Carbohydr. Polym.* **2014**, *103*, 456−465.
(83) Doi, N.; Jo, J. I.; Tabata, Y. Preparation of Biodegradable Gelatin Nanospheres with a Narrow Size Distribution for Carrier of Cellular Internalization of Plasmid DNA. *J. Biomater. Sci. Polym. Ed.* **2012**, *23*, 901−1004.
(84) Curcio, M.; Altimari, I.; Spizzirri, U. G.; Cirillo, G.; Vittorio, O.; Puoci, F.; Picci, N.; Iemma, F. Biodegradable gelatin-based nanospheres as pH-responsive drug delivery systems. *J. Nanopart. Res.* **2013**, *15*, 1−11.
(85) Kanmani, P.; Rhim, J. W. Antimicrobial and physical-mechanical properties of agar-based films incorporated with grapefruit seed extract. *Carbohydr. Polym.* **2014**, *102*, 708−716.
(86) Andreani, L.; Cercená, R.; Ramos, B.; Soldi, V. Development and characterization of wheat gluten microspheres for use in a controlled release system. *Mater. Sci. Eng. C* **2009**, *29*, 524−531.
(87) Liao, L.; Luo, Y.; Zhao, M.; Wang, Q. Preparation and characterization of succinic acid deamidated wheat gluten micro-

DOI: 10.1021/acs.jafc.5b01403
J. Agric. Food Chem. 2015, 63, 4699−4707

spheres for encapsulation of fish oil. *Colloid Surface B* **2012**, *92*, 305−314.
(88) Mauguet, M. C.; Legrand, J.; Brujes, L.; Carnelle, G.; Larre, C.; Popineau, Y. Gliadin matrices for microencapsulation processes by simple coacervation method. *J. Microencapsul.* **2002**, *19*, 377−384.
(89) Duclairoir, C.; Orecchioni, A. M.; Depraetere, P.; Osterstock, F.; Nakache, E. Evaluation of gliadins nanoparticles as drug delivery systems: a study of three different drugs. *Int. J. Pharm.* **2003**, *253*, 133−144.
(90) Ezpeleta, I.; Irache, J. M.; Stainmesse, S.; Chabenat, C.; Gueguen, J.; Popineau, Y.; Orecchioni, A.-M. Gliadin nanoparticles for the controlled-release of all-trans-retinoic acid. *Int. J. Pharm.* **1996**, *131*, 191−200.
(91) Gulfam, M.; Kim, J. E.; Lee, J. M.; Ku, B.; Chung, B. H.; Chung, B. G. Anticancer drug-loaded gliadin nanoparticles induce apoptosis in breast cancer cells. *Langmuir* **2012**, *28*, 8216−8223.
(92) Gorty, A. V.; Barringer, S. A. Electrohydrodynamic spraying of chocolate. *J. Food Process. Preserv.* **2011**, *35*, 542−549.
(93) Milda, E. E.; Kerry, C. H. *Edible Films and Coatings for Food Applications*; Springer: Dordrecht Heidelberg London New York, 2009; Vol. *1*, Chapter 1, p 1.
(94) Du, W. X.; Olsen, C. W.; Avena-Bustillos, R. J.; McHugh, T. H.; Levin, C. E.; Friedman, M. Storage stability and antibacterial activity against Escherichia coli O157:H7 of carvacrol in edible apple films made by two different casting methods. *J. Agric. Food Chem.* **2008**, *56*, 3082−3088.
(95) Ravishankar, S.; Zhu, L.; Olsen, C. W.; McHugh, T. H.; Friedman, M. Edible apple film wraps containing plant antimicrobials inactivate foodborne pathogens on meat and poultry products. *J. Food Sci.* **2009**, *74*, 440−445.
(96) Morsy, M. K.; Khalaf, H. H.; Sharoba, A. M.; El-Tanahi, H. H.; Cutter, C. N. Incorporation of essential oils and nanoparticles in pullulan films to control foodborne pathogens on meat and poultry products. *J. Food Sci.* **2014**, *79*, 675−684.
(97) Kurt, A.; Kahyaoglu, T. Characterization of a new biodegradable edible film made from salep glucomannan. *Carbohydr. Polym.* **2014**, *104*, 50−58.
(98) Khazaei, N.; Esmaiili, M.; Djomeh, Z. E.; Ghasemlou, M.; Jouki, M. Characterization of new biodegradable edible film made from basil seed (*Ocimum basilicum L.*) gum. *Carbohydr. Polym.* **2014**, *102*, 199−206.
(99) Yan, Q.; Hou, H.; Guo, P.; Dong, H. Effects of extrusion and glycerol content on properties of oxidized and acetylated corn starch-based films. *Carbohydr. Polym.* **2012**, *87*, 707−712.
(100) Xiao, Q.; Tong, Q. Thermodynamic properties of moisture sorption in pullulan sodium alginate based edible films. *Food Res. Int.* **2013**, *54*, 1605−1612.
(101) Sirviö, J. A.; Kolehmainen, A.; Liimatainen, H.; Niinimäki, J.; Hormi, O. E. Biocomposite cellulose-alginate films: promising packaging materials. *Food Chem.* **2014**, *151*, 343−351.
(102) Masotti, A.; Ortaggi, G. Chitosan micro- and nanospheres: fabrication and applications for drug and DNA delivery. *Mini. Rev. Med. Chem.* **2009**, *9*, 463−469.
(103) Paques, J. P.; van der Linden, E.; van Rijn, C. J.; Sagis, L. M. Preparation methods of alginate nanoparticles. *Adv. Colloid Interface Sci.* **2014**, *209*, 163−171.
(104) Liu, L.; Wu, F.; Ju, X. J.; Xie, R.; Wang, W.; Niu, C. H.; Chu, L. Y. Preparation of monodisperse calcium alginate microcapsules via internal gelation in microfluidic-generated double emulsions. *J. Colloid Interface Sci.* **2013**, *404*, 85−90.
(105) Espitia, P. J.; Avena-Bustillos, R. J.; Du, W. X.; Chiou, B. S.; Williams, T. G.; Wood, D.; McHugh, T. H.; Soares, N. F. Physical and antibacterial properties of açaí edible films formulated with thyme essential oil and apple skin polyphenols. *J. Food Sci.* **2014**, *79*, 903−910.
(106) Jridi, M.; Hajji, S.; Ayed, H. B.; Lassoued, I.; Mbarek, A.; Kammoun, M.; Souissi, N.; Nasri, M. Physical, structural, antioxidant and antimicrobial properties of gelatin-chitosan composite edible films. *Int. J. Biol. Macromol.* **2014**, *67*, 373−379.
(107) Fakhreddin, H. S.; Rezaei, M.; Zandi, M.; Ghavi, F. F. Preparation and functional properties of fish gelatin-chitosan blend edible films. *Food Chem.* **2013**, *136*, 1490−1495.
(108) Jouki, M.; Mortazavi, S. A.; Yazdi, F. T.; Koocheki, A. Characterization of antioxidant-antibacterial quince seed mucilage films containing thyme essential oil. *Carbohydr. Polym.* **2014**, *99*, 537−546.
(109) Torres-Giner, S.; Martinez-Abad, A.; Ocio, M. J.; Lagaron, J. M. Stabilization of a nutraceutical omega-3 fatty acid by encapsulation in ultrathin electrosprayed zein prolamine. *J. Food Sci.* **2010**, *75*, 69−79.
(110) Chen, L.; Xie, Z.; Zhuang, X.; Chen, X.; Jing, X. Controlled release of urea encapsulated by starch-g-poly(L-lactide). *Carbohydr. Polym.* **2008**, *72*, 342−348.

DOI: 10.1021/acs.jafc.5b01403
J. Agric. Food Chem. 2015, 63, 4699−4707

JOURNAL OF AGRICULTURAL AND FOOD CHEMISTRY

Article

pubs.acs.org/JAFC

Water Stress Alters Lignin Content and Related Gene Expression in Two Sugarcane Genotypes

Adriana Brombini dos Santos,[†,‡] Alexandra Bottcher,[†,§] Eduardo Kiyota,[†] Juliana Lischka Sampaio Mayer,[†] Renato Vicentini,[∥] Michael dos Santos Brito,[†,⊥] Silvana Creste,[⊥] Marcos G. A. Landell,[⊥] and Paulo Mazzafera*[,†]

[†]Departamento de Biologia Vegetal, Instituto de Biologia, CP 6109, Universidade Estadual de Campinas, CEP 13083-970 Campinas, SP, Brazil

[‡]Embrapa Soja, Rodovia Carlos João Strass, s/n°, Acesso Orlando Amaral, Distrito de Warta, CP 231, CEP 86001-970 Londrina, PR, Brazil

[§]Centro de Tecnologia Canavieira (CTC), Rua Santo Antônio, Centro, CEP 13400-160 Piracicaba, SP, Brazil

[∥]Centro de Biologia Molecular e Engenharia Genética, Universidade Estadual de Campinas, CEP 13083-875 Campinas, SP, Brazil

[⊥]Centro de Cana, Instituto Agronômico de Campinas, CEP 14001-970 Ribeirão Preto, SP, Brazil

Supporting Information

ABSTRACT: The lignin deposition in the stem of two sugarcane genotypes was assessed on exposure to water stress. The lignin content and the morphoanatomical characterization of the stem indicated that IACSP94-2094 plants are more lignified than those of IACSP95-5000 genotype, under normal water supply conditions, which was especially associated with higher lignin contents in the rind of mature internodes. Water deficit had negative impact on the biomass production, mostly with IACSP94-2094 plants, possibly due to stress severity or higher susceptibility of that genotype during the stem-lengthening phase. Water deficit led to significant alterations in the expression levels of lignin biosynthesis genes and led to an approximate 60% increase of lignin content in the rind of young internodes in both genotypes. It is concluded that the young rind region was more directly affected by water stress and, depending on the genotype, a higher lignin accumulation may occur in the stem, thus implying lower quality biomass for bioethanol production.

KEYWORDS: *Saccharum, lignocellulosic biomass, gene expression, genetic variability, water stress*

INTRODUCTION

Sugarcane (*Saccharum* spp.) is a C4 grass accounting for an abundant and promising source of plant biomass for the production of biofuels. Residual sugarcane biomass (mainly bagasse and tops + young leaves) accounts for two-thirds of the total energy of the plant, the potential of which is partially used with the incineration of the bagasse, so as to generate electricity at alcohol and sugar mills.[1] It is estimated that a mill currently and daily producing 1000000 L of ethanol from sugarcane juice, rich in sucrose, is potentially capable of initially generating an additional 150000 L of ethanol from the bagasse, provided that the cellulose there contained was available by means of acid hydrolysis, for fermentation with microorganisms.[1] Ethanol derived from bagasse is called second-generation ethanol or cellulosic ethanol, the use of which is restricted by the recalcitrance of the cell wall.

Sugarcane bagasse consists of approximately 50% cellulose, 25% hemicellulose, and 25% lignin.[2] The recalcitrance of sugarcane bagasse and other biomasses is partially attributed to lignin, which serves as a natural mechanical barrier preventing the access of hydrolytic enzymes to cellulose fibrils. Additionally, lignin can absorb the enzymes used during hydrolysis of lignocellulosic material, thus impairing process efficiency. Furthermore, some polymer degradation products may inhibit subsequent fermentation phases.[3]

Lignin is a phenolic polymer complex derived mainly from three hydroxycinnamoyl alcohols varying in methoxylation rate: monolignol *p*-coumaryl, coniferyl, and sinapyl. After incorporation in the lignin polymer, via combinatorial coupling reactions, monolignols originate the subunits *p*-hydroxyphenyl (H), guaiacyl (G), and syringyl (S), respectively.[4,5] Polymerization takes place by means of addition of new monolignol radicals to the growing polymer, usually via a connection in position β, such as β-O-4, β-5, and β-β. The interunit linkage β-O-4 (β-aryl ether) is the most frequent and also the most easily cleaved by chemical processes, whereas condensed linkages (β-5, β-β, 5-5, 5-O-4, and β-1) are more resistant to chemical degradation.[4,6]

Lignin content and composition vary among different taxons, cellular types, and cellular wall layers and are modified by environmental factors throughout plant development.[7] In gymnosperms (softwood), lignin is formed basically by G units and traces of H units, whereas in dicotyledonous angiosperms (hardwood) it consists mainly of G and S units, with few traces of H units. In grasses (monocotyledonous), G

Received: December 24, 2014
Revised: May 1, 2015
Accepted: May 3, 2015
Published: May 4, 2015

ACS Publications © 2015 American Chemical Society

DOI: 10.1021/jf5061858
J. Agric. Food Chem. 2015, 63, 4708−4720

and S units are incorporated at similar levels, while H units are relatively higher, in comparison to dicotyledonous species.[4]

Research into grasses has revealed that the incorporation of H, G, and S units in the lignin polymer is regulated spatiotemporally, varying in primary and secondary cellular walls and also in different tissues.[8,9] Lignin topology and composition in different sugarcane internodes vary among the main cellular types present in the stem: fibers incorporate a significant amount of sinapyl alcohol, forming lignin at a S > G > H proportion; in xylem vessels, G and H units prevail in the protoxylem, whereas metaxylem features a fiberlike composition; parenchyma cells have a great deal of phenolic acids, thus preventing accurate determination of the proportion of each lignin unit.[8] Similarly to other grasses, sugarcane features a significant amount of hydroxycinnamic acids associated with the cellular wall, at higher levels in the parenchyma tissue than in the vascular bundles. Sinapyl, ferulic, and *p*-coumaric acids are preferably deposited in the early stages of lignification, presenting different relative proportions as tissues mature.[8]

Sugarcane internode anatomy shows that it consists basically of parenchyma cells and vascular bundles, featuring two different morphological regions, the rind and the pith. The rind is the region containing mostly vascular bundles, in turn constituted by vessels surrounded by a great number of fibers. The pith is formed by parenchyma cells (which store sucrose), where the vascular bundles are distributed, at a lower number than in the rind.[10]

A recent systematic study reported on physiological, morphological, biochemical, and molecular data for the investigation of lignin deposition throughout sugarcane stem development.[11] The outcome was a detailed profile of lignin and phenolic compounds related to the formation of the cellular wall in two contrasting genotypes for lignin content, highlighting differences regarding polymer content and composition, S/G ratio, and gene expression of lignin biosynthesis in the rind and in the pith of sugarcane internodes.

Alteration in lignin biosynthesis is induced by a range of environmental stresses, such as drought, low temperature, UV-B radiation, mineral deficiency, and pathogen infection.[12] Several studies in corn reported an increased gene expression in lignin biosynthesis and varied content and composition in plants exposed to water deficit.[13,14] Other studies have revealed that the gene expression and presence of enzymes related to lignin and its deposition on the cellular walls can be differentially regulated during water stress. cDNA-AFLP (amplified fragment length polymorphism) and Northern blot analyses have evidenced that the expression of the genes playing a role in cellular growth and extensibility of the cell wall in rice roots was potentiated in the early stages of water stress, whereas gene expression related to lignin biosynthesis was considerably higher during the intermediate and final stages of water deficit.[15] A proteomic study of *Citrullus lanatus* roots submitted to water deficit has proven that proteins related to lignin synthesis, such as CCoAOMT and various class III peroxidases (involved in lignification), were induced mainly in the final stages of the stress.[16]

Supported by a previous systematic study of lignin deposition in sugarcane,[11] the present work has looked into the effects of water deficit on lignin metabolism in the stem of two sugarcane genotypes.

MATERIALS AND METHODS

Plant Material and Growth Conditions. The experiment was carried out at the experimental area of the Department of Plant Biology of the State University of Campinas, at Campinas, SP, Brazil (22°81′77′′ latitude S; 47°03′83′′ longitude W). Two commercial *Saccharum* spp. genotypes were used: IACSP94-2094, deemed drought-resistant,[17,18] and IACSP95-5000, which has not been characterized for drought tolerance so far. Plants were obtained from single nodes of mature culms collected from plants in the field. These "one eye setts" were left to germinate (January 2011) on trays containing vermiculite, and after approximately 1 month 15 plants of each genotype were transferred to 25 L plastic (35 cm height × 25 cm top diameter × 28 cm bottom diameter) vases containing 20 L of commercial organic soil mixture and kept in a greenhouse under no temperature, light, or air humidity control. Secondary sprouts were removed, and only the main stem remained in each vase. The plants were irrigated on a daily basis until the beginning of the water-restriction treatment, on May 2011.

Water-Stress Treatment and Plant Collection. At the age of 5 months, the plants were submitted to three water regimes: namely, severe drought (SD), moderate drought (MD), and control (daily irrigation). SD and MD correspond to maintenance of the water content in the substratum at 40% and 80% of the total water storage capacity of the soil (C_w). Five plants of each genotype were used in each treatment. The C_w value was estimated using the fresh mass of the soil after water saturation (C_{fm}) and the dry mass (C_{dm}) after soil drying in a greenhouse for 24 h at 105 °C and applied in the equation $C_w = (C_{fm} - C_{dm})/C_{fm} \times 100$. At the beginning of the treatments, the vases were water-saturated, drained of water, and weighed. From that moment on, irrigation was suspended and the vases were weighed every second day, assuring maintenance of C_w at 40% or 80% by water addition, considering 1 mL = 1 g. The plants were kept under such conditions for 60 days. Figure S1 in the Supporting Information shows water replacement volumes throughout the stress period, as well as temperature and relative air humidity variation. The average maximum and minimum air temperatures in the greenhouse were 28.4 ± 3.8 and 11.8 ± 2.6 °C, respectively; the relative humidity was not controlled.

By the end of a 60 day period (July 6th, 2011) the following parameters were obtained for each replicate in each treatment: number of green leaves (N_l), number of stem internodes (N_i), stem lengths (L_s), fresh stem mass (FM_s), dry leaf mass (DM_l), and dry root mass (DM_r). For N_l determination only leaves featuring over 50% of leaf blade colored green were considered. Measurements of the leaves and root dry mass were determined after drying the material at 72 °C for 72 h. Stems were numbered from apex to base, so that internode 1 (I1) corresponded to the internode in which the leaf +1 was inserted. The internode stem diameter was measured by means of a digital caliper rule. Then two distinct internode maturation stages were selected for analysis: young or immature region, made of a pool of internodes I1−I3, and mature region, a pool of internodes I8 and I9. Each sample of these stages was separated in rind and pith, as previously identified.[19] The stem material was frozen in liquid nitrogen and divided into two parts, one for biochemical analyses and the other for molecular analyses. The samples for biochemical analyses were lyophilized at −60 °C for 72 h and stored at −80 °C, whereas the samples for molecular analyses were kept at −80 °C.

Biochemical Analyses. Approximately 50 mg of lyophilized (pith) and pulverized material was extracted twice with 1 mL of 80% ethanol in a water bath at 40 °C for 30 min with occasional vortexing. The supernatants were recovered by centrifugation at 8000*g* for 15 min, and the extracts were combined and dried in a SpeedVac (Savant, São Paulo, Brazil). The residue was solubilized in 1 mL of Milli-Q water. For soluble sugar determination 50 μL of each sample was homogenized in 950 μL of 80% acetonitrile in water and an aliquot of 4 μL was injected in an Acquity UPLC-MS (Micromass-Waters, Manchester, U.K.) mass spectrometer coupled to a TDQ triple quadrupole. The chromatographic separation was carried out in an Acquity UPLC C18-BEH column (2.1 mm × 50 mm, 1.7 μm) at a 0.2 mL min^{-1} flow rate. A gradient of 20−35% of 0.1% NH_4OH solution

DOI: 10.1021/jf5061858
J. Agric. Food Chem. 2015, 63, 4708−4720

Table 1. Gene Identification, Sugarcane Assembled Sequences (SAS-SUCEST Database), Primer Sequences, and Amplicon Sizes

gene	SAS[a]	primer (5′→ 3′)	amplicon (bp)
ShPAL1	SCCCLR194D07.g	for: AGGAGGAGAAGAGGAGGAAAATAC rev: AGAAGAAAGAACAACGCCACA	150
ShC4H1	SCCCCL4009H01.g	for: CCGCAGATCCAGCACTATG rev: ATCCAACACCATTCCTCAGC	148
Sh4CL2	SCVPLB1015F12.g	for: CACACTGGGGACATTGGTT rev: CATTGAGACAACAGCAGCATC	162
ShHCT-like	SCVPRT2082B07.g	for: GCAGGTGGTAGAGTCGTCGT rev: ATGAGGTCCAGGGGAGAGAG	81
ShC3H1	SCVPCL6041E07.g	for: TCACTGCTGGAATGGACACA rev: TGTAGGTAGGGGAGGTTCTGG	163
ShCCoAOMT1	SCAGCL6012G12.g SCCCLR1069B09.g SCCCLR1079A02.g SCRUFL4024C06.b	for: GACGCCGACAAGGACAAC rev: CACGAAGTCGCGGTAGAAG	162
ShCCoAOMT3	SCJFRZ2010H06.g	for: CAGGACCAGTGCCAACATC rev: TTTCAGCGTCTCTTTCATTACTTG	157
ShCCR1	SCCCRZ2C01A04.g SCBFRT1064A01.g	for: GCTGGTCGGTCTCTTATCATC rev: CTGACGGTTCCCTTGACAG	214
ShF5H	SCJLRT1022E04.g	for: GCACTACGGTCCCTTCTGG rev: TCACGTTCTTGGTCAGGTTG	194
ShCOMT1	SCRFLR1012F12.g SCJLRT1023B09.g	for: GAGGACAAGGACGGCAAGT rev: AGTACCAGCTCTCCATGAGGAC	139
ShCAD2	SCBFAM2021E08.g SCEPRZ1011A02.g	for: CCCCTACACCTACACCCTCA rev: CACCTCACCGACCACCTC	157
ShCAD8	SCEQLR1029E05.g	for: ACGGCTGGAGAAGAACGAC rev: GCAAAGCACCAACTCATCAA	154
ShGAPDH	SCCCCL3001G02	for: TTGGTTTCCACTGACTTCGTT rev: CTGTAGCCCCACTCGTTGT	122

[a]Sugarcane assembled sequence.

in water (solvent B) and acetonitrile containing 0.1% NH_4OH (solvent A) was used to elute the compounds from the column. The electrospray ionization in the mass spectrometer was set to the negative mode under the following conditions: capillary 3.0 kV and cone 30 V, temperature at ionization source 150 °C, and desolvation temperature 350 °C. The sugar content was estimated from calibration curves obtained with pure standards of glucose, fructose, and sucrose. Free proline content was determined spectrophotometrically.[20]

Morphoanatomical Analyses. Transversal sections of the middle of the third (I3) and ninth (I9) stem internodes in plants of both genotypes, not submitted to water stress, were obtained manually and treated with phloroglucinol[21] for lignin analysis with an optical microscope (Olympus BX51).

Lignin Analyses. The analyses of soluble lignin oligomers in the stem were carried out with 100 mg of lyophilized material according to ref 22. Lignin content was estimated by derivatization with thioglycolic acid from 15 mg of lyophilized material,[23] using lignin alkali, 2-hydroxypropyl ether (Sigma-Aldrich), to build a calibration curve.

Gene Expression Analyses. Gene expression was assayed only in samples from severe drought (SD) treatment. Approximately 200−300 mg of tissue (pith and rind) pulverized in liquid nitrogen was used for the extraction of total RNA.[24] After DNase treatment (Ambion), total RNA was quantified in a spectrophotometer at 260 nm and the quality checked in 1% agarose gel with ethidium bromide and UV visualization. The first cDNA strand was synthesized from 1 μg of total RNA using a Superscript III Reverse Transcriptase kit (Invitrogen, Carlsbad, CA, USA), in accordance with the manufacturer's instructions. The relative number of transcripts was estimated for 12 genes related to lignin biosynthesis. The analyzed genes and their primers are given in Table 1.[11] Quantitative RT-PCR (qPCR) analyses were carried out with a QuantiFast SYBR Green PCR kit (Qiagen, São Paulo, Brazil) on 96-well plates using 50×-diluted cDNA. The reactions were analyzed with an iCycler iQ5Multicolor Real-Time PCR Detection system (Bio-Rad USA) and the correction of the C_t (cycle threshold) values among the plates in the same assay (the same gene) was based on an intercalibrating sample and automatically performed by an iQ5 software tool. Calculation of the relative gene

DOI: 10.1021/jf5061858
J. Agric. Food Chem. 2015, 63, 4708−4720

Table 2. Number of Green Leaves (N_l), Number of Internodes (N_i), Stem Length (L_s), Fresh Stem Mass (FM_s), Dry Leaf Mass (DM_l), and Dry Root Mass (DM_r) in Plants of Sugarcane Genotypes IACSP94-2094 and IACSP95-5000 Grown with Normal Water Supply (C) and Moderate (MD) and Severe (SD) Water Stress

	IACSP94-2094[a]			IACSP95-5000		
param	C	MD	SD	C	MD	SD
N_l	9.8 ± 0.4 Aa	8.0 ± 0.5 Ba	6.0 ± 0.3 Ca	7.8 ± 0.4 Ab	7.2 ± 0.6 Aa	3.8 ± 0.3 Bb
N_i	15.8 ± 0.4 Aa	15.2 ± 0.2 Aa	14.2 ± 0.2 Ba	12.4 ± 0.2 Ab	12.8 ± 0.6 Ab	12.5 ± 0.3 Ab
L_s (m)	1.5 ± 0.10 Aa	1.3 ± 0.1 Aa	1.2 ± 0.1 Ba	0.63 ± 0.03 Ab	0.55 ± 0.04 Ab	0.64 ± 0.02 Ab
FM_s (g)	491 ± 35 Aa	411 ± 16 Aa	369 ± 18 Ba	241 ± 5 Ab	188 ± 17 Bb	210 ± 4 Ab
DM_l (g)	92.6 ± 4.3 Aa	80.1 ± 3.1 Aa	68.8 ± 4. Four Ba	76.3 ± 3.3 Ab	68.5 ± 3.1 Ab	57.3 ± 1.4 Ba
DM_r (g)	56.5 ± 4.9 Aa	49.3 ± 5.1 Aa	38.9 ± 3.7 Ba	66.9 ± 6.1 Aa	65.8 ± 5.6 Aa	43.5 ± 2.2 Ba

[a]Different uppercase letters indicate significant differences among water regimes within the same genotype; different lowercase letters indicate differences between the two genotypes under the same water regime. Means were compared by the Tukey test, $P \leq 0.05$. Each value represents the mean ± standard error of five replications.

expression was based on the $\Delta\Delta C_t$ method,[25] and *GAPDH* (glyceraldehyde 3-phosphate dehydrogenase) was the reference gene to normalize expression values in the different samples.[11,26]

Statistics. The experiment was carried out in an entirely randomized design, in a 2 × 3 factorial (two genotypes and three water regimes), with five biological replications. For lignin quantification, data were analyzed as a 2 × 3 factorial (two internode maturation stages and three water regimes) for each sugarcane genotype. Each experimental unit consisted of one plant per vase. Data were submitted to variance analysis (Statistics software, version 10), and significant differences in treatment means were compared by means of the Tukey test and the *F* test ($P \leq 0.05$). Results were presented as means + standard error. For the biochemical and molecular analyses, each replication represents the average of three technical determinations of each sample.

RESULTS

Biometry. Except for dry root mass (DM_r), we have observed that control IACSP94-2094 genotype plants featured better growth rates than those of the IACSP95-5000 genotype (Table 2). We have verified, for instance, that, regarding the number of internodes (N_i), stem length (L_s), and fresh stem mass (FM_s), the performance of IACSP94-2094 plants was 22%, 58%, and 51% better than that of IACSP95-5000 plants, respectively.

Water restriction negatively and progressively (regarding stress intensity) affected plant growth parameters in both sugarcane genotypes (Table 2). Moderate drought (MD) had few effects on plant growth, so that only N_l (in IACSP94-2094) and FM_s parameters (in IACSP95-5000) were reduced. Under severe drought (SD) conditions, IACSP94-2094 plants had significant reduction of all analyzed parameters, in comparison with irrigated plants. N_l, DM_l, and DM_r also decreased in IACSP95-5000 plants under SD, nevertheless without significant alteration in stem-related parameters (N_i and L_s).

The internode stem diameter of stressed plants had a growth profile resembling that of control plants (Figure 1), although the average stem diameter was greater in IACSP95-5000 genotype plants (21.25 mm) than in IACSP94-2094 (19.98 mm). In these plants, intermediate internodes (I4−I8) presented an average diameter above those of the other stem regions, in both sugarcane genotypes. Regardless of the water regime, the plants tended to present lower basal internode (mature) diameters, with values approaching those obtained for apical internode (immature) diameters (Figure 1).

Water deficit caused a reducion of the internode diameter along the stem. IACSP94-2094 plants appear to have been more strongly affected, especially during severe drought. The

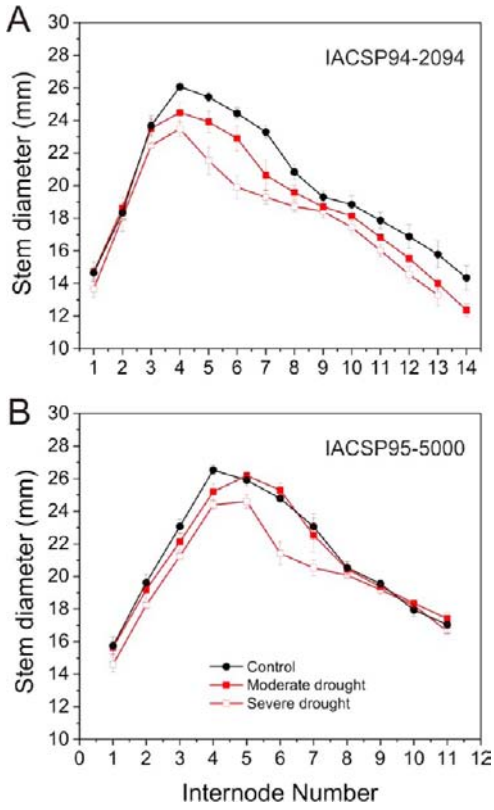

Figure 1. Diameters of stem internodes of plants of sugarcane genotypes IACSP94-2094 and IACSP95-5000 grown under different water regimes. Data are means ± standard error of five replicates.

intermediate internode region presented the most significant reductions: i.e. 14.3% in IACSP94-2094 and 9.3% in IACSP95-5000 (Figure 1). Morphological alterations, such as shortening and/or thinning of the internodes, were observed in both sugarcane genotypes, possibly as a result of cultivation conditions in the vegetation house.

Soluble Sugars and Proline. Sucrose content in the well-watered control plants was higher in immature internodes of IACSP94-2094 genotype, as opposed to IACSP95-5000 genotype, while in mature internodes similar values were observed in the two genotypes (Figure 2A). The amount of sucrose in control plants of both genotypes was approximately 5−6 times higher in mature internodes than in immature internodes. Plants under water restriction (MD and/or SD) posed significantly increased sucrose content in immature

DOI: 10.1021/jf5061858
J. Agric. Food Chem. 2015, 63, 4708−4720

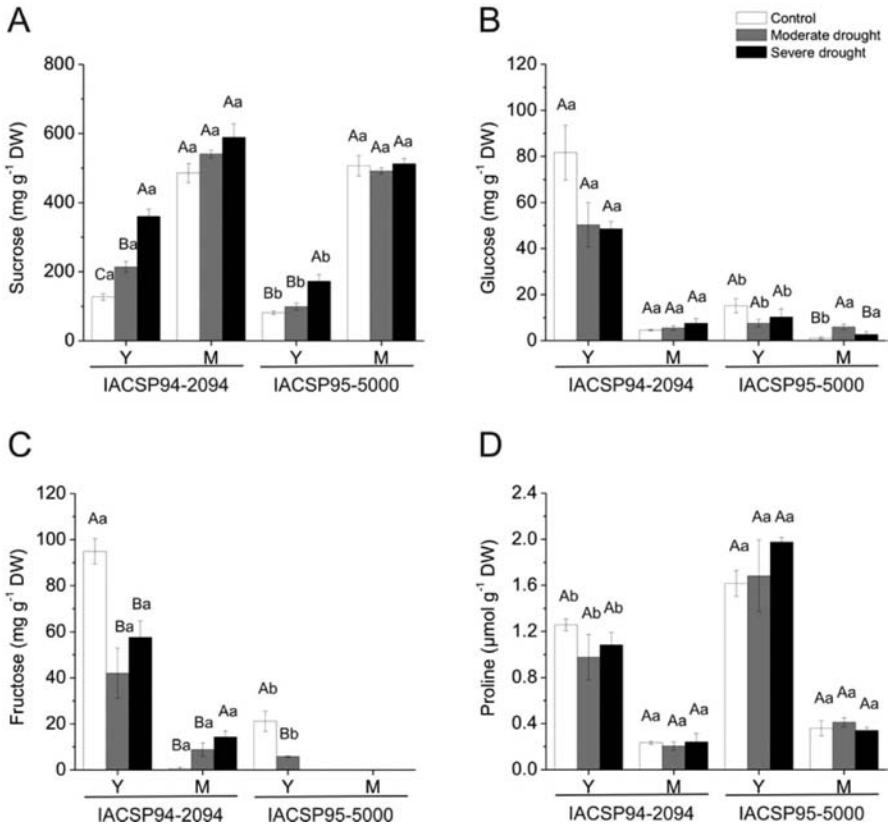

Figure 2. Contents of sucrose (A), glucose (B), fructose (C), and proline (D) in immature internodes (Y) and in mature internodes (M) of plants of sugarcane genotypes IACSP94-2094 and IACSP95-5000 grown under different water regimes. Different uppercase letters indicate significant differences among water regimes within the same genotype, whereas different lowercase letters indicate differences between the genotypes under the same water regime. Data are means ± standard error of four replicates.

internodes. No significant difference was observed in mature internodes of the two sugarcane genotypes under the same water regime (Figure 2A).

Control plants presented higher contents of reducing sugars in immature internodes, in relation to mature internodes (Figures 2B,C). In those plants, we observed that the relative amounts of glucose and fructose were higher in IACSP94-2094 than in IACSP95-5000 in immature and mature internodes. Under water deficit, glucose and fructose contents tended to be reduced in immature internodes, in comparison with that in control plants; however, this reduction was only significant for fructose, in both sugarcane genotypes (Figure 2C). In mature internodes, such sugars posed values similar to those observed in control plants in both genotypes (except for IACSP94-2094 plants under severe drought, which featured higher glucose content in relation to control plants). It was not possible to detect fructose contents in mature internodes of IACSP95-5000 plants (Figure 2C).

Regardless of the water regime, IACSP95-5000 genotype plants always had higher proline content in immature internodes than IACSP94-2094 genotype plants. Free proline contents were higher in immature internodes in comparison with those of mature internodes in both genotypes. Proline content in the stem was not significantly affected by water deficit in either evaluated sugarcane genotype (Figure 2D).

Morphoanatomical Analyses. The analyses of the internal morphology revealed that the sugarcane stem of both varieties studied here consists basically of parenchyma cells, concentrated on the pith region, and of vascular bundles, more abundant in the rind region. Reaction with phloroglucinol evidenced a differentiated lignin deposition pattern in the sugarcane genotypes analyzed in this study. IACSP94-2094 genotype stems present a premature and more intense lignification process, in comparison to IACSP95-5000 genotype plants, as indicated by the thickening of cellular walls and the lignification level of the epidermis and of the vascular bundle elements of the xylem in immature internodes (Figures 3A,C,E,G and 4A,C,E,G).

We have observed that, in immature internodes of IACSP94-2094 plants, the tracheal elements of protoxylem and metaxylem are already lignified (Figures 3E,G), while fibers and subepidermal layers happen to be in an early lignification phase (Figure 3A). In mature internodes, lignin is present in practically all tissues, except for chlorophyllin parenchyma cells (Figure 3B) and phloem cells in the vascular bundles (Figure 3F,H). Tissues tend to become too rigid, because parenchyma cells feature thicker and more lignified walls all over the organ; in addition, xylem fibers also present rather thick and lignified cellular walls (Figure 3F,H).

Stems of IACSP95-5000 plants presented a discrete lignification degree in immature internodes, in which only protoxylem tracheal elements of the vascular bundles were lignified (Figure 4A,E,G). In mature internodes, parenchyma cells were lignified (Figure 4F,H); nevertheless, they posed a less intense reaction in the presence of phloroglucinol, in comparison to IACSP94-2094 plants. Similarly, fibers also became less stained in vascular bundles located both in the rind (Figure 4B,F) and in the pith (Figure 4H).

DOI: 10.1021/jf5061858
J. Agric. Food Chem. 2015, 63, 4708−4720

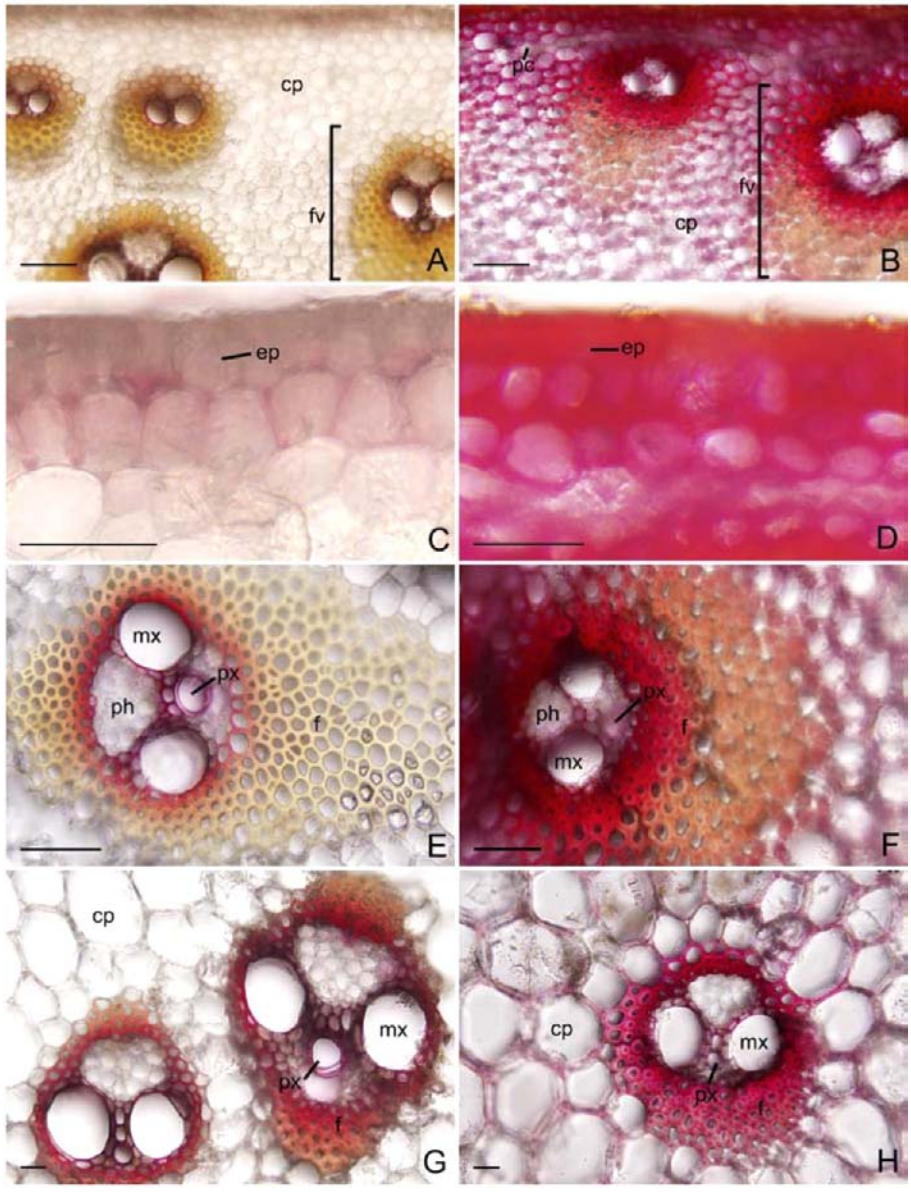

Figure 3. Transversal sections of different regions of sugarcane stems of genotype IACSP94-2094 submitted to acid phloroglucinol for lignin detection: (left column) immature internode; (right column) mature internode; (A, B) rind region; (C, D) detail of epidermis and adjacent cellular layers; (E, F) detail of rind vascular bundle; (G, H) detail of pith vascular bundle. Abbreviations: pc = parenchymal cell; ep = epidermis; f = fibers; mx = metaxylem; cp = chlorophyllin parenchyma; ph = phloem; vb = vascular bundle; px = protoxylem. Bars: (A, B and E, F) 50 μm; (C, D and G, H) 20 μm.

Soluble Lignin Oligomers. The analyses of soluble lignin enabled outlining the profiles of monomer and oligomer precursors of sugarcane polymer, on the basis of the frequency of such structures, as indicated in Table 3. We have identified G and S monolignols and their aldehydes (coniferyl and sinapyl aldehyde) and four dimers and four trimers of lignin. Type 8-O-4 linkages (less recalcitrant) were relatively frequent among the identified structures; however, linkages 8-5 and 8-8 (more recalcitrant) were also found.

G monomers (coniferyl alcohol, m/z 179) were found more frequently than S monomers (sinapyl alcohol, m/z 209), while H units (*p*-coumaryl alcohol, m/z 149) were not detected (Figure 5), thus confirming previous results.[11] In both genotypes, lignin dimers tended to prevail in the rind and in the pith of immature internodes (YR and YP) in comparison to their content in mature internodes; trimers, in turn, tended to prevail in mature internodes.

In IACSP94-2094 plants, G monomers were more frequently detected in mature internodes than in immature internodes (Figure 5A). Under stressing conditions, G levels tended to decrease in mature internodes (rind). Dimers predominated in immature internodes (YR), and their frequency did not appear to be affected by water deficit. Among dimers, G(8-5)H (m/z 327) was the rarest, while S(8-O-4)G (m/z 435) was the most abundant. Among trimers, G(8-O-4)S(8-8)S (m/z 613) was the least frequent, detected only in mature internodes. In contrast, S(8-O-4)G(8-O-4)S (m/z 631) appeared to be the most frequent trimer, being absent only in the pith immature internodes. Structures G(8-O-4)G(8-5)G (m/z 553) and G(8-O-4)S(8-5)G (m/z 583) were found in immature internodes only under water restriction (MD and SD).

DOI: 10.1021/jf5061858
J. Agric. Food Chem. 2015, 63, 4708−4720

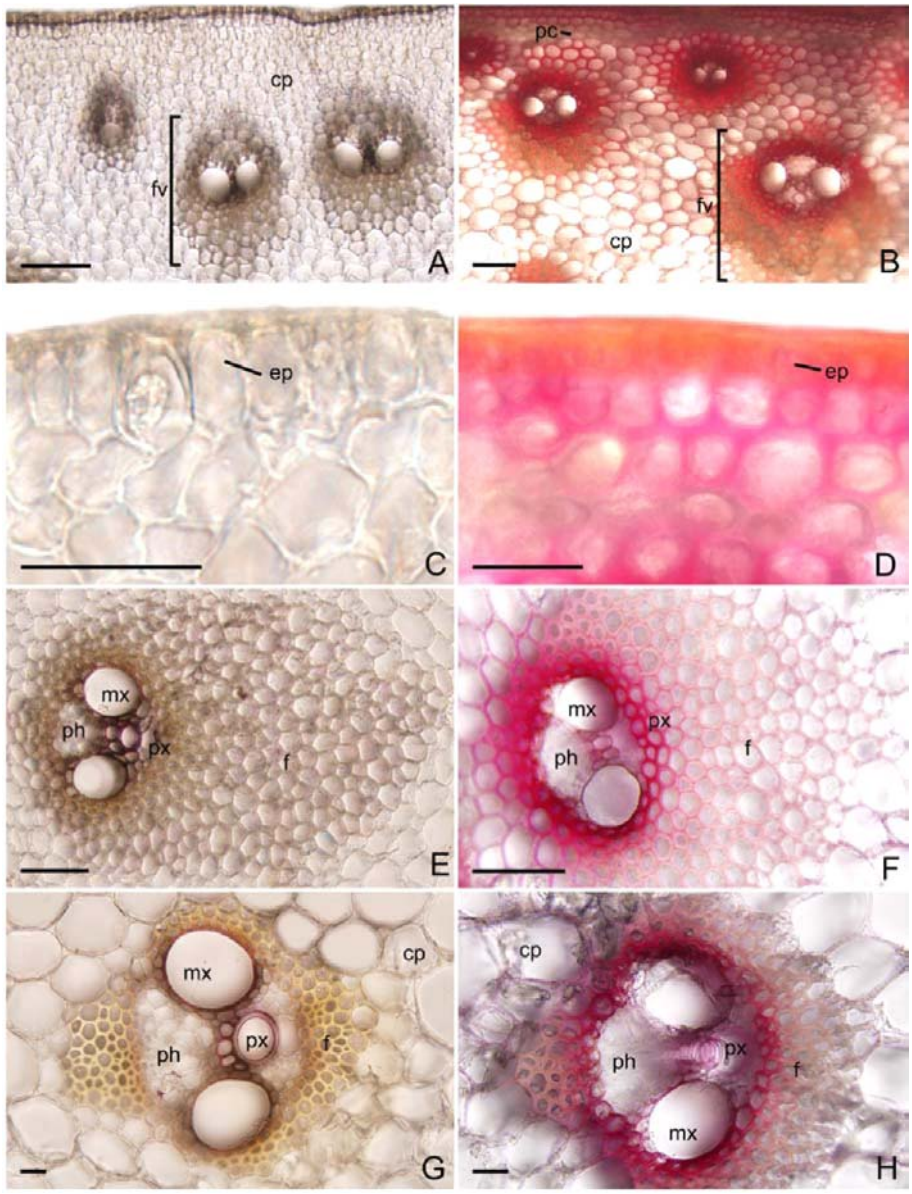

Figure 4. Transversal sections of different regions of sugarcane stems of genotype IACSP95-5000 submitted to acid phloroglucinol for lignin detection; (left column) immature internode; (right column) mature internode; (A, B) rind region; (C, D) detail of epidermis and adjacent cellular layers; (E, F) detail of rind vascular bundle; (G, H) detail of pith vascular bundle. Abbreviations: pc = parenchymal cell; ep = epidermis; f = fibers; mx = metaxylem; cp = chlorophyllin parenchyma; ph = phloem; vb = vascular bundle; px = protoxylem. Bars: (A, B and E, F) 50 μm; (C, D and G, H) 20 μm.

In the IACSP95-5000 genotype, G levels in immature and mature internodes appeared to be negatively affected by water deficit (Figure 5B). Dimers also tended to prevail in immature internodes; their abundance posed no apparent correlation with water stress. In mature internodes, G(8-O-4)S(8-5)G (m/z 583) and S(8-O-4)G(8-O-4)S (m/z 631) were the most abundant trimers. In this tissue region, the presence of G(8-O-4)G(8-5)G (m/z 553) was apparently influenced by the water regime, tending to be more frequent in MR and MP, under drought conditions (MD and SD). On the other hand, S(8-O-4)G(8-O-4)S (m/z 631) tended to be less frequent under water stress.

Lignin Content. Lignin content was positively associated with the maturation status of stem internodes, so that the amount of lignin was higher in mature internodes than in immature internodes (Figure 6). IACSP94-2094 genotype control plants featured lignin content 4.6 times higher in mature internodes in comparison to that in immature internodes (rind region); on the other hand, IACSP95-5000 genotype control plants posed a 3.2× ratio. In mature internodes, the pith was also approximately 2.7× as lignified as in immature internodes, in both sugarcane genotypes (Figure 6). Lignin contents measured in the stems of irrigated plants were similar in the two sugarcane genotypes analyzed, except for MR, which proved to be more lignified in IACSP94-2094, in comparison to that in IACSP95-5000 plants.

Water deficit has induced discrete lignin accumulation in immature internodes (YR and YP) in both sugarcane genotypes (Figure 6). In mature internodes, IACSP95-5000 plants featured significantly increased MR lignin content, on submission to severe water restriction (SD) (Figure 6B).

DOI: 10.1021/jf5061858
J. Agric. Food Chem. 2015, 63, 4708−4720

Table 3. Lignin Precursor Monomers and Oligomers and Respective *m/z* Values Obtained by UPLC-MS/MS

unit	structure	*m/z*
monomer	coniferyl aldehyde	177
	coniferyl alcohol (G)	179
	sinapyl aldehyde	207
	sinapyl alcohol (S)	209
dimer	G(8-5)H	327
	G(8-5)G	357
	S(8-8)S	417
	S(8-O-4)G	435
trimer	G(8-O-4)G(8-5)G	553
	G(8-O-4)S(8-5)G	583
	G(8-O-4)S(8-8)S	613
	S(8-O-4)G(8-O-4)S	631

Gene Expression. The analyses of the expression pattern of the genes coding for enzymes of the lignin biosynthesis pathway in sugarcane showed that the number of transcripts varied in accordance with the developmental phase of stem internodes, tissue type (rind or pith) and water regime (Figure 7). In the control plants, i.e. under irrigation, most analyzed genes were more strongly expressed in mature internodes (MR and/or MP), except for *Sh4CL2* and *ShCCoAOMT3* genes, which featured a higher number of transcripts in immature internodes for some tissues (Figure 7C,H). *ShCAD8* had similar expression patterns in immature and mature internodes (YR, YP, MR, and MP) in control plants (Figure 7L). When comparing transcript levels in the rind and in the pith, we observed that the expression of the analyzed genes was higher in the rind, independently of the maturation phase of stem internodes.

Water deficit has induced alterations in the expression of various genes in lignin biosynthesis (Figure 7). The expression patterns of all analyzed genes were similar in IACSP94-2094 and IACSP95-5000 plants, although stress response intensities differed. In a general way, severe water restriction (SD) has led to increased transcripts of various genes in immature internodes, mainly in YR. Under water stress, except for *ShCCoAOMT3* (Figure 7H) and *ShCAD8* (Figure 7L), all other genes were significantly more expressed in immature internodes (YR), in comparison to the control conditions, in at least one of the analyzed genotypes. Similarly, genes *ShPAL1*, *Sh4CL2*, *ShCOMT1*, *ShCCoAOMT3*, and *ShCCR1* also featured a higher number of transcripts, due to drought in YP (Figure 7A,C,F,H,J). In contrast, mature internodes presented an overall reduction in the expression of the analyzed genes, in comparison to watered control plants. Transcripts of *ShPAL1*, *ShC4H1*, *ShC3H1*, *ShCOMT1*, *ShCCoAOMT1*, *ShCCoAOMT3*, *ShF5H*, *ShCCR1*, and *ShCAD2* genes were significantly decreased in MP under stress, in one or both sugarcane genotypes (Figure 7A,B,E−K). Such reduction in the expression levels was also observed for *ShPAL1*, *ShC3H1*, *ShCOMT1*, *ShCCoAOMT1*, *ShCCoAOMT3*, *ShF5H*, and *ShCAD2* genes in MR, in comparison to irrigated control plants (Figures 7A,E−I,K). Apparently, *ShHCT-like* and *ShCAD8* were slightly affected or not affected at all by the drought, maintaining practically unaltered expression levels (Figure 7D,L). Figure S1 in the Supporting Information shows the summarized main changes in gene expression levels in plants submitted to severe water deficit (SD) and their effects on lignin content in stem internodes.

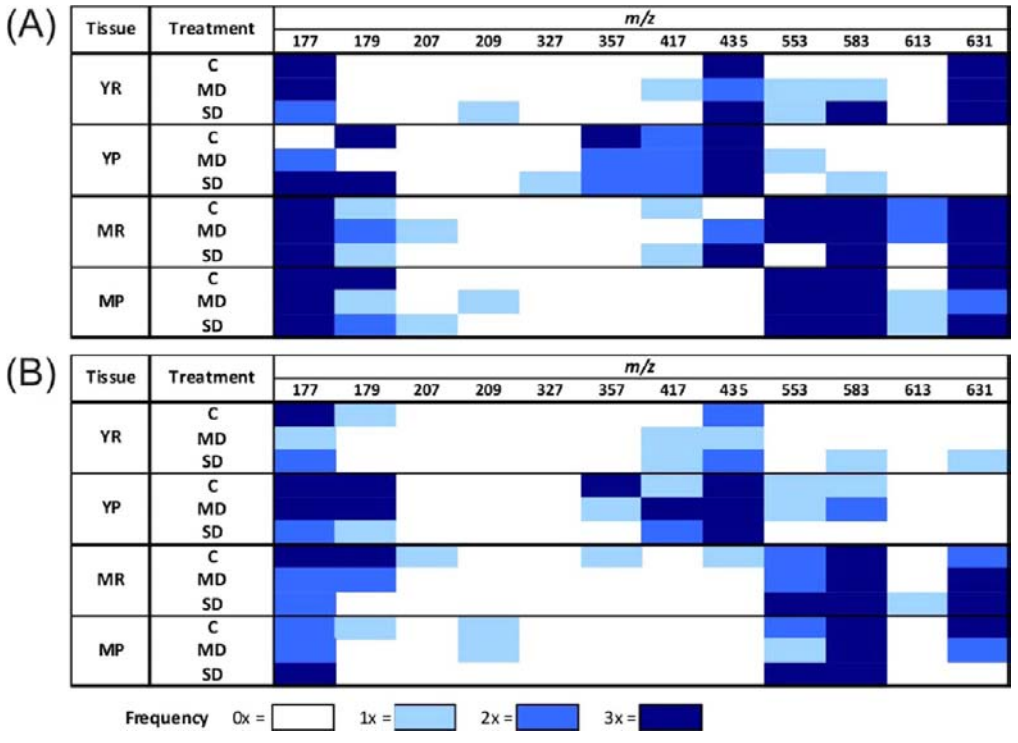

Figure 5. Soluble lignin detection pattern obtained by UPLC-MS analyses in plants of sugarcane genotypes IACSP94-2094 and IACSP95-5000 grown under different water regimes. The frequency of each structure is represented in the diagram by different hues, thus, 0× (white) indicates that the structure was not detected in any biological replicate, and 1×−3× indicate that the structure was detected in one, two, or three biological replicates. Abbreviations: YR = young rind; YP = young pith; MR = mature rind; MP = mature pith.

DOI: 10.1021/jf5061858
J. Agric. Food Chem. 2015, 63, 4708−4720

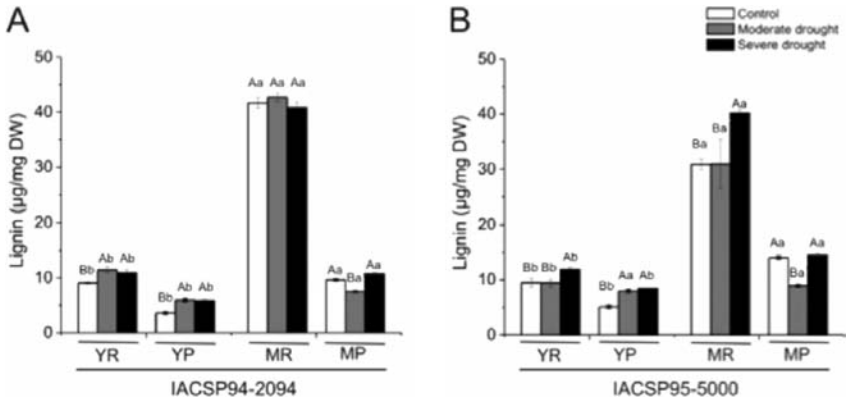

Figure 6. Lignin content in the rind and pith from the stem of plants of sugarcane genotypes IACSP94-2094 (A) and IACSP95-5000 (B) grown under different water regimes. Different uppercase letters indicate significant differences among the water regimes in the same internode, whereas different lowercase letters indicate differences among the internodes (immature or mature) under the same water regime. Data are means ± standard error of four or five replications. Abbreviations: YR = young rind; YP = young pith; MR = mature rind; MP = mature pith.

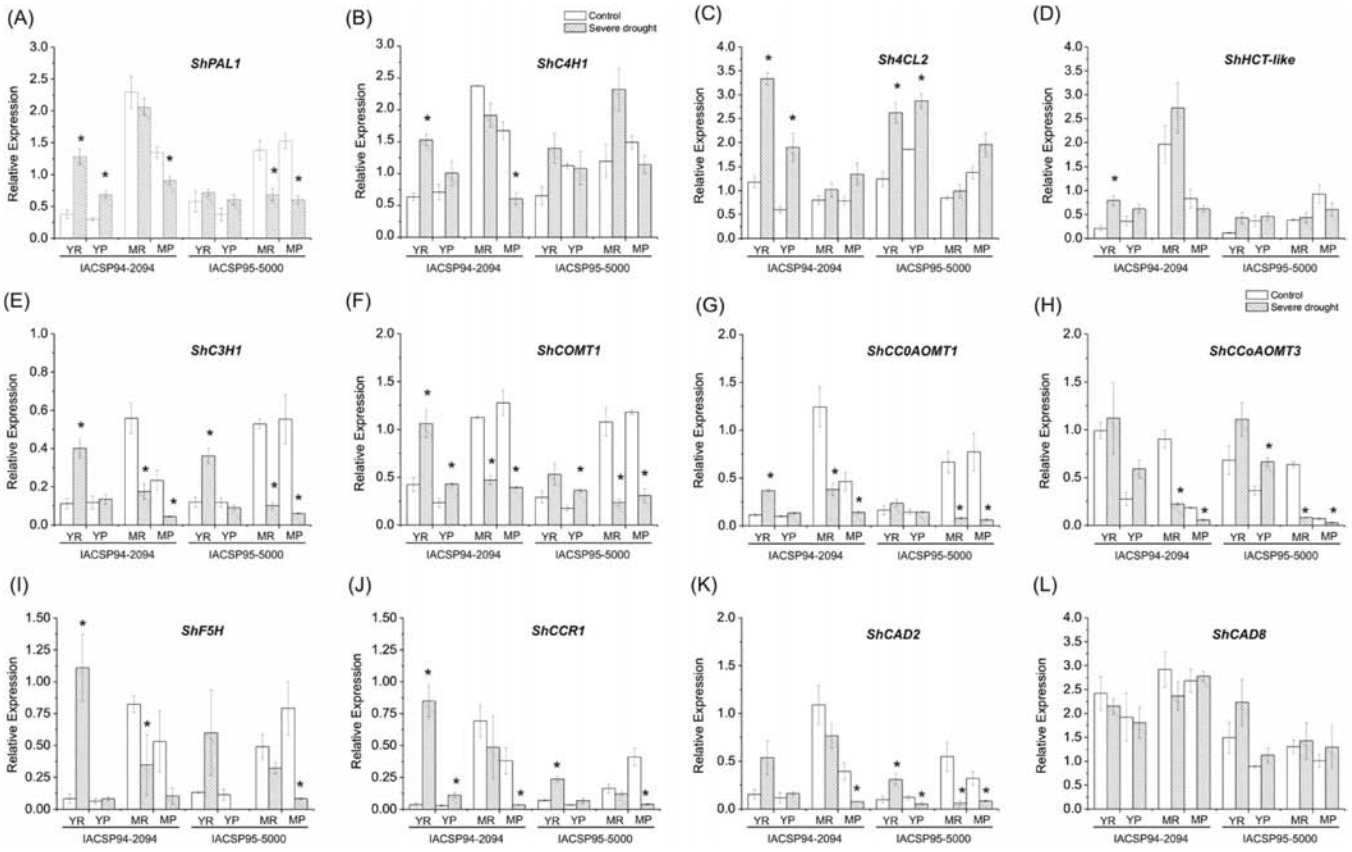

Figure 7. Relative expressions of lignin biosynthesis related genes in the pith and rind from the stem of plants of IACSP94-2094 and IACSP95-5000 sugarcane genotypes grown under different water regimes (A–L). Expression values were normalized by means of *GAPDH* as a reference gene; relative expression was calculated by the $\Delta\Delta C_t$ method. Severely stressed plants (SD) marked with an asterisk differ from the respective control plants (C) within the same genotype group. Data are means ± standard error of three replicates. Abbreviations: YR = young rind; YP = young pith; MR = mature rind; MP = mature pith.

DISCUSSION

Sugarcane bagasse is a material that is coproduced by sucro-alcohol industries, readily available for utilization in the production of cellulosic ethanol. The conversion of the vegetative biomass into ethanol is mainly limited by biomass recalcitrance to chemical, enzymatic, or microbial attack.[27,28] Studies involving gene manipulation in the lignin biosynthesis pathway have indicated that both polymer content and composition influence vegetative biomass recalcitrance.[27,29,30]

The present study has evaluated two commercial sugarcane genotypes, regarding the "modulating" effect of water deficit on lignin content and structure in the stem. Some papers have reported the effect of water stress on lignin biosynthesis in different plant species, indicating complex genetic regulation, the influence of the severity/time of exposure to stress, phenological phase, and organ/tissue of the plant, among other

DOI: 10.1021/jf5061858
J. Agric. Food Chem. 2015, 63, 4708–4720

factors.[14,15,31] As far as we are concerned, there is no available information on the mechanisms regulating lignin biosynthesis and deposition on the cellular wall or on how environmental stress, such as droughts, may affect the lignification process.

The sugarcane genotypes used in our study, IACSP94-2094 and IACSP95-5000, were affected by water stress in different manners. Although IACSP94-2094 genotype is deemed to be drought-resistant,[17,18] plants submitted to severe and prolonged water restriction presented significant reduction in all assessed biometric parameters (N_l, N_i, L_s, FM_s, DM_l, and DM_r), while IACSP95-5000 was less affected, posing decreased N_l, DM_l, and DM_r values (Table 2). The number of green leaves (N_l) and root biomass (DM_r) had the highest reductions, in both sugarcane genotypes: i.e., 39% and 31% in IACSP94-2094 plants and 51% and 35% in IACSP95-5000 plants, respectively. The impact of drought on sugarcane growth accounted for losses of up to 35%.[32]

Additionally, the low performance of IACSP94-2094 plants under water restriction might be related to severity and/or time of exposure to water stress, since only N_l was significantly reduced under moderate stress (MD). The reduction in the number of leaves and leaf senescence in sugarcane plants during water deficit might indicate a strategy to diminish transpiration surface, thus also mitigating energetic expenditure and ensuring basal tissue metabolism.[33−35]

The impact of water deficit on sugarcane productivity is related to specific plant growth stages. Some studies indicate that sugarcane becomes more vulnerable to water deficit during early growth, characterized by accelerated growth and tillering.[18,36] At the same time, other authors claim that higher susceptibility to drought occurs during the stem-lengthening phase, with significant reductions of both mass and sucrose accumulation.[33,37] Our results confirm that water restriction imposed during the stem-lengthening phase has caused stress, expressed in lower growth rates and consequent lower biomass production.

Sugarcane accumulates sucrose in its stem, raising contents as internodes mature.[38] Sucrose and reducing sugars account for the highest fraction of total soluble sugars present in the stem. The proportions of such sugars are altered throughout the different internode maturation stages, being negatively correlated to one another.[39] The results obtained for IACSP94-2094 and IACSP95-5000 plants confirm that in the early stages of development, when growth rates are at their apex, reducing sugar contents (fructose and glucose) were proportionally higher than sucrose contents in immature internodes. The opposite was observed during maturity, when sucrose accumulation was potentiated and reducing sugar contents became significantly low (Figure 2A−C).

Water stress is well known for negatively affecting photosynthesis in plants, as a result of stomatal and nonstomatal limitations.[40] Our data have clearly shown that low water availability has caused sugar balance alterations in the stem, which causes a major drain of photoassimilates in sugarcane. In immature internodes, the accumulation of sucrose contents and the reduction of fructose contents were simultaneously induced by lack of water in both genotypes (Figures 2A−C), which is probably related to reduced growth rates of these internodes during water deficit. On the other hand, the results obtained with Q117 sugarcane genotype revealed that water deficit did not cause significant alteration in the amount of sucrose and reducing sugars in young internodes.[41]

In mature internodes, the contents of sucrose and reducing sugars were not affected by water stress. Considering that photosynthesis is usually affected by drought and consequently the sucrose biosynthesis and export to the culms, the maintenance of the sugar pool in those internodes might be related to cleavage dynamics and sucrose cellular resynthesis, a process regulated by the activity of sucrose phosphate synthase, sucrose synthase, and invertase enzymes.[42] Additionally, our results are partially in agreement with those obtained by others,[41] demonstrating that, despite the absence of alteration in sucrose contents, glucose and fructose contents happened to increase in mature internodes of sugarcane plants during water deficit. The intensity and/or time of exposure to water stress, in addition to the genotypes employed, might explain the different physiological responses.

We aimed here to characterize water stress, rather than tolerance, as information in that respect is available solely for the IACSP94-2094 genotype.[17,18] Free proline contents in the stem were similar in irrigated control plants for both analyzed genotypes; under severe water deficit conditions, no significant alteration in the amount of that amino acid was detected in the stem (Figure 2D). Such results indicate that proline plays no osmoprotective role in the stem, in the event of prolonged water deficit, when the plant might recruit more effective mechanisms. Likewise, the adoption of proline as a biochemical indicator for water stress must be seen with caution;[43] when it comes to sugarcane, contents of such amino acid may vary according to severity and/or time of exposure to stress,[44] as well as the developmental phase of the plant.[45]

Our anatomy analyses are consistent with those previously described,[10] evidencing typical internode organization in two morphologically distinct regions: the rind, characterized by a great number of vascular bundles, and the pith, where predominates reserve parenchyma cells. An estimate of the number of vascular bundles in sugarcane internodes has shown that approximately 50% are located within 3 mm from the rind,[46] thus constituting a region naturally enriched with such types of cellular organization, a rather interesting object for the study of lignin biosynthesis.

A comparison of different lignin deposition patterns in stem internodes in two sugarcane genotypes showed that lignification in IACSP94-2094 plants occurs earlier than that in IACSP95-5000 plants (Figures 3 and 4). The analysis of immature internodes supports such findings: while only protoxylem was lignified in the vascular bundles of IACSP95-5000, both protoxylem and metaxylem were lignified in IACSP94-2094, in addition to the initial lignification of fibers and subepidermal layers. Likewise, parenchyma cells of mature internodes are also lignified, and xylem fibers feature rather thickened and lignified walls. Walsh et al.[46] have revealed that parenchyma cell walls are lignified as internodes mature; in the fourth internode the lignification level is around 5%, while in the tenth internode it may reach 60%.

The lignin contents found in the genotypes studied here confirmed that polymer accumulation varied according to internode maturation (immature or mature) and also according to the tissue region in the stem (rind or pith). Mature internodes were more lignified than immature internodes, and inside each internode, the rind featured higher lignin content than the pith, which was associated with the higher concentration of vascular bundles in the rind region of the internode and with progressive epidermal and hypodermal lignification. We have also observed that mature rind was up to

DOI: 10.1021/jf5061858
J. Agric. Food Chem. 2015, 63, 4708−4720

4.6 times as lignified as young rind in IACSP94-2094, whereas this increase was 3.2 times in IACSP95-5000; in the pith region, lignin content was 2.7 times higher in mature pith than in young pith, in both sugarcane genotypes (Figure 6). Higher rind lignification, as identified in sugarcane stems, is consistent with higher peroxidase activity rates detected in this region, which might be involved in lignin polymerization.[19]

Lignin biosynthesis is under a complex genetic control, resulting in different adaptive responses, which may vary during plant growth and development.[12,47] As for water stress, a number of studies have revealed that gene expression of the biosynthesis pathway and/or lignin content may be altered according to stress time and/or intensity,[15,16] organ and its specific regions,[13,14] and certain cellular types.[48]

The water stress imposed in our study induced significant accumulation of lignin in the rind and pith of immature internodes of both genotypes, in comparison to the respective irrigated control plants. Additionally, IACSP95-5000 plants submitted to severe drought have accumulated 30% more lignin in mature rind, in comparison to irrigated plants. The lignin accumulation in IACSP95-5000, particularly in the rind, might indicate a strategy to enhance xylem vessel resistance, so as to cope with higher tension during water deficit, by reducing water loss. Voelker et al.[49] have shown that the reduced lignification level of transgenic *Populus* spp. plants silenced to *4CL* gene increased xylem vulnerability to embolism.

Different methodologies,[50] among other major factors, such as tissue type, plant age,[48] and genotypic variation[51] may explain the differences found in the literature regarding lignin content in sugarcane. In the present study, lignin content was determined with thioglycolic acid and ranged from 0.4% in young pith to 4.2% in mature rind. Using the same method, de Souza et al.[48] found 4.9% in the leaves and 2.5% in the stem of young sugarcane plants. The high specificity associated with the method, added to the fact that a significant fraction of lignin in grasses has an acid-soluble property (thus remaining in solution during the precipitation phase in acid), might lead to underestimated total lignin values.[50] Regardless of method-related inquiries, our results demonstrate differential lignin accumulation in immature and mature internodes and also between the pith and the rind.

The analysis of soluble lignin in IACSP94-2094 and IACSP95-5000 has shown that, regardless of maturation level (young or mature) and stem region (rind or pith), the frequency of G monomer (coniferyl) was constantly higher than that of S (sinapyl). As observed by Bottcher et al.,[11] H units (*p*-hydroxyphenyl) were not found in sugarcane, probably due to low concentration (typically <5%), even in grasses.[52] Lignin oligomers identified in the present study were positively correlated to the maturation level of sugarcane internodes, so that dimers were more frequent in immature internodes, whereas trimers were more abundant in mature internodes (Figure 5). Similarly, Bottcher et al.[11] have observed that lignin oligomers were preferably accumulated in mature internodes in both sugarcane genotypes, owing to higher lignin deposition, associated with tissue maturation.

Our results also indicated that the oligomer profile varied between rind and pith. For instance, S(8-O-4)G was more abundant in young internodes and, relatively, was the only dimer found in the rind, while the pith featured other structures, such as G(8-5)G and S(8-8)S, in proportions similar to that of S(8-O-4)G. The frequency of some oligomers was also affected by water deficit, featuring structures such as S(8-8)S, G(8-O-4)G(8-5)G, and G(8-O-4)S(8-5)G in young rind solely under stressing conditions, while other oligomers such as G(8-O-4)G(8-5)G and G(8-O-4)S(8-8)S tended to be less abundant in mature rind, in comparison to those in the irrigated control.

Lignin structural complexity appears to be directly associated with the relative frequency of different interunit linkages, which in turn depend upon the abundance of each monomer during the polymerization process. Therefore, lignins constituted mainly by G units, as in conifers, contain a higher number of resistant linkages, such as 8-5, 8-8, 5-5 and 5-O-4, than lignin rich in S units and thus are more resistant to chemical degradation.[4] Unfortunately, we have not determined the ratio S/G, but given the consistencies between our results and those by Bottcher et al.,[11] the observed pattern is very likely to occur in the genotypes studied here.

Lignin deposition is associated with vegetative organ maturity and final differentiating stages of cellular types,[4] which naturally tends to raise the levels of gene expression of lignin biosynthesis in those regions. In irrigated control plants, we have observed that transcript accumulation in mature sugarcane internodes was higher than that in immature internodes (Figure 7). A comparative analysis between the expression profiles of the two sugarcane genotypes has evidenced that, in IACSP94-2094 plants, the abundance of transcripts in mature rinds was higher than that in IACSP95-5000 plants (except for *Sh4CL2* and *ShC3H1*). The high levels of expression observed in IACSP94-2094 support the results of the anatomical analysis of lignin, thus suggesting that this sugarcane genotype features a higher stem lignification level.

When plants of both sugarcane genotypes were submitted to severe water deficit (SD), there were significant alterations in the expression levels of most analyzed genes, with generalized increased transcripts in young internodes (except for *ShCAD8*) and reduced expression in mature internodes, as opposed to the findings in control plants, which tended to feature higher levels of gene expression of lignin biosynthesis in mature internodes (Figure 7). Such data were consistent with the higher lignin content (>60%, when compared to control plants) observed in the pith of young internodes for both sugarcane genotypes under water deficit (Figure 6).

On the other hand, reduced expression of most lignin biosynthesis genes (except for *ShC4H1*) in mature internodes of the stem under drought conditions fails to explain the approximately 30% increase of lignin content in mature rind of IACSP95-5000 plants, in comparison to that in irrigated sugarcane plants. The high-complexity genomes of modern sugarcane cultivars (allopolyploid hybrids), associated with possible functional redundancies among the various members of the same gene family,[11] might justify the apparent lack of correlation between low gene expression and high lignin content observed in this context.

Under severe water restriction, *ShF5H* and *ShCCR1* have proven to be the most differentially expressed genes in IACSP94-2094, approximately 13 and 24 times more expressed in young rind under severe water deficit in comparison with control plants, respectively (Figure 7I,J). *ShF5H* codes for a key enzyme in the production of lignin S units, and the accumulation of its transcripts in the rind region (rich in vascular bundles) might be related to intensified lignin deposition in young internodes induced by stress.

In conclusion, we have demonstrated here that lignin deposition in stem internodes is affected by severe water stress

DOI: 10.1021/jf5061858
J. Agric. Food Chem. 2015, 63, 4708−4720

in two sugarcane genotypes. The results on the lignin content and anatomical characterization indicate that, under normal growth conditions, IACSP94-2094 plants are more lignified than IACSP95-5000 plants. The gene expression profile related to lignin biosynthesis confirmed that the accumulation of transcripts of the analyzed genes rises as internodes mature and that, generally speaking, the expression level is constantly higher in the rind than in the pith. The approximately 60% increase in lignin content induced by water deficit in the pith of young internodes, in both genotypes, is positively related to the accumulation of *Sh4CL2* and *ShCOMT1* transcripts, thus suggesting that those genes might play a crucial role in the control of lignin deposition in sugarcane. Our data reinforce the complexity of the mechanisms involved in the spatiotemporal control of lignin deposition.

Regarding the differences in lignin content between rind and pith, there is a correlation between the topochemical distribution of lignin and hydroxycinnamic acids and the efficiency of the enzymatic hydrolysis of sugars released from sugarcane bagasse biomass.[53] Pith samples were promptly hydrolyzed by cellulase, reaching a 63% cellulose conversion after a 72 h hydrolysis, whereas rind samples reached only a 20% conversion. On the other hand, the rind treatment with an acetic/chlorite acid solution, so as to remove lignin and hydroxycinnamic acids, enabled significant increase in cellulose conversion: i.e., approximately 60% after a 4 h hydrolysis. Altogether, such data confirm that sugarcane internode rinds are more recalcitrant than piths and that their high endurance to cellular wall saccharification is probably associated with higher rind lignification, owing to the abundance of vessels in the xylem and fibers. Therefore, our data show that water stress changes lignin deposition in these tissues and therefore might affect recalcitrance and hydrolysis efficiency. Complementary studies are required to further investigate the effect of these changes on the final quality of sugarcane lignocellulosic biomass.

■ ASSOCIATED CONTENT

Supporting Information

Figure S1, showing water replacement in plants of sugarcane genotypes IACSP94-2094 and IACSP95-5000 grown under moderate (MD) and severe drought (SD). The Supporting Information is available free of charge on the ACS Publications website at DOI: 10.1021/jf5061858.

■ AUTHOR INFORMATION

Corresponding Author

*P.M.: e-mail, pmazza@unicamp.br; tel, +55 19 35216213.

Funding

The authors thank Fundação de Amparo à Pesquisa do Estado de São Paulo for financial support (FAPESP, 2008/58035-6) and the Conselho Nacional de Desenvolvimento Científico e Tecnológico (CNPq) for doctorate (A.B.S.) and research (P.M.) fellowships.

Notes

The authors declare no competing financial interest.

■ ACKNOWLEDGMENTS

The authors thank Laerti Reis Roque and Viviam Moura da Silva for help the lignin analyses.

■ REFERENCES

(1) Marques, F. O alvo é o bagaço - subproduto abundante da indústria da cana dá vantagem competitiva ao Brasil na busca do etanol de segunda geração. *Pesq. FAPESP* **2009**, *163*, 16−20.

(2) Pandey, A.; Soccol, C. R.; Nigam, P.; Soccol, V. T. Biotechnological potential of agro-industrial residues. I: sugarcane bagasse. *Bioresour. Technol.* **2000**, *74*, 69−80.

(3) Keating, J. D.; Panganiban, C.; Mansfield, S. D. Tolerance and adaptation of ethanologenic yeasts to lignocellulosic inhibitory compounds. *Biotechnol. Bioeng.* **2006**, *93*, 1196−1206.

(4) Boerjan, W.; Ralph, J.; Baucher, M. Lignin biosynthesis. *Annu. Rev. Plant Biol.* **2003**, *54*, 519−546.

(5) Ralph, J.; Lundquist, K.; Brunow, G.; Lu, F.; Kim, H.; Schatz, P. F.; Marita, J. M.; Hatfield, R. D.; Ralph, S. A.; Christensen, J. H.; Boerjan, W. Lignins: natural polymers from oxidative coupling of 4-hydroxyphenyl- propanoids. *Phytochem. Rev.* **2004**, *3*, 29−60.

(6) Morreel, K.; Ralph, J.; Kim, H.; Lu, F. C.; Goeminne, G.; Ralph, S.; Messens, E.; Boerjan, W. Profiling of oligolignols reveals monolignol coupling conditions in lignifying poplar xylem. *Plant Physiol.* **2004**, *136*, 3537−3549.

(7) Campbell, M. M.; Sederoff, R. R. Variation in lignin content and composition - mechanism of control and implications for the genetic improvement of plants. *Plant Physiol.* **1996**, *110*, 3−13.

(8) He, L.; Terashima, N. Formation and structure of lignin in monocotyledons. III. Heterogeneity of sugarcane (*Saccharum officinarum*) lignin with respect to the composition of structural units in different morphological regions. *J. Wood Chem. Technol.* **1990**, *10*, 435−459.

(9) He, L.; Terashima, N. Formation and structure of lignin in monocotyledons. IV. Deposition process and structural diversity of the lignin in the cell wall of sugarcane and rice plant studied by ultraviolet microscopic spectroscopy. *Holzforschung* **1991**, *45*, 191−198.

(10) Moore, P. H. 1987. Anatomy and morphology. In *Sugarcane improvement through breeding*; Heinz, D. J., Ed.; Elsevier: Amsterdam, The Netherlands, 1987; pp 85−142.

(11) Bottcher, A.; Cesarino, I.; Santos, A. B.; Vicentini, R.; Mayer, J. L. S.; Vanholme, R.; Morreel, K.; Goemmine, G.; Moura, J. C. M. S.; Nobile, P. M.; Carmello-Guerreiro, S. M.; Anjos, I. A.; Creste, S.; Boerjan, W.; Landell, M. G. A.; Mazzafera, P. Lignification in sugarcane: biochemical characterization, gene discovery and expression analysis in two genotypes contrasting for lignin content. *Plant Physiol.* **2013**, *163*, 1539−1557.

(12) Moura, J. C. M. S.; Bonine, C. A. V.; Viana, J. D. F.; Dornelas, M. C.; Mazzafera, P. Abiotic and biotic stresses and changes in the lignin content and composition in plants. *J. Integr. Plant Biol.* **2010**, *52*, 360−376.

(13) Vincent, D.; Lapierre, C.; Pollet, B.; Cornic, G.; Negroni, L.; Zivy, M. Water deficits affect caffeate *O*-methyltransferase, lignification, and related enzymes in maize leaves. A proteomic investigation. *Plant Physiol.* **2005**, *137*, 949−960.

(14) Fan, L.; Linker, R.; Gepstein, S.; Tanimoto, E.; Yamamoto, R.; Neumann, P. M. Progressive inhibition by water deficit of cell wall extensibility and growth along the elongation zone of maize roots is related to increased lignin metabolism and progressive stelar accumulation of wall phenolics. *Plant Physiol.* **2006**, *140*, 603−612.

(15) Yang, L.; Wang, C. C.; Guo, W. D.; Li, X. B.; Lu, M.; Yu, C. L. Differential expression of cell wall related genes in the elongation zone of rice roots under water deficit. *Russ. J. Plant Physiol.* **2006**, *53*, 390−395.

(16) Yoshimura, K.; Masuda, A.; Kuwano, M.; Yokota, A.; Akashi, K. Programmed proteome response for drought avoidance/tolerance in the root of a C_3 xerophyte (wild watermelon) under water deficits. *Plant Cell Physiol.* **2008**, *49*, 226−241.

(17) Machado, R. S.; Ribeiro, R. V.; Marchiori, P. E. R.; Machado, D. F. S. P.; Machado, E. C.; Landell, M. G. A. Biometric and physiological responses to water deficit in sugarcane at different phenological stages. *Pesqui. Agropecu. Bras.* **2009**, *44*, 1575−1582.

(18) Ribeiro, R. V.; Machado, R. S.; Machado, E. C.; Machado, D. F. S. P.; Magalhães Filho, J. R.; Landell, M. G. A. Revealing drought-

DOI: 10.1021/jf5061858
J. Agric. Food Chem. 2015, 63, 4708−4720

resistance and productive patterns in sugarcane genotypes by evaluating both physiological responses and stalk yield. *Exp. Agric.* **2013**, *49*, 212−224.
(19) Cesarino, I.; Araujo, P.; Mayer, J. L. S.; Leme, A. F. P.; Mazzafera, P. Enzymatic activity and proteomic profile of class III peroxidases during sugarcane stem development. *Plant Physiol. Biochem.* **2012**, *55*, 66−76.
(20) Bates, L. S.; Waldren, R. P.; Teare, I. D. Rapid determination of free proline for water-stress studies. *Plant Soil* **1973**, *39*, 205−207.
(21) Johansen, D. A. *Plant microtechnique*; McGraw-Hill: New York, 1940.
(22) Kiyota, E.; Mazzafera, P.; Sawaya, A. C. H. F. Analysis of soluble lignin in sugarcane by ultrahigh performance liquid chromatography-tandem mass spectrometry with a do-it-yourself oligomer database. *Anal. Chem.* **2012**, *84*, 7015−7020.
(23) Lange, B. M.; Lapierre, C.; Sandermann, H. Elicitor-induced spruce stress lignin - structural similarity to early developmental lignins. *Plant Physiol.* **1995**, *108*, 1277−1287.
(24) Chang, S.; Puryear, J.; Cairney, J. A simple and efficient method for isolating RNA from pine trees. *Plant Mol. Biol. Rep.* **1993**, *11*, 113−116.
(25) Livak, K. J.; Schmittgen, T. D. Analysis of relative gene expression data using real-time quantitative PCR and the $2^{-\Delta\Delta Ct}$ method. *Methods* **2001**, *25*, 402−408.
(26) Iskandar, H.; Simpson, R.; Casu, R.; Bonnett, G.; Maclean, D.; Manners, J. Comparison of reference genes for quantitative real-time polymerase chain reaction analysis of gene expression. *Plant Mol. Biol. Rep.* **2004**, *22*, 325−337.
(27) Chen, F.; Dixon, R. A. Lignin modification improves fermentable sugar yields for biofuel production. *Nat. Biotechnol.* **2007**, *25*, 759−761.
(28) Himmel, M. E.; Ding, S.-Y.; Johnson, D. K.; Adney, W. S.; Nimlos, M. R.; Brady, J. W.; Foust, T. D. Biomass recalcitrance: engineering plants and enzymes for biofuels production. *Science* **2007**, *315*, 804−807.
(29) Davison, B. H.; Drescher, S. R.; Tuskan, G. A.; Davis, M. F.; Nghiem, N. P. Variation of S/G ratio and lignin content in a *Populus* family influences the release of xylose by dilute acid hydrolysis. *Appl. Biochem. Biotechnol.* **2006**, *130*, 427−435.
(30) DeMartini, J. D.; Pattathil, S.; Miller, J. S.; Li, H. J.; Hahn, M. G.; Wyman, C. E. Investigating plant cell wall components that affect biomass recalcitrance in poplar and switchgrass. *Energy Environ. Sci.* **2013**, *6*, 898−909.
(31) Alvarez, S.; Marsh, E. L.; Schroeder, S. G.; Schachtman, D. P. Metabolomic and proteomic changes in the xylem sap of maize under drought. *Plant, Cell Environ.* **2008**, *31*, 325−340.
(32) Inman-Bamber, N. G. Sugarcane water stress criteria for irrigation and drying off. *Field Crops Res.* **2004**, *89*, 107−122.
(33) Inman-Bamber, N. G.; Smith, D. M. Water relations in sugarcane and response to water deficits. *Field Crops Res.* **2005**, *92*, 185−202.
(34) Smit, M. A.; Singels, A. The response of sugarcane canopy development to water stress. *Field Crops Res.* **2006**, *98*, 91−97.
(35) Inman-Bamber, N. G.; Bonnett, G. D.; Spillman, M. F.; Hewitt, M. L.; Jackson, J. Increasing sucrose accumulation in sugarcane by manipulating leaf extension and photosynthesis with irrigation. *Aust. J. Agric. Res.* **2008**, *59*, 13−26.
(36) Ramesh, P. Effect of different levels of drought during the formative phase on growth parameters and its relationship with dry matter accumulation in sugarcane. *J. Agron. Crop Sci.* **2000**, *185*, 83−89.
(37) Robertson, M. J.; Inman-Bamber, N. G.; Muchow, R. C.; Wood, A. W. Physiology and productivity of sugarcane with early and mid-season water deficit. *Field Crops Res.* **1999**, *64*, 211−227.
(38) Rose, S.; Botha, F. C. Distribution patterns of neutral invertase and sugar content in sugarcane internodal tissues. *Plant Physiol. Biochem.* **2000**, *38*, 819−824.
(39) Pan, Y. Q.; Luo, H. L.; Li, Y. R. Soluble acid invertase and sucrose phosphate synthase: Key enzymes in regulating sucrose accumulation in sugarcane stalk. *Sugar Tech* **2009**, *11*, 28−33.
(40) Ghannoum, O. C4 photosynthesis and water stress. *Ann. Bot.* **2009**, *103*, 635−644.
(41) Iskandar, H. M.; Casu, R. E.; Fletcher, A. T.; Schmidt, S.; Xu, J.; Maclean, D. J.; Manners, J. M.; Bonnett, G. D. Identification of drought-response genes and a study of their expression during sucrose accumulation and water deficit in sugarcane culms. *BMC Plant Biol.* **2011**, *11*, 12.
(42) Botha, F. C.; Black, K. G. Sucrose phosphate synthase and sucrose synthase activity during maturation of internodal tissue in sugarcane. *Aust. J. Plant Physiol.* **2000**, *27*, 81−85.
(43) Bertolli, S. C.; Mazzafera, P.; Souza, G. M. Why is it so difficult to identify a single indicator of water stress in plants? A proposal for a multivariate analysis to assess emergent properties. *Plant Biol.* **2014**, *16*, 578−585.
(44) Cia, M. C.; Guimaraes, A. C. R.; Medici, L. O.; Chabregas, S. M.; Azevedo, R. A. Antioxidant responses to water deficit by drought-tolerant and -sensitive sugarcane varieties. *Ann. Appl. Biol.* **2012**, *161*, 313−324.
(45) Queiroz, R. J. B.; Santos, D. M. M.; Ferraudo, A. S.; Carlin, S. D.; Silva, M. D. Biochemical and physiological responses of sugarcane cultivars to soil water deficiencies. *Sci. Agric.* **2011**, *68*, 469−476.
(46) Walsh, K. B.; Sky, R. C.; Brown, S. M. The anatomy of the pathway of sucrose unloading within the sugarcane stalk. *Funct. Plant Biol.* **2005**, *32*, 367−374.
(47) Rogers, L. A.; Campbell, M. M. The genetic control of lignin deposition during plant growth and development. *New Phytol.* **2004**, *164*, 17−30.
(48) de Souza, A. P.; Leite, D. C. C.; Pattathil, S.; Hahn, M. G.; Buckeridge, M. S. Composition and structure of sugarcane cell wall polysaccharides: implications for second-generation bioethanol production. *BioEnergy Res.* **2013**, *6*, 564−579.
(49) Voelker, S. L.; Lachenbruch, B.; Meinzer, F. C.; Kitin, P.; Strauss, S. H. Transgenic poplars with reduced lignin show impaired xylem conductivity, growth efficiency and survival. *Plant, Cell Environ.* **2011**, *34*, 655−668.
(50) Hatfield, R.; Fukushima, R. Can lignin be accurately measured? *Crop Sci.* **2005**, *45*, 832−839.
(51) Masarin, F.; Gurpilhares, D. B.; Baffa, D. C. F.; Barbosa, M. H. P.; Carvalho, W.; Ferraz, A.; Milagres, A. M. F. Chemical composition and enzymatic digestibility of sugarcane clones selected for varied lignin content. *Biotechnol. Biofuels* **2011**, *4*, 55.
(52) Vanholme, R.; Morreel, K.; Darrah, C.; Oyarce, P.; Grabber, J. H.; Ralph, J.; Boerjan, W. Metabolic engineering of novel lignin in biomass crops. *New Phytol.* **2012**, *196*, 978−1000.
(53) Siqueira, G.; Milagres, A. M. F.; Carvalho, W.; Koch, G.; Ferraz, A. Topochemical distribution of lignin and hydroxycinnamic acids in sugar-cane cell walls and its correlation with the enzymatic hydrolysis of polysaccharides. *Biotechnol. Biofuels* **2011**, *4*, 7.

DOI: 10.1021/jf5061858
J. Agric. Food Chem. 2015, 63, 4708−4720

JOURNAL OF AGRICULTURAL AND FOOD CHEMISTRY

Article

pubs.acs.org/JAFC

Isolation and Characterization of a Novel Imidacloprid-Degrading *Mycobacterium* sp. Strain MK6 from an Egyptian Soil

Mahrous M. Kandil,*[,†] Carmen Trigo,[‡] William C. Koskinen,[‡] and Michael J. Sadowsky[‡,§]

[†]Department of Soil and Water, Faculty of Agriculture, Alexandria University, Alexandria 21545, Egypt

[‡]Department of Soil, Water, and Climate, and [§]BioTechnology Institute, University of Minnesota, St. Paul, Minnesota 55108, United States

ABSTRACT: Thus far, only a small number and types of bacteria with limited ability in degrading imidacloprid have been reported. Also, genes regulating imidacloprid (IMDA) degradation have yet to be discovered. To study this in more detail, an enrichment technique was used to isolate consortia and pure cultures of IMDA-degrading bacteria. Through this approach, we successfully isolated a novel bacterium capable of completely degrading IMDA as a sole nitrogen source. The bacterium was subsequently identified as *Mycobacterium* sp. strain MK6 by sequence analysis of its 16S rRNA gene (Genbank accession number KR052814). BLASTn searches indicated that 16S rRNA gene from *Mycobacterium* sp. strain MK6 was 99% identical to several *Mycobacterium* spp. *Mycobacterium* sp. strain MK6 transformed 99.7% added IMDA (150 μg mL^{-1}) in <2 weeks ($t_{1/2}$ = 1.6 days) to 6-chloronicotinic acid (6-CNA) as its major metabolite. Although the isolated strain and mixed bacterial consortia were able to degrade IMDA, they failed to grow further on 6-CNA, indicating a lack of IMDA mineralization to carbon dioxide. Small amounts of the desnitro-olefin and desnitro-degradates of IMDA were observed during the incubation but did not accumulate in culture medium.

KEYWORDS: *imidacloprid, 6-chloronicotinic acid, desnitro-olefin, Mycobacterium sp. strains, biodegradation, HFERP*

INTRODUCTION

Insecticides are globally used in agriculture to combat the loss of crops as a result of attack by microbial and insect pests. Insect damage to plants is a severe problem and results in the annual use of 940 million pounds of active ingredients worldwide.[1] It has been reported, however, that more than 99% of applied pesticides do not reach their target pests and may affect non-target species or contaminate the environment.[2] Following their deposition, many factors control the fate of pesticides in the environment, including retention, transport, and transformation processes.[3−5]

The interaction of pesticides with different environmental abiotic and biotic factors results in the transformation of parent compounds. Microorganisms use many pesticides as a source of carbon, nitrogen, and energy, often transforming them into carbon dioxide, water, and diverse sets of metabolites.[6−8] These compounds may be less or sometimes more toxic to target and non-target pests and organisms.[6] For instance, to determine the effect of insecticides on soil microorganisms, various assays, such as nitrification, denitrification, or N_2 fixation, have been commonly used.[9−11] Cycoń et al.[12] used two culture-independent [phospholipid fatty acid analysis (PLFA) and polymerase chain reaction−denaturing gradient gel electrophoresis (PCR-DGGE)], and culture-dependent [community-level physiological profiling (CLPP)] approaches to show that imidacloprid [1-(6-chloro-3-pyridylmethyl)-*N*-nitroimidazolidin-2-ylideneamine (IMDA)] induced significant changes in the composition of microbial communities and their metabolic activity, which, in turn, can influence the maintenance of soil quality.

IMDA is one of the most widely used neonicotinoid insecticides in agriculture.[13−17] While IMDA is mainly applied via foliar application for insect control, it is also used as a seed dressing or stem treatment.[14] IMDA is characterized by variable persistence in soil, with a half-life up to 229 days in the field.[18] In contrast, Wu et al.[19] found under laboratory conditions that the degradation of IMDA was rapid, with half-lives of 4−5 days. The persistence of IMDA in water increased with increasing application rates and pH values.[20] In aquatic environments, it was found that IMDA was more persistent in sediment than in water, with half-lives of 160 and 30 days, respectively.[21−24]

The persistence of IMDA in soil depends upon different physicochemical and biological parameters, such as organic matter, pH, temperature, crops, time, and microbial activity. Oi[25] and Cox et al.[26] established that sorption increased with contact time in soil, thereby decreasing potential availability to degrading organisms in soil. Decreased availability, would, in turn, increase persistence in soil. Dissolved organic carbon reduces IMDA sorption by competing with the pesticide molecules for sorption sites on the soil surface, increasing availability for degradation by microorganism and for leaching of IMDA and potentially increasing groundwater contamination.[27]

The metabolism of IMDA has been studied mainly in plants and mammals, and the proposed pathways for IMDA transformation have mostly been based on studies performed using eukaryotes.[28] However, a few studies have focused on the transformation of IMDA by pure or mixed cultures of soil microorganisms.[29−32] It is crucial to isolate and identify

Received: February 8, 2015
Revised: April 27, 2015
Accepted: May 1, 2015
Published: May 1, 2015

ACS Publications © 2015 American Chemical Society

DOI: 10.1021/acs.jafc.5b00754
J. Agric. Food Chem. 2015, 63, 4721−4727

microorganisms capable of degrading different pesticides for their potential use in bioremediation strategies either directly or via use of their enzymes.

The objectives of this study were to (1) isolate mixed cultures of bacteria-degrading IMDA from an Egyptian soil, (2) purify and characterize unique isolates with the ability to transform IMDA, and (3) identify IMDA metabolites produced during the degradation process. Results of this study are crucial for our understanding of IMDA transformation in the environment and for the development of possible bioremediation strategies.

MATERIALS AND METHODS

Chemicals and Pesticide. Analytical standards of IMDA (99.5% purity) and 6-chloronicotinic acid (6-CNA; 99.5% purity) were purchased from Sigma-Aldrich (St, Louis, MO) and desnitro-imidacloprid 1-(2-chloro-pyridin-5-yl-methyl)-2-imino-imidazolidine (DSN-IMDA; >97% purity), and desnitro-olefin imidacloprid 1-(6-chloro-pyridin-3yl-methyl)-*N*-nitro-1*H*-imidazol-2-imine (DSN-olefin−IMDA; >97% purity) were provided by Bayer Corporation (Stilwell, KS). IMDA and metabolite stock solutions (50 mg mL^{-1}) were prepared in high-performance liquid chromatography (HPLC)-grade acetonitrile (ACN) to ensure full solubility and were stored in the dark at 4 °C until used.

Soil Sample Collection. Soil samples were collected from the Abis Agricultural Research Farm, Alexandria University, Alexandria, Egypt. Five surface (top 15 cm) soil samples of about 1 kg each were collected randomly from an area following a traditional agricultural rotation farming system of wheat and clover. The area was selected on the basis of the farm's record showing no history of IMDA application for the 5 years prior to sampling. Samples were collected using a bleach-sterilized hand shovel, placed in sterile polyethylene bottles, transferred to the lab on ice, and stored at 4 °C until used. The soil samples were mixed to form a composite sample that was used within 24 h for IMDA enrichment cultures. Following standard methods of soil analysis,[33] the composite soil sample was classified as a sandy clay loam texture of 27.9% clay, 10.1% silt, and 62.0% sand with pH 7.6, electrical conductivity (EC), 1.52 mS cm^{-1}; organic matter, 0.75%; and cation-exchange capacity (CEC), 33 $cmol^{(+)}$ kg^{-1} of soil.

Culture Medium and Growth Conditions. An enrichment culture technique was used to isolate IMDA-degrading bacteria from the soil described above. Isolation and degradation experiments were conducted using R-salts minimal medium (RSM) as previously described.[34] The liquid RSM consists of solutions (1) 67.0 mL of 1 M KH_2PO_4 (pH 6.9), (2) 5 mL of R-salt mixture (16.0 g of $MgSO_4 \cdot 7H_2O$, 0.4 g of $FeSO_4 \cdot 7H_2O$, and 0.8 mL of HCl per 200 mL of H_2O), (3) 200 μL of 1 M $CaCl_2 \cdot 2H_2O$, and (4) 1.0 mL of trace element solution (10.0 mg of $ZnSO_4 \cdot 7H_2O$, 3.0 mg of $MnCl_2 \cdot 4H_2O$, 30 mg of H_3BO_4, 20.0 mg of $CoCl_2 \cdot 6H_2O$, 1.0 mg of $CuCl_2 \cdot 2H_2O$, 2.0 mg of $NiCl_2 \cdot 6H_2O$, and 3.0 mg of $Na_2MoO_4 \cdot 2H_2O$ per liter). Glucose stock solution (20%) was prepared and filter-sterilized by polytetrafluoroethylene (PTFE) membrane filters (0.22 μm) and stored at 4 °C. Stock solution (10%) of ammonium nitrate (NH_4NO_3) was prepared. These solutions were autoclaved separately at 121 °C for 20 min and mixed after cooling to 60 °C in a water bath, as needed. Solutions of glucose, NH_4NO_3, and IMDA were added by PTFE syringe filters, as described below.

Isolation of IMDA-Degrading Bacteria by Enrichment Techniques. All experiments were prepared under aseptic conditions. IMDA, $C_9H_{10}ClN_5O_2$, contains carbon and nitrogen on its pyridine and imidazolidine rings and side chain, which might be used as a source of carbon, nitrogen, or both for soil microorganisms. Therefore, various enrichment cultures with or without carbon and nitrogen sources were prepared to isolate bacteria using IMDA as a sole N or C source or both, including all possible control treatments. Nitrogen-free RSM was supplemented with 150 μg mL^{-1} IMDA as a sole nitrogen source and 2 g L^{-1} glucose (10 mL of 20% stock solution) as a carbon source. Carbon-free RSM was supplemented with 150 μg mL^{-1} IMDA as a carbon source and 1 g L^{-1} NH_4NO_3 (10 mL of 10% stock solution) as a nitrogen source.

Enrichment cultures of treatments described above were conducted in 250 mL Erlenmeyer flasks containing 100 mL of respective RSM inoculated with 5 g of fresh weight soil and incubated in the dark at 27 °C on a G24 (New Brunswick, NJ) environmental incubator shaker at 150 rpm for a 3 week period for the first run. This period was implemented to increase the chance of creating a favorable condition for IMDA-degrading bacteria while building a growth-limiting culture for other soil microorganisms after they consume soil organic matter and nutrients, thus ensuring the adaptability of IMDA-degrading bacteria to IMDA and its degradation byproducts. Successive enrichment subcultures were renewed every 2 weeks by transferring 1 mL from the old culture into a fresh enrichment flask containing 100 mL of the corresponding treatment medium. This step was repeated 5 more times to eliminate any impurities of organic matter originating from the soil sample and to attempt to isolate a mixed culture of IMDA-degrading microorganisms.

Isolation and Purification of IMDA-Degrading Bacterial Isolates. A microbial consortium isolated on IMDA was examined for growth and IMDA degradation. After confirmation of the ability of the consortium to degrade IMDA, individual bacterial isolates were obtained by serial dilution and pour plating of the consortium onto RSM solid medium supplemented with 1.5% Noble agar and IMDA (150 μg mL^{-1}) as the sole nitrogen source. Plates were incubated at 28 °C for 15 days. On the basis of morphological features, discrete unique bacterial colonies were picked and further purified by successive streaking on the same medium. This process was repeated several times to ensure isolation of pure cultures and the ability of isolates to grow on IMDA as a sole N source. Pure cultures were preserved in 20% sterile glycerol and stored at −70 °C until used.

IMDA Degradation Assay and Its Kinetics. The consortium and later individual pure culture isolates were tested for their ability to degrade 150 μg mL^{-1} IMDA in RSM liquid medium. Growth was determined by measuring an optical density at 600 nm (OD_{600}), and degradation was determined from analysis of IMDA in solution. Initially, the IMDA concentration in the supernatant of cultures was monitored spectrophotometrically at 270 nm,[28,35] followed by HPLC analysis under the conditions described below. For this assay, 250 mL flasks containing 100 mL of RSM liquid media were inoculated with individual isolates or a consortium and maintained for 15 days under the incubation conditions described above. Aliquots (5 mL) were taken every 2 days under aseptic conditions for measuring bacterial growth by OD_{600} and IMDA concentration in the culture medium. The kinetic parameters for IMDA degradation were calculated using the exponential formula $C_t = C_o e^{kt}$, where C_t is the concentration of IMDA at a time t, C_o is its initial concentration, k is its decay constant, and t is its half-life time ($t_{1/2}$).

HPLC Analysis for IMDA and Its Degradation Products. Culture samples were centrifuged at 10000*g* for 10 min to separate cell pellets from the supernatant. IMDA was measured in the supernatant by HPLC using a Waters HPLC (Milford, MA) with a reverse-phase C-18 (RP18) symmetry shield column (Waters−Millipore) (3.9 mm × 150 cm) and an ultraviolet (UV) detector. A 1.0 mL aliquot of growth medium was taken under aseptic conditions, centrifuged to remove bacterial cells, and filtered through a 0.22 μm sterile Millipore membrane. A 0.5 mL aliquot of filtered supernatant was diluted to 2.5 mL using ultrapure water prior to injection. The HPLC operational conditions used were as previously described:[31] 30 min gradient of HPLC-grade ACN and acidified (pH 3) ultrapure water [0 min, 20:80 (%) ACN/H_2O; 7 min, 22:78 (%) ACN/H_2O; 14 min, 30:70 (%) ACN/H_2O; 21 min, 40:60 (%) ACN/H_2O; and 30 min, 20:80 (%) ACN/H_2O], injection volume of 20 μL, flow rate of 0.6 mL min^{-1}, and UV detection at 270 nm for IMDA and 220 and 247 nm for metabolites. The HPLC column temperature was maintained at 24 °C. Analytical-grade IMDA, DSN-IMDA, DSN-olefin−IMDA, IMDA−urea, and 6-CNA were used to prepare a series of standard solutions. Standards of IMDA and 6-CNA (0−100 μg mL^{-1}) were run at each time of analysis. Standards of metabolites were run only after corresponding peaks were observed in solution. Linear calibration

DOI: 10.1021/acs.jafc.5b00754
J. Agric. Food Chem. 2015, 63, 4721−4727

curves for IMDA and 6-CNA were observed in the range of 1−100 μg mL^{-1} with 0.99 correlations. Retention times were 7.50, 2.50, 2.19, 6.4, and 5.51 min for IMDA, DSN-olefin−IMDA, DSN-IMDA, IMDA−urea, and 6-CNA, respectively. Peak area was plotted against its calibrated linear fitted standards (0−100 μg mL^{-1}) to quantitatively measure the IMDA concentration in culture flasks.

Clustering and Selection of Unique IMDA-Degrading Isolates by Horizontal Fluorophore-Enhanced Rep-PCR (HFERP). A total of 20, morphologically distinct, pure culture isolates were subjected to the HFERP DNA fingerprinting technique.[36] Rep-PCR was performed using a MJ research PTC 100 (MJ Research, Waltham, MA) thermocycler according to a published and well described protocol.[36] Electrophoresis was performed at 4 °C for 17 h at 70 V as previously described, with constant buffer recirculation for separating DNA fragments.[37] All HFERP experiments contained a positive control (*Escherichia coli*) and a negative control (no DNA). DNA fingerprints were captured using a Typhoon 8600 variable mode imager (Molecular Dynamics/Amersham Biosciences, Sunnyvale, CA), and images were subjected to analysis using BioNumerics, version 2.5, software (Applied Maths, Sint-Martens-Latem, Belgium) as previously described.[36]

Amplification of 16S rRNA Gene for the Identification of Unique Isolates. The taxonomic identity of unique bacterial isolates degrading IMDA was determined by sequencing near-full-length copies of 16S rRNA gene. Universal primers 27f (5′-AGAGTTT-GATCMTGGCTCAG-3′) and 1492r (5′-GGTTACCTTGTTAC-GACTT-3′) (Integrated DNA Technologies, Coralville, IA) were used for 16S rRNA gene amplification as described.[38] The amplified 16S rRNA fragment was extracted and purified following the protocol of the QIAquick PCR purification kit (Qiagen, Valencia, CA). PCR reaction conditions were performed as described.[39] The concentration of the purified DNA was determined by a NanoDrop 2000 spectrophotometer (Thermo Scientific, Wilmington, DE), and DNA was sequenced at the Genome Sequencing Center, University of Minnesota (St. Paul, MN). Sequences were assembled using BioEdit software.[40] Assembled contigs were compared to known 16S rRNA gene sequences in the GenBank database by BLASTn search. MEGA4 software was used for multiple alignment and phylogenetic tree generation to examine interrelationships among strains.[41] The sequence of 16S rRNA gene was used for assigning taxonomic status to the isolated strains. The 16S rRNA gene sequence of isolated IMDA-degrading MK6 strain was deposited in the National Center of Biological Information (NCBI) GenBank database under accession number KR052814.

RESULTS AND DISCUSSION

Enrichment of IMDA-Degrading Bacteria. An enrichment culture was used to isolate consortia and eventually pure cultures of bacteria that were capable of transforming IMDA (150 μg mL^{-1}) when used as a sole N source for growth. The enrichment technique has an advantage over direct isolation methods in its high probability of success in isolation because of acclimatization and providing favorable conditions for some species while suppressing the growth of others.[42−44] After 5 cycles of enrichment renewal, we obtained a mixed culture of microorganisms capable of growing on IMDA.

The addition of glucose as the sole source of carbon produced considerable microbial growth through the 5 rounds of subculturing, indicating that IMDA was most likely being used as a nitrogen source. As shown in Figure 1A, growth (OD_{600}) of the mixed culture supplemented with both IMDA and glucose was much greater than other treatments, including those supplemented with both IMDA and nitrogen. Other treatments provided limited and often insignificant growth. As a consequence, the biodegradation of IMDA as a nitrogen source was further investigated throughout this study. HPLC analyses were used to follow the IMDA concentration in mixed culture

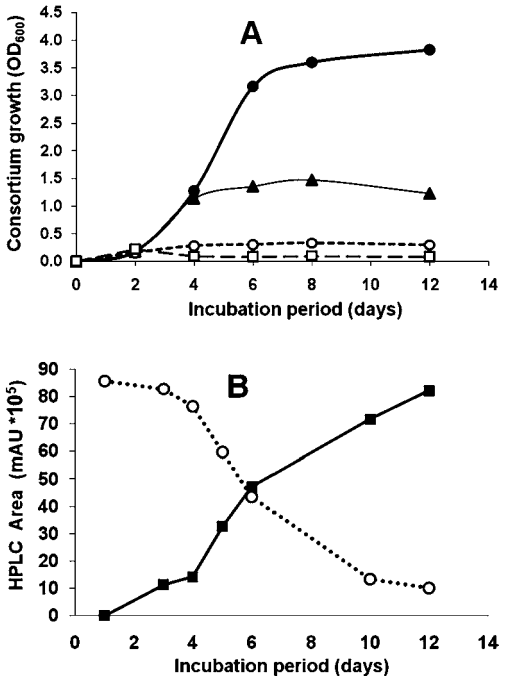

Figure 1. (A) Growth of the isolated bacterial consortium on (○) IMDA (150 μg mL^{-1}) alone, (▲) IMDA + nitrogen, and (●) IMDA + glucose compared to (□) control with none. (B) Biodegradation of (○) IMDA into (■) initially unknown metabolite by the isolated stable consortium in a minimal medium supplemented with glucose (2%).

growth in RSM, where IMDA served as the sole N source. Results in Figure 1B show that, as the quantity of IMDA decreased in the glucose-supplemented culture significantly with time, a single degradate accumulated in the growth medium.

Isolation and Purification of IMDA-Degrading Bacteria from Mixed Culture. A dilution series of the consortium was performed to isolate individual bacterial isolates capable of IMDA degradation. About 20 morphologically distinct colony isolates were selected and subjected to HFERP DNA fingerprint analysis to select for unique clones. Results in Figure 2 show the HFERP DNA fingerprints of these isolates. All 20 isolates could be divided into seven distinct groups that individually degraded IMDA. Strains in each DNA fingerprint group were individually tested for their ability to degrade IMDA. Results in Figure 3 show the growth of the IMDA-degrading consortium and individual isolates grown in minimal medium containing IMDA as a sole nitrogen source. One of these isolates (isolate MK6) showed rapid growth and had IMDA degradation rates similar to that seen with the consortium, while the other isolates showed slower growth on IMDA.

Identification of the Unique Isolates Degrading IMDA. Isolate MK6 was confirmed for IMDA transformation ability and was further identified by analysis of 16S rRNA gene sequence. Sequence similarities were determined by BLASTn analysis and indicated that the near-full-length 16S rRNA gene sequence of isolate MK6 was 99.9% identical to that of *Mycobacterium cosmeticum*, strain LTA-388. To our knowledge, this is the first report of an IMDA-degrading *Mycobacterium* sp. strain. In addition, BLASTn searches showed that the sequence of 16S rRNA gene of this strain was 98−99% identical to those of *Mycobacterium neoaurum* VKM Ac-1815D (CP006936.2),

DOI: 10.1021/acs.jafc.5b00754
J. Agric. Food Chem. 2015, 63, 4721−4727

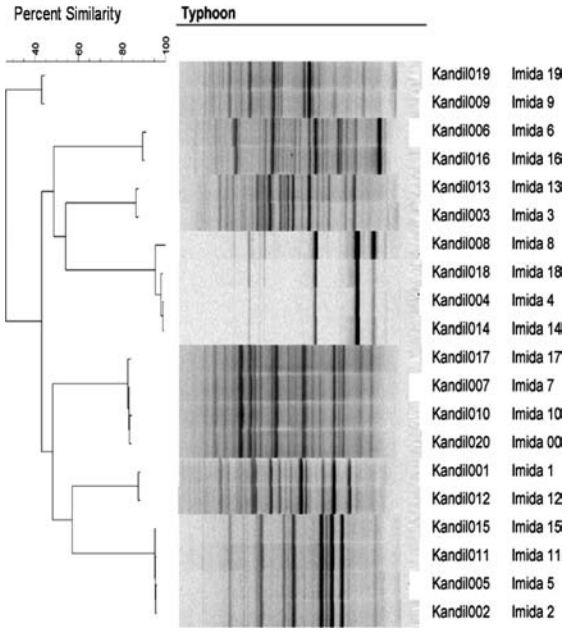

Figure 2. Pearson correlation of HFERP clusters for pure isolates growing on solid minimal medium supplemented with IMDA and glucose.

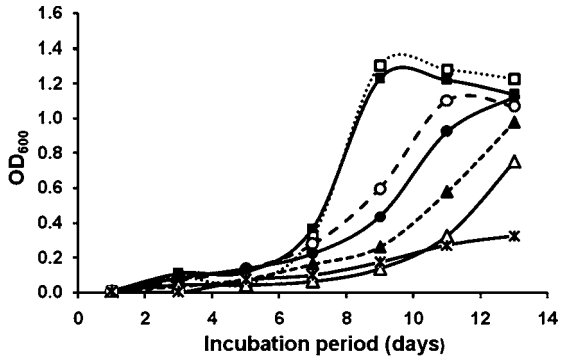

Figure 3. Growth of (□) consortium and its individual isolates, (■) MK6, (○) E4, (●) MK7, (▲) MK10, (△) E12, and (∗) E5, on IMDA as a sole nitrogen source in liquid minimal medium at 27 °C.

Mycobacterium rhodesiae NBB3 (CP003169.1), *Mycobacterium gilvum* Spyr1 (CP002385.1), *Mycobacterium smegmatis* str. MC2 155 (CP000480.1), *Mycobacterium smegmatis* strain INHR2 (CP009496.1), and *Mycobacterium gilvum* PYR-GCK (CP000656.1), whose genomes were completely sequenced. A phylogenetic tree (Figure 4) of the IMDA degrading strain was constructed using MEGA4 software (http://www.megasoftware.net/mega4/mega41.html).[41]

Kinetics of IMDA Biodegradation. Results in Figure 5A show that the reduction of the concentration of IMDA in supernatant was concomitant with a continuously rising growth (growth rate, μ = 0.375 day^{-1}) of isolate MK6. On the basis of HPLC analysis, more than 99% of the initial concentration of IMDA (150 μg mL^{-1}) was degraded within 2 weeks by this strain at 27 °C, making it among the most efficient IMDA-degrading bacterium reported to date. For instance, a *Klebsiella* sp. strain was only reported to degrade 78% of 50 μg mL^{-1} IMDA.[45] Figure 5B shows the percentage of IMDA degradation and the concurrent production of its major metabolite. While the IMDA concentration was reduced to traces (<2 μg mL^{-1})

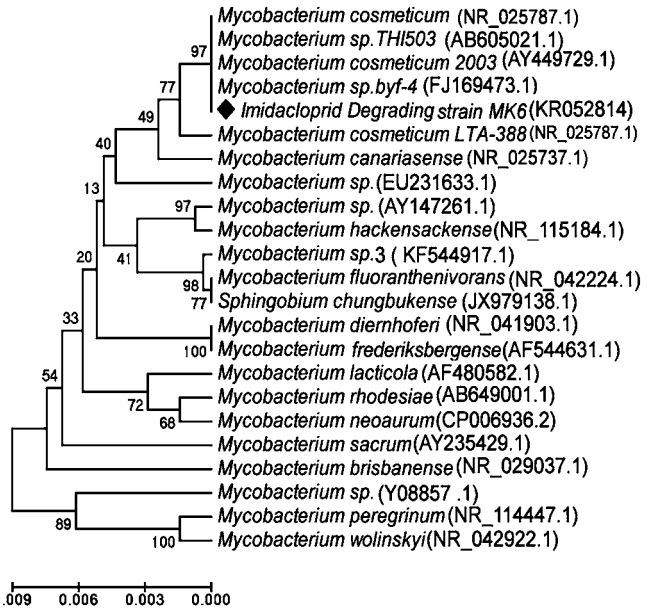

Figure 4. Phylogenetic tree for the confirmed (♦) IMDA-degrading strain MK6. The bootstrap values (%) are indicated at the nodes and are based on unweighted pair group method with arithmetic mean (UPGMA) analysis. The scale bar indicates the genetic distance among strains. Accession numbers of closely related strains are indicated in parentheses.

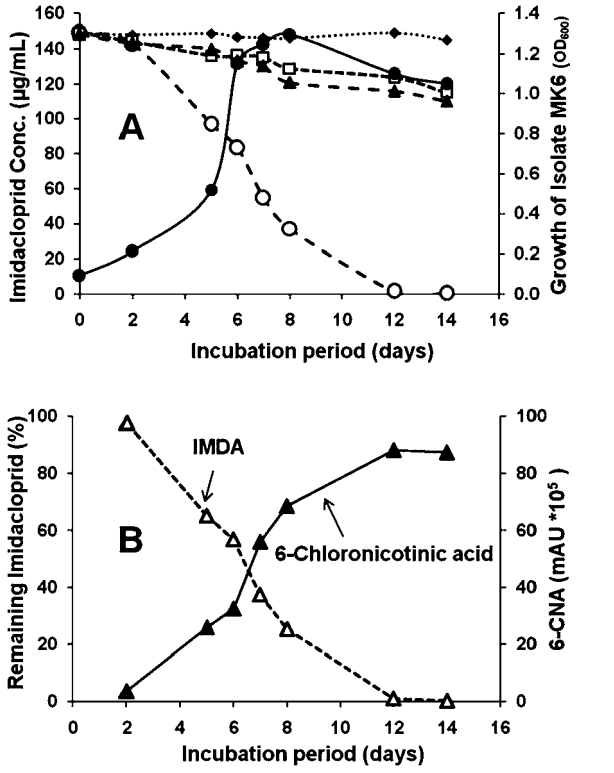

Figure 5. (A) Biodegradation of IMDA by the isolated *Mycobacterium* sp. strain MK6 growing on (□) IMDA alone, (○) IMDA + glucose, and (▲) IMDA + NH_4NO_3 compared to (◆) uninoculated control of IMDA + glucose. Only the growth (OD_{600}) of isolated *Mycobacterium* sp. strain MK6 with (●) IMDA + glucose treatment was shown. (B) Concurrent dissipation of (△) IMDA and production of (▲) 6-CNA by *Mycobacterium* sp. strain MK6 in a minimal medium.

DOI: 10.1021/acs.jafc.5b00754
J. Agric. Food Chem. 2015, 63, 4721−4727

in minimal medium, one major unknown biodegradation byproduct was increasingly produced (Figure 5B). Using the exponential formula $C_t = C_o e^{kt}$, as described above, the kinetics parameters (k and $t_{1/2}$) of IMDA degradation and the formation of 6-CNA as its major metabolite were calculated and are shown in Table 1. Degradation of IMDA followed a

Table 1. Kinetic Parameters of IMDA Degradation by *Mycobacterium* sp. Strain MK6

parameters[a]	control	IMDA + glucose	IMDA only
k (day^{-1})	0.001	0.442	0.017
$t_{1/2}$ (day)	693.2	1.6	41.0
R^2	0.258	0.844	0.97
IMDA degradation (%)	0	99.8	20
6-CNA production (%)	0	100	31

[a] k, decay constant; $t_{1/2}$, half-life time in days.

first-order decay reaction at the above-described growth conditions in a minimal medium. Data showed that the addition of glucose accelerated the degradation of IMDA and reducing its $t_{1/2}$ to 1.6 days compared to 41 days with IMDA alone.

Identification of Main Byproducts of IMDA Biodegradation. Supernatant samples of IMDA-grown *Mycobacterium* sp. strain MK6 were analyzed by HPLC. Various compounds have been previously reported as degradates of IMDA transformation by microorganisms,[26,29,46,47] plants,[25,48] termites,[49] and mice[50,51] or by photodegradation.[52,53] Results in Figure 6 show the disappearance of IMDA [retention time

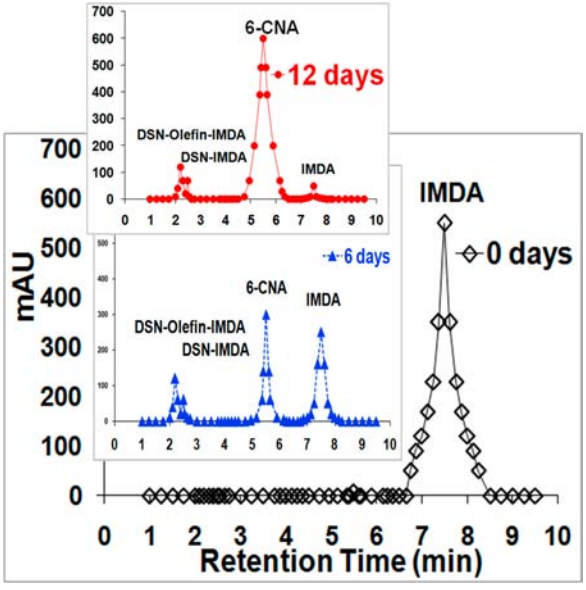

Figure 6. Retention time and HPLC area changes of IMDA and its metabolites at different incubation times, (black ◇) 0 days, (blue ▲) 6 days, and (red ●) 12 days, with *Mycobacterium* sp. strain MK6.

(RT) of 7.50] and appearance of three degradates DSN-olefin–IMDA (RT of 2.19 min), DSN-IMDA (RT of 2.50 min), and 6-CNA (RT of 5.51 min). Another previously observed degradate IMDA–urea, with an RT of 6.14 min,[54,55] was not observed in this study. While the concentration of 6-CNA increased with time, DSN-olefin–IMDA and DSN-IMDA remained relatively constant, suggesting that these two degradates may be intermediate metabolites in the transformation of IMDA to 6-CNA. Also consistent with the findings of this study, olefin–IMDA was previously reported as one of the major IMDA biodegradation byproducts by *Stenotrophomonas maltophilia* CGMCC 1.1788 but substrate mineralization was not reported.[30] Although the degradation of IMDA into other byproducts has been previously reported in some studies, the percent degradation was much lower than that of this study. For instance, IMDA was reported to be co-metabolically transformed by *Leifsonia* sp. strain PC-21 into 6-CNA, but there was no evidence of mineralization of IMDA into CO_2.[31] Shetti and Kaliwal[47] were able to isolate from soil *Brevundimonas* sp. MJ 15, which degraded up to 38% IMDA with no sign of mineralization to CO_2. The mineralization of IMDA was investigated in a water–sediment system, and its disappearance was associated with minimum mineralization into CO_2.[56]

It is significant to point out that results of the present study indicated that IMDA was completely degraded to 6-CNA, but was not further degraded by *Mycobacterium* sp. strain MK6 or mineralized to CO_2 in the time frame of the incubation. It is proposed that the isolated strain metabolizes IMDA through oxidative cleavage of the methylene bridge to form 6-CNA or reduction of the nitro group through a fast process of oxidation of desnitro-olefin as previously concluded.[28,45] Using Using different growth substrates, such as sucrose and succinate, it was suggested that *Stenotrophomonas maltophilia* CGMCC 1.1788 used different degradation pathways via 5-hydroxy-IMDA.[30]

In summary, we isolated a mixed culture capable of biodegrading IMDA using an enrichment culture technique. A single, pure culture of isolate MK6 that fully degraded IMDA was subsequently isolated and purified from the mixed culture. This bacterium was identified as *Mycobacterium* sp. strain MK6 through sequence analysis of its 16S rRNA gene. Although IMDA was transformed completely to 6-CNA by the identified strain, there was no evidence of mineralization to CO_2 in the time frame of the incubation. A proposed biodegradation pathway of IMDA considers DSN-olefin–IMDA and DNS-IMDA as degradation intermediates. Because relatively few species of bacteria degrading IMDA have been identified, we propose to completely sequence *M. cosmeticum* strain MK6, so that genes and enzymes responsible for IMDA degradation can be identified and studied in detail.

AUTHOR INFORMATION

Corresponding Author

*E-mail: mahrouskan@yahoo.com.

Notes

The authors declare no competing financial interest.

ACKNOWLEDGMENTS

This work was performed in collaboration between the Alexandria University, Egypt, and the University of Minnesota, St. Paul, MN.

ABBREVIATIONS USED

IMDA, imidacloprid; 6-CNA, 6-chloronicotinic acid; DSN-olefin–IMDA, desnitro-olefin imidacloprid; DSN-IMDA, desnitro-imidacloprid; HFERP, horizontal fluorophore-enhanced Rep-PCR; OD_{600}, optical density at 600 nm; RSM, R-salts minimal medium; HPLC, high-performance liquid chromatography; ACN, acetonitrile; C_t, concentration of imidacloprid at

DOI: 10.1021/acs.jafc.5b00754
J. Agric. Food Chem. 2015, 63, 4721–4727

time t; C_o, imidacloprid initial concentration; k, decay constant; $t_{1/2}$, half-life time; μ, growth rate; NCBI, National Center of Biological Information; CEC, cation-exchange capacity, EC, electrical conductivity; PLFA, phospholipid fatty acid analysis; CLPP, community level physiological profiling; PCR-DGGE, polymerase chain reaction-denaturing gradient gel electrophoresis

REFERENCES

(1) Wadhwa, B. K.; Singh, P.; Arora, S.; Sharma, V. Analysis of pesticide residues in soils. In *Handbook of Pesticides: Methods of Pesticide Residues Analysis*; Nollet, L. M. L., Rathore, H. S., Eds.; CRC Press (Taylor & Francis Group): Boca Raton, FL, 2010; pp 583−595.

(2) Pimentel, D.; Livetan, L. Pesticides: Amounts applied and amounts reaching target pests. *BioScience* **1986**, *36* (2), 86−91.

(3) Khan, S. U. The interaction of organic matter with pesticides. In *Soil Organic Matter*; Schnitzer, M., Khan, S. U., Eds.; Elsevier Publishing Co.: New York, 1978; pp 137−172.

(4) Delle Site, A. Factors affecting sorption of organic compounds in natural sorbent/water systems and sorption coefficients for selected pollutants. A review. *J. Phys. Chem. Ref. Data* **2001**, *30* (1), 187−439.

(5) Gavrilescu, M. Fate of pesticides in the environment and its bioremediation. *Eng. Life Sci.* **2005**, *5* (6), 497−526.

(6) Alexander, M. Aging, bioavailability and overestimation of risk from environmental pollutants. *Environ. Sci. Technol.* **2000**, *34*, 4259−4265.

(7) Reginato, J. B.; Koskinen, W. C.; Sadowsky, M. J. Influence of soil aging on sorption and bioavailability of simazine. *J. Agric. Food Chem.* **2006**, *54*, 1373−1379.

(8) Van der Wal, L.; Tjallig, J.; Fleuren, R.; Barendregt, A.; Sinnige, T.; van Gestel, C.; Hermens, J. Solid-phase microextraction to predict bioavailability and accumulation of organic micropollutants in terrestrial organisms after exposure to a field-contaminated soil. *Environ. Sci. Technol.* **2004**, *38*, 4842−4844.

(9) Ingram, C. W.; Coyne, M. S.; William, D. W. Effects of commercial diazinon and imidacloprid on microbial urease activity in soil and sod. *J. Environ. Qual.* **2005**, *34*, 1573−1580.

(10) Vig, K.; Singh, D. K.; Agarwal, H. C.; Dhawan, A. K.; Dureja, P. Soil microorganisms in cotton fields sequentially treated with insecticides. *Ecotoxicol. Environ. Saf.* **2008**, *69*, 263−276.

(11) Cycoń, M.; Piotrowska-Seget, Z.; Kozdrój, J. Microbial characteristics of sandy soils exposed to diazinon under laboratory conditions. *World J. Microbiol. Biotechnol.* **2010**, *26*, 409−418.

(12) Cycoń, M.; Markowicz, A.; Borymski, S.; Wójcik, W.; Piotrowska-Seget, Z. Imidacloprid induces changes in the structure, genetic diversity and catabolic activity of soil microbial communitites. *J. Environ. Manage.* **2013**, *131*, 55−65.

(13) Anatra-Cordone, M.; Durkin, P. *Imidacloprid—Human Health Assessment and Ecological Risk Assessment—Final Report*; Syracuse Environmental Research Associates, Inc.: New York, 2005; SERA TR 05-43-24-03a.

(14) Matsuda, K.; Kanaoka, S.; Akamatsu, M.; Sattelle, D. B. Diverse actions and target-site selectivity of neonicotinoids: Structural insights. *Mol. Pharmacol.* **2009**, *76* (1), 1−10.

(15) Jeschke, P.; Nauen, R.; Schindler, M.; Elbert, A. Overview of the status and global strategy for neonicotinoids. *J. Agric. Food Chem.* **2011**, *59*, 2897−2908.

(16) Tomizawa, M.; Casida, J. E. Neonicotinoid insecticide toxicology: Mechanisms of selective action. *Annu. Rev. Pharmacol. Toxicol.* **2005**, *45*, 247−68.

(17) Zabar, R.; Dolenc, D.; Jerman, T.; Franko, M.; Trebše, P. Photolytic and photocatalytic degradation of 6-chloronicotinic acid. *Chemosphere* **2011**, *85*, 861−868.

(18) Kalpana, P.; Gajbhiye, V. T.; Agnihotri, N. P. Persistence and leaching of imidacloprid in soil. *Ann. Plant Prot. Sci.* **2002**, *10*, 176−178.

(19) Wu, J.; Wei, H.; Xue, J. Degradation of imidacloprid in chrysanthemi flos and soil. *Bull. Environ. Contam. Toxicol.* **2012**, *88*, 776−780.

(20) Sarkar, M. A.; Biswas, P. K.; Roy, S.; Kole, R. K.; Chowdhury, A. Effect of pH and type of formulation on the persistence of imidacloprid in water. *Bull. Environ. Contam. Toxicol.* **1999**, *63*, 604−609.

(21) Tišler, T.; Jemec, A.; Mozetic, B.; Trebše, P. Hazard identification of imidacloprid to aquatic environment. *Chemosphere* **2009**, *76*, 907−914.

(22) Drobne, D.; Blažič, M.; Van Gestel, C. A. M.; Leŝer, V.; Zidar, P.; Jemec, A.; Trebŝe, P. Toxicity of imidacloprid to the terrestrial isopod *Porcellio scaber* (Isopoda, Crustacea). *Chemosphere* **2008**, *71*, 1326−1334.

(23) Van Dijk, T. C.; Van Staalduinen, M. A.; Van der Sluijs, J. P. Macro-invertebrate decline in surface water polluted with imidacloprid. *PLoS One* **2013**, *8* (5), No. e62374.

(24) Liu, W.; Zheng, W.; Ma, Y.; Liu, K. K. Sorption and degradation of imidacloprid in soil and water. *J. Environ. Sci. Health, Part B* **2006**, *41* (5), 623−634.

(25) Oi, M. Time-dependent sorption of imidacloprid in two different soils. *J. Agric. Food Chem.* **1999**, *47*, 327−332.

(26) Cox, L.; Koskinen, W.; Yong Yen, P. Changes in sorption of imidacloprid with incubation time. *Soil Sci. Soc. Am. J.* **1998**, *62*, 342−347.

(27) Flores-Cespedes, F.; González-Pradas, E.; Fernández-Pérez, M.; Villafranca-Sánchez, M.; Socías-Viciana, M.; Ureña-Amate, M. D. Effects of dissolved organic carbon on sorption and mobility of imidacloprid in soil. *J. Environ. Qual.* **2002**, *31* (3), 880−888.

(28) Sur, R.; Stork, A. Uptake, translocation and metabolism of imidacloprid in plants. *Bull. Insectol.* **2003**, *56* (1), 35−40.

(29) Dai, Y. J.; Yuan, S.; Ge, F.; Chen, T.; Xu, S. C.; Ni, J. P. Microbial hydroxylation of imidacloprid for the synthesis of highly insecticidal olefin imidacloprid. *Appl. Microbiol. Biotechnol.* **2006**, *71*, 927−934.

(30) Liu, Z.; Dai, Y.; Huan, Y.; Sun, L.; Zhou, Q.; Zhang, W.; Sang, Q.; Wei, H.; Yuan, S. Different utilizable substrates have different effects on cometabolic fate of imidacloprid in *Stenotrophomonas maltophilia*. *Appl. Microbiol. Biotechnol.* **2013**, *97*, 6537−6547.

(31) Anhalt, J. C.; Moorman, T. B.; Koskinen, W. C. Biodegradation of imidacloprid by an isolated soil microorganism. *J. Environ. Sci. Health, Part B* **2007**, *42*, 509−514.

(32) Meleiro-Porto, A. L.; Melgar, G. Z.; Kasemodel, M. C.; Nitschke, M. Biodegradation of pesticides. In *Pesticides in the Modern World—Pesticides Use and Management*; Stoytcheva, M., Ed.; InTech: Rijeka, Croatia, 2011; pp 407−439, ISBN: 978-953-307-459-7.

(33) Page, A. L.; Miller, R. H.; Keeney, D. R. *Methods of Soil Analysis*, 2nd ed.; American Society of Agronomy (ASA) and Soil Science Society of America (SSSA): Madison, WI, 1982; Agronomy Monograph 9.

(34) Kandil, M. M. Genetic diversity of soil bacteria degrading cyanuric acid: An intermediate in the atrazine biodegradation pathway. Ph.D. Thesis, University of Minnesota, St. Paul, MN, 2006.

(35) Anhalt, J. C.; Moorman, T. B.; Koskinen, W. C. Degradation and sorption of imidacloprid in dissimilar surface and subsurface soils. *J. Environ. Sci. Health, Part B* **2008**, *43*, 207−213.

(36) Johnson, L. K.; Brown, M. B.; Carruthers, E. A.; Ferguson, J. A.; Dombek, P. E.; Sadowsky, M. J. Sample size, library composition, and genotypic diversity among natural populations of *Escherichia coli* from different animals influence accuracy of determining sources of fecal pollution. *Appl. Environ. Microbiol.* **2004**, *70*, 4478−4485.

(37) Rademaker, J. L. W.; Louws, F. J.; de Bruijn, F. J. Characterization of the diversity of ecologically important microbes by rep-PCR genomic fingerprinting. In *Molecular Microbial Ecology Manual*; Akkermans, A. D. L., van Elsas, J. D., de Bruijn, F. J., Eds.; Kluwer Academic Publishers: Dordrecht, Netherlands, 1998; Supplement 3, pp 1−26.

DOI: 10.1021/acs.jafc.5b00754
J. Agric. Food Chem. 2015, 63, 4721−4727

(38) Lane, D. J. 16S/23S rRNA sequencing. In *Nucleic Acids Techniques in Bacterial Systematics*; Stackebrandt, E., Goodfellow, M., Eds.; John Wiley & Sons: Chichester, U.K., 1991; pp 115−147.
(39) Rousseaux, S.; Hartmann, A.; Soulas, G. Isolation and characterization of new Gram-negative and Gram-positive atrazine degrading bacteria from different French soils. *FEMS Microbiol. Ecol.* **2001**, *36* (2−3), 211−222.
(40) Hall, T. *BioEdit, Version 7.0.9*; Ibis Biosciences: Carlsbad, CA, 2007; http://www.mbio.ncsu.edu/BioEdit/page2.html.
(41) Tamura, K.; Dudley, J.; Nei, M.; Kumar, S. MEGA4: Molecular evolutionary genetics analysis (MEGA) software version 4.0. *Mol. Biol. Evol.* **2007**, *24*, 1596−1599.
(42) Jackson, C. R.; Roden, E. E.; Churchill, P. F. Changes in bacterial species composition in enrichment cultures with various dilutions of inoculum as monitored by denaturing gradient gel electrophoresis. *Appl. Environ. Microbiol.* **1998**, *64*, 5046−5048.
(43) Probst, A.; Vaishampayan, P.; Osman, S.; Moissl-Eichinger, C.; Andersen, G. L.; Venkateswaran, K. Diversity of anaerobic microbes in spacecraft assembly clean rooms. *Appl. Environ. Microbiol.* **2010**, *76*, 2837−2845.
(44) Sayler, G. S.; Hooper, S. W.; Layton, A. C.; Henry King, J. M. Catabolic plasmids of environmental and ecological significance. *Microb. Ecol.* **1990**, *19*, 1−20.
(45) Phugare, S. S.; Kalyani, D. C.; Gaikwad, Y. B.; Jadhav, J. P. Microbial degradation of imidacloprid and toxicological analysis of its biodegradation metabolites in silkworm (*Bombyx mori*). *Chem. Eng. J.* **2013**, *230*, 27−35.
(46) Pandey, G.; Dorrian, S. J.; Russell, R. J.; Oakeshott, J. G. Biotransformation of the neonicotinoid insecticides imidacloprid and thiamethoxam by *Pseudomonas* sp. 1G. *Biochem. Biophys. Res. Commun.* **2009**, *380* (3), 710−714.
(47) Shetti, A. A.; Kaliwal, B. B. Biodegradation of imidacloprid by soil isolate *Brevundimonas* sp. MJ15. *Int. J. Curr. Res.* **2012**, *4* (10), 100−106.
(48) Nix, K.; Lambdin, P.; Grant, J.; Coots, C.; Merten, P. Concentration levels of imidacloprid and dinotefuran in five tissue types of black walnut, *Juglans nigra*. *Forests* **2013**, *4*, 887−897.
(49) Tomalski, M.; Leimkuehler, W.; Schal, C.; Vargo, E. L. Metabolism of imidacloprid in workers of *Reticulitermes flavipes* (Isoptera: Rhinotermitidae). *Ann. Entomol. Soc. Am.* **2010**, *103* (1), 84−95.
(50) Chao, S. L.; Casida, J. E. Interaction of imidacloprid metabolites and analogs with the nicotinic acetylcholine receptor of mouse brain in relation to toxicity. *Pestic. Biochem. Physiol.* **1997**, *58*, 77−88.
(51) Swenson, T. L.; Casida, J. E. Aldehyde oxidase importance in vivo in xenobiotic metabolism: imidacloprid nitroreduction in mice. *Toxicol. Sci.* **2013**, *133* (1), 22−28.
(52) Agüera, A.; Almansa, E.; Malato, S.; Maldonado, M. I.; Fernández-Alba, A. R. Evaluation of photocatalytic degradation of imidacloprid in industrial water by GC−MS and LC−MS. *Analusis* **1998**, *26* (7), 245−251.
(53) Zabar, R.; Komel, T.; Fabjan, J.; Kralj, M. B.; Trebše, P. Photocatalytic degradation with immobilised TiO_2 of three selected neonicotinoid insecticides: Imidacloprid, thiamethoxam and clothianidin. *Chemosphere* **2012**, *89*, 293−301.
(54) Bacey, J. *Environmental Fate of Imidacloprid*; Environmental Monitoring and Pest Management Branch, California Department of Pesticide Regulation, Sacramento, CA, 2000; www.cdpr.ca.gov/docs/empm/pubs/fatememo/imid.pdf.
(55) Fossen, M. *Environmental Fate of Imidacloprid*; California Department of Pesticide Regulation: Sacramento, CA, 2006; www.cdpr.ca.gov/docs/emon/pubs/fatememo/Imidclprdfate2.pdf.
(56) Krohn, J.; Hellpointner, E. Environmental fate of imidacloprid. *Pflanzenschutz-Nachr. Bayer (Engl. Ed.)* **2002**, *55*, 3−26.

DOI: 10.1021/acs.jafc.5b00754
J. Agric. Food Chem. 2015, 63, 4721−4727

JOURNAL OF AGRICULTURAL AND FOOD CHEMISTRY

Article

pubs.acs.org/JAFC

Conjugation of the Mycotoxins Alternariol and Alternariol Monomethyl Ether in Tobacco Suspension Cells

Andreas A. Hildebrand, Beate N. Kohn, Erika Pfeiffer, Daniel Wefers, Manfred Metzler, and Mirko Bunzel*

Institute of Applied Biosciences, Department of Food Chemistry and Phytochemistry, Karlsruhe Institute of Technology (KIT), Adenauerring 20a, 76131 Karlsruhe, Germany

Supporting Information

ABSTRACT: The mycotoxins alternariol (AOH) and alternariol-9-*O*-methyl ether (AME) carry three and two phenolic hydroxyl groups, respectively, which makes them candidates for the formation of conjugated metabolites in plants. Such conjugates may escape routine methods of analysis and have therefore been termed masked or, more recently, modified mycotoxins. We report now that AOH and AME are extensively conjugated in suspension cultures of tobacco BY-2 cells. Five conjugates of AOH were identified by MS and NMR spectroscopy as β-D-glucopyranosides (attached in AOH 3- or 9-position) as well as their 6′-malonyl derivatives, and as a gentiobiose conjugate. For AME, conjugation resulted in the D-glucopyranoside (mostly attached in the AME 3-position) and its 6′- and 4′-malonyl derivatives. Pronounced differences were noted for the quantitative pattern of AOH and AME conjugates as well as for their phytotoxicity. Our *in vitro* study demonstrates for the first time that masked mycotoxins of AOH and AME can be formed in plant cells.

KEYWORDS: *masked mycotoxins, modified mycotoxins, Alternaria toxins, malonyl glucosides, plant cell culture*

INTRODUCTION

The cosmopolitan genus *Alternaria* contains many species that are important plant pathogens, infesting all the aerial parts of plants and causing, e.g., early blight diseases of vegetables, brown spot of tangerines, or postharvest black rot of fruit.[1] In addition to economic losses due to preharvest and postharvest decay, *Alternaria* species produce several groups of toxins, which contaminate food and feed and may pose a health problem.[2] For example, *Alternaria* toxins have been associated with an increased incidence of esophageal cancer in certain areas of China.[3] In 2011, the European Food Safety Authority (EFSA) published a Scientific Opinion on the risks for animal and public health related to the presence of *Alternaria* toxins in feed and food.[4] The analysis of 11 730 occurrence data showed that the most frequently detected *Alternaria* toxins were the dibenzo-α-pyrones alternariol (AOH) and alternariol-9-*O*-monomethyl ether (AME) (Figure 1A,B), which were common contaminants of cereals, sunflower seeds, oilseed rape, olives, various fruits, and other food items.[4] AOH and AME exhibit genotoxicity *in vitro* by inducing gene mutations, DNA strand breaks, and inhibition of topoisomerase I and IIα.[5−8]

Both AOH and AME have free hydroxyl groups available for metabolic conjugation (Figure 1A,B). In the mammalian organism, formation of glucuronides is a major pathway of detoxification and excretion. *In vitro* studies have shown that AOH and AME are readily converted to glucuronides upon incubation with hepatic and intestinal microsomes from humans, rats, and pigs in the presence of UDPGA.[9] Whereas AOH gave rise to comparable amounts of the 3-*O*-glucuronide and 9-*O*-glucuronide, AME was predominantly converted to the 3-*O*-glucuronide. In the same study, the activities of 10 recombinant human UDP-glucuronosyltransferases for AOH and AME were determined; nine were found to be active for AOH and eight for AME.

Over the past years, researchers and regulators have become aware that conjugation of mycotoxins (and other compounds such as pesticides) may also occur in plants. Such conjugation reactions are believed to be part of the detoxification system of the plant.[10] Xenobiotic and endogenous compounds carrying hydroxyl groups are frequently converted to glucosides and further processed by addition of a malonyl, hexose, or pentose moiety to facilitate compartmentation and storage.[10] Conjugated compounds escape routine methods of analysis if the method aims exclusively at the detection of the parental compounds. However, upon ingestion of the conjugate by humans or animals, the parental form may be released in the digestive tract and absorbed, thereby increasing the total exposure to the compound. For the first time, this has been unambiguously demonstrated for a glucoside of the mycotoxin zearalenone, and the term "masked mycotoxin" has been coined.[11] Today, several masked forms of zearalenone and other mycotoxins, in particular of trichothecenes like deoxynivalenol and nivalenol are known.[12,13] More recently, the term "modified mycotoxins" has been proposed for a comprehensive definition including, e.g., derivatives formed by thermal reactions or by plant metabolism (so-called "masked" mycotoxins).[14]

Because it is yet unknown whether AOH and AME are converted to conjugated metabolites in plants, the aim of this

Received: February 11, 2015
Revised: April 23, 2015
Accepted: April 25, 2015
Published: April 25, 2015

ACS Publications © 2015 American Chemical Society

DOI: 10.1021/acs.jafc.5b00806
J. Agric. Food Chem. 2015, 63, 4728−4736

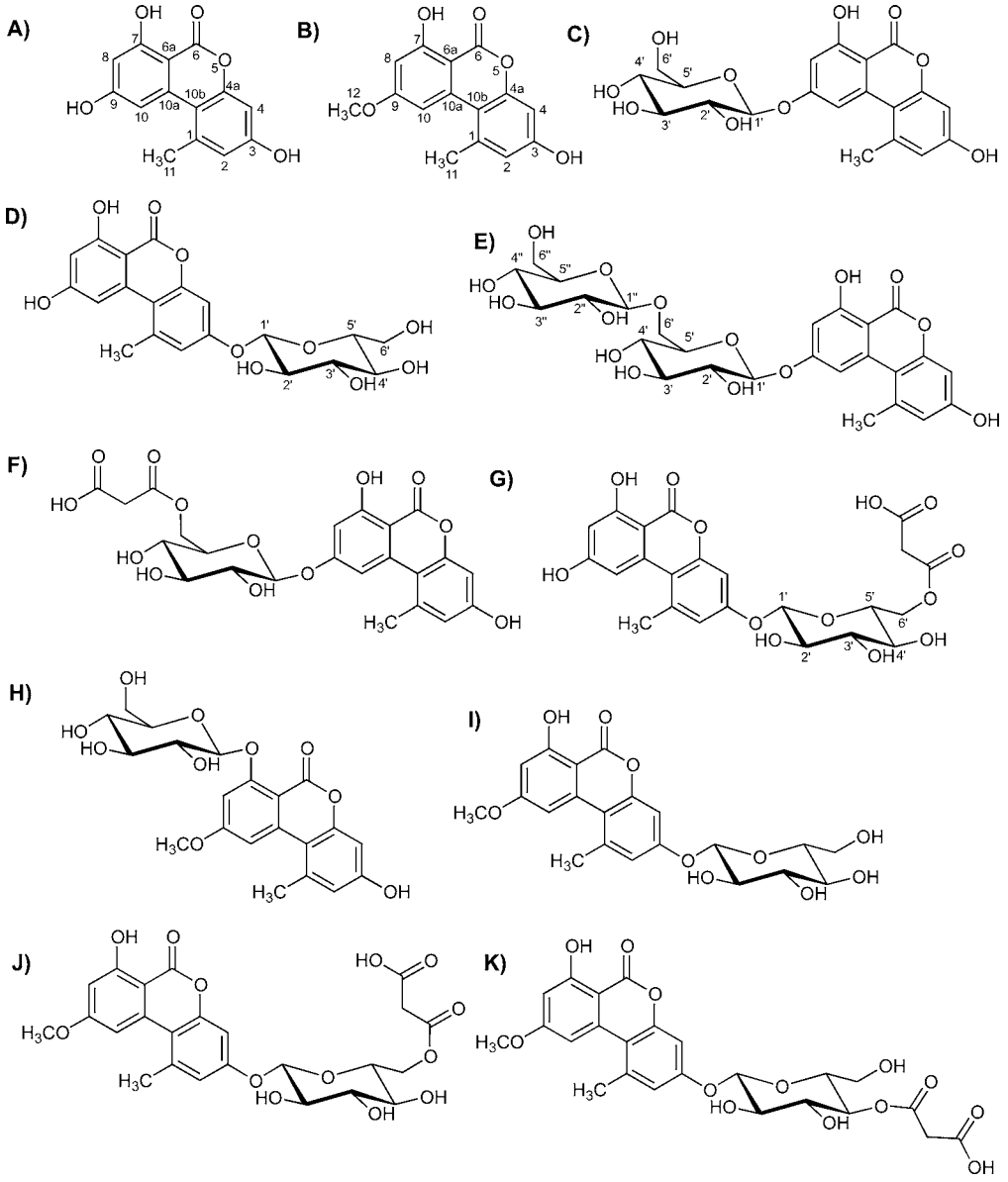

Figure 1. Chemical structures of alternariol (AOH, A), alternariol-9-*O*-monomethyl ether (AME, B), and AOH and AME metabolites formed in a tobacco suspension cell culture system. 9-*O*-*β*-D-glucopyranosyl-AOH (AOH-2, C); 3-*O*-*β*-D-glucopyranosyl-AOH (AOH-3, D); 9-*O*-{*β*-D-glucopyranosyl(1 → 6)-*β*-D-glucopyranosyl}AOH (AOH-1, E); 9-*O*-(6-*O*-malonyl-*β*-D-glucopyranosyl)AOH (AOH-4, F); 3-*O*-(6-*O*-malonyl-*β*-D-glucopyranosyl)AOH (AOH-5, G); 7-*O*-*β*-D-glucopyranosyl-AME (AME-2, H); 3-*O*-*β*-D-glucopyranosyl-AME (AME-5, I); 3-*O*-(6-*O*-malonyl-*β*-D-glucopyranosyl)AME (AME-6, J); 3-*O*-(4-*O*-malonyl-*β*-D-glucopyranosyl)AME (AME-7, K).

study was to analyze AOH and AME conjugation in a tobacco BY-2 suspension cell culture as a model system.

MATERIALS AND METHODS

Chemicals and Reagents. AOH and AME were isolated from a culture of *Alternaria alternata* strain TA7 grown on rice flour containing media for 24 days at 25 °C as described earlier for the isolation of other *Alternaria* toxins.[15] The crude extract was analyzed by LC-MS, and the fractions containing AOH and AME were isolated by preparative HPLC. Identity was confirmed by NMR (see below), and the purity was >98% according to HPLC analysis with UV detection at 254 nm.

Chemicals for the tobacco cell culture and other chemicals and reagents were obtained from Sigma-Aldrich/Fluka (Taufenkirchen, Germany) and Duchefa (Haarlem, The Netherlands) and were of the highest quality available (96−100% depending on the chemical, with the exception of Evan's Blue (>75% purity)). HPLC-MS grade acetonitrile and methanol were purchased from VWR International (Bruchsal, Germany). NMR solvents were from Deutero GmbH (Kastellaun, Germany) and VWR International.

Tobacco Suspension Cell Culture. Tobacco BY-2 cells (*Nicotiana tabacum* L. cv. Bright Yellow 2) were kindly provided by Dr. Jan Maisch (Institute of Botany, KIT). The cells were cultured in the dark at 25 °C on an orbital shaker at 150 rpm in 100 mL Erlenmeyer flasks containing 30 mL of Murashige and Skoog medium supplemented with 30 g/L sucrose, 200 mg/L KH_2PO_4, 100 mg/L inositol, 1 mg/L thiamine, and 0.2 mg/L 2,4-dichlorophenoxyacetic acid. The medium was adjusted to pH 5.8. The cells were subcultured weekly, transferring 1.5 mL (about 0.5 g cell wet weight) of the suspension into 30 mL of fresh medium. The exponential growth phase of the cells started after 3 days and was finished on day seven (about 10 g of cell wet weight or 0.4−0.5 g of cell dry weight in the stationary phase).

Incubation of Tobacco Cells with AOH and AME. Stock solutions (10 mM) of AOH or AME in DMSO were stable at ambient

DOI: 10.1021/acs.jafc.5b00806
J. Agric. Food Chem. 2015, 63, 4728−4736

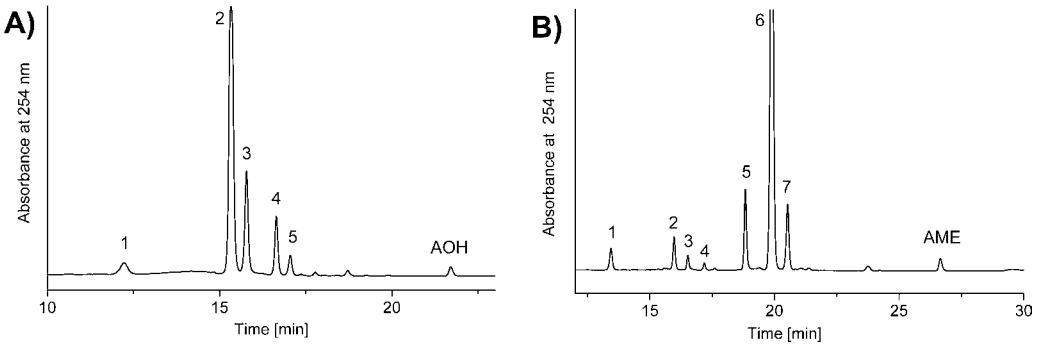

Figure 2. HPLC profiles of metabolites of alternariol (AOH) (A) and alternariol-9-*O*-monomethyl ether (AME) (B) in extracts of cultured tobacco BY-2 cells after 48 h incubation (UV detection at 254 nm). The abbreviations used for the metabolites (AOH-X, AME-X) indicate which metabolite is represented by which peak in the chromatogram (with X describing the peak number).

temperature in the dark for up to two months. The concentration of the mycotoxin in the incubation medium was 50 or 100 μM. The DMSO concentration did not exceed 1%. Control incubations were carried out with DMSO but without mycotoxin. After 24, 48, or 96 h of incubation, cells and medium were separated by filtration and freeze-dried. The dried medium was dissolved in MeOH for chromatographic analysis. The dried cells (10−12 g wet cells yield about 0.6 g dry cells) were ground using mortar and pestle. To extract AOH, AME, and their metabolites, an optimized extraction procedure was used: 0.1 g of the ground material was extracted twice for 2 h at 25 °C with horizontal shaking. For the first extraction, 4.5 mL of MeOH/CH_2Cl_2 (2:1, v/v) was used, whereas 4.5 mL of MeOH/H_2O/acetic acid (79/20/1, v/v/v) was used for the second extraction. The combined extracts were evaporated to dryness using a vacuum evaporator, and the residues were dissolved in 0.4 mL of MeOH and analyzed by using HPLC-photo diode array (PDA)-MS.

Assay To Determine Cell Death. Cells that accumulated Evans blue were considered as dead cells.[16] An aliquot of the cell suspension (200 μL) was incubated with 1.5 mL of 0.05% (w/v) Evans blue at room temperature for 15 min, subsequently washed twice with 1 mL of PBS, and resuspended in 500 μL of PBS. An aliquot of the suspension (20 μL) was transferred on microscope slides, and a total of 500 cells was scored under the light microscope, discriminating between living (uncolored) and dead (blue stained) cells.

HPLC-PDA-MS Analysis. An LXQ Linear Ion Trap MS^n system (Thermo Fisher Scientific, Waltham, MA, USA) equipped with a Finnigan Surveyor HPLC-PDA system was used. Separation was carried out on a reversed phase column (Phenomenex Luna C8(2), 250 × 4.6 mm i.d.). Solvent A was H_2O with 0.1% formic acid, solvent B was acetonitrile with 0.1% formic acid, and the flow rate was 0.5 mL/min. The linear gradient started with 20% B, held for 5 min, ramped to 50% B in 10 min, ramped to 70% B in 9 min, ramped to 100% B in 5 min, held for 2 min, decreased to 20% B in 1 min, and equilibrated for 2 min before the next injection. The metabolites were detected at 254 nm and characterized with MS operating in ESI positive mode. Full scan mass spectra were recorded from m/z 100−1000, MS^2 of the $[M + H]^+$ ions was conducted at CID 35 (35% of 5 V). Nitrogen was used as the sheath gas, auxiliary gas, and sweep gas with flow rates of 30.0, 15.0, and 0.02 L/min, respectively. Spray voltage was 4.47 kV, spray current 3.15 mA, capillary voltage 45.10 V, capillary temperature 350 °C, and the tube lens voltage was 125.58 V. Semiquantitative analyses were carried out by determining peak areas at 254 nm, using AOH or AME as external standard compounds.

Isolation of the Metabolites of AOH and AME. About 12 g of dry cells were collected from several incubations of each mycotoxin and extracted by scaling up the procedure described above, yielding about 40 mL of crude extracts dissolved in MeOH. These extracts were fractionated in portions of 1.5 mL using a preparative HPLC-UVD system (LC-8A pumps, SPD-20A UV detector, Shimadzu, Kyoto, Japan) and a reversed phase column (Phenomenex, Luna C18(2), 5 μm, 250 × 25.0 mm i.d.). Solvent A was water with 0.1% formic acid, solvent B was MeOH with 0.1% formic acid, and the flow rate was 8 mL/min. A linear gradient was started with 20% B held for 5 min, then ramped to 65% B in 20 min, ramped to 90% B in 1 min, and held for 4 min. Fractions of the separated metabolites were collected manually according to the chromatograms. After vacuum-concentration to about half of their volumes, the fractions were freeze-dried for HPLC-PDA-MS and NMR analysis. HPLC-PDA-MS was conducted as described above and showed that the purity of the AOH and AME metabolites used for NMR analysis was >97% (based on UV chromatograms at 254 nm).

Carbohydrate Analysis. Carbohydrate analysis was performed by high performance anion exchange chromatography (HPAEC) with pulsed amperometric detection (PAD) after acidic hydrolysis with 2 M trifluoroacetic acid for 30 min at 121 °C. After evaporation of the acid, the sample was redissolved in water and analyzed on an ICS-5000 HPAEC system (Thermo Scientific Dionex, Sunnyvale, CA, USA) using a CarboPac PA-20 column. The exact chromatographic conditions are described in Wefers et al. (2014).[17] To determine D-/L-configuration of the glucose unit in 9-*O*-β-glucopyranosyl-AOH, the glycosidic linkage was cleaved as described above. The residue after evaporation was derivatized with 150 μL of (*R*)-2-octanol and 5 μL of TFA at 130 °C overnight. After removal of the derivatization reagents, the sample was silylated by using 80 μL of *N*,*O*-bis(trimethylsilyl) trifluoroacetamide and 20 μL of pyridine. Sample analysis was performed by GC-MS (GC-2010 Plus and GCMS-QP2010 Ultra, Shimadzu, Kyoto, Japan) equipped with an Rxi-5Sil MS column (30 m × 0.25 mm i.d., 0.25 μm film thickness, Restek, Bad Homburg, Germany). Detailed chromatographic conditions are given in Wefers et al. (2014).[17]

NMR Spectroscopy. NMR spectra were recorded on a Bruker Ascend^M 500 spectrometer (Rheinstetten, Germany) equipped with a Prodigy cryoprobe. Freeze-dried samples were dissolved in 500 μL of DMSO-d_6. The structures of the isolated oligosaccharides were identified by using ^{1}H, H,H-correlated spectroscopy (COSY), heteronuclear single quantum coherence (HSQC), and heteronuclear multiple bond correlation (HMBC) experiments. Standard Bruker pulse sequences were used; spectra were acquired at 298 K. Chemical shifts (δ) were referenced to the central solvent signals (δH 2.50 ppm and δC 39.5 ppm).[18]

RESULTS AND DISCUSSION

Metabolite Patterns of AOH and AME Obtained from Tobacco BY-2 Cells. AOH and AME were incubated in tobacco BY-2 cell suspensions for 2 days during the exponential growth phase. The incubation medium after cell separation did not contain detectable amounts of free AOH and AME, suggesting complete mycotoxin uptake into the cells. Analysis of the cell extracts after disruption of the intact cells revealed the presence of small amounts of parental AOH and AME. The major part of the mycotoxins was, however, metabolized as demonstrated by five and seven peaks with spectroscopic

DOI: 10.1021/acs.jafc.5b00806
J. Agric. Food Chem. 2015, 63, 4728−4736

Table 1. ^{1}H and ^{13}C NMR Data of Alternariol (AOH) and Its Metabolites[a]

	AOH (Figure 1A)			AOH-1 (Figure 1E)			AOH-2 (Figure 1C)			AOH-3 (Figure 1D)			AOH-4 (Figure 1F)			AOH-5 (Figure 1G)		
	δ_H	J	δ_C	δ_H	J	δ_C	δ_H	J	δ_C	δ_H	J	δ_C	δ_H	J	δ_C	δ_H	J	δ_C
1			138.10			138.33			138.36			138.07			138.12			138.33
2	6.72	d (2.3)	117.32	6.74	d (2.3)	117.44	6.74	d (2.2)	117.50	6.96	d (2.4)	117.82	6.73	d (2.1)	117.30	6.94	d (2.6)	117.50
3			158.25			158.44			158.42			157.42			158.62			157.15
3-OH	10.35	s		10.66	s		10.46	s					10.44	s				
4	6.64	d (2.3)	101.36	6.67	d (2.3)	101.38	6.66	d (2.2)	101.28	6.97	d (2.4)	102.16	6–64	d (2.1)	101.31	6.97	d (2.6)	102.16
4a			152.51			152.37			152.55			152.27			152.70			153.80
6			163.99			nd			nd			nd			nd			nd
6a			97.21			99.29			99.42			97.25			99.75			98.09
7			164.44			163.75			163.49			163.90			164.11			164.33
7-OH	11.77	s					11.76	s		nd			11.78	s		11.74	s	
8	6.37	d (1.6)	100.63	6.75	d (1.8)	101.33	6.64	d (1.5)	101.45	6.41	d (1.3)	101.27	6.70	d (1.2)	101.41	6.42	d (1.7)	101.16
9			165.29			163.70			163.78			165.66			163.48			165.59
9-OH	10.92	s								nd						nd		
10	7.25	d (1.6)	104.07	7.37	d (1.8)	104.15	7.40	d (1.5)	103.97	7.30	d (1.3)	104.84	7.32	d (1.2)	103.95	7.32	d (1.7)	104.62
10a			138.10			138.33			138.36			138.07			138.12			138.33
10b			108.75			108.36			108.61			111.04			108.75			111.65
11	2.71	s	24.97	2.75		24.93	2.76	s	24.86	2.76	s	24.99	2.75	s	24.82	2.77	s	24.94
1′				5.14	d (7.2)	99.41	5.13	d (7.3)	99.62	5.02	d (7.4)	99.75	5.14	d (7.4)	99.46	5.08	d (7.4)	99.24
2′				3.29		72.80	3.29		72.85	3.25		72.93	3.31		72.74	3.29		72.75
3′				3.31		75.85	3.32		76.06	3.28		76.33	3.35		75.68	3.32		75.93
4′				3.24		69.18	3.17		69.39	3.16		69.40	3.18		69.49	3.20		69.33
5′				3.69		75.28	3.43		77.19	3.42		76.93	3.73		73.75	3.75		73.43
6′				3.97		68.38	3.72		60.45	3.70		60.42	4.40		63.80	4.37		63.83
6′				3.62		68.37	3.47		60.45	3.45		60.43	4.07		63.75	4.12		63.78
1″				4.16	d (7.8)	103.37												
2″				2.95		73.24												
3″				3.05		76.66												
4″				3.05		69.74												
5″				3.10		76.44												
6″				3.64		60.77												
6″				3.42		60.74												
Mal-CH_2													3.24		42.19	3.39		41.20
Mal-*COOR*															167.37			nd
Mal-*COOH*													12.20		167.80	11.00		167.80

[a]AOH-1:9-*O*-{*β*-D-glucopyranosyl(1 → 6)-*β*-D-glucopyranosyl}AOH; AOH-2:9-*O*-*β*-D-glucopyranosyl-AOH; AOH-3:3-*O*-*β*-D-glucopyranosyl-AOH; AOH-4:9-*O*-(6-*O*-malonyl-*β*-D-glucopyranosyl)AOH; AOH-5:3-*O*-(6-*O*-malonyl-*β*-D-glucopyranosyl)AOH. δ_H/δ_c are given in ppm, J in Hz. nd = not determined, s = singlet, d = doublet

DOI:10.1021/acs.jafc.5b00806
J. Agric. Food Chem. 2015, 63, 4728−4736

characteristics suggesting AOH and AME conjugates, respectively (Figure 2). None of these peaks was present in control incubations without mycotoxins. Variation of the mycotoxin concentration, incubation time, and cell mass did not change the number of potential conjugates, although slight changes in the size of the peaks were observed. All potential conjugates eluted earlier than AOH or AME from the reversed-phase column and had characteristic UV spectra similar to that of the parental mycotoxins, i.e., with absorption bands at about 254, 288, 299, and 340 nm. The m/z values of the quasi-molecular ions of the potential conjugates were higher than those of the parental compounds, but their MS^2 spectra showed the m/z values of the corresponding mycotoxins as major fragments.

To obtain sufficient quantities of the metabolites for structure elucidation, the combined cell extracts of several incubations were fractionated using preparative HPLC. All five metabolites of AOH and four dominant AME metabolites represented by peaks 2, 5, 6, and 7 (Figure 2) were isolated in quantities and purities that allowed for unambiguous structural characterization by NMR spectroscopy. The minor AME metabolites 1, 3, and 4 were isolated in small amounts only. Tentative structures could, however, be proposed based on their UV and mass spectrometric data as discussed later.

Structure Elucidation of the Major AOH and AME Conjugates. *AOH Metabolites.* The molecular mass of the AOH metabolite representing the dominant peak 2 (Figure 2A) was determined as 420 (quasi-molecular ion with m/z 421 $[M + H]^+$) consistent with a metabolite built of AOH and a hexose sugar. The mass difference between the quasi-molecular ion and the fragment m/z 259 $[AOH + H]^+$ also suggests AOH being attached to a hexose. HPAEC-PAD analysis after acidic hydrolysis revealed the hexose to be glucose. The aromatic region of the ^1H NMR spectrum of AOH metabolite 2 showed four AOH doublets with 2 Hz *meta* coupling constants. The carbons shifts of AOH were assigned by using the HSQC and HMBC spectra. Comparison of the ^1H and ^{13}C chemical shifts (Table 1) with those of parental AOH showed larger differences for C9, H8, and H10 suggesting a modification at the phenolic hydroxyl group attached to C9. Because DMSO was used as a solvent, intermolecular proton exchanges were slowed down resulting in several discrete OH signals in most samples. By using the HMBC experiment the phenolic OH protons can be assigned to specific carbons. Here, HMBC correlation peaks showed coupling of the phenolic proton in position 7, demonstrating that this phenolic group was not conjugated. The anomeric proton signal of the glucose moiety showed a coupling constant of 7.3 Hz implicating the β-anomer of the glucose unit. The appearance of one anomeric proton only and comparison of the ^1H and ^{13}C NMR data with those of glucose suggested the glucose to be bound via its lactol group to AOH. An HMBC correlation peak (Figure 3A) between the anomeric proton and C9 of AOH confirmed the glycosidic linkage in the suggested position and proved this compound to be 9-*O*-β-D-glucopyranosyl-AOH (Figure 1C).

Structure elucidation of the compound representing peak 3 (Figure 2A) showed many similarities to 9-*O*-β-D-glucopyranosyl-AOH. However, NMR data clearly demonstrate the linkage between the β-anomer of the glucose unit and the phenolic hydroxyl group in position C3 of AOH via a glycosidic linkage, identifying this compound as 3-*O*-β-D-glucopyranosyl-AOH (Figure 1D).

The remaining three potential AOH conjugates had molecular masses different from AOH glucosides. The mass

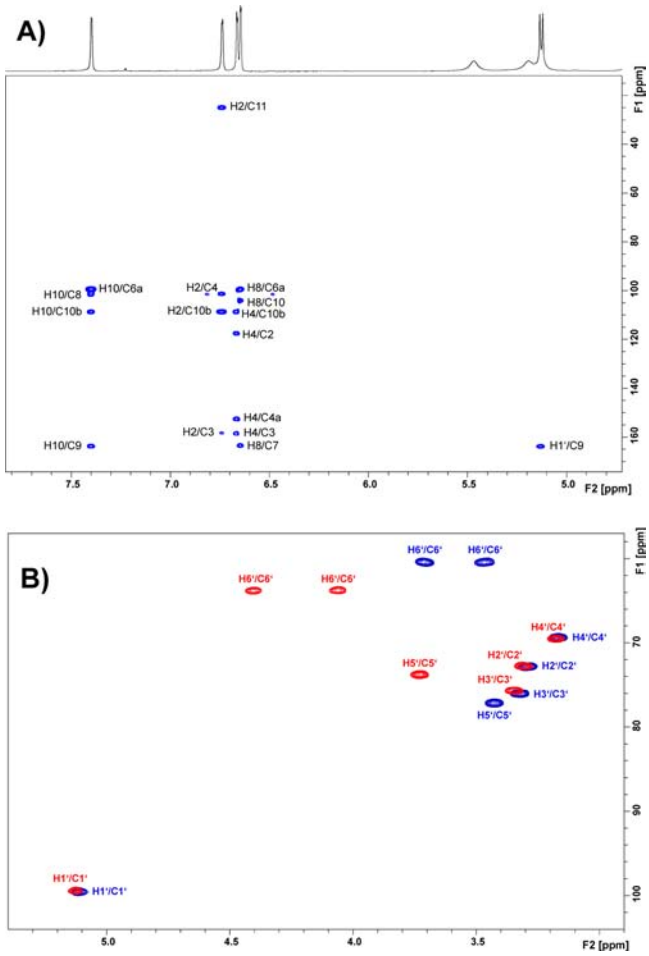

Figure 3. (A) HMBC spectrum (aglycone and anomeric region) of 9-*O*-β-D-glucopyranosyl-alternariol. (B) Overlay of the carbohydrate regions of the HSQC spectra of 9-*O*-β-D-glucopyranosyl-alternariol (blue correlation peaks) and 9-*O*-(6-*O*-malonyl-β-D-glucopyranosyl)-alternariol (red correlation peaks).

spectrum of peak 1 showed quasi-molecular ions with m/z 583 ($[M + H]^+$) and m/z 605 ($[M + Na]^+$), indicating a molecular mass of 582. Two mass losses of 162 Da resulting in m/z 421 and m/z 259 suggested that AOH is attached to a hexose disaccharide. NMR data confirmed this assumption and demonstrated an (1 → 6)-linkage between the two glucopyranose units (diagnostic HMBC signals, downfield shift of about 8 ppm for C6 of one glucose unit). Again, the coupling constants of the anomeric protons (7.2 Hz, 7.8 Hz) demonstrated both glucose anomers to be in their β-position. NMR data of the aglycone suggested its conjugation via the phenolic OH group at C9, which was unambiguously verified by interpretation of the HMBC spectrum. Thus, the compound representing peak 1 was identified as 9-*O*-{β-D-glucopyranosyl-(1 → 6)-β-D-glucopyranosyl}AOH (Figure 1E).

The quasi-molecular ions of the compounds representing peaks 4 and 5 (m/z 507, $[M + H]^+$; m/z 529, $[M + Na]^+$) suggest a molecular mass of 506 that cannot be explained by the formation of simple AOH glycosides. The MS^2 spectra showed a 248 Da mass loss resulting in a fragment with m/z 259 $[AOH + H]^+$. A mass loss of 248 Da indicates the elimination of an anhydro malonylglucoside as was also observed for isoflavone malonylglucosides.[19] Interpretation of the NMR spectra confirmed the substitution of the glucose unit

DOI: 10.1021/acs.jafc.5b00806
J. Agric. Food Chem. 2015, 63, 4728−4736

Table 2. ^{1}H and ^{13}C NMR Data of Alternariol-9-*O*-monomethyl Ether (AME) and Its Metabolites[a]

	AME (Figure 1B)			AME-2 (Figure 1H)			AME-5 (Figure 1I)			AME-6 (Figure 1J)			AME-7 (Figure 1K)		
	δ_H	*J*	δ_C	δ_H	*J*	δ_C	δ_H	*J*	δ_C	δ_H	*J*	δ_C	δ_H	*J*	δ_C
1			138.30			137.75			138.22			138.08			138.48
2	6.73	d (2.3)	117.42	6.68	d (2.4)	116.70	6.98	d (2.4)	117.94	6.96	d (1.8)	117.71	7.01	d (2.5)	117.95
3			158.33			158.30			157.60			157.18			157.65
3-OH	10.39	s		10.33	s										
4	6.65	d (2.3)	101.29	6.56	d (2.4)	100.72	6.99	d (2.4)	102.21	6.98	d (1.8)	102.28	7.03	d (2.5)	102.21
4a			152.52			152.67			152.22			152.11			152.19
6			nd			nd			nd			nd			nd
6a			98.47			nd			98.62			98.54			99.02
7			164.00			161.30			164.04			163.94			164.16
7-OH	11.83	s					11.78			11.80			11.81		
8	6.63	d (1.9)	98.94	6.97	d (2.1)	101.33	6.69	d (1.9)	99.56	6.68	d (1.1)	99.54	6.71	d (2.1)	99.60
9			165.89			164.17			165.92			165.71			166.07
10	7.23	d (1.9)	103.23	7.37	d (2.1)	104.21	7.30	d (1.9)	103.88	7.3	d (1.1)	103.89	7.32	d (2.1)	103.94
10a			138.30			137.75			138.22			138.08			138.48
10b			108.60			108.70			110.79			110.79			111.33
11	2.74	s	24.81	2.75		24.70	2.80		24.77	2.80		24.78	2.81		24.80
12	3.91	s	55.60	3.93		55.44	3.93		55.69	3.93		41.23	3.93		55.72
1′				5.01	d (7.7)	101.68	5.03	d (7.4)	99.74	5.1	d (7.3)	99.29	5.17	d (7.8)	99.31
2′				3.39		73.14	3.26		72.91	3.29		72.78	3.37		72.84
3′				3.31		76.04	3.28		76.30	3.32		76.03	3.76		74.04
4′				3.16		69.64	3.16		69.39	3.20		69.37	4.68		71.43
5′				3.43		77.33	3.44		76.92	3.75		73.46	3.55		73.46
6′				3.73		60.60	3.71		60.39	4.37		63.87	3.57		59.79
6′				3.45		60.60	3.45		60.38	4.12		63.87	3.35		59.74
Mal-CH_2										3.39		41.23	3.42		41.47
Mal-*COOR*												166.68			166.34
Mal-*COOH*										nd		167.30			168.22

[a]AME-2:7-*O*-*β*-D-glucopyranosyl-AME; AME-5:3-*O*-*β*-D-glucopyranosyl-AME; AME-6:3-*O*-(6-*O*-malonyl-*β*-D-glucopyranosyl)AME; AME-7:3-*O*-(4-*O*-malonyl-*β*-D-glucopyranosyl)AME. δ_H/δ_c are given in ppm, J in Hz. nd = not determined, s = singlet, d = doublet.

with a malonyl group. Linkage of the malonyl group to the glucose 6 position was obvious from the ^{1}H and ^{13}C data if compared to data of the non-malonyl conjugated AOH glucoside (Figure 3B, Table 1) and was confirmed by HMBC correlation peaks showing coupling of the malonyl carbonyl carbon and glucose 6 protons. Again, the glucose unit was proven to be in its *β*-configuration. NMR also revealed that the compounds representing peaks 4 and 5 differ in the AOH position to which the 6-*O*-malonyl-*β*-D-glucopyranosyl unit is attached. HMBC correlation peaks show the attachment to AOH position 9 (compound representing peak 4) and 3 (compound representing peak 5) identifying these AOH metabolites as 9-*O*-(6-*O*-malonyl-*β*-D-glucopyranosyl)AOH and 3-*O*-(6-*O*-malonyl-*β*-D-glucopyranosyl)AOH, respectively (Figure 1F,G).

AME Metabolites. Different from AOH, AME carries two phenolic hydroxyl groups only. Because of the methoxyl group in position 9, glycosidation in this position as shown for AOH is not an option. The quasi-molecular ion of peak 2 (Figure 2B) (*m*/*z* 457, $[M + Na]^+$) and the fragment *m*/*z* 273 ($[AME + H]^+$, mass loss of 162 Da) suggested AME to be conjugated with a hexose. NMR data (Table 2) indicated glucose conjugation of AME in position 7, which was confirmed by an HMBC correlation peak between the anomeric proton (*β*-configuration) and carbon 7 of AME identifying this compound as 7-*O*-*β*-D-glucopyranosyl-AME (Figure 1H).

The compound representing peak 5 has a molecular weight of 434 (quasi-molecular ion *m*/*z* 435, $[M + H]^+$), and its NMR-data are closely comparable to those of 3-*O*-*β*-D-glucopyranosyl-AOH with the exception of those data showing the difference between AOH and AME. Complete interpretation of the data including the HMBC correlation peak between the anomeric glucose proton and the AME C3 identified this compound as 3-*O*-*β*-D-glucopyranosyl-AME (Figure 1I).

The mass spectrum of the compound representing peak 6 suggested a malonyl conjugated AME glucoside (quasi-molecular ions of *m*/*z* 521 $[M + H]^+$ and *m*/*z* 543 $[M + Na]^+$, MS^2: *m*/*z* 273 $[AME + H]^+$). Independent interpretation of the NMR data but also comparison to the data of 3-*O*-(6-*O*-malonyl-*β*-D-glucopyranosyl)AOH suggested this compound to be 3-*O*-(6-*O*-malonyl-*β*-D-glucopyranosyl)AME. The linkage positions between AME, glucose, and the malonyl group were unambiguously confirmed by HMBC signals, identifying this compound as 3-*O*-(6-*O*-malonyl-*β*-D-glucopyranosyl)AME (Figure 1J).

Another malonyl glucoside of AME was obtained from peak 7. Again, both the quasi-molecular of *m*/*z* 521 ($[M + H]^+$) and the loss of 248 Da (representing an anhydro malonylglycoside) were indicative for such a structure. NMR data of the AME moiety of this compound were closely comparable to those of 3-*O*-(6-*O*-malonyl-*β*-D-glucopyranosyl)AME; however, large differences were found for the NMR data of the glucose moiety. A downfield shift of the glucose C4 signal and upfield shifts of both the C3 and C5 signals indicate the attachment of the malonyl group to the glucose 4 position, which was also confirmed by interpretation of the HMBC spectrum. Using the described information, this compound was identified as 3-*O*-(4-*O*-malonyl-*β*-D-glucopyranosyl)AME (Figure 1K).

Thus, all metabolites of AOH and AME contain *β*-glucopyranose linked through a glycosidic bond to various

DOI: 10.1021/acs.jafc.5b00806
J. Agric. Food Chem. 2015, 63, 4728−4736

hydroxyl groups of the mycotoxins. To prove that glucose was in its D-configuration, 9-*O*-*β*-D-glucopyranosyl-AOH was hydrolyzed under acidic conditions. The liberated glucose was derivatized with (*R*)-2-octanol, silylated, and analyzed by GC-MS confirming that glucose was present in its D-form. From these results it was assumed that all glucose units in the identified AOH and AME conjugates were in their D-configuration. Whereas both available phenolic hydroxyl groups (in 3- and 7-position) of AME were found conjugated with glucose, a conjugate in which the phenolic hydroxyl group in position 7 of AOH was substituted with glucose was not found as a major AOH conjugate. Lack of conjugation may be due to the hydroxyl group being engaged in hydrogen bonding with the neighboring carbonyl group at C6 (Figure 1). In contrast, 7-*O*-glucosylation occurred in the conjugation of AME to a small extent; 3-*O*-glucosylation was, however, predominant (see below). A similar difference in the conjugation of AOH and AME was observed in an *in vitro* study on the glucuronidation with human hepatic microsomes and recombinant human UDP-glucuronosyl transferases (UGTs). AOH was glucuronidated at the C3 and C9, but not C7 hydroxyl groups, and the rate and ratio of C3 and C9 conjugation were dependent on the individual UGT isoform.[9] For AME, glucuronidation was clearly preferred at C3 by most UGT isoforms, but a few isoforms, e.g., UGT1A7, catalyzed the conjugation at C7. Similar differences in the conjugation can be assumed for plant cells, which are known to differ in their pattern of UDP-glucosyltranferases.[12] For example, Kovalsky Paris et al. (2014) recently identified an UDP-glucosyltransferase from barley, which did not catalyze the common glucosylation of zearalenone at the 14-hydroxyl group only, which is equivalent to the 9-hydroxyl of AOH, but also at the 16-hydroxyl group, which is neighboring a carbonyl group similar to the 7-hydroxyl groups of AOH and AME.[20]

The monoglucosides are, in part, further conjugated at the glucopyranoside moiety with another *β*-D-glucopyranose (forming a gentiobiose conjugate). A gentiobiose conjugate was unambiguously identified for AOH only. However, the MS spectra and HPLC retention times of AME peaks 1 and 3 (Figure 2B) also suggest the existence of an AME-7-diglucoside and an AME-3-diglucoside, respectively. Because NMR spectra were not obtained from the minor quantities of these metabolites, the position of conjugation was deduced from the observation that metabolites with identical conjugate moiety are eluted earlier if conjugated at C7 as compared to those conjugated at C3. In addition, two malonyl glucosides of AOH and two malonyl glucosides of AME were unambiguously identified. On the basis of its mass spectrum and elution behavior a fifth malonyl glucoside was tentatively identified as 7-*O*-(6-*O*-malonyl-*β*-D-glucopyranosyl)AME. Earlier studies describe a malonyl migration for malonyl glucosides of various phytochemicals such as isoflavones. Acyl migration, especially 4 → 6 migrations, are frequently described in the literature.[21] Exemplarily, 4 → 6 migration was observed for malonylgenistin.[19] Therefore, solutions of the isolated AME malonyl glucosides in MeOH and DMSO were tested for their stability. Both compounds 3-*O*-(6-*O*-malonyl-*β*-D-glucopyranosyl)AME and 3-*O*-(4-*O*-malonyl-*β*-D-glucopyranosyl)AME were stable within the test period of up to 2 weeks.

Quantitative Aspects of AOH and AME Conjugation in Tobacco BY-2 Cells. Although it was not the aim of this study to exactly quantitate the metabolites and investigate the kinetics of their formation, a striking difference in the quantitative pattern of the metabolites of AOH and AME was noted. After 48 h incubation of AME (50 μM in medium), about 75% of the applied amount was recovered in the form of extractable conjugates. Conjugation with glucose took place at the phenolic hydroxyl groups located at positions C3 (about 90%) and C7 (10%) (Figure 2B). About 10% of the recovered metabolites remained as the monoglucoside 3-*O*-*β*-D-glucopyranosyl-AME, whereas 80% were further metabolized by malonylation, preferentially (70%) at the glucose 6 position but also at the 4 position (10%). The only notable change in the pattern of AME metabolites due to varying incubation times concerned the proportion of 3-*O*-*β*-D-glucopyranosyl-AME, which decreased from 25% after 24 h incubation to 5% after 96 h, with a concomitant increase of 3-*O*-(6-*O*-malonyl-*β*-D-glucopyranosyl)AME (data not shown).

After 48 h incubation of AOH (50 μM in medium), the total recovery of the applied amount as extractable conjugates was only about 50%, and the major proportion (80%) of the recovered material consisted of the monoglucosides 9-*O*-*β*-D-glucopyranosyl-AOH (60%) and 3-*O*-*β*-D-glucopyranosyl-AOH (20%). Notably, the corresponding malonylated 9-*O*- and 3-*O*-glucosides of AOH together accounted for only 13% of the extractable conjugates. This pattern did not differ much at incubation times of 24 and 96 h. The major difference was an increase of 9-*O*-{*β*-D-glucopyranosyl(1 → 6)-*β*-D-glucopyranosyl}AOH from 7% at 24 h to 25% at 96 h, accompanied by a decrease of 9-*O*-*β*-D-glucopyranosyl-AOH (data not shown). In addition, the total recovery of extractable AOH metabolites decreased to about 35%.

Implications. Our study demonstrated that the *Alternaria* toxins AOH and AME are efficiently conjugated in cultured tobacco BY-2 cells, a widely used *in vitro* model for plant cell metabolism. The first metabolic step for both mycotoxins is conjugation with glucose. Metabolic conjugation during phase II metabolism is comparable in mammals and plants and considered an important first detoxification step for endogenous and exogenous compounds.[22] Major differences, however, between mammals and plants exist in the fate of such conjugated metabolites. Whereas animals and humans are able to rapidly excrete phase II metabolites via urine and bile, plants are basically unable to excrete phase II metabolites. Thus, storage of the metabolites either as soluble conjugates in vacuoles or as insoluble conjugates bound to cell wall components becomes essential. Both options require further modification of the primary conjugates. Whereas malonylation of the glucoside is considered a signal for transport into vacuoles, further glycosylation is supposed to enable incorporation into the cell wall.[22] Both processes are, however, not well understood on a molecular and cellular level. From our first semiquantitative data it appears that malonyl conjugation of the primarily formed glucosides is the preferred pathway for AME, whereas AOH is glycosylated, but less readily malonylated. Thus, it can be assumed that AME detoxification through conjugation and storage in the vacuole is a more efficient process for AME as compared to AOH. The efficient formation of malonyl glucosides and their potential storage in the vacuole may also explain the comparatively high recoveries for AME in our experiments, whereas much less AOH was recovered. Thus, it can be assumed that AOH is preferentially stored in the cell wall, a hypothesis that, however, needs to be investigated in future studies.

Another difference observed between AOH and AME incubations was related to cell growth. Growth of cells

DOI: 10.1021/acs.jafc.5b00806
J. Agric. Food Chem. 2015, 63, 4728−4736

incubated with AME was comparable to control cells without mycotoxin; a reduction of cell mass was, however, noted if the cells were incubated with AOH. Therefore, cell cultures were treated during the lag phase of growth with the mycotoxins (50 μM in medium) for 24, 48, and 72 h, and the wet weight of cells was determined. An aliquot of the cells was stained with Evans blue to indicate dead cells and scored by light microscopy. Whereas the cell mass of AME-treated cells increased up to 6 fold with a slight decrease of dead cells, no significant increase in the cell mass was observed in AOH-treated cells, but the percentage of dead cells increased up to 40% over time. Thus, the impact of *Alternaria* toxins and their conjugates on phytotoxicity is another factor that needs to be investigated in future studies.

While we unambiguously proved the formation of conjugates of *Alternaria* toxins in cell suspensions, the formation of these conjugates also needs to be demonstrated in field plants as a first step to evaluate a potential impact of AOH and AME conjugates on food and feed safety. A very first approach to measure conjugated *Alternaria* toxins was performed by Walravens and co-workers who developed an UPLC-MS/MS method to analyze glucosylated AOH and AME using synthesized standard compounds.[23] Syntheses of 9-*O*-β-D-glucopyranosyl-AOH, 3-*O*-β-D-glucopyranosyl-AOH, and 3-*O*-β-D-glucopyranosyl-AME were described by Mikula et al.,[24] but only 3-*O*-β-D-glucopyranosyl-AOH and 3-*O*-β-D-glucopyranosyl-AME were used for the method development mentioned above. Analyses of 24 cereal-based food products did not detect any 3-*O*-β-D-glucopyranosyl-AOH (the less abundant glucose-conjugated AOH metabolite in our study) or 3-*O*-β-D-glucopyranosyl-AME in these samples, which, however, did not contain AME, too, and only trace amounts of AOH. Therefore, more studies that include the full array of metabolites identified in our study using food products from different plant families are required to estimate the impact of AOH and AME conjugates on food and feed safety.

■ ASSOCIATED CONTENT

Supporting Information

HSQC and HMBC spectra of all AOH and AME metabolites identified in this study. The Supporting Information is available free of charge on the ACS Publications website at DOI: 10.1021/acs.jafc.5b00806.

■ AUTHOR INFORMATION

Corresponding Author

*Tel: +4972160842936. E-mail: mirko.bunzel@kit.edu.

Notes

The authors declare no competing financial interest.

■ ACKNOWLEDGMENTS

The authors are grateful to Dr. Jan Maisch (Institute of Botany, KIT) for providing BY-2 cells.

■ ABBREVIATIONS

AME, alternariol-9-*O*-monomethyl ether; AOH, alternariol; HPAEC, high performance anion exchange chromatography; PAD, pulsed amperometric detection; PDA, photo diode array; UGT, UDP-glucuronosyl transferase

■ REFERENCES

(1) Logrieco, A.; Moretti, A.; Solfrizzo, M. Alternaria toxins and plant diseases: An overview of origin, occurrence and risks. *World Mycotoxin J.* **2009**, *2*, 129−140.

(2) Ostry, V. Alternaria mycotoxins: An overview of chemical characterization, producers, toxicity, analysis and occurrence in foodstuffs. *World Mycotoxin J.* **2008**, *1*, 175−188.

(3) Liu, G. T.; Qian, Y. Z.; Zhang, P.; Dong, W. H.; Qi, Y. M.; Guo, H. T. Etiological role of Alternaria alternata in human esophageal cancer. *Chin. Med. J. (Engl)* **1992**, *105*, 394−400.

(4) EFSA. Scientific opinion on the risks for animal and public health related to the presence of *Alternaria* toxins in feed and food. *EFSA J.* **2011**, *9* (2407), 97.

(5) Lehmann, L.; Wagner, J.; Metzler, M. Estrogenic and clastogenic potential of the mycotoxin alternariol in cultured mammalian cells. *Food Chem. Toxicol.* **2006**, *44*, 398−408.

(6) Brugger, E. M.; Wagner, J.; Schumacher, D. M.; Koch, K.; Podlech, J.; Metzler, M.; Lehmann, L. Mutagenicity of the mycotoxin alternariol in cultured mammalian cells. *Toxicol. Lett.* **2006**, *164*, 221−230.

(7) Pfeiffer, E.; Eschbach, S.; Metzler, M. *Alternaria* toxins: DNA strand-breaking activity in mammalian cells in vitro. *Mycotoxin Res.* **2007**, *23*, 152−157.

(8) Fehr, M.; Pahlke, G.; Fritz, J.; Christensen, M. O.; Boege, F.; Altemoller, M.; Podlech, J.; Marko, D. Alternariol acts as a topoisomerase poison, preferentially affecting the IIalpha isoform. *Mol. Nutr. Food Res.* **2009**, *53*, 441−451.

(9) Pfeiffer, E.; Schmit, C.; Burkhardt, B.; Altemöller, M.; Podlech, J.; Metzler, M. Glucuronidation of the mycotoxins alternariol and alternariol-9-methyl ether in vitro: Chemical structures of glucuronides and activities of human UDP-glucuronosyltransferase isoforms. *Mycotoxin Res.* **2009**, *25*, 3−10.

(10) Sandermann, H. Plant metabolism of xenobiotics. *Trends Biochem. Sci.* **1992**, *17*, 82−84.

(11) Gareis, M.; Bauer, J.; Thiem, J.; Plank, G.; Grabley, S.; Gedek, B. Cleavage of zearalenone-glycoside, a masked mycotoxin, during digestion in swine. *J. Vet. Med. B* **1990**, *37*, 236−240.

(12) Berthiller, F.; Crews, C.; Dall'Asta, C.; De Saeger, S.; Haesaert, G.; Karlovsky, P.; Oswald, I. P.; Seefelder, W.; Speijers, G.; Stroka, J. Masked mycotoxins: A review. *Mol. Nutr. Food Res.* **2013**, *57*, 165−186.

(13) EFSA. Scientific opinion on the risks for human and animal health related to the presence of modified forms of certain mycotoxins in food and feed. *EFSA J.* **2014**, *12* (3916), 107.

(14) Rychlik, M.; Humpf, H. U.; Marko, D.; Danicke, S.; Mally, A.; Berthiller, F.; Klaffke, H.; Lorenz, N. Proposal of a comprehensive definition of modified and other forms of mycotoxins including "masked" mycotoxins. *Mycotoxin. Res.* **2014**, *30*, 197−205.

(15) Fleck, S. C.; Burkhardt, B.; Pfeiffer, E.; Metzler, M. Alternaria toxins: Altertoxin II is a much stronger mutagen and DNA strand breaking mycotoxin than alternariol and its methyl ether in cultured mammalian cells. *Toxicol. Lett.* **2012**, *214*, 27−32.

(16) Turner, J. G.; Novacky, A. Quantitative relation between plant and bacterial cells involved in hypersensitive reaction. *Phytopathology* **1974**, *64*, 885−890.

(17) Wefers, D.; Tyl, C. E.; Bunzel, M. Novel arabinan and galactan oligosaccharides from dicotyledonous plants. *Front. Chem.* **2014**, *2*, 100.

(18) Gottlieb, H. E.; Kotlyar, V.; Nudelman, A. NMR chemical shifts of common laboratory solvents as trace impurities. *J. Org. Chem.* **1997**, *62*, 7512−7515.

(19) Yerramsetty, V.; Mathias, K.; Bunzel, M.; Ismail, B. Detection and structural characterization of thermally generated isoflavone malonylglucoside derivatives. *J. Agric. Food. Chem.* **2011**, *59*, 174−83.

(20) Kovalsky Paris, M. P.; Schweiger, W.; Hametner, C.; Stuckler, R.; Muehlbauer, G. J.; Varga, E.; Krska, R.; Berthiller, F.; Adam, G. Zearalenone-16-*O*-glucoside: a new masked mycotoxin. *J. Agric. Food. Chem.* **2014**, *62*, 1181−1189.

DOI: 10.1021/acs.jafc.5b00806
J. Agric. Food Chem. 2015, 63, 4728−4736

(21) Yoshimoto, K.; Tsuda, Y. General path of *O*-acyl migration in D-glucose derivatives: acyl migration of methyl mono-*O*-myristoyl-α- and β-D-glucopyranosides and mono-O-myristoyl-D-glucopyranoses. *Chem. Pharm. Bull.* **1983**, *31*, 4324−34.
(22) Sandermann, H. Higher-plant metabolism of xenobiotics-the green liver concept. *Pharmacogenetics* **1994**, *4*, 225−241.
(23) Walravens, J.; Mikula, H.; Rychlik, M.; Asam, S.; Ediage, E. N.; Di Mavungu, J. D.; Van Landschoot, A.; Vanhaecke, L.; De Saeger, S. Development and validation of an ultra-high-performance liquid chromatography tandem mass spectrometric method for the simultaneous determination of free and conjugated Alternaria toxins in cereal-based foodstuffs. *J. Chromatogr. A* **2014**, *1372*, 91−101.
(24) Mikula, H.; Skrinjar, P.; Sohr, B.; Ellmer, D.; Hametner, C.; Froehlich, J. Total synthesis of masked Alternaria mycotoxins-sulfates and glucosides of alternariol (AOH) and alternariol-9-methyl ether (AME). *Tetrahedron* **2013**, *69*, 10322−10330.

DOI: 10.1021/acs.jafc.5b00806
J. Agric. Food Chem. 2015, 63, 4728−4736

JOURNAL OF AGRICULTURAL AND FOOD CHEMISTRY

Article

pubs.acs.org/JAFC

Use of Fluoride-Containing Water for the Irrigation of Soil–Plant Systems

Lisa M. Scholz,[†] Peter M. Kopittke,*[,†] Neal W. Menzies,[†] Scott A. Dalzell,[‡] David C. Macfarlane,[‡] and J. Bernhard Wehr[†]

[†]The University of Queensland, School of Agriculture and Food Sciences, St Lucia, Queensland 4072, Australia

[‡]Santos, Queensland Business Unit Environment, Brisbane, Queensland 4000, Australia

Supporting Information

ABSTRACT: Many groundwaters used for irrigation contain elevated concentrations of F, but much remains unknown regarding how this F behaves within soils and plants. The present study investigated the adsorption and desorption of F from several soils in short- to medium-term irrigation systems and related foliar F concentrations in three forage plant species to the maximum tolerable level (MTL) in the diets of grazing animals (being 1.8 μmol/g for young cattle, for example). Although adsorption isotherms could be successfully used to predict the behavior (adsorption and desorption) of F within the soil, this was not related to the subsequent accumulation of F in plant foliage. In addition, the extent to which F accumulated in the foliage depended on the plant species. Regardless, F generally did not accumulate in plant foliage to levels exceeding the MTL when used at rates equivalent to irrigation for 25 years. In addition to uptake by roots, F may accumulate in foliar tissues directly due to retention from overhead irrigation. The data presented here regarding the behavior of F in soils and plants will assist in the rigorous regulation of F-containing irrigation water to ensure maximum plant growth while simultaneously minimizing potential harm.

KEYWORDS: *adsorption and desorption, fluoride toxicity, fluoride uptake, lucerne, leucaena, Rhodes grass*

INTRODUCTION

Fluoride (F) is present naturally in the environment and is a common constituent of groundwater. However, agricultural activities, particularly the use of phosphatic fertilizers,[1] and industrial activities can also result in its accumulation to levels which are of concern in both soils and waters. At a concentration of ca. 0.053 mM (1 mg/L), F can mitigate against dental decay and is often added to potable water supplies. However, consumption of excess F can cause dental fluorosis or, in extreme cases, skeletal fluorosis. The concentration of F in groundwater is typically <0.053 mM, but concentrations of 0.25−1.0 mM are not uncommon.[2] The maximum concentration of F permitted in groundwater used for irrigation varies substantially depending upon the country and the conditions under which the water is to be irrigated (for example, soil type), ranging from 0.053 mM (1 mg/L) to 0.79 mM (15 mg/L).[3] In irrigated areas, the use of groundwater containing elevated levels of F is of concern not only due to direct ingestion of water by livestock but also due to its consumption in plant matter following its plant uptake from irrigated soils. The maximum tolerable level (MTL) of F in plant material has been developed as a guideline for the upper limit of F that different classes of animals may consume without a high risk of developing fluorosis, with the MTL for F ranging from 1.8 μmol/g (35 mg/kg) for young beef calves and heifers to >5.3 μmol/g (100 mg/kg) for swine and poultry.[4]

Given the worldwide problem regarding the irrigation of waters containing elevated F, the focus of this study was the Great Artesian Basin (Australia) which is the largest artesian basin in the world, containing an estimated 65000 million ML of groundwater.[5] The groundwater and coal seam water in this basin can be used for agriculture, and concentrations of F are typically <0.26 mM (5 mg/L).[6,7] Of particular interest to this study, the coal seam water, which is released during production of coal seam gas (also termed coal bed methane) can be used beneficially to increase agricultural production, although production of coal seam water only lasts for 10−15 years, after which no further irrigation is possible. Although the general irrigation of groundwater for agricultural production would typically exceed these timeframes, these traditional agricultural systems are not the focus of the present study.

In order to understand the risk of F uptake into forages, three factors are of interest: (i) adsorption and desorption of F by soils, (ii) uptake of F from soils by plant roots, and (iii) retention of F on the foliage of plants grown using overhead irrigation. Although numerous studies have investigated the F adsorption capacities of soils,[8−15] few have investigated desorption of F from soil surfaces back into the soil solution (as required for subsequent plant uptake).[9−12] The accumulation of F in foliar tissues resulting from irrigation with water containing F has also received comparatively little investigation.[16−22] Singh et al.[23] found that irrigation with 6.3 mM F will not harm okra (*Abelmorchus esculentus*) plants and that irrigation with 0.53 mM F resulted in fruit containing F at a concentration of 0.11 μmol/g. Another study investigating

Received: February 24, 2015
Revised: April 24, 2015
Accepted: April 30, 2015
Published: April 30, 2015

ACS Publications © 2015 American Chemical Society

DOI: 10.1021/acs.jafc.5b01001
J. Agric. Food Chem. 2015, 63, 4737−4745

uptake and concentration of F in rice (*Oryza sativa* L.) irrigated with water containing up to 0.21 mM F found the concentration of F in the leaves to be >2.6 μmol/g.[24] Unfortunately, these studies do not differentiate between F taken up by plant roots and that accumulated by foliar tissues through direct contact with irrigation water. Indeed, we are aware of only one study examining the retention of F by foliar tissues as a result of direct contact between F in irrigation water and foliar surfaces.[25] These authors found that the accumulation of F on the foliar surfaces of bush beans (*Phaseolus vulgaris* L.) increased with increased F concentration of irrigation water and increases in irrigation frequency.

The aim of the present study was to investigate the risk of F accumulation above the lowest recommended MTL (young beef calves and heifers, 1.8 μmol F/g) in three forage plant species grown on a range of soils irrigated with groundwater containing concentrations of F above the current conservative regulated limit of 0.053 mM, as used in Australia, the USA, and Canada.[3] In doing so, three key factors were examined: (i) adsorption/desorption of F in soils (and hence concentrations of plant-available F in the soil solution), (ii) plant root uptake of F from the soil solution and translocation to foliar tissues, and (iii) the accumulation of F in foliar tissues from direct contact between F in irrigation water and foliar surfaces. Of particular interest were irrigated systems of short- to medium-term duration (i.e., < 20 years where water resources are limited), such as irrigation of coal seam water, irrigation to establish forestry/grazing systems, or irrigation to supplement the water supply in variable rainfall environments.

MATERIALS AND METHODS

Selection and Preparation of soils. Three experiments were conducted to investigate the movement of F within soils and plants. Experiment 1 was conducted in the laboratory and investigated the adsorption and desorption of F by soils. Experiment 2 was conducted in the greenhouse and investigated the uptake of F from F-loaded soils, and experiment 3 investigated the retention of F due to overhead irrigation. Six soils were used for these experiments: an alfisol, a red vertisol, a brown vertisol, a red ultisol, a yellow ultisol, and a spodosol. These soils were collected from various regions within the Great Artesian Basin and were representative of typical soils used for agricultural production (Table S1, Supporting Information), with the mineralogy being examined using quantitative X-ray diffraction (Table S2, Supporting Information).[26] A washed white quartz sand from North Stradbroke Island (Australia) was included as a control (the sand treatment is referred to as a "soil" for brevity). These soils had not previously been irrigated with groundwater and were selected as they were expected to vary in their F adsorption capacities. All soils were collected, air-dried, mixed, and ground to pass a 1 mm sieve.

Experiment 1: Soil F Adsorption and Desorption. First, a laboratory experiment was conducted to investigate the adsorption of F by soils. The NaF was added to the soil at seven rates, with seven soils (five soils had three separate layers and two soils had only a single layer; Tables S1 and S2, Supporting Information), and three replicates per treatment, yielding a total of 357 experimental units. Triplicate blanks (controls) containing no soil were also included and measured in the same manner as that for the soil samples. Soil subsamples (2 g) were weighed into 15 mL tubes, and 8 mL of deionized water and 2 mL of F solution was added. The solutions added contained F at concentrations of 0, 0.26, 1.1, 2.6, 6.6, 13, and 26 mM, yielding final nominal F concentrations of 0, 0.053, 0.22, 0.52, 1.3, 2.6, and 5.2 mM (0, 1, 4, 10, 25, 50, and 100 mg/L) with corresponding pH values ranging from 6.5 to 7.3. The lower F concentrations used were similar to those of irrigation waters, but much higher values were also used because preliminary experiments showed that these concentrations were required in order to reach maximum sorption. For each soil, a control (i.e., without soil) was included to allow for the measurement of the F added. Samples were shaken for 24 h on an end-over-end mixer[13] and centrifuged for 5 min. Then, 2 mL of the supernatant was mixed with 2 mL of total ionic strength adjusting buffer (TISAB, containing 1 M acetic acid, 1 M NaCl, and 4 g/L CDTA),[27] and the activity of the F^- was measured using an F^- ion selective electrode (TPS IONODE IJ-F, Australia). The pH of the supernatant was measured following shaking, with the pH increasing an average of 0.64 unit following addition of F (Figure S1, Supporting Information).

Second, following its adsorption to the soil matrix, desorption of F was investigated. Subsamples of untreated soils (2 g) were weighed into 15 mL tubes, and 10 mL of artificial groundwater was added containing F at a concentration of either 0.26 or 6.6 mM. Thus, the desorption study consisted of two F concentrations with seven soils (some with three layers), each with three replicates, and with triplicate blanks (controls, with no soil). Soils were allowed to equilibrate with F solution in an end-over-end mixer for 7 days and the samples centrifuged. The supernatant was removed, and the F^- activity was measured following the same procedure outlined above. The supernatant was replaced with 10 mL of deionized water, the sample was resuspended, and the tube was shaken for 1 h before the supernatant was again removed for the measurement of F^-, determining the F desorbed. This desorption process (i.e., addition of water, resuspension, and subsequent removal of supernatant) was repeated a total of seven times.

For statistical analysis of adsorption and desorption, the free F^- (mM) and bound F (mmol/kg) of the adsorption experiment were fitted by nonlinear regression to the Langmuir adsorption isotherm (SigmaPlot 12.3, Systat Software Inc., Chicago, IL, USA) given as

$$Q = Q_{max}\frac{K[A]}{1 + K[A]} \quad (1)$$

where Q is the adsorption capacity, Q_{max} is the maximum adsorption capacity, K is the binding strength, and A is the concentration of F at equilibrium (or free F). Relationships between K and Q_{max} were investigated using Pearson's correlation coefficient (Minitab 16, Minitab Inc., State College, PA, USA).

Experiment 2: Uptake of F by Roots. This experiment aimed to investigate the root uptake of F from four F-loaded soils using leucaena (*Leucaena leucocephala* (Lam.) de Wit ssp. *glabrata* cv. Tarramba), lucerne (*Medicago sativa* L. cv. L91), and Rhodes grass (*Chloris gayana* cv. Top Cut). The three plant species were grown on four of the soils used in experiment 1 (red Ultisol (0−15 cm), yellow Ultisol (0−15 cm), red Vertisol (0−15 cm), and sand) which were loaded with four levels of F: control (0), 2.6, 7.9, and 26 mmol of F/kg of soil (0, 50, 150, and 500 mg of F/kg). The maximum concentration used (26 mmol of F/kg soil) was equivalent to the application of 200 ML/ha water containing 0.26 mM F (5 mg/L F) to the top 20 cm of the soil (assuming an annual irrigation rate of 8 ML/ha, this a loading for ca. 25 years). Thus, there were 12 treatments per soil type (three species and four F concentrations) with four replicates. In addition, there were also three pots of each treatment with no plants. This gave a total of 51 pots per soil and 204 pots across the entire study, which were arranged in a completely randomized design.

In order to incorporate the F, each soil (excluding sand) was weighed and divided into four samples. For three of these samples, F (as NaF) was dissolved into 5 L of deionized water and sprayed evenly across the surface of the soil. The soil was mixed thoroughly while the 5 L of F solution was being applied. Due to its low adsorption capacity, F was added to sand by adding the F to the amount of water required for each pot to reach field capacity (1 L). The soil was placed in pots (200 mm, holding ca. 6 kg of soil per pot), and the pot was wrapped in reflective insulation foil and positioned on a capillary watering bench to reduce leaching through the pot and maintain constant water content within the soil. White polypropylene beads were placed on the top of the soil to reduce evaporation, and a basal application of "Flowfeed EX7" (21 N:3.3 P:17.4 K + trace elements) fertilizer (1 g/L) was added every 2−3 weeks.

DOI: 10.1021/acs.jafc.5b01001
J. Agric. Food Chem. 2015, 63, 4737−4745

Approximately 20 seeds were sown in each pot, and germination was good for all treatments other than the F-containing sand treatments, where no seeds were observed to germinate in the 7.9 and 26 mmol F/kg treatments (and only low germination took place in the 2.6 mmol of F/kg treatment). For these sand treatments, seeds of all species were germinated in the laboratory before transplanting; however, there was again 100% mortality. Following their establishment, seedlings were thinned to three plants per pot and grown for 8 weeks during summer. During this growth period, average minimum temperatures were 22 °C with average maximum temperatures of 33 °C, with typical photosynthetically active radiation levels during the middle of the day of 1500 μmol of photons m^{-2} s^{-1}. The above-ground plant material was harvested, weighed, and dried in an oven at 60 °C for 4 days.

Soil solution was extracted from the soil using centrifugation.[28] The solution was analyzed for pH and F (1:1 with TISAB). To determine the concentration of F within the plant tissues, samples were prepared for NaOH fusion.[29] Prior to the measurement of F, the solution was mixed 10:4 with concentrated TISAB buffer to ensure pH 5.4 and to prevent the F from forming complexes that would interfere with the measurement of F. Our calculations indicate a 10-fold excess of CDTA over Al ions in the assays, with CDTA effectively complexing all soluble Al in soil solution. Activities of the free F^- ion in the solutions were determined by a F ion selective electrode.

The data were analyzed using a two-way analysis of variance (ANOVA) to investigate the relationships between F additions to soils, soil types, and plant species. The F concentration of soil solutions of the four soils was also investigated by conducting a two-way ANOVA, although sand treatments were removed for the soil F concentrations, as the variance did not conform to the normal distribution. Statistical analysis was conducted using Genstat (VSN International, Hemel Hempstead, U.K.) and Minitab 16.

Experiment 3: Foliar Retention of F. This experiment aimed to investigate foliar retention of F from direct contact between foliar surfaces and groundwater containing F. In systems irrigated with coal seam water (as with other systems), foliage will also occasionally be rinsed with low-F water (for example, rainfall). This would potentially remove much of the F previously accumulated on the foliage. To separate the effect of root uptake from foliar adsorption, we grew plants in an oxisol (Table S2, Supporting Information), since this soil had a very high F adsorption capacity and limited plant uptake of F from the soil. Furthermore, the soil surface of the pots was covered with plastic sheets to minimize the infiltration of irrigation water into the soil.

This experiment consisted of the three plant species utilized in experiment 2 and four F concentrations in artificial groundwater (0, 0.053, 0.16, or 0.26 mM, added using NaF and verified by measurement using an ion-selective electrode), each with three replicates arranged in a randomized block design totaling 36 pots (each pot containing three plants). The highest concentration of F utilized for experiment 3 (0.26 mM) represents the highest concentration of F generally found in the groundwater of the Great Artesian Basin (95% of groundwater wells having ≤0.26 mM F).[6] After an initial growing period of ca. 8 weeks, plants were overhead-irrigated twice weekly using irrigation chambers connected to a pump and a 100 L drum containing one of the four F treatments. The 100 L of water was irrigated per treatment, taking around 30 min. Plants were irrigated with the F-containing solutions a total of eight times. To investigate whether any F retained on the leaf surface could be subsequently leached by application of good-quality water following these eight F irrigations, the plants were irrigated with deionized water for 10 min to simulate a rainfall event, allowed to dry overnight, and harvested. Plants were allowed to grow for a further 2 weeks to see if any F remaining in the plant foliage was volatilized and lost over time.

Plant foliage was randomly harvested after 0, 4, and 8 irrigations with F treatments. Plant tissue samples were also collected following irrigation with deionized water and after the subsequent 2 week growth period. Foliar concentrations of F were measured after NaOH fusion (see experiment 2) using an F ion selective electrode, as discussed previously. Approximately 300 g of soil from five randomly selected pots of each treatment (20 pots in total) was collected and the soil solution extracted by centrifugation, as outlined in experiment 2.

Statistical analyses were conducted in Genstat and Minitab 16, with the relationship between number of irrigations and plant F concentrations investigated using a two-way ANOVA. Similarly, the relationship between plant species and F in irrigation water was investigated using a two-way ANOVA.

RESULTS

Experiment 1: Soil F Adsorption and Desorption. The seven soils varied substantially in their capacity to adsorb F—a Langmuir adsorption isotherm could not be fitted to the sand due to its low adsorption capacity (Figure 1 and Table 1). The

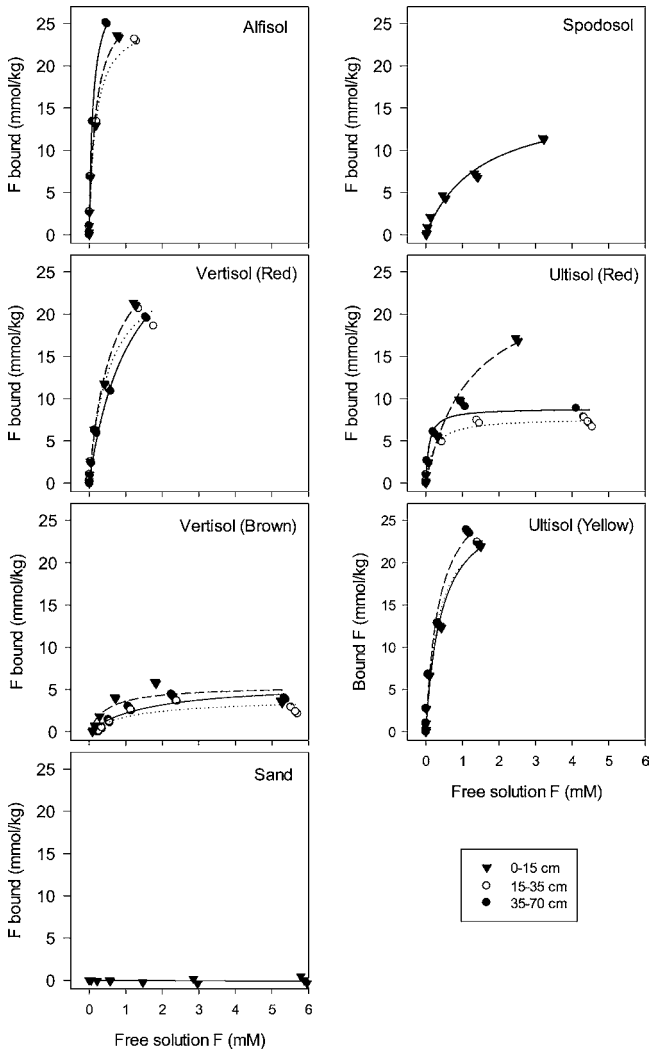

Figure 1. Adsorption isotherms of F for seven different soils (experiment 1) fitted using the Langmuir equation.

lowest binding strength was observed for the brown vertisol (K = 0.6−2.0 mmol/L) and spodosol (K = 0.7 L/mmol), suggesting that these soils weakly bind F. The highest sorption capacity (Q_{max}) was determined for the yellow ultisol (Q_{max} = 26.7−30.3 mmol/kg), alfisol (Q_{max} = 25.8−30.6 mmol/kg), and red vertisol (Q_{max} = 26.7−34.2 mmol/kg) (Figure 1 and Table 1). Interestingly, the red ultisol was the only soil to differ substantially in F sorption on comparison of different layers through the soil profile, with the surface layer (0−15 cm) having a Q_{max} value of 24.7 mmol/kg, decreasing to 8.8 mmol/

DOI: 10.1021/acs.jafc.5b01001
J. Agric. Food Chem. 2015, 63, 4737−4745

Table 1. Langmuir Sorption Parameters Q_{max} (Maximum F Adsorption Capacity) and K (F Binding Strength) For Six Soils (All with Three Layers Excluding the Spodosol) Investigated in Experiment 1[a]

soil	depth (cm)	Q_{max} ± SE (mmol/kg)	K ± SE (L/mmol)	R^2
ultisol (red)	0–15	25 ± 1.5	0.8 ± 0.1	0.987
	15–35	7.7 ± 0.2	4.9 ± 0.6	0.986
	35–70	8.8 ± 0.3	11 ± 2.2	0.960
ultisol (yellow)	0–15	30 ± 2.0	2.7 ± 0.5	0.974
	15–35	27 ± 1.3	2.9 ± 0.4	0.981
	35–70	30 ± 2.0	2.7 ± 0.5	0.974
vertisol (brown)	0–15	5.4 ± 0.7	2.0 ± 0.7	0.768
	15–35	4.0 ± 0.7	0.8 ± 0.3	0.736
	35–70	5.8 ± 0.8	0.6 ± 0.2	0.854
vertisol (red)	0–15	31 ± 1.4	1.6 ± 0.2	0.992
	15–35	27 ± 1.4	1.9 ± 0.2	0.985
	35–70	34 ± 1.8	0.8 ± 0.1	0.994
alfisol	0–15	29 ± 1.0	5.5 ± 0.6	0.991
	15–35	26 ± 0.7	5.7 ± 0.5	0.990
	35–70	31 ± 1.0	9.0 ± 0.8	0.990
spodosol	0–25	16 ± 1.2	0.7 ± 0.1	0.979

[a]The values were determined by nonlinear regression, and the regression parameter R^2 is shown in the last column. The sand is excluded due to inability to fit data to the Langmuir equation with low adsorption capacity.

kg at 35–70 cm depth, whereas the binding strength increased with depth, from K = 0.8 L/mmol in the 0–15 cm layer to 11.4 L/mmol in the 35–70 cm layer.

Next, the desorption of F was investigated. As expected, the extent of F desorption increased with increasing washing steps, with ca. 20–80% of the F desorbed after seven washes (Table 2 and Figure S2 in the Supporting Information). A notable exception was the brown vertisol, which desorbed more F than was initially added in the 15–35 cm (188%) and 35–70 cm (159%) layers (Table 2), thereby indicating that this soil already contained appreciable F. In general, more F was desorbed from soil treated with a higher F concentration (6.6 mM vs 0.26 mM) (Table 2). Importantly, the desorption of F was significantly correlated (negatively) to the K value estimated by the Langmuir equation for both low (0.26 mM) and high (6.6 mM) F treatments (r = −0.54 and −0.68, respectively; P < 0.05), thereby indicating that the binding strength (K) would appear to be a useful measure for predicting the F retention capacity of the soils examined. For example, in the red ultisol, as K increased from 0.8 (0–15 cm depth) to 11.4 (35–70 cm depth), the extent of F desorption decreased from 63 to 38% (Tables 1, and 2 and Figure S2 in the Supporting Information).

Table 2. Desorption of F from Six Soils to Which F Had Initially Been Equilibrated for 7 Days using Solutions Containing F at a Concentration of either 0.26 mM (Low) or 6.6 mM (High) (Experiment 1)

		cumulative F desorbed (%)	
soil	depth (cm)	low F addition	high F addition
ultisol (red)	0–15	30.0 ± 0.3	62.9 ± 0.2
	15–35	20.0 ± 0.4	47.6 ± 0.4
	35–70	17.3 ± 0.8	38.0 ± 0.1
ultisol (yellow)	0–15	29.0 ± 0.4	53.3 ± 0.7
	15–35	25.2 ± 0.2	46.0 ± 0.5
	35–70	23.4 ± 0.0	36.1 ± 0.0
vertisol (brown)	0–15	64.3 ± 0.1	49.3 ± 0.3
	15–35	188.0 ± 8.0	99.0 ± 2.3
	35–70	159.0 ± 0.0	59.1 ± 0.0
vertisol (red)	0–15	48.6 ± 0.9	52.8 ± 0.2
	15–35	52.3 ± 0.5	55.8 ± 0.8
	35–70	77.4 ± 2.6	43.7 ± 1.1
alfisol	0–15	38.4 ± 0.9	45.4 ± 0.4
	15–35	43.5 ± 2.2	40.3 ± 1.4
	35–70	25.6 ± 0.6	27.1 ± 0.1
spodosol	0–15	79.0 ± 2.0	78.5 ± 1.6

Experiment 2: Uptake of F by Roots. The addition of F influenced plant growth to varying extents depending upon the soil type. For the sand, growth was reduced substantially, with almost complete mortality in most of the F-containing treatments. In the yellow ultisol, dry matter of lucerne and Rhodes grass decreased significantly as the F-application rate was increased from 0 to 26 mmol/kg but the dry matter of leucaena was unaffected. In the red ultisol and red vertisol, the addition of F to the rooting environment had no significant effect on the dry matter of the plants (P > 0.05).

For this experiment, increases in soil solution F concentrations followed trends expected from the Q_{max} and K values obtained in the laboratory-based study (i.e., experiment 1). For example, when F was added at a rate of 26 mmol/kg, soil solution concentrations of F were highest in the sand (96 mM), followed by the red ultisol with 4.5 mM, the yellow ultisol with 1.0 mM, and the red vertisol with 0.58 mM (see Figures 1 and 2 and Table 1). For the red ultisol, the addition of F increased the pH of soil solution by ca. 3 pH units, with the increase in the other soils being ca. 1 pH unit (Figure S3, Supporting Information). Interestingly, the pH in the solutions of soils growing Rhodes grass was higher than those for lucerne and leucaena in red ultisol, yellow ultisol and red vertisol in every F treatment (excluding red ultisol 26 mmol F/kg; Figure S2, Supporting Information)—this requires further investigation.

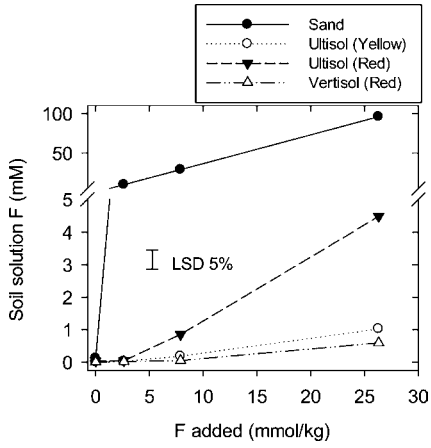

Figure 2. Soil solution F concentration (averaged across all three plant species) for four soils treated with increasing concentrations of F (0, 2.6, 7.9, or 26 mmol F/kg, experiment 2). The vertical bar represents the least significant difference (LSD, 5%) to allow comparison either between soils at a single rate of F or between F rates for the same soil.

DOI: 10.1021/acs.jafc.5b01001
J. Agric. Food Chem. 2015, 63, 4737–4745

Given the increase in soil solution F concentrations (see above), it was also not surprising that the addition of F to soils increased the foliar concentrations of F (Figure 3). A significant

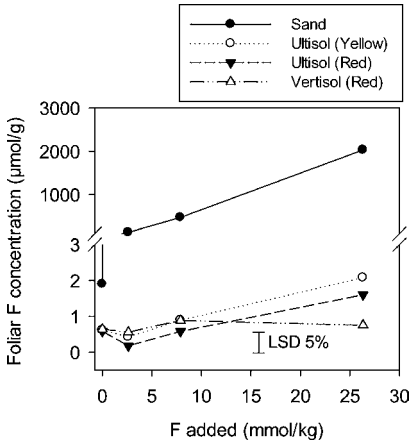

Figure 3. Concentration of F in plant foliar material (averaged across all three species) grown on four soils treated with increasing concentrations of F (0, 2.6, 7.9, or 26 mmol F/kg, experiment 2). The vertical bar represents the least significant difference (LSD, 5%) to allow comparison either between soils at constant F or between F concentrations for the same soil.

interaction ($P < 0.001$) was found between the soil type and the rate of F addition, indicating that while the addition of F to the soil significantly influenced the concentration of F in plant material, the pattern of this response varied for each soil (Figure 3). Indeed, the increase in foliar F was greatest in sand (increasing from an average of 1.9 to 2000 μmol F/g) and least for the red vertisol (increasing from an average of 0.63 to 0.74 μmol F/g) (Figure 3). The uptake of F was influenced not only by soil type but also by plant species. For the yellow ultisol, red ultisol, and sand (but not the red vertisol), analyses of individual plant species identified a significant interaction between the rate of F addition and plant species ($P < 0.001$) (Figure 4). For example, in the sand, yellow ultisol and red ultisol treated with 26 mmol of F/kg, lucerne accumulated significantly more F in the foliage than did Rhodes grass or leucaena.

To determine the factors regulating the uptake of F from the soil solution, the foliar concentrations were first related to total concentrations of F in the soil solution. When the foliar concentrations of F were examined across the different soils, data for the sand had to be excluded from linear regressions, as these high F concentrations had statistically high leverage. Across the remaining three soils, the foliar F concentration was not related to the total concentration of F in the soil solution for either Rhodes grass ($R^2 = 0.079$) or leucaena ($R^2 < 0.001$), although a weak relationship was found for lucerne ($R^2 = 0.539$) (Figure 5). These differences between species are perhaps not surprising, given that lucerne was the only species in which tissue F concentrations increased substantially (excluding the sand treatments) (Figure 4). Unsurprisingly, when the foliar F concentrations were examined for each soil individually, the relationship was also generally poor (other than for the sand) (Figure S4, Supporting Information). Given the lack of relationship with the total soluble F concentrations, thermodynamic modeling was also conducted using PhreeqcI v3.1.2 (Minteq database) to determine if the F concentration in the foliage was related to the speciation of F in the soil solution.

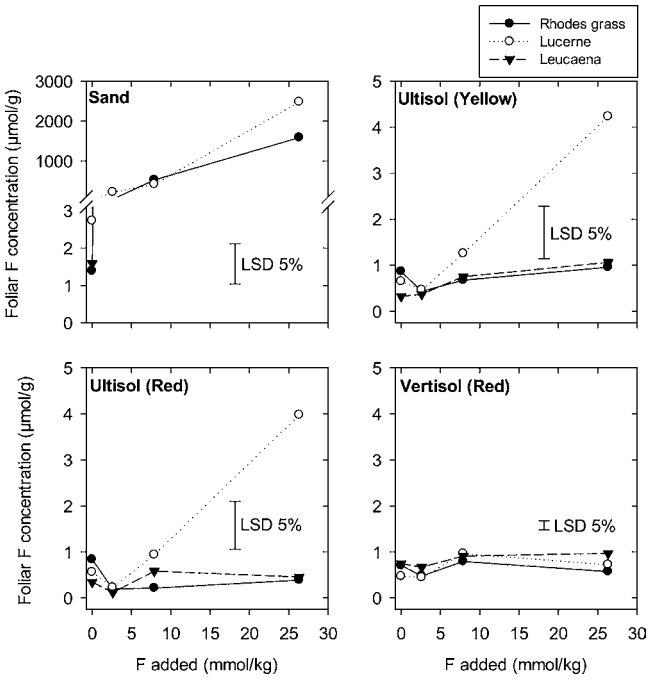

Figure 4. Foliar F concentrations of Rhodes grass, lucerne, and leucaena grown on four soils (a sand, a yellow ultisol, a red ultisol, and a red vertisol) treated with 0, 2.6, 7.9, or 26 mmol F/kg (experiment 2). Due to greatly reduced growth, leucaena plants in the 2.6, 7.9, and 26 mmol F/kg treatments could not be analyzed in the sand due to insufficient dry plant material. The vertical bar represents the least significant difference (LSD, 5%) to allow comparison either between plant species at constant F or between F concentrations for the same species.

As expected, the speciation of F varied substantially between soils, with F present predominantly as the free F^- ion in both the Red Ultisol and the Sand but as Al−F complexes in the yellow ultisol (data not presented). Although various relationships were observed using this thermodynamic modeling, no consistent relationship was found across all four soils and three plant species (data not presented).

Experiment 3: Foliar Retention of F. Overhead irrigation of F-containing groundwater was found to influence the foliar F concentration (Figure 6a). The accumulation of F in the foliage resulting from soil uptake was negligible, given that the concentration of F within the soil solution of the oxisol averaged across all four treatments was <0.003 mM (cf. experiment 2; see Figure 2 for example).

A significant interaction was found between increasing irrigations of F-containing water and plant species ($P < 0.001$), indicating that not only does the cumulative application of F in irrigation water increase foliar F concentrations but also the pattern of response differs between plant species (Figure 6a). Lucerne was found to retain the highest concentration of F in the foliar material; after four irrigations (second harvest) with 0.26 mM irrigation water, the concentration of F in lucerne foliar tissues increased from 0.37 to 1.7 μmol F/g, and following eight irrigations (third harvest) the plant material increased further to 2.3 μmol F/g: a ca. 6-fold increase ($P < 0.05$, Figure 6a). Conversely, increases in tissue concentrations were more modest for the other two plant species, increasing from 0.53 to 0.79 μmol of F/g for Rhodes grass and 0.37 to 1.1 μmol of F/g for leucaena after eight irrigations at ca. 0.26 mM (Figure 6a). The concentration of F within the irrigation water

DOI: 10.1021/acs.jafc.5b01001
J. Agric. Food Chem. 2015, 63, 4737−4745

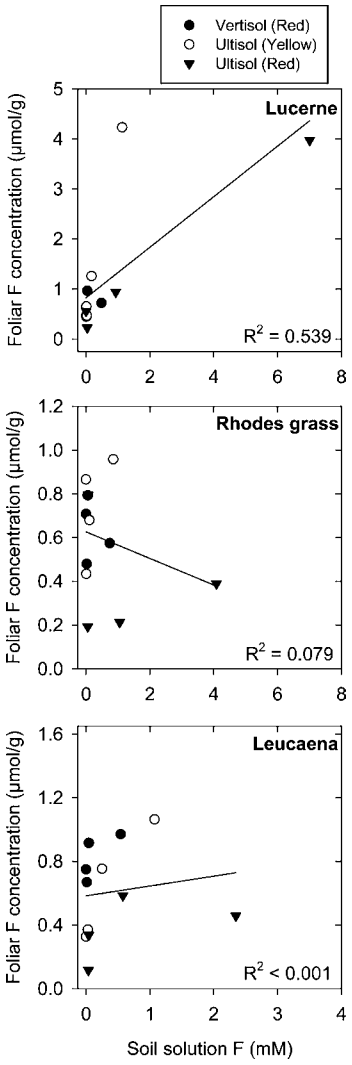

Figure 5. Relationship between the concentration of F in the foliar tissues of three plant species (lucerne, Rhodes grass, and leucaena) with the total concentration of F in the soil solution (experiment 2). Data are presented for three soils, but the data for the sand were excluded because these values had statistically high leverage. Note that the scales are not constant.

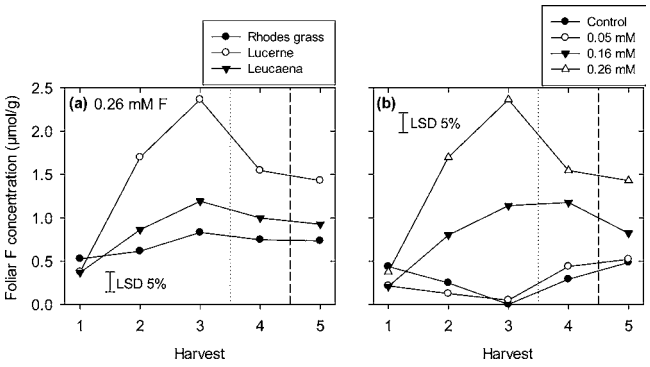

Figure 6. Concentrations of F in plant foliage following four irrigations (harvest 2) or eight irrigations (harvest 3) with artificial groundwater containing F (experiment 3). Plants were then irrigated with deionized water (harvest 4) and grown for a further 2 weeks without overhead irrigation (harvest 5). (a) Concentrations of F in foliage of Rhodes grass, lucerne, and leucaena irrigated with water containing F at a concentration of 0.26 mM. (b) Concentrations of F in the foliage of lucerne irrigated with water containing F at a concentration of 0, 0.053, 0.16, or 0.26 mM. The vertical bar represents the least significant difference (LSD, 5%) to allow comparison between harvests for a single treatment or between treatments for a single harvest.

also had a significant effect on foliar F concentrations, with a significant increase in tissue F concentrations when the F concentration of the water was raised from 0 to ca. 0.16 and 0.26 mM (Figure 6b).

After eight irrigations with F-containing groundwater, deionized water was applied to simulate rainfall and to investigate the potential leaching of F from the foliage. Relative to tissue concentrations after eight irrigations with water containing ca. 0.26 mM, tissue concentrations decreased significantly (from 2.4 to 1.5 μmol of F/g) for lucerne but there were no significant differences for the two other plant species (Figure 6a). For groundwaters containing lower concentrations of F, the effect of rainfall on tissue F concentrations was not clear (Figure 6b). Allowing the plants to grow undisturbed (i.e., no overhead irrigation) for a further 2 weeks after the simulated rainfall generally had no significant effect on tissue concentrations (Figure 6, $P > 0.05$).

DISCUSSION

Both the direct addition of F to soils and the foliar retention of F-containing irrigation water resulted in increases in the foliar F concentration. However, under the current experimental conditions, these increases in foliar F concentrations through either pathway were modest and concentrations generally remained lower than the MTL of 1.8 μmol/g (35 mg/kg) for cattle (excluding plants grown on sand). For example, even when F was added at a rate of 26 mmol/kg (this soil concentration would be reached after irrigation with water containing 0.26 mM at a rate of 5 ML/(ha year) for 25 years), most plant tissue concentrations were <1 μmol/g (with the highest values being for lucerne, 4.2 μmol/g; Figure 4) and hence were generally was less than the MTL of mature beef cattle (2.6 μmol/g), sheep (3.2 μmol/g), chickens (10 μmol/g), and swine (7.9 μmol/g).[4] Furthermore, with addition of F at a rate of 7.9 mmol/kg (i.e., reached after 8 years of irrigation at 5 ML/(ha year) with 0.26 mM) plant foliar tissues did not increase above 1.3 μmol F/g in any treatment, this being less than the MTL for young beef calves and heifers, 1.8 μmol F/g.[4] Therefore, for short- to medium-term irrigation projects (for example, irrigation to establish forestry or grazing systems), the addition of realistic rates of F-containing groundwater is unlikely to increase the soil F concentrations in soils (excluding highly sandy soils) to levels above which plant uptake of F from the soil may affect grazing animals.

These conclusions need to be considered carefully before extrapolating to other situations. For example, the present study examined the irrigation of F-containing water in short- to medium-term systems, but long-term irrigation with water containing high concentrations of F would result in the addition of F at levels higher than those considered here. Also, it is apparent that both the soil type and the plant species influences the retention and uptake of F, with the present study only examining seven soils and three plant species. Finally, irrigation of water with F concentrations lower or higher than this value would also alter the volume of water that could be safely irrigated.

DOI: 10.1021/acs.jafc.5b01001
J. Agric. Food Chem. 2015, 63, 4737−4745

Variation in the Concentration of F in the Soil Solution Depending upon the Soil Type. The extent to which F was available in the soil solution varied substantially depending upon the soil (Figure 1). In the laboratory (experiment 1), the relationship between F adsorbed and F remaining free in the soil solution could be estimated using the Langmuir equation, with Q_{max} providing an estimate of maximum adsorption capacity and K providing an estimate of the binding strength (Figure 1 and Table 1). Similarly, in the greenhouse (experiment 2), the concentrations of soluble F in the soil solutions were related to the Langmuir parameters determined in experiment 1, with total soil solution F present in the 26 mmol of F/kg treatment in the order (decreasing) sand > red ultisol > yellow ultisol = red vertisol (Figure 2). Thus, adsorption isotherms are likely to be useful for (i) identification of soils which are likely to be unsuitable for irrigation with F-containing waters (such as the sand in the current study) and (ii) estimation of the volume of irrigation water which could be applied before the concentration of F in the soil solution exceeds a given threshold (for example, the concentration of F permitted in drainage water). However, within the range of relevance to the MTLs, the relationship between the concentration of F in the foliage and the concentration of F in the soil solution was comparatively poor (see next section). It is known that adsorption (and therefore the amount of F remaining in solution) is determined by a number of factors, among them pH, ionic strength, presence of poorly crystalline Fe and Al hydrous oxides, and clay mineralogy,[13,14,17,30−32] and these factors have differed between the soils used in this study (Tables S1 and S2, Supporting Information). However, there were no clear relationships between these soil factors and the F uptake in this study, likely due to the limited number of soils used.

It was also decided to investigate the desorption of F, given that it is this desorption (i.e., movement back into the soil solution) which will result in a buffering of the F concentration in the soil solution. The desorption of F from all soils was significantly correlated (negatively) to the estimated K, indicating that desorption capacity of soils can be estimated from the Langmuir adsorption parameters. The desorption of F was in the range of ca. 20−40% for soils with high K values, increasing to 60−80% for soils with low K values (Tables 1 and 2). As expected, the proportion of F that desorbed increased as the rate of F addition increased (Table 2), most likely due to the fact that high affinity binding sites for F become saturated, resulting in F being less strongly bound as the rate of F addition increases. It was also noted that the desorption of F decreased when adsorption equilibrium time increased (data not presented) due to the occurrence of slower reactions such as CaF_2 (fluorite) precipitation and diffusion into pores.[9,11] This indicates that desorption rates observed in the present study would likely be reduced further following an increase in equilibration time, as would occur in the field.

Uptake of F from the Soil Solution and Its Accumulation in the Foliage. The accumulation of F in the foliage varied substantially depending upon both the plant species and the soil type (Figures 3 and 4). Under the present experimental conditions, lucerne was the only plant species which accumulated F in the foliage to concentrations >1.3 μmol F/g (excluding sand), although the reason as to why lucerne accumulates more F than other species is not known. Interestingly, Hansen et al.[33] also found lucerne concentrated high F in foliar material, with 5.3 μmol of F/g observed when soils were loaded with ca. 84 mmol of F/kg. Similarly, tissue concentrations of up to 3.4 μmol of F/g were found in lucerne grown in acid soil amended with flue gas desulfurization gypsum.[34] More study is required in this regard, but it is possible that Rhodes grass and leucaena are F excluders, and hence the concentration of F within their tissues was not closely related to F availability within the soil. It is also possible that water use efficiency is lower for lucerne than for other species, resulting in greater F uptake; alternatively, translocation of F complexes in the xylem differs between plant species and it has been suggested that Ca limits translocation from roots to shoots either by membrane effects or by precipitation on the root surface.[30,34,35]

The accumulation of F in the foliage varied substantially depending upon the soil type (Figure 3). This was expected, given the differences observed in the adsorption capacities of these soils (Figure 1) and the resultant variations in soil solution F concentrations (Figure 2). However, despite being the immediately "plant available" fraction, soluble F in the soil solution was not generally related to the concentration of F in the foliage (Figure 5). Similarly, there was no consistent relationship between F uptake and F speciation in the soil solution, with F uptake closely related to F^- activity in some soils but to the activity of Al−F complexes in other soils (data not presented).

Foliar Retention of F from Overhead Irrigation. The overhead irrigation of water containing F at a concentration of 0 or 0.053 mM had no observable impact on the foliar concentrations of F (Figure 6). However, for water containing F at a concentration of either 0.16 or 0.26 mM, overhead irrigation resulted in significant increases in the foliar F concentration (Figure 6). This finding is in agreement with the study of Wallender and Keller,[25] who found that foliar concentrations of F in bush beans increased with increasing concentrations of F in the irrigation water. In the present study, lucerne was the only species to concentrate F in foliar material above the MTL (1.8 μmol/g) following eight consecutive irrigations with water containing 0.26 mM (Figure 6)—further investigation is needed in this regard. For example, it is known that cuticular thickness, cuticular composition, and stomatal density influence the uptake/absorption of foliar applied elements.[36]

The finding that overhead irrigation with good-quality water reduced foliar F concentrations (at least somewhat) is similar to the observation of Maclean et al.,[37] who, in a study of lucerne and tall fescue grass (*Festuca arundinacea*) exposed to atmospheric F, also found that rainfall (or washing with detergent) reduced the foliar concentration of F. Several mechanisms may result in a decrease in tissue F concentrations, including growth dilution, leaf death, translocation, or volatilization, with the last mechanism considered a major contributor of F removal from plants.[38] Therefore, to investigate this possibility, plants were grown without overhead irrigation for another 2 weeks following the irrigation with deionized water. During this time, foliar F further reduced slightly for plants in the 0.16 and 0.26 mM treatments (although this decrease was significant only in lucerne irrigated with 0.16 mM F) (Figure 6). It is known that HF is volatile, and hence if F is on the leaf surface or within foliar material, it is possible that volatilization will occur. However, in the present study, allowing the plants to grow undisturbed (i.e., without overhead irrigation) generally had no significant effect on tissue concentrations of F (Figure 6), possibly because plants were

DOI: 10.1021/acs.jafc.5b01001
J. Agric. Food Chem. 2015, 63, 4737−4745

only grown for 2 weeks before harvest, thereby potentially limiting volatilization.

The present study has examined the accumulation of F within soils and plants on irrigatation with F-containing groundwater. Generally, under the current experimental conditions, F did not accumulate in plant foliage to levels likely to be deleterious to grazing fauna, even when used at rates equivalent to irrigation for 25 years (assuming irrigation at a rate of 5 ML/(ha year) with water containing F at a concentration of 0.26 mM). First, when the F was added to the soil, the extent to which the soluble F concentration increased varied significantly between soils. Given that the extent to which F accumulated in the foliage did not appear to be related to the total concentration of F in the soil solution, it would be difficult to accurately predict the amount of F which could be added to the soil before the MTL would be exceeded. In addition, the extent to which F accumulated in the plant foliage varied depending upon the species (being greatest in lucerne). Second, when water was overhead-irrigated, foliar F concentrations increased in all three species due to foliar contact with F-containing water. However, lucerne was again the only species which accumulated foliar F above MTL for young beef cattle. The data presented here regarding the behavior of F in soils and plants will assist in the rigorous regulation of the maximum volume of F-containing water per soil type and crop species to ensure maximum productivity while simultaneously minimizing potential environmental harm.

■ ASSOCIATED CONTENT

Supporting Information

Detailed description of the chemical properties of the soils used in the experiments (Table S1), soil mineralogy (Table S2), changes in soil solution pH following addition of F in experiment 1 (Figure S1), cumulative desorption of F from the soils (Figure S2), changes in soil solution pH following addition of F in experiment 2 (Figure S3), and the effect of soil solution F concentrations of foliar F concentrations (Figure S4). The Supporting Information is available free of charge on the ACS Publications website at DOI: 10.1021/acs.jafc.5b01001.

■ AUTHOR INFORMATION

Corresponding Author

*P.M.K.: e-mail, p.kopittke@uq.edu.au; tel, +61 7 3346 9149; fax, +61 7 3365 1177.

Notes

The authors declare no competing financial interest.

■ ABBREVIATIONS USED

ANOVA, analysis of variance; *K*, Langmuir binding strength for F; MTL, maximum tolerable level; Q_{max}, Langmuir maximum sorption capacity for F

■ REFERENCES

(1) McLaughlin, M. J.; Tiller, K. G.; Naidu, R.; Stevens, D. P. Review: The behaviour and environmental impact of contaminants in fertilizers. *Aust. J. Soil Res.* **1996**, *34*, 1−54.

(2) Brindha, K.; Elango, L., Fluoride in groundwater: Causes, implications and mitigation measures. In *Fluoride Properties, Applications and Environmental Management*; Monroy, S. D., Ed.; Nova Science: Hauppauge, NY, USA, 2011; pp 111−136.

(3) Weinstein, L. H.; Davison, A. W. *Fluorides in the environment: Effects on plants and animals*; CABI: Cambridge, MA, USA, 2004; p 287.

(4) National Research Council (U.S.), *Mineral Tolerance of Animals*, 2nd ed.; National Academy of Sciences: Washington, D.C., USA, 2005; p 510.

(5) Nevill, J. C.; Hancock, P. J.; Murray, B. R.; Ponder, W. F.; Humphreys, W. F.; Phillips, M. L.; Groom, P. K. Groundwater-dependent ecosystems and the dangers of groundwater overdraft: A review and an Australian perspective. *Pac Conserv Biol.* **2010**, *16*, 187−208.

(6) Harvey, J. M.; Moule, G. R. Fluorosis of merino sheep in Queensland. Part 1. How the disease is caused. *Queensland Agricultural Journal* **1954**, *79*, 291−298.

(7) *Great Artesian Basin Resource Study*; Great Artesian Basin Consultative Council: Canberra, ACT, Australia, 1998; p 235.

(8) Bower, C. A.; Hatcher, J. T. Adsorption of fluoride by soils and minerals. *Soil Sci.* **1967**, *103*, 151−154.

(9) Barrow, N. J.; Shaw, T. C. Slow reactions between soil and anions: 6. Effect of time and temperature of contact on fluoride. *Soil Sci.* **1977**, *124*, 265−278.

(10) Fluhler, H.; Polomski, J.; Blaser, P. Retention and movement of fluoride in soils. *Journal of Environmental Quality* **1982**, *11*, 461−468.

(11) Peek, D. C.; Volk, V. V. Fluoride sorption and desorption in soils. *Soil Science Society of America Journal* **1985**, *49*, 583−586.

(12) Arnesen, A. K. M.; Krogstad, T. Sorption and desorption of fluoride in soil polluted from the aluminium smelter at Ardal in Western Norway. *Water, Air, Soil Pollut.* **1998**, *103*, 357−373.

(13) Harrington, L. F.; Cooper, E. M.; Vasudevan, D. Fluoride sorption and associated aluminum release in variable charge soils. *J. Colloid Interface Sci.* **2003**, *267*, 302−313.

(14) Pickering, W. F. The mobility of soluble fluoride in soils. *Environ. Pollut., Ser. B* **1985**, *9*, 281−308.

(15) Barrow, N. J.; Ellis, A. S. Testing a mechanistic model 0.3. The effects of pH on fluoride retention by a soil. *J. Soil Sci.* **1986**, *37*, 287−293.

(16) Stevens, D. P.; McLaughlin, M. J.; Alston, A. M. Limitations of acid digestion techniques for the determination of fluoride in plant-material. *Commun. Soil Sci. Plant Anal.* **1995**, *26*, 1823−1842.

(17) Arnesen, A. K. M. Availability of fluoride to plants grown in contaminated soils. *Plant Soil* **1997**, *191*, 13−25.

(18) Stevens, D. P.; McLaughlin, M. J.; Randall, P. J.; Keerthisinghe, G. Effect of fluoride supply on fluoride concentrations in five pasture species: Levels required to reach phytotoxic or potentially zootoxic concentrations in plant tissue. *Plant Soil* **2000**, *227*, 223−233.

(19) Jha, S. K.; Nayak, A. K.; Sharma, Y. K. Response of spinach (*Spinacea oleracea*) to the added fluoride in an alkaline soil. *Food Chem. Toxicol.* **2008**, *46*, 2968−2971.

(20) Manoharan, V.; Loganathan, P.; Tillman, R. W.; Parfitt, R. L. Interactive effects of soil acidity and fluoride on soil solution aluminium chemistry and barley (*Hordeum vulgare* L.) root growth. *Environ. Pollut.* **2007**, *145*, 778−786.

(21) Ruan, J. Y.; Ma, L. F.; Shi, Y. Z.; Han, W. Y. The impact of pH and calcium on the uptake of fluoride by tea plants (*Camellia sinensis* L.). *Ann. Bot.* **2004**, *93*, 97−105.

(22) Stevens, D. P.; McLaughlin, M. J.; Alston, A. M. Phytotoxicity of aluminium-fluoride complexes and their uptake from solution culture by *Avena sativa* and *Lycopersicon esculentum*. *Plant Soil* **1997**, *192*, 81−93.

(23) Singh, V.; Gupta, M. K.; Rajwanshi, P.; Mishra, S.; Srivastava, S.; Srivastava, R.; Srivastava, M. M.; Prakash, S.; Dass, S. Plant uptake of fluoride in irrigation water by ladyfinger (*Abelmorchus esculentus*). *Food Chem. Toxicol.* **1995**, *33*, 399−402.

(24) Gupta, S.; Banerjee, S. P. Fluoride accumulation in Paddy (*Oryza sativa*) irrigation with fluoride-contaminated groundwater in an endemic area of the Birbhum district, West Bengal. *Fluoride* **2009**, *42*, 224−227.

(25) Wallender, W. W.; Keller, J. Foliar fluoride accumulation under sprinkle irrigation. *Transactions of the Asae* **1984**, *27*, 449−455.

DOI: 10.1021/acs.jafc.5b01001
J. Agric. Food Chem. 2015, 63, 4737−4745

(26) Moore, D. M.; Reynolds, R. C. *X-Ray Diffraction and the Identification and Analysis of Clay Minerals*; Oxford University Press: New York, 1997; p 378.
(27) Menzies, N. W.; Edwards, D. G.; Bell, L. C. The use of total ionic-strength adjusting buffers in determining fluoride concentration in soil solutions by ion-selective electrometry. *Commun. Soil Sci. Plant Anal.* **1993**, *24*, 1865−1882.
(28) Gillman, G. P. *A centrifuge method for obtaining soil solution*; CSIRO: Melbourne, Australia, 1976.
(29) McQuaker, N. R.; Gurney, M. Determination of total fluoride in soil and vegetation using an alkali fusion selective ion electrode technique. *Anal. Chem.* **1977**, *49*, 53−56.
(30) Ruan, J. Y.; Ma, L. F.; Shi, Y. Z.; Han, W. Y. The impact of pH and calcium on the uptake of fluoride by tea plants (*Camellia sinensis* L.). *Ann. Bot.* **2004**, *93*, 97−105.
(31) Robbins, C. W. Fluoride adsorption by a saline sodic soil irrigated with a high F water. *Irrig. Sci.* **1986**, *7*, 107−112.
(32) Kau, P. M. H.; Smith, D. W.; Binning, P. Experimental sorption of fluoride by kaolinite and bentonite. *Geoderma* **1998**, *84*, 89−108.
(33) Hansen, E. D.; Wiebe, H. H.; Thorne, W. Air pollution with relation to agronomic crops: VII. Fluoride uptake from soils. *Agronomy Journal* **1958**, *50*, 565−568.
(34) Alvarez-Ayuso, E.; Gimenez, A.; Ballesteros, J. C. Fluoride accumulation by plants grown in acid soils amended with flue gas desulphurisation gypsum. *J. Hazard. Mater.* **2011**, *192*, 1659−1666.
(35) Mackowiak, C. L.; Grossl, P. R.; Bugbee, B. G. Biogeochemistry of fluoride in a plant-solution system. *J. Environ. Qual.* **2003**, *32*, 2230−2237.
(36) Fernández, V.; Brown, P. H., From plant surface to plant metabolism: the uncertain fate of foliar-applied nutrients. *Frontiers in Plant Science* **2013**, *4*,10.3389/fpls.2013.00289
(37) Maclean, D. C.; Schneider, R. E.; Hansen, K. S.; Troiano, J. J. Effects of simulated acid-rain on uptake, accumulation, and retention of fluoride in forage crops. *Water, Air, Soil Pollut.* **1989**, *43*, 191−198.
(38) Davison, A. W.; Weinstein, L. H. Some Problems Relating to Fluorides in the Environment: Effects on Plants and Animals. In *Advances in Fluorine Science*; Alain, T., Ed.; Elsevier: Amsterdam, 2006; Chapter 8, Vol. *1*, pp 251−298.

DOI: 10.1021/acs.jafc.5b01001
J. Agric. Food Chem. 2015, 63, 4737−4745

JOURNAL OF AGRICULTURAL AND FOOD CHEMISTRY

Article

pubs.acs.org/JAFC

One-Step Fabrication of a Multifunctional Magnetic Nickel Ferrite/Multi-walled Carbon Nanotubes Nanohybrid-Modified Electrode for the Determination of Benomyl in Food

Qiong Wang, Jichun Yang, Yuanyuan Dong, and Lei Zhang*

College of Chemistry, Liaoning University, 66 Chongshan Middle Road, Shenyang, Liaoning 110036, People's Republic of China

ABSTRACT: Benomyl, as one kind of agricultural pesticide, has adverse impact on human health and the environment. It is urgent to develop effective and rapid methods for quantitative determination of benomyl. A simple and sensitive electroanalytical method for determination of benomyl using a magnetic nickel ferrite ($NiFe_2O_4$)/multi-walled carbon nanotubes (MWCNTs) nanohybrid-modified glassy carbon electrode (GCE) was presented. The electrocatalytic properties and electroanalysis of benomyl on the modified electrode were investigated by cyclic voltammetry (CV) and differential pulse voltammetry (DPV). In the phosphate-buffered saline (PBS) of pH 6.0, this constructed biosensor exhibited two linear relationships with the benomyl concentration range from 1.00×10^{-7} to 5.00×10^{-7} mol/L and from 5.00×10^{-7} to 1.00×10^{-5} mol/L, respectively. The detection limit was 2.51×10^{-8} mol/L (S/N = 3). Moreover, the proposed method was successfully applied to determine benomyl in real samples with satisfactory results. The $NiFe_2O_4$/MWCNTs/GCE showed good reproducibility and stability, excellent catalytic activity, and anti-interference.

KEYWORDS: *benomyl, $NiFe_2O_4$ nanoparticles, multi-walled carbon nanotubes, cyclic voltammetry*

1. INTRODUCTION

The fungicide benomyl, i.e., methyl 1-(butylcarbamoyl)-2-benzimidazole carbamate, is a synthetic benzimidazole. It is known to exert selective toxicity against fungal cells because of its higher affinity for fungal tubulin than mammalian tubulin.[1] Benomyl is widely used for sterilizing seeds of vegetables as an agricultural chemical against a range of fungal diseases.[2,3] Because of the occurrences of benomyl and carbendazim in the environment and the potential exposure to them through diet, there continues to be ongoing concern over the risks to human health of these fungicides.[4−7] Numerous studies have been conducted to determine the fate of benomyl and its associated residues in soils, plants, and mammals.[8] Further, in mammals, benomyl is known for its ability to induce structural changes in the chromosomes and hepatocyte microtubule cytoskeleton,[9] inhibit protein synthesis[10] and lipid peroxidation, and cause glutathione depletion.[11] Recently, benomyl and carbendazim were reported as endocrine disruptors that increased both expression and activity of aromatase in the human ovarian granulose-like tumor cell line KGN.[12] There has been concern that this compound might influence human health and cause diseases. Further, benomyl is quite unstable, and it decomposes in aqueous solutions into more stable compounds, such as carbendazim and *N*,*N*′-dibutyl urea.[13,14] The determination of benomyl residue in vegetables, fruits, and environmental water samples is a difficult task. To protect consumers from the risk related to benomyl in food and environmental water, the development of a simple, rapid, and reliable method for the determination of benomyl is of great importance.

Thus far, various techniques for the detection of benomyl have been reported in the literature, such as high-performance liquid chromatography (HPLC),[15] frequency domain fluorescence,[16] fluorescence polarization,[17,18] and in-layer chromatography[19] methods. These methods have high accuracy, well reproducibility, and reliable ability of qualitative analysis. However, these methods also suffer from some disadvantages, such as expensive experimental instruments, sophisticated laboratory procedures, trained personnel, and complex sample pretreatment. In comparison to other techniques, electrochemical methods have aroused great interests among researchers because of their relatively high sensitivity, fast response, and ability to be miniaturized.[20] The literature reported that the OV-17 silicon-modified carbon paste electrodes and bare glassy carbon electrode (GCE) were used in the determination of benomyl by differential pulse voltammetry,[21,22] and the detection limit was 6.9×10^{-5} and 1.5×10^{-4} g/L, respectively. Recently, the electroanalysis method is reported for the determination of benomyl by square-wave adsorptive stripping voltammetry,[23] and the detection limit was 2.4×10^{-5} g/L. According to our knowledge, magnetic nickel ferrite/multi-walled carbon nanotubes nanohybrid-modified glassy carbon electrode ($NiFe_2O_4$/MWCNTs/GCE) for determination of benomyl had not been reported. The main objective of this paper is to develop a new method with high sensitivity, simplicity, and efficiency for the detection of benomyl.

In this paper, $NiFe_2O_4$/MWCNTs nanohybrids were synthesized through a one-step hydrothermal method and employed as a modified electrode material for the analysis of benomyl. This method is based on the different properties of the mediators plus nanoparticles, such as strong adsorptive ability, huge specific area, and subtle electronic properties.[24−26] In addition, Ni and Fe have excellent electrocatalytic activity in

Received: February 25, 2015
Revised: April 20, 2015
Accepted: April 27, 2015
Published: May 7, 2015

ACS Publications © 2015 American Chemical Society

DOI: 10.1021/acs.jafc.5b00973
J. Agric. Food Chem. 2015, 63, 4746−4753

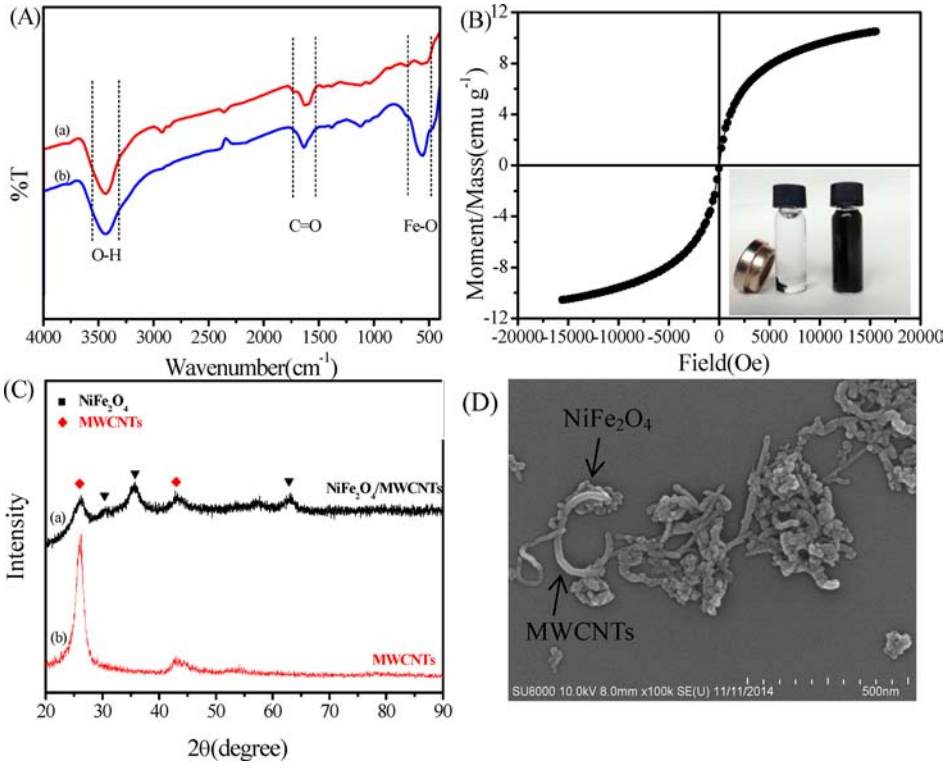

Figure 1. Characterization of MWCNTs and $NiFe_2O_4$/MWCNTs: (A) FTIR spectra of (a) MWCNTs and (b) $NiFe_2O_4$/MWCNTs, (B) VSM image of $NiFe_2O_4$/MWCNTs, (C) XRD patterns of (a) $NiFe_2O_4$/MWCNTs and (b) MWCNTs, and (D) SEM image of $NiFe_2O_4$/MWCNTs.

the catalyst of reactions of organic materials based on their electronic arrangement.[27,28] The results showed that the proposed method is simple, rapid, sensitive, and selective for the quantitative determination of benomyl at the $NiFe_2O_4$/MWCNTs/GCE.

2. EXPERIMENTAL SECTION

2.1. Chemicals and Reagents. MWCNTs (length, 0.5−2.0 μm; specific surface area, >500 m^2/g; outer diameter, <8 nm; and 95% purity) were purchased from Chengdu Organic Chemicals Co., Ltd., Chinese Academy of Sciences, Beijing, China. Benomyl (95% purity) was purchased from HEOWNS Biochemical Technology Co., Ltd. (Tianjin, China). The 5% Nafion ethanol solution (D520) was from HESEN Co., Ltd. (Shanghai, China). All other chemicals were of analytical reagent grade and produced by Shenyang Chemical Company, China.

2.2. Apparatus. A CHI660D electrochemical workstation (Shanghai ChenHua Instruments Co., China) coupled with a conventional three-electrode cell, including a platinum wire auxiliary electrode, a saturated calomel reference electrode (SCE), and a working electrode, was used for electrochemical measurements. X-ray diffraction patterns were recorded on a X-ray diffractometer (XRD, Siemens D5000, Germany) at 40 kV and 150 mA with Cu Kα radiation. The diffraction data were recorded for 2θ angles between 20° and 90°. Fourier transform infrared spectroscopy (FTIR, Avatar 330, Nicolet, Thermo Electron Scientific, Madison, WI) was used to characterize MWCNTs and $NiFe_2O_4$/MWCNTs within a 500−4000 cm^{-1} spectral domain with a resolution of 4 cm^{-1} using a KBr pellet technique at room temperature. A vibrating sample magnetometer (VSM, Lake Shore 7407, Lake Shore Cryotronics, Inc., Westerville, OH) was used to measure the magnetic prosperities of $NiFe_2O_4$/MWCNTs in the field of ±15 kOe at room temperature. The morphologies and microstructures of the material were characterized using scanning electron microscopy (Hitachi SU8000, Japan) under the voltage of 10.0 kV. A S-3C model pH meter (Shanghai Precision Scientific Instrument Co., China) was used for measuring the pH of solutions. Deionized water used throughout experiments was purified using a Sartorius Arium 611 system (Sartorius, Göttingen, Germany).

2.3. Synthesis of $NiFe_2O_4$/MWCNTs. The $NiFe_2O_4$/MWCNTs composite was fabricated by a one-step hydrothermal method. Briefly, 2.0193 g of $Fe(NO_3)_3 \cdot 9H_2O$ (0.005 mol) and 0.7017 g of $NiSO_4 \cdot 7H_2O$ (0.0025 mol) were dissolved in 50 mL of ethanol, and subsequently, 0.5 g of MWCNTs was added. Prior to that, MWCNTs were acidified with HNO_3. The obtained mixture was stirred vigorously for 1.0 h to obtain a homogeneous black solution. Then, it was transferred into a 100 mL Teflon-lined stainless-steel autoclave, heated to 180 °C, and reacted for 12 h. After that, the magnetic composite was separated by a magnet, washed repeatedly with deionized water until neutrality, and then dried at 60 °C for 12 h.

2.4. Preparation of a $NiFe_2O_4$/MWCNTs-Modified Electrode. Before modification, the bare GCE was carefully polished with three grades of alumina slurrys (0.05, 0.30, and 1.00 mm) on polishing cloth, respectively, rinsed thoroughly with deionized water between each polishing step, then washed successively with deionized water, anhydrous alcohol, and deionized water in an ultrasonic bath, and dried in air. A 4 mg/mL $NiFe_2O_4$/MWCNTs dispersion was prepared by dissolving 8.0 mg of $NiFe_2O_4$/MWCNTs in 2 mL of 1% Nafion solution prepared in ethanol. The mixture was then sonicated for 30 min to obtain a stable and well-distributed $NiFe_2O_4$/MWCNTs/Nafion suspension. A 6.0 μL drop of 4.0 mg/mL $NiFe_2O_4$/MWCNTs/Nafion suspension solution was coated on the surface of the GCE, and then the solvent was evaporated under the infrared lamp to obtain the $NiFe_2O_4$/MWCNTs/GCE.

2.5. Procedure for Benomyl Analysis. The electrochemical behavior of benomyl was studied by cyclic voltammetry (CV), and the determination of benomyl was performed by differential pulse voltammetry (DPV). All of the experiments were carried out in a conventional electrochemical cell holding 5.00 mL of 0.2 mol/L phosphate-buffered saline (PBS) at pH 6.0 and a certain amount of benomyl at room temperature. Before benomyl analysis, the 5 mL PBS solution was purged with highly purified nitrogen for 10 min.

2.6. Real Samples. Three samples of apple, mushroom, and spinach were bought in a local supermarket. Suitable amounts of three

DOI: 10.1021/acs.jafc.5b00973
J. Agric. Food Chem. 2015, 63, 4746−4753

kinds of samples were added to a 50.00 mL beaker; then a suitable amount of ethanol was added to dissolve them for 30 min with ultrasonic assistance; and sample solutions were filtrated. All of the above sample solutions were stored in a refrigerator at 4 °C and determined by DPV according to the standard addition method.

3. RESULTS AND DISCUSSION

3.1. Characterization of the $NiFe_2O_4$/MWCNTs Electrode. Curve a in Figure 1A is the FTIR spectra of MWCNTs. Two characteristic peaks of MWCNTs were observed at 1650 and 3430 cm^{-1} corresponding to C═O and O−H band stretching vibrations.[29] Curve b in Figure 1A displays the FTIR spectra of the $NiFe_2O_4$/MWCNTs nanohybrid sample. The new characteristic peak at around 556 cm^{-1} is associated with the Fe−O−Ni stretching vibration.[30] This evidence confirmed that $NiFe_2O_4$ was successfully loaded to MWCNTs. Figure 1B presents the magnetic properties of $NiFe_2O_4$/MWCNTs analyzed by room-temperature VSM with an applied field of $-15.0 \leq H \leq 15.0$ kOe. The value of saturation magnetization (Ms) is about 10.48 emu g^{-1} (inset is the photo of magnetic separation).

The XRD patterns of $NiFe_2O_4$/MWCNTs and pure MWCNTs are shown in Figure 1C. The peaks at 25.9° and 43.2° were attributed to the characteristic peaks of MWCNTs (which can be seen in both curves a and b in Figure 1C).[31] Besides, from curve b in Figure 1C, it could be seen that the diffraction peaks of $NiFe_2O_4$ could be assigned to spinel-type $NiFe_2O_4$ [Joint Committee on Powder Diffraction Standards (JCPDS) 54-0964]. The peaks at the 2θ values of 30.2, 35.5, and 62.4 could be indexed to (220), (311), and (440) crystal planes of spinel $NiFe_2O_4$, respectively. The results indicated that $NiFe_2O_4$ was successfully loaded to MWCNTs.

The morphology of $NiFe_2O_4$/MWCNTs was investigated by scanning electron microscopy (SEM). From Figure 1D, it is observed that $NiFe_2O_4$ nanoparticles were deposited on the surface of MWCNTs.

3.2. Electrochemical Characterization of Benomyl. The CV behavior of benomyl on the bare GCE, $NiFe_2O_4$/GCE, MWCNTs/GCE, and $NiFe_2O_4$/MWCNTs/GCE are illustrated in Figure 2 (curves a, b, c, and d, respectively). As seen, no visible signal was found on the bare GCE (curve a), only a small and broad redox peaks of benomyl occur on the $NiFe_2O_4$/GCE (curve b) and the MWCNTs/GCE (curve c). Meanwhile, a pair of well-defined and quasi-reversible redox peaks was observed at $NiFe_2O_4$/MWCNTs/GCE (curve d), which indicates that the electrochemical reaction of benomyl is a reversible process, and the $NiFe_2O_4$/MWCNTs composite has a strong enhancement ability for the electric signal of benomyl.[32,33] This is most likely to be attributed to the large surface area of $NiFe_2O_4$/MWCNTs, which may provide many favorable sites for electron transfer to molecules, and the $NiFe_2O_4$/MWCNTs nanohybrid has a good synergic effect,[34−36] which may be ascribed to the specific and preferable properties of the magnetic nanoparticles and MWCNTs.

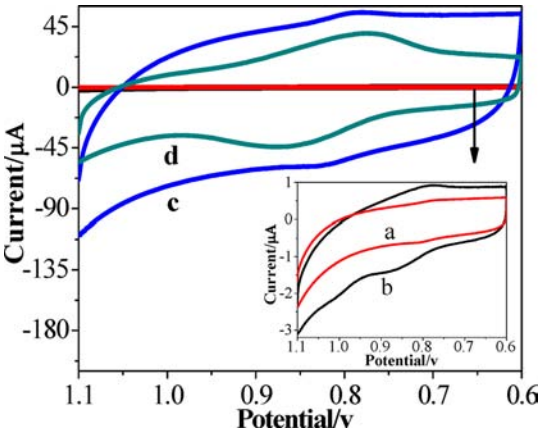

Figure 2. CVs of benomyl in 0.2 mol/L PBS at pH 6.0 solution ($C_{benomyl} = 3.5 \times 10^{-6}$ mol/L). (Inset) (a) benomyl on the bare GCE, (b) benomyl on the $NiFe_2O_4$/GCE, (c) benomyl on the MWCNTs/GCE, and (d) benomyl on the $NiFe_2O_4$/MWCNTs/GCE. Scan rate, 0.1 V/s; quiet time, 600 s.

3.3. Effect of the Modifier Amount on the Oxidation Peak Current. From the experiment, it was found that the redox peak current increased significantly with the amount of modifier (4.0 mg/mL $NiFe_2O_4$/MWCNTs/Nafion suspension solution) increasing from 4.0 to 6.0 μL, and when the amount of the suspension exceeded 6.0 μL, the current decreased. It was ascribed that the active sites for the accumulation of benomyl increased with the increment of modifier amount. The peak current decreased when the volume exceeded 6.0 μL, because the conductivity of the electrode reduced, and the film unstable as $NiFe_2O_4$/MWCNTs could leave off the electrode surface when the film was too thick. Thus, the modifier amount of 6.0 μL was chosen in the experiment.

3.4. Effect of the Accumulation Time. It is important to fix the accumulation time when adsorption studies were undertaken. Bearing this in mind, the effect of the accumulation time has been studied by the DPV method. The accumulation time can improve the amount of benomyl adsorbed on the electrode surface, then improve determination sensitivity, and decrease the detection limit. The DPV peak currents increase rapidly with the increase of the accumulation time from 0 to 600 s. However, for a longer accumulation time, there is no significant increase in the current response. This phenomenon could be attributed to the saturated adsorption of benomyl at the electrode surface. Thus, the accumulation time of 600 s was chosen in the experiment.

3.5. Effect of the pH. The effect of solution pH on the redox peak of benomyl on $NiFe_2O_4$/MWCNTs/GCE investigated at the pH range from 4.0 to 8.0 by CV is shown in Figure 3. As seen, with increasing the pH, the peak currents of benomyl increased and the potentials shifted negatively because of the participation of protons in the electrode reaction. The potentials of benomyl followed the linear regression equations with pH: E_{pa} (V) = −0.060pH + 1.14 (r = 0.9992). The value of the slope was 0.060 pH^{-1}, which is approximately close to the theoretical value of 0.0585 pH^{-1}; therefore, it can be deduced that the proton number is equal to that of the number of transferred electrons. The peak currents of benomyl increase from pH 4.0 and reach a maximum value at pH 6.0; therefore, a pH of 6.0 was chosen for the subsequent analytical experiments.

3.6. Electrochemical Properties of Benomyl. Useful information involving the electrochemical mechanism can generally be acquired from the relationship between the peak current and scan rate.[37,38] Therefore, CVs of benomyl on $NiFe_2O_4$/MWCNTs/GCE with different scan rates ranging from 0.050 to 0.20 V/s in PBS at pH 6.0 were recorded, and results are shown in Figure 4. It can be found that the peak current increased linearly with the scan rate in the range of 0.050−0.20 V s^{-1} (as shown in Figure 4A). The linear regression equations were expressed as follows: I_{pc} (μA) = 100.15v (V/s) − 4.83 (r = 0.996) and I_{pa} (μA) = −132.13v (V/

DOI: 10.1021/acs.jafc.5b00973
J. Agric. Food Chem. 2015, 63, 4746−4753

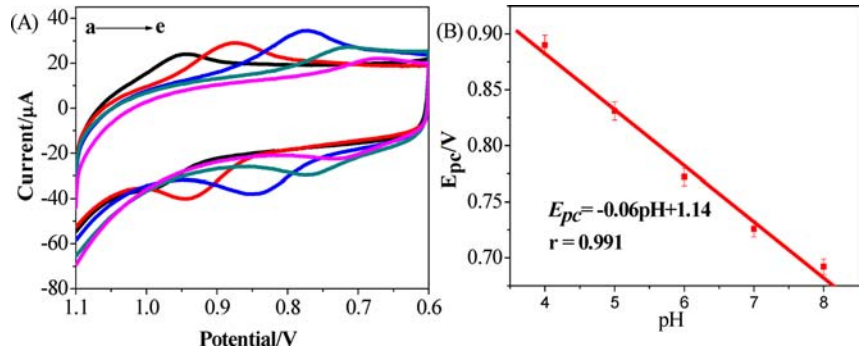

Figure 3. (A) Influence of pH on CVs of benomyl at the $NiFe_2O_4$/MWCNTs/GCE, with the pH range from a to e being 4.0−8.0, at the scan rate of 0.1 V/s, and (B) effects of pH on the potential response.

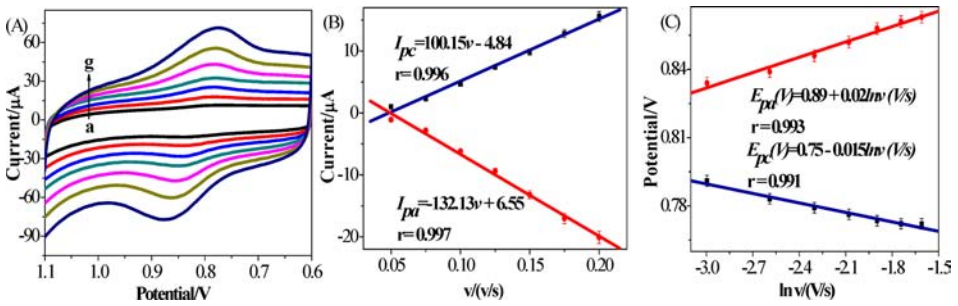

Figure 4. CVs of benomyl at different scan rates, with benomyl at 3.5×10^{-6} mol/L. (A) Scan rates from a to g are 0.050, 0.075, 0.10, 0.125, 0.15, 0.175, and 0.20 V/s, respectively. (B) Dependence of the peak current on the scan rate. (C) Dependence of the plots of E_p versus ln v.

s) + 6.55 (r = 0.997) (as shown in Figure 4B), respectively. It indicates that the redox of benomyl on $NiFe_2O_4$/MWCNTs/GCE is an adsorption-controlled process.[39,40] The ratio of the redox peak current (I_{pa}/I_{pc}) was approximately found to be 1, suggesting that the redox reaction of benomyl on $NiFe_2O_4$/MWCNTs/GCE was a quasi-reversible electrochemical behavior. In this work, the scan rate was chosen as 0.10 V s^{-1}. For an adsorption-controlled and quasi-reversible electrode process, the relationship between peak potentials and the scan rate follows Laviron's equation[41,42]

$$E_{pc} = E^0 - \frac{RT}{anF} \ln v \quad (1)$$

$$E_{pa} = E^0 + \frac{RT}{(1-a)nF} \ln v \quad (2)$$

$$\log K_s = a \log(1-a) + (1-a)\log a - \log \frac{RT}{nFv} - \frac{(1-a)anF\Delta E_p}{2.3RT} \quad (3)$$

where E_{pa} and E_{pc} are the anodic and cathodic peak potentials (V), E^0 is the formal potential (V), n is the number of electron transferred, α is the electron transfer coefficient, K_s is the standard rate constant of the surface reaction (s^{-1}), v is the scan rate (V/s), ΔE_p is the peak−peak potential separation, R is the universal gas constant (8.314 J mol^{-1} K^{-1}), T is the temperature (298 K), and F is the Faraday constant (96 500 C/mol). Figure 4C shows the plots of E_p versus ln v; the equations of the straight line were as follows: E_{pc} (V) = 0.75 − 0.015 ln v (V/s) (r = 0.991), and E_{pa} (V) = 0.87 + 0.020 ln v (V/s) (r = 0.993). The values of α and n can be determined from the slope, respectively. The electron transfer number n is close to 2, and the value of α is 0.528. Moreover, the values of K_s were calculated to be 0.951 s^{-1}. The pH effect on E_{pa} demonstrated that the number of electrons and protons involved in the benomyl oxidation process is equal (see section 3.3). Therefore, the redox of benomyl on $NiFe_2O_4$/MWCNTs/GCE is proven participation of a two protons ($2H^+$) and two electron ($2e^-$) process. The mechanism of the electrode process could be described as follows (Scheme 1).

Scheme 1. Proposed Mechanism of Electroreduction of Benomyl on the $NiFe_2O_4$/MWCNTs/GCE

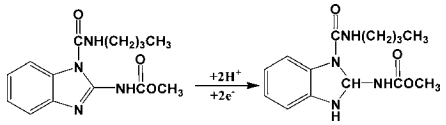

3.7. Estimation of Electrode Real Surface Areas and Γ_s.

The electrochemically effective surface areas of bare GCE and $NiFe_2O_4$/MWCNTs/GCE were determined by the chronocoulometric method according to the formula given by Anson[43]

$$Q(t) = \frac{2nFAcD^{1/2}t^{1/2}}{\pi^{1/2}} + Q_{dl} + Q_{ads} \quad (4)$$

where A is surface area of the working electrode, c is the concentration of the substrate, D is the diffusion coefficient, Q_{dl} is the double-layer charge, and Q_{ads} is the Faradaic charge. Other symbols have their usual meanings. A 0.1 mM $K_3[Fe(CN)_6]$ solution containing 1 mM KCl has a D[44] of $K_3[Fe(CN)_6]$ of 7.60×10^{-6} cm^2 s^{-1}. According to the experimental results (as shown in panels A and B of Figure 5), on the basis of the slope of the linear relationship between Q

DOI: 10.1021/acs.jafc.5b00973
J. Agric. Food Chem. 2015, 63, 4746−4753

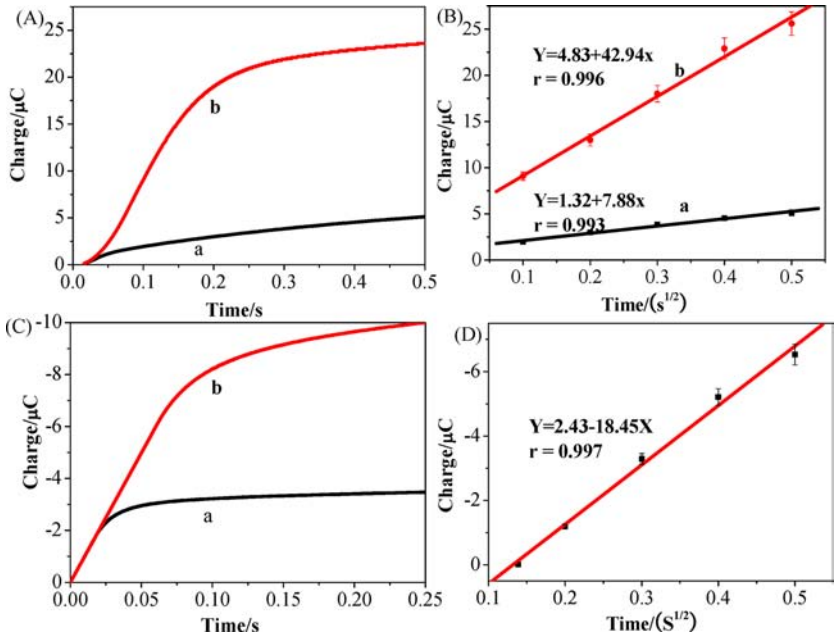

Figure 5. (A) Plot of $Q-t$ curves of (a) GCE and (b) $NiFe_2O_4$/MWCNTs/GCE in 0.1 mM $K_3[Fe(CN)_6]$ containing 1 M KCl. (B) Plot of $Q-t^{1/2}$ curves on (a) GCE and (b) $NiFe_2O_4$/MWCNTs/GCE). (C) Plot of $Q-t$ curves of the modified electrode in 0.2 M PBS at pH 6.0 in the (a) absence and (b) presence of 3.5×10^{-6} mol/L benomyl. (D) Plot of $Q-t^{1/2}$ curve on $NiFe_2O_4$/MWCNTs/GCE after the background is subtracted.

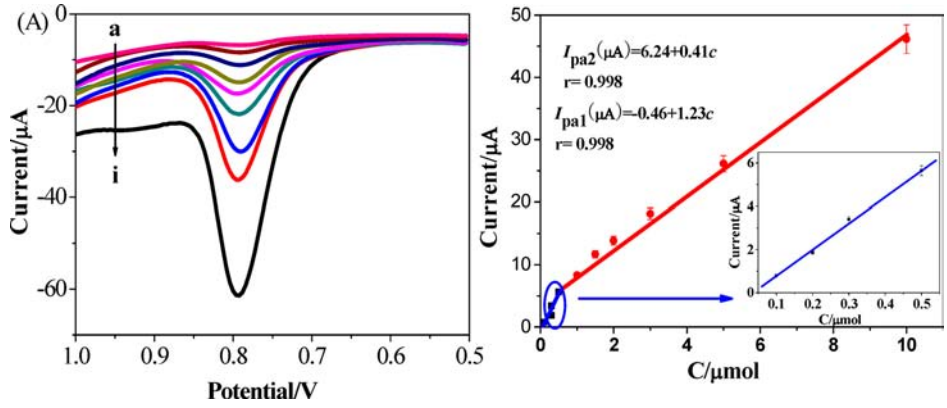

Figure 6. (A) DPVs of benomyl at different concentrations. The concentrations of benomyl from a to l are 1×10^{-7}, 2×10^{-7}, 3×10^{-7}, 5×10^{-7}, 1×10^{-6}, 1.5×10^{-6}, 3×10^{-6}, 5×10^{-6}, 1×10^{-5} mol/L, respectively. (B) Related calibration curve.

Table 1. Comparison of the Developed Method to Some Other Methods for the Determination of Benomyl

method	linear range (g/L)	detection limit (g/L)	recovery (%)	reference
liquid chromatographic	from 1.0×10^{-5} to 2.5×10^{-2}	3.3×10^{-6}		45
GC/MS	from 2.0×10^{-6} to 1.0×10^{-5}	2.0×10^{-8}	74−107	46
fluorescence polarization	from 3.0×10^{-7} to 3.0×10^{-4}	1.1×10^{-7}	104−113	47
bare GCE	from 8.1×10^{-5} to 1.5×10^{-3}	2.4×10^{-5}	99	21
OV-17 silicon-modified carbon paste electrodes	from 1.0×10^{-5} to 4.0×10^{-4}	6.9×10^{-5}	31−83	23
$NiFe_2O_4$/MWCNTs-modified GCE	from 2.9×10^{-5} to 2.9×10^{-3}	7.2×10^{-6}	93−103	present work

and $t^{1/2}$, A was calculated to be 0.013 and 0.072 cm^2 for bare GCE and $NiFe_2O_4$/MWCNTs/GCE, respectively. These results indicated that the specific area of the modified electrodes is nearly 6 times that of the bare electrode, which would enhance the current response and decrease the detection limit.

The diffusion coefficient D and Faradaic charge Q_{ads} of benomyl at $NiFe_2O_4$/MWCNTs/GCE can also be determined by chronocoulometry based on eq 4. As shown in panels C and D of Figure 5, after background subtraction, the plot of Q against $t^{1/2}$ showed a linear relationship. With $n = 2$, $A = 0.072$ cm^2, and $c = 3.5 \times 10^{-6}$ mol/L, D was calculated to be 1.13×10^{-7} cm^2 s^{-1}. According to the equation $Q_{ads} = nFA\Gamma_s$, the adsorption capacity, Γ_s, can be obtained as 1.75×10^{-10} mol cm^{-2}.

3.8. Electrochemical Determination of Benomyl Using DPV. As a highly sensitive and low detection limit electrochemical method, DPV was used for the determination of benomyl. Figure 6 presents DPV curves of benomyl at different concentrations on the $NiFe_2O_4$/MWCNTs/GCE under the

DOI: 10.1021/acs.jafc.5b00973
J. Agric. Food Chem. 2015, 63, 4746−4753

optimum conditions. It can be seen that an increase in the benomyl concentration is accompanied by an increase in anodic current, but there are two linear sections in the regression line that fit the following equations: for concentrations in the range from 1.00×10^{-7} to 5.00×10^{-7} mol/L, I_{pa} (μA) = −0.46 + 1.23c (μmol/L) (r = 0.998), and for concentrations in the range from 5.00×10^{-7} to 1.00×10^{-5} mol/L, I_{pa} (μA) = 6.24 + 0.41c (μmol/L) (r = 0.995). The detection limit was 2.51×10^{-8} mol/L based on 3 times that of the background noise. It could be seen that the proposed method showed a rational linear range and an acceptable detection limit.

The comparison of the developed method to some other methods for the determination of benomyl is listed in Table 1, which showed excellent sensitivity and a wide linear range of the proposed method.

3.9. Reproducibility, Stability, and Interference Study. The $NiFe_2O_4$/MWCNTs/GCE showed good reproducibility, and the relative standard deviation (RSD) was 3.3%, which was evaluated by six repetitive measurements of 3.5×10^{-6} mol/L benomyl in PBS at pH 6.0 (accumulation time, 600 s; scan rate, 0.10 V s^{-1}; and accumulation potential, open circuit potential), which indicates that the electrochemical response of benomyl at the $NiFe_2O_4$/MWCNTs/GCE was highly reproducible. The DPV responses remained 91% of the initial current after the $NiFe_2O_4$/MWCNTs/GCE electrode was stored in a refrigerator at 4 °C for 7 days, suggesting good stability.

Under the optimized conditions, the redox peaks current of 3.5×10^{-6} mol/L benomyl was individually measured in the presence of different interferents and their influence on the analytical signal was investigated. As shown in Figure 7, it was found that 100-fold concentrations of carbendazim, thiabendazole, and tricyclazole, 300-fold concentrations of vitamin C, glucose, and CO_3^{2-}, and 1000-fold concentrations of Ca^{2+}, Mg^{2+}, K^+, Na^+, Zn^{2+}, Cl^-, and NO_3^- have no influence on the signal of benomyl. The results indicated that the peak current of benomyl was not significantly affected by the presence of common existing substances, suggesting a great anti-interference ability of the $NiFe_2O_4$/MWCNTs/GCE.

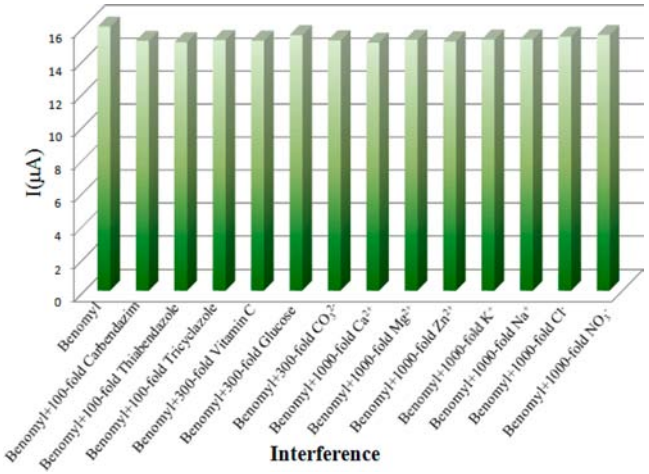

Figure 7. Signal of benomyl in the presence of interfering compounds.

3.10. Analysis of the Real Sample. To evaluate the practical application of $NiFe_2O_4$/MWCNTs/GCE for real sample analysis, apple, mushroom, and spinach were analyzed and detected by DPV under the optimal conditions using the standard addition method. The results are given in Table 2, and the recoveries were determined in the range from 93 to 103%. As indicated by the results, the developed sensor was proven to be a promising and reliable tool for the determination of benomyl in food and possesses potential applications in the analysis of the relevant real samples.

Table 2. Determination of Benomyl in Real Samples

sample	added ($\times 10^{-5}$, mol/L)	found[a] ($\times 10^{-5}$, mol/L)	RSD[b] (%)	recovery (%)
apple	0	0		
	0.482	0.479	3.5	99.3
	3.445	3.500	3.8	101.6
mushroom	0	0		
	0.482	0.496	2.6	96.9
	3.445	3.500	4.1	98.5
spinach	0	0		
	0.482	0.463	5.3	96.1
	3.445	3.211	4.5	93.2

[a]Mean of three measurement. [b]Relative standard deviation for n = 5.

4. CONCLUSION

In this work, a sensitive and reliable electrochemical method was proposed to determine benomyl. The electrochemical sensor based on $NiFe_2O_4$/MWCNTs/GCE displays an electrocatalytic performance to the oxidation of benomyl with a low detection limit. The electrochemical sensor shows good sensitivity, selectivity, and reproducibility. The $NiFe_2O_4$/MWCNTs/GCE is proven to be an accurate and reliable method because of the determination of benomyl in real samples with satisfactory results.

AUTHOR INFORMATION

Corresponding Author

*Telephone: +86-24-62207809. Fax: +86-24-62202380. E-mail: zhanglei63@126.com.

Funding

This project was supported by the National Natural Science Foundation of China (NSFC, 51178212), the Science and Technology Foundation of Ocean and Fisheries of Liaoning Province (201408 and 201406), and the Foundation of 211 Project for Innovative Talent Training, Liaoning University.

Notes

The authors declare no competing financial interest.

REFERENCES

(1) Kilmartin, J. V. Purification of yeast tubulin by self-assembly in vitro. *Biochemistry* **1981**, *20*, 3629−3633.

(2) Peres, N. A.; Timmer, L. W.; Adaskaveg, J. E.; Correll, J. C. Lifestyle of *Colletotrichum acutatum*. *Plant Dis.* **2005**, *89*, 784−796.

(3) Davidse, L. C. Benzimidazole fungicides—Mechanism of action and biological impact. *Annu. Rev. Phytopathol.* **1986**, *24*, 43−65.

(4) Rathinasamy; Panda, D. Kinetic stabilization of microtubule dynamic instability by benomyl increases the nuclear transport of p53. *Biochem. Pharmacol.* **2008**, *76*, 1669−1680.

(5) Davidse, L. C.; Flach, W. Differential binding of methyl benzimidazole-2-yl carbamate to fungal tubulin as a mechanism of resistance to this antimitotic agent in mutant strains of *Aspergillus nidulans*. *J. Cell Biol.* **1977**, *72*, 174−193.

(6) Zhou, J.; Xiong, K.; Yang, Y.; Ye, X.; Liu, J.; Li, F. Deleterious effects of benomyl and carbendazim on human placental trophoblast cells. *Reprod. Toxicol.* **2014**, *51*, 64−71.

DOI: 10.1021/acs.jafc.5b00973
J. Agric. Food Chem. 2015, 63, 4746−4753

(7) Zelesco, P. A.; Barbieri, I.; Graves, J. A. M. Use of a cell hybrid test system to demonstrate that benomyl induces aneuploidy and polyploidy. *Mutat. Res., Genet. Toxicol. Test.* **1990**, *242*, 329−335.
(8) Baude, F. J.; Pease, H. L.; Holt, R. F. Fate of benomyl on field soil and turf. *J. Agric. Food Chem.* **1974**, *22*, 413−418.
(9) Urani, C.; Chiesara, E.; Galvani; Marabini, L.; Santagostino, A.; Camatini, M. Benomyl affects the microtubule cytoskeleton and the glutathione level of mammalian primary cultured hepatocytes. *Toxicol. Lett.* **1995**, *76*, 135−144.
(10) Marinovich, M.; Ghilardi, F.; Galli, C. L. Effect of pesticide mixtures on in vitro nervous cells: comparison with single pesticides. *Toxicology* **1996**, *108*, 201−206.
(11) Banks, D.; Soliman, M. R. Protective effects of antioxidants against benomyl-induced lipid peroxidation and glutathione depletion in rats. *Toxicology* **1997**, *116*, 177−181.
(12) Morinaga, H.; Yanase, T.; Nomura, M.; Okabe, T.; Goto, K.; Harada, N.; Nawata, H. A benzimidazole fungicide, benomyl, and its metabolite, carbendazim, induce aromatase activity in a human ovarian granulose-like tumor cell line (KGN). *Endocrinology* **2004**, *145*, 1860−1869.
(13) Sassman, S. A.; Lee, L. S.; Bischoff, M.; Turco, R. F. Assessing *N*,*N*′-dibutylurea (DBU) formation in soils after application of *n*-butylisocyanate and benlate fungicides. *J. Agric. Food Chem.* **2004**, *52*, 747−54.
(14) Garcia Sanchez, F.; Aguilar Gallardo, A. Fluorimetric determination of the fungicide benomyl after solvolysis. *Microchim. Acta* **1994**, *116*, 211−218.
(15) Bernal, J. L.; Nozala, M. J.; Toribio, L.; Jiménez, J. J.; Atienza, J. High-performance liquid chromatographic determination of benomyl and carbendazim residues in apiarian samples. *Journal of Chromatography A* **1997**, *787*, 129−136.
(16) Navas Díaz, A.; García Sánchez, F.; López Guerrero, M. M. Modulated anisotropy fluorescence for quantitative determination of carbaryl and benomyl. *Talanta* **2003**, *60*, 629−634.
(17) García Reyes, J. F.; Ortega Barrales, P.; Molina Díaz, A. Gel-surface enhanced fluorescence sensing system coupled to a continuous-flow assembly for simultaneous monitoring of benomyl and carbendazim. *Anal. Chim. Acta* **2003**, *493*, 35−45.
(18) García Sánchez, F.; Navas Díaz, A.; Torijas, M. C. Selective determination of carbaryl and benomyl by fluorescence polarization. *Anal. Chim. Acta* **2000**, *414*, 25−32.
(19) MacNeil, J. D.; Hikichi, M. A rapid method for the quantitive analysis of benomyl on cherries by thin-layer chromatography and in situ fluorometry. *J. Chromatogr. A* **1974**, *101*, 33−37.
(20) Zima, J.; Svancara, I.; Barek, J.; Vytras, K. Recent advances in electroanalysis of organic compounds at carbon paste electrodes. *Crit. Rev. Anal. Chem.* **2009**, *39*, 204−227.
(21) Sarigül, T.; Inam, R.; Demir, E.; Aboul-Enein, H. Y. Electro-oxidation and determination of benomyl by square-wave adsorptive stripping voltammetry. *J. AOAC Int.* **2014**, *97*, 995−1000.
(22) Muñíz Alvarez, J. L.; García Calzón, J. A.; López Fonseca, J. M. Catalytic polarographic prewave of cobalt(II) induced by carbendazim. Application to the voltammetric determination of benomyl. *Electroanalysis* **1997**, *9*, 500−502.
(23) Hernindez, P.; Garcia, S.; Hernindez, L. Voltammetric use of a graphite electrode modified with OV-17 silicone for the determination of organic compounds. *Anal. Chim. Acta* **1992**, *259*, 325−331.
(24) Shipway, A. N.; Lahav, M.; Willner, I. Nanostructured gold colloid electrodes. *Adv. Mater.* **2000**, *12*, 993.
(25) Wang, L.; Ji, H.; Wang, S.; Kong, L.; Jiang, X.; Yang, G. Preparation of Fe_3O_4 with high specific surface area and improved capacitance as a supercapacitor. *Nanoscale* **2013**, *5*, 3793.
(26) Anwar, S.; Muthu, K. S.; Ganesh, V.; Lakshminarasimhan, N. J. A comparative study of electrochemical capacitive behavior of $NiFe_2O_4$ synthesized by different routes. *J. Electrochem. Soc.* **2011**, *158*, A976−A981.
(27) Wang, R.; Xie, M.; Li, P.; Fai, N. G. Catalytic and electrocatalytic oxidation of propane on V−Mg−O and V−Mg−O (Ag) catalysts. *Catal. Lett.* **1994**, *24*, 67−77.
(28) Ehsania, A.; Vaziri-Rad, A.; Babaei, F.; Shiri, H. M. Electrosynthesis, optical modeling and electrocatalytic activity of Ni−MWCNT−PT nanocomposite film. *Electrochim. Acta* **2015**, *159*, 140−148.
(29) Gordani, G. R.; Ghasemi, A.; Saidi, A. Optimization of carbon nanotube volume percentage for enhancement of high frequency magnetic properties of $SrFe_8MgCoTi_2O_{19}$/MWCNTs. *J. Magn. Magn. Mater.* **2014**, *363*, 49−54.
(30) Cao, N.; Zou, X. Y.; Huang, Y. Q.; Zhao, Y. B. Preparation of $NiFe_2O_4$ architectures for affinity separation of histidine-tagged proteins. *Mater. Lett.* **2015**, *144*, 161−164.
(31) Chen, C. H.; Liang, Y. H.; Zhang, W. D. $ZnFe_2O_4$/MWCNTs composite with enhanced photocatalytic activity under visible-light irradiation. *J. Alloys Compd.* **2010**, *501*, 168−172.
(32) Gunjakar, J. L.; More, A. M.; Shinde, V. R.; Lokhande, C. D. Synthesis of nanocrystalline nickel ferrite ($NiFe_2O_4$) thin films using low temperature modified chemical method. *J. Alloys Compd.* **2008**, *465*, 468−473.
(33) Jauhar, S.; Singhal, S. Substituted cobalt nano-ferrites, $CoM_xFe_{2-x}O_4$ (M = Cr^{3+}, Ni^{2+}, Cu^{2+}, Zn^{2+}; $0.2 \leq x \leq 1.0$) as heterogeneous catalysts for modified Fenton's reaction. *Ceram. Int.* **2014**, *40*, 11845−11855.
(34) Xiong, P.; Hu, C. Y.; Fan, Y.; Zhang, W. Y.; Zhu, J. W.; Wang, X. Ternary manganese ferrite/graphene/polyaniline nanostructure with enhanced electrochemical capacitance performance. *J. Power Sources* **2014**, *266*, 384−392.
(35) Cai, W. H.; Lai, T.; Dai, W. L.; Ye, J. S. A facile approach to fabricate flexible all-solid-state supercapacitors based on $MnFe_2O_4$/graphene hybrids. *J. Power Sources* **2014**, *255*, 170−178.
(36) Fu, M.; Jiao, Q. Z.; Zhao, Y. In situ fabrication and characterization of cobalt ferrite nanorods/graphene composites. *Mater. Charact.* **2013**, *86*, 303−315.
(37) Zhang, Y. Y.; Hu, L. T.; Liu, X.; Liu, B. F.; Wu, K. B. Highly-sensitive and rapid detection of ponceau 4R and tartrazine in drinks using alumina microfibers-based electrochemical sensor. *Food Chem.* **2015**, *166*, 352−357.
(38) Wang, X.; Yang, J. C.; Wang, Y. J.; Li, Y. H.; Wang, F.; Zhang, L. Studies on electrochemical oxidation of estrogenic disrupting compound bisphenol AF and its interaction with human serumalbumin. *J. Hazard. Mater.* **2014**, *276*, 105−111.
(39) Yang, X.; Feng, B.; Yang, P.; Ding, Y. L.; Chen, Y.; Fei, J. J. Electrochemical determination of toxic ractopamine at an ordered mesoporous carbon modified electrode. *Food Chem.* **2014**, *145*, 619−624.
(40) Gu, X. F.; Jiang, G. M.; Jiang, G. Q.; Chen, T. T.; Zhan, W. Y.; Li, X.; Wu, S. J.; Tian, S. Detection of dopamine on a mercapto-terminated hexanuclear Fe(III) cluster modified gold electrode. *Talanta* **2015**, *137*, 189−196.
(41) Laviron, E. J. Adsorption autoinhibition and autocatalysis in polarography and linear potential sweep voltammetry. *J. Electroanal. Chem. Interfacial Electrochem.* **1974**, *52*, 355−393.
(42) Laviron, E. J. General expression of the linear potential sweep voltammogram in the case of diffusionless electrochemical systems. *J. Electroanal. Chem. Interfacial Electrochem.* **1979**, *101*, 19−28.
(43) Anson, F. C. Application of potentiostatic current integration to the study of the adsorption of cobalt(III)−(ethylenedinitrilo-(tetraacetate) on mercury electrodes. *Anal. Chem.* **1964**, *36*, 932−934.
(44) Yu, L. L.; Shi, M. X.; Yue, X.; Qu, L. B. A novel and sensitive hexadecyltrimethyl ammonium bromide functionalized graphene supported platinum nanoparticles composite modified glassy carbon electrode for determination of sunset yellow in soft drinks. *Sens. Actuators, B* **2015**, *209*, 1−8.
(45) Navickiene, S.; Possidônio de, O.; Junior, A.; Brito, N. M.; Graciolli, L. A.; Lúcia Ribeiro, M. Determination of benomyl residues in shiitake mushrooms (*Lentinula edodes*) by liquid chromatography with UV detection. *J. Chromatogr. Sci.* **2007**, *45*, 340−344.
(46) Shin, H. S.; Hong, J. E.; Pyo, H.; Park, S. J.; Lee, W. Sensitive determination of benomyl in environmental samples by GC/MSD. *Anal. Chem.* **2001**, *17*, 49−52.

DOI: 10.1021/acs.jafc.5b00973
J. Agric. Food Chem. 2015, 63, 4746−4753

(47) García Sánchez, F.; Navas Díaz, A.; Torijas, M. C. Selective determination of carbaryl and benomyl by fluorescence polarization. *Anal. Chim. Acta* **2000**, *414*, 25−32.

DOI: 10.1021/acs.jafc.5b00973
J. Agric. Food Chem. 2015, 63, 4746−4753

JOURNAL OF AGRICULTURAL AND FOOD CHEMISTRY

Article

pubs.acs.org/JAFC

Photodegradation of Imidacloprid in Aqueous Solution by the Metal-Free Catalyst Graphitic Carbon Nitride using an Energy-Saving Lamp

Xue Liu, Xiaoli Wu, Zhen Long, Che Zhang, Yongqiang Ma,* Xianghong Hao, Hongyan Zhang,* and Canping Pan

Department of Applied Chemistry, College of Science, China Agricultural University, No. 2 Yuanmingyuanxi Road, Beijing 100193, People's Republic of China

Supporting Information

ABSTRACT: Imidacloprid has become a research hotspot, due to its high toxicity to bees and other nontarget organisms. Photodegradation is a common method for removing imidacloprid in an aquatic environment. Traditional methods of pesticide photodegradation have generally been confined by many factors, such as response to only high-energy ultraviolet light. Herein, the visible-light-driven photocatalyst graphitic carbon nitride (g-C_3N_4) was applied to the photodegradation of imidacloprid. Visible-light illumination (λ >400 nm) resulted in nearly 90% substrate transformation in 5 h. With the illumination of an energy-saving lamp, imidacloprid has also been mostly removed. 1-((6-chloropyridin-3-yl)methylhydroxy)imidazolidin-2-ylidene nitramide) and 4,5-dihydro-*N*-nitro-1-(3-pyridinylmethyl)-1*H*-imidazol-2-amine were the main photoproducts identified by LC-MS analysis. The photocatalytic mechanism has also been discussed. This work could provide new perspective that g-C_3N_4, as a good visible-light photocatalyst could be applied to the cleanup of environmental pesticide pollution.

KEYWORDS: *imidacloprid, graphitic carbon nitride, metal-free, photodegradation, visible light, mechanism*

INTRODUCTION

Under typical field application conditions, only a small portion of the applied pesticide reaches its biological target[1] and the remaining contaminates the land, the air, and particularly the water.[2] It is generally known that less than 1% of the world's fresh water resources are readily available for human use. Worse, it was found in 2012 that 748 million people still rely on unimproved drinking water sources.[3] Thus, there is a pressing need for methods to remove pesticides and their derivatives from wastewater. Imidacloprid has become the most widely used neonicotinoid insecticide for over 140 agricultural crops.[4] In 2011, about 11.4 thousand tons of products containing imidacloprid was applied in China alone.[5] Aside from its benefits to agricultural production and pest control,[6] it has become a threat to agroecosystems and human health.[7] There is evidence that imidacloprid can be toxic to nontarget soil organisms and aquatic arthropods.[8−10] Imidacloprid also could reduce bumblebee colony growth and queen production, which result in further worsening global malnutrition.[4,11] The European Council decided in April 2013 to impose a temporary ban of imidacloprid.[12] In addition, the mobility of imidacloprid in the environment and its high solubility and persistent stability in water have placed a damper on its natural degradation.[13,14]

Various treatment processes have been studied to address the pollution of wastewater by pesticides. Different advanced oxidation processes (AOPs) have been proven to be some of the most commonly used techniques.[15,16] Photocatalytic oxidation (TiO_2/UV) and photo-Fenton or Fenton-like systems (H_2O_2/UV/Fe^{3+}) are the most widely used AOPs for pesticide degradation.[17] However, there are also many drawbacks to these traditional strategies, such as the formation of iron sludge, acidic pH requirements,[18] and high operating costs.[19] Most of these processes use metal catalysts, which may lead to secondary pollution.[20] In addition, it is worth noting that only UV light (4% of the solar spectrum) can be used in those processes.[21] From the standpoint of solar energy availability, visible light (more than 43% of the solar spectrum) active photocatalysts have great prospects in this field.[17]

Graphitic carbon nitride (g-C_3N_4) has been a novel "metal-free", visible-light-induced semiconductor.[22,23] Constructed from tri-*s*-triazine units and connected by planar amino groups, graphitic carbon nitride has been regarded as the most stable allotrope of carbon nitrides under ambient conditions, both on heating and in solutions of pH 1−14.[23] The ideal g-C_3N_4 consists solely of an assembly of C−N bonds without electron localization in the π state.[24] With a band gap of about 2.70 eV, g-C_3N_4 was found to show an intrinsic absorption in the visible region. Recently it has attracted intense attention for hydrogen and oxygen evolution via water splitting,[25] photosynthesis,[26] biosensing,[27] detection of metal ions,[28] and photocatalytic contaminant degradation.[29] Consisting of carbon and nitrogen, g-C_3N_4 is thus environmentally friendly and sustainable[30] and can be easily obtained by direct heat treatment of several precursors, such as melamine, urea, dicyandiamide, etc.[31−33]

Herein, g-C_3N_4 was used as a visible-light catalyst for the degradation of imidacloprid. Synthesized from low-cost and abundant urea, g-C_3N_4 showed an exceptionally high imidacloprid degradation ratio of nearly 90% under visible light over 5 h. Furthermore, optimized supported g-C_3N_4 showed an exceptionally high imidacloprid degradation ratio

Received: March 2, 2015
Revised: April 26, 2015
Accepted: April 29, 2015
Published: April 29, 2015

ACS Publications © 2015 American Chemical Society

DOI: 10.1021/acs.jafc.5b01105
J. Agric. Food Chem. 2015, 63, 4754−4760

of 83.4% under real indoor illumination using an energy-saving lamp, which could promote the practical environmental application of the g-C_3N_4 photocatalyst. As another commonly used precursor, g-C_3N_4 synthesized by melamine was also prepared under identical conditions. It was found that different precursors have a significant impact on the photocatalysis efficiency of g-C_3N_4. Further discussion was also made on the basis of this result. More importantly, the possible mechanism of imidacloprid degradation was deduced on the basis of the interaction between chemical scavengers and different active species.

MATERIALS AND METHODS

Materials. All reagents for synthesis and analysis were commercially available and were used without further treatments. Deionized water was used throughout the experiments.

Preparation of g-C_3N_4 Photocatalyst. g-C_3N_4 materials were prepared by polymerization of urea and melamine molecules under high temperature. Typically, 10 g of precursor powder was placed in a crucible with a cover and then calcined at 550 °C for 4 h in a muffle furnace, at a heating rate of 10 °C min^{-1}. After it was naturally cooled to room temperature, the resulting product was washed with 0.1 M HNO_3 and deionized water several times. Then the pure products were dried at 105 °C for 10 h. The resultant yellow product was collected and milled into powder for further use. The as-prepared g-C_3N_4 samples were labeled as U-g-C_3N_4 (from urea) and M-g-C_3N_4 (from melamine), respectively.

Characterization. Powder X-ray diffraction (XRD) patterns of the as-synthesized samples were recorded with a Bruker D/MAX 2500 X-ray diffractometer. The microstructure was observed using a scanning electron microscope (SEM; FEI, Sirion 200, 10 kV) and transmission electron microscopy (TEM; FEI Tecnai G2F20, 200 kV). Fourier transform infrared (FT-IR) spectra of products were obtained in the range of 400−4000 cm^{-1} (FTIR, PerkinElmer 2000). X-ray photoelectron spectroscopy (XPS) measurements were done using an Escalab 250Xi XPS system. The specific surface areas of the samples were measured by nitrogen sorption at 77 K on a Micromeritics ASAP 2020 analyzer and calculated by the Brunauer−Emmett−Teller (BET) method. For photodegradation, a 300 W xenon lamp (CEL-HFX300W, Beijing) with cutoff filter (λ >400 nm) was used. An Agilent 1100 series high-performance liquid chromatograph (HPLC) with a UV detector was used to determine the concentrations of imidacloprid. An Agilent 1100 LC/MSD ion trap was employed to identify byproducts.

Imidacloprid Photocatalytic Degradation. The photocatalytic degradation of imidacloprid was performed under visible-light (λ >400 nm) irradiation. In a typical experiment, the 0.05 g of the catalyst was suspended in an aqueous solution of imidacloprid (100 mL, 20 mg L^{-1}). The indoor light photocatalytic study was performed using an 8 W energy-saving lamp (commercially available) as the light source. A 0.1 g portion of the catalyst was added to 100 mL of imidacloprid solution (5 mg L^{-1}) with constant stirring. All tests were carried out in a 150 mL reactor fitted with a circulating water system to maintain a constant temperature. Prior to irradiation, the suspensions were magnetically stirred in the dark for 30 min to create an absorption−desorption equilibrium between the catalyst and imidacloprid. To investigate the possible mechanisms involved in the photocatalytic degradation process, a series of experiments were carried out by adding individual scavengers to the photocatalytic reaction system.

RESULTS AND DISCUSSION

Characterization of g-C_3N_4 Samples. The X-ray diffraction (XRD) patterns of U-g-C_3N_4 and M-g-C_3N_4 are presented in Figure 1. The patterns all exhibit peaks at 13.0° (d = 0.676 nm) and 27.7° (d = 0.322 nm), corresponding to the approximate dimension of the tri-*s*-triazine unit and the interlayer stacking peak of aromatic systems, respectively. It is worth noting that

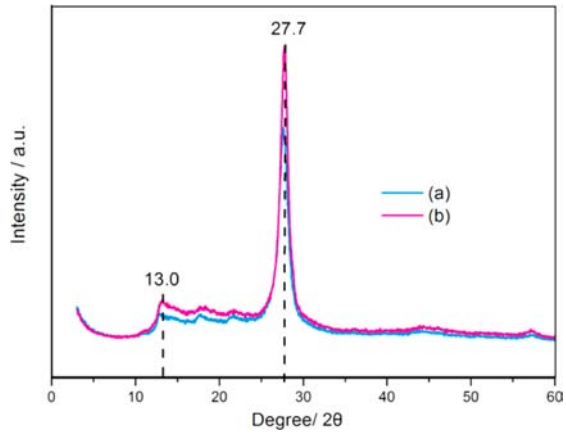

Figure 1. XRD patterns of (a) U-g-C_3N_4 and (b) M-g-C_3N_4.

the intensity of the 27.7° peak varies between urea and melamine samples. A more intense peak suggests a decreased polymerization in M-g-C_3N_4 in comparison to U-g-C_3N_4.[34]

Figure S1 in the Supporting Information displays the FT-IR spectra of U-g-C_3N_4 and M-g-C_3N_4 samples. From the spectra, it can be seen that all photocatalysts have absorption bands at 810 cm^{-1}, corresponding to the breathing mode of the triazine units. The peaks observed at 1200−1650 cm^{-1} are representative of the stretching and bending modes of nitrogen-containing heterocycles. The broad band in the range 3000−3700 cm^{-1} is assigned to stretching modes of −NH− groups and surface-adsorbed water molecules.[21,34,35]

The morphology and microstructure of samples were investigated by SEM, as shown in Figure 2. Figure 2a shows that U-g-C_3N_4 consists of smooth paper-thin sheets, while M-g-C_3N_4 (Figure 2b) is composed of large particles with a layer. The morphological difference between U-g-C_3N_4 and M-g-C_3N_4 is distinctive.

The morphological difference between U-g-C_3N_4 and M-g-C_3N_4 was also consistent with TEM images (Figure 3). As can be seen from the images, U-g-C_3N_4 exhibits two-dimensional smooth and thin layers with typical porouslike morphology. M-g-C_3N_4 exhibits a dense and thick sheetlike morphology with irregular shape. This fact indicates that different heteroatom-containing precursors can result in different morphologies and microstructures of the resultant g-C_3N_4.

The specific bonding and structure of the samples were investigated by X-ray photoelectron spectroscopy (XPS). Figure 4 depicts the high-resolution XPS spectra for the N 1s peak. The N 1s peak has been resolved to three main peaks at 398.7, 399.7, and 400.9 eV correspond to sp^2 C−N−C, sp^3 H−N−$[C]_3$ and C−NH_x, respectively.[36] The 404.4 eV peak was weak and was attributed to the π excitations.[37] C 1s and O 1s XPS spectra of the two samples (U-g-C_3N_4 and M-g-C_3N_4) are shown in Figure S3 of the Supporting Information. A residual O 1s peak could be ascribed to the tiny amount of O_2 adsorbed on the surface of the synthetic product during the calcination process. The C 1s spectra show adventitious carbon species, the tertiary carbon, and a trace amount of C−O bonding at 284.9, 288.2, and 289.2 eV, respectively.[35]

The ratio of sp^2 C−N−C bonds to the sum of sp^3 H−N−$[C]_3$ and C−NH_x bonds is 2.84 in U-g-C_3N_4 and only 1.83 in M-g-C_3N_4 (Tables S1 and S2 in the Supporting Information), which means the former has a lower proton concentration. It might be the key factors affecting the degradation efficiency.

DOI: 10.1021/acs.jafc.5b01105
J. Agric. Food Chem. 2015, 63, 4754−4760

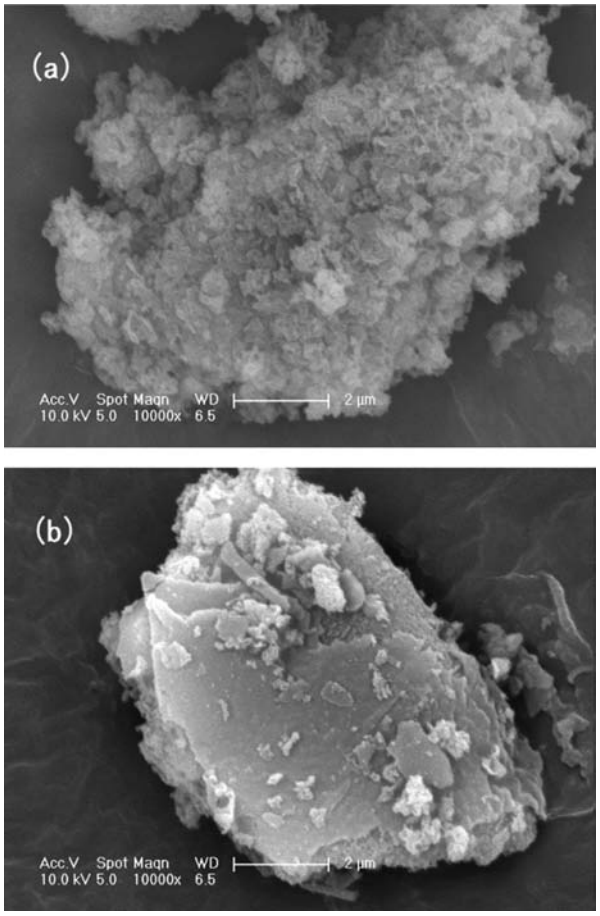

Figure 2. SEM images of (a) U-g-C_3N_4 and (b) M-g-C_3N_4.

Figure 5 shows the nitrogen adsorption−desorption isotherms for U-g-C_3N_4 and M-g-C_3N_4. Type IV hysteresis loops can be observed, indicating the presence of mesopores. The specific surface area of g-C_3N_4 greatly increased after acid treatment.[38] The BET surface areas and pore volumes of U-g-C_3N_4 (393.8 m^2g^{-1} and 0.62 cm^3 g^{-1}) are slightly higher than those of M-g-C_3N_4 (303.9 m^2g^{-1} and 0.44 cm^3 g^{-1}), indicating that the surface area is not the main reason for the photocatalytic activity, in accordance with the results reported in previous papers.[34]

Photocatalytic Degradation. The photocatalytic degradation of imidacloprid in the presence of photocatalyst in the dark could be negligible under the consistent experimental conditions (Figure 6). The photocatalytic activities of U-g-C_3N_4 and M-g-C_3N_4 under visible-light irradiation are shown in Figure 7. After 5 h of visible-light irradiation, the photocatalytic degradation rate of U-g-C_3N_4 for imidacloprid is nearly 90%. The photocatalytic efficiency of M-g-C_3N_4 is only 42.9%.

The photodegradation process has been fitted to pseudo-first-order models, in which the value of rate constant k is equal to the corresponding slope of the fitting line. As indicated in Figure 8, the values for the apparent reaction rate constant k are 0.3941 and 0.1179 h^{-1}, respectively, for U-g-C_3N_4 and M-g-C_3N_4. Even under irradiation with visible light (λ >400 nm), the U-g-C_3N_4 degradation of imidacloprid is more than twice as fast as that of M-g-C_3N_4. On the basis of the results, it is clear that U-g-C_3N_4 shows excellent performance in the photocatalytic degradation of imidacloprid in aqueous solution.

Figure 9 compares the indoor-light-induced photocatalytic degradation of imidacloprid over U-g-C_3N_4 and M-g-C_3N_4. The activity of the M-g-C_3N_4 sample was quite poor, with almost no degradation effect of imidacloprid even after 24 h of indoor-light irradiation. However, the photocatalytic degradation rate of U-g-C_3N_4 for imidacloprid actually reached 83.4%. This result could imply that only relatively low energy is needed for U-g-C_3N_4 to start its photoactivity. This characteristic of U-g-C_3N_4 could provide new perspectives for promoting its large-scale applications in real, natural environments for the degradation of pollutants.

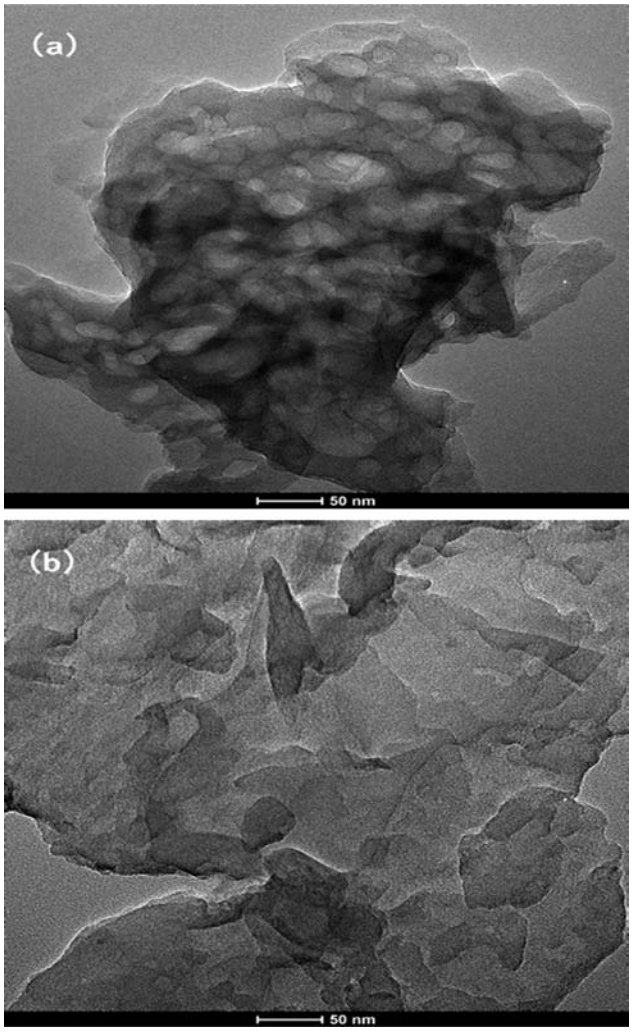

Figure 3. TEM images of (a) U-g-C_3N_4 and (b) M-g-C_3N_4.

Proposed Mechanism of g-C_3N_4 for Degradation of Imidacloprid. $^{\bullet}OH$, h^+, and $^{\bullet}O_2^-$ have been reported as major reactive species for photocatalytic oxidation. When the as-prepared samples are irradiated under visible light, g-C_3N_4 samples can easily absorb visible light and be excited to produce photogenerated electron−hole pairs. After capture by oxygen adsorbed on the surface of g-C_3N_4, the photogenerated electrons can generate $^{\bullet}O_2^-$.

Ethylenediaminetetraacetic acid disodium salt (EDTA-2Na), ammonium oxalate (AO), and potassium iodide (KI) were used as the hole scavengers.[39−41] *tert*-butyl alcohol (TBA) and isopropyl alcohol (IPA) were used as hydroxyl free radical ($^{\bullet}OH$) scavengers.[42,43] Benzoquinone (BQ) was used to remove superoxide radical ($^{\bullet}O_2^-$).[44]

As shown in Figure 10, the photocatalytic efficiencies of imidacloprid are 85.4% and 42.9% without scavengers for

DOI: 10.1021/acs.jafc.5b01105
J. Agric. Food Chem. 2015, 63, 4754−4760

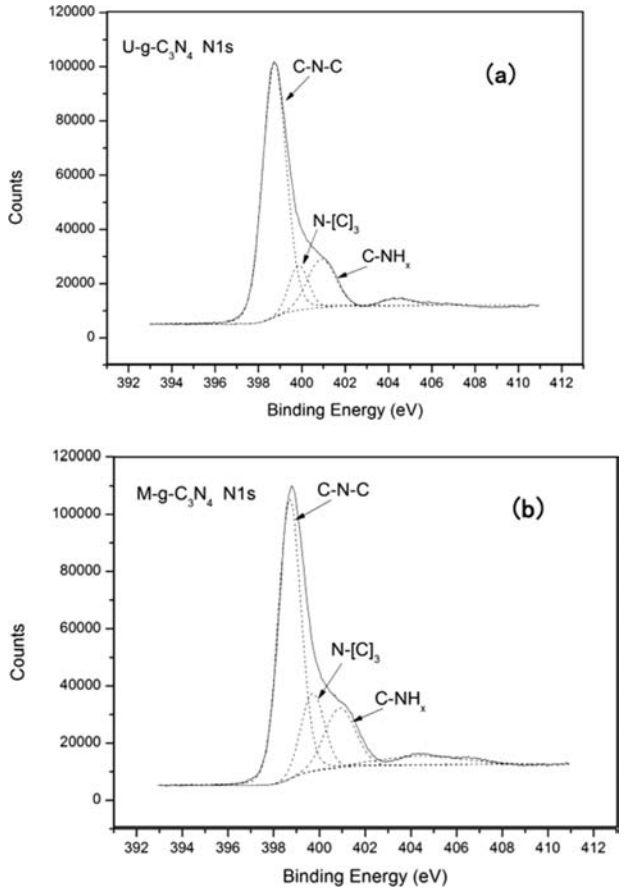

Figure 4. XPS spectra from samples of (a) U-g-C_3N_4 and (b) M-g-C_3N_4.

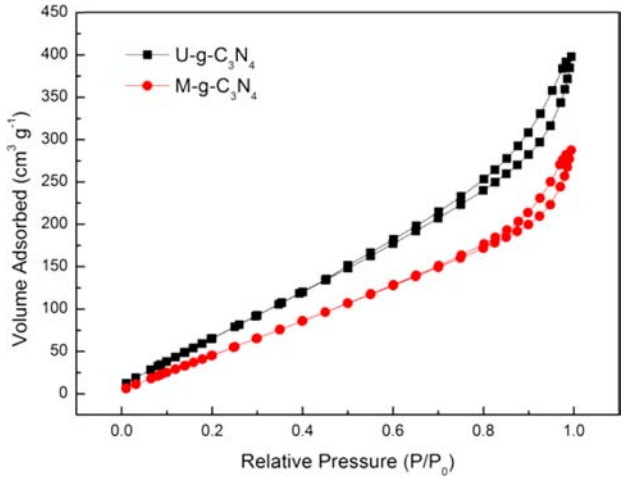

Figure 5. N_2 adsorption−desorption isotherms of U-g-C_3N_4 and M-g-C_3N_4.

U-g-C_3N_4 and M-g-C_3N_4, respectively. The photocatalytic activity of g-C_3N_4 was largely inhibited by the addition of hole capture. However, $^{\bullet}OH$ scavengers have almost no effect on the degradation process. Therefore, the hole is the main oxidative species for g-C_3N_4 samples, rather than $^{\bullet}OH$. Another point is that when benzoquinone (BQ) was used to remove superoxide radical ($^{\bullet}O_2^-$), the photocatalytic activity of g-C_3N_4 was slightly increased. This is because the consumption of superoxide radical ($^{\bullet}O_2^-$) was accompanied by the loss of electrons (e^-), which enhanced the separation efficiency of photoexcited electron−hole pairs.

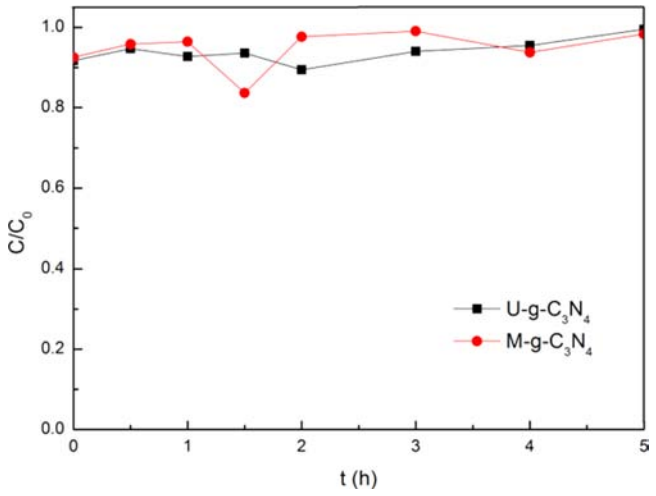

Figure 6. Photocatalytic activities of U-g-C_3N_4 and M-g-C_3N_4 in the degradation of imidacloprid in the absence of light.

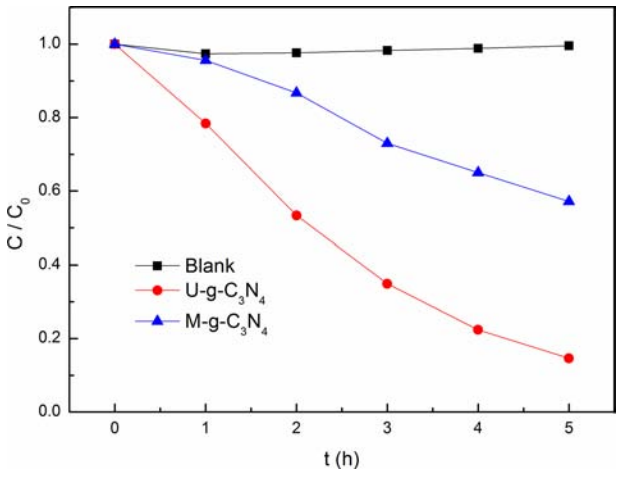

Figure 7. Photocatalytic activities of U-g-C_3N_4 and M-g-C_3N_4 in the degradation of imidacloprid under visible-light irradiation (λ >400 nm).

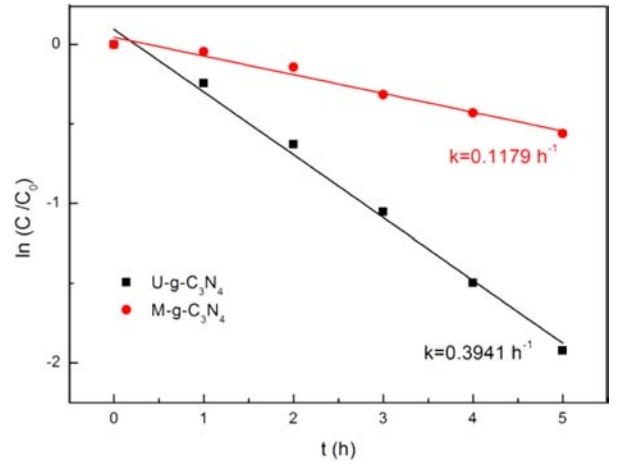

Figure 8. Kinetic analysis for the determination of apparent rate constants of the reaction between imidacloprid and photocatalysts.

On the basis of the above analysis, the photocatalytic degradation mechanism of g-C_3N_4 for imidacloprid is different from that of traditional techniques. Aqueous imidacloprid

DOI: 10.1021/acs.jafc.5b01105
J. Agric. Food Chem. 2015, 63, 4754−4760

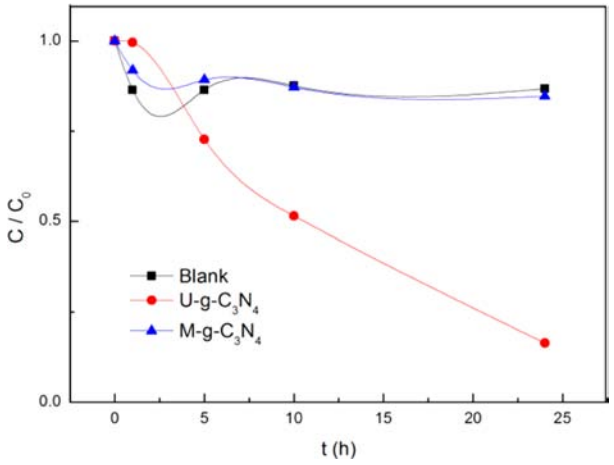

Figure 9. Indoor-light-induced photocatalytic degradation of imidacloprid over various photocatalysts.

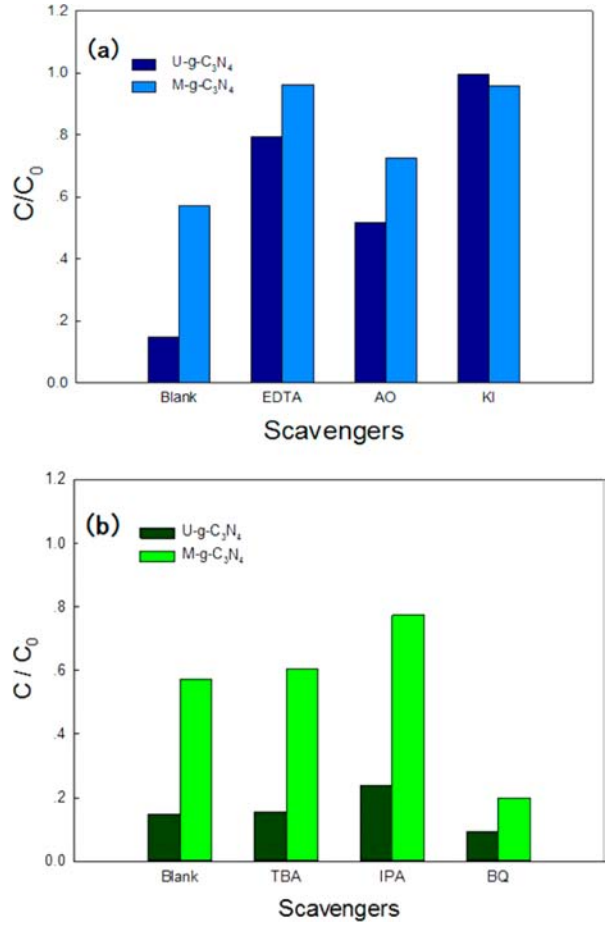

Figure 10. Effects of a series of scavengers on the photocatalytic efficiency of samples (dosage of scavengers 6×10^{-3} mol L^{-1}, illumination time t = 5 h): (a) hole scavengers; (b) radical scavengers.

degradation may be clarified by a mechanistic explanation using eqs 1−5.

$$g\text{-}C_3N_4 \rightarrow e^- + h^+ \quad (1)$$

Possible Degradation Pathway and Main Degradation Products. In this work, LC/MS analysis of the irradiated

$$h^+ + H_2O \rightarrow {}^{\bullet}OH + H^+ \quad (2)$$

$$e^- + O_2 \rightarrow O_2^{\bullet -} \quad (3)$$

$$h^+(g\text{-}C_3N_4) + \text{imidacloprid} \rightarrow \text{degradation product (compound } \mathbf{1}) \quad (4)$$

$${}^{\bullet}OH + \text{imidacloprid} \rightarrow \text{degradation product (compound } \mathbf{2}) \quad (5)$$

imidacloprid aqueous solution revealed two main products. The formation of 4,5-dihydro-*N*-nitro-1-(3-pyridinylmethyl)-1*H*-imidazol-2-amine (compound **1**) could be due to the mechanisms of holes (h^+). Addition of $^{\bullet}OH$ to the imidazolidine ring allows the formation of 1-((6-chloropyridin-3-yl)methylhydroxy)-imidazolidin-2-ylidene nitramide (compound **2**)[45] (Figure 11).

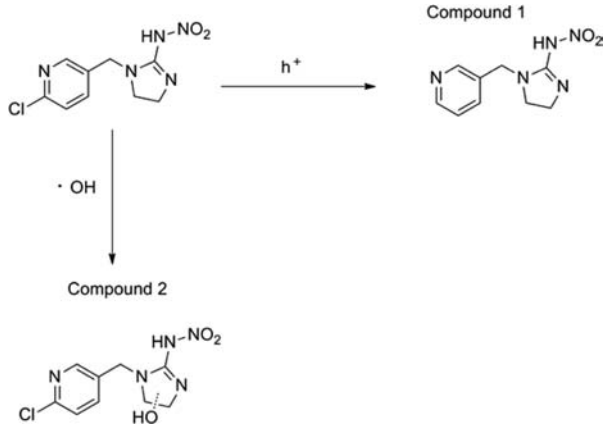

Figure 11. Proposed degradation pathway for imidacloprid using g-C_3N_4 as a visible-light photocatalyst.

To the best of our knowledge, compound **1** has not been reported previously, as a type of imidacloprid degradation product.

The stability of photocatalysts is important for their practical application. The renewable catalytic activity of U-g-C_3N_4 photocatalysts was further investigated. As shown in Figure 12, after three cycles, the high photodegradation rate of imidacloprid

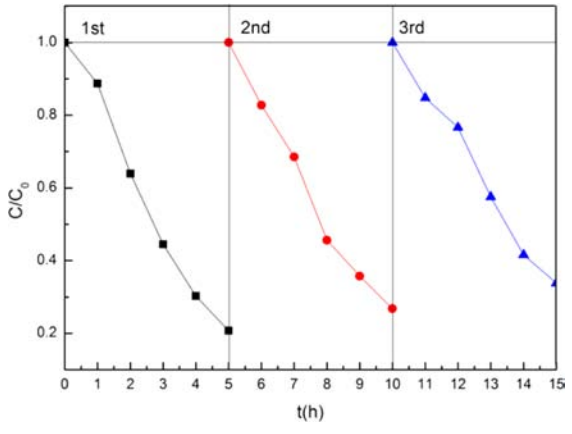

Figure 12. Cycling runs for the photocatalytic degradation of imidacloprid in the presence of U-g-C_3N_4 under visible light.

DOI: 10.1021/acs.jafc.5b01105
J. Agric. Food Chem. 2015, 63, 4754−4760

could be maintained. There was no significant loss of activity with the extension of reaction time, even on irradiation for 15 h. Thus, the present work could promote a new strategy dealing with the pollution of wastewater by pesticides. For the synergy between the reduced proton concentration and the increased polymerization, U-g-C_3N_4 possessed significant photodegradation activity for imidacloprid under both visible- and indoor-light irradiation. The main reactive species responsible for g-C_3N_4 photodegradation was a photogenerated hole. As it is economically feasible and sustainable, U-g-C_3N_4 has promising prospects for environmental applications.

■ ASSOCIATED CONTENT

Supporting Information

FT-IR spectra of M-g-C_3N_4 and U-g-C_3N_4 samples (Figure S1), C1s and O1s XPS spectra of g-C_3N_4 synthesized from different precursors (Figure S2), ratios of bonds within the N1s core level peak in different samples and their comparisons to the photodegradation activity (Table S1), and percentage breakdown of different bonds within the N1s spectrum (Table S2). The Supporting Information is available free of charge on the ACS Publications website at DOI: 10.1021/acs.jafc.5b01105.

■ AUTHOR INFORMATION

Corresponding Authors

*Y.M.: e-mail, mayongqiang@cau.edu.cn; tel, +86-010-62733620; fax, +86-010-62733620.

*H.Z.: e-mail, hongyan@cau.edu.cn.

Funding

This work was supported by the National Science Foundation for Fostering Talents in Basic Research of China (no. J1210064) and the National Instrumentation Program of China (No. 2013YQ510391).

Notes

The authors declare no competing financial interest.

■ REFERENCES

(1) Wamhoff, H.; Schneider, V. Photodegradation of imidacloprid. *J. Agric. Food Chem.* **1999**, *47*, 1730−1734.

(2) Kitsiou, V.; Filippidis, N.; Mantzavinos, D.; Poulios, I. Heterogeneous and homogeneous photocatalytic degradation of the insecticide imidacloprid in aueous solutions. *Appl. Catal., B* **2009**, *86*, 27−35.

(3) Water and Sanitation. http://www.who.int/gho/mdg/environmental_sustainability/en/.

(4) Whitehorn, P. R.; O'Connor, S.; Wackers, F. L.; Goulson, D. Neonicotinoid pesticide reduces bumble bee colony growth and queen production. *Science* **2012**, *336*, 351−352.

(5) Yu, C. H.; Lin, R. H.; Fu, M. R.; Zhou, Y. M.; Zong, F. L.; Jiang, H.; Lv, N.; Piao, X. Y.; Zhang, J.; Liu, Y. Q.; Brock, T. C. M. Impact of imidacloprid on life-cycle development of *Coccinella septempunctata* in laboratory microcosms. *Ecotoxicol. Environ. Saf.* **2014**, *110*, 168−173.

(6) Pérez-Iglesias, J. M.; Ruiz de Arcaute, C.; Nikoloff, N.; Dury, L.; Soloneski, S.; Natale, G. S.; Larramendy, M. L. The genotoxic effects of the imidacloprid-based insecticide formulation Glacoxan Imida on Montevideo tree frog *Hypsiboas pulchellus* tadpoles (Anura, Hylidae). *Ecotoxicol. Environ. Saf.* **2014**, *104*, 120−126.

(7) Malato, S.; Blanco, J.; Cáceres, J.; Fernández-Alba, A. R.; Agüera, A.; Rodríguez, A. Photocatalytic treatment of water-soluble pesticides by photo-Fenton and TiO_2 using solar energy. *Catal. Today* **2002**, *76*, 209−220.

(8) Alves, P. R. L.; Cardoso, E. J. B. N.; Martines, A. M.; Sousa, J. P.; Pasini, A. seed dressing pesticides on springtails in two ecotoxicological laboratory tests. *Ecotoxicol. Environ. Saf.* **2014**, *105*, 65−71.

(9) Alves, P. R. L.; Cardoso, E. J. B. N.; Martines, A. M.; Sousa, J. P.; Pasini, A. Earthworm ecotoxicological assessments of pesticides used to treat seeds under tropical conditions. *Chemosphere* **2013**, *90*, 2674−2682.

(10) Song, M. Y.; Stark, J. D.; Brown, J. J. Comparative toxicity of four insecticides, including imidacloprid and tebufenozide, to four aquatic arthropods. *Environ. Toxicol. Chem.* **1997**, *16*, 2494−2500.

(11) Chaplin-Kramer, R.; Dombeck, E.; Gerber, J.; Knuth, K. A.; Mueller, N. D.; Mueller, M.; Ziv, G.; Klein, A. M. Global malnutrition overlaps with pollinator-dependent micronutrient production. *Proc. R. Soc. London, Ser. B* **2014**, *281*, 1799−1805.

(12) L 139/12EN Official Journal of the European Union, 25.5.2013.

(13) Malato, S.; Caceres, J. Degradation of imidacloprid in water by photo-Fenton and TiO_2 photocatalysis at a solar pilot plant: a comparative study. *Environ. Sci. Technol.* **2001**, *35*, 4359−4366.

(14) Main, A. R.; Headle, J. V.; Peru, K. M.; Michel, N. L.; Cessna, A. J.; Morrissey, C. A. Widespread use and frequent detection of neonicotinoid insecticides in wetlands of Canada's prairie pothole region. *PLoS One* **2014**, DOI: 10.1371/journal.pone.0092821.

(15) Gonzalez-Olmos, R.; Martin, M. J.; Georgi, A.; Kopinke, F.; Oller, I.; Malato, S. Fe-zeolites as heterogeneous catalysts in solar Fenton-like reactions at neutral pH. *Appl. Catal., B* **2012**, *125*, 51−58.

(16) Xi, B. J.; Verma, L. K.; Li, J.; Bhatia, C. S.; Danner, A. J.; Yang, H.; Zeng, H. C. TiO_2 thin films prepared via adsorptive self-assembly for self-cleaning applications. *ACS Appl. Mater. Interfaces* **2012**, *4*, 1093−1102.

(17) Aragay, G.; Pino, F.; Merkoçi, A. Nanomaterials for sensing and destroying pesticides. *Chem. Rev.* **2012**, *112*, 5317−5338.

(18) Zhao, H. Y.; Wang, Y. J.; Wang, Y. B.; Cao, T. C.; Zhao, G. H. Electro-Fenton oxidation of pesticides with a novel Fe_3O_4@Fe_2O_3/activated carbon aerogel cathode: high activity, wide pH range and catalytic mechanism. *Appl. Catal., B* **2012**, *125*, 120−127.

(19) Chu, W.; Lau, T. K.; Fung, S. C. Effects of combined and sequential addition of dual oxidants (H_2O_2/$S_2O_8^{2-}$) on the aqueous carbofuran photodegradation. *J. Agric. Food Chem.* **2006**, *54*, 10047−10052.

(20) Fenoll, J.; Hellín, P.; Martínez, C. M.; Flores, P.; Navarro, S. Semiconductor-sensitized photodegradation of s-triazine and chloroacetanilide herbicides in leaching water using TiO_2 and ZnO as catalyst under natural sunlight. *J. Photochem. Photobiol., A* **2012**, *238*, 81−87.

(21) Li, H. P.; Liu, J. Y.; Hou, W. G.; Du, N.; Zhang, R. J.; Tao, X. T. Synthesis and characterization of g-C_3N_4/Bi_2MoO_6 heterojunctions with enhanced visible light photocatalytic activity. *Appl. Catal., B* **2014**, *160−161*, 89−97.

(22) Wang, X. C.; Maeda, K.; Thomas, A.; Takanabe, K.; Xin, G.; Carlsson, J. M.; Domen, K.; Antonietti, M. A metal-free polymeric photocatalyst for hydrogen production from water under visible light. *Nat. Mater.* **2009**, *8*, 76−80.

(23) Tian, J. Q.; Ning, R.; Liu, Q.; Asiri, A. M.; Al-Youbi, A. O.; Sun, X. P. Three-dimensional porous supramolecular architecture from ultrathin g-C_3N_4 nanosheets and reduced graphene oxide: solution self-assembly construction and application as a highly efficient metal-free electrocatalyst for oxygen reduction reaction. *ACS Appl. Mater. Interfaces* **2014**, *6*, 1011−1017.

(24) Zhu, J. J.; Xiao, P.; Li, H. L.; Carabineiro, S. A. C. Graphitic carbon nitride: synthesis, properties, and applications in catalysis. *ACS Appl. Mater. Interfaces* **2014**, *6*, 16449−16465.

(25) Su, F. Z.; Mathew, S. C.; Lipner, G.; Fu, X. Z.; Antonietti, M.; Blechert, S.; Wang, X. C. mpg-C_3N_4-catalyzed selective oxidation of alcohols using O_2 and visible light. *J. Am. Chem. Soc.* **2010**, *132*, 16299−16301.

(26) Xu, J.; Zhang, L. W.; Shi, R.; Zhu, Y. F. Chemical exfoliation of graphitic carbon nitride for efficient heterogeneous photocatalysis. *J. Mater. Chem. A* **2013**, *1*, 14766−14772.

(27) Tian, J. Q.; Liu, Q.; Ge, C. G.; Xing, Z. C.; Asiri, A. M.; Al-Youbi, A. O.; Sun, X. P. Ultrathin graphitic carbon nitride nanosheets: a low-cost, green, and highly efficient electrocatalyst toward the

reduction of hydrogen peroxide and its glucose biosensing application. *Nanoscale* **2013**, *5*, 8921−8924.
(28) Tian, J. Q.; Liu, Q.; Asiri, A. M.; Al-Youbi, A. O.; Sun, X. P. Ultrathin graphitic carbon nitride nanosheet: a highly efficient fluorosensor for rapid, ultrasensitive detection of Cu^{2+}. *Anal. Chem.* **2013**, *85*, 5595−5599.
(29) Chen, N. Y.; Tian, J. Q.; Liu, Q.; Ge, C. J.; Qusti, A. H.; Asiri, A. M.; Al-Youbi, A. O.; Sun, X. P. Au-nanoparticle-loaded graphitic carbon nitride nanosheets: green photocatalytic synthesis and application toward the degradation of organic pollutants. *ACS Appl. Mater. Interfaces* **2013**, *5*, 6815−6819.
(30) Yan, S. C.; Li, Z. S.; Zou, Z. G. Photodegradation performance of g-C_3N_4 fabricated by directly heating melamine. *Langmuir* **2009**, *25*, 10397−10401.
(31) He, F.; Chen, G.; Yu, Y. G.; Hao, S.; Zhou, Y. S.; Zheng, Y. Facile approach to synthesize g-PAN/g-C_3N_4 composites with enhanced photocatalytic H_2 evolution activity. *ACS Appl. Mater. Interfaces* **2014**, *6*, 7171−7179.
(32) Zhang, M.; Xu, J.; Zong, R. L.; Zhu, Y. F. Enhancement of visible light photocatalytic activities via porous structure of g-C_3N_4. *Appl. Catal., B* **2014**, *147*, 229−235.
(33) Xu, H.; Yan, J.; Xu, Y. G.; Song, S. H.; Li, H. M.; Xia, J. X.; Huang, C. J.; Wan, H. L. Novel visible-light-driven AgX/graphite-like C_3N_4(X = Br, I) hybrid materials with synergistic photocatalytic activity. *Appl. Catal., B* **2013**, *129*, 182−193.
(34) Martin, D. G.; Qiu, K. P.; Shevlin, S. A.; Handoko, A. D.; Chen, S. W.; Guo, Z. X.; Tang, J. W. Highly efficient photocatalytic H_2 evolution from water using visible light and structure-controlled graphitic carbon nitride. *Angew. Chem., Int. Ed.* **2014**, *53*, 9240−9245.
(35) Dong, F.; Zhao, Z. W.; Xiong, T.; Ni, Z. L.; Zhang, W. D.; Sun, Y. J.; Ho, W. K. In situ construction of g-C_3N_4/g-C_3N_4 metal-free heterojunction for enhanced visible-light photocatalysis. *ACS Appl. Mater. Interfaces* **2013**, *5*, 11392−11401.
(36) Xiang, Q. J.; Yu, J. G.; Jaroniec, M. Preparation and enhanced visible-light photocatalytic H_2-production activity of graphene/C_3N_4 composites. *J. Phys. Chem. C* **2011**, *115*, 7355−7363.
(37) Dong, G. H.; Zhao, K.; Zhang, L. Z. Carbon self-doping induced high electronic conductivity and photoreactivity of g-C_3N_4. *Chem. Commun.* **2012**, *48*, 6178−6180.
(38) Wu, S. Z.; Chen, C. H.; Zhang, W. D. Etching graphitic carbon nitride by acid for enhanced photocatalytic activity towards degradation of 4-nitrophenol. *Chin. Chem. Lett.* **2014**, *25*, 1247−1251.
(39) Li, X.; Kikugawa, N.; Ye, J. Nitrogen-doped lamellar niobic acid with visible light-responsive photocatalytic activity. *Adv. Mater.* **2008**, *20*, 3816−3819.
(40) Chen, S. F.; Hu, Y. F.; Meng, S. G.; Fu, X. L. Study on the separation mechanisms of photogenerated electrons and holes for composite photocatalysts g-C_3N_4-WO_3. *Appl. Catal., B* **2014**, *150*−*151*, 564−573.
(41) Zhao, H. X.; Yu, H. T.; Quan, X.; Chen, S.; Zhang, Y. B.; Zhao, H. M.; Wang, H. Fabrication of atomic single layer graphitic-C_3N_4 and its high performance of photocatalytic disinfection under visible light irradiation. *Appl. Catal., B* **2014**, *152*−*153*, 46−50.
(42) Yan, S. C.; Li, Z. S.; Zou, Z. G. Photodegradation of rhodamine B and methyl orange over boron-doped g-C_3N_4 under visible light irradiation. *Langmuir* **2010**, *26*, 3894−3901.
(43) Lee, H.; Choi, W. Y. Photocatalytic oxidation of arsenite in TiO_2 suspension: kinetics and mechanisms. *Environ. Sci. Technol.* **2002**, *36*, 3872−3878.
(44) Li, W. J.; Li, D. Z.; Lin, Y. M.; Wang, P. X.; Chen, W.; Fu, X. Z.; Shao, Y. Evidence for the active species involved in the photodegradation process of methyl orange on TiO_2. *J. Phys. Chem. C* **2012**, *116*, 3552−3560.
(45) Turabik, M.; Oturan, N.; Gözmen, B.; Oturan, M. A. Efficient removal of insecticide "imidacloprid" from water by electrochemical advanced oxidation processes. *Environ. Sci. Pollut. Res.* **2014**, *21*, 8387−8397.

NOTE ADDED AFTER ISSUE PUBLICATION

The incorrect Supporting Information was attached to this Article on May 12, 2015. The corrected version was published on the Web on September 16, 2015. An Addition and Correction was published in volume 63, issue 38.

DOI: 10.1021/acs.jafc.5b01105
J. Agric. Food Chem. 2015, 63, 4754−4760

JOURNAL OF AGRICULTURAL AND FOOD CHEMISTRY

Article

pubs.acs.org/JAFC

Characterization of the Key Aroma Compounds in a Commercial Amontillado Sherry Wine by Means of the Sensomics Approach

Pauline Marcq and Peter Schieberle*

Deutsche Forschungsanstalt für Lebensmittelchemie, Lise-Meitner-Straße 34, D-85354 Freising, Germany

ABSTRACT: An aroma extract dilution analysis (AEDA) carried out on the volatile fraction isolated by extraction/solvent-assisted flavor evaporation (SAFE) distillation from a commercial Amontillado sherry wine revealed 37 odor-active compounds with flavor dilution (FD) factors in the range of 16−4096. Among them, 2-phenylethanol (flowery, honey-like) and ethyl methylpropanoate (fruity) showed the highest FD factors, followed by ethyl (2*S*,3*S*)-2-hydroxy-3-methylpentanoate (fruity) reported for the first time in sherry wine. A total of 36 aroma-active compounds located by AEDA were then quantitated by a stable isotope dilution assay, and their odor activity values (OAVs; ratio of concentration to odor threshold) were calculated. The highest OAV was displayed by 1,1-diethoxyethane (2475; fruity), followed by 2- and 3-methylbutanals (574; malty) and methylpropanal (369; malty). Aroma reconstitution experiments and a comparative aroma profile analysis revealed that the entire orthonasal aroma profile of the Amontillado sherry wine could be closely mimicked.

KEYWORDS: *GC−O, AEDA, static headspace−olfactometry, OAV, ethyl (2S,3S)-2-hydroxy-3-methylpentanoate, aroma recombinate*

INTRODUCTION

Sherry is a fortified wine produced in the Jerez region in southern Spain. Three different white grape varieties are used in its production, Palomino Fino, Pedro Ximénez, and Moscatel, with the first being the most abundant in dry sherry production, while the others are commonly used to produce sweet sherry wines. Although made from the same grape variety, namely, Palomino Fino, different types of dry sherry wines are manufactured by three different maturation processes: Fino, Amontillado, and Oloroso. Fino is processed by a dynamic biological aging with a layer of yeast, also called *flor*, developing on the surface of the wine, thus protecting it from oxidation. Fino is fortified to 15.5% (v/v) ethanol and results in a pale, yellow product with a sharp and delicate bouquet.[1] Oloroso, which is dark, brown, and full-bodied,[1] is aged under oxidative conditions and fortified to at least 17% ethanol (v/v), hindering the formation of a *flor*, thus allowing direct contact between the wine and ambient air. Amontillado is aged by means of two consecutive steps: a biological step and an oxidative step. Its color is in between that of Fino and Oloroso, and it has been reported to possess a complex flavor.[2] Amontillado is the oldest and most valued of the three wine styles made from the Palomino Fino grape.[3]

A particularity of sherry wine is a dynamic aging system called "*criaderas* and *solera*". The wine is stored in American oak casks (500−600 L) stacked in several levels, with the lowest level containing the older wine and the highest level containing the youngest wine. This technique involves many transfers of wine of different ages and vintages, enabling the production of a consistent and homogeneous sherry aroma. A detailed description of the system can be found in various textbooks cited in reviews.[3,4]

Data on the volatile composition of sherry wine were published as early as 1976,[5] and over 130 volatile components were identified. Subsequently, numerous studies mainly involving gas chromatographic analysis were undertaken, attempting to correlate the entire volatile fraction of sherry wine with its aroma profile.[6−8] Thus, today more than 300 volatiles are known in sherry.[9]

It is well-accepted in state-of-the-art aroma analysis that only a small subset of volatiles cause the aroma perception in the brain initiated by an interaction of odorants with the human olfactory receptors.[10−12] Therefore, it can be assumed that only a few of the numerous volatiles identified in sherry wine are probably odor-active. To characterize the key aroma compounds in foods, the sensomics analysis was suggested by Schieberle and Hofmann[11] as a molecular sensory analysis approach to differentiate the key aroma compounds from the bulk of odorless volatiles. By combination of sensory-supported analysis, such as gas chromatography−olfactometry (GC−O), with modern instrumental techniques, it is possible to determine the combinatorial food aroma code, also called the "aroma blueprint", and various aromas have already successfully been decoded by means of the sensomics analysis.[12]

By application of GC−O, Zea et al.[13] have monitored the aroma profile of Fino during aging; however, no quantitative analysis was performed in this study. In a recent work by Moyano et al.,[14] Amontillado sherry wine was analyzed by GC−O to identify the odorants generated during the sequential biological and oxidative aging steps. A total of 25 compounds were monitored and based on so-called odor spectrum values, and ethyl octanoate, ethyl butanoate, eugenol, ethyl methylpropanoate, and sotolon were proposed as the most potent odorants in Amontillado sherry wine. Several further studies on sherry wines applied the odor activity value concept (OAV; ratio of concentration to odor threshold), however, without performing a preliminary screening of aroma compounds by

Received: March 19, 2015
Revised: April 28, 2015
Accepted: April 28, 2015
Published: April 28, 2015

ACS Publications © 2015 American Chemical Society

DOI: 10.1021/acs.jafc.5b01418
J. Agric. Food Chem. 2015, 63, 4761−4770

GC−O.[2,15−17] Moreno et al.[18] monitored volatile compounds with OAV > 5 in Fino sherry wine during aging on the basis of GC/flame ionization detector (FID) quantitation. In addition to acetaldehyde, these authors suggested sotolon, 1,1-diethoxyethane, and *cis*-whiskylactone as markers of aging.

Although several studies have been performed aimed at identifying important odorants by either applying GC−O or the OAV concept, up to now, no comprehensive studies employing the full sensomics approach[12] have been performed on a sherry wine. Therefore, this research consisted of (i) the identification of the key aroma compounds in an Amontillado sherry wine by means of aroma extract dilution analysis, (ii) the quantitation of these compounds by a stable isotope dilution assay (SIDA), (iii) the determination of the importance of each odorant on the basis of OAVs, and (iv) a validation of the results through aroma reconstitution experiments and sensory evaluation.

MATERIALS AND METHODS

Sherry Wine. The investigated commercial sherry wine was an Amontillado produced in Spain in the Sanlúcar de Barrameda region (Jerez region). The wine was called Don Benigno and has been produced and bottled by Pedro Rodriguez e Hijos. On the basis of the label, it contained 17.5% (v/v) ethanol and carried the Jerez-Xérès-Sherry denomination of origin. The wine was purchased at a local spirit shop. This selection was not performed for advertising purposes nor does it imply a research contract with the manufacturer.

Chemicals. Reference compounds of the odorants were obtained from the sources given in parentheses: acetaldehyde, acetic acid, 4-allyl-2-methoxyphenol (eugenol), 2,3-butanedione, butanoic acid, ethyl butanoate, ethyl 2-hydroxyhexanoate, ethyl propanoate, ethyl octanoate, 4-ethyl-2-methoxyphenol, ethyl methylpropanoate, 4-ethylphenol, hexanoic acid, 4-hydroxy-2,5-dimethylfuran-3(2*H*)-one, 4-hydroxy-3-methoxyacetophenone (acetovanillone), 4-hydroxy-3-methoxybenzaldehyde (vanillin), 2-methyl-1-butanal, 3-methyl-1-butanal, 2-methylbutanoic acid, 3-methylbutanoic acid, 2-methyl-1-butanol, 3-methyl-1-butanol, methylpropanal, methylpropanol, methylpropanoic acid, 3-(methylthio)-propanal, 2-phenylacetic acid, 2-phenylethanol, octanoic acid, and whiskylactone (Sigma-Aldrich, St. Louis, MO); 1,1-diethoxyethane, ethyl hexanoate, ethyl 2-methylbutanoate, ethyl 3-methylbutanoate, and 3-hydroxy-4,5-dimethylfuran-2(5*H*)-one (sotolon) (Fisher Scientific, Pittsburgh, PA); ethyl 2-hydroxy-4-methylpentanoate (TCI America, Portland, OR); and (*E*)-*β*-damascenone (Vigon, East Stroudsburg, PA).

The isotopically labeled standards were obtained commercially from the sources given in parentheses: [$^2H_3$]-acetaldehyde, [$^2H_5$]-butanoic acid, [$^2H_4$]-1,1-diethoxyethane, [$^2H_3$]-ethyl butanoate, [$^2H_{11}$]-ethyl hexanoate, [$^2H_{15}$]-ethyl octanoate, [$^2H_{10}$]-4-ethylphenol, [$^2H_4$]-pentanoic acid, [$^2H_2$]-3-methylbutanoic acid, [$^2H_2$]-3-methyl-1-butanal, [$^2H_4$]-3-methyl-1-butanol, [$^2H_3$]-methylpropanoic acid, [$^2H_5$]-2-phenylethanol, and [$^2H_{15}$]-octanoic acid (CDN Isotopes, Inc., Pointe Claire, Canada); [$^{13}C_2$]-acetic acid and [$^{13}C_2$]-2-phenylacetic acid (Isotech Stable Isotopes, Sigma-Aldrich, St. Louis, MO); [$^2H_3$]-2,3-pentanedione, [$^2H_2$]-ethyl methylpropanoate, [$^2H_2$]-methylpropanal, and [$^2H_4$]-(*E*)-*β*-damascenone (Adesis, Inc., New Castle, DE); and [$^2H_3$]-4-allyl-2-methoxyphenol, [$^2H_5$]-ethyl propanoate, [$^2H_5$]-ethyl (2*S*,3*S*)-2-hydroxy-3-methylpentanoate, [$^2H_2$]-ethyl 2-methylbutanoate, [$^{13}C_2$]-3-hydroxy-4,5-dimethylfuran-2(5*H*)-one, [$^{13}C_2$]-4-hydroxy-2,5-dimethylfuran-3(2*H*)-one, [$^2H_3$]-4-hydroxy-3-methoxybenzaldehyde, and [$^2H_3$]-3-(methylthio)-propanal (AromaLab AG, Freising, Germany). [$^2H_2$]-*cis*-Whiskylactone was synthesized as previously reported.[19]

Anhydrous sodium carbonate, anhydrous sodium sulfate, and hydrochloric acid (37%) were obtained from Fisher Scientific (Pittsburgh, PA). Sodium chloride, sodium hydroxide, sodium nitrite, L-isoleucine, and concentrated sodium chloride (26%) were obtained from Sigma-Aldrich (St. Louis, MO). Diethyl ether (Acros, Fisher Scientific, Pittsburgh, PA) and *n*-pentane (Merck, Darmstadt, Germany) were freshly distilled prior to use. Dichloromethane was obtained from Fisher Scientific (Pittsburgh, PA). Silica 60 was purified according to a procedure described by Esterbauer.[20] For chromatographic separation, water was purifed with a Milli-Q Advantage A10 system (Millipore, Molsheim, France). For sensory reconstitution experiments, Deer Park bottled water was used (Nestlé Water North America, Inc., Stamford, CT). D-Glucose and L-(+)-tartaric acid were supplied by Sigma-Aldrich (St. Louis, MO), and glycerol was supplied by Fisher Scientific (Pittsburgh, PA).

Synthesis of Ethyl (2*S*,3*S*)-2-Hydroxy-3-methylpentanoate. This was carried out in two steps and was based on previously published procedures,[21,22] with some modification.

(2S,3S)-2-Hydroxy-3-methylpentanoic Acid. L-Isoleucine (22.9 mmol) was dissolved in aqueous hydrochloric acid (1 mol/L, 22.9 mL), and concentrated acetic acid (45.8 mL) was added with stirring. Then, an aqueous solution of sodium nitrite (23 mmol in 27.6 mL) was added dropwise at 0 °C to the mixture within 30 min with stirring. The solution was stirred for another 20 min at 0 °C and then stirred overnight at room temperature under an argon atmosphere. The solution was concentrated, and the residue was dissolved in water (50 mL) and adjusted to a pH of ∼2 with concentrated hydrochloric acid. After extraction with diethyl ether (3 × 100 mL), the combined organic extracts were washed with saturated sodium chloride solution and dried over anhydrous sodium sulfate. After filtration, the solvent was distilled off using a Vigreux column at 40 °C to yield the target compound.

Ethyl (2S,3S)-2-hydroxy-3-methylpentanoate. The acid was mixed with ethanol (20 mL) and concentrated hydrochloric acid (50 μL) and was refluxed for 150 min. After the mixture was cooled, diethyl ether (50 mL) was added and the organic phase was consecutively washed with sodium carbonate (0.75 mol/L, 20 mL) and bidistilled water (15 mL). The organic layer was dried over anhydrous sodium sulfate and then concentrated using a Vigreux column (60 × 1 cm). The target compound was purified using a water-cooled glass column (30 × 1 cm) containing 20 g of purified silica gel,[20] conditioned in *n*-pentane. For this purpose, the solution (0.2 mL) was placed on the top of the column and separation was performed using the following *n*-pentane/diethyl ether gradient: *n*-pentane (I; 100 mL), *n*-pentane/diethyl ether (II; 95:5, 100 mL), *n*-pentane/diethyl ether (III; 80:20, 100 mL), and finally, diethyl ether (IV; 100 mL). The target compound was detected by GC−O in fraction III and was further purified using flash chromatography (40 g of Lichroprep DIOL phase; particle size of 40−63 μm) under pressure with a flow rate of 2 mL/min and the *n*-pentane/diethyl ether gradient.

MS (EI), *m*/*z* (%): 87 (100), 76 (66), 104 (53), 45 (37), 69 (24), 57 (17), 41 (10), 88 (7), 75 (6), 58 (5), 103 (5), 105 (5), 71 (4), 55 (3), 77 (3), 85 (3), 86 (3), 43 (2), 47 (2), 70 (2), 99 (2), 117 (2), 131 (2), 145 (2), 46 (1), 53 (1), 59 (1), 67 (1), 68 (1), 89 (1), 97 (1), 98 (2), 106 (1), 113 (1), 114 (1).

MS (CI), *m*/*z* (%): 161 (100).

The concentration of ethyl (2*S*,3*S*)-2-hydroxy-3-methylpentanoate was determined by GC/FID using 1-octanol as the internal standard. Its odor threshold was determined in a 17% (v/v) hydroalcoholic solution according to the procedure described previously,[23] with 12 panelists participating in this session (4 males and 8 females, ranging in age from 29 to 51 years old).

Isolation of the Volatiles. The sherry (100 mL) was mixed with sodium chloride (10 g) and was extracted with diethyl ether (total volume of 250 mL). The organic layers as well as the emulsion formed were combined, dried over anhydrous sodium sulfate, and concentrated to 100 mL using an automated solvent evaporator system operating at 25 °C, 0.7 bar, and using nitrogen gas vortex shearing (TurboVap II, Biotage, Uppsala, Sweden). The volatiles were then separated from the non-volatile compounds by high-vacuum distillation using the solvent-assisted flavor evaporation (SAFE) apparatus,[24] and the distillate was separated into an acidic fraction (AF) and a neutral-basic fraction (NBF) by treatment with an aqueous sodium carbonate solution.[25] AF and NBF were washed with saturated sodium chloride solution, dried over anhydrous sodium sulfate, and concentrated to ∼4 mL using the automated solvent evaporator system described above. The distillate was further concentrated to ∼1 mL under a subtle stream of nitrogen at 37 °C.

DOI: 10.1021/acs.jafc.5b01418
J. Agric. Food Chem. 2015, 63, 4761−4770

Table 1. Selected Ions (m/z) of Analytes and Isotopically Labeled Standards Used in the SIDA

odorant	ion (m/z)	labeled standard	ion (m/z)	Rf
acetaldehyde	43	[$^2H_3$]-acetaldehyde	46	0.70
acetic acid	60	[$^{13}C_2$]-acetic acid	62	1.09
4-allyl-2-methoxyphenol	164	[$^2H_3$]-4-allyl-2-methoxyphenol	167	0.93
2,3-butanedione	86	[$^2H_3$]-2,3-pentanedione	103	1.24
butanoic acid	73	[$^2H_5$]-butanoic acid	75	1.00
cis-whiskylactone	157	[$^2H_2$]-*cis*-whiskylactone	159	0.59
1,1-diethoxyethane	73	[$^2H_4$]-1,1-diethoxyethane	77	1.33
ethyl butanoate	116	[$^2H_3$]-ethyl butanoate	119	1.16
ethyl hexanoate	99	[$^2H_{11}$]-ethyl hexanoate	110	1.07
ethyl propanoate	102	[$^2H_5$]-ethyl propanoate	107	1.10
ethyl octanoate	88	[$^2H_{15}$]-ethyl octanoate	91	1.14
4-ethyl-2-methoxyphenol	152	[$^2H_2$]-4-ethyl-2-methoxyphenol	154	1.00
ethyl (2*S*,3*S*)-2-hydroxy-3-methylpentanoate	104	[$^2H_5$]-ethyl (2*S*,3*S*)-2-hydroxy-3-methylpentanoate	109	1.10
ethyl 2-hydroxy-4-methylpentanoate	87	[$^2H_5$]-ethyl (2*S*,3*S*)-2-hydroxy-3-methylpentanoate	77	0.96
ethyl 2-methylbutanoate	102	ethyl 3-methylbutanoate	88	0.99
ethyl 3-methylbutanoate	88	[$^2H_2$]-ethyl 2-methylbutanoate	59	1.03
ethyl methylpropanoate	116	[$^2H_2$]-ethyl methylpropanoate	118	1.06
4-ethylphenol	107	[$^2H_{10}$]-4-ethylphenol	113	1.01
hexanoic acid	60	[$^2H_4$]-pentanoic acid	62	0.98
3-hydroxy-4,5-dimethylfuran-2(5*H*)-one (sotolon)	128	[$^{13}C_2$]-3-hydroxy-4,5-dimethylfuran-2(5*H*)-one	130	0.96
4-hydroxy-2,5-dimethylfuran-3(2*H*)-one	128	[$^{13}C_2$]-4-hydroxy-2,5-dimethylfuran-3(2*H*)-one	130	1.10
4-hydroxy-3-methoxyacetophenone (acetovanillone)	151	[$^2H_3$]-4-hydroxy-3-methoxybenzaldehyde	154	0.82
4-hydroxy-3-methoxybenzaldehyde (vanillin)	151	[$^2H_3$]-4-hydroxy-3-methoxybenzaldehyde	154	1.03
2- and 3-methylbutanoic acids	60	[$^2H_2$]-3-methylbutanoic acid	62	1.05
2- and 3-methyl-1-butanals	71	[$^2H_2$]-3-methylbutanal	73	0.78
2- and 3-methyl-1-butanols	70	[$^2H_4$]-3-methyl-1-butanol	74	0.99
methylpropanal	70	[$^2H_2$]-methylpropanal	74	1.09
methylpropanol	43	[$^2H_4$]-3-methyl-1-butanol	74	0.94
methylpropanoic acid	88	[$^2H_3$]-methylpropanoic acid	91	1.02
3-(methylthio)-propanal	104	[$^2H_3$]-3-(methylthio)-propanal	107	0.91
2-phenylacetic acid	136	[$^{13}C_2$]-2-phenylacetic acid	138	1.03
2-phenylethanol	122	[$^2H_5$]-2-phenylethanol	127	1.04
octanoic acid	60	[$^2H_{15}$]-octanoic acid	63	0.94
(*E*)-*β*-damascenone	190	[$^2H_4$]-(*E*)-*β*-damascenone	194 + 195	0.89

GC−O. GC−O was performed using an Agilent gas chromatograph type 6890 (Agilent Technologies, Inc., Santa Clara, CA) and the following fused silica capillaries: J&W Scientific DB-FFAP and DB-5 (30 m × 0.32 mm inner diameter, 0.25 μm film thickness) (Folsom, CA). The sample (1 μL) was applied by cool on-column injection at 40 °C using helium as the carrier gas with a flow rate of 2.5 mL/min. The temperature programs were as follow: 40 °C for 2 min, 8 °C/min up to 80 °C, 5 °C/min up to 120 °C, 8 °C/min up to 230 °C, and 230 °C for 15 min (DB-FFAP) and 40 °C for 2 min, 8 °C/min up to 80 °C, 5 °C/min up to 120 °C, 8 °C/min up to 250 °C, and 250 °C for 15 min (DB-5). GC−O was performed with simultaneous flame ionization and olfactometric detection by evenly splitting the effluent using a Y-type glass splitter and two deactivated fused silica glass capillaries of the same length. Both FID and sniffing port temperature were at 220 °C. Linear retention indices (RIs) of the aroma compounds were calculated from the retention times of a series of *n*-alkanes (C_5−C_{26}) as described previously.[26]

Aroma Extraction Dilution Analysis (AEDA). AEDA was performed on the DB-FFAP column. The original NBF and AF were first sniffed by four panelists to ensure a consistency of detection and aroma language selection. Each fraction was then stepwise-diluted with diethyl ether (1:1, v/v) and subjected to GC−O. The flavor dilution (FD) factor of an odorant represented the last dilution in which it could be perceived. Each panelist was trained on a weekly basis by means of solutions of reference odorants in water using a common aroma language.[23]

Static Headspace−Olfactometry (SHO) and Aroma Dilution Analysis (ADA). GC of static headspace samples was carried out by means of a Thermo Trace Ultra gas chromatograph in connection with a cryotrap system type 915 (Braunschweig, Germany), cooled with liquid nitrogen. An aliquot of the sherry wine (10 mL) was equilibrated in a septum-sealed vessel (120 mL) for 15 min at 30 °C. From different samples of the same volume, decreasing headspace volumes (10−0.1 mL) were withdrawn with a gastight syringe, injected by cold on-column injection, and subsequently trapped at −150 °C. The trap was then rapidly heated to 250 °C, and the sample was flushed onto a J&W Scientific DB-5 fused silica column (30 m × 0.25 mm inner diameter, 0.5 μm film thickness) (Folsom, CA). After injection, the temperature of the oven was held at 0 °C for 2 min, then raised at 6 °C/min to 100 °C, followed by 40 °C/min to 240 °C, and held at 240 °C for 2 min. At the end of the column, the effluent was split evenly between an FID and a sniffing port held at 250 and 220 °C, respectively. The flow rate of the carrier gas helium was 0.8 mL/min. The FD factors were calculated by dividing the largest volume analyzed to the lowest volume in which the odorant could be detected.

Gas Chromatography/Mass Spectrometry (GC/MS). Dependent upon the concentration of the aroma compound and the presence of co-eluting compounds, several GC/MS systems were used for identification. The majority of the compounds was identified by means of a gas chromatograph type 6890 coupled to a MS type 5975 (Agilent Technologies, Inc., Santa Clara, CA) operated in the electron impact mode (MS−EI) at 70 eV. Separation was performed at a constant flow (average velocity of 37 cm/s), and the scan was between 35 and 350 amu with 4.45 scans/s. Trace analytes were identified using a two-dimensional GC/MS instrument consisting of an Agilent GC1 and GC2 system type 7890A and 6890N, respectively (Santa Clara, CA).

DOI: 10.1021/acs.jafc.5b01418
J. Agric. Food Chem. 2015, 63, 4761−4770

The column combination consisted of a BP-20 (SGE, Inc., Austin, TX) in the first dimension and a J&W Scientific DB-5 (Folsom, CA) in the second dimension (30 m × 0.32 mm inner diameter, 0.25 μm film thicknesses each). For the identification of low boiling substances, the system used for the SHO described above was coupled to a Varian Saturn 2100 ion trap mass spectrometer (Darmstadt, Germany), and mass spectra were generated by MS−EI at 70 eV. Separation was performed at a constant pressure with an average velocity of 45.103 cm/s. The MS was operated with a scan mode between 45 and 400 amu and a scan speed of 3.99 scans/s.

Quantitation by a SIDA in Combination with GC/MS. Aliquots of the labeled standard in dichloromethane were added to different amounts of sherry wine (1−100 mL) depending upon the concentration of the target compound estimated in preliminary experiments. The samples were stirred for 30 min and then extracted with diethyl ether. Volatiles were isolated according to the method described above, and quantitation of the aroma compounds in the extracts was performed using both the two-dimensional GC/MS system as described above as well as a one-dimensional GC/MS system with an Agilent 6890 gas chromatograph and an Agilent 5973 mass spectrometer (Santa Clara, CA). Separation was performed using a J&W Scientific DB-FFAP column (30 m × 0.32 mm inner diameter, 0.25 μm film thickness) (Folsom, CA) using the following temperature program: 40 °C for 2 min, 5 °C/min up to 240 °C, and 240 °C for 5 min. The temperature of the injector (splitless mode) was at 180 °C, and the flow rate of the carrier gas helium was 1.5 mL/min. Details of the ions selected for the SIDA and the correction factors are given in Table 1. Separation was performed at a constant flow (average velocity of 44 cm/s), and the mass spectrometer was operated in the selected ion monitoring (SIM) mode with a dwell time of 100 ms.

Static Headspace Analysis. The analysis was performed using the GC/MS system described above equipped with an unpolar Restek RT-Q-Bond capillary column (30 m × 0.32 mm inner diameter, 10 μm film thickness) (Bellefonte, PA). The sample (5 mL) was mixed with NaCl (1 g) in a septum-sealed vessel (20 mL), and the labeled standards dissolved in ethanol (17%, v/v) were added to the wine sample (5 mL). To quantitate acetaldehyde, the wine (0.1 mL) was diluted with water to reach a final volume of 5 mL and [$^2H_3$]-acetaldehyde was added. The headspace was generated for 20 min at 40 °C with automatic agitation at 500 rpm, and 1 mL was injected in the splitless mode using a gastight syringe at 50 °C and an injector temperature of 80 °C. The temperature program was as follows: 40 °C for 0 min, 12 °C/min up to 220 °C, 20 °C/min up to 260 °C, and 260 °C for 5 min. The flow rate of the carrier gas helium was 2 mL/min. A calibration factor was determined for each compound by analyzing mixtures of defined amounts of labeled and unlabeled compounds in ratios of 1:3, 1:1, and 3:1, respectively (Table 1). All quantitative analyses were performed in MS−EI at 70 eV, except for *cis*-whiskylactone, which was quantitated in chemical ionization (CI) mode as described previously.[19]

Determination of Ethanol. Ethanol was enzymatically quantitated using a test kit (R-Biopharm, Darmstadt, Germany).

Determination of Isomeric Distribution. 2- and 3-methylbutanoic acids were quantitated according to the procedure described by Frank et al.[25] Ethyl 2-methylbutanoate and ethyl 3-methylbutanote were quantitated in two steps because of the availability of only one labeled standard (Table 1) and mass fragment interferences between the two esters and the labeled standard. First, ethyl 3-methylbutanoate was quantitated (Table 1). Then, the ion intensities of the mass fragments m/z 102 and 88 for ethyl 2-methylbutanoate and ethyl 3-methylbutanoate, respectively, were monitored by MS−EI, and finally, the concentration of ethyl 2-methylbutanoate was calculated using a calibration curve prepared by analyzing defined mixtures of both isomers.

Aroma Profile Analysis. Panelists who participated in the study were all trained for at least 3 months on a weekly basis to recognize and describe the odor qualities of a wide range of odorants and products. In a first step, the wine was evaluated orthonasally by a small panel to generate a list of aroma attributes that were later on ranked on the basis of their frequency of citation as well as their intensity. The following nine aroma attributes were selected for the descriptive analysis: fruity, cooked apple, dark/dry fruit, honey, caramel, alcohol-like, sour/pungent, smoky, and malty. Aqueous solutions of each of the following compounds (OAV = 100) were provided to the panelists as references during each session: ethyl 3-methylbutanoate (fruity), (*E*)-β-damascenone (cooked apple), 2-phenylethanol (flowery, honey-like), 4-hydroxy-2,5-dimethylfuran-3(2*H*)-one (caramel), ethanol (alcohol-like), acetic acid (sour/pungent), 2-methoxyphenol (smoky), and 3-methylbutanol (malty). For the dark/dry fruit descriptor, dry figs and raisins were provided. The wine (20 mL) was poured into a glass vessel (45 mL) and analyzed by ranking the intensity of each attribute on a seven-point scale (steps of 0.5) from 0 (not perceivable) to 3 (strongly perceivable). The aroma profile

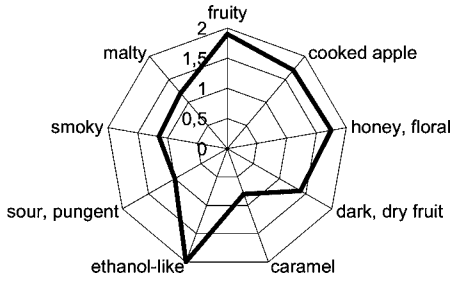

Figure 1. Aroma profile analysis of Amontillado sherry wine.

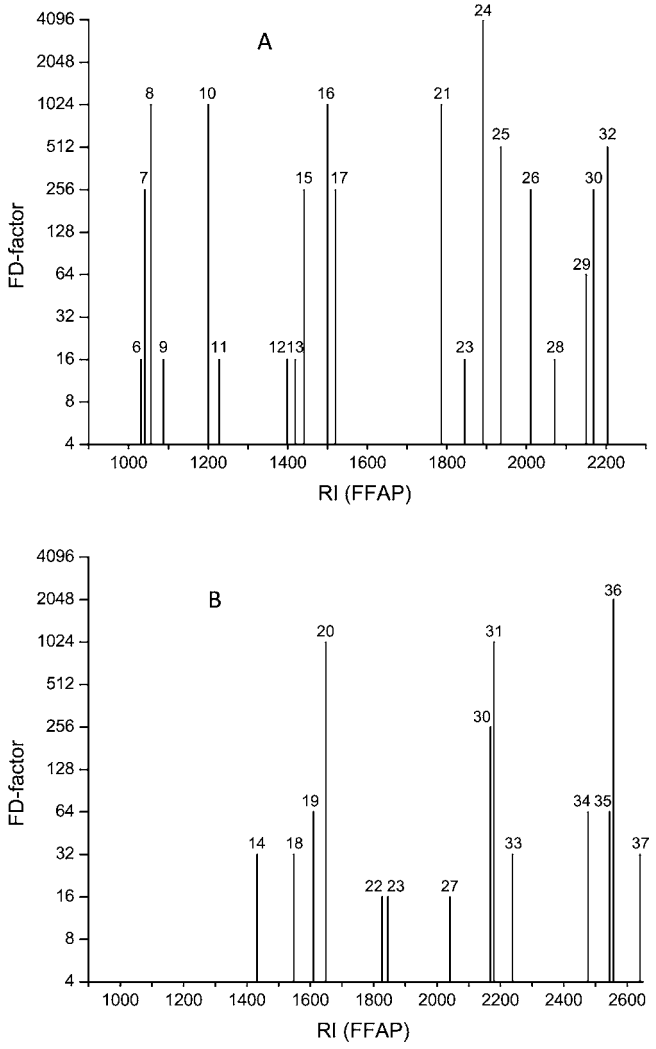

Figure 2. FD chromatogram of (A) NBF and (B) AF isolated from Amontillado sherry wine (FD factors are given as a function of the linear retention indices). Numbering refers to Table 2.

DOI: 10.1021/acs.jafc.5b01418
J. Agric. Food Chem. 2015, 63, 4761−4770

Table 2. Most Odor-Active (FD ≥ 16) Volatile Constituents Identified in Amontillado Sherry Wine

compound number	odorant[b]	odor quality[c]	RI[a] FFAP	RI[a] DB5	fraction[d]	FD factor[e]
1	1,1-diethoxyethane	green/fruity	<1000	716	NBF	256
2	2- and 3-methylbutanals	malty	<1000	660	NBF	16
3	ethyl propanoate	fruity/green	<1000	715	NBF	16
4	ethyl methylpropanoate	fruity	<1000	745	NBF	4096
5	2,3-butanedione	buttery	<1000	<700	NBF	64
6	ethyl butanoate	fruity	1031	806	AF	16
7	ethyl 2-methylbutanoate	fruity	1041	844	NBF	256
8	ethyl 3-methylbutanoate	fruity	1056	847	NBF	1024
9	methylpropanol	malty	1088	647	NBF	16
10	2- and 3-methylbutanols	malty	1200	753	NBF	1024
11	ethyl hexanoate	fruity	1228	995	NBF	16
12	unknown	fruity	1398	nd	NBF	16
13	ethyl octanoate	fruity	1419	1195	NBF	16
14	acetic acid	sour	1432	nd	NBF	32
15	3-(methylthio)-propanal	cooked potato	1441	898	AF	256
16	ethyl (2*S*,3*S*)-2-hydroxy-3-methylpentanoate	fruity	1500	1064	NBF	1024
17	ethyl 2-hydroxy-4-methylpentanoate	fruity	1520	1060	NBF	256
18	methylpropanoic acid	sweaty	1548	nd	NBF	32
19	butanoic acid	sweaty	1610	nd	AF	64
20	2- and 3-methylbutanoic acids	sweaty	1649	877	AF	1024
21	(*E*)-*β*-damascenone	cooked apple	1786	1385	AF	1024
22	hexanoic acid	sweaty	1827	999	NBF	16
23	2-methoxyphenol	sweet, burnt	1845	1089	AF	16
24	2-phenylethanol	flowery/honey-like	1891	1163	NBF	4096
25	*cis*-whiskylactone	coconut	1936	1328	NBF	512
26	4-ethyl-2-methoxyphenol	clove-like	2011	1272	NBF	256
27	octanoic acid	fatty	2041	nd	AF	16
28	*p*-cresol	horse stable	2071	1086	AF	16
29	4-allyl-2-methoxyphenol	clove	2150	1363	NBF	64
30	4-ethylphenol	horse stable	2168	1169	NBF	256
31	3-hydroxy-4,5-dimethylfuran-2(5*H*)-one (sotolon)	seasoning-like	2180	1119	AF/NBF	1024
32	wine lactone[f]	coconut	2203	1455	NBF	512
33	decanoic acid	fatty	2238	1373	AF	32
34	unknown	woody	2477	nd	AF	64
35	phenylacetic acid	honey	2544	1248	AF	64
36	4-hydroxy-3-methoxybenzaldehyde (vanillin)	vanilla	2557	1405	AF	2048
37	4-hydroxy-3-methoxyacetophenone (acetovanillone)	sweet/vanilla	2640	nd	AF	32

[a]RI = retention index. [b]Chemical structure identified on the basis of odor quality and intensity at the sniffing port, with retention indices and mass spectra compared to reference compounds on capillaries FFAP and DB-5. [c]Odor quality perceived at the sniffing port. [d]Fraction in which the aroma compound was detected. [e]FD factor = flavor dilution factor. [f]No unequivocal mass spectrum was obtained. Identification is based on the remaining criteria in footnote *b*.

analysis of Amontillado wine was performed by 21 panelists, and the single evaluations of the panelists were averaged.

Aroma Reconstitution Experiment. An aroma mixture was prepared consisting of all quantitated aroma compounds in the same concentration as determined in the wine. For the isomers quantitated as sum (2- and 3-methylbutanols and 2- and 3-methylbutanals), a mixture of 60:40 of the isomers was used, because their corresponding esters (ethyl 2- and 3-methylbutanoates) and acids (2- and 3-methylbutanoic acids) were found in a similar ratio. For *cis*-whiskylactone, the commercial reference was used, which consisted of a mixture of ∼1:1 *cis*- and *trans*-whiskylactone. The pH was adjusted to 3.6 with hydrochloric acid (0.1 mol/L). The model solution was equilibrated at 4 °C overnight and presented to the panelists at room temperature for evaluation against a control. A volume of 10 mL from the control and from the sample was placed in amber glass containers (30 mL). The control was a freshly opened bottle of Amontillado wine (<1 week, stored at 4 °C under nitrogen gas after opening). The intensities of each attribute determined during the descriptive analysis of the wine (Figure 1) were used as a reference. Panelists were first asked to rate each attribute compared to the reference, and then the panelists were asked to evaluate the similarity between the two samples using a seven-point scale with the following end anchors: "very different" (0) and "very similar" (3), respectively.

Sensory Evaluation of Aroma and Taste Interactions. The model solution described above was prepared in either an aqueous solution of ethanol (17%, v/v) adjusted to pH 3.6 by hydrochloric acid (0.1 mol/L) (recombinate A) or an aqueous solution of ethanol (17%, v/v; pH 3.6) containing L-tartaric acid, D-glucose, and glycerol, each at a concentration falling within the range of concentrations commonly found in dry sherry wines[1,27] (recombinate B). Recombinate B was adjusted to pH 3.6 with sodium hydroxide (5 mol/L). Descriptive aroma profiles were performed as described above with a maximum of two sessions per day. In a last session, Amontillado wines from different bottles were compared. The sherry wine sample was labeled as the "control", whereas the recombinates as well as the sherry wine from a different bottle were labeled as "sample", followed by a sample code. Between 9 and 10 panelists participated in these sessions, and the results obtained were averaged.

DOI: 10.1021/acs.jafc.5b01418
J. Agric. Food Chem. 2015, 63, 4761−4770

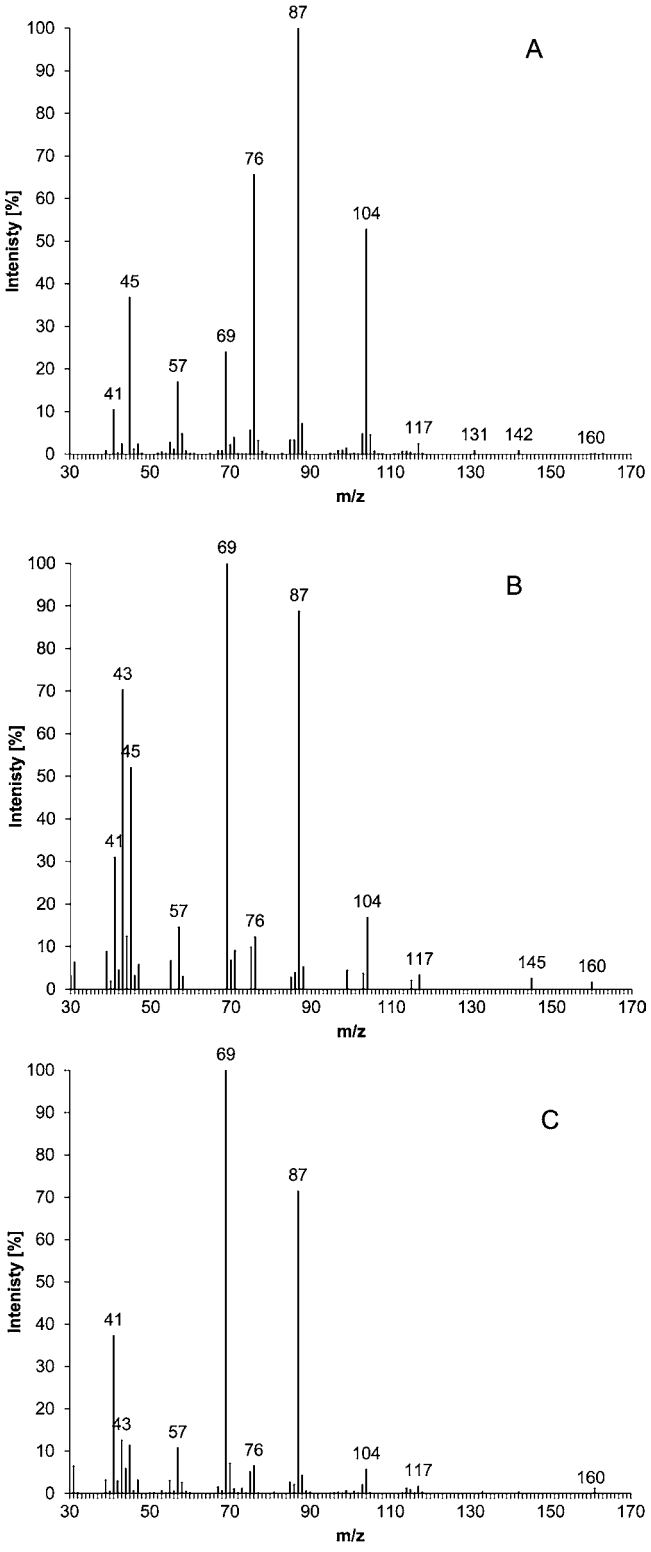

Figure 3. Mass spectrum (MS−EI) of ethyl (2*S*,3*S*)-2-hydroxy-3-methylpentanoate isolated from (A) Amontillado sherry wine. Comparison to (B) mass spectrum of ethyl 2-hydroxyhexanoate and (C) mass spectrum of ethyl 2-hydroxy-4-methylpentanoate.

RESULTS AND DISCUSSION

The aroma profile analysis of the Amontillado sherry wine was carried out by evaluating the intensity of nine aroma attributes on a scale from 0 (not perceivable) to 3 (strongly perceivable) (Figure 1). The sample was characterized by a moderate to strong ethanol-like aroma, followed by moderate fruity, honey/floral, and cooked apple attributes. The odor characteristic dark/dry fruit was also perceived but only as weak to moderate.

Table 3. Most Odor-Active Volatile Constituents in the Headspace above the Amontillado Sherry Wine

odorant[a]	odor quality[b]	RI on DB5[c]	FD factor[d]
acetaldehyde	green/fresh	<500	20
ethanol	solvent/green	500	4
methylpropanal	malty	561	10
2,3-butanedione	buttery	601	10
2- and 3-methylbutanals	malty	660	10
ethyl propanoate	fruity/green	719	2
1,1-diethoxyethane	green/fruity	740	100
2- and 3-methylbutanols	malty	753	20
ethyl methylpropanoate	fruity/liquor	765	100
ethyl butanoate	fruity	803	40
ethyl 2-methylbutanoate	fruity	847	100
ethyl 3-methylbutanoate	fruity	853	100

[a]Chemical structure identified on the basis of odor quality and intensity at the sniffing port, with retention index and mass spectrum compared to reference compounds on a DB-5 capillary column. [b]Odor quality perceived at the sniffing port. [c]RI = retention index. [d]FD factor = flavor dilution factor.

The volatiles were then isolated by solvent extraction followed by SAFE distillation,[24] and a drop of the volatile fraction was applied on a filter paper strip and evaluated by six panelists, who confirmed the presence of the typical aroma of the sherry wine. The method of volatile isolation was thus proven to be adequate for aroma isolation.

Identification of Odor-Active Compounds. GC−O was separately applied on the NBF and AF obtained from 100 mL of wine. A total of 24 compounds with FD factors ranging from 16 to 4096 were detected as the most odor-active compounds in the NBF (Figure 2A), and 13 odorants were additionally found in the AF with FD factors between 16 and 2048 (Figure 2B). The highest FD factors were found for a fruity compound (**4**; FD of 4096) eluting with a retention index below 1000, a flowery, honey-like smelling odorant (**24**), followed by a vanilla-smelling compound (**36**; FD of 2048). In addition, two fruity-smelling compounds (**8** and **16**), a malty-smelling compound (**10**), a sweaty-smelling compound (**20**), a cooked-apple-like-smelling compound (**21**), and a seasoning-like-smelling compound (**31**) appeared with high FD factors.

To identify the compounds responsible for the odors perceived at the sniffing port, first, the retention indices of the odor-active areas were determined on two different stationary GC phases. Thus, by comparison to retention indices of ∼1000 food odorants compiled in an in-house database, a chemical structure could be suggested for most of the odorants. Subsequently, the respective reference compounds were subjected to GC−O and GC/MS, and the identification was confirmed on the basis of odor quality and intensity matching at the sniffing port as well as mass spectra (MS−EI) matching between the reference and analyte. In some cases, the use of two-dimensional GC/MS was necessary to identify trace compounds co-eluting with volatiles present in a high concentration. For example, compound **21** did not yield a signal at the flame ionization detector (data not shown) but was perceived with a FD factor of 1024, indicating a low odor threshold.

On the basis of this approach, the most odor-active compounds in the Amontillado sherry wine were characterized

DOI: 10.1021/acs.jafc.5b01418
J. Agric. Food Chem. 2015, 63, 4761−4770

Table 4. Concentrations of 36 Important Aroma Compounds in Amontillado Sherry Wine

odorant	concentration[a] (μg/L)	relative standard deviation (%)	method[b]
ethanol	134000000	2.5	enzymatic
acetic acid	377241	7.7	GC/MS
1,1-diethoxyethane	123765	1.5	HS−GC/MS
2- and 3-methylbutanols	149863	7.2	GC/MS
acetaldehyde	56880	4.0	HS−GC/MS
methylpropanol	55069	0.3	GC/MS
2-phenylethanol	12242	1.1	2D GC/MS
ethyl propanoate	6311	1.7	HS−GC/MS
methylpropanoic acid	2298	3.4	GC/MS
hexanoic acid	1767	2.0	GC/MS
2,3-butanedione	1602	3.9	HS−GC/MS
butanoic acid	1302	1.5	GC/MS
octanoic acid	645	1.7	GC/MS
3-methylbutanoic acid	504	4.7	GC/MS
ethyl methylpropanoate	449	2.2	HS−GC/MS
ethyl butanoate	380	3.8	HS−GC/MS
ethyl hexanoate	379	3.4	HS−GC/MS
ethyl 2-hydroxy-4-methylpentanoate	352	3.1	GC/MS
2- and 3-methylbutanals	287	2.4	HS−GC/MS
2-methylbutanoic acid	283	3.8	GC/MS
3-hydroxy-4-methoxybenzaldehyde	239	6.9	GC/MS
4-hydroxy-3-methoxyacetophenone	201	12.8	GC/MS
methylpropanal	181	3.8	HS−GC/MS
ethyl 3-methylbutanoate	122	1.7	HS−GC/MS
ethyl octanoate	110	2.5	GC/MS
phenylacetic acid	108	6.8	GC/MS
ethyl 2-methylbutanoate	81.0	1.1	HS−GC/MS
4-ethylphenol	73.9	0.7	GC/MS
ethyl (2*S*,3*S*)-2-hydroxy-3-methylpentanoate	60.8	0.8	GC/MS
3-hydroxy-4,5-dimethylfuran-2(5*H*)-one	41.5	3.9	2D GC/MS
3-(methylthio)-propanal	36.5	0.8	2D GC/MS
4-ethyl-2-methoxyphenol	19.3	5.0	GC/MS
cis-whiskylactone	18.1	6.9	2D GC/MS (CI)
4-hydroxy-2,5-dimethylfuran-3(2*H*)-one	3.8	10.1	2D GC/MS
4-allyl-2-methoxyphenol	2.3	0.8	2D GC/MS
(*E*)-*β*-damascenone	1.4	2.2	2D GC/MS

[a]Calculated as a mean value of three different workups. [b]Quantitative method used. MS−EI was used for GC/MS methods, except for *cis*-whiskylactone, which was quantitated in MS−CI.

as ethyl methylpropanoate (**4**) and 2-phenylethanol (**24**) (Table 2). With somewhat lower FD factors, 4-hydroxy-3-methoxybenzaldehyde (**36**), ethyl 3-methylbutanoate (**8**), 2- and 3-methylbutanols (**10**), 2- and 3-methylbutanoic acids (**20**), (*E*)-*β*-damascenone (**21**), and 3-hydroxy-4,5-dimethylfuran-2(5*H*)-one (**31**) were suggested as potential contributors to the overall aroma. For compound **16**, no reference spectrum was available. The mass spectrum obtained (Figure 3A) somewhat matched with the mass spectra of ethyl 2-hydroxyhexanoate (Figure 3B) and ethyl 2-hydroxy-4-methylpentanoate (Figure 3C), respectively. However, the first mentioned compound was excluded, because it elicited a green/rubber-like aroma, but the latter had the same fruity character as compound **16**. However, ethyl 2-hydroxy-4-methylpentanoate was not eluted at the same retention index (RI) as the target analyte (RI_{FFAP} of 1520; Table 2), thus also excluding this structure. A fruity-smelling compound with a similar mass spectrum as found for compound **16** was previously reported in sherry wine;[28] however, its structure remained unknown, despite several attempts of the authors; e.g., different isomers of ethyl 2-hydroxy-4-methylpentanoate were compared to the target analyte, but only ethyl (2*R*,3*R*)-2-hydroxy-3-methylpentanaote was found to have a similar RI and mass spectrum. Thus, we concluded that an enantiomer of ethyl (2*R*,3*R*)-2-hydroxy-3-methylpentanaote might correspond to the fruity-smelling compound **16**. Ethyl 2-hydroxy-3-methylpentanoate has been identified for the first time in Cognac and other grape brandies; however, its stereochemistry was not specified in this study.[29] More recently, Poisson identified ethyl (2*S*,3*S*)-2-hydroxy-3-methylpentanoate in whisky.[21] Because the ester was not commercially available, the compound was synthesized and analyzed by GC−O and GC/MS using two different capillary columns. A complete match of RI, MS, and odor properties with the target analyte finally confirmed the identity of compound **16** as ethyl (2*S*,3*S*)-2-hydroxy-3-methylpentanoate (Table 2). Poisson suggested[21] that the ester may be generated by transamination of L-isoleucine through the action of yeast during fermentation. In the case of Amontillado wine, which undergoes biological aging, it is very likely that this compound is also generated at this production stage.

A total of 35 aroma compounds could be identified in the Amontillado sherry wine (Table 2). It was interesting to find

DOI: 10.1021/acs.jafc.5b01418
J. Agric. Food Chem. 2015, 63, 4761−4770

Table 5. Orthonosal Odor Thresholds and OAVs for 36 Odorants in Amontillado Sherry Wine

odorant	odor threshold[a] (μg/L)	OAVs[b]
1,1-diethoxyethane	50[30]	2475
2- and 3-methylbutanals	0.5[23 c]	574
methylpropanal	0.49[23]	369
ethanol	990000[23]	135
ethyl (2*S*,3*S*)-2-hydroxy-3-methyl pentanoate	0.47[d]	129
acetaldehyde	500[30]	114
3-(methylthio)-propanal	0.43[23]	93
ethyl 2-methylbutanoate	1[30]	81
ethyl hexanoate	5[30]	76
ethyl octanoate	2[30]	55
ethyl 3-methylbutanoate	3[30]	41
ethyl methylpropanoate	15[30]	30
(*E*)-β-damascenone	0.05[30]	26
ethyl butanoate	20[30]	19
2,3-butanedione	100[30]	16
3-methylbutanoic acid	33.4[35]	15
3-hydroxy-4,5-dimethylfuran-2(5*H*)-one	5[30]	8
butanoic acid	173[35]	8
ethyl 2-hydroxy-4-methylpentanoate	55[36 e]	7
4-ethylphenol	13[23]	6
2- and 3-methylbutanols	30000[30 c]	5
acetic acid	200000[30]	2
methylpropanol	40000[30]	1
octanoic acid	500[35]	1
ethyl propanoate	5000[18]	1
4-hydroxy-3-methoxybenzaldehyde	200[30]	1
2-phenylethanol	10000[30]	1
methylpropanoic acid	2300[35]	1
2-methylbutanoic acid	2200[23]	<1
4-ethyl-2-methoxyphenol	33[35]	<1
4-allyl-2-methoxyphenol	5[30]	<1
cis-whiskylactone	35[15]	<1
hexanoic acid	3000[30]	<1
phenylacetic acid	2500[37]	<1
4-hydroxy-3-methoxyacetophenone	1000[38]	<1
4-hydroxy-2,5-dimethylfuran-3(2*H*)-one	500[30]	<1

[a]Odor thresholds were taken from the literature. Odor thresholds from ref 23 were determined in water, while all of the others were determined in hydroalcoholic solutions. [b]OAVs = odor activity values calculated by dividing the concentrations (Table 4) by the respective odor threshold. [c]The odor threshold of the (3) isomer was selected. [d]The odor threshold was determined in the laboratory in a 17% (v/v) water/ethanol mixture. [e]The odor threshold of the (*S*) isomer was used.

that the two vanilla-smelling compounds, vanillin (**36**) and acetovanillone (**37**), as well as wine lactone (**32**) have not been mentioned in any of the previous studies on sherry aroma. While the first two odorants are known to be extracted from the barrel during aging, wine lactone has also been found as an important contributor to white wine aroma because of its very low odor threshold (0.01 μg/L).[30] With the exception of these compounds, all odorants were previously identified in various sherry wines corroborating the assumption that the differences in aroma profiles of the same type of food are due to quantitative rather than qualitative differences in the key odorants.[12]

In addition, a SHO analysis was applied on Amontillado wine to address possible losses in higher volatile compounds during sample preparation. A total of 12 odor-active areas were detected in 10 mL of headspace, while only 4, all with a fruity character, could be detected in the lowest volume (0.1 mL), confirming their importance in the aroma of the Amontillado sherry wine (Table 3), namely, 1,1-diethoxyethane, ethyl methylpropanoate, ethyl 2-methylbutanoate, and ethyl 3-methylbutanoate. Ethanol, methylpropanal, and acetaldehyde were detected as additional odorants to those already detected by the AEDA.

Table 6. Average Similarity Scores of the Aroma Recombinates and Amontillado Wine from Bottle 2 to the Amontillado from Bottle 1 (Control)

sample	*n*[a]	similarity[b]
recombinate A[c]	9	2.5
recombinate B[d]	9	2.7
bottle 2[e]	10	2.8

[a]Number (*n*) of participants. [b]Similarity to sherry wine rated on a seven-point scale from 0 (very different) to 3 (very similar). [c]Model mixture with odorants in their natural concentration (Table 4) in an aqueous solution of ethanol (17%, v/v; pH 3.6). [d]Model mixture (Table 4) with L-tartaric acid (5 g/L), D-glucose (0.05 g/L), and glycerol (5 g/L) dissolved in an aqueous solution of ethanol (17%, v/v; pH 3.6). [e]Amontillado wine from a different bottle.

Quantitation of Aroma Compounds. None of the compounds identified with high FD factors elicited an aroma reminding of sherry wine. Thus, it can be assumed that the overall aroma is generated by a set of key odorants present in a defined concentration. A total of 36 compounds were quantitated in the sherry wine by means of a SIDA. The caramel-like smelling compound 4-hydroxy-2,5-dimethylfuran-3(2*H*)-one was included in the quantitative assay because it occurs in wine,[25,30] and the aroma attribute caramel was selected by the sensory panel to describe the aroma profile of Amontillado wine (Figure 1). The highest concentration was determined for ethanol, followed by acetic acid, 1,1-diethoxyethane, and 2- and 3-methylbutanols (Table 4). With the exception of 1,1-diethoxyethane, these compounds are known metabolites of yeast, with 2- and 3-methylbutanols known to be formed by an enzymatic degradation of the amino acids isoleucine and leucine, respectively. 1,1-Diethoxyethane is formed as an acetal from ethanol and acetaldehyde. Because Amontillado sherry wine is aged under a layer of yeast, acetaldehyde might be formed during this stage by oxidation of ethanol via the action of alcohol dehydrogenase from the yeast. A concentration of 56.9 mg/L was measured (Table 4), but in Fino wines, concentrations up to 1000 mg/L have previously been found.[31] Moyano et al.[14] measured the highest concentration of 409 mg/L acetaldehyde during the aging of an Amontillado wine after 8 years of aging, but its concentration decreased to 196 mg/L after 24 years. The Amontillado wine investigated in their study was from the Montilla-Moriles region and was produced from a Pedro Ximénez grape, which could explain the observed differences. A total of 22 compounds were present in concentrations higher than 200 μg/L (Table 4), and 3 showed concentrations below 5 μg/L, namely, 4-hydroxy-2,5-dimethylfuran-3(2*H*)-one, 4-allyl-2-methoxyphenol (eugenol), and (*E*)-β-damascenone.

Then, OAVs were calculated for all 36 compounds to identify the most potent odorants. With the exception of the threshold for ethyl (2*S*,3*S*)-2-hydroxy-3-methylpentanoate, all odor threshold values were taken from the literature (Table 5). The results

DOI: 10.1021/acs.jafc.5b01418
J. Agric. Food Chem. 2015, 63, 4761−4770

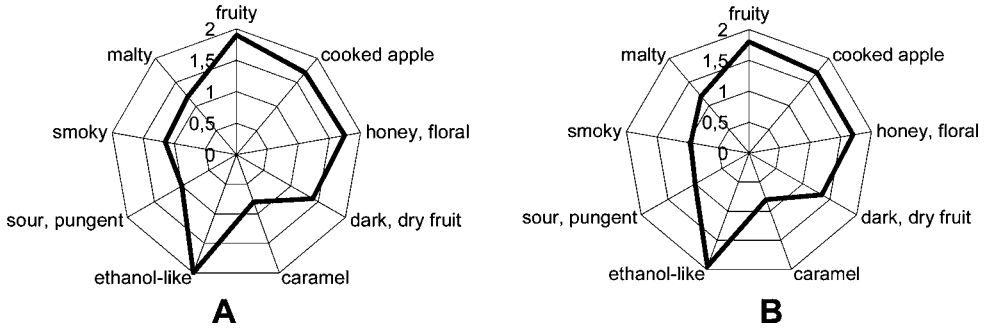

Figure 4. Comparison of (A) aroma profiles of Amontillado wine and (B) aroma recombinate B.

suggested that 28 odorants should contribute to the characteristic aroma of the sherry wine, because their concentrations clearly exceeded their odor thresholds. With an OAV of 2475, 1,1-diethoxyethane is potentially the most important odorant, and high OAVs were also calculated for 2- and 3-methylbutanals, methylpropanal, and ethanol (Table 5). The odor threshold of the newly identified compound ethyl (2*S*,3*S*)-2-hydroxy-3-methylpentanoate was determined in an aqueous matrix with 17% (v/v) ethanol. Its value (0.47 μg/L) is within the range of the odor threshold values determined, in water (0.18 μg/L)[21] and in 40% ethanol (8.0 μg/L). Therefore, with a concentration of 60 μg/L in the wine (Table 4), ethyl (2*S*,3*S*)-2-hydroxy-3-methylpentanoate is a clear contributor to the Amontillado sherry wine aroma. Also, ethyl octanoate, ethyl butanoate, ethyl methylpropanoate, and 3-hydroxy-4,5-dimethylfuran-2(5*H*)-one were found with an OAV above 1 in the sherry wine (Table 5). These four aroma compounds were also previously identified as key odorants in an Amontillado sherry wine from the Montilla-Moriles region.[14] On the other hand, 2-methylbutanoic acid, 4-ethyl-2-methoxyphenol, 4-allyl-2-methoxyphenol, *cis*-whisky-lactone, hexanoic acid, phenylacetic acid, 4-hydroxy-3-methoxyacetophenone (acetovanillone), and 4-hydroxy-2,5-dimethylfuran-3(2*H*)-one showed OAVs below 1, suggesting that these have no or only little contribution to the overall aroma.

Aroma Reconstitution Experiments. To validate the quantitative results, an aroma recombinate containing all key odorants in the "natural" concentrations measured in Amontillado wine (Table 4) was prepared in an ethanolic solution (17%, v/v; pH 3.6). The aroma profile analysis of recombinate A was performed in comparison to the Amontillado wine by rating the intensity of nine odor attributes as well as the overall similarity. On the basis of the intensity ratings of each aroma attribute, recombinate A had a very similar profile compared to the wine (data not shown). However, taking the overall similarity rating (2.5; Table 6) into consideration, it was clear that differences do exist, which could not be explained on the basis of the analytical data. With regard to the comments of the panelists, an overall lower aroma intensity was perceived in recombinate A compared to the wine. It is well-known from the literature that the presence of non-volatile constituents in wine may affect the release of aroma compounds and, therefore, the aroma perceived from the headspace. Therefore, a mixture of non-volatile constituents was added to the recombinate (recombinate B). The mixture consisted of L-tartaric acid, glycerol, and D-glucose at concentrations typically found in dry sherry wines (Table 6). Now, the aroma profile of this recombinate was very close to the wine (Figure 4) and was perceived as more similar to the wine than recombinate A (2.7 versus 2.5 respectively; Table 6). The presence of the non-volatile tastants may have affected the release of the aroma compounds by influencing their air−liquid partitioning. Several studies have demonstrated that different compounds present in wine matrices can change the odorant volatility and concentration in the headspace.[32,33] Frank et al.[25] on the other hand, suggested a strong influence of the non-volatile tastants on the intensity of certain aroma qualities in an aroma recombinate in ethanol.

In a final experiment, the aroma profile of Amontillado wine was compared to the same wine but from a different bottle. This test was performed to investigate the magnitude of the difference, which can be perceived by panelists between two very similar samples. The similarity value was the highest (2.8) compared to recombinate A and recombinate B (Table 6) but not the highest possible degree of similarity as 3.0. This result could be explained by a slight variation in the concentrations of the key aroma compounds between the two bottles or by the well-known tendency of the panelists to avoid end anchors of scale.[34] Without further investigation of the reason for this observation and consideration that a similarity of 2.8 is the maximum value obtained for identical or nearly identical wines, it can be concluded the composition of odorants in that recombinate B closely mimicked the aroma profile of Amontillado sherry wine.

AUTHOR INFORMATION

Corresponding Author

*Telephone: +49-8161-71-2932. Fax: +49-8161-71-2970. E-mail: peter.schieberle@ch.tum.de.

Notes

The authors declare no competing financial interest.

ACKNOWLEDGMENTS

The authors thank all panelists who participated in this study as well as Jörg Stein for his skilfull contribution to the flash chromatography purification procedure.

REFERENCES

(1) Consejo Regulador de las Denominaciones de Origen. *"Jerez-Xeres-Sherry"—"Manzanilla-Sanlucar de Barrameda"—"Vinagre de Jerez" Generoso Wines (The Wines—Diversity and Classification)*; 2014; http://www.sherry.org/en/generosos.cfm.

(2) Zea, L.; Moyano, L.; Moreno, J.; Cortes, B.; Medina, M. Discrimination of the aroma fraction of Sherry wines obtained by oxidative and biological ageing. *Food Chem.* **2001**, *75*, 79−84.

(3) Pozo-Bayón, Á. M.; Moreno-Arribas, V. M. Sherry wines. *Adv. Food Nutr. Res.* **2011**, *63*, 17−40.

(4) Clarke, R. J.; Bakker, J. Volatile components. In *Wine Flavour Chemistry*; Blackwell Publishing, Ltd.: Ames, IA, 2004; pp 120−188.

DOI: 10.1021/acs.jafc.5b01418
J. Agric. Food Chem. 2015, 63, 4761−4770

(5) Webb, A. D.; Noble, A. C. Aroma of sherry wines. *Biotechnol. Bioeng.* **1976**, *18*, 939−952.
(6) Castro, R.; Natera, R.; Benitez, P.; Barroso, C. G. Comparative analysis of volatile compounds of 'fino' sherry wine by rotatory and continuous liquid−liquid extraction and solid-phase microextraction in conjunction with gas chromatography−mass spectrometry. *Anal. Chim. Acta* **2004**, *513*, 141−150.
(7) Begoña Cortes, M.; Moreno, J. J.; Zea, L.; Moyano, L.; Medina, M. Response of the aroma fraction in Sherry wines subjected to accelerated biological aging. *J. Agric. Food Chem.* **1999**, *47*, 3297−3302.
(8) Martinez De La Ossa, E.; Perez, L.; Caro, I. Variations of the major volatiles through aging of Sherry. *Am. J. Enol. Vitic.* **1987**, *38*, 293−297.
(9) Nijssen, L. M.; Ingen-Visscher, C. A. v.; Donders, J. J. H. *VCF Volatile Compounds in Food: Database*; 2014; http://www.vcf-online.nl/VcfHome.cfm.
(10) Grosch, W. Evaluation of the key odorants of foods by dilution experiments, aroma models and omission. *Chem. Senses.* **2001**, *26*, 533−545.
(11) Schieberle, P.; Hofmann, T Mapping the combinatorial code of food flavors by means of molecular sensory science approach. In *Food Flavors*; CRC Press: Boca Raton, FL, 2011; pp 413−438.
(12) Dunkel, A.; Steinhaus, M.; Kotthoff, M.; Nowak, B.; Krautwurst, D.; Schieberle, P.; Hofmann, T. Nature's chemical signatures in human olfaction: A foodborne perspective for future biotechnology. *Angew. Chem., Int. Ed.* **2014**, *53*, 7124−7143.
(13) Zea, L.; Moyano, L.; Ruiz, M. J.; Medina, M. Chromatography−olfactometry study of the aroma of Fino Sherry wines. *Int. J. Anal. Chem.* **2010**, *2010*, 1.
(14) Moyano, L.; Zea, L.; Moreno, J. A.; Medina, M. Evaluation of the active odorants in Amontillado sherry wines during the aging process. *J. Agric. Food Chem.* **2010**, *58*, 6900−6904.
(15) Chaves, M.; Zea, L.; Moyano, L.; Medina, M. Changes in color and odorant compounds during oxidative aging of Pedro Ximenez sweet wines. *J. Agric. Food Chem.* **2007**, *55*, 3592−3598.
(16) Munoz, D.; Peinado, R. A.; Medina, M.; Moreno, J. Biological aging of sherry wines under periodic and controlled microaerations with *Saccharomyces cerevisiae* var. *capensis*: Effect on odorant series. *Food Chem.* **2007**, *100*, 1188−1195.
(17) Moyano, L.; Zea, L.; Villafuerte, L.; Medina, M. Comparison of odor-active compounds in sherry wines processed from ecologically and conventionally grown Pedro Ximenez grapes. *J. Agric. Food Chem.* **2009**, *57*, 968−973.
(18) Moreno, J. A.; Zea, L.; Moyano, L.; Medina, M. Aroma compounds as markers of the changes in sherry wines subjected to biological ageing. *Food Control* **2005**, *16*, 333−338.
(19) Poisson, L.; Schieberle, P. Characterization of the key aroma compounds in an American Bourbon whisky by quantitative measurements, aroma recombination, and omission studies. *J. Agric. Food Chem.* **2008**, *56*, 5820−5826.
(20) Esterbauer, H. Autoxidation of methyl linoleate in water. III. Chromatographic separation of water-soluble reaction products. *Fette, Seifen, Anstrichm.* **1968**, *70*, 1−4.
(21) Poisson, L. Key odorants as indicators for quality and origin of whiskies. Dissertation, Technische Universität München, München, Germany, 2003 (in German).
(22) Roeder, M.; Spiegelstein, O.; Schurig, V.; Bialer, M.; Yagen, B. Absolute configuration of the four stereoisomers of valnoctamide (2-ethyl-3-methyl valeramide), a potentially new stereospecific anti-epileptic and CNS drug. *Tetrahedron: Asymmetry* **1999**, *10*, 841−853.
(23) Czerny, M.; Christlbauer, M.; Christlbauer, M.; Fischer, A.; Granvogl, M.; Hammer, M.; Hartl, C.; Hernandez, N. M.; Schieberle, P. Re-investigation on odour thresholds of key food aroma compounds and development of an aroma language based on odour qualities of defined aqueous odorant solutions. *Eur. Food Res. Technol.* **2008**, *228*, 265−273.
(24) Engel, W.; Bahr, W.; Schieberle, P. Solvent assisted flavour evaporation—A new and versatile technique for the careful and direct isolation of aroma compounds from complex food matrices. *Eur. Food Res. Technol.* **1999**, *209*, 237−241.
(25) Frank, S.; Wollmann, N.; Schieberle, P.; Hofmann, T. Reconstitution of the flavor signature of Dornfelder red wine on the basis of the natural concentrations of its key aroma and taste compounds. *J. Agric. Food Chem.* **2011**, *59*, 8866−8874.
(26) Hinterholzer, A.; Schieberle, P. Identification of the most odour-active volatiles in fresh, hand-extracted juice of Valencia late oranges by odour dilution techniques. *Flavour Fragrance J.* **1998**, *13*, 49−55.
(27) Villamiel, M.; Polo, M. C.; Moreno-Arribas, M. V. Nitrogen compounds and polysaccharides changes during the biological ageing of sherry wines. *LWT - Food Sci. Technol.* **2008**, *41*, 1842−1846.
(28) Campo, E.; Cacho, J.; Ferreira, V. Multidimensional chromatographic approach applied to the identification of novel aroma compounds in wine. Identification of ethyl cyclohexanoate, ethyl 2-hydroxy-3-methylbutyrate and ethyl 2-hydroxy-4-methylpentanoate. *J. Chromatogr., A* **2006**, *1137*, 223−230.
(29) Schreier, P.; Drawert, F.; Winkler, F. Composition of neutral volatile constituents in grape brandies. *J. Agric. Food Chem.* **1979**, *27*, 365−372.
(30) Guth, H. Quantitation and sensory studies of character impact odorants of different white wine varieties. *J. Agric. Food Chem.* **1997**, *45*, 3027−3032.
(31) Martinez, P.; Valcarcel, M. J.; Perez, L.; Benitez, T. Metabolism of *Saccharomyces cerevisiae* flor yeasts during fermentation and biological aging of Fino sherry: By-products and aroma compounds. *Am. J. Enol. Vitic.* **1998**, *49*, 240−250.
(32) Jones, P. R.; Gawel, R.; Francis, I. L.; Waters, E. J. The influence of interactions between major white wine components on the aroma, flavour and texture of model white wine. *Food Qual. Pref.* **2008**, *19*, 596−607.
(33) Tsachaki, M.; Linforth, R. S. T.; Taylor, A. J. Aroma release from wines under dynamic conditions. *J. Agric. Food Chem.* **2009**, *57*, 6976−6981.
(34) Lawless, H. T.; Heymann, H. Scaling. In *Sensory Evaluation of Food: Principles and Practices*; Springer: New York, 1999; pp 208−264.
(35) Ferreira, V.; Lopez, R.; Cacho, J. F. Quantitative determination of the odorants of young red wines from different grape varieties. *J. Sci. Food Agric.* **2000**, *80*, 1659−1667.
(36) Lytra, G.; Tempere, S.; De Revel, G.; Barbe, J. C. Distribution and organoleptic impact of ethyl 2-hydroxy-4-methylpentanoate enantiomers in wine. *J. Agric. Food Chem.* **2012**, *60*, 1503−1509.
(37) Ferreira, V.; Ortin, N.; Escudero, A.; Lopez, R.; Cacho, J. Chemical characterization of the aroma of Grenache rose wines: Aroma extract dilution analysis, quantitative determination, and sensory reconstitution studies. *J. Agric. Food Chem.* **2002**, *50*, 4048−4054.
(38) Cullere, L.; Escudero, A.; Cacho, J.; Ferreira, V. Gas chromatography−olfactometry and chemical quantitative study of the aroma of six premium quality Spanish aged red wines. *J. Agric. Food Chem.* **2004**, *52*, 1653−1660.

DOI: 10.1021/acs.jafc.5b01418
J. Agric. Food Chem. 2015, 63, 4761−4770

JOURNAL OF AGRICULTURAL AND FOOD CHEMISTRY

Article

pubs.acs.org/JAFC

Use of Pollen Solid-Phase Extraction for the Determination of *trans*-Resveratrol in Peanut Oils

Qian Lu,[†,§] Qin Zhao,[‡,§] Qiong-Wei Yu,[†] and Yu-Qi Feng*[,†]

[†]Key Laboratory of Analytical Chemistry for Biology and Medicine (Ministry of Education), Department of Chemistry, Wuhan University, Wuhan 430072, China

[‡]Department of Preventive Medicine, School of Medicine, Wuhan University of Science and Technology, Wuhan 430074, China

Supporting Information

ABSTRACT: In this study, a simple and convenient method for the determination of *trans*-resveratrol (TRA) in peanut oils based on pollen grain solid-phase extraction (SPE) was developed. Pollen grains were used as normal-phase SPE sorbent to separate TRA from peanut oils for the first time. As a naturally occurring material, pollen grains exhibited an excellent adsorption capacity for polyphenolic compounds due to their particular functional structures such as hydroxyl groups, saturated and unsaturated aliphatic chains with aromatics. Their stable compositions as well as adequate particle size (30−40 μm) also make them suitable for SPE. Several parameters influencing extraction performance were investigated. Coupled with high-performance liquid chromatography-ultraviolet detection (HPLC-UV), a green purification method for fast determination of TRA in peanut oils using pollen grain cartridges as sorbents was established. The linearity range of the proposed method was 10−2500 ng·g^{-1} with a satisfactory correlation coefficient (r^2) of 0.9999. The limit of detection (LOD) for TRA in peanut oils was 2.7 ng·g^{-1}, and the recoveries in spiked oil samples were from 70.2% to 98.4% with the relative standard deviations (RSDs) less than 4.9% (intraday) and 5.2% (interday). This method was successfully applied to the analysis of TRA in several peanut oils with different brands from local market as well as other kinds of vegetable oils.

KEYWORDS: *pollen grains, trans-resveratrol, peanut oils, normal-phase solid-phase extraction, HPLC-UV*

INTRODUCTION

Resveratrol (3,5,4′-trihydroxystilbene) is a phytoalexin, which is produced by a wide variety of plants including grapes, blueberries, knotweed, pistachio nuts, and peanuts.[1] Due to its benefits to human health, such as antioxidative effect,[2] analgesic effect,[3] cardiovascular protective effect,[4] cancer prevention,[5] and antiaging property,[6] resveratrol has been widely studied over the past few decades. Resveratrol exists in two isomeric forms, *trans*- and *cis*-isomers, and *trans*-resveratrol (TRA) appears predominantly and has been proved to be more biologically active.[7]

Peanut oil as one of the main vegetable oils in human diet contains a well-balanced fatty acid profile and antioxidants, which provide protection against harmful substances especially free radicals.[8] Some scientific data showed that the antioxidative effect of peanut oil is due to the presence of phenolic compounds like TRA.[9] However, much attention was focused on the content of TRA in peanut skins,[10] peanut hulls,[11] peanut roots,[12] and peanut leaves[13] in recent years, and analysis of TRA in peanut oils was less reported.[14]

The content of TRA in peanut oil is much lower than that in peanut kernels or peanut skins, and the high-fat matrix cause the main difficulties for the analysis of trace amounts of TRA in oil matrices. Therefore, an effective sample pretreatment method for TRA separation and enrichment before instrument analysis is needed. Very recently, Zhao et al. employed a mixed-mode SPE cartridge purchased from Waters Oasis WCX for direct separation of TRA from soybean and peanut oils.[15] The method was effective, and high recoveries were achieved. However, in their experiment, the cartridge was used only one time, and the price of this commercial cartridge was expensive for routine analysis. Ma et al. utilized homemade hydrophilic multiwalled carbon nanotubes (HMWCNTs) as sorbents for magnetic solid-phase extraction of TRA in vegetable oils.[16] The sample pretreatment procedure was simple and rapid, whereas the preparation of HMWCNTs involved large amount of concentrated acid (H_2SO_4/HNO_3), which was harmful to the manipulator and violates several rules of green analytical chemistry such as the application of less toxic reagents, generating as less waste as possible, increasing safety for operators, among others.[17,18] Therefore, the development of new selective sorbents obtained from renewable source for TRA separation was still desirable.

Pollen grains are naturally occurring material from plants and are the carriers of plant's genetic substance needed for pollination.[19] Exine, the outer pollen wall, consists of an extremely stable and complex biopolymer known as sporopollenin, which is highly resistant to chemical attack and high temperature.[20] Because of the diverse chemical composition of exine, pollen grains have been used in drug deliveries,[21,22] in novel materials as templates,[23,24] as carbon microspheres,[25] in protein chromatography,[26] and during removal of organic pollutants.[27] The particle size of pollen grains is 30−40 μm, and the Fourier transform infrared (FT-IR) spectrum revealed the existence of numerous hydroxyl groups on the surface of pine

Received: December 9, 2014
Revised: April 26, 2015
Accepted: April 27, 2015
Published: April 27, 2015

ACS Publications © 2015 American Chemical Society

DOI: 10.1021/jf505938w
J. Agric. Food Chem. 2015, 63, 4771−4776

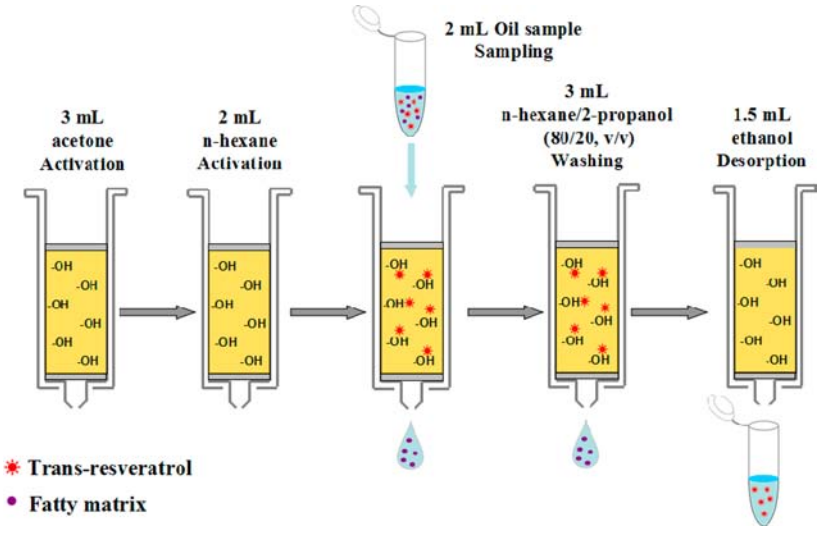

Figure 1. Schematic diagram for the extraction of TRA by NP-SPE.

pollen grains. Therefore, pollen grains are a promising normal-phase SPE (NP-SPE) sorbent. Recently, we reported a green method for determination of 16 plant growth regulators in fruits and vegetables by using pollen grains as SPE sorbent.[28] Herein, we expand this natural sorbent to the extraction of TRA from peanut and other vegetable oils. When nonpolar solvent was used for sampling and washing, TRA in peanut oils was retained on the pollen grains as a result of the hydrogen-bonding interaction, whereas the matrix of peanut oils such as neutral and nonpolar lipids were removed. Parameters that affect the extraction efficiency were investigated and discussed in detail. By coupling with HPLC-UV analysis, a rapid, simple, and convenient method for the determination of TRA in peanut oils was established.

EXPERIMENTAL PROCEDURES

Chemicals and Materials. Pine pollen (*Pinus massoniana Lamb.*) was obtained from Anhui Guzhitang Edible Fungus Co., Ltd. (Anhui, China). Before use, pollen grains were placed in a thimble holder inside a Soxhlet extractor and then refluxed in methanol for 24 h to remove pigments and fats. The resultant pollen grains were dried under reduced pressure at 60 °C for 12 h.

Methanol, ethanol, acetonitrile, acetone, *n*-hexane, and 2-propanol were purchased from Sinopharm Chemical Reagent (Shanghai, China). 2-Propanol (HPLC grade) and acetonitrile (HPLC grade) were obtained from Tedia Company Inc. (Fairfield, OH, U.S.A.). Purified water was obtained using a Millipore Milli-Q apparatus (Bedford, MA, U.S.A.).

trans-Resveratrol (TRA, 99%) was purchased from Aladdin (Shanghai, China). TRA stock solution was prepared in 2-propanol (HPLC grade) at a concentration of 50 $\mu g \cdot mL^{-1}$ and stored at −20 °C in darkness. With the stock solution, the sample solution was spiked to the desired concentration for the following experiments.

Sample Preparation. Oil samples were prepared by spiking TRA at a known concentration (25 $ng \cdot g^{-1}$) to study the SPE performance under different conditions.

Various kinds of peanut oils were purchased from local markets in Wuhan (China) and stored at room temperature. One refined soybean oil sample which was detected to be free of TRA was used as blank matrix for calibration and validation purposes. Oil sample (2.0 g) was directly spiked with TRA. After mixing uniformly, the sample was diluted to 10 mL with *n*-hexane.

Extraction Procedure. SPE was performed on a Supelco 12-port model SPE Vacuum Manifold (Bellefonte, PA, U.S.A.).

Oil (2.00 ± 0.01 g) was accurately weighed into a 10 mL volumetric flask. It was diluted to the required volume with *n*-hexane and shaken for 1 min. Then, 2 mL of the sample solution was loaded onto a 300 mg pollen grain SPE cartridge (sorbent materials were packed into a 3 mL polypropylene syringe and retained by two polyethylene frits), which was sequentially preconditioned with 3 mL of acetone and 2 mL of *n*-hexane for activation (in Figure 1). After the cartridge was washed with 3 mL of *n*-hexane/2-propanol (80/20, v/v), 1.5 mL of ethanol was used for elution, and the eluate was collected into a centrifuge tube. The collected fraction was evaporated to dryness under a mild nitrogen stream at 35 °C. The residue was dissolved in 200 μL of 2-propanol, and 10 μL of the solution was injected into the HPLC system for analysis.

Analytical Conditions. The HPLC apparatus (Shimadzu, Kyoto, Japan) used in this study consisted of binary LC-20AT pumps, a DGU-20A3 degasser, a SPD-20A ultraviolet detector, a SIL-20A autosampler, and a CTO-20AC column oven. The chromatographic data were acquired by Shimadzu LC Solution (Kyoto, Japan).

The HPLC separation was accomplished on a Hisep C18-T column (150 mm × 4.6 mm i.d., 5 μm), which was obtained from Weltech Co., Ltd. (Wuhan, China). The column temperature was set at 40 °C and the injection volume was 10 μL. A mixture of acetonitrile/0.2% acetic acid in water (30/70, v/v) was used as mobile phase at a flow rate of 1 $mL \cdot min^{-1}$ in isocratic mode. The detection wavelength was set at 306 nm, and the analysis was completed within 15 min.

RESULTS AND DISCUSSION

Optimization of SPE Conditions. Several parameters that might affect the extraction efficiency of SPE were investigated, including sorbent amount, washing volume, and the type and volume of desorption solvent. The oily solution spiked with TRA at the concentration of 5 $ng \cdot mL^{-1}$ was used to study the SPE performance under different conditions, and a total of three replicates were performed in all optimization experiment to obtain a mean value. The extraction efficiency was calculated as the ratio of the peak area obtained in redissolved solution (2-propanol) to the standard solution (2-propanol) spiked with TRA at the concentration of 50 $ng \cdot mL^{-1}$.

Effect of Sorbent Amount. The amount of sorbent is an important factor influencing the extraction efficiency in SPE. Therefore, the cartridges packed with different pollen amounts from 100 to 500 mg were evaluated. The extraction efficiency increased as the amount of sorbents increased from 100 to 300 mg, and then reached a plateau as the sorbent amount further

DOI: 10.1021/jf505938w
J. Agric. Food Chem. 2015, 63, 4771−4776

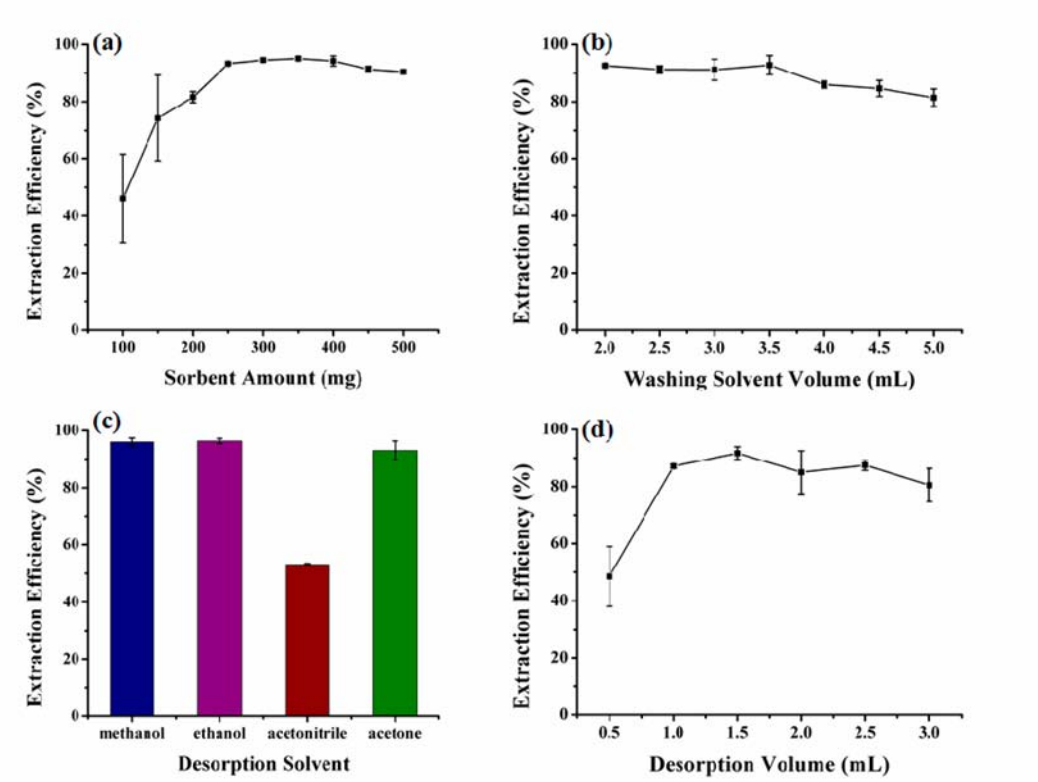

Figure 2. Influence of several parameters on the extraction efficiency: (a) sorbent amount, (b) washing solvent volume, (c) desorption solvent, and (d) desorption volume.

increased (Figure 2a). Consequently, the cartridge of 300 mg was employed in the subsequent experiment.

Effect of Washing Volume. The removal of lipid which was adsorbed on pollen grain SPE cartridge is essential not only to minimize its maintenance in the chromatographic system but also to obtain low detection limits. In this work, *n*-hexane/2-propanol (80/20, v/v) was used as washing solution, and its volume on TRA extraction efficiency was investigated. The result showed that the extraction efficiency of TRA decreased when the volume was higher than 3.5 mL (Figure 2b). Therefore, 3 mL of washing solvent was adopted to avoid significant loss of TRA in the washing step.

Effect of Desorption Solvent. Four different kinds of polar solvents (methanol, ethanol, acetonitrile, and acetone) were investigated as desorption solvent. The adsorption of TRA onto pollen grains behaved as typical normal phase chromatography, and the extraction efficiency increased when more polar solvents were used. The hydroxyl-rich solvents (methanol and ethanol) showed higher extraction efficiency (Figure 2c), indicating that TRA was retained based on the hydrogen bonding interactions. Ethanol was selected as eluent for further experiments due to its low-toxin content.

Effect of Desorption Volume. Desorption volumes ranging from 0.5 to 3.0 mL were investigated. The results showed that extraction efficiency for TRA reached a plateau with 1.0 mL of ethanol (Figure 2d), viz., 1.0 mL of desorption solvent was enough to elute TRA. To ensure complete desorption of TRA, 1.5 mL of ethanol was employed in the following experiment.

Reusability of Pollen SPE Cartridge. The reusability of pollen grain cartridge was evaluated by repeating the extraction procedure with the same SPE cartridge. The results showed that pine pollen grains were highly stable and reusable under the analysis conditions, with RSD of TRA recovery less than 5.0% in 10 cycles of repeated experiments (Table S1), which further demonstrated the known robust nature of the sporopollenin materials. The ability to regenerate and reuse pollen grains using common organic solvents to extract TRA from peanut oils is of value because it will reduce the overall cost and confirm its environmentally friendly merit.

Comparison with Other NP-SPE Sorbents. In order to compare the extraction efficiency of TRA by this novel NP-SPE sorbent with some traditional NP-SPE sorbents, 300 mg of silica gel (~50 μm) or aluminum oxide (neutral, ~100 μm) was loaded in the cartridges separately. Then, three different NP-SPE sorbents were compared following the same extraction protocol as in Figure 1. Each sorbent was performed in triplicate and the recoveries as well as RSD values were recorded in Table 1. When comparing sorbents purification properties, the sampling and washing effluent were collected together in a 10 mL centrifuge tube and then evaporated under a mild nitrogen stream at 35 °C to get rid of the organic solvent. By weighing the residues, we can conclude that 90% of oil matrix components were eluted out by these sorbents, which

Table 1. Comparison of Purification and Extraction Efficiencies among Different NP-SPE Sorbents[a]

sorbent	pollen grains	aluminum oxide	silica gel	silica gel	silica gel	silica gel
amount (mg)	300	300	300	400	500	600
oil removal (g)	0.34	0.32	0.36	/	/	/
recovery%	103.2	0	4.2	5.3	5.8	7.4
RSD%	7.2	/	6.9	4.9	2.5	4.7

[a]The total oil sampling amount was 0.40 g.

DOI: 10.1021/jf505938w
J. Agric. Food Chem. 2015, 63, 4771−4776

demonstrated that pollen grains have the similar cleanup efficiency for the samples in high-fat matrix like silica gel or aluminum oxide. When comparing retention properties of TRA on sorbents, eluate from these three sorbents was evaporated to dryness under a nitrogen stream and redissolved for HPLC analysis. The result showed that aluminum oxide has no retention for TRA, whereas the retention on silica gel was weak. The extraction efficiency did not increase significantly as the amount of silica gel sorbents increased from 300 to 600 mg, which may be ascribed to the fact that silica gel sorbents lack aromatic groups possessed by pollen grains.[28] This result further proved that the selective extraction of TRA from peanut oils by pollen grains is based on the hydrogen-bond and $\pi-\pi$ interaction.

Matrix Effect of Pollen SPE. The matrix effect of the proposed method was evaluated by comparing the assay result obtained with or without oil matrix. As shown in Figure 3b–d,

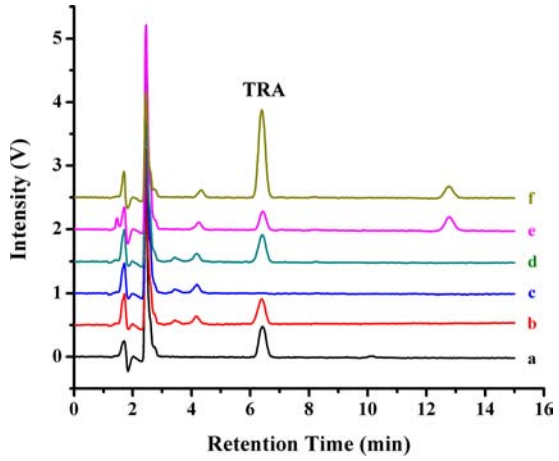

Figure 3. HPLC chromatogram of the following: (a) the standard solution (2-propanol) spiked with TRA at the concentration of 50 ng·mL^{-1}; (b) a *n*-hexane sample spiked with TRA at the concentration of 5 ng·mL^{-1}; (c) a blank soybean oil sample; (d) a blank soybean oil solution spiked with TRA at the concentration of 5 ng·mL^{-1}; (e) peanut oil sample 6; (f) peanut oil solution 6 spiked with TRA at the concentration of 10 ng·mL^{-1}.

the chromatograms of the spiked *n*-hexane sample (5 ng·mL^{-1}) and the oily solution spiked with TRA at the concentration of 5 ng·mL^{-1} were practically the same, which demonstrated that the assay result is not influenced by the presence of oil matrix. Besides, we compared three recoveries of TRA, with one in the standard solution (2-propanol, 50 ng·mL^{-1}) and the other two in blank soybean oil sample spiked before (5 ng·mL^{-1}) and after (50 ng·mL^{-1}) pollen SPE extraction. Those three recoveries were nearly the same (RSD < 4.9%, Table S2), which indicated that the oil matrix can be effectively removed by pollen SPE extraction.

Method Validation. Experiments with regard to linearity, limit of detection (LOD), limit of quantification (LOQ), and reproducibility were performed to validate the proposed method under optimized conditions. The linearity was studied using a blank soybean oil sample spiked with TRA at 10 different concentrations ranging from 10 to 2500 ng·g^{-1} (10, 15, 20, 25, 50, 100, 250, 500, 1000, and 2500 ng·g^{-1}). In the construction of the calibration curve, triplicate measurements of each concentration level of the calibration samples were performed, and the calibration curve was obtained by plotting mean peak area versus concentrations (Figure S1). The linear range, regression data, LOD, and LOQ from the validation are listed in Table 2 (raw data in Table S3). A good linearity was obtained with r^2 up to 0.9999 for the target TRA. A blank soybean oil sample spiked with TRA at 10 ng·g^{-1} gave a peak response with signal-to-noise of ~11.2 (triplicate experiments with the SD of 1.0). The LOD for TRA, calculated at a signal-to-noise of 3, was ~2.7 ng·g^{-1} and the LOQ, calculated at a signal-to-noise of 10, was ~8.9 ng·g^{-1}.

The reproducibility of the method was investigated by determining the intra- and interday precisions. The intra- and interday relative standard deviations (RSDs) were calculated with blank soybean oil spiked with TRA at three different concentrations (25, 100, and 250 ng·g^{-1}). Six parallel extractions of a sample solution over 1 day provided the intraday RSDs, and interday RSDs were determined by extracting sample solutions that had been independently prepared for three continuous days. The RSD and recovery values were recorded in Table 3 (raw data in Table S4). The results showed that the finally adopted experimental protocol for the analysis of TRA is characterized by significantly high recovery values (min 93.7%) as well as low RSD values (max 5.2%). This pollen SPE method shows high accuracy (as recovery%) and well precision (as RSD%) of detection.

Analysis of Real Samples. Ten peanut oil samples with different brands and another five kinds of vegetable oils were analyzed to demonstrate the applicability of the method. All samples obtained were analyzed in three replicates, and the detailed results are outlined in Table 4. The recoveries were obtained by comparing the amount of TRA calculated from the calibration curve with the corresponding spiking amount. As shown in Table 4, the recoveries of the target TRA from various real samples were in the range from 70.2 to 98.4% with RSDs less than 8.7%, indicating the good applicability of the present method in different kinds of vegetable oils. In addition, six peanut oil samples were found to contain a certain amount of TRA with the concentration ranging from 10.9 to 16.9 ng·g^{-1}. Therefore, TRA could be potential biomarker constituents for

Table 2. Linear Range, Regression Data, Limit of Detection (LOD), Limit of Quantification (LOQ) for the Determination of TRA in Oil Samples

Analyte	Structure	Linear Range (ng·g^{-1})	Regression Line		LOD (ng·g^{-1})	LOQ (ng·g^{-1})
			Linear Equation	r^2 Value		
Trans-resveratrol	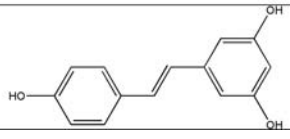	10-2500	Y= -814.29664+174.12348X	0.9999	2.7	8.9

DOI: 10.1021/jf505938w
J. Agric. Food Chem. 2015, 63, 4771–4776

Table 3. Method Precisions (Intra- and Interday) and Recoveries at Three Different Concentrations for the Determination of TRA in Oil Samples

	intraday assay (n = 6)			interday assay (n = 3)		
	low (25 ng·g^{-1})	medium (100 ng·g^{-1})	high (250 ng·g^{-1})	low (25 ng·g^{-1})	medium (100 ng·g^{-1})	high (250 ng·g^{-1})
RSD%	4.9	3.1	2.7	2.9	5.2	3.6
recovery%	93.7	95.2	100.9	95.0	98.0	102.7

Table 4. Concentrations (concn, ng·g^{-1}), Accuracy (recovery%), and Precision (RSD%, n = 3) in Real Samples[a]

	peanut oil 1	peanut oil 2	peanut oil 3	peanut oil 4	peanut oil 5
concn (ng·g^{-1}, RSD%, n = 3)	16.6 (4.3)	16.9 (2.4)	11.0 (0.9)	11.0 (0.8)	10.9 (1.8)
found (ng·g^{-1}, RSD%, n = 3)	63.8 (5.8)	63.2 (0.7)	56.3 (2.8)	48.8 (0.2)	46.0 (2.2)
recovery%	94.3	92.7	90.5	75.7	70.2
	peanut oil 6	peanut oil 7	peanut oil 8	peanut oil 9	peanut oil 10
concn (ng·g^{-1}, RSD%, n = 3)	14.2 (1.6)	N.d.	N.d.	N.d.	N.d.
found (ng·g^{-1}, RSD%, n = 3)	53.8 (0.2)	40.7 (0.1)	41.3 (2.5)	46.0 (7.1)	44.3 (5.3)
recovery%	79.1	81.4	82.6	92.1	88.6
	soybean oil	corn oil	rapeseed oil	rice bran oil	flax seed oil
concn (ng·g^{-1}, RSD%, n = 3)	N.d.	N.d	N.d.	N.d.	N.d.
found (ng·g^{-1}, RSD%, n = 3)	49.2 (2.3)	48.0 (1.3)	47.1 (5.1)	44.2 (8.7)	45.2 (7.6)
recovery%	98.4	96.0	94.2	88.5	90.5

[a]The concentrations of the spiked TRA was 50 ng·g^{-1}. N.d., not detected.

Table 5. Comparison of Sample Preparation Procedures among Different Methods

sample pretreatment (sorbents)	determination	LOD (ng·g^{-1})	recovery% (RSD%)	advantages and drawbacks	ref
MSPE (h-MWCNT-MNPs)	LC−MS/MS	0.60	90.0−110.0 (4.0−17.5)	simple and rapid but sorbent preparation is tedious and not environmental friendly	16
SPE (Waters Oasis WCX)	LC−MS/MS	0.12	84.6−103.1 (1.3−2.4)	applicable and effective but the commercial sorbent is expensive and cannot be recycled	15
SPE (pollen grains)	HPLC-UV	2.70	70.2−94.3 (0.2−5.8)	simple, effective, natural sorbent, environmental friendly, regenerable and low cost	this work

quality assessment of peanut oils adulterated with other vegetable oils. Figure 3e showed the HPLC chromatogram of TRA detected in peanut oil sample 6. The results confirmed the feasibility of the proposed method for determination of TRA in real samples.

A comparative study of our developed pollen grains NP-SPE method for TRA analysis in peanut oils to previously reported methods was performed, and the results are presented in Table 5. Comparing to those two sorbents, these natural pollen sorbents obtained from a renewable source avoid cumbersome material synthesis steps, which fully meet the needs of green analytical chemistry. Besides, this pollen SPE cartridge can be reused for at least 10 times, which will reduce the overall cost for routine analysis. The results demonstrate that using pollen grains as constituent of SPE sorbents directly is simple, effective, eco-friendly, and inexpensive. Although the LOD in this developed methodology is not as good as other methods using LC-MS/MS for determination, the HPLC-UV detection possesses several merits like reduced cost, lower power consumption, and easier maintainability. For the next work, we will try to improve the detection sensitivity, and the related study will be conducted in our following experiment.

In conclusion, using pollen grains as a novel normal-phase solid-phase extraction sorbent, coupled with HPLC-UV detection, was demonstrated to be an environmentally friendly and effective method for the determination of TRA in peanut oils. Oil samples after pretreatment can be directly injected for HPLC analysis. The results show that these natural materials have the potential to be applied for the separation and purification of other polar analytes due to its good adsorption properties and low cost.

■ ASSOCIATED CONTENT

Supporting Information

recycling experiment data (Table S1), matrix effect experiment data (Table S2), data for calibration, LOD and LOQ (Table S3), intraday and interday assays (Table S4), calibration curve (Figure S1). The Supporting Information is available free of charge on the ACS Publications website at DOI: 10.1021/jf505938w.

■ AUTHOR INFORMATION

Corresponding Author

*E-mail: yqfeng@whu.edu.cn. Tel.: +86-27-68755595. Fax: +86-27-68755595.

Author Contributions

§These authors contributed equally to this work (Q.L. and Q.Z.).

Funding

This work was supported by the National Key Technologies R&D Program (2012BAK08B03) and the National Natural Science Foundation of China (21475098, 91217309).

Notes

The authors declare no competing financial interest.

DOI: 10.1021/jf505938w
J. Agric. Food Chem. 2015, 63, 4771−4776

■ ACKNOWLEDGMENTS

The authors wish to thank the lab members (Zheng Zhang, Hao-Bo Zheng and Li-Jing Mao) for critiques and advice.

■ REFERENCES

(1) Sales, J. M.; Resurreccion, A. V. A. Resveratrol in Peanuts. *Crit. Rev. Food Sci. Nutr.* **2014**, *54*, 734−770.
(2) Kim, H. J.; Chang, E. J.; Cho, S. H.; Chung, S. K.; Park, H. D.; Choi, S. W. Antioxidative activity of resveratrol and its derivatives isolated from seeds of Paeonia lactiflora. *Biosci., Biotechnol., Biochem.* **2002**, *66*, 1990−1993.
(3) Bertelli, A.; Falchi, M.; Dib, B.; Pini, E.; Mukherjee, S.; Das, D. K. Analgesic resveratrol? *Antioxid. Redox Signaling* **2008**, *10*, 403−404.
(4) Bradamante, S.; Barenghi, L.; Villa, A. Cardiovascular protective effects of resveratrol. *Cardiovasc. Drug Rev.* **2004**, *22*, 169−188.
(5) Aggarwal, B. B.; Bhardwaj, A.; Aggarwal, R. S.; Seeram, N. P.; Shishodia, S.; Takada, Y. Role of resveratrol in prevention and therapy of cancer: Preclinical and clinical studies. *Anticancer Res.* **2004**, *24*, 2783−2840.
(6) Valenzano, D. R.; Terzibasi, E.; Genade, T.; Cattaneo, A.; Domenici, L.; Cellerino, A. Resveratrol prolongs lifespan and retards the onset of age-related markers in a short-lived vertebrate. *Curr. Biol.* **2006**, *16*, 296−300.
(7) Goncalves, J.; Camara, J. S. New method for determination of (E)-resveratrol in wine based on microextraction using packed sorbent and ultra-performance liquid chromatography. *J. Sep. Sci.* **2011**, *34*, 2376−2384.
(8) Ozcan, M. M. Some Nutritional Characteristics of Kernel and Oil of Peanut (Arachis hypogaea L.). *J. Oleo Sci.* **2010**, *59*, 1−5.
(9) Tuberoso, C. I. G.; Kowalczyk, A.; Sarritzu, E.; Cabras, P. Determination of antioxidant compounds and antioxidant activity in commercial oilseeds for food use. *Food Chem.* **2007**, *103*, 1494−1501.
(10) Yu, J. M.; Ahmedna, M.; Goktepe, P. Effects of processing methods and extraction solvents on concentration and antioxidant activity of peanut skin phenolics. *Food Chem.* **2005**, *90*, 199−206.
(11) Chung, I. M.; Park, M. R.; Chun, J. C.; Yun, S. J. Resveratrol accumulation and resveratrol synthase gene expression in response to abiotic stresses and hormones in peanut plants. *Plant Sci.* **2003**, *164*, 103−109.
(12) Chen, R. S.; Wu, P. L.; Chiou, R. Y. Y. Peanut roots as a source of resveratrol. *J. Agric. Food Chem.* **2002**, *50*, 1665−1667.
(13) Lin, L. L.; Lien, C. Y.; Cheng, Y. C.; Ku, K. L. An effective sample preparation approach for screening the anticancer compound piceatannol using HPLC coupled with UV and fluorescence detection. *J. Chromatogr. B: Anal. Technol. Biomed. Life Sci.* **2007**, *853*, 175−182.
(14) Akhtar, S.; Khalid, N.; Ahmed, I.; Shahzad, A.; Suleria, H. A. R. Physicochemical Characteristics, Functional Properties, and Nutritional Benefits of Peanut Oil: A Review. *Crit. Rev. Food Sci. Nutr.* **2014**, *54*, 1562−1575.
(15) Zhao, X.; Ma, F.; Li, P.; Li, G.; Zhang, L.; Zhang, Q.; Zhang, W.; Wang, X. Simultaneous determination of isoflavones and resveratrols for adulteration detection of soybean and peanut oils by mixed-mode SPE LC−MS/MS. *Food Chem.* **2015**, *176*, 465−471.
(16) Ma, F.; Li, P.; Zhang, Q.; Yu, L.; Zhang, L. Rapid determination of trans-resveratrol in vegetable oils using magnetic hydrophilic multiwalled carbon nanotubes as adsorbents followed by liquid chromatography−tandem mass spectrometry. *Food Chem.* **2015**, *178*, 259−266.
(17) Ibrahim, W. A. W.; Abd Ali, L. I.; Sulaiman, A.; Sanagi, M. M.; Aboul-Enein, H. Y. Application of Solid-Phase Extraction for Trace Elements in Environmental and Biological Samples: A Review. *Crit. Rev. Anal. Chem.* **2014**, *44*, 233−254.
(18) Gałuszka, A.; Migaszewski, Z.; Namieśnik, J. The 12 principles of green analytical chemistry and the significance mnemonic of green analytical practices. *TrAC, Trends Anal. Chem.* **2013**, *50*, 78−84.
(19) Diego-Taboada, A.; Beckett, S. T.; Atkin, S. L.; MacKenzie, G. Hollow pollen shells to enhance drug delivery. *Pharmaceutics* **2014**, *6*, 80−96.
(20) Diego-Taboada, A.; Cousson, P.; Raynaud, E.; Huang, Y.; Lorch, M.; Binks, B. P.; Queneau, Y.; Boa, A. N.; Atkin, S. L.; Beckett, S. T.; MacKenzie, G. Sequestration of edible oil from emulsions using new single and double layered microcapsules from plant spores. *J. Mater. Chem.* **2012**, *22*, 9767−9773.
(21) Paunov, V. N.; Mackenzie, G.; Stoyanov, S. D. Sporopollenin micro-reactors for in-situ preparation, encapsulation and targeted delivery of active components. *J. Mater. Chem.* **2007**, *17*, 609−612.
(22) Hamad, S. A.; Dyab, A. F. K.; Stoyanov, S. D.; Paunov, V. N. Encapsulation of living cells into sporopollenin microcapsules. *J. Mater. Chem.* **2011**, *21*, 18018−18023.
(23) Hall, S. R.; Bolger, H.; Mann, S. Morphosynthesis of complex inorganic forms using pollen grain templates. *Chem. Commun.* **2003**, 2784−2785.
(24) Hall, S. R.; Swinerd, V. M.; Newby, F. N.; Collins, A. M.; Mann, S. Fabrication of Porous Titania (Brookite) Microparticles with Complex Morphology by Sol−Gel Replication of Pollen Grains. *Chem. Mater.* **2006**, *18*, 598−600.
(25) Wang, Y.; Liu, Z.; Han, B.; Huang, Y.; Yang, G. Carbon Microspheres with Supported Silver Nanoparticles Prepared from Pollen Grains. *Langmuir* **2005**, *21*, 10846−10849.
(26) Erzengin, M.; Ünlü, N.; Odabaşı, M. A novel adsorbent for protein chromatography: Supermacroporous monolithic cryogel embedded with Cu2+-attached sporopollenin particles. *J. Chromatogr. A* **2011**, *1218*, 484−490.
(27) Thio, B. J. R.; Clark, K. K.; Keller, A. A. Magnetic pollen grains as sorbents for facile removal of organic pollutants in aqueous media. *J. Hazard. Mater.* **2011**, *194*, 53−61.
(28) Lu, Q.; Wu, J.-H.; Yu, Q.-W.; Feng, Y.-Q. Using pollen grains as novel hydrophilic solid-phase extraction sorbents for the simultaneous determination of 16 plant growth regulators. *J. Chromatogr. A* **2014**, *1367*, 39−47.

DOI: 10.1021/jf505938w
J. Agric. Food Chem. 2015, 63, 4771−4776

JOURNAL OF AGRICULTURAL AND FOOD CHEMISTRY

Article

pubs.acs.org/JAFC

Easy Extraction Method To Evaluate $\delta^{13}C$ Vanillin by Liquid Chromatography–Isotopic Ratio Mass Spectrometry in Chocolate Bars and Chocolate Snack Foods

Monica Bononi,*[,†] Giancarlo Quaglia,[‡] and Fernando Tateo[†]

[†]Department of Agricultural and Environmental Sciences—Production, Landscape, Agroenergy, University of Milan, Via Celoria 2, 20133 Milan, Italy

[‡]Floramo Corporation Laboratories, Via Lime 4, 12047 Rocca de' Baldi, Cuneo, Italy

Supporting Information

ABSTRACT: An easy extraction method that permits the use of a liquid chromatography–isotopic ratio mass spectrometry (LC–IRMS) system to evaluate $\delta^{13}C$ of vanillin in chocolate products and industrial flavorings is presented. The method applies the determination of stable isotopes of carbon to discriminate between natural vanillin from vanilla beans and vanillin from other sources (mixtures from beans, synthesis, or biotechnology). A series of 13 chocolate bars and chocolate snack foods available on the Italian market and 8 vanilla flavorings derived from industrial quality control processes were analyzed. Only 30% of products considered in this work that declared "vanilla" on the label showed data that permitted the declaration "vanilla" according to European Union (EU) Regulation 1334/2008. All samples not citing "vanilla" or "natural flavoring" on the label gave the correct declaration. The extraction method is presented with data useful for statistical evaluation.

KEYWORDS: *LC–IRMS, $\delta^{13}C$, vanillin, chocolate, snack foods*

INTRODUCTION

Numerous studies have been devoted to the authentication of natural flavoring extracts derived from the tropical orchid of the genus *Vanilla*, of which *Vanilla planifolia* and *Vanilla tahitensis* are the most widely used.[1] The increased demand for natural vanilla extracts[2] has encouraged research for new sources of vanillin (4-hydroxy-3-methoxybenzaldehyde), the major flavoring component of vanilla.[1,3] Commercial vanillin available on the market can be derived from chemically synthesized processes, starting from eugenol, guaiacol, or lignin. Another commercial vanillin is the so-called biovanillin, produced through a biotechnological pathway and classified as a "natural flavor" because of the utilization of natural precursors or raw materials.[4] The biovanillin production by microbial fermentation or enzymatic reaction starts from naturally derived precursors, such as ferulic acid, isoeugenol, or curcumin.[1,3,5,6] Agro-wastes are potential sources for biovanillin production, including cereal bran, sugar beet pulp, rice bran oil, and palm oil biomass.[5]

To discriminate between vanillin from authentic vanilla extracts and vanillin derived from extracts adulterated with vanillin from different sources, investigations by chromatographic methods have been proposed and, recently, the Direction Générale de la Concurrence, de la Consommation et de la Répression des Fraudes (DGCCRF) revised the ranges for the vanilla aromatic ratios.[7]

Site-specific natural isotope fractionation combined with nuclear magnetic resonance (SNIF–NMR) measurements has produced data that define the site-specific abundance of deuterium or carbon-13.[8,9] Several reports have shown that ^{2}H NMR spectroscopy allows for the determination of the synthetic or natural origin of vanillin as well as providing information about the starting materials.[6,8−12]

The determination of stable isotope ratio mass spectrometry of carbon is presently a useful method for discrimination between natural vanillin from vanilla beans and synthetic vanillin or that produced from biotechnological methods. Indeed, vanillin from vanilla beans is naturally enriched in ^{13}C and can be distinguished from vanillin produced from other sources. Various authors have therefore suggested the application of the isotope ratio measurements of $^{13}C/^{12}C$, expressed as $\delta^{13}C$,[6,9,13−15] to demonstrate the origin to the various vanillins.

The European Union (EU) Regulation 1334/2008[16] permits the citation of the flavoring source (in our case "vanilla") only if the flavoring component has been obtained exclusively or by at least 95% (w/w) from the referenced source material. The citation in the label "natural flavoring", following the same EU Regulation,[16] may only be used if the flavoring component is derived from a different source material.

$\delta^{13}C$ can be determined by elemental analysis–isotopic ratio mass spectrometry (EA–IRMS) or gas chromatography–isotopic ratio mass spectrometry (GC–IRMS).

Reference values for $\delta^{13}C$ ratios concerning vanillin from various origins can be found in several publications.[9,14,15,17] According to the range reported in the literature, values of $\delta^{13}C$ greater than −21.5[18] or −21.8[17] for vanillin are used as a criterion of authenticity (vanillin from vanilla beans).

Received: January 22, 2015
Revised: May 2, 2015
Accepted: May 4, 2015
Published: May 12, 2015

ACS Publications © 2015 American Chemical Society

DOI: 10.1021/acs.jafc.5b02136
J. Agric. Food Chem. 2015, 63, 4777−4781

Application of a precautionary judgment and consideration of the possible implications of the curing stage,[18] the lower limit of −22.6 may be adopted.

Data referring to vanillin of different origins, i.e., from isoeugenol, lignin, guaiacol, and ferulic acid, result in ratio values lower than −26.8.[6,9,14]

Herein, we report the data produced by analysis of $\delta^{13}C$ for vanillin in 13 chocolate bars and chocolate snack foods available on the Italian market. Applying the suggested extraction method and the LC−IRMS analytical technique made it possible to confirm the lawful use of the term "vanilla" in these labels. Moreover, we report the results from 8 vanilla flavorings from the European flavoring market used for quality control in three food industries. We also included extracts from two sources of authentic vanilla beans. The label declarations of the considered samples are reported.

MATERIALS AND METHODS

Samples. Samples of snack foods and chocolate were directly purchased on the Italian market and represent well-known consumer products. The industrial vanilla flavorings were obtained from industrial suppliers. Two samples of genuine vanilla beans (source Madagascar) were obtained from a direct trader, and the corresponding extracts were produced by a percolation method (50:50 ethanol/water solution) under vacuum for 3 days.

Chemicals. Hexane, ethanol, water, sodium persulfate, and orthophosphoric acid (Sigma-Aldrich, Italy) were analytical-reagent-grade and used without any purification.

Helium (5.6 grade) as the carrier gas and carbon dioxide (4.5 grade) as the reference gas were produced by Messer (Turin, Italy); carbon dioxide was calibrated and controlled using calibrated materials. Solutions and dilutions were prepared with ultrapure Milli-Q water (Milan, Italy). Synthetic vanillin (99%) was a Sigma-Aldrich product.

Sample Preparation. The chocolate bar or chocolate snack food matrix (Table 1) was finely crushed after freezing (T = −20 °C). A portion (50−100 g) of matrix was extracted for 6 h with a Soxhlet device using hexane as the solvent (150−300 mL).

About 10 mL of industrial flavoring samples (samples 14−21 in Table 2) and two vanilla bean extracts produced in our laboratory (samples 22 and 23 in Table 2) were extracted 3 times for 5 min with hexane (30 mL each time) in a 100 mL graduated cylinder. The samples were also subjected to ultrasonic extraction (USE) each time for 15 min (T = 25 °C) at a fixed frequency of 35 kHz. The three hexane fractions are collected and combined.

The hexane extracts were concentrated by rotary evaporation under vacuum to a final volume of 90−100 mL and treated in a separatory funnel 3 times with 5 mL of water/ethanol (30:70), shaking for 5 min. The three water/ethanol phases were collected and pooled. The aqueous−alcoholic phase was concentrated by rotary evaporation to a final volume of 0.1−0.2 mL. For a better control of the concentration and to recover the residue, the round-bottom flask can be fitted in the bottom with a graduated conical tube. Dependent upon the vanillin concentration, the aqueous residue may be appropriately diluted with water and filtered (0.45 μm) before the IRMS analysis.

Instrumentation. *LC−IRMS.* A Delta V Advantage (Thermo Fisher, Bremen, Germany) isotope ratio mass spectrometer was used coupled to a high-performance liquid chromatography (HPLC) system and the LC IsoLink interface (Thermo Fisher, Bremen, Germany).

A P 1000 Thermo Fisher HPLC (Bremen, Germany) was used in conjunction with a Surveyor MS pump, a HTC PAL autosampler (CTC, Zwingen, Switzerland), and a column oven (Mistral, Spark Holland B.V., Emmen, Netherlands). The oxidation reagent consisted of sodium persulfate in water (1.5 M, 30 μL min^{-1}), and the acid reagent was phosphoric acid (1.5 M, 50 μL min^{-1}) pumped by two pump heads. The mixture of these reagents, added by a T piece to the mobile phase, flowed through a capillary oxidation reactor at 100 °C, as described by Krummen et al.[19] for the LC IsoLink. After the oxidation reactor, the mobile phase was cooled and the individual CO_2 peaks were transferred to a counter flow of helium; thereby, the liquid phase was completely degassed. The fluxing helium introduced CO_2 to the mass spectrometer.

For chromatographic separation, a Phenomenex HPX-87C Bio-Rad (Italy) column (300 × 7.8 mm) was used, with ultrapure water as the mobile phase; the flow rate was 0.3 mL min^{-1}, and the injection volume was 15 μL. The column temperature was 50 °C. Water was used to prepare samples and standard solutions for LC−IRMS analysis; all samples were filtered through a polypropylene membrane filter with 0.45 μm porosity and 25 mm diameter. The Isodat 3.0 software (Thermo Scientific Bremen, Germany) was the controlling system. The analysis was repeated twice for each sample, and the average values of these two measurements are listed in Tables 1 and 2.

Table 1. LC−IRMS Data (Averages of Two Measurements) for $\delta^{13}C$ (‰) of Vanillin in a Series of Chocolate Bars and Chocolate Snack Food Samples Available on the Italian Market

	sample	label	$\delta^{13}C$ (‰)	judgment[a]
1	chocolate snack	natural vanilla extract	−23.7	not correct
2	chocolate snack	vanillin	−30.3	correct
3	chocolate snack	vanilla natural flavoring	−22.5	correct
4	chocolate snack	flavoring	−27.5	correct
5	chocolate snack	natural flavoring	−32.5	?
6	chocolate nutmeg	flavorings	−27.6	correct
7	chocolate nutmeg	vanilla flavoring	−24.0	not correct
8	chocolate nutmeg	vanilla extract	−32.3	not correct
9	dark chocolate	vanilla beans	−28.3	not correct
10	milk chocolate	vanilla extract	−29.7	not correct
11	milk chocolate	vanilla extract	−21.8	correct
12	milk chocolate	vanilla Bourbon	−23.4	not correct
13	white chocolate	natural flavoring	−26.9	?

[a]Judgment concerning the outcomes with respect to EU Regulation 1334/2008 is also reported.

Table 2. LC−IRMS Data (Averages of Two Measurements) for $\delta^{13}C$ (‰) of Vanillin in a Series of Industrial Flavorings and Two Laboratory Extracts from Vanilla Beans for a Useful Comparison

	sample	label	$\delta^{13}C$ (‰)	judgment[a]
14	industrial flavor	vanilla extract	−23.1	not correct
15	industrial flavor	natural flavoring	−36.0	correct
16	industrial flavor	vanilla extract	−21.4	correct
17	industrial flavor	natural flavoring	−30.3	?
18	industrial flavor	vanilla extract	−26.1	not correct
19	industrial flavor	vanilla extract	−18.5	correct
20	vanillin (powder)	natural flavoring	−32.6	?
21	industrial flavor	vanilla extract	−25.5	not correct
22	laboratory extract from vanilla beans		−20.3	
23	laboratory extract from vanilla beans		−20.7	

[a]Judgment concerning the outcomes with respect to EU Regulation 1334/2008 is also reported.

DOI: 10.1021/acs.jafc.5b02136
J. Agric. Food Chem. 2015, 63, 4777−4781

The $\delta^{13}C$ values (‰) were calibrated to Vienna Pee Dee Belemnite (VPDB) by three pulses of CO_2 reference gas, calibrated against the international standard, and performed at the beginning of the elution run.

EA–IRMS. $\delta^{13}C$ values of synthetic vanillin were measured with an Flash 2000 elemental analyzer coupled to a Delta V Advantage via a ConFlo IV interface. The EA worked under 100 mL min^{-1} helium flux and temperatures of 950 °C in the oxidation tube and 850 °C in the reduction tube. The outlet was equipped with a column that physically retained CO_2 at 70 °C; carbon dioxide was released by increasing the temperature to 210 °C. The overall experiment duration was 600 s.

RESULTS AND DISCUSSION

Method Validation. To evaluate the chemical oxidation of eluted compounds and CO_2 extraction from the IRMS system, the linearity was verified from 0.50 to 20.00 mg L^{-1} synthetic vanillin (99%), analyzing each solution in triplicate. The corresponding area averages by IRMS were reported versus the vanillin concentration in Figure 1, and the correlation indicated the complete oxidation of the eluted molecule to CO_2; also, we demonstrated the complete recovery of the gas.

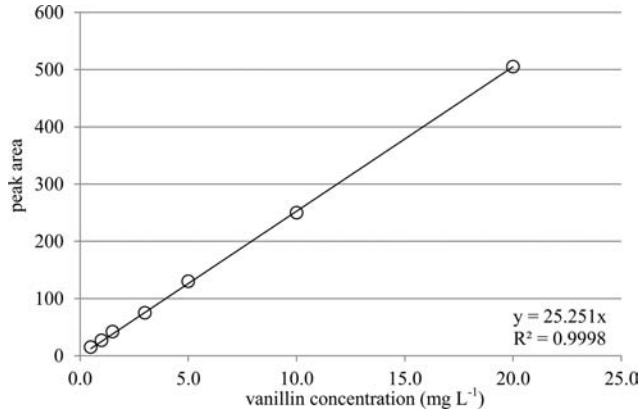

Figure 1. Values of CO_2 peak area LC–IRMS produced by vanillin synthetic solutions at concentrations ranging from 0.5 to 20.0 mg L^{-1}.

The agreement between $\delta^{13}C$ values produced by a sample of synthetic vanillin, determined from the solid by EA–IRMS, and expressed as a mean of five measurements (target value) and the $\delta^{13}C$ values determined by the LC–IRMS method on the same vanillin specimen at different concentration values were also evaluated. The data were distributed in the range ±0.4‰ for concentration values from 0.05 to 20 mg L^{-1} (Figure 2). Therefore, undetectable isotopic fractionation was observable. Reproducibility was checked adopting the Nordic Committee on Food Analysis (NMKL) method[20] and with consideration of the relative repeatability standard deviation (RSDr = 0.011) derived from all data in duplicate obtained for all samples listed in Tables 1 and 2 (see Table S1 of the Supporting Information).

The samples considered in the present study, following the suggested extraction method, had all been previously analyzed by HPLC–diode array detection (DAD) to evaluate the possible influence of other compounds; we were able to demonstrate that the vanillin peak and, consequently, $\delta^{13}C$ values of vanillin in the analyzed samples were not influenced by the nature of the sample matrix.

Furthermore, in all samples analyzed, the *p*-hydroxybenzaldehyde (pHB) peak was at least 25–30 times lower than the vanillin peak because of the partition coefficient of pHB under

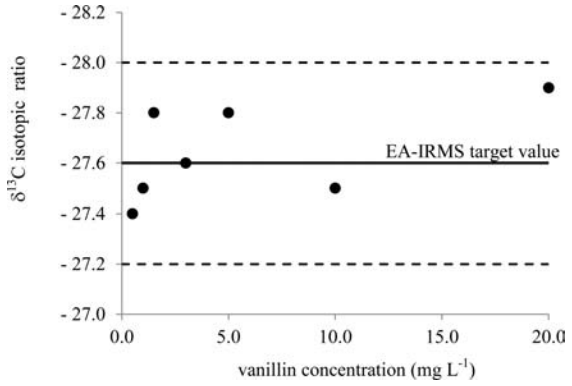

Figure 2. $\delta^{13}C$ values of a sample of synthetic vanillin at concentrations from 0.05 to 20.0 mg L^{-1} produced by LC–IRMS compared to the EA–IRMS mean target value measured on the solid vanillin.

the extraction conditions. Therefore, any influence on the $\delta^{13}C$ value by natural pHB ($\delta^{13}C$ from −15.2 to −17.0) would be irrelevant on the decision concerning the vanillin origin, even if traces of pHB were eluted with vanillin peak. The same observation is even more valid for all other compounds present in the considered matrices. Moreover, under the chromatographic conditions adopted for LC–IRMS, the retention time of pHB was sufficiently differentiated from that of vanillin. In fact, in the LC–IRMS chromatogram, pHB can be coeluted only with caffeine, when this last compound is present. Moreover, the caffeine peak is well-resolved in LC–IRMS from the vanillin peak. Thus, the extraction method adopted in this work allowed us to selectively avoid the influence of other volatile compounds present in the considered matrices. Figure 3 shows two examples of LC–IRMS traces of the vanillin peak that illustrate the good resolution of vanillin from caffeine when the latter substance is present.

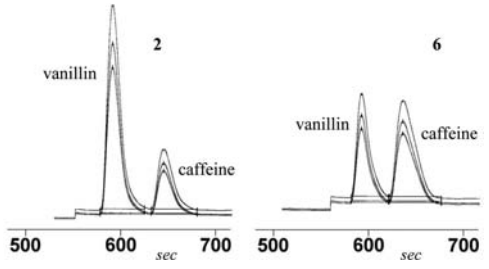

Figure 3. Examples of resolution between vanillin and caffeine peaks in LC–IRMS traces for two samples, where their ratios were different, adopting the suggested operative conditions (samples 2 and 6 in Table 1).

Sample Measurements. The results of the stable isotope ratio analysis of the samples (Tables 1 and 2) identified some discrepancies with the product declaration on the label of the food or flavoring agent.

Of the chocolate bars and chocolate snack foods in Table 1, the samples 1, 3, 7, 8, 9, 10, 11, and 12 were declared as "vanilla" on the label. Only samples 3 and 11 gave results that agreed with this declaration.[16]

Of the other samples 2, 4, 5, 6, and 13, only 2, 4, and 6 reported a lawful declaration[16] because no reference was made to the terms "vanilla" or "natural flavoring". The samples 5 and 13 reported the declaration "natural flavoring", but the data

DOI: 10.1021/acs.jafc.5b02136
J. Agric. Food Chem. 2015, 63, 4777–4781

(−32.5 and −26.9, respectively) did not permit the confirmation that a natural source of vanillin was used. These values may be justified if the flavoring agent was derived from a mixture of biovanillin from ferulic acid and vanillin from vanilla beans. Such a designation would be valid if biovanillin is considered as "natural".

Data reported in Table 2 showed that two samples (16 and 19) of five industrial flavoring agents declared as "vanilla" (14, 16, 18, 19, and 21) were really derived from vanilla beans. Samples 14, 18, and 21 produced data lower than −22.6,[20] which is the lower limit compatible with vanillin from vanilla beans; therefore, for these three samples, the label declaration was not lawful.

The other three samples, 15, 17, and 20, declared "natural flavoring" and showed very low values. Only sample 15 was clearly compatible with biovanillin from ferulic acid,[9] while the other two data values permitted the declaration "natural flavoring" only if derived from a mixture of biovanillin from ferulic acid and vanillin from vanilla beans.

The same analytical method was applied for the two samples produced by laboratory extraction from two samples of genuine vanilla beans (23 and 24) and the values produced results that were strictly included in the range cited by the literature for vanillin from vanilla beans.

From the results of Tables 1 and 2, we deduced that of the 13 samples citing the term "vanilla" on the label, only four of them (3, 11, 16, and 19) were in compliance with the EU Regulation 1334/2008.[16] Three samples not citing the terms "vanilla" or "natural" (2, 4, and 6) showed the correct label.

Accepting that the biovanillin from ferulic acid, which produces a $\delta^{13}C$ value of absolute −36.0, may actually be considered as a "natural flavoring", we were unable to assign a definite judgment for the four samples 5, 13, 17, and 20, which cited the term "natural flavoring", on their labels. Indeed, a wide range of data (from −22.7 to −36.1) corresponded to the various putative mixtures of vanillin from vanilla beans, synthetic vanillin, and biovanillin.

In conclusion, for the food matrices examined in the present work, the suggested method was able to distinguish between flavorings derived from authentic vanilla beans and those flavorings from other sources. Data reported in Tables 1 and 2 permitted us to conclude that only ca. 30% of the samples citing the term "vanilla" were in accordance with the EU Regulation 1334/2008[16] and all of the samples not citing the terms "vanilla" or "natural" agreed with the same regulation.

Only for sample 15, which showed a $\delta^{13}C$ value of −36.0 characteristic of biovanillin from ferulic acid, was it possible to confirm the classification as "natural flavoring".

■ ASSOCIATED CONTENT

Supporting Information

Vanillin isotope ratio determined on all of the samples listed in Tables 1 and 2 and RSDr derived from data in duplicate (Table S1) (PDF). The Supporting Information is available free of charge on the ACS Publications website at DOI: 10.1021/acs.jafc.5b02136.

■ AUTHOR INFORMATION

Corresponding Author

*Telephone: +39-0250316538. Fax: +39-0250316539. E-mail: monica.bononi@unimi.it.

Notes

The authors declare no competing financial interest.

■ REFERENCES

(1) Ramachandra Rao, S.; Ravishankar, G. A. Vanilla flavour: Production by conventional and biotechnological routes. *J. Sci. Food Agric.* **2000**, *80*, 289−304.

(2) Brownell, R. New approaches to a sustainable vanilla supply chain. *Perfum. Flavor.* **2014**, *39*, 28−30.

(3) Kaur, B.; Chakraborty, D. Biotechnological and molecular approaches for vanillin production: A review. *Appl. Biochem. Biotechnol.* **2013**, *169*, 1353−1372.

(4) Schreier, P. Bioflavours: An overview. In *Biotransformation of Flavours*; Patterson, R. L. S., Charlwoods, B. V., MacLeod, G., Williams, A. A., Eds.; Royal Society of Chemistry (RSC): Cambridge, U.K., 1992; pp 1−20.

(5) Zamzuri, N. A.; Abd-Aziz, S. Biovanillin from agro wastes as an alternative food flavour. *J. Sci. Food Agric.* **2013**, *93*, 429−438.

(6) Benz, I.; Muheim, A. Biotechnological production of vanillin. In *Flavour Science—Recent Developments*; Taylor, A. G., Mottram, D. S., Eds.; Royal Society of Chemistry (RSC): Cambridge, U.K., 1996; pp 111−117.

(7) Ministry of Economy, Finance, and Industry. *Directorate General for Competition, Consumption, and Fraud Repression*; Ministry of Economy, Finance, and Industry: Paris, France, June 16, 2003; Information Note 2003-61.

(8) Remaud, G.; Martin, Y. L.; Martin, G. G.; Martin, G. J. Detection of sophisticated adulterations of natural vanilla flavors and extracts: Application of the SNIF−NMR method to vanillin and *p*-hydroxybenzaldehyde. *J. Agric. Food Chem.* **1997**, *45*, 859−866.

(9) Bensaid, F. F.; Wietzerbin, K.; Martin, G. J. Authentication of natural vanilla flavorings: Isotopic characterization using degradation of vanillin into guaiacol. *J. Agric. Food Chem.* **2002**, *50*, 6271−6275.

(10) Martin, G.; Remaud, G.; Martin, G. J. Isotopic methods for control of natural flavours authenticity. *Flavour Fragrance J.* **1993**, *8*, 97−107.

(11) John, T. V.; Jamin, E. Chemical investigation and authenticity of Indian vanilla beans. *J. Agric. Food Chem.* **2004**, *52*, 7644−7650.

(12) Tenailleau, E. J.; Lancelin, P.; Robins, R. J.; Akoka, S. Authentication of the origin of vanillin using quantitative natural abundance ^{13}C NMR. *J. Agric. Food Chem.* **2004**, *52*, 7782−7787.

(13) Culp, R. A.; Legat, J. M.; Otero, E. Carbon dioxide composition of selected flavoring compounds for the determination of natural origin by gas chromatography/isotope ratio mass spectrometer. *ACS Sym. Ser.* **1998**, *705*, 260−287.

(14) Godin, J. P.; MacCullagh, J. S. O. Review: Current applications and challenges for liquid chromatography coupled to isotope ratio mass spectrometry (LC/IRMS). *Rapid Commun. Mass Spectrom.* **2011**, *25*, 3019−3028.

(15) Lamprecht, G.; Pichlmayer, F.; Schmidt, E. R. Determination of the authenticity of vanilla extracts by stable isotope ratio analysis and component analysis by HPLC. *J. Agric. Food Chem.* **1994**, *42*, 1722−1727.

(16) European Union (EU).. Regulation (EC) No 1334/2008 of the European Parliament and of the Council of 16 December 2008 on flavourings and certain food ingredients with flavouring properties for use in and on foods and Amending Council Regulation (EEC) No 1601/91, Regulations (EC) No 2232/96 and (EC) No 110/2008. *Off. J. Eur. Union, L: Legis.* **2008**, *51*, 34−50.

(17) Hansen, A. M. S.; Fromberg, A.; Frandsen, H. L. Authenticity and traceability of vanilla flavors by analysis of stable isotopes of carbon and hydrogen. *J. Agric. Food Chem.* **2014**, *62*, 10326−10331.

(18) Gassenmeier, K.; Binggeli, E.; Kirsch, T.; Otiv, S. Modulation of the $^{13}C/^{12}C$ ratio of vanillin from vanilla beans during curing. *Flavour Fragrance J.* **2013**, *28*, 25−29.

(19) Krummen, M.; Hilkert, A. W.; Juchelka, D.; Duhr, A.; Schluter, H. J.; Pesch, R. A new concept for isotope ratio monitoring liquid chromatography/mass spectrometry. *Rapid Commun. Mass Spectrom.* **2004**, *18*, 2260−2266.

DOI: 10.1021/acs.jafc.5b02136
J. Agric. Food Chem. 2015, 63, 4777−4781

(20) Nordic Committee on Food Analysis (NMKL). *Estimation and Expression of Measurement Uncertainty in Chemical Analysis*; NMKL: Oslo, Norway, 1997; NMKL Procedure 5.

DOI: 10.1021/acs.jafc.5b02136
J. Agric. Food Chem. 2015, 63, 4777−4781

JOURNAL OF AGRICULTURAL AND FOOD CHEMISTRY

Article

pubs.acs.org/JAFC

Hyperspectral Deep Ultraviolet Autofluorescence of Muscle Fibers Is Affected by Postmortem Changes

Caroline Chagnot,[†,‡] Annie Vénien,[†] Frédéric Jamme,[§,∥] Matthieu Réfrégiers,[∥] Mickaël Desvaux,[‡] and Thierry Astruc*[,†]

[†]UR370 Qualité des Produits Animaux, and [‡]UR454 Microbiologie, Institut National de la Recherche Agronomique (INRA), F-63122 Saint-Genès Champanelle, France

[§]BP48, Synchrotron SOLEIL, L'Orme des Merisiers, F-91120 Gif-sur-Yvette, France

[∥]UAR1008 CEPIA, Institut National de la Recherche Agronomique (INRA), Rue de la Géraudière, F-44316 Nantes, France

Supporting Information

ABSTRACT: After slaughter, muscle cells undergo biochemical and physicochemical changes that may affect their autofluorescence characteristics. The autofluorescent response of different rat extensor digitorum longus (EDL) and soleus muscle fiber types was investigated by deep ultraviolet (UV) synchrotron microspectroscopy immediately after animal sacrifice and after 24 h of storage in a moist chamber at 20 °C. The glycogen content decreased from 23 to 18 μmol/g of fresh muscle in 24 h postmortem. Following a 275 nm excitation wavelength, the spectral muscle fiber autofluorescence response showed discrimination depending upon postmortem time (t_0 versus $t_{24\,h}$) on both muscles at 346 and 302 nm and, to a lesser extent, at 408 and 325 nm. Taken individually, all fiber types were discriminated but with variable accuracy, with type IIA showing better separation of $t_0/t_{24\,h}$ than other fiber types. These results suggest the usefulness of the autofluorescent response of muscle cells for rapid meat-aging characterization.

KEYWORDS: *rat muscle fibers, postmortem, meat, UV spectroscopy, histology, fiber types*

INTRODUCTION

Meat comes from skeletal muscle, which generally contains different proportions of the four pure myofiber types: type I, type IIA, type IIX, and type IIB. These contain the myosin heavy-chain isoforms (MyHC) I, IIa, IIx, and IIb, respectively.[1,2] Hybrid fibers intermediate between two pure types and containing two different myosin isoforms (I−IIA, IIA−IIX, and IIX−IIB) are also found. The muscle fibers are characterized by their metabolism (oxidative or glycolytic) and their contraction speed (slow or fast). Type I fibers are slow-twitch fibers, and all type II fibers are fast-twitch fibers. Type I and IIA fibers have an oxidative metabolism, and type IIX and IIB fibers have a glycolytic metabolism.[1,2]

After slaughter of farm animals, muscle undergoes significant metabolic, physical, structural, and biochemical changes that determine the quality of meat and meat products.[3,4] After bleeding, the muscle is deprived of oxygen and nutrients. Muscle cells will try to survive by degrading their glycogen stock through anaerobic glycolysis. Lactate accumulation in cells is accompanied by a drop in pH. When the energy reserves are depleted, muscle pH stabilizes at values generally between 5.7 and 6.2, termed the ultimate pH. The kinetics of change in pH is species-dependent, and the time to reach the ultimate pH can range from 2 h in poultry to 24 h in cattle. After this first phase of postmortem changes, additional biochemical changes and significant ultrastructural alterations are observed, related to the improvement of meat quality, especially meat tenderness.[5,6] The speed of these postmortem changes (also called meat maturation) is dependent upon the species and mostly the metabolic and contractile types of the muscles considered. Degradation of the myofibrillar structure is faster in white fibers than in red fibers.[5,7]

Postmortem changes can be assessed by mechanical measurements and biochemical and/or ultrastructural analyses, but these methods are usually destructive and time-consuming. Some authors have exploited the variation in the physical properties of muscles to characterize differences in composition by fluorescence spectroscopy.[8−10] This highly sensitive method detects fluorophores naturally present in muscle whose properties are very sensitive to changes in their environment. Collagen, tryptophan, tyrosine, or NADH are among the most abundant autofluorescent molecules in muscle.[8] Several years ago, the autofluorescence of the tryptophan signal following meat sample excitation at 290 nm allowed for a correct discrimination of non-aged from aged meat samples.[11] However, the analysis was performed on a macroscopic scale and did not address the metabolic and contractile properties of muscles. The analysis at the cell or even the ultrastructural scale is more difficult because of the low availability fluorescence microscopes that allow for an excitation in the deep ultraviolet (UV), which is relevant for studying biomacromolecules that have a strong absorption in this energy range. Indeed, although spectrometers can often go down to 250 nm, microscopes are usually very limited in this range with either 350 nm cutoff or access to only a limited number of excitation wavelengths.

Received: February 4, 2015
Revised: April 22, 2015
Accepted: April 27, 2015
Published: April 27, 2015

ACS Publications © 2015 American Chemical Society

DOI: 10.1021/acs.jafc.5b00668
J. Agric. Food Chem. 2015, 63, 4782−4789

However, the combination of a microscope with a UV fluorescence spectrometer coupled to synchrotron radiation allows for an excitation range of 200−600 nm that has been used to characterize animal tissues at the ultrastructural level.[12−15]

Thanks to the availability of these tools, it becomes theoretically possible to detect small changes of the tissue and cells and, therefore, characterize the degree of postmortem change in muscle cells. Our goal was to investigate the autofluorescence changes of individual muscle fibers from rat skeletal muscles stored under anoxia during 24 h regarding their metabolism and ultrastructure changes.

MATERIALS AND METHODS

Animals and Samples. The rat model was chosen because it allows for a better control of rearing and slaughter conditions; it is easy to extract entire muscles and obtain early samples in the laboratory by controlling the best kinetic sampling and temperature conditions.

A total of 24 male Wistar rats aged 5 months and weighing about 500 g were bought from Janvier (Saint-Berthevin, France) and housed at 22 °C under 12 h dark/12 h light cycles with water and food *ad libitum* at an INRA animal facility (Installation Expérimentale de Nutrition, Unité de Nutrition Humaine, INRA Theix, Agreement C 63345.14). Rats were anaesthetized by isoflurane gas and decapitated with a guillotine according to the recommendation of our Regional Ethics Committee (C2E2A 2) and French national legislation (JO 87-848). As no act of pain was performed, because the sampling took place after the death of animals, the experimental project was outside the scope of the European Union Directive 2010/63 and, therefore, did not require ethics review. However, the experimental project was followed by the animal welfare structure integrated in the INRA animal facility installation according to French law (Article JO R. 214-103).

Immediately after death, the lower limbs were severed and dissected under sterile conditions. Extensor digitorum longus (EDL), tibialis anterior, gastrocnemius, and soleus muscles from the right and left hindlegs were extracted from tendon to tendon, avoiding any lesions.

Muscle Postmortem Kinetics. Muscles from three rats were immediately cryofixed post-dissection (10 min after decapitation). For the other 21 rats, muscles were suspended at 20 °C in a sterile moist chamber to prevent drying of the muscle and contamination from microorganisms. Lead ballast was attached at the caudal tendon of each muscle (1.5 g for soleus and EDL and 4.5 g for tibialis and gastrocnemius) to preserve the anatomical muscle length (Figure 1).

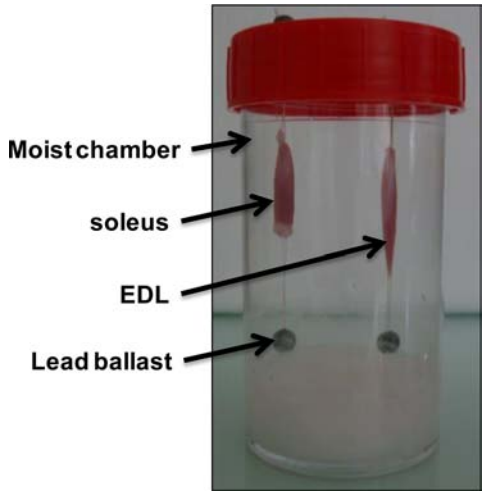

Figure 1. Positioning of the muscles in a moist chamber. Muscles equipped with lead ballast were suspended in a bottle, the bottom of which was lined with a moistened paper towel. The flask was placed in an oven at a temperature maintained at 20 °C.

After 30 min, 1 h, 2 h, 4 h, 8 h, 12 h, and 24 h postmortem, muscles of three rats were removed from their moist chambers and prepared for biochemical and imaging analysis.

pH Measurements. Because EDL and soleus muscles are too small, pH measurements were made on tibialis anterior and gastrocnemius muscles localized around EDL and soleus muscles. pH measurements were made according to the study by Fernandez et al.,[16] adapting to the small quantity of muscle available. Briefly, muscles were weighed and ground in 5 mM idoacetate buffer (2.5 mL/g of muscle), and pH was measured in the muscle suspension at room temperature.

Glycogen Determination. The glycogen content was determined on each right EDL and soleus rat muscle at each time postmortem by enzymatic procedures according to Bergmeyer,[17] with slight modifications. About 0.15 g of muscle tissue was homogenized with 1.8 mL of 0.55 M perchloric acid. On two 0.5 mL aliquots, glycogen was hydrolyzed in glucose with amyloglycosidase. Glucose was converted into 6-phosphogluconolactone after hexokinase and G-6-P dehydrogenase action accompanied by NADH H^+ production. NADH, proportional to glucose content, was determined by spectrophotometry at 340 nm and compared to standards to calculate the glucose concentration. Results are expressed in micromoles per gram of fresh tissue.

Histology. *Cryofixation and Histological Sections.* Parts of left EDL and soleus muscles at 0 (t_0) and 24 h ($t_{24\,h}$) postmortem were positioned on a cork plate with embedding medium (Tissue-Tek) and cryofixed by immersion at −160 °C in isopentane cooled with liquid nitrogen (−196 °C). Serial cross-sections of entire muscles (10 μm thick) were cut using a cryostat (Microm, HM 560) and collected on glass slides for histological stains and quartz coverslips for deep UV (DUV) microspectroscopy fluorescence analyses. Sections were stored at −20 °C under vacuum until use. Periodic acid Schiff (PAS) staining was performed for glycogen characterization.[18]

Muscle Fiber Type Determination. Fiber types were identified by highlighting the different MyHC using specific mouse monoclonal antibodies BA-D5, SC-71, and BFF3 (AGRO-BIO France). The different primary MyHC antibodies were visualized by an Alexa Fluor 488 labeled goat anti-mouse IgG secondary antibody (A 11001, Invitrogen). In addition, the extracellular matrix (ECM) protein laminin, surrounding the muscle fiber, was stained using an anti-laminin primary polyclonal antibody (L9393 Sigma) and a cyanine-3-labeled secondary antibody (111-165-008, Jackson). The myofiber response to the different MyHC antibodies identified fiber types I, IIA, IIB, and hybrid IIX−IIB. IIX fiber types corresponded to the remaining unmarked cells. Controls were performed with no primary antibody to validate the results.

Image Acquisitions. Observations and image acquisitions were performed using a light microscope (Olympus BX 61) coupled to a high-resolution digital camera (Olympus DP 71) and the Cell F software. PAS-stained sections were examined, and images were acquired in bright-field mode. Immunohistochemistry images were acquired in fluorescence mode (Alexa Fluor 488, 495/519 nm; cyanine 3, 550/570 nm).

Transmission Electron Microscopy. Analysis was conducted on EDL and soleus muscles at 0 and 24 h postmortem from six rats (three rats per postmortem time). Pieces of EDL and soleus muscles of about 4 × 1 mm were fixed overnight at 4 °C by immersion in 2.5% glutaraldehyde in 0.1 M sodium cacodylate buffer at pH 7.2, taking into account muscle fiber direction. Small cubes of about 1 mm^3 were post-fixed in 1% osmium tetroxide in 0.1 M sodium cacodylate buffer for 1 h at room temperature. These cubes were dehydrated through a graded ethanol series and embedded in epoxy resin (TAAB, Eurobio France). Ultrathin longitudinal sections (90 nm) (parallel to the fiber direction) were stained with uranyl acetate and lead citrate and examined with a transmission electron microscope (Hitachi HM 7650) using a 80 kV acceleration voltage at the CICS cellular imaging lab on the Clermont-Ferrand University campus (France). Micrographs were acquired with a Hamamatsu AMT digital camera system coupled with the microscope.

DOI: 10.1021/acs.jafc.5b00668
J. Agric. Food Chem. 2015, 63, 4782−4789

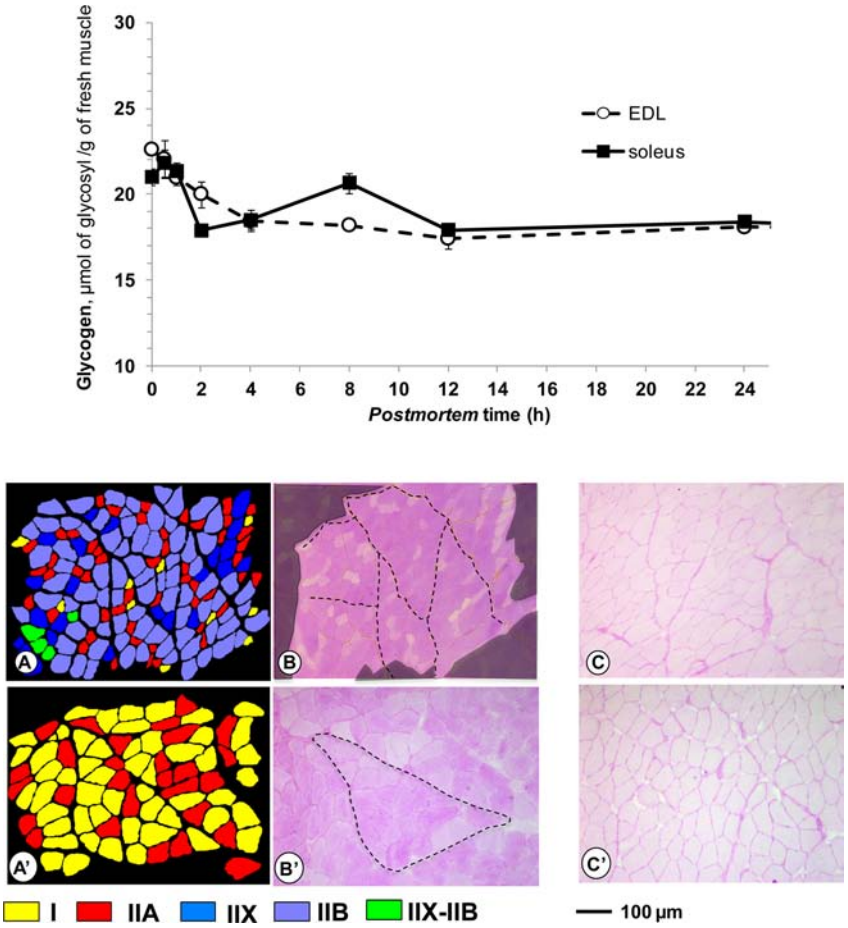

Figure 2. Postmortem evolution of glycogen content in EDL and soleus muscles. The glycogen is degraded in the first hours after slaughter and then stabilizes. Histology revealed the lower glycogen content in oxidative metabolism fibers, particularly in Type IIA fibers. A and A′: Fiber type identification of EDL and soleus muscles, respectively. B and B′: Glycogen staining of EDL and soleus muscle, respectively, 10 min after animal sacrifice. C and C′: Glycogen staining of EDL and soleus muscle, respectively, 24 h after animal sacrifice.

DUV Fluorescence Microspectrocopy. *Spotting of Cell Types on Unstained Muscle Serial Cross-Section.* From two rat soleus and EDL muscles (0 and 24 h postmortem), an unstained serial section was deposited on quartz coverslips, and using fiber-type identification by immunohistofluorescence on other serial sections, 20 soleus muscle fibers (10 type I and 10 type IIA) and 21 EDL muscle fibers (3 type I, 2 type IIA, 5 type IIX, 8 type IIX–IIB, and 3 type IIB) were spotted for fluorescence spectra acquisition by DUV microspectroscopy.

Spectrum Acquisition. Synchrotron DUV microspectroscopy was performed on the DISCO beamline of the SOLEIL synchrotron radiation facility (Saint-Aubin, France).[19,20] DUV monochromatized light was used at 275 nm excitation wavelength to excite tissue sections. The emission spectra were acquired from 290 to 540 nm. For each excited pixel, a fluorescence spectrum was recorded. On each spotted cell, 20 acquisitions were made in the intracellular space.

Spectrum Processing and Statistical Analysis. Autofluorescence spectra were spike- and noise-filtered using an in-house program written in MATLAB, version 7.3 (The MathWorks, Natick, MA). The Unscrambler software (version 9.8, Camo Software AS, Norway) was used to perform a baseline adjustment to zero, apply unit vector normalization that normalizes sample-wise the spectral data to unit vectors, and analyze the processed spectra by principal component analysis (PCA). After analysis, the family label of each spectrum was revealed and the two first of the 10 components tested were plotted. The mean spectrum of each group was also plotted for better referencing of the spectral discriminants. Score plots were used to show similarity maps for comparison of spectra, regardless of sample categories. Loading plots derived from the first principal components (PC1) and second principal components (PC2) were used to reveal and identify characteristic fluorescence peaks.

Numerical variables of fluorescence intensity for wavelengths of interest identified on the PCA loadings were expressed as the mean ± standard error of the mean (SEM). Variance analysis and mean comparisons were performed using one-way variance analysis and the Student–Newman–Keuls test under the XLSTAT software 2010 (Microsoft Office, Redmond, WA).

RESULTS AND DISCUSSION

Postmortem Metabolism Time Course. The level of EDL and soleus muscle glycogen was about 23 μmol/g of fresh muscle at 10 min postmortem and decreased slightly with time for both muscles (Figure 2). The decrease in contrast of PAS staining with time postmortem reflects a decrease in intracellular glycogen, in agreement with our biochemical data and the literature.[3,4] However, soon after animal sacrifice, PAS staining intensity depended upon the fiber type. Glycolytic fibers (IIX and IIB) of the EDL were systematically richer in glycogen than oxidative fibers (I and IIA), fully consistent with the literature on the subject.[3,4] The soleus, which contains only oxidative fibers (I and IIA), also showed a heterogeneous distribution. In this muscle, the IIA fibers contained less glycogen than type I fibers. This result is surprising at first sight because generally IIA fast-twitch fibers have more glycogen reserves than type I slow-twitch fibers to cope with high energy consumption during vigorous exercise. This finding is explained

DOI: 10.1021/acs.jafc.5b00668
J. Agric. Food Chem. 2015, 63, 4782–4789

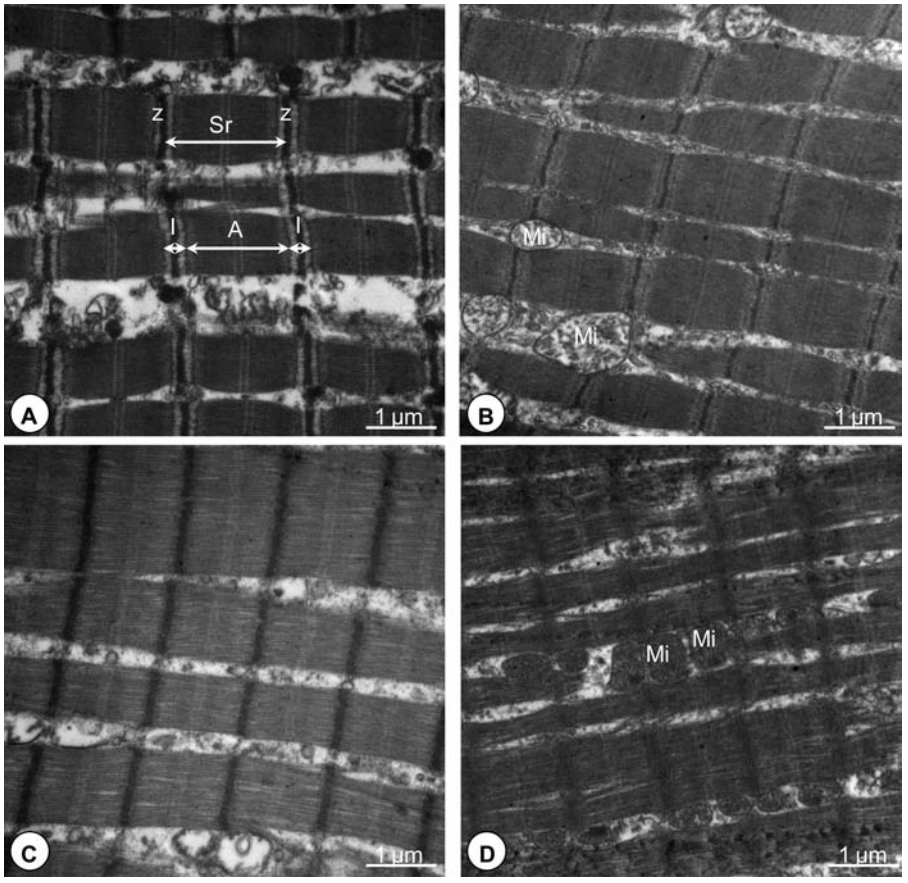

Figure 3. Postmortem ultrastructure changes of EDL and soleus muscles. A, B: EDL muscle at 0 and 24 h postmortem, respectively. C, D: Soleus muscle at 0 and 24 h postmortem, respectively. At slaughter soleus muscle has contracted sarcomeres, which may be the result of cold shortening. The ultrastructure has changed little at 24 h postmortem whatever the considered muscle. Z: Z line, Sr: sarcomere, A: A band, I: I band, Mi: mitochondria.

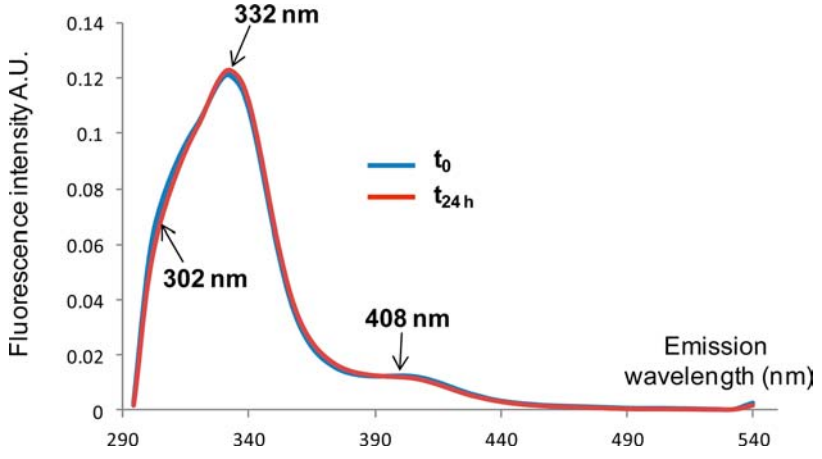

Figure 4. Mean emission fluorescence spectra of 0 (t_0) and 24 h ($t_{24\,h}$) postmortem soleus muscle fibers (excitation wavelength of 275 nm). The UV-excited spectra show peaks at 332 nm and 408 nm with shoulders at 302 nm. Fluorescence emission at 302 and 332 are assigned to tyrosine and tryptophan, respectively. Compounds emitting at 408 nm could be NADH. The postmortem time causes a slight shift of the spectrum.

by a specific feature of rodent muscles (rats and mice), whose type IIA fibers are richer in mitochondria and, thus, more oxidative than their type I fibers.[21,22] It is therefore logical for it to be less richly supplied with glycogen. The initial level of glycogen (around 23 μmol/g of fresh muscle) was lower than reported by others, who found 30−40 μmol/g of fresh muscle in the rat muscle.[23,24] This difference is probably due to the delay of 10 min necessary for muscle dissection when part of the glycogen was depleted; 60% of muscle glycogen is degraded within 5 min after the death of the animal.[23] This hypothesis is in accordance with the initial pH (6.9 in tibialis and gastrocnemius muscles), slightly lower than usual *in vivo* pH (7.2), as a consequence of glycogen degradation associated with a release of protons in the tissue.

The rat muscle glycogen content appeared to be considerably lower than seen in farm animal species, where values of

DOI: 10.1021/acs.jafc.5b00668
J. Agric. Food Chem. 2015, 63, 4782−4789

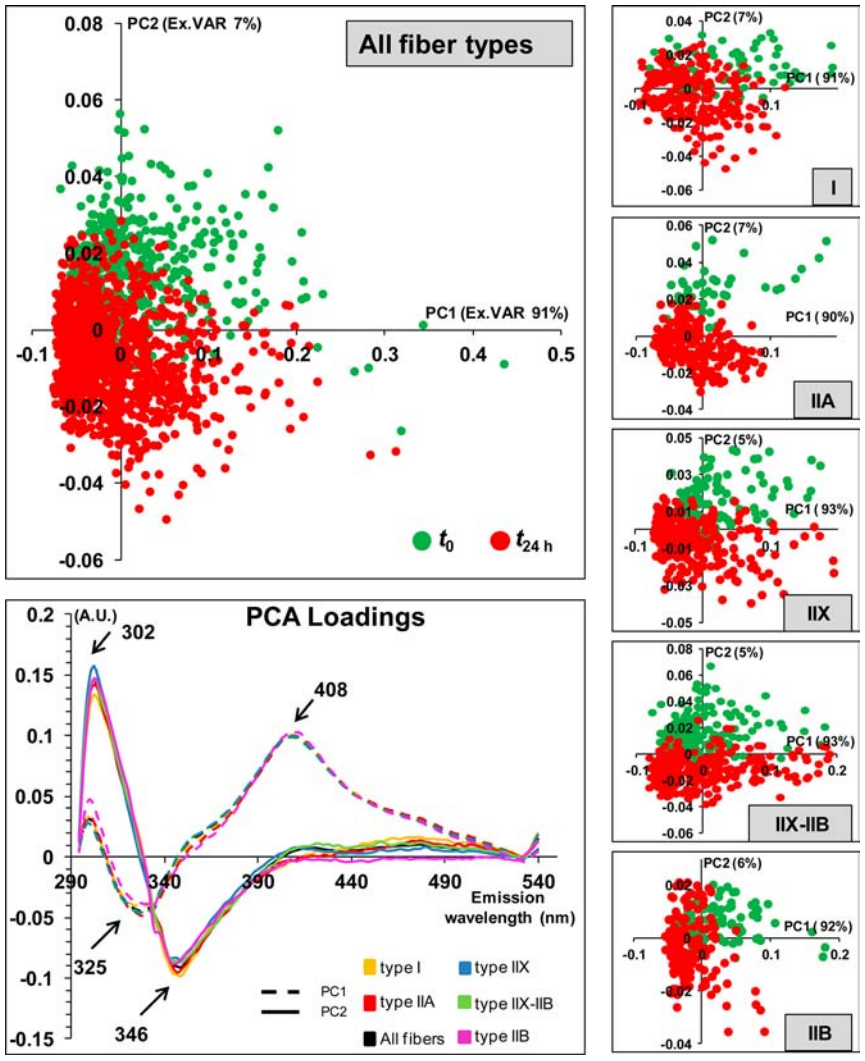

Figure 5. PCA score plots and loadings of fluorescence response of fresh (t_0) and 24 h postmortem ($t_{24\,h}$) EDL muscle. Ex.VAR: explained variance. Postmortem time was most discriminated on the PC2 (346 nm and 302 nm bands) for IIA, IIX, and IIX-IIB fibers and on the PC1 (408 nm and 346 nm bands) for I and IIB fiber types.

glycogen are about 60−70 μmol/g in rabbits,[25] 85−100 μmol/g in pigs,[26,27] 45−50 μmol/g in turkeys,[28] 80−100 μmol/g in cattle,[29,30] and about 70 μmol/g in sheep.[31] Glycogen reserves remained relatively high in rat muscle (Figure 2), unlike in farm animals, whose meat glycogen reserves fall to less than 10 μmol/g after rigor mortis, with a pH stabilization around 5.6−6.0 depending upon the type of muscle.[3,4]

The initial pH of the gastrocnemius and tibialis muscle decreased and has reached its minimum (6.06 ± 0.12 and 6.15 ± 0.03, respectively) after 2.5 h postmortem, which is consistent with the postmortem time of the stopped glycogen consumption in soleus and EDL muscles (Figure 2).

Postmortem Ultrastructural Changes. Representative images of ultrastructural analysis are shown in Figure 3. Shortly after animal sacrifice, the myofibrils were well-preserved with well-defined sarcomeres and aligned Z lines. However, the soleus showed contracted myofibrils that prevented the I bands from being distinguished. This contraction may be related to mechanical stimulation during sampling but also to cold shortening, despite our precautions to avoid this problem (fixative immersion at room temperature). The fact that only the soleus muscle showed this state leads us to believe that it was due to cold shortening because only red muscles are sensitive to cold shortening.[3]

After 24 h postmortem, the myofibrils showed no significant change in their structure. Soleus myofibrils were still contracted; however, Z lines remained aligned, and mitochondria were well-preserved, despite the storage temperature of 20 °C, which promotes the action of endogenous proteases.

Appreciable changes were observed at 48 h postmortem on the muscle sample prepared exactly in the same conditions (see Supplementary Figure S1 of the Supporting Information).

Fluorescence Response of Muscle Fibers According to Time Postmortem. Figure 4 shows the profile of fluorescence spectra acquired in soleus muscle fibers at death (t_0) and 24 h postmortem ($t_{24\,h}$) (spectra acquired on the EDL muscle show the same general pattern). The spectra show a peak at 332 nm characteristic of tryptophan and a shoulder at 302 nm assigned to tyrosine.[12,20,32] The compound that emits fluorescence at 408 nm could not be identified with certainty. Collagen and elastin fluoresce in this wavelength range,[14] but these proteins are located in the ECM, which excludes the involvement of these compounds in the observed fluorescence, because our spectral acquisitions were strictly intracellular. The fluorescence

DOI: 10.1021/acs.jafc.5b00668
J. Agric. Food Chem. 2015, 63, 4782−4789

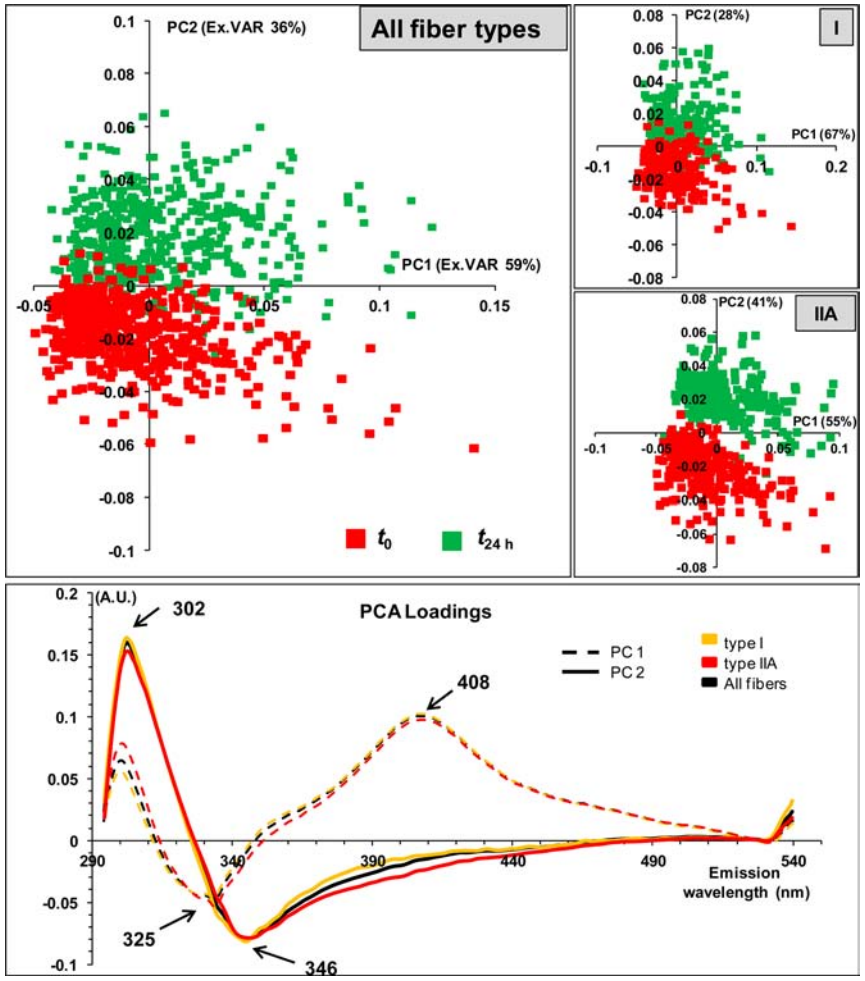

Figure 6. PCA score plots and loadings of fluorescence response of fresh (t_0) and 24 h postmortem ($t_{24\,h}$) soleus muscle. Ex.VAR: explained variance. Postmortem time was best discriminated on the PC2 (346 nm and 302 nm bands) whatever the fiber type of the soleus muscle (I and IIA).

peak at 408 nm could be attributed to NADH, because in living cells, this compound is suspected to fluoresce in this wavelength range.[20]

The superposition of the spectra acquired at t_0 and $t_{24\,h}$ shows some shifts that are however difficult to see with the naked eye. However, these differences are highlighted by the PCA and variance analysis that are presented in Figures 5−7. PCA and loadings indicate a separation of the two postmortem times (t_0 and $t_{24\,h}$) essentially in the PC2 on the fluorescence intensities at 302 and 346 nm and to a lesser extent on the PC1 at 325 and 408 nm, whichever the muscle considered (Figures 5 and 6). In general, 302 and 408 nm fluorescence intensities were higher and 346 and 325 nm fluorescence intensities were lower for t_0 than for $t_{24\,h}$ samples. Separation on the EDL PCA was less clear-cut than in the soleus, mainly because the EDL is composed of four types of fiber plus IIX−IIB hybrid fibers, while the soleus is composed of only I and IIA fibers.

Some cell types allow for a better separation of postmortem times, such as type IIA fibers, which show excellent discrimination of postmortem times on both the EDL and soleus muscles. IIX−IIB hybrid fibers and IIX fibers (absent in the soleus muscle) also show a good separation with regard to postmortem time. Postmortem time of soleus muscle type I fiber discrimination was somewhat less marked than for type IIA but still very sharp. In contrast, postmortem time discrimination of EDL type I and type IIB fibers was not as sharp on PC2. For these fiber types, the postmortem time was discriminating on both PC2 at 302 and 346 nm and PC1 at 408 and 325 nm.

Discriminatory wavelengths of PC1 and PC2 were exactly the same for the two muscles (EDL and soleus) and all types of fibers: 325 and 408 nm for PC1 and 302 and 346 for PC2. Hence, it seems that only few fluorophores are concerned in postmortem time discrimination.

Significant differences in emission fluorescence intensities regarding the postmortem time were amplified by the 346/302 and 408/325 ratios, which were systematically lower and higher, respectively, for t_0 than $t_{24\,h}$ muscle fibers (Figure 7). Soleus t_0 fibers I and IIA have a lower 408/325 ratio than EDL t_0 I and IIA fibers (Figure 7). The fluorescence intensity at 408 nm is significantly higher ($p < 0.01$) in the EDL (0.0195 ± 0.0009 and 0.0170 ± 0.0015 for I and IIA fibers, respectively) than in the soleus (0.0114 ± 0.0002 and 0.0113 ± 0.0002 for I and IIA fibers, respectively), while that at 325 nm has very low variations (around 0.110). Therefore, the difference in response is related to the fluorescence emission at 408 nm suspected to correspond to NADH. Moreover, soleus fluorescence at 408 nm is less affected by postmortem time than that of EDL. These results indicate that, within the same type of fiber, the response of some fluorophores may depend upon the muscle origin. Therefore, it seems that the composition or the

DOI: 10.1021/acs.jafc.5b00668
J. Agric. Food Chem. 2015, 63, 4782−4789

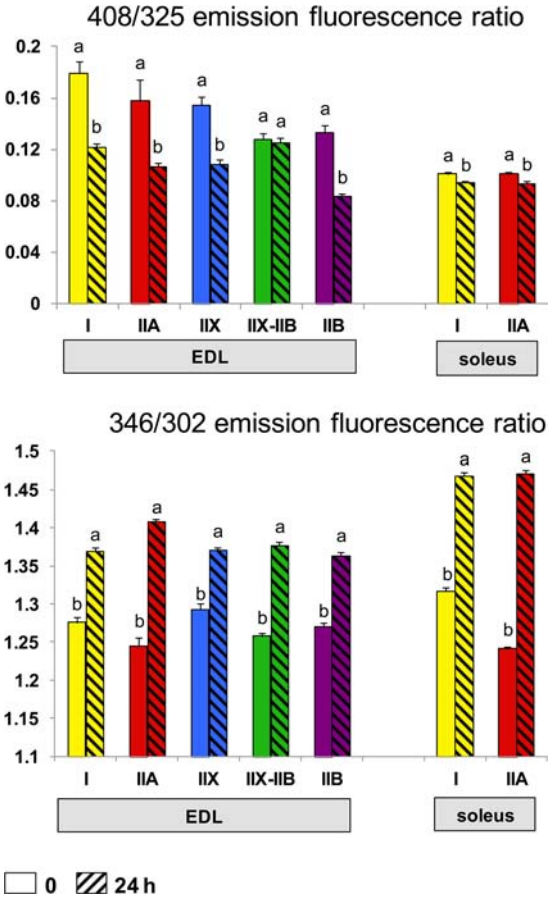

Figure 7. Ratio of fluorescence intensity wavelength evidenced by loadings of PCA regarding the postmortem time. Fluorescence intensity ratio of wavelengths corresponding to discrimination peaks evidenced by PCA allow an amplification of differences. Twenty-four hours postmortem time muscle fibers ($t_{24\,h}$) show higher 346/302 and lower 408/325 values than fresh muscles fibers (t_0). For a given fiber type, different letters indicate a significant difference between 0 and 24 h postmortem samples for $p < 0.01$ (less than 1% that the observed difference is due to coincidence and more than 99% chance that it is related to postmortem time).

intracellular environment of a given fiber type is dependent upon its muscle source.

If the discrimination on 302 and 408 nm is coming from range in fluorescence intensity of tyrosine and NADH, the discrimination on 325 and 346 nm probably originates from slight shifts in the emission fluorescence of tryptophan around 332 nm related to changes in its physicochemical environment.[33,34] Indeed, after animal slaughter, muscle undergoes structural, biochemical, and physicochemical changes.[3,4] The pH drop is accompanied by glycogen decrease, lactate accumulation in cells, and muscle contraction. The plasma membranes are quickly perforated,[35] and ionic gradients gradually collapse, culminating in ion concentration equilibrium in the cells. Nucleus and organelles (mitochondria, lysosome sarcoplasmic reticulum, etc.) degrade, and muscle proteins are degraded into peptides under the action of endogenous proteolytic enzymes.[5,6] All of these phenomena substantially change the intracellular physicochemical environment and, therefore, the fluorescent properties of molecules[33,34] that may explain the t_0 and $t_{24\,h}$ differences in fluorescence intensity of aromatic amino acids.

The level of discrimination seems dependent upon both muscle (EDL or soleus) and fiber type. In comparison to type I fibers, the better postmortem time separation on IIA fibers suggests more marked environmental changes in these cells.

Postmortem time discrimination being less clear-cut on the EDL than on the soleus muscle is probably related to the fact that the EDL contains four pure types of fibers and IIX−IIB hybrids. In the EDL, the postmortem time of types I, IIB, and IIX fibers was discriminated on both PC1 and PC2, with the $t_{24\,h}$ showing a lower fluorescence intensity at 408 nm and a higher fluorescence at 325 nm than the t_0.

In comparison to t_0, the decrease in fluorescence intensity at 408 nm for $t_{24\,h}$ strengthens our hypothesis that this band corresponds to NADH. We know that NADH (fluorescent) is completely oxidized to NAD (non-fluorescent) after a short period of anoxia and all the more so after 24 h postmortem,[36,37] which would explain the difference in 408 nm intensity as demonstrated on the PC1 loading. The fact that the discrimination at 408 nm was not as clear-cut on some types of fiber may be due to the rate of oxidation of NADH depending upon the fiber type.

Our results demonstrate the benefit of exploiting the variation in DUV autofluorescence feature to characterize some postmortem changes in muscle cells. Despite low spectral differences, multivariate analyzes have identified the wavelengths capable of discriminating muscle samples collected at slaughter from those taken 24 h postmortem. A kinetic study will show whether the evolution of postmortem muscle can be characterized by its autofluorescent answer.

■ ASSOCIATED CONTENT

Ⓢ Supporting Information

At 48 h postmortem ultrastructure changes in EDL and soleus muscles (Figure S1). The Supporting Information is available free of charge on the ACS Publications website at DOI: 10.1021/acs.jafc.5b00668.

■ AUTHOR INFORMATION

Corresponding Author

*Telephone: +33-4-73-62-41-56. Fax: +33-4-73-62-42-68. E-mail: thierry.astruc@clermont.inra.fr.

Funding

This work was supported by the French National Institute for Agronomical Research (INRA) with the MICEL project funded by divisions CEPIA and MICA (Science and Process Engineering of Agricultural Products/Microbiology and Food Chain). Caroline Chagnot is a Ph.D. Research Fellow supported by the Région Auvergne (Contrat de Projet État-Région)−FEDER (Fonds Européen de Développement Régional).

Notes

The authors declare no competing financial interest.

■ ACKNOWLEDGMENTS

Experiments were performed at the SOLEIL synchrotron on the beamline DISCO in the framework of Project 20120364. The authors thank Christophe De l'Homme from the "Installation Expérimentale de Nutrition" (INRA de Theix, Saint-Genès Champanelle, France) for housing rats and technical assistance during animal sacrifice and Claude Ferreira for technical assistance in glycogen determination.

DOI: 10.1021/acs.jafc.5b00668
J. Agric. Food Chem. 2015, 63, 4782−4789

REFERENCES

(1) Astruc, T. Muscle fiber types and meat quality. In *Encyclopedia of Meat Science*, 2nd ed.; Devine, C., Dikeman, M., Eds.; Elsevier: Oxford, U.K., 2014; Vol. 2, pp 442−448.

(2) Lefaucheur, L. A second look into fibre typing—Relation to meat quality. *Meat Sci.* **2010**, *84*, 257−270.

(3) Bendall, J. R. Post mortem changes in muscle. In *Structure and Function of Muscle*; Bourne, G. H., Ed.; Academic Press: New York, 1973; pp 243−309.

(4) Greaser, M. L. Conversion of muscle to meat. In *Muscle as Food*; Bechtel, P., Ed.; Academic Press: New York, 1986.

(5) Ouali, A. Meat tenderrization: Possible causes and mechanisms. A review. *J. Muscle Foods* **1990**, *1*, 129−165.

(6) Koohmaraie, M. Muscle proteinases and meat aging. *Meat Sci.* **1994**, *36*, 93−104.

(7) Dutson, T. R.; Pearson, A. M.; Merkel, A. A. Ultrastructural *postmortem* changes in normal and low quality porcine muscle fibers. *J. Food Sci.* **1974**, *39*, 32−37.

(8) Dufour, E.; Frencia, J. P.; Kane, E. Development of a rapid method based on front-face fluorescence spectroscopy for the monitoring of fish freshness. *Food Res. Int.* **2003**, *36*, 415−423.

(9) Swatland, H. J. Measurement of the gristle content in beef by macroscopic ultraviolet fluorimetry. *J. Anim Sci.* **1987**, *65*, 158−164.

(10) Skjervold, P. O.; Taylor, R. G.; Wold, J. P.; Berge, P.; Abouelkaram, S.; Culioli, J.; Dufour, E. Development of intrinsic fluorescent multispectral imagery specific for fat, connective tissue, and myofibers in meat. *J. Food Sci.* **2003**, *68*, 1161−1168.

(11) Frencia, J. P.; Thomas, E.; Dufour, E. Measure of meat tenderness using front-face fluorescence spectroscopy. *Sci. Aliments* **2003**, *23*, 142−145.

(12) Theron, L.; Venien, A.; Jamme, F.; Fernandez, X.; Peyrin, F.; Molette, C.; Dumas, P.; Refregiers, M.; Astruc, T. Protein matrix involved in the lipid retention of *foie gras* during cooking: A multimodal hyperspectral imaging study. *J. Agric. Food Chem.* **2014**, *62*, 5954−5962.

(13) Pallu, S.; Rochefort, G. Y.; Jaffre, C.; Refregiers, M.; Maurel, D. B.; Benaitreau, D.; Lespessailles, E.; Jamme, F.; Chappard, C.; Benhamou, C. L. Synchrotron ultraviolet microspectroscopy on rat cortical bone: Involvement of tyrosine and tryptophan in the osteocyte and its environment. *PLoS One* **2012**, *7*, No. e43930.

(14) Jamme, F.; Kascakova, S.; Villette, S.; Allouche, F.; Pallu, S.; Rouam, V.; Refregiers, M. Deep UV autofluorescence microscopy for cell biology and tissue histology. *Biol. Cell* **2013**, *105*, 277−288.

(15) Chagnot, C.; Venien, A.; Peyrin, F.; Jamme, F.; Refregiers, M.; Desvaux, M.; Astruc, T. Deep UV excited muscle cell autofluorescence varies with fibre type. *Analyst* **2015**, DOI: 10.1039/C5AN00172B.

(16) Fernandez, X.; Sante, V.; Baeza, E.; Lebihan-Duval, E.; Berri, C.; Remignon, H.; Babile, R.; Le Pottier, G.; Astruc, T. Effects of the rate of muscle post mortem pH fall on the technological quality of turkey meat. *Br. Poult. Sci.* **2002**, *43*, 245−252.

(17) Bergmeyer, H. U. *Methods of Enzymatic Analysis*; New York Academic Press: New York, 1974.

(18) Pearse, A. G. E. *Histochemistry. Theoretical and Applied*, 4th ed.; Churchill Livingstone: Edinburgh, U.K., 1985; Vol. 2.

(19) Giuliani, A.; Jamme, F.; Rouam, V.; Wien, F.; Giorgetta, J. L.; Lagarde, B.; Chubar, O.; Bac, S.; Yao, I.; Rey, S.; Herbeaux, C.; Marlats, J. L.; Zerbib, D.; Polack, F.; Refregiers, M. DISCO: A low-energy multipurpose beamline at synchrotron SOLEIL. *J. Synchrotron Radiat.* **2009**, *16*, 835−841.

(20) Jamme, F.; Villette, S.; Giuliani, A.; Rouam, V.; Wien, F.; Lagarde, B.; Refregiers, M. Synchrotron UV fluorescence microscopy uncovers new probes in cells and tissues. *Microsc. Microanal.* **2010**, *16*, 507−514.

(21) Punkt, K.; Naupert, A.; Asmussen, G. Differentiation of rat skeletal muscle fibres during development and ageing. *Acta Histochem.* **2004**, *106*, 145−154.

(22) Bloemberg, D.; Quadrilatero, J. Rapid determination of myosin heavy chain expression in rat, mouse, and human skeletal muscle using multicolor immunofluorescence analysis. *PLoS One* **2012**, *7*, No. e35273.

(23) Calder, P. C.; Geddes, R. Post mortem glycogenolysis is a combination of phosphorolysis and hydrolysis. *Int. J. Biochem.* **1990**, *22*, 847−856.

(24) Manabe, Y.; Gollisch, K. S.; Holton, L.; Kim, Y. B.; Brandauer, J.; Fujii, N. L.; Hirshman, M. F.; Goodyear, L. J. Exercise training-induced adaptations associated with increases in skeletal muscle glycogen content. *FEBS J.* **2013**, *280*, 916−926.

(25) Astruc, T.; Talmant, A.; Fernandez, X.; Monin, G. Temperature and catecholamine effects on metabolism of perfused isolated rabbit muscle. *Meat Sci.* **2002**, *60*, 287−293.

(26) Fernandez, X.; Neyraud, E.; Astruc, T.; Sante, V. Effects of halothane genotype and pre-slaughter treatment on pig meat quality. Part 1. Post mortem metabolism, meat quality indicators and sensory traits of m. Longissimus lumborum. *Meat Sci.* **2002**, *62*, 429−437.

(27) Kocwin-Podsiadla, M.; Przybylski, W.; Kuryl, J.; Talmant, A.; Monin, G. Muscle glycogen level and meat quality in pigs of different halothane genotypes. *Meat Sci.* **1995**, *40*, 121−125.

(28) Fernandez, X.; Sante, V.; Baeza, E.; Lebihan-Duval, E.; Berri, C.; Remignon, H.; Babile, R.; Le Pottier, G.; Millet, N.; Berge, P.; Astruc, T. Post mortem muscle metabolism and meat quality in three genetic types of turkey. *Br. Poult. Sci.* **2001**, *42*, 462−469.

(29) McVeigh, J. M.; Tarrant, P. V. Glycogen content and repletion rates in beef muscle, effect of feeding and fasting. *J. Nutr.* **1982**, *112*, 1306−1314.

(30) Immonen, K.; Ruusunen, M.; Hissa, K.; Puolanne, E. Bovine muscle glycogen concentration in relation to finishing diet, slaughter and ultimate pH. *Meat Sci.* **2000**, *55*, 25−31.

(31) Diaz, M. T.; Vieira, C.; Perez, C.; Lauzurica, S.; de Chavarri, E. G.; Sanchez, M.; De la Fuente, J. Effect of lairage time (0 h, 3 h, 6 h or 12 h) on glycogen content and meat quality parameters in suckling lambs. *Meat Sci.* **2014**, *96*, 653−660.

(32) Petit, V. W.; Refregiers, M.; Guettier, C.; Jamme, F.; Sebanayakam, K.; Brunelle, A.; Laprevote, O.; Dumas, P.; Le Naour, F. Multimodal spectroscopy combining time-of-flight-secondary ion mass spectrometry, synchrotron-FT-IR, and synchrotron-UV micro-spectroscopies on the same tissue section. *Anal. Chem.* **2010**, *82*, 3963−3968.

(33) Lakowicz, J. R. *Principles of Fluorescence Spectroscopy*, 3rd ed.; Springer: New York, 2006; p 954.

(34) Valeur, B.; Berberan-Santos, M. N. *Molecular Fluorescence: Principes and Applications*; Wiley-VCH Verlag GmbH: Weinheim, Germany, 2001.

(35) Astruc, T., Muscle structure and digestive enzyme bioaccessibility to intracellular compartment. In *Food Structure Digestion & Health*, 1st ed.; Boland, M., Golding, M., Singh, H., Eds.; Academic Press: London, U.K., 2014; pp 193−222.

(36) Ren, J. M.; Henriksson, J.; Katz, A.; Sahlin, K. NADH content in type I and type II human muscle fibres after dynamic exercise. *Biochem. J.* **1988**, *251*, 183−187.

(37) Mayevsky, A.; Rogatsky, G. G. Mitochondrial function in vivo evaluated by NADH fluorescence: From animal models to human studies. *Am. J. Physiol.: Cell Physiol.* **2007**, *292*, C615−C640.

DOI: 10.1021/acs.jafc.5b00668
J. Agric. Food Chem. 2015, 63, 4782−4789

JOURNAL OF AGRICULTURAL AND FOOD CHEMISTRY

Article

pubs.acs.org/JAFC

Application of Single-Stage Orbitrap Mass Spectrometry and Differential Analysis Software to Nontargeted Analysis of Contaminants in Dog Food: Detection, Identification, and Quantification of Glycoalkaloids

Jack J. Lohne,*[,†] Sherri B. Turnipseed,[†] Wendy C. Andersen,[†] Joseph Storey,[†] and Mark R. Madson[†,‡]

[†]Animal Drugs Research Center and [‡]Denver Laboratory, U.S. Food and Drug Administration, Denver Federal Center Building 20, West Sixth Avenue and Kipling Street, Denver, Colorado 80225-0087, United States

ABSTRACT: The objective of this study was to perform a preliminary investigation of the nontargeted search and quantitative capabilities of a single-stage Exactive High-Resolution Mass Spectrometer (HRMS). To do this, the instrument and its associated software performed a non-targeted search for deleterious substances in a dog food sample suspected of causing gastrointestinal problems in dogs. A single-stage Orbitrap/high-performance liquid chromatography method and differential expression analysis software (Sieve) was used to detect and identify, and subsequently quantify, nontargeted compounds occurring only in the suspect dog food sample. When combined with an online database (ChemSpider), a preliminary identification of one of the nontargeted compounds was determined to be potato glycoalkaloids. The diagnostic product ion ratios and quantitative data accuracy generated by the single-stage Orbitrap MS were shown to be similar to results obtained using a triple quadrupole LC-MS/MS. Additionally, the ability of the single-stage Orbitrap instrument to provide precursor and product ion accurate masses and isotope patterns was also investigated.

KEYWORDS: *glycoalkaloids, HRMS, nontargeted search, Orbitrap, Sieve, dog food*

INTRODUCTION

With the introduction of relatively inexpensive high-resolution mass spectrometer (HRMS) instruments, such as time-of-flight (TOF) and Orbitrap mass spectrometers, new capabilities in sample analysis have emerged.[1−3] In addition to the traditional data supplied by triple quadrupole and ion trap instruments (nominal mass/charge measurements and precursor to product ion transition ratios), these HRMS instruments can also provide accurate mass data for precursor and product ions and their corresponding isotopolog ions.[2] Additional data from HRMS measurements not only allow for screening of known compounds, but, more importantly, they allow for the structural elucidation of unknown low molecular weight compounds using the inferred elemental composition of precursor/product ions and the isotope patterns[4] derived from the accurate mass measurements. The full scan data acquisition of HRMS enables the instrument to record virtually all ions[4,5] that reach the detector. This allows for postacquisition identification not only for targeted compounds but also for any other nontargeted compounds with mass/charge values within the scan range of the method.[2,3,6] With proper resolution settings (e.g., ≥ 50 000), the resulting data is also highly selective because narrow ion extraction windows (e.g., ± 5 ppm) can be constructed around the theoretical mass/charge of the compound(s) of interest.[2]

This preliminary investigation was done to determine the nontargeted search capabilities of the single-stage Exactive HRMS and the identification capabilities of its associated Sieve software. Also, the ability of the Exactive to quantify and positively identify (according to FDA and EU guidelines) compounds was also studied. HRMS analysis is a powerful tool for the identification of unknown nontargeted contaminants in a food safety laboratory. A good example of a nontargeted search is the analysis of a food or drug sample for potential contaminants suspected of causing illness or death in humans and/or animals.[7] In these cases, there may be little or no information available to the analyst, only the information provided by the sample packaging and the people involved in the case (i.e., consumer, patient, doctor, etc.). In the past, this type of nontargeted sample analysis was done by using a wide range of analytical instrumentation and extraction techniques to compare the suspect sample against a very similar sample (e.g., the same product from the same manufacturer but from a different lot that was not causing adverse effects). The results from these analyses were then manually compared, and differences between the two were investigated. This approach has led to the successful identification of many contaminants in food and drugs, such as the recent economic adulteration of Chinese protein products with melamine in 2007−2008[7] and the adulteration of Tylenol capsules with cyanide in 1982.[8] However, because it can be time-consuming and is not always successful, a better approach to nontargeted analysis is needed.

One new approach can involve HRMS instruments and their associated software. Analysis using HRMS has been applied to environmental testing,[9] forensics,[10] and food safety.[11] These instruments provide the selectivity and sensitivity required for efficient wide-range screening of samples by combining high,

Received: February 20, 2015
Revised: April 24, 2015
Accepted: April 27, 2015
Published: April 27, 2015

ACS Publications © 2015 American Chemical Society

DOI: 10.1021/acs.jafc.5b00959
J. Agric. Food Chem. 2015, 63, 4790−4798

full-spectral sensitivity with sufficient mass resolution for accurate mass measurements of any ionizable component in a sample. Elemental composition for nontargeted compounds can be deduced from these results. Then a user defined database can be searched (targeted search), or as in this study, a large online database such as ChemSpider[12] can be searched (nontargeted search) for potential matches. These database searches (both targeted and nontargeted) can be done automatically using the equipment manufacturers software.[4]

There are numerous papers describing the use of HRMS methods and data processing using differential analysis software,[13,14] but most are associated with the fields of proteomics or metabolomics.[4,13−16] These analyses are often targeted in nature because the class of compounds is usually known and the analytical methods are more specific. There are few papers addressing low-molecular-weight compounds in adulterated samples where the contaminant is a total unknown. This "small molecule, totally unknown" sample type can be especially difficult as the extraction procedure, instrument method and data processing parameters must all be set to capture a wide range of possible compounds. This results in a massive amount of data that must then be subjected to some type of reduction process to make the number of possible adulterants identified manageable.

This paper describes a high-resolution accurate mass/mass spectrometry (HRMS) analytical method for potential contaminants in dog food and subsequent data analysis using differential analysis software to identify compounds that were only found in the suspect sample. In general, differential analysis software compares the magnitudes of matching chromatographic peaks (i.e., same mass/charge and retention time using user defined limits) found in a suspect sample versus a control sample. These magnitude differences can then be used to filter the data. As an example, the data can be filtered to show only ions that were at least 10 times more abundant in the suspect dog food. Using this approach, only one instrument was needed in this study to identify the unknown compound that could be causing the illness in dogs, as opposed to the multiple analytical techniques used in the past. In addition, the tedious job of comparing the data generated was evaluated automatically in a matter of hours by the software.

MATERIALS AND METHODS

Study Design. A truly nontargeted analysis implies no foreknowledge of what compounds are to be detected, and therefore, generalized extraction and chromatographic parameters need to be used. With this in mind, a simple liquid/solid extraction using common solvents that span a wide range of polarities, followed by filtration, was chosen as the initial extraction procedure. Each extraction solvent (ACN, ACN/H_2O 70:30 (v/v) and MTBE) was used to extract the suspect and control dog food samples in triplicate. The set of three injections of the extracted suspect dog food sample was then compared to the set of three injections of the extracted control dog food sample using Sieve differential analysis software to determine what ions were present in the suspect dog food compared to the control dog food. The software then assigned values to the magnitude of the differences between the suspect sample and the control sample using parameters such as the peak area ratio (treatment peak area/control peak area) or the statistical probability ("p" value) that they come from the same population; the "difference magnitudes" were then used to filter the results. This procedure was applied for each of the three data sets of the extraction solvents.

To further investigate the capabilities of the Orbitrap/Sieve software combination, four additional experiments were performed: (1) the effect of differing resolution settings on the ability of Sieve to correctly identify compounds, (2) the effect of molecular weight cutoff filter (MWCO) during sample extract cleanup, (3) specificity of the Sieve software (i.e., were there any glycoalkaloids identified in a Blank vs Blank Sieve test), (4) lowest concentration at which the nontargeted compounds could be positively identified by the Sieve software. Once glycoalkaloids were identified as the suspect compounds, in addition to the suspect sample, five additional potato-containing and four nonpotato-containing dog foods were purchased to determine the prevalence and range of concentrations of glycoalkaloids. Fortified dog food samples, at various concentrations (0.01 ppm to 20 ppm), were also prepared and analyzed.

Three instrumental methods were used in this study, two for the Orbitrap and one for the triple quadrupole. The initial Orbitrap method was used for nontargeted searching and consisted of a liquid/liquid extraction using three separate solvents mixtures that encompassed a wide range of polarities with a slow HPLC linear mobile phase gradient from low to high organic content. Upon review of the initial data, a second Orbitrap analytical method was developed which better separated the compounds of interest. The second Orbitrap method (extraction, HPLC, and Orbitrap parameters) was then used to generate all quantification and confirmation data presented here. Lastly, some samples were divided into two aliquots to allow for additional analysis using a triple quadrupole LC-MS/MS to compare quantitative and qualitative data obtained by both instrument types; therefore, a third instrument method was required for the additional LC-MS/MS analysis.

Reagents and Supplies. Water (H_2O), acetonitrile (ACN), and methanol (MeOH) were of LC/MS grade, whereas *tert*-butyl methyl ether (MTBE) was of HPLC grade; all were purchased from Fisher Scientific (Pittsburgh, PA, U.S.A.). Nylon syringe filters, 13 mm, 0.2 μm, GD/X disposable, were also purchased from Fisher Scientific. Molecular weight cutoff filters, 3K, were purchased from EMD Millipore (Billerica, MA, U.S.A.). Analytical standards were obtained as follows; solanine (≥95%) and solanidine (≥97%) were purchased from Sigma (St. Louis, MO, U.S.A.), Chaconine (≥95%) was purchased from Chromadex (Irvine, CA, U.S.A.), and solamargine (98%) was purchased from Stanford Materials Corporation (Irvine, CA, U.S.A.)

Standard Solutions. Solanine, solanidine, solamargine, and chaconine standard stock solutions were prepared individually at a concentration of approximately 0.1 mg/mL by dissolving approximately 1 mg of each in 10 mL of 70:30 MeOH/H_2O (v/v). Intermediate stock standards were prepared by various combinations and dilutions of these stock standard solutions in 70:30 H_2O/ACN (v/v). The diluent used for the final dilution before injection of all samples was 95:5 H_2O:ACN (v/v). All solutions were corrected for purity and no internal standard was used in this study.

Calibrant and Fortified Sample Preparation. Powdered dog food, similar to the suspect dog food and previously shown to be free of glycoalkaloids, was spiked in duplicate with varying amounts of intermediate stock standard solutions to prepare fortified extracted standard samples at 0.5, 1.0, 1.25, 2.5, 5.0, 10.0, and 20.0 ppm and fortified extracted samples ranging from 2 to 300 ppb. The fortified samples were allowed to sit uncapped for 20 min. The calibrants were then extracted as described below in the section Final Extraction Procedure.

Sample Preparation. The suspect dog food was obtained personally from the dog owner and consisted of approximately 5 lb of dry brown pellets. The negative control dog food sample, purchased at a commercial pet food chain, was nearly identical to the suspect sample with similar texture, color, and ingredients listed in the same order. The only major difference between the suspect and control samples was that the control dog food contained sweet potatoes, and the suspect dog food contained regular potatoes. After the initial analysis of suspect versus negative control dog food was completed, standards and additional dry dog food samples, with and without potatoes, were purchased to determine the ability of the method to consistently isolate, identify, and quantify compounds present only in the suspect sample. Approximately 5 lb of each dry dog food sample

DOI: 10.1021/acs.jafc.5b00959
J. Agric. Food Chem. 2015, 63, 4790−4798

was ground (approximately 5 min) to a fine homogeneous powder using a food processor (Robot Coupe, Ridgeland, MS, U.S.A.).

Initial Extraction Procedure. In the initial dog food extraction procedure, three extraction solvents of differing polarities (100% ACN, 70:30 v/v ACN/H_2O and 100% MTBE) were used. Five grams of the suspect and control dog food powder and 10 mL of each solvent were added to individual 15 mL polypropylene centrifuge tubes. The samples were vortex mixed at high speed for 15 min, then centrifuged at 4270*g* for 5 min. The supernatant from each sample was transferred to a clean 15 mL centrifuge tube. Each pellet was then washed with an additional 5 mL of the appropriate extraction solvent, centrifuged, and the supernatant was added to the initial extraction solvent. The combined extract was dried under 15 psi nitrogen (Turbo Vap, Hopkinton, MA, U.S.A.) at 40 °C to less than 1 mL and reconstituted to 1 mL with 95:5 (v/v) H_2O/ACN. The resulting liquid was filtered through a 0.2 μm, 13 mm nylon filter (Millipore, Billerica, MA, U.S.A.).

Final Extraction Procedure. In the final extraction procedure, 1 g of dog food powder was extracted, as described in the section Initial Extraction Procedure (above), using only the 70:30 (v/v) ACN/H_2O extraction solvent mixture. The resulting 10 mL of liquid was then dried, reconstituted, and filtered, as described above. The reconstituted solution was then additionally filtered through a 3K amu molecular weight cutoff filter using a microcentrifuge (HERMLE Labortechnik, Wehingen, GmbH) set at 21 000*g* for 15 min.

Initial LC-MS/MS Orbitrap Procedure. The LC system consisted of a Thermo (San Jose, CA, U.S.A.) Accela 1250 HPLC pump/degasser and a Thermo Pal HTC-Accela1-TMO autosampler. The HPLC conditions for the initial nontargeted phase of the analysis consisted of an Agilent (Santa Clara, CA, U.S.A.) Eclipse XDB 4.6 × 150 mm, 5 μm HPLC column with a Phenomenex (Torrance, CA, U.S.A.) Security Guard C18 4 × 2.0 mm guard column. Mobile phase "A" was 0.1% formic acid, and "B" was ACN. The gradient started at 95% "A" and 5% "B", was held for 3 min, then ramped linearly to 5% "A" and 95% "B" over 23 min, held there for 2 min, then brought back to initial conditions over 2 min, and held for 3 min. The flow rate was 0.5 mL/min. Five microliters of extract was injected onto the HPLC column, and the column was kept at room temperature.

A Thermo single-stage Exactive Orbitrap equipped with Xcalibur version 2.1, and Sieve version 2.0 software was used for the initial nontargeted phase of the study; the "Lock Masses" feature was not used. A generic tune file was created by tuning on the Total Ion Chromatogram (TIC) of the Orbitrap positive ion calibration solution. Three scan events were created, all with a mass range of 95 to 900 atomic mass units (u), a resolution setting of 50 000 at full width at half-maximum (fwhm), an automatic gain control (AGC) setting of 1 000 000, and a maximum injection time of 50 ms (ms). The first scan event used no fragmentation (i.e., neither in-source collision induced dissociation (CID) nor higher energy collision dissociation (HCD) was used), the second scan used HCD collision cell energy of 25.0 electron volts (eV), and the third scan used HCD collision cell energy of 40.0 electron volts (eV). The following source settings were used: spray voltage was 4500 (+), capillary temperature was 380 °C, sheath gas was 60 (arbitrary units), Aux gas was not used, and the heated electrospray ionization (HESI) temperature was 350 °C. A 5 ppm mass accuracy window was used to extract all compound masses used for calculations.

Final LC-MS/MS Orbitrap Procedure. The same HPLC as described above was used. Conditions for the analysis phase of the study consisted of an Agilent ODS Prodigy 2.0 × 150, 5 μm HPLC column with a Phenomenex Security Guard C18 4 × 2.0 mm guard column. Mobile phase "A" was 0.1% formic acid, and "B" was ACN. With a flow rate of 0.75 mL/min, the initial pump conditions were isocratic at 81% "A" and 19% "B" for 10 min, then the mobile phase was ramped linearly to 10% "A" and 90% "B" over 2 min, held there for 3 min, then brought back to initial conditions over 2 min, and held for 3 min.

For the final Orbitrap analysis, a tune file was created by tuning on solanidine (m/z 398.3417), which was the least responsive of the glycoalkaloids. Two scan events were created, both used a mass range of 95 to 900 amu with a resolution setting of 25 000 at fwhm, an AGC setting of 1 000 000 and a maximum injection time of 20 ms. The first (full) scan used no fragmentation, whereas the second (fragmentation) scan used an HCD setting of 90 eV. The source settings were the following: spray voltage, 4500 (+); capillary temperature, 380 °C; sheath gas, 60 (arbitrary units); Aux gas, not used; and the HESI temperature was 350 °C. A 5 ppm mass extraction window was used to extract all masses/compounds for calculations.

LC-MS/MS Sciex 5500 Procedure. The HPLC system was an Agilent 1200 series and consisted of a G1379B degasser, a G1312B binary pump, a G1316B column heater (kept at room temperature), and a Leap HTC Pal autosampler. The same LC parameters, injection volume, and HPLC column used in the "Final LC-MS/MS Procedure" of the Orbitrap study above were also used in this study.

An Applied Biosystems (Foster City, CA, U.S.A.) ABSciex 5500 QTrap mass spectrometer with Analyst software version 1.5.1 was used with electrospray ionization (ESI) in the positive ion mode. A tune file was created by tuning on the least responsive glycoalkaloid (solanidine). The precursor and product ions monitored were the same as those extracted from the Orbitrap data. The instrument settings were as follows; resolution for Q1 and Q3 was set at unit resolution; curtain gas (CUR), 25.0; collision gas (CAD), medium; ion spray voltage (IS), 5500.0; temperature (TEM), 600.0; ion source gas 1 (GS1), 60.0; ion source gas 2 (GS2), 50.0; declustering potential (DP), 100.0; entrance potential (EP), 10.0; and collision cell exit potential (CXP), 20.0; fragmentation parameters can be found in Table 1.

Table 1. Masses Monitored

analyte	Orbitrap m/z	Sciex 5500 m/z	Sciex 5500 collision energy (v)
solanine	868.5053[a]	868.5	N/A
frag. 1	98.0965[a]	98.1[a]	160
frag. 2	706.4513	706.5	95
frag. 3	722.446	722.4	95
chaconine	852.5104[a]	852.5	N/A
frag. 1	98.0965	98.1	160.0
frag. 2	398.3417	398.3	100.0
frag. 3	706.4513[a]	706.5[a]	90.0

[a]Product ion used for quantitation, Orbitrap precursor ion also used for quantitation.

Data Analysis with Differential Expression Software. Thermo Sieve (2.0) Automated Label-Free Differential Expression software was used with the "Small molecule", "Chromatographic Alignment and Framing", and "Two Sample Differential analysis" options. Analytical results from three replicate analyses of the suspect dog food (the "Treatment" sample in the Sieve software) were compared against triplicate analyses of a dog food with very similar ingredients to the suspect sample (the "Control" sample in the Sieve software). Sieve first aligns the Control and Treatment chromatograms along the retention time or "*X*" axis (Figure 1a,b). Then, using recursive base-peak framing and user-defined constraints (e.g., allowable variability in mass and retention time), Sieve constructs frames using retention time as the *X* axis and m/z as the *Y* axis (Figure 2). Each frame in the "Treatment" chromatogram(s) is compared to the corresponding frame in the "Control" chromatogram(s). All peaks (masses) detected in the consumer complaint and control sample were then sent to ChemSpider for tentative identification. The compounds identified by ChemSpider can then be filtered using various parameters offered by the Sieve software to limit or expand the amount of data generated such as the ratio of "Treatment" sample peak area/"Control" sample peak area.[17−19]

RESULTS AND DISCUSSION

Analytical Methodology. The objective of this study was to determine the ability of a single-stage Exactive HRMS

DOI: 10.1021/acs.jafc.5b00959
J. Agric. Food Chem. 2015, 63, 4790−4798

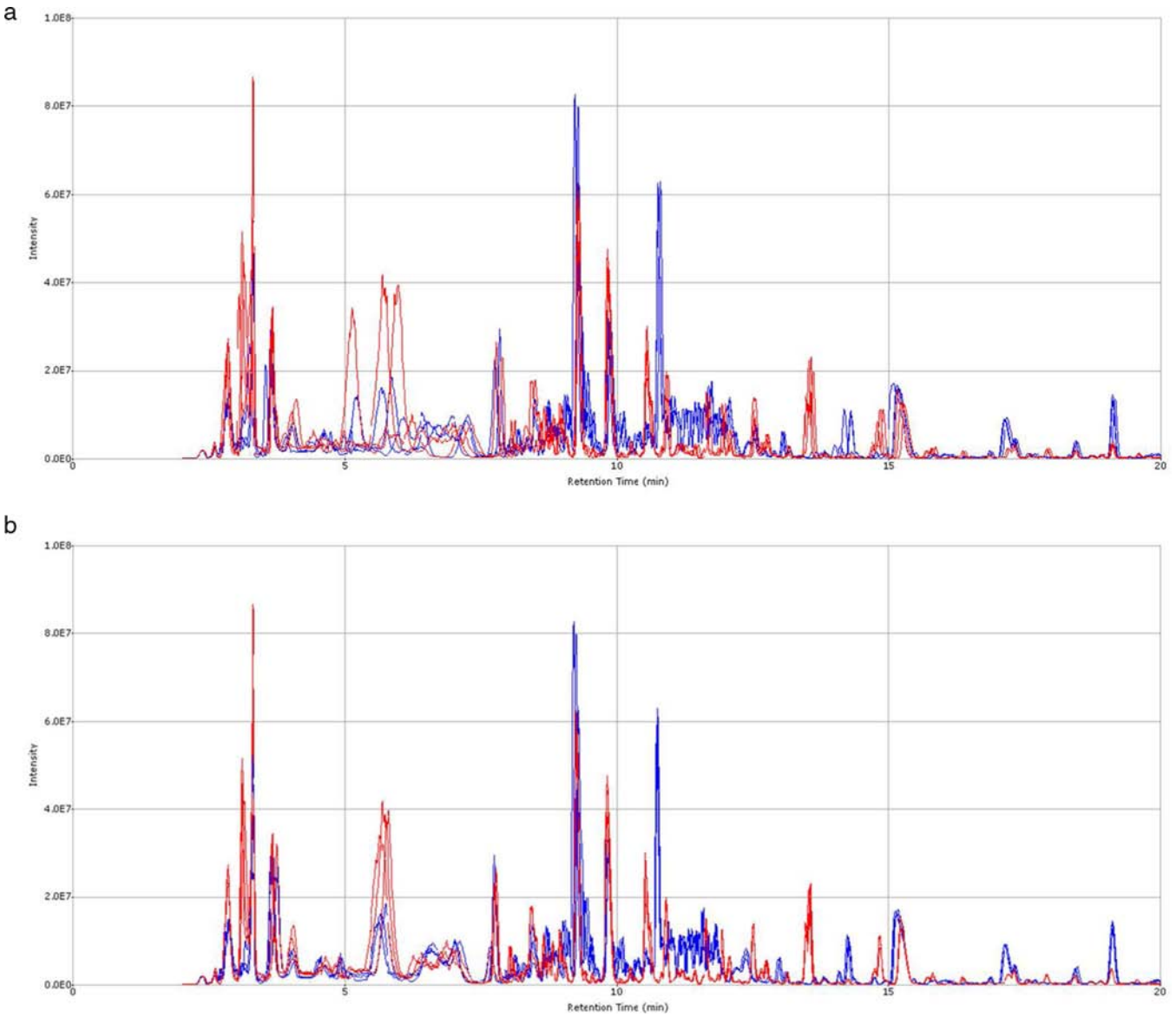

Figure 1. (a) Sieve unaligned chromatograms. (b) Sieve aligned chromatograms.

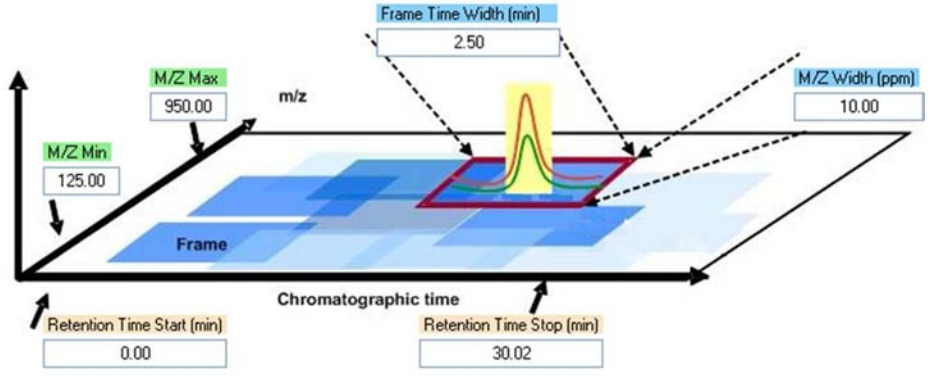

Figure 2. User defined frames constructed using retention time as the X axis and m/z as the Y axis.

instrument to positively identify what compound, if any, in a dog food sample could be causing gastrointestinal problems in dogs and the ability to quantify that compound. The analytical methodology evolved during the course of the study as the focus changed from unknown compound discovery to a more targeted procedure for glycoalkaloids. Initially, this was a true nontargeted analysis utilizing a single-stage Orbitrap and its associated Sieve differential analysis software for sample analysis. The sample extraction consisted of several different solvents covering a wide range of polarities with simple

DOI: 10.1021/acs.jafc.5b00959
J. Agric. Food Chem. 2015, 63, 4790−4798

filtration as the only cleanup in order to facilitate the extraction of a wide range of compounds. With no indication of how much background interference the dog food extracts would have, the Orbitrap resolution was set to 50 000. This resolution reduced the probability of mass errors caused by isobaric interferences, leading to more accurate identification of compounds with the Sieve software. Upon review of the initial data and tentative identification of potato glycoalkaloids as the potential contaminating agent, the instrument resolution was reduced to 25 000 because there was no indication of isobaric interferences. This reduction in resolution increased scan speed with no increase in mass error and no reduction in the ability of the Sieve software to correctly identify all glycoalkaloids. Filtration of the reconstituted sample through a 3K amu molecular weight cutoff filter was added to the extraction procedure resulting in a slight reduction in absolute recovery (glycoalkaloid peak areas were reduced by approximately 5%) but lessened the amount of unwanted material from entering the analytical system. The Sieve software detected glycoalkaloids in all three sample extracts (i.e., ACN, ACN/H2O; 70:30 (v/v) and MTBE) with ACN/H2O giving the greatest response; therefore ACN/H2O was used as the extraction solvent throughout the rest of the study. The HPLC method was adjusted to separate the coeluting glycoalkaloid isomers solanine and solamargine (Figure 3a,b) to ensure accurate calculation of concentrations and product ion ratios.

Differential Analysis. The suspect and negative control dog food samples were injected in triplicate and then analyzed by the Sieve software. The large number of possible compounds initially found by the Sieve software was reduced using the "Ratio" filter (ratio of suspect sample response to control sample response, set at >10:1) and the "PValue" filter (the probability, or "*p*" value, that the set of suspect chromatograms came from the same population as those from the Control chromatograms, set at ≤0.01) available in the software. Although instrument software programs are designed to evaluate large amounts of information generated by HRMS instruments, it can be difficult to set parameters to detect low levels of contaminants without generating a large positive identification list that must then be carefully evaluated. To reduce the extremely large number of compounds generated by this comparison, some assumptions were made: (1) the compound causing the sickness in dogs would be present in the suspect sample at a much higher concentration than in the control sample (at least 10×); (2) it would be present and detected in all three replicates of the suspect sample at approximately the same concentration in each replicate; and (3) that the compound would have a common name in addition to its International Union of Pure and Applied Chemistry (IUPAC) name. The first two assumptions did reduce the number of possible compounds from approximately 6000 to 2000, but this was still too large a number to manually search; therefore, assumption number three was included. It must be remembered that the use of the "common name" restriction may remove from consideration the compound actually causing the sickness in dogs (this assumption can easily be removed to revert to the approximately 2000 compound list). These three assumptions reduced the number or possible contaminants/adulterants to approximately 200 in the suspect dog food examined. These candidates were then either removed from the list due to their known benign nature or a literature search was done to determine the nature of the unknown substance; if benign, they were removed from the list.

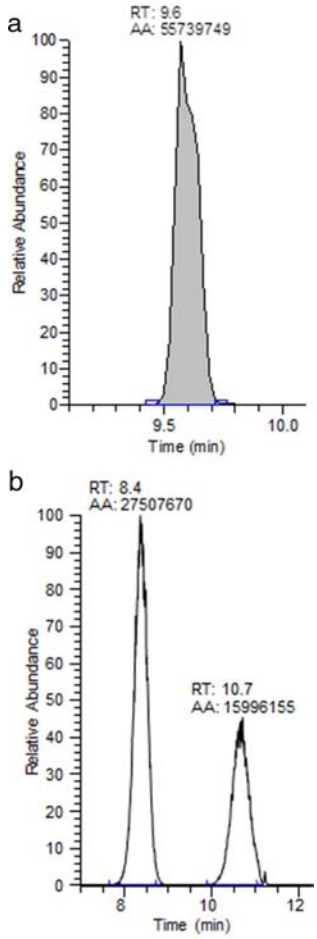

Figure 3. (a) LC-MS chromatogram of solanine and solamargine coeluting. (b) LC-MS chromatogram of solanine and solamargine separated.

Of the remaining substances, those that could cause symptoms similar to those exhibited by the sick dogs (i.e., drowsiness, vomiting, and ataxia) were studied further. One class of compounds detected by the Sieve software that matched all these criteria and was an ingredient in the dog food was potato glycoalkaloids.

All potato glycoalkaloids except solanidine were tentatively identified as occurring in only the suspect sample regardless of the extraction solvent used. An example of Sieve software results for solanine can be seen in Figure 4. Solanine and solamargine are structural isomers (Figure 5 and 6); therefore, the two compounds were indistinguishable to the Sieve/ChemSpider search and both were listed as possibilities.

Identification of Glycoalkaloids. The single-stage Orbitrap does not have the ability to isolate precursor ions (no isolation quadrupole) but was equipped with an HCD cell which was used for the fragmentation of all precursor ions entering the cell over a certain time interval. Extracted ion chromatograms of pertinent precursor and product ions were created using a 5 ppm mass accuracy extraction window; these data were then used for subsequent calculations. A literature search revealed that the masses (Table 1) of parent and product ions generated by the Orbitrap for the tentatively identified glycoalkaloids matched those in the literature[20−22] and that the actual and theoretical isotope patterns also matched (Figure 7a,b). Also, the symptoms exhibited by the sick dogs matched

DOI: 10.1021/acs.jafc.5b00959
J. Agric. Food Chem. 2015, 63, 4790−4798

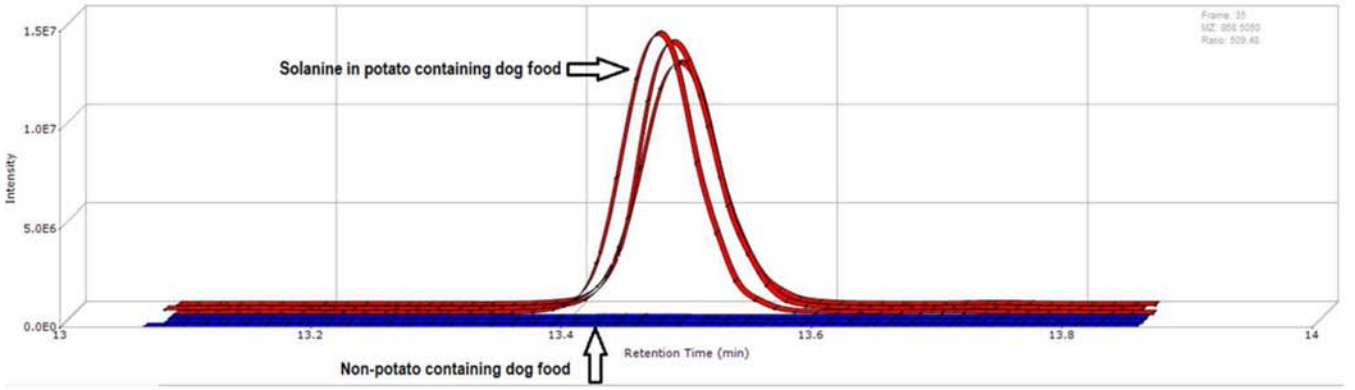

Figure 4. Sieve analysis results of suspect dog food sample vs control sample.

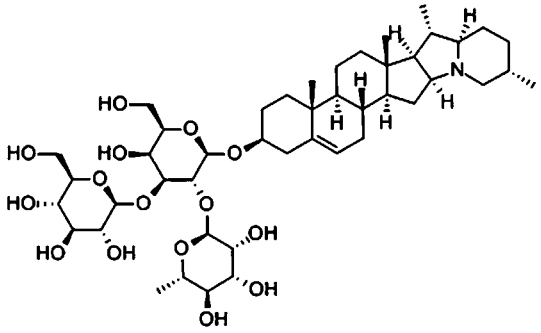

Figure 5. Solanine structure.

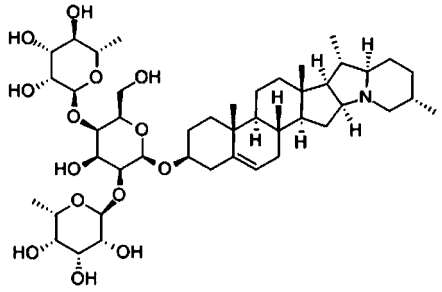

Figure 6. Chaconine structure.

the symptoms of potato glycoalkaloid poisoning.[23] At this point in the study, we determined that there was enough evidence to purchase standards for comparison against the suspect compound. Spectra (Figure 8a,b), accurate mass and retention time of the standard and sample were compared, the identity of solanine, chaconine, solamargine, and solanidine was then confirmed according to the U.S. Food and Drug Administration's Guidance to Industry 118 "Mass Spectrometry for Confirmation of the Identity of Animal Drug Residues"[24] and the European Union Commission Decision 2002/657/EC of 12 August 2002.[25]

Glycoalkaloids are naturally produced by all potatoes, but the amount produced is determined by many factors such as the potato strain, response to environmental stresses such as insect infestation, temperature extremes, physical bruising, and others.[26−28] Solanine and chaconine make up approximately 95% of the total glycoalkaloids produced, whereas solanidine and solamargine make up only about 5%;[20] therefore, quantitative results for these two lesser compounds are not

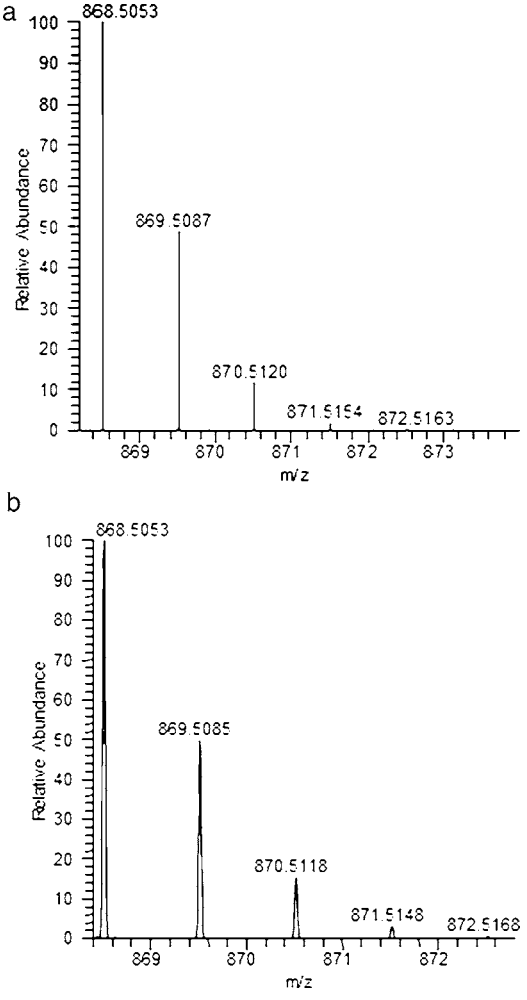

Figure 7. (a) Theoretical isotope pattern of solanine. (b) Measured isotope pattern of solanine.

reported here. The United States Department of Agriculture has set informal guidelines recommending the total glycoalkaloids concentration of potatoes for human consumption be no more than 200 ppm,[29] although no suggested limit could be found for animal feeds. This recommended limit in humans is thought to be too high by many researchers[26−30] and does not take into account various possible aggravating factors such as the synergistic effects of the solanine/chaconine ratio[26,29,31] and differences in species tolerance.[27] Also, the recommended 200

DOI: 10.1021/acs.jafc.5b00959
J. Agric. Food Chem. 2015, 63, 4790−4798

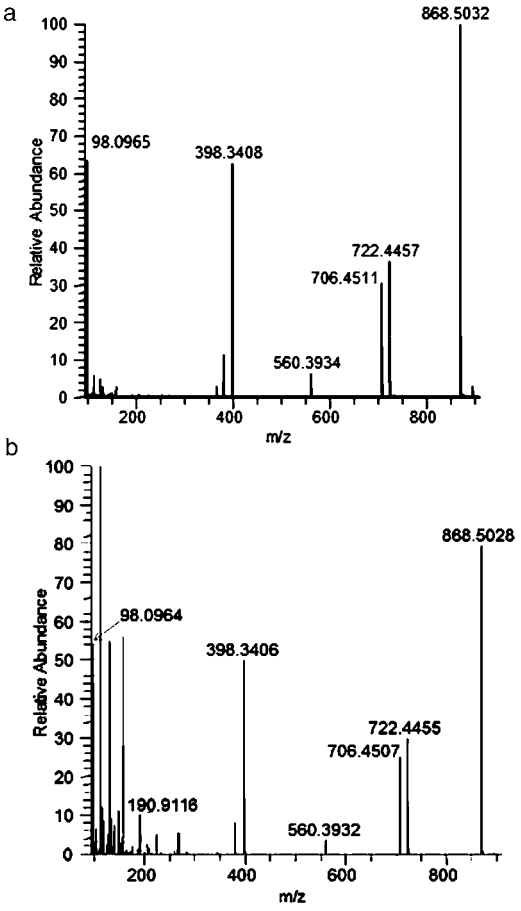

Figure 8. (a) Spectra of a 1 ppm solanine standard suspect dog food using HCD. (b) Spectra of suspect potato-containing dog food using HCD.

ppm limit refers to an acute dose of glycoalkaloids but does not address the effects of chronic toxicity of glycoalkaloids.[26,30] This chronic toxicity aspect of glycoalkaloids should be kept in mind when considering the following: (1) dog owners are often loyal to one brand of dog food; (2) this single brand of dog food may be the sole source of nutrition; and (3) the dog food may be bought in "bulk" quantities. The concentration of glycoalkaloids in the suspect dog food was 100 times lower than that suggested as safe by the USDA, but it cannot be ruled out as the offending substance because of its chronic toxicity in conjunction with the feeding habits of some dog owners.

Determination of Potato Glycoalkaloids in Dog Food Samples. Once it was determined that potato glycoalkaloids were the compounds of interest, further analysis (quantification and confirmation of identity) for these contaminants in dog food was performed using both the Orbitrap and a triple quadrupole LC-MS. For both mass spectrometers, a linear curve (i.e., $y = mx + b$) was constructed to calculate concentrations using fortified extracted matrix standards. Total glycoalkaloid concentrations (total of solanine and chaconine) ranged from approximately 5 ppm to 180 ppm in the six potato-containing dog foods tested (Table 2), and no glycoalkaloids were detected in the nonpotato-containing dog foods. Linearity (R^2) of all calibration curves, including those from the Sciex 5500 triple quadrupole, was greater than 0.992. Average recovery (using either precursor or product ion data) of solanine and chaconine in dog food samples fortified at 1.0, 1.25, 2.5, 5.0, and 10 ppm ranged from 101.6 to 98.8 (%RSD $\leq$ 20.6%, $n = 18$) for both compounds when calculated against a fortified extracted matrix curve. There was no statistical difference in recovery at the 95% confidence interval ($p \geq 0.71$) between the results generated using precursor or product ion data.

The quantitative and qualitative identification abilities of the single-stage Orbitrap was explored by comparing the data for glycoalkaloids in various potato samples generated by the Orbitrap to data generated by the Sciex 5500 triple quadruple LC-MS/MS. Extracted potato-containing dog food samples were prepared, and the final reconstituted sample was split in half; one sample was analyzed on the Orbitrap and the other on the Sciex 5500 system. There was no statistical difference in concentration results produced by the two instruments at the 95% confidence interval except for the solanine concentration in dog food sample no. 6 and both compounds in sample no. 4 (Table 2). The quantitative data generated by the Orbitrap's precursor ion peak area was compared to that generated by the most abundant product ion peak area of solanine and chaconine. There was no statistical difference at the 95% confidence interval except for one analytical run where the Orbitrap concentration calculation using the precursor ion differed from the calculation using the product ion by only 5.5%.

For both instruments used in this study, positive identification of solanine and chaconine was established by comparing product ion ratios of standards (average of solvent standards and fortified extracted dog food), commercial dog food samples, and fortified control dog food samples. Using the three precursor and three product ion transitions listed in Table 1, solanine and chaconine were confirmed in 99% of the 50 potato-containing dog food samples examined using FDA guidelines[24] and in 92% of samples using EU guidelines.[25] These samples included multiple potato-containing dog food samples analyzed unaltered ($n = 34$) and altered investigative dog food samples ($n = 16$) that had been fortified with various

Table 2. Solanine and Chaconine Concentrations in Potato-Containing Dog Food Samples

	solanine concentrations (m/z 868)				chaconine concentrations (m/z 852)			
	av (ppm)		%RSD (n)		av (ppm)		%RSD (n)	
	Orbitrap	5500	Orbitrap	5500	Orbitrap	5500	Orbitrap	5500
sample no. 1	2.7	2.7	6.5 (9)	2.6 (3)	2.6	2.7	7.4 (9)	1.4 (3)
sample no. 2	5.4	5.5	4.4 (5)	4.6 (3)	6.0	6.3	3.2 (5)	0.1 (3)
sample no. 3	13.3	13.5	1.9 (5)	1.7 (3)	12.3	13.1	4.4 (5)	0.1 (3)
sample no. 4	78.4	71.9	2.7 (5)	3.3 (3)	103.9	93.0	1.8 (5)	5.0 (3)
sample no. 5	9.7	10.2	6.0 (5)	4.6 (3)	14.0	15.5	10.7 (5)	1.2 (3)
sample no. 6	9.2	8.8	2.2 (5)	6.8 (3)	9.4	9.5	2.7 (5)	0.5 (3)

DOI: 10.1021/acs.jafc.5b00959
J. Agric. Food Chem. 2015, 63, 4790−4798

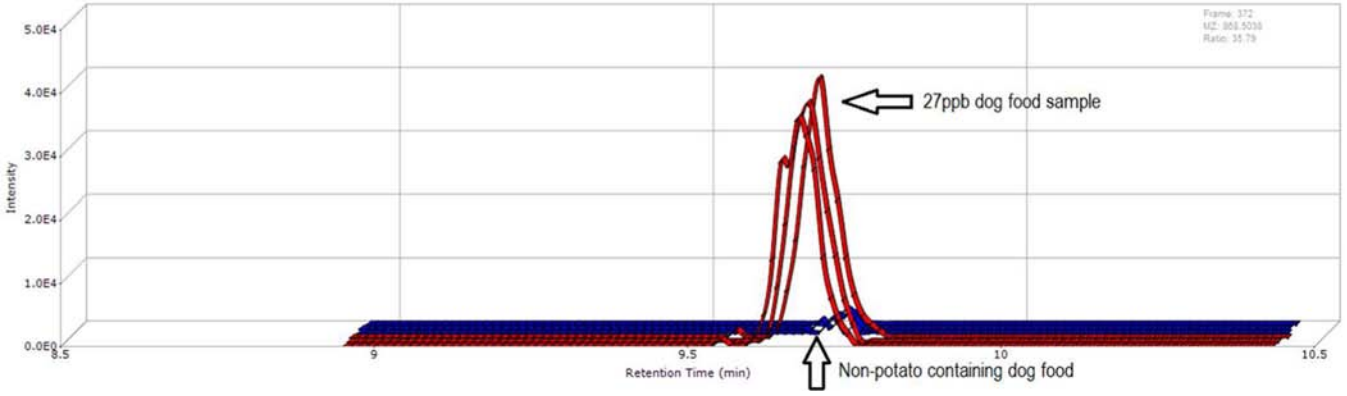

Figure 9. Sieve results for a dog food sample containing solanine at 27 ppb and a nonpotato-containing dog food.

glycoalkaloid standards or diluted with dog food extract previously shown to be free of glycoalkaloids. The concentrations of these altered/unaltered samples ranged from 0.01 to 180 ppm.

Finally, the "non-targeted search" capabilities of the Orbitrap/Sieve software combination to detect low levels of contaminants were further explored by analyzing extracts from fortified and positive samples with different concentrations of glycoalkaloids. To vary concentrations, two dilution schemes were tested: (1) dilution of potato-containing dog food sample extract with nonpotato-containing extract and (2) fortification of nonpotato-containing dog food sample with various amounts of glycoalkaloids prior to extraction. Both of these sample types were then compared to nonpotato-containing dog food samples. The resulting concentrations of diluted (no. 1 above) and fortified (no. 2 above) samples ranged from 2.7 to 500 ppb. The Sieve software was able to identify solanine and chaconine in all samples down to the 27 ppb level using either dilution scheme (Figure 9).

The single-stage Exactive performed well in this study, and the only possible drawback is the large amount of data generated by HRMS (both TOF and Orbitrap) instruments.[4,9,10] With targeted searches, the challenge lies in the time-consuming process of examining the data for false positive and false negative results.[32,33] Nontargeted searches, such as the one presented here using the Sieve differential analysis software, initially found 10 000 compounds, and this was the limit placed on the software by the user; however, more compounds could have been found by increasing the maximum limit. Both of these "data" problems must be addressed by instrument/software manufacturers before these instruments can reach their full potential.

The results presented here indicate the ability of the single-stage Orbitrap HRMS, and its associated differential analysis software, to compare two analytical sample extracts and determine what chemical compounds are unique to each sample at the ppb level. We have also shown that the Orbitrap is capable of correctly quantifying those compounds using the accurate mass extraction of either the precursor or major product ion.

AUTHOR INFORMATION

Corresponding Author

*E-mail: Jack.Lohne@fda.hhs.gov. Tel.: +1-303-236-9612.

Notes

The authors declare no competing financial interest.

REFERENCES

(1) Lehotay, S. J.; Mastovska, K.; Amirav, A.; Fialkov, A. B.; Alon, T.; Martos, P. A.; De Kok, Andre.; Fernandez-Alba, A. R. Identification and confirmation of chemical residues in food by chromatography-mass spectrometry and other techniques. *TrAC, Trends Anal. Chem.* **2008**, *27*, 1070−1090.

(2) Rochat, B. Quantitative/qualitative analysis using LC−HRMS: the fundamental step forward for clinical laboratories and clinical practice. *Bioanalysis* **2012**, *4*, 1709−1710.

(3) Malik, A. K.; Blasco, C.; Pico, Y. Liquid chromatography-mass spectrometry in food safety. *J. Chromatogr. A* **2010**, *1217*, 4018−4040.

(4) Katajamaa, M.; Oresic, M. Data processing for mass spectrometry-based metabolomics. *J. Chromatogr. A* **2007**, *1158*, 318−328.

(5) Maurer, H. H. What is the future of (ultra) high performance liquid chromatography coupled to low and high resolution mass spectrometry for toxicological drug screening? *J. Chromatogr. A* **2013**, *1292*, 19−24.

(6) Barbara, J.; Buckley, D. B.; Horrigan, M. J. Exploring the utility of high-resolution MS with post-acquisition data mining for simultaneous exogenous and endogenous metabolite profiling. *Bioanalysis* **2013**, *5*, 1211−1228.

(7) Everstine, K.; Spink, J.; Kennedy, S. Economically Motivated Adulteration (EMA) of Food: Common Characteristics of EMA Incidents. *J. Food Prot.* **2013**, *76*, 723−735.

(8) Wolnik, K. A.; Fricke, F. L.; Bonnin, E.; Gaston, C. M.; Satzger, R. D. The Tylenol tampering incident. *Anal. Chem.* **1984**, *56*, 466A−474A.

(9) Krauss, M.; Singer, H.; Hollender, J. LC-high resolution MS in environmental analysis: from targeted screening to the identification of unknowns. *Anal. Bioanal. Chem.* **2010**, *397*, 943−951.

(10) Favretto, D.; Pascali, J. P.; Tagliaro, F. New challenges and innovation in forensic toxicology: Focus on the "New Psychoactive Substances. *J. Chromatogr. A* **2013**, *1287*, 84−95.

(11) Kaufmann, A. The current role of high-resolution mass spectrometry in food analysis. *Anal. Bioanal. Chem.* **2012**, *403*, 1233−1249.

(12) Little, J. L.; Williams, A. J.; Pshenichnov, A.; Tkachenko, V. Identification of "known unknowns" utilizing accurate mass data and ChemSpider. *J. Am. Soc. Mass Spectrom.* **2012**, *23*, 179−185.

(13) Weiss, J. M.; Simon, E.; Stroomberg, G. J.; de Boer, R.; de Boer, J.; van der Linden, S. C.; Leonards, P. E. G.; Lamoree, M. H. Identification strategy for unknown pollutants using high-resolution mass spectrometry: Androgen-disrupting compounds identified through effect-directed analysis. *Anal. Bioanal. Chem.* **2011**, *400*, 3141−3149.

(14) Watson, D. G. The potential of mass spectrometry for the global profiling of parasite metabolomes. *Parasitology* **2010**, *137*, 1409−1423.

(15) Opperman, M.; Damoc, N. E.; Crone, C.; Moehring, T.; Muenster, H.; Hornshaw, M. High precision measurement and fragmentation analysis for metabolite identification. In *Methods in*

DOI: 10.1021/acs.jafc.5b00959
J. Agric. Food Chem. 2015, 63, 4790−4798

Molecular Biology; Plant Metabolomics: Methods and Protocols; Hardy, N. W., Halls, R. D., Eds.; Springer Science+Business Media: New York, 2012; Vol. *860*, p 145.
(16) Aronov, P. A.; Luo, F. J. G.; Plummer, N. S.; Quan, Z.; Holmes, S.; Hostetter, T. H.; Meyer, T. W. Colonic contribution to uremic solutes. *J. Am. Soc. Nephrol.* **2011**, *22*, 1769−1776.
(17) Antignac, J. P.; Courant, F.; Pinel, G.; Bichon, E.; Monteau, F.; Elliot, C.; Le Bizec, B. Mass spectrometry-based metabolomics applied to the chemical safety of food. *TrAC, Trends Anal. Chem.* **2011**, *30*, 292−301.
(18) Malysheva, S. V.; Arroyo-Manzanares, N.; Cary, J. W.; Ehrlich, K. C.; Vanden Bussche, J.; Vanhaecke, L.; Bhatnagar, D.; Di Mavungu, J. D.; De Saeger, S. Identification of novel metabolites from Aspergillus flavus by high resolution and multiple stage mass spectrometry. *Food Addit. Contam., Part A* **2014**, *31*, 111−120.
(19) Tarr, P. T.; Dryer, M. L.; Athanas, M.; Shahgholi, M.; Saarloos, K.; Second, T. P. A metabolomics based approach for understanding the influence of terroir in Vitis Vinifera L. *Metabolomics* **2013**, *9*, S170−S177.
(20) Zywicki, B.; Catchpole, G.; Draper, J.; Fiehn, O. Comparison of rapid liquid chromatography-electrospray ionization-tandem mass spectrometry methods for determination of glycoalkaloids in transgenic Weld-grown potatoes. *Anal. Biochem.* **2005**, *336*, 178−186.
(21) Shakya, R.; Navarre, D. A. LC-MS Analysis of Solanidane Glycoalkaloid Diversity among Tubers of Four Wild Potato Species and Three Cultivars (*Solanum tuberosum*). *J. Agric. Food Chem.* **2008**, *56*, 6949−6958.
(22) Stobieck1, M.; Matysiak-Kata, I.; Franski, R.; Skala, J.; Szopa, J. Monitoring changes in anthocyanin and steroid alkaloid glycoside content in lines of transgenic potato plants using liquid chromatography/mass spectrometry. *Phytochemistry* **2003**, *62*, 959−969.
(23) Hellenas, K.-E.; Branzell, C.; Johnsson, H.; Slanina, P. High levels of glycoalkaloids in the established Swedish potato variety magnum bonum. *J. Sci. Food Agric.* **1995**, *68*, 249−255.
(24) U.S. Food and Drug Administration (FDA). Center for Veterinary Medicine. *Guideline for industry: Mass spectrometry for confirmation of the identity of animal drug residues*. Federal Register (FR) No. 68 FR 25617; Center for Vetrinary Medicine, FDA: Laurel, MD, 2003; Vol. *68*, pp 25617−25618. http://www.fda.gov/cvm/guidance/guide118.pdf
(25) Commission Decision 2002/657/EC of 12 August 2002 implementing Council Directive 96/23/EC concerning performance of analytical methods and the interpretation of results. *Official Journal of the European Union*, 2002; *Vol.* 45, Legislation No. L221/8. http://eur-lex.europa.eu/legal-content/EN/ALL/?uri=CELEX:32002D0657.
(26) Smith, D. B.; Roddick, J. G.; Jones, J. L. Potato glycoalkaloids: some unanswered questions. *Trends Food Sci. Technol.* **1996**, *7*, 126−131.
(27) Slanina, P. Solanine (glycoalkaloids) in potatoes: toxilogical evaluation. *Food Chem. Toxicol.* **1990**, *28*, 759−761.
(28) Mensinga, T. T.; Sips, A. J. A. M.; Rompelberg, C. J. M.; van Twillert, K.; Meulenbelt, J.; van den Top, H. J.; van Egmond, H. P. Potato glycoalkaloids and adverse effects in humans: an ascending dose study. *Regul. Toxicol. Pharmacol.* **2005**, *41*, 66−72.
(29) Friedman, M.; Roitman, J. N.; Kozukue, N. Glycoalkaloid and calystegine content of eight potato cultivars. *J. Agric. Food Chem.* **2003**, *51*, 2964−2973.
(30) Korpan, Y. I.; Nazarenco, E. A.; Skryshevskaya, I. V.; Martelet, C.; Jaffrezic-Renault, N.; El skaya, A. V. Potato glycoalkaloids: true safety or false sense of security? *Trends Biotechnol.* **2004**, *22*, 147−151.
(31) Langkilde, S.; Mandimika, T.; Schroder, M.; Meyer, O.; Slob, W.; Peijnenburg, A.; Poulsen, M. A 28-day repeat dose toxicity study of steroidal glycoalkaloids, α-solanine and α-chaconine in Syrian Golden hamster. *Food Chem. Toxicol.* **2009**, *47*, 1099−1108.
(32) Kaufmann, A.; Butcher, p.; Maden, K.; Walker, S.; Widmer, M. Semi-targeted residue screening in complex matrices with liquid chromatography coupled to high resolution mass spectrometry: current possibilities and limitations. *Analyst* **2011**, *136*, 1898−1909.
(33) Turnipseed, S. B.; Lohne, J. J.; Storey, J. M.; Andersen, W. C.; Young, S. L.; Carr, J. R.; Madson, M. R. Challenges in implementing a screening method for veterinary drugs in milk using liquid chromatography quadrupole time-of-flight mass spectrometry. *J. Agric. Food Chem.* **2014**, *62*, 3660−3674.

DOI: 10.1021/acs.jafc.5b00959
J. Agric. Food Chem. 2015, 63, 4790−4798

JOURNAL OF AGRICULTURAL AND FOOD CHEMISTRY

Article

pubs.acs.org/JAFC

Development and Evaluation of a Monoclonal Antibody-Based Inhibition ELISA for the Quantification of Chymosin in Solution

O. Rolet-Répécaud,[†] C. Arnould,[†] D. Dupont,[‡,§] S .Gavoye,[∥] E. Beuvier,[†] and C. Achilleos*[,†]

[†]INRA, UR342 Technologie et Analyses Laitières, F-39800 Poligny, France

[‡]INRA, UMR1253 Science et Technologie Lait & Oeuf, F-35042 Rennes, France

[§]AGROCAMPUS OUEST, UMR1253 Science & Technologie Lait & Oeuf, F-35042 Rennes, France

[∥]ACTALIA, F-25620 Mamirolle, France

ABSTRACT: Chymosin is the major enzyme of natural rennet, traditionally used in cheese making for its high milk-clotting activity. For technical reasons, an accurate characterization of rennet should include its total clotting activity and also its enzymatic composition. Monoclonal antibodies specific to chymosin were obtained from mice immunized with purified bovine chymosin, and an inhibition enzyme-linked immunosorbent assay (ELISA) was developed for the quantification of chymosin in solution. No cross-reactivity was observed with other milk-clotting enzymes commonly used in cheese making. The limit of detection and limit of quantification were 125 and 400 ng/mL, respectively. The values of precision within and among runs were 7.23 and 7.39%, respectively, and satisfying recovery, from 92 to 119%, was found for spiked samples. The inhibition ELISA was successfully applied to commercial rennets, and the results were consistent with those obtained using the standard chromatographic method (IDF 110: A, 1987).

KEYWORDS: *chymosin, inhibition ELISA, monoclonal antibody, rennet*

INTRODUCTION

Chymosin (EC 3.4.23.4) is a neonatal gastric aspartic proteinase and is of commercial importance in cheese making. Chymosin is secreted in the abomasal mucosa of newborn ruminants during the first days of life. Its natural function is the hydrolysis of κ-casein once the milk is in the calf's stomach, leading to the formation of a coagulum that can be easily digested.

Once extracted from gastric tissues, chymosin and pepsin (EC 3.4.23.1) constitute the main clotting enzymes of calf, kid, and lamb rennets. In cheese technology, rennet is traditionally added to the vat during the first stage of cheese making to coagulate the milk. Chymosin hydrolyses the Phe^{105}–Met^{106} bond of κ-casein which stabilizes the casein micelles and thereby induces an aggregation reaction leading to a gel and a phase separation of the milk into cheese curd and whey. A fraction of the added chymosin is retained in the curd,[1] which, in most types of cheese, catalyzes the slower hydrolysis of other peptide bonds in casein.[2,3] In the dairy industry, milk-clotting enzymes are characterized by their milk-clotting activity (MCA) and their general proteolytic activity. The ratio between those two properties gives an overview of the essential quality of a milk-clotting enzyme. Only the enzymes with a high MCA/general proteolytic activity ratio are considered suitable for cheese manufacturing; high levels of nonspecific proteolysis lead to a weak gel structure, high losses of protein and fat in the whey, and reduced cheese yield.[4] Depending on technological factors for cheese making, residual active enzymes remain in the curd and can affect cheese maturation and its final quality of flavor/texture.[1,4] In comparison to other milk-clotting enzymes, chymosin is superior in combining a high MCA with a low general proteolytic activity. Chymosin represents >90% of the MCA of a good-quality calf rennet, the remaining activity being due to pepsin.[5]

Rennets available on the market have different values for cheese making because of their enzymatic composition. The relative proportion of the enzymes varies, depending on the age of the animal and its diet. In rennets extracted from young milk-fed calves, chymosin represents 88–94% of the clotting enzymes and pepsin represents 6–12%, whereas pepsin predominates in extracts from older fodder-eating bovines.[6] Rennets are generally prepared from multiple calf stomachs and are heterogeneous in their chymosin content and chymosin/pepsin ratio. Moreover, chymosin and pepsin have different reaction rates in their specific hydrolysis of κ-casein and show quite different effects in their proteolytic action during cheese ripening.[7] Therefore, for economic and quality reasons, the most important parameters of rennet to be analyzed are the MCA and the composition, i.e., the nature and the concentration of the enzymes. To define a rennet accurately, information should be given on its total MCA with its chymosin/pepsin ratio or its composition in active chymosin and pepsin. Today, the total MCA of a bovine rennet is determined according to an international standard method[8] and is expressed in international milk-clotting units (IMCU). For commercialization in France, current regulations require the MCA to be expressed in milligrams of active enzyme, chymosin, and pepsin per liter[9] to give information on the enzyme composition whereas IMCU expresses a global activity.

Received: February 23, 2015
Revised: April 17, 2015
Accepted: April 23, 2015
Published: April 23, 2015

ACS Publications © 2015 American Chemical Society

DOI: 10.1021/acs.jafc.5b00990
J. Agric. Food Chem. 2015, 63, 4799–4804

The enzyme composition has been determined with different methods based on spectrophotometric measurements of the proteolytic activities,[10] chromatographic separation with MCA determination,[11] selective inactivation,[12] and rocket immunoelectrophoresis.[13] More recently, rennets have been characterized by high-performance liquid chromatography (HPLC)[14] and by mass spectrometry.[15] The conventional method for the enzymatic characterization of rennets is a chromatographic one.[9,16,17] First, a desalted sample of rennet is separated by chromatography into two fractions, chymosin and pepsin. Then, the MCA of each of the separated enzymes is measured and converted to weight contents of chymosin and pepsin calculated in percentages[16,17] or in mg of active enzyme/L.[9] Despite being sensitive, the chromatographic method is time-consuming with laborious pretreatment procedures.

Antibodies have widely been used as analytical tools in various methods developed for the detection and quantification of proteins, enzymes, vitamins, allergenic ingredients, and contaminants such as toxins, pesticides, and drugs in food.[18] Immunoassays are easy to perform, rapid, with a large number of samples analyzed at the same time, and give very high sensitivity and specificity, in particular when based on monoclonal antibodies (mAbs). The high specificity of these methods decreases the need for thorough cleanup; therefore, sample-preparation procedures in immunoassays are generally rather simple. Furthermore, mAbs have the advantage of a continuous supply of constant quality.

The aim of the present study was to produce and characterize mAbs specific to bovine chymosin. An mAb-based inhibition enzyme-linked immunosorbent assay (ELISA) specific to the quantification of chymosin in solution was developed. The described assay was applied to the analysis of rennet samples and compared to the IDF standard method (chromatography and MCA measurement)[16] to assess its applicability to the direct quantification of chymosin. Moreover, inhibition ELISA may allow measurements of low chymosin concentrations in complex matrices such as milk, whey, and cheese curd in order to determine chymosin inactivation according to cheese-making steps and its remaining activity in the cheese curd, provided that an efficient method of enzyme extraction is developed.

MATERIALS AND METHODS

Chemicals and Samples. Analytical-grade chemicals were purchased from VWR International (Fontenay-sous-Bois, France). Purified chymosin (rennin from calf stomach) and porcine pepsin were purchased from Sigma-Aldrich (Saint Louis, MO, USA). Calf, kid, and lamb rennets, recombinant chymosin, bovine pepsin, and microbial coagulants were obtained from different suppliers (Chr. Hansen, Denmark; Danisco, Denmark; Laboratoires ABIA, France; Laboratoire Central des Présures S.A.S., France; and Österreichische Laberzeugung Hundsbichler GmbH, Austria).

Production, Purification, and Isotyping of mAbs. Immunization with chymosin was carried out by the foot pad route according to Jeanson et al.[19] Lyophilized chymosin (1.2 mg/mL in 10 mM phosphate-buffered saline pH 7.2 (PBS)) was 1.5-fold diluted in physiological water in order to obtain a 800 μg protein/mL solution. This solution was then emulsified 1:1 (v/v) in Freund adjuvant (Difco Laboratories, Detroit, MI, USA), complete for the first immunization, incomplete for the booster injection 14 days later. Fifty microliters of the emulsion (i.e., 20 μg of proteins) were injected into two female BALB/c mice (Iffa-Credo, St-Germain sur l'Arbresle, France) per foot pad. Three days after the booster injection, popliteal lymph nodes from immunized mice were removed and pooled. Lymphocytes were fused in a 5:1 ratio with Sp2/O-Ag14 myeloma cells using filter fusion according to Buttin et al.[20] Poly(ethylene glycol) (PEG 1000, Merck Millipore, Darmstadt, Germany) was allowed to permeate monolayers of mixed cells adsorbed on membrane filters. The fused cells were propagated in an azaserine/hypoxanthine (AH) selection medium containing 10% horse serum (Life Technologies SAS, Saint-Aubin, France) and plated in 48-well microculture plates incubated at 37 °C with a 6% CO_2 atmosphere. Culture supernatants of resulting hybridomas were collected during the log growth phase of cells and screened for the presence of antibodies that recognized chymosin by indirect ELISA. To avoid cross-reactivity, secreting hybridomas were also screened for bovine and porcine pepsins by indirect ELISA. Selected positive hybridomas were subsequently subcloned by the limiting dilution method and then cryopreserved in liquid nitrogen.

The ascites from the selected clones were obtained according to Jones et al.[21] and purified by a saturated ammonium sulfate (SAS) precipitation followed by affinity chromatography. Briefly, 75 g of ammonium sulfate were dissolved in 100 mL of distilled water at 80 °C and cooled. Four volumes of SAS were added drop to drop with gentle stirring to 6 volumes of ascite. Stirring was continued at 4 °C for at least 60 min; then the mixture was centrifuged at 3220*g* for 6 min at 4 °C. The supernatant was removed, and the precipitated fraction was suspended in 5 volumes of 100 mM phosphate buffer, 150 mM NaCl, pH 7.4. Then, 5 volumes of SAS were added as previously described, followed by a centrifugation at 3220*g* for 6 min at 4 °C. The supernatant was removed, and finally the precipitated fraction of immunoglobulins was suspended in 4 volumes of 100 mM phosphate buffer, 150 mM NaCl, pH 7.4. The resultant solution was dialyzed overnight at 4 °C in a dialysis bag (molecular weight cutoff 10 kDa) against 1000 volumes of 10 mM PBS, 150 mM NaCl.

To purify mAbs, affinity chromatography was used with a HiTrap NHS-activated HP column (GE Healthcare Bio-Sciences, Uppsala, Sweden) as described by Muller-Renaud et al.[22] Briefly, 50 mg of chymosin in 5 mL of coupling buffer (200 mM $NaHCO_3$, 500 mM NaCl, pH 8) were covalently immobilized on the column. Any excess active groups were deactivated by washing with 500 mM ethanolamine, 500 mM NaCl, pH 8.3, and the nonspecifically bound ligands were washed out with 100 mM acetate, 500 mM NaCl pH 4. One milliliter of ascitic fluid prepurified by SAS precipitation, diluted in 7 mL of running buffer (50 mM PBS, pH 7.3), was then injected. The column was washed with running buffer. Antichymosin mAbs were eluted with 10 mM glycine-HCl buffer, pH 2.1, and the eluted fraction was neutralized by the addition of 1:15 (v/v) 1 M Tris-HCl, pH 9. The purified mAbs were then divided into aliquots and stored at −20 °C. The isotypes of the produced mAbs were determined by a mouse monoclonal antibody isotyping kit (RD-Biotech, Besançon, France) according to the manufacturer's instructions.

All animals were maintained in accordance with the French Ministry of Agriculture ethical guidelines for the care and use of laboratory animals (B 21 231 010 EA).

Characterization of mAbs. *By Indirect ELISA.* Culture supernatants were screened by indirect ELISA to assess their specificity for chymosin and their possible cross-reactivity against other milk-clotting enzymes: rennets from different animal sources (calf, kid, and lamb), recombinant chymosin, bovine and porcine pepsins, and microbial coagulants. Microtiter plates (NUNC F96 Maxisorp, 4000 Roskilde, Denmark) coated with 100 μL/well of milk-clotting enzymes (1 μg/mL in 100 mM sodium bicarbonate buffer, pH 9.6 (CB)) were incubated for 90 min at 37 °C. The remaining binding sites were blocked by incubation with 10 g/L gelatin (Merck Millipore, Darmstadt, Germany) in PBS 0.05% Tween 20 (PBS-T) (250 μL/well) for 1 h at 37 °C. Culture supernatants (100 μL/well) previously diluted 1:2 in PBS-T were then added. After 1 h of incubation at 37 °C, 100 μL/well of donkey antimouse immunoglobulin alkaline phosphatase conjugate (Jackson Immunoresearch, Interchim, Montluçon, France) diluted 1:3000 in PBS-T were added. Bound immunoglobulins were detected after 1 h of incubation at 37 °C. Between each incubation step, the plate was rinsed four times for 15 s with PBS-T (250 μL/well) using a HydroFlex microplate washer (TECAN, Männedorf, Switzerland). Finally, 100 μL/well of *p*-nitrophenyl phosphate (Interchim, Montluçon, France) containing 1 g/L of a solution of 1 M diethanolamine-HCl, 1 mM $MgCl_2$, and 0.1

DOI: 10.1021/acs.jafc.5b00990
J. Agric. Food Chem. 2015, 63, 4799−4804

mM zinc acetate were added to the wells. After 30 min, the absorbance at 405 nm ($A_{405\,nm}$) was read against a blank (substrate only) using a NanoQuant Infinite F200 Pro microplate spectrophotometer (TECAN, Männedorf, Switzerland).

By Western Blotting. Chymosin and milk-clotting enzymes were subjected to sodium dodecyl sulfate polyacrylamide gel electrophoresis (SDS-PAGE) using a 12% acrylamide Novex Tris-glycine gel (Life Technologies SAS, Saint-Aubin, France) according to the manufacturer's instructions. All samples were reduced before analysis using 100 mM DL-dithiothreitol and loaded onto each lane (10 μg/lane). Electrophoresis was performed at 125 V, variable intensity, for 2 h at 10 °C in 25 mM Tris, 192 mM glycine, 0.1% SDS buffer, pH 8.4. Precision Plus Protein Kaleidoscope standards (Life Technologies SAS, Saint Aubin, France) were used as the molecular-weight standard. Immediately after separation, proteins were transferred onto a 0.2-μm-pore-size nitrocellulose membrane (Protran BA83 NC, Whatman GE Healthcare Life Sciences − Europe GmbH, Velizy-Villacoublay, France) for immunoblotting using a TE22 Mighty Small Transfer Tank (Hoefer, Inc., Holliston, MA, USA) at 100 V, variable intensity, for 70 min at 10 °C in 25 mM Tris, 200 mM glycine, 0.01% SDS buffer in 200 mL/L ethanol. The immunodetection was performed as described by Dupont et al.[23]

By Biacore. Real-time binding assays between purified chymosin and purified mAbs were performed using a Biacore 3000 optical biosensor (GE Healthcare Life Sciences − Europe GmbH, Velizy-Villacoublay, France) equipped with a carboxymethyl-dextran-coated (CM5) research-grade sensor chip. The experiments were performed at 21 °C in HBS-EP running buffer (GE Healthcare Life Sciences). Standard amine coupling[24] was used to covalently immobilize rabbit antimouse antibodies (RAM) (GE Healthcare Life Sciences) at a final density of 10 000 response units (RUs). First, mAbs (20 μL) were injected over the RAM surface, and then 20 μL of purified chymosin, 1 mg/mL in HBS-EP buffer, was injected over the flow cell and were able to bind to mAbs in a continuous, pulse-free, controlled flow at a flow rate of 20 μL/min. Data were collected during the 60 s association and 100 s dissociation phases. Regeneration of the chip was achieved with 5 μL of 10 mM glycine-HCl buffer, pH 1.7. A flow cell saturated with 1 M ethanolamine was used as a reference for background subtraction and to check for nonspecific binding. Data analysis was performed using BIAevaluation v3.2 software (GE Healthcare Life Sciences). The binding ability of an mAb toward chymosin was defined as the percentage of chymosin bound compared to the theoretical maximum binding capacity of the mAb (R_{max}).[25]

Reactivity against Active Chymosin. The specificity of mAbs against active chymosin was evaluated by indirect ELISA against heat-treated rennet samples. Two different rennets, A and B, pH adjusted to 6.54, were split into four aliquots (500 μL). One aliquot was used as reference, and the other three aliquots were submitted to a heat treatment by incubation in a block heater (Lab-line, Thermo Fisher Scientific Inc., Ashville, NC, USA): 60 °C/2 min 30 s; 80 °C/2 min, and 100 °C/2 min. For each aliquot, indirect ELISA was performed as described previously, and the MCA was estimated as described in ref 9.

Quantitative Inhibition ELISA. ELISA plates NUNC F96 Maxisorp were coated with 1 μg/mL chymosin in CB (100 μL/well) and incubated for 1 h at 37 °C. Blocking of the remaining binding sites was performed as previously described. Serial dilutions of a rennet of known chymosin concentration (determined according to an IDF standard[16]) in PBS-T were used as standards (concentrations ranging from 0 to 20 000 ng/mL). The chymosin standards or the samples diluted in PBS-T (150 μL) were incubated in test tubes with 150 μL of purified antichymosin mAb (1:10 000 in PBS-T) for 1 h at 37 °C. The mixture (100 μL/well) was then added to the ELISA plate and further incubated for 1 h at 37 °C. The plate washing steps, the revelation of the reaction, and the measurement of the absorbance were performed as already described. The standard curve was obtained by plotting the $A_{405\,nm}$ obtained from each standard against its chymosin concentration (ng/mL). The unknown concentration of chymosin in samples was calculated from the standard curve and adjusted for the dilution factor. Each sample concentration resulted from the mean of three diluted samples analyzed in duplicate.

Validation of the Assay. Immunoassay validation was performed using the limit of detection (LOD), the limit of quantification (LOQ), the precision, and the accuracy. LOD and LOQ were expressed as the chymosin concentration corresponding to the average measured content of 20 blank samples plus 3 or 10 times the standard deviation (SD) of the average value, respectively.[26] The precision was expressed as the relative standard deviation (RSD), measured as the % ratio between the standard deviation of independent results and their mean value. It was estimated with independent results obtained by the same operator in 1 day on 10 successive analyses of the same rennet sample (intra-assay RSD) and on 12 analyses of the same rennet sample in a small time interval (interassay RSD). The interassay RSD was calculated for a low-chymosin rennet (179 mg/L) and a high-chymosin rennet (676 mg/L). All measurements were made in duplicate at three different dilutions. The accuracy was measured as the recovery of exogenous amounts of chymosin, 22, 45, 90, 225, and 450 mg/L, added to a rennet sample (179 mg/L). The accuracy was expressed as the % recovery between the ELISA value and the theoretical value ((detected concentration/concentration of added chymosin) × 100).

Statistical Analyses. Chymosin concentrations in commercial rennet samples determined by IDF standard chromatography[16] and inhibition ELISA were evaluated and compared using Deming regression analysis and the paired samples *t* test (Analyze-it 3.90.2, Analyze-it Software Ltd., U.K.). For Deming regression, the intercept value reflects the constant bias and the slope reflects the proportional bias. Agreement was considered to be good if the 95% confidence interval (CI) of the intercept and slope included 0 and 1, respectively.

RESULTS AND DISCUSSION

mAbs Production and Characterization. One fusion experiment yielded 847 hybridomas. Screening by chymosin-coated indirect ELISA allowed a selection of 42 clones which secreted chymosin-specific mAbs. These clones were used for further investigations based on mAbs specificity. The mAbs tested were of IgG isotypes: 60% IgG1, 20% IgG2a, and 20% IgG2b.

Cross-Reactivity Measurements. Cross-reactivity of mAbs was evaluated by indirect ELISA and immunoblotting against purified chymosin and other milk-clotting enzymes commonly used in cheese making: rennets extracted from different animal sources (calf, kid, and lamb), recombinant chymosin, bovine pepsin, porcine pepsin, and microbial coagulants. Specific mAbs recognized chymosin present in rennets from all of the different animal sources (calf, kid, and lamb) and in recombinant chymosins whereas no cross-reactivity was detected with bovine and porcine pepsins and microbial coagulants with both methods. As observed by immunoblotting (Figure 1), specific mAbs recognized a protein band of 35 kDa, which coincided well with the expected size of chymosin. mAbs also recognized minor bands between 35 and 25 kDa which were identified as degraded chymosin in rennets and recombinant chymosins.[27] These results indicated that mAbs were specific to chymosin whatever its source and thus were suitable for use in the immunoassay.

Binding Interactions between mAbs and Chymosin. To investigate the binding ability of selected mAbs to chymosin, mAbs were screened with a Biacore 3000 optical biosensor. An overview of the assay is shown in Figure 2. Late binding, at the end of the association phase, gives information about the affinity of chymosin for the bound mAb. Late stability, at the end of the dissociation phase, corresponds to the stability of the interaction between chymosin and the bound mAb. The best mAb for further ELISA development should present a high affinity for chymosin with a slow dissociation rate. The binding

DOI: 10.1021/acs.jafc.5b00990
J. Agric. Food Chem. 2015, 63, 4799−4804

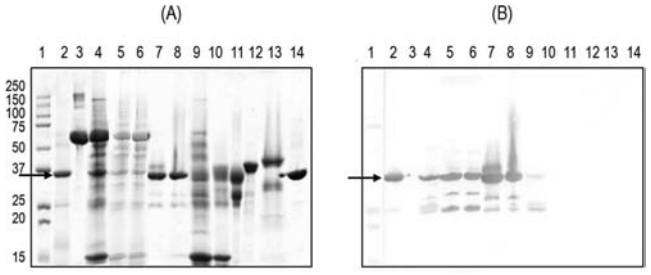

Figure 1. mAbs specificity was characterized by immunoblotting. (A) SDS-PAGE of different milk-clotting preparations. The amount of sample loaded onto each lane of the 12% gel was 10 μg. (B) Western immunoblot of the fractions obtained in (A) incubated with antichymosin mAb (1:1500). Band 1, protein molecular weight marker (kDa); band 2, purified chymosin (highlighted by an arrow); band 3, bovine serum albumin; band 4, calf rennet; band 5, lamb rennet; band 6, kid rennet; bands 7 and 8, recombinant chymosin; band 9, bovine pepsin/chymosin extract; bands 10 and 11, bovine pepsin; band 12, porcine pepsin; bands 13 and 14, microbial coagulants.

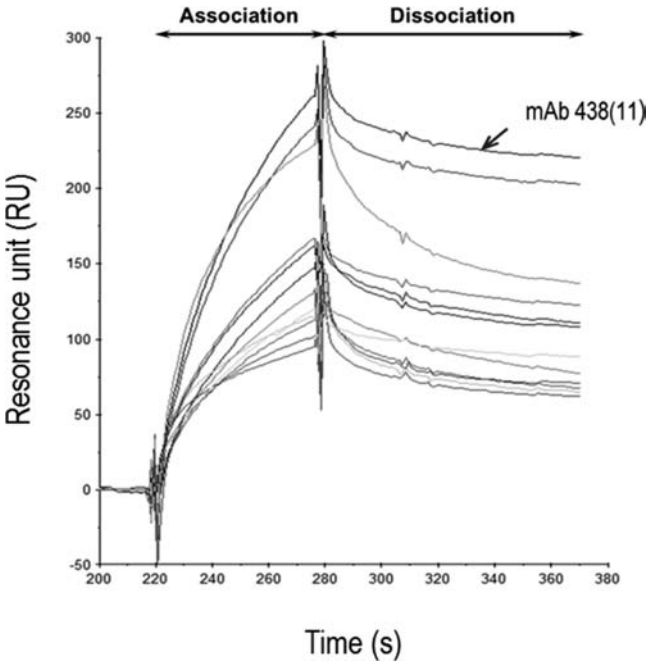

Figure 2. Association and dissociation curves for purified chymosin (1 mg/mL) binding to different mAbs. mAbs were bound to rabbit antimouse antibodies immobilized on a Biacore CM5 sensor chip. Data were collected during the 60 s association and the 100 s dissociation phases. In the association phase, chymosin interacts with the bound mAbs. In the dissociation phase, the complex resulting from the interaction starts to dissociate.

ability of mAbs was calculated from the binding of purified chymosin in percent of maximum theoretical binding, R_{max}. Assuming that the interaction between chymosin and mAb is monovalent, the binding abilities of the tested mAbs varied between 23.03 and 139.80% R_{max}. All tested mAbs were shown to bind to chymosin, but some mAbs had low binding abilities. Values >100% R_{max} may be attributed to the mass transport effect between the chymosin in the flow and the mAbs immobilized on the surface of the sensor chip which can potentially perturb the 1:1 interaction. Only mAbs with a binding ability of >85% R_{max} were kept for further analyses.

Thermal Inactivation of Chymosin. The MCA was affected by the temperature. Holding the rennet at 60 °C for 2 min 30 s decreased its MCA. The clotting time was higher for heat-treated rennet samples: 2.25 and 1.97-times higher for rennet A and B, respectively. A 2 min heating at 80 and 100 °C totally inactivated chymosin: no coagulation was observed after 6 h 30 min for both rennets. The optimum temperature for the coagulation of milk by calf rennet at pH 6.6 is around 45 °C.[5] Indirect ELISA performed on heat-treated rennets showed that the different mAbs tested were specific to chymosin in its active form (Figure 3). The absorbance decreased for high temperatures, 80 and 100 °C. At these temperatures, the inactivated chymosin was not detected by the different mAbs in rennet A but was partially detected in rennet B.

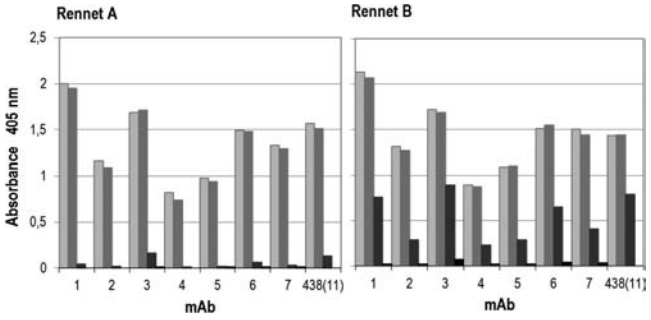

Figure 3. Reactivity of antichymosin mAbs evaluated by indirect ELISA against two different rennets submitted to heat treatment. (Light-gray) not heated; (medium-gray) 60 °C/2 min 30 s; (dark-gray) 80 °C/2 min; (black) 100 °C/2 min. The pH of rennet samples was adjusted to 6.54.

Finally, one positive clone named mAb 438(11) was selected for the development of the inhibition ELISA. This selected mAb was of the IgG1 isotype. It showed a high specificity for chymosin according to indirect ELISA and immunoblotting and a high binding ability toward chymosin according to Biacore results: 98.84% R_{max}.

Characteristics of the Assay. The assay was validated by investigating the LOD, the LOQ, the precision, and the accuracy. The standard curve for the quantification of chymosin was obtained from serial dilutions of a rennet of known chymosin concentration (Figure 4). A good linear correlation between $A_{405\,nm}$ and the chymosin concentration was represented by $A_{405\,nm}$ = 1.093−0.0005[chymosin], R^2 = 0.882, in the range of 200−2000 ng/mL. The LOD and LOQ were 125 and 400 ng chymosin/mL, respectively. The precision was measured by the relative standard deviation (RSD) of samples within and among runs. The RSDs within runs and among runs were 7.23 and 7.39%, respectively, for both low- and high-chymosin rennets, which indicated that there were minimum variations between wells and limited day-to-day variability. The assay had good precision values. Moreover, the level of precision of the immunoassay remained competitive compared to the standard chromatography: 7 vs 5%.[17] ELISA recovery values of chymosin from the spiked rennet samples ranged from 92 to 119% (Figure 5) with a mean recovery value of 102% for a chymosin range from 22 to 450 mg/L. Inhibition ELISA gave acceptable recovery efficiency. These results demonstrated the potential application of immunoassay for the quantification of chymosin in solution.

Application to Commercial Rennets. To assess the applicability of inhibition ELISA for quantification of chymosin

DOI: 10.1021/acs.jafc.5b00990
J. Agric. Food Chem. 2015, 63, 4799−4804

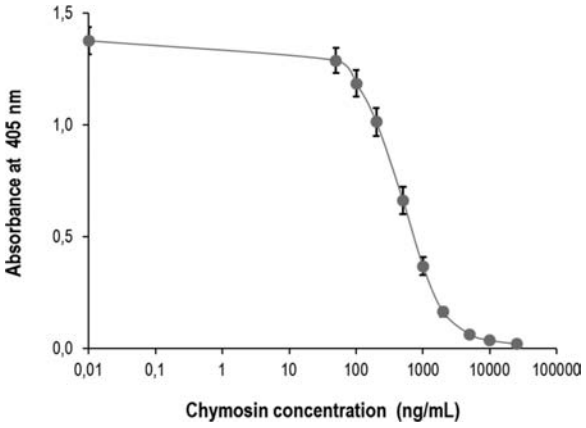

Figure 4. Representative chymosin standard curve obtained with the optimized ELISA. Data are summarized from seven independent curves generated over a 1 month period. The error bar represents the standard deviation of the mean.

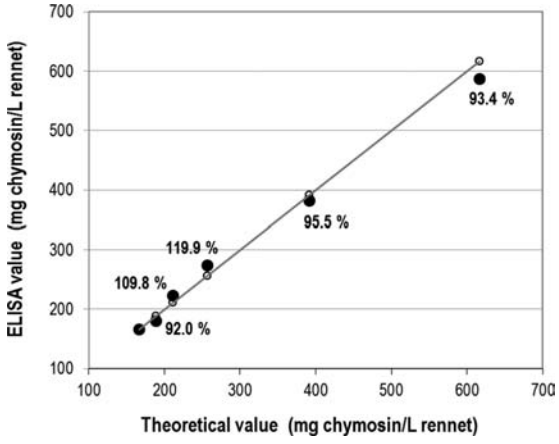

Figure 5. Recovery of chymosin (%) from artificially spiked rennet samples determined by ELISA. Five different amounts of chymosin (22, 45, 90, 225, and 450 mg/L) were added to a rennet sample.

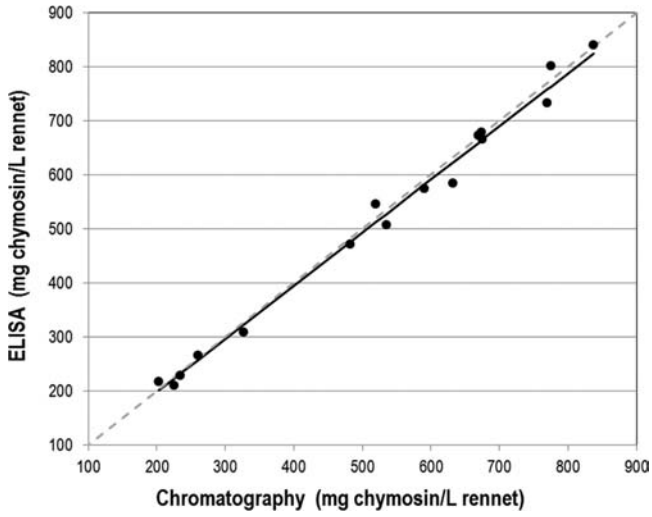

Figure 6. Deming regression fit between chymosin concentrations (mg/L) measured by inhibition ELISA and chromatography in different rennet samples. Sixteen commercial rennets over the range of 200 to 840 mg chymosin/L representative of the diversity available on the market were analyzed. The black line represents the fitted regression line ($[\text{chymosin}]_{\text{ELISA}} = 1.004 + 0.984\text{-}[\text{chymosin}]_{\text{chromatography}}$), and the dotted gray line represents the identity line (methods equal).

Table 1. Correlation between the Developed Immunoassay and the Standard Chromatographic Method by Deming Regression

parameter	estimate	jackknife 95% CI[a]	jackknife SE[a]	p value[b]
slope	0.984	0.922 to 1.045	0.029	0.575
intercept	1.004	−29.25 to 31.26	14.107	0.944

[a]Confidence intervals (CI) and standard errors of the parameter estimates (SE) were calculated with the jackknife (leave one out resampling) method. [b]Significantly equal to 1 (slope) and 0 (intercept): $p > 0.05$.

in solution, 16 commercial rennets, with low and high chymosin contents representative of the diversity available on the market, were analyzed. The concentration of chymosin in the samples was determined with both inhibition ELISA and standard chromatography.[16] Concentrations obtained by ELISA were statistically similar to concentrations obtained with the standard chromatographic method (Figure 6) using the Deming regression analysis, which considers both methods to be subject to measurement error whereas simple regression allows only the immunoassay concentration to be measured with error.[28] The Deming regression equation between ELISA and chromatography results was $[\text{chymosin}]_{\text{ELISA}} = 1.004 + 0.984[\text{chymosin}]_{\text{chromatography}}$ ($R^2 = 0.995$). The 95% CI for the slope and the intercept contained the values 1 ($p = 0.575$) and 0 ($p = 0.944$), respectively (Table 1). In addition to the Deming regression analysis, a comparative evaluation test was carried out to measure how different the immunoassay and the chromatographic method are. A paired-samples t test was performed with the following results: $t(15) = 1.34$, $p = 0.200$. These results indicated that there was no significant difference at the 5% significance level between the two methods. These statistical results indicated that the developed inhibition ELISA could be useful in quantifying chymosin in solution without any pretreatments and that it provided a noticeable advantage over methods requiring laborious pretreatment procedures.

In conclusion, a hybridoma cell line secreting mAbs specific to chymosin was obtained, and chymosin-specific mAbs were used to develop an inhibition ELISA for the quantification of chymosin in solution. The immunoassay has been characterized, optimized, and validated using rennet samples. The comparison of the developed inhibition ELISA with the reference chromatographic method showed the potential of the immunoassay. It provides a versatile alternative tool with high sample throughput and with no pretreatment of the sample for a direct quantification of chymosin, unlike the reference method which is a two-step method with time-consuming pretreatment procedures. Besides, work is underway to quantify (1) bovine pepsin in solution by ELISA in order to completely characterize rennets regarding their enzymatic composition and (2) residual chymosin in cheese by ELISA in order to characterize its remaining activity in the cheese.

AUTHOR INFORMATION

Corresponding Author

*Tel: 33 3 84 73 63 00. Fax: 33 3 84 37 37 81. E-mail: Christine.Achilleos@poligny.inra.fr.

DOI: 10.1021/acs.jafc.5b00990
J. Agric. Food Chem. 2015, 63, 4799−4804

Funding

This work was supported by funding from the Direction Régionale de l'Alimentation, de l'Agriculture et de la Forêt Franche-Comté (Besançon, France), and the Centre National Interprofessionnel de l'Economie Laitière (CNIEL, Paris, France).

Notes

The authors declare no competing financial interest.

■ ACKNOWLEDGMENTS

We thank M. H. Duployer (INRA UR342, URTAL Poligny, France) for technical assistance and R. Berges and C. Belloir (INRA UMR1324, CSGA, Dijon, France) for providing access to the animal housing facility and the cell culture laboratory.

■ ABBREVIATIONS USED

$A_{405\ nm}$, absorbance at 405 nm; CB, bicarbonate buffer; CI, confidence interval; ELISA, enzyme-linked immunosorbent assay; IDF, International Dairy Federation; IMCU, international milk-clotting unit; mAb, monoclonal antibody; MCA, milk-clotting activity; PBS, phosphate-buffered saline; RAM, rabbit antimouse; RU, response unit; SAS, saturated ammonium sulfate

■ REFERENCES

(1) Bansal, N.; Fox, P. F.; McSweeney, P. L. H. Comparison of the level of residual coagulant activity in different cheese varieties. *J. Dairy Res.* **2009**, *76*, 290−293.

(2) Sousa, M. J.; Ardö, Y.; McSweeney, P. L. H. Advances in the study of proteolysis during cheese ripening. *Int. Dairy J.* **2001**, *11*, 327−345.

(3) Upadhyay, V. K.; McSweeney, P. L. H.; Magboul, A. A. A.; Fox, P. F. Proteolysis in Cheese during Ripening. In *Cheese: Chemistry, Physics and Microbiology*, 3rd ed.; Fox, P. F., McSweeney, P. L. H., Cogan, T. M., Guinee, T. P., Eds.; Elsevier Academic Press: Amsterdam, Netherlands, 2004; Vol. *1*, 391−433.

(4) Jacob, M.; Jaros, D.; Rohm, H. Recent advances in milk clotting enzymes. *Int. J. Dairy Technol.* **2011**, *64*, 14−33.

(5) Fox, P. F.; Guinee, T. P.; Cogan, T. M.; McSweeney, P. L. H. Enzymatic Coagulation of Milk. *Fundamentals of Cheese Science*; Aspen Publishers, Inc.: Gaithersburg, MD, 2000; pp 98−137.

(6) Robinson, R. K.; Wilbey, R. A. Coagulants and Precipitants. In *Cheesmaking Practice*, 3rd ed.; Scott, R., Robinson, R. K., Wilbey, R. A., Eds.; Springer: New York, 1998; pp 146−164.

(7) Pirisi, A.; Pinna, G.; Addis, M.; Piredda, G.; Mauriello, R.; De Pascale, S.; Caira, S.; Mamone, G.; Ferranti, P.; Addeo, F.; Chianese, L. Relationship between the enzymatic composition of lamb rennet paste and proteolytic, lipolytic pattern and texture of PDO Fiore Sardo ovine cheese. *Int. Dairy J.* **2007**, *17*, 143−156.

(8) Standard IDF 157A/ISO 11815. Milk - Determination of total Milk-Clotting Activity in Bovine Rennets. 1997.

(9) Journal Officiel de la République Française. Méthode Officielle d'Analyse pour la Détermination de la Teneur en Chymosine et en Pepsine Bovines. 1981.

(10) Visser, S.; Rollema, H. S.; Friedenthal, M. K.; Van Alebeek, G. J. Spectrophotometric method for the determination of chymosin and pepsin in calf and adult bovine rennets. *Netherlands Milk Dairy J.* **1988**, *287*, 221−232.

(11) Martin, P.; Collin, J. C.; Garnot, P.; Ribadeau Dumas, B.; Mocquot, G. Evaluation of bovine rennets in terms of absolute concentrations of chymosin and pepsin A. *J. Dairy Res.* **1981**, *48*, 447−456.

(12) Mulvihill, D. M.; Fox, P. F. Selective denaturation of milk coagulants in 5 M-Urea. *J. Dairy Res.* **1977**, *44*, 319−324.

(13) Rothe, G. A. L.; Harboe, M. K.; Martiny, S. C. Quantification of milk-clotting enzymes in 40 commercial bovine rennets, comparing rocket immunoelectrophoresis with an activity ratio assay. *J. Dairy Res.* **1977**, *44*, 73−77.

(14) Rampilli, M.; Larsen, R.; Harboe, M. Natural heterogeneity of chymosin and pepsin in extracts of bovine stomachs. *Int. Dairy J.* **2005**, *15*, 1130−1137.

(15) Lilla, S.; Caira, S.; Ferranti, P.; Addeo, F. Mass spectrometric characterisation of proteins in rennet and in chymosin-based milk-clotting preparations. *Rapid Commun. Mass Spectrom.* **2001**, *15*, 1101−1112.

(16) Standard IDF 110A. Milk and Milk Products - Calf Rennet and Adult Bovine Rennet - Determination by Chromatography of Chymosin and Bovine Pepsin Contents. 1987.

(17) Standard IDF 110B/ISO 15163. Milk and Milk Products - Calf Rennet and Adult Bovine Rennet - Determination by Chromatography of Chymosin and Bovine Pepsin Contents. 2012.

(18) Samarajeewa, U.; Wei, C. I.; Huang, T. S.; Marshall, M. R. Application of immunoassay in the food industry. *Crit. Rev. Food Sci. Nutr.* **1991**, *29*, 403−434.

(19) Jeanson, S.; Dupont, D.; Grattard, N.; Rolet-Répécaud, O. Characterization of the Heat Treatment Undergone by Milk Using Two Inhibition ELISAs for Quantification of Native and Heat Denatured α-Lactalbumin. *J. Agric. Food Chem.* **1999**, *47*, 2249−2254.

(20) Buttin, G.; LeGuern, G.; Phalente, L.; Lin, E. C.; Medrano, L.; Cazenave, P. A. Production of hybrid lines secreting monoclonal anti-idiotypic antibodies by cell fusion on membrane filters. *Curr. Top. Microbiol. Immunol.* **1978**, *81*, 27−36.

(21) Jones, S. L.; Cox, J. C.; Pearson, J. E. Increased monoclonal-antibody ascites production in mice primed with Freund incomplete adjuvant. *J. Immunol. Methods* **1990**, *129*, 227−231.

(22) Muller-Renaud, S.; Dupont, D.; Dulieu, P. Development of a biosensor immunoassay for the quantification of alpha(S1)-casein in milk. *J. Dairy Res.* **2005**, *72*, 57−64.

(23) Dupont, D.; Arnould, C.; Rolet-Repecaud, O.; Duboz, G.; Faurie, F.; Martin, B.; Beuvier, E. Determination of bovine lactoferrin concentrations in cheese with specific monoclonal antibodies. *Int. Dairy J.* **2006**, *16*, 1081−1087.

(24) Johnsson, B.; Löfås, S.; Lindquist, G. Immobilization of proteins to a carboxymethyldextran-modified gold surface for biospecific interaction analysis in surface plasmon resonance sensors. *Anal. Biochem.* **1991**, *198*, 268−277.

(25) Dupont, D.; Johansson, A.; Marchin, S.; Rolet-Repecaud, O.; Marchesseau, S.; Leonil, J. Topography of the Casein Micelle Surface by Surface Plasmon Resonance (SPR) Using a Selection of Specific Monoclonal Antibodies. *J. Agric. Food Chem.* **2011**, *59*, 8375−8384.

(26) Feinberg, M. La validation des méthodes d'analyse. *Le Cahier Techniques l'INRA* **2000**, *44*, 19−49.

(27) Rolet-Répécaud, O.; Berthier, F.; Beuvier, E.; Gavoye, S.; Notz, E.; Roustel, S.; Gagnaire, V.; Achilleos, C. Characterization of the non-coagulating enzyme fraction of different milk-clotting preparations. *LWT - Food Sci. Technology* **2013**, *50*, 459−468.

(28) Linnet, K. Evaluation of Regresion Procedures for Methods Comparison Studies. *Clin. Chem.* **1993**, *39*, 424−432.

DOI: 10.1021/acs.jafc.5b00990
J. Agric. Food Chem. 2015, 63, 4799−4804

JOURNAL OF AGRICULTURAL AND FOOD CHEMISTRY

Article

pubs.acs.org/JAFC

Comparison of Milk Oligosaccharides Pattern in Colostrum of Different Horse Breeds

E. Difilippo,[†] H. A. M. Willems,[†] J. C. Vendrig,[‡] J. Fink-Gremmels,[‡] H. Gruppen,[†] and H. A. Schols*[,†]

[†]Laboratory of Food Chemistry, Wageningen University , P.O. Box 17, 6700 AA Wageningen, The Netherlands

[‡]Faculty of Veterinary Medicine, Institute for Risk Assessment Sciences, Subdivision of Veterinary Pharmacology, Pharmacotherapy, and Toxicology, Utrecht University, 3584 CM Utrecht, The Netherlands

Supporting Information

ABSTRACT: Colostrum oligosaccharides are known to exhibit prebiotic and immunomodulatory properties. Oligosaccharide composition is species-specific, and equine colostrum has been reported to contain unique oligosaccharides. Therefore, equine oligosaccharides (EMOS) from colostrum from different horse breeds were analyzed by CE-LIF, CE-MS^n, HILIC-MS^n, and exoglycosidase degradation. Sixteen EMOS were characterized and quantified, of which half were neutral and half were acidic. EMOS showed about 63% structural overlap with human milk oligosaccharides, known for their bioactivity. Seven EMOS were not reported before in equine oligosaccharides literature: neutral Gal(β1−4)HexNAc, Gal(β1−4)Hex-Hex, β4′-galactosyllactose, and lactose-*N*-hexaose, as well as acidic 6′-Sialyl-Hex-Ac-HexNAc, sialyllacto-*N*-tetraose-a, and disialylacto-*N*-tetraose (isomer not further specified). In all colostrum samples, the average oligosaccharide concentration ranged from 2.12 to 4.63 g/L; with β 6′and 3′- galactosyllactose, 3′-sialyllactose, and disialyllactose as the most abundant of all oligosaccharides (27−59, 16−37, 1−8, and 1−6%, respectively). Differences in presence and in abundance of specific EMOS were evident not only between the four breeds but also within the breed.

KEYWORDS: *milk, CE-MS, HILIC-MS, exoglycosidases, mass analysis, chromatography*

INTRODUCTION

Mammalian milk and colostrum contain many structures, which are essential for the nutrition and health of the suckling neonate. Throughout the past decades, specific oligosaccharides, which have been identified in milk and colostrum, have been shown to beneficially affect health.[1] For example, human milk oligosaccharides (HMOS) carrying the so-called bifidogenic factor (Gal(β1−3)GlcNAc) have been illustrated to enhance the growth of bifidobacteria in the intestine of neonates.[2] When bifidobacteria selectively ferment HMOS, they produce short-chain fatty acids (SCFA), leading to a pH decrease in the intestine. The lowered pH in the intestine creates a less favorable environment for the growth of the pathogens and stimulates the production of mucin, which in turn, enhances the host's resistance to infections.[3] The production of SCFA also leads to a stimulation of the immune system through a direct interaction with the immune cells of the intestine.[3,4] Moreover, increasing evidence has come forward to demonstrate direct immunomodulatory properties of oligosaccharides derived from milk and colostrum. Some properties could derive from interaction with specific receptors on intestinal epithelial cells and immune cells, such as carbohydrate receptors and Toll-like receptors.[4−6] In addition, milk oligosaccharides serve as soluble ligands for pathogens, preventing viral and bacterial attachment to the intestinal mucosa.[5]

The core structure of mammalian milk oligosaccharides (MMOs) is, in most cases, a lactose unit (Gal(β1−4)Glc) at the reducing end. However, in cow's, horse's, and goat's milk, *N*-acetyllactosamine (Gal(β1−4)GlcNAc) is also found at the reducing end instead of the lactose unit.[7,8] Starting from these disaccharides, glycosyltransferases can elongate the core structure with neutral and charged sugars. The neutral sugars that can be attached to the core structure are D-galactose (Gal), L-fucose (Fuc), *N*-acetylglucosamine (GlcNAc), and with the exception of HMOS, also *N*-acetylgalactosamine (GalNAc).[7]

The charged sugars that can decorate the core structure are sialic acids, both *N*-acetyl- and *N*-glycolyl-neuraminic acids, and glucose or *N*-acetylglucosamine substituted with one phosphoric group (e.g., in milk oligosaccharides of horses and cattle).[7−9] Depending on the linkage present in their chains, the MMOs are divided into two groups: Type I group contains Gal(β1−3)GlcNAc, and Type II group contains Gal(β1−4)GlcNAc.[10]

The reported mature-milk oligosaccharide concentration is 12−13 g/L for human milk and approximately 0.05 g/L for cow's milk.[8,11] The oligosaccharide concentration in colostrum is higher than the concentration in mature milk: 24 g/L in human colostrum and more than 1 g/L in cattle's colostrum.[7,12] So far, 43 equine milk oligosaccharides (EMOS) have been reported, of which 31 are neutral and 12 are acidic.[7,8,13] Compared to the HMOS, the EMOS have a higher degree of sialylation (20−30% and 60%, respectively)[11] and a lower degree of fucosylation (70% and 5%, respectively).[11] The previously documented EMOS showed a 17% overlap with oligosaccharides present in human milk. Although not reported so far, the presence and relative abundance of individual EMOS

Received: March 3, 2015
Revised: April 29, 2015
Accepted: April 30, 2015
Published: April 30, 2015

ACS Publications © 2015 American Chemical Society

DOI: 10.1021/acs.jafc.5b01127
J. Agric. Food Chem. 2015, 63, 4805−4814

may vary between individual animal breeds, comparable to the variations in HMOS in different human populations.[14−16]

This study focuses on the analysis of EMOS in colostrum samples of four different horse breeds: Dutch Warmblood horse, Shetland pony, Crossbred Arabian/New Forest pony, and Friesian horse. After isolation from the colostrum samples, the EMOS were identified and quantified, highlighting the interbreed (EMOS for the different horse breeds) and the intrabreed (EMOS for the same breed) variations.

MATERIALS AND METHODS

Materials. Colostrum samples of horses belonging to four different breeds were obtained from private Dutch owners with consent. Five colostrum samples were available for the Crossbred Arabian/New Forest pony (Nederlands Rijpaarden and Pony Stamboek), four colostrum samples were available for the Dutch Warmblood horse (Royal Warmblood Studbook of The Netherlands), two colostrum samples were available for the Friesian horse, and one colostrum sample was available for the Shetland pony. Each colostrum was collected within 12 h postpartum and frozen (−20 °C) until use.

The standards 3′-, and 6′-sialyllactose, 3′-, and 6′-sialyl-*N*-acetyllactosamine, lacto-*N*-tetraose, sialyllacto-*N*-tetraose-a, and lacto-*N*-hexaose were purchased from Dextra Laboratories (Reading, U.K.). The standards β 3′-, 4′- , and 6′-galactosyllactose, lacto-*N*-tetraose, and lacto-*N*-neotetraose were bought from Carbosynth (Compton, U.K.). The labeling of the oligosaccharides was accomplished using the Carbohydrate Labeling and Analysis Kit (Beckman Coulter, Fullerton, CA, U.S.A.). All other chemicals used were of analytical grade. Millipore water (Millipore, Darmstadt, Germany) was referred to as water in the text.

Extraction of Equine Colostral Sugars. The Dutch Warmblood colostrum samples were available in larger quantities than those of other breeds. Therefore, a mixture of the Dutch Warmblood colostrum samples was used to optimize the extraction method and to obtain enough material to be loaded in the preparative Size Exclusion Chromatography. Specifically, 1.25 mL of each colostrum sample was pooled together and mixed with a vortex for 2 min. After method optimization, EMOS were extracted from 1 mL of the 12 individual colostrum samples. The optimized sugar extraction from the colostrum samples was performed by modification of the method of Nakamura et al.[13] Briefly, colostrum (5 mL) was treated with 4 volumes of chloroform. After 2 h of head over tail mixing, the sample was centrifuged (5000*g*, 30 min, 5 °C), and the supernatant was treated with 2 volumes of methanol. After the same mixing and centrifugation procedure, the methanol−water solution was concentrated by vacuum evaporation. The remaining water solution was freeze-dried.

Purification and Fractionation of EMOS. Size Exclusion Chromatography (SEC) was used to remove lactose from the extracted carbohydrates of the pooled Dutch Warmblood colostrum, in order to obtain pools containing EMOS with difference degrees of polymerization (DP). In total, four pools were obtained, and they were analyzed for the characterization of the EMOS. The fractionation was carried out at 35 °C on three Superdex 30 Hiload 26/60 preparative grade columns (GE Healthcare, Pittsburgh, PA, U.S.A.) connected in series on a AKTA Purifier (GE Healthcare). After manual injection, the EMOS (200 mg) were eluted with water containing 0.5% (v/v) EtOH and collected in 9 mL fractions. The fractions were pooled as follows: pool 1: 290−492 mL, pool 2: 493−688 mL, pool 3: 689−730 mL, and pool 4: 731−758 mL. Using water solution as eluent, charged oligosaccharides were excluded from the column material and were eluted first. Neutral oligosaccharides were instead fractionated based on their size. Lactose and monomers were the last to be eluted and were excluded from further analysis. The neutral oligosaccharides were pooled according to the retention times shown by a mixture of neutral galacto-oligosaccharides (DP from 1 to 6) (Vivinal GOS syrup) (FrieslandCampina Domo, Borculo, The Netherlands), which was considered a reference for its retention time. After freeze-drying, the resulting powders were rehydrated with 1 mL of water prior to analysis.

Solid Phase Extraction (SPE) was used to reduce the lactose content from the 12 individual colostrum samples. The extracted carbohydrates (1 mg) were solubilized in 1 mL of water and loaded onto activated graphitized carbon cartridge (150 mg bed weight, 4 mL tube size; Grace, Deerfield, IL, U.S.A.). Elution with water (1.5 mL) was used to remove salts, and 2% (v/v) acetonitrile (ACN) (1.5 mL) was used in order to elute monomers and lactose. The EMOS, still bound to the graphitized carbon cartridge, were recovered with 1.5 mL of 40/60% (v/v) ACN/water solution containing 0.05% (v/v) trifluoroacetic acid. The obtained EMOS were dried overnight under a stream of nitrogen and subsequently solubilized in 0.5 mL of water.

Capillary Electrophoresis with Laser-Induced Fluorescent and Mass Spectrometry Detection. The EMOS fractionated either by SEC or SPE were labeled with a fluorescent label (9-aminopyrene-1,4,6-trisulfonate, APTS) for their analysis by capillary electrophoresis (CE) with laser-induced fluorescence (LIF) detection as reported previously with minor modifications.[17] Briefly, 100 μL of sample containing 5 nmol of xylose, as internal standard, was dried and labeled with APTS. Each oligosaccharide standard (10 nmol), containing 5 nmol of xylose, was labeled with the APTS and run together with the EMOS samples. The labeled samples were diluted 40 times before the analysis. The experiment was performed using a ProteomeLab PA 800 system (Beckman Coulter), equipped with a LIF detector (Beckman Coulter). During the run, the sample was loaded hydrodynamically (7 s at 0.5 psi) into a polyvinyl alcohol (NCHO) coated capillary (50 μm × 50.2 cm (Beckman Coulter). Resultant peaks were integrated manually using Chromeleon software 6.8 (Dionex, Sunnyvale, CA, U.S.A.). In the CE technique, the oligosaccharides are linked in a molar ratio of 1:1 with the fluorescent, negatively charged label (APTS). The resulting migration times of the linked oligosaccharides depend on their size and on their net charge.

The SEC-fractionated, labeled EMOS were also analyzed for their masses by the PA 800 plus system (Beckman Coulter) coupled to a Velos Pro mass spectrometer (LTQ Velos Pro ion trap MS, Thermo Scientific, Waltham, MA, U.S.A.), after 20 times dilution. The CE-MS^n experiment conditions were performed as reported by Albrecht et al.[18]

HILIC-ESI-MS^n. The EMOS pools, derived from SEC, were also analyzed through hydrophilic interaction liquid chromatography (HILIC) with mass spectrometry detection (MS^n) as described by Remoroza et al. with some minor modifications.[19]

Briefly, an Accela UHPLC system (Thermo Scientific) coupled to a mass spectometer (LTQ Velos Pro ion trap MS, Thermo Scientific) was used. The chromatographic separation was performed on an Acquity HILIC BEH Amide column (1.7 μm, 2.1 mm × 150 mm) combined with a Van Guard precolumn (1.7 μm, 2.1 mm × 5 mm; Waters Corporation, Milford, MA, U.S.A.). The acquisition time was 72 min, and the eluents had a flow rate of 600 μL/min. The injection volume was 5 μL. The composition of the three mobile phases were (A) water with 1% (v/v) ACN, (B) 100% (v/v) ACN and (C) 200 mM ammonium formate (pH 3.0). The elution program was performed as follows: 2 min isocratic 80% B; 58 min linear gradient from 80% to 30% B; followed by 12 min of column washing with a linear gradient from 30% to 20% B and column re-equilibration form 20 to 80% B. The eluent C was kept at 5% during the elution.

Exoglycosidase Degradation. To determine the linkage type of the sialic acid decorating the EMOS, two types of sialidases were used: Sialidase S and Sialidase T (ProZyme, Hayward, CA, U.S.A.). Sialidase S is specific for the α2−3 linked neuraminic acid, while Sialidase T splits α 2−3 and α 2−6 linked neuraminic acid. For the structural analysis of the neutral EMOS Glyco(β1−3)galactosidase, Glyco(β1−4)galactosidase, Glyco(β1−4,6)galactosidase, and Glykoβ-*N*-acetylhexosaminidase (ProZyme) were used. All reactions were performed as suggested by the manufacturer. After the enzyme degradation at 37 °C overnight, the solutions were centrifuged (5000*g*, 5 min, 25 °C), and the supernatants were analyzed by HILIC-MS^n.

Quantification of the EMOS. In CE-LIF, the quantification of the oligosaccharides was enabled by the use of an internal standard and by a 1:1 stoichiometry between the oligosaccharide and the APTS

DOI: 10.1021/acs.jafc.5b01127
J. Agric. Food Chem. 2015, 63, 4805−4814

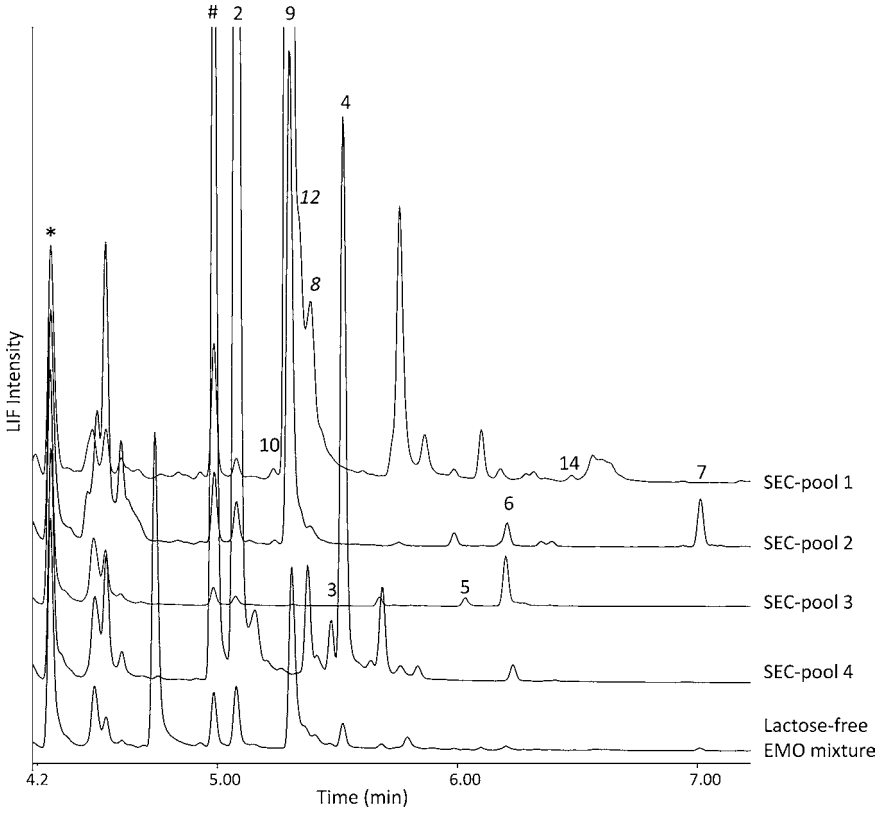

Figure 1. CE-LIF electropherograms of lactose-free EMO mixture and the EMO SEC pools 1−4. *: Internal standard xylose, #: Lactose, 1−14: identified peaks as named in Table 1

molecule. A linear correlation between concentration and CE-LIF peak area has been shown.[17] CE-LIF peak areas were converted to the corresponding EMOS nanomoles and their concentrations in the colostrum samples (g/L). The samples were run in duplicate, and the quantification was validated with the help of labeled neutral and acidic oligosaccharides standards. The quantification of 3′-sialyl-*N*-acetyllactosamine (3′-SLN) and Gal(β1−4)Hex-Hex, annotated by HILIC-MS^n and not assigned in the CE-LIF electropherograms, was performed with HILIC-MS^n. A calibration curve was made based on the peak areas in mass spectrometry of the 3′-SLN and β 4′-galactosyllactose (β 4′-GL) standards, respectively. The curves fitting the 3′-SLN and β 4′-GL standards had a linear correlation with R^2 of 0.997 and 0.998, respectively.

RESULTS AND DISCUSSION

Structural Characterization of the Equine Milk Oligosaccharides. In order to elucidate the structure of the EMOS, a colostrum mixture was prepared using Dutch Warmblood colostrum. After sugar extraction, part of the oligosaccharides was fractionated using Size Exclusion Chromatography (SEC). A lactose-free EMO mixture was obtained pooling part of the SEC fractions. Lactose-free EMO mixture and four SEC pools obtained were labeled with the fluorescent dye APTS and subsequently analyzed by CE-LIF and CE-MS^n.

In Figure 1, CE electropherograms of labeled lactose-free EMO mixture and SEC pools are shown. The migration times of labeled EMOS were compared with available standards and with HMOS elution patterns, which have been described in literature.[20] In total, 24 peaks were counted of which 11 peaks were annotated (numbers 2−14, Figure 1). Together with remaining lactose after SEC (symbol #, Figure 1), the annotation of five oligosaccharides was confirmed by CE-MS^n analysis. Acidic oligosaccharides were the first eluted from the SEC columns, and they were mainly pooled in pool 1. Pool 2 contained sialyllactose together with neutral pentamer and hexamer oligosaccharides. Pool 3 and pool 4 contained neutral tetramer and trimer, respectively.

In the CE-MS^2, the APTS-labeled oligosaccharides showed a specific fragmentation behavior due to the fluorescent molecule attached at their reducing end and a multiple charge state in their fragments spectrum. One example of CE-MS^n identification is given for lacto-*N*-novo-pentaose I, previously identified in equine milk, and shown in Figure 2.[8,21] APTS-lacto-*N*-novo-pentaose I loses one terminal galactose yielding a APTS-tetramer fragment, with m/z 573 and m/z 382, having charge states −2 and −3, respectively. The APTS-tetramer fragment loses a terminal galactose producing the fragment GlcNAc-Gal-Glc-APTS with m/z 492 and 328, having charge states −2 and −3, respectively. The GlcNAc-Gal-Glc-APTS subsequently forms APTS-lactose, with m/z 391, having charge state −2, via the loss of the terminal *N*-acetyl-glucosamine. From the fragmentation of the APTS-lactose, a molecule of APTS-glucose was formed, with m/z 310, having charge state −2.

In order to enhance the characterization of the EMOS, the mass analysis was also performed with HILIC-MS^n with non-labeled oligosaccharides obtained after SEC fractionations. With this technique, five more EMOS were annotated. All found molecules had a charge state of −1. One example for HILIC-MS^n identification of 3′-sialyl-*N*-acetyllactosamine (3′-SLN) is shown in Figure 3. Two peaks are highlighted for the sialyl-*N*-acetyllactosamine (Figure 3a). The highest peak refers to 3′-SLN, while the lowest peak refers to 6′-SLN. Each of the molecules were found as a double peak. It is hypothesized that

DOI: 10.1021/acs.jafc.5b01127
J. Agric. Food Chem. 2015, 63, 4805−4814

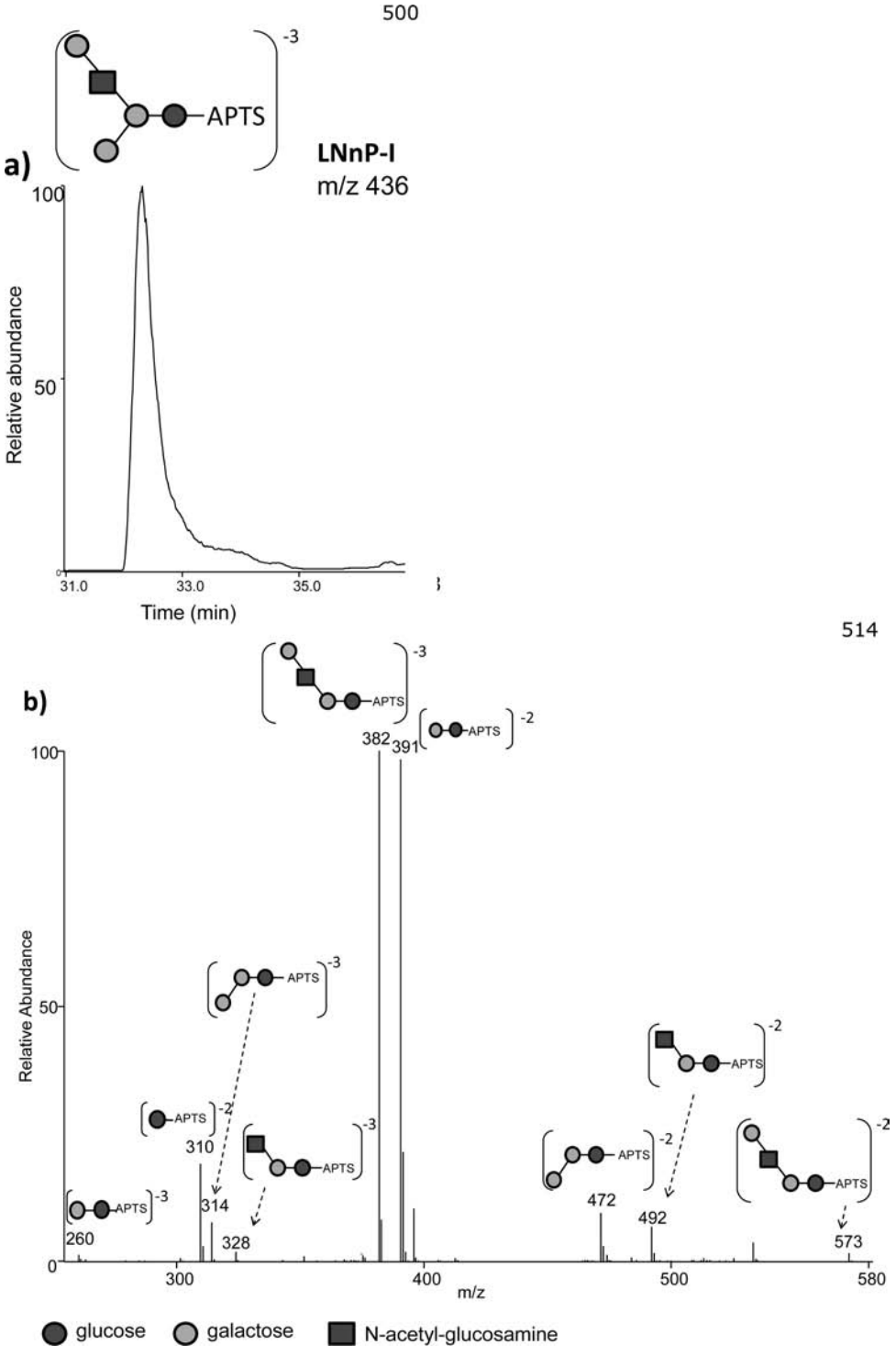

Figure 2. Selected base peak for the lacto-*N*-novo-pentaose-I (LNnP-I) in CE-MSn as present in lactose-free EMO mixture (a). Corresponding MS2 fragmentation patterns and structural composition of LNnP-I (b). m/z 436 precursor ion in CE-MS^n. [−2], [−3]: charge state of the molecules formed after fragmentation.

the double peaks correspond to the α/β conformation of the reducing end.[22] The MS^2 fragmentation of the 3′-SLN was compared with existing literature and with MS^2 fragmentation of available standard.[23] The 3′-SLN loses water (Figure 3b), forming thereby the fragment with m/z 655. A characteristic intraring fragmentation of the molecule leads to the formation of the fragment with m/z 572. The fragment with the highest intensity refers to the *N*-acetylneuraminic acid, with m/z 290.

With respect to four milk oligosaccharides, enzymatic degradation was necessary to determine their linkages. The neutral dimer Gal(β1−4) HexNAc and the trimer Gal(β1−4)Hex-Hex could be characterized only by using Glyco-galactosidases specific for β1−3, 1−4, and 1−4, 6 linkages, in addition to using the Glykoβ-*N*-acetylhexosaminidase. The acidic 6′-sialyl-Hex[Ac]-HexNAc and 3′-sialyllacto-*N*-tetraose a (LSTa), could be characterized only by using Sialidase S

DOI: 10.1021/acs.jafc.5b01127
J. Agric. Food Chem. 2015, 63, 4805−4814

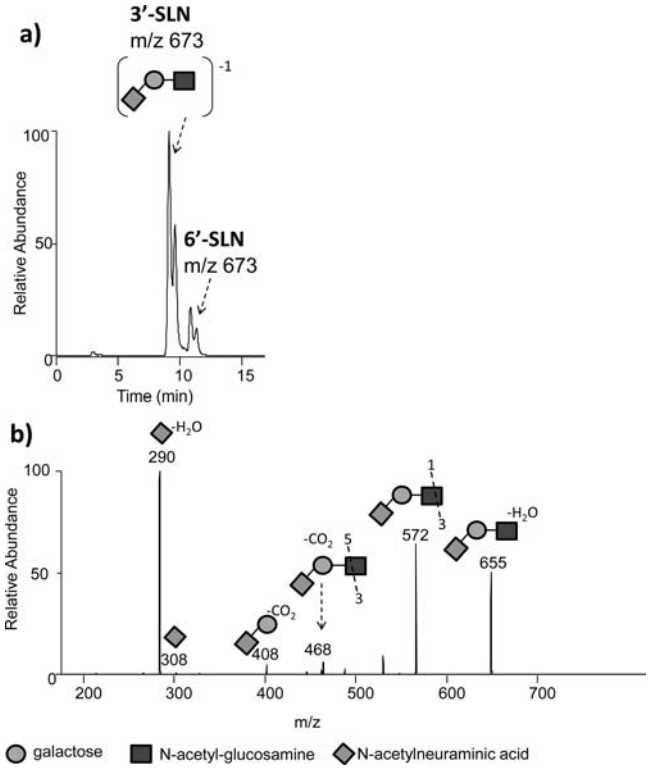

Figure 3. Selected base peak for the 3′-sialyl-*N*-acetyllactosamine (3′-SLN) in HILIC-MS^n as present in lactose-free EMO mixture (a). Corresponding MS^2 fragmentation patterns and structural composition of 3′-SLN as found in the lactose-free EMO mixture (b). *m*/*z* 673 precursor ion in HILIC-MS^n. [−1]: charge state of molecules.

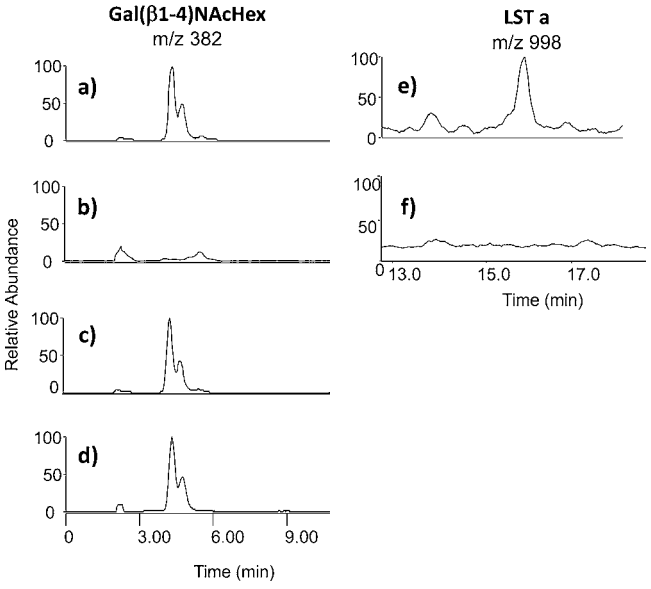

Figure 4. Selected base peak for the Gal(*β*1−4)HexNAc in HILIC-MS^n (a) as present in lactose-free EMO mixture. Corresponding base peak after degradation by Glyco-galactosidases specific for *β*1−4 linkage (b), by Glyco-galactosidases specific for *β*1−3 linkage (c), by Glyko*β*−*N*-acetylhexosaminidase (d). Selected base peak for the 3′-sialyllacto-*N*-tetraose-a (LSTa) in HILIC- MS^n as present in lactose-free EMO mixture (e). Corresponding base peak after degradation by Sialidase S specific for the *α*2−3 linkage (f). *m*/*z* 382 precursor ion for Gal(*β*1−4)HexNAc in HILIC-MS^n; *m*/*z* 998 precursor ion for LSTa in HILIC-MS^n.

(specific for the *α*2−3 linked *N*-acetylneuraminic acid), Sialidase T (specific for *α*2−3 and 6 linked *N*-acetylneuraminic acid), and Glyko*β*-*N*-acetylhexosaminidase. After their enzyme degradation, the samples were analyzed by HILIC-MS^n. As an example, Figure 4 illustrates the enzymatic degradation of Gal(*β*1−4)HexNAc and LSTa prior to analysis by HILIC-MS^n. The Gal(*β*1−4)HexNAc was found as double peak (Figure 4a), as consequence of *α*/*β* conformation of the reducing end. Using the enzymes tested, Gal(*β*1−4)HexNAc was digested by Glyco(*β*1−4)galactosidase (Figure 4b), while neither Glyco-(*β*1−3)galactosidase nor Glyko-*N*-acetylhexosaminidase showed any activity, indicating the presence of a *β*1−4 linked, terminal galactose. The LST molecule, as found in the mare colostrum samples, was digested by Sialidase S (Figure 4f), proving the presence of a terminal *N*-acetylneuraminic acid *α* 2−3 linked. Moreover, the identification of LSTa was confirmed by its migration time in CE, similar to commercially available LSTa standard (Table S1, Supporting Information).

Through the combination of CE and HILIC mass analysis and enzyme degradation of the SEC pools, it was possible to identify 16 EMOS. All identified EMOS are listed in Table 1, and an overview of methods used in order to characterize them (CE migration time, mass over charge values, and retention times in CE-MS^n, and HILIC-MS^n, and enzymes) are described in Supporting Information (Table S1). Comparing the outcomes of this study with previous data, seven EMOS were not reported previously and were presented in Table 1 in **bold**: the neutral oligosaccharides Gal(*β*1−4)HexNAc, Gal(*β*1−4)Hex-Hex, *β*4′-galactosyllactose, and lactose-*N*-hexaose, as well as the acidic oligosaccharides 6′-sialyl-Hex-Ac-HexNAc, LSTa, and disialylacto-*N*-tetraose (isomer not further specified).[7,8] Full identification was possible for six of the novel EMOS, while partial identification was possible for three of the novel EMOS. For 6′-sialyl-Hex-Ac-HexNAc, the presence of an additional acetyl group (Ac) was confirmed by mass fragmentation. An additional acetyl group linked to acidic milk oligosaccharides has previously been reported in equine colostrum.[8] The additional acetyl group was reported to be linked to the sialic acid group, while in our study it was found to be linked to the hexose moiety.

Comparison of the Equine Milk Oligosaccharides per Breed. After annotation of the EMOS, peaks in the CE-LIF electropherogram of the lactose-free EMO mixture were assigned. The peaks assigned were used as a reference for the identification of EMOS in the CE profiles of the 12 colostrum samples of the four horse breeds. In Figure 5, the EMO profiles of the four breeds are shown, including the peak assignments. The CE-LIF electropherograms of the labeled EMOS showed high reproducibility and high peak resolution.

Interbreed EMOS Comparison. The comparison of the EMO profiles for the four breeds (A, B, C, and D in Figure 5) reveals that the presence and relative abundance of the different oligosaccharides varied depending on the breed. Quantification was carried out after manual integration of CE-LIF peaks area. For two compounds, Gal(*β*1−4)Hex-Hex and 3′-sialyl-*N*-acetyllactosamine, the assignment in the CE-LIF EMO profiles was not possible. For these two molecules, the quantification was obtained with HILIC-MS^n.

The total concentrations of EMOS varied between the different colostrum samples: 4.63 g/L for the Shetland pony, 1.81−6.71 g/L for the Crossbred Arabian/New Forest ponies, 1.42−2.75 for the Dutch Warmblood horses, and 1.76−2.48 g/

DOI: 10.1021/acs.jafc.5b01127
J. Agric. Food Chem. 2015, 63, 4805−4814

Table 1. Presence and Concentration of Equine Milk Oligosaccharides for the Four Breeds' Colostrum Samples[a]

degree of polymerization	EMOS structures	abbreviation	MW	peak CE-LIF (Figure 1)	concentration of equine milk oligosaccharide (g/L)											
					Dutch Warmblood				crossbred Arabian/New Forest ponies					Shetland pony	Friesian	
					A1	A2	A3	A4	B1	B2	B3	B4	B5	C1	D1	D2
	neutral															
dimer	**Gal(β1−4)HexNAc**		383	1	0.11	0.14	0.05	0.08	0.14	0.11	0.38	0.09	0.51	0.22	0.29	0.13
trimer	**Gal(β1−4)Hex-Hex**		504	na	++	++	++	+	+	+	+	++	+	+	——	——
	β6′-galactosyllactose	β6′-GL		2	0.98	2.08	0.65	0.84	0.83	0.55	1.64	0.83	3.15	1.91	1.20	0.88
	β4′-galactosyllactose	β4′-GL		3	tr	tr	tr	tr	tr	tr	——	——	——	——	tr	tr
	β3′-galactosyllactose	β3′-GL		4	0.16	0.16	0.10	0.09	0.23	0.08	0.04	0.14	0.23	0.11	0.05	0.05
tetramer	lacto-*N*-neotetraose	LNnT	708	5	0.02	tr	0.13	0.02	0.39	0.21	0.13	0.26	0.09	0.10	0.07	0.03
pentamer	lacto-*N*-novo-pentaose I	LNnP I	870	6	0.03	0.08	0.09	tr	0.05	0.04	0.04	0.04	0.11	0.06	tr	tr
hexamer	**lacto-*N*-hexaose**	LNH	1073	7	0.03	0.05	0.02	tr	0.04	0.03	0.02	0.04	0.07	0.04	tr	0.01
	acidic															
trimer	6′-sialyl-*N*-acetyllactosamine	6′-SLN	675	8	0.07	——	——	0.01	0.12	0.02	0.06	0.01	0.02	0.02	0.07	0.19
	3′-sialyl-*N*-acetyllactosamine	3′-SLN		na	0.05	0.03	0.02	0.02	0.01	0.003	0.01	0.02	0.03	0.02	——	——
	3′-sialylactose	3′-SL	633	9	1.00	1.16	0.71	0.29	0.48	0.38	0.69	0.44	1.75	1.73	0.53	0.33
	6′-sialyllactose	6′-SL		10	0.10	0.15	0.07	0.03	0.12	0.06	0.12	0.03	0.23	0.09	0.09	0.02
	6′-sialyl-Hex-Ac-HexNAc		716	11	tr	tr	tr	tr	0.10	0.05	0.01	0.06	0.02	0.03	tr	0.02
tetramer	disialyllactose	DSL	925	12	0.16	0.13	0.04	0.02	0.09	0.06	0.21	0.02	0.40	0.23	0.13	0.07
pentamer	**sialyllacto-*N*-tetraose-a**	LSTa	999	13	0.02	0.03	0.06	0.02	0.27	0.16	0.83	0.16	0.06	0.07	0.05	tr
hexamer	**disialyllacto-*N*-tetraose***	DS-LNT*	1290	14	0.02	tr	tr	tr	0.15	0.06	0.03	0.05	0.04	tr	tr	0.03
total oligosaccharides concentration					2.75	4.01	1.94	1.42	3.02	1.81	4.21	2.19	6.71	4.63	2.48	1.76
average oligosaccharides concentration per breed						2.52					3.58			4.63	2.12	

[a]na = peak not assigned in CE-LIF and quantified by HILIC-MS^n; ++ = 0.001−0.002; + = 0.001−0.0002 g/L; tr = detectable but not quantifiable; —— = not detected; the symbol * = isomer not further specified. Structures in **bold**: oligosaccharides novel for the equine milk literature.[8,21,34]

DOI: 10.1021/acs.jafc.5b01127
J. Agric. Food Chem. 2015, 63, 4805−4814

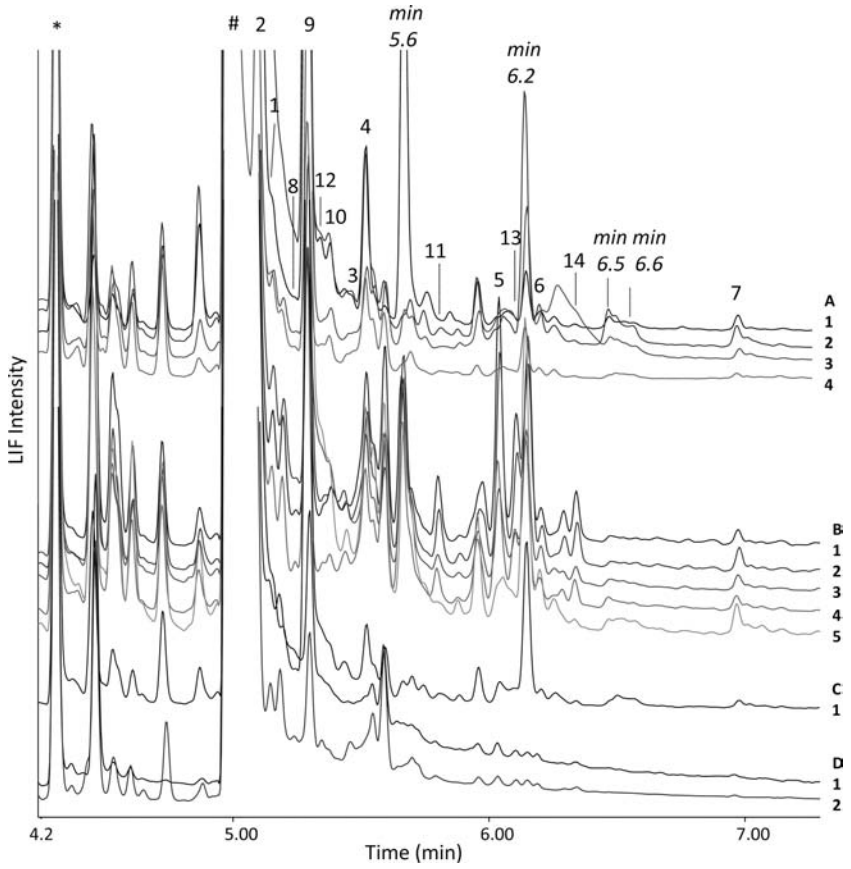

Figure 5. CE-LIF electropherograms of APTS-derivatized oligosaccharides for the four breeds. A: Dutch Warmblood horse; B: Crossbred Arabian/New Forest pony; C: Shetland Pony; D: Friesian horse. *: Internal standard xylose, #: Lactose, 1−14: identified peaks as named in Table 1

L for the Friesian horses (Table 1). Oligosaccharide concentrations found in this study are higher than concentration found in cow colostrum (about 1 g/L).[8] For other animals, the oligosaccharide concentration has only been reported for mature milks with levels (0.02 to 0.25 g/L), as expected, lower than the values obtained in this study for equine colostrum.[24] Although a large variation in the total concentration of EMOS was observed, it was noticed that the ponies' colostrum samples contained the highest concentration of EMOS, followed by the Dutch Warmblood horses' and the Friesian horses' colostrum samples.

Twelve out of the 16 EMOS were present in all colostrum samples. Gal(β1−4)Hex-Hex and 3′-sialyl-*N*-acetyllactosamine were absent in the Friesian horses' colostrum samples, β4′-galactosyllactose was absent in the Crossbred ponies' colostrum samples, and 6′-sialyl-*N*-acetyllactosamine was absent in the Dutch Warmblood horses' colostrum samples (Table 1).

In all breeds, the most abundant oligosaccharides were β3′-galactosyllactose, β6′-galactosyllactose, 3′-sialyllactose, and disialyllactose (numbers 2, 4, 9, and 12 in Table 1). The highest concentrations of β6′-galactosyllactose, β3′-sialyllactose, and disialyllactose were found in the colostrum sample of the Shetland pony (concentrations of 1.91 g/L, 1.73 g/L, and 0.23 g/L, respectively). These values for EMOS present in Shetland pony colostrum are only an indication, because only one colostrum sample was available for the analysis. The highest concentration of the β3′-galactosyllactose was found in the colostrum samples of the Crossedbred ponies, with an average concentration of 0.14 g/L.

In profiles A1 and B1−5 (Figure 5) high concentrations of non-characterized EMOS, migrating at 5.6 and 6.2 min, were observed. From the CE migration time, it could be suggested that these are neutral trimers and pentamers, respectively. The unidentified peaks with a retention time of 6.5 and 6.6 min (Figure 5), suggesting acidic or neutral hexamers, were present in all colostrum samples.

The oligosaccharide with the lowest observed concentration in all colostrum samples was 3′-sialyl-*N*-acetyllactosamine with an average concentration of 0.02 g/L.

Intrabreed EMOS Comparison. Evaluating the EMOS profiles within the same breed, differences were also noticed. Specifically, for the Dutch Warmblood profiles, β6′-galactosyllactose and 3′-sialylactose (numbers 2 and 9 in Table 1) were the most abundant oligosaccharides, and their concentrations varied by a factor 3.2 and 4, respectively. β6′-Galactosyllactose was present with a concentration of 0.65−2.08 g/L, while 3′-sialylactose with was present with a concentration of 0.29−1.16 g/L.

Looking at the overall electropherograms, the Crossbred ponies' colostrum samples contained the same EMOS structures, although they highly varied in concentration. β4′-Galactosyllactose, however, was not detected in three colostrum samples (B3−5, Table 1). In the Crossbred ponies' colostrum samples, similarly to the Dutch Warmblood horses' colostrum samples, the most abundant oligosaccharides were the β6′-galactosyllactose and the 3′-sialylactose. The β6′-galactosyllactose was present in a concentration of 0.55−3.15 g/L, while the 3′-sialylactose with was present in a concentration of 0.38−1.75 g/L, exhibiting a 5.7 and a 4.6 factor, respectively. Intrabreed

DOI: 10.1021/acs.jafc.5b01127
J. Agric. Food Chem. 2015, 63, 4805−4814

Table 2. EMOS Found in the Dutch Warmblood Horses' Colostrum and Their Presence in Other Mammalian Milk Samples[a]

degree of polymerization	EMOS structures (Dutch Warmblood milk)[8,21,34]	milk			
		cow[7,9]	sheep[7,27]	goat[7,27]	human[10,20]
	neutral equine milk oligosaccharides				
dimer	**Gal(β1−4)HexNAc**	——	——	——	——
trimer	**Gal(β1−4)Hex-Hex**	——	——	——	——
	β6′-galactosyllactose	X	X	X	X
	β4′-galactosyllactose	X	——	——	X
	β3′-galactosyllactose	X	X	X	X
tetramer	lacto-*N*-neotetraose	——	——	——	X
pentamer	lacto-*N*-novo-pentaose I	X	——	——	——
hexamer	**lacto-*N*-hexaose**	——	——	X	X
	acidic equine milk oligosaccharides				
trimer	6′-sialyl-*N*-acetyllactosamine	X	——	——	——
	3′-sialyl-*N*-acetyllactosamine	X	X	X	——
	3′-sialylactose	X	X	X	X
	6′-sialyllactose	X	——	X	X
	6′-sialyl-Hex-Ac-HexNAc	——	——	——	——
tetramer	disialyllactose	X	——	X	X
pentamer	**sialyllacto-*N*-tetraose-a**	——	——	——	X
hexamer	**disialyllacto-*N*-tetraose***	——	——	——	X

[a]X = present; —— = not present; the symbol * = isomer not further specified. Structures in **bold**: oligosaccharides novel for the equine milk literature.[8,21,34]

analysis showed relatively high variation in EMOS concentration (Table 1). Most probably the variation in EMOS concentration could be dependent on the intrinsic variation in composition and in quality of colostrum among individuals, as shown before for cow milk and colostrum.[25,26]

Presence of Equine Milk Oligosaccharides Structures in Comparison with the Profile in Milk of Other Mammals. Ten out of the 16 EMOS found in this study were also found in milk samples from other domestic animals (Table 2). So far, β6′- and 3′- galactosyllactose, 3′-sialylactose, and 3′-sialyl-*N*-acetyllactosamine have been found in bovine, caprine, and ovine milk, while 6′-sialyllactose and disialyllactose have been found both in bovine and caprine milk.[7,27] Lacto-*N*-hexaose was characteristic for caprine milk, while β4′-galactosyllactose, lacto-*N*-novo-pentaose I, and 6′-sialyl-*N*-acetyllactosamine were present in bovine milk.[7,9,27] Ten out of 16 milk oligosaccharide structures present in equine colostrum were previously reported to be present in human milk: the neutral trimers, tetramer, and hexamer, and the acidic 3′-, 6′-sialyllactose, tetramer, pentamer, and hexamer.[10,20]

The presence of milk oligosaccharides carrying the bifidogenic factor (Gal(β1−3)GlcNAc) (numbers 6, 7, and 13 in Table 1) and the presence of eight EMOS decorated with sialic acids suggest bioactivity of the EMOS, such as being bifidogenic and soluble ligands for intestinal pathogens.[2,28−31] In this study, EMOS decorated with *N*-glycolylneuraminic acid (Neu5Gc) were not detected, while they were reported to count for less than 1% in previous study.[8] The presence of Neu5Gc linked to milk oligosaccharides is not rare in oligosaccharides derived from domestic animals. For example, such oligosaccharides account for about 6% of the oligosaccharides in cows' colostrum.[8] On the contrary, milk oligosaccharides decorated with Neu5Gc are absent in human colostrum, which is considered as beneficial because blood antibodies against Neu5Gc are present in several diseases such as acute and chronic hepatitis, hyperacute transplant rejection, and cancer.[10,31−33]

In summary, oligosaccharide profile of colostrum from horses showed significant differences between breeds as well as per individual. EMOS identified showed quite some overlap with oligosaccharides present in milk from human and other mammals, although also horse specific structures were identified. The presence of EMOS carrying the bifidogenic factor and/or the *N*-acetylneuraminic acid, together with low concentrations of EMOS with *N*-glycolylneuraminic acid, could make equine colostrum a good source for further research into in vitro bioactive effects of milk oligosaccharides.

■ ASSOCIATED CONTENT

Supporting Information

Analytical techniques used for the identification of EMOS in the Dutch Warmblood horses' colostrum, and EMOS' liquid chromatography and mass spectrometry characteristics. The Supporting Information is available free of charge on the ACS Publications website at DOI: 10.1021/acs.jafc.5b01127.

■ AUTHOR INFORMATION

Corresponding Author

*E-mail: henk.schols@wur.nl. Phone: +31 317 482239. Fax: +31 317 484893.

Funding

This project is jointly financed by the European Union, European Regional Development Fund and The Ministry of Economic Affairs, Agriculture and Innovation, Peaks in the Delta, the Municipality of Groningen, the Provinces of Groningen, Fryslân and Drenthe, the Dutch Carbohydrate Competence Center (CCC WP25; www.cccresearch.nl), Danone Nutricia Research and FrieslandCampina.

Notes

The authors declare no competing financial interest.

DOI: 10.1021/acs.jafc.5b01127
J. Agric. Food Chem. 2015, 63, 4805−4814

■ ACKNOWLEDGMENTS

We would like to thank Edwin Bakx (Laboratory of Food Chemistry, Wageningen University) for the fruitful discussions on the interpretation of the mass spectra.

■ ABBREVIATIONS

DSL,Disialyllactose; DS-LNnT,Disialyllacto-*N*-neotetraose; Fuc,Fucose; Gal,D-Galactose; GalNAc,*N*-Acetylgalactosamine; *β*3′-GL,*β*3′-Galactosyllactose; *β*4′-GL,*β*4′-Galactosyllactose; *β*6′-GL,*β*6′-Galactosyllactose; Glc,D-Glucose; GlcNAc,*N*-Acetylglucosamine; Hex,Hexaose; HexNAc,*N*-Acetyl-hexosamine; LNH,Lacto-*N*-hexaose; LNnT,Lacto-*N*-neo-tetraose; LNnP I,lacto-*N*-novo-pentaose I; LSTa,Sialyllacto-*N*-tetraose a; 3′-SL,3′-Sialylactose; 6′-SL,6′-Sialyllactose; 3′-SLN,3′-Sialyl-*N*-acetyllactosamine; 6′-SLN,6′-Sialyl-*N*-acetyllactosamine

■ REFERENCES

(1) German, J. B.; Freeman, S. L.; Lebrilla, C. B.; Mills, D. A. Human milk oligosaccharides: evolution, structures and bioselectivity as substrates for intestinal bacteria. *Nestle Nutr Workshop Ser. Pediatr Program* **2008**, *62*, 205−218 discussion 218−22. .

(2) Asakuma, S.; Hatakeyama, E.; Urashima, T.; Yoshida, E.; Katayama, T.; Yamamoto, K.; Kumagai, H.; Ashida, H.; Hirose, J.; Kitaoka, M. Physiology of consumption of human milk oligosaccharides by infant gut-associated bifidobacteria. *J. Biol. Chem.* **2011**, *286*, 34583−92.

(3) Preidis, G. A.; Versalovic, J. Targeting the human microbiome with antibiotics, probiotics, and prebiotics: gastroenterology enters the metagenomics era. *Gastroenterology* **2009**, *136*, 2015−31.

(4) Seifert, S.; Watzl, B. Inulin and oligofructose: review of experimental data on immune modulation. *J. Nutr.* **2007**, *137*, 2563S−2567S.

(5) Bode, L. Human milk oligosaccharides: every baby needs a sugar mama. *Glycobiology* **2012**, *22*, 1147−62.

(6) He, Y.; Liu, S.; Kling, D. E.; Leone, S.; Lawlor, N. T.; Huang, Y.; Feinberg, S. B.; Hill, D. R.; Newburg, D. S. The human milk oligosaccharide 2′-fucosyllactose modulates CD14 expression in human enterocytes, thereby attenuating LPS-induced inflammation. *Gut* **2014**, DOI: 10.1136/gutjnl-2014-307544.

(7) Urashima, T.; Saito, T.; Nakamura, T.; Messer, M. Oligosaccharides of milk and colostrum in non-human mammals. *Glycoconjugate J.* **2001**, *18*, 357−71.

(8) Albrecht, S.; Lane, J. A.; Marino, K.; Al Busadah, K. A.; Carrington, S. D.; Hickey, R. M.; Rudd, P. M. A comparative study of free oligosaccharides in the milk of domestic animals. *Br. J. Nutr.* **2014**, *111*, 1313−28.

(9) Parkkinen, J.; Finne, J. Isolation of sialyl oligosaccharides and sialyl oligosaccharide phosphates from bovine colostrum and human urine. *Methods Enzymol* **1987**, *138*, 289−300.

(10) Urashima, T.; Asakuma, S.; Messer, M., Milk oligosaccharides. In *Comprehensive glycoscience. From chemistry to system biology*, Kamerling, J. P.; Boons, G. J.; Lee, Y. C.; Suzuki, A.; Taniguchi, N.; Voragen, A. G. J., Eds. Elsevier: Oxford, U.K., 2007; Vol. *4*, pp 695−722.

(11) Tao, N.; DePeters, E. J.; German, J. B.; Grimm, R.; Lebrilla, C. B. Variations in bovine milk oligosaccharides during early and middle lactation stages analyzed by high-performance liquid chromatography-chip/mass spectrometry. *J. Dairy Sci.* **2009**, *92*, 2991−3001.

(12) Albrecht, S. Gastrointestinal-active oligosaccharides from human milk and functional foods. Ph.D. thesis, Wageningen University, Wageningen, The Netherlands, 2011.

(13) Nakamura, T.; Amikawa, S.; Harada, T.; Saito, T.; Arai, I.; Urashima, T. Occurrence of an unusual phosphorylated N-acetyllactosamine in horse colostrum. *Biochim. Biophys. Acta, Gen. Subj.* **2001**, *1525*, 13−8.

(14) Chaturvedi, P.; Warren, C. D.; Altaye, M.; Morrow, A. L.; Ruiz-Palacios, G.; Pickering, L. K.; Newburg, D. S. Fucosylated human milk oligosaccharides vary between individuals and over the course of lactation. *Glycobiology* **2001**, *11*, 365−72.

(15) Kunz, C.; Rudloff, S.; Baier, W.; Klein, N.; Strobel, S. Oligosaccharides in human milk: structural, functional, and metabolic aspects. *Annu. Rev. Nutr.* **2000**, *20*, 699−722.

(16) Erney, R. M.; Malone, W. T.; Skelding, M. B.; Marcon, A. A.; Kleman-Leyer, K. M.; O'Ryan, M. L.; Ruiz-Palacios, G.; Hilty, M. D.; Pickering, L. K.; Prieto, P. A. Variability of human milk neutral oligosaccharides in a diverse population. *J. Pediatr. Gastroenterol. Nutr.* **2000**, *30*, 181−92.

(17) Albrecht, S.; van Muiswinkel, G. C. J.; Schols, H. A.; Voragen, A. G. J.; Gruppen, H. Introducing capillary electrophoresis with laser-induced fluorescence detection (CE-LIF) for the characterization of konjac glucomannan oligosaccharides and their in vitro fermentation behavior. *J. Agric. Food Chem.* **2009**, *57*, 3867−3876.

(18) Albrecht, S.; Schols, H. A.; van Zoeren, D.; van Lingen, R. A.; Groot Jebbink, L. J. M.; van den Heuvel, E. G. H. M.; Voragen, A. G. J.; Gruppen, H. Oligosaccharides in feces of breast- and formula-fed babies. *Carbohydr. Res.* **2011**, *346*, 2173−2181.

(19) Remoroza, C.; Buchholt, H. C.; Gruppen, H.; Schols, H. A. Descriptive parameters for revealing substitution patterns of sugar beet pectins using pectolytic enzymes. *Carbohydr. Polym.* **2014**, *101*, 1205−1215.

(20) Albrecht, S.; Schols, H. A.; van den Heuvel, E. G. H. M.; Voragen, A. G. J.; Gruppen, H. Occurrence of oligosaccharides in feces of breast-fed babies in their first six months of life and the corresponding breast milk. *Carbohydr. Res.* **2011**, *346*, 2540−2550.

(21) Urashima, T.; Saito, T.; Kimura, T. Chemical structures of three neutral oligosaccharides obtained from horse (thoroughbred) colostrum. *Comparative Biochemistry and Physiology Part B: Comparative Biochemistry* **1991**, *100*, 177−183.

(22) Hernandez-Hernandez, O.; Calvillo, I.; Lebron-Aguilar, R.; Moreno, F. J.; Sanz, M. L. Hydrophilic interaction liquid chromatography coupled to mass spectrometry for the characterization of prebiotic galactooligosaccharides. *J. Chromatogr A* **2012**, *1220*, 57−67.

(23) Wheeler, S. F.; Harvey, D. J. Negative ion mass spectrometry of sialylated carbohydrates: discrimination of N-acetylneuraminic acid linkages by MALDI-TOF and ESI-TOF mass spectrometry. *Anal. Chem.* **2000**, *72*, 5027−5039.

(24) Martinez-Ferez, A.; Rudloff, S.; Guadix, A.; Henkel, C. A.; Pohlentz, G.; Boza, J. J.; Guadix, E. M.; Kunz, C. Goats' milk as a natural source of lactose-derived oligosaccharides: Isolation by membrane technology. *Int. Dairy J.* **2006**, *16*, 173−181.

(25) Parrish, D. B.; Wise, G. H.; Hughes, J. S.; Atkeson, F. W. Properties of the Colostrum of the Dairy Cow. V. Yield, Specific Gravity and Concentrations of Total Solids and its Various Components of Colostrum and Early Milk1. *J. Dairy Sci.* **1950**, *33*, 457−465.

(26) Kehoe, S. I.; Jayarao, B. M.; Heinrichs, A. J. A Survey of Bovine Colostrum Composition and Colostrum Management Practices on Pennsylvania Dairy Farms1. *J. Dairy Sci.* **2007**, *90*, 4108−4116.

(27) Kiskini, A.; Difilippo, E. Oligosaccharides in goat milk: structure, health effects and isolation. *Cell Mol. Biol. (Noisy-le-grand)* **2013**, *59*, 25−30.

(28) Kitaoka, M.; Tian, J.; Nishimoto, M. Novel putative galactose operon involving lacto-N-biose phosphorylase in Bifidobacterium longum. *Appl. Environ. Microbiol.* **2005**, *71*, 3158−62.

(29) Wada, J.; Ando, T.; Kiyohara, M.; Ashida, H.; Kitaoka, M.; Yamaguchi, M.; Kumagai, H.; Katayama, T.; Yamamoto, K. Bifidobacterium bifidum lacto-N-biosidase, a critical enzyme for the degradation of human milk oligosaccharides with a type 1 structure. *Appl. Environ. Microbiol.* **2008**, *74*, 3996−4004.

(30) Sela, D. A.; Li, Y.; Lerno, L.; Wu, S.; Marcobal, A. M.; German, J. B.; Chen, X.; Lebrilla, C. B.; Mills, D. A. An infant-associated bacterial commensal utilizes breast milk sialyloligosaccharides. *J. Biol. Chem.* **2011**, *286*, 11909−18.

(31) Bode, L. Recent advances on structure, metabolism, and function of human milk oligosaccharides. *J. Nutr.* **2006**, *136*, 2127−30.

DOI: 10.1021/acs.jafc.5b01127
J. Agric. Food Chem. 2015, 63, 4805−4814

(32) Morito, T.; Nishimaki, T.; Masaki, M.; Yoshida, H.; Kasukawa, R.; Nakarai, H.; Kano, K. Studies on Hanganutziu-Deicher Antigens-Antibodies. *Int. Arch. Allergy Immunol.* **1986**, *81*, 204−209.
(33) Tangvoranuntakul, P.; Gagneux, P.; Diaz, S.; Bardor, M.; Varki, N.; Varki, A.; Muchmore, E. Human uptake and incorporation of an immunogenic nonhuman dietary sialic acid. *Proc. Natl. Acad. Sci. U. S. A.* **2003**, *100*, 12045−12050.
(34) Urashima, T.; Saito, T.; Nakamura, T.; Messer, M. Oligosaccharides of milk and colostrum in non-human mammals. *Glycoconjugate J.* **2001**, *18*, 357−71.

DOI: 10.1021/acs.jafc.5b01127
J. Agric. Food Chem. 2015, 63, 4805−4814

JOURNAL OF AGRICULTURAL AND FOOD CHEMISTRY

Article

pubs.acs.org/JAFC

Influence of Coffee Genotype on Bioactive Compounds and the in Vitro Capacity To Scavenge Reactive Oxygen and Nitrogen Species

Naira Poerner Rodrigues,[†] Terezinha de Jesus Garcia Salva,[§] and Neura Bragagnolo*[,†]

[†]Faculty of Food Engineering, University of Campinas (UNICAMP), 13083-862 Campinas, São Paulo, Brazil

[§]Coffee Center, Agronomic Institute of Campinas (IAC), P.O. Box, 28, 13001-970 Campinas, São Paulo, Brazil

Supporting Information

ABSTRACT: The influence of green coffee genotype on the bioactive compounds and the in vitro antioxidant capacity against the principal reactive oxygen ($ROO^{\bullet}$, H_2O_2, $HO^{\bullet}$, and HOCl) and nitrogen ($NO^{\bullet}$ and $ONOO^{-}$) species of biological relevance was investigated. This is the first report on the capacity of green coffee to scavenge H_2O_2, HOCl, and $NO^{\bullet}$. Variations in the contents of total chlorogenic acids (22.9−37.9 g/100 g), cinnamoyl−amino acid conjugates (0.03−1.12 g/100 g), trigonelline (3.1−6.7 g/100 g), and caffeine (3.9−11.8 g/100 g) were found. Hydrophilic extracts of *Coffea canephora* and *Coffea kapakata* were the most potent scavengers of $ROO^{\bullet}$, H_2O_2, $HO^{\bullet}$, $NO^{\bullet}$, and $ONOO^{-}$ due to their chlorogenic acid contents, which were, on average, 30% higher than those found in *Coffea arabica* and *Coffea racemosa*. The results showed that genotype is a determinant characteristic in the bioactive compound contents and consequently in the antioxidant capacity of green coffee.

KEYWORDS: *Rubiaceae, cultivars, varieties, germplasm bank, reducing capacity, phenolic compounds, methylxanthines*

INTRODUCTION

Coffee plants belong to the Rubiaceae family and to the genus *Coffea*, which has 103 species. *Coffea arabica* (arabica coffee) and *Coffea canephora* (robusta coffee) are the only species used for commercial production, representing about 60 and 40%, respectively, of the world coffee market.[1,2] The other coffee species, although having no commercial relevance, are important for genetic improvement of coffee plants, because they constitute gene reserves for resistance against pests, diseases, and adverse environmental conditions. Coffee species show considerable variation in their morphological, agronomical, and biochemical characteristics.[3] The biochemical differences are responsible for the variations in chemical composition of the coffee fruits and even between genotypes of the same coffee species.[3,4]

Green coffee beans are rich in bioactive compounds, with a highlight on caffeine, trigonelline, chlorogenic acids,[5] tocopherols (α, β, γ), and diterpenes (mainly kawheol and cafestol).[6] A number of health properties were reported for these specific compounds in the literature. Caffeine presents various biological activities such as stimulation of the central nervous system, diuretic effect, peripheral vasoconstriction, smooth muscle relaxation, and myocardial stimulation.[7] Trigonelline exerts antidiabetic action by decreasing serum glucose and increasing the insulin sensitivity index.[8] Chlorogenic acids have been related to a series of health benefits such as reduction in type 2 diabetes[9] and antihypertensive activity,[10] as well as antibacterial, anti-inflammatory[11,12] and antioxidant[13] activities. Vitamin E, represented by the tocotrienols and the tocopherols, is a potent antioxidant, anti-inflammatory, and anticarcinogenic agent.[14] Diterpenes present anticarcinogenic properties and stimulate the intracellular antioxidant defense mechanisms.[15]

The inverse relationship between the ingestion of foods rich in antioxidants and the decreased risk for the development of some chronic-degenerative diseases has already been well established.[16] Oxidative and nitrosative stress, resulting from a disequilibrium between the antioxidant defense of the cells and the generation of oxygen (ROS) and nitrogen (RNS) reactive species, causes damage to some important cell components, including lipids, proteins, and DNA. Due to these effects, oxidative and nitrosative stress can cause human diseases such as heart and degenerative diseases, diabetes, cancer, and nearly all liver pathologies and also take part in the aging process.[17,18] Antioxidants consumed in the diet are important to maintain the equilibrium of ROS and RNS, especially when the endogenous antioxidant defense system is not capable of efficiently deactivating the reactive species generated during oxidative and nitrosative stress.[18]

Several epidemiological studies indicated that the consumption of green coffee extracts had an antihypertensive effect in rats and humans,[19] improved vasoreactivity in humans,[20] had an inhibitory effect on the accumulation of fat and on the increase in body weight in rats and humans,[21,22] and modulated glucose metabolism in humans.[9] Health effects associated with coffee consumption largely depend on the bioacessibility and bioavailability of its bioactive compounds. After coffee ingestion, chlorogenic acids appear in the circulatory system as methylated, sulfated, and glucuronated metabolites in plasma concentrations that rarely exceeds nanomolar. Substantial quantities of both the parent compounds and their metabolites pass to the colon, where they are degraded by the action of the local microbiota, giving rise principally to small phenolic acid and aromatic catabolites that are absorbed into the circulatory system.[23] With regard to caffeine bioavailability, rapid absorption, metabolization, and

Received: January 28, 2015
Revised: April 23, 2015
Accepted: April 24, 2015
Published: April 24, 2015

ACS Publications © 2015 American Chemical Society

DOI: 10.1021/acs.jafc.5b00530
J. Agric. Food Chem. 2015, 63, 4815−4826

excretion of caffeine and its derived methylxanthines and methyluric acids have been observed after consumption of a green/roasted coffee product.[24] It is extremely important to take into account that the plasma antioxidant activity measured after the intake of coffee could be related to both the parent compounds and their metabolites.[23]

The bioactive compound profile of green coffee beans is mainly influenced by genetic aspects, such as species and variety, and by physiological aspects, such as maturity degree.[25] For example, green coffee beans from *C. canephora*, *C. liberica*, *C. congensis*, *C. eugenioides*, *C. stenophylla*, *C. racemosa*, and *C. kapakata* present considerable variation in their chlorogenic acid (3.29−6.22 g/100 dry weight) and caffeine (0.96−2.12 g/100g dry weight) contents.[3]

Considering the importance of the genotype on the bioactive compound contents of coffee endosperm and consequently on the antioxidant capacity of the coffee extract, in this work we first evaluated the influence of coffee genotype on the bioactive compound qualitative and quantitative profiles. Second, we evaluated the in vitro scavenging capacity of coffee genotypes against the main biological relevant ROS and RNS, namely, peroxyl radical ($ROO^{\bullet}$), hydrogen peroxide (H_2O_2), hydroxyl radical ($HO^{\bullet}$), hypochlorous acid (HOCl), nitric oxide radical ($NO^{\bullet}$), and peroxynitrite anion ($ONOO^{-}$). This is the first time that the capacity of green coffee to scavenge H_2O_2, HOCl, and $NO^{\bullet}$ is reported. In addition, we estimated the contribution of each bioactive compound (5-caffeoylquinic acid, caffeic acid, trigonelline, caffeine, and theophylline) to the antioxidant capacity of the hydrophilic extracts from the 12 evaluated coffee genotypes.

MATERIALS AND METHODS

Reagents. Caffeine, 5-caffeoylquinic acid (5-CQA), caffeic acid, *p*-coumaric acid, ferulic acid, trigonelline, theobromine, theophylline, trolox, ascorbic acid, quercetin, cysteine, and rutin standards were acquired from Sigma-Aldrich (St. Louis, MO, USA), presenting a minimum of 95% of purity as determined by HPLC-DAD. HPLC grade methanol, glacial acetic acid, and formic acid were acquired from J. T. Baker (Phillipsburg, NJ, USA), and analytical grade formic acid was from Merck (Darmstadt, Germany). Folin−Ciocalteu reagent, fluorescein, α,α'-azodiisobutyramidine dihydrochloride (AAPH), lucigenin, 30% hydrogen peroxide solution (w/v), luminol, dihydrorhodamine 123 (DHR), *N*,*N*-dimethylformamide (DMF), sodium hypochlorite solution with 10−15% available chlorine, 4,5-diaminofluorescein (DAF-2), and 3-(aminopropyl)-1-hydroxy-3-isopropyl-2-oxo-1-triazene (NOC-5) were acquired from Sigma-Aldrich. Sodium carbonate, sodium phosphate monobasic monohydrate, sodium phosphate dibasic, sodium hydroxide, sodium nitrite, sodium chloride, potassium chloride, and sodium carbonate were acquired from Synth (São Paulo, Brazil). Sodium phosphate tribasic dodecahydrate and 2-amino-2-(hydroxymethyl)-1,3-propanodiol (TRIS) were acquired from Sigma-Aldrich, ferrous chloride tetrahydrate was from J. T. Baker, and citric acid and ethylenediaminetetraacetic acid (EDTA) were from Quemis (Joinville, Brazil). Ultrapure water was obtained from a Millipore purification and filtration system (Billerica, MA, USA).

Coffee Samples. Twelve green coffee samples belonging to four different species were evaluated: one *C. kapakata*; one *C. racemosa*; three cultivars of *C. arabica*, Catuaí Vermelho IAC 144 (Caturra Amarelo IAC 476-11 × Mundo Novo IAC 374-19), IAC Ouro Verde (Catuaí Amarelo IAC H2077-2-12-70 × Mundo Novo IAC 515-20), and Tupi IAC 1669-33 (Vila Sarchi × Híbrido de Timor CIFC 832/2); and seven varieties of *C. canephora* (Robusta IAC 3597, Robusta IAC 1655, Robusta IAC 1650, Kouilou IAC 70-14A, Kouilou IAC 70-14B, Laurentii, and Bukobensis). The term "genotype" will be used to denominate the different species, cultivars, and varieties of coffee throughout this paper. Eight of the 12 evaluated coffee genotypes are commercially cultivated (3 *C. arabica* and 5 *C. canephora* of the varieties Robusta and Kouilou).

All of the plants are maintained in the Coffee Germplasm Bank and are cultivated in the experimental center of the Campinas Agronomy Institute (IAC) in Campinas, SP, Brazil, located at a latitude of 22°54′ S, a longitude of 47°05′ W, and an altitude of 640 m. Coffee fruits were harvested in the cherry maturation stage during the 2010/2011 harvest.

Sample Preparation. After harvesting, hulling, and manual removal of the mucilage, the coffee endosperms with their parchment were immediately frozen in liquid nitrogen. The parchment and silver skin were manually removed; the endosperms were frozen in liquid nitrogen and freeze-dried for 129 h at −65 °C below 40 μm Hg (Liobras, São Paulo, Brazil). The freeze-dried endosperms were ground, sieved through a 0.5 mm sieve (ABNT 35, Tyler 32), vacuum packed (Jumbo Plus, Selovac, São Paulo, Brazil) in polyethylene bags, and stored in the dark at −80 °C until extraction.

Preparation of Hydrophilic Extracts. The hydrophilic extract was obtained according to the method of Prior et al.[26] with some modifications. The freeze-dried ground coffee (2.0 g) was weighed in a 50 mL Teflon tube, defatted three times with 20 mL of hexane, and centrifuged (Beckman Coulter Allegra 64R, Palo Alto, CA, USA) at 9000*g* for 15 min at 20 °C, and the supernatants were discarded. The solid residue was extracted three times with 20 mL of an acetone/water/acetic acid solution (70:29.5:0.5, v/v/v). The extraction consisted of vortexing for 30 s followed by sonication for 4 min and finally centrifugation at 9000*g* for 15 min at 20 °C, collecting the supernatant. The three supernatants were combined in a round-bottom flask, and the organic solvent was removed in a rotary evaporator (T < 30 °C). The concentrated extract (aqueous phase) was frozen at −80 °C and freeze-dried for 120 h at −92 °C below 60 μmHg. After freeze-drying, the hydrophilic extract was transferred to an amber flask and stored at −80 °C.

The yield of the hydrophilic extract was calculated according to eq 1:

$$\text{yield (\%, w/w)} = \left(\frac{\text{mass of hydrophilic extract (g)}}{\text{mass of freeze-dried coffee (g)}}\right) \times 100 \quad (1)$$

Determination of the Hydrophilic Extract Composition by HPLC-DAD and HPLC-DAD-MS^n. The hydrophilic extract was suspended in a water/methanol (80:20, v/v) solution in the proportion of 5 mg of hydrophilic extract/1250 μL of solution, vortexed for 30 s, and centrifuged at 25000*g* for 10 min at 10 °C. The supernatant was filtered through a 0.45 μm membrane (Millipore, São Paulo, Brazil) and injected into a HPLC-DAD or HPLC-DAD-MS^n.

The quantitative analyses of the hydrophilic extract composition were carried out in a high-performance liquid chromatograph (HPLC, Shimadzu HPLC, Kyoto, Japan) equipped with a binary pump system (LC-10AD), helium gas degasser (DGU-2A), automatic injection system (SIL-10A), and diode array detector (DAD) (SPD-M10A). Trigonelline, theobromine, theophylline, caffeine, and the chlorogenic acids were separated on an ODS-C_{18} Shim-pack column (5 μm, 250 × 4.6 mm, Shimadzu) coupled to an ODS-C_{18} precolumn (5 μm, 4 × 3 mm, Phenomenex, Torrance, CA, USA), using a mixture of 80% (v/v) 10 mM citric acid (pH 2.5) and 20% (v/v) methanol (solvent A) and methanol (solvent B).[27] The gradient was programmed as follows: 100:0 (solvent A/solvent B) for 19 min, from 100:0 to 80:20 in 10 min, then to 60:40 in 15 min, maintaining this condition for 10 min, changing to 100:0 in 1 min, and finaly maintaining this proportion for 9 min. The flow rate was 1.0 mL/min and the column temperature 30 °C.

Trigonelline was quantified at 262 nm; theobromine, theophylline, and caffeine were quantified at 272 nm and the chlorogenic acids and caffeic acid at 325 nm. Quantitation was performed using analytical curves with six concentrations prepared in triplicate, and all of the analytical curves were linear (R^2 = 0.99, p < 0.05). The limits of detection (LOD) and quantification (LOQ) were calculated on the basis of the parameters of the analytical curves (Table S1 of the Supporting Information). The chlorogenic acids and their derivatives were quantified using the area of the 5-CQA standard combined with

DOI: 10.1021/acs.jafc.5b00530
J. Agric. Food Chem. 2015, 63, 4815−4826

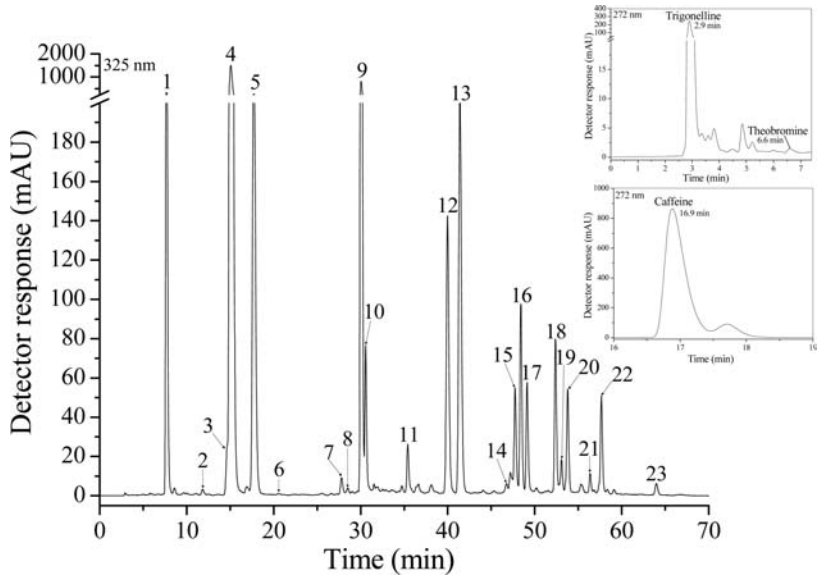

Figure 1. Chromatograms, obtained by HPLC-DAD, of the hydrophilic extract of *C. canephora* var. Kouilou IAC 70-14B recorded at 325 and 272 nm. Compound identification is shown in Table 1.

the molar extinction coefficients as described by Farah et al.[27] Due to the lack of a molar extinction coefficient for *p*-coumaroylquinic acid, this compound was quantified using the area of the 5-CQA standard. The cinnamoyl−amino acid conjugates were quantified using the molar extinction coefficient for 5-CQA as correction factor,[28] and caffeoylferuloylquinic, *p*-coumaroylcaffeoylquinic, dimethoxycaffeoylquinic, and dimethoxyferuloylquinic acids were quantified using the mean of the molar extinction coefficient of the three dicaffeoylquinic acid isomers.[29]

The compounds present in the hydrophilic extract were identified using an HPLC (Shimadzu) equipped with a quaternary pump (LC-20AD), an online degasser (DGU-20A5), a Rheodyne valve with a 20 μL sample loop, a DAD detector (Shimadzu, SPD-M20A) connected to a mass spectrometer (MS) with an electrospray ionization source (ESI), and an ion trap analyzer (Bruker Daltonics, model Esquire 4000, Bremen, Germany). The chromatographic conditions were the same as described for quantification analyses, except that citric acid in solvent A was substituted by 0.3% formic acid (pH 2.5) because citric acid generates fragments at m/z 191, which interfere in compound identification. The mass spectra were acquired in the range from m/z 70 to 600, and the parameters used were as follows: ESI in the negative mode, capillary voltage of 2500 V, drying gas (N_2) temperature of 310 °C and flow of 8 L/min, nebulizer = 30 psi, and the fragmentation energy of the MS^2 and MS^3 = 1.6 V.

Trigonelline, theobromine, theophylline, caffeine, 5-CQA, and caffeic acid were identified on the basis of the combined results of the following parameters: elution order on reversed phase column, cochromatography with standards and characteristics of UV−visible and mass spectra as compared with those obtained with the standards analyzed under the same conditions. The other chlorogenic acids and their derivatives, for which no commercial standards were available, were tentatively identified on the basis of their elution order on the reversed phase column and characteristics of UV−visible and mass spectra (m/z of the deprotonated molecule, fragmentation pattern of the MS^2 and MS^3 spectra) as compared to those found in the literature.[28,30−32]

Assays to Determine the Reducing Capacity and ROS/RNS Scavenging Capacity. The hydrophilic extract was suspended in the specific buffer solution for each method in the proportion of 5 mg of hydrophilic extract/1250 μL of buffer, vortexed for 30 s, and centrifuged at 25000*g* for 10 min at 10 °C, and the supernatant was used in the reducing capacity and ROS/RNS scavenging capacity analyses.

The assays were carried out in a microplate reader (Synergy Mx, Bio-Tek, Winooski, VT, USA) equipped with a thermostat and two reagent dispensers. The following control assays were carried out for all microplates: (i) without the addition of the radical generator or reactive species, such that no interaction between the probe and the extract was observed, and (ii) inclusion of an analytical quality control (positive control), that is, a compound with antioxidant capacity known to scavenge the specific reactive species. Each assay corresponded to three experiments carried out in triplicate. The variation in the responses of the positive controls was below 15% during the assays. With the exception of the reducing capacity and the $ROO^•$ scavenging assay, the results were expressed in IC_{50} values, calculated by nonlinear regression analysis using the software GraphPad Prism 5.03.

Reducing Capacity. The reducing capacity of the hydrophilic extract was determined using the Folin−Ciocalteu colorimetric method,[33] which was adapted for analysis using a microplate reader.[32] The reaction mixture contained the following reagents (final volume = 300 μL): hydrophilic extract dissolved in ultrapure water (33 and 73 μg/mL), Folin−Ciocalteu reagent (8.3%, v/v), and sodium carbonate solution (2.3%, w/v). The absorbance was monitored at 765 nm for 120 min at 25 °C, and quantification was done by way of an analytical curve for gallic acid in the range between 2 and 12.5 μg/mL, with the results expressed in milligrams of gallic acid equivalents per gram of extract (mg GAE/g).

Peroxyl Radical Scavenging Assay. The $ROO^•$ was generated by the thermal decomposition of AAPH at 37 °C. The $ROO^•$ scavenging capacity was measured by monitoring the effect of the hydrophilic extract on the fluorescence decay due to fluorescein oxidation induced by $ROO^•$.[34,35] The reaction mixture contained fluorescein (61 nM), hydrophilic extract (five concentrations, 0.5−5.2 μg/mL), and AAPH (19 mM) dissolved in 75 mM phosphate buffer (pH 7.4). The mixture was pre-incubated in the microplate reader during 10 min before AAPH addition. The fluorescence signal (excitation at 485 ± 20 nm and emission at 528 ± 20 nm) was monitored every minute until it reached 0.5% of the initial fluorescence signal. Quantification was carried out using an analytical curve for trolox in the range from 1 to 12 μmol, and the results were expressed in micromoles of trolox equivalents per gram of extract (μmol TE/g).

Hydrogen Peroxide Scavenging Assay. The H_2O_2 scavenging capacity was measured by monitoring the effect of the hydrophilic extract on reducing the luminescence resulting from lucigenin oxidation induced by H_2O_2.[34] The reaction mixture contained lucigenin (0.8 mM) and hydrophilic extract (five concentrations, 350−2400 μg/mL) dissolved in 50 mM Tris-HCl buffer (pH 7.4) and

DOI: 10.1021/acs.jafc.5b00530
J. Agric. Food Chem. 2015, 63, 4815−4826

Table 1. Chromatographic and Mass Spectroscopy Characteristics of Chlorogenic Acids and Derivatives Identified in Hydrophilic Extracts from Coffee Beans, Obtained by HPLC-DAD-MS^n

peak[a]	t_R (min)[b]	compound (abbrev)	$[M-H]^-$ (m/z)	fragments (m/z)[c]	identity confirmation
1	7.7	3-caffeoylquinic acid (3-CQA)	353	MS^2 [353]: **191**, 179, 135, 173 MS^3 [353→191]: **127**, 173, 85, 93	30
2	11.9	3-*p*-coumaroylquinic acid (3-*p*CoQA)	337	MS^2 [337]: **163** MS^3 [337→163]: **119**	30
3	14.4	3-feruloylquinic acid (3-FQA)	367	MS^2 [367]: **193**, 133, 173 MS^3 [367→193]: **133**, 149	30
4	15.1	5-caffeoylquinic acid (5-CQA)	353	MS^2 [353]: **191**, 179 MS^3 [353→191]: **127**, 173, 85, 111	analytical standard
5	17.7	4-caffeoylquinic acid (4-CQA)	353	MS^2 [353]: **173**, 179, 191, 135 MS^3 [353→173]: **93**, 111, 155, 71	30
6	20.6	caffeic acid (CA)	179	MS^2 [179]: **135**	standard
7	27.8	5-*p*-coumaroylquinic acid (5-*p*CoQA)	337	MS^2 [337]: **191**, 163 MS^3 [337→191]: **127**, 172, 85	30
8	28.5	4-*p*-coumaroylquinic acid (4-*p*CoQA)	337	MS^2 [337]: **173**, 191, 163 MS^3 [337→173]: **93**, 111, 155	30
9	30.0	5-feruloylquinic acid (5-FQA)	367	MS^2 [367]: **191**, 173 MS^3 [367→191]: **127**, 173, 85, 93	30
10	30.6	4-feruloylquinic acid (4-FQA)	367	MS^2 [367]: **173**, 191 MS^3 [367→173]: **93**, 111, 155	30
11	35.4	caffeoyltyrosine (CTyr)	342	MS^2 [342]: **207**, 163, 135, 119 MS^3 [342→207]: **163**, 119	28
12	40.0	3,4-dicaffeoylquinic acid (3,4-diCQA)	515	MS^2 [515]: **353**, 173, 179, 191, 335 MS^3 [515→353]: **173**, 179, 191, 135	30
13	41.4	3,5-dicaffeoylquinic acid (3,5-diCQA)	515	MS^2 [515]: **353**, 191 MS^3 [515→353]: **191**, 179, 135, 173	30
14	46.8	3-*p*-coumaroyl-4-caffeoylquinic acid (3*p*Co,4CQA)	499	MS^2 [499]: **353**, 335, 337, 173, 179 MS^3 [499→353]: **173**, 179, 135, 191	32
15	47.7	3-caffeoyl-4-feruloylquinic acid (3C,4FQA)	529	MS^2 [529]: **367**, 173, 335, 193 MS^3 [529→367]: **173**, 193	30
16	48.4	4,5-dicaffeoylquinic acid (4,5-diCQA)	515	MS^2 [515]: **353**, 173, 203 MS^3 [515→353]: **173**, 179, 191, 135	30
17	49.1	3-caffeoyl-5-feruloylquinic acid (3C,5FQA)	529	MS^2 [529]: **353**, 367, 191 MS^3 [529→353]: **191**, 179, 135	30
18	52.4	caffeoyltryptophan (CTrp)	366	MS^2 [366]: **229**, 135, 185 MS^3 [366→229]: **185**, 100, 142	28
19	53.1	4-feruloyl-5-caffeoylquinic acid (4F,5CQA)	529	MS^2 [529]: **367**, 173 MS^3 [529→367]: **173**, 193, 134	30
20	53.8	4-caffeoyl-5-feruloylquinic acid (4C,5FQA)	529	MS^2 [529]: **353**, 367, 173, 191 MS^3 [529→353]: **173**, 179, 191, 135	30
21	56.4	*p*-coumaroyltryptophan (*p*-CoTrp)	350	MS^2 [350]: **229**, 185 MS^3 [350→229]: **185**, 100, 142	28
22	57.7	4-dimethoxycinnamoyl-5-caffeoylquinic acid (4D,5CQA)	543	MS^2 [543]: **381**, 367, 173, 207, 349, 335 MS^3 [543→381]: **173**, 207	31
23	64.0	4-dimethoxycinnamoyl-5-feruloylquinic acid (4D,5FQA)	557	MS^2 [557]: **381**, 349, 207, 173 MS^3 [557→381]: **173**, 207	31

[a]Numbered according to the chromatogram shown in Figure 1. [b]Retention time on C_{18} column. [c]The base peaks are shown in bold.

1% H_2O_2 (v/v). The chemiluminescence signal was measured after 5 min of incubation at 37 °C.

Hydroxyl Radical Scavenging Assay. The HO$^\bullet$ was generated by the Fenton reaction ($FeCl_2$−EDTA−H_2O_2). The HO$^\bullet$ scavenging capacity was measured by monitoring the effect of the hydrophilic extract on reducing the luminescence resulting from luminol oxidation induced by HO$^\bullet$.[34] The reaction mixture contained hydrophilic extract (five concentrations, 0.4−8.0 μg/mL) dissolved in ultrapure water, luminol (20 μM) in 0.5 M carbonate buffer (pH 10), $FeCl_2$−EDTA (25 μM, 100 μM) solution in ultrapure water, and H_2O_2 (3.5 mM). The chemiluminescence signal was measured after 5 min of incubation at 37 °C.

Hypochlorous Acid Scavenging Assay. The HOCl scavenging capacity was measured by monitoring the effect of the hydrophilic extract on reducing the fluorescence resulting from the oxidation of DHR to rhodamine 123 induced by HOCl.[34] The HOCl was prepared by adjusting the pH of a 1% NaOCl (w/v) solution to 6.2 with 10% H_2SO_4 (v/v). The HOCl concentration was determined spectrophotometrically at 235 nm using the molar absorption coefficient of 100 M^{-1} cm^{-1}, and the other dilutions were made in 100 mM phosphate buffer (pH 7.4). The reaction mixture contained hydrophilic extract (five concentrations, 0.7−71 μg/mL), DHR (5 μM), and HOCl (5 μM) dissolved in 100 mM phosphate buffer (pH 7.4). The fluorescence signal (excitation at 485 ± 20 nm and emission at 528 ± 20 nm) was measured immediately after the addition of HOCl at 37 °C.

Nitric Oxide Scavenging Assay. NO$^\bullet$ was generated by thermal decomposition of NOC-5. The NO$^\bullet$ scavenging capacity was

DOI: 10.1021/acs.jafc.5b00530
J. Agric. Food Chem. 2015, 63, 4815−4826

Table 2. Yield and Contents of the Main Chlorogenic Acid Subgroups (CQA, FQA, *p*-CoQA, di-CQA, and CFQA), Total Chlorogenic Acids (CGA), Cinnamoyl−Amino Acid Conjugates (TCTrp), and Caffeic Acid in the Hydrophilic Extracts of the Different Coffee Genotypes

hydrophilic extract origin[a]	yield (%, w/w)	CQA total[b]	FQA total[c]	*p*-CoQA total[d]	di-CQA total[e]	CFQA total[f]	CGA[g]	TCTrp total[h]	caffeic acid
C. kapakata	24.1	25709 ± 194a	1829 ± 12fg	231 ± 3c	4951 ± 21c	647 ± 3e	33391 ± 225de	nd[i]	nd
C. racemosa	23.9	19863 ± 457d	803 ± 14i	185 ± 9d	3708 ± 112e	126 ± 4f	24693 ± 595g	nd	9.9 ± 0.2a
C. arabica cv. Catuaí Vermelho IAC 144	22.4	17929 ± 409e	1696 ± 39gh	284 ± 6b	2792 ± 78f	117 ± 3f	22869 ± 536g	26.5 ± 0.8f	6.3 ± 0.3c
C. arabica cv. IAC Ouro Verde	22.6	19066 ± 369de	1382 ± 26h	273 ± 6b	2994 ± 58f	94.5 ± 2.4f	23854 ± 463g	27.0 ± 1.0f	5.7 ± 0.2cd
C. arabica cv. Tupi IAC 1669-33	25.1	20030 ± 54d	1748 ± 16gh	366 ± 11a	2869 ± 107f	109 ± 4f	25183 ± 194g	101 ± 5e	5.9 ± 0.1cd
C. canephora var. Robusta IAC 3597	26.3	18866 ± 687de	4985 ± 170de	113 ± 4e	4929 ± 177c	1441 ± 59a	30397 ± 1111f	672 ± 28d	4.3 ± 0.2ef
C. canephora var. Robusta IAC 1655	23.6	19054 ± 544de	8189 ± 217a	120 ± 3e	4574 ± 159d	1273 ± 41b	33276 ± 979cde	741 ± 20cd	4.2 ± 0.3f
C. canephora var. Robusta IAC 1650	24.1	22117 ± 196bc	5859 ± 50c	70.6 ± 0.6f	5850 ± 79b	1218 ± 6bc	35172 ± 324bcd	758 ± 16c	7.5 ± 0.4b
C. canephora var. Kouilou IAC 70-14A	28.4	21663 ± 766c	5686 ± 204c	185 ± 6d	3859 ± 163e	951 ± 35d	32421 ± 1175ef	745 ± 28c	4.5 ± 0.2ef
C. canephora var. Kouilou IAC 70-14B	28.9	24844 ± 483a	6744 ± 159b	170 ± 4d	4245 ± 104d	1449 ± 39a	37965 ± 799a	1026 ± 33b	5.1 ± 0.2de
C. canephora var. Laurentii	25.1	23124 ± 290b	4698 ± 61e	234 ± 4c	6326 ± 137a	1150 ± 31bc	35593 ± 523bc	1116 ± 26a	6.2 ± 0.5c
C. canephora var. Bukobensis	29.0	25413 ± 288a	5230 ± 30d	183 ± 5d	4565 ± 81d	1162 ± 49ab	36824 ± 393ab	768 ± 17c	4.2 ± 0.3f

[a]The results correspond to the average of triplicate ± standard deviation, expressed as mg/100 g of hydrophilic extract. Means with different letters in the same column are significantly different ($p < 0.05$). [b]CQA total, caffeoylquinic acid (sum of 3-CQA, 4-CQA, and 5-CQA). [c]FQA total, feruloylquinic acid (sum of 3-FQA, 4-FQA, and 5-FQA). [d]*p*-CoQA total, *p*-coumaroylquinic acid (sum of 3-*p*CoQA, 4-*p*CoQA, and 5-*p*CoQA). [e]di-CQA total, dicaffeoylquinic acid (sum of 3,4-diCQA, 3,5-diCQA, and 4,5-diCQA). [f]CFQA total, caffeoylferuloylquinic acid (sum of 3C,4FQA, 3C,5FQA, 4F,5CQA, and 4C,5FQA). [g]CGA, total chlorogenic acid (sum of CQA, FQA, *p*-CoQA, di-CQA, CFQA, *p*-coumaroylcaffeoylquinic acid, and dimethoxycinnamoylquinic acid). [h]TCTrp, cinnamoyl−amino acid conjugates (sum of caffeoyltyrosine, caffeoyltryptophan, and *p*-coumaroyltryptophan). [i]nd, not detected (limit of detection, caffeic acid = 0.09 μg/mL).

measured by monitoring the effect of the hydrophilic extract in the reduction of the fluorescence resulting from the oxidation of 4,5-diaminofluoresceine (DAF-2) to triazolofluoresceine induced by $NO^{\bullet}$.[34] The reaction mixture contained DAF-2 (5 μM), hydrophilic extract (five concentrations, 0.7−85 μg/mL), and NOC-5 (60 μM) dissolved in 50 mM phosphate buffer (pH 7.4). The fluorescence signal (excitation at 485 ± 20 nm and emission at 528 ± 20 nm) was measured after 30 min of incubation at 37 °C.

Peroxynitrite Anion Scavenging Assay. The $ONOO^-$ scavenging capacity was measured by monitoring the effect of the hydrophilic extract on the reduction of the fluorescence resulting from the oxidation of DHR to rodamine 123 induced by $ONOO^-$.[34] The $ONOO^-$ was synthesized as previously described by Gomes et al.[36] The reaction mixture contained DHR (5 μM) in phosphate buffer (90 mM NaCl, 50 mM Na_3PO_4, 5 mM KCl, pH 7.4), the hydrophilic extract (five concentrations, 0.3−35 μg/mL) dissolved in phosphate buffer, and $ONOO^-$ (600 nM). The fluorescence signal (excitation at 485 ± 20 nm and emission at 528 ± 20 nm) was measured after 5 min of incubation at 37 °C. To simulate the physiological CO_2 concentration, an assay was carried out in parallel in the presence of 25 mM $NaHCO_3$.

Contribution of Each Bioactive Compound to the Antioxidant Capacity. The contribution of each bioactive compound (5-CQA, caffeic acid, trigonelline, caffeine, and theophylline) to the antioxidant capacity of the hydrophilic extract was calculated considering the antioxidant capacity of the extract, the antioxidant capacity of the analytical standard of each bioactive compound previously evaluated by Rodrigues et al.,[34] and the concentration of each bioactive compound present in the extract. In the assays of reducing capacity and $ROO^{\bullet}$ scavenging capacity, the percent contribution (a) was calculated using eq 2. In the assays of H_2O_2, $HO^{\bullet}$, HOCl, $NO^{\bullet}$, and $ONOO^-$ scavenging capacity, for which the antioxidant capacity was expressed as the IC_{50}, the following steps were used to calculate the percent contribution (b): (1) calculation of the concentration of the bioactive compound in the fraction of the hydrophilic extract responsible for inhibiting 50% of the probe oxidation (eq 3) and calculation of the decimal logarithm of this concentration; (2) calculation of the percent inhibition of the bioactive compound present in the extract using the equation of the dose−response curve obtained for each analytical standard (eq 4).

$$\%\ \text{contribution}\ (a) = \frac{[\text{concentration}] \times \text{reducing capacity of the standard}}{\text{reducing capacity of the extract}} \quad (2)$$

$$\text{concentration}\ (\mu\text{g/mL}) = \frac{[\text{concentration}] \times IC_{50}\ \text{of extract}}{100} \quad (3)$$

$$\%\ \text{contribution}\ (b) = 100/1 + 10^{(\log IC_{50} - X) \times \text{Hill slope}} \quad (4)$$

where [concentration] = concentration of the bioactive compound in the extract (g/100 g), log IC_{50}= logarithm of the IC_{50} of the analytical standard, and X = logarithm of the concentration of the bioactive compound present in the extract.

Statistical Analysis. The results obtained for the contents of bioactive compounds, reducing capacity, and ROS/RNS scavenging capacities of the hydrophilic extracts were submitted to an analysis of variance (ANOVA), and the means were compared by Tukey's test using Origin 8 software. The similarity of the hydrophilic extracts with respect to reducing capacity and scavenging capacity against ROS/RNS was determined using the method of hierarchical clustering by nonpondered average and the Euclidean distance as similarity index. The principal component analysis was applied to characterize the hydrophilic extracts according to their reducing capacity, scavenging capacity against ROS/RNS, and the content of bioactive compounds using Statistica 6.0 software. The reducing capacity and ROS/RNS scavenging capacity were used as the active variables. The chlorogenic acid (sum of caffeoylquinic, feruloylquinic, *p*-coumaroylquinic, dicaffeoylquinic, caffeoylferuloylquinic, *p*-coumaroylcaffeoylquinic, dimethoxycaffeoylquinic, and dimethoxyferuloylquinic acids), cinnamoyl−amino

DOI: 10.1021/acs.jafc.5b00530
J. Agric. Food Chem. 2015, 63, 4815−4826

Table 3. Trigonelline, Theobromine, Theophylline, and Caffeine Contents in the Hydrophilic Extracts of the Different Coffee Genotypes

hydrophilic extract origin[a]	trigonelline	theobromine	theophylline	caffeine
C. kapakata	6712 ± 70a	nd[b]	7.8 ± 0.3c	3923 ± 46g
C. racemosa	5438 ± 105b	43.2 ± 1.3a	3.3 ± 0.03d	4780 ± 54e
C. arabica cv. Catuaí Vermelho IAC 144	4719 ± 101cd	nd	nd	4616 ± 112ef
C. arabica cv. IAC Ouro Verde	4578 ± 69de	nd	nd	4163 ± 84fg
C. arabica cv. Tupi IAC 1669-33	4436 ± 62e	3.9 ± 0.1b	nd	4482 ± 24efg
C. canephora var. Robusta IAC 3597	3838 ± 151f	nd	nd	6600 ± 265d
C. canephora var. Robusta IAC 1655	4934 ± 120c	nd	11.5 ± 0.5a	8937 ± 207c
C. canephora var. Robusta IAC 1650	4686 ± 28cde	nd	9.3 ± 0.2b	9321 ± 71c
C. canephora var. Kouilou IAC 70-14A	4019 ± 133f	4.6 ± 0.4b	nd	9963 ± 299b
C. canephora var. Kouilou IAC 70-14B	3952 ± 67f	4.9 ± 0.2b	nd	11776 ± 402a
C. canephora var. Laurentii	3922 ± 54f	nd	12.2 ± 0.5a	9467 ± 125bc
C. canephora var. Bukobensis	3091 ± 25g	nd	nd	9210 ± 153c

[a]The results correspond to the average of triplicate ± standard deviation, expressed as mg/100 g of hydrophilic extract. Means with different letters in the same column are significantly different ($p < 0.05$). [b]nd, not detected (limit of detection, theobromine = 0.07 μg/mL; theophylline = 0.04 μg/mL).

Table 4. Peroxyl Radical ($ROO^{\bullet}$), Hydrogen Peroxide (H_2O_2), Hydroxyl Radical ($HO^{\bullet}$), and Hypochlorous Acid (HOCl) Scavenging Capacities and Reducing Capacity of the Hydrophilic Extracts from Different Coffee Genotypes and Positive Controls

			IC_{50}[a] (μg/mL)		
	reducing capacity[b]	$ROO^{\bullet}$[c]	H_2O_2	$HO^{\bullet}$	HOCl
hydrophilic extracts origin					
C. kapakata	205 ± 14bcd	3738 ± 246cd	877 ± 31b	1.49 ± 0.04cd	4.26 ± 0.28a
C. racemosa	152 ± 10e	2643 ± 190g	1083 ± 27ef	2.15 ± 0.10f	5.08 ± 0.33a
C. arabica cv. Catuaí Vermelho IAC 144	145 ± 11e	2453 ± 161g	1526 ± 19g	2.96 ± 0.07h	16.07 ± 0.19e
C. arabica cv. IAC Ouro Verde	149 ± 8e	3008 ± 261ef	1133 ± 20f	2.76 ± 0.06g	11.96 ± 0.51d
C. arabica cv. Tupi IAC 1669-33	147 ± 9e	2700 ± 231fg	863 ± 33b	2.82 ± 0.07gh	13.22 ± 0.77d
C. canephora var. Robusta IAC 3597	192 ± 10d	3204 ± 220e	941 ± 4c	1.77 ± 0.06e	7.47 ± 0.35b
C. canephora var. Robusta IAC 1655	202 ± 11cd	4111 ± 404bc	1022 ± 24de	1.61 ± 0.01d	10.60 ± 0.40c
C. canephora var. Robusta IAC 1650	215 ± 10abc	3689 ± 276d	984 ± 8cd	1.56 ± 0.03d	9.72 ± 0.56c
C. canephora var. Kouilou IAC 70-14a	206 ± 14bcd	4230 ± 350b	831 ± 17ab	1.39 ± 0.03bc	9.88 ± 0.34c
C. canephora var. Kouilou IAC 70-14B	225 ± 12a	4735 ± 370a	779 ± 25a	1.33 ± 0.05ab	15.26 ± 0.87e
C. canephora var. Laurentii	219 ± 12ab	4020 ± 322bcd	868 ± 16b	1.33 ± 0.01ab	9.57 ± 0.40c
C. canephora var. Bukobensis	226 ± 14a	3681 ± 246d	824 ± 9ab	1.25 ± 0.01a	14.62 ± 0.26e
positive controls					
ascorbic acid	721 ± 45		155 ± 18		
quercetin		28032 ± 2025			
gallic acid				0.16 ± 0.01	
cysteine					66.46 ± 6.37

[a]IC_{50} = in vitro inhibitory concentration necessary to decrease by 50% the oxidative effect of the reactive species in the tested media (mean of triplicate ± standard deviation). Means with the different letters in the same column are significantly different ($p < 0.05$). [b]Milligrams of gallic acid equivalents per gram of hydrophilic extract or gram of standard compound (mean of triplicate ± standard deviation). [c]Micromoles of trolox equivalents per gram of hydrophilic extract or gram of standard compound (mean of triplicate ± standard deviation).

acid conjugates (sum of caffeoyltyrosine, caffeoyltryptophan, and *p*-coumaroyltryptophan), caffeic acid, trigonelline, theobromine, theophylline, and caffeine contents were used as the supplementary variables in the derivation of the principal components, being projected in the same space.

RESULTS

Bioactive Compounds in the Hydrophilic Extracts. Figure 1 shows a typical chromatogram of the separation of trigonelline, theobromine, caffeine, and chlorogenic acids and derivatives in the hydrophilic coffee extract. A total of 23 hydroxycinnamic derivatives were identified and quantified in the hydrophilic extracts (Table 1), 19 being chlorogenic acids, 3 cinnamoyl–amino acid conjugates, and 1 free cinnamic acid. A detailed description of the identification of each hydroxycinnamic derivative by HPLC-DAD-MS^n in green coffee beans was previously presented in the literature, and the references for these papers can be found in Table 1. The UV–visible spectra of the compounds identified in hydrophilic coffee extracts are presented in Figure S1 of the Supporting Information. The nomenclature of all chlorogenic acid isomers cited in the present work was based on the recommended IUPAC numbering system.[37]

In general, the qualitative profiles of the bioactive compounds were similar in all of the coffee genotypes (Tables 2 and 3), and the differences occurred in relation to the concentrations of these compounds in the extracts. On average, the hydrophilic extracts of *C. canephora* (34.5 g/100 g) and *C. kapakata* (33.4 g/100 g) showed 30% more chlorogenic acids

DOI: 10.1021/acs.jafc.5b00530
J. Agric. Food Chem. 2015, 63, 4815–4826

than those of *C. arabica* (24 g/100 g) and *C. racemosa* (24.7 g/100 g) (Table 2).

In addition to the differences in total chlorogenic acid contents, differences were found in the contributions of the subgroups of the compounds making up the chlorogenic acids. For example, the subgroups CQA, FQA, *p*-CoQA, di-CQA, and CFQA represented, on average, 79, 6.7, 1.3, 12, and 0.4% of the total chlorogenic acid contents of the *C. arabica* extracts, whereas they represented, on average, 64, 17, 0.4, 14, and 3.6% of the *C. canephora* extracts. Among the chlorogenic acid subgroups, the elevated contents of FQA and CFQA in the *C. canephora* extracts stood out, being, on average, 4 and 12 times higher than the respective values found in the *C. arabica* extracts. On the other hand, the *C. arabica* extracts contained, on average, twice the amount of *p*-CoQA found in the *C. canephora* extracts. In general, the hydrophilic extracts presented 5-CQA, 5-FQA, 5-*p*CoQA, 3,5-diCQA, and 3C,5FQA as the majority isomers of each subgroup (Tables S2 and S3 of the Supporting Information).

The cinnamoyl−amino acid conjugates were not found in the hydrophilic extracts of *C. kapakata* or *C. racemosa*, and the contents found in *C. canephora* (832 mg/100 g) were, on average, 16 times higher than those found in *C. arabica* (51 mg/100 g) (Table 2). Caffeine was the major alkaloid found in the hydrophilic extracts of all the coffee genotypes studied (Table 3). *C. racemosa* beans presented a distinct behavior, because in addition to caffeine, which was the major alkaloid, the theobromine contents were, on average, 10 times higher than those found in C. *arabica* (Tupi cultivar) and *C. canephora* (Kouilou varieties). The hydrophilic extracts of *C. canephora* presented twice the amounts of caffeine found in the other coffee species. On the other hand, *C. kapakata* and *C. racemosa* stood out for their elevated contents of trigonelline.

Reducing Capacity and ROS/RNS Scavenging Capacity of the Hydrophilic Extracts. The 12 hydrophilic coffee extracts presented reducing capacity and were able to scavenge all of the evaluated ROS ($ROO^{\bullet}$, H_2O_2, $HO^{\bullet}$, and HOCl) (Table 4) and RNS ($NO^{\bullet}$ and $ONOO^-$) (Table 5), always in a dose-dependent manner and with IC_{50} values to the order of micrograms per milliliter. On average, the reducing capacity and $ROO^{\bullet}$, H_2O_2, $HO^{\bullet}$, $NO^{\bullet}$, and $ONOO^-$ scavenging capacities of the hydrophilic extracts were, respectively, 3, 8, 6, 12, 17, and 8 times lower than that of the positive control used in each assay. On the other hand, the capacity of the hydrophilic extracts to scavenge HOCl was, on average, 6 times higher than that of the cysteine standard used as positive control.

The capacity of the hydrophilic extracts to scavenge $ONOO^-$ was also evaluated in the presence of $NaHCO_3$ with the objective of simulating the physiological CO_2 concentrations. Under this condition, the CO_2 could modulate the reactivity of $ONOO^-$ due to the rapid reaction between these two compounds, generating nitrogen dioxide radical ($NO_2^{\bullet}$) and the carbonate radical anion ($CO_3^{\bullet -}$), which are the main radicals responsible for the oxidation and nitration reactions observed in vivo.[38] In general, the hydrophilic extracts maintained their IC_{50} values in the assays carried out in the presence of $NaHCO_3$ (Table 5), indicating that they are also effective in scavenging $NO_2^{\bullet}$ and $CO_3^{\bullet -}$.

The antioxidant capacity of the hydrophilic coffee extracts was influenced both by the coffee genotype and by the evaluated reactive species. When the cluster analysis was applied using the reducing capacity and ROS/RNS scavenging capacity of the hydrophilic extracts as the variables, two large groups were formed (Figure 2). The first group was formed by the three *C. arabica* extracts and the *C. racemosa* extract. The second group was formed by the seven *C. canephora* extracts and the *C. kapakata* extract.

Table 5. Nitric Oxide ($NO^{\bullet}$) and Peroxynitrite Anion ($ONOO^-$) Scavenging Capacities of the Hydrophilic Extracts from Different Coffee Genotypes and Positive Controls

	$IC_{50}{}^A$ (μg/mL)		
	$NO^{\bullet}$	$ONOO^-$	
		absence of $NaHCO_3$	presence of 25 mM $NaHCO_3$
hydrophilic extracts			
C. kapakata	9.96 ± 0.81c	1.20 ± 0.09ab	1.43 ± 0.06a
C. racemosa	13.90 ± 0.94d	1.94 ± 0.08ef	2.13 ± 0.07b
C. arabica cv. Catuaí Vermelho IAC 144	17.62 ± 0.51ef	2.36 ± 0.09g	3.06 ± 0.24c
C. arabica cv. IAC Ouro Verde	15.57 ± 0.84de	1.86 ± 0.12ef	2.20 ± 0.14b
C. arabica cv. Tupi IAC 1669-33	18.26 ± 1.25f	2.00 ± 0.16f	2.21 ± 0.14b
C. canephora var. Robusta IAC 3597	6.86 ± 0.55a	1.68 ± 0.04de	1.99 ± 0.10b
C. canephora var. Robusta IAC 1655	6.11 ± 0.38a	1.40 ± 0.10bc	1.39 ± 0.08a
C. canephora var. Robusta IAC 1650	7.35 ± 0.34ab	1.57 ± 0.05cd	2.09 ± 0.15b
C. canephora var. Kouilou IAC 70-14A	9.41 ± 0.57bc	1.28 ± 0.06abc	1.52 ± 0.15a
C. canephora var. Kouilou IAC 70-14B	9.18 ± 0.74bc	1.08 ± 0.05a	1.21 ± 0.08a
C. canephora var. Laurentii	6.40 ± 0.56a	1.09 ± 0.03a	1.28 ± 0.08a
C. canephora var. Bukobensis	6.77 ± 0.60a	1.10 ± 0.03a	1.24 ± 0.07a
positive controls			
rutin	0.78 ± 0.05		
trolox		0.20 ± 0.005	0.20 ± 0.01

$^A IC_{50}$ = *in vitro* inhibitory concentration necessary to decrease by 50% the oxidative effect of the reactive species in the tested media (mean of triplicate ± standard deviation). Means with the different superscript letters at the same column are significantly different ($p < 0.05$).

The same two groups formed in the cluster analysis were also formed in the principal components analysis. The first group, formed by the three *C. arabica* extracts and the *C. racemosa* extract, was located to the right of the first principal component (PC1), and the second, formed by the seven *C. canephora* extracts and the *C. kapakata* extract, was to the left of PC1 (Figure 3c). The hydrophilic extracts from the second group presented higher reducing capacity and higher scavenging capacity against $ROO^{\bullet}$, H_2O_2, $HO^{\bullet}$, $NO^{\bullet}$, and $ONOO^-$ than the hydrophilic extracts from the first group (Figure 3a,c). The higher capacity to scavenge these five reactive species was positively correlated with chlorogenic acid, cinnamoyl−amino acid conjugate, and caffeine contents (Figure 3b).

Estimate of the Contribution of Each Bioactive Compound to the Antioxidant Capacity. 5-CQA was mainly responsible for the reducing capacity and ROS/RNS scavenging capacity of the hydrophilic extracts, with the exception of HOCl (Table 6), among the five analytical standards of bioactive compounds present in the evaluated

DOI: 10.1021/acs.jafc.5b00530
J. Agric. Food Chem. 2015, 63, 4815−4826

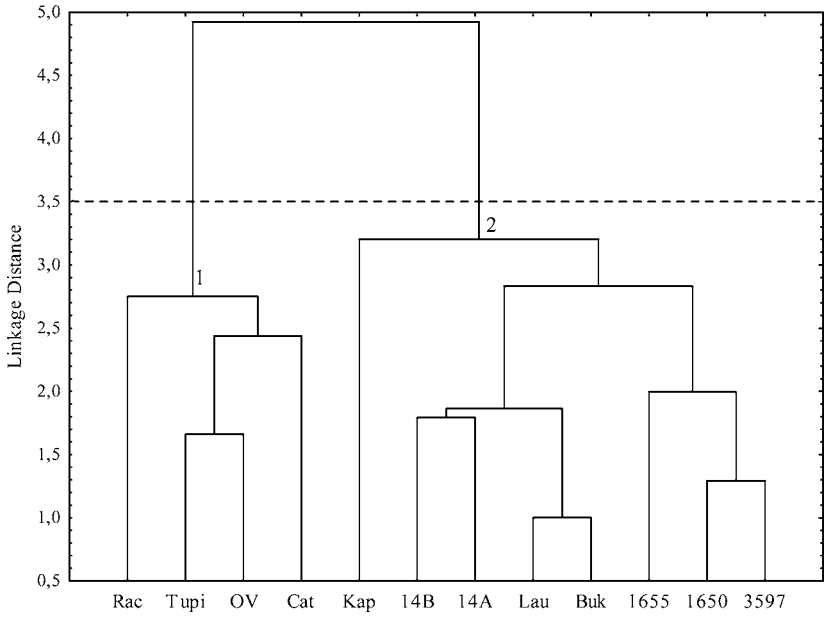

Figure 2. Dendrogram obtained by hierarchical cluster analysis of the reducing capacity and ROS/RNS scavenging capacity of hydrophilic extracts. Rac, *C. racemosa*; Tupi, *C. arabica* cv. Tupi IAC 1669-33; OV, *C. arabica* cv. IAC Ouro Verde; Cat, *C. arabica* cv. Catuaí Vermelho IAC 144; Kap, *C. kapakata*; 14B, *C. canephora* var. Kouilou IAC 70-14B; 14A, *C. canephora* var. Kouilou IAC 70-14A; Lau, *C. canephora* var. Laurentii; Buk, *C. canephora* var. Bukobensis; 1655, *C. canephora* var. Robusta IAC 1655; 1650, *C. canephora* var. Robusta IAC 1650; 3597, *C. canephora* cv. Robusta IAC 3597.

hydrophilic extracts. Caffeic acid, trigonelline, caffeine, and theophylline did not contribute to the ROS/RNS scavenging capacity of the extracts, with the exception of the contribution of trigonelline to scavenge H_2O_2 (2.4−14.6%) and of caffeic acid to scavenge HOCl (1.5−2.0%).

DISCUSSION

Studies carried out with green coffee beans of the two main species cultivated in the world, *C. arabica* and *C. canephora*, showed that the *C. canephora* beans contained higher amounts of chlorogenic acids, cinnamoyl−amino acid conjugates, and caffeine.[29,39,40] The results of the present study confirmed this information and also showed that the quantitative profile of each chlorogenic acid subgroup was also an important factor in discriminating between *C. arabica*, *C. canephora*, *C. kapakata*, and *C. racemosa* beans. The chlorogenic acid subgroups that aided in the discrimination between the coffee species evaluated in this study were caffeoylferuloylquinic and feruloylquinic acids (both with higher contents in *C. canephora* beans) and *p*-coumaroylquinic acid (with a higher content in *C. arabica* beans). In addition, cinnamoyl−amino acid conjugates and caffeine (both with higher contents in *C. canephora* beans) and trigonelline (with a higher content in *C. kapakata* and *C. racemosa* beans) also contributed to differentiating among the species (Tables 2 and 3).

The quantitative profile of the bioactive compounds was also used to explain the high antioxidant capacity of the hydrophilic extracts from different coffee genotypes against $ROO^{\bullet}$, H_2O_2, $HO^{\bullet}$, HOCl, $NO^{\bullet}$, and $ONOO^-$ and possibly against $NO_2^{\bullet}$ and $CO_3^{\bullet-}$ (indirectly evaluated reactive species). The hydrophilic extracts of coffee could be considered potent antioxidants due to (i) the low IC_{50} values required to scavenge the reactive species, to the order of micrograms per milliliter, and (ii) the similar or higher antioxidant capacity when compared to coffee brews and fruit and plant extracts (with recognized antioxidant capacity against ROS and RNS IC_{50} values cited by Rodrigues et al.[34]).

The hydrophilic extracts from the seven *C. canephora* varieties and from *C. kapakata* stood out for their elevated reducing capacities and capacities to scavenge $ROO^{\bullet}$, H_2O_2, $HO^{\bullet}$, $NO^{\bullet}$, and $ONOO^-$ (Figure 3). These green coffee hydrophilic extracts presented higher capacities to scavenge $ROO^{\bullet}$ (3.20−4.74 μmol TE/mg), $HO^{\bullet}$ (IC_{50} = 1.25−1.77 μg/mL), $NO^{\bullet}$ (IC_{50} = 6.11−9.96 μg/mL), and $ONOO^-$ (IC_{50} = 1.08−1.68 μg/mL) than mana-cubiu pulp extracts ($ROO^{\bullet}$, 0.32 μmol TE/mg; $HO^{\bullet}$, 36 μg/mL; $ONOO^-$, 20 μg/mL)[41] and artichoke leaf extracts ($NO^{\bullet}$, 5.5−11.0 μg/mL; $ONOO^-$, 3.4−5.1 μg/mL),[42] 5-CQA being the main phenolic compound identified in both of these extracts. The greater scavenging capacity of the green coffee hydrophilic extracts was probably related to their higher 5-CQA concentration (15−23%, w/w) when compared to mana-cubiu (0.4%, w/w) and artichoke (4.0−6.4%, w/w) extracts. In addition, the study of the estimated contribution of each bioactive compound to the antioxidant capacity showed that 5-CQA was the main component responsible for the scavenging capacity of the hydrophilic extracts against ROS and RNS (Table 6). In fact, 5-CQA was the major phenolic compound found in coffee, corresponding respectively to 52 and 68% of the total chlorogenic acids present in the hydrophilic extracts of *C. canephora* and *C. kapakata* (Table S2 of the Supporting Information).

This group of results indicates 5-CQA as the main contributor to the reducing capacity and $ROO^{\bullet}$, $HO^{\bullet}$, $NO^{\bullet}$, and $ONOO^-$ scavenging capacities of coffee hydrophilic extracts. Some studies have reported the mechanism by which phenolic compounds such as 5-CQA scavenge some of these reactive species. Phenolic compounds can scavenge $ROO^{\bullet}$ and $HO^{\bullet}$ by transfer of hydrogen atoms or electrons and by addition to double bonds.[43,44] The three mechanisms can occur, but the $ROO^{\bullet}$ scavenging by phenolic compounds occurs mainly due to the transference of a hydrogen atom.[35]

DOI: 10.1021/acs.jafc.5b00530
J. Agric. Food Chem. 2015, 63, 4815−4826

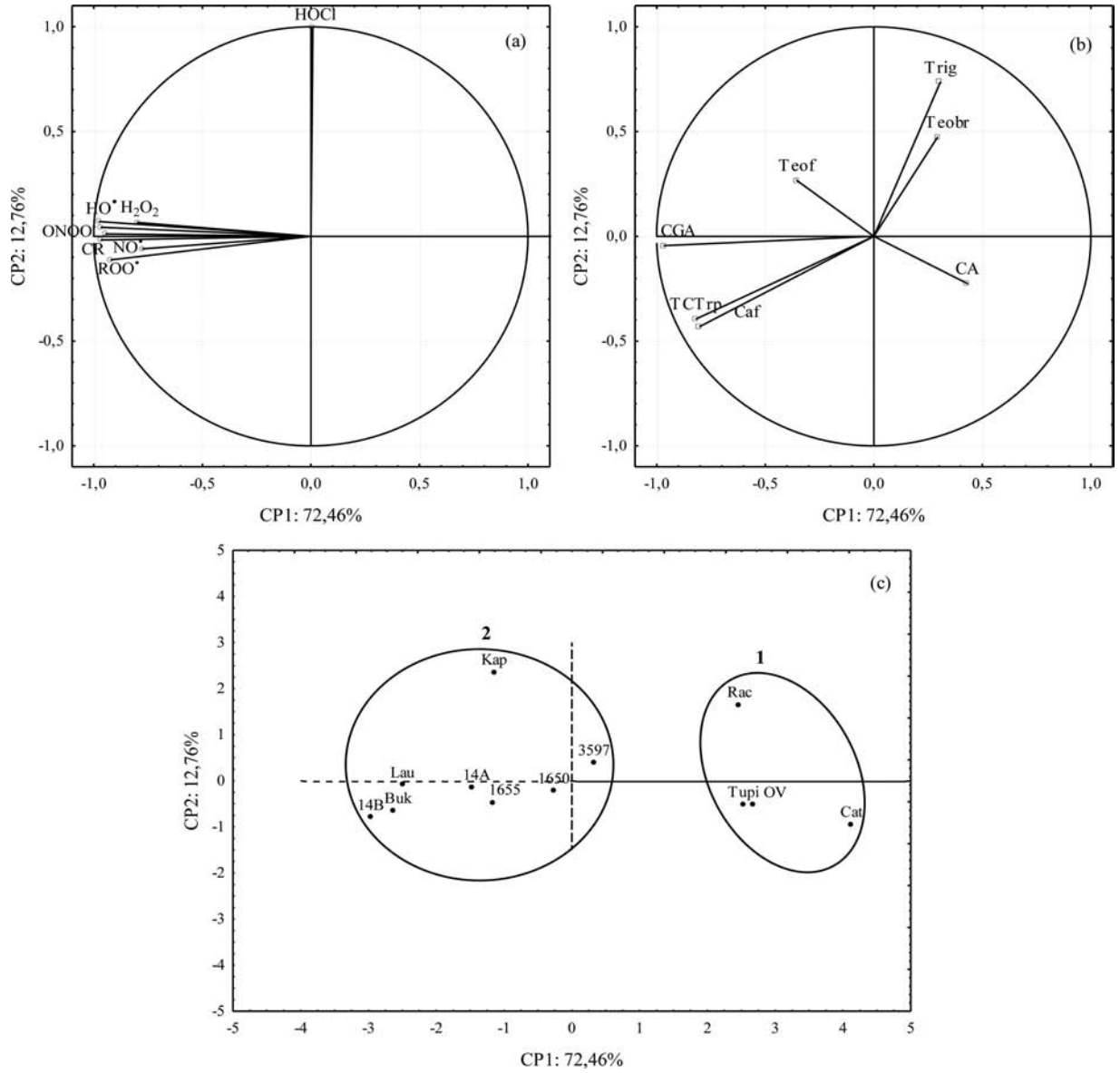

Figure 3. Principal component analysis of the reducing capacity and ROS/RNS scavenging capacity of hydrophilic extracts: (a) active variable projection; (b) supplementary variable projection; (c) scatter plot for the hydrophilic extracts. CR, reducing capacity; $ROO^{\bullet}$, peroxyl radical; H_2O_2, hydrogen peroxide; $HO^{\bullet}$, hydroxyl radical; HOCl, hypochlorous acid; $NO^{\bullet}$, nitric oxide; $ONOO^{-}$, peroxynitrite anion; CGA, chlorogenic acids; TCTrp, cinnamoyl−amino acid conjugates (caffeoyltyrosine, caffeoyltryptophan, and *p*-coumaroyltryptophan); CA, caffeic acid; Trig, trigonelline; Caf, caffeine; Teobr, theobromine; Teof, theophylline; Rac, *C. racemosa*; Tupi, *C. arabica* cv. Tupi IAC 1669-33; OV, *C. arabica* cv. IAC Ouro Verde; Cat, *C. arabica* cv. Catuaí Vermelho IAC 144; Kap, *C. kapakata*; 14B, *C. canephora* var. Kouilou IAC 70-14B; 14A, *C. canephora* var. Kouilou IAC 70-14A; Lau, *C. canephora* var. Laurentii; Buk, *C. canephora* var. Bukobensis; 1655, *C. canephora* var. Robusta IAC 1655; 1650, *C. canephora* var. Robusta IAC 1650; 3597, *C. canephora* cv. Robusta IAC 3597.

The literature has also reported the $ONOO^{-}$ scavenging capacity of phenolic compounds, which can occur by two mechanisms depending on the structural characteristcs of the phenolic compound. Monophenols, such as feruloylquinic and *p*-coumaroylquinic acids, act preferably by nitration, and the catechols, such as the caffeic, caffeoylquinic, and dicaffeoylquinic acids and the cinnamoyl−amino acid conjugates, act by electron donation.[45] On the other hand, the elevated reducing capacity of the hydrophilic extracts is related to the electron transfer mechanism carried out by the phenolic compounds. The study of reducing capacity is important because some ROS and RNS can be scavenged after they receive one or more electrons.

The compounds 5-CQA, 3-CQA, and 4-CQA are formed by the esterification of a caffeic acid molecule with quinic acid and present a catechol in their structure. The catechol group of the phenolic compounds has an important role in scavenging ROS and RNS, because it can act in the transference of hydrogen atoms and electrons. Other compounds containing catechol groups in their structures are also present in the green coffee hydrophilic extracts, such as dicaffeoylquinic acids, caffeoylferuloylquinic acid, caffeoyltyrosine, and caffeoyltryptophan. Within this group, the dicaffeoylquinic acids stand out because they present two catechol groups in their structure, conferring a high antioxidant capacity with respect to the radical DPPH and the superoxide anion radical.[46] This structural characteristic of the dicaffeoylquinic acids allied to an elevated concentration in the hydrophilic *C. canephora* and *C. kapakata* extracts (Table 2) probably contributed to the high reducing capacity and $ROO^{\bullet}$,

DOI: 10.1021/acs.jafc.5b00530
J. Agric. Food Chem. 2015, 63, 4815−4826

Table 6. Estimate (Percent) of the Contribution of the Standards of Each Bioactive Compound on the Reducing Capacity and ROS and RNS Scavenging Capacity of the Hydrophilic Coffee Extracts

scavenging capacity assay	5-CQA	caffeic acid	trigonelline	caffeine	theophylline
reducing capacity	53−74	0.03−0.07	NC	0.1−0.4	NC
$ROO^{\bullet}$	47−74	0.03−0.08	NC	0.01−0.02	NC
H_2O_2 [a]	15−26	NC	2.4−14.6	NC	NC
$HO^{\bullet}$ [a]	18−41	NC	NC	NC	NC
HOCl[a]	0.7−2.9	1.5−2.0	NC	NC	NC
$NO^{\bullet}$ [a]	9−25	0.08−0.39	NC	NC	NC
$ONOO^-_a$ [a]	36−48	0.06−0.22	NC	NC	NC
$ONOO^-_p$ [a]	33−49	0.004−0.02	NC	NC	NC

[a]The estimate is based on concentration necessary to decrease by 50% the oxidative effect of the reactive species in the tested media (IC_{50}). NC, no contribution; $ROO^{\bullet}$, peroxyl radical; H_2O_2, hydrogen peroxide; $HO^{\bullet}$, hydroxyl radical; HOCl, hypochlorous acid; $NO^{\bullet}$, nitric oxide; $ONOO^-_a$, peroxynitrite anion in the absence of $NaHCO_3$; $ONOO^-_p$, peroxynitrite anion in the presence of 25 mM $NaHCO_3$; 5-CQA, 5-caffeoylquinic acid.

H_2O_2, $HO^{\bullet}$, $NO^{\bullet}$, and $ONOO^-$ scavenging capacities of these extracts.

The hydrophilic extracts were potent HOCl scavengers, presenting a scavenging capacity on average 6 times higher than that of cysteine, the positive control used in the method. Despite contributing <3% of the IC_{50} value, among the evaluted bioactive compounds 5-CQA and caffeic acid were the only ones that contributed to this ROS scavenging (Table 6). It has already been reported that phenolic compounds are capable of scavenging HOCl by donating two electrons from the phenolic ring, forming an *o*-quinone.[47] HOCl, an oxidant with two electrons, is particularly active with thiols and methionine residues and can also convert amine groups to chloramines.[48] Thus, the presence of other compounds capable of donating two electrons in the extract, such as proteins and amino acids, could explain the HOCl scavenging by the hydrophilic extracts.

The present work was focused on the screening of the in vitro scavenging capacity of hydrophilic coffee extracts against the main ROS and RNS produced in biological systems. Considering that each reactive species has specific chemical properties and distinct mechanisms of action, this screening becomes relevant in establishing the complete in vitro antioxidant capacity profile of hydrophilic green coffee extracts. On the other hand, this kind of assay presents some limitations; thus, the extrapolation of the in vitro antioxidant capacity to possible in vivo effects should always be made with extreme care. For instance, in general, the concentrations of bioactive compounds used in antioxidant capacity assays are higher than the physiological concentrations of these compounds in cells. Moreover, other bioactive compounds derived from the ingested compounds could be also bioavailable and possess antioxidant capacity.

The results of this study show that the genotype is a determinant factor in the bioactive compound contents and consequently in the antioxidant capacity of the green coffee. The hydrophilic extracts of *C. canephora* and *C. kapakata* were the most potent scavengers of $ROO^{\bullet}$, H_2O_2, $HO^{\bullet}$, $NO^{\bullet}$, and $ONOO^-$ due to the fact that they contained, on average, 30% more chlorogenic acids than *C. arabica* and *C. racemosa*. Among the studied coffees, the species *C. canephora* and *C. kapakata* stood out as sources of hydrophilic antioxidant compounds for the food, pharmaceutical, and cosmetics industries. In addition, the study carried out to estimate the contribution of each bioactive compound in the antioxidant capacity of the hydrophilic coffee extracts showed that the chlorogenic acids and derivatives were responsible for the potent antioxidant capacity against the studied reactive species ($ROO^{\bullet}$, H_2O_2, $HO^{\bullet}$, $NO^{\bullet}$, and $ONOO^-$) and that HOCl was probably scavenged by the presence of other compounds in the extract, such as proteins and amino acids.

■ ASSOCIATED CONTENT

Supporting Information

Linearity range, limits of detection (LOD) and quantification (LOQ) of standard compounds, and contents of caffeoylquinic acid isomers (CQA), feruloylquinic acid isomers (FQA), *p*-coumaroylquinic acid isomers (*p*-CoQA), dicaffeoylquinic acid isomers (diCQA), caffeoylferuloylquinic acid isomers (CFQA), *p*-coumaroylcaffeoylquinic acid (*p*CoCQA), dimethoxycinnamoylquinic acid (DCQA and DFQA), and cinnamoyl−amino acid conjugates (CTir, CTrp, and *p*-CoTrp) in the hydrophilic extracts; UV spectra of the compounds identified in hydrophilic coffee extracts. The Supporting Information is available free of charge on the ACS Publications website at DOI: 10.1021/acs.jafc.5b00530.

■ AUTHOR INFORMATION

Corresponding Author

*(N.B.) Phone: +55 19 3521 2162. Fax: +55 19 3521 2153. E-mail: neurabragagnolo@gmail.com.

Funding

This research was supported by FAPESP (São Paulo Research Foundation Grant 2011/01335-0), CAPES (Coordination for the Improvement of Higher Education Personnel), and CNPq (Brazilian National Research Council).

Notes

The authors declare no competing financial interest.

■ REFERENCES

(1) Davis, A. P.; Govaerts, R.; Bridson, D. M.; Stoffelen, P. An annotated taxonomic conspectus of the genus *Coffea* (Rubiaceae). *Bot. J. Linn. Soc.* **2006**, *152*, 465−512.

(2) International Coffee Organization. Coffee market report − September 2014; http://dev.ico.org/documents/cy2013-14/cmr-0914-e.pdf (accessed Oct 24, 2014).

(3) Aguiar, A. T. E.; Fazuoli, L. C.; Salva, T. J. G.; Favarin, J. L. Chemical diversity in coffee species of genebank of Instituto Agronômico do estado de São Paulo. *CBAB, Crop Breed. Appl. Biotechnol.* **2005**, *5*, 460−466.

(4) Bertrand, B.; Guyot, B.; Anthony, P.; Lachermes, P. Impact of the *Coffea canephora* gene introgression on beverage quality of *C. arabica*. *Theor. Appl. Genet.* **2003**, *107*, 387−394.

(5) Esquivel, P.; Jiménez, V. M. Functional properties of coffee and coffee by-products. *Food Res. Int.* **2012**, *46*, 488−495.

DOI: 10.1021/acs.jafc.5b00530
J. Agric. Food Chem. 2015, 63, 4815−4826

(6) Speer, K.; Kölling-Speer, I. The lipid fraction of the coffee bean. *Braz. J. Plant Physiol.* **2006**, *18*, 201−216.
(7) Heck, C. I.; Mejia, E. G. Yerba mate tea (*Ilex paraguariensis*): a comprehensive review on chemistry, health implications, and technological considerations. *J. Food Sci.* **2007**, *72*, 138−151.
(8) Zhou, J.; Chan, L.; Zhou, S. Trigonelline: a plant alkaloid with therapeutic potential for diabetes and central nervous system disease. *Curr. Med. Chem.* **2012**, *19*, 3523−3531.
(9) Butt, M. S.; Sultan, M. T. Coffee and its consumption: benefits and risks. *Crit. Rev. Food Sci. Nutr.* **2011**, *51*, 363−373.
(10) Chen, Z.; Peng, C.; Jiao, R.; Wong, Y. M.; Yang, N.; Huang, Y. Anti-hypertensive nutraceuticals and functional foods. *J. Agric. Food Chem.* **2009**, *57*, 4485−4499.
(11) Almeida, A. A.; Farah, A.; Silva, D. A. M.; Nunam, E. A.; Glória, M. B. A. Antibacterial activity of coffee extracts and selected coffee chemical compounds against enterobacteria. *J. Agric. Food Chem.* **2006**, *54*, 8738−8743.
(12) Santos, M. D.; Almeida, M. C.; Lopes, N. P.; Souza, G. E. P. Evaluation of the anti-inflamatory, analgesic and antypiretic activities of the natural polyphenol chlorogenic acid. *Biol. Pharm. Bull.* **2006**, *29*, 2236−2240.
(13) Shahidi, F.; Chandrasekara, A. Hydroxycinnamates and their in vitro and in vivo antioxidant activities. *Phytochem. Rev.* **2010**, *9*, 147−170.
(14) Ju, J.; Picinich, S. C.; Yang, Z.; Zhao, Y.; Suh, N.; Kong, A.; Yang, C. S. Cancer-preventive activities of tocopherols and tocotrienols. *Carcinogenesis* **2010**, *31*, 533−542.
(15) Nkondjock, A. Coffee consumption and the risk of cancer: an overview. *Cancer Lett.* **2009**, *277*, 121−125.
(16) Fernandez-Panchon, M. S.; Villano, D.; Troncoso, A. M.; Garcia-Parrilla, M. C. Antioxidant activity of phenolic compounds: from *in vitro* results to *in vivo* evidence. *Crit. Rev. Food Sci. Nutr.* **2008**, *48*, 649−671.
(17) Almeida, I. F.; Fernandes, E.; Lima, J. L.; Costa, P. C.; Bahia, M. F. *In vitro* protective efect of *Hypericum androsaemum* extract against oxygen and nitrogen reactive species. *Basic Clin. Pharmacol. Toxicol.* **2009**, *105*, 222−227.
(18) Halliwell, B.; Gutteridge, J. M. Chapter 2. The chemistry of free radicals and related reactive species. In *Free Radicals in Biology and Medicine*, 4th ed.; Halliwell, B., Gutteridge, J. M., Eds.; Oxford University Press: New York, 2007; pp 30−78.
(19) Kozuma, K.; Tsuchiya, S.; Kohori, J.; Hase, T.; Tokimitsu, I. Antihypertensive effect of green coffee bean extract on mildly hypertensive subjects. *Hypertens. Res.* **2005**, *28*, 711−718.
(20) Ochiai, R.; Jokura, H.; Suzuki, A.; Tokimitsu, I.; Ohishi, M.; Komai, N.; Rakugi, H.; Ohigara, T. Green coffee bean extract improves human vasoreactivity. *Hypertens. Res.* **2004**, *27*, 731−737.
(21) Tanaka, K.; Nishizono, S.; Tamaru, S.; Kondo, M.; Shimoda, H.; Tanaka, J.; Okada, T. Anti-obesity and hypotriglyceridemic properties of coffee bean extract in SD rats. *Food Sci. Technol. Res.* **2009**, *15*, 147−152.
(22) Vinson, J. A.; Burnham, B. R.; Nagendran, M. V. Randomized, double-blind, placebo-controlled, linear dose, crossover study to evaluate the efficacy and safety of a green coffee bean extract in overweight subjects. *Diabetes, Metab. Syndr. Obes.: Targets Ther.* **2012**, *5*, 21−27.
(23) Heleno, S. A.; Martins, A.; Queiroz, M. J. R. P.; Ferreira, I. C. F. R. Bioactivity of phenolic acids: metabolites *versus* parent compounds: a review. *Food Chem.* **2015**, *173*, 501−513.
(24) Martínez-López, S.; Sarriá, B.; Baeza, G.; Mateos, R.; Bravo-Clemente, L. Pharmacokinetics of caffeine and its metabolites in plasma and urine after consuming a soluble green/roasted coffee blend by healthy subjects. *Food Res. Int.* **2014**, *64*, 125−133.
(25) Farah, A. Chapter 15. Coffee as a speciality and functional beverage. In *Functional and Speciality Beverage Technology*, 1st ed.; Paquin, P., Ed.; Woodhead Publishing: Cambridge, UK, 2009; pp 370−395.
(26) Prior, R. L.; Hoang, H.; Gu, L.; Wu, X.; Bacchiocca, M.; Howard, L.; Hampsch-Woodill, M.; Huang, D.; Ou, B.; Jacob, R. Assays for hydrophilic and lipophilic antioxidant capacity (oxygen radical absorbance capacity (ORACFL)) of plasma and other biological and food samples. *J. Agric. Food Chem.* **2003**, *51*, 3273−3279.
(27) Farah, A.; De Paulis, T.; Trugo, L. C.; Martin, P. R. Effect of roasting on the formation of chlorogenic acid lactones in coffee. *J. Agric. Food Chem.* **2005**, *53*, 1505−1513.
(28) Clifford, M. N.; Knight, S. The cinnamoyl-amino acid conjugates of green robusta coffee beans. *Food Chem.* **2004**, *87*, 457−463.
(29) Perrone, D.; Farah, A.; Donangelo, C. M.; De Paulis, T.; Martin, P. R. Comprehensive analysis of major and minor chlorogenic acids and lactones in economically relevant Brazilian coffee cultivars. *Food Chem.* **2008**, *106*, 859−867.
(30) Clifford, M. N.; Johnston, K. L.; Knight, S.; Kuhnert, N. Hierarchical scheme for LC-MS identification of chlorogenic acids. *J. Agric. Food Chem.* **2003**, *51*, 2900−2911.
(31) Clifford, M. N.; Knight, S.; Surucu, B.; Kuhnert, N. Characterization by LC-MS^n of four new classes of chlorogenic acids in green coffee beans: dimethoxycinnamoylquinic acids, diferuloylquinic acids, caffeoyl-dimethoxycinnamoylquinic acids, and feruloyl-dimethoxycinnamoylquinic acids. *J. Agric. Food Chem.* **2006**, *54*, 1957−1969.
(32) Clifford, M. N.; Marks, S.; Knight, S.; Kuhnert, N. Characterization by LC-MS^n of four new classes of *p*-coumaric acid-containing diacyl chlorogenic acids in green coffee beans. *J. Agric. Food Chem.* **2006**, *54*, 4095−4101.
(33) Singleton, V. L.; Rossi, J. A. Colorimetry of total phenolics with phosphomolybdic-phosphotungstic acid reagents. *Am. J. Enol. Vitic.* **1965**, *16*, 144−158.
(34) Rodrigues, N. P.; Benassi, M. T.; Bragagnolo, N. Scavenging capacity of coffee brews against oxygen and nitrogen reactive species and the correlation with bioactive compounds by multivariate analysis. *Food Res. Int.* **2014**, *61*, 228−235.
(35) Ou, B.; Hampsch-Woodill, M.; Prior, R. L. Development and validation of an improved oxygen radical absorbance capacity assay using fluorescein as the fluorescent probe. *J. Agric. Food Chem.* **2001**, *49*, 4619−4626.
(36) Gomes, A.; Fernandes, E.; Silva, A. M. S.; Santos, C. M. M.; Pinto, D. C. G. A.; Cavaleiro, J. A. S.; Lima, J. L. F. C. 2-Styrylchromones: novel strong scavengers of reactive oxygen and nitrogen species. *Bioorg. Med. Chem.* **2007**, *15*, 6027−6036.
(37) IUPAC. Nomenclature of cyclitols. *Biochem. J.* **1976**, *153*, 23−31.
(38) Squadrito, G. L.; Pryor, W. A. Oxidative chemistry of nitric oxide: the roles of superoxide, peroxynitrite, and carbon dioxide. *Free Radical Biol. Med.* **1998**, *25*, 392−403.
(39) Alonso-Salces, R. M.; Serra, F.; Reniero, F.; Héberger, K. Botanical and geographical characterization of green coffee (*Coffea arabica* and *Coffea canephora*): chemometric evaluation of phenolic and methylxanthine contents. *J. Agric. Food Chem.* **2009**, *57*, 4224−4235.
(40) Bicho, N. C.; Leitão, A. E.; Ramalho, J. C.; Alvarenga, N. B.; Lidon, F. C. Identification of chemical clusters discriminators of arabica and robusta green coffee. *Int. J. Food Prop.* **2013**, *16*, 895−904.
(41) Rodrigues, E.; Mariutti, L. R. B.; Mercadante, A. Z. Carotenoids and phenolic compounds from *Solanum sessiliflorum*, an unexploited Amazonian fruit, and their scavenging capacity against reactive oxygen and nitrogen species. *J. Agric. Food Chem.* **2013**, *61*, 3022−3029.
(42) Pistón, M.; Machado, I.; Branco, C. S.; Cesio, V.; Heinzen, H.; Ribeiro, D.; Fernandes, E.; Chisté, R. C.; Freitas, M. Infusion, decoction and hydroalcoholic extracts of leaves from artichoke (*Cynara cardunculus* L. subsp. *cardunculus*) are effective scavengers of physiologically relevant ROS and RNS. *Food Res. Int.* **2014**, *64*, 150−156.
(43) Horstman, J. A.; Wrona, M. Z.; Dryhurst, G. Further insights into the reaction of melatonin with hydroxyl radical. *Bioorg. Chem.* **2002**, *30*, 371−382.

DOI: 10.1021/acs.jafc.5b00530
J. Agric. Food Chem. 2015, 63, 4815−4826

(44) Anouar, E.; Kosinová, P.; Kozlowski, D.; Mokrini, R.; Duroux, J. L.; Trouillas, P. New aspects of the antioxidant properties of phenolic acids: a combined theoretical and experimental approach. *Phys. Chem. Chem. Phys.* **2009**, *11*, 7659−7668.
(45) Pannala, A. S.; Razaq, R.; Halliwell, B.; Singh, S.; Rice-Evans, C. A. Inhibition of peroxynitrite dependent tyrosine nitration by hydroxycinnamates: nitration or electron donation? *Free Radical Biol. Med.* **1998**, *24*, 594−606.
(46) Iwai, K.; Kishimoto, N.; Kakino, Y.; Mochida, K.; Fujita, T. In vitro antioxidative effects and tyrosinase inhibitory activities of seven hydroxycinnamoyl derivatives in green coffee beans. *J. Agric. Food Chem.* **2004**, *52*, 4893−4898.
(47) Kono, Y.; Shibata, H.; Kodama, Y.; Ueda, A.; Sawa, Y. Chlorogenic acid as a natural scavenger for hypochlorous acid. *Biochem. Biophys. Res. Commun.* **1995**, *217*, 972−978.
(48) Winterbourn, C. C. Reconciling the chemistry and biology of reactive oxygen species. *Nat. Chem. Biol.* **2008**, *4*, 278−286.

DOI: 10.1021/acs.jafc.5b00530
J. Agric. Food Chem. 2015, 63, 4815−4826

JOURNAL OF AGRICULTURAL AND FOOD CHEMISTRY

Article

pubs.acs.org/JAFC

Lipid-Encapsulated Echium Oil (*Echium plantagineum*) Increases the Content of Stearidonic Acid in Plasma Lipid Fractions and Milk Fat of Dairy Cows

Melissa L. Bainbridge,[†] Adam L. Lock,[§] and Jana Kraft*[,†]

[†]Department of Animal Science, University of Vermont, 570 Main Street, Burlington, Vermont 05405, United States

[§]Department of Animal Science, Michigan State University, 474 South Shaw Lane, East Lansing, Michigan 48824, United States

Supporting Information

ABSTRACT: The objective of this study was to evaluate the impact of feeding lipid-encapsulated echium oil (EEO) on animal performance and milk fatty acid profile. Twelve Holstein dairy cows were used in a 3 × 3 Latin Square design with 14 day periods. Treatments were a control diet (no supplemental fat), 1.5% dry matter (DM) as EEO and 3.0% DM as EEO. Treatments had no negative effect on animal performance (dry matter intake, milk yield, and fat yield). The milk fat content of total n-3 fatty acids and stearidonic acid (SDA) increased with EEO supplementation ($P < 0.001$). The proportion of SDA increased in all plasma lipid fractions with EEO supplementation ($P < 0.001$). Transfer of SDA from EEO into milk fat was 3.4 and 3.2% for the 1.5 and 3% EEO treatments, respectively. In conclusion, EEO increases the content of n-3 fatty acids in milk fat; however, the apparent transfer efficiency was low.

KEYWORDS: *blood metabolites, γ-linolenic acid, bioactive fatty acids, plasma lipid fractions, transfer efficiency*

INTRODUCTION

The increased understanding of the relationship between nutrition and health has led to a growing interest in promoting functional foods enriched with bioactive compounds. One class of bioactive compounds is n-3 fatty acids (n-3 FA), which are known for their protective effects against inflammation,[1] neurological disorders,[2] and cardiovascular diseases,[3,4] as well as their importance to growth and development.[5] Current dietary sources do not meet the requirements for n-3 FA in the human diet,[6] driving the pursuit to develop functional foods enriched with n-3 FA.

The fatty acid profile of milk is predominantly influenced by the diet of dairy cows,[7] and research has demonstrated that FA derived from supplemental oils can be incorporated into milk fat.[8,9] There are several challenges, however, when supplementing dairy cows with oils rich in polyunsaturated FA (PUFA). One is the extensive biohydrogenation of dietary unsaturated FA by rumen bacteria, which often exceeds 85%.[10] This produces *trans*-fatty acid isomers that decrease lipogenesis in the mammary gland, leading to milk fat depression, and reduce the amount of unsaturated FA available to the mammary gland for milk fat synthesis.[10] Various protection methods have been developed to try to minimize ruminal biohydrogenation of feed-derived unsaturated FA, such as chemical treatment, calcium salt, protein aldehyde matrix, and encapsulation with saturated lipid. Hence, protecting n-3 FA from bacterial degradation in the rumen is essential to increase the amount of n-3 FA in milk while maintaining animal performance.[11]

Docosahexaenoic acid (DHA; 22:6 4*c*,7*c*,10*c*,13*c*,16*c*,19*c*) and eicosapentaenoic acid (EPA; 20:5 5*c*,8*c*,11*c*,14*c*,17*c*) are long-chain, highly unsaturated n-3 FA that are preferentially incorporated into plasma cholesterol esters and phospholipids.[12] Both plasma lipid fractions are unavailable to the mammary gland for production of milk fat,[13] resulting in a low transfer efficiency of EPA and DHA into milk.[14] Recent research demonstrates the two shorter carbon chain n-3 FA, *α*-linolenic acid (ALA; 18:3 9*c*,12*c*,15*c*) and stearidonic acid (SDA; 18:4 6*c*,9*c*,12*c*,15*c*), show similar health benefits to EPA and DHA.[15,16] SDA bypasses the initial rate-limiting step of *δ*-6-desaturase in the biosynthesis of EPA and DHA and, thus, is converted 4−5-fold more efficiently to EPA than ALA.[17] Moreover, recent research suggests that uptake of FA by the mammary gland is based on the fatty acid composition of plasma triacylglyceride (TAG), as an intravenous infusion of a TAG emulsion of ALA exhibited a higher transfer efficiency (28%) to milk fat when compared to DHA (11%).[18]

Echium oil (EO) from the seed of *Echium plantagineum*, a member of the Boraginaceae family, is a plant-based source of SDA (13% of total FA), ALA (31% of total FA), and *γ*-linolenic acid (GLA; 18:3 6*c*,9*c*,12*c*; 9% of total FA). GLA has been shown to possess anticarcinogenic and anti-inflammatory properties,[19,20] and several studies have shown the health benefits of echium oil, as well as its promise as an alternative to fish oils.[21,22] Kitessa and Young[23] demonstrated an increase in the n-3 FA content of milk with inclusion of a formaldehyde-treated EO on a pasture-based diet using five dairy cows. Lipid protection may provide more resilience against rumen biohydrogenation and thus may result in higher incorporation into milk fat.[11] There can also be considerable variation in response to supplementation depending upon basal diet and inclusion level;[24] thus, an evaluation of EO fed at incremental

Received: February 15, 2015
Revised: April 22, 2015
Accepted: April 22, 2015
Published: April 22, 2015

ACS Publications © 2015 American Chemical Society

DOI: 10.1021/acs.jafc.5b00857
J. Agric. Food Chem. 2015, 63, 4827−4835

levels on conserved forages is needed to determine the optimal inclusion rate for commercial feasibility. It is necessary to determine which plasma lipid fractions EO-derived FA are preferentially incorporated into and hence to what extent they can be incorporated into milk fat. We hypothesized that the inclusion of lipid-encapsulated echium oil (EEO) in the diet of dairy cows fed a total mixed ration (TMR) would increase the ALA, SDA, EPA, DHA, and GLA contents of milk fat. Our objectives were to (1) evaluate the effects of feeding an EEO supplement on milk production parameters, (2) determine the transfer efficiency of EO-derived FA to milk fat by supplementing incremental levels of EEO, and (3) assess the incorporation of EO-derived FA into plasma lipid fractions.

MATERIALS AND METHODS

Experimental Design. All experimental procedures were approved by the Michigan State Institutional Animal Care and Use Committee. Twelve multiparous Holstein dairy cows in late lactation (229 ± 62 DIM) were used in a 3 × 3 Latin Square design with 14 day experimental periods. Cows averaged body weights of 749 ± 69 kg and body condition scores of 3.56 ± 0.39 (1−5 in 0.25 increments[25]) at the start of the study. Diets were formulated to meet NRC (2001) nutrient requirements (Table 1) and fed as TMRs. Treatments were diets containing no supplemental fat (control; CON), diets supplemented with EEO at 1.5% of DM (low EEO; LEO), and EEO at 3% of DM (high EEO; HEO). EEO replaced soy hulls in the diet. EO was purchased from Technology Crops International (Winston-Salem, NC, USA) and lipid-encapsulated with hydrogenated vegetable oil by Jefo (Saint-Hyacinthe, Canada) using the spray cooling method with a prilling automizer. Lipid encapsulation technology is based on the inherent property of saturated lipids being resistant to enzymes in the rumen, yet susceptible to enzymatic digestion in the small intestine.[11] EO contained 35% ALA, 15% 18:1 9*c*, 15% SDA, 10% 18:2 9*c*,12*c*, 10% GLA, and 3% 18:0. The lipid-encapsulated supplement contained 25% EO, and the fatty acid profile of the supplement is presented in Table 2. A 10 day period before the start of the trial served as a preliminary period. Milk samples were collected during the last 3 days of this period, and cows were subsequently blocked by fat-corrected milk (FCM) yield and assigned to treatments. Cows were housed in individual tie stalls, blocked from feed at 8:00 a.m., fed once daily at 10:00 a.m., and milked twice daily at 4:00 a.m. and 3:00 p.m. Corn silage and alfalfa silage DM were determined twice weekly, and TMR was adjusted accordingly. Diets were fed ad libitum (12−17% orts) throughout the experiment. Fresh drinking water was available continuously.

Table 1. Ingredient and Nutrient Composition of the Treatment Diets

	treatment		
	CON[a]	LEO[b]	HEO[c]
ingredient, % of DM			
corn silage	33.9	33.9	33.9
alfalfa silage	17.0	17.0	17.0
dry ground corn	23.8	23.8	23.8
soybean meal	12.7	12.7	12.7
soyhulls	9.2	7.7	6.2
vitamin−mineral mix[d]	3.5	3.5	3.5
echium oil supplement	0.0	1.5	3.0
nutrient composition			
DM, %	48.8	47.7	47.4
NDF,[e] % of DM	27.2	26.2	25.3
CP,[f] % of DM	17.0	15.9	16.3
starch, % of DM	28.5	28.4	28.5
total fatty acids, % of DM	2.72	3.71	4.94
cis-9,*cis*-12 18:2	1.33	1.25	1.31
cis-6,*cis*-9,*cis*-12 18:3	0.00	0.03	0.06
cis-9,*cis*-12,*cis*-15 18:3	0.20	0.31	0.43
cis-6,*cis*-9,*cis*-12,*cis*-15 18:4	0.0	0.04	0.08
total SFA	0.58	1.49	2.39
total MUFA	0.59	0.59	0.65
total PUFA	1.54	1.63	1.89
total n-3	0.20	0.35	0.51
total n-6	1.34	1.28	1.37
n-6/n-3 ratio	6.61	3.63	2.69

[a]CON, control (0% of DM as lipid-encapsulated echium oil). [b]LEO, 1.5% of DM as lipid-encapsulated echium oil. [c]HEO, 3% of DM as lipid-encapsulated echium oil. [d]Vitamin−mineral mix contained (DM basis) 30.1% limestone, 25.3% sodium bicarbonate, 10.1% salt, 7.07% urea, 6.00% potassium chloride, 5.98% dicalcium phosphate, 5.68% magnesium sulfate, 5.68% animal fat, 3.94% trace mineral premix and vitamins, and 0.21% selenium yeast 600 (600 mg of Se/kg). [e]NDF, neutral detergent fiber. [f]CP, crude protein.

Table 2. Fatty Acid Composition (Grams per Kilogram) of Lipid-Encapsulated Echium Oil (EEO)

fatty acid	EEO
12:0	0.12
14:0	0.81
16:0	41.5
18:0	33.4
cis-9 18:1	4.33
cis-11 18:1	0.14
cis-9,*cis*-12 18:2	3.96
20:0	0.39
cis-6,*cis*-9,*cis*-12 18:3	2.65
cis-9,*cis*-12,*cis*-15 18:3	9.03
cis-6,*cis*-9,*cis*-12,*cis*-15 18:4	3.40
22:0	0.06
cis-11,*cis*-14,*cis*-17 20:3	0.12
24:0	0.06
cis-15 24:1	0.04

Data and Sample Collection. Milk weights and samples were taken at each milking during the last 4 days of each period; an aliquot was preserved with 2-bromo-2-nitropropane-1,3-diol and analyzed for fat, protein, lactose, and milk urea nitrogen (MUN) by mid-infrared spectroscopy by the Michigan Herd Improvement Association (Universal Lab Services, Lansing, MI, USA). Another aliquot was stored at −20 °C without preservative for fatty acid analysis. Feed offered and refusals were weighed and recorded daily. Feed ingredients and TMR were sampled during the last 4 days of each period and stored at −20 °C until further analysis. Blood was collected from coccygeal vessels into evacuated tubes containing K_2EDTA (Becton Dickenson, Franklin Lakes, NJ, USA) at 9:00 a.m. on the last day of each period. Blood samples were placed immediately on ice, and plasma was obtained within 2 h of blood collection by centrifugation at 900*g* for 15 min at 4 °C and stored at −20 °C.

Feed and Orts Samples. Samples for each period were composited and dried in a forced-air oven at 65 °C for 48 h. Dried samples were weighed to determine dry matter and ground with a Wiley mill using a 1 mm screen (Arthur H. Thomas, Philadelphia, PA, USA). Individual feed ingredients and orts were analyzed for neutral detergent fiber (NDF) with heat-stable α-amylase and sodium sulfite,[26] crude protein (CP),[27] and starch composition[28] (Cumberland Valley Analytical Services Inc., Hagerstown, MD, USA). Reported NDF values are inclusive of ash. The fatty acid composition of feed samples was determined according to a modified method of Sukhija and Palmquist.[29] Glyceryl tridecanoate (Nu-Check Prep, Elysian, MN, USA) was used as an internal standard (1 mg/mL in acetone). Two milliliters of toluene and 2 mL of 5% methanolic sulfuric acid (Sigma-

DOI: 10.1021/acs.jafc.5b00857
J. Agric. Food Chem. 2015, 63, 4827−4835

Table 3. Fatty Acid Intake (Grams per Day) of Treatments

	treatment				
	CON[a]	LEO[b]	HEO[c]	SE	*P* value
total fatty acids	726a	1000b	1329c	27.0	<0.001
16:0	114a	250b	382c	7.54	<0.001
18:0	21.5a	125b	228c	4.48	<0.001
cis-9 18:1	145a	146a	162b	3.94	<0.001
cis-9,*cis*-12 18:2	358a	338b	356a	8.24	<0.001
cis-9,*cis*-12,*cis*-15 18:3	50.4a	84.5b	116c	2.34	<0.001
cis-6,*cis*-9,*cis*-12 18:3	0.30a	8.50b	17.1c	0.32	<0.001
cis-6,*cis*-9,*cis*-12,*cis*-15 18:4	0.04a	10.6b	21.7c	0.40	<0.001
$\sum$ other[d]	35.7a	34.8a	44.5b	1.02	<0.001
total SFA[e]	157a	400b	641c	12.6	<0.001
total MUFA[f]	156a	158a	176b	3.91	<0.001
total PUFA[g]	413a	442b	512c	11.1	<0.001
total n-3	54.9a	95.6b	138c	2.75	<0.001
total n-6	358a	347b	373c	8.51	<0.001

[a]CON, control (0% of DM as lipid-encapsulated echium oil). [b]LEO, 1.5% of DM as lipid-encapsulated echium oil. [c]HEO, 3% of DM as lipid-encapsulated echium oil. [d]$\sum$ other, 12:0, 14:0, 15:0, *cis*-9 16:1, 17:0, *cis*-11 18:1, 20:0, 20:1 n-9, 21:0, 20:2 n-6, 22:0,22:1 n-9, 20:4 n-6, 23:0, 24:0. [e]Total SFA, sum of saturated fatty acids (4:0 to 26:0). [f]Total MUFA, sum of monounsaturated fatty acids (14:1 to 24:1). [g]Total PUFA: sum of polyunsaturated fatty acids (18:2 to 22:5).

Aldrich, St. Louis, MO, USA) were added to 500 mg of ground sample and shaken overnight at 50 °C. Samples were cooled to room temperature, and 5 mL of 5% sodium chloride solution and 2 mL of *n*-hexane were added. The extraction procedure was repeated twice with 1 mL of *n*-hexane each. The samples were washed with 4 mL of saturated potassium bicarbonate solution; the *n*-hexane phase was removed, dried over 1 g of anhydrous sodium sulfate, and purified using silica gel and activated charcoal. A 1% fatty acid methyl ester (FAME) solution was prepared in *n*-hexane, and samples were stored −20 °C until gas chromatography (GC) analysis.

Milk FA Analysis. Milk samples from the last 4 days of each period were composited by fat yield, and an aliquot was centrifuged at 17800*g* for 30 min at 8 °C to collect the cream. Milk lipids were extracted using the method of Hara and Radin,[30] and FAME were prepared by base-catalyzed transmethylation. Briefly, a total of 25 mg of lipid extract was solubilized in 2.5 mL of *n*-hexane, and 0.5 mL of 0.5 M sodium methoxide was added to the lipid solution and subsequently vortexed for 5 min. Following, enough sodium bisulfate monohydrate was added to the vial to cover the lower layer. The supernatant containing the FAME was transferred into a 2 mL vial and directly used for GC analysis.

Plasma Lipid Fraction FA Analysis. Plasma lipids were extracted according to the method of Folch et al.,[31] using chloroform/methanol in a 2:1 ratio (v/v). The chloroform layer, containing the lipids, was dried down under nitrogen gas, and the lipids were resuspended in 1 mL of *n*-hexane/methyl *tert*-butyl ether/acetic acid (100:3:0.3; v/v) and stored at −20 °C. Lipid classes were separated by solid-phase extraction (SPE) using aminopropyl cartridges (Fisher Scientific, Waltham, MA, USA). The columns (100 mg matrix) were preconditioned with 1.2 mL of acetone/water (7:1; v/v) and 4 mL of *n*-hexane prior to use. The lipid solution was loaded onto the column, and 14 mL of *n*-hexane was added to elute cholesterol esters (CE) at a flow rate of 0.3 mL/min. TAG were extracted with 8 mL of *n*-hexane/chloroform/ethyl acetate (100:5:5; v/v). The column was then washed with 6 mL of chloroform/isopropanol (2:1; v/v), and this solution was discarded. Free FA (FFA) were eluted in 8 mL of chloroform/methanol/acetic acid (100:2:2; v/v), and phospholipids (PL) were eluted by adding 10 mL of methanol/chloroform/water (10:5:4; v/v) to the column. All fractions except for the PL were dried down under nitrogen gas, redissolved in chloroform, and then stored at −20 °C until transesterification. PL were washed with 5% sodium chloride before being dried down under nitrogen gas and redissolved in chloroform and stored at −20 °C for further analysis. The TAG fraction was methylated with sodium methoxide as described above. PL, CE, and FFA fractions were methylated with 1 mL of sodium hydroxide at 100 °C for 10 min. One milliliter of 10% (w/w) boron trifluoride−methanol solution (Sigma-Aldrich) was added and incubated at 100 °C for 10 min. Once these fractions had cooled to room temperature, 2 mL of saturated potassium bicarbonate and 2 mL of *n*-hexane were added. The extraction step was repeated twice with 2 mL of *n*-hexane each and then transferred over anhydrous sodium sulfate. The samples were dried under nitrogen gas and resuspended in *n*-hexane to achieve a 0.1% FAME solution and stored at −20 °C for GC analysis.

Gas Chromatography. The total fatty acid composition covering ca. 110 FA in the range from C4:0 to C24:0, including branched-chain FA, isomers of octadecenoic acid (18:1) and conjugated linoleic acids (CLA), were determined by GC analysis of the FAME on a GC-2010 gas chromatograph (Shimadzu, Kyoto, Japan) equipped with a split injector (1:100 split ratio) and a flame ionization detector (FID) using an SP-2560 fused-silica capillary column (100 m × 0.25 m × 0.2 μm). Hydrogen was used as the carrier gas at a flow rate of 1 mL/min and for the FID at 40 mL/min. The other gases were purified air at 400 mL/min and nitrogen makeup gas at 30 mL/min. Injector and detector temperatures were kept at 250 °C. The oven program was as follows: initial temperature of 45 °C, held for 4 min, programmed at 13 °C/min to 175 °C, held for 27 min, then programmed at 4 °C/min to 215 °C, and held for 35 min[32] The injection volume was 1 μL of the FAME mixture containing about 1−2 μg/μL. Integration and quantitation were accomplished with GCsolution software (version 2.30.00) and based on the FID response. FAME were identified by comparison of retention times with known FAME standards (Nu-Check Prep 463, 674, CLA mixture; Supelco PUFA-3 mixture and linoleic and linolenic acid mixture). The short-chain FAME were corrected for mass discrepancy using the correction factors published by Wolff et al.[33]

Plasma Metabolite Quantification. Commercially available kits were used to analyze the plasma concentrations of FFA (Serum/Plasma Fatty Acid Detection Kit, ZenBio; Research Triangle Park, NC, USA), β-hydroxybutyrate (BHBA) (β-Hydroxybutyrate assay kit, Sigma-Aldrich), and glucose (Glucose (GO) Assay Kit, Sigma-Aldrich) according to the manufacturers' instructions. Samples were analyzed in duplicate, and all coefficients of variance were <5%.

Calculations. Apparent transfer efficiency was determined as

DOI: 10.1021/acs.jafc.5b00857
J. Agric. Food Chem. 2015, 63, 4827−4835

$$100 \times \left[\frac{\mathrm{MFA(t)} - \mathrm{MFA(c)}}{\mathrm{EOFA(t)}}\right] \quad (1)$$

where MFA is the FA yield (g/day) in milk, EOFA is the amount (g/day) of FA supplied by the EEO supplement, t is treatment (i.e., LEO and HEO), and c is control (CON).

Statistical Analyses. Data were analyzed using the fit model program of JMP Pro (version 11; SAS Institute, Cary, NC, USA). The following model was used for all data:

$$Y_{ijk} = \mu + S_i + C(S)_{ij} + P_k + T_l + e_{ijkl}$$

Y_{ijk} = dependent variable, μ = overall mean, S_i = fixed effect of square (i = 1−4), $C(S)_{ij}$ = random effect of cow nested within square (j = 1−12), P_k = fixed effect of period (k = 1−3), T_l = fixed effect of treatment (l = 1−3), and e_{ijk} = residual error. Treatment by period interactions were evaluated and removed because $P > 0.15$. A post hoc Tukey's honestly significantly difference (HSD) test was used to determine differences between dietary treatments. Differences between plasma lipid fractions were determined by an unpaired t test. Reported values are least-squares (LS) means and standard error (SE). Significance was declared at $P \leq 0.05$ and trends at $0.05 \leq P \leq 0.10$.

RESULTS

Animal Performance. FA intakes are shown in Table 3. CON, LEO, and HEO treatments provided 50.4, 84.5, and 116.4 g/day of ALA, respectively (Table 3; $P < 0.001$). The intakes of SDA were 0.0, 10.6, and 21.7 g/day for CON, LEO, and HEO treatments, respectively ($P < 0.001$). Treatments had no effect on DMI, which averaged 26.6 kg/day (Table 4). Milk yield (30.7 kg/day), energy-corrected milk (34.0 kg/day), and feed efficiency (1.3) were unaffected by EEO supplementation (Table 4). There was a trend toward increased 3.5% fat-corrected milk in the HEO treatment ($P = 0.09$; Table 4). The percentage of milk fat (4.1 vs 4.3%; $P = 0.03$) and fat yield (1.25 vs 1.32 kg/day; $P = 0.04$) was higher in the HEO treatment compared to CON. Milk protein percentage decreased between CON and HEO treatments (3.56 and 3.47%, respectively; $P = 0.002$; Table 4); however, protein yield did not differ among treatments and averaged 1.1 kg/day. Milk urea nitrogen was lower in the HEO treatment when compared to CON (10.1 and 10.9 mg/dL, respectively; $P = 0.01$). Percentage of milk lactose and lactose yield were unaffected by treatment. There was no difference between treatments for plasma glucose (74.0 mg/dL), FFA (0.12 mmol/L), or BHBA (0.67 mmol/L) (Table 5).

Table 4. Daily Dry Matter Intake (DMI), Milk Yield, Milk Components, and Feed Efficiency of Dairy Cows[a] in Response to Dietary CON,[b] LEO,[c] and HEO[d] Treatments

	treatment				
	CON	LEO	HEO	SE	P value
DMI (kg/day)	26.4	26.5	26.8	0.58	ns
milk yield (kg/day)	30.6	30.3	31.1	0.92	ns
3.5% fat-corrected milk (FCM)[e]	33.5	33.8	35.5	0.75	0.09
energy-corrected milk (ECM)[f]	33.6	33.8	34.6	0.85	ns
milk components yield (kg/day)					
fat	1.25a	1.27ab	1.32b	0.03	0.04
protein	1.08	1.07	1.08	0.03	ns
lactose	1.39	1.38	1.43	0.05	ns
milk components (%)					
fat	4.10a	4.22ab	4.25b	0.10	0.03
protein	3.56a	3.54ab	3.47b	0.04	0.002
lactose	4.53	4.54	4.55	0.06	ns
feed efficiency[g]	1.28	1.28	1.31	0.04	ns
milk urea nitrogen (mg/dL)	10.9a	10.4ab	10.1b	0.44	0.01

[a]LS means are based on 12 dairy cows per treatment. LS means without a common letter differ significantly ($P < 0.05$). [b]CON, control (0% of DM as lipid-encapsulated echium oil). [c]LEO, 1.5% of DM as lipid-encapsulated echium oil. [d]HEO, 3% of DM as lipid-encapsulated echium oil. [e]3.5% FCM = [0.43 × milk yield (kg/day)] + [16.22 × fat yield (kg/day)]. [f]ECM = [12.82 × fat yield (kg/day)] + [7.13 × protein yield (kg/day)] + [0.32 × milk yield (kg/day)]. [g]Feed efficiency = kg of 3.5% FCM/kg DMI.

Table 5. Plasma Metabolites[a] of Dairy Cows in Response to Dietary CON,[b] LEO,[c], and HEO[d] Treatments

	treatment				
	CON	LEO	HEO	SE	P value
FFA (mmol/L)	0.11	0.12	0.12	0.01	ns
glucose (mg/dL)	75.8	74.5	71.7	1.20	0.07
BHBA (mmol/L)	0.71	0.69	0.61	0.06	ns

[a]LS means are based on 12 dairy cows per treatment. LS means without a common letter differ significantly ($P < 0.05$). [b]CON, control (0% of DM as lipid-encapsulated echium oil). [c]LEO, 1.5% of DM as lipid-encapsulated echium oil. [d]HEO, 3% of DM as lipid-encapsulated echium oil.

Milk FA Composition. Supplementation with EEO altered the milk FA profile (Table 6 and Supplemental Table 1). LEO and HEO treatments decreased the content of de novo synthesized FA (<16 carbon atoms) by 5 and 12%, respectively, relative to CON ($P < 0.001$). The EEO treatments increased the preformed fatty acid (>16 carbon atoms) content in milk fat by 9% (LEO) and 16% (HEO) when compared to CON ($P < 0.001$). Total saturated fatty acid (SFA) content of milk fat was reduced in LEO and HEO relative to CON (Table 6; $P < 0.001$). The content of MUFA in milk fat increased from CON to LEO treatment (by 6%) and from CON to HEO treatment (by 12%; $P < 0.001$). The largest change in MUFA was seen in the *trans*-18:1 isomers; increasing 18% (LEO) and 37% (HEO), respectively, relative to CON ($P < 0.001$; Table 6). Total PUFA content increased in milk fat with increasing EEO supplementation ($P < 0.001$). Total n-3 FA showed the largest percentage change of all PUFA when compared to CON, increasing by 34% for the LEO treatment and by 66% for the HEO treatment ($P < 0.001$), compared to CON. The content of n-6 FA decreased in LEO (by 5%) and HEO (by 7%), compared to CON ($P < 0.001$). Similarly, the n-6/n-3 ratio decreased from 5.9 in CON to 4.1 and 3.3 for LEO and HEO treatments, respectively ($P < 0.001$). Both LEO and HEO treatments increased the content of FA derived from EO in milk fat. Compared with CON, the ALA content in milk fat increased 25 and 53% for LEO and HEO ($P < 0.001$), respectively. GLA increased, relative to CON, in LEO (by 80%) and HEO (by 145%) treatments ($P < 0.001$). The SDA content of milk fat increased 3.4-fold in the LEO treatment and 5.4-fold in the HEO treatment when compared to CON ($P < 0.001$). Milk fat from EEO-treated cows had a higher content of EPA than CON, increasing 43 and 61% for LEO and HEO, respectively ($P < 0.001$). DHA was not detected in milk fat. Total CLA increased 14% in the LEO treatment and 36% in the HEO treatment compared to CON ($P < 0.001$). Branched-chain FA decreased, relative to CON, by 6 and by 12% for LEO and HEO, respectively ($P < 0.001$).

DOI: 10.1021/acs.jafc.5b00857
J. Agric. Food Chem. 2015, 63, 4827−4835

Table 6. Milk Fat Content[a] of Select Fatty Acids (Grams per 100 g of FA) in Response to Dietary CON,[b] LEO,[c], and HEO[d] Treatments

	treatment				
fatty acid	CON	LEO	HEO	SE	*P* value
16:0	34.8a	34.1b	34.5ab	0.62	0.04
18:0	6.80a	7.99b	8.58c	0.21	<0.001
trans-11 18:1	0.54a	0.62a	0.77b	0.08	<0.001
cis-9 18:1	14.8a	15.9b	16.7c	0.28	<0.001
cis-9,*cis*-12 18:2	2.46a	2.29b	2.24b	0.07	<0.001
cis-6,*cis*-9,*cis*-12 18:3	0.03a	0.06b	0.08c	0.00	<0.001
cis-9,*cis*-12,*cis*-15 18:3	0.38c	0.47c	0.58c	0.02	<0.001
cis-9,*trans*-11 18:2	0.29a	0.30a	0.37b	0.03	<0.001
cis-6,*cis*-9,*cis*-12,*cis*-15 18:4	0.02a	0.06b	0.09c	0.00	<0.001
cis-5,*cis*-8,*cis*-11,*cis*-14 20:4	0.16a	0.15b	0.15b	0.00	<0.001
cis-8,*cis*-11,*cis*-14,*cis*-17 20:4	0.02a	0.03b	0.04c	0.00	<0.001
cis-5,*cis*-8,*cis*-11,*cis*-14,*cis*-17 20:5	0.03a	0.05b	0.05b	0.00	<0.001
cis-7,*cis*-10,*cis*-13,*cis*-16,*cis*-19 22:5	0.06a	0.07b	0.06ab	0.00	0.03
unknown	0.29a	0.30a	0.32b	0.01	<0.001
de novo[e]	29.8a	28.7b	26.6c	0.53	<0.001
mixed[f]	36.4a	35.6ab	35.9b	0.65	0.03
preformed[g]	29.0a	31.5b	33.6c	0.70	<0.001
total SFA[h]	73.7a	72.4b	71.1c	0.53	<0.001
total MUFA[i]	20.5a	21.6b	22.6c	0.42	<0.001
total PUFA[j]	3.98a	4.05a	4.37b	0.12	<0.001
total n-6 PUFA[k]	2.85a	2.69b	2.64b	0.07	<0.001
total n-3 PUFA[l]	0.49a	0.65b	0.81c	0.02	<0.001
n-6:n-3 ratio	5.88a	4.11b	3.28c	0.07	<0.001
total *trans* 18:1	1.75a	1.91a	2.22b	0.17	<0.001
total CLA[m]	0.31a	0.33a	0.39b	0.03	<0.001
total odd and branched-chain FA	3.85a	3.41b	3.15c	0.11	<0.001
18:0 δ-9-desaturase index[n]	0.69a	0.67b	0.66b	0.01	<0.01

[a]LS means are based on 12 dairy cows per treatment. LS means without a common letter differ significantly ($P < 0.05$). [b]CON, control (0% of DM as lipid-encapsulated echium oil). [c]LEO, 1.5% of DM as lipid-encapsulated echium oil. [d]HEO, 3% of DM as lipid-encapsulated echium oil. [e]De novo, sum of fatty acids <16 carbons. [f]Mixed, sum of 16:0 and *cis*-9 16:1. [g]Preformed, sum of fatty acids >16 carbons. [h]Total SFA, sum of saturated fatty acids (4:0 to 26:0). [i]Total MUFA, sum of monounsaturated fatty acids (14:1 to 24:1). [j]Total PUFA, sum of polyunsaturated fatty acids (18:2 to 22:5). [k]Total n-6 PUFA, sum of n-6 PUFA: *cis*-9,*cis*-12 18:2, *cis*-6,*cis*-9,*cis*-12 18:3, *cis*-11,*cis*-14 20:2, *cis*-8,*cis*-11,*cis*-14 20:3, *cis*-5,*cis*-8,*cis*-11,*cis*-14 20:4, and *cis*-7,*cis*-10,*cis*-13,*cis*-16 22:4. [l]Total n-3 PUFA: sum of n-3 PUFA: *cis*-9,*cis*-12,*cis*-15 18:3, *cis*-6,*cis*-9,*cis*-12,*cis*-15 18:4, *cis*-11,*cis*-14,*cis*-17 20:3, *cis*-8,*cis*-11,*cis*-14,*cis*-17 20:4, *cis*-5,*cis*-8,*cis*-11,*cis*-14,*cis*-17 20:5, and *cis*-7,*cis*-10,*cis*-13,*cis*-16,*cis*-19 22:5. [m]Total CLA, sum of conjugated linoleic acids: *cis*-9,*trans*-11-CLA, *cis*-9,*cis*-11-CLA, *trans*-7,*trans*-9-CLA, and *trans*-10,*trans*-12-CLA. [n]18:0 δ-9-desaturase index: (*cis*-9 18:1/(18:0 + *cis*-9 18:1)).

The apparent transfer efficiencies of ALA from the EEO supplement to milk fat were 3.4 and 3.9% for LEO and HEO treatments, respectively (Table 7). SDA showed similar transfer efficiencies of 3.2% for LEO and 3.4% for HEO. The apparent transfer efficiencies of GLA were 3.0 and 2.8% for LEO and HEO, respectively.

Plasma Lipid Fraction FA Composition. The fatty acid composition of plasma lipid fractions, TAG, FFA, CE, and PL, are presented in Figure 1 and Supplemental Tables 2−5. Overall, 18:0 and 16:0 made up the predominant proportion of TAG and FFA fractions (Supplemental Tables 2 and 3), whereas 18:2 n-6 was the most abundant fatty acid in the CE and PL fractions (Supplemental Tables 4 and 5). The ALA ($P = 0.02$) content increased in plasma TAG in response to LEO (18%) and HEO (33%) treatments. SDA was not detected in CON plasma TAG and increased ($P < 0.001$) in response to LEO and HEO treatments. The GLA content of plasma TAG increased from CON to HEO (48%; $P < 0.01$) but not between CON and LEO (Figure 1). There was no increase of EPA in plasma TAG. Changes in the composition of most plasma FFA were negligible; however, there was a 41% increase in GLA ($P < 0.05$) between CON and HEO treatments, a 13-fold increase in SDA from CON to LEO, and a 39-fold increase from CON to HEO ($P < 0.001$). Plasma CE had the highest proportions of

Table 7. Transfer Efficiencies[a] of FA from the Echium Oil Supplement to Milk Fat

	treatment			
	LEO[b]	HEO[c]	SE	*P* value
cis-6,*cis*-9,*cis*-12 18:3, %	3.0	2.8	0.32	ns
cis-9,*cis*-12,*cis*-15 18:3, %	3.4	3.9	0.59	ns
cis-6,*cis*-9,*cis*-12,*cis*-15 18:4, %	3.4	3.2	0.23	ns
cis-6,*cis*-9,*cis*-12,*cis*-15 18:4 plus *cis*-5, *cis*-8,*cis*-11,*cis*-14,*cis*-17 20:5, %[d]	4.7	4.1	0.38	ns

[a]LS means are based on 12 dairy cows per treatment. LS means without a common letter differ significantly ($P < 0.05$). [b]LEO, 1.5% of DM as lipid-encapsulated echium oil. [c]HEO, 3% of DM as lipid-encapsulated echium oil. [d]*cis*-6,*cis*-9,*cis*-12,*cis*-15 18:4 (SDA) plus *cis*-5,*cis*-8,*cis*-11,*cis*-14,*cis*-17 20:5 (EPA): [((SDA + EPA in milk fat of treatment) − (SDA + EPA in milk fat of control))/ SDA in diet *100].

DOI: 10.1021/acs.jafc.5b00857
J. Agric. Food Chem. 2015, 63, 4827−4835

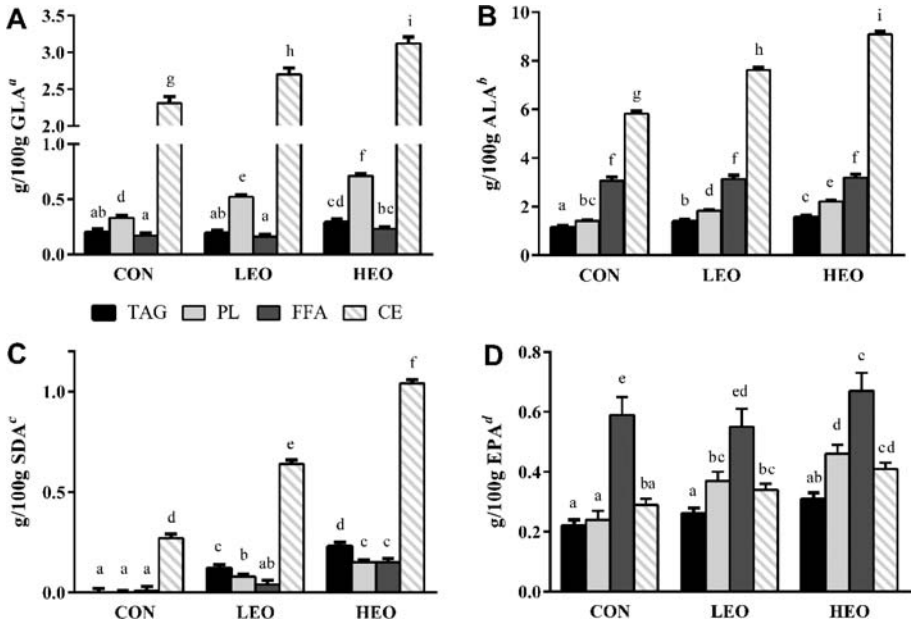

Figure 1. Content (g/100 g within plasma lipid fraction) of γ-linoleic acid (GLA) (A), α-linolenic acid (B), (ALA) stearidonic acid (C) (SDA), and eicosapentaenoic acid (D) (EPA) in plasma lipid fractions of dairy cows supplemented 0% DM as lipid-encapsulated echium oil (EO) (CON), 1.5% DM as EO (LEO), and 3% DM as EO (HEO). TAG, triacylglycerols; CE, cholesterol esters; PL, phospholipids; FFA, free fatty acids. Data are presented as least-squares means (n = 12) and standard error. LS means within fatty acids without a common letter differ significantly (P < 0.05).

ALA, GLA, and SDA of all plasma lipid fractions. ALA was 30% higher in plasma CE of LEO than CON and 55% higher in plasma CE of HEO than CON (P < 0.001). GLA increased 15 and 34% from CON to LEO and HEO treatments, respectively (P < 0.001). There was a 2.4-fold increase in SDA of plasma CE from CON to LEO and a 3.9-fold increase from CON to HEO (P < 0.001). EPA increased 20 and 44% in plasma CE from CON for LEO and HEO treatments, respectively (P < 0.01). Plasma PL showed a similar pattern of incorporation with significant increases in ALA, GLA, SDA, and EPA with increasing EEO inclusion in the diet (P < 0.001). There was a 56% (LEO) and 111% (HEO) increase in the content of GLA in plasma PL from CON (P < 0.001). ALA increased 30% in plasma PL from CON to LEO and 56% from CON to HEO (P < 0.001). EPA content of plasma PL increased 55 and 92% from CON to LEO and HEO, respectively (P < 0.001).

DISCUSSION

Animal Performance. Increasing the inclusion of EEO in the diet increased the intake of EO-derived FA (ALA, SDA, GLA) in the LEO and HEO treatment groups. Intakes of 18:0 and 16:0 also increased due to the lipid encapsulation of the EEO supplement. A primary consideration when supplementing dietary FA to dairy cows is their effect on production and performance. Inclusion of EEO in the diet of dairy cows at 1.5 and 3% of DM increased milk fat concentration and yield. These results are consistent with some experiments supplementing oil containing SFA or n-3 FA;[34,35] however, others have shown no change or a decrease in milk fat with n-3 FA supplementation.[9,15] This observation can be explained by the increase in fat content of the treatment diets. There was a slight decrease in milk protein percentage, but no change in the protein yield.

Milk FA Profile. Milk fat from cows supplemented with EEO contained less de novo synthesized FA and more preformed FA, which is similar to results observed with linseed oil or fish oil in the diet.[8,9] Unsaturated FA are known to inhibit de novo synthesis of milk fat, resulting in a greater uptake of preformed FA by the mammary gland.[36] A decrease in total SFA was observed despite the increase in SFA intake supplied by the lipid-encapsulated product. This can also be attributed to a reduction in de novo synthesized FA as they are composed primarily of SFA. The MUFA content of milk fat increased, mainly due to an increase in *trans* 18:1 isomers and a greater content of *cis*-9 18:1. The 18:0 δ-9-desaturase index [*cis*-9 18:1/(18:0 + *cis*-9 18:1)] decreased due to treatments; thus, the higher proportion of *cis*-9 18:1 in milk fat is explained by the increased supply of its precursor, 18:0, from the diet.

As expected, supplementation with EEO enhanced the content of PUFA in milk fat, particularly GLA, ALA, SDA, and their downstream metabolites: *cis*-8,*cis*-11,*cis*-14,*cis*-17 20:4, EPA, and *cis*-7,*cis*-10,*cis*-13,*cis*-16,*cis*-19 22:5 (docosapentaenoic acid; DPA). Similar results were seen by Kitessa and Young[23] when supplementing formaldehyde-treated EO for 10 days on a pasture-based diet. They noted, however, a decrease in milk production that was not observed in the present study. DHA was not detected in milk fat, despite the increase in DPA, which is consistent with Kitessa and Young.[23] Bernal-Santos et al.[37] also saw no change in the content of DHA in milk with abomasal infusion of SDA-rich soybean oil, containing 27.1% SDA. δ-6-Desaturase acts in both the pathways of converting ALA to SDA and EPA to DHA, and thus increasing ALA in the diet could saturate δ-6-desaturase in the conversion of ALA to SDA and cause a lower activity of this enzyme in the conversion of EPA to DHA.[38] Angulo et al. demonstrated the ability to increase DHA in milk fat by supplementing DHA-rich marine algae at 0.4% of DM for 10 weeks.[39]

Apparent Transfer Efficiency and Plasma Lipid Fraction Incorporation of EO-Derived FA. Apparent transfer efficiencies of dietary FA to milk fat vary with individual FA, diet, length of supplementation, protection method, and stage of lactation.[40,41] The apparent transfer

DOI: 10.1021/acs.jafc.5b00857
J. Agric. Food Chem. 2015, 63, 4827−4835

efficiencies of ALA from the EEO supplement into milk fat were 3.4 and 3.9% for LEO and HEO treatments, respectively. This is similar to reports using formaldehyde-treated flax oil[42] and extruded or micronized flaxseed.[43] The apparent transfer efficiencies of SDA to milk fat were 3.4% for the LEO treatment and 3.2% for the HEO treatment. The metabolism of SDA to EPA, however, is not accounted for in this model; thus, when the increase in EPA from CON to treatments was included in the apparent transfer efficiency equation of SDA, values were 4.7 and 4.1% for LEO and HEO, respectively. Bernal-Santos et al.[37] infused SDA-enriched soybean oil into the abomasum of dairy cows and reported an apparent transfer efficiency for SDA of 39.3%, whereas ruminal infusion of SDA-enriched oil resulted in a 1.7% apparent transfer efficiency to milk fat. Therefore, there is potential for a greater transfer efficiency if the FA successfully bypass the rumen, as with abomasal infusion. The apparent transfer efficiency of GLA was similar to those of ALA and SDA, being 3.0 and 2.8% for LEO and HEO, respectively, indicating consistent transfer efficiencies among n-6 and n-3 PUFA.

The overall low transfer of FA from EEO to milk may be due to (1) partial ruminal biohydrogenation of the n-3 FA in the supplement, (2) low release and/or decreased absorption of EO-derived FA in the intestine, or (3) incorporation of FA into plasma lipid fractions unavailable to the mammary gland. Our data support a combination of these factors. *trans* 18:1 isomers, a marker of incomplete biohydrogenation, were significantly increased from LEO to HEO, but no difference was observed between CON and LEO, suggesting biohydrogenation of the unsaturated FA in the HEO treatment despite the lipid encapsulation. The release of encapsulated oil and absorption of EO-derived FA in the small intestine could not be assessed in this study; however, others have noted that lipid-protected oils may have lower digestibility.[14]

Mammary lipoprotein lipase utilizes TAG from circulating chylomicrons and LDL; thus, TAG are the main source of preformed FA for milk fat synthesis.[44] Supplementing n-3 FA in the diet of dairy cows can saturate the normal esterification capacity of the small intestine and cause an increased uptake of n-3 FA into plasma TAG.[44] In our study ALA, SDA, and GLA contents increased in plasma TAG, demonstrating potential for these FA to be incorporated into milk fat. This increase, however, was small, compared to the increase in the CE and FFA fractions, suggesting not enough of these FA were available to substantially increase enterocyte esterification of n-3 FA into TAG. Plasma CE had the highest contents of SDA, GLA, and total n-3 FA, demonstrating preferential incorporation of SDA and GLA into plasma CE, which are unavailable to the mammary gland for milk fat synthesis.[12,13] Plasma FFA are also available to the mammary gland for milk fat synthesis.[45] The only n-3 FA to show a significant increase in incorporation into plasma FFA was SDA; however, the concentration of FFA available to the mammary gland of mid-late lactation dairy cows in positive energy balance is negligible.[46] To our knowledge, there are no studies delineating the incorporation of SDA into plasma lipid fractions and only a few studies evaluating the incorporation of other n-3 FA. Stamey et al.[14] supplemented mid-lactation Holstein dairy cows with a lipid-encapsulated algal oil and algal biomass for 7 days and showed that DHA was preferentially incorporated into plasma PL, with very little DHA found in plasma TAG. Sterk et al.[35] supplied 1.6% DM as ALA to early-lactation dairy cows via a formaldehyde-treated linseed oil and demonstrated a 2-fold higher content of ALA in plasma TAG than the HEO treatment in the current study that supplied 0.4% DM as ALA. The increased incorporation of ALA into plasma TAG coincided with a 13% apparent transfer efficiency of ALA to milk fat;[35] differences could be due to supplementation level, oil protection method, or the use of early-lactation dairy cows, as previous research has demonstrated an increased availability of preformed FA to the mammary gland in early lactation.[47]

Human Health Considerations. The increase of n-3 FA in the diet of dairy cows led to a decrease in the n-6/n-3 ratio in milk fat of the LEO and HEO treatments when compared to CON. The n-6/n-3 balance is critical as dietary n-6 and n-3 FA compete for the same enzymes in the production of eicosanoids, and in general n-6 FA produce inflammatory signaling molecules, whereas eicosanoids derived from n-3 FA have anti-inflammatory properties.[48] A lower n-6/n-3 FA ratio in the diet of humans is associated with improved health and reduced risk of disease.[49] The milligrams of n-3 FA per gram of milk fat were estimated by mass correcting FA values to triglyceride equivalents using a correction factor of 0.87; one serving of EO-FA enriched whole milk [1 cup (244 g) of 3.25% milk fat] would provide 56 mg of n-3 FA. The amount of n-3 FA provided in EO-FA enriched milk is comparable to levels of n-3 FA supplied by commercially available whole-milk products with added marine oils (50 mg of EPA/DHA per serving; Organic Valley Omega-3 Milk, Organic Valley, La Farge, WI, USA; 32 mg DHA per serving; Horizon Organic DHA Omega-3 Milk, Horizon Organic, Broomfield, CO, USA). Supplementing dairy cows with EEO increased the milk fat content of GLA but did not increase the content of its downstream pro-inflammatory metabolite arachidonic acid. Human studies have demonstrated that consuming GLA leads to increased serum arachidonic acid; however, because EO also contains SDA, this conversion is inhibited, allowing for the accumulation of the anti-inflammatory GLA.[50] Moreover, research shows that consuming GLA along with EPA and DHA reduces risk of heart attack and lowers blood TAG levels more effectively than EPA and DHA alone.[51] Milk fat from cows supplemented with EEO had an increased proportion of *trans*18:1 FA in milk. *trans* 18:1 FA have been generally associated with increased risk of cardiovascular disease in humans by increasing low-density lipoprotein (LDL) and decreasing high-density lipoprotein (HDL).[52] However, the majority of these trials were conducted with *trans* FA from partially hydrogenated vegetable oils (PHVO). Ruminant-derived *trans* FA do not show the same negative health effects as *trans* FA from PHVO due to the difference in the composition of *trans* 18:1 isomers.[53] The predominant *trans* 18:1 in milk fat is vaccenic acid (VA), and epidemiological studies suggest that consumption of VA may impart health benefits.[54] Thus, the increase in the content of *trans* FA in the EO-enriched milk does not influence the healthfulness of the product.

Conclusion. Developing functional food products enriched with n-3 FA is a challenging endeavor in ruminants. The n-3 FA must be both protected from ruminal biohydrogenation and released in the small intestine and then subsequently incorporated into plasma TAG to be available to the mammary gland for milk fat synthesis. Supplementing an EEO at 1.5 and 3% of DM increased the content of n-3 FA in milk fat; whereas percentage increases of n-3 FA were high, the actual content of these FA in milk is still relatively low. ALA, and SDA showed the highest incorporation into plasma TAG and milk, whereas EPA also increased in milk but not in plasma TAG. The

DOI: 10.1021/acs.jafc.5b00857
J. Agric. Food Chem. 2015, 63, 4827−4835

greatest increase in content of n-3 FA occurred in the plasma PL and CE, explaining the low apparent transfer efficiency of ALA and SDA to milk fat. High transfer efficiencies are feasible only if rumen protection and postrumen absorption are optimized; thus, further research is needed to assess the protection of the EEO supplement in the rumen and digestibilily in the small intestine and whether longer term supplementation or increasing the SDA content of the oil would increase the apparent transfer efficiency to milk fat.

■ ASSOCIATED CONTENT

Supporting Information

Tables of the complete fatty acid profiles of milk fat and plasma lipid fractions, TAG, CE, PL, and FFA in response to dietary treatment. The Supporting Information is available free of charge on the ACS Publications website at DOI: 10.1021/acs.jafc.5b00857.

■ AUTHOR INFORMATION

Corresponding Author

* (J.K.) Phone: (802) 656-5489. Fax: (802) 656-8196. E-mail: Jana.Kraft@uvm.edu.

Notes

The authors declare no competing financial interest.

■ ACKNOWLEDGMENTS

We thank C. L. Preseault, J. P. Boerman, J. E. Rico, L. C. Nagengast, R. Smith, and the staff at the MSU Dairy Teaching and Research Center for their assistance in this work.

■ ABBREVIATIONS USED

ALA, alpha-linolenic acid; BCFA, branched-chain fatty acids; BHBA, beta-hydroxybutyrate; CE, cholesterol esters; CLA, conjugated linoleic acids; CON, control; CP, crude protein; DHA, docosahexaenoic acid; DIM, days in milk; DM, dry matter; DPA, docosapentaenoic acid; ECM, energy-corrected milk; EEO, lipid-encapsulated echium oil; EO, echium oil; EPA, eicosapentaenoic acid; FA, fatty acid; FCM, fat-corrected milk; FAME, fatty acid methyl esters; FFA, free fatty acids; GC, gas chromatography; GLA, gamma-linolenic acid; HDL, high-density lipoprotein; HEO, high-echium oil; LDL, low-density lipoprotein; LEO, low-echium oil; NDF, neutral detergent fiber; MUFA, monounsaturated fatty acids; MUN, milk urea nitrogen; PHVO, partially hydrogenated vegetable oil; PL, phospholipids; PUFA, polyunsaturated fatty acids; SDA, stearidonic acid; SFA, saturated fatty acids; SPE, solid phase extraction; TAG, triacylglycerol; TMR, total mixed ration; VA, vaccenic acid

■ REFERENCES

(1) Wall, R.; Ross, R. P.; Fitzgerald, G. F.; Stanton, C. Fatty acids from fish: the anti-inflammatory potential of long-chain omega-3 fatty acids. *Nutr. Rev.* **2010**, *68*, 280−289.

(2) Denis, I.; Potier, B.; Vancassel, S.; Heberden, C.; Lavialle, M. Omega-3 fatty acids and brain resistance to ageing and stress: body of evidence and possible mechanisms. *Ageing Res. Rev.* **2013**, *12*, 579−594.

(3) De Caterina, R. N-3 Fatty acids in cardiovascular disease. *N. Engl. J. Med.* **2011**, *364*, 2439−2450.

(4) De Oliveira Otto, M. C.; Wu, J. H. Y.; Baylin, A.; Vaidya, D.; Rich, S. S.; Tsai, M. Y.; Jacobs, D. R.; Mozaffarian, D. Circulating and dietary omega-3 and omega-6 polyunsaturated fatty acids and incidence of CVD in the Multi-Ethnic Study of Atherosclerosis. *J. Am. Heart Assoc.* **2013**, *2* (6), 1−17.

(5) Koren, N.; Simsa-Maziel, S.; Shahar, R.; Schwartz, B.; Monsonego-Ornan, E. Exposure to omega-3 fatty acids at early age accelerate bone growth and improve bone quality. *J. Nutr. Biochem.* **2014**, *25*, 623−633.

(6) Papanikolaou, Y.; Brooks, J.; Reider, C.; Fulgoni, V. L. U.S. adults are not meeting recommended levels for fish and omega-3 fatty acid intake: results of an analysis using observational data from NHANES 2003−2008. *Nutr. J.* **2014**, *13* (31), 1−6.

(7) Lock, A. L.; Bauman, D. E. Modifying milk fat composition of dairy cows to enhance fatty acids beneficial to human health. *Lipids* **2004**, *39*, 1197−1206.

(8) Vahmani, P.; Fredeen, A.; Glover, K. Effect of supplementation with fish oil or microalgae on fatty acid composition of milk from cows managed in confinement or pasture systems. *J. Dairy Sci.* **2013**, *96*, 6660−6670.

(9) Benchaar, C.; Romero-Pérez, G.; Chouinard, P.; Hassanat, F.; Eugene, M.; Petit, H.; Côrtes, C. Supplementation of increasing amounts of linseed oil to dairy cows fed total mixed rations: effects on digestion, ruminal fermentation characteristics, protozoal populations, and milk fatty acid composition. *J. Dairy Sci.* **2012**, *95*, 4578−4590.

(10) Jenkins, T.; Wallace, R.; Moate, P. J.; Mosley, E. E. Board-invited review: Recent advances in biohydrogenation of unsaturated fatty acids within the rumen microbial ecosystem. *J. Anim. Sci.* **2008**, *86*, 397−412.

(11) Papas, A.; Wu, S. Rumen-stable delivery systems. *Adv. Drug Delivery Rev.* **1997**, *28*, 323−334.

(12) Brumby, P. E.; Storry, J. E.; Sutton, J. D. Metabolism of cod-liver oil in relation to milk fat secretion. *J. Dairy Res.* **1972**, *39*, 167−182.

(13) Offer, N. W.; Speake, B. K.; Dixon, J.; Marsden, M. Effect of fish-oil supplementation on levels of (n-3) poly-unsaturated fatty acids in the lipoprotein fractions of bovine plasma. *Anim. Sci.* **2001**, *73*, 523−531.

(14) Stamey, J.; Shepherd, D.; de Veth, M.; Corl, B. Use of algae or algal oil rich in n-3 fatty acids as a feed supplement for dairy cows. *J. Dairy Sci.* **2012**, *95*, 5269−5275.

(15) Surette, M. E. Dietary omega-3 PUFA and health: stearidonic acid-containing seed oils as effective and sustainable alternatives to traditional marine oils. *Mol. Nutr. Food Res.* **2013**, *57*, 748−759.

(16) Fleming, J. A.; Kris-Etherton, P. M. The evidence for α-linolenic acid and cardiovascular disease benefits: comparisons with eicosapentaenoic acid and docosahexaenoic acid. *Adv. Nutr.* **2014**, *5* (6), 863−876.

(17) Whelan, J. Dietary stearidonic acid is a long chain (n-3) polyunsaturated fatty acid with potential health benefits. *J. Nutr.* **2009**, *139* (1), 5−10.

(18) Stamey Lanier, J.; Suagee, J. K.; Becvar, O.; Corl, B. A. Mammary uptake of fatty acids supplied by intravenous triacylglycerol infusion to lactating dairy cows. *Lipids* **2013**, *48*, 469−479.

(19) Kapoor, R.; Huang, Y. Gamma linolenic acid: an antiinflammatory omega-6 fatty acid. *Curr. Pharm. Biotechnol.* **2006**, *7*, 531−534.

(20) Xu, Y.; Qian, S. Y. Anti-cancer activities of ω-6 polyunsaturated fatty acids. *Biomed. J.* **2014**, *37*, 112−119.

(21) Kuhnt, K.; Fuhrmann, C.; Köhler, M.; Kiehntopf, M.; Jahreis, G. Dietary echium oil increases long-chain n-3 PUFAs, including docosapentaenoic acid, in blood fractions and alters biochemical markers for cardiovascular disease independently of age, sex, and metabolic syndrome. *J. Nutr.* **2014**, *144* (4), 447−460.

(22) Kavanagh, K.; Flynn, D. M.; Jenkins, K. A.; Wilson, M. D.; Chilton, F. H. Stearidonic and γ-linolenic acids in echium oil improves glucose disposal in insulin resistant monkeys. *Prostaglandins, Leukotrienes Essent. Fatty Acids* **2013**, *89* (1), 39−45.

(23) Kitessa, S.; Young, P. Enriching milk fat with n−3 polyunsaturated fatty acids by supplementing grazing dairy cows with ruminally protected echium oil. *Anim. Feed Sci. Technol.* **2011**, *170* (1−2), 35−44.

DOI: 10.1021/acs.jafc.5b00857
J. Agric. Food Chem. 2015, 63, 4827−4835

(24) Dewhurst, R. J.; Shingfield, K. J.; Lee, M. R. F.; Scollan, N. D. Increasing the concentrations of beneficial polyunsaturated fatty acids in milk produced by dairy cows in high-forage systems. *Anim. Feed Sci. Technol.* **2006**, *131*, 168−206.
(25) Wildman, E. E.; Jones, G. M.; Wagner, P. E.; Boman, R. L.; Troutt, H. F.; Lesch, T. N. A dairy cow body condition scoring system and its relationship to selected production characteristics. *J. Dairy Sci.* **1982**, *65*, 495−501.
(26) Van Soest, P. J.; Roberson, J. B.; Lewis, B. A. Methods for dietary fiber, neutral detergent fiber, and nonstarch polysaccharides in relation to animal nutrition. *J. Dairy Sci.* **1991**, *74*, 3583−3597.
(27) *Official Methods of Analysis of AOAC International*, 17th ed.; AOAC International: Gaithersburg, MD, USA, 2000; Official Method 990.03.
(28) Hall, M. B. Determination of starch, including maltooligosaccharides, in animal feeds: a comparison of methods and a recommended method for AOAC collaborative study. *J. AOAC Int.* **2009**, *92*, 42−49.
(29) Sukhija, P. S.; Palmquist, D. L. Rapid method for determination of total fatty acid content and composition of feedstuffs and feces. *J. Agric. Food Chem.* **1988**, *36*, 1202−1206.
(30) Hara, A.; Radin, N. S. Lipid extraction of tissues with a low-toxicity solvent. *Anal. Biochem.* **1978**, *90*, 420−426.
(31) Folch, J.; Lees, M.; Stanley, G. H. S. A simple method for the isolation and purification of total lipids from animal tissues. *J. Biol. Chem.* **1957**, *226*, 497−509.
(32) Kraft, J.; Collomb, M.; Möckel, P.; Sieber, R.; Jahreis, G. Differences in CLA isomer distribution of cow's milk lipids. *Lipids* **2003**, *38*, 657−664.
(33) Wolff, R. L.; Bayard, C. C.; Fabien, R. J. Evaluation of sequential methods for the determination of butterfat fatty acid composition with emphasis on trans-18:1 acids. Application to the study of seasonal variations in French butters. *J. Am. Oil Chem. Soc.* **1995**, *72*, 1471−1483.
(34) Lock, A. L.; Preseault, C. L.; Rico, J. E.; DeLand, K. E.; Allen, M. S. Feeding a C16:0-enriched fat supplement increased the yield of milk fat and improved conversion of feed to milk. *J. Dairy Sci.* **2013**, *96*, 6650−6659.
(35) Sterk, A.; Vlaeminck, B.; van Vuuren, A.; Hendriks, W.; Dijkstra, J. Effects of feeding different linseed sources on omasal fatty acid flows and fatty acid profiles of plasma and milk fat in lactating dairy cows. *J. Dairy Sci.* **2012**, *95*, 3149−3165.
(36) Grummer, R.; Carroll, D. Effects of dietary fat on metabolic disorders and reproductive performance of dairy cows. *J. Anim. Sci.* **1991**, *69*, 3838−3852.
(37) Bernal-Santos, G.; O'Donnell, A. M.; Vicini, J. L.; Hartnell, G. F.; Bauman, D. E. Hot topic: Enhancing omega-3 fatty acids in milk fat of dairy cows by using stearidonic acid-enriched soybean oil from genetically modified soybeans. *J. Dairy Sci.* **2010**, *93*, 32−37.
(38) Portolesi, R.; Powell, B. C.; Gibson, R. A. Competition between 24:5n-3 and ALA for Delta 6 desaturase may limit the accumulation of DHA in HepG2 cell membranes. *J. Lipid Res.* **2007**, *48*, 1592−1598.
(39) Angulo, J.; Mahecha, L.; Nuernberg, K.; Nuernberg, G.; Dannenberger, D.; Olivera, M.; Boutinaud, M.; Leroux, C.; Albrecht, E.; Bernard, L. Effects of polyunsaturated fatty acids from plant oils and algae on milk fat yield and composition are associated with mammary lipogenic and SREBF1 gene expression. *Animal* **2012**, *6*, 1961−1972.
(40) Chilliard, Y.; Glasser, F.; Ferlay, A.; Bernard, L.; Rouel, J.; Doreau, M. Diet, rumen biohydrogenation and nutritional quality of cow and goat milk fat. *Eur. J. Lipid Sci. Technol.* **2007**, *109*, 828−855.
(41) Chilliard, Y.; Ferlay, A.; Doreau, M. Effect of different types of forages, animal fat or marine oils in cow's diet on milk fat secretion and composition, especially conjugated linoleic acid (CLA) and polyunsaturated fatty acids. *Livest. Prod. Sci.* **2001**, *70*, 31−48.
(42) Hawkins, A.; Yuan, K.; Armendariz, C.; Highland, G.; Bello, N.; Winowiski, T.; Drouillard, J.; Titgemeyer, E.; Bradford, B. Effects of urea formaldehyde condensation polymer treatment of flaxseed on ruminal digestion and lactation in dairy cows. *J. Dairy Sci.* **2013**, *96*, 3907−3915.
(43) Gonthier, C.; Mustafa, A. F.; Ouellet, D. R.; Chouinard, P. Y.; Berthiaume, R.; Petit, H. Feeding micronized and extruded flaxseed to dairy cows: effects on blood parameters and milk fatty acid composition. *J. Dairy Sci.* **2005**, *88*, 748−756.
(44) Bauchart, D. Lipid absorption and transport in ruminants. *J. Dairy Sci.* **1993**, *76*, 3864−3881.
(45) Palmquist, D. L. Milk fat: origin of fatty acids and influence of nutritional factors thereon. In *Advanced Dairy Chemistry*, 3; Fox, P. F., McSweeney, P. L. H., Eds.; Springer: New York, 2006; Vol. 2, pp 43−93.
(46) Emery, R. S. Biosynthesis of milk fat. *J. Dairy Sci.* **1973**, *56*, 1187−1195.
(47) Palmquist, D. L.; Beaulieu, A. D.; Barbano, D. M. Feed and animal factors influencing milk fat composition. *J. Dairy Sci.* **1993**, *76*, 1753−1771.
(48) Poudyal, H.; Panchal, S. K.; Diwan, V.; Brown, L. Omega-3 fatty acids and metabolic syndrome: effects and emerging mechanisms of action. *Prog. Lipid Res.* **2011**, *50*, 372−387.
(49) Duan, Y.; Li, F.; Li, L.; Fan, J.; Sun, X.; Yin, Y. n-6:n-3 PUFA ratio is involved in regulating lipid metabolism and inflammation in pigs. *Br. J. Nutr.* **2014**, *111*, 445−451.
(50) Miquel, M. Echium oil: a valuable source of n-3 and n-6 fatty acids. *Ol., Corps Gras, Lipides* **2008**, *15*, 252−256.
(51) Laidlaw, M.; Holub, B. J. Effects of supplementation with fish oil derived n-3 fatty acids and γ-linolenic acid on circulating plasma lipids and fatty acid profiles. *Am. J. Clin. Nutr.* **2003**, *77*, 37−42.
(52) Mozaffarian, D.; Aro, A.; Willett, W. C. Health effects of trans-fatty acids: experimental and observational evidence. *Eur. J. Clin. Nutr.* **2009**, *63*, 5−21.
(53) Rice, B. H.; Kraft, J.; Bauman, D. E.; Lock, A. L. Ruminant-produced trans-fatty acids raise plasma total and small HDL particle concentrations in male Hartley guinea pigs. *J. Nutr.* **2010**, *140*, 2173−2179.
(54) Field, C. J.; Blewett, H. H.; Proctor, S.; Vine, D. Human health benefits of vaccenic acid. *Appl. Physiol., Nutr., Metab.* **2009**, *34*, 979−991.

DOI: 10.1021/acs.jafc.5b00857
J. Agric. Food Chem. 2015, 63, 4827−4835

JOURNAL OF AGRICULTURAL AND FOOD CHEMISTRY

Article

pubs.acs.org/JAFC

Quantitative Analysis of Phenylpropanoid Glycerol Glucosides in Different Organs of Easter Lily (*Lilium longiflorum* Thunb.)

John P. Munafo, Jr. and Thomas J. Gianfagna*

Plant Biology Department, Rutgers—The State University of New Jersey, 59 Dudley Road, New Brunswick, New Jersey 08901, United States

ABSTRACT: The Easter lily (*Lilium longiflorum* Thunb.) is esteemed worldwide as an attractive ornamental plant, and the flower buds and bulbs are used for both culinary and medicinal purposes in many parts of the world. *L. longiflorum* contains significant amounts of phenylpropanoid glycerol glucosides, a group of compounds that may contribute to plant pathogen defense, ultraviolet/high-intensity visible light (UV/high light) protection, and the purported medicinal uses of lilies. To define the natural distribution of these compounds within the plant, a liquid chromatography−mass spectrometry (LC-MS) method performed in selected ion monitoring (SIM) mode was employed for the quantitative analysis of five phenylpropanoid glycerol glucosides, namely, (2*S*)-1-*O*-caffeoyl-2-*O*-*β*-D-glucopyranosylglycerol, **1**; (2*R*)-1-*O*-*β*-D-glucopyranosyl-2-*O*-*p*-coumaroylglycerol, **2**; (2*S*)-1-*O*-*p*-coumaroyl-2-*O*-*β*-D-glucopyranosylglycerol, **3**; (2*S*)-1-*O*-caffeoyl-2-*O*-*β*-D-glucopyranosyl-3-*O*-acetylglycerol, **4**; and (2*S*)-1-*O*-*p*-coumaroyl-2-*O*-*β*-D-glucopyranosyl-3-*O*-acetylglycerol, **5**, in the different organs of *L. longiflorum*. The *p*-coumaroyl-based **3** and its acetylated derivative **5** were determined to be the most abundant of the phenylpropanoid glycerol glucosides found in Easter lily bulbs, at 776.3 ± 8.4 and 650.7 ± 32.6 *μ*g/g dry weight, respectively. The acetylated *p*-coumaroyl- and caffeoyl-based derivatives, **5** and **4**, accumulated to the highest concentration in the closed flower buds, at 4925.2 ± 512.8 and 3216.8 ± 406.4 *μ*g/g dry weight, respectively. Compound **4**, followed by **5** and **1**, proved to be the most abundant in the mature flowers, occurring at 6006.2 ± 625.8, 2160.3 ± 556.5, and 1535.8 ± 174.1 *μ*g/g dry weight, respectively. Total concentrations of the phenylpropanoid glycerol glucosides were 10−100-fold higher in the above-ground plant organs as compared to the bulbs and fleshy roots. Two of the five compounds, **1** and **2**, were identified in *L. longiflorum* for the first time. The quantitative analysis of phenylpropanoid glycerol glucosides in the different plant organs of *L. longiflorum* will establish the direction of investigations aimed at defining how these compounds function in the physiology and chemical ecology of the plant and also as a starting point for determining their possible effects on human health, which has not been investigated.

KEYWORDS: *Lilium longiflorum Thunb., Liliaceae, Easter lily, phenylpropanoid glycerol glucosides, regalosides*

INTRODUCTION

The Easter lily (*Lilium longiflorum* Thunb., family Liliaceae) is primarily grown as an ornamental plant because of its large, fragrant, white flowers. Although not well-known as a food in the United States, lily flower buds and bulbs are used as both food and medicine in many Asian countries, especially China and Japan. In Chinese cuisine the bulbs of various lily species, including *L. longiflorum*, are a common ingredient in soups, stir-fries, and stew-like dishes such as "hot pot". Lily bulbs and flower buds are an important part of the Asian diet and are consumed on a regular basis. Despite this fact, very little is known about their chemical composition and impact on human health. In addition to their culinary value, lily bulbs have a long history of documented medicinal use as sedatives, anti-inflammatory agents, and antitussives.[1−3] In fact, preparations of lily bulbs from *Lilium* species, referred to in China as "Bai-he," are employed in Traditional Chinese Medicine (TCM) as effective treatments for inflammation and some lung ailments.[1,2] However, although the medicinal use of *L. longiflorum* is well documented, the bioactive phytochemicals responsible for the putative medicinal properties as well as their mechanisms of action remain elusive.

Plants from the *Lilium* genus are an abundant source of a number of natural products. Many classes of compounds have been reported from the genus, including phenolics,[4] alkaloids,[5] flavonoids,[6] carotenoids,[7] sterols,[7] steroidal saponins,[2,8−17] and steroidal glycoalkaloids.[15,17−19] In addition, the *Lilium* genus contains an abundant supply of cinnamic acid derivatives, in particular, phenylpropanoid glycerol glucosides, a group of natural products, with many structural analogues, first isolated and characterized from *Lilium regale* E. H. Wilson and thus trivially named regalosides.[20] Cinnamic acid derivatives, most notably *p*-coumaric, caffeic, and ferulic acids, are widely distributed in plants and naturally occur as both esters and glycosides. Regalosides are acylated glycerol glucosides. As such, they characteristically contain *p*-coumaric, caffeic, or ferulic acids, but less often cinnamic acid. Typically, they are esterified at the C1 or C2 carbon of a glucosylated glycerol backbone, with *S* configuration at the 2-position, (2*S*)-regalosides, being the most common, and *R* configuration, (2*R*)-regalosides, less usual. Moreover, a few acetylated and methylated regalosides have been described.[6,9,20−22] Regalosides have been identified in members of the Liliaceae family including *L. regale*,[20] *Lilium henryi* Baker,[21] *Lilium pardalinum* Kellogg,[3] *Lilium auratum* Lindl.,[3,23] *Lilium lancifolium* Thunb.,[22]

Received: February 16, 2015
Revised: April 23, 2015
Accepted: April 23, 2015
Published: April 23, 2015

ACS Publications © 2015 American Chemical Society

DOI: 10.1021/acs.jafc.5b00893
J. Agric. Food Chem. 2015, 63, 4836−4842

L. longiflorum,[6,22] *Lilium brownii* F. E. Br. ex Miellez,[2,15] *Lilium speciosum* Thunb.,[14] and *Lilium mackliniae* Sealy.[9]

Earlier studies have identified phenylpropanoid glycerol glucosides in the bulbs of *L. longiflorum*, specifically, (2*S*)-1-*O*-*p*-coumaroyl-2-*O*-*β*-D-glucopyranosylglycerol, **3**; (2*S*)-1-*O*-caffeoyl-2-*O*-*β*-D-glucopyranosyl-3-*O*-acetylglycerol, **4**; and (2*S*)-1-*O*-*p*-coumaroyl-2-*O*-*β*-D-glucopyranosyl-3-*O*-acetylglycerol, **5**.[22] Additionally, a 4-acetyl derivative of (2*S*)-1-*O*-*p*-coumaroyl-2-*O*-*β*-D-glucopyranosylglycerol has been reported from *L. longiflorum* flowers that exhibited mild cyclooxygenase and lipid peroxidation inhibition activities.[6] Although these compounds may be involved in plant pathogen defense, ultraviolet/high-intensity visible light (UV/high light) protection, and the putative medicinal activities of lilies,[1−3,17] reports on the biological activities of phenylpropanoid glycerol glucosides are scarce. Phenylpropanoid glycerol glucosides are reported to be bitter in taste,[20] which may suggest a possible role in antiherbivory; however, the bitter taste thresholds of the compounds have not been quantitated nor have the antiherbivory activities of the compounds been investigated.

The dual aim of our present investigation has been to develop a liquid chromatography−mass spectrometry (LC-MS) method for the quantitative analysis of five phenylpropanoid glycerol glucosides in plant tissues and to identify and quantitate the concentration of the compounds in the different plant organs of Easter lily. The results were anticipated to lay the groundwork for defining how these compounds function in the physiology and chemical ecology of the plant and also as a starting point for determining their possible effects on human health when consumed as a food, which has not been investigated.

MATERIALS AND METHODS

Plant Material. Cultivar 7-4 *L. longiflorum* bulbs were cultivated, harvested, lyophilized, and milled according to the methods described in Munafo et al.[19] Three fully mature plants, containing all stages of the vegetative and reproductive organs, were harvested and dissected into fleshy bulb scales, fleshy roots, leaves, lower stems, upper stems, flower buds, and mature flowers. The fleshy bulb scales were 0.8−2.0 cm in width and 0.9−4.0 cm in length. The fleshy roots were approximately 2−4 mm in diameter and the leaves about 6−14 cm in length. Lower stems (the part growing below the soil surface) ranged in size from 6 to 10 cm and were white to yellow in color. Upper stems (the part growing above the soil surface) ranged in size from 19 to 31 cm and were green. The flower buds were approximately 3−6 cm in length, fully closed, and green in appearance. The mature flowers ranged between 6 and 14 cm in length, were fully open, and were white in appearance. Each of the organ types from an individual plant were pooled together. Three individual plants were used in the analysis (n = 3). After harvest, all samples were immediately frozen under liquid nitrogen, lyophilized, and stored at −80 °C prior to analysis.

Chemicals. All solvents, acetonitrile, 1-butanol, dimethyl sufoxide (DMSO), ethyl acetate, ethanol, formic acid, methanol, tetrohydrofuran (THF), and pentanes were of chromatographic grade and were obtained from Thermo Fisher Scientific Inc., Fair Lawn, NJ, USA. Methanol-d_4 (0.03% v/v TMS) was obtained from Sigma-Aldrich, St. Louis, MO, USA. Deionized (DI) water (18 MΩ cm) was generated using a Milli-Q-water purification system (Millipore, Bedford, MA, USA).

Purification of Phenylpropanoid Glycerol Glucosides 1−5 as Analytical Standards. *Sequential Solvent Extraction of Lyophilized L. longiflorum Bulbs.* Lyophilized lily bulbs (100 g) were milled to a fine powder after freezing in liquid nitrogen. To remove lipids, the bulb powder was extracted with pentanes (3 × 100 mL) at room temperature for 15 min each time on a shaker. The extract was centrifuged (5000 rpm) for 10 min and the solvent was decanted. The residue was then allowed to dry overnight in a fume hood. The dried defatted residue was extracted with ethanol and DI water (7:3, v/v; 2 × 150 mL) for 45 min at room temperature on a shaker. The extract was centrifuged (5000 rpm) for 10 min and the supernatant was saved and vacuum filtered. The supernatant was rotary evaporated (30 °C; 1.0×10^{-3} bar) and lyophilized, yielding a crude bulb extract (fraction I, 12.4 g). Next, the lyophilized crude bulb extract was dissolved in DI water (100 mL) and extracted with ethyl acetate (5 × 100 mL), and the aqueous phase, containing the highly polar compounds such as carbohydrates and steroidal glycosides, was discarded. The organic phase was rotary evaporated to dryness (30 °C; 1.0×10^{-3} bar) (fraction II), redissolved in DI water (100 mL), and sonicated for 10 min. The extract was centrifuged (5000 rpm) for 10 min, vacuum filtered, and the supernatant was collected. The aqueous phase was then extracted with 1-butanol (5 × 100 mL). The organic phase was rotary evaporated (30 °C; 1.0×10^{-3} bar) and lyophilized, yielding 1-butanol extract (fraction III, 1.9 g).

Semipreparative Reverse-Phase High-Performance Liquid Chromatography (RP-HPLC). The 1-butanol extract (fraction III) was fractionated by semipreparative RP-HPLC on a 250 mm × 21.2 mm i.d., 10 μm, Luna C18 column (Phenomenex, Torrance, CA) to afford **1**−**5** (Figure 1) using an LC-6AD liquid chromatograph (Shimadzu

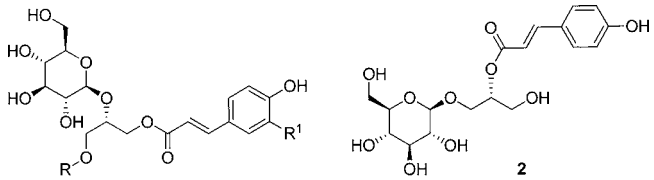

	R	R^1
1	H	OH
3	H	H
5	Ac	H
4	Ac	OH

Figure 1. Structures of compounds **1**−**5** quantitated in the various *L. longiflorum* organs.

Scientific Instruments Inc., Columbia, MD, USA) equipped with a UV/vis detector and a 2 mL injection loop. The mobile phases were mixtures of (A) 0.1% formic acid in DI water and (B) 0.1% formic acid in acetonitrile. The flow rate was set to 20 mL/min, column temperature was 23 ± 2 °C, and UV detection was recorded at λ 210 nm. The 1-butanol extract (fraction III, 200 mg) was dissolved in a mixture of mobile phase A and mobile phase B (90:10, v/v; 2 mL) and filtered through a 0.45 μm PTFE syringe filter prior to injection (injection volume = 1 mL). The butanol extract was fractionated using a linear gradient of 5−24.4% B for 35 min and then ramped to 90% B in 5 min, with a hold at 90% B for additional 5 min. The solvent mixture was reset to 5% B for 10 min before subsequent injections. Fractions containing the compounds of interest were collected (Figure 2), and the solvent was rotary evaporated (30 °C; 1.0×10^{-3} bar) and lyophilized, yielding **1** (15.2 mg), **2** (12.1 mg), **3** (39.6 mg), **4** (10.2 mg), and **5** (40.3 mg) as pale yellow amorphous powders with >98% purity as determined by LC-MS and NMR.

*Compound **1**, (2S)-1-O-Caffeoyl-2-O-β-D-glucopyranosylglycerol (regaloside K).* 1D and 2D NMR data were consistent with ^{1}H NMR and ^{13}C NMR reported in the literature.[9]

*Compound **2**, (2R)-1-O-β-D-Glucopyranosyl-2-O-p-coumaroylglycerol (regaloside H).* 1D and 2D NMR data were consistent with ^{1}H NMR and ^{13}C NMR reported in the literature.[23]

*Compound **3**, (2S)-1-O-p-Coumaroyl-2-O-β-D-glucopyranosylglycerol (regaloside D).* 1D and 2D NMR data were consistent with ^{1}H NMR and ^{13}C NMR reported in the literature.[3]

*Compound **4**, (2S)-1-O-Caffeoyl-2-O-β-D-glucopyranosyl-3-O-acetylglycerol (regaloside E).* 1D and 2D NMR data were consistent with ^{1}H NMR and ^{13}C NMR reported in the literature.[3]

DOI: 10.1021/acs.jafc.5b00893
J. Agric. Food Chem. 2015, 63, 4836−4842

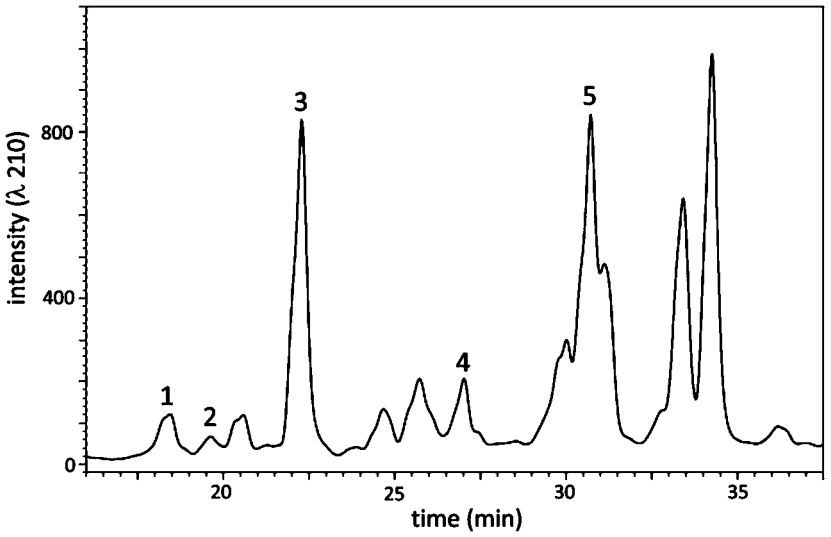

Figure 2. Semipreparative RP-HPLC chromatogram (λ 210 nm) of **1**−**5** purified from *L. longiflorum* 1-butanol extract (fraction III).

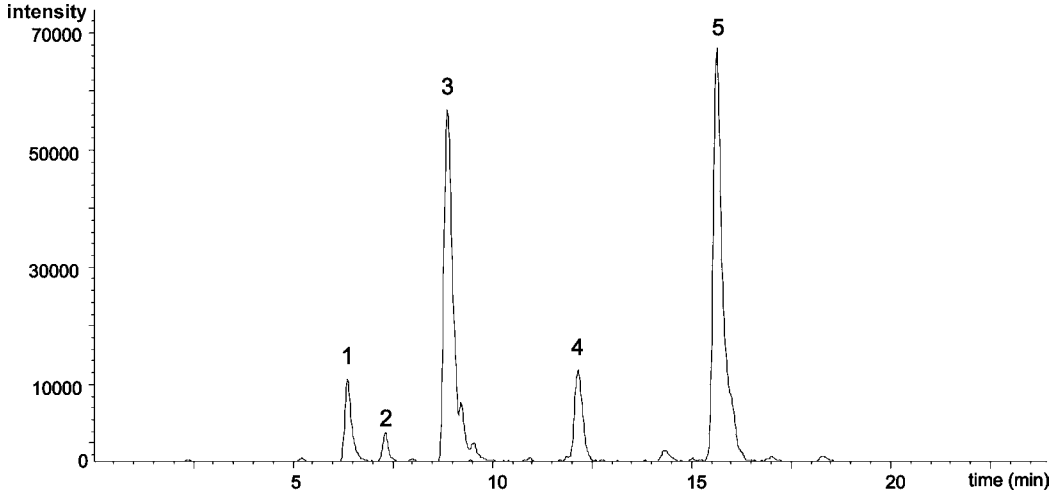

Figure 3. LC-MS chromatogram for the quantitative analysis of compounds **1**−**5** in a *L. longiflorum* bulb scale operating in selective ion monitoring (SIM) mode.

Compound **5**, *(2S)-1-O-p-Coumaroyl-2-O-β-D-glucopyranosyl-3-O-acetylglycerol (regaloside B).* 1D and 2D NMR data were consistent with ^{1}H NMR and ^{13}C NMR reported in the literature.[20]

Nuclear Magnetic Resonance Spectroscopy (NMR). 1D ^{1}H NMR spectra was acquired with a 400 MHz spectrometer (Bruker, Rheinstetten, Germany). 2D heteronuclear multiple-bond coherence (HMBC), heteronuclear single-quantum coherence (HSQC), and H−H correlation spectroscopy (H−H COSY) spectra were acquired on a 500 MHz spectrometer (Bruker). Samples for NMR analysis were dissolved in methanol-d_4, and chemical shifts were calculated as δ values with reference to tetramethylsilane (TMS).

Optimization of Sample Extraction Parameters for Quantitative Analysis. *Solvent Composition and Extraction Efficiency Determination.* Six neat organic solvents (methanol, ethanol, DMSO, acetone, acetonitrile, and THF) as well as different ratios of methanol and DI water (1:0, 9:1. 8:2, 7:3, 6:4, 5:5, 4:6, 3:7, 2:8, 1:9, and 0:1, v/v) were used for experiments aimed at optimization of the extraction solvent system for phenylpropanoid glycerol glucosides **1**−**5** from lyophilized *L. longiflorum* tissue. Performing successive extraction of the same plant tissue from one to three times determined extraction efficiency. Lyophilized lily bulb tissue was extracted with methanol and DI water (8:2, v/v) solvent mixture. Results from each successive extraction were collected separately and filtered through a 0.45 μm PTFE syringe filter prior to LC-MS analysis.

Quantitative Analysis of Phenylpropanoid Glycerol Glucosides 1−5 in *L. longiflorum*. *Sample Preparation.* Following removal from the freezer, lyophilized lily organ samples were thawed to ambient temperature. The samples (40 mg each) were milled to pass through a 200 mesh sieve, weighed separately, transferred into a 15 mL centrifuge tube, and covered with methanol and DI water (8:2, v/v; 7 mL each). The samples were extracted with shaking (10 min), sonicated (10 min), and filled to final volume (10 mL) with methanol and DI water (8:2, v/v). The samples were vortexed (1 min), and centrifuged (5000 rpm for 10 min), and the supernatant was collected. The pellet was re-extracted with methanol and DI water (8:2, v/v; 10 mL), shaken (10 min), sonicated (10 min), centrifuged (5000 rpm for 10 min), and the supernatants were combined (total volume ∼ 20 mL). Prior to LC-MS analysis, all samples were filtered through a 0.45 μm PTFE syringe filter.

Analytical Standard Preparation. Phenylpropanoid glycerol glucosides **1**−**5**, isolated and purified as described above, were used as analytical standards. Each compound was weighed into volumetric flasks (10 mL), dissolved with methanol and DI water (8:2, v/v; 7 mL each), and sonicated for 5 min before taken to full volume. Working solutions were prepared for calibration equations by diluting the stock solutions. External standard equations were calculated from six data points covering a concentration range of 1−300 μg/mL. To establish calibration equations, mean peak areas (n = 3) from the standard

DOI: 10.1021/acs.jafc.5b00893
J. Agric. Food Chem. 2015, 63, 4836−4842

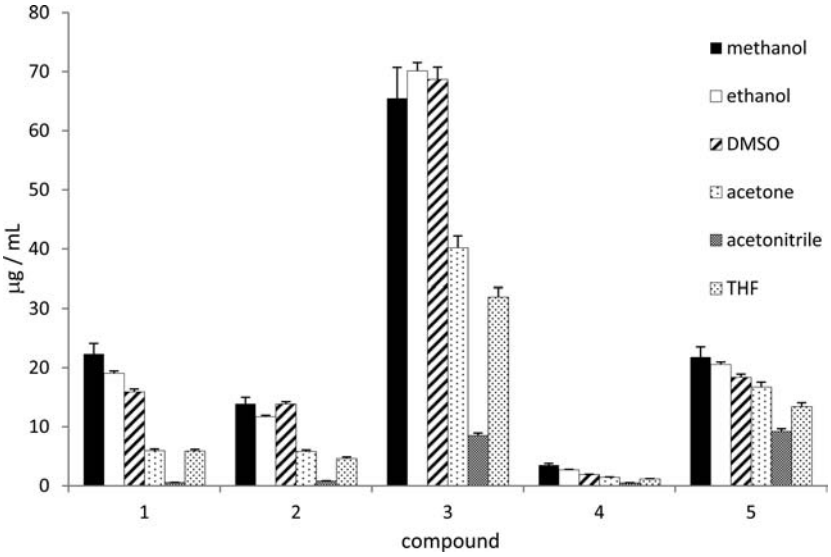

Figure 4. Evaluation of six organic solvents on the extraction of compounds **1**−**5** from *L. longiflorum* bulbs. Concentrations are means of triplicates ± SD.

solutions were plotted versus concentration. Standard solutions were stored at 4 °C and equilibrated to ambient temperature before use.

Liquid Chromatography–Mass Spectrometry (LC-MS). LC-MS analysis of *L. longiflorum* extracts was performed using an Agilent 1100 series HPLC system (Agilent Technologies Inc., Santa Clara, CA, USA) equipped with an autoinjector, quaternary pump, column heater, diode array detector and interfaced to a 1100 series single-quadruple mass selective detector (MSD) equipped with an API-ESI ionization source. Chromatographic separations were made on a 250 mm × 4.6 mm i.d., 5 μm Prodigy C18 column (Phenomenex) operated at a flow rate of 1.0 mL/min, column temperature set to 23 ± 2 °C, and an injection volume of 10 μL. The binary mobile phase consisted of (A) 0.1% formic acid in DI water and (B) 0.1% formic acid in acetonitrile. Phenylpropanoid glycerol glucosides were separated using a linear gradient of 15−34.6% B for 28 min and then ramped to 95% B in 5 min with a hold at 95% B for 5 min. The system was reset to 15% B for 10 min before each sample injection. ChemStation software was used for data acquisition and analysis. Negative ionization mode was used to quantify the phenylpropanoid glycerol glucosides using SIM. The following ions were selected for each compound: **1**, *m*/*z* 415; **2**, *m*/*z* 399; **3**, *m*/*z* 399; **4**, *m*/*z* 457; and **5**, *m*/*z* 441 (Figure 3). Ionization conditions were as follows: capillary voltage, 3.5 kV; nebulizer pressure, 35 psi; drying gas flow, 10.0 mL/min; and drying gas temperature, 350 °C. MSD signal parameters included mode, SIM; polarity, negative; fragmentor voltage, 70 V; gain, 1.0; dwell time, 144 ms; and percent relative dwell time, 25.

Recovery. The standard addition method was used to calculate recovery rates.[24] Lyophilized lily organs were milled to pass through a 200 mesh sieve, separately weighed (40 mg), and transferred into 15 mL centrifuge tubes containing one of three different concentrations (50, 100, and 200 μg/g) of pure compounds dissolved in methanol and DI water (8:2, v/v). To the sample tubes was added a solution of methanol and DI water (8:2, v/v; 7 mL), and the extract was shaken (10 min), sonicated (10 min), and then filled to final volume (10 mL) with the same solvent. The samples were vortexed (1 min) centrifuged (5000 rpm for 10 min), and the supernatant was recovered. For a second time, the centrifuge tube containing the pellet was filled to final volume (10 mL), extracted with shaking (10 min), sonicated (10 min), and centrifuged (5000 rpm for 10 min), and the supernatants from the two extractions were pooled (total volume ∼ 20 mL). All samples were syringe filtered (0.45 μm PTFE) and the phenylpropanoid glycerol glucosides quantified as described above. The percentage recovery for each of the phenylpropanoid glycerol glucosides **1**−**5** in vegetative and reproductive organs was determined by subtracting the amount found in the lily organ sample that was not spiked with additional standards (control) from the amount of standard found in the spiked sample, with three replicate samples for each analysis.

Statistical Analysis. To compare differences in phenylpropanoid glycerol glucosides content in the lily plant organs, LC-MS data were first transformed to the logarithmic function, and an analysis of variance (ANOVA) was conducted. Means were separated with Tukey's test (α = 0.05) using JMP 10 software (SAS Institute Inc., Cary, NC, USA). Two-way hierarchal cluster analysis (HCA) and the resulting color map, visually depicting the differences in concentration of compounds **1**−**5** throughout the lily plant organs, were generated using JMP 10 software (SAS Institute Inc.).

RESULTS AND DISCUSSION

Isolation and Identification of Compounds 1 and 2 from *L. longiflorum* Bulbs. The crude 1-butanol extract was fractionated by repeated semipreparative RP-HPLC to yield compounds **1**−**5**. On the basis of 1D ^{1}H and 2D (HMBC, HSQC, and H−H COSY) NMR, compounds **3**, **4**, and **5** were confirmed to be (2*S*)-1-*O*-*p*-coumaroyl-2-*O*-*β*-D-gucopyranosylglycerol, (2*S*)-1-*O*-caffeoyl-2-*O*-*β*-D-glucopyranosyl-3-*O*-acetylglycerol, and (2*S*)-1-*O*-*p*-coumaroyl-2-*O*-*β*-D-glucopyranosyl-3-*O*-acetylglycerol, respectively. All three of these compounds have been previously reported from *L. longiflorum* bulbs.[22] On the basis of 1D ^{1}H and 2D (HMBC, HSQC, and H−H COSY) NMR, compounds **1** and **2** were confirmed to be (2*S*)-1-*O*-caffeoyl-2-*O*-*β*-D-glucopyranosylglycerol, **1**, and (2*R*)-1-*O*-*β*-D-glucopyranosyl-2-*O*-*p*-coumaroylglycerol, **2**, respectively. Compound **1** was previously reported from fresh bulb scales of *L. mackliniae*[9] and **2** from *L. auratum*.[23] This is the first report of **1** and **2** as natural products identified in *L. longiflorum*.

Optimization of Quantitative Extraction Parameters. *Solvent Composition Determination.* The determination of an effective extraction solvent system for the quantitative analysis of **1**−**5** was achieved by first analyzing the resulting extracts prepared from six neat organic solvents, namely, methanol, ethanol, DMSO, acetone, acetonitrile, and THF (Figure 4). Various combinations of methanol and DI water were then evaluated with the goal of determining a solvent system that effectively extracted **1**−**5**. On the basis of these data, the combination of methanol and DI water (8:2, v/v) was chosen

DOI: 10.1021/acs.jafc.5b00893
J. Agric. Food Chem. 2015, 63, 4836−4842

as the optimum solvent system of the solvent combinations evaluated (Figure 5).

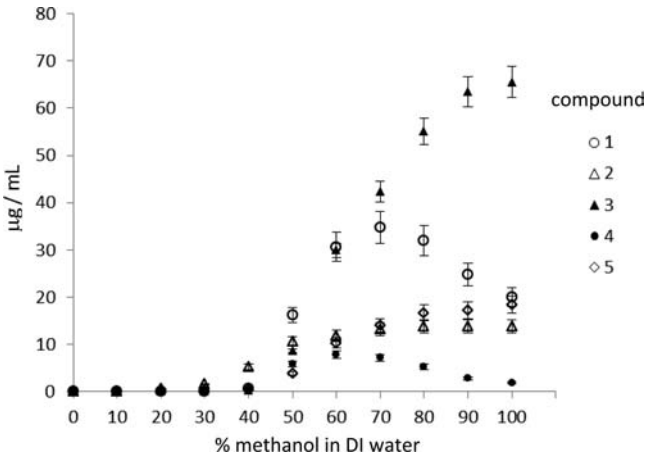

Figure 5. Evaluation of various ratios of methanol and DI water on the extraction of compounds **1**−**5** from *L. longiflorum* bulbs. Concentrations are means of triplicates ± SD.

Extraction Efficiency. Sequential solvent extraction of the lyophilized lily bulb powder using methanol and DI water (8:2, v/v) was employed to estimate the optimal number of extraction cycles for quantitative analysis. The results indicated that between 77.6 and 89.6% of compounds **1**−**5** were recovered in the first extraction. An additional 9.3−17.7% was found with the second extraction and approximately 0−5.1% after the third cycle. On the basis of these observations, the combined supernatants generated from two successive extraction cycles were chosen for further quantitative analysis, resulting in an estimation of 94.4−98.9% extraction efficiency for compounds **1**−**5**.

Method Validation. To quantitate the distribution of five phenylpropanoid glycerol glucosides in *L. longiflorum* organs, **1**−**5** were purified from lily bulbs as analytical reference standards. For quantitative analysis, extracts were prepared from lyophilized plant parts and analyzed using LC-MS in SIM mode. To determine linear relationships between peak area and concentration for the quantitative method, six-point calibration plots were constructed, which demonstrated good linearity over the concentration range of 1.0−300 μg/mL for compounds **1**−**5**. The correlation coefficients ranged from R^2 = 0.9998 to 0.9999. Accuracy of the method was assessed by calculating recovery rates for **1**−**5** in each of the plant organs using the standard addition method.[24] Recovery rates were calculated for each of the plant organs (bulb scales, 94.7−100.8%; roots, 94.8−101.4%; leaves, 96.7−102.9%; lower stems, 93.7−99.8%; upper stems, 94.9−103.3%; flower buds, 96.3−102.0%; and mature flowers, 95.2−101.9%). For compounds **1**−**5** the recovery rates in all of the plant organs assayed were between 93.7 and 103.3%. The precision of the method was evaluated by analyzing the same sample multiple times (bulb; n = 6) and subsequently calculating the relative standard deviation (RSD) of **1**−**5** in the sample. The RSD values for **1**−**5** were 4.14, 3.53, 2.81, 2.73, and 3.57%, respectively. These data demonstrate satisfactory linearity, recovery rates, and RSD, which suggests that the LC-MS method operating in SIM mode is a suitable method for the quantitation of phenylpropanoid glycerol glucosides **1**−**5** in *L. longiflorum* plant organs.

Quantitation of Phenylpropanoid Glycerol Glucosides 1−5 in the Different Organs of *L. longiflorum*. Concentrations of **1**−**5** were quantitatively determined in all plant organs of *L. longiflorum* (Table 1; Figure 6). The *p*-coumaroyl-based compound **3** and its acetylated derivative **5** were determined to be the most abundant of the phenylpropanoid glycerol glucosides found in Easter lily bulbs, at 776.3 ± 8.4 and 650.7 ± 32.6 μg/g dry weight (dw), respectively. As previously mentioned, lily bulbs are regularly consumed as a food, and preparations from lily bulbs, referred to in China as "Bai-he", are employed as effective treatment for various inflammations and some lung ailments; however, the bioactive phytochemicals responsible for the putative medicinal properties remain unknown.[1,2] Compounds **3** and **5** occurred at the highest concentration in the root tissues at 584.4 ± 34.3 and 345.8 ± 32.6 μg/g dw, respectively. Similar to the bulbs and roots, **3** and **5** occurred at the highest concentration in the upper stem and lower stem. Compound **3** occurred at higher concentrations in the lower stem versus the upper stem, and the concentrations of compound **5** were similar in both the lower and upper stems.

The above-ground plant organs of Easter lily (upper stems, leaves, buds, and flowers) showed a different trend of phenylpropanoid glycerol glucoside concentrations from that of the below-ground plant organs (bulbs, roots, and lower stem). The above-ground organs displayed more caffeoyl-based compounds and a greater abundance of acetylation than the below-ground organs. The caffeoyl-based compounds **1** and **4** were the highest in the leaves, at 2007.4 ± 207.5 and 1786.0 ± 200.9 μg/g dw, followed by the *p*-coumaroyl-based compounds **3**, **2**, and **5**, at 1074.8 ± 53.1, 1003.5 ± 36.4, and 935.1 ± 103.9 μg/g dw, respectively. The acetylated *p*-coumaroyl- and caffeoyl-based derivatives, **5** and **4**, had the highest concentrations in the closed flower buds, at 4925.2 ± 512.8 and 3216.8

Table 1. Concentrations of Compounds 1−5 in the Different Organs of *L. longiflorum*

	compound concentration[a] (μg/g dw)				
organ	1	2	3	4	5
bulb	68.4c ± 11.4[b]	80.3bc ± 8.43	776.3a ± 8.4	116.7b ± 29.1	650.7a ± 32.6
root	95.7c ± 12.6	62.8d ± 1.70	584.4a ± 34.3	85.5c ± 12.5	345.8b ± 17.1
leaf	2007.4a ± 207.5	1003.5b ± 36.4	1074.8b ± 53.1	1786.0a ± 200.9	935.1b ± 103.9
lower stem	381.3c ± 49.0	152.8e ± 13.0	1281.7a ± 26.5	275.8d ± 14.1	860.0b ± 47.2
upper stem	274.1c ± 15.6	242.7c ± 25.4	1011.3a ± 35.2	619.0b ± 34.6	1125.0a ± 105.7
bud	762.9d ± 34.0	636.7d ± 40.5	1771.2c ± 104.3	3216.8b ± 406.4	4925.2a ± 512.8
flower	1535.8b ± 174.1	385.9d ± 10.6	736.2c ± 16.4	6006.2a ± 625.8	2160.3b ± 556.5

[a]Concentrations are means of triplicates ± SD, expressed on a dry weight basis (dw). [b]Values with the same letter in each row are not significantly different (p < 0.05).

DOI: 10.1021/acs.jafc.5b00893
J. Agric. Food Chem. 2015, 63, 4836−4842

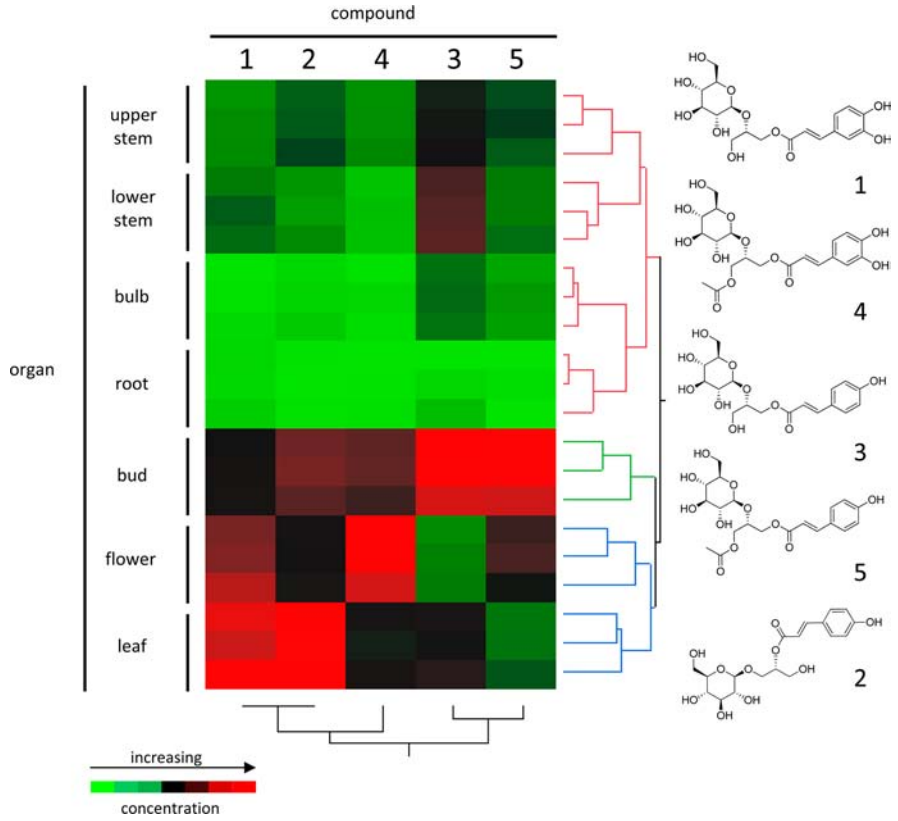

Figure 6. Two-way hierarchal cluster analysis (HCA). Color map visually depicting the differential concentrations of compounds **1**−**5** in the different plant organs of *L. longiflorum*. Colored branches on the dendrogram denote clusters. Upper stem, lower stem, root, and bulb, red cluster; flower and leaf, blue cluster; bud, green cluster.

± 406.4 μg/g dw, respectively. In parts of Asia, lily flower buds, similarly to lily bulbs, are commonly consumed as snacks and in soups, stir-fries, and stew-like dishes. Easter lily flower buds are rich in acetylated phenylpropanoid glycerol glucosides **5** and **4** and differ dramatically from the phytochemical profile of the bulbs. Most abundant in the mature flowers was compound **4**, followed by **5** and **1**, occurring at 6006.2 ± 625.8, 2160.3 ± 556.5, and 1535.8 ± 174.1 μg/g dw, respectively. Interestingly, mature Easter lily flowers are also a plentiful source of acetylated phenylpropanoid glycerol glucosides.

The *p*-coumaroyl-based compound **3** and its acetylated derivative compound **5** had similar distribution profiles in *L. longiflorum* plant parts; however, compound **5** occurred in higher concentrations than compound **3** in the flower buds and mature flowers. Compounds **3** and **5** were the highest occurring phenylpropanoid glycerol glucosides measured in the bulb scales, but their highest concentrations were determined to be in the flower buds as compared to the other plant organs. Notably, compounds **3** and **5** were both higher in the flower buds as compared to mature flowers.

Compound **2** was determined to be a structural isomer of compound **3**, differing only in the linkage arrangement of the glucose and *p*-coumaroyl moiety to the glycerol backbone. In compound **2**, the acyl group is linked to the C2 carbon and the glucose to the C1 carbon, (2*R*)-1-*O*-*β*-D-glucopyranosyl-2-*O*-*p*-coumaroylglycerol, whereas in compound **3**, the acyl group is linked to the C1 carbon and the glucose to the C2 carbon of the glycerin backbone, (2*S*)-1-*O*-*p*-coumaroyl-2-*O*-*β*-D-glucopyranosylglycerol. An acetylated derivative of compound **2** was not identified in the present investigation. Its natural distribution differed from that of the other compounds investigated in the study. The highest concentration of compound **2** was determined to be in the leaves as compared to the other plant organs (Table 1).

The caffeyol-based compound **1** and its acetylated derivative compound **4** had similar profiles in the various organs of *L. longiflorum*; however, as with compounds **3** and **5**, the acetylated derivative, compound **4**, occurred in higher concentrations than compound **1** in the flower buds and mature flowers (Table 1). Compound **4** was the most abundant phenylpropanoid glycerol glucoside measured in the mature flowers.

Upon comparison of the total phenylpropanoid glycerol glucoside concentrations in the plant organs, it is clear that the highest concentrations of these compounds are found in the above-ground portions of the plant (Figure 6). Leaves, flower buds, and flowers have 10−100 times the concentrations of phenylpropanoid glycerol glucosides compared to bulbs and roots, suggesting possible functions for these compounds unique to the above-ground environment. In general, free phenylpropanoid acids do not accumulate in plants, but are usually found as glycosides or esterified to glycerol or organic, fatty, and amino acids. In *Arabidopsis*, malic acid esters and glucosides of the phenylpropanoid sinapic acid accumulate in the leaves, where they provide protection from UV-B light stress and function as sunscreens.[24] It is possible that phenylpropanoid glycerol glucosides may play a similar role in Easter lily, a plant native to the unshaded rocky shores of the subtropical Ryukyu Islands of Japan. The high concentrations of phenylpropanoid glycerol glucosides in the leaves and flower buds may also serve as a constitutive reserve of fungitoxic phenolic acids as in cucumber leaves, where attack by a

DOI: 10.1021/acs.jafc.5b00893
J. Agric. Food Chem. 2015, 63, 4836−4842

powdery mildew fungus triggers the hydrolysis of glucosides of *p*-coumaric acid methyl ester and other phenylpropanoid acid conjugates, significantly reducing disease symptoms.[26]

The unequal distribution pattern of the phenylpropanoid glycerol glucosides between above- and below-ground organs is similar to the distribution of two types of steroidal glycosides of lily bulbs. The proportion of the steroidal glycoalkaloids to furostanol saponins in light-exposed organs was greater; moreover, this ratio decreased from the above-ground organs to those growing farther below the soil surface, suggesting that these compounds may be involved in different physiological processes particular to their growing environment.[27]

In conclusion, this is the first report of the natural distribution of phenylpropanoid glycerol glucosides within the different organs of a plant and the first report that these compounds are present in plant organs other than the bulbs and flowers. The *p*-coumaroyl-based compound **3** and its acetylated derivative **5** were determined to be the most plentiful of the phenylpropanoid glycerol glucosides found in Easter lily bulbs, whereas the acetylated *p*-coumaroyl- and caffeoyl-based derivatives **5** and **4** were found in the highest concentrations in the flower buds. Quantitative analysis of phenylpropanoid glycerol glucosides in the component parts of *L. longiflorum* is a prelude to understanding their function in plant physiology, development, and pathogen defense. The results of this study will also form the basis for research on the benefits of lily bulb consumption to human health and for the development of functional foods, cosmetics, and pharmaceuticals containing lily bulb compounds.

AUTHOR INFORMATION

Corresponding Author

*(T.J.G.) Phone: (848) 932-6369. Fax: (732) 932-6441. E-mail: gianfagna@aesop.rutgers.edu.

Notes

The authors declare no competing financial interest.

ACKNOWLEDGMENTS

We are very grateful to Dr. Karsten Siems from AnalytiCon Discovery GmbH (Potsdam, Germany) for the skillful acquisition of the NMR spectra.

REFERENCES

(1) Ori, K.; Mimaki, Y.; Mito, K.; Sashida, Y.; Nikaido, T.; Ohmoto, T.; Masuko, A. Jatropham derivatives and steroidal saponins from the bulbs of *Lilium hansonii*. *Phytochemistry* **1992**, *31*, 2767−2775.

(2) Mimaki, Y.; Sashida, Y. Steroidal saponins from the bulbs of *Lilium brownii*. *Phytochemistry* **1990**, *29*, 2267−2271.

(3) Shimomura, H.; Sashida, Y.; Mimaki, Y.; Kudo, Y.; Maeda, K. New phenylpropanoid glycerol glucosides from the bulbs of *Lilium* species. *Chem. Pharm. Bull.* **1988**, *36*, 4841−4848.

(4) Sang Tai, C.; Uemoto, S.; Shoyama, Y.; Nishioka, I. Biologically active phenolics from *Lilium longiflorum*. *Phytochemistry* **1981**, *20*, 2565−2568.

(5) Shimomura, H.; Sashida, Y.; Mimaki, Y.; Minegishi, Y. Jatropham glucoside from the bulbs of *Lilium hansonii*. *Phytochemistry* **1987**, *26*, 582−583.

(6) Francis, J. A.; Rumbeiha, W.; Nair, M. G. Constituents in Easter lily flowers with medicinal activity. *Life Sci.* **2004**, *76*, 671−683.

(7) Tsukida, K.; Ikeuchi, K. Epoxycarotenoids. VIII. Pollen carotenoids of *Lilium longiflorum* and of its cultivated hybrid. *Bitamin* **1965**, *32*, 222−226.

(8) Shimomura, H.; Sashida, Y.; Mimaki, Y. Steroidal saponins, pardarinoside A−G from the bulbs of *Lilium pardarinum*. *Phytochemistry* **1989**, *28*, 3163−3170.

(9) Sashida, Y.; Ori, K.; Mimaki, Y. Studies on the chemical constituents of the bulbs of *Lilium mackliniae*. *Chem. Pharm. Bull.* **1991**, *39*, 2362−2368.

(10) Nakamura, O.; Mimaki, Y.; Nishino, H.; Sashida, Y. Steroidal saponins from the bulbs of *Lilium speciosum* x *L. nobilissimum* 'Star Gazer' and their antitumour-promoter activity. *Phytochemistry* **1994**, *36*, 463−467.

(11) Mimaki, Y.; Satou, T.; Kuroda, M.; Sashida, Y.; Hatakeyama, Y. Steroidal saponins from the bulbs of *Lilium candidum*. *Phytochemistry* **1999**, *51*, 567−573.

(12) Mimaki, Y.; Satou, T.; Kuroda, M.; Sashida, Y.; Hatakeyama, Y. New steroidal constituents from the bulbs of *Lilium candidum*. *Chem. Pharm. Bull.* **1998**, *46*, 1829−1832.

(13) Mimaki, Y.; Sashida, Y.; Nakamura, O.; Nikaido, T.; Ohmoto, T. Steroidal saponins from the bulbs of *Lilium regale* and *Lilium henryi*. *Phytochemistry* **1993**, *33*, 675−682.

(14) Mimaki, Y.; Sashida, Y. Steroidal and phenolic constituents of *Lilium speciosum*. *Phytochemistry* **1991**, *30*, 937−940.

(15) Mimaki, Y.; Sashida, Y. Steroidal saponins and alkaloids from the bulbs of *Lilium brownii* var. *colchesteri*. *Chem. Pharm. Bull.* **1990**, *38*, 3055−9.

(16) Mimaki, Y.; Nakamura, O.; Sashida, Y.; Satomi, Y.; Nishino, A.; Nishino, H. Steroidal saponins from the bulbs of *Lilium longiflorum* and their antitumour-promoter activity. *Phytochemistry* **1994**, *37*, 227−232.

(17) Munafo, J. P., Jr.; Gianfagna, T. J. Chemistry and biological activity of steroidal glycosides from the Lilium genus. *Nat. Prod. Rep.* **2015**, *32*, 454−477.

(18) Munafo, J. P., Jr.; Gianfagna, T. J. Antifungal activity and fungal metabolism of steroidal glycosides of Easter lily (*Lilium longiflorum* Thunb.) by the plant pathogenic fungus, *Botrytis cinerea*. *J. Agric. Food Chem.* **2011**, *59*, 5945−5954.

(19) Munafo, J. P., Jr.; Ramanathan, A.; Jimenez, L. S.; Gianfagna, T. J. Isolation and structural determination of steroidal glycosides from the bulbs of Easter lily (*Lilium longiflorum* Thunb.). *J. Agric. Food Chem.* **2010**, *58*, 8806−8813.

(20) Shimomura, H.; Sashida, Y.; Mimaki, Y.; Iida, N. Regaloside A and B, acylated glycerol glucosides from *Lilium regale*. *Phytochemistry* **1988**, *27*, 451−454.

(21) Shimomura, H.; Sashida, Y.; Mimaki, Y.; Iitaka, Y. Studies on the chemical constituents of *Lilium henryi* Baker. *Chem. Pharm. Bull.* **1988**, *36*, 2430−2446.

(22) Shimomura, H.; Sashida, Y.; Mimaki, Y. New phenolic glycerol glucosides, regaloside D, E, and F from the bulbs of *Lilium* species. *Chem. Pharm. Bull.* **1989**, *43*, 64−70.

(23) Mimaki, Y.; Sashida, Y.; Shimomura, H. Lipid and steroidal constituents of *Lilium auratum* var. *platyphyllum* and *Lilium tenuifolium*. *Phytochemistry* **1989**, *28*, 3453−3458.

(24) Skoog, D.; Holler, F.; Nieman, T. Introduction. In *Principles of Instrumental Analysis*, 5th ed.; Brooks/Cole Publishing: Belmont, CA, USA, 1997.

(25) Li, J.; Ou-Lee, T.-M.; Raba, R.; Amundson, R. G.; Last, R. L. Arabidopsis flavonoid mutants are hypersensitive to UV-B irradiation. *Plant Cell* **1993**, *5*, 171−179.

(26) Daayf, F.; Ongena, M.; Boulanger, R.; El Hadrami, I.; Bélanger, R. R. Induction of phenolic compounds in two cultivars of cucumber by treatment of healthy and powdery mildew-infected plants with extracts of *Reynoutria sachalinensis*. *J. Chem. Ecol.* **2000**, *26*, 1579−1593.

(27) Munafo, J. P., , Jr.; Gianfagna, T. J. Quantitative analysis of steroidal glycosides in different organs of Easter lily (*Lilium longiflorum* Thunb.) by LC-MS/MS. *J. Agric. Food Chem.* **2011**, *59*, 995−1004.

DOI: 10.1021/acs.jafc.5b00893
J. Agric. Food Chem. 2015, 63, 4836−4842

JOURNAL OF AGRICULTURAL AND FOOD CHEMISTRY

Article

pubs.acs.org/JAFC

Carnosic Acid as a Major Bioactive Component in Rosemary Extract Ameliorates High-Fat-Diet-Induced Obesity and Metabolic Syndrome in Mice

Yantao Zhao, Rashin Sedighi, Pei Wang, Huadong Chen, Yingdong Zhu, and Shengmin Sang*

Center for Excellence in Post-Harvest Technologies, North Carolina Agricultural and Technical State University, North Carolina Research Campus, 500 Laureate Way, Kannapolis, North Carolina 28081, United States

ABSTRACT: In this study, we investigated the preventive effects of carnosic acid (CA) as a major bioactive component in rosemary extract (RE) on high-fat-diet-induced obesity and metabolic syndrome in mice. The mice were given a low-fat diet, a high-fat diet or a high-fat diet supplemented with either 0.14% or 0.28% (w/w) CA-enriched RE (containing 80% CA, RE#1L and RE#1H), or 0.5% (w/w) RE (containing 45% CA, RE#2), for a period of 16 weeks. There was the same CA content in the RE#1H and RE#2 diets and half of this amount in the RE#1L diet. The dietary RE supplementation significantly reduced body weight gain, percent of fat, plasma ALT, AST, glucose, insulin levels, liver weight, liver triglyceride, and free fatty acid levels in comparison with the mice fed with a HF diet without RE treatment. RE administration also decreased the levels of plasma and liver malondialdehyde, advanced glycation end products (AGEs), and the liver expression of receptor for AGE (RAGE) in comparison with those for mice of the HF group. Histological analyses of liver samples showed decreased lipid accumulation in hepatocytes in mice administrated with RE in comparison with that of HF-diet-fed mice. Meanwhile, RE administration enhanced fecal lipid excretion to inhibit lipid absorption and increased the liver GSH/GSSG ratio to perform antioxidant activity compared with HF group. Our results demonstrate that rosemary is a promising dietary agent to reduce the risk of obesity and metabolic syndrome.

KEYWORDS: *rosemary, carnosic acid, obesity, metabolic syndrome, high-fat diet, oxidative stress*

INTRODUCTION

Obesity is now a global epidemic and is a high risk factor for chronic diseases such as type 2 diabetes, cardiovascular disease, hypertension, nonalcoholic fatty liver disease (NAFLD), osteoarthritis, cancer, and stroke.[1] More than one-third (34.9%, more than 78 million) of adults in the United States were obese in 2011−2012.[2] In addition, 90% of type 2 diabetic patients are overweight or obese.[3,4] A poor dietary habit is one of the most common causes of obesity and type 2 diabetes.[5,6] Dietary intervention with functional food has been proven to be an effective approach to reduce the risk of obesity and related type 2 diabetes.[7,8] Much research is currently being devoted to the bioactive food components to improve metabolic syndrome.

Rosemary (*Rosmarinus officinalis* L.) is well-known for its antioxidant properties and has been widely employed and commercialized as a preserving agent in the food industry, cosmetic additives, and nutritional supplements.[9−12] The rosemary extract (RE) has been approved by the European Union (EU) for use in food preservation and has been categorized by the FDA as "generally recognized as safe". Rosemary itself contains a variety of polyphenolic compounds, including carnosic acid (CA), carnosol, rosemanol, rosmarinic acid (RA), and many others.[13−15] CA has been used as a principal component for the standardization of commercial rosemary extract in food or supplements.[11]

Only a few studies have investigated the beneficial effects of RE on obesity and metabolic disorders in various rodent models of high-fat (HF)-diet-induced[16,17] and genetic obesity.[18,19] Ibarra et al.[17] demonstrated that RE (containing 20% CA) supplement at 500 mg of RE/kg of body weight for 16 weeks inhibited weight gain and improved glucose and lipid homeostasis in HF-diet-fed male C57BL/6J mice. In another study, the male C57BL/6J mice were fed HF diet for 11 weeks and then given RE (containing 2.5% CA, 4% RA, and 5.6% carnosol) for 50 days. This 200 mg/kg of RE administration significantly reduced weight and fat mass gain and protected obesity-induced liver steatosis.[16] In those two HF-diet-induced obesity studies, even though the body weight was limited by oral RE administration, two different kinds of rosemary extract were used and it is hard to determine which component is the major active compound in rosemary. The objective of the present study was to determine whether CA is a major active component in RE and the dose−response effect of CA against HF-induced obesity and related metabolic syndrome in mice.

MATERIALS AND METHODS

Chemicals and Reagents. Commercial RE with 45% CA was purchased from Changsha Yaying Biotechnology Inc. (Changsha, People's Republic of China). The CA content of rosemary extracts was determined by high-performance liquid chromatography (HPLC), and the main compounds of RE were determined by liquid chromatography/mass spectrometry (LC/MS). Antibodies against RAGE were purchased from Santa Cruz Biotechnology (Dallas, TX, USA). Antibodies against β-actin and horseradish peroxidase (HRP) conjugated donkey antirabbit IgG were purchased from Cell Signaling

Received: March 10, 2015
Revised: April 30, 2015
Accepted: April 30, 2015
Published: April 30, 2015

ACS Publications © 2015 American Chemical Society

DOI: 10.1021/acs.jafc.5b01246
J. Agric. Food Chem. 2015, 63, 4843−4852

Table 1. Compositions of the Experimental Low-Fat Diet (LF), High-Fat Diet (HF), and HF plus Rosemary Extract (RE) Diets (RE#1L, RE#1H, and RE#2)

	LF		HF		RE#1L		RE#1H		RE#2	
	g %	kcal %	g %	kcal %	g %	kcal %	g %	g %	g %	g %
protein	19.2	20	26.2	20	26.2	20	26.2	20	26.1	20
carbohydrate	67.3	70	26.3	20	26.3	20	26.3	20	26.2	20
fat	4.3	10	34.9	60	34.8	60	34.8	60	34.7	60
total		100		100		100		100		100
kcal/g	3.85		5.24		5.24		5.23		5.22	

	LF		HF		RE#1L		RE#1H		RE#2	
ingredient	g	kcal	g	kcal	g	kcal	g	kcal	g	kcal
casein/80 mesh	200	800	200	800	200	800	200	800	200	800
L-cystine	3	12	3	12	3	12	3	12	3	12
corn starch	506.2	2024.8	0	0	0	0	0	0	0	0
maltodextrin 10	125	500	125	500	125	500	125	500	125	500
sucrose	68.8	275.2	68.8	275.2	68.8	275.2	68.8	275.2	68.8	275.2
cellulose, BW200	50	0	50	0	50	0	50	0	50	0
soybean oil	25	225	25	225	25	225	25	225	25	225
lard	20	180	245	2205	245	2205	245	2205	245	2205
mineral mix, S10026	10	0	10	0	10	0	10	0	10	0
D calcium phosphate	13	0	13	0	13	0	13	0	13	0
calcium carbonate	5.5	0	5.5	0	5.5	0	5.5	0	5.5	0
potassium citrate, 1 H_2O	16.5	0	16.5	0	16.5	0	16.5	0	16.5	0
vitamin mix, V10001	10	40	10	40	10	40	10	40	10	40
choline biartrate	2	0	2	0	2	0	2	0	2	0
RE#1	0	0	0	0	1.09	0	2.18	0	0	0
RE#2	0	0	0	0	0	0	0	0	3.9	0
dye (different color)	0.05		0.05		0.05		0.05		0.05	
total	1055.05	4057	773.85	4057	774.94	4057	776.03	4057	777.75	4057

(Danvers, MA, USA). CA standard and other chemicals were purchased from Sigma (St. Louis, MO, USA). HPLC-grade solvents and other reagents were obtained from VWR Scientific (South Plainfield, NJ, USA). LC/MS-grade methanol and water were obtained from Thermo Fisher Scientific (Waltham, MA, USA).

Preparation of RE with 80% CA. RE with 80% CA was prepared from the commercial RE (45% CA) in our laboratory according to the method described in the US patent 5,256,700[20] with modification. In brief, 50 g of RE (45% CA) was subjected to column chromatography over silica gel (230−400 mesh, Sorbent Technologies Inc., Atlanta, GA) and eluted with a gradient of hexane/acetone (50/2, 50/3, 50/4, 50/5, and 0/100) to give five fractions (Fr A−E). Fraction B (23.3 g) was applied to reverse-phase C_{18} silica gel medium-pressure column chromatography (35 mm × 400 mm, 60 Å, Sigma) eluted with 75% methanol/25% water containing 0.05% formic acid to give four subfractions (Fr. B_1−B_4). Fraction B_2 (6.85 g) was identified as the CA-enriched fraction (80% CA) by HPLC. These steps were repeated five times in order to accumulate enough samples for the mouse study.

Determination of the Major Components in RE by LC/MS. LC/MS was carried out with a Thermo-Finnigan Spectra System, consisting of an Accela high-speed MS pump, an Accela refrigerated autosampler, and an LTQ Velos ion trap mass detector (Thermo Electron, San Jose, CA, USA) incorporated with an electrospray ionization (ESI) interface. A Gemini C18 column (150 × 4.6 mm, 5 μm; Phenomenex, Torrance, CA) was used for separation at a flow rate of 200 μL/min. The column was eluted with 100% solvent A (5% aqueous methanol with 0.2% acetic acid) for 3 min, followed by linear increases in B (95% aqueous methanol with 0.1% acetic acid) to 60% from 3 to 8 min, then to 75% from 8 to 30 min to 82% from 30 to 48 min, and then with 100% from 48 to 55 min. The column was then re-equilibrated with 100% A for 5 min. The injection volume was 10 μL for each sample. Nitrogen gas was used as the sheath gas and auxiliary gas. The collision-induced dissociation (CID) was conducted with an isolation width of 2 Da and normalized collision energy of 35 for MS^2 and MS^3. The mass range was measured from m/z 50 to 1000. Data acquisition was performed with Xcalibur version 2.0 (Thermo Electron, San Jose, CA, USA).

Animals, Diets, and Experimental Design. Male C57BL/6J mice (5 weeks old) were obtained from Jackson Laboratory (Bar Harbor, ME, USA) and were acclimated for 1 week before being randomly assigned to different experimental groups. All of the mice were maintained on a 12 h light/dark cycle on a standard chow diet until experimental analysis. Control low-fat diet (10% kcal energy from fat, D12450J, LF), high-fat diet (60% kcal energy from fat, D12492, HF), and HF mixed with 0.14% or 0.28% of CA-enriched RE (80% CA, RE#1L and RE#1H) and 0.5% of commercial RE (45% CA, RE#2) were produced from Research Diets (New Brunswick, NJ). All diets were pelleted, and the composition of diets is shown in Table 1. The experimental animal protocol was approved by the Institutional Animal Care and Use Committee of the North Carolina Research Campus (No. 12-012). After adaptation for 1 week, mice were randomly divided into five groups (n = 15 in each group, 5 mice per cage): (1) control low fat (LF); (2) control high fat (HF); (3) HF + 0.14% (w/w) CA-enriched RE (RE#1L); (4) HF + 0.28% (w/w) CA-enriched RE (RE#1H); (5) HF + 0.5% (w/w) commercial RE (RE#2). The RE#1H and RE#2 diets contain the same concentration of CA, and the RE#1L diet has half the amount of CA in comparison with those in RE#1H and RE#2 diets. Water and food were available to the animals ad libitum. Body weight and food intake were recorded weekly. At the end of the experiment, the animals were sacrificed by euthanization with isofluorane after fasting for 8 h, and plasma, liver, kidney, and adipose tissue (epididymal, retroperitoneal, and mesenteric) were collected, weighed, frozen under liquid nitrogen, and stored at −80 °C until further analyses.

Body Composition-MRI Analysis. Whole body composition (fat and lean tissues) was determined using nuclear magnetic resonance technology with an EchoMRI Analyzer system (Model MRI-100, Houston, TX, USA) at week 15 (day 102). The EchoMRI-100 instrument provides measurements of whole body composition parameters: total fat, lean mass, and total body water in live mice without the need for anesthesia or sedation in about 2 min.

DOI: 10.1021/acs.jafc.5b01246
J. Agric. Food Chem. 2015, 63, 4843−4852

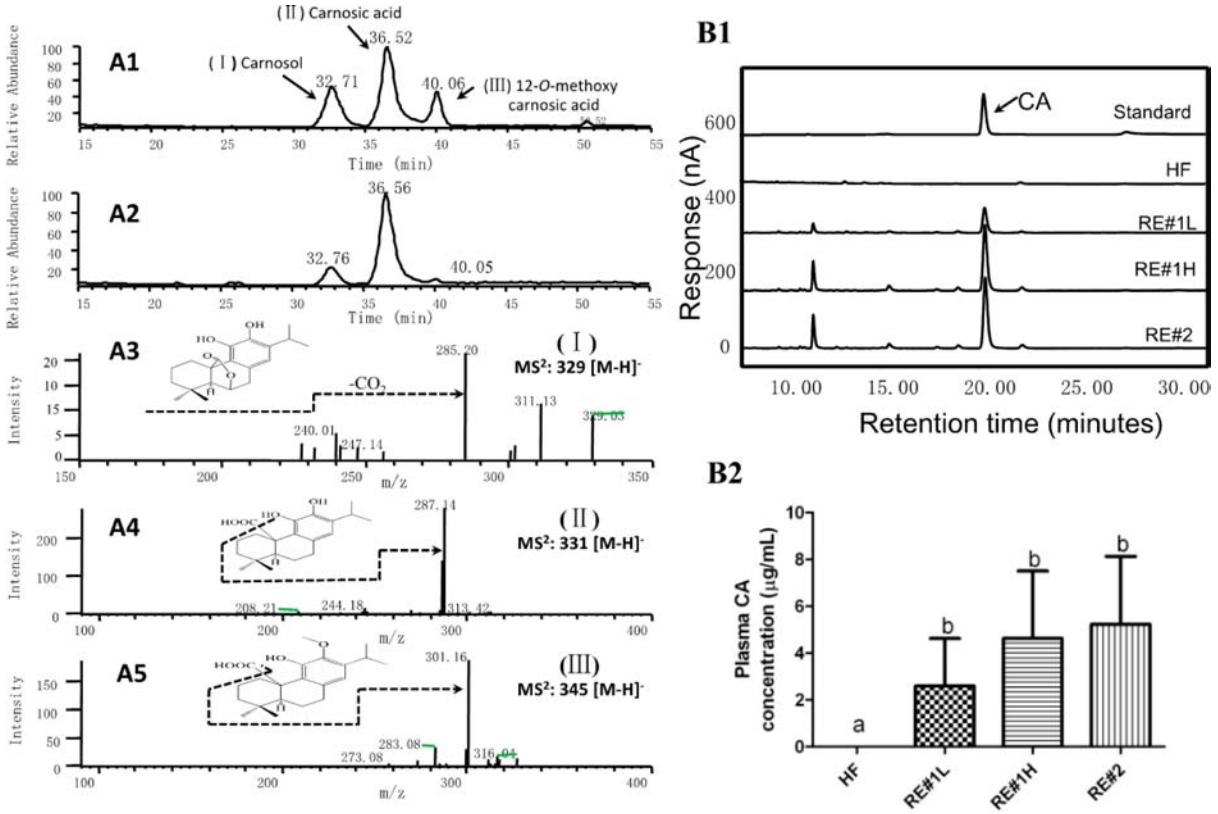

Figure 1. Chemical profiles of rosemary extracts (REs) used in this study and plasma carnosic acid (CA) concentrations in mice treated with REs. LC chromatograms of commercial RE (A1) and CA-enriched RE (A2) with negative ESI-MS as detector and MS/MS (negative) spectra of peaks I–III (A3–A5). Representative HPLC-ECD chromatograms of CA standard and the corresponding CA peak in plasma samples from mice in HF, RE#1L, RE#1H, and RE#2 groups (B1) and plasma CA concentrations of different groups (B2). Results are means ± standard deviations (n = 15), represented by vertical bars. Significant differences (p < 0.05, ANOVA) are identified by the different letters among HF, RE#1L, RE#1H, and RE#2 groups.

Plasma CA Concentrations Determined by HPLC Coupled with an Electrochemical Detector (ECD). Enzymatic deconjugation of the plasma samples was performed as described before, but with slight modification.[21] In brief, plasma samples (100 μL) were treated with β-glucuronidase (250 U) and sulfatase (3 U) for 45 min at 37 °C. This mixture was extracted with 2.5 mL of *n*-hexane by shaking for 5 min and centrifuged at 16.1 (×1000*g*) for 10 min at 4 °C, and then the supernatant was transferred to another tube and evaporated to dryness under a gentle stream of nitrogen at room temperature. The pellet was reconstituted in 150 μL of methanol containing 0.2% acetic acid and filtered through a 0.22 μm filter prior to injecting to the HPLC-ECD system.

CA was quantified using an HPLC-ECD system (ESA, Chelmsford, MA, USA) consisting of an ESA Model 584 HPLC pump, an ESA Model 542 autosampler, an ESA organizer, and an ESA CoulArray detector coupled with two ESA Model 6210 four-sensor cells. A Gemini C_{18} column (150 × 4.6 mm, 5 μm; Phenomenex, Torrance, CA, USA) was used for chromatographic analysis at a flow rate of 1.0 mL/min. The mobile phases consisted of solvent A (30 mM sodium phosphate buffer containing 1.75% acetonitrile and 0.125% tetrahydrofuran, pH 3.35) and solvent B (15 mM sodium phosphate buffer containing 58.5% acetonitrile and 12.5% tetrahydrofuran, pH 3.45). The gradient elution had the following profile: 30% B from 0 to 3 min; 30–65% B from 3 to 10 min; 65–100% B from 10 to 40 min; 100% B from 40 to 45 min; and 30% B from 45 to 50 min. The cells were then cleaned at a potential of 1000 mV for 2 min. The injection volume of the samples was 10 μL. The eluent was monitored by the Coulochem electrode array system (CEAS) with potential settings at −50, 0, 100, 200, 300, 400, 500, and 600 mV. Data for Figure 2B1 was from the channel set at 200 mV of the CEAS. For CA, the limit of detection (LOD) and the limit of quantification (LOQ) were 0.1 and 0.5 μg/mL, respectively. The linearity ranged from LOQ to 10 μg/mL (the upper limit was not tested) with a correlation coefficient of 0.999.

Biochemical Analyses of Blood Samples. Blood samples were collected by cardiac puncture, and plasma was obtained by centrifuging the blood at 8000*g* for 15 min at 4 °C. Plasma alanine aminotransferase (ALT) and aspartate aminotransferase (AST) activities were colorimetrically measured using Infinity ALT and AST Reagent provided by Thermo Scientific (Waltham, MA). Plasma TNF-α was measured using a Mouse TNF-α ELISA kit (Millipore, Temecula, CA). To measure blood glucose, mice were fasted for 8 h before measurement. Blood was collected from the tail vein, and glucose concentrations were measured using a OneTouch Ultra2 Blood Glucose Meter (LifeScan, Milpitase, CA, USA) at weeks 0, 10, and 16. Insulin levels were determined using an Ultrasensitive Insulin ELISA kit (ALPCO, Salem, NH, USA). Homeostasis model assessment of insulin resistance (HOMA-IR) was calculated using the following formula: [fasting glucose (mg/dL) × insulin (mU/L)]/405.[22]

Hepatic Lipid Analyses. Quantitative assay of lipids was conducted by measuring triglyceride and free fatty acids (FFA) concentrations in the liver. Hepatic lipids are extracted by homogenizing liver tissue in chloroform using 1% Triton X-100. The organic extracts were air-dried, vacuumed, and dissolved in Trition X-100. Triglyceride and FFA concentrations in extracts were determined using commercial kits (BioVision, Milpitase, CA).

Fecal Lipid Excretion. The feces harvested during a 24 h period were collected at week 16, frozen at −80 °C, and pulverized. Total lipids were extracted from 100 mg of dried feces using the following method.[23] The feces were cleaned and dried for 24 h by a freeze-dryer, incubated with 2 mL of chloroform/methanol (2/1) for 30 min at 60 °C with constant agitation, and then centrifuged. Water (1 mL) was added to the supernatant, and following vortexing, phase separation was induced by low-speed centrifugation (500*g* for 10 min). The lower chloroform

DOI: 10.1021/acs.jafc.5b01246
J. Agric. Food Chem. 2015, 63, 4843–4852

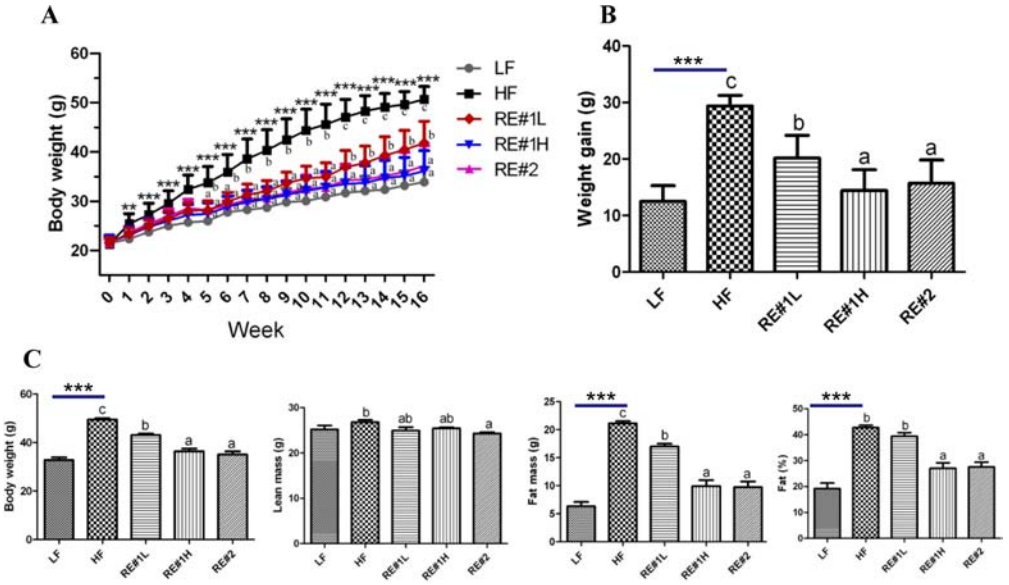

Figure 2. Effects of long-term carnosic acid (CA) enriched rosemary extract (RE) (RE#1L, RE#1H, and RE#2) administration on body weight (BW) (A), weight gain (B), and body composition (C) in high-fat-diet-fed C57BL/6J mice. Results are means ± standard deviations (n = 15 for A and B; n = 5 for C) represented by vertical bars. The asterisk (*) denotes a significant difference of the HF group in comparison with the LF group: (*) $p < 0.05$, (**) $p < 0.01$, (***) $p < 0.001$. Significant differences ($p < 0.05$, ANOVA) are identified by the different letters among HF, RE#1L, RE#1H, and RE#2 groups.

phase was then removed and transferred to a new tube, and the sample was evaporated to dryness by a nitrogen evaporator and weighed.

Hepatic GSH/GSSG and Oxidative Stress Levels. The ratio of GSH/GSSG in the liver was determined by a commercial Glutathione Assay Kit (Trevigen, Gaithersburg, MD, USA). The lipid peroxidation product malondialdehyde (MDA) in the plasma and liver was measured by the thiobarbituric acid reactive substances (TBARS) method using a commercial kit (Cayman Chemical, Ann Arbor, MI, USA).

Liver Histology. Liver tissues were fixed with 10% formalin and processed for paraffin embedding. Tissue sections were cut to 5 μm and stained with hematoxylin and eosin (H&E) for assessing histopathological changes.

Plasma and Liver AGEs. The plasma AGE level was measured on the basis of the methods of Henle,[24] Munch,[25] and Raposeiras-Roubin.[26] In brief, plasma was diluted 1/20 with PBS (pH 7.4), and the fluorescence intensity was recorded at 360 nm excitation and 460 nm emission wavelengths by a multimode microplate reader (Synergy 2, Biotek). Fluorescence intensity was expressed in arbitrary units (AU), and the fluorescence was normalized with the LF group.

The liver AGE level was determined according to the methods of Nakayama[27] and Yamabe.[28] In brief, minced liver tissue was delipidated with chloroform and methanol (2/1, v/v) with overnight shaking. After it was washed with methanol and distilled water, the tissue was homogenized in 0.1 N NaOH, followed by centrifugation at 8000g for 15 min at 4 °C. The amounts of AGEs in these alkali-soluble samples were determined by measuring fluorescence at 360 nm excitation and 460 nm emission wavelengths. The fluorescence reading of 1 mg/mL of BSA was defined as 1 unit. The fluorescence values of samples were measured at a protein concentration of 1 mg/mL and expressed in arbitrary units (AU) normalized by the reading from 1 mg/mL of BSA.

Western Blot Assay of Proteins. Whole protein lysates of liver tissue were extracted using RIPA buffer (25 mM Tris-HCl (pH 7.6), 150 mM NaCl, 1% NP-40, 1% sodium deoxycholate, 0.1% SDS, Thermo Fisher Scientific) supplemented with 1% protease inhibitor cocktail and 1% phenylmethylsulfonyl fluoride. Protein concentrations were measured using a BCA Protein Assay Kit (Thermo Scientific, Rockford, IL, USA). Aliquots containing 50 μg of protein were loaded onto a 10−12% sodium dodecyl sulfatepolyacrylamide gel, transblotted onto a polyvinylidene difluoride (PVDF) membrane (Bio-Rad), blocked with Tris-buffered saline with 1% Casein with 0.1% Tween-20, and then incubated with each of the primary antibodies of RAGE and β-actin. The membrane was then incubated with horseradish peroxidase conjugated donkey antirabbit or goat antimouse IgG (Cell signaling, Danvers, MA, USA). The bound complexes were detected with SuperSignal Chemiluminescent Subtract (Thermo Scientific, Rockford, IL, USA). The immunoblot bands were quantified by densitometry analysis, and the ratio to β-actin was calculated and presented, setting the values of low-fat diet fed mice as 1.

Statistical Analysis. All results are presented as means ± standard deviation. A Student's t test was performed using GraphPad Prism version 5.04. An asterisk (*) means a significant difference of HF group in comparison with the LF group: (*) $p < 0.05$, (**) $p < 0.01$, (***) $p < 0.001$. The intergroup variation was measured by one-way ANOVA with Tukey's test. Significant differences are identified by the different letters among HF, RE#1L, RE#1H, and RE#2 groups, and a p value of <0.05 was considered statistically significant.

The inhibition of gains and biochemical parameters by RE-treated groups is expressed as a percentage calculated as inhibition percentage (%) = ((HF − RE)/(HF − LF)) × 100.

RESULTS

Preparation of CA-Enriched RE. In order to determine whether CA is the active component in RE against obesity and related metabolic syndrome, we further enriched CA from commercial RE using different column chromatography techniques. The three major peaks in the commercial RE were identified as carnosol, CA, and 12-*O*-methoxy carnosic acid by analyzing their tandem mass (Figure 1A). The CA concentrations of commercial RE and CA enriched RE were quantified by HPLC-ECD and determined to be 45% and 80%, respectively.

Plasma CA Concentrations in RE-Treated Mice. The plasma CA concentrations were quantified by HPLC-ECD. The CA levels of mice in the RE#1L group were much lower than those in RE#1H and RE#2 groups; even though the difference is not significant (Figure 1B), the results are consistent with the levels of CA in the RE#1L, RE#1H, and RE#2 diets.

Effects of Long-Term RE Supplementation on Body Weights and Organ Weights. Three different RE treatments, RE#1L, RE#1H, and RE#2, were used in this study. RE#1H and RE#2 had the same amount of CA (0.224% in the diet), which was twice that in RE#1L (0.112% in the diet). Body weights

DOI: 10.1021/acs.jafc.5b01246
J. Agric. Food Chem. 2015, 63, 4843−4852

Table 2. Organ Weights of Mice Fed with Low-Fat Diet (LF), High-Fat Diet (HF), and HF plus Rosemary Extract (RE) Diets (RE#1L, RE#1H, and RE#2) for 16 Weeks[a]

	weight (g)				
	LF	HF	RE#1L	RE#1H	RE#2
liver	1.18 ± 0.26	2.78 ± 0.61***b	1.30 ± 0.27a	1.19 ± 0.41a	1.28 ± 0.15a
liver/BW (%)	3.53 ± 1.00	5.45 ± 0.97***b	3.10 ± 0.37a	3.01 ± 0.22a	3.45 ± 0.30a
kidney	0.32 ± 0.03	0.37 ± 0.03**b	0.34 ± 0.03ab	0.33 ± 0.02a	0.32 ± 0.03a
kidney/BW (%)	0.95 ± 0.10	0.73 ± 0.04***a	0.82 ± 0.07b	0.94 ± 0.10c	0.87 ± 0.11bc
epididymal fat	1.17 ± 0.50	1.54 ± 0.25*a	2.63 ± 0.34c	1.97 ± 0.75ab	2.21 ± 0.69bc
mesenteric fat	0.48 ± 0.16	1.72 ± 0.24***c	0.78 ± 0.22b	0.54 ± 0.13a	0.56 ± 0.22a
retroperitoneal fat	0.48 ± 0.21	1.58 ± 0.34***c	1.17 ± 0.24b	0.84 ± 0.27a	0.86 ± 0.33a
total fat	2.13 ± 0.83	4.85 ± 0.47***b	4.59 ± 0.68b	3.43 ± 1.05a	3.64 ± 1.05a

[a]Values are means ± SD. The asterisks (*) denote significant difference of the HF group in comparison with the LF group: (*) $p < 0.05$; (**) $p < 0.01$; (***) $p < 0.001$. Significant differences ($p < 0.05$, ANOVA) are identified by the different letters among HF, RE#1L, RE#1H, and RE#2 groups.

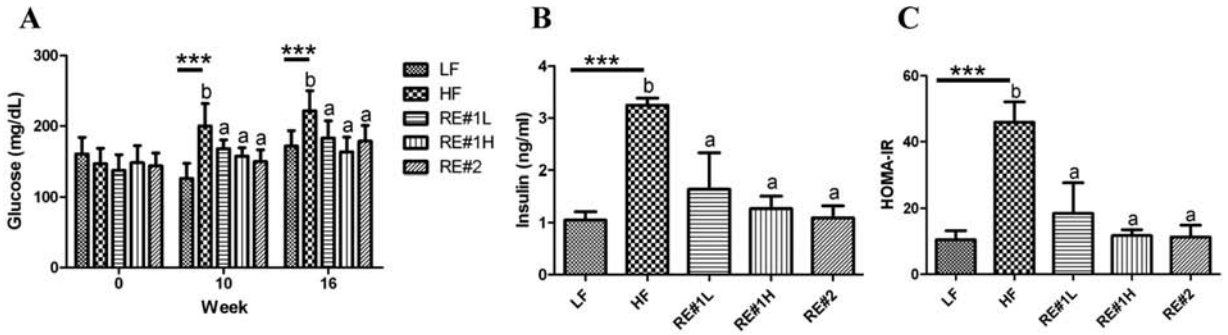

Figure 3. Effects of long-term rosemary extract (RE) dietary treatments on glucose (A), insulin (B), and HOMA-IR (C) in high-fat-diet-fed C57BL/6J mice. HOMA-IR was calculated on the basis of the formula [fasting glucose (mg/dL) × insulin (mU/L)]/405 to express the degree of insulin resistance. Values are presented as mean ± standard deviations ($n = 15$ for A and $n = 5$ for B and C) represented by vertical bars. The asterisk (*) denotes a significant difference of the HF group in comparison with the LF group: (*) $p < 0.05$, (**) $p < 0.01$, (***) $p < 0.001$. Significant differences ($p < 0.05$, ANOVA) are identified by the different letters among the HF, RE#1L, RE#1H, and RE#2 groups.

between the HF and LF groups began to differ significantly after the first week of treatment ($p < 0.01$). RE supplementation significantly decreased body weight gain induced by the HF diet after the fifth week of treatment ($p < 0.05$). Meanwhile, body weights of RE#1H- and RE#2-treated mice were significantly lower than those in the RE#1L group after 12 weeks of treatment ($p < 0.05$). After 16 weeks of treatment of LF, HF, and HF plus RE diets, HF-treated mice showed a significantly higher body weight and body weight gain in comparison with those of LF-treated control (BW, 50.67 ± 2.58 g vs 33.89 ± 3.05 g, $p < 0.001$, Figure 2A; BW gain, 29.39 ± 1.88 g vs 12.49 ± 2.78 g, $p < 0.001$, Figure 2B). HF plus RE diet treated mice showed a significantly lower final body weight (41.80 ± 4.40, 36.13 ± 4.14, and 37.10 ± 4.18 g, respectively, $P < 0.05$) and body weight gain (20.17 ± 4.00, 14.41 ± 3.70, and 15.67 ± 4.16 g, respectively, $p < 0.05$) with 54.5%, 88.7%, and 81.2% inhibition of weight gain by RE#1L, RE#1H, and RE#2 treatments, respectively, in comparison with those of HF mice. Meanwhile, the RE#1H and RE#2 mice had lower body weight than RE#1L mice ($p < 0.05$) at the end of the 16 week experimental period.

HF mice had significantly increased liver weight ($p < 0.001$) and liver/body weight ratio ($p < 0.001$) in comparison with those of LF mice, which were normalized by RE supplementation (Table 2). Similar effects of RE supplementation were observed on kidney weight ($p < 0.01$) and kidney/body weight ratio ($p < 0.001$, Table 2). Consistent with the body weight results, the weights of epididymal ($p < 0.05$), mesenteric ($p < 0.001$), and retroperitoneal fat ($p < 0.001$) significantly increased in the HF group in comparison with the LF group. RE supplementation significantly decreased the weights of mesenteric ($p < 0.05$) and retroperitoneal fat ($p < 0.05$); however, the weight of epididymal fat was increased by the RE supplementation. The total body fat weights of mice in RE#1H and RE#2 groups were decreased significantly ($p < 0.05$) but not for the RE#1L group (Table 2). These results were further confirmed by the MRI data (Figure 2C). HF mice had a significantly increased percent body fat (42.72 ± 2.08%) in comparison with LF mice (19.17 ± 4.88%, $p < 0.001$). RE-treated mice had significantly lower percent body fat (39.41 ± 3.00%, 27.00 ± 4.78%, and 27.57 ± 4.06% for RE#1L, RE#1H, and RE#2, respectively, $p < 0.05$) in comparison with HF mice; meanwhile, the percent body fat values for RE#1H and RE#2 mice were much lower than those of RE#1L mice ($p < 0.05$). Altogether, CA-enriched RE supplementation could dose-dependently limit body weight and total fat mass gains. RE#1H and RE#2 had almost identical effects and were much more potent than RE#1L.

RE Supplementation Improved Blood Glucose and Insulin Levels and HOMA-IR Index in HF Diet Fed Mice. We determined the fasting blood glucose levels at weeks 0, 10, and 16 (Figure 3A). HF mice had significantly higher blood glucose levels in comparison with those of LF mice after 10 and 16 weeks of treatment ($P < 0.001$). CA-enriched RE supplementation significantly decreased the fasting blood glucose levels elevated by the HF diet ($P < 0.05$).

At the end of the experiment, a higher insulin level (3.24 ± 0.14 ng/mL) was observed in the HF group in comparison with

DOI: 10.1021/acs.jafc.5b01246
J. Agric. Food Chem. 2015, 63, 4843−4852

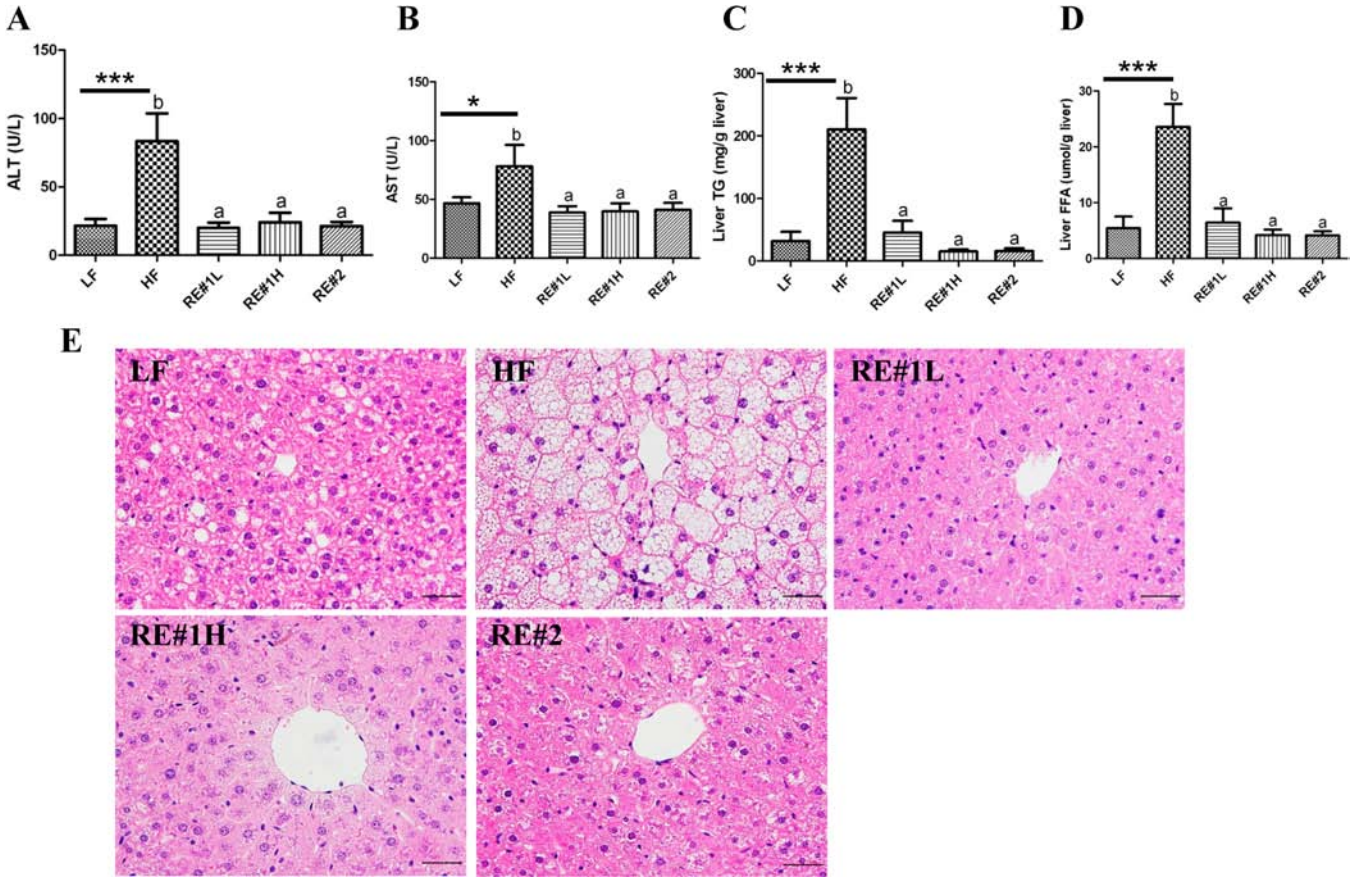

Figure 4. Effects of long-term rosemary extract (RE) dietary treatments on biomarkers of liver injury, liver lipid levels, and liver histology in high-fat-diet-fed C57BL/6J mice. Plasma ALT (A), AST (B), liver triglyceride (TG) (C) and liver free fatty acid (FFA) (D) were determined using commercial kits. Histological examination (E) was determined using H&E staining for liver samples of LF, HF, RE#1L, RE#1H, and RE#2 feeding mice. Scale bar: 50 μm. Values are presented as mean ± standard deviations (n = 6 for A–D and n = 8 for E) represented by vertical bars. The asterisk (*) denotes a significant difference of the HF group in comparison with the LF group: (*) $p < 0.05$, (**) $p < 0.01$, (***) $p < 0.001$. Significant differences ($p < 0.05$, ANOVA) are identified by the different letters among HF, RE#1L, RE#1H, and RE#2 groups.

that of the LF group (1.05 ± 0.16 ng/mL) (Figure 3B). The insulin levels were almost normalized to the levels in the LF group by RE supplementation in RE#1L, RE#1H, and RE#2 groups (1.64 ± 0.69, 1.27 ± 0.24, and 1.09 ± 0.23 ng/mL, respectively). The mice of RE#1L, RE#1H, and RE#2 groups experienced 72.9%, 90.0%, and 98.1% less increase in plasma insulin levels ($p < 0.05$). HOMA-IR index was calculated on the basis of the final blood glucose and insulin concentrations. HF mice had a significantly higher HOMA-IR index than LF mice ($p < 0.001$; Figure 3C), whereas RE supplementation dramatically decreased the HOMA-IR index at 71.9%, 96.4%, and 97.7% of RE#1L, RE#1H, and RE#2, respectively, in comparison with HF mice ($p < 0.05$; Figure 3C).

RE Supplementation Attenuated HF-Induced Liver Injury and Lipid Accumulation. HF mice had a significantly larger liver size in comparison to LF mice ($P < 0.001$; Table 2). These mice also had elevated plasma ALT ($p < 0.001$; Figure 4A) and AST ($p < 0.05$; Figure 4B) concentrations and liver triglycerides ($p < 0.001$; Figure 4C) and free fatty acids (FFA, $p < 0.001$; Figure 4D) levels. RE supplementation significantly reduced liver weight (53%, 57%, and 54% inhibition of RE#1L, RE#1H, and RE#2, respectively), plasma ALT (102.7%, 96.1%, and 100.5% inhibition, respectively) and AST (96.8%, 121.8%, and 117.6% inhibition, respectively) concentrations, and liver triglyceride (92.4%, 109.4%, and 108.9% inhibition, respectively) and FFA (94.3%, 106.7%, and 107.1% inhibition, respectively) levels.

Histological analysis of liver sections from the five groups of mice demonstrated enlargement of hepatocytes and steatosis represented by the vacuolation in hepatocytes of the HF mice in comparison with those in the LF mice, and fat deposits were obviously reduced by RE#1L, RE#1H, and RE#2 treatments in comparison with those in the HF group (Figure 4E). There was no obvious difference among RE#1L, RE#1H, and RE#2 groups with regard to liver histology.

RE Supplementation Increased Fecal Lipid Excretion. The fecal lipid excretion of the mice in the HF group was significantly higher than that of the mice in the LF group after 16 weeks of treatment ($p < 0.05$; Figure 5). Dietary RE supplementation significantly inhibited lipid absorption and increased the fecal lipid excretion in comparison with the HF group (52.4%, 91.5%, and 96.2% increase of RE#1L, RE#1H, and RE#2, respectively). The fecal lipid excretions of mice in RE#1H and RE#2 groups were significantly higher than that in the RE#1L group.

RE Supplementation Attenuated HF-Induced Oxidative Stress and Inflammation. As an indicator of oxidative stress, the lipid peroxidation product MDA was significantly increased by HF diet feeding in plasma (30.92 ± 7.15 μM, $p < 0.05$) and liver (1.39 ± 0.41 nmol/mg protein, $p < 0.05$) in comparison with that in the LF group (19.99 ± 4.16 μM and 0.86

DOI: 10.1021/acs.jafc.5b01246
J. Agric. Food Chem. 2015, 63, 4843–4852

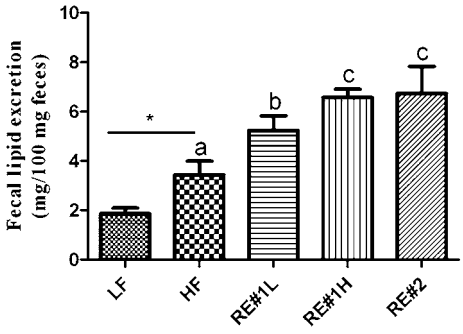

Figure 5. Effects of long-term rosemary extract (RE) dietary treatments on fecal lipid excretion in high-fat-diet-fed C57BL/6J mice at week 16. Values are presented as mean ± standard deviations ($n = 3$) represented by vertical bars. The asterisk (*) denotes a significant difference of the HF group in comparison with the LF group: (*) $p < 0.05$, (**) $p < 0.01$, (***) $p < 0.001$. Significant differences ($p < 0.05$, ANOVA) are identified by the different letters among HF, RE#1L, RE#1H, and RE#2 groups.

± 0.098 nmol/mg protein, respectively), and these increases were significantly inhibited by RE supplementation (52.4%, 89.7%, and 93.0% inhibition in plasma, 100.5%, 119.9%, and 119.9% inhibition in liver of RE#1L, RE#1H, and RE#2, respectively; Figure 6A,B). The plasma MDA levels were normalized to that of the LF mice in the RE#1H and RE#2 groups (21.12 ± 2.39 and 20.75 ± 5.31 μM, respectively) but not in the RE#1L group (25.19 ± 2.12 μM). The GSH/GSSG ratio in liver of mice in the HF group was significantly lower than that of the LF group ($p < 0.01$), and this decrease was normalized by RE supplementation (Figure 6C). However, there was no difference among the three RE-treated groups. Proinflammatory cytokine TNF-α level was measured using ELISA. RE supplementation significantly decreased the proinflammatory TNF-α levels elevated by HF-diet treatment (86.4%, 87.2%, and 91.3% inhibition of RE#1L, RE#1H, and RE#2, respectively; Figure 6D).

RE Supplementation Attenuated HF-Induced AGEs Accumulation and RAGE Activation. A HF diet induced significant AGE accumulation in plasma ($p < 0.001$) and liver (p

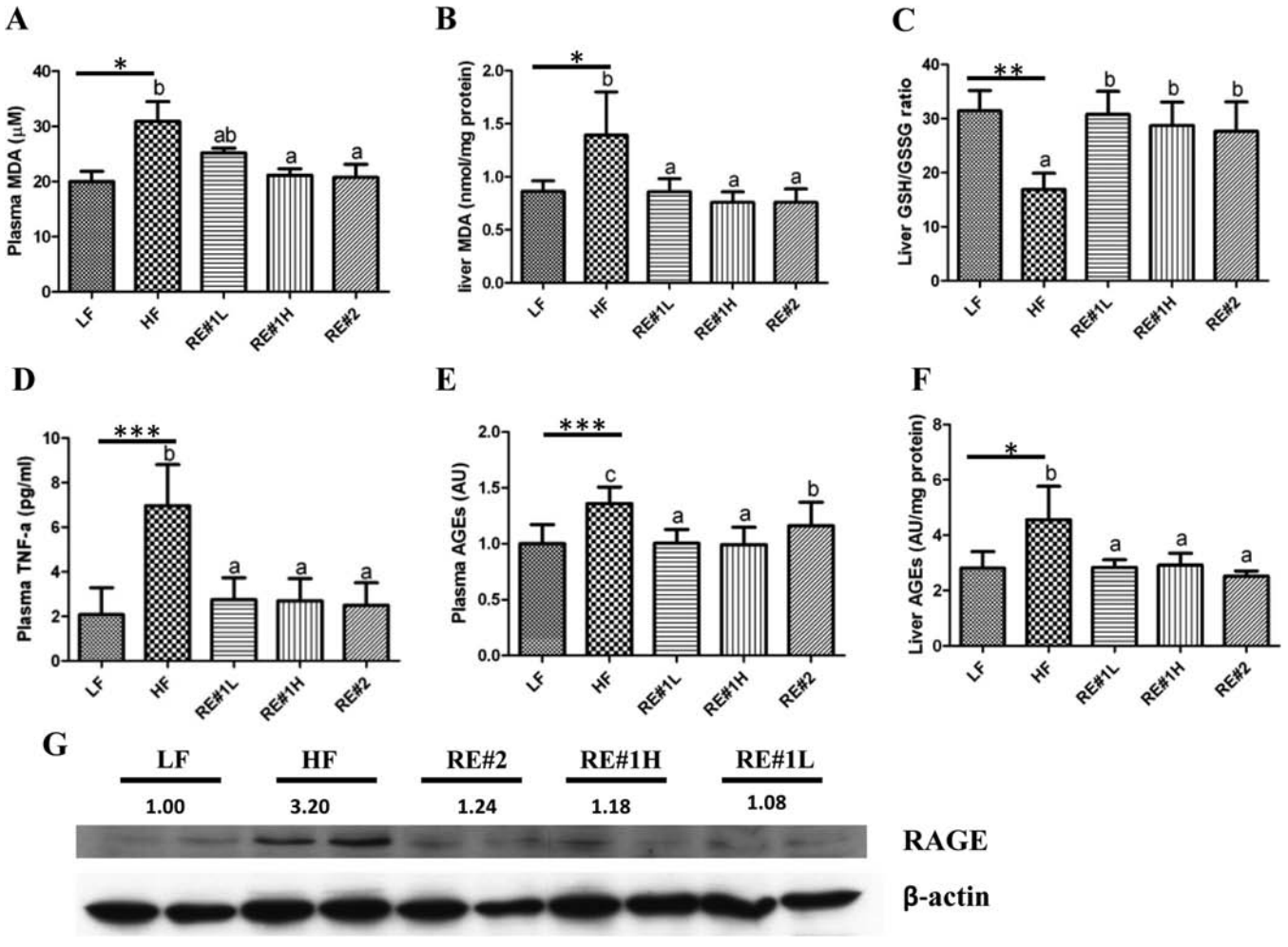

Figure 6. Effects of long-term rosemary extract (RE) dietary treatments on biomarkers of oxidative stress, inflammation, and protein glycation. The levels of plasma and liver malondialdehyde (MDA) (plasma, A; liver, B), liver GSH/GSSG (C), and plasma TNF-α (D) were measured using a commercial kit. The AGE levels (plasma, E; liver, F) were determined by a fluorescence method. The expression of liver RAGE (G) was determined by Western blot; the immunoblot bands were quantified by densitometry analysis, and the ratio to β-actin was calculated by setting the value of LF as 1. Values are presented as mean ± standard deviations ($n = 6$ for A–C and E, $n = 12$ for D, $n = 15$ for E, and $n = 2$ for G). The asterisk (*) denotes a significant difference of the HF group in comparison with the LF group: (*) $p < 0.05$, (**) $p < 0.01$, (***) $p < 0.001$. Significant differences ($p < 0.05$, ANOVA) are identified by the different letters among HF, RE#1L, RE#1H, and RE#2 groups.

DOI: 10.1021/acs.jafc.5b01246
J. Agric. Food Chem. 2015, 63, 4843–4852

< 0.05) in comparison with the LF group, and this accumulation was significantly inhibited by dietary RE supplementation (52.1%, 99.8%, and 102.3% inhibition in plasma and 116.4%, 94.0%, and 98.3% inhibition in liver of RE#1L, RE#1H, and RE#2, respectively; Figure 6E,F). There was a significant difference in plasma AGE levels of RE#1H and RE#1L groups in comparison with those of the RE#2 group, but there was no difference between the RE#1H and RE#1L groups. Meanwhile, HF diet feeding for 16 weeks induced a significant increase of liver RAGE expression by 3.20-fold in comparison with the LF group (Figure 6G). This increase induced by HF was significantly reduced by dietary RE supplementation.

DISCUSSION

In this study, we gave male C57BL/6J mice a HF diet containing 60% kcal of fat for 16 weeks to induce obesity and type 2 diabetes. The body weight gain of the mice fed this HF diet was dramatically increased in comparison with that of LF diet fed mice. The liver weight, fat mass, and other metabolic parameters of the obese mice, such as plasma ALT, AST, glucose, insulin levels, and liver TG and FFA levels, were significantly elevated by HF treatment. RE supplementation significantly decreased body weight gain of HF-treated mice. We provide the first evidence that CA is a major active component of rosemary which effectively and dose-dependently attenuates body weight gain and counteracts metabolic disorders, especially obesity-associated liver damage, induced by a HF diet in mice.

The dose of commercial RE (RE#2 with 45% CA) at 0.5% (w/w) was selected on the basis of a literature study which reported that 0.5% of RE with 20% CA could limit weight gain in mice on a high-fat diet.[17] The dose of 0.28% CA-enriched RE (RE#1H with 80% CA) was calculated on the basis of the amount of CA in 0.5% commercial RE in order to have the same amount of CA in RE#1H and RE#2 to determine whether CA is a major bioactive component of RE against obesity induced by HF. In order to elucidate the dose-dependent effect of CA-enriched RE, we also included the half-dose of RE#1H, 0.14% CA-enriched RE (RE#1L with 80% CA). Considering the difference between mice and humans in terms of calorie consumption, the 0.5% dose in diet (w/w) (500 mg/kg of BW per day calculated on the basis of each mouse with 30 g of BW eats 3 g of diet) in mice approximately equals 40 mg/kg BW per day in humans (on the basis of 60 kg BW).[29] However, this estimated human dose needs to be validated experimentally, since humans and mice are different at least in terms of absorption and metabolism of compounds in RE.

Body weight was significantly decreased by RE supplementation in comparison to the HF group, and an almost complete prevention of body weight gain was observed in the groups receiving diets containing higher CA content (RE#1H and RE#2), without affecting food intake (data not shown). Our finding is in agreement with the two previous rosemary extract supplementation studies in HF-diet-fed mice, in which it was shown that RE supplementation apparently reduced weight gain in comparison to the control.[16,17] In the Harach et al. study, administration of 200 mg/kg of BW per day RE supplementation for 50 days reduced body weight gain in diet-induced obese mice. However, the RE used in that study contained 2.5% CA, 4% RA, and 5.6% carnosol, which is very different from the RE used in the present study. Ibarra et al. reported that the RE (containing 20% CA) supplementation in the HF diet (45% kcal from fat) for 16 weeks inhibited the weight gain in HF-diet-fed mice, but only one dose of RE (500 mg/kg) was used and the inhibitory effect by RE with 20% CA was not as dramatic as that observed in the present study.

We found that the 16 week RE treatment also significantly decreased total fat, percent body fat, and visceral fat weight. The weights of the mesenteric and retroperitoneal fat depots were significantly decreased by RE supplementation, with the larger decrease occurring in the mesenteric depot. Interestingly, the weight of epididymal fat was not significantly decreased but increased by the RE treatment. This is the opposite of the findings from Harach's and Ibarra's studies. Further studies are warranted to pinpoint the mechanism behind this observation. It has been reported that decreases in body fat may be partially due to the inhibitory effects of RE on lipid absorption and lipase activity.[16,17] Indeed, we found that long-term RE treatment increased fecal lipid excretion in RE supplementation groups in comparison with HF-diet-fed mice, supporting the hypothesis that RE decreased lipid absorption.

Metabolic syndrome is a group of pathological conditions related to obesity, dislipidemia, insulin resistance, and prediabetes. We found that long-term dietary RE administration significantly decreased blood glucose, insulin, and insulin resistance in HF-diet-fed mice. A significant decrease in glucose by RE treatment was also observed in Ibarra's study.[17] However, RE administration did not alter glucose and insulin levels in Harach's study, in which the RE had a very low level of CA (2.5%),[16] indicating that CA is the potential active component altering glucose and insulin levels.

Meanwhile, RE treatment histologically and biochemically prevented hepatic steatosis induced by the HF diet. The liver weights of RE-treated mice were significantly lower than these of HF-diet-fed mice. However, there was no alteration of liver weight observed after the treatment of RE with 20% CA or 2.5% CA,[16,17] further indicating that CA is the major active component in RE. The liver TG and FFA levels were also significantly decreased by RE treatment, which agrees with the findings from a chronic CA administration mouse study.[30] Park et al.[30] reported that dietary CA suppressed HF-diet-induced hepatic steatosis through downregulation of the expression of hepatic lipogenic genes (SREBP-1c, L-FABP, SCD-1, and FAS) to decrease de novo lipogenesis and increase fatty acid β-oxidation-related genes (PPAR-α, CPT-1, and ACO), as well as fatty acid elongation. Wang et al.[31,32] also reported that CA prevented obesity and hepatic steatosis in *ob/ob* mice and inhibited lipid accumulation in hepatocytes through the EGFR/MAPK signaling pathway to inhibit expression of protein and activity of PPARγ. Tu et al.[33] reported that RE increased glucose consumption in HepG2 cells and potentially increased liver glycolysis and fatty acid oxidation through activating AMPK and PPAR pathways. Thus, the likely mechanisms of the preventive effect on fatty liver of RE are inhibition of lipid absorption, decrease of de novo lipogenesis, increase of fatty acid β-oxidation, and regulation of lipid metabolism in liver of mice.

In the present study, we determined MDA levels as an indicator of oxidative stress in plasma and liver and proinflammatory cytokine TNF-α in plasma. A significant increase of MDA levels in plasma and liver was observed in HF-diet-fed mice in comparison with those in LF-diet-fed mice, which confirms previous reports.[34,35] The elevated MDA levels were normalized by all of the RE treatments (RE#1L, RE#1H, and RE#2) in liver and by RE treatments with higher levels of CA (RE#1H and RE#2) in plasma. The RE supplementation significantly decreased the elevated TNF-α in plasma induced by HFD feeding. We also demonstrated that RE treatments

DOI: 10.1021/acs.jafc.5b01246
J. Agric. Food Chem. 2015, 63, 4843−4852

significantly increased the GSH/GSSG ratio in comparison with that of the HF group. It is well-known that the Nrf2 signaling pathway plays a key role in regulating GSH levels.[36,37] However, we did not observe the translocation of Nrf2 from cytoplasm to nucleus in liver using immunohistochemical (IHC) and immunofluorescent (IF) staining (data not shown). It is possible that CA can activate the Nrf2 pathway at early stages of the treatment, which needs to be proved experimentally.

Protein damage due to reaction with carbohydrates, the nonenzymatic formation of advanced glycation end products (AGEs), is thought to be the major pathogenesis cause of diabetic complications. Therefore, we measured AGE levels in plasma and liver tissue in the present investigation. The HFD significantly induced AGE accumulation in plasma and liver in comparison with that of LF-diet-fed mice. This concurs with a previous report that HF induced AGE accumulation in mice.[38] These elevated AGE levels in plasma and liver were decreased by the RE administrations. HF-diet feeding also induced overexpression of RAGE in the liver, which was significantly decreased by RE treatment. Even though there have been some reports that rosemary exhibited antiglycative effects in vitro,[39−41] we demonstrated for the first time that RE administration lowered the AGE levels in plasma and liver in HF-diet-induced obese and diabetic mice.

In conclusion, our present study demonstrated that CA is a major active component of rosemary extract and could dose-dependently ameliorate obesity and metabolic syndrome induced by HF diet in mice. It will be worthwhile to further study the underlying molecular mechanisms of CA against obesity and identify the effective dose range of CA. Whether CA or RE can prevent/treat obesity in humans is another topic of future study.

AUTHOR INFORMATION

Corresponding Author

*S.S.: tel, 704-250-5710; fax, 704-250-5709; e-mail, ssang@ncat.edu or shengminsang@yahoo.com.

Funding

This study was supported by funding from the USDA National Institute of Food and Agriculture (Grant No. 2011-38821-31131) to S.S.

Notes

The authors declare no competing financial interest.

ACKNOWLEDGMENTS

We thank the UNC Nutrition Obesity Research Center (Grant No. ID-P30 DK 056350) for providing the MRI body composition service.

ABBREVIATIONS USED

RE, rosemary extract; CA, carnosic acid; LF, low fat; HF, high fat; ALT, alanine aminotransferase; AST, aspartate aminotransferase; TG, triglyceride; FFA, free fatty acid; MDA, malondialdehyde; AGEs, advanced glycation end products; RAGE, receptor for AGEs; GSH, reduced glutathione; GSSG, oxidized glutathione; GSH-Px, glutathione peroxidase; NFκB, nuclear factor kappa B; Nrf2, nuclear factor E2-related factor-2; AMPK, AMP-activated protein kinase; SREBP-1c, sterol regulating element binding protein-1c; L-FABP, liver-fatty acid binding protein; SCD-1, stearoyl-CoA desaturase 1; FAS, fatty acid synthase; PPAR, peroxisome proliferator-activated receptor; CPT-1, carnitine palmitoyltransferase 1; ACO, acyl-CoA oxidase; EGFR, epithelium growth factor receptor; MAPK, mitogen-activated protein kinase; TNF-α, tumor necrosis factor-alpha

REFERENCES

(1) World Health Organization. Obesity: preventing and managing the global epidemic. *Report of a WHO consultation*. 2000; pp 1−253.

(2) Ogden, C. L.; Carroll, M. D.; Kit, B. K.; Flegal, K. M. Prevalence of obesity among adults: United States, 2011−2012. *NCHS Data Brief* **2013**, *131*, 1−8.

(3) Whitmore, C. Type 2 diabetes and obesity in adults. *Br J. Nurs.* **2010**, *19*, 880−886.

(4) World Health Organization. Obesity and Overweight Fact sheet. URL(http://www.who.int/dietphysicalactivity/media/en/gsfs_obesity.pdf). October 2013.

(5) Roblin, L. Childhood obesity: food, nutrient, and eating-habit trends and influences. *Appl. Physiol., Nutr., Metab.* **2007**, *32*, 635−645.

(6) Anders, S.; Schroeter, C. Diabetes, diet-health behavior, and obesity. *Front. Endocrinol.* **2015**, DOI: 10.3389/fendo.2015.00033.

(7) Fabricatore, A. N.; Wadden, T. A. Treatment of obesity: An overview. *Clinical Diabetes* **2003**, *21*, 67−72.

(8) Riccardi, G.; Capaldo, B.; Vaccaro, O. Functional foods in the management of obesity and type 2 diabetes. *Curr. Opin. Clin. Nutr. Metab. Care* **2005**, *8*, 630−635.

(9) Panda, H. Cultivation of Rosmarinus officinalis. *In Aromatic Plants Cultivation, Processing and Uses*; Asia Pacific Business Press: New Delhi, 2009; pp 22−28.

(10) Calabrese, V.; Scapagnini, G.; Catalano, C.; Catalano, C.; Dinotta, F.; Geraci, D.; Morganti, P. Biochemical studies of a natural antioxidant isolated from rosemary and its application in cosmetic dermatology. *Int. J. Tissue React.* **2000**, *22*, 5−13.

(11) Aguilar, F.; Autrup, H.; Barlow, S.; Castle, L.; Crebelli, R.; Dekrant, W.; Engel, K. H.; Gontard, N.; Gott, D.; Grilli, S.; Gurtler, R.; Larsen, J. C.; Leclerq, C.; Leblanc, J.; Malcata, F. X.; Mennes, W.; Milana, M. R.; Pratt, I.; Rietjens, I.; Tobback, P.; Toldra, F. Use of rosemary extracts as food additive scientific opinion of panel on food additives, flavourings, processing aids and materials in contact with food. *EFSA Journal* **2008**, *721*, 1−29.

(12) Etter, S. C. Rosmarinus officinalis as an Antioxidant. *J. Herbs, Spices Med. Plants* **2004**, *11*, 121−159.

(13) Ho, C. T.; Wang, M.; Wei, G. J.; Huang, T. C.; Huang, M. T. Chemistry and antioxidative factors in rosemary and sage. *BioFactors* **2000**, *13*, 161−166.

(14) Cuvelier, M.-E.; Richard, H.; Berset, C. Antioxidative activity and phenolic composition of pilot-plant and commercial extracts of sage and rosemary. *J. Am. Oil Chem. Soc.* **1996**, *73*, 645−652.

(15) Razboršek, M. I.; Vončina, D. B.; Doleček, V.; Vončina, E. Determination of major phenolic acids, phenolic diterpenes and triterpenes in rosemary (*Rosmarinus officinalis* L.) by gas chromatography and mass spectrometry. *Acta Chim Slov.* **2007**, *54*, 60−67.

(16) Harach, T.; Aprikian, O.; Monnard, I.; Moulin, J.; Membrez, M.; Beolor, J. C.; Raab, T.; Mace, K.; Darimont, C. Rosemary (Rosmarinus officinalis L.) leaf extract limits weight gain and liver steatosis in mice fed a high-fat diet. *Planta Med.* **2010**, *76*, 566−571.

(17) Ibarra, A.; Cases, J.; Roller, M.; Chiralt-Boix, A.; Coussaert, A.; Ripoll, C. Carnosic acid-rich rosemary (Rosmarinus officinalis L.) leaf extract limits weight gain and improves cholesterol levels and glycaemia in mice on a high-fat diet. *Br. J. Nutr.* **2011**, *106*, 1182−1189.

(18) Romo-Vaquero, M.; Selma, M. V.; Larrosa, M.; Obiol, M.; Garcia-Villalba, R.; Gonzalez-Barrio, R.; Issaly, N.; Flanagan, J.; Roller, M.; Tomas-Barberan, F. A. A rosemary extract rich in carnosic acid selectively modulates caecum microbiota and inhibits beta-glucosidase activity, altering fiber and short chain fatty acids fecal excretion in lean and obese female rats. *PLoS One* **2014**, *9*, e94687.

(19) Romo Vaquero, M.; Yanez-Gascon, M. J.; Garcia Villalba, R.; Larrosa, M.; Fromentin, E.; Ibarra, A.; Roller, M.; Tomas-Barberan, F.; Espin de Gea, J. C.; Garcia-Conesa, M. T. Inhibition of gastric lipase as a

DOI: 10.1021/acs.jafc.5b01246
J. Agric. Food Chem. 2015, 63, 4843−4852

mechanism for body weight and plasma lipids reduction in Zucker rats fed a rosemary extract rich in carnosic acid. *PLoS One* **2012**, *7*, e39773.
(20) Robert Aeschbach, V.; Georges Philippossian, L. Carnosic acid obtention and uses. U.S. Patent 5,256,700, Oct 26, 1993.
(21) Chen, H.; Lv, L.; Soroka, D.; Warin, R. F.; Parks, T. A.; Hu, Y.; Zhu, Y.; Chen, X.; Sang, S. Metabolism of [6]-shogaol in mice and in cancer cells. *Drug Metab. Dispos.* **2012**, *40*, 742−753.
(22) Bose, M.; Lambert, J. D.; Reuhl, K. R.; Shapses, S. A.; Yang, C. S. The major green tea polyphenol, (−)-epigallocatechin-3-gallate, inhibits obesity, metabolic syndrome, and fatty liver disease in high-fat-fed mice. *J. Nutr.* **2008**, *138*, 1677−1683.
(23) Folch, J.; Lees, M.; Sloane Stanley, G. H. A simple method for the isolation and purification of total lipides from animal tissues. *J. Biol. Chem.* **1957**, *226*, 497−509.
(24) Henle, T.; Deppisch, R.; Beck, W.; Hergesell, O.; Hansch, G. M.; Ritz, E. Advanced glycated end-products (AGE) during haemodialysis treatment: discrepant results with different methodologies reflecting the heterogeneity of AGE compounds. *Nephrol Dial Transplant.* **1999**, *14*, 1968−1975.
(25) Munch, G.; Keis, R.; Wessels, A.; Riederer, P.; Bahner, U.; Heidland, A.; Niwa, T.; Lemke, H. D.; Schinzel, R. Determination of advanced glycation end products in serum by fluorescence spectroscopy and competitive ELISA. *Eur. J. Clin Chem. Clin Biochem.* **1997**, *35*, 669−677.
(26) Raposeiras-Roubin, S.; Rodino-Janeiro, B. K.; Grigorian-Shamagian, L.; Moure-Gonzalez, M.; Seoane-Blanco, A.; Varela-Roman, A.; Alvarez, E.; Gonzalez-Juanatey, J. R. Soluble receptor of advanced glycation end products levels are related to ischaemic aetiology and extent of coronary disease in chronic heart failure patients, independent of advanced glycation end products levels: New Roles for Soluble RAGE. *Eur. J. Heart Failure* **2010**, *12*, 1092−1100.
(27) Nakayama, H.; Mitsuhashi, T.; Kuwajima, S.; Aoki, S.; Kuroda, Y.; Itoh, T.; Nakagawa, S. Immunochemical detection of advanced glycation end products in lens crystallins from streptozocin-induced diabetic rat. *Diabetes* **1993**, *42*, 345−350.
(28) Yamabe, N.; Kang, K. S.; Park, C. H.; Tanaka, T.; Yokozawa, T. 7-O-galloyl-D-sedoheptulose is a novel therapeutic agent against oxidative stress and advanced glycation endproducts in the diabetic kidney. *Biol. Pharm. Bull.* **2009**, *32*, 657−664.
(29) Reagan-Shaw, S.; Nihal, M.; Ahmad, N. Dose tranlation from animal to human studies revisited. *FASEB J.* **2008**, *22*, 659−661.
(30) Park, M. Y.; Mun, S. T. Dietary carnosic acid suppresses hepatic steatosis formation via regulation of hepatic fatty acid metabolism in high-fat diet-fed mice. *Nutr. Res. Pract.* **2013**, *7*, 294−301.
(31) Wang, T.; Takikawa, Y.; Satoh, T.; Yoshioka, Y.; Kosaka, K.; Tatemichi, Y.; Suzuki, K. Carnosic acid prevents obesity and hepatic steatosis in ob/ob mice. *Hepatol. Res.* **2011**, *41*, 87−92.
(32) Wang, T.; Takikawa, Y.; Tabuchi, T.; Satoh, T.; Kosaka, K.; Suzuki, K. Carnosic acid (CA) prevents lipid accumulation in hepatocytes through the EGFR/MAPK pathway. *J. Gastroenterol.* **2012**, *47*, 805−813.
(33) Tu, Z.; Moss-Pierce, T.; Ford, P.; Jiang, T. A. Rosemary (Rosmarinus officinalis L.) extract regulates glucose and lipid metabolism by activating AMPK and PPAR pathways in HepG2 cells. *J. Agric. Food Chem.* **2013**, *61*, 2803−2810.
(34) Fraulob, J. C.; Ogg-Diamantino, R.; Fernandes-Santos, C.; Aguila, M. B.; Mandarim-de-Lacerda, C. A. A Mouse Model of Metabolic Syndrome: Insulin Resistance, Fatty Liver and Non-Alcoholic Fatty Pancreas Disease (NAFPD) in C57BL/6 Mice Fed a High Fat Diet. *J. Clin. Biochem. Nutr.* **2010**, *46*, 212−223.
(35) Milagro, F. I.; Campion, J.; Martinez, J. A. Weight gain induced by high-fat feeding involves increased liver oxidative stress. *Obesity* **2006**, *14*, 1118−1123.
(36) Lu, S. C. Glutathione synthesis. *Biochim. Biophys. Acta, Gen. Subj.* **2013**, *1830*, 3143−3153.
(37) Lu, J.; Holmgren, A. The thioredoxin antioxidant system. *Free Radical Biol. Med.* **2014**, *66*, 75−87.
(38) Li, S. Y.; Liu, Y.; Sigmon, V. K.; McCort, A.; Ren, J. High-fat diet enhances visceral advanced glycation end products, nuclear O-Glc-Nac modification, p38 mitogen-activated protein kinase activation and apoptosis. *Diabetes, Obes. Metab.* **2005**, *7*, 448−454.
(39) Dearlove, R. P.; Greenspan, P.; Hartle, D. K.; Swanson, R. B.; Hargrove, J. L. Inhibition of protein glycation by extracts of culinary herbs and spices. *J. Med. Food* **2008**, *11*, 275−281.
(40) Kim, H. Y.; Kim, K. Protein glycation inhibitory and antioxidative activities of some plant extracts in vitro. *J. Agric. Food Chem.* **2003**, *51*, 1586−1591.
(41) Hsieh, C. L.; Peng, C. H.; Chyau, C. C.; Lin, Y. C.; Wang, H. E.; Peng, R. Y. Low-density lipoprotein, collagen, and thrombin models reveal that Rosemarinus officinalis L. exhibits potent antiglycative effects. *J. Agric. Food Chem.* **2007**, *55*, 2884−2891.

DOI: 10.1021/acs.jafc.5b01246
J. Agric. Food Chem. 2015, 63, 4843−4852

JOURNAL OF AGRICULTURAL AND FOOD CHEMISTRY

Article

pubs.acs.org/JAFC

Structural and Gel Textural Properties of Soy Protein Isolate When Subjected to Extreme Acid pH-Shifting and Mild Heating Processes

Qian Liu,[†,‡,§] Rui Geng,[†,‡] Juyang Zhao,[‡] Qian Chen,[‡] and Baohua Kong*[,‡,§]

[‡]College of Food Science, Northeast Agricultural University, Harbin, Heilongjiang 150030, People's Republic of China

[§]Synergetic Innovation Center of Food Safety and Nutrition, Harbin, Heilongjiang 150030, People's Republic of China

ABSTRACT: Changes in the structural and gel textural properties were investigated in soy protein isolate (SPI) that was subjected to extreme acid pH-shifting and mild heating processes. The SPI was incubated up to 5 h in pH 1.5 solutions at room temperature or in a heated water bath (50 or 60 °C) to lead to protein structural unfolding, followed by refolding at pH 7.0 for 1 h. The combination of pH-shifting and heating treatments resulted in drastic increases in the SPI gel penetration force ($p < 0.05$). These treatments also significantly enforced the conversion of sulphydryl groups into disulfides, increased the particle size and hydrophobicity values, reduced the protein solubility ($p < 0.05$), and strengthened the disulfide-mediated aggregation of SPI. The intrinsic fluorescence spectroscopy results indicated structural unravelling when protein was subjected to acidic pH-shifting in combination with heating processes. The slight loss of secondary structure was observed by circular dichroism. These results suggested that pH-shifting combined with heating treatments provide great potential for the production of functionality-improved SPI, with the improved gelling property highly related to changes in the protein structure and hydrophobic aggregation.

KEYWORDS: *pH shifting, heating, soy protein isolate, protein structure, gel textural property*

INTRODUCTION

Soy protein as a health-promoting and inexpensive functional composition is widely used in meat products, nutraceutical products, and beverages.[1] In general, untreated soy proteins display only limited functionality, such as emulsifying, gelation, and other processing properties.[2] Therefore, additional studies are needed to modify the soy protein isolate (SPI) structures to exhibit broadened functionality, such as solubility, emulsification, and gelation.

The ability of SPI to form gel is usually regarded as a very important functional property of SPI, and thus, it is worth probing into the inner link between the structure and gel characteristics of soy protein.[3] The thermal-induced protein gel is a complicated process that includes protein aggregation and unfolding before forming a complex network structure.[4] The molecular weight and size of the protein aggregates have a relationship to the gel network and gel properties.[5] As the major components in the SPI, 7S and 11S play a decisive role in the gelling property. One study found that 7S and 11S mainly affect the gel viscoelasticity and hardness and that the B subunit of 11S and β subunit of 7S undergo macromolecule aggregation by electrostatic interactions, which were considered to have an important effect on the gel properties.[6] Damodaran and Kinsella[7] reported that the existence of 7S definitely inhibits the dissociation of the 11S subunits. Hence, both protein aggregation and each subunit play an important role in gelation. In recent years, numerous researchers have made some effects to change the protein structures to produce certain conformations that are in favor of producing a desirable functionality.[8] When exposed to extreme pH conditions, many globular proteins undergo significant conformational changes, typically referred to as the molten globule (MG) state.[8] The discovery of an extreme pH-shifting-induced intermediate state in SPI has resulted in an interest in investigating acid or alkaline treatments to improve the functionality of these protein.[9−13] Jiang et al.[13] proved that acidic or alkaline pH treatments could cause MG structure formation in SPI, resulting in enhanced emulsifying ability. Some studies have revealed that extreme pH treatments might dissect protein into subunits, thus leading to improved SPI functional properties,[13] particularly the enhanced gelation of mixed myofibrillar and soy protein sols.[14]

Heating is the easiest method to enhance the functional properties of protein, producing numerous desirable structural changes in the SPI, in favor of protein gel formation.[14] It is conceivable that SPI becomes more sensitive to temperature changes after exposure to extreme pH values. The heating temperature in the present study was 50 or 60 °C. The SPI is substantially but not completely denatured (unfolded) by the extreme pH treatment. However, the MG state (a metastable state) induced by pH shifting renders soy proteins more susceptible to further structural changes and hydrophobic aggregation. Hence, the low temperatures of 50 and 60 °C, which would not normally affect the structure of 7S or 11S globulins in control SPI, now become effective. When the pH shifting is combined with mild heating, a number of desirable structural and functional changes can occur. A clear knowledge of the gel textural profiles of soy proteins treated by acidic pH shifting alone or pH shifting combined with heating is crucial for the food industry. The aim of this research was to evaluate the effect of extreme acid pH-shifting combined with 50 or 60 °C heating treatments on the gelation and structural properties

Received: December 15, 2014
Revised: May 3, 2015
Accepted: May 4, 2015
Published: May 4, 2015

ACS Publications © 2015 American Chemical Society

DOI: 10.1021/acs.jafc.5b01331
J. Agric. Food Chem. 2015, 63, 4853−4861

of SPI and to identify the relative structural contributions that produced the functionality improvements.

MATERIALS AND METHODS

Materials. Defatted soy flakes were obtained from Harbin High-Tech Group (Harbin, Heilongjiang, China). Ethylenediaminetetraacetic acid (EDTA), 2-nitro-5-thiobenzoate (NTB), and 1-anilino-8-naphthalene-sulfonate (ANS) were obtained from Sigma Chemical Co. (St. Louis, MO). All of the reagents and chemicals were of analytical grade.

Preparation of SPI. SPI was prepared according to the method of Jiang et al.[13] and Chen et al.[15] The samples were freeze-dried and stored in a 4 °C cooler. The protein content of the prepared SPI was 94.76% (w/w), as determined by the Kjeldahl method.

pH-Shifting and Heating Process-Treated SPI. The pH-treated SPI was prepared according to Jiang and Xiong.[13] Suspensions of SPI (30 mg/mL protein) was centrifuged at 12000*g* for 15 min at 4 °C. The supernatant was adjusted to pH 1.5 with 2 M HCl. After holding at pH 1.5 for 0, 1, 3, or 5 h under different temperature conditions, room temperature (20 ± 2 °C), 50, or 60 °C, to unfold the protein, the solutions were neutralized with 2 M NaOH to pH 7 and kept at this pH for 1 h to make partial refolding. Meanwhile, to remove any salts brought from the pH adjustments, proteins from the treatments were precipitated at pH 4.5, washed 3 times, and then resolubilized at neutral pH.[14] The control sample did not treat with pH shifting and heating. The SPI samples treated in a 50 or 60 °C water bath were used for comparison.

Testing of Gel Strength. The SPI (120 mg/mL) samples were suspended in deionized water, and gels were formed in 25 × 40 mm (length × diameter) glass vials in a 90 °C water bath for 30 min. Then, the gels were stored overnight at 2−4 °C. Before analysis, the gels were equilibrated at room temperature (22−24 °C) for 30 min. Gel strength of the SPI gels was analyzed with a model TA-XT2 texture analyzer (Stable Micro Systems, Ltd., Godalming, U.K.) attached to a 5 kg load cell. The gels were axially penetrated to a depth of 12 mm at a speed of 50 mm/min with a P/0.5 flat-surface cylindrical probe (12 mm in diameter). The penetration force, defined as the force required to rupture the gel, was expressed as gel strength.

Protein Solubility. Protein samples (treated and control SPI) were completely dispersed (20 mg/mL) in sodium phosphate buffer (10 mM, pH 7.0). Then, the protein solutions were centrifuged at 10000*g* for 15 min. Protein concentrations of the supernatants and whole suspensions were determined by the Biuret method. Protein solubility was calculated according to the method of Jiang et al.[13]

Particle Size Distribution. Each SPI suspension (0.2 mg/mL, in 10 mM sodium phosphate buffer at pH 7.0) was transferred to a square cuvette for dynamic laser light scattering analysis (Zetasizer Nano-ZS, Malvern Instruments, Worcestershire, U.K.). The particle size was expressed as the average of at least six readings of the volume surface mean diameter (D_{32}) and volume mean diameter (D_{43}).

Total Sulfhydryl (SH) and Exposed SH Contents. SH content was measured according to the method of Beveridge et al.[16] SPI samples (15 mg) were suspended in 5.0 mL reaction buffer (0.09 M glycine, 0.086 M Tris, and 4 mM EDTA at pH 8.0) with (total SH) or without (exposed SH) 8 M urea. After the addition of 50 μL of Ellman's reagent, the resultant suspensions were incubated for 1 h at room temperature (23 ± 1 °C) with occasional vibrating and then centrifuged for 15 min at l0000*g*. The absorbance of the supernatant was read at 412 nm with the reagent buffer as the blank. The protein content of samples was measured by the micro-Kjeldahl method. The total SH and exposed SH contents in micromoles per gram of protein were calculated using the extinction coefficient of NTB, which is 13 600 M^{-1} cm^{-1}.

Surface Hydrophobicity. The surface hydrophobicity of the samples was measured using ANS as a fluorescence probe.[17] Briefly, 4 mL aliquots of the SPI samples (0.005−0.5 mg/mL) were dissolved in 0.01 M phosphate buffer at pH 7.0 and mixed with 50 μL of 8 × 10^3 M ANS. After the reaction had proceeded for 10 min at room temperature, the fluorescence intensity (FI) was determined with an emission at 484 nm and excitation at 365 nm (both with a slit width of 5 nm) on a fluorescence spectrophotometer (Hitachi F-4500, Hitachi, Ltd., Tokyo, Japan). The initial FI slope versus protein concentration plot was used to determine the protein surface hydrophobicity.

Intrinsic Fluorescence Emission Spectra. The intrinsic emission fluorescence spectra of the protein solutions were obtained using a fluorometer (F-4500 model, Hitachi, Tokyo, Japan). The protein solutions (0.2 mg/mL) were prepared in 10 mM phosphate buffer (pH 7.0). The protein solutions were excited at 295 nm, and the emission spectra were recorded from 300 to 400 nm with a constant slit of 2.5 nm for both excitation and emission.

Circular Dichroism (CD). Far-ultraviolet (UV) CD spectra of the protein samples were determined at 25 °C using a CD spectropolarimeter (Mos-450, Biologic, Claix, France) to measure the influence of the different treatments on the secondary structure according to the methods of Jiang et al.,[13] with some modification. Each SPI sample (0.5 mg/mL) was dissolved in 10 mM phosphate buffer at pH 7.0 and scanned 5 times between 190 and 250 nm to obtain an averaged value. Phosphate buffer was used as the blank solution. The bandwidth, step resolution, and scan rate were 1.0 nm, 0.2 nm, and 100 nm/min, respectively. The residue ellipticity (θ) values were calculated as $[\theta]$ (deg cm^2 dmol) = $(100XM)/LC$, where X is the signal (millidegrees) obtained by the CD spectrometer, M is the average molecular weight (MW) of amino acid residues (assumed to be 115), C is the protein concentration (mg/mL) of the sample, and L is the cell path length (1 cm).

Electrophoresis. Sodium dodecyl sulfate−polyacrylamide gel electrophoresis (SDS−PAGE) was conducted as described by Liu and Xiong.[18] The stacking gel and resolving gel contained 5 and 12% acrylamide, respectively. Electrophoresis samples were prepared both without and with β-mercaptoethanol. For the SDS−PAGE samples without β-mercaptoethanol, 1 mM *N*-ethylmaleimide (NEM) was added to prevent the formation of disulfide artifacts.

Statistical Analyses. The experiment was replicated 3 times, and for each of the replications, at least triplicate samples were analyzed. The data were analyzed using the general linear model procedure. An analysis of variance (AOV) was performed to determine the significance of the main effects. Tukey's procedures were used to identify the significant differences ($p < 0.05$) between the means.

RESULTS AND DISCUSSION

Penetration Testing. Penetration testing is useful way to determine gel properties. For samples treated with pH-shifting alone or 50 °C mild heating alone, there were no significant changes ($p > 0.05$) in the penetration force with the increased incubation time (Figure 1). The penetration force of the sample

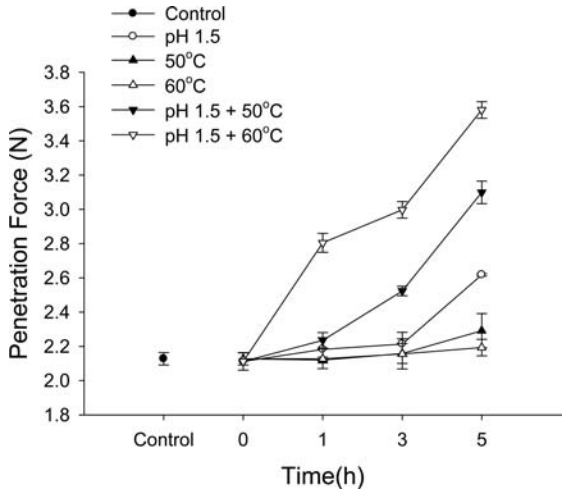

Figure 1. Penetration force of SPI after acidic pH-shifting combined with heating treatments at various holding times.

DOI: 10.1021/acs.jafc.5b01331
J. Agric. Food Chem. 2015, 63, 4853−4861

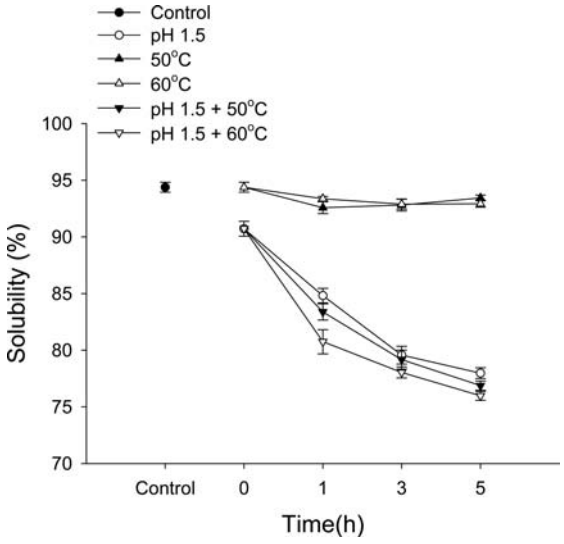

Figure 2. Solubility of SPI after pH-shifting combined with heating treatments at various holding times.

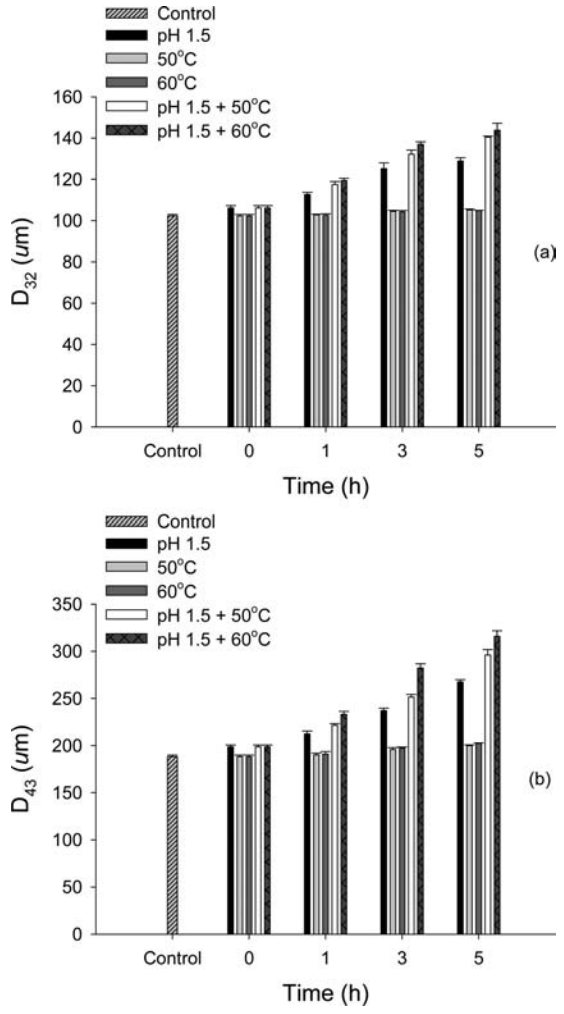

Figure 3. Particle size of SPI solutions after pH-shifting combined with heating treatments at various holding times: (a) volume surface mean diameter (D_{32}) and (b) volume mean diameter (D_{43}).

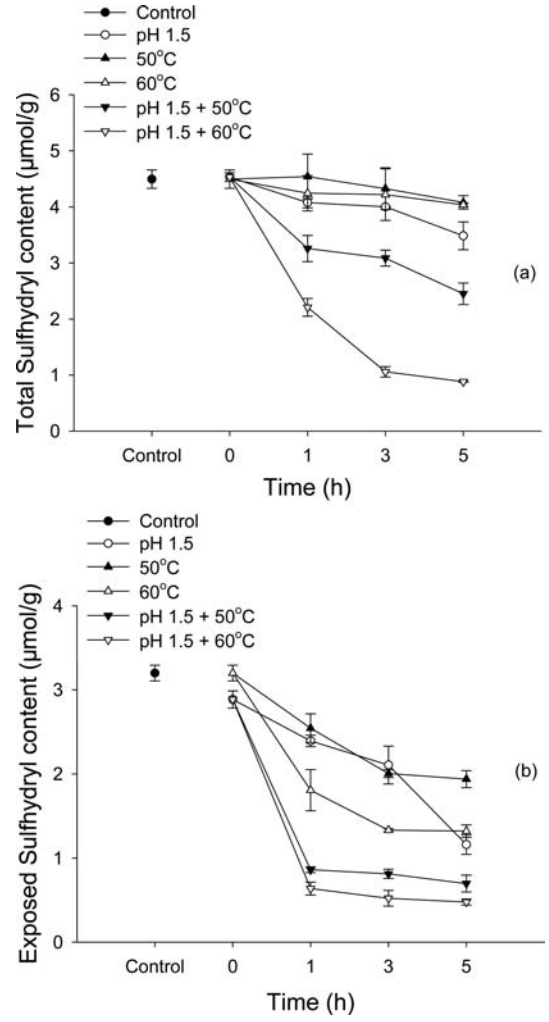

Figure 4. Total and exposed SH contents of SPI after pH-shifting combined with heating treatments at various holding times.

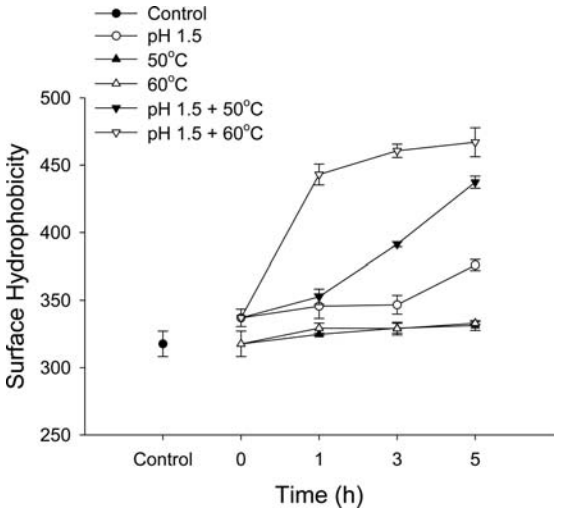

Figure 5. Surface hydrophobicity of SPI after acidic pH-shifting combined with heating treatments at various holding times.

with 60 °C heating alone for 5 h was 2.26 N, and it was significantly higher than that of control samples (2.13 N) ($p <$ 0.05). However, the combination of pH-shifting with 50 and 60 °C heating treatments led to drastic increases in the penetration force of SPI gels ($p < 0.05$), with the value increased by 44.1

DOI: 10.1021/acs.jafc.5b01331
J. Agric. Food Chem. 2015, 63, 4853−4861

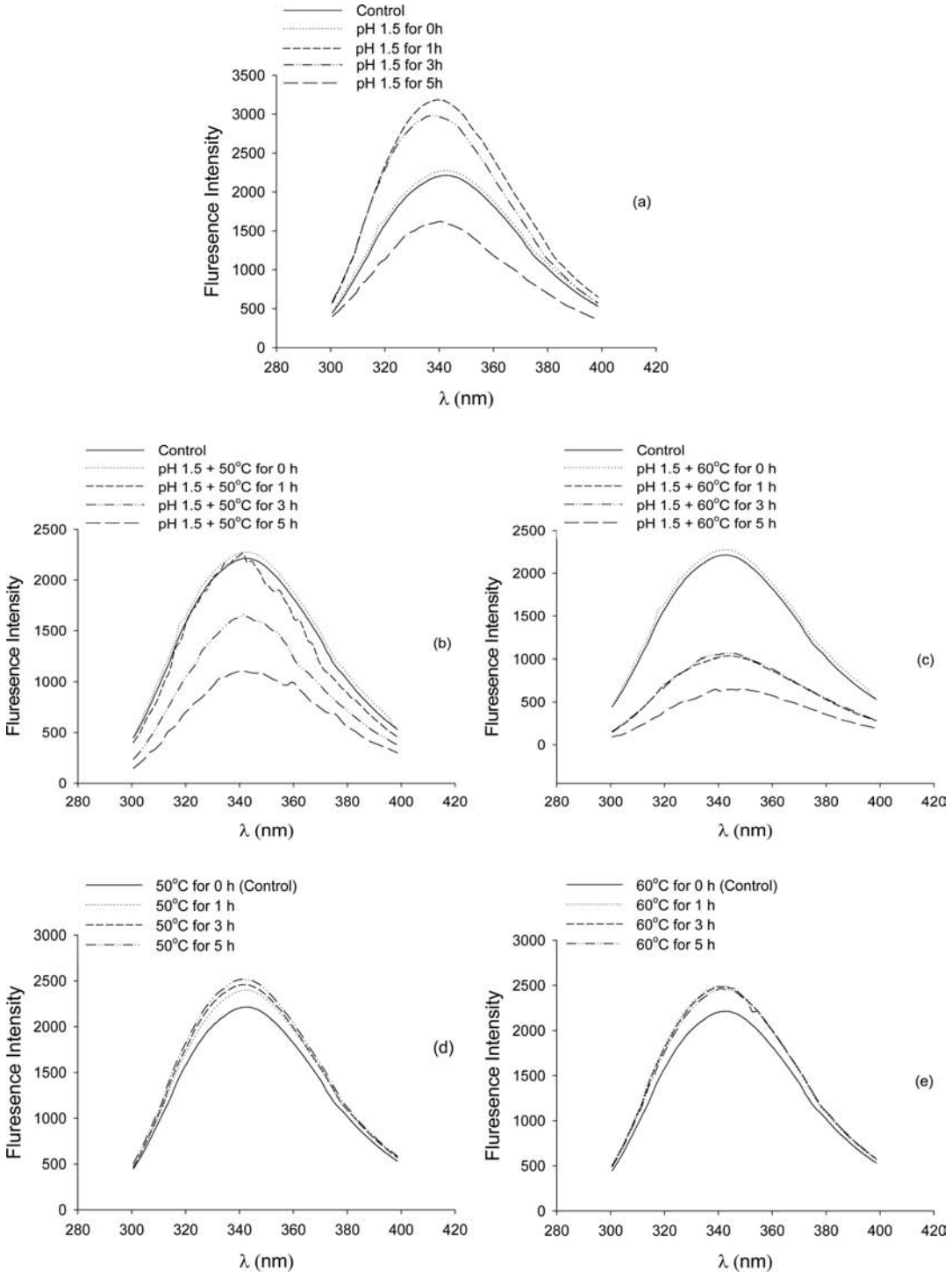

Figure 6. Intrinsic emission fluorescence spectra of SPI after acidic pH-shifting combined with heating treatments at various holding times.

and 69.0% after holding for 5 h, respectively, compared to control SPI.

A protein gel can be stabilized by both non-covalent and covalent forces. The gelation or coagulation of SPI was shown to include covalent cross-links and hydrophobic interactions.[19] Results from SDS−PAGE (Figure 8) and SH content measurements (Figure 4) confirmed the formation of disulfide bonds during heating. Some researchers have suggested that this disulfide bond formation helps to reinforce the gel structure.[20] Furthermore, O'Kane et al.[21] also showed that network formation by the legumin proteins was caused by hydrogen and hydrophobic bonds, and Mleko and Foegeding[22] revealed the increase in shear moduli of whey protein gels and increase in temperature during heating mainly to the presence of hydrophobic forces.

Protein Solubility. Solubility can affect protein surface-active properties. As depicted in Figure 2, the solubility of control SPI was 94.4%, with heating the SPI at 50 and 60 °C alone causing no significant change in solubility ($p > 0.05$). When the sample was treated with pH 1.5 shifting, the solubility decreased sharply with increasing incubation times ($p < 0.05$), which dropped to 77.9% after 5 h. Yuan et al.[23]

DOI: 10.1021/acs.jafc.5b01331
J. Agric. Food Chem. 2015, 63, 4853−4861

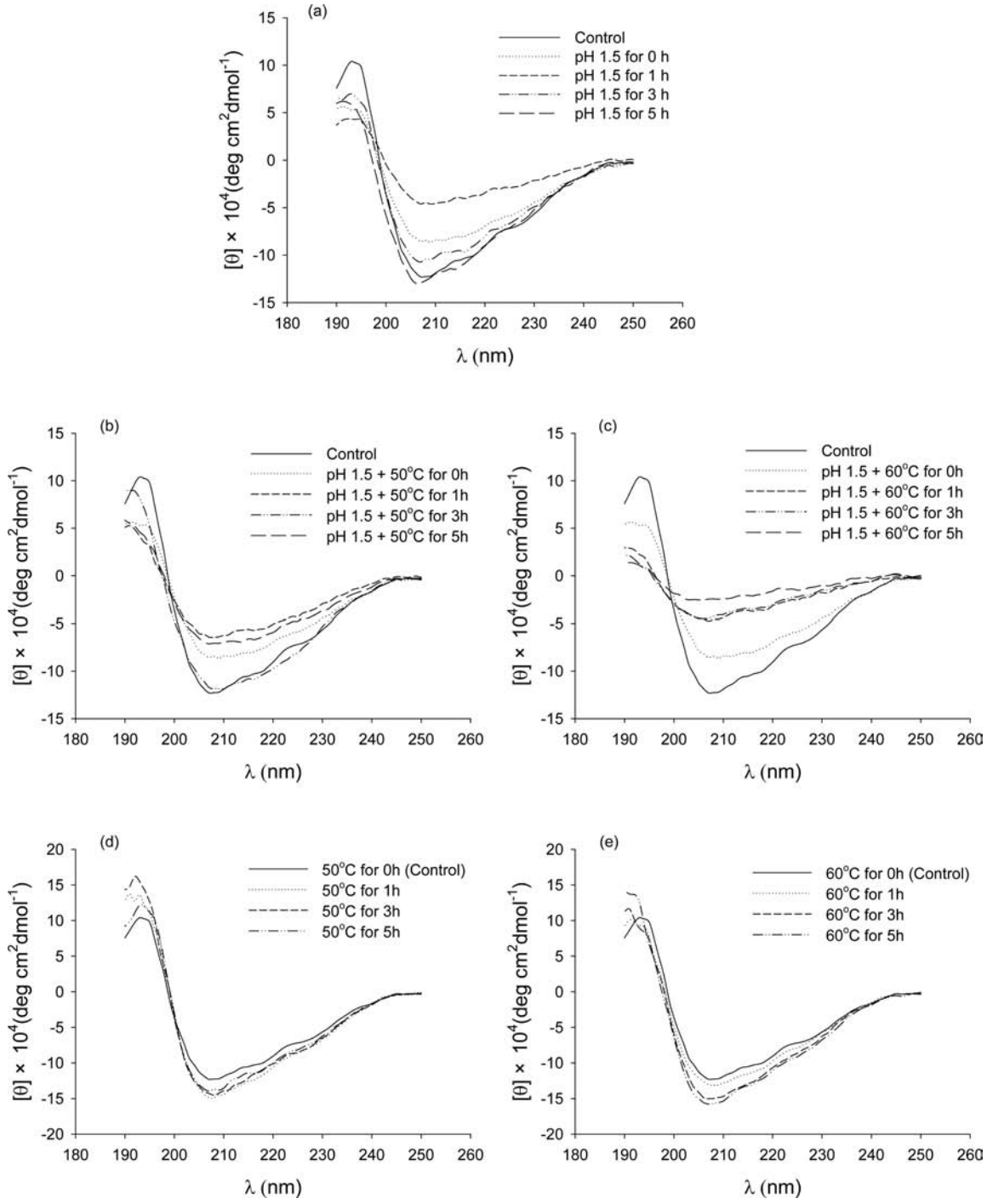

Figure 7. CD spectra of SPI after acidic pH-shifting combined with heating treatments at various holding times.

reported that, because of the effect of acid (pH 2.0) treatment, SPI would unfold, aggregate, and expose more hydrophobic residues. Meanwhile, similar trends were observed for samples treated with pH 1.5 + 50 or 60 °C, which rendered more solubility reduction than that for the pH 1.5 shifting treatment alone for 1, 3, and 5 h, respectively ($p < 0.05$). This phenomenon indicated that SPI was more susceptible to denaturation under extremely low pH-shifting combined with heating conditions. Jiang et al.[13] suggested that the decrease in protein solubility was mainly contributed to the formation of disulfide cross-linking and hydrophobic aggregation under the extremely low pH-shifting treatments. Liu et al.[24] also noted that the solubility had a obvious correlation with surface hydrophobicity of whey protein, which was affected by the aggregation state of the protein. The results were also supported by SH contents, surface hydrophobicity, and SDS–PAGE analysis, as discussed below.

Particle Size Determination. The volume surface mean diameter (D_{32}) and volume mean diameter (D_{43}) of control or modified SPI dispersions were measured by a dynamic laser light scattering instrument (Figure 3). The D_{32} and D_{43} of control SPI were 102.3 and 188.2 μm, respectively, and heating the SPI at 50 and 60 °C alone caused no significant change in particle size ($p > 0.05$). As expected, pH-shifting treatment

DOI: 10.1021/acs.jafc.5b01331
J. Agric. Food Chem. 2015, 63, 4853−4861

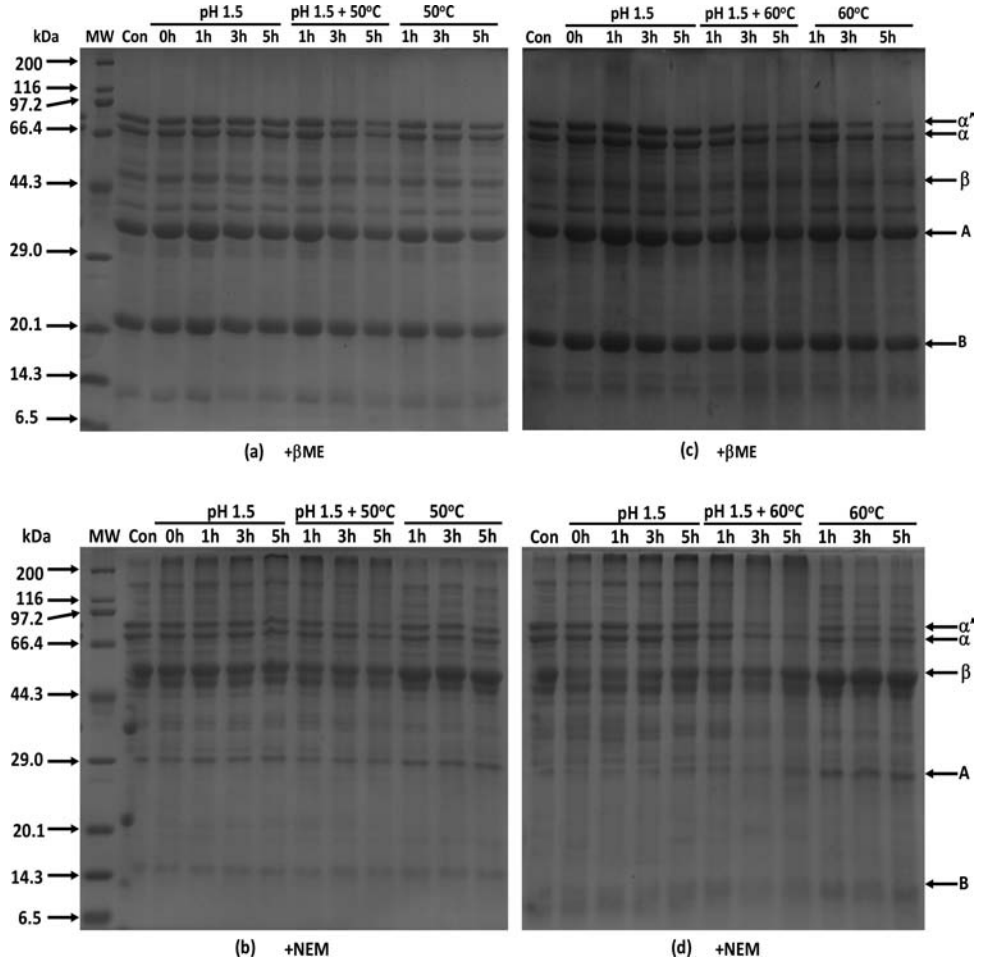

Figure 8. SDS−PAGE pattern of SPI after acidic pH-shifting combined with heating treatments at various holding times. Con: SPI solutions at pH 7.0 without pH-shifting and heating treatment. The SDS−PAGE samples were prepared (a and c) with or (b and d) without β-mercaptoethanol. MW: molecular weight marker (Da). SPI constituents: α' (86 kDa), α (66 kDa), and β (51 kDa) for conglycinin; A, the acidic subunit (34−43 kDa), B, the basic subunit (17−26 kDa) for glycinin.

significantly increased the particle size of SPI ($p < 0.05$), and D_{32} and D_{43} increased 1.26- and 1.42-fold after 5 h of incubation, respectively. Moreover, SPI samples treated with pH 1.5 + 50 or 60 °C exhibited a larger particle size than that with the pH 1.5 shifting treatment alone ($p < 0.05$). Yuan et al.[23] pointed out that the mean hydrodynamic diameter of SPI obviously increased after acid (pH 2.0) treatment for 1 h. Gulseren et al.[25] found that non-covalent interactions were the immediate driving force for the protein aggregation. In addition, according to Kohyama et al.,[26] hydrophobic interactions between protein molecules induced by the aggregation of the protein were the predominant factors for a fine gel network structure. Hu et al.[27] also suggested that exposition of hydrophobic residues might facilitate the formation of protein−protein aggregates, leading to a better gel network and water-holding capacity. Consequently, it can be concluded that complicated hydrophobic aggregation of SPI occurs under pH-shifting combined with mild heating treatments.

SH Contents. The pH-shifting and heating treatments caused some changes in the SH contents that seemed to have some relation to protein unfolding. The total SH and exposed SH in the SPI samples decreased with increasing incubation times ($p < 0.05$; Figure 4). The total SH in control SPI samples was 4.495 μmol/g of protein, and the value significantly decreased ($p < 0.05$) by 22.6, 9.2, 10.18, 45.5, and 80.23% at 5 h for the samples treated with pH 1.5 shifting, 50 °C heating, 60 °C heating, pH 1.5 + 50 °C, and pH 1.5 + 60 °C, respectively. The acidic pH-shifting treatments alone had little effect ($p > 0.05$) on the total SH after treating for 5 h, which was in accordance with the results of Jiang et al.[13] The heating treatment at 50 °C alone also had minimal effect on decreasing the total SH ($p > 0.05$), and the effect of 60 °C treatment was larger than the effect observed for 50 °C treatment ($p < 0.05$). However, the acidic pH-shifting or heating treatments alone had significant effects in decreasing the exposed SH ($p < 0.05$) of SPI for 5 h of incubation, which were different from the effects on the total SH. The combination of pH-shifting and heating treatments could significantly enforce the conversion of SH groups into disulfides ($p < 0.05$). The amount of detectable total SH and exposed SH in the pH 1.5 + 60 °C samples after incubation exhibited more decreases than observed in the pH 1.5 + 50 °C samples.

The decreased number of SH contents can be used to explain the improved gel texture of SPI gel in Figure 1. It was noteworthy that incubations over 1 h resulted in a loss of SH contents, which were mainly due to protein structure opening in control proteins being particularly sensitive to the heating as well as the formation of S−S bonds leading to a decreased number of total and exposed SH. The disulfide covalent

DOI: 10.1021/acs.jafc.5b01331
J. Agric. Food Chem. 2015, 63, 4853−4861

polymers have been illustrated by the SDS−PAGE results (Figure 8). Some researchers reported that acidation leads to the removal of disulfide bonds; however, with consistent heating treatments, the repeated formation of intra- and intermolecular disulfide bonds and the occurrence of oxidation may give rise to the loss of total SH and reaction SH contents.[28] The reason that total SH contents have no significant changes in pH 1.5 shifting treated samples may be due to the lower pH-treated samples only displaying limited denaturation (as proven by the hydrophobicity and CD analysis; Figures 5 and 7) and disulfide bonds being relatively stable at acidic conditions.[29] The decrease in the SH content incubation of pH-shifting + heating samples was maybe due to the formation of disulfide bonds by SH oxidation and SH/SS interchange reactions, which is favored by heating.[30] This result revealed that the SH contents or disulfide linkages in SPI were important residue factors for the protein conformational stability.

Surface Hydrophobicity. Surface hydrophobicity allows for the detection of changes in the distribution of hydrophobic groups at the surface, which are caused by changes in the molecular structure of protein upon denaturation. The other factors that may cause an increase in surface hydrophobicity include the expansion of peptide chains or the dissociation of protein subunits.[31] Studies had reported that treatment conditions, including temperature, time, and protein concentration, influenced protein surface hydrophobicity.[32] In our study, acidic pH-shifting treatment alone showed a slight effect on the surface hydrophobicity of soy protein, and surface hydrophobicity rose significantly ($p < 0.05$) only after 5 h of treatment (Figure 5). Conversely, the acidic pH-shifting combined with heating (50 °C for more than 3 h or 60 °C for more than 1 h) markedly increased the hydrophobicity values of SPI ($p < 0.05$), where the pH 1.5 + 60 °C treatment samples had the highest hydrophobicity.

As Jiang et al.[8] reported, at the extreme acidic pH conditions, most of the proteins in SPI might be deacetylated and the removal of charged COO− groups would mainly account for the increased surface hydrophobicity, which resulting in enhanced attractive interactions between individual protein molecules. Temperature increases cause proteins to unfold, exposing the SH and hydrophobic groups. For example, glycinin has secondary structure alterations and a surface hydrophobicity that increases upon heating.[33,34] Heating the SPI, which consists of both glycinin and β-conglycinin, induces the development of specific interactions among the subunits[35] and leads to the formation of soluble complexes between the β subunit of β-conglycinin and the basic subunit of glycinin.[36] However, in Figure 3, heating the SPI at 50 and 60 °C alone caused no significant change in the hydrophobicity value ($p > 0.05$). Hence, acidic pH-shifting treatment might cause proteins to unravel their spatial structure and render a MG state[13,37] when combined with mild heating and would further disrupt the structure, with more hydrophobic groups exposed on the surface, as the temperature and time increase.

Emission Fluorescence Spectroscopy Analysis. Intrinsic fluorescence spectroscopy reflect the movement of protein side chains.[38] As depicted in panels a, b, and c of Figure 6, the λ_{max} of the samples treated with pH 1.5 shifting, pH 1.5 + 50 °C, and pH 1.5 + 60 °C, respectively, had marked shifts in the maximum emission wavelength compared to the control SPI, while the fluorescence spectra of both 50 and 60 °C heating samples had no obvious blue shift (panels d and e of Figure 6). The blue shift was mainly attributed to an alter in the three-dimensional positions and the shift of the Trp microenvironment toward a more hydrophobic microenvironment.[39] Jiang et al.[13] reported that some buried side chains could be exposed to the polar surface after acid pH-shifting treatments. Wu et al.[40] noted that blue shifts of the maximum emission wavelength revealed that the previously exposed Trp residues of SPI were buried in the interior of the modified SPI molecules. As expected, the intrinsic fluorescence results are consistent with those from the ANS analyses (Figure 5), which expressed the gradual exposure of hydrophobic clusters initially buried in the extreme pH-shifting combined with heating processes.

CD Spectra. To understand the impact of acidic pH and heating processes on the secondary structure of SPI, the soy protein samples were subjected to CD determination. According to Kelly and Price,[41] the ellipticities at 222 and 208 nm allow for the evaluation of the α-helix content in a protein. Moreover, the blue shift of the peak wavelength and the attenuation of the 210 nm negative peaks suggest losses in the α-helical structure content. As shown in Figure 7a, the CD spectra for the pH-shifting samples were not markedly altered during the first 1 h of incubation; however, after 3−5 h of treatment, the negative peak changed and blue shifted. Jiang et al.[8,13] noted that the CD spectra of the pH-shifted SPI samples incubated for shorter times exhibited only slight changes. However, after acidic pH-shifting combined with heating treatments, considerable changes occurred in the SPI (panels b and c of Figure 7). The negative peak attenuated with the holding time and the peak minimum shifted from 209 to 207 nm in the pH-shifting + 50 °C sample incubated for 5 h, which indicates partial disruption of the α helix. A similar result was obtained for samples under pH-shifting + 60 °C treatment, where the peak minimum reduced to 206 nm. To prove that this change was not exclusively caused by heating, the controls for 50 and 60 °C heating alone were measured and are shown in panels d and e of Figure 7. Clearly, no obvious changes in the CD spectra were observed, and the secondary α-helix conformation did not appear to be disrupted by mild heating treatments alone. These results indicate that a change in secondary structure is commonly observed among samples subjected to a combination of pH 1.5 shifting and mild heating processes. In addition, there was a negatively linear correlation between surface hydrophobicity and the α-helix structure content of SPI, which was supported by the results of Hou and Chang.[42]

SDS−PAGE. SDS−PAGE of the protein samples treated with β-mercaptoethanol or *n*-ethylmaleimide (NEM) was used to study the role of S−S linkages in forming protein aggregates in protein samples incubated under acidic pH and heating conditions (Figure 8). The SDS−PAGE patterns of the control SPI had the characteristic bands corresponding to the subunits of β-conglycinin (α', α, and β) and glycinin (A and B). As shown in panels b and d of Figure 8, under non-reducing conditions (+NEM), large polymers were observed in both the pH-shifting and pH-shifting and heating samples that accumulated at the top of the gel. These high-molecular-weight (MW) bands were disulfide covalent polymers and aggregates from soy globulins. The gradual disappearance of the α', α, and β subunits in the pH 1.5 + heating samples during incubation suggested that β-conglycinin was the precursor of those high-MW polymers. Moreover, the glycinin subunits (A and B) showed unremarkable changes during incubation.

DOI: 10.1021/acs.jafc.5b01331
J. Agric. Food Chem. 2015, 63, 4853−4861

For the reducing SDS−PAGE (panels a and c of Figure 8), the large MW aggregates and polymers were completely dissociated into the corresponding α', α, and β subunits of β-conglycinin. All protein samples expressed a similar electrophoretic pattern. These results demonstrate that disulfide cross-linking of β-conglycinin was responsible for the production of protein aggregates and polymers during the pH-shifting and heating processes, which also explains the increased protein gelation observed in Figure 1. Both inter- and intramolecular SH/SS interchanges are dynamic and are expected in the observed protein polymer formation.[14] Such reactions more likely would result in less SH groups and more S−S linkages, which might lead to some favorable changes in the protein functional properties.

In conclusion, our results demonstrated that the pH treatments under extremely acidic (pH 1.5) conditions combined with proper heating (50 and 60 °C) produced structurally modified SPI samples that displayed enhanced gelling ability. The pH-shifting and heating denaturation induced an increase in the particle size, surface hydrophobicity, and SH content and a decrease in the solubility, resulting in protein cross-linking. The CD and fluorescence spectroscopy analyses revealed secondary and tertiary structural changes in pH-shifting and heating samples. Overall, the improvement in the protein gelling property induced by pH-shifting combined with heating treatments was party related to the change in secondary and tertiary structures and mainly attributed to the connection and interaction between protein subunits through hydrophobic association, hydrogen bonds, and disulfide bonds. The pH-shifting combined with mild heating treatments give great potential for the production of functionality-improved SPI.

AUTHOR INFORMATION

Corresponding Author

*Telephone: +86-451-55191794. Fax: +86-451-55190577. E-mail: kongbh63@hotmail.com.

Author Contributions

†Qian Liu and Rui Geng contributed equally to this work.

Funding

This study was supported by the Development Program of China (863 Program) (Grant 2013AA102208-2), the Program for Young Talents of Northeast Agricultural University (Grant 14QC40), and the Foundation of Science and Technology in Heilongjiang (Grant GC13B212).

Notes

The authors declare no competing financial interest.

REFERENCES

(1) Kinsella, J. Functional properties of soy proteins. *J. Am. Oil Chem. Soc.* **1979**, *56*, 242−258.

(2) Nishinari, K.; Fang, Y.; Guo, S.; Phillips, G. O. Soy proteins: A review on composition, aggregation and emulsification. *Food Hydrocolloids* **2014**, *39*, 301−318.

(3) Hua, Y.; Cui, S. W.; Wang, Q.; Mine, Y.; Poysa, V. Heat induced gelling properties of soy protein isolates prepared from different defatted soybean flours. *Food Res. Int.* **2005**, *38*, 377−385.

(4) Hermansson, A. M. Soy protein gelation. *J. Am. Oil Chem. Soc.* **1986**, *63*, 658−666.

(5) Subirade, M.; Kelly, I.; Guéguen, J.; Pézolet, M. Molecular basis of film formation from a soybean protein: comparison between the conformation of glycinin in aqueous solution and in films. *Int. J. Biol. Macromol.* **1998**, *23*, 241−249.

(6) German, B.; Damodaran, S.; Kinsella, J. E. Thermal dissociation and association behavior of soy proteins. *J. Agric. Food Chem.* **1982**, *30*, 807−811.

(7) Damodaran, S.; Kinsella, J. E. Effect of conglycinin on the thermal aggregation of glycinin. *J. Agric. Food Chem.* **1982**, *30*, 812−817.

(8) Jiang, J.; Xiong, Y. L.; Chen, J. Role of β-conglycinin and glycinin subunits in the pH-shifting-induced structural and physicochemical changes of soy protein isolate. *J. Food Sci.* **2011**, *76*, C293−302.

(9) Matsudomi, N.; Sasaki, T.; Kato, A.; Kobayashi, K. Conformational changes and functional properties of acid-modified soy protein. *Agric. Biol. Chem.* **1985**, *49*, 1251−1256.

(10) Wagner, J. R.; Sorgentini, D. A. Thermal and electrophoretic behavior, hydrophobicity, and some functional properties of acid-treated soy isolates. *J. Agric. Food Chem.* **1996**, *44*, 1881−1889.

(11) Wagner, J. R.; Guéguen, J. Surface functional properties of native, acid-treated, and reduced soy glycinin. 1. Foaming properties. *J. Agric. Food Chem.* **1999**, *47*, 2173−2180.

(12) Liang, Y.; Kristinsson, H. G. Structural and foaming properties of egg albumen subjected to different pH-treatments in the presence of calcium ions. *Food Res. Int.* **2007**, *40*, 668−678.

(13) Jiang, J.; Chen, J.; Xiong, Y. L. Structural and emulsifying properties of soy protein isolate subjected to acid and alkaline pH-shifting processes. *J. Agric. Food Chem.* **2009**, *57*, 7576−83.

(14) Jiang, J.; Xiong, Y. L. Extreme pH treatments enhance the structure-reinforcement role of soy protein isolate and its emulsions in pork myofibrillar protein gels in the presence of microbial transglutaminase. *Meat Sci.* **2013**, *93*, 469−76.

(15) Chen, N. N.; Zhao, M. M.; Sun, W. Z.; Ren, J. Y.; Cui, C. Effect of oxidation on the emulsifying properties of soy protein isolate. *Food Res. Int.* **2013**, *52*, 26−32.

(16) Beveridge, T.; Toma, S. J.; Nakai, S. Determination of SH- and SS-groups in some food proteins using Ellman's reagent. *J. Food Sci.* **1974**, *39*, 49−51.

(17) Sorgentini, D. A.; Wagner, J. R. Comparative study of structural characteristics and thermal behavior of whey and isolate soybean proteins. *J. Food Biochem.* **1999**, *23*, 489−507.

(18) Liu, G.; Xiong, Y. L. Electrophoretic pattern, thermal denaturation, and in vitro digestibility of oxidized myosin. *J. Agric. Food Chem.* **2000**, *48*, 624−630.

(19) Tang, C. H.; Wu, H.; Yu, H. P.; Li, L.; Chen, Z.; Yang, X. Q. Coagulation and gelation of soy protein isolates induced by microbial transglutaminase. *J. Food Biochem.* **2006**, *30*, 35−55.

(20) Zhou, F.; Zhao, M.; Su, G.; Cui, C.; Sun, W. Gelation of salted myofibrillar protein under malondialdehyde-induced oxidative stress. *Food Hydrocolloids* **2014**, *40*, 153−162.

(21) O'Kane, F. E.; Happe, R. P.; Vereijken, J. M.; Gruppen, H.; van Boekel, M. A. J. S. Heat-induced gelation of pea legumin: Comparison with soybean glycinin. *J. Agric. Food Chem.* **2004**, *52*, 5071−5078.

(22) Mleko, S.; Foegeding, E. A. pH induced aggregation and weak gel formation of whey protein polymers. *J. Food Sci.* **2000**, *65*, 139−143.

(23) Yuan, B. E.; Ren, J. Y.; Zhao, M. M.; Luo, D. H.; Gu, L. J. Effects of limited enzymatic hydrolysis with pepsin and high-pressure homogenization on the functional properties of soybean protein isolate. *LWT - Food Sci. Technol.* **2012**, *46*, 453−459.

(24) Liu, C. M.; Zhong, J. Z.; Liu, W.; Tu, Z. C.; Wan, J.; Cai, X. F.; Song, X. Y. Relationship between functional properties and aggregation changes of whey protein induced by high pressure microfluidization. *J. Food Sci.* **2011**, *76*, E341−E347.

(25) Gulseren, I.; Guzey, D.; Bruce, B. D.; Weiss, J. Structural and functional changes in ultrasonicated bovine serum albumin solutions. *Ultrason. Sonochem.* **2007**, *14*, 173−183.

(26) Kohyama, K.; Sano, Y.; Doi, E. Rheological characteristics and gelation mechanism of tofu (soybean curd). *J. Agric. Food Chem.* **1995**, *43*, 1808−1812.

(27) Hu, H.; Fan, X.; Zhou, Z.; Xu, X. Y.; Fan, G.; Wang, L. F.; Huang, X. J.; Pan, S. Y.; Zhu, L. Acid-induced gelation behavior of soybean protein isolate with high intensity ultrasonic pre-treatments. *Ultrason. Sonochem.* **2013**, *20*, 187−195.

DOI: 10.1021/acs.jafc.5b01331
J. Agric. Food Chem. 2015, 63, 4853−4861

(28) Hwang, D. C.; Damodaran, S. Metal-chelating properties and biodegradability of an ethylenediaminetetraacetic acid dianhydride modified soy protein hydrogel. *J. Appl. Polym. Sci.* **1997**, *64*, 891−901.
(29) Zapun, A.; Creighton, T. E. Effects of DsbA on the disulfide folding of bovine pancreatic trypsin inhibitor and α-lactalbumin. *Biochemistry* **1994**, *33*, 5202−5211.
(30) Monahan, F. J.; German, J. B.; Kinsella, J. E. Effect of pH and temperature on protein unfolding and thiol/disulfide interchange reactions during heat-induced gelation of whey proteins. *J. Agric. Food Chem.* **1995**, *43*, 46−52.
(31) Laligant, A.; Dumay, E.; Casas Valencia, C.; Cuq, J. L.; Cheftel, J. C. Surface hydrophobicity and aggregation of β-lactoglobulin heated near neutral pH. *J. Agric. Food Chem.* **1991**, *39*, 2147−2155.
(32) Petruccelli, S.; Anon, M. C. Thermal aggregation of soy protein isolates. *J. Agric. Food Chem.* **1995**, *43*, 3035−3041.
(33) Renkema, J. M. S.; Lakemond, C. M. M.; de Jongh, H. H. J.; Gruppen, H.; van Vliet, T. The effect of pH on heat denaturation and gel forming properties of soy proteins. *J. Biotechnol.* **2000**, *79*, 223−230.
(34) Tezuka, M.; Yagasaki, K.; Ono, T. Changes in characters of soybean glycinin groups I, IIa, and IIb caused by heating. *J. Agric. Food Chem.* **2004**, *52*, 1693−1699.
(35) Utsumi, S.; Damodaran, S.; Kinsella, J. E. Heat-induced interactions between soybean proteins: Preferential association of 11S basic subunits and β subunits of 7S. *J. Agric. Food Chem.* **1984**, *32*, 1406−1412.
(36) Morr, C. V. Current status of soy protein functionality in food systems. *J. Am. Oil Chem. Soc.* **1990**, *67*, 265−271.
(37) Kristinsson, H. G.; Hultin, H. O. The effect of acid and alkali unfolding and subsequent refolding on the pro-oxidative activity of trout hemoglobin. *J. Agric. Food Chem.* **2004**, *52*, 5482−5490.
(38) Keerati-u-rai, M.; Corredig, M. Heat-induced changes in oil-in-water emulsions stabilized with soy protein isolate. *Food Hydrocolloids* **2009**, *23*, 2141−2148.
(39) Viseu, M. I.; Carvalho, T. I.; Costa, S. M. B. Conformational transitions in β-lactoglobulin induced by cationic amphiphiles: Equilibrium studies. *Biophys. J.* **2004**, *86*, 2392−2402.
(40) Wu, W.; Zhang, C. M.; Hua, Y. F. Structural modification of soy protein by the lipid peroxidation productmalondialdehyde. *J. Sci. Food Agric.* **2009**, *89*, 1416−1423.
(41) Kelly, S. M.; Price, N. C. The use of circular dichroism in the investigation of protein structure and function. *Curr. Protein Pept. Sci.* **2000**, *1*, 349−384.
(42) Hou, H. J.; Chang, K. C. Structural characteristics of purified β-conglycinin from soybeans stored under four conditions. *J. Agric. Food Chem.* **2004**, *52*, 7931−7937.

DOI: 10.1021/acs.jafc.5b01331
J. Agric. Food Chem. 2015, 63, 4853−4861

This is an open access article published under an ACS AuthorChoice License, which permits copying and redistribution of the article or any adaptations for non-commercial purposes.

JOURNAL OF AGRICULTURAL AND FOOD CHEMISTRY

Article

pubs.acs.org/JAFC

Rheological Profiling of Organogels Prepared at Critical Gelling Concentrations of Natural Waxes in a Triacylglycerol Solvent

Ashok R. Patel,*[,†] Mehrnoosh Babaahmadi,[†] Ans Lesaffer,[‡] and Koen Dewettinck[†]

[†]Vandemoortele Centre for Lipid Science and Technology, Laboratory of Food Technology and Engineering, Faculty of Bioscience Engineering, Ghent University, Coupure Links 653, 9000 Gent, Belgium

[‡]Vandemoortele R &D Izegem, Prins Albertlaan 79, 8870 Izegem, Belgium

Supporting Information

ABSTRACT: The aim of this study was to use a detailed rheological characterization to gain new insights into the gelation behavior of natural waxes. To make a comprehensive case, six natural waxes (differing in the relative proportion of chemical components: hydrocarbons, fatty alcohols, fatty acids, and wax esters) were selected as organogelators to gel high-oleic sunflower oil. Flow and dynamic rheological properties of organogels prepared at critical gelling concentrations (C_g) of waxes were studied and compared using drag (stress ramp and steady flow) and oscillatory shear (stress and frequency sweeps) tests. Although, none of the organogels satisfied the rheological definition of a "strong gel" (G''/G' $(\omega) \leq 0.1$), on comparing the samples, the strongest gel (highest critical stress and dynamic, apparent, and static yield stresses) was obtained not with wax containing the highest proportion of wax esters alone (sunflower wax, SFW) but with wax containing wax esters along with a higher proportion of fatty alcohols (carnauba wax, CRW) although at a comparatively higher C_g (4%wt for latter compared to 0.5%wt for former). As expected, gel formation by waxes containing a high proportion of lower melting fatty acids (berry, BW, and fruit wax, FW) required a comparatively higher C_g (6 and 7%wt, respectively), and in addition, these gels showed the lowest values for plateau elastic modulus (G'_{LVR}) and a prominent crossover point at higher frequency. The gelation temperatures ($T_{G'=G''}$) for all the studied gels were lower than room temperature, except for SFW and CRW. The yielding-type behavior of gels was evident, with most gels showing strong shear sensitivity and a weak thixotropic recovery. The rheological behavior was combined with the results of thermal analysis and microstructure studies (optical, polarized, and cryo-scanning electron microscopy) to explain the gelation properties of these waxes.

KEYWORDS: *organogels, natural waxes, rheological characterization, cryo-SEM, microstructure, wax-based gels*

INTRODUCTION

Organogels are a class of soft matter systems that are considered to be at an interface of complex fluids and phase-separated states of matter. They comprise an organic liquid that is physically immobilized by a network of dispersed, self-assembled aggregates of gelator molecules.[1,2] The normal phase separation into aggregated gelator molecules and liquid solvent phase is avoided in organogels due to the organization of aggregated gelator molecules into an interconnected solid-like, three-dimensional (3D) network, resulting in the formation of strong or weak gels depending on the gelator−gelator interactions as well as the solvent properties.[1,3,4] The possibility of transforming different types of organic liquids into solid-like viscoelastic gels (at relatively lower mass fractions of gelator molecules) makes organogelation an attractive subject of investigation in varied research domains for many different applications. For example, systems where triacylglycerol solvents (vegetable oils) are gelled using natural components, have found potential applications in biorelated fields such as drug delivery,[5−7] cosmetics,[8−10] and foods.[11−13] Among various gelators explored for gelling vegetable oils, natural waxes are considered to be the most promising ones because of their excellent oil binding properties,[14] economical value (capable of gelling oils at a significantly lower mass fractions, $w_c \ll 0.1$),[15,16] and availability of a number of waxes approved for use in humans.[17,18] Moreover, the gels formed using waxes have interesting properties such as themoreversibility[19,20] and emulsion stabilization,[21−23] which further justifies their popularity as organogelators for vegetable oils.

In spite of such widespread interest in these systems, a clear fundamental understanding of the physical properties of wax-based organogels is still missing. Unlike other low molecular weight gelators, waxes have a multicomponent chemical nature, comprising of components such as hydrocarbons (HCs), wax esters (WEs), fatty acids (FAs), and fatty alcohols (FALs), and such chemical diversity makes characterization of wax-based organogels very complicated. Some fundamental studies have been published in recent years where the gelation behavior of waxes was explored based on the chemical properties of waxes (composition, impurities),[15] thermodynamics and kinetic aspects of wax crystallization (fractal aggregation, thermal properties, crystal morphology, and cooling rates),[14,24,25] and some rheological[26−28] and large deformation studies (texture analysis) of the formed gels.[20] As seen with fats (high-melting triacylglycerols, TAGs), waxes also crystallize in low-melting TAGs (liquid oil) when the temperature is decreased well below their melting temperatures. Fundamentally, this type of

Received: January 23, 2015
Revised: April 28, 2015
Accepted: May 1, 2015
Published: May 1, 2015

 © 2015 American Chemical Society

DOI: 10.1021/acs.jafc.5b01548
J. Agric. Food Chem. 2015, 63, 4862−4869

crystallization includes characteristics of both melt crystallization (crystallization due to supercooling) and crystallization of solute from the solvent (crystallization due to the decreased solubility of waxes in oils at lower temperatures). Similar to fat crystallization, the formed crystallites of waxes undergo further thermodynamically induced structural reorganization including clustering and aggregation. These crystalline aggregates can act as building blocks to trap the liquid oil into a gel-like structure, resulting in organogel formation. The structure is stabilized via weak interactions (among the neighboring building blocks) such as H-bonding and polar−polar interactions among constituents with polar moieties as well as weak intermolecular interactions such as induced dipole−induced dipole interactions (London dispersion force) among nonpolar components.

In our opinion, there is a need for a comprehensive comparative rheological profiling of wax-based organogels in order to further probe the link between the macroscopic flow/deformation response of gels and the microscopic interactions between the constituent building blocks (crystalline aggregates). In the present study, we report a detailed rheological characterization using a range of steady and dynamic shear measurements to understand the gelation behavior of natural waxes. To make a comprehensive case, six natural waxes (differing in the relative proportion of chemical components: HCs, WEs, FAs, and FALs) were selected to prepare organogels using high-oleic sunflower oil as the triacylglycerol solvent. The critical gelling concentrations (C_g) for different waxes were identified, and the flow and dynamic rheological properties of organogels prepared at C_g of waxes were studied and compared using drag (stress ramp), steady flow (flow and 3ITT (3 interval thixotropy test)), oscillatory shear (stress and frequency sweeps), and mixed flow−oscillatory shear tests. The results obtained from these measurements were combined with the results from thermal behavior and microstructure studies to characterize the physical properties of organogels. The C_g is the minimum concentration of wax at which the gelation of solvent occurs, and since we are considering wax-based organogels as fractal gels, the C_g in this case corresponds to the minimum volume fraction of crystalline particles at which a space-filling network of rarefied fractal flocs is formed.[29] Below this concentration, the dispersed particles contribute only in increasing the viscosity of the sol, whereas at concentrations higher than C_g a decrease in the size of fractal flocs is observed with a resultant increase in fractal dimensions due to the densification of flocs.[30] Thus, the viscoelasticity of fractal gels is best studied at C_g in order to better understand the nature of molecular interactions involved in gel formation at low volume fractions of particles.

MATERIALS AND METHODS

Materials. Refined high-oleic sunflower oil, HOS (TAGs > 99% wt), was received from Vandemoortele Lipids N.V. (Izegem, Belgium). Sunflower wax, *Helianthus Annuus Seed Cera* (SFW, acid value: 2−8 mg KOH/g, saponification value: 75−95 mg KOH/g), carnauba wax, *Copernicia Cerifera Cera* (CRW, acid value: 2−7 mg KOH/g, saponification value: 78−95 mgKOH/g), candelilla wax, *Euphorbia Cerifera Cera* (CLW, acid value: 12−22 mg KOH/g, saponification value: 43−65 mgKOH/g), bees wax, *Cera Alba* (BZW, acid value: 17−22 mg KOH/g, saponification value: 70−80 mgKOH/g), berry wax, *Rhus Verniciflua Peel Cera* (BW, acid value: 48−54 mg KOH/g, saponification value: 180−220 mgKOH/g), and fruit wax, *Myrica Cerifera* (FW, acid value: 5−25 mg KOH/g, saponification value: 210−240 mgKOH/g) were received as gift samples from Kalh GmbH & Co. KG (Trittau, Germany). Chemical composition of waxes was determined in-house using HPLC-ELSD to understand the distribution of main components. The main components of six waxes are listed in Table S1. More details on the experimental setup and result analysis will be published elsewhere.

Preparation of Organogels. Waxes were dispersed in HOS at varying concentrations by heating above their melting points until complete melting of waxes was achieved. The clear oily dispersions were subsequently cooled to 5 °C at a rate of approximately 2 °C/min under mild stirring (200 rpm) using a magnetic stirrer (model EM3300T, Labotech Inc., Germany). The critical gelling concentration (C_g) for all six waxes was identified using rheological characterization (oscillatory frequency sweeps). Samples prepared at different concentrations of waxes were subject to frequency sweeps at a constant stress of 0.02 Pa. The resultant values of elastic and viscous modulus (G' and G'', respectively) were compared at low frequency, and the corresponding concentrations at which $G' > G''$ were identified as C_g for individual waxes. The samples were stored at 5 °C until used further for characterization. The photograph of gels prepared at the respective C_g of waxes is shown in Figure S1.

Thermal Characterization. The thermal behavior of neat waxes and wax-based organogels was determined in triplicate using a Q1000 DSC (TA Instruments, New Castle, DE, USA) equipped with a refrigerated cooling system. Nitrogen was used as purge gas. The cell constant and temperature were set with indium (TA Instruments). An additional temperature calibration was done using azobenzene (Sigma-Aldrich, Bornem, Belgium) and undecane (Acros Organics, Geel, Belgium). The wax samples were heated at 90 °C in sealed aluminum pans (TA Instruments) before being cooled to 0 °C, kept isothermally at 0 °C for 20 min, and reheated to 90 °C. Heating and cooling were done at a constant rate of 2 °C/min. Characteristic parameters of the thermal curves, including onset and peak maximum temperatures for crystallization and melting (T_c onset, T_m onset, T_c peak, and T_m peak), were obtained using the software TA Universal Analysis provided by the instrument supplier.

Microstructure Studies. The microstructure of wax crystals was observed under normal and polarized light (PLM) using a Leica DM2500 microscope (Wetzlar, Germany) equipped with a Leica MC170 HD color camera. For cryo-scanning electron microscopy (cryo-SEM), deoiling of organogel samples was carried out using butanol to remove the surface liquid oil in order to visualize the wax crystals. Precisely, the deoiling was carried out in two different ways: (1) A known quantity of organogel was weighed in a glass vial followed by addition of butanol (at a gel:butanol ratio of 1:50 w/w approximately), which led to the collapse of the gel structure and resultant sedimentation of the crystalline fraction. After overnight storage, the supernatant liquid was decanted to collect the sediment, which was then placed on the sample holder. (2) The organogel sample was directly placed on a specialized stub (sample holder with grooves) followed by a dropwise addition of butanol to remove the liquid oil. The stub was left for overnight drying in inverted position to drain out all the solvent. The stub was then plunge-frozen in liquid nitrogen and transferred into the cryo-preparation chamber (PP3010T Cryo-SEM Preparation System, Quorum Technologies, UK), where it was freeze-fractured and subsequently sputter-coated with Pt and examined in a JEOL JSM 7100F SEM (JEOL Ltd., Tokyo, Japan).

Rheological Measurements. An advanced rheometer AR 2000ex (TA Instruments, USA) equipped with a Peltier system for temperature control was used for all rheological measurements. A parallel plate cross-hatched geometry of diameter 40 mm was used (geometry gap = 1000 μm) for the following tests: (a) amplitude sweeps: oscillatory stress = 0.001−1000 Pa, frequency = 1 Hz, and temperature = 5 °C; (b) frequency sweeps: oscillatory stress = 0.02 Pa, angular frequency = 0.6−240 rads^{-1}, and temperature = 5 °C; (c) temperature ramps: oscillatory stress = 0.02 Pa, frequency = 1 Hz, and temperature = 90−5 °C; (d) stress ramp: shear stress (0.08−300 Pa) and temperature = 5 °C; (e) flow-frequency test: samples were subjected to a range of shear rate = 0.01−20 s^{-1} followed by frequency sweeps (ν = 0.01−10 Hz); and (f) 3-ITT: samples were subjected to alternating intervals of low and high shear rates (0.1 s^{-1} for 10 min, 1

DOI: 10.1021/acs.jafc.5b01548
J. Agric. Food Chem. 2015, 63, 4862−4869

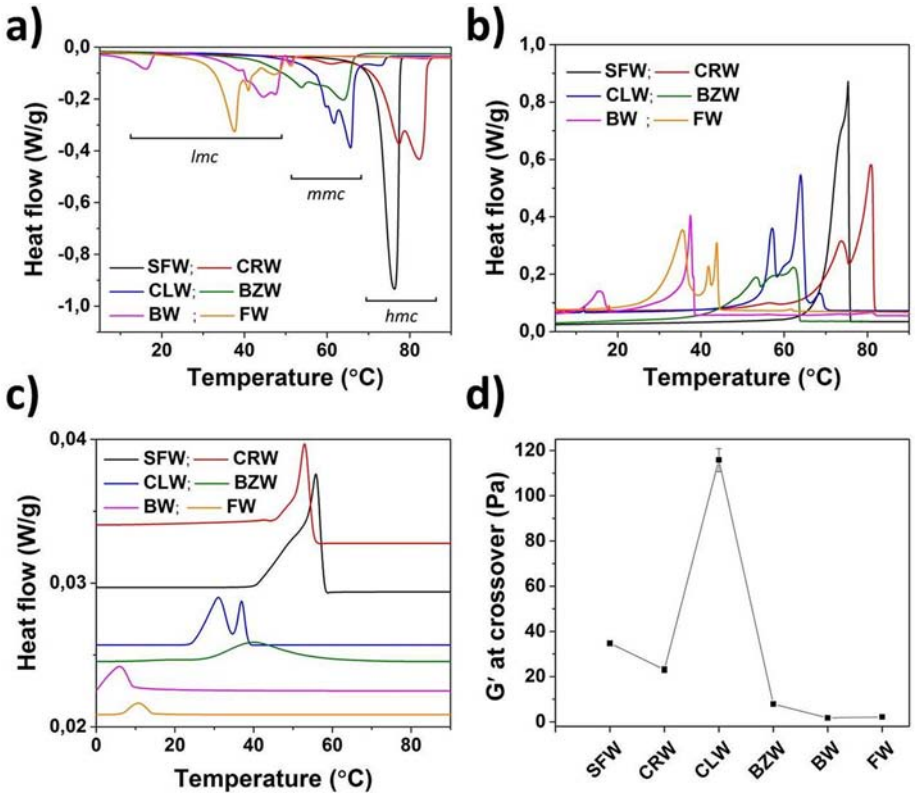

Figure 1. Comparative heating (a) and cooling (b) curves of neat waxes; (c) cooling curves of organogels prepared at the C_g of respective waxes; and (d) elastic modulus (G') at crossover point for organogels prepared at the C_g of respective waxes (also refer to Figure S3).

s^{-1} for next 5 min, followed by 0.1 s^{-1} for 10 min) at a temperature of 5 °C. The apparent yield stress was measured by fitting the stress versus shear rate data to a three-parameter model (Hershel Bulkley model) as discussed later.

Statistical Analysis. Data from texture and sensorial evaluation of cakes were compared using statistical analysis. An unpaired, two-tailed Student's *t* test was used on the data (SPSS Statistics) to establish the statistical significance in the differences observed.

RESULTS AND DISCUSSION

Waxes are a complex mixtures of a number of nonpolar and polar components with major components being HCs, WEs, FAs, and FALs with varying carbon chain lengths (representative molecular structures of main components are shown in Figure S2). When a liquid dispersion of a melted wax in an apolar solvent is cooled to temperatures well below the melting temperatures of wax (supercooling), the components separate out into crystalline phase that aggregate and further interconnect to form a 3D network that physically traps the liquid solvent into a gel structure.[31,32] Depending on the major component(s) as well as the carbon chain lengths of these components, the waxes display strikingly different gelation properties. The goal of this study was to have a detailed rheological profiling of wax-based physical gels in order to better understand their physical properties. To accomplish the goal, we selected six chemically diverse (differing in the proportions of major components) natural waxes: SFW, CRW, CLW, BZW, BW, and FW as listed in Table S1. DSC melting and cooling curves of neat waxes are shown in Figure 1a and b. On the basis of the melting peaks, the samples were categorized into waxes containing high-, mid-, and low-melting components (*hmc*, *mmc*, and *lmc*, respectively). SFW was predominantly rich (>95%wt) in WEs and showed single melting and crystallization peaks and, hence, was considered as a monocomponent wax, while the other five waxes contained at least two chemical components in high proportions as follows: CRW (WEs, ∼62% wt; FALs, ∼30%wt), CLW (HCs, ∼73%wt; WEs, ∼16%wt; FAs, ∼9%wt), BZW (WEs, ∼58%wt; HCs, ∼27%wt; FAs, ∼9% wt); BW (FAs, ∼96%wt; FALs, ∼4%wt), and FW (FAs, ∼36% wt; FALs, ∼63%wt). Please note that some FAs in BW and FW are esterified to a glycerol backbone. The multicomponent nature of these waxes is further confirmed from multiple melting and crystallization peaks seen in Figure 1a and b.

To identify the critical gelling concentration (Table 1), a series of oily dispersions were made by varying the concentration of waxes, heating them at 90 °C, and subsequently cooling the dispersion to 5 °C at a constant rate of 2 °C/min. The gelation was noted first by simple tube flipping observation to identify the concentration ranges where the gels did not flow under the influence of gravity, followed by

Table 1. Critical Gelling Concentration (C_g) and Crystallization Onset (T_c Onset) and Peak (T_c Peak) and Crossover ($T_{G'=G''}$) Temperatures (Mean ± SD) for Waxes in Organogels Prepared at Their Respective C_g

axis	C_g (% wt)	T_c onset (°C)	T_c peak (°C)	$T_{G'=G''}$ (°C)
SFW	0.5	57.27 ± 0.05	55.97 ± 0.31	45.9 ± 2.1
CRW	4	54.61 ± 0.05	52.83 ± 0.44	32.7 ± 1.3
CLW	0.75	38.72 ± 0.82 (I)	37.76 ± 0.84 (I)	13.1 ± 0.9
		34.06 ± 0.12 (II)	31.14 ± 0.42 (II)	
BZW	1	42.69 ± 0.35	40.98 ± 0.75	19.0 ± 0.7
BW	6	8.92 ± 0.41	6.27 ± 0.03	7.3 ± 0.2
FW	7	14.87 ± 0.11	10.55 ± 0.07	17.3 ± 1.0

DOI: 10.1021/acs.jafc.5b01548
J. Agric. Food Chem. 2015, 63, 4862−4869

oscillatory rheological measurements (amplitude sweeps) to distinguish between a gel ($G' > G''$) and a viscous sol ($G'' > G'$) at low applied shear (τ_o). Oscillatory measurements offer a convenient way of measuring the flow and deformation properties of viscoelastic samples and also facilitate the classification of samples into strong gels, weak gels, and viscous sols based on frequency sweeps.[33]

For viscoelastic materials, the frequency-dependent functions G' and G'' give a measure of solid-like and liquid-like characteristics, respectively. Typically, for gels the elastic component (G') dominates over the viscous component (G'') at small applied shear and attains a plateau (G'_{LVR}) in the linear response region (LVR, or linear viscoelastic region).[34] The end of the LVR is marked by the first point where the G' varies by 10% of the G'_{LVR} value, and the corresponding stress at this point is referred to as the critical stress (τ^*). As the applied shear increases further, a permanent deformation (yielding) of the materials may occur ($G' = G''$), and the corresponding stress value at this point is referred to as oscillatory or dynamic yield stress (τ_{dy}).[35] The τ^* represents the onset of nonlinearity (and hence structure breakdown), while τ_{dy} represents the transition from solid- to liquid-like behavior, and the zone spanning these two events is referred to as the yield zone.[36,37]

There is a significant discussion in the literature relating that the monocomponent gel formation in apolar solvents by low molecular weight gelators is usually achieved by a competitive interplay of fibrous structure formation and crystallization. The gelator−gelator interactions (mediated via hydrogen bonding, electron transfer, etc.) need to be anisotropic (unidirectional) to promote assembly into 1D fibers, and the relative absence of such interactions in the other two dimensions prevents lateral growth and subsequent crystallization.[38,39] The self-assembly gets more complicated when dealing with multicomponent systems; when more than one self-assembling components are present, they can either coassemble (heterogeneous assembly) or undergo "self-sorting" (coexisting, monomolecular assemblies) depending on the intermolecular interactions arising from similarities and dissimilarities in the chemical structures.[40] As the concentration of the gelator(s) exceeds a certain concentration (C_g), the equivalent spherical volumes of self-assembled linear aggregates (of anisotropically stacked gelator molecules) start overlapping and an interconnected 3D network is formed, leading to the formation of physical gels.[1,2] Such a behavior can be compared to the overlapping of hydrodynamic volumes of polymeric chains in semidilute solutions at a defined overlap concentration (C^*) that is specific for a polymer−solvent combination.[41]

As seen from Table 1, SFW, CLW, and BZW could form a gel at a significantly lower concentration ($C_g \leq 1$%wt), whereas BW and FW required concentrations as high as 6 and 7%wt, respectively to gel the liquid oil. The higher C_g values for BW and FW were expected since these waxes are devoid of components with a larger "carbon backbone"; they are mainly composed of low-melting short-chain FAs ($C_{14:0}$, $C_{16:0}$, $C_{18:0}$) and FALs (C_{20-22}). The relatively higher solubility of these components is also confirmed from the crystallization peaks of BW and FW organogels (Figure 1c), where the peaks are shifted to much lower temperatures compared to the peaks of neat waxes. To further understand the relationship between crystallization and gelation, a single frequency test was done on samples where the material functions (G' and G'') were measured as a function of temperature (at constant $\tau = 0.02$ Pa and $\nu = \omega/2\pi = 1$ Hz). The temperature ($T_{G'=G''}$) and G' at the crossover point (or sol−gel transformation point) for organogel samples at C_g of individual waxes are shown in Figure 1d. Interestingly, for waxes containing high- and mid-melting components, a prominent delay in gelation was evident with $T_{G'=G''}$ being much lower than T_c peak (Table 1), while for BW and FW the gelation and crystallization occurred simultaneously. On comparing the G' values for the gels at their respective crossover points, one can assume that the gelation of BW and FW gels ($G' < 2.5$ Pa) is not preceded by extensive microstructure development, in contrast to the gels formed by waxes containing high- and mid-melting components. In BW and FW, most FAs are not free but esterified to a glycerol backbone, and these nonlinear molecules display lateral packing leading to the formation of large crystals.

Due to the formation of relatively larger spherical crystal/crystalline aggregates (Figure 2a−f) by BW and FW (along with a comparatively higher crystalline weight fraction), the possibility of creating loose entanglements is higher. These entanglements can act as transient junction points, which can contribute to the elasticity but sustain only a very low magnitude of stress, as confirmed from amplitude and frequency sweeps discussed later in the text. The platelet-like crystals are clearly distinguishable in spherical crystalline aggregates of BW (Figure 2c), while flat crystals are seen radiating outward from the center to form spherical units in the case of FW (Figure 2f). Among the other four waxes, the most striking results were observed for the CLW gel, where the G' at the crossover point was exceptionally high (~115 Pa), while the gelation occurred only after completion of the crystallization event, indicating that gel formation is a result of a significant reorganization of the crystalline phase at lower temperatures. As seen from Figure 2h and i, CLW crystallizes into very fine linear particles that are further organized into an open aggregate-like structure (Figure 2g). The sparse (noncompacted) packing is also evident from a low birefringence seen in the polarized light microscopy image (Figure 2h). The formation of such crystalline particles by CLW is attributed to a high proportion of linear hydrocarbons (*n*-alkanes).[42] The formation of gels with higher elasticity at lower crystalline mass

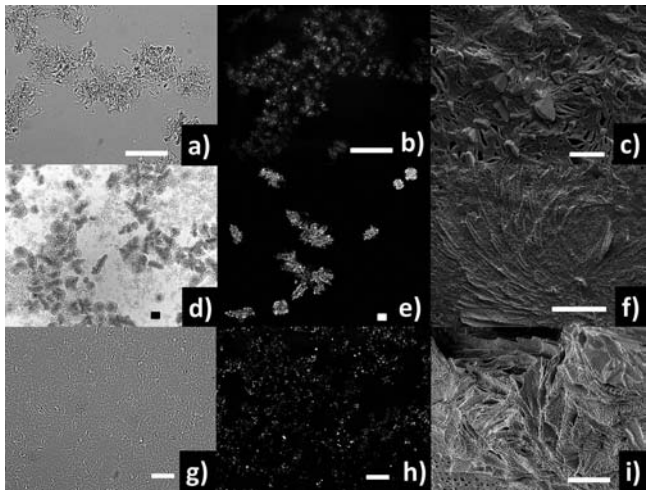

Figure 2. Optical microscopy (under normal and polarized light) and cryo-SEM images of gels of (a−c) BW; (d−f) FW, and (g−i) CLW. Scale bars = 50 μm (a, b, g, and h); 20 μm (d and e); 10 μm (f); and 1 μm (i and c).

DOI: 10.1021/acs.jafc.5b01548
J. Agric. Food Chem. 2015, 63, 4862−4869

fraction is in agreement with previously reported studies on CLW-oil organogels.[16,20]

The plots from oscillatory amplitude and frequency sweeps done on organogels are shown in Figure 3. As seen from the

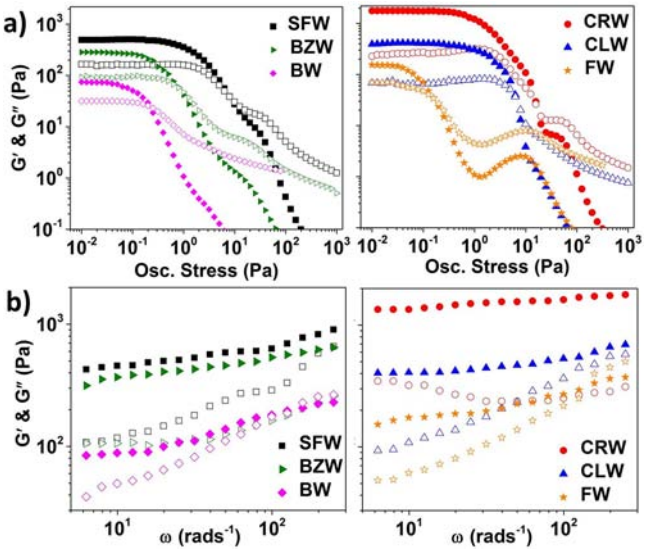

Figure 3. (a and b) Amplitude (at ν = 1 Hz) and frequency (at τ = 0.02 Pa) sweeps for gels made at the C_g of respective waxes. G' and G'' are shown as filled and open symbols, respectively.

graphs, none of the studied samples satisfied the rheological definition of a "strong gel" (G''/G' (ω) $\leq$ 0.1). However, the CRW gel did show the least frequency dependence (more or less linear curve in Figure 3b), higher G'_{LVR} value, and higher oscillatory yield stress in comparison to other gels. As discussed earlier, the elasticity of BW and FW organogels is attributed to loose entanglements of large crystals, and because of this structure, the gels can sustain only a lower magnitude of stress, which is confirmed from low values of dynamic moduli in the linear response region. Moreover, these gels also showed very low values of τ^* (<0.05 Pa) and a narrow yield zone with τ_{dy} <0.25 Pa.

The yield zone or, more specifically, the slope of the curve in the yield zone gives information about the breakage of intermolecular forces holding up the structure. A narrow yield zone points at the fact that the structure breakdown occurs at once (all bonds break at the same force). The weak structure of BW and FW gels is further evident from a prominent crossover (tan $\delta = G''/G' > 1$) at higher ω, which is a confirmation of structure breakdown at high rates of deformation. When comparing the gels made with waxes containing *hmc*, it can be seen that SFW gel was much softer than CRW and yielded at much lower force (τ_{dy} = 9.9 Pa compared to 19.8 Pa for the CRW gel). However, it should be noted that SFW gel was formed at a C_g of only 0.5%wt, whereas a high C_g of 4%wt was required for CRW.

The differences in C_g can be explained from the morphology of crystals formed in these two gels (Figure 4a–f). SFW crystals had an anisotropic, rod-like morphology (with lengths spanning the micrometer range), which is considered to be the most desirable shape of elementary assemblies (building blocks) to immobilize a large volume of solvent for efficient gelation.[35] The rod-like morphology of SFW is attributed to its high content (>95%wt) of wax esters, which are known to be the

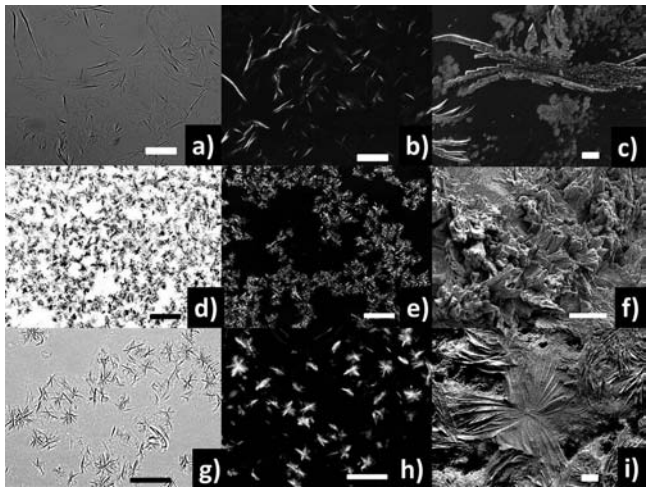

Figure 4. Optical microscopy (under normal and polarized light) and cryo-SEM images of gels of (a–c) SFW; (d–f) CRW; and (g–i) BZW. Scale bars = 50 μm (a, b, d, and e); 20 μm (g and h); 10 μm (c and f); and 1 μm (i).

main components responsible for excellent gelation behavior of most natural waxes.[14,15,25] Interestingly, in recently published work by Blake and Marangoni,[43] they have concluded based on cryo-SEM imaging that the morphology of SFW (along with other waxes such as CLW and rice bran wax) was "platelet-like", contrary to the observed morphology in the current work. In the case of CRW, the three-dimensional crystals of less than 10 μm in size are seen stacked closely together into larger aggregates (50–100 μm), and thus, a relatively higher crystalline mass fraction is required for gelation because the network formation is expected to be a result of the overlapping of spherical volumes of these aggregates. For waxes with *mmc*, both CLW and BZW gels showed similar frequency dependence, but the gel formed by BZW was comparatively more brittle and showed breakdown and yielding at lower stress values. The crystal morphology in the BZW gel was quite different from other waxes, showing a distinct "sea urchin"-like morphology (Figure 4i). Formation of such interestingly organized structures has been explained through crystal design and engineering and is attributed to a two-stage crystallization process initiated by a three-dimensional spherulite formation at the nucleation center followed by the organization of needle-like crystals in the outer layer, resulting in a radially oriented growth.[44,45] Such structures are also easily identifiable when viewed under an optical microscope (Figure 4g and h).

The yielding-type behavior with a strong shear thinning nature of all the gels is evident from the curves of apparent viscosity (η_{app}) versus shear rate ($\dot{\gamma}$) as shown in Figure 5b. Flow parameters such as apparent yield stress ($_{app}\tau_y$) and flow index (n) were calculated by fitting the data to a three-parameter model (Hershel Bulkley, eq 1).

$$\tau = {}_{app}\tau_y + K\dot{\gamma}^n \quad (1)$$

where K = consistency coefficient and $\dot{\gamma}$ = shear rate.

The Hershel Bulkley model is one of the most commonly used models for characterizing materials that display non-Newtonian behavior after yielding, and the value of n can be used as a measure to define the degree of shear thinning (n < 1) or shear thickening (n > 1) of the material. All the gel samples showed a prominent shear thinning flow behavior (n < 1), but the degree of shear thinning was highest for CRW gels, which

DOI: 10.1021/acs.jafc.5b01548
J. Agric. Food Chem. 2015, 63, 4862–4869

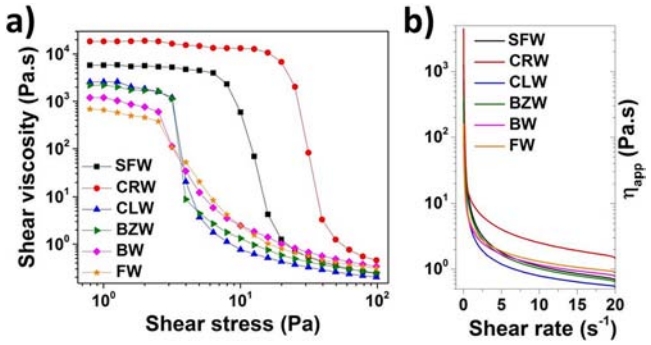

Figure 5. (a) Data from stress ramp shown as shear viscosity versus shear stress and (b) apparent viscosity (η_{app}) versus shear rate.

incidentally also had the highest ${}_{app}\tau_y$ (Table S2). In addition, the CRW gel also showed the highest static yield stress (τ_{sy}) determined from the plots of the stress ramp (Figure 5a). The τ_{sy} measured using methods such as stress ramp and stress growth is defined as the minimum stress required for initiating flow, whereas the ${}_{app}\tau_y$ determined by model fitting is defined as the minimum stress required for maintaining flow and is often lower in values than the former.[37,46,47] The τ_{sy} and ${}_{app}\tau_y$ for all the gels were close to each other except for the CRW gel, where the τ_{sy} was almost 3 times larger than ${}_{app}\tau_y$. Such a big difference in stresses required for initiating and maintaining flow is taken as an indication of the existence of more than one structure that makes up the body of a material.[37,47] One of these structures is built up only during rest and can undergo breakdown under relatively lower shear, while a more robust structure that can withstand moderate shear rates contributes to the ${}_{app}\tau_y$.[46,47] Since τ_{sy} is a consequence of combined structures, it is expected to be higher than ${}_{app}\tau_y$. The high zero-shear viscosity of CRW gel (Figure 5b) confirms that the network structure is built up by overlapping spherical volumes of large aggregates, and a strong shear thinning behavior is a consequence of the disruption of aggregate clusters into smaller ones, which is driven by the mechanical energy. It is also important to note that although the yield stress values of these gels are rather low, they are still appreciably high to prevent gravitational settling of the particle network that structures the gels,[32] which was also confirmed from the absence of any phase separation in our samples stored for more than a month at 5 °C. Moreover, the stored samples were also periodically tested using oscillatory rheological measurements to evaluate any structure changes over 4 weeks of storage, and the results (Figure S4) confirm the stability of these gels.

Thixotropy has been defined in different ways by different authors over the years. While some authors refer to thixotropy simply as a time-dependent decrease in viscosity at a constant shear rate, other authors also include the reversible and gradual recovery of the consistency (which was lost on shearing) when the stress or shear rate is removed.[48−50] The term "gradual" when understood in terms of "finite time" required for structure recovery, makes the definition of thixotropy complete by enabling the inclusion of shear-thinning materials that show a rapid recovery (near zero time of recovery), which were previously known by the term "structural viscosity".[50] The word "reversible" could mean both a complete recovery (viscosity attains the original values or almost close to the original values on removal of shear) or a less desirable, partial recovery (flow-induced irreversible structural changes leading to an irreversible loss in viscosity on removal of shear). Thus, the thixotropic behavior is best studied by tracking the material response resulting from stepwise changes in shear rate, as the coupled effect of time and shear rate can be clearly separated in such experiments.[51,52] A specific rheological test that is utilized to measure thixotropy is known as 3-ITT; it consists of three consecutive steps in control rate mode with alternating low and high shear rates.[36] The fraction of η_{app} recovered in the third step or interval gives a measure of thixotropic recovery of the material.[22,53] The plots from 3-ITT done on organogels are shown in Figure S5. The thixotropic recovery for the gels were as follows: SFW (43.52%), CRW gel (15.84%), CLW (58.64%), BZW (67.34%), BW (80.77%), FW (56.52%). The CRW gel showed the least thixotropic recovery among the studied gels in spite of having a comparatively highest viscosity at rest as well as the highest τ_{sy} and ${}_{app}\tau_y$. Such behavior is usually associated with brittle gels that display a high gel strength and a narrow LVR as well as yield zone. However, from the results discussed in Figure 3, the CRW gel did not show a "brittle-type" failure, as confirmed from a broader yield zone, which indicates that the bonding in the network of crystalline particles is more heterogeneous, leading to a nonuniformity in bonding strength and consequent "ductile-type" failure.[54] This nonuniformity in the bonding strength is also evident from almost a 3-fold difference between τ_{sy} (~20.06 Pa) and ${}_{app}\tau_y$ (6.99 Pa), which basically tells us that 3 times higher force is required to initiate the flow compared to maintaining flow. The network structure in CRW can thus be assumed to be a random agglomeration of aggregated crystalline particles, and the local bonding strength among the aggregates may be stronger in certain regions compared to other regions due to localized crowding of aggregates. As the gel is sheared, with time, the structure breaks down into smaller clusters of aggregates that can contribute to the viscosity enhancement of the solvent, but the restructuring of these clusters into a coherent network is avoided because the Brownian motion is overcome by shear forces. In contrast, BW and BZW gels showed a reasonable thixotropic recovery (80.77% and 67.34%, respectively). From the microstructure studies, these two gels show spherical-type building units that are connected together into a network by a weak yet more uniform type of bonding (homogeneous bonding strength), and thus, all bonds can be broken down at the same applied force (supported well by narrow yield zone seen for these samples), resulting in a flow-induced structure breakdown that is non-time-dependent (linear curves in first and third interval of 3ITT, Figure S5). To further understand the structure of the sheared sample, mixed flow-oscillatory measurements were carried out on samples by first subjecting them to increasing shear rates from 0.01 to 20 s^{-1} followed by frequency sweeps (0.01−10 Hz or 0.06−62.8 $rads^{-1}$). The graphs of shear moduli plotted as a function of angular frequency are shown in Figure 6. As seen from the figure, the quick recovery from flow-induced structure breakdown was seen only in BW and BZW samples ($G' > G''$ at ω_0 = 0.06 rad s^{-1}), while the rest of the gels showed liquid-like behavior at low frequency. CRW gels, on the other hand, showed complete liquification, with a viscous component dominating over the entire frequency range. On comparing these curves with results from frequency sweeps done on unsheared samples, it can be seen that, out of the six waxes studied in this work, CRW showed a maximum loss of structure (G' values showing more than 100-fold reduction after the flow step), while BW showed the least structure loss

DOI: 10.1021/acs.jafc.5b01548
J. Agric. Food Chem. 2015, 63, 4862−4869

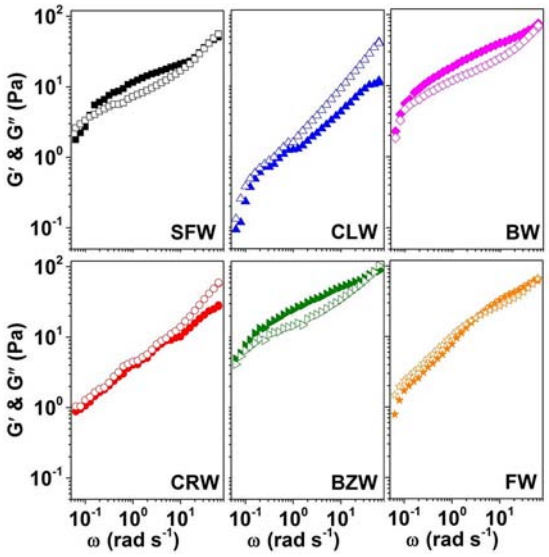

Figure 6. Data from frequency sweeps (from the flow-frequency tests) done on samples that were subjected to the flow test.

(G' values showing close to 2-fold reduction after the flow step), which is in agreement with 3ITT results.

To conclude, the rheological behavior of wax-based physical gels can be assumed to have characteristics of a flocculated suspension (at low volume fractions of colloidal particles) as well as a semidilute polymer solution. At a certain concentration, C_g (analogous to C^* in the case of a semidilute polymer solution), a 3D network or agglomeration of aggregated crystalline particles is created to form a viscoelastic gel, which might show "ductile-type" or "brittle-type" deformation under applied shear depending on the uniformity of bonding strength connecting the aggregated particles (as seen in a flocculated suspension). The C_g and the rheological behavior are strongly influenced by the morphology of the primary crystalline particles as well as the subsequent aggregation of these primary particles, which, in turn, depends on the chemical components present in waxes. The waxes studied in this work are of natural origins, and thus, they can be used for potential applications in biorelated fields such as food, pharmaceutical, and cosmetics industries.[55] For instance, the gelling of edible oils at such low concentrations of waxes can be exploited in the formulation of food products with low saturated fat content. The information obtained through this work will help us in setting criteria for selecting waxes. For instance, it is not the melting range but the relative proportion of individual chemical constituents that determines the rheological properties of obtained gels. However, since these gels are rather "weak" in nature with high shear sensitivity and low thixotropic recovery, incorporation of high-melting fats will be necessary to obtain structured oil systems (i.e., hybrid systems) with desired properties for actual food applications.[56]

■ ASSOCIATED CONTENT

Supporting Information

Chemical composition of waxes (Table S1); flow parameters of gels (Table S2); photograph of organogels (Figure S1); chemical structures of main wax components (Figure S2); plots of temperature ramps (Figure S3); graph of tan δ at v = 1 Hz measured at periodic intervals for all gels over a storage period of 1 month (Figure S4); and data from 3 ITT (Figure S5). The Supporting Information is available free of charge on the ACS Publications website at DOI: 10.1021/acs.jafc.5b01548.

■ AUTHOR INFORMATION

Corresponding Author

*Tel: +32 (0) 9 264 6209. Fax: +32 (0) 9 264 6218. E-mail: Patel.Ashok@Ugent.be.

Funding

This research is supported by the Marie Curie Career Integration Grant (Project: SAT-FAT-FREE) within the 7th European Community Framework Programme. The Hercules Foundation is acknowledged for its financial support in the acquisition of the JEOL JSM-7100F scanning electron microscope equipped with a Quorum PP3000T cryo-transfer system and Oxford Instruments Aztec EDS (grant number AUGE-09-029).

Notes

The authors declare no competing financial interest.

■ REFERENCES

(1) Terech, P.; Weiss, R. G. Low molecular mass gelators of organic liquids and the properties of their gels. *Chem. Rev.* **1997**, *97*, 3133−3160.

(2) Weiss, R. G. The past, present, and future of molecular gels. What is the status of the field, and where is it going? *J. Am. Chem. Soc.* **2014**, *136*, 7519−7530.

(3) Terech, P.; Pasquier, D.; Bordas, V.; Rossat, C. Rheological properties and structural correlations in molecular organogels. *Langmuir* **2000**, *16*, 4485−4494.

(4) Bui, A.; Virgilio, N. Tuning organogel properties by controlling the organic-phase composition. *Ind. Eng. Chem. Res.* **2013**, *52*, 14185−14191.

(5) Wang, D.; Zhao, J.; Liu, X.; Sun, F.; Zhou, Y.; Teng, L.; Li, Y. Parenteral thermo-sensitive organogel for schizophrenia therapy, in vitro and in vivo evaluation. *Eur. J. Pharm. Sci.* **2014**, *60*, 40−48.

(6) Główka, E.; Wosicka-Frąckowiak, H.; Hyla, K.; Stefanowska, J.; Jastrzębska, K.; Klapiszewski, Ł.; Jesionowski, T.; Cal, K. Polymeric nanoparticles-embedded organogel for roxithromycin delivery to hair follicles. *Eur. J. Pharm. Biopharm.* **2014**, *88*, 75−84.

(7) Vintiloiu, A.; Leroux, J.-C. Organogels and their use in drug delivery - A review. *J. Controlled Release* **2008**, *125*, 179−192.

(8) Raut, S.; Bhadoriya, S. S.; Uplanchiwar, V.; Mishra, V.; Gahane, A.; Jain, S. K. Lecithin organogel: A unique micellar system for the delivery of bioactive agents in the treatment of skin aging. *Acta Pharm. Sin. B* **2012**, *2* (1), 8−15.

(9) Morales, M. E.; Gallardo, V.; Clarés, B.; García, M. B.; Ruiz, M. A. Study and description of hydrogels and organogels as vehicles for cosmetic active ingredients. *Int. J. Cosmet. Sci.* **2010**, *32* (4), 314−314.

(10) Puigmartí-Luis, J.; Laukhin, V.; Pérez del Pino, Á.; Vidal-Gancedo, J.; Rovira, C.; Laukhina, E.; Amabilino, D. B. Supramolecular conducting nanowires from organogels. *Angew. Chem., Int. Ed.* **2007**, *46* (1−2), 238−241.

(11) Hughes, N. E.; Marangoni, A. G.; Wright, A. J.; Rogers, M. A.; Rush, J. W. E. Potential food applications of edible oil organogels. *Trends Food Sci. Technol.* **2009**, *20* (10), 470−480.

(12) Pernetti, M.; van Malssen, K. F.; Flöter, E.; Bot, A. Structuring of edible oils by alternatives to crystalline fat. *Curr. Opin. Colloid Interface Sci.* **2007**, *12* (4−5), 221−231.

(13) Marangoni, A. G.; Garti, N. *Edible Oleogels: Structure and Health Implications*; AOCS Press: Urbana, IL, 2011.

(14) Blake, A.; Co, E.; Marangoni, A. Structure and physical properties of plant wax crystal networks and their relationship to oil binding capacity. *J. Am. Oil Chem. Soc.* **2014**, *91* (6), 885−903.

DOI: 10.1021/acs.jafc.5b01548
J. Agric. Food Chem. 2015, 63, 4862−4869

(15) Hwang, H.-S.; Kim, S.; Singh, M.; Winkler-Moser, J.; Liu, S. Organogel formation of soybean oil with waxes. *J. Am. Oil Chem. Soc.* **2012**, *89* (4), 639−647.
(16) Toro-Vazquez, J. F.; Morales-Rueda, J.; Torres-Martínez, A.; Charó-Alonso, M. A.; Mallia, V. A.; Weiss, R. G. Cooling rate effects on the microstructure, solid content, and rheological properties of organogels of amides derived from stearic and (R)-12-hydroxystearic acid in vegetable oil. *Langmuir* **2013**, *29* (25), 7642−7654.
(17) Dassanayake, L. S. K.; Kodali, D. R.; Ueno, S. Formation of oleogels based on edible lipid materials. *Curr. Opin. Colloid Interface Sci.* **2011**, *16* (5), 432−439.
(18) Parish, E. J.; Shengrong, L.; Bell, A. D. Chemistry of waxes and sterols. In *Food Lipids: Chemistry, Nutirtion and Biotechnology*; Akoh, C. C., Min, D. B., Eds.; CRC Press: Boca Raton, FL, USA, 2000; pp 99−123.
(19) Patel, A. R.; Schatteman, D.; Vos, W. H. D.; Dewettinck, K. Shellac as a natural material to structure a liquid oil-based thermo reversible soft matter system. *RSC Adv.* **2013**, *3*, 5324−5327.
(20) Toro-Vazquez, J. F.; Morales-Rueda, J. A.; Dibildox-Alvarado, E.; Charó-Alonso, M.; Alonzo-Macias, M.; González-Chávez, M. M. Thermal and textural properties of organogels developed by candelilla wax in safflower oil. *J. Am. Oil Chem. Soc.* **2007**, *84*, 989−1000.
(21) Patel, A. R.; Rajarethinem, P. S.; Gredowska, A.; Turhan, O.; Lesaffer, A.; De Vos, W. H.; Van de Walle, D.; Dewettinck, K. Edible applications of shellac oleogels: spreads, chocolate paste and cakes. *Food Function* **2014**, *5*, 645−652.
(22) Patel, A. R.; Schatteman, D.; De Vos, W. H.; Lesaffer, A.; Dewettinck, K. Preparation and rheological characterization of shellac oleogels and oleogel-based emulsions. *J. Colloid Interface Sci.* **2013**, *411*, 114−121.
(23) Hwang, H.-S.; Singh, M.; Bakota, E.; Winkler-Moser, J.; Kim, S.; Liu, S. Margarine from organogels of plant wax and soybean oil. *J. Am. Oil Chem. Soc.* **2013**, *90*, 1705−1712.
(24) Jana, S.; Martini, S. Effect of high-Intensity ultrasound and cooling rate on the crystallization behavior of beeswax in edible oils. *J. Agric. Food Chem.* **2014**, *62*, 10192−10202.
(25) Dassanayake, L. S. K.; Kodali, D. R.; Ueno, S.; Sato, K. Crystallization kinetics of organogels prepared by rice bran wax and vegetable oils. *J. Oleo Sci.* **2012**, *61*, 1−9.
(26) Alvarez-Mitre, F. M.; Toro-Vázquez, J. F.; Moscosa-Santillán, M. Shear rate and cooling modeling for the study of candelilla wax organogels' rheological properties. *J. Food Eng.* **2013**, *119*, 611−618.
(27) Alvarez-Mitre, F. M.; Morales-Rueda, J. A.; Dibildox-Alvarado, E.; Charó-Alonso, M. A.; Toro-Vazquez, J. F. Shearing as a variable to engineer the rheology of candelilla wax organogels. *Food Res. Int.* **2012**, *49*, 580−587.
(28) Morales-Rueda, J.; Dibildox-Alvarado, E.; Charó-Alonso, M.; Toro-Vazquez, J. Rheological properties of candelilla wax and dotriacontane organogels measured with a true-gap system. *J. Am. Oil Chem. Soc.* **2009**, *86*, 765−772.
(29) Pieter, W. Fractal particle gels in foods. In *Supramolecular and Colloidal Structures in Biomaterials and Biosubstrates*; Lal, M., Lillford, P. J., Naik, V. M.., Prakash, V., Eds.; Imperal College Press and the Royal Society: London, UK, 2000; pp 157−173.
(30) Johansson, D. Weak gels of fat crystals in oils at low temperatures and their fractal nature. *J. Am. Oil Chem. Soc.* **1995**, *72*, 1235−1237.
(31) Visintin, R. F. G.; Lapasin, R.; Vignati, E.; D'Antona, P.; Lockhart, T. P. Rheological behavior and structural interpretation of waxy crude oil gels. *Langmuir* **2005**, *21*, 6240−6249.
(32) Emanuele, V.; Roberto, P.; Ruben, F. G. V.; Romano, L.; Paolo, D. A.; Thomas, P. L. Wax crystallization and aggregation in a model crude oil. *J. Phys.: Condens. Matter* **2005**, *17*, S3651.
(33) *Rheology: Concepts, Methods and Applications*; Chemtech Publishing: Toronto, Canada, 2006.
(34) Menard, K. P. *Dynamic Mechanical Analysis*; CRC Press: Boca Raton, FL, USA, 2008.
(35) Mewis, J.; Wagner, N. *Colloidal Suspension Rheology*; Cambridge University Press: Cambridge, UK, 2012.
(36) Mezger, T. G. *The Rheology Handbook: For Users of Rotational and Oscillatory Rheometers*; Vincentz Network GmbH & Co. KG: Hannover, Germany, 2006.
(37) Cheng, D. C. H. Yield stress: A time-dependent property and how to measure it. *Rheol. Acta* **1986**, *25*, 542−554.
(38) Wang, Y.; Tang, L.; Yu, J. Investigation of spontaneous transition from low-molecular-weight hydrogel into macroscopic crystals. *Cryst. Growth Des.* **2008**, *8*, 884−889.
(39) Houton, K. A.; Morris, K. L.; Chen, L.; Schmidtmann, M.; Jones, J. T. A.; Serpell, L. C.; Lloyd, G. O.; Adams, D. J. On crystal versus fiber formation in dipeptide hydrogelator systems. *Langmuir* **2012**, *28*, 9797−9806.
(40) Morris, K. L.; Chen, L.; Raeburn, J.; Sellick, O. R.; Cotanda, P.; Paul, A.; Griffiths, P. C.; King, S. M.; O'Reilly, R. K.; Serpell, L. C.; Adams, D. J. Chemically programmed self-sorting of gelator networks. *Nat. Commun.* **2013**, *4*, 1480.
(41) Gennes, P. G. D. *Scaling Concepts in Polymer Physics*; Cornell University Press: Ithaca, NY, 1979.
(42) Toro-Vazquez, J.; Morales-Rueda, J.; Mallia, V. A.; Weiss, R. Relationship between molecular structure and thermo-mechanical properties of candelilla wax and amides derived from (R)-12-hydroxystearic acid as gelators of safflower oil. *Food Biophys.* **2010**, *5*, 193−202.
(43) Blake, A. I.; Marangoni, A. G. Plant wax crystals display platelet-like morphology. *Food Struct.* **2015**, *3*, 30−34.
(44) Heijna, M. C. R.; Theelen, M. J.; van Enckevort, W. J. P.; Vlieg, E. Spherulitic growth of hen egg-white lysozyme crystals. *J. Phys. Chem. B* **2007**, *111*, 1567−1573.
(45) Ueno, S.; Nishida, T.; Sato, K. Synchrotron radiation microbeam X-ray analysis of microstructures and the polymorphic transformation of spherulite crystals of trilaurin. *Cryst. Growth Des.* **2008**, *8*, 751−754.
(46) Galindo-Rosales, F. J.; Rubio-Hernandez, F. J. Static and dynamic yield stresses of Aerosil® 200 suspensions in polypropylene glycol. *Appl. Rheol.* **2010**, *20*, 22787.
(47) Galindo-Rosales, F. J.; Rubio-Hernández, F. J.; Velázquez-Navarro, J. F.; Gómez-Merino, A. I. Structural level of silica-fumed aqueous suspensions. *J. Am. Ceram. Soc.* **2007**, *90*, 1641−1643.
(48) Mewis, J. Thixotropy - A general review. *J. Non-Newtonian Fluid Mech.* **1979**, *6*, 1−20.
(49) Mewis, J.; Wagner, N. J. Thixotropy. *Adv. Colloid Interface Sci.* **2009**, *147−148*, 214−227.
(50) Barnes, H. A. Thixotropy - A review. *J. Non-Newtonian Fluid Mech.* **1997**, *70*, 1−33.
(51) Weltmann, R. N. Breakdown of thixotropic structure as function of time. *J. Appl. Phys.* **1943**, *14*, 343−350.
(52) Coussot, P.; Nguyen, Q. D.; Huynh, H. T.; Bonn, D. Viscosity bifurcation in thixotropic, yielding fluids. *J. Rheol.* **2002**, *46*, 573−589.
(53) Patel, A. R.; Schatteman, D.; Lesaffer, A.; Dewettinck, K. A foam-templated approach for fabricating organogels using a water-soluble polymer. *RSC Adv.* **2013**, *3*, 22900−22903.
(54) Uhlherr, P. H. T.; Guo, J.; Tiu, C.; Zhang, X. M.; Zhou, J. Z. Q.; Fang, T. N. The shear-induced solid−liquid transition in yield stress materials with chemically different structures. *J. Non-Newtonian Fluid Mech.* **2005**, *125*, 101−119.
(55) Doan, C. D.; Van de Walle, D.; Dewettinck, K.; Patel, A. R. Evaluating the oil-gelling properties of natural waxes in rice bran oil: rheological, thermal, and microstructural study. *J. Am. Oil Chem. Soc.* **2015**, DOI: 10.1007/s11746-015-2645-0.
(56) Patel, A. R.; Dewettinck, K. Comparative evaluation of structured oil systems: shellac oleogel, HPMC oleogel and HIPE gel. *Eur. J. Lipid Sci. Technol.* **2015**, DOI: 10.1002/ejlt.201400553.

DOI: 10.1021/acs.jafc.5b01548
J. Agric. Food Chem. 2015, 63, 4862−4869

JOURNAL OF AGRICULTURAL AND FOOD CHEMISTRY

Article

pubs.acs.org/JAFC

Identification and Characterization of Terpene Synthases Potentially Involved in the Formation of Volatile Terpenes in Carrot (*Daucus carota* L.) Roots

Mosaab Yahyaa,[†] Dorothea Tholl,[‡] Guy Cormier,[§] Roderick Jensen,[§] Philipp W. Simon,[∥] and Mwafaq Ibdah*,[†]

[†]Newe Ya'ar Research Center, Agriculture Research Organization, Post Office Box 1021, Ramat Yishay 30095, Israel

[‡]Department of Biological Sciences, Virginia Polytechnic Institute and State University, 409 Latham Hall, 220 Agquad Lane, Blacksburg, Virginia 24061, United States

[§]Department of Biological Sciences, Virginia Polytechnic Institute and State University, 119 Life Sciences I, 970 Washington Street, Blacksburg, Virginia 24061, United States

[∥]Vegetable Crops Research Unit, Department of Horticulture, University of Wisconsin—Madison, 1575 Linden Drive, Madison, Wisconsin 53706, United States

Supporting Information

ABSTRACT: Plants produce an excess of volatile organic compounds, which are important in determining the quality and nutraceutical properties of fruit and root crops, including the taste and aroma of carrots (*Daucus carota* L.). A combined chemical, biochemical, and molecular study was conducted to evaluate the differential accumulation of volatile terpenes in a diverse collection of fresh carrots (*D. carota* L.). Here, we report on a transcriptome-based identification and functional characterization of two carrot terpene synthases, the sesquiterpene synthase, *Dc*TPS1, and the monoterpene synthase, *Dc*TPS2. Recombinant *Dc*TPS1 protein produces mainly (*E*)-β-caryophyllene, the predominant sesquiterpene in carrot roots, and α-humulene, while recombinant *Dc*TPS2 functions as a monoterpene synthase with geraniol as the main product. Both genes are differentially transcribed in different cultivars and during carrot root development. Our results suggest a role for *DcTPS* genes in carrot aroma biosynthesis.

KEYWORDS: *Daucus carota, terpenes, (E)-β-caryophyllene, geraniol, terpene synthase*

INTRODUCTION

Carrots (*Daucus carota* L.) are popular vegetables because of their health benefits and characteristic flavor.[1,2] Carrot quality is determined by several traits that affect taste, aroma, and nutritional value.[3] In particular, terpene secondary metabolites, which are synthesized during carrot root development, have a direct effect on root quality and flavor.

Terpenes constitute the largest class of plant secondary metabolites, represent major components of floral scents and essential oils of herbs,[4] and are important in determining the quality and nutraceutical properties of horticultural food products, including the taste and aroma of wine and melon.[5,6] Plants produce terpenoids that function in primary metabolism, such as phytohormones (absisic acid, gibberellins, and brassinosteroids), and are part of photosynthetic pigments (phytol and carotenoids).[7] Terpenes can serve as phytoalexins in defense against plant pathogens[8] or direct defense against herbivores.[9] In addition, volatile terpenoids can function as indirect defensive compounds by attracting predators or parasitoids of the attracting insect.[10]

All plant terpenes are made from the 5-carbon precursor, isopentenyl diphosphate (IPP), and its isomer, dimethylallyl diphosphate (DMAPP), both of which are derived from two alternative pathways, the mevalonate (MVA) pathway in the cytosol or the methylerythritol phosphate (MEP) pathway in plastids. Condensation of the C_5 precursors leads to the formation of C_{10}, C_{15}, and C_{20} *trans*- or *cis*-prenyl diphosphate intermediates, such as geranyl diphosphate (GPP), neryl diphosphate (NPP), *trans,trans*-farnesyl diphosphate or *cis,cis*-farnesyl diphosphate [(*E,E*)-FPP or (*Z,Z*)-FPP], and all-*trans*-geranylgeranyl diphosphate (GGPP) that are converted into monoterpenes (C_{10}), sesquiterpenes (C_{15}), and diterpenes (C_{20}), respectively, by the activity of terpene synthase (TPS) enzymes.[11] GGPP also functions as a precursor in the carotenoid biosynthetic pathway by condensation of two GGPP units to C_{40}-phytoene.[12] TPSs are the primary enzymes in the formation of low-molecular-weight terpene metabolites. To date, TPSs have been identified and characterized in many species,[13,14] including *Arabidopsis thaliana*,[15] *Cucumis melo* L.,[6] *Gossypium hirsutum* L.,[16] *Solanum lycopersicum*,[17] *Vitis vinifera* L.,[18] *Coriandrum sativum*,[19] and *Thapsia garganica*. TPSs are encoded by large gene families and have the ability to produce multiple terpene products from a single substrate. The formation of mixtures of structurally diverse compounds contributes to the specific aroma and flavor characteristics of

Received: January 29, 2015
Revised: April 13, 2015
Accepted: April 30, 2015
Published: April 30, 2015

ACS Publications © 2015 American Chemical Society

DOI: 10.1021/acs.jafc.5b00546
J. Agric. Food Chem. 2015, 63, 4870−4878

Table 1. Quantification of of Mono- and Sesquiterpene Volatile Compounds in Different Raw Colored Carrot Varieties at 10 Weeks after Sowing[a]

compounds	level of mono- and sesquiterpene volatile compounds [ng/g of fresh weight (FW)]					IC[b]
	Nairobi	Rothild	Purple Haze	Yellowstone	Crème de Lite	
α-pinene	110.72 ± 0.74	214.22 ± 1.25	227.15 ± 1.63	110.93 ± 0.97	89.55 ± 0.27	RI, MS, STD
camphene	17.26 ± 0.25	22.91 ± 0.25	27.00 ± 0.19	12.44 ± 0.28	17.02 ± 0.23	RI, MS, STD
sabinene	16.56 ± 0.16	348.87 ± 0.67	30.67 ± 0.28	604.89 ± 1.51	168.92 ± 1.58	RI, MS, STD
β-pinene	60.51 ± 0.63	100.50 ± 0.94	182.31 ± 1.44	181.36 ± 0.94	57.83 ± 0.45	RI, MS, STD
β-myrcene	168.21 ± 0.51	688.81 ± 1.02	219.81 ± 0.45	440.44 ± 0.94	233.10 ± 1.1	RI, MS, STD
α-phellandrene	47.18 ± 0.20	47.44 ± 0.31	22.39 ± 0.29	71.69 ± 0.20	26.98 ± 0.433	RI, MS, STD
α-terpinene	35.51 ± 0.55	129.32 ± 0.12	21.75 ± 0.16	223.01 ± 0.61	63.21 ± 0.75	RI, MS,STD
p-cymene	194.21 ± 0.97	186.31 ± 0.73	156.70 ± 1.01	109.27 ± 0.47	85.73 ± 0.87	RI, MS, STD
limonene	68.85 ± 0.55	99.17 ± 0.52	47.21 ± 0.44	82.02 ± 0.29	55.55 ± 0.846	RI, MS, STD
Z-β-ocimene	35.12 ± 0.33	28.49 ± 0.22	35.38 ± 0.05	49.33 ± 0.31	18.91 ± 0.12	RI, MS, STD
E-β-ocimene	9.81 ± 0.26	15.98 ± 0.42	8.46 ± 0.24	26.00 ± 0.42	6.77 ± 0.28	RI, MS, STD
γ-terpinene	348.11 ± 1.32	496.98 ± 0.76	417.69 ± 1.31	361.53 ± 1.38	160.71 ± 0.77	RI, MS, STD
terpinolene	566.80 ± 1.23	516.53 ± 0.9	80 ± 0.16	744.23 ± 0.65	304.92 ± 0.99	RI, MS, STD
borneol	1.72 ± 0.12	1.38 ± 0.05	T	1.88 ± 0.05	2.42 ± 0.07	RI, MS, STD
geraniol	0.78 ± 0.17	5.10 ± 0.39	T	6.28 ± 0.89	1.88 ± 0.02	RI, MS, STD
thymol	3.12 ± 0.25	T	T	5.98 ± 0.29	T	RI, MS, STD
β-elemene	T	8.18 ± 1.3	T	2.51 ± 0.22	T	RI, MS, STD
β-caryophyllene	622.66 ± 2.85	696.40 ± 1.08	993.55 ± 0.75	412.84 ± 1.09	1048.32 ± 0.93	RI, MS, STD
α-humulene	66.80 ± 0.76	83.71 ± 0.64	103.30 ± 1.24	88.07 ± 0.18	124.47 ± 0.55	RI, MS, STD

[a]Volatile terpenes were measured by auto-HS−SPME−GC−MS. T = traces. The results shown are an average of three biological replicates. [b]IC = identification criteria. The identification criteria were based on mass spectra matching with the standard NIST-98.L and Wiley 7N.I libraries (MS), comparison of the retention index (RI), and comparison to the authentic standard (STD).

plant tissues.[17] Transcriptional regulation plays an important role in controlling volatile organic compound biosynthesis, but it is not the only mechanism involved. While little is known about post-transcriptional regulation of volatile organic compound formation, recent comprehensive reviews provide a thorough discussion of the regulation of the MVA and MEP pathways.[7,20] Recently, it has been reported that the progressive biosynthesis of (*E*)-β-caryophyllene in *Arabidopsis* inflorescence after flowering is regulated by miR156-targeted SQUAMOSA promoter binding protein-like (SPL), which directly activates TPS21 expression.[21]

Carrots produce a large number of different mono- and sesquiterpene volatiles in leaf and root tissues.[22] In carrot roots, terpenes are more abundant in mature tissues and primarily synthesized in an interconnected network of oil ducts located in the phloem.[23] Labeling experiments with stable isotope precursors also indicated *de novo* biosynthesis of terpenes in the xylem.[24]

Despite the characterization of a large number of plant TPSs, surprisingly, no carrot TPSs have been described to date. Here, we report on the isolation and functional characterization of two carrot terpene synthase genes, *Daucus carota* terpene synthase 1 (*DcTPS1*) and *D. carota* terpene synthase 2 (*DcTPS2*), whose encoded enzymes catalyze the formation of the sesquiterpene, (*E*)-β-caryophyllene, and the monoterpene alcohol, geraniol, respectively. We show that *DcTPS1* is expressed in all five cultivars investigated in this study and is most likely associated with the production of high amounts of (*E*)-β-caryophyllene in these cultivars. *DcTPS1* gene transcript levels peak at week 12 post-germination in correlation with highest concentrations of terpene compounds at this developmental stage.

MATERIALS AND METHODS

Chemicals. Unlabeled FPP and GPP (1 mg/mL), terpene standards, other chemicals, and reagents were purchased from Sigma-Aldrich, unless noted otherwise.

Plant Material. Commercial colored carrot cultivars, orange "Nairobi", orange "Rothild", purple "Purple Haze", yellow "Yellowstone", and white "Crème de Lite" (Kiepenkerl Profi-Line, www.kiepenkerl.com), were grown in the "Newe Ya'ar" Research Center in northern Israel, under standard field irrigation and fertigation conditions. Freshly harvested 9−12-week-old carrot roots were crushed in liquid nitrogen and stored at −80 °C for terpene and transcript analysis.

Statistical Analysis. Amounts of terpenes are presented as means ± standard error (SE). Chemical terpene data were analyzed by multivariate data analysis [principle component analysis (PCA)] using the JMP software (SAS Institute, Inc.).

Extraction of Volatile Compounds from Fresh Carrot Roots. Three replicates of fresh 10-week-old root carrots (1 g) of each cultivar were ground into a uniform powder under liquid nitrogen with a mortar and pestle. The fine powder was placed in a 20 mL DuPont autosampler vial (DuPont Performance Elastomers, http://www.dupontelastomers.com) with a white solid-top polypropylene cap (Alltech, http://www.alltech.com). Samples were overlaid with 5 mL of NaCl (25%) solution and 1 g of NaCl (for inhibition of enzyme activity). Each sample was supplemented with 1 mg/kg [1 part per million (ppm)] of 2-heptenone as an internal standard. Samples were incubated at room temperature (25 °C) for 1 h, and thereafter, volatile compounds were collected with a solid-phase microextraction (SPME) device PDMS-100 with a polydimethylsiloxane fiber (Supelco, http://www.sigmaaldrich.com) by inserting the fiber into the tube and leaving it in place for 20 min at room temperature. After this incubation step, the SPME fiber was injected directly into gas chromatography−mass spectrometry (GC−MS).

Auto-Head Space (HS)−SPME−GC−MS Analysis of Carrot Root Volatile Compounds. Volatile compounds were analyzed on a GC−MS apparatus (Agilent Technologies, Santa Clara, CA) equipped with an Rtx-5SIL MS (30 m × 0.25 mm × 0.25 μm) fused-silica capillary column. He (1 mL min^{-1}) was used as a carrier gas. The

DOI: 10.1021/acs.jafc.5b00546
J. Agric. Food Chem. 2015, 63, 4870−4878

injector temperature was 250 °C, set for splitless injection. The oven was set to 50 °C for 1 min, and then the temperature was increased to 220 °C at a rate of 5 °C min^{-1}. For SPME analysis, thermal desorption was allowed for 40 min. The detector temperature was 280 °C. The mass range was recorded from m/z 41 to 450, with an electron energy of 70 eV. Identification of the main components was performed by comparison of mass spectra and retention times to those of authentic standards and supplemented with a Wiley GC−MS library. Quantification of absolute amounts was performed for (*E*)-*β*-caryophyllene, *α*-humulene, and the monoterpenes listed in Table 1 by comparing their retention time and mass spectra to those of authentic standards.

For the construction of the calibration curves, a mixture of straight-chain alkanes (C_7−C_{23}) was run under the above-mentioned conditions to determine retention indices. The amount of each compound in the sample was calculated as (peak area × internal standard response factor) divided by (response factor × internal standard peak area).[25] For compounds for which no standards were available, only normalized peak areas are shown. Total terpene levels were based on normalized peak areas of all compounds.

Isolation and Characterization of Carrot Terpene Synthases. Putative carrot *TPS* encoding genes were identified using Blastx to compare known *TPS* genes in *Arabidopsis* (*At2g24210* and *At5g23960*) to the *de novo* assembled RNA-Seq carrot transcriptome contigs from Iorizzo et al.[26] The expression levels of these candidate genes in the purple (B7262) cultivar and an orange cultivar (B6274) were estimated by mapping the Illumina GAII reads for each sample from Iorizzo et al.,[26] (SRA accessions SRR187758−SRR187763) using the "Map to Reference" feature of the Geneious (BioMatters, Ltd.) alignment software.

Two specific primers corresponding to the 5′ and 3′ ends of the *DcTPS1* coding sequence (P1: 5′-ATG TCT CTC AAT GTT CTG GC-3′) and (P2: 5′-TGA TGG AAC CCG ATC AAT GA-3′) were designed. *DcTPS2* was obtained using the forward primer P3 (5′-ATG GCC CTC CCA GCT CTG TTT T-3′) and the reverse primer P4 (5′-CTG GCT AAG AGT AAA GGG TTC GAC C-3′).

RNA from carrot roots of all colored cultivar was isolated using the Spectrum Plant Total RNA Kit (Sigma-Aldrich). To produce a cDNA clone, 5 *μ*g of total RNA from the Nairobi (orange) cultivar was reverse-transcribed using the SuperScript one-step reverse transcriptase polymerase chain reaction (RT-PCR). The DNA molecule was then amplified using Platinum *Taq* DNA polymerase (Invitrogen), yielding a 1683 bp specific fragment for *DcTPS1* and a 1782 pb fragment for *DcTPS2*, respectively. The cDNAs were ligated into the pEXP5-CT/TOPO TA expression vector (Invitrogen Corporation, Carlsbad, CA), producing pEXP-*DcTPS1*, and pEXP-*DcTPS2*, respectively, in which the *DcTPS1* and *DcTPS2* coding sequences were fused with a His-tag-coding extension at the C terminus and transformed into *Escherichia coli* TOP10 cells. The constructs were verified by DNA sequencing.

Preparation of Bacterial Lysates. A 3 mL preculture of *E. coli* BL21 (DE3) was grown overnight at 37 °C in lysogeny broth (LB) medium containing 100 g/mL ampicillin. The culture was used to inoculate 500 mL of fresh medium to which 500 *μ*M isopropyl-1-thio-*β*-D-galactopyranoside (IPTG) was added after 3 h to induce protein expression. Cells were further grown for 12 h at 30 °C. After centrifugation for 10 min at 11000*g*, the bacteria were resuspended in 50 mM Bis-Tris at pH 6.9, containing 10% (v/v) glycerol, 10 mM dithiothreitol (DTT), and 5 mM $Na_2S_2O_5$. Cells were lysed by a combination of a 30 min lysozyme treatment (1 mg/500 mL of culture) and subsequent ultrasonication (five pulses of 20 s at 20 W, at 4 °C). After the cells lysed, the suspensions were centrifuged (20000*g* for 30 min at 4 °C). The supernatant containing the soluble recombinant *Dc*TPS1 and *Dc*TPS2 proteins, respectively, were purified by metal (nickel) affinity chromatography (Qiagen, Valencia, CA) with a stepwise gradient of increasing imidazole concentrations using standard procedures. The *Dc*TPS1- and *Dc*TPS2-containing fractions were pooled and desalted with 50 mM Bis-Tris at pH 7.0 containing 10% (v/v) glycerol and 10 mM DTT, using Vivaspin 20 [GE Healthcare, molecular weight cutoff (MWCO) of 10 kDa]. Proteins were checked for purity by sodium dodecyl sulfate−polyacrylamide gel electrophoresis (SDS−PAGE). Protein concentrations were determined by the method of Bradford[27] using reagent obtained from Bio-Rad. Bovine serum albumin was used for calibration.

Assay for Terpene Synthase Activity. Enzyme activity assays were performed in screw-capped 2 mL GC glass vials, using 1 to 500 ng of purified recombinant proteins, 10 *μ*M substrate (GPP or FPP), 10 mM $MgCl_2$, 10 *μ*M $MnCl_2$, and 50 mM Bis-Tris at pH 7.0 assay buffer in a total volume of 100 *μ*L. The reactions were incubated for 30 min at 30 °C. After incubation, the samples were analyzed by auto-HS−SPME−GC−MS for the identification of volatile terpenes generated during the 30 °C incubation. As controls, *E. coli* cells transformed with control plasmids devoid of the *DcTPS1* and *DcTPS2* genes, and heat-inactivated DcTPS1 and DcTPS2 proteins or assays without GPP/FPP as a substrate were used.

***DcTPS* Transcript Analysis.** For quantitative RT-PCR (qRT-PCR) analysis of *DcTPS1* and *DcTPS2*, total RNA (5 *μ*g) from the orange carrot cultivar Nairobi was extracted (Spectrum Plant Total RNA Kit, Sigma-Aldrich) and reverse-transcribed using an oligo-dT primer and the SuperScript II first-strand system (Invitrogen).

qRT-PCR was performed on an Applied Biosystems StepOnePlus real-time PCR system (Life Technologies) using ABsolute Blue qPCR SYBR Green ROX Mix (Tamar Laboratory Supplies, Ltd., Israel), 5 ng of reverse-translated total RNA, and 100 ng of each primers. Primers for *DcTPS1* were *DcTPS1*-qRT-F (5′- CCTCTACTGTGTTCCG-CAAATA-3′) and *DcTPS1*-qRT-R (5′-CTGAAGTGCTTCCTC-CAGTATC-3′), and primers for *DcTPS2* were *DcTPS2*-qRT-F (5′-AAAGATGACACAGCGGGTAAA-3′), and *DcTPS2*-qRT-R (5′-GCCTCTGAAACCGAAGAAAGA-3′). A relative quantification of gene expression was performed using the housekeeping gene tubulin from carrot as a reference gene. The primers used for tubulin were Tubulin_F_qPCR (5′-TCTTGGAGGTGGCACAGGAT-3′) and Tubulin_R_qPCR (5′-ACCTTAGGAGACGGGAACACAGA-3′).

The difference in relative expression levels of *DcTPS1* and *DcTPS2* were calculated from the $2^{-\Delta\Delta C_t}$ value after normalization of *DcTPS1* and *DcTPS2* data to tubulin. All analyses were performed using at least three biological replicates.

RESULTS AND DISCUSSION

Terpene Profiles in Colored Carrot Cultivars. We previously demonstrated that variation in norisoprenoid accumulation in different colored carrot cultivars is genotype-dependent.[2] Also, variation in the total content of carrot terpenes has been reported.[28−31] However, to the best of our knowledge, the role of TPSs in the formation of mono- and sesquiterpene volatiles and their flavor properties in carrots has not been reported. Our primary goal is to decipher the role of individual TPSs in terpene flavor variation in different carrot cultivars. To this end, we first examined the volatile compound composition of freshly harvested (10 week old) tissue of five colored cultivars (orange "Nairobi", orange "Rothild", purple "Purple Haze", yellow "Yellowstone", and white "Crème de Lite") using SPME−GC−MS. More than 41 volatile compounds were detected, among which 23 were identified or predicted to be monoterpenes and 17 were found or predicted to be sesquiterpenes (Table 1 and Supplemental Table 1 of the Supporting Information). The orange carrot cultivar, Rothild, accumulated the highest levels of total volatile compounds, and the yellow carrot cultivar, Yellowstone, accumulated the lowest level of total terpenes (see Supplemental Table 1 of the Supporting Information). Our analyses unveiled the presence of different terpenes in carrot roots according to the variety analyzed (Table 1 and Supplemental Table 1 of the Supporting Information). The main sesquiterpene compounds found in all cultivars were (*E*)-*β*-caryophyllene, (*E*)-*γ*-bisabolene, and *α*-humulene, and the main monoterpenes were terpinolene, *γ*-

DOI: 10.1021/acs.jafc.5b00546
J. Agric. Food Chem. 2015, 63, 4870−4878

terpinene, myrcene, *p*-cymene, and *α*-pinene (Table 1 and Supplemental Table 1 of the Supporting Information).

To determine whether the terpene volatile compositions in carrot cultivars of diverse color are influenced by the genotypes, PCA was applied. The results are visualized by mean values and as bi-plot (PC1 versus PC2) (Figure 1), showing the first two

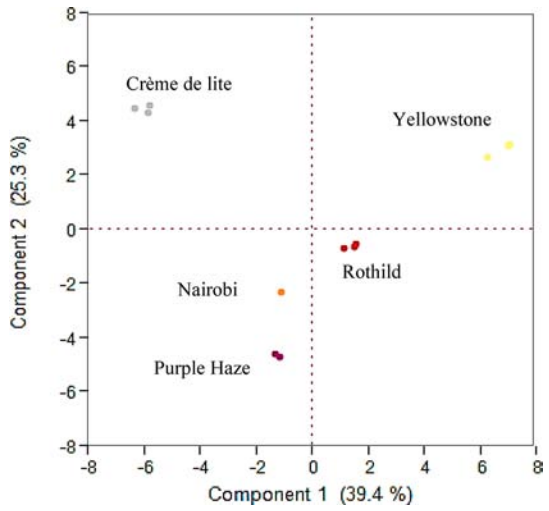

Figure 1. PCA analysis of 41 volatile compounds in five different colored carrot cultivars: orange "Nairobi", orange "Rothild", purple "Purple Haze", yellow "Yellowstone", and white "Crème de Lite". All analyses were performed using three biological replicates.

PCs to explain 64% of the variation. A large proportion of the variation in the terpene volatiles is found in PC1 (39.4%), whereas PC2 (25.3%) mainly explains a chemical variation in the terpene content. Our analysis showed that mono- and sesquiterpene profiles varied widely among different genetic stocks (Figure 1). These findings of genotypic differences are supported by other previous analyses of diverse carrot varieties.[28−31]

Analysis of Terpene Levels during Carrot Root Development. To better understand the pattern of terpene accumulation during carrot root development, we determined the total terpene content of the orange carrot cultivar Nairobi between 9 and 12 weeks after sowing (Figure 2). This time period of root maturation overlaps with the time of harvest 10−14 weeks post-seeding.[32]

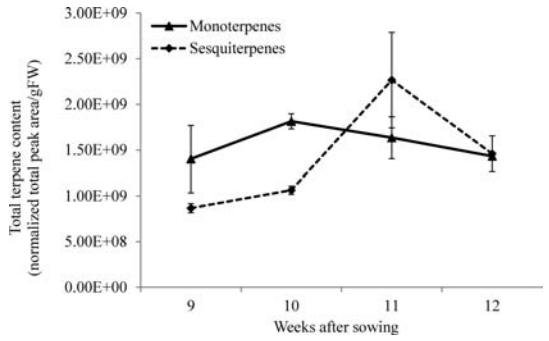

Figure 2. Terpene volatile accumulation during carrot root development in the orange cultivar Nairobi. The authenticity of mono- and sesquiterpenes was confirmed by comparing their retention time and mass spectra to those of authentic standards. Values are the mean ± standard error (n = 4).

Auto-HS−SPME−GC−MS analysis of total terpene volatile accumulation demonstrated that mono- and sesquiterpene concentrations consistently increased between the 9th and 11th week of carrot root development prior to a slight decrease in week 12 (Figure 2). The accumulation of sesquiterpenes was more rapid than that of monoterpenes between weeks 10 and 11. The reduced concentration observed after week 11 may be attributable to a period where root growth outpaced terpene accumulation. The composition of compounds during carrot root development further depends upon the different soils, climates, and genetic variability of the carrot cultivars.[32,33]

The chemical profile of terpenes found in carrot roots was first assessed to facilitate the design of PCR primers for the isolation of *TPS* genes catalyzing the biosynthesis of particular classes of terpenes. Interestingly, (*E*)-*β*-caryophyllene account as the main sesquiterpene compounds found in all cultivars (Table 1). A possible rationale would be to identify the TPSs that are responsible for producing the predominant terpene products in carrot roots. Therefore, two candidate *DcTPS1* and *DcTPS2* genes were chosen on the basis of sequence homology to other known plant TPSs for further characterization (see below).

Isolation and Functional Characterization of Carrot TPSs. Despite the characterization of a large number of plant TPSs, surprisingly no TPS enzymes or their encoding genes have been isolated and characterized from *D. carota*. Moreover, the role of TPSs in the formation of mono- and sesquiterpene volatiles and their flavor properties in carrots have not been reported. To identify the genes responsible for mono- and sesquiterpene volatile formation in carrot roots, we performed a homology search of RNA-Seq carrot transcriptome sequences, which had previously been obtained by Iorizzo et al.[26] Blastx searches of the assembled contigs in the "additional file 2" (1471-2164-12-389-S2.FASTA) from Iorizzo et al.,[26] against *TPS* genes in Genbank identified more than a dozen candidate *TPS* genes. At least six were full-length carrot *TPS* cDNAs, of which three are predicted to be monoterpene synthases and three may be sesquiterpene synthases (Table 2). The wide variation observed in the number of mapped reads for these genes in the purple (B7262) and orange (B6275) cultivars suggests substantial differences in gene expression between the two cultivars (Table 2).

Table 2. Detection of Carrot *TPS* Genes Based on *de Novo* Assembly of Illumina Sequences of Two Carrot Genotypes[26] [a]

	number of mapped reads per *TPS* contig		
carrot EST contig	cultivar B6274 (orange)	cultivar B7262 (purple)	predicted TPS function according to best Blast Match (Genbank) >50% amino acid
1324	1079	2160	monoterpene synthase
21245	2392	6925	monoterpene synthase
43814	3119	940	monoterpene synthase
4929	5726	304	sesquiterpene synthase
52846	1045	3478	sesquiterpene synthase
58617	602	598	sesquiterpene synthase
	total RNA-Seq reads per cultivar = 28363561	total RNA-Seq reads per cultivar = 33029462	

[a]Six contigs correspond to full-length *TPS*.

DOI: 10.1021/acs.jafc.5b00546
J. Agric. Food Chem. 2015, 63, 4870−4878

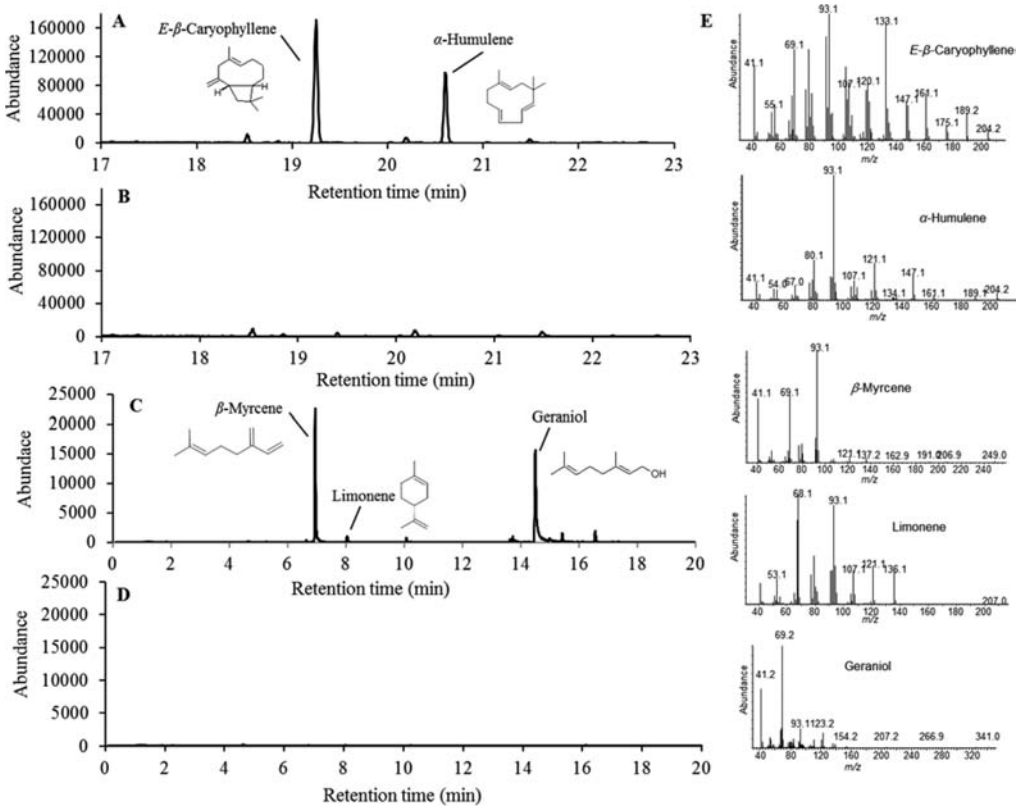

Figure 3. GC−MS of the products generated *in vitro* by nickel−nitrilotriacetic acid (Ni−NTA)-purified recombinant *Dc*TPS1 protein. (A) GC−MS analysis of *Dc*TPS1 with FPP as a substrate and measured by auto-HS−SPME−GC−MS. (B) GC−MS analysis of boiled *Dc*TPS1 with FPP as a substrate and measured by auto-HS−SPME−GC−MS. (C) GC−MS analysis of *Dc*TPS1 with GPP as a substrate and measured by auto-HS−SPME−GC−MS. (B) GC−MS analysis of boiled *Dc*TPS1 with GPP as a substrate. Identification of the products was performed by GC−MS comparing to authentic standards and according to the retention time and by mass spectral library comparison. (E) Mass spectra of enzymatic reaction products of *E*-*β*-caryophyllene, *α*-humulene, *β*-myrcene, limonene, and geraniol. *m*/*z* = mass-to-charge ratio. The inset shows the structure of the products *E*-*β*-caryophyllene, *α*-humulene, *β*-myrcene, limonene, and geraniol.

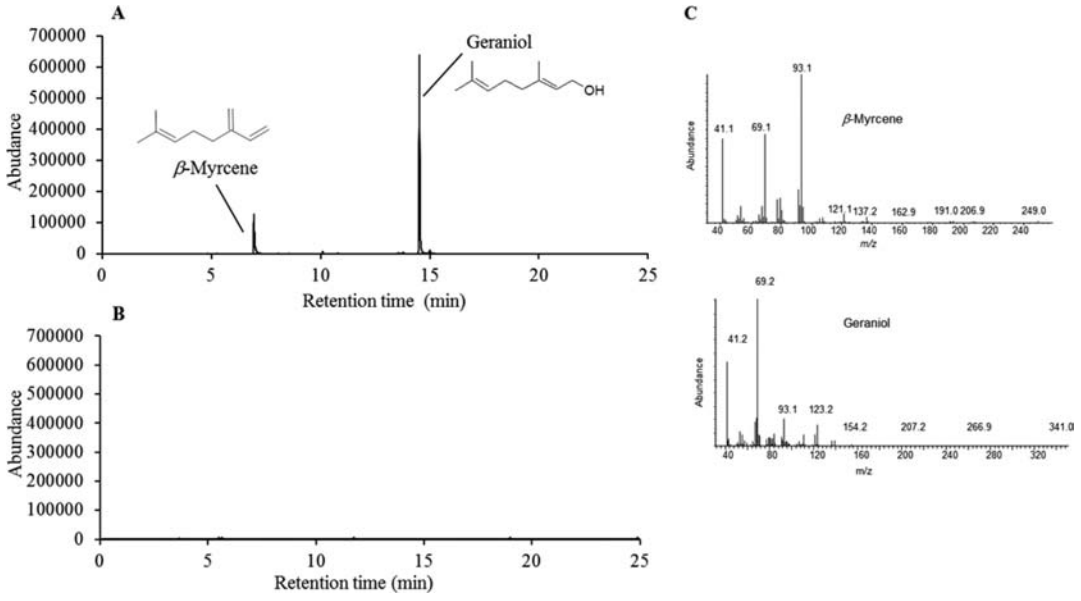

Figure 4. GC−MS of the products generated *in vitro* by Ni−NTA-purified recombinant *Dc*TPS2 protein. (A) GC−MS analysis of *Dc*TPS2 with GPP as a substrate and measured by auto-HS−SPME−GC−MS. (B) GC−MS analysis of boiled *Dc*TPS2 with GPP as a substrate and measured by auto-HS−SPME−GC−MS. Identification of the products was performed by GC−MS comparing to authentic standards and according to the retention time and by mass spectral library comparison. (C) Mass spectrum of enzymatic reaction products of *β*-myrcene and geraniol. *m*/*z* = mass-to-charge ratio. The inset shows the structure of the products *β*-myrcene and geraniol.

DOI: 10.1021/acs.jafc.5b00546
J. Agric. Food Chem. 2015, 63, 4870−4878

We then generated cDNAs for the *DcTPS* contig 4929 (called *DcTPS1* from here on) and *DcTPS* contig 43814 (called *DcTPS2* from here on) from RNA isolated from the orange cultivar Nairobi in our cultivar collection. Amino acid sequences encoded by *DcTPS1* and *DcTPS2* were 90% identical to those identified from the B7262 and B6274 cultivars. Recombinant *Dc*TPS1 protein expressed in *E. coli* converted (*E*,*E*)-FPP to (*E*)-β-caryophyllene, the predominant sesquiterpene in all cultivars (Table 1), as the primary product, along with α-humulene (Figure 3A). Incubation of *Dc*TPS1 with GPP led to the production of several monoterpenes, including β-myrcene, limonene, and geraniol (Figure 3C). *E. coli* cells transformed with control plasmids devoid of the *DcTPS1* gene, and heat-inactivated DcTPS1 protein or assays without GPP/FPP as a substrate were used as a control (panels B and D of Figure 3).

Our results confirm previous findings in other plants indicating that sesquiterpene synthases, e.g., β-caryophyllene synthase from *Artemisia annua*, produced monoterpenes[34] and 9-*epi*-caryophyllene from *Lavandula* × *interminda*,[35] and *trans*-α-bergamotene synthase from *Lavandula angustifolia*,[36] produced monoterpenes when assayed with GPP as a substrate. The mono- and sesquiterpenes formed by *Dc*TPS1 were found as constituents of the carrot volatile blend in all carrot cultivars (Table 1). However, it can be assumed that *Dc*TPS1 most likely functions as a sesquiterpene synthase *in vivo* because of the lack of a plastidial targeting sequence (Figures 3A and 7). TPS enzymes producing (*E*)-β-caryophyllene and α-humulene have been reported primarily from aboveground tissues of a variety of plants, where these sesquiterpenes are assumed to function in mutualistic interactions and in plant defense.[37,38] Functions of root-specific (*E*)-β-caryophyllene synthases have been less well-described, with the exception of a maize (*E*)-β-caryophyllene synthase that is involved in indirect defense against root herbivores.[39]

Analysis of reaction products formed after incubation of the *Dc*TPS2 protein with GPP showed the presence of two monoterpene compounds, geraniol and β-myrcene (Figure 4A). As control experiments, heat-inactivated DcTPS2 protein and *E. coli* cells transformed with control plasmids devoid of the *DcTPS2* gene or assays without GPP as a substrate were used (Figure 4B). Geraniol and β-myrcene are not actually the major monoterpenes accumulated. Besides terpinolene, some monoterpene hydrocarbons, e.g. *E*-β-ocimene, β-myrcene, and sabinene, are the major compounds in all carrot cultivars investigated in this study (Table 1 and Supplemental Table 1 of the Supporting Information).

Volatile mono- and sesquiterpenes have been reported to be synthetized and accumulated in roots and rhizomes of various plant species.[40,41] It has been reported that root-emitted volatile compounds can be involved in the plant defense by directly repelling herbivores or pathogens or recruiting enemies of their aggressors to limit or eliminate further damage.[42,43] Besides their ecological benefits to plants, terpene-specialized compounds are widely used by humans as flavors, fragrances, or pharmaceuticals.[6] However, terpene oils produced in carrot root tissues are assumed to contribute significantly to the aroma and flavor of carrots,[1,28,29] and they could also play interesting defensive roles in belowground biotic stress. The terpene products found for *Dc*TPS1 and *Dc*TPS2 represent only a fraction of the terpene constituents detected in carrot roots. Additional *TPS* gene transcript analysis, enzyme characterization, and subsequent targeted gene silencing will provide a better understanding of the individual or overlapping functions of root carrot *TPS* genes in terpene biosynthesis.

Cultivar-Specific and Developmental Expression Patterns of *DcTPS1* and *DcTPS2* Genes. To examine whether terpene volatile compound accumulation during carrot root development and differences in terpene composition between carrot cultivars could be related to the expression of terpene biosynthetic genes, transcript levels of *DcTPS1* and *DcTPS2* were analyzed by qRT-PCR (Figure 5) in the same samples as used for auto-HS−SPME−GC−MS analysis.

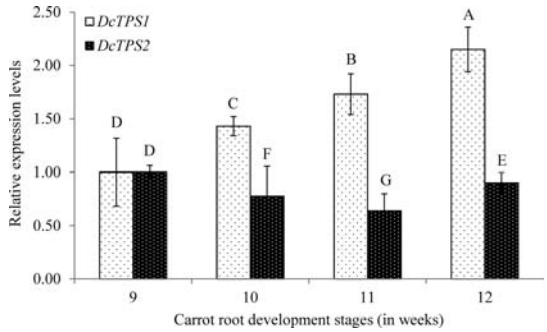

Figure 5. Expression patterns of *DcTPS1* and *DcTPS2* during carrot root development from 9 to 12 weeks after sowing in the orange carrot cultivar Nairobi. Quantification of *DcTPS1* and *DcTPS2* transcript levels by real-time RT-PCR analysis normalized to equal levels of tubulin transcripts. All analyses were performed using three biological replicates. Bars labeled with different letters indicate significant differences as determined by JMP statistic software [$F < 0.0001$; Tukey−Kramer honestly significant difference (HSD) test].

Transcripts of *DcTPS1* and *DcTPS2* were observed in all four stages in the Nairobi cultivar, demonstrating that these two genes were expressed at all developmental stages. Furthermore, transcript abundance increased during root maturation for the *DcTPS1* gene, with maximum transcript levels occurring in 12-week-old roots (Figure 5), which is consistent with the accumulation of high terpene levels in this time period (Figure 2). The expression level of *DcTPS1* and *DcTPS2* varied statistically between carrot tissues at all developmental stages (Figure 5).

We also examined possible differences in the expression of *DcTPS1* and *DcTPS2* in the five different carrot cultivars (Figure 6). Transcript abundance was highest for both genes in the Rothild cultivar, consistent with high levels of total terpenes in this cultivar (see Supplemental Table 1 of the Supporting Information). The lowest level of both gene transcripts was observed in the cultivar Yellowstone (Figure 6), correlating with lowest terpene concentrations in this cultivar (see Supplemental Table 1 of the Supporting Information). Also, the expression level varied statistically between *DcTPS1* and *DcTPS2* in the five different carrot cultivars investigated in this study (Figure 6). However, *DcTPS1* and *DcTPS2* expression levels did not directly correlate with the amounts of (*E*)-β-caryophyllene and geraniol in the different cultivars, which indicates the presence of other TPSs producing the same compounds or possible post-transcriptional/translational regulatory mechanisms. Post-transcriptional regulation of TPS enzymes[44] as well as light-dependent substrate availability[45] are also discussed as regulatory steps in terpene formation.

***Dc*TPS1 and *Dc*TPS2 Are Members of the TPS-a and TPS-b Families.** The predicted *Dc*TPS1 protein sequence

DOI: 10.1021/acs.jafc.5b00546
J. Agric. Food Chem. 2015, 63, 4870−4878

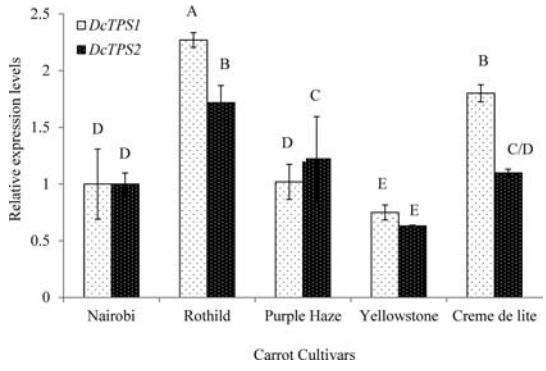

Figure 6. Quantitative RT-PCR analysis of *DcTPS1* and *DcTPS2* expression in roots of five different colored carrot varieties. Bars labeled with different letters indicate the significant differences as determined by JMP statistic software ($F < 0.0001$; Tukey–Kramer HSD test).

consists of 560 amino acids, with a calculated molecular mass of 64.7 kDa (see Supplemental Figure 1 of the Supporting Information). No chloroplast-targeting sequence was identified for *Dc*TPS1, which is indicative for the function of this enzyme as a cytosolic sesquiterpene synthase. The *Dc*TPS2 protein consists of 593 amino acids with a calculated molecular mass of 68.4 kDa. In contrast to *Dc*TPS1, *Dc*TPS2 appears to carry a 53 amino acid N-terminal plastidial transit peptide (see Supplemental Figure 1 of the Supporting Information), as predicted by the ChloroP 1.1 software (http://www.cbs.dtu.dk/services/ChloroP/), suggesting a function of *Dc*TPS-2 as a monoterpene synthase *in vivo*.

Both *Dc*TPS1 and *Dc*TPS2 sequences contain the conserved features of plant TPSs, including the asparate-rich motif DDxxD and the RxR motif, both of which are involved in catalysis (see Supplemental Figure 1 of the Supporting Information).[13,1446] A RR(x)8W motif is present in the N-terminal region of *Dc*TPS1 and downstream of the N-terminal transit peptide of *Dc*TPS2 (see Supplemental Figure 1 of the Supporting Information). The motif is assumed to participate in the ionization of the substrate[47] and is characteristic of most TPS members of the subfamilies TPS-a and TPS-b.[4849]

To analyze the phylogenetic relationship of the carrot TPS proteins (*Dc*TPS1, *Dc*TPS58617, *Dc*TPS52846, *Dc*TPS2, *Dc*TPS1324, and *Dc*TPS21245) with known TPSs of other plants, a phylogenetic tree was constructed using the neighbor-joining method (Figure 7). On the basis of protein sequence and function, plant TPSs were recently organized into seven subfamilies. These include three angiosperm-specific clades (TPS-a, TPS-b, and TPS-g), a gymnosperm-specific subfamily (TPS-d), a subfamily most conserved among land plants (TPS-c), two subfamilies most conserved among vascular plants (TPS-e and TPS-f), and a subfamily specific to *Selaginella moellendorffii* (TPS-h).[13]

*Dc*TPS1, *Dc*TPS58617, and *Dc*TPS52846, along with some TPSs from Apiaceae, the same plant family as *D. carota*, e.g., the sesquiterpene cyclase from *Centella asiatica* (55% identity of amino acids), STS1 and STS2 from *Thapsia garganica* (51 and 55% identity of amino acids, respectively),[50] β-caryophyllene synthases from *Solanum lycopersicom*[37] and *Vitis vinifera*, and pinene synthase from *Malus* × *domestica*,[51] belong to the TPS-a group of the terpene synthase superfamily (Figure 7). Furthermore, the *Dc*TPS1 protein displays a high degree of sequence similarity to the α-copaene synthase (62% identity)

Figure 7. Phylogenetic tree of deduced amino acid sequences of plant sesquiterpene synthases. The sequences were aligned using phylogeny analysis (http://www.phylogeny.fr). The evolutionary history was inferred using the neighbor-joining methods and drawn by TreeView. The TPS family was subdivided into six subfamilies, designated TPS-a–TPS-f, each distinguished by sharing a minimum of 40% identity among members.[49] Cu is *Citrus unshiu*; Vv is *Vitis vinifera*; Md is *Malus* × *domestica*; Rc is *Ricinus communis*; Ch is *Citrus hystrix*; Sh is *Solanum habrochaites*; Sl is *Solanum lycopersicum*; Fv is *Fragaria vesca*; Ga is *Gossypium arboretum*; Lh is *Lycopersicon hirsutum*; Mt is *Medicago truncatula*; At is *Artemisia annua*; Cb is *Clarkia breweri*; Cc is *Clarkia concinna*; Pg is *Picea glauca*; Pt is *Populus trichocarpa*; Ta is *Triticum aestivum*; Ag is *Abies grandis*; Ob is *Ocimum basilicum*; Am is *Antirrhinum majus*; La is *Lavandula angustifolia*; Os is *Oryza sativa*; Aa is *Artemisia annua*; Mg is *Magnolia grandiflora*; Eg is *Eucalyptus grandis*; Cs is *Coriandrum sativum*; Ca is *Centella asiatica*; and Tg is *Thapsia garganica*. The black bold underline indicates the carrot TPSs, *Dc*TPS1, *Dc*TPS2, *Dc*TPS58617, *Dc*TPS52846, *Dc*TPS1324, and *Dc*TPS21245 proteins, identified in this study.

from *Eleutherococcuc trifoliatus*, a sesquiterpene synthase (60% identity) from *Panax ginseng*, and (*E*)-β-caryophyllene synthase (54% identity) from *Vitis vinifera*.

*Dc*TPS2, *Dc*TPS1324, and *Dc*TPS21245 cluster in the TPS-b clade, together with *S*-linalool synthase (39% identity of amino acids) and γ-terpinene synthase (41% identity of amino acids) from *Coriandrum sativum* (Apiaceae family),[19] α-terpinol synthase and myrcene synthase from *Vitis vinifera*,[48] and D-limonene synthase from *Citrus* (Figure 7).[52] *Dc*TPS2 showed the highest amino acid similarity to terpene synthase (63% identity) from *Jatropha curcas*, (*R*)-limonene synthase (59%

DOI: 10.1021/acs.jafc.5b00546
J. Agric. Food Chem. 2015, 63, 4870–4878

identity) from *Ricinus communis*, and α-terpineol synthase (54% identity) and β-bisabolene synthase (52% identity) from *Eucalyptus grandis*.

In conclusion, several terpene volatile compounds and the total volatile terpene content varied widely among different colored carrot genotypes. Two TPSs (*Dc*TPS1 and *Dc*TPS2) of a larger carrot TPS family were found to produce (*E*)-β-caryophyllene, the predominant sesquiterpene constituent of carrot roots, and the monoterpene component, geraniol, respectively. The identification of carrot *TPS* cDNAs will facilitate the cloning of additional genes of the *TPS* family in *D. carota* and will allow for future molecular, physiological, and biochemical studies of the regulation of flavor and aroma formation during carrot root development. The *TPS* genes described here and potential other *TPS* genes from *D. carota* may be developed into molecular markers to aid in breeding and improvement of cultivars with superior carrot flavor and aroma.

■ ASSOCIATED CONTENT

Supporting Information

Levels of mono- and sesquiterpene volatile compounds, for which no authentic standards are available, and total content of all terpene compounds in different carrot varieties at 10 weeks (Supplemental Table 1) (PDF) and comparison of deduced amino acid sequences of *Dc*TPS1 and *Dc*TPS2 (Supplemental Figure 1) (PDF). The Supporting Information is available free of charge on the ACS Publications website at DOI: 10.1021/acs.jafc.5b00546.

■ AUTHOR INFORMATION

Corresponding Author

*Telephone/Fax: 00972-4-953-9509. E-mail: mwafaq@volcani.agri.gov.il.

Funding

This research was supported by the United States−Israel Binational Agricultural Research and Development Fund (BARD) (Grant IS-4745-14R to Mwafaq Ibdah, Dorotha Tholl, and Philipp W. Simon).

Notes

The authors declare no competing financial interest.

■ ACKNOWLEDGMENTS

The authors are grateful to Efraim Lewinsohn for critical reading of the manuscript and many discussions during the preparation of this work. The authors are very grateful to Einat Bar for support in the GC−MS analysis. The authors are grateful for Jackline Abu-Nassar for taking care of the carrot plants.

■ ABBREVIATIONS USED

*Dc*TPS, *Daucus carota* terpene synthase; DMAPP, dimethylallyl diphosphate; (*E*,*E*)-FPP, *trans*,*trans*-farnesyl diphosphate; (*Z*,*Z*)-FPP, *cis*,*cis*-farnesyl diphosphate; FW, fresh weight; GC−MS, gas chromatography−mass spectrometry; GGPP, geranylgeranyl diphosphate; GPP, geranyl diphosphate; HS, head space; IPTG, isopropyl-1-thio-β-D-galactopyranoside; IPP, isopentenyl diphosphate; MEP, methylerythritol phosphate; MVA, mevalonate; *m*/*z*, mass-to-charge ratio; NPP, neryl diphosphate; ppm, part per million; qRT-PCR, quantitative reverse transcriptase polymerase chain reaction; SPME, solid-phase microextraction; TPS, terpene synthase

■ REFERENCES

(1) Fukuda, T.; Okazaki, K.; Shinano, T. Aroma characteristic and volatile profiling of carrot varieties and quantitative role of terpenoid compounds for carrot sensory attributes. *J. Food Sci.* **2013**, *78*, S1800−S1806.

(2) Yahyaa, M.; Bar, E.; Dubey, N. K.; Meir, A.; Davidovich-Rikanati, R.; Hirschberg, J.; Aly, R.; Tholl, D.; Simon, P. W.; Tadmor, Y.; Lewinsohn, E.; Ibdah, M. Formation of norisoprenoid flavor compounds in carrot (*Daucus carota* L.) roots: Characterization of a cyclic-specific carotenoid cleavage dioxygenase 1 gene. *J. Agric. Food Chem.* **2013**, *61*, 12244−12252.

(3) Simon, P. W.; Peterson, C. E.; Lindsay, R. C. Genotype, soil, and climate effects on sensory and objective components of carrot flavor. *J. Am. Soc. Hortic. Sci.* **1982**, *107*, 644−648.

(4) Dudareva, N.; Pichersky, E.; Gershenzon, J. Biochemistry of plant volatiles. *Plant Physiol.* **2004**, *135*, 1893−1902.

(5) Matarese, F.; Cuzzola, A.; Scalabrelli, G.; D'Onofrio, C. Expression of terpene synthase genes associated with the formation of volatiles in different organs of *Vitis vinifera*. *Phytochemistry* **2014**, *105*, 12−24.

(6) Portnoy, V.; Benyamini, Y.; Bar, E.; Harel-Beja, R.; Gepstein, S.; Giovannoni, J. J.; Schaffer, A. A.; Burger, J.; Tadmor, Y.; Lewinsohn, E.; Katzir, N. The molecular and biochemical basis for varietal variation in sesquiterpene content in melon (*Cucumis melo* L.) rinds. *Plant Mol. Biol.* **2008**, *66*, 647−661.

(7) Tholl, D.; Lee, S. Terpene specialized metabolism in *Arabidopsis thaliana*. *Arabidopsis Book* **2011**, *9*, e0143.

(8) Hasegawa, M.; Mitsuhara, I.; Seo, S.; Imai, T.; Koga, J.; Okada, K.; Yamane, H.; Ohashi, Y. Phytoalexin accumulation in the interaction between rice and the blast fungus. *Mol. Plant-Microbe Interact.* **2010**, *23*, 1000−1011.

(9) Heiling, S.; Schuman, M. C.; Schoettner, M.; Mukerjee, P.; Berger, B.; Schneider, B.; Jassbi, A. R.; Baldwin, I. T. Jasmonate and ppHsystemin regulate key malonylation steps in the biosynthesis of 17-hydroxygeranyllinalool diterpene glycosides, an abundant and effective direct defense against herbivores in *Nicotiana attenuata*. *Plant Cell* **2010**, *22*, 273−292.

(10) Walling, L. L. The myriad plant responses to herbivores. *J. Plant Growth Regul.* **2000**, *19*, 195−216.

(11) Tholl, D. Terpene synthases and the regulation, diversity and biological roles of terpene metabolism. *Curr. Opin. Plant Biol.* **2006**, *9*, 297−304.

(12) Cunningham, F. X. J.; Gantt, E. Genes and enzymes of carotenoid biosynthesis in plants. *Annu. Rev. Plant Physiol. Plant Mol. Biol.* **1998**, *49*, 557−583.

(13) Chen, F.; Tholl, D.; Bohlmann, J.; Pichersky, E. The family of terpene synthases in plants: a mid-size family of genes for specialized metabolism that is highly diversified throughout the kingdom. *Plant J.* **2011**, *66*, 212−229.

(14) Degenhardt, J.; Kollner, T. G.; Gershenzon, J. Monoterpene and sesquiterpene synthases and the origin of terpene skeletal diversity in plants. *Phytochemistry* **2009**, *70*, 1621−1637.

(15) Tholl, D.; Chen, F.; Petri, J.; Gershenzon, J.; Pichersky, E. Two sesquiterpene synthases are responsible for the complex mixture of sesquiterpenes emitted from *Arabidopsis* flowers. *Plant J.* **2005**, *42*, 757−771.

(16) Huang, X.; Xiao, Y.; Kollner, T.; Zhang, W.; Wu, J.; Wu, J.; Guo, Y.; Zhang, Y. Identification and characterization of (*E*)-β-caryophyllene synthase and α/β-pinene synthase potentially involved in constitutive and herbivore-induced terpene formation in cotton. *Plant Physiol. Biochem.* **2013**, *73*, 302−308.

(17) Falara, V.; Akhtar, T. A.; Nguyen, T. T. H.; Spyropoulou, E. A.; Bleeker, P. M.; Schauvinhold, I.; Matsuba, Y.; Bonini, M. E.; Schilmiller, A. L.; Last, R. L.; Schuurink, R. C.; Pichersky, E. The tomato terpene synthase gene family. *Plant Physiol.* **2011**, *157*, 770−789.

(18) Martin, D. M.; Aubourg, S.; Schouwey, M. B.; Daviet, L.; Schalk, M.; Toub, O.; Lund, S. T.; Bohlmann, J. Functional annotation, genome organization and phylogeny of the grapevine (*Vitis vinifera*)

DOI: 10.1021/acs.jafc.5b00546
J. Agric. Food Chem. 2015, 63, 4870−4878

terpene synthase gene family based on genome assembly, FLcDNA cloning, and enzyme assays. *BMC Plant Biol.* **2010**, *10*, 226.
(19) Galata, M.; Sarker, L. S.; Mahmoud, S. S. Transcriptome profiling, and cloning and characterization of the main monoterpene synthases of *Coriandrum sativum* L. *Phytochemistry* **2014**, *102*, 64−73.
(20) Hemmerlin, A.; Harwood, J. L.; Bach, T. J. A raison d'etre for two distinct pathways in the early steps of plant isoprenoid biosynthesis? *Prog. Lipid Res.* **2012**, *51*, 95−148.
(21) Yu, Z.-X.; Wang, L.-J.; Zhao, B.; Shan, C.-M.; Zhang, Y.-H.; Chen, D.-F.; Chen, X.-Y. Progressive regulation of sesquiterpene biosynthesis in Arabidopsis and Patchouli (*Pogostemon cablin*) by the miR156-targeted SPL transcription factors. *Mol. Plant* **2015**, *8*, 98−110.
(22) Habegger, R.; Schnitzler, W. H. Aroma compounds in essential oils of carrots (*Daucus carota* L. ssp. *sativus*) leaves in comparison with roots. *J. Appl. Bot.* **2000**, *74*, 220−223.
(23) Senalik, D. A.; Simon, P. W. Relationship between oil ducts and volatile terpenoid content in carrot roots. *Am. J. Bot.* **1986**, *73*, 60−63.
(24) Hampel, D.; Mosandl, A.; Wust, M. Biosynthesis of mono- and sesquiterpenes in carrot roots and leaves (*Daucus carota* L.): Metabolic cross talk of cytosolic mevalonate and plastidial methylerythritol phosphate pathways. *Phytochemistry* **2005**, *66*, 305−311.
(25) Rand, K.; Bar, E.; Ben-Ari, M.; Lewinsohn, E.; Inbar, M. The mono- and sesquiterpene content of aphid-induced galls on *Pistacia palaestina* is not a simple reflection of their composition in intact leaves. *J. Chem. Ecol.* **2014**, *40*, 632−642.
(26) Iorizzo, M.; Senalik, D. A.; Grzebelus, D.; Bowman, M.; Cavagnaro, P. F.; Matvienko, M.; Ashrafi, H.; Van Deynze, A.; P.W, S. *De novo* assembly and characterization of the carrot transcriptome reveals novel genes, new markers, and genetic diversity. *BMC Genomics* **2011**, *12*, 389.
(27) Bradford, M. M. A rapid and sensitive method for the quantitation of microgram quantities of protein utilizing the principle of protein-dye binding. *Anal. Biochem.* **1976**, *72*, 248−254.
(28) Alasalvar, C.; Grigor, J. M.; Quantick, P. C. Method for the static headspace analysis of carrot volatiles. *Food Chem.* **1999**, *65*, 391−397.
(29) Kjeldsen, F.; Christensen, L. P.; Edelenbos, M. Quantitative analysis of aroma compounds in carrot (*Daucus carota* L.) cultivars by capillary gas chromatography using large-volume injection technique. *J. Agric. Food Chem.* **2001**, *49*, 4342−4348.
(30) Kjeldsen, F.; Christensen, L. P.; Edelenbos, M. Changes in volatile compounds of carrots (*Daucus carota* L.) during refrigerated and frozen storage. *J. Agric. Food Chem.* **2003**, *51*, 5400−5407.
(31) Kreutzmann, S.; Thybo, A. K.; Edelenbos, M.; Christensen, L. P. The role of volatile compounds on aroma and flavour perception in coloured raw carrot genotypes. *Int. J. Food Sci. Technol.* **2008**, *43*, 1619−1627.
(32) Rosenfeld, H. J.; Knut S. Dalen, K. S.; Haffner, K. The growth and development of carrot roots. *Gartenbauwissenschaft* **2002**, *67*, 11−16.
(33) Nicolle, C.; Simon, G.; Rock, E.; Amouroux, P.; Remesy, C. Genetic variability influences carotenoid, vitamin, phenolic, and mineral content in white, yellow, purple, orange, and dark-orange carrot cultivars. *J. Am. Soc. Hortic. Sci.* **2004**, *129*, 523−529.
(34) Cai, Y.; Jia, J.-W.; Crock, J.; Lin, Z.-X.; Chen, X.-Y.; Croteau, R. A cDNA clone for β-caryophyllene synthase from *Artemisia annua*. *Phytochemistry* **2002**, *61*, 523−529.
(35) Sarker, L.; Demissie, Z.; Mahmoud, S. Cloning of a sesquiterpene synthase from *Lavandula* × *intermedia* glandular trichomes. *Planta* **2013**, *238*, 983−989.
(36) Landmann, C.; Fink, B.; Festner, M.; Dregus, M.; Engel, K.-H.; Schwab, W. Cloning and functional characterization of three terpene synthases from lavender (*Lavandula angustifolia*). *Arch. Biochem. Biophys.* **2007**, *465*, 417−429.
(37) Bleeker, P. M.; Spyropoulou, E. A.; Diergaarde, P. J.; Volpin, H.; Both, M. J.; Zerbe, P.; Bohlmann, J.; Falara, V.; Matsuba, Y.; Pichersky, E.; Haring, M. A.; Schuurink, R. C. RNA-seq discovery, functional characterization, and comparison of sesquiterpene synthases from *Solanum lycopersicum* and *Solanum habrochaites* trichomes. *Plant Mol. Biol.* **2011**, *77*, 323−336.
(38) Huang, M.; Abel, C.; Sohrabi, R.; Petri, J.; Haupt, I.; Cosimano, J.; Gershenzon, J.; Tholl, D. Variation of herbivore-induced volatile terpenes among *Arabidopsis* ecotypes depends on allelic differences and subcellular targeting of two terpene synthases, TPS02 and TPS03. *Plant Physiol.* **2010**, *153*, 1293−1310.
(39) Koellner, T. G.; Held, M.; Lenk, C.; Hiltpold, I.; Turlings, T. C. J.; Gershenzon, J.; Degenhardt, J. A maize (*E*)-β-caryophyllene synthase implicated in indirect defense responses against herbivores is not expressed in most American maize varieties. *Plant Cell* **2008**, *20*, 482−494.
(40) Bos, R.; Koulman, A.; Woerdenbag, H. J.; Quax, W. J.; Pras, N. Volatile components from *Anthriscus sylvestris* (L.) Hoffm. *J. Chromatogr. A* **2002**, *966*, 233−238.
(41) Chen, F.; Ro, D. K.; Petri, J.; Gershenzon, J.; Bohlmann, J.; Pichersky, E.; Tholl, D. Characterization of a root-specific *Arabidopsis* terpene synthase responsible for the formation of the volatile monoterpene 1,8-cineole. *Plant Physiol.* **2004**, *135*, 1956−1966.
(42) Kessler, A.; Baldwin, I. T. Defensive function of herbivore-induced plant volatile emissions in nature. *Science* **2001**, *291*, 2141−2144.
(43) Rasmann, S.; Köllner, T. G.; Degenhardt, J.; Hiltpold, I.; Toepfer, S.; Kuhlmann, U.; Gershenzon, J.; Turlings, T. C. J. Recruitment of entomopathogenic nematodes by insect-damaged maize roots. *Nature* **2005**, *434*, 732−737.
(44) Schnee, C.; Kollner, T. G.; Gershenzon, J.; Degenhardt, J. The maize gene terpene synthase 1 encodes a sesquiterpene synthase catalyzing the formation of (*E*)-β-farnesene, (*E*)-nerolidol, and (*E*,*E*)-farnesol after herbivore damage. *Plant Physiol.* **2002**, *130*, 2049−2060.
(45) Arimura, G. I.; Koepke, S.; Kunert, M.; Volpe, V.; David, A.; Brand, P.; Dabrowska, P.; Maffei, M. E.; Boland, W. Effects of feeding *Spodoptera littoralis* on lima bean leaves: IV. Diurnal and nocturnal damage differentially initiate plant volatile emission. *Plant Physiol.* **2008**, *146*, 965−973.
(46) Davis, E. M.; Croteau, R. Cyclization enzymes in the biosynthesis of monoterpenes, sesquiterpenes, and diterpenes. *Biosynthesis* **2000**, *209*, 53−95.
(47) Williams, D. C.; McGarvey, D. J.; Katahira, E. J.; Croteau, R. Truncation of limonene synthase preprotein provides a fully active 'pseudomature' form of this monoterpene cyclase and reveals the function of the amino-terminal arginine pair. *Biochemistry* **1998**, *37*, 12213−12220.
(48) Martin, D. M.; Bohlmann, J. Identification of *Vitis vinifera* (−)-α-terpineol synthase by in silico screening of full-length cDNA ESTs and functional characterization of recombinant terpene synthase. *Phytochemistry* **2004**, *65*, 1223−1229.
(49) Bohlmann, J.; Meyer-Gauen, G.; Croteau, R. Plant terpenoid synthases: Molecular biology and phylogenetic analysis. *Proc. Natl. Acad. Sci. U. S. A.* **1998**, *95*, 4126−4133.
(50) Pickel, B.; Drew, D. P.; Manczak, T.; Weitzel, C.; Simonsen, H. T.; Ro, D. K. Identification and characterization of a kunzeaol synthase from *Thapsia garganica*: Implications for the biosynthesis of the pharmaceutical thapsigargin. *Biochem. J.* **2012**, *448*, 261−271.
(51) Nieuwenhuizenm, N. J.; Green, S. A.; Chen, X.; Bailleul, E. J.; Matich, A. J.; Wang, M. Y.; Atkinson, R. G. Functional genomics reveals that a compact terpene synthase gene family can account for terpene volatile production in apple. *Plant Physiol.* **2013**, *161*, 787−804.
(52) Lucker, J.; El Tamer, M. K.; Schwab, W.; Verstappen, F. W. A.; van der Plas, L. H. W.; Bouwmeester, H. J.; Verhoeven, H. A. Monoterpene biosynthesis in lemon (*Citrus limon*)—cDNA isolation and functional analysis of four monoterpene synthases. *Eur. J. Biochem.* **2002**, *269*, 3160−3171.

DOI: 10.1021/acs.jafc.5b00546
J. Agric. Food Chem. 2015, 63, 4870−4878

JOURNAL OF AGRICULTURAL AND FOOD CHEMISTRY

Article

pubs.acs.org/JAFC

In Vitro Production of Fumonisins by *Fusarium verticillioides* under Oxidative Stress Induced by H_2O_2

Davide Ferrigo,[†] Alessandro Raiola,[†] Sara Bogialli,[‡] Claudio Bortolini,[‡] Andrea Tapparo,[‡] and Roberto Causin*[,†]

[†]Department of Land, Environment, Agriculture and Forestry, University of Padua, Campus of Agripolis, Viale Università 16, 35020 Legnaro, Padua, Italy

[‡]Department of Chemical Science, University of Padua, via Marzolo 1, 35131 Padua, Italy

Supporting Information

ABSTRACT: The effects of oxidative stress induced by H_2O_2 were tested in liquid cultures in the fumonisin-producing fungus *Fusarium verticillioides*. The quantitative analysis of fumonisins B_1, B_2, B_3, and B_4 was achieved by means of liquid chromatography coupled to high-resolution mass spectrometry. Two effects in *F. verticillioides*, consisting of different abilities to produce fumonisins in response to oxidative stress, were identified. Following H_2O_2 addition, two *F. verticillioides* strains produced significantly more fumonisin (>300%) while three other strains produced significantly less (<20%) in comparison to control cultures. Transcriptional studies with seven biosynthetic genes showed a significant increase in transcript levels in the strain that made more fumonisin and either no or minimal changes in the strain that made less fumonisin. Our data indicate the important role of oxidative stress toward the modulation of the fumonisin biosynthesis and suggest the necessity to verify the presence of such divergent behavior in *F. verticillioides* populations under natural conditions.

KEYWORDS: *Fusarium verticillioides, fumonisins, oxidative stress, fum genes, H_2O_2, LC-high-resolution MS analysis*

INTRODUCTION

Fusarium verticillioides is one of the most common pathogenic fungi affecting maize,[1] characterized by low virulence. *F. verticillioides* is often endophytically seed borne[2] but can also penetrate through damaged tissues, causing severe ear rot and accumulation of fumonisins in kernels.[3] Fumonisins, the most common mycotoxins in maize, are primarily produced by *F. verticillioides* and *F. proliferatum*.[4] They occur at biologically significant levels both on maize grains and on a variety of derived human and animal food products worldwide.[5]

Fumonisin B_1 (FB_1) is the most abundant and toxicologically active type B fumonisin produced by *F. verticillioides*, followed by the other congeners FB_2, FB_3, and FB_4 (Figure 1).[6]

One of the most investigated research areas in relation to mycotoxin production is the influence of stress factors. Abiotic stress, such as unfavorable temperature, water activity (a_w), and pH, can influence mycotoxin biosynthetic pathways.[7] Previous experiments have shown that intracellular oxidative stress can affect aflatoxin[8] and trichothecene production,[9] and a positive correlation between these mycotoxins and the accumulation of reactive oxygen species has been observed.[10,11] In particular, in *Fusarium graminearum* during in vitro growth, both mycotoxin accumulation and expression of *tri*-cluster genes were modulated by oxidative stress induced by H_2O_2. It has been proposed that the differential modulation of toxin biosynthesis is linked to the fungal ability to protect itself from oxidative damage.[12]

In response to biotic and abiotic stresses,[13−15] plants have developed a broad range of strategies to protect themselves. Plant responses include rapid production of reactive oxygen species (ROS),[16] such as superoxide anion (O_2^-), hydrogen peroxide (H_2O_2), hydroxyl radical (HO^-), and lipoperoxides (LOOH). A correlation is known to exist between environmental stress and mycotoxin biosynthesis.[7,17] The ability of antioxidant phenolic compounds and scavenging oxidative chemical species to decrease in vitro mycotoxin biosynthesis[18,19] suggest the involvement of ROS compounds. Moreover, it was previously hypothesized that plant compounds, including ROS, involved in plant−pathogen interactions during the infection process by *Fusarium* spp. could modulate mycotoxin production in host tissues.[12]

In our study, we investigated the in vitro effect of oxidative stress induced by hydrogen peroxide on fumonisin production in *F. verticillioides*. We have also analyzed, under the same conditions, the expression of several fumonisin cluster genes involved in the fumonisin biosynthetic pathway, including *fum1* (polyketide synthase), *fum6* (cytochrome P450 monooxygenase), *fum10* (acyl-CoA synthetase), *fum14* (peptide synthase), and *fum19* (ABC-transporter), the regulatory gene *fcc1*, a C-type cyclin, and *fum21*, a transcription factor.

MATERIALS AND METHODS

Strain Isolation and Experimental Conditions. Five *F. verticillioides* strains (named *Fv*1, *Fv*3, *Fv*4, *Fv*7, and *Fv*8) isolated from maize kernels grown in Veneto (Italy) were chosen for this study, and monoconidial cultures were obtained as reported previously.[20] To confirm the identification at the species level, the *Fusarium*

Received: January 22, 2015
Revised: April 21, 2015
Accepted: April 24, 2015
Published: April 24, 2015

ACS Publications © 2015 American Chemical Society

DOI: 10.1021/acs.jafc.5b00113
J. Agric. Food Chem. 2015, 63, 4879−4885

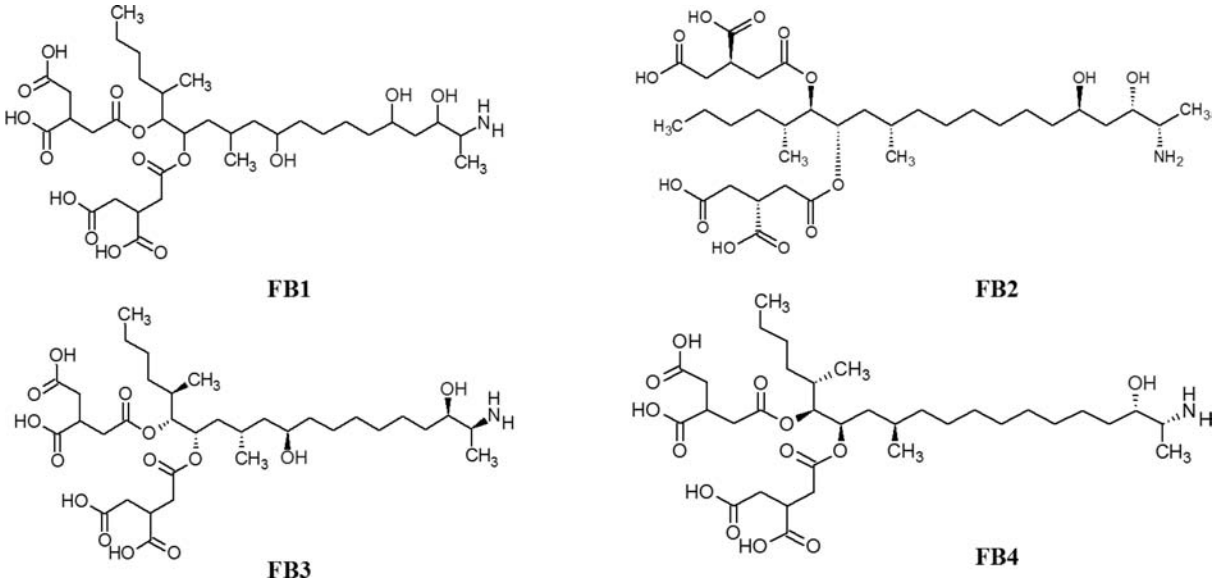

Figure 1. Chemical structures of the type B fumonisins.

monoconidial strains were submitted to molecular analysis by PCR using VER1 and VER2 primers.[21]

Five randomly chosen monoconidial strains were grown on PDA at 25 °C under dark conditions for 8 days before spore collection. For each strain, 100 μL of a conidial suspension at the density of 10^8 conidia/mL was inoculated in 100 mL of GYAM medium (8 mM L-asparagine, 1.7 mM NaCl, 4.4 mM K_2HPO_4, 2 mM $MgSO_4$, 8.8 mM $CaCl_2$, 0.05% yeast extract, 0.24 M glucose, and 5.0 mM malic acid) and incubated at 25 °C on a rotary shaker at 150 rpm in the dark. Cultures were grown for 2 days before H_2O_2 treatments. These treatments consisted of H_2O_2 addition every 24 h to obtain a final concentration of 0.5, 2, or 0.5 mM supplemented with 100 units of catalase (Sigma–Aldrich, St. Louis, MO). Control cultures were supplemented with sterile water.

The incubation period was 21 days for biomass and fumonisin quantitation and 5 days for gene expression analysis.

For gene expression analysis, *Fv*8 and *Fv*1 were selected as fumonisin-promoted and -inhibited representative strains, respectively.

Effect of H_2O_2 on Fungal Growth and Fumonisin Production. Fungal strains were grown for 21 days as previously described; biomass and supernatant were collected by centrifugation at 3000*g* for 5 min. The supernatant was filtered through Whatman paper No. 4 and stored at −20 °C before LC-MS analysis. Fungal mycelia were dried and weighed to normalize fumonisin production and to analyze the effect of H_2O_2 treatment on fungal growth. Each experiment was performed in triplicate.

Reagents and Chemicals. Analytical standard solutions of FB_1 and FB_2 and of FB_3, both at 50 μg/mL in acetonitrile/water (50/50, v/v), were from Sigma-Aldrich. All standard dilutions were made with the same solution. The isotope-labeled fumonisin B_1 $^{13}C_{34}$ (25.1 μg/mL in acetonitrile/water 50/50, v/v) (Sigma-Aldrich) was diluted to 0.5 μg/mL and used as an internal standard (IS) for quality control purposes. A composite working standard solution of FB_1, FB_2, and FB_3 at 83.3 ng/mL was obtained from appropriate dilution of stock solutions. Formic acid (reagent grade, min 99%) and LC-MS grade acetonitrile and methanol were purchased from Sigma-Aldrich. Water was purified (18 MΩ cm) using a Milli-Q Water System (Millipore, Darmstadt, Germany).

Fumonisin Extraction and HPLC-MS Analysis. One milliliter of each cultured strain was centrifuged for 10 min at 10000 rpm and 25 °C. A 100 μL aliquot of supernatant was diluted 1/10 with a solution of LC mobile phases (50/50 v/v) and spiked with IS at a concentration of 4 ng/mL, and finally 5 μL was injected into the LC-MS detection system. An Ultimate 3000 UHPLC (Thermo Fisher Scientific, Waltham, MA), consisting of a vacuum degasser, autosampler, quaternary pump, and column oven, was coupled to a Q-Exactive mass analyzer with an HESI source (Thermo Fisher Scientific) in positive ionization mode.

Optimization of peak separation was achieved with a 150 mm × 2 mm i.d., 2.6 μm Kinetex C18 column (Phenomenex, Bologna, Italy) thermostated at 30 °C. The mobile phase components A and B were water and acetonitrile, respectively, both acidified with 0.1% of formic acid. The eluent flow rate was 0.3 mL/min. The mobile phase gradient profile is as follows: 0–5 min, 0% B; 5–16 min, 0–100% B; 16–19 min, 100% B; 19–20 min, 100–0% B; 20–27 min, 0% B. MS parameters were as follows: spray voltage 4 kV; sheath gas 40 psi; auxiliary gas 20 arbitrary units; ion transfer tube temperature 320 °C; vaporizer temperature 310 °C; S-lens RF level 60 V.

The mass calibration was performed weekly using the manufacturer's solution. For all chromatographic runs, m/z 391.2843 relative to the $[M + H]^+$ ion from diisooctyl phthalate, always present as an impurity, was set as the lock mass for accurate mass analysis. A simultaneous MS (resolution 70000 at m/z 200) and MS/MS (resolution 17500 at m/z 200) acquisition was performed with the data-dependent feature, using the $[M + H]^+$ pseudomolecular ions of the selected analytes in the preferred inclusion list with an isolation width of 4 amu. Centroid MS spectra were recorded over the range m/z 150–1000, setting the normalized collision energies at 50. The highest fragment ion obtained was used for confirmatory purposes, while the pseudomolecular ion $[M + H]^+$ was used for quantitative analysis. The automatic gain control was set at 3×10^6 ions with a maximum injection time of 200 ms for MS and at 1×10^5 ions with a maximum injection time of 50 ms for MS/MS. Mass spectra acquisition and data analysis were processed with Excalibur 2.2 Software (Thermo Fisher Scientific).

All analyses performed showed a mass accuracy better than 0.1 ppm, allowing the correct identification of the target (FB_1, FB_2, and FB_3) and nontarget (FB_4) fumonisins. The quantitation of fumonisins was performed using the corresponding external calibration curve with least-squares regression, obtained by plotting the area of each analyte normalized with the internal standard area (A/A_{IS}), related to the extracted ion chromatogram (extraction accuracy 10 ppm) of the molecular ion $[M + H]^+$. A five-point calibration curve, ranging from 0.2 to 50 ng/mL, was injected in duplicate for each set of analysis, showing that R^2 was always higher than 0.9995.

Quantitation of fumonisin B_4 was made by assuming the same molar response of the B_2 variant, since a commercial standard was not available. Limits of detection, assessed from the lowest point of the calibration curve and corresponding to an S/N value of 3, were estimated to be 0.5 ng/mL in the matrix.

DOI: 10.1021/acs.jafc.5b00113
J. Agric. Food Chem. 2015, 63, 4879–4885

Table 1. Fumonisin Content after Treatment with H_2O_2 and H_2O_2 plus Catalase[a]

		H_2O_2 0.5 mM		H_2O_2 2 mM		H_2O_2 0.5 mM + catalase	
	control fumonisins (ng/mg ± SE)	fumonisins (ng/mg ± SE)	rel yield (%)	fumonisins (ng/mg ± SE)	rel yield (%)	fumonisins (ng/mg ± SE)	rel yield (%)
*Fv*1	75 ± 7[a]	12 ± 1[c]	16	35 ± 4[b]	47	7 ± 2[d]	9
*Fv*3	65 ± 7[c]	357 ± 44[a]	549	297 ± 34[b]	457	13 ± 2[d]	20
*Fv*4	98 ± 11[a]	19 ± 2[b]	19	24 ± 5[b]	24	10 ± 2[c]	10
*Fv*7	317 ± 31[a]	26 ± 4[c]	8	50 ± 3[b]	16	31 ± 4[c]	10
*Fv*8	131 ± 15[c]	301 ± 23[a]	230	183 ± 18[b]	140	25 ± 4[d]	19

[a]Fumonisins expressed as percent values relative to their level in the control culture. Fumonisin values were normalized on dry weight fungal biomass. Values with different letters in the rows are significantly different ($p < 0.05$) on the basis of ANOVA and Tukey's HSD tests. Statistical analyses were performed separately per strain.

Gene Expression Analysis. A set of genes involved in both the fumonisin regulatory (*fcc1* and *fum21*) and biosynthetic pathways (*fum1*, *fum6*, *fum10*, *fum14*, and *fum19*) was analyzed by quantitative real-time PCR (qPCR). *Fv*8 and *Fv*1 were grown on GYAM as previously described, and RNAs were extracted on 5 day old mycelium according to Brown et al.[22] A 30 mg portion of fresh mycelium was ground in a mortar with liquid nitrogen, and the total RNA was extracted using an Illustra RNAspin Mini Kit (GE Healthcare, Chalfont St. Giles, U.K.) according to the manufacturer's instructions. RNA concentrations were determined by both spectrophotometer and densitometric analysis of RNA bands following agarose gel electrophoresis. Total RNA (10 μg) was treated with 10 units of RQ1 RNase-free DNase (Promega, Madison, WI) and 2 units of RNasin Ribonuclease Inhibitor (Promega) for 30 min and then purified by phenol−chloroform extraction and precipitated in isopropyl alcohol. For cDNA synthesis, DNase-treated RNA (2 μg) was reverse-transcribed using the Reverse Transcription System according to the manufacturer's instructions (Promega). Real-time PCR was performed by a 7500 real-time PCR detection system (Applied Biosystems) according to the manufacturer's guidelines. A total of 1 μL of a cDNA dilution (corresponding to 25 ng of total RNA) was amplified in a 25 μL reaction containing Power SYBR Green PCR Master Mix (Applied Biosystem) and 200 μM in each primer.

Primer pairs used for gene expression were designed from published sequences available in the NCBI database using software Primer3 v0.4.0 software.[23] Primers for each gene were designed to anneal at 56−60 °C and amplify a fragment of approximately 150 bp. Gene expression analyses were performed with a real-time PCR 7500 Applied Biosystem using Power SYBR Green PCR Master Mix (Applied Biosystems). One-tenth of a cDNA reaction mixture was used to optimize PCR amplification and primer efficiency. Each amplification reaction was conducted according to the manufacturer's instructions with a primer concentration of 200 nM.

The amplification conditions consisted of 40 cycles as follows: 95 °C for 15 s, annealing at 56 °C for 30 s, and extension at 72 °C for 35 s, followed by a final extension step of 4 min at 72 °C. All reactions were performed in triplicate. The absence of dimer formation was checked in nontemplate samples by product dissociation analysis and electrophoretic separation in agarose gel. Relative expression of the RT-PCR products was determined using the method described by Pfaffl[24] by Q-Gene 4.3.10 software.[25] β-Tubulin (β-tub) was used as a reference gene to normalize quantitative expression data.

Statistical Analysis. Values of fungal growth, fumonisin content, and gene expression were log-transformed before statistical analysis, the Kolmogorov−Smirnov test was performed to verify that the data had a normal distribution, and the Levene test was used to check the homogeneity of variance.

Statistical analysis of the effect of H_2O_2 supplementation on *F. verticillioides* growth and fumonisin content was performed by ANOVA followed by Tukey's HSD test, in which treatment (T) and strain (S) were independent variables. Gene expressions were statistically analyzed by ANOVA followed by Tukey's HSD test. All analyses were conducted using the software SPSS 14.0. These results were computed from experiments performed in triplicate. Data on fumonisin levels and dry biomass obtained from separate experiments were expressed as percent values relative to the treatment controls.

RESULTS AND DISCUSSION

Fumonisin Accumulation under Oxidative Stress by H_2O_2 from Different *F. verticillioides* Strains. As a first approach to clarify the influence of ROS in fumonisin modulation, our study has examined the in vitro impact of oxidative stress induced by hydrogen peroxide treatment on five strains of *F. verticillioides*. Further, catalase, which degrades H_2O_2, was applied to the fungus to verify the link between fumonisin biosynthesis and oxidative stress. Fumonisin production was measured in culture medium supplemented with two concentrations of H_2O_2 (0.5 and 2 mM) and also in the presence of catalase. The results indicate that different oxidative stress conditions can modulate production of fumonisins in relation to the fungal strain; in particular *Fv*3 and *Fv*8, on treatment with the two concentrations of H_2O_2, were stimulated to produce fumonisins, while in the other three strains analyzed (*Fv*1, *Fv*4, and *Fv*7), fumonisin production was strongly inhibited.

For promoted strains, treatment with 0.5 mM H_2O_2 increased fumonisin yields (549% and 230% for strains *Fv*3 and *Fv*8, respectively), while the effect was slightly lower with the higher H_2O_2 concentration (457% and 140%, respectively), as reported in Table 1.

Results obtained for two out of five *F. verticillioides* strains studied for fumonisin synthesis were similar to those reported for *Aspergillus flavus* synthesis of aflatoxin[8] and *F. graminearum* synthesis of trichothecenes:[10] that oxidative stress positively influences toxin production. However, here, for the first time, we report that the response to oxidative stress is strain dependent. Moreover, we also confirm what was previously reported for *Aspergillus flavus* and *F. verticillioides*: that mild stress caused by environmental factors increases mycotoxin production but severe stress conditions can reduce it.[7,26]

In addition to promoted strain, we found that the synthesis of fumonisin was inhibited in three other strains by the same oxidative conditions. Inhibited cultures suppressed fumonisin biosynthesis almost completely at lower H_2O_2 concentration (84% and 92% reduction for *Fv*1 and *Fv*7, respectively), whereas the 2 mM treatment caused a slight increase of fumonisin production of 47% and 16% for *Fv*1 and *Fv*7, respectively, but no significant changes were observed for *Fv*4 strain (Table 1). Statistical analysis showed a significant influence of fungal strain (F 4.533, $p < 0.016$) and treatment (F 4.864, $p < 0.035$) on fumonisin production as well as the interaction between the two factors (F 4.124, $p < 0.008$). Finally, our analysis showed that FB_1 was the major fumonisin

DOI: 10.1021/acs.jafc.5b00113
J. Agric. Food Chem. 2015, 63, 4879−4885

analogue produced by *F. verticillioides* strains. The isoform composition for each strain (Table 2) indicates that all strains

Table 2. Type B Fumonisin Composition[a]

	composition (%)			
	$FB_1 \pm SE$	$FB_2 \pm SE$	$FB_3 \pm SE$	$FB_4 \pm SE$
*Fv*1	62 ± 6	12 ± 4	25 ± 1	1 ± 1
*Fv*3	68 ± 1	3 ± 1	27 ± 1	2 ± 1
*Fv*4	56 ± 1	8 ± 1	32 ± 1	4 ± 1
*Fv*7	57 ± 2	9 ± 1	27 ± 2	7 ± 1
*Fv*8	59 ± 2	16 ± 2	23 ± 1	2 ± 1

[a]Average type B fumonisin composition estimated on total fumonisin for *F. verticillioides* strains. Fumonisin composition percentages were not significantly different upon treatments.

in this study belong to *F. verticillioides* chemotype $FB_1 > FB_3 > FB_2 > FB_4$ according to the Szécsi classification.[27] Type B fumonisin ratios were not significantly different upon treatments (data not shown).

In catalase-treated cultures, all *F. verticillioides* strains reduced mycotoxin biosynthesis, thus reducing fumonisin levels from 80 to 91% in comparison to the control culture, independent of their response to H_2O_2 supplementation. Our results for *Fv* strains promoted or inhibited by hydrogen peroxide demonstrate that the addition of an antioxidant-activity enzyme causes a low production of fumonisins. On the other hand, the addition of chemical antioxidant compounds has also been reported to counteract the fumonisin accumulation.[28,29]

Studies on *F. graminearum* provide evidence that catalases affect the exogenous H_2O_2 treatment, which work as an inducer of deoxynivalenol or as an inhibitor of nivalenol and fusarenon-X biosynthesis, supporting the notion that this enzyme, acting as a scavenger for the oxidant compounds, can modulate the mycotoxin biosynthesis.[30] Furthermore, in the same fungus the chemotypes could be related to virulence[31] and to the different abilities to detoxify hydrogen peroxide.[30] On the basis of our study, it appears evident that different sensitivities to oxidative stress in *F. verticillioides* determine the variable responses to fumonisin production; however, these experiments were not performed to discriminate the sensitivity of different *Fv* isolates to H_2O_2, and we cannot advance a hypothesis regarding whether inhibited strains are more susceptible or resistant to this stress with respect to promoted strains.

Since fumonisin production seems to be required for *F. verticillioides* virulence,[32] the investigation of fumonisin modulation by oxidative stress on the fitness and virulence may represent a future challenge. Different sensitivities to oxidative stress affecting fumonisin production open the question as to the benefit of having an adaptive system toward oxidative stress. The *F. verticillioides* population presenting different sensitivities to the oxidative stress under field conditions remains to be investigated.

Oxidative balance status during plant−fungus interactions can play a role in the establishment of plant defense responses.[33] Since virulent fungal pathogens appear able to suppress the plant oxidative response,[34] the modulation of oxidative stress, as observed for some strains in our study, could be part of the fungal capability to establish the endophytic phase, the typical habit of this species in maize.

Relation of Fumonisin Production to Fungal Biomass. Treatment with an oxidative agent at the adopted doses affected the *Fv* strains differently. The effect of lower levels of H_2O_2 on fungal growth was similar among *Fv* strains, although the capability to produce mycotoxins varied greatly; in contrast, when the concentration of H_2O_2 was increased to 2 mM, two strains (*Fv*1 and *Fv*4) showed a biomass decrease of approximately 10% (Table 3). Furthermore, when 100 U of catalase was added to the cultures, the fungal biomass of each strain was found to be comparable to that of the control culture.

No correlation between fungal biomass and fumonisin accumulation was observed: *F. verticillioides* strains with similar growth (*Fv*1 with *Fv*8; *Fv*3 with *Fv*4 and *Fv*7) accumulate very different amounts of fumonisins; however, while the strains *Fv*1 and *Fv*4 were both inhibited in biomass and fumonisin production by the higher concentration of H_2O_2, this behavior was not observed for the *Fv*7 strain. This result suggests a lack of correlation between fungal growth changes and the levels of fumonisin production under mild oxidative stress conditions. Differently, at the highest oxidative stress levels the reduced growth in two strains out of the five analyzed suggests the possibility of differences in sensitivity to H_2O_2 treatment.

During growth, the final pH values of each fungal culture did not show variation between treatments (data not shown).

Correlation of Gene Expression Analisys upon H_2O_2 with the in Vitro Fumonisin Production. The variability in fumonisin accumulation in different *Fv* strains may be due to a different epigenetic regulation of *fum* cluster[35] or to different positions and numbers of cis-acting promoter elements.[36] In our work, we provide evidence that oxidative stress induced by H_2O_2 can affect the kinetics of *fum* gene expression. Moreover, sublethal doses of azole fungicides, known to trigger oxidative stress, has been demonstrated to upregulate *fum1* gene in *F. verticillioides*.[37]

This study also indicates that changes in fumonisin accumulation in different *Fv* strains seem to be linked to an up- or downregulation of some genes involved in the fumonisin biosynthesis pathway in response to oxidative stress. In contrast to *F. graminearum*, where exogenous H_2O_2 treatment increases

Table 3. Fungal Biomass Content after Treatment with H_2O_2 and H_2O_2 plus Catalase

		H_2O_2 0.5 mM		H_2O_2 2 mM		H_2O_2 0.5 mM + catalase	
	control biomass (mg ± SE)	biomass (mg ± SE)	rel yield (%)	biomass (mg ± SE)	rel yield (%)	biomass (mg ± SE)	rel yield (%)
*Fv*1	141 ± 8[a]	144 ± 4[a]	102	125 ± 6[b]	89	138 ± 2[a]	98
*Fv*3	127 ± 5[a]	128 ± 5[a]	101	125 ± 7[a]	99	127 ± 6[a]	100
*Fv*4	119 ± 6[a]	119 ± 5[a]	100	106 ± 3[b]	89	114 ± 5[a]	96
*Fv*7	123 ± 5[a]	127 ± 4[a]	103	122 ± 3[a]	99	123 ± 4[a]	100
*Fv*8	143 ± 3[a]	150 ± 5[a]	105	149 ± 9[a]	104	149 ± 7[a]	103

Dry weight fungal biomass expressed as percent values relative to their level in the control culture. Values with different letters on the rows are significantly different ($p < 0.05$) based on ANOVA and Tukey's HSD tests. Statistical analyses were performed separately per strain.

DOI: 10.1021/acs.jafc.5b00113
J. Agric. Food Chem. 2015, 63, 4879−4885

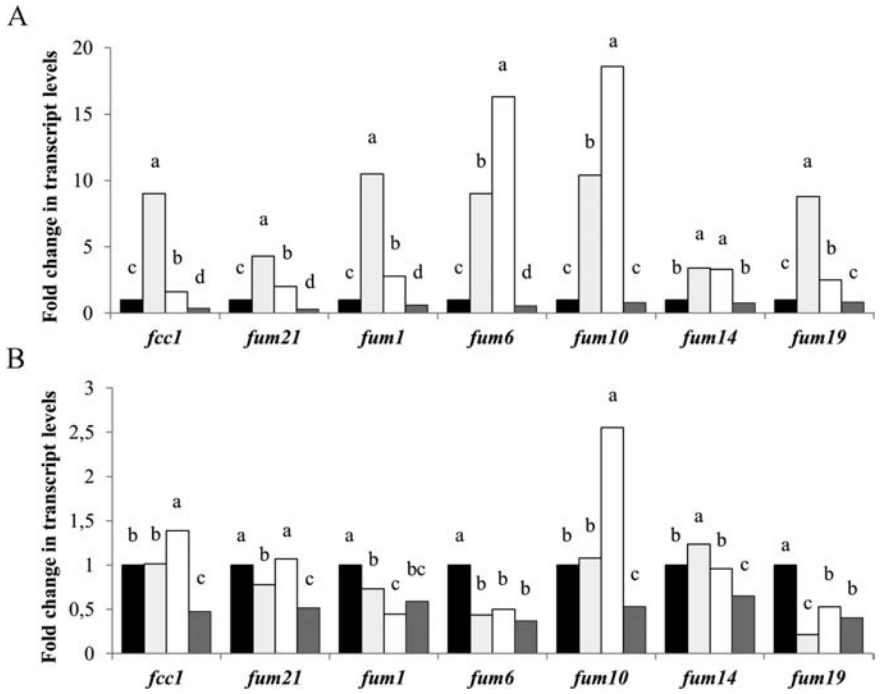

Figure 2. Fold changes in fumonisin gene levels for (A) promoted *Fv*8 and (B) inhibited *Fv*1 strains after hydrogen peroxide treatment. Treatments considered were as follows: control (black bar); 0.5 mM H_2O_2 (light gray bar); 2 mM H_2O_2 (white bar); 0.5 mM H_2O_2 plus catalase (dark gray bar). The fold change was normalized to control gene expression. Tubulin expression was used as the reference gene. Mean values for gene expression were analyzed by an ANOVA test with $\alpha = 0.05$. Bars represent the average of three independent experiments, and different letters indicate data sets significantly different according to ANOVA followed by Tukey's test ($P < 0.05$).

mycotoxin production,[30] inducing the expression of trichothecene biosynthetic genes,[12,38] in *F. verticillioides* two different responses were observed, after exogenous H_2O_2 treatment.

Two *F. verticillioides* representative strains, *Fv*8 as the promoted strain and *Fv*1 as the inhibited strain, were grown under stress conditions induced by H_2O_2 treatment. In addition, the expression levels of genes involved in the fumonisin biosynthetic pathway were analyzed in the absence or presence of catalase treatment.

In the promoted strain *Fv*8, the transcription of genes involved in fumonisin biosynthesis was generally enhanced by both H_2O_2 concentrations with some differences (Figure 2A). Supplementation with 0.5 mM H_2O_2 appeared to increase expression of all seven genes between 3.4- and 10.5-fold, relative to their expression in the control culture. In contrast, supplementation with 4-fold more H_2O_2 (2 mM) appeared to minimally increase five genes (1.6- to 3.3-fold) while significantly increasing the expression of two genes between 16.3- and 18.6-fold. The inclusion of catalase to a culture supplemented with 0.5 mM H_2O_2 led to a slight decrease or minimal change in transcript levels for all seven genes, relative to the control culture.

In contrast, under the same conditions, the inhibited *Fv*1 strain showed a generalized decrease of fumonisin-related transcripts to levels similar to or lower than those observed in the control cultures (Figure 2B). Supplementation with 0.5 mM H_2O_2 led to insignificant differences in transcription of two genes relative to the control culture; four genes were inhibited (0.2- to 0.7-fold), while a slight increase was reported for one gene (1.25-fold). In contrast, supplementation with 2 mM H_2O_2 appeared to minimally increase two genes (1.4- to 2.5-fold) while the others reported no significant changes or a slight decrease (0.5-fold) relative to the control culture. The inclusion of catalase to a culture supplemented with 0.5 mM H_2O_2 led to a general decrease (0.3- to 0.6-fold) in transcript levels for all seven genes, relative to the control culture. This result shows that this fungal species could be composed of a heterogeneous population of toxigenic fungi that differentially respond to oxidative stress for the gene expression.

The regulatory *fcc1* gene encodes a putative receptor to sense environment or extracellular stress and interacts with other regulatory genes involved in conidiation and FB biosynthesis.[39,40] Until now, *fcc1p* has been found to be activated by pH signaling or nitrogen starvation;[40,41] however, we provide evidence that this gene is also differentially affected by oxidative stress in a strain-dependent manner. Comparable behavior was also evident under oxidative stress conditions for *fum21*, which encodes a $Zn^{II}_2Cys_6$ binuclear DNA-binding transcription factor for most of the genes involved in the fumonisin biosynthetic pathway.[22] Under lower stress conditions, *fum21* and *fum1* were upregulated in the promoted strains; the same behavior but with downregulation was observed in the inhibited strain, as expected for the role of FUM21, an upstream transcription factor of the *fum* cluster. The *fum1* gene encodes a polyketide synthase (PKS) required for fumonisin production. Changes in *fum1* expression during the stress conditions correlate with other PKS proteins that, although not linked to mycotoxin biosynthesis, are involved in detoxification, pigmentation, and virulence and are found to be responsive to H_2O_2.[42,43] As *fum19*, as well as *fum1*, is considered to be a good marker for fumonisin production,[44] its expression was surveyed. Expression of *fum19*, an ABC transporter involved in extracellular export of fumonisins and responsive to stress challenges,[45] appears to be more or less sensitive at lower or higher levels of H_2O_2, respectively, in promoted or inhibited strains; however, its regulation could depend on either the

DOI: 10.1021/acs.jafc.5b00113
J. Agric. Food Chem. 2015, 63, 4879−4885

oxidative stress or the amount of mycotoxin produced, and our results do not permit us to clarify this model. *Fum14* encodes a nonribosomal peptide synthetase (NRPS) necessary to confer toxicity to fumonisin, and its lack leads to the accumulation of hydrolyzed forms of FB_3 and FB_4.[46] The present results suggested an enhancement of *fum14* transcription in the presence of H_2O_2 supplementation, even if it was not strong relative to the other studied genes; this behavior is in accordance with previous findings in which the synthesis of fumonisins was reduced at high expression levels of *fum14*.[17] *Fum6* encodes a bifunctional cytochrome P450 monooxygenase-NADP reductase,[47] and *fum10* encodes an acyl-CoA synthase required for tricarballylic ester formation;[48] both were overexpressed with H_2O_2 concentrations of 2 mM. *Fum10* is upregulated, in both promoted and inhibited strains, whereas *fum6* follows the same behavior as *fum10* only in the promoted strain, indicating that the regulation of *fum6* is strain dependent. Further studies will be necessary to elucidate the role of these stress conditions on enzymatic activities of the *fum* gene products.

Since catalase has been proven to drastically reduce the *tri* gene expression levels in *F. graminearum*,[30] we investigated the effect of the enzyme on fumonisin gene expression in *F. verticillioides*. Here, we report that catalase downregulates the expression of *fum* genes in both the inhibited and promoted *Fv* strains in comparison to the control cultures, and this result correlates with the low amount of fumonisins produced in all of the five isolates studied.

■ ASSOCIATED CONTENT

Supporting Information

Tables and a figure giving optimized experimental parameters for LC-MS detection of fumonisins B_1−B_4, mass spectra of the pseudomolecular Ions $[M + H]^+$ of fumonisins B_1−B_4, recorded in high-resolution full-scan MS mode, and primers used for fumonisin-related gene expression analysis. The Supporting Information is available free of charge on the ACS Publications website at DOI: 10.1021/acs.jafc.5b00113.

■ AUTHOR INFORMATION

Corresponding Author

*R.C.: tel, +39-0498272887; fax, +39-0498272890; e-mail, roberto.causin@unipd.it.

Notes

The authors declare no competing financial interest.

■ REFERENCES

(1) Leslie, J. F. Mating population in *Gibberella fujikuroi* (Fusarium section Liseola). *Phytopathology.* **1991**, *81*, 1058−1060.
(2) Bacon, C. W.; Hinton, D. M. Symptomless endophytic colonization of maize by *Fusarium moniliforme*. *Can. J. Bot.* **1996**, *74*, 1195−1202.
(3) White, D. G. *Compendium of Corn Diseases*, 3rd ed.; American Phytopathological Society Press: Saint Paul, MN, 1999; p 128.
(4) Placinta, C.; D'Mello, J. P.; Macdonald, A. M. A review of worldwide contamination of cereal grains and animal feed with *Fusarium* mycotoxins. *Anim. Feed Sci. Technol.* **1999**, *78*, 21−37.
(5) Marasas, W. F. O. Fumonisins: Their implications for human and animal health. *Nat. Toxins* **1995**, *3*, 193−198.
(6) Logrieco, A.; Mulè, G.; Moretti, A.; Bottalico, A. Toxigenic *Fusarium* species and mycotoxins associated with maize ear rot in Europe. *Eur. J. Plant Pathol.* **2002**, *108*, 597−609.
(7) Schmidt-Heydt, M.; Magan, N.; Geisen, R. Stress induction of mycotoxin biosynthesis genes by abiotic factors. *FEMS Microbiol. Lett.* **2008**, *284*, 142−149.
(8) Jayashree, T.; Subramanyam, C. Oxidative stress as a prerequisite for aflatoxin production by *Aspergillus parasiticus*. *Free Radical Biol. Med.* **2000**, *29*, 981−985.
(9) Boutigny, A. L.; Richard-Forget, F.; Barreau, C. Natural mechanisms for cereal resistance to the accumulation of *Fusarium* trichothecenes. *Eur. J. Plant Pathol.* **2008**, *121*, 411−423.
(10) Ponts, N.; Pinson-Gadais, L.; Verdal-Bonnin, M. N.; Barreau, C.; Richard-Forget, F. Accumulation of deoxynivalenol and its 15-acetylated form is significantly modulated by oxidative stress in liquid cultures of *Fusarium graminearum*. *FEMS Microbiol. Lett.* **2006**, *258*, 102−107.
(11) Reverberi, M.; Punelli, M.; Smith, C. A.; Zjalic, S.; Scarpari, M.; Scala, V.; Cardinali, G.; Aspite, N.; Pinzari, F.; Payne, G. A.; Fabbri, A. A.; Fanelli, A. How peroxisomes affect aflatoxin biosynthesis in *Aspergillus flavus*. *PLoS One* **2012**, *7*, e48097.
(12) Ponts, N.; Pinson-Gadais, L.; Barreau, C.; Richard-Forget, F.; Ouellet, T. Exogenous H_2O_2 and catalase treatments interfere with *Tri* genes expression in liquid cultures of *Fusarium graminearum*. *FEBS Lett.* **2007**, *581*, 443−447.
(13) Apel, K.; Hirt, H. Reactive oxygen species, metabolism, oxidative stress, and signal transduction. *Annu. Rev. Plant Biol.* **2004**, *55*, 373−399.
(14) Zhao, Z.; Chen, G.; Zhang, C. Interaction between reactive oxygen species and nitric oxide in drought-induced abscisic acid synthesis in root tips of wheat seedlings. *Funct. Plant Biol.* **2001**, *28*, 1055−1061.
(15) Torres, M. A.; Jones, J. D. G.; Dangl, J. L. Reactive oxygen species signaling in response to pathogens. *Plant Physiol.* **2006**, *141*, 373−378.
(16) Dat, J.; Vandenabeele, S.; Vranová, E.; Montagu, M. V.; Inzé, D.; Breusegem, F. V. Dual action of the active oxygen species during plant stress responses. *Cell. Mol. Life Sci.* **2000**, *57*, 779−795.
(17) Medina, A.; Schmidt-Heydt, M.; Cárdenas-Chávez, D. L.; Parra, R.; Geisen, R.; Magan, N. Integrating toxin gene expression, growth and fumonisin B_1 and B_2 production by a strain of *Fusarium verticillioides* under different environmental factors. *J. R. Soc., Interface* **2013**, *10*, 20130320.
(18) Coma, V.; Portes, E.; Gardrat, C.; Richard-Forget, F.; Castellan, A. In vitro inhibitory effect of tetrahydrocurcuminoids on *Fusarium proliferatum* growth and fumonisin B_1 biosynthesis. *Food Addit. Contam., Part A* **2011**, *28*, 218−225.
(19) Pani, G.; Scherm, B.; Azara, E.; Balmas, V.; Jahanshiri, Z.; Carta, P.; Fabbri, D.; Dettori, M. A.; Fadda, A.; Dessì, A.; Dallocchio, R.; Migheli, Q.; Delogu, G. Natural and natural-like phenolic inhibitors of type B trichothecene *in vitro* production by the wheat (*Triticum* sp.) pathogen *Fusarium culmorum*. *J. Agric. Food Chem.* **2014**, *62*, 4969−4978.
(20) Tuite, J. In *Plant Pathological Methods: Fungi and Bacteria*; Tuite, J., Ed., Burgess: Minneapolis, MN, 1969; p 239.
(21) Mulè, G.; Susca, A.; Stea, G.; Moretti, A. A species-specific PCR assay based on the calmodulin partial gene for identification of *Fusarium verticillioides*, *F. proliferatum* and *F. subglutinans*. In *Molecular Diversity and PCR-detection of Toxigenic Fusarium Species and Ochratoxigenic Fungi*; Mulè, G., Bailey, J. A., Cooke, B. M., Logrieco, A., Eds.; Springer: Dordrecht, The Netherlands, 2004; pp 495−502.
(22) Brown, D. W.; Butchko, R. A. E.; Busman, M.; Proctor, R. H. The *Fusarium verticillioides* FUM gene cluster encodes a Zn(II)2Cys6 protein that affects *FUM* gene expression and fumonisin production. *Eukaryotic Cell* **2007**, *6*, 1210−1218.
(23) Rozen, S.; Skaletsky, H. Primer3 on the WWW for general users and for biologist programmers. In *Bioinformatics Methods and Protocols*; Misener, S., Krawetz, S. A., Eds.; Humana Press: New York, 1999; Vol. *132*, pp 365−386.
(24) Pfaffl, M. W. A new mathematical model for relative quantification in real-time RT−PCR. *Nucleic Acids Res.* **2001**, *29*, e45.

DOI: 10.1021/acs.jafc.5b00113
J. Agric. Food Chem. 2015, 63, 4879−4885

(25) Muller, P. Y.; Janovjak, H.; Miserez, A.; Dobbie, Z. Processing of gene expression data generated by quantitative real-time RT-PCR. *BioTechniques.* **2002**, *32*, 1372−1379.
(26) Jurado, M.; Marín, P.; Magan, N.; González-Jaén, M. T. Relationship between solute and matric potential stress, temperature, growth, and *FUM1* gene expression in two *Fusarium verticillioides* strains from Spain. *Appl. Environ. Microbiol.* **2008**, *74*, 2032−2036.
(27) Szécsi, Á.; Szekeres, A.; Bartók, T.; Oros, G.; Bartók, M.; Mesterházy, Á. Fumonisin B_{1-4}-producing capacity of Hungarian *Fusarium verticillioides* isolates. *World Mycotoxin J.* **2010**, *3*, 67−76.
(28) Etcheverry, M.; Torres, A.; Ramirez, M. L.; Chulze, S.; Magan, N. In vitro control of growth and fumonisin production by *Fusarium verticillioides* and *F. proliferatum* using antioxidants under different water availability and temperature regimes. *J. Appl. Microbiol.* **2002**, *92*, 624−632.
(29) Picot, A.; Barreau, C.; Pinson-Gadais, L.; Caron, D.; Lannou, C.; Richard-Forget, F. Factors of the *Fusarium verticillioides*-maize environment modulating fumonisin production. *Crit. Rev. Microbiol.* **2010**, *36*, 221−231.
(30) Ponts, N.; Couedelo, L.; Pinson-Gadais, L.; Verdal-Bonnin, M. N.; Barreau, C.; Richard-Forget, F. *Fusarium* response to oxidative stress by H_2O_2 is trichothecene chemotype-dependent. *FEMS Microbiol. Lett.* **2009**, *293*, 255−262.
(31) Carter, J. P.; Rezanoor, H. N.; Holden, D.; Desjardins, A. E.; Plattner, R. D.; Nicholson, P. Variation in pathogenicity associated with the genetic diversity of *Fusarium graminearum*. *Eur. J. Plant Pathol.* **2002**, *108*, 573−583.
(32) Glenn, A. E.; Zitomer, N. C.; Zimeri, A. M.; Williams, L. D.; Riley, R. T.; Proctor, R. H. Transformation-mediated complementation of a *FUM* gene cluster deletion in *Fusarium verticillioides* restores both fumonisin production and pathogenicity on maize seedlings. *Mol. Plant-Microbe Interact.* **2007**, *21*, 87−97.
(33) Overmyer, K.; Brosché, M.; Kangasjärvi, J. Reactive oxygen species and hormonal control of cell death. *Trends Plant Sci.* **2003**, *8*, 335−342.
(34) Eaton, C. J.; Cox, M. P.; Scott, B. What triggers grass endophytes to switch from mutualism to pathogenism? *Plant Sci.* **2011**, *180*, 190−195.
(35) Visentin, I.; Montis, V.; Döll, K.; Alabouvette, C.; Tamietti, G.; Karlovsky, P.; Cardinale, F. Transcription of genes in the biosynthetic pathway for fumonisin mycotoxins is epigenetically and differentially regulated in the fungal maize pathogen *Fusarium verticillioides*. *Eukaryotic Cell* **2012**, *11*, 252−259.
(36) Montis, V.; Pasquali, M.; Visentin, I.; Karlovsky, P.; Cardinale, F. Identification of a cis-acting factor modulating the transcription of *FUM1*, a key fumonisin-biosynthetic gene in the fungal maize pathogen *Fusarium verticillioides*. *Fungal Genet. Biol.* **2013**, *51*, 42−49.
(37) Marín, P.; de Ory, A.; Cruz, A.; Magan, N.; González-Jaén, M. T. Potential effects of environmental conditions on the efficiency of the antifungal tebuconazole controlling *Fusarium verticillioides* and *Fusarium proliferatum* growth rate and fumonisin biosynthesis. *Int. J. Food Microbiol.* **2013**, *165*, 251−258.
(38) Ochiai, N.; Tokai, T.; Nishiuchi, T.; Takahashi-Ando, N.; Fujimura, M.; Kimura, M. Involvement of the osmosensor histidine kinase and osmotic stress-activated protein kinases in the regulation of secondary metabolism in *Fusarium graminearum*. *Biochem. Biophys. Res. Commun.* **2007**, *363*, 639−644.
(39) Shim, W. B.; Woloshuk, C. P. Regulation of fumonisin B_1 biosynthesis and conidiation in *Fusarium verticillioides* by a cyclin-like (C-Type) gene, *FCC1*. *Appl. Environ. Microbiol.* **2001**, *67*, 1607−1612.
(40) Bluhm, B. H.; Woloshuk, C. P. Fck1, a C-type cyclin-dependent kinase, interacts with Fcc1 to regulate development and secondary metabolism in *Fusarium verticillioides*. *Fungal Genet. Biol.* **2006**, *43*, 146−154.
(41) Kohut, G.; Ádám, A. L.; Fazekas, B.; Hornok, L. N-starvation stress induced *FUM* gene expression and fumonisin production is mediated via the HOG-type MAPK pathway in *Fusarium proliferatum*. *Int. J. Food Microbiol.* **2009**, *130*, 65−69.
(42) Langfelder, K.; Jahn, B.; Gehringer, H.; Schmidt, A.; Wanner, G.; Brakhage, A. A. Identification of a polyketide synthase gene (*pksP*) of *Aspergillus fumigatus* involved in conidial pigment biosynthesis and virulence. *Med. Microbiol. Immunol.* **1998**, *187*, 79−89.
(43) Brakhage, A. A.; Liebmann, B. *Aspergillus fumigatus* conidial pigment and cAMP signal transduction, significance for virulence. *Med. Mycol.* **2005**, *43*, 75−82.
(44) López-Errasquín, E.; Vázquez, C.; Jiménez, M.; González-Jaén, M. T. Real-Time RT-PCR assay to quantify the expression of *fum1* and *fum19* genes from the fumonisin-producing *Fusarium verticillioides*. *J. Microbiol. Methods* **2007**, *68*, 312−317.
(45) Cruz, A.; Marín, P.; Magan, N.; González-Jaén, M. T. Combined effects of benomyl and environmental factors on growth and expression of the fumonisin biosynthetic genes *FUM1* and *FUM19* by *Fusarium verticillioides*. *Int. J. Food Microbiol.* **2014**, *191*, 17−23.
(46) Zaleta-Rivera, K.; Xu, C.; Yu, F.; Butchko, R. A. E.; Proctor, R. H.; Hidalgo-Lara, M. E.; Raza, A.; Dussault, P. H.; Du, L. A bidomain nonribosomal peptide synthetase encoded by *FUM14* catalyzes the formation of tricarballylic esters in the biosynthesis of fumonisins. *Biochemistry* **2006**, *45*, 2561−2569.
(47) Seo, J. A.; Proctor, R. H.; Plattner, R. D. Characterization of four clustered and coregulated genes associated with fumonisin biosynthesis in *Fusarium verticillioides*. *Fungal Genet. Biol.* **2001**, *34*, 155−165.
(48) Butchko, R. A. E.; Plattner, R. D.; Proctor, R. H. Deletion analysis of *FUM* genes involved in tricarballylic ester formation during fumonisin biosynthesis. *J. Agric. Food Chem.* **2006**, *54*, 9398−9404.

DOI: 10.1021/acs.jafc.5b00113
J. Agric. Food Chem. 2015, 63, 4879−4885

JOURNAL OF AGRICULTURAL AND FOOD CHEMISTRY

Article

pubs.acs.org/JAFC

Ptaquiloside, the Major Carcinogen of Bracken Fern, in the Pooled Raw Milk of Healthy Sheep and Goats: An Underestimated, Global Concern of Food Safety

Antonella Virgilio,[†] Annamaria Sinisi,[†] Valeria Russo,*[,‡] Salvatore Gerardo,[§] Adriano Santoro,[‡] Aldo Galeone,[†] Orazio Taglialatela-Scafati,[†] and Franco Roperto[#]

[†]Department of Pharmacy, Naples University Federico II, Via D. Montesano 49, 80131 Naples, Italy

[‡]Department of Veterinary Medicine and Animal Productions, Naples University Federico II, Via Delpino 1, 80137 Naples, Italy

[§]Assessorato Politiche della Persona, Ufficio Veterinario, Igiene Alimenti, Tutela Sanitaria Consumatori, Regione Basilicata, Viale Verrastro 9, 85100 Potenza, Italy

[#]Department of Biology, Naples University Federico II, Via Cinzia 21, 80126 Naples, Italy

ABSTRACT: Bracken fern (*Pteridium aquilinum*) is a worldwide plant containing toxic substances, which represent an important chemical hazard for animals, including humans. Ptaquiloside, **1**, a norsesquiterpenoid glucoside, is the major carcinogen of bracken detected in the food chain, particularly in the milk from farm animals. To date, ptaquiloside has been shown in the milk of cows feeding on a diet containing bracken fern. This is the first study that shows the systematic detection of ptaquiloside, **1**, and reports its direct quantitation in pooled raw milk of healthy sheep and goats grazing on bracken. Ptaquiloside, **1**, was detected by a sensitive method based on the chemical conversion of ptaquiloside, **1**, into bromopterosine, **4**, following gas chromatography−mass spectrometry (GC−MS) analysis. The presence of ptaquiloside, **1**, possibly carcinogenic to humans, in the milk of healthy animals is an unknown potential health risk, thus representing a harmful and potential global concern of food safety.

KEYWORDS: *bracken fern, ptaquiloside, pterosine, milk, sheep, goats*

INTRODUCTION

Bracken fern (*Pteridium aquilinum*) is a ubiquitous fern, one of the five most common plants on the planet.[1] This plant contains a number of toxic components, the consumption of which produces acute and chronic toxic syndromes in different animal species. Acute bracken poisoning is characterized by a thiamine deficiency in horses and pigs and a depression of bone marrow activity leading to severe leucopenia, thrombocytopenia, and acute hemorrhagic crisis in cattle. Chronic bracken poisoning is responsible for a progressive retinal degeneration, resulting in blindness in sheep, and is associated with tumors of the upper alimentary tract in cattle;[2] furthermore, it causes a syndrome known as chronic enzootic hematuria in cattle and in water buffaloes characterized morphologically by urothelial tumors of the urinary bladder and clinically by the presence of blood in the urine.[3,4]

Ptaquiloside, **1**, a norsesquiterpene glucoside of the illudane type, is known to be the major carcinogen of bracken, readily undergoing glucose elimination to form an unstable conjugated dieneone intermediate, named ptaquilodienone, **2**, and pterosine B, **3** (Figure 1).[5] The reactive cyclopropane moiety of ptaquilodienone, **2**, is capable of breaking DNA strands and/or alkylating selected DNA bases. Thus, the biological properties of ptaquiloside, **1**, are characterized by mutagenic, clastogenic, and carcinogenic effects.[6,7]

It has been suggested that bracken fern increases the oncogenic risk also in humans.[8,9] Indeed, ptaquiloside, **1**, is responsible for severe human chromosomal abnormalities[10,11] and is suspected of causing cancer in humans.[7,12−16]

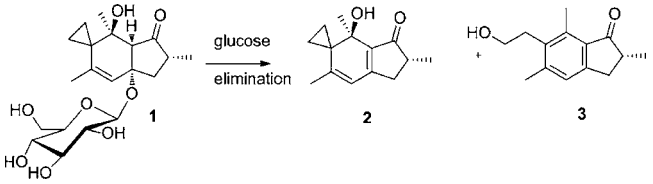

Figure 1. Structure of ptaquiloside, **1**, and of its degradation products ptaquilodienone, **2**, and pterosine B, **3**.

Epidemiological surveys revealed that bracken consumption is positively correlated with esophageal cancer in many geographical areas of the world[17] and with stomach cancer in population of farmers living in some rural regions of Wales and Costa Rica.[17−21]

Several routes may led to human exposure to ptaquiloside, **1**, namely, eating the plant,[22] breathing air containing bracken spores,[23] and consumption of milk and meat of affected animals.[24−26] Drinking water appears to be an additional important route of transmission.[27] Indeed, ptaquiloside, **1**, has been detected in both groundwater below bracken vegetation and surface water.[28]

Ptaquiloside, **1**, is responsible for H-Ras activation via an initial alkylation of adenine of the codon 61, resulting in a

Received: February 11, 2015
Revised: April 30, 2015
Accepted: May 1, 2015
Published: May 1, 2015

ACS Publications © 2015 American Chemical Society

DOI: 10.1021/acs.jafc.5b01937
J. Agric. Food Chem. 2015, 63, 4886−4892

transition (A to G) or transversion (A to T/C).[6] Any amino acid substitution at this position, except glutamic acid, blocks the guanosine triphosphate (GTP) hydrolysis of the Ras−GTP complex. The deregulation of hydrolysis is believed to result in the aberrant Ras signaling pathway, which causes an abnormal cell growth, proliferation, and survival.[29] Although oncogenic pathways remain to be elucidated, recent molecular studies provided new insights. Indeed, ptaquiloside, **1**, has been shown to induce a deregulation of the expression of a panel of genes related to cell cycle arrest in gastric epithelial cells. Furthermore, ptaquiloside, **1**, has been found to be responsible for glycophenotypic alterations of gastric mucosa and play a synergistic effect with *Helycobacter pylori* infection, leading to the gastric carcinogenesis process.[30,31]

Thus far, ptaquiloside, **1**, has been detected in milk of cows experimentally fed on a diet containing bracken fern.[32−34] It has been shown that the administration of milk from bracken-fed cows to mice was responsible for a high incidence of pulmonary and mammary tumors.[33] No systematic data are available about the naturally occurring presence of ptaquiloside, **1**, in milk of farm animals other than cows. The aim of the present paper is to report the detection and direct quantitation of ptaquiloside, **1**, in the pooled raw milk of healthy sheep and goats grazing on bracken fern-infested pastures, using a gas chromatography−mass spectrometry (GC−MS)-based method.

MATERIALS AND METHODS

Materials, Chemicals, and Reagents. Acetonitrile, ethyl ether, and ethyl acetate were purchased from Sigma-Aldrich (Milan, Italy). All solvents were of analytical grade and used as supplied. Ultrapure water was obtained from a Milli-Q plus system (Millipore, Bedford, MA). Sulfuric acid (Suprapur grade) was purchased from Merck (Darmstadt, Germany). Cartridges (1.2 cm inner diameter) filled with graphitized carbon black (500 mg of Carbograph 4) were prepared and provided by LARA (Rome, Italy). Carbograph 4 has a surface area of 200 m^2/g, and it is commercially also referred to as Carboprep (Resteck, Bellefonte, PA). Polyethylene frits (20 μm) were included. d_4-Bromopterosine, used as an internal standard in the calibration procedure, was synthesized according to a recent protocol.[35] Solutions of deuterated standard were prepared in methanol or ethyl acetate and stored at −20 °C.

Instrumentation. An Agilent Technologies 6850 Series II gas chromatograph, coupled with a 5973 mass selective detector (MSD) (Agilent Technologies, Santa Clara, CA), was used. The carrier gas was helium at 1.7 mL/min of 99.999% purity. The HP-5MS capillary column used was a 30 m × 0.25 mm inner diameter, 0.25 μm film thickness (Agilent, 5% phenyl methyl siloxane). The GC oven temperature was initially held at 100 °C for 1 min, then ramped at 20 °C/min to 280 °C, and held at this temperature for 2 min. Temperatures of injector and transfer line were 280 °C. Analyses were performed in splitless mode, and 0.5 μL was injected. The software MSDchem (Agilent Technologies) has been used to obtain graphics and quantitative data.

Calibration Procedure for Milk Samples. For the quantitative analysis of milk, a five-point calibration curve was obtained by spiking milk, free from ptaquiloside, **1**, with known amounts of internal standard to cover a concentration range of 3−20 ng/mL ptaquiloside, **1**. The amount of ptaquiloside, **1**, was determined in each experiment as previously described,[36] namely, by comparing the sum of the areas of three ions monitored m/z 187, 201, and 280 for the bromopterosine and m/z 189, 205, and 284 for the deuterated reference (d_4-bromopterosine). Each experimental value corresponds to the average of three independent measurements.

The limit of detection (LOD) and limit of quantitation (LOQ), calculated following the directives of the International Union of Pure and Applied Chemistry (IUPAC) and American Chemical Society's Committee on Environmental Analytical Chemistry, were 0.3 and 0.4 ng/mL, respectively. For comparison, the method recently published by Aranha and co-workers[34] declared a LOQ of 5.8 ng/mL.

Sample Preparation. Sample preparation was carried out following a protocol reported elsewhere.[37] The carbograph cartridge was washed with 6 mL of a mixture of acetonitrile/water (7:3, v/v); it was subsequently activated with diluted HCl (pH 2, 20 mL) and, finally, washed with 6 mL of water. A total of 10 mL of milk was passed through the cartridge; the eluate was discarded; and the cartridge was washed with 6 mL of water. The cartridge was then eluted with 7 mL of a mixture of acetonitrile/water (7:3, v/v), and 20 ng of d_4-bromopterosine and 2 g of NaBr were added to this eluate. After evaporation of the upper phase (acetonitrile) in nitrogen stream, the solution was made alkaline (pH 12) and heated at 45 °C for 1 h. The solution was cooled, acidified at pH 2, and extracted 3 times with ethyl ether. The resulting ether solution was evaporated to dryness, and finally, the extract was diluted to 20 μL in a micro (conical) test tube with ethyl acetate.

Collection of Milk Samples. For this study, flocks composed of both goats and sheep that had grazed on pasturelands covered by an abundance of bracken fern in several topographically distinct territories in southern Italy were selected. Milk samples were collected in different periods of the year from healthy sheep and goats sharing the same pastures located within 300−500 m above sea level (asl) (Martirano), within 500−800 m asl (Decollatura), and within 800−1000 m asl (Serrastretta and Carlopoli) altitudinal ranges. In Martirano, the flocks were composed of 117 crossbred sheep and 115 goats that have grazed on lands where bracken fern germinates in March−mid-April. Furthermore, in these lands, borage (*Borago officinalis* L.), Rowan tree (*Sorbus domestica* L.), myrtle (*Myrtus communis* L.), Scotch broom (*Spartium junceum* L.), poppy (*Papaver rhoeas* L.), chicory (*Cichorium intybus* L.), fennel (*Foeniculum vulgare* Mill.), blackberry bush (*Rubus ulmifolius* Schott), clover (*Trifolium pratense* L.), white clover (*Trifolium repens* L.), and sulla clover (*Hedysarum coronarium* L.) were also present. Flocks from Decollatura were composed of 124 Sarda sheep and 46 Maltese and Syria-derived goats that have grazed of lands covered with bracken fern, the fronds of which start to emerge from underground rhizomes in May. Amaranth (*Amaranthus retroflexus* L.), heather (*Erica arborea* L.), clematis (*Clematis vitalba* L.), butcher's broom (*Ruscus aculeatus* L.), ivy (*Hedera helix* L.), and hawthorn (*Crataegus monogyna* Jacq.) are the prevailing herbaceous plants of those lands. Flocks from Serrastretta were composed of 60 crossbred sheep and 67 Nicastrese goats; Carlopoli flocks were composed of 109 Sarda sheep and 100 crossbred, Saanen and Alpine, goats. Pigweed (*Portulaca oleracea* L.), asparagus (*Asparagus acutifolius* L.), aniseed (*Pimpinella anisum* L.), watercress (*Nasturtium officinale* R.), Italian ryegrass (*Lolium multiflorum* L.), tall fescue (*Festuca pratensis* Huds.), oregano (*Origanum heracleoticum* L.), bush (*Rubus canescens* DC.), strawberry (*Fragaria vesca* L.), wild rose (*Rosa canina* L.), horsetail (*Equisetum telmateia* Ehrh.), milk thistle [*Silybum marianum* (L.) Gaertn.], nettle (*Urtica dioica* L.), and wild lettuce [*Reichardia picroides* (L.) Roth.] were herbs prevalently found in the lands of Serrastretta and Carlopoli.

Furthermore, we collected pooled raw ovine and caprine milk samples from flocks composed of 90 crossbred sheep and 86 Nicastrese goats grazing on bracken fern-free lands located near the sea (Sant'Eufemia Gulf of Calabria, southern Italy). In these samples, no ptaquiloside, **1**, has been detected in either ovine or caprine milk.

In each flock, bulk ovine milk was harvested and separately kept from pooled caprine milk. The daily average of milk production for each flock was 60−80 L for ovine milk and 80−100 L for caprine milk. Following milking of all animals, the samples were obtained from tanks containing the pooled raw milk before undergoing any physical and/or other treatments. According to European Union (EU) legislation, "raw milk" is defined as milk produced by the secretion of the mammary gland of farmed animals that has not been heated to more than 40 °C or undergone any treatment that has an equivalent effect [Regulation (EC) No. 853/2004]. All milk samples were investigated within 1 week since harvesting.

Determination of Ptaquiloside, 1, Content. Determination of ptaquiloside, **1**, content in milk samples was obtained with the

DOI: 10.1021/acs.jafc.5b01937
J. Agric. Food Chem. 2015, 63, 4886−4892

previous method,[37] with small modifications. All of the analyses were made as triplicates. This method takes advantage of the click conversion of ptaquiloside, **1**, into bromopterosine, **4**, in the presence of bromide ions (Figure 2) and the stability and easy detectability of bromopterosine, **4**, by conventional GC−MS techniques.

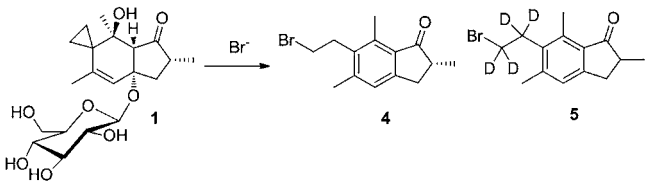

Figure 2. Structure of bromopterosine, **4**, obtained upon treatment of ptaquiloside, **1**, with bromide ions. On the right, the structure (**5**) represents the tetradeuterated standard obtained by total synthesis.

Fresh milk has been filtered over cartridges filled with graphitized carbon black, a matrix with high affinity toward free sugars and glycosylated compounds (such as ptaquiloside, **1**). Freezing and subsequent unfreezing of the milk resulted in a dense sample, likely because of protein precipitation, whose filtration over cartridges gave nonreproducible results, and therefore, this procedure was avoided.

Cartridges were then eluted with a mixture of acetonitrile/water (7:3, v/v), and the reference compound d_4-bromopterosine (**4**) (in place of d_2-bromopterosine used in the previous method) and NaBr were added to the eluate. After evaporation of the acetonitrile phase and workup, the resulting ethyl acetate solution was injected in the GC−MS instrument, using helium as the carrier gas and a HP-5MS capillary column.

RESULTS AND DISCUSSION

The amount of ptaquiloside, **1**, present was determined as a result of the comparison of the sum of the areas of three ions for bromopterosine (m/z 187, 201, and 280) and the corresponding ions of the deuterated reference compound (m/z 189, 205, and 284) (Figure 3). The obtained data, reported in Table 1, show a significant presence of ptaquiloside, **1**, in the milk of both goats and sheep and an absence in the milk from animals as controls. Ptaquiloside, **1**, was detected earlier in milk of goats that have grazed on lowlands (Martirano), which may suggest that the higher the altitude of land where the animals are at pasture, the later bracken fern toxin in the milk can be detected. Furthermore, higher doses have been detected in goat's milk rather than sheep's milk from the same mixed flocks and in the same seasonal period. Very likely, this is because goats more than sheep tend to browse young leaves and nibble the palatable shoots, such as bracken crosiers. It has been shown that ptaquiloside, **1**, occurs in the highest concentrations in the young developing part parts of bracken, such as the crosiers, and the unfolding parts during the spring and early summer.[7] Furthermore, it has been suggested that a few herbaceous plants other than bracken fern contain high levels of ptaquiloside, **1**.[38,39] The variety of herbs of all lands that we examined allowed us to suggest that ptaquiloside, **1**, came from bracken fern only. *Pteridium aquilinum* ssp. *aquilinum* (L.) Kuhn is the only species of bracken fern contaminating all of the lands where the animals, the milk of which we examined, have grazed. Therefore, also edaphic and/or environmental causes might influence the ptaquiloside, **1**, content detected in milk in different seasonal periods.

This is the first study that shows the systematic detection and reports the direct quantitation of ptaquiloside, **1**, in the pooled raw milk of healthy sheep and goats sharing pasturelands covered by bracken fern. The ptaquiloside, **1**, amount was detected by a sensitive method based on the chemical conversion of ptaquiloside, **1**, into bromopterosine, **4**, and following GC−MS analysis,[36,37] easily reproducible in non-specialized laboratories. Because this method has been reported to be able to quantitate up to 80% of ptaquiloside, **1**, present in the sample,[37] it is reasonable to presume that the real ptaquiloside, **1**, values in the pooled raw milk are even higher than we found. We have no data about the amount of bracken fern ingested daily; therefore, experimental procedures are needed to know ptaquiloside, **1**, metabolism in small animals too. It has been experimentally shown that the average value of total ptaquiloside, **1**, excreted in milk of cows is 8.6 ± 1.2% of the amount ingested; furthermore, ptaquiloside, **1**, was detected in milk, for the first time, 38 h after feeding cows with bracken fronds.[33] Direct quantitation of ptaquiloside, **1**, was evaluated in plasma and several tissues (liver, kidney, and skeletal muscle) after feeding two daily cows with a diet containing about 19% of *P. esculentum* for 25 days.[26] New sensitive methods allowing ptaquiloside, **1**, and its decay product, pterosine B, **3**, to be quantified directly and simultaneously in both soil, groundwater, and surface water[27,28] and biological fluids, such as plasma, urine, and milk, have been proposed.[34] All of these methods, including ours, showing low detection limits, have important implications for studies of ptaquiloside, **1**, toxicokinetics in animals and for screening animal tissues suitable for human consumption.

It has been recommended that the priority to reduce the risk to consumers from bracken should be the identification of the amount of ptaquiloside, **1**, that occurs in meat, offal, milk, and dairy products from animals naturally exposed to bracken without any signs of toxicity.[40] Thus far, reports about the presence of ptaquiloside, **1**, in milk and tissues have been from cows in experimental procedures.[26,32,33] No information was available on the amount of ptaquiloside, **1**, or other components of bracken that can occur in milk from animals naturally grazing on bracken fern-infested lands.[40] It is believed that the toxicity of bracken toward domestic animals may affect people too, particularly in the case of ptaquiloside-induced carcinogenesis.[12] Indeed, it has been suggested that ptaquiloside, **1**, can be potentially carcinogenic to humans at all levels of ingestion.[40]

Currently, the International Agency for Research on Cancer (IARC) assigned ptaquiloside, **1**, to Group 2B (possibly carcinogenic to humans) on the basis of epidemiological and experimental evidence. However, the sixth IARC Monographs Advisory Group on priorities for future evaluations made a urgency list of agents and exposures to be considered in the future IARC Monographs Programme. The IARC Group considers ptaquiloside, **1**, and bracken fern high priorities among "naturally occurring substances". Furthermore, the IARC Group recommends that new animal carcinogenicity data should be collected soon and encourages the need to have more defined molecular, epidemiological, and ecological aspects of the impact of bracken fern.[41] In this context, it is worthwhile remembering that urinary bladder tumors caused by ptaquiloside, **1**, intoxication have recently been described, for the first time, in captive fallow deer.[42] Furthermore, a novel syndrome characterized by intestinal adenocarcinomas in adult farmed Sika deer that have grazed on bracken-infested pastures has just been described. Therefore, it has been suggested that ptaquiloside, **1**, plays a crucial role in deer intestinal tumorigenesis too.[43]

DOI: 10.1021/acs.jafc.5b01937
J. Agric. Food Chem. 2015, 63, 4886−4892

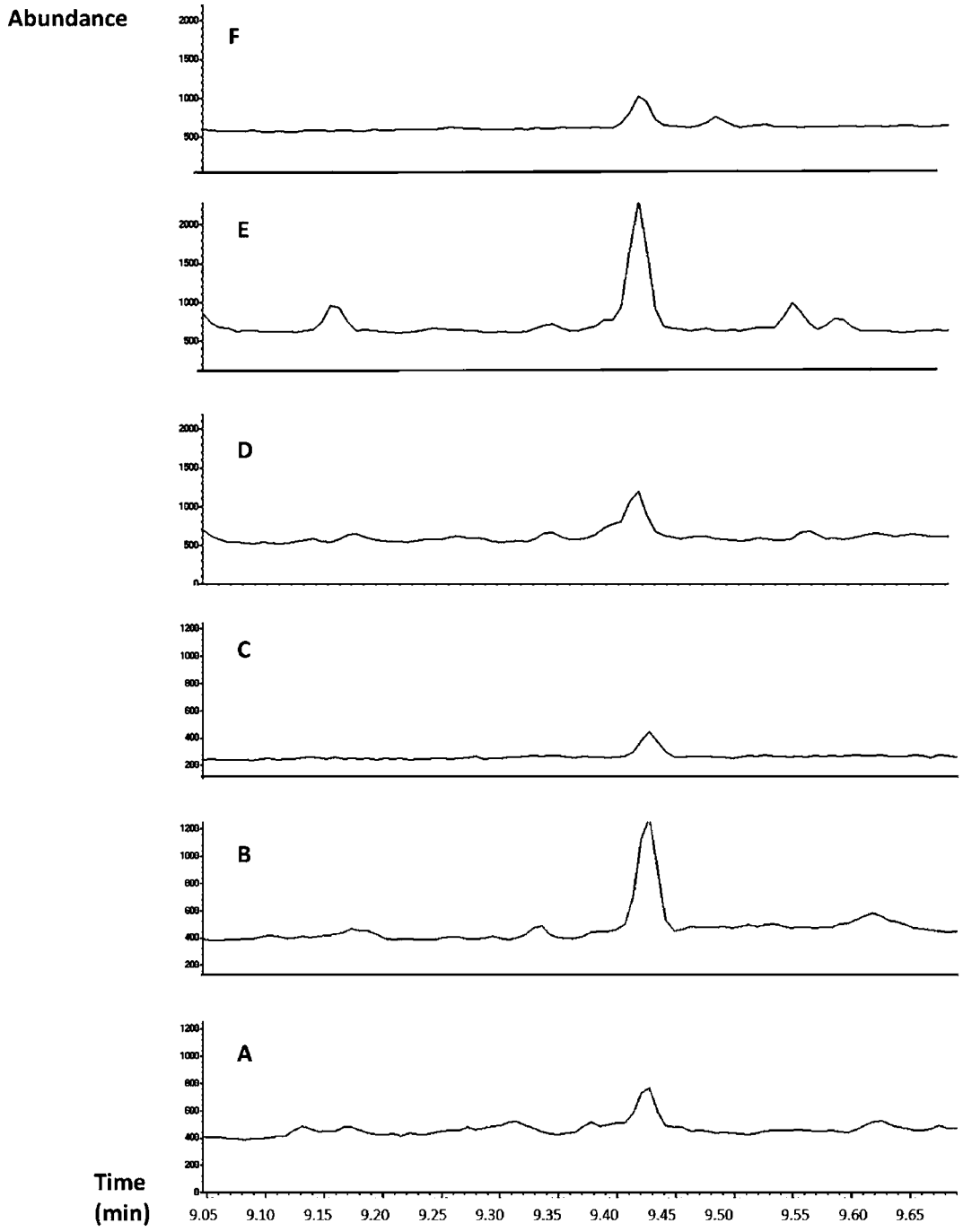

Figure 3. Representative GC traces of the monitored ions. The graphic corresponds to the sample goat/Decollatura/June 2014 in Table 1. Panels A, B, and C refer to the monitoring of ions at m/z 187, 201, and 280. Panels D, E, and F refer to the corresponding deuterated ions at m/z 189, 205, and 284. The retention time of the analyte is 9.42 min.

Finally, it is well-known that thousands of chemicals to which humans are exposed have inadequate data useful to predict their potential for toxicological effects.[44] Risk assessment of ptaquiloside, **1**, presents particular difficulties because the effects of some substances are normally regarded as being without a threshold.[45] Therefore, how long ptaquiloside, **1**, takes to reach toxicological thresholds necessary for its identification and characterization as hazardous, two important steps in the concept of "safe levels of exposure", remains to be elucidated.[46]

Recent epidemiological studies emphasize the potential role of sheep's milk and goats' milk as a risk factor for esophageal squamous cell carcinoma in the high risk area of northern Iran.[47,48] It has been shown that low doses of diterpene ester toxins can be detected in the milk of small ruminants fed by a family of Euphorbiaceae flower plants; therefore, it has been suggested that the high incidence of esophageal cancer observed in certain areas in the Caspian littoral of Iran may be associated with a greater consumption of sheep's milk and goats' milk contaminated by these toxins.[49]

The stability of ptaquiloside, **1**, and its hydrolysis have already been carefully analyzed according to different pH conditions in aqueous solutions.[5] Further interesting aspects to be investigated in the near future are (i) the effect of thermal

DOI: 10.1021/acs.jafc.5b01937
J. Agric. Food Chem. 2015, 63, 4886−4892

Table 1. Amounts of Ptaquiloside Content Found in Milk Samples

animal	collection and analysis date	place (farm) of collection	bromopterosine content (ng/mL)[a]	ptaquiloside content (ng/mL)[b]
goat	March 2014	Martirano	<LOD[c]	
goat	May 2014	Martirano	0.68 ± 0.14	0.97 ± 0.20
goat	June 2014	Martirano	0.45 ± 0.12	0.64 ± 0.17
goat	April 2014	Decollatura	<LOD	
goat	May 2014	Decollatura	<LOD	
goat	June 2014	Decollatura	1.45 ± 0.25	2.06 ± 0.35
goat	July 2014	Decollatura	1.29 ± 0.18	1.83 ± 0.26
goat	June 2014	Serrastretta	0.40 ± 0.09	0.57 ± 0.13
goat	July 2014	Serrastretta	0.43 ± 0.11	0.61 ± 0.16
goat	September 2014	Serrastretta	0.40 ± 0.08	0.57 ± 0.11
goat	July 2013	Carlopoli	0.77 ± 0.15	1.09 ± 0.21
goat	December 2013	Carlopoli	2.21 ± 0.27	3.14 ± 0.38
sheep	March 2014	Martirano	<LOD	
sheep	June 2014	Martirano	<LOD	
sheep	April 2014	Decollatura	<LOD	
sheep	May 2014	Decollatura	<LOD	
sheep	June 2014	Decollatura	0.60 ± 0.12	0.85 ± 0.17
sheep	July 2014	Decollatura	<LOD	
sheep	June 2014	Serrastretta	<LOD	
sheep	July 2014	Serrastretta	<LOD	
sheep	September 2014	Serrastretta	<LOD	
sheep	July 2013	Carlopoli	0.96 ± 0.18	1.36 ± 0.26
sheep	December 2013	Carlopoli	1.15 ± 0.21	1.63 ± 0.30
goat/C[d]	April 2015	Sant'Eufemia	<LOD	
sheep/C	April 2015	Sant'Eufemia	<LOD	

[a]Each value corresponds to the average of three distinct experiments. [b]Indirectly derived from the bromopterosine content. [c]LOD = limit of detection. [d]C = control.

treatment on ptaquiloside, **1**, dose naturally present in milk of farm animals, (ii) determination of naturally occurring ptaquiloside, **1**, in meat and dairy products for human consumption in animals naturally grazing on pasturelands with bracken abundance, and (iii) functional studies in an attempt to show the relationship, if any, between ptaquiloside, **1**, and intracellular catabolic systems, such autophagy and apoptosis. The design and implementation of the analytical methods useful to reach the above goals are underway in our laboratories.

AUTHOR INFORMATION

Corresponding Author

*Telephone: +39-081-2536468. Fax: +39-081-2536186. E-mail: valeria.russo@unina.it.

Funding

This work was sponsored in part by grants from the Ministero Italiano delle Politiche Agricole, Agroalimentari e Forestali (MIPAAF), the Regione Campania, and the Regione Basilicata.

Notes

The authors declare no competing financial interest.

ACKNOWLEDGMENTS

The authors are grateful to M. S. Campo, Professor Emeritus, University of Glasgow, U.K., and M. Alonso-Amelot, Universidad of Los Andes (ULA), Mérida, Venezuela, for reading the manuscript and their useful comments and G. Sindona, Unical University, Cosenza, Italy, for providing us d_4-bromopterosine.

REFERENCES

(1) Tailor, J. A. The bracken problem: A global perspective. In *Bracken Biology and Management*; Thomson, J. A., Smith, R. T., Eds.; The Australian Institute of Agricultural Science: Wahroonga, New South Wales, Australia, 1990; Vol. *40*, pp 3−20.

(2) Smith, B. L. Bracken fern and animal health in Australia and New Zealand. In *Bracken Biology and Management*; Thomson, J. A., Smith, R. T., Eds.; The Australian Institute of Agricultural Science: Wahroonga, New South Wales, Australia, 1990; Vol. *40*, pp 227−232.

(3) Campo, M. S.; Jarrett, W. F. H.; Barron, R.; O'Neil, B. W.; Smith, K. T. Association of bovine papillomavirus type 2 and bracken fern with bladder cancer in cattle. *Cancer Res.* **1992**, *52*, 6898−6904.

(4) Roperto, S.; Russo, V.; Ozkul, A.; Sepici-Dincel, A.; Maiolino, P.; Borzacchiello, G.; Marcus, I.; Esposito, I.; Riccardi, M. G.; Roperto, F. Bovine papillomavirus type 2 infects the urinary bladder of water buffalo (*Bubalus bubalis*) and plays a crucial role in bubaline urothelial carcinogenesis. *J. Gen. Virol.* **2013**, *94*, 403−408.

(5) Ayala-Luis, K. B.; Hansen, H. C. B.; Rasmussen, L. H.; Hansen, H. C. B. Kinetics of ptaquiloside hydrolysis in aqueous solution. *Environ. Toxicol. Chem.* **2006**, *25*, 2623−2629.

(6) Prakash, A. S.; Pereira, T. N.; Smith, B. L.; Shaw, G.; Seawright, A. A. Mechanism of bracken fern carcinogenesis: Evidence for H-ras activation via initial adenine alkylation by ptaquiloside. *Nat. Toxins* **1996**, *4*, 221−227.

(7) Yamada, K.; Ojika, M.; Kigoshi, H. Ptaquiloside, the major toxin of bracken, and related terpene glycosides: Chemistry, biology and ecology. *Nat. Prod. Rep.* **2007**, *24*, 798−813.

(8) Kamon, S.; Hirayama, T. Epidemiology of cancer of the oesophagus in Miye, Nara and Wakayama prefectures with special reference to the role of bracken fern. *Proc. Jpn. Cancer Assoc.* **1975**, *34*, 211.

(9) Hirayama, T. Diet and cancer. *Nutr. Cancer* **1979**, *1*, 67−81.

(10) Recouso, R. C.; Stocco dos Santos, R. C.; Freitas, R.; Santos, R. C.; de Freitas, A. C.; Brunner, O.; Beçak, W.; Lindsey, C. J. Clastogenic effect of bracken fern (*Pteridium aquilinum* v.

DOI: 10.1021/acs.jafc.5b01937
J. Agric. Food Chem. 2015, 63, 4886−4892

arachnoideum) diet in peripheral lymphocytes of human consumers: Preliminary data. *Vet. Comp. Oncol.* **2003**, *1*, 22−29.
(11) Gil da Costa, R. M.; Coelho, P.; Sousa, R.; Bastos, M. M.; Porto, B.; Teixeira, J. P.; Malheiro, I.; Lopes, C. Multiple genotoxic activities of ptaquiloside in human lympocytes aneugenesis, clastogenesis and induction of sister chromatid exchange. *Mutat. Res., Genet. Toxicol. Environ. Mutagen.* **2012**, *747*, 77−81.
(12) Gil da Costa, R. M.; Bastos, M. M. S. M.; Oliveira, P. A.; Lopes, C. Bracken-associated human and animal health hazards: Chemical, biological and pathological evidence. *J. Hazard. Mater.* **2012**, *203*−*204*, 1−12.
(13) Rasmussen, L. H.; Schmidt, B.; Sheffield, E. Ptaquiloside in bracken spores from Britain. *Chemosphere* **2013**, *90*, 2539−2541.
(14) Sharma, R.; Bhat, T. K.; Sharma, O. P. The environmental and human effects of ptaquiloside-induced enzootic bovine hematuria: A tumorous disease of cattle. *Rev. Environ. Contam. Toxicol.* **2013**, *224*, 53−95.
(15) Tourchi-Roudsari, M. Multiple effects of bracken fern under *in vivo* and *in vitro* conditions. *Asian Pac. J. Cancer Prev.* **2014**, *15*, 7505−7513.
(16) Vetter, J. A biological hazard of our age: Bracken fern [*Pteridium aquilinum* (L.) Khun]—A review. *Acta Vet. Hung.* **2009**, *57*, 183−196.
(17) Marliére, C. A.; Wathern, P.; Castro, M. C.; O'Connor, P.; Galvao, M. A. Bracken fern (*Pteridium aquilinum*) ingestion and oesophageal and stomach cancer. *IARC Sci. Publ.* **2002**, *156*, 379−380.
(18) Alonso-Amelot, M. E.; Avendaño, M. Possible association between gastric cancer and bracken fern in Venezuela: An epidemiologic study. *Int. J. Cancer* **2001**, *91*, 252−259.
(19) Alonso-Amelot, M. E.; Avendaño, M. Human carcinogenesis and bracken fern: A review of the evidence. *Curr. Med. Chem.* **2002**, *9*, 675−685.
(20) Alonso-Amelot, M. E.; Avendaño Meza, M. Gastric cancer conglomerates in Mérira State, Venezuela. *Intercencia* **2009**, *34*, 617−622.
(21) Potter, D. M.; Baird, M. S. Carcinogenic effects of ptaquiloside in bracken fern and related compounds. *Br. J. Cancer* **2000**, *83*, 914−920.
(22) Hirono, I.; Yamada, K. Bracken fern. In *Natural Occurring Carcinogens of Plant Origin—Toxicology, Pathology and Biochemistry*; Hirono, I., Ed.; Kodanska: Tokyo, Japan, 1987; pp 87−120.
(23) Galpin, O. P.; Whitaker, C. J.; Whitaker, R.; Kassab, J. Y. Gastric cancer in Gwynedd. Possible link with bracken. *Br. J. Cancer* **1990**, *61*, 737−740.
(24) Alonso-Amelot, M.; Castillo, U. F.; De Jong, F. Passage of the bracken fern carcinogen ptaquiloside into bovine milk. *Lait* **1993**, *73*, 323−332.
(25) Alonso-Amelot, M. The link between bracken fern and stomach cancer: Milk. *Nutrition* **1997**, *13*, 694−696.
(26) Fletcher, M. T.; Reichmann, K. G.; Brock, I. J.; McKenzie, R. A.; Blaney, B. J. Residue potential of norsesquiterpene glycosides in tissues of cattle fed austral bracken (*Pteridium esculentum*). *J. Agric. Food Chem.* **2011**, *59*, 8518−8523.
(27) Jensen, P. H.; Jacobsen, O. S.; Hansen, H. C. B.; Juhler, R. K. Quantification of ptaquiloside and pterosin B in soil and groundwater using liquid chromatography−tandem mass spectrometry (LC−MS/MS). *J. Agric. Food Chem.* **2008**, *56*, 9848−9854.
(28) Clauson-Kaas, F.; Jensen, P. H.; Jacobsen, O. S.; Juhler, R. K.; Hansen, H. C. B. The naturally occurring carcinogen ptaquiloside is present in groundwater below bracken vegetation. *Environ. Toxicol. Chem.* **2014**, *33*, 1030−1034.
(29) Schubbert, S.; Shannon, K.; Bollag, G. Hyperactive Ras in developmental disorders and cancer. *Nat. Rev. Cancer* **2007**, *7*, 295−308.
(30) Gomes, J.; Magalhães, A.; Carvalho, A. S.; Hernandez, G. E.; Papp, S. L.; Head, S. R.; Michel, V.; David, L.; Gärtner, F.; Touati, E.; Reis, C. A. Glycophenotypic alterations induced by Pteridium aquilinum in mice gastric mucosa: synergistic effect with *Helicobacter pylori* infection. *PLoS One* **2012**, *7* (6), No. e38353.
(31) Gomes, J.; Magalhães, A.; Michel, V. E.; Amado, I. F.; Aranha, P.; Ovesen, R. G.; Hansen, H. C. B.; Gärtner, F.; Reis, C. A.; Touati, E. *Pteridium aquilinum* and its ptaquiloside toxin induce DNA damage response in gastric epithelial cells, a link with gastric carcinogenesis. *Toxicol. Sci.* **2012**, *126*, 60−71.
(32) Alonso-Amelot, M. E.; Castillo, U.; Smith, B. L.; Lauren, D. R. Bracken ptaquiloside in milk. *Nature* **1996**, *382*, 587.
(33) Villalobos Salazar, J.; Hernandez, H.; Meneses, A.; Salazar, G. Factors which may affect ptaquiloside levels in milk: Effects of altitude, bracken fern growth stage, and milk processing. In *Bracken: Toxicity, Biology and Control*; Thomson, J. A., Smith, R. T., Eds.; International Group: Manchester, U.K., 2000; pp 68−73.
(34) Aranha, P. C. R.; Hansen, H. C. B.; Rasmussen, L. H.; Strobel, B. W.; Friis, C. Determination of ptaquiloside and pterosin B derived from bracken (*Pteridium aquilinum*) in cattle plasma, urine and milk. *J. Chromatogr. B: Anal. Technol. Biomed. Life Sci.* **2014**, *951*−*952*, 44−51.
(35) Attya, M.; Nardi, M.; Tagarelli, A.; Sindona, G. A new facile synthesis of d4-pterosin B and d4-bromopterosin, deuterated analogues of ptaquiloside. *Molecules* **2012**, *17*, 5795−5802.
(36) Bonadies, F.; Borzacchiello, G.; Dezzi, S.; Nicoletti, R.; Roperto, S. Mass spectrometric analysis of ptaquiloside, the toxic sesquiterpene from bracken fern. *Rapid Commun. Mass Spectrom.* **2004**, *18*, 825−828.
(37) Francesco, B.; Giorgio, B.; Rosario, N.; Saverio, R. F.; Francesco, D. G.; Romano, M.; Adriano, S.; Cinzia, R.; Antonio, T.; Franco, R.; Valeria, R.; Sante, R. A new, very sensitive method of assessment of ptaquiloside, the major bracken carcinogen in the milk of farm animals. *Food Chem.* **2011**, *124*, 660−665.
(38) Rasmussen, L. H.; Donnelly, E.; Strobel, B. W.; Holm, P. E.; Hansen, H. C. B. Land management of bracken needs to account for bracken carcinogens—A case study from Britain. *J. Environ. Manage.* **2015**, *151*, 258−266.
(39) Somvanshi, R.; Lauren, D. R.; Smith, B. L.; Dawra, R. K.; Sharma, O. P.; Sharma, V. K.; Singh, A. K.; Gangwar, N. K. Estimation of the fern toxin, ptaquiloside, in certain Indian ferns other than bracken. *Curr. Sci.* **2006**, *11*, 1547−1552.
(40) Committees on the Toxicity (COT), Mutagenicity (COM) and Carcinogenicity (COC) of Chemicals in Food, Consumer Products and the Environment. *Annual Report*; COT, COM, and COC: London, U.K., 2008; http://tna.europarchive.org/20130802141804/http://cot.food.gov.uk/cotreports/.
(41) International Agency for Research on Cancer (IARC). *Report of an Ad-Hoc IARC Monographs Advisory Group on Priorities for Future Evaluations*; IARC: Lyon, France, Feb 11−14, 2003; IARC Internal Report 03/001.
(42) Scala, C.; Ortiz, K.; Catinaud, J.; Lemberger, K. Hematuria and urinary bladder lesions compatible with bracken fern (*Pteridium aquilinum*) intoxication in captive fallow deer (*Dama dama*). *J. Zoo Wildl. Med.* **2014**, *45*, 380−385.
(43) Kelly, P. A.; Toolan, D.; Jahns, H. Intestinal adenocarcinoma in a herd of farmed Sika deer (*Cervus nippon*): A novel syndrome. *Vet. Pathol.* **2015**, *52*, 193−200.
(44) Tice, R. R.; Austin, C. P.; Kavlock, R. J.; Bucher, J. R. Improving to human hazard characterization of chemicals: A Tox21 update. *Environ. Health Perspect.* **2013**, *121*, 756−765.
(45) Pratt, I.; Barlow, S.; Kleiner, J.; Larsen, J. C. The influence of thresholds on the risk assessment of carcinogen in food. *Mut. Res.* **2009**, *678*, 113−117.
(46) Dybing, E.; O'Brien, J.; Renwick, A. G.; Sanner, T. Risk assessment of dietary exposure to compounds that are genotoxic and carcinogenic—An overview. *Toxicol. Lett.* **2008**, *180*, 110−117.
(47) Hormozdiari, H.; Day, N. E.; Aramesh, B.; Mahboubi, E. Dietary factors and esophageal cancer in the Caspian littoral of Iran. *Cancer Res.* **1975**, *35*, 3493−3498.
(48) Nasrollahzadeh, D.; Ye, W.; Shakeri, R.; Sotoudeh, M.; Merat, S.; Kamangar, F.; Abnet, C. C.; Islami, F.; Boffetta, P.; Dawsey, S. M.; Brennan, P.; Malekzadeh, R. Contact with ruminants is associated with esophageal squamous cell carcinoma risk. *Int. J. Cancer* **2015**, *136*, 1468−1474.

DOI: 10.1021/acs.jafc.5b01937
J. Agric. Food Chem. 2015, 63, 4886−4892

(49) Zayed, S. M.; Farghaly, M.; Taha, H.; Gminski, R.; Hecker, E. Dietary cancer risk from conditional cancerogens in produce of livestock fed on species of spurge (*Euphorbiaceae*). III. Milk of lactating goats fed on the skin irritant herb *Euphorbia peplus* is polluted by tumor promoters of the ingenane diterpene ester type. *J. Cancer Res. Clin. Oncol.* **1998**, *124*, 301−306.

DOI: 10.1021/acs.jafc.5b01937
J. Agric. Food Chem. 2015, 63, 4886−4892

JOURNAL OF AGRICULTURAL AND FOOD CHEMISTRY

Article

pubs.acs.org/JAFC

Excretory, Secretory, and Tissue Residues after Label and Extra-label Administration of Flunixin Meglumine to Saline- or Lipopolysaccharide-Exposed Dairy Cows

David J. Smith,*[,†] Weilin L. Shelver,[†] Ronald E. Baynes,[#] Lisa Tell,[§] Ronette Gehring,[⊥] Mengjie Li,[⊥] Terry Dutko,[Δ] J. W. Schroeder,[‡] Grant Herges,[†] and Jim E. Riviere[⊥]

[†]Biosciences Research Laboratory, USDA-ARS, 1605 Albrecht Boulevard, Fargo, North Dakota 58102, United States

[#]College of Veterinary Medicine, North Carolina State University, Raleigh, North Carolina 27607, United States

[§]School of Veterinary Medicine, University of California, Davis, California 95616, United States

[⊥]Institute of Computational Comparative Medicine, College of Veterinary Medicine, Kansas State University, Manhattan, Kansas 66506, United States

[Δ]Office of Public Health Science, Midwestern Laboratory, USDA-FSIS, 4300 Goodfellow Boulevard, St. Louis, Missouri 63120, United States

[‡]Department of Animal Sciences, North Dakota State University, P.O. Box 6050, Fargo, North Dakota 58108, United States

Supporting Information

ABSTRACT: Twenty lactating dairy cattle were intravenously infused with either lipopolysaccharide (LPS) (n = 10) or sterile saline (n = 10). Five cattle in each group received three doses of flunixin meglumine administered by either intravenous infusion or intramuscular injection at 24 h intervals. Milk, urine, and tissues were collected. Thirty-six hours after the last flunixin administration, milk from six cows contained 5-hydroxyflunixin (5OHF) levels greater than the milk tolerance of 2 ng/mL; by 48 h, milk from two cows, a saline and a LPS-treated animal, had violative milk concentrations of 5OHF. A single animal treated with LPS and intramuscular flunixin contained violative flunixin residues in liver. The ratio of urinary flunixin/5OHF was correlated (P < 0.01; R^2 = 0.946) with liver flunixin residues in LPS-treated animals, but not (P = 0.96; R^2 = 0.003) in cows treated with saline in lieu of LPS. Violative residues of flunixin in dairy cattle may be related to LPS inhibition of flunixin metabolism.

KEYWORDS: *dairy, extra-label, flunixin, holstein, liver, metabolite ratio, milk, residue*

INTRODUCTION

Flunixin meglumine is a nonsteroidal anti-inflammatory analgesic with antipyretic activities. Approval for flunixin use in cattle to treat pyrexia associated with bovine respiratory disease and to treat pyrexia and inflammation in endotoxemia has been granted[1] by the U.S. Food and Drug Administration (FDA) Center for Veterinary Medicine (CVM). The label was extended in 2004[2] to include lactating dairy cattle for the control of pyrexia associated with mastitis. Under label specifications, flunixin meglumine may be administered to cattle as an intravenous infusion (iv) of 1.1−2.2 mg/kg body weight. Infusion should occur either once per day as a single dose or twice per day as two doses separated by approximately 12 h for a maximum of three consecutive days. In practice it is often difficult to administer flunixin meglumine or other drugs by iv infusion to cattle, especially on a repeated basis. As a consequence, flunixin meglumine is commonly administered via intramuscular (im) or subcutaneous (sc) injection. In 2007, the CVM reminded veterinarians that im flunixin meglumine has the potential to cause violative residues in meat or milk products of cattle and that convenience is not an acceptable basis for extra-label flunixin use.[3] Due to the persistent problem of violative flunixin residues, especially in dairy cattle,[4,5] the bases for these violations remains to be of interest to producers, regulatory agencies, and consumers.

Although the United States has an excellent regulatory system for minimizing drug residues in meat and milk products, instances of violative residues do occur. For example, in 2011 the USDA FSIS confirmed 974 instances of violative chemical residues in inspector-generated samples screened using the kidney inhibition swab (KIS).[4] Of these violations, 15% (142) were violations with flunixin. All of the flunixin violations were in cattle, with no violations in hogs. The major contributor to total flunixin violations was in dairy cows, comprising 63% of the total violations, with veal calves (23%) and beef cows and steers (14%) accounting for the remaining violations.[4] Data from 2012[5] indicated a similar trend with 928 instances of violative chemical residues in inspector-generated samples screened using the KIS assay and confirmed with selective assays. Of these violations, 11% (101) were due to excessive flunixin residue. Similar to 2011, all of the flunixin residue violations occurred in cattle. Dairy cows comprised 58% of the

Received: March 25, 2015
Revised: April 24, 2015
Accepted: April 27, 2015
Published: May 7, 2015

ACS Publications © 2015 American Chemical Society

DOI: 10.1021/acs.jafc.5b01509
J. Agric. Food Chem. 2015, 63, 4893−4901

2011 flunixin violations; veal calves (19%) and beef cows and steers (14%) were the bulk of the remaining violations. The magnitude of flunixin residues has been reported sufficient to cause the contamination of bulk milk. For example, Kissell et al.[6] measured a violation rate of 0.2% for residues of 5-hydroxyflunixin (5OHF, the marker residue for flunixin in milk) in bulk milk from tanker trucks. Deyrup et al.[7] have suggested that the probability of a violative flunixin residue increases in cull dairy cows that appear as "suspect", with suspect including animals that appear to be lame, that appear to have mastitis, metritis, or that have lesions associated with injection. Kinetic studies in beef cattle[8] have shown that rates of plasma flunixin depletion did not differ ($P > 0.05$) after subcutaneous or intravenous administration, but a study with larger numbers of dairy cattle indicated that the dosing route did influence terminal half-lives of flunixin.[9]

Another contributing factor to flunixin violations could be drug use with an insufficient preslaughter withdrawal period. Alternatively, violations could occur after flunixin is dosed to sick animals even after observation of the required 4 day withdrawal period. The latter instance could occur if illness affects the kinetics of flunixin elimination, as suggested by the data of Kissell et al.[10] in mastitic cows treated with flunixin. For example, because flunixin tends to accumulate in inflamed tissues,[11,12] its release from those tissues in animals with systemic infection could be altered significantly. In addition, flunixin efficacy is maintained even when plasma or serum concentrations are very low.[13] Collectively, such observations suggest that nonplasma tissue pools of flunixin exist, but the locations of these "deep compartments" are unknown. Pharmacokinetic parameters of serum flunixin, however, did not differ after experimental induction of mastitis by mammary inoculation with *Escherichia coli*.[14] In cows having naturally occurring mastitis, however, flunixin clearance (mL/h/kg) decreased and area under the curve (μg·h/mL) increased, relative to healthy cows.[10]

We hypothesized that route of administration or systemic inflammation could significantly alter flunixin kinetics and tissue residues in lactating dairy cows. If true, flunixin violations could occur in healthy or sick animals dosed intramuscularly with the maximum label dose (2.2 mg/kg bw) for the maximum dosing period of three consecutive days, but slaughtered with the label withdrawal period of 4 days. The systemic inflammatory responses observed during mastitis in cows can be mimicked by systemic lipopolysaccharide (LPS) administration.[15] Therefore, the objective of this study was to determine the tissue residues of flunixin after intravenous (label) and intramuscular (off-label) administration of flunixin meglumine to healthy and LPS-challenged dairy cows in regulated (milk, muscle, liver, kidney, adipose) and nonregulated (offal) tissues and urine.

MATERIALS AND METHODS

Study Overview. The study was designed and conducted as a 2 × 2 factorial experiment (Table 1) with main factors being route of drug administration (iv or im) and lipopolysaccharide challenge (LPS or saline). The study was conducted as five replicate trials for a total "*n*" of five cows per treatment, with each treatment being replicated once in each trial. Lactating Holstein cows were randomly assigned to receive either an iv infusion of 0.2 μg/kg BW of LPS (endotoxin) or saline. Two hours after LPS or saline infusion, each cow received 2.2 mg/kg BW of flunixin meglumine either by iv infusion or by im injection. Flunixin administration was repeated 24 and 48 h after the first flunixin dose; cows were slaughtered 96 h after the final flunixin administration. During the dosing and withdrawal periods, blood, milk, urine, and saliva were serially collected at predetermined intervals. Saliva data, however, are not reported in this treatise. A detailed animal use protocol was reviewed and approved by the North Dakota State University Institutional Animal Care and Use Committee (IACUC) prior to the initiation of the live phase of the study.

Table 1. Study Design and Replication

	treatment			
	intravenous		intramuscular	
replicate[a]	−LPS[b]	+LPS	−LPS	+LPS
trial A	1	1	1	1
trial B	1	1	1	1
trial C	1	1	1	1
trial D	1	1	1	1
trial E	1	1	1	1
total *n*	5	5	5	5

[a]Each treatment was replicated five times using a single cow per treatment per trial. [b]Lipopolysaccharide (0.2 μg/kg BW).

Animals and Animal Husbandry. Lactating dairy cattle were purchased from either the North Dakota State University dairy herd (8 animals) or from a commercial dairy (12 animals) located in Jamestown, ND, USA. Upon delivery to the NDSU Animal Nutrition and Physiology Center (ANPC), each cow was weighed and placed in a tie stall with full access to water and a corn silage-based ration. Cows were milked twice daily at approximate 12 h intervals using a single-cow portable milking machine (InterPuls, Albinea, Italy). Animals were adapted to the ANPC barn facility for a minimum of 7 days prior to the start of the study. Animal weights, used as the basis for dosing LPS and flunixin, were collected 2−3 days prior to the actual dose date. Cow weights did not differ ($P = 0.83$) between the iv-saline, iv-LPS, im-saline, and im-LPS treatment groups (645 ± 75, 607 ± 92, 606 ± 62, and 636 ± 93 kg, respectively; mean ± SD).

LPS or Saline Administration. LPS purified from *E. coli* 0111:B4 (Sigma Chemical Co., St. Louis, MO, USA) was dissolved (10 μg/mL) in sterile saline. Immediately prior to administration of LPS or saline, cows were placed into a squeeze chute, and an 18 gauge, 6.25 cm, catheter (Milcath, Elanger, KY, USA) was placed into the jugular vein. Animals selected for LPS treatment were administered 0.2 μg/kg BW LPS (0.02 mL/kg BW) via iv infusion over a 1−2 min period; cows randomly selected for saline treatment were infused with 0.02 mL/kg saline in the same manner as LPS-dosed cows. Catheters were removed immediately after LPS or saline infusion.

Flunixin Administration. Intramuscular flunixin meglumine (Banamine; Merck Animal Health; Millsboro, DE, USA) was delivered via 3.8 cm, 18 gauge, needles into neck muscles in locations caudal to the head and 7.6−10.2 cm abaxial to the spine (Supporting Information Figure S1). Sites for flunixin administration, and subsequent "injection site" recovery at slaughter, were marked by shaving a series of three sequential, vertically oriented patches (~16 cm^2 for each patch) for each injection day. Patches were also shaved on the necks of iv-treated animals to facilitate collection of equivalent muscles at slaughter. Between-day injections alternated between right and left aspects with separation between day 1 and 3 injections of approximately 10 cm (Figure S1). The maximum volume for a single injection site was 10 mL; because all animals required total daily doses of >10 mL, separate injections were delivered to the required volume in a vertical alignment with respect to the initial, within-day injection. The time of each flunixin treatment was recorded.

Milk Collection. Cows were milked twice daily before and after the initiation of the study protocol with milk yield being measured gravimetrically. Milk was thoroughly mixed, and multiple aliquots (~10 mL) of milk from each time point were frozen (≤ −20 °C) until analysis.

Urine Collection. Urine samples were collected prior to dosing and at 2, 4, 8, 12, and 24 h on the initial dosing day and on dosing day 2; subsequent to dosing on day 3, urine was collected at 2, 4, 8, 12, 24,

DOI: 10.1021/acs.jafc.5b01509
J. Agric. Food Chem. 2015, 63, 4893−4901

36, 48, 60, 72, and 96 h. Urine was collected by inducing micturition or during nonstimulated urination; samples were frozen (≤ −20 °C) until analysis.

Blood Collection. Blood samples were collected by jugular venipuncture (21 ga needles) on treatment day 1 at 0, 0.25, 0.5, 0.75, 1, 1.5, 2, 3, 4, 6, 8, 12, 18, and 24 h. Subsequent to dosing on day 2, blood was drawn at 0.5, 1, 2, 4, 8, 12, and 24 h. After dosing on treatment day 3, blood was drawn at 0.5, 1, 2, 4, 8, 12, 24, 36, 48, 60, 72, 84, and 96 h. Blood samples were collected into BD Vacutainer tubes containing 158 units of sodium heparin, gently inverted eight times, and centrifuged at 1160*g* for 10 min. Plasma aliquots were distributed into replicate, labeled, 2 mL polypropylene vials and were placed in a freezer (≤ −20 °C) until analysis.

Tissue Collection. Cows were slaughtered by captive bolt stunning followed by rapid exsanguination[16] 96 h after the last flunixin administration. Cattle were exsanguinated and eviscerated using standard industry practices. Day 1, 2, and 3 injection sites were removed so that approximately 500 g of tissue was gathered per site. Liver, kidney, skeletal muscle (longissimus dorsi), and adipose tissue were collected, diced, and placed into labeled containers. Livers were sampled, after removal of the gall bladder, by removing a cross section of 6 ± 2 cm width across all lobes. Kidneys were collected in their entirety, and the fibrous capsule was removed, diced, pooled, and frozen. All tissue samples were frozen at ≤ −20 °C until analysis.

Specialty tissues including lung, tongue, heart, brain, tail base (oxtail), reticulum, abomasum, ileum, and mammary tissue were collected. Aliquots of the gastrointestinal tissues were removed, and contents were removed by rinsing with water, placed in labeled containers, and frozen until analyses.

Sample Stability. On the basis of stability data published by Boner et al.[17] flunixin in nonhepatic tissues is stable for a minimum of 2 months and in hepatic tissues is stable for a minimum of 1 year when stored at ≤ −20 °C. In addition, flunixin residues have been demonstrated to be stable after three freeze−thaw cycles.[17] Jedziniak et al.[18] established that 5OHF is stable when stored at −20 ± 2 °C for 9 months. Thus, additional stability studies were not conducted. Nevertheless, all tissue analyses were conducted within 1 year of tissue collection.

Analyses. Milk flunixin and 5OHF concentrations were determined at the North Carolina State University Center for Chemical Toxicology Research and Pharmacokinetics as described by Kissell et al.[10] The milk assay limit of quantitation was 0.1 ng/mL for each analyte.

Plasma flunixin and 5OHF concentrations were quantified at the University of California Davis School of Veterinary Medicine, Veterinary Drug Residue Laboratory, as described by Buur et al.[19] and modified with respect to the UPLC system by Shelver et al.[8] In addition, the flunixin standard curve was expanded to include points at 0.5, 1, 2, 20, 200, 500, 1000, and 2000 ng/mL in the current study. Limits of detection and quantification were 0.1 and 0.5 ng/mL for flunixin and 0.3 and 0.9 ng/mL for 5OHF, respectively.

Flunixin residues in liver and skeletal muscle were determined at both the USDA FSIS Midwestern Laboratory in St. Louis, MO, USA, and at the Biosciences Research Laboratory in Fargo, ND, USA. The FSIS Midwestern Laboratory used slight modifications of method CLG-FLX4.03.[20] Briefly, the method employed a Waters Acquity UPLC triple-quadrupole instrument with a 1.7 μm, BEH C18, 2.1 × 50 mm column and gradient mobile phase consisting of 0.4% formic acid (solvent A) and 4 parts of CH_3CN in 5 parts of MeOH with 0.18% formic acid (solvent B) at a flow rate of 0.650 mL/min. The solvent gradient (8 min total) was as follows: 0 min, 55:45 A/B; 0.42 min, 65:35 A/B; 5.53 min, 65:35 A/B; 5.64 min, 5:95 A/B; 6.36 min, 5:95 A/B; 6.42 min, 55:45 A/B; 8.00 min, 55:45 A/B. The FSIS method quantifies tissue residues to only half of the tolerance of 125 ng/g in liver and 25 ng/g in skeletal muscle.

Flunixin free acid in edible tissues, injection sites, and specialty tissues was determined at the USDA ARS Fargo laboratory using the method of Boner et al.[17] on which method CLG-FLX4[20] is based. However, matrix-matched standard curves were prepared at 0.25, 1.25, 6.25, 12.5, and 18.75 ng flunixin free acid/mL of extract corresponding to tissue concentrations of 1, 5, 25, 50, and 75 ng/g, which allows quantitative analyses well below half the tolerance of skeletal muscle. With each sample set, blank tissues were fortified at 5 and 50 ng/g and extracted contemporaneously with incurred samples. Flunixin was measured using ultrahigh-performance liquid chromatography (Acquity, Waters, Milford, MA, USA) coupled to a tandem quadrupole mass spectrometer (Acquity; Waters) using the conditions described in FSIS method CLG-FLX4.03.[20] Liver 5OHF concentrations were measured exactly as described for flunixin except that a water-based external standard curve equivalent to 1, 5, 25, 50, and 75 ng/g of tissue was used for quantitation based on the m/z 313 → 295 ion transition with qualifier m/z transitions of 313 → 280 and 313 → 109.

Details of urinary flunixin and 5OHF analyses will be described elsewhere (Shelver et al., in preparation). Briefly, 1 part of urine and 4 parts of 6 N formic acid were mixed and heated at 120 °C for 2 h. Urine samples were then diluted to 1:100 in 50% acetonitrile in water containing 250 ng/mL of flunixin-d_3 and 5-hydroxyflunixin-d_3 as internal standards. If analyte concentration for a given urine sample was outside the range of the calibration curve, fresh urine aliquots were rediluted at either 1:10 in 50% aqueous acetonitrile or 1:250 using 1:100 control urine as diluent, depending on approximations from the original analysis, and reanalyzed. A matrix-matched calibration curve with appropriate dilution strength was run concurrently with all incurred samples. Within each set, blank urine was fortified at 1, 20, and 500 ng/mL each of flunixin and 5OHF and analyzed concurrently with unknowns. Quantitative analyses were performed on an Acquity UPLC (Waters Corp., Milford, MA, USA) coupled to a tandem quadrupole mass spectrometer with a heated electrospray ionization source operated in the positive ion mode (Acquity; Waters). The column was an Acquity UPLC HSS T3 (1.8 μm, 2.1 × 100 mm) maintained at 35 °C. The mobile phase was 0.1% acetic acid/acetonitrile (32:68) at a flow rate of 0.4 mL/min. Ions were monitored in the multiple reaction monitoring mode with flunixin 297 → 279, flunixin-d_3 300 → 282, 5OHF 313 → 295, and 5OHF-d_3 316 → 298 serving as quantified transitions. Flunixin 297 → 264 and 297 → 259, flunixin-d_3 300 → 264 and 300 → 112, 5OHF 313 → 280 and 313 → 109, and 5OHF-d_3 316 → 280 and 316 → 112 transitions each served as qualifiers.

Pharmacokinetic Parameter Estimates. Noncompartmental pharmacokinetic analyses of flunixin plasma concentration versus time profiles were performed on an individual cow basis using Phoenix NCA module (version 1.3; Certara, Cary, NC, USA). Estimates of C_{max} and t_{max} after im injection, flunixin clearance at steady state (CL_{ss}/F), volume of distribution at steady state (V_{ss}/F), area under the plasma concentration−time curve from time zero to the time of the last observation (AUC_{last}), mean residence time (MRT), and half-life ($t_{1/2}$) were calculated using standard procedures.

Statistical Analyses. Within collection time, the effects of LPS treatment and route of flunixin administration on milk yield were evaluated using a two-way analysis of variance (ANOVA). Across time points, there was no effect of route of flunixin administration ($P > 0.05$) on milk yield, but significant ($P < 0.05$) effects of LPS administration on milk yield were measured. Therefore, milk yield data are presented in terms of main effects only.

The main effect of LPS on the milk flunixin/5OHF ratio was tested at each collection time point by a simple one-way ANOVA. For the 12, 24, 36, 48, and 72 h collection points, ratios were non-normally distributed (Shapiro−Wilk, $P < 0.05$) so the Kruskal−Wallis analysis of variance on ranks was employed. For the 84, 96, and 108 h collection points, ratios were normally distributed ($P > 0.05$) and ordinary one-way ANOVAs were conducted.

Within tissue, flunixin concentrations were analyzed using a two-way ANOVA with main effects of endotoxin status (+LPS or saline) and route of flunixin administration (iv or im). Data were transformed if normality or equal variance assumptions were not met. The method of transformation for a particular set of means is included in tables summarizing means. For instances in which the ANOVA returned a significant main effect, the Holm−Sidak test was employed to infer differences in treatment means.

DOI: 10.1021/acs.jafc.5b01509
J. Agric. Food Chem. 2015, 63, 4893−4901

RESULTS AND DISCUSSION

Milk Yield. There was no ($P > 0.05$) effect of route of flunixin administration on milk yield (Figure 1; Supporting Information Table S1); however, administration of LPS to lactating dairy cows reduced ($P < 0.05$) milk yield relative to the milk yield of saline-treated cows (Figure 1). The magnitudes and duration of milk yield reductions following iv LPS administration were comparable to those observed after iv infusion of *E. coli* LPS to lactating Holstein cows by Waldron et al.[21] LPS-associated reduction in milk yields or milk fat yields are well characterized after dietary induction of ruminal LPS and the resulting inflammatory response in dairy cattle.[22,23] Such results in cows used for the present study strongly suggest that LPS infusion was successful in mediating a systemic, but temporary, inflammatory response.

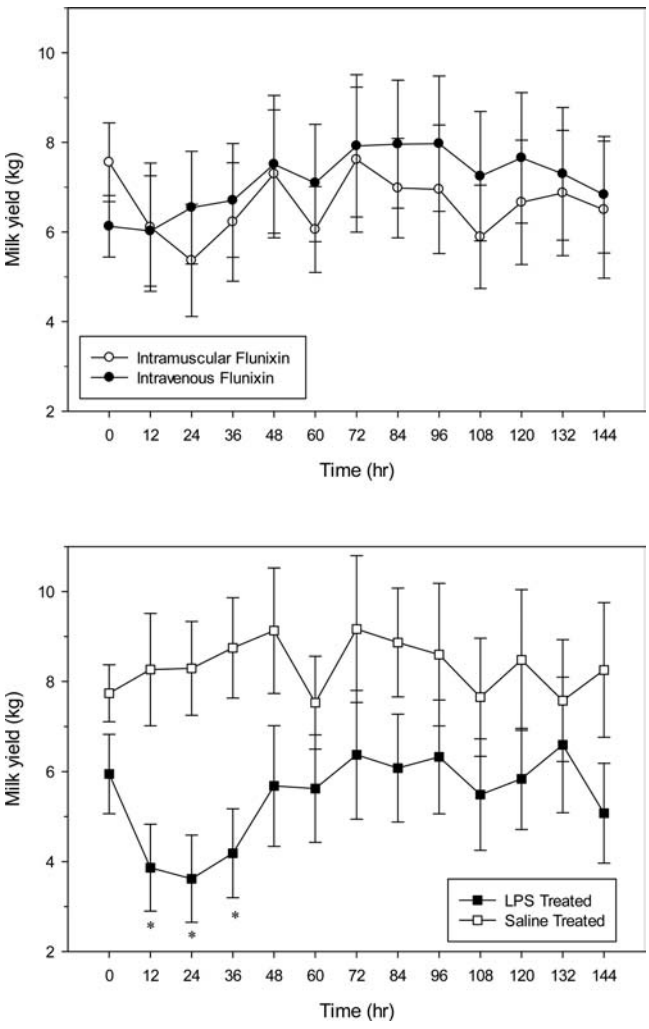

Figure 1. Effects of route of flunixin administration (top panel) or lipopolysaccharide (LPS) treatment (bottom panel) on mean milk yield (±SE) during the study period (10 cows per treatment group for each main effect). Route of drug administration had no effects ($P > 0.05$) on milk yield, but LPS treatment caused reductions (*) in milk yields at 12 ($P = 0.012$), 24 ($P = 0.004$), and 36 h ($P = 0.007$). By 48 h, the effect of LPS on milk yield was marginal ($P = 0.091$) and, thereafter, negligible ($P > 0.1$).

Kinetic Parameter Estimates. Estimated pharmacokinetic parameters for parent flunixin are shown in Table 2. Across treatments, terminal plasma half-life, AUC_{last}, Vd_{ss}/F, and MRT were larger than parameter estimates of previous studies in lactating dairy cattle.[9,10,14,24−26] This study differed from earlier studies in several respects: (a) cows were sequentially dosed with flunixin over a 3 day period; (b) the plasma flunixin assay was very sensitive, with an LOQ of 0.5 ng/mL, and blood samples were collected for 96 h after the final flunixin dose. In many instances, quantifiable flunixin residues were present 84−96 h after dosing with the resulting pharmacokinetic parameters being influenced by the prolonged concentration−time curve relative to other studies. Within these data, however, LPS administration increased ($P < 0.05$) AUC_{last}, clearance, and the volume of distribution in cows dosed with iv flunixin. For cows dosed im with flunixin, LPS administration increased ($P < 0.05$) clearance (CL_{ss}/F) and mean residence time.

Milk Residues. Concentrations of 5OHF and flunixin in milk after withdrawal periods of 36, 48, and 96 h are shown in Table 3; there were no effects of either route ($P > 0.50$) or LPS status ($P > 0.45$) on 5OHF concentrations at either 36 or 48 h. Consistent with the results of Feely et al.,[27] 5OHF was typically measurable in milk for longer periods of time than was parent flunixin (Supporting Information Tables S2 and S3), corroborating the metabolite as an appropriate marker for milk. At the minimum milk discard time of 36 h, 6 of the 20 cattle (30%) had 5OHF concentrations that met or exceeded the 2.0 ng/mL tolerance for 5OHF in milk. Similarly, 5OHF exceeded 2 ng/mL 36 h after the last flunixin dose in 25% of the eight cattle studied by Feely et al.[27] and in 8 of 20 cattle studied by Kissell et al.[10] With a 48 h withdrawal time, 2 of the 20 animals (10%) in the present study had 5OHF levels greater than allowable under U.S. statutory limits: a single cow from the iv-flunixin (−)LPS group (label conditions; cow 1) and a single cow from the im-flunixin (+)LPS group (off-label conditions; cow 18). Again, this result does not seem remarkable given the fact that of the eight cows dosed by Feely et al.,[27] a single cow secreted 17 ng/g of total radioactive residue (TRR) after a 48 h withdrawal period; assuming that 5OHF represented 20% of the total TRR in this milk, 5OHF would have exceeded tolerance levels at 3.4 ng/mL. In recent studies, Kissell et al.[9] measured violative 5OHF levels in milk of two cows 36 h after the last im or subcutaneous flunixin administration, but residues were not present at a 48 h withdrawal time. In contrast, 5OHF residues were measurable in milk from 3 of 10 mastitic cows after a 48 h withholding time.[10]

Milk yield was considered a significant ($P < 0.1$) covariate with the rate of 5OHF elimination in cows by Kissell et al.[9] Cows producing <20 kg of milk/day eliminated 5OHF at slower rates than cows producing >30 kg of milk per day. In the current study, average daily milk production across *all* cows was 13.8 ± 7.5 kg/day (mean ± SD), indicative of the fact that each cow used for the study represented an animal selected for culling because of age, poor reproductive performance, or low milk production. None of the animals were selected for elimination from the herd because of mastitis. For these low-producing cows, there was no relationship ($R^2 = 0.1509$, $P = 0.09$) between milk yield and milk 5OHF concentration at 36 h of withdrawal.

Kissell et al.[10] noted that for mastitic animals, the relative quantity and duration of parent flunixin secreted into milk was surprisingly great, with three cows eliminating 13 ± 11 ng/mL after a 60 h withdrawal period. In the current study, parent flunixin was detectable in 12 of 20 milk samples collected 60 h after the last flunixin administration, but average concentrations

DOI: 10.1021/acs.jafc.5b01509
J. Agric. Food Chem. 2015, 63, 4893−4901

Table 2. Flunixin Plasma Pharmacokinetic Parameter Estimates (Estimates Are Means ± Standard Deviations of Five Cows per Treatment)

		route of administration			
		intravenous		intramuscular	
parameter	unit	−LPS	+LPS	−LPS	+LPS
$t_{1/2}$	h	11.6 ± 8.0	5.6 ± 1.7[a]	15.5 ± 8.0	14.2 ± 6.11
t_{max}	h			0.25 ± 0.01	0.89 ± 0.68
C_{max}	μg/mL	11.9 ± 4.7	9.7 ± 1.2	5.5 ± 2.3	3.1 ± 1.5
AUC_{last}	μg·h/mL	40.2 ± 16.7	29.5 ± 11.6[a]	33.2 ± 9.1	37.0 ± 13.0
CL_{ss}	mL/h/kg	151 ± 62.8	205 ± 42.4[a]		
Vd_{ss}	L/kg	5.82 ± 3.11	8.19 ± 1.62[a]		
CL_{ss}/F	mL/h/kg			188 ± 48.7	210 ± 69.7[b]
Vd_{ss}/F	L/kg			4.19 ± 2.69	4.21 ± 1.83
MRT	h	36.7 ± 10.4	41.1 ± 12.0	44.3 ± 8.3	62.1 ± 23.0[b]

[a]Means differed ($P < 0.05$) between saline and LPS treatments within the iv flunixin group. [b]Means differed ($P < 0.05$) between saline and LPS treatments within the im flunixin group.

Table 3. Concentrations of 5-Hydroxyflunixin (5OHF) and Flunixin and in Milk of Cows at 36, 48, and 96 h after the Last Administration of Flunixin Meglumine[a]

	intravenous										intramuscular									
	saline (ng/mL)					+LPS (ng/mL)					saline (ng/mL)					+LPS (ng/mL)				
withdrawal period (h)	1	6	12	13	19	3	8	10	15	17	2	5	11	14	20	4	7	9	16	18
5-Hydroxyflunixin																				
36	**19.1**	**2.0**	0.6	0.4	0.7	0.4	1.0	0.5	0.4	**2.8**	0.9	**2.4**	**4.7**	0.9	1.8	1.8	1.3	1.4	0.9	**8.3**
48	**34.4**	0.5	0.3	0.1	0.1	0.4	0.2	0.2	0.1	0.6	0.4	0.2	1.4	0.3	0.8	0.4	0.4	0.7	0.3	**2.5**
96	**4.4**		0.1				0.1						0.3		0.1		0.1	0.2		0.7
Flunixin																				
36	1.9	0.3	0.2		0.3	0.6	1.1	0.1	0.3	0.7	0.5	0.2	0.8	0.4	0.6	1.0	1.7	1.3	0.6	10.3
48	4.1		0.1			1.0	0.1		0.1	0.2	0.5		0.4	0.1	0.3	0.5	0.5	0.9	0.2	4.6
96	1.6										0.1					0.2	0.2	0.1		2.4

[a]The tolerance for 5OHF in milk is 2.0 ng/mL; a minimum 36 h milk discard time is required. Milk values of 5OHF shown in bold exceed the tolerance at the indicated times. Concentrations of 5OHF and flunixin in milk collected from 0 to 96 h are shown in Tables S2 and S3 of the Supporting Information.

were only 0.9 ng/mL. For cows 1 and 18 (which had violative milk residues at 48 h), parent flunixin remained at relatively high levels (>1 ng/mL) until slaughter at 96 h. On the basis of the data of Kissell et al.[10] one might predict that cow 1 was mastitic or sick, and the milk record of cow 1 does suggest that this cow was not well. On the first day of dosing, cow 1 produced a total of 16 kg of milk; thereafter, the daily milk production decreased progressively from 8.3, 4.0, 3.2, 1.1, 0.2, to 0.1 kg on days 2−7, respectively (Supporting Information Table S1). Although the cows were not mastitic when purchased, we cannot rule out the development of mastitis during the study period. Cow 18 was in the im flunixin (+)LPS treatment group and was a low-producing cow, secreting an average of 2.0 kg of milk per day.

Figure 2 shows the ratio of flunixin to 5OHF secreted into milk across the study period for the control and LPS-treated cows. Cows pretreated with 0.2 μg/kg LPS consistently secreted greater ($P < 0.05$) ratios of flunixin/5OHF in milk than control cows, suggesting that either the transport or metabolism of flunixin in LPS-treated animals was altered relative to control animals. These data are consistent with the findings of Kissell et al.,[10] who demonstrated that mastitic cows secreted flunixin and 5OHF in ratios ranging from 6 to 45 from 2 to 48 h after flunixin dosing, whereas control cows had milk secretions containing ratios ranging from 0.4 to 0.8 for 24 h after dosing (neither flunixin nor 5OHF was detected in milk of

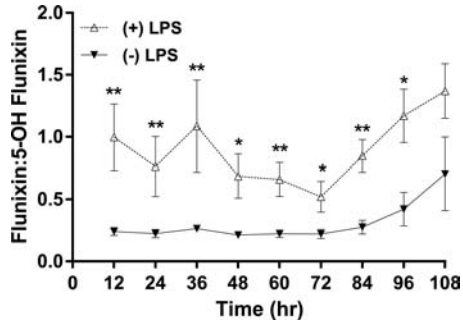

Figure 2. Ratio of flunixin to 5OHF secreted into milk by cows treated with LPS [(+)LPS] or with saline [(−)LPS]. Data are expressed as the mean ratios ± SEM of the concentration of flunixin to 5OHF in milk ($n = 10$ per treatment) by collection time. Asterisks indicate probabilities of significant differences between treatment means (*, $P < 0.05$; **, $P < 0.01$).

control animals after 24 h). Similarly, healthy cows used by Jedziniak et al.[28] secreted flunixin and 5OHF into milk at ratios estimated to be on the order of 0.1. Metabolite ratios in the current study were not as pronounced as those measured by Kissell et al.[10] but were highly consistent with the notion that inflammation may alter flunixin metabolism and disposition.

Tissue Residues. Mean concentrations of flunixin in edible and specialty tissues are shown in Table 4. There was no effect

DOI: 10.1021/acs.jafc.5b01509
J. Agric. Food Chem. 2015, 63, 4893−4901

Table 4. Residues of Flunixin in Traditionally Edible and Specialty Tissues of Cows Treated with 2.2 mg/kg Body Weight of Flunixin Meglumine for Three Consecutive Days and Slaughtered 96 h after the Final Flunixin Dose

	route of administration							
	intravenous		intramuscular			*P* value		
item	−LPS	+LPS	−LPS	+LPS	pooled SEM	route	LPS	route × LPS
n	5	5	5	5				
liver[a] (ng/g)	31.3	41.4	39.1	73.0	15.3	0.248	0.107	0.463
kidney[a] (ng/g)	15.4	14.5	17.7	41.5	12.6	0.204	0.521	0.408
skeletal muscle[a] (ng/g)	1.9	1.7	1.3	1.9	0.4	0.295	0.931	0.357
adipose tissue[b] (ng/g)	3.3	5.3	3.1	2.9	2.1	0.190	0.928	0.754
injection site[c] (ng/g)	4.6[x]	4.7[x]	400[y]	12000[z]	5500	<0.001	0.038	0.043
mammary[a] (ng/g)	9.2	7.1	6.6	10.7	2.0	0.979	0.940	0.135
lung[a] (ng/g)	17.5	12.0	9.7	17.0	3.3	0.362	0.895	0.044
heart[a] (ng/g)	7.1	8.1	5.2	7.8	1.4	0.280	0.353	0.512
tongue (ng/g)	6.2	5.5	4.3	6.0	1.1	0.539	0.671	0.301
reticulum (ng/g)	5.2	5.4	4.8	8.2	1.3	0.443	0.167	0.220
abomasum (ng/g)	7.1	7.0	5.5	10.1	2.2	0.917	0.238	0.429
ileum[c] (ng/g)	9.6	6.5	6.3	9.9	2.6	0.539	0.856	0.168
brain (ng/g)	<LOQ[d]	<LOQ	<LOQ	<LOQ				

[a]Data were transformed [(log *X*)] prior to statistical analyses to meet normal variance and normality assumptions. [b]Data were transformed [(log *X*)] prior to statistical analysis to meet ($P > 0.05$) normal variance and approach ($P = 0.032$) normality assumptions. Two animals each in the (IM −LPS) and (IM + LPS) groups had residues less than the LOQ. These animals were included at 0.5 ng/g (half the LOQ) for purposes of calculating mean adipose tissue values. [c]Data were transformed [$(\log X)^{-2}$] prior to statistical analyses to meet normal variance and normality assumptions. [d]All animals in the −LPS treatments had residues less than the LOQ (1.0 ng/g); a single animal each in the (IV + LPS) and (IM + LPS) groups had residues above the LOQ (1 ng/g).

($P > 0.05$) of route of flunixin administration or pretreatment of cows with LPS on tissue flunixin concentrations, with the exception of flunixin residues at the injection site. That is, im administration of flunixin caused greater ($P < 0.001$) injection site residues than in equivalent muscles of iv-treated cows. Within the im group, cows dosed with LPS had greater ($P < 0.05$) injection site residues than cows treated with saline in lieu of LPS. However, it should be noted that with only five cows per treatment, the statistical power for observing treatment differences in this study was limited. In a larger study ($n = 12$), Kissel et al.[9] observed that the plasma half-life of flunixin was greater in sc-treated cows relative to iv-treated cows; the implication of such data is that given sufficient numbers of animals, tissue residues could also be greater in animals treated extravascularly such as im or sc with flunixin.

As a portion of this study, liver and muscle tissues were sent to the USDA FSIS Midwestern Laboratory for flunixin analysis using the validated FSIS regulatory flunixin method.[20] Hepatic flunixin concentrations less than half the tolerance (62.5 ng/g) were interpolated from the standard curve at the FSIS laboratory without the benefit of regressions based on low-concentration standards. Aliquots of the same livers were also extracted and analyzed at the Fargo laboratory, but with an extended standard curve so that residues below half the tolerance values could be accurately quantified. Measured liver flunixin concentrations returned by the FSIS and ARS laboratories did not differ ($P = 0.686$; $n = 20$), demonstrating the linearity of the FSIS method, even in the absence of low-level analytical standards. Analytical results obtained from the analysis of skeletal muscles were not compared because of the low concentrations of flunixin in skeletal muscle.

Whereas average concentrations of flunixin across treatment (Table 4) did not indicate treatment-related causes for residue violations, a singular instance of a tissue flunixin violation occurred (Supporting Information Table S4). The liver of cow 18, (im-flunixin + LPS treatment) contained 177.5 ng/g of flunixin residue, which exceeded the liver tolerance of 125 ng/g by approximately 50 ng/g. Flunixin residues in other tissues of cow 18 were also consistently numerically greater than flunixin residues of the same tissues in other cows (Table S4). For this reason, cow 18 was treated as an "outlier", and statistical analyses were rerun to determine whether route of flunixin administration or the presence of LPS influenced tissue flunixin residues. After removal of cow 18 from the statistical analyses, no treatment effects ($P > 0.05$), other than the effect of im administration on injection site residues, were apparent.

Although statistical analyses between tissues were not performed, the rank order of flunixin among tissues (excluding injection site) was liver > kidney ≈ lung > mammary, ileum, abomasum, heart, reticulum, tongue > skeletal muscle, adipose tissue > brain. Residue analysis of specialty tissues indicated that flunixin residues would not represent a food safety risk for consumers of those tissues. This assertion is based on the fact that flunixin concentrations in specialty tissues were <20 ng/g, the consumption of specialty tissues relative to skeletal muscle, and the established tolerance of 25 ng/g for skeletal muscle.[2]

Urine Residues. Figure 3 shows urinary excretion of flunixin and its major metabolite, 5OHF, across the dosing and withdrawal periods. Error bars are not shown in Figure 3 for the sake of clarity; in addition, it should be recalled that prior to analysis conjugates of flunixin were hydrolyzed by acid digestion. Flunixin and 5OHF were detectable in the urine of most cows throughout the 96 h depuration period. Such detection is not surprising because flunixin was present in most tissues at the 96 h withdrawal period and because renal excretion tends to concentrate residues in urine relative to tissues. Jones et al.[29] also were able to detect flunixin in urine of beef heifers as long as 96 h after a single iv flunixin administration. Of note is the fact that urinary flunixin concentrations accurately reflect the rapid absorption and elimination described by previous kinetic studies.[9,10] In addition, the graphical data (Figure 3) do not strongly suggest

DOI: 10.1021/acs.jafc.5b01509
J. Agric. Food Chem. 2015, 63, 4893−4901

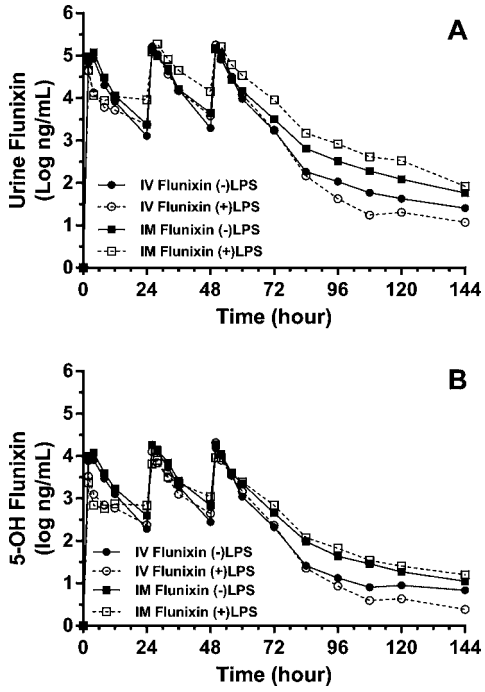

Figure 3. Urinary excretion of flunixin (A) and 5OHF (B) as a function of time. Data are expressed as the log analyte concentrations in ng/mL.

treatment differences with respect to flunixin or 5OHF excretion during the 3 day dosing period. Only at about 72 h (24 h after the last flunixin dose) does it appear that concentrations of both flunixin and 5OHF are at least numerically greater in im-dosed cows. Such results are likely due to the slower release of residual flunixin from the injection sites, relative to its distribution into the body after iv infusion. The second observation gleaned from the urinary data was the fact that flunixin was present in urine at concentrations about 10 times higher than the metabolite, 5OHF, again with the im-treated animals having numerically higher concentrations of 5OHF than iv-treated animals.

Figure 4 show the ratios of flunixin to 5OHF excreted in urine during the dosing and depuration periods. Cow 18, a member of the im (+)LPS treatment group, was not included in the means shown for the im (+)LPS treatment group, but cow 18 is included as a stand-alone element of Figure 4. Across all time points, mean (±SEM) flunixin/5OHF ratios for the iv saline, iv (+)LPS, im saline, and im (+LPS) treatment groups were 8.9 ± 0.4, 9.8 ± 0.4, 7.4 ± 0.4, and 13.4 ± 0.5, respectively. Within the cows treated with iv flunixin, there was no difference (P = 0.06) between the LPS and saline groups, but for the im-treated cows, the LPS-exposed animals had a greater (P < 0.001) mean flunixin/5OHF urinary ratio than the saline-treated cows. Within the group of cows that did not receive LPS (saline controls), im-treated cows had a higher (P = 0.009) mean ratio than iv-treated cows, whereas for cows infused with LPS the im group also had a greater (P < 0.001) mean ratio than the saline-treated group. Thus, these data suggest that LPS pretreatment may have altered either the hydroxylation or the excretion of flunixin. Circumstantial evidence presented in Figure 5, supports, but by no means proves, such a supposition. When the average urinary flunixin/5OHF ratio of saline-treated cows was regressed against the respective liver flunixin concentrations (Figure 5A), no relationship (P = 0.96; R^2 = 0.0003) could be discerned. In

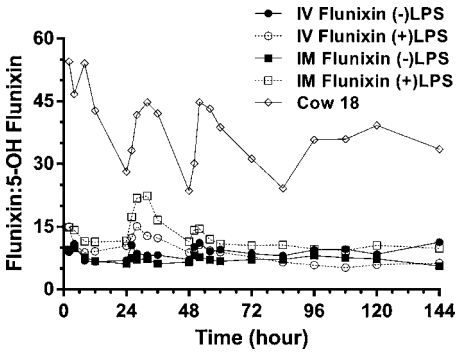

Figure 4. Urinary flunixin/5OHF ratio by treatment with cow 18 excluded from the mean of the im (+)LPS treatment group and plotted independently.

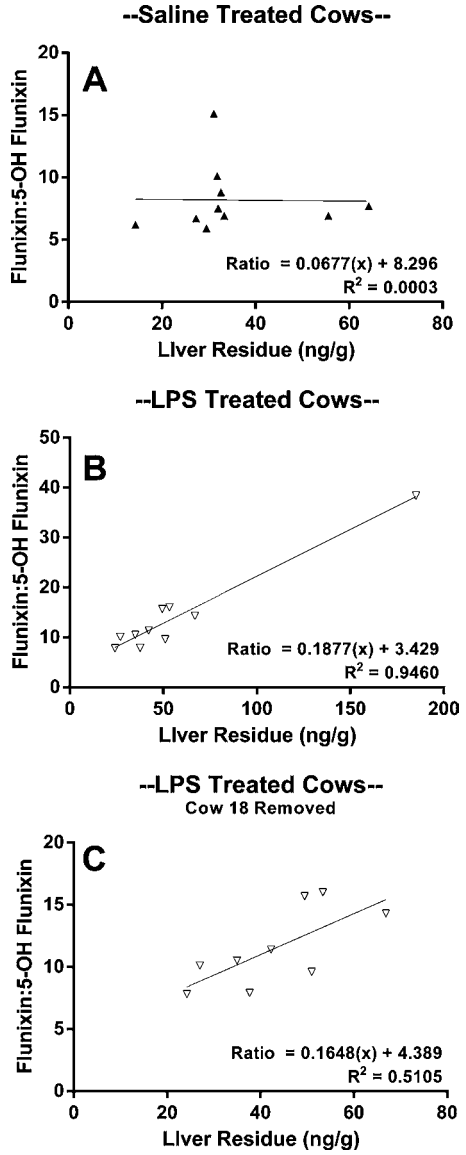

Figure 5. Relationship between lipopolysaccharide (LPS) treatment and the level of liver flunixin residues in dairy cows: (A) control cows; (B) LPS-treated cows; (C) LPS-treated cows without cow 18.

DOI: 10.1021/acs.jafc.5b01509
J. Agric. Food Chem. 2015, 63, 4893−4901

contrast, when the average urinary flunixin/5OHF ratios of LPS-treated cows were regressed with the respective liver flunixin concentrations (Figure 5B), a significant linear ($P < 0.0001$; $R^2 = 0.9460$) relationship was apparent. Recognizing that cow 18, which had a very high urinary flunixin/5OHF ratio and liver flunixin concentration, could greatly bias the least-squares regression, the regression was repeated with data from cow 18 removed (Figure 5C). Even with the influence of cow 18 removed, a linear relationship ($P = 0.03$) between the flunixin/5OHF ratio and liver flunixin residues remained, albeit with a much lower correlation coefficient ($R^2 = 0.5105$).

Such data suggest that LPS treatment could affect the metabolism or excretion of flunixin in cows. To be sure, the role of LPS in the down-regulation of several cytochrome P_{450} (CYP) isoforms has been well established in rodents and human cell models,[30−32] with the systemic administration of LPS generally down-regulating several constitutive[33] and inducible hepatic CYPs[34] at the transcription and protein levels.[32] It is unknown what CYPs metabolize flunixin in dairy cows or other livestock species. Indeed, the idea that flunixin is metabolized by CYPs in livestock is a presumption because no studies have been published investigating the enzymes responsible for flunixin clearance in livestock. Nevertheless, inhibition of hepatic CYP expression or activity by LPS would be consistent with the correlation between the flunixin/5OHF ratio in urine and hepatic flunixin levels in LPS-treated cows observed in this study. Likewise, such a supposition would also explain the greater propensity for mastitic cows to secrete violative 5OHF residues in milk than healthy cows,[10] presumably because of slower clearance. Finally, the inhibition of CYP-mediated hydroxylation of flunixin in LPS-treated cows would be consistent with the fact that 5OHF was measurable in livers of 5 of 10 control cows in this study but in only 1 of 10 LPS-treated cows (see the Supporting Information).

Collectively, data from this study strongly suggest that cattle undergoing inflammatory processes, especially those mediated by infection with LPS-producing organisms, could be contributing to the inventory of animals that test positive for flunixin at the slaughterhouse. The data reported herein suggest that even with observation of the appropriate regulatory withdrawal period, such animals could still test positive for violative flunixin residues. Further study with larger numbers of observations will be necessary to either support or refute such a supposition.

■ ASSOCIATED CONTENT

Supporting Information

Tables containing milk production, milk residue, and tissue residue data by animal and treatment. The Supporting Information is available free of charge on the ACS Publications website at DOI: 10.1021/acs.jafc.5b01509.

■ AUTHOR INFORMATION

Corresponding Author

*(D.J.S.) Phone: (701) 239-1238. Fax: (701) 239-1430. E-mail: david.j.smith@ars.usda.gov.

Funding

Support for the Food Animal Residue Avoidance Databank program (FARAD) at KSU, UC−Davis, and NCSU was provided by USDA-NIFA. The use of trade, firm, or corporation names in this publication is for the information and convenience of the reader. Such use does not constitute an official endorsement or approval by the U.S. Department of Agriculture, the Agricultural Research Service, or the Food Safety and Inspection Service of any product or service to the exclusion of others that may be suitable.

Notes

The authors declare no competing financial interest.

■ ACKNOWLEDGMENTS

The technical expertise of Missy Berry, Carlotta Bruns, Dee Ellig, Austen Germolous, Justin Gilbertson, Michael Giddings, Kelsey Heiberg, Jason Holthusen, Erin Loeb, Sara Lupton, Amy McGarvey, Colleen Pfaff, Malinda Scherf, Terry Skunberg, and Michael Woodworth is greatly appreciated as are the efforts of student employees of the North Dakota State University Meats Laboratory and Animal Nutrition and Physiology Center. The excellent analyses of milk samples by Jim Yeatts and Jim Brooks of the North Carolina State University Center for Chemical Toxicology/Residue Pharmacology are greatly appreciated as are the efforts of Scott Wetzlich at the Department of Medicine and Epidemiology, University of California, Davis, for analyzing plasma samples.

■ REFERENCES

(1) FOIS. Freedom of information summary. Supplemental New Animal Drug Application, NADA 101-479, 1998; http://www.fda.gov/downloads/AnimalVeterinary/Products/ApprovedAnimalDrugProducts/FOIADrugSummaries/ucm064905.pdf (accessed Feb 13, 2015).

(2) FOIS. Freedom of information summary. Supplemental New Animal Drug Application, NADA 101-479, 2004; http://www.fda.gov/downloads/AnimalVeterinary/Products/ApprovedAnimalDrugProducts/FOIADrugSummaries/ucm064910.pdf (accessed Feb 13, 2015).

(3) JAVMA. FDA issues reminder on correct use of flunixin meglumine. JAVMA News, July 1, 2007; http://www.avma.org/onlnews/javma/jul07/070701e_pf.asp.

(4) FSIS. United States National Residue Program for Meat, Poultry and Egg Products, 2011 Residue Sample Results, May 2013; http://www.fsis.usda.gov/wps/wcm/connect/f511ad0e-d148-4bec-95c7-22774e731f7c/2011_Red_Book.pdf?MOD=AJPERES (accessed Feb 13, 2015).

(5) FSIS. United States National Residue Program for Meat, Poultry and Egg Products, 2012 Residue Sample Results, Sept 2014; http://www.fsis.usda.gov/wps/wcm/connect/be77fe0d-2295-417f-9472-6b43052068b9/2012-Red-Book.pdf?MOD=AJPERES (accessed Feb 13, 2015).

(6) Kissell, L. W.; Baynes, R. E.; Riviere, J. E.; Smith, G. W. Occurrence of flunixin residues in bovine milk samples from the USA. *Food Addit. Contam., Part A* **2013**, *30*, 1513−1516.

(7) Deyrup, C. L.; Southern, K. J.; Cornett, J. A.; Shultz, C. E.; Cera, D. A. Examining the occurrence of residues of flunixin meglumine in cull dairy cows by use of the flunixin cull cow survey. *J. Am. Vet. Med. Assoc.* **2012**, *241*, 249−253.

(8) Shelver, W. L.; Tell, L. A.; Wagner, S.; Wetzlich, S.; Baynes, R. E.; Riviere, J. E.; Smith, D. J. Comparison of ELISA and LC-MS/MS for the measurement of flunixin plasma concentrations in beef cattle after intravenous and subcutaneous administration. *J. Agric. Food Chem.* **2013**, *61*, 2679−2686.

(9) Kissell, L. W.; Smith, G. W.; Leavens, T. L.; Baynes, R. E.; Wu, H.; Riviere, J. E. Plasma pharmacokinetics and milk residues of flunixin and 5-hydroxy flunixin following different routes of administration in dairy cattle. *J. Dairy Sci.* **2012**, *95*, 7151−7157.

(10) Kissell, L. W.; Leavens, T. L.; Baynes, R. E.; Riviere, J. E.; Smith, G. W. Comparison of pharmacokinetics and milk elimination of flunixin in healthy cows and cows with mastitis. *J. Am. Vet. Med. Assoc.* **2015**, *246*, 118−125.

DOI: 10.1021/acs.jafc.5b01509
J. Agric. Food Chem. 2015, 63, 4893−4901

(11) Landoni, M. F.; Cunningham, F. M.; Lees, P. Determination of pharmacokinetics and pharmacodynamics of flunixin in calves by use of pharmacokinetic/pharmacodynamics modeling. *Am. J. Vet. Res.* **1995**, *56*, 786−794.
(12) Intervet. Banamine Product Information; http://intervetus.naccvp.com/?m=product_view&id=1047018 (accessed March 28, 2012).
(13) Odensvisk, K. Pharmacokinetics of flunixin and its effect on prostaglandin $F_{2\alpha}$ metabolite concentrations after oral and intravenous administration in heifers. *J. Vet. Pharmacol. Ther.* **1995**, *18*, 254−259.
(14) Rantala, M.; Kaartinen, L.; Välimäki, E.; Stryrman, M.; Hiekkaranta, M.; Niemi, A.; Saari, L.; Pyörälä, S. Efficacy and pharmacokinetics of enrofloxacin and flunixin meglumine for treatment of cows with experimentally induced *Escherichia coli* mastitis. *J. Vet. Pharmacol. Ther.* **2002**, *25*, 251−258.
(15) Shuster, D. E.; Harmon, R. J.; Jackson, J. A.; Hemken, R. W. Reduced lactational performance following intravenous endotoxin administration to dairy cows. *J. Dairy Sci.* **1991**, *74*, 3407−3411.
(16) AVMA. *AVAMA Guidelines for the Euthanasia of Animals*; American Veterinary Medical Association: Schaumburg, IL, USA, 2013.
(17) Boner, P. L.; Lui, D. D. W.; Feely, W. F.; Robinson, R. A.; Wu, J. Determination of flunixin in edible bovine tissues using liquid chromatography coupled with tandem mass spectrometry. *J. Agric. Food Chem.* **2003**, *51*, 7555−7559.
(18) Jedziniak, P.; Szprengier-Juszkiewicz, T.; Olejnik, M. In-house reference materials: 5-hydroxyflunixin and meloxicam in cow milk-preparation and evaluation. *Anal. Chim. Acta* **2009**, *637*, 346−350.
(19) Buur, J. L.; Baynes, R. E.; Smith, G.; Riviere, J. E. Pharmacokinetics of flunixin meglumine in swine after intervenous dosing. *J. Vet. Pharmacol. Ther.* **2006**, *29*, 437−440.
(20) FSIS. Determination and confirmation of flunixin by HPLC/ESI-MS/MS, CLG-FLX4.03, 7/16/2012; http://www.fsis.usda.gov/wps/wcm/connect/c8cf4faf-58c2-4268-be5e-3a2d2a8ee556/CLG_FLX_4_03.pdf?MOD=AJPERES (accessed Feb 13, 2015).
(21) Waldron, M. R.; Nishida, T.; Nonnecke, B. J.; Overton, T. R. Effect of lipopolysaccharide on indices of peripheral and hepatic metabolism in lactating cows. *J. Dairy Sci.* **2003**, *86*, 3447−3459.
(22) Khafipour, E.; Krause, D. O.; Plaizier, J. C. A grain-based subacute ruminal acidosis challenge causes translocation of lipopolysaccharide and triggers inflammation. *J. Dairy Sci.* **2009**, *92*, 1060−1070.
(23) Zebeli, Q.; Ametaj, B. N. Relationships between rumen lipopolysachharide and mediators of inflammatory response with milk fat production and efficiency in dairy cows. *J. Dairy Sci.* **2009**, *92*, 3800−3809.
(24) Odensvisk, K.; Johansson, I. M. High-performance liquid chromatography method for determination of flunixin in bovine plasma and pharmacokinetics after single and repeated doses of the drug. *Am. J. Vet. Res.* **1995**, *56*, 489−495.
(25) Anderson, K. L.; Neff-Davis, C. A.; Davis, L. E.; Bass, V. D. Pharmacokinetics of flunixin-meglumine in lactating cattle after single and multiple intramuscular and intravenous administrations. *Am. J. Vet. Res.* **1990**, *51*, 1464−1467.
(26) Hardee, G. E.; Smith, J. A.; Harris, S. J. Pharmacokinetics of flunixin meglumine in the cow. *Res. Vet. Sci.* **1985**, *39*, 110−112.
(27) Feely, W. F.; Chester-Yansen, C.; Thompson, K.; Campbell, J. W.; Boner, P. L.; Liu, D. D.W; Couch, L. S. Flunixin residues in milk after intravenous treatment of dairy cattle with ^{14}C-flunixin. *J. Agric. Food Chem.* **2002**, *50*, 7308−7313.
(28) Jedziniak, P.; Olejnik, M.; Szprengierl-Juszkiewicz, T.; Smulski, S.; Kaczmarowski, M.; Zmudzki, J. Identification of flunixin glucuronide and depletion of flunixin and its marker residue in bovine milk. *J. Vet. Pharmacol. Ther.* **2013**, *36*, 571−575.
(29) Jones, S. A.; Salter, R. S.; Goldsmith, T.; Quintana, J.; Rapnicki, P.; Shuck, K.; Wells, J. E.; Schneider, M.; Griffin, D. Development and model testing of antemortem screening methodology to predict required drug withholds in heifers. *J. Food Prot.* **2014**, *77*, 292−298.
(30) Yang, K. H.; Lee, M. G. Effect of endotoxin derived from *Escherichia coli* lipopolysaccharide on the pharmacokinetics of drugs. *Arch. Pharmacal Res.* **2008**, *31*, 1073−1086.
(31) Morgan, E. T.; Goralski, K. B.; Piquette-Miller, M.; Renton, K. W.; Robertson, G. R.; Chaluvadi, M. R.; Charles, K. A.; Clarke, S. J.; Kacevska, M.; Liddle, C.; Richardson, T. A.; Sharma, R.; Sinal, C. J. Regulation of drug metabolizing enzymes and transporters in infection, inflammation, and cancer. *Drug Metab. Dispos.* **2008**, *36*, 205−216.
(32) Aitken, A. A.; Richardson, T. A.; Morgan, E. T. Regulation of drug-metabolizing enzymes and transporters in inflammation. *Annu. Rev. Pharmacol. Toxicol.* **2006**, *46*, 123−149.
(33) Moriya, N.; Kataoka, H.; Fujino, H.; Nishikawa, J.; Kugawa, F. Different expression patterns of hepatic cytochrome P450s during anaphylactic or lipopolysaccharide-induced inflammation. *Pharmazie* **2014**, *69*, 142−147.
(34) Moriya, N.; Kataoka, H.; Fujino, H.; Nishikawa, J.; Kugawa, F. Effect of lipopolysaccharide on the xenobiotic-induced expression and activity of hepatic cytochrome P450 in mice. *Biol. Pharm. Bull.* **2012**, *35*, 473−480.
(35) Mølgaard, L.; Damgaard, B. M.; Bjerre-Harpøth, V.; Herskin, M. S. Effects of percutaneous needle liver biopsy on dairy cow behaviour. *Res. Vet. Sci.* **2012**, *93*, 1248−1254.

DOI: 10.1021/acs.jafc.5b01509
J. Agric. Food Chem. 2015, 63, 4893−4901

JOURNAL OF AGRICULTURAL AND FOOD CHEMISTRY

Article

pubs.acs.org/JAFC

Chlorogenic Acid Biosynthesis Appears Linked with Suberin Production in Potato Tuber (*Solanum tuberosum*)

Matías Ariel Valiñas, María Luciana Lanteri, Arjen ten Have, and Adriana Balbina Andreu*

Instituto de Investigaciones Biológicas-CONICET, Universidad Nacional de Mar del Plata, CC 1245, 7600 Mar del Plata, Argentina

Supporting Information

ABSTRACT: Potato (*Solanum tuberosum* L.) is a good source of dietary antioxidants. Chlorogenic acid (CGA) and caffeic acid (CA) are the most abundant phenolic acid antioxidants in potato and are formed by the phenylpropanoid pathway. A number of CGA biosynthetic routes that involve hydroxycinnamoyl-CoA quinate hydroxycinnamoyl transferase (HQT) and/or hydroxycinnamoyl-CoA shikimate/quinate hydroxycinnamoyl transferase (HCT) have been proposed, but little is known about their path in potato. CA production requires a caffeoyl shikimate esterase (CSE), and CA serves as a substrate of lignin precursor ferulic acid via the action of caffeic/5-hydroxyferulic acid *O*-methyltransferase (COMT I). CGA is precursor of caffeoyl-CoA and, via caffeoyl-CoA O-methyltransferase (CCoAOMT), of feruloyl-CoA. Feruloyl-CoA is required for lignin and suberin biosynthesis, crucial for tuber development. Here, metabolite and transcript levels of the mentioned and related enzymes, such as cinnamate 4-hydroxylase (C4H), were determined in the flesh and skin of fresh and stored tubers. Metabolite and transcript levels were higher in skin than in flesh, irrespective of storage. CGA and CA production appear to occur via *p*-coumaroyl-CoA, using HQT and CSE, respectively. HCT is likely involved in CGA remobilization toward suberin. The strong correlation between CGA and CA, the correspondence with *C4H*, *HQT*, *CCoAOMT2*, and *CSE*, and the negative correlation of *HCT* and *COMT I* in potato tubers suggest a major flux toward suberin.

KEYWORDS: *antioxidant, caffeic acid, flavonoid metabolism, phenolic acids metabolism, Solanum tuberosum, storage*

INTRODUCTION

Potato (*Solanum tuberosum* L.) is an important food crop worldwide. It is considered a cheap source of high-quality proteins, minerals, and antioxidants, including vitamin C, carotenoids, and phenolic compounds such as chlorogenic acid (CGA) and flavonoids.[1] Phenolic acids have been extensively studied because they are involved in defense mechanisms induced upon biotic and abiotic stresses in plants.[2] Recently, they have been associated with health-promoting effects, mainly related to their antioxidant activity.[3,4] In particular, CGA has been reported to protect against degenerative diseases, cancer, heart disease,[5] hypertension,[6] and viral and bacterial diseases. Since differences in CGA levels of 1−2 orders of magnitude among varieties have been reported,[4] the biosynthesis of CGA in potato appears to be an important subject of study.

CGA and other phenolic acids, as caffeic acid (CA), are derived from the complex phenylpropanoid biosynthesis, part of the secondary metabolism. In the first steps of the "core phenylpropanoid pathway", primary metabolite phenylalanine is converted to *p*-coumaroyl-CoA by the consecutive action of phenylalanine-ammonia-lyase (PAL), cinnamate 4-hydroxylase (C4H), and 4-coumarate-CoA ligase (4CL). *p*-Coumaroyl-CoA is the general precursor of the flavonoid metabolism, a precursor of lignin biosynthesis, and the starting point for two routes of CGA production (Figure 1).[7,8] Route I consists of esterification of quinic acid with *p*-coumaroyl-CoA, followed by hydroxylation of *p*-coumaroylquinic acid to form CGA (Figure 1). Route II requires four consecutive steps: esterification of shikimic acid with *p*-coumaroyl-CoA, hydroxylation of *p*-coumaroyl shikimate to form caffeoyl shikimic acid, and then de-esterification to produce caffeoyl-CoA, which in turn is re-esterified with quinic acid to form CGA (Figure 1). It has long been assumed that caffeoyl-CoA can also be synthesized from *p*-coumaric acid (CouA) via CA,[9] which is the second most abundant phenolic in potato tuber. Furthermore, a heteromeric C3H/C4H complex that converts CouA to CA has been identified in *Populus trichocarpa* (route III, Figure 1).[10] A fourth route, producing CGA via caffeoyl-glucose, has been proposed in sweet potato tuber (not shown in Figure 1).[11] Key enzymes appear to be hydroxycinnamoyl-CoA quinate hydroxycinnamoyl transferase (HQT) and hydroxycinnamoyl-CoA shikimate/quinate hydroxycinnamoyl transferase (HCT), two very closely related, homologous enzymes. Note that two reactions supposedly require HCT, one reaction may utilize HQT or HCT, and in one reversible reaction HQT and HCT catalyze opposite reactions (Figure 1). Using gene silencing and overexpression, HQT was shown to be the principal enzyme for CGA accumulation in tomato leaves.[8] Tobacco HCT is involved in CGA remobilization toward caffeoyl-CoA, as silenced *HCT* tobacco plants were shown to accumulate large amounts of CGA in the stem.[12]

Recently, caffeoyl shikimate esterase (CSE) was shown to be involved in the biosynthesis of CA and, via 4CL, caffeoyl-CoA in *Arabidopsis thaliana*, bypassing the second HCT reaction.[13] Activity of caffeic/5-hydroxyferulic acid *O*-methyltransferase (COMT I) and caffeoyl-CoA *O*-methyltransferase

Received: December 3, 2014
Revised: April 24, 2015
Accepted: April 29, 2015
Published: April 29, 2015

ACS Publications © 2015 American Chemical Society

DOI: 10.1021/jf505777p
J. Agric. Food Chem. 2015, 63, 4902−4913

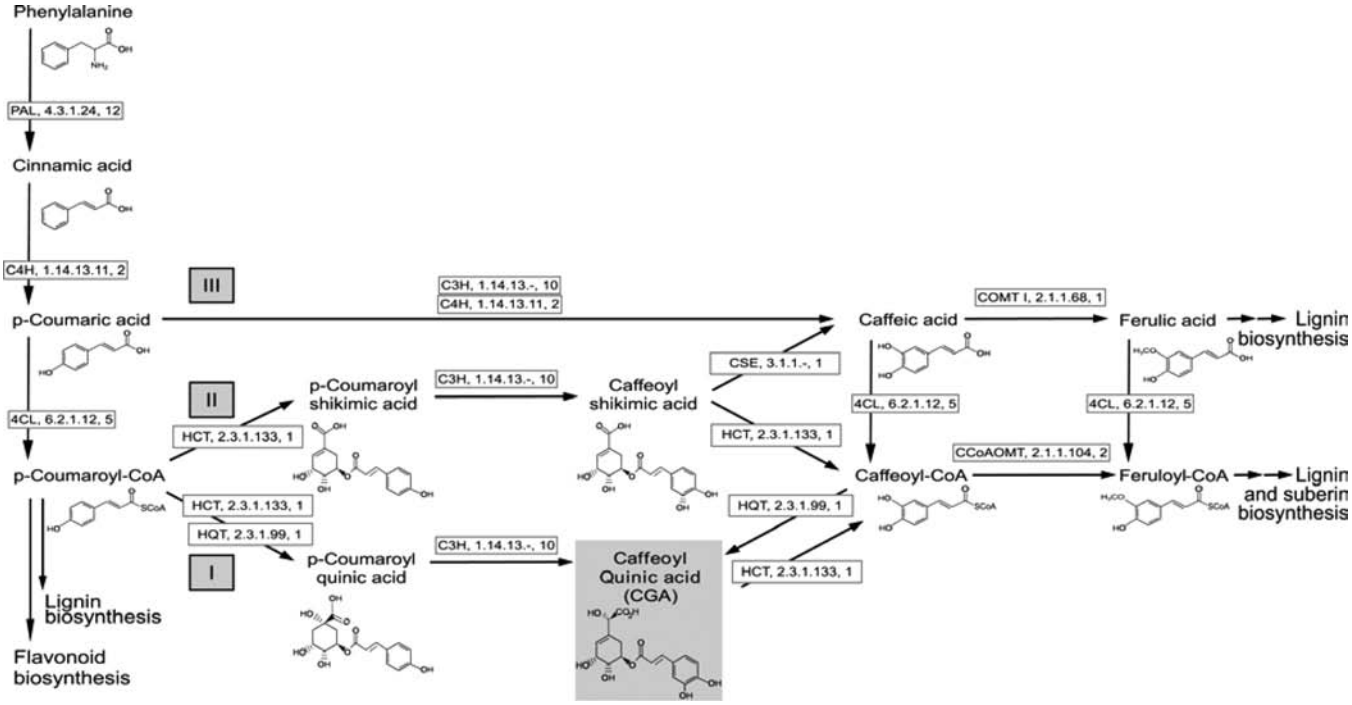

Figure 1. Chlorogenic acid biosynthetic pathways in plants. I, II, and III indicate possible biochemical routes toward CGA. The abbreviated enzyme names are boxed and followed by the corresponding EC number and the number of possible isoenzymes identified in the potato genome. Abbreviations: PAL, phenylalanine-ammonia-lyase; C4H, cinnamate 4-hydroxylase; 4CL, 4-coumarate-CoA ligase; HCT, hydroxycinnamoyl-CoA shikimate/quinate hydroxycinnamoyltransferase; C3H, *p*-coumarate 3′-hydroxilase; HQT, hydroxycinnamoyl-CoA quinate hydroxycinnamoyl transferase; CSE, caffeoyl shikimate esterase; COMT I, caffeic/5-hydroxyferulic acid *O*-methyltransferase; CCoAOMT, caffeoyl-CoA *O*-methyltransferase.

(CCoAOMT), respectively, results in ferulic acid (FA), a lignin precursor, and feruloyl-CoA, a precursor of both lignin and suberin (Figure 1).

It has been generally accepted that phenylpropanoid biosynthesis is mostly regulated by transcriptional control.[14] Several studies performed in CGA-accumulating plant families (i.e., Asteraceae, Rubiaceae, and Solanaceae) show that transcript levels reflect metabolites levels.[15−21] Relatively little is known about the regulation of the phenolic acids biosynthesis in potato tuber. André et al.[22] studied the expression of various genes involved in the phenylpropanoid pathway in tubers under normal and drought stress conditions. Constitutive and drought-induced expression profiles of *PAL*, *HCT*, and *C3H* genes were coordinated and correlated with phenolic acids levels, suggesting that also in potato tuber these enzymes are regulated at the transcriptional level; curiously, this was less clear for *C4H* and *HQT*. In a similar study, Payyavula et al.[23] found that phenylpropanoid gene expression appeared coordinately regulated and was well correlated with metabolite pools. In accordance with André et al.,[22] the correlation observed between *HQT* and CGA was less clear than that between the other phenylpropanoid genes and CGA. Enzymes that act downstream of CGA synthesis, such as CCoAOMT, were shown to be involved in suberization of potato tuber skin.[24] However, it is not clear how downstream events catalyzed by COMT I and CCoAOMT affect CGA levels. To the best of our knowledge, there are no studies regarding the role of CSE in CGA synthesis nor secondary metabolism in potato.

The phenolic acids contents of potato tuber are determined by both intrinsic and extrinsic factors. Genotype, developmental stage, and tissue are the major intrinsic factors.[25−36] It should be noted that most studies on the regulation of CGA synthesis have been carried out in whole tubers, although it has been shown that metabolite levels between flesh and skin differ significantly.[25,30,33,34] The major extrinsic factors, cultivation conditions (e.g., location, year of cultivation, and fertilization)[29,37,38] and cold storage, have not yet been studied extensively. The literature suggests that during cold storage, a period in which potatoes may undergo high metabolic changes,[39] their phenolics content either remains constant or increases.[40−42] A similar observation has been reported for antioxidant activity.[43−45] However, there are no studies on the effect of cold storage on transcription levels of genes involved in CGA biosynthesis in potato tubers. The aim of this work was to determine the transcriptional regulation of the synthesis of CGA and related phenolics, such as CA, through a comparative analysis of flesh and skin tissues of fresh and stored tubers of five carefully selected processing potato varieties.

MATERIALS AND METHODS

Plant Material. Twelve white- or yellow-fleshed processing varieties of *Solanum tuberosum* ssp. *tuberosum* were grown in fields located in Balcarce, Buenos Aires, Argentina, during the 2009/2010 campaign of McCain Argentina S.A. All varieties were planted on the same date in random plots and harvested at the end of their respective cycles. For each variety, skin and flesh from 10 tubers that were either freshly harvested ("fresh") or stored for 3 months in darkness at 8 °C and a relative humidity of 80−90% with forced air ventilation ("stored") were pooled to generate a representative sample. The material was immediately frozen in liquid nitrogen and stored at −80 °C until analysis.

Total Phenolics. Total phenolics were determined using the Folin−Ciocalteu reagent following the procedure described by Campos et al.[46] with minor modifications. Briefly, a 300 mg sample

DOI: 10.1021/jf505777p
J. Agric. Food Chem. 2015, 63, 4902−4913

Table 1. Primer Sequences Used for qRT-PCR

gene	primer	sequence (5′−3′)	potato genome contig
C4H1	fw	CCAGCTGAAAGCAAAATCTTA	PGSC0003DMS000000597
	rv	GAAAGGAAGAAATCTGAAGTCG	
C4H2	fw	CTGGATACGATATTCCAGCTGAG	PGSC0003DMS000000597
	rv	ACCGAAAGGAAGAAATCTAAAGTCA	
HCT	fw	ACGACTTATTCCGGCAGTTG	PGSC0003DMS000000559
	rv	CCATGTGTTGATGAAGTGAAGAC	
HQT	fw	CACCATGTTTGGAACTTAAGAAAC	PGSC0003DMS000000585
	rv	TGGAGGGATGAGAGACCATC	
CSE	fw	CCGGATACTTGGACAGGGTT	PGSC0003DMS000001550
	rv	ATAGCCTTGCCCACCATCTT	
COMT I	fw	CTTTGATTTGCCACATGTTATTGA	PGSC0003DMS000000587
	rv	AAGCAATGTTCATCGCTCCA	
CCoAOMT1	fw	CTGGCTATTCTCTTCTTGCTACT	PGSC0003DMS000001250
	rv	GTAAAGCAGGTCCCTCTCG	
CCoAOMT2	fw	TGGCTACTCCCTTCTTGCTACC	PGSC0003DMS000001261
	rv	GCAAAGCAGGGCCTTCTCT	
ACTIN	fw	CTAGCAGCATGAAGATTAAGGTG	PGSC0003DMS000000503
	rv	GGACAATAGAAGGACCAGATTCG	
L2	fw	CGAAGGAGCTGTTGTTTGTAAC	PGSC0003DMS000002000
	rv	GGGCACAATCTTTTTGGC	

was homogenized in a mortar with liquid nitrogen, suspended in 3 mL of 95% ethanol, and subsequently incubated at 4 °C for 24 h. A 0.5 mL aliquot of extract was diluted with 7.5 mL of water, mixed with 0.5 mL of water-diluted Folin−Ciocalteu reagent (1:7), and allowed to react for 3 min. Next, 1 mL of 0.5 M Na_2CO_3 was added and allowed to react for 10 min. The absorbance at 725 nm was measured in a visible light spectrophotometer (Hitachi U-1900). Chlorogenic acid (Sigma-Aldrich) was used as standard for the calibration curve, and total phenolics contents were expressed as micrograms of CGA equivalents per gram fresh weight (FW). Blank samples consisted of 95% ethanol.

Antioxidant Activity. Antioxidant activity was measured using the 2,2-diphenyl-1-picrylhydrazyl (DPPH) assay described by Reddivari et al.[28] with minor modifications. A 100 mg sample, homogenized in a mortar with liquid nitrogen, was suspended in 1 mL of methanol and incubated at 4 °C for 24 h. The extract was obtained by centrifugation at 10000*g* for 10 min at 4 °C. A DPPH solution was freshly prepared by dissolving 4 mg of DPPH in 100 mL of methanol to obtain an absorbance of ∼1.1 at 515 nm. Next, 150 μL of the extract was mixed with 2850 μL of DPPH solution and incubated for 24 h at room temperature in the dark. The absorbance at 515 nm was measured using a visible light spectrophotometer (Hitachi U-1900). Blank samples consisted of methanol. Trolox (6-hydroxy-2,5,7,8-tetramethylchroman-2-carboxylic acid) was used as standard for the calibration curve. The results were expressed as micrograms of Trolox equivalents per gram FW.

Phenolic Acids Analysis. One gram of tissue homogenized in a mortar with liquid nitrogen was incubated with extraction buffer (25 mL of 90% methanol with 0.1% HCl) for 60 min at 4 °C in darkness with constant agitation. After centrifugation at 4000*g* for 20 min at 4 °C, the extract was first concentrated using a rotary evaporator, and the remaining solvent was then completely evaporated in a vacuum centrifuge (Savant AES 1010 Automatic Environmental Speed Vac). The residue was dissolved in 1 mL of extraction buffer and filtered through a 0.45 μm PVDF syringe filter. Quantification of phenolic compounds was carried out using an Agilent 1100 system equipped with a quaternary pump, an autosampler, and a diode array detector (DAD). A flow rate of 1 mL min^{-1} was used, and 20 μL samples were injected onto a C-18 Phenomenex Luna column (250 × 4.6 mm i.d.; 5 μm particle size). The mobile phases were (A) acetonitrile and (B) buffer, pH 2.3 (HPLC-grade water acidified with H_3PO_4). The solvent gradient was as follows: 0 to 20 min, linear gradient of A 20% to 100% then back to 20% to 25 min and held until 30 min. Identification of phenolic compounds was carried out by comparing retention times and spectra of authentic standards. The external standard method of calibration and peak areas were used for quantitation. Phenolic acids were expressed in μg g^{-1} FW.

Primer Design. A BLAST analysis[47] was performed at the Web site of the Potato Genome Sequencing Consortium (http://potato.plantbiology.msu.edu/blast.shtml) in order to identify the phenolic acids' biosynthetic genes, *PAL*, *C4H*, *4CL*, *HCT*, *C3H*, *HQT*, *CSE*, *COMT*, and *CCoAOMT*, from the *Solanum phureja* genome. Housekeeping genes *ACTIN* and *L2*, previously used to normalize transcript levels of genes involved in the phenylpropanoid pathway in potato tubers,[22,23,35,36,48−50] were identified by BLAST at NCBI. Primers were designed with Fast-PCR software[51] and the Primer3 online primer design tool.[52] Amplicon sizes were selected around 150 bp, and temperatures of annealing were set around 60 °C. The *HCT*, *HQT*, *CSE*, *COMT I*, and *CCoAOMT* primers are intron spanning. Primers (sequences given in Table 1) were tested by BLAST at NCBI, and against *Solanum* DNA and cDNA. When possible, primer sequences were designed to anneal in regions conserved among *S. tuberosum*, *S. lycopersicum*, *S. melongena*, *S. pinnatisectum*, and *S. cardiophyllum*.

RNA Extraction and cDNA Synthesis. RNA was extracted from tuber samples using the cetyltrimethylammonium bromide (CTAB) method.[53] Samples were ground to fine powders in mortars precooled with liquid nitrogen. Next, 100 mg portions of the powders were transferred to RNase-free tubes filled with 1 mL of prewarmed extraction buffer, including 20 μL of β-mercaptoethanol, and vortex-mixed. The samples were incubated at 65 °C for 20 min and vortex-mixed every 5 min. An equal volume of chloroform/isoamyl alcohol (24:1) was added prior to the final vortex-mix. After centrifugation for 10 min at 15000*g* at 4 °C, the aqueous phase was extracted twice with an equal volume of chloroform/isoamyl alcohol. The supernatant was then mixed with 1/3 volume of 8 M lithium chloride. RNA was precipitated overnight at −20 °C and harvested by centrifugation for 10 min at 15000*g* at 4 °C. The pellet was dissolved in 400 μL of distilled, RNase-free water (dH_2O), reprecipitated with 1/10 volume of 3 M sodium acetate (pH 5.2) and 3 volumes of 100% ethanol at −20 °C for 30 min, and harvested by centrifugation for 10 min at 15000*g* at 4 °C. The RNA pellet was washed with 75% ethanol and finally dissolved in 30 μL of dH_2O. RNA was quantified by measuring the OD260 and OD280 values using a spectrophotometer (Hitachi U-1900), and quality was assessed by agarose gel electrophoresis. cDNA was synthesized using 2 μg of total RNA, previously treated with RNase-free DNase I (Invitrogen), anchored oligo(dT) 15 VN primers, and MMuLV reverse transcriptase according to the manufacturer's description (Invitrogen).

DOI: 10.1021/jf505777p
J. Agric. Food Chem. 2015, 63, 4902−4913

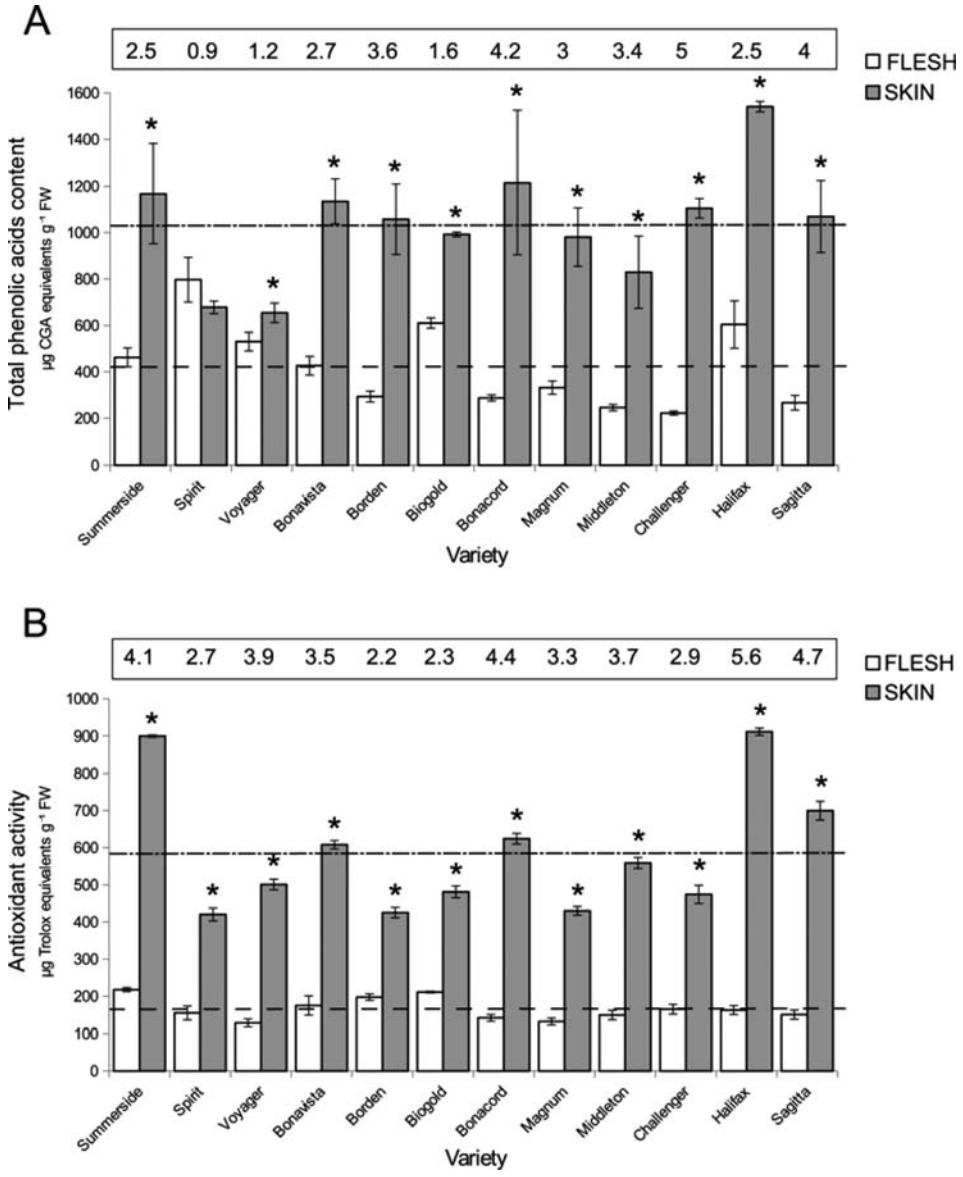

Figure 2. Phenolic acids contents and total hydrophilic antioxidant activity in flesh and skin of tubers from 12 processing potato varieties. (A) Total phenolic acids contents determined by the Folin−Ciocalteu reaction, and (B) total antioxidant activity determined by the DPPH assay in flesh (white bars) and skin (gray bars). Values are presented as the mean ± SD of three independent extractions. Dashed and dash-dotted lines indicate the mean values considering the 12 varieties in flesh and skin, respectively. Numbers in the upper boxes represent the skin-to-flesh ratios. Asterisks denote significant differences between flesh and skin by Student's *t* test ($p < 0.05$).

qRT-PCR Experiments. Relative transcript levels were determined by qRT-PCR in a 10 μL reaction volume with 20 ng of RNA equivalent cDNA, 300 nM gene-specific primers, and 5 μL of SYBR Green Mix (Roche, Mannheim, Germany). Amplification was done using a StepOne real-time PCR system (Applied Biosystem) according to the manufacturer's description, with a 10 min preincubation step at 95 °C, followed by 40 cycles of 15 s denaturation at 95 °C and 1 min annealing/extension at 60 °C. Relative expression was calculated by the ΔCT method[54] by normalizing the CT levels of target genes to the geometric mean of CT levels of both housekeeping genes, *ACTIN* and *L2*. Specificity of amplification was assessed by dissociation curve analysis and agarose gel electrophoresis. qRT-PCR data represent the normalized means ± SD of two independent experiments with two technical replicates each.

C4H2 Sequencing. Genomic DNA (gDNA) was extracted from leaves of *in vitro* grown potato plants using the PureLink genomic plant DNA purification kit (Invitrogen) according to the manufacturer's instructions. The *C4H2* locus was amplified with specific primers C4H2seqfw (5′ GTGCAGCAGTATAGAGGG 3′) and C4H2seqrv (5′ CCTTGCAAATCTTCAAGTAC 3′) from purified gDNA by standard PCR conditions. PCR products were purified from agarose gel using the DNA PuriPrep-GP kit (Inbio, Tandil, Argentina). Purified fragments were sequenced using an internal primer C4H2seqint1rv (5′ AAAGCTCTGAGCCAATCTACTCC 3′) by the sequencing service of Unidad de Genómica, Instituto de Biotecnología, INTA Castelar, Argentina.

Statistical Analysis. Pearson product moment correlation coefficients (*r* values) were calculated with Microsoft Excel using the means of metabolite concentrations or relative gene expression values and visualized with HeatMapper Plus.[55] Differences in the contents of metabolites and transcripts between flesh and skin were evaluated with *t* test.[56] For all statistical analyses, normality and homoscedasticity of the data set were tested using the Kolmogorov−Smirnov and Cochran tests, respectively.[56] When necessary, data were transformed to fit parametric assumptions.

DOI: 10.1021/jf505777p
J. Agric. Food Chem. 2015, 63, 4902−4913

Table 2. Phenolic Acids Content in Flesh and Skin of Fresh and Stored Tubers of Five Potato Varieties[a]

	metabolite													
	CGA			CA			CouA			FA			total	
condition	flesh	skin	*R*	flesh	skin	*R*	flesh	skin	*R*	flesh	skin	*R*	flesh	skin
							Summerside							
fresh	9.8 ± 1.1 (95.4)	142.0 ± 15.4* (95.5)	14.5	0.26 ± 0.04 (2.5)	6.24 ± 1.27* (4.2)	24.0	0.11 ± 0.03 (1.0)	0.14 ± 0.04 (0.1)	1.3	0.11 ± 0.02 (1.1)	0.31 ± 0.09* (0.2)	2.8	10.28 ± 1.19	148.69 ± 16.8
stored	5.6 ± 1.5 (95.1)	94.7 ± 13.2* (94.7)	17.0	0.15 ± 0.03 (2.6)	4.88 ± 0.75* (4.9)	32.5	0.05 ± 0.00 (0.9)	0.18 ± 0.02* (0.2)	3.5	0.09 ± 0.02 (1.5)	0.20 ± 0.09 (0.2)	2.2	5.89 ± 1.55	99.96 ± 14.06
							Voyager							
fresh	9.0 ± 1.5 (96.5)	97.8 ± 10.1* (95.5)	10.9	0.22 ± 0.09 (2.4)	4.21 ± 0.11* (4.1)	19.1	0.03 ± 0.00 (0.3)	0.27 ± 0.10* (0.3)	9.0	0.08 ± 0.02 (0.9)	0.18 ± 0.03* (0.2)	2.2	9.33 ± 1.61	102.46 ± 10.34
stored	5.3 ± 0.9 (92.9)	62.0 ± 7.3* (96.0)	11.6	0.22 ± 0.10 (3.8)	1.73 ± 1.11 (2.7)	7.8	0.11 ± 0.04 (1.9)	0.07 ± 0.01 (0.1)	0.7	0.08 ± 0.04 (1.4)	0.81 ± 0.10* (1.3)	9.7	5.71 ± 1.08	64.61 ± 8.52
							Challenger							
fresh	4.6 ± 0.1 (93.6)	91.5 ± 14.7* (94.7)	20.0	0.11 ± 0.03 (2.3)	4.78 ± 1.10* (4.9)	43.5	0.06 ± 0.01 (1.2)	0.24 ± 0.03* (0.2)	4.0	0.14 ± 0.03 (2.9)	0.13 ± 0.05 (0.1)	0.9	4.91 ± 0.17	96.65 ± 15.88
stored	4.4 ± 1.3 (93.4)	57.2 ± 15.9* (94.4)	12.9	0.07 ± 0.01 (1.5)	3.00 ± 0.75* (5.0)	42.9	0.05 ± 0.02 (1.1)	0.04 ± 0.01 (0.1)	0.8	0.19 ± 0.04 (4.1)	0.36 ± 0.06* (0.6)	1.8	4.71 ± 1.37	60.6 ± 16.72
							Halifax							
fresh	14.4 ± 2.1 (97.2)	175.4 ± 24.9* (92.2)	12.2	0.24 ± 0.00 (1.6)	14.16 ± 1.51* (7.4)	59.0	0.04 ± 0.01 (0.3)	0.27 ± 0.07* (0.1)	6.8	0.14 ± 0.02 (0.9)	0.49 ± 0.14* (0.3)	3.5	14.82 ± 2.13	190.32 ± 26.62
stored	16.5 ± 2.5 (96.8)	175.7 ± 19.4* (96.1)	10.6	0.15 ± 0.04 (0.9)	6.8 ± 1.32* (3.7)	44.3	0.28 ± 0.06 (1.6)	0.10 ± 0.01* (0.1)	0.4	0.11 ± 0.01 (0.6)	0.20 ± 0.04 (0.1)	1.9	17.04 ± 2.61	182.8 ± 20.77
							Sagitta							
fresh	5.9 ± 0.4 (93.0)	118.4 ± 11.3* (89.6)	20.1	0.18 ± 0.03 (2.8)	12.86 ± 1.48* (9.7)	71.4	0.08 ± 0.02 (1.2)	0.56 ± 0.13* (0.4)	7.4	0.19 ± 0.02 (3.0)	0.27 ± 0.10 (0.2)	1.4	6.35 ± 0.47	132.09 ± 13.01
stored	3.4 ± 0.4 (91.9)	119.8 ± 34.2* (95.6)	35.1	0.11 ± 0.02 (3.1)	5.21 ± 1.97* (4.2)	46.0	0.08 ± 0.02 (2.0)	0.07 ± 0.01 (0.1)	0.9	0.11 ± 0.03 (3.1)	0.26 ± 0.05* (0.2)	2.3	3.70 ± 0.47	125.34 ± 36.23

[a]Data represent the mean ± SD from three independent extractions. Metabolite levels were determined by HPLC-DAD and are expressed as $\mu g\ g^{-1}$ FW. Numbers in parentheses indicate the percentage of each metabolite with respect to the total. *R* indicates skin-to-flesh ratio. Abbreviations: CGA, chlorogenic acid; CA, caffeic acid; CouA, *p*-coumaric acid; FA, ferulic acid. Asterisk denotes significant differences between flesh and skin by Student's *t*-test ($p < 0.05$).

J. Agric. Food Chem. 2015, 63, 4902−4913
DOI: 10.1021/jf505777p

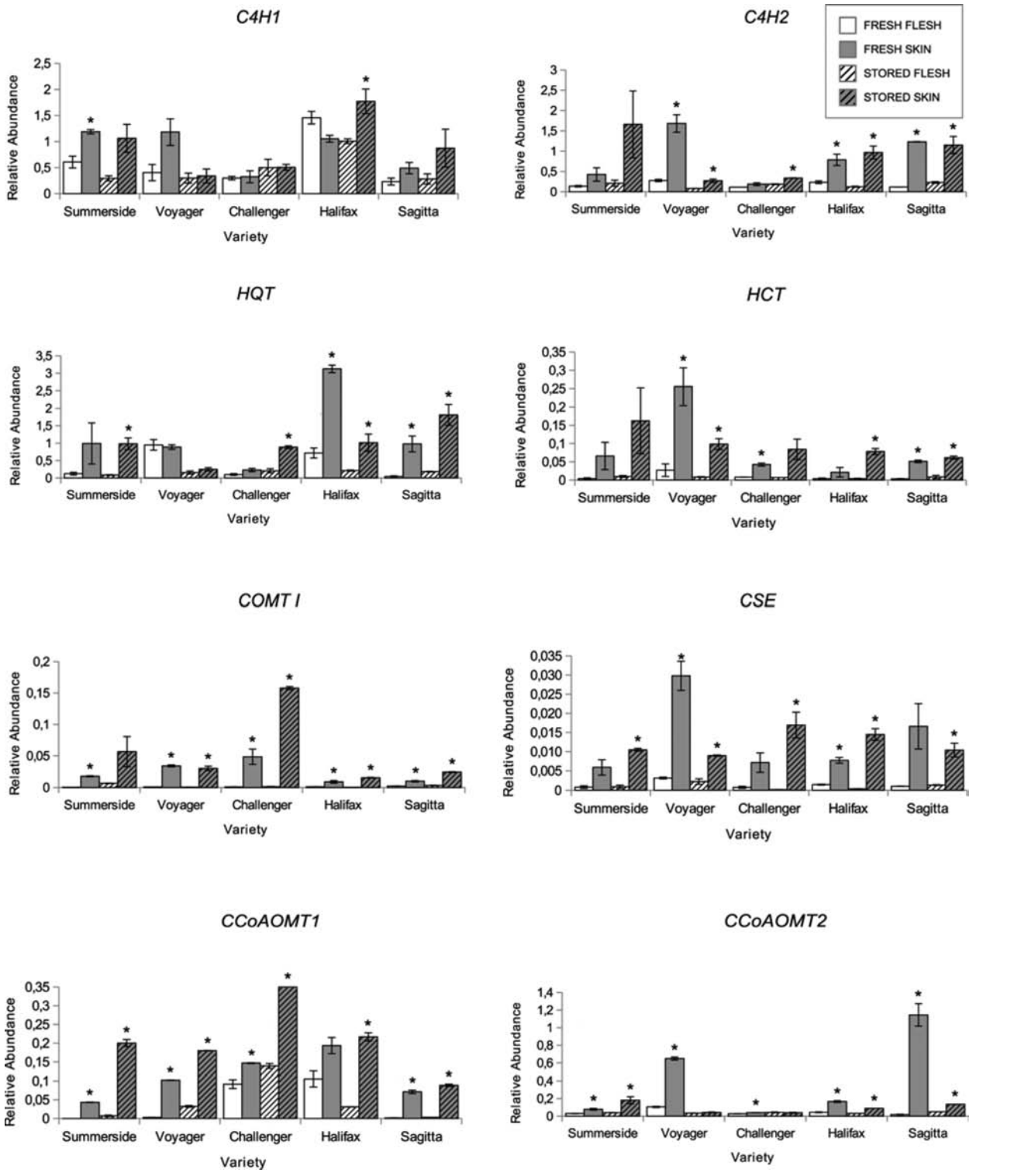

Figure 3. Transcript levels of phenolic acids' biosynthetic genes by qRT-PCR in flesh and skin of fresh and stored tubers from five selected processing potato varieties. qRT-PCR data represent the normalized means ± SD of two independent experiments with two technical replicates each. Asterisk denotes significant differences between flesh and skin by Student's t test ($p < 0.05$).

RESULTS

Selection of Potato Varieties with Different Phenolic Acids Profiles. In order to study the aspects that determine the levels of CGA, it is necessary to have a group of potato varieties with different levels of CGA and related metabolites. Therefore, and since CGA is the major phenolic acid in potato tuber,[57] varieties with different contents of total phenolic acids were selected, taking into account differences in skin and flesh tissue content. Phenolic acids contents in flesh and skin of fresh tubers of 12 processing potato varieties were determined by means of the Folin−Ciocalteu reaction (Figure 2A). Total phenolic acids in flesh ranged from 220 (Challenger) to 800 (Spirit) μg CGA equivalents g^{-1} FW (mean concentration 423.2 μg), whereas in skin the content varied between 650

DOI: 10.1021/jf505777p
J. Agric. Food Chem. 2015, 63, 4902−4913

(Voyager) and 1550 (Halifax) μg CGA equivalents g^{-1} FW (mean concentration 1035.6 μg). Total phenolics were 1.2 (Voyager) to 5 (Challenger) times more abundant in skin than in flesh (Figure 2A). Curiously, Spirit showed slightly higher phenolic acids levels in flesh than in skin.

Five potato varieties were selected for subsequent in-depth analysis on the basis of differences in their skin-to-flesh ratios. Briefly, Voyager shows a low, Summerside and Halifax an intermediate, and Challenger and Sagitta a high skin-to-flesh ratio.

Phenolic acids form a major source of hydrophilic antioxidants. In order to demonstrate the contribution of phenolic acids to antioxidant levels, the hydrophilic antioxidant activity was quantified in both tissues by the DPPH assay (Figure 2B). Antioxidant activity was 2.2 (Borden) to 5.6 (Halifax) times higher in skin than in flesh. Antioxidant activity in flesh ranged from 130 (Voyager) to 220 (Summerside) μg Trolox equivalents g^{-1} FW (mean concentration 165.4 μg), while in skin it varied between 420 (Spirit) and 910 (Halifax) μg Trolox equivalents g^{-1} FW (mean concentration 586.2 μg; Figure 2B). There is a weak positive correlation between total phenolic content and antioxidant activity in skin but not in flesh (data not shown). These results indicate that there are differences in either the phenolic acids or the non-phenolic acids antioxidant composition.

Chlorogenic and Caffeic Acids Levels Are Higher in Skin than in Flesh and Largely Independent of Storage. Because producing fresh potatoes throughout the year is unfeasible, storage is essential[58] but might affect phenolic acids content. Therefore, the levels of CGA, CA, CouA, FA, and cinnamic acid (CinA) were quantified via HPLC-DAD in flesh and skin of both fresh and 3 months stored tubers of the five selected potato varieties (Table 2).

Table 2 shows that CGA is the major phenolic acid in the skin and flesh of both fresh and stored potato tubers (89.6−97.2%). CA, CouA, and FA are minor components (0.1−9.7%), whereas CinA could not be detected by HPLC-DAD. In correspondence to what was found for total phenolics in the initial Folin−Ciocalteu screening, the abundance of most compounds was higher in skin than in flesh. For instance, CGA levels were 10.9 (Voyager) to 20.1 (Sagitta) times more abundant in skin than in flesh. Skin-to-flesh ratios of CA were even higher, reaching up to 71-fold in fresh tubers of the Sagitta variety. In general, CouA and FA exhibited minor differences among tissues, as reflected by their skin-to-flesh ratios. During storage, the levels of CGA and CA either diminished or did not alter significantly. The levels of CouA and FA fluctuated without a clear pattern (Table 2).

CGA Synthesis Is Regulated at the Transcriptional Level in Potato Tuber and Is the Result of a Dynamic Balance between the Influx via C4H and HQT and the Outward Flux through CSE and HCT, Irrespective of the Effect of Storage. With the aim to explore the molecular mechanisms that determine the levels of CGA and CA, a qRT-PCR transcript level analysis of key enzymes *C4H*, *HQT*, *HCT*, *CSE*, *COMT I*, and *CCoAOMT* was performed on the skin and flesh of both fresh and stored tubers of the five selected potato varieties. *CCoAOMT* appears to be encoded by two nearly identical (86%) genes, which were both evaluated. *C4H* shows two 98% identical genes, of which *C4H2* initially appeared to be a pseudogene. The genome sequence of *Solanum phureja*[59] shows that *C4H2* has a single nucleotide deletion, resulting in a reading frame shift. SNP analysis of publicly available EST data could not unequivocally show that *C4H2* is a pseudogene in all *S. tuberosum* varieties (data not shown). Part of the *C4H2* locus from the *S. phureja* variety that was sequenced by the Potato Genome Sequencing Consortium as well as two varieties used in our analysis was amplified and sequenced with locus-specific primers. Surprisingly, none of the obtained sequences demonstrates the single nucleotide deletion identified in the genome sequence (see Supporting Information, Figure S1). Hence, gene-specific primers for both *C4H* genes were designed and used in qRT-PCR analysis. *ACTIN* and cytoplasmic ribosomal protein *L2* transcript levels were used for normalization (Figure 3). In general, the results show that transcript levels were higher in skin than in flesh, in both fresh and stored tubers (Figure 3). Levels in stored and fresh tubers were of the same order of magnitude. Transcript levels of *C4H1*, *C4H2*, *HQT*, and *CCoAOMT2* were of the same order of magnitude, although *CCoAOMT2* levels showed larger fluctuations. *HCT* and *CCoAOMT1* levels were about 1−2 orders of magnitude lower (skin and flesh, respectively), whereas the lowest transcript levels were found for *CSE* and *COMT I* (Figure 3). Transcript levels of the genes involved in CGA synthesis were tissue- and condition-specific. Expression patterns of *C4H1*, *C4H2*, and *HQT* were similar in flesh of fresh tubers (Figure 3) and in accordance with the levels of CGA (Table 2) in all studied varieties except for Voyager. Voyager showed the highest expression levels of *C4H2* and *HQT*, but intermediate levels of *C4H1* and CGA (Figure 3 and Table 2). The transcript level of *HQT* reflects CGA levels in skin of fresh potato tubers in four of the five varieties (Figure 3 and Table 2). Nevertheless, Voyager has intermediate transcript levels of *HQT* but lower CGA levels.

A Pearson correlation analysis was performed in order to quantify associations between metabolite and transcript levels. Figure 4 shows the correlation between fresh flesh transcript and metabolite levels as well as fresh skin metabolite levels of four of the five initially selected varieties. The Voyager data were not included since this cultivar exhibits a different behavior which might hinder detecting otherwise obvious trends. The complete set of analysis of all four conditions of the four selected varieties can be found in the Supporting Information, Figure S2.

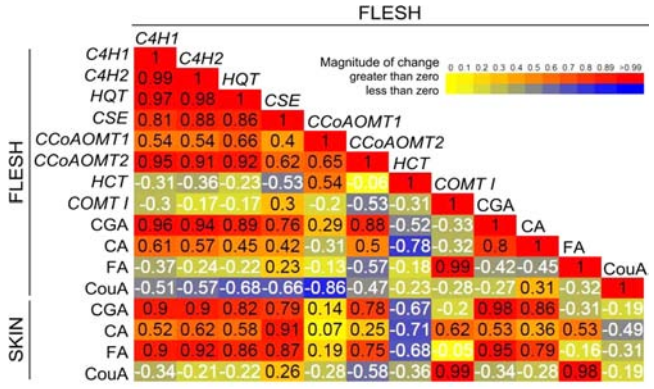

Figure 4. Correlation analysis of transcript and metabolite levels of fresh tubers from four selected processing potato varieties. Pearson correlation coefficients were calculated using the means of metabolite concentrations from fresh flesh and/or fresh skin and/or relative gene expression values from fresh flesh and used to generate a heatmap. Abbreviations are listed in Figure 1 and Table 2.

DOI: 10.1021/jf505777p
J. Agric. Food Chem. 2015, 63, 4902−4913

In fresh flesh, transcript levels of *C4H1*, *C4H2*, *HQT*, *CSE*, and *CCoAOMT2* show mutual positive correlations and exhibit positive correlations with the major metabolites CGA and, to a lesser extent, CA. In contrast, *HCT* and *COMT I* show an almost consistent negative correlation with all other transcripts and most metabolites. An important exception to the latter is the mutual positive correlation between *COMT I* and *CSE* transcripts and FA, the metabolite downstream of the consecutive action of the corresponding enzymes. *CCoAOMT1* shows lower *r* values than *CCoAOMT2* and exhibits a positive correlation with *HCT* (Figure 4).

The metabolite levels in skin are higher than in flesh, in correspondence with transcript levels. Nevertheless, Figure 4 also shows the correlation between fresh flesh transcript and metabolite levels with fresh skin metabolite levels in order to analyze putative metabolite transport. A high correlation between CGA levels in skin and flesh (r = 0.98; Figure 4) suggests metabolite contribution from flesh toward skin. Accordingly, flesh *C4H1*, *CH42*, and *HQT* transcript levels correlate well with skin CGA levels (r = 0.90, 0.90, and 0.82, respectively). Furthermore, skin FA levels show a better correlation with flesh than with skin *C4H* transcript levels (Figures 4 and S2; also see Discussion section).

DISCUSSION

The present study was directed at the elucidation of the biosynthesis of the dietary antioxidant CGA in the staple crop potato. Metabolite and transcript levels in flesh and skin from fresh and stored tubers from five carefully selected potato varieties were determined. The initial selection of five from 12 varieties was made on the basis of total phenolic acids contents determined by Folin−Ciocalteu assay. Total phenolic acids in flesh were in accordance with reports for white- or yellow-fleshed cultivars by Al-Saikhan et al.[60] and Reddivari et al.[29] Antioxidant activity in flesh was similar to or slightly lower than that in previous reports.[28,61] As with total phenolic acids content, antioxidant activity was higher in skin than in flesh and correlated well with it in skin but not in flesh. Differences in the composition of phenolics and other antioxidants present in methanol extracts may cause the lack of correlation in flesh. It has been shown that CA has higher antioxidant activity than CGA[28] and vitamin C is an abundant, methanol-soluble antioxidant in potato.[62]

The Folin−Ciocalteu assay showed higher values for total phenolic contents than the sum of all the individual phenolic compounds quantified by HPLC-DAD. These results fit with those obtained by other groups[33,63] and can be explained by the fact that compounds like thiol derivatives, vitamins, and amino acids may interact with the Folin−Ciocalteu assay.[64] A strong correlation was found between the results obtained by the two different methods (r = 0.93 for flesh, r = 0.83 for skin), as previously reported by André et al.,[27] even though fold differences between samples appear less clear in the Folin−Ciocalteu assay. This supports the idea that the Folin−Ciocalteu assay remains a rapid and economic alternative for comparative purposes.

CGA and CA Levels Are Significantly Higher in Skin Tissue. CGA is the predominant phenolic acid in both skin and flesh. CA contributes significantly, around 1−10%, whereas other phenolic acids contribute little to the total phenolic content. This is in agreement with other reports that show CGA is the most abundant phenolic acid in potatoes, followed by CA,[27,32,33,42,65] with CouA and FA being the least abundant.[33,66] We could not identify CinA in skin nor in flesh. CinA was earlier identified only in tuber skin.[25]

Both CGA and CA levels are 10−70 times higher in skin than in flesh. Similar results were obtained by Im et al.[30] in skin and flesh of five commercial potato varieties. Other previous data indicated that phenolic compounds are found mostly between the cortex and potato skin[67] or in the potato skin and adjoining tissues, with decreasing concentrations toward the center of potato tubers.[68] This is likely related to suberin deposition in skin tissue during tuber growth.[69]

During storage, the levels of CGA and CA diminished or remained unaffected. Conversely, Madiwale et al.[61] reported that 90 days of storage at 4 °C led to a 1.3- to 4-fold increase of CGA and CA content. These differences might be attributed either to cultivar-dependent storage responses or to storage conditions.

Transcript and Metabolite Levels Are Highly Correlated. Transcript levels of phenolic acids biosynthetic genes were also, in general, higher in skin than in flesh (see Figure 3). The good correspondence between transcript and metabolite levels suggests that the control of gene expression is essential in the control of CGA biosynthesis and that the enzymes are coordinately regulated, at least in part, at the transcriptional level. This confirms earlier work[14−21] and is fundamental in the use of Pearson correlation analysis for metabolic modeling. Interestingly, *HCT* shows a consistent negative correlation, whereas *COMT I* shows a prevalent negative correlation with most metabolites, FA forming the obvious exception (Figure 4).

Of particular interest is C4H, encoded by two genes. The close proximity of the two genes in the *S. phureja* genome combined with the high sequence identity suggests that these genes are under concerted evolution.[70] Although the genome sequence of *S. phureja* shows *C4H2* has a fatal deletion, resequencing of the locus amplified by locus-specific primers indicates that *C4H2* is a functional gene (see Figure S1). André et al.[22] used indiscriminative primers, which might explain the lack of positive correlation between *C4H* transcript and CGA levels they demonstrated. The consistent positive correlation of the *C4H* transcripts corresponds with a major role for the sink in the metabolism of both CA and CGA. *HQT* transcripts correspond very well with CGA, which indicates that HQT is the principal enzyme for CGA accumulation. This is in correspondence with results found in tomato leaves, where overexpression of *HQT* increased CGA content, whereas *HQT* silencing caused a reduction but had no detectable effects on lignin accumulation.[8] An in-depth study of *HCT*-silenced *Nicotiana benthamiana* plants revealed that lignin biosynthesis depends on HCT activity *in vivo*.[12] In correspondence, we found that CGA shows a negative correlation with *HCT* transcript levels in all studied conditions (Figure S2).

Toward a Model for CGA and CA Metabolism. CGA is the major phenolic acid in potato tuber, and its biosynthesis is very well explained by the transcript levels of its structural genes, as shown in Figure 4. We did not analyze transcript levels of structural genes of the flavonoid pathway, but previously CGA was shown to correlate better with flavonoid biosynthetic enzymes than with *HQT* transcript levels.[22,23] Thus, phenolic acid and flavonoid metabolism are linked, under direct transcriptional control, and must be subject to metabolic regulation. Using the Pearson correlation analysis shown in Figure 4, we developed an initial model of CGA and CA biosynthesis that appears to be driven by both the source CouA

DOI: 10.1021/jf505777p
J. Agric. Food Chem. 2015, 63, 4902−4913

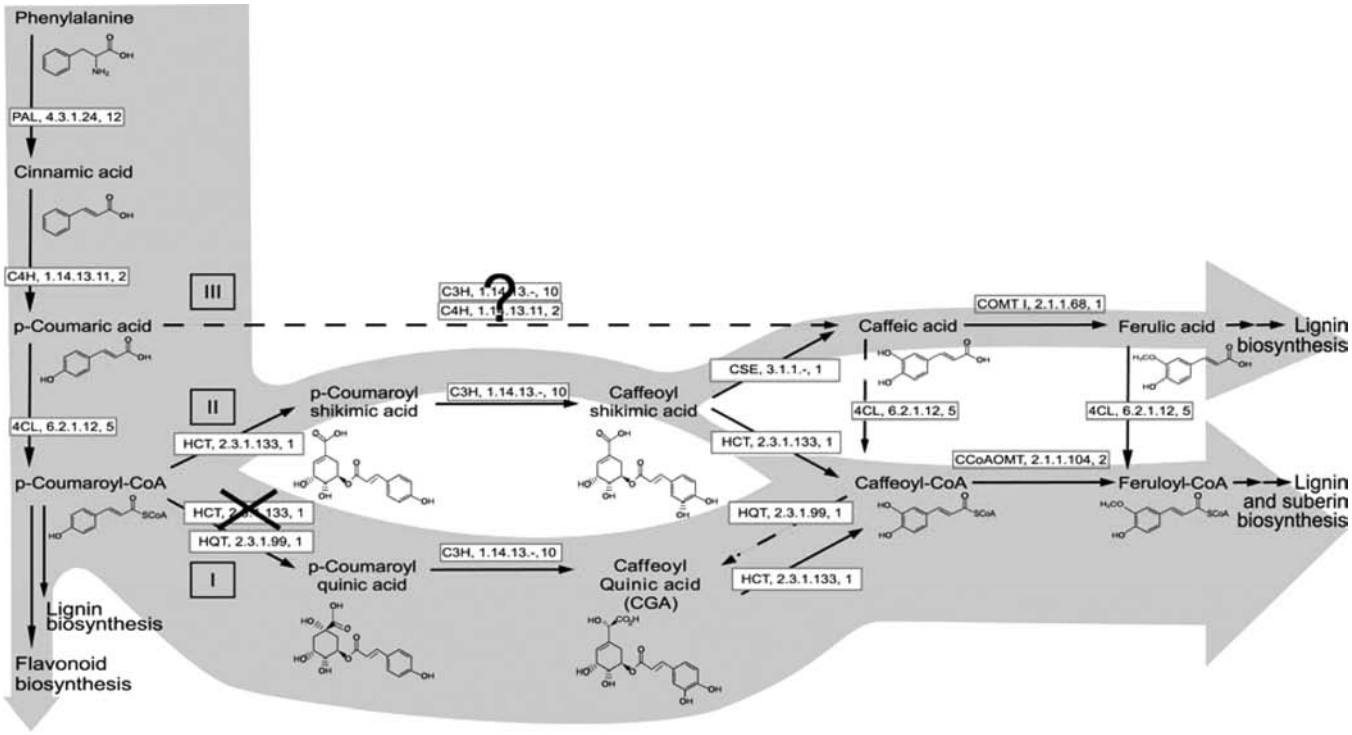

Figure 5. Proposed flux model of biochemical pathways leading to CGA and CA production in potato tuber. Dashed lines, question mark, and cross indicate unlikely routes, uncertain enzyme complexes, and unfeasible reaction, respectively. Enzyme names are listed in Figure 1.

and the sink suberin (Figure 5). The model explains the correlation between CA and CGA ($r = 0.8$, see Figure 4) by the high correlation of both metabolites with *C4H* transcript levels and, hence, the sink via CouA. Then, the positive correlation between *CSE* and CA indicates route II is actively involved in CA biosynthesis. Note that HCT and CSE will compete for substrate, which contributes to the negative correlation of *HCT* with CA, which can further be explained by additional or alternative CA formation via route III. Although, theoretically, CGA biosynthesis could occur via CA and caffeoyl-CoA, the negative correlation of *HCT* points toward a role for HCT in CGA remobilization toward lignin and suberin. Thus, route I would be the major route, and HQT is the major enzyme in CGA biosynthesis. Note also that *HCT* transcript levels are consistently low in flesh and show up to ~18-fold induction in skin, where suberin is deposited in the primary cell wall. This suggests that CGA is transported to the skin. The positive correlation of *CCoAOMT*, required for feruloyl-CoA and downstream suberin, and the negative correlation of *COMT I*, required for FA and downstream lignin, also suggest a central role for suberin deposition in potato tuber. It should be mentioned that, given the complexity of the phenylpropanoid, lignin, and suberin biosynthetic pathways, this merely a trend, and other fluxes can and likely will occur.

The model was based on the fresh flesh data set but also explains the fresh skin data set quite well, albeit that the correlation values are not so high. This could be caused by metabolite transport, suggested by the correlations between flesh transcript and skin metabolite levels (Figure 4). Such metabolite transport would have a minor effect on the voluminous flesh tissue but a major effect on skin metabolite levels. On that proposition, the skin data are not reliable resources for model construction. Then, the stored tuber data sets shows less clear patterns. Nevertheless, the stored flesh data correspond with the model. *C4H2*, *HCT*, *CSE*, and *COMT I* correlate well to each other. On the other hand, *C4H1*, *HQT*, and CGA correspond well, whereas *CCoAOMT* appears to have an inconsistent correlation. Within the proposed model, this would mean that, upon storage, there is more emphasis on lignin production, or less emphasis on suberin production. This is not reflected in the levels of CA, CGA, and FA but might be reflected in the levels of caffeoyl-CoA and feruloyl-CoA. It should be mentioned that the model corresponds with poor rather than negative correlations of *HCT*. However, in all likelihood, no model can account for the consistent negative correlation of *HCT*. Then, the model was made on the basis of an incomplete data set since we ignored the Voyager data set in the Pearson correlation analysis, this in order to more easily detect the major trends. However, the Voyager data set does actually also correspond quite well with the model. An increased flux toward lignin and suberin, reflected by the highest levels of *CSE* and *HCT* observed in fresh tubers of Voyager variety, would explain why even though it showed high expression levels of *C4H* and *HQT*, it has intermediate levels of CGA. In other words, CGA levels are the result of a dynamic balance between the influx via C4H and HQT and the outward flux through CSE and HCT.

The model in Figure 5 should be seen as an initial model that requires both substantiation and elaboration. The model is clearly based on the oversimplification that transcript levels reflect metabolite levels and that no post-translational regulation is involved. Hence, for instance, differences in enzyme kinetics between various cultivars cannot be captured by such a simple model but would require a more delicate systems biology approach. The same should be mentioned regarding the proposed metabolite transport and the Voyager data set, which complicate Pearson correlation analysis but can readily be included in more delicate and elaborate analyses such

DOI: 10.1021/jf505777p
J. Agric. Food Chem. 2015, 63, 4902−4913

as flux balance analysis, thereby contributing to an improved, possibly even semiquantitative model.

■ ASSOCIATED CONTENT

Supporting Information

Figure S1, showing multiple sequence alignment of the *C4H2* subsequences surrounding the nucleotide deletion reported in the genome sequence of *S. tuberosum* group *phureja* (2_PGSC_Sp); Figure S2, showing correlation analysis of transcript and metabolite levels in tubers from four selected processing potato varieties. The Supporting Information is available free of charge on the ACS Publications website at DOI: 10.1021/jf505777p.

■ AUTHOR INFORMATION

Corresponding Author

*Telephone: +54-223-4753030. Fax: +54-223-4724143. E-mail: abandreu@mdp.edu.ar.

Funding

This work was financially supported by grants from Agencia Nacional de Promoción Científica y Tecnológica (PICT 2010 No. 511 and PICT 2010 No. 1812), Consejo Nacional de Investigaciones Científicas y Técnicas (CONICET) (PIP No. 0226), and Universidad Nacional de Mar del Plata (EXA 539/11). A.B.A., A.T.H., and M.L.L. are career members and M.A.V. is a Ph.D. fellow of CONICET, Argentina.

Notes

The authors declare no competing financial interest.

■ ACKNOWLEDGMENTS

We thank Daniel Caldiz (Global Director of Agronomy (R&D), McCain Foods Limited) and Carolina de Lasa (Agronomy Chief for Argentina and Colombia, McCain Argentina S.A.) for providing the potato tubers used in this study. We also thank Hernán Bondino for primer design used in qRT-PCR assay.

■ ABBREVIATIONS USED

qRT-PCR, quantitative real-time polymerase chain reaction; HPLC-DAD, high-performance liquid chromatography with diode-array detection; CGA, chlorogenic acid; CA, caffeic acid; CoA, coenzyme A; CouA, *p*-coumaric acid; FA, ferulic acid; CinA, cinnamic acid; PAL, phenylalanine-ammonia-lyase; C4H, cinnamate 4-hydroxylase; 4CL, 4-coumarate-CoA ligase; HCT, hydroxycinnamoyl-CoA shikimate/quinate hydroxycinnamoyltransferase; C3H, *p*-coumarate 3′-hydroxylase; HQT, hydroxycinnamoyl-CoA quinate hydroxycinnamoyltransferase; CSE, caffeoyl shikimate esterase; COMT I, caffeic/5-hydroxyferulic acid *O*-methyltransferase; CCoAOMT, caffeoyl-CoA *O*-methyltransferase

■ REFERENCES

(1) Camire, M. E.; Kubow, S.; Donnelly, D. J. Potatoes and human health. *Crit. Rev. Food Sci. Nutr.* **2009**, *49*, 823−840.

(2) Dixon, R. A.; Paiva, N. L. Stress-Induced Phenylpropanoid Metabolism. *Plant Cell* **1995**, *7*, 1085−1097.

(3) Evers, D.; Deußer, H. *Potato Antioxidant Compounds: Impact of Cultivation Methods and Relevance for Diet and Health*, 2009; www.cdn.intechopen.com/books/.

(4) Ezekiel, R.; Singh, N.; Sharma, S.; Kaur, A. Beneficial phytochemicals in potato—a review. *Food Res. Int.* **2013**, *50*, 487−496.

(5) Nogueira, T.; do Lago, C. L. Determination of caffeine in coffee products by dynamic complexation with 3,4-dimethoxycinnamate and separation by CZE. *Electrophoresis* **2007**, *28*, 3570−3574.

(6) Yamaguchi, T.; Chikama, A.; Mori, K.; Watanabe, T.; Shioya, Y.; Katsuragi, Y.; Tokimitsu, I. Hydroxyquinone-free coffee: A double-blind, randomized controlled dose-response study of blood pressure. *Nutr. Metab. Cardiovasc. Dis.* **2008**, *18*, 408−414.

(7) Schoch, G.; Goepfert, S.; Morant, M.; Hehn, A.; Meyer, D.; Ullmann, P.; Werck-Reichhart, D. CYP98A3 from Arabidopsis thaliana Is a 3′-Hydroxylase of Phenolic Esters, a Missing Link in the Phenylpropanoid Pathway. *J. Biol. Chem.* **2001**, *276*, 36566−36574.

(8) Niggeweg, R.; Michael, A. J.; Martin, C. Engineering plants with increased levels of the antioxidant chlorogenic acid. *Nat. Biotechnol.* **2004**, *22*, 746−754.

(9) Matsuda, F.; Morino, K.; Ano, R.; Kuzawa, M.; Wakasa, K.; Miyagawa, H. Metabolic flux analysis of the phenylpropanoid pathway in elicitor-treated potato tuber tissue. *Plant Cell Physiol.* **2005**, *46*, 454−466.

(10) Chen, H.-C.; Li, Q.; Shuford, C. M.; Liu, J.; Muddiman, D. C.; Sederoff, R. R.; Chiang, V. L. Membrane protein complexes catalyze both 4- and 3-hydroxylation of cinnamic acid derivatives in monolignol biosynthesis. *Proc. Natl. Acad. Sci. U.S.A.* **2011**, *108*, 21253−21258.

(11) Villegas, R. J. A.; Kojima, M. Purification and characterization of hydroxycinnamoyl D-glucose. Quinate hydroxycinnamoyl transferase in the root of the sweet potato, Ipomoea batatas Lam. *J. Biol. Chem.* **1986**, *261*, 8729−8733.

(12) Hoffmann, L.; Besseau, S.; Geoffroy, P.; Ritzenthaler, C.; Meyer, D.; Lapierre, C.; Pollet, B.; Legrand, M. Silencing of hydroxycinnamoyl-coenzyme A shikimate/quinate hydroxycinnamoyltransferase affects phenylpropanoid biosynthesis. *Plant Cell* **2004**, *16*, 1446−1465.

(13) Vanholme, R.; Cesarino, I.; Rataj, K.; Xiao, Y.; Sundin, L.; Goeminne, G.; Kim, H.; Cross, J.; Morreel, K.; Araujo, P.; Welsh, L.; Haustraete, J.; McClellan, C.; Vanholme, B.; Ralph, J.; Simpson, G. G.; Halpin, C.; Boerjan, W. Caffeoyl shikimate esterase (CSE) is an enzyme in the lignin biosynthetic pathway in Arabidopsis. *Science* **2013**, *341*, 1103−1106.

(14) Mol, J.; Grofewold, E.; Koes, R. How genes paint flowers and seeds. *Trends Plant Sci.* **1998**, *3*, 212−217.

(15) Comino, C.; Lanteri, S.; Portis, E.; Acquadro, A.; Romani, A.; Hehn, A.; Larbat, R.; Bourgaud, F. Isolation and functional characterization of a cDNA coding a hydroxycinnamoyltransferase involved in phenylpropanoid biosynthesis in Cynara cardunculus L. *BMC Plant Biol.* **2007**, *7*, 14.

(16) Comino, C.; Hehn, A.; Moglia, A.; Menin, B.; Bourgaud, F.; Lanteri, S.; Portis, E. The isolation and mapping of a novel hydroxycinnamoyltransferase in the globe artichoke Chlorogenic acid pathway. *BMC Plant Biol.* **2009**, *9*, 30.

(17) Koshiro, Y.; Jackson, M. C.; Katahira, R.; Wang, M. L.; Nagai, C.; Ashihara, H. Biosynthesis of chlorogenic acids in growing and ripening fruits of Coffea arabica and Coffea canephora plants. *Z. Naturforsch., Sect. C: J. Biosci.* **2007**, *62*, 731−742.

(18) Lepelley, M.; Cheminade, G.; Tremillon, N.; Simkin, A.; Caillet, V.; McCarthy, J. Chlorogenic acid synthesis in coffee: an analysis of CGA content and real-time RT-PCR expression of HCT, HQT, C3H1, and CCoAOMT1 genes during grain development in C. canephora. *Plant Sci.* **2007**, *172*, 978−996.

(19) Salmona, J.; Dussert, S.; Descroix, F.; De Kochko, A.; Bertrand, B.; Joët, T. Deciphering transcriptional networks that govern Coffea arabica seed development using combined cDNA array and real-time RT-PCR approaches. *Plant Mol. Biol.* **2008**, *66*, 105−124.

(20) Joët, T.; Laffargue, A.; Salmona, J.; Doulbeau, S.; Descroix, F.; Bertrand, B.; De Kochko, A.; Dussert, S. Metabolic pathways in tropical dicotyledonous albuminous seeds: Coffea arabica as a case study. *New Phytol.* **2009**, *182*, 146−162.

(21) Joët, T.; Salmona, J.; Laffargue, A.; Descroix, F.; Dussert, S. Use of the growing environment as a source of variation to identify the quantitative trait transcripts and modules of co-expressed genes that determine chlorogenic acid accumulation. *Plant Cell Environ.* **2010**, *33*, 1220−1233.

(22) André, C. M.; Schafleitner, R.; Legay, S.; Lefevre, I.; Aliaga, C. A. A.; Nomberto, G.; Hoffmann, L.; Hausman, J. F.; Larondelle, Y.; Evers, D. Gene expression changes related to the production of phenolic compounds in potato tubers grown under drought stress. *Phytochemistry* **2009**, *70*, 1107−1116.
(23) Payyavula, R. S.; Navarre, D. A.; Kuhl, J. C.; Pantoja, A.; Pillai, S. S. Differential effects of environment on potato phenylpropanoid and carotenoid expression. *BMC Plant Biol.* **2012**, *12*, 39.
(24) Barel, G.; Ginzberg, I. Potato skin proteome is enriched with plant defence components. *J. Exp. Bot.* **2008**, *59*, 3347−3357.
(25) Lewis, C. E.; Walker, J. R. L.; Lancaster, J. E.; S, K. Determination of anthocyanins, flavonoids and phenolic acids in potatoes. I: Coloured cultivars of Solanum tuberosum L. *J. Sci. Food Agric.* **1998**, *77*, 45−57.
(26) André, C. M.; Ghislain, M.; Bertin, P.; Oufir, M.; Herrera, M. D. R.; Hoffmann, L.; Hausman, J. F.; Larondelle, Y.; Evers, D. Andean potato cultivars (Solarium tuberosum L.) as a source of antioxidant and mineral micronutrients. *J. Agric. Food Chem.* **2007**, *55*, 366−378.
(27) André, C. M.; Oufir, M.; Guignard, C.; Hoffmann, L.; Hausman, J. F.; Evers, D.; Larondelle, Y. Antioxidant profiling of native Andean potato tubers (Solanum tuberosum L.) reveals cultivars with high levels of β-carotene, α-tocopherol, chlorogenic acid, and petanin. *J. Agric. Food Chem.* **2007**, *55*, 10839−10849.
(28) Reddivari, L.; Hale, A. L.; Miller, J. C. Determination of phenolic content, composition and their contribution to antioxidant activity in specialty potato selections. *Am. J. Potato Res.* **2007**, *84*, 275−282.
(29) Reddivari, L.; Hale, A. L.; Miller, J. C. Genotype, location, and year influence antioxidant activity, carotenoid content, phenolic content, and composition in specialty potatoes. *J. Agric. Food Chem.* **2007**, *55*, 8073−8079.
(30) Im, H. W.; Suh, B. S.; Lee, S. U.; Kozukue, N.; Ohnisi-Kameyama, M.; Levin, C. E.; Friedman, M. Analysis of phenolic compounds by high-performance liquid chromatography and liquid chromatography/mass spectrometry in potato plant flowers, leaves, stems, and tubers and in home-processed potatoes. *J. Agric. Food Chem.* **2008**, *56*, 3341−3349.
(31) André, C. M.; Oufir, M.; Hoffmann, L.; Hausman, J.-F.; Rogez, H.; Larondelle, Y.; Evers, D. Influence of environment and genotype on polyphenol compounds and in vitro antioxidant capacity of native Andean potatoes (Solanum tuberosum L.). *J. Food Compos. Anal.* **2009**, *22*, 517−524.
(32) Navarre, D. A.; Pillai, S. S.; Shakya, R.; Holden, M. J. HPLC profiling of phenolics in diverse potato genotypes. *Food Chem.* **2011**, *127*, 34−41.
(33) Deußer, H.; Guignard, C.; Hoffmann, L.; Evers, D. Polyphenol and glycoalkaloid contents in potato cultivars grown in Luxembourg. *Food Chem.* **2012**, *135*, 2814−2824.
(34) Narváez-Cuenca, C. E.; Vincken, J. P.; Zheng, C.; Gruppen, H. Diversity of (dihydro) hydroxycinnamic acid conjugates in Colombian potato tubers. *Food Chem.* **2013**, *139*, 1087−1097.
(35) Navarre, D. A.; Payyavula, R. S.; Shakya, R.; Knowles, N. R.; Pillai, S. S. Changes in potato phenylpropanoid metabolism during tuber development. *Plant Physiol. Biochem.* **2013**, *65*, 89−101.
(36) Payyavula, R. S.; Navarre, D. A.; Kuhl, J. C.; Pantoja, A. Developmental effects on phenolic, flavonol, anthocyanin, and carotenoid metabolites and gene expression in potatoes. *J. Agric. Food Chem.* **2013**, *61*, 7357−7365.
(37) Lachman, J.; Hamouz, K.; Orsák, M.; Pivec, V.; Dvořák, P. The influence of flesh colour and growing locality on polyphenolic content and antioxidant activity in potatoes. *Sci. Hortic. (Amsterdam)* **2008**, *117*, 109−114.
(38) Hamouz, K.; Lachman, J.; Hejtmánková, K.; Pazderů, K.; Čížek, M.; Dvořák, P. Effect of natural and growing conditions on the content of phenolics in potatoes with different flesh colour. *Plant Soil Environ.* **2010**, *8*, 368−374.
(39) Pinhero, R.; Coffin, R.; Yada, R. Post-harvest storage of potatoes. In *Advances in potato chemistry and technology*; Elsevier: Amsterdam, 2009; pp 339−370.
(40) Lewis, C. E.; Walker, J. R. L.; Lancaster, J. E. Changes in anthocyanin, flavonoid and phenolic acid concentrations during development and storage of coloured potato (Solanum tuberosum L) tubers. *J. Sci. Food Agric.* **1999**, *79*, 311−316.
(41) Stushnoff, C.; Holm, D.; Thompson, M. D.; Jiang, W.; Thompson, H. J.; Joyce, N. I.; Wilson, P. Antioxidant Properties of Cultivars and Selections from the Colorado Potato Breeding Program. *Am. J. Potato Res.* **2008**, *85*, 267−276.
(42) Blessington, T.; Nzaramba, M. N.; Scheuring, D. C.; Hale, A. L.; Reddivari, L.; Miller, J. C. Cooking Methods and Storage Treatments of Potato: Effects on Carotenoids, Antioxidant Activity, and Phenolics. *Am. J. Potato Res.* **2010**, *87*, 479−491.
(43) Spychalla, J. P.; Desborough, S. L. Superoxide Dismutase, Catalase, and α-Tocopherol Content of Stored Potato Tubers 1. *Plant Physiol.* **1990**, *94*, 1214−1218.
(44) Mizuno, M.; Kamei, M.; Tsuchida, H. Ascorbate peroxidase and catalase cooperate for protection against hydrogen peroxide generated in potato tubers during low-temperature storage. *Biochem. Mol. Biol. Int.* **1998**, *44*, 717−726.
(45) Rosenthal, S.; Jansky, S. Effect of production site and storage on antioxidant levels in specialty potato (Solanum tuberosum L.) tubers. *J. Sci. Food Agric.* **2008**, *88*, 2087−2092.
(46) Campos, D.; Noratto, G.; Chirinos, R.; Arbizu, C.; Roca, W.; Cisneros-Zevallos, L. Antioxidant capacity and secondary metabolites in four species of Andean tuber crops: Native potato (Solanum sp.), mashua (Tropaeolum tuberosum Ruiz & Pavón), Oca (Oxalis tuberosa Molina) and ulluco (Ullucus tuberosus Caldas). *J. Sci. Food Agric.* **2006**, *86*, 1481−1488.
(47) Altschul, S. F.; Madden, T. L.; Schäffer, A. A.; Zhang, J.; Zhang, Z.; Miller, W.; Lipman, D. J. Gapped BLAST and PSI-BLAST: A new generation of protein database search programs. *Nucleic Acids Res.* **1997**, *25*, 3389−3402.
(48) Rommens, C. M.; Richael, C. M.; Yan, H.; Navarre, D. A.; Ye, J.; Krucker, M.; Swords, K. Engineered native pathways for high kaempferol and caffeoylquinate production in potato. *Plant Biotechnol. J.* **2008**, *6*, 870−886.
(49) Payyavula, R. S.; Singh, R. K.; Navarre, D. A. Transcription factors, sucrose, and sucrose metabolic genes interact to regulate potato phenylpropanoid metabolism. *J. Exp. Bot.* **2013**, *64*, 5115−5131.
(50) Payyavula, R.; Shakya, R. Synthesis and regulation of chlorogenic acid in potato: Rerouting phenylpropanoid flux in HQT-silenced lines. *Plant Biotechnol. J.* **2014**, *13*, 551−564.
(51) Kalendar, R.; Lee, D.; Schulman, A. H. FastPCR software for PCR primer and probe design and repeat search. *Genes Genomes Genomics* **2009**, *3*, 1−14.
(52) Rozen, S.; Skaletsky, H. Primer3 on the WWW for general users and for biologist programmers. *Methods Mol. Biol.* **2000**, *132*, 365−386.
(53) Li, X.; Wang, C.; Sun, H.; Li, T. Establishment of the total RNA extraction system for lily bulbs with abundant polysaccharides. *African J. Biotechnol.* **2011**, *10*, 17907−17915.
(54) Livak, K. J.; Schmittgen, T. D. Analysis of relative gene expression data using real-time quantitative PCR and the 2(-Delta Delta C(T)). *Methods* **2001**, *25*, 402−408.
(55) Verhaak, R. G. W.; Sanders, M. A.; Bijl, M. A.; Delwel, R.; Horsman, S.; Moorhouse, M. J.; van der Spek, P. J.; Löwenberg, B.; Valk, P. J. M. HeatMapper: powerful combined visualization of gene expression profile correlations, genotypes, phenotypes and sample characteristics. *BMC Bioinformatics* **2006**, *7*, 337.
(56) Zar, J. H. *Biostatistical Analysis*; Prentice Hall: Englewood Cliffs, NJ, 2010; p 663.
(57) Dao, L.; Friedman, M. Chlorogenic acid content of fresh and processed potatoes determined by ultraviolet spectrophotometry. *J. Agric. Food Chem.* **1992**, *40*, 2152−2156.
(58) Sonnewald, U. Control of potato tuber sprouting. *Trends Plant Sci.* **2001**, *6*, 333−335.
(59) Xu, X.; Pan, S.; Cheng, S.; Zhang, B.; Mu, D.; Ni, P.; Zhang, G.; Yang, S.; Li, R.; Wang, J.; Orjeda, G.; Guzman, F.; Torres, M.; Lozano,

DOI: 10.1021/jf505777p
J. Agric. Food Chem. 2015, 63, 4902−4913

R.; Ponce, O.; Martinez, D.; De la Cruz, G.; Chakrabarti, S. K.; Patil, V. U.; Skryabin, K. G.; Kuznetsov, B. B.; Ravin, N. V.; Kolganova, T. V.; Beletsky, A. V.; Mardanov, A. V.; Di Genova, A.; Bolser, D. M.; Martin, D. M.; Li, G.; Yang, Y.; Kuang, H.; Hu, Q.; Xiong, X.; Bishop, G. J.; Sagredo, B.; Mejía, N.; Zagorski, W.; Gromadka, R.; Gawor, J.; Szczesny, P.; Huang, S.; Zhang, Z.; Liang, C.; He, J.; Li, Y.; He, Y.; Xu, J.; Zhang, Y.; Xie, B.; Du, Y.; Qu, D.; Bonierbale, M.; Ghislain, M.; Herrera, M. D. R.; Giuliano, G.; Pietrella, M.; Perrotta, G.; Facella, P.; O'Brien, K.; Feingold, S. E.; Barreiro, L. E.; Massa, G.; Diambra, L.; Whitty, B. R.; Vaillancourt, B.; Lin, H.; Massa, A. N.; Geoffroy, M.; Lundback, S.; DellaPenna, D.; Buell, C. R.; Sharma, S. K.; Marshall, D. F.; Waugh, R.; Bryan, G. J.; Destefanis, M.; Nagy, I.; Milbourne, D.; Thomson, S. J.; Fiers, M.; Jacobs, J. M. E.; Nielsen, K. L.; Sønderkær, M.; Iovene, M.; Torres, G. A.; Jiang, J.; Veilleux, R. E.; Bachem, C. W. B.; de Boer, J.; Borm, T.; Kloosterman, B.; van Eck, H.; Datema, E.; Hekkert, B. T. L.; Goverse, A.; van Ham, R. C. H. J.; Visser, R. G. F. Genome sequence and analysis of the tuber crop potato. *Nature* **2011**, *475*, 189−195.

(60) Al-Saikhan, M. S.; Howard, L. R.; Miller, J. C., Jr. Antioxidant activity and total phenolics in different genotypes of potato (Solanum tuberosum, L.). *J. Food Sci.* **1995**, *60*, 341−343.

(61) Madiwale, G. P.; Reddivari, L.; Holm, D. G.; Vanamala, J. Storage elevates phenolic content and antioxidant activity but suppresses antiproliferative and pro-apoptotic properties of colored-flesh potatoes against human colon cancer cell lines. *J. Agric. Food Chem.* **2011**, *59*, 8155−8166.

(62) Hale, A. L.; Reddivari, L.; Nzaramba, M. N.; Bamberg, J. B.; Miller, J. C. Interspecific Variability for Antioxidant Activity and Phenolic Content Among Solanum Species. *Am. J. Potato Res.* **2008**, *85*, 332−341.

(63) Escarpa, A.; González, M. Approach to the content of total extractable phenolic compounds from different food samples by comparison of chromatographic and spectrophotometric methods. *Anal. Chim. Acta* **2001**, *427*, 119−127.

(64) Everette, J. D.; Bryant, Q. M.; Green, A. M.; Abbey, Y. A.; Wangila, G. W.; Walker, R. B. Thorough study of reactivity of various compound classes toward the Folin-Ciocalteu reagent. *J. Agric. Food Chem.* **2010**, *58*, 8139−8144.

(65) Navarre, D. A.; Shakya, R.; Holden, J.; Kumar, S. The effect of different cooking methods on phenolics and vitamin C in developmentally young potato tubers. *Am. J. Potato Res.* **2010**, *87*, 350−359.

(66) Verde Méndez, C. d. M.; Rodríguez Delgado, M. A.; Rodríguez Rodríguez, E. M.; Díaz Romero, C. Content of free phenolic compounds in cultivars of potatoes harvested in Tenerife (Canary Islands). *J. Agric. Food Chem.* **2004**, *52*, 1323−1327.

(67) Reeve, R. M.; Hautala, E.; Weaver, M. L. Anatomy and compositional variation within potatoes II. Phenolics, enzymes and other minor components. *Am. Potato J.* **1969**, *46*, 374−386.

(68) Hasegawa, S.; Johnson, R.; Gould, W. Effect of Cold Storage on Chlorogenic Acid Content of Potatoes. *J. Agric. Food Chem.* **1966**, *14*, 165−169.

(69) Bernards, M. A.; Lewis, N. G. The macromolecular aromatic domain in suberized tissue: A changing paradigm. *Phytochemistry* **1998**, *47*, 915−933.

(70) Nei, M.; Rooney, A. P. Concerted and birth-and-death evolution of multigene families. *Annu. Rev. Genet.* **2005**, *39*, 121−152.

DOI: 10.1021/jf505777p
J. Agric. Food Chem. 2015, 63, 4902−4913

JOURNAL OF AGRICULTURAL AND FOOD CHEMISTRY

Article

pubs.acs.org/JAFC

Imidacloprid Sorption Kinetics, Equilibria, and Degradation in Sandy Soils of Florida

Jorge A. Leiva,[†] Peter Nkedi-Kizza,*[,†] Kelly T. Morgan,[‡] and Jawwad A. Qureshi[§]

[†]Soil and Water Science Department, Institute of Food and Agricultural Sciences, University of Florida, Post Office Box 110290, Gainesville, Florida 32611, United States

[‡]Soil and Water Science Department, Southwest Florida Research and Education Center, and [§]Entomology and Nematology Department, Southwest Florida Research and Education Center, University of Florida, 2685 State Road 29 North, Immokalee, Florida 34142, United States

ABSTRACT: Imidacloprid (IMD) is a neonicotinoid insecticide soil-drenched on sandy soils of southwest Florida for the control of *Diaphorina citri* Kuwayama or Asian citrus psyllid (ACP). The ACP vectors causal pathogens of a devastating citrus disease called citrus greening. Understanding the behavior of IMD in these soils and plants is critical to its performance against target pests. Samples from Immokalee fine sand (IFS) were used for sorption kinetics and equilibria experiments. IMD kinetics data were described by the one-site mass transfer (OSMT) model and reached equilibrium between 6 and 12 h. Batch equilibrium and degradation studies revealed that IMD was weakly sorbed (K_{OC} = 163−230) and persistent, with a half-life of 1.0−2.6 years. Consequently, IMD has the potential to leach below the citrus root zone after the soil-drench applications.

KEYWORDS: *one-site mass transfer, soil partition coefficient, zero-order transformation, pesticide transport, Asian citrus psyllid, integrated pest management*

INTRODUCTION

Imidacloprid [1-(6-chloro-3-pyridylmethyl)-*N*-nitroimidazolin-2-ylideneamine (IMD)] is a systemic insecticide of the neonicotinoid class. Neonicotinoids are synthetic derivatives of nicotine, an alkaloid found in the leaves of many plants in addition to tobacco.[1] IMD translocates through plant tissue after application, acting by contact and ingestion to control plant-sucking pests, such as psyllids and aphids, and some chewing insects, including termites and soil insects, and even fleas on pets.[2,3] IMD targets post-synaptic nicotinic acetylcholine receptors in the insect nervous system.[4] The binding affinity of IMD at the nicotinic receptors in mammals is much less than that of insect nicotinic receptors.[5] IMD has been extensively applied to many crops, such as sugar beet, tomato, eggplant, cabbage, and mustard.[1,6−8] In Florida, IMD is used to control the Asian citrus psyllid (ACP), *Diaphorina citri* Kuwayama, the vector of the pathogens believed to cause the devastating huanglongbing or citrus greening disease.[9] Insecticides, including IMD, are soil-drenched around the trunk of the citrus tree, so that they are absorbed by the roots and translocate to growing tender shoots, where the insects feed and reproduce.[9,10]

IMD data on the soil sorption coefficient normalized to the soil organic carbon content (K_{OC}) range from 156 to 960, with a half-life of several weeks to years.[11−14] The half-life increases with an increase in the initial applied concentration of IMD as observed with non-agricultural application rates (>50 $\mu g\ g^{-1}$) to control termites.[15] On the other hand, much shorter IMD half-lives have been reported for agricultural application rates (e.g., 0.56 kg ha^{-1} around the root biomass of perennial commodities, such as citrus) or concentrations higher than 10 $\mu g\ g^{-1}$.[10,16,17]

Moderate to high leaching potential has been observed for IMD and most other neonicotinoids.[18] From 1999 to 2005, the U.S. Geological Survey (USGS) detected IMD in 13% of groundwater monitoring wells located in citrus orchards of the Central Florida Ridge.[19] This area is dominated by sandy, deep, and excessively drained Entisols.[20] In southwest Florida, the dominant soils are Spodosols, which are sandy, low-lying, flat, and poorly drained, with shallow water tables.[20,21] One example of these soils is Immokalee fine sand (IFS) that is excessively permeable, with a low organic carbon content in its A and E diagnostic horizons.[20] It also has a poorly drained spodic layer (Bh), high in organic matter, with accumulation of Fe and Al.[20]

Currently, it is unclear how IMD reacts with these soils, and there are no data describing IMD transport and persistency in southwest Florida soils treated to control ACP. To address these questions, the study goals were to characterize IMD sorption and degradation in Florida sandy soils, specifically IFS diagnostic horizons A, E, and Bh. The data will provide a technical basis for IMD transport studies in the field regarding IMD application rates to citrus, leaching potential, and ACP control. The hypotheses tested were that (a) IMD has a small soil sorption coefficient (K_D) and slow degradation rate (k) in IFS, (b) the spodic layer has a higher IMD sorption coefficient and faster degradation rate than the overlaying A and E horizons, because of its higher organic matter and clay contents, and (c) there is high leaching potential beyond the citrus root zone (0−45 cm) after IMD soil-drench applications (and

Received: January 28, 2015
Revised: March 26, 2015
Accepted: May 4, 2015
Published: May 4, 2015

ACS Publications © 2015 American Chemical Society

DOI: 10.1021/acs.jafc.5b00532
J. Agric. Food Chem. 2015, 63, 4915−4921

Table 1. Some Physical and Chemical Properties of IFS at the SWFREC

horizon	depth (cm)	pH[a]	SOC[b] (g g^{-1})	CEC[c] (cmol$_c$ kg^{-1})	sand (%)	silt (%)	clay (%)
A	0−15	4.4	8.0×10^{-3}	7.63	93.8	5.0	1.2
E1	15−30	4.5	1.9×10^{-3}	0.74	97.2	2.7	0.1
E1	30−45	4.4	1.0×10^{-3}	0.33	98.4	0.5	1.1
E2	45−60	4.4	8.8×10^{-3}	2.56	98.0	1.2	0.8
Bh	60−75	4.6	1.9×10^{-2}	6.85	96.4	2.6	1.0

[a]pH in water at a soil/solution ratio of 10:25. [b]SOC = soil organic carbon. [c]CEC = cation-exchange capacity.

subsequent irrigation and rainfall events), during ACP-integrated pest management programs.

MATERIALS AND METHODS

Soil Sampling. The soil used in this study was IFS classified as sandy, siliceous, hyperthermic, Arenic Alaquods.[21] Soil samples were taken at the Southwest Florida Research and Education Center (SWFREC), University of Florida (UF), Immokalee, FL (latitude, 26° 27.75′ N; longitude, 81° 26.83′ W). The soil organic carbon (SOC) content was determined using the Walkley−Black method,[22] and the soil pH was determined with electrometric methods using a soil/solution ratio of 10:25 in water.[23] Soil cation-exchange capacity (CEC) and texture data were obtained from the Florida Soil Characterization Database of the Institute of Food and Agricultural Sciences (IFAS), UF.[24] The selected physical and chemical properties of IFS are presented in Table 1.

In a SWFREC experimental plot, planting beds for young citrus trees were built to conduct studies on IMD leaching and ACP control. During planting bed construction, soils from the A horizon (surface) and E horizon (albic, subsurface) were somewhat mixed. Soil samples from the planting beds were collected from five depths using a bucket auger with dimensions of 5.0 cm (inner diameter) × 15.0 cm. The soil samples from the planting beds were used for the sorption kinetics study (Table 2) to generate transport parameters to model IMD movement in the field during ACP control.

Table 2. OSMT Model Parameters (α and K_D) Optimized for IMD Sorption Kinetics Using an Initial Concentration (C_o) of 2.5 μg mL^{-1} Equilibrated in IFS Diagnostic Horizons A, E, and Bh[a]

		OSMT		
horizon	depth (cm)	α	K_D	isotherm K_D[b] (mL g^{-1})
A	0−15	0.67 (0.2)	0.18 (0.01)	0.14
E1	15−30	0.97 (0.2)	0.30 (0.01)	0.24
E1	30−45	0.95 (0.2)	0.08 (0.01)	0.07
E2	45−60	0.60 (0.1)	0.19 (0.01)	0.18
Bh	60−75	0.83 (0.1)	1.07 (0.02)	0.78

[a]Soil samples are from citrus planting beds. Standard deviations are in parentheses. [b]K_D values are from 24 h batch sorption equilibrium isotherms.

The batch equilibria and degradation studies were conducted on IFS samples taken from a site with secondary forest regrowth. The soil samples were collected from a pit, from five depths divided in 15 cm increments from the soil surface. The five depths were representative of the A, E, and Bh soil diagnostic horizons of IFS (Table 1).

Soil Sorption Kinetics Experiments. A kinetic batch study was conducted to estimate equilibration times for the IMD concentration in solution using samples from disturbed (bedded) flatwood soils, from IFS diagnostic horizons A, E, and Bh. Triplicate 5 g samples of air-dried soil (m) were weighed in 50 mL centrifuge tubes (Nalgene, Thermo Scientific). The equilibration volume (v) was 10 mL of 0.01 M $CaCl_2$ spiked with three IMD concentrations of 2.5, 12.5, and 25 μg mL^{-1}, representing three initial soil solution concentrations (C_o; eq 1). The highest initial concentration used in the kinetics and batch studies was based on the label-recommended application rate for young non-bearing citrus trees in Florida, where IMD is soil-drenched around the tree trunk. Blank samples (no added IMD) were also prepared in 0.01 M $CaCl_2$. The centrifuge tubes (and soil samples) were equilibrated in the dark using an Eberbach horizontal shaker, for 2, 6, 14, and 24 h. After shaking, the tubes were centrifuged at 6000 rpm for 20 min, and then the supernatant was filtered with Whatman 42 filter paper. The filtrate was refiltered with a Fisherbrand 0.45 μm nylon sterile syringe filter before analysis by high-performance liquid chromatography with ultraviolet detection (HPLC−UV).

Batch Sorption Kinetics Model. The sorption kinetics phenomena in soils may be caused by the hydrophobicity or hydrophilicity of the organic chemical, the natural heterogeneity of sorption sites, and the diffusion pathways in the porous media.[25] In this study, the kinetic parameters were optimized using the one-site mass transfer model (OSMT; eqs 1−3). This model assumes that all sites in the soil have rate-limited sorption or type 2 sites.[26,27] The model is a special case of the two-site non-equilibrium (TSNE) model[28,29]

$$\frac{C_t}{C_o} = \frac{1}{R} + \left(1 - \frac{1}{R}\right)\exp[-\alpha R t] \quad (1)$$

$$R = 1 + (m/v)K_D \quad (2)$$

$$\beta = 1/R \quad (3)$$

where C_t is the solute concentration in solution (μg mL^{-1}) at any time, C_o is the initial IMD solution concentration (μg mL^{-1}), m is the mass of soil (g), v is the volume of soil solution (mL), R is the expression for retardation, β represents the fraction of retardation as a result of kinetic sites, α is the kinetic rate coefficient for desorption from type 2 sites (h^{-1}), t is the time (h), and K_D is the sorption coefficient at equilibrium (mL g^{-1}). The parameters α and K_D in the OSMT were optimized using nonlinear regression procedures.[30]

Soil Sorption Equilibria. The batch slurry equilibrium study was conducted using triplicated soil samples for each soil depth (0−15, 15−30, 30−45, 45−60, and 60−75 cm) and each equilibrium concentration. Triplicate 10 g samples of air-dried soil were weighed in 50 mL polycarbonate centrifuge tubes (Nalgene, Thermo Scientific). The soil samples were equilibrated with 10 mL of 0.01 M $CaCl_2$ solution spiked with IMD initial concentrations of 2, 4, 6, and 8 μg mL^{-1} (C_o; eq 4). Blank samples were also equilibrated in 0.01 M $CaCl_2$. All samples were equilibrated for 24 h in an Eberbach horizontal shaker. After equilibration, the tubes were centrifuged for 20 min at 6000 rpm and then filtered with Whatman 42 filter paper. Before analysis by HPLC−UV, the aqueous filtrate was refiltered with a Fisherbrand 0.45 μm nylon sterile syringe filter. The measured solution concentration was considered as equilibrium concentrations (C_e, μg mL^{-1}; eq 4). The IMD-sorbed equilibrium concentration (S_e, μg g^{-1}) is given by eq 4 based on mass balance

$$S_e = \frac{V}{m}(C_o - C_e) \quad (4)$$

$$S_e = K_D C_e \quad (5)$$

$$K_{OC} = K_D/OC \quad (6)$$

DOI: 10.1021/acs.jafc.5b00532
J. Agric. Food Chem. 2015, 63, 4915−4921

where v is the volume of solution added (mL) and m is the mass of oven-dry soil (g). The sorption coefficient K_D (mL g^{-1}) was calculated using simple linear regressions (eq 5) and then normalized to account for the influence of OC (soil organic carbon, g g^{-1}) on the sorption phenomena for hydrophobic organic compounds, such as IMD (eq 6).

Soil Degradation Study. IFS soil samples were maintained at the initial moisture content found in the field for the degradation study, to keep microbial communities as intact as possible. The samples from five depths (0−15, 15−30, 30−45, 45−60, and 60−75 cm) were thoroughly mixed, and the moisture content was measured. Triplicate 10 g samples of soil were weighed into polycarbonate centrifuge tubes (Nalgene, Thermo Scientific) and kept at room temperature (21 °C). The samples were spiked with an IMD solution in deionized water and homogenized with vortex for 2 min. The intended initial spiking concentration S_o was 10 μg of IMD/g of oven-dry soil. The tubes were stored in the dark, loosely capped, and maintained at a constant field capacity (FC) of 10% moisture content on a gravimetric basis. The FC water content (or mass) for each tube was checked every other week during the entire study period (514 days), by replacing any lost moisture with deionized water using a dropper. The final soil mass and moisture contents were checked before sample extraction.

The IMD degradation experiments consisted of soil samples from 0 to 15, from 15 to 30, and from 30 to 45 cm depths that were extracted at 9, 52, 120, 241, and 514 days after spiking. The soil samples from 45 to 60 and from 60 to 75 cm were extracted roughly every 12 weeks at 85, 168, 246, 329, and 434 days. Also, alongside the degradation experiment samples, autoclaved soil samples were spiked with the same solution, kept in a freezer, and then extracted to estimate IMD extraction efficiency as a function of time.

The spiked samples were extracted using a soil/solution ratio of 1:2, adding 20 mL of acetonitrile/water (80:20) to the centrifuge tubes. The samples were shaken for 2 h, centrifuged for 20 min at 6000 rpm, and then filtered with Whatman 42 filter paper. Before the analysis by HPLC−UV, the filtrates were diluted with HPLC-grade water (1:1) and refiltered with Fisherbrand 0.45 μm nylon sterile syringe filters. The fraction of organic solvent in the extracting solutions of acetonitrile/water was based on the solvophobic theory, which states that the sorption coefficient for hydrophobic organic compounds (HOCs) decreases exponentially as the fraction of organic co-solvent increases in the extracting mixture.[31,32]

Extraction Efficiency (ε), Degradation Rate (k), and Half-Life ($t_{1/2}$). The extraction efficiency was assumed constant during the degradation experiment for all soil depths. The initial IMD concentration in the soil sample was defined as S_o^* (μg g^{-1}), and the concentration at a given time was defined as S_t^* (μg g^{-1}). The asterisk (∗) denoted the measured extracted concentration not corrected for extraction efficiency ε (eq 7). The ε was the absolute extraction efficiency estimated for each soil depth at each extraction date, using autoclaved control samples to eliminate microbial degradation. After autoclaving, these samples were spiked with the same solution (to obtain an approximate initial concentration of 10 μg g^{-1}), and were frozen alongside unspiked samples. We assumed that the baseline to calculate ε was the concentration from the autoclaved frozen samples extracted about 9 days after spiking, because no IMD metabolites were observed from the autoclaved samples during analysis by HPLC−UV. This was conducted during the first 8 months of the degradation experiment (241 days), to ensure analytical consistency[15] and to avoid estimation errors for IMD degradation rates. Our study showed that IMD degradation followed a zero-order process for soil samples from all depths (eqs 7 and 8).

$$\frac{S_t^*}{\varepsilon} = \frac{S_o^*}{\varepsilon} - kt \tag{7}$$

$$S_t^* = S_o^* - k^*t \tag{8}$$

Here, we propose that the overall ε was constant during the experiment, affecting the estimate of k in the zero-order process (eqs 8 and 9). Assuming that ε was constant, the correct IMD degradation rate value (k) would be given by eq 9. Consequently, S_o ($S_o = S_o^*/\varepsilon$) and k (eq 9) were used in this study to estimate IMD half-life (eq 10) for each soil depth.

$$k = k^*/\varepsilon \tag{9}$$

$$t_{1/2} = S_o/2k \tag{10}$$

Analytical Procedures and Statistics. Analytical-grade standards for IMD were obtained from ChemService, Inc., West Chester, PA. A 100 ppm standard stock solution was prepared in 0.01 M $CaCl_2$, and mixed thoroughly. The sorption equilibrium batch spikes (2, 4, 6, and 8 μg mL^{-1}) were serially diluted in 0.01 M $CaCl_2$ using HPLC-grade water. The HPLC calibration curve for the batch samples had IMD concentrations of 0, 2.5, 5.0, and 10.0 μg mL^{-1}.

On each sampling date during the degradation experiment, freshly made calibration standards were prepared from a stock solution of 100 μg of IMD mL^{-1} in pure acetonitrile. The HPLC−UV calibration curve standards were serially diluted to solutions of 1.25, 2.5, 5.0, 10.0, and 20.0 μg of IMD mL^{-1} in a matrix of acetonitrile/water (40:60). The IMD soil extracts (degradation study) and equilibration solutions (sorption kinetics and sorption equilibria studies) were analyzed using an Agilent Infiniti 1260 HPLC−UV with a mobile phase of HPLC-grade acetonitrile/water (40:60), a Supelcosil LC-18 column (150 × 4.6 mm; Sigma-Aldrich Co.), an injection volume of 20 μL, a flow rate of 1 mL min^{-1}, and an absorption wavelength of 270 nm. The analysis by HPLC−UV for the sorption and degradation studies had limit of detection and quantitation (LOD and LOQ) values of 0.40 and 1.25 μg mL^{-1}, respectively (eqs 11 and 12)

$$\mathrm{LOD} = \mathrm{sd}t \tag{11}$$

$$\mathrm{LOQ} = 3\mathrm{LOD} \tag{12}$$

where sd is the standard deviation of the recovered spikes and t is the one-tailed statistic for 99% confidence using six replications. All degradation extracts were diluted with HPLC-grade water to obtain a mixture of acetonitrile/water of 40:60. All solutions were filtered before analysis by HPLC−UV using Fisherbrand 0.45 μm non-sterile syringe filters. The retention time for IMD under the above conditions was 2.70 min.

The K_D values and IMD degradation rate (k) values were obtained by a simple linear regression conducted in JMP Pro 9.[33] The linear regression fitted parameters were checked using analysis of variance (ANOVA) and t tests. Multiple comparison Tukey honestly significant difference (HSD) tests on the sorption coefficients (K_D) and degradation rates (k) were conducted using an analysis of covariance (ANCOVA) procedure to assess the effect of the covariate (soil depth) on the linear regression slopes between soil depths.[34]

RESULTS AND DISCUSSION

IMD Sorption Kinetics. IMD sorption kinetics data were fitted properly by the OSMT model.[28,35] The fitted parameters are summarized in Table 2 for each of the five soil depths. To avoid crowding the figures, the data presented correspond only to the 2.5 μg mL^{-1} initial concentration (C_o). Data in Figure 1 show that the OSMT model provided a good fit for IMD kinetic data, with a sharp decrease in the solution concentration and then reaching equilibrium between 6 and 12 h when the concentration in solution remained relatively constant. This trend was observed in every combination of C_o and soil depth. IMD has been reported to have a rapid equilibration time of 6 h or less in soils with low organic matter content, but the sorption kinetics data were described with various models.[36] However, the OSMT model has been reported to describe sorption kinetics of hydrophobic organic chemicals in soils and organoclays.[28,35]

The OSMT parameter α value was highest in the upper part of the E horizon (15−45 cm), which has the lowest organic matter content. The parameter α had lower values in the other sampling depths (A, E2, and Bh). Also, β values (eq 3) were

DOI: 10.1021/acs.jafc.5b00532
J. Agric. Food Chem. 2015, 63, 4915−4921

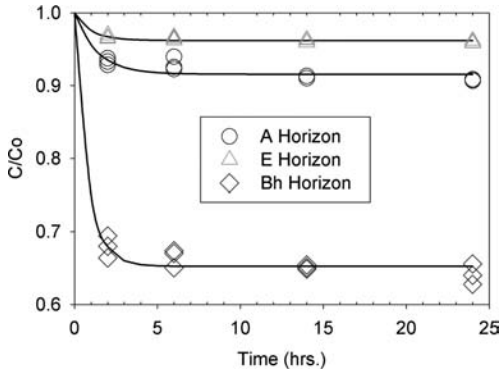

Figure 1. IMD sorption kinetics with an initial spiking concentration (C_o) of 2.5 μg mL^{-1} in IFS samples from A, E, and Bh soil horizons. Symbols indicate observed relative concentrations as a function of time. Solid lines represent the OSMT kinetic model.

close to 1 for all depths. This is in agreement with the OSMT model assumption that most sorption sites were kinetic. In essence, IMD showed that sorption equilibrium was reached much sooner than 24 h, which is the standard protocol for sorption equilibrium studies, confirming the validity of our batch equilibrium experiments and the obtained distribution coefficients (K_D).

IMD Sorption Equilibria. The sorption isotherms for IMD are shown in Figure 2. In Table 3, K_D values are compared

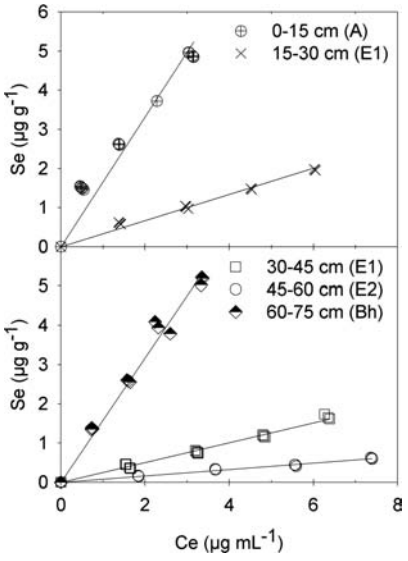

Figure 2. IMD sorption isotherms in samples from five soil depths (0−15, 15−30, 30−45, 45−60, and 60−75 cm) comprising IFS horizons A, E, and Bh (Table 3). Symbols represent equilibrium concentrations in solution (C_e) and soil sorbed (S_e).

between different depths and horizons. The K_D values for the 0−15 cm (A horizon) and 60−75 cm (Bh horizon) samples were very similar (1.66 ± 0.042 and 1.59 ± 0.032 mL g^{-1}, respectively). This was confirmed by Tukey's HSD test showing no significant differences between the two (q = 1.7; p > 0.50). The soil samples from the E horizon (15−30, 30−45, and 45−60 cm) were statistically different from each other (q = 36.8; p < 0.001). The sorption coefficients were lowest in the E horizon samples (0.08−0.31), as was expected because this soil horizon has the lowest organic matter content in IFS.

Table 3. IMD Sorption Coefficients (K_D and K_{OC}) for Different Depths (cm) and Diagnostic Horizons in IFS[a]

horizon	depth (cm)	K_D ± SE[b] (mL g^{-1})[c]	K_{OC}	log K_{OC}
A	0−15	1.66 ± 0.04 a	208	2.3
E1	15−30	0.31 ± 0.01 b	163	2.2
E1	30−45	0.23 ± 0.01 c	230	2.4
E2	45−60	0.08 ± 0.001 d	13	1.1
Bh	60−75	1.59 ± 0.03 a	63	1.8

[a]Soil samples are from IFS with secondary forest regrowth. [b]SE = standard error. [c]Different letters indicate significant difference between K_D values.

In essence, sorption equilibrium data confirmed that IMD was a weakly sorbed chemical in IFS (Table 3). However, the K_{OC} values for 45−60 cm (E2) and 60−75 cm (Bh) were much lower than the layers above (A and E1) and were not consistent with the K_{OC} concept. Initially, we hypothesized that the spodic layer would show higher IMD sorption. In contrast, the surface horizon samples (0−15 cm) showed higher K_{OC} value than the Bh horizon. It is possible that the nature and functional groups of the organo-mineral complexes in the Bh horizon could have reduced IMD sorption on this layer.

Previous studies have suggested that IMD sorption in soils is predominantly explained by the soil organic carbon content,[11] which is a characteristic for hydrophobic organic chemicals partitioning in soils.[37] IMD studies on soil sorption have found similar values for IMD K_{OC} in soils with low organic matter content. Liu et al.[38] found values averaging 220 in soils with low organic matter content (0.25−0.71%).

IMD Degradation. The extraction efficiency (ε) data obtained from the autoclaved−frozen soil samples did not show a significant relationship with time based on the linear regression (p > 0.31; Table 4). The data confirmed the assumption that our degradation experiments had an extraction efficiency (ε) constant as a function of time, as was previously reported for IMD.[15] However, the co-solvents used in our study (80:20 acetonitrile/water) yielded ε values very close to 100% during the first 8 months of the degradation experiment, especially in the A and E horizons (Table 4). Therefore, if ε is 100%, then $k = k^*$ and $S_o = S_o^*$ (eqs 7−10).

Data in Figures 3 and 4 show the linear relationship between extracted concentrations and time (p < 0.0001) based on a zero-order degradation rate. The t tests on the regression slopes showed that k values were significantly different from zero (p < 0.0001). The degradation rates were also significantly different from each other, with p < 0.0001 (Table 5 and Figures 3 and 4). IMD degraded at different rates in the A horizon samples (0−15 cm) compared to the other depths. The E1 horizon samples (15−30 and 30−45 cm) showed very similar degradation rates as well as the highest $t_{1/2}$ values. The E2 layer (45−60 cm) and the Bh layer (60−75 cm) showed no significant difference in degradation rates and had the lowest $t_{1/2}$ values.

IMD half-life ($t_{1/2}$) ranged from 0.98 to 2.60 years across all sampling depths. The insecticide was very persistent at the rate used, and degradation was not a function of the concentration (i.e., a zero-order process). Baskaran et.al.[15] data were somewhat similar to ours, showing that IMD had $t_{1/2}$ values of 2.71 years in soils and 2.95−3.37 years in construction bedding materials (sand).

This is the first study evaluating IMD sorption and degradation in sandy soils of Florida. The data revealed that

DOI: 10.1021/acs.jafc.5b00532
J. Agric. Food Chem. 2015, 63, 4915−4921

Table 4. Extraction Efficiency ε (%) as a Function of Time for IMD in IFS Incubated for 514 Days (A and E1) and 434 Days (E2 and Bh)

			extraction time (days)					
horizon	depth (cm)		9	52	85	120	168	241
A	0−15	ε (%)	100	100	*a*	100	*a*	100
E1	15−30	ε (%)	100	100	*a*	88	*a*	101
E1	30−45	ε (%)	100	97	*a*	109	*a*	110
E2	45−60	ε (%)	100	*a*	100	*a*	109	96
Bh	60−75	ε (%)	100	*a*	100	*a*	115	89

[a]Not measured.

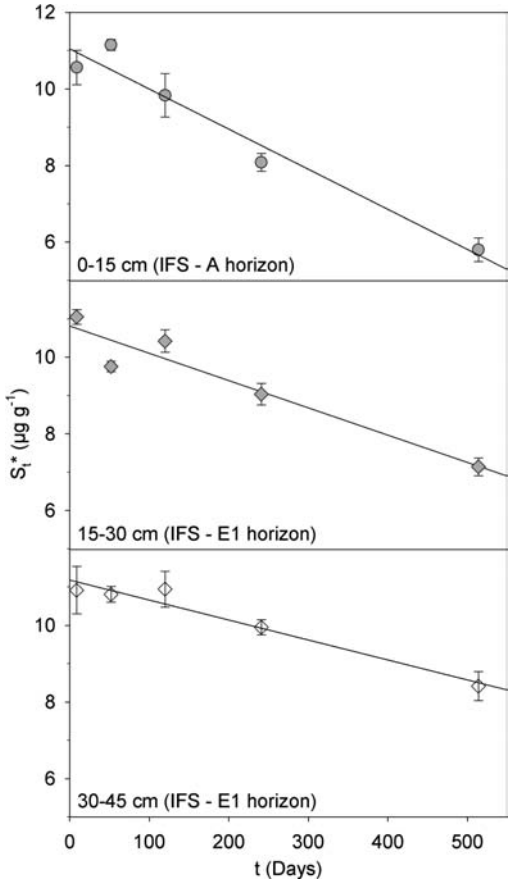

Figure 3. IMD degradation as a function of time in samples from soil depths of 0−15, 15−30, and 30−45 cm (IFS horizons A and E1). IMD extracted concentrations S_t^* (symbols) and linear regression fits (solid lines).

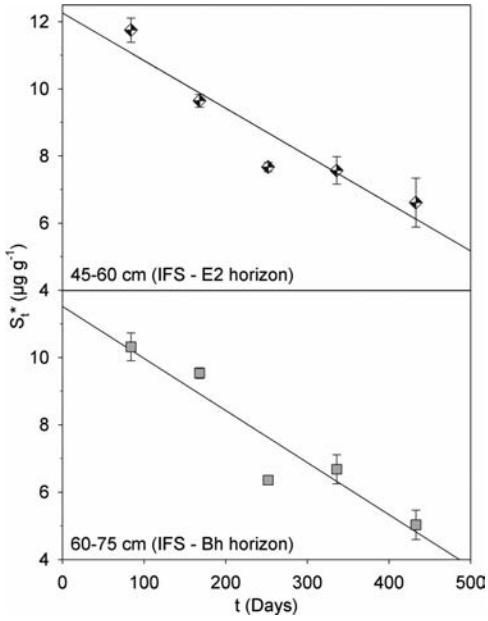

Figure 4. IMD degradation as a function of time in samples from soil depths of 45−60 and 60−75 cm (IFS horizons E2 and Bh). IMD extracted concentrations S_t^* (symbols) and linear regression fits (solid lines).

Table 5. IMD Degradation Rates (k) in IFS Incubated for 514 Days (A and E1) and 434 Days (E2 and Bh)

horizon	depth (cm)	$k^a \pm$ SE^b (μg g^{-1} day^{-1})^c	$S_o{}^d \pm$ SE (μg g^{-1})	$t_{1/2}{}^e$ (day)	$t_{1/2}$ (year)
A	0−15	0.011 ± 0.001 a	11.24 ± 0.33	511	1.40
E1	15−30	0.008 ± 0.001 b	10.98 ± 0.16	686	1.88
E1	30−45	0.006 ± 0.001 b	11.38 ± 0.25	948	2.60
E2	45−60	0.014 ± 0.002 c	12.31 ± 0.55	440	1.21
Bh	60−75	0.016 ± 0.002 c	11.50 ± 0.54	359	0.98

[a]k = degradation rate. [b]SE = standard error. [c]Different letters indicate significant difference between soil depths. [d]S_o = initial concentration. [e]$t_{1/2}$ = half-life.

IMD undergoing sorption kinetics is a weakly sorbed chemical with K_{OC} values of 163−230 in the A and E horizons and is very persistent, with $t_{1/2}$ of 0.98−2.60 years. The main concern in Florida Spodosols after IMD soil-drench applications is the shallow and fluctuating water table. This study showed that IMD sorption (and, therefore, retardation) would be lowest in the E horizon. Consequently, once the chemical moves beyond the first 15 cm of soil (A horizon), the potential for leaching beyond the citrus root zone increases considerably. This was an expected outcome for IFS that has a very low organic matter content, especially in the eluviated horizon (E), which is generally stripped of colloidal coatings (clay and organic matter) that could help to retain important plant nutrients[20] and possibly organic solutes, such as IMD.

Our data on IMD sorption and degradation confirmed a high potential for IMD leaching beyond the citrus root zone and that it is necessary to establish field studies to evaluate different IMD soil-drench application rates, to monitor irrigation and rainfall events after soil drenching, and to estimate how much leaching is occurring under such conditions. Furthermore, IMD fate and transport modeling in sandy soils of Florida will have to consider the plant uptake component, not only to avoid loss by leaching but also to ensure ACP control across seasons. In the event that IMD is actually leaching, one strategy would be to increase the residence time in the citrus root zone with

DOI: 10.1021/acs.jafc.5b00532
J. Agric. Food Chem. 2015, 63, 4915−4921

amendments of pyrolyzed organic matter (biochar) or organic composts.[39] These amendments as agricultural practices need further research and validation.

AUTHOR INFORMATION

Corresponding Author

*E-mail: kizza@ufl.edu.

Funding

The study was funded by a United States Department of Agriculture (USDA)−Tropical and Subtropical Agriculture Research (TSTAR) grant.

Notes

The authors declare no competing financial interest.

REFERENCES

(1) Jeschke, P.; Nauen, R. Neonicotinoids: From zero to hero in insecticide chemistry. *Pest Manage. Sci.* **2008**, *64*, 1084−1098.

(2) Tomlin, C. D. S. *The Pesticide Manual: A World Compendium*; British Crop Protection Council: Alton, U.K., 2006.

(3) Fossen, M. *Environmental Fate of Imidacloprid*; California Department of Pesticide Regulation: Sacramento, CA, 2006.

(4) Buckingham, S.; Lapied, B.; Corronc, H.; Grolleau, F.; Sattelle, F. Imidacloprid actions on insect neuronal acetylcholine receptors. *J. Exp. Biol.* **1997**, *200*, 2685−2692.

(5) Tomizawa, M.; Casida, J. Imidacloprid, thiacloprid, and their imine derivatives up-regulate the $\alpha4\beta2$ nicotinic acetylcholine receptor in M10 cells. *Toxicol. Appl. Pharmacol.* **2000**, *169*, 114−120.

(6) Rouchaud, J.; Gustin, F.; Wauters, A. Imidacloprid insecticide soil metabolism in sugar beet field crops. *Bull. Environ. Contam. Toxicol.* **1996**, *56*, 29−36.

(7) Mukherjee, I.; Gopal, M. Environmental behavior and translocation of imidacloprid in eggplant, cabbage and mustard. *Pest Manage. Sci.* **2000**, *56*, 932−936.

(8) Alsayeda, H.; Pascal-Lorber, S.; Nallanthigal, C.; Debrauwer, L.; Laurent, F. Transfer of the insecticide C-14 imidacloprid from soil to tomato plants. *Environ. Chem. Lett.* **2008**, *6*, 229−234.

(9) Qureshi, J. A.; Kostyk, B. C.; Stansly, P. A. Insecticidal suppression of Asian citrus psyllid *Diaphorina citri* (Hemiptera: Liviidae) vector of huanglongbing pathogens. *PLoS One* **2014**, *9*, No. e112331.

(10) Leiva, J. A. Imidacloprid fate and transport in Florida flatwoods soils and plants during control of the Asian citrus psyllid. Doctoral Dissertation, University of Florida, Gainesville, FL, 2014.

(11) Cox, L.; Koskinen, W. C.; Yen, P. Y. Changes in sorption of Imidacloprid with incubation time. *Soil Sci. Soc. Am. J.* **1998**, *62*, 342−347.

(12) Oi, M. Time-dependent sorption of imidacloprid in two different soils. *J. Agric. Food Chem.* **1999**, *47*, 327−332.

(13) Kamble, S. T.; Saran, R. K. Effect of concentration on the adsorption of three termiticides in soil. *Bull. Environ. Contam. Toxicol.* **2005**, *75*, 1077−1085.

(14) Oliver, D. P.; Kookana, R. S.; Quintana, B. Sorption of pesticides in tropical and temperate soils from Australia and the Philippines. *J. Agric. Food Chem.* **2005**, *53*, 6420−6425.

(15) Baskaran, S.; Kookana, R. S.; Naidu, R. Degradation of bifenthrin, chlorpyrifos and imidacloprid in soil and bedding materials at termiticidal application rates. *Pestic. Sci.* **1999**, *55*, 1222−1228.

(16) Cox, L.; Koskinen, W. C.; Yen, P. Y. Sorption−desorption of imidacloprid and its metabolites in soils. *J. Agric. Food Chem.* **1997**, *45*, 1468−1472.

(17) Sarkar, M.; Roy, S.; Kole, R.; Chowdhury, A. Persistence and metabolism of imidacloprid in different soils of West Bengal. *Pest Manage. Sci.* **2001**, *57*, 598−602.

(18) Bonmatin, J. M.; Giorio, C.; Girolami, V.; Goulson, D.; Kreutzweiser, D. P.; Krupke, C.; Liess, M.; Long, E.; Marzaro, M.; Mitchell, E. A. D.; Noome, D. A.; Simon-Delso, N.; Tapparo, A. Environmental fate and exposure; neonicotinoids and fipronil. *Environ. Sci. Pollut. Res.* **2015**, *22*, 35−67.

(19) Choquette, A. F. *Pesticides and Nitrate in Groundwater Underlying Citrus Croplands, Lake Wales Ridge, Central Florida, 1999−2005*; U.S. Geological Survey: Reston, VA, 2014.

(20) Obreza, T. A.; Morgan, K. T. *Nutrition of Florida Citrus Trees*; Florida Cooperative Extension Service, Institute of Food and Agricultural Sciences (IFAS), University of Florida: Gainesville, FL, 2008.

(21) United States Department of Agriculture (USDA)−Natural Resources Conservation Service (NRCS). *Soil Survey of Collier County Area Florida*; USDA, Institute of Food and Agricultural Sciences (IFAS), University of Florida: Gainesville, FL, 1998.

(22) Nelson, D. W.; Sommers, L. E. Total carbon, organic carbon, and organic matter. In *Methods of Soil Analysis, Part 2. Chemical and Microbiological Properties*; Page, A. L., Miller, R. H., Keeney, D. R., Eds.; American Society of Agronomy (ASA)−Soil Science Society of America (SSSA): Madison, WI, 1982; pp 539−579.

(23) Thomas, G. W. Soil pH and soil acidity. In *Methods of Soil Analysis Part 3—Chemical Methods*; Sparks, D. L., Page, A. L., Helmke, P. A., Loeppert, R. H., Eds.; American Society of Agronomy (ASA)−Soil Science Society of America (SSSA): Madison, WI, 1996; pp 475−490.

(24) Grunwald, S.; Harris, W. G.; Hurt, W.; Bloom, S. A.; Deich, W.; Hoover, B.; Rivero, R.; Ramasundaram, V.; Gao, M.; Murphy, B.; Bloom, K. *Florida Soil Characterization: Data Retrieval System*; Soil and Water Science Department, University of Florida: Gainesville, FL, 2007; http://soils.ifas.ufl.edu/flsoils/index.asp (accessed March 10, 2015).

(25) Skaggs, T. H.; Wilson, G. V.; Shouse, P. J.; Leij, F. J. Solute transport: Theoretical background. In *Methods of Soil Analysis Part 4. Physical Methods*; Dane, J. H., Topp, G. C., Eds.; Soil Science Society of America (SSSA): Madison, WI, 2002; pp 1353−1380.

(26) Nkedi-Kizza, P.; Biggar, J. W.; Selim, H. M.; Van Genuchten, M. T.; Wierenga, P. J.; Davidson, J. M.; Nielsen, D. R. On the equivalence of two conceptual models for describing ion exchange during transport through an aggregated Oxisol. *Water Resour. Res.* **1984**, *20*, 1123−1130.

(27) Brusseau, M.; Jessup, R.; Rao, P. Nonequilibrium sorption of organic chemicals: Elucidation of rate-limiting processes. *Environ. Sci. Technol.* **1991**, *25*, 134−142.

(28) Nzengung, V. A.; Nkedi-Kizza, P.; Jessup, R. E.; Voudrias, E. A. Organic cosolvent effects on sorption kinetics of hydrophobic organic chemicals by organoclays. *Environ. Sci. Technol.* **1997**, *31*, 1470−1475.

(29) van Genuchten, M. T. *Non-equilibrium Transport Parameters from Miscible Displacement Experiments*; U.S. Salinity Laboratory: Riverside, CA, 1981.

(30) Skaggs, T. H.; Wilson, G. V.; Šimunek, J.; Van Genuchten, M. T.; Jacques, D.; Hopmans, J. W.; Inoue, M.; Flury, M. Solute transport: Data analysis and parameter estimation. In *Methods of Soil Analysis Part 4. Physical Methods*; Dane, J. H., Topp, G. C., Eds.; Soil Science Society of America (SSSA): Madison, WI, 2002; pp 1403−1434.

(31) Nkedi-Kizza, P.; Rao, P. S. C.; Hornsby, A. G. Influence of organic cosolvents in sorption of hydrophobic organic chemicals in soils. *Environ. Sci. Technol.* **1985**, *19*, 975−979.

(32) Rao, P. S. C.; Hornsby, A. G.; Kilcrease, D. P.; Nkedi-Kizza, P. Sorption and transport of hydrophobic organic chemicals in aqueous and mixed solvent systems: Model development and preliminary evaluation. *J. Environ. Qual.* **1985**, *14*, 376−383.

(33) SAS Institute, Inc. *JMP 9.0.2 Basic Analysis and Graphing*; SAS Institute, Inc.: Cary, NC, 2010.

(34) Zar, J. H. *Biostatistical Analysis*; Prentice-Hall/Pearson: Upper Saddle River, NJ, 2010.

(35) Nkedi-Kizza, P.; Shinde, D.; Savabi, M. R.; Ouyang, Y.; Nieves, L. Sorption kinetics and equilibria of organic pesticides in carbonatic soils from south Florida. *J. Environ. Qual.* **2006**, *35*, 268−276.

(36) Fernandez-Bayo, J. D.; Nogales, R.; Romero, E. Evaluation of the sorption process for imidacloprid and diuron in eight agricultural

DOI: 10.1021/acs.jafc.5b00532
J. Agric. Food Chem. 2015, 63, 4915−4921

soils from southern Europe using various kinetic models. *J. Agric. Food Chem.* **2008**, *56*, 5266−5272.
(37) Katayama, A.; Bhula, R.; Burns, G. R.; Carazo, E.; Felsot, A.; Hamilton, D.; Harris, C.; Kim, Y.; Kleter, G.; Koedel, W.; Linders, J.; Peijnenburg, J. W.; Sabljic, A.; Stephenson, R. G.; Racke, D. K.; Rubin, B.; Tanaka, K.; Unsworth, J.; Wauchope, R. D. Bioavailability of xenobiotics in the soil environment. In *Reviews of Environmental Contamination and Toxicology*; Whitacre, D. M., Ed.; Springer, New York, 2010; Vol. *203*, pp 1−86.
(38) Liu, W. P.; Zheng, W.; Ma, Y.; Liu, K. K. Sorption and degradation of imidacloprid in soil and water. *J. Environ. Sci. Health, Part B* **2006**, *41*, 623−634.
(39) Fernández-Bayo, J. D.; Nogales, R.; Romero, E. Winery vermicomposts to control the leaching of diuron, imidacloprid and their metabolites: Role of dissolved organic carbon content. *J. Environ. Sci. Health, Part B* **2015**, *50*, 190−200.

DOI: 10.1021/acs.jafc.5b00532
J. Agric. Food Chem. 2015, 63, 4915−4921

JOURNAL OF AGRICULTURAL AND FOOD CHEMISTRY

Article

pubs.acs.org/JAFC

Behavior of Multiclass Pesticide Residue Concentrations during the Transformation from Rose Petals to Rose Absolute

Oriane Tascone,[†,‡] Yoann Fillâtre,[†] Céline Roy,[†] and Uwe J. Meierhenrich*[,‡]

[†]European Research Institute on Natural Ingredients (ERINI), 06130 Grasse, France

[‡]University Nice Sophia Antipolis, Institut de Chimie de Nice, UMR 7272 CNRS, 06108 Nice, France

ABSTRACT: This study investigates the concentrations of 54 multiclass pesticides during the transformation processes from rose petal to concrete and absolute using roses spiked with pesticides as a model. The concentrations of the pesticides were followed during the process of transforming the spiked rose flowers from an organic field into concrete and then into absolute. The rose flowers, the concrete, and the absolute, as well as their transformation intermediates, were analyzed for pesticide content using gas chromatography/tandem mass spectrometry. We observed that all the pesticides were extracted and concentrated in the absolute, with the exception of three molecules: fenthion, fenamiphos, and phorate. Typical pesticides were found to be concentrated by a factor of 100−300 from the rose flowers to the rose absolute. The observed effect of pesticide enrichment was also studied in roses and their extracts from four classically phytosanitary treated fields. Seventeen pesticides were detected in at least one of the extracts. Like the case for the spiked samples in our model, the pesticides present in the rose flowers from Turkey were concentrated in the absolute. Two pesticides, methidathion and chlorpyrifos, were quantified in the rose flowers at approximately 0.01 and 0.01−0.05 mg kg^{-1}, respectively, depending on the treated field. The concentrations determined for the corresponding rose absolutes were 4.7 mg kg^{-1} for methidathion and 0.65−27.25 mg kg^{-1} for chlorpyrifos.

KEYWORDS: *pesticides, rose flowers, concrete, absolute, natural extracts, dispersive SPE, aroma and perfume chemistry, cosmetic industry*

INTRODUCTION

Extracts of roses, such as essential oils (EOs) or absolutes, are among the leading products in the field of perfumes. Perfumes generated by the most prestigious brands use rose absolute in their formulations. More than approximately 10 tons of concrete and 4 tons of essential oils are produced worldwide each year despite their low extraction yields: 0.03% (w/w) for EO and 0.3% (w/w) for concrete.[1] The most commonly used roses are *Rosa damascena* species from Turkey, Bulgaria, and Morocco. Fewer roses are produced in France. *Rosa centifolia* is the only species cultivated in France.

In general, the EO from roses is obtained by steam distillation and mainly contains monoterpene alcohol (citronellol, linalool, nerol, geraniol).[2] The concrete from roses is obtained by maceration of rose flowers in *n*-hexane. This complex sample contains alcohols, terpenes, terpenoids, and stearoptenes.[3,4] The concrete is then extracted with ethanol to produce the absolute.[1,5] During this process, stearoptenes are usually removed from the concrete, while compounds such as phenylethyl alcohol, citronellol, geraniol, nerol, eugenol, nonadecane, nonadecene, and many others are extracted and concentrated in the absolute.

The crop production of these flowers is habitually based on monoculture and involves the use of pesticides. The raw materials intended for perfume, aroma, and cosmetic products have been increasingly regulated in terms of the residual levels of chemicals allowed because of their impact on public health and on the environment. During the processes of extraction, treatment, and concentration of the natural ingredients, pesticides have the potential to be coextracted with the target olfactory compounds.[6] However, presently, the behavior of the pesticides during the extraction and transformation of the natural ingredients remains unknown and requires a systematic analysis of the pesticides at each step during the process. As highlighted in a recent review, little research has been dedicated to the analysis of pesticides in natural extracts:[7] three studies mentioned multiclass pesticide analyses in essential oils,[8−10] three investigations were performed on concrete,[6,11,12] and there are no studies regarding absolutes.

Due to the extraction recovery and the few studies on absolutes, we describe here the concentration of pesticide during the extraction process from rose flowers to rose absolute. The first stage of our work was to develop new analytical methodologies based on dispersive solid phase extraction (d-SPE) to determine the pesticide content in those extracts.[13,14]

The study of pesticides was performed on spiked roses from an organic field and their extracts and on real samples of roses and their extracts from classically treated Turkish fields. Fifty-four pesticides that are representative of multiclass pesticide residues used in agricultural phytosanitary treatments, mainly in the form of organophosphates, organochlorines, and pyrethroids, were selected for the development of the method. Due to the chemical nature of the targeted molecules, a gas chromatograph/tandem mass spectrometry system (GC-MS/MS) was employed to quantify the pesticide residues.

Received: February 23, 2015
Revised: April 30, 2015
Accepted: May 5, 2015
Published: May 5, 2015

ACS Publications © 2015 American Chemical Society

DOI: 10.1021/acs.jafc.5b00985
J. Agric. Food Chem. 2015, 63, 4922−4932

MATERIALS AND METHODS

Chemicals and Materials. Acetonitrile (Optima LCMS grade) and acetic acid (HOAc Optima) were purchased from Fisher Scientific (Illkirch, France). Toluene (Chromasolv for HPLC 99.9% grade) was obtained from Sigma-Aldrich (Saint-Quentin Fallavier, France).

A modified QuEChERS approach for the sample preparation was developed. For the extraction/partitioning step, pouches (DisQuE) containing 1 g of sodium citrate, 1 g of sodium chloride, 4 g of magnesium sulfate ($MgSO_4$), and 0.5 g of sodium sesquihydrate were purchased from Waters (Wexford, Ireland). For the d-SPE cleanup, tubes containing 900 mg of $MgSO_4$, 150 mg of primary and secondary amines (PSAs), and 150 mg of C18 were obtained from Waters (Wexford, Ireland). A 150 μg graphitized carbon black (GCB) sorbent purchased from Agilent Technologies (Massy, France) was added to the cleanup tubes. The reconstituted matrix contained phenethyl alcohol from Yinghai (Canghzou, People's Republic of China), citronellol from BASF (Ludwigshafen, Germany), linalool from DSM Nutritional (Heerlen, Netherlands), geranyl acetate, citronellyl acetate, and eugenol that were internally prepared, and alkanes (C_7−C_{40}), geraniol, and fatty acid esters from Sigma-Aldrich (Saint-Quentin Fallavier, France).

The pesticide reference standards (mixture and individual standards) were of ≥95% purity and were obtained from CPI International (Santa Rosa, USA) and Dr. Ehrenstorfer GmbH (Augsburg, Germany).

Preparation of the Standard Solution. Individual pesticide standard stock solutions were prepared at 1000 μg mL^{-1} in toluene and stored at −18 °C. From these solutions, a 100 μg mL^{-1} working standard mixture (mix 1) in toluene was prepared. Two other mixtures of pesticides from CPI International at 1000 μg mL^{-1} were mixed and diluted in toluene to 100 μg mL^{-1} (mix 2). Mix 1 and mix 2 were stored at −18 °C and used for the preparation of the matrix-matched calibration levels.

A third mixture (mix 3) was prepared to spike the roses. One milliliter of each individual pesticide standard (1000 μg mL^{-1}) and the two mixtures of pesticide standards from CPI International (1000 μg mL^{-1}) were mixed in 200 mL of ethanol.

Origin and Transformation of the Rose Flowers. Rose flowers from both organic and nonorganic origins were collected to produce concretes and absolutes following the process described in Figure 1. To study the behavior of pesticides during the illustrated transformation process, 22.5 kg of French *centifolia* roses was picked from a French organic field at the Musée International de la Parfumerie (MIP) in Grasse. From the 22.5 kg of rose flowers, 10 kg was spiked (MIP spiked flowers) with 54 pesticides at a concentration of 0.1 mg kg^{-1}. To improve the uniformity and to simplify the spiking, flowers were divided into five barrels with exactly 2 kg each. In each one, the flowers were spiked by pulverization with 40 mL of mix 3. Small quantities of spiked flowers were spiked gradually and mixed until all 2 kg of the flowers was spiked. After 24 h of permeation, the MIP spiked flowers were combined and extracted for the production of the concrete. The remaining 12.5 kg of MIP organic flowers was used as a blank.

To evaluate the results obtained from the MIP organic spiked flowers, *damascena* rose flowers coming from four different nonorganic fields in Turkey were collected. These fields were chosen according to the confidence in the farmers regarding the veracity of their field treatments. To be consistent with our previous article, we named these fields B−E.[13]

All six rose flower samples (MIP organic flowers, MIP spiked flowers, and field B−E flowers) were transformed into concrete by a maceration of the roses in *n*-hexane followed by a filtration step and finally solvent evaporation. The absolute was produced by extracting 20 g of the concrete with ethanol followed by freezing of the mixture, filtration, and solvent evaporation. For each step of the process, the weights of the initial sample and the final extract, as well as the extraction recoveries, were recorded as indicated in Figure 2. For the MIP experiments, samples of fresh and spent roses, extracts, waste, and solvents (before and after the process) were taken at each step of the transformation for analysis of the pesticide residues. For Turkish fields, samples of fresh roses, the concrete, and the absolute were analyzed.

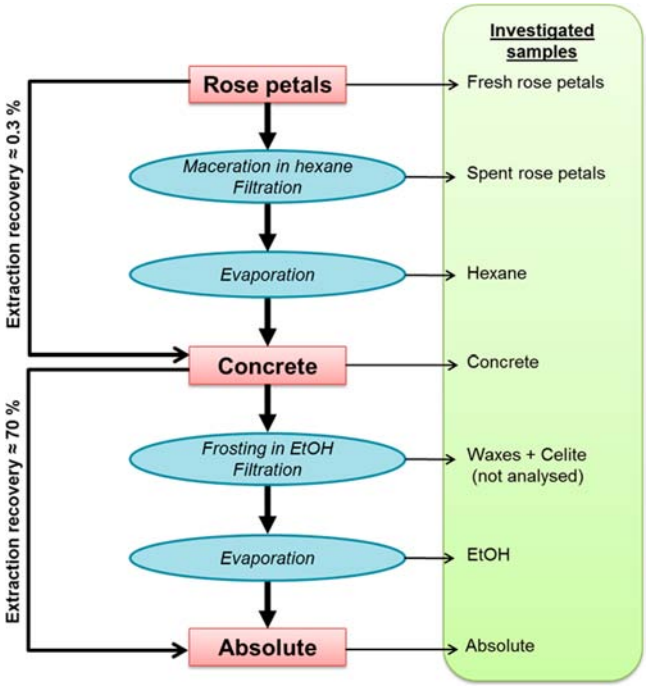

Figure 1. Transformation process from rose flowers to absolute and a list of the investigated samples for each transformation step. The average total mass recoveries of the concrete and absolute extractions are indicated.

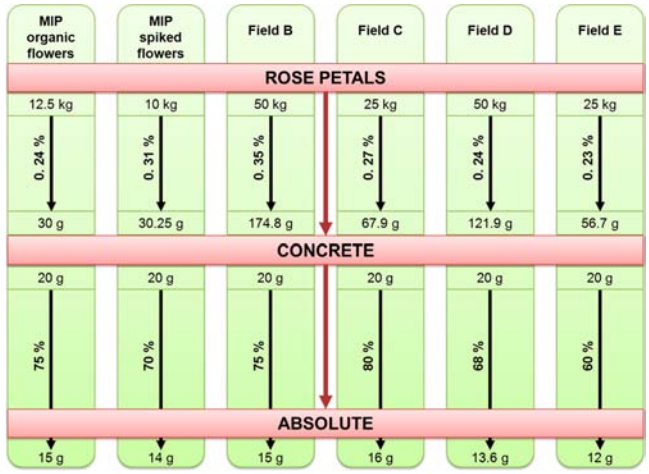

Figure 2. Total mass recoveries for the extraction of each rose. The recoveries for the transformation of rose from petal to concrete varied between 0.23% and 0.35%. In each case, 20 g of concrete was extracted. This step was performed on a laboratory scale, and the recoveries showed relatively large variation between 60% and 80%.

Sample Preparation. The rose flowers were cut and immediately stored in the freezer at −18 °C. Due to the close dry weight of fresh flowers and spent rose flowers (approximately 20%), fresh and spent rose flowers were prepared using the previously published validated protocol.[13] Briefly, 100 g of the rose flowers was ground and homogenized after freezing. A 5.0 g subsample of the rose flowers was transferred into a 50 mL centrifuge tube, and 15 mL of acetonitrile was added. The tube was shaken by hand for 1 min and placed in the refrigerator at 4 °C for 4 h. The contents of a pouch ($MgSO_4$, sodium citrate, NaCl, and sodium sesquihydrate) were added to the tube to remove any residual water and to assist in the extraction of the

DOI: 10.1021/acs.jafc.5b00985
J. Agric. Food Chem. 2015, 63, 4922−4932

pesticides from the matrix. The tube was vigorously shaken with a vortex mixer for approximately 30 s. Subsequently, the mixture was centrifuged for 10 min at 2630 rcf. Then, 8.0 mL of the supernatant was transferred into a d-SPE cleanup tube containing $MgSO_4$ (900 mg), PSA (150 mg), C18 (150 mg), and GCB (150 mg), and 3 mL of toluene was added. The tube was vigorously shaken with a vortex mixer for 1 min. Subsequently, the mixture was centrifuged for 10 min at 2630 rcf. The extract was transferred into a second purification tube that also contained $MgSO_4$, PSA, C18, and GCB and shaken with a vortex mixer. After centrifugation, 4 mL of the resulting solution was evaporated under nitrogen flow at 35 °C until approximately 200 μL remained. Then, the residue was transferred into a GC vial. The tube was washed with a small amount of toluene. The final volume was adjusted to 1 mL.

For the concretes and absolutes, the protocol previously described and validated was applied with slight modifications.[14] The main modifications of the protocol used for the rose flower samples were the weight of the subsample, 2.5 g of the concrete and 2.5 g of the absolute (compared to 5.0 g used for the rose flowers), and the addition of 2.5 g of water. Additionally, a 2-fold dilution of the final extract was performed just before analysis of the absolute.

For analysis of the *n*-hexane and ethanol solvents, 50 mL of the solvent was evaporated under a nitrogen flow to 500 μL and analyzed by GC-MS/MS. The quantification was performed using external calibration.

Each described sample (roses, concrete, absolute, and solvents) was prepared and analyzed in duplicate.

GC-MS/MS Analysis. GC-MS/MS analyses were performed on an Agilent 7000 triple-quadrupole mass spectrometer interfaced with an Agilent 7890A GC system. The GC was equipped with a fused silica 95% dimethylpolysiloxane 5% phenyl capillary ZB5-MSi (30 m × 0.25 mm i.d. × 0.25 μm film thickness) column from Phenomenex (Le Pecq, France). The carrier gas was helium at a constant flow of 1 mL min^{-1}. The GC was equipped with an Agilent 7683 autosampler and a split/splitless injector. The temperature program was as follows: initial temperature of 90 °C, held at 90 °C for 1 min, 30 °C min^{-1} ramped to 180 °C, then 3 °C min^{-1} ramped to 280 °C, and held at 280 °C for 5 min. The temperature of the injection port was 280 °C, and a 1 μL volume was injected in pulsed splitless mode.

The MS transfer line and ion source temperatures were both set to 280 °C. An electron ionization energy of 70 eV was used.

Analyses were performed in the selected reaction monitoring (SRM) mode on the basis of the use of one transition for quantification (quantifier) and one transition to confirm the compound identity (qualifier). For each analyte, the collision energy (CE) was optimized. To optimize the sensitivity of the detection of each pesticide, the SRM method was divided into 20 time segments.

RESULTS AND DISCUSSION

Pesticide Concentrations in MIP Spiked Flowers. The first step of the study was to determine the initial concentration of pesticides in the MIP spiked flowers (c_0) after a theoretical spiking of 0.1 mg kg^{-1}. It is important to precisely determine the amount of pesticides absorbed by the rose flowers, which is likely to be extracted in the concrete and then in the absolute. The analysis of the blank sample of the MIP organic flowers showed that no pesticides were present (limit of quantification: 0.01 mg kg^{-1}) prior to spiking.

For the MIP spiked flowers, the pesticide concentrations (c_0) determined, along with their recovery rates (R_0), calculated from a theoretical spiking of 0.1 mg kg^{-1}, are detailed in columns 3 and 4 of Table 1.

The bar charts in Figure 3 depict the number of active substances as a function of the recovery rate (R_0).

As shown in Figure 3, 52 molecules were quantified, 17 molecules of which showed $R_0 < 50\%$ (undetected < c_0 < 0.05 mg kg^{-1}); 5 molecules showed $50\% \le R_0 < 70\%$ (0.05 mg $kg^{-1} \le c_0 <$ 0.070 mg kg^{-1}), and 29 molecules showed $70\% \le R_0 \le 120\%$ (0.07 mg $kg^{-1} \le c_0 \le$ 0.12 mg kg^{-1}). The 2,4-D isopropyl ester and acetochlor were undetected (ND) (signal to noise ratio <3). One pesticide, endosulfan sulfate, showed $R_0 > 120\%$ ($c_0 >$ 0.12 mg kg^{-1}). It should be noted that, according to our previous article,[13] the determinations of pesticides in flowers are validated with a reporting limit of quantification of 0.05 mg kg^{-1} for all pesticides. However, for most of the pesticides, the analytical sensitivity was sufficient to enable an accurate quantification below 0.05 mg kg^{-1}. Therefore, we considered it important to report the results for the 19 pesticides with $c_0 <$ 0.05 mg kg^{-1}, although they should be considered with caution.

As shown in Table 1, most of the low recovery rates were observed for the pesticides that eluted early. Indeed, 19 pesticides among the first 23 eluted pesticides had recoveries ND < R_0 < 59%. This phenomenon can be attributed to both the volatility of the residues and the experimental conditions for the pesticide application. The spiking solution, which was made from pesticide standards without a fixing agent, as in commercial solutions, was sprayed on the MIP rose flowers stocked in barrels outside where the temperature was approximately 20−25 °C. Then, the barrels were left half-opened to avoid maceration and they remained outside for 24 h before the concrete extraction. Therefore, the probability of volatilization of some of the pesticides is rather high. Another explanation could be the degradation of the residues containing a thioether group (for example, fenthion and fenamiphos), which are known to be prone to oxidation.[15] Under the conditions found in the environment, they usually quickly degrade to sulfoxide and sulfones. Thiophosphate sulfides (for example, malathion and parathion-methyl) can be oxidized to oxons.[15]

Endosulfan sulfate is a particular case, because it is the only pesticide that exhibits a high recovery rate (R_0 = 135%) and a high concentration (c_0 = 0.135 mg kg^{-1}) in the rose flowers. Endosulfan sulfate is known to be the main metabolite resulting from the degradation of endosulfans.[16] The low α-endosulfan concentration (c_0 = 0.043 mg kg^{-1}, R_0 = 43%) corroborates the hypothesis for the degradation of endosulfan. α,Endosulfan is known to be less stable than β-endosulfan (c_0 = 0.109 mg kg^{-1}, R_0 = 109%).

A complete explanation of these results would require further investigations that are beyond the scope of this paper. The aim was to determine the amount of pesticides likely to be extracted during the production of concretes and absolutes. Therefore, the previously determined pesticide concentrations c_0 in MIP spiked rose flowers will serve as a reference for the rest of the study.

Pesticide Concentrations in the Concrete from the MIP Spiked Roses. To examine pesticide concentrations during the extraction of the MIP spiked rose flowers in the concretes, samples of concretes, spent roses, *n*-hexane before extraction, and *n*-hexane after extraction were analyzed.

The analysis of the concrete from the MIP organic flowers (blank matrix) showed that no pesticide was present and/or introduced during the process. Analyses of *n*-hexane showed that no pesticides were present before the extraction, but some traces of pesticides were found in the *n*-hexane after the extraction (Table 1 column 9, c_{hexane}). Twenty-two pesticides were detected below the limit of quantification (LOQ), and six pesticides (phorate, lindane, fenitrothion, chlorpyrifos, parathion, and triazophos) were quantified at 0.01 mg L^{-1}.

The analysis of spent roses showed the presence of all the pesticides except 2,4-D isopropyl ester, acetochlor, and

DOI: 10.1021/acs.jafc.5b00985
J. Agric. Food Chem. 2015, 63, 4922−4932

Table 1. Pesticide Distribution during the Extraction Process for the MIP Spiked Flowers[a]

		MIP spiked flowers		concrete extraction step							absolute extraction step				
	retention time (min)	c_0 (mg kg^{-1})	R_0 (%)	c_2' ($c_0 \times 323$) (mg kg^{-1})	c_2 (mg kg^{-1})	R_2 (%)	$c_{1,\text{spent}}$ (mg kg^{-1})	c_{hexane} (mg L^{-1})	$c_{2,\text{corrected}}$ (mg kg^{-1})	$R_{2,\text{corrected}}$ (%)	c_3' ($c_2 \times 1.4$) (mg kg^{-1})	c_3 (mg kg^{-1})	R_3 (%)	c_{ethanol} (mg L^{-1})	concentration factor
2-phenylphenol	6.62	0.020	20	6.45	15.65	243	<LOQ	<LOQ	6.45	243	22.38	17.51	78	0.03	875
phorate	8.29	0.013	13	4.19	8.71	208	<LOQ	0.01	4.19	208	12.45	0.22	2	0.01	17
2,4-D isopropyl ester	8.65	<LOD			0.85		<LOD	<LOQ			1.22	0.98	80	<LOQ	
propetamphos	9.37	0.031	31	10.00	14.91	149	<LOQ	<LOQ	10.00	149	21.32	17.83	84	0.01	575
lindane	9.53	0.079	79	25.49	18.87	74	<LOQ	0.01	25.49	74	26.99	22.76	84	0.04	288
diazinon	9.64	0.013	13	4.19	11.94	285	<LOQ	<LOQ	4.19	285	17.07	11.77	69	0.01	905
acetochlor	11.26	<LOQ			2.68		<LOD	<LOQ			3.84	2.99	78	<LOD	
chlorpyrifos-methyl	11.43	0.037	37	11.94	16.11	135	<LOQ	<LOQ	11.94	135	23.04	17.40	76	0.02	470
parathion-methyl	11.53	0.016	16	5.16	16.26	315	<LOQ	<LOQ	5.16	315	23.25	15.88	68	0.01	992
pirimiphos-methyl	12.39	0.059	59	19.03	17.52	92	0.01	<LOQ	16.45	107	25.06	19.40	77	0.01	329
fenitrothion	12.50	0.046	46	14.84	17.20	116	<LOQ	0.01	14.84	116	24.60	18.75	76	0.01	408
malathion	12.72	0.013	13	4.19	8.74	208	<LOQ	<LOQ	4.19	208	12.50	9.47	76	<LOD	729
fenthion	13.23	0.044	44	14.19	9.26	65	<LOQ	<LOQ	14.19	65	13.24	0.30	2	<LOQ	7
chlorpyrifos	13.25	0.087	87	28.07	16.77	60	0.03	0.01	17.10	98	23.97	18.63	78	0.01	214
parathion	13.37	0.056	56	18.07	16.72	93	0.01	0.01	14.19	118	23.91	20.47	86	0.01	366
isofenphos	14.97	0.088	88	28.39	17.74	62	<LOQ	<LOQ	28.39	62	25.37	19.37	76	<LOQ	220
chlorfenvinphos	14.99	0.086	86	27.74	16.07	58	0.01	<LOQ	24.20	66	22.98	18.22	79	<LOQ	212
mecarbam	15.06	0.043	43	13.87	13.93	100	<LOQ	<LOQ	13.87	100	19.92	15.23	76	<LOD	354
phenthoate	15.14	0.037	37	11.94	14.45	121	<LOQ	<LOQ	9.36	121	20.66	15.87	77	0.01	429
quinalphos	15.23	0.077	77	24.84	17.84	72	<LOQ	<LOQ	24.84	72	25.51	19.61	77	<LOD	255
methidathion	15.89	0.024	24	7.74	12.29	159	<LOQ	<LOQ	7.74	159	17.58	13.28	76	<LOQ	553
endosulfan I	16.28	0.043	43	13.87	14.95	108	0.03	<LOQ	5.48	273	21.37	17.11	80	0.01	398
fenamiphos	16.95	0.017	17	5.48	5.93	108	<LOD	<LOD	5.48	108	8.48	0.16	2	<LOD	9
prothiofos	17.16	0.099	99	31.94	14.80	46	0.06	<LOQ	12.26	121	21.17	16.82	79	0.00	170
profenofos	17.33	0.086	86	27.74	17.01	61	0.01	<LOD	24.84	68	24.32	18.40	76	<LOD	214
p,p′-DDE	17.55	0.100	100	32.26	13.43	42	0.07	<LOQ	10.65	126	19.20	15.29	80	<LOQ	153
buprofezin	17.93	0.063	63	20.32	17.30	85	<LOQ	<LOD	20.32	85	24.74	17.93	72	<LOD	285
o,p′-DDT	18.01	0.112	111	36.13	15.14	42	0.04	<LOD	21.94	69	21.65	12.38	57	<LOD	111
chlorfenapyr	18.88	0.116	116	37.42	17.51	47	0.02	<LOD	30.00	58	25.04	20.25	81	<LOD	175
chlorobenzilate	19.20	0.065	65	20.97	18.74	89	0.01	<LOD	17.42	108	26.80	21.04	79	<LOQ	324
endosulfan II	19.19	0.109	109	35.16	17.14	49	0.01	<LOQ	31.94	54	24.51	19.23	78	<LOD	176
p,p′-DDT	19.72	0.116	116	37.42	13.05	35	0.08	<LOD	12.26	106	18.66	15.82	85	<LOD	136
ethion	19.76	0.102	102	32.91	16.32	50	0.05	<LOD	18.07	90	23.33	19.36	83	<LOD	190
triazophos	20.67	0.087	87	28.07	18.12	65	<LOQ	0.01	28.07	65	25.92	20.24	78	<LOD	233
endosulfan sulfate	21.38	0.136	135	43.87	17.82	41	0.01	<LOD	40.97	43	25.48	21.69	85	<LOD	159
Propargite	22.49	0.084	84	27.10	14.85	55	0.05	<LOD	11.29	132	21.24	17.12	81	<LOD	204
pyridaphenthion	24.01	0.070	70	22.58	17.93	79	<LOQ	<LOD	22.58	79	25.64	17.79	69	<LOD	254
iprodione	24.18	0.117	117	37.74	18.09	48	0.01	<LOD	34.20	53	25.88	19.12	74	<LOD	163
phosmet	24.22	0.045	45	14.52	14.91	103	<LOQ	<LOD	14.52	103	21.32	15.25	72	<LOD	339

DOI: 10.1021/acs.jafc.5b00985
J. Agric. Food Chem. 2015, 63, 4922−4932

Table 1. continued

		MIP spiked flowers		concrete extraction step							absolute extraction step				
	retention time (min)	c_0 (mg kg^{-1})	R_0 (%)	c_2' ($c_0 \times 323$) (mg kg^{-1})	c_2 (mg kg^{-1})	R_2 (%)	$c_{1,spent}$ (mg kg^{-1})	c_{hexane} (mg L^{-1})	$c_{2,corrected}$ (mg kg^{-1})	$R_{2,corrected}$ (%)	c_3' ($c_2 \times 1.4$) (mg kg^{-1})	c_3 (mg kg^{-1})	R_3 (%)	$c_{ethanol}$ (mg L^{-1})	concentration factor
bromopropylate	24.31	0.117	117	37.74	18.18	48	0.03	<LOD	29.36	62	25.99	19.68	76	<LOD	168
bifenthrin	24.33	0.112	112	36.13	14.20	39	0.08	<LOD	10.97	129	20.31	15.33	75	<LOD	137
fenpropathrin	24.76	0.104	104	33.55	15.93	47	0.06	<LOD	13.23	120	22.78	16.93	74	<LOD	163
tetradifon	25.89	0.101	101	32.58	18.75	58	0.01	<LOD	29.03	65	26.82	20.60	77	<LOD	204
phosalone	26.34	0.064	64	20.65	17.53	85	0.01	<LOD	18.07	97	25.07	18.80	75	<LOD	294
azinphos-methyl	26.41	0.048	48	15.48	15.10	98	0.01	<LOD	12.58	120	21.59	15.41	71	<LOD	321
cyfluthrin I	31.61	0.109	109	35.16	14.28	41	0.06	<LOD	15.81	90	20.42	16.10	79	<LOD	148
cyfluthrin II	31.95	0.103	103	33.23	14.60	44	0.06	<LOD	15.48	94	20.87	16.30	78	<LOD	158
cyfluthrin III	32.14	0.106	106	34.20	14.45	42	0.06	<LOD	15.48	93	20.66	16.39	79	<LOD	155
cyfluthrin IV	32.30	0.104	104%	33.55	14.27	43%	0.05	<LOD	16.78	85	20.40	16.28	80	<LOD	157
cypermethrin I	32.55	0.089	89	28.71	12.17	42	0.06	<LOD	10.97	111	17.41	14.39	83	<LOD	162
cypermethrin II	32.90	0.083	83	26.78	12.41	46	0.05	<LOD	10.65	117	17.75	14.64	82	<LOD	176
cypermethrin III	33.08	0.091	91	29.36	11.52	39	0.05	<LOD	12.26	94	16.47	13.85	84	<LOD	152
cypermethrin IV	33.24	0.089	89	28.71	11.97	42	0.05	<LOD	12.58	95	17.12	14.31	84	<LOD	161
deltamethrin	37.72	0.033	32	10.65	5.17	49	0.02	<LOD	4.19	123	7.39	5.57	75	<LOD	169

[a]Definitions: c_0, pesticide concentrations in the MIP spiked roses; R_0, recovery rates between the theoretical spiked concentration on the roses and the pesticide concentration in the MIP spiked roses; c_2', maximum pesticide concentration in the concrete from the MIP spiked roses (assuming a 100% pesticide transfer from the MIP spiked roses to the concrete); c_2, pesticide concentrations quantified in the concrete; R_2, recovery rates between the maximum theoretical concentrations of pesticides in the concrete and the pesticide concentrations quantified in the concrete; $c_{1,spent}$, pesticide concentrations in the spent MIP spiked roses; c_{hexane}, pesticide concentrations in the hexane used to extract the MIP spiked roses; $c_{2,corrected}$, theoretical pesticide concentrations in the concrete taking into account the pesticide concentrations in the spent MIP spiked roses ($c_{2,corrected} = 323(c_2 - c_{1,spent})$); $R_{2,corrected}$, recovery rates between the corrected theoretical concentrations of pesticides in the concrete and quantified pesticide concentrations in the concrete; c_3', maximum pesticide concentration in the absolute from the concrete (assuming a 100% pesticide transfer from the concrete to the absolute); c_3, pesticide concentrations quantified in the absolute; R_3, recovery rates between the maximum theoretical concentrations of pesticides in the absolute and the quantified pesticide concentrations in the absolute; $c_{ethanol}$, pesticide concentrations in the ethanol used to extract the concrete.

DOI: 10.1021/acs.jafc.5b00985
J. Agric. Food Chem. 2015, 63, 4922−4932

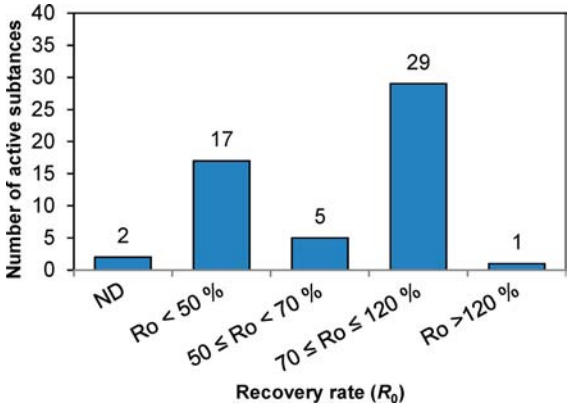

Figure 3. Distribution of recovery rates (R_0) of the pesticides in the MIP spiked roses.

fenamiphos. The respective concentrations of each pesticide found in the spent roses ($c_{1,spent}$) are reported in Table 1, column 8, and in the bar charts of Figure 4, which depict the

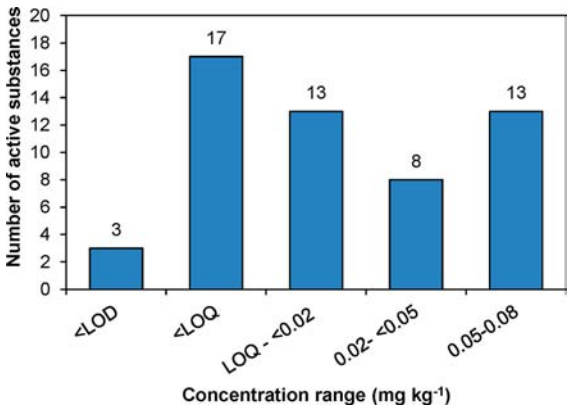

Figure 4. Distribution of the pesticide concentrations in the spent roses ($c_{1,spent}$). Thirty-three pesticides showed concentrations lower or close to the limit of quantification. Seventeen molecules were detected below the LOQ (0.01 mg kg^{-1}).

number of pesticides found within different concentration ranges in the spent roses.

As shown in Figure 4, 33 of the 54 pesticides have $c_{1,spent}$ < 0.02 mg kg^{-1}. Twenty pesticides had $c_{1,spent}$ < LOQ. Most of these 20 pesticides corresponded to the pesticides showing the lowest concentrations in the rose flowers (c_0). More than half of the pesticide content remained in the spent roses for the 13 pesticides quantified between 0.05 and 0.08 mg kg^{-1}.

The analysis of the concrete showed that all of the pesticides were detected in the concrete. The determined concentrations c_2 for each pesticide are shown in Table 1, column 6. On the basis of the experimental results for the fresh roses (c_0) *and* of the recoveries from the concrete extraction (Figure 2), the maximum concentration of the pesticides in the concrete (c_2'), corresponding to 100% pesticide transfer from the MIP spiked roses to the rose concrete, can be calculated. Assuming that a pesticide is fully extracted following an average concrete extraction yield of 0.31% (see Figure 2), the theoretical concentration of a pesticide in the concrete (c_2') is 323-fold the concentration of a pesticide in the rose flowers (Table 1, column 5):

$$c_2' = 323c_0$$

On the basis of this value, the corresponding recovery rates (R_2) were calculated: $R_2 = 100c_2/c_2' = 100c_2/(323\ c_0)$. The observed concentrations of pesticides in the concrete vary from c_2 = 0.85 mg kg^{-1} (2,4-D isopropyl ester) to c_2 = 18.87 mg kg^{-1} (lindane), and the recovery rates span from R_2 = 35% (*p,p′*-DDT) to R_2 = 315% (parathion-methyl).

The results are illustrated in the bar charts of Figure 5, which show the superposition of the pesticide amounts in the spent roses and in the concrete ($c_0 + c_2$) in comparison to the theoretical pesticide amounts in the concrete (c_2'). This representation shows the amount of each pesticide (in mg) coextracted into the concrete, the amount that remained in the spent roses, and the comparison of the total of these two with the theoretical value, assuming a 100% transfer of the pesticides into the concrete.

In Figure 5, two groups of pesticides can be distinguished. Group G1 contains the 46 pesticides whose levels found in the concrete and the spent roses agree with the theoretical quantity. Within this group, 2 subgroups can be distinguished.

G1a: 11 pesticides were quantified in the concrete and had a low concentration in the spent roses ($c_{1,spent}$ < LOQ). Their concentrations varied from c_2 = 5.96 mg kg^{-1} (fenamiphos) to c_2 = 18.87 mg kg^{-1} (lindane), and the recovery rates ranged from R_2 = 62% (isofenphos) to R_2 = 116% (fenitrothion).

G1b: 35 pesticides, including chlorpyrifos, prothiofos, DDT isomers, ethion, cypermethrin isomers, and cyfluthrin isomers, were found to be distributed between the spent roses and the concrete. Between 2% (endosulfan sulfate) and 84% (*p,p′*-DDE) of the pesticide content remained in the spent roses.

The second group, G2, is composed of 8 pesticides (o-phenylphenol, phorate, propetamphos, diazinon, chlorpyrifos-methyl, parathion-methyl, malathion, and methidathion) that have concentrations c_2 above the maximum concentration c_2' and recovery rates R_2 of between 135% (chlorpyrifos-methyl) and 315% (parathion-methyl). With the exception of chlorpyrifos-methyl, none of these pesticides were found in the spent roses. All of these pesticides had the 11 lowest concentrations in the MIP spiked roses (near LOQ or not detected). As mentioned in the previous section, the concentrations of these pesticides in the MIP spiked roses were lower than the reporting limit of 0.05 mg kg^{-1}, and the results are subject to errors. These recovery rates can be explained by considering the low concentrations in the fresh roses and the potentially high concentration factor in the concrete (323-fold concentrated). A difference of 0.01 mg kg^{-1} in the quantification of the pesticides in the fresh roses leads to a difference of 3.23 mg kg^{-1} in the concrete and could therefore have a significant impact on R_2. The effect is presented in Table 2 for 4 of the pesticides. According to these results, an underestimation of 0.01 mg kg^{-1} in the pesticide concentrations in the MIP rose flowers yields recoveries in the concrete closest to 100%. For example, taking into account an underestimation of 0.01 mg kg^{-1} in the rose (c_{0max} = 0.023 mg kg^{-1}) for phorate yields a theoretical concentration of c_{2max}' = 7.42 mg kg^{-1} in the concrete. Thus, the corresponding recovery rate would be $R_{2,min}$ = 117%. Similar phenomena were observed for the 3 other pesticides (chlorpyrifos-methyl, $R_{2,min}$ = 106%; methidathion, $R_{2,min}$ = 113%; propetamphos, $R_{2,min}$ = 113%).

Pesticide Concentrations in the Absolute from the MIP Concrete. To examine the concentrations of pesticide during the transformation from the concrete to the absolute, samples of the absolute, as well as ethanol (before and after extraction), were analyzed for pesticide levels.

DOI: 10.1021/acs.jafc.5b00985
J. Agric. Food Chem. 2015, 63, 4922−4932

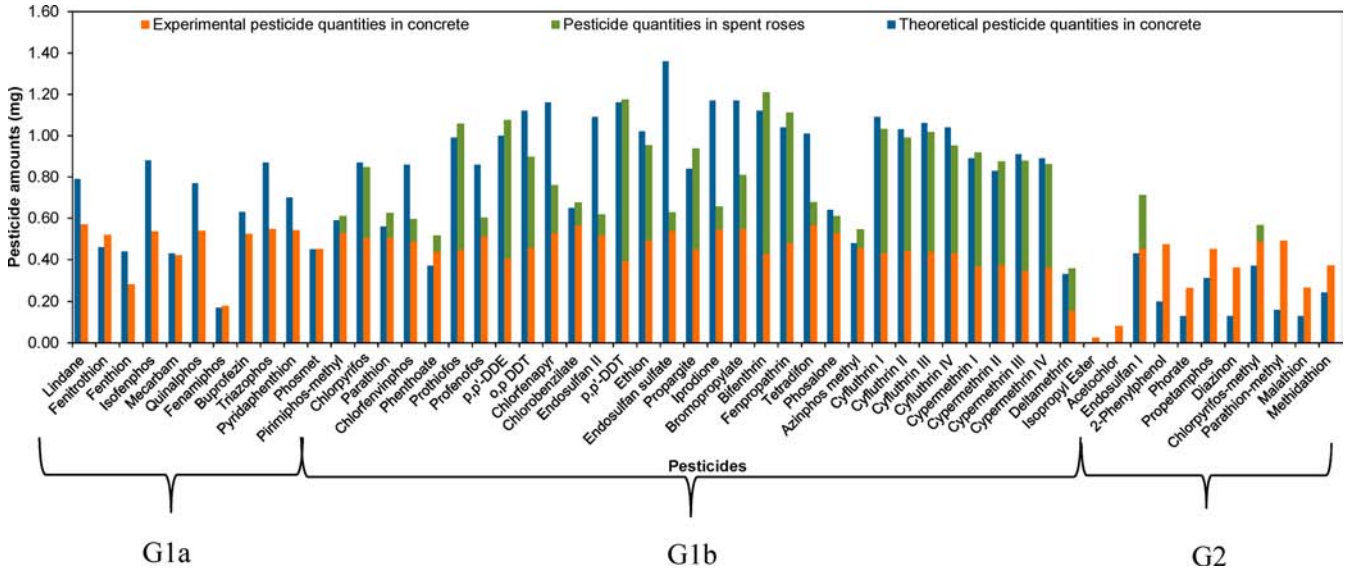

Figure 5. Pesticide content in the spent roses (green) and in the concrete (orange) in comparison to the theoretical pesticide content in the concrete (blue). Pesticide quantities in the fresh roses were distributed in the concrete and in the spent roses for most of the investigated molecules. Two groups can be distinguished: G1 with G1a and G1b, in which the theoretical pesticide amounts are in agreement with the total pesticide amounts in the spent roses and the concrete, and G2, in which the pesticide content in the concrete is above theoretical amounts.

Table 2. Examples of the Effect of the Variation in the Pesticide Concentrations in the MIP Spiked Roses on the Pesticide Concentrations in the Concrete and on the Recovery Rate R_2[a]

	c_0 ($c_{0,min}$–$c_{0,max}$) (mg kg^{-1})	c_2' ($c_{2,min}'$–$c_{2,max}'$) (mg kg^{-1})	c_2 (mg kg^{-1})	R_2 ($R_{2,min}$–$R_{2,max}$) (%)
chlorpyrifos-methyl	0.037 (0.027–0.047)	11.94 (8.71–15.17)	16.11	135 (106–185)
phorate	0.013 (0.003–0.023)	4.19 (0.96–7.42)	8.71	208 (117–907)
propetamphos	0.031 (0.021–0.041)	10.00 (6.77–13.23)	14.91	149 (113–220)
methidathion	0.024 (0.014–0.034)	7.74 (4.51–10.97)	12.29	159 (113–272)

[a]Abbreviations: c_0 ($c_{0,min}$–$c_{0,max}$), pesticide concentrations in the MIP spiked roses (concentration taking into account a variation of 0.01 mg kg^{-1} in c_0); c_2' ($c_{2,min}'$–$c_{2,max}'$), maximum pesticide concentration in the concrete from MIP spiked roses (theoretical concentration in the concrete from the MIP spiked roses taking into account a variation of 3.23 mg kg^{-1} in c_2'); c_2, pesticide concentrations quantified in the concrete; R_2 ($R_{2,min}$–$R_{2,max}$), recovery rates between the maximum theoretical concentrations of pesticides in the concrete and quantified pesticide concentrations in the concrete (recovery rate taking into account the variation in c_2').

The analysis of the blank matrix (the absolute from the concrete that originated from the MIP organic flowers) showed that no pesticide was present or introduced during the transformation process.

Analyses of the ethanol showed that no pesticides were present prior to extraction and some traces of pesticides were found in the ethanol after the extraction, $c_{ethanol}$ (Table 1, column 15). Seven of the pesticides had levels below the LOQ, and 13 of the pesticides were determined to be $c_{ethanol} \geq 0.01$ mg L^{-1}. Two of the pesticides, *o*-phenylphenol and lindane, were determined to be $c_{ethanol} = 0.03$ and 0.04 mg L^{-1}, respectively. The $c_{ethanol}$ values measured are considered relatively small and are therefore negligible for this pesticide study.

The analyses of the absolute from the MIP spiked roses showed the presence of all the pesticides in this extract, as indicated by c_3 (Table 1, column 13). The calculated concentrations, c_3', that correspond to a 100% pesticide transfer from the concrete to the absolute are shown in Table 1 column 12. As shown in Figure 2, the recovery from the absolute extraction was 70%. Thus, the extracted pesticides are potentially concentrated 1.4-fold from the concrete to the absolute:

$$c_3' = 1.4c_2$$

All of the pesticides were extracted in the absolute with recovery rates R_3 between 69 and 88%, with the exception of *o,p'*-DDT ($R_3 = 57\%$), phorate ($R_3 = 2\%$), fenthion ($R_3 = 2\%$), and fenamiphos ($R_3 = 2\%$). The levels of phorate ($c_{ethanol} = 0.1$ mg L^{-1}), fenthion ($c_{ethanol} <$ LOQ), and fenamiphos ($c_{ethanol} <$ LD) in ethanol are not sufficient to explain the very low R_3 values. More probable explanations are that the pesticides were retained in waxes blended with Celite, which were not analyzed, or were degraded during the concrete transformation process.

The model on MIP spiked roses showed that some pesticides were lost during the spiking of pesticides. During the transformation of the rose flowers to the concrete, we observed that the majority of the pesticides are extracted and concentrated into the concrete, although some of the pesticides did partially remain in the spent roses. With the exceptions of phorate, fenthion, and fenamiphos, all of the pesticides present in the concrete were also extracted into the absolute with $R_3 > 57\%$. Therefore, during the entire process, the pesticides present in flowers were found to be at least 100-fold concentrated in the absolute (Table 1, column 16). To verify this trend, the same study was performed on 4 samples from the Turkish fields.

Real Samples Cultivated in Turkey. The behavior of the pesticides was studied in roses and their extracts were obtained from classically treated crops. Four fields were investigated, and in each case, the rose flowers, concretes, and absolutes were analyzed for their pesticide content. For consistency with our

DOI: 10.1021/acs.jafc.5b00985
J. Agric. Food Chem. 2015, 63, 4922–4932

previous article, we named these samples B−E, corresponding to the 4 different fields.[13] The treatment was performed on the selected fields at least 3 weeks before harvest (rose tree with rose bud, before rose blooming). To our knowledge, only chlorpyrifos among the 54 targeted pesticides was applied to fields D and E. The other pesticides applied to these fields, including imidacloprid, thiacloprid, and hexaconazole, are not in our list and are amenable to liquid chromatography. Table 3 summarizes the results of the pesticide content found in the rose flowers, the concrete, and the absolute for each field.

Samples Cultivated from Field B. Among the 54 targeted pesticides, 11 pesticides were detected in at least one of the 3 samples (rose, concrete, or absolute). Most of them were present in amounts below the LOQ. Only cypermethrin isomers ($c_{3,B} \approx 0.25$ mg kg^{-1} in the absolute), methidathion ($c_{2,B} = 0.22$ mg kg^{-1} in the concrete, $c_{3,B} = 0.22$ mg kg^{-1} in the absolute), and chlorpyrifos ($c_{0,B} = 0.01$ mg kg^{-1} in the rose flowers, $c_{2,B} = 1.63$ mg kg^{-1} in the concrete, $c_{3,B} = 1.73$ mg kg^{-1} in the absolute) could be quantified. Thus, the corresponding recovery rates during the concrete extraction ($R_{2,B}$) and during the absolute extraction ($R_{3,B}$) were calculated for methidathion ($R_{3,B} = 75\%$) and for chlorpyrifos ($R_{2,B} = 47\%$; $R_{3,B} = 79\%$).

These recovery rates for the transformation from the concrete to the absolute are consistent with our previous results in our model spiked samples, in which chlorpyrifos and methidathion were extracted at $R_3 = 78\%$ and 76% into the absolute, respectively. A more significant difference was observed for the recovery rate of chlorpyrifos during the concrete extraction for the sample from field B. In our spiked model, chlorpyrifos was extracted at $R_2 = 60\%$ in the concrete, whereas it was extracted at $R_{2,B} = 47\%$ in the concrete from field B.

Samples Cultivated from Field C. Among the 54 targeted pesticides, 14 pesticides were detected in at least one of the 3 samples (rose, concrete, or absolute). Unlike the results for field B, most of them were present in amounts above the limit of quantification. Cypermethrin isomers (in the rose flowers, concrete, and absolute), chlorpyrifos, malathion, methidathion, *p,p′*-DDT, *o,p′*-DDT, and *p,p′*-DDE (all in the concrete and absolute) were quantified. Thus, the recovery rates could only be determined for the cypermethrin isomers ($R_{2,C} = 16\%$; $R_{3,C} = 120\%$) during concrete extraction and absolute extraction. For the other pesticides, only the recovery rates for the absolute extraction ($R_{3,C}$) could be determined.

For chlorpyrifos ($R_{3,C} = 80\%$), malathion ($R_{3,C} = 76\%$), and methidathion ($R_{3,C} = 80\%$), the recovery rates observed for the transformation process from the concrete to the absolute were consistent with our previous results using our MIP spiked samples, in which chlorpyrifos, malathion, and methidathion were extracted at $R_3 = 78\%$, 76%, and 76%, respectively, in the absolute. More significant differences were observed for the recovery rates of *p,p′*,-DDT, *o,p′*-DDT, *p,p′*-DDE, and cypermethrin isomers, with differences between 11% for *p,p′*-DDE and 49% for cypermethrin isomers and *p,p′*-DDT. As in our MIP spiked samples, less than 50% of *o,p′*-DDT was extracted during the absolute extraction.

Samples Cultivated from Field D. With the exception of acetochlor, the same 13 pesticides found for samples from field C were detected in at least 1 of the 3 samples (rose, concrete, or absolute). Most of the pesticides were present in amounts above the limit of quantification. Only chlorpyrifos and methidathion were quantified in all three samples ($c_{0,D}$ = 0.05 and 0.01 mg kg^{-1} in the rose flowers, $c_{2,D} = 18.87$ and 3.42 mg kg^{-1} in the concrete, and $c_{3,D} = 27.78$ and 5.03 mg kg^{-1} in the absolute, respectively). The other pesticides were quantified in the concrete and the absolute, with recovery rates of extraction in the absolute of $32\% < R_{3,D} < 141\%$.

The observed recovery rates for malathion, *p,p′*-DDT, *o,p′*-DDT, and *p,p′*-DDE were within the same order of magnitude as those previously obtained for the samples from field C. More significant differences were observed for the recovery rates of chlorpyrifos ($R_{2,D} = 100\%$) and methidathion ($R_{2,D} = 64\%$) during the extraction from the rose flowers in comparison to those obtained in our MIP spiked samples ($R_2 = 60\%$ and 159%, respectively). These differences were also significant for the recovery rates of chlorpyrifos ($R_{3,D} = 98\%$) and methidathion ($R_{3,D} = 93\%$) during the absolute extraction in comparison to those obtained in our MIP spiked samples ($R_3 = 78\%$ and 76%, respectively). The chlorpyrifos recovery rates were higher than those obtained for the samples from the other studied fields for this pesticide.

Samples Cultivated from Field E. Among the 54 targeted pesticides, 11 pesticides were detected in at least one of the 3 samples (rose, concrete, or absolute). Four pesticides were detected in amounts below the limit of quantification. As in the case of field D, only chlorpyrifos and methidathion were quantified in all three samples ($c_{0,E}$ = 0.05 and 0.01 mg kg^{-1} in the rose flowers, $c_{2,E} = 4.74$ and 1.64 mg kg^{-1} in the concrete, and $c_{3,E} = 9.52$ and 2.60 mg kg^{-1} in the absolute, respectively). The levels of malathion ($c_{2,E} = 0.07$ mg kg^{-1} in the concrete, $c_{3,E} = 0.10$ mg kg^{-1} in the absolute) and cypermethrin isomers ($c_{3,E} = 0.16$ mg kg^{-1} in the absolute) were also quantified. Thus, the corresponding recovery rates for the concrete extraction ($R_{2,E}$) and for the absolute extraction ($R_{3,E}$) were calculated for malathion ($R_{3,B} = 84\%$), methidathion, and chlorpyrifos.

The corresponding recovery rates obtained for methidathion ($R_{2,E} = 31\%$; $R_{3,E} = 95\%$) and chlorpyrifos ($R_{2,E} = 23\%$; $R_{3,E} = 120\%$) were significantly different from those obtained for our MIP spiked samples ($R_2 = 159\%$ and 60%, $R_3 = 76\%$ and 78%, respectively). The recovery rates obtained for the 2 pesticides chlorpyrifos and methidathion were respectively 4-fold and 2-fold lower than those obtained for the samples from field D.

Table 4 summarizes the minimum and maximum concentrations and recovery rates for each detected pesticide in each sample and for all the fields. Among the 54 targeted pesticides, 17 pesticides were identified. The pesticide concentrations varied between 0.01 mg kg^{-1} (chlorpyrifos, methidathion, and cypermethrin) and 0.05 mg kg^{-1} (chlorpyrifos) in the roses, between 0.04 mg kg^{-1} (diazinon, methidathion, and *p,p′*-DDE) and 18.9 mg kg^{-1} (chlorpyrifos) in the concrete, and between 0.03 mg kg^{-1} (*p,p′*-DDE) and 27.25 mg kg^{-1} (chlorpyrifos) in the absolute. Only chlorpyrifos and methidathion were detected in every field and in every sample. The observed recovery rates for the pesticide extraction during the rose extraction show a large range for chlorpyrifos, with values between 23% and 100%. Significant differences between the recovery rates of methidathion in the concrete from real samples (31−64%) and from MIP spiked roses (159%) are also noted.

Among the 17 pesticides identified in the 4 Turkish fields, nine pesticides are not approved in Europe under the regulation EC 1107/2009 (methidathion, DDT isomers, diazinon, parathion-methyl, acetochlor, profenofos, *p,p′*-DDE, and phosalone). Although Turkey is not subject to European regulations, it is important for importation. Two pesticides, chlorpyrifos and methidathion, were detected and quantified in each field throughout the transformation process from the rose flowers to the absolute via the concrete. In these 4 fields, the pesticides

DOI: 10.1021/acs.jafc.5b00985
J. Agric. Food Chem. 2015, 63, 4922−4932

Table 3. Pesticides Present in the Samples Cultivated in Turkish Fields B–E[a]

	sample from field B					sample from field C					sample from field D					sample from field E				
	$c_{0,B}$ (mg kg^{-1})	$c_{2,B}$ (mg kg^{-1})	$R_{2,B}$ (%)	$c_{3,B}$ (mg kg^{-1})	$R_{3,B}$ (%)	$c_{0,C}$ (mg kg^{-1})	$c_{2,C}$ (mg kg^{-1})	$R_{2,C}$ (%)	$c_{3,C}$ (mg kg^{-1})	$R_{3,C}$ (%)	$c_{0,D}$ (mg kg^{-1})	$c_{2,D}$ (mg kg^{-1})	$R_{2,D}$ (%)	$c_{3,D}$ (mg kg^{-1})	$R_{3,D}$ (%)	$c_{0,E}$ (mg kg^{-1})	$c_{2,E}$ (mg kg^{-1})	$R_{2,E}$ (%)	$c_{3,E}$ (mg kg^{-1})	$R_{3,E}$ (%)
acetochlor						<LOQ														
buprofezin									<LOQ					<LOQ					<LOQ	
chlorpyrifos	0.01	1.63	47	1.73	79	<LOQ	0.65		0.65	80	0.05	18.90	100	27.25	98	0.05	4.74	23	9.52	120
cypermethrin I		<LOQ		0.25		0.014	0.96	19	1.39	116				0.18			<LOQ		0.24	
cypermethrin II		<LOQ		0.22		0.013	0.70	15	1.15	131				0.12			<LOQ		0.16	
cypermethrin III		<LOQ		0.32		0.015	0.76	14	1.17	123				0.50			<LOQ		0.10	
cypermethrin IV		<LOQ		0.25		0.014	0.83	16	1.34	130				0.15			<LOQ		0.15	
diazinon		<LOQ		<LOQ			<LOQ		<LOQ			0.04		0.05	91		<LOQ		<LOQ	
malathion		<LOQ					0.34		0.36	85		0.25		0.32	86		0.07		0.10	84
methidathion	<LOQ	0.22		0.22	75	<LOQ	0.04		0.04	80	0.01	3.42	64	4.70	93	0.01	1.64	31	2.60	95
o,p DDT							0.19		0.08	33		0.15		0.07	32					
p,p′-dde	<LOQ	<LOQ					0.05		0.04	69		0.04		0.03	58		<LOQ			
p,p′-ddT		<LOQ					0.16		0.27	134		0.13		0.27	141					
parathion-methyl												0.12		0.10	55					
phosalone																	<LOQ		<LOQ	
plrimiphos-methyl						<LOQ														
profenofos	<LOQ																			

[a]Abbreviations: $c_{0,B}$, $c_{0,C}$, $c_{0,D}$ and $c_{0,E}$, initial concentrations of the pesticides in the roses; $c_{2,B}$, $c_{2,C}$, $c_{2,D}$, and $c_{2,E}$, quantified concentrations of the pesticides in the concrete; $c_{3,B}$, $c_{3,C}$, $c_{3,D}$, and $c_{3,E}$, quantified concentrations of the pesticides in the absolute; $R_{2,B}$, $R_{2,C}$, $R_{2,D}$, and $R_{2,E}$, recovery rates between the maximum theoretical concentrations of pesticides in the concrete and the quantified pesticide concentrations in the concrete; $R_{3,B}$, $R_{3,C}$, $R_{3,D}$, and $R_{3,E}$, recovery rates between the maximum theoretical concentrations of pesticides in the absolute and the quantified pesticide concentrations in the absolute.

DOI: 10.1021/acs.jafc.5b00985
J. Agric. Food Chem. 2015, 63, 4922−4932

Table 4. Summary of the Minimum and Maximum Pesticide Concentrations in Each Sample from the Turkish Fields and Corresponding Recovery Rates[a]

	in rose		in concrete				in absolute			
	times detected (>LOQ)	$c_{0,min}$–c_{0max} (mg kg^{-1})	times detected (>LOQ)	$c_{2,min}$–$c_{2,max}$ (mg kg^{-1})	$R_{2,min}$–$R_{2,max}$ (%)	$R_{2,model}$ (%)	times detected (>LOQ)	$c_{3,min}$–$c_{3,max}$ (mg kg^{-1})	$R_{3,min}$–$R_{3,max}$ (%)	$R_{3,model}$ (%)
diazinon	0		4 (1)	0.04			4(1)	0.05	91	69
acetochlor	1 (0)		0				0			
parathion-methyl	0		1 (1)	0.12			1 (1)	0.09	55	68
pirimiphos-methyl	1 (0)		0				0			
malathion	0		4 (3)	0.07–0.34			3 (3)	0.10–0.36	84–86	76
chlorpyrifos	4 (3)	0.01–0.05	4 (4)	0.65–18.9	23–100	65	4 (4)	0.65–27.25	79–120	78
methidathion	4 (2)	0.01	4 (4)	0.04–3.42	31–64	159	4 (4)	0.04–4.70	75–95	76
buprofezin	0		0				3 (0)			
profenofos	1 (0)		0				0			
p,p′-DDE	1 (0)		4 (2)	0.04–0.05			2 (2)	0.03–0.04	58–69	80
o,p-DDT	0		2 (2)	0.15– 0.19			2 (2)	0.07–0.08	32–33	57
p,p′-DDT	0		2 (2)	0.13– 0.16			2 (2)	0.27	134–141	85
phosalone	0		1 (0)				1 (0)			
cypermethrin I		0.01		0.96	19	42		0.18–1.39	116	83
cypermethrin II	1 (1)	0.01	3 (1)	0.7	15	46	4 (4)	0.12–1.15	131	82
cypermethrin III		0.02		0.76	14	39		0.5–1.17	123	84
cypermethrin IV		0.01		0.83	16	42		0.15–1.34	130	84

[a]Abbreviations: $c_{0,min}$–$c_{0,max}$, minimum and maximum pesticide concentrations observed in roses from Turkish fields; $c_{2,min}$–$c_{2,max}$, minimum and maximum pesticide concentrations observed in the concrete from the roses cultivated in Turkish fields; $c_{3,min}$–$c_{3,max}$, minimum and maximum pesticide concentrations observed in the absolute from the roses cultivated in Turkish fields; $R_{2,min}$–$R_{2,max}$, minimum and maximum recovery rates between the theoretical concentrations of pesticides in the concrete and the quantified pesticide concentrations in the concrete; $R_{3,min}$–$R_{3,max}$, minimum and maximum recovery rates between the theoretical concentrations of the pesticides in the absolute and the quantified pesticide concentrations in the absolute; $R_{2,model}$, recovery rate observed in model obtained from MIP spiked roses, Table 1, column 7; $R_{3,model}$, recovery rate observed in model obtained from MIP spiked roses, Table 1, column 14.

that were present in the rose flowers were extracted and concentrated in the concrete and in the absolute. Their recovery rates were found to vary during the transformation process from one field to another and, in some cases, were significantly different from the recovery rates observed for our MIP spiked samples. Several parameters should be taken into account to explain these results. As previously detailed, the uncertainty of the quantification of the pesticides in the rose flowers near the LOQ combined with the high concentration factor that occurs during the concrete extraction is one possible explanation. Other explanations include the variation in the recoveries for the concrete extraction (Figure 2: 0.24–0.31%) and the absolute transformation (Figure 2: 60–80%) as well as the variation in rose species (MIP, *Rosa centifolia*; Turkey, *Rosa damascena*) and the differences in the industrial processes. For example, new *n*-hexane was used for each rose extraction of our MIP spiked samples, whereas in Turkey, the solvent was recycled, and cross-contamination could occur. A test of the *n*-hexane before extraction of the roses from field D revealed that chlorpyrifos was present in the solvent. To our knowledge, a different solvent batch was used for the extraction of the roses from field E.

CONCLUSION

This study systematically investigated the behavior of 54 pesticides during the extraction process from rose flowers to rose absolute via rose concrete. We showed that pesticides in the MIP spiked rose flowers were extracted with matrix molecules during the transformation process. With an initial concentration $c_0 \leq 0.1$ mg kg^{-1} in the MIP spiked rose flowers, the pesticides were concentrated to reach approximately 20 mg kg^{-1} in the final absolute. Thus, 34 of the targeted pesticides were concentrated between 100- and 300-fold from the MIP spiked roses to the MIP rose absolute. Three pesticides, fenthion, phorate, and fenamiphos, were concentrated less than 100-fold. Some pesticides, such as pirimiphos-methyl, fenitrothion, mecarbam, chlorobenzilate, phosmet, and azinphos-methyl, were concentrated more than 300-fold in the final absolute.

These results were confirmed by the analysis of rose flowers, concrete, and absolute from 4 treated Turkish fields. Indeed, 17 of the 54 pesticides were detected in at least one of the samples. In the process from the concrete to the absolute, the pesticides were concentrated with recovery rates between 32% (*o,p′*-DDT) and 130% (cypermethrin). In these Turkish fields, the concentration factor from the rose flowers to the absolute varied from 87 (cypermethrin in field C) to 545 (chlorpyrifos in field D). It is important to highlight that, with the exception of chlorpyrifos in fields D and E, none of the detected pesticides were applied to the fields during the year of crop. However, concentrations for these pesticides above 1 mg kg^{-1} were found in the concrete and the absolute. One hypothesis that explains their presence could be the persistence of pesticides over time due to old treatments or cross-contamination resulting from bag storage, solvents, or other crops in the same area as the rose fields.

Although some variation was observed in terms of recovery rates, this study shows for the first time that most of the investigated pesticides present in the raw materials (rose flowers) are extracted into the concrete and the absolute, leading to a significant concentration in these extracts. These results from the rose samples show the importance of controlling pesticide levels in natural extracts. Further investigation should be performed on the nonextracted pesticides, such as fenamiphos, which is approved by regulation, in the absolutes. Moreover, other phenomena, such as pesticide degradations and pesticide transformation, could occur in the plant crop or during the processing of the plant extraction and require further investigation.

DOI: 10.1021/acs.jafc.5b00985
J. Agric. Food Chem. 2015, 63, 4922–4932

AUTHOR INFORMATION

Corresponding Author

*U.J.M.: tel, +33 4 92 07 61 77; fax, +33 4 92 07 61 51; e-mail, Uwe.Meierhenrich@unice.fr; web, www.unice.fr/meierhenrich/.

Notes

The authors declare no competing financial interest.

Funding

We thank the "Association Nationale de la Recherche et de la Technologie" (ANRT) for the CIFRE funding of the Ph.D. thesis of O.T. We acknowledge the financial and scientific support of Waters Co. and International Flavors & Fragrances, LMR Naturals division.

ACKNOWLEDGMENTS

We thank the "Jardins du Musée International de la Parfumerie" for the organic flowers.

REFERENCES

(1) Naves, Y. R. *Technologie et chimie des parfums naturels: essences concrètes, résinoïdes, huiles, et pommades aux fleurs*; Masson: Paris, 1974.

(2) Bayrak, A.; Akgül, A. Volatile oil composition of Turkish rose (Rosa damascena). *J. Sci. Food Agric.* **1994**, *64*, 441−448.

(3) Aycı, F.; Aydınlı, M.; Bozdemir, Ö. A.; Tutaş, M. Gas chromatographic investigation of rose concrete, absolute and solid residue. *Flavour Fragrance J.* **2005**, *20*, 481−486.

(4) Kurkcuoglu, M.; Baser, K. Studies on Turkish rose concrete, absolute, and hydrosol. *Chem. Nat. Compd.* **2003**, *39*, 457−464.

(5) Aydinli, M.; Tutaş, M. Production of rose absolute from rose concrete. *Flavour Fragrance J.* **2003**, *18*, 26−31.

(6) Garland, S. M.; Menary, R. C.; Davies, N. W.; Oliver, G. S. Practical approaches to the analyses for pesticide residues in essential oils; Rural Industries Research and Development Corporation, Australian Government, Publication No. 04/109, 2004; p 105.

(7) Tascone, O.; Roy, C.; Filippi, J.-J.; Meierhenrich, U. J. Use, analysis, and regulation of pesticides in natural extracts, essential oils, concretes, and absolutes. *Anal. Bioanal. Chem.* **2014**, *406*, 971−980.

(8) Fillatre, Y.; Rondeau, D.; Bonnet, B.; Daguin, A.; Jadas-Hécart, A.; Communal, P.-Y. Multiresidue analysis of multiclass pesticides in lavandin essential oil by LC/MS/MS using the scheduled selected reaction monitoring mode. *Anal. Chem.* **2010**, *83*, 109−117.

(9) Fillâtre, Y.; Rondeau, D.; Daguin, A.; Jadas-Hecart, A.; Communal, P.-Y. Multiresidue determination of 256 pesticides in lavandin essential oil by LC/ESI/sSRM: advantages and drawbacks of a sampling method involving evaporation under nitrogen. *Anal. Bioanal. Chem.* **2014**, *406*, 1541−1550.

(10) Barrek, S.; Paisse, O.; Grenier-Loustalot, M.-F. Analysis of pesticide residues in essential oils of citrus fruit by GC−MS and HPLC−MS after solid-phase extraction. *Anal. Bioanal. Chem.* **2003**, *376*, 157−161.

(11) Garland, S. M.; Davies, N. W.; Menary, R. C. The dissipation of tebuconazole and propiconazole in boronia (Boronia megastigma Nees). *J. Agric. Food Chem.* **2004**, *52*, 6200−6204.

(12) Groenewoud, K. M.; Davies, N. W.; Menary, R. C. Determination of propiconazole residue in boronia extract (concrete). *J. Agric. Food Chem.* **1995**, *43*, 1230−1232.

(13) Tascone, O.; Shirshikova, M.; Roy, C.; Meierhenrich, U. J. Pesticide determination in rose petals using dispersive solid-phase extraction followed by gas chromatography-tandem mass spectrometry. *Anal. Bioanal. Chem.* **2014**, *406*, 8041−8048.

(14) Tascone, O.; Roy, C.; Uwe, M. Pesticide determination in rose concrete and rose absolute using dispersive solid-phase extraction followed by gas chromatography-tandem mass spectrometry. *Flavour and Fragrance Journal* **2015**, DOI: 10.1007/s00216-014-8270-1.

(15) Maštovská, K.; Lehotay, S. J. Evaluation of common organic solvents for gas chromatographic analysis and stability of multiclass pesticide residues. *Journal of Chromatography A* **2004**, *1040*, 259−272.

(16) Jayashree, R.; Vasudevan, N. Persistence and distribution of endosulfan under field condition. *Environ. Monit. Assess.* **2007**, *131*, 475−487.

DOI: 10.1021/acs.jafc.5b00985
J. Agric. Food Chem. 2015, 63, 4922−4932

JOURNAL OF AGRICULTURAL AND FOOD CHEMISTRY

Article

pubs.acs.org/JAFC

Analysis of Polynuclear Aromatic Hydrocarbons in Olive Oil after Solid-Phase Extraction Using a Dual-Layer Sorbent Cartridge Followed by High-Performance Liquid Chromatography with Fluorescence Detection

Katherine K. Stenerson,* Olga Shimelis, Michael R. Halpenny, Ken Espenschied, and Maochun M. Ye

Sigma-Aldrich, 595 North Harrison Road, Bellefonte, Pennsylvania 16823, United States

ABSTRACT: A simple and easy direct solid-phase extraction (SPE) method was developed for the analysis of polynuclear aromatic hydrocarbons (PAHs) in olive oil using a dual-layer cartridge containing activated Florisil and a mixture of octadecyl (C_{18})-bonded and zirconia-coated silicas. Undiluted olive oil was applied directly to the SPE cartridge, and the sample was eluted with acetonitrile solvent. Background in the extract was found to be low enough for either gas chromatography–mass spectrometry (GC–MS) or high-performance liquid chromatography with fluorescence detection (HPLC–FLD) analysis. Average recoveries for 16 different PAHs from spiked olive oil replicates were >75%, with intraday precisions of <20% relative standard deviation (% RSD). Detection limits ranged from 0.2 to 1.0 μg/kg and, specifically for the PAHs listed in EC Regulation 835/2011, benzo(*a*)anthracene, chrysene, benzo(*b*)fluoranthene, and benzo(*a*)pyrene, were from 0.3 to 0.7 μg/kg. The method was then applied to determine the PAH content present in commercial samples of refined versus extra-virgin olive oils.

KEYWORDS: *polynuclear aromatic hydrocarbons, PAHs, olive oil, solid-phase extraction, SPE, HPLC*

INTRODUCTION

Polynuclear aromatic hydrocarbons (PAHs) are a group of lipophilic compounds comprised of two or more fused aromatic rings. They are ubiquitous in the environment, resulting from natural combustion, such as volcanic eruptions and forest fires, and from man-made activities such as cigarette smoke, automobile exhaust, coal production, and other industrial processes.[1−3] Their occurrence in edible oils can be a result of environmental exposure to particulates contaminated with PAHs and of processes used to produce the oil, such as exposure to combustion gases in drying steps.[2−4] In the case of olive oil, PAH contamination can occur directly on the fruit itself through exposure to exhaust from harvesting equipment and from air pollution in the vicinity of the olive grove.[1] Processes used in the production of refined grades of olive oils can influence PAH content, such as processing steps prior to refining, and decolorization with carbon or clay. In the latter case, PAH content can be reduced as a result of decolorization and/or bleaching.[1,5,6]

A major source of human exposure to PAHs is through food, and in 2002, the European Scientific Committee on Food recommended the monitoring of food for these compounds. It was concluded that benzo(*a*)pyrene could be used as a marker of the content of carcinogenic PAHs present.[7] This recommendation was then adopted by the International Olive Oil Council for olive oil and olive pomace oil and by the European Union (EU) for oils and fats intended for human consumption, with both setting a maximum contaminant level of 2 μg/kg for benzo(*a*)pyrene.[8−10] More recently, the European Union has amended its regulation of PAH content in edible oils to include maximum contaminant levels for additional PAHs. Specifically, a maximum level of 10 μg/kg for the sum of benzo(*a*)anthracene, chrysene, benzo(*b*)-fluoranthene, and benzo(*a*)pyrene together, in addition to the 2 μg/kg level for benzo(*a*)pyrene only.[11] These regulations have driven the requirement for routine testing of olive oils for PAHs and created a need for a simple and rapid testing method.

Established methods (ISO and CEN) exist for the analysis of PAHs in edible oils, and encompass a variety of somewhat complicated and laborious extraction and cleanup techniques, including column chromatography, liquid extraction followed by solid-phase extraction (SPE), online SPE, and direct dilution followed by gel permeation chromatography (GPC).[11−15] Alternate sample preparation methods have also been proposed. A review of methodology performed by Moret and Conte in 2000 for PAHs in fats and oils found three of the most common procedures for extraction to be liquid–liquid partition, caffeine complexation, and saponification.[4] With all of these approaches, a second step for purification of the sample extracts was required, most commonly using column chromatography with silica gel, Florisil, alumina, or polymeric resins.[4,16,17] Since 2000, researchers have more frequently used SPE in place of column chromatography for cleanup. These newer approaches include direct dilution of the oil followed by silica gel SPE and/or GPC, and liquid–liquid extraction (LLE) followed by SPE with C_{18}, silica gel, or amino-phase sorbents.[2,5,18−22] While SPE cleanup requires less solvent than column chromatography, all of these methodologies still require a separate extraction step. Also, if GPC cleanup is used, special instrumentation is required. A more recent method-

Received: January 6, 2015
Revised: April 29, 2015
Accepted: May 4, 2015
Published: May 4, 2015

ACS Publications © 2015 American Chemical Society

DOI: 10.1021/jf506299f
J. Agric. Food Chem. 2015, 63, 4933−4939

ology review performed in 2010 by Plaza-Bolaños et al. for analysis of PAH in food and beverages included reference to a quick and easy direct SPE method for the analysis of benzo(*a*)pyrene in olive oil using a dual-layer SPE cartridge.[3] This method, introduced by Bogusz et al. in 2004, describes a combination of the extraction and cleanup steps by direct loading of undiluted olive oil on a dual-layer SPE cartridge containing Florisil and C_{18}. Subsequent elution of PAHs was accomplished with acetonitrile. The resulting extract was then concentrated and analyzed by both high-performance liquid chromatography (HPLC) and gas chromatography−mass spectrometry (GC−MS).[23] This simplified combined extraction and cleanup procedure did not require the use of large solvent volumes or special instrumentation; however, data were not presented for PAHs other than benzo(*a*)pyrene. This direct SPE approach provides an easy and inexpensive method for benzo(*a*)pyrene analysis; however, in light of the amended EU regulation that requires monitoring of additional PAHs, a need exists for a method that can be used to test a wider range of these compounds.

The purpose of this study was to develop a quick and easy direct SPE method based on the work performed by Bogusz et al. for the extraction of 2−6-ring PAHs from olive oil. The goals of the method were adequate sensitivity to allow testing for EU regulations, speed, ease of use, and reduced solvent consumption over other methods. In addition to conventional Florisil and C_{18} sorbents, the addition of zirconia-coated silica was investigated for retention of a fatty matrix. Zirconia-coated silica was originally developed for removing phospholipids from biological samples prior to analysis of drugs and other small molecules. The empty d orbitals of zirconia act as a Lewis acid (i.e., electron acceptor) and interact with phospholipids through the electron pair on the oxygen atom within the phosphate moiety.[24] When that concept was extended to other types of lipids, it was believed that zirconia should be able to interact in a similar manner with the OH groups found in acylglycerols, which are a major component of fats. This has been applied in recently published works in which zirconia-coated silica was used as a cleanup sorbent in quick, easy, cheap, effective, rugged, and safe (QuEChERS) methodology with fat-containing food samples. It was successfully applied as a sorbent in the cleanup of catfish samples for analysis of PAHs, polychlorinated biphenyls, and flame retardants and in the cleanup of avocado and almond extracts in the analysis of pesticides.[25,26] For these reasons, it was theorized that the retention mechanism provided by the zirconia-coated silica, combined with C_{18} and Florisil, would be useful in the retention of the fats present in olive oil. At the same time, the zirconia-coated silica was not expected to be detrimental to the recovery of the PAHs. The final optimized method used a simple SPE cartridge format to provide direct extraction of PAHs from olive oil without the need for special instrumentation or additional cleanup steps.

MATERIALS AND METHODS

Samples. Samples of olive oils were obtained at local supermarkets. Labeling indicated the oils to be either "extra-light olive oil" or "extra-virgin olive oil". All samples were stored at room temperature prior to extraction and analysis.

A single brand of extra-light olive oil was used for all validation studies. Spiked samples were prepared by the addition of a PAH spiking solution in methylene chloride to the oil, followed by thorough mixing. Samples were then allowed to sit for a minimum of 1 day at room temperature prior to extraction.

Standards. A standard mixture containing the United States Environmental Protection Agency (U.S. EPA) PAHs listed on the target compound list (TCL) at 2000 μg/mL in methylene chloride was obtained from Supelco (Bellefonte, PA) and used for preparation of spiking and calibration standards. Spiking solutions for the olive oil samples were prepared by dilution of the standard in methylene chloride. Calibration standards were prepared by dilution of the PAH standard into acetonitrile. Benzo(*b*)chrysene was used as an internal standard (IS) and obtained from Accustandard (New Haven, CT) as a neat material. An IS mother solution was prepared by dissolving 3 mg of benzo(*b*)chrysene into 10 mL of 1:1 benzene/methylene chloride. This solution was then diluted into acetonitrile to prepare a spiking solution for samples and standards.

Materials. Dual-layer SPE cartridges were obtained from Supelco (Bellefonte, PA). The cartridges consisted of 12 mL polypropylene tubes containing 1.25 g of activated Florisil in the top sorbent bed and 1.25 g of a mixture of zirconia-coated silica and C_{18} in a ratio of 1:2.5 in the bottom bed. Acetone and acetonitrile solvents were obtained from Aldrich Chemical Co. (Milwaukee, WI) and of the highest purity available.

Sample Preparation. The SPE cartridges were first conditioned by allowing 10 mL of acetone to flow through under gravity and then dried by applying vacuum at −15 in. Hg for 10 min. Samples (500 μL, approximately 0.4 g) of olive oil were weighed directly onto the dried SPE cartridge and allowed to penetrate the frit. The IS, benzo(*b*)-chrysene in acetonitrile, was then added directly. Direct addition of the IS to the oil on the SPE cartridge was found to be easier and more reproducible than spiking the oil prior to loading. Elution was performed using 15 mL of acetonitrile solvent, setting a collection rate of approximately 1 drop/s. The eluent was concentrated under nitrogen purge at 40 °C to a final volume of 0.2 mL and analyzed directly by GC−MS for background evaluation during method development, or by HPLC−fluorescence detection (FLD) for PAH detection and quantitation.

Instrumentation. The background remaining in the olive oil extracts was evaluated using GC on an Agilent (Little Falls, DE) 6890 gas chromatograph connected to a 5973N mass spectral detector. The GC column used was a SLB-5 ms (Supelco, Bellefonte PA), bonded and highly cross-linked silphenylene polymer, with polarity equivalent to poly(5% diphenyl/95% dimethylsiloxane). Column dimensions were 20 m × 0.18 mm inner diameter, 0.18 μm. The GC oven conditions were 60 °C, hold for 1 min, ramp at 15 °C/min to 250 °C, ramp at 8 °C/min to 330 °C, and hold for 10 min. The MS interface temperature was 330 °C, and source and quadrupole temperatures were 250 and 200 °C, respectively. Helium was used as the carrier gas at 1 mL/min, with constant flow. The injection port temperature was set to 300 °C. The injection volume was 1 μL and was introduced into a 4 mm inner diameter tapered FocusLiner using a pressure-pulsed injection of 50 psi until 0.75 min, at which point the splitter was opened. The total flow to the inlet was set to 75 mL/min. The mass spectrometer was run in full-scan mode, with a scan range of m/z 40−450, and tuned using a standard autotune macro.

The PAH content was analyzed by HPLC on a Dionex Ultimate 3000 UHPLC system connected to a 3000RS programmable fluorescence detector (Thermo Scientific, Sunnyvale, CA). The system was equipped with a quaternary pumping system and an autosampler. Chromeleon Client 6.8 SR11 software was used for instrumental control and data analysis. Chromatographic analysis was performed on a Supelcosil LC-PAH column (Supelco, Bellefonte, PA) with dimensions of 25 cm × 4.6 mm inner diameter, 5 μm particle size. A water/acetonitrile gradient was used at a flow rate of 1.4 mL/min, starting at 40% acetonitrile, holding 5 min, ramp to 100% acetonitrile over 15 min, and holding at 100% acetonitrile for 12 min. The excitation and emission wavelengths were programmed as described in Table 1. The sample injection volume was 20 μL, and the column temperature was held at 30 °C.

Sample Analysis for PAH Content. As shown in the chromatogram of a spiked olive oil sample in Figure 1, no background interference was noted co-eluting with any of the analyte peaks. This allowed PAHs to be identified in all samples by retention time match

DOI: 10.1021/jf506299f
J. Agric. Food Chem. 2015, 63, 4933−4939

Table 1. Acquisition and Detector Parameters for PAHs Analyzed by HPLC−FLD

peak number	compound	t_R[a] (min)	excitation/emission wavelengths (nm)
1	naphthalene	13.08	225/320
2	acenaphthene	15.38	225/320
3	fluorene	15.65	225/320
4	phenanthrene	16.53	250/368
5	anthracene	17.30	250/368
6	fluoranthene	18.15	237/440
7	pyrene	18.86	237/440
8	benzo(*a*)anthracene	20.56	265/380
9	chrysene	21.00	265/380
10	benzo(*b*)fluoranthene	22.43	280/420
11	benzo(*k*)fluoranthene	23.08	280/420
12	benzo(*a*)pyrene	24.03	280/420
13	dibenzo(*a*,*h*)anthracene	24.89	280/420
14	benzo(*g*,*h*,*i*)perylene	26.62	300/466
15	indeno(1,2,3-*cd*)pyrene	27.03	300/466
16	benzo(*b*)chrysene (IS)	28.12	300/466

[a] t_R = retention time.

to peaks in the mid-level calibration standard (Table 1). Quantitation of sample extracts was performed against a multi-point calibration curve prepared in acetonitrile. Corresponding concentrations for each identified PAH peak were determined using peak area and were calculated relative to the peak area of the IS. Concentrations were then corrected for sample weight to a final concentration of micrograms of PAH per kilogram of sample (μg/kg). Olive oil blanks (unspiked extra-light olive oil) were analyzed during method validation studies and used for blank correction where indicated. SPE method blanks (solvent and IS, no olive oil) were used to monitor PAH background in the laboratory during the extraction process.

Method Validation. Validation was performed following procedures and protocols described by the International Union of Pure and Applied Chemistry (IUPAC) and the Eurachem guide to method validation.[27,28] Method linearity was determined with samples of extra-light olive oil spiked at five levels from 0.5 to 20 μg/kg and analyzed in triplicate. Unspiked olive oil was analyzed and used for blank subtraction. The average amount of each PAH was measured in μg/kg, blank-corrected when necessary, and plotted against the spiked concentration. Correlation values (r^2) were determined for each compound using regression analysis in Excel. Method accuracy (percent recovery) and intraday precision [percent relative standard deviation (% RSD)] were determined using replicates of extra-light olive oil samples spiked at 2 μg/kg, prepared and analyzed in a single day (n = 8).[29] The spiking level was chosen based on the maximum levels for PAHs in edible oils listed in the amendment to EC Regulation 1881/2006.[11] The approaches for calculation of limit of detection (LOD) and limit of quantitation (LOQ) were taken from the Eurachem guide. LOD and LOQ were calculated for each PAH using 3× and 10× the standard deviation of the average amounts measured in the n = 8 set of 2 μg/kg of spiked olive oil samples. Standard deviation values were blank-corrected using the equation: $s'_o = s_o(1/n + 1/n_b)^{1/2}$, where s_o is the standard deviation of the average amount of PAH measured in the set of spiked replicates (without blank correction), n is the number of sample replicates (n = 8), and n_b is the number of blank or unspiked olive oil replicates (n_b = 3).[28] Interday precision (% RSD) was determined from duplicate olive oil spikes (2 μg/kg) prepared and analyzed on three different days (n = 6).

RESULTS AND DISCUSSION

Method Optimization. Optimization of the final SPE method involved evaluation of the elution solvent, maximum sample capacity, and cartridge conditioning. These parameters were optimized to balance acceptable PAH recovery and low background. While HPLC was used to determine PAH recovery, background was evaluated using GC−MS in full-scan mode. This later analytical technique was chosen because of its ability to detect fatty components that may not produce a signal by HPLC−FLD but can still lead to chromatographic anomalies, such as an unstable baseline or band broadening.

For the elution step, 10 mL of acetonitrile was used initially; however, recoveries for 5- and 6-ring PAHs were <50%. The addition of methylene chloride to the elution solvent was then investigated, and it was found that the addition of ≥10% methylene chloride to the acetonitrile elution solvent was necessary to increase recoveries. However, methylene chloride had the unwanted effect of increasing background, as determined by GC−MS. The total ion chromatogram (TIC) in Figure 2 shows the background remaining in an olive oil extract after elution from the SPE cartridge using 15 mL of acetonitrile. The TIC in Figure 3 shows the same sample after elution with 10 mL of a mixture of 90:10 acetonitrile/methylene chloride. The peaks eluting in the 12−13 min region were determined by spectral match to be fatty acid esters, and the large peak eluting after 16 min was determined by spectral match to be squalene. This indicated that methylene chloride in the elution solvent was preventing adsorption of fatty components in the olive oil onto the Florisil bed. The fatty

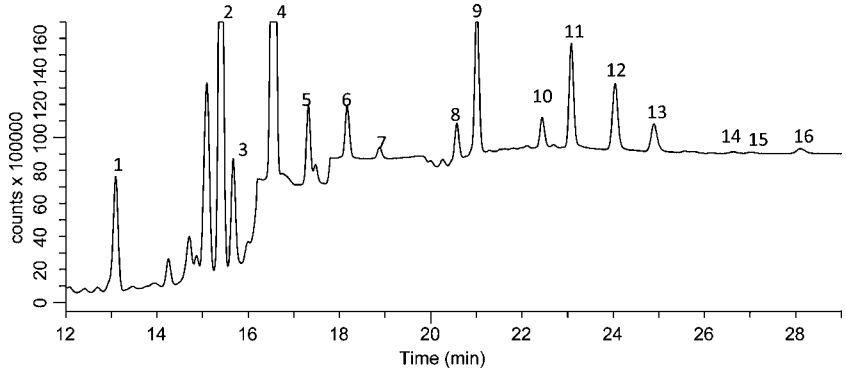

Figure 1. HPLC−FLD analysis of 2 μg/kg of spiked olive oil sample extract. Identities of PAH peaks: (1) naphthalene, (2) acenaphthene, (3) fluorene, (4) phenanthrene, (5) anthracene, (6) fluoranthene, (7) pyrene, (8) benzo(a)anthracene, (9) chrysene, (10) benzo(*b*)fluoranthene, (11) benzo(*k*)fluoranthene, (12) benzo(*a*)pyrene, (13) dibenzo(*a*,*h*)anthracene, (14) benzo(*g*,*h*,*i*)peryelene, (15) indeno(1,2,3-*cd*)pyrene, and (16) benzo(*b*)chrysene (IS).

DOI: 10.1021/jf506299f
J. Agric. Food Chem. 2015, 63, 4933−4939

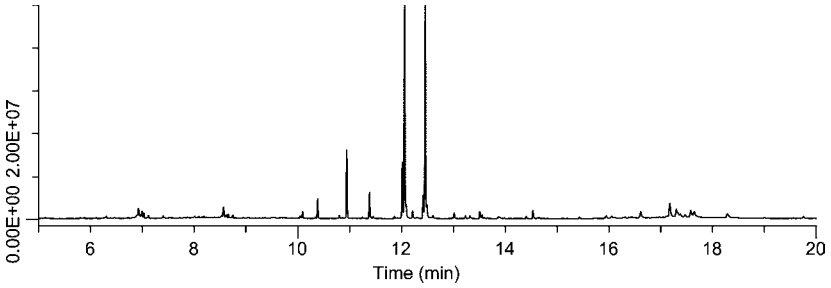

Figure 2. TIC of olive oil extract eluted with 15 mL of acetonitrile, with no acetone conditioning step prior to sample loading. The peaks eluting in the 11−13 min range are primarily C_{16} and C_{18} fatty acid esters.

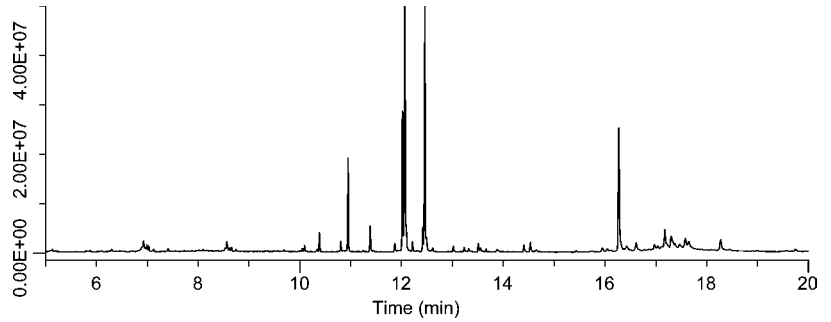

Figure 3. TIC of olive oil extract eluted with 10 mL of 90:10 acetonitrile/methylene chloride, with no acetone conditioning step prior to sample loading. The largest peaks eluting in the 11−13 min range are C_{16} and C_{18} fatty acid esters. Squalene is the large peak eluting just after 16 min.

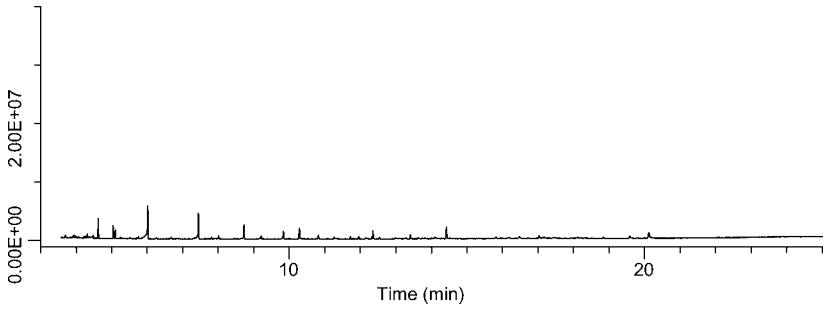

Figure 4. TIC of olive oil extract with the final optimized method, acetone conditioning and drying step, and elution with 15 mL of acetonitrile.

Table 2. Method Linearity in the Range of 0.5−20 μg/kg

	average concentration measured at the indicated spiking level (each n = 3)					
	0.5 μg/kg	1 μg/kg	5 μg/kg	10 μg/kg	20 μg/kg	r^2
naphthalene	6.4	1.3	4.5	8.3	28.1	0.929
acenaphthene	1.5	0.7	3.6	8.0	10.3	0.963
fluorene	2.0	1.0	3.8	8.5	24.7	0.978
phenanthrene	4.3	0.6	4.3	9.2	16.1	0.968
anthracene	0.8	0.9	3.9	8.4	22.9	0.989
fluoranthene	1.5	1.1	4.4	8.5	25.3	0.981
pyrene	1.0	1.2	4.4	8.9	24.8	0.987
benzo(*a*)anthracene	0.8	0.9	4.4	8.9	25.6	0.986
chrysene	0.9	1.0	4.4	8.4	15.1	0.999
benzo(*b*)fluoranthene	1.1	1.1	4.6	8.5	25.1	0.983
benzo(*k*)fluoranthene	0.5	0.8	4.2	8.2	22.6	0.989
benzo(*a*)pyrene	0.5	0.8	4.4	8.0	23.5	0.987
dibenzo(*a*,*h*)anthracene	0.5	0.8	4.2	7.9	18.5	0.997
benzo(*g*,*h*,*i*)perylene	0.2	0.7	3.9	6.4	18.4	0.990
indeno(1,2,3-*cd*)pyrene	0.2	0.7	4.1	6.6	18.9	0.992

acid esters form as a result of these components breaking through the Florisil bed and contacting the zirconia-coated silica/C_{18} sorbent mix in the bottom bed. A combination of residual methanol in this sorbent along with the zirconia (which

DOI: 10.1021/jf506299f
J. Agric. Food Chem. 2015, 63, 4933−4939

Table 3. Method Accuracy (Percent Recovery), LOD, LOQ, and Intraday (n = 8) and Interday (n = 6) Precision Measurements (% RSD)[a]

	average amount recovered (μg/kg)	s'_o[b]	percent recovery (%)	LOD[c] (μg/kg)	LOQ[d] (μg/kg)	% RSD[e] intraday (n = 8) (%)	% RSD[e] interday (n = 6) (%)
naphthalene	1.65	0.34	83	1.01	3.38	9	27
acenaphthene	1.67	0.10	83	0.30	1.00	7	36
fluorene	1.83	0.14	92	0.43	1.45	9	17
phenanthrene	2.25	0.20	113	0.61	2.04	6	68
anthracene	1.58	0.11	79	0.32	1.07	8	23
fluoranthene	2.19	0.09	110	0.26	0.88	5	24
pyrene	2.19	0.12	109	0.37	1.23	6	21
benzo(*a*)anthracene	2.08	0.22	104	0.66	2.19	15	10
chrysene	2.09	0.09	104	0.26	0.85	5	10
benzo(*b*)fluoranthene	2.36	0.11	118	0.33	1.11	7	12
benzo(*k*)fluoranthene	2.54	0.06	127	0.19	0.65	4	16
benzo(*a*)pyrene	2.19	0.10	110	0.30	1.01	6	24
dibenzo(*a*,*h*)anthracene	2.31	0.13	116	0.40	1.33	9	15
benzo(*g*,*h*,*i*)perylene	2.07	0.19	103	0.57	1.91	14	15
indeno(1,2,3-*cd*)pyrene	2.07	0.22	103	0.67	2.24	16	13

[a]Parameters were measured using extra-light olive oil samples spiked at 2 μg/kg. [b]s'_o = standard deviation (n = 8). [c]LOD = limit of detection. [d]LOQ = limit of quantitation. [e]% RSD = percent relative standard deviation (%).

acts as a Lewis acid catalyst) results in transesterification of the fatty components to form fatty acid esters. The elution volume using 100% acetonitrile was then increased from 10 to 15 mL. This increased volume produced PAH recoveries comparable to the addition of 10% methylene chloride but did not have the same effect on the background.

Using 15 mL of acetonitrile for elution, the capacity of the SPE cartridge was studied with different sample sizes of olive oil from 0.4 to 1.4 g. Squalene was detected by GC−MS in extracts prepared from sample sizes of >0.7 g. Sample sizes of >0.9 g exhibited breakthrough, which was observed as oil droplets in the final extract. On the basis of these findings, a sample size of 0.4 g was chosen for the final method, to ensure that the capacity of the sorbents for retaining background was not exceeded.

The final step in method optimization was investigation of a conditioning step prior to loading the olive oil sample onto the SPE cartridge. Because of the mixed functionality of the sorbents used in the cartridge, a traditional conditioning scheme was not employed. Instead, conditioning with acetone followed by drying of the cartridge was used. This step produced extracts with lower background, as determined by GC−MS. The TIC in Figure 4 shows the background in an olive oil extract prepared using an acetone conditioning step as part of the SPE procedure. A significant reduction in background was observed over the same procedure without the acetone conditioning step (Figure 2). It is believed that the acetone conditioning removes residual water present on the Florisil, making it more adsorptive to fatty acids. It could also be expelling residual methanol from the zirconia-coated silica/C_{18} sorbent mix, thus preventing the catalytic transesterification reaction discussed earlier. The dry time for the SPE cartridges of 10 min was increased from an initial time of 5 min to ensure that all residual acetone was removed prior to sample loading.

Method Validation Parameters and Detection Levels. Parameters determined for method linearity are summarized in Table 2. The average values measured at each spiking level are reported after blank subtraction. Correlation values were >0.92 for all PAHs and >0.98 for 11 of the 15 target compounds. The highest deviations in measured versus spiked values were observed at the 0.5 μg/kg spiking level, indicating that this is below the LOQ for the method. Especially for the lighter PAHs (naphthalene through pyrene), accurate quantitation could not be obtained at 0.5 μg/kg. These PAHs were detected in the unspiked olive oil and, subsequently, affected low-level quantitation.

Method parameters summarizing accuracy, standard deviation, LOD, LOQ, and intraday (n = 8) and interday (n = 6) precision are presented in Table 3. Accuracy, determined as recovery, was >75% for all PAHs, which meets requirements described in ISO Method 15753 and CEN 16621 and for benzo(*a*)pyrene in EU Regulation EC 333/2007.[13,15,29] Recoveries were better than those obtained by Moret using silica gel SPE and comparable to methods using GPC cleanup.[2,5,18,22] In the case of benzo(*a*)pyrene, recovery was higher than that reported previously by direct SPE using the Florisil/C_{18} dual-layer tube.[24] Looking specifically at the four PAHs designated in EU Regulation 835/2011, benzo(*a*)-anthracene, chrysene, benzo(*b*)fluoranthene, and benzo(*a*)-pyrene, all had recoveries of 100−110%. LOD values were <1 μg/kg for all PAHs, except naphthalene, and LOQ values ranged from 0.5 to 3.4 μg/kg. Higher LOD and LOQ values for naphthalene and phenanthrene could be attributed to the baseline levels of 3.9 and 2.8 μg/kg, respectively, present in the olive oil used for spiking.

Intraday precision was acceptable, with % RSD values of <20% for all PAHs. Interday precision over 3 different days with two different analysts performing the method and spanning a 9 month time period was <25% RSD for most of the PAHs. In the case of naphthalene, acenaphthene, and phenanthrene, high background levels of these PAHs were detected in SPE method blanks on one of the test days (11.6, 1.1, and 3.6 ng/cartridge, respectively) and contributed to variation in the measurement of samples.

Analysis of Commercial Olive Oil Samples. Virgin olive oils cannot be processed in any way that will alter them from their natural composition. Refined olive oils are defined as those obtained from the processing of virgin olive oils, as long as the processes do not alter the glyceridic structure of the oil.[30] Previous studies have shown that the refining process, which

DOI: 10.1021/jf506299f
J. Agric. Food Chem. 2015, 63, 4933−4939

Table 4. PAH Levels in Commercially Purchased Olive Oil Samples, Measured in μg/kg, with Each at an Average of Three Replicate Samples

type[a]	extra-light		extra-light		extra-virgin, first cold press		extra-virgin, first cold press	
origin[a]	Spain, Turkey, and Morocco		Italy, Spain, Greece, and Tunisia		Italy		United States	
	μg/kg	% RSD (%)[b]	μg/kg	% RSD (%)[b]	μg/kg	% RSD (%)[b]	μg/kg	% RSD (%)[b]
naphthalene	5.20	8	<LOD[c]		14.9	6	7.4	7
acenaphthene	0.3	11	0.3	0.7	1.6	11	0.9	13
fluorene	ND[d]		3.9	19	ND		ND	
phenanthrene	3.3	20	8.3	0.3	18.9	10	6.5	11
anthracene	<LOD		0.4	11	0.6	42	<LOD	
fluoranthene	0.5	16	0.8	12	5.4	8	1.4	12
pyrene	0.6	26	0.8	12	5.7	14	1.1	11
benzo(*a*)anthracene	ND		ND		<LOD		ND	
chrysene	ND		ND		1.2	12	<LOD	
benzo(*b*)fluoranthene	ND		ND		<LOD		<LOD	
benzo(*k*)fluoranthene	ND		ND		<LOD		<LOD	
benzo(*a*)pyrene	<LOD		<LOD		<LOD		<LOD	
dibenzo(*a,h*)anthracene	ND		ND		ND		ND	
benzo(*g,h,i*)perylene	ND		ND		<LOD		<LOD	
indeno(1,2,3-*cd*)pyrene	ND		ND		ND		<LOD	

[a]Per product label. [b]% RSD = percent relative standard deviation (%) (n = 3). [c]<LOD = peak detected but below the calculated LOD. [d]ND = no peak detected.

can include neutralization, bleaching, and deodorization of the oil using activated charcoal and/or clays, reduces PAH content.[6,31] Several different samples of commercially purchased olive oils were extracted and analyzed using the described method. Products described as "extra-light olive oil" and "extra-virgin, first cold press" were selected to see if a difference in PAH content could be detected. Information on the product labels of the samples indicated their countries of origin. The extra-light samples consisted of a blend of oils from several different countries. Oils described as "olive oil" are blends of refined and virgin olive oils. Thus, it was expected that the extra-virgin olive oils (EVOOs) would show more PAH content than the refined oils. Samples were analyzed in triplicate, and the average PAH levels measured are reported in Table 4. SPE method blanks were analyzed alongside the olive oil samples and used for blank subtraction of each olive oil analyzed. All PAHs present above the calculated LOD were reported. PAHs indicated as "<LOD" were detected but at levels below the method LOD. "ND" indicates that no PAH was detected. PAH levels were found to be higher in the two EVOO samples than in the "extra-light" oils. This is in agreement with previous data comparing PAH levels in virgin and refined olive oils.[6,32] This difference was attributable mainly to the lighter PAHs of 2−4 rings, which are known to be reduced by the deodorization step used in the processing of refined olive oil.[31] For PAHs of 4−6 rings, chrysene was detected above the LOD in one EVOO sample. None of the PAHs listed in EU Regulation 235/2011 was detected above the 2 and 10 μg/kg total limits described.[11]

The direct SPE method described includes the first use of a zirconia-coated silica in a dual-layer cartridge configuration in the simultaneous extraction and cleanup of olive oil samples for analysis of PAH content. Zirconia was combined with C_{18} and Florisil to retain most of the fatty constituents of olive oil while allowing elution of PAHs with acetonitrile. The matrix background in olive oil extracts was low, as evidenced by GC−MS analysis. The resulting extract in acetonitrile can thus be analyzed directly by either GC−MS or HPLC−FLD without the need for a solvent exchange step. The LOD of the method ranged from 0.2 to 1 μg/kg, and the LOQ of the method ranged from 0.65 to 3.4 μg/kg. At a 2 μg/kg spiking level, recoveries of PAHs were >75%, with precision of <20% RSD for replicate analyses. The method, when applied to olive oils of different origins, was able to detect differences in PAH content between EVOO and refined samples. The number and complexity of process steps in the method is minimal, and solvent usage is reduced compared to previously described methodologies.[2,5,6,12,13,17−22] The method required less time than approaches such as column chromatography, liquid−liquid extraction, and GPC. In addition, the use of expensive glassware, chlorinated solvents, and special instrumentation with associated calibration procedures was not required.

AUTHOR INFORMATION

Corresponding Author

*Telephone: 1-814-359-5781. Fax: 1-814-359-5459. E-mail: katherine.stenerson@sial.com.

Notes

The authors declare the following competing financial interest(s): Zirconia-coated silica is patent-pending technology. The intellectual property rights belong to Sigma-Aldrich. Olga Shimelis and Michael Ye are listed as inventors in patent application number 12/785,160.

REFERENCES

(1) Mafra, I.; Amaral, J.; Oliviera, M. Polycyclic aromatic hydrocarbons in olive oils and other vegetable oils; potential for carcinogenesis. In *Olives and Olive Oil in Health and Disease Prevention*; Preedy, V., Watson, R., Eds.; Oxford Academic Press: London, U.K., 2010; pp 489−498.

(2) Węgrzyn, E.; Grześkiewicz, S.; Poplawska, W.; Glód, B. Modified analytical method for polycyclic aromatic hydrocarbons, using SEC for sample preparation and RP-HPLC with fluorescence detection. Application to different food samples. *Acta Chromatogr.* **2006**, *17*, 233−249.

DOI: 10.1021/jf506299f
J. Agric. Food Chem. 2015, 63, 4933−4939

(3) Plaza-Bolaños, P.; Frenich, A.; Vidal, J. Polycyclic aromatic hydrocarbons in food and beverages. Analytical methods and trends. *J. Chromatogr. A* **2010**, *1217*, 6303−6326.
(4) Moret, S.; Conte, L. J. Polycyclic aromatic hydrocarbons in edible fats and oils: Occurrence and analytical methods. *J. Chromatogr. A* **2000**, *882*, 245−253.
(5) Ballesteros, E.; Sánchez, A.; Martos, N. Simultaneous multi-determination of residues of pesticides and polycyclic aromatic hydrocarbons in olive and olive-pomace oils by gas chromatography/tandem mass spectrometry. *J. Chromatogr. A* **2006**, *1111*, 89−96.
(6) Menichini, E.; Bocca, A.; Merli, F.; Ianni, D.; Monfredini, F. Polycyclic aromatic hydrocarbons in olive oils on the Italian market. *Food Addit. Contam.* **1991**, *8*, 363−369.
(7) European Commission. *Opinion of the Scientific Committee on Food, on the Risks to Human Health of Polycyclic Aromatic Hydrocarbons in Food*; Health and Consumer Protection Directorate General, European Commission: Brussels, Belgium, 2002; Scientific Committee of Food Report SCF/CS/CNTM/PAH/29 Final, pp 63−64.
(8) International Olive Oil Council (IOC). *Detection of Polycyclic Aromatic Hydrocarbons in Edible Olive Oils and Olive-Pomace Oils*; IOC: Madrid, Spain, 2005; Resolution RES-1/93-IV/05.
(9) European Union Commission.. Regulation EC/208/2005 of 4 February 2005 amending Regulation EC/466/2001 as regards polycyclic aromatic hydrocarbons. *Off. J. Eur. Union, L: Legis.* **2005**, *34*, 3−5.
(10) European Union Commission. *Regulation EC/1881/2006 of 19 December 2006 Setting Maximum Levels for Certain Contaminants in Foodstuffs*; European Union Commission: Brussels, Belgium, 2006; Document 2006R1881-EN-01.07.2007-001.001-1, Section 6.1.1.
(11) European Union Commission.. Regulation EC/835/2011 of 19 August 2011 amending Regulation EC/1881/2006 as regards maximum levels for polycyclic aromatic hydrocarbons in foodstuffs. *Off. J. Eur. Union, L: Legis.* **2011**, *215*, 9−16.
(12) International Standard Organization (ISO). *ISO 15302. Animal and Vegetable Fats and Oils—Determination of Benzo(a)pyrene—Reverse Phase High Performance Liquid Chromatography Method*; ISO: Geneva, Switzerland, 2007.
(13) International Standard Organization (ISO). *ISO 15753. Animal and Vegetable Fats and Oils—Determination of Polycyclic Aromatic Hydrocarbons*; ISO: Geneva, Switzerland, 2006.
(14) International Standard Organization (ISO). *ISO 22959. Animal and Vegetable Fats and Oils—Determination of Polycyclic Aromatic Hydrocarbons by On-Line Donor−Acceptor Complex Chromatography and HPLC with Fluorescence Detection*; ISO: Geneva, Switzerland, 2009.
(15) European Committee for Standardization (CEN). *European Technical Specification CEN/TS 16621. Determination of Benzo(a) pyrene, Benzo(a)anthracene, Chrysene, and Benzo(b)fluoranthene in Foodstuffs by High Performance Liquid Chromatography with Fluorescence Detection (HPLC-FD)*; CEN: Brussels, Belgium, 2014.
(16) Cert, A.; Moreda, W.; Pérez-Camino, M. Chromatographic analysis of minor constituents in vegetable oils. *J. Chromatogr. A* **2000**, *881*, 131−148.
(17) Speer, K.; Steeg, E.; Horstmann, P.; Kühn, Th. Determination and distribution of polycyclic aromatic hydrocarbons in native vegetable oils, smoked fish products, mussels and oysters, and bream from the River Elbe. *J. High Resolut. Chromatogr.* **1990**, *13*, 104−111.
(18) Moret, S.; Conte, L. A rapid method for polycyclic aromatic hydrocarbon determination in vegetable oils. *J. Sep. Sci.* **2002**, *25*, 96−100.
(19) Barranco, A.; Alonso-Salces, R.; Bakkali, A.; Berrueta, L.; Gallo, B.; Vicente, F.; Sarobe, M. Solid-phase clean-up in the liquid chromatographic determination of polycyclic aromatic hydrocarbons in edible oils. *J. Chromatogr. A* **2003**, *988*, 33−40.
(20) Guillén, M.; Sopelana, P.; Palencia, G. Polycyclic aromatic hydrocarbons and olive pomace oil. *J. Agric. Food Chem.* **2004**, *52*, 2123−2132.
(21) Moreda, W.; Rodríguez-Acuña, R.; Pérez-Camino, M.; Cert, A. Determination of high molecular mass polycyclic aromatic hydrocarbons in refined olive pomace and other vegetable oils. *J. Sci. Food Agric.* **2004**, *84*, 1759−1764.
(22) Martinez-López, A.; Morales-Noé, A.; Pastor-Garcia, A.; Morales-Rubio, A.; de la Guardia, M. Sample preparation improvement in polycyclic aromatic hydrocarbons determination in olive oils by gel permeation chromatography and liquid chromatography with fluorescence detection. *J. AOAC Int.* **2005**, *88*, 1247−1254.
(23) Bogusz, M.; El Hajj, S.; Ehaideb, Z.; Hassan, H.; Al-Tufail, M. Rapid determination of benzo(*a*)pyrene in olive oil samples with solid-phase extraction and low-pressure, wide-bore gas chromatography−mass spectrometry and fast liquid chromatography with fluorescence detection. *J. Chromatogr. A* **2004**, *1026*, 1−7.
(24) Aurand, C.; Trinh, A.; Ye, C.; Mi, C. *Introducing HybridSPE—Precipitation Technology for Pharmaceutical Bioanalytical Sample Preparation*; Supelco, Division of Sigma-Aldrich: Bellefonte, PA, 2008; Reporter 26.3, pp 3−6.
(25) Sapozhnikova, E.; Lehotay, S. Multi-class, multi-residue analysis of pestcides, polychlorinated biphenyls, polycyclic acromatic hydrocarbons, polybrominated diphenylethers and novel flame retardants in fish using fast, low-pressure gas chromatography−tandem mass spectrometry. *Anal. Chim. Acta* **2013**, *758*, 80−92.
(26) Rajaski, Ł.; Lozano, A.; Uclés, A.; Ferrer, C.; Fernández-Alba, A. Determination of pesticide residues in high oil vegetal commodities by using various multi-residue methods and clean-ups followed by liquid chromatography tandem mass spectrometry. *J. Chromatogr. A* **2013**, *1304*, 109−120.
(27) Thompson, M.; Ellison, S.; Wood, R. Harmonized guidelines for single laboratory validation of methods of analysis (IUPAC Technical Report). *Pure Appl. Chem.* **2002**, *74* (5), 835−855.
(28) *Eurachem Guide: The Fitness of Purpose of Analytical Methods—A Laboratory Guide to Method Validation and Related Topics*, 2nd ed.; Magnusson, B., Örnemark, U., Eds.; Eurachem: Leoben, Austria, 2014; ISBN: 978-91-87461-59-0, www.eurachem.org.
(29) European Union Commission.. Regulation EC/333/2007 of 28 March 2007 laying down the methods of sampling and analysis for the official control of the levels of lead, cadmium, mercury, inorganic tin, 3-MCPD and benzo(*a*)pyrene in foodstuffs. *Off. J. Eur. Union, L: Legis.* **2007**, *88*, 29−39.
(30) International Olive Council (IOC). *Trade Standard Applying to Olive Oils and Olive-Pomace Oils*; IOC: Madrid, Spain, 2013; COI/T.15/NC No. 3/Rev. 7.
(31) Texeira, V.; Casal, S.; Oliveira, M. PAHs content in sunflower, soybean and virgin olive oils: Evaluation in commercial samples and during refining process. *Food Chem.* **2007**, *104*, 106−112.
(32) Fromberg, A.; Højgård, A.; Duedahl-Olesen, L. Analysis of polycyclic aromatic hydrocarbons in vegetable oils combining gel permeation chromatography with solid phase extraction cleanup. *Food Addit. Contam.* **2007**, *24*, 758−767.

DOI: 10.1021/jf506299f
J. Agric. Food Chem. 2015, 63, 4933−4939

JOURNAL OF AGRICULTURAL AND FOOD CHEMISTRY

Article

pubs.acs.org/JAFC

Development of a Screening Fluorescence Polarization Immunoassay for the Simultaneous Detection of Fumonisins B_1 and B_2 in Maize

Chenglong Li,[†] Tiejun Mi,[†,‡] Gea Oliveri Conti,[§] Qing Yu,[†] Kai Wen,[†] Jianzhong Shen,[†,#] Margherita Ferrante,[§] and Zhanhui Wang*[,†,#]

[†]College of Veterinary Medicine, China Agricultural University, Beijing Key Laboratory of Detection Technology for Animal-Derived Food Safety, Beijing Laboratory for Food Quality and Safety, 100193 Beijing, People's Republic of China

[‡]College of Veterinary Medicine, Northwest A&F University, 712100 Yangling, People's Republic of China

[§]Department "GF Ingrassia", Hygiene and Public Health, Laboratory of Environmental and Food Hygiene, University of Catania, 87 Avenue S. Sofia, 95123 Catania, Italy

[#]National Reference Laboratory for Veterinary Drug Residues, 100193 Beijing, People's Republic of China

Supporting Information

ABSTRACT: This paper reports the development of a screening fluorescence polarization immunoassay (FPIA) for the simultaneous detection of fumonisins B_1 (FB_1) and B_2 (FB_2) in maize. Three FB_1 tracers including FB_1-fluorescein isothiocyanate isomer I (FB_1-FITC), FB_1-5-([4,6-dichlorotriazine-2-yl]amino)-fluorescein (FB_1-5-DTAF), and FB_1-Texas Red-X succinimidyl ester (FB_1-TRX) were synthesized and studied to select appropriate tracer−antibody pairs using seven previously produced monoclonal antibodies (mAbs). An FPIA employing the pair of FB_1-FITC and mAb 4B9 showing 98.9% cross-reactivity (CR) toward FB_2 was used to simultaneously detect FB_1 and FB_2. Maize flour samples were extracted with methanol/water (2:3, v/v). After optimization, the FPIA revealed a limit of detection (LOD) of 157.4 μg/kg for FB_1 and an LOD of 290.6 μg/kg for FB_2, respectively. Recoveries were measured for spiked samples of FB_1 or FB_2 separately, ranging from 84.7 to 93.6%, with a coefficient of variation (CV) of <9.9%. Total time needed for FPIA including sample pretreatment was <30 min. The FPIA was used to screen naturally contaminated maize samples. Results detected by FPIA showed good agreement with that of HPLC-MS/MS with a fit of R^2 = 0.99 for the simultaneous detection of FB_1 and FB_2. The established method offered a rapid, simple, sensitive, and high-throughput screening tool for the detection of fumonisins in maize.

KEYWORDS: *fumonisin B_1, fumonisin B_2, fluorescence polarization immunoassay, maize, detection*

INTRODUCTION

Fumonisins are a class of mycotoxins produced as secondary metabolites by fungi of the genus *Fusarium*, notably *Fusarium verticillioides* and *Fusarium proliferatum*.[1,2] Since the first description and characterization of fumonisins in 1988, at least 18 different fumonisin analogues classified into A, B, C, and P groups have been identified.[3−6] The B group, mainly fumonisins B_1 (FB_1) and B_2 (FB_2) with a ratio of 10:3, is believed to be the most prevalent and toxic in naturally contaminated cereals throughout the world.[7,8]

Fumonisins have received much attention due to their hepatotoxicity and carcinogenic effects on animals by interfering with sphingolipid metabolism. For example, fumonisins have been implicated as contributors to leukoencephalomalacia in equines and rabbits, pulmonary edema syndrome and hydrothorax in swine, and apoptosis in the liver of rats.[4,9] In humans, there is a correlation between the consumption of FB_1 highly contaminated home-grown maize and an incidence of esophageal and liver cancer in those regions of China.[10] On the basis of these available data, the International Agency for Research on Cancer has assessed the cancer risk of FB_1 and rated it as a group 2B human carcinogen.[11]

To protect public health from unacceptable contamination, guidance or regulations for fumonisins have been enforced in many countries. The U.S. Food and Drug Administration issued recommended maximum levels of 2−4 mg/kg for total FB_1, FB_2, and fumonisin B_3 (FB_3) in human foods.[12] The scientific committee for food of the European Commission has set action levels for the sum of FB_1 and FB_2, which ranged from 200 μg/kg in processed maize-based foods and baby foods to 4000 μg/kg in unprocessed maize.[13,14]

Several analytical methods for fumonisin detection have currently been developed, including high-performance liquid chromatography (HPLC) with fluorescence detection and liquid chromatography coupled to mass spectrometry (LC-MS) or tandem mass spectrometry (LC-MS/MS).[15−17] These instrumental methods, generally suffering from sophisticated instrumentation, tedious sample preparation, and the need for highly trained/skilled technicians, especially are expensive and time-consuming for routine screening of suspected contami-

Received: January 18, 2015
Revised: May 4, 2015
Accepted: May 5, 2015
Published: May 5, 2015

ACS Publications © 2015 American Chemical Society

DOI: 10.1021/acs.jafc.5b01845
J. Agric. Food Chem. 2015, 63, 4940−4946

nants in many samples. Immunoassays, mainly enzyme-linked immunosorbent assay (ELISA), have frequently been reported for the determination of fumonisins because they are highly sensitive, cost-effective, and easy to use.[18−24] However, ELISA is a heterogeneous method in solid phase, which is limited by requiring multiple incubation and washing steps, and generally needs from 15 to 60 min for the analysis of fumonisins. Thus, with the increasing demand for quicker, easier, and high-throughput screening of contaminants, much effort has been focused on exploring alternatives.

Fluorescence polarization immunoassay (FPIA) is a homogeneous assay based on the competition between unlabeled analyte and fluorescein-labeled tracer for specific antibody in solution phase, which uses changes in fluorescence polarization (FP) to detect the presence of target.[25] Compared with ELISA, FPIA takes only as little as a few seconds or minutes before measuring, and no separation or washing steps are required, which makes the method rapid and simple with high-throughput suitable for the analysis of large numbers of samples. Recently, FPIA has been applied to detect mycotoxins, including aflatoxins (AFs), fumonisins, deoxynivalenol (DON), T-2 toxin, ochratoxin A (OTA), and zearalenone (ZEA).[18,19,25−32] Maragos et al.[18] initially developed an FPIA method in tube format for the measurement of FB_1 by utilizing tracer FB_1-6-([4,6-dichlorotriazine-2-yl]amino)-fluorescein (FB_1-6-DTAF) and monoclonal antibody (mAb) P2A5-3-F3 with a limit of detection (LOD) of 500 μg/kg in maize. After this pioneering work, Nasir et al.[19] improved the sensitivity of the assay, which employed the same immunoreagents with an LOD of 100 μg/kg by refining the tracer and each step of the FPIA. However, the FPIAs reported were both performed in glass tubes, which are low throughput as samples need to be inserted into the instrument one after another, and only FB_1 was detected in maize.

In the current work, an FPIA in a microplate reader format was developed for the simultaneous detection of FB_1 and FB_2 in maize samples. For this purpose, we synthesized three tracers and paired them with seven already produced mAbs. After optimization, the developed FPIA was applied to detect FB_1 and FB_2 in spiked maize and in naturally contaminated maize samples.

MATERIALS AND METHODS

Safety Information. Mycotoxins and related samples used in studies should be handled with extreme caution to avoid exposure to all of these contaminants.

Reagents and Materials. FB_1 was purchased from Pribolab Pte. Ltd. (Singapore City, Singapore), and FB_2 was obtained from LKT Laboratories, Inc. (St. Paul, MN, USA). FB_3, fluorescein isothiocyanate isomer I (FITC), and 5-([4,6-dichlorotriazine-2-yl]amino)-fluorescein hydrochloride (5-DTAF) were supplied by Sigma-Aldrich (St. Louis, MO, USA). Texas Red-X succinimidyl ester (TRX) was acquired from Life Technologies (Carlsbad, CA, USA). Aflatoxin B_1 (AFB_1), ZEA, OTA, DON, and T-2 toxin were purchased from Fermentek Biotechnology (Jerusalem, Israel). Water was obtained from a Milli-Q system (Bedford, MA, USA). All other reagents were of analytical grade or better unless specified otherwise and were acquired from Sinopharm Chemical Reagent Co., Ltd. (Shanghai, China). Precoated TLC silica gel 60 F_{254} aluminum sheets were acquired from Merck (Darmstadt, Germany). Black opaque 96-well microtiter plates with a nonbinding surface were purchased from Corning (Oneonta, NY, USA). The 0.45 μm syringe filters were obtained from Tianjin Jinteng Experiment Equipment Co., Ltd. (Tianjin, China).

Seven mAbs to FB_1, named 2B9, 4B9, 7C9, 2D7, 4F5, 5F8, and 2H8, were previously prepared.[23] Two batches of flour samples of naturally contaminated maize were kindly provided by Prof. Sarah De Saeger (Ghent University) and were stored at −20 °C.[33]

Borate buffer (50 mM, pH 8.0) with 0.1% sodium azide was used as a working buffer solution in this study. Stock solutions (5 mg/mL) of FB_1 and FB_2 were prepared by dissolving 1 mg of standard in 200 μL of methanol, respectively, and were stored at −20 °C until use.

Apparatus. FPIA was performed using a Spectramax M5 microplate reader obtained from Molecular Devices (Sunnyvale, CA, USA) to measure FP and fluorescence intensity (FI) signal.

Preparation of Fluorescein-Labeled FB_1 Tracers. As FB_1 has a single primary amine to enable coupling reactions, it was directly conjugated to fluorescein according to the protocol with minor modifications.[34] Briefly, a stock solution of FB_1 (50 μL) was added to FITC (2 mg) dissolved in 50 μL of methanol followed by the addition of triethylamine (10 μL). After overnight reaction at room temperature in the dark, a small portion (20 μL) of crude product was purified by thin layer chromatography (TLC) using a trichloromethane/methanol/acetic acid (40:10:1, v/v/v) mobile phase. The major yellow band at R_f 0.1 was scraped from the plate and eluted with 100 μL of methanol. Other tracers FB_1-5-DTAF and FB_1-TRX were prepared in the same way and were stored in the dark at −20 °C. All of the tracer solutions were further diluted with borate buffer to get the working concentration with FI about 20 times that of borate buffer background.

Sample Preparation. An amount of 1 g of maize flour sample was added into a 50 mL plastic centrifuge tube. Then the samples were extracted with 5 mL of methanol/water (2:3, v/v) at room temperature. After 1 min of vortexing and ultrasonication for 5 min, the mixtures were centrifuged at 10000 rpm at 4 °C for 10 min. The supernatant (2 mL) was filtered through a 0.45 μm syringe filter, and 1 mL of filtrate was mixed with 3 mL of borate buffer. Finally, 70 μL of the diluted extract was analyzed by FPIA without further treatment.

To acquire the accuracy and repeatability of the FPIA method, 1 g of blank maize flour was spiked with known amounts of standard solutions of FB_1 or FB_2 to obtain samples with different concentrations ranging from 300 to 2000 μg/kg before extraction.

Fluorescence Polarization Immunoassay. *Antibody Dilution Curve.* The antibody dilution curve was performed by mixing 70 μL per well of tracer solution at a working concentration with 70 μL per well of 2-fold serially diluted mAb. Borate buffer was added to reach an overall volume of 210 μL per well.

Maize Matrix-Based Calibration Curve. The concentration of fumonisins in naturally contaminated maize samples was determined relative to the maize matrix-based calibration curve of FB_1 or FB_2 prepared in blank matrix extracts.

The assay was conducted by adding 70 μL per well of tracer working solution and 70 μL per well of prepared standards (or samples) to the microplate, followed by the addition of 70 μL per well of optimal diluted mAb corresponding to a 70% tracer binding based on the antibody dilution curve. After the mixture was shaken for 10 s in the microplate reader, FP values were measured at λ_{ex} 485 nm and λ_{em} 530 nm with emission cutoff of 515 nm for FB_1-FITC and FB_1-5-DTAF or at λ_{ex} 585 nm and λ_{em} 620 nm with emission cutoff of 610 nm for FB_1-TRX, respectively.

The sigmoidal curve was obtained by plotting the measured FP values against the concentration of fumonisins and fitting them to a four-parameter logistic equation by OriginPro 8.0 (Northampton, MA, USA). The LOD was experimentally defined as IC_{10}, the concentration of standard inhibiting 10% of tracer binding with antibody, that is, the concentration corresponding to 10% inhibition of the maximal FP signal.[35] The detectable range corresponds to the concentration of standard varying from IC_{20} to IC_{80}.

Cross-Reactivity (CR) Determination. To determine the specificity of this method, CR with other mycotoxins including FB_2, FB_3, AFB_1, ZEA, OTA, DON, and T-2 toxin were calculated by the following equation, where the IC_{50} value was the concentration of standard inhibiting tracer binding by 50%.

$$\mathrm{CR}\ (\%) = (\mathrm{IC}_{50}\ \text{of}\ \mathrm{FB}_1)/(\mathrm{IC}_{50}\ \text{of other mycotoxins}) \times 100\%$$

DOI: 10.1021/acs.jafc.5b01845
J. Agric. Food Chem. 2015, 63, 4940−4946

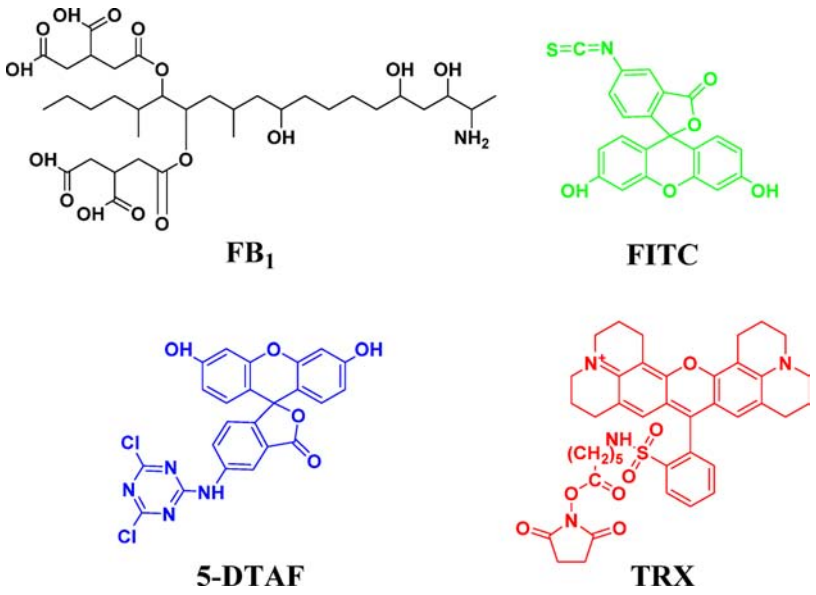

Figure 1. Chemical structures of fluorescein (FITC, 5-DTAF, and TRX) and FB_1 used in this study.

Accuracy and Precision. The accuracy (expressed as recovery), the precision containing repeatability (denoted by coefficient of variation (CV)), and reproducibility were measured for the developed FPIAs. Correlation studies were conducted to determine the reproducibility. Samples of naturally contaminated maize already detected by HPLC-MS/MS were analyzed by the developed FPIA.

RESULTS AND DISCUSSION

Synthesis and Characterization of Tracers. In previous papers, several tracers of FB_1 were prepared and used in FPIA for the determination of fumonisins, including FB_1-DTAF, FB_1-iodoacetamido-fluorescein (FB_1-IAF), and FB_1-carboxy-fluorescein (FB_1-FAM).[18,19] Different tracers have shown different performances in FPIA when using the same mAb P2A5-3-F3. Among these tracers, FB_1-DTAF had the most rigid structure as well as the least "propeller effect" and was found to be the best one.

In this study, three tracers (hapten labeled with three fluorescein including FITC, 5-DTAF, and TRX) were synthesized to achieve the most sensitive FPIA (Figure 1). After purification by TLC, tracers were primarily characterized for binding with seven mAbs by the addition of saturating amount of mAbs (dilution of 1/100) to tracer working solutions. The main bands of TLC at R_f 0.1 for both FB_1-FITC and FB_1-5-DTAF and R_f 0.5 for FB_1-TRX were used as tracers in the following studies because they have an affinity with antibodies as FP signals significantly increased before and after mAbs were added (Figure 2). The couple of FB_1-TRX and mAb 2H8 gave the largest increase in FP signal with δ FP (FP_{bind} minus FP_{free}) of about 392.4 mP (millipolarization units) showing the highest affinity. Meanwhile, FP values of other combinations were also increased and ranged from 49 to 218 mP.

Selection of Tracer–Antibody Pairs. It is reported that the combination of tracer and antibody may have a significant impact on the sensitivity and specificity in the development of an FPIA.[35,36] In this assay, IC_{50} values of FPIA calibration curves for FB_1 in borate buffer, which were obtained by using working concentration of tracers and diluted mAbs that correspond to a 50% tracer binding, was mainly applied to select the optimal tracer–antibody pairs. The highest sensitivity

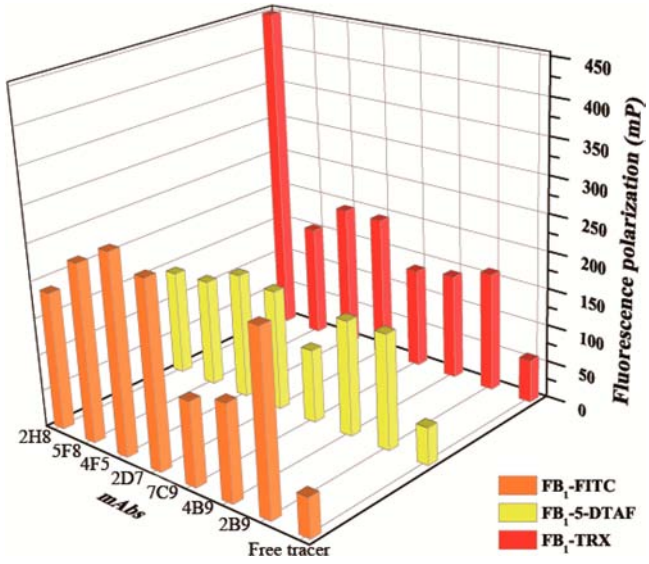

Figure 2. Results of three tracers binding with 100-fold diluted mAbs.

(lowest IC_{50} = 18.8 ng/mL) was achieved when using FB_1-FITC and the 4F5 mAb produced by immunogen FB_1-KLH via conjugating the carboxylic group of FB_1 to the carrier protein (Table 1). Also, this combination gave the widest assay window (δ FP, FP_{max} minus FP_{min}) and lowest background compared with other mAbs and FB_1-FITC pairs. Among the tracers we prepared, FB_1-FITC gave the best performance followed by FB_1-5-DTAF and then FB_1-TRX when seven mAbs were used (Table 1). It should be noted that FB_1-TRX could specifically bind to all of these mAbs and gave an adequate increase in FP signals. However, obvious inhibitions of FB_1 were not found for most of these antibodies. This may be because FB_1-TRX has the most "propeller effect" based on its flexible chemical structure in accordance with previous studies.[19]

Remarkable differences in sensitivity and specificity may be achieved by using the same tracer and different antibodies.[37] The specificity of FB_1-FITC and mAb combinations was obtained by evaluating CR with other occurring mycotoxins (FB_2, FB_3, AFB_1, ZEA, OTA, DON, and T-2 toxin) by FPIA.

DOI: 10.1021/acs.jafc.5b01845
J. Agric. Food Chem. 2015, 63, 4940–4946

Table 1. IC_{50} Parameter (Nanograms per Milliliter) of Competitive FPIA Calibration Curves of FB_1 in Borate Buffer Using Three Tracers and Seven mAbs

	mAbs						
tracer	2B9	4B9	7C9	2D7	4F5	5F8	2H8
FB_1-FITC	23.3	90.1	491.3	23.9	18.8	50.7	158.4
FB_1-5-DTAF	34.4	93.0	552.4	24.2	21.4	246.1	202.0
FB_1-TRX	–[a]	–[a]	–[a]	79.0	60.9	–[a]	223.0

[a]No obvious concentration-dependent FP changes were observed.

Unlike the 4F5 mAb, 4B9 was obtained using immunogen FB_1-GA–BSA through conjugation of the amino group of FB_1 to the carrier protein as reported.[23] The sensitivity of the FB_1-FITC and 4B9 pair was lower than that of the FB_1-FITC and 4F5 combination. However, high CR to FB_2 (98.9% in maize matrix) was acquired when using the FB_1-FITC and 4B9 combination (Table 2). Thus, method 1 employing FB_1-FITC and 4B9 was used for the simultaneous detection of FB_1 and FB_2 in maize. In addition, method 2 employing the pair of FB_1-FITC and 4F5 could be used for specific determination of FB_1 due to its low CR toward FB_2 (2.3% in maize matrix). The results also showed negligible CR of both mAbs 4F5 and 4B9 coupled with FB_1-FITC to AFB_1, ZEA, OTA, DON, and T-2 toxin.

Table 2. Cross-Reactivity of FB_1-FITC and mAb Combinations to FB_1 and Other Mycotoxins by FPIA in Maize Matrix

Mycotoxins	Structures	mAbs			
		4B9		4F5	
		IC_{50} (ng/mL)	CR (%)	IC_{50} (ng/mL)	CR (%)
FB_1	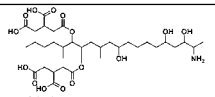	118.5	100.0	18.0	100.0
FB_2	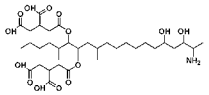	119.8	98.9	770.7	2.3
FB_3	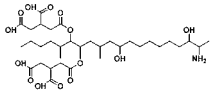	203.7	58.2	28.1	64.1
AFB_1	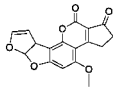	-[a]	< 1%	-[a]	<0.1%
ZEA	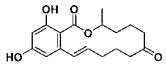	-[a]	< 1%	-[a]	<0.1%
OTA	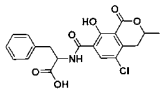	-[a]	< 1%	-[a]	<0.1%
DON	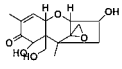	-[a]	< 1%	-[a]	<0.1%
T-2 toxin	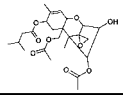	-[a]	< 1%	-[a]	<0.1%

[a]IC_{50} > 10000 ng/mL.

Investigation of Matrix Effect. In general, fumonisins can be extracted from maize with a mixture of organic solvent and water (methanol/water or acetonitrile/water).[38] In this study, methanol/water (2:3, v/v) was used to extract fumonisins from maize samples according to the previous paper.[24]

As a homogeneous assay, FPIA was more susceptible to interference by matrix effects than other heterogeneous assays. Therefore, the investigation of matrix effect is an important part of FPIA. For the purpose of acquiring information on matrix effects of maize samples, calibration curves were performed in both borate buffer and diluted sample extracts. Results show that the matrix effect could not be reduced simply through a dilution of the extract. The main reason may be that varieties of colored or fluorescent contents are also extracted along with fumonisins when using organic solvent.[39] In FPIA, PBS substantially free of organic solvent was also used for the extraction of FB_1 in maize samples, but the matrix effect still exists with the protocol that 150 μL of extract was added to 150 μL of antibody in PBS and then 200 μL was taken out and mixed with 1.4 mL of tracer.[18] Therefore, a maize matrix-based calibration curve was used to determine the concentration of fumonisins in naturally contaminated maize samples to reduce the background interference of maize extracts.

Development of FPIA in Maize Matrix. Because tracer concentration influences the sensitivity of an assay markedly, the lowest possible concentration should be used to get the most sensitive assay, but this also resulted in low precision of FP signal.[35,36,40] Generally, optimal concentration of tracer was chosen when FI was at least 10 times higher than that of borate buffer background.[41] According to the manual of the microplate reader used in this assay, it was recommended that the precision expressed as standard deviation (SD) of FP be <5 mP. The working concentration of tracer was optimized in borate buffer when the FI of tracer was about 5, 10, 20, and 40 times higher than background following the procedure previously published.[42] The results show that the precision of the FP signal depended on tracer concentration. When FI was about 20 times higher than that of background, tracer at this concentration was selected as working concentration because the SD of FP values of both free and bound tracer was <5 mP.

Antibody dilution curves in the maize matrix were obtained for the FB_1-FITC and 4B9 combination, as well as the pair of FB_1-FITC and 4F5. Theoretically, the optimal concentration of antibody corresponding to a 50% tracer binding would receive the best sensitivity. However, in this research antibody dilution that corresponds to 70% tracer binding was chosen as optimum concentration so as to get a wider analytical range according to previous studies.[43] The best antibody dilution was observed for FB_1-FITC with 4B9 (1/46) and 4F5 (1/2900) in maize matrix.

Under optimal conditions, calibration curves were plotted in blank maize matrix (Figure 3). FP signals were read every 5 min for 90 min. No incubation time was needed as the equilibrium of competition was quickly completed just after samples, tracer, and antibody were mixed (data not shown). Method 1 employing the combination of FB_1-FITC and 4B9 could be used to detect FB_1 and FB_2 in maize samples simultaneously with an LOD of 157.4 μg/kg for FB_1 or 290.6 μg/kg for FB_2 (Table 3). Meanwhile, method 2 showed an LOD of 53.6 μg/

DOI: 10.1021/acs.jafc.5b01845
J. Agric. Food Chem. 2015, 63, 4940–4946

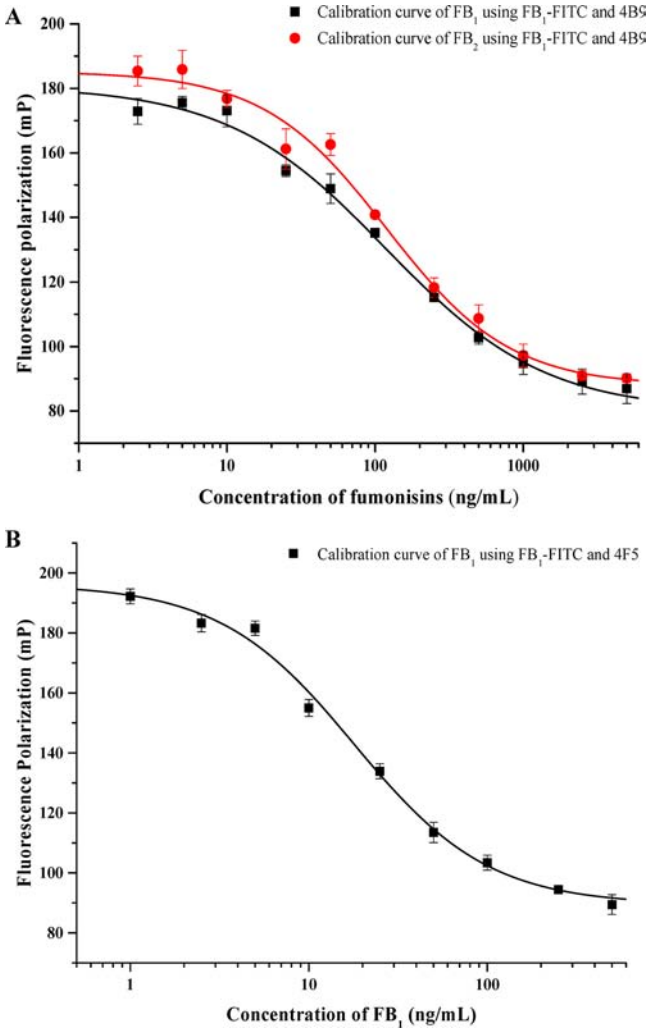

Figure 3. Calibration curves based on optimal conditions in maize matrix of (A) FB_1-FITC and 4B9 pair and (B) FB_1-FITC and 4F5 pair. Each point represents the average of triplicates for a given concentration (n = 3).

Table 3. Analytical Characteristics of Calibration Curves in Maize Matrix

			parameters		
fumonisin	tracer	mAb	LOD (μg/kg)	IC_{50} (μg/kg)	detectable range (μg/kg)
FB_1	FB_1-FITC	4B9	157.4	2370	426.8−13166
FB_2			290.6	2396	632.8−9072
FB_1	FB_1-FITC	4F5	53.6	360.4	108.0−1201

kg for FB_1 specifically in maize samples by using the FB_1-FITC and 4F5 pair. This LOD is about 2-fold lower than that of the published FPIA method (0.1 mg/kg in maize samples) for the determination of FB_1.[19] Also, the detectable ranges in method 1 were 426.8−13166 μg/kg for FB_1 and 632.8−9072 μg/kg for FB_2, whereas in method 2 it was 108.0−1201 μg/kg for FB_1 in maize. Moreover, the whole analysis could be completed within 30 min, including extraction time. Its unrivalled speed and high throughput make it ideally suited for screening for targets in large numbers of samples.

Recovery and Precision Study. The recoveries of method 1 spiked with FB_1 or FB_2 separately at 500, 1000, and 2000 μg/kg were 84.7−93.6%, with CV values <9.9% (Table 4). In spiked maize samples of FB_1 at 300, 500, and 1000 μg/kg, the recoveries of method 2 ranged from 68.5 to 87.0%, with CV values of no more than 3.6%. Acceptable recoveries and CV values were acquired for this assay system.

Table 4. Recoveries and CVs of Fumonisin-Spiked Blank Maize Samples (n = 3)

fumonisin	tracer	mAb	spiked concentration (μg/kg)	recovery (%)	CV (%)
FB_1	FB_1-FITC	4B9	2000	89.2	6.1
			1000	89.9	4.0
			500	93.6	3.9
FB_2			2000	87.3	3.2
			1000	85.4	7.6
			500	84.7	9.9
FB_1	FB_1-FITC	4F5	1000	68.5	3.6
			500	87.0	1.6
			300	80.2	2.7

Two batches of naturally contaminated maize samples, one contaminated with multiple mycotoxins including FB_1 and FB_2, the other with FB_1 and DON, were analyzed by FPIA and HPLC-MS/MS (Table 5). The total concentrations of FB_1 and FB_2 in the first batch of maize were determined relative to the maize matrix-based calibration curve of FB_1 standard using the FB_1-FITC and 4B9 combination. Meanwhile, the concentrations of FB_1 in the second batch of maize were determined by the maize matrix-based calibration curve of FB_1 standard using the combination of FB_1-FITC and 4F5. The results between FPIA and HPLC-MS/MS were compared using a correlation test, which showed good agreement with a fit of R^2

Table 5. Naturally Contaminated Maize Flour Samples

no.	mycotoxin	HPLC-MS/MS (μg/kg)	FPIA (μg/kg)	CV (%)
1-1	FB_1+FB_2	602	982	10
1-2	FB_1+FB_2	67	−[a]	−[d]
1-3	FB_1+FB_2	−[b]	−[a]	−[d]
1-4	FB_1+FB_2	−[b]	−[a]	−[d]
1-5	FB_1+FB_2	328	560.6	4.3
1-6	FB_1+FB_2	1082	1422	3.6
1-7	FB_1+FB_2	1668	1422	5.8
1-8	FB_1+FB_2	525	966.8	4.4
1-9	FB_1+FB_2	10422	7012	6.8
2-1	FB_1	297	210.4	6.2
2-2	FB_1	291	389.2	13
2-3	FB_1	742	880.8	5.0
2-4	FB_1	236	135.6	4.0
2-5	FB_1	−[b]	−[a]	−[d]
2-6	FB_1	1686	+[c]	−[d]
2-7	FB_1	308	466.6	13
2-8	FB_1	92	−[a]	−[d]
2-9	FB_1	2285	+[c]	−[d]
2-10	FB_1	−[b]	−[a]	−[d]
2-11	FB_1	96	−[a]	−[d]
2-12	FB_1	328	445.6	4.4

[a]Samples with concentrations below the detection range. [b]Concentration of sample was about half of the LOD. [c]Samples with concentrations outside the detection range. [d]Not calculated.

DOI: 10.1021/acs.jafc.5b01845
J. Agric. Food Chem. 2015, 63, 4940−4946

= 0.99 for the simultaneous detection of FB_1 and FB_2 in maize and 0.80 for the specific determination of FB_1 in maize samples, respectively. Therefore, the developed FPIA could be potentially applied to screen fumonisins in maize.

■ ASSOCIATED CONTENT

Supporting Information

Table of data for three tracers binding with 100-fold diluted mAbs and figures depicting selection of tracer/antibody combinations, matrix effect, optimization of tracer/antibody concentration, and correlation analysis between HPLC-MS/MS and the developed FPIA. The Supporting Information is available free of charge on the ACS Publications website at DOI: 10.1021/acs.jafc.5b01845.

■ AUTHOR INFORMATION

Corresponding Author

*(Z.W.) Phone: +86-10-6273 4565. Fax: +86-10-6273 1032. E-mail: wangzhanhui@cau.edu.cn.

Funding

This work was supported by grants from the Natural Science Foundation of China (U1301214), the Special Fund for Agro-scientific Research in the Public Interest (201203040), and the International Science & Technology Cooperation Program of China (2012DFG31840).

Notes

The authors declare no competing financial interest.

■ ACKNOWLEDGMENTS

We are very thankful to Prof. Sarah De Saeger (Laboratory of Food Analysis, Faculty of Pharmaceutical Sciences, Ghent University) for providing naturally contaminated maize samples.

■ REFERENCES

(1) Marasas, W. F. O.; Miller, J. D.; Riley, R. T.; Visconti, A. Fumonisins − occurrence, toxicology, metabolism and risk assessment. In *Fusarium: Paul E. Nelson Memorial Symposium*; Summerell, B. A., Leslie, J. F., Backhouse, D., Bryden, W. L., Burgess, L. W., Eds.; APS Press: St. Paul, MN, USA, 2001; pp 332−359.

(2) Rheeder, J. P.; Marasas, W. F. O.; Vismer, H. F. Production of fumonisin analogs by *Fusarium* species. *Appl. Environ. Microbiol.* **2002**, *68*, 2101−2105.

(3) Bezuidenhout, S. C.; Gelderblom, W. C. A.; Gorstallman, C. P.; Horak, R. M.; Marasas, W. F. O.; Spiteller, G.; Vleggaar, R. Structure elucidation of the fumonisins, mycotoxins from *Fusarium moniliforme*. *J. Chem. Soc., Chem. Commun.* **1988**, 743−745.

(4) Gelderblom, W. C. A.; Jaskiewicz, K.; Marasas, W. F. O.; Thiel, P. G.; Horak, R. M.; Vleggaar, R.; Kriek, N. P. J. Fumonisins-novel mycotoxins with cancer-promoting activity produced by *Fusarium moniliforme*. *Appl. Environ. Microbiol.* **1988**, *54*, 1806−1811.

(5) Plattner, R. D.; Weisleder, D.; Poling, S. M. Analytical determination of fumonisins and other metabolites produced by *Fusarium moniliforme* and related species on corn. In *Advances in Experimental Medicine and Biology: Fumonisins in Food*; Jackson, L. S., DeVries, J. W., Bullerman, L. B., Eds.; Plenum Press: New York, 1996; pp 57−64.

(6) Sewram, V.; Mshicileli, N.; Shephard, G. S.; Vismer, H. F.; Rheeder, J. P.; Lee, Y. W.; Leslie, J. F.; Marasas, W. F. O. Production of fumonisin B and C analogues by several *Fusarium* species. *J. Agric. Food Chem.* **2005**, *53*, 4861−4866.

(7) Weidenborner, M. Foods and fumonisins. *Eur. Food Res. Technol.* **2001**, *212*, 262−273.

(8) Joint FAO/WHO Expert Committee on Food Additives, Evaluation of certain mycotoxins in food: fifty-sixth report of the Joint FAO/WHO Expert Committee on Food Additives. WHO technical report series 906, Geneva, 2002; http://www.who.int/iris/handle/10665/42448 (accessed May 5, 2015).

(9) Bennett, J. W.; Klich, M. Mycotoxins. *Clin. Microbiol. Rev.* **2003**, *16*, 497−516.

(10) Sun, G.; Wang, S.; Hu, X.; Su, J.; Huang, T.; Yu, J.; Tang, L.; Gao, W.; Wang, J. Fumonisin B_1 contamination of home-grown corn in high-risk areas for esophageal and liver cancer in China. *Food Addit. Contam.* **2007**, *24*, 181−185.

(11) International Agency for Research on Cancer. Toxins derived from *Fusarium moniliforme*: fumonisins B_1 and B_2 and fusarin C, In *IARC Monographs on the Evaluation of Carcinogenic Risks to Humans*; Lyon, France, 1993; pp 445.

(12) *Guidance for Industry: Fumonisin Levels in Human Foods and Animal Feeds*; U.S. Food and Drug Administration: Washington, DC, USA, 2001.

(13) Commission Regulation (EC) No. 1881/2006 of 19 December 2006 Setting maximum levels for certain contaminants in foodstuffs. *Off. J. Eur. Union* **2006**, *L364*, 5−24.

(14) Commission Regulation (EC) No. 1126/2007 of 28 September 2007 Amending Regulation (EC) No. 1881/2006 Setting maximum levels for certain contaminants in foodstuffs as regards *Fusarium* toxins in maize and maize products. *Off. J. Eur. Union* **2007**, *L255*, 14−17.

(15) Arranz, I.; Baeyens, W. R. G.; Weken, G.; Saeger, S.; Peteghem, C. Review: HPLC determination of fumonisin mycotoxins. *Crit. Rev. Food Sci. Nutr.* **2004**, *44*, 195−203.

(16) Sforza, S.; Dallasta, C.; Marchelli, R. Recent advances in mycotoxin determination in food and feed by hyphenated chromatographic techniques/mass spectrometry. *Mass Spectrom. Rev.* **2006**, *25*, 54−76.

(17) Silva, L.; Franzon, M. F.; Font, G.; Pena, A.; Silveira, I.; Lino, C.; Manes, J. Analysis of fumonisins in corn-based food by liquid chromatography with fluorescence and mass spectrometry detectors. *Food Chem.* **2009**, *112*, 1031−1037.

(18) Maragos, C. M.; Jolley, M. E.; Plattner, R. D.; Nasir, M. S. Fluorescence polarization as a means for determination of fumonisins in maize. *J. Agric. Food Chem.* **2001**, *49*, 596−602.

(19) Nasir, M. S.; Jolley, M. E. Fluorescence polarization (FP) assays for the determination of grain mycotoxins (fumonisins, DON vomitoxin and aflatoxins). *Comb. Chem. High Throughput Screen* **2003**, *6*, 267−273.

(20) Quan, Y.; Zhang, Y.; Wang, S.; Lee, N.; Kennedy, I. R. A rapid and sensitive chemiluminescence enzyme-linked immunosorbent assay for the determination of fumonisin B_1 in food samples. *Anal. Chim. Acta* **2006**, *580*, 1−8.

(21) Wang, S.; Quan, Y.; Lee, N.; Kennedy, I. R. Rapid determination of fumonisin B_1 in food samples by enzyme-linked immunosorbent assay and colloidal gold immunoassay. *J. Agric. Food Chem.* **2006**, *54*, 2491−2495.

(22) Shiu, C. M.; Wang, J. J.; Yu, F. Y. Sensitive enzyme-linked immunosorbent assay and rapid one-step immunochromatographic strip for fumonisin B_1 in grain-based food and feed samples. *J. Sci. Food Agric.* **2010**, *90*, 1020−1026.

(23) Sheng, Y.; Jiang, W.; Saeger, S. D.; Shen, J.; Zhang, S.; Wang, Z. Development of a sensitive enzyme-linked immunosorbent assay for the detection of fumonisin B_1 in maize. *Toxicon* **2012**, *60*, 1245−1250.

(24) Wang, Z.; Li, H.; Li, C.; Yu, Q.; Shen, J.; Saeger, S. D. Development and application of a quantitative fluorescence-based immunochromatographic assay for fumonisin B_1 in maize. *J. Agric. Food Chem.* **2014**, *62*, 6294−6298.

(25) Smith, D. S.; Eremin, S. A. Fluorescence polarization immunoassays and related methods for simple, high-throughput screening of small molecules. *Anal. Bioanal. Chem.* **2008**, *391*, 1499−1507.

(26) Nasir, M. S.; Jolley, M. E. Development of a fluorescence polarization assay for the determination of aflatoxins in grains. *J. Agric. Food Chem.* **2002**, *50*, 3116−3121.

(27) Lippolis, V.; Pascale, M.; Visconti, A. Optimization of a fluorescence polarization immunoassay for rapid quantification of

deoxynivalenol in durum wheat-based products. *J. Food Prot.* **2006**, *69*, 2712−2719.
(28) Maragos, C. Fluorescence polarization immunoassay of mycotoxins: a review. *Toxins* **2009**, *1*, 196−207.
(29) Zezza, F.; Longobardi, F.; Pascale, M.; Eremin, S. A.; Visconti, A. Fluorescence polarization immunoassay for rapid screening of ochratoxin A in red wine. *Anal. Bioanal. Chem.* **2009**, *395*, 1317−1323.
(30) Choi, E. H.; Kim, D. M.; Choi, S. W.; Eremin, S. A.; Chun, H. S. Optimisation and validation of a fluorescence polarisation immunoassay for rapid detection of zearalenone in corn. *Int. J. Food Sci. Technol.* **2011**, *46*, 2173−2181.
(31) Lippolis, V.; Pascale, M.; Valenzano, S.; Pluchinotta, V.; Baumgartner, S.; Krska, R.; Visconti, A. A rapid fluorescence polarization immunoassay for the determination of T-2 and HT-2 toxins in wheat. *Anal. Bioanal. Chem.* **2011**, *401*, 2561−2571.
(32) Sheng, Y.; Eremin, S. A.; Mi, T.; Zhang, S.; Shen, J.; Wang, Z. The development of a fluorescence polarization immunoassay for aflatoxin detection. *Biomed. Environ. Sci.* **2014**, *27*, 126−129.
(33) Monbaliu, S.; Poucke, C. V.; Detavernier, C.; Dumoulin, F.; Velde, M. V. D.; Schoeters, E.; Dyck, S. V.; Averkieva, O.; Peteghem, C. V.; Saeger, S. D. Occurrence of mycotoxins in feed as analyzed by a multi-mycotoxin LC-MS/MS method. *J. Agric. Food Chem.* **2010**, *58*, 66−71.
(34) Wang, Z.; Zhang, S.; Nesterenko, I. S.; Eremin, S. A.; Shen, J. Monoclonal antibody-based fluorescence polarization immunoassay for sulfamethoxypyridazine and sulfachloropyridazine. *J. Agric. Food Chem.* **2007**, *55*, 6871−6878.
(35) Eremin, S. A.; Bochkareva, A. E.; Popova, V. A.; Abad, A.; Manclus, J. J.; Mercader, J. V.; Montoya, A. Fluorescence polarization immunoassay for the insecticide DDT and its metabolites. *Anal. Lett.* **2002**, *35*, 1835−1850.
(36) Kolosova, A. Y.; Park, J. H.; Eremin, S. A.; Kang, S. J.; Chung, D. H. Fluorescence polarization immunoassay based on a monoclonal antibody for the detection of the organophosphorus pesticide parathion-methyl. *J. Agric. Food Chem.* **2003**, *51*, 1107−1114.
(37) Wang, Z.; Zhang, S.; Ding, S.; Eremin, S. A.; Shen, J. Simultaneous determination of sulphamerazine, sulphamethazine and sulphadiazine in honey and chicken muscle by a new monoclonal antibody-based fluorescence polarisation immunoassay. *Food Addit. Contam., Part A* **2008**, *25*, 574−582.
(38) Kulisek, E. S.; Hazebroek, J. P. Comparison of extraction buffers for the detection of fumonisin B_1 in corn by immunoassay and high-performance liquid chromatography. *J. Agric. Food Chem.* **2000**, *48*, 65−69.
(39) Nasir, M. S.; Jolley, M. E. Fluorescence polarization-based homogeneous assay for fumonisin determination in grains. U.S. Patent 6482601, 2002.
(40) Mi, T.; Wang, Z.; Eremin, S. A.; Shen, J.; Zhang, S. Simultaneous determination of multiple (fluoro)quinolone antibiotics in food samples by a one-step fluorescence polarization immunoassay. *J. Agric. Food Chem.* **2013**, *61*, 9347−9355.
(41) Yakovleva, J.; Zeravik, J.; Michura, I. V.; Formanovsky, A. A.; Franek, M.; Eremin, S. A. Hapten design and development of polarization fluoroimmunoassay for nonylphenol. *Int. J. Environ. Anal. Chem.* **2003**, *83*, 597−607.
(42) Mi, T.; Liang, X.; Ding, L.; Zhang, S.; Eremin, S. A.; Beier, R. C.; Shen, J.; Wang, Z. Development and optimization of a fluorescence polarization immunoassay for orbifloxacin in milk. *Anal. Methods* **2014**, *6*, 3849−3857.
(43) Deryabina, M. A.; Yakovleva, Y. N.; Popova, V. A.; Eremin, S. A. Determination of the herbicide acetochlor by fluorescence polarization immunoassay. *J. Anal. Chem.* **2005**, *60*, 80−85.

DOI: 10.1021/acs.jafc.5b01845
J. Agric. Food Chem. 2015, 63, 4940−4946

JOURNAL OF AGRICULTURAL AND FOOD CHEMISTRY

Article

pubs.acs.org/JAFC

Development of a Sandwich ELISA for Quantification of Gly m 4, a Soybean Allergen

Tao Geng,* Kang Liu, Ronald Frazier, Lifang Shi, Erin Bell, Kevin Glenn, and Jason M. Ward

Monsanto Company, 800 North Lindbergh Boulevard, St. Louis, Missouri 63167, United States

ABSTRACT: Gly m 4 is a key soybean allergen that causes allergic symptoms in the skin, gastrointestinal tract, or respiratory tract of sensitive individuals. To understand naturally variable levels of Gly m 4 among conventional soybean varieties, a sandwich ELISA was developed and validated using a mouse anti-Gly m 4 monoclonal antibody and a goat anti-Gly m 4 polyclonal antibody as capture and detection antibodies, respectively. The ELISA shows high specificity to Gly m 4 without any cross-reactivity to other soybean proteins and has a quantification range of 7.8−250 ng/mL using an *Escherichia coli*-produced recombinant Gly m 4, with 2.1 ng/mL being the limit of detection. Within the quantification range, the coefficients of variation of the intra-assay and interassay precision are less than 5 and 12%, respectively. Moreover, extraction efficiency and dilutional parallelism experiments were completed to demonstrate the assay is accurate. The validated assay was used to quantify Gly m 4 levels in 128 soybean samples from 24 conventional soybean varieties grown at 8 distinct geographical locations. There was a 13-fold difference between the least and greatest amounts of Gly m 4 concentrations among the samples, and the results demonstrate that the most significant sources of variability in Gly m 4 levels in the conventional varieties were related to location and variety.

KEYWORDS: *soybean, allergy, Gly m 4, ELISA, natural variability*

INTRODUCTION

Soybean (*Glycine max*) seed has protein constituting 34.1−56.8% of total content on a dry weight basis,[1] which makes it a good source of nutritional protein for animal and human consumption. Soybean and its byproducts are widely used in the food, feed, and pharmaceutical industries because of their nutritional values and physicochemical properties.[2] Because of the extensive use and need for protecting crop productivity, genetically modified (GM) soybeans have become the overwhelming majority of soybean varieties grown. In 2014, 82% (90.7 million of the 111 million hectares) of the soybeans planted globally were GM soybean.[3] To enable the commercialization of a GM soybean variety, an extensive safety assessment that includes an allergy safety assessment is completed.[4] This assessment includes a comparison of endogenous allergen levels in the GM soybean and conventional control. To evaluate this comparison of endogenous allergen levels, an understanding of the variability in allergen levels would be useful for supporting eventual determinations of exposure levels. Therefore, quantification of endogenous allergens from variable non-GM varieties is needed.

To date, eight soybean endogenous proteins have been shown to cause allergic symptoms in soybean-allergic individuals, including Gly m 3, Gly m 4, Gly m 5 (β-conglycinin), Gly m 6 (glycinin), Gly m 8 (2S albumin), Gly m Bd 28K, Gly m Bd 30K, and Kunitz trypsin inhibitor.[5]

Gly m 4, also called SAM22, is a pathogenesis-related (PR) protein that is specifically expressed in response to plant pathogens or environmental factors that affect plant physiology.[6] It belongs to the family of PR proteins that also includes several other pollen and food allergens[7−10] and thus shows high amino acid sequence identity (>50%) to birch (53% with Bet v 1),[11] hazelnut (58% with Cor a 1.0401),[12] apple (53% with Mal d 1),[13] and cherry (54% with Pru av 1)[14] pollen or food allergens. In addition to high amino acid sequence identity, Gly m 4 showed almost identical three-dimensional structure and cross-reaction to a major birch pollen allergen, Bet v 1,[8,15−17] suggesting a possible causal association between exposure to birch pollen and soy food allergy.

Although several studies have focused on Gly m 4 structure and its clinical implications, little is known about its expression levels in soybeans grown under different environmental conditions. Julka et al.[18] developed and validated a two-dimensional liquid chromatography approach with ultraviolet and mass spectrometry to quantify Gly m 4 from soybean seeds, but the method requires time-consuming processes and expensive equipment. Although Mittag et al.[17] generated a rabbit anti-Gly m 4 antibody and performed a quantitative Western blot, the method is low throughput and hard to validate. The enzyme-linked immunosorbent assay (ELISA), the most common method used by food industries and food control agencies to identify and quantify allergens,[2,19−21] could be the best approach to quantify a large amount of samples because of its sensitivity and high throughput. For these reasons ELISA methods for the detection of several soy allergens have been developed, including Gly m Bd 30K,[22,23] Gly m Bd 28K,[24,25] glycinin/Gly m 5,[26] β-conglycinin,[27,28] and Kunitz trypsin inhibitor.[29] However, to date, there is no validated ELISA method to detect and quantify Gly m 4 levels from soybean seeds.

Received: February 10, 2015
Revised: April 27, 2015
Accepted: May 6, 2015
Published: May 6, 2015

ACS Publications © 2015 American Chemical Society

DOI: 10.1021/acs.jafc.5b00792
J. Agric. Food Chem. 2015, 63, 4947−4953

In this study, a recombinant Gly m 4 (rGly m 4) protein was expressed, purified, and used as a reference standard protein for an ELISA. Mono- and polyclonal antibodies were generated using the rGly m 4 as an antigen and used to develop and validate a sandwich ELISA. The experiments completed during the assay validation demonstrated that the ELISA is sensitive, specific, accurate, and precise for Gly m 4 levels in soybean samples. Following the validation, the newly developed assay was used to quantify Gly m 4 levels from different soybean varieties grown under a variety of environmental conditions. The result showed that this key soybean food allergen has high variability across conventional soybean varieties grown in different locations.

MATERIALS AND METHODS

Soybean Varieties. Conventional soybean varieties (24 varieties) were grown in a U.S. field trial during the 2010 growing season at eight geographically diversified sites (one site each in Arkansas, Illinois, Missouri, Indiana, and Pennsylvania and three sites in Iowa), with each site planted in a randomized complete block design with four replicated blocks. Normal agronomic practices were followed for each site. Seed was harvested at the R8 growth stage[30] (95% of the pods had reached mature pod color) when the moisture content was approximately 12−15% and was stored at ambient temperature after harvest.

Protein Extraction from Soybean Seeds. Soybean seed samples were ground using a mega grinder (Monsanto Co., St. Louis, MO, USA) for approximately 1 min. Protein was extracted from about 100 mg of each ground sample by using a Harbil Mixer (Fluid Management, Inc., Wheeling, IL, USA) with 10 mL (1:100 tissue to buffer ratio) of 0.01 M phosphate-buffered saline with 0.05% (v/v) Tween-20, pH 7.4 (PBST), and 8 chrome beads (0.25 in. in diameter) for 3.5 min at 1500 rpm. Insoluble material was removed from soybean seed extract using a 16 mm × 4 in. serum filter (catalog no. 02-681-51, Fisher Scientific, Pittsburgh, PA, USA).

Expression, Purification, and Characterization of rGly m 4. The Gly m 4 cDNA sequence (GI 134194, NCBI) fused with a His tag at C-terminal was synthesized by Integrated DNA Technologies, Inc. (Coralville, IA, USA) and then ligated into pET24 vector (Novagen, Madison, WI, USA) using *Nde*I/*Xho*I restriction sites. The *Escherichia coli* BL21 (DE3) strain harboring pET24 rGly m 4 was grown in 800 mL of Terrific Broth (Sigma, St. Louis, MO, USA) containing 50 μg/mL kanamycin (Fisher Scientific). The cells were grown overnight at 37 °C with rotary shaking (250 rpm). The cultures were induced by the addition of IPTG (Invitrogen, Grand Island, NY, USA) to 200 μM and then grown for another 48 h at 15 °C. The cells were harvested by centrifugation at 20000*g* for 30 min.

The cell paste was homogenized in 1 L of 50 mM Tris-HCl, 100 mM NaCl, pH 8, using a cell disruptor (Constant Systems Inc., Kennesaw, GA, USA) at 15000 psi. The cell lysate was centrifuged at 20000*g* for 30 min, and the supernatant was incubated with 25 mL of NiNTA resin (Qiagen, Valencia, CA, USA) on an orbital shaker for 1 h at 4 °C. The resin slurry was then poured into a column and washed with an additional 200 mL of lysis buffer. The resin was washed with 100 mL of lysis buffer containing 20 mM imidazole and then eluted with 75 mL of lysis buffer containing 200 mM imidazole. The eluted protein was dialyzed into 50 mM Tris-HCl, 100 mM NaCl, pH 8, and stored at −80 °C.

The purified rGly m 4 protein concentration was determined by ACQUITY UPLC amino acid analysis using an AccQ-tag Ultra derivatization kit (Waters, Milford, MA, USA) and measured by a UPLC-UV detector (Waters). The protein was first acetone precipitated to get rid of the Tris-HCl buffer and then vapor phase acid hydrolyzed in 6 N HCl at 150 °C for 90 min. The hydrolyzed amino acids were precolumn derivatized with the AccQ-tag Ultra kit according to the manufacturer's protocol and then injected into the ACQUITY UPLC. Individual amino acid concentration was determined by an amino acid standard H calibration curve (Life Technology, Rochester, NY, USA). The final protein concentration was determined by total amino acid concentration on the average of five replicates. BSA standard (Sigma) with known concentration was used as control to evaluate the system suitability.

The purified rGly m 4 protein was diluted with Laemmli buffer with β-mercaptoethanol and separated on a precast Tris−glycine 4−20% polyacrylamide gradient gel (Invitrogen). Gel was stained with colloidal Brilliant Blue G (Sigma). Gel image was captured and the protein purity analyzed using a GS-800 scanning densitometer equipped with Quantity One software (Bio-Rad, Hercules, CA, USA).

N-terminal sequence analysis of rGly m 4 protein was performed for 15 cycles. The analysis was conducted using an Applied Biosystems 494 Procise Sequencing System (Applied Biosystems, Foster City, CA, USA).

The purified rGly m 4 protein was also characterized by mass spectrometry. Briefly, the protein was run on a 4−20% SDS-PAGE Tris−glycine gel (Invitrogen), and the band corresponding to rGly m 4 at ∼17 kDa was excised. The protein was extracted, reduced, alkylated, and digested. The digest was applied to an Applied Biosystems Voyager DE-Pro Biospectrometry Workstation with the supplied Data Explorer software for the mass spectrometry (MS) analysis.

Preparation of the Polyclonal Antibody. The production of goat polyclonal antibody (pAb) for Gly m 4 was conducted by Harlan Bioproducts for Science, Inc. (Madison, WI, USA). Briefly, two goats, G1195 and G1196, were immunized with the purified rGly m 4 by four subcutaneous injections. The first injection contained 1 mg of rGly m 4 emulsified in complete Freund's adjuvant (FCA; Sigma). The three subsequent boosts contained 500 μg of rGly m 4 emulsified in incomplete Freund's adjuvant (IFA; Sigma) and were given every 3 weeks. Blood was harvested from each goat 2 weeks after the final booster. The titers and the specificity of sera were determined by using the direct binding ELISA and Western blots as described below, respectively.

The goat sera were then affinity purified by a 5 mL HiTrap protein G column (GE Healthcare, Piscataway, NJ, USA) with an AKTA FPLC (GE Healthcare) according to the manufacturer's instruction. The purified total IgG was further purified by a rGly m 4 conjugated HiTrap NHS-Activated HP column (GE Healthcare) with an AKTA FPLC (GE Healthcare) according to the manufacturer's instruction. Briefly, about 10 mg of rGly m 4 was conjugated by amide linkage to a 5 mL prepacked column of *N*-hydroxysuccinimide (NHS) cross-linked to HP Sepharose beads. The total IgG in PBS (pH 7.4) was flowed through the rGly m 4 column. Unbound IgG was washed out by using PBS, and Gly m 4 specific IgG was eluted out with 100 mM glycine (pH 2.5). To prevent antibody still binding to the column, 3.5 M $MgCl_2$ in PBS was used to wash the column after elution. The specificity of the rGly m 4 column-purified IgG was assessed by Western blots by using soybean seed extract. The purified Gly m 4 specific IgG was dialyzed overnight by using 10K molecular weight cutoff (MWCO) dialysis cassettes (Thermo Scientific, Rockford, IL, USA) in the 4 L of PBS, with three changes of buffer, and then biotinylated by using an EZ-link Sulfo-NHS-LC-biotin kit (Thermo Scientific) according to the manufacturer's instruction. The ratio of antibody and biotin was determined as 1:7 by using a Biotin Quantitation kit (Thermo Scientific). The biotin-conjugated pAb served as the detection antibody in the sandwich ELISA for Gly m 4.

Preparation of the Monoclonal Antibody. The production of mouse monoclonal antibody (mAb) for Gly m 4 was conducted by Rockland Immunochemicals, Inc. (Gilbertsville, PA, USA). Prior to primary immunization, five BALB/c mice were fed a soybean-free diet for 2 weeks. The mice were then subcutaneously immunized with 50 μg of emulsified in CFA (Sigma). Two weeks later, the mice were reimmunized with 25 μg of rGly m 4 emulsified in IFA (Sigma). Three more boosts were given every 3 weeks with 25 μg of rGly m 4 emulsified in IFA. The titer of the test bleed of each boost was determined by using the direct coating ELISA, and the specificity of bleeds was assessed by using Western blots. The mouse with the highest antibody titer and specific to Gly m 4 was selected for cell fusion.

DOI: 10.1021/acs.jafc.5b00792
J. Agric. Food Chem. 2015, 63, 4947−4953

One week following cell fusion, the supernatant culture fluid from all wells was tested by the direct coating ELISA and Western blots. Cell lines with high affinity and specificity for Gly m 4 were selected for subcloning. Two stable subclones were injected intraperitoneally into five mice for each clone to produce ascites. Finally, the monoclonal antibodies were purified from the ascites by a 5 mL HiTrap protein G column (GE Healthcare) with an AKTA FPLC (GE Healthcare). After screening by direct plate binding ELISAs, the mAb with the highest titer was selected and applied as the capture antibody in the sandwich ELISA for Gly m 4.

Direct Binding ELISA To Measure Gly m 4. A direct binding ELISA was carried out to determine the titers of goat sera, mouse sera, and the hybridoma cell lines. rGly m 4 was used as the plate-coating antigen. A 96-well microtiter plate (Thermo Fisher Scientific, Rochester, NY, USA) was coated with a solution (100 μL/well) containing rGly m 4 (10 μg/mL) in 0.05 M carbonate/bicarbonate buffer with 0.15 M NaCl (pH 9.6) and incubated overnight at 4 °C. The plates were washed three times with 300 μL/well washing buffer (PBST, PBS containing 0.05% (v/v) Tween-20, pH 7.4) using a plate washer (ELC405, Biotek, Winooski, VT, USA) to remove unbound antigen. The plates were then blocked by 200 μL/well 1% (w/v) casein in PBS (Thermo Fisher Scientific) for 1 h at 37 °C. All plates were subsequently washed three times. Serially diluted goat sera, mouse sera, and the supernatants of hybridoma cell lines in PBST with 0.1% (w/v) BSA were added (100 μL/well) and incubated at 37 °C for 1 h. After three washings of the plate with PBST, rabbit anti-goat IgG-HRP (Thermo Fisher Scientific), or goat anti-mouse IgG-HRP (Cell Signaling) diluted to 1:2000 using PBST with 0.1% (w/v) BSA was added (100 μL/well) and incubated at 37 °C for 1 h, followed by three washings with PBST; peroxidase substrate TMB solution (KPL, Gaithersburg, MD, USA) was added (100 μL/well) and incubated at room temperature for 10 min. The reaction was terminated by 6 M H_3PO_4 solution (100 μL/well), and the optical density (OD) was measured at 450 nm with reference wavelength at 620 nm by a plate reader (SpectraMax 384 Plus, Molecular Devices, Sunnyvale, CA, USA) with a SoftMax software (version 5.4).

SDS-PAGE and Western Blot. Western blot was performed to assess the specificity of the goat sera, mouse sera, the hybridoma cell lines, monoclonal antibody, and polyclonal antibody for Gly m 4. The rGly m 4 and the soybean seed extract were diluted initially in PBST and further diluted 1:2 (v/v) in Bio-Rad 2X Laemmli Buffer and then heated in a 95 °C metal block for approximately 5 min. The denatured proteins and prestained protein ladder (BenchMark, Invitrogen) or Bio-Rad broad range protein markers were subjected to SDS-PAGE using a midi-gel apparatus (Invitrogen) with precast Novex Tris−glycine 4−20% (w/v) polyacrylamide gels (Invitrogen). The separated proteins were eletrophoretically transferred from the gels to a 0.45 μm polyvinylidene fluoride (PVDF) microporous membrane (Invitrogen) in a vertical midi-format electrophoresis cell (Criterion, Bio-Rad). Blotting was performed at 100 V for 60 min. The membrane was blocked overnight at 4 °C in PBS containing 0.3% (v/v) Tween-20. The membrane was rinsed three times for 10 min each in PBST and probed for 1 h at room temperature with either antisera or purified IgG in PBST with 0.1% (w/v) BSA. After three washings with PBST for 10 min each, the membrane was probed with rabbit anti-goat IgG-HRP (Thermo Fisher Scientific) or goat anti-mouse IgG-HRP (Cell Signaling) for 1 h at room temperature. After three rinses with PBST, SuperSignal West Pico Chemiluminescent Substrate (Thermo Scientific) was added onto the membrane. The luminescence signals were captured by photographic films (Amersham Hyperfilm ECL, GE Healthcare, Buckinghamshire, UK) in a dark room using a Konica SRX-101A automated film processor (Tokyo, Japan). Different exposures were taken, and a single exposure was scanned using a Bio-Rad GS-800 densitometer with the supplied Quantity One software (version 4.6.7).

Indirect Sandwich ELISA. An indirect sandwich ELISA was developed and validated to detect Gly m 4 from soybean seed quantitatively. Ninety-six-well microtiter plates were coated with 100 μL/well of purified mAb (2 μg/mL) in 0.05 M carbonate/bicarbonate buffer with 0.15 M NaCl (pH 9.6) and incubated overnight at 4 °C. The plates were washed three times with 300 μL/well PBST using a plate washer (ELC405, Biotek) to remove unbound mAb. Excess binding sites were blocked with 200 μL/well of Poly-HRP dilution buffer (Thermo Scientific) for 1 h at 37 °C. The plates were subsequently washed three times, and 100 μL of rGly m 4 standards and samples diluted in PBST with 0.1% (w/v) BSA at various concentrations was added into each well and incubated for 1 h at 37 °C. After three washings of the plate with PBST, biotinylated pAb with 1:4000 dilution in PBST with 0.1% (w/v) BSA was added (100 μL/well) and incubated for 1 h at 37 °C. Following three washings of the plates, a Poly-HRP streptavidin conjugate (Thermo Scientific) with 1:10000 dilution in Poly-HRP dilution buffer (Thermo Scientific) was added to each well (100 μL/well) and incubated for 0.5 h at 37 °C. Following three washings with PBST, peroxidase substrate 3,3′,5,5′-tetramethylbenzidine (TMB) solution (KPL, Gaithersburg, MD, USA) was added (100 μL/well) and incubated at room temperature for 10 min. The reaction was terminated by 6 M H_3PO_4 solution (100 μL/well), and the optical density (OD) was measured at 450 nm with reference wavelength at 620 nm. Calibration curve was obtained by plotting the OD values against Gly m 4 concentrations. A buffer blank, a negative control (QC−), and a positive control (QC+, 60 ng of rGly m 4 in PBST with 0.1% (w/v) BSA) were also included on every ELISA plate. All samples were run in triplicate. The sandwich ELISA was subsequently validated for its precision, limits of detection and quantitation (LOD and LOQ), dilutional parallelism, and extraction efficiency.[6,31]

Statistical Analysis of Gly m 4 Levels from Conventional Soybean Varieties. The Gly m 4 level was calculated according to the following equation:

$$\text{ppm} = (\text{ng/mL of extract}) \times (\text{dilution factor}) \times (\text{buffer to tissue ratio mL/g}) \div 1000\ \text{ng/μg}$$

Variance components analysis (VCA) was conducted for Gly m 4 from 24 soybean varieties to estimate the proportion of random effects contributing to the total variance, on the basis of the following analysis of variance (ANOVA) model by combining all eight sites:

$$Y_{ijk} = U + T_i + L_j + B(L)_{jk} + LT_{ij} + e_{ijk}$$

Y_{ijk} is the unique individual observation, U is the overall mean, T_i is the soybean variety effect, L_j is the location effect, $B(L)_{jk}$ is the block within location effect, LT_{ij} is the location by variety interaction effect, and e_{ijk} is the residual error.

In this application, all of the effects in the ANOVA model were set as random effects. The SAS procedure PROC MIXED was employed to run the analysis. The output table of covariance parameter estimates from SAS PROC MIXED procedure gives estimates of the variance component parameters.[32] The variance component parameters of each model component were divided by the total variance to get the variance proportions for each of the components.

RESULTS

Expression, Purification, and Characterization of rGly m 4. The soybean protein was expressed in *E. coli* with a histidine tag to facilitate purification (Figure 1). The cell lysates of pET24 rGly m 4/BL21 (DE3) showed a His-tagged rGly m 4 at 17 kDa with other proteins from *E. coli* (lane 3, Figure 1). After elution with imidazole in a NiNTA resin column, a single rGly m 4 band at the expected molecular weight was observed by SDS-PAGE (lanes 5 and 6, Figure 1). The rGly m 4 was stored in the buffer with 50 mM Tris-HCl, 100 mM NaCl, pH 8. By calculating rGly m 4 protein band intensity over total intensity on lane 6 (Figure 1), its purity was determined as 97%. The purity-corrected concentration was used to prepare ELISA standard curves.

The N-terminal sequence of rGly m 4 showed exact matches of 15 amino acids to the predicted amino acid sequence. MS

DOI: 10.1021/acs.jafc.5b00792
J. Agric. Food Chem. 2015, 63, 4947−4953

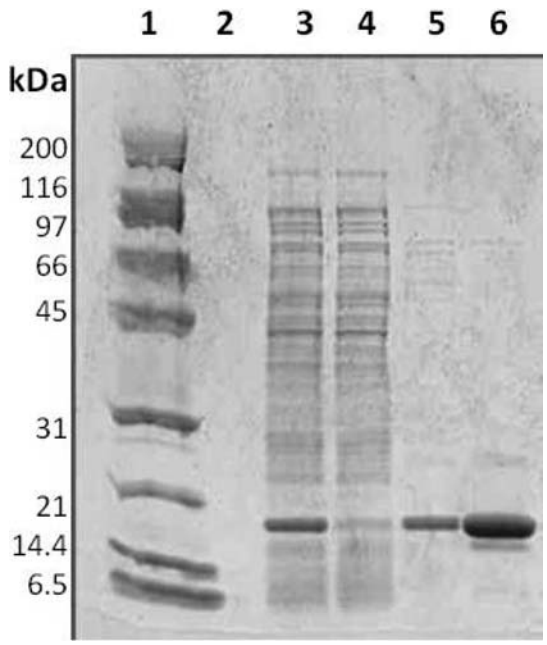

Figure 1. SDS-PAGE analysis of the expression and purification of rGly m 4 protein from *E. coli*. Lanes: 1, molecular weight markers; 2, blank; 3, lysates of pET24 rGly m 4/BL21 (DE3); 4, NiNTA flowthrough; 5, elution with 20 mM imidazole; 6, elution with 200 mM imidazole. The purity of rGly m 4 was determined as 97%.

result showed 41.8% sequence coverage. Overall, the identity of the rGly m 4 was confirmed by N-terminal sequence analysis and mass spectrometry.

Characterization of Antibodies. Monoclonal antibodies were purified from ascites of clone 46F8.B4 that showed the highest titer of 1:102,400. Similarly, polyclonal antibodies, purified from sera of two goats, were screened by using direct plate binding ELISA. The goat with the highest titer (1:6400) was selected for further characterization. Western blots were used to determine the specificity of both antibodies to the rGly m 4 and Gly m 4 in soybean extract (Figure 2). For these Western blots the rGly m 4 protein and soybean seed extract were serially diluted and loaded onto SDS-PAGE gels. Following the transfer of separated proteins onto the membranes, the blots were probed by using either monoclonal antibody (Figure 2a) or goat polyclonal antibody (Figure 2b). The Western blot results show both antibodies react with His-tagged rGly m 4 (approximate 17 kDa band in lanes 2−6) and Gly m 4 in soybean extract (approximate 16 kDa band in lanes 7−10). The monoclonal antibody showed more band intensity compared to the polyclonal antibody as expected on the basis of their respective titers. There were very faint cross-reaction bands (lanes 2−3) at approximately 49 kDa (Figure 2a) or at 60 and 26 kDa (Figure 2b) from rGly m 4, indicating both antibodies could have very slight immunoreactions with proteins from *E. coli*. This could be due to the small amount of impurities present in the rGly m 4 that was used as an immunogen for the antibody productions. Most importantly, both antibodies showed negligible cross-reaction with other soy proteins in the soybean seed extracts (Figure 2, lanes 7−10), indicating they were specific for Gly m 4 and could be used for the development of a Gly m 4 sandwich ELISA for soybean seed samples. From these experiments a monoclonal antibody and a polyclonal antibody were selected as capture and detection antibodies, respectively.

ELISA Method Optimization and Validation. A sandwich ELISA was optimized to use 2 μg/mL of mAb to capture Gly m 4 and a 1:4000 dilution of the pAb to detect Gly m 4. Using these antibody amounts, the assay showed low background values and high sensitivity. The quantification range of the standard curve was established from 7.8 to 125 ng/mL with anchor points of 0 and 500 ng/mL (Figure 3). A 60 ng/mL positive quality control (QC+) was used to evaluate the accuracy of the assay.

The precision of the assay across the entire working range of rGly m 4 protein levels was determined both within a run (intra-assay precision of technical replicates) and across runs (interassay precision of assay plates over a period of time). To do this the seven-point standard curve of rGly m 4 (at concentrations shown in Table 1) and the QC+ sample were assayed in triplicate wells over 36 assay runs carried out on three different days by three different analysts. Assay precision was calculated as the percentage coefficient of variation (%CV) using the interpreted concentrations of the QC+ samples and the standards observed over all assay runs (Table 1). The %CV of intra-assay and interassay precisions of standards and QC+ were much less than 15%, the commonly accepted limit in industry bioanalytical method validation.[33]

To ensure accurate detection of Gly m 4 in the soybean seed, it was also important to determine the lowest concentration of

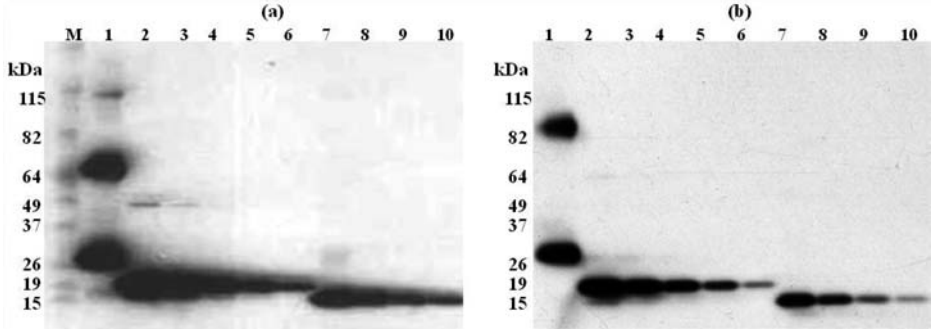

Figure 2. Western blot analyses of monoclonal antibody (a) and polyclonal antibody (b) with rGly m 4 and soybean seed extract. Lanes: M, prestained protein ladder; 1, mouse IgG (a) or goat IgG (b) as positive controls; 2, antibodies reacted with 32 ng of rGly m 4; 3, 16 ng of rGly m 4; 4, 8 ng of rGly m 4; 5, 4 ng of rGly m 4; 6, 2 ng of rGly m 4; 7, soybean extract with 1:200 total dilution; 8, soybean extract with 1:400 total dilution; 9, soybean extract with 1:800 total dilution; 10, soybean extract with 1:1600 total dilution. These Western blots demonstrate that the monoclonal and polyclonal antibodies are specific for both rGly m 4 and Gly m 4 from soybean.

DOI: 10.1021/acs.jafc.5b00792
J. Agric. Food Chem. 2015, 63, 4947−4953

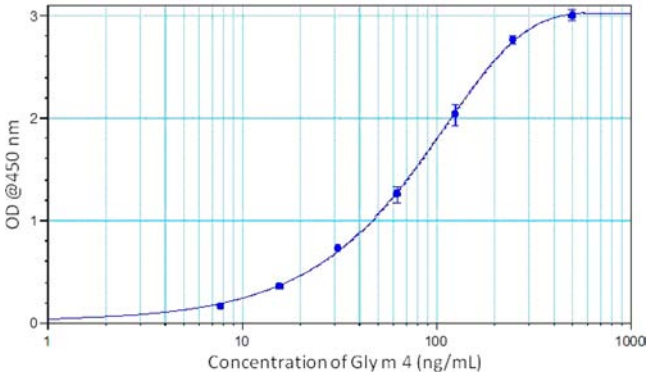

Figure 3. Standard curve of sandwich ELISA for Gly m 4. Each point represents the optical density (OD) of each Gly m 4 concentration with mean ± standard deviation from three determinations. The coefficient of determination (R^2) is 1.00. The quantification range of the standard curve is 7.8−125 ng/mL.

Table 1. Gly m 4 ELISA Dose-Dependent Intrarun and Inter-run Precisions of Seven Standard Points and the QC+ Sample

concentration of standard (ng/mL)	%CV intrarun	%CV inter-run
250.0	3.9	3.9
125.0	1.1	2.4
62.5	1.0	1.8
31.3	1.3	1.9
15.6	1.7	2.8
7.8	4.0	5.0
QC+	4.3	11.5

Gly m 4 that can reliably be detected above the assay's background level. Because no negative matrix could be used to determine this lowest concentration, 21 replicate buffer samples (seven in one assay buffer, total three lots of the assay buffer) were analyzed in triplicate wells on three ELISA runs by three different analysts. The limit of detection (LOD) was defined as the average concentration of Gly m 4 that could be calculated from the background OD observed in the assay buffers plus three standard deviations of the concentration. By these criteria, the LOD for Gly m 4 in the soybean seed samples was determined to be 2.1 ng/mL. The limit of quantification (LOQ) for Gly m 4 was defined as the lowest concentration on the standard curve with a %CV ≤ 15% and was determined to be 7.8 ng/mL.

In addition to assay precision using a standard curve and QC +, it is important to confirm that the Gly m 4 ELISA is accurate across a range of expression levels in soybean seed samples. Dilutional parallelism is a method used to demonstrate the accuracy of an ELISA assay. Dilutional parallelism was demonstrated by testing multiple dilutions of a soybean protein extract to demonstrate that the ELISA method is accurate regardless of the sample dilution being tested. To test dilutional parallelism of Gly m 4, five independently extracted samples were analyzed at four dilution factors (20-, 30-, 40-, and 50-fold) that were within the quantitative range of the standard curve. Each result was then corrected for the appropriate dilution factor and compared to the average concentration of all dilutions for that sample. The recovery of Gly m 4 across the multiple dilutions of five soybean seed samples ranged from 89 to 104% (Figure 4), indicating that this assay can accurately detect Gly m 4 from soybean seed samples across a range of working concentrations.

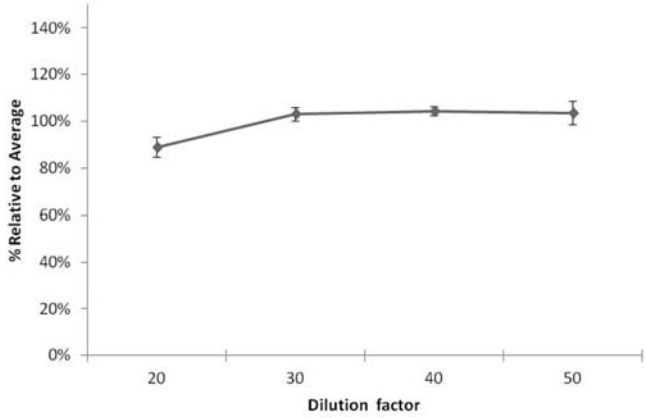

Figure 4. Dilutional parallelism of the sandwich ELISA for Gly m 4. The recovery of Gly m 4 across the multiple dilutions of soybean seed extracts ranged from 94 to 103%, indicating that this assay can accurately detect Gly m 4 from soybean seed samples across a range of working concentrations.

Finally, an extraction efficiency experiment was also performed to estimate the efficiency of the procedure used to extract Gly m 4 from soybean seed. This experiment is completed by performing successive extractions on the same material and analyzing each extract to determine the amount of Gly m 4 protein that remains after the first extraction. The extraction efficiency is expressed as the percent of Gly m 4 protein recovered in the first extraction (supernatant, E1) compared to the total recovered from the consecutive re-extractions of the same sample. For this evaluation, Gly m 4 from three soybean seed samples was extracted, and the average extraction efficiency was calculated to be 76%.

Overall, the validation results demonstrate that this sandwich ELISA is precise and accurate and provides sensitive and reliable reproducible quantification of Gly m 4 levels in soybean seed samples.

Gly m 4 Levels in Soybean Varieties Grown at Eight Locations. The ELISA assay was used to measure Gly m 4 levels in 24 different soybean varieties grown across eight different commercial soybean growing locations in the United States. The results showed that the range of Gly m 4 levels was about 13-fold difference (from 24 to 311 ppm; Figure 5a). Variance component analysis showed location and substance as well as residual (from uncontrolled systematic variability, including biological variability) are the three main contributions to the total variability of Gly m 4 expression in soybeans, indicating that both environmental and germplasm differences do affect endogenous allergen levels (Figure 5b).

DISCUSSION

Gly m 4 has been identified as a key allergen in soybean.[34] Here a Gly m 4-specific sandwich ELISA is described, using antibodies generated by immunization of a histidine-tagged recombinant form of soy Gly m 4 (Figure 1). The ELISA shows high specificity and sensitivity to Gly m 4 in soybean seed extract, without any cross-reactivity to other soybean seed proteins (Figures 2 and 3). The intra- and interassay precisions of this Gly m 4 ELISA were well within the limit of variability accepted by industry bioanalytical method validation criteria

DOI: 10.1021/acs.jafc.5b00792
J. Agric. Food Chem. 2015, 63, 4947−4953

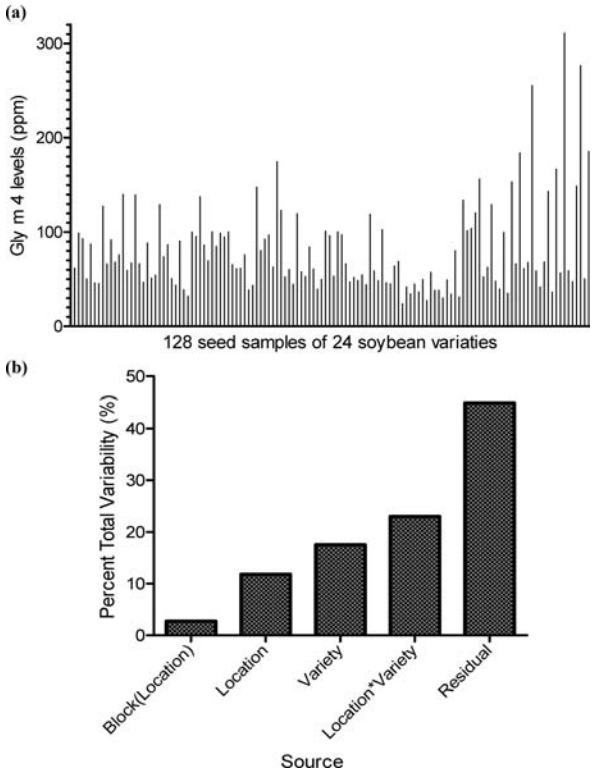

Figure 5. Gly m 4 levels in soybean seed samples: (a) Gly m 4 levels from 24 soybean varieties from 8 locations representing the major U.S. commercial growing areas; (b) sources of variation estimates from variance component analysis (VCA). Location is the environmental effect from eight growing locations; variety is the variety effect soybean from 24 soybean varieties; block is the block effect within each location; location × variety is the location by variety interaction effect, and the residual is the residual error from uncontrolled systematically variation.

(Table 1).[33] Additionally, extraction efficiency and dilutional parallelism experiments demonstrated the high level of accuracy that the ELISA method has in quantifying Gly m 4 (Figure 4) in soybean seed extracts. Taken together, the Gly m 4 ELISA described is shown to have the specificity, sensitivity, accuracy, and precision required for use in the assessment of this soybean allergen in samples from both GM and conventional soybean samples.

The purpose of the endogenous allergen assessment for GM soybean varieties is to compare the endogenous allergen levels in the GM variety to those in non-GM varieties. To evaluate this comparison of endogenous allergen levels, an understanding of the variability in allergen levels safely consumed by nonallergic individuals must be established. For this reason, the developed ELISA method was used to measure Gly m 4 in 24 conventional soybean varieties planted in different locations. The result showed that Gly m 4 levels could vary up to 13-fold (from 24 to 311 ppm) for soybean seed samples from different varieties and grown in different locations. This high level of natural variability of Gly m 4 is similar to those previously reported by Mittag et al. using a quantitative Western blot method, which showed Gly m 4 level ranged from 8 to 224 ppm.[17] Similar observations were obtained for other soybean allergens. By using SDS-PAGE, Martinez-Villaluenga et al. found β-conglycinin and glycinin of 15 soybean genotypes ranged from 0.0 to 35.7% and from 23.1 to 50.8% of total protein, respectively.[35] By using ELISA, Hei et al. observed that β-conglycinin ranged from 3.99 to 14.78% of total weight from 469 soybean seed samples,[36] and Chen et al. found that glycinin ranged from 2.72 to 19.56% of total weight from the same set of soybean seed samples.[37] For Gly m Bd 30k (P34) determined by ELISA in 138 soybean cultivars from a diverse germplasm collection from 10 different countries, the lowest and highest levels were 2.32 and 27.75 mg/g defatted flour, respectively.[38] The effects of environment and genotype on Gly m 4 levels from conventional soybeans are also consistent with previous studies on compositional differences.[39−43] Further investigation of environmental and genotypic effects on allergenicity is needed for other endogenous allergens.

In conclusion, a robust sandwich ELISA for Gly m 4 has been developed and validated for soybean seed extracts. Use of this ELISA has shown that this common soybean food allergen has high variability across conventional soybean varieties grown in different locations.

AUTHOR INFORMATION

Corresponding Author

*(T.G.) E-mail: tao.geng@monsanto.com. Phone: (314) 694-7695.

Notes

The authors declare no competing financial interest.

ACKNOWLEDGMENTS

We thank Luis Burzio, George Harrigan, and John Vicini for excellent technical review. We also thank Emily Barr, Holly Chapman, and Cunxi Wang for technical assistance.

REFERENCES

(1) Wilson, R. F. Seed composition. In *Soybeans: Improvement, Production and Uses*, 3rd ed.; Boerma, H. R., Specht, J. E., Eds.; ASA, CSSA, SSA: Madison, WI, USA, 2004.

(2) L'Hocine, L.; Boye, J. I. Allergenicity of soybean: new developments in identification of allergenic proteins, cross-reactivities and hypoallergenization technologies. *Crit. Rev. Food Sci. Nutr.* **2007**, *47* (2), 127−143.

(3) James, C. Global status of commercialized biotech/GM crops. *ISAAA Brief 49*; 2014.

(4) Alimentarius, C. *Foods Derived from Modern Biotechnology*; Codex Alimentarius Commission, Joint FAO/WHO Food Standards Programme: Rome, Italy, 2009.

(5) Ladics, G. S.; Budziszewski, G. J.; Herman, R. A.; Herouet-Guicheney, C.; Joshi, S.; Lipscomb, E. A.; McClain, S.; Ward, J. M. Measurement of endogenous allergens in genetically modified soybeans − short communication. *Regul. Toxicol. Pharmacol.* **2014**, *70* (1), 75−79.

(6) Crowell, D. N.; John, M. E.; Russell, D.; Amasino, R. M. Characterization of a stress-induced, developmentally regulated gene family from soybean. *Plant Mol. Biol.* **1992**, *18* (3), 459−466.

(7) Wen, J.; Vanek-Krebitz, M.; Hoffmann-Sommergruber, K.; Scheiner, O.; Breiteneder, H. The potential of Betv1 homologues, a nuclear multigene family, as phylogenetic markers in flowering plants. *Mol. Phylogenet. Evol.* **1997**, *8* (3), 317−333.

(8) Berkner, H.; Neudecker, P.; Mittag, D.; Ballmer-Weber, B. K.; Schweimer, K.; Vieths, S.; Rosch, P. Cross-reactivity of pollen and food allergens: soybean Gly m 4 is a member of the Bet v 1 superfamily and closely resembles yellow lupine proteins. *Biosci. Rep.* **2009**, *29* (3), 183−192.

(9) Karamloo, F.; Scheurer, S.; Wangorsch, A.; May, S.; Haustein, D.; Vieths, S. Pyr c 1, the major allergen from pear (*Pyrus communis*), is a new member of the Bet v 1 allergen family. *J. Chromatogr., Biomed. Appl.* **2001**, *756* (1−2), 281−293.

DOI: 10.1021/acs.jafc.5b00792
J. Agric. Food Chem. 2015, 63, 4947−4953

(10) Pinto, M. P.; Ricardo, C. P. *Lupinus albus* L. pathogenesis-related proteins that show similarity to PR-10 proteins. *Plant Physiol.* **1995**, *109* (4), 1345−1351.
(11) Breiteneder, H.; Pettenburger, K.; Bito, A.; Valenta, R.; Kraft, D.; Rumpold, H.; Scheiner, O.; Breitenbach, M. The gene coding for the major birch pollen allergen Betv1, is highly homologous to a pea disease resistance response gene. *EMBO J.* **1989**, *8* (7), 1935−1938.
(12) Luttkopf, D.; Muller, U.; Skov, P. S.; Ballmer-Weber, B. K.; Wuthrich, B.; Skamstrup Hansen, K.; Poulsen, L. K.; Kastner, M.; Haustein, D.; Vieths, S. Comparison of four variants of a major allergen in hazelnut (*Corylus avellana*) Cor a 1.04 with the major hazel pollen allergen Cor a 1.01. *Mol. Immunol.* **2002**, *38* (7), 515−525.
(13) Vanek-Krebitz, M.; Hoffmann-Sommergruber, K.; Laimer da Camara Machado, M.; Susani, M.; Ebner, C.; Kraft, D.; Scheiner, O.; Breiteneder, H. Cloning and sequencing of Mal d 1, the major allergen from apple (*Malus domestica*), and its immunological relationship to Bet v 1, the major birch pollen allergen. *Biochem. Biophys. Res. Commun.* **1995**, *214* (2), 538−551.
(14) Scheurer, S.; Metzner, K.; Haustein, D.; Vieths, S. Molecular cloning, expression and characterization of Pru a 1, the major cherry allergen. *Mol. Immunol.* **1997**, *34* (8−9), 619−629.
(15) Kleine-Tebbe, J.; Wangorsch, A.; Vogel, L.; Crowell, D. N.; Haustein, U. F.; Vieths, S. Severe oral allergy syndrome and anaphylactic reactions caused by a Bet v 1-related PR-10 protein in soybean, SAM22. *J. Allergy Clin. Immunol.* **2002**, *110* (5), 797−804.
(16) Kleine-Tebbe, J.; Martin, A.; Wangorsch, A.; Crowell, D. N.; Haustein, U. F.; Vieths, S. Histamine release from human basophils in vitro and IgE-binding to recombinant (r) pathogenesis-related (PR) Bet v 1-homologue soybean protein rSAM22: Explanation for soy-induced anaphylactic reactions and severe oral allergy syndrome (OAS) in birch pollen-allergic subjects. *J. Allergy Clin. Immunol.* **2002**, *109* (1), S304−S305.
(17) Mittag, D.; Vieths, S.; Vogel, L.; Becker, W. M.; Rihs, H. P.; Helbling, A.; Wuthrich, B.; Ballmer-Weber, B. K. Soybean allergy in patients allergic to birch pollen: clinical investigation and molecular characterization of allergens. *J. Allergy Clin. Immunol.* **2004**, *113* (1), 148−154.
(18) Julka, S.; Kuppannan, K.; Karnoup, A.; Dielman, D.; Schafer, B.; Young, S. A. Quantification of Gly m 4 Protein, a major soybean allergen, by two-dimensional liquid chromatography with ultraviolet and mass spectrometry detection. *Anal. Chem.* **2012**, *84* (22), 10019−10030.
(19) Poms, R. E.; Klein, C. L.; Anklam, E. Methods for allergen analysis in food: a review. *Food Addit. Contam.* **2004**, *21* (1), 1−31.
(20) Kirsch, S.; Fourdrilis, S.; Dobson, R.; Scippo, M.-L.; Maghuin-Rogister, G.; De Pauw, E. Quantitative methods for food allergens: a review. *Anal. Bioanal. Chem.* **2009**, *395* (1), 57−67.
(21) Schubert-Ullrich, P.; Rudolf, J.; Ansari, P.; Galler, B.; Fuehrer, M.; Molinelli, A.; Baumgartner, S. Commercialized rapid immunoanalytical tests for determination of allergenic food proteins: an overview. *Anal. Bioanal. Chem.* **2009**, *395* (1), 69−81.
(22) Liu, B.; Teng, D.; Wang, X. M.; Yang, Y. L.; Wang, J. H. Expression of the soybean allergenic protein P34 in Escherichia coli and its indirect ELISA detection method. *Appl. Microbiol. Biotechnol.* **2012**, *94* (5), 1337−1345.
(23) Tsuji, H.; Okada, N.; Yamanishi, R.; Bando, N.; Kimoto, M.; Ogawa, T. Measurement of Gly-M-Bd-30k, a major soybean allergen, in soybean products by a sandwich enzyme-linked-immunosorbent-assay. *Biosci., Biotechnol., Biochem.* **1995**, *59* (1), 150−151.
(24) Liu, B.; Teng, D.; Wang, X. M.; Wang, J. H. Detection of the soybean allergenic protein Gly m Bd 28K by an indirect enzyme-linked immunosorbent assay. *J. Agric. Food Chem.* **2013**, *61* (4), 822−828.
(25) Bando, N.; Tsuji, H.; Hiemori, M.; Yoshizumi, K.; Yamanishi, R.; Kimoto, M.; Ogawa, T. Quantitative analysis of Gly m Bd 28K in soybean products by a sandwich enzyme-linked immunosorbent assay. *J. Nutr. Sci. Vitaminol.* **1998**, *44* (5), 655−664.
(26) Ma, X.; Sun, P.; He, P. L.; Han, P. F.; Wang, J. J.; Qiao, S. Y.; Li, D. F. Development of monoclonal antibodies and a competitive ELISA detection method for glycinin, an allergen in soybean. *Food Chem.* **2010**, *121* (2), 546−551.
(27) Liu, B.; Teng, D.; Yang, Y. L.; Wang, X. M.; Wang, J. H. Development of a competitive ELISA for the detection of soybean alpha subunit of beta-conglycinin. *Process Biochem.* **2012**, *47* (2), 280−287.
(28) You, J. M.; Li, D.; Qiao, S. Y.; Wang, Z. R.; He, P. L.; Ou, D. Y.; Dong, B. Development of a monoclonal antibody-based competitive ELISA for detection of β-conglycinin, an allergen from soybean. *Food Chem.* **2008**, *106* (1), 352−360.
(29) Brandon, D. L.; Bates, A. H.; Friedman, M. ELISA analysis of soybean trypsin inhibitors in processed foods. *Adv. Exp. Med. Biol.* **1991**, *289*, 321−337.
(30) ISU (Iowa State University). *Soybean Growth and Development*; Ames, IA, USA, 2004; Vol. PM 45.
(31) Deshpande, S. S. *Enzyme Immunoassays: From Concept to Product Development*; Chapman and Hall: New York, 1996.
(32) Littell, R. C.; Milliken, G. A.; Stroup, W. W.; Wolfinger, R. D.; Schabenberger, O. *SAS for Mixed Models*; SAS Institute: Cary, NC, USA. 2006.
(33) FDA. *Guidance for Industry Bioanalytical Method Validation*; U.S. GPO: Washington, DC, USA, 2001.
(34) Berneder, M.; Bublin, M.; Hoffmann-Sommergruber, K.; Hawranek, T.; Lang, R. Allergen chip diagnosis for soy-allergic patients: Gly m 4 as a marker for severe food-allergic reactions to soy. *Int. Arch. Allergy Immunol.* **2013**, *161* (3), 229−233.
(35) Martinez-Villaluenga, C.; Bringe, N. A.; Berhow, M. A.; de Mejia, E. G. β-Conglycinin embeds active peptides that inhibit lipid accumulation in 3T3-L1 adipocytes in vitro. *J. Agric. Food Chem.* **2008**, *56* (22), 10533−10543.
(36) Hei, W.; Li, Z.; Ma, X.; He, P. Determination of β-conglycinin in soybean and soybean products using a sandwich enzyme-linked immunosorbent assay. *Anal. Chim. Acta* **2012**, *734* (0), 62−68.
(37) Chen, J.; Wang, J.; Song, P.; Ma, X. Determination of glycinin in soybean and soybean products using a sandwich enzyme-linked immunosorbent assay. *Food Chem.* **2014**, *162* (0), 27−33.
(38) Wilson, S.; Martinez-Villaluenga, C.; De Mejia, E. G. Purification, thermal stability, and antigenicity of the immunodominant soybean allergen P34 in soy cultivars, ingredients, and products. *J. Food Sci.* **2008**, *73* (6), T106−T114.
(39) Harrigan, G. G.; Lundry, D.; Drury, S.; Berman, K.; Riordan, S. G.; Nemeth, M. A.; Ridley, W. P.; Glenn, K. C. Natural variation in crop composition and the impact of transgenesis. *Nat. Biotechnol.* **2010**, *28* (5), 402−404.
(40) Berman, K. H.; Harrigan, G. G.; Nemeth, M. A.; Oliveira, W. S.; Berger, G. U.; Tagliaferro, F. S. Compositional equivalence of insect-protected glyphosate-tolerant soybean MON 87701 x MON 89788 to conventional soybean extends across different world regions and multiple growing seasons. *J. Agric. Food Chem.* **2011**, *59* (21), 11643−11651.
(41) Zhou, J.; Berman, K. H.; Breeze, M. L.; Nemeth, M. A.; Oliveira, W. S.; Braga, D. P.; Berger, G. U.; Harrigan, G. G. Compositional variability in conventional and glyphosate-tolerant soybean (*Glycine max* L.) varieties grown in different regions in Brazil. *J. Agric. Food Chem.* **2011**, *59* (21), 11652−11656.
(42) Zhou, J.; Harrigan, G. G.; Berman, K. H.; Webb, E. G.; Klusmeyer, T. H.; Nemeth, M. A. Stability in the composition equivalence of grain from insect-protected maize and seed from glyphosate-tolerant soybean to conventional counterparts over multiple seasons, locations, and breeding germplasms. *J. Agric. Food Chem.* **2011**, *59* (16), 8822−8828.
(43) Harrigan, G. G.; Culler, A. H.; Culler, M.; Breeze, M. L.; Berman, K. H.; Halls, S. C.; Harrison, J. M. Investigation of biochemical diversity in a soybean lineage representing 35 years of breeding. *J. Agric. Food Chem.* **2013**, *61* (45), 10807−10815.

DOI: 10.1021/acs.jafc.5b00792
J. Agric. Food Chem. 2015, 63, 4947−4953

This is an open access article published under a Creative Commons Attribution (CC-BY) License, which permits unrestricted use, distribution and reproduction in any medium, provided the author and source are cited.

JOURNAL OF AGRICULTURAL AND FOOD CHEMISTRY

Article

pubs.acs.org/JAFC

International Ring Trial for the Validation of an Event-Specific Golden Rice 2 Quantitative Real-Time Polymerase Chain Reaction Method

Sara Jacchia,[†] Elena Nardini,[†] Niccolò Bassani,[†] Christian Savini,[†] Jung-Hyun Shim,[‡] Kurniawan Trijatmiko,[‡] Joachim Kreysa,[†] and Marco Mazzara*[,†]

[†]Molecular Biology and Genomics Unit, Institute for Health and Consumer Protection, European Commission Joint Research Centre, Via E. Fermi 2749, 21027 Ispra, Varese, Italy

[‡]Plant Breeding, Genetics and Biotechnology Division, International Rice Research Institute, Los Baños, 4031 Laguna, Philippines

Supporting Information

ABSTRACT: This article describes the international validation of the quantitative real-time polymerase chain reaction (PCR) detection method for Golden Rice 2. The method consists of a taxon-specific assay amplifying a fragment of rice Phospholipase D α2 gene, and an event-specific assay designed on the 3′ junction between transgenic insert and plant DNA. We validated the two assays independently, with absolute quantification, and in combination, with relative quantification, on DNA samples prepared in haploid genome equivalents. We assessed trueness, precision, efficiency, and linearity of the two assays, and the results demonstrate that both the assays independently assessed and the entire method fulfill European and international requirements for methods for genetically modified organism (GMO) testing, within the dynamic range tested. The homogeneity of the results of the collaborative trial between Europe and Asia is a good indicator of the robustness of the method.

KEYWORDS: *international validation, Golden Rice 2 (GR2), quantitative real-time PCR (qPCR), genetically modified organism (GMO), endogenous taxon-specific gene, event-specific method*

INTRODUCTION

In rice the biosynthetic pathway of β-carotene, a precursor of vitamin A, is normally active in leaves but not in the eaten part of the plant, the grain, mainly constituted by endosperm. Golden Rice 2 (GR2) produces and accumulates β-carotene in the endosperm and was engineered with the aim of fighting vitamin A deficiency, which affects the life of millions of people who do not have access to enough fresh vegetables, dairy product, eggs and meat, but rely on rice as a staple food.[1−5] GR2 belongs to the second generation of Golden Rice plants and accumulates significantly more β-carotene in the endosperm than the first generation of Golden Rice. The International Rice Research Institute in the Philippines (IRRI) is coordinating the introgression (i.e., introduction by conventional breeding) of the GR2 trait into local varieties widely used by farmers and fit for the target growing conditions.[6] Cultivation in the target countries will require authorization by the responsible authorities, which in most cases is guaranteed only if a method for the detection and, in case of labeling requirements, quantification of the GM event is available.

The use of DNA-based methods, and in particular polymerase chain reaction (PCR), is preferred to other analytical approaches for genetically modified organisms (GMOs) screening and quantification because PCR has been proven to be very accurate, both when applied to raw ingredients and to processed food/feed samples.[7−11] PCR and real-time PCR are internationally recognized and recommended for GMO analysis.[12,13] For the development of a method for the detection of GR2, IRRI asked for the collaboration of the Molecular Biology and Genomics (MBG) Unit of the Institute for Health and Consumer Protection of the European Commission Joint Research Centre. The MBG Unit hosts the European Union Reference Laboratory for Genetically Modified Food and Feed (EU-RL GMFF), which has 10 years of experience in validation of quantitative real-time PCR (qPCR) methods and has fully validated about 60 methods for GMO detection.[14−17] The EU-RL GMFF, together with the European Network of GMO Laboratories (ENGL), defined globally accepted performance requirements for analytical methods of GMO testing.[18] These requirements are also in line with the Codex Alimentarius guidelines for methods for detection, identification, and quantification of specific DNA sequences and proteins in food.[19] The developed method is a simplex TaqMan event-specific method for the determination of the relative content of GR2 DNA to total rice DNA and is composed of two qPCR assays: a new rice taxon-specific assay, PLD-GR, which amplifies a 124 bp fragment of rice Phospholipase D α2 (PLD) gene, and an event-specific assay, GR2, which amplifies a 121 bp fragment across the 3′ junction between transgenic insert and plant DNA. Detailed information on the development and single laboratory validation of the method, including assessment of the copy number and stability of the taxon-specific assay, and of the specificity, limit of detection (LOD), limit of quantification (LOQ), dynamic range, and robustness of the PLD-GR and GR2 assays, can be found in the dedicated article.[20]

Received: February 19, 2015
Revised: April 29, 2015
Accepted: May 6, 2015
Published: May 6, 2015

 © 2015 American Chemical Society

DOI: 10.1021/acs.jafc.5b00951
J. Agric. Food Chem. 2015, 63, 4954−4965

This paper reports on the subsequent international validation of the method through a collaborative trial. Such a validation trial is a fundamental step to ensure that the method performance measured during single laboratory validation is reproducible when the method is run by different laboratories, operators, instruments, and conditions, and in this study notably in different geographic regions. It verifies the robustness and fitness for purpose of the method, by testing that its performance matches pre-established criteria when it is used in a population of laboratories that is representative of the target users.[21−23] The immediate purpose of the development of the detection method for GR2 is the authorization for cultivation and for food use of the GM rice in the Philippines, where labeling is mandatory for foods containing GM ingredients above a 5% threshold,[24] and at later stages in other Asian countries (e.g., Indonesia and Bangladesh). However, the method could in the future be needed by European control laboratories to check for the presence of GR2 in rice imports from Asia.[25−29] Thus, for the validation of the GR2 detection method, we selected eight laboratories in Europe, of which seven are European national reference laboratories and one operates in Switzerland,[30] and eight laboratories in Asia, belonging to the official GMO control networks including universities, national institutes, and food safety authorities. The 16 laboratories were selected among those potentially going to use the method on the basis of their geographic location, with the aim of obtaining a good distribution of test results across the European and Asian territory.

The analytical procedures for the detection of GMOs, from sampling to determination of GM content, are composed of distinct successive or parallel steps, termed modules. Different modules can be validated separately and combined together afterward, provided that the pre-established performance criteria are respected for the preceding or parallel module.[23,31−33] This approach allows higher flexibility than the validation of the full method because independently validated modules (e.g., DNA extraction and qPCR) can be combined together according to their availability or appropriateness for the target material. In many cases it allows reducing the costs of method validation: when one or more modules that constitute a method are already validated there is no need to include them in the validation study. We considered that the taxon- and the event-specific PCR-assays that constitute a qPCR method can also be regarded as modules and, thus, chose to validate them independently.[31−34] The validation samples were prepared in haploid genome equivalents (hge), calculated by taking into account a rice haploid genome size of 0.5 pg.[35] The rice material used for this study was homozygous, with a ratio between the GM event and the taxon-specific gene of 1;[20] the GM percentages expressed in hge percentages are thus equivalent to mass GM percentages.

The experimental design and results of the validation of the qPCR detection method for GR2 are presented and discussed in the following paragraphs.

MATERIALS AND METHODS

Material and ***DNA extraction*** are described in the Supporting Information.

Quantitative Real-Time PCR. The qPCR reactions for the PLD-GR taxon-specific assay and the GR2 event-specific assay are optimized to be performed in a volume of 25 μL including 5 μL of DNA sample; the primers and probe sequences for each assay are reported in Table S1, Supporting Information. The qPCR reaction mixtures of PLD-GR and GR2 assays contained the following reagents: 1× TaqMan universal master mix (Applied Biosystems, Warrington, United Kingdom), 300 nM primer forward, 300 nM primer reverse (Eurofins Genomics, Ebesberg, Germany), 150 nM probe (Applied Biosystems, Warrington, United Kingdom), 5 μL DNA solution (between 0.02 ng and 200 ng of template DNA per reaction), and nuclease free water (Promega, Madison, USA) to reach the volume of 25 μL. The thermal profile was as follows: 50 °C for 2 min; 95 °C for 10 min; 45 cycles of 95 °C for 15 s, and 60 °C for 60 s; fluorescence data were acquired at the end of the elongation step of each cycle.

Sample Preparation. Two sets of samples were prepared, one for the validation of the taxon-specific assay, labeled PLD, and one for the validation of the GR2 event-specific assay and for a test of the performance of the entire method, labeled GR2. The two sets of samples, consisting of five standard curve samples and 20 blind samples each, were prepared and shipped to all laboratories. PLD and GR2 standard curve samples were prepared from non-GM and GM DNA, respectively, by serial dilution and were labeled S1−S5 PLD/GR2. The hge content and DNA concentration of the standard curve samples are described in Tables S2 and S4, Supporting Information. PLD and GR2 blind samples were prepared independently and consisted of five samples at different DNA concentrations labeled B1−B5 PLD/GR2, which were then subdivided into four samples each and randomly labeled from U1 to U20 PLD/GR2. PLD blind samples were prepared with non-GM DNA, diluted to obtain the desired hge content; GR2 blind samples were prepared with GM DNA, diluted in a background of non-GM DNA to obtain the desired GM hge content in the defined total hge content. The hge content and DNA concentration of the blind samples are described in Tables S3 and S5, Supporting Information. All dilutions were prepared with 0.1× TE and all samples were thoroughly homogenized before any subsequent use. After preparation the samples were tested with a qPCR experiment and divided into 21 aliquots each. The validation kits were prepared from those aliquots and one randomly chosen kit was tested in accordance to the validation protocol prior to the shipment of kits to participating laboratories.

International Collaborative Trial. The collaborative trial was organized by the EU-RL GMFF: 16 laboratories evenly distributed over European and Asian countries were selected to participate to the study (see list of participating laboratories in Table S6, Supporting Information). Each laboratory received a kit for the validation study that included all reagents and samples needed for the validation, with the exception of the no-template control sample, that had to be prepared. Kits were shipped in dry ice to all laboratories with the exception of those located in China and India, for which blue ice had to be used due to the impossibility to ship in dry ice to those countries. All participating laboratories also received a detailed protocol to follow and an excel file for reporting results and were requested to report any deviation from the protocol which may have occurred during the preparation and execution of the qPCR experiments. The laboratories had to run three qPCR plates: one loaded with PLD standard curve samples and PLD blind samples (plate A), for the quantification of PLD blind samples with the PLD-GR assay; one for the quantification of GR2 blind samples with the GR2 assay, loaded with GR2 standard curve samples and GR2 blind samples (plate B); and one for the quantification of the amount of rice taxon-specific PLD target in GR2 blind samples with the PLD-GR assay, loaded with PLD standard curve samples and GR2 blind samples (plate C). Each sample was pipetted in three adjacent wells and the three resulting Cq values were averaged. A no template control was included in the plate, also pipetted in triplicate. The four blind samples with the same hge content were considered as independent replicates, yielding a total of four replicated measurements per laboratory for each blind sample. The layout of the plate setup is available in Figures S1−S3, Supporting Information.

Performance Parameters. In accordance with ISO 5725-1[21] we evaluated two measures of accuracy: trueness and precision. Trueness was expressed as mean percent bias (difference between the mean value of the test results and the accepted reference value divided by the

DOI: 10.1021/acs.jafc.5b00951
J. Agric. Food Chem. 2015, 63, 4954−4965

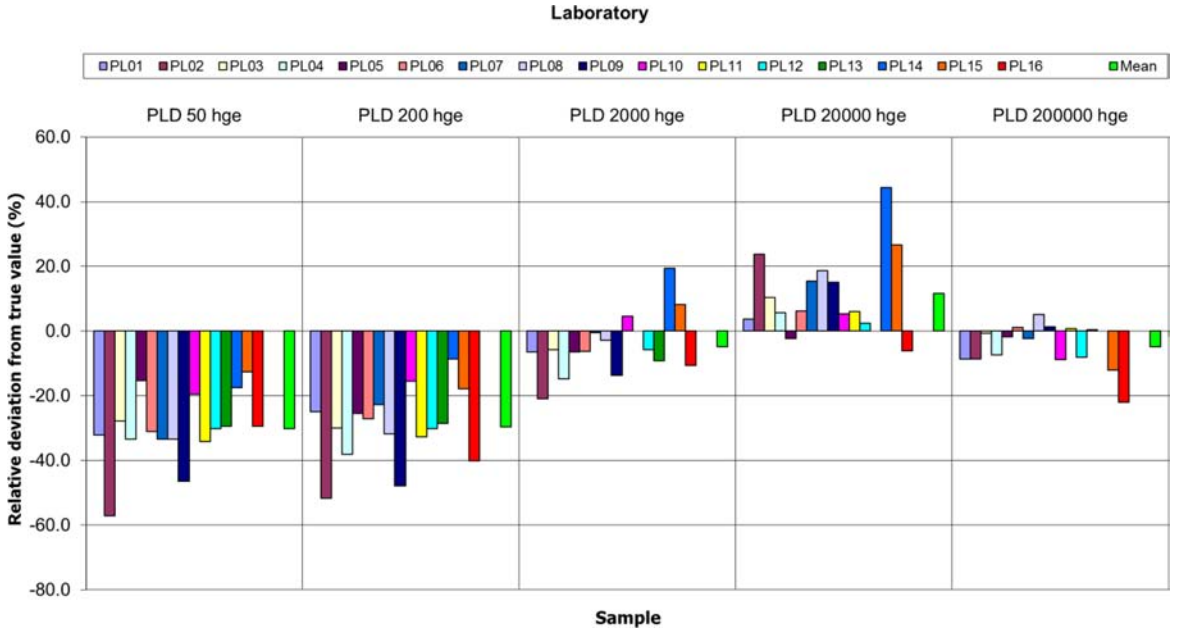

Figure 1. Relative percent deviation from the target hge content for PLD-GR taxon-specific assay. Colored bars represent the difference between the hge measured by each laboratory and the true hge content in percentage of the latter; the green bar on the right represents the mean of the relative deviations of all laboratories for each level of hge content. PL01-PL16: codes assigned to the 16 testing laboratories; PL11 at 2000 hge, PL13 at 20 000 hge, and PL14 at 200 000 hge do not show up in the graph because their results for those levels were excluded from the analysis as outliers.

Table 1. Summary of Validation Results for the PLD-GR Taxon-Specific Assay (16 Laboratories)

	test sample haploid genome equivalents				
	level 5 50	level 4 200	level 3 2000	level 2 20000	level 1 200000
number of outliers	0	0	1	1	1
reason for exclusion[a]			C	C	S/D
measured hge content	**35**	**141**	**1905**	**22335**	**190438**
(95% CI)	(32; 38)	(129; 153)	(1795; 2014)	(20911; 23758)	(182734; 198143)
relative repeatability standard deviation, RSD_r %	19.6	13.9	9.0	7.1	8.1
relative reproducibility standard deviation, RSD_R %	23.2	20.0	13.0	13.0	10.1
bias %	−30.2	−29.6	−4.8	11.7	−4.8
(95% CI)	(−36.1; −24.3)	(−35.6; −23.6)	(−10.2; 0.7)	(4.6; 18.8)	(−8.6; −0.9)

[a]C, Cochran test; S, single Grubbs test; D, double Grubbs test.

accepted reference value). Precision was expressed as relative repeatability standard deviation (RSD_r) in percent relative to the accepted reference value, and as relative reproducibility standard deviation (RSD_R) in percent relative to the accepted reference value. We evaluated also two other performance parameters associated with each assay: the amplification efficiency, in percent, and the linearity, expressed as coefficient of determination, R^2. The amplification efficiency was calculated from the slope of the standard calibration curve using the formula: efficiency = $((10^{(-1/\text{slope})}) - 1) \times 100$. Linearity was calculated as coefficient of determination of the standard curve obtained by linear regression analysis. The ENGL minimum performance requirements for analytical methods of GMO testing (MPR) set the criteria that a method must meet to be accepted for validation, and the criteria to be respected to declare the method valid after the international validation. These criteria are in line with Codex Alimentarius guidelines.[18,19] We referred to the criteria set in the MPR and Codex documents to evaluate the performance of the qPCR assays and method. According to them the percent bias should be within ±25% of the accepted reference value over the whole dynamic range assessed; the RSD_r should be below or equal to 25% over the whole dynamic range and the RSD_R should be below 35% over the whole dynamic range, or below 50% at relative concentrations minor than 0.2% or hge lower than 100; the average slope values of the standard curves should be in the range between −3.6 and −3.1, corresponding to amplification efficiencies between 90% and 110%; average R^2 values of the standard curves should be equal to or above 0.98.

Data Analysis. The results of the collaborative trial were analyzed following the steps described in ISO 5725-2.[36] The identified outlying results and/or laboratories were excluded from the analysis, in accordance with ISO 5725-2, and were evidenced throughout the text. For the PLD-GR assay, results from plate A and C were compared by evaluating differences in slope, linearity, and efficiency of the standard curves through Bland−Altman plots for agreement. Limits of agreement were obtained as the average difference between paired values from plates A and C plus/minus twice the standard deviation of all paired differences, following the Bland−Altman approach.[37] Homogeneity of results between European and Asian laboratories was assessed by comparing method performance parameters such as mean measured hge/GM % content, RSD_r, RSD_R, and bias. Mean measured GM content and bias were compared by means of two-tailed Student's 95% confidence intervals, whereas variability was evaluated by estimating the coefficient of variation of the measured GM content alongside the 95% confidence interval using the modified McKay method.[38]

DOI: 10.1021/acs.jafc.5b00951
J. Agric. Food Chem. 2015, 63, 4954−4965

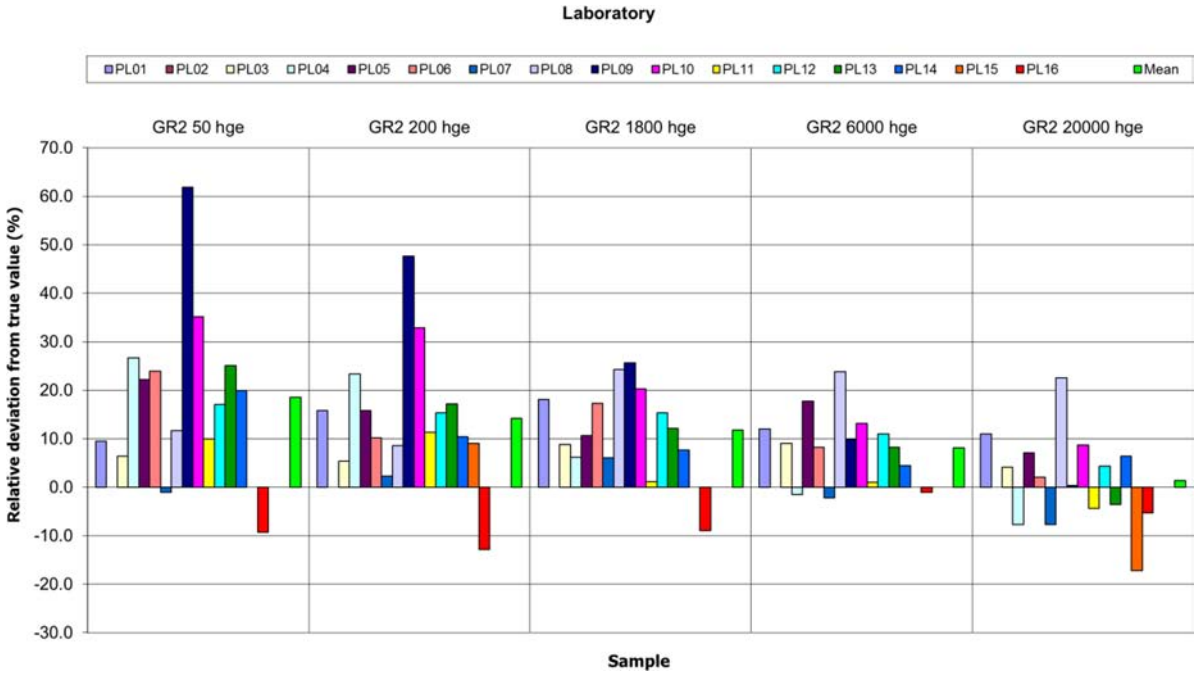

Figure 2. Relative percent deviation from the target hge content for GR2 event-specific assay. Colored bars represent the difference between the hge content measured by each laboratory and the true hge content in percentage of the latter; the green bar on the right represents the mean of the relative deviations for each level of hge content over the analyzed laboratories. PL01−PL16: codes assigned to the 16 testing laboratories. The following values do not show up in the graph: PL2 results for the five levels because they were excluded from the analysis as outliers; PL15 results at 50, 1800, and 6000 hge because they were excluded from the analysis as outliers.

RESULTS

Validation of PLD-GR Taxon-Specific Assay. Results submitted by one laboratory for level 3, and from a second laboratory for level 2, were identified as outliers by the Cochran test at 1% significance level and discarded; results from a third laboratory for level 1 were identified as outliers from the single/double Grubbs test at 1% significance level and discarded from the analysis. The relative deviation from the target hge content (accepted reference value) for each blind sample tested for each laboratory is shown in Figure 1. Mean measured hge content, RSD_r, RSD_R, and bias are reported in Table 1. The measured RSD_r, RSD_R, and the bias measured for three out of five samples meet the criteria, but the two blind samples with lower hge content showed a bias of −30.2% and −29.6%, thus above the limit of −25% set by MPR and Codex guidelines.[18,19] The 95% confidence intervals calculated around the measured hge content include the accepted reference value for level 3, while the accepted reference value for level 2 is higher than the calculated 95% confidence interval and those for levels 1, 4, and 5 are lower. The 95% confidence intervals calculated around the measured bias overlap with the range of values considered acceptable for all tested levels (see Table 1). The full set of quantification results submitted by laboratories is available in Tables S7 and S8, Supporting Information. In addition to the experiment described above (plate A), PLD standard curve samples were tested in a second plate for the relative quantification experiment (plate C) that is described in the paragraph Relative Quantification below. The values obtained by participating laboratories for the slope, amplification efficiency and linearity (R^2) of PLD-GR standard curves are reported in Table S9, Supporting Information. One laboratory could not run plate C, thus standard curve parameters were not reported for plate C for that laboratory. Standard curve parameter values were within the established criteria, ranging from −3.52 to −3.28, with an average of −3.43 for slope, from 92.4 to 101.8, with an average of 95.7% for PCR efficiency and from 0.995 to 0.999, with an average of 0.998 for linearity. Additionally, since plate A and C were performed independently, we compared the slope, PCR efficiency and linearity of the PLD-GR standard curve measured for plate A and C for each laboratory, to identify possible differences between the two plates, yet none was identified. Bland−Altman plots are presented in Figure S4, Supporting Information, and suggest a satisfactory level of concordance between the plates having narrow limits of agreement.

Validation of GR2 Event-Specific Assay. One laboratory was identified as outlier at all hge levels for both Cochran and single/double Grubbs tests at a 1% significance level, thus results from this laboratory were excluded from the analysis. Additionally, results submitted by one laboratory for level 5 were identified as outlier by all outlier tests considered at a 1% significance level and discarded; results from the same laboratory for levels 2 and 3 were identified as outliers by the Cochran test considered at a 1% significance level and discarded. The relative deviation from the target hge content for each blind sample tested for each retained laboratory is shown in Figure 2. In Table 2 the mean hge content, the percentage RSD_r, RSD_R, and bias, all meeting the established criteria, are reported. The accepted reference value for level 1 is included in the 95% confidence interval calculated around the measured hge content, while for levels 2, 3, 4, and 5 the accepted reference value is lower than the calculated 95% confidence interval. The 95% confidence intervals calculated around the measured bias overlap with the range of values considered acceptable for all tested levels (see Table 2). The full set of quantification results submitted by laboratories is available in Tables S10 and S11, Supporting Information. Table

DOI: 10.1021/acs.jafc.5b00951
J. Agric. Food Chem. 2015, 63, 4954−4965

Table 2. Summary of Validation Results for the GR2 Event-Specific Assay (15 Laboratories)

	test sample haploid genome equivalents				
	level 5 50	level 4 200	level 3 1800	level 2 6000	level 1 20000
number of outliers	1	0	1	1	0
reason for exclusion[a]	all tests		C	C	
measured hge content	**59**	**228**	**2012**	**6489**	**20277**
(95% CI)	(54; 64)	(213; 243)	(1915; 2109)	(6228; 6750)	(19218; 21336)
relative repeatability standard deviation, RSD_r %	10.5	5.3	4.1	4.6	5.1
relative reproducibility standard deviation, RSD_R %	17.1	12.8	9.1	8.0	10.4
bias %	18.5	14.2	11.8	8.2	1.4
(95% CI)	(8.6; 28.4)	(6.6; 21.7)	(6.4; 17.2)	(3.8; 12.5)	(−3.9; 6.7)

[a]C, Cochran test; S, single Grubbs test; D, double Grubbs test.

S12, Supporting Information, reports the slope, amplification efficiency, and linearity values obtained by the participating laboratories for the GR2 standard curve with the GR2 event-specific assay (plate B). Slope values ranged from −3.50 to −3.93, with an average of −3.65; the PCR efficiency ranged from 79.8 to 93.1%, with an average of 88.0%. These values of slope and efficiency slightly exceed the MPR and Codex guidelines.[18,19] However, one laboratory presented outstanding deviation in terms of slope and PCR efficiency for the GR2 assay, very likely due to fact that it received the validation samples with some delay. If we exclude the values of slope and PCR efficiency for that laboratory we obtain an average slope of −3.63 and an average efficiency of 89% for the GR2 assay. Measured linearity, which ranged from 0.993 to 1.000 with an average of 0.997, indicates that the GR2 assay has a linear response over the dynamic range tested.

Relative Quantification. GR2 blind samples were designed to have a variable GM content in a fixed total amount of rice DNA, and the relative GM % content of these samples was calculated by dividing the measured GR2 hge content by the measured PLD taxon-specific gene hge content and multiplying by 100 (GM % = GR2/PLD × 100). The measured GR2 hge content of GR2 blind samples was obtained from the plate run for GR2 event-specific assay validation (plate B); the measured PLD taxon-specific gene hge content was obtained from the plate for the quantification of GR2 blind samples with PLD-GR taxon-specific assay (plate C, see Figures S2 and S3, Supporting Information). Out of 16 laboratories, 14 were retained for the analysis. One laboratory could not run plate C and did not present results for the relative quantification of GR2 samples. Additionally, since the relative quantification of the GM % content of GR2 samples relied on the results of both plates B and C, the outliers discarded during the analysis of the results of plate B were discarded also from this analysis. We thus discarded all results from one laboratory and the results submitted by another laboratory for levels 2, 3, and 5. The relative deviation from the target GM % content for each blind sample tested for each laboratory is shown in Figure 3. Table 3 reports the mean GM % content measured, the percentage RSD_r, RSD_R, and bias calculated for the laboratories retained for the analysis. The 95% confidence intervals calculated around

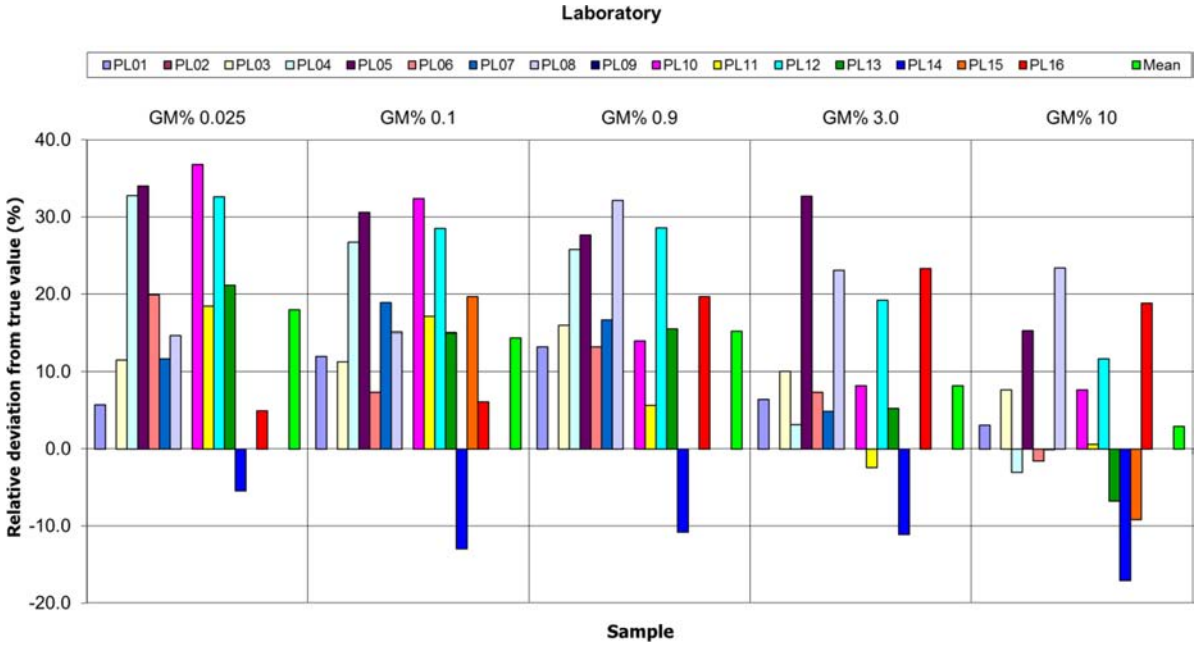

Figure 3. Relative percent deviation from the target value of GM percentage (% hge/hge, equivalent to mass/mass) for all laboratories. Colored bars represent the difference between the GM % content measured by each laboratory and the true GM % content in percentage of the latter; the green bar on the right represents the mean of the relative deviations over the analyzed laboratories for each level of GM % content. PL01-PL16: codes assigned to the 16 testing laboratories; the following values do not show up in the graph: PL2 results for the five levels because they were excluded from the analysis as outliers; PL9 results for the five levels because they were not available for this analysis; PL07 results at GM level 10% because they have very small relative deviation from the target value and the corresponding histogram is not evident in the graph, PL15 results at GM percentages 0.025%, 0.9%, and 3.0% because they were excluded from the analysis as outliers.

DOI: 10.1021/acs.jafc.5b00951
J. Agric. Food Chem. 2015, 63, 4954−4965

Table 3. Summary of Validation Results for the Entire Method Relative Content Quantification (14 Laboratories)

	test sample GM %[a]				
	level 5 0.025	level 4 0.1	level 3 0.9	level 2 3.0	level 1 10
number of outliers	1	0	1	1	0
reason for exclusion	all tests		C	C	
measured GM % content	**0.0296**	**0.12**	**1.05**	**3.3**	**10.4**
(95% CI)	(0.0276; 0.0316)	(0.11; 0.12)	(0.99; 1.11)	(3.1; 3.5)	(9.7; 11.0)
relative repeatability standard deviation, RSD_r %	11.5	7.6	5.6	6.7	7.0
relative reproducibility standard deviation, RSD_R %	14.8	12.1	10.7	12.2	12.4
bias %	18.4	16.3	16.7	10.0	3.6
(95% CI)	(10.5; 26.2)	(9.4; 23.1)	(9.9; 23.5)	(2.9; 17.1)	(−2.9; 10.1)

[a]GM % expressed as hge/hge, equivalent to mass/mass. C, Cochran test; S, single Grubbs test; D, double Grubbs test.

the measured GM % content include the accepted reference value for level 1, while the accepted reference values for levels 2, 3, 4, and 5 are lower than the calculated 95% confidence interval. The 95% confidence intervals calculated around the bias measured overlap with the range of values considered acceptable for all levels tested (see Table 3). The full set of GM % contents calculated on the basis of data submitted by all laboratories is available in Tables S13 and S14, Supporting Information.

Homogeneity of Validation Results. The two geographical areas included in the validation study, Europe and Asia, present differences in terms of climate (e.g., average temperature and relative humidity), length of samples traveling time, and quality certification requirements for GMO testing laboratories. We hypothesized that these differences might have influenced the results presented by laboratories, introducing a factor of nonuniformity that would limit the significance of the results of the validation study. To verify the homogeneity of the results received we compared data presented by the laboratories located in Europe (laboratories from Austria, Belgium, France, Germany, Italy, Slovenia, Spain, and Switzerland; see Table S6, Supporting Information) with the results of the laboratories located in Asia (two laboratories from China, one from India, Japan, Korea, Malaysia, Philippines, and Singapore). The results that were identified as outliers and removed from the analysis of the full set of validation data presented above were removed also from this analysis. Detailed results for the two assays and the complete method are reported in Tables 4−6 and in Figure 4.

PLD-GR. For PLD-GR taxon-specific assay the results presented in Table 4 and Figure 4a are based on eight laboratories for both groups. Consistently with the overall analysis, results submitted by two European laboratories, one for level 3 and another for level 2 and from one Asian laboratory for level 1 were discarded from the analysis. No significant difference was identified between the two groups for the measured hge content, bias and coefficient of variation of the measured PLD hge content, at a 95% confidence level, for any of the levels tested. As observable in Figure 4a, for the taxon-specific assay the coefficient of variation of the measured hge content is generally higher for the Asian group than for the European group, and it tends to decrease with the increase of hge content for both groups. The RSD_r and RSD_R are within MPR and Codex guidelines for both groups, the percent bias is slightly higher than recommended for the two levels with a lower DNA content for both groups, in line with the results of the overall analysis.[18,19]

GR2. For GR2 event-specific assay the results presented in Table 5 and Figure 4b are based on eight laboratories for the European group and on seven laboratories for the Asian group. Consistently with the overall analysis, results submitted by one Asian laboratory for levels 2, 3, and 5 were discarded from the analysis. No significant difference was identified between the two groups for the measured hge content, for bias, and for the coefficient of variation of the measured hge content, at a 95% confidence level, for any of the levels tested. For the GR2 assay the coefficient of variation of the measured hge content is generally higher for the Asian group than for the European

Table 4. Summary of Validation Results for the PLD-GR Taxon-Specific Assay Grouped by Geographical Area (8 Laboratories for Each Group)

	European laboratories test sample hge					Asian laboratories test sample hge				
	level 5 50	level 4 200	level 3 2000	level 2 20000	level 1 200000	level 5 50	level 4 200	level 3 2000	level 2 20000	level 1 200000
number of outliers	0	0	1	1	0	0	0	0	0	1
reason for exclusion[a]			C	C						S/D
measured mean	**36**	**144**	**1900**	**21689**	**196354**	**34**	**138**	**1909**	**22900**	**183678**
(95% CI)	(33; 39)	(132; 155)	(1784; 2015)	(20387; 22991)	(188833; 203875)	(28; 40)	(113; 163)	(1697; 2122)	(20160; 25639)	(168845; 198511)
coefficient of variation	0.100	0.096	0.066	0.065	0.046	0.211	0.214	0.133	0.143	0.087
(95% CI)	(0.066; 0.206)	(0.063; 0.197)	(0.042; 0.146)	(0.042; 0.144)	(0.030; 0.093)	(0.138; 0.452)	(0.140; 0.460)	(0.088; 0.277)	(0.094; 0.298)	(0.056; 0.194)
$RSD_{r\ \%}$	19.9	11.4	8.1	7.5	9.0	19.2	16.2	9.7	6.8	6.9
$RSD_{R\ \%}$	19.9	13.8	9.6	9.2	9.0	26.8	25.6	15.7	15.5	10.6
bias %	−28.3	−28.1	−5.0	8.4	−1.8	−32.0	−31.1	−4.5	14.5	−8.2
(95% CI)	(−34.3; −22.3)	(−33.9; −22.3)	(−10.8; 0.8)	(1.9; 15.0)	(−5.6; 1.9)	(−44.0; −20.1)	(−43.4; −18.7)	(−15.2; 6.1)	(0.8; 28.2)	(−15.6; −0.7)

[a]C, Cochran test; S, single Grubbs test; D, double Grubbs test.

DOI: 10.1021/acs.jafc.5b00951
J. Agric. Food Chem. 2015, 63, 4954−4965

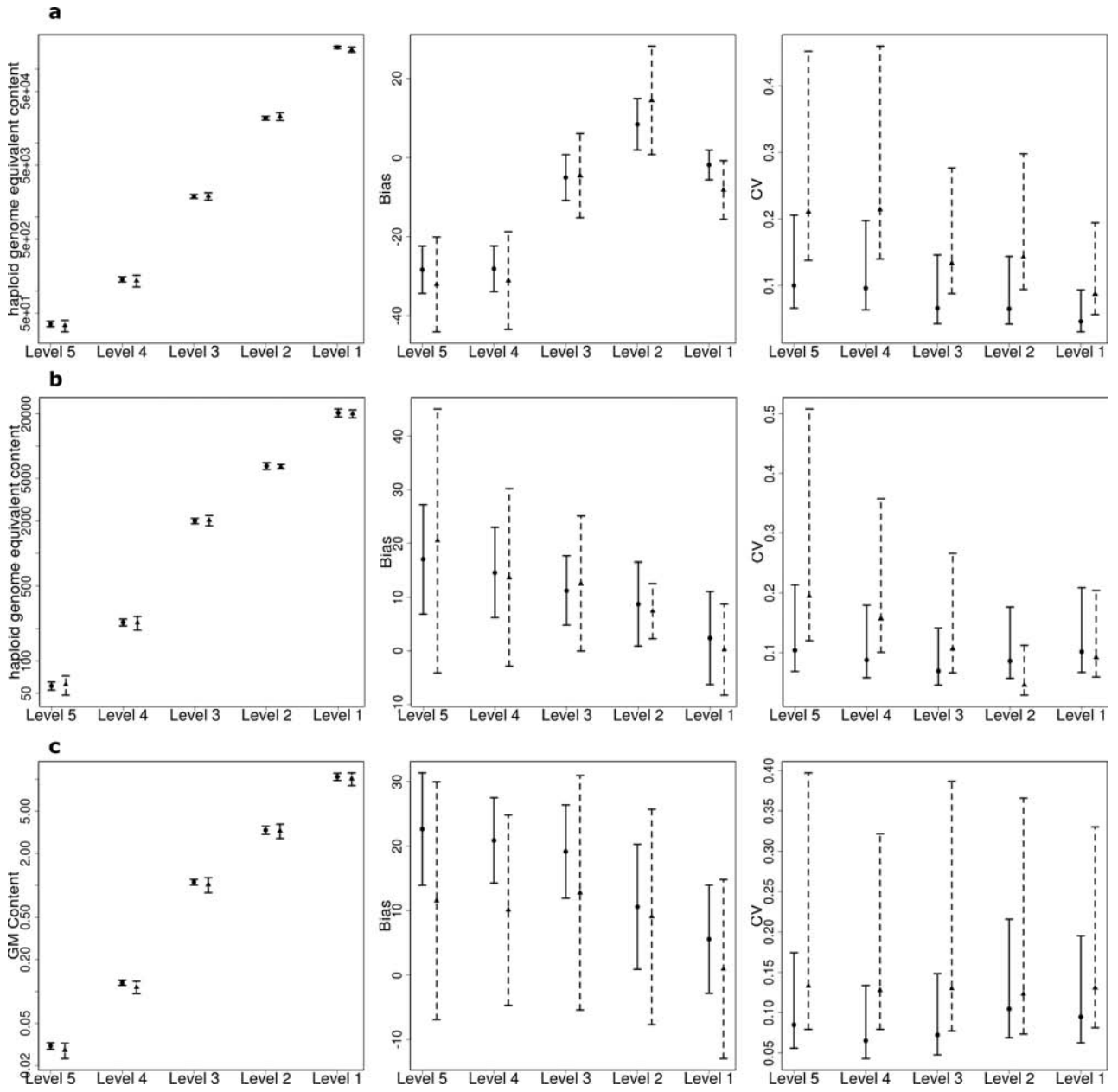

Figure 4. Scatterplots of the measured hge/GM content, bias and coefficient of variation of the measured hge/GM content with 95% confidence intervals for European (dot) and Asian (triangle) laboratories. (a) PLD-GR taxon-specific assay; (b) GR2 event-specific assay; (c) GR2 complete method. The *y* axis of the measured hge/GM content scatterplots is in logarithmic scale.

group only for levels 3, 4, and 5, and it remains constant across the levels for European laboratories, while it decreases with the increase of GR2 hge content for Asian laboratories (Figure 4b). The RSD_r, RSD_R, and percent bias are within the acceptance criteria for both groups.

GM %. For the entire method the results presented in Table 6 and Figure 4c for the European group are based on eight laboratories, those for the Asian group on six laboratories. Results submitted by one Asian laboratory for levels 2, 3, and 5 were discarded from the analysis. No significant difference was identified between the two groups for the measured GM % content, bias, and coefficient of variation of the measured GM % content, at a 95% confidence level, for any of the levels tested. For the entire method the coefficient of variation of the measured GM % content is generally higher for Asian laboratories and rather constant across the GM % levels for both groups (Figure 4c). The RSD_r, RSD_R, and percent bias are in line with the requirements for both Asian and European laboratories.

DISCUSSION

We presented the results of the international validation of the two modules that constitute a qPCR detection method for GR2, the PLD-GR taxon-specific assay and the GR2 event specific assay. These results show that the two assays have a good performance in terms of RSD_r, RSD_R, and bias when assessed with an international collaborative trial, both as independent modules, with absolute quantification, and when combined together, with relative quantification. The dynamic range assessed goes from 50 to 200 000 hge for the PLD-GR taxon-specific assay, from 50 to 20 000 hge for the GR2 event-specific assay and from 0.025% to 10% relative hge/hge GM %

DOI: 10.1021/acs.jafc.5b00951
J. Agric. Food Chem. 2015, 63, 4954−4965

Table 5. Summary of Validation Results for the GR2 Event-Specific Assay Grouped by Geographical Area (8 Laboratories for Europe and 7 Laboratories for Asia)

	European laboratories test sample hge					Asian laboratories test sample hge				
	level 5 50	level 4 200	level 3 1800	level 2 6000	level 1 20000	level 5 50	level 4 200	level 3 1800	level 2 6000	level 1 20000
number of outliers	0	0	0	0	0	1	0	1	1	0
reason for exclusion[a]						all tests		C	C	
measured mean	**59**	**229**	**2002**	**6523**	**20478**	**60**	**227**	**2025**	**6445**	**20047**
(95% CI)	(53; 64)	(212; 246)	(1887; 2118)	(6054; 6992)	(18741; 22215)	(48; 73)	(194; 260)	(1799; 2251)	(6136; 6753)	(18346; 21749)
coefficient of variation	0.104	0.087	0.069	0.086	0.101	0.194	0.157	0.106	0.046	0.092
(95% CI)	(0.068; 0.214)	(0.058; 0.180)	(0.046; 0.141)	(0.057; 0.176)	(0.067; 0.209)	(0.120; 0.508)	(0.101; 0.358)	(0.066; 0.266)	(0.028; 0.112)	(0.059; 0.204)
$RSD_{r\ \%}$	8.4	4.9	4.4	2.9	3.4	12.7	5.7	3.8	6.2	6.6
$RSD_{R\ \%}$	12.7	9.7	7.9	9.0	10.6	22.3	16.5	11.1	7.0	10.8
bias %	17.0	14.6	11.2	8.7	2.4	20.5	13.7	12.5	7.4	0.2
(95% CI)	(6.9; 27.2)	(6.2; 23.0)	(4.8; 17.6)	(0.9; 16.5)	(−6.3; 11.1)	(−4.1; 45.1)	(−2.8; 30.2)	(0.0; 25.1)	(2.3; 12.6)	(−8.3; 8.7)

[a]C, Cochran test; S, single Grubbs test; D, double Grubbs test.

Table 6. Summary of Validation Results for the Entire Method Relative Content Quantification Grouped by Geographical Area (8 Laboratories for Europe and 6 Laboratories for Asia)

	European laboratories test sample GM %[a]					Asian laboratories test sample GM %[a]				
	level 5 0.025	level 4 0.1	level 3 0.9	level 2 3.0	level 1 10	level 5 0.025	level 4 0.1	level 3 0.9	level 2 3.0	level 1 10
number of outliers	0	0	0	0	0	1	0	1	1	0
reason for exclusion						all tests		C	C	
measured GM %	**0.031**	**0.12**	**1.07**	**3.3**	**10.6**	**0.028**	**0.11**	**1.01**	**3.3**	**10.1**
(95% CI)	(0.028; 0.033)	(0.11; 0.13)	(1.01; 1.14)	(3.0; 3.6)	(9.7; 11.4)	(0.023; 0.032)	(0.10; 0.12)	(0.85; 1.18)	(2.8; 3.8)	(8.7; 11.5)
coefficient of variation	0.085	0.065	0.072	0.105	0.095	0.133	0.128	0.130	0.123	0.131
(95% CI)	(0.056; 0.174)	(0.043; 0.134)	(0.048; 0.148)	(0.069; 0.216)	(0.063; 0.195)	(0.079; 0.397)	(0.079; 0.322)	(0.077; 0.387)	(0.073; 0.366)	(0.081; 0.330)
$RSD_{r\ \%}$	10.8	8.0	6.2	7.4	7.1	12.8	7.0	4.2	5.5	6.8
$RSD_{R\ \%}$	12.6	9.5	9.0	12.3	11.3	17.3	14.1	13.5	13.2	14.4
bias %	22.6	20.9	19.2	10.6	5.6	11.5	10.1	12.8	9.0	1.0
(95% CI)	(13.9; 31.3)	(14.3; 27.5)	(11.9; 26.4)	(0.9; 20.3)	(−2.8; 14.0)	(−6.9; 30.0)	(−4.7; 24.8)	(−5.4; 30.9)	(−7.7; 25.7)	(−12.9; 14.8)

[a]GM % expressed as hge/hge, equivalent to mass/mass. C, Cochran test; S, single Grubbs test; D, double Grubbs test.

content for the combined method. The RSD_r, RSD_R, and bias measured meet the MPR and Codex guidelines for all tested levels and assays/methods, with the exception of the samples at 50 and 200 hge of the PLD-GR taxon-specific assay. For those levels the percentage bias measured was of −30.2% and −29.6%, respectively. However, the 95% confidence interval calculated for the bias of these two levels includes the limit of −25% suggested for bias.[18,19] Thus, from a purely statistical point of view it cannot be excluded that their measured bias lies inside the accepted range. It is also important to note that 50 and 200 rice hge correspond to 0.025 and 0.1 ng of rice DNA, respectively, and that while it is important that the event-specific method is able to reliably quantify very small amounts of DNA, it is in practice very unlikely that the taxon-specific assay is used to quantify such small amounts of rice DNA. Therefore, the limitation mentioned above for the PLD-GR assay is of negligible relevance for the practical application of the method. In fact, hypothesizing a 5% GM labeling threshold, 200 rice hge per reaction would correspond to 10 GM event hge per reaction, far below the LOQ of the GR2 assay (50 hge). At 2000 rice hge per reaction the number of GM hge would instead correspond to 100, thus reliably quantifiable with the GR2 assay, and generally with any GM event-specific assay. The RSD_r measured with this validation study for PLD-GR taxon-specific and GR2 event-specific assays is in line with the RSD_r measured during the single laboratory validation of two assays, whose data is presented in the article on the development and single laboratory validation of GR2 qPCR detection method.[20] In fact, for the PLD-GR assay the RSD_r for samples at 50 and 200 000 hge was 19.8% and 4.2%, respectively, in the single laboratory validation and 19.6% and 8.1%, respectively, in this collaborative trial (Table 1). The RSD_r for the GR2 assay was 13.5% and 11.7%, respectively, in the single laboratory validation for samples containing 50 and 20 000 hge of the GR2 event and 10.5% and 5.1%, respectively, in this collaborative study (Table 2). The efficiency and linearity of

DOI: 10.1021/acs.jafc.5b00951
J. Agric. Food Chem. 2015, 63, 4954−4965

the PLD-GR taxon-specific assay and the linearity of the GR2 event-specific assay were fully within the established performance criteria, while the efficiency of the GR2 assay was slightly lower than recommended, with an average slope of −3.65 and an average efficiency of 88.0%.[18,19] Given that GR2 blind samples were quantified correctly with the event-specific assay, both with absolute and relative quantification, this slight underperformance in terms of efficiency does not constitute a serious problem. In addition to this, if we exclude from the calculation of the GR2 assay average slope and efficiency the values measured by Lab 9, which presented deviations for those parameters, we obtain an average slope of −3.63 and an average efficiency of 89%, even nearer to the recommended value range.

In this validation study, we adopted the principle of modularity, according to which the different assays that constitute a detection method can be validated separately, provided that the pre-established performance criteria are respected for the preceding or parallel assay,[31−34] and we validated the taxon-specific and the event-specific assays that constitute the GR2 detection method independently. Validating the taxon-specific and event-specific assays independently has different advantages. Establishing the dynamic range of the two assays separately allows the users of the method complete freedom in the choice of GM percentages and DNA concentrations to test and establishes clearer limits on the highest and lower DNA concentrations that can be used in function of the target GM percentage. This is important when countries with different labeling regulations regarding GMO presence in the food or feed chain and different labeling thresholds set for unintended GMO presence are going to use the method.[7,11,24,39−41] The independent validation of the taxon-specific and event-specific assays also allows the users of the method to decide whether to use a delta Ct method or a two-standard curves method, depending on sample availability and quality, screening strategies or the experience of laboratory personnel. For example, a delta Ct method normally requires more DNA than a two-standard curves method for the preparation of standard curve samples, but it may be preferred for other reasons. The taxon-specific assay can be immediately used for other rice GM event-specific detection methods, without the need to revalidate both assays; in this case only the event-specific qPCR method would need to be developed and validated. On the other hand, if a GMO testing laboratory has already implemented the use of one rice taxon-specific assay, it may adopt only the event-specific assay and use it in combination with the pre-existent taxon-specific assay. Among the taxon-specific assays previously developed for rice GM quantification[42−48] only the qPCR assay developed on the sucrose phosphate synthase gene (SPS) was internationally validated independently from an event-specific GM detection method.[45,46] However, to our knowledge this is the first time that both the assays that constitute a GM event-specific qPCR detection method have been developed and validated independently, in absolute hge, and that a relative quantification experiment was performed to confirm the results obtained with the independent assays. The relative quantification experiment was performed by running the taxon-specific and the event-specific assays on two different plates with two independently prepared standard curves; some laboratories run the two plates on different days. Despite these factors are potential sources of variability, the results showed that when the two assays were combined to quantify GR2 DNA in relation to total rice DNA content, their performance in terms of accuracy was comparable, if not better, to the one of the single assays and in line with MPR and Codex guidelines,[18,19] confirming the robustness of the two assays. The samples tested were designed to comply with the European legislation on GMOs,[25−30] so that this qPCR detection method will be available in case of need.

According to ISO 5725-1 and to the IUPAC protocol for the design, conduct and interpretation of method-performance studies,[21,22] if a method is intended for international use, the laboratories participating to the collaborative trial should be from different countries. We chose to include laboratories from the two main areas where the method was developed and is likely to be used: Asia and Europe. These two geographical areas, however, present differences in terms of climate, distance from the organizing laboratory and quality certification requirements for GMO testing laboratories. The assumption behind a collaborative study is that the measured repeatability should be homogeneous between participating laboratories, in order to be able to consider the repeatability standard deviation (RSD_R) obtained with the study applicable to any laboratory.[21] We thus considered important to verify the homogeneity of the results of the collaborative study, by comparing the two subgroups that presented possible sources of variability, Europe and Asia. This analysis did not identify any significant difference between the results of the two groups for what concerns the measured hge/GM percentage content, bias and coefficient of variation, thus confirming the homogeneity of the results received. However, the coefficient of variation of the measured hge/GM percentage content was generally higher for Asian laboratories, a factor that does not compromise the homogeneity of results and that was expected, given that the group covers an area that is wider and more heterogeneous than Europe. To our knowledge, this is the first time that the homogeneity of the results of the international validation of a qPCR detection method was verified.

In conclusion, with the cooperation of the laboratories that participated to this collaborative trial, we have validated the taxon-specific and the event-specific assays that constitute the qPCR detection method for the GR2 event. The two assays were validated independently, a factor that will allow the users of the GR2 detection method to test a wide range of GM concentrations with flexibility on starting sample DNA concentration. This method, developed in collaboration with IRRI, optimized, single laboratory-tested[1] and validated by the EU-RL GMFF can be reliably used for the quantification of GR2 DNA in a sample, over the validated dynamic range.

■ ASSOCIATED CONTENT

Supporting Information

Description of the samples for the validation of the PLD-GR taxon-specific assay, of the GR2 event-specific assay, and of the combined GR2 detection method (Tables S2−S5); list of the laboratories that participated to the collaborative trial (Table S6); the full set of quantification results for the PLD-GR assay (Tables S7−S8), for the GR2 assay (Tables S10−S11), and for the relative quantification (Tables S13−S14); standard curve parameters values obtained for the PLD-GR assay (Table S9) and the GR2 assay (Table S12); layout of plate set up for the validation (Figures S1−S3); scatterplots of the comparison of PLD-GR standard curve parameters measured for plate A and C (Figure S4). The Supporting Information is available free of charge on the ACS Publications website at DOI: 10.1021/acs.jafc.5b00951.

DOI: 10.1021/acs.jafc.5b00951
J. Agric. Food Chem. 2015, 63, 4954−4965

AUTHOR INFORMATION

Corresponding Author

*E-mail: marco.mazzara@ec.europa.eu.

Funding

We acknowledge funding for this project from the European Commission (budget lines BGUE-B2012-10.020100-C1-JRC A7001050016 and BGUE-B2013-10.020100-C1-JRC A7001050016), the Bill and Melinda Gates Foundation, the United States Agency for International Development (USAID), and the Rockefeller Foundation.

Notes

The authors declare no competing financial interest.

ACKNOWLEDGMENTS

We thank the following collaborators for their participation in the collaborative trial: Wensheng Huang (Agro-Product Safety Research Center, Chinese Academy of Inspection and Quarantine No A3, Beijing, China), Vincent Herau (ANSES Laboratoire de la Santé des Végétaux, unité bactériologie, virologie et OGM, France), Rupert Hochegger (Austrian Agency for Health and Food Safety, Competence Centre for Biochemistry, Austria), Hae-Yeong Kim (Department of Food Science & Biotechnology, Kyung Hee University, South Korea), Geoffrey Cottenet (Food Safety & Quality Microbial & Molecular Analytics, Nestec Ltd, Nestlé Research Center, Switzerland), Kazumi Kitta and Reona Takabatake (GMO Analytical Evaluation Laboratory, National Food Research Institute, Japan), Elliza Mat Nor (GMO Unit, Environmental Health Division, Department of Chemistry Malaysia, Malaysia), Dabing Zhang and Litao Yang (Joint Center for Life Sciences, School of life science and Biotechnology, Shanghai Jiao Tong University, Shanghai, China), Dietrich Mäde and Stefa Kahle (Landesamt für Verbraucherchutz des Landes Sachsen-Anhalt, Fachbereich Lebensmittelsicherheit, Germany), Isabel Prieto (National Centre for Food, Spanish Food Safety Agency and Nutrition, Biotechnology Unit, Spain), Jana Žel and Dejan Stebih (National Institute of Biology, Slovenia), Geronima P. Eusebio and Lorelie U. Agbagala (Post Entry Quarantine Station Molecular and Biotechnology Laboratory, Bureau of Plant Industry, Philippines), Gurinder Jit Randhawa (Referral Centre for Molecular Diagnosis of Transgenic Planting Material, National Bureau of Plant Genetic Resources, India), Ilaria M. Ciabatti and Ugo Marchesi (Veterinary Public Health Institute for Lazio and Toscana Regions, National Reference Centre for GMO Analysis, Italy), Wang Zheng Ming (Veterinary Public Health Laboratory, Agri-Food & Veterinary Authority of Singapore, Singapore), and Gilbert Berben and Eric Janssen (Walloon Agricultural Research Centre−Department Valorization of Agricultural Products, Belgium). We thank Roberta Brustio and Lorella Vidmar who coordinated the shipment of the validation kits and all those who contributed to the design, preparation, and shipment of the samples for the collaborative trial. We also thank Gerard Barry for his supervision of the Golden Rice Project at IRRI and Parminder Virk for his participation to the project.

ABBREVIATIONS USED

ENGL, European Network of GMO Laboratories; EU-RL GMFF, European Union Reference Laboratory for Genetically Modified Food and Feed; GMO, genetically modified organism; GR2, Golden Rice 2; hge, haploid genome equivalents; IRRI, International Rice Research Institute; LOD, limit of detection; LOQ, limit of quantification; MBG, Molecular Biology and Genomics; MPR, ENGL minimum performance requirements for analytical methods of GMO testing; PCR, polymerase chain reaction; qPCR, quantitative real time PCR; PLD, Phospholipase D α2; RSD_r, relative repeatability standard deviation; RSD_R, relative reproducibility standard deviation

REFERENCES

(1) Ye, X.; Al-Babili, S.; Klöti, A.; Zhang, J.; Lucca, P.; Beyer, P.; Potrykus, I. Engineering the provitamin A (beta-carotene) biosynthetic pathway into (carotenoid-free) rice endosperm. *Science* **2000**, *287*, 303−305.

(2) Mayer, J. E. Delivering golden rice to developing countries. *J. AOAC Int.* **2007**, *90*, 1445−1449.

(3) Haskell, M. J. The challenge to reach nutritional adequacy for vitamin A: β-carotene bioavailability and conversion-evidence in humans. *Am. J. Clin. Nutr.* **2012**, *96*, 1193S−1203S.

(4) Tang, G.; Hu, Y.; Yin, S. A.; Wang, Y.; Dallal, G. E.; Grusak, M. A.; Russell, R. M. β-Carotene in Golden Rice is as good as β-carotene in oil at providing vitamin A to children. *Am. J. Clin. Nutr.* **2012**, *96*, 658−664.

(5) Paine, J. A.; Shipton, C. A.; Chaggar, S.; Howells, R. M.; Kennedy, M. J.; Vernon, G.; Wright, S. Y.; Hinchliffe, E.; Adams, J. L.; Silverstone, A. L.; Drake, R. Improving the nutritional value of Golden Rice through increased pro-vitamin A content. *Nat. Biotechnol.* **2005**, *23*, 482−487.

(6) Beyer, P.; Al-Babili, S.; Ye, X.; Lucca, P.; Schaub, P.; Welsch, R.; Potrykus, I. Golden Rice: introducing the beta-carotene biosynthesis pathway into rice endosperm by genetic engineering to defeat vitamin A deficiency. *J. Nutr.* **2002**, *132*, 506S−510S.

(7) Miraglia, M.; Berdal, K. G.; Brera, C.; Corbisier, P.; Holst-Jensen, A.; Kok, E. J.; Marvin, H. J. P.; Schimmel, H.; Rentsch, J.; van Rie, J. P. P. F.; Zagon, J. Detection and traceability of genetically modified organisms in the food production chain. *Food Chem. Toxicol.* **2004**, *42*, 1157−1180.

(8) Rodríguez-Lázaro, D.; Lombard, B.; Smith, H.; Rzezutka, A.; D'Agostino, M.; Helmuth, R.; Schroeter, A.; Malorny, B.; Miko, A.; Guerra, B.; Davison, J.; Kobilinsky, A.; Hernández, M.; Bertheau, Y.; Cook, N. Trends in analytical methodology in food safety and quality: monitoring microorganisms and genetically modified organisms. *Trends Food Sci. Technol.* **2007**, *18*, 306−319.

(9) Elenis, D. S.; Kalogianni, D. P.; Glynou, K.; Ioannou, P. C.; Christopoulos, T. K. () Advances in molecular techniques for the detection and quantification of genetically modified organisms. *Anal. Bioanal. Chem.* **2008**, *392*, 347−354.

(10) Marmiroli, N.; Maestri, E.; Gullì, M.; Malcevschi, A.; Peano, C.; Bordoni, R.; De Bellis, G. Methods for detection of GMOs in food and feed. *Anal. Bioanal. Chem.* **2008**, *392*, 369−384.

(11) Michelini, E.; Simoni, P.; Cevenini, L.; Mezzanotte, L.; Roda, A. New trends in bioanalytical tools for the detection of genetically modified organisms: an update. *Anal. Bioanal. Chem.* **2008**, *392*, 355−367.

(12) *Foodstuffs−Methods of analysis for the detection of genetically modified organisms and derived products−Qualitative nucleic acid based methods*; International Organization for Standardization: Geneva, 2005; International Standard (ISO) 21569:2005.

(13) *Foodstuffs−Methods of analysis for the detection of genetically modified organisms and derived products−Quantitative nucleic acid based methods*; International Organization for Standardization: Geneva, 2005, International Standard (ISO) 21570:2005.

(14) European Union Reference Laboratory for GM food and Feed. Status of dossiers. http://gmo-crl.jrc.ec.europa.eu/StatusOfDossiers.aspx (accessed February 12, 2015).

(15) Kluga, L.; Folloni, S.; Kagkli, D. M.; Bogni, A.; Foti, N.; Savini, C.; Mazzara, M.; Van den Eede, G.; Van den Bulcke, M. Combinatory SYBR® Green Real-Time PCR Screening Approach for Tracing

DOI: 10.1021/acs.jafc.5b00951
J. Agric. Food Chem. 2015, 63, 4954−4965

Materials Derived from Genetically Modified Rice. *Food Anal. Method* **2013**, *6*, 361−369.
(16) Querci, M.; Foti, N.; Bogni, A.; Kluga, L.; Broll, H.; Van den Eede, G. Real-time PCR based ready-to-use multi-target analytical system for GMO detection. *Food Anal. Method* **2009**, *2*, 325−336.
(17) Leimanis, S.; Hamels, S.; Florence, Nazé F.; Mbella, G. M.; Sneyers, M.; Hochegger, R.; Broll, H.; Roth, L.; Dallmann, K.; Micsinai, A.; La Paz, J. L.; Pla, M.; Brünen-Nieweler, C.; Papazova, N.; Taverniers, I.; Hess, N.; Kirschneit, B.; Bertheau, Y.; Audeon, C.; Laval, V.; Busch, U.; Pecoraro, S.; Neumann, K.; Rösel, S.; van Dijk, J.; Kok, E.; Bellocchi, G.; Foti, N.; Mazzara, M.; Moens, W.; Remacle, J.; Van Den Eede, G. Validation of the performance of a GMO multiplex screening assay based on microarray detection. *Eur. Food Res. Technol.* **2008**, *227*, 1621−1632.
(18) European Network of GMO Laboratories. Definition of minimum performance requirements for analytical methods of GMO testing. http://gmo-crl.jrc.ec.europa.eu/doc/Min_Perf_Requirements_Analytical_methods.pdf (accessed February 12, 2015).
(19) Codex Committee on Methods of Analysis and Sampling. *Guidelines on performance criteria and validation of methods for detection, identification and quantification of specific dna sequences and specific proteins in foods*; 2010; CAC/GL 74-2010.
(20) Jacchia, S.; Nardini, E.; Savini, C.; Petrillo, M.; Angers-Loustau, A.; Shim, J. H.; Trijatmiko, K.; Kreysa, J.; Mazzara, M. Development, optimization and single laboratory validation of an event-specific real-time PCR method for the detection and quantification of Golden Rice 2 using a novel taxon-specific assay. *J. Agric. Food Chem.* **2015**, *63*, 1711−21.
(21) *Accuracy (trueness and precision) of measurement methods and results−Part 1: General principles and definitions*; International Organization for Standardization: Geneva, 1994; International Standard (ISO) 5725-1:1994.
(22) Horwitz, W. Protocol for the design, conduct and interpretation of method-performance studies. *Pure Appl. Chem.* **1995**, *67*, 331−343.
(23) Bellocchi, G.; Bertheau, Y.; De Giacomo, M.; Holst-Jensen, A.; Macarthur, R.; Mazzara, M.; Onori, R.; Taverniers, I.; van den Bulcke, M.; Trapmann, S. Method Validation and Reference Materials. In *Genetically Modified and Non-Genetically Modified Food Supply Chains: Co-Existence and Traceability*, 1st ed.; Bertheau, Y., Ed.; Wiley-Blackwell, 2012; pp 383−402.
(24) Zhang, D.; Guo, J. The development and standardization of testing methods for genetically modified organisms and their derived products. *J. Integr. Plant Biol.* **2011**, *53*, 539−551.
(25) European Parliament and the Council of the European Union.. Regulation (EC) No 1829/2003 of 22 September 2003 on genetically modified food and feed. *Off. J. Eur. Union* **2003**, *L268*, 1−23.
(26) European Parliament and the Council of the European Union.. Regulation (EC) No 882/2004 on official controls performed to ensure the verification of compliance with feed and food law, animal health and animal welfare rules. *Off. J. Eur. Union* **2004**, *L165*, 1−141.
(27) European Parliament and the Council of the European Union.. Regulation (EC) No 641/2004 on detailed rules for the implementation of Regulation (EC) No 1829/2003. *Off. J. Eur. Union* **2004**, *L102*, 14−25.
(28) European Commission.. Commission Regulation (EU) No 619/2011 laying down the methods of sampling and analysis for the official control of feed as regards presence of genetically modified material for which an authorisation procedure is pending or the authorisation of which has expired. *Off. J. Eur. Union* **2011**, *L166*, 9−15.
(29) European Parliament and the Council of the European Union.. Regulation (EU) No 503/2013 of 3 April 2013 on applications for authorisation of genetically modified food and feed in accordance with Regulation (EC) No 1829/2003 of the European Parliament and of the Council and amending Commission Regulations (EC) No 641/2004 and (EC) No 1981/2006. *Off. J. Eur. Union* **2013**, *L157*, 1−48.
(30) European Parliament and the Council of the European Union.. Regulation (EC) No 1981/2006 of 22 December 2006 on detailed rules for the implementation of Article 32 of Regulation (EC) No 1829/2003 of the European Parliament and of the Council as regards the Community reference laboratory for genetically modified organisms. *Off. J. Eur. Union* **2006**, *L368*, 99−109.
(31) Holst-Jensen, A.; Berdal, K. G. The modular analytical procedure and validation approach and the units of measurement for genetically modified materials in foods and feeds. *J. AOAC Int.* **2004**, *87*, 927−936.
(32) Holst-Jensen, A.; Bertheau, Y.; de Loose, M.; Grohmann, L.; Hamels, S.; Hougs, L.; Morisset, D.; Pecoraro, S.; Pla, M.; Van den Bulcke, M.; Wulff, D. Detecting un-authorized genetically modified organisms (GMOs) and derived materials. *Biotechnol. Adv.* **2012**, *30*, 1318−1835.
(33) Van den Bulcke, M.; Bellocchi, G.; Berben, G.; Burns, M.; Cankar, K.; De Giacomo, M.; Gruden, K.; Holst-Jensen, A.; Malcewsky, A.; Mazzara, M.; Onori, R.; Papazova, N.; Parlouer, E.; Taverniers, I.; Trapmann, S.; Wulff, D.; Zhang, D. The Modular Approach in GMO Quality Control and Enforcement Support Systems. In *Genetically Modified and Non-Genetically Modified Food Supply Chains: Co-Existence and Traceability*, 1st ed.; Bertheau, Y., Ed.; Wiley-Blackwell, 2012; pp 293−306.
(34) Kagkli, D. M.; Weber, T. P.; Van den Bulcke, M.; Folloni, S.; Tozzoli, R.; Morabito, S.; Ermolli, M.; Gribaldo, L.; Van den Eede, G. Application of the modular approach to an in-house validation study of real-time PCR methods for the detection and serogroup determination of verocytotoxigenic Escherichia coli. *Appl. Environ. Microbiol.* **2011**, *77*, 6954−6963.
(35) Bennett, M. D.; Leitch, I. J. Plant DNA C-values database, Release 6.0, December, 2012. http://www.kew.org/cvalues/ (accessed February 12, 2015).
(36) *Accuracy (trueness and precision) of measurement methods and results−Part 2: Basic method for the determination of repeatability and reproducibility of a standard measurement method*; International Organization for Standardization: Geneva, 1994; International Standard (ISO) 5725-2:1994.
(37) Bland, J. M.; Altman, D. G. Statistical methods for assessing agreement between two methods of clinical measurement. *Lancet* **1986**, *327*, 307−310.
(38) Vangel, M. G. Confidence intervals for a normal coefficient of variation. *Am. Stat.* **1996**, *50*, 21−26.
(39) Gruère, G. P.; Rao, S. R. A Review of International Labeling Policies of Genetically Modified Food to Evaluate India's Proposed Rule. *AgBioForum* **2007**, *10*, 51−64.
(40) Gruère, G. P.; Carter, C. A.; Farzin, Y. H. Explaining International Differences in Genetically Modified Food Labeling Policies. *Review of International Economics* **2009**, *17*, 393−408.
(41) Albert, J. New technologies and food labelling: the controversy over labelling of foods derived from genetically modified crops. In *Innovations in food labelling*; Food and Agriculture Organization of the United Nations and Woodhead Publishing Limited, 2010.
(42) Mazzara, M.; Grazioli, E.; Savini, C.; Van Den Eede, G. *Event-specific Method for the Quantitation of Rice Line LLRICE62 Using Real-time PCR—Validation Report and Protocol—Sampling and DNA Extraction of Rice*; 2006; EUR 22490 EN.
(43) Chaouachi, M.; Giancola, S.; Romaniuk, M.; Laval, V.; Bertheau, Y.; Brunel, D. A strategy for designing multi-taxa specific reference gene systems. Example of application — ppi phosphofructokinase (ppi-PPF) used for the detection and quantification of three taxa: maize (Zea mays), cotton (Gossypium hirsutum) and rice (Oryza sativa). *J. Agric. Food Chem.* **2007**, *55*, 8003−8010.
(44) Jeonga, S. C.; Packa, I. S.; Choa, E. Y.; Youka, E. S.; Parkb, S.; Yoona, W. K.; Kima, C. G.; Choic, Y. D.; Kimd, J. K.; Kim, H. M. Molecular analysis and quantitative detection of a transgenic rice line expressing a bifunctional fusion TPSP. *Food Control* **2007**, *18*, 1434−1442.
(45) Ding, J.; Jia, J.; Yang, L.; Wen, H.; Zhang, C.; Liu, W.; Zhang, D. Validation of a rice specific gene, sucrose phosphate synthase, used as the endogenous reference gene for qualitative and real-time quantitative PCR detection of transgenes. *J. Agric. Food Chem.* **2004**, *52*, 3372−3377.

DOI: 10.1021/acs.jafc.5b00951
J. Agric. Food Chem. 2015, 63, 4954−4965

(46) Jiang, L.; Yang, L.; Zhang, H.; Guo, J.; Mazzara, M.; Van den Eede, G.; Zhang, D. International collaborative study of the endogenous reference gene, sucrose phosphate synthase (SPS), used for qualitative and quantitative analysis of genetically modified rice. *J. Agric. Food Chem.* **2009**, *57*, 3525−3532.
(47) Hernández, M.; Esteve, T.; Pla, M. Real-time polymerase chain reaction based assays for quantitative detection of barley, rice, sunflower, and wheat. *J. Agric. Food Chem.* **2005**, *53*, 7003−7009.
(48) Grohmann, L.; Maede, D. Detection of genetically modified rice: collaborative validation study of a construct-specific real-time PCR method for detection of transgenic Bt rice. *Eur. Food Res. Technol.* **2009**, *228*, 497−500.

DOI: 10.1021/acs.jafc.5b00951
J. Agric. Food Chem. 2015, 63, 4954−4965

JOURNAL OF AGRICULTURAL AND FOOD CHEMISTRY

Article

pubs.acs.org/JAFC

Development of Fluorescence Sensing Material Based on CdSe/ZnS Quantum Dots and Molecularly Imprinted Polymer for the Detection of Carbaryl in Rice and Chinese Cabbage

Can Zhang,*[,†] Hanyu Cui,[†] Jianrong Cai,[†] Yuqing Duan,[†] and Yuan Liu[‡]

[†]School of Food & Biological Engineering, Jiangsu University, Zhenjiang 212013, P. R. China

[‡]Zhenjiang Institute for Drug Control, Zhenjiang, 212000, P. R. China

ABSTRACT: A fluorescence sensing material based on quantum dots with excellent optical properties and molecularly imprinted polymer (QDs@MIP) with specific recognition has been developed. First the surface of CdSe/ZnS QDs was modified with ionic liquids (ILs) by electrostatic interaction. The fluorescence sensing material was constructed from anchoring the MIP layer on IL modified CdSe/ZnS QDs by copolymerization, which had been developed for the detection of carbaryl in rice and Chinese cabbage. The MIP fluorescence was more strongly quenched by carbaryl than the non-imprinted polymer (NIP) fluorescence, which indicated that the QDs@MIP could selectively recognize the corresponding carbaryl. Furthermore, the developed QDs@MIP method was validated by HPLC and ELISA respectively, and the results of these methods were well correlated (R^2 = 0.98). The fluorescence sensing material had obvious advantages, such as being easily prepared and having specific recognition and photostability. The developed method was simple and effective for the detection of carbaryl. And, it could also provide the technical support for the rapid detection in food safety fields.

KEYWORDS: *quantum dots, molecularly imprinted polymer, carbaryl, fluorescence sensing material*

INTRODUCTION

Molecular imprinted polymers (MIPs) are prepared by the template molecule, functional monomer, cross-linker, and initiator with a heat or light trigger. After the template molecules are eluted from the MIPs, they have a cavity match, in such aspects as size and shape in space and chemical action, which can specifically combine with the template molecules. For the structure−activity reservation, specific recognition and extensive applicability, MIPs are being researched and developed in many fields such as solid-phase extraction,[1−4] chromatography,[5,6] and sensor technology.[7,8]

Quantum dots (QDs) are semiconductor nanoparticles composed of groups II−VI or III−V elements with unique optical properties. QDs have unique quantum size and surface effect, showing good spectral characteristics and chemical stability. Consequently, they have been widely applied as fluorescence labels for biomolecules and as optoelectronic devices for sensitive detection of analytes.[9]

On the basis of quantum dots with excellent optical properties and an MIP with specific recognition, fluorescence sensing material (QDs@MIP) have been developed and have drawn considerable attention. Many researchers have constructed fluorescence materials based on QDs for determination of analytes. It is reasonably believed that the molecular imprinting technique will be a powerful tool to improve the selectivity of the optical detection. For example, Wang et al. proposed MIPs coated with QD fluorescence materials for highly selectivity and sensitive determination of ractopamine,[10] vitamin E,[11] and tocopherol.[12] Xie et al.[13] developed a high affinity dipheolic acid (DPA)-MIPs-QD sensor using DPA as a dummy template, for selective determination of trace tetrabromobisphenol A in water and soil samples. Li et al.[14] reported a simple procedure for the synthesis of molecularly imprinted silica nanosphere-embedded mercaptosuccinic acid-coated CdTe quantum dots for selective recognition of λ-cyhalothrin.

To illustrate the usefulness of the MIPs combined with QD materials, carbaryl was chosen as a target. Carbaryl (1-naphthol-*N*-methylcarbamate) was the first successful carbamate insecticide used due to its broad-spectrum efficacy to control insecticide pests. It is widely used in Chinese agricultural systems to combat amounts of pests. Through inhibiting the activity of cholinesterase and the accumulation of acetylcholine in the organization, the normal secretion of biological systems was disrupted.[15−17] Various methods have been explored to detect carbaryl, such as chromatographic techniques,[18] biosensors,[19] enzyme-linked immunosorbent assay,[20,21] et al. MIP-capped QD fluorescence sensing material for analytical applications is still in rapid developed. As far as we know QDs@MIP fluorescence material for the quantitative analysis of carbaryl has not been reported. In this study, we synthesized fluorescence material for detection of carbaryl. The sensing material is based on fluorescence quenching when carbaryl are selectively recognized and combined with QDs@MIP. The participation of QDs exhibits a Stern−Volmer quenching behavior.[22] This method is prospected to realize a fast and efficient detection method for carbaryl without derivation.

Received: February 27, 2015
Revised: April 7, 2015
Accepted: May 6, 2015
Published: May 6, 2015

ACS Publications © 2015 American Chemical Society

DOI: 10.1021/acs.jafc.5b01072
J. Agric. Food Chem. 2015, 63, 4966−4972

MATERIALS AND METHODS

Materials and Reagents. Carbaryl, metolcarb, and isoprocarb were purchased from J&K Chemicals (Shanghai, China) (shown in Figure 1). CdSe/ZnS QDs (catalog Q1565) were purchased from

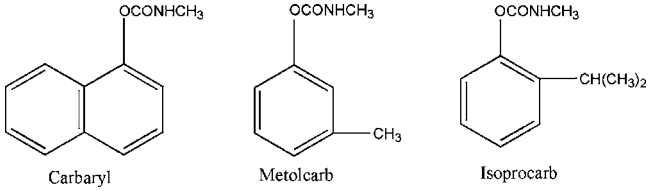

Figure 1. Structures of carbaryl, metolcarb, and isoprocarb.

Jiayuan (Wuhan, China). The 1-vinyl-3-hexyllimidazoliumhexafluorophosphate ILs was purchased from the Chinese Academy of Sciences (Lanzhou, China). Whatman filter paper no. 1 was purchased from GE Healthcare Worldwide. The functional monomer methacrylic acid (MAA), the cross-linker ethylene glycol dimethacrylate (EDGMA, 98%), and the initiator 2, 2-azobis(isobutyronitrile) (AIBN, 99%) were purchased from J&K Chemicals (Shanghai, China). The MAA and EDGMA were distilled under reduced pressure and AIBN was recrystallized in ethanol before use. All of the reagents were analytical grade.

Instruments. Fluorescence (FL) spectrophotometry was performed on an FLR Varian Cary Eclipse (Varian, USA) equipped with a quartz cell (1 cm × 1 cm). Ultraviolet−visible (UV−vis) spectra (200−800 nm) were recorded on a Cary 100-Bio UV spectrometer (Victoria, Australia). Scanning electron microscopy (S-4800, JEOL) was used to observe the surface morphologies of QDs@MIP and fluorescence material based on quantum dots and non-imprinted polymer (QDs@NIP). Fourier-transform infrared (FT-IR) spectra (4000−400 cm^{-1}) were recorded using a Thermo Scientific Nicolet IS 50 (Thermo Fisher Scientific, USA).

Synthesis of Fluorescence Material QDs@MIP. ILs are considered to be a green reaction media because of their nonvolatility, nonflammability, high ionic density, and high ionic conductivity, and they are widely used in areas such as synthesis, separation, and catalytic chemistry. In this study, ILs were used as the medium in the preparation of MIPs. They were anchored on the surface of QDs by electrostatic interaction. Under dark conditions, CdSe/ZnS QDs (50 μmol) were dissolved in chloroform (10 mL), mixed with 1-vinyl-3-hexyllimidazolium hexafluorophosphate IL (3 mmol), and stirred for 3 h at room temperature. Then, synthesis of molecularly imprinted fluorescence material based on IL-modified CdSe/ZnS QDs was carried out as follows: The carbaryl (1 mmol) and MAA (4 mmol) were added. The mixture was stirred overnight before adding cross-linker (EDGMA; 20 mmol) and AIBN (40 mg). After purging with nitrogen 5 min, the mixture was placed in a water bath at 60 °C for 24 h. When the polymerization reaction finished, the template molecules were removed by Soxhlet extraction with methanol and acetic acid (200 mL, v:v = 9:1) until no analyte was detected by UV−vis spectrophotometry. Finally, the polymers were dried in a vacuum oven at 55 °C. And, the QDs@MIP was obtained. The QDs@NIP was prepared without the template molecules.

Fluorescence Analysis. In the adsorption experiments, QDs@MIP and QDs@NIP nanoparticles (20 mg, 200 mesh screens) were dispersed in a 15 mL plug centrifuge tube, containing carbaryl standard solution (10 mL) with the concentration of 0−100 mg L^{-1}. After shaking for a certain time at room temperature, the templates were bound to the QDs@MIP, causing fluorescence quenching of the QDs. To further evaluate the analytical performance of the fluorescence sensing material, the detection limit and linear range were investigated. The detection limit (LOD) was calculated as the concentration of carbaryl that quenched three times the standard deviation of the blank signal divided by the slope of the standard curve. Metolcarb and isoprocarb were used as structural analogues in selectivity experiments. In the experiment, all the FL detections were performed under the same conditions: the excitation wavelength was set at 280 nm with a recording emission range of 450−650 nm, and the slit widths of the excitation and emission were both 2.5 nm. Then the mixture was mixed thoroughly and quickly scanned by the Cary Eclipse spectrophotometer.

RESULTS AND DISCUSSION

Preparation and Characterization of QDs@MIP and QDs@NIP. The general scheme for the synthesis of QDs@MIP and QDs@NIP was illustrated in Figure 2. First, the CdSe/ZnS QDs were modified with the ILs through electrostatic interactions. Then the ILs-modified CdSe/ZnS QDs were reacted with MAA through covalent bonding and the carbaryl was reacted with the MAA by hydrogen-bond interactions. The C═C bonds of ILs, anchored on the surface of QDs, participated in the polymerization process of MIPs. The introduction of ILs could increase the surface functional groups of QDs and improve the fluorescence stability of QDs.

After the template molecules were extracted from the composites by decomposing the hydrogen bonds, the identification of specific cavity sites was made in the composites and the QDs@MIP was obtained. Before removal of the

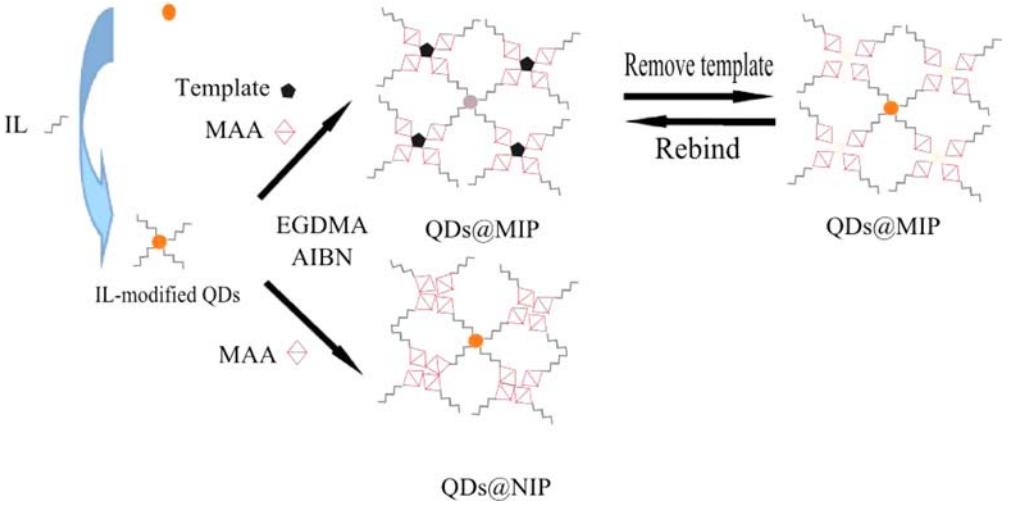

Figure 2. Schematic illustration of the preparation of QDs@MIP.

DOI: 10.1021/acs.jafc.5b01072
J. Agric. Food Chem. 2015, 63, 4966−4972

template molecules, the FL intensity of the QDs@MIP was about 24.4% of that of the QDs@NIP, while after removal of it, the FL intensity of the QDs@MIP increased to 96.6% of that of the QDs@NIP (Figure 3). This result indicated that the template molecule (carbaryl) was removed cleanly from the composites.

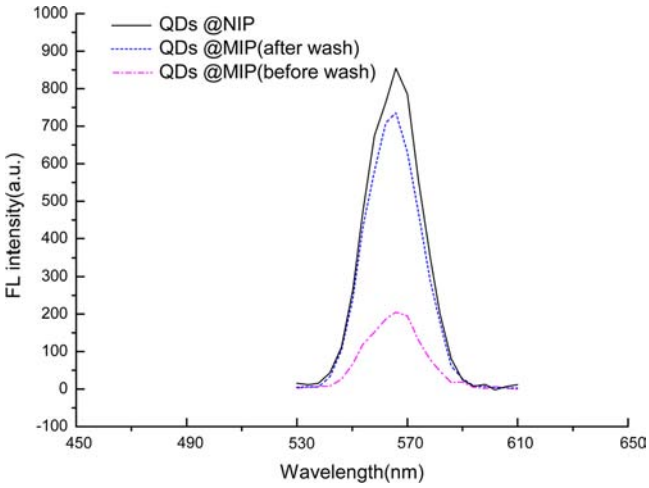

Figure 3. FL spectra of QDs@NIP, QDs@MIP (after wash), and QDs@MIP (before wash).

Characterization of QDs@MIP and QDs@NIP. The surface morphologies of QDs@MIP and QDs@NIP were observed by SEM (Figure 4). The QDs@ MIP (Figure 4a) had better uniformity and spherical structure and a rougher surface than QDs@NIP (Figure 4b), indicating that the template molecules' sites were left in the QDs@MIP.

FT-IR spectroscopy is performed to further characterize the QDs@MIP (Figure 5). The characteristic peaks of IL-QDs were shown in Figure 5b: the bands at 3173 and 3113 cm^{-1}were the stretching vibrations of aromatic C−H, the 2963 and 2940 cm^{-1} were the stretching vibrations of saturated C−H, the strong bands at 1666 cm^{-1} were the stretching vibrations of C═C, the bands at 1554, 1465, and 1178 cm^{-1} were the stretching vibrations of C═N, aromatic C═C, and C−N, respectively. The characteristic peaks of QDs@MIP were shown in Figure 5a: the peaks at 2981 and 2958 cm^{-1} were the stretching vibrations of saturated C−H, the bands at 1456 and 1159 cm^{-1} were respectively the stretching vibrations of aromatic C═C and C−N in ILs. The strong peak at around 1731 cm^{-1} of C═O, indicating that the cross-linker (EDGMA) had been successfully incorporated into the polymers.

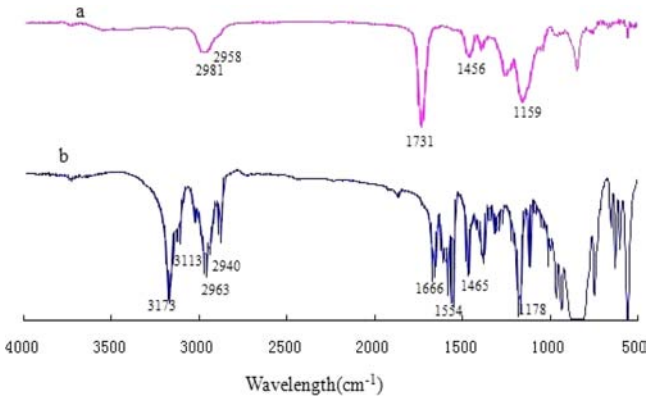

Figure 5. FT-IR spectra of (a) QDs@MIP and (b) IL-QDs.

Furthermore, the characteristic C═C peaks of 1666 cm^{-1} in IL-QDs disappeared markedly from the QDs@MIP, which showed the covalent interactions between the ILs and MAA. All these results indicated that the QDs@MIP was successfully grafted on the surface of the IL-coated CdSe/ZnS QDs.

Adsorption Capacity of the QDs@MIP and the QDs@NIP. In order to investigate the binding performance of the QDs@MIP and QDs@NIP, an equilibrium binding analysis was carried out using 10 mg L^{-1} carbaryl. First, to compare the effects of different solvents on the adsorption, acetonitrile, ethanol, methanol, and chloroform were selected. The difference in FL intensity between the QDs@MIP and the QDs@NIP was obvious when acetonitrile as solvent, showing that acetonitrile was a more suitable solvent for adsorption of carbaryl than the others. Therefore, acetonitrile was chosen as the adsorption solvent in the following experiments.

Effect of Adsorption Time. The influence of adsorption time on the fluorescence intensity investigated at different times was showed in Figure 6. It was found that the mixture showed a rapid decrease in fluorescence intensity after the carbaryl was added. The reaction reached equilibrium within 30 min, and the fluorescence intensity was kept constant with the rise of adsorption time beyond 30 min (Figure 6a). In addition, the UV−vis spectra of carbaryl (Figure 6b) decreased gradually until no carbaryl was detected after 30 min. This result was in accordance with the FL result. This further indicated that the optimal adsorption time was 30 min.

Optosensing of Carbaryl by QDs@MIP. QDs@MIP was used in this study as a sensing material to detect carbaryl. As shown in the absorption spectrum of the carbaryl and QDs@MIP (Figure 7), the UV absorption band of carbaryl is close to the band gap of the QDs@MIP and there is no spectral overlap

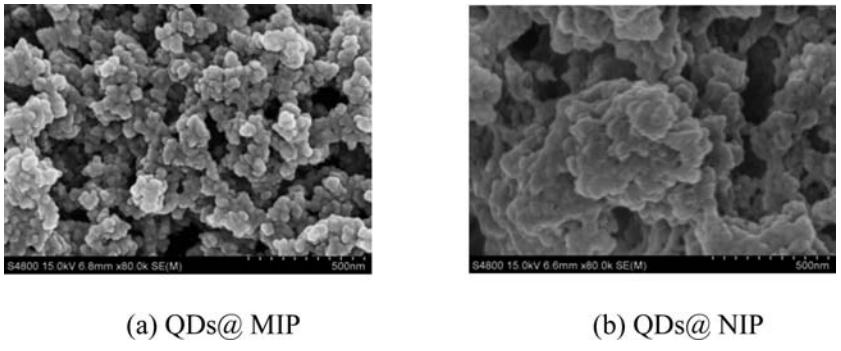

Figure 4. SEM images of (a) QDs@MIP and (b) QDs@NIP.

DOI: 10.1021/acs.jafc.5b01072
J. Agric. Food Chem. 2015, 63, 4966−4972

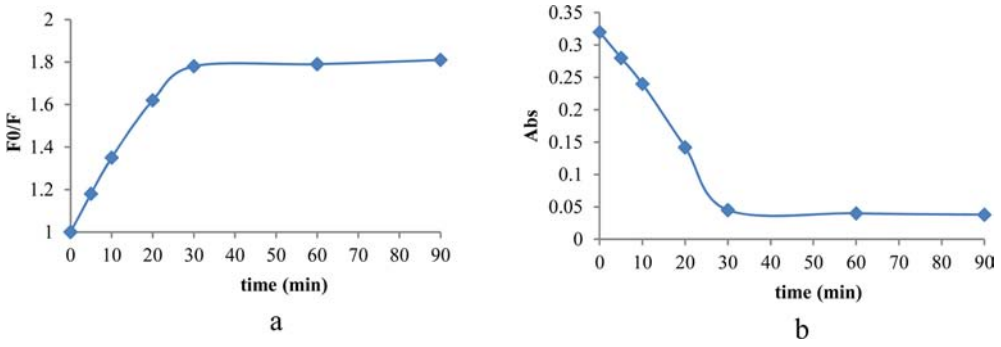

Figure 6. Dynamic adsorption of QDs@MIP for carbaryl (10 mg L^{-1}): (a) fluorescence; (b) UV−visible.

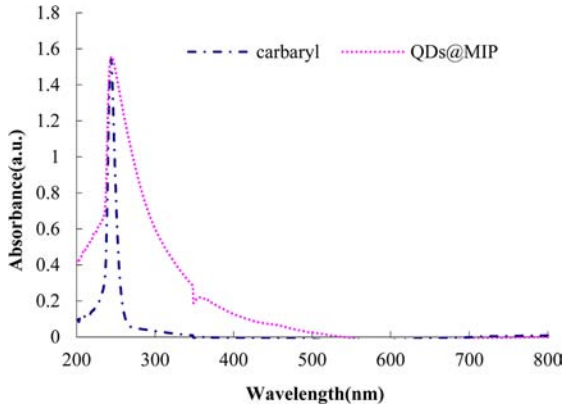

Figure 7. UV−vis spectra of carbaryl and QDs@MIP.

between the absorption spectrum of the carbaryl and the emission spectrum of the QDs@MIP (Em 565 nm). On the basis of former studies,[23,24] the mechanism of the decrease in fluorescence intensity may be charge transfer instead of energy transfer from the QDs to carbaryl. The QD valence band is full of charges; when a beam of light shines on the QDs, the charges tranfer to the conduction band. Charges in the conduction band are usually instable and can go back to the valence band, emitting photons and causing fluorescence. When carbaryl was presented, the charges of the conductive bands of the QDs could transfer to the lowest unoccupied molecular orbital of the UV band of carbaryl. They could not go back to the valence band, and there was no more fluorescence. That was FL quenching between carbaryl and QDs. The FL quenching in this system followed the Stern−Volmer equation.

$$F_0/F = 1 + K_{SV}[Q] \quad (1)$$

F_0 and F were the FL intensity of the QDs in the absence and presence of carbaryl, respectively, K_{SV} was the Stern−Volmer constant, and $[Q]$ was the concentration of carbaryl. This equation was used to quantify the different quenching constants in this research, and the ratio of the K_{SV} values of the MIP and NIP ($K_{SV,MIP}/K_{SV,NIP}$) was defined as the imprinting factor to evaluate the selectivity of the materials.

Selectivity Adsorption of QDs@MIP. Metolcarb and isoprocarb were selected as structural analogues to evaluate the selectivity of QDs@MIP (Figure 8). In Figure 8a and b, the FL changes of QDs@MIP were obvious between carbaryl and its structural analogues but less obvious in QDs@NIP. There are customized recognition sites in QDs@MIP after removing templates molecule that can specifically adsorb carbaryl, while

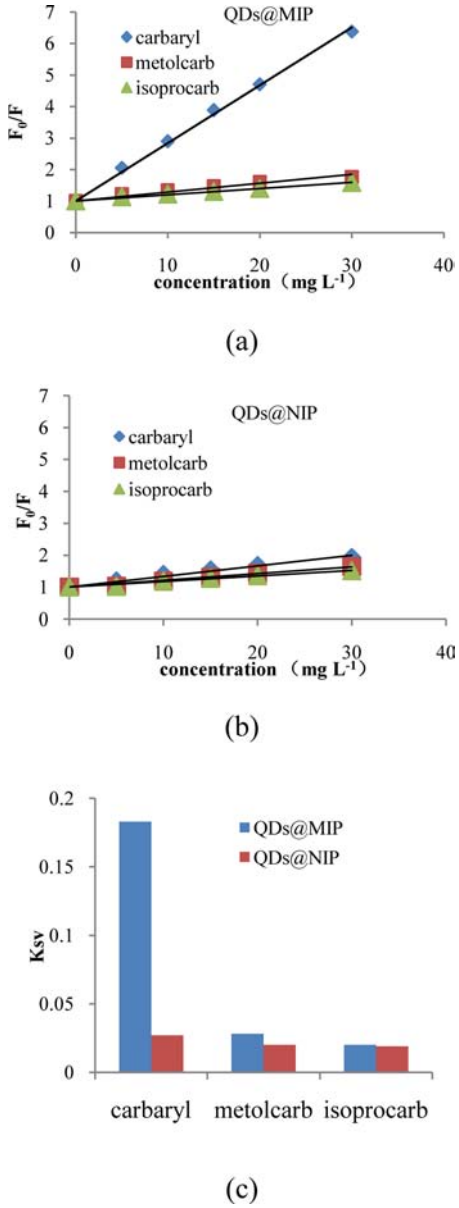

Figure 8. Selectivity of QDs@MIP (a) and QDs@NIP (b) for carbaryl, metolcarb, and isoprocarb and quenching constant of QDs@MIP and QDs@NIP (c) for carbaryl, metolcarb, and isoprocarb.

metolcarb and isoprocarb are not easy to identify. And there are no customized recognition sites formed in the QDs@NIP. This demonstrated the recognition mechanism of QDs@MIP is

DOI: 10.1021/acs.jafc.5b01072
J. Agric. Food Chem. 2015, 63, 4966−4972

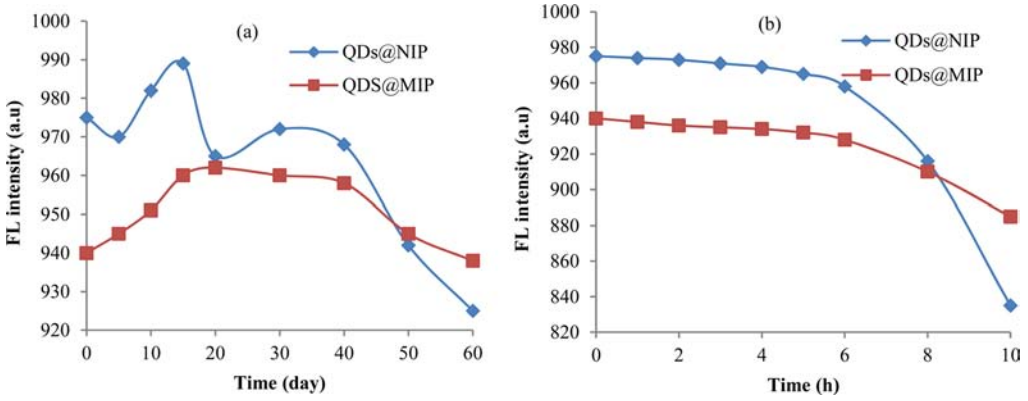

Figure 9. FL stability of QDs@ MIP and QDs@ NIP: (a) room temperature away from light for 60 days, (b) continuous UV irradiation for 10 h.

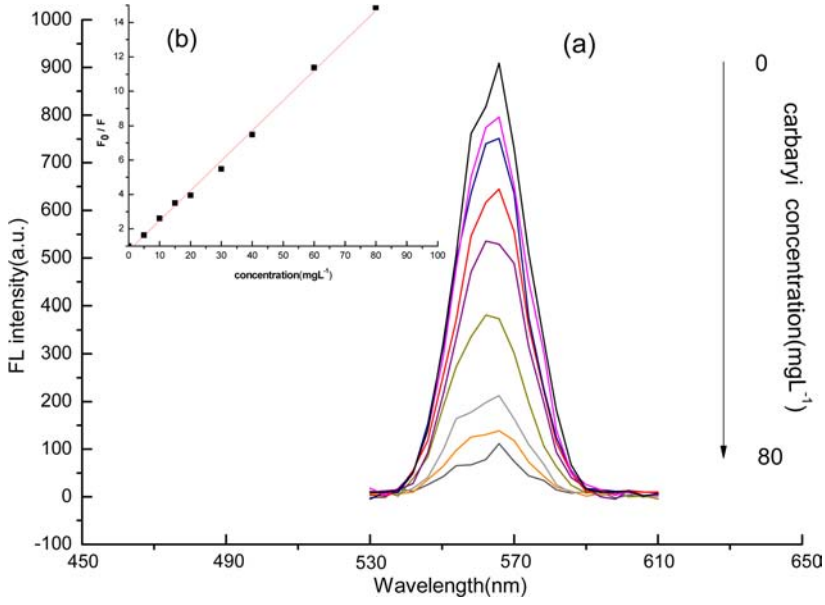

Figure 10. (a) FL spectra of QDs@MIP with increasing concentration of carbaryl. (b) Effect of carbaryl concentration on the FL intensity of QDs@ MIP.

based on the interactions of the structure and function of the templates. As shown in Figure 8c, the QDs@MIP exhibited a larger K_{SV} than the QDs@NIP. And the K_{SV} of carbaryl was much higher than its structural analogues. The ratio of $K_{SV,\ MIP}$ to $K_{SV,NIP}$ was the highest for carbaryl, at 6.78, indicating efficient imprinting.

Stability of QDs@MIP. The stability of QDs@MIP was also studied. The FL stabilities of QDs@MIP and QDs@NIP are shown in Figure 9 under the conditions of room temperature away from light for 60 days and with continuous UV irradiation for 10 h, respectively. It could be seen that for QDs@MIP in Figure 9a, FL decreased less than 5% at room temperature away from light for 60 days. For UV irradiation, the FL change was not obvious within 6 h. After 10 h, the FL of QDs@MIP reduced by 5.8%, and QDs@NIP was down 14.4%. It was known that the shelf life of bare QDs was very short and the solution turned to opaque black easily without surface-modification. However, the sensing material of QDs@MIP had better photostability. It could be explained that the package of an MIP layer outside might protect the photo stability of QDs.

QDs@MIP for the FL Detection of Carbaryl. In this system, the FL quenching followed the Stern−Volmer equation. Under optimum conditions, the QDs@MIP exhibited linear fluorescent quenching for carbaryl in the concentration range from 4.97×10^{-7} to 3.98×10^{-4} mol L^{-1}, with a correlation $R^2 = 0.9954$, as shown in Figure 10b. The LOD for carbaryl was 1.47×10^{-7} mol L^{-1}. The precision for five replicate detections of carbaryl (10 mg L^{-1}) was 2.4% (relative standard deviation). The reproducibility of QDs@MIP was also investigated. Three replicate measurements were carried out under the same conditions. The relative standard deviation was 3.8%.This indicates that the FL sensing method with QDs@ MIP could be used for simple, rapid determination of carbaryl with efficiency and sensitivity.

Application of the QDs@MIP to the Detection of Carbaryl in Real Samples. The ability of the developed FL method to quantify concentration of carbaryl in a real sample was examined. Samples of rice and Chinese cabbage were purchased from a supermarket. No response corresponding to carbaryl was observed by HPLC. Furthermore, three levels of carbaryl at 5, 10, and 20 mg L^{-1} were spiked. The sample pretreatment procedures were performed as follows: 2 g of spiked sample was treated by mixing 6 mL of methanol and shaking at 200 rpm on the rotary shaker for 30 min. The extracts were purified by filter paper. The filtrate was concentrated to near dryness and redissolved with acetonitrile

DOI: 10.1021/acs.jafc.5b01072
J. Agric. Food Chem. 2015, 63, 4966−4972

before analysis. A summary of the spiked concentration for samples and the corresponding analysis results is shown in Table 1. The concentrations of carbaryl in the spiked samples

Table 1. Spiked Recovery Results for the Determination of Carbaryl in Rice and Chinese Cabbage Samples by QDs@MIP, HPLC, and ELISA

sample	spiked level (mg kg^{-1})	QDs@MIP (mean ± SD; n = 3, mg kg^{-1})	ELISA (mg kg^{-1})	HPLC (mg kg^{-1})
rice	5	4.22 ± 0.30	4.36 ± 0.15	4.27 ± 0.10
	10	8.14 ± 0.65	8.47 ± 0.24	8.70 ± 0.13
	20	15.72 ± 1.04	16.10 ± 0.50	16.29 ± 0.28
Chinese cabbage	5	4.01 ± 0.35	4.14 ± 0.17	4.08 ± 0.14
	10	8.56 ± 0.79	8.87 ± 0.27	8.65 ± 0.20
	20	14.19 ± 1.09	14.94 ± 0.35	14.78 ± 0.27

determined by the developed FL method based on QDs@MIP were in good agreement with those of carbaryl spiked. The recoveries of carbryl were between 74% and 88%. The detected results were also validated by HPLC and ELISA, respectively. And the correlation between these methods was good (Figure 11, R^2 = 0.98).

In summary, we here reported an optosensing material which is a simple and effective method to detect carbaryl. The material had attractive advantages, such as being easily prepared and highly selective and photostable. The high selectivity of the analytical method based on QDs@MIP as the sensing material was successfully applied to analyze carbaryl in rice and Chinese cabbage samples. The study could also provide the technical support for the rapid detection in food safety fields.

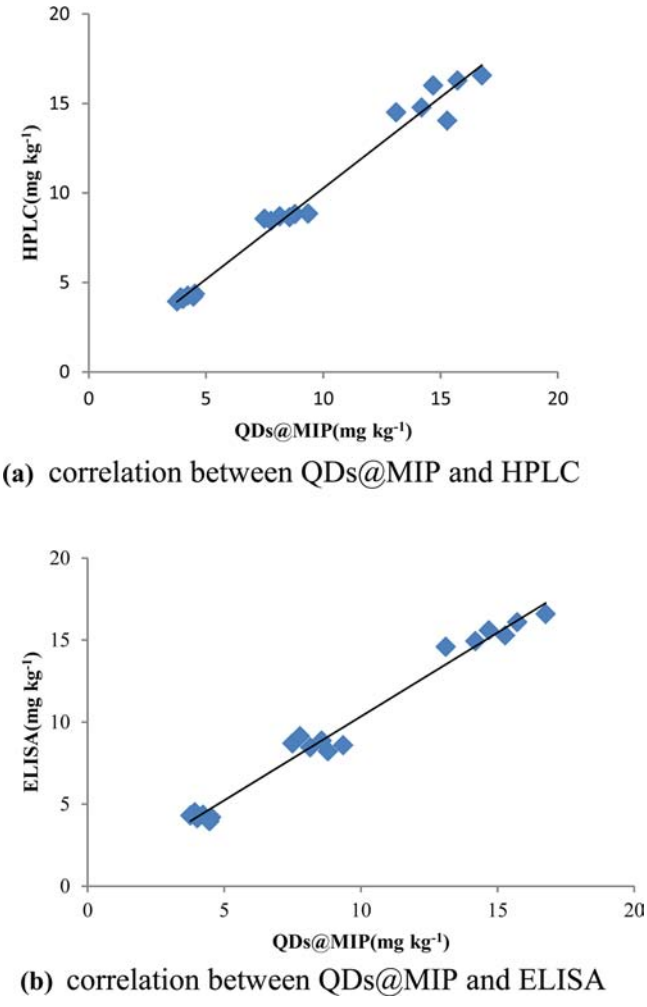

Figure 11. Correlation curves of the results.

AUTHOR INFORMATION

Corresponding Author

*E-mail address: zhangcan@mail.ujs.edu.cn. Tel.: +86 0511 88780201.

Notes

The authors declare no competing financial interest.

ACKNOWLEDGMENTS

This work was supported by the National Natural Science Foundation of China (Nos.31000783), the Jiangsu Planned Projects for Postdoctoral Research Funds (No.1202010B), the Project Funded by the Priority Academic Program Development of Jiangsu Higher Education Institutions (PAPD), Zhenjiang Social Developing Fund Program (SH2014019), and the Talent Foundation of Jiangsu University (No.09JDG052).

REFERENCES

(1) Euterpio, M. A.; Pagano, I.; Piccinelli, A. L.; Rastrelli, L.; Crescenzi, C. Development and Validation of a Method for the Determination of (E)-Resveratrol and Related Phenolic Compounds in Beverages Using Molecularly Imprinted Solid Phase Extraction. *J. Agric. Food Chem.* **2013**, *61*, 1640−1645.

(2) Yan, H. Y.; Cheng, X. L.; Yang, G. L. Dummy Molecularly Imprinted Solid-Phase Extraction for Selective Determination of Five Phthalate Esters in Plastic Bottled Functional Beverages. *J. Agric. Food Chem.* **2012**, *60*, 5524−5531.

(3) Sun, X. L.; Wang, J. C.; Li, Y.; Jin, J.; Yang, J. J.; Li, F.; Shah, S. M.; Chen, J. P. Highly class-selective solid-phase extraction of bisphenols in milk, sediment and human urine samples using well-designed dummy molecularly imprinted polymers. *J. Chromatogr. A* **2014**, *1360*, 9−16.

(4) Sadeghi, S.; Jahani, M. Selective solid-phase extraction using molecular imprinted polymer sorbent for the analysis of Florfenicol in food samples. *Food Chem.* **2013**, *141*, 1242−1251.

(5) Wang, X. L.; Qiao, X. G.; Ma, Y.; Zhao, T.; Xu, Z. X. Simultaneous Determination of Nine Trace Organophosphorous Pesticide Residues in Fruit Samples Using Molecularly Imprinted Matrix Solid-Phase Dispersion Followed by Gas Chromatography. *J. Agric. Food Chem.* **2013**, *61*, 3821−3823.

(6) Denderz, N.; Lehotay, J. Using of molecularly imprinted polymers for determination of gallic and protocatechuic acids in red wines by high performance liquidchromatography. *J. Chromatogr. A* **2014**, *1372*, 72−80.

(7) Dai, J.; Zhang, Y.; Pan, M. F.; Kong, L. J.; Wang, S. Development and Application of Quartz Crystal Microbalance Sensor Based on Novel Molecularly Imprinted Sol−Gel Polymer for Rapid Detection of Histamine in Foods. *J. Agric. Food Chem.* **2014**, *62*, 5269−5274.

(8) Sun, X. L.; Zhang, L. J.; Zhang, H. X.; Qian, H.; Zhang, Y. Z.; Tang, L. L.; Li, Z. J. Development and Application of 3-Chloro-1,2-propandiol Electrochemical Sensor Based on a Polyaminothiophenol Modified Molecularly Imprinted Film. *J. Agric. Food Chem.* **2014**, *62*, 4552−4557.

(9) Karakoti, A. S.; Shukla, R.; Shanker, R.; Singh, S. Surface functionalization of quantum dots for biological applications. *Adv. Colloid Interface Sci.* **2015**, *215*, 28−45.

(10) Liu, H. L.; Liu, D. R.; Fang, G. Z.; Liu, F. F.; Liu, C. C.; Yang, Y. K.; Wang, S. A novel dual-function molecularly imprinted polymer on

DOI: 10.1021/acs.jafc.5b01072
J. Agric. Food Chem. 2015, 63, 4966−4972

CdTe/ZnSquantum dots for highly selective and sensitive determination of ractopamine. *Anal. Chim. Acta* **2013**, *762*, 76−82.
(11) Liu, H. L.; Fang, G. Z.; Zhu, H. D.; Li, C. M.; Liu, C. C.; Wang, S. A novel ionic liquid stabilized molecularly imprinted optosensing material based on quantum dots and graphene oxide for specific recognition of vitamin E. *Biosens. Bioelectron.* **2013**, *47*, 127−132.
(12) Liu, H. L.; Fang, G. Z.; Li, C. M.; Pan, M. F.; Liu, C. C.; Fan, C.; Wang, S. Molecularly imprinted polymer on ionic liquid-modified CdSe/ZnS quantum dots for the highly selective and sensitive optosensingoftocopherol. *J. Mater. Chem.* **2012**, *22*, 19882−19887.
(13) Chen, Y. P.; Wang, D. N.; Yin, Y. M.; Wang, L. Y.; Wang, X. F.; Xie, M. X. Quantum Dots Capped with Dummy Molecularly Imprinted Film as Luminescent Sensor for the Determination of Tetrabromobisphenol A in Water and Soils. *J. Agric. Food Chem.* **2012**, *60*, 10472−10479.
(14) Wei, X.; Meng, M. J.; Song, Z. L.; Gao, L.; Li, H. J.; Dai, J. D.; Zhou, Z. P.; Li, C. X.; Pan, J. M.; Yu, P.; Yan, Y. S. Synthesis of molecularly imprinted silica nanospheres embedded mercaptosuccinic acid-coated CdTe quantum dots for selective recognition of λ-cyhalothrin. *J. Lumin.* **2014**, *153*, 326−332.
(15) Nayak, M. K.; Collins, P. J.; Kopittke, R. A. Residual toxicities and persistence of organophosphorus insecticides mixed with carbaryl as structural treatments against three liposcelididpsocid species (Psocoptera: Liposcelididae) infesting stored grain. *J. Stored Prod. Res.* **2003**, *39*, 343−353.
(16) Moreno, A. J.M.; Serafim, T. L.; Oliveira, P. J.; Madeira, V. M. C. Inhibition of mitochondrial bioenergetics by carbaryl is only evident for higher concentrations − Relevance for carbaryl toxicity mechanisms. *Chemosphere* **2007**, *66*, 404−411.
(17) Jeon, J. H.; Escher, A. K. B. I.; Hollender, J. Characterization of acetylcholinesterase inhibition and energy allocation in Daphnia magna exposed to carbaryl. *Ecotoxicol. Environ. Saf.* **2013**, *98*, 28−35.
(18) Zhang, J.; Lee, H. K. Application of liquid-phase microextraction and on-column derivatization combined with gas chromatographymass spectrometry to the determination of carbamate pesticides. *J.Chromatogr. A* **2006**, *1117*, 31−37.
(19) Mauriz, E.; Calle, A.; Abad, A.; Montoya, A.; Hildebrandt, A.; Barceló, D.; Lechuga, L. M. Determinationofcarbaryl in natural water samples by a surface plasmon resonance flow-through immunosensor. *Biosens. Bioelectron.* **2006**, *21*, 2129−2136.
(20) Wang, S.; Yu, C. D.; Wang, J. P. Enzyme immunoassay for the determination of carbaryl residues in agricultural products. *Food Addit. Contam.* **2005**, *22*, 735−742.
(21) Sun, J. W.; Dong, T. T.; Zhang, Y.; Wang, S. Development of enzyme linked immunoassay for the simultaneousdetection of carbaryl and metolcarb in different agricultural products. *Anal. Chim. Acta* **2010**, *666*, 76−82.
(22) Durán, T. V.; Gran, S. A.; Órdenes, A. N.; Monrás, J. P.; Saona, L. A.; Venegas, F. A.; Chasteen, T. G.; Bravo, D.; Pérez, D. J.M. Quantum dot-based assay for Cu^{2+} quantification in bacterial cell culture. *Anal. Biochem.* **2014**, *450*, 30−36.
(23) Tu, R. Y.; Liu, B. H.; Wang, Z. Y.; Gao, D. M.; Wang, F.; Fang, Q. L.; Zhang, Z. P. Amine-Capped $ZnS^{-}Mn^{2+}$ Nanocrystals for Fluorescence Detection of Trace TNT Explosive. *Anal. Chem.* **2008**, *80*, 3458−3465.
(24) Wang, H. F.; He, Y.; Ji, T. R.; Yan, X. P. Surface Molecular Imprinting on Mn-DopedZnS Quantum Dots for Room-Temperature Phosphorescence Optosensing of Pentachlorophenolin Water. *Anal. Chem.* **2009**, *81*, 1615−1621.

DOI: 10.1021/acs.jafc.5b01072
J. Agric. Food Chem. 2015, 63, 4966−4972

JOURNAL OF AGRICULTURAL AND FOOD CHEMISTRY

Article

pubs.acs.org/JAFC

Bioaccessibility of the Bioactive Peptide Carnosine during in Vitro Digestion of Cured Beef Meat

Elena Marcolini,[†] Elena Babini,[†,‡] Alessandra Bordoni,[†,‡] Mattia Di Nunzio,[†] Luca Laghi,[†,‡] Anita Maczó,[§] Gianfranco Picone,[‡] Emoke Szerdahelyi,[§] Veronica Valli,[‡] and Francesco Capozzi*[,†,‡,⊥]

[†]Interdepartmental Centre for Industrial Agri-Food Research, University of Bologna, Piazza Goidanich 60, 47521 Cesena, Forlì Cesena, Italy

[‡]Department of Agri-Food Sciences and Technologies, University of Bologna, Piazza Goidanich 60, 47521 Cesena, Forlì Cesena, Italy

[§]National Agricultural Research and Innovation Centre-Food Science Research Institute, Herman Ottó út 15, H-1022 Budapest, Hungary

[⊥]Centre of Magnetic Resonance, University of Florence, via L. Sacconi 6, 50019 Sesto Fiorentino, Florence, Italy

ABSTRACT: A bioactive compound is a food component that may have an impact on health. Its bioaccessibility, defined as the fraction released from the food matrix into the gastrointestinal tract during digestion, depends on compound stability, interactions with other food components, and supramolecular organization of food. In this study, the effect of pH on the bioaccessibility of the bioactive dipeptide carnosine was evaluated in two commercial samples of the Italian cured beef meat bresaola at two key points of digestion: before the gastric and after the duodenal phases. The digestion process was simulated using an in vitro static system, whereas capillary zone electrophoresis (CZE) and ^{1}H nuclear magnetic resonance (NMR) were used for quantitative analysis. The gap between the total carnosine content, measured by CZE, and its free diffusible fraction observable by NMR spectroscopy, was 11 and 19% for two independent bresaola products, where such percentages represent the fraction of carnosine not accessible for intestinal absorption because it was adsorbed to the food matrix dispersed in the digestion fluid.

KEYWORDS: *carnosine, bresaola, in vitro digestion, bioaccessibility, bioactive compounds, ^{1}H NMR, CZE*

INTRODUCTION

Bioactive compounds are extra nutritional constituents of food that typically occur in small quantities but can have a positive impact on body functions or conditions and may ultimately influence health.[1] For their potential positive effects, they have been extensively studied in the past decade, isolated from different food sources and chemically and functionally characterized. Most of the research has focused on secondary plant materials such as phytosterols or polyphenols; meat and meat products, despite being recognized as good suppliers of high-grade proteins, vitamins, and minerals, are generally not considered as sources of bioactive substances. Yet, research has made progress in the meat segment, too, and today many compounds found in meat, such as, small peptides, carnosine, anserine, taurine, creatinine, and coenzyme Q10, have been recognized as bioactives with a wide spectrum of physiological actions.[2−4]

Carnosine is a β-alanine and L-histidine dipeptide, which is distributed widely and abundantly in the excitable tissues (particularly muscle and nervous tissues) of several animal species. Although its physiological role is not been completely understood yet, many beneficial actions have been attributed to carnosine, such as being an antioxidant and a free radical scavenger, an antiglycating and an ion-chelating agent, and a wound-healing promoter.[5] These biological activities may explain the ability of carnosine to exert an antiaging activity at cellular and whole animal levels[6] and to restrain some oxidative-based diseases such as diabetes,[7−9] atherosclerosis,[10] metabolic distress syndrome,[11] and also ischemia−reperfusion damage in different organs.[12−14]

After meat digestion, the amount of dietary carnosine becoming available for intestinal absorption depends not only on its original concentration in food (related to animal species and tissue type) but also on its bioaccessibility, that is, the fraction of the compound that is released from the food matrix in the gastrointestinal tract during digestion and is available for intestinal absorption.[15] Nutrient bioaccessibility is affected by digestion conditions (pH, enzyme concentration, and activity), compound stability, and interactions with other food components, as well as the supramolecular organization of the food.[16] Particularly, the pH of the environment is a critical parameter, being able to modify the net charge of a molecule, its structure, and consequently the degree of interaction with the solvent and other food molecules.

In this work, the effect of pH on the solubility and in turn bioaccessibility of carnosine was assessed in bresaola, a typical beef-based product of northern Italy (Valtellina), which is produced by curing the intact beef muscle through different processing steps including a careful selection and skillful trimming of cuts of meat, followed by a dry salting step, during which wine, spices, and sugar (with the aim of encouraging

Received: March 5, 2015
Revised: May 11, 2015
Accepted: May 13, 2015
Published: May 13, 2015

ACS Publications © 2015 American Chemical Society

DOI: 10.1021/acs.jafc.5b01157
J. Agric. Food Chem. 2015, 63, 4973−4978

microbial phenomena responsible for much of the aging of the product) are added, and then the meat is stuffed into natural or artificial casings and sent to the next stage of drying in special cells for a slow maturation. As this substrate is consumed crude, the evaluation of carnosine content is not expected to be affected by alterations due to the cooking process, which can cause a reduction of carnosine of up to 50% in other beef products, depending on the cooking procedure.[17,18] The digestion of bresaola occurring in vivo in the human gastrointestinal tract was simulated using an in vitro static system,[19] and the soluble free compound in the digestion fluid was evaluated by coupling ^{1}H nuclear magnetic resonance spectroscopy (^{1}H NMR) and capillary zone electrophoresis (CZE). These techniques were operated at different pH values to obtain a global description of the free fraction of the molecule at three key points of digestion, those being the end of the oral phase and after 180 and 300 min of duodenal digestion.

To the best of our knowledge this research work represents the first study estimating the effect of pH on the interactions of carnosine with the digested meat matrix and, therefore, on its bioaccessibility. The presence of emulsifiers, metal ions, fats, biopolymers, and other chemical species able to bind the bioactive compounds could sequester them, thus limiting their free diffusion through the extracting digestion fluid, from the food matrix, where bioactive molecules are embedded, to the gut mucosa where their absorption occurs. The modification of bioaccessibility due to interactions with the food matrix is a key factor that should be considered while evaluating the potential significance of bioactives in human health. Each compound, indeed, is susceptible to chemical exchange between environments, being either freely diffusible in the digestion fluids or being adsorbed on the surfaces of the macromolecular food matrix; this could affect the bioactive bioaccessibility and, therefore, effectiveness, when it is delivered in the human diet as part of a complex food matrix and not as a discrete molecule.

MATERIALS AND METHODS

All chemicals and solvents were of the highest analytical grade and were purchased from Sigma-Aldrich (St. Louis, MO, USA), except where indicated. The two types of commercial bresaola, named B1 and B2, were bought in a local market.

Cured Meat Sample Preparation for Carnosine Quantification in Raw Material. Bresaola meat samples were prepared for carnosine quantification by grinding them with a common mincer. Five grams of minced meat was then homogenized with 10 mL of distilled water for 4 min at 25000 rpm using a homogenizer. Thereafter, the pH was adjusted to 2.5 with 37% HCl and, after centrifugation for 30 min at 11500 rpm at 4 °C, the supernatant was filtered through a 0.45 μm filter, boiled for 10 min, centrifuged for 20 min at 11500 rpm and 4 °C, and filtered again using a 0.22 μm filter. For CZE analysis the filtered sample was diluted 1:20 with 100 mM phosphate buffer, pH 2.5 (BioRad Laboratories, Hercules, CA, USA). For ^{1}H NMR spectroscopy 160 μL of deuterium oxide (D_2O), containing 10 mM 3-trimethylsilyl-propanoic-2,2,3,3-d_4 acid sodium salt (TSP), as chemical shift calibration standard, was added to 1 mL of filtered sample, and the pH was adjusted to the investigated value by adding 10% NaOH or 1 M HCl.

Cured Meat Sample Preparation for Carnosine pH Dependence Evaluation. The pH dependence of carnosine in bresaola meat was analyzed by ^{1}H NMR in samples prepared as described in the previous section. In these experiments, before the first centrifugation, the pH was adjusted, by adding 10% NaOH or 1 M HCl, to the following values: 2, 2.5, 3.5, 5, 6, 7, and 8. Afterward, the samples were centrifuged at 14000 rpm for 5 min to remove precipitates.

Cured Meat in Vitro Digestion. The bresaola samples were digested in triplicate according to the method of Bordoni,[19] following the scheme reported in Figure 1.

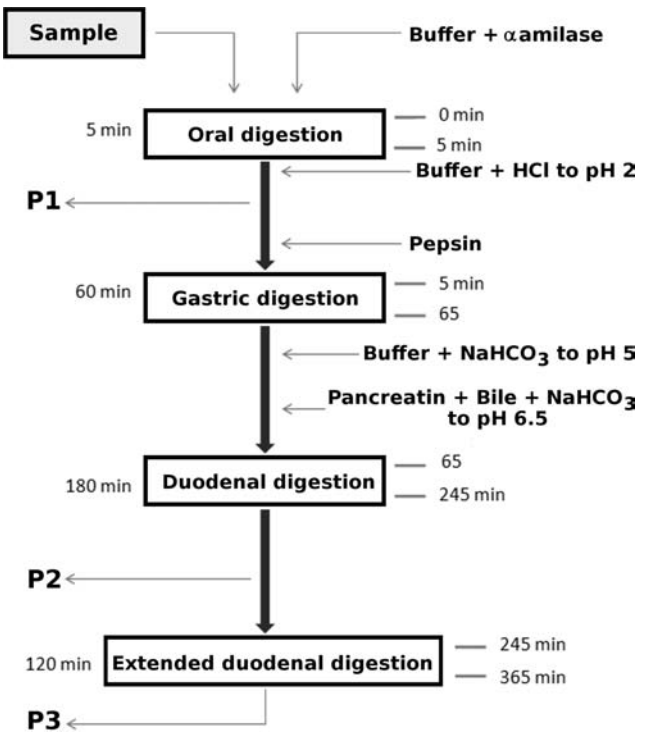

Figure 1. Flowchart of human in vitro digestion. P1, P2, and P3 are the labels of samples collected at the beginning of the gastric phase (P1) and after 180 min (P2) and 300 min (P3) from the beginning of the duodenal phase.

In detail, human digestion was simulated in vitro inside a 100 mL flask, kept at 37 °C in a water bath on a magnetic stirrer equipped with a heating plate.[20] The chemical composition of the digestive fluid, pH, and residence periods were adjusted to mimic physiological conditions. Three samples were collected during digestion: P1, before the gastric phase, when the food enters the stomach and the pH decreases to 2; P2 and P3, at 180 and 300 min from the beginning of the duodenal phase, respectively.

Samples P2 and P3 were acidified to pH 2 with 37% HCl to stop hydrolysis by the pancreatic enzymes. P1, P2, and P3 samples were stored at −80 °C before CZE and ^{1}H NMR experiments, before any further treatment.

For CZE, 500 μL of samples P1−P3 was boiled for 10 min, immediately cooled, and then centrifuged for 30 min at 9500g and 4 °C; the supernatant was filtered through a 0.22 μm before analysis.

Samples P1−P3 were prepared for ^{1}H NMR by adding 160 μL of D_2O, containing 10 mM TSP, as chemical shift calibration standard, to 1 mL of each sample. After adjustment of the pH to 7, the samples were centrifuged at 14000 rpm for 5 min to remove precipitates.

Carnosine Quantification by CZE. CZE analysis and data processing were performed on a Biofocus 2000 from Bio-Rad Laboratories. Uncoated fused-silica capillaries with a diameter of 50 μm and an effective length of 51 cm were used for the analysis. The temperature during the analysis was maintained constant at 38 °C, and samples were analyzed in a 110 mM phosphate buffer at pH 2.5 (Bio-Rad Laboratories). The voltage was kept at 15 kV, and the separated components were detected at 200 nm (UV), without derivatization. The quantification was performed in duplicate by area integration.

^{1}H NMR Evaluation of Carnosine Concentration and Carnosine pH Dependence. All ^{1}H NMR spectra were recorded at 25 °C on a Bruker US+ Avance III spectrometer operating at 600 MHz, equipped with a BBI-z probe and a B-ACS 60 sampler for

DOI: 10.1021/acs.jafc.5b01157
J. Agric. Food Chem. 2015, 63, 4973−4978

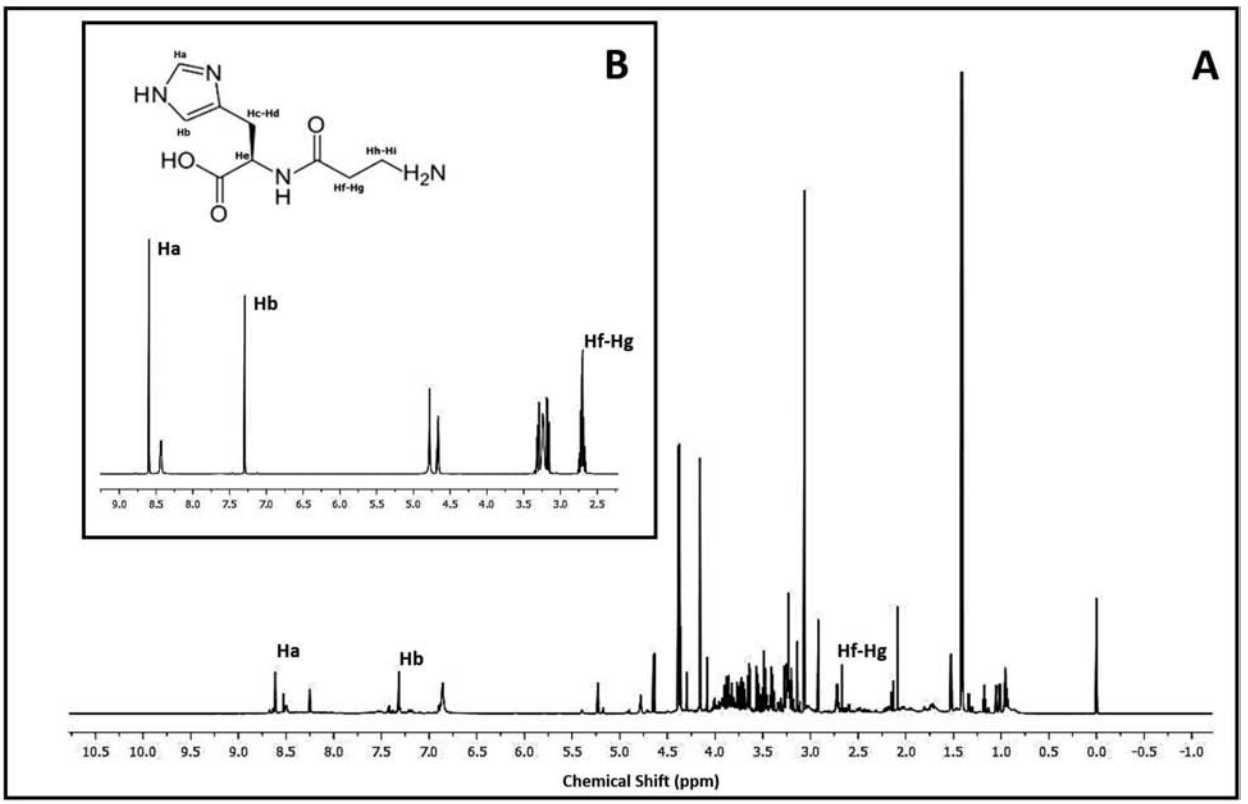

Figure 2. ^{1}H NMR spectrum of (A) bresaola B1 sample at P1 digestion point (pH 7.0) and (B) carnosine standard, showing the signals from L-histidine (Ha, Hb, Hc, Hd, and He) and β-alanine (Hh, Hi, Hf, and Hg) residues.

automation (Bruker BioSpin, Karlsruhe, Germany). Spectra were collected with a 90° pulse of 14 μs with a power of 10 W, a relaxation delay of 5 s, and an acquisition time of 2.28 s.

Spectra were registered by means of the first increment of a NOESY sequence, designed to suppress the HOD residual signal while giving, for each proton, signals proportional to the concentration of the substance they belong.

Statistical Analysis. Data normality and homogeneity of the variances were assessed by means of Shapiro−Wilks and Barlett tests, respectively. Sample and pH effects on carnosine concentration were investigated through an ANOVA test, followed by a post hoc LSD test. Every calculation was performed by means of the correspondent packages implemented in R computational language. A trim value of 0.05 was considered, unless differently stated.

RESULTS AND DISCUSSION

Carnosine Quantification in Raw Bresaola Meat by CZE and ^{1}H NMR Spectroscopy. In undigested raw samples, carnosine content was measured by both CZE and ^{1}H NMR, using the purified compound as reference standard. Measurements were performed at pH 2.5, which optimizes carnosine resolution through CZE.[21]

By CZE the content of carnosine was estimated at 628 and 671 mg/100 g in raw B1 and B2, respectively.

A typical ^{1}H NMR spectrum of bresaola extract, with carnosine highlighted, is reported in Figure 2. For the quantification of this molecule the signals at 7.30 and 8.60 ppm, corresponding to imidazole hydrogens Ha and Hb of the histidine residue, were considered, because they are singlets (thus granting the highest signal-to-noise ratio) and well resolved from signals ascribable to other molecules. In all of the registered spectra it was possible to observe a 1:2 ratio between the area of these signals and those from β-alanine appearing in the range of 2.65−2.80 ppm, corresponding to the two protons Hf and Hg, indicating that the amount of free histidine in all samples was negligible.

By ^{1}H NMR the amount of measured carnosine was estimated as 623.3 and 664.1 mg/100 g of raw products, in B1 and B2 samples, respectively. The very low difference in carnosine concentration detected by ^{1}H NMR and CZE values (Δ = 0.7 and 1.0% for B1 and B2 samples, respectively) clearly indicates a good agreement between the two techniques when working at the same acidic pH.

These values are higher than those reported in the literature for beef meat, for which carnosine content ranged from 32.6 mg/100 g in heart to 452 mg/100 g in semitendinosus muscle,[22,23] being generally higher in anaerobic, glycolitic, white muscle than in red, aerobic muscle.[6] It is conceivable that the higher carnosine content is related to the dehydration process that raw meat undergoes during bresaola production, which increases the protein content from 20.5 to 32 g/100 g.[24]

Effect of pH on Carnosine Quantification in Bresaola Meat. Previous investigations have shown that the solubility of low molecular weight molecules during food digestion depends on the physiological pH of the different digestion environments, which can be modulated by the interaction with the food matrix undergoing digestion.[25] This especially holds for carnosine, the net charge of which strongly depends on pH for the presence of three ionizable groups, namely, the histidine α carboxylic group (pK_a = 2.64), the histidine imidazolic group (pK_a = 6.83), and the alanine β aminic group (pK_a = 9.51).

To better elucidate the relationship between carnosine bioaccessibility and pH, the dipeptide concentration in raw B1 and B2 samples was quantified by ^{1}H NMR in the pH 2−8 range. As reported in Figure 3, in both samples the amount of

DOI: 10.1021/acs.jafc.5b01157
J. Agric. Food Chem. 2015, 63, 4973−4978

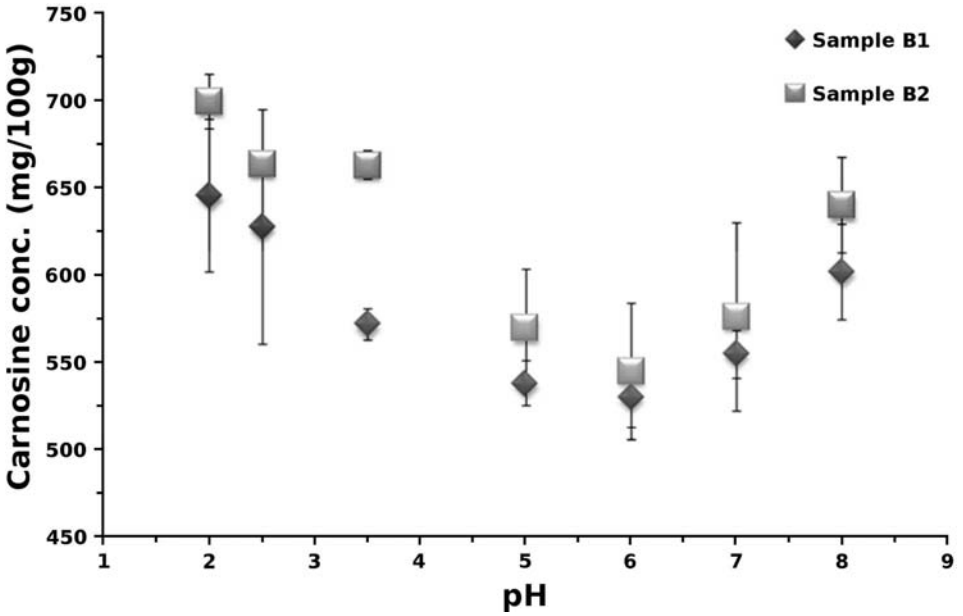

Figure 3. Carnosine concentration as assessed by ^{1}H NMR in the presence of meat samples B1 and B2 at different pH values. The error bars indicate the standard deviation calculated on three replicates.

Table 1. Carnosine Concentration of Bresaola B1 and B2, Measured by CZE and ^{1}H NMR, at the Beginning of the Gastric Digestion (P1) and at 180 and 300 min from the Beginning of the Duodenal Phase (P2 and P3)[a]

		CZE (pH 2.5), mg/100 g		^{1}H NMR (pH 7), mg/100 g		Δ CZE − ^{1}H NMR, %
B1						
	P1	620.30	600.73 ± 19.70	514.70	543.82 ± 30.02	10.50
		601.00		574.66		
		580.90		542.09		
	P2	638.94	654.43 ± 13.85	519.57	557.81 ± 33.93	17.32
		658.76		584.29		
		665.60		569.58		
	P3	608.89	631.78 ± 20.64	524.70	555.80 ± 28.56	13.67
		637.50		580.85		
		648.96		561.86		
B2						
	P1	595.32	607.18 ± 17.44	519.30	518.02 ± 4.50	17.21
		599.02		513.01		
		627.20		521.74		
	P2	712.73	659.57 ± 63.92	519.57	542.02 ± 10.52	21.60
		588.64		584.29		
		677.34		569.58		
	P3	681.68	640.74 ± 57.41	524.70	555.02 ± 24.03	15.32
		575.12		580.85		
		665.42		561.86		

[a]The values of three replicates of digestion and their average ± standard deviation are presented, expressed in mg/100 g of meat.

free carnosine was maximum at pH <2.5 or >8 and was characterized by a curvilinear relationship with pH, with a minimum around pH 5.3, corresponding to the isoelectric point of meat proteins. In detail, carnosine concentration in solution appeared significantly different between pH 2 and 7 ($P < 0.05$).

The quantification of carnosine alone in water solution did not show any change of concentration depending on pH (data not reported), pointing out that such behavior was peculiarly ascribable to the interaction between carnosine and the food matrix. The lowest recovery around meat proteins' isoelectric point suggested in particular the interaction of carnosine with the hydrophobic patches over the surface of meat proteins.

Meat is characterized by its own pH, depending on the quality and manufacturing processes in the case of curing, aging, or other technological transformations. The purpose of this study was to describe the effect of the digested meat matrix on the solubility of carnosine, which modulates its accessibility, for example, the diffusion of the dipeptide toward the gut mucosa where the absorption will occur. The possible implication of this phenomenon on the kinetics of absorption should be taken into account in the development of new meat products, by considering that matrix could be modified, thus reacting to digestion in different ways.

Carnosine Bioaccessibility during in Vitro Bresaola Digestion. To study carnosine bioaccessibility during

DOI: 10.1021/acs.jafc.5b01157
J. Agric. Food Chem. 2015, 63, 4973−4978

digestion, its concentration was measured in the soluble fraction of samples collected at different phases of an in vitro static digestion process. CZE and ^{1}H NMR were used in parallel at pH 2.5 and 7, respectively. pH values were adjusted before sample injection (CZE) or transfer to the NMR tube, respectively. As mentioned above, measurement at pH 2.5 optimizes carnosine resolution through CZE;[21] furthermore, it allowed a direct comparison between data obtained on raw samples and digestates. Measurement by ^{1}H NMR were performed at pH 7 to focus on the carnosine concentration at pH values similar to those found in the intestine, where absorption takes place.

Carnosine concentrations in the soluble fractions of digestate obtained at three different time points (P1, P2, and P3), as the result of three repetitions of in vitro digestion processes of B1 and B2 products, are reported in Table 1.

Carnosine concentration at P1 corresponds to the amount of compound brought into solution after the oral step, during which the meat is chewed in the presence of saliva. CZE analysis allowed the comparison of carnosine content at P1 and in raw, undigested samples, evidencing that in both samples the simple action of chewing and subsequent acidification actually released most of the dipeptide (96 and 90% in B1 and B2, respectively).

In both samples carnosine concentration measured by ^{1}H NMR at pH 7 was lower than by CZE, in agreement with the above-reported data on the effect of pH on carnosine quantification. Comparison was made between the gastric samples analyzed by CZE at pH 2.5 and the same samples analyzed by NMR after bringing the pH to 7. This change of pH may parallel the jump occurring when the bolus exits the stomach and enters the duodenum.

As well, carnosine concentration at P2 and P3 (at 180 and 300 min from the beginning of the duodenal digestion, respectively) was higher by CZE than by ^{1}H NMR. It is important to consider that the pH of the intestinal environment is close to 7, so ^{1}H NMR analysis actually mirrors the amount of carnosine available for absorption (i.e., the bioaccessible carnosine), values obtained with CZE being an artifact due to the condition of analysis. ^{1}H NMR showed that, after 180 min of duodenal digestion, the amount of compound found as the bioaccessible soluble fraction was 89 and 81% of the total extracted from the raw samples B1 and B2, respectively. Prolongation of the in vitro duodenal digestion for a further 120 min (P3) did not lead to any significant increase in carnosine concentration, indicating that carnosine release from the food matrix is almost completed after 3 h of duodenal digestion.

In summary, in the present work two different techniques, CZE and NMR spectroscopy, were used in parallel to evaluate the carnosine concentration in two samples of a typical Italian cured meat based product, bresaola. Evaluation was performed on both the raw material and after in vitro digestion of samples. Both analyses were performed on raw bresaola at pH 2.5, and results evidenced a good agreement between the two techniques. In digested samples, CZE analysis was still performed at pH 2.5, which represents the optimum pH value for the analysis, whereas NMR spectroscopy was performed at a pH value resembling the one in the intestine (pH 7). In this way, it was possible to evidence the influence exerted by the matrix on carnosine transfer from the food to the soluble fraction, avoiding interference due to the herein evidenced effect of pH on carnosine quantification.

The nutritional evaluation of a food as a source of specific nutrients is usually based on the chemical composition of the food itself. This approach does not take into account the digestion process, which regulates the amount of nutrients that can be absorbed, leading to a handy approximation often exceeding the real role of the food in the satisfaction of human metabolic needs. The availability of nutrients depends on the food matrix in which they are embedded and on food processing, which can interfere with the digestion process. An exhaustive evaluation of the nutritional meaning of a food should take into account, among others, the modifications occurring during the digestion process, becaise only nutrients that are absorbed have the possibility to modulate the physiological processes occurring in the human body.

Although the present study aimed to investigate the concentration of free carnosine in the gastric and duodenal digestion fluids, the same phenomenon may occur in meat samples before digestion. It is interesting to note that pH 5.3 is typical of meat, and at this pH carnosine has the lowest fraction as free diffusible molecule, which could prevent depletion of such dipeptide during drip loss.

The potential of NMR spectroscopy to describe the interactions between a bioactive compound and the food matrix, directly in the digestion fluid and at the physiological pH, provides a tool that may help to differentiate meat products on the basis of their matrix effect. Matrix is difficult to study during digestion, but its definition may be inferred through the study of its chemical interactions with soluble molecules. The simple quantification of the total amount of each compound extracted from the meat prevents the differentiation of meat products on the supramolecular scale, that is, on the basis of its matrix. NMR spectroscopy offers the opportunity to leave the molecules in their physiological environments, including those characterizing the digestion process and for which the food matrix may play an important role for the diffusibility of the bioactive molecules from food to the gut mucosa.

An omic approach is needed to describe the food system and its relationship with the human system. This approach, known as foodomics, has gained momentum in recent years because it allows reaching a deeper level of knowledge about the nutritional value of a food and of the relationship between food and health.

AUTHOR INFORMATION

Corresponding Author

*(F.C.) Phone: +39 0547 338105. Fax: +39 0547 382348. E-mail: francesco.capozzi@unibo.it.

Funding

This work was supported by COST action INFOGEST (FA1005).

Notes

The authors declare no competing financial interest.

ABBREVIATIONS USED

NMR, nuclear magnetic resonance; CZE, capillary zone electrophoresis; NOESY, nuclear Overhauser effect spectroscopy

REFERENCES

(1) Kitts, D. D.; Weiler, K. Bioactive proteins and peptides from food sources. Applications of bioprocesses used in isolation and recovery. *Curr. Pharm. Design* **2003**, *9*, 1309−1323.

DOI: 10.1021/acs.jafc.5b01157
J. Agric. Food Chem. 2015, 63, 4973−4978

(2) Schmid, A. Bioactive substances in meat and meat products. *Fleischwirtschaft Int.* **2009**, *89*, 83−90.
(3) Szterk, A.; Roszko, M. Simultaneous determination of free amino acids, L-carnosine, purine, pyrimidine, and nucleosides in meat by liquid chromatography/single quadrupole mass spectrometry. *J. Liq. Chromatogr. Relat. Technol.* **2013**, *37*, 664−680.
(4) Saiga, A.; Kanda, K.; Wei, Z.; Okumura, T.; Kaneko, T.; Nishimura, T. Hypotensive activity of muscle protein and gluten hydrolysates obtained by protease treatment. *J. Food Biochem.* **2002**, *26*, 391−401.
(5) Bellia, F.; Vecchio, G.; Cuzzocrea, S.; Calabrese, V.; Rizzarelli, E. Neuroprotective features of carnosine in oxidative driven diseases. *Mol. Aspects Med.* **2011**, *32*, 258−266.
(6) Hipkiss, A. R. Carnosine and its possible roles in nutrition and health. In *Advances in Food and Nutrition Research*; Steve, L. T., Ed.; Academic Press: San Diego, CA, USA, 2009; Vol. 57, pp 87−154.
(7) Riedl, E.; Pfister, F.; Braunagel, M.; Brinkkötter, P.; Sternik, P.; Deinzer, M.; Bakker, S. J. L.; Henning, R. H.; van den Born, J.; Krämer, B. K.; Navis, G.; Hammes, H. P.; Yard, B.; Koeppel, H. Carnosine prevents apoptosis of glomerular cells and podocyte loss in STZ diabetic rats. *Cell. Physiol. Biochem.* **2011**, *28*, 279−288.
(8) Lee, Y.-t.; Hsu, C.-c.; Lin, M.-h.; Liu, K.-s.; Yin, M.-c. Histidine and carnosine delay diabetic deterioration in mice and protect human low density lipoprotein against oxidation and glycation. *Eur. J. Pharmacol.* **2005**, *513*, 145−150.
(9) Pfister, F.; Riedl, E.; Wang, Q.; vom Hagen, F.; Deinzer, M.; Harmsen, M. C.; Molema, G.; Yard, B.; Feng, Y.; Hammes, H. P. Oral carnosine supplementation prevents vascular damage in experimental diabetic retinopathy. *Cell. Physiol. Biochem.* **2011**, *28*, 125−136.
(10) Rashid, I.; van Reyk, D. M.; Davies, M. J. Carnosine and its constituents inhibit glycation of low-density lipoproteins that promotes foam cell formation in vitro. *FEBS Lett.* **2007**, *581*, 1067−1070.
(11) Aldini, G.; Orioli, M.; Rossoni, G.; Savi, F.; Braidotti, P.; Vistoli, G.; Yeum, K.-J.; Negrisoli, G.; Carini, M. The carbonyl scavenger carnosine ameliorates dyslipidaemia and renal function in Zucker obese rats. *J. Cell. Mol. Med.* **2011**, *15*, 1339−1354.
(12) Pekcetin, C.; Kiray, M.; Ergur, B.; Tugyan, K.; Bagriyanik, H.; Erbil, G.; Baykara, B.; Camsari, U. Carnosine attenuates oxidative stress and apoptosis in transient cerebral ischemia in rats. *Acta Biol. Hung.* **2009**, *60*, 137−148.
(13) Dobrota, D.; Fedorova, T.; Stvolinsky, S.; Babusikova, E.; Likavcanova, K.; Drgova, A.; Strapkova, A.; Boldyrev, A. Carnosine protects the brain of rats and mongolian gerbils against ischemic injury: after-stroke-effect. *Neurochem. Res.* **2005**, *30*, 1283−1288.
(14) Lee, J. W.; Miyawaki, H.; Bobst, E. V.; Hester, J. D.; Ashraf, M.; Bobst, A. M. Improved functional recovery of ischemic rat hearts due to singlet oxygen scavengers histidine and carnosine. *J. Mol. Cell. Cardiol.* **1999**, *31*, 113−121.
(15) Fernández-García, E.; Carvajal-Lérida, I.; Pérez-Gálvez, A. In vitro bioaccessibility assessment as a prediction tool of nutritional efficiency. *Nutr. Res. (N. Y., NY, U. S.)* **2009**, *29*, 751−760.
(16) Bordoni, A.; Laghi, L.; Babini, E.; Di Nunzio, M.; Picone, G.; Ciampa, A.; Valli, V.; Danesi, F.; Capozzi, F. The foodomics approach for the evaluation of protein bioaccessibility in processed meat upon in vitro digestion. *Electrophoresis* **2014**, *35*, 1607−1614.
(17) Purchas, R. W.; Busboom, J. R.; Wilkinson, B. H. P. Changes in the forms of iron and in concentrations of taurine, carnosine, coenzyme Q_{10}, and creatine in beef longissimus muscle with cooking and simulated stomach and duodenal digestion. *Meat Sci.* **2006**, *74*, 443−449.
(18) Peiretti, P. G.; Medana, C.; Visentin, S.; Dal Bello, F.; Meineri, G. Effect of cooking method on carnosine and its homologues, pentosidine and thiobarbituric acid-reactive substance contents in beef and turkey meat. *Food Chem.* **2012**, *132*, 80−85.
(19) Bordoni, A.; Picone, G.; Babini, E.; Vignali, M.; Danesi, F.; Valli, V.; Di Nunzio, M.; Laghi, L.; Capozzi, F. NMR comparison of in vitro digestion of Parmigiano Reggiano cheese aged 15 and 30 months. *Magn. Reson. Chem.* **2011**, *49*, S61−S70.
(20) Szterk, A. Chemical state of heterocyclic aromatic amines in grilled beef: evaluation by in vitro digestion model and comparison of alkaline hydrolysis and organic solvent for extraction. *Food Chem. Toxicol.* **2013**, *62*, 653−660.
(21) Žunić, G.; Spasić, S. Capillary electrophoresis method optimized with a factorial design for the determination of glutathione and amino acid status using human capillary blood. *J. Chromatogr. B: Anal. Technol. Biomed. Life Sci.* **2008**, *873*, 70−76.
(22) Purchas, R. W.; Rutherfurd, S. M.; Pearce, P. D.; Vather, R.; Wilkinson, B. H. P. Concentrations in beef and lamb of taurine, carnosine, coenzyme Q10, and creatine. *Meat Sci.* **2004**, *66*, 629−637.
(23) Cornet, M.; Bousset, J. Free amino acids and dipeptides in porcine muscles: differences between 'red' and 'white' muscles. *Meat Sci.* **1999**, *51*, 215−219.
(24) INRA Tabella di composizione di alimenti; http://www.inran.it/.
(25) Laghi, L.; Babini, E.; Bordoni, A.; Ciampa, A.; Danesi, F.; Nunzio, M. D.; Picone, G.; Valli, V.; Capozzi, F. Time domain measurements and high resolution spectroscopy are powerful nuclear magnetic resonance approaches suitable to evaluate the in vitro digestion of protein-rich food products. In *Magnetic Resonance in Food Science: Food for Thought*; van Duynhoven, J., Van As, H., Belton, P. S., Webb, G., Eds.; RSC Publishing: London, UK, 2013; pp 201−212.

DOI: 10.1021/acs.jafc.5b01157
J. Agric. Food Chem. 2015, 63, 4973−4978

JOURNAL OF AGRICULTURAL AND FOOD CHEMISTRY

Article

pubs.acs.org/JAFC

Fisetin Suppresses Lipid Accumulation in Mouse Adipocytic 3T3-L1 Cells by Repressing GLUT4-Mediated Glucose Uptake through Inhibition of mTOR-C/EBPα Signaling

Marina Watanabe,[‖] Mitsuhiro Hisatake,[‖] and Ko Fujimori*

Laboratory of Biodefense and Regulation, Osaka University of Pharmaceutical Sciences, 4-20-1 Nasahara, Takatsuki, Osaka 569-1094, Japan

Supporting Information

ABSTRACT: 3,7,3′,4′-Tetrahydroxyflavone (fisetin) is a flavonoid found in vegetables and fruits having broad biological activities. Here the effects of fisetin on adipogenesis and its regulatory mechanism in mouse adipocytic 3T3-L1 cells are studied. Fisetin inhibited the accumulation of intracellular lipids and lowered the expression of adipogenic genes such as peroxisome proliferator-activated receptor γ and CCAAT/enhancer-binding protein (C/EBP) α and fatty acid-binding protein 4 (aP2) during adipogenesis. Moreover, the mRNA levels of genes such as acetyl-CoA carboxylase, fatty acid synthase, and stearoyl-CoA desaturase involved in the fatty acid biosynthesis (lipogenesis) were reduced by the treatment with fisetin. The expression level of the glucose transporter 4 (GLUT4) gene was also decreased by fisetin, resulting in down-regulation of glucose uptake. Furthermore, fisetin inhibited the phosphorylation of the mammalian target of rapamycin (mTOR) and that of p70 ribosomal S6 kinase, a target of the mTOR complex, the inhibition of which was followed by a decreased mRNA level of the C/EBPα gene. The results obtained from a chromatin immunoprecipitation assay demonstrated that the ability of C/EBPα to bind to the GLUT4 gene promoter was reduced by the treatment with fisetin, which agreed well with those obtained when 3T3-L1 cells were allowed to differentiate into adipocytes in medium in the presence of rapamycin, an inhibitor for mTOR. These results indicate that fisetin suppressed the accumulation of intracellular lipids by inhibiting GLUT4-mediated glucose uptake through inhibition of the mTOR-C/EBPα signaling in 3T3-L1 cells.

KEYWORDS: *fisetin, glucose uptake, mTOR, C/EBPα, adipocytes*

INTRODUCTION

Obesity is now an important public health problem[1] and is closely linked to the trigger of various metabolic diseases such as cardiovascular disease, hypertension, and type II diabetes.[2,3] Obesity occurs by an energy imbalance of intake and expenditure that leads to growth and enlargement of adipose cells. Excess body fat is accumulated in adipose cells as lipids (mostly triglycerides), resulting in an elevated triglyceride level in plasma as well as liver and muscle. Accumulation of body fat and differentiation of adipocytes are closely associated with obesity. In contrast, recent studies have demonstrated that adipocytes are important cells for the regulation of energy homeostasis, as well as for that of endocrine cells that secrete a number of adipocytokines.[4−6]

Adipogenesis is controlled by various factors through complex processes. The molecular mechanisms regulating adipogenesis have been well-studied, and many transcription factors are involved in the control of adipocyte differentiation.[7] Peroxisome proliferator-activated receptor (PPAR) γ, CCAAT/enhancer-binding proteins (C/EBPs), and sterol regulatory element-binding protein (SREBP) play central roles in adipogenesis.[8−10] C/EBPβ and C/EBPδ are expressed in preadipocytes and in the early phase of adipogenesis. They sequentially enhance the expression of C/EBPα and PPARγ genes, which are involved in the differentiation of adipose cells.[8,11] SREBP-1 regulates the expression of various genes involved in fatty acid metabolism in adipocytes.[12]

Various antiobesity drugs have been utilized clinically.[13,14] However, aside from their antiobesity effects, in some cases such drugs show unexpected side effects.[13,14] Defining the mechanisms underlying the suppressive regulation of adipogenesis is critical for the development of antiobesity drugs without side effects or with minimal ones. Natural compounds from plants display various biological and pharmacological activities such as anti-inflammatory, anticancer, and antioxidant ones.[15] Moreover, these activities are often useful for weight management when such compounds are used as nutritional supplements.[16,17] 3,7,3′,4′-Tetrahydroxyflavone (fisetin; Figure 1A) is a flavonoid that is found in fruits and vegetables, especially apples, strawberries, kiwis, cucumbers, and onions,[18] and it has various biological effects resulting from its antimicrobial and antioxidant activities, as well as other cellular regulatory properties.[19] Fisetin has been found as a novel regulator of the mammalian target of rapamycin (mTOR) signaling in prostate cancer cells.[19,20] Moreover, fisetin prevents adipocyte differentiation and obesity through inhibition of mTOR signaling in high fat diet fed mice.[21]

The mTOR protein is a serine/threonine kinase and is a member of the phosphoinositide 3-kinase (PI3K)-related kinase

Received: February 11, 2015
Revised: May 6, 2015
Accepted: May 6, 2015
Published: May 6, 2015

ACS Publications © 2015 American Chemical Society

DOI: 10.1021/acs.jafc.5b00821
J. Agric. Food Chem. 2015, 63, 4979−4987

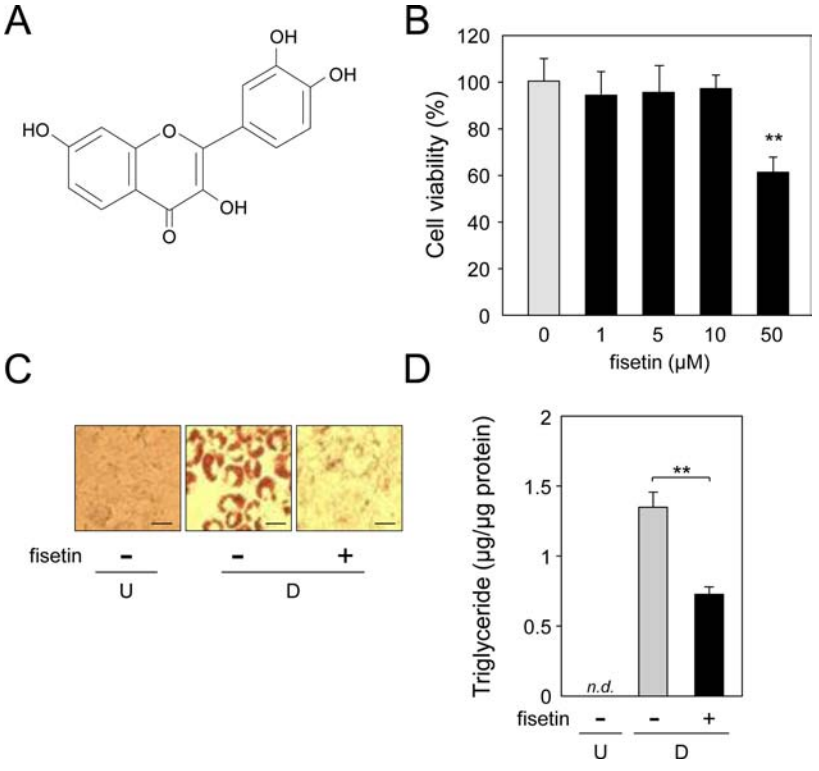

Figure 1. Repression of accumulation of intracellular lipids by fisetin. (A) Structure of fisetin. (B) Cell toxicity of fisetin toward 3T3-L1 cells. Cells were incubated with various concentrations of fisetin (0−50 μM) for 6 days, and cell toxicity was then measured in terms of cell viability. DMSO [final concentration is 0.01% (v/v)] was added as the vehicle. Data are the means ± SD (n = 3). (**) $p < 0.01$, as compared with that of the vehicle (0 μM). (C) Staining for intracellular lipids in 3T3-L1 cells with Oil Red O. The cells (undifferentiated cells, U) were caused to differentiate into adipocytes (D) for 6 days in DMEM with or without fisetin (10 μM). Intracellular lipid droplets were stained with Oil Red O. (D) Fisetin-mediated suppression of the intracellular triglyceride level in 3T3-L1 cells. The cells (undifferentiated cells, U) were caused to differentiate (D) into adipocytes for 6 days in the absence (gray bar) or presence of fisetin (10 μM; black bar). Data are the means ± SD (n = 3). (**) $p < 0.01$, as indicated by the bracket. n.d., not detected.

family, which is involved in the regulation of cell growth and cell proliferation.[22] mTOR consists of two functionally different protein complexes: mTOR complex 1 (mTORC1) and mTORC2.[22] mTORC1 responds to nutrient signals such as glucose and amino acids[23] and is composed of mTOR, raptor, mammalian lethal with sec-13 (mLST8), and proline-rich Akt substrate of 40 kDa (PRAS40); this complex is involved in cellular processes triggered by external signals such as growth factors, oxygen, and amino acids. Recently, the involvement of mTOR signaling in adipogenesis and lipid metabolism has been well recognized.[22] Rapamycin, an mTOR inhibitor, suppresses the progression of adipogenesis.[24,25] Moreover, rapamycin-sensitive mTOR signaling regulates adipocyte differentiation via regulation of PPARγ activity in response to nutritional signals such as insulin and amino acids.[25−28] Constitutive activation of mTORC1 via deletion of tuberous sclerosis 2 enhances adipocyte differentiation.[29]

In this study, we showed a molecular mechanism of fisetin-repressed accumulation of intracellular lipids in adipose cells. We found that fisetin repressed the accumulation of intracellular lipids by down-regulating glucose transporter 4 (GLUT4)-mediated glucose uptake through repression of mTOR-C/EBPα signaling in 3T3-L1 cells.

MATERIALS AND METHODS

Materials. Fisetin, Oil Red O, insulin, 3-isobutyl-1-methylxanthine, and dexamethasone were purchased from Sigma (St. Louis, MO, USA). Rapamycin and deoxy-2-[(7-nitro-2,1,3-benzoxadiazol-4-yl)-amino]-D-glucose (2-NBDG) were obtained from Cayman Chemical (Ann Arbor, MI, USA). Anti-C/EBPα (C-18) and p70 S6 kinase (S6K: C-18) polyclonal antibodies and normal rabbit IgG were obtained from Santa Cruz Biotech (Santa Cruz, CA, USA). Monoclonal antibodies against mTOR (2983), phospho-mTOR (5536), and phospho-S6K (9234) were from Cell Signaling (Danvers, MA, USA). Anti-fatty acid-binding protein 4 (aP2) was purchased from Epitomics (Burlingame, CA, USA). Anti-GLUT4 polyclonal and anti-β-actin (AC-15) monoclonal antibodies were from Sigma. Secondary antibodies such as anti-mouse or anti-rabbit IgG antibody conjugated with horseradish peroxidase were purchased from Santa Cruz Biotech. Other reagents were obtained from Wako Pure Chemicals (Osaka, Japan), Nacalai Tesque (Kyoto, Japan), and Sigma.

Cell Culture. Mouse adipocytic 3T3-L1 cells were obtained from Human Science Research Resources Bank, (Osaka, Japan) and were cultured in Dulbecco's modified Eagle's medium (DMEM; Sigma) supplemented with 10% (v/v) fetal calf serum and antibiotics and in a humidified atmosphere of 5% CO_2 at 37 °C.

Adipocyte differentiation of 3T3-L1 cells was started by incubation of the cells for 2 days in DMEM containing adipocyte differentiation cocktail: insulin (10 μg/mL), 0.5 mM IBMX, and 1 μM dexamethasone. On day 2, the medium was changed to DMEM containing insulin (10 μg/mL) alone and replaced every 2 days.

Fisetin was added to the culture medium at the start of incubation, and when the medium was replaced, fisetin was also added every 2 days.

Cell Toxicity Test. 3T3-L1 cells were cultured in 96-well plates overnight at 37 °C. Then, cells were cultured in DMEM with various concentrations of fisetin (0−50 μM) for 6 days. Cell toxicity was measured by the use of Cell Count Reagent SF (Nacalai Tesque).

DOI: 10.1021/acs.jafc.5b00821
J. Agric. Food Chem. 2015, 63, 4979−4987

Table 1. Primers Used in This Study

gene	accession no.	forward	reverse
PPARγ	NM_011146	5′-CAAGAATACCAAAGTGCGATCAA-3′	5′-GAGCTGGGTCTTTTCAGAATAATAAG-3′
C/EBPα	NM_007678	5′-CTGGAAAGAAGGCCACCTC-3′	5′-AAGAGAAGGAAGCGGTCCA-3′
aP2	NM_024406	5′-GCCAGACACCCCTGCTA-3′	5′-GTTCTGGGCGTCACTCC-3′
ACC	NM_133360	5′-GCGTCGGGTAGATCCAGTT-3′	5′-CTCAGTGGGGCTTAGCTCTG-3′
FAS	NM_007988	5′-GTTGGGGGTGTCTTCAACC-3′	5′-GAAGAGCTCTGGGGTCTGG-3′
SCD	NM_009127	5′-TTCCCTCCTGCAAGCTCTAC-3′	5′-CAGAGCGCTGGTCATGTAGT-3′
ATGL	NM_001163689	5′-TGACCATCTGCCTTCCAGA-3′	5′-TGTAGGTGGCGCAAGACA-3′
HSL	NM_010719	5′-GCACTGTGACCTGCTTGGT-3′	5′-CTGGCACCCTCACTCCATA-3′
MGL	NM_011844	5′-TCGGAACAAGTCGGAGGT-3′	5′-TCAGCAGCTGTATGCCAAAG-3′
GLUT4	NM_009204	5′-GACGGACACTCCATCTGTTG-3′	5′-GCCACGATGGAGACATAGC-3′
TBP	NM_013684	5′-GTGATGTGAAGTTCCCCATAAG-3′	5′-CTACTGAACTGCTGGTGGGTCA-3′

Measurement of Intracellular Triglyceride Level. 3T3-L1 cells were allowed to differentiate into adipocytes for 6 days in DMEM in the presence or absence of fisetin. Cells were disrupted in 5% (v/v) Triton-X100 for 3 min at 90 °C after sonication. The extracts were centrifuged for 15 min at 12000*g* at 20 °C. The supernatant was utilized for measurement of the intracellular triglyceride levels (WAKO LabAssay Triglyceride Kit; Wako Pure Chemical) and protein concentration (Pierce BCA Protein Assay Reagent; Thermo Scientific, Rockford, IL, USA).

Measurement of mRNA Levels. Total RNA was extracted from the cells by the use of TriPure Isolation Reagent (Roche Diagnostics, Mannheim, Germany). cDNAs were synthesized from total RNA (1 μg) with ReverTra Ace Reverse Transcriptase (Toyobo, Osaka, Japan) and random hexamer (Takara-Bio, Kyoto, Japan) at 42 °C for 1 h after denaturation at 72 °C for 3 min. After the reverse transcription, the enzyme was denatured at 99 °C for 5 min.

Transcription levels of the desired genes were measured by using a LightCycler system (Roche Diagnostics) with THUNDERBIRD SYBR qPCR Mix (Toyobo) and gene-specific primer sets (Table 1). PCR was conducted under the following condition: 95 °C for 30 s, followed by 40 cycles of 95 °C for 5 s and 60 °C for 30 s. After PCR, the products were heated at 95 °C for 15 s and then cooled to 40 °C, followed by melting at 0.2 °C/s to 95 °C with fluorescence data acquisition.

The expression levels of the genes were normalized to that of the TATA-binding protein (TBP).

Chromatin Immunoprecipitation (ChIP) Assay. ChIP assays were carried out as described previously.[30] The precipitated DNA fragments were further utilized for PCR amplification with a specific primer set: 5′-GCAGGCGGGAACCTTAGGGGCG-3′ (from −184 to −163; transcription initiation site as +1) and 5′-CCAAGGCTC-TCCGGGATCTAGTG-3′ (from −4 to +18). PCR was performed with KOD FX DNA Polymerase (Toyobo) under the following conditions: initial denaturation at 94 °C for 2 min, followed by 32 cycles of 98 °C for 10 s, 55 °C for 20 s, and 68 °C for 20 s. The input control DNA that was prepared from samples prior to immunoprecipitation was diluted 10-fold before PCR amplification. The PCR products (expected size of amplicons was 202 bp) were analyzed by 1% (w/v) agarose gel electrophoresis.

Western Blot Analysis. Crude cell extracts were prepared as described previously[31] with slight modification. Phosphatase inhibitors 1 mM NaF, 50 μM Na_2MoO_4, and 1 mM Na_3VO_4 were added to the extraction buffer. Protein concentration was measured as described above.

The proteins were separated on SDS-PAGE gels (10%) and then transferred onto nylon PVDF membranes (Immobilon; Millipore, Bedford, MA, USA). Blots were first incubated with each primary antibody. After the membranes had been washed, they were incubated with the appropriate secondary antibody, that is, anti-rabbit or anti-mouse IgG antibody conjugated with horseradish peroxidase. The signals were detected by using Pierce Western Blotting Substrate (Thermo Scientific) and an LAS-3000 Image Analyzer (Fujifilm, Tokyo, Japan) and analyzed with Multi Gauge software (Fujifilm).

2-Deoxyglucose Uptake Assay. 3T3-L1 cells were allowed to differentiate into adipocytes in a 96-well plate in DMEM with or without fisetin for 6 days. After removal of the medium, the cells were washed three times with PBS(−) and then cultured for 30 min at 37 °C in PBS(−) containing 150 μg/mL of a fluorescent glucose analogue, 2-NBDG. After the buffer had been discarded, the cells were washed three times with PBS(−), and the fluorescence was observed in PBS(−) under a fluorescence microscope (CKX-41FL, Olympus, Tokyo, Japan). The fluorescence was measured by use of an Enspire Multimode Plate Reader (excitation and emission wavelengths of 485 and 535 nm; PerkinElmer, Waltham, MA, USA). Then, the cells were disrupted, and the protein concentration was determined as described above. The uptake level of 2-NBDG was normalized to the protein concentration.

Statistical Analysis. Comparison of two groups was analyzed by using Student's *t* test. For comparison of more than two groups with comparable variances, one-way ANOVA and Tukey's post hoc test were performed. $p < 0.05$ was considered significant.

RESULTS

Effects of Fisetin on Lipid Accumulation of 3T3-L1 Cells. First, we examined the effect of fisetin (Figure 1A), a plant flavonoid, on the growth of 3T3-L1 cells. Cells were incubated for 6 days in DMEM containing various concentrations of fisetin (0−50 μM), and then cell toxicity was measured. No significant cell toxicity was detected up to 10 μM fisetin (Figure 1B). However, when the cells were cultured in medium with 50 μM fisetin, the cell viability was decreased about 38% as compared with that of the untreated cells (0 μM; Figure 1B).

Next, we investigated the effects of fisetin on lipid accumulation in adipose cells. 3T3-L1 cells were allowed to differentiate into adipocytes for 6 days in DMEM in the presence or absence of fisetin, and thereafter the intracellular lipids were stained with Oil Red O. The number of lipid droplets in the differentiated cells was elevated as compared with that in the undifferentiated cells (Figure 1C). In contrast, when we differentiated the cells into adipocytes in DMEM containing fisetin, the number of intracellular lipid droplets was clearly and drastically decreased (Figure 1C).

Then, the level of intracellular triglycerides was measured. When 3T3-L1 cells were differentiated into adipocytes for 6 days in DMEM in the presence or absence of fisetin, the intracellular triglyceride level in the differentiated cells was increased as compared with that in the undifferentiated cells (Figure 1D). However, when fisetin was present during the adipocyte differentiation of 3T3-L1 cells, the intracellular triglyceride level was decreased to approximately 48% of that in the differentiated cells (Figure 1D). These results, taken

DOI: 10.1021/acs.jafc.5b00821
J. Agric. Food Chem. 2015, 63, 4979−4987

together, reveal that fisetin repressed the accumulation of intracellular lipids in adipocytes.

Suppression of Expression of Adipogenic Genes by Fisetin. Next we studied the effects of fisetin on the transcription of adipogenic genes such as PPARγ, C/EBPα, aP2, and SREBP-1c by quantitative PCR. We differentiated 3T3-L1 cells into adipocytes for 6 days in DMEM containing fisetin, and RNA was then prepared. The expression level of the PPARγ, C/EBPα, aP2, and SREBP-1c genes in the control cells was enhanced approximately 22-, 1.8-, 134-, and 5.0-fold, respectively, during adipogenesis (Figure 2). In contrast,

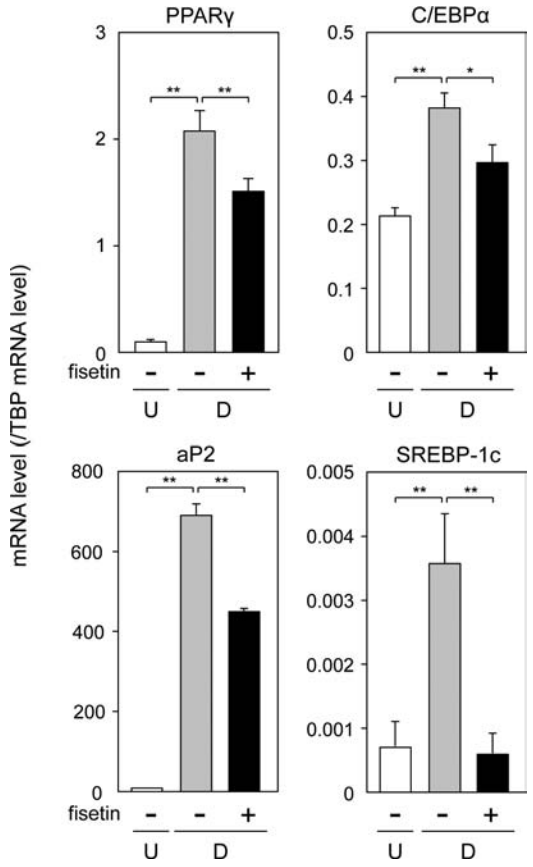

Figure 2. Suppressed expression of adipogenic genes in fisetin-treated 3T3-L1 cells: expression levels of adipogenic genes of PPARγ, C/EBPα, aP2, and SREBP-1c in fisetin-treated cells. 3T3-L1 cells (undifferentiated cells, U; bars) were caused to differentiate (D) into adipocytes for 6 days in DMEM in the absence (gray bars) or presence of fisetin (10 μM; black bars). The mRNA levels were measured by quantitative PCR analysis. Data are the means ± SD (n = 3). (**) p < 0.01, as indicated by the brackets.

mRNA levels of the PPARγ, C/EBPα, aP2, and SREBP-1c genes in the fisetin-treated cells were decreased about 27, 22, 35, and 82%, respectively, as compared with those in the vehicle-treated differentiated cells (Figure 2). These results indicate that fisetin repressed the mRNA levels of adipogenic genes in 3T3-L1 cells.

Repression of Expression of Lipogenic Genes by Fisetin. To assess the effect of fisetin on fatty acid metabolism, we examined the alteration in the mRNA level of lipogenic genes in the fisetin-treated 3T3-L1 cells. When we differentiated 3T3-L1 cells into adipocytes for 6 days in DMEM without fisetin, the mRNA levels of lipogenic genes such as acetyl-CoA carboxylase (ACC), fatty acid synthase (FAS), and stearoyl-CoA desaturase (SCD) were elevated about 1.2-, 1.2-, and 1.8-fold, respectively, as compared with each of those of the undifferentiated cells (Figure 3). In contrast, when fisetin was

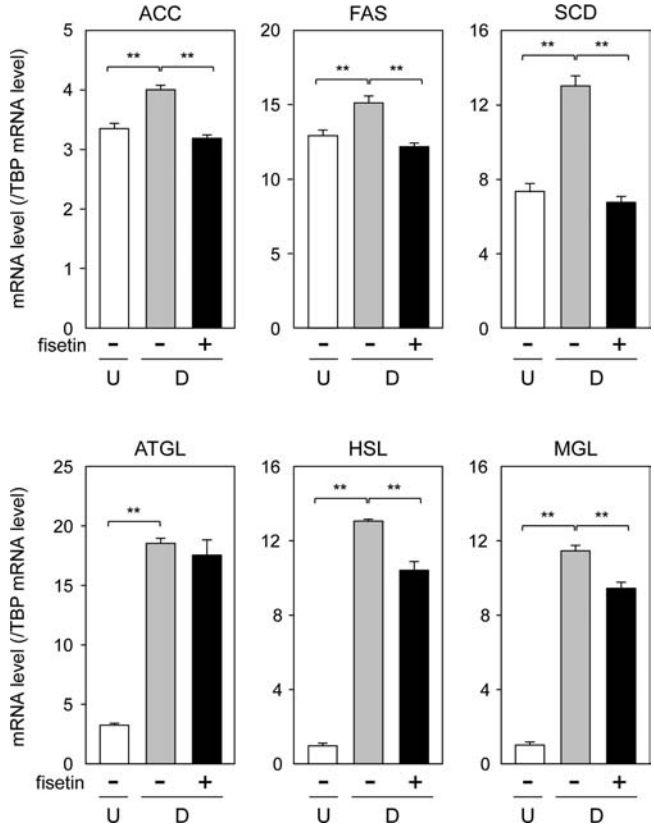

Figure 3. Expression of lipogenic and lipolytic genes in fisetin-treated 3T3-L1 cells: expression in fisetin-treated 3T3-L1 cells of ACC, FAS, and SCD of lipogenic genes and ATGL, HSL, and MGL genes involved in lipolysis. The cells (undifferentiated cells, U; white bars) were caused to differentiate (D) into adipocytes for 6 days in DMEM without (gray bars) or with (black bars) fisetin (10 μM). Transcription levels were measured by quantitative PCR analysis. Data are the means ± SD from three independent experiments. (**) p < 0.01, as indicated by the brackets.

present during the differentiation, the transcription levels of the ACC, FAS, and SCD genes were reduced about 20, 19, and 47%, respectively, as compared with those of the vehicle-treated differentiated cells (Figure 3). These results suggest that lipogenesis was suppressed by fisetin in adipocytes.

Next, we studied the mRNA level of genes involved in lipolysis, that is, adipocyte triglyceride lipase (ATGL), hormone-sensitive lipase (HSL), and monoacyl glyceride lipase (MGL). In the absence of fisetin, the transcription levels of the ATGL, HSL, and MGL genes were up-regulated during adipogenesis, about 5.7-, 13-, and 11-fold, respectively, as compared with those of the undifferentiated cells (Figure 3). Moreover, when we differentiated the cells into adipocytes in DMEM containing fisetin, the transcription levels of the HSL and MGL genes were decreased to about 80 and 83%, respectively, of those of the differentiated cells (Figure 3). However, the expression level of the ATGL gene in these cells was not altered (Figure 3). These results indicate that lipolysis in 3T3-L1 cells may have been slightly repressed by fisetin.

Fisetin Inhibits GLUT4-Mediated Glucose Uptake in Adipocytes. Next we examined the glucose uptake in fisetin-

DOI: 10.1021/acs.jafc.5b00821
J. Agric. Food Chem. 2015, 63, 4979−4987

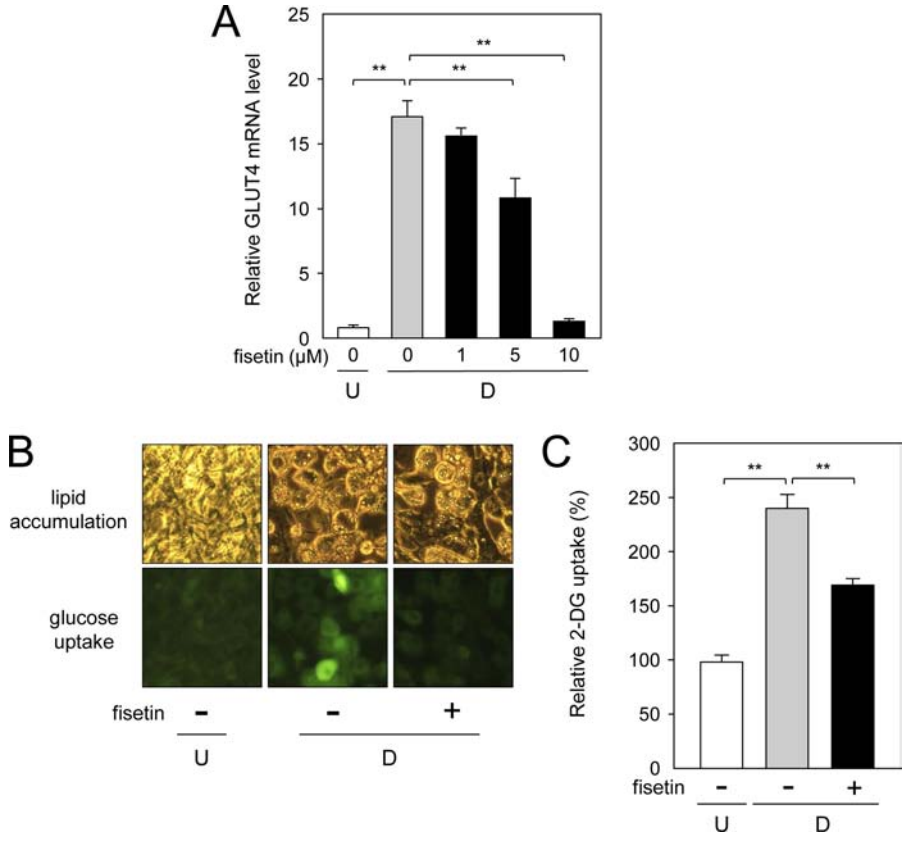

Figure 4. Fisetin-mediated decrease in glucose uptake in 3T3-L1 cells. (A) Repression of GLUT4 expression in fisetin-treated cells. 3T3-L1 cells (undifferentiated cells, U; white bars) were caused to differentiate (D) into adipocytes for 6 days in DMEM without (gray bars) or with various concentrations of fisetin (1−10 μM; black bars). The mRNA level of the GLUT4 gene was measured by quantitative PCR analysis. Data are the means ± SD (n = 3). (**) $p < 0.01$, as indicated by the brackets. (B) Suppression of glucose uptake by fisetin. 3T3-L1 cells (undifferentiated cells, U) were caused to differentiate into adipocytes for 6 days in DMEM without (differentiated cells, D) or with fisetin (10 μM; fisetin-treated differentiated cells, D/fisetin), and glucose uptake was then observed under fluorescence microscope by the use of the fluorescent 2-NDBG (upper, phase contrast; lower, fluorescent). (C) Quantification of glucose uptake in fisetin-treated 3T3-L1 cells. Cells were prepared as described for panel B. The data are presented as the value relative to that of the undifferentiated cells and are shown as the means ± SD (n = 3). (**) $p < 0.01$, as indicated by the brackets.

treated 3T3-L1 cells. First, we investigated the change in the expression level of the GLUT4 gene in fisetin-treated 3T3-L1 cells. Without fisetin, the mRNA level of the GLUT4 gene was elevated about 21-fold, as compared with that of the undifferentiated cells (Figure 4A). However, when fisetin was present during the adipocyte differentiation of 3T3-L1 cells, the mRNA level of the GLUT4 gene was reduced in a concentration-dependent manner of fisetin and decreased to about 18% (at 10 μM fisetin) of that for the vehicle-treated differentiated cells (Figure 4A).

Then, we examined glucose uptake in the fisetin-treated 3T3-L1 cells by the use of the fluorescent 2-NBDG. 3T3-L1 cells were differentiated into adipocytes in DMEM with or without fisetin, and then the cells were incubated with 2-NBDG, followed by observation with the fluorescence microscope. The fluorescence of 2-NBDG was clearly enhanced in the vehicle-treated differentiated cells, as compared with that of the undifferentiated cells (Figure 4B). On the contrary, the fisetin-treated cells showed a decrease in fluorescence, as compared with the fluorescence of the vehicle-treated differentiated cells (Figure 4B). Moreover, we measured the fluorescence in the cells to quantify the uptake of glucose. Glucose uptake in the absence of the fisetin was activated about 2.3-fold during adipogenesis (Figure 4C). In contrast, in its presence, the uptake was suppressed approximately 37%, as compared with that by the vehicle-treated differentiated cells (Figure 4C). These results reveal that glucose uptake was suppressed by fisetin through down-regulation of the GLUT4 expression in 3T3-L1 cells.

Fisetin-Reduced Ability of C/EBPα To Bind to the GLUT4 Promoter. To elucidate the molecular mechanism of the repression of accumulation of intracellular lipids by fisetin in 3T3-L1 cells, we investigated the effect of fisetin on the regulatory mechanism of GLUT4 gene expression. The GLUT4 gene expression is enhanced by C/EBP in 3T3-L1 cells.[32,33] As the C/EBPα gene was expressed in 3T3-L1 cells and its expression level was repressed by fisetin (Figure 2A), we carried out a ChIP assay to study the involvement of the C/EBPα in the fisetin-mediated transcriptional suppression of GLUT4 gene expression. The expected size (202 bp; Figure 5A) of PCR products containing the C/EBP-binding element at −92 to −88 from the mouse GLUT 4 promoter was detected when anti-C/EBPα antibody was added (Figure 5B). The efficiency of binding of C/EBPα to this C/EBP-binding element in the differentiated cells was clearly enhanced, as compared with that for the undifferentiated cells (Figure 5B). In contrast, when the cells were allowed to differentiate into adipocytes in DMEM with fisetin, the band intensity was decreased as compared with that for the vehicle-treated differentiated cells (Figure 5B). No detectable signal was

DOI: 10.1021/acs.jafc.5b00821
J. Agric. Food Chem. 2015, 63, 4979−4987

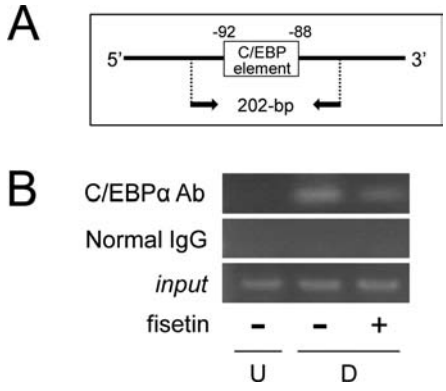

Figure 5. Decrease in the ability of C/EBPα to bind to the GLUT4 promoter in fisetin-treated 3T3-L1 cells. (A) Scheme for the ChIP assay of the GLUT4 promoter. (B) ChIP assay. The cells (undifferentiated cells, U) were caused to differentiate (D) into adipocytes in DMEM with or without fisetin (10 μM) for 6 days, and the ChIP assay was then carried out. The profile of the amplicon is shown, and the input control (*input*) means that a small diluted aliquot before immunoprecipitation was used for PCR amplification.

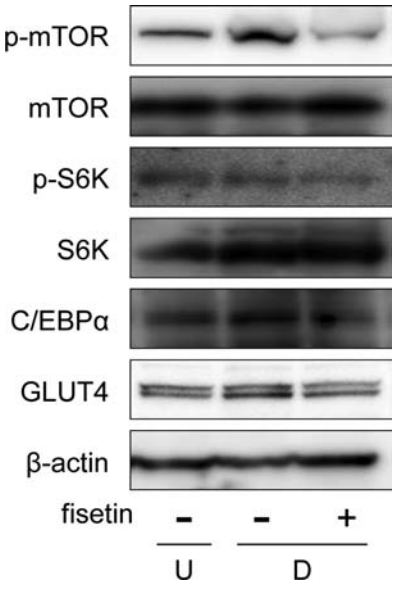

Figure 6. Suppression of GLUT4 expression by fisetin through mTOR-C/EBPα signaling. Expression of mTOR, S6K, C/EBPα, and GLUT4 and phosphorylation of mTOR and S6K in fisetin-treated 3T3-L1 cells. The cells were caused to differentiate (D) into adipocytes in DMEM with or without fisetin (10 μM) for 6 days. Western blot analysis was performed (10 or 15 μg/lane).

observed when normal IgG was used in the immunoprecipitation (Figure 5B). In addition, when the input control was used as the template for PCR analysis, the signals were detected in all samples. These results suggest that C/EBPα bound to the C/EBP-binding element of the GLUT4 gene promoter. Moreover, its binding ability was suppressed by the treatment with fisetin. Therefore, fisetin repressed the C/EBPα-activated GLUT4-mediated glucose uptake in 3T3-L1 cells.

Suppression of mTOR-C/EBPα Signaling by Fisetin. As fisetin is involved in the regulation of obesity through mTORC1 signaling,[34] we further examined the involvement of mTOR signaling in the regulation of the C/EBPα-activated GLUT4-mediated glucose uptake in 3T3-L1 cells. We differentiated 3T3-L1cells into adipocytes in DMEM with or without fisetin for 6 days, after which the expressions of mTOR, S6K, C/EBPα, and GLUT4 and the phosphorylation of mTOR and S6K proteins were examined by Western blot analysis (Figure 6 and Figure S1). The phosphorylation level of mTOR was enhanced in the control differentiated cells as compared with that of the undifferentiated cells. Moreover, its phosphorylation level was clearly decreased when the cells were allowed to differentiate into adipocytes in DMEM with fisetin. The total mTOR protein level was almost the same in all samples. On the contrary, the phosphorylation of S6K was slightly decreased in the cells treated with fisetin, although the pan-S6K level was not changed in any of the samples. Moreover, when we allowed the cells to differentiate into adipocytes for 6 days without fisetin, the protein levels of C/EBPα and GLUT4 were enhanced, whereas a decrease in both was observed when fisetin was present. All of these results agree well with those obtained from the quantitative PCR analysis (Figures 2 and 4A), indicating that fisetin repressed the phosphorylation of mTOR and S6K, thus causing a decrease in the expression of C/EBPα and GLUT4 in adipocytes.

In addition, to confirm the involvement of mTOR signaling in the regulation of C/EBPα-activated GLUT4 gene expression, we utilized rapamycin, an mTOR inhibitor. 3T3-L1 cells were allowed to differentiate into adipocytes in DMEM with rapamycin for 6 days, after which the intracellular lipids were stained with Oil Red O. Rapamycin suppressed the accumulation of intracellular lipid in 3T3-L1 cells, revealing that mTOR signaling is involved in the accumulation of intracellular lipids in these cells (Figure 7A). Moreover, when we added rapamycin during the adipocyte differentiation process at play in the cells, the mRNA level of C/EBPα and GLUT4 genes was reduced approximately 33 and 96%, respectively, in the fisetin-treated cells as compared with those in the vehicle-treated differentiated cells (Figure 7B). In addition, glucose uptake was decreased to about 68% of that in the vehicle-treated differentiated cells by the treatment with rapamycin (Figure 7C,D). Furthermore, the ability of C/EBPα to bind to the promoter region of GLUT4 gene was decreased by rapamycin, as revealed by the results of a ChIP assay (Figure 7E). Thus, rapamycin, an mTOR inhibitor, deceased the accumulation of intracellular lipids via inhibition of the binding of C/EBPα to the GLUT4 promoter, which is in agreement with the results obtained when fisetin was added to the medium during adipogenesis.

■ DISCUSSION

Obesity is a trigger factor for the development of various metabolic diseases[2,3] and is defined as an overaccumulation of body fat; adipose cells in obese individuals contain a large amount of lipids. Excess adipose tissue is the result of an increased number (hyperplasia) and enlarged size (hypertrophy) of adipocytes. Therefore, treatments that inhibit either hyperplasia or hypertrophy, or both, may be a new therapeutic approach for obesity. Recently, it was reported that some flavonoids have antiadipogenic activities.[16,17] Apigenin[35] and quercetin[36] repress adipogenesis through activation of AMP-activated protein kinase (AMPK) and the mitogen-activated protein kinase pathway. Curcumin[37] and genistein, a soy-derived isoflavone,[38,39] suppress adipocyte differentiation. Fisetin represses adipocyte differentiation by inhibiting mTOR signaling in high fat diet fed mice.[19,34] However, the regulatory mechanism of fisetin-mediated suppression of adipogenesis has never been identified. Our present study

DOI: 10.1021/acs.jafc.5b00821
J. Agric. Food Chem. 2015, 63, 4979−4987

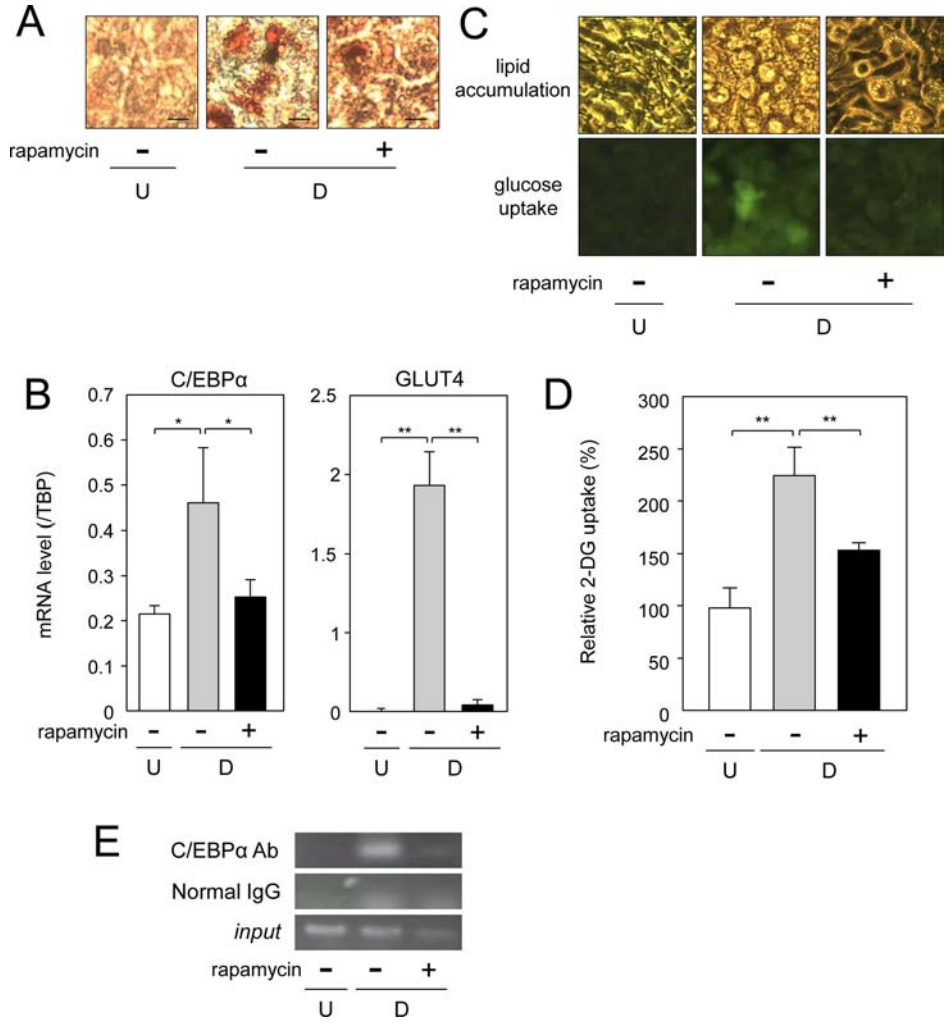

Figure 7. Inhibition of adipogenesis by rapamycin. (A) Staining of intracellular lipids in 3T3-L1 cells with Oil Red O. The cells (undifferentiated cells, U) were caused to differentiate into adipocytes (D) for 6 days in DMEM with or without rapamycin (20 nM). Intracellular lipid droplets were stained with Oil Red O. (B) Transcription levels of the C/EBPα and GLUT4 genes in rapamycin-treated cells. 3T3-L1 cells (undifferentiated cells, U; white bars) were caused to differentiate (D) into adipocytes for 6 days in DMEM without (gray bars) or with (black bars) rapamycin (20 nM). The mRNA level was then measured by quantitative PCR analysis. Data are the means ± SD ($n = 3$). (**) $p < 0.01$ and (*) $p < 0.05$, as indicated by the brackets. (C) Reduction in glucose uptake by rapamycin. Cells (undifferentiated cells, U) were caused to differentiate into adipocytes for 6 days in DMEM without (differentiated cells, D) or with rapamycin (20 nM; rapamycin-treated differentiated cells, D/rapamycin), and glucose uptake was then observed under fluorescence microscope by the use of the fluorescent 2-NDBG (upper, phase contrast; lower, fluorescent). (D) Quantification of glucose uptake in rapamycin-treated 3T3-L1 cells. Cells were prepared as described for panel C. The data are represented as the value relative to that of the undifferentiated cells and are shown as the means ± SD ($n = 3$). (**) $p < 0.01$, as indicated by the brackets. (E) ChIP assay. 3T3-L1 cells (undifferentiated cells, U) were caused to differentiate (D) into adipocytes in DMEM with or without rapamycin (20 nM) for 6 days, and the ChIP assay was then carried out. The profile of the amplicon is shown, and the input control (*input*) means that a small diluted aliquot before immunoprecipitation was used for PCR amplification.

showed a regulatory mechanism by which fisetin suppressed adipogenesis by inhibiting C/EBPα-activated GLUT4-mediated glucose uptake through suppression of mTOR signaling.

Glucose is incorporated into the cells by glucose transporter proteins, the GLUT family in mammals.[40] Glucose transport is the rate-limiting step in glucose uptake, which is responsible for glucose metabolism.[41] GLUT4, a member of the glucose transporter family, plays a dominant role in adipocytes, and the increased intrinsic activity of GLUT4 induces elevated glucose incorporation into 3T3-L1 cells.[42] As incorporation of an excess amount of glucose into the cells causes an increase in the intracellular lipids, the control of glucose transport is critical for its regulation and therefore is closely related to obesity. In this study, we demonstrated that fisetin repressed the glucose uptake with the marked decrease of GLUT4 mRNA level (Figure 4A) and slight reduction of GLUT4 protein (Figure 6) in 3T3-L1 cells, resulting in decreased accumulation of intracellular lipids. The difference of GLUT4 mRNA and protein level (Figures 4A and 6) may be derived from their distinct stabilities.[43,44] Thus, fisetin is a useful flavonoid for the regulation of the accumulation of intracellular lipids via suppression of glucose uptake. Some other flavonoids also have the potential to regulate glucose uptake in adipocytes, for example, apigenin, avicularin, quercetin, genistein, and epigallocatechin gallate.[27,33]

mTOR is a key regulator that integrates hormonal and nutritional inputs,[22] and it is involved in the regulation of various cellular functions. The hormonal and nutritional activation of the mTORC1 complex and its downstream signaling molecule, S6K, a member of the ribosomal S6K family

DOI: 10.1021/acs.jafc.5b00821
J. Agric. Food Chem. 2015, 63, 4979−4987

of serine/threonine kinases, is inhibited by rapamycin.[22] mTOR plays critical roles in the regulation of both lipid metabolism and adipogenesis. The inhibition of this pathway represses the PI3K/Akt pathway through insulin-activated insulin receptor substrate 1 (IRS-1) signaling, resulting in the suppression of glucose uptake in adipocytes.[26,45−48] The mTOR-S6K1 signaling is activated in obesity, overnutrition, and insulin resistance.[21,49] In vivo analysis of mTOR signaling has been performed by the use of gene-knockout mice. Ablation of S6K1 decreases body weight gain in mice on a high-fat diet[50,51] and represses insulin resistance through decreased phosphorylation of IRS-1;[50] in the absence of Raptor, a component of mTORC1, the mice became lean.[52] Akt-mediated phosphorylation of TSC2 activates mTORC1 signaling, followed by elevation of adipogenesis.[29] Therefore, the inhibition of mTOR-S6K1 signaling is useful for the improvement of insulin resistance and antiobesity.

mTOR and PI3K/Akt signalings are involved in the activation of PPARγ in adipogenesis.[28] C/EBPα and PPARγ regulate each other to enhance adipogenesis.[7] Moreover, activation of mTORC1 increases the expression of PPARγ.[29] In this study, we revealed that fisetin reduced the expression of C/EBPα through mTOR signaling. Therefore, this fisetin-mediated decrease in C/EBPα expression may have been regulated through PPARγ. Moreover, although fisetin suppressed the phosphorylation of mTOR and S6K, ae well as the expression of C/EBPα and GLUT4, when the cells were cultured for 6 days in its presence, these levels were not altered when the cells were cultured for just 1 day in DMEM containing fisetin (data not shown). Thus, fisetin-mediated suppression of mTOR signaling may be dependent on the differentiation stage of adipogenesis. Furthermore, the intracellular energy homeostasis is regulated by mTORC1 through AMPK, a master sensor of intracellular energy homeostasis. In addition, when energy was depleted, AMPK reduces mTORC1 activity via phosphorylation of Raptor.[53] Thus, fisetin-mediated suppression of the accumulation of intracellular lipid may be associated with the AMPK signaling. In further study, the signal network such as AMPK and PI3K/Akt pathways involved in fisetin-mediated inhibition of the accumulation of intracellular lipid will be elucidated.

In summary, fisetin, a plant flavonoid, represses the accumulation of intracellular lipids by suppressing direct regulation of the expression of GLUT4 gene by C/EBPα, followed by decreasing GLUT4-mediated glucose uptake through inhibition of mTOR signaling in 3T3-L1 cells. In a future study, we plan to evaluate the action of fisetin as an antiobesity agent in vivo. Additionally, the molecular mechanism underlying the suppression of activation of mTOR by fisetin will be investigated to elucidate the molecular mechanism of fisetin-mediated suppression of glucose uptake in adipocytes.

■ ASSOCIATED CONTENT

Supporting Information

Figure S1. The Supporting Information is available free of charge on the ACS Publications website at DOI: 10.1021/acs.jafc.5b00821.

■ AUTHOR INFORMATION

Corresponding Author

*(K.F.) Phone/fax: +81-72-690-1215. E-mail: fujimori@gly.oups.ac.jp.

Author Contributions

‖M.W. and M.H. contributed equally.

Funding

This work was supported in part by grants from the programs Grant-in-Aid for Scientific Research (21570151) and Scientific Research on Innovative Areas (23116516) of the Ministry of Education, Culture, Sports, Science and Technology of Japan and Technology of Japan (MEXT) and by grants from the Japan Foundation for Applied Enzymology, The Naito Foundation, The Research Foundation for Pharmaceutical Sciences, and Daiwa Securities Health Foundation (K.F.).

Notes

The authors declare no competing financial interest.

■ ACKNOWLEDGMENTS

We acknowledge Dr. Fumio Amano (Osaka University of Pharmaceutical Sciences) for valuable discussion.

■ ABBREVIATIONS USED

PPAR, peroxisome proliferator-activated receptor; C/EBP, CCAAT/enhancer-binding protein; SREBP, sterol regulatory element-binding protein; mTOR, mammalian target of rapamycin; PI3K, phosphoinositide 3-kinase; mTORC, mTOR complex; GLUT, glucose transporter 4; 2-NBDG, deoxy-2-[(7-nitro-2,1,3-benzoxadiazol-4-yl)amino]-D-glucose; S6K, p70 S6 kinase; DMEM, Dulbecco's modified Eagle's medium; TBP, TATA-binding protein; ChIP, chromatin immunoprecipitation; aP2, fatty acid-binding protein 4; ACC, acetyl-CoA carboxylase; FAS, fatty acid synthase; SCD, stearoyl-CoA desaturase; ATGL, adipocyte triglyceride lipase; HSL, hormone-sensitive lipase; MGL, monoacyl glyceride lipase

■ REFERENCES

(1) Friedman, J. M. Modern science versus the stigma of obesity. *Nat. Med.* **2004**, *10*, 563−569.

(2) Cornier, M. A.; Dabelea, D.; Hernandez, T. L.; Lindstrom, R. C.; Steig, A. J.; Stob, N. R.; Van Pelt, R. E.; Wang, H.; Eckel, R. H. The metabolic syndrome. *Endocr. Rev.* **2008**, *29*, 777−822.

(3) Pi-Sunyer, X. The medical risks of obesity. *Postgrad. Med.* **2009**, *121*, 21−33.

(4) Galic, S.; Oakhill, J. S.; Steinberg, G. R. Adipose tissue as an endocrine organ. *Mol. Cell. Endocrinol.* **2010**, *316*, 129−139.

(5) Rasouli, N.; Kern, P. A. Adipocytokines and the metabolic complications of obesity. *J. Clin. Endocrinol. Metab.* **2008**, *93*, S64−73.

(6) Antuna-Puente, B.; Feve, B.; Fellahi, S.; Bastard, J. P. Adipokines: the missing link between insulin resistance and obesity. *Diabetes Metab.* **2008**, *34*, 2−11.

(7) Farmer, S. R. Transcriptional control of adipocyte formation. *Cell Metab.* **2006**, *4*, 263−273.

(8) Lefterova, M. I.; Lazar, M. A. New developments in adipogenesis. *Trends Endocrinol. Metab.* **2009**, *20*, 107−114.

(9) Rosen, E.; Eguchi, J.; Xu, Z. Transcriptional targets in adipocyte biology. *Expert Opin. Ther. Targets* **2009**, *13*, 975.

(10) White, U. A.; Stephens, J. M. Transcriptional factors that promote formation of white adipose tissue. *Mol. Cell. Endocrinol.* **2010**, *318*, 10−14.

(11) Sharma, A. M.; Staels, B. Review: Peroxisome proliferator-activated receptor gamma and adipose tissue–understanding obesity-related changes in regulation of lipid and glucose metabolism. *J. Clin. Endocrinol. Metab.* **2007**, *92*, 386−395.

(12) Eberle, D.; Hegarty, B.; Bossard, P.; Ferre, P.; Foufelle, F. SREBP transcription factors: master regulators of lipid homeostasis. *Biochimie* **2004**, *86*, 839−848.

DOI: 10.1021/acs.jafc.5b00821
J. Agric. Food Chem. 2015, 63, 4979−4987

(13) Rodgers, R. J.; Tschop, M. H.; Wilding, J. P. Anti-obesity drugs: past, present and future. *Dis. Models & Mech.* **2012**, *5*, 621−626.
(14) Kang, J. G.; Park, C. Y. Anti-obesity drugs: a review about their effects and safety. *Diabetes Metab J.* **2012**, *36*, 13−25.
(15) Nijveldt, R. J.; van Nood, E.; van Hoorn, D. E.; Boelens, P. G.; van Norren, K.; van Leeuwen, P. A. Flavonoids: a review of probable mechanisms of action and potential applications. *Am. J. Clin. Nutr.* **2001**, *74*, 418−425.
(16) Nishiumi, S.; Miyamoto, S.; Kawabata, K.; Ohnishi, K.; Mukai, R.; Murakami, A.; Ashida, H.; Terao, J. Dietary flavonoids as cancer-preventive and therapeutic biofactors. *Front. Biosci., Scholar Ed.* **2011**, *3*, 1332−1362.
(17) Pandey, K. B.; Rizvi, S. I. Plant polyphenols as dietary antioxidants in human health and disease. *Oxid. Med. Cell. Longevity* **2009**, *2*, 270−278.
(18) Kimira, M.; Arai, Y.; Shimoi, K.; Watanabe, S. Japanese intake of flavonoids and isoflavonoids from foods. *J. Epidemiol.* **1998**, *8*, 168−175.
(19) Adhami, V. M.; Syed, D. N.; Khan, N.; Mukhtar, H. Dietary flavonoid fisetin: a novel dual inhibitor of PI3K/Akt and mTOR for prostate cancer management. *Biochem. Pharmacol.* **2012**, *84*, 1277−1281.
(20) Suh, Y.; Afaq, F.; Khan, N.; Johnson, J. J.; Khusro, F. H.; Mukhtar, H. Fisetin induces autophagic cell death through suppression of mTOR signaling pathway in prostate cancer cells. *Carcinogenesis* **2010**, *31*, 1424−33.
(21) Jia, G.; Aroor, A. R.; Martinez-Lemus, L. A.; Sowers, J. R. Overnutrition, mTOR signaling, and cardiovascular diseases. *Am. J. Physiol. Regul. Integr. Comp. Physiol.* **2014**, *307*, R1198−R1206.
(22) Laplante, M.; Sabatini, D. M. Regulation of mTORC1 and its impact on gene expression at a glance. *J. Cell Sci.* **2013**, *126*, 1713−1719.
(23) Dibble, C. C.; Manning, B. D. Signal integration by mTORC1 coordinates nutrient input with biosynthetic output. *Nat. Cell Biol.* **2013**, *15*, 555−564.
(24) Yeh, W. C.; Bierer, B. E.; McKnight, S. L. Rapamycin inhibits clonal expansion and adipogenic differentiation of 3T3-L1 cells. *Proc. Natl. Acad. Sci. U. S. A.* **1995**, *92*, 11086−11090.
(25) Gagnon, A.; Lau, S.; Sorisky, A. Rapamycin-sensitive phase of 3T3-L1 preadipocyte differentiation after clonal expansion. *J. Cell. Physiol.* **2001**, *189*, 14−22.
(26) Gulati, P.; Thomas, G. Nutrient sensing in the mTOR/S6K1 signalling pathway. *Biochem. Soc. Trans.* **2007**, *35*, 236−238.
(27) Nomura, M.; Takahashi, T.; Nagata, N.; Tsutsumi, K.; Kobayashi, S.; Akiba, T.; Yokogawa, K.; Moritani, S.; Miyamoto, K. Inhibitory mechanisms of flavonoids on insulin-stimulated glucose uptake in MC3T3-G2/PA6 adipose cells. *Biol. Pharm. Bull.* **2008**, *31*, 1403−1409.
(28) Kim, J. E.; Chen, J. Regulation of peroxisome proliferator-activated receptor-gamma activity by mammalian target of rapamycin and amino acids in adipogenesis. *Diabetes* **2004**, *53*, 2748−2756.
(29) Zhang, H. H.; Huang, J.; Duvel, K.; Boback, B.; Wu, S.; Squillace, R. M.; Wu, C. L.; Manning, B. D. Insulin stimulates adipogenesis through the Akt-TSC2-mTORC1 pathway. *PLoS One* **2009**, *4*, e6189.
(30) Kobayashi, T.; Fujimori, K. Very long-chain-fatty acids enhance adipogenesis through coregulation of Elovl3 and PPARgamma in 3T3-L1 cells. *Am. J. Physiol. Endocrinol. Metab.* **2012**, *302*, E1461−E1471.
(31) Fujimori, K.; Yano, M.; Miyake, H.; Kimura, H. Termination mechanism of CREB-dependent activation of COX-2 expression in early phase of adipogenesis. *Mol. Cell. Endocrinol.* **2014**, *384*, 12.
(32) Kaestner, K. H.; Christy, R. J.; Lane, M. D. Mouse insulin-responsive glucose transporter gene: characterization of the gene and trans-activation by the CCAAT/enhancer binding protein. *Proc. Natl. Acad. Sci. U. S. A.* **1990**, *87*, 251−255.
(33) Fujimori, K.; Shibano, M. Avicularin, a plant flavonoid, suppresses lipid accumulation through repression of C/EBPalpha-activated GLUT4-mediated glucose uptake in 3T3-L1 cells. *J. Agric. Food Chem.* **2013**, *61*, 5139−5147.
(34) Jung, C. H.; Kim, H.; Ahn, J.; Jeon, T. I.; Lee, D. H.; Ha, T. Y. Fisetin regulates obesity by targeting mTORC1 signaling. *J. Nutr. Biochem.* **2013**, *24*, 1547−1554.
(35) Ono, M.; Fujimori, K. Antiadipogenic effect of dietary apigenin through activation of AMPK in 3T3-L1 cells. *J. Agric. Food Chem.* **2011**, *59*, 13346−52.
(36) Ahn, J.; Lee, H.; Kim, S.; Park, J.; Ha, T. The anti-obesity effect of quercetin is mediated by the AMPK and MAPK signaling pathways. *Biochem. Biophys. Res. Commun.* **2008**, *373*, 545−549.
(37) Ejaz, A.; Wu, D.; Kwan, P.; Meydani, M. Curcumin inhibits adipogenesis in 3T3-L1 adipocytes and angiogenesis and obesity in C57/BL mice. *J. Nutr.* **2009**, *139*, 919−925.
(38) Bazuine, M.; van den Broek, P. J.; Maassen, J. A. Genistein directly inhibits GLUT4-mediated glucose uptake in 3T3-L1 adipocytes. *Biochem. Biophys. Res. Commun.* **2005**, *326*, 511−514.
(39) Zhang, M.; Ikeda, K.; Xu, J. W.; Yamori, Y.; Gao, X. M.; Zhang, B. L. Genistein suppresses adipogenesis of 3T3-L1 cells via multiple signal pathways. *Phytother. Res.* **2009**, *23*, 713−718.
(40) Karim, S.; Adams, D. H.; Lalor, P. F. Hepatic expression and cellular distribution of the glucose transporter family. *World J. Gastroenterol.* **2012**, *18*, 6771−6781.
(41) Muretta, J. M.; Mastick, C. C. How insulin regulates glucose transport in adipocytes. *Vitam Horm* **2009**, *80*, 245−286.
(42) Kanzaki, M. Insulin receptor signals regulating GLUT4 translocation and actin dynamics. *Endocr. J.* **2006**, *53*, 267−293.
(43) Hager, S. R.; Pastorek, D.; Jochen, A. L.; Meier, D. Divergence between GLUT4 mRNA and protein abundance in skeletal muscle of insulin resistant rats. *Biochem. Biophys. Res. Commun.* **1991**, *181*, 240−245.
(44) Flores-Riveros, J. R.; McLenithan, J. C.; Ezaki, O.; Lane, M. D. Insulin down-regulates expression of the insulin-responsive glucose transporter (GLUT4) gene: effects on transcription and mRNA turnover. *Proc. Natl. Acad. Sci. U. S. A.* **1993**, *90*, 512−516.
(45) Veilleux, A.; Houde, V. P.; Bellmann, K.; Marette, A. Chronic inhibition of the mTORC1/S6K1 pathway increases insulin-induced PI3K activity but inhibits Akt2 and glucose transport stimulation in 3T3-L1 adipocytes. *Mol. Endocrinol.* **2010**, *24*, 766−778.
(46) Tremblay, F.; Gagnon, A.; Veilleux, A.; Sorisky, A.; Marette, A. Activation of the mammalian target of rapamycin pathway acutely inhibits insulin signaling to Akt and glucose transport in 3T3-L1 and human adipocytes. *Endocrinology* **2005**, *146*, 1328−1337.
(47) Adochio, R.; Leitner, J. W.; Hedlund, R.; Draznin, B. Rescuing 3T3-L1 adipocytes from insulin resistance induced by stimulation of Akt-mammalian target of rapamycin/p70 S6 kinase (S6K1) pathway and serine phosphorylation of insulin receptor substrate-1: effect of reduced expression of p85alpha subunit of phosphatidylinositol 3-kinase and S6K1 kinase. *Endocrinology* **2009**, *150*, 1165−1173.
(48) Copps, K. D.; White, M. F. Regulation of insulin sensitivity by serine/threonine phosphorylation of insulin receptor substrate proteins IRS1 and IRS2. *Diabetologia* **2012**, *55*, 2565−2582.
(49) Um, S. H.; D'Alessio, D.; Thomas, G. Nutrient overload, insulin resistance, and ribosomal protein S6 kinase 1, S6K1. *Cell Metab.* **2006**, *3*, 393−402.
(50) Um, S. H.; Frigerio, F.; Watanabe, M.; Picard, F.; Joaquin, M.; Sticker, M.; Fumagalli, S.; Allegrini, P. R.; Kozma, S. C.; Auwerx, J.; Thomas, G. Absence of S6K1 protects against age- and diet-induced obesity while enhancing insulin sensitivity. *Nature* **2004**, *431*, 200−205.
(51) Carnevalli, L. S.; Masuda, K.; Frigerio, F.; Le Bacquer, O.; Um, S. H.; Gandin, V.; Topisirovic, I.; Sonenberg, N.; Thomas, G.; Kozma, S. C. S6K1 plays a critical role in early adipocyte differentiation. *Dev. Cell* **2010**, *18*, 763−774.
(52) Polak, P.; Cybulski, N.; Feige, J. N.; Auwerx, J.; Ruegg, M. A.; Hall, M. N. Adipose-specific knockout of raptor results in lean mice with enhanced mitochondrial respiration. *Cell Metab.* **2008**, *8*, 399−410.
(53) Laplante, M.; Sabatini, D. M. mTOR signaling at a glance. *J. Cell Sci.* **2009**, *122*, 3589−3594.

DOI: 10.1021/acs.jafc.5b00821
J. Agric. Food Chem. 2015, 63, 4979−4987

JOURNAL OF AGRICULTURAL AND FOOD CHEMISTRY

Article

pubs.acs.org/JAFC

Ellagic Acid, a Dietary Polyphenol, Inhibits Tautomerase Activity of Human Macrophage Migration Inhibitory Factor and Its Pro-inflammatory Responses in Human Peripheral Blood Mononuclear Cells

Souvik Sarkar,[†] Asim A. Siddiqui,[†] Somnath Mazumder,[†] Rudranil De,[†] Shubhra J. Saha,[†] Chinmoy Banerjee,[†] Mohd. S. Iqbal,[†] Susanta Adhikari,[‡] Athar Alam,[†] Siddhartha Roy,[§] and Uday Bandyopadhyay*[,†]

[†]Division of Infectious Diseases and Immunology, CSIR-Indian Institute of Chemical Biology, 4, Raja S. C. Mullick Road, Jadavpur, Kolkata 700032, West Bengal, India

[‡]Department of Chemistry, University of Calcutta, 92, A. P. C. Road, Kolkata 700 009, West Bengal, India

[§]Division of Structural Biology and Bioinformatics, CSIR-Indian Institute of Chemical Biology, 4, Raja S. C. Mullick Road, Jadavpur, Kolkata 700032, West Bengal, India

Supporting Information

ABSTRACT: Ellagic acid (EA), a phenolic lactone, inhibited tautomerase activity of human macrophage migration inhibitory factor (MIF) noncompetitively (K_i = 1.97 ± 0.7 μM). The binding of EA to MIF was determined by following the quenching of tryptophan fluorescence. We synthesized several EA derivatives, and their structure−activity relationship studies indicated that the planar conjugated lactone moiety of EA was essential for MIF inhibition. MIF induces nuclear translocation of NF-κB and chemotaxis of peripheral blood mononuclear cells (PBMCs) to promote inflammation. We were interested in evaluating the effect of EA on nuclear translocation of NF-κB and chemotactic activity in human PBMCs in the presence of MIF. The results showed that EA inhibited MIF-induced NF-κB nuclear translocation in PBMCs, as evident from confocal immunofluorescence microscopic data. EA also inhibited MIF-mediated chemotaxis of PBMCs. Thus, we report MIF-inhibitory activity of EA and inhibition of MIF-mediated proinflammatory responses in PBMCs by EA.

KEYWORDS: *ellagic acid, macrophage migration inhibitory factor, tautomerase activity, gallic acid, inflammation, chemotaxis*

INTRODUCTION

Phenolic compounds or polyphenols comprise one of the most plentiful and widely distributed groups of phytochemicals. More than 8000 different chemical structures have been identified and reported.[1] Plants produce phenolic compounds as secondary metabolites (i.e., they are not essential for growth or reproduction), which exist mostly in their storage tissues. Phenolic compounds may play roles as antioxidants as well as modulators of several biological macromolecules. As a chemical family, polyphenols can be classified into several groups on the basis of their basic structures.[1] These groups can be distinguished according to the number of aromatic rings and the structural moieties that connect them. The phenolics contain at least one aromatic ring bearing one hydroxyl (phenol) or more hydroxyl (polyphenol) groups. Thus, polyphenolic compounds include a large array of molecules, including phenols, phenolic acids, tannins, lignans, flavonoids, stilbenes, and lignins. A wide range of biological actions have been reported for different polyphenols, including antimicrobial, analgesic, antibiotic, anticancer, and anti-inflammatory properties.[2−5] Their biological actions are mostly attributes of the antioxidant effects of their phenolic groups. Blocking of the phenolic group results in decreased activity, whereas extended unsaturated bond conjugation, proper ester linkage, and an extended fused ring system increased the activity of these polyphenolics.[6−8]

Ellagic acid (EA), a polyphenolic tannin-based dilactone (4,4′,5,5′,6,6′-hexahydroxydiphenic acid 2,6,2′,6′-dilactone) is reportedly known to possess a broad range of beneficial human health (antiviral,[9] antibacterial,[10] gastro-protective,[11] cardio-protective,[12] antimutagenic,[13] antimicrobial,[14] antimalarial,[15] anti-inflammatory,[16] and anticancer[17]) properties. Previous studies revealed that aromatic conjugated −OH groups of EA are the main scaffold responsible for its antioxidant nature.[18,19] Apart from its −OH mediated antioxidant activity, recent literature suggests several other modes of action of EA, which may not be directly linked to its antioxidant property.[20,21] EA interacts with receptors, cytokines, and enzymes.[22−24] Macrophage migration inhibitory factor (MIF) is one of the pivotal cytokines that plays an important role in both innate and acquired immunity. In certain cancers, proinflammatory cytokines serve as the major mediators of intercellular communication in the tumor microenvironment,[25] thus paving the way for developing malignancy; in others, oncogenic changes drive a tumor-promoting inflammatory microenvironment. With intricate and various activities, MIF has been considered to be a missing link between inflammation and

Received: February 18, 2015
Revised: April 27, 2015
Accepted: April 29, 2015
Published: May 1, 2015

ACS Publications © 2015 American Chemical Society

DOI: 10.1021/acs.jafc.5b00921
J. Agric. Food Chem. 2015, 63, 4988−4998

tumorigenesis.[26] Moreover, MIF has been proposed to regulate proliferation, DNA-damage response, apoptosis, senescence, and invasion during carcinogenesis.[27−30] Studies revealed that MIF, via regulating nuclear translocation of NF-κB, plays an important role in inflammatory diseases.[31] NF-κB signaling has long been known as a significant event regulating inflammation, mainly due to the role of NF-κB in regulating the expression of several proinflammatory mediators, including cytokines, chemokines, and adhesion molecules.[32] Inhibition of MIF has been shown to reduce activation of NF-κB and consequent activation of other cytokines.[33] During inflammatory disorders PBMCs enhance the proinflammatory cytokines and suppress the anti-inflammatory cytokines.[34] Secreted proinflammatory cytokines such as MIF further recruit PBMCs to the site of inflammation through chemotactic migration.[35] Therefore, the involvement of PBMCs via chemotactic migration in response to a concentration gradient of MIF is an essential event involved in the inflammatory response. Several natural product polyphenolics such as curcumin, eugenol, resveratrol, and caffeic acid have been found to inhibit MIF, mainly via blocking the tautomerase activity of the cytozyme.[36]

Here we report that EA, a naturally occurring polyphenolic compound, binds to MIF and inhibits its tautomerase activity. Spatiotemporal inhibition of EA on MIF tautomerase activity is solely dependent on the dimensionally conformed lactone moiety. We further report that EA significantly inhibits MIF-induced nuclear translocation of NF-κB and MIF-mediated chemotactic migration in human PBMCs, two signature events associated with tissue inflammation.

MATERIALS AND METHODS

Chemicals. Ellagic acid, pyrene, DMSO, paraformaldehyde, kanamycin, chloramphenicol, and protease inhibitor cocktail were procured from Sigma (St. Louis, MO, USA). PBS (Hyclone), isopropyl-β-D-thiogalactopyranoside (IPTG), prestained marker and unstained protein ladders, rapid DNA ligation kit, NcoI, and *Hin*dIII were purchased from Fermentas (Thermo Scientific, USA). Luria−Berteni medium was obtained from Hi-Media (Mumbai, India). A gel extraction kit and MiniElute PCR purification kit was procured from Qiagen USA. pET28a was purchased from Novagen (Merck KGaA, Darmstadt, Germany). Gallic acid and benzyl bromide were procured from SRL (New Delhi, India). NF-κB antibodies were obtained from Santa Cruz Biotechnology (Santa Cruz, CA, USA). AlexaFluor 647 conjugated secondary antibody was purchased from Invitrogen (Carlsbad, CA, USA). All other chemicals were of analytical grade.

Overexpression and Purification of Human MIF. Human MIF was cloned by following the protocol as described earlier with slight modification.[37] In brief, full length MIF cDNA was cloned using pCMV6-XL5 cloning vector obtained from ORIGENE USA. Complete ORF from the clone pCMV6-XL5 was PCR amplified with the forward primer 5′-CTAACCATGGCCCCGATGTTCATTGTAAATACCAACGTGCCCC-3′ (NcoI restriction site underlined) and reverse primer 5′-TTAAAGCTTCTGCGGTTCTTAGGCGAAGGTAGAGTTGTTCCAGCCC-3′ (*Hin*dIII restriction site underlined). PCR was performed with initial denaturation at 95 °C for 3 min and then 35 cycles of denaturation (95 °C for 30 s), annealing (52 °C for 30 s), and extension (72 °C for 1 min) with a final extension of 72 °C for 10 min. PCR product was then cloned in *Escherichia coli* expression vector pET28a (Novagen). Ligation mix was transformed in competent DH5α cells, and clones were screened by colony PCR and double-digestion release of insert from positive colonies.

Host strain *E. coli* Rosetta (Novagen) was used for recombinant MIF overexpression and purification. Lysogency Broth (LB; 1 L) was inoculated with 1% (v/v) of overnight (16 h) grown culture on the following morning and incubated at 37 °C with shaking at a rate of 200 rpm. Culture was induced with IPTG (1 mM final concentration) in the OD_{600} range 0.6−0.8 and was further allowed to grow for 4 h. Cells were harvested (11000*g*, 5 min, 4 °C) and reconstituted in 10 mL of lysis buffer (PBS with 10% (v/v) glycerol) containing protease inhibitor cocktail. Cells were incubated on ice for 60 min and subsequently lysed by sonication (30 cycles of pulse rest at 60% amplitude; pulse duration 10 s and rest duration 1 min), after which supernatant was collected by centrifuging the lysate at 40000*g*. Overexpression of MIF in the soluble fraction was confirmed by 15% SDS-PAGE of the supernatant. All further steps were performed at 4 °C. The obtained supernatant was concentrated to 4 mL by an Amicon Ultra Centrifugal Filter Ultracel-3K (Millipore Ireland Ltd.) and then passed through a 0.2 μm filter. Finally, MIF was purified by performing gel filtration chromatography through a Sephadex G50 (GE Life Sciences, Uppsala, Sweden) column using PBS as the solvent with a flow rate of 6 mL/h.

MALDI-TOF and Peptide Fingerprinting. Purified protein was processed by μ-C18 ZipTip tips (Millipore) for removal of salts as per the manufacturer's instructions and subjected to MALDI-TOF mass analysis. In short, trifluoroacetic acid (TFA) was added to the purified protein solution to 0.1% (the pH should be less than 4) and then aspirated in pre-equilibrated (with 0.1% TFA) tips in a 10 μL pipet to the maximum volume. The solution was dispensed and aspirated again in the tip. This cycle was repeated 10 times for maximum binding. Washing was performed twice with 0.1% TFA with 5% methanol, and elution was done in 4 μL of 0.1% TFA with 50% acetonitrile. This protein was directly used for MALDI-TOF analysis using an Applied Biosystems 4700 Proteomics Analyzer170 instrument. For confirmation of the identity of the protein, peptide mass fingerprinting was performed. The protein band was excised from the gel and destained followed by reduction, alkylation, and digestion into peptides using an In-Gel Tryptic Digestion Kit (Thermo Scientific) as instructed by the manufacturer. Briefly, a gel piece was treated with reducing buffer (50 mM TCEP and 25 mM ammonium bicarbonate) and then with alkylation buffer (100 mM iodoacetamide and 25 mM ammonium bicarbonate) and then shrunk using acetonitrile, air-dried, and swelled by activated trypsin with digestion buffer added after 15 min (kept overnight at 30 °C with shaking). Buffer was collected back the next day without gel. This contained peptides released and could be directly used for MALDI MS/MS. 1% trifluoroacetic acid was used to extract the remaining peptides and deactivate trypsin. This final product was used for MALDI MS/MS. The spectrum obtained was searched in the NCBI database by GPS explorer using a MASCOT browser.

L-Dopachrome Methyl Ester (L-DOPA) Preparation To Follow MIF Tautomerase Activity Assay. The tautomerase activity of MIF was followed as described earlier.[38] Activity was determined at 25 °C by adding L-DOPA (0.25−1.5 mM) to a cuvette containing 60 nM MIF in 10 mM potassium phosphate buffer, pH 6.2, containing 0.5 mM EDTA. The activity of MIF was monitored by measuring the conversion of L-DOPA (colored) to indolecarboxylic acid methyl ester (colorless) at 475 nm. Inhibitory activities of the synthesized EA derivatives were measured by dissolving in dry DMSO, subsequently adding to the cuvette containing MIF at different concentrations, and finally incubating the mixture for 30 min before addition of L-DOPA. The IC_{50} values were obtained with different concentrations of compounds, and finally K_i (inhibition constant) values were determined using nonlinear regression analysis with Prism4 (GraphPad Prism).

Fluorescence Spectroscopy. The concentration-dependent response of EA on MIF tryptophan fluorescence was monitored as mentioned earlier[39] by serial addition of EA to MIF (7.5 μM). The resulting solution was excited at 295 nm for the tryptophan residue, and the intrinsic fluorescence emission was scanned at 300−400 nm. Fluorescence quenching was determined by analyzing the data by the classical Stern−Volmer equation

$$F_0/F = 1 + k_q\tau_0[Q] = 1 + K_{SV}[Q] \quad (1)$$

where F_0 and F are the fluorescence intensities in the absence and the presence of the quencher respectively, K_q and K_{SV} are the quenching rate constant and dynamic quenching constant, respectively, the

DOI: 10.1021/acs.jafc.5b00921
J. Agric. Food Chem. 2015, 63, 4988−4998

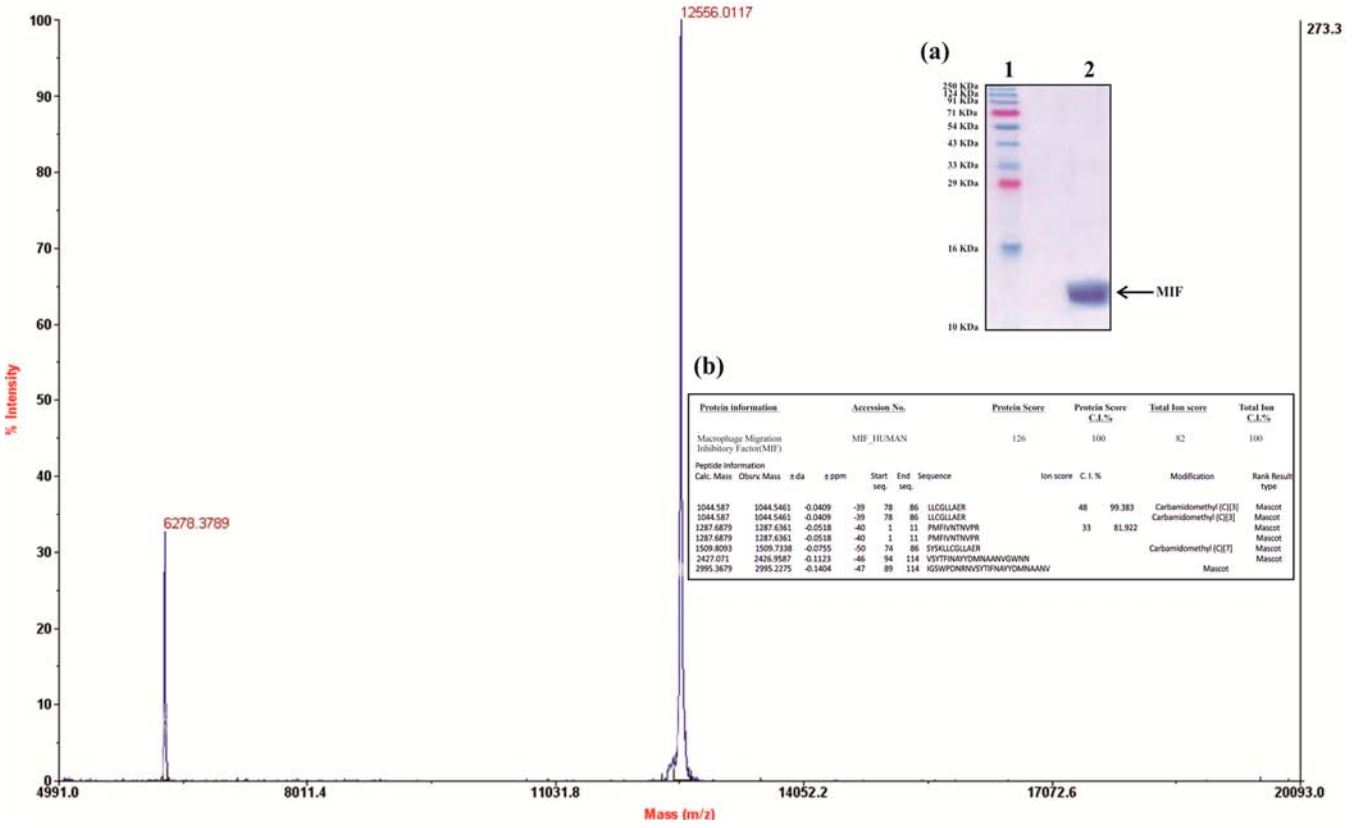

Figure 1. Purification of recombinant MIF: MALDI spectrum showing the molecular mass of MIF. Inset a: 15% SDS-PAGE, (lane 1) prestained molecular weight marker and (lane 2) MIF. Inset b: MALDI MS/MS for confirmation of protein identity by peptide fingerprinting and matching fragmented sequences with the database.

average lifetime of the protein in the absence of the quencher is expressed in terms of τ_0, and [Q] is the concentration of the free quencher, as mentioned earlier.[40] When small molecules interact with several comparable sites in a protein, the equilibrium between liberated and bound molecules is expressed by the equation

$$\log((F_0 - F)/F) = \log K_b + n \log[Q] \quad (2)$$

where K_b represents the binding constant for a quencher−protein interaction and n is the number of binding sites per molecule of MIF. Utilizing K_b, the free energy change (ΔG°) value can be estimated from the equation

$$\Delta G^\circ = -RT \ln K_b \quad (3)$$

The negative sign of the ΔG° value validates the spontaneity of the quencher−protein interaction.

Circular Dichroism (CD) Spectroscopy. CD spectroscopy was used to evaluate the structural changes in MIF as mentioned before.[41] The secondary structure of MIF was evaluated in the presence of different concentrations of EA (10, 25, and 50 μM) in the far-UV range by a J-810 CD spectrometer. CD spectra were recorded at a range of 190−270 nm from 10 μM of MIF in optically clear buffer. Spectra represented an average of five scans (a step size of 0.2 nm, an averaging time of 3 s) with buffer baseline subtracted, smoothed over four data points to generate the data reported in units of mean residue ellipticity. Secondary structure analysis of the CD spectra was performed by the Dichroweb online server (http://dichroweb.cryst.bbk.ac.uk/html/home.shtml).

Molecular Docking. Ideal coordinates for EA (PubChem CID 5281855) and MIF (PDB code 3L5S; 1.86 Å resolution) were obtained from the PDB. Molecular docking calculations were performed using SwissDock, based on the docking software EADock DSS.[42] A grid (box size 40 × 40 × 40 Å) was designed in which many binding modes were generated and their CHARMM energies were estimated on the grid.[43] The docking type was accurate, and MIF was treated as rigid during docking calculations. Each docking experiment was a composite of 250 different consecutive runs. Fast analytical continuum treatment of solvation (FACTS) was used to evaluate the modes of binding with the most favorable energies and finally clustered. Clusters were then ranked according to the average full fitness of their elements.[44] The results of SwissDock were visualized and rendered by a PyMOL molecular viewer.

General Procedure for Formation of Esters by EDC Coupling. Reactions of 1-ethyl-3-(3-(dimethylamino)propyl)carbodiimide (EDC) coupling were carried out as described earlier with slight modification.[45] To a solution of benzoic acid (1 equiv), amine (hydrochloride)/alcohol (1.5 equiv), 1-hydroxybenzotriazole (HOBt) (1 equiv, for amine), and Et_3N (5 equiv, for amine)/DMAP (1 equiv, for alcohol) in *N*,*N*-dimethylformamide was added EDC hydrochloride (1.5 equiv) at 0 °C. Then the reaction mixture was stirred at room temperature until completion of the reaction (12 h) as monitored by TLC. The reaction was terminated by the addition of ice and the mixture extracted with ethyl acetate. The ethyl acetate layer was washed with brine and dried over Na_2SO_4. The solvent was then removed in a rotavap under vacuum, and the crude mass was chromatographed over a silica gel column.

General Procedure of Debenzylation (Hydrogenolysis). A combination of benzylated compound and 10% palladium on carbon (catalytic) in a methanol/chloroform mixture (4/1) (10 mL) was stirred under a hydrogen atmosphere (using a hydrogen balloon) until completion of the reaction (2 h) as monitored by TLC. The reaction mixture was passed through a small pad of Celite. The filtrate was evaporated in vacuo to dryness to obtain the product.

Peripheral Blood Mononuclear Cell (PBMC) Isolation. Human PBMCs were isolated using Histopaque density gradient centrifugation following the instruction of the manufacturer. Briefly, 10 mL of blood was collected from the median cubital vein of a healthy volunteer by sterile disposable syringe and dispensed in tubes containing heparin.

DOI: 10.1021/acs.jafc.5b00921
J. Agric. Food Chem. 2015, 63, 4988−4998

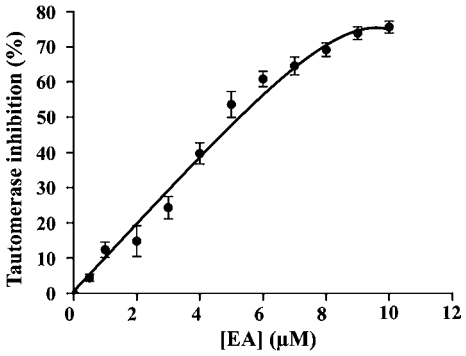

Figure 2. Inhibition of MIF tautomerase activity by EA. MIF (60 nM) is treated with different concentrations of EA for 30 min to measure the tautomerase activity at 474 nm. Data are presented as mean ± SD.

Next 6 mL of blood was carefully layered on a preformed Histopaque gradient (6 mL) prepared by layering Histopaque 1077 over Histopaque 11191 in a 1/1 ratio. The tubes were next centrifuged at 700*g* for 30 min at room temperature. The mononuclear cell fraction was carefully aspirated out and collected in a fresh tube. The cells were washed three times in phosphate buffered saline (PBS) and checked for cell viability by Trypan blue. A total of 90−95% of the isolated cells were alive. Finally an aliquot of the isolated cells was stained by crystal violet and observed under a microscope to check the purity of the isolated PBMCs. Isolated PBMCs were resuspended in RPMI-1640 containing 5% FBS (Gibco) and maintained at 37 °C in a 5% CO_2 environment for all subsequent experiments.

Confocal Microscopy. Isolated PBMCs were used for immunofluorescence microscopy as mentioned earlier[46,47] with minor modifications. Briefly, about 1 × 10^6 cells/mL were plated in RPMI-1640 containing 10% FBS and treated in four sets: control, MIF (1 μg/mL), EA (50 μM), and EA+MIF for 4 h at 37 °C and 5% CO_2. Cells after treatment were washed with prewarmed PBS (HyClone) and fixed with 4% paraformaldehyde at room temperature for 10 min. Cells were next washed with PBS by a swirling motion and permeabilized with 0.1% Triton X-100 at room temperature for 10 min. After washing, the cells were blocked in a solution containing 2% BSA in PBS for 2 h at room temperature. Immunostaining of the fixed cells was performed by incubating the cells in the blocking solution containing rabbit anti-NF-κB (p65) antibody overnight. The next day the cells were stained with antirabbit Alexa Fluor 647-conjugated secondary antibody (1/2000; Invitrogen). The nucleus was stained with DAPI. Cells were imaged at 512 × 512 resolution with a Leica TCS-SP8 confocal microscope. Samples were viewed under a 63× oil immersion lens, and digital zooming was performed according to the requirements. The overlap of red (NF-κB) and blue (nucleus) signals was quantified using the software provided with the microscope. Pearson's correlation coefficient was considered to present the intranuclear NF-κB. The data presented are a representation of one of four experiments showing similar values.

Chemotaxis Assay. A chemotactic assay was performed with human PBMCs as mentioned before[47,48] with minor modifications. Briefly, isolated PBMCs (2.5 × 10^5 cells/well) were loaded into the inserts (having a polycarbonate membrane with 5 μm pore size) of a Transwell cell migration chamber (Corning) in a 24-well plate format. The chemoattractant MIF (1 μg mL^{-1}) was added into the lower chambers in the presence and/or absence of increasing concentrations of EA (10−50 μM). Cells without any treatment were used as a control, and macrophage inflammatory protein-1 alpha (MIP-1α), a chemoattractant cytokine, was used as a positive control. Heat-inactivated MIF (MIF heated to 65 °C for 30 min) was also used as a negative control. Transwell plates were incubated for 4 h at 37 °C in 5% CO_2. PBMCs that had migrated through the membrane were dislodged using 2 mM EDTA and fixed with methanol. The number of cells that migrated from the upper chamber into the filter and reached its lower side was determined by staining with crystal violet and counting under a microscope (Leica). To compare the results from different experiments, a chemotaxis index (CI = number of PBMCs migrating toward MIF or MIF plus EA-loaded wells divided by the number of PBMCs migrating toward control medium) was calculated. The counts provided were the results observed in five randomly selected fields under a microscope. The results were reported as the mean CI ± SD change with respect to control of at least three independent experiments.

Statistical Analysis. For IC_{50} determination, respective experiments were repeated in triplicate. Data were presented as mean ± SD. Student's *t* test was used to analyze the data in GraphPadPrism 4. Values of $p < 0.05$ were considered significant.

RESULTS

Purification of MIF. MIF was cloned in pET28a vector, overexpressed in *E. coli*, and purified using gel permeation chromatography. The purity of the protein was checked by 15% SDS-PAGE, and the molecular weight (12.556 kDa) was confirmed by MALDI-TOF mass spectrometry (Figure 1, inset a). Peptide fingerprinting (Figure 1, inset b) finally confirmed the identity of MIF by MALDI MS/MS with a perfect match from the NCBI database.

Inhibition of MIF Tautomerase by Ellagic Acid (EA): Kinetics and Mode of Inhibition. The tautomerase activity of recombinant MIF was measured by following the tautomerization of L-DOPA in the absence or presence of increasing concentrations of EA. Data indicated that EA

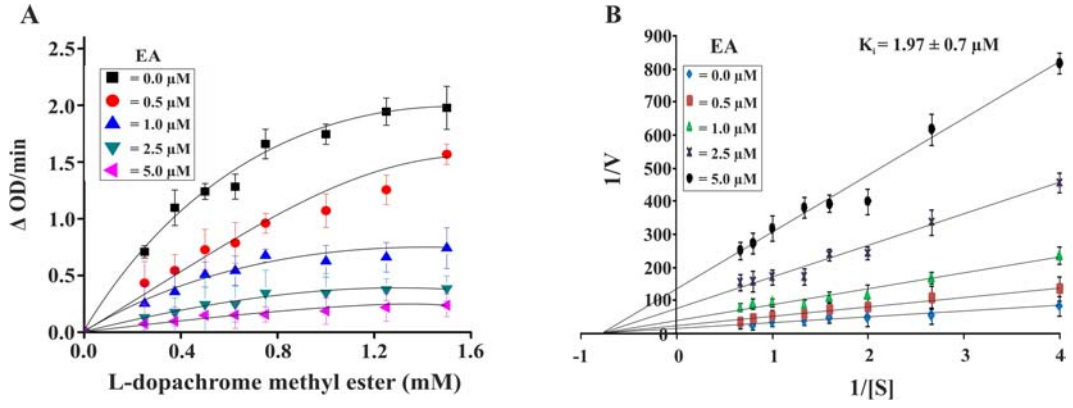

Figure 3. Kinetics of inhibition of MIF by EA: (A) concentration−response curve of EA versus substrate L-DOPA; (B) inhibition constant (K_i) of EA against L-DOPA. The noncompetitive inhibition pattern of EA with MIF is revealed by a Lineweaver−Burk plot. The details of the methodologies are described in Materials and Methods. Data are presented as means ± SD of three independent experiments.

DOI: 10.1021/acs.jafc.5b00921
J. Agric. Food Chem. 2015, 63, 4988−4998

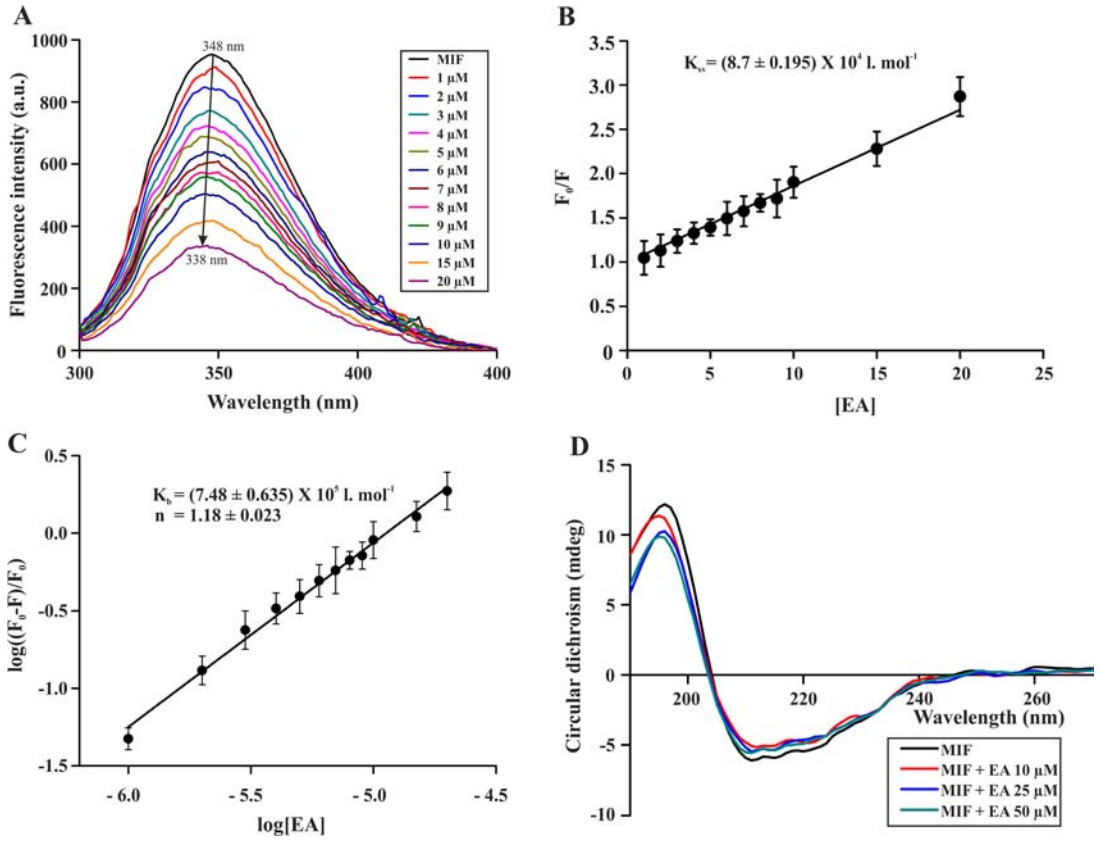

Figure 4. Binding of EA to MIF. (A) Fluorescence quenching spectra of MIF. The protein solution is excited and quenching of fluorescence is recorded in the presence of varying concentrations of EA (1−20 μM). (B) Stern−Volmer plot of decrease in fluorescence of MIF in the presence of varying concentrations of EA. The dynamic quenching rate constant K_{sv} is evaluated from the slope of the line. (C) Logarithmic plots of relative fluorescence quenching of MIF against logarithmic concentrations of EA to calculate K_b. K_b is calculated from the intersection of the line with the y axis and the number of binding sites (n) from the slope of the line. (D) CD spectra of MIF in the presence or absence of EA.

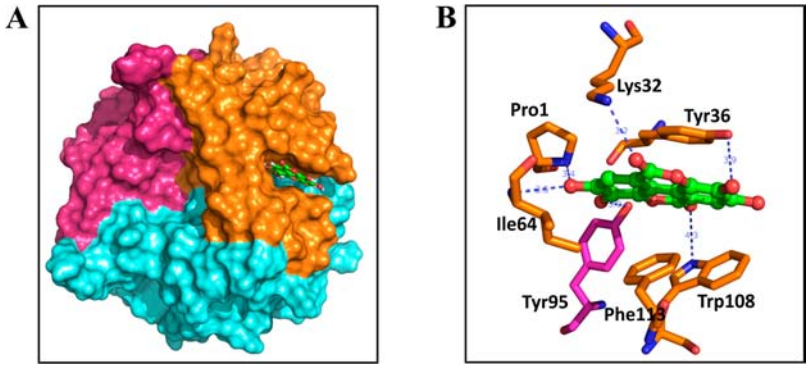

Figure 5. Molecular docking of EA with MIF. (A) Surface diagram of MIF homotrimers docked with EA. Each monomer is indicated by a different color: chain A, orange; chain B, cyan; chain C, magenta. EA is shown in green. The docked conformation produced by SwissDock indicates that EA interacts with MIF in a pocket formed at the interface of chains A and B. (B) Interacting side chains of amino acid residues shown by sticks and the ligand by a ball and stick model. Hydrogen bonds are depicted as blue dashed lines. The binding pocket is formed by the side chains of Pro-1, Lys-32, Tyr-36, Ile-64, Trp-108, Phe-113, and Tyr-95 from two neighboring subunits. The figures were generated using PyMOL.

significantly inhibited the tautomerase activity of MIF (IC_{50} = 4.77 ± 0.52 μM) (Figure 2). Next, we were interested in analyzing the type of inhibition offered by EA. A concentration−response curve and Lineweaver−Burk plot were plotted (Figure 3). A Lineweaver−Burk plot of concentration−response curves revealed a noncompetitive mode of inhibition of MIF by EA. The inhibition constant (K_i) was determined from the concentration−response curve and found to be 1.97 ± 0.7 μM. Binding of EA to MIF was assessed by following the quenching of tryptophan (Trp-108) fluorescence in the presence of increasing concentrations of EA. The only tryptophan in human MIF is distantly located from the catalytic Pro-1 and is exposed to the solvent. MIF in optically clear assay buffer was excited at 295 nm for recording the fluorescence spectra, which were mainly attributed to the only tryptophan residue. MIF showed an emission maximum at 348 nm. The protein solution was titrated by consecutive additions of EA (1−20 μM), and its fluorescence intensity was gradually found to decrease with

DOI: 10.1021/acs.jafc.5b00921
J. Agric. Food Chem. 2015, 63, 4988−4998

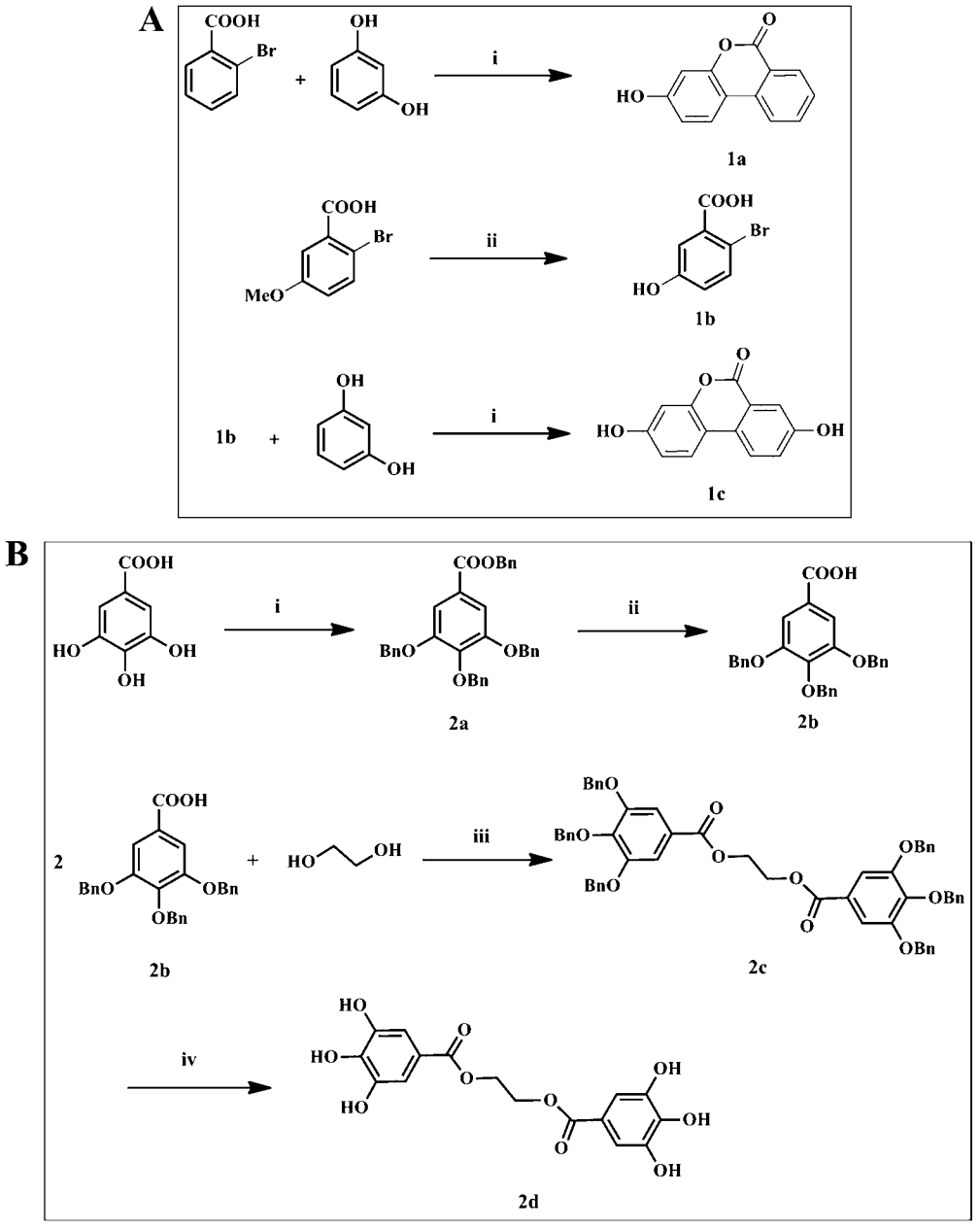

Figure 6. (A) Reagents and conditions: (i) (a) aqueous NaOH, 30 min, reflux, (b) $CuSO_4$, 10 min, reflux, (ii) $AlCl_3$, chlorobenzene, 2.5 h, reflux. (B) Reagents and conditions: (i) BnCl, K_2CO_3, $(n\text{-Bu})_4N^+I^-$, acetone, 6 h, reflux; (ii) 20% KOH, ethanol, 2 h, reflux; (iii) EDC-HCl, HOBt, Et_3N, DMF, overnight, room temperature; (iv) 10% Pd−C, methanol/chloroform, room temperature, 30 min.

increasing concentrations of EA (Figure 4A). A small blue shift of the λ_{max} value was also observed with increasing concentrations of EA. The nature of fluorescence quenching of the MIF−EA (0−20 μM) interaction was analyzed using the Stern−Volmer equation (Figure 4B). Subsequently K_{SV} was calculated from the linear regression curve of F_0/F versus [Q]. The binding constant (K_b), number of binding sites (n), and free energy change (ΔG°) of the EA−MIF interaction were determined from eqs 2 and 3, respectively (Figure 4C). The binding affinity of EA was found to be quite strong, and its value was found to be $\Delta G^\circ = -33.53 \pm 0.729$ kJ mol^{-1}. We analyzed the conformation of MIF in the presence of 10, 25, and 50 μM EA by CD spectroscopy to confirm any effect of EA on the MIF secondary structure (manifested as a gradual decrease in MIF fluorescence). Secondary structural elements such as α-helices, β-sheets, and random coils absorb specific components of the circularly polarized light of a CD spectrum, thereby providing information about specific structural elements within a protein. The addition of EA did not alter much of the basic secondary structure of MIF (Figure 4D). For further confirmation of minimum changes in structure we analyzed the spectral data in a DICHROWEB web server by four widely used algorithms. The outcome of these algorithms established (data not shown) that EA did not significantly alter the secondary structure of MIF.

To get the exact binding location of EA with MIF, we tried to cocrystallize EA with MIF but failed to get the cocrystallized product. Hence, molecular docking was performed to get a preliminary idea about the possible interaction between MIF and EA. Structural details for human MIF (Protein Data Bank

DOI: 10.1021/acs.jafc.5b00921
J. Agric. Food Chem. 2015, 63, 4988−4998

code 3L5S; 1.86 Å resolution) and EA (PubChem CID 5281855) were obtained from the respective databases. For molecular docking studies, the homotrimer of MIF was docked with EA. Each docking experiment was a composite of 250 independent runs. Molecular docking outputs showed that EA interacted at or close to the active site of the N terminal of MIF. EA binds in a pocket formed by the N terminal (Pro-1, Lys-32, Tyr-36) and C terminal (Ile-64, Trp-108, Phe-113) residues of chain A and Tyr-95 of chain B (Figure 5A). In this orientation EA formed hydrogen-bond interactions with MIF through the amino acids Pro-1, Lys-32, Tyr-36, Ile-64, Tyr-95, Trp-108, and Tyr-95 (Figure 5B). The ligand was also stabilized by hydrophobic interactions with the aromatic side chains of Tyr-36, Ile-64, Tyr-95, Trp-108, and Phe-113. In addition, the aromatic side chain of Tyr-36 makes a $\pi-\pi$ stacking interaction with EA. These hydrogen bonds and hydrophobic interactions were thought to play a role in the binding of EA with MIF.

Functional Group Pattern Recognition Study: Orientation and Role of Lactone Moiety. Following the identification of EA as a new MIF inhibitor, we were now interested in identifying the active pharmacophore. We therefore synthesized several molecules as structural dissects/parts of EA and screened them for MIF tautomerase activity. Gallic acid, a unit structural scaffold of EA, did not show any activity. Synthesized EA metabolites urolithin B and urolithin A (Figure 6A) contained only three fused rings with one lactone group and showed inhibitory activity with higher IC_{50} values (Table 1). To check the specific involvement of the lactone moiety on tautomerase inhibition, we synthesized a distant dimeric gallic acid derivative (compound **2d**). Compound **2d**, a dimer of GA comprising two labile ester groups and six free hydroxyl groups (like EA), was synthesized using the distant linker ethylene glycol (Figure 6B). Compound **2d** showed very low activity against MIF (IC_{50} = 35.9 ± 0.72 μM) (Table 1). To explore the role of planar conjugated fused systems, we took pyrene, a planar polycyclic, fused aromatic hydrocarbon without any functional group. Pyrene did not show any tautomerase inhibitory activity. Thus, compounds having lactone or ester groups were found to be active and hydroxyl groups had no effect on MIF tautomerase inhibition.

Prevention of MIF-Mediated Nuclear Translocation of NF-κB by EA: Molecular Event Essential for Proinflammatory Signaling. MIF promotes inflammation by activating signaling cascades involving NF-κB. MIF is known to cause translocation of NF-κB into the nucleus. Therefore, nuclear translocation of NF-κB was followed by confocal microscopy in PBMCs. Blue fluorescence represented the nucleus (Figure 7, first column), while red fluorescence represented cells immunostained with NF-κB primary antibody and Alexa Fluor 647 conjugated secondary antibody (Figure 7, second column). The third column represent the merged images of the red and blue fluorescence, while the area of intranuclear NF-κB is depicted as white dots in the fourth column. In the fifth column, intranuclear versus non-intranuclear NF-κB is presented as a bar diagram. In the control set (Figure 7, first row), there was a basal level of NF-κB (red fluorescence) in the nucleus; however, the red signal was confined mostly in the cytosol. PBMCs with exogenously treated MIF (Figure 7, second row) showed a significantly higher level of NF-κB in the nucleus depicting the role of MIF on nuclear translocation of NF-κB. In contrast, PBMCs treated with MIF preincubated with EA (50 μM) showed a much lower intranuclear NF-κB, as evident from reduced overlap of the red and blue signals and the white dots. Because PBMCs normally secrete a basal level of MIF,[34] treatment of PBMCs with EA alone also resulted in lowering of nuclear NF-κB in comparison to the control. Thus, the data showed that the stimulatory effect of MIF on the nuclear translocation of NF-κB was significantly compromised upon treatment with EA.

Table 1. Chemical Structure and Activities of EA Derivatives against MIF Tautomerase

Compounds	Inhibition of tautomerase activity of MIF (IC_{50}) (μM) Mean ± S.D
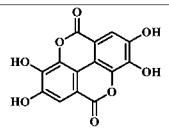 EA	4.77 ± 0.52
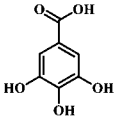 GA	Not active
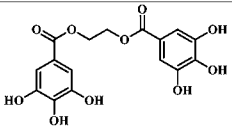 Compound 2d	35.9 ± 0.72
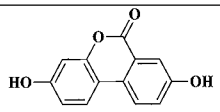 Urolithin A	50.03 ± 4.37
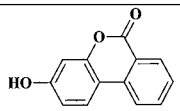 Urolithin B	57.42 ± 3.93
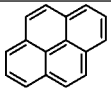 Pyrene	Not active

Prevention of MIF-Mediated Chemotaxis of Human Peripheral Blood Mononuclear Cells (PBMCs) by EA: Cellular Event Necessary for Inflammation. MIF promotes macrophage chemotactic migration and also plays an important role in neutrophil infiltration during inflammatory diseases. To check any probable effect of EA on MIF-mediated chemotactic activity, we performed a chemotactic migration assay using PBMCs in the presence or absence of increasing concentrations of EA. EA showed a potent concentration-dependent inhibitory effect on MIF-induced chemotactic migration of PBMCs (CI = 2.31, 1.93, and 1.14 for EA 10, 25, and 50 μM, respectively, in comparison with CI = 3.38 for MIF-treated cells where the control set CI was fixed at 0.0) (Figure 8). We validated the chemotactic migration assay using heat-inactivated MIF, which further showed negligible chemotactic migration of PBMCs in comparison to the control (Figure 8). MIP-1α, a classical chemoattractant, used in this assay also resulted in significant chemotactic migration (CI = 2.96) of the PBMCs. However, it is interesting to note that EA even at a high concentration (50 μM) failed to inhibit the MIP-1α-induced

DOI: 10.1021/acs.jafc.5b00921
J. Agric. Food Chem. 2015, 63, 4988−4998

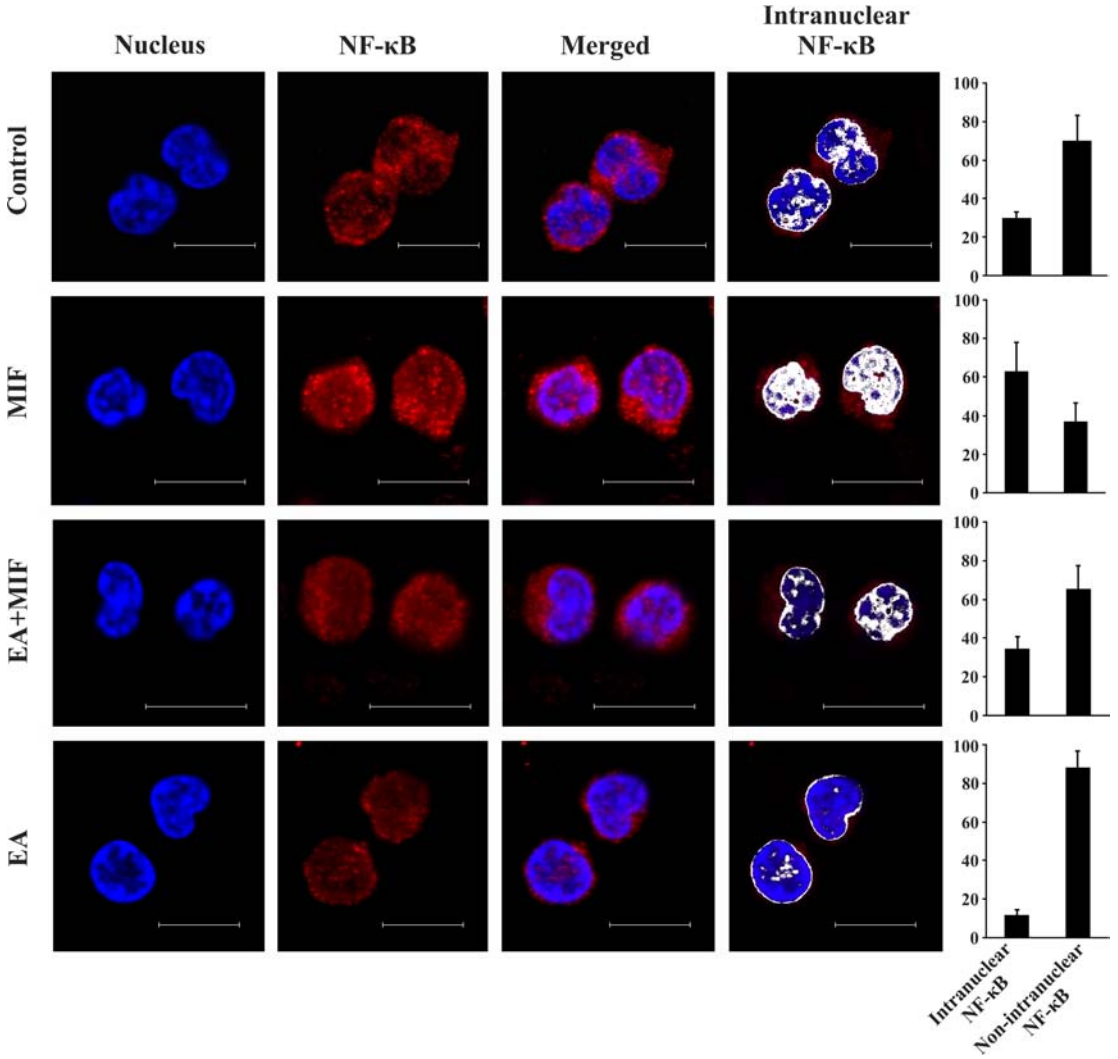

Figure 7. Inhibition of MIF-mediated nuclear translocation of NF-κB in PBMCs by EA. Localization of NF-κB (red) into the nucleus (blue) is calculated from Pearson's correlation coefficient (fifth column). The white spots in the fourth column indicate the area of maximum intranuclear NF-κB. Scale bars indicate 10 μm. Data are presented as means ± SD of three independent experiments.

chemotactic migration of PBMCs (Figure 8), suggesting the specificity of EA for MIF-mediated chemotaxis.

DISCUSSION

EA is long since known for its antioxidant and anti-inflammatory activity. However, here we report that EA inhibits tautomerase activity of human MIF, a proinflammatory protein. Further, we identified that the planar conjugated lactone moiety is responsible for tautomerase inhibition after performing extensive structure−function analysis. EA also inhibited MIF-mediated proinflammatory responses in PBMCs.

The inhibitory action of EA against MIF followed a concentration gradient. Moreover, EA noncompetitively inhibited MIF, as there was no structural similarity between the EA and MIF assay substrate L-DOPA. This suggested that EA might bind to the allosteric site (away from the active site) or close to the active site with slack binding of MIF, which did not block it from binding to the substrate but inhibited the tautomerase activity of MIF. Binding of EA to MIF was evaluated by fluorescence spectroscopy. Structural conformations of a globular protein may change upon binding of a small molecule due to alterations in the intramolecular forces responsible for maintaining the secondary and tertiary structures. A decrease in Trp-108 fluorescence λ_{max} value therefore suggested that the EA−MIF interaction might alter the microenvironment of Trp. Emission spectra of MIF were measured using an excitation wavelength at 295 nm to ensure that light caused excitation of Trp residues only. A blue shift of the λ_{max} of Trp emission spectra indicated a decrease in hydrophilicity in its surrounding region within the globular protein, indicating that Trp residue might have shifted to a more hydrophobic environment due to a presumptive change in the secondary structure of the protein. Moreover, the free energy change having a negative sign indicated the spontaneity and stability of the EA−MIF interaction. Since human MIF has only one Trp, which is distant from the catalytic Pro-1 and exposed to the solvent, therefore the results of the fluorimetric quenching of Trp λ_{max} may result in either a change in microenvironment around Trp or a gross alteration in the secondary structure of MIF upon addition of EA.[49] This change in protein structure is expected to be reflected in circular dichroism (CD) spectra. Our CD data, however, indicated almost no changes in the secondary structure of MIF even in the presence of high concentrations of EA (50 μM), therefore showing that quenching of MIF fluorescence was

DOI: 10.1021/acs.jafc.5b00921
J. Agric. Food Chem. 2015, 63, 4988−4998

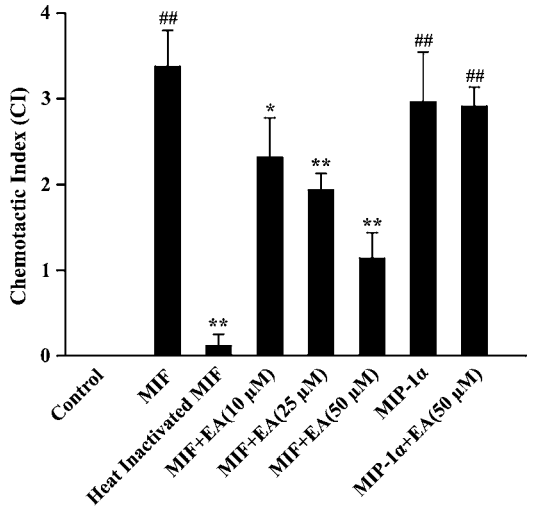

Figure 8. Inhibition of MIF-mediated chemotactic migration of PBMCs by EA. The chemotactic index is plotted with the number of cells migrated toward the lower chamber and expressed as change over control, keeping the control value at 0. Data are presented as mean ± SD ((##) $p < 0.001$ versus control; (*) $p < 0.01$; (**) $p < 0.001$ versus MIF).

probably due to alteration in the microenvironment around Trp-108 and was not due to the alteration in the secondary structure of the whole protein. Molecular docking of EA to MIF revealed that the NH backbone of Pro-1, Lys-32, and Tyr-36, the CO terminal of Ile-64, Trp-108, Phe-113, and Tyr-95 and $\pi-\pi$ interactions with Tyr-36, Ile-64, Tyr-95, Trp-108, and Phe-113 allowed a favorable interaction of EA with MIF. These interactions shown in the docking study were consistent with our previous kinetics of tautomerase inhibition and fluorimetric binding.

Next, we were interested in identifying the active functional scaffold of EA responsible for MIF tautomerase inhibition. Gallic acid (GA), a unit structural motif of EA previously shown to exhibit anti-inflammatory and antioxidant activity,[50,51] may also inhibit MIF tautomerase activity. To test this hypothesis, we performed a dopachrome tautomerization assay to screen the inhibitory activity of GA and all synthetic GA-related polyphenolic compounds. We found EA to be the most potent inhibitor among all of the compounds, followed by compound **2d**, urolithin A, and urolithin B. GA, however, exhibited no inhibitory activity at all. Therefore, it appears that the difference in activity between EA and GA probably arises from the two lactone groups present in EA, although both have free hydroxyl groups. Compound **2d**, having an ester group, was also found to be active. The conjugated aromatic system was also not responsible for the inhibition of tautomerase activity, because pyrene did not exhibit any inhibitory activity. Therefore, ester groups play an important role, whereas hydroxyl groups do not have any impact on inhibition of MIF tautomerase activity. Although free ester groups are capable of inhibiting MIF, their activity is much less than that of a cyclic ester group, i.e. lactone, as is evident from the IC_{50} values. The presence of a higher inhibitory activity of EA (having two lactone groups) in comparison to urolithin A and urolithin B (both having a single lactone group) indicates the importance of conformationally restricted lactones as well as the role of lactones in MIF inhibition. Thus, the structurally restricted lactone group of EA is probably the most essential scaffold responsible for MIF inhibition.

MIF is an inflammatory cytokine.[52] Therefore, we investigated the effect of EA on MIF-mediated inflammatory response such as nuclear translocation of NF-κB in PBMCs. It has been reported that binding of MIF to a CD74 complex involving CD44 leads to the release of the intracellular domain of CD74 (CD74 ICD), which triggers the downstream signaling pathway leading to the activation of NF-κB.[53] Activation of the NF-κB in turn plays a central role in inflammation by switching on the transcription of a plethora of proinflammatory target genes. As NF-κB is a transcription factor, which enters the nucleus and binds to the DNA of its targets to mediate its actions,[54] we therefore investigated the inhibitory effect of EA on MIF-induced translocation of NF-κB into the nucleus. The data clearly indicated that MIF greatly induced NF-κB translocation to the nucleus in PBMCs, whereas the control (without MIF) and EA (50 μM) treated cells did not show such NF-κB translocation, as is evident from confocal images. Interestingly ISO-1, which is a well-established MIF inhibitor reported to bind the tautomerase active site of MIF, inhibits its proinflammatory activity and also significantly reduces the nuclear translocation of NF-κB.[55] Inhibition of MIF tautomerase activity or interference in the tautomerase active site might therefore be a restraining factor behind the inhibition of MIF-induced nuclear translocation of NF-κB. However, we cannot exclude other possibilities of anti-inflammatory properties of EA that can mediate the inhibition of nuclear translocation of NF-κB.

Chemotactic migration plays a major role during inflammation by leucocyte recruitment to the site of inflammation. MIF promotes macrophage chemotactic migration and also plays an important role in leukocyte recruitment during inflammation.[56] EA inhibited MIF-induced chemotaxis of PBMCs, and this inhibition was specific, as no inhibition was found when MIP-1α was used as the chemoattractant. However, knowledge about the exact mechanism of inhibition of MIF-mediated chemotaxis by EA needs further detailed investigation. Blocking of tautomerase activity or the tautomerase active site of MIF by EA might be a reason behind this inhibition. This study therefore reports that the naturally occurring antioxidant EA inhibits the tautomerase activity of MIF and MIF-mediated proinflammatory responses in PBMCs.

■ ASSOCIATED CONTENT

Supporting Information

Text and figures giving experimental procedures for the synthesis of compounds and ^{1}H and ^{13}C NMR spectra. The Supporting Information is available free of charge on the ACS Publications website at DOI: 10.1021/acs.jafc.5b00921.

■ AUTHOR INFORMATION

Corresponding Author

*U.B.: tel, +91-33-24995735; e-mail, ubandyo_1964@yahoo.com or udayb@iicb.res.in.

Funding

We thank the Council of Scientific and Industrial Research, New Delhi, India, for offering a fellowship to S.S. to carry out this work. This work was supported by Council of Scientific and Industrial Research, New Delhi, India (Grant No. BEnD, BSC 0206).

Notes

The authors declare no competing financial interest.

DOI: 10.1021/acs.jafc.5b00921
J. Agric. Food Chem. 2015, 63, 4988−4998

REFERENCES

(1) Stalikas, C. D. Extraction, separation, and detection methods for phenolic acids and flavonoids. *J. Sep. Sci.* **2007**, *30*, 3268−95.

(2) Lee, J. H.; Cho, S.; Paik, H. D.; Choi, C. W.; Nam, K. T.; Hwang, S. G.; Kim, S. K. Investigation on antibacterial and antioxidant activities, phenolic and flavonoid contents of some thai edible plants as an alternative for antibiotics. *Asian-Australas. J. Anim. Sci.* **2014**, *27*, 1461−8.

(3) de Araujo, A. A.; Soares, L. A.; Assuncao Ferreira, M. R.; de Souza Neto, M. A.; da Silva, G. R.; de Araujo, R. F., Jr.; Guerra, G. C.; de Melo, M. C. Quantification of polyphenols and evaluation of antimicrobial, analgesic and anti-inflammatory activities of aqueous and acetone-water extracts of Libidibia ferrea, Parapiptadenia rigida and Psidium guajava. *J. Ethnopharmacol.* **2014**, *156*, 88−96.

(4) Adedapo, A. A.; Adeoye, B. O.; Sofidiya, M. O.; Oyagbemi, A. A. Antioxidant, antinociceptive and anti-inflammatory properties of the aqueous and ethanolic leaf extracts of Andrographis paniculata in some laboratory animals. *J. Basic Clin. Physiol. Pharmacol.* **2014**, DOI: 10.1515/jbcpp-2014-0051.

(5) Rodrigo, R.; Libuy, M.; Feliu, F.; Hasson, D. Polyphenols in disease: from diet to supplements. *Curr. Pharm. Biotechnol* **2014**, *15*, 304−317.

(6) Li, B. H.; Ma, X. F.; Wang, Y.; Tian, W. X. Structure-activity relationship of polyphenols that inhibit fatty acid synthase. *J. Biochem.* **2005**, *138*, 679−85.

(7) Rahman, I.; Biswas, S. K.; Kirkham, P. A. Regulation of inflammation and redox signaling by dietary polyphenols. *Biochem. Pharmacol.* **2006**, *72*, 1439−52.

(8) Xiao, J.; Ni, X.; Kai, G.; Chen, X. A review on structure-activity relationship of dietary polyphenols inhibiting alpha-amylase. *Crit. Rev. Food Sci. Nutr.* **2013**, *53*, 497−506.

(9) Goodwin, E. C.; Atwood, W. J.; DiMaio, D. High-throughput cell-based screen for chemicals that inhibit infection by simian virus 40 and human polyomaviruses. *J. Virol* **2009**, *83*, 5630−9.

(10) Nohynek, L. J.; Alakomi, H. L.; Kahkonen, M. P.; Heinonen, M.; Helander, I. M.; Oksman-Caldentey, K. M.; Puupponen-Pimia, R. H. Berry phenolics: antimicrobial properties and mechanisms of action against severe human pathogens. *Nutr. Cancer* **2006**, *54*, 18−32.

(11) Beserra, A. M.; Calegari, P. I.; Souza Mdo, C.; Dos Santos, R. A.; Lima, J. C.; Silva, R. M.; Balogun, S. O.; Martins, D. T. Gastroprotective and ulcer-healing mechanisms of ellagic acid in experimental rats. *J. Agric. Food Chem.* **2011**, *59*, 6957−65.

(12) Iakovleva, L. V.; Ivakhnenko, A. K.; Buniatian, N. D. [The protective action of ellagic acid in experimental myocarditis]. *Eksp Klin Farmakol* **1998**, *61*, 32−4.

(13) Kaur, R.; Sharma, U.; Singh, B.; Arora, S. Antimutagenic and antioxidant characteristics of Chukrasia tabularis A Juss extracts. *Int. J. Toxicol.* **2011**, *30*, 21−34.

(14) Iqbal, J.; Zaib, S.; Farooq, U.; Khan, A.; Bibi, I.; Suleman, S. Antioxidant, Antimicrobial, and Free Radical Scavenging Potential of Aerial Parts of Periploca aphylla and Ricinus communis. *ISRN Pharmacol* **2012**, *2012*, 563267.

(15) Dell'Agli, M.; Parapini, S.; Basilico, N.; Verotta, L.; Taramelli, D.; Berry, C.; Bosisio, E. In vitro studies on the mechanism of action of two compounds with antiplasmodial activity: ellagic acid and 3,4,5-trimethoxyphenyl(6′-O-aalloyl)-beta-D-glucopyranoside. *Planta Med.* **2003**, *69*, 162−4.

(16) Yoon, C. H.; Chung, S. J.; Lee, S. W.; Park, Y. B.; Lee, S. K.; Park, M. C. Gallic acid, a natural polyphenolic acid, induces apoptosis and inhibits proinflammatory gene expressions in rheumatoid arthritis fibroblast-like synoviocytes. *Joint Bone Spine* **2012**, DOI: 10.1016/j.jbspin.2012.08.010.

(17) Forester, S. C.; Choy, Y. Y.; Waterhouse, A. L.; Oteiza, P. I. The anthocyanin metabolites gallic acid, 3-O-methylgallic acid, and 2,4,6-trihydroxybenzaldehyde decrease human colon cancer cell viability by regulating pro-oncogenic signals. *Mol. Carcinog* **2012**, DOI: 10.1002/mc.21974.

(18) Barch, D. H.; Rundhaugen, L. M.; Stoner, G. D.; Pillay, N. S.; Rosche, W. A. Structure-function relationships of the dietary anticarcinogen ellagic acid. *Carcinogenesis* **1996**, *17*, 265−9.

(19) Galano, A.; Francisco Marquez, M.; Perez-Gonzalez, A. Ellagic acid: an unusually versatile protector against oxidative stress. *Chem. Res. Toxicol.* **2014**, *27*, 904−18.

(20) Mishra, S.; Vinayak, M. Ellagic acid checks lymphoma promotion via regulation of PKC signaling pathway. *Mol. Biol. Rep.* **2013**, *40*, 1417−28.

(21) Mishra, S.; Vinayak, M. Ellagic acid induces novel and atypical PKC isoforms and promotes caspase-3 dependent apoptosis by blocking energy metabolism. *Nutr. Cancer* **2014**, *66*, 675−81.

(22) Wang, N.; Wang, Z. Y.; Mo, S. L.; Loo, T. Y.; Wang, D. M.; Luo, H. B.; Yang, D. P.; Chen, Y. L.; Shen, J. G.; Chen, J. P. Ellagic acid, a phenolic compound, exerts anti-angiogenesis effects via VEGFR-2 signaling pathway in breast cancer. *Breast Cancer Res. Treat.* **2012**, *134*, 943−55.

(23) Tang, B.; Chen, G. X.; Liang, M. Y.; Yao, J. P.; Wu, Z. K. Ellagic acid prevents monocrotaline-induced pulmonary artery hypertension via inhibiting NLRP3 inflammasome activation in rats. *Int. J. Cardiol* **2014**, *180C*, 134−141.

(24) Lee, J. H.; Won, J. H.; Choi, J. M.; Cha, H. H.; Jang, Y. J.; Park, S.; Kim, H. G.; Kim, H. C.; Kim, D. K. Protective Effect of Ellagic Acid on Concanavalin A-Induced Hepatitis via Toll-Like Receptor and Mitogen-Activated Protein Kinase/Nuclear Factor kappaB Signaling Pathways. *J. Agric. Food Chem.* **2014**, *62*, 10110−7.

(25) Candido, J.; Hagemann, T. Cancer-related inflammation. *J. Clin. Immunol.* **2013**, *33* (Suppl 1), S79−84.

(26) Bucala, R.; Donnelly, S. C. Macrophage migration inhibitory factor: a probable link between inflammation and cancer. *Immunity* **2007**, *26*, 281−5.

(27) Welford, S. M.; Bedogni, B.; Gradin, K.; Poellinger, L.; Broome Powell, M.; Giaccia, A. J. HIF1alpha delays premature senescence through the activation of MIF. *Genes Dev.* **2006**, *20*, 3366−71.

(28) Lue, H.; Thiele, M.; Franz, J.; Dahl, E.; Speckgens, S.; Leng, L.; Fingerle-Rowson, G.; Bucala, R.; Luscher, B.; Bernhagen, J. Macrophage migration inhibitory factor (MIF) promotes cell survival by activation of the Akt pathway and role for CSN5/JAB1 in the control of autocrine MIF activity. *Oncogene* **2007**, *26*, 5046−59.

(29) Verjans, E.; Noetzel, E.; Bektas, N.; Schutz, A. K.; Lue, H.; Lennartz, B.; Hartmann, A.; Dahl, E.; Bernhagen, J. Dual role of macrophage migration inhibitory factor (MIF) in human breast cancer. *BMC Cancer* **2009**, *9*, 230.

(30) Dessein, A. F.; Stechly, L.; Jonckheere, N.; Dumont, P.; Monte, D.; Leteurtre, E.; Truant, S.; Pruvot, F. R.; Figeac, M.; Hebbar, M.; Lecellier, C. H.; Lesuffleur, T.; Dessein, R.; Grard, G.; Dejonghe, M. J.; de Launoit, Y.; Furuichi, Y.; Prevost, G.; Porchet, N.; Gespach, C.; Huet, G. Autocrine induction of invasive and metastatic phenotypes by the MIF-CXCR4 axis in drug-resistant human colon cancer cells. *Cancer Res.* **2010**, *70*, 4644−54.

(31) Salminen, A.; Kaarniranta, K. Control of p53 and NF-kappaB signaling by WIP1 and MIF: role in cellular senescence and organismal aging. *Cell. Signalling* **2011**, *23*, 747−52.

(32) Lawrence, T. The nuclear factor NF-kappaB pathway in inflammation. *Cold Spring Harbor Perspect. Biol.* **2009**, *1*, a001651.

(33) Chuang, C. C.; Chuang, Y. C.; Chang, W. T.; Chen, C. C.; Hor, L. I.; Huang, A. M.; Choi, P. C.; Wang, C. Y.; Tseng, P. C.; Lin, C. F. Macrophage migration inhibitory factor regulates interleukin-6 production by facilitating nuclear factor-kappa B activation during Vibrio vulnificus infection. *BMC Immunol.* **2010**, *11*, 50.

(34) Dicker, D.; Salook, M. A.; Marcoviciu, D.; Djaldetti, M.; Bessler, H. Role of peripheral blood mononuclear cells in the predisposition of obese individuals to inflammation and infection. *Obes. Facts* **2013**, *6*, 146−51.

(35) Cho, Y.; Crichlow, G. V.; Vermeire, J. J.; Leng, L.; Du, X.; Hodsdon, M. E.; Bucala, R.; Cappello, M.; Gross, M.; Gaeta, F.; Johnson, K.; Lolis, E. J. Allosteric inhibition of macrophage migration inhibitory factor revealed by ibudilast. *Proc. Natl. Acad. Sci. U. S. A.* **2010**, *107*, 11313−8.

DOI: 10.1021/acs.jafc.5b00921
J. Agric. Food Chem. 2015, 63, 4988−4998

(36) Molnar, V.; Garai, J. Plant-derived anti-inflammatory compounds affect MIF tautomerase activity. *Int. Immunopharmacol.* **2005**, *5*, 849−56.
(37) Alam, A.; Haldar, S.; Thulasiram, H. V.; Kumar, R.; Goyal, M.; Iqbal, M. S.; Pal, C.; Dey, S.; Bindu, S.; Sarkar, S.; Pal, U.; Maiti, N. C.; Bandyopadhyay, U. Novel anti-inflammatory activity of epoxyazadiradione against macrophage migration inhibitory factor: inhibition of tautomerase and proinflammatory activities of macrophage migration inhibitory factor. *J. Biol. Chem.* **2012**, *287*, 24844−61.
(38) Alam, A.; Pal, C.; Goyal, M.; Kundu, M. K.; Kumar, R.; Iqbal, M. S.; Dey, S.; Bindu, S.; Sarkar, S.; Pal, U.; Maiti, N. C.; Adhikari, S.; Bandyopadhyay, U. Synthesis and bio-evaluation of human macrophage migration inhibitory factor inhibitor to develop anti-inflammatory agent. *Bioorg. Med. Chem.* **2011**, *19*, 7365−73.
(39) Santini, S.; Bizzarri, A. R.; Yamada, T.; Beattie, C. W.; Cannistraro, S. Binding of azurin to cytochrome c 551 as investigated by surface plasmon resonance and fluorescence. *J. Mol. Recognit.* **2014**, *27*, 124−30.
(40) Lucie Trnkova, I. B. Vladimir Kubicek, Jaroslav Drsata, Binding of naturally occurring hydroxycinnamic acids to bovine serum albumin. *Nat. Sci.* **2010**, *2*, 563−570.
(41) Alam, A.; Goyal, M.; Iqbal, M. S.; Bindu, S.; Dey, S.; Pal, C.; Maity, P.; Mascarenhas, N. M.; Ghoshal, N.; Bandyopadhyay, U. Cysteine-3 and cysteine-4 are essential for the thioredoxin-like oxidoreductase and antioxidant activities of Plasmodium falciparum macrophage migration inhibitory factor. *Free Radical Biol. Med.* **2011**, *50*, 1659−68.
(42) Grosdidier, A.; Zoete, V.; Michielin, O. SwissDock, a protein-small molecule docking web service based on EADock DSS. *Nucleic Acids Res.* **2011**, *39*, W270−7.
(43) Grosdidier, A.; Zoete, V.; Michielin, O. Fast docking using the CHARMM force field with EADock DSS. *J. Comput. Chem.* **2011**, *32*, 2149.
(44) Grosdidier, A.; Zoete, V.; Michielin, O. EADock: docking of small molecules into protein active sites with a multiobjective evolutionary optimization. *Proteins: Struct., Funct., Genet.* **2007**, *67*, 1010−25.
(45) Pal, C.; Bindu, S.; Dey, S.; Alam, A.; Goyal, M.; Iqbal, M. S.; Sarkar, S.; Kumar, R.; Halder, K. K.; Debnath, M. C.; Adhikari, S.; Bandyopadhyay, U. Tryptamine-gallic acid hybrid prevents non-steroidal anti-inflammatory drug-induced gastropathy: correction of mitochondrial dysfunction and inhibition of apoptosis in gastric mucosal cells. *J. Biol. Chem.* **2012**, *287*, 3495−509.
(46) Bindu, S.; Pal, C.; Dey, S.; Goyal, M.; Alam, A.; Iqbal, M. S.; Dutta, S.; Sarkar, S.; Kumar, R.; Maity, P.; Bandyopadhyay, U. Translocation of heme oxygenase-1 to mitochondria is a novel cytoprotective mechanism against non-steroidal anti-inflammatory drug-induced mitochondrial oxidative stress, apoptosis, and gastric mucosal injury. *J. Biol. Chem.* **2011**, *286*, 39387−402.
(47) Bindu, S.; Mazumder, S.; Dey, S.; Pal, C.; Goyal, M.; Alam, A.; Iqbal, M. S.; Sarkar, S.; Azhar Siddiqui, A.; Banerjee, C.; Bandyopadhyay, U. Nonsteroidal anti-inflammatory drug induces proinflammatory damage in gastric mucosa through NF-kappaB activation and neutrophil infiltration: anti-inflammatory role of heme oxygenase-1 against nonsteroidal anti-inflammatory drug. *Free Radical Biol. Med.* **2013**, *65*, 456−67.
(48) Dey, S.; Bindu, S.; Goyal, M.; Pal, C.; Alam, A.; Iqbal, M. S.; Kumar, R.; Sarkar, S.; Bandyopadhyay, U. Impact of intravascular hemolysis in malaria on liver dysfunction: involvement of hepatic free heme overload, NF-kappaB activation, and neutrophil infiltration. *J. Biol. Chem.* **2012**, *287*, 26630−46.
(49) Swope, M. D.; Sun, H. W.; Klockow, B.; Blake, P.; Lolis, E. Macrophage migration inhibitory factor interactions with glutathione and S-hexylglutathione. *J. Biol. Chem.* **1998**, *273*, 14877−84.
(50) Yang, H. L.; Huang, P. J.; Liu, Y. R.; Kumar, K. J.; Hsu, L. S.; Lu, T. L.; Chia, Y. C.; Takajo, T.; Kazunori, A.; Hseu, Y. C. Toona sinensis inhibits LPS-induced inflammation and migration in vascular smooth muscle cells via suppression of reactive oxygen species and NF-kappaB signaling pathway. *Oxid Med. Cell Longev* **2014**, *2014*, 901315.
(51) Pal, C.; Bindu, S.; Dey, S.; Alam, A.; Goyal, M.; Iqbal, M. S.; Maity, P.; Adhikari, S. S.; Bandyopadhyay, U. Gallic acid prevents nonsteroidal anti-inflammatory drug-induced gastropathy in rat by blocking oxidative stress and apoptosis. *Free Radical Biol. Med.* **2010**, *49*, 258−67.
(52) Bank, M.; Stein, A.; Sison, C.; Glazer, A.; Jassal, N.; McCarthy, D.; Shatzer, M.; Hahn, B.; Chugh, R.; Davies, P.; Bloom, O. Elevated circulating levels of the pro-inflammatory cytokine macrophage migration inhibitory factor in individuals with acute spinal cord injury. *Arch. Phys. Med. Rehabil.* **2015**, *96*, 633−44.
(53) Shi, X.; Leng, L.; Wang, T.; Wang, W.; Du, X.; Li, J.; McDonald, C.; Chen, Z.; Murphy, J. W.; Lolis, E.; Noble, P.; Knudson, W.; Bucala, R. CD44 is the signaling component of the macrophage migration inhibitory factor-CD74 receptor complex. *Immunity* **2006**, *25*, 595−606.
(54) Lee, S.; Shin, S.; Kim, H.; Han, S.; Kim, K.; Kwon, J.; Kwak, J. H.; Lee, C. K.; Ha, N. J.; Yim, D. Anti-inflammatory function of arctiin by inhibiting COX-2 expression via NF-kappaB pathways. *J. Inflammation (London, U. K.)* **2011**, *8*, 16.
(55) Al-Abed, Y.; Dabideen, D.; Aljabari, B.; Valster, A.; Messmer, D.; Ochani, M.; Tanovic, M.; Ochani, K.; Bacher, M.; Nicoletti, F.; Metz, C.; Pavlov, V. A.; Miller, E. J.; Tracey, K. J. ISO-1 binding to the tautomerase active site of MIF inhibits its pro-inflammatory activity and increases survival in severe sepsis. *J. Biol. Chem.* **2005**, *280*, 36541−4.
(56) Fan, H.; Hall, P.; Santos, L. L.; Gregory, J. L.; Fingerle-Rowson, G.; Bucala, R.; Morand, E. F.; Hickey, M. J. Macrophage migration inhibitory factor and CD74 regulate macrophage chemotactic responses via MAPK and Rho GTPase. *J. Immunol.* **2011**, *186*, 4915−24.

DOI: 10.1021/acs.jafc.5b00921
J. Agric. Food Chem. 2015, 63, 4988−4998

JOURNAL OF AGRICULTURAL AND FOOD CHEMISTRY

Article

pubs.acs.org/JAFC

Inhibition of Human Neutrophil Responses by the Essential Oil of *Artemisia kotuchovii* and Its Constituents

Igor A. Schepetkin,[†] Svetlana V. Kushnarenko,[§] Gulmira Özek,[#] Liliya N. Kirpotina,[†] Gulzhakhan A. Utegenova,[§,Δ] Yuriy A. Kotukhov,[⊥] Alevtina N. Danilova,[⊥] Temel Özek,[#] K. Hüsnü Can Başer,[#,○] and Mark T. Quinn*[,†]

[†]Department of Microbiology and Immunology, Montana State University, Bozeman, Montana 59717, United States

[§]Institute of Plant Biology and Biotechnology, Almaty 050040, Republic of Kazakhstan

[#]Department of Pharmacognosy, Faculty of Pharmacy, Anadolu University, Eskisehir 26470, Turkey

[Δ]Faculty of Biology and Biotechnology, Al-Farabi Kazakh National University, 71 al-Farabi Avenue, 050038 Almaty, Republic of Kazakhstan

[⊥]Altai Botanical Garden, 07130 Ridder, Republic of Kazakhstan

[○]Botany and Microbiology Department, College of Science, King Saud University, Riyadh 11451, Saudi Arabia

ABSTRACT: Essential oils were obtained by hydrodistillation of the flowers+leaves and stems of *Artemisia kotuchovii* Kupr. ($AKEO_{f+l}$ and $AKEO_{stm}$, respectively) and analyzed by gas chromatography (GC) and gas chromatography−mass spectrometry (GC-MS). The primary components of the oils were estragole, (*E*)- and (*Z*)-*β*-ocimenes, methyleugenol, limonene, spathulenol, *β*-pinene, myrcene, and (*E*)-methyl cinnamate. Seventy-four constituents were present at concentrations from 0.1 to 1.0%, and 34 compounds were identified in trace (<0.1%) amounts in one or both plant components. Screening of the essential oils for biological activity showed that $AKEO_{stm}$, but not $AKEO_{f+l}$, inhibited *N*-formyl-Met-Leu-Phe (*f*MLF)-stimulated Ca^{2+} flux and chemotaxis and phorbol-12-myristate-13-acetate (PMA)-induced reactive oxygen species (ROS) production in human neutrophils. Selected pure constituents, representing >96% of the $AKEO_{stm}$ composition, were also tested in human neutrophils and HL-60 cells transfected with *N*-formyl peptide receptor 1 (FPR1). One component, 6-methyl-3,5-heptadien-2-one (MHDO), inhibited *f*MLF- and interleukin 8 (IL-8)-stimulated Ca^{2+} flux, *f*MLF-induced chemotaxis, and PMA-induced ROS production in human neutrophils. MHDO also inhibited *f*MLF-induced Ca^{2+} flux in FPR1-HL60 cells. These results suggest that MHDO may be effective in modulating some innate immune responses, possibly by inhibition of neutrophil migration and ROS production.

KEYWORDS: *Artemisia kotuchovii, calcium flux, chemotaxis, essential oil, neutrophil, N-formyl peptide receptor 1 (FPR1), reactive oxygen species*

INTRODUCTION

Artemisia is one of largest genera in the Asteraceae family, with approximately 500 species. Many of these species produce essential oils used in folk and modern medicine and in the cosmetics and pharmaceutical industries.[1,2] Extracts or compounds isolated from *Artemisia* have been shown to exhibit a wide range of biological properties, including anti-inflammatory activities that help to reduce inflammation.[3,4] Essential oils from several species of this genus have also been reported to decrease the production of pro-inflammatory mediators.[5,6] Extensive studies of the chemical components of these oils have demonstrated that they contain diverse bioactive secondary metabolites, including volatile monoterpenes and sesquiterpenes, with artemisinin as one of the best studied.[1,2,7,8] However, the chemical composition and biological properties of many endemic *Artemisia* spp. have not been evaluated.

Artemisia kotuchovii Kupr. is endemic in the Kazakhstan Altai. This perennial herb was described in 1999 and is closely related to *Artemisia dracunculus* L. (tarragon).[9] To date, the chemical composition and biological properties of *A. kotuchovii* have not been analyzed. Although ethnobotanical and ethnopharmacological data on medicinal usage of this herb are unknown, the related herb tarragon has been reported to have a wide range of applications in traditional medicine because of its therapeutic properties for a variety of ailments.[1] For example, pharmacological evaluation of tarragon extracts demonstrated anti-inflammatory activity.[1,10] Although tarragon essential oil was inactive in modulating human neutrophil phagocytosis,[11] essential oils from other *Artemisia* spp. exhibited some immunomodulatory properties, such as inhibition of nuclear factor (NF)-*κ*B transcriptional activity and stimulation of nitric oxide and prostaglandin E_2 production by macrophages.[5,6]

Neutrophils are a key cellular component of the immune response to infection or tissue injury.[12] These phagocytes are recruited to sites of injury or infection by a variety of factors, including formyl-Met-Leu-Phe (*f*MLF), a bacterial or mitochondria-derived peptide, and chemokines such as

Received: March 13, 2015
Revised: May 4, 2015
Accepted: May 9, 2015
Published: May 9, 2015

ACS Publications © 2015 American Chemical Society

DOI: 10.1021/acs.jafc.5b01307
J. Agric. Food Chem. 2015, 63, 4999−5007

interleukin 8 (IL-8).[13] IL-8 and *f*MLF activate G-protein coupled receptors (GPCR) to induce neutrophil chemotaxis and the release of various mediators, such as reactive oxygen species (ROS), proteases, and cytokines.[13] Growing evidence supporting the anti-inflammatory and tissue-protective effects of chemokine antagonists led to the design and screening of synthetic compounds and plant-derived constituents for novel small-molecule *N*-formyl peptide receptor (FPR) and α-chemokine receptor (CXCR) antagonists.[14,15] Human neutrophil elastase (HNE) also plays an important role in regulation of inflammation, and some plant-derived compounds have been identified as elastase inhibitors.[16]

In the present work, we defined the composition of essential oils from *A. kotuchovii* and evaluated their biological activity.

MATERIALS AND METHODS

Chemicals. The major and several minor constituents of essential oils were obtained from commercial sources. Sabinene, (−)-linalool, hexanal, *p*-cymen-8-ol, 3,7-dimethyl-1,3,6-octatriene (β-ocimene), and MHDO were purchased from Sigma-Aldrich Chemical Co. (St. Loius, MO, USA). Citronellol, (+)-limonene, *trans*-anethole, (−)-caryophyllene oxide, 4-allylanisole (estragole), 1,2-dimethoxy-4-(2-propenyl) (methyleugenol), myrcene, isopropyl myristate, *p*-cymene, α-terpinene, and (−)-limonene were purchased from Acros Organics (Geel, Belgium). Myristic acid, α-pinene, and terpinolene were from Santa Cruz Biotechnology (Dallas, TX, USA). Methyl cinnamate, 4-methoxystyrene (4-vinylanisole), palmitic (hexadecanoic) acid, and (1*S*)-(−)-β-pinene were from Alfa Aesar (Ward Hill, MA, USA). For biological evaluation, compounds were dissolved in dimethyl sulfoxide (DMSO; 20 mM stock solutions) and stored at −20 °C.

Materials. 8-Amino-5-chloro-7-phenylpyridol[3,4-*d*]pyridazine-1,4-(2*H*,3*H*)-dione (L-012) was obtained from Wako Chemicals (Richmond, VA, USA). DMSO, *f*MLF, HEPES, bacterial lipopolysaccharide (LPS) from *Escherichia coli* K-235, phorbol-12-myristate-13-acetate (PMA), and Histopaque 1077 were purchased from Sigma-Aldrich Chemical Co. (St. Louis, MO, USA). Roswell Park Memorial Institute (RPMI) 1640 medium and penicillin−streptomycin solution were purchased from Mediatech (Herdon, VA, USA). Human neutrophil elastase, *N*-methylsuccinyl-Ala-Ala-Pro-Val-7-amino-4-methylcoumarin, ionomycin, and bovine serum albumin were purchased from EMD Biosciences (San Diego, CA, USA). Fetal bovine serum (FBS) was purchased from Atlas Biologicals (Fort Collins, CO, USA). Human IL-8 was purchased from Peprotech Inc. (Rocky Hill, NJ, USA). Tween-20 was from VWR (Radnor, PA, USA). Tris was from J. T. Baker (Phillipsburg, NJ, USA). Blasticidin S and zeocin were obtained from Invivogen (San Diego, CA, USA). Hanks' balanced salt solution (HBSS; 0.137 M NaCl, 5.4 mM KCl, 0.25 mM Na_2HPO_4, 0.44 mM KH_2PO_4, 4.2 mM $NaHCO_3$, 5.56 mM glucose, and 10 mM HEPES, pH 7.4) and G418 were from Life Technologies (Grand Island, NY, USA). HBSS containing 1.3 mM $CaCl_2$ and 1.0 mM $MgSO_4$ is designated $HBSS^+$; HBSS without ions Ca^{2+} and Mg^{2+} is designated $HBSS^-$.

Plant Material. Aerial parts of *A. kotuchovii* were collected at the end of the blossoming stage in August 2013 in the southern Altai on the Tarbagatai range at altitude 1709 m above sea level (latitude, N 49°03′52″; longitude, W 85°59′35″). The plant was identified by Dr. Yuriy Kotukhov, and voucher specimens were deposited at the Institute of Plant Biology and Biotechnology (Almaty, Kazakhstan). Plant components were air-dried for 7−10 days at room temperature away from direct sunlight. Weighed samples were cut under laboratory conditions before hydrodistillation.

Essential Oil Extraction. Two types of air-dried material (inflorescence+leaves or stems) were separately subjected to hydrodistillation for 3 h using a Clevenger type apparatus to yield essential oils. Conventional hydrodistillation is considered the primary method for essential oil extraction.[17] Although hydrodistillation could lead to artifacts when performed at higher temperatures over long hydrodistillation times at low pH,[18] we applied only conditions accepted by the European Pharmacopoeia (European Directorate for the Quality of Medicines, Council of Europe, Strasbourg, France, 2014) and thus avoided these artifacts. Solutions of the essential oils were made in DMSO (10 mg/mL stock solutions) for biological evaluation, and in *n*-hexane (10 % w/v) for gas-chromatographic analysis.

Gas Chromatography−Mass Spectrometry (GC-MS) Analysis. GC-MS analysis of the oils was carried out with an Agilent 5975 GC-MSD system, as reported previously.[19,20] An Innowax FSC column (60 m × 0.25 mm, 0.25 μm film thickness) was used with He as carrier gas (0.8 mL/min). GC oven temperature was kept at 60 °C for 10 min, increased to 220 °C at a rate of 4 °C/min, kept constant at 220 °C for 10 min, and then increased to 240 °C at a rate of 1 °C/min. The split ratio was adjusted to 40:1, and the injector temperature was at 250 °C. MS were taken at 70 eV. Mass range was from m/z 35 to 450.

GC analysis was carried out using an Agilent 6890N GC system. To obtain the same elution order as with GC-MS, simultaneous injection was performed using the same column and appropriate operational conditions. Flame ionization detector (FID) temperature was 300 °C. The components of essential oils were identified by co-injection with standards (whenever possible), which were purchased from commercial sources or isolated from natural sources. In addition, compound identities were confirmed by comparison of their mass spectra with those in the Wiley GC/MS Library (Wiley, New York), MassFinder software 4.0 (Dr. Hochmuth Scientific Consulting, Hamburg, Germany), Adams Library, and NIST Library. A C_8−C_{40} *n*-alkane standard solution (Fluka, Buchs, Switzerland) was used to spike the samples for the determination of relative retention indices (RRI). Relative percentage amounts of the separated compounds were calculated from FID chromatograms.

Cell Culture. Human MonoMac-6 monocytic cells (DSMZ, Germany) were grown in RPMI 1640 supplemented with 10% (v/v) endotoxin-free FBS, 10 μg/mL bovine insulin, 100 μg/mL streptomycin, and 100 U/mL penicillin. Human monocytic THP-1Blue cells obtained from InvivoGgen were cultured in RPMI 1640 medium supplemented with 10% (v/v) endotoxin-free FBS, 100 μg/mL streptomycin, 100 U/mL penicillin, 100 μg/mL zeocin, and 10 μg/mL blasticidin S. These cells are stably transfected with a secreted embryonic alkaline phosphatase gene that is under the control of a promoter inducible by NF-κB and AP-1. Human promyelocytic leukemia HL-60 cells stably transfected with human FPR1 (FPR1-HL60 cells) were cultured in RPMI-1640 medium supplemented with 10% heat-inactivated fetal calf serum, 10 mM HEPES, 100 μg/mL streptomycin, 100 U/mL penicillin, and G418 (1 mg/mL).[15]

Measurement of TNF Production. MonoMac-6 cells were plated in culture medium supplemented with 3% (v/v) endotoxin-free FBS in 96-well plates at a density of 2×10^5 cells in 100 μL per well. The cells were pretreated with or without essential oil or DMSO (vehicle control) for 30 min, followed by treatment with LPS (200 ng/mL) and incubation for 24 h at 37 °C and 5% CO_2. An enzyme-linked immunosorbent assay kit for human tumor necrosis factor (TNF) (Biolegend; San Diego, CA, USA) was used to measure cytokine levels in the cell supernatants.

Analysis of NF-κB/AP-1 Activation. Activation of NF-κB/AP-1 transcriptional activity was measured using an alkaline phosphatase reporter gene assay in THP1-Blue cells (2×10^5 cells in 100 μL per well). The cells were pretreated with or without essential oil or DMSO (vehicle control) for 30 min, followed by treatment with LPS (200 ng/mL) and incubation for 24 h at 37 °C and 5% CO_2. Alkaline phosphatase activity was measured in cell supernatants using QUANTI-Blue mix (Invivogen). Activation of NF-κB is reported as absorbance at 655 nm and compared with positive control samples (LPS).

Human Neutrophil Elastase (HNE) Inhibition Assay. Essential oils and individual compounds were dissolved in 100% DMSO at 5 mM stock concentrations. The final concentration of DMSO in the reactions was 1%, and this level of DMSO had no effect on enzyme activity. One of our previously described HNE inhibitors (compound **5b**) was used as a positive control.[21] The inhibition assay was performed, as described previously.[22] Briefly, a buffer solution

DOI: 10.1021/acs.jafc.5b01307
J. Agric. Food Chem. 2015, 63, 4999−5007

Table 1. Composition of the Volatile Compounds Identified in the Essential Oils from *A. kotuchovii*[a]

compd no.	RRI	compound name	A (%)	B (%)	compd no.	RRI	compound name	A (%)	B (%)
1	1032	**α-pinene**[b]	0.6	0.6	**9**	1783	β-sesquiphellandrene[c]	0.2	0.2
2	1035	α-thujene[c]	tr	tr	**60**	1786	*ar*-curcumene[c]	0.1	0.1
3	1093	**hexanal**[b]	tr	0.1	**61**	1798	methyl salicylate[b]		tr
4	1118	**β-pinene**[b]	0.9	1.0	**62**	1804	myrtenol[b]		tr
5	1132	**sabinene**[b]	0.3	0.3	**63**	1815	2,6-dimethyl-3(*E*),5(*Z*),7-octatrien-2-ol[c]	tr	tr
6	1174	**myrcene**[b]	1.5	0.7	**64**	1827	(*E*,*E*)-2,4-decadienal		tr
7	1188	**α-terpinene**[b]	tr	0.4	**65**	1830	2,6-dimethyl-3(*E*),5(*E*),7-octatrien-2-ol[c]	0.1	tr
8	1195	dehydro-1,8-cineole[c]	tr	0.1	**66**	1845	**(*E*)-anethole**[b]	tr	0.1
9	1203	**limonene**[b]	1.0	1.0	**67**	1857	geraniol[b]		tr
10	1218	β-phellandrene[c]	0.2	0.1	**68**	1864	***p*-cymen-8-ol**[b]	0.1	tr
11	1244	amylfuran[c]	tr	tr	**69**	1868	(*E*)-geranyl acetone[b]	tr	tr
12	1246	**(*Z*)-β-ocimene**[b]	3.9	3.8	**70**	1885	1-phenyl-3-methylpenta-1,2,4-triene[c]	0.1	
13	1255	γ-terpinene[b]	tr	tr	**71**	1893	(*Z*)-methyl cinnamate[c]	tr	tr
14	1266	**(*E*)-β-ocimene**[b]	5.3	4.4	**72**	1958	(*E*)-β-ionone[b]	tr	tr
15	1280	***p*-cymene**[b]	0.3	0.5	**73**	1988	**isopropyl myristate**[b]		0.1
16	1290	**terpinolene**[b]	0.3	0.1	**74**	1990	anisaldehyde[b]		tr
17	1348	6-methyl-5-hepten-2-one[b]		tr	**75**	2001	isocaryophyllene oxide[c]	tr	tr
18	1362	*cis*-rose oxide[c]		tr	**76**	2008	**caryophyllene oxide**[b]	0.4	0.2
19	1376	*trans*-rose oxide[c]		tr	**77**	2014	(*E*)-cinnamaldehyde[b]	tr	
20	1382	*cis*-alloocimene[c]	tr	tr	**78**	2030	**methyleugenol**[b]	4.3	4.6
21	1413	rose furan[c]	0.1	0.1	**79**	2037	salvial-4(14)-en-1-one[c]	tr	0.1
22	1416	4,8-dimethyl-1,3,7-nonatriene[c]	tr		**80**	2041	pentadecanal[c]		tr
23	1429	perillene[c]	tr	tr	**81**	2065	salviadienol[c]	tr	
24	1446	2,6-dimethyl-1,3(*E*),5(*Z*),7-octatetraene[c]	tr		**82**	2071	humulene epoxide-II[c]	tr	
25	1452	α,*p*-dimethylstyrene[b]	tr		**83**	2096	**(*E*)-methyl cinnamate**[b]	1.9	0.5
26	1452	1-octen-3-ol[b]		tr	**84**	2097	(*E*)-ethyl cinnamate[c]		tr
27	1458	*cis*-1,2-limonene epoxide[b]	tr		**85**	2124	zingiberenol[c]	tr	tr
28	1460	2,6-dimethyl-1,3(*E*),5(*E*),7-octatetraene[c]		tr	**86**	2131	hexahydrofarnesyl acetone[c]	tr	tr
29	1468	*trans*-1,2-limonene epoxide[c]	tr		**87**	2139	chavibetol[c]	tr	
30	1474	*trans*-sabinene hydrate[c]	tr		**88**	2144	spathulenol[c]	0.8	1.0
31	1476	(*Z*)-β-ocimene epoxide[c]	tr	tr	**89**	2179	3,4-dimethyl-5-pentylidene-2(5*H*)-furanone[c]		tr
32	1479	(*E*,*Z*)-2,4-heptadienal[c]	tr		**90**	2187	T-cadinol[c]	tr	tr
33	1487	isoneroloxide[c]	tr		**91**	2204	alismol[c]	0.1	0.2
34	1498	(*E*)-β-ocimene epoxide[c]	tr	tr	**92**	2214	*ar*-turmerol[c]	tr	
35	1520	3,5-octadien-2-one[c]	tr	tr	**93**	2228	isospathulenol[c]	tr	
36	1535	β-bourbonene[c]	tr		**94**	2232	α-bisabolol[b]	tr	
37	1541	benzaldehyde[b]	tr	tr	**95**	2245	elemicin[c]	0.2	0.1
38	1542	α-isocomene[c]		tr	**96**	2247	*trans*-α-bergamotol[c]	tr	0.1
39	1553	**linalool**[b]		0.2	**97**	2255	α-cadinol[c]	tr	
40	1586	pinocarvone[c]		tr	**98**	2257	β-eudesmol[b]		tr
41	1602	**6-methyl-3,5-heptadien-2-one (MHDO)**[b]		0.1	**99**	2259	eudesma-4(15),7-dien-1-ol[b]		0.1
42	1611	terpinen-4-ol[b]	tr	tr	**100**	2268	torilenol[c]	tr	tr
43	1612	β-caryophyllene[b]	0.1	tr	**101**	2269	(6*S*,7*R*)-bisabolone[c]		tr
44	1639	*trans*-*p*-mentha-2,8-dien-1-ol[c]	tr		**102**	2281	chavicol[c]	tr	
45	1670	benzeneacetaldehyde[b]	tr		**103**	2290	(2*E*,6*Z*)-farnesol[b]	tr	
46	1672	*trans*-pinocarveol[b]	tr		**104**	2375	eudesma-4(15),7-dien-1-β-ol[c]	0.1	0.1
47	1671	acetophenone[b]	tr		**105**	2300	tricosane[b]		tr
48	1687	α-humulene[b]	tr	tr	**106**	2309	farnesylacetone[b]	tr	
49	1687	estragole[b]	75.1	76.6	107	2360	6-dodecen-4-olide[c]	tr	
50	1694	*p*-vinylanisole[b]		0.1	108	2369	(2*E*,6*E*)-farnesol[b]		tr
51	1706	α-terpineol[b]	tr	0.1	**109**	2392	caryophylla-2(12),6-dien-5β-ol[c]	tr	
52	1726	α-zingiberene[c]		tr	**110**	2415	demethoxyencecaline[c]	0.1	0.1
53	1726	germacrene D[c]	0.2	0.1	**111**	2500	pentacosane[b]		tr
54	1733	neryl acetate[b]	tr		**112**	2528	(*E*)-*p*-methoxycinnamaldehyde[c]	tr	
55	1755	bicyclogermacrene[c]		tr	**113**	2622	phytol[b]	tr	
56	1765	geranyl acetate[b]	tr	tr	**114**	2670	**myristic acid**[b]	0.2	0.1
57	1772	**citronellol**[b]	tr	0.1	**115**	2700	heptacosane[b]		tr

DOI: 10.1021/acs.jafc.5b01307
J. Agric. Food Chem. 2015, 63, 4999−5007

Table 1. continued

compd no.	RRI	compound name	A (%)	B (%)	compd no.	RRI	compound name	A (%)	B (%)
58	1773	δ-cadinene[c]	tr		**116**	2931	**palmitic acid**[b]	tr	0.4

[a]The data are presented as relative % for components of essential oil from flowers+leaves (A) and essential oil from stems (B). RRI, relative retention indices calculated against *n*-alkanes; % calculated from flame ionization detector data. Trace amounts (tr) are present at <0.1%. [b]Identification based on comparison with co-injected with standards. [c]Tentatively identified using Wiley and MassFinder mass spectra libraries and published RRI. Compounds that were selected for further biological screening are indicated in bold.

containing 200 mM Tris-HCl, pH 7.5, 0.01% bovine serum albumin, and 0.05% Tween-20 and 20 mU/mL of human neutrophil elastase was added to black, flat-bottom 96-well microtiter plates containing different concentrations of test compounds. Reactions were initiated by the addition of 25 μM elastase substrate *N*-methylsuccinyl-Ala-Ala-Pro-Val-7-amino-4-methylcoumarin in a final reaction volume of 100 μL/well. Kinetic measurements were obtained every 30 s for 10 min at 25 °C using a Fluoroskan Ascent FL fluorescence microplate reader (Thermo Electron) with excitation and emission wavelengths at 355 and 460 nm, respectively. The concentration of inhibitor that caused 50% inhibition of the enzymatic reaction (IC_{50}) was calculated by plotting percent inhibition versus logarithm of inhibitor concentration.

Neutrophil Isolation. For isolation of human neutrophils, blood was collected from healthy donors in accordance with a protocol approved by the Institutional Review Board at Montana State University. Neutrophils were purified from the blood using dextran sedimentation, followed by Histopaque 1077 gradient separation and hypotonic lysis of red blood cells, as described previously.[15] Isolated neutrophils were washed twice and resuspended in HBSS. Neutrophil preparations were routinely >95% pure, as determined by light microscopy, and >98% viable, as determined by trypan blue exclusion.

Ca^{2+} Mobilization Assay. Changes in intracellular Ca^{2+} were measured with a FlexStation II scanning fluorometer using fluorescent dye Fluo-4AM (Invitrogen). Neutrophils or FPR1-HL60 cells, suspended in HBSS, were loaded with Fluo-4AM dye (final concentration, 1.25 μg/mL) and incubated for 30 min in the dark at 37 °C. After dye loading, the cells were washed with HBSS, resuspended in $HBSS^+$, separated into aliquots, and deposited into the wells of flat-bottom, half-area well black microtiter plates (2×10^5 cells/well). The compound source plate contained dilutions of test essential oil or pure compound in $HBSS^+$, and changes in fluorescence were monitored (λ_{ex} = 485 nm, λ_{em} = 538 nm) every 5 s for 240 s at room temperature after automated addition of compounds. Maximum change in fluorescence, expressed in arbitrary units over baseline, was used to determine agonist response. Responses were normalized to the response induced by 5 nM *f*MLF, which was assigned a value of 100%. Curve fitting (at least five or six points) and calculation of median effective concentration values (EC_{50} or IC_{50}) were performed by nonlinear regression analysis of the dose−response curves generated using Prism 5 (GraphPad Software, Inc., San Diego, CA, USA).

Chemotaxis Assay. Human neutrophils were suspended in $HBSS^+$ containing 2% (v/v) heat-inactivated fetal bovine serum (2×10^6 cells/mL), and chemotaxis was analyzed in 96-well ChemoTx chemotaxis chambers (Neuroprobe, Gaithersburg, MD, USA), as described previously.[23] In brief, neutrophils were preincubated with the indicated concentrations of the test sample (oil or pure compound) or DMSO for 30 min at room temperature and added to the upper wells of the ChemoTx chemotaxis chambers. The lower wells were loaded with 30 μL of $HBSS^+$ containing 2% (v/v) FBS and the indicated concentrations of test sample, DMSO (negative control), or 1 nM *f*MLF as a positive control. Neutrophils were added to the upper wells and allowed to migrate through the 5.0 μm pore polycarbonate membrane filter for 60 min at 37 °C and 5% CO_2. The number of migrated cells was determined by measuring ATP in lysates of transmigrated cells using a luminescence-based assay (CellTiter-Glo; Promega, Madison, WI, USA), and luminescence measurements were converted to absolute cell numbers by comparison of the values with standard curves obtained with known numbers of neutrophils. Curve fitting (at least eight or nine points) and calculation of median effective concentration values (IC_{50}) were performed by nonlinear regression analysis of the dose−response curves generated using Prism 5.

ROS Production. ROS production was determined by monitoring L-012-enhanced chemiluminescence, which represents a sensitive and reliable method for detecting superoxide anion ($O_2^{\bullet-}$) production.[23] Human neutrophils were resuspended at 2×10^5 cells/mL in $HBSS^+$ supplemented with 40 μM L-012. Cells (100 μL) were aliquoted into wells of 96-well flat-bottom microtiter plates containing essential oil or compounds at different concentrations (final DMSO concentration, 1%). Cells were preincubated for 30 min, and 200 nM PMA was added to each well to stimulate ROS production. Luminescence was monitored for 60 min (2 min intervals) at 37 °C using a Fluoroscan Ascent FL microtiter plate reader (Thermo Electron, Waltham, MA, USA). The curve of light intensity (in relative luminescence units) was plotted against time, and the area under the curve was calculated as total luminescence. The compound concentration that inhibited ROS production by 50% of the PMA-induced response (positive control) was determined by graphing the percentage inhibition of ROS production versus the logarithm of concentration of test sample (IC_{50}). Each curve was determined using five to seven concentrations.

Compound Cytotoxicity. Cytotoxicity was analyzed with a CellTiter-Glo Luminescent Cell Viability Assay Kit (Promega), according to the manufacturer's protocol. Briefly, MonoMac-6 cells were cultured at a density of 1×10^5 cells/well with different concentrations of essential oil or compound for 4 or 24 h at 37 °C and 5% CO_2. Following treatment, the cells were allowed to equilibrate to room temperature for 30 min, substrate was added, and the samples were analyzed with a Fluoroscan Ascent FL microplate reader.

RESULTS

Composition of the Essential Oils from *A. kotuchovii*. Essential oils were obtained by conventional hydrodistillation of the dried stems or flowers+leaves of *A. kotuchovii* (designated $AKEO_{stm}$ and $AKEO_{f/l}$, respectively) and analyzed by GC and GC-MS techniques simultaneously to determine their chemical compositions. Hydrodistillation of the stems and flowers+leaves produced 0.096 and 1.010% (v/w on the basis of the weight of dried material) essential oils, respectively. The main constituents of $AKEO_{f/l}$ and $AKEO_{stm}$ were estragole (75.1 and 76.6%), (*E*)- and (*Z*)-β-ocimene (9.2 and 8.2%), methyleugenol (4.3 and 4.6%), limonene (1.0 and 1.0%), spathulenol (0.8 and 1.0%), β-pinene (0.9 and 1.0%), myrcene (1.5 and 0.7%), and (*E*)-methyl cinnamate (1.9 and 0.5%, respectively). Seventy-four constituents were present at concentrations from 0.1 to <1.0% in one or both plant sources. The remaining 34 volatile compounds were identified in trace amounts, and their relative percentage amounts are indicated in Table 1. Thus, the major components of the $AKEO_{f/l}$ and $AKEO_{stm}$ are phenylpropanoids (81.5 and 79.6%, respectively) and monoterpene hydrocarbons (13.0 and 14.4%, respectively). Sesquiterpenes compose around 2−2.2% in both plant components. It should be noted that $AKEO_{stm}$ had more oxygenated monoterpenes and fatty acids compared to $AKEO_{f/l}$ (0.5 vs 0.1% and 0.5 vs 0.2%, respectively).

Evaluation of Essential Oil Effect on Phagocyte Function. The essential oils from *A. kotuchovii* were screened

DOI: 10.1021/acs.jafc.5b01307
J. Agric. Food Chem. 2015, 63, 4999−5007

for modulatory activity in various cell and enzymatic systems related to mechanisms of innate immunity (Table 2). Essential oils and their components have been reported previously to modulate intracellular Ca^{2+} levels[24] and inhibit leukocyte migration.[25,26] We found that $AKEO_{stm}$, but not $AKEO_{f/l}$, inhibited *f*MLF-stimulated Ca^{2+} flux and *f*MLF-induced chemotaxis in human neutrophils, with IC_{50} values of 12.5 and 10.1 μg/mL, respectively (Figure 1 and Table 2). Recently, several essential oils were reported to modulate ROS production in neutrophils.[27,28] Thus, we evaluated the effect of $AKEO_{stm}$ and $AKEO_{f/l}$ on PMA-induced ROS production by human neutrophils and found that $AKEO_{stm}$ inhibited ROS production with an IC_{50} of 49.2 μg/mL, whereas $AKEO_{f/l}$ had no activity (Table 2). Although some essential oils and their components were previously identified as HNE inhibitors,[29] evaluation of $AKEO_{stm}$ and $AKEO_{f/l}$ showed that they did not inhibit HNE, even at concentrations up to 50 μg/mL.

Table 2. Biological Screening of the Essential Oils from *A. kotuchovii*

biological activity	IC_{50} (μg/mL)	
	$AKEO_{f/l}$	$AKEO_{stm}$
LPS-induced NF-κB/AP-1 activity in THP-1Blue cells	NA[a]	NA
LPS-induced TNF production in MonoMac-6 cells	NA	NA
neutrophil elastase enzymatic activity	NA	NA
*f*MLF-induced Ca^{2+} flux in human neutrophils[b]	NA	12.5 ± 2.7
*f*MLF-induced chemotaxis in human neutrophils[c]	NA	10.1 ± 3.1
PMA-induced ROS production in human neutrophils[d]	NA	49.2 ± 5.4

[a]NA, no activity was observed, even at the highest concentration tested (50 μM). [b]Activity was evaluated as inhibition of Ca^{2+} flux induced by 5 nM *f*MLF in neutrophils. [c]Inhibition of chemotactic activity in neutrophils was evaluated in the presence of 0.5 nM *f*MLF. [d]Inhibition of ROS production in neutrophils was evaluated in the presence of 200 nM PMA and 40 μM L-012.

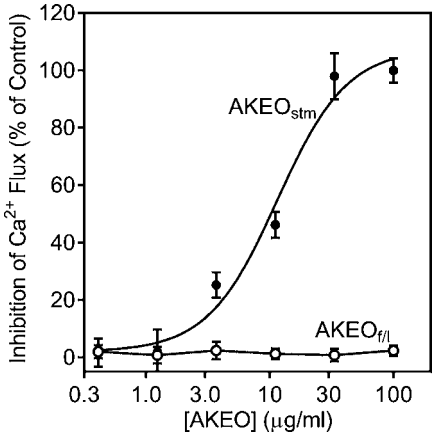

Figure 1. Effect of essential oils from *A. kotuchovii* on Ca^{2+} mobilization in human neutrophils. Neutrophils were preincubated with the indicated concentrations of essential oils isolated from stems ($AKEO_{stm}$) (solid circles) and flowers+leaves ($AKEO_{f/l}$) (open circles) of *A. kotuchovii* for 30 min at 25 °C and then stimulated with 5 nM *f*MLF. The response induced by the peptide agonist alone was assigned a value of 100%. Values are the mean ± SD of triplicate samples from one experiment that is representative of three independent experiments.

Because various essential oils have been reported to inhibit NF-κB/AP-1 transcriptional activity and production of pro-inflammatory cytokines,[30,31] we also evaluated the effects of $AKEO_{stm}$ and $AKEO_{f/l}$ on these responses using cultures of monocytic cells. However, we found that $AKEO_{stm}$ and $AKEO_{f/l}$ did not alter NF-κB/AP-1 activity or TNF production in monocytic cells (Table 2).

Although our functional cell-based assays suggested that the essential oils were relatively nontoxic, we evaluated their potential cytotoxic effects to determine if the results might be influenced by background cytotoxicity. Using a cytotoxicity assay, we determined that neither of the essential oils significantly affected the viability of MonoMac-6 cells over a concentration range up to 50 μg/mL, further demonstrating that $AKEO_{stm}$ and $AKEO_{f/l}$ were not cytotoxic (data not shown).

Effect of $AKEO_{stm}$ Components on Neutrophil Function. Because $AKEO_{stm}$ inhibited neutrophil functional responses, we focused on analysis of the effects of $AKEO_{stm}$ constituents to possibly identify the active compound(s). Twenty-five commercially available components of $AKEO_{stm}$, including 8 major (≥1%) and 17 minor compounds, were tested. Note that among the minor constituents tested, hexanal, α-terpinene, *p*-cymene, MHDO, (*E*)-anethole, isopropyl myristate, and palmitic acid were all present at higher levels in $AKEO_{stm}$ compared to $AKEO_{f/l}$ (Table 1).

All selected compounds were evaluated for agonist and antagonist effects on Ca^{2+} flux in human neutrophils. We found that four compounds from different chemical classes, including β-pinene, sabinene, palmitic acid, and myristic fatty acid, had direct but weak agonist activity, as determined by monitoring Ca^{2+} flux (Table 3). Of all of the component compounds tested, only MHDO inhibited *f*MLF-stimulated Ca^{2+} mobilization in neutrophils (IC_{50} = 8.2 μM), which is far below our common hit threshold of 50 μM,[15] and this inhibition was concentration-dependent (Table 2 and Figure 2A). MHDO did not directly activate Ca^{2+} flux, suggesting it was not down-regulating the subsequent response to *f*MLF but was directly inhibiting *f*MLF-stimulated Ca^{2+} mobilization via a different mechanism. Furthermore, MHDO inhibited Ca^{2+} flux in *f*MLF-stimulated FPR1-HL60 cells (Table 2) and IL-8-induced Ca^{2+} mobilization in human neutrophils (IC_{50} = 3.2 μM) (Figure 2B). On the other hand, MHDO did not inhibit nonspecific Ca^{2+} flux induced by 10 μM ionomycin (data not shown). Thus, these data indicate that MHDO can modulate intracellular signaling pathways that are common to both FPR1 and CXCR1/2 chemokine receptors, but it is not an ion channel inhibitor or a calcium chelator.

Consistent with its effect on Ca^{2+} mobilization, MHDO also inhibited neutrophil chemotaxis with an IC_{50} in the low micromolar range (Table 3). Among the other compounds tested, β-pinene, sabinene, β-citronellol, and elemicin were weak inhibitors of neutrophil chemotaxis (Table 3).

All 25 compounds were also evaluated for their effect on neutrophil ROS production. As with the other responses, only MHDO inhibited PMA-induced ROS production in human neutrophils (IC_{50} = 2.8 μM) (Table 3).

To ensure that the results on inhibition of Ca^{2+} flux and neutrophil chemotaxis were not influenced by possible compound toxicity, cytotoxicity of MHDO was evaluated at various concentrations (up to 100 μM) in MonoMac-6 cells during a 4 h incubation, which is relevant for relatively short times used to measure Ca^{2+} mobilization (up to 35 min) and

DOI: 10.1021/acs.jafc.5b01307
J. Agric. Food Chem. 2015, 63, 4999−5007

Table 3. Effect of Selected Volatile Compounds on Functional Responses in Human Neutrophil and FPR1-HL60 Cells

	Ca^{2+} flux (μM (μg/mL))				
	neutrophils		FPR1-HL60 cells		
compound name	activation (EC_{50})	inhibition[a] (IC_{50})	inhibition[a] (IC_{50})	inhibition of chemotaxis[b] (IC_{50}) (μM (μg/mL))	inhibition of ROS production[c] (IC_{50}) (μM (μg/mL))
(1*R*)-(+)-α-pinene	NA[d]	NA	NA	NA	NA
hexanal	NA	NA	NA	NA	NA
β-pinene	23.8 ± 3.1 (3.2 ± 0.4)	NA	NA	22.7 ± 2.6 (3.1 ± 0.4)	NA
sabinene (±)	49.4 ± 6.3 (6.7 ± 0.86)	N.A.	N.A.	37.4 ± 4.3 (5.1 ± 0.6)	N.A.
myrcene	NA	NA	NA	NA	NA
α-terpinene	NA	NA	NA	NA	NA
(*R*)-(+)-limonene	NA	NA	NA	NA	NA
(*S*)-(−)-limonene	NA	NA	NA	NA	NA
(*E*/*Z*)-β-ocimene	NA	NA	NA	NA	NA
p-cymene	NA	NA	NA	NA	NA
terpinolene	NA	NA	NA	NA	NA
(−)-linalool	NA	NA	NA	NA	NA
MHDO	NA	8.2 ± 2.5 (1.02 ± 0.31)	18.0 ± 5.4 (2.2 ± 0.7)	3.6 ± 0.5 (0.45 ± 0.16)	2.8 ± 0.4 (0.35 ± 0.05)
estragol	NA	NA	NA	NA	NA
4-vinylanisole	NA	NA	NA	NA	NA
(±)-β-citronellol	NA	NA	NA	48.6 ± 3.7 (7.6 ± 0.6)	NA
(*E*)-anethole	NA	NA	NA	NA	NA
p-cymen-8-ol	NA	NA	NA	NA	NA
isopropyl myristate	NA	NA	NA	NA	NA
(−)-caryophyllene oxide	NA	NA	NA	NA	NA
methyleugenol	NA	NA	NA	NA	NA
(*E*)-methyl cinnamate	NA	NA	NA	NA	NA
elemicine	NA	NA	NA	46.9 ± 4.2 (9.8 ± 0.9)	NA
myristic acid	46.7 ± 5.3 (10.7 ± 1.2)	NA	12.9 ± 3.4 (3.0 ± 0.8)	NA	NA
palmitic acid	40.7 ± 4.6 (10.4 ± 1.2)	NA	NA	NA	NA

[a]Inhibition of Ca^{2+} flux induced by 5 nM *f*MLF. [b]Inhibition of chemotactic activity in neutrophils was evaluated in the presence of 0.5 nM *f*MLF. [c]Inhibition of ROS production in neutrophils was evaluated in the presence of 200 nM PMA and 40 μM L-012. [d]NA, no activity was observed, even at the highest concentration tested (50 μM).

chemotaxis (up to 90 min). As shown in Figure 3, MHDO did not affect cell viability, even at the highest tested concentration, thereby verifying that this compound, like the parent essential oil, was also not cytotoxic, at least during the 4 h incubation period.

DISCUSSION

Essential oils are natural mixtures of terpenes, mainly monoterpenes and sesquiterpenes, which have a wide range of pharmacological activities.[11,32−34] Furthermore, essential oils from various plants, including *Artemisia* spp., have been reported to exhibit various biological effects in vitro and in vivo.[2,35] In the present study, we defined the chemical profile of essential oils isolated from *A. kotuchovii* and evaluated their effects on phagocyte function.

Similar to the composition of essential oils from *A. dracunculus*,[1] we found that estragole, (*E*)- and (*Z*)-β-ocimenes, and methyleugenol were the primary constituents of *A. kotuchovii* essential oils. Other primary constituents present at lower concentrations (1−1.9% total weight) were limonene, spathulenol, β-pinene, myrcene, and methyl cinnamate. These compounds, with the exception of methyl cinnamate, are also present in tarragon essential oils.[1,36]

Although various essential oils have previously been found to inhibit NF-κB/AP-1 transcription and production of pro-inflammatory cytokines[5,30] and HNE activity,[29,37] we did not find these activities in *A. kotuchovii* essential oils. Indeed, none of the major components of *A. kotuchovii* essential oils (>1% by total weight) have been reported previously to inhibit HNE, NF-κB/AP-1 activity, or TNF production. Among the minor compounds (~1%), only limonene has been reported to inhibit NF-κB activation in vivo during acute lung injury.[38]

Evaluation of biological activities of *A. kotuchovii* essential oils revealed that only $AKEO_{stm}$ inhibited Ca^{2+} flux and chemotaxis in human neutrophils. To date, there are no publications on the modulation of Ca^{2+} mobilization in neutrophils by essential oils. Because intercellular Ca^{2+} flux is involved in chemotaxis, the inhibitory effect of $AKEO_{stm}$ on neutrophil chemotaxis is likely

DOI: 10.1021/acs.jafc.5b01307
J. Agric. Food Chem. 2015, 63, 4999−5007

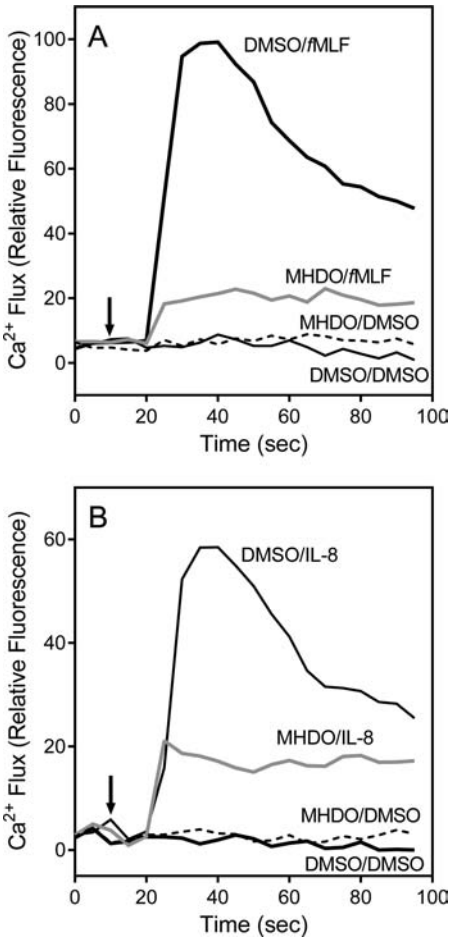

Figure 2. Effect of MHDO on *f*MLF-induced Ca^{2+} mobilization in human neutrophils. (A) Human neutrophils were preincubated for 30 min (at 25 °C) with 15 μM MHDO or DMSO (vehicle control), followed by treatment with 5 nM *f*MLF or DMSO (vehicle control). (B) Effect of MHDO on IL-8-induced Ca^{2+} mobilization in human neutrophils. Human neutrophils were preincubated for 30 min (at 25 °C) with 15 μM MHDO or DMSO (vehicle control), followed by treatment with 25 nM IL-8 or DMSO (vehicle control). Arrows indicate time of treatment additions. The data shown in both panels are representative of three independent experiments.

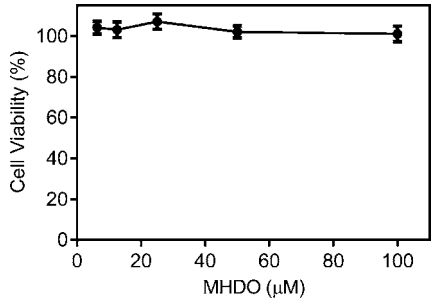

Figure 3. Effect of MHDO on cell viability. MonoMac-6 cells were incubated for 4 h with the indicated concentrations of MHDO, and cell viability was determined using a luminescent cell viability assay kit, as described. Values are the mean ± SD of triplicate samples from one experiment that is representative of two independent experiments. No statistically significant differences between untreated cells (DMSO alone) and cells treated with the compound were found.

due to a primary effect on Ca^{2+} flux. Previously, other essential oils or their constituents have been reported to inhibit cell migration. For example, rosemary and geranium essential oils inhibited leukocyte recruitment and chemotaxis.[39,40] In addition, *Thymus vulgaris* L. and *Citrus latifolia* (Yu. Tanaka) Tanaka essential oils also inhibited leukocyte migration.[25,41] Although we found that $AKEO_{stm}$ also inhibited PMA-induced ROS production in human neutrophils, the potency of this effect was relatively low compared to that of essential oils from *Sideritis italica* (Miller) Greuter et Burdet.[27]

To further define the active component(s) in $AKEO_{stm}$, we evaluated 25 of its constituents and found that β-citronellol, elemicin, β-pinene, and sabinene had low activity, whereas MHDO was a relatively potent inhibitor of neutrophil chemotaxis (Table 3), suggesting that it could be one of the primary essential oil components responsible for the inhibitory effects of $AKEO_{stm}$ on human neutrophils in vitro (Table 2). Indeed, only MHDO inhibited the other neutrophil responses tested (i.e., PMA-induced ROS production and *f*MLF- and IL-8-induced Ca^{2+} flux). Furthermore, MHDO was not present in $AKEO_{f/l}$ (Table 1). Thus, these data provide a molecular basis to explain at least part of the inhibitory activity of $AKEO_{stm}$ on neutrophil chemotaxis. However, on the basis of the molecular weight of MHDO (124.18 Da), its relative percentage (~0.1%) in $AKEO_{stm}$, and the IC_{50} values for biological activities of $AKEO_{stm}$ (~10−50 μg/mL) (see Tables 1 and 2), effective concentrations of this component would be in the range of 0.08−0.4 μM, which is several-fold lower than the IC_{50} values for the biological activity profiles of MHDO (2.8−8.2 μM, see Table 3). Thus, we could not exclude possible synergetic effects of other minor compounds, which are higher in $AKEO_{stm}$ (dehydro-1,8-cineole, *trans*-α-bergamotol, etc.) versus $AKEO_{f/l}$. Because β-pinene and sabinene directly activated Ca^{2+} mobilization in neutrophils, albeit with low efficacy, it is possible that they could contribute to receptor desensitization and/or intracellular Ca^{2+} store depletion. Recently, Siani et al.[42] reported that effective inhibition of eosinophil migration by essential oils from *Syzygium cumini* Skells and *Psidium guajava* L. correlated with the presence of β-pinene. Because α-pinene was completely inactive in all of our test systems (Table 3), we suggest that human neutrophils can discriminate between α- and β-isomers of this bicyclic monoterpene. In support of this isomer preference, α-pinene inhibited inflammatory pathways in human chondrocytes, whereas β-pinene was inactive.[43] Thus, various cell and/or molecular targets may determine the potency of the biological activities of these isomers.

Although previous papers indicate estragole and limonene can inhibit neutrophil and eosinophil migration,[25,26,44] we did not observe inhibition of neutrophil function by *R*- and *S*-enantiomers of limonene. Likewise, we did not observe any effects of anethole on neutrophil function, although it was reported to inhibit paw edema in mice in acute and persistent inflammation models.[45] These discrepancies may be explained by differences in methodologies and species specificity. For example, Kummer et al.[26] used murine neutrophils, which respond differently from human neutrophils to *f*MLF and other agonists.

Neutrophils express a large number of receptors for the recognition of pathogen invasion and communication, including chemosensory, chemoattractant, and chemokine GPCR, Fc-receptors, various cytokine receptors, and adhesion receptors as well as innate immune receptors, such as Toll-like receptors.[46,47] Here, we found that MHDO inhibited both *f*MLF- and IL-8-induced Ca^{2+} fluxes in neutrophils and the *f*MLF-induced response in FPR1-HL60 cells. Thus, MHDO may

DOI: 10.1021/acs.jafc.5b01307
J. Agric. Food Chem. 2015, 63, 4999−5007

interfere with intracellular signaling pathways common for both FPR1 and CXCR1/2. Nevertheless, further studies will be necessary to determine the precise molecular targets for MHDO in human neutrophils. It should be noted that MHDO is found in paprika and tomato oleoresins[48] and can be formed by thermal degradation of lycopene (ψ,ψ-carotene),[49] a red pigment of some fruits and vegetables. Although there are many publications describing the anti-inflammatory and antioxidant effects of lycopene,[50] our studies suggest that inhibition of leukocyte activation and/or migration could also contribute to the biological effects of paprika and tomato oleoresins, including lycopene metabolites and products of its thermal degradation.

In summary, we have defined the essential oil composition of *A. kotuchovii* and shown that these essential oils and a primary component compound are able to inhibit human neutrophil responses, including Ca^{2+} mobilization, chemotaxis, and ROS production. Further studies are now needed to determine the molecular targets for MHDO, as well as the biological activity of other minor constituents of the oil and evaluation of therapeutic efficacy of $AKEO_{stm}$ and MHDO in animal models of acute or chronic inflammatory diseases.

AUTHOR INFORMATION

Corresponding Author

*(M.T.Q.) Phone: (406) 994-4707. Fax: (406) 994-4303. E-mail: mquinn@montana.edu.

Funding

This research was supported in part by National Institutes of Health IDeA Program COBRE Grant GM110732; Grants 0504/GF3 and 2117/GF4 from The Ministry of Education and Science, Kazakhstan; a USDA National Institute of Food and Agriculture Hatch project; and the Montana State University Agricultural Experiment Station.

Notes

The authors declare no competing financial interest.

ACKNOWLEDGMENTS

We thank Professor Andrei Khlebnikov, Tomsk Polytechnic University, Tomsk, Russia, for advice on compound structure interpretation.

ABBREVIATIONS USED

AKEO, essential oils of *A. kotuchovii*; DMSO, dimethyl sulfoxide; fetal bovine serum, FBS; FID, flame ionization detector; FPR1, *N*-formyl peptide receptor 1; GC, gas chromatography; GPCR, G-protein coupled receptors; HBSS, Hanks' balanced salt solution; HNE, human neutrophil elastase; IL, interleukin; LPS, lipopolysaccharide; MHDO, 6-methyl-3,5-heptadien-2-one; MS, mass spectrometry; PMA, phorbol-12-myristate-13-acetate; ROS, reactive oxygen species; TNF, tumor necrosis factor

REFERENCES

(1) Obolskiy, D.; Pischel, I.; Feistel, B.; Glotov, N.; Heinrich, M. *Artemisia dracunculus* L. (tarragon): a critical review of its traditional use, chemical composition, pharmacology, and safety. *J. Agric. Food Chem.* **2011**, *59*, 11367−11384.

(2) Abad, M. J.; Bedoya, L. M.; Apaza, L.; Bermejo, P. The *Artemisia* L. genus: a review of bioactive essential oils. *Molecules* **2012**, *17*, 2542−2566.

(3) Mubashir, K.; Ganai, B. A.; Ghazanfar, K.; Akbar, S.; Malik, A. H.; Masood, A. Evaluation of *Artemisia amygdalina* D. for anti-inflammatory and immunomodulatory potential. *ISRN Inflammation* **2013**, *2013*, No. 483646.

(4) Moufid, A.; Eddouks, M. *Artemisia herba* alba: a popular plant with potential medicinal properties. *Pak. J. Biol. Sci.* **2012**, *15*, 1152−1159.

(5) Yoon, W. J.; Moon, J. Y.; Song, G.; Lee, Y. K.; Han, M. S.; Lee, J. S.; Ihm, B. S.; Lee, W. J.; Lee, N. H.; Hyun, C. G. *Artemisia fukudo* essential oil attenuates LPS-induced inflammation by suppressing NF-κB and MAPK activation in RAW 264.7 macrophages. *Food Chem. Toxicol.* **2010**, *48*, 1222−1229.

(6) Cha, J. D.; Moon, S. E.; Kim, H. Y.; Lee, J. C.; Lee, K. Y. The essential oil isolated from *Artemisia capillaris* prevents LPS-induced production of NO and PGE(2) by inhibiting MAPK-mediated pathways in RAW 264.7 Macrophages. *Immunol. Invest.* **2009**, *38*, 783−497.

(7) Li, T.; Chen, H.; Wei, N.; Mei, X.; Zhang, S.; Liu, D. L.; Gao, Y.; Bai, S. F.; Liu, X. G.; Zhou, Y. X. Anti-inflammatory and immunomodulatory mechanisms of artemisinin on contact hypersensitivity. *Int. Immunopharmacol.* **2012**, *12*, 144−150.

(8) Ho, W. E.; Peh, H. Y.; Chan, T. K.; Wong, W. S. Artemisinins: pharmacological actions beyond anti-malarial. *Pharmacol. Ther.* **2014**, *142*, 126−139.

(9) Kupriyanov, A. N. New species of genus *Artemisia* (Asteraceae) from Altay and Kazakhstan. *Artemisia kotuchovii* Kupr. Sp. nov. *Botanical J.* **1999**, *84*, 114−116.

(10) Vandanmagsar, B.; Haynie, K. R.; Wicks, S. E.; Bermudez, E. M.; Mendoza, T. M.; Ribnicky, D.; Cefalu, W. T.; Mynatt, R. L. *Artemisia dracunculus* L. extract ameliorates insulin sensitivity by attenuating inflammatory signalling in human skeletal muscle culture. *Diabetes, Obes. Metab.* **2014**, *16*, 728−738.

(11) Perez-Roses, R.; Risco, E.; Vila, R.; Penalver, P.; Canigueral, S. Effect of some essential oils on phagocytosis and complement system activity. *J. Agric. Food Chem.* **2015**, *63*, 1496−1504.

(12) Beyrau, M.; Bodkin, J. V.; Nourshargh, S. Neutrophil heterogeneity in health and disease: a revitalized avenue in inflammation and immunity. *Open Biol.* **2012**, *2*, No. 120134.

(13) Bokoch, G. M. Chemoattractant signaling and leukocyte activation. *Blood* **1995**, *86*, 1649−1660.

(14) Maeda, D. Y.; Quinn, M. T.; Schepetkin, I. A.; Kirpotina, L. N.; Zebala, J. A. Nicotinamide glycolates antagonize CXCR2 activity through an intracellular mechanism. *J. Pharmacol. Exp. Ther.* **2010**, *332*, 145−152.

(15) Schepetkin, I. A.; Kirpotina, L. N.; Khlebnikov, A. I.; Cheng, N.; Ye, R. D.; Quinn, M. T. Antagonism of human formyl peptide receptor 1 (FPR1) by chromones and related isoflavones. *Biochem. Pharmacol.* **2014**, *92*, 627−641.

(16) Ryoo, I. J.; Yun, B. S.; Lee, I. K.; Kim, Y. H.; Lee, I. S.; Ahn, J. S.; Bae, K.; Yoo, I. D. Hydoroxyhibiscone A, a novel human neutrophil elastase inhibitor from *Hibiscus syriacus*. *J. Microbiol. Biotechnol.* **2010**, *20*, 1189−1191.

(17) Kubeczka, K.-H. History and sources of essential oil research. In *Handbook of Essential Oils: Science, Technology and Applications*, Baser, K. H. C., Buchbauer, G., Eds.; CRC Press Taylor & Francis Group: Boca Raton, FL, USA, 2010; pp 3−30.

(18) Mastelic, J.; Politeo, O.; Jerkovic, I. Contribution to the analysis of the essential oil of *Helichrysum italicum* (Roth) G. Don. Determination of ester bonded acids and phenols. *Molecules* **2008**, *13*, 795−803.

(19) Ali, A.; Tabanca, N.; Özek, G.; Özek, T.; Aytac, Z.; Bernier, U. R.; Agramonte, N. M.; Baser, K. H. C.; Khan, I. A. Essential oils of *Echinophora lamondiana* (Apiales: Umbelliferae): a relationship between chemical profile and biting deterrence and larvicidal activity against mosquitoes (Diptera: Culicidae). *J. Med. Entomol.* **2015**, *52*, 93−100.

(20) Özek, G.; Demirci, F.; Özek, T.; Tabanca, N.; Wedge, D. E.; Khan, S. I.; Baser, K. H.; Duran, A.; Hamzaoglu, E. Gas chromatographic-mass spectrometric analysis of volatiles obtained by four different techniques from *Salvia rosifolia* Sm., and evaluation for biological activity. *J. Chromatogr. A* **2010**, *1217*, 741−748.

DOI: 10.1021/acs.jafc.5b01307
J. Agric. Food Chem. 2015, 63, 4999−5007

(21) Crocetti, L.; Schepetkin, I. A.; Cilibrizzi, A.; Graziano, A.; Vergelli, C.; Giomi, D.; Khlebnikov, A. I.; Quinn, M. T.; Giovannoni, M. P. Optimization of *N*-benzoylindazole derivatives as inhibitors of human neutrophil elastase. *J. Med. Chem.* **2013**, *56*, 6259−72.
(22) Schepetkin, I. A.; Khlebnikov, A. I.; Quinn, M. T. *N*-Benzoylpyrazoles are novel small-molecule inhibitors of human neutrophil elastase. *J. Med. Chem.* **2007**, *50*, 4928−4938.
(23) Schepetkin, I. A.; Kirpotina, L. N.; Khlebnikov, A. I.; Quinn, M. T. High-throughput screening for small-molecule activators of neutrophils: identification of novel *N*-formyl peptide receptor agonists. *Mol. Pharmacol.* **2007**, *71*, 1061−1074.
(24) Chan, A. S.; Pang, H.; Yip, E. C.; Tam, Y. K.; Wong, Y. H. Carvacrol and eugenol differentially stimulate intracellular Ca^{2+} mobilization and mitogen-activated protein kinases in Jurkat T-cells and monocytic THP-1 cells. *Planta Med.* **2005**, *71*, 634−639.
(25) Hirota, R.; Roger, N. N.; Nakamura, H.; Song, H. S.; Sawamura, M.; Suganuma, N. Anti-inflammatory effects of limonene from yuzu (*Citrus junos* Tanaka) essential oil on eosinophils. *J. Food Sci.* **2010**, *75*, H87−H92.
(26) Kummer, R.; Fachini-Queiroz, F. C.; Estevao-Silva, C. F.; Grespan, R.; Silva, E. L.; Bersani-Amado, C. A.; Cuman, R. K. Evaluation of anti-inflammatory activity of *Citrus latifolia* Tanaka essential oil and limonene in experimental mouse models. *Evid. Based Complement. Alternat. Med.* **2013**, *2013*, No. 859083.
(27) Basile, A.; Senatore, F.; Gargano, R.; Sorbo, S.; Del Pezzo, M.; Lavitola, A.; Ritieni, A.; Bruno, M.; Spatuzzi, D.; Rigano, D.; Vuotto, M. L. Antibacterial and antioxidant activities in *Sideritis italica* (Miller) Greuter et Burdet essential oils. *J. Ethnopharmacol.* **2006**, *107*, 240−248.
(28) Cosentino, M.; Luini, A.; Bombelli, R.; Corasaniti, M. T.; Bagetta, G.; Marino, F. The essential oil of bergamot stimulates reactive oxygen species production in human polymorphonuclear leukocytes. *Phytother. Res.* **2014**, *28*, 1232−1239.
(29) Mori, M.; Ikeda, N.; Kato, Y.; Minamino, M.; Watabe, K. Inhibition of elastase activity by essential oils in vitro. *J. Cosmet. Dermatol.* **2002**, *1*, 183−187.
(30) Tabanca, N.; Ma, G.; Pasco, D. S.; Bedir, E.; Kirimer, N.; Baser, K. H.; Khan, I. A.; Khan, S. I. Effect of essential oils and isolated compounds from *Pimpinella* species on NF-κB: a target for antiinflammatory therapy. *Phytother. Res.* **2007**, *21*, 741−745.
(31) Hua, K. F.; Yang, T. J.; Chiu, H. W.; Ho, C. L. Essential oil from leaves of *Liquidambar formosana* ameliorates inflammatory response in lipopolysaccharide-activated mouse macrophages. *Nat. Prod. Commun.* **2014**, *9*, 869−872.
(32) de Cassia da Silveira, E. S. R.; Andrade, L. N.; Dos Reis Barreto de Oliveira, R.; de Sousa, D. P. A review on anti-inflammatory activity of phenylpropanoids found in essential oils. *Molecules* **2014**, *19*, 1459−1480.
(33) Seow, Y. X.; Yeo, C. R.; Chung, H. L.; Yuk, H. G. Plant essential oils as active antimicrobial agents. *Crit. Rev. Food Sci. Nutr.* **2014**, *54*, 625−644.
(34) Bhalla, Y.; Gupta, V. K.; Jaitak, V. Anticancer activity of essential oils: a review. *J. Sci. Food Agric.* **2013**, *93*, 3643−3653.
(35) Takaki, I.; Bersani-Amado, L. E.; Vendruscolo, A.; Sartoretto, S. M.; Diniz, S. P.; Bersani-Amado, C. A.; Cuman, R. K. Anti-inflammatory and antinociceptive effects of *Rosmarinus officinalis* L. essential oil in experimental animal models. *J. Med. Food* **2008**, *11*, 741−6.
(36) Sayyah, M.; Nadjafnia, L.; Kamalinejad, M. Anticonvulsant activity and chemical composition of *Artemisia dracunculus* L. essential oil. *J. Ethnopharmacol.* **2004**, *94*, 283−287.
(37) Khan, M. S.; Ahmad, I. In vitro antifungal, anti-elastase and anti-keratinase activity of essential oils of *Cinnamomum*-, *Syzygium*- and *Cymbopogon*-species against *Aspergillus fumigatus* and *Trichophyton rubrum*. *Phytomedicine* **2011**, *19*, 48−55.
(38) Chi, G.; Wei, M.; Xie, X.; Soromou, L. W.; Liu, F.; Zhao, S. Suppression of MAPK and NF-κB pathways by limonene contributes to attenuation of lipopolysaccharide-induced inflammatory responses in acute lung injury. *Inflammation* **2013**, *36*, 501−511.
(39) Abe, S.; Maruyama, N.; Hayama, K.; Inouye, S.; Oshima, H.; Yamaguchi, H. Suppression of neutrophil recruitment in mice by geranium essential oil. *Mediators Inflammation* **2004**, *13*, 21−24.
(40) Nogueira de Melo, G. A.; Grespan, R.; Fonseca, J. P.; Farinha, T. O.; Silva, E. L.; Romero, A. L.; Bersani-Amado, C. A.; Cuman, R. K. *Rosmarinus officinalis* L. essential oil inhibits in vivo and in vitro leukocyte migration. *J. Med. Food* **2011**, *14*, 944−946.
(41) Fachini-Queiroz, F. C.; Kummer, R.; Estevao-Silva, C. F.; Carvalho, M. D.; Cunha, J. M.; Grespan, R.; Bersani-Amado, C. A.; Cuman, R. K. Effects of thymol and carvacrol, constituents of *Thymus vulgaris* L. essential oil, on the inflammatory response. *Evid. Based Complement. Alternat. Med.* **2012**, *2012*, No. 657026.
(42) Siani, A. C.; Souza, M. C.; Henriques, M. G.; Ramos, M. F. Anti-inflammatory activity of essential oils from *Syzygium cumini* and *Psidium guajava*. *Pharm. Biol.* **2013**, *51*, 881−887.
(43) Rufino, A. T.; Ribeiro, M.; Judas, F.; Salgueiro, L.; Lopes, M. C.; Cavaleiro, C.; Mendes, A. F. Anti-inflammatory and chondroprotective activity of (+)-α-pinene: structural and enantiomeric selectivity. *J. Nat. Prod.* **2014**, *77*, 264−269.
(44) Silva-Comar, F. M. D.; Wiirzler, L. A. M.; Silva, S. E.; Kummer, R.; Pedroso, R. B.; Spironello, R. A.; Silva, E. L.; Bersani-Amado, C. A.; Cuman, R. K. N. Effect of estragole on leukocyte behavior and phagocytic activity of macrophages. *Evid. Based Complement. Alternat. Med.* **2014**, *2014*, 1.
(45) Ritter, A. M.; Domiciano, T. P.; Verri, W. A., Jr.; Zarpelon, A. C.; da Silva, L. G.; Barbosa, C. P.; Natali, M. R.; Cuman, R. K.; Bersani-Amado, C. A. Antihypernociceptive activity of anethole in experimental inflammatory pain. *Inflammopharmacology* **2013**, *21*, 187−197.
(46) Futosi, K.; Fodor, S.; Mocsai, A. Neutrophil cell surface receptors and their intracellular signal transduction pathways. *Int. Immunopharmacol.* **2013**, *17*, 638−650.
(47) Malki, A.; Fiedler, J.; Fricke, K.; Ballweg, I.; Pfaffl, M. W.; Krautwurst, D. Class I odorant receptors, TAS1R and TAS2R taste receptors, are markers for subpopulations of circulating leukocytes. *J. Leukocyte Biol.* **2015**, *97*, 533−545.
(48) Rios, J. J.; Fernandez-Garcia, E.; Minguez-Mosquera, M. I.; Perez-Galvez, A. Description of volatile compounds generated by the degradation of carotenoids in paprika, tomato and marigold oleoresins. *Food Chem.* **2008**, *106*, 1145−1153.
(49) Kanasawud, P.; Crouzet, J. C. Mechanism of formation of volatile compounds by thermal-degradation of carotenoids in aqueous-medium. 2. Lycopene degradation. *J. Agric. Food Chem.* **1990**, *38*, 1238−1242.
(50) He, Q.; Zhou, W.; Xiong, C.; Tan, G.; Chen, M. Lycopene attenuates inflammation and apoptosis in post-myocardial infarction remodeling by inhibiting the nuclear factor-κB signaling pathway. *Mol. Med. Rep.* **2015**, *11*, 374−378.

DOI: 10.1021/acs.jafc.5b01307
J. Agric. Food Chem. 2015, 63, 4999−5007

JOURNAL OF AGRICULTURAL AND FOOD CHEMISTRY

Article

pubs.acs.org/JAFC

Se-Methyl-L-selenocysteine Induces Apoptosis via Endoplasmic Reticulum Stress and the Death Receptor Pathway in Human Colon Adenocarcinoma COLO 205 Cells

Yen-Chen Tung,[†] Mei-Ling Tsai,[‡] Fang-Ling Kuo,[‡] Ching-Shu Lai,[§] Vladimir Badmaev,[∥] Chi-Tang Ho,[†] and Min-Hsiung Pan*[,§,⊥,#]

[†]Department of Food Science, Rutgers, The State University of New Jersey, New Brunswick, New Jersey 08901, United States

[‡]Department of Seafood Science, National Kaohsiung Marine University, Kaohsiung 811, Taiwan

[§]Institute of Food Sciences and Technology, National Taiwan University, Taipei 106, Taiwan

[∥]American Medical Holdings Incorporated, 1440 Forest Hill Road, New York, New York 10314, United States

[⊥]Department of Medical Research, China Medical University Hospital, China Medical University, Taichung 40402, Taiwan

[#]Department of Health and Nutrition Biotechnology, Asia University, Taichung 413, Taiwan

ABSTRACT: Selenomethionine (SeMet) and Se-methyl-L-selenocysteine (MSeC) are natural organoselenium compounds found in garlic, onion, and broccoli. In addition, these compounds have lower toxicity and better anticancer activities than inorganic Se. This study investigated the effects of MSeC treatment on the growth of COLO 205 human colorectal adenocarcinoma cells and evaluated the mechanisms related to the MSeC-induced effects. When COLO 205 cells were treated with 200 μM MSeC for 24 h, MSeC caused 80% apoptosis in cells. MSeC increased the expression of Fas and FasL, followed by the cleavage of caspase-3, caspase-8, DNA fragmentation factor (DFF45), and poly(ADP-ribose) polymerase (PARP). MSeC also increased the levels of Bax protein and decreased the levels of Bid and Bcl-2 proteins. However, MSeC did not cause apoptosis through reactive oxygen species (ROS) stress but instead through endoplasmic reticulum (ER) stress. The cleavage of caspase-12 and caspase-9 was shown to increase the growth arrest and protein levels of DNA-damage inducible genes (GADD) 153 and 45. MSeC also downregulated the ERK1/2 and PI3K/AKT protein levels and upregulated the p38 and JNK protein levels in COLO 205 cells. These results showed that the mechanism by which MSeC induced apoptosis in COLO 205 cells involved caspase activation, the extrinsic apoptotic pathway, and the regulation of ER-stress-induced apoptosis.

KEYWORDS: *Se-methyl-L-selenocysteine, apoptosis, endoplasmic reticulum stress, COLO 205 cells*

INTRODUCTION

Colorectal cancer (CRC) is the third most common cancer worldwide and the second most frequent cause of cancer death in men and women.[1] Most cases of CRC are thought to arise from adenomatous polyps, and a routine colonoscopy may be a good tool for detecting adenomatous polyps early, thereby decreasing the incidence and mortality of CRC.[2] However, CRC may arise between two colonoscopy examinations.[3] The occurrence of CRC is highly related to diet. Red meat and alcohol consumption are recognized dietary risk factors for the development of CRC.[4]

Selenium (Se) is an essential micronutrient required by the human body and is an important element of glutathione peroxidase, which protects the body.[5,6] Se can be obtained from inorganic compounds, such as selenites and selenates, or in organic forms, such as selenoamino acids, selenopeptides, and selenoproteins.[5,7,8] Although the inorganic forms of Se are common sources of Se and have been shown to effectively induce apoptosis in different cancer cells, they may also cause toxicity in normal cells.[9] An increasing number of studies have shown that organic Se, such as selenomethionine (SeM) and Se-methyl-L-selenocysteine (MSeC), have better anticancer activities and lower toxicities than inorganic Se.[10] In 1971, Shamberger and Willis indicated that people living in areas with high dietary Se consumption have lower mortality rates because of gastrointestinal tract, lung, and breast cancers.[11,12] Moreover, epidemiological surveys have also demonstrated that selenium deficiency in the body can increase the risk of colonic, gastric, lung, and prostate carcinomas.[7] Se can be obtained from food and is abundant in natural foods, such as nuts, eggs, fish, liver, chicken, and garlic.[5] It seems that Se may be a supplement for CRC prevention. Thus, in the present study, we investigated the organoselenium compounds SeM, MSeC, *N*-γ-(L-glutamyl)-L-selenomethioine (GSeM), and *N*-γ-(L-glutamyl)-Se-methyl-L-selenocysteine (GMSeC) for their inhibitory activities on the cell growth of human COLO 205 colorectal adenocarcinoma cells. We identified the most potential anticancer compound and explored the mechanism underlying the promotion of apoptosis in cancer cells. MSeC was shown to inhibit COLO 205 cancer cell growth through multiple underlying mechanisms to promote apoptosis. Altogether, these results indicate a potential application for MSeC in the prevention of colon cancer.

Received: April 9, 2015
Revised: May 5, 2015
Accepted: May 5, 2015
Published: May 5, 2015

ACS Publications © 2015 American Chemical Society

DOI: 10.1021/acs.jafc.5b01779
J. Agric. Food Chem. 2015, 63, 5008−5016

MATERIALS AND METHODS

Cell Culture. The cell line COLO 205 [CCL-222, American Type Culture Collection (ATCC), Rockville, MD] was cultured in the RPMI-1640 medium with 10% fetal bovine serum (Gibco, Grand Island, NY) and penicillin–streptomycin (Biowest, Nuaille, France) and maintained in a humidified 5% CO_2 atmosphere at 37 °C.

Chemicals and Reagents. SeM, GSeM, MSeC, and GMSeC are kindly provided by American Medical Holdings, Inc. (New York, NY) (Figure 1). The purity of those compounds is over 99.2% according to

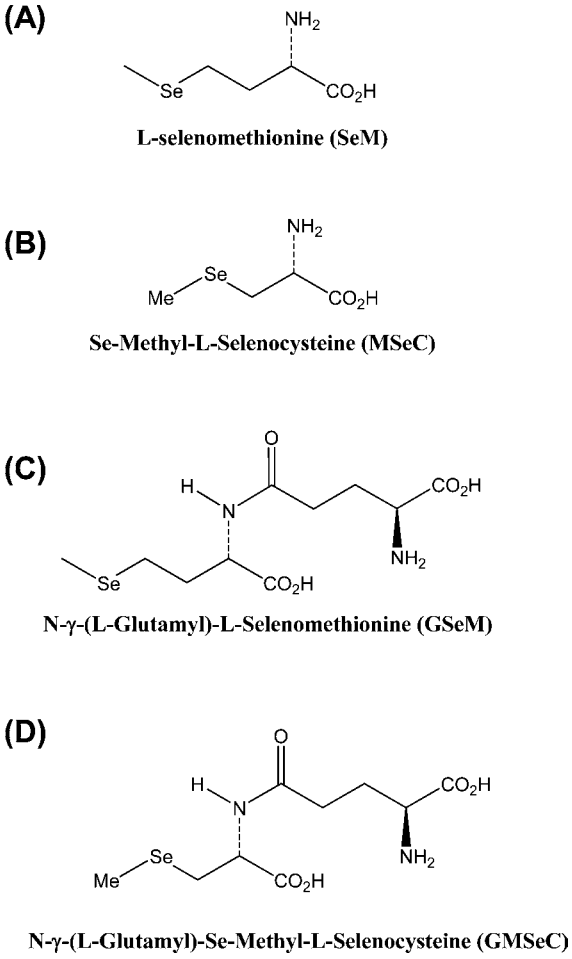

Figure 1. Chemical structures of (A) SeM, (B) MSeC, (C) GSeM, and (D) GMSeC.

high-performance liquid chromatography analysis. Trypan blue, acridine orange (AO), and propidium iodide (PI) were purchased from Sigma-Aldrich (St. Louis, MO). Anti-Akt and anti-PARP antibodies were purchased from Merck (Whitehouse Station, NJ); anti-Bcl-2 and anti-Bax were purchased from Santa Cruz Biotechnology (Dallas, TX); anti-Bid, anti-Fas, and anti-FasL were purchased from Becton-Dickinson (San Jose, CA); anti-DFF-45/ICAD and anti-caspase 8 were purchased from MBL (Woburn, MA); anti-p44/42 (ERK1/2) was purchased from Cell Signaling Technology (Danvers, MA); anti-p53 was purchased from Oncogen (La Jolla, CA); and anti-phospho-Akt and anti-caspase 3 were purchased from Novus (Littleton, CO).

Cytotoxicity Assay. COLO 205 cells were seeded in the 24 well plate with the density of 2×10^4 cells/mL overnight. Cells were treated with 0, 50, 100, 200, and 250 μM SeM, GSeM, MSeC, and GMSeC for 24 h. Cell viability was assayed by 3-(4,5-dimethylthiazol-2-yl)-2,5-diphenyl tetrazolium bromide (MTT) and determined by scanning with an enzyme-linked immunosorbent assay (ELISA) reader at 570 nm.

Trypan Blue Exclusion Assay. COLO 205 cells were cultured in the 24 well plate with the 2×10^5 cells/mL density. After overnight growth, cells were treated with 0, 50, 100, 200, and 250 μM MSeC for 24 h. After a 24 h co-culture with different concentrations of MSeC, the cell suspension was collected and dyed with trypan blue by a 1:1 ratio. Cells were then counted in a hemacytometer by a microscope (Olympus America, Inc., Lake Success, NY).

Flow Cytometry. Incubated COLO 205 cells were seeded with the 2×10^5 cells/mL density in the 24 well plate overnight and treated with different concentrations of MSeC for 24 h. After 24 h, cells were harvested with phosphate-buffer saline (PBS), fixed with iced 100% ethanol, and then stored in −20 °C. Cells were resuspended with hypotonic buffer (0.5% Triton X-100 in PBS and 0.5 μg/mL RNase) and then stained with PI at 37 °C for 15 min, individually. Fluorescence intensity was quantified by flow cytometry (Becton-Dickinson, San Jose, CA).

AO Staining Assay. COLO 205 cells were cultured in the 24 well plate with 2×10^5 cells/mL density overnight and treated with 200 μM MSeC for another 24 h. After 24 h, cells were harvested and suspended in the PBS. Equal volumes of cell suspension and AO were mixed, and the fluorescence intensity was observed by a microscope (Olympus America, Inc., Lake Success, NY).

DNA Fragmentation. COLO 205 cells were seeded with the 2×10^5 cells/mL density in a 100 mm Petri dish overnight and then treated with different concentrations of MSeC for 24 h. Cells were also treated with 200 μM MSeC for 0, 3, 6, 9, 12, 18, and 24 h. Cells were harvested, centrifuged, and suspended in PBS. The cell solution was centrifuged, and then the cell lysate was collected and mixed with DNA lysis-PK buffer at 56 °C overnight. RNase A (0.5 μg/mL) was added to the cell lysate solution at 50 °C for 3 h, and an equal volume of phenol/chloroform/isoamyl (25:24:1) was added in the cell lysate solution to obtain DNA. DNA was loaded in the 2% agarose gel electrophoresis and run at 50 V for 120 min in Tris–borate/ethylenediaminetetraacetic acid (EDTA) electrophoresis buffer (TBE). The gel was stained by ethidium bromide, visualized under ultraviolet (UV) light, and photographed.

Caspase Activity. COLO 205 cells were seeded in 100 mm with the 2×10^5 cells/mL density Petri dish overnight and then treated with 200 μM MSeC for 0, 3, 6, 9, 12, 18, and 24 h. Harvest cells were washed by PBS and centrifuged, and then the supernatant was removed. Protein was extracted by mixing cell pellet with gold lysis buffer [50 mM tris(hydroxymethyl)aminomethane (Tris)–HCl at pH 7.4, 1 mM NaF, 150 mM NaCl, 1 mM ethylene glycol bis(2-aminoethyl ether)-*N*,*N*,*N*′,*N*′-tetraacetic acid (EGTA), 1 mM phenylmethanesulfonyl fluoride, 1% NP-40, and 10 g/mL leupeptin] and then centrifuged at 12 000 rpm for 30 min at 4 °C. A total of 50 μg of each sample was mixed with the caspase substrate (acetyl-Asp-Glu-Val-Asp-7-amino-4-methylcoumarin) at 30 °C for 1 h, and the fluorescence intensity was quantified by the ELISA reader at 360 nm excitation wavelength and 460 nm emission wavelength.

Determination of Superoxide, Hydroperoxide, Glutathione, and Mitochondrial Transmembrane Potential. COLO 205 cells were incubated with the 2×10^5 cells/mL density in the 24 well plate overnight and treated with 200 μM MSC for 0, 15, 30, 60, and 120 min. Cells were harvested and washed by PBS twice and mixed separately with dihydroethidium (DHE), 5-cholomethylfluoroescein diacetate (CMFDA), 2′,7′-dicholofluoroescein diacetate (DCFHDA), and 3,3′-dihexyloxacarbocyanine iodide (DiOC6) for 30 min, and the reactions were stopped by trypsin–EDTA at 37 °C and then analyzed by flow cytometry.

Analysis of Antioxidant and Apoptosis. COLO 205 cells (2×10^5 cells/mL) were seeded in the 24 well plate overnight and 50 and 100 μM allopurinol (ALL), 200 and 400 units/mL catalase (CAT), 10 and 20 μM diphenylene iodonium (DPI), 2.5 and 5 μM *N*-acetylcysteine (NAC), and 100 and 200 μg/mL superoxide dismutase (SOD) were added for 1 h, individually. After the treatment with different antioxidants, the cells were treated with 200 μM MSeC for 24 h and the reaction was stopped by trypsin–EDTA and analyzed by flow cytometry.

DOI: 10.1021/acs.jafc.5b01779
J. Agric. Food Chem. 2015, 63, 5008–5016

Western Blotting. COLO 205 cells were seeded in 100 mm with the 2×10^5 cells/mL density Petri dish overnight and then treated with 0, 50, 100, 200, and 250 μM for 24 h and 200 μM MSeC for 0, 3, 6, 9, 12, 18, 24 h, individually. Protein was extracted with gold lysis buffer (50 mM Tris−HCl at pH 7.4, 1 mM NaF, 150 mM NaCl, 1 mM EGTA, 1 mM phenylmethanesulfonyl fluoride, 1% NP-40, and 10 μg/mL leupeptin) by mixing the cells and gold lysis buffer on ice for 30 min, followed by centrifugation at 10000*g* for 30 min at 4 °C. The total protein (50 μg) was used in the 12% sodium dodecyl sulfate−polyacrylamide gel electrophoresis (SDS−PAGE) at a constant current of 20 mA. Proteins were electrotransferred from gel to immobile membrane [polyvinylidene fluoride (PVDF), Millipore Corp., Bedford, MA] with transfer buffer (25 mM Tris−HCl at pH 8.9, 192 mM glycine, and 20% methanol). The membranes were blocked with blocking solution [20 mM Tris−base, 125 mM NaCl, 0.2% Tween 20, 1% bovine serum albumin (BSA), and 0.1% sodium azide] and then immunoblotted with primary antibodies [including Anti-Akt and anti-PARP antibodies purchased from Merck (Whitehouse Station, NJ), anti-Bcl-2 and anti-Bax purchased from Santa Cruz Biotechnology (Dallas, TX), anti-Bid, anti-Fas, and anti-FasL purchased from Becton-Dickinson (San Jose, CA), anti-DFF-45/ICAD and anti-caspase 8 purchased from MBL (Woburn, MA), anti-p44/42 (ERK1/2) purchased from Cell Signaling Technology (Danvers, MA), anti-p53 purchased Oncogen (La Jolla, CA), and anti-phospho-Akt and anti-caspase 3 purchased from Novus (Littleton, CO)] at 4 °C overnight. Detection was achieved by measuring the chemiluminescence of the blotting agent [electrochemiluminescence (ECL), Amersham Corp., Arlington Heights, IL], after exposure of the filters to Kodak X-Omat films.

Statistical Analysis. All results were presented as means ± standard error of the mean (SE) in the independently performed experiments. The differences between the control group and different concentrations of Se compounds were analysis by Student's *t* test. Data were considered statistically significant at a p value of <0.05.

RESULTS

Cytotoxic Effects of SeM, MSeC, GSeM, and GMSeC in Human COLO 205 Cells. The cytotoxic effects of SeM, MSeC, GSeM, and GMSeC in human colorectal adenocarcinoma (COLO 205) cells were evaluated using the MTT assay. As shown in Figure 2A, the viability of COLO 205 cells was reduced by MSeC treatment but not by treatment with the other three organoselenium compounds. The cell viabilities were 60.6 ± 12.9, 31.3 ± 9.4, and 24.8 ± 5.4% after treatment with 150, 200, and 250 μM MSeC, respectively. The cytotoxic effects of MSeC in COLO 205 cells were further confirmed by trypan blue analysis. Figure 2B shows that MSeC induced significant cell death in COLO 205 cells in a dose-dependent manner. These results clearly revealed the cytotoxic effect of MSeC in COLO 205 cells.

MSeC Induced Apoptosis in Human COLO 205 Cells. Because MSeC-induced cytotoxic effects in COLO 205 cells were found in our study, the mechanism of these cytotoxic effects was evaluated by treating COLO 205 cells with MSeC and examining the cellular morphology. After the cells were treated with 200 μM MSeC for 24 h, membrane blebbing and apoptotic bodies were clearly observed (top panels of Figure 3A). MSeC also caused chromatin condensation that was detected through the use of the fluorescent dye AO (bottom panels of Figure 3A). DNA fragmentation is considered to be a hallmark of apoptosis. Thus, DNA fragmentation analysis was also performed in the present study. As shown in Figure 3B, significant DNA ladders were observed in COLO 205 cells treated with 150 μM MSeC for 24 h (left). In addition, DNA ladders were observed after treatment with 200 μM MSeC after 18 or 24 h (right). The MSeC-induced apoptotic effect in

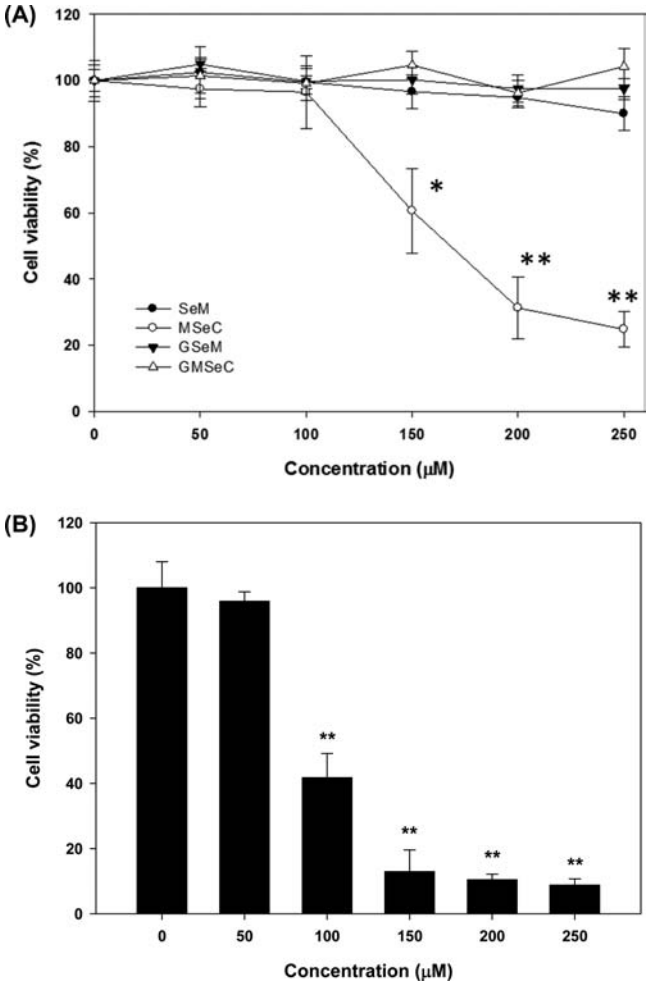

Figure 2. Cytotoxic effects of SeM, MSeC, GSeM, and GMSeC in COLO 205 cells. COLO 205 cells were treated with various concentrations (0, 50, 100, 150, 200, and 250 μM) of SeM, MSeC, GSeM, and GMSeC for 24 h. The cells were harvested, and the cell viability was determined by (A) MTT assay and (B) trypan blue exclusion assay. (*) $p < 0.01$ and (**) $p < 0.001$ indicate statistically significant differences relative to the control group.

COLO 205 cells was confirmed using flow cytometry. As seen in Figure 3C, the number of apoptotic cells was markedly increased by MSeC treatment. The quantitative results for the percentage of apoptotic cells showed that MSeC significantly induced apoptosis (Figure 3D). These results suggested that the cytotoxic effect caused by MSeC in human COLO 205 cells occurred mainly through the induction of apoptosis.

MSeC Induced Cleavage of PARP, DFF45, and Caspase Activation. To explore the mechanism of MSeC-induced apoptosis, the enzymatic activity of caspase was measured using fluorescent substrates. After treatment with 200 μM MSeC, the activities of caspase-8 and caspase-9 significantly increased by 6 h and continued to increase until 24 h (Figure 4A). After treatment with 200 μM MSeC, caspase-3 was activated by 12 h and markedly increased in activation by 18 and 24 h. Figure 4B shows the COLO 205 cells that were treated with MSeC for 24 h, which resulted in the proteolytic cleavage of PARP and DFF45 in a dose-dependent manner. A decreased level of procaspase-3 protein also occurred when cells were treated with MSeC (lower). Moreover, the COLO 205 cells treated with 200 μM MSeC showed marked PARP and DFF45 cleavage by

DOI: 10.1021/acs.jafc.5b01779
J. Agric. Food Chem. 2015, 63, 5008−5016

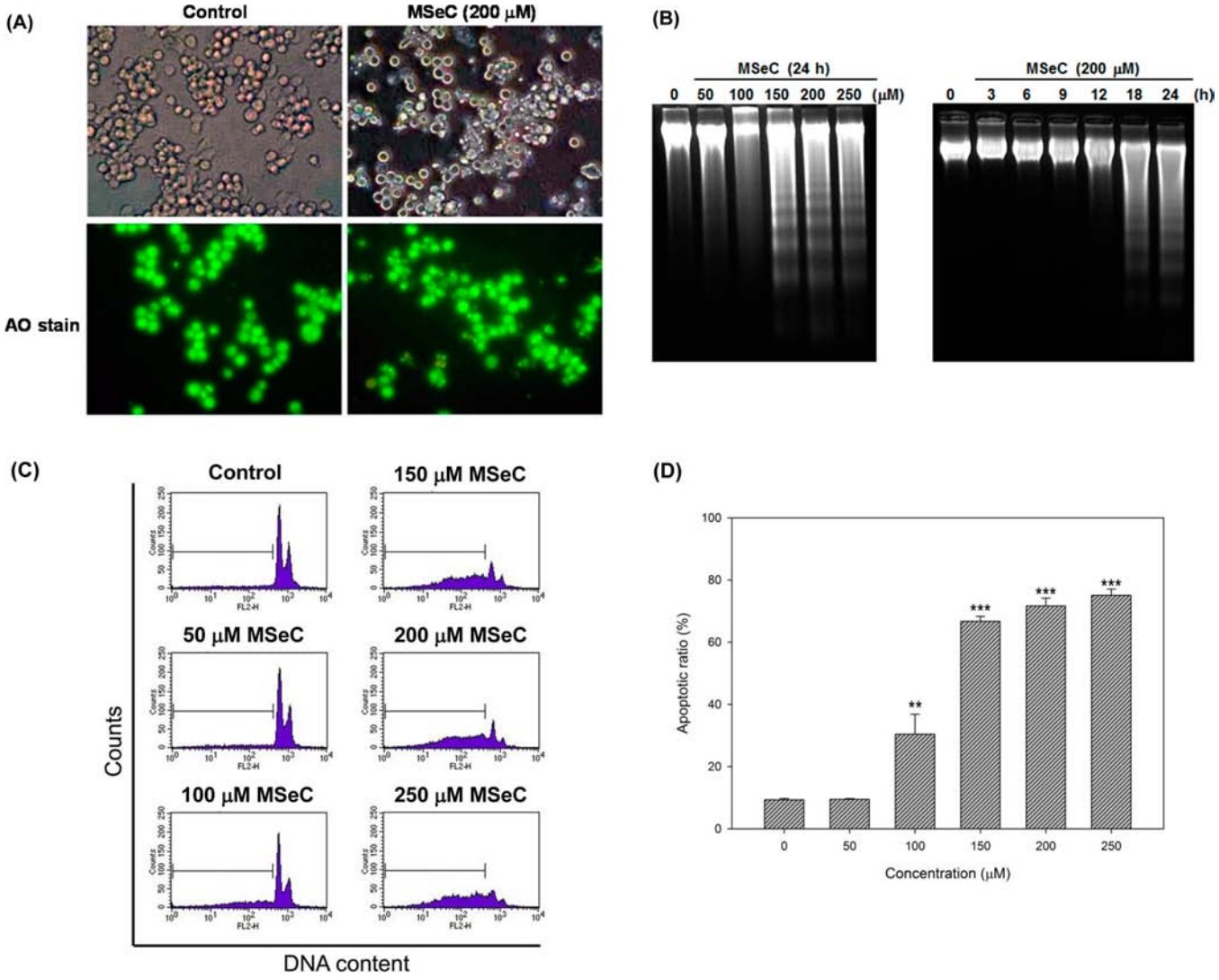

Figure 3. MSeC-induced apoptosis in COLO 205 cells. COLO 205 cells were treated with different concentrations of MSeC for 24 h or with 200 μM MSeC for the indicated time. (A) Cells were stained with AO, and the morphological changes and chromatin condensation were examined using fluorescence microscopy. (B) DNA was extracted, and the DNA fragmentation was analyzed using agarose gel electrophoresis. (C and D) Cells were harvested and fixed with ethanol overnight and stained with PI. Apoptotic cells were detected by flow cytometry and presented as the apoptotic ratio (%). (*) $p < 0.01$ and (**) $p < 0.001$ indicate statistically significant differences compared to the control group.

12 h, which continued until 24 h (Figure 4C). This result was consistent with the DNA fragmentation results (Figure 3B). These findings suggested that the activation of caspases participated in the MSeC-induced apoptosis of human COLO 205 cells.

MSeC Induced Apoptosis via the Death Receptor and Mitochondrial Signaling Pathways. To further investigate the mechanism underlying MSeC-induced apoptosis, the total protein was extracted and analyzed by western blot analysis. The activation of Fas results in FasL signaling, which promotes the autocatalytic activation of procaspase-8 and initiates death signaling.[13] Figure 5A shows that the treatment of COLO 205 cells with 200 μM MSeC caused the increased expression of Fas and FasL proteins by 9 h, which continued until 24 h. Meanwhile, the cleavage of procaspase-8 also occurred from 9 to 24 h (top panel of Figure 5B). MSeC also caused the time-dependent cleavage of procaspase-9 by the early time point of 3 h, whereas cleaved procaspase-3 was detected by 18 h (middle and bottom panels of Figure 5B). The protein expression of the Bcl-2 family members, which plays an important role in regulating mitochondria-dependent apoptosis, was also measured in the MSeC-treated cells.[14] As illustrated in Figure 5C, the MSeC treatment caused an increase in the protein level of Bax. However, MSeC treatment reduced the protein expression levels of Bcl-2 and Bid. These data suggested that MSeC-induced apoptosis in human COLO 205 cells may have occurred through both the intrinsic and extrinsic pathways.

Effects of MSeC on the Mitochondrial Membrane Potential ($\Delta\Psi_m$) and the Levels of Hydrogen Peroxide, Superoxide, and Glutathione (GSH). Mitochondria are the main source of reactive oxygen species (ROS), such as hydrogen peroxide and superoxide, which are known to cause cell death under conditions in which excess ROS are generated.[15] The imbalance of redox systems, such as reduced GSH, results in oxidative stress that also participates in the regulation of apoptosis.[16,17] To understand whether MSeC-induced cell apoptosis occurred through the upregulation of ROS, the intracellular hydrogen peroxide and superoxide levels were detected using flow cytometry with the fluorescent dyes DCFHDA and DHE. As illustrated in Figure 6A, MSeC did not

DOI: 10.1021/acs.jafc.5b01779
J. Agric. Food Chem. 2015, 63, 5008−5016

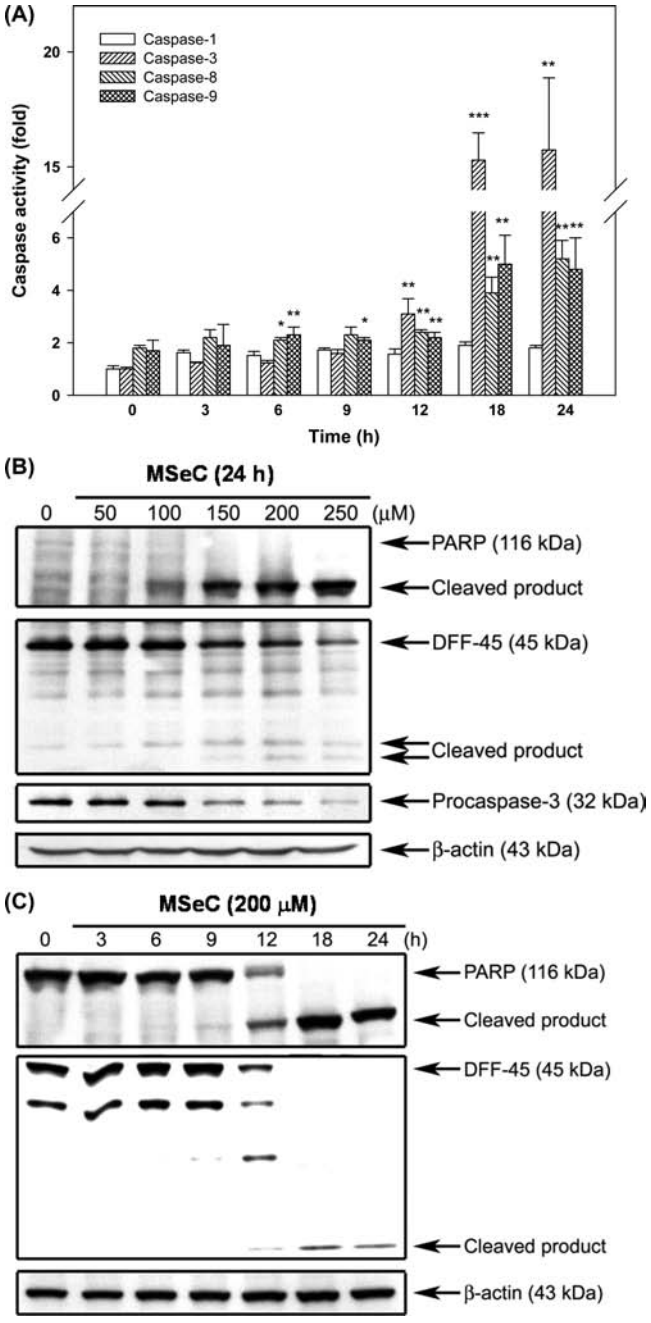

Figure 4. MSeC-induced PARP cleavage, DFF-45 degradation, and activation of caspases in COLO 205 cells. COLO 205 cells were treated with various concentrations of MSeC for 24 h or 200 μM MSeC for the indicated time. The total protein was extracted, and the enzymatic activities of caspase-1, caspase-3, caspase-8, and caspase-9 were determined using fluorogenic substrates, as described in the Materials and Methods. (B and C) Cleavage of PARP and DFF-45 was analyzed by western blot analysis. The values are expressed as the means ± standard deviation (SD) of triplicate tests. (*) $p < 0.05$, (**) $p < 0.01$, and (***) $p < 0.001$ indicate statistically significant differences compared to the control group.

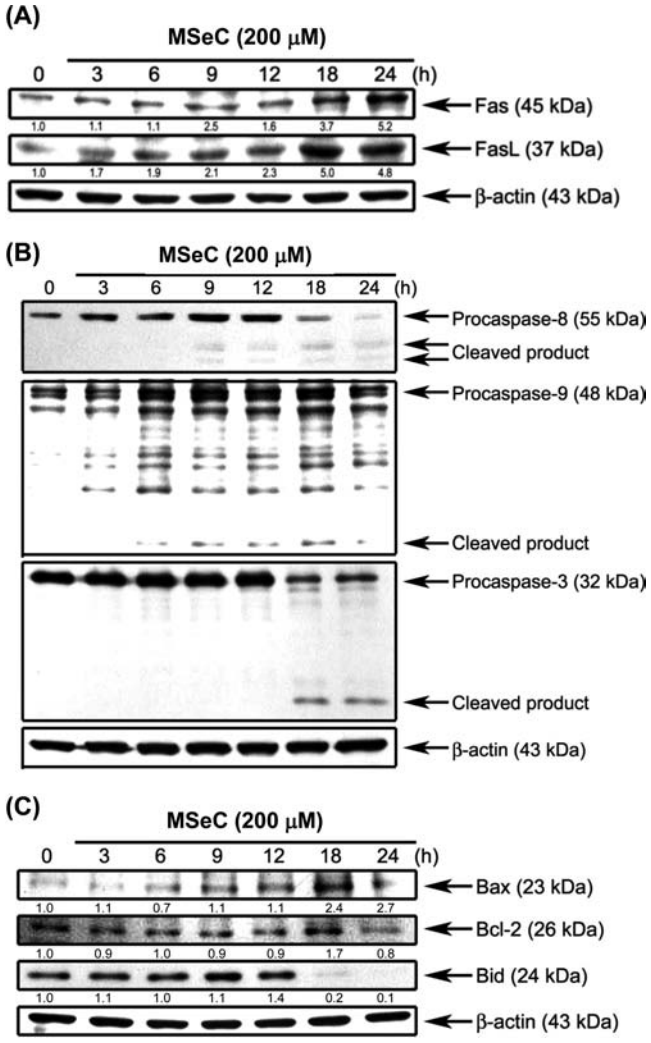

Figure 5. MSeC-induced apoptosis in COLO 205 cells through the death receptor and mitochondrial pathways. Cells were treated with 200 μM MSeC for the indicated time. The total protein was extracted, and the protein levels of (A) Fas and FasL, (B) caspase-8 and caspase-3, and (C) Bcl-2 family proteins were analyzed by western blot analysis. This experiment was repeated 3 times with similar results.

increase the levels of either hydrogen peroxide or superoxide by 6 and 12 h. However, after treatment with MSeC, a slight reduction in the level of GSH was observed through the use of the fluorescent probe CMFDA (right panel of Figure 6A). Although increased levels of ROS were not detected, a slight disruption of the mitochondrial membrane potential ($\Delta\Psi_m$) occurred after MSeC treatment, which was evidenced by the reduced levels of DiOC6 fluorescence intensity (left panel of Figure 6A). To further examine the role of ROS in MSeC-induced apoptosis, COLO 205 cells were preincubated with various antioxidants and treated with MSeC and then the apoptotic ratio was measured. As shown in Figure 6B, none of the antioxidant treatments reduced the MSeC-induced apoptosis, suggesting that ROS may not play a major role in MSeC-induced apoptosis. The treatment with MSeC dramatically induced the expression of both DNA-damage inducible genes (GADD) 153 and 45 proteins in a time-dependent manner (Figure 6C). This result indicated that the induction of DNA damage or endoplasmic reticulum (ER) stress may be one of mechanisms involved in MSeC-induced apoptosis.

Effects of MSeC on the Phosphorylation of MAPK Kinases and PI3K/Akt. The mitogen-activated protein kinases (MAPKs), including extracellular signal-regulated kinase (ERK), c-Jun NH2-terminal kinase (JNK), and p38 MAPK, play critical roles in the regulation of gene expression, mitosis, proliferation, motility, metabolism, and apoptosis in the cells.

DOI: 10.1021/acs.jafc.5b01779
J. Agric. Food Chem. 2015, 63, 5008−5016

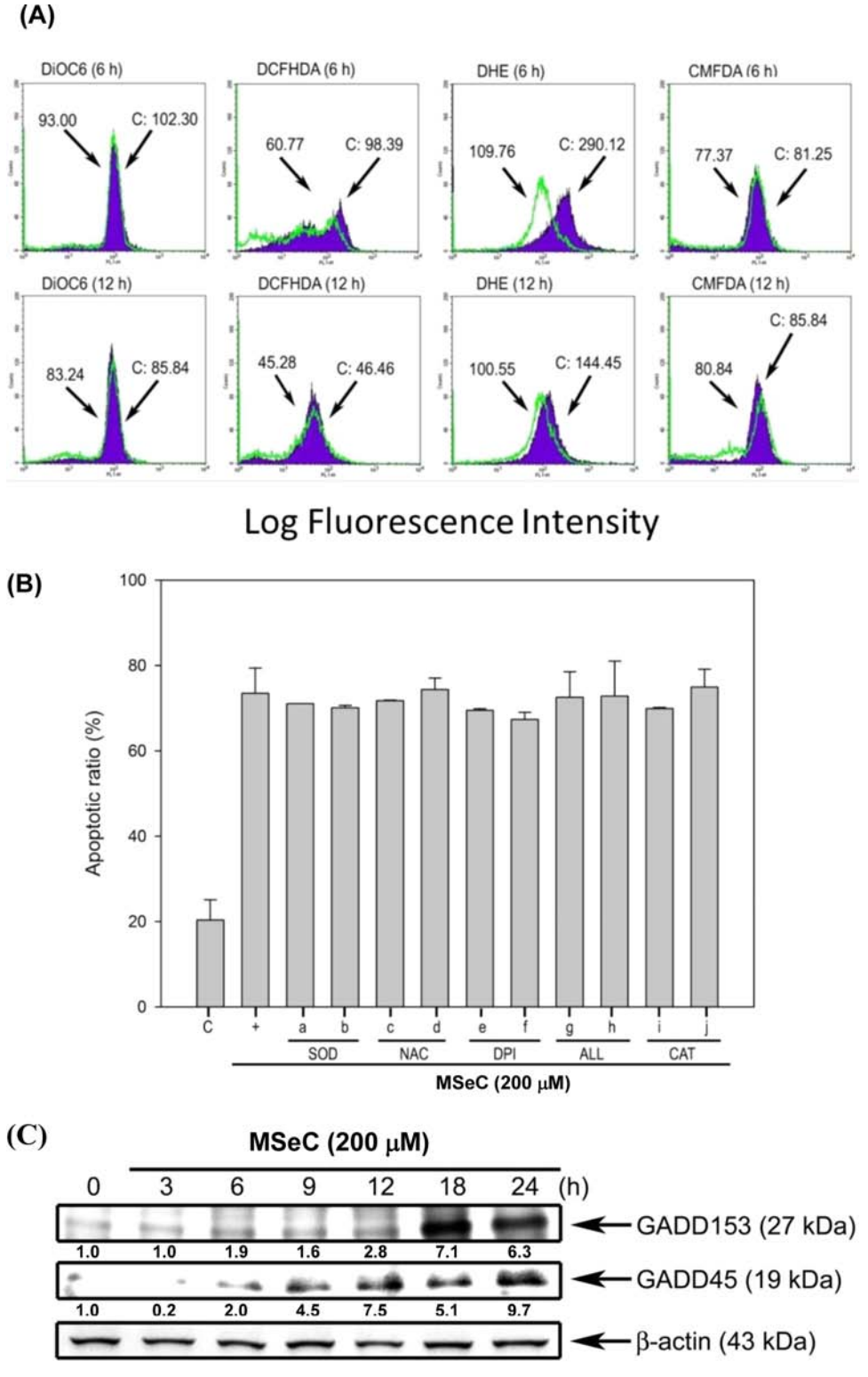

Figure 6. MSeC-induced mitochondrial dysfunction and ROS generation in COLO 205 cells. (A) COLO 205 cells were treated with MSeC for 6 or 12 h, incubated with DiOC6, DCFHDA, DHE, or CMFDA and then analyzed by flow cytometry. The data are presented as the log fluorescence intensity and expressed as the means ± standard error (SE). (B) COLO 205 cells were treated with different concentrations of SOD (a, 100 μg/mL; b, 200 μg/mL), NAC (c, 2.5 mM; d, 5 mM), DPI (e, 10 μM; f, 20 μM), ALL (g, 100 μM; h, 50 μM), or CAT (i, 200 units/mL; j, 400 units/mL) for 1 h, followed by 200 μM MSC treatment for another 24 h. Apoptotic cells were detected by flow cytometry and presented as the apoptotic ratio (%). (∗) $p < 0.01$ and (∗∗) $p < 0.001$ indicate statistically significant differences from the control group. (C) MSeC upregulated the expression of GADD153 and GADD45 proteins in COLO 205 cells. Cells were treated with 200 μM MSeC for the indicated time, and the total protein was extracted. The protein levels of GADD153 and GADD45 were analyzed by western blot analysis. This experiment was repeated 3 times with similar results.

DOI: 10.1021/acs.jafc.5b01779
J. Agric. Food Chem. 2015, 63, 5008−5016

Previous studies have reported the anti-apoptotic role of ERK1/2,[18−20] whereas p38 MAPK and JNK have been shown to be stress-responsive proteins that tend to induce apoptosis.[21] Here, we found that MSeC treatment downregulated the protein level of phospho-ERK1/2 while markedly increasing the protein levels of phospho-p38 MAPK and phospho-JNK (Figure 7A). PI3K and its downstream kinase Akt, which are

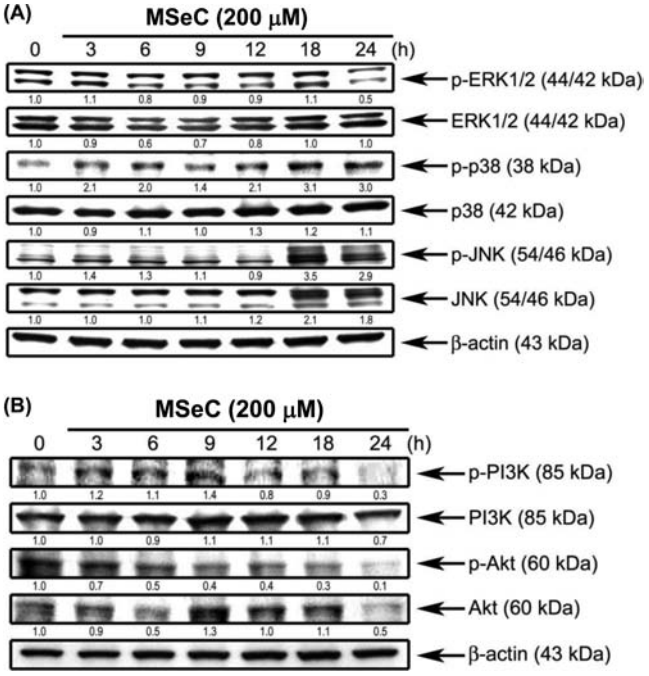

Figure 7. Effects of MSeC on MAPKs and PI3K/Akt signaling in COLO 205 cells. The cells were treated with 200 μM MSeC for an indicated time, and the total protein was extracted. The protein levels of (A) ERK, phospho-ERK, p38, phospho-p38, JNK, and phospho-JNK and (B) PI3K, phospho-PI3K, Akt, and phosph-Akt were analyzed by western blot analysis. This experiment was repeated 3 times with similar results.

pivotal to cell survival and cell growth, are highly upregulated in various human cancers.[22] When the cells were treated with MSeC, the phosphorylation of both PI3K and Akt were decreased (Figure 7B). These results indicated that the modulation of stress and survival signaling was one of the possible mechanisms contributing to MSeC-induced apoptosis.

DISCUSSION

MSeC, a naturally occurring monomethylated selenoamino acid, is the most valuable form of Se found in vegetables, such as garlic. Studies have shown that MSeC has a high oral bioavailability and metabolizes to methylselenol, which is known to be an excellent anticarcinogen.[23] The chemopreventive effects of MSeC have been suggested to occur through mechanisms, such as anti-inflammation,[24] anti-tumorigenesis,[25] and anti-angiogenesis.[26] Several studies have reported that MSeC inhibits cell growth in various cancer cells through the induction of cell cycle arrest and apoptosis.[27,28] In the present study, MSeC displayed more potent cytotoxic effects than three other Se compounds that were tested in COLO 205 cells. The cytotoxic effects caused by MSeC contributed to the induction of apoptosis, which was evidenced by morphological changes, nuclear condensation, and DNA fragmentation (Figure 2). At the molecular level, the upregulation of Fas and FasL and the activation of caspase-8 occurred in MSeC-treated cells, suggesting a role for the death receptor pathway in MSeC-induced apoptosis. Although alterations in the expression of Bcl-2 family proteins were also observed after MSeC treatment, this may not be an early signaling event because altered protein levels were observed at a later time point (Figure 5). Moreover, MSeC induced a slight decrease in the mitochondrial membrane potential but did not increase the production of ROS. This finding was also confirmed by pretreatment with various antioxidants (Figure 6), implying that the ROS-triggered intrinsic signaling was not a major mechanism contributing to the MSeC-mediated apoptosis.

Accumulating evidence has suggested that ER stress signaling involves the modulation of the intrinsic (mitochondrial) and/or the extrinsic (death receptor) apoptotic pathways. The ER stress-induced expression of GADD genes, including GADD34, GADD45, and GADD153, are known to promote apoptosis. GADD153, which is also known as CEBP homology protein (CHOP), is rapidly induced by UV irradiation, oxidative stress, genotoxic agents, and ER stress. Studies using the overexpression of a plasmid have demonstrated that GADD153 functions in the initiation of apoptosis,[29] although one study has suggested that GADD153 expression alone does not trigger cell death and, instead, sensitizes cells to ER-stress-induced death.[30] The mechanism by which GADD153 promotes apoptosis is complicated and indistinct, whereas the overexpression of GADD153 has been shown to downregulate the transcription of Bcl-2.[30] Although no evidence has confirmed the existence of a GADD153 binding site in the Bcl-2 promoter, GADD153 may regulate the transcription of Bcl-2 through interactions with other transcription factors.[31,32] In the present study, MSeC induced the early expression of GADD153, which may have initiated apoptotic signaling and further repressed the Bcl-2 protein levels (Figure 6C). Another GADD protein, GADD45, which also has a role in controlling the cell cycle, apoptosis, and DNA repair, has been shown to respond to stress signaling.[33] In the present study, the expression of GADD45 was upregulated by treatment with MSeC. A previous study has demonstrated that the activation of JNK and ERK is involved in the induction of the GADD45 promoter activity, while other studies have suggested that GADD45 is required for the activation of JNK and apoptosis via modulation of the upstream JNK kinase.[34] Here, after the cells were treated with MSeC, the phosphorylation of JNK1/2 occurred far later than the upregulation of GADD45, indicating that MSeC increased GADD45 prior to the activation of JNK1/2 and the JNK-dependent apoptosis signaling pathway. Another study has implicated p38 MAPK in the induction of GADD45 transcription.[35] GADD45 was found to be upregulated early by MSeC treatment in the present study, which suggested the possibility that MSeC mediates the activation of p38 MAPK to regulate GADD45. However, we cannot exclude the possible role of p38 MAPK in modulating other molecules and signaling cascades involved in MSeC-induced apoptosis. The anti-apoptotic role of PI3K/Akt signaling, which is pivotal in regulating cell survival in response to ER stress, has been previously documented.[36] Studies have also suggested that the inactivation of PI3K/Akt induces GADD153 expression and cell death under conditions of ER stress.[37] In the present study, we found that MSeC treatment caused the early downregulation of Akt, implying that the MSeC-induced expression of GADD153 was associated with the inactivation of PI3K/Akt.

DOI: 10.1021/acs.jafc.5b01779
J. Agric. Food Chem. 2015, 63, 5008−5016

However, more experiments are needed to investigate this mechanism in detail.

In conclusion, MSeC-induced apoptosis in human colorectal adenocarcinoma COLO 205 cells may occur through the death receptor and ER stress signaling pathways via the modulation of multiple kinase signaling events. These findings suggest that MSeC could be a potential compound for the prevention and treatment of colon cancer.

AUTHOR INFORMATION

Corresponding Author

*Telephone: 886-2-3366-4133. Fax: 886-2-3366-1771. E-mail: mhpan@ntu.edu.tw.

Funding

This study was supported by the National Taiwan University (104R7777) and the National Science Council (NSC, 101-2628-B-022-001-MY4 and 102-2628-B-002-053-MY3).

Notes

The authors declare no competing financial interest.

REFERENCES

(1) Tárraga López, P. J. T.; Albero, J. S.; Rodríguez-Montes, J. A. Primary and secondary prevention of colorectal cancer. *Clin. Med. Insights Gastroenterol.* **2014**, *7*, 33−46.

(2) Singh, H.; Nugent, Z.; Demers, A. A.; Kliewer, E. V.; Mahmud, S. M.; Bernstein, C. N. The reduction in colorectal cancer mortality after colonoscopy varies by site of the cancer. *Gastroenterology* **2010**, *139*, 1128−1137.

(3) Sanduleanu, S.; Masclee, A. M.; Meijer, G. A. Interval cancers after colonoscopy—Insights and recommendations. *Nat. Rev. Gastroenterol. Hepatol.* **2012**, *9*, 550−554.

(4) Kiedrowski, M.; Mroz, A. The effects of selected drugs and dietary compounds on proliferation and apoptosis in colorectal carcinoma. *Contemp. Oncol.* **2014**, *18*, 222−226.

(5) Maseko, T.; Callahan, D. L.; Dunshea, F. R.; Doronila, A.; Kolev, S. D.; Ng, K. Chemical characterisation and speciation of organic selenium in cultivated selenium-enriched *Agaricus bisporus*. *Food Chem.* **2013**, *141*, 3681−3687.

(6) Pieczyńska, J.; Grajeta, H. The role of selenium in human conception and pregnancy. *J. Trace Elem. Med. Biol.* **2015**, *29*, 31−38.

(7) Finley, J. W. Bioavailability of selenium from foods. *Nutr. Rev.* **2006**, *64*, 146−151.

(8) Amoako, P. O.; Uden, P. C.; Tyson, J. F. Speciation of selenium dietary supplements; formation of *S*-(methylseleno)cysteine and other selenium compounds. *Anal. Chim. Acta* **2009**, *652*, 315−323.

(9) Letavayová, L.; Vlasáková, D.; Spallholz, J. E.; Brozmanová, J.; Chovanec, M. Toxicity and mutagenicity of selenium compounds in *Saccharomyces cerevisiae*. *Mutat. Res., Fundam. Mol. Mech. Mutagen.* **2008**, *638*, 1−10.

(10) Zhao, R.; Domann, F. E.; Zhong, W. Apoptosis induced by selenomethionine and methioninase is superoxide mediated and p53 dependent in human prostate cancer cells. *Mol. Cancer Ther.* **2006**, *5*, 3275−3284.

(11) Shamberger, R. J.; Willis, C. E. Selenium distribution and human cancer mortality. *Crit. Rev. Clin. Lab. Sci.* **1971**, *2*, 211−221.

(12) Whanger, P. Selenium and its relationship to cancer: an update. *Br. J. Nutr.* **2004**, *91*, 11−28.

(13) Huang, D. C.; Hahne, M.; Schroeter, M.; Frei, K.; Fontana, A.; Villunger, A.; Newton, K.; Tschopp, J.; Strasser, A. Activation of Fas by FasL induces apoptosis by a mechanism that cannot be blocked by Bcl-2 or Bcl-x_L. *Proc. Natl. Acad. Sci. U. S. A.* **1999**, *96*, 14871−14876.

(14) Kuwana, T.; Newmeyer, D. D. Bcl-2-family proteins and the role of mitochondria in apoptosis. *Curr. Opin. Cell Biol.* **2003**, *15*, 691−699.

(15) Suski, J. M.; Lebiedzinska, M.; Bonora, M.; Pinton, P.; Duszynski, J.; Wieckowski, M. R. Relation between mitochondrial membrane potential and ROS formation. *Methods Mol. Biol.* **2012**, *810*, 183−205.

(16) Schafer, F. Q.; Buettner, G. R. Redox environment of the cell as viewed through the redox state of the glutathione disulfide/glutathione couple. *Free Radical Biol. Med.* **2001**, *30*, 1191−1212.

(17) Circu, M. L.; Aw, T. Y. Reactive oxygen species, cellular redox systems, and apoptosis. *Free Radical Biol. Med.* **2010**, *48*, 749−762.

(18) Porras, A.; Zuluaga, S.; Black, E.; Valladares, A.; Alvarez, A. M.; Ambrosino, C.; Benito, M.; Nebreda, A. R.P38α mitogen-activated protein kinase sensitizes cells to apoptosis induced by different stimuli. *Mol. Biol. Cell* **2004**, *15*, 922−933.

(19) Wada, T.; Penninger, J. M. Mitogen-activated protein kinases in apoptosis regulation. *Oncogene* **2004**, *23*, 2838−2849.

(20) Lu, Z.; Xu, S. ERK1/2 MAP kinases in cell survival and apoptosis. *IUBMB Life* **2006**, *58*, 621−631.

(21) Ono, K.; Han, J. The p38 signal transduction pathway activation and function. *Cell. Signalling* **2000**, *12*, 1−13.

(22) Chang, F.; Lee, J.; Navolanic, P.; Steelman, L.; Shelton, J.; Blalock, W.; Franklin, R.; McCubrey, J. Involvement of PI3K/Akt pathway in cell cycle progression, apoptosis, and neoplastic transformation: A target for cancer chemotherapy. *Leukemia* **2003**, *17*, 590−603.

(23) Ip, C.; Ganther, H. E. Activity of methylated forms of selenium in cancer prevention. *Cancer Res.* **1990**, *50*, 1206−1211.

(24) Pan, M. H.; Hong, H. M.; Lin, C. L.; Jhang, A. Z.; Tsai, J. H.; Badmaev, V.; Nagabhushanam, K.; Ho, C. T.; Chen, W. J. Se-methylselenocysteine inhibits lipopolysaccharide-induced NF-κB activation and iNOS induction in RAW 264.7 murine macrophages. *Mol. Nutr. Food Res.* **2011**, *55*, 723−732.

(25) Ip, C. Lessons from basic research in selenium and cancer prevention. *J. Nutr.* **1998**, *128*, 1845−1854.

(26) Jiang, C.; Jiang, W.; Ip, C.; Ganther, H.; Lu, J. Selenium-induced inhibition of angiogenesis in mammary cancer at chemopreventive levels of intake. *Mol. Carcinog.* **1999**, *26*, 213−225.

(27) Kim, T.; Jung, U.; Cho, D.-Y.; Chung, A.-S. Se-methylselenocysteine induces apoptosis through caspase activation in HL-60 cells. *Carcinogenesis* **2001**, *22*, 559−565.

(28) Dong, Y.; Ganther, H. E.; Stewart, C.; Ip, C. Identification of molecular targets associated with selenium-induced growth inhibition in human breast cells using cDNA microarrays. *Cancer Res.* **2002**, *62*, 708−714.

(29) Maytin, E. V.; Ubeda, M.; Lin, J. C.; Habener, J. F. Stress-inducible transcription factor CHOP/gadd153 induces apoptosis in mammalian cells via p38 kinase-dependent and-independent mechanisms. *Exp. Cell Res.* **2001**, *267*, 193−204.

(30) McCullough, K. D.; Martindale, J. L.; Klotz, L.-O.; Aw, T.-Y.; Holbrook, N. J. Gadd153 sensitizes cells to endoplasmic reticulum stress by down-regulating Bcl2 and perturbing the cellular redox state. *Mol. Cell. Biol.* **2001**, *21*, 1249−1259.

(31) Wolfgang, C. D.; Chen, B.; Martindale, J. L.; Holbrook, N. J.; Hai, T. gadd153/Chop10, a potential target gene of the transcriptional repressor ATF3. *Mol. Cell. Biol.* **1997**, *17*, 6700−6707.

(32) Ron, D.; Habener, J. F. CHOP, a novel developmentally regulated nuclear protein that dimerizes with transcription factors C/EBP and LAP and functions as a dominant-negative inhibitor of gene transcription. *Genes Dev.* **1992**, *6*, 439−453.

(33) Salvador, J. M.; Brown-Clay, J. D.; Fornace, A. J., Jr. Gadd45 in stress signaling, cell cycle control, and apoptosis. *Adv. Exp. Med. Biol.* **2013**, *793*, 1−19.

(34) Tong, T.; Fan, W.; Zhao, H.; Jin, S.; Fan, F.; Blanck, P.; Alomo, I.; Rajasekaran, B.; Liu, Y.; Holbrook, N. J. Involvement of the MAP kinase pathways in induction of GADD45 following UV radiation. *Exp. Cell Res.* **2001**, *269*, 64−72.

(35) Sarkar, D.; Su, Z.-Z.; Lebedeva, I. V.; Sauane, M.; Gopalkrishnan, R. V.; Valerie, K.; Dent, P.; Fisher, P. B. mda-7 (IL-24) Mediates selective apoptosis in human melanoma cells by inducing the coordinated overexpression of the GADD family of genes by means of p38 MAPK. *Proc. Natl. Acad. Sci. U. S. A.* **2002**, *99*, 10054−10059.

DOI: 10.1021/acs.jafc.5b01779
J. Agric. Food Chem. 2015, 63, 5008−5016

(36) Srinivasan, S.; Ohsugi, M.; Liu, Z.; Fatrai, S.; Bernal-Mizrachi, E.; Permutt, M. A. Endoplasmic reticulum stress-induced apoptosis is partly mediated by reduced insulin signaling through phosphatidylinositol 3-kinase/Akt and increased glycogen synthase kinase-3β in mouse insulinoma cells. *Diabetes* **2005**, *54*, 968−975.
(37) Hyoda, K.; Hosoi, T.; Horie, N.; Okuma, Y.; Ozawa, K.; Nomura, Y. PI3K-Akt inactivation induced CHOP expression in endoplasmic reticulum-stressed cells. *Biochem. Biophys. Res. Commun.* **2006**, *340*, 286−290.

DOI: 10.1021/acs.jafc.5b01779
J. Agric. Food Chem. 2015, 63, 5008−5016

JOURNAL OF AGRICULTURAL AND FOOD CHEMISTRY

Article

pubs.acs.org/JAFC

Electrochemical Genosensor To Detect Pathogenic Bacteria (*Escherichia coli* O157:H7) As Applied in Real Food Samples (Fresh Beef) To Improve Food Safety and Quality Control

Mandour H. Abdalhai, António Maximiano Fernandes, Xiaofeng Xia, Abubakr Musa, Jian Ji, and Xiulan Sun*

State Key Laboratory of Food Science and Technology, School of Food Science and Technology, Synergetic Innovation Center of Food Safety and Nutrition, Wuxi, Jiangsu 214122, China

ABSTRACT: The electrochemical genosensor is one of the most promising methods for the rapid and reliable detection of pathogenic bacteria. In a previous work, we performed an efficient electrochemical genosensor detection of *Staphylococcus aureus* by using lead sulfide nanoparticles (PbSNPs). As a continuation of this study, in the present work, the electrochemical genosensor was used to detect *Escherichia coli* O157:H7. The primer and probes were designed using NCBI database and Sigma-Aldrich primer and probe software. The capture and signalizing probes were modified by thiol (SH) and amine (NH_2), respectively. Then, the signalizing probe was connected using cadmium sulfide nanoparticles (CdSNPs), which showed well-defined peaks after electrochemical detection. The genosensor was prepared by immobilization of complementary DNA on the gold electrode surface, which hybridizes with a specific fragment gene from pathogenic to make a sandwich structure. The conductivity and sensitivity of the sensor were increased by using multiwalled carbon nanotubes (MWCNT) that had been modified using chitosan deposited as a thin layer on the glass carbon electrode (GCE) surface, followed by a deposit of bismuth. The peak currents of *E. coli* O157:H7 correlated in a linear fashion with the concentration of tDNA. The detection limit was 1.97×10^{-14} M, and the correlation coefficient was 0.989. A poorly defined current response was observed as the negative control and baseline. Our results showed high sensitivity and selectivity of the electrochemical DNA biosensor to the pathogenic bacteria *E. coli* O157:H7. The biosensor was also used to evaluate the detection of pathogen in real beef samples contaminated artificially. Compared with other electrochemical DNA biosensors, we conclude that this genosensor provides for very efficient detection of pathogenic bacteria. Therefore, this method may have potential application in food safety and related fields.

KEYWORDS: *electrochemical genosensor, sandwich structure, cadmium sulfide nanoparticle, E. coli O157:H7, beef sample*

INTRODUCTION

Foodborne bacterial infections and diseases are a major cause of illness and death worldwide[1] *Escherichia coli* is a common bacterium in both food and humans and a predominant species of facultative anaerobes in the gut of animals. *E. coli* O157:H7 (designated by its somatic, O, and flagellar, H, antigens) was first recognized as a human pathogen following two hemorrhagic colitis outbreaks in 1982.[2,3] There is an enterohemorrhagic strain of the bacterium and Gram-negative pathogen that has been responsible for several diseases, such as hemorrhagic colitis (HC) and hemolytic uremic syndrome (HUS), caused by the presence and expression of Shiga toxins that can occur with very low exposure (<10 cells) to the bacterium.[3−5] Some of the *E. coli* strains found in human feces also are themselves pathogenic.

E. coli is associated with infection in both food and humans; it has been associated with food-related outbreaks in many countries and often involves contaminated beef or fresh produce. It exists in soils, fruits, and raw vegetables, and it is a significant foodborne pathogen carried in the intestinal tract of cattle and other animals. The bacteria may be transmitted to humans through fecal contamination of food.[5] The common source of infection is the consumption of contaminated food, especially meats, untreated water, unpasteurized milk, and foods that have been in direct contact with animals. *E. coli* O157:H7 is commonly found in the intestinal tract of warm-blooded animals, and the contamination depends on interaction with gut tissues where the pathogens adhere to the host cells. Consumption of foods contaminated with this pathogen can cause gastroenteritis as well as life-threatening diseases. Therefore, food safety becomes an issue of worldwide interest when we have repeated outbreaks of bacterial pathogens. Food safety in many countries requires monitoring, and more consumers and organizations now pay attention to food safety issues, which may prevent complication.

Testing of food and food raw materials for the presence of pathogenic microorganisms and toxin producers is classically done using traditional methods such as plate samples. This is widely used and relies on a series of selective or nonselective media, each of which allows for growth of a certain group of pathogens. The detection of microorganisms using this traditional method (conventional plate count) is time-consuming, taking at least 2−5 days for results and up to 7−10 days for the final confirmation. Therefore, polymerase chain reaction (PCR) has been used to amplify the target DNA.

Received: February 4, 2015
Revised: May 7, 2015
Accepted: May 12, 2015
Published: May 12, 2015

ACS Publications © 2015 American Chemical Society

DOI: 10.1021/acs.jafc.5b00675
J. Agric. Food Chem. 2015, 63, 5017−5025

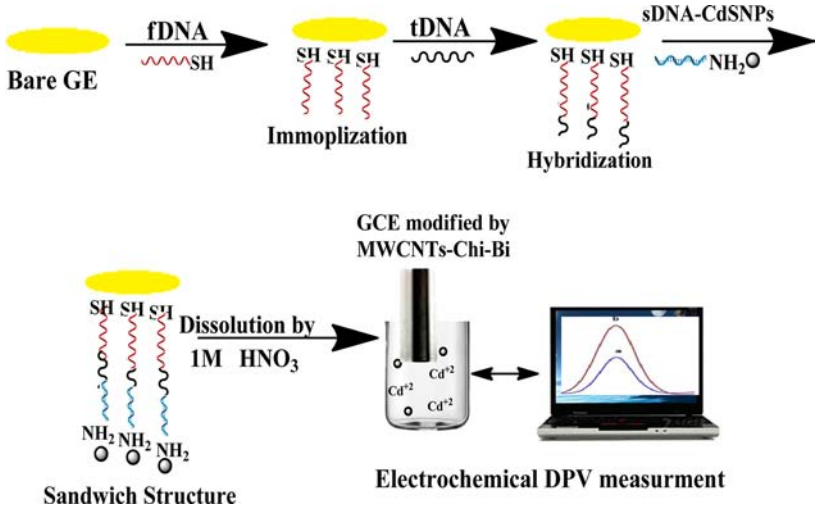

Figure 1. Schematic performance of the electrochemical detection of target DNA based on CdSNPs-labeled oligonucleotides DNA probes.

However, this method is time consuming and requires expensive instrument.[6] In recent years, research has developed new methods.[7] However, these methods often fail to differentiate pathogenic species from nonpathogenic ones. Presently, the electrochemical method for DNA detection of pathogenic microorganisms in food safety has been receiving more attention because of its advantages of speed, sensitivity, selectivity, and lower cost. In a method based on nanoparticles, the specific gene can be detected.[8] Another method developed is the biosensor. Much literature has focused on the biosensor, especially the genosensor due to its high specificity, which avoids false results as happen in traditional methods and biochemical methods. This approach is crucial in connection with research efforts directed at gene analysis as well as in detection of genetic disorders and tissue matching. Electrochemical sensors have received considerable attention due to their quick response, remarkably higher sensitivity, good selectivity, and strong operability for the detection of pathogenic microorganisms.[9,10] The target DNA must be hybridized with a fixing probe (which is conjugated with nanoparticles). Another signalizing probe must be used that is fixed on a gold electrode surface that has been modified by a thiol group. To be clear, the most critical step in the preparation of DNA electrochemical biosensors is the immobilization of DNA strands on the surface of the gold electrode.[11] If the hybridization step is successful and creates a sandwich structure, the signal can be measured electronically. The development of nanotechnology and nanoscience has produced different nonmaterials that can be used for sensor design to develop sensitivity and selectivity. The use of a heavy metal to develop electrochemical biosensors is done to differentiate signals from the sandwich hybridization using a stripping method.[12] The nanoparticle was used as a marker to label a sequence known as the oligonucleotide.[13] For example, one study used the Cd nanocrystal based electrochemiluminescence biosensor cadmium sulfide (CdS), one of the most important binary semiconductors that we have, which has been extensively studied in the field of sensors.[14] Another study[15] used multiwalled carbon nanotubes (MWCNT) to increase the sensitivity of the electrode. The carbon nanotube (CNT) is one of the most widely studied nonmaterials. Numerous researchers have investigated the biocompatibility of functional CNTs, both in vitro and in vivo. However, the toxicological effects of MWCNT have not been thoroughly investigated, and some of the findings remain controversial.[16] MWCNT provide a large surface area, significant mechanical strength, efficient electrocatalytic activity, and high electrical conductivity that enhance electron transfer with the electrode surface. In addition, they may serve as catalysts.[17] Specific nucleic acid sequences were detected by single-stranded DNA probes complementary to the target DNA.[15] The key step in setting up such systems is the employment of high-efficiency testing methods, which must be accurate and sensitive enough to detect even low levels of contamination in a given commodity to prevent pathogens from being transmitted through the food chain to the consumer. In the present study, we measure a highly sensitive electrochemical genosensor for the rapid detection of *E. coli* O157:H7. We used complementary probes to construct a sandwich structure, CdNPs, and glass carbon electrode (GCE) decorated with MWCNT-Chi. Figure 1 shows the preparation of the sandwich structure on a GE surface and depicts electrochemical DNA detection using cadmium sulfide nanoparticles (CdSNPs) labels.

MATERIALS AND METHODS

Materials and Reagents. Cadmium chloride ($CdCl_2$), sodium sulfide (Na_2S), sodium hydroxide (NaOH), and 3-mercaptoacetic acid were used for the synthesis of CdSNPs. Tri(2-carboxyethyl)-phosphinehydrochloride (TCEP) and [1-ethyl-3-(3-dimethylaminopropyl)carbodiimide hydrochloride (EDC)] purchased from Sigma-Aldrich were used as carboxyl activating agents for the coupling of primary amines to create amide bonds with carboxylic group on the surface of NPs. Salmon sperm DNA was used as blocking agent during the hybridization. Sodium dodecyl sulfate (SDS) was used to remove the unhybridized DNA after immobilization and hybridization. Multiwalled carbon (purity > 95%, diameter = 50 nm, length = 10−20 μm) was obtained from Nanjing Xianfeng Nanomaterials Technology, China. Bismuth nitrate obtained from Scharlau Chewwice S.A. (Spain) was applied to the surface of the electrode to increase the sensitivity. All of the oligonucleotides used in the sensor were purchased from Takara Co. (Dalian, China) and Sangon Biotechnology Co., Ltd. (Shanghai, China), with HPLC purification. All of the solutions were prepared using ultrapure water from a Millipore Milli-Q system.

Apparatus. A centrifuge was used to concentrate and wash the NPs. A vortex mixer was used to combine the amine group with the CdSNPs. An incubator was used for the hybridization reaction and a refrigerator for the preservation of the CdSNPs. A Nanodrop 1000

DOI: 10.1021/acs.jafc.5b00675
J. Agric. Food Chem. 2015, 63, 5017−5025

Table 1. Oligonucleotide Sequences Used in Amplification, Immobilization, and Hybridization Experiments Specific for the *E. coli* O157:H7

target	accession no.	oligonucleotide	sequence (5′−3′)	length (bp)	amplicon size (bp)
Aeromonas hidrophyla	M84709	forward primer	5′-CCAATATGTCGGTGAAGA-3′	18	161
		reverse primer	5′-CATGTTTGAAGCTGTCAG-3′	18	
E. coli O157:H7	JX206444.1	forward primer	5′-GATAAATCGCCATTCG-3′	16	752
		reverse primer	5′-GTCACAGTAACAAACC-3′	16	
E. coli O157:H7	JX206444.1	capture probe	5′-GGAACCTCACTGACGC-SH-3′	16	
		detection probe	5′-NH_2-TGTGGCAAGAGCGATG-3′	16	

spectrophotometer (Thermo Scientific, Ashville, NC, USA) was used to measure the concentration and purity DNA. Electrochemical experiments were performed on potentiostat/galvanostat (Shanghai CH Instruments Co.) The three-electrode electrochemical detection system consisted of a GCE as a working electrode, an Ag/AgCl (saturated KCl) as a reference electrode, and platinum wire as a counter electrode. Scanning and transmission electron microscopes (SEM and TEM, respectively) were used to obtain images and morphologies of the CdSNPs and GCE surfaces, respectively.

Bacteria Culture and Genomic DNA Extraction. *E. coli* O157:H7 (accession no. JX206444.1) was obtained from the Zhangjiagang Entry-Exit Inspection and Quarantine Bureau (Suzhou, Jiangsu province, China). *Aeromonas hydrophila* (accession no. M84709) was obtained from the Freshwater Fisheries Research Center (Wuxi, China) and used as a negative control in this biosensor. The other strains were obtained from Jiangnan University laboratory. *A. hydrophila* was grown in ampicillin starch agar phenol red, whereas *E. coli* O157:H7 was grown in MacConkey agar (CM908) obtained from Beijing Land Bridge Technology Co., Ltd. Inoculum media strains were grown aerobically and incubated at 37 °C for 24 h in tryptic soy broth media (TSB). Genomic DNA was extracted after incubation for 18 h. Then, the DNA was extracted using a modified boiling method.[18] Briefly, the culture was boiled for 10 min to kill all pathogenic bacteria, and 1 mL of the culture was transferred into an Eppendorf tube and centrifuged at 13000 rpm for 5 min at 4 °C to pellet the cells. The supernatant was discarded, and the pellet obtained was suspended in 500 μL of sterile deionized water with a vigorous vortex. The cell suspension was boiled in a water bath for 15 min and immediately cooled at −20 °C for 10 min to cause a shock to the cells. Then, the sample was centrifuged a second time at 12000 rpm for 3 min. Finally the supernatant containing genomic DNA was harvested into another sterile Eppendorf and used as the DNA template for the PCR amplification.

Oligonucleotides, PCR Condition, and DNA Purification. All oligonucleotides used in this study were synthesized using the integrated DNA technology of Takara Co. and were purified by HPLC. The DNA probes for the *E. coli* were established by designing the primers used for the insertion element gene of *E. coli* to be complementary with the probes. For the amplification of the DNA samples, two primers (forward and reverse) were used. The pairs of primers were designed according to the target bacterial gene using the databases of the National Center for Biotechnology Information (NCBI) and the Basic Local Alignment Tool (BLAST) software (http://www.ncbi.nlm.nih.gov/)[19] DNA calculator from Sigma-Aldrich. The specificity of the primer sequences was further verified using software (http://www.sigmagenosys.com/calc/DNACalc.asp). All primer and probe sequences used in this study are listed in Table 1.

The reaction solution for PCR was performed in a total reaction volume of 25 μL, containing 2.5 μL of 10× PCR buffer, 2 μL of 10 mM of each dNTP (10 mM of each dNTP), 1 μL of each of the forward and reverse primers (0.4 μM concentration), 0.25 μL of Qiagen Taq, 17.25 μL DNase-free deionized water, and 1 μL of tDNA. *A. hydrophila* (ATCC 7966) was used as a negative control. The amplifications were carried out in a thermal cycler (TAkaRa, GRADIENT PCR, Japan) using the following conditions: an initial denaturation at 94 °C for 2 min, followed by 30 cycles of denaturation at 94 °C for 30 s, annealing at 45−53 °C for 30 s for *E. coli* O157:H7 and *A. hydrophila*, respectively, and, finally, extension at 72 °C for 5 min and holding at 4 °C. PCR amplifications were run on 2% agarose gel electrophoresis. Then, the bands were stained with Andy Safe, and the images were obtained using ultraviolet light using the Bio-Rad Gel doc 1000. A DNA fragment of 100 bp was used as the molecular size. A fragment (752 pb) of the *E. coli* O157:H7 (accession no. JX206444.1) was used, along with one (161 pb) of *A. hydrophila*. A PCR-purified kit purchased from Sangon Biotech Co. (Shanghai, China) was set up to purify the DNA products after PCR amplification and used according to the manufacturer's guidelines.

Synthesis of Nanoparticles. Glassware used in the procedure was cleaned in a bath of freshly prepared 3:1 HCl/HNO_3, rinsed thoroughly in twice-distilled water, and dried in an oven. CdSNPs were prepared according to the literature[20,21] with a slight modification. Specifically, 0.023 g of cadmium chloride ($CdCl_2$) was dissolved into 100 mL of deionized water to yield an aqueous solution at a concentration of 0.1 mM. Then 2 μL of mercaptoacetic acid ($C_2H_4O_2S$) was added as a stabilizer using vigorous stirring. The pH was adjusted to a final level of pH 11 using additional concentrated 0.5 mol L^{-1} NaOH. The solution was bubbled with nitrogen for 30 min, and then 50 mL of 1.34 mmol L^{-1} freshly prepared sodium sulfide (Na_2S) was added dropwise. Solutions were filtered prior to use with a 0.22 μm microporous membrane filter. The mixture turned yellow immediately due to the formation of CdS, and after additional stirring, the reaction was carried out for 24 h under bubbled nitrogen. The prepared colloid CdSNPs were stored in brown glass bottles at 4 °C until being used.

TEM, SEM. TEM has been found to be an excellent tool for characterizing the morphology of nanoparticles. A drop of the mixed solution was put on a TEM specimen and lit until it dried; then, TEM and SEM images were performed. This equipment was chosen to characterize the morphology of the electrode surface.

Conjugation between CdSNPs and NH_2-Modified Oligonucleotides. CdS was conjugated to the NH_2-modified oligonucleotides by using imidazole and EDC according to ref 22 with slight modifications. Briefly, 2 OD of NH_2-modified oligonucleotides was mixed with 200 μL of 0.1 M imidazole buffer and stirring for 30 min. Then 100 μL of freshly prepared EDC (0.1 M) was added. Washed CdSNPs were added and incubated at room temperature for 24 h with gentle stirring. Afterward, the solution was centrifuged at 10000 rpm for 30 min to purify the CdNP-NH_2-modified oligonucleotide. The precipitate was washed and centrifuged at 13000 rpm, and the pellet was resuspended and stored at −20 °C.

DNA Immobilization. Prior to the immobilization step, the gold electrode was heated in a piranha solution (3:7 H_2O_2/concentrated H_2SO_4), rinsed with DD water, and dried under nitrogen flow. Then, the gold electrodes were polished to a mirror-like finish using a microcloth with alumina powder of grain sizes 0.03 μm and 0.05 nm. Then, the electrodes were washed with water and 95% ethanol, respectively, for 5 min to remove the residual alumina powder and adsorbed impurities. To achieve the maximum cleaning process, the bare gold electrode was cleaned electrochemically in 0.5 mol/L H_2SO_4 until a repeatable cyclic voltammogram was obtained. The clean electrodes were washed with ultrapure water and dried under a pure nitrogen stream. The dried electrodes were initially immersed in a

DOI: 10.1021/acs.jafc.5b00675
J. Agric. Food Chem. 2015, 63, 5017−5025

fixing probe modified with a thiol group at 4 °C overnight to allow adsorption onto the gold surface. Finally, the electrodes modified with fixing probes were thoroughly rinsed with 10 mM PBS solution (1 M NaCl, pH 7.4) to remove unbound fDNA.[8,11,23]

DNA Hybridization. Prior to hybridization, the purified tDNA was denatured in a water bath (95 °C) and immediately chilled in ice for 5 min. The product was diluted with a PBS buffer solution (pH 7.0) and serial dilution. The first hybridization was performed by immersing the gold electrodes in tDNA and incubating at 45 °C for 1 h to allow the hybridization between the fixing probe and the tDNA. Then the electrodes were immersed in 0.1% sodium dodecyl sulfate (SDS) for 10 min to remove the unhybridized tDNA. In the second hybridization, the electrodes were incubated again for 1 h with a signalizing probe containing sDNA-CdSNPs. Then, the sandwich structure (fDNA-tDNA-sDNA-CdSNPs) was constructed. The electrochemical response was performed using an electrochemical analyzer at room temperature.[8,23,24]

Dissolution of CdS and Electrochemical Measurements. After immobilization and hybridization, the gold electrode with a sandwich structure was immersed in 150 μL of 1.0 mol L^{-1} HNO_3 solution for 5 min to dissolve the CdSNPs fixed on the surface of the electrode. The released CdSNPs ions were then ready for electrochemical measurement. For the decoration step, MWCNT-Chi was dropped onto the GCE surface and dried at room temperature. Then bismuth layer was deposited electrochemically by immersing the modified electrode into a solution containing 0.1 M acetate buffer solution and 100 μL of bismuth ions, and a negative potential for 100 s was applied.[25] Electrochemical measurements including DPV, clean electrode, cyclic votammetry (CV), and electrochemical impedance spectroscopy (EIS) were performed using an electrochemical analyzer (CHI Inc., Shanghai, China) and a three-electrode system at room temperature. All experiments were carried out at room temperature, and all measurements were replicated three times. All curves were the average of at least three test results. Different bacteria concentrations were used, and each bacterial concentration was plotted against the current peak. The deposition potential used in this study was −1.2 Vvs for 100 s, whereas the DPV potential was −1.2 Vvs.

Real Application of Sensor in Food Matrix. Fresh beef meat was purchased from a local market in Wuxi, China. The sample was prepared and examined according to the literature.[26] Briefly, the sample was divided into different parts and sterilized with radiation. Then, 10 g of beef sample was inoculated with 100 μL of different bacterial concentrations (*E. coli* O157:H7) ranging from 10 to 10^5 CFU/mL onto the surface of the beef sample and stored at 4 °C for 4 h. In the same manner, controls consisting of uninoculated samples were used. Afterward, each beef sample was transferred to a sterile 250 mL Erlenmeyer flask, and 90 mL of TSB was added to obtain the proportion 1:10 (sample weight/total weight). Then, a 1.5 mL portion of rinse fluid was removed from each bottle and placed in a sterile 2 mL microcentrifuge tube for DNA extraction. The DNA of the pellet was extracted using a boiling method, and the PCR products were checked as above.

RESULTS AND DISCUSSION

Characterization of Nanoparticles and Electrode. The morphologies and size of the CdSNPs were estimated using TEM (Figure 2). The image of the CdSNPs shows the average length ranged from 8 to 11 nm with good dispersion. Furthermore, the image shows that the particles did not aggregate after synthesis and storage. The size of the NPs affected the quality and connection with the signalizing probe.[27] We found that the size of the CdS was approximately 7−53 nm, which agrees with research[28] documenting use of CdSNPs with size >10 nm. After electrode polish, the GE was cleaned electrochemically by scan in 0.5 mol/L H_2SO_4; Figure 3 shows the scan of electrode. The modified GCE was characterized by SEM in different steps. Figure 4A shows the image of the bare GCE (blank control) and shows only a blurred background of

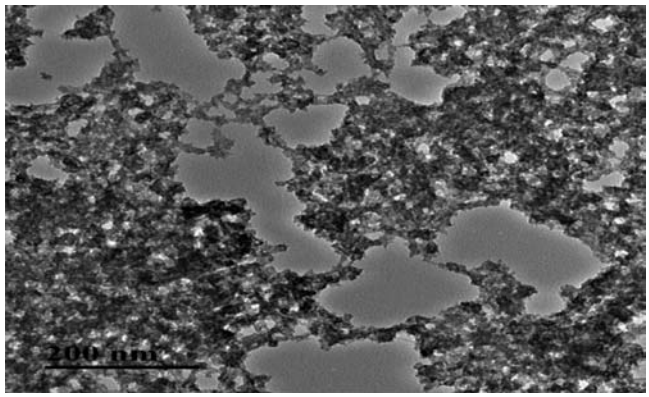

Figure 2. TEM micrographs of the synthesized CdSNPs.

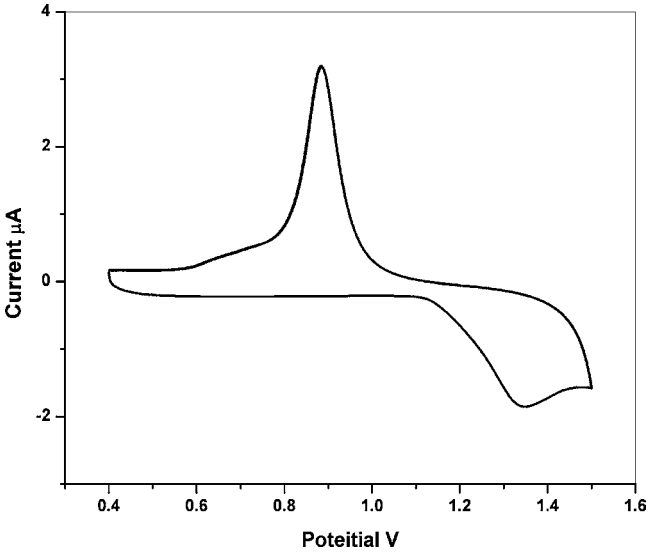

Figure 3. Cleaning gold electrode by using 0.5 mol/L H_2SO_4.

the electrode surface. Figure 4B shows the GCE covered with MWCNT-Chi after being dried. There was an electrochemical deposition of bismuth to the GCE modified by the MWCNT, as Figure 4C confirms.

PCR Amplification. A pair of primers was designed to be specific to *E. coli* O157:H7. The specificity of the PCR products of the pure culture using positive and negative bacteria is shown in Figure 5. The results indicate that the primer pair was specific for the corresponding target organisms. It used the amplification reactions for the PCR detection of the target genes of *E. coli* O157:H7 at approximately 752 bp and at 161 bp for *A. hydrophila*. It produced a high yield of specific DNA target sequences. This yield was verified by gel electrophoresis, which revealed a band that did not appear in any PCR reaction with another DNA template (negative control). The band's intensity was different when the genome was extracted from pure culture and real sample. The PCR product had double-stranded DNA oligonucleotides with a complementary sequence of both fDNA and sDNA.

Eectrochemical Impedance Spectroscopy (EIS) and Cyclic Voltammetry (CV). EIS experiments were performed to characterize a modified electrode surface in different steps. It was extensively used for the study of electron transfer on the modified surface. It also measured the sensitive electrode surface phenomena and changes in bulk properties.[10] EIS data

DOI: 10.1021/acs.jafc.5b00675
J. Agric. Food Chem. 2015, 63, 5017−5025

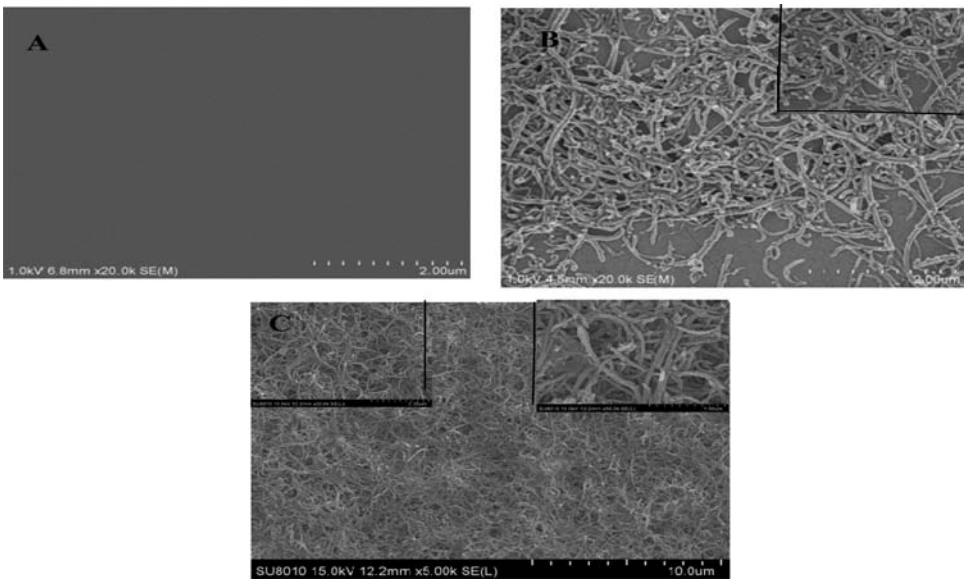

Figure 4. SEM images of GCE morphological changes in different resolutions: (A) bare electrode; (B) GCE covered with MWCNT-Chi; (C) MWCNT-Chi-Bi.

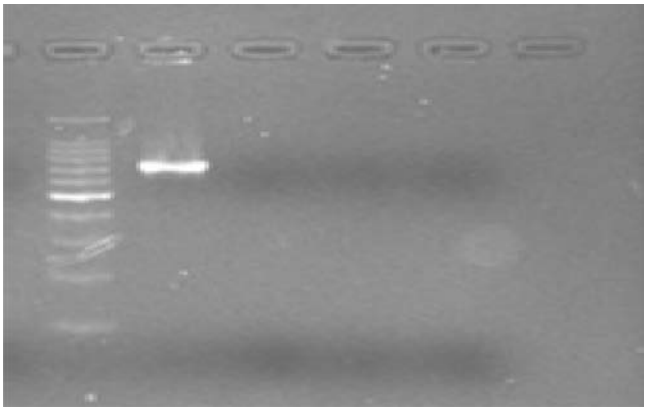

Figure 5. Agarose gel electrophoresis analysis (2%) of PCR amplicon. Lanes: 1, molecular marker (100 bp); 2, positive test sample *E. coli* 157:H7 (accession no. JX206444.1); 3, negative control containing PCR mixture with *Aeromonas hydrophila* (ATCC 7966); 4, negative control containing PCR mixture with *Staphylococcus aureus* (accession no. EF529607.1).

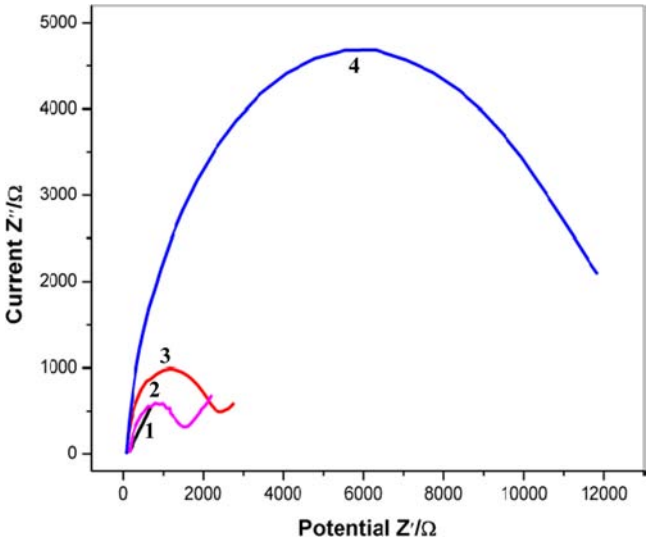

Figure 6. EIS of the electrode at different stages (different film modified electrodes) in potassium ferricyanide $[K_3OFe(CN)_6]$: (1) on the bare gold electrode surface; (2) gold electrode and fixing probe; (3) gold electrode, fixing probe, and tDNA; (4) gold electrode, fixing probe, tDNA, and capture probe.

were measured from 100 kHz to 1 Hz at a wave amplitude of 5 mV and an electrode potential of 0.20 V in $Fe(CN)_6^{3-/4-}$. Figure 6 shows the EIS in various modified GE steps. In this study, we selected thiol-terminated fDNA because of the strong affinity of thiol−metal (SH−Au) linkages, which provides connection with the gold surface.[11] The bare electrode showed a straight line. The R_{et} increased after being modified and hybridized, which indicated that electron transfer became more difficult. This phenomenon resulted from the negative charge on the sDNA that made the electron transfer of ferricyanide probes difficult due to electrostatic repulsion[8] and interaction between the material and ferricyanide anion.

Figure 7 characterizes modified GCE measured by EIS. The bare GCE showed a clear well-defined reversible redox peaks corresponding to the $[Fe(CN)_6]^{3-/4-}$ electron transfer process. When GCE was modified with MWCNT-Chi, the semicircular curve was observed. The bismuth layer formed during electrodeposition showed a slight decrease in peak currents and a negligible semicircle was observed. The bismuth slightly inhibits the electron transfer process in solution. The combination of MWCNT-Chi-Bi enhanced the sensitivity, adherence, and electrodeposition of released Cd^{2+}. GCE decorated by MWCNT-Chi can allow several uses. Prior to another detection, a potential of +0.3 V for 30 s can be applied to remove the Bi-CdSNPs from the electrode surface, and then a new bismuth layer could be generated by electrodeposition.

The effect of the scan rate on the electrochemical performance (redox reaction) of modified GCE (MWCNT-Chi-Bi) was investigated, using CV at different scan rates from 10 to 150 mV, to measure the current response of a ferricyanide solution exposed to different potentials. It was found that the sharp increase in peak currents was observed with an increase of scan rate, and the relationship was linearly related to the scan

DOI: 10.1021/acs.jafc.5b00675
J. Agric. Food Chem. 2015, 63, 5017−5025

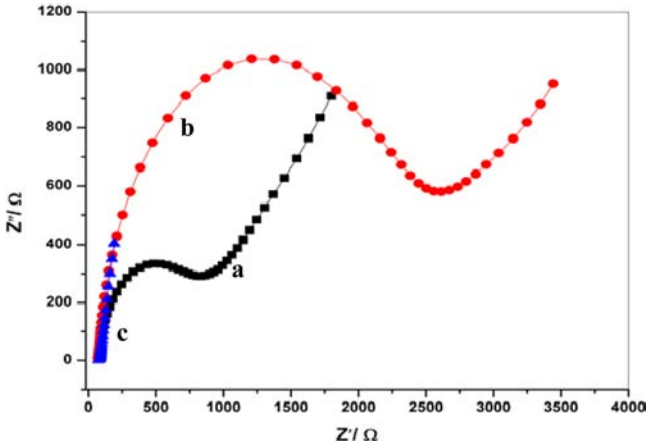

Figure 7. Impedance spectroscopy EIS for GCE in different modification steps obtained in 1 mM $K_3Fe(CN)_6$ solution: (a) bare GCE; (b) GCE modified by MWCNT-Chi; (c) GCE modified by MWCNT-Chi-Bi.

rate, indicating that the sensor has a good electrochemical conductivity. After the deposition of bismuth, the charge transfer decreased, which indicates that the electron transfer of $[Fe(CN)_6]^{3-/4-}$ was blocked. Bismuth has poor electrical conductivity, so the electrical characteristics were improved by using MWCNT in the GCE surface to enhance the efficiency. Figure 8 shows the scan rate in a different current.

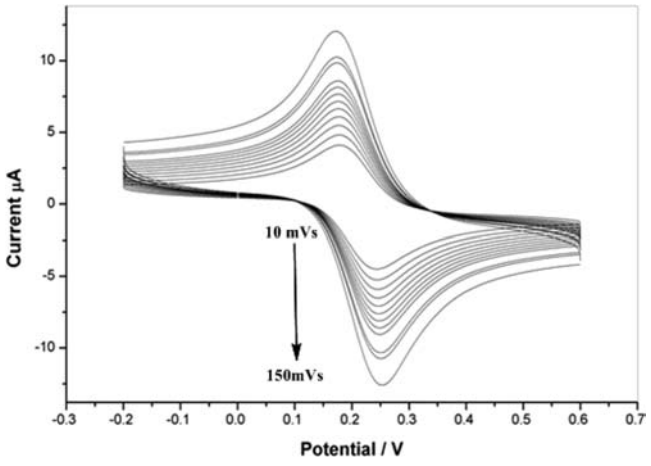

Figure 8. Cyclic voltammetry acquired on modified GCE in a solution containing $Fe(CN)_6^{3-/4-}$, at different scan rates from 10 to 150 mV s^{-1}. Scan range was between −0.2 and 0.6 V.

Electrochemical. The DNA detection process was performed in two main steps. The first was immobilization to allow the modified fixing probe on the GE surface to connect the thiol group with the GE.[15] Prior to immobilization, fDNA was mixed with tri(2-carboxyethyl)phosphine hydrochloride at a proportion of 1:2 and incubated at room temperature for 1 h to allow the thiol group bond to be free. This procedure facilitated the attachment to the GE surface. Bovine serum albumin (BSA) blocking was carried out after the probe immobilization and washed with PBS. Then, hybridization was accomplished by first adding serial concentrations of tDNA to connect with fDNA and then adding signalizing DNA containing CdSNPs. To conjugate and complete the sandwich structure, sDNA modified by CdSNPs with EDC was used to cross-link the CdSNPs and the amine group[22] and washed with GE to remove any unhybridized DNA. In the next step, the GE was submerged in 1 M HNO_3 solution[20] to release the sandwich structure content CdNPs to be measured by DPV. GCE was decorated with MWCNT-Chi-Bi, which improves the deposition release of cadmium ions on the electrode surface. CNT accelerates electron transfer due to the high conductivity. Therefore, it increases the sensitivity of MWCNT and characterizes the different steps, as shown in Figure 4. The electrochemical behavior of the CdSNPs ion was measured to investigate the sandwich using differential pulse voltammetry at the GCE surface and taking measurements of peak current. The DPV responses of the sensor to various concentrations of *E. coli* O157:H7 are shown in Figure 8. The negative control *A. hydrophila* was measured, and both steps (immobilization and hybridization) were included in tests.

Electrochemical DPV Measurements. DPV is a useful method for the sensitive detection of micro amounts of metal ion. Therefore, it is used in the measurement of Cd^{2+}.[20] The electrochemical behavior of the sandwich structure of the genosensor was detected as shown in Figure 9. The peak

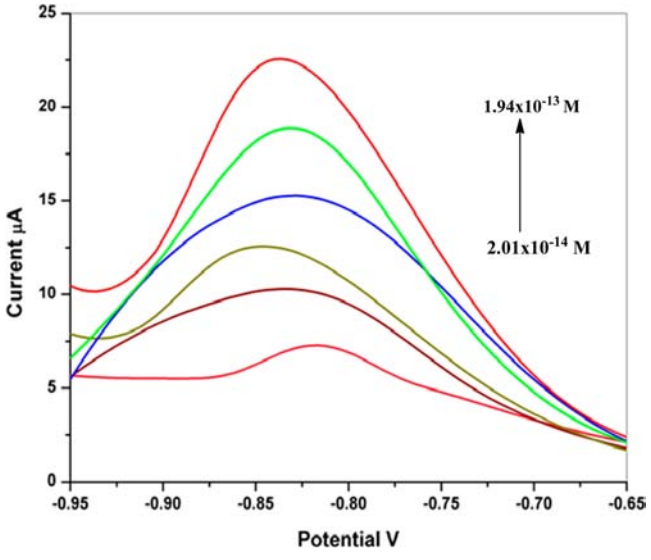

Figure 9. DPV analysis of electrochemical DNA sensors to detect tDNA with different concentration using CdSNPs for *E. coli* O157:H7 genomic DNA labeling, with sandwich structure fDNA−tDNA−cDNA−CdSNPs. The tDNA concentration ranged between 1.94×10^{-13} and 2.01×10^{-14} M.

current of various tDNA concentrations was observed, and we observed that the signal intensities increased dynamically with the increase of the concentration of tDNA. The calibration plot in Figure 10 shows that the signals of released Cd^{2+} had a good linear relationship with the peak currents and serial dilution of tDNA, with a correlation coefficient of 0.981 and the linear equation of $y = 113.9x + 5.86$), where y is the concentration of *E. coli* O157:H7 and x is the current. However, the peak appears at approximately −0.85 V. The detection limit of this study was 1.97×10^{-14} M with the ratio of signal-to-noise (s/n) equal to 3. The hybridization selectivity of the genosensor was investigated by the negative control sample (noncomplementary sequence), and the results did not show response at 0.8−0.9 V (CdSNPs). The results indicate that the MWCNT had a remarkable enhancement effect on the electrochemical response. The synergistic effect of the electronic conductivity

DOI: 10.1021/acs.jafc.5b00675
J. Agric. Food Chem. 2015, 63, 5017−5025

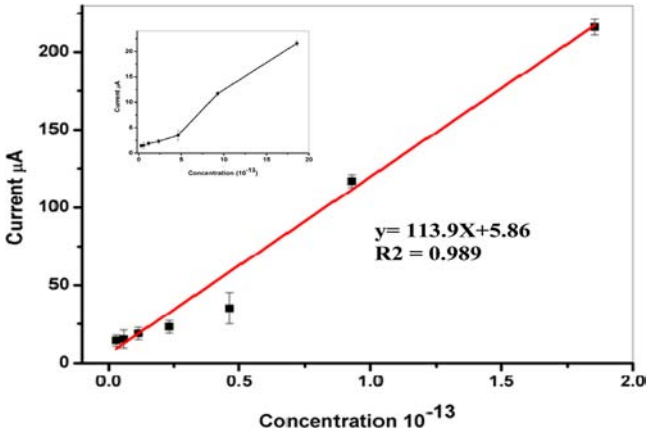

Figure 10. Corresponding calibration plots of peak current versus the concentration of *E. coli* O157H7 genomic DNA detection. The presented values are an average of triplicates with standard deviation. The resulting standard calibration curve is for different target DNA concentrations.

and electrocatalytic activity of the MWCNT enhanced ionic conductivity and ion-exchange capacity.[17] Overall, these results showed that this genosensor has good specificity and that only the complementary DNA sequence could form a sandwich structure. Therefore, the DNA genosensor sensitivity for the detection of *E. coli* O157:H7 has a limit of 1.97×10^{-14} M, whereas in the previous study,[29] the limit of detection was 3.17×10^{-14} M using *S. aureus* and PbNPs. The sensor is highly sensitive and has high specificity compared to other studies. Table 3 shows the detection limits of other studies and shows that this method performs better in sensitivity and specificity with regard to tDNA. Positive correlation was observed when the signal generated by CdSNPs was compared to the positive sample. The peaks showed a slight shift when using different tDNA concentrations. This phenomenon occurred in the interaction between the deposited materials and the metals formed during electrodeposition.

Application of Genosensor in a Food Matrix. The application of the present system is tested for enumeration of bacteria in six samples. The time between sampling and analysis has to be controlled to prevent changes in the concentration of the target microorganism that occur naturally over time.[4] The counts ranged from $(6.00 \pm 0.24) \times 10^2$ to $(2.47 \pm 0.75) \times 10^4$ cfu/mL for *E. coli* O157:H7. Although the infectious dose varies among pathogen types, it is generally believed that most bacterial pathogens are able to cause infection when $>10^3$ cfu/mL is ingested.[26] There were significant growth increases for different dilutions. Table 2 shows the enrichment for bacteria inoculated onto a beef sample. The DNA was extracted and amplified as described above. The gel electrophoresis detection of PCR products for serial dilution inoculums in beef samples is shown in Figure 11. The PDV obtained for the beef samples is shown in Figure 12. Measurement of the electrochemical response of the positive samples was indicated at −0.85 V, and the peak increased with the increase in concentration. On the

Table 2. Enumeration of *E. coli* O157:H7 in Artificially Contaminated Fresh Beef Sample and after Inoculation of Samples (Number Was Counted after Incubation for 24 h at 37° C)[a]

dilution factor	*E. coli* O157:H7 ± SD (cfu/mL)
10^1	$(2.47 \pm 0.75) \times 10^4$
10^2	$(1.08 \pm 0.38) \times 10^4$
10^3	$(7.09 \pm 1.45) \times 10^3$
10^4	$(2.09 \pm 0.52) \times 10^3$
10^5	$(6.00 \pm 0.24) \times 10^2$

[a]Data are expressed as the mean ± standard deviation (average of three replications for *E. coli* O157:H7). PCR analysis was carried out after overnight culture.

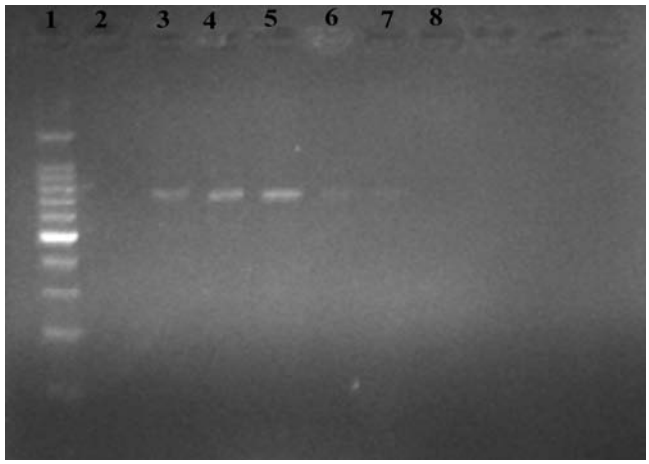

Figure 11. Agarose gel electrophoresis analysis (2%) of PCR amplicon extraction from fresh beef sample. Lanes: 1, molecular marker (100 bp); 2, negative test sample *Areomonas hydrophila* (M84709); 3−8, positive sample containing PCR mixture with *E. coli* (JX206444.1) in different concentrations.

Table 3. Limit Detection Sensitivity and Comparison of the Performance of the Genosensor with Other Electrochemical DNA Biosensor

target	method	detection limit	ref
synthesized oligonucleotide	DNA BIosensor	1.0×10^{-10} mol L^{-1}	12
low-density lipoprotein	CdS nanocrystal-based electrochemiluminescence biosensor	0.006 ng mL^{-1}	21
synthesized DNA	elongated hexagonal-pyramid CdS (eh-CdS) modified	3.9×10^{-15} M	14
syntheses (NOS) terminator gene sequence	differential pulse anodic stripping voltammetric method	2.75×10^{-12} M	20
S. aureus nuc gene	chitosan−Co_3O_4 nanorod− graphene	4.3×10^{-13} M	30
S. aureus	electrochemical genosensor based on multiwalled carbon nanotubes, chitosan, and bismuth	3.17×10^{-14} M	29
E. coli O157:H7	electrochemical genosensor based on multiwalled carbon nanotubes, chitosan, and bismuth	1.97×10^{-14} M	this study

DOI: 10.1021/acs.jafc.5b00675
J. Agric. Food Chem. 2015, 63, 5017−5025

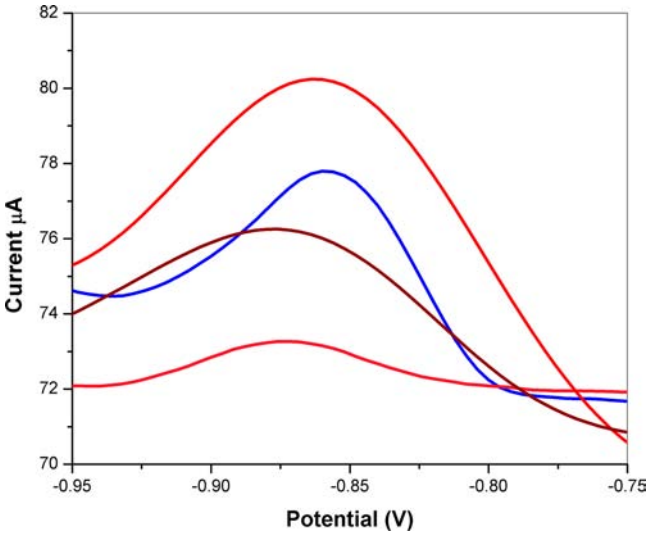

Figure 12. Differential pulse voltammogram responses for real samples (beef sample) in different concentrations.

other hand, the negative control *A. hydrophila* produced a negligible current. The electrochemical genosensor detection method has many advantages: it is quick, specific, and sensitive for pathogenic bacteria detection. In the present study, the electrochemical genosensor detection method was used to detect *E. coli* O157:H7 and showed high precision in *E. coli* O157:H7 detection. It could detect a very small amount of *E. coli* O157:H7. The genosensor was also applied in real samples (beef samples contaminated artificially) and showed good sensitivity and selectivity to pathogenic bacteria. The fDNA modified by a thiol group was enhanced and immobilized on GE. CdSNPs were synthesized using chemical methods and characterized by TEM; they were then conjugated with an amine group on the modified probe. Modification of MWCNT-chitosan with bismuth on the GCE surface increased electrochemical detection capacity. The signal of the released cadmium ions increased with increasing tDNA concentration. Therefore, this method will be very useful in food safety and quality control as an efficient and quick method for monitoring pathogenic bacteria in samples.

AUTHOR INFORMATION

Corresponding Author

*(X.S.) Mail: School of Food Science and Technology, Center of Food Safety and Quality control, Jiangnan University, 1800 Lihu Road, Wuxi 214122, China. Phone: 13915294105. Fax: +86 51085328726. E-mail: sxlzzz@jiangnan.edu.cn, mabdalhai1@hotmail.

Funding

This work has been supported by the National Natural Science Foundation of China (no. 31371768), the national research program (no. 201203069-1), the Program for New Century Excellent Talents in Jiangnan University, Qinglan Project, Synergetic Innovation Center of Food Safety and quality control, and the Priority Academic Program Development of Jiangsu Higher Education Institutions.

Notes

The authors declare no competing financial interest.

REFERENCES

(1) Scallan, E.; Hoekstra, R. M.; Angulo, F. J.; Tauxe, R. V.; Widdowson, M.-A.; Roy, S. L.; Jones, J. L.; Griffin, P. M. Foodborne illness acquired in the United States—major pathogens. *Emerg. Infect. Dis.* **2011**, *17*, P11101.

(2) Mendonça, R. C. S.; Morelli, A. M. F.; Pereira, J. A. M.; de Carvalho, M. M.; de Souza, N. L. Prediction of *Escherichia coli* O157:H7 adhesion and potential to form biofilm under experimental conditions. *Food Control* **2012**, *23*, 389−396.

(3) Hu, J.; Wang, B.; Fang, X.; Means, W. J.; McCormick, R. J.; Gomelsky, M.; Zhu, M.-J. c-di-GMP signaling regulates *E. coli* O157:H7 adhesion to colonic epithelium. *Vet. Microbiol.* **2013**, *164*, 344−351.

(4) Ngwa, G.; Schop, R.; Weir, S.; León-Velarde, C.; Odumeru, J. Detection and enumeration of *E. coli* O157:H7 in water samples by culture and molecular methods. *J. Microbiol. Methods* **2013**, *92*, 164−172.

(5) Zhu, P.; Shelton, D. R.; Li, S.; Adams, D. L.; Karns, J. S.; Amstutz, P.; Tang, C.-M. Detection of *E. coli* O157:H7 by immunomagnetic separation coupled with fluorescence immunoassay. *Biosens. Bioelectron.* **2011**, *30*, 337−341.

(6) Zhu, W.; Su, X.; Gao, X.; Dai, Z.; Zou, X. A label-free and PCR-free electrochemical assay for multiplexed micro RNA profiles by ligase chain reaction coupling with quantum dots barcodes. *Biosens. Bioelectron.* **2014**, *53*, 414−419.

(7) Li, Y.; Fang, L.; Cheng, P.; Deng, J.; Jiang, L.; Huang, H.; Zheng, J. An electrochemical immunosensor for sensitive detection of *Escherichia coli* O157:H7 using C 60 based biocompatible platform and enzyme functionalized Pt nanochains tracing tag. *Biosens. Bioelectron.* **2013**, *49*, 485−491.

(8) Wang, H.-B.; Zhang, H.-D.; Xu, S.-P.; Gan, T.; Huang, K.-J.; Liu, Y.-M. A sensitive and label-free electrochemical impedance biosensor for protein detection based on terminal protection of small molecule-linked DNA. *Sens. Actuators, B* **2014**, *194*, 478−483.

(9) Yola, M. L.; Eren, T.; Atar, N. Molecular imprinted nanosensor based on surface plasmon resonance: application to the sensitive determination of amoxicillin. *Sens. Actuators, B* **2014**, *195*, 28−35.

(10) Chen, Y.; Xu, J.; Su, J.; Xiang, Y.; Yuan, R.; Chai, Y. In situ hybridization chain reaction amplification for universal and highly sensitive electrochemiluminescent detection of DNA. *Anal. Chem.* **2012**, *84*, 7750−7755.

(11) Xu, H.-B.; Ye, R.-F.; Yang, S.-Y.; Li, R.; Yang, X. Electrochemical DNA nano-biosensor for the detection of genotoxins in water samples. *Chin. Chem. Lett.* **2014**, *25*, 29−34.

(12) Mao, X.; Yang, L.; Su, X.-L.; Li, Y. A nanoparticle amplification based quartz crystal microbalance DNA sensor for detection of *Escherichia coli* O157: H7. *Biosens. Bioelectron.* **2006**, *21*, 1178−1185.

(13) Zhu, N.; Zhang, A.; Wang, Q.; He, P.; Fang, Y. Electrochemical detection of DNA hybridization using methylene blue and electrodeposited zirconia thin films on gold electrodes. *Anal. Chim. Acta* **2004**, *510* (2), 163−168.

(14) Zheng, D.; Wang, Q.; Gao, F.; Wang, Q.; Qiu, W.; Gao, F. Development of a novel electrochemical DNA biosensor based on elongated hexagonal-pyramid CdS and poly-isonicotinic acid composite film. *Biosens. Bioelectron.* **2014**, *60*, 167−174.

(15) Ligaj, M.; Tichoniuk, M.; Gwiazdowska, D.; Filipiak, M. Electrochemical DNA biosensor for the detection of pathogenic bacteria *Aeromonas hydrophila*. *Electrochim. Acta* **2014**, *128*, 67−74.

(16) Liu, Z.; Liu, Y.; Peng, D. Hydroxylation of multi-walled carbon nanotubes reduces their cytotoxicity by limiting the activation of mitochondrial mediated apoptotic pathway. *J. Mater. Sci.: Mater. Med.* **2014**, *25*, 1033−1044.

(17) Nigović, B.; Sadiković, M.; Sertić, M. Multi-walled carbon nanotubes/Nafion composite film modified electrode as a sensor for simultaneous determination of ondansetron and morphine. *Talanta* **2014**, *122*, 187−194.

(18) Pui, C. F.; Wong, W. C.; Chai, L. C.; Nillian, E.; Ghazali, F. M.; Cheah, Y. K.; Nakaguchi, Y.; Nishibuchi, M.; Radu, S. Simultaneous detection of *Salmonella* spp., *Salmonella* Typhi and *Salmonella*

DOI: 10.1021/acs.jafc.5b00675
J. Agric. Food Chem. 2015, 63, 5017−5025

Typhimurium in sliced fruits using multiplex PCR. *Food Control* **2011**, *22*, 337−342.
(19) Sguazza, G. H.; Reynaldi, F. J.; Galosi, C. M.; Pecoraro, M. R. Simultaneous detection of bee viruses by multiplex PCR. *J. Virol. Methods* **2013**, *194* (1), 102−106.
(20) Sun, W.; Zhong, J.; Zhang, B.; Jiao, K. Application of cadmium sulfide nanoparticles as oligonucleotide labels for the electrochemical detection of NOS terminator gene sequences. *Anal. Bioanal. Chem.* **2007**, *389* (7−8), 2179−2184.
(21) Jie, G.; Liu, B.; Pan, H.; Zhu, J.-J.; Chen, H.-Y. CdS nanocrystal-based electrochemiluminescence biosensor for the detection of low-density lipoprotein by increasing sensitivity with gold nanoparticle amplification. *Anal. Chem.* **2007**, *79*, 5574−5581.
(22) Zhang, D.; Huarng, M. C.; Alocilja, E. C. A multiplex nanoparticle-based bio-barcoded DNA sensor for the simultaneous detection of multiple pathogens. *Biosens. Bioelectron.* **2010**, *26*, 1736−1742.
(23) Jarczewska, M.; Ziółkowski, R.; Górski, Ł.; Malinowska, E. Electrochemical uranyl cation biosensor with DNA oligonucleotides as receptor layer. *Bioelectrochemistry* **2014**, *96*, 1−6.
(24) Shi, A.; Wang, J.; Han, X.; Fang, X.; Zhang, Y. A sensitive electrochemical DNA biosensor based on gold nanomaterial and graphene amplified signal. *Sens. Actuators, B* **2014**, *200*, 206−212.
(25) Cai, J.; Zhou, X.; Tu, Y.; Feng, G.; Huang, C. Application of bismuth-film modified glassy carbon electrode for solid-phase extraction of Sudan I. *Adv. Mater. Lett.* **2012**, *3*, 87−91.
(26) Guan, Z. P.; Jiang, Y.; Gao, F.; Zhang, L.; Zhou, G. H.; Guan, Z. J. Rapid and simultaneous analysis of five foodborne pathogenic bacteria using multiplex PCR. *Eur. Food Res. Technol.* **2013**, *237* (4), 627−637.
(27) Hassan, M.; Ali, A. Synthesis of nanostructured cadmium and zinc sulfides in aqueous solutions of hyperbranched polyethyleneimine. *J. Cryst. Growth* **2008**, *310*, 5252−5258.
(28) Bhardwaj, R.; Kushwaha, H.; Gaur, J.; Upreti, T.; Bharti, V.; Gupta, V.; Chaudhary, N.; Sharma, G.; Banerjee, K.; Chand, S. A green approach for direct growth of CdS nanoparticles network in poly(3-hexylthiophene-2,5-diyl) polymer film for hybrid photovoltaic. *Mater. Lett.* **2012**, *89*, 195−197.
(29) Abdalhai, M. H.; Maximiano Fernandes, A.; Bashari, M.; He, Q.; Sun, X.; Jing, J. A rapid and sensitive detection of foodborne pathogenic bacteria (*Staphylococcus aureus*) by using electrochemical DNA genomic biosensor and its application in beef products. *J. Agric. Food Chem.* **2014**, *62*, 12659−12667.
(30) Qi, X.; Gao, H.; Zhang, Y.; Wang, X.; Chen, Y.; Sun, W. Electrochemical DNA biosensor with chitosan-Co_3O_4 nanorod-graphene composite for the sensitive detection of staphylococcus aureus nuc gene sequence. *Bioelectrochemistry* **2012**, *88*, 42−47.

DOI: 10.1021/acs.jafc.5b00675
J. Agric. Food Chem. 2015, 63, 5017−5025

JOURNAL OF AGRICULTURAL AND FOOD CHEMISTRY

Article

pubs.acs.org/JAFC

From Producer to Consumer: Greenhouse Tomato Quality As Affected by Variety, Maturity Stage at Harvest, Transport Conditions, and Supermarket Storage

Michèl J. Verheul,* Rune Slimestad, and Irene Holta Tjøstheim

Norwegian Institute for Agricultural and Environmental Research—Bioforsk Vest Særheim, Postvegen 213, N-4353 Klepp Station, Norway

ABSTRACT: Possible causes for differences in quality traits at the time of buying were studied in two widely different red tomato types. Three maturity stages were harvested from commercial greenhouses and transferred immediately to controlled environments simulating different storage, transport, and supermarket conditions. Results show significant differences in development of color, fruit firmness, contents of soluble solids (SSC), titratable acids (TTA), phenolics, and carotenoids from harvest to sale, as related to postharvest conditions. Fruit firmness, SSC, and TTA of vine-ripened red cherry tomatoes was 30, 55 and 11% higher than for those harvested at breakers and ripened to red. Temperature, light, UVC radiation, or ethylene during 4 days transport affected tomato quality traits, and differences persisted during 3 weeks of supermarket storage. Ethylene exposure gave a 3.7-fold increase in lycopene content in cherry tomatoes, whereas UVC hormesis revealed a 6-fold increase compared with the control. Results can be used to update recommendations concerning optimal handling.

KEYWORDS: *Lycopersicon esculentum Mill., quality, on-vine ripening, postharvest treatment, color, firmness, taste, soluble solid content, total acid content, carotenoids, flavonoids*

INTRODUCTION

Tomato fruit quality is usually understood as a combination of some or all of the following parameters: visual appearance, firmness and texture, dry matter content, organoleptic compounds, and health influencing compounds.[1] Research on tomato fruit storage has mostly focused on shelf life in terms of appearance and firmness.[2] However, taste and health-influencing compounds of fresh tomatoes are of high relevance from a consumer perspective.[3] The initial decision to buy fruit and vegetables is usually made on the basis of appearance and firmness, while the frequency and magnitude of subsequent purchases depend largely on consumer assessment of eating quality. In the case of tomatoes, taste is mainly defined by the content of reducing sugars and organic acids.[4−6] Both sugars and acids contribute to the sweetness and to the overall aroma intensity.[7] Firmness is appreciated by Norwegian consumers who consider firmness and texture to be strongly related.[3]

Tomatoes together with processed products thereof are important parts of the traditional Mediterranean diet associated with low mortality of cardiovascular diseases.[8] Lycopene, the main carotenoid in red tomato, has received special attention because of results from epidemiological studies as well as from cell culture and animal studies that suggest that lycopene may lower the risk of cancer and cardiovascular diseases.[9] In addition, tomato is a valuable source of β-carotene, a pro-vitamin A compound, which, like lycopene, is a strong lipophilic antioxidant. Because of the high consumption of tomato-based products worldwide, attention has also been given to other phytochemicals from this species. The flavonol rutin (quercetin 3-(6″-rhamnosyl)-glucoside), together with chalconaringenin (a chalcone), was found at higher concentrations than lycopene in fresh cherry tomatoes.[10] Both compounds exhibit antiradical and antioxidant properties. Because rutin and apiorutin (quercetin 3-(2″apiosyl-6″-rhamnosyl)-glucoside)[11] are hydrophilic compounds, they are supposed to work differently from the carotenoids. Chlorogenic acid (5′-caffeoyl quinic acid) is an aromatic acid in fresh tomatoes that occurs together with isomeric compounds and other minor phenylpropanoids. Together, these compounds may account for concentrations similar to rutin in fresh tomatoes. As a result of the orto-catechol structure of chlorogenic acid, it is supposed to have some of the same antioxidant functions as rutin.

Early harvesting is a common practice employed to obtain firmer fruit suitable for transport. In Norway, wholesalers demand fruits to be harvested at maturity stage "breakers". A storage temperature of 10−13 °C in the dark is often chosen to guarantee a long shelf life.[12] Wholesalers obtain firmer fruits suitable for long distance transport and a longer marketable period. This commercial practice was justified by Lin and Block.[13] Because newer varieties often have a longer shelf life, this practice also leads to long-time storage, up to 3 weeks, in the supermarket before red ripe tomatoes reach the consumer.[14] Little is known about the effects of storage conditions on organoleptic and health-influencing compounds of fresh tomatoes. Consumers complain about the lack of taste of tomatoes in numerous newspaper and magazine articles.[15] The number of tomato varieties and types grown in Norwegian greenhouses for fresh consumption has increased dramatically the last 5 years. All types and varieties are stored the same way, and it is not known whether different tomato varieties and types react differently to storage conditions.

Received: November 25, 2014
Revised: April 23, 2015
Accepted: April 28, 2015
Published: April 28, 2015

ACS Publications © 2015 American Chemical Society

DOI: 10.1021/jf505450j
J. Agric. Food Chem. 2015, 63, 5026−5034

Variables such as maturity stage at harvest and environmental conditions during transport and supermarket storage might be crucial for tomato quality. Earlier studies have shown that maturity stage at harvest may influence postharvest quality.[1] The effects of growing conditions on the quality of different tomato cultivars were reviewed earlier.[16]

Postharvest treatment with UVC radiation might increase tomato quality, and sunlight might decrease tomato quality.[17] Long-distance transport in Norway often includes suboptimal storage conditions because of joint transport with other products that require low temperature (2−8 °C) or give off ethylene. Little is known about the effects and possible aftereffects of transportation on the quality of the tomato that reaches the consumer.

We carried out an experiment to quantify the effects of (1) maturity stage at harvest and (2) environmental conditions during transport on tomato quality during simulated supermarket storage at 22 °C. Two widely different tomato varieties were used. Storage at 22 °C was compared to standard storage conditions at 12 °C in the dark. The effects of postharvest treatment with UVC radiation or ethylene were elucidated.

MATERIALS AND METHODS

Plant material. Fully developed cherry tomatoes (*Lycopersicon esculentum* Mill. 'Susanne') and round tomatoes (*Lycopersicon esculentum* Mill. 'Dometica') at maturity stage "breakers", "pink", or "red"[18] were harvested from two commercial greenhouses in southwestern Norway (58°47′ N, 5°41′ E) on August 30 and September 8, 2010 and stored at 12 °C (±0.2 °C) in the dark at a relative humidity (RH) of 85% (±3%). Only undamaged fruits were harvested and handled carefully to decrease possible effects on flavor perception.[15] Fruit age at harvest was respectively 40, 47, and 54 days after flowering for 'Susanne', and 50, 57, and 64 days after flowering for 'Dometica' for maturity stages breakers, pink and red. Fruit size was 17 ± 3 g for 'Susanne' and 80 ± 5 g for 'Dometica'. Samples for analyses were taken on August 31 and September 3, 6, 14, and 20 for first harvest and on September 9, 13, 16, 23, and 30 for second harvest. All treatments included three maturity stages and three replications. Each sample consisted of six fruits, giving a total number of 9720 fruits.

Storage Conditions. Fruits from both cultivars and all three maturity stages were transferred randomly to 20 m^3 storage rooms with forced ventilation and different temperature and light conditions. In the time period from day 1 until day 4 after harvesting, different transport conditions were simulated. Conditions, selected after communication with Norwegian wholesalers, included different temperatures: 2, 8, 12, and 15 °C, all in the dark, exposure to light provided by fluorescent tubes (Osram L58W/21) with a light intensity of 150 μmol m^{-2} s^{-1} at fruit height while kept at a temperature of 12 °C, or exposure to ethylene (150 ppm) at a temperature of 2 °C in the dark. To elucidate the effects of UVC radiation, fruits were exposed to UVC radiation provided by UV lamps (Osram HNS 15W OFR) with a light intensity of 350 μmol m^{-2} s^{-1} at fruit height for 15 or 90 s at 12 °C and thereafter kept at 12 °C in the dark. All treatments were kept at a relative humidity of 85% (±3%). Temperature fluctuations in all storage rooms were kept within ±0.2 °C.

After simulated transportation for 96 h (day 4), the fruits were transferred to a storage room with a temperature of 22 °C, a light intensity of 40 μmol m^{-2} s^{-1} at fruit height provided by fluorescent tubes (Osram L58W/21), and a relative humidity of 85% (±3%) for 17 days, thus simulating storage conditions measured in Norwegian supermarkets in August 2010. As a control, fruits were kept in a storage room at 12 °C and 85% relative humidity in the dark. Fruits showing microbiological decay were excluded from the quality analysis.

Chemicals. Chalconaringenin (CN) and rutin were isolated from cherry tomatoes as described previously.[10] All other chemicals were obtained from Sigma-Aldrich, Norway.

Quality Traits. Color, firmness, soluble solid content (SSC), and total titratable acid (TTA) were measured following the methods of Mitcham and co-workers,[19] and the mean value from the measurements of four to six individual tomatoes was used to describe the quality of a sample. Tomato color was determined in accordance with a color sheet scaling from 1, which is equivalent to full green, to 12 which is fully red fruit. Colors 4, 8, as 12 represent maturity stages "breakers", "pink", and "red".[18] Firmness was measured on two opposite sides at a maximum distance from the columella for each of four tomatoes by use of a durometer (Durofel, Agro-Technologies, France). Complete lack of firmness is given number 1, whereas 100 means full firmness. Fruit firmness below 40 is considered to be nonsaleable in a Norwegian supermarket. SSC was determined by the use of a digital PR-100α refractometer (Atago Co., Japan) of tomato juice at ambient temperature. Juice was pressed by hand and measured; the data were expressed as the equivalent °Brix (or percent SSC). For the assessment of TTA, four to six tomatoes for each sample were chopped in a food processor until maximum homogenization was achieved. The sample was transferred to a 0.5 L plastic bag, sealed, and stored at −20 °C until further analyses. Within 2 weeks, ∼5 g of each sample was thawed, mixed with ∼20 mL of deionized water, and titrated (Basic Titrini 794, Metrohm, Switzerland) against 0.1 M NaOH until end equivalence point at pH 8.5−8.9. Total acid was expressed as citric acid equivalents (milligrams of CAE per 100 g FW).

HPLC Analyses. HPLC analyses were made on samples from the second harvest. A liquid chromatograph (Agilent 1100 system, Agilent Technologies) supplied with an autosampler and a photodiode array detector was used for the analysis of individual phenolics and carotenoids. Separation of the phenolics was achieved by an Eclipse XDB-C8 (4.6 × 150 mm, 5 μm) column (Agilent Technologies) and the use of a binary solvent system consisting of (A) 0.05% TFA in water and (B) 0.05% TFA in acetonitrile. The gradient (B in A) was linear from 5% to 10% in 5 min; from 10% to 25% for the next 5 min; from 25% to 85% in 6 min; from 85% to 5% in 2 min; and finally, reconditioning of the column by 5% for 2 min. The flow rate was 0.8 mL min^{-1}; 10 μL samples were injected onto the column, and separation took place at 30 °C. Flavonoids were detected at 370 nm, whereas aromatic acids were detected at 320 nm. Carotenoids were separated over the same column by use of the binary solvent system (A) methanol−acetonitrile−water−0.2 M Tris−HCl (pH 7.4) (15:65:18:2 v/v) and (B) methanol-*n*-hexane (7:1) with the gradient (B in A) linear from 0% to 100% in 15 min; 100% isocratic for 10 min; linear from 100% to 0% in 3 min; and finally, reconditioning of the column for 2 min.[20] The flow rate was 1.0 mL min^{-1}, 20 μL samples were injected onto the column, and separation took place at 30 °C. Lycopene and β-carotene were detected at 450 nm. All HPLC samples were filtered through a 13 mm syringe filter (Whatman Nylon filter 0.45 μm, Sigma-Aldrich) prior to injection. Individual standard curves were used to quantify chalconaringenin, rutin, chlorogenic acid, lycopene, and β-carotene. Quercetin 3-(2″-apiosyl-6″-rhamnosyl)-glucoside (apiorutin) was quantified as an equivalent of rutin, whereas the phenolic compounds **1**−**3** (Figure 7) exhibiting chromatographic and spectral properties similar to that of chlorogenic acid were quantified as equivalents of chlorogenic acid.

Statistics. Statistical analysis included two sampling dates at harvesting, three replications, two cultivars, three maturity stages, nine treatments (nine storage conditions during simulated transport and two storage conditions after transport) and five sampling dates after harvesting. For statistical analysis, mean values for six fruits were used. To evaluate the effects of supermarket conditions, fruits kept from day 1 to day 4 at 12 °C in the dark before transfer to 22 °C in the light were compared with fruits kept at 12 °C in the dark for 21 days. The effects of simulated transport conditions were evaluated after transfer to 22 °C in the light. Results were subjected to analysis of variance using the GLM procedure from the SAS statistical computer program (version 9.2). The SNK test was used to determinate significant differences between cultivars, maturity stages, storage conditions, transport conditions and days after harvesting at a level of significance of $P < 0.05$.

DOI: 10.1021/jf505450j
J. Agric. Food Chem. 2015, 63, 5026−5034

Table 1. Tomato Quality Traits at Harvest[a]

cultivar (V)	maturity stage (M)	color (1−12)	firmness (1−100)	SSC (°Brix)	TTA	chalco-naringenin	apiorutin	rutin	lycopene	β-carotene
Susanne	breakers	1.9 ± 0.5	88 ± 1	6.2 ± 0.1	741 ± 10	6.5 ± 4.2	0.7 ± 0.2	2.2 ± 1.6	0.3 ± 0.5	0.1 ± 0.1
	pink	6.6 ± 0.8	71 ± 2	7.4 ± 0.3	680 ± 21	5.9 ± 6.2	0.7 ± 0.1	2.7 ± 1.6	1.3 ± 0.6	0.2 ± 0.1
	red	10.1 ± 0.6	62 ± 2	8.5 ± 0.2	624 ± 16	3.8 ± 1.6	0.6 ± 0.1	1.6 ± 0.4	8.4 ± 3.3	0.5 ± 0.1
Dometica	breakers	3.9 ± 0.6	88 ± 2	5.4 ± 0.1	440 ± 38	5.4 ± 4.4	0.9 ± 0.6	1.7 ± 1.1	0.2 ± 0.5	0.1 ± 0.0
	pink	8.0 ± 0.5	84 ± 1	5.2 ± 0.1	370 ± 26	2.1 ± 1.9	0.7 ± 0.1	1.4 ± 0.6	0.2 ± 0.3	0.2 ± 0.0
	red	11.7 ± 0.1	79 ± 2	5.2 ± 0.1	335 ± 9	1.3 ± 0.6	0.8 ± 0.1	1.3 ± 0.2	3.1 ± 0.1	0.3 ± 0.1
V[b]		***	***	***	***	n.s.	n.s.	n.s.	*	***
M[b]		***	***	***	***	n.s.	n.s.	n.s.	**	***
V*M[b]		n.s.	**	***	n.s.	n.s.	n.s.	n.s.	*	*

[a]Mean values ± SD (n = 6). Phytochemical content is given as milligrams per 100 grams FW ± SD (n = 3). [b]Significance of differences between cultivar (V), maturity stage (M) and significance of interaction between cultivar and maturity stage (V*M) is given: n.s., not significant; *, $P < 0.1$; **, $P < 0.01$; ***, $P < 0.001$.

RESULTS AND DISCUSSION

Tomato Quality at Harvest. Tomato quality traits at the start of the experiment are given in Table 1. Maturity stage at harvest had a significant effect on color; taste; and taste-related factors, such as firmness, soluble solid content (SSC), and total titratable acid concentration (TTA). The effects were different for the two tomato types. In 'Susanne', SSC was considerably higher when harvested more mature, whereas this effect was absent in 'Dometica'. TTA was lower in more mature fruits of both cultivars. As expected, fruits were less firm when harvested more mature, but this effect was more pronounced in 'Susanne'. In addition, the content of flavonoids and carotenoids increased with increasing maturity stage. The highest contents of lycopene and β-carotene were found in red cherry tomatoes ('Susanne'), as expected from earlier observations.[21,22] Earlier studies with respect to taste-related components for tomato at harvesting time show contrasting results. Watada and Aulenbach could not find significant differences in SSC between fruits of round tomatoes harvested at different maturity stages.[23] Lopez et al. found the highest concentrations of sugars and acids in tomatoes at the breakers stage.[6] According to Davies and Hobson, a decrease in sugar content as the fruit approaches full ripeness was most frequently found, whereas Roberts et al., Raffo et al., and Cantwell found higher SSC in fruits of specialty tomatoes that were harvested more mature.[24−27] It is well established that tomato varieties can vary markedly in acidity. Titratable acidity has earlier been reported both to increase and to decrease with ripening stage.[6,24] Contrasting results might be explained by the use of different tomato types or cultivars in the experiments. Specialty tomato types and newer varieties might be more sensitive to changes in taste-related components at harvesting time than common round tomatoes or older varieties.[25]

Development of Tomato Quality during Storage. The main effects of the development of tomato quality during storage at simulated supermarket conditions when compared with storage at a temperature of 12 °C in the dark (control) are shown in Table 2. The color value increased at 22 °C when compared with 12 °C. The color development of 'Susanne' was severely reduced for all three maturity stages when kept in the dark, whereas 'Dometica' fruits harvested at breakers stage were not able to reach a fully red color in the "supermarket" (Figure 1). Color development in tomatos is reported to depend on the temperature. The optimal temperature for lycopene synthesis is between 16 and 26 °C.[28,29] Firmness decreased more when the tomatoes were stored at 22 °C compared with 12 °C, and the firmness decreased more in 'Susanne' when compared with 'Dometica', resulting in considerable losses of saleable fruits for "Susanne" harvested red after 14−21 days at 22 °C (Figure 2). The SSC content in both tomato cultivars decreased during storage, and even more at 22 °C compared with 12 °C (Figure 3). This might correspond to a higher respiration rate at the higher temperature.[25] The initial differences in SSC in tomatoes harvested at different maturity stages persisted during storage. Particularly, tomatoes harvested at the breakers stage retained a higher SSC when stored at 12 °C as compared with those

Table 2. Main Effects of Storage Conditions[a] on Tomato Color, Firmness, Soluble Solid Content and Titratable Acid Concentration (milligrams per 100 g) of Two Tomato Cultivars with Three Maturity Stages at 4, 7, 14, and 21 Days after Harvesting (n = 288)

	color (1−12)	firmness (1−100)	SSC (°Brix)	TTA
storage (S)				
supermarket	9.9 (a)[b]	62 (b)	5.9 (b)	502 (a)
control	9.1 (b)	70 (a)	6.2 (a)	494 (a)
days after harvest (D)				
4	7.6 (c)	75 (a)	6.3 (a)	554 (a)
7	9.6 (b)	65 (b)	6.0 (b)	570 (a)
14	11.0 (a)	55 (c)	5.8 (c)	425 (b)
21	11.2 (a)	54 (c)	5.4 (d)	411 (b)
cultivar (V)				
Susanne	8.8 (b)	58 (b)	6.9 (a)	668 (a)
Dometica	10.5 (a)	70 (a)	5.0 (b)	342 (b)
maturity stage at harvest (M)				
breakers	7.6 (c)	69 (a)	5.4 (c)	568 (a)
pink	10.3 (b)	63 (b)	6.0 (b)	474 (b)
red	11.4 (a)	59 (c)	6.4 (a)	450 (b)
S*D[c]	*	***	**	n.s.
S*V[c]	***	***	n.s.	n.s
S*M[c]	*	n.s	*	n.s.
S*D*V[c]	***	**	n.s.	n.s.
S*D*M[c]	***	*	n.s.	n.s.
S*V*M[c]	*	n.s.	n.s	n.s.
S*D*V*M[c]	*	*	n.s.	n.s.

[a]Simulated supermarket conditions versus storage at 12 °C in the dark (control), both after transport at 12 °C. [b]Values followed by different letters are significantly different according to SNK-test at $P < 0.05$ level. [c]Significance of interaction between storage conditions (S), days after harvesting (D), cultivar (V), and maturity stage at harvest (M) is given: n.s., not significant. *, $P < 0.1$; **, $P < 0.01$; ***, $P < 0.001$.

DOI: 10.1021/jf505450j
J. Agric. Food Chem. 2015, 63, 5026−5034

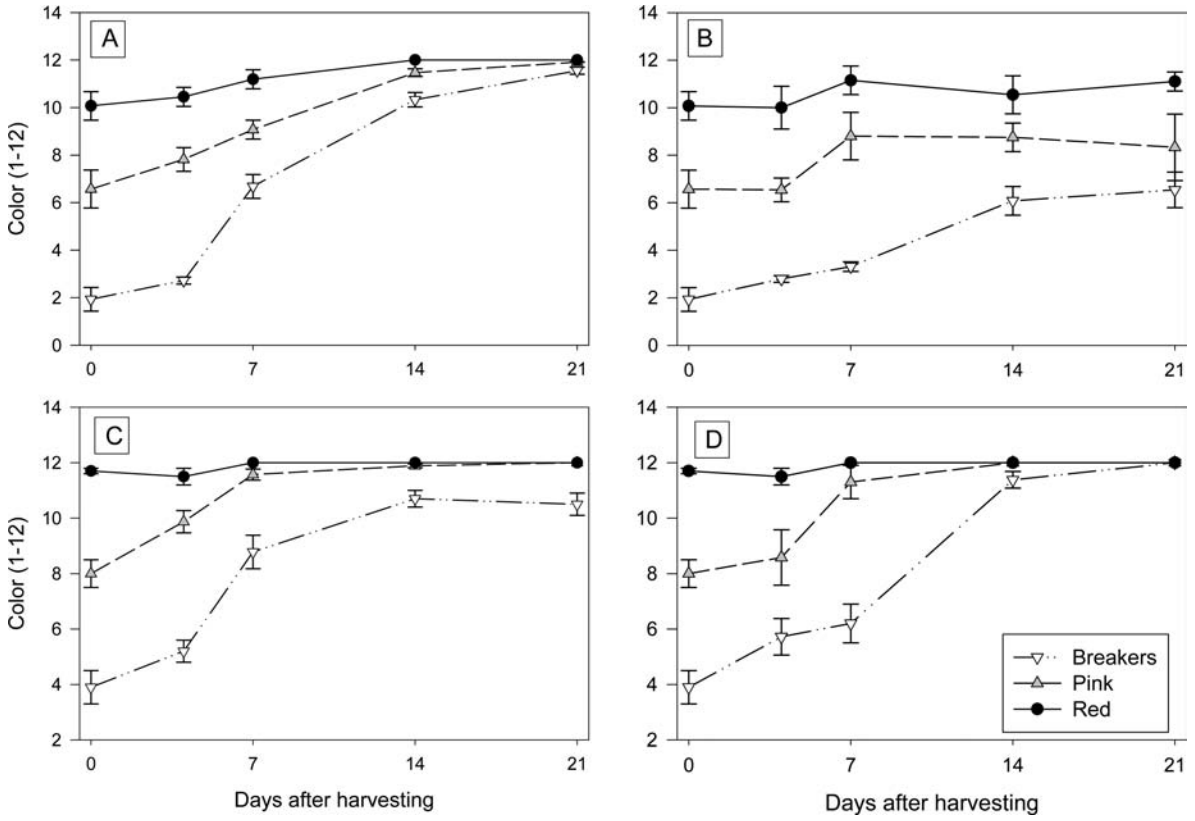

Figure 1. Color value of tomato 'Susanne' (A,B) and "Dometica" (C,D) harvested at different ripening stages (—··· breakers, - - - pink, — red) and stored under simulated supermarket conditions (A,C) or in the dark at 12 °C (B,D) for 21 days (mean values ± s.e., n = 6).

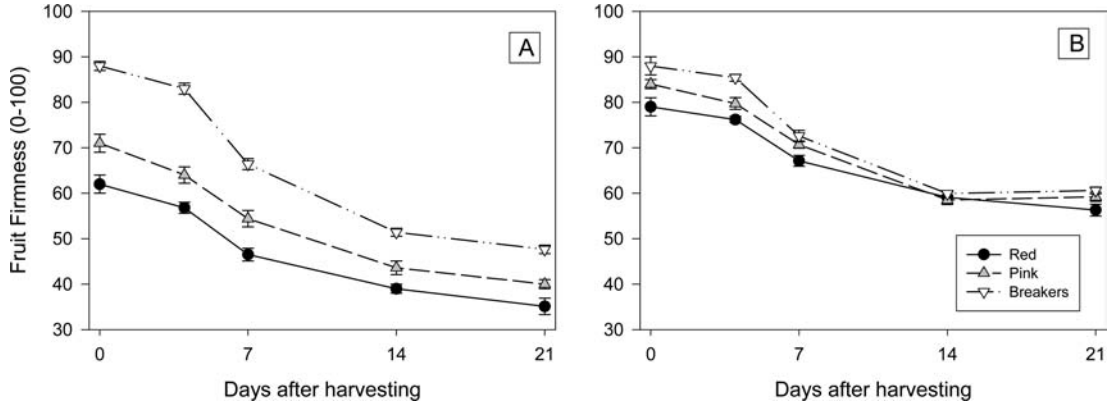

Figure 2. Fruit firmness of tomato 'Susanne' (A) and 'Dometica' (B) harvested at different ripening stages (—··· breakers, - - - pink, — red) and stored under simulated supermarket conditions for 21 days (mean values ± s.e., n = 6).

stored at 22 °C (Table 3). The TTA also decreased during storage (Table 1). Fruit firmness, SSC, and TTA of vine-ripened red 'Susanne' were 30, 55, and 11% higher than for those harvested at breakers and ripened to red. For 'Dometica', this was 32, 15, and 12%, respectively.

Mention of a decrease in firmness after harvesting tomatoes is commonly found in literature. Earlier experiments show contrasting results for taste-related components. Lin and Block concluded that vine-ripe red round tomatoes have quality attributes similar to that of tomatoes room-ripened at 20−22 °C.[13] Bui et al. pointed out that SSC and TTA did not change during postharvest.[30] The present experiment shows that the taste attributes of vine-ripened red tomatoes are considerably better than those of tomatoes harvested at breakers or pink and ripened to red, particularly for 'Susanne' (Figure 4). A better taste of vine-ripened tomatoes is confirmed by earlier observations by Betancourt et al.[31] and Roberts et al.[25]

Color, firmness, and taste are important quality parameters for consumers' willingness to pay.[3] Results in the present experiment show that fruits of a tomato variety with the same color and firmness may have different taste-related components. The uncertainty about taste may reduce consumers' willingness to pay. More knowledge on the effects of storage conditions on taste of high-quality tomato types is required to compete in lucrative markets. Reaching this market will also bring more challenges. The vine-ripened red cherry tomato type 'Susanne' in the present experiment had the best taste-

DOI: 10.1021/jf505450j
J. Agric. Food Chem. 2015, 63, 5026−5034

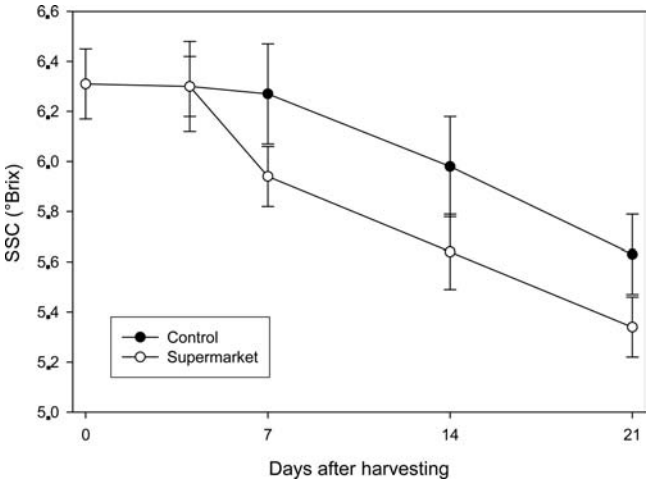

Figure 3. SSC of tomatoes stored under simulated supermarket conditions or in the dark at 12 °C for 21 days (mean values ± s.e., n = 36).

Table 3. Soluble Solid Content (°Brix) in Tomato Fruits Harvested at Three Maturity Stages and Kept under Supermarket or Control Conditions from Day 4 to Day 21[a]

maturity stage at harvest	supermarket	control
breakers	5.3 ± 0.1	5.6 ± 0.1
pink	6.0 ± 0.1	6.0 ± 0.2
red	6.3 ± 0.2	6.5 ± 0.2

[a]Mean value ± s.e. (n = 48).

related properties but shorter shelf life and will therefore require quicker handling to reach consumers.

Breaker tomatoes with no initial extractable lycopene exhibited a slow production of lycopene upon storage in darkness at 12 °C (Figure 4). After 2 weeks, a slight increase in this content was recognized in 'Susanne', whereas 'Dometica' during the first week seemed to initiate a certain production, but this faded during the rest of the storage period. Tomatoes harvested as pink had a higher initial lycopene concentration but followed the same pattern with respect to lycopene content. Red controls gave an abrupt decrease in lycopene content for both tomato types. From the 4th to the 15th day of storage, the content of extractable lycopene was low, but content increased rapidly at the end of the storage period, especially in 'Susanne'. The metabolism of β-carotene closely followed that of lycopene for the two tomato types; however, at a concentration level about one-tenth that of lycopene. The content of extractable lycopene did not correlate well with tomato color under some circumstances, especially not for breakers and red tomatoes (Figures 1b,d and 5). Correlation coefficients (R) were found to be −0.30 and −0.87 for breaker and red tomatoes of 'Dometica', and 0.32 and 0.09 for breaker and red tomatoes of 'Susanne'. In most of the analyzed samples, the content of lycopene is in agreement with their visible maturity stage or it is lower. In some cases. the content of extractable lycopene is higher than what would be expected on the basis of fruit color. For example, in 'Susanne', 21 days after harvesting, the content of extractable lycopene is 8 times higher than those analyzed at day 15, but this difference was not measurable as a color change. The results show that color by itself is not necessarily a good marker for extractable lycopene. Among the tomatoes that were stored in the darkness, those that were harvested fully ripened and had been stored for 3 weeks revealed the highest content of extractable lycopene. During fruit ripening, lycopene accumulates in the outer skin layer. One reason for low extractivity of the compound is the compactness of the tomato peel tissue, which hinders solvent penetration and transport to the chromoplasts. Furthermore, lycopene is tightly bound to membranous structures inside the organelle. These structures seem to be broken by action of cellulases, hemicellulases, and pectinases, which thus enhances the extractability of lycopene.[32] It seems that tomato carotenoids in ripened and mature fruit are not so strongly connected to membranous structures compared with the content found in less-ripened tomatoes. This might be an important issue with respect to impact of lycopene on human health because extractability of lycopene has been shown to correlate with the bioavailability of lycopene.[33]

Effects of Transport Conditions on Tomato Quality in the Supermarket. The main effects of transport conditions on tomato quality in the supermarket are shown in Table 4. No significant interactions were found between transport conditions and storage duration. Thus, differences in tomato quality traits directly after transport (sampling date 4) were also evident afterward at 22 °C (sampling dates 7, 14, and 21). Color development was highest after a transport temperature of 15 °C and lowest when tomatoes were submitted to ethylene

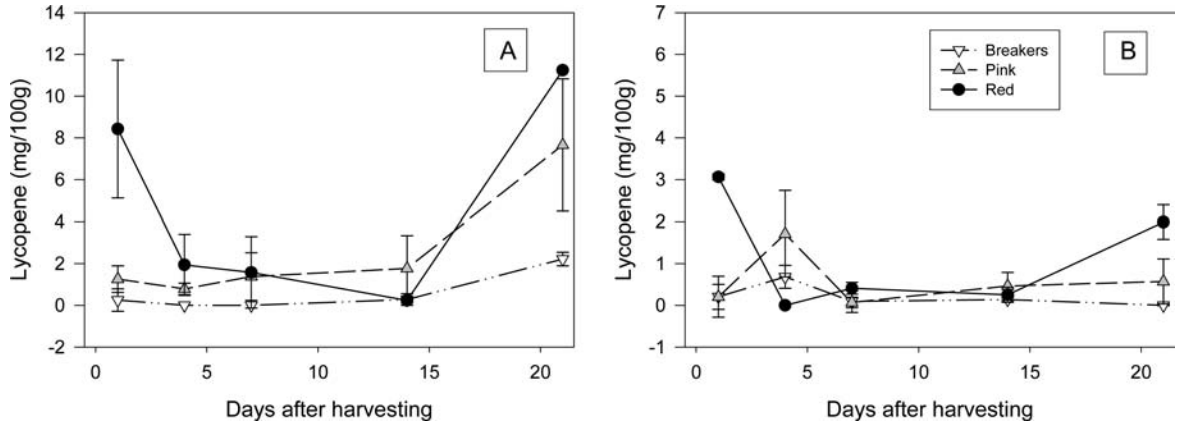

Figure 4. Content of lycopene in 'Susanne' (A) and 'Dometica' (B) of tomatoes harvested at different ripening stages (—··· breakers, - - - pink, — red) and stored in the dark at 12 °C during 21 days (mean values ± SD, n = 3).

DOI: 10.1021/jf505450j
J. Agric. Food Chem. 2015, 63, 5026−5034

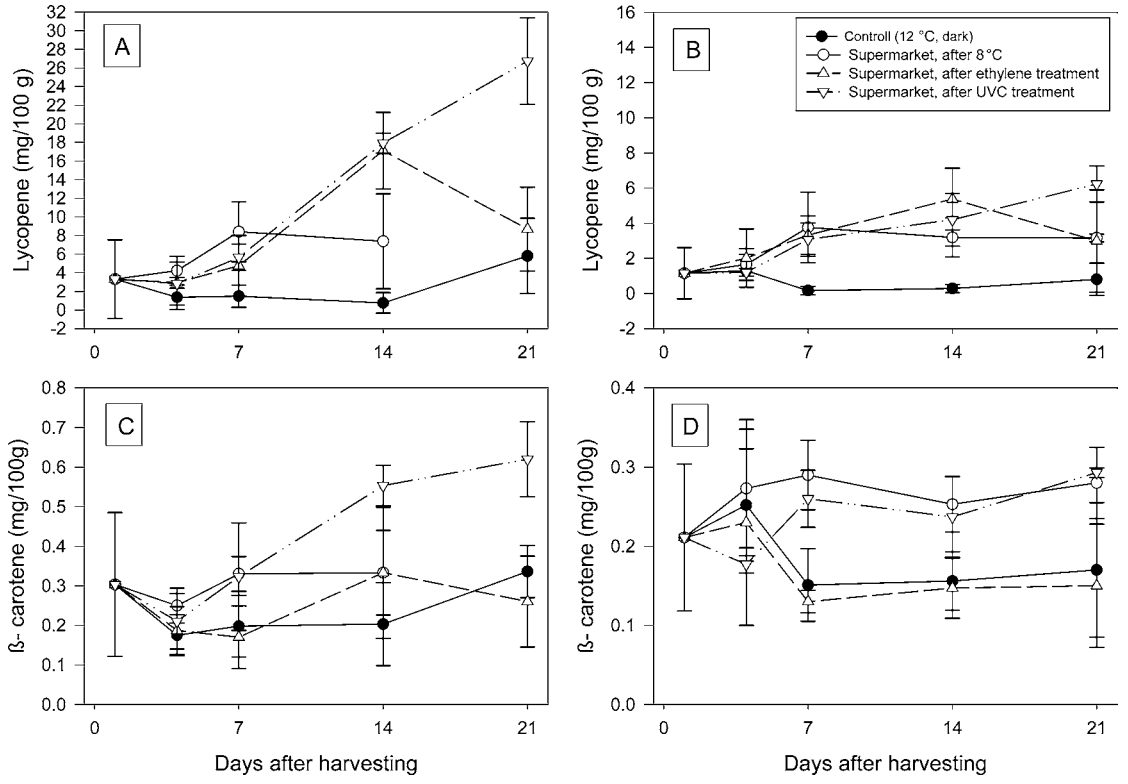

Figure 5. Content of lycopene (A,B) and β-carotene (C,D) in samples of 'Susanne' (A,C) and 'Dometica' (B,D) as a function of transport and storage conditions: supermarket, after transport at 8 °C in the dark (−o−), ethylene treatment (−Δ−), or 90 s UVC treatment (−V−) or control at 12 °C in the dark (−●−). All tomatoes were harvested at ripening stage pink. Mean values ± SD (n = 3).

Table 4. Main Effects of Transport Conditions on Color, Firmness, SSC, and TTA of Tomatoes in the Supermarket[a]

transport conditions	color (1−12)	firmness (1−100)	SSC (°Brix)	TTA (milligrams per 100 g)
2 °C	9.6 (cd)[b]	62 (ab)	5.9 (ab)	480 (b)
8 °C	9.5 (cd)	64 (a)	5.8 (ab)	520 (a)
12 °C	9.5 (cd)	64 (a)	5.8 (ab)	520 (a)
15 °C	10.5 (a)	58 (b)	5.9 (a)	472 (b)
light exposure	9.6 (cd)	61 (ab)	5.7 (bc)	475 (b)
ethylene exposure	9.0 (d)	62 (ab)	5.6 (c)	498 (ab)
UVC; 15 s	10.3 (ab)	59 (b)	5.9 (a)	466 (c)
UVC; 90 s	9.9 (bc)	62 (ab)	5.9 (ab)	493 (b)

[a]Two tomato cultivars with three maturity stages; 4,7,14, and 21 days after harvest; n = 144. [b]Values followed by different letters are significantly different according to SNK-test at $P < 0.05$ level.

during 4 days of transport. Transport at 15 °C and submission to UVC radiation for 15 s reduced tomato firmness compared with other transport conditions. Soluble solid content at 22 °C was higher for fruits transported at 15 °C or submitted to UVC radiation for 15 s and significantly lower for fruits transported when submitted to ethylene or fluorescent light. The TTA content at 22 °C was highest for fruits kept at 8 or 12 °C during transport and lowest for fruits submitted to 15 s of UVC radiation.

The results of the present experiment show that transport conditions during 4 days after harvest can have measurable effects on tomato quality in the supermarket. However, the effects are small compared with the effects of the cultivar and maturity stage at harvest on tomato quality (Table 2).

Earlier research has indicated that tomatoes should be stored at 10 °C or higher to avoid chilling injury.[25,34] Kader et al. provided evidence of adverse effects of low temperature (5 °C) on tomato flavor.[35] Even storage temperatures of 12.5 °C or lower may be detrimental to tomato flavor quality.[15] The present experiments shows that a temperature of 2−12 °C during transport had only a limited effect on tomato quality parameters such as color, firmness, SSC, and TTA. Kader reported a positive effect of ethylene on tomato quality, but the opposite was the case in the present experiment.[36] Charles et al. found that UV-treated fruits stored at 13 °C for 21 days had better texture and taste than nontreated fruits, although their appearance and color were rated poorer.[37]

Optimal storage conditions might be dependent on cultivar and maturity stage.[12] This could be confirmed in the present experiment. Significant interaction was found between conditions during transport and cultivar for color ($p < 0.05$), SSC ($p < 0.001$), and TTA ($p < 0.001$) and between transport conditions and maturity stage for SSC ($p < 0.01$) (data not shown). Recommended transport and storage conditions for tomatoes might therefore have to be reconsidered, depending on cultivars and maturity stage at harvest, to provide better-tasting tomatoes for the consumer.

Postharvest effects on carotenoids and flavonoids. Tomatoes harvested at maturity stage "pink" and kept at 8 °C in the dark for the first 4 days before being transferred to supermarket conditions (22 °C, light), exhibited a linear increase in lycopene and β-carotene production compared with control samples, kept at 12 °C in the dark, during the first 3 days after transfer to supermarket conditions (Figure 5).

DOI: 10.1021/jf505450j
J. Agric. Food Chem. 2015, 63, 5026−5034

Thereafter, the increase in the amount of both metabolites in both cultivars stagnated. In tomatoes initially exposed to ethylene, the amount of lycopene exceeded that found in nontreated fruits, and the concentrations increased continuously until 2 weeks after harvest. The effect of ethylene exposure on the development of β-carotene was different, however, and followed the low-concentration path found in control samples. The effects of initial UVC radiation for 90 s were even more pronounced than those of ethylene. The rise in concentration of lycopene and β-carotene prolonged during the whole storage period and was most pronounced for 'Susanne'.

Carotenoids are present in the thylakoid membranes of plants.[38] One part of their function is to serve as accessory pigments for light-harvesting in photosynthesis. Because they are part of light-harvesting complexes, the level of carotenoids will, in general, increase as a function of light irradiation. The dependence on light and temperature was demonstrated upon transfer of nontreated fruits to supermarket conditions (Figure 5). Alba et al. demonstrated the role of light quality on tomato phytochromes in the production of lycopene in tomato cultivars.[39] It was found that red light induced lycopene 2.3-fold, whereas far-red light reversed this production. The proportion of far-red light in the lamps used in the present experiment was lower than the proportion of red light. This might in part explain the rise in carotenoid content during the "supermarket" storage period.

The increase in content of tomato lycopene follows the general fruit ripening process. In addition, specific environmental factors make an impact on this metabolism. The most common stimulators of lycopene synthesis in harvested fruits are storage temperature and ethylene.[40] In general, storage temperatures of 20−30 °C stimulate lycopene production, whereas temperatures of 5 °C or less reduce lycopene.[2,41] Storage at 22 °C may thus have stimulated the carotenoid production in the tomatoes. Together with the light effect, this may explain the rise in lycopene during the simulated supermarket storage period; however, the temperature effect is reported to be specific for the different carotenoids, and an increase in temperature from 21 to 26 °C has been found to reduce the content of β-carotene without affecting lycopene.[42]

Ethylene acts as a plant hormone that stimulates ripening, cell wall softening, and subsequent lycopene formation in tomatoes and bitter melon.[40] In watermelon, subsequent use of ethylene caused cellular breakdown of placental tissue in immature and mature fruit and increased lycopene content by 10%. Here, ethylene treatment of 'Susanne' displayed a 3.7-fold enhancement in lycopene toward the control. Because the exposure took place at 2 °C (for 2 days), followed by 2 days without ethylene but at same low temperature and in darkness, the effect of temperature alone could give a decrease in lycopene.[2,41] It is therefore reasonable to conclude that the increase in lycopene is an effect of ethylene alone. The initial effect of ethylene might explain the prolonged increase in lycopene level of the "supermarket" storage of both tomato types versus the control.

The effectiveness of UVC hormesis for manipulation of tomato lycopene and β-carotene content has been found to depend on dosage(s) and combined treatments.[43] Liu and coworkers reported a strong increase in lycopene content after daily irradiation of mature green (breaker) tomatoes, whereas the concentration of β-carotene was unaffected.[17] Others reported a negative effect on lycopene and color development.[44,45] In addition to these results, the present data reveal a hormesis effect on both carotenoids in both tomato types.

Breaker cherry tomatoes were found to contain higher levels of flavonoids than fruits harvested at pink and red stages (Table 1). Chalconaringenin (CN) is the major compound among the flavonoids in breakers and pink tomatoes, and its content increased in pink tomatoes under simulated transportation conditions, especially at 8 °C in darkness. During storage at 22 °C, the concentration of CN declined, irrespective of simulated transport conditions (Figure 6). This is consistent with

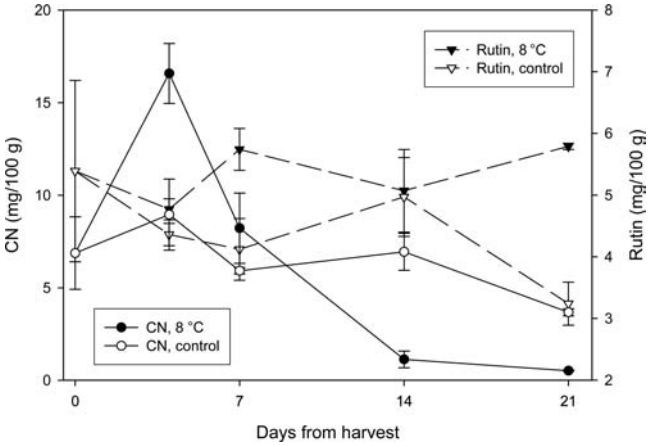

Figure 6. Content of chalconaringenin (CN) (−●−) and rutin (−▼−) in 'Susanne' harvested at breaker stage, pretreated at 8 °C, and stored under simulated supermarket conditions for 21 days. Controls (−o−, −V−) were stored at 12 °C in the darkness. Mean values ± SD (n = 3).

previous observations of the cherry cultivar Jennita.[21] However, controls (12 °C, darkness) of 'Susanne' gave no significant reduction in either CN or total flavonoid contents. This may imply that the CN metabolic turnover relies on genetic differences for otherwise close cultivars. Rutin is the major flavonoid in red cherry tomatoes, and its content, together with those of quercetin 3-apiosylrutinoside and kaempferol 3-rutinoside, were found to be stable during simulated transportation and supermarket conditions. This is in agreement with earlier observations.[21] Chlorogenic acid is the major aromatic acid in tomatoes.[16] Its concentration declined as a function of maturity stage upon harvest and during "supermarket" storage irrespective of "transport" conditions (Figure 7). This seems to follow a recognized pattern of caffeic acid derivatives in tomatoes.[21,26] Three more compounds were tentatively identified as more hydrophilic caffeic acid derivatives than chlorogenic acid, according to their HPLC retention factors, online UV-spectra, and previous detection of such compounds in tomatoes.[46] In contrast to chlorogenic acid, a weak rise in concentration was observed both as a function of ripening degree at harvest and during postharvest ripening, that is, under simulated supermarket conditions.

The results might explain discrepancies found in earlier research in postharvest tomato quality, and this justifies a need to update earlier recommendations concerning optimal handling conditions for high-quality tomatoes in the consumers' market.

DOI: 10.1021/jf505450j
J. Agric. Food Chem. 2015, 63, 5026−5034

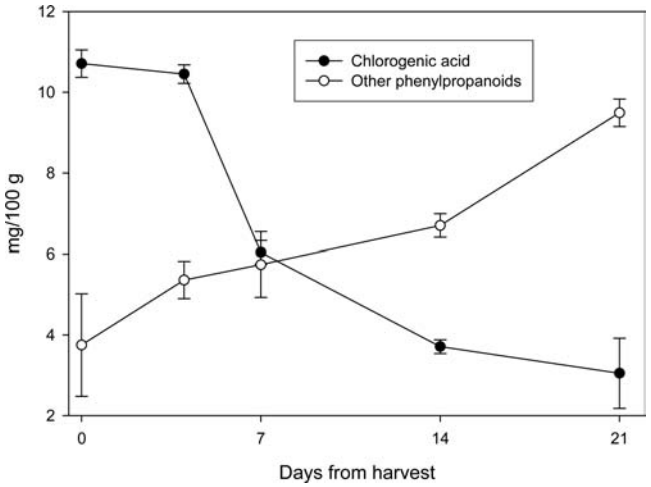

Figure 7. Content of chlorogenic acid (−●−) and other phenylpropanoids (−o−) in 'Susanne' harvested at breaker stage, pretreated at 8 °C and stored under simulated supermarket conditions for 21 days. Mean values ± SD (n = 3).

AUTHOR INFORMATION

Corresponding Author

*Phone: +47-934-08-525. Fax: +47-5142-6744. E-mail: michel.verheul@bioforsk.no.

Funding

The authors want to thank the Research Council of Norway, the Foundation for Research Levy on Agricultural Products and the Agricultural Agreement Research Fund for financial support.

Notes

The authors declare no competing financial interest.

REFERENCES

(1) Dorais, M.; Papadopoulos, A. P.; Gosselin, A. Greenhouse tomato fruit quality. *Hortic. Rev.* **2001**, *26*, 239−319.

(2) Hobson, G. E. Low-temperature injury and the storage of ripening tomatoes. *J. Hortic. Sci.* **1987**, *62*, 55−62.

(3) Alfnes, F.; Guttormsen, A. G.; Asche, F.; Verheul, M. J. Important factors for buying behavior of Norwegian consumers. *Gartneryrket* **2011**, *5*, 24−27 (in Norwegian).

(4) Stevens, M. A.; Kader, A. A.; Albright-Holton, M.; Algazi, M. Genotypic variation of flavor and composition in fresh market tomatoes. *J. Am. Soc. Hortic. Sci.* **1977**, *102*, 680−689.

(5) Malundo, T. M. M.; Shewfelt, R. L.; Scott, J. W. Flavor quality of fresh tomato (Lycopersicon esculentum Mill.) as affected by sugar and acid levels. *Postharvest Biol. Technol.* **1995**, *6*, 103−110.

(6) López, M. D.; Contreras, M.; Fernández-Alba, A. R. Time evolution of tomato quality parameters versus storage conditions. *Acta Hortic.* **2003**, *604*, 619−624.

(7) Baldwin, E. A.; Scott, J. W.; Einstein, M. A.; Malundo, T. M. M.; Carr, B. T.; Shewfelt, R. L.; Tandon, K. S. Relationship between sensory and instrumental analysis for tomato flavor. *J. Am. Soc. Hortic. Sci.* **1998**, *123*, 906−915.

(8) Bilton, R.; Gerber, M.; Grolier, P.; Leoni, C., Eds. *The White Book on Antioxidants in Tomatoes and Tomato Products and Their Health Benefits*; 2001, ISSN 0021-8561.

(9) Story, E. N.; Kopec, R. E.; Schwartz, S. J.; Harris, G. K. An update on the health effects of tomato lycopene. *Annu. Rev. Food Sci. Technol.* **2010**, *1*, 189−210.

(10) Slimestad, R.; Verheul, M. Properties of chalconaringenin and rutin isolated from cherry tomatoes. *J. Agric. Food Chem.* **2011**, *59*, 3180−3185.

(11) Slimestad, R.; Fossen, T.; Verheul, M. The flavonoids of tomatoes. *J. Agric. Food Chem.* **2008**, *56*, 2436−2441.

(12) Sargent, S. A.; Moretti, C. L. Tomato. USDA Agriculture Handbook Number 66: *The Commercial Storage of Fruits, Vegetables, and Florist and Nursery Stocks*; U.S. Department of Agriulture: Washington, DC, 2005; http://www.ba.ars.usda.gov/hb66/tomato.pdf.

(13) Lin, W. C.; Block, G. S. The effects of cultural practice and storage temperature on quality and flavor volatiles of greenhouse tomatoes. *Acta Hortic.* **1998**, *464*, 213−218.

(14) Verheul, M. J. Inventory of taste related properties of tomatoes grown in Norway. Kartlegging av smaksegenskaper i tomat. *Bioforsk Report* **2008**, *3*, 113−130 (in Norwegian).

(15) Maul, F.; Sargent, S. A.; Sims, C. A.; Baldwin, E. A.; Balaban, M. O.; Huber, D. J. Tomato flavor and aroma quality as affected by storage temperature. *J. Food Sci.* **2000**, *65*, 1228−1237.

(16) Slimestad, R.; Verheul, M. Review of flavonoids and other phenolics from fruits of different tomato (Lycopersicon esculentum Mill.) cultivars. *J. Sci. Food Agric.* **2009**, *89*, 1255−1270.

(17) Liu, L. H.; Zabaras, D.; Bennett, L. E.; Aguas, P.; Woonton, B. W. Effects of UV-C, red light and sun light on the carotenoid content and physical qualities of tomatoes during post-harvest storage. *Food Chem.* **2009**, *115*, 495−500.

(18) *USDA Tomato Ripeness Color Chart*; U.S. Department of Agriculture: Washington, DC, 1975; http://postharvest.ucdavis.edu/pfvegetable/TomatoPhotos/?repository=30014&a=83755.

(19) Mitcham, B.; Cantwell, M.; Kader, A. Methods for determining quality of fresh commodities. *Perishables Handling Newsletter* **1996**, *85*, 1−5.

(20) Francis, G. W.; Huseby, B.; Andersen, Ø.M. An improved HPLC system for the analysis of photosynthetic pigments. *Chromatographia* **1993**, *35*, 189−192.

(21) Slimestad, R.; Verheul, M. J. Content of chalconaringenin and chlorogenic acid in cherry tomatoes is strongly reduced during postharvest ripening. *J. Agric. Food Chem.* **2005**, *53*, 7251−7256.

(22) Giovanelli, G.; Lavelli, V.; Peri, C.; Nobili, S. Variation in antioxidant components of tomato during vine and post-harvest ripening. *J. Sci. Food Agric.* **1999**, *79*, 1583−1588.

(23) Watada, A. E.; Aulenbach, B. E. Chemical and sensory qualities of fresh market tomatoes. *J. Food Sci.* **1979**, *44*, 1013−1016.

(24) Davies, J. N.; Hobson, G. E. The constituents of tomato fruit − the influence of environment, nutrition and genotype. *CRC Crit. Rev. Food Sci. Nutr.* **1981**, *15*, 205−280.

(25) Roberts, K. P.; Sargent, S. A.; Fox, A. J. Effect of storage temperature on ripening and postharvest quality of grape and mini-pear tomatoes. *Proc. Fla. State Hortic. Soc.* **2002**, *115*, 80−84.

(26) Raffo, A.; Leonardi, C.; Fogliano, V.; Ambrosino, P.; Salucci, M.; Gennaro, L.; Bugianesi, R.; Giuffrida, F.; Quaglia, G. Nutritional value of cherry tomatoes (Lycopersicon esculentum cv. Naomi F1). *J. Agric. Food Chem.* **2002**, *50*, 6550−6556.

(27) Cantwell, M. Optimum procedures for ripening tomatoes. In: Arpaia, M. L.; Mitcham, E. J.; Cantwell, M.; Crisosto, C.; Kader, A., Reid, M.; Thomson, J. Fruit ripening and ethylene management. *UC Postharvest Hortic. Series* 2008, *9*, 85−92.

(28) Robertson, G. H.; Mahoney, N. E.; Goodman, N.; Pavlath, A. E. Regulation of lycopene formation in cell-suspension culture of VFNT tomato (Lycopersicon esculentum) by CPTA, growth regulators, sucrose and temperature. *J. Exp. Bot.* **1995**, *46*, 667−673.

(29) Türk, R.; Seniz, V.; Ozdemir, N.; Suzen, M. A. Changes in chlorophyll carotenoid and lycopene content of tomatoes in relation to temperature. *Acta Hortic.* **1994**, *368*, 856−862.

(30) Bui, H. T.; Makhlouf, J.; Ratti, C. Postharvest ripening characterisation of greenhouse tomatoes. *Int. J. Food Prop.* **2010**, *13*, 830−846.

(31) Betancourt, L. A.; Stevens, M. A.; Kader, A. A. Accumulation and loss of sugars and reduced ascorbic acid in attached and detached tomato fruits. *J. Am. Soc. Hortic. Sci.* **1977**, *102*, 721−723.

DOI: 10.1021/jf505450j
J. Agric. Food Chem. 2015, 63, 5026−5034

(32) Laveccia, R.; Zuorro, A. Enhancement of lycopene extraction from potato peels by enzymatic treatment. *Chem. Eng. Trans.* **2008**, *14*, 301−308.
(33) Gupta, R.; Balasubramaniam, V. M.; Schwartz, S. J.; Francis, D. M. Storage stability of lycopene in tomato juice subjected to combined pressure-heat treatments. *J. Agric. Food Chem.* **2010**, *58*, 8305−8313.
(34) Jiminez, M.; Trejo, E.; Cantwell, M. Cherry tomato storage and quality evaluations. Vegetable Research Report; Dept. Vegetable Crops, University of California: Davis, CA, 1996. http//cetulare.ucdavis.edu/pubveg/che96.htm.
(35) Kader, A. A.; Morris, L. L.; Stevens, M. A.; Albright-Holton, M. Composition and flavor quality of fresh marked tomatoes as influences by some postharvest handling procedures. *J. Am. Soc. Hortic. Sci.* **1978**, *103*, 6−13.
(36) Kader, A. A. Effects of postharvest handling procedures on tomato quality. *Acta Hortic.* **1986**, *190*, 209−222.
(37) Charles, M. T.; Kalantari, S.; Corcuff, R.; Arul, J. Postharvest quality and sensory evaluation of UV-treated tomato fruit. *Acta Hortic.* **2005**, *682*, 537−542.
(38) Davies, B. H.; Köst, H.-P. In *Handbook of chromatography* Köst, H.-P., Ed.; CRC Press: Boca Raton, FL; Vol. *1*, Plant pigments, 1988; p 3.
(39) Alba, R.; Cordonnier-Pratt, M.-M.; Pratt, L. H. Fruit-localized phytochromes regulate lycopene accumulation independently of ethylene production in tomato. *Plant Physiol.* **2000**, *123*, 363−370.
(40) Collins, J. K.; Perkins-Veazie, P. Lycopene: From plants to humans. *Hortic. Sci.* **2006**, *41*, 1135−1144.
(41) Soto-Zamora, G.; Yahia, E. M.; Brecht, J. K.; Gardea, A. Effects of postharvest hot air treatments on the quality and antioxidant levels in tomato fruit. *LWT* **2005**, *38*, 657−663.
(42) Gautier, H.; Diakou-Verdin, V.; Bénard, C.; Reich, M.; Buret, M.; Gourgaud, F.; Poëssel, J. L.; Caris-Veyrat, C.; Génard, M. How does tomato quality (sugar, acid and nutritional quality) vary with ripening stage, temperature and irradiance? *J. Agric. Food Chem.* **2008**, *56*, 1241−1250.
(43) Shama, G.; Alderson, P. UV hormesis in fruits: a concept ripe for commercialisation. *Trends Food Sci. Technol.* **2005**, *16*, 128−136.
(44) Maharaj, R.; Arul, J.; Nadeau, P. Effect of photochemical treatment in the preservation of fresh tomato (Lycopersicon esculentum cv. Capello) by delaying senescence. *Postharvest Biol. Technol.* **1999**, *15*, 13−23.
(45) Jagadeesh, S. L.; Charles, M. T.; Gariepy, Y.; Goyette, B.; Raghavan, G. S. V.; Vigneault, C. Influence of postharvest UV-C hormesis on the bioactive components of tomato during post-treatment handling. *Food Bioprocess Technol.* **2011**, *4*, 1463.
(46) Moco, S.; Capanoglu, E.; Tikunov, Y.; Bino, R. J.; Boyacioglu, D.; Hall, R. D.; Vervoort, J.; De Vos, R. C. H. Tissue specialization at the metabolite level is perceived during the development of tomato fruit. *J. Exp. Bot.* **2007**, *58*, 4131−4146.

DOI: 10.1021/jf505450j
J. Agric. Food Chem. 2015, 63, 5026−5034

JOURNAL OF AGRICULTURAL AND FOOD CHEMISTRY

Article

pubs.acs.org/JAFC

Inhibition of the Aggregation of Lactoferrin and (−)-Epigallocatechin Gallate in the Presence of Polyphenols, Oligosaccharides, and Collagen Peptide

Wei Yang, Fuguo Liu, Chenqi Xu, Cuixia Sun, Fang Yuan, and Yanxiang Gao*

Beijing Key Laboratory of Functional Food from Plant Resources, College of Food Science & Nutritional Engineering, China Agricultural University, Beijing 100083, People's Republic of China

ABSTRACT: The aggregation of lactoferrin and (−)-epigallocatechin gallate (EGCG) was inhibited by polyphenols, oligosaccharides, and collagen peptide in this study. Polyphenols, oligosaccharides, or collagen peptide can effectively prevent the formation of lactoferrin−EGCG aggregates, respectively. The addition sequence of lactoferrin, polyphenols (oligosaccharides or collagen peptide) and EGCG can affect the turbidity and particle size of the ternary complexes in the buffer solution; however, it hardly affected the ζ-potential and fluorescence characteristics. With either positive or negative charge, polyphenols and collagen peptide disrupted the formation of lactoferrin−EGCG aggregate mainly through the mechanism of its competition with EGCG molecules which surrounded the lactoferrin molecule surface with weaker binding affinities, forming polyphenols or a collagen peptide−lactoferrin−EGCG ternary complex; for neutral oligosaccharides, the ternary complex was generated mainly through steric effects, accompanied by a change in the lactoferrin secondary structure induced by gallic acid, chlorogenic acid, and xylo-oligosaccharide. Polyphenols, oligosaccharides, or collagen peptide restraining the formation of lactoferrin−EGCG aggregate could be applied in the design of clear products in the food, pharmaceutical, and cosmetic industries.

KEYWORDS: *aggregation inhibitors, lactoferrin, (−)-epigallocatechin gallate, polyphenols, oligosaccharides, collagen peptide*

INTRODUCTION

Polyphenol may interact with protein reversibly by usually noncovalent forces such as hydrogen bonding, hydrophobic bonding, and van der Waals forces.[1−3] Turbidity is generally due to the binding of polyphenol present in beverage and food products from plant origin with proteins to form aggregates. At the same time, the protein−polyphenol complexes are considered to be responsible for the sensation of astringency on the human palate. Astringency is often perceived as an undesirable quality factor in some beverages such as fruit juices and red wine if they are too intense.[4] The interaction between polyphenol and proteins has been proven to generate negative effects, reducing the palate lubrication, causing an unpleasant sensation of roughness, dryness, and constriction and reducing absorption of nutrients.[5−7]

There exist a number of factors, such as pH, ionic strength, alcohol, nature of the solvent, and presence of carbohydrates, affecting the protein−polyphenol haze formation in food systems.[8] Several studies have demonstrated that some polysaccharides, such as pectin, xanthan gum, and arabic gum, can be applied as food colloids, to disrupt polyphenol and protein interaction in food systems.[7,9−13] There are three mechanisms responsible for the inhibition of protein−polyphenol aggregation by some polysaccharides: (1) molecular association between polysaccharides, such as arabic gum, β-cyclodextrin, and polyphenols, competing with protein aggregation;[7,13] (2) the formation of a protein−polyphenol−polysaccharide ternary complex, enhancing its solubility in aqueous medium, such as pectin;[13] (3) steric effects, limiting the number of available binding sites of proteins to readily fit polyphenols, such as dextran.[9]

It is well-known that EGCG can act as a multidentate ligand and bridge protein,[2,14] forming a lactoferrin−EGCG aggregate. Yang et al. reported that EGCG was spontaneously bound to lactoferrin by a two-stage mechanism: first EGCG molecules were bound within the hydrophobic pockets of lactoferrin with strong binding affinities, and then EGCG molecules surrounded the lactoferrin molecule surface with weaker binding affinities. A further increase in EGCG concentration led to phase separation (haze formation).[15]

Some functional food ingredients, such as polyphenols, oligosaccharides, and collagen peptide, are widely used in beverage, food, and pharmaceutical formulations. Proteins are thought to have a number of sites bound by polyphenols, oligosaccharides, or peptides.[16−18] Oligosaccharides and collagen peptide, on the other hand, have a number of ends that could bind polyphenols. Therefore, polyphenols, oligosaccharides, or peptides might affect the interaction between the protein and polyphenol when these components are intergrated together. So far, the effect of polyphenols, polysaccharides, and collagen peptide on the interaction of the polyphenol with protein has been largely overlooked. Phenolic compounds are chemically structured as a hydroxyl group bonded to an aromatic ring. Dietary polyphenols, natural compounds largely in fruits, vegetables, and cereals, are consumed as part of the human diet in significant amounts[19,20] and have become an intense focus of research interest due to their health-beneficial effects, especially in the treatment and prevention of several chronic diseases. Oligosaccharides,

Received: December 7, 2014
Accepted: May 4, 2015
Published: May 4, 2015

ACS Publications © 2015 American Chemical Society

DOI: 10.1021/acs.jafc.5b01881
J. Agric. Food Chem. 2015, 63, 5035−5045

especially xylo-oligosaccharide (XOS) and fructo-oligosaccharide (FOS), with a mouthfeel similar to that of sugar but being only 20−70% as sweet as table sugar, have received much attention recently as functional food ingredients.[21] They are often applied to enhance the survivability and colonization of probiotic bacteria when they are enriched in foods.[22] Because of its nutritional and medical benefits, collagen peptide is easily absorbed by the human body due to its low molecule weight and is often used as an ingredient and additive of functional foods and nutraceuticals.[23]

The objective of this work was to elucidate the effect of polyphenols, oligosaccharides, and collagen peptide on the aggregation of EGCG with lactoferrin. A clear dispersion containing lactoferrin, EGCG, and polyphenols (oligosaccharides or collagen peptide) can be applied in many fields, such as the food, pharmaceutical, and cosmetic industries.

MATERIALS AND METHODS

Materials and Chemicals. Lactoferrin (purity ≥92.0%) from bovine whey was purchased from New Image International Limited (New Zealand). EGCG (purity ≥95.0%), gallic acid (purity ≥98.0%), and chlorogenic acid (purity ≥99.0%) was purchased from BSZH Science (Beijing, People's Republic of China). Glucose (purity ≥99.0%) was purchased from Beijing Chemical Reagent (Beijing, People's Republic of China). XOS (purity ≥95.0%) was supplied by Longlive Biotechnology Co., Ltd. (Shandong, People's Republic of China). FOS (purity ≥95.0%) was supplied by Baolingbao Biotechnology Co., Ltd. (Shandong, People's Republic of China). Collagen peptide (purity ≥99.0%; 2000 Da) from tilapia skin was supplied by Beijing Semnl Biotechnologies Co., Ltd. (Beijing, People's Republic of China).

Sample Preparation. Lactoferrin (1.6% w/v, 0.2 mM) and EGCG (0.1832 w/v, 4.0 mM) were dissolved in 10 mM potassium phosphate buffer solution (pH 6.0), and the solutions were each stirred constantly at 25 °C for at least 2 h.

Preparation of Ternary Complexes Containing Lactoferrin, EGCG, and a Polyphenol, Oligosaccharide, or Collagen Peptide. Three addition sequences were applied to prepare the ternary complexes in the buffer solution. Different volumes of polyphenols, oligosaccharides, or collagen peptide stock solutions were mixed with designed volumes of potassium phosphate buffer solution. For the experiments, stock solutions of polyphenols (0.3% gallic acid, 1.0% chlorogenic acid), glucose and oligosaccharides (21.0%), and collagen peptide (9.0%) were prepared with potassium phosphate buffer solution.

Method I (M1). Briefly, 2.0 mL of lactoferrin (1.6% w/v, 0.2 mM) and 1.0 mL of EGCG (0.1832% w/v, 4.0 mM) solutions were mixed on a vortex shaker (QL-866, Haimen QILINBEIER Instruments Co., Ltd., Haimen, People's Republic of China) at 3000 rpm for 1 min. The mixture was allowed to stand for 2 h. After that, 1.0 mL of polyphenol, oligosaccharide, or collagen peptide solution in different concentrations was added and mixed for 1 min, and the mixture was allowed to stand for 2 h before the measurement.

The abbreviation X-1 (X = gallic acid, chlorogenic acid, glucose, XOS, FOS, collagen peptide) is used to represent the ternary complexes containing lactoferrin, EGCG, and a polyphenol, oligosaccharide, or collagen peptide prepared by M1.

Method II (M2). Briefly, 2.0 mL of lactoferrin (1.6% w/v, 0.2 mM) and 1.0 mL of a polyphenol, oligosaccharide, or collagen peptide solution in different concentrations were mixed on a vortex shaker (QL-866, Haimen QILINBEIER Instruments Co., Ltd., Haimen, People's Republic of China) at 3000 rpm for 1 min. These mixtures were allowed to stand for 2 h. Then, 1.0 mL of EGCG (0.1832% w/v, 4.0 mM) solution was added to the different mixtures. After that, these mixtures were blended for 1 min and allowed to stand for 2 h before the measurement.

The abbreviation X-2 (X = gallic acid, chlorogenic acid, glucose, XOS, FOS, collagen peptide) is used to represent the ternary complexes containing lactoferrin, EGCG, and a polyphenol, oligosaccharide, or collagen peptide prepared by M2.

Method III (M3). In brief, 1.0 mL of EGCG (0.1832% w/v, 4.0 mM) and 1.0 mL of a polyphenol, oligosaccharide, or collagen peptide solution in different concentrations were mixed on a vortex shaker (QL-866, Haimen QILINBEIER Instruments Co., Ltd., Haimen, People's Republic of China) at 3000 rpm for 1 min. The mixtures were allowed to stand for 2 h. After that, 2.0 mL of lactoferrin (1.6% w/v, 0.2 mM) solution was added to these mixtures. Then these mixtures were blended for 1 min and allowed to stand for 2 h before the measurement.

The abbreviation X-3 (X = gallic acid, chlorogenic acid, glucose, XOS, FOS, collagen peptide) is used to represent the ternary complexes containing lactoferrin, EGCG, and a polyphenol, oligosaccharide, or collagen peptide prepared by M3.

Turbidity Measurements. Nephelometry experiments were performed with a HACH 2100N Laboratory Turbidimeter (Loveland, USA), and the aggregation behavior of lactoferrin and EGCG in the absence and presence of polyphenol, oligosaccharide, or collagen peptide solution in buffer solution was evaluated. The optical apparatus was equipped with a tungsten-filament lamp with three detectors: a 90° scattered-light detector, a forward-scatter light detector, and a transmitted light detector. The calibration was performed using a Gelex Secondary Turbidity Standard Kit (HACH, Loveland, USA), which consists of stable suspensions of a metal oxide in a gel. All experiments were performed in triplicate.

Particle Size Measurements. Particle size and size distribution of the ternary complexes in the buffer solution were determined by dynamic light scattering (DLS) using a Zetasizer Nano-ZS90 (Malvern Instruments, Worcestershire, U.K.). The intensity of light scattered was monitored at a 90° angle. Results are described as cumulant mean diameter (size, nm) for particle size and polydispersity index (PdI) for size distribution. All experiments were performed in triplicate.

ζ-Potential Measurements. The ζ potential of ternary complexes in the buffer solution was determined by a Zetasizer Nano-ZS90 particle electrophoresis instrument (Malvern Instruments, Worcestershire, U.K.). Samples were loaded in the cell, and the temperature was set at 25 °C without further dilution. The ζ-potential values are reported as the average of measurements for three freshly prepared samples, with three readings recorded for each sample.

Fluorescence Spectroscopy Measurements. Fluorescence measurements were carried out using a fluorescence spectrophotometer (F-7000, Hitachi, Japan). Spectra were collected when the mixtures were kept at 25 °C for 2 h.

Fluorescence emission spectra of the ternary complexes were recorded with an excitation wavelength at 292 nm. The synchronous fluorescence spectra were determined in the continuous range of 300−600 nm with $\Delta\lambda$ at 60 nm. Both excitation and emission band widths were set at 10 nm.

Circular Dichroism Measurements. The CD spectra were recorded using a CD spectropolarimeter (Pistar π-180, Applied Photophysics Ltd. U.K.) in rhw far-UV (190−250 nm) region under constant nitrogen flush. The path length was 0.1 cm for the far-UV region. Ellipticity was recorded at a speed of 100 nm/min, 0.2 nm resolution, 20 accumulations, and 2.0 nm bandwidth. The collected data were analyzed using Dichroweb, the online Circular Dichroism Web site (http://dichroweb.cryst.bbk.ac.uk).[24,25] Each spectrum presented was obtained as the average of three consecutive scans with automatic subtraction of the buffer and/or polyphenol, oligosaccharide, or collagen peptide spectra. The concentrations of polyphenols, oligosaccharides, or collagen peptide in ternary complexes were 0.75% for gallic acid, 0.25% for chlorogenic acid, 10.25% for glucose, FOS, and XOS, and 2.25% for collagen peptide.

Statistical Analysis. The experiments were conducted in duplicate, and all analyses were done in triplicate. The results are presented as the means ± standard deviation. Data were analyzed by one-way analysis of variance using the SPSS 16.0 package (SPSS Inc., Chicago, IL, USA), and significant differences of means ($p < 0.05$) were determined using the Duncan multiple-range test. The correlation analysis was carried out using the Pearson mode. The

DOI: 10.1021/acs.jafc.5b01881
J. Agric. Food Chem. 2015, 63, 5035−5045

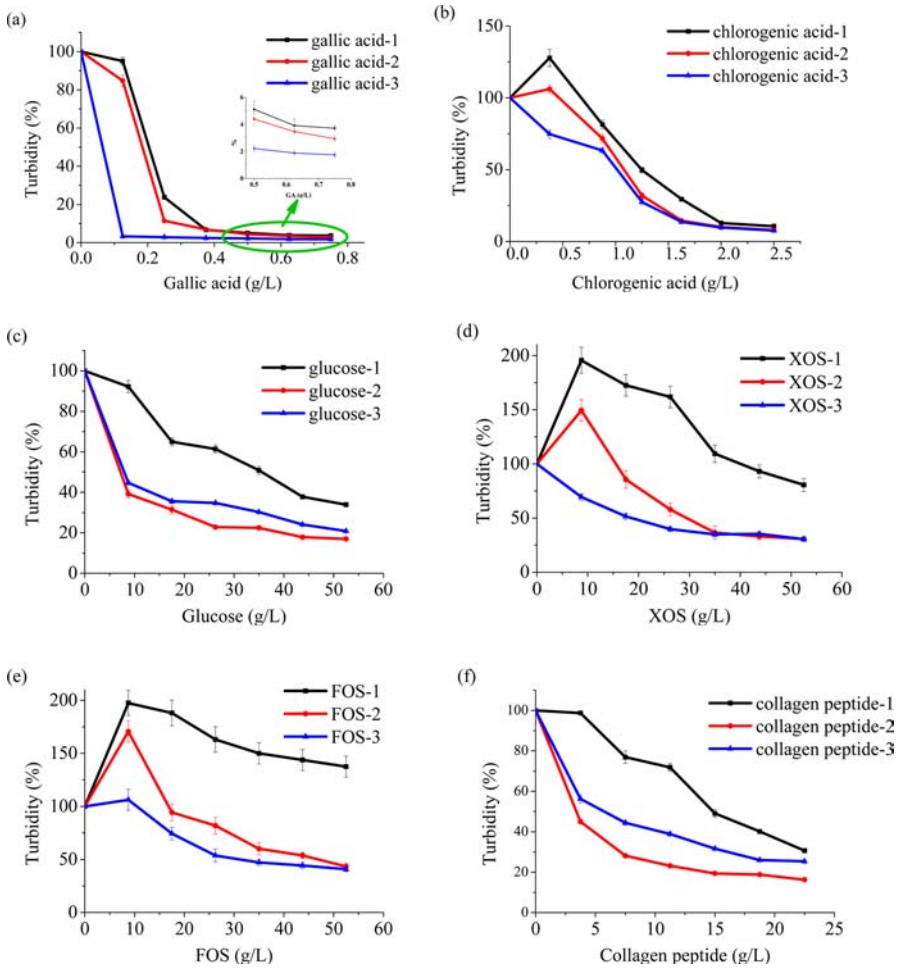

Figure 1. Variation (%) in turbidity of lactoferrin−EGCG aggregate (containing 1.0 mM EGCG) with increasing concentrations of polyphenols, oligosaccharides, or collagen peptide.

concordance between experimental data and calculated values was established by the root-mean-squared deviation.

RESULTS AND DISCUSSION

The turbidity of the lactoferrin−EGCG aggregate in the buffer solution was around 160 NTU when the EGCG concentration was 1.0 mM. It should be noted that the ζ potential of the lactoferrin and lactoferrin−EGCG aggregate was around 0 mV, despite the pH of the buffer being below the reported isoelectric point of lactoferrin (pI ≈ 8). The most likely explanation for this effect is that the cationic groups on the adsorbed lactoferrin bound some anionic phosphate ions present in the buffer.[26]

Several assays were performed with progressively increasing concentrations of polyphenols, oligosaccharides, or collagen peptide, until practically no changes in the amount of insoluble lactoferrin−EGCG aggregate were observed. The effect of the component addition sequence on the turbidity, particle size, and structure of the ternary complexes was also investigated.

Nephelometry Measurements. Nephelometry measures the formation of the structures of high-molecular-weight substances at a macromolecular level, taking into account all physicochemical driving forces involved in the formation of aggregates. It is very interesting to find that, except for a few cases, the presence of the polyphenols, oligosaccharides, or collagen peptide in the solution restrained the formation of lactoferrin−EGCG insoluble aggregates (Figure 1).

The turbidity of the aggregates in the buffer solution prepared by three addition sequences progressively decreased with an increase in gallic acid, chlorogenic acid, and collagen peptide concentrations, respectively, which indicated that smaller particles were formed to scatter light for the ternary complexes. M3 was the most effective method to inhibit the formation of lactoferrin−EGCG aggregate for gallic acid and chlorogenic acid, while M2 was the most effective method for collagen peptide. These results revealed that gallic acid was the most effective (the gallic acid amount required was about 10-fold lower than that of chlorogenic acid and about 100-fold lower than that of collagen peptide) in restraining the interaction between lactoferrin and EGCG.

The presence of glucose, XOS, and FOS, respectively, in the solution retarded the formation of insoluble lactoferrin−EGCG aggregate with use of M2 and M3. M2 was the most effective method for glucose, while M3 was the most effective method for XOS and FOS.

It should be noted that some exception was observed for chlorogenic acid, XOS, and FOS by M1 and M2. Significant ($p < 0.05$) increases of the insoluble aggregates were found at low concentrations, 0−0.5 g/L for chlorogenic acid and 0−10 g/L for XOS and FOS, which could be explained by their size increase, resulting from the adsorption of chlorogenic acid,

DOI: 10.1021/acs.jafc.5b01881
J. Agric. Food Chem. 2015, 63, 5035−5045

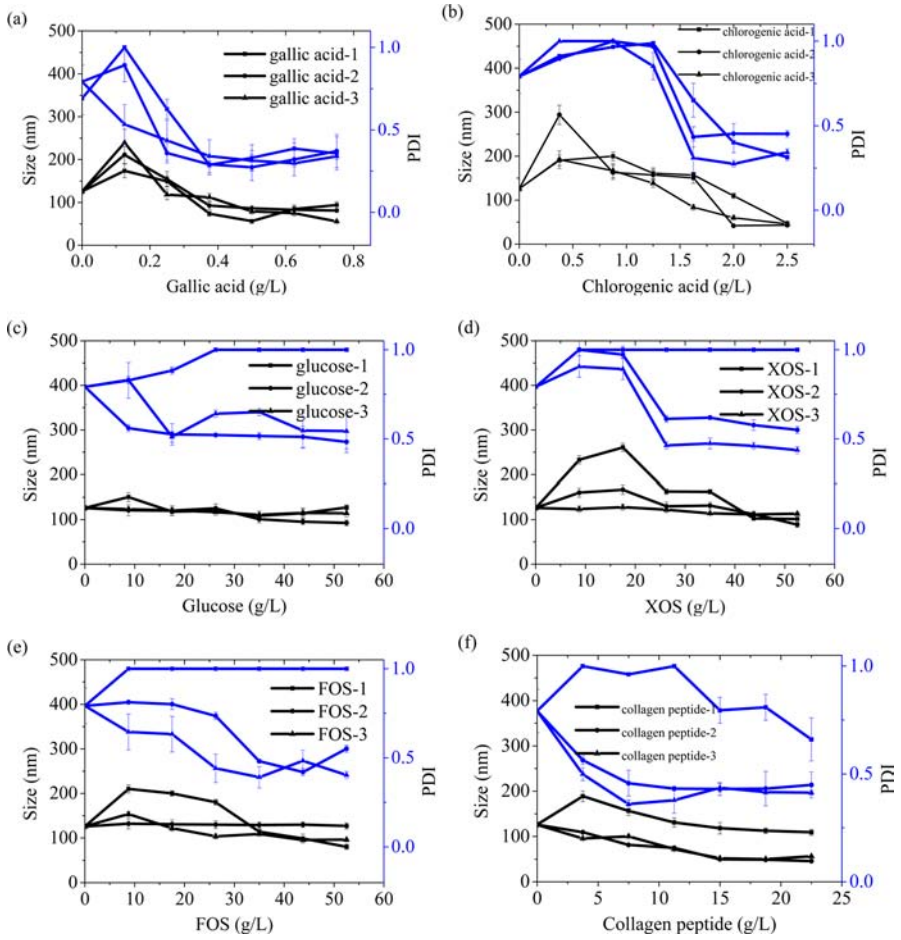

Figure 2. Influence of polyphenol, oligosaccharide, or collagen peptide concentration on the particle size of lactoferrin−EGCG aggregate (containing 1.0 mM EGCG).

XOS, or FOS molecules on the surface of lactoferrin−EGCG aggregate. This result was similar to that in the report of de Freitas et al., which showed that the presence of dextran in the insoluble aggregates formed by procyanidins and bovine serum albumin tended to remain constant or to slightly increase.[9] In particular, for XOS and FOS by M1, but not by M2, a further increase in the concentration of XOS and FOS did not show an effective inhibition of the aggregation between lactoferrin and EGCG. These results obviously revealed that the turbidity of the ternary complexes in the buffer solution was mostly related to the addition sequence of lactoferrin, polyphenol (oligosaccharide or collagen peptide), and EGCG, especially for XOS and FOS.

On the basis of the aforementioned results, it was possible to classify the capacity of polyphenols, oligosaccharides, and collagen peptide in retarding the aggregation: gallic acid > chlorogenic acid > collagen peptide > glucose > XOS > FOS.

Size Measurements of Ternary Complexes. The measurement of ternary complex size in the buffer solution resulting from the interaction between lactoferrin and EGCG in the absence and presence of polyphenols, oligosaccharides, or collagen peptide was performed by DLS. Figure 2 shows the mean particle size and polydispersity of aggregates. As expected, with an increase in polyphenol, oligosaccharide, or collagen peptide concentration, the mean particle size showed changes synchronous with the turbidity.

It is interesting to find that, as the aggregation decreased, a narrow range of particle size distribution was observed for gallic acid, chlorogenic acid, and collagen peptide, respectively, by M1, M2, and M3 (a decreased PDI value, from 0.792 to 0.34 for gallic acid, to 0.314 for chlorogenic acid, and to 0.413 for collagen peptide), indicating a homogeneous population of these aggregates.

As glucose, XOS, and FOS concentrations increased, the aggregation of the ternary complexes decreased and a narrow range of the particle size distribution was also observed (a decreased PDI value, from 0.792 to 0.483 for glucose, to 0.437 for XOS, and to 0.403 for FOS) by M2 and M3, also implying a heterogeneous population of these aggregates. An opposite phenomenon was observed by using M1; that is, the PDI value was increased to around 1.0 as the concentrations of glucose, XOS, and FOS, respectively, were increased, indicating the formation of more heterogeneous aggregates.

Yang et al. reported that EGCG molecules might be first bound within the hydrophobic pockets of lactoferrin with strong binding affinities. As the concentration of EGCG increased, it surrounded the lactoferrin molecule surface with weaker binding affinities, acting as multidentate ligands and bridge proteins or as a protein−polyphenol complex, leading to the formation of metastable dispersions of particles; further, an increase of polyphenols led to phase separation (haze formation).[15] Therefore, it is hypothesized that when lactoferrin and EGCG were mixed together in the absence of

DOI: 10.1021/acs.jafc.5b01881
J. Agric. Food Chem. 2015, 63, 5035−5045

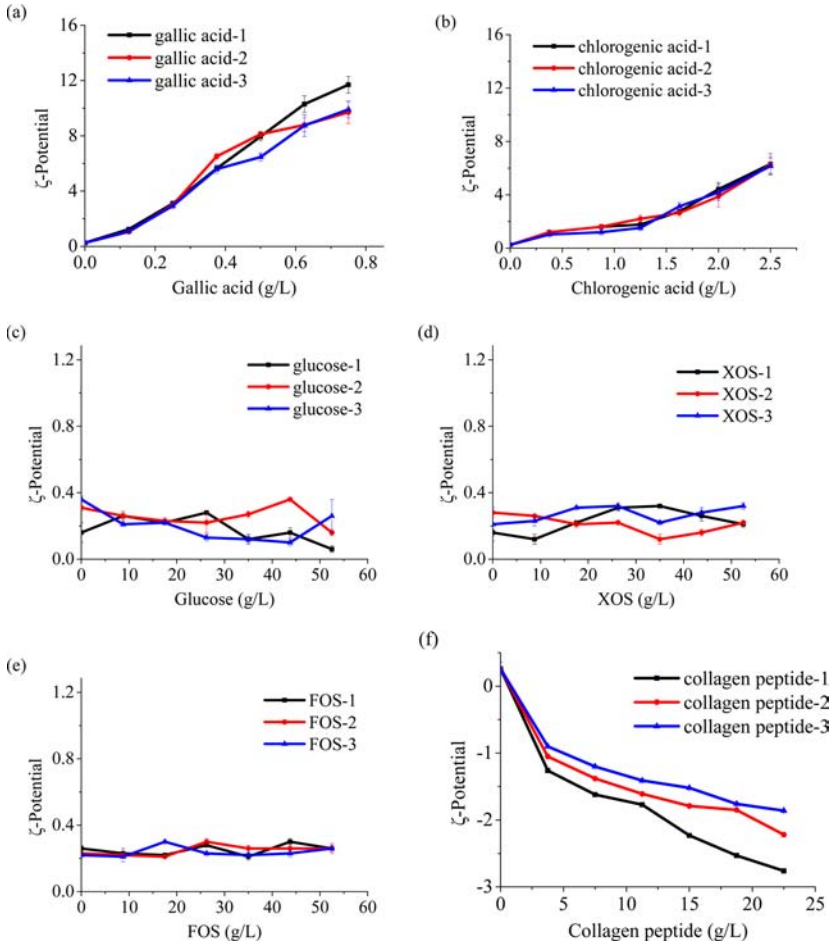

Figure 3. Influence of polyphenol, oligosaccharide, or collagen peptide concentration on the ζ potential of lactoferrin−EGCG aggregate (containing 1.0 mM EGCG).

polyphenols, oligosaccharides, or collagen peptide (M1), a large network structure with high PDI value was first formed, leading to phase separation. After the addition of a certain amount of polyphenols, oligosaccharides, or collagen peptide, the network was gradually disrupted by EGCG molecules which covered the lactoferrin molecule surface with weaker binding affinities, forming new smaller networks or complexes with low PDI value (for example, gallic acid and chlorogenic acid) or larger networks with a PDI value of around 1.0 (for example, XOS and FOS). When lactoferrin or EGCG and a polyphenol, oligosaccharide, or collagen peptide were first mixed together (M2 and M3, respectively), the interaction between lactoferrin and EGCG was disrupted by the polyphenol, oligosaccharide, or collagen peptide through a competition mechanism or steric effects, forming new smaller networks accompanied by a decreased PDI value.

ζ-Potential Measurements. The ζ potential plays an important role in the stability of protein−polysaccharide or protein−polyphenol complexes in aqueous solution. Figure 3 shows the ζ potential of complexes presented in the solution resulting from the interaction between lactoferrin and EGCG in the absence and presence of polyphenols, oligosaccharides, or collagen peptide.

In this study, the ζ-potential values of the ternary complexes increased with an increase of gallic acid and chlorogenic acid and decreased with an increase of collagen peptide, leading to particle deaggregation at higher concentration. Unlike the case for gallic acid, chlorogenic acid, and collagen peptide, it was interestingly found that the ζ potential of the ternary complexes was around 0 mV, also leading to particle deaggregation at higher concentrations of glucose, XOS, and FOS, respectively. However, the concentrations of a neutral carbohydrate, such as glucose, XOS, or FOS, were much higher in comparison to those of gallic acid, chlorogenic acid, and collagen peptide, which are thought to have an ionic character. This result interpreted the low affinity of neutral carbohydrates for polyphenols, as reported by other authors.[27,28]

There might be a simple relationship between the ability to inhibit the formation of lactoferrin−EGCG aggregate and ζ potential; that is, charged polyphenols and collagen peptide (whether positively or negatively charged) were more effective in the decrease of aggregation than noncharged oligosaccharides.

Fluorescence Spectroscopy Measurements. There are 13 tryptophan residues in the lactoferrin structure.[29] The emission of tryptophan may be blue-shifted if the group is buried within a native protein, and its emission may be red-shifted when the protein is unfolded.[30] By monitoring of the emission peak change, some information could be obtained concerning the structural change and the microenvironment surrounding the fluorophore in the protein. Synchronous fluorescence spectra supplied some information about the molecular environment in the vicinity of the chromophore molecules. When $\Delta\lambda$ = 60 nm, spectral characteristics of

DOI: 10.1021/acs.jafc.5b01881
J. Agric. Food Chem. 2015, 63, 5035−5045

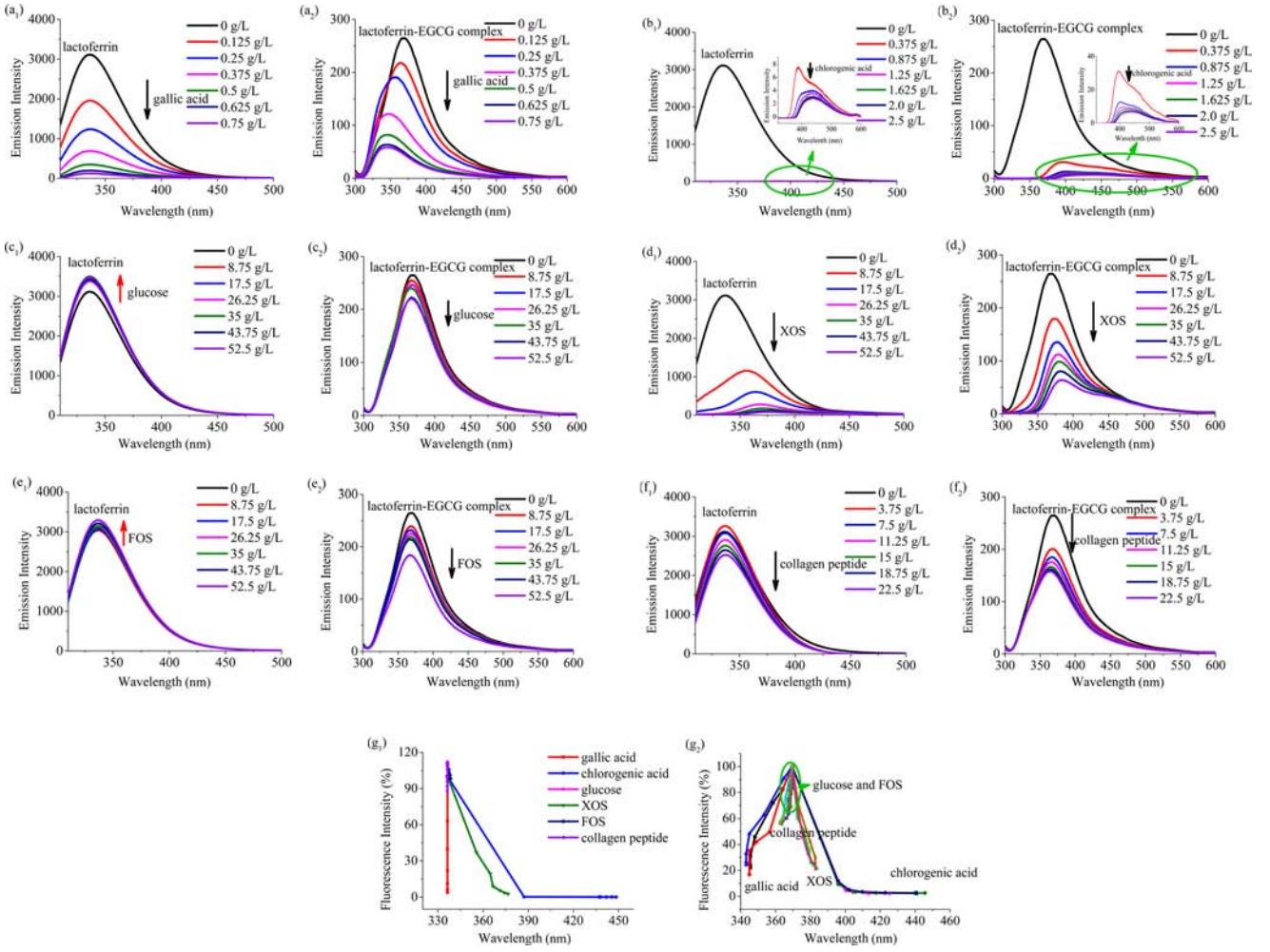

Figure 4. Fluorescence emission spectra of lactoferrin, in the absence and presence of polyphenols, oligosaccharides, or collagen peptide (a_1–f_1), influence of increasing concentrations of polyphenols, oligosaccharides, or collagen peptide on the variation of the fluorescence of lactoferrin solution (g_1), fluorescence emission spectra of lactoferrin–EGCG aggregate (containing 1.0 mM EGCG), in the absence and presence of polyphenols, oligosaccharides, or collagen peptide (a_2–f_2), and the influence of increasing concentrations of polyphenols, oligosaccharides, or collagen peptide on variation of the fluorescence of lactoferrin–EGCG aggregate (containing 1.0 mM EGCG) (g_2).

tryptophan residues in the protein were observed.[31] The shift in the position of the emission maximum (λ_{max}) corresponded to the change in polarity around the chromophore molecule. Thus, the conformation change of lactoferrin could be estimated by this measurement.[32,33]

The fluorescence emission spectrum (at λ_{ex} 292 nm) obtained for lactoferrin in the absence and presence of polyphenols, oligosaccharides, or collagen peptide is shown in Figure 4a_1–f_1. A high degree of fluorescence quenching was observed for gallic acid (from 100% to 3.9%), chlorogenic acid (from 100% to 0.09%), and XOS (from 100% to 2.7%). However, as the concentrations of glucose, FOS, and collagen peptide were respectively increased, the intensity of the fluorescence only slightly increased (for glucose and FOS) or decreased (for collagen peptide). Similar trends were also observed with synchronous fluorescence (Figure 5a_1–f_1). This implied that binding behavior existed between lactoferrin and gallic acid, chlorogenic acid, or XOS, respectively but that there was hardly any interaction between lactoferrin and glucose, FOS, or collagen peptide, respectively. Since M2 and M3 showed fluorescent properties closely similar to those of M1 (the fluorescence spectra data of M2 and M3 are not shown), only M1 is used for analysis in the following sections.

The fluorescence emission spectrum obtained for lactoferrin–EGCG aggregate in the absence and presence of polyphenols, oligosaccharides, or collagen peptide is shown in Figure 4a_2–f_2. Similar to the effect of polyphenols, oligosaccharides, or collagen peptide on lactoferrin, a high degree of fluorescence quenching of lactoferrin–EGCG aggregate was observed for gallic acid (from 100% to 2.4–2.6%), chlorogenic acid (from 100% to 16.8–24.3%), and XOS (from 100% to 20.8–24%) (Figure 4g_1,g_2). At the same time, there were obvious blue shifts of the maximum λ_{em} of fluorescence for gallic acid (from 369.6 to 343.2–351.4 nm), obvious red shifts with chlorogenic acid (from 369.6 to 440.6–445.6 nm), and red shifts with XOS (from 369.6 to 382.4–383.8 nm), accompanied by significant quenching of the fluorescence, which implied that binding behaviors existed between lactoferrin–EGCG aggregate and gallic acid, chlorogenic acid, or XOS, respectively. Therefore, it was inferred that the interactions of lactoferrin–EGCG aggregate with gallic acid, chlorogenic acid, or XOS, respectively, led to the compact structure of lactoferrin and increase of the hydrophobicity in the microenvironment of tryptophan residues with gallic acid, while the protein structure was unfolded and the hydrophilicity of the microenvironment of tryptophan residues for chloro-

DOI: 10.1021/acs.jafc.5b01881
J. Agric. Food Chem. 2015, 63, 5035–5045

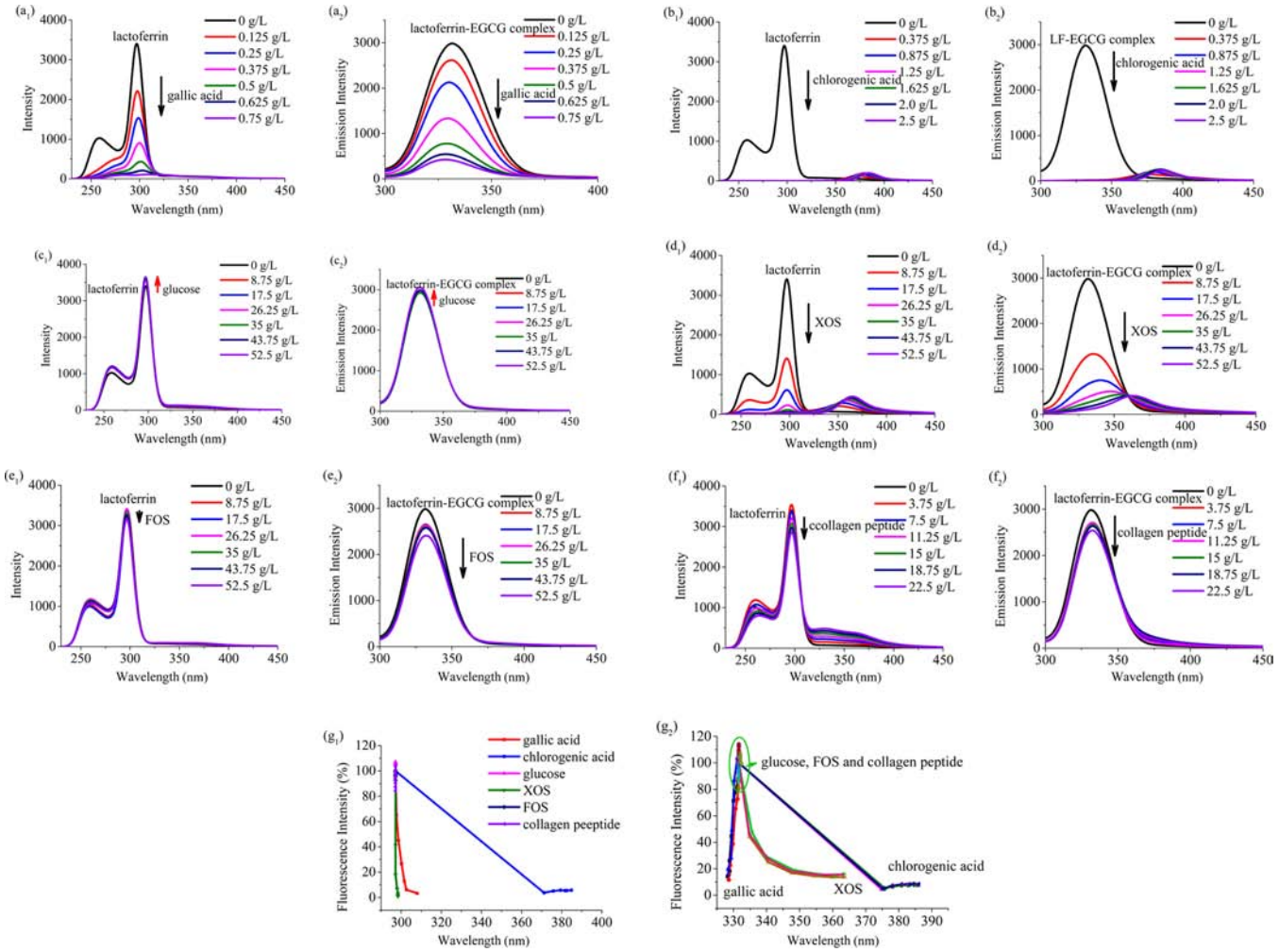

Figure 5. Synchronous fluorescence spectra of lactoferrin, in the absence and presence of polyphenols, oligosaccharides, or collagen peptide (a_1–f_1), influence of polyphenols, oligosaccharides, or collagen peptide concentration on the variation of the synchronous fluorescence of lactoferrin (g_1), synchronous fluorescence spectra of lactoferrin–EGCG aggregate (containing 1.0 mM EGCG), in the absence and presence of polyphenols, oligosaccharides, or collagen peptide (a_2–f_2), and the influence of polyphenols, oligosaccharides, or collagen peptide concentration on the variation of the synchronous fluorescence of lactoferrin–EGCG aggregate (containing 1.0 mM EGCG) (g_2).

genic acid and XOS increased. Additionally, this also suggested that gallic acid, chlorogenic acid, or XOS was situated in close proximity to the tryptophan residues for quenching to occur, and the microenvironment of tryptophan residues was changed.

The fluorescence intensity of lactoferrin–EGCG aggregate also regularly decreased with an increase in glucose, FOS, or collagen peptide concentration. Unlike the case for gallic acid, chlorogenic acid, and XOS, a low degree of fluorescence quenching was observed for glucose (from 100% to 66.9–89.9%), FOS (from 100% to 64.5–69.3%), and collagen peptide (from 100% to 46.8–59.6%). Meanwhile, there were only slight blue shifts for glucose (from 369.6 to 366.2–367 nm), FOS (from 369.6 to 366–367 nm), and collagen peptide (from 369.6 to 363.4 nm). These results revealed that glucose, FOS, and collagen peptide might enhance the interaction of lactoferrin and EGCG but there was hardly any binding behavior between lactoferrin and glucose, FOS, and collagen peptide, respectively, and the structure of lactoferrin interacting with 1.0 mM EGCG was not altered significantly in the presence of glucose, FOS, and collagen peptide, respectively. Additionally, this also implied that the microenvironment of tryptophan residues did not change after the addition of glucose, FOS, or collagen peptide, respectively.

The synchronous fluorescence spectra of lactoferrin–EGCG aggregate in the absence and presence of polyphenols, oligosaccharides, or collagen peptide are shown in Figure 5a_2–f_2, which show synchronous fluorescence trends similar to those obtained for lactoferrin in the absence and presence of polyphenols, oligosaccharides, or collagen peptide (Figure 5g_1,g_2). It was apparent that the emission maximum of tryptophan residues had a slight blue shift for gallic acid (from 331.6 to 328.2–328.8 nm) but a stronger red shift for chlorogenic acid (from 331.6 to 385.4–385.8 nm) and XOS (from 331.6 to 363.6 nm). These shifts revealed that the conformation of lactoferrin changed, the polarity around the tryptophan residues decreased, and the hydrophobicity increased with gallic acid, while the presence of chlorogenic acid or XOS modified the microenvironment from a nonpolar into a polar state; in other words, tryptophan residues were located in a less hydrophobic environment and were more exposed to the solution.[34] These shifts in the spectra expressed some changes in conformation of lactoferrin upon binding with gallic acid, chlorogenic acid, and XOS, respectively.

DOI: 10.1021/acs.jafc.5b01881
J. Agric. Food Chem. 2015, 63, 5035–5045

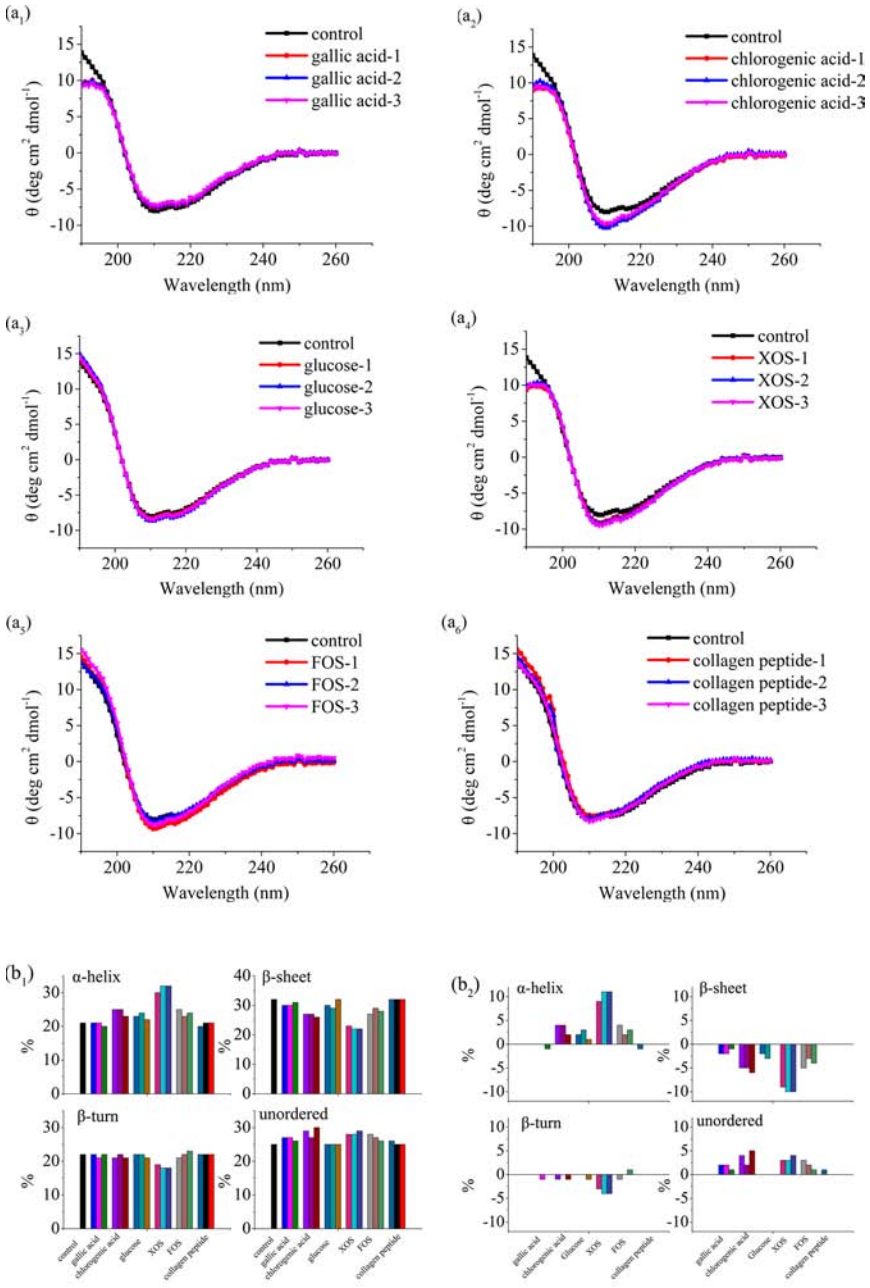

Figure 6. Far-UV CD spectra of lactoferrin in the absence and presence of polyphenols, oligosaccharides, or collagen peptide with 1.0 mM EGCG (a_1−a_6), secondary structure of lactoferrin in the absence and presence of polyphenols, oligosaccharides, or collagen peptide with 1.0 mM EGCG (b_1), changes in the secondary structure of lactoferrin in the presence of polyphenols, oligosaccharides, or collagen peptide with 1.0 mM EGCG (b_2), and near-UV CD spectra of lactoferrin in the absence and presence of polyphenols, oligosaccharides, or collagen peptide with 1.0 mM EGCG (c_1−c_6). "Control" represents the lactoferrin−EGCG complex (containing 1.0 mM EGCG) in the absence of polyphenols, oligosaccharides or collagen peptide.

The conformation of lactoferrin in lactoferrin−EGCG aggregate was not monitored when glucose, FOS, or collagen peptide was added, respectively, since no shifts in fluorescence quenching spectra and synchronous fluorescence spectra were found.

On the basis of the fluorescence results, we hypothesize that gallic acid, chlorogenic acid, and XOS not only interacted with lactoferrin and/or EGCG molecules which surrounded the lactoferrin molecule surface with weaker binding affinities via being substituted and/or adsorbed by them but also affected the internal structure of lactoferrin and/or EGCG which were bound within the hydrophobic pockets of lactoferrin with strong binding affinities, leading to a decrease in turbidity and blue or red shifts of the maximum λ_{em} value of lactoferrin fluorescence as their concentrations were increased (except for XOS by M1, which showed increases in the turbidity with increasing concentrations of XOS). However, glucose, FOS, or collagen peptide only interacted with the surface of lactoferrin and EGCG molecules which surrounded the lactoferrin molecule surface, leading to a decrease in turbidity but no shift of the maximum λ_{em} value of lactoferrin fluorescence (except for FOS by M1, which showed an increase of the turbidity as the concentration of FOS was increased).

DOI: 10.1021/acs.jafc.5b01881
J. Agric. Food Chem. 2015, 63, 5035−5045

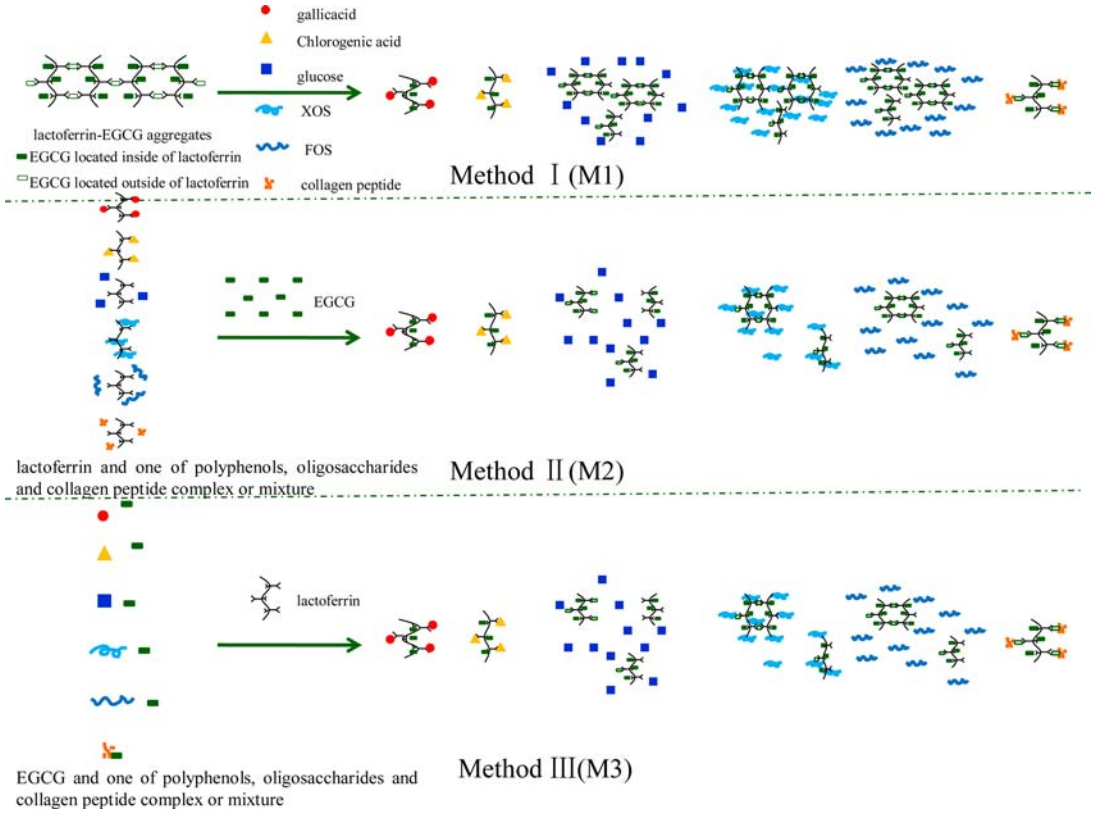

Figure 7. Possible mechanisms and structures involved in the inhibition of the aggregation of lactoferrin and EGCG in the presence of polyphenols, oligosaccharides, or collagen peptide.

Analysis of the Secondary Structure of Lactoferrin Using Circular Dichroism (CD). To obtain more information about the secondary structural changes of lactoferrin induced by EGCG and a polyphenol, oligosaccharide, or collagen peptide, the ternary complexes were analyzed by far-UV CD.

As shown in Figure 6a_1−a_6, in the region of 190−260 nm, the spectrum of lactoferrin in the presence of 1.0 mM EGCG was composed of a broad negative band centered at 208−210 nm and a shoulder at 218−220 nm. In the presence of chlorogenic acid, gallic acid, and XOS, the peak showed a significant ($p < 0.05$) decrease for chlorogenic acid and XOS and a slight increase for gallic acid in negative ellipticities, which is characteristic of a lactoferrin secondary structure conformation change, and the peak showed little change for glucose, FOS, and collagen peptide in negative ellipticities, which indicated no change in lactoferrin secondary structure.

The secondary structure contents were estimated using the DICHROWEB procedure, which is an online server for protein secondary structure analyses, from circular dichroism spectroscopic data.[35] The fractions of α-helix, β-sheet, turn, and unordered coil were estimated by CDSSTR and are shown in Figure 6b_1. In the presence of 1.0 mM EGCG, lactoferrin had 21% α-helix, 32% β-sheet, 22% β-turn, and 25% unordered. In the ternary complexes, lactoferrin had a relatively higher content of α-helix for chlorogenic acid, XOS, and FOS, a lower content of β-sheet for chlorogenic acid, XOS, and FOS, a lower content of β-turn for XOS, and a higher content of unordered for gallic acid, chlorogenic acid, XOS, and FOS, while the contents remained relatively unchanged for glucose and collagen peptide (Figure 6b_2). The protein conformational analysis based on CD data indicated that the presence of polyphenols or oligosaccharides in the ternary complexes led to a change in lactoferrin secondary structure; that is, polyphenols or oligosaccharides induced a progressive increase in the proportion of α-helix structure at the cost of the β-sheet structure of lactoferrin and the conformation became slightly looser due to an increase in the unordered coil fraction. These results showed that lactoferrin secondary conformational changes were consistent with the findings from fluorescence spectra.

Figure 7 shows the possible mechanisms and structures involved in the inhibition of the aggregation of lactoferrin and EGCG by polyphenols, oligosaccharides, or collagen peptide. Polyphenols, such as gallic acid and chlorogenic acid, could form a protein−polyphenol complex with lactoferrin by cooperative hydrogen bonding and hydrophobic interactions. Gallic acid and chlorogenic acid molecules are too small to form insoluble aggregates with lactoferrin through effective cross-linking (data not shown). Therefore, the results obtained for gallic acid and chlorogenic acid strongly suggested that the main mechanism by which these two compounds inhibited the aggregation of lactoferrin and EGCG was to compete with EGCG molecules, which were bound on the surface of lactoferrin. The ternary complex structures EGCG−lactoferrin−gallic acid and EGCG−lactoferrin−chlorogenic acid were formed and exhibited a smaller particle size accompanied by the change of lactoferrin structure (compacting structure of lactoferrin for EGCG−lactoferrin−gallic acid aggregate and unfolding structure of lactoferrin for EGCG−lactoferrin−chlorogenic acid aggregate).

Carbohydrates should have a suitable structure and composition (ionic character) and sufficient size and flexibility to be able to complex with polyphenols. The association of the neutral carbohydrates with polyphenols was thought to be

DOI: 10.1021/acs.jafc.5b01881
J. Agric. Food Chem. 2015, 63, 5035−5045

primarily a surface effect, resulting from a cooperative hydrogen-bonding interaction between the hydroxyl groups of these carbohydrates and the phenolic hydroxyl groups of polyphenols.[13] According to M1, with increasing glucose concentration, there was a gradual disruption of the binding between lactoferrin and EGCG molecules which surrounded the lactoferrin molecule surface with weaker binding affinities; new smaller networks were formed. By M2 and M3, glucose limited the number of available binding sites of lactoferrin to readily fit EGCG through steric effects, leading to a decrease in the turbidity. The disruption or reconstitution of the lactoferrin−EGCG aggregate by glucose might be the main mechanism to form smaller aggregates with higher PDI values in comparison to those for gallic acid and chlorogenic acid.

As mentioned above, the amount of aggregates precipitated tended to increase significantly ($p < 0.05$) with increasing concentration of XOS by M1, while this amount decreased by M2 and M3, which indicated that XOS, unlike gallic acid, chlorogenic acid, and glucose, did not have the ability to compete with EGCG molecules which were bound on the surface of lactoferrin. Fluorescence spectra of lactoferrin with XOS were generally similar to those of lactoferrin with chlorogenic acid, since it could form a lactoferrin−XOS complex. The results obtained strongly suggested that the main mechanism for XOS influence on the lactoferrin−EGCG aggregation was to form a complex or simple ternary complex by an interaction between lactoferrin and XOS. For example, $(\text{lactoferrin−EGCG})_n$-XOS, a more complex structure, exhibiting a larger particle size accompanied by a change in lactoferrin structure, was formed by M1; lactoferrin−EGCG−XOS with a ternary structure, exhibiting a smaller particle size accompanied by a change in lactoferrin structure, was formed by M2 and M3.

Unlike XOS, FOS did not have the ability to influence the fluorescence characteristics of lactoferrin, only interacting with the surface of lactoferrin and EGCG molecules which surrounded the lactoferrin molecule surface. The fluorescence spectra of FOS were generally similar to those of glucose. FOS, whose molecular weight was greater than that of glucose, could adsorb onto the lactoferrin−EGCG aggregate surface (associative interaction) and the larger complex $(\text{lactoferrin−EGCG})_n$−FOS was formed by M1, leading to the insolubilization of the ternary complex. By M2 and M3, in addition to the formation of soluble ternary complex, another explanation could be attributed to the steric effects in solution, limiting the number of available binding sites of lactoferrin to readily fit EGCG, which was able to prevent the interaction between proteins and polyphenols, as suggested for glucose.

XOS species are oligomers containing 2−10 xylose molecules linked by β 1−4-bonds;[36] FOS species are composed of 2,1-linked or 2,6-linked β-D-fructofuranosyl units.[37] Therefore, the chemical composition of these oligosaccharides may affect their interactions with proteins or polyphenols. A more in-depth investigation should be performed to support these findings.

Collagen peptide had changes of fluorescence similar to those of glucose and FOS. However, two significant differences were observed between collagen peptide and glucose or FOS: first, unlike glucose and FOS, collagen peptide could interact with EGCG, forming a new collagen peptide−EGCG complex;[38] second, the PDI values of the ternary complex fabricated by collagen peptide, lactoferrin, and EGCG (0.41−0.66), similar to those of gallic acid and chlorogenic acid (0.34−0.372 for gallic acid, 0.314−0.452 for chlorogenic acid), were lower than those fabricated by glucose or FOS, lactoferrin, and EGCG (0.483−1.0 for glucose, 0.403−1.0 for FOS) as their concentrations were increased. A competition mechanism was postulated between collagen peptide and lactoferrin with EGCG molecules, which surrounded the lactoferrin molecule surface, leading to a decrease in turbidity. A ternary complex structure, lactoferrin−EGCG−collagen peptide, was formed and exhibited a smaller particle size without a change in lactoferrin structure.

The aforementioned findings imply that polyphenols, oligosaccharides, or collagen peptide, like some anionic polysaccharides, were able to resolubilize the protein−polyphenol aggregates. Charged oligosaccharides or collagen peptide, with either positive or negative charge, disrupted the lactoferrin−EGCG aggregate mainly through the mechanism of competition of EGCG molecules which surrounded the lactoferrin molecule surface with weaker binding affinities, forming a ternary complex, accompanied by changes in lactoferrin structure (for gallic acid and chlorogenic acid) or no change (for collagen peptide), while neutral molecules disrupted the aggregate mainly through steric effects and formation of ternary complexes, also accompanied by changes in lactoferrin structure (for XOS) or no change (for glucose and FOS).

Polyphenols, oligosaccharides, or collagen peptide effectively inhibit the formation of lactoferrin−EGCG aggregate by M2 or M3 instead of M1: that is, adding polyphenols, oligosaccharides, or collagen peptide to lactoferrin or EGCG buffer solution before the formation of lactoferrin−EGCG aggregate. Therefore, the pros and cons of polyphenols, oligosaccharides, or collagen peptide on the turbidity and particle size of the ternary complexes mostly depended on the addition sequence of lactoferrin, polyphenols (oligosaccharide or collagen peptide), and EGCG.

Overall, the exceptional properties of polyphenols, oligosaccharides, and collagen peptide, present at high levels in food and beverage products, exhibit a possible additional contribution for reducing the astringent response or turbidity of polyphenols. The inhibition of polyphenols, oligosaccharides, and collagen peptide for the formation of lactoferrin−EGCG aggregate could be applied to the design of clear products in specific food, pharmaceutical, and cosmetic industries.

AUTHOR INFORMATION

Corresponding Author

*Y.G.: tel, +86-10-62737034; fax, +86-10-62737986; e-mail, gyxcau@126.com.

Funding

The research work was funded by the National Natural Science Foundation of China under Grant No. 31371835.

Notes

The authors declare no competing financial interest.

REFERENCES

(1) Frazier, R. A.; Papadopoulou, A.; Mueller-Harvey, I.; Kissoon, D.; Green, R. J. Probing protein-tannin interactions by isothermal titration microcalorimetry. *J. Agric. Food Chem.* **2003**, *51*, 5189−5195.

(2) Le Bourvellec, C.; Renard, C. M. G. C. Interactions between polyphenols and macromolecules: quantification methods and mechanisms. *Crit. Rev. Food Sci. Nutr.* **2012**, *52*, 213−248.

(3) Ozdal, T.; Capanoglu, E.; Altay, F. A review on protein−phenolic interactions and associated changes. *Food Res. Int.* **2013**, *51*, 954−970 2013 .

DOI: 10.1021/acs.jafc.5b01881
J. Agric. Food Chem. 2015, 63, 5035−5045

(4) Jöbstl, E.; O'Connell, J.; Fairclough, J. P. A.; Williamson, M. P. Molecular model for astringency produced by polyphenol/protein interactions. *Biomacromolecules* **2004**, *5*, 942−949.
(5) Prinz, J. F.; Lucas, P. W. Saliva tannin interactions. *J. Oral Rehabil.* **2000**, *27*, 991−994.
(6) McManus, J. P.; Davis, K. G.; Lilley, T. H.; Haslam, E. The association of proteins with polyphenols. Journal of the Chemical Society. *J. Chem. Soc., Chem. Commun.* **1981**, 309b−311.
(7) Gonçalves, R.; Mateus, N.; De Freitas, V. Influence of carbohydrates on the interaction of procyanidin B3 with trypsin. *J. Agric. Food Chem.* **2011**, *59*, 11794−11802.
(8) Fontoin, H.; Saucier, C.; Teissedre, P. L.; Glories, Y. Effect of pH, ethanol and acidity on astringency and bitterness of grape seed tannin oligomers in model wine solution. *Food Qual. Prefer.* **2008**, *19*, 286−291.
(9) De Freitas, V.; Carvalho, E.; Mateus, N. Study of carbohydrate influence on protein−tannin aggregation by nephelometry. *Food Chem.* **2003**, *81*, 503−509.
(10) Mateus, N.; Carvalho, E.; Luís, C.; de Freitas, V. Influence of the tannin structure on the disruption effect of carbohydrates on protein−tannin solutions. *Anal. Chim. Acta* **2004**, *513*, 135−140.
(11) Carvalho, E.; Mateus, N.; Plet, B.; Pianet, I.; Dufourc, E.; De Freitas, V. Influence of wine pectic polysaccharides on the interactions between condensed tannins and salivary proteins. *J. Agric. Food Chem.* **2006**, *54*, 8936−8944.
(12) Soares, S. I.; Goncalves, R. M.; Fernandes, I. V. A.; Mateus, N.; de Freitas, V. Mechanistic approach by which polysaccharides inhibit α-amylase/procyanidin aggregation. *J. Agric. Food Chem.* **2009**, *57*, 4352−4358.
(13) Soares, S.; Mateus, N.; de Freitas, V. Carbohydrates Inhibit Salivary Proteins Precipitation by Condensed Tannins. *J. Agric. Food Chem.* **2012**, *60*, 3966−3972.
(14) Pascal, C.; Poncet-Legrand, C.; Cabane, B.; Vernhet, A. Aggregation of a proline-rich protein induced by epigallocatechin gallate and condensed tannins: effect of protein glycosylation. *J. Agric. Food Chem.* **2008**, *56*, 6724−6732.
(15) Yang, W.; Liu, F.; Xu, C.; Yuan, F.; Gao, Y. Molecular interaction between (−)-epigallocatechin-3-gallate and bovine lactoferrin using multi-spectroscopic method and isothermal titration calorimetry. *Food Res. Int.* **2014**, *64*, 141−149 2014 .
(16) Bandyopadhyay, P.; Ghosh, A. K.; Ghosh, C. Recent developments on polyphenol−protein interactions: effects on tea and coffee taste, antioxidant properties and the digestive system. *Food Funct.* **2012**, *3*, 592−605.
(17) Corredig, M.; Sharafbafi, N.; Kristo, E. Polysaccharide−protein interactions in dairy matrices, control and design of structures. *Food Hydrocolloids* **2011**, *25*, 1833−1841.
(18) Shemetov, A. A.; Nabiev, I.; Sukhanova, A. Molecular interaction of proteins and peptides with nanoparticles. *ACS Nano* **2012**, *6*, 4585−4602.
(19) Graf, B. A.; Milbury, P. E.; Blumberg, J. B. Flavonols, flavones, flavanones, and human health: epidemiological evidence. *J. Med. Food* **2005**, *8*, 281−290.
(20) Pandey, K. B.; Rizvi, S. I. Plant polyphenols as dietary antioxidants in human health and disease. *Oxid. Med. Cell. Longevity* **2009**, *2*, 270−278.
(21) Chou, Y. T.; Lin, K. W. Effects of xylooligosaccharides and sugars on the functionality of porcine myofibrillar proteins during heating and frozen storage. *Food Chem.* **2010**, *121*, 127−131.
(22) Cummings, C. H.; Macfarlane, G. T.; Englyst, H. N. Prebiotic digestion and fermentation. *Am. J. Clin. Nutr.* **2001**, *73*, 415−420.
(23) Pei, X.; Yang, R.; Zhang, Z.; Gao, L. F.; Wang, J. B.; Xu, Y. J.; Zhao, M.; Han, X. L.; Liu, Z. G.; Li, Y. Marine collagen peptide isolated from Chum Salmon (Oncorhynchus keta) skin facilitates learning and memory in aged C57BL/6J mice. *Food Chem.* **2010**, *118*, 333−340.
(24) Lobley, A.; Whitmore, L.; Wallace, B. A. DICHROWEB: an interactive website for the analysis of protein secondary structure from circular dichroism spectra. *Bioinformatics* **2002**, *18*, 211−212.
(25) Whitmore, L.; Wallace, B. A. DICHROWEB, an online server for protein secondary structure analyses from circular dichroism spectroscopic data. *Nucleic Acids Res.* **2004**, *32*, W668−W673.
(26) Tokle, T.; Lesmes, U.; McClements, D. J. Impact of electrostatic deposition of anionic polysaccharides on the stability of oil droplets coated by lactoferrin. *J. Agric. Food Chem.* **2010**, *58*, 9825−9832.
(27) Haslam, E.; Lilley, T. H. Natural astringency in foodstuffs-a molecular interpretation. *Crit. Rev. Food Sci. Nutr.* **1998**, *27*, 1−41.
(28) Luck, G.; Liao, H.; Murray, N. J.; Grimmer, H. R.; Warminski, E. E.; Williamson, M. P.; Haslam, E. Polyphenols, astringency and proline-rich proteins. *Phytochemistry* **1994**, *37*, 357−371.
(29) Stănciuc, N.; Aprodu, I.; Râpeanu, G.; van der Plancken, I.; Bahrim, G.; Hendrickx, M. Analysis of the thermally induced structural changes of bovine lactoferrin. *J. Agric. Food Chem.* **2013**, *61*, 2234−2243.
(30) Xiao, J.; Chen, L.; Yang, F.; Liu, C. X.; Bai, Y. L. Green, yellow and red emitting CdTe QDs decreased the affinities of apigenin and luteolin for human serum albumin in vitro. *J. Hazard. Mater.* **2010**, *182*, 696−703.
(31) Hu, Y. J.; Liu, Y.; Sun, T. Q.; Bai, A. M.; Lu, H. Q.; Pi, Z. B. Binding of anti-inflammatory drug cromolyn sodium to bovine serum albumin. *Int. J. Biol. Macromol.* **2006**, *39*, 280−285.
(32) Liu, X.; Wu, X.; Yang, J. Protein determination using methylene blue in a synchronous fluorescence technique. *Talanta* **2010**, *81*, 760−765.
(33) Zhang, J.; Yan, Q.; Liu, J.; Lu, X.; Zhu, Y.; Wang, J.; Wang, S. Study of the interaction between 5-sulfosalicylic acid and bovine serum albumin by fluorescence spectroscopy. *J. Lumin.* **2013**, *134*, 747−753.
(34) Guo, M.; Zhang, L. Y.; Lü, W. J.; Cao, H. R. Analysis of the spectroscopic characteristics on the binding interaction between tosufloxacin and bovine lactoferrin. *J. Lumin.* **2011**, *131*, 768−775.
(35) Liu, F.; Sun, C.; Yang, W.; Yuan, F.; Gao, Y. Structural characterization and functional evaluation of lactoferrin−polyphenol conjugates formed by free-radical graft copolymerization. *RSC Adv.* **2015**, *5*, 15641−15651.
(36) Mäkeläinen, H.; Forssten, S.; Saarinen, M.; Stowell, J.; Rautonen, N.; Ouwehand, A. C. Xylo-oligosaccharides enhance the growth of bifidobacteria and Bifidobacterium lactis in a simulated colon model. *Benefic. Microbes* **2010**, *1*, 81−91.
(37) Zhang, M.; Du, W.; Bi, H. Physicochemical Characterization of a Low-Molecular-Weight Fructooligosaccharide from Chinese Cangshan Garlic (Allium sativum L.). *J. Agric. Food Chem.* **2012**, *60*, 9462−9467.
(38) Yang, W.; Yuan, F.; Gao, Y. Interaction of fish collagen peptide with (−)-epigallocatechin-3-gallate. *Spectrosc. Spect. Anal.* **2014**, *34*, 12 2014 .

DOI: 10.1021/acs.jafc.5b01881
J. Agric. Food Chem. 2015, 63, 5035−5045

JOURNAL OF AGRICULTURAL AND FOOD CHEMISTRY

Article

pubs.acs.org/JAFC

Fabrication Mechanism and Structural Characteristics of the Ternary Aggregates by Lactoferrin, Pectin, and (−)-Epigallocatechin Gallate Using Multispectroscopic Methods

Wei Yang, Chenqi Xu, Fuguo Liu, Cuixia Sun, Fang Yuan, and Yanxiang Gao*

Beijing Key Laboratory of Functional Food from Plant Resources, College of Food Science & Nutritional Engineering, China Agricultural University, P.O. Box 112, No. 17 Qinghua East Road, Beijing 100083, People's Republic of China

ABSTRACT: The ternary aggregates were fabricated by lactoferrin (LF), pectin (high methylated pectin (HMP)/low methylated pectin (LMP)), and (−)-epigallocatechin gallate (EGCG) through three different fabrication methods at pH 5.0. The turbidity, particle size, and ζ-potential of ternary aggregates were influenced by the types of pectin, the concentration of EGCG, and fabrication methods. The fluorescence intensity of LF decreased with an increase in EGCG concentration for all ternary aggregates. Far-UV circular dichroism results indicated that EGCG could alter the secondary structure of LF with an increase in the proportion of β-sheet structure at the cost of unordered coil structure. According to near-UV circular dichroism results, EGCG could also modulate the tertiary structure of LF at the presence of pectin. In addition, EGCG could increase the viscoelasticity of the ternary aggregates with HMP, leading to better stability of the ternary aggregates. An opposite result was observed for the ternary aggregates with LMP. These findings should provide an insight into the fabrication mechanism and applications of ternary aggregates formed by protein, polysaccharide, and polyphenol in the food, pharmaceutical, and cosmetic industries.

KEYWORDS: *fabrication mechanism, structural characteristics, lactoferrin, pectin, (−)-epigallocatechin gallate, multispectroscopic*

INTRODUCTION

Polyphenols can bind noncovalently to proteins.[1−3] Some researchers have focused on the disadvantage of the use of polyphenols, since they can precipitate proteins to form an insoluble state, resulting in undesirable turbidity and colloidal haze products.[4] From a nutritional point of view, the interaction between polyphenols and proteins, such as α-amylase and trypsin, has been shown to have negative effects, reducing the palate lubrication, causing an unpleasant sensation of roughness, dryness, and constriction, and reducing absorption of nutrients.[5,6] Polyphenols also affect the conformational changes of proteins. It was pointed out that the conformation of proteins (such as β-lactoglobulin, casein, collagen, bovine serum albumin, and lysozyme) was modified by polyphenols (such as tea polyphenols, resveratrol, genistein, curcumin, and procyanidin).[7−11] The conformational changes of proteins, signs of a partial protein unfolding upon protein−polyphenol complexes, might affect the formation and properties of the electrostatic complexes between protein and polysaccharide.

Polysaccharides are widely used as stabilizers, thickening, or gelling agents in the food industry.[12] The interaction between polysaccharides and polyphenols might result from cooperative hydrogen bonding between the hydroxyl groups of polysaccharide and polyphenols and from hydrophobic interactions.[13−16] Sun-Waterhouse et al. reported the effect of fruit polyphenols and pectin on the properties of bread and suggested possible polyphenol complexes, via nonbinding interactions such as hydrogen bonding, with pectin.[17] Hayashi et al. showed that the presence of pectin mitigated the astringency of tea infusions and attributed the observed behavior to pectin−catechin complex formation.[18] Mercedes Lataza Rovaletti et al. indicated that polysaccharides could react with tannic acid in beer, and this reaction actually caused a considerable increase in turbidity.[19]

Several studies have demonstrated the ability of some polysaccharides to disrupt polyphenol−protein interactions in dilute solution.[6,15,16,20−22] Two hypotheses were proposed for this disrupting effect of polysaccharides toward protein and polyphenol interactions: (i) the ability of polysaccharides to form a protein−polyphenol−polysaccharide ternary complex with enhanced solubility in aqueous medium and (ii) the ability of polysaccharides to encapsulate polyphenols, competing with the binding to proteins.[23] Recent studies have shown that the complexation of preheated whey protein isolate−pectin complexes inhibited the protein precipitation with polyphenols.[24]

As main components of foods, proteins and polysaccharides play a key role in the formation of the building blocks of structure and texture. The interactions occurring between polysaccharides and proteins are influenced by their surface charge, hydrophobicity, and the rheological characteristics. The formation of aggregates between proteins and polysaccharides might be the starting point for the development of delivery systems in the food, cosmetics, and pharmaceutical industries. These aggregates could be used to encapsulate, protect, and deliver functional or bioactive components, such as minerals, polyphenols, vitamins, enzymes, drugs, and peptides,[25−31] to specific sites, controlling the rate or extent of their digestibility in different regions of the human digestive system within the

Received: December 16, 2014
Accepted: May 8, 2015
Published: May 8, 2015

ACS Publications © 2015 American Chemical Society

DOI: 10.1021/acs.jafc.5b01592
J. Agric. Food Chem. 2015, 63, 5046−5054

consumer's body: e.g., mouth, stomach, small intestine, or colon.[25,32−34]

Pectins are normally extracted from several raw materials (such as apple pomace, sugar beet chips, and citrus peels) and are used in the food industry as thickening, gelling, and stabilizing agents. Chemically, they are mainly composed of D-galacturonic acid linked by α-(1,4)-glycosidic bonds, forming polygalacturonic acid. Pectins have different degrees of esterification (DE), with those higher or lower than 50% methylation corresponding to high or low methoxyl pectins, respectively.[35] Lactoferrin (LF) has attracted strong interest as a functional bioactive ingredient for applications in food, personal care, and pharmaceutical products. It has a relatively high p*I* (8−9) and therefore tends to be cationic at a pH value below 8.0. Thus, the electrostatic interaction between LF and pectin has been harnessed to form various particulate systems and modulate emulsion functionality over a wide pH range.[36,37]

Recently, there has been increasing interest in the incorporation of polyphenols into protein−polysaccharide aggregates and the functionality of the ternary electrostatic aggregates between polysaccharides and proteins might be affected by the presence of polyphenols. An understanding of the fabrication mechanism and structural characteristics of the ternary aggregates is a key step for optimizing the formation of aggregates with applications in coatings, emulsions, etc. In the present work, ternary aggregates fabricated from lactoferrin (LF), pectin, and (−)-epigallocatechin gallate (EGCG) were designed to form a novel delivery systems for foods and other products. The effect of binding sequence for LF, pectin, and EGCG on the physical characteristics of the aggregates was also investigated.

MATERIALS AND METHODS

Materials and Chemicals. Lactoferrin (purity ≥92%) from bovine whey was purchased from New Image International Limited (Auckland, New Zealand). EGCG (purity ≥95%) from green tea was purchased from BSZH Science (Beijing, People's Republic of China). High methoxylated pectin (HMP) with a DE value of 72% (GENU pectin type YM-150-H) and low methoxylated pectin (LMP) with a DE value of 36% (GENU pectin type LM-101-AS) were obtained from CP Kelco (Copenhagen, Denmark). All other chemicals used were of analytical grade, unless otherwise stated.

Solution Preparation. LF (3.2% w/v), EGCG (8.0 mM), and pectin (1.8% w/v) were dissolved in 10 mM acetate buffer (pH 5.0), and the mixture was stirred constantly at room temperature for 2 h and then stored overnight at 4 °C to achieve complete dissolution.

Formation of the Ternary Aggregate Solutions (Fabricated from LF, Pectin, and EGCG). The ternary aggregate solutions were formed with three addition sequences of LF, pectin, and EGCG. All solutions were mixed on a vortex shaker (QL-866, Haimen QILINBEIER Instruments Co., Ltd., Haimen, People's Republic of China) at 3000 rpm for 2 min.

Method I (M1). First, 1.0 mL of LF (3.2% w/v) and 2.0 mL of pectin (1.8% w/v) solutions were mixed and allowed to stand for 2 h. After that, 1.0 mL of EGCG solutions with different concentrations (0−2.0 mM) were mixed with LF−pectin complexes and the mixtures allowed to stand for 2 h before the measurement.

Method II (M2). First, 1.0 mL of LF (3.2% w/v) solution and 1.0 mL of EGCG solutions with different concentrations (0−2.0 mM) were mixed and allowed to stand for 2 h. After that, 2.0 mL of pectin solution (1.8% w/v) was mixed with different LF−EGCG complexes, and the mixtures were allowed to stand for 2 h before the measurement.

Method III (M3). First, 2.0 mL of pectin (1.8% w/v) solution and 1.0 mL of EGCG solutions with different concentrations (0−2.0 mM) were mixed and allowed to stand for 2 h. After that, 1.0 mL of LF (3.2% w/v) solution was mixed with the pectin−EGCG complexes, and the mixtures were allowed to stand for 2 h before the measurement.

The abbreviations TA_{Pectin}, TA_{HMP}, and TA_{LMP} represent the ternary aggregates prepared using LF, EGCG, and pectin (both HMP and LMP), HMP, and LMP, respectively. TA_{Pectin}-*x*, TA_{HMP}-*x*, and TA_{LMP}-*x* (*x* = 1−3) were used to represent the ternary aggregates prepared by M1, M2, and M3, respectively.

Turbidity Measurements. Nephelometry experiments were performed in a HACH 2100N Laboratory Turbidimeter (Loveland, TX, USA). All samples were diluted 1/10 (v/v) with acetate buffer solution (pH 5.0). The optical apparatus was equipped with a tungsten-filament lamp with three detectors: a 90° scattered-light detector, a forward-scattering light detector, and a transmitted light detector. The calibration was performed using a Gelex Secondary Turbidity Standard Kit (HACH, Loveland, TX, USA), which consists of stable suspensions of a metal oxide in a gel. All experiments were performed in triplicate.

Particle Size and ζ-Potential Measurements. Particle size and ζ-potential were determined using a combined dynamic light scattering (DLS) and particle electrophoresis instrument (Nano-ZS90, Malvern Instruments, Worcestershire, U.K.). Basically, all samples were diluted 1/10 (v/v) with acetate buffer solution (pH 5.0) and then equilibrated for 1 min inside the instrument before dynamic light backscattering, and then data were collected over at least 10 sequential readings. The *Z*-average particle diameter was calculated by the instrument using the Stokes−Einstein equation. The ζ-potential of the particles was calculated using the Smoluchowski model through electrophoretic mobility measurements performed in a capillary electrophoresis device inserted into the DLS instrument.

Fluorescence Spectroscopy. Fluorescence measurements were carried out using a fluorescence spectrophotometer (F-7000, Hitachi, Japan). All samples were diluted 1/3 (v/v) with acetate buffer solution. Spectra were collected when the diluted solutions were kept at 25 °C for 2 h. Fluorescence emission spectra of LF were recorded with the excitation wavelength at 292 nm. Both excitation and emission slit widths were set at 10 nm.

Circular Dichroism Measurements. The CD spectra were recorded using a CD spectropolarimeter (Pistar π-180, Applied Photophysics Ltd., Surrey, U.K.) at both far-UV (190−250 nm) and near-UV (250−320 nm) regions under a constant nitrogen flush. Path lengths were 0.1 cm for the far-UV region and 1 cm for the near-UV region. Ellipticity was recorded at a speed of 100 nm/min, 0.2 nm resolution, 20 accumulations, and 2.0 nm bandwidth. The collected data were analyzed using Dichroweb: the online circular dichroism web site (http://dichroweb.cryst.bbk.ac.uk.) The fractions of α-helix, β-sheet, turn, and unordered coil were estimated by SELCON3. Each spectrum presented is the average of three consecutive measurements.

Viscoelastic Properties. The viscoelastic properties of the samples were evaluated by optical microrheology (Rheolaser LAb from Formulaction, Union, France). In the experiment, 20 mL of samples was injected by a syringe into a flat-bottomed cylindrical glass tube (height 70 mm, external diameter 27.5 mm). The tube was immediately placed in the sample chamber of the Rheolaser LAb instrument. During the measurement, the speckle pattern of the sample, which was generated by the interfering backscattering wave of the incident laser at 650 nm caused by the Brownian motion of the particles, was collected by a multipixel detector for 3 min. The generated speckle image was treated to plot the decorrelation curve, which could quantify the particle mobility and displacement and in turn be used to characterize the viscoelastic properties of the samples.

Physical Stability Measurements. The stabilities of the solutions were measured by the LUMi-Sizer (L.U.M. GmbH, Berlin, Germany), an instrument employing centrifugal sedimentation to accelerate the occurrence of instability phenomena such as sedimentation, flocculation, and creaming. The samples were subjected to centrifugal force, while near-infrared light illuminated the entire sample cell to measure the intensity of transmitted light as a function of time and position over the entire sample length simultaneously. The sample stability was shown as a space- and time-related transmission profile

DOI: 10.1021/acs.jafc.5b01592
J. Agric. Food Chem. 2015, 63, 5046−5054

over the sample length. At the start of the measurement, the solutions were intact. As the sample was centrifuged, however, the heavier and less transparent aqueous phase moved to the bottom, which gave higher transmission; the lighter and more transparent phase moved to the top. The instrumental parameters used for the measurement were as follows: volume, 1.8 mL of dispersion; 3000 rpm; $time_{Exp}$, 3600 s; time interval, 30 s; temperature, 25 °C.

Statistical Analysis. The experiments were conducted in duplicate, and all of the analyses were done in triplicate. The results are presented as the means ± standard deviation. Data were analyzed by one-way analysis of variance using the SPSS 16.0 package (SPSS Inc., Chicago, IL, USA), and significant differences of means ($p < 0.05$) were determined using the Duncan multiple-range test. The correlation analysis was carried out using the Pearson mode. The concordance between experimental data and calculated values was established by the root-mean-squared deviation (RMSD).

RESULTS AND DISCUSSION

A fixed concentration of pectin (0.9% w/v) was used in the experiments to saturate the LF (0.8% w/v) molecules, as no further change in ζ-potential was observed above this concentration (data not shown).

Effect of Addition Sequence of LF, Pectin, and EGCG on Turbidity, Particle Size, and ζ-Potential of the Ternary Aggregates. It is well-known that EGCG can bind to LF with strong affinity and form nanosized particles at pH 5.0.[38] At the same time, pectin and EGCG can form a pectin−EGCG complex by cooperative hydrogen bonding between the hydroxyl groups of polysaccharide and groups of polyphenols. Therefore, the addition sequence of LF, pectin, and EGCG may directly affect the interactions of these compounds, thereby affecting the structural characteristics of the ternary aggregates. The turbidity, particle size, and ζ-potential of the ternary aggregates are shown in Figure 1. The magnitude of the

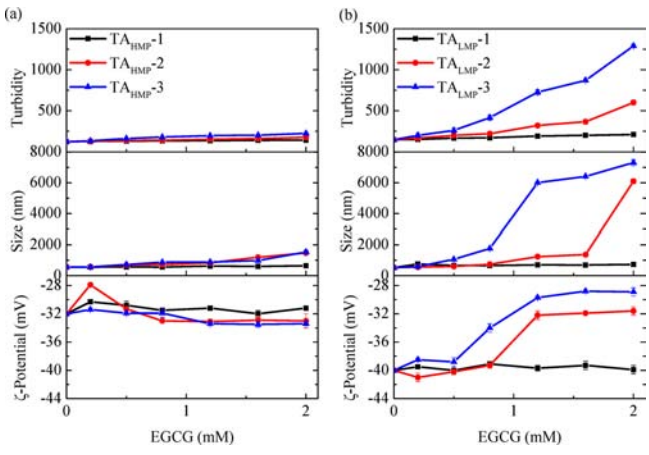

Figure 1. Turbidity, particle size, and ζ-potential of TA_{HMP} (a) and TA_{LMP} (b) as a function of EGCG concentration (0−2.0 mM) at pH 5.0.

negative charge on the LF−pectin complexes was greater for LMP than for HMP, which could be attributed to the fact that LMP has a higher linear charge density: i.e., more carboxylic acid groups per unit chain length. The turbidity and particle size exhibited a synchronous trend with the rise of EGCG concentration.

For TA_{Pectin}-1, the turbidity, particle size, and ζ-potential were not apparently changed with different concentrations of EGCG; in other words, the aggregates large enough to scatter light strongly were not formed, and EGCG hardly affected the structural properties of TA_{HMP}-1 and TA_{LMP}-1. Our results were similar to those of Thongkaew et al., who showed that the presence of catechin, grape seed extract, and hibiscus extract to whey protein isolate−pectin complex at pH 3.5 did not show a obvious difference of mean particle diameter and the addition of catechin, grape seed extract, and tannic acid did not affect the ζ-potential of preheated whey protein isolate−pectin complex at pH 5.2.[23] The increasing concentration of EGCG exhibited some effects on the turbidity and particle size of TA_{Pectin}-2 and TA_{Pectin}-3, which suggested that the ternary aggregates were formed to be large to scatter light. The larger turbidity and particle size of TA_{Pectin}-3 in comparison to those of TA_{Pectin}-2 indicated that more complex structures were formed by M3 than by M2.

The effect of EGCG on the formation of large aggregates was more prominent for TA_{LMP} than for TA_{HMP}, which was consistent with the greater change in ζ-potential of TA_{LMP} than of TA_{HMP} (discussed below). The particle sizes of TA_{HMP}-1, TA_{HMP}-2, and TA_{HMP}-3 were smaller than those of TA_{LMP}-1, TA_{LMP}-2, and TA_{LMP}-3, respectively, which suggested that the aggregates formed with HMP were more numerous than those formed with LMP. A possible explanation of this phenomenon is that LMP, containing a higher charge density than HMP, may have a greater propensity to form large complexes or sediments through neutralization of LF−EGCG complexes. On the other hand, more localized interactions between protein and polysaccharide molecules led to the formation of complexes of more limited size, because there are free segments of biopolymers that promote complex repulsion through electrostatic or steric hindrance effects.[39] Thus, the particles formed with HMP were likely less compact and possessed more biopolymer segments extending into solutions in comparison to LMP particles.

For TA_{Pectin}-2 and TA_{Pectin}-3, the presence of EGCG significantly ($p < 0.05$) affected the ζ-potential of the ternary aggregates. Interestingly, the addition of EGCG resulted in a decrease in negatively charged ζ-potential for TA_{HMP}-2 and TA_{HMP}-3 but an increase for TA_{LMP}-2 and TA_{LMP}-3. The charges of HMP, LMP, and EGCG at pH 5.0 were −32 ± 0.1, −40 ± 0.6, and −16 ± 1.0 mV, respectively. Therefore, it was estimated that the types of pectin and electrostatic repulsion between pectin and EGCG might have some effect on the charge distribution of those ternary aggregates. However, an EGCG concentration of more than 1.2 mM had almost no effect on the ζ-potential of the ternary aggregates, indicating that the aggregates formed may retain their charged functional groups.

Fluorescence Spectroscopy Measurements. There are 13 tryptophan residues in the LF molecule.[40] By monitoring of the emission peak change, some useful information could be obtained concerning the structural changes of LF.

It was obvious that, for all ternary aggregates, the fluorescence intensity of LF regularly decreased with an increase in EGCG concentration, and this implied that there existed binding behavior between LF and EGCG (Figure 2a,b). The maximum λ_{em} was slightly red-shifted (from 334.4 to 335.8 nm for TA_{HMP} and from 334.4 to 337.2−338 nm for TA_{LMP}, more red-shifted emission in comparison to TA_{HMP}) in the presence of EGCG (Figure 2c). These results revealed that there were some changes in the immediate environment of the tryptophan residues of LF in TA_{HMP} and TA_{LMP} and that EGCG was situated in closer proximity to the tryptophan residues in TA_{LMP} than in TA_{HMP} for quenching to occur.

DOI: 10.1021/acs.jafc.5b01592
J. Agric. Food Chem. 2015, 63, 5046−5054

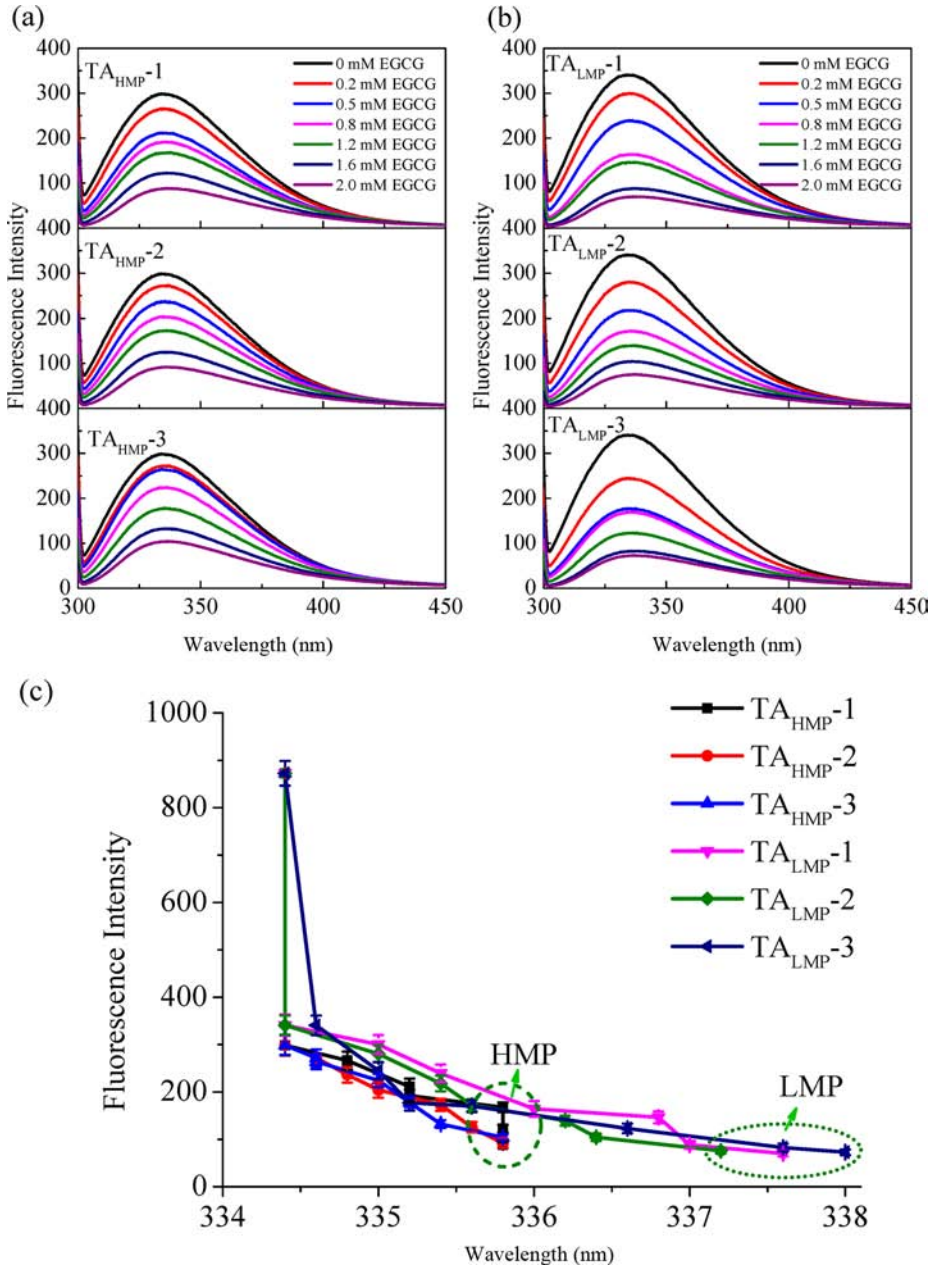

Figure 2. Fluorescence spectra of LF in TA_{HMP} (a) and TA_{LMP} (b) at different EGCG concentrations (0−2.0 mM) at pH 5.0. Influence of increasing concentration of EGCG on the fluorescence variation of LF in TA_{HMP} and TA_{LMP} (c).

In the solution prepared by M1, LF−pectin aggregates were formed first; then, EGCG was added to the aggregates, and it might be embedded in the gaps of LF−pectin aggregates and interact with LF, leading to almost complete loss of fluorescence intensity in TA_{Pectin}-1, as in TA_{Pectin}-2 and TA_{Pectin}-3. Meanwhile, with increasing concentrations of EGCG, the outer layer of pectin prevented the formation of a larger "$-(LF-EGCG)_n-$" network structure, leading to little change in turbidity, particle size, and ζ-potential of TA_{Pectin}-1 (see Figure 1). Therefore, the structure of TA_{Pectin}-1 was LF in the inner layer, pectin in the outer layer, and EGCG in the middle layer (Figure 3a).

In the solution prepared by M2, "$-(LF-EGCG)_n-$" complex showed a small or large particle size formed at relatively low or high concentration of EGCG first; after pectin was added to the solution, the pectin had a sufficient capacity to coat the "$-(LF-EGCG)_n-$" complex. Therefore, the structure of TA_{Pectin}-2 was "$-(LF-EGCG)_n-$" complex in the inner layer

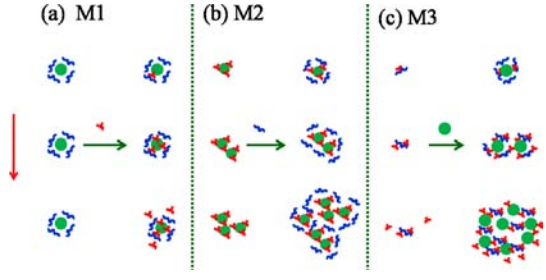

Figure 3. Schematic representation of possible mechanisms (a−c) involved in the formation of the ternary aggregates with LF, pectin, and EGCG. Legend: LF, green square; pectin, blue ribbon; EGCG, red streak. The red arrow indicates increasing concentrations of EGCG.

DOI: 10.1021/acs.jafc.5b01592
J. Agric. Food Chem. 2015, 63, 5046−5054

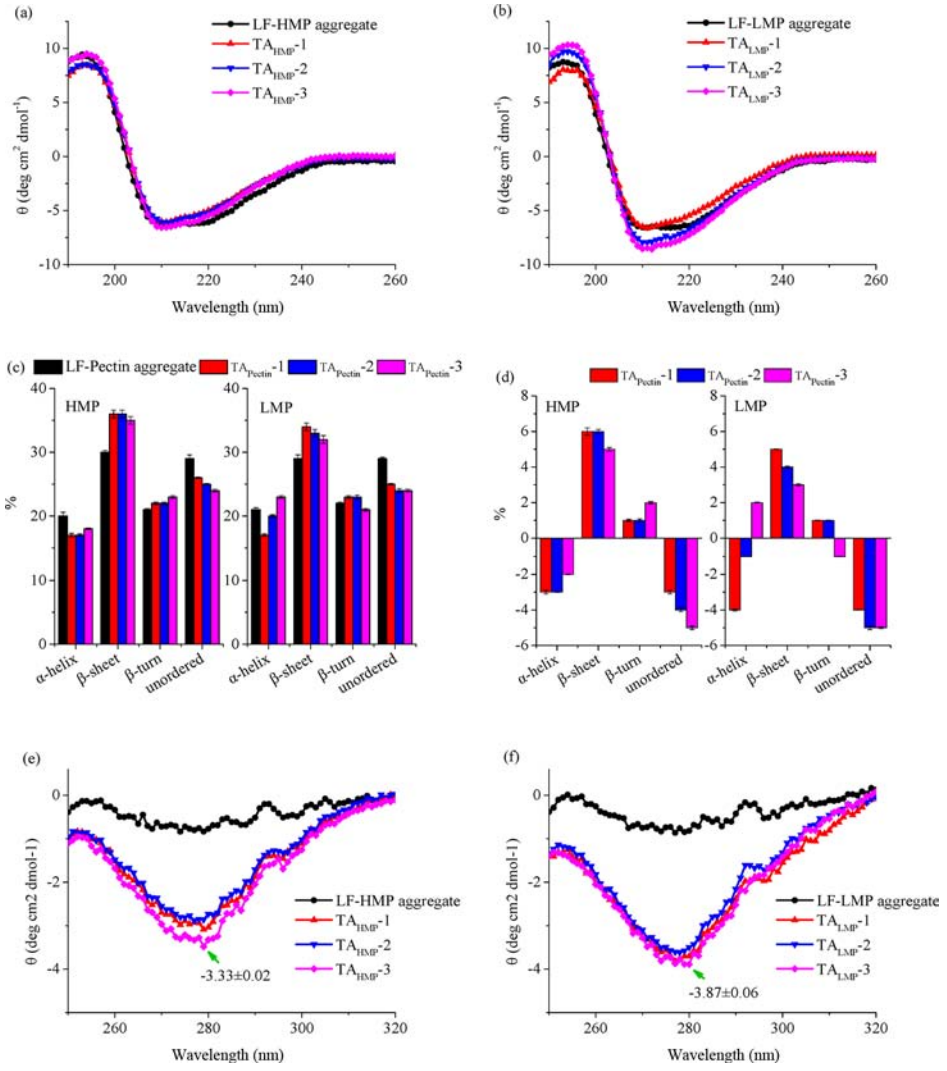

Figure 4. Far-UV CD spectra of LF in LF−pectin aggregates and TA_{Pectin} containing 1.0 mM EGCG (a, b). Secondary structure of LF in LF−pectin aggregates and TA_{Pectin} containing 1.0 mM EGCG (c). Changes in secondary structure of LF in TA_{Pectin} containing 1.0 mM EGCG (d). Near-UV CD spectra of LF in LF−pectin aggregates and TA_{Pectin} containing 1.0 mM EGCG (e, f).

and pectin in the outer layer (Figure 3b). Pectin, which forms the outer layer of TA_{Pectin}-2, also could prevent further aggregation of these compounds; thus, TA_{Pectin}-2 exhibited a particle size relatively larger than that of TA_{Pectin}-1 but a smaller particle size than TA_{Pectin}-3 (see Figure 1).

In the solution prepared by M3, "−pectin−EGCG−" complex was formed first; after LF was added to the solution, "$-[LF-EGCG-pectin-EGCG-LF]_n-$" aggregates, more complicated than those of TA_{Pectin}-2, were formed and showed the greatest turbidity and largest particle size at corresponding concentrations of EGCG (see Figure 1). The structure of TA_{Pectin}-3 was a complex network structure fabricated by LF, EGCG, and pectin (Figure 3c).

Circular Dichroism (CD) Measurements. Far-UV CD is used to obtain the information about the changes occurring at a secondary folding level of proteins. In this section, the influence of pectin type on the secondary structure of LF- and EGCG-induced conformational transitions of LF in TA_{HMP} and TA_{LMP} (containing 1.0 mM EGCG) was monitored by far-UV CD spectroscopy (Figure 4a,b). The fractions of α-helix, β-sheet, turn, and unordered coil are shown in Figure 4c,d.

It was found that LF in the LF−HMP aggregate contained 20% α-helix, 30% β-sheet, 21% β-turn, and 29% unordered, and 21% α-helix, 29% β-sheet, 22% β-turn, and 29% unordered fractions occurred in LF−LMP aggregate. The slight difference in the secondary structure of LF in LF−HMP and LF−LMP aggregates might be attributed to the different physiochemical characteristics of HMP and LMP.

It is well-known that the noncovalent interactions of EGCG and proteins affect the structure of proteins.[7,8,41,42] Hence, in the presence of EGCG, the secondary structural composition of LF in TA_{HMP} and TA_{LMP} possibly changed when LF−EGCG complex was formed. As is shown in Figure 4a,b, in the presence of 1.0 mM EGCG, the broad negative band centered at 208−210 nm showed a slight decrease in negative ellipticities for TA_{HMP} and TA_{LMP}, while the shoulder at 218−220 nm showed a decrease or an increase in negative ellipticities, which is a characteristic of LF secondary structure conformation change.

The protein conformational analysis based on CD data indicated that the addition of EGCG led to changes in the secondary structure of LF in TA_{HMP} and TA_{LMP}. In the presence of 1.0 mM EGCG, the β-sheet and β-turn contents

DOI: 10.1021/acs.jafc.5b01592
J. Agric. Food Chem. 2015, 63, 5046−5054

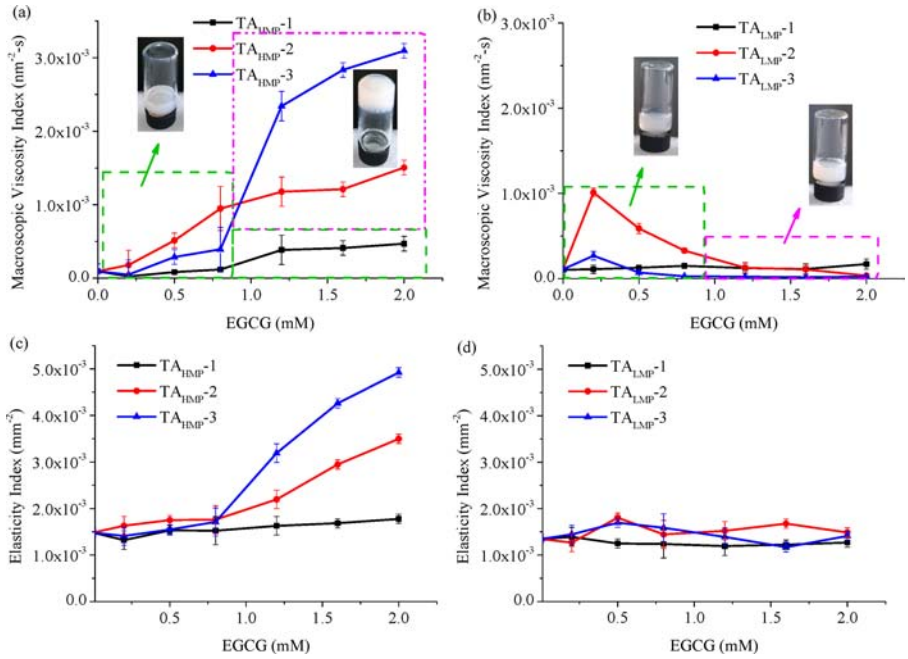

Figure 5. MVI and EI of TA_{HMP} (a, c) and TA_{LMP} (b, d) as a function of EGCG concentration (0−2.0 mM) at pH 5.0.

increased with a concomitant reduction of α-helical and unordered coil fractions in TA_{HMP}-1, TA_{HMP}-2, TA_{HMP}-3, TA_{LMP}-1, and TA_{LMP}-2. Therefore, it could be concluded that, for these ternary aggregates, EGCG contributed largely to the stability of LF β-sheet conformation and LF assumed a slightly compact conformation due to the decrease of unordered coil fraction.

It is interesting to find that an inverse result, an increase of α-helix (about 2%) and decrease of β-turn (about −1%), was observed in TA_{LMP}-3, which might be one reason for the lower viscoelasticity and less stability of TA_{LMP}-3 in comparison to TA_{HMP}-3.

Near-UV CD is a powerful tool for probing the tertiary structure of proteins. CD spectra in the region of 250−320 nm were attributed to aromatic amino acids, and the real shape and magnitude of the near-UV CD spectrum of a protein were determined by the number of each type of aromatic amino acids present, their mobility, the nature of the environment (hydrogen bonds, polar groups, and polarizability), and spatial disposition in the protein.[43] From Figure 4e,f, the near-UV CD spectra of LF in TA_{HMP} and TA_{LMP} showed a broad distribution range from 250 to 300 nm, comprising four maxima at 254, 277, 285, and 292 nm, which were attributed to phenylalanine (Phe), tyrosine (Tyr), and tryptophan (Trp), respectively.[43] The presence of EGCG led to a remarkable decrease in the ellipticities, which suggested that the LF tertiary conformation had changed. It should be noted that LF in TA_{LMP} showed a greater decrease in the magnitudes of the near-UV CD bands in comparison to that in TA_{HMP}, which indicated that the LMP−EGCG complex had a greater impact than HMP−EGCG complex on the structure of LF.

As EGCG caused different changes of LF secondary and tertiary structures in TA_{HMP} and TA_{LMP}, respectively, it may alter the stoichiometry of the LF−pectin complexes, which might increase the tendency for charge neutralization and lead to stronger bridging forces between LMP and LF and therefore the nature of ternary aggregates with larger particle size formed by LMP in comparison to HMP (see Figure 1).

Thus, EGCG could interact with LF in TA_{HMP} and TA_{LMP}, leading to changes of LF secondary and tertiary structures, and the effects of EGCG on LF secondary structure mainly depended on the types of pectin and fabrication methods.

Viscoelastic Properties. Passive particle tracking is a direct method consisting of monitoring the Brownian motion of tracer particles within a system and interpreting such movements in terms of the local viscoelasticity, or microrheology.[44] Particle tracking microrheology is a powerful technique that enables researchers to measure the viscoelastic properties of complex fluids with relatively low viscoelastic moduli (typically <1 Pa) in small sample volumes which are inaccessible to macrorheology and to spatially map structural heterogeneities at a microlevel.[45] Therefore, particle tracking microrheology has considerable potential in food gels, since the system is commonly inhomogeneous.[46]

Biopolymer particles increased the overall system viscosity when they were incorporated into the aqueous solution. The LF−HMP and LF−LMP aggregates had very similar viscoelastic properties. The initial macroscopic viscosity indexes (MVIs) of LF−HMP and LF−LMP aggregates were $0.96 \times 10^{-4} \pm 1 \times 10^{-5}$ and $1.09 \times 10^{-4} \pm 1 \times 10^{-5}$ nm^{-2} s, respectively. The initial elasticity indexes (EIs) of LF−HMP and LF−LMP aggregates were $1.48 \times 10^{-3} \pm 1 \times 10^{-4}$ and $1.34 \times 10^{-3} \pm 1 \times 10^{-4}$ mm^{-2}, respectively. Since EGCG could noncovalently bind to protein and polysaccharide, respectively, therefore, it might be incorporated into LF−pectin biopolymer particles to modify their viscoelastic characteristics.

As shown in Figure 5, EGCG exhibited a slight effect on MVI and EI for TA_{HMP}-1 and TA_{LMP}-1. For TA_{HMP}-2 and TA_{HMP}-3, the values of MVI and EI were relatively small at low EGCG concentrations but steeply increased when the EGCG concentration was more than 0.8 mM. However, TA_{LMP}-2 and TA_{LMP}-3 showed a somewhat sinuous behavior: at low EGCG concentration (less than 0.2 mM), the values of MVI and EI increased. When the EGCG concentration was 0.5 mM for TA_{LMP}-2 and 1.6 mM for TA_{LMP}-3, MVI values decreased to the initial levels and then decreased significantly ($p < 0.05$) to

DOI: 10.1021/acs.jafc.5b01592
J. Agric. Food Chem. 2015, 63, 5046−5054

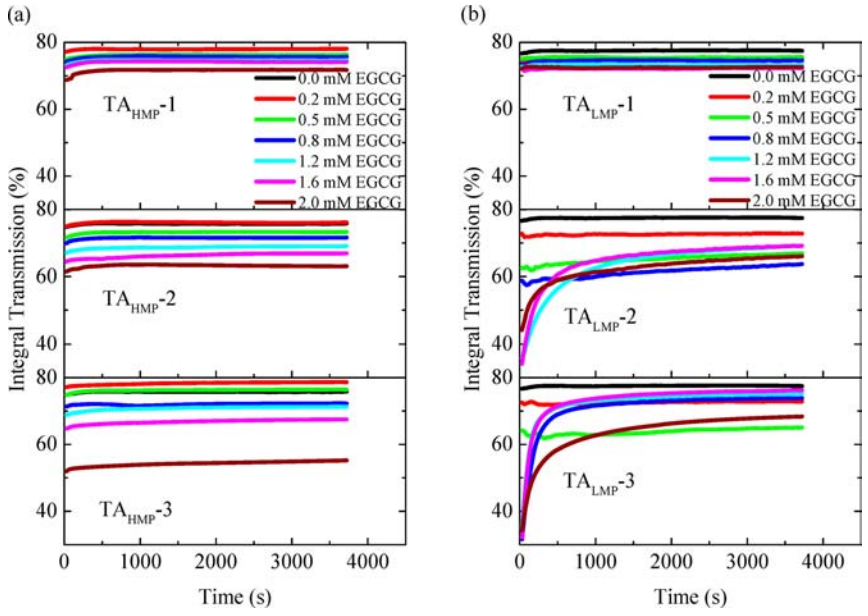

Figure 6. Evolution of transmission profiles of TA_{HMP} (a) and TA_{LMP} (b) as a function of EGCG concentration (0–2.0 mM) at pH 5.0.

31.9% and 22.4% of the initial levels when the EGCG concentration was 2.0 mM for TA_{LMP}-2 and TA_{LMP}-3, respectively. EI showed the similar trend as MVI with a rise of EGCG concentration.

Aberkane et al. reported that the presence of quercetin increased β-lactoglobulin–acacia gum binding and improved the stability of the β-lactoglobulin–acacia gum complex and coacervates.[47] However, in our study, we interestingly found that the viscoelastic properties of the ternary aggregates fabricated by LF, pectin, and EGCG were mainly affected by the types of pectin and fabrication methods. The increase in MVI and EI for TA_{HMP}-2 and TA_{HMP}-3 could be attributed to the fact that the presence of EGCG increased the binding of LF to HMP and improved the stability of the LF–HMP aggregates. An inverse result was observed for TA_{LMP}.

Influence of EGCG on the Physical Stability of LF–Pectin Aggregates. According to Stokes' law ($V_0 = a\Delta\rho d^2/18\eta$, where V_0 is the floating rate of solution droplets, d is the particle diameter, $\Delta\rho$ is the density contrast between the two phases, a is the acceleration of centrifugation, and η is the viscosity of the continuous phase),[48] a smaller particle size and a greater viscosity resulted in a slower floating rate of droplets and , thus enhanced physical stability of the aggregates. The stabilities of aggregates were expressed as space- and time-related transmission profiles over the sample length (Figure 6). The greater the change of the transmission with centrifugation, the less stable the ternary aggregates. The stability of aggregates could be reflected quantitatively by plotting the integrated transmission profiles against the measuring time, and the slope of the resultant curve was inversely related to the stability.[49]

There were appreciable differences in the influence of types of pectin on the stability of ternary aggregates. From Figure 6, it could be found that TA_{HMP} exhibited less change in the transmission profiles and low slope values over space and time, resulting in better stability of the aggregates. TA_{LMP}-2 and TA_{LMP}-3, with high slope values, showed less stability than TA_{HMP}-2 and TA_{HMP}-3, respectively, when the EGCG concentration was more than a critical value (1.2 mM for TA_{LMP}-2 and 0.8 mM for TA_{LMP}-3), despite having a greater negative charge.

Three possible reasons could be used to explain why TA_{LMP}-2 and TA_{LMP}-3 were more prone to aggregation and sedimentation than TA_{HMP}, with the rise of EGCG concentration. First, the ternary aggregates had different changes in ζ-potential: a decrease for TA_{HMP} and an increase for TA_{LMP}. Second, both TA_{LMP}-2 and TA_{LMP}-3 had larger particle sizes and lower viscosity in comparison to those of TA_{HMP}. Finally, the LF structures in TA_{HMP} and TA_{LMP} were different, including the secondary structure, especially for α-helix and β-turn, and the tertiary structure.

CONCLUSION

In the present study, the turbidity and viscoelastic properties of ternary aggregates could be manipulated by controlling the concentration of EGCG, types of pectin, and especially fabrication methods. EGCG always interacted with LF and affected the secondary and tertiary structures of LF in LF–pectin aggregates. TA_{HMP}-2 and TA_{HMP}-3 had better transparency and higher viscoelasticity and could be applied in clear beverages or gel-like solutions. In contrast, TA_{LMP}-2 and TA_{LMP}-3 had higher turbidity and lower viscoelasticity and could be applied in cloudy beverages or liquid foods. Overall, the ternary aggregates containing EGCG could have prospective potential in the food, pharmaceutical, and cosmetic industries, as delivery systems to encapsulate, protect, and release bioactive components or as functional ingredients to modify optical, rheological, and sensorial properties of food products.

AUTHOR INFORMATION

Corresponding Author

*Y.G.: tel, +86-10-62737034; fax, +86-10-62737986; e-mail, gyxcau@126.com.

Funding

The research was funded by the National Natural Science Foundation of China under Grant No. 31371835.

DOI: 10.1021/acs.jafc.5b01592
J. Agric. Food Chem. 2015, 63, 5046–5054

Notes

The authors declare no competing financial interest.

REFERENCES

(1) Frazier, R. A.; Papadopoulou, A.; Mueller-Harvey, I.; Kissoon, D.; Green, R. J. Probing protein-tannin interactions by isothermal titration microcalorimetry. *J. Agric. Food Chem.* **2003**, *51*, 5189−5195.

(2) Le Bourvellec, C.; Renard, C. M. G. C. Interactions between polyphenols and macromolecules: quantification methods and mechanisms. *Crit. Rev. Food Sci. Nutr.* **2012**, *52*, 213−248.

(3) Ozdal, T.; Capanoglu, E.; Altay, F. (2013). A review on protein−phenolic interactions and associated changes. *Food Res. Int.* **2013**, *51*, 954−970.

(4) Siebert, K. J. Haze formation in beverages. *LWT-Food Sci. Technol.* **2006**, *39*, 987−994.

(5) McManus, J. P.; Davis, K. G.; Lilley, T. H.; Haslam, E. The association of proteins with polyphenols. Journal of the Chemical Society. *J. Chem. Soc., Chem. Commun.* **1981**, *7*, 309b−311.

(6) Gonçalves, R.; Mateus, N.; De Freitas, V. Influence of carbohydrates on the interaction of procyanidin B3 with trypsin. *J. Agric. Food Chem.* **2011**, *59*, 11794−11802.

(7) Kanakis, C. D.; Hasni, I.; Bourassa, P.; Tarantilis, P. A.; Polissiou, M. G.; Tajmir-Riahi, H. A. Milk β-lactoglobulin complexes with tea polyphenols. *Food Chem.* **2011**, *127*, 1046−1055.

(8) Hasni, I.; Bourassa, P.; Hamdani, S.; Samson, G.; Carpentier, R.; Tajmir-Riahi, H. A. Interaction of milk α-and β-caseins with tea polyphenols. *Food Chem.* **2011**, *126*, 630−639.

(9) Zhang, J.; Mi, Q.; Shen, M. Resveratrol binding to collagen and its biological implication. *Food Chem.* **2012**, *131*, 879−884.

(10) Bourassa, P.; Kanakis, C. D.; Tarantilis, P.; et al. Resveratrol, Genistein, and Curcumin Bind Bovine Serum Albumin. *J. Phys. Chem. B* **2010**, *114*, 3348−3354.

(11) Liang, M.; Liu, R.; Qi, W.; et al. Interaction between lysozyme and procyanidin: Multilevel structural nature and effect of carbohydrates. *Food Chem.* **2013**, *138*, 1596−1603.

(12) Akhtar, M.; Dickinson, E.; Mazoyer, J.; Langendorff, V. Emulsion stabilizing properties of depolymerized pectin. *Food Hydrocolloids* **2002**, *16*, 249−256.

(13) McManus, J. P.; Davis, K. G.; Beart, J. E.; Gaffney, S. H.; Lilley, T. H.; Haslam, E. Polyphenol interactions. Part 1. Introduction; some observations on the reversible complexation of polyphenols with proteins and polysaccharides. *J. Chem. Soc., Perkin Trans. 2* **1985**, *2*, 1429−1438.

(14) Vernhet, A.; Pellerin, P.; Prieur, C.; Osmianski, J.; Moutounet, M. Charge properties of some grape and wine polysaccharide and polyphenolic fractions. *Am. Soc. Enology. Viticulture* **1996**, *47*, 25−30.

(15) de Freitas, V.; Carvalho, E.; Mateus, N. Study of carbohydrate influence on protein−tannin aggregation by nephelometry. *Food Chem.* **2003**, *81*, 503−509.

(16) Soares, S. I.; Goncalves, R. M.; Fernandes, I. V. A.; Mateus, N.; de Freitas, V. Mechanistic approach by which polysaccharides inhibit α-amylase/procyanidin aggregation. *J. Agric. Food Chem.* **2009**, *57*, 4352−4358.

(17) Sun-Waterhouse, D.; Sivam, A. S.; Cooney, J.; Zhou, J.; Perera, C. O.; Waterhouse, G. I. N. Effects of added fruit polyphenols and pectin on the properties of finished breads revealed by HPLC/LC-MS and size-exclusion HPLC. *Food Res. Int.* **2011**, *44*, 3047−3056.

(18) Hayashi, N.; Ujihara, T.; Kohata, K. Reduction of catechin astringency by the complexation of gallate-type catechins with pectin. *Biosci., Biotechnol., Biochem.* **2005**, *69*, 1306.

(19) Mercedes Lataza Rovaletti, M.; Benítez, E. I.; Martinez Amezaga, N. M.; Peruchena, N. M.; Sosa, G. L.; Lozano, J. E. Polysaccharides influence on the interaction between Tannic Acid and haze active proteins in beer. *Food Res. Int.* **2014**, *72*, 779−785.

(20) Mateus, N.; Carvalho, E.; Luís, C.; de Freitas, V. Influence of the tannin structure on the disruption effect of carbohydrates on protein−tannin solutions. *Anal. Chim. Acta* **2004**, *513*, 135−140.

(21) Carvalho, E.; Mateus, N.; Plet, B.; Pianet, I.; Dufourc, E.; De Freitas, V. Influence of wine pectic polysaccharides on the interactions between condensed tannins and salivary proteins. *J. Agric. Food Chem.* **2006**, *54*, 8936−8944.

(22) Soares, S.; Mateus, N.; de Freitas, V. Carbohydrates Inhibit Salivary Proteins Precipitation by Condensed Tannins. *J. Agric. Food Chem.* **2012**, *60*, 3966−3972.

(23) Luck, G.; Liao, H.; Murray, N. J.; Grimmer, H. R.; Warminski, E. E.; Williamson, M. P.; Haslam, E. Polyphenols, astringency and proline-rich proteins. *Phytochemistry* **1994**, *37*, 357−371.

(24) Thongkaew, Chutima; et al. Polyphenol Interactions with Whey Protein Isolate and Whey Protein Isolate-Pectin Coacervates. *Food Hydrocolloids* **2014**, *2014*, 103−112.

(25) Chen, L.; Remondetto, G. E.; Subirade, M. Food protein-based materials as nutraceutical delivery systems. *Trends Food Sci. Technol.* **2006**, *17*, 272−283.

(26) Gallo, M.; Vinci, G.; Graziani, G.; De Simone, C.; Ferranti, P. The interaction of cocoa polyphenols with milk proteins studied by proteomic techniques. *Food Res. Int.* **2013**, *54*, 406−415.

(27) Luo, Y.; Zhang, B.; Whent, M.; Yu, L. L.; Wang, Q. Preparation and characterization of zein/chitosan complex for encapsulation of α-tocopherol, and its *in vitro* controlled release study. *Colloids Surf., B* **2011**, *85*, 145−152.

(28) Liu, H.; Nakagawa, K.; Kato, D. I.; Chaudhary, D.; Tadé, M. O. Enzyme encapsulation in freeze-dried bionanocomposites prepared from chitosan and xanthan gum blend. *Mater. Chem. Phys.* **2011**, *129*, 488−494.

(29) Koupantsis, T.; Pavlidou, E.; Paraskevopoulou, A. Flavour encapsulation in milk proteins−CMC coacervate-type complexes. *Food Hydrocolloids* **2014**, *37*, 134−142.

(30) Lacerda, L.; Parize, A. L.; Fávere, V.; Laranjeira, M. C. M.; Stulzer, H. K. Development and evaluation of pH-sensitive sodium alginate/chitosan microparticles containing the antituberculosis drug rifampicin. *Mater. Sci. Eng., C* **2014**, *39*, 161−167.

(31) O'Neill, G. J.; Egan, T.; Jacquier, J. C.; O'Sullivan, M.; Dolores O'Riordan, E. Whey microbeads as a matrix for the encapsulation and immobilisation of riboflavin and peptides. *Food Chem.* **2014**, *160*, 46−52.

(32) McClements, D. J.; Decker, E. A.; Park, Y.; Weiss, J. Designing food structure to control stability, digestion, release and absorption of lipophilic food components. *Food Biophys* **2008**, *3*, 219−228.

(33) Ubbink, J.; Burbidge, A.; Mezzenga, R. Food structure and functionality: a soft matter perspective. *Soft Matter* **2008**, *4*, 1569−1581.

(34) Parada, J.; Aguilera, J. M. Food microstructure affects the bioavailability of several nutrients. *J. Food Sci.* **2007**, *72* (2), R21−R32.

(35) Asker, D.; Weiss, J.; McClements, D. J. Formation and stabilization of antimicrobial delivery systems based on electrostatic complexes of cationic-non-ionic mixed micelles and anionic polysaccharides. *J. Agric. Food Chem.* **2011**, *59*, 1041−1049.

(36) Peinado, I.; Lesmes, U.; Andrés, A.; et al. Fabrication and morphological characterization of biopolymer particles formed by electrostatic complexation of heat treated lactoferrin and anionic polysaccharides. *Langmuir* **2010**, *26*, 9827−9834.

(37) Tokle, T.; Lesmes, U.; McClements, D. J. Impact of electrostatic deposition of anionic polysaccharides on the stability of oil droplets coated by lactoferrin[J]. *J. Agric. Food Chem.* **2010**, *58*, 9825−9832.

(38) Yang, W.; Xu, C.; Liu, F.; et al. Native and thermally modified protein-polyphenol co-assemblies: lactoferrin-based nano-particles and sub-micrometer particles as protective vehicles for (−)-epigallocatechin-3-gallate. *J. Agric. Food Chem.* **2014**, *62*, 10816−10827.

(39) Dickinson, E. Interfacial structure and stability of food emulsions as affected by protein−polysaccharide interactions. *Soft Matter* **2008**, *4*, 932−942.

(40) Stănciuc, N.; Aprodu, I.; Râpeanu, G.; et al. Analysis of the thermally induced structural changes of bovine lactoferrin. *J. Agric. Food Chem.* **2013**, *61*, 2234−2243.

(41) Hudson, S. A.; Ecroyd, H.; Dehle, F. C.; Musgrave, I. F.; Carver, J. A. −)-Epigallocatechin-3-Gallate (EGCG) Maintains κ-Casein in Its Pre-Fibrillar State without Redirecting Its Aggregation Pathway. *J. Mol. Biol.* **2009**, *392*, 689−700.

DOI: 10.1021/acs.jafc.5b01592
J. Agric. Food Chem. 2015, 63, 5046−5054

(42) Shpigelman, A.; Israeli, G.; Livney, Y. D. Thermally-induced protein−polyphenol co-assemblies: beta-lactoglobulin-based nano-complexes as protective nanovehicles for EGCG. *Food Hydrocolloids* **2010**, *24*, 735−743.
(43) Kelly, S. M.; Jess, T. J.; Price, N. C. How to study proteins by circular dichroism. *Biochim. Biophys. Acta, Proteins Proteomics* **2005**, *1751*, 119−139.
(44) Waigh, T. A. Microrheology of complex fluids. *Rep. Prog. Phys.* **2005**, *68*, 685. Ward, P. P.; Uribe-Luna, S.; Conneely, O. M. Bovine lactoferrin and host defense. *Biochem. Cell Biol.* **2002**, *80*, 95−102.
(45) Moschakis, T.; Murray, B. S.; Dickinson, E. (2010). On the kinetics of acid sodium caseinate gelation using particle tracking to probe the microrheology. *J. Colloid Interface Sci.* **2010**, *345*, 278−285.
(46) Moschakis, T. Microrheology and particle tracking in food gels and emulsions. *Curr. Opin. Colloid Interface Sci.* **2013**, *18*, 311−323.
(47) Aberkane, L.; Jasniewski, J.; Gaiani, C.; Hussain, R.; Scher, J.; Sanchez, C. Structuration mechanism of β-lactoglobulin−acacia gum assemblies in presence of quercetin. *Food Hydrocolloids* **2012**, *29*, 9−20.
(48) Walstra, P. Dispersed systems: basic considerations. In *Food Chemistry*, 3rd ed.; Fennema, O. R., Ed.; Marcel Dekker: New York, 1996.
(49) Petzold, G.; Goltzsche, C.; Mende, M.; Schwarz, S.; Jaeger, W. Monitoring the stability of nanosized silica dispersions in presence of polycations by a novel centrifugal sedimentation method. *J. Appl. Polym. Sci.* **2009**, *114*, 696−704.

DOI: 10.1021/acs.jafc.5b01592
J. Agric. Food Chem. 2015, 63, 5046−5054

JOURNAL OF AGRICULTURAL AND FOOD CHEMISTRY

Article

pubs.acs.org/JAFC

Development of Iron-Chelating Poly(ethylene terephthalate) Packaging for Inhibiting Lipid Oxidation in Oil-in-Water Emulsions

David R. Johnson,[†] Fang Tian,[†] Maxine J. Roman,[†] Eric A. Decker,[†,§] and Julie M. Goddard*[,†]

[†]Department of Food Science, 228 Chenoweth Laboratory, University of Massachusetts—Amherst, 100 Holdsworth Way, Amherst, Massachusetts 01003, United States

[§]Bioactive Natural Products Research Group, Department of Biochemistry, Faculty of Science, King Abdulaziz University, P.O. Box 80203, Jeddah 21589, Saudi Arabia

ABSTRACT: Foods such as bulk oils, salad dressings, and nutritionally fortified beverages that are susceptible to oxidative degradation are often packaged in poly(ethylene terephthalate) (PET) bottles with metal chelators added to the food to maintain product quality. In the present work, a metal-chelating active packaging material is designed and characterized, in which poly(hydroxamic acid) (PHA) metal-chelating moieties were grafted from the surface of PET. Biomimetic PHA groups were grafted in a two-step UV-initiated process without the use of a photoinitiator. Surface characterization of the films by attenuated total reflective Fourier transform infrared spectroscopy (ATR-FTIR) and scanning electron microscopy (SEM) suggested successful grafting and conversion of poly(hydroxyethyl acrylate) (PHEA) to PHA chelating moieties from the surface of PET. Colorimetric (ferrozine) and inductively coupled plasma mass spectroscopy (ICP-MS) assays demonstrated the ability of PET-*g*-PHA to chelate iron in a low-pH (3.0) environment containing a competitive metal chelator (citric acid). Lipid oxidation studies demonstrated the antioxidant activity of PET-*g*-PHA films in inhibiting iron-promoted oxidation in an acidified oil-in-water (O/W) emulsion model system (pH 3.0). Particle size and ζ-potential analysis indicated that the addition of PET-*g*-PHA films did not affect the physical stability of the emulsion system. This work suggests that biomimetic chelating moieties can be grafted from PET and effectively inhibit iron-promoted degradation reactions, enabling removal of metal-chelating additives from product formulations.

KEYWORDS: *active packaging, metal chelation, lipid oxidation, poly(ethylene terephthalate), poly(hydroxamic acid)*

INTRODUCTION

The presence of transition metals (e.g., iron) enhances lipid oxidation in foods containing lipids, leading to nutrient loss and the generation of off-flavors. This is due to the ability of iron to promote the breakdown of lipid hydroperoxides to generate reactive radicals that degrade bioactive molecules such as fatty acids, antioxidants, and carotenoids.[1] Synthetic metal chelators (e.g., ethylenediaminetetraacetic acid, EDTA) are commonly used in food and beverage products and have been shown to be potent inhibitors of lipid oxidation in emulsion-based systems.[2] However, growing consumer concern over the use of synthetic additives has led researchers to seek alternative solutions to prevent lipid oxidation, such as natural additives and active packaging.[3−5] Unfortunately, natural additives are often not as effective as their synthetic counterparts, and their safety limits are largely unknown.[6,7] Active packaging represents an attractive strategy for protecting labile food ingredients, but in some cases may involve migration of active compounds or alteration of the bulk properties (mechanical strength, appearance) of the packaging material.[8−10] Therefore, nonmigratory covalent modifications to packaging materials capable of chelating prooxidative transition metals have been investigated.[11]

Our group previously reported grafting of nonmigratory biomimetic hydroxamic acid (PHA) chelating groups from a polypropylene (PP) surface.[12] The resulting materials chelated iron across a pH range relevant to foods and performed better than EDTA in inhibiting volatile lipid oxidation product formation in oil-in-water (O/W) emulsions.[11] However, PP-*g*-PHA synthesis requires the use of an added chemical photoinitiator (e.g., benzophenone) to enable grafting from the PP surface. To expand the industrial potential of nonmigratory chelating packaging, the overall goal of this work was to graft PHA from an alternative food packaging material and determine its efficacy in an acidified (pH 3.0) model food emulsion system. Poly(ethylene terephthalate) (PET) was chosen because of its lower oxygen transmission rate, clarity, moisture barrier, temperature tolerance, lightweight nature, and widespread use in the food and beverage industry.[13,14] In addition, an advantage of PET is that its chemical structure can be leveraged to graft polymerize a monomer without the need for a photoinitiator. The challenge in hydroxamic acid grafted PET (PET-*g*-PHA) is that it requires an alternative chemical synthesis to polymerize a monomer PHA precursor from the PET surface.

Herein, we describe a two-step grafting procedure in which hydroxyethyl acrylate (HEA) was grafted from the surface of PET films via UV-induced graft polymerization. Poly(hydroxyethyl acrylate) (PHEA) groups were then converted to PHA groups by exposure to hydroxylamine. The resulting PET-*g*-PHA was capable of chelating iron at pH 3.0 in the

Received: February 10, 2015
Revised: May 5, 2015
Accepted: May 8, 2015
Published: May 19, 2015

ACS Publications © 2015 American Chemical Society

DOI: 10.1021/acs.jafc.5b00796
J. Agric. Food Chem. 2015, 63, 5055−5060

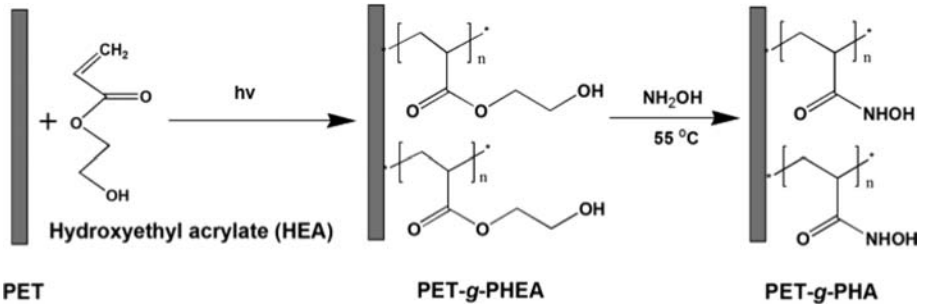

Figure 1. Schematic of two-step UV-initiated graft polymerization and conversion of (poly)hydroxamic acid from the surface of poly(ethylene terephthalate) PET-*g*-PHA.

presence of a competitive chelator (citric acid). Materials were characterized for changes in surface chemistry, and the ability to inhibit lipid oxidation was demonstrated in an acidified (pH 3.0) O/W emulsion. This work demonstrates that biomimetic chelating moieties can be grafted from PET and effectively inhibit iron-promoted degradation reactions.

MATERIALS AND METHODS

Materials. Commercial soybean oil (Wesson 100% natural vegetable oil) was purchased from a local grocer. A PET (oriented) sheet with a thickness of 178 ± 18 μm was purchased from McMaster-Carr (Elmhurst, IL, USA). Acetone, ferric chloride anhydrous, hydrochloric acid, trichloroacetic acid (TCA), 4-(2-hydroxyethyl)-1-piperazineethane sulfonic acid (HEPES), water (HPLC), 2-propanol, isooctance, 1-butanol, methanol, sodium citrate dihydrate, sodium acetate trihydrate, sodium hydroxide, disodium EDTA, and Brij 35 (a nonionic surfactant) were purchased from Fisher Scientific (Fair Lawn, NJ, USA). Citric acid monohydrate and hydroxyethyl acrylate (HEA, 97%, stabilized) were purchased from Acros Organics (Morris Plains, NJ, USA). 3-(2-Pyridyl)-5,6-diphenyl-1,2,4-triazine-*p*,*p*′-disulfonic acid monosodium salt hydrate (ferrozine, 97%), imidazole, hydroxylamine solution (50 wt % in water), barium chloride dihydrate, ammonium thiocyanate, cumene hydroperoxide (80%), and hexanal (98%) were purchased from Sigma-Aldrich (St. Louis, MO, USA). All chemicals and solvents were used without further purification.

Grafting of PHA from the PET Film Surface. PET film was cut into 1 cm × 2 cm coupons, which were cleaned sequentially in isopropanol, acetone, and deionized water (2 × 10 min cleanse per solvent) by sonication. Cleaned PET films were dried in a desiccator overnight (25 °C, 15% relative humidity) for future use. PHA was grafted from the surface of PET films using a two-step process (Figure 1). In the first step, PHEA was grafted from the PET film surface using UV-induced graft polymerization. Briefly, PET coupons were submerged in 6 mL of 30 wt % HEA in water using individual septum screw cap vials. The monomer solution was purged with nitrogen for 15 min to remove oxygen, followed by sonication to disrupt air bubble formation on the films. Films were then subjected to ultraviolet (UV) irradiation for 2.5 min in a Dymax light-curing system (model 5000 flood, 320−395 nm, 200 mW/cm^2, Dymax Corp., Torrington, CT, USA) to graft PHEA from the surface of PET. The resulting PET-*g*-PHEA films were then washed in deionized water for 30 min at room temperature followed by washing for 1 h at 60 °C followed by the same washing overnight at room temperature to remove adsorbed HEA monomers and PHEA homopolymers.

PHEA grafts were then converted to PHA grafts by a modification of the method reported by Polomoscanik et al.[15] PET-*g*-PHEA films were submerged in an aqueous solution of hydroxylamine (16.67 wt %) at a surface area to volume ratio of 1 cm^2 to 2.5 mL and stirred at 55 °C for 1 h (Figure 1). The resulting PET-*g*-PHA films were then rinsed three times in deionized water followed by 30 min of exposure to acidic water (adjusted by HCl, pH 3.0) to protonate hydroxamic acid groups and finally rinsed again in copious deionized water. The obtained PET-*g*-PHA films were dried and stored over anhydrous calcium sulfate (25 °C, 15% RH) until further use.

Surface Characterization. The surface chemistry of films, before and after PHA grafting, was characterized using attenuated total reflectance Fourier transform infrared spectroscopy (ATR-FTIR) by an IRPrestige-21 FTIR spectrometer (Shimadzu Scientific Instruments, Inc., Kyoto, Japan) equipped with a diamond ATR crystal. Using clean, native PET as background spectrum, each spectrum was generated from 32 scans at a 4 cm^{-1} resolution and collected from three independent films. Representative spectra were replotted with SigmaPlot 12.2 (Systat Software, Inc., Chicago, IL, USA). The surface morphology of films was analyzed by field emission scanning electron microscopy (SEM) (JCM-6000 NeoScope, JEOL, Japan) at 10 kV. Prior to imaging, samples were sputter-coated with gold to prevent charging.

Iron Chelating by the Ferrozine Assay. The ferric iron (Fe^{3+}) chelating activity of PET-*g*-PHA films was determined at pH 3.0 in citric acid/citrate buffer (10 mM) as described previously.[16,17] Citrate was used to both mimic the acid used in many foods and also to help maintain iron solubility. Films (native PET, PET-*g*-PHEA, and PET-*g*-PHA) were submerged in 0.06 mM Fe^{3+} (from ferric chloride anhydrous) in citric acid/citrate buffer, with Fe^{3+} solution without films serving as a control. Films were allowed to chelate in the dark for 24 h at room temperature while on an orbital shaker (200 rpm). The Fe^{3+}-chelating activity of films was calculated by the difference of the Fe^{3+} concentration (determined by ferrozine assay, described below) in Fe^{3+} solution with films against the control group (Fe^{3+} solution with no films).[11]

A modification of the ferrozine assay was performed to quantify the Fe^{3+} concentration of chelating solutions, in which a colorimetric complex is formed between Fe^{2+} and ferrozine reagent.[16,17] First, Fe^{3+} was reduced to Fe^{2+} by exposure to 5 wt % hydroxylamine hydrochloride in 10 wt % trichloroacetic acid followed by the addition of ferrozine reagent (18 mM in 0.05 M HEPES buffer, pH 7.0) and mixing for 1 h at room temperature to enable color formation. Absorbance was measured at 562 nm. Fe^{3+} concentration was quantified by comparison to a standard curve made from ferric chloride anhydrous. Results are representative of two experiments performed on independent days.

Inductively Coupled Plasma−Mass Spectroscopy (ICP-MS). As a direct quantification of iron chelation to support results from ferrozine assay, native and modified PET films (performed in duplicates) were subjected to ICP-MS analysis after films were exposed to iron in the ferrozine assay (see above). Films were prepared for ICP-MS using a standard method.[18] Approximately 100 mg of the PET film was weighed directly into microwave digestion vessels, followed by the addition of nitric acid (5.0 mL). Microwave digestion by a Mars Xpress (CEM, Matthews, NC, USA) was carried out at 210 °C for 10 min. Digested samples were then diluted with deionized water and held at 4 °C until analysis. ICP-MS analysis was conducted on a PerkinElmer Elan 9000 equipped with an autosampler (Waltham, MA, USA). Iron concentration was determined by a standard curve prepared using an iron ICP-MS standard (Ricca Chemical Co., Arlington, TX, USA).

DOI: 10.1021/acs.jafc.5b00796
J. Agric. Food Chem. 2015, 63, 5055−5060

Effect of PET-*g*-PHA films of the Oxidative Stability of O/W Emulsions. To demonstrate the effectiveness of chelating PET-*g*-PHA films in preventing iron-promoted degradation reactions, an accelerated lipid oxidation study was performed using an acidified O/W emulsion as a model food system. Emulsions were prepared by dissolving Brij 35 (0.10% w/w) and commercial soybean oil (1.0% w/w) in a 0.05 M sodium acetate/imidazole buffer (pH 3.0), followed by homogenization with a hand-held homogenizer (Biospec Products, Inc., Bartlesville, OK, USA) at 7000 rpm for 2 min. The coarse emulsion then underwent three passes through a microfluidizer (Microfluidics, Newton, MA, USA) at 9 kbar. Films (1 cm^2) were submerged in 1 mL of emulsion and stored in the dark at 55 °C for 29 days. Emulsions without films served as a negative control; emulsions containing the synthetic chelator EDTA at two concentrations (0.01 mM, equivalent to the chelating capacity of the PET-*g*-PHA films, and 0.08 mM, the maximum legal limit) served as positive controls (FDA Food Additive Regulation 21 CFR 172.120).

The formation of primary and secondary lipid oxidation products (lipid hydroperoxides and hexanal, respectively) were quantified throughout the study to determine the oxidative stability of the O/W emulsions. Lipid hydroperoxides were quantified according to the method reported by Waraho et al.[19] Briefly, 0.30 mL of emulsion was mixed with 1.5 mL of iso-octane/isopropanol (3:1 v/v) by vortex for 3 × 10 s and then centrifuged at 3000*g* for 2 min. The upper layer, containing the lipid hydroperoxides, was collected and added to 2.8 mL of methanol/1-butanol (2:1 v/v), followed by the addition of 30 μL of thiocyanate/Fe^{2+} solution (obtained from mixing an equal volume of 3.94 M thiocyanate solution with 0.072 M Fe^{2+}). The reaction samples were held for 20 min at room temperature to enable color formation. Absorbances were read at 510 nm, and lipid hydroperoxide concentrations were determined by comparison to a standard curve prepared using six concentrations of cumene hydroperoxide between 0 and 600 mmol/kg oil (r^2 = 0.99, linear regression). Samples were diluted with methanol/1-butanol to maintain their absorbance within the prepared concentration range.

The secondary lipid oxidation product hexanal was quantified by gas chromatography (GC, model GC-2014, Shimadzu, Tokyo, Japan) equipped with an autosampler and flame ionization detector (FID) as in Tian et al.[11] Samples (1 mL) were incubated at 55 °C for 10 min to allow volatile compounds from the emulsion to enter the headspace of the 10 mL headspace gas chromatography vial. A divinylbenzene/carboxen/polydimethylsiloxane (DVB/carboxen/PDMS) solid-phase microextraction (SPME) fiber (50/30 μm, Supelco, Bellefonte, PA, USA) was exposed to the headspace above the sample for 2 min to adsorb volatile components, followed by desorption for 3 min at 250 °C in the injector at a split ratio of 1:7. Volatile compounds were separated on a fused-silica capillary column (30 m × 0.32 mm inner diameter × 1 μm) coated with 100% poly(dimethylsiloxane) (Equity-1, Supelco). The run time was 10 min per sample with temperatures of 250, 65, and 250 °C for the injector, oven, and detector, respectively. Hexanal concentration was calculated from the peak areas using a standard curve prepared using authentic hexanal (concentrations ranging from 0 to 43.6 mmol/kg oil, r^2 = 0.91, linear regression)

Time to lipid oxidation was quantified by determining the lag phase, defined as the day before a statistically significant increase in concentration of primary or secondary oxidation products as compared to initial concentrations.

To demonstrate that the PET-*g*-PHA films did not affect emulsion stability, emulsion particle size distribution and electrical charge were characterized using a Zetasizer Nano ZS (Malvern Instruments, Worcestershire, UK). Particle size was determined by dynamic light scattering (DLS) after 10-fold dilution of the emulsion with sodium acetate/imidazole buffer (0.05 M, pH 3.0). The diluted emulsion was equilibrated for 60 s before particle size measurements were recorded with an average of 11 readings, reported as the *Z*-average in mean diameter (nm). Size measurements were followed immediately by electrical charge measurements (10 readings for each measurement) with an equilibration time of 60 s, and the zeta (ζ) potential (mV) of the emulsion droplets was collected. Stability tests were both performed for two measurements per sample and performed in duplicates.

Statistical Analysis. Results are presented as means and standard deviations of analysis conducted in triplicate, unless otherwise stated. Oxidation lag phases were defined as the first data point statistically greater than the 0 time within each treatment tested using one-way analysis of variance (ANOVA) with comparison of the means performed using Tukey's HSD post hoc test ($p < 0.05$). Calculations were performed using IBM SPSS Statistics version 22 (IBM SPSS, Chicago, IL, USA).

RESULTS AND DISCUSSION

Characterization of Biomimetic PET-*g*-PHA Active Packaging Films. Metal-chelating active packaging films were produced in a two-step process in which PHEA was grafted from the surface of PET by UV-initiated graft polymerization followed by conversion to PHA by exposure to hydroxylamine (Figure 1). The surface chemistry at each step in the modification was analyzed by ATR-FTIR (Figure 2).

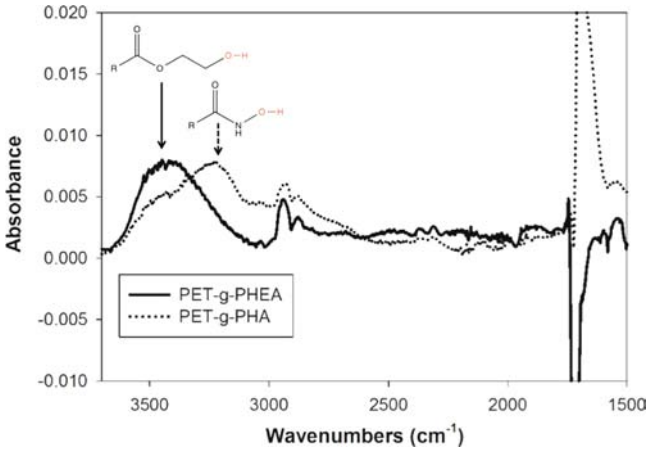

Figure 2. ATR-FTIR spectra of PET-*g*-PHEA and PET-*g*-PHA films using native PET as the background. Each spectrum is representative of measurements collected from three independent films.

Using clean, native PET as the background, the spectrum of PET-*g*-PHEA showed a strong absorption band at 3500−3300 cm^{-1} characteristic of an −OH stretch and two smaller peaks at 2900−2800 cm^{-1} corresponding to −CH stretch, suggesting successful covalent grafting of PHEA from PET. Conversion of PHEA to chelating hydroxamate groups (PHA) was confirmed by the introduction of an −OH stretch at 3300−3100 cm^{-1} typical of a hydroxyl group adjacent to an amide as present in the hydroxamic acid chelating moiety (Figure 2). The absorption in the 3000−2900 cm^{-1} range, attributed to the −CH stretching for the long alkyl backbone of PHEA, did not change, suggesting specific conversion of the ester to a hydroxamic acid moiety. ATR-FTIR spectroscopy on both sides of the film confirmed that grafting did not occur on the backside of PET films.

The effect of PHA grafting on the film surface morphology was determined by electron microscopy (Figure 3). Native PET (Figure 3A) exhibited small irregularities, similar to those observed by others in commercial PET films.[20] PET-*g*-PHEA films had uniform surface morphology across and between samples (Figure 3B), exhibiting ridge-like structures typical of hydrophilic polymer/hydrogels that shrink upon dehydration.[11,21] As expected, the films lost the ridge-like structure after conversion to PET-*g*-PHA (Figure 3C) due to the change

DOI: 10.1021/acs.jafc.5b00796
J. Agric. Food Chem. 2015, 63, 5055−5060

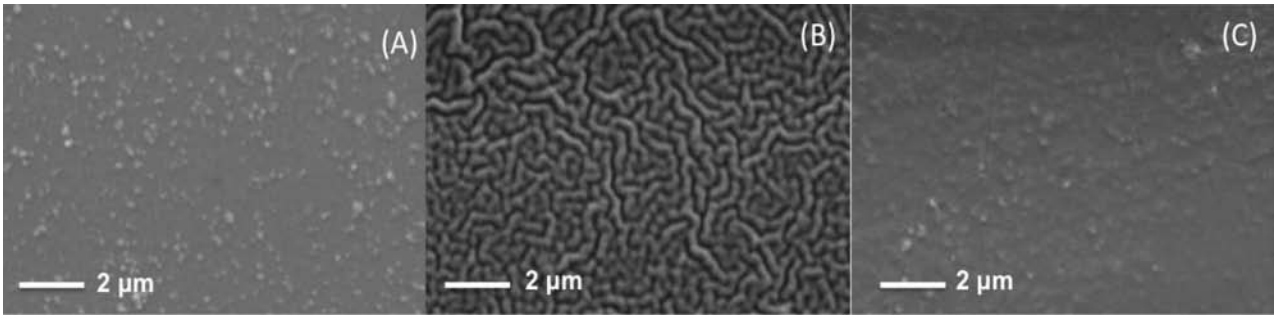

Figure 3. SEM surface analysis (9000×) of (A) PET, (B) PET-*g*-PHEA, and (C) PET-*g*-PHA films.

in surface hydrophilicity by conversion to the relatively hydrophobic hydroxamate groups. Qualitatively, the effect of grafting from the surface of PET had no influence on film visual character (images not shown).

Iron Chelation by Biomimetic PET-*g*-PHA Active Packaging Films. The ability of the hydroxamic acid grafted PET (PET-*g*-PHA) films to chelate iron was quantified by the colorimetric ferrozine iron-binding assay (Figure 4). Iron

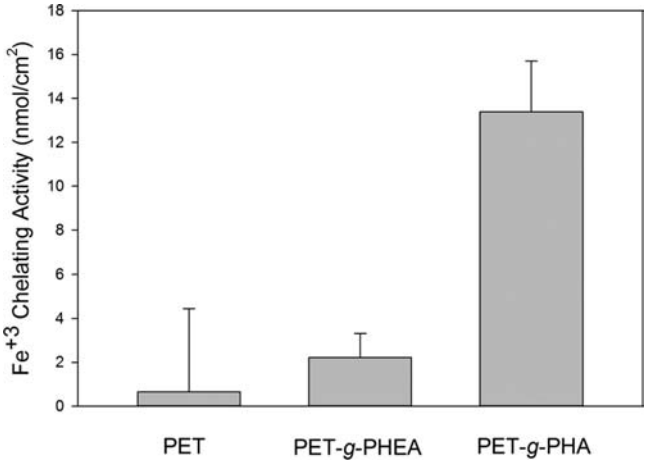

Figure 4. Ferric iron chelation by PET, PET-*g*-PHEA, and PET-*g*-PHA films (24 h of incubation, pH 3.0 citric acid/citrate buffer). Values represent means ± standard deviation (n = 4). Results are representative of two experiments performed on independent days.

chelating of native PET was not detectable (PET, 0.60 ± 3.80 nmol Fe^{3+}/cm^2), and grafted PHEA exhibited statistically negligible activity (PET-*g*-PHEA, 2.22 ± 1.10 nmol Fe^{3+}/cm^2). PET-*g*-PHA films demonstrated significant iron-chelating activity (13.39 ± 2.30 nmol Fe^{3+}/cm^2) in competitively chelated citrate−Fe^{3+} solutions. Given these data, the density of the chelating groups on the PET-*g*-PHA film can be estimated between 13 and 39 nmol HA groups, assuming a HA/Fe^{3+} ratio of between 1:1 and 3:1. The lack of chelating by native PET and PET-*g*-PHEA suggests that chelating shown by PET-*g*-PHA groups is due to specific iron−HA interactions. The minimal chelation of PET-*g*-PHEA films was likely the result of nonspecific absorption or swelling into the grafted layer. Previously, our group demonstrated the effectiveness of grafted PHA from polypropylene (PP-*g*-PHA).[12] The chelating activity of the PET-*g*-PHA materials reported herein is lower than found in our previous studies on PP-*g*-PHA materials; however, it is important to note that those studies were performed at a higher pH value (pH 5.0), at which the film chelated 21.39 ± 1.28 nmol Fe^{3+}/cm^2. In this work, we have demonstrated the ability of the synthesized PET-*g*-PHA films to maintain chelating abilities in an environment representative of an acidified liquid food system (pH 3.0), in which citric acid was used as an acidulant (10 mM) and competitive chelator.

Direct quantification of iron chelation by ICP-MS was performed to complement ferrozine assay results. After exposure to ferric iron solution, native PET films presented insignificant iron (−1.00 ± 1.70 nmol Fe^{3+} cm^{-2}), whereas PET-*g*-PHA films presented 7.20 ± 1.10 nmol Fe^{3+} cm^{-2}. These values are on the order of, but lower than, those obtained using the ferrozine assay. This discrepancy may be a result of differences in assay sensitivities or incomplete microwave digestion of the PET-*g*-PHA films during the preparation step for ICP-MS analysis.

Controlling Lipid Oxidation by Iron Chelating PET-*g*-PHA Films. The ability of PET-*g*-PHA films to delay lipid oxidation in acidified (pH 3.0) soybean O/W emulsions was determined by quantifying the formation of lipid hydroperoxides and hexanal during storage at 55 °C in the dark (Figures 5 and 6). Effective inhibition of lipid oxidation was determined by extension of lag phase, defined as the day before a statistically significant increase in concentration of primary or secondary oxidation products as compared to initial concentrations. Once lipid oxidation had occurred, samples were therefore removed from the study and not further characterized for oxidation products. As expected, emulsions in the absence of metal chelators (control and native PET samples) oxidized rapidly with a lag phase of 3 days for both lipid hydroperoxide and hexanal production. The addition of PET-*g*-PHA films to the emulsions extended the lag phase to 5 days for lipid hydroperoxide production and to 7 days for hexanal production. The PET-*g*-PHA films were less effective than emulsions containing the positive controls (EDTA and no film), which at both concentrations extended lag phase to 20 days and 26 days for lipid hydroperoxides and hexanal, respectively.

The effective inhibition of lipid oxidation by EDTA suggests that transition metal-promoted degradation was a major oxidative instability mechanism in the O/W emulsions. The iron content of the commercial soybean oil was determined to be 330 ppb by ICP-MS analysis, which is in agreement with prior reports on iron content of refined soybean oil (200 ppb).[22] The results indicated that both EDTA concentrations were in excess of the transition metals (e.g., iron or copper) present in the emulsion system because an increase in EDTA concentration did not extend the lag phase of lipid hydroperoxide or hexanal production. It is interesting to note that although the PET-*g*-PHA film had theoretical equivalent

DOI: 10.1021/acs.jafc.5b00796
J. Agric. Food Chem. 2015, 63, 5055−5060

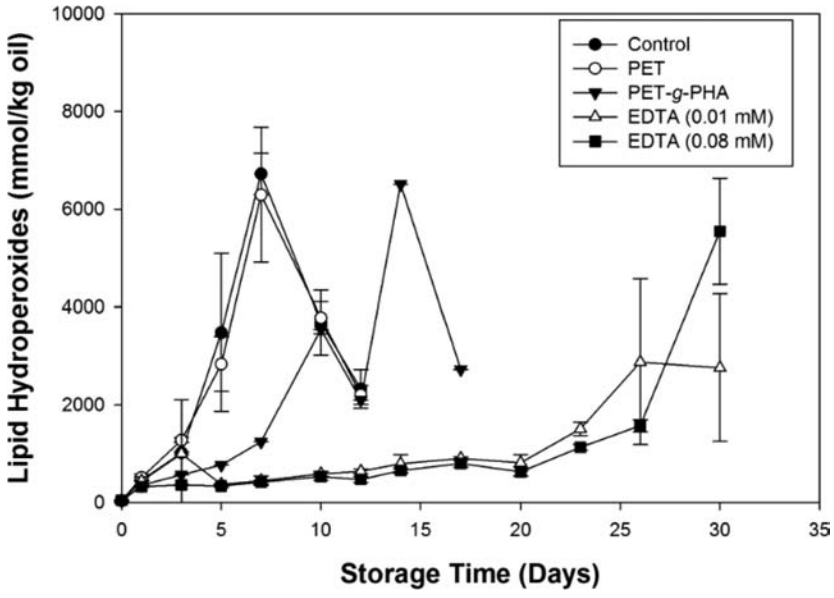

Figure 5. Formation of lipid hydroperoxides in 0.05 M sodium acetate−imidazole-buffered (pH 3.0) soybean O/W emulsions stored at 55 °C: in the absence of a metal chelator (control and native PET), a metal chelator (EDTA 0.01 and 0.08 mM), or PET-*g*-PHA film. Values represent means ± standard deviation (n = 3).

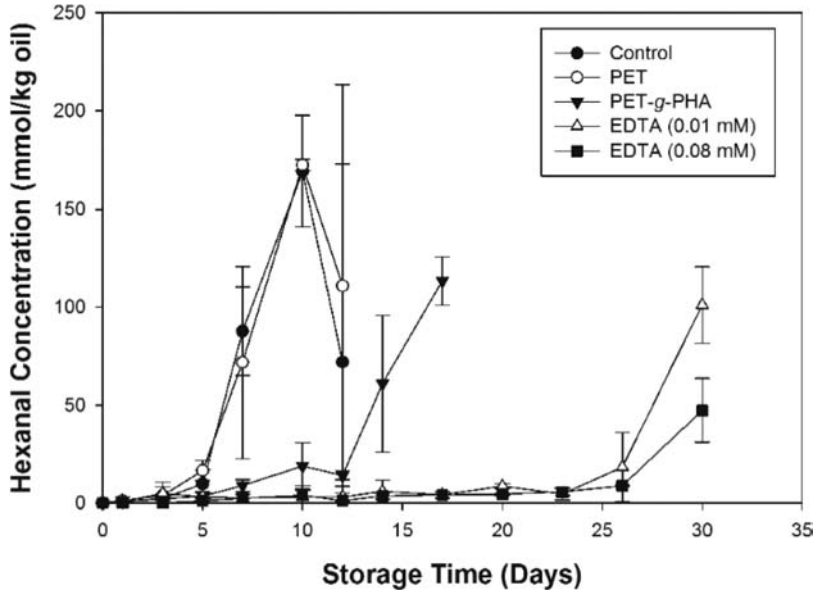

Figure 6. Formation of hexanal in 0.05 M sodium acetate−imidazole-buffered (pH 3.0) soybean O/W emulsions stored at 55 °C: in the absence of a metal chelator (control and native PET), a metal chelator (EDTA 0.01 and 0.08 mM), or PET-*g*-PHA film. Values represent means ± standard deviation (n = 3).

chelating capacity to the emulsion containing 0.01 mM EDTA, it was significantly less effective at inhibiting lipid oxidation. A possible explanation for the higher efficacy of EDTA, as compared to PET-*g*-PHA, may be related to the physical structure and chelation geometry.[23] PET-*g*-PHA chelating groups are tethered to the PET polymer, and chelating may be dependent upon iron diffusion to the HA groups, whereas EDTA molecules are uniformly dispersed in the solution. In addition, the enhanced oxidative stability of emulsions containing EDTA could be due to EDTA's low $pK_{1,2}$ (1.99, 2.67) that allows greater chelating capacity under acidic conditions (pH 3.0).

Previously, our group demonstrated the effectiveness of grafted PHA from polypropylene (PP-*g*-PHA) in controlling lipid oxidation in an O/W emulsion system (pH 3.0) composed of stripped soybean oil.[11] Although PP-*g*-PHA films were unable to effectively inhibit lipid hydroperoxide development, they demonstrated better performance than EDTA (0.01 mM) in preventing the formation of hexanal. Herein, the developed PET-*g*-PHA film demonstrated ability to delay development of both lipid hydroperoxide and hexanal, albeit to a lesser extent than EDTA. In this study, an acidified food or beverage system using commercial oil was studied to demonstrate the potential application of PET-*g*-PHA modified packaging in extending the shelf life of an O/W emulsion system.

The physical stability of the emulsions at days 0 and 19 was evaluated to confirm that the physicochemical properties of the emulsion did not change during the course of lipid oxidation.

DOI: 10.1021/acs.jafc.5b00796
J. Agric. Food Chem. 2015, 63, 5055−5060

Throughout the study, there was no significant change in the size and charge of the Brij 35-stabilized emulsion, suggesting that the reported PET-*g*-PHA films do not influence the physical stability of emulsions (Table 1).

Table 1. Physical Stability of 0.05 M Sodium Acetate−Imidazole-Buffered (pH 3.0) Soybean O/W Emulsions Stored at 55 °C at Days 0 and 19 for Particle Size Diameter and ζ Potential[a]

sample emulsion	particle size diameter (nm)	ζ potential (mV)
original emulsion (day 0)	290 ± 61a	−1.13 ± 0.62
no film	221 ± 18b	0.24 ± 0.10
PET	224 ± 17b	0.08 ± 0.04
PET-*g*-PHA	198 ± 14bc	0.57 ± 0.45
EDTA (0.01 mM)	182 ± 3c	−0.99 ± 0.30
EDTA (0.08 mM)	180 ± 2c	−0.58 ± 0.12

[a]Values are means ± standard deviation of two measurements per sample, performed in duplicate (n = 4).

In conclusion, the potential applicability of a biomimetic iron-chelating moiety (PHA), grafted from a commercially applicable food-packaging polymer (PET), was demonstrated in controlling lipid oxidation of a commercial soybean oil-in water emulsion system. Herein, we developed a synthesis method to graft iron-chelating group precursors and convert them into active iron-chelating HA groups. PET-*g*-PHA films demonstrated strong iron-chelating activity in buffered systems relevant for chelating iron levels found in acidified food and beverages (pH 3.0) with competitive chelators. Results from this study demonstrate the applicability of biomimetic active packaging technology that can be utilized to protect foods and beverages from iron-promoted degradation.

AUTHOR INFORMATION

Corresponding Author

*(J.M.G.) Phone: (413) 545-2275. Fax: (413) 545-1262. E-mail: goddard@foodsci.umass.edu.

Funding

This research was funded by PepsiCo, Inc. The views expressed in this paper are those of the authors and do not necessarily represent position or policy or PepsiCo, Inc. M.J.R. acknowledges the Peter Salmon Graduate Fellowship and the Northeast Alliance Fellowships for their support.

Notes

The authors declare no competing financial interest.

ACKNOWLEDGMENTS

We gratefully acknowledge D. Julian McClements for the use of his emulsion preparation equipment and Zetasizer Nano ZS. ICP-MS sample preparation and analysis were conducted in the laboratories of Julian Tyson and David Reckhow with technical assistance from Nan Wang, Joe Goodwill, and Rassil Sayess.

REFERENCES

(1) Gutteridge, J. M. Lipid peroxidation and antioxidants as biomarkers of tissue damage. *Clin. Chem.* **1995**, *41*, 1819−1828.

(2) Mancuso, J. R.; McClements, D. J.; Decker, E. A. The effects of surfactant type, pH, and chelators on the oxidation of salmon oil-in-water emulsions. *J. Agric. Food Chem.* **1999**, *47*, 4112−4116.

(3) Frankel, E. N.; Finley, J. W. How to standardize the multiplicity of methods to evaluate natural antioxidants. *J. Agric. Food Chem.* **2008**, *56*, 4901−4908.

(4) López-de-Dicastillo, C.; Pezo, D.; Nerín, C.; López-Carballo, G.; Catalá, R.; Gavara, R.; Hernández-Muñoz, P. Reducing oxidation of foods through antioxidant active packaging based on ethyl vinyl alcohol and natural flavonoids. *Packag. Technol. Sci.* **2012**, *25*, 457−466.

(5) Tian, F.; Decker, E. A.; Goddard, J. M. Controlling lipid oxidation of food by active packaging technologies. *Food Funct.* **2013**, *4*, 669−680.

(6) Medina, I.; Satué-Gracia, M. T.; German, J. B.; Frankel, E. N. Comparison of natural polyphenol antioxidants from extra virgin olive oil with synthetic antioxidants in tuna lipids during thermal oxidation. *J. Agric. Food Chem.* **1999**, *47*, 4873−4879.

(7) Pokorný, J. Are natural antioxidants better—and safer—than synthetic antioxidants? *Eur. J. Lipid Sci. Technol.* **2007**, *109*, 629−642.

(8) Goddard, J. M.; McClements, D. J.; Decker, E. A. Innovative technologies in the control of lipid oxidation. *Lipid Technol.* **2012**, *24*, 275−277.

(9) Pereira de Abreu, D.; Paseiro Losada, P.; Maroto, J.; Cruz, J. Natural antioxidant active packaging film and its effect on lipid damage in frozen blue shark *Prionace glauca*. *Innovative Food Sci. Emerging Technol.* **2011**, *12*, 50−55.

(10) Vermeiren, L.; Devlieghere, F.; Van Beest, M.; De Kruijf, N.; Debevere, J. Developments in the active packaging of foods. *Trends Food Sci. Technol.* **1999**, *10*, 77−86.

(11) Tian, F.; Decker, E. A.; Goddard, J. M. Controlling lipid oxidation via a biomimetic iron chelating active packaging material. *J. Agric. Food Chem.* **2013**, *61*, 12397−12404.

(12) Tian, F.; Roman, M. J.; Decker, E. A.; Goddard, J. M. Biomimetic design of chelating interfaces. *J. Appl. Polym. Sci.* **2015**, *132*, DOI: 10.1002/APP.41231.

(13) Lange, J.; Wyser, Y. Recent innovations in barrier technologies for plastic packaging—a review. *Packag. Technol. Sci.* **2003**, *16*, 149−158.

(14) Uchida, E.; Uyama, Y.; Ikada, Y. Grafting of water-soluble chains onto a polymer surface. *Langmuir* **1994**, *10*, 481−485.

(15) Polomoscanik, S. C.; Cannon, C. P.; Neenan, T. X.; Holmes-Farley, S. R.; Mandeville, W. H.; Dhal, P. K. Hydroxamic acid-containing hydrogels for nonabsorbed iron chelation therapy: synthesis, characterization, and biological evaluation. *Biomacromolecules* **2005**, *6*, 2946−2953.

(16) Bou, R.; Guardiola, F.; Codony, R.; Faustman, C.; Elias, R. J.; Decker, E. A. Effect of heating oxymyoglobin and metmyoglobin on the oxidation of muscle microsomes. *J. Agric. Food Chem.* **2008**, *56*, 9612−9620.

(17) Tian, F.; Decker, E. A.; Goddard, J. M. Control of lipid oxidation by nonmigratory active packaging films prepared by photoinitiated graft polymerization. *J. Agric. Food Chem.* **2012**, *60*, 7710−7718.

(18) Talbot, J.; Weiss, A. *Laboratory Methods for ICP-MS Analysis of Trace Metals in Precipitation*; Hazardous Waste Research and Information Center: Champaign, IL, USA, 1994

(19) Waraho, T.; Cardenia, V.; Rodrigues-Estrada, M. T.; McClements, D. J.; Decker, E. A. Prooxidant mechanisms of free fatty acids in stripped soybean oil-in-water emulsions. *J. Agric. Food Chem.* **2009**, *57*, 7112−7117.

(20) Fasce, L.; Costamagna, V.; Pettarin, V.; Strumia, M.; Frontini, P. Poly (acrylic acid) surface grafted polypropylene films: near surface and bulk mechanical response. *eXPRESS Polym. Lett.* **2008**, *2*, 779−790.

(21) Curti, P. S.; Moura, M.R.d.; Veiga, W.; Radovanovic, E.; Rubira, A. F.; Muniz, E. C. Characterization of PNIPAAm photografted on PET and PS surfaces. *Appl. Surf. Sci.* **2005**, *245*, 223−233.

(22) Choe, E.; Min, D. B. Mechanisms and factors for edible oil oxidation. *Compr. Rev. Food Sci. Food Saf.* **2006**, *5* (4), 169−86.

(23) Winston, A.; McLaughlin, G. R. Hydroxamic acid polymers. II. Design of a polymeric chelating agent for iron. *J. Polym. Sci., Polym. Chem. Ed.* **1976**, *14*, 2155−2165.

DOI: 10.1021/acs.jafc.5b00796
J. Agric. Food Chem. 2015, 63, 5055−5060

JOURNAL OF AGRICULTURAL AND FOOD CHEMISTRY

Article

pubs.acs.org/JAFC

Lutein and Lutein Esters in Whole Grain Flours Made from 75 Genotypes of 5 *Triticum* Species Grown at Multiple Sites

Jochen U. Ziegler,[†] Sabine Wahl,[†] Tobias Würschum,[‡] C. Friedrich H. Longin,[‡] Reinhold Carle,[†,§] and Ralf M. Schweiggert*[,†]

[†]Institute of Food Science and Biotechnology, University of Hohenheim, Garbenstraße 25, D-70599 Stuttgart, Germany

[‡]State Plant Breeding Institute, University of Hohenheim, Fruwirthstraße 21, D-70599 Stuttgart, Germany

[§]Faculty of Science, Biological Science Department, King Abdulaziz University, P.O. Box 80257, Jeddah 21589, Saudi Arabia

Supporting Information

ABSTRACT: Concentrations of lutein and lutein esters were determined in an ample collection of 75 wheat genotypes comprising bread wheat (*Triticum aestivum* L.), durum (*Triticum durum* Desf.), spelt (*Triticum spelta* L.), emmer (*Triticum dicoccum* Schrank), and einkorn (*Triticum monococcum* L.) grown in five different environments. Einkorn genotypes showed the highest total amounts of lutein (4.5−7.8 μg/g dry matter), followed by durum (2.0−4.6 μg/g), spelt (0.9−2.0 μg/g), emmer (0.8−1.9 μg/g), and bread wheat (0.7−2.0 μg/g). Due to the observed highly significant genetic variance and high heritability, lutein contents of wheat genotypes may be increased by future plant breeding. Detailed HPLC-DAD-APCI(±)-MS^n data allowing the identification of six lutein monoesters and nine diesters are presented. Linoleic, palmitic, and oleic acids were the most abundant fatty acids in both the lutein esters and total free lipid fractions. Lutein esters were virtually absent in the tetraploid durum and emmer species, whereas their concentrations considerably differed among the genotypes belonging to the other species.

KEYWORDS: *carotenoid ester, heritability, xanthophylls, mass spectrometry, fatty acids*

INTRODUCTION

Wheat (*Triticum* spp.) is one of the most important cereal crops in Europe and worldwide.[1] Although this staple food is mainly consumed as an energy supplier due to its high starch and protein contents, it also contains nutritionally relevant compounds, such as vitamin E and carotenoids.[2] Among the present carotenoids, lutein is predominant in wheat (Figure 1A), accounting for 90−100% of the total carotenoids.[3] Lutein also occurs at high concentrations in the human macula, and its increased dietary intake has been associated with a reduced incidence of eye diseases, such as age-related macular degeneration (AMD), cataract, and retinitis pigmentosa.[4,5] The prevention of mild cognitive impairment and Alzheimer's disease in elderly people by lutein has also been discussed.[6−8] A yet unknown function of lutein in the infant brain has recently been hypothesized, as approximately 60% of the total carotenoids in their brain have been assigned to lutein, and its levels were found to be depleted in preterm infants.[9]

Although lutein concentrations in most wheat products are rather low (0.1−0.5 mg/100 g fresh weight (FW))[10] compared to common lutein-rich foods, such as green leafy vegetables (>2 mg/100 g FW)[11] and egg yolk (approximately 1 mg/100 g FW),[12] their high per capita consumption makes them an important dietary source. In 2007, annual per capita consumption of wheat products in Germany has been estimated to be 87 kg (women) and 114 kg (men), respectively.[13] In addition to its nutritional relevance, the carotenoid content in wheat is an important prerequisite for the product's color, substantially differing when processing flours from different species and genotypes.[3,14] In particular, durum wheat (*Triticum durum* Desf.) was bred for a high carotenoid content, due to its use for the production of semolina and pasta, where the resulting yellowish color hue is highly desirable.[15] Nevertheless, the carotenoid content in einkorn (*Triticum monococcum* L.), an ancient diploid wheat species, was previously reported to be up to 4-fold higher than in other wheat species.[3,14] However, investigations into carotenoid levels of flours from different wheat species are so far limited to a low number of included species and genotypes, additionally lacking multiyear and multisite studies.

According to the semisystematic carotenoid nomenclature,[16] lutein is characterized by hydroxylated β- and ε-rings (Figure 1A). Due to their asymmetric esterification with fatty acids, regioisomers of lutein esters are frequently observed. Recent studies of different nonwheat sources provided detailed information about lutein esters, including their regioisomers.[17−19] Although an earlier study demonstrated that lutein in wheat may occur in both the nonesterified and esterified forms,[20] comprehensive reports about the occurrence and identification of lutein acyl esters in wheat and cereals in general are scarce.[19,20] Particularly, a comprehensive study on carotenoid esters in old wheat species, such as spelt, emmer, and einkorn, has not been carried out to date.

In the present study, the determination of lutein and its esters in an ample set of 75 genotypes from 5 wheat species

Received: March 23, 2015
Revised: April 27, 2015
Accepted: May 6, 2015
Published: May 6, 2015

ACS Publications © 2015 American Chemical Society

DOI: 10.1021/acs.jafc.5b01477
J. Agric. Food Chem. 2015, 63, 5061−5071

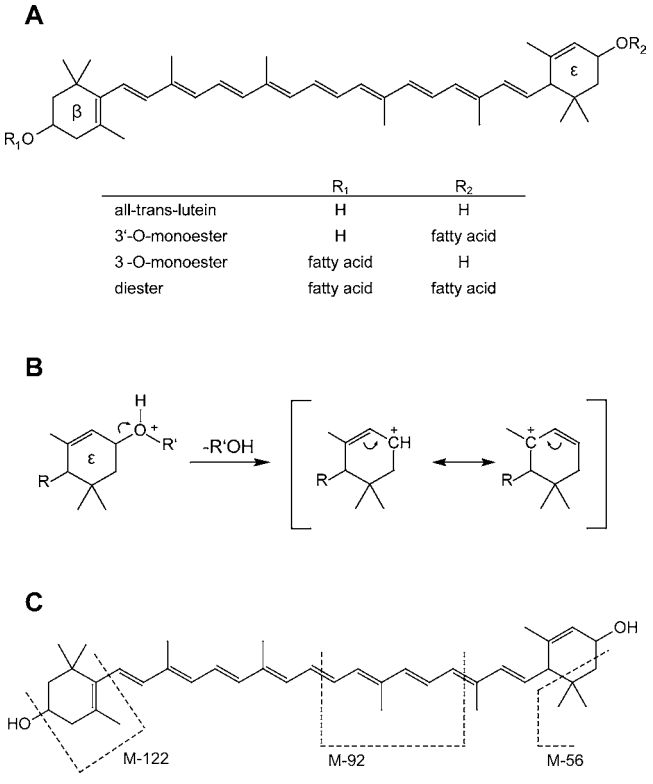

Figure 1. (A) Chemical structure of free and esterified lutein. (B) Fragmentation scheme of lutein at the ε-ring applying positive atmospheric pressure chemical ionization (APCI). (C) Characteristic lutein fragments produced by positive APCI.

grown in 5 different environments should illustrate the genetic variation and modificatory variability, that is, diversity of xanthophyll contents among different and identical species as affected by both genotype and environment. Considering the applied HPLC-DAD-MS^n method, the advantages of combining positive and negative ionization techniques for the identification of lutein ester regioisomers are additionally discussed.

MATERIALS AND METHODS

Plant Material and Sample Preparation. Fifteen genotypes each of bread wheat (*Triticum aestivum* L.), durum (*Triticum durum* Desf.), spelt (*Triticum spelta* L.), einkorn (*Triticum monococcum* L.), and emmer (*Triticum dicoccum* Schrank) were grown at four sites in Germany (Hohenheim, Eckartsweier, Oberer Lindenhof, Seligenstadt). All samples originated from harvest 2013, except for those from Hohenheim, which were from 2012 and 2013. A detailed sample list and further information about the different sites are provided in Supplemental Tables 1−6. Cereal samples used in this study were produced by the State Plant Breeding Institute (University of Hohenheim, Stuttgart, Germany) in separate but adjacent trials with two replicates for each species. After harvest, all spelt, einkorn, and emmer samples were dehulled and cleaned with a laboratory seed cleaner (Samatec-Roeber, Bad Oeynhausen, Germany) to remove hulls, straw, and damaged kernels. For chemical analyses, the kernels of the two replicates of one site were combined. The samples were stored under identical conditions (≤18 °C, ≤40% relative humidity) prior to milling to a particle size ≤0.5 mm by a laboratory mill ZM1 (Retsch, Haan, Germany). Subsequently, whole grain flour was stored at −20 °C until further analysis. Dry matter content was determined using an infrared moisture analyzer MA 40 (Sartorius, Göttingen, Germany).

Chemicals. Methanol, methyl *tert*-butyl ether (MTBE), potassium hydroxide (KOH), sodium chloride (NaCl), and ammonium acetate were purchased from VWR International (Darmstadt, Germany). Acetone, diethyl ether, and *n*-hexane were from Merck (Darmstadt, Germany). Lutein (purity ≥ 95%) originated from CaroteNature (Lupsingen, Switzerland). Fatty acids (FAs), their respective methyl esters (FAMEs) of GC purity, and a methanolic boron trifluoride solution (10% BF_3 in methanol) were obtained from Sigma-Aldrich (Steinheim, Germany). A marigold (*Tagetes erecta* L.) extract (10% lutein esters) was kindly provided by BioActives Europe (Frankfurt, Germany). Purified water was prepared using a Sartorius arium 611 Ultrapure Water System.

Extraction of Carotenoids. Carotenoids were extracted for their quantification according to a previously described method.[21] Briefly, an

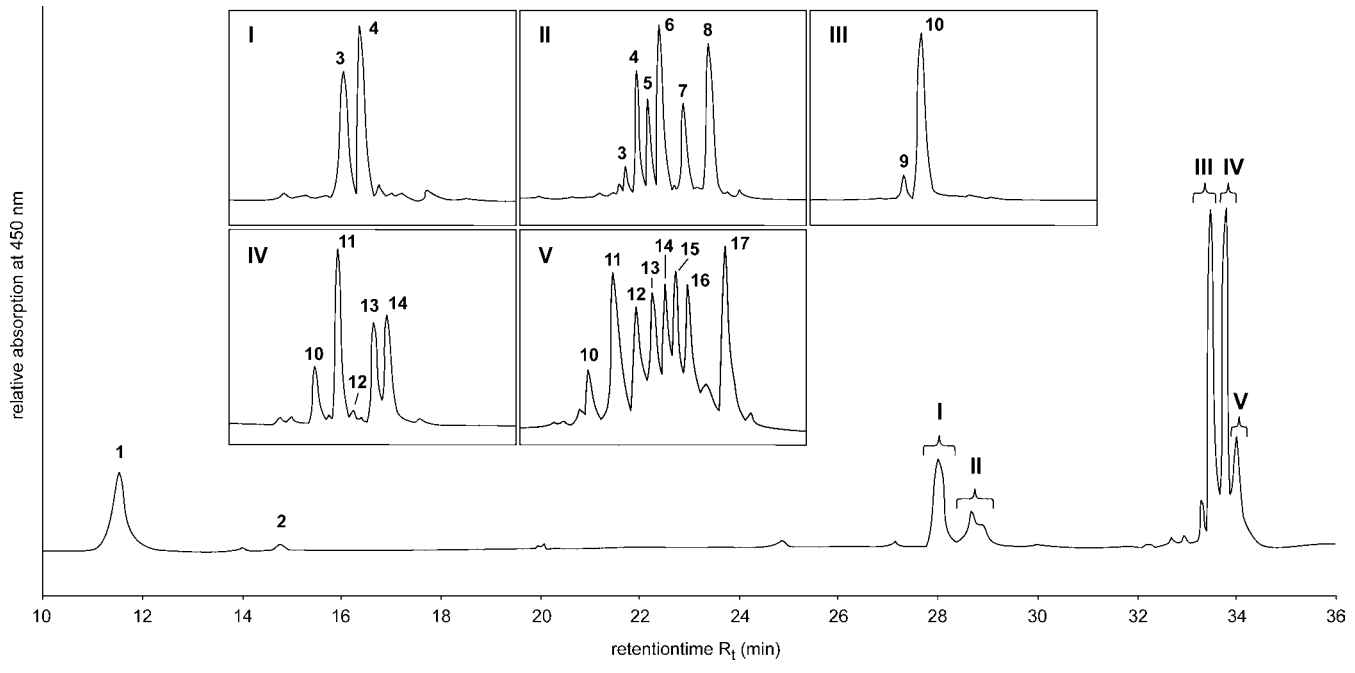

Figure 2. C_{18} HPLC chromatogram of a carotenoid extract from einkorn and C_{30} HPLC chromatograms of the isolated lutein ester fractions (I−V).

DOI: 10.1021/acs.jafc.5b01477
J. Agric. Food Chem. 2015, 63, 5061−5071

aliquot of 0.70 ± 0.05 g of whole grain flour was extracted three times with acetone (2, 1.5, and 1.5 mL, respectively) using an Ultra Turrax T-25 homogenizer (IKA-Werke, Staufen, Germany). Separation of the acetone extracts from the solid extraction residue was enhanced by centrifugation at 1750*g* for 2 min (Heraeus Labofuge 400R, Thermo Fisher Scientific, Osterode, Germany). The combined acetone extracts were dried under a gentle nitrogen stream and stored at −80 °C until HPLC analyses. As described by Burkhard and Böhm,[22] a soaking step was applied prior to the exhaustive extraction of carotenoids from the tetraploid wheat species durum and emmer. For this purpose, 0.7 mL of water was added to the wheat flour and soaked for 5 min prior to extraction. After the application of this soaking step, average carotenoid yields were increased by 44.5 and 39.1% for durum and emmer when all samples from genotypes of these species were compared, respectively (data not shown). In contrast, total carotenoid contents were decreased by 2.4−17.9% in the case of bread wheat, spelt, and einkorn. Therefore, the data reported for the latter species refer to an extraction omitting the soaking step.

For semipreparative isolation and subsequent identification of lutein esters, the extraction procedure described was scaled up to 40 g of extracted flour. The dried extract was redissolved in 5 mL of MeOH/MTBE (1:1, v/v) and, subsequently, lutein esters were fractionated by semipreparative HPLC using a 250 × 21.2 mm i.d. Phenomenex Aqua 5 μm C_{18} 125 Å column (Phenomenex, Torrance, CA, USA). For this purpose, a linear gradient from MeOH/water (90:10, v/v) to MTBE/MEOH/water (60:36:4, v/v/v) within 40 min was applied. As shown in Figure 2, the lipophilic wheat extracts were separated into five fractions (I−V), evaporated in vacuo (T = 25 °C), and analyzed by HPLC-DAD-MS^n as described below.

Saponification of Carotenoid Extracts. Confirming the occurrence of lutein esters, saponification of carotenoid extracts was conducted as follows. After carotenoid extraction as described above, the dried extracts were saponified following a method described by Mellado-Ortega and Hornero-Méndez.[19] Briefly, the dried extracts were redissolved in 2 mL of diethyl ether. Subsequently, 0.5 mL of methanolic KOH (10%, w/v) was added, and the mixture was stirred (ca. 500 rpm) for 1 h under a nitrogen atmosphere. After the addition of 1 mL of $NaCl_{aq}$ (30%, w/v), carotenoids were extracted with diethyl ether. The combined ether phases were evaporated in vacuo (T = 25 °C), and the dried extracts were stored at −80 °C until HPLC analyses.

HPLC-DAD-MS^n Analyses of Lutein and Lutein Esters. Prior to HPLC-DAD-MS^n analyses, the dried carotenoid extracts were redissolved in MeOH/MTBE (1:1, v/v) and membrane-filtered (0.45 μm, PTFE) into amber glass vials. Separation of carotenoids was performed on a series 1100 HPLC (Agilent, Waldbronn, Germany) equipped with a G1315B diode array detector. The carotenoid C_{30} column (150 × 3.0 mm i.d., 3 μm particle size, YMC, Dinslaken, Germany) with a YMC C_{30} guard column (10 × 3.0 mm i.d.) of the same material was operated at 25 °C. The mobile phase consisted of two different mixtures of MeOH/MTBE/10 g/L ammonium $acetate_{aq}$ (80:18:2 (v/v/v), solvent A; 6:92:2 (v/v/v), solvent B). The gradient program was as follows: 0−60% B (45 min), 60−100% B (5 min), 100% B isocratic (2 min), 100−0% B (3 min). Re-equilibration of the column was achieved at 0% B within 5 min. Total run time was 60 min at a flow rate of 0.42 mL/min. Injection volume was 20 μL. All carotenoids and carotenoid esters were monitored at 450 nm. Additionally, UV−vis spectra were recorded in the range of 220−700 nm. The HPLC system was coupled online to a Bruker (Bremen, Germany) model Esquire 3000+ ion trap mass spectrometer. MS^n analyses of carotenoids were performed using an atmospheric pressure chemical ionization (APCI) source in positive and negative mode in the range of m/z 200−1200 at a scan speed of 13000 Th/s. Nitrogen was used both as drying gas at a flow rate of 5 L/min and as nebulizer gas at a pressure of 55 psi. Vaporizer and dry temperature were set at 350 °C with a capillary voltage of ±2800 V, and the corona was set at 3000 nA in both positive and negative modes. Helium was used as the collision gas for collision-induced dissociation (CID) experiments at a pressure of 4.9×10^{-6} mbar. The fragmentation amplitude was set at 1.0 V.

Identification of carotenoids was carried out by comparing their retention times, UV−vis absorption, and mass spectra with those of authentic standards. Because commercial standards of lutein esters were unavailable, they were identified by their UV−vis absorption matching free lutein and by their characteristic mass spectral behavior as discussed below.[17−19,23] The identification of lutein esters was confirmed by cochromatographic analyses of a marigold (*Tagetes erecta* L.) extract containing known lutein esters (lutein dimyristate, lutein palmitate-myristate, lutein dipalmitate, lutein stearate-palmitate, and lutein distearate).[17] The respective chromatogram and corresponding identification parameters are provided in the Supporting Information.

The quantification of free, mono-, and diesterifed lutein was conducted by RP-C_{18}-HPLC-DAD using an authentic lutein standard recently described.[21] Due to their coelution on RP-C_{18} columns, zeaxanthin was quantitated together with free lutein. However, zeaxanthin contributes only 0−10% to the total carotenoids in *Triticum* according to previous studies[3] and our observations using a C_{30} column. Therefore, peak 1 was assigned to free lutein. Because the chromophore of xanthophylls remains identical after esterification,[24] the concentrations of lutein esters were determined by using the linear calibration for free lutein and molecular weight correction factors when data were converted from micromoles to micrograms. Limits of detection (LOD) and quantitation (LOQ) were determined[25] to be 0.01 and 0.03 μmol lutein/g DM, respectively.

Fatty Acid Extraction, Derivatization, and Analyses by GC-FID. Fatty acids (FAs) were determined according to a previously published protocol[26] with some modifications. Briefly, total free lipids of wheat flours were extracted in a Soxhlet apparatus for 2 h with boiling *n*-hexane. The organic solvent was evaporated in vacuo at 30 °C, and the total free lipid content was gravimetrically determined. Subsequently, an aliquot of 20−30 mg of the obtained total free lipids was combined with 1 mL of methanolic KOH (0.5 M) and heated at 80 °C for 10 min. After the mixture had cooled to room temperature, 1 mL of methanolic BF_3 reagent was added and heated for another 5 min at 80 °C. The samples were subsequently cooled to room temperature, and then 2 mL of $NaCl_{aq}$ (30%, w/v) was added. The fatty acid methyl esters (FAMEs) obtained were then extracted with *n*-hexane prior to GC-FID analyses. Heptadecanoic acid was added as internal standard prior to saponification.

For determination of FAMEs, a Chrompack CP 9001 gas chromatograph (Chromopack, Middleburg, The Netherlands) equipped with a CP 9010 autosampler and a FID detector was used. Separation was performed on a Supelcowax-10 fused silica capillary column (30 m × 0.25 mm i.d., 0.25 μm; Supelco, Bellafonte, PA, USA). Helium (purity 5.0) was used as carrier gas with a constant flow of 0.92 mL/min, and the injection volume was 1 μL at a split ratio of approximately 1:55. The oven temperature was ramped from 180 to 240 °C at a heating rate of 3 K/min. The final temperature was held for 3 min. The temperature of both the injector and detector was set at 250 °C. FAMEs were identified by comparison of their retention times with those of authentic standards. Quantitation was performed using linear calibrations of authentic reference compounds, additionally corrected by the internal standard signal (heptadecanoic acid).

Statistical Analysis. Variance components were determined by the restricted maximum likelihood (REML) method, assuming a random model using classical one-stage analyses.[27] Significance of variance component estimates was tested by model comparison with likelihood ratio tests in which halved P values were used as approximation.[28] Heritability h^2 was calculated according to eq 1

$$h^2 = 1 - \frac{\vartheta}{2\sigma_G^2} \quad (1)$$

where ϑ is the mean variance of a difference of two best linear unbiased predictors (BLUP) and σ_G^2 the genetic variance.[29,30] All analyses were performed with the statistical software R (R Development Core Team 2011) and the software ASReml 3.0.[31]

DOI: 10.1021/acs.jafc.5b01477
J. Agric. Food Chem. 2015, 63, 5061−5071

Table 1. Chromatographic and Spectroscopic Properties of the Lutein and Lutein Esters Isolated from Einkorn

peak[a]	t_R[b] (min)	identity	HPLC-DAD UV−vis spectrum λ_{max} (nm)	APCI(−) $[M]^-$ m/z	APCI(+) $[M + H]^+$ m/z (relative intensity)	HPLC-APCI(+)-MS^2 m/z (relative intensity)[c]
std	9.0	(*all-E*)-lutein standard	445, 473	568	551	[551]: 533 (100), 495 (79), 429 (24), 411 (22), 459 (12), 477 (11), 345 (10)
1	9.0	(*all-E*)-lutein	445, 473	568	551	[551]: 533 (100), 495 (28), 429 (24), 411 (17), 459 (12), 477 (11), 345 (8)
2	10.3	lutein (*Z*)-isomer	329, 441, 468	568	551	
3	21.5	lutein 3′-*O*-linoleate	445, 473	830	551 (100), 533 (13), 831 (4)	[551]: 533 (100), 495 (26) 429 (24), 411 (16), 477 (10) 459 (9), 345 (8)
4	22.4	lutein 3-*O*-linoleate	445, 473	830	813 (100), 533 (51), 831 (8)	[813]: 533 (100), 411 (11), 477 (8)
5	23.3	lutein 3′-*O*-oleate	445, 473	832	551 (100), 533 (21), 833 (9)	[551]: 533 (100), 495 (92), 411 (27), 429 (23), 477 (12), 345 (10), 459 (9)
6	24.1	lutein 3-*O*-oleate	445, 473	832	815 (100), 533 (53), 833 (10)	[815]: 533 (100), 411 (12), 477 (6), 441 (6)
7	25.8	lutein 3′-*O*-palmitate	445, 473	806	551 (100), 533 (36)	[551]: 533 (100), 495 (35), 429 (19), 441 (18), 477 (8), 345 (6), 459 (4)
8	27.7	lutein 3-*O*-palmitate	445, 473	806	789 (100), 533 (43), 808 (5)	[789]: 533 (100), 411 (10), 477 (8), 441 (4)
9	31.6	lutein linoleate-linolenate[d]	445, 473	1090	813 (100), 811 (96), 533 (63)	[813]: 533 (100), 411 (15)
10	32.4	lutein dilinoleate	445, 473	1092	813 (100), 533 (17)	[813]: 533 (100), 411 (12), 477 (7)
11	33.5	lutein 3′-*O*-linoleate- 3-*O*-oleate	445, 473	1094	815 (100), 813 (47), 533 (41)	[815]: 533 (100), 411 (8), 477 (4), 441 (3)
12	34.6	lutein dioleate	445, 473	1096	815 (100), 533 (46)	[815]: 533 (100), 411 (10), 441 (4)
13	35.3	lutein 3′-*O*-palmitate- 3-*O*-linoleate	445, 473	1068	813 (100), 533 (33), 789 (4)	[813]: 533 (100), 411 (13)
14	36.0	lutein 3′-*O*-linoleate- 3-*O*-palmitate	445, 473	1068	789 (100), 533 (42), 813 (8)	[789]: 533 (100), 411 (14), 477 (7)
15	36.5	lutein 3′-*O*-palmitate- 3-*O*-oleate	445, 473	1070	815 (100), 533 (62), 789 (45)	[815]: 533 (100), 411 (9), 477 (6), 441 (4)
16	37.0	lutein 3′-*O*-oleate-3-*O*-palmitate	445, 473	1070	789 (100), 533 (69), 815 (29)	[789]: 533 (100), 411 (9), 477 (6), 441 (5)
17	38.7	lutein dipalmitate	445, 473	1044	789 (100), 533 (52)	[789]: 533 (100), 411 (14), 477 (5), 441 (3)

[a]Peak assignment according to Figure 2 and Supplemental Figure 1. [b]Retention times (t_R) refer to the analytical runs on the C_{30} column. [c]Carotenoid-specific fragments. [d]Identification of regioisomer was impossible.

RESULTS AND DISCUSSION

Identification of Lutein and Its Fatty Acid Esters. *General Considerations.* All compounds monitored at 450 nm revealed identical UV−vis absorption spectra with maxima at 445 and 473 nm, also being identical to that of an authentic lutein standard (Table 1). In contrast to compounds **1** and **2**, compounds **3**−**17** were absent in the saponified carotenoid extracts (Supplemental Figure 1B,C). The highest concentrations of these compounds (**3**−**17**), presumably lutein mono- and diesters as described below (Table 2), were found in the einkorn breeding line '8.103/04', the bread wheat genotype 'Tabasco', and the spelt genotype 'Oberkulmer Rotkorn'. Thus, these genotypes were used for the identification of lutein esters.

For identification by RP-C_{30}-HPLC-DAD-MS^n as described above, the lutein ester-rich extracts were first divided into five fractions (I−V) by RP-C_{18} semipreparative HPLC (Figure 2). For the identification of lutein esters, mass spectral data obtained from an authentic lutein standard were helpful. Because the hydroxyl group of the ε-ring is in an allylic position (Figure 1A), the *in source*-formation of the dehydrated fragment at m/z 551 $[M + H - H_2O]^+$ is highly favored in the positive APCI experiments due to mesomeric effects (Figure 1B). The abundance of this ion at m/z 551 was drastically higher than that of the protonated pseudomolecular ion at m/z 569 $[M + H]^+$ (Table 1), being in agreement with previous studies.[32−34] CID experiments of the *in source*-fragment $[M + H - H_2O]^+$ at m/z 551 revealed several characteristic fragments (Figure 1C),[33,34] such as the predominant daughter ion $[M + H - 2H_2O]^+$ at m/z 533 (base peak), resulting from an additional loss of water from the hydroxyl group of the β-ring. The carotenoid-specific elimination of toluene from the central polyene chain of the carotenoid skeleton resulted in a characteristic loss of 92 amu,[32] leading to product ions at m/z 459 $[M + H - H_2O - 92]^+$ and 441 $[M + H - 2H_2O - 92]^+$. As shown in Figure 1C, the neutral loss of 56 amu may be due to an ε-ring-specific fragmentation following a retro-Diels−Alder reaction as described previously.[32,33] Consequently, the product ions detected at m/z 495 and 477 may correspond to $[M + H - H_2O - 56]^+$ and $[M + H - 2H_2O - 56]^+$, respectively (Table 1). The elimination of the cyclic β- or ε-end groups from the carotenoid skeleton resulted in the fragment ions $[M + H - H_2O - 122]^+$ at m/z 429 and $[M + H - 2H_2O - 122]^+$ at m/z 411 (Figure 1C),[33] whereas the ion at m/z 345 was previously described to be a fragment of $[M + H - H_2O]^+$ at m/z 551.[35]

The described fragmentation pattern of lutein was instrumental for the identification of lutein esters, particularly their regioisomers. By analogy to the *in source* water loss from C3′ of the ε-ring, acyl residues were separated from the ε-ring of lutein esters during APCI(+) experiments. As a result, the protonated molecular ion $[M + H]^+$ of 3′-*O*-monoesters and diesters is commonly observed at poor intensity. However, the differing fragmentation patterns of the β- and ε-ring hydroxyl and acyl moieties allow the differentiation of lutein ester

DOI: 10.1021/acs.jafc.5b01477
J. Agric. Food Chem. 2015, 63, 5061−5071

Table 2. Total Lutein Content and Relative Composition of Free, Mono-esterified, and Di-esterified Lutein in Different Wheat Species and Genotypes

			total lutein content[a] (μg/g DM)		lutein composition[b] (%)			
species	genotype	n[c]	mean[d]	range	free	monoesterified	diesterified	esterified
bread wheat	Altigo	5	1.35 ± 0.27	0.92−1.57	100.0	0.0	0.0	0.0
	Colonia	5	1.48 ± 0.24	1.18−1.77	74.3	20.2	5.5	25.7
	Cubus	5	1.30 ± 0.29	0.87−1.54	100.0	0.0	0.0	0.0
	Event	5	0.87 ± 0.28	0.56−1.32	71.8	17.8	10.5	28.2
	Genius	5	1.07 ± 0.21	0.74−1.23	74.4	18.1	7.5	25.6
	JBAsano	5	1.35 ± 0.28	0.91−1.61	69.2	19.8	11.0	30.8
	Julius	5	0.69 ± 0.15	0.44−0.81	100.0	0.0	0.0	0.0
	Lear	4	2.01 ± 0.36	1.51−2.36	100.0	0.0	0.0	0.0
	Meister	5	1.34 ± 0.31	0.88−1.71	100.0	0.0	0.0	0.0
	Mulan	5	1.57 ± 0.40	0.98−2.11	100.0	0.0	0.0	0.0
	Orcas	5	1.28 ± 0.31	0.82−1.57	77.3	17.1	5.7	22.7
	Skalmeje	5	1.39 ± 0.37	0.84−1.83	70.4	20.6	9.0	29.6
	Tabasco	5	1.50 ± 0.20	1.20−1.70	61.7	22.3	16.1	38.3
	Tobak	5	1.26 ± 0.28	0.90−1.64	100.0	0.0	0.0	0.0
	Tommi	5	1.52 ± 0.26	1.16−1.84	71.9	19.3	8.8	28.1
	median		1.35		77.3	17.1	5.5	22.7
durum	Auradur	5	3.36 ± 0.70	2.42−4.39	100.0	0.0	0.0	0.0
	Elsadur	4	3.58 ± 0.84	2.65−4.69	100.0	0.0	0.0	0.0
	Karur	5	2.95 ± 0.51	2.16−3.37	100.0	0.0	0.0	0.0
	Logidur	5	2.22 ± 0.38	1.69−2.73	100.0	0.0	0.0	0.0
	Lunadur	5	2.01 ± 0.45	1.41−2.64	100.0	0.0	0.0	0.0
	Lupidur	5	2.35 ± 0.57	1.63−3.20	100.0	0.0	0.0	0.0
	W-05005/02	5	3.46 ± 0.84	2.68−4.88	100.0	0.0	0.0	0.0
	W-05006/01	5	3.00 ± 0.42	2.48−3.62	100.0	0.0	0.0	0.0
	W-05018/04	5	3.56 ± 0.50	3.07−4.38	100.0	0.0	0.0	0.0
	W-05020/01	5	3.02 ± 0.52	2.49−3.79	100.0	0.0	0.0	0.0
	W-05024/01	5	4.56 ± 1.06	3.62−6.33	100.0	0.0	0.0	0.0
	W-05025/01	5	3.37 ± 0.60	2.69−4.33	100.0	0.0	0.0	0.0
	W-05026/03	5	3.25 ± 0.65	2.44−4.17	100.0	0.0	0.0	0.0
	W-05029/02	5	4.28 ± 0.77	3.36−5.49	100.0	0.0	0.0	0.0
	Wintergold	5	3.26 ± 0.56	2.53−4.03	100.0	0.0	0.0	0.0
	median		3.26		100.0	0.0	0.0	0.0
spelt	Badengold	5	1.51 ± 0.21	1.26−1.76	70.9	19.7	9.5	29.1
	Badenkrone	5	1.96 ± 0.43	1.32−2.42	70.0	21.5	8.5	30.0
	Badenstern	5	1.53 ± 0.26	1.15−1.82	70.3	19.9	9.8	29.7
	D-04004/03	5	1.56 ± 0.42	1.07−2.13	71.6	19.3	9.1	28.4
	D-04004/04	5	1.64 ± 0.43	1.11−2.20	69.9	19.0	11.1	30.1
	D-04004/08	5	1.77 ± 0.47	1.18−2.37	68.6	20.5	10.9	31.4
	D-04004/09	5	1.50 ± 0.39	1.00−2.02	71.6	18.6	9.8	28.4
	D-05015/03	5	0.87 ± 0.18	0.62−1.05	74.3	17.1	8.6	25.7
	Divimar	5	1.57 ± 0.36	1.10−1.97	68.6	21.1	10.3	31.4
	Filderstolz	5	1.23 ± 0.28	0.94−1.58	71.0	19.0	10.0	29.0
	Franckenkorn	5	1.28 ± 0.21	1.11−1.63	76.3	17.5	6.3	23.7
	Oberkulmer Rotkorn	5	1.54 ± 0.23	1.30−1.80	64.2	21.9	13.9	35.8
	Samir	5	1.65 ± 0.41	1.20−2.16	72.2	19.0	8.8	27.8
	Schwabenkorn	5	1.51 ± 0.34	1.07−1.89	67.3	21.6	11.1	32.7
	Zollernspelz	5	1.43 ± 0.16	1.29−1.65	68.2	22.0	9.8	31.8
	median		1.53		70.3	19.7	9.8	29.7
einkorn	8.103/04	4	5.56 ± 0.37	5.14−6.05	41.7	18.1	40.2	58.3
	8.108/04	5	5.56 ± 1.01	4.28−7.07	92.7	7.0	0.3	7.3
	8.116/04	5	7.33 ± 0.59	6.92−8.33	88.5	10.1	1.3	11.5
	M-03021/03	5	5.92 ± 0.50	5.44−6.69	89.7	9.3	1.0	10.3
	M-04003/01	5	6.24 ± 0.53	5.73−7.12	94.1	5.6	0.4	5.9
	M-04018/01	5	4.69 ± 0.49	4.03−5.35	93.3	6.4	0.3	6.7
	M-04018/02	5	4.47 ± 0.47	4.03−5.19	94.0	5.7	0.3	6.0

DOI: 10.1021/acs.jafc.5b01477
J. Agric. Food Chem. 2015, 63, 5061−5071

Table 2. continued

species	genotype	n^c	total lutein content[a] (μg/g DM) mean[d]	range	lutein composition[b] (%) free	monoesterified	diesterified	esterified
	M-04018/03	5	4.69 ± 0.63	4.09−5.62	93.8	6.0	0.2	6.2
	M-04033/01	5	7.66 ± 0.80	6.75−8.83	89.7	9.1	1.1	10.3
	M-04033/03	5	7.83 ± 0.85	6.95−8.95	89.3	9.4	1.2	10.7
	M-07006/01	4	6.06 ± 0.41	5.71−6.64	95.4	4.6	0.0	4.6
	Monlis	3	5.65 ± 0.20	5.42−5.77	95.6	4.4	0.0	4.4
	MVMenket	4	5.72 ± 0.28	5.35−5.96	92.4	6.9	0.7	7.6
	Terzino	5	5.49 ± 0.38	4.89−5.92	90.6	8.2	1.2	9.4
	Tifi	5	5.51 ± 0.48	4.82−5.87	90.5	8.6	0.9	9.5
	median		5.65		92.4	7.0	0.7	7.6
emmer	9.105/06/01	5	1.31 ± 0.18	1.04−1.52	100.0	0.0	0.0	0.0
	9.118/05/01	5	1.13 ± 0.22	0.91−1.44	100.0	0.0	0.0	0.0
	9.121/05	5	1.15 ± 0.17	0.92−1.35	100.0	0.0	0.0	0.0
	9.131/05	5	0.90 ± 0.09	0.76−0.99	100.0	0.0	0.0	0.0
	9.199/06/01	5	1.62 ± 0.15	1.40−1.81	100.0	0.0	0.0	0.0
	CC1E-04058/01	5	1.90 ± 0.19	1.63−2.13	100.0	0.0	0.0	0.0
	CC1E-04059/02	5	1.86 ± 0.32	1.30−2.13	100.0	0.0	0.0	0.0
	CC1E-04059/04	5	1.61 ± 0.21	1.27−1.83	100.0	0.0	0.0	0.0
	CC1E-04059/06	5	1.85 ± 0.22	1.47−2.05	100.0	0.0	0.0	0.0
	CC1E-04059/07	5	1.57 ± 0.26	1.25−1.82	100.0	0.0	0.0	0.0
	E-07086/01	4	1.93 ± 0.31	1.55−2.27	100.0	0.0	0.0	0.0
	E-07087/01	4	1.19 ± 0.14	1.08−1−39	100.0	0.0	0.0	0.0
	E-07087/02	4	0.79 ± 0.10	0.64−0.88	100.0	0.0	0.0	0.0
	Osiris	5	1.53 ± 0.07	1.41−1.58	100.0	0.0	0.0	0.0
	Ramses	5	1.27 ± 0.14	1.13−1.44	100.0	0.0	0.0	0.0
	median		1.52		100.0	0.0	0.0	0.0

[a]Up to 10% of the total lutein content may be zeaxanthin. [b]Mean. [c]Number of environments where the respective genotype was grown. [d]Mean ± standard deviation.

regioisomers, as the predominant *in source*-fragment ion indicates the position of the fatty acid moiety.[17−19] Briefly, lutein 3′-*O*-monoesters showed *in source*-fragments $[M + H - \text{fatty acid}]^+$ at m/z 551 as the most abundant ion, whereas $[M + H - H_2O]^+$ at higher m/z represented the predominant positive fragment ion of 3-*O*-monoesters, for example, at m/z 789 for lutein 3-*O*-palmitate. Similarly, the most abundant *in source*-fragment ion of lutein diesters indicated the loss of the fatty acid located at position 3′ (ε-ring). Consequently, the identity of the fatty acid attached to position 3 (β-ring) can be deduced by exclusion principle. However, this identification strategy requires the unambiguous assignment of the m/z of the (pseudo)molecular ion, which may be intricate when only APCI(+) is used. Therefore, APCI(−) experiments were conducted as described previously.[36,37] Under the chosen MS conditions, the authentic lutein standard showed a predominant ion in the negative mode at m/z 568, corresponding to its molecular ion $[M]^-$. Among others, Breithaupt[36] reported that APCI(−) produced a higher abundance of the negatively charged molecular ions $[M]^-$ of astaxanthin esters than the corresponding $[M - H]^-$ ions.

Identification of Lutein Monoesters. Following the identification strategy described above, six compounds (**3**−**8**) contained in fractions I and II were assigned to lutein monoesters by RP-C_{30}-HPLC-MS^n (Figure 2). Lutein being the core carotenoid of diverse esters was identified on the basis of its characteristic UV−vis absorption spectrum identical to that of free lutein (Table 1) as well as the disappearance of lutein esters after saponification and the concomitant increase of the signal of free lutein. Both 3′-*O*- and 3-*O*-regioisomers of lutein linoleate (**3**, **4**), oleate (**5**, **6**), and palmitate (**7**, **8**) were identified, because characteristic molecular ions $[M]^-$ at m/z 830, 832, and 806 were observed during APCI(−)-MS experiments, respectively. With regard to the 3′-*O*-regioisomers, the *in source*-fragment $[M + H - \text{acyl}]^+$ at m/z 551 was the prevailing ion, whereas the 3-*O*-regioisomers showed predominant dehydrated *in source*-fragment ions corresponding to $[M + H - H_2O]^+$ of lutein linoleate (m/z 813), lutein oleate (m/z 815), and lutein palmitate (m/z 789), respectively. In contrast to APCI(−)-MS, molecular ions $[M + H]^+$ were detected only at very low intensity, if they were detectable at all. However, CID experiments of the above-mentioned predominant *in source*-fragment ions of 3′-*O*-regioisomers provided characteristic daughter ions at m/z 495, 459, and 429, thus indicating the occurrence of a free hydroxyl group at the β-ring as described above. After fragmentation of 3-*O*-regioisomers, the lutein backbone $[M + H - H_2O - \text{fatty acid}]^+$ at m/z 533 was the most abundant ion, followed by product ions at m/z 411 and 477, corresponding to a further lutein-specific fragmentation. In addition, identification of 3′-*O*-regioisomers of lutein monoesters was confirmed by their elution before the respective 3-*O*-isomers as has been previously reported for the RP-C_{30} conditions applied.[17−19]

Identification of Lutein Diesters. Eight compounds (**9**−**17**) present in the isolated fractions III−V (Figure 2) were identified to be lutein diesters due to their characteristic UV−vis absorption spectra identical to that of free lutein (Table 1), their disappearance after saponification, and their characteristic mass spectral behavior.

DOI: 10.1021/acs.jafc.5b01477
J. Agric. Food Chem. 2015, 63, 5061−5071

The first eluting diester (compound **9**) showed a negative ion $[M]^-$ at m/z 1090. The occurrence of the positive *in source*-fragment ions $[M + H - 278 \text{ (linolenic acid)}]^+$ at m/z 813 and $[M + H - 280 \text{ (linoleic acid)}]^+$ at m/z 811 indicated a lutein linolenate-linoleate. Unexpectedly, elucidation of its regioconfiguration was impossible, due to the almost identical intensities of the above-mentioned *in source*-fragments $[M + H - \text{acyl}]^+$. Possibly, this finding may be explained by the coelution of both regioisomers.

Compound **10** exhibited a predominant molecular ion $[M]^-$ at m/z 1092 in APCI(−), whereas APCI(+) produced corresponding *in source*-fragments $[M + H - 280]^+$ at m/z 813 (100%) and $[M + H - 280 - 280]^+$ at m/z 533 (17%). After CID of the ion at m/z 813, a prevailing fragment at m/z 533 confirmed the relationship of both ions. Due to the absence of a second *in source*-fragment $[M + H - \text{fatty acid}]^+$ indicating the loss of a fatty acid other than linoleic acid, compound **10** was identified as a homogeneous diester, namely, lutein dilinoleate.

Due to its $[M]^-$ at m/z 1094 and characteristic *in source*-fragments $[M + H - 282 \text{ (oleic acid)}]^+$ at m/z 815, $[M + H - 280]^+$ at m/z 813, and $[M + H - 282 - 280]^+$ at m/z 533 (Table 1), compound **11** was assigned to lutein 3′-*O*-linoleate-3-*O*-oleate.

Compound **12** revealed a molecular ion $[M]^-$ at m/z 1096. The *in source*-fragments $[M + H - 282]^+$ at m/z 815 allowed its identification as lutein dioleate (**12**), particularly because additional losses of fatty acids other than oleic acid were missing.

A negative molecular ion $[M]^-$ at m/z 1068 was observed for both compounds **13** and **14**, indicating related regioisomers. As described above, the relative ion abundances of the two $[M + H - \text{acyl}]^+$ *in source*-fragments were used for the identification of the regioconfiguration. The occurrence of product ions $[M + H - 256 \text{ (palmitic acid)}]$ at m/z 813 (100%) and $[M + H - 280]^+$ at m/z 789 (4%) identified compound **13** as lutein 3′-*O*-palmitate-3-*O*-linoleate, whereas compound **14** producing ions at m/z 789 (100%) and m/z 813 (8%) occurring at reversed intensity was assigned to lutein 3′-*O*-linoleate-3-*O*-palmitate. By analogy, peaks **15** and **16** were identified as lutein 3′-*O*-palmitate-3-*O*-oleate (**15**) and lutein 3′-*O*-oleate-3-*O*-palmitate (**16**). Compound **17** revealed a molecular ion $[M]^-$ at m/z 1044 as well as a characteristic *in source*-fragment $[M + H - 256]^+$ at m/z 789. Because neutral losses of other fatty acids were not observed, compound **17** was identified as lutein dipalmitate.

In addition to these observations, the CID spectra presented in Table 1 confirmed our proposed structures of compounds **9**−**17**. The identity of the carotenoid core molecule lutein was supported by CID spectra of the respective *in source*-fragments, consisting of a characteristic product ion at m/z 411, which corresponds to the lutein backbone after elimination of one cyclic end group (β- or ε-ring).[33] Furthermore, compounds **10**, **11**, and **14**−**17** revealed a product ion at m/z 477 corresponding to a retro-Diels−Alder fragment of the ε-ring of the lutein backbone. Notably, further fragment ions less important for structure elucidation were observed (data not shown).

Lutein Content and Degree of Esterification in *Triticum* spp. Lutein contents of whole grain flours from 15 genotypes of wheat species comprising bread wheat, durum, spelt, einkorn, and emmer were determined after their cultivation in five different environments, that is, different sites and harvest years. Concentrations of free lutein (compound **1**), total lutein monoesters (fractions I and II, Figure 2), total lutein diesters (fractions III−V), and total lutein (free + esterified) were determined using the whole sample set, whereas concentrations of single lutein esters were determined only in a representative subset of samples (see below).

Table 2 shows the lutein contents and their degree of esterification of the investigated 75 genotypes belonging to 5 species of bread wheat, durum, spelt, einkorn, and emmer. The einkorn genotypes clearly showed the highest total lutein content (total median = 5.65 μg/g DM), followed by the 1.7-fold lower content of durum (3.26 μg/g DM). Spelt (1.53 μg/g DM) and emmer (1.52 μg/g DM) contained comparable amounts, being slightly higher than in bread wheat (1.35 μg/g DM). The highest total lutein contents were found for the einkorn breeding line M-04033/03, consistently over all environments investigated (6.95−8.95 μg/g DM), although not being significantly different from the also lutein-rich einkorn genotypes M-04033/01 (6.75−8.83 μg/g DM) and 8.116/04 (6.92−8.33 μg/g DM). The lutein contents determined in *Triticum* spp. are comparable to previously reported values.[3,14] Similarly, einkorn was previously reported to be the most lutein-rich *Triticum* species.[3,38] Due to its high carotenoid content, the production of pasta may be a promising application of einkorn, because the resulting yellow color is highly desirable. Hence, lutein concentrations up to 0.6 mg/100 g could be reached in vegan pasta, being even higher than in egg pasta (0.5 mg/100 g).[39,40]

The degree of lutein esterification varied strongly among and within species. Interestingly, lutein esters were completely absent in all durum and emmer genotypes. Because durum and emmer are both tetraploid wheat species, the inability to form carotenoid esters may be congenital. However, further investigations may be intricate, because, to the best of our knowledge, the genes and enzymes responsible for carotenoid esterification have not yet been reported. Although the absence of lutein esters in emmer has been reported for the first time, sporadic reports about a few durum genotypes lacking lutein esters are available.[15,23]

With regard to bread wheat, lutein esters were absent in seven genotypes, whereas 22.7−38.3% of total lutein was esterified in the remaining eight genotypes (Table 2). In contrast, all spelt and einkorn genotypes consistently contained lutein esters. However, the degree of esterified lutein in spelt (median = 29.7%) was significantly higher than in einkorn (7.6%). Furthermore, the ratio of mono- to diesters was about 2:1 in spelt. In einkorn, this ratio was even higher, ranging from 7:1 to 20:1, with the einkorn breeding line 8.103/04 being the only exception. The latter contained 48.7−72.6% lutein esters, mainly diesters. A correlation between the amount of esterified lutein and the total lutein content could not be revealed (data not shown).

Notably, the simultaneous occurrence of lutein and its esters in significant amounts, as shown for *Triticum* in the present work, is very unusual. In photosynthetically active tissues, lutein commonly occurs only in its free form, whereas it is predominantly esterified in chromoplasts of diverse fruits or petals.[41]

In previous studies, the occurrence of lutein esters in cereals has been hypothesized to be related to storage conditions such as temperature, humidity, and time.[23,42−44] Because all samples investigated in the presented study were stored under the same conditions and originated from five different environments, we

DOI: 10.1021/acs.jafc.5b01477
J. Agric. Food Chem. 2015, 63, 5061−5071

hypothesize a significant genetic factor to be responsible for the observed differences among genotypes and species.

Genetic Variance and Heritability of Total Lutein Contents. In all five wheat species, a highly significant genetic variance (σ^2_G) was determined for the total lutein content (Table 3). Furthermore, a very high heritability (h^2) exceeding 0.93 was calculated for all wheat species, thus confirming previous studies of tetraploid wheats.[45,46] Accordingly, total lutein contents in einkorn, emmer, spelt, durum, and bread wheat appear to be mainly affected by genetic factors, whereas environmental effects play a minor role. The variability of the total lutein content of individual genotypes is illustrated in Supplemental Tables 2−6, showing comparatively small differences among the different cultivation sites or harvest years. However, over all environments, the same einkorn genotypes revealed the highest total lutein contents (M-04033/03, M-04033/01, and 8.116/04), whereas the bread wheat genotypes Julius and Event consistently showed the lowest lutein contents. The wheat species durum and einkorn both exhibiting the highest average lutein contents also showed the largest genetic variance. Thus, especially in the latter species, a future increase of total lutein content by plant selection efforts seems to be promising.

Table 3. Genetic Variance (σ^2_G), Heritability (h^2), and Least Significant Difference (LSD) of Total Lutein Content across Five Locations, Which Have Been Separately Determined for Each Species

variable	bread wheat	durum wheat	spelt	einkorn	emmer
σ^2_G	0.09*[a]	0.46*	0.06*	0.94*	0.12*
h^2	0.98	0.97	0.93	0.97	0.94
LSD	0.13	0.32	0.19	0.51	0.26

[a]*, significant at the 0.001 probability level.

Quantification of Individual Lutein Esters in Selected Genotypes. Concentrations of individual lutein esters were determined in bread wheat (var. Tabasco), spelt (var. Oberkulmer Rotkorn), and einkorn (var. 8.103/04). As shown in Table 4, all esters so far identified were found in einkorn, which exhibited the highest total ester content of the investigated genotypes (7.7 μg/g DM). The monoesters lutein 3-*O*-oleate (**6**) and lutein 3-*O*-palmitate (**8**), as well as the diesters lutein dioleate (**12**) and lutein 3′-*O*-oleate-3-*O*-palmitate (**16**), could not be detected in bread wheat and spelt. In the latter species, lutein linoleate-linolenate (**9**) and lutein 3′-*O*-palmitate-3-*O*-oleate (**15**) were found only in traces (<LOQ). Lutein dilinoleate was the prevailing ester in all three species, with particularly high concentrations in einkorn (2.637 μg/g DM). This lutein diester seems to be characteristic of cereals, because it has previously been described in bread wheat and tritordeum (×*Tritordeum* Ascherson et Graebener).[19,42] To the best of our knowledge, its occurrence in other plants has not been reported so far.

In agreement with a previous study on lutein regioisomers from tritordeum grains,[19] 3-*O*-regioisomers of lutein monoesters occurred at higher concentrations than their related 3′-*O*-regioisomers, displaying a ratio of about 2:1 in einkorn (Table 4). However, because bread wheat and spelt showed the opposite with lower or even undetectable amounts of 3-*O*-regioisomers, conclusions about preferred regiospecific esterification cannot be drawn. By analogy, this specific einkorn genotype contained 3.8-fold higher diester levels than monoesters, whereas bread wheat and spelt contained almost equal amounts of both forms.

Fatty Acid Composition in Lutein Esters and Total Free Lipids. To reveal putative similarities, the fatty acid pattern of the carotenoid esters was compared to that of total free lipids in wheat after saponification of a limited subset of samples (Table 5). Linoleic acid was the predominant fatty acid

Table 4. Contents of Individual Lutein Esters in Einkorn, Bread Wheat, and Spelt

		content[a] (μg/g DM)		
peak	identity	bread wheat (Tabasco)	spelt (Oberkulmer Rotkorn)	einkorn (8.103/04)
1	(*all-E*)-lutein	0.666 ± 0.018	0.616 ± 0.005	1.551 ± 0.187
2	lutein *Z*-isomer	0.113 ± 0.007	0.057 ± 0.005	0.187 ± 0.013
3	lutein 3′-*O*-linoleate	0.151 ± 0.004	0.132 ± 0.008	0.441 ± 0.010
4	lutein 3-*O*-linoleate	0.103 ± 0.008	0.123 ± 0.017	0.732 ± 0.021
5	lutein 3′-*O*-oleate	0.040 ± 0.002	0.038 ± 0.007	0.062 ± 0.003
6	lutein 3-*O*-oleate	nd[b]	nd	0.122 ± 0.014
7	lutein 3′-*O*-palmitate	0.152 ± 0.009	0.148 ± 0.003	0.086 ± 0.006
8	lutein 3-*O*-palmitate	nd	nd	0.160 ± 0.009
9	lutein linoleate-linolenate	tr[c]	tr	0.365 ± 0.009
10	lutein dilinoleate	0.195 ± 0.002	0.165 ± 0.003	2.637 ± 0.063
11	lutein 3′-*O*-linoleate- 3-*O*-oleate	0.067 ± 0.001	0.068 ± 0.001	1.015 ± 0.025
12	lutein dioleate	nd	nd	0.178 ± 0.014
13	lutein 3′-*O*-palmitate-3-*O*-linoleate	0.174 ± 0.005	0.164 ± 0.005	0.681 ± 0.019
14	lutein 3′-*O*-linoleate-3-*O*-palmitate	0.059 ± 0.004	0.057 ± 0.003	0.772 ± 0.21
15	lutein 3′-*O*-palmitate-3-*O*-oleate	tr	tr	0.162 ± 0.015
16	lutein 3′-*O*-oleate-3-*O*-palmitate	nd	nd	0.112 ± 0.015
17	lutein dipalmitate	0.053 ± 0.003	0.051 ± 0.005	0.202 ± 0.003
	total monoesters	0.446	0.440	1.604
	total diesters	0.550	0.504	6.126
	total lutein esters	0.996	0.945	7.729

[a]Mean ± standard deviation (n = 3). [b]nd, not detectable, ≤LOD. [c]tr, traces, ≥LOD, ≤LOQ.

DOI: 10.1021/acs.jafc.5b01477
J. Agric. Food Chem. 2015, 63, 5061−5071

Table 5. Fatty Acid Composition in the Total Free Lipids of Different Wheat Species and Genotypes

species (genotype)	fatty acid composition[a] (%) palmitic (C 16:0)	stearic (C 18:0)	oleic (C 18:1)	linoleic (C 18:2)	linolenic (C 18:3)	arachidic (C 20:0)	eicosenoic (C 20:1)
bread wheat (Tabasco)	17.68 ± 0.11	0.92 ± 0.01	14.36 ± 0.02	61.57 ± 0.04	4.67 ± 0.05	0.15 ± 0.01	0.65 ± 0.01
durum (Auradur)	13.98 ± 0.12	1.34 ± 0.02	18.72 ± 0.03	58.94 ± 0.12	5.88 ± 0.13	0.21 ± 0.04	0.93 ± 0.02
spelt (Oberkulmer Rotkorn)	15.33 ± 0.32	1.10 ± 0.02	22.98 ± 0.07	55.99 ± 0.20	3.52 ± 0.19	0.17 ± 0.01	0.90 ± 0.05
einkorn (8.103/04)	13.39 ± 0.08	0.85 ± 0.01	29.22 ± 0.08	50.73 ± 0.04	4.15 ± 0.04	0.19 ± 0.01	1.47 ± 0.03
emmer (Ramses)	15.84 ± 0.14	1.19 ± 0.02	21.96 ± 0.08	55.51 ± 0.19	4.44 ± 0.40	0.26 ± 0.02	0.81 ± 0.07

[a]Mean ± standard deviation (n = 2).

(50.7−61.6%) of the total free lipids in all five genotypes investigated. As previously reported,[47,48] palmitic acid was the second most common fatty acid in bread wheat (17.7%), followed by oleic acid (14.4%), whereas it was vice versa in the other four species investigated (13.4−15.8% palmitic and 18.7−29.2% oleic acid). Linolenic acid accounted for 3.5−5.9% of the total fatty acids. Stearic acid, eicosenoic acid, and arachidic acid occurred only in minor amounts. Major fatty acids of the total free lipids were found to be identical with those being esterified with lutein. Figure 3 illustrates the strong correlation (Pearson

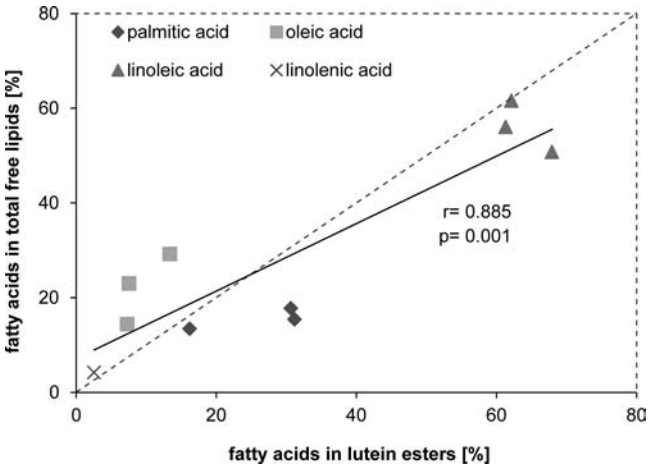

Figure 3. Correlation between the abundance of fatty acids in the total free lipids and of lutein esters.

correlation coefficient r = 0.885, p = 0.001) between the fatty acids present in carotenoid esters and those of total free lipids. As demonstrated by the dashed reference line (slope = 1), the abundance of linoleic and palmitic acid in the lutein esters was significantly higher (61−68 and 16−31%, respectively), that of oleic and linolenic acid being relatively underrepresented (7−13 and 2%, respectively). However, these findings do not yet allow the hypothesis of a highly fatty acid-specific xanthophyll acyltransferase in wheat, as has previously been suggested for tritordeum.[19,23] Briefly, Mellado-Ortega and Hornero-Méndez[19] found palmitic acid to be the most common fatty acid in lutein esters, whereas its relative abundance among the fatty acids of the total free lipids was lower. In addition, oleic acid was found to be present at high concentrations in the total lipids of tritordeum, being absent in its lutein esters. Therefore, they suggested a highly specified enzyme involved in the esterification of lutein.

In our study, the relative amounts of fatty acids being esterified with carotenoids were determined, showing that only up to 0.06% w/w of the total fatty acids in all wheat species was esterified with lutein.

In conclusion, einkorn genotypes showed the highest lutein contents among all genotypes belonging to five *Triticum* species investigated in the present study. The presence of lutein esters was demonstrated to be a characteristic trait of specific genotypes and species, being independent of their total carotenoid content. The absence of lutein esters in tetraploid wheat species (i.e., durum, emmer) was found to be a general trait, which merits further investigation. Genotypes devoid of and being rich in lutein esters may be useful tools for the identification of the yet unknown genes and enzymes responsible for carotenoid esterification. Whether the bioavailabilities of lutein and its esters from wheat differ is yet unknown, although their esterification should impart a highly distinct solubility in dietary lipids and, thus, also different liberation and absorption behaviors from wheat products. In addition, lutein and lutein esters may be deposited in different plastidal substructures, which may further affect their bioavailability.[49,50] Therefore, a nutritional preference of lutein ester-containing sources to those mainly containing free lutein should be based on in vitro and in vivo experiments. Although the lutein contents in vegetables and fruits are by far higher than in wheat (i.e., up to 20-fold higher in spinach or kale than in einkorn),[51] wheat products are generally consumed more frequently and in higher quantities in many countries worldwide. Therefore, wheat and, in particular, the yet underutilized species einkorn and durum should be considered as valuable sources of lutein in the human diet. In addition, manufacture of yellow-tinted vegan wheat products may become feasible without the addition of egg yolk or other colorants by the sole use of einkorn flours.

■ ASSOCIATED CONTENT

Supporting Information

Supplemental Tables 1−7 and Supplemental Figure 1. The Supporting Information is available free of charge on the ACS Publications website at DOI: 10.1021/acs.jafc.5b01477.

■ AUTHOR INFORMATION

Corresponding Author

*(R.M.S.) Phone: +49-(0) 711 459 22995. Fax: +49-(0) 711 459 24110.

Notes

The authors declare no competing financial interest.

■ ACKNOWLEDGMENTS

J.U.Z. is grateful for funding of the present research by the Landesgraduiertenförderung Baden-Württemberg (State Graduate Scholarships).

DOI: 10.1021/acs.jafc.5b01477
J. Agric. Food Chem. 2015, 63, 5061−5071

ABBREVIATIONS USED

amu, atomic mass unit; APCI, atmospheric pressure chemical ionization; CID, collision-induced dissociation; DM, dry matter; FA, fatty acid; FAME, fatty acid methyl ester; FW, fresh weight; LOD, limit of detection; LOQ, limit of quantitation

REFERENCES

(1) Food and Agriculture Organization of the United Nations. *FAO (Database)* 2014; http://faostat3.fao.org/faostat-gateway/go/to/home/E (accessed July 24, 2014).

(2) Fardet, A. New hypotheses for the health-protective mechanisms of whole-grain cereals: what is beyond fibre? *Nutr. Res. Rev.* **2010**, *23*, 65−134.

(3) Abdel-Aal, E.-S. M.; Young, J. C.; Rabalski, I.; Hucl, P.; Fregeau-Reid, J. Identification and quantification of seed carotenoids in selected wheat species. *J. Agric. Food Chem.* **2007**, *55*, 787−794.

(4) Landrum, J. T.; Bone, R. A. Lutein, zeaxanthin, and the macular pigment. *Arch. Biochem. Biophys.* **2001**, *385*, 28−40.

(5) Fullmer, L. A.; Shao, A. The role of lutein in eye health and nutrition. *Cereal Foods World* **2001**, *46*, 408−413.

(6) Johnson, E. J. A possible role for lutein and zeaxanthin in cognitive function in the elderly. *Am. J. Clin. Nutr.* **2012**, *96*, 1161−1165.

(7) Kiko, T.; Nakagawa, K.; Tsuduki, T.; Suzuki, T.; Arai, H.; Miyazawa, T. Significance of lutein in red blood cells of Alzheimer's disease patients. *J. Alzheimer's Dis.* **2012**, *28*, 593−600.

(8) Nolan, J. M.; Loskutova, E.; Howard, A. N.; Moran, R.; Mulcahy, R.; Stack, J.; Bolger, M.; Dennison, J.; Akuffo, K. O.; Owens, N.; Thurnham, D. I.; Beatty, S. Macular pigment, visual function, and macular disease among subjects with alzheimer's disease: An exploratory study. *J. Alzheimer's Dis.* **2014**, *42*, 1191−1202.

(9) Vishwanathan, R.; Kuchan, M. J.; Sen, S.; Johnson, E. J. Lutein and preterm infants with decreased concentrations of brain carotenoids. *J. Pediatr. Gastroenterol. Nutr.* **2014**, *59*, 659−665.

(10) Abdel-Aal, E.-S. M.; Young, J. C.; Akhtar, H.; Rabalski, I. Stability of lutein in wholegrain bakery products naturally high in lutein or fortified with free lutein. *J. Agric. Food Chem.* **2010**, *58*, 10109−10117.

(11) Britton, G.; Khachik, F. Carotenoids in food. In *Carotenoids. Vol. 5: Nutrition and Health*; Britton, G., Liaaen-Jensen, S., Pfander, H., Eds.; Birkhäuser: Basel, Switzerland, 2009; pp 45−66.

(12) Nimalaratne, C.; Lopes-Lutz, D.; Schieber, A.; Wu, J. Effect of domestic cooking methods on egg yolk xanthophylls. *J. Agric. Food Chem.* **2012**, *60*, 12547−12552.

(13) Max Rubner Institut. *Nationale Verzehrsstudie II (NVS II)*, 2008.

(14) Leenhardt, F.; Lyan, B.; Rock, E.; Boussard, A.; Potus, J.; Chanliaud, E.; Remesy, C. Genetic variability of carotenoid concentration, and lipoxygenase and peroxidase activities among cultivated wheat species and bread wheat varieties. *Eur. J. Agron.* **2006**, *25*, 170−176.

(15) Hentschel, V.; Kranl, K.; Hollmann, J.; Lindhauer, M. G.; Böhm, V.; Bitsch, R. Spectrophotometric determination of yellow pigment content and evaluation of carotenoids by high-performance liquid chromatography in durum wheat grain. *J. Agric. Food Chem.* **2002**, *50*, 6663−6668.

(16) Weedon, B.; Moss, G. Structure and nomenclature. In *Carotenoids. Vol. 1A: Isolation and Analysis*; Britton, G., Liaaen-Jensen, S., Pfander, H., Eds.; Birkhäuser: Basel, Switzerland, 1995; pp 27−70.

(17) Breithaupt, D. E.; Wirt, U.; Bamedi, A. Differentiation between lutein monoester regioisomers and detection of lutein diesters from marigold flowers (*Tagetes erecta* L.) and several fruits by liquid chromatography−mass spectrometry. *J. Agric. Food Chem.* **2002**, *50*, 66−70.

(18) Young, J. C.; Abdel-Aal, E.-S. M.; Rabalski, I.; Blackwell, B. A. Identification of synthetic regioisomeric lutein esters and their quantification in a commercial lutein supplement. *J. Agric. Food Chem.* **2007**, *55*, 4965−4972.

(19) Mellado-Ortega, E.; Hornero-Méndez, D. Isolation and identification of lutein esters, including their regioisomers, in tritordeum (×*Tritordeum* Ascherson et Graebner) grains: evidence for a preferential xanthophyll acyltransferase activity. *Food Chem.* **2012**, *135*, 1344−1352.

(20) Lepage, M.; Sims, R. P. A. Carotenoids of wheat flour: their identification and composition. *Cereal Chem.* **1968**, 600−604.

(21) Ziegler, J. U.; Schweiggert, R. M.; Carle, R. A method for the simultaneous extraction and quantitation of lipophilic antioxidants in *Triticum* sp. by HPLC-DAD/FLD-MS^n. *J. Food Compos. Anal.* **2015**, *39*, 94−102.

(22) Burkhardt, S.; Böhm, V. Development of a new method for the complete extraction of carotenoids from cereals with special reference to durum wheat (*Triticum durum* Desf.). *J. Agric. Food Chem.* **2007**, *55*, 8295−8301.

(23) Mellado-Ortega, E.; Hornero-Méndez, D. Carotenoid profiling of *Hordeum chilense* grains: the parental proof for the origin of the high carotenoid content and esterification pattern of tritordeum. *J. Cereal Sci.* **2015**, *62*, 15−21.

(24) Britton, G. UV/visible spectroscopy. In *Carotenoids. Vol. 1B: Spectroscopy*; Britton, G., Liaaen-Jensen, S., Pfander, H., Eds.; Birkhäuser: Basel, Switzerland, 1995; pp 13−62.

(25) ICH. Validation of analytical procedures: test and Methodology Q2(R1), 1994; http://www.ich.org/fileadmin/Public_Web_Site/ICH_Products/Guidelines/Quality/Q2_R1/Step4/Q2_R1__Guideline.pdf (accessed Aug 20, 2013).

(26) Fromm, M.; Bayha, S.; Carle, R.; Kammerer, D. R. Comparison of fatty acid profiles and contents of seed oils recovered from dessert and cider apples and further Rosaceous plants. *Eur. Food Res. Technol.* **2012**, *234*, 1033−1041.

(27) Cochran, W.; Cox, G. *Experimental Designs*; Wiley: New York, 1957.

(28) Stram, D. O.; Jae Won Lee. Variance components testing in the longitudinal mixed effects model. *Biometrics* **1994**, *50*, 1171−1177.

(29) Cullis, B. R.; Smith, A. B.; Coombes, N. E. On the design of early generation variety trials with correlated data. *JABES* **2006**, *11*, 381−393.

(30) Piepho, H.-P.; Möhring, J. Computing heritability and selection response from unbalanced plant breeding trials. *Genetics* **2007**, *177*, 1881−1888.

(31) Gilmour, A.; Gogel, B.; Cullis, B. R.; Thompson, R. *ASReml User Guide, Release 3.0*; VSN International Ltd.: Hemel Hempstead, UK, 2009.

(32) Enzell, C. R.; Francis, G. W.; Liaaen-Jensen, S. Mass spectrometric studies of carotenoids. 2. A survey of fragmentation reactions. *Acta Chem. Scand.* **1969**, *23*, 727−750.

(33) Enzell, C. R.; Back, S. Mass spectrometry. In *Carotenoids. Vol. 1B: Spectroscopy*; Britton, G., Liaaen-Jensen, S., Pfander, H., Eds.; Birkhäuser: Basel, Switzerland, 1995; pp 261−320.

(34) Rivera, S.; Canela-Garayoa, R. Analytical tools for the analysis of carotenoids in diverse materials. *J. Chromatogr., A* **2012**, *1224*, 1−10.

(35) Kopec, R. E.; Schweiggert, R. M.; Riedl, K. M.; Carle, R.; Schwartz, S. J. Comparison of high-performance liquid chromatography/tandem mass spectrometry and high-performance liquid chromatography/photo-diode array detection for the quantitation of carotenoids, retinyl esters, α-tocopherol and phylloquinone in chylomicron-rich fractions of human plasma. *Rapid Commun. Mass Spectrom.* **2013**, *27*, 1393−1402.

(36) Breithaupt, D. E. Identification and quantification of astaxanthin esters in shrimp (*Pandalus borealis*) and in a microalga (*Haematococcus pluvialis*) by liquid chromatography−mass spectrometry using negative ion atmospheric pressure chemical ionization. *J. Agric. Food Chem.* **2004**, *52*, 3870−3875.

(37) Tian, Q.; Duncan, C. J. G.; Schwartz, S. J. Atmospheric pressure chemical ionization mass spectrometry and in-source fragmentation of lutein esters. *J. Mass Spectrom.* **2003**, *38*, 990−995.

DOI: 10.1021/acs.jafc.5b01477
J. Agric. Food Chem. 2015, 63, 5061−5071

(38) Hidalgo, A.; Brandolini, A.; Pompei, C.; Piscozzi, R. Carotenoids and tocols of einkorn wheat (*Triticum monococcum* ssp. *monococcum* L.). *J. Cereal Sci.* **2006**, *44*, 182−193.
(39) Werner, S.; Böhm, V. Bioaccessibility of carotenoids and vitamin e from pasta: evaluation of an in vitro digestion model. *J. Agric. Food Chem.* **2011**, *59*, 1163−1170.
(40) Hidalgo, A.; Brandolini, A.; Pompei, C. Carotenoids evolution during pasta, bread and water biscuit preparation from wheat flours. *Food Chem.* **2010**, *121*, 746−751.
(41) Schweiggert, R. M.; Carle, R. Carotenoid deposition in plant and animal foods and its impact on bioavailability. *Crit. Rev. Food Sci.* **2015**, accepted for publication.
(42) Kaneko, S.; Nagamine, T.; Yamada, T. Esterification of endosperm lutein with fatty acids during the storage of wheat seeds. *Biosci., Biotechnol., Biochem.* **1995**, *59*, 1−4.
(43) Ahmad, F. T.; Asenstorfer, R. E.; Soriano, I. R.; Mares, D. J. Effect of temperature on lutein esterification and lutein stability in wheat grain. *J. Cereal Sci.* **2013**, *58*, 408−413.
(44) Mellado-Ortega, E.; Atienza, S. G.; Hornero-Méndez, D. Carotenoid evolution during postharvest storage of durum wheat (*Triticum turgidum* conv. *durum*) and tritordeum (×*Tritordeum* Ascherson et Graebner) grains. *J. Cereal Sci.* **2015**, *62*, 134−142.
(45) Digesù, A. M.; Platani, C.; Cattivelli, L.; Mangini, G.; Blanco, A. Genetic variability in yellow pigment components in cultivated and wild tetraploid wheats. *J. Cereal Sci.* **2009**, *50*, 210−218.
(46) Patil, R. M.; Oak, M. D.; Tamhankar, S. A.; Sourdille, P.; Rao, V. S. Mapping and validation of a major QTL for yellow pigment content on 7AL in durum wheat (*Triticum turgidum* L. ssp. *durum*). *Mol. Breed.* **2008**, *21*, 485−496.
(47) Hidalgo, A.; Brandolini, A.; Ratti, S. Influence of genetic and environmental factors on selected nutritional traits of *Triticum monococcum*. *J. Agric. Food Chem.* **2009**, *57*, 6342−6348.
(48) Gabrovská, D.; Fiedlerová, V.; Holasová, M.; Mašková, E.; Smrčinov, H.; Rysová, J.; Winterová, R.; Michalová, A.; Hutař, M. The nutritional evaluation of underutilized cereals and buckwheat. *Food Nutr. Bull.* **2002**, *23*, 246−249.
(49) Schweiggert, R. M.; Mezger, D.; Schimpf, F.; Steingass, C. B.; Carle, R. Influence of chromoplast morphology on carotenoid bioaccessibility of carrot, mango, papaya, and tomato. *Food Chem.* **2012**, *135*, 2736−2742.
(50) Schweiggert, R. M.; Kopec, R. E.; Villalobos-Gutierrez, M. G.; Högel, J.; Quesada, S.; Esquivel, P.; Schwartz, S. J.; Carle, R. Carotenoids are more bioavailable from papaya than from tomato and carrot in humans: a randomised cross-over study. *Br. J. Nutr.* **2014**, *111*, 490−498.
(51) Humphries, J. M.; Khachik, F. Distribution of lutein, zeaxanthin, and related geometrical isomers in fruit, vegetables, wheat, and pasta products. *J. Agric. Food Chem.* **2003**, *51*, 1322−1327.

DOI: 10.1021/acs.jafc.5b01477
J. Agric. Food Chem. 2015, 63, 5061−5071

JOURNAL OF AGRICULTURAL AND FOOD CHEMISTRY

Article

pubs.acs.org/JAFC

Structural and Nutritional Properties of Pasta from *Triticum monococcum* and *Triticum durum* Species. A Combined ^{1}H NMR, MRI, and Digestibility Study

Gabriella Pasini,[†] Fulvia Greco,[‡] Mauro A. Cremonini,[§,#] Andrea Brandolini,[∥] Roberto Consonni,[‡] and Maristella Gussoni*[,‡,⊥]

[†]DAFNAE, Dipartimento di Agronomia, Animali, Alimenti, Risorse Naturali ed Ambiente, Università degli Studi di Padova, 35020 Legnaro (PD), Italy

[‡]Laboratorio NMR, Istituto per lo Studio delle Macromolecole, Consiglio Nazionale delle Ricerche, 20133 Milano, Italy

[§]Dipartimento di Scienze degli Alimenti, Università di Bologna, 47023 Cesena, Italy

[∥]Unità per la Selezione dei Cereali e la Valorizzazione delle varietà vegetali, Consiglio per la Ricerca e la Sperimentazione in Agricoltura (CRA-SCV), Via Forlani 3, 26866 S. Angelo Lodigiano (LO), Italy

[⊥]Dipartimento di Fisiopatologia Medico Chirurgica e dei Trapianti, Università degli Studi di Milano, Via F.lli Cervi, 93, 20090 Segrate (MI), Italy

ABSTRACT: The aim of the present study was to characterize the structure of two different types of pasta, namely *Triticum turgidum* ssp. *durum* (cv. Saragolla) and *Triticum monococcum* ssp. *monococcum* (cv. Monlis), under different processing conditions. MRI analysis and NMR spectroscopy (i.e., T_1 and T_2 NMR relaxation times and diffusion parameters) were conducted on pasta, and ^{1}H NMR spectroscopic analysis of the chemical compounds released by pasta samples during the cooking process was performed. In addition, starch digestibility (enzimatically determined) was also investigated. The NMR results indicated that Saragolla pasta has a more compact structure, ascribed to pasta network and in particular to different technological gluten properties, that mainly determine the lower ability of Monlis pasta in binding water. These results correlate well with the lower rate of starch hydrolysis measured for Monlis pasta compared to Saragolla when both are dried at high temperature.

KEYWORDS: *pasta microstructure, MRI, ^{1}H NMR spectroscopy, T_1/T_2 relaxation times, diffusion, in vitro starch digestibility*

INTRODUCTION

Wheat provides a significant amount of carbohydrates and proteins and constitutes a good source of lipids, antioxidants and minerals that, although present in a limited concentration, cover most of the human requirements.[1] Einkorn (*Triticum monococcum* L. ssp. *monococcum*), a diploid hulled wheat with high protein,[2] carotenoids, tocols,[3] and microelements, is a promising candidate for the development of bakery products, baby food and enriched foods.[5,3] In addition, the French-led Protected Geographical Indication[6] in Italy led to the development of a new einkorn variety called Monlis. Monlis is characterized by excellent bread-making aptitude, high tocol and carotenoid content and good yielding ability.

The digestibility of starch products is widely studied due to its positive correlation with the glycemic response in humans. Recently, the European Food Safety Authority, via the Panel on Dietetic Products, Nutrition and Allergies, concluded that high postprandial glycemic responses may be detrimental to human physiology. The panel concluded that slowly digestible starch (SDS) in cereal products, compared to rapidly digestible starch (RDS), has a reduced post-prandial glycemic response.[7] The digestibility of pasta, a very common starchy food, was reported to depend on both intrinsic properties of the wheat ingredients and the processing conditions during extrusion, drying and cooking.[8,9] For example, extrusion leads to the formation of starch−protein and starch−lipid complexes,[10] which decreases digestibility. Similarly, the high-temperature drying process leads to highly aggregated proteins that are cross-linked via covalent bonds and disulfide bridges, thereby also decreasing starch digestibility.[9] Starch gelatinization occurs during cooking, causing swelling of starch granules that in turn leads to an increased enzymatic activity during starch digestion. The efficiency of enzymes also depends on starch hydration[11,12] and limited amylase affinity and catalytic efficiency have been observed in conditions with low water content.[13] Finally, inherent characteristics of the wheat, linked to geographical and botanical origins, play important roles, as these characteristics have been shown to be correlated with starch architecture[11] and metabolic profile.[14]

All of these processes further influence the pasta structure. Nuclear magnetic resonance (NMR) is a widely recognized innovative methodology used in the molecular characterization of food. It is a noninvasive and nondestructive technique capable of probing molecular processes occurring over a wide range of time scales.

Received: November 25, 2014
Revised: April 30, 2015
Accepted: May 5, 2015
Published: May 5, 2015

ACS Publications © 2015 American Chemical Society

DOI: 10.1021/acs.jafc.5b01993
J. Agric. Food Chem. 2015, 63, 5072−5082

High-resolution NMR spectroscopy can be combined with magnetic resonance imaging (MRI) approaches to characterize the molecular structure as well as the state of water in heterogeneous systems as a food matrix. Specific for the MRI technique, image contrast is governed by spatial variation of the NMR parameters. Depending on the imaging protocol, spin−lattice (T_1) and spin−spin (T_2) relaxation times or self-diffusion coefficient (D) maps can be obtained for a defined sample region. For example, the ^{1}H relaxation properties of starch samples exhibit a complex multiexponential behavior and show an increase in the more mobile fractions upon gelatinization.[15,16] The application of NMR was extended to the study of starch in complex systems that contain fat and sucrose in large amount such as cakes,[17] while water diffusion analysis has been applied to pasta,[18] cooked rice,[19] and spaghetti.[20] However, while some information is available on the behavior of durum wheat pasta during digestion,[8] very few data are reported in the literature on einkorn pasta.

The present study aims at investigating the physical, microstructural, and digestibility properties of different types of pasta prepared from *Triticum turgidum* ssp. *durum* (cv. Saragolla) and *Triticum monococcum* ssp. *monococcum* (cv. Monlis) processed at two drying temperatures, 92 and 40 °C. Microstructural characterization was performed by MRI, via analysis of T_1 and T_2 relaxation and diffusion parameters, in combination with NMR T_2 relaxation and free induction decay (FID) analysis. In addition, ^{1}H NMR analysis of the chemical compounds released by cooking pasta was performed. NMR results correlated well with starch digestibility data, enzymatically determined. Finally, the MRI results were confirmed with Environmental Scanning Electron Microscopy (ESEM) images.

MATERIALS AND METHODS

Samples. The kernels of *T. turgidum* L. ssp. *durum* Desf (cv. Saragolla) and *T. monococcum* L. ssp. *monococcum* (cv. Monlis) were harvested from 100 m^2 plots that were cropped in 2008−2009 at Sant'Angelo Lodigiano (Po Plain, Italy) following standard agronomic practices. Before milling, the seeds of Monlis (M) were de-hulled with an Otake FC4S thresher (Satake, Japan); de-hulling was not necessary for the free-threshing durum wheat Saragolla (S). Overnight tempering was performed at 14% moisture for M and at 16% for S. The kernels were milled with a Bona 4RB (Bona, Italy) experimental mill, which separates the flour fraction from bran and germ.

Pasta Preparation. Approximately 4 kg samples of M and S flours were processed into short-cut pasta (macaroni) with a P630VR lab pasta maker (Parmasel, Parma, Italy). Dough mixing, performed under vacuum (−60 kPa), lasted 7 min. The pre-extrusion moisture of the dough was 30% for M and 32% for S; the extrusion was performed under 8000 kPa pressure. Pasta drying was carried out at two different temperatures, specifically low (peak temperature 40 °C, 24 h) and high (peak temperature 92 °C, 4 h), in a dark drying cabinet (Braibanti, Padova, Italy) at a constant 75% relative humidity. Samples of S and M pasta at both drying conditions of 92 and 40 °C were obtained. Hereafter, the different S and M pasta species, dried at 40 and 92 °C will be referred to as S40, S92, M40, and M92, respectively.

Cooking Parameters. Pasta samples were cooked in deionized boiling water at a ratio of 1:10. The "al dente" cooking time was determined by observing the disappearance of the white core of the pasta squeezed between two glass plates, according to the AACC 16−50 method (AOAC, 2000).

Chemical Composition of Cooked Pasta. Protein, starch and ash quantifications were performed in duplicate for all types of pasta cooked at 11 and 15 min. Protein quantification was carried out using the Kjeldahl method, as reported in the official method of analysis 976.05.[21] The total starch content was measured according to method 996.11. Ash content was determined as described in method 923.03.[21]

ESEM Analysis. The microscopic structure of cooked pasta samples was assessed using a TM-1000 Tabletop environmental electronic scanning microscope (Hitachi High-Technology, Tokyo, Japan) at 15 kV accelerating voltage and 28.6 mA emission current. Samples were placed in a metallic support without coating under low vacuum. Images were captured at different magnifications and in triplicate.

^{1}H NMR Relaxation and MRI. Proton NMR T_1 and T_2 relaxation, free induction decay (FID), and MRI experiments were carried out on a Bruker AM 200 WB spectrometer (Bruker, Karlsruhe, Germany) operating at 4.7 T, equipped with a standard microimaging accessory consisting of a ^{1}H tunable probe-head and a gradient drive unit. Orthogonal field gradient coils were capable of achieving gradients up to 150 G·cm^{-1} with a trigger pulse of 5 μs. Each pasta sample (1 g) was boiled in 100 mL of distilled water for 11, 15, or 20 min. For each time point, the sample was drained in a steel colander and, after removing surface water, inserted into a 10 mm NMR tube. The same protocol was applied to pasta samples with an identical mass boiled in 100% D_2O. Three repetitions were performed for each boiling time. T_1, T_2 and diffusion MRI experiments were performed in a single experimental session. T_1 and T_2 weighted images were recorded by employing the standard phase/frequency encoding 2D spin−echo sequence. A spectral width of 33 kHz was employed together with an 11 mm field of view (FOV) and a voxel resolution of 86 × 86 × 1000 μm^3. Selective radiofrequency pulses (1000 Hz bandwidth, Gaussian shaped, truncated at 5% level) were used for slice selection. Other acquisition parameters are reported in the figure captions. T_1-weighted images were recorded by adopting an echo time of 6.07 ms to minimize the T_2 effect. For each experiment, 15 images (number of averages (NE) = 4) were collected, by varying the repetition time (TR) between 0.05 and 60 s. The two equally spaced echo times were systematically varied in the range of 6−80 ms to collect T_2-weighted images with a TR = 20 s to eliminate T_1 artifacts. A total of 15 images (NE = 4) were sequentially collected. Diffusion-weighted images were acquired by adopting a modified STEAM sequence specifically tailored for imaging of biological samples characterized by long T_1 and short T_2 relaxations. Seven images (NE = 4) were recorded: a reference image with Z gradient = 0 T·m^{-1} and six images with the Z-diffusion encoding gradients with little delta (δ) of 3 ms in the 0−340 mT·m^{-1} range separated by a big delta (Δ) of 50 ms. All the images were processed on the O2 Workstation (Silicon Graphics, California) with the Paravision software package (Version 2.6, Bruker).

Proton relaxation times and FID analyses were carried out on identical weighed S92 and M92 samples, boiled for 15 min in H_2O or 100% D_2O. The longitudinal magnetization decay (T_1) was measured by the inversion recovery sequence by adopting the following acquisition parameters: inversion recovery time (2τ) from 50 ms to 10 s, NE = 15, NS = 8, TR = 20s. The transversal magnetization decay (T_2) was measured by the common Hahn spin−echo sequence: echo times from 5 μs to 5 s, NE = 45, NS = 4. The CPMG sequence was also employed: 90° = 9 μs, 180° = 19 μs, 180° interpulse delay = 1.1 ms. The CPMG train was varied between 2 and 80 ms. FIDs were determined with one transient in single channel detection mode, 4096 data points, acquisition time = 0.4096 s, dwell time = 100 μs, TR = 30 s. All experiments were carried out in triplicate at 297 K.

Relaxometric and Diffusion Data Analysis. Two or more circular regions of interest (ROIs) of approximately 2 × 10^6 μm^2 and a ROI on the entire surface were tracked over each T_1, T_2 and diffusion weighed recorded image. The software returned the maps containing the signal intensity values to be used for the calculation of the T_1, T_2 and diffusion parameters. Normalized peak intensities of the Fourier-transformed ^{1}H spectra recorded by using the spin−echo and/or the CPMG pulse sequences were used versus the corresponding time, 2τ, to calculate the T_1 and T_2 relaxation values. All relaxometric data were fitted to a multiexponential function, whose rate constant represented, respectively, the parameters T_1, T_2, and D. The experimental data were fitted using the Maquardt−Levenberg algorithm, implemented by the Sigma Plot (Version 1.02) software (Jandel).

^{1}H NMR Spectroscopy of Boiling Water. Each pasta sample (1 g) was boiled in 100 mL of distilled water for 11 and 15 min. The

DOI: 10.1021/acs.jafc.5b01993
J. Agric. Food Chem. 2015, 63, 5072−5082

boiling water was carefully withdrawn, centrifuged and lyophilized; 15 mg of each sample was then dissolved in phosphate-buffered (pH 7.0) D_2O and inserted into a 5 mm NMR tube (550 μL) for ^{1}H NMR experiments. ^{1}H NMR spectra were recorded on a Bruker DMX 500 spectrometer (Bruker Biospin GmbH Rheinstetten, Karlsruhe, Germany) operating at 11.7 T and equipped with a 5 mm inverse probe and *z*-gradient. All spectra were acquired in triplicate at 300 K. The spectral width was 6500 Hz, and 32K data points were collected using the standard one-dimensional NOESY pulse sequence.[22] We employed a water presaturation scheme with low radiofrequency power during the mixing time (100 ms) and the relaxation delay (1.2 s). An exponential function with a line broadening of 0.3 Hz was applied before Fourier transformation. Processing (phase and spectra baseline correction) was performed with TOPSPIN software (Bruker Biospin). Integrals were normalized to sodium 3-trimethylsilyl propionate (TSP) as a reference.

***In Vitro* Starch Digestion.** Starch digestion of each pasta type was performed *in vitro* following 11 and 15 min of cooking time, modifying the method of Kim et al.[23] Briefly, cooked pasta was minced to mimic the oral food breakdown. Approximately 1 g of minced sample was put into glass vials, each representing a single point of starch digestion. The extent of digestion was assessed at five time points (0, 20, 60, 120, and 150 min). All samples were subjected to a 30 min incubation with pepsin (pepsin from hog stomach, 3348 U·mL^{-1}, Fluka; enzyme:protein ratio 1:30, pH 2.5) to simulate the gastric phase. Afterward, the pH was adjusted to 7.2 and 4 mL of (10 mg·mL^{-1}) pancreatic amylase (Megazyme, Ireland) was added to perform starch digestion. Samples were incubated at 37 °C while being shaken at 170 rpm for 20, 120, and 150 min. The digestion reaction was stopped by ethanol addition. The samples were then centrifuged at 5000 rpm for 10 min at 8 °C and supernatants diluted to 100 mL with 100 mM sodium acetate buffer (pH 4.5). A 100 μL aliquot was treated with 10 μL of amyloglucosidase (300 U·mL^{-1}) and incubated at 50 °C for 20 min. Subsequently, 3 mL of glucose oxidase/peroxidase (Megazyme, Ireland) was added, and the samples were incubated for an additional 20 min at 50 °C prior to absorbance detection. The glucose released during digestion was quantified as hydrolyzed starch during the amount of time elapsed, multiplying the absorbance by 0.9. From this value, the rapidly digestible starch (RDS) content was estimated.[24] The experiments were performed in triplicate.

Statistical Analysis. Statistical analysis for relaxation and diffusion data was performed by the Prism program Version 4 (GraphPad Software Inc., La Jolla, CA, USA) and the Sigma Plot software (Jandel). The results were compared by one-way analysis of variance (ANOVA). Tukey-Kramer multiple comparison test was used to determine significant differences between samples. $P < 0.05$ was accepted as the level for statistical significance.

RESULTS AND DISCUSSION

Chemical Composition of Cooked Pasta. Chemical and nutritional compositions of M and S pasta samples dried at 40 and 92 °C after 11 and 15 min cooking times were determined, and the results are reported in Table 1. In all tested conditions, S and M samples exhibited significantly different ($p < 0.001$) protein contents, which was not affected by the cooking time. The total starch in cooked pasta was quantified and the results suggest that for S pasta starch content increased significantly ($P < 0.001$) with cooking time. Although a significantly higher ($p < 0.001$) ash content was found in S (mean value of all S samples = 0.60%) compared to M (mean = 0.29%), both these figures fall into the typical range for plain flour.

ESEM Analysis. ESEM experiments were carried out for all pasta samples. Representative results from M92 and S92 are displayed in Figure 1. A different structural matrix for the two pasta types: S (Figure 1A) and M (Figure 1B) at each processing phase can be observed. Dried S (a) and M (b) both showed the presence of partially gelatinized starch. It is well known that the gelatinization process during pasta preparation (in particular, during kneading−extrusion and drying) can cause a transition of the starch structure from crystalline to amorphous.[25] This phenomenon was more evident at the high drying temperature (92 °C) and in S (a) compared to M (b). The different matrix characteristics were preserved after cooking. At 11 min, in S pasta, some defects were apparent, as observed by the big inhomogeneity in the matrix (see arrow, (c)). These defects were probably introduced during the mixing and/or forming steps and can be ascribed to not completely hydrated and mixed dough and/or to the extrusion process. The relevance of structuring of pasta components at each processing step has been widely reported in the literature.[26] Release of starch degradation products was found to be slower in pasta than in other cereal products mainly due to pasta compact structure resulting from the extrusion process.[27] The relationship between mixing time and structural homogeneity, in relation to fine gluten structure formation was investigated as well.[28] In the present study in-homogeneities partially disappeared with overcooking, giving rise to holes endowed with a regular roundish shape of lower dimension (not shown). Moreover, at 11 min the compact structure of the kneading matrix displayed a cluster-like structure of durum wheat as well as swollen but not disrupted starch granules embedded on a protein matrix. These features show up in the cross section ESEM image displayed in e). In contrast, several cracks were easily detectable on the external surface of the M92 pasta sample (d) as well as in the cross section image (f) most likely due to the lower technological gluten properties. At 15 min, integral starch granules were localized in the internal matrix and were clearly observable in S (g). Zones of gelatinized starch filaments and fibrils close to the cracks were detectable in M (h), suggesting microstructural changes of the inner layer.

Table 1. Chemical and Nutritional Compositions of Monlis (M) and Saragolla (S) Pasta Types, Dried at 40 and 92 °C, at Cooking Times of 11 and 15 min[a]

sample	protein (%)	ash (%)	total starch (%)	rapidly digestible starch (RDS) (%)
		Cooking Time = 11 min		
M92	15.22 $^{b,c,d\#}$ (±0.02)	0.25 $^{b,c,d\#}$ (±0.02)	72.69 $^{b,c\#}$ (±0.68)	28.27 $^{b\#,A\#}$ (±1.30)
S92	14.43 $^{a,c\#}$ (±0.05)	0.55 $^{a,c,d\#,B*}$ (±0.04)	71.09 $^{a,c\#,d*}$ (±0.13)	36.41 $^{a,c,d\#}$ (±0.39)
M40	15.11 $^{a*b,d\#}$ (±0.06)	0.36 $^{a,b,d\#,C*}$ (±0.01)	74.23 $^{a,b,d\#}$ (±0.38)	30.79 $^{b\#,C\#}$ (±2.77)
S40	14.45 $^{a,c\#,D*}$ (±0.03)	0.67 $^{a,b,c\#,D\#}$ (±0.01)	72.15 $^{b*,c\#}$ (±0.25)	30.22 $^{b\#,C\#}$ (±0.21)
		Cooking Time = 15 min		
M92	15.22 $^{b,c,d\#}$ (±0.02)	0.26 $^{b,d\#,c*}$ (±0.01)	73.39 $^{b\#}$ (±0.08)	33.08 $^{b,c\#}$ (±0.01)
S92	14.49 $^{a,c\#}$ (±0.01)	0.65 $^{a,c\#,d*}$ (±0.01)	72.11 $^{a,c\#,B\#}$ (±0.55)	36.52 $^{a,c\#}$ (±1.70)
M40	15.12$^{a,b,d\#}$ (±0.05)	0.32 $^{a*,b,d\#}$ (±0.02)	74.11 $^{b,d\#}$ (±0.54)	36.00 $^{a\#}$ (±1.10)
S40	14.52 $^{a,c\#}$ (±0.03)	0.54 $^{a,c\#,b*}$ (±0.07)	72.83 $^{c\#,D*}$ (±0.23)	34.98 (±1.60)

[a]Standard deviations are given in parentheses. Different lowercase letters (a, b, c, d) indicate significant differences of the types of pasta within each boiling time. Different capital letters (A, B, C, D) indicate significant differences of the same type of pasta at the different boiling times. Symbols: $^*P < 0.05$, $^\#P < 0.001$.

DOI: 10.1021/acs.jafc.5b01993
J. Agric. Food Chem. 2015, 63, 5072−5082

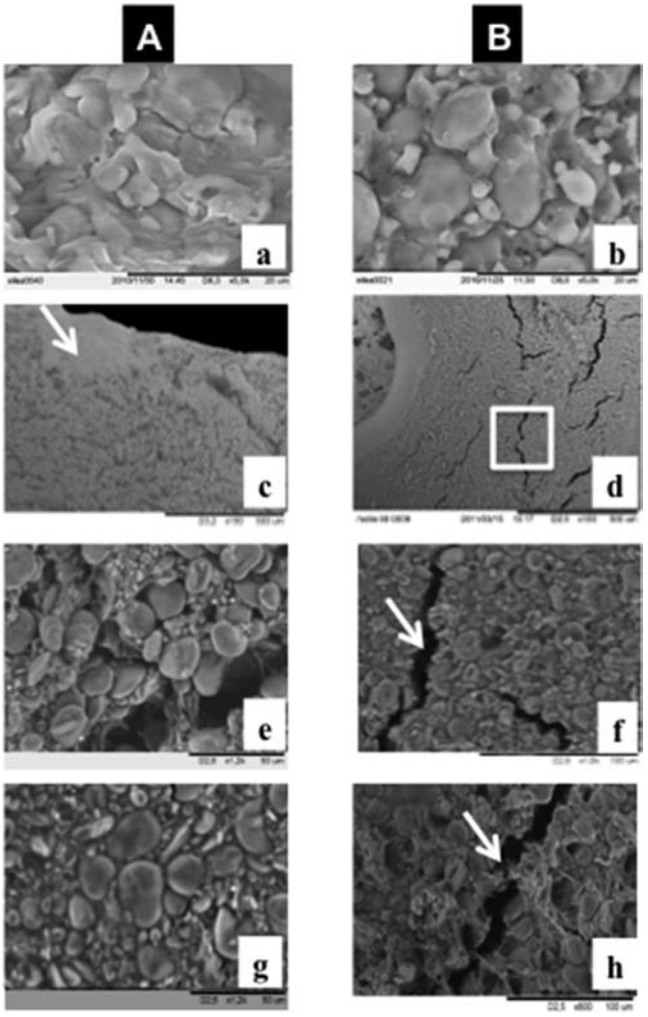

Figure 1. Coupled ESEM images of (A) S92 and (B) M92 pasta samples. S92 (a) and M92 (b) dried pasta sections, scale bar 20 μm. For 11 min cooking: surface sections of S92 (c) and M92 (d), scale bar 500 μm. A big inhomogeneity is shown in (c) (see arrow); gelatinized cracks are visible in (d) (see square). Cross sections of S92 (e), scale bar 50 μm, and M92 (f), scale bar 100 μm. For 15 min cooking: cross sections of S92 (g), scale bar 50 μm, and M92 (h), scale bar 100 μm. Internal cracks are shown (see arrows).

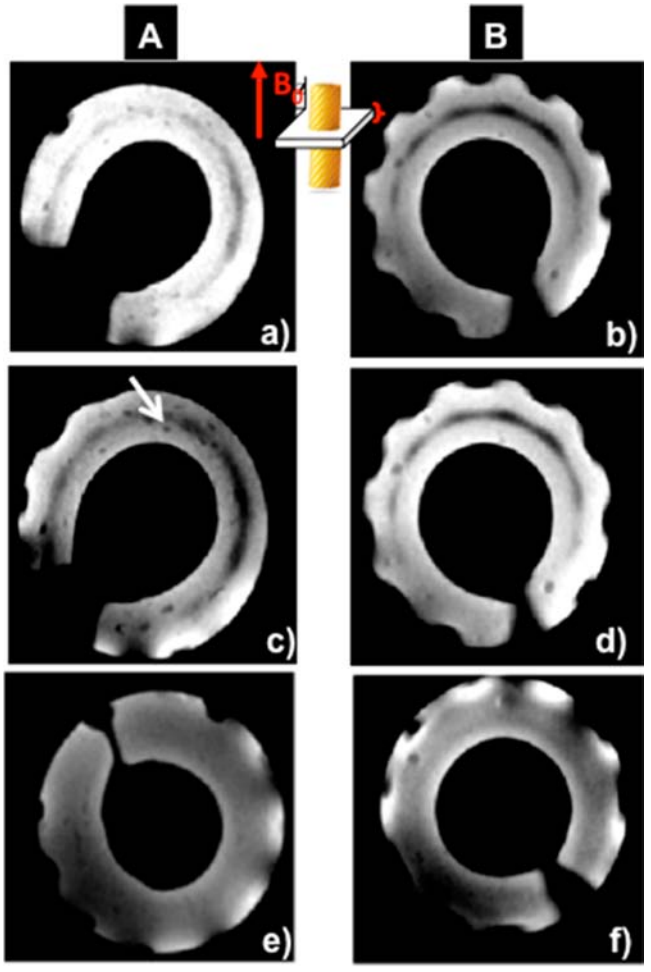

Figure 2. Coupled MRI transversal *xy* spin echo images of (A) S92 and (B) M92 pasta samples. The sketch shows the *xy* imaging plane cutting the pasta sample that is orthogonally placed in the NMR tube. All images were recorded with 128 × 128 matrix, FOV = 11 mm × 11 mm, voxel resolution = 86 × 86 × 1000 μm^3, NE = 4, RG = 4, and are displayed at the same gray levels for comparison. For 11 min cooking: S92 (a) and M92 (b) T_1 (TR = 1s) weighed images. A central dark region, ascribable to the "al dente" texture, is visible in both the images. S92 (c) and M92 (d) T_2 (TR = 10 ms) weighed images. A magnification of the defects attributed to the processing phases is shown (indicated by the arrow in (c)). For 15 min cooking: S92 (e) and M92 (f) T_1 weighed image (TR = 1s). The central dark region due to the pasta matrix not being uniformly cooked disappeared with overcooking.

MRI Analysis. Figure 2 shows T_1- and T_2-weighted *xy* transversal spin−echo MRI images collected from S92 (A) and M92 (B) pasta samples after 11 and 15 min of cooking. At 11 min, a central dark region throughout the whole sample was observable in the T_1-weighted images of both S92 (a) and M92 (b) pasta samples, ascribable to the so-called "al dente" pasta texture, namely to regions that were not completely cooked. In addition, in-homogeneities were present in the T_2-weighted image displayed in (c) (see arrow) and (d) and were ascribed to processing dough defects that were also observed by ESEM (Figure 1). A dimension of about 400 μm was estimated from Figure 1c, which should also be detectable by the MRI technique. A more homogeneous pasta reticulate, with an increased signal-to-noise ratio (SNR) could be observed by lengthening the cooking time to 15 min in S92 (e) and M92 (f). It is clear from both the images that there was disappearance of the central dark region observed at 11 min. As observed in ESEM images, inhomogeneities changed their shape and reduced with overcooking at dimensions below MRI resolution.

T_1 MRI Relaxation. The T_1 mean data values (±SD) and signal percentages for the different pasta types (11, 15, and 20 min) are reported in Table 2. T_1 magnetization decay resulted in a single exponential for all pasta types at 11 min, with significantly shorter values for S pasta compared to M pasta ($P < 0.05$), suggesting, even after short cooking time, S pasta network endowed with a greater rigidity than M. All pasta types resulted in significantly different T_1 values ($P < 0.05$) on the basis of Tukey's multiple comparison test. In particular, M92 exhibited the longest T_1 value and the greatest variability (SD). This latter could be ascribed to the presence of not uniformly cooked pasta regions as highlighted also by the T_1- and T_2-weighted images (see Figure 2). At 15 min, two relaxation

DOI: 10.1021/acs.jafc.5b01993
J. Agric. Food Chem. 2015, 63, 5072−5082

Table 2. Proton Longitudinal Relaxation Time Values (T_1, in s) and Signal Percentages of Monlis (M) and Saragolla (S) Pasta Types, Dried at 40 and 92 °C and at Cooking Times of 11, 15, and 20 min[a]

		sample			
cooking time (min)		M92	M40	S92	S40
11		1.02 $^{d*,B\#}$	0.91 $^{d*B\#}$	0.85 $^{B\#}$	0.76 $^{a,b*,B\#}$
		(±0.13)	(±0.09)	(±0.07)	(±0.04)
		100%	100%	100%	100%
15	short	0.76 $^{b\#,d*,A\#}$	0.47 $^{a,c\#,d*,A\#}$	0.71 $^{b\#,A\#}$	0.63 $^{b,a*,A\#}$
		(±0.04)	(±0.02)	(±0.05)	(±0.08)
	long	1.50 $^{D\#}$	1.61	1.23 $^{D\#}$	1.27 $^{D\#}$
		(±0.56)	(±0.58)	(±0.24)	(±0.52)
		82.56%	67.78%	15.75%	81.70%
		(±10.0)	(±28.2)	(±1.78)	(±19.6)
20	short	1.28 ^{b,d*}		1.03 ^{a*}	0.97 ^{a*}
		(±0.12)		(±0.19)	(±0.04)
	long	2.43 $^{C\#}$	1.33	2.74 $^{C\#}$	1.99 $^{C\#}$
		(±0.56)	(±0.20)	(±0.74)	(±0.03)
		52.44%	100%	30.13%	18.22%
		(±7.22)		(±4.30)	(±8.19)

[a]Standard deviations are given in parentheses. Different lowercase letters (a, b, c, d) indicate significant differences of the types of pasta within each boiling time. Different capital letters (A, B, C, D) indicate significant differences of the same type of pasta at the different boiling times. Symbols: $^{*}P < 0.05$, $^{\#}P < 0.001$.

components could be identified for all pasta types: a short component (significantly shorter than at 11 min, $p < 0.001$) and a long component with different signal percentages (approximately 70−80% in M and 15% in S92). Both short and long components of T_1 values lengthened after 20 min of cooking, with the short component of S92 being significantly shorter ($P < 0.05$) than M92. Upon lengthening the cooking time, the S92 pasta type maintained its compact network.

In heterogeneous systems, relaxation is affected by the interior structure as a result of water-macromolecules interaction. Therefore, not only translation and rotation of water molecules affect relaxation, but also a diffusive and chemical exchange process between water molecules and biopolymers strongly contributes to relaxation values. Starch, the most abundant biopolymer in pasta systems, together with proteins, plays an important role in these processes.[29] As a consequence relative populations of the components cannot necessarily be taken as accurately reflecting the number of spin in a particular environment.[30] Only under the slow diffusion limit ($a^2\Delta R_2/D \ll 1$, where a is the size of the environment and $R_2 = 1/T_2$) NMR signals will be characterized by several components signature of different local environments, each with its own relaxation time.[31] Multiexponential relaxation behavior for water has been consistently reported in starch−water systems because of slow diffusive exchange and this regimen is also suggested by combining ESEM (30 μm for granule size) and diffusion (in the order of 10^{-10}) results in the current study. The distribution and dynamic state of water, following swelling and gelatinization, was previously studied in rice starch granules.[32] By the analysis of the longitudinal magnetization decay curve during the swelling process the authors identified two components, and the short T_1 value was ascribed to water−starch interaction. After gelatinization, only one T_1 value associated with water in the gel state was observed. A similar trend could be identified in the present study by the T_1 analysis (Table 2). Two components were identified even when the cooking time was extended to 20 min, with the exception of M40 whose relaxation was fitted to a single exponential. Indeed, we hypothesize that, upon lengthening the cooking time, the pasta matrix mobility can be enhanced by an increase in the gelatinization processes, thereby causing a progressive passage from a inhomogeneous network toward a more uniform carbohydrate gel phase. However, gelatinization appeared to take place to a greater extent in M pasta type, generally showing a longer T_1 relaxation value and particularly in M40 after 20 min of cooking. The different behavior of M, compared to S, might be ascribed to the different protein reticulate and, at the same time, this feature might be at the basis of a greater accessibility of starch granules to the enzymatic attack in M compared to S (see below).

MRI Diffusion. At 11 min, for all types of pasta, water diffusion resulted in a single exponential. A significantly higher ($p < 0.05$) diffusion value for M40 with respect to S pasta type was calculated (Table 3). In contrast, two components could be identified at 15 min, with the short component of M92 reaching a D value close to free water (2.22×10^{-9} m·s^{-2}, $r^2 = 0.98$). Both M92 short and long components attained significantly higher values with respect to S92 ($P < 0.05$), suggesting greater translational mobility. The diffusion data at 20 min resulted in a single exponential with D values far from those found for pure water and significantly lower ($P < 0.05$) than the short components calculated at 15 min.

T_1 relaxation and diffusion parameters indicated that the S pasta endowed a more compact structure than M pasta at all cooking times. The different components identified might be related to the starch gelatinization process occurring during cooking.

As pointed out, gelatinization, by far the most common and impactful transformation in starch (pasting, baking), results from the input of heat in the presence of water. Water enters the granule and plasticizes the amorphous component of the starch. The lengthening of the cooking time is known to cause an increase in the degree of gelatinization through swelling of starch granules and rupture and ultimately produces the gel

DOI: 10.1021/acs.jafc.5b01993
J. Agric. Food Chem. 2015, 63, 5072−5082

Table 3. Water Diffusion Data (D, in $\times 10$ $m^2 \cdot s^{-1}$) and Signal Percentages of Monlis (M) and Saragolla (S) Pasta Types, Dried at 40 and 92 °C at Cooking Times of 11, 15, and 20 min[a]

cooking time (min)		sample M92	M40	S92	S40
11		3.51 $^{B\#}$	4.51 $^{d,c*,B\#}$	3.07 $^{b*,B\#}$	3.00 $^{b*,B\#}$
		(±0.70)	(±0.49)	(±0.88)	(±0.19)
		100%	100%	100%	100%
15	short	17 $^{b,c,d*,A\#}$	7.48 $^{a*,A\#}$	8.08 $^{a*,A\#}$	9.08 $^{a*,A\#}$
		(±5.56)	(±1.77)	(±1.33)	(±1.14)
		21.10%	11.89%	36.95%	20.54%
	long	3.53 $^{c,d*,D\#}$	3.21 $^{D\#}$	2.56 $^{a*,D\#}$	2.55 $^{a*,D\#}$
		(±0.02)	(±0.05)	(±0.04)	(±0.03)
		78.89%	88.10%	63.04%	79.45%
		(±0.03)	(±0.06)	(±0.08)	(±0.14)
20		4.16 $^{d*,C\#}$	4.46 $^{d*,C\#}$	4.31 $^{d*,C\#}$	5.80 $^{a,b,c*,C\#}$
		(±0.03)	(±0.03)	(±0.01)	(±0.09)
		100%	100%	100%	100%

[a]Standard deviations are given in parentheses. Different lowercase letters (a, b, c, d) indicate significant differences of the types of pasta within each boiling time. Different capital letters (A, B, C, D) indicate significant differences of the same type of pasta at different boiling times. Symbols: $^*P < 0.05$, $^\#P < 0.001$.

state. To observe the starch through the complete process of gelatinization, the cooking time for the pasta was extended up to 20 min, well beyond the usually adopted cooking time. Indeed, the gelatinization process is strongly affected by many parameters, including botanical species, source, presence and amount of solutes (such as sugars) that lead to changes in many functional properties such as viscosity, solubility and digestibility. At the same time, functional changes are expected to be determined by structural modifications of the pasta network that can be monitored by MRI, throughout an estimation of rotational (T_1) and translational (D) mobility, mainly of water. The enhanced rotational and translational mobility of water, probed by T_1 relaxation and diffusion data, indicated a greater network mobility of M compared to S, taking into account exchange effects. In other words, the constituents of M (protein bodies, filaments, and fibrils) are less effective at restricting water movement. Water mobility significantly increased at 15 min, while further differences were not observed at 20 min. This result suggests similar interactions between water and macromolecules at 15 and 20 min but not unrestricted diffusion, which would be observed if there was complete disruption of the starch granule. In fact, self-diffusion constants (D) were in the order of 10^{-10} $m^2 \cdot s^{-1}$, significantly slower than that of free water. At the same time, the root-mean-square distance in one-dimensional diffusion, $(2D\Delta)^{1/2}$ was approximately 6−7 μm. This distance is considerably below the mean granule size of approximately 30 μm calculated by ESEM analysis (Figure 1e,g), thus confining diffusion pathway within the granule. On the other hand, if the internal granule structure was ruptured by gelatinization, water would display diffusion parameters similar to those in a normal three-dimensional pathway. We can therefore conclude that hindered diffusion within the starch gels takes place as a consequence of incomplete gelatinization.

T_2 Relaxation Analysis. Different from longitudinal relaxation, transverse relaxation is sensitive to dipole−dipole interactions. Thus, T_2-weighted images are effective at highlighting sample inhomogeneities (Figure 2c,d). However, even if image contrast clearly pointed to the presence of regions endowed with different mobility, all T_2 decays calculated from MRI data were fitted to a single exponential. The calculated T_2 values (13−20 ms range, data not shown) lengthened when the cooking time increased but were shorter than bulk water, therefore reflecting the interactions between water and macromolecules. It is well known that water molecules with a near isotropic motion are characterized by a T_1/T_2 ratio value near unity and T_2 values that are low compared to those of bulk

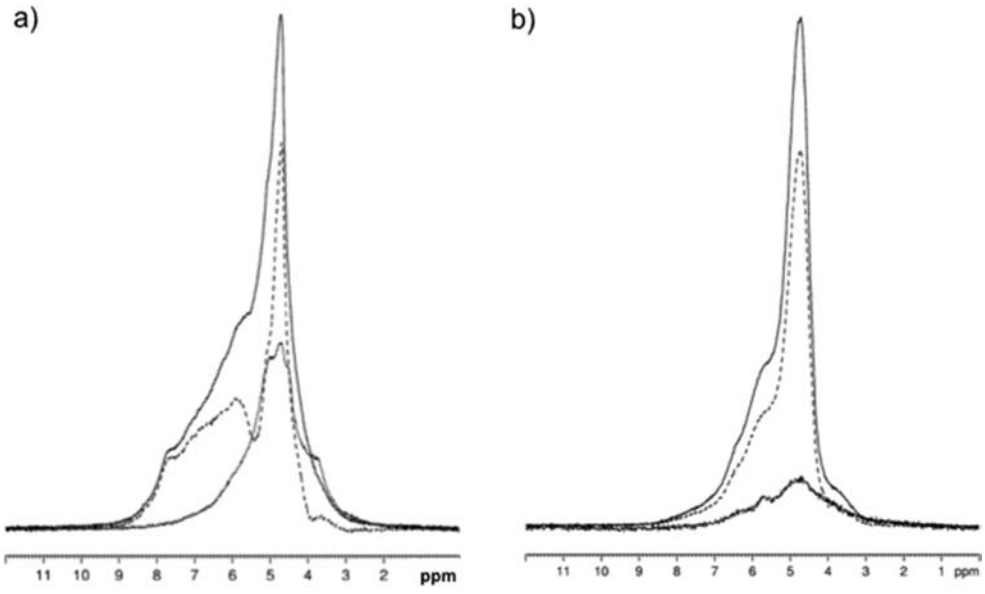

Figure 3. 200 MHz ^{1}H NMR 1D spectra recorded from identically weighing S92 (a) and M92 (b) pasta samples cooked for 15 min in H_2O (continuous line) and D_2O (dotted line). The calculated difference spectra are also displayed (dashed line).

DOI: 10.1021/acs.jafc.5b01993
J. Agric. Food Chem. 2015, 63, 5072−5082

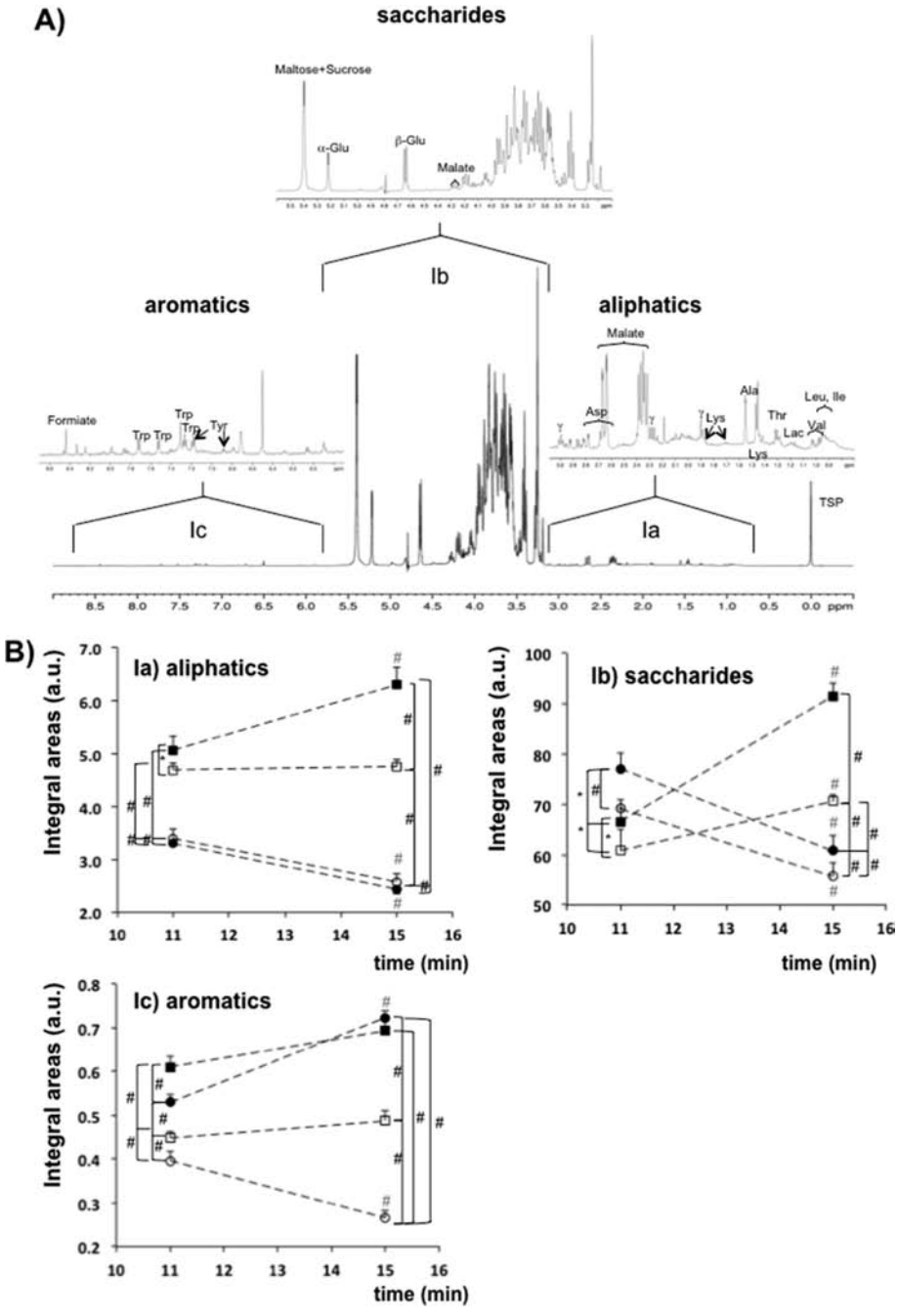

Figure 4. (A) 500 MHz 1D ^{1}H NMR spectrum recorded from the cooking water of a S92 sample at 15 min of cooking time. The integrated spectral regions are shown into brackets: Ia, aliphatics (1−3 ppm); Ib, saccharides (3−5.6 ppm); and Ic, aromatics (5.8−8 ppm). The regions are zoomed-in in the insets with labeling of the main assigned compounds. (B) Plots of the integral areas (arbitrary units) versus the cooking time (11−15 min) of the three integrated spectral regions (Ia−Ic): M92 (■), M40 (□), S92 (●), and S40 (○). Results are expressed as mean ± SD. Significant differences of types of pasta at the same cooking time are indicated by brackets; significant differences at different cooking times are displayed in gray. Symbols: $^*P < 0.05$, $^\#P < 0.001$. Dotted straight lines are drawn to guide the eye.

water were ascribed to an interaction of water molecules with starch.[32] In the present study, the T_2 values calculated from T_2-weighted images reflected the presence of a water-biopolymer interactions, mainly by starch. Unfortunately, the echo time adopted by the spin−echo MRI method (TE = 6.07 ms) prevented the determination of fast T_2 relaxation mechanisms. Therefore, the relaxation mechanism was further investigated by spectroscopic analysis. The dynamics were monitored on a short time scale (10−1000 μs) using the spin−echo sequence and on a longer time scale (2−80 ms) using the CPMG pulse sequence. The study focused on S92 and M92 samples at 15 min of cooking time. Two main relaxation time components resulted from the spin−echo analysis; the long component (M92, 26.35 ± 6.15 ms; S92, 20.19 ± 3.95 ms) with a greater percentage signal (approximately 80%) in both pasta types. By contrast, the short component (M92, 6.00 ± 0.7 ms; S92, 1.99 ± 0.99 ms) was significantly shorter for S92 ($P < 0.01$), thereby suggesting a more rigid structure for this latter. Intriguingly, although one might expect the solid part of the FID of the spin−echo decay to have a significant Gaussian component, all

DOI: 10.1021/acs.jafc.5b01993
J. Agric. Food Chem. 2015, 63, 5072−5082

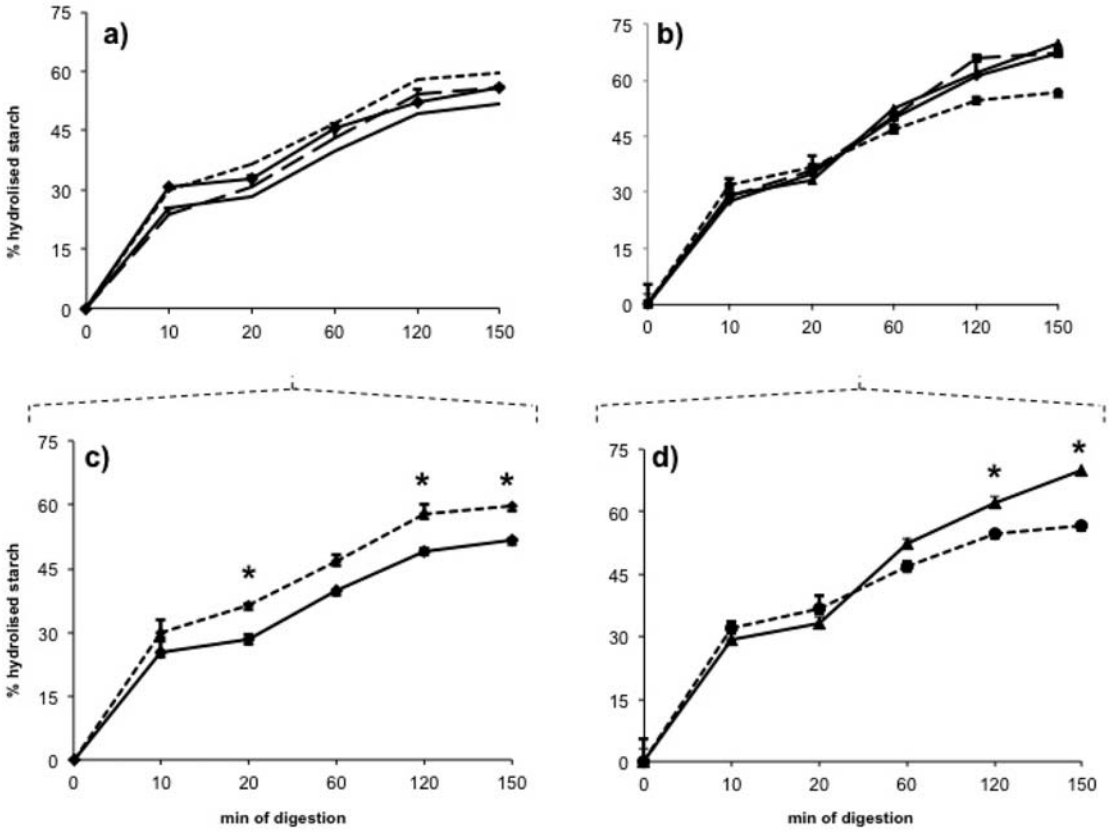

Figure 5. (a) Digestion curves of M92 (▲), S92 (●), M40 (■), and S40 (◆) samples after 11 min of cooking time. Abscissa: 0 (no digestion), 10, 20, 60, 120, and 150 indicate the time points of digestion (in min; mean of triplicate analysis for each time point). (b) Digestion curves of the four species of pasta at 15 min (mean of triplicate analysis ± SD). Abscissa and symbols as in (a). (c) Zoom-in of the starch digestibility curves, to better enhance the differences, of the S92 and M92 samples shown in (a); significant differences ($p < 0.05$) at time points 20, 120, and 150 min. (d) Zoom-in of the starch digestibility curves of S92 and M92 shown in (b); significant differences ($p < 0.05$) at time points 120 and 150 min.

data were well represented as a biexponential decay with no evidence of a solid-like dipolar component, independently of the cooking time, in agreement with the results obtained by Tang et al. on fully swollen native potato starch granules at 295 K.[33]

Pasta is an extremely complex matrix. It includes carbohydrates, proteins and fiber elements that cannot be analyzed individually. Therefore, the structural network as a whole was further investigated by the comparison of the FIDs recorded from M92 and S92 pasta samples of identical weight cooked for 15 min in either H_2O or D_2O (100%). After D_2O exchange, the NMR signal of pasta samples mainly originates from the nonexchanging protons, i.e., those of CH groups involved in the H-bonded network that will contribute to the rigid component of the decay.

Figure 3 shows the 1D ^{1}H NMR spectra from S92 (a) and M92 (b) samples in H_2O (continuous line) and D_2O (dotted line) and the difference spectra (dashed line) The spectral signals of these latter originate from water and exchangeable protons mainly starch, and in a lower amount from proteins (see Table 1), while a contribution of fats could be almost excluded, due to the absence of the wheat germ in both pasta types. A dry matter percentage of 92.33 ± 0.001 and 93.25 ± 0.001% was calculated for raw M92 and S92, respectively, while measuring the sample weight at both the end of cooking and raw a ratio of 2.69 ± 0.08 and 2.28 ± 0.09 on dry basis for S92 and M92 was calculated. Based on these data, from the normalized spectral areas, the amount of water and mobile protons was calculated as 58 ± 0.5 and 41 ± 0.7% of the cooked weight on dry basis for M92 and S92 respectively. The results enabled us to conclude that, during the cooking process, water is absorbed by starch of both pasta types in the same way. However, this water is then distributed in the pasta matrix differently, essentially owing to the lower ability of M92 matrix in binding water and this was ascribed to the lower technological gluten properties of M92 pasta, with respect to S92 type.

^{1}H NMR Spectroscopy of Cooking Water. The pasta–water interaction was also elucidated by high-resolution ^{1}H NMR spectroscopy. Data were acquired from samples of the water in which the pasta was boiled (11 and 15 min) to identify and quantify the chemical compounds released by the different types of pasta that were calculated from the spectra via integral areas.

Figure 4A shows the ^{1}H NMR spectrum recorded from a S92 cooked water sample at 15 min. The resonance assignments of the main signals were made with an internal database of standard compounds and by the aid of two-dimensional experiments (TOCSY and HSQC). All samples were found to contain the same chemical compounds: amino and organic acids (malate and formate) and saccharides (α- and β-glucose, sucrose, and maltose). However, these components were in different amounts depending on the duration of the cooking time. The plots of the calculated integrals are displayed in Figure 4B. A clear separation of M with respect to S species could be observed in both aliphatic (organic and amino acids)

DOI: 10.1021/acs.jafc.5b01993
J. Agric. Food Chem. 2015, 63, 5072−5082

region (a): M showed a greater amount of released compounds than S, independent of the drying temperature and cooking time. An opposite trend was observed for M and S pasta as concerns saccharides, whose release, between 11 and 15 min, was found to significantly ($P < 0.001$) increase and decrease, respectively. The behavior of the compounds investigated by NMR spectroscopy (i.e., amino acids, saccharides, and low-molecular-weight molecules released in water during the cooking process) can be viewed as complementary to that involved in the digestibility analysis, where the chemical components retained in the pasta matrix (i.e., those not released into the water during the cooking process) contribute to the measurement. Demonstrating this phenomenon, when increasing the duration of the cooking time, M92 was found to release the most compounds into the cooking water, in agreement with the more mobile matrix that was suggested with relaxation and diffusion data (Tables 2 and 3).

In conclusion, our results enabled us to establish a correlation between matrix structures and low-molecular-weight compounds released into water while boiling (i.e., water-soluble compounds). Our data suggest a greater release of compounds from matrices with higher mobility, as observed for M. Accordingly, a lower tendency to release compounds with a longer cooking time was found for S, which is inherently poorer in proteins and exhibited significantly shorter values for T_1 (Tables 1 and 2).

Starch Digestibility Analysis. The effect of cooking time on S and M pasta both low and high temperature dried on starch digestibility was assessed. Starch digestibility was measured by detecting saccharides released during *in vitro* starch digestion. Figure 5a shows the kinetics of starch hydrolysis (digestion curves) for the four pasta types cooked for 11 min. The trend of starch hydrolysis appeared to be similar for each sample. However, M92 pasta seemed to be less digested than the analogous durum (S92), as shown by the lower hydrolyzed starch value at each time point (Figure 5c). Specifically, a significant difference between the two curves was observed at 20 min of starch digestion ($P < 0.05$), corresponding to the rapidly digestible starch (RDS) fraction. This fraction is nutritionally important because it correlates with high postprandial blood glucose levels. The presence of higher amounts of readily digestible sugars and starches contributes to a high glycemic index.[7]

The degree of starch hydrolysis of pasta cooked for 15 min (Figure 5b) increased for M92, M40, and S40 compared to pasta cooked for 11 min. However, no significant differences ($P > 0.05$) were detected during the first 20 min of digestion, suggesting that RDS did not increase as a consequence of increasing the duration of the cooking time. Nevertheless, a significant difference between M92 and S92 pasta (Figure 5d) at 120 and 150 min was detected. In particular, the digestibility did not change for S92 between 120 and 150 min of digestion, as shown by the hydrolyzed starch values at these time points. These results suggest that starch hydrolysis was likely not enhanced from overcooking, but more likely that there was a synergic effect of the high temperature drying process and the presence of the strong protein network.[9] As a result, there was a delay in the accessibility of amylolitic enzymes to the starch. On the other hand, the starch hydrolysis drastically increased between 120 and 150 min of digestion in M92 pasta. NMR data in general suggested a less compact structure of M with respect to S. In particular, as already pointed out, M and S saccharide release showed an opposite trend at 11 versus 15 min.

These results are in agreement with the NMR, MRI and ESEM analyses where an increase in the cooking time corresponded to a rise in starch gelatinization of the inner part of M pasta (Figure 1h). By contrast, ESEM analysis did not show relevant differences of the internal microstructure in S pasta (Figure 1e), suggesting that starch gelatinization was limited. Additionally, NMR data suggested a reduced water mobility of S92 with respect to M92 pasta, mainly ascribable to the different ability of the gluten proteins to bind water (see Figure 3). At the same time, diffusion data suggested that water movement was restricted to the inner part of the starch granule.

Currently, durum wheat semolina is the preferred ingredient for the production of high quality pasta due to its color, flavor and cooking quality. Its structure is complex, with starch granules incorporated in a protein matrix. In particular, it is believed that gluten protein aids in the formation of network surrounding the starch granules, thereby acting as a barrier to starch digestion.[34] This can explain why S92 pasta was not more susceptible to amylolitic digestion at a prolonged cooking time. ESEM analysis also confirmed this result, showing that at 15 min of cooking, starch granules were partially gelatinized and entrapped in the protein network (Figure 1g). MRI analysis also indicated that S pasta is endowed with a more packed structure ascribable to the protein reticulate; M pasta was characterized by water with greater rotational and translational mobility. In addition, this is the reason that for M92, starch hydrolysis increased with increasing incubation time with digestive enzymes, while this was not observed for S92. Water availability in the food matrix is important for amylase activity: the more the water diffuses into the system, the higher is the catalytic efficiency.[13]

Analysis of the cooking water by NMR spectroscopy showed that a higher release of compounds into the water was found from the network with higher mobility. With respect to S, at 11 min, M pasta demonstrated a high leakage of aliphatic compounds from the pasta matrix, while the leakage of polysaccharides required at least 15 min, in agreement with the starch digestibility data. The present study highlighted significant differences in starch digestion of pasta made with *T. monococcum* (cv. Monlis), compared to the commonly used durum wheat (cv. Saragolla) dried at 92 °C cooked to "al dente" texture. These results suggest a synergic effect between wheat genotype and processing. As reported in the literature, drying is essential for maintaining the pasta structure, especially during overcooking. The protein network of LT (55 °C) dried and then cooked pasta was found partially disrupted. On the contrary, the protein network was found preserved after VHT (100 °C) together with a lower extent of starch swelling.[35] High drying levels could play an effect on microstructure by enhancing protein cross-link thereby highlighting the protective role played by proteins, limiting water absorption by granules.[36] In agreement with literature data, in this study, NMR relaxation and diffusion results suggested a considerable effect of drying temperature mainly with overcooking as well. Moreover the release of compounds in the aliphatic region (Figure 4B) differed significantly ($p < 0.001$) for M and S pasta species at both 11 and 15 min cooking times.

NMR analysis suggested that S pasta has a more compact structure, ascribable to different network properties. More generally, this study demonstrates that investigating the food structure aids to understand its behavior during gastro-intestinal digestion. For this purpose, we propose NMR, in conjunction with enzymatic digestibility methods as valid methodologies for

DOI: 10.1021/acs.jafc.5b01993
J. Agric. Food Chem. 2015, 63, 5072−5082

estimating how starch may behave during cooking and subsequently during its degradation in the human body.

AUTHOR INFORMATION

Corresponding Author

*E-mail: maristella.gussoni@unimi.it. Phone: ++39 02 23699723. Fax: ++39 02 2369961.

Present Address

#M.A.C.: Agilent Technologies Italia, 20063 Milano, Italy

Funding

The study was partially supported by Progetto AGER, grant no. 2010-0278.

Notes

The authors declare no competing financial interest.

ABBREVIATIONS USED

MRI, magnetic resonance imaging; ESEM, environmental scanning electron microscopy; NMR, nuclear magnetic resonance; T_1, spin−lattice relaxation time; T_2, spin−spin relaxation time; ROI, region of interest; TE, echo time; D, diffusion; FID, free induction decay; AQ, acquisition time; RG, receiver gain; M, Monlis; S, Saragolla; RDS, rapidly digestible starch; LT, low temperature; VHT, very high temperature

REFERENCES

(1) Hemery, Y.; Xavier, R.; Lullien-Pellerin, V.; Barron, C.; Abecassis, J. Dry processes to develop wheat fractions and products with enhanced nutritional quality. *J. Cereal Sci.* **2007**, *46*, 327−347.

(2) Borghi, B.; Castagna, R.; Corbellini, M.; Heun, M.; Salamini, F. Breadmaking Quality of Einkorn Wheat (*Triticum monococcum* ssp. *monococcum*). *Cereal Chem.* **1996**, *73*, 208−214.

(3) Hidalgo, A.; Brandolini, A.; Pompei, C.; Piscozzi, R. Carotenoids and tocols of einkorn wheat (Triticum monococcum ssp. monococcum L.). *J. Cereal Sci.* **2006**, *44*, 182−193.

(4) Erba, D.; Hidalgo, A.; Bresciani, J.; Brandolini, A. Environmental and genotypic influences on trace element and mineral concentrations in whole meal flour of einkorn (Triticum monococcum L. subsp. monococcum). *J. Cereal Sci.* **2011**, *54*, 250−254.

(5) Corbellini, M.; Empilli, S.; Vaccino, P.; Brandolini, A.; Borghi, B.; Heun, M.; Salamini, S. Einkorn Characterization for Bread and Cookie Production in Relation to Protein Subunit Composition. *Cereal Chem.* **1999**, *76*, 727−733.

(6) EC. Commission Regulation (EC) No 418/2009 of 20 May 2009 entering a name in the register of protected designations of origin and protected geographical indications . *Off. J. Eur. Union* **2009**, *52*, L 125.

(7) EFSA. Panel on Dietetic Products, Nutrition and Allergies (NDA). *EFSA J.* **2011**, *9*, 2292.

(8) De Zorzi, M.; Curioni, A.; Simonato, B.; Giannattasio, M.; Pasini, G. Effect of pasta drying temperature on gastrointestinal digestibility and allergenicity of durum wheat proteins. *Food Chem.* **2007**, *104*, 353−363.

(9) Petitot, M.; Brossard, C.; Barron, C.; Larré, C.; Morel, M. H.; Micard, V. Modification of pasta structure induced by high drying temperatures. Effects on in vitro digestibility on protein and starch fractions on the potential allergenicity of protein hydrolysates. *Food Chem.* **2009**, *116*, 401−412.

(10) Singh, J.; Dartois, A.; Kaur, L. Starch digestibility in food matrix: a review. *Trends Food Sci. Technol.* **2010**, *21*, 168−180.

(11) Dona, A. C.; Pages, G.; Gilbert, R. G.; Kuchel, P. W. Digestion of starch: In vivo and in vitro kinetic models used to characterise oligosaccharide or glucose release. *Carbohydr. Polym.* **2010**, *80*, 599−617.

(12) Miyazawa, T.; Ohtsu, S.; Nakagawa, Y.; Funazukuri, T. Solvothermal treatment of starch for the production of glucose and maltooligosaccharides. *J. Mater. Sci.* **2006**, *41*, 1489−1494.

(13) Roder, N.; Gerard, C.; Verel, A.; Bogracheva, T.; Hedley, C. Factors affecting the action of α-amylase on wheat starch: Effects of water availability. An enzymic and structural study. *Food Chem.* **2009**, *113*, 471−478.

(14) Lamanna, R.; Cattivelli, L.; Miglietta, M. L.; Troccoli, A. Geographical origin of durum wheat studied by ^{1}H-NMR profiling. *Magn. Reson. Chem.* **2011**, *49*, 1−5.

(15) Chatakanonda, P.; Chinachoti, P.; Sriroth, K.; Piyachomkwan, K.; Chotineeranat, S.; Tang, H. R.; Hills, B. The influence of time and conditions of harvest on the functional behaviour of cassava starch-a proton NMR relaxation study. *Carbohydr. Polym.* **2003**, *53*, 233−240.

(16) Tang, H. R.; Godward, J.; Hills, B. The distribution of water in native starch granules-a multinuclear NMR study. *Carbohydr. Polym.* **2000**, *43*, 375−387.

(17) Le Grand, F.; Cambert, M.; Mariette, F. NMR Signal Analysis To Characterize Solid, Aqueous, and Lipid Phases in Baked Cakes. *J. Agric. Food Chem.* **2007**, *55*, 10947−10952.

(18) Hills, B. P.; Babonneau, F.; Quantin, V. M.; Gaudet, F.; Belton, P. S. Radial NMR Microimaging Studies of the Rehydration of Extruded Pasta. *J. Food Eng.* **1996**, *27*, 71−86.

(19) Frías, J. M.; Foucat, L.; Bimbenet, J. J.; Bonazzi, C. Modeling of moisture profiles in paddy rice during drying mapped with magnetic resonance imaging. *Chem. Eng. J.* **2002**, *86*, 173−178.

(20) Horigane, A. K.; Naito, S.; Kurimoto, M.; Irie, K.; Yamada, M.; Motoi, H.; Yoshida, M. Moisture Distribution and Diffusion in Cooked Spaghetti Studied by NMR Imaging and Diffusion Model. *Cereal Chem.* **2006**, *83*, 235−242.

(21) *Official Methods of Analysis of AOAC International*, 17th ed.; Horwitz, W., Ed.; AOAC: Washington, DC, 2000.

(22) Nicholson, J. K.; Foxall, P. J. D.; Spraul, M.; Farrant, R. D.; Lindon, J. C. 750 MHz 1H and 1H-13C NMR Spectroscopy of Human Blood Plasma. *Anal. Chem.* **1995**, *67*, 793−811.

(23) Kim, E. H. J.; Petrie, J. R.; Motoi, L.; Morgenstern, M. P.; Sutton, K. H.; Mishra, S.; Simmons, L. D. Effect of Structural and Physico-Chemical Characteristics of the Protein Matrix in Pasta on in Vitro Starch Digestibility. *Food Biophys.* **2008**, *3*, 229−234.

(24) Englyst, H. N.; Kingman, S. M.; Cummings, J. H. Classification and Measurement of Nutritionally Important Starch Fractions. *Eur. J. Clin. Nutr.* **1992**, *46*, S33−S50.

(25) Zweifel, C.; Conde-Petit, B.; Escher, F. Thermal Modifications of Starch During High-Temperature Drying of Pasta. *Cereal Chem.* **2000**, *77*, 645−651.

(26) Petitot, M.; Abecassis, J.; Micard, V. Structuring of pasta components during processing: impact on starch and protein digestibility and allergenicity. *Trends in Food Sci. Technol.* **2009**, *20*, 521−532.

(27) Tudorica, C. M.; Kuri, V.; Brennan, C. S. Nutritional and Physicochemical Characteristics of Dietary Fiber Enriched Pasta. *J. Agric. Food Chem.* **2002**, *50*, 347−356.

(28) Peighambardoust, S. H.; Dadpour, M. R.; Dokouhaki, M. Application of epifluorescence light microscopy (EFLM) to study the microstructure of wheat dough: a comparison with confocal scanning laser microscopy (CSLM) technique. *J. Cereal Sci.* **2010**, *51*, 21−27.

(29) Hills, B. P.; Wright, K. M.; Belton, P. S. Proton N.M.R. studies of chemical and diffusive exchange in carbohydrate systems. *Mol. Phys.* **1989**, *67*, 1309−1326.

(30) Belton, P. S.; Ratcliffe, R. G. NMR and compartmentation in biological tissues. *Prog. NMR Spectrosc.* **1985**, *17*, 241−79.

(31) Mariette, F. Investigations of food colloids by NMR and MRI. *Curr. Opin. Colloid Interface Sci.* **2009**, *14*, 203−211.

(32) Ritota, M.; Gianferri, R.; Bucci, R.; Brosio, E. Proton NMR relaxation study of swelling and gelatinisation process in rice starch-water samples. *Food Chem.* **2008**, *110*, 14−22.

(33) Tang, H. R.; Brun, A.; Hills, B. A proton NMR relaxation study of the gelatinisation and acid hydrolysis of native potato starch. *Carbohydr. Polym.* **2001**, *46*, 7−18.

(34) Aravind, N.; Sission, M.; Fellows, C. Can variation in durum wheat pasta protein and starch composition affect in vitro starch hydrolysis? *Food Chem.* **2011**, *124*, 816−821.

DOI: 10.1021/acs.jafc.5b01993
J. Agric. Food Chem. 2015, 63, 5072−5082

(35) Zweifel, C.; Handschin, S.; Escher, F.; Conde-Petit, B. Thermal modifications of starch during high-temperature drying of pasta. *Cereal Chem.* **2003**, *80*, 159−167.
(36) Colonna, P.; Barry, J. L.; Cloarec, D.; Bornet, F.; Gouilloud, S.; Galmiche, J. P. Enzymic susceptibility of starch from pasta. *J. Cereal Sci.* **1990**, *11*, 59−70.

DOI: 10.1021/acs.jafc.5b01993
J. Agric. Food Chem. 2015, 63, 5072−5082

JOURNAL OF AGRICULTURAL AND FOOD CHEMISTRY

Article

pubs.acs.org/JAFC

Structure Elucidation, Relative LC−MS Response and In Vitro Toxicity of Azaspiracids 7−10 Isolated from Mussels (*Mytilus edulis*)

Jane Kilcoyne,*[,†,‡] Michael J. Twiner,[§] Pearse McCarron,[⊥] Sheila Crain,[⊥] Sabrina D. Giddings,[⊥] Barry Foley,[‡] Frode Rise,[∥] Philipp Hess,[▽] Alistair L. Wilkins,[○] and Christopher O. Miles[○,#]

[†]Marine Institute, Rinville, Oranmore, County Galway, Ireland

[‡]School of Chemical and Pharmaceutical Sciences, Dublin Institute of Technology, Kevin Street, Dublin 8, Ireland

[§]School of Medicine, Wayne State University, Detroit, Michigan 48202, United States

[⊥]Measurement Science and Standards, Biotoxin Metrology, National Research Council Canada, 1411 Oxford Street, Halifax, Nova Scotia B3H 3Z1, Canada

[∥]Department of Chemistry, University of Oslo, N-0315 Oslo, Norway

[▽]Ifremer, Laboratoire Phycotoxines, Rue de l'Ile d'Yeu, 44311 Nantes, France

[○]Norwegian Veterinary Institute, P.O. Box 750 Sentrum, 0106 Oslo Norway

[#]Department of Pharmaceutical Chemistry, School of Pharmacy, University of Oslo, P.O. Box 1068 Blindern, N-0316 Oslo Norway

Supporting Information

ABSTRACT: Azaspiracids (AZAs) are marine biotoxins produced by dinoflagellates that can accumulate in shellfish, which if consumed can lead to poisoning events. AZA7−10, **7**−**10**, were isolated from shellfish and their structures, previously proposed on the basis of only LC−MS/MS data, were confirmed by NMR spectroscopy. Purified AZA4−6, **4**−**6**, and **7**−**10** were accurately quantitated by qNMR and used to assay cytotoxicity with Jurkat T lymphocyte cells for the first time. LC−MS(MS) molar response studies performed using isocratic and gradient elution in both selected ion monitoring and selected reaction monitoring modes showed that responses for the analogues ranged from 0.3 to 1.2 relative to AZA1, **1**. All AZA analogues tested were cytotoxic to Jurkat T lymphocyte cells in a time- and concentration-dependent manner; however, there were distinct differences in their EC_{50} values, with the potencies for each analogue being: AZA6 > AZA8 > AZA1 > AZA4 ≈ AZA9 > AZA5 ≈ AZA10. This data contributes to the understanding of the structure−activity relationships of AZAs.

KEYWORDS: *azaspiracid, structure confirmation, LC−MS molar response, NMR, mass spectrometry, purification, Jurkat T, toxicity*

INTRODUCTION

The consumption of shellfish contaminated with azaspiracids (AZAs) leads to the syndrome azaspiracid poisoning (AZP).[1] Poisoning incidents associated with this toxin group have been reported in Europe and in the United States.[2,3] In these cases, the source of the implicated shellfish was Ireland, where the levels and number of AZA occurrences have been most problematic.[4] AZAs have been reported to produce "neurotoxin-like" symptoms via intraperitoneal injection in mice, with death in 20−90 min.[5] Oral administration was found to produce clinical disease that was dose- and time-dependent, in addition to damaging the intestinal organs.[6−9] AZA1, **1**, (Figure 1) is a K^+ channel blocker[10] and is highly cytotoxic to multiple cell types, which undergo atypical apoptosis after exposure.[11]

AZAs were first identified in the late 1990s, and since then, more than 30 analogues have been observed in shellfish,[12] phytoplankton,[13−15] crabs,[16] and a marine sponge.[17] Only **1**; AZA2, **2**; and AZA3, **3** (Figure 1), are currently regulated in raw shellfish.[18] Compounds **1** and **2** are produced by the dinoflagellate *Azadinium spinosum*,[13] whereas many of the other analogues are shellfish metabolites.[19,20] Compounds **1**;[21] **2**; **3**;[22] AZA4, **4**; AZA5, **5**;[23] and AZA6, **6**,[24] have been isolated and their structures elucidated through a combination of NMR spectroscopy and chemical reactions. More recently, 37-*epi*-**1** was isolated from shellfish extracts and found to differ structurally from **1** with respect to the orientation of the methyl group at C-37 and to be 5-fold more toxic than **1** using the Jurkat T lymphocyte cell assay.[25]

LC−MS analysis revealed the presence of hitherto unknown AZAs in the dinoflagellates *Amphidoma languida*,[13] *Azadinium poporum*[14] and *Azadinium spinosum*.[15] The AZAs identified in *A. spinosum*, subsequently named AZA33 and -34, were found to be the same structurally at the amine end of the molecule (C-21−40) compared with **1**, producing the characteristic *m*/*z* 362 fragment during LC−MS/MS analysis.[15] AZAs from *A. poporum* (AZA36 and −37), on the other hand, differ by the lack of a methyl or methylene group in the I-ring, resulting in an equivalent fragment with *m*/*z* 348.[9] The AZAs (with molecular masses of 815 and 829 Da) detected in the *A. languida* also displayed fragment ions with *m*/*z* 348, suggesting that these compounds also may lack a methyl or methylene group in the I-ring.[14]

Received: March 16, 2015
Revised: April 22, 2015
Accepted: April 24, 2015
Published: April 24, 2015

ACS Publications © 2015 American Chemical Society

DOI: 10.1021/acs.jafc.5b01320
J. Agric. Food Chem. 2015, 63, 5083−5091

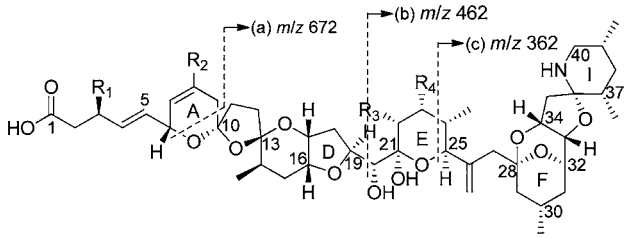

	R_1 (C-3)	R_2 (C-8)	R_3 (C-22)	R_4 (C-23)	$[M+H]^+$ *m/z*	Origin	Status
AZA1 (**1**)	H	H	CH_3	H	842.5	*A. spinosum*	phycotoxin
AZA2 (**2**)	H	CH_3	CH_3	H	856.5	*A. spinosum*	phycotoxin
AZA3 (**3**)	H	H	H	H	828.5	shellfish	metabolite
AZA4 (**4**)	OH	H	H	H	844.5	shellfish	metabolite
AZA5 (**5**)	H	H	H	OH	844.5	shellfish	metabolite
AZA6 (**6**)	H	CH_3	H	H	842.5	shellfish	metabolite
AZA7 (**7**)	OH	H	CH_3	H	858.5	shellfish	metabolite
AZA8 (**8**)	H	H	CH_3	OH	858.5	shellfish	metabolite
AZA9 (**9**)	OH	CH_3	H	H	858.5	shellfish	metabolite
AZA10 (**10**)	H	CH_3	H	OH	858.5	shellfish	metabolite

Figure 1. Structures of **1**−**10**, their protonated masses, and origin. The *m*/*z* values of the fragments are for **1**; corresponding fragments were observed for **2**−**10**.

To protect shellfish consumers while at the same time avoiding unnecessary closures of shellfish farms, more information is required about the type and toxity of AZAs found in shellfish and how to quantitate them. Here, we describe the isolation of **4**, **5** and for the first time AZA7, **7**; AZA8, **8**; AZA9, **9**; and AZA10, **10** (Figure 1), from shellfish, with confirmation by NMR of the structures previously postulated on the basis of LC−MS/MS. Relative molar response studies using mass spectrometry were performed following the preparation of reference standards, which had concentrations assigned using quantitative NMR (qNMR). The toxicity of **4**−**10** was assessed using the Jurkat T lymphocyte cell assay and the results used to discern structure−activity relationships (SARs).

MATERIALS AND METHODS

Chemicals. All solvents (pesticide analysis grade) were from Labscan (Dublin, Ireland) and Caledon (Georgetown, Ontario, Canada). Distilled H_2O was further purified using a Barnstead nanopure diamond UV purification system (Thermo Scientific, Waltham, MA). Sodium chloride (99+%), triethylamine (99%), ammonium acetate (97+%), ammonium formate (reagent grade), formic acid (>98%), silica gel (10−40 μm, type H), sodium chloride (99+%), sodium periodate, Trace CERT caffeine, and CD_3OD (100.0 atom % D) were from Sigma−Aldrich (Steinheim, Germany). Sephadex LH-20 was from GE Healthcare (Uppsala, Sweden), LiChroprep RP C8 (25−40 μm) was from Merck (Darmstadt, Germany), Luna Phenyl-Hexyl (15 μm) was from Phenomenex (Cheshire, UK), CD_3OH (99.5 atom % D) for qNMR was from Cambridge Isotope Laboratories (Tewksbury, MA). AZA certified reference materials (CRMs) were obtained from the National Research Council (Halifax, NS, Canada).

Isolation and Purification of 4−10. The isolation procedure was described previously.[24] Final purification of AZAs was achieved by semi-preparative chromatography on a model 1200 instrument (Agilent Technologies, Santa Clara, CA) with photodiode array detection (210 nm) using a 250 mm × 4.6 mm i.d., 5 μm, Cosmosil C18 column (Nacalai tesque, Kyoto, Japan) eluted with CH_3CN/H_2O (1:1, plus 2 mM ammonium acetate) at 1 mL/min. The column temperature was 30 °C. Because of the presence of co-eluting compounds, two additional semipreparative steps using CH_3CN/H_2O (0.8:1, plus 2 mM ammonium acetate) were required to attain sufficient purity for NMR. Purified AZAs were recovered by diluting the fractions with H_2O (to 20% CH_3CN), loading onto solid-phase extraction cartridges (Oasis HLB, 200 mg), washing with $MeOH/H_2O$ (1:9, 10 mL) to remove the buffer, and eluting with $MeOH/H_2O$ (9:1, 20 mL). Removal of solvent by evaporation in vacuo afforded purified AZAs as white solids.

Accurate reference standards of the purified AZAs were prepared by diluting the qNMR stock solutions in high-purity degassed MeOH. The concentrations of the working solutions were ∼1 μM for all analogues.

Periodate Cleavage. Dilutions (∼100 ng/mL) of purified **1**−**10** in MeOH were used. To 100 μL of each sample was added 50 μL of 0.2 M sodium periodate solution, and the reactions were analyzed immediately by LC−MS (method B), including traces at *m*/*z* 448.4 (for the **7** oxidation product), *m*/*z* 464.4 (for the **8** oxidation product), *m*/*z* 434.4 (for the **9** oxidation product), and at *m*/*z* 450.4 (for the **10** oxidation product).

Mass Spectrometry. *Method A.* Recoveries were determined by quantitative analysis of fractions on a model 2695 LC instrument (Waters, Manchester, UK) coupled to a triple-stage quadrupole (TSQ) Ultima instrument (Micromass, Manchester, UK) operated in selected reaction monitoring (SRM) mode for the following transitions: *m*/*z* 842.5 → 824.5/362.3 (**1** and **6**); *m*/*z* 856.5 → 838.5/362.3 (**2**); *m*/*z* 828.5 → 810.5/362.3 (**3**); *m*/*z* 844.5 → 826.5/362.3 (**4** and **5**), and *m*/*z* 858.5→ 840.5/362.3 (**7**−**10**). The cone voltage was 60 V; collision energy was 50 V; the cone and desolvation gas flows were set at 100 and 800 L/h, respectively; and the source temperature was 150 °C.

Binary gradient elution was used, with phase A consisting of H_2O and phase B of CH_3CN (95%) in H_2O (both containing 2 mM ammonium formate and 50 mM formic acid). The column used was a 50 mm × 2.1 mm i.d., 3 μm, Hypersil BDS C8 column with a 10 mm × 2.1 mm i.d. guard column of the same stationary phase (Thermo Scientific, Waltham, MA). The gradient was from 30% to 90% B over 8 min at 0.25 mL/min, held for 5 min, then held at 100% B at 0.4 mL/min for 5 min, before returning to the initial for equilibration. The

DOI: 10.1021/acs.jafc.5b01320
J. Agric. Food Chem. 2015, 63, 5083−5091

Table 1. NMR Assignments for 4, 5, and 7−10 in CD_3OH

	4		5		7		8		9		10	
position	^{13}C	^{1}H	^{13}C	^{1}H	^{13}C	^{1}H	^{13}C	^{1}H	^{13}C	^{1}H	^{13}C	^{1}H
1	179.9		181.7		179.7		181.6		179.9		181.5	
2	45.3	2.32, 2.36	38.5	2.23, 2.23	45.3	2.32, 2.36	38.5	2.23, 2.23	45.2	2.32, 2.36	38.6	2.22, 2.22
3	70.4	4.42	30.4	2.32, 2.32	70.5	4.43	30.4	2.33, 2.33	70.5	4.42	30.4	2.32, 2.32
4	135.0	5.77	133.9	5.75	135.0	5.77	133.9	5.75	134.7	5.75	133.6	5.72
5	130.5	5.67	130.6	5.43	130.5	5.68	130.6	5.43	131.0	5.65	131.0	5.40
6	71.8	4.86	72.5	4.79	71.8	4.86	72.5	4.79	72.0	4.79	72.7	4.72
7	129.0	5.67	129.4	5.64	129.0	5.66	129.5	5.64	122.6	5.37	123.1	5.34
8	123.4	5.74	123.2	5.73	123.4	5.74	123.2	5.72	131.2		131.0	
9	35.8	2.12, 2.48	35.7	2.11, 2.47	35.8	2.13, 2.48	35.7	2.12, 2.48	40.4	1.98, 2.42	40.4	1.96, 2.42
10	107.1		107.2		107.1		107.2		107.4		107.4	
11	33.2	1.65, 2.31	33.2	1.63, 2.32	33.2	1.65, 2.31	33.2	1.64, 2.33	33.3	1.64, 2.32	33.3	1.63, 2.32
12	37.6	1.96, 2.15	37.5	1.95, 2.13	37.6	1.96, 2.15	37.5	1.96, 2.13	37.5	1.97, 2.16	37.4	1.96, 2.15
13	111.3		111.3		111.3		111.3		111.2		111.2	
14	30.9	2.01	31.0	2.00	30.9	2.03	31.0	2.01	31.0	2.00	31.0	1.99
15	32.7	1.74, 1.83	32.6	1.75, 1.83	32.7	1.75, 1.83	32.6	1.76, 1.83	32.7	1.73, 1.82	32.6	1.73, 1.82
16	77.9	3.92	78.0	3.90	78.0	3.90	78.2	3.89	77.9	3.91	78.0	3.90
17	73.3	4.18	73.1	4.20	73.1	4.19	73.2	4.22	73.1	4.16	73.1	4.17
18	38.4	1.99, 2.06	38.2	2.00, 2.00	38.7	2.00, 2.04	37.9	2.00, 2.00	38.4	2.00, 2.06	38.2	2.01, 2.01
19	79.8	4.41	79.4	4.38	79.3	4.41	78.9	4.38	79.6	4.41	79.3	4.38
20	80.2	3.29	79.3	3.49	77.3	3.48	76.7	3.77	80.2	3.30	79.4	3.50
21	97.9		99.5		99.8		102.2		97.8		99.5	
22	31.9	1.51, 2.11	38.5	1.80, 2.29	36.1	2.28	40.0	2.18	31.9	1.51, 2.11	38.5	1.80, 2.28
23	29.4	1.58, 1.62	71.1	3.93	38.7	1.41, 1.41	76.5	3.60	29.4	1.58, 1.62	71.1	3.93
24	39.5	1.33	44.5	1.48	42.0	1.36	46.7	1.49	39.5	1.33	44.5	1.48
25	80.6	3.96	74.1	4.35	79.7	3.92	73.6	4.33	80.5	3.96	74.1	4.36
26	147.2		147.6		148.0		148.0		147.1		147.5	
27	48.5	2.17, 2.36	48.9	2.23, 2.42	49.3	2.15, 2.35	49.3	2.24, 2.43	48.5	2.17, 2.36	48.9	2.23, 2.42
28	98.0		98.5		98.0		98.6		98.1		98.5	
29	44.3	1.33, 1.98	44.2	1.37, 2.05	44.8	1.30, 1.97	44.3	1.36, 2.06	44.4	1.33, 1.98	44.2	1.37, 2.05
30	26.7	2.24	26.5	2.25	26.7	2.24	26.4	2.24	26.7	2.25	26.5	2.25
31	35.8	1.48, 1.77	35.5	1.52, 1.82	35.9	1.47, 1.77	35.4	1.52, 1.83	35.8	1.48, 1.78	35.5	1.51, 1.81
32	72.7	4.24	72.8	4.33	72.9	4.23	72.9	4.35	72.7	4.24	72.8	4.33
33	79.3	3.72	ND[a]	3.93	79.4	3.72	81.2	4.01	79.4	3.72	79.7	3.93
34	75.6	4.80	75.2	4.94	75.5	4.79	75.0	4.99	75.6	4.80	75.2	4.94
35	43.1	1.90, 2.38	42.1	2.29, 2.52	43.0	1.90, 2.38	41.8	2.42, 2.56	43.1	1.90, 2.39	42.1	2.11, 2.52
36	95.9		96.4		96.0		96.5		95.9		96.4	
37	37.9	1.74	ND[a]	1.88	37.7	1.74	36.0	1.93	37.9	1.75	36.5	1.88
38	40.0	1.14, 1.54	38.2	1.24, 1.63	39.9	1.14, 1.53	38.0	1.27, 1.65	40.0	1.14, 1.54	38.6	1.24, 1.63
39	31.7	1.66	ND[a]	1.83	31.8	1.65	29.6	1.88	31.7	1.66	30.3	1.83
40	47.8	2.51, 2.57	46.2	2.74, 2.74	47.5	2.48, 2.52	46.3	2.77, 2.82	47.8	2.51, 2.57	46.3	2.74, 2.74
14-Me	16.7	0.938	16.6	0.941	16.7	0.942	16.6	0.944	16.7	0.927	16.6	0.930
22-Me					16.5	0.890	13.7	1.097				
24-Me	18.2	0.819	14.7	0.918	18.1	0.813	14.9	0.924	18.2	0.818	14.7	0.917
26=CH_2	116.1	5.14, 5.22	117.1	5.21, 5.35	115.3	5.09, 5.25	117.1	5.20, 5.39	116.1	5.14, 5.23	117.0	5.21, 5.35
30-Me	23.9	0.928	23.6	0.952	23.8	0.929	23.5	0.958	23.9	0.929	23.7	0.951
37-Me	16.1	0.860	15.7	0.929	16.1	0.855	15.5	0.952	16.1	0.860	15.7	0.927
39-Me	19.5	0.855	18.9	0.921	19.4	0.850	18.7	0.940	19.5	0.862	18.9	0.922
8-Me									23.0	1.70	23.0	1.69

[a]Not detected because of limited signal-to-noise.

injection volume was 5 μL, and the column and sample temperatures were 25 and 6 °C, respectively.

Method B. Structures and purities were assessed on a model 2795 LC instrument (Waters, Manchester, UK) coupled to a quadrapole time-of-flight (QToF) Ultima instrument (Micromass, Manchester, UK) by running MS scans (m/z 100−1000) using the same chromatographic conditions as method A. The possible presence of other AZA contaminants was determined by performing product ion scans, in which the precursor ions were selected and then fragmented, for all the known AZA analogues.

Method C. For a relative molar response study, analysis was performed on a model 1200 LC instrument (Agilent Technologies, Santa Clara, CA) connected to a model API4000 QTRAP mass spectrometer (AB Sciex, Framingham, MA) equipped with a Turbospray ionization source. The MS was operated in positive ion mode, and SRM transitions were as follows: m/z 842.5 → 824.5/672.5/462.3/362.3 (**1**); m/z 844.5 → 826.5/658.5/362.3 (**4**); m/z 844.5 → 826.5/674.5/362.3 (**5**); m/z 842.5 → 824.5/658.5/362.3 (**6**); m/z 858.5 → 840.5/672.5/362.3 (**7**); m/z 858.5 → 840.5/688.5/362.3 (**8**); m/z 858.5 → 840.5/658.5/362.3 (**9**), and m/z 858.5 →

DOI: 10.1021/acs.jafc.5b01320
J. Agric. Food Chem. 2015, 63, 5083−5091

840.5/674.5/362.3 (**10**). For selected ion monitoring (SIM) experiments, *m/z* 842.5 (**1** and **6**), 844.5 (**4** and **5**), and 858.5 (**7**−**10**) were analyzed. Typical parameters were 5500 V electrospray voltage, 400 °C source temperature, 70 V declustering potential, and collision energies of 45−70 V (where applicable). Method C (i) used gradient elution with the same acidic mobile phase as method A. The column used was a 2.1 mm × 50 mm i.d., 2.5 μm Luna C18(2) HST column (Phenomenex, Cheshire, UK). The gradient was from 25 to 100% B over 5 min at 300 μL/min and held at 100% B for 2 min, before re-equilibration for the next run. The injection volume was 1−5 μL, and the column and sample temperatures were 25 and 6 °C, respectively. Method C (ii) used isocratic elution with the acidic mobile phase on the same Luna column, with 60% B at 300 μL/min.

Method D. For separation of the 37-epimers,[25] a neutral gradient elution was used.[27] The column used was a 2.1 mm × 50 mm i.d., 2.5 μm, Luna C18(2) HST column (Phenomenx, Cheshire, UK), operated at 15 °C, injecting 1−5 μL samples. A binary mobile phase of H_2O (A) and CH_3CN (95%) in H_2O (B), each containing 5 mM ammonium acetate (pH 6.8), was used with a linear gradient from 25 to 100% B over 5 min at 350 μL/min and held at 100% B for 2 min before re-equilibration for the next run.

Method E. Accurate mass measurements were performed on an Acquity UPLC instrument coupled to a Xevo G2-S QToF (Waters, Manchester, UK) operated in MS^e mode, scanning from *m/z* 100−1200 and using leucine enkephalin as the reference compound. The cone voltage was 40 V; collision energy was 50 V; the cone and desolvation gas flows were set at 100 and 1000 L/h, respectively; and the source temperature was 120 °C.

The column used was a 50 mm × 2.1 mm i.d., 1.7 μm, Acquity UPLC BEH C18 (Waters, Wexford, Ireland), using the same mobile phase as that described in method A. The gradient was from 30 to 90% B over 5 min at 0.3 mL/min, held for 0.5 min, and returned to the initial conditions and held for 1 min to equilibrate the system. The injection volume was 2 μL and the column and sample temperatures were 25 and 6 °C, respectively.

NMR Spectroscopy. NMR experiments for structure elucidation were run using Avance I and Avance II 600 MHz spectrometers (Bruker, Fällanden, Switzerland) equipped with TCI cryoprobes and Z-gradient coils, at 30 °C, and a Bruker DRX-500 spectrometer (Milton, Ontario, Canada) with a TXI probe and Z-gradient coils at 20 °C was used for qNMR. Structures were determined by analysis of ^1H, COSY, TOCSY, NOESY, ROESY, HSQC, HMBC, ^{13}C, and DEPT135 NMR spectra. Samples of **4**−**10** (∼0.1 mg) were dissolved in ∼0.5 mL CD_3OD at 30 °C, and chemical shifts were referenced to internal CHD_2OD (3.31 ppm) or CD_3OD (49.0 ppm). Single- or double-frequency pre-saturation of solvent resonances was performed using continuous wave or excitation sculpting, as required.

Quantitation of **1** and **4**−**10** was performed on aliquots of the purified compounds by dissolving in CD_3OH. The samples were run against external standards of caffeine dissolved in H_2O (4.1 mM) as described previously for AZA CRMs.[28]

Toxicology. *Cell Culturing.* Human Jurkat E6−1 T lymphocyte cells (American Type Culture Collection TIB-152, Manassas, VA) were grown as described by Twiner et al.[29] Briefly, cells were grown in RPMI medium (Invitrogen, Carlsbad, CA) supplemented with 10% (v/v) fetal bovine serum (Invitrogen, Carlsbad, CA) and maintained in a humidified incubator with 5% CO_2 in air at 37 °C. Cells were subcultured with fresh medium at an inoculum ratio of 1:4 every 3−4 days by transferring 2.5 mL of the cells to 7.5 mL of fresh supplemented medium in 75 cm^2 screw-cap culture flasks.

Cytotoxicity Assay. To determine the effect of **1**, **4**−**6**, and **8**−**10** on cellular toxicity, Jurkat T lymphocyte cells were continuously exposed to toxins, and the viability was determined. The non-adherent human cell line Jurkat T lymphocyte was grown in RPMI medium supplemented with 10% (v/v) fetal bovine serum. Cells were maintained in humidified 5% CO_2 in air at 37 °C and subcultured with fresh medium at an inoculum ratio of 1:10 every 5−7 days by transferring 1 mL of the cells to 9 mL of fresh supplemented medium in 75 cm^2 screw-cap culture flasks. Cells were seeded in a volume of 100 μL of the supplemented medium at a density of 35 000 cells per well in black, sterile, 96-well culture plates for 24 h to allow for recovery and settling. Each AZA was added at a single concentration (10 nM) for 24, 48, or 72 h of continuous exposure prior to assessment of cytotoxicity. Parallel controls of equivalent amounts of MeOH/phosphate buffered saline were used to normalize the viability data for each treatment. Cellular viability/cytotoxicity was assessed using the 3-(4,5-dimethylthiazol-2-yl)-5-(3-carboxymethoxyphenyl)-2-(4-sulfophenyl)-2*H*-tetrazolium (MTS) assay (Promega Biosciences, Sunnyvale, CA). Like other tetrazolium-based assays, MTS in the presence of an electron coupling reagent (phenazine methosulfate; PMS) measures cellular viability by determining the activity of mitochondrial dehydrogenase.[30] As a substrate for dehydrogenases, MTS becomes reduced into a soluble, purple dye that can be quantitated colorimetrically to determine the relative level of cellular viability/cytotoxicity per well. Following exposure of the cells to the AZA analogues for the specified period of time, each well received 10 μL of a PMS/MTS (1:20) solution. Cells were incubated for 4 h, after which absorbance readings at 485 nm were obtained using a FluoStar microplate reader (BMG Lab Technologies, Cary, NC). Data are presented as means ± SE (n = 3−5). In addition, each cytotoxicity experiment was performed using duplicate wells. Cytotoxicity data were blank-corrected and normalized to the control (% viability) and plotted using GraphPad Prism (version 5.0c).

RESULTS AND DISCUSSION

The isolation of **6** has previously been described.[24] Hydroxylated analogs **4**, **5**, and **7**−**10** are less lipophilic than **1**−**3** and **6**

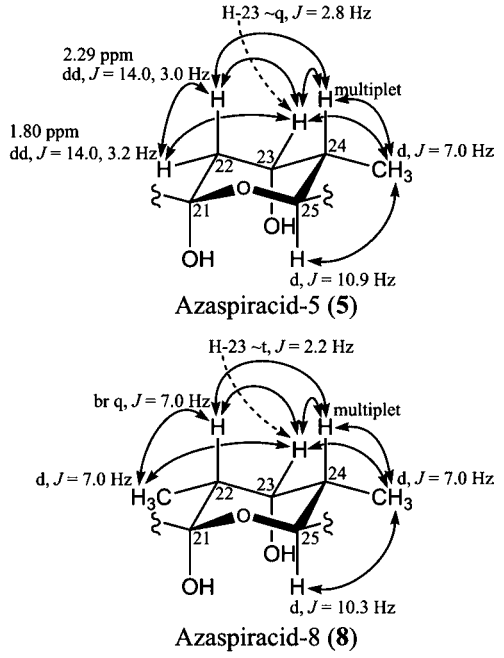

Figure 2. Structures for the E-rings of **5** and **8** showing dispositions of substituents. Observed $^1H-^1H$ coupling constants and correlations (arrows) in the ROESY NMR spectra are also shown.

and, therefore, eluted earlier[12] and were more difficult to separate from the other contaminants in the sample. In the initial semipreparative HPLC step, **4** and **5** and **7**−**10** were collected as two separate fractions. Individual analogues were separated in a second chromatographic step, and a third was required to achieve sufficient purity for NMR spectroscopy. The amounts purified ranged from ∼100 to 200 μg. Each analogue also contained its corresponding 37-epimer (∼2−15%) as recently reported.[25] Sufficient purity for the cytotoxicity assay was achieved for all AZAs except for **7**

DOI: 10.1021/acs.jafc.5b01320
J. Agric. Food Chem. 2015, 63, 5083−5091

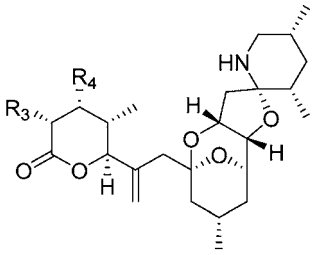

Precursor	R_3	R_4	m/z [MH]$^+$
1, **2**, **7**	CH_3	H	448.3
3, **4**, **6**, **9**	H	H	434.3
5, **10**	H	OH	450.3
8	CH_3	OH	464.3

Figure 3. Products detected by LC−MS after periodate cleavage of purified samples on **1**−**10**, and their calculated m/z values.

(purity ∼63%), which was contaminated with **5** and another hitherto unreported AZA (∼20%) with a molecular mass of 825 Da, which was also detected in the initial hepatopancreas extract. Compounds **4**, **5**, **6**, **8** and **10** had purities (including the 37-epimers) of >95%; **9** had a purity of 89%.

Structure Determination. The AZAs isolated in this study showed typical AZA mass spectral fragmentation patterns, namely, a protonated molecular ion, retro Diels−Alder (RDA), and m/z 362 fragments (Figure 1), all of which appeared in clusters, indicative of several H_2O losses. NMR structure elucidation was done using 1D and 2D-homonuclear ^{1}H, ^{13}C, and heteronuclear ^{1}H{^{13}C} spectroscopy to assign the ^{1}H and ^{13}C resonances, the chemical shifts of which were then compared with the published ^{1}H (for **1**−**6**) and ^{13}C NMR (for **1**−**3** and **6**) data for **1**−**6**.[21−24] The majority of chemical shifts in Table 1 are from 1D-NMR spectra, but some chemical shifts were from 2D-spectra where necessary because of weak or overlapping signals. All samples inevitably contained low percentages of the corresponding 37-epimer,[25] but this did not interfere with NMR analyses and is not discussed further. Other minor AZAs were sometimes present as contaminants in the samples but not at levels sufficient to prevent spectrometric analysis.

*AZA4 (**4**) and AZA5 (**5**).* Structure assignments for **4** have been published on the basis of ^{1}H NMR and fast atom bombardment MS,[23] which was considered to show C-3 hydroxylation. This study confirmed those findings. In addition to the expected fragments, the MS spectra showed a molecular ion cluster (m/z 782.5), suggesting a loss of CO_2, followed by several H_2O losses, that is indicative of C-3 hydroxylation. NMR spectroscopic analysis also demonstrated that **4** is 3-hydroxylated. We also determined ^{13}C NMR assignments for **4** (Table 1). Although it is not possible to determine the configuration at C-3 from ROESY correlations or coupling constants, **4** has been shown to be 3*R*-hydroxyazaspiracid-3 by degradation reactions and synthesis of the degradation products.[21] ^{1}H NMR assignments for **4** closely paralleled those of Ofuji et al.,[23] apart from variations[25] attributable to the degree of protonation on the amino group and to the reversal of the resonances for H-7 and H-9 due to the revised position of the double bond in the A-ring.[24,31,32] The ^{13}C and ^{1}H chemical shifts for the 22-positions of **4** were markedly different from those reported recently for **6** (39.0, and 2.13 (2H) ppm).[24] However, examination of the original NMR data[24] for **6** indicates that these signals resonate at 31.5 ppm and at 1.50 and 2.10 ppm, in accord with the published NMR data for **3**,[22] as well as that presented here for **4**.

The MS/MS spectrum of **5** showed a fragment peak at m/z 408 that is indicative of C-23 hydroxylation.[33] As with **4**, the ^{1}H NMR assignments (Table 1) for **5** closely paralleled those of Ofuji et al.[23] Analyses of the ^{1}H NMR data that we recorded for **5** confirmed the presence of a hydroxyl group at C-23 and showed that H-23 (3.93 ppm, ∼q, J = 2.7 Hz) was equatorially oriented toward the upper (β) face of the C-21—C-25 ring (Figure 2) and that the 23-hydroxyl group was therefore axially inclined toward the lower (α) face of this ring.

*AZA7 (**7**) and AZA9 (**9**).* Analogously to **4**, the MS, MS/MS, periodate cleavage and NMR data showed C-3 hydroxylation (Table 1, Figure 3).

*AZA8 (**8**) and AZA10 (**10**).* Analogously to **5**, the MS, MS/MS, periodate cleavage, and NMR data showed C-23 hydroxylation (Table 1, Figures 2 and 3).

Examination of the assignments within Table 1 and comparison with NMR assignments for **1**−**3**[21,22] and **6**[24] obtained under the same conditions and calibrated identically reveals diagnostic effects on chemical shifts arising from the hydroxylations and methylations of the AZA skeleton. Hydroxylation at C-3 leads not only to marked changes in the C-3 and H-3 resonances but also to significant changes (≥∼1 ppm for ^{13}C, ≥∼0.05 ppm for ^{1}H) to the nearby C-2, C-4, H-2, H-5, and H-6 resonances. Similarly, hydroxylation at C-23 leads to consistent alterations in the chemical shifts of C-22−C-25 and H-22−H-25 as well as the appended 22- (if present) and 24-methyl groups in the E-ring. Addition of a methyl group at C-8 also results in characteristic changes to the C-7−C-9 and H-6−H-9 resonances. Similarly, the presence or absence of a 22-methyl has a pronounced effect on the chemical shifts of C-22−C-24 and H-22 and H-23.

The previously reported effect attributed to the state of ionization of the amino group[23] is evident in Table 1, leading to

Table 2. Relative (to 1) Molar Responses of 4−10 by LC−MS(MS) under Acidic Conditions

	SIM		SRM isocratic[a]			SRM gradient[b]		
AZA	isocratic[a]	gradient[b]	H_2O loss	RDA	m/z 362	H_2O loss	RDA	m/z 362
4	0.88	0.75	0.80	0.81	0.86	0.96	0.96	1.03
5	0.77	0.70	0.55	0.47	0.47	0.61	0.54	0.53
6	0.95	0.93	1.06	1.21	1.17	1.05	1.21	1.13
7	0.45	0.40	0.37	0.33	0.37	0.40	0.37	0.40
8	0.84	0.81	0.58	0.41	0.47	0.59	0.47	0.51
9	0.53	0.49	0.45	0.48	0.61	0.50	0.53	0.68
10	0.49	0.48	0.34	0.33	0.35	0.34	0.35	0.36

[a]Method C (i). [b]Method C (ii).

DOI: 10.1021/acs.jafc.5b01320
J. Agric. Food Chem. 2015, 63, 5083−5091

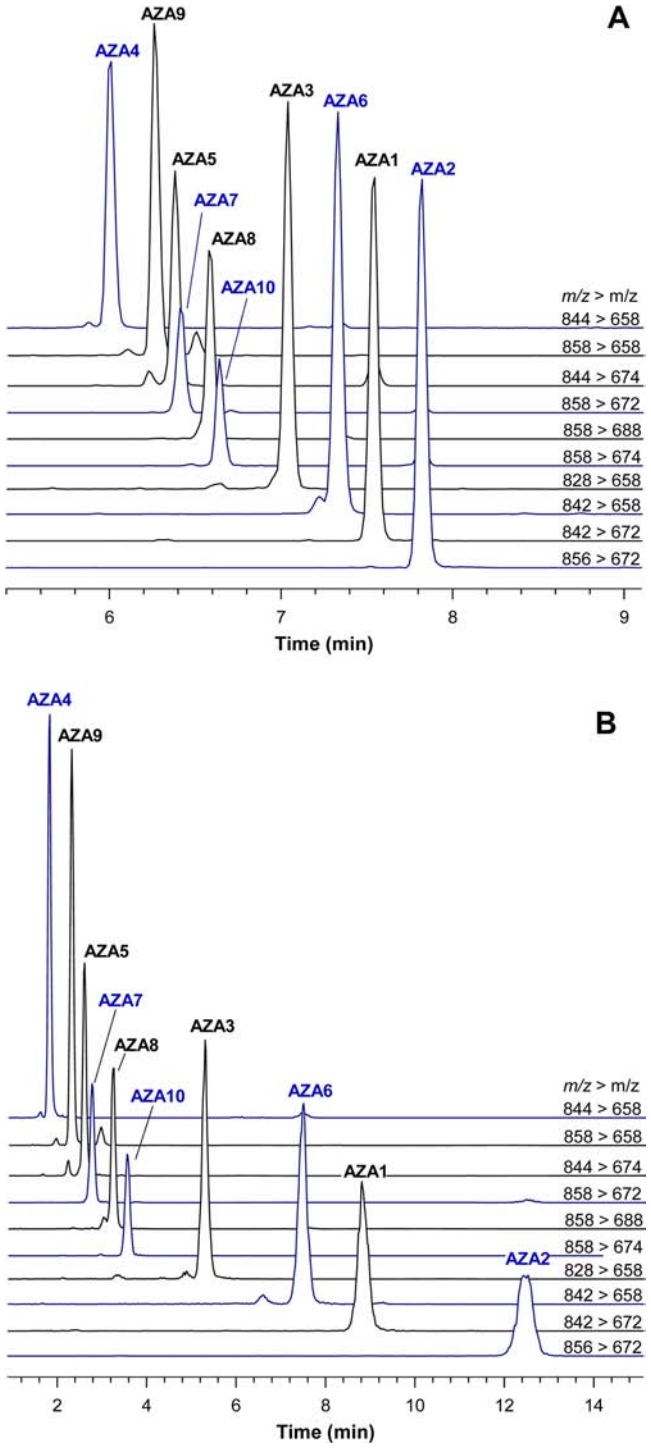

Figure 4. LC–MS/MS analysis (method C) of reference standards prepared for **1**–**10** under (A) gradient and (B) isocratic conditions. Note: two combined reference standards were prepared, as indicated by the colors (blue, black).

systematic changes to most of the resonances of rings F–I (C-35, C-37–C-40, H-29, H-31–H-40, and the 37- and 39-methyl groups). This effect is also observable on a number of remote resonances (H-18, H-19, and the olefinic methylene at C-26), consistent with molecular modeling and ROESY correlations indicating the ring systems F–I to be folded over in such a way that the amino group is near H-19 so that **1**, **2**,[23] **4**, **5**, and **7**–**10** showed ROESY correlations between H-19 and H-40$_{eq}$. Knowledge of these consistent substituent effects on the AZA skeleton will be helpful during NMR structure analysis of other AZA congeners and metabolites.

Further structural evidence was obtained by treatment with periodate that cleaves whenever a diol moiety is present. LC–MS analysis showed that treatment of **7**–**10** with periodate yielded C-20–C-21-cleavage products at m/z 448.4 for **7** (with the same retention time as the cleavage products from **1** and **2**), m/z 464.4 for **8**, m/z 434.4 for **9** (same retention time as products from **3** and **6**), and m/z 450.4 for **10** (same retention time as the product from **5**) (Figure 3). Because the structures of **1**–**6** are well established,[21−24] these results confirm the C-20–C-40 substructures of **7**, **9**, and **10** that were determined by NMR spectroscopy shown (Figure 1).

Because **4**, **5**, **7**, **8**, **9**, and **10** are produced in mussels by enzymatic oxidations and decarboxylations of **1** and **2** biosynthesized by dinoflagellates, it follows that their absolute configurations are as shown in Figure 1. Analogs **4**, **5**, **7**, and **8** are proposed to be bioconversion products of **1**, whereas **9** and **10** appear to be bioconversion products of **2**.[20,34]

Relative Molar Response Study. For the AZAs studied, differences in response factors were less significant in SIM mode under isocratic conditions (Table 2). In LC–MS/MS, the mobile phase composition can influence the ionization efficiency; therefore, analysis under isocratic conditions produces more accurate results. The response factor for **6** was very similar to that of **1**. All the hydroxylated AZAs gave lower response factors, with **7**, **9**, and **10** being the lowest at ~0.5 (Figure 4).

The data shows that the SRM transition selected for analysis of all the AZAs, including **6**, can significantly impact quantitation when using **1** as a calibration standard (Table 2). The H_2O loss transition for **6** was similar to that of **1**; however, the RDA cleavage of the A-ring resulted in significantly higher response factors under both isocratic and gradient conditions. For all the other AZAs, the differences in SRM mode were even greater. The results suggest that, in the absence of standards for the hydroxylated analogues, quantitation will be more accurate in SIM mode under isocratic conditions and that the concentration of hydroxylated AZAs may be significantly underestimated when AZA1 alone is used for calibration (Table 2).

Toxicology. All available AZA analogues tested were cytotoxic to Jurkat T lymphocyte cells in a time- and concentration-dependent manner (Figure 5). However, there were distinct differences in the relative potencies of each analogue, as revealed by their EC_{50} values (Table 3). The range of EC_{50} values for the eight analogues tested in this study were 0.1–3.1 nM, a 31-fold range. On the basis of the EC_{50} values, the relative potencies were **2**[35] > **6** > **8** ≈ **3**[35] > **1** > **4** ≈ **5** ≈ **9** > **10**. Impurities in **7** prevented it from being subjected to the Jurkat cell assay.

In the present study, the AZAs tested represented differing sites of methylation and hydroxylation. Collectively, SAR analysis using these data and published data for **2** and **3**[35] suggest that AZA potency was somewhat increased by methylation at C-8 or C-22 (i.e., **2**, **6**), whereas potency was reduced somewhat by hydroxylation at C3 or C23 (i.e., **4**, **5**) (Table 3, Figure 5). These findings allow us to speculate on the relative potencies of other analogues, such as AZA12 (predicted to have relatively higher potency) and AZA13 (predicted to have relatively lower potency), on the basis of their structures. Interestingly, reduced potencies of **4** and **5** relative to **1** in the

DOI: 10.1021/acs.jafc.5b01320
J. Agric. Food Chem. 2015, 63, 5083–5091

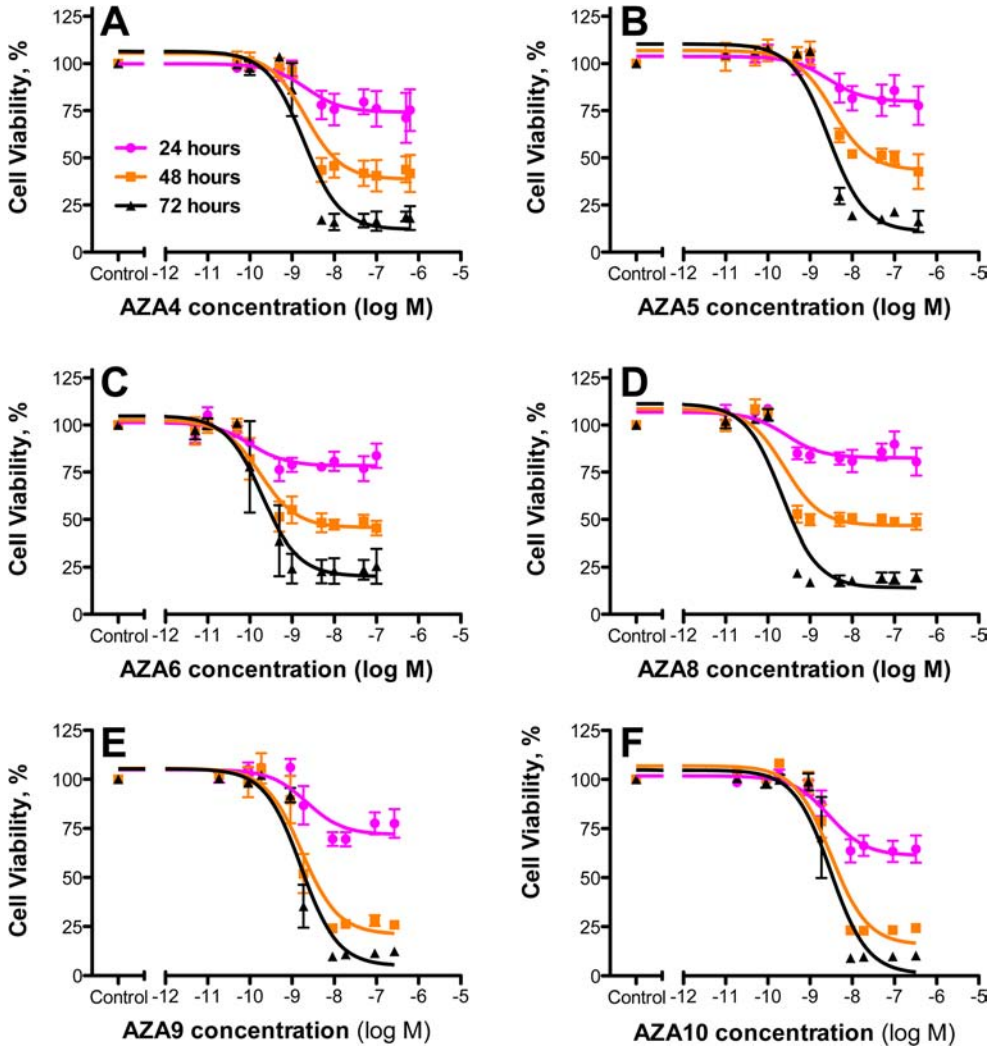

Figure 5. Effect of various AZA analogues on T lymphocyte cell viability. Jurkat T cells were exposed to various concentrations of (A) **4**, (B) **5**, (C) **6**, (D) **8**, (E) **9**, and (F) **10** for 24, 48, or 72 h and viability was assessed using the MTS assay. All data (mean ± SE; n = 3−5) were normalized to the control (10% MeOH vehicle).

Table 3. Calculated EC_{50} Values and Relative Potencies for AZA Analogues Based on T-Lymphocyte Cytotoxicity

	24 h		48 h		72 h			
AZA	EC_{50} (nM)	95% CI	EC_{50} (nM)	95% CI	EC_{50} (nM)	95% CI[a]	mean EC_{50} (nM)	relative potency to AZA1[b]
4	2.1	0.3−15	2.1	1.0−4.4	1.9	1.0−3.5	2.0	0.6
5	2.7	0.5−15	3.4	1.7−6.9	2.8	1.6−4.7	3.0	0.4
6	0.1	0.03−0.4	0.2	0.1−0.4	0.2	0.1−0.5	0.2	7.0
8	0.3	0.1−1.2	0.3	0.1−0.5	0.2	0.1−0.4	0.3	4.5
9	2.2	0.7−7.4	1.7	1.0−3.0	1.7	1.1−2.6	1.9	0.4
10	2.9	1.2−6.8	3.2	2.1−4.8	3.1	1.8−5.5	3.1	0.2

[a]Confidence interval. [b]Comparisons between analogues should be done cautiously as data were collected from different experiments during which minor changes in in vitro AZA1 potency were observed. Relative potency values for AZA4, -5, -6, and -8 were compared to AZA1 EC_{50} values of 0.96, 1.1, and 1.3 for 24, 48, and 72 h. Relative potency values for AZA9 and -10 were compared to AZA1 EC_{50} values of 0.51, 0.89, and 0.88 for 24, 48, and 72 h.

Jurkat cell assay are the same as those determined by intraperitoneal injection in mice.[23] The utility of this in vitro cytotoxicity assay for relative analogue potencies (i.e., TEFs) are further corroborated by previous in vitro and in vivo studies whereby both techniques also clearly demonstrated increased potencies of **2** and **3** relative to **1**.[21,22,35] However, recent in vivo studies (mouse intraperitoneal and mouse oral) showed that **1** is more toxic than **2** (mouse intraperitoneal ≈ oral; TEF = 0.6−0.7) and **3** (mouse intraperitoneal = oral; TEF = 0.5).[9] Furthermore, the toxicity of **6** was determined by mouse intraperitoneal for the first time and was found to be less toxic (TEF = 0.7) than **1**.[9] Although the reason for this discrepancy is unknown at this time, the oral in vivo studies probably have more relevance for protecting shellfish consumers. However, oral dosing experiments are difficult to perform because of the high mass of toxins needed. Hence, further studies should be

DOI: 10.1021/acs.jafc.5b01320
J. Agric. Food Chem. 2015, 63, 5083−5091

conducted to isolate more of the minor analogues to conclusively clarify their toxicological importance.

In summary, compounds **4**−**10** were purified from shellfish, with the structures of **7**−**10** being elucidated for the first time by NMR, which confirmed the previously postulated structures based on LC−MS/MS studies. qNMR was performed on all purified samples and subsequent LC−MS(MS) relative molar response factors and cytotoxicity were determined. Differences in the molar responses relative to **1** were observed, particularly for the hydroxylated analogues (up to 3-fold). The differences were least significant when analyzing in SIM mode under isocratic conditions. Combining all the cytotoxicity data published to date for AZAs using the Jurkat T lymphocyte cell assay, the order of potencies is **2** > **6** ≈ AZA34[15] ≈ 37-*epi*-**1**[25] > **8** ≈ **3** > **1** > **4** ≈ **9** > **5** ≈ **10** > AZA33.[15]

■ ASSOCIATED CONTENT

Supporting Information

Mass spectrum of AZA analogue with *m*/*z* of 826 Da; mass spectra of **4**, **5** and **7**−**10**; table of isolated compounds and their purities; NMR spectra of **4**, **5** and **7**−**10**. The Supporting Information is available free of charge on the ACS Publications website at DOI: 10.1021/acs.jafc.5b01320.

■ AUTHOR INFORMATION

Corresponding Author

*Phone: + 353 91 387376. E-mail: jane.kilcoyne@marine.ie.

Funding

This project (PBA/AF/08/001(01)) was carried out under the *Sea Change* strategy with the support of the Marine Institute and the Marine Research Sub-Programme of the National Development Plan 2007−2013, co-financed under the European Regional Development Fund and supported in part by a Marie Curie International Incoming Fellowship (to C.O.M.) within the seventh European Community Framework Programme (FP7/2007−2013) under grant agreement no. 221117.

Notes

The authors declare no competing financial interest.

■ ACKNOWLEDGMENTS

We thank the biotoxin chemistry team at the Marine Institute, Galway, in particular, O. Finch, for assistance in the laboratory. We also thank I. Burton at the National Research Council of Canada for providing original NMR data for AZA6.

■ REFERENCES

(1) Twiner, M. J.; Rehmann, N.; Hess, P.; Doucette, G. J. Azaspiracid shellfish poisoning: a review on the chemistry, ecology, and toxicology with an emphasis on human health impacts. *Mar. Drugs* **2008**, *6*, 39−72.

(2) Furey, A.; O'Doherty, S.; O'Callaghan, K.; Lehane, M.; James, K. Azaspiracid poisoning (AZP) toxins in shellfish: toxicological and health considerations. *Toxicon* **2010**, *56*, 173−190.

(3) Klontz, K. C.; Abraham, A.; Plakas, S. M.; Dickey, R. W. Mussel-associated azaspiracid intoxication in the United States. *Ann. Intern. Med.* **2009**, *150*, 361.

(4) Marine Insitute shellfish safety database. http://www.marine.ie/home/publicationsdata/data/Habs+Search+Database/HabsSearch.htm. Accessed 6 March, 2015.

(5) McMahon, T.; Silke, J. Winter toxicity of unknown aetiology in mussels. *Harmful Algae News*, **1996**, *14*.

(6) Aune, T.; Espenes, A.; Aasen, J. A. B.; Quilliam, M. A.; Hess, P.; Larsen, S. Study of possible combined toxic effects of azaspiracid-1 and okadaic acid in mice via the oral route. *Toxicon* **2012**, *60*, 895−906.

(7) Ito, E.; Satake, M.; Ofuji, K.; Higashi, M.; Harigaya, K.; McMahon, T.; Yasumoto, T. Chronic effects in mice caused by the oral administration of sub-lethal doses of azaspiracid, a new marine toxin isolated from mussels. *Toxicon* **2002**, *40*, 193−203.

(8) Aasen, J. A. B.; Espenes, A.; Hess, P.; Aune, T. Sub-lethal dosing of azaspiracid-1 in female NMRI mice. *Toxicon* **2010**, *56*, 1419−1425.

(9) Kilcoyne, J.; Jauffrais, T.; Twiner, M.; Doucette, G.; Aasen Bunæs, J. A.; Sosa, S.; Krock, B.; Séchet, V.; Nulty, C.; Salas, R.; Clarke, D.; Geraghty, J.; Duffy, C.; Foley, B.; John, U.; Quilliam, M. A.; McCarron, P.; Miles, C. O.; Silke, J.; Cembella, A.; Tillmann, U.; Hess, P. *Azaspiracids − toxicological evaluation, test methods and identifcation of the source organisms (ASTOX II)*; Marine Institute − Marine Research Sub-Programme (NDP 2007−2013) series (http://oar.marine.ie/handle/10793/970), 2014. Accessed 27 March 2015.

(10) Twiner, M. J.; Doucette, G. J.; Rasky, A.; Huang, P. X.; Roth, B. L.; Sanguinetti, M. C. The marine algal toxin azaspiracid is an open state blocker of hERG potassium channels. *Chem. Res. Toxicol.* **2012**, *25*, 1975−1984.

(11) Twiner, M. J.; Hanagriff, J. C.; Butler, S.; Madhkoor, A. K.; Doucette, G. J. Induction of apoptosis pathways in several cell lines following exposure to the marine algal toxin azaspiracid-1. *Chem. Res. Toxicol.* **2012**, *25*, 1493−1501.

(12) Rehmann, N.; Hess, P.; Quilliam, M. A. Discovery of new analogs of the marine biotoxin azaspiracid in blue mussels (*Mytilus edulis*) by ultra-performance liquid chromatography/tandem mass spectrometry. *Rapid Commun. Mass Spectrom.* **2008**, *22*, 549−558.

(13) Krock, B.; Tillmann, U.; John, U.; Cembella, A. D. Characterization of azaspiracids in plankton size-fractions and isolation of an azaspiracid-producing dinoflagellate from the North Sea. *Harmful Algae* **2009**, *8*, 254−263.

(14) Krock, B.; Tillmann, U.; Voß, D.; Koch, B. P.; Salas, R.; Witt, M.; Potvin, É.; Jeong, H. J. New azaspiracids in *Amphidomataceae* (Dinophyceae). *Toxicon* **2012**, *60*, 830−839.

(15) Kilcoyne, J.; Nulty, C.; Jauffrais, T.; McCarron, P.; Herve, F.; Wilkins, A. L.; Foley, B.; Rise, F.; Crain, S.; Twiner, M. J.; Hess, P.; Miles, C. O. Isolation, structure elucidation, relative LC−MS response, and in vitro toxicity of azaspiracids from the dinoflagellate *Azadinium spinosum*. *J. Nat. Prod.* **2014**, *77*, 2465−2474.

(16) Torgersen, T.; Bremnes, N. B.; Rundberget, T.; Aune, T. Structural confirmation and occurrence of azaspiracids in Scandinavian brown crabs (*Cancer pagurus*). *Toxicon* **2008**, *51*, 93−101.

(17) Ueoka, R.; Ito, A.; Izumikawa, M.; Maeda, S.; Takagi, M.; Shinya, K.; Yoshida, M.; Van Soest, R. W. M.; Matsunaga, S. Isolation of azaspiracid-2 from a marine sponge *Echinoclathria* sp. as a potent cytotoxin. *Toxicon* **2009**, *53*, 680−684.

(18) Anon. Commission Regulation (EU) No 15/2011 of 10th January 2011 amending Regulation (EC) No 2074/2005 as regards recognised testing methods for detecting marine biotoxins in live bivalve molluscs. *Official Journal of the European Union*, **2011**, *L6*, 3−6.

(19) Salas, R.; Tillmann, U.; John, U.; Kilcoyne, J.; Burson, A.; Cantwell, C.; Hess, P.; Jauffrais, T.; Silke, J. The role of *Azadinium spinosum* (Dinophyceae) in the production of azaspiracid shellfish poisoning in mussels. *Harmful Algae* **2011**, *10*, 774−783.

(20) Jauffrais, T.; Marcaillou, C.; Herrenknecht, C.; Truquet, P.; Séchet, V.; Nicolau, E.; Tillmann, U.; Hess, P. Azaspiracid accumulation, detoxification and biotransformation in blue mussels (*Mytilus edulis*) experimentally fed *Azadinium spinosum*. *Toxicon* **2012**, *60*, 582−595.

(21) Satake, M.; Ofuji, K.; Naoki, H.; James, K. J.; Furey, A.; McMahon, T.; Silke, J.; Yasumoto, T. Azaspiracid, a new marine toxin having unique spiro ring assemblies, isolated from Irish mussels. *J. Am. Chem. Soc.* **1998**, *120*, 9967−9968.

(22) Ofuji, K.; Satake, M.; McMahon, T.; Silke, J.; James, K. J.; Naoki, H.; Oshima, Y.; Yasumoto, T. Two analogs of azaspiracid isolated from mussels, *Mytilus edulis*, involved in human intoxications in Ireland. *Nat. Toxins* **1999**, *7*, 99−102.

(23) Ofuji, K.; Satake, M.; McMahon, T.; James, K. J.; Naoki, H.; Oshima, Y.; Yasumoto, T. Structures of azaspiracid analogs,

DOI: 10.1021/acs.jafc.5b01320
J. Agric. Food Chem. 2015, 63, 5083−5091

azaspiracid-4 and azaspiracid-5, causative toxins of azaspiracid poisoning in Europe. *Biosci., Biotechnol., Biochem.* **2001**, *65*, 740−742.
(24) Kilcoyne, J.; Keogh, A.; Clancy, G.; LeBlanc, P.; Burton, I.; Quilliam, M. A.; Hess, P.; Miles, C. O. Improved isolation procedure for azaspiracids from shellfish, structural elucidation of azaspiracid-6, and stability studies. *J. Agric. Food Chem.* **2012**, *60*, 2447−2455.
(25) Kilcoyne, J.; McCarron, P.; Twiner, M. J.; Nulty, C.; Wilkins, A. L.; Rise, F.; Quilliam, M. A.; Miles, C. O. Epimers of azaspiracids: isolation, structural elucidation, relative LC−MS response, and *in vitro* toxicity of 37-*epi*-azaspiracid-1. *Chem. Res. Toxicol.* **2014**, *27*, 587−600.
(26) Krock, B.; Tillmann, U.; Witt, M.; Gu, H. Azaspiracid variability of *Azadinium poporum* (Dinophyceae) from the China Sea. *Harmful Algae* **2014**, *36*, 22−28.
(27) McCarron, P.; Giddings, S. D.; Quilliam, M. A. A mussel tissue certified reference material for multiple phycotoxins. Part 2: liquid chromatography−mass spectrometry, sample extraction and quantitation procedures. *Anal. Bioanal. Chem.* **2014**, *400*, 835−846.
(28) Burton, I.; Quilliam, M. A.; Walter, J. A. Quantitative ^{1}H NMR with external standards: use in preparation of calibration solutions for algal toxins and other natural products. *Anal. Chem.* **2005**, *77*, 3123−3131.
(29) Twiner, M. J.; Hess, P.; Bottein Dechraoui, M. Y.; McMahon, T.; Samons, M. S.; Satake, M.; Yasumoto, T.; Ramsdell, J. S.; Doucette, G. J. Cytotoxic and cytoskeletal effects of azaspiracid-1 on mammalian cell lines. *Toxicon* **2005**, *45*, 891−900.
(30) Mosmann, T. Rapid colorimetric assay for cellular growth and survival: application to proliferation and cytotoxicity assays. *J. Immunol. Methods* **1983**, *65*, 55−63.
(31) Nicolaou, K. C.; Li, Y. W.; Uesaka, N.; Koftis, T. V.; Vyskocil, S.; Ling, T. T.; Govindasamy, M.; Qian, W.; Bernal, F.; Chen, D. Y. K. Total synthesis of the proposed azaspiracid-1 structure, part 1: construction of the enantiomerically pure C1-C20, C21-C27, and C28-C40 fragments. *Angew. Chem., Int. Ed.* **2003**, *42*, 3643−3648.
(32) Nicolaou, K. C.; Chen, D. Y. K.; Li, Y. W.; Qian, W. Y.; Ling, T. T.; Vyskocil, S.; Koftis, T. V.; Govindasamy, M.; Uesaka, N. Total synthesis of the proposed azaspiracid-1 structure, part 2: coupling of the C1-C20, C21-C27, and C28-C40 fragments and completion of the synthesis. *Angew. Chem., Int. Ed.* **2003**, *42*, 3649−3653.
(33) James, K. J.; Diaz Sierra, M.; Lehane, M.; Braña Magdalena, A.; Furey, A. Detection of five new hydroxyl analogues of azaspiracids in shellfish using multiple tandem mass spectrometry. *Toxicon* **2003**, *41*, 277−283.
(34) McCarron, P.; Kilcoyne, J.; Miles, C. O.; Hess, P. Formation of azaspiracids-3, −4, −6, and −9 via decarboxylation of carboxyazaspiracid metabolites from shellfish. *J. Agric. Food Chem.* **2009**, *57*, 160−169.
(35) Twiner, M. J.; El-Ladki, R.; Kilcoyne, J.; Doucette, G. J. Comparative effects of the marine algal toxins azaspiracid- 1, −2, and −3 on Jurkat T lymphocyte cells. *Chem. Res. Toxicol.* **2012**, *25*, 747−754.

NOTE ADDED AFTER ASAP PUBLICATION

Due to a production error, this paper was published on the Web on May 12, 2015, with footnote b to Table 3 missing. The corrected version was reposted on May 13, 2015.

DOI: 10.1021/acs.jafc.5b01320
J. Agric. Food Chem. 2015, 63, 5083−5091

JOURNAL OF AGRICULTURAL AND FOOD CHEMISTRY

Article

pubs.acs.org/JAFC

Comparative Toxicokinetics, Absolute Oral Bioavailability, and Biotransformation of Zearalenone in Different Poultry Species

Mathias Devreese,*[,†] Gunther Antonissen,[†,‡] Nathan Broekaert,[†] Siegrid De Baere,[†] Lynn Vanhaecke,[§] Patrick De Backer,[†] and Siska Croubels[†]

[†]Department of Pharmacology, Toxicology and Biochemistry, [‡]Department of Pathology, Bacteriology and Avian Diseases, and [§]Department of Veterinary Public Health and Food Safety, Faculty of Veterinary Medicine, Ghent University, Salisburylaan 133, B-9820 Merelbeke, Belgium

Supporting Information

ABSTRACT: After oral (PO) and intravenous (IV) administration of zearalenone (ZEN) to broiler chickens, laying hens, and turkey poults, the mycotoxin was rapidly absorbed (T_{max} = 0.32−0.97 h) in all three species; however, the absolute oral bioavailability was low (F% = 6.87−10.28%). Next, also a rapid elimination of the mycotoxin in all poultry species was observed ($T_{1/2el}$ = 0.29−0.46 h). Both α- and β-zearalenone (ZEL) were formed equally after IV administration in all species studied, whereas an increased biotransformation to β-ZEL was demonstrated after PO administration, indicating presystemic biotransformation mainly in broiler chickens and laying hens. In comparison to the latter, turkey poults demonstrated a more extensive biotransformation of ZEN to α-ZEL after PO administration which could, in combination with the observed higher volume of distribution of ZEN, indicate a higher sensitivity of this species to the effects of ZEN in comparison to other poultry species.

KEYWORDS: *poultry, laying hen, turkey, broiler chicken, zearalenone, toxicokinetics, biotransformation*

INTRODUCTION

Mycotoxins are secondary metabolites produced by different fungal species contaminating several food and feed commodities. Over 400 mycotoxins have been identified, although only a few of them are known to have distinct toxic effects. The most prevalent mycotoxin producing fungi in moderate climates are *Fusarium* species. Zearalenone (ZEN) is one of the most frequently occurring *Fusarium* mycotoxins. In a recent study by Streit,[1] 87% of the 83 investigated feed and feed raw material samples were contaminated with ZEN, with a median contamination level of 14 μg/kg and a maximum of 5.3 mg/kg. ZEN can be listed as a nonsteroidal estrogen or myco-estrogen.[2] It resembles 17β-estradiol, the principal hormone produced by the ovary, which allows ZEN to bind to estrogen receptors in target cells.[3] Once the estrogen receptor is bound, it undergoes a conformational change allowing the receptor to interact with chromatin and to modulate transcription of target genes.[4] Not all compounds have the same affinity for estrogen receptors. It has been shown that some phase I metabolites of ZEN can express lower or even higher affinities to estrogen receptors than the parent compound. In general, ZEN is metabolized by 3α- and 3β-hydroxysteroid dehydrogenase (HSD) into α- and β-zearalenol (ZEL), respectively. β-ZEL has a 2.5 times lower affinity for the estrogen receptor, whereas α-ZEL has a 92 times higher binding affinity in comparison to ZEN. The biotransformation to β-ZEL can therefore be regarded as an inactivation pathway, whereas the biotransformation to α-ZEL can be seen as a bioactivation.[5] The rate and extent of α- or β-ZEL production, and consequently the susceptibility, is species dependent. Pigs are regarded as the most sensitive species, as suggested by in vitro data demonstrating that pig liver microsomes dominantly convert ZEN into α-ZEL.[5] This has been confirmed in vivo, where α-ZEL was the only phase I metabolite detected in plasma, urine, and faeces of pigs intravenously (IV) dosed with ZEN.[6] Next, in a study by Zöllner[7] the α-ZEL/β-ZEL ratios were 2.5/1 and 3/1 in pig liver and urine, respectively, after oral intake of ZEN. In vitro results suggest that laying hens and cattle metabolize ZEN to a large extent into β-ZEL, which confirms that they are less prone to the effects of ZEN.[5,8] Next, also phase II biotransformation (conjugation) is regarded as a detoxification pathway. The extent of conjugation has also been found to have major interspecies variation. Migdalof[9] reported that glucuronidated metabolites account for 99% of the total ZEN recovered in humans, whereas in dogs glucuronidation only accounts for 1% of the excreted ZEN metabolites.

To date, no in vivo data are available in poultry regarding the phase I and phase II biotransformation of ZEN after oral exposure, which is mandatory to confirm the in vitro findings and the species-dependent sensitivity. Also, limited information on in vivo toxicokinetics and absolute oral bioavailability is available. Osselaere[10] reported a rapid elimination of ZEN after IV administration of 0.3 mg of ZEN/kg body weight (BW) to broiler chickens ($T_{1/2el}$ = 0.53 h), whereas after oral (PO) administration of the same dose, no ZEN or phase I metabolites could be detected in plasma (limit of quantification: 1−5 ng/mL). The rapid elimination and the assumed low oral bioavailability of the mycotoxin supports the limited toxicity of ZEN in this animal species. Furthermore, Dailey[11] administered 10 mg of [^{14}C]ZEN/kg BW to laying hens and demonstrated

Received: March 31, 2015
Revised: May 6, 2015
Accepted: May 7, 2015
Published: May 7, 2015

ACS Publications © 2015 American Chemical Society

DOI: 10.1021/acs.jafc.5b01608
J. Agric. Food Chem. 2015, 63, 5092−5098

that 94% of the administered dose was eliminated via the excreta within 72 h, with one-third as unchanged [^{14}C]ZEN and the other part as unidentified metabolites. Feeding mature laying hens a diet contaminated with ZEN up to 800 mg/kg did not affect their reproductive performance.[12,13] In contrast, feeding 100 mg of ZEN/kg of feed to mature female turkeys reduced the egg production by 20%.[14] Next, feeding 800 mg of ZEN/kg of feed to male turkeys for 2 weeks induced strutting behavior and an increased size and coloration of caruncles and dewlaps, which was not present in birds fed the uncontaminated diet.[15] This difference in sensitivity between broiler chickens and turkey poults is most probably attributed to differences in toxicokinetics and/or biotransformation processes.

Therefore, the aim of the present study was to unravel the toxicokinetic behavior, absolute oral bioavailability, and biotransformation of ZEN after PO as well as IV administration in the economically most important poultry species, namely broiler chickens, laying hens, and turkey poults.

MATERIALS AND METHODS

Chemicals, Products, and Reagents. The analytical standard of ZEN, used for both plasma analysis and the animal experiment, was obtained from Fermentek (Jerusalem, Israel). The analytical standards of α-ZEL, β-ZEL, α-zearalanol (α-ZAL), β-zearalanol (β-ZAL), and zearalanone (ZAN) used for the analytical experiments were obtained from Sigma-Aldrich (Bornem, Belgium). The internal standard (IS), $^{13}C_{18}$-ZEN, used for the analytical experiments was obtained from Romer Laboratories (Tulln, Austria). All analytical standards were stored at ≤−15 °C. Working solutions of ZEN, the described metabolites, and the IS were prepared by appropriate dilution of the stock solutions with acetonitrile (ACN) and stored at 2−8 °C. Water, methanol (MeOH), ACN, and glacial acetic acid used for the plasma analysis were of LC-MS grade and were obtained from Biosolve (Valkenswaard, The Netherlands). Water and dimethyl sulfoxide (DMSO) used for the animal experiment were of analytical grade and were obtained from Filterservice (Eupen, Belgium). Millex-GV PVDF filter units (0.22 μm) were obtained from Merck-Millipore (Overijse, Belgium).

Animals and Experimental Procedure. Six turkey Hybrid Converter poults (3 ♂/3 ♀, 0.95 ± 0.06 kg BW), broiler chickens (Ross 308, 3 ♂/3 ♀, 1.05 ± 0.05 kg BW) and laying hens (Brown Leghorn, 6 ♀, 1.04 ± 0.05 kg BW) were obtained from a commercial breeder. During the experiment, animals were housed in group and a 16 h light/8 h dark light cycle was applied. Feed and water were given ad libitum throughout the 1 week acclimatization period. Subsequently, 12 h before the start of the experiment, the animals were deprived of feed. After this period, three birds per species were administered ZEN (3 mg/kg BW) by oral gavage (PO), whereas the other three birds/species were injected the same dose of ZEN in the wing vein (IV). The PO and IV bolus solution was prepared by dissolving the ZEN standard in DMSO (10 mg/mL) and further diluted with water (PO) or physiological saline (IV) up to a volume of 1 mL. Following administration of the mycotoxin, 0.5 mL of blood was drawn from the leg vein at various time points: 0 (just before administration) and 2, 5, 10, 20, 30, 40, 50, 60, 120, 180, and 240 min postadministration. Samples were centrifuged (2851*g*, 10 min, 4 °C), and aliquots of plasma (150 μL) were stored at ≤−15 °C until analysis. After a 2 day wash-out period, the protocol was repeated in a two-way crossover design. The birds that received an IV injection of the mycotoxin then received a PO bolus and vice versa. The dosing, blood collection, and sample storage was performed in the same way as the first administration. The animal experiment was approved by the Ethical Committee of the Faculty of Veterinary Medicine and Bioscience Engineering of Ghent University (EC 2014/118).

LC-MS/MS Analysis. Sample treatment and quantification of ZEN, and its phase I metabolites (α-ZEL, β-ZEL, α-ZAL, β-ZAL and ZAN; see Figure 1 in the Supporting Information), in poultry plasma were performed as previously described by De Baere et al. with minor modifications. Briefly, 50 μL of IS working solution (50 ng/mL) was added to 150 μL of plasma, followed by the addition of ACN up to 1 mL. Next, the sample was vortex mixed (15 s) and centrifuged (8517*g*, 10 min, 4 °C). The supernatant was evaporated to dryness using nitrogen (N_2, 45 ± 5 °C). The dry residue was reconstituted in 200 μL of water/MeOH (85/15, v/v), vortex mixed (15 s), filtered through a Millex GV-PVDF syringe filter, and transferred into a conical autosampler vial. An aliquot (5 μL) was injected onto the LC-MS/MS instrument.

Chromatographic separation was achieved on a Hypersil Gold column (50 mm × 2.1 mm i.d., dp 1.9 μm) in combination with a guard column of the same type (10 mm × 2.1 mm i.d., dp 3 μm), both from ThermoFisher Scientific (Breda, The Netherlands). Mobile phase A consisted of 0.1% acetic acid in water, whereas mobile phase B was ACN. The following gradient elution program was run: 0−0.5 min (70% A, 30% B), 0.5−5.0 min (linear gradient to 70% B), 5.0−6.4 min (30% A, 70% B), 6.4−6.5 min (linear gradient to 30% B), 6.5−8.5 min (70% A, 30% B). The flow rate was set at 300 μL/min, and the temperatures of the column oven and autosampler tray were set at 45 and 5 °C, respectively.

Detection was performed on a Waters Xevo TQ-S triple-quadrupole mass spectrometer by means of electrospray ionization (ESI) in the negative ionization mode. The instrument was tuned by direct infusion of a 10 ng/mL working solution of ZEN, the metabolites, and the IS. The following parameters were retained for optimal detection: capillary voltage, 2.5 kV; cone voltage, 15 V; source temperature, 150 °C; desolvation temperature, 600 °C; cone gas flow, 150 L/h; desolvation gas flow, 1000 L/h. Acquisition was performed in the selected reaction monitoring (SRM) mode. The following transitions (m/z) were used as quantifier and qualifier ion, respectively: for ZEN, 317.1 > 175.0 and 317.1 > 131.0; for α-ZEL, 319.0 > 275.0 and 319.0 > 159.9; for β-ZEL, 319.0 > 159.9 and 319.0 > 275.0; for ZAN, 319.0 > 205.0 and 319.0 > 275.0; for α-ZAL, 321.1 > 277.1 and 321.1 > 303.0; for β-ZAL, 321.1 > 277.1 and 321.1 > 303.0; for IS, 335.2 > 168.9 and 335.2 > 185.0. The method was validated for the compounds listed above according to a validation protocol described by De Baere[16] based on European[17] and international[18] guidelines. The validation protocol encompassed the following parameters: linearity (correlation coefficient and goodness-of-fit), within- and between-run accuracy and precision, carryover, limit of quantification (LOQ), and limit of detection (LOD). The LOQ was set at 0.5 ng/mL for ZEN, 0.2 ng/mL for α-ZEL and α-ZAL, and 0.1 ng/mL for β-ZEL, β-ZAL, and ZAN.

UHPLC-HRMS Analysis. The extracted samples were also analyzed by UHPLC coupled to HRMS analysis for identification and semiquantification of the glucuronide conjugates of ZEN and of its phase I metabolites as previously described by De Baere.[19] This was performed on the basis of the peak area ratios of the metabolites, versus the IS. The UHPLC system consisted of an Accela type 1250 high-speed LC and autosampler, both from ThermoFisher Scientific. The same HPLC column and mobile phases were used as described above. The UHPLC was interfaced to an Exactive Orbitrap HR mass spectrometer, equipped with a heated ESI probe operating in the negative ionization mode (ThermoFisher Scientific). Accurate masses were based on the predicted masses (m/z; $[M - H]^-$) described by De Baere[19] and Stevenson:[20] ZEN-glucuronide (ZEN-GlcA, $C_{24}H_{30}O_{11}$), 493.17153; ZAN-GlcA, α-ZEL-GlcA and β-ZEL-GlcA ($C_{24}H_{32}O_{11}$, no chromatographic separation or distinction between these compounds based on accurate masses possible), 495.18718; α-ZAL-GlcA and β-ZAL-GlcA ($C_{24}H_{34}O_{11}$, no chromatographic separation or distinction between these compounds based on accurate masses possible), 497.20283. Confirmation of the GlcA peaks observed in the extracted ion chromatogram (EIC) was performed by comparing the theoretically calculated $^{13}C/^{12}C$ isotope ratios for the $[M - H]^-$ ion with the corresponding isotope ratios detected in the analyzed samples, as described by De Baere.[19]

Toxicokinetic Analysis. Noncompartmental toxicokinetic analysis of ZEN and α- and β-ZEL was performed with WinNonlin 6.3 (Pharsight, St. Louis, MO, USA). For ZEN, the following toxicokinetic parameters were calculated for IV and PO administration: maximum plasma concentration for PO (C_{max}), plasma concentration at time 0 for IV (C_0), time to maximum plasma concentration (T_{max}), area under the

DOI: 10.1021/acs.jafc.5b01608
J. Agric. Food Chem. 2015, 63, 5092−5098

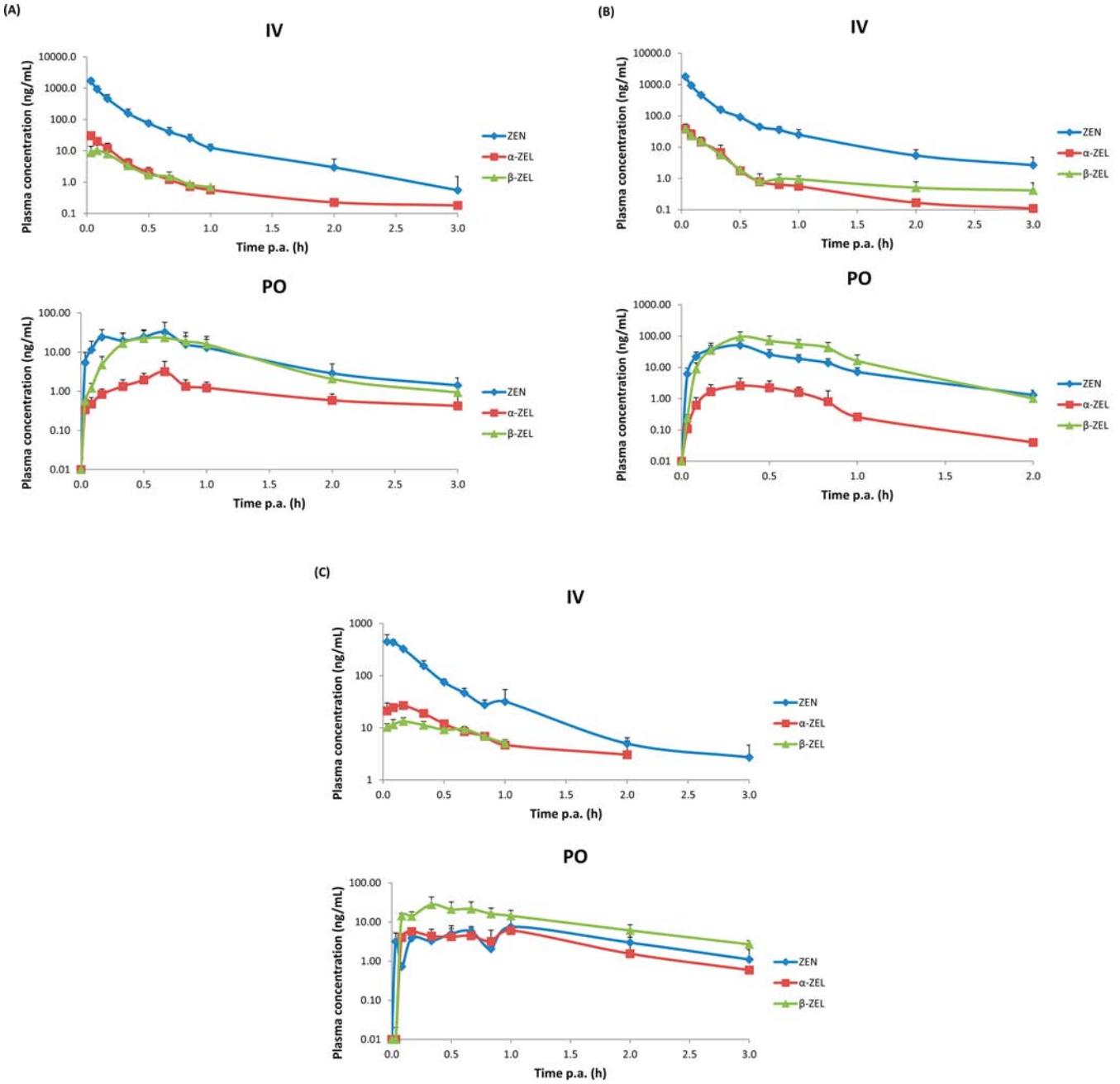

Figure 1. Plasma concentration−time profile of zearalenone (ZEN), α-zearalenol (α-ZEL), and β-zearalenol (β-ZEL) after intravenous (IV) and oral (PO) administration of 3 mg of ZEN/kg of body weight to broiler chickens (A), laying hens (B), and turkey poults (C) ($n = 6$). Values are presented as means + SD.

plasma concentration−time curve from time 0 to 3 h (AUC_{0-t}), area under the plasma concentration−time curve from time 0 to infinite (AUC_{0-inf}), elimination rate constant (k_{el}), elimination half-life ($T_{1/2el}$), total body clearance (Cl), volume of distribution (V_d), and mean residence time (MRT).

The absolute oral bioavailability (F, expressed as %, F%) for each individual bird was calculated according to the formula

$$F\% = AUC_{0-inf\,PO}/AUC_{0-inf\,IV} \times 100$$

The Cl and V_d values after PO administration were calculated by multiplying the data generated by the toxicokinetic software (i.e., V_d/F and Cl/F) by the F value from each individual bird.

The mean absorption time (MAT) was calculated according to the formula

$$MAT = MRT_{PO} - MRT_{IV}$$

The absorption rate constant (k_a) and absorption half-life ($T_{1/2a}$) were derived from the MAT:

$$k_a = MAT^{-1}$$

$$T_{1/2a} = 0.693/k_a$$

For α- and β-ZEL, the C_{max}, T_{max}, AUC_{0-t} (from time 0 to the last time point above the LOQ, i.e. 2 or 3 h) and AUC_{0-inf} values were determined after both IV and PO administration of ZEN. Next, ZEL/ZEN ratios were calculated according to the formulas

$$\alpha\text{-ZEL/ZEN} = AUC_{0-inf\,\alpha\text{-ZEL}}/AUC_{0-inf\,ZEN}$$

$$\beta\text{-ZEL/ZEN} = AUC_{0-inf\,\beta\text{-ZEL}}/AUC_{0-inf\,ZEN}$$

DOI: 10.1021/acs.jafc.5b01608
J. Agric. Food Chem. 2015, 63, 5092−5098

Table 1. Main Toxicokinetic Parameters of Zearalenone after Oral (PO) and Intravenous (IV) Administration (3 mg/kg BW) to Broiler Chickens, Laying Hens, And Turkey Poults ($n = 6$)[a]

	broiler chicken		laying hen		turkey poult	
	PO	IV	PO	IV	PO	IV
C_{max}(PO)[b] or C_0(IV)[c] (ng/mL)	39.17 ± 18.67[a,b]	2607.0 ± 506.03[a]	54.12 ± 22.90[a]	2789.2 ± 189.78[a]	8.33 ± 2.21[b]	700.5 ± 301.18[b]
T_{max} (h)[d]	0.35 ± 0.16[a]		0.32 ± 0.08[a]		0.97 ± 0.36[b]	
AUC_{0-t} ((h ng)/mL)[e]	21.87 ± 12.12[a,b]	290.9 ± 72.78[a]	29.31 ± 6.78[a]	322.8 ± 37.27[a]	8.53 ± 3.07[b]	180.0 ± 21.12[b]
AUC_{0-inf} ((h ng)/mL)[f]	23.59 ± 15.62[a]	292.1 ± 72.50[a]	30.04 ± 6.45[a]	324.9 ± 35.94[a]	10.21 ± 5.57[b]	183.1 ± 18.92[b]
k_a (h^{-1})[g]	3.36 ± 1.52[a]		3.50 ± 1.41[a]		3.68 ± 2.28[a]	
$T_{1/2a}$ (h)[h]	0.26 ± 0.10[a]		0.24 ± 0.09[a]		0.30 ± 0.19[a]	
MRT (h)[i]	0.53 ± 0.13[a]	0.16 ± 0.02[a]	0.53 ± 0.07[a]	0.22 ± 0.04[a,b]	0.68 ± 0.19[a]	0.33 ± 0.09[b]
MAT (h)[j]	0.37 ± 0.14[a]		0.35 ± 0.13[a]		0.44 ± 0.27[a]	
Cl (L/(h kg))[k]	9.06 ± 4.61[a]	11.1 ± 2.91[a]	11.38 ± 3.03[a]	9.39 ± 1.08[a]	19.66 ± 3.87[b]	16.57 ± 1.64[b]
k_{el} (h^{-1})[l]	2.14 ± 0.35[a]	2.86 ± 1.06[a]	1.98 ± 0.37[a]	1.72 ± 0.07[a]	2.04 ± 0.57[a]	1.83 ± 0.10[a]
$T_{1/2el}$ (h)[m]	0.34 ± 0.07[a]	0.29 ± 0.11[a]	0.36 ± 0.07[a]	0.46 ± 0.12[a]	0.35 ± 0.10[a]	0.38 ± 0.02[a]
V_d (L/kg)[n]	3.21 ± 2.13[a]	4.16 ± 0.75[a]	6.18 ± 2.52[a]	6.24 ± 0.92[a]	10.65 ± 1.05[b]	9.03 ± 1.43[b]
F (%)[o]	8.34 ± 5.96[a]	100[a]	10.28 ± 2.53[a]	100[a]	6.87 ± 3.54[a]	100[a]

[a]Values are presented as means ± SD. A different superscript (a or b) denotes a significant difference between animal species for each administration route at $p < 0.05$. [b]C_{max} = maximum plasma concentration. [c]C_0 = plasma concentration at time 0. [d]T_{max} = time to maximum plasma concentration. [e]AUC_{0-t} = area under the plasma concentration−time curve from time 0 to 3 h. [f]AUC_{0-inf} = area under the plasma concentration−time curve from time 0 to infinite. [g]k_a = absorption rate constant. [h]$T_{1/2a}$: = absorption half-life. [i]MRT = mean residence time. [j]MAT = mean absorption time. [k]Cl = total body clearance. [l]k_{el} = elimination rate constant. [m]$T_{1/2el}$ = elimination half-life. [n]V_d = volume of distribution. [o]F = absolute oral bioavailability.

$$\text{ZEL/ZEN} = (\text{AUC}_{0-\text{inf}\,\alpha\text{-ZEL}} + \text{AUC}_{0-\text{inf}\,\beta\text{-ZEL}})/\text{AUC}_{0-\text{inf ZEN}}$$

Finally, the α-ZEL/β-ZEL ratio was calculated according to the formula

$$\alpha\text{-ZEL}/\beta\text{-ZEL} = \text{AUC}_{0-\text{inf}\,\alpha\text{-ZEL}}/\text{AUC}_{0-\text{inf}\,\beta\text{-ZEL}}$$

Statistical Analysis. All toxicokinetic parameters from each compound (ZEN, α- and β-ZEL) and each administration route were compared between animal species using one-way analysis of variance (ANOVA) (SPSS 21, IBM, USA). The level of significance was set at 0.05.

RESULTS AND DISCUSSION

The goal of this study was to unravel the toxicokinetic behavior, absolute oral bioavailability, and biotransformation of ZEN in different poultry species in order to assess potential species-dependent sensitivity to this mycotoxin. During the animal experiment, no clinical symptoms were observed after PO or IV administration of ZEN to the birds. Furthermore, no sex differences in toxicokinetic parameters were observed for broiler chickens and turkey poults. In Figure 1, the plasma concentration−time profiles of ZEN and α- and β-ZEL after IV and PO administration of ZEN to broiler chickens, laying hens, and turkey poults are presented. Only trace amounts of α- and β-ZAL and ZAN were detected, but none were above the LOQ of 0.2, 0.1, and 0.1 ng/mL, respectively. As can be seen in Figure 1 and Table 1, ZEN is rapidly absorbed in all studied poultry species, namely broiler chickens (T_{max} = 0.35 h, MAT = 0.37 h), laying hens (T_{max} = 0.32 h, MAT = 0.35 h), and turkey poults (T_{max} = 0.97 h, MAT = 0.44 h). However, the F% is low in all studied poultry species: 8.34%, 10.28%, and 6.87%, in broiler chickens, laying hens, and turkey poults, respectively. This might indicate either a low extent of absorption and/or extensive presystemic biotransformation, and is attributed to the generally accepted high tolerance of poultry to ZEN, since F is a measurement for systemic exposure. Next to rapid absorption, the mycotoxin is rapidly eliminated in all species as well with $T_{1/2el}$ values between 0.34 and 0.36 h and between 0.29 and 0.46 h after PO and IV administration, respectively. Osselaere[10] reported a similar $T_{1/2el}$ value of 0.53 h after IV administration of 0.3 mg of ZEN/kg of BW to broiler chickens. Furthermore, a high V_d value is observed after PO and IV administration in all animal species (V_d = 3.21−10.65 L/kg). For broiler chickens, an even higher V_d value has been reported previously by Osselaere,[10] namely 22.26 L/kg; however, this value was reported with a high uncertainty (15.15 L/kg). Of interest here is that turkey poults have a significant higher V_d value (9.03−10.65 L/kg) in comparison to broiler chickens (3.21−4.16 L/kg) and laying hens (6.18−6.24 L/kg), which supports the hypothesis of a higher sensitivity to ZEN of this species. Furthermore, the higher V_d value explains why the C_0 value is significantly lower in turkey poults (C_0 = 700.5 ng/mL) in comparison to broiler chickens (C_0 = 2607.0 ng/mL) and laying hens (C_0 = 2789.2 ng/mL), although they were administered the same dose of ZEN (3 mg/kg BW). In addition, pigs display a high V_d value of ZEN, comparable to that of turkey poults, after IV administration, namely 10.84 L/kg, leading to a high tissue distribution of the mycotoxin.[6] In addition to a higher V_d value in turkey poults, also a significantly higher Cl value in turkeys (Cl = 16.57−19.66 L/h/kg) in comparison to those in broiler chickens (Cl = 9.06−11.1 L/(h kg)) and laying hens (Cl = 9.39−11.38 L/(h kg)) was noticed. Since both V_d and Cl values are higher in turkey poults, this leads to comparable $T_{1/2el}$ values between the latter ($T_{1/2el}$ = 0.35−0.38 h) and broiler chickens ($T_{1/2el}$ = 0.29−0.34 h) and laying hens ($T_{1/2el}$ = 0.36−0.46 h). Next, due to the higher Cl values in turkey poults and comparable F values, the AUC_{0-inf} value is significantly lower in this species after both administration routes ($AUC_{0-inf\,PO}$ = 10.21 (h ng)/mL, $AUC_{0-inf\,IV}$ = 183.12 (h ng)/mL) in comparison to broiler chickens ($AUC_{0-inf\,PO}$ = 23.59 (h ng)/mL, $AUC_{0-inf\,IV}$ = 292.10 (h ng)/mL) and laying hens ($AUC_{0-inf\,PO}$ = 30.04 (h ng)/mL, $AUC_{0-inf\,IV}$ = 324.93 (h ng)/mL). Similarly, also the AUC_{0-t} value was significantly lower.

As described above, species-dependent biotransformation of ZEN has a distinct impact on sensitivity to this mycotoxin, and the in vitro estrogenic potency of its phase I metabolites is as follows: α-ZAL > α-ZEL > β-ZAL > ZEN > β-ZEL.[21] Phase I biotransformation of ZEN consists of reduction of the ketone group of ZEN to its corresponding alcohol by 3α-/3β-HSD,

DOI: 10.1021/acs.jafc.5b01608
J. Agric. Food Chem. 2015, 63, 5092−5098

Table 2. Main Toxicokinetic Parameters of α- and β-Zearalenol (α-/β-ZEL) after Oral (PO) and Intravenous (IV) Administration of Zearalenone (3 mg/kg BW) to Broiler Chickens, Laying Hens, and Turkey Poults ($n = 6$)[a]

	broiler chicken		laying hen		turkey poult	
	PO	IV	PO	IV	PO	IV
α-ZEL						
C_{max} (ng/mL)[b]	3.99 ± 2.53[a]	30.31 ± 10.23[a]	3.20 ± 1.99[a]	37.91 ± 10.07[a]	6.45 ± 0.33[a]	27.32 ± 2.21[a]
T_{max} (h)[c]	0.63 ± 0.11[a]	0.03 ± 0.00[a]	0.27 ± 0.08[a]	0.03 ± 0.00[a]	0.58 ± 0.08[a]	0.09 ± 0.03[b]
AUC_{0-t} ((h ng)/mL)[d]	2.44 ± 0.80[a]	5.68 ± 1.61[a]	1.57 ± 0.87[a]	6.81 ± 1.80[a]	11.60 ± 0.14[b]	17.71 ± 2.35[b]
AUC_{0-inf} ((h ng)/mL)[e]	2.79 ± 1.37[a]	5.93 ± 1.68[a]	1.63 ± 0.89[a]	6.99 ± 1.75[a]	15.58 ± 8.39[b]	20.04 ± 5.12[b]
β-ZEL						
C_{max} (ng/mL)[b]	25.25 ± 13.96[a]	13.30 ± 6.48[a]	96.16 ± 38.95[b]	38.92 ± 16.14[b]	28.52 ± 15.36[a]	15.14 ± 1.61[a]
T_{max} (h)[c]	0.61 ± 0.11[a]	0.07 ± 0.19[a]	0.42 ± 0.08[a,b]	0.03 ± 0.00[a]	0.37 ± 0.14[b]	0.15 ± 0.03[b]
AUC_{0-t} (h.ng/mL)[d]	24.55 ± 15.09[a]	3.50 ± 1.51[a]	58.48 ± 14.60[a]	6.64 ± 2.81[b]	29.66 ± 13.43[a]	9.83 ± 1.43[b]
AUC_{0-inf} (h.ng/mL)[e]	27.36 ± 17.51[a]	4.09 ± 1.87[a]	58.84 ± 14.54[a]	6.90 ± 2.71[a]	38.83 ± 20.04[a]	15.36 ± 3.42[b]
α-ZEL/ZEN[f]	0.138 ± 0.073[a]	0.020 ± 0.001[a]	0.057 ± 0.026[a]	0.021 ± 0.004[a]	1.015 ± 0.369[b]	0.109 ± 0.033[b]
β-ZEL/ZEN[g]	1.607 ± 1.159[a]	0.018 ± 0.011[a]	2.029 ± 0.262[a]	0.021 ± 0.006[a]	4.888 ± 3.124[a]	0.089 ± 0.028[b]
ZEL/ZEN[h]	1.149 ± 0.525[a]	0.032 ± 0.009[a]	2.086 ± 0.271[a]	0.042 ± 0.009[a]	5.226 ± 2.898[b]	0.152 ± 0.040[b]
α-ZEL/β-ZEL[i]	0.153 ± 0.049[a]	1.629 ± 0.566[a]	0.027 ± 0.013[a]	1.073 ± 0.151[a]	0.749 ± 0.292[b]	1.076 ± 0.243[a]

[a]Values are presented as means ± SD. A different superscript (a or b) denotes a significant difference between animal species for each administration route at $p < 0.05$. [b]C_{max} = maximum plasma concentration. [c]T_{max} = time to maximum plasma concentration. [d]AUC_{0-t} = area under the plasma concentration−time curve from time 0 to 2 or 3 h. [e]AUC_{0-inf} = area under the plasma concentration−time curve from time 0 to infinite. [f]α-ZEL/ZEN = $AUC_{0-inf\,\alpha\text{-ZEL}}/AUC_{0-inf\,ZEN}$. [g]β-ZEL/ZEN = $AUC_{0-inf\,\beta\text{-ZEL}}/AUC_{0-inf\,ZEN}$. [h]ZEL/ZEN = $(AUC_{0-inf\,\alpha\text{-ZEL}} + AUC_{0-inf\,\beta\text{-ZEL}})/AUC_{0-inf\,ZEN}$. [i]α-ZEL/β-ZEL = $AUC_{0-inf\,\alpha\text{-ZEL}}/AUC_{0-inf\,\beta\text{-ZEL}}$.

thereby forming α-/β-ZEL, and aromatic hydrogenation of α-/β-ZEL to α-/β-ZAL by cytochrome P450 (CYP450) enzymes. Finally, α-/β-ZAL can be oxidized by 3α-/3β-HSD to ZAN. The biotransformation of ZEL to ZAL and ZAN has been reported for pigs and humans; however, the extent is negligible.[21] In addition, in the present study only trace amounts of α-/β-ZAL and ZAN were detected, demonstrating that formation of α- and β-ZEL is also the predominant phase I biotransformation in poultry. In all three poultry species both α- and β-ZEL could be detected, although the extent differed between species and routes of administration (Figure 1 and Table 2). Turkey poults have a more efficient biotransformation of ZEN to α- and β-ZEL in comparison to broiler chickens and laying hens, with higher α-ZEL/ZEN and β-ZEL/ZEN ratios after both PO and IV administration (although not significant for β-ZEL/ZEN after PO), whereas these ratios are comparable between broiler chickens and laying hens (Table 2). Consequently, also the ZEL/ZEN ratio in turkey poults is significantly higher after PO (ZEL/ZEN_{PO} = 5.226) as well as IV administration (ZEL/ZEN_{IV} = 0.152) in comparison to broiler chickens (ZEL/ZEN_{PO} = 1.149, ZEL/ZEN_{IV} = 0.032) and laying hens (ZEL/ZEN_{PO} = 2.086, ZEL/ZEN_{IV} = 0.042). Furthermore, the biotransformation of ZEN to α- and β-ZEL occurs to a greater extent after PO than after IV administration in all animal species. This difference in ZEL formation between both administration routes indicates presystemic biotransformation of ZEN in the gut and/or the liver. After IV administration, the α-ZEL/β-ZEL ratio is not statistically different between bird species and is around 1 (α-ZEL/$\beta\text{-ZEL}_{IV}$ = 1.073 to 1.629). In contrast, after PO administration the β-ZEL isomer is predominantly formed in broiler chickens (α-ZEL/$\beta\text{-ZEL}_{PO}$ = 0.153) and laying hens (α-ZEL/$\beta\text{-ZEL}_{PO}$ = 0.027), but this is significantly different in turkey poults (α-ZEL/$\beta\text{-ZEL}_{PO}$ = 0.749). Again, this indicates presystemic formation of mainly β-ZEL, especially in broiler chickens and laying hens. These data confirm the in vitro findings in laying hen: namely, a predominant β-ZEL formation.[5] Since the α-ZEL/ZEN ratio after PO and IV ZEN administration is significantly higher in turkey poults in comparison to both other bird species, this supports the hypothesis of increased sensitivity of turkey poults to the estrogenic effects of the mycotoxin.

Phase II biotransformation of ZEN and its phase I metabolites comprises glucuronidation which is catalyzed by uridine 5′-diphosphate glucuronosyltransferase (UGT).[22] Since no analytical standards of glucuronidated ZEN (ZEN-GlcA) or glucuronidated α- or β-ZEL (ZEL-GlcA) are commercially available, no accurate quantitative analysis could be performed. However, a semiquantitative using HR-MS was done (Figure 2). After IV administration of ZEN, ZEN-GlcA is the predominant phase II metabolite in all three bird species. Although the ZEL/ZEN ratio is higher in turkey poults, namely 0.152, in comparison to broiler chickens and laying hens, 0.032 and 0.042, respectively, no ZEL-GlcA could be detected in this species after IV administration, which is in contrast to the other species. After oral ZEN administration, comparable amounts of ZEN-GlcA and ZEL-GlcA were detected in broiler chickens and laying hens, whereas in turkey poults only ZEL-GlcA was detected, attributed to the high ZEL/ZEN ratio in this species after PO administration (ZEL/ZEN = 5.226). This confirms the phase I biotransformation data: namely, a presystemic ZEL formation and consequent predominant ZEL glucuronidation. Differences in phase II biotransformation might also account for differences in sensitivity. For the mycotoxin DON, for instance, limited sulfation was described for turkeys in contrast to broiler chickens, which might explain the increased sensitivity of turkeys to deoxynivalenol.[23] In addition, for the mycotoxin aflatoxin B1 (AFB1), turkeys are more sensitive in comparison to other poultry and animal species on the basis of differences in biotransformation of AFB1. In turkeys, the phase I bioactivation of AFB1 to AFB1-8,9-epoxide is highly efficient and the epoxide metabolite is held responsible for the hepatotoxic and carcinogenic effects of AFB1.[24] Furthermore, turkeys have a glutathione-*S*-transferase deficiency (phase II biotransformation) which adds to the sensitivity of this species.[25]

In conclusion, this paper describes—for the first time—the toxicokinetic behavior, absolute oral bioavailability, and comparative phase I and II biotransformation of ZEN in broiler

DOI: 10.1021/acs.jafc.5b01608
J. Agric. Food Chem. 2015, 63, 5092−5098

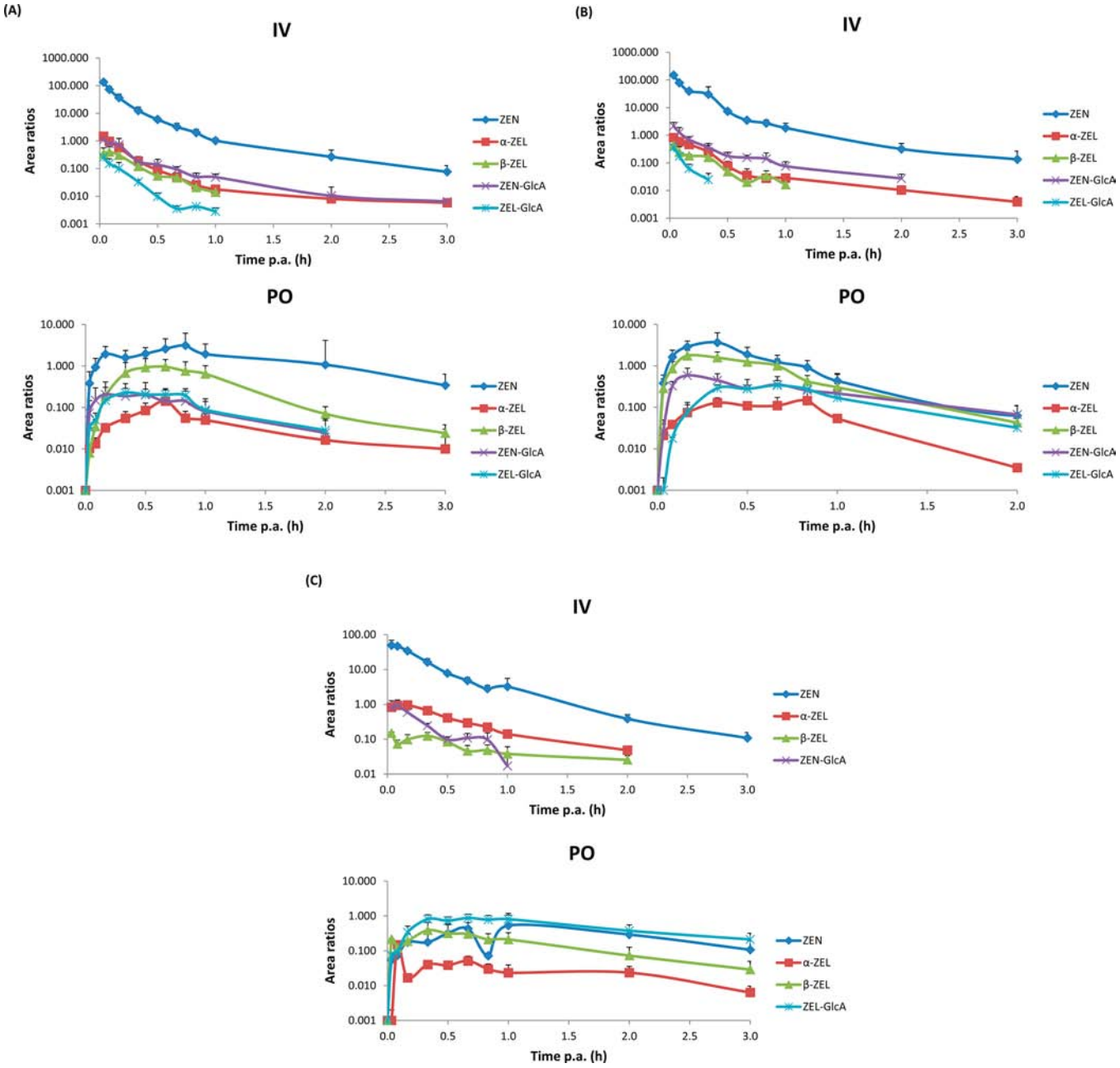

Figure 2. Ratio of the peak area detected by ultrahigh-performance liquid chromatography coupled to high-resolution mass spectrometry of zearalenone (ZEN) or its metabolites, namely α-zearalenol (α-ZEL), β-zearalenol (β-ZEL), ZEN-glucuronide (ZEN-GlcA), and ZEL-glucuronide (ZEL-GlcA), and the internal standard ($^{13}C_{18}$-ZEN) plotted against the time after intravenous (IV) or oral (PO) administration (p.a.) of 3 mg of ZEN/kg of body weight to broiler chickens (A), laying hens (B), or turkey poults (C) (n = 6). Values are presented as means + SD.

chickens, laying hens, and turkey poults. ZEN is rapidly absorbed in all studied poultry species, but the absolute oral bioavailability of the mycotoxin is low. Furthermore, it is rapidly eliminated as well after both PO and IV administration. Both α- and β-ZEL were formed equally after IV administration in all bird species, whereas an increased biotransformation to β-ZEL was demonstrated after oral administration, indicating presystemic biotransformation processes, primarily in broiler chickens and laying hens. Finally, the presented data suggest that turkey poults might be more sensitive to the effects of ZEN on the basis of the higher V_d value of ZEN and the more extensive presystemic biotransformation of ZEN to α-ZEL in comparison to the two other poultry species.

■ ASSOCIATED CONTENT

Supporting Information

A figure giving the chemical structure and phase I biotransformation pathways of zearalenone (adapted from Mukherjee[21]). The Supporting Information is available free of charge on the ACS Publications website at DOI: 10.1021/acs.jafc.5b01608.

■ AUTHOR INFORMATION

Corresponding Author

*M.D.: e-mail, mathias.devreese@ugent.be; tel, + 32 9 264 73 24; fax, +32 9 264 74 97.

Notes

The authors declare no competing financial interest.

DOI: 10.1021/acs.jafc.5b01608
J. Agric. Food Chem. 2015, 63, 5092−5098

REFERENCES

(1) Streit, E.; Schwab, C.; Sulyok, M.; Naehrer, K.; Krska, R.; Schatzmayr, G. Multi-mycotoxin screening reveals the occurrence of 139 different secondary metabolites in feed and feed ingredients. *Toxins* **2013**, *5*, 504−23.

(2) Tiemann, U.; Danicke, S. In vivo and in vitro effects of the mycotoxins zearalenone and deoxynivalenol on different non-reproductive and reproductive organs in female pigs: A review. *Food Addit. Contam.* **2007**, *24*, 306−314.

(3) Greenman, D. L.; Mehta, R. G.; Wittliff, J. L. Nuclear interaction of Fusarium mycotoxins with estradiol binding sites in the mouse uterus. *J. Toxicol. Environ. Health* **1979**, *5*, 593−8.

(4) Kuiper, G. G. J. M.; Lemmen, J. G.; Carlsson, B.; Corton, J. C.; Safe, S. H.; van der Saag, P. T.; van der Burg, P.; Gustafsson, J. A. Interaction of estrogenic chemicals and phytoestrogens with estrogen receptor beta. *Endocrinology* **1998**, *139*, 4252−4263.

(5) Malekinejad, H.; Maas-Bakker, R.; Fink-Gremmels, J. Species differences in the hepatic biotransformation of zearalenone. *Vet. J.* **2006**, *172*, 96−102.

(6) Dänicke, S.; Valenta, H.; Doll, S. On the toxicokinetics and the metabolism of deoxynivalenol (DON) in the pig. *Arch. Anim. Nutr.* **2004**, *58*, 169−180.

(7) Zollner, P.; Jodlbauer, J.; Kleinova, M.; Kahlbacher, H.; Kuhn, T.; Hochsteiner, W.; Lindner, W. Concentration levels of zearalenone and its metabolites in urine, muscle tissue, and liver samples of pigs fed with mycotoxin-contaminated oats. *J. Agric. Food Chem.* **2002**, *50*, 2494−2501.

(8) Zinedine, A.; Soriano, J. M.; Molto, J. C.; Manes, J. Review on the toxicity, occurrence, metabolism, detoxification, regulations and intake of zearalenone: an oestrogenic mycotoxin. *Food Chem. Toxicol.* **2007**, *45*, 1−18.

(9) Migdalof, B. H.; Dugger, H. A.; Heider, J. G.; Coombs, R. A.; Terry, M. K. Biotransformation of zeranol: disposition and metabolism in the female rat, rabbit, dog, monkey and man. *Xenobiotica* **1983**, *13*, 209−21.

(10) Osselaere, A.; Devreese, M.; Goossens, J.; Vandenbroucke, V.; De Baere, S.; De Backer, P.; Croubels, S. Toxicokinetic study and absolute oral bioavailability of deoxynivalenol, T-2 toxin and zearalenone in broiler chickens. *Food Chem. Toxicol.* **2013**, *51*, 350−5.

(11) Dailey, R. E.; Reese, R. E.; Brouwer, E. A. Metabolism of [Zearalenone-C-14 in Laying Hens. *J. Agric. Food Chem.* **1980**, *28*, 286−291.

(12) Allen, N. K.; Aakhusallen, S.; Mirocha, C. J. Effect of Zearalenone on Reproduction of Chickens. *Poultry Sci.* **1980**, *59*, 1577−1577.

(13) Allen, N. K.; Mirocha, C. J.; Aakhusallen, S.; Bitgood, J. J.; Weaver, G.; Bates, F. Effect of Dietary Zearalenone on Reproduction of Chickens. *Poult. Sci.* **1981**, *60*, 1165−1174.

(14) Allen, N. K.; Peguri, A.; Mirocha, C. J.; Newman, J. A. Effects of Fusarium Cultures, T-2-Toxin, and Zearalenone on Reproduction of Turkey Females. *Poult. Sci.* **1983**, *62*, 282−289.

(15) Olsen, M.; Mirocha, C. J.; Abbas, H. K.; Johansson, B. Metabolism of High-Concentrations of Dietary Zearalenone by Young Male Turkey Poults. *Poult. Sci.* **1986**, *65*, 1905−1910.

(16) De Baere, S.; Goossens, J.; Osselaere, A.; Devreese, M.; Vandenbroucke, V.; De Backer, P.; Croubels, S. Quantitative determination of T-2 toxin, HT-2 toxin, deoxynivalenol and deepoxy-deoxynivalenol in animal body fluids using LC-MS/MS detection. *J. Chromatogr. B: Anal. Technol. Biomed. Life Sci.* **2011**, *879*, 2403−2415.

(17) European Union. The rules governing medicinal products in the European Union Volume 8: Notice to applicants and guideline on the establishment of maximum residue limits (MRLs) for residues of veterinary medicinal products in foodstuffs of animal origin; weblink http://ec.europa.eu/health/files/eudralex/vol-8/pdf/vol8_10-2005_en.pdf (consulted on May 4, 2015).

(18) VICH GL49(R). Guidance for Industry Studies to Evaluate the Metabolism and Residue Kinetics of Veterinary Drugs in Food-Producing Animals: Validation of Analytical Methods Used in Residue Depletion Studies; weblink http://www.fda.gov/downloads/AnimalVeterinary/GuidanceComplianceEnforcement/GuidanceforIndustry/UCM207942.pdf (consulted on May 4, 2015).

(19) De Baere, S.; Osselaere, A.; Devreese, M.; Van Haecke, L.; De Backer, P.; Croubels, S. Quantitative determination of zearalenone and its major metabolites in animal plasma using LC-MS/MS and (U)HPLC-HR-MS detection. *Anal. Chim. Acta* **2012**, *756*, 37−48.

(20) Stevenson, D. E.; Hansen, R. P.; Loader, J. I.; Jensen, D. J.; Cooney, J. M.; Wilkins, A. L.; Miles, C. O. Preparative enzymatic synthesis of glucuronides of zearalenone and five of its metabolites. *J. Agric. Food Chem.* **2008**, *56*, 4032−4038.

(21) Mukherjee, D.; Royce, S. G.; Alexander, J. A.; Buckley, B.; Isukapalli, S. S.; Bandera, E. V.; Zarbl, H.; Georgopoulos, P. G., Physiologically-Based Toxicokinetic Modeling of Zearalenone and Its Metabolites: Application to the Jersey Girl Study. *PLoS One* **2014**, 9.e11363210.1371/journal.pone.0113632

(22) Pfeiffer, E.; Hildebrand, A.; Mikula, H.; Metzler, M. Glucuronidation of zearalenone, zeranol and four metabolites in vitro: Formation of glucuronides by various microsomes and human UDP-glucuronosyltransferase isoforms. *Mol. Nutr. Food Res.* **2010**, *54*, 1468−1476.

(23) Devreese, M.; Antonissen, G.; Broekaert, N.; De Mil, T.; De Baere, S.; Vanhaecke, L.; De Backer, P.; Croubels, S. Toxicokinetic study and oral bioavailability of deoxynivalenol in turkey poults, and comparative biotransformation between broilers and turkeys. *World Mycotoxin J.* **2015**, *1*, 1.

(24) Rawal, S.; Coulombe, R. A., Jr. Metabolism of aflatoxin B1 in turkey liver microsomes: the relative roles of cytochromes P450 1A5 and 3A37. *Toxicol. Appl. Pharmacol.* **2011**, *254*, 349−54.

(25) Chen, C.-H. *Activation and Detoxification Enzymes: Functions and Implications*; Springer: New York, 2012.

DOI: 10.1021/acs.jafc.5b01608
J. Agric. Food Chem. 2015, 63, 5092−5098

JOURNAL OF AGRICULTURAL AND FOOD CHEMISTRY

Symposium Introduction

pubs.acs.org/JAFC

51st North American Chemical Residue Workshop

ABSTRACT: Manuscripts collected in this 51st North American Chemical Residue Workshop (NACRW) Symposium issue of the *Journal of Agricultural and Food Chemistry* (*JAFC*) were originally presented at the 51st NACRW meeting. The 2014 NACRW *JAFC* symposium collects 14 publications representing the broad range of topics in chemical analyses presented at the 2014 meeting. These include the analysis of chemical residues and contaminants in food, environment, feed, botanical, and bee samples as well as the application of quality control/quality assurance protocols in routine and method development.

The 51st North American Chemical Residue Workshop (NACRW, www.nacrw.org) was held July 20−23, 2014, in its traditional location at the TradeWinds Island Grand Resort in St. Pete Beach, FL, USA. The NACRW has been sponsored by the FLAG Works Inc. (www.flagworks.org) since 1963, as well as manufacturers of laboratory consumables, analytical standards and reference materials, sample preparation kits, and analytical equipment. Formerly known as the Florida Pesticide Residue Workshop (FPRW), the new name NACRW was established in 2013 to reflect the increasing scope of the workshop. This year, the NACRW attracted 310 registered attendees representing academics, government and industrial sectors from 17 countries worldwide. Together, the Program Committee put together a four day program encompassing 5 keynotes, 29 oral presentations, 106 posters, 41 exhibitors, and a short course.

Under the general theme "Science without Borders", scientists from 17 countries delivered 140 oral and poster presentations. The workshop started with a short course, "Fundamentals of Gas and Liquid Chromatography for Residue Analysis", on Sunday; followed by 10 scientific sessions including veterinary drug residue analysis, new approaches to ensure quality, pesticide and bees, state laboratory forum, tools and toxicological effects, high-throughput sample preparation and analysis methods, perfluorinated compounds, and two sessions dedicated to general topics; it ended Wednesday evening with a special mass spectrometry forum focusing on issues associated with targeted and nontargeted screening methods. Papers published in this 51st NACRW Group of *JAFC* were originally presented and/or derived from intensive discussions at the 4 day workshop.

The papers included in this NACRW symposium of *JAFC* are a good representation of topics presented and discussed at the 51st NACRW and should provide an open invitation to all for the future meetings, especially for the 2015 NACRW to be held July 19−22, 2015, also at the TradeWinds in St. Pete Beach. Please come to learn, discuss, network, enjoy the science with your colleagues, and take advantage of the many opportunities the NACRW has to offer.

Paul Yang*[,†]
Perry Martos[‡]
Brad Barrett[§]

[†]Laboratory Services Branch, Ontario Ministry of the Environment, 125 Resources Road, Etobicoke, Ontario M9P 3V6, Canada

[‡]Laboratory Services, University of Guelph, 95 Stone Road West, Guelph, Ontario N1H 8J7, Canada

[§]Americas Business Unit, AB SCIEX, 500 Old Connecticut Path, Framingham, Massachusetts 01701, United States

AUTHOR INFORMATION

Notes

The authors declare no competing financial interest.

Special Issue: 51st North American Chemical Residue Workshop

Received: January 10, 2015
Published: February 14, 2015

ACS Publications © 2015 American Chemical Society

DOI: 10.1021/acs.jafc.5b00159
J. Agric. Food Chem. 2015, 63, 5099−5099

JOURNAL OF AGRICULTURAL AND FOOD CHEMISTRY

Article

pubs.acs.org/JAFC

Single-Laboratory Ruggedness Testing and Validation of a Modified QuEChERS Approach To Quantify 185 Pesticide Residues in Salmon by Liquid Chromatography– and Gas Chromatography–Tandem Mass Spectrometry

Brittany Holmes,* Arlene Dunkin, Royal Schoen, and Chris Wiseman

Chemical and Hop Laboratory, Washington State Department of Agriculture, Suite 106, 21 North First Avenue, Yakima, Washington 98902, United States

Supporting Information

ABSTRACT: In this study, we successfully applied a previously modified version of the QuEChERS approach to quantify pesticide residues in samples of fresh salmon. Analysis was performed using a combination of liquid and gas chromatography–tandem mass spectrometry (LC-MS/MS and GC-MS/MS). The validated QuEChERS method used ethyl acetate for the extraction solvent and involved two freezing steps and a C18 dispersive solid phase extraction for removal of lipids. Of the 228 pesticides initially screened, only 185 passed the method validation criteria (103 on LC-MS/MS and 82 on GC-MS/MS). In a quantitative validation, acceptable performances were achieved with overall recoveries of 70–120% and <20% RSD for 179 analytes (n = 7) over the course of five different extractions at 2 times the limit of quantification. Over 12 months, this method was used in the analysis of 708 salmon samples collected as part of the U.S. Department of Agriculture's Pesticide Data Program. Ruggedness testing conducted throughout the entire study showed this method to be robust and suitable for long-term use.

KEYWORDS: *salmon, QuEChERS, USDA, PDP, pesticide residues, LC-MS/MS, GC-MS/MS, method validation*

INTRODUCTION

Accurate pesticide dietary risk assessments by the U.S. Environmental Protection Agency (EPA) require incidence and level pesticide residue data. The Pesticide Data Program (PDP) is a voluntary, federal–state pesticide residue monitoring program administered by the U.S. Department of Agriculture (USDA) Agricultural Marketing Service since 1991. The purpose of PDP is to collect and report pesticide residue data on commodities selected from the U.S. food supply. Commodities included in PDP surveys are selected on the basis of consumption rates compiled from the Continuing Survey of Food Intakes by Individuals, with an emphasis on foods most consumed by children and infants. PDP food sampling is based on a rigorous statistical design that ensures the data are reliable for use in dietary exposure assessments.[1] Pesticides included in the PDP survey are prioritized on the basis of input from data users, stakeholders EPA, FDA private grower groups, industry, consumer/environmental groups), and current U.S. tolerances and action levels, but data are collected for any additional pesticides tested by the participating laboratory. Analytical methods used for PDP sample analyses must fulfill PDP's stringent method validation and ongoing quality control requirements.[2]

Analytical methods have been developed for assessing various chemical residues in fish tissue, with the distinguishing factor being the sample preparation technique. Common preparations include solid–liquid extraction, Soxhlet extraction, sonication-assisted extraction, or accelerated solvent extraction coupled to a cleanup step involving solid phase extraction or gel permeation chromatography.[3−5] With these methods come high costs and low sample throughput; the labor-, time-, and solvent-intensive procedures also require advanced analytical expertise and laboratory equipment. To overcome these challenges the "quick, easy, cheap, effective, rugged, and safe" (QuEChERS) approach, originally developed for the determination of pesticide residues in fruits and vegetables,[6] has been modified over the years for different compounds and matrices.[7−9] There are hundreds of publications in the scientific literature that have utilized QuEChERS for sample preparation and analysis. The original approach is characterized by an extraction step using the polar solvent acetonitrile followed by subsequent liquid–liquid partitioning of residues through the addition of salts and buffering agents. Samples are then subjected to various cleanup steps to remove coextractives and further isolate pesticide residues for analysis by either liquid or gas chromatography coupled to a tandem mass spectrometer. As part of PDP, the National Science Laboratory in Gastonia, NC, USA, modified the QuEChERS approach to analyze pesticide residues in catfish.[10] Major modifications included changing the extraction solvent from acetonitrile to ethyl acetate and incorporating two freezing steps for removal of lipids. Figure 1 provides a complete comparison of these two approaches. Changing to a less polar solvent improves partitioning of analytes from the fatty lipid layer in fish tissue.[11] However, this will also increase the amount of coextractives

Special Issue: 51st North American Chemical Residue Workshop

Received: November 14, 2014
Revised: February 19, 2015
Accepted: February 23, 2015
Published: February 26, 2015

ACS Publications © 2015 American Chemical Society

DOI: 10.1021/jf5055276
J. Agric. Food Chem. 2015, 63, 5100−5106

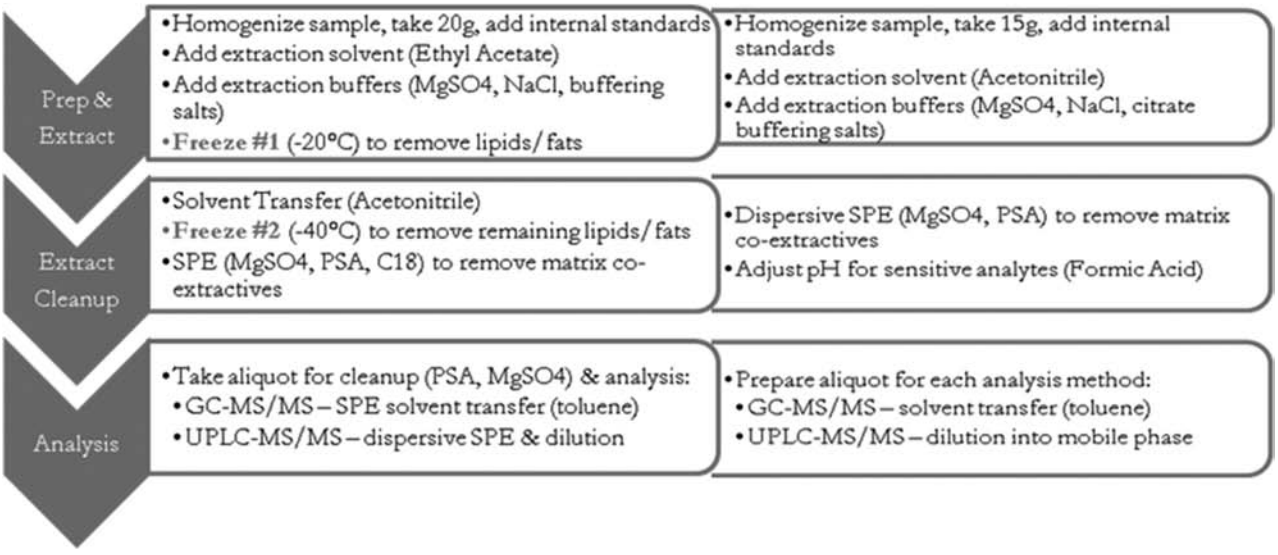

Figure 1. Modified QuEChERS for salmon (left) compared to original QuEChERS approach (right).

(especially lipids),[12] which can be removed by freezing the extract to below −20 °C.[11] To ensure complete lipid removal, two separate freezing steps were added. The objective of this study was to apply this method originally developed for catfish to the salmon matrix and evaluate its efficiency and robustness. One major concern was the lipid content of salmon, as it can be 2−3 times higher than that of catfish.[13] The two freezing steps in the original method should be enough to reduce matrix interferences from the additional lipid content in salmon, but to ensure that matrix effects are reduced as much as possible, C18 sorbent was added to the LC-MS/MS dispersive solid phase extraction (dSPE) cleanup step. The pigments that give salmon its trademark pink color could cause interference with analytes of interest if included in the final extract. Most commercial dSPE kits use a combination of primary−secondary amine and/or graphitized carbon black (GCB) to remove pigments. GCB is known to remove planar pesticides,[6] and because the goal of PDP is to provide as much data as possible, this sorbent was not investigated for any of the dSPE cleanup steps.

Method validation was accomplished by assessing selectivity and conducting single-laboratory intra- and interday precision and accuracy studies. The performance of the method validation was evaluated using criteria outlined in Table 1, set by the USDA-PDP quality assurance program and based on EPA Good Laboratory Practices. Once validated, this modified approach extends the scope of previously validated multiresidue methods for fish[5,7,8] and salmon[3,4,11] tissue in terms of instrumentation (both LC- and GC-MS/MS), number of samples (60 samples per month), length of study (1 year), and size of pesticide screen. The initial screen includes all of the major chemical classes: carbamates (n = 21), ureas (n = 12), organophosphorus (n = 44), organochlorines (n = 35), pyrethroids (n = 22), conazoles (n = 66), pyrethroids (n = 22), triazines (n = 5), and dinitroanilines (n = 6).

Table 1. Method Validation Criteria Set for PDP by USDA Agricultural Marketing Service

	criteria	range[a]
analysis selectivity	LC retention time	±0.5 min
	GC retention time	±0.05 min
	minimum no. of MS/MS transitions	quantitative, 2; qualitative, 1
	MS/MS ion response ratio	%CV < 20%
analysis accuracy	calibration STD linearity	R^2 > 0.990
	calibration STD range	1×, 5×, and 10× LOQ
	linearity range	80−120% of the test concentrations
	calibration STD accuracy	80−120% of actual concentration
	fortification recovery	50−150% at 2 × LOQ
analysis precision	calibration STD precision	%CV < 30%
	interday: fortification recovery	%CV < value predicted by Horwitz
	interday: matrix-matched STD recovery	
method LOQ	quantitative MS/MS transition	>10:1 S:N ratio
	qualitative MS/MS transition	>3:1 S:N ratio

[a]%CV = coefficient of variation, defined as a ratio of the standard deviation (s) of a set of numbers (n), to their average (x), expressed as a percentatge: $s/x \times 100\%$; LOQ = limit of quantitation, at least 10:1 signal: noise; Horwitz %CV = $2^{(1-0.5\log C)}$, where C is concentration.

MATERIALS AND METHODS

Reagents and Chemicals. Acetonitrile, ethyl acetate, toluene, acetone, and acetic acid (HPLC grade or better) and methanol and formic acid (LCMS grade Optima) were purchased from Fischer Scientific. Magnesium sulfate, anhydrous reagent grade ($MgSO_4$), sodium chloride, reagent grade (NaCl), primary−secondary amine (PSA), 1 mL mini-centrifuge tubes, polypropylene (PPE) 15 and 50 mL centrifuge tubes, and solid phase extraction (SPE) columns were purchased from UCT.

Standards with valid certificates of analysis were obtained from the National Pesticide Standard Repository, EPA, and ChemService. All neat standards were stored in a freezer at −20 °C or lower, unless degradation occurred, in which case standard was stored at the recommended temperature. Individual stock solutions at 1.0 mg/mL were prepared in methanol or acetone depending on solubility and instrumentation. Mixed standard solutions containing about 140 pesticides for LC and 90 pesticides for GC were prepared from the stock standards in methanol and acetone, respectively. All standard solutions were stored in a freezer at 0 °C; all cold-storage devices were secured and monitored according to ANSI/ISO/IEC 17025. Anytime a neat standard or solution was removed from cold storage, it was first

DOI: 10.1021/jf5055276
J. Agric. Food Chem. 2015, 63, 5100−5106

brought to room temperature before being used. Individual standard solutions were good for 1 year, whereas mixed solutions were used for only 6 months and then remade accordingly.

Sample Collection and Processing. Using a rigorous statistical design, PDP has developed extensive procedures that ensure samples are randomly selected from the national food distribution system and reflect what is typically available to the consumer. PDP State sample collectors and State testing facilities are trained to adhere to detailed program Standard Operating Procedures that provide criteria for site selection and specific instructions for sample selection, collection, shipping, and handling. Samples are collected year-round from markets, terminal markets, distribution centers, and retail sites selected by the National Agricultural Statistics Service (NASS) using probability proportional to size methodology so that the data reported are a statistically defensible representation of the U.S. food supply. State population figures are used to assign the number of samples scheduled for collection each month.[1] These population and distribution network-based numbers result in the following monthly collection assignments for each state: California, 13; Colorado, 2; Florida, 7; Maryland, 4; Michigan, 6; New York, 9; Ohio, 6; Texas, 8; and Washington, 4. This schedule results in a monthly target of 59 salmon samples, for a target of 708 total samples to be collected beginning July 2013 and ending June 2014.

Acceptable samples included farm-raised, wild, organic, conventional, domestic, and imported Atlantic or Pacific salmon for the following species: Chinook (King), Chum (Dog, Keta, Silverbite), Coho (Silver), Pink (Humpback), and Sockeye (Red). Each sample consisted of 1 pound fresh or frozen (raw, uncooked) fillets, nuggets, steaks, or strips. Salmon with guts and/or heads, breading, seasonings, or flavoring (i.e., smoked) were excluded, but both bone-in/out and skin/skinless were included in sampling. Sample collectors rely solely upon the label for identification of collected samples. To ensure samples arrived at the laboratory in a frozen or cold-to-the-touch condition, they were collected in pesticide-free polyethylene bags, frozen overnight, and then shipped the following day by next-day air with ample frozen cold packs and insulating materials surrounding all sample units. Any samples that were no longer frozen or cold-to-the-touch once they arrived at Yakima Laboratory were discarded, and a resample was requested.

Frozen salmon samples were held in a freezer at 0 °C or lower until the sample could be homogenized. Samples could also be refrigerated overnight before cutting approximately 1 pound portions into approximately 1 in. squares and frozen in labeled ziplock bags in a −20 °C freezer until homogenization. Each sample was then homogenized in a Retsch food processor for approximately 45 s in reverse and forward mode at 2200−4500 rpm until homogeneous. Portions of the homogenized sample were transferred into two labeled 8 oz polypropylene (PPE) sample cups, and 20 ± 0.2 g (±1%) was weighed out into two labeled 50 mL PPE centrifuge tubes containing a ceramic homogenizer; exact weight was recorded. Homogenized samples were stored at −20 °C for up to 72 h and moved to a −40 °C freezer for long-term storage (>72 h).

GC-MS/MS Instrumentation. The GC system (Agilent 7890A, Palo Alto, CA, USA) was equipped with an autosampler (Agilent 7693) and coupled to a quadrapole mass spectrometer (Agilent MSD 7000B). MassHunter software was used for instrument control and data acquisition. Analytes were separated using two HP-1 ms columns (15 m long × 0.25 mm i.d. × 0.25 μm df) (J&W Scientific, Folsom, CA, USA), connected through a backflush union for a total column length of 30 m. The column head pressure was set at 16.727 psi at a total flow rate of 34.6 mL/min, using helium as carrier gas. The injection volume was 1 μL in splitless mode at 220 °C with a 3.5 min solvent delay. The oven temperature was programmed as follows: oven held at 90 °C for 1 min, then raised at 50 °C/min to 150 °C, then 6 °C/min to 200 °C, then 16 °C/min to 280 °C, and held at 280 °C for 9 min. Total run time was 21.533 min. The ion source and transfer line and source temperatures were set at 300 °C. Electron multiplier voltage was set by automatic tuning. Nitrogen and helium were used as the collision gases for all MS/MS experiments, and the flow in the collision cell was set at 1.5 and 2.25 mL/min, respectively. For each analyte a scheduled multiple reaction monitoring (MRM) was optimized for two ion transitions in a 60 s detection window with a 10 ms dwell time. Complete method details can be found in the Supporting Information.

LC-MS/MS Instrumentation. The LC system (Acquity UPLC, Waters Corp., Milford, MA, USA) was coupled to a tandem quadrapole mass spectrometer (Xevo TQ-S, Waters Corp.). MassLynx software (version 4.1) was used for instrument control and data acquisition. Analytes were separated on a universal, silica-based bonded phase Acquity HSS T3 column (2.1 mm × 50 mm, 1.8 μm particle size, Waters Corp.) at 40 °C with a sample injection of 4 μL. A binary mobile phase was composed of 0.1% v/v formic acid and 10 mM ammonium formate in water (A) and in methanol (B). A mobile phase gradient at 0.45 mL/min started at 5% B and went to 100% B in 9.5 min, was held for 1.5 min, and concluded by column equilibration at initial conditions for 4 min for a total run time of 15 min. The MS source operated using positive electrospray mode with the following conditions: capillary voltage of 1000 V, source offset of 25 V, desolvation gas flow of 850 L/h, desolvation and cone temperatures of 550 and 150 °C (respectively), cone gas flow of 150 L/h, collision gas flow of 0.15 mL/min, and nebulizer gas of 5 bar. For each analyte, at least one scheduled MRM with a 60 s detection window was optimized for qualitative analysis, and two were optimized for quantitative analysis. Complete method details can be found in the Supporting Information.

Sample Extraction. For reagent blank, 20 mL of deionized water was used. The previously weighed out 20 g samples were thawed at 4 °C overnight or in cold water on the day of extraction. Thirty milliliters of ethyl acetate was added using an automated liquid dispensing unit verified before use by gravimetric check. Samples were then shaken for 5 min on a SPEX 2000 Geno grinder (SPEX Sample Prep, LLC, Metuchen, NJ, USA) at 1200 rpm and then centrifuged (1000 rcf, 5 min, ambient temperature) to compact the contents, allowing for addition of extraction buffers (8 g of $MgSO_4$ and 2 g of NaCl). Samples were shaken for another 5 min at the same speed and inspected for air or liquid pockets; for tubes with visible air or liquid pockets, a disposable PPE transfer pipet was used to disperse the pocket and ensure complete mixing of buffer salts with sample. Sealed tubes were placed into a −20 °C freezer for 30 min and then centrifuged (3000 rcf, 5 min, ambient temperature); the upper ethyl acetate layer was decanted through a funnel and filter paper into a calibrated 50 mL glass graduated centrifuge tube. Target recovery for this layer is 18 mL (A1); excess liquid was aspirated to waste, or if <18 mL was recovered, the exact volume collected was recorded. A1 was concentrated to 3 mL under a stream of nitrogen set at no more than 10 L/min with a water bath at 60−70 °C. Samples were diluted to 15 mL with acetonitrile, capped and vortexed for 30 s, and then frozen for a second time at −40 °C for 30 min. To facilitate layer separation after freezing, samples were centrifuged (1000 rcf, 3 min, ambient temperature) immediately before they were thawed out.

SPE columns were prepared by adding 1 g of $MgSO_4$ to the top of SPE cartridges containing 1000 mg of C18. Conditioning involved 1% acetic acid in acetonitrile using a positive pressure or vacuum SPE manifold and eluting to waste. Ten milliliters (A2) of the extract was loaded onto the SPE column and eluted in a dropwise manner into a calibrated 15 mL glass centrifuge tube. Each SPE column was washed with two 2.5 mL volumes of 1% acetic acid in acetonitrile; after the second washing, the column was kept under pressure for about 1 min to completely elute the extract from the column. Eluted extract was concentrated to 2 mL under a stream of nitrogen set at no more than 10 L/min with a water bath set at 50 °C. Final extract volume adjustments were made with acetonitrile. Target sample concentration was 4 g/mL if all target volumes were met for aliquots A1 and A2, as shown by eqs 1 and 2.

$$\text{sample concn}\left(\frac{\text{g}}{\text{mL}}\right) = \frac{\text{sample size (g)}}{\text{extraction solvent (mL)}} \times \frac{\text{A1}}{15\ \text{mL}} \times \frac{\text{A2}}{2\ \text{mL}} \quad (1)$$

DOI: 10.1021/jf5055276
J. Agric. Food Chem. 2015, 63, 5100−5106

$$\text{target sample concn} = \frac{20\text{ g}}{30\text{ mL}} \times \frac{18\text{ mL}}{15\text{ mL}} \times \frac{10\text{ mL}}{2\text{ mL}} = 4\text{ g/mL} \quad (2)$$

Sample Cleanup. Due to the sensitivity of the instrumentation, samples were subjected to additional cleanup and dilution steps prior to analysis. For LC-MS/MS 1 mL of final extract was quantitatively transferred into a mini-centrifuge tube containing 150 mg of $MgSO_4$, 50 mg of PSA, and 50 mg of C18, vortexed for 1 min, and centrifuged (1000 rcf, 2 min, ambient temperature). Samples were diluted 1:8 in the following fashion: 125 μL of clean sample extract, 20 μL of 1.55 ppm TPP (internal standard), 355 μL of acetonitrile, 500 μL of methanol, and 1000 μL of 0.67 mM formic acid. Samples were filtered through a nylon 0.2 mm syringe filter into a maximum recovery LC vial. Remaining extract in mini-centrifuge tubes was held in reserve at 0 °C or lower. Final LC-MS/MS sample concentration was 0.25 g/mL.

For GC-MS/MS, 1 mL of final extract was quantitatively transferred to a conditioned (4 mL, 3:1 acetone/toluene) SPE column containing 500 mg of PSA. Each SPE column was washed three times with 4 mL of 3:1 acetone/toluene. After the last washing, the column was kept under pressure for about 1 min to completely elute extract from the column. Samples were then concentrated to 0.5 mL under a stream of nitrogen set at no more than 10 L/min with a water bath set at 50 °C. To completely displace the other solvents from the final extract, 3 mL of toluene was added, and samples were concentrated again to 0.5 mL. Final volume was adjusted to 1 mL with toluene, and the sample was vortexed for 30 s. About half of the extracts were transferred to GC autosampler vials with 0.5 mL glass inserts; remaining extract was held in reserve at 0 °C or lower. Final GC-MS/MS sample concentration was 4 g/mL.

Standard matrix blank homogenate followed the same extraction procedure for LC-MS/MS samples, but for GC-MS/MS it was doubly concentrated during the cleanup step by transferring 2 mL instead of 1 to create an 8 g/mL matrix blank for use in preparing GC-MS/MS calibration standards.

Pesticide Residue Quantitation. Following extraction and cleanup, samples were analyzed for pesticide residues using both LC- and GC-MS/MS instrumentation. For quantification, a matrix-matched standard of blank salmon extract was prepared at 1, 5, and 10 times the limit of quantification (LOQ) for each pesticide by adding appropriate volumes of mixed fortification standard to the blank sample extract (after each instrument's specific cleanup). The peak area of the primary transition was used to generate an external, three-point calibration curve using least-squares linear regression analysis. A matrix-matched standard at 2 × LOQ was used to assess the validity of the generated calibration curve; method recoveries were not background subtracted.

Quality Assurance/Control. Confirmation of pesticides found in fortified and incurred samples was determined by comparing expected retention time and the ratio of the two transition results to matrix-matched standards, per PDP criteria for identification and acceptable recovery as shown in Table 1. The stability of chromatography was assessed by analyzing continuing calibration verification standards every 7−11 samples. The accuracy and precision of continuing calibration standards were typically within ±20% of expected values. The presence of artifact pesticide residues arising from laboratory-associated procedures, reagents, and/or matrix was assessed through the analysis of laboratory reagent and matrix blanks. Additionally, interday accuracy and precision were monitored throughout the entire study by means of statistical process control charting and review.

RESULTS AND DISCUSSION

Method Validation. First, different samples of salmon were extracted and analyzed to find the lowest contaminated matrix for use in blanks and fortified samples. The interday precision and accuracy of recoveries for 88 GC and 142 LC analytes were determined by spiking a matrix blank in triplicate with a mixture of these pesticides at concentrations of 1, 5, and 10 times the LOQ for each analyte. Spiked samples were then extracted and cleaned up using the modified QuEChERS approach for salmon. At the lowest level validated, 85% of GC and 91% of LC analytes had acceptable recoveries (70−120%). At the highest level validated, these values improved to 95% of GC and 97% of LC analytes. Of the 228 analytes initially screened by this method, 7 were not detected at any spike level, 5 were not detected at the lowest spiking level, 5 were detected but had recoveries outside the 50−150% range, 2 had irreproducible results (%CV > 30%), and 25 had poor peak shape or resolution between matrix coextractive peaks. These analytes were subsequently dropped from analysis, resulting in a final screen of 103 analytes by LC-MS/MS and 82 analytes by GC-MS/MS. Of the compounds that were not detected or had poor recovery at the lowest spike level, a pesticide group that stood out included the highly lipophilic pesticides (i.e., acephate, chlorthalonil, imazalil, oxidemeton methyl, methamidophos, thiabendazole). This group of pesticides is liable to partition into the fat layer[9] that formed during extraction procedure and settled out of the final extract, as shown in Figure 2. Extract pH was not controlled in this method, thus compromising the stability of base-sensitive and/or acid-labile pesticides (i.e., thiodicarb, chlorthalonil, 1-naphthol). Complete details on the results of the interday experiment can be found in the Supporting Information (Table S3).

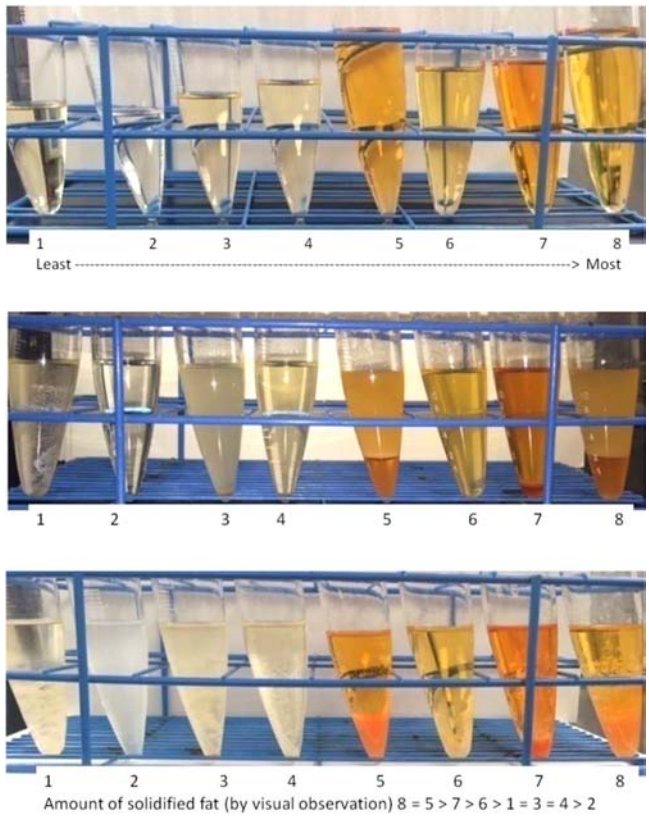

Figure 2. Sample diversity is apparent throughout the extraction: not only did the color vary between salmon samples but varying amounts were recovered for A1 (top) and different amounts of fat were separated and removed from extract after solvent exchange from ethyl acetate to acetonitrile (middle) and at the conclusion of the second freezing step (bottom).

The accuracy of this method was confirmed by a blind, internal proficiency sample using the same matrix material as the blank. Ideally, a standard reference material would be used,

DOI: 10.1021/jf5055276
J. Agric. Food Chem. 2015, 63, 5100−5106

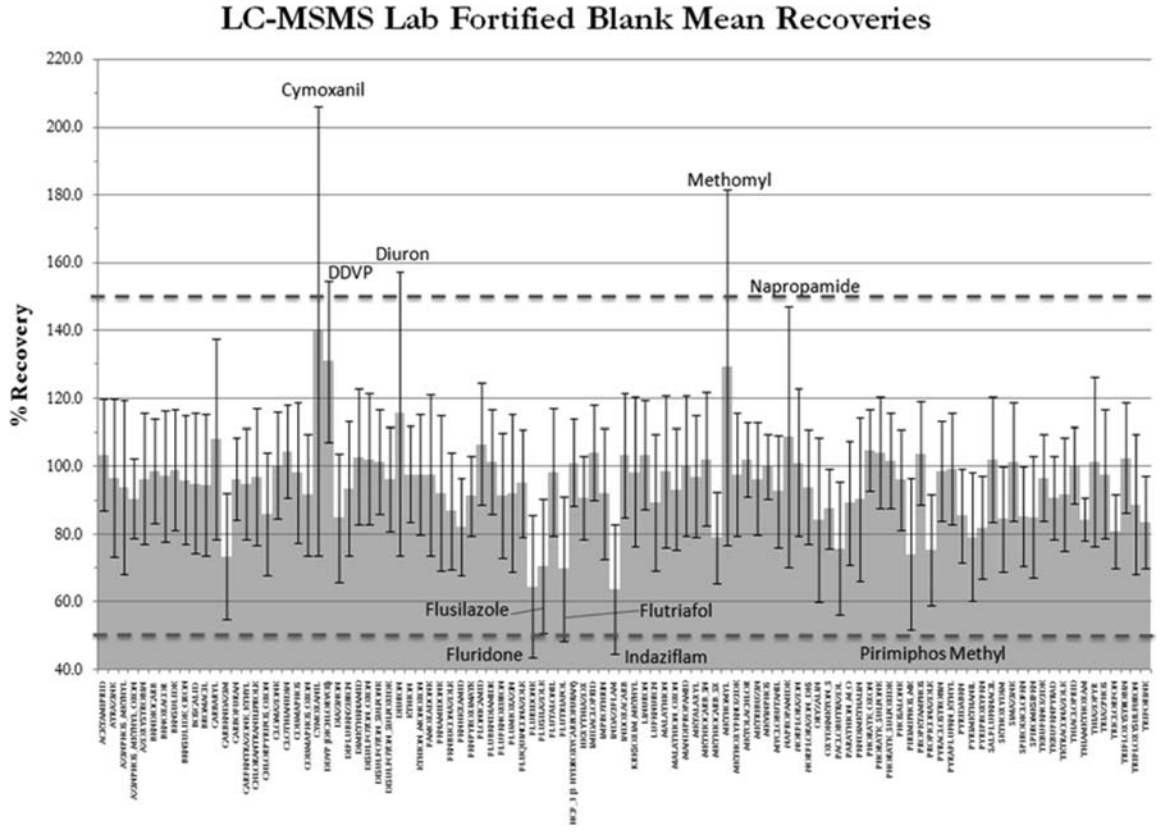

Figure 3. Average recoveries of laboratory-fortified blank analyzed by LC-MS/MS (n = 18−19 depending on analyte). Error bars represent standard deviation for analyte.

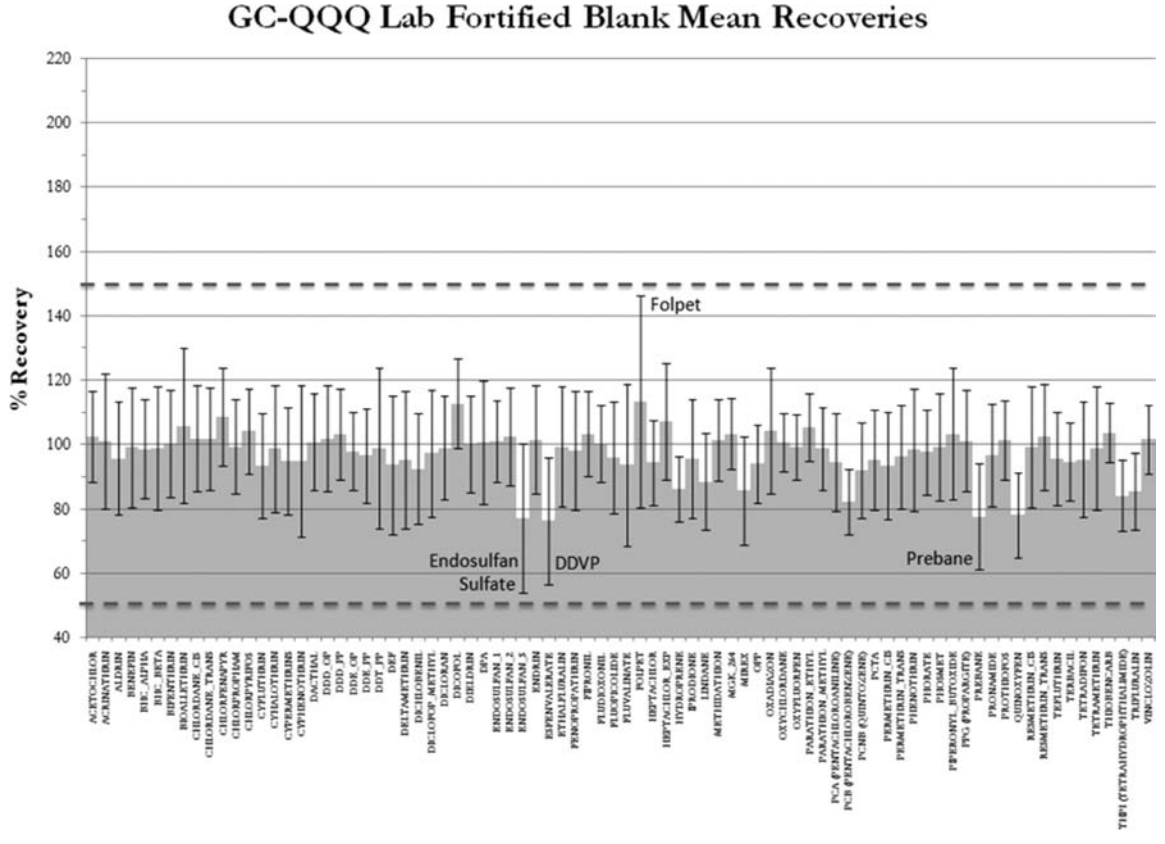

Figure 4. Average recoveries of laboratory-fortified blanks by GC-MS/MS analysis (n = 16−17 depending on analyte). Error bars represent standard deviation for analyte.

DOI: 10.1021/jf5055276
J. Agric. Food Chem. 2015, 63, 5100−5106

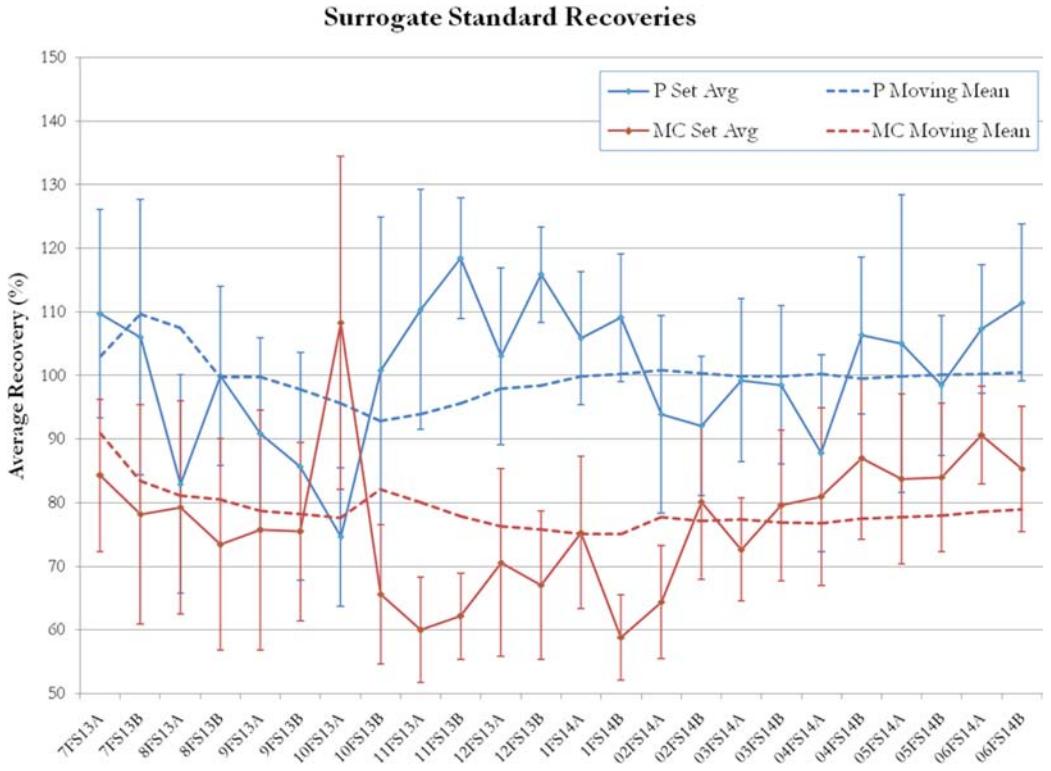

Figure 5. Surrogate standard recovery for propoxur (P) and methyl chlorpyrifos (MC). Average and standard deviation were determined for each analysis set (n = 30 for each set, n = 24 complete sets).

but none that met the scope of method (different fish species, incomplete analyte list) were available at the time of study. Internal proficiency testing consisted of two blind samples; each contained a mixture of seven analytes at concentrations ranging from 0.020 to 0.080 μg/mL. These samples were included with a regularly scheduled analysis set and subjected to the same extraction procedure as a regular sample, including the addition of quality controls and analysis by LC- and GC-MS/MS. Amounts found were reported to a quality control officer for evaluation; overall, the recoveries were 70−100% with a minimum recovery of 71% for parathion ethyl by GC-MS/MS. Complete proficiency testing results are included in the Supporting Information (Table S4).

Intraday precision and accuracy for the final screen of 185 analytes were determined by monitoring a sample fortified at 2 × LOQ throughout the entire study duration for a total of about 18 data points for each analyte. Analysis by LC-MS/MS, summarized in Figure 3, had higher variability (expressed as % CV) than GC-MS/MS, summarized in Figure 4. Despite this, some compounds had irreproducible peak shapes as a result of interfering matrix coextractives that resulted in a subjective analysis. Of these compounds, five were eventually dropped from the GC-MS/MS screen; they were bioallethrin, folpet, hydroprene, oxychlordane, and prothiofos. Even with the addition of a C18 cleanup step, the amount of coextractives in the final sample was enough to negatively impact the precision of recovery for cymoxanil, dichlorvos (DDVP), diuron, endosulfan sulfate, fluridone, flusilazole, indaziflam, methomyl, napropamide, Prebane, and pirimiphos methyl, as shown in Figures 3 and 4.

Method Ruggedness. The goal of this study was to survey salmon for pesticide residues over the course of a year; the diversity of samples collected over such a long period was going to be large. To account for varying matrix effects from different salmon species (Atlantic, Pacific, King, Chinook, etc.) and origin (import, domestic, farmed, wild), two internal standards were spiked into every sample at 5 × LOQ: methyl chlorpyrifos (MC) and propoxur (P) for GC and LC analysis, respectively. The observed sample diversity was apparent throughout the entire study as shown in Figure 2, with extract color, volume extracted, and visible fat content being the most discernible features. The samples shown in Figure 2 are from a single analysis set of 30 samples; observed extract color varied from clear and colorless, clear and colored, and opaque and colorless to opaque and clear and remained throughout the extraction process. However, all of the data sets analyzed with this method successfully met PDP's criteria listed in Table 1 for interlaboratory precision with average set recoveries of 101 and 77% for P and MC, respectively. During the course of this study several lots of reagents, materials, consumables, and standards were used, and a total of six operators were included to test the overall robustness of the written procedure. The statistical process control chart in Figure 5 shows that as the study progressed, the process variation decreased from around 20%CV to 10%CV, and the moving mean stabilized for both analyses. Initially the moving mean changed significantly between sample sets and %CV was high; after investigation, it was found that the standard operating procedure contained steps that were either confusing or had engineering controls that were not clearly defined (i.e., nitrogen flow rate and temperature for N-Evap). The procedure was revised in January 2014 and implemented starting with the second October data set (10FS13B). Sets analyzed with the new written procedure had improved precision, thereby stabilizing the moving mean. This demonstrates the significance a clear, concise, and

DOI: 10.1021/jf5055276
J. Agric. Food Chem. 2015, 63, 5100−5106

thoroughly documented procedure has on ensuring a method's ruggedness.

During the course of this study, the analytical instruments had decreased sensitivity and poor intra- and interbatch precision as a result of source (LC) and inlet (GC) contamination by the salmon matrix. To reduce contamination and improve stability of instrument between runs, the frequency of routine maintenance tasks such as changing the GC liner, trimming the GC column, and cleaning the LC-MS/MS source components was increased from one to two times per month to daily at around the October data sets. Nonroutine maintenance tasks for the LC-MS/MS were also increased from one to two times per year to after every 200−300 injections of salmon matrix; this included cleaning the ion block heater and ion optics. This increased maintenance suggests that the final salmon extract should have been subjected to an additional cleanup or dilution step to minimize instrument downtime.

The observed process variation throughout the study cannot be attributed to just unclear written directions or contamination of analytical instrumentation by matrix coextractives; additional testing to isolate each source of error is needed before a statement can be made. However, the ruggedness testing results presented here support the claim that these extraction and analysis methods are suitable for long-term use by different operators and analysts using different lots of reagents and materials. Before this method can be considered official, it is recommended that it should be compared with reference methods in side-by-side analysis of the same sample and an interlaboratory study should also be performed.

■ ASSOCIATED CONTENT

Supporting Information

Files 1 and 2 are the complete method details for GC-MS/MS and LC-MS/MS analytical instrumentation, respectively; Table S3 lists the method range and precision results for each of the 228 pesticides included in initial screen, as well as the ruggedness testing at 2 × LOQ for final screen of 185 pesticides; Table S4 lists the complete results of the internal proficiency testing samples. This material is available free of charge via the Internet at http://pubs.acs.org.

■ AUTHOR INFORMATION

Corresponding Author

*(B.H.) E-mail: bholmes@agr.wa.gov.

Notes

Mention of brand or firm names does not constitute an endorsement by either the U.S. or Washington States Department's of Agriculture above others of a similar nature not mentioned.

The authors declare no competing financial interest.

■ ACKNOWLEDGMENTS

We thank the National Scientific Laboratory, Gastonia, NC, USA, for their work on modifying the QuEChERS approach used in this study. Sample preparation and method optimization tests were supported through the technical assistance of Tammy Best, Justin Chambers, Jorge Contreras, and Karen Lowe of the WSDA Chemical and Hop Laboratory.

■ ABBREVIATIONS USED

GC-MS/MS, gas chromatography−triple-quadrapole mass spectrometer; LC-MS/MS, liquid chromatography−mass spectrometry; PSA, primary−secondary amine; QuEChERS, quick, easy, cheap, effective, rugged, and safe; SPE, solid phase extraction; USDA, U.S. Department of Agriculture; FDA, U.S. Food and Drug Administration; EPA, U.S. Environmental Protection Agency

■ REFERENCES

(1) Punzi, J. S.; Lamont, M.; Haynes, D.; Epstein, R. L. *Outlooks on Pest Management*; Research Information Ltd.: Burnham, UK, June 2005; pp 131−137.

(2) U.S. Department of Agriculture, Agricultural Marketing Service, Pesticide Data Program, Standard Operating Procedures Page; http://www.ams.usda.gov/AMSv1.0/ams.fetchTemplateData.do?template=TemplateG==ScienceandLaboratories=PDPProgramSOPs=PDP+Standard+Operating+Procedures+(SOPs)=pestcddataprg (accessed May 14, 2014).

(3) Forsberg, N. D.; Wilson, G. R.; Anderson, K. A. *J. Agric. Food Chem.* **2011**, *59*, 8108−8116.

(4) Berntssen, M. H.G.; Maage, A.; Julshamn, K.; Oeye, B. E.; Lundebye, A.-K. *Chemospere* **2011**, *83*, 95−103.

(5) Schenck, F.; Calderon, L.; Podhorniak, L. V. *J. AOAC Int.* **1996**, *79*, 1209−1214.

(6) Anastassiades, M.; Lehotay, S. J. *J. AOAC Int.* **2003**, *86*, 412−431.

(7) Lazartigues, A.; Wiest, L.; Baudot, R.; Thomas, M.; Feidt, C.; Cren-Olive, C. *Anal. Bioanal. Chem.* **2011**, *400*, 2185−2193.

(8) Rawn, D. F. K.; Judge, J.; Roscoe, V. *Anal. Bioanal. Chem.* **2010**, *397*, 2525−2531.

(9) Chamkasem, N.; Ollis, L. W.; Harmon, T.; Lee, S.; Mercer, G. *J. Agric. Food Chem.* **2013**, *61*, 2315−2329.

(10) USDA-AMS-S&T National Science Laboratory, Gastonia, NC, USA. *Pesticide Residue Analysis of Plant and Animal Tissues*, MET-100, revision 04, 2010.

(11) Norli, H. R.; Christiansen, A.; Deribe, E. *J. Chromatogr., A* **2011**, *1218*, 7234−7241.

(12) Koesukwiwat, U.; Lehotay, S.; Mastovska, K.; Dorweiler, K. J.; Leepipatpiboon, N. *J. Agric. Food Chem.* **2010**, *58*, 5950−5958.

(13) U.S. Department of Agriculture, Agricultural Research Service, 2014. USDA National Nutrient Database for Standard Reference, release 26; Nutrient Data Laboratory Home Page, http://www.ars.usda.gov/ba/bhnrc/ndl (accessed Feb 27, 2014).

DOI: 10.1021/jf5055276
J. Agric. Food Chem. 2015, 63, 5100−5106

JOURNAL OF AGRICULTURAL AND FOOD CHEMISTRY

Article

pubs.acs.org/JAFC

Development of an Automated Column Solid-Phase Extraction Cleanup of QuEChERS Extracts, Using a Zirconia-Based Sorbent, for Pesticide Residue Analyses by LC-MS/MS

Bruce D. Morris* and Richard B. Schriner

Food and Bioanalytical Division, R. J. Hill Laboratories, Private Bag 3205, Hamilton East, New Zealand

Supporting Information

ABSTRACT: A new, automated, high-throughput, mini-column solid-phase extraction (c-SPE) cleanup method for QuEChERS extracts was developed, using a robotic X-Y-Z instrument autosampler, for analysis of pesticide residues in fruits and vegetables by LC-MS/MS. Removal of avocado matrix and recoveries of 263 pesticides and metabolites were studied, using various stationary phase mixtures, including zirconia-based sorbents, and elution with acetonitrile. These experiments allowed selection of a sorbent mixture consisting of zirconia, C_{18}, and carbon-coated silica, that effectively retained avocado matrix but also retained 53 pesticides with <70% recoveries. Addition of MeOH to the elution solvent improved pesticide recoveries from zirconia, as did citrate ions in CEN QuEChERS extracts. Finally, formate buffer in acetonitrile/MeOH (1:1) was required to give >70% recoveries of all 263 pesticides. Analysis of avocado extracts by LC-Q-Orbitrap-MS showed that the method developed was removing >90% of di- and triacylglycerols. The method was validated for 269 pesticides (including homologues and metabolites) in avocado and citrus. Spike recoveries were within 70−120% and 20% RSD for 243 of these analytes in avocado and 254 in citrus, when calibrated against solvent-only standards, indicating effective matrix removal and minimal electrospray ionization suppression.

KEYWORDS: *QuEChERS, SPE, LC-MS/MS, ITSP, Z-Sep, zirconia, pesticide, multiresidue, avocado, citrus*

INTRODUCTION

The "quick, easy, cheap, effective, rugged, and safe" (QuEChERS) method for the analysis of multiclass pesticide residues in fruits and vegetables introduced the use of dispersive solid-phase extraction (d-SPE) cleanup, to reduce the amounts of coextracted matrix in extracts, before instrumental analysis, using a mixture of $MgSO_4$ and PSA sorbents, with C_{18} and graphitized carbon black (GCB) added if required to improve removal of nonpolar matrix and chlorophyll.[1−4] In the original QuEChERS method, d-SPE was used instead of column SPE (c-SPE) to provide a quicker and cheaper cleanup.[1] Recently the zirconia-based sorbent HybridSPE, in well-plates or columns, has been utilized for the removal of phopholipids from plasma[5−7] and eggs.[8] The zirconia materials Z-Sep and Z-Sep+ have been evaluated for d-SPE cleanup of QuEChERS extracts for analysis of environmental pollutants and pesticides in fish and shrimp[9−11] and pesticides from oily fruits or vegetable oils,[12−16] due to their abilities to remove the lipophilic matrix. However, in our experience, used routinely, Z-Sep d-SPE can result in the transfer of solid phase into analysis vials and subsequently into the HPLC, building up over time to cause retention of some analytes and poor peak shapes or carry-over. Consequently, we investigated the development of an automated c-SPE cleanup, based on zirconia-coated silica, using Instrument Top Sample Preparation (ITSP) mini-cartridges, on a robotic X-Y-Z instrument autosampler. This could be as quick and cheap as d-SPE, as many instruments are already equipped with robotic autosamplers; however, it could also give the improved matrix removal that is possible with c-SPE[17] and avoid zirconia transfer to the LC-MS/MS.

Avocado extracts were selected as a matrix with high oil content,[18,19] and experiments were carried out to evaluate the weight of matrix removed after acetonitrile (MeCN) elution through ITSP c-SPE cartridges with six different stationary phases. Recoveries of 263 pesticides and metabolites spiked on avocado were determined through five of these sorbents and, along with matrix weight-removal results, allowed selection of a Z-Sep/C_{18}/CarbonX mixture for further method development. Investigation of the effect of different elution solvents (MeCN, MeCN/MeOH (1:1), MeOH, coextracted citrate in a CEN (European Committee for Standardization method,[20]), QuEChERS extract, and formate buffer at three concentrations in MeCN/MeOH (1:1), on pesticide recoveries through Z-Sep/C_{18}/CarbonX, resulted in a method using elution of CEN QuEChERS extracts with 100 mM formate buffer in MeCN/MeOH (1:1). To the best of our knowledge, this study is the first to use ITSP mini-cartridges for cleanup of QuEChERS extracts and zirconia solid phase in an SPE column, rather than used dispersively, for pesticide residue analysis. Removal of avocado di- and triacylglycerols by Z-Sep, monitored by LC-Q-Orbitrap-MS, is also presented. The method was validated for the analysis of 269 pesticides, including homologues and metabolites, in avocado and citrus, to give spike recovery and reproducibility data.

Special Issue: 51st North American Chemical Residue Workshop

Received: November 17, 2014
Revised: February 7, 2015
Accepted: February 9, 2015
Published: February 23, 2015

ACS Publications © 2015 American Chemical Society

DOI: 10.1021/jf505539e
J. Agric. Food Chem. 2015, 63, 5107−5119

MATERIALS AND METHODS

Reagents and Consumables. MeCN and MeOH (Lichrosolv grade), formic acid (98−100%), NaCl (99.5%), trisodium citrate dihydrate, disodium hydrogen citrate sesquihydrate, and ammonium formate were purchased from Merck (Darmstadt, Germany). $MgSO_4$ (anhydrous) used for QuEChERS extractions was from Scharlau (Sentmenat, Spain). Water was purified using a Sartorius (Goettingen, Germany) Arium 611UV unit. Formate buffer (100 mM) for c-SPE was prepared in MeOH/MeCN (1:1) by dissolving ammonium formate (70 mM) and adding 30 mM formic acid. Lower concentrations of formate buffer (50 and 10 mM) were prepared by dilution of the 100 mM solution with MeOH/MeCN (1:1). Two zirconia-coated silica sorbents, Supel Que Z-Sep and Z-Sep+, were obtained from Supelco (Bellefonte, PA, USA), as was Supel-Select HLB SPE. Z-Sep+ is a zirconia-coated silica, with octadecyl derivatization of silanol groups. Silanols are underivatized in Z-Sep material. PSA and C_{18}-functionalized silicas, and anhydrous $MgSO_4$ used for SPE experiments were from UCT (Bristol, PA, USA). The carbon-coated silica, CarbonX was supplied by United Science Corp (Center City, MN, USA). Ceramic grinding rods ($^3/_8$ in. × $^7/_8$ in.) to aid QuEChERS extractions were sourced from SPEX (Metuchen, NJ, USA).

Analytical Standards. High-purity analytical standards were obtained from Dr. Ehrenstorfer (LGC Standards, Middlesex, UK), Sigma-Aldrich (St. Louis, MO, USA), Wako (Osaka, Japan), Accustandard (New Haven, CT, USA), and Chemservice (West Chester, PA, USA). Penthiopyrad was purchased from Kanto Chemical Co. (Tokyo, Japan). Atrazine-d_5, used as an internal standard, and triphenylphosphate, added as a system monitoring compound (SMC), were from Sigma-Aldrich. A 20 mg/L solution of triphenylphosphate was prepared in MeOH and a 2 mg/L solution of atrazine-d_5 in MeCN. Pesticides were separated into 10 mixes, prepared in MeCN with 0.05% formic acid (10 mg/L). These were used for spiking experiments and diluted in 10 mM formate buffer (aqueous, pH 4)/MeOH/MeCN (13:2:1) to give calibration standards (0.02, 0.05, 0.1, 0.2, 0.4, 1, 2, 5, 10, 20, 40 μg/L).

Samples and Extraction. Samples, for analyte recovery experiments and method validation, of avocado (cv. Hass), citrus (orange, mandarin, and lemon) and buttercup squash were obtained from New Zealand growers. Avocados were mature, but unripe, and citrus fruits were without wax coating. Real samples of avocado, navel orange, and mandarin were purchased from local markets in Hamilton, New Zealand, and used to demonstrate the application of the validated method for recovery of incurred residues. Extraction was based on the citrate-buffered CEN QuEChERS method.[4,20] Frozen samples were homogenized using a Blixer 6 blender (Robot Coupe, Vincennes, France). Subsamples (5 g for avocado and citrus, 20 g for squash) were weighed into 50 mL polypropylene tubes containing two ceramic rods. SMC (100 μL of 20 mg/L) was added to each. Spikes (50 μL of each 10 mg/L mix) were split between two samples, with approximately 50% (five mixes) of the pesticides in each, which separated parents from breakdown products (e.g., acephate from methamidophos, naled from dichlorvos, furathiocarb from carbofuran). Water (10 mL) and MeCN (9.65 mL, to give 10 mL total volume including spikes, or 10 mL for unspiked blanks), were added, and tubes were shaken by hand for 1 min. After the addition of salt mixture (13 g of $MgSO_4$/NaCl/trisodium citrate dihydrate/disodium hydrogen citrate sesquihydrate (8:2:2:1)), tubes were shaken on a horizontal shaker for 15 min. For citrus an additional 4 g of trisodium citrate was added along with the salt mixture, to compensate for the citric acid in samples and bring the pH back into the buffer region. Tubes were centrifuged at 2000 rpm, for 5 min, and then 1 mL of the MeCN layer was transferred into autosampler vials, to which 100 μL of atrazine-d_5 (2 mg/L) was added. For validation, three samples of avocado, and samples of lemon, orange, or mandarin, were extracted without spiking, plus in triplicate or quadruplicate with spikes, using different technicians, in three batches, over a more than 2 week period, to give a total of 10 replicates. Lemons, oranges, and mandarins were extracted in separate batches.

Automated Mini-Column SPE and Dispersive SPE. Miniaturized c-SPE cartridges, for use on X-Y-Z autosamplers, were supplied by ITSP Solutions (Hartwell, GA, USA), with 30 mg of Z-Sep/C_{18}/CarbonX (2:5:0.24), 45 mg of PSA/C_{18}/CarbonX/$MgSO_4$ (3:3:0.25:5), and 10 mg of Z-Sep or 30 mg of Z-Sep+ sorbents, the first two as homogeneous mixtures. Cartridges with 20 mg of HLB/Z-Sep/CarbonX (1:1:0.22) were handmade in the laboratory. ITSP c-SPE cartridges were 3.5 cm long, including a 0.6 cm tip, with a sorbent bed 6 mm in diameter × 2.5 mm in height (0.5 mm bed height for 10 mg of Z-Sep). Sorbent weights for each mixture were amounts that could fit into the fixed cartridge volume. The upper section of the cartridge comprised a syringe needle guide with a sealing septum on top (Figure 1). Robotic c-SPE used a PAL HTS-xt, X-Y-Z

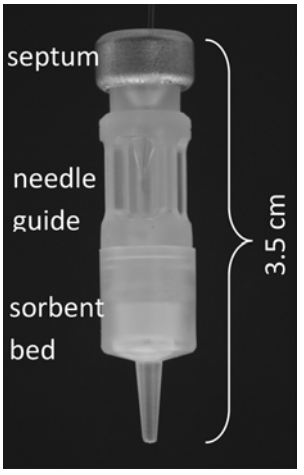

Figure 1. Automated ITSP c-SPE cartridge.

autosampler (CTC Analytics, Zwingen, Switzerland), with HW-54P and HW-96P aluminum trays (ITSP Solutions) and a 250 μL syringe (CTC Analytics). c-SPE cartridges were conditioned (with 150 μL of elution solvent) in the HW-96P tray, then transferred, on the end of the syringe needle, to the HW-54P tray, where they were inserted into 2 mL amber glass vials with split-septa clip caps. Extract (150 μL) was then loaded onto the cartridge followed by elution solvent (150 μL), with the combined eluent collected. For cartridges with 30 mg of sorbent (Z-Sep/C_{18}/CarbonX and Z-Sep+) or 45 mg of PSA/C_{18}/CarbonX/$MgSO_4$, approximately 75 μL of solvent was retained; therefore, 150 μL was 2 column void volumes. Elution rate was 2 μL/s. Cleaned up extracts were diluted 5-fold for analysis, with 10 mM formate buffer (aqueous, pH 4)/MeOH/MeCN (13:2:1).

D-SPE used 30 mg of Z-Sep/C_{18}/CarbonX (2:5:0.24) in a 2 mL glass vial. Two-fold diluted avocado extract (150 μL) was added, plus 150 μL of MeCN, to match the dilution on c-SPE. The vial was vortexed for 1 min, the solid-phase was allowed to settle for 5 min, and then 200 μL of extract was transferred to a second vial for 5-fold dilution with 10 mM formate buffer (aqueous, pH 4)/MeOH/MeCN (13:2:1) for analysis.

Gravimetric Recovery Experiments. Glass 2 mL vial inserts (350 μL flat-bottomed) were weighed on a five-figure analytical balance (Sartorius CPA225D), then either 150 μL of 2-fold-diluted crude avocado extract or the eluent from 150 μL of the same extract passed through automated ITSP c-SPE was collected in the preweighed inserts. Solvent was evaporated at 40 °C under a gentle flow of nitrogen, and the inserts were allowed to re-equilibrate to room temperature (15 min) before reweighing to determine the dry weight of avocado matrix recovered.

LC-MS/MS Parameters. LC-MS/MS was carried out on Triple Quad 5500 and 6500 triple-quadrupole instruments (AB Sciex, Toronto, ON, Canada), coupled to 1200 HPLC systems (Agilent, Palo Alto, CA, USA) with PAL HTS-xt autosamplers and DLW syringes (CTC Analytics). The MS/MSs were operated in positive electrospray ionization (ESI) mode, with source temperatures of 350 °C (Triple Quad 5500)

DOI: 10.1021/jf505539e
J. Agric. Food Chem. 2015, 63, 5107−5119

and 285 °C (Triple Quad 6500), and an ionspray voltage of 5500 V. Multiple reaction monitoring (MRM) transitions are given in Supporting Information Table SI-B and were optimized by undertaking multiple injections with differing declustering potential (DP) and collision energy (CE) parameters. HPLC used Ascentis Express C18 columns (10 cm × 2.1 mm, 2.7 μm particle size) from Supelco at a flow rate of 0.4 mL/min and a column oven temperature of 50 °C. Mobile phase A was 10 mM ammonium formate/formic acid buffer (pH 4) in H_2O/MeOH (9:1), and mobile phase B was MeOH. Gradient elution started at 12.5% B (held for 0.5 min) and ramped to 40% B over 1.5 min, then to 62.7% B over 6 min, followed by a final ramp to 95% B over 6 min (held at 95% for 2 min), to give an even spread of peaks across the chromatogram. Injection volume was 10 μL.

Validated Method. The final method validated used QuEChERS extraction of 5 g subsamples of homogenized fruit, with citrate buffering, as outlined under Samples and Extraction. Automated c-SPE was carried out with ITSP cartridges containing 30 mg of Z-Sep/C_{18}/CarbonX (2:5:0.24). Extracts (150 μL) were loaded onto cartridges and eluted with 150 μL of 100 mM formate buffer in MeOH/MeCN (1:1), with loading and elution volumes collected. After 5-fold dilution with 10 mM formate buffer (aqueous, pH 4)/MeOH/MeCN (13:2:1), extracts were analyzed by LC-MS/MS. Details are provided in the relevant c-SPE and LC-MS/MS sections.

LC-Q-Orbitrap-MS Analysis. The LC consisted of an Ultimate 3000 UHPLC pump, autosampler, degasser, and column compartment and was coupled to a Q-Exactive quadrupole-orbitrap mass spectrometer (Thermo Fisher Scientific, San Jose, CA, USA) operated in positive ESI mode. A Kinetex C18, 10 cm × 2.1 mm, 2.6 μm particle size, HPLC column (Phenomenex, Torrance, CA, USA) was used. Mobile phase A was 10 mM ammonium formate/formic acid buffer (pH 4) in water/MeOH (9:1), and mobile phase B was 10 mM ammonium formate/0.015% formic acid in MeOH/isopropanol (1:1). The flow rate was 0.4 mL/min, and the column oven held at 50 °C. The injection volume was 5 μL. The elution gradient started at 30% B (held for 0.5 min) with a ramp to 60% B at 2 min, followed by a second ramp to 98% B at 10 min (held for 8 min before returning to 30% B for re-equilibration). The Q-Exactive was tuned using LTQ ESI Positive Ion Calibration Solution <24 h before use, and data were acquired by full-scan MS (range set at m/z 75−1000), with mass resolution set to 17500 fwhm (m/z 200). This resolution was adequate to separate and identify (to <5 ppm accuracy) the triacylglycerols (TAGs) and diacylglycerols (DAGs) being targeted while giving a high enough scan rate to give the number of points per peak desired. The source sheath gas flow was set to 60, auxiliary gas flow to 20, sweep gas flow to 5, spray voltage to 3 kV, capillary temperature to 380 °C, S-lens RF level to 50, and heater temperature to 350 °C. Crude QuEChERS avocado extract was diluted 40-fold with MeCN for analysis or was diluted 2-fold before automated ITSP c-SPE, or d-SPE, with both using 30 mg of Z-Sep/C_{18}/CarbonX (2:5:0.24). C-SPE and d-SPE extracts were finally diluted 10-fold with MeCN, to match the dilution of crude extract, before injection. Data analysis used Thermo Xcalibur Qual Browser. Extracted ion chromatograms were constructed by entering the accurate masses of each TAG or DAG peak, with a 10 ppm range. To identify TAGs and DAGs, accurate masses were entered into ChemSpider Advanced Search.[21]

RESULTS AND DISCUSSION

Automated C-SPE Method Development. Initial gravimetric recovery experiments were aimed at assessing the retention of nonpolar coextracted matrix by various c-SPE stationary phase mixtures, using avocado as a sample with high oil content, comprising mono-, di-, and triacylglycerides, free fatty acids, sterols, and tocopherols.[18,19] Five different stationary phase packings were compared in the first weight-recovery experiment (extract 1, Table 1): PSA/C_{18}/CarbonX/$MgSO_4$ (45 mg), Z-Sep (10 mg), HLB/Z-Sep/CarbonX (20 mg), Z-Sep+ (30 mg), and Z-Sep/C_{18}/CarbonX (30 mg), with each sorbent weight being the maximum amount that could be packed into the bed volume of the cartridges. Z-Sep (10 mg) was included to show the effect it alone was having in the Z-Sep/C_{18}/CarbonX (30 mg) mixture. Comparison of dry weights recovered after MeCN elution of 2-fold diluted avocado, extract 1, indicated Z-Sep+ retained the greatest amount of matrix (79%), followed by Z-Sep/C_{18}/CarbonX (56%, Table 1). Matrix retention by 10 mg of Z-Sep alone (47%) indicated it was responsible for the greatest proportion (84%) of this retention in the Z-Sep/C_{18}/CarbonX mixture, meaning the increased removal by Z-Sep+ may have been partly due to the greater weight of zirconia material in these cartridges (30 mg compared with 10 mg). To investigate this, a second extract, extract 2, was passed through 30 mg of Z-Sep, which resulted in 70% matrix removal (Table 1), slightly poorer than for 30 mg of Z-Sep+, but greater than the 47% removed by 10 mg of Z-Sep. These results indicated that the C_{18} functional group of Z-Sep+ was improving avocado matrix removal over Z-Sep, as was addition of C_{18}-silica to Z-Sep in the mixed Z-Sep/C_{18}/CarbonX cartridge. The cartridge with PSA/C_{18}/CarbonX/$MgSO_4$, a mixture similar to that used in many studies for d-SPE cleanup of oily extracts,[2,22,23] showed poorer retention of avocado matrix (32%) than those containing Z-Sep, in agreement with previous d-SPE results for avocado extracts comparing Z-Sep with PSA/C_{18}.[12,13] Two-fold dilution of avocado extract was used as it gave measurable breakthrough of matrix, even for the most retentive Z-Sep+ stationary phase.

Table 1. Dry Weight Recoveries for 150 μL of 2-Fold-Diluted Avocado Extract, before and after Automated C-SPE, Using Various Stationary Phase Mixtures, Eluted with MeCN or MeCN/MeOH (1:1)

		Avocado Extract 1[a]				
		elution solvent: MeCN (150 μL)				
	crude extract	PSA/C_{18}/CarbonX (45 mg)	Z-Sep/C_{18}/CarbonX (30 mg)	Z-Sep+ (30 mg)	Z-Sep (10 mg)	Z-Sep/HLB/CarbonX (20 mg)
dry wt recovered (mg)	0.34	0.23	0.15	0.07	0.18	0.20
% dry wt recovered		68	44	21	53	59

		Avocado Extract 2			
		elution solvent: MeCN (150 μL)		elution solvent: MeCN/MeOH (1:1) (150 μL)	
	crude extract	Z-Sep (30 mg)	C_{18} (30 mg)	Z-Sep/C_{18}/CarbonX (30 mg)	
dry wt recovered (mg)	0.40	0.12	0.32	0.11	
% dry wt recovered		30	80	28	

[a]50 of the 300 μL eluted volume was taken for LC-MS/MS analysis (Table 2), prior to evaporation of solvent. The weight of crude extract was also corrected for this and was 0.41 mg for 150 μL of 2-fold-diluted extract.

DOI: 10.1021/jf505539e
J. Agric. Food Chem. 2015, 63, 5107−5119

Table 2. LC-MS/MS Percent Spike Recoveries for Selected Pesticides (of 263 Tested), Spiked at 100 μg/kg on Avocado, after QuEChERS Extraction, 2-Fold Dilution of Extract, and Automated C-SPE, or D-SPE, Using Various Stationary Phases, Eluted with Acetonitrile, and Quantified against Solvent-Only Calibration Standards[a]

	automated c-SPE (ITSP)					d-SPE
compound	PSA/C_{18}/CarbonX (45 mg)	Z-Sep (10 mg)	HLB/Z-Sep/CarbonX (20 mg)	Z-Sep+ (30 mg)	Z-Sep/C_{18}/CarbonX (30 mg)	Z-Sep/C_{18}/CarbonX (30 mg)
acephate	77	**39**	**65**	**8**	**16**	**56**
aldicarb	98	95	95	94	99	97
aldicarb sulfone	96	95	97	97	99	101
aldicarb sulfoxide	89	**50**	**59**	**17**	**58**	**62**
atrazine	94	95	91	93	96	90
avermectin B1a	91	**42**	**57**	**8**	**5**	**58**
azaconazole[b]	93	85	87	**12**	80	84
azadirachtin	88	**57**	72	**56**	**39**	80
bifenthrin	72	82	91	105	**49**	86
bitertanol	91	74	75	**16**	**70**	86
bromopropylate	116	96	109	**7**	88	115
cadusafos	89	88	91	**58**	86	92
carbendazim	**51**	73	**15**	**18**	**32**	78
carboxin	74	**68**	71	**63**	71	74
chlorfluazuron	96	84	**62**	88	**62**	119
clofentezine	87	91	**53**	91	81	86
cyfluthrin	94	97	107	106	112	111
cypermethrin	113	106	122	104	122	110
cyproconazole A	98	**40**	**55**	**1**	**8**	**45**
cyproconazole B	97	**30**	**44**	**1**	**3**	**41**
cyprodinil	76	87	**46**	79	**66**	108
DDAC	**0**	**64**	**47**	**7**	**0**	**64**
demeton-*S*-methyl	89	88	88	**63**	85	92
dichlofluanid	**25**	84	96	97	97	94
dichlorvos	109	**52**	**63**	**21**	**30**	81
dicrotophos	97	**62**	71	**5**	**59**	**67**
difenoconazole[b]	90	84	81	**21**	79	87
dimethoate	100	93	92	90	94	107
dimethomorph A	89	87	86	**51**	85	91
dimethomorph B	92	86	86	**39**	83	88
dodine	**0**	**24**	**0**	**0**	**0**	**49**
edifenphos	94	78	87	**44**	80	96
emamectin B1a	**0**	**1**	**0**	**1**	**0**	**9**
epoxiconazole	94	90	90	**46**	88	95
fenamiphos	84	83	85	**3**	80	86
fenarimol	87	81	77	**20**	73	94
fenbuconazole	**45**	**43**	**42**	**29**	**42**	**47**
fenhexamid	**0**	**14**	**20**	**3**	**0**	**49**
fenpropimorph	**47**	77	**55**	**49**	**13**	75
fensulfothion	93	85	88	**27**	83	82
fenvalerate	97	110	149	104	77	133
flumethrin	**35**	**50**	**43**	72	**49**	**40**
flusilazole	88	85	89	**33**	82	99
flutriafol	94	**24**	**34**	**4**	**2**	**37**
fluvalinate	103	124	150	112	**65**	138
forchlorfenuron	**18**	97	**2**	93	**21**	84
halfenprox	**69**	85	85	119	**46**	72
hexaconazole	91	**33**	**42**	**0**	**4**	**41**
imazalil	70	**37**	**27**	**1**	**9**	**29**
metconazole	87	**50**	**60**	**3**	**26**	72
methabenzthiazuron	80	94	**40**	**66**	71	94
methamidophos	72	**14**	**14**	**1**	**2**	**32**
methomyl	97	98	98	93	99	97
milbemycin A3	85	**65**	76	**7**	**40**	**61**
milbemycin A4	94	**65**	77	**4**	**35**	**58**
monocrotophos	96	77	84	**22**	75	80
myclobutanil	91	88	87	**58**	88	84

DOI: 10.1021/jf505539e
J. Agric. Food Chem. 2015, 63, 5107−5119

Table 2. continued

	automated c-SPE (ITSP)					d-SPE
compound	PSA/C_{18}/CarbonX (45 mg)	Z-Sep (10 mg)	HLB/Z-Sep/CarbonX (20 mg)	Z-Sep+ (30 mg)	Z-Sep/C_{18}/CarbonX (30 mg)	Z-Sep/C_{18}/CarbonX (30 mg)
naled	**35**	**17**	**30**	**6**	**2**	**61**
octhilinone	87	**64**	**69**	**1**	**39**	**55**
omethoate	90	**48**	**58**	**4**	**41**	**53**
paclobutrazol	98	**69**	86	**12**	**59**	85
penconazole	93	89	88	**12**	85	87
permethrin A	**25**	**40**	**44**	74	**48**	**28**
permethrin B	**70**	**62**	72	74	**67**	**64**
phosphamidon A	97	85	92	**51**	82	100
phosphamidon B	96	78	89	**22**	**69**	93
prochloraz	83	73	**63**	**4**	**58**	74
propamocarb	**0**	**0**	**0**	**4**	**0**	**14**
propiconazole	95	91	90	**21**	88	89
pymetrozine	**3**	**0**	**0**	**1**	**0**	**6**
pyrifenox A	80	75	80	**28**	78	77
pyrifenox B	82	77	80	**28**	79	74
sethoxydim peak 1	**4**	**20**	**33**	**3**	**27**	**56**
sethoxydim peak 2	**7**	**47**	77	**7**	**46**	**48**
spinetoram major	**0**	**14**	**0**	**8**	**0**	**34**
spinetoram minor	**0**	**17**	**0**	**7**	**0**	**45**
spinosyn A	**0**	**14**	**0**	**12**	**1**	**37**
spinosyn D	**0**	**14**	**0**	**9**	**0**	**41**
spirotetramat	87	88	91	**48**	86	89
spirotetramat-*cis*-enol	**0**	**6**	**5**	**6**	**0**	**39**
spirotetramat-*cis*-ketohydroxy	86	**42**	**58**	**17**	**17**	**64**
spirotetramatenol-glucoside	**3**	**0**	**0**	**16**	**0**	**13**
spirotetramatmonohydroxy	94	76	80	**35**	79	86
sulfentrazone	**0**	97	93	95	93	100
tebuconazole	91	**57**	**65**	**4**	**32**	**67**
terbumeton	95	88	93	**63**	92	94
tetraconazole	93	87	90	70	93	102
thiabendazole	**39**	**37**	**3**	**1**	**8**	**44**
thiophanate-methyl	**61**	**59**	**43**	70	71	81
tolylfluanid	**36**	87	95	97	94	95
triadimefon	90	91	93	72	88	96
triadimenol A	88	75	84	**12**	71	93
triadimenol B	96	77	93	**14**	74	83
trichlorfon	83	**3**	**0**	**0**	**0**	**10**
triphenylphosphate (SMC)	101	97	91	95	97	100
uniconazole	87	**53**	**61**	**4**	**28**	71

[a]Recoveries <70% are highlighted in bold type. [b]Mean of isomers A and B.

Although Z-Sep+ removed the highest percentage of avocado matrix, it also gave the poorest pesticide recoveries (Table 2). Recoveries were low for the 18 triazoles, with cyproconazole (1%), flutriafol (4%), hexaconazole (0%), metconazole (3%), and tebuconazole (4%) most strongly retained (Figure 2). These 5 fungicides have an acidic −OH group on the carbon α to the aromatic ring, missing from the other 13 triazoles, suggesting retention via lone-pair electron interactions with zirconia vacant d-orbitals or electrostatic interactions with zirconia. Zirconia has vacant 3d orbitals, which have Lewis acid character, and can form coordination bonds with Lewis bases (electron donors), one of the main retention mechanisms for zirconia,[5,12,24,25] along with electrostatic interactions with a positively charged zirconium surface, present at pH <5.9.[24,25] Previous studies[9,12,14] obtained >70% recoveries for triazole pesticides, using Z-Sep d-SPE cleanup. D-SPE, using the same Z-Sep/C_{18}/CarbonX mixture as packed into cartridges and the same extract to sorbent ratio as c-SPE, also gave greater recoveries of these analytes than c-SPE (Table 2, final column), reflecting the relatively poor retention of d-SPE, although recoveries were still <70% for cyproconazole, fenbuconazole, flutriafol, hexaconazole, and tebuconazole from d-SPE. These lower d-SPE recoveries, compared with those of other authors, possibly reflect the lower weight ratio of avocado to zirconia used (9:1), compared with the 28.6:1 ratio of Lozano et al.[12] and Rajski et al.,[14] our inclusion of C_{18} sorbent, or differing sample matrices.

Several organophosphate insecticides (acephate, dicrotophos, methamidophos, omethoate, and trichlorfon) were strongly retained on Z-Sep and Z-Sep+ (Table 2). Comparison of the structures of omethoate and dimethoate (4 and 90% recoveries, respectively, from Z-Sep+) indicates that lone pairs on the phosphate P═O of omethoate may have been interacting with the zirconia, with a weaker interaction for the equivalent thiophosphate P═S of dimethoate. Similar relative recoveries of omethoate and dimethoate were previously found for shrimp

DOI: 10.1021/jf505539e
J. Agric. Food Chem. 2015, 63, 5107−5119

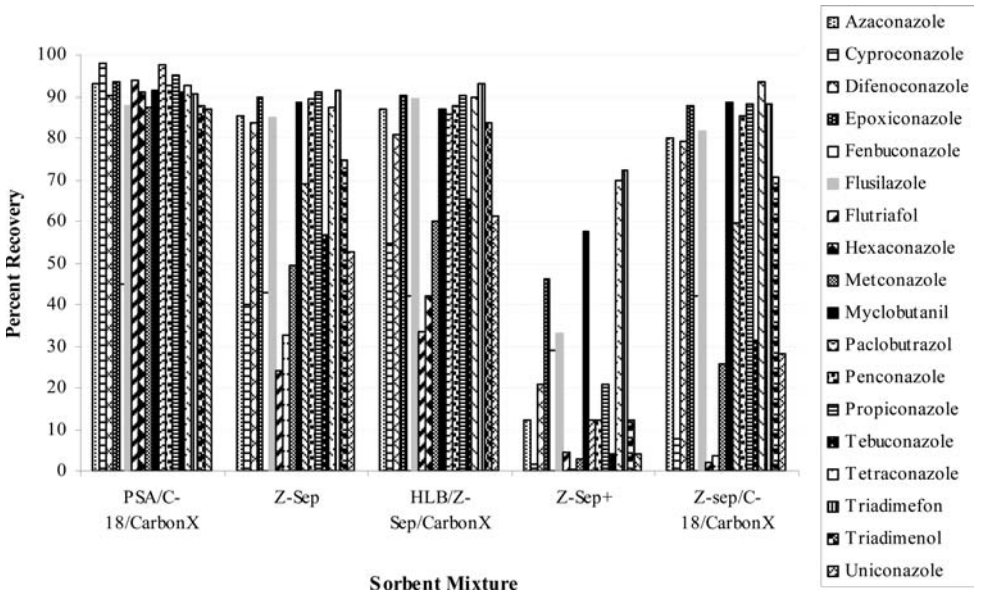

Figure 2. Triazole pesticide recoveries from avocado spiked at 100 μg/kg, extracted by QuEChERS and passed through automated c-SPE with different sorbent mixtures, eluted with MeCN, and analyzed by LC-MS/MS.

extracts cleaned up using PSA/Z-Sep/C_{18} d-SPE in filter vials,[10] whereas low recoveries of dicrotophos were observed after Z-Sep d-SPE of catfish extracts.[9]

Macrocyclic lactones (avermectin B1a, emamectin B1a, milbemycins A3 and A4, spinetoram, spinosyns A and D), all showed low recoveries from Z-Sep and Z-Sep+. This is in agreement with the poor recoveries of spinosyns A and D of Han et al.,[10] although >70% recoveries were obtained from Z-Sep d-SPE by Rajski et al.,[14] possibly reflecting the relatively poor retention of d-SPE compared with c-SPE, as recoveries from Z-Sep/C_{18}/CarbonX were 37 and 41% for d-SPE and 1 and 0% for automated c-SPE, for spinosyns A and D, respectively (Table 2).

The quaternary ammonium analyte DDAC was retained on stationary phase mixtures containing C_{18} in combination with zirconia or PSA material, with greater recoveries from Z-Sep alone, and HLB/Z-Sep/CarbonX, suggesting primarily hydrophobic interaction with C_{18} (Table 2).

Of the 280 analytes (including isomers and homologues, comprising 263 pesticides and metabolites) tested with the five different stationary phase packings (results for selected pesticides shown in Table 2), 71 showed <70% recovery from Z-Sep+, whereas 53 were below 70% recovery from Z-Sep/C_{18}/CarbonX. Therefore, the Z-Sep/C_{18}/CarbonX mixture was chosen for further method development, as a compromise between matrix removal and analyte recoveries. This is similar to the conclusions reached by other authors using d-SPE, to use Z-Sep rather than Z-Sep+ for final method development, due to higher analyte recoveries.[11,12,14] A lower weight of zirconia-based sorbent in the Z-Sep/C_{18}/CarbonX cartridges than in the Z-Sep+ cartridges could also improve recoveries of analytes being retained on zirconia, whereas inclusion of 70% by weight of C_{18} may improve removal of citrus matrix[2,15] and sterols.[26]

Methods developed using zirconia-based SPE for phospholipid removal from plasma, serum, or tissue samples have used formic or citric acids in MeCN to recover analytes with acidic functional groups, as formate and citrate are stronger Lewis bases than most analytes and cause their displacement from zirconia.[5,6] Ammonium formate in MeOH has been used for elution of basic compounds from HybridSPE, by blocking interaction with negatively charged silanols, or Zr-bound formate;[6] however, ammonium formate has poor solubility in MeCN, used for QuEChERS extractions, requiring MeOH in the elution solution. To investigate the effects of adding MeOH to the elution solvent, spikes were prepared in MeCN only and eluted with MeCN, MeCN/MeOH (1:1), or MeOH. Results of these experiments (Table 3) showed 57 compounds were retained (having <70% recovery) on Z-Sep/C_{18}/CarbonX cartridges, with MeCN elution, and only 8 showed <70% recovery with MeCN/MeOH (1:1) or MeOH elution (Table 3). This suggests that MeOH is disrupting the interactions of analytes with Z-Sep, either Lewis acid−Lewis base or electrostatic interactions. The percent dry weight of avocado matrix recovered with MeCN/MeOH (1:1) elution was 28%, compared with 44% for MeCN elution (Table 1), likely due to decreased solubility of avocado oils in MeOH, resulting in an improvement in cleanup. Elution with MeOH only showed lower recoveries of many nonpolar analytes (those with long retention times), such as cyfluthrin, cypermethrin, fenvalerate, fluvalinate, halfenprox, and permethrin (Table 3), due to lower solubility in MeOH compared with MeCN, favoring partitioning onto the sorbents.

The effect of citrate ions, present in CEN QuEChERS extracts, and ammonium formate/formic acid buffer on compound recoveries was investigated by spiking a pesticide-free squash extract (100 μg/L) and then passing it through Z-Sep/C_{18}/CarbonX automated c-SPE cartridges, eluted with MeCN, MeCN/MeOH (1:1), or 10, 50, or 100 mM buffer solutions in MeCN/MeOH (1:1). Squash was selected as giving a QuEChERS extract with low levels of matrix acids, sugars, or nonpolar compounds and lack of significant LC-MS/MS suppression. Elution of the squash extract with MeCN resulted in increased recoveries of all of the analytes that were lost from MeCN-only spikes, when eluted with MeCN (Table 3). Recoveries of the macrocyclic lactones avermectin B1a, emamectin B1a, milbemycins A3 and A4, spinetoram, and spinosyns A and D increased from between 0 and 1% to between 62 and 76% with the presence of citrate. Similarly, triazole

DOI: 10.1021/jf505539e
J. Agric. Food Chem. 2015, 63, 5107−5119

Table 3. LC-MS/MS Percent Spike Recoveries for Selected Pesticides, Using Automated C-SPE (Z-Sep/C_{18}/CarbonX sorbent), Eluted with MeCN, MeCN/MeOH (1:1), or MeOH[a]

		MeCN-only spike (100 μg/L)			squash postextraction spike (100 μg/L)
compound	t_R (min)	MeCN	MeCN/MeOH (1:1)	MeOH	MeCN
acephate	0.93	**0**	95	98	84
aldicarb sulfoxide	1.08	**0**	98	98	84
avermectin B1a	13.86	**0**	81	82	73
azaconazole[c]	5.20, 5.96	**42**	100	99	100
azadirachtin	5.35	**15**	90	83	94
bitertanol	10.59	**8**	89	85	96
bromopropylate	12.34	**18**	88	84	116
carbendazim	2.81	**0**	80	84	**68**
clethodim[d]	7.75, 11.18	**42**	113	107	82
clofentezine	10.49	77	73	**66**	97
cyfluthrin	13.11	109	98	84	116
cypermethrin	13.26	109	102	87	119
cyproconazole[c]	7.92, 8.34	**0**	85	88	86
cyprodinil	9.65	**64**	74	70	86
DDAC	12.04	**3**	74	75	83
dicrotophos	2.33	**0**	99	100	89
difenoconazole[c]	10.95	**46**	90	88	102
dodine	9.90	**37**	**46**	**53**	91
emamectin B1a	11.90	**1**	**60**	**65**	**62**
epoxiconazole	8.86	**61**	82	82	110
fenamiphos	9.34	**20**	79	72	97
fenhexamid	8.60	**2**	73	78	75
fenpropimorph	9.97	**0**	83	79	86
fensulfothion	5.85	**13**	95	95	102
fenvalerate	13.52	111	98	82	113
flusilazole	9.40	**57**	85	82	102
flutriafol	5.64	**0**	91	92	86
fluvalinate	13.78	121	101	84	123
halfenprox	14.69	120	102	83	116
hexaconazole	10.26	**0**	84	86	76
hexazinone	4.27	**48**	106	101	102
imazalil	6.61	**0**	87	81	79
metconazole	10.39	**0**	85	86	83
methabenzthiazuron	5.36	**65**	75	70	87
methamidophos	0.84	**0**	93	100	**49**
milbemycin A3	13.64	**1**	83	87	76
milbemycin A4	14.07	**1**	79	85	72
monocrotophos	1.99	**0**	97	100	95
myclobutanil	8.07	80	90	88	98
naled	6.13	**1**	**6**	**15**	**47**
octhilinone	8.61	**0**	79	85	74
omethoate	1.01	**0**	96	96	88
paclobutrazol	7.77	**3**	89	90	102
penconazole	9.69	**53**	87	89	101
permethrin A	13.85	111	103	88	111
permethrin B	14.15	113	101	87	110
prochloraz	10.45	**2**	85	83	85
propamocarb	1.05	**24**	**48**	**55**	**35**
propiconazole	10.10	71	92	91	99
pymetrozine	1.54	**0**	**67**	**66**	**32**
pyrifenox A	8.47	**68**	85	83	91
pyrifenox B	8.98	70	84	80	86
sethoxydim[d]	7.46, 11.68	**28**	103	96	75
spinetoram major	11.52	**0**	80	75	**69**
spinetoram minor	12.14	**0**	83	74	**69**
spinosyn A	10.79	**0**	81	76	72
spinosyn D	11.43	**0**	83	75	71
spirotetramat	8.71	**68**	87	83	98

DOI: 10.1021/jf505539e
J. Agric. Food Chem. 2015, 63, 5107−5119

Table 3. continued

compound	t_R (min)	MeCN-only spike (100 μg/L)			squash postextraction spike (100 μg/L)
		MeCN	MeCN/MeOH (1:1)	MeOH	MeCN
spirotetramat-*cis*-enol	5.07	**0**	89	90	**67**
spirotetramat-*cis*-ketohydroxy	6.20	**2**	88	92	73
spirotetramat-enol-glucoside	2.46	**0**	**28**	**47**	**9**
spirotetramat-monohydroxy	4.25	**2**	98	96	103
tebuconazole	9.89	**0**	82	82	94
tetraconazole	8.90	77	86	83	95
thiabendazole	3.26	**0**	**62**	**67**	**46**
triadimefon	8.01	86	90	85	103
triadimenol A	8.35	**8**	86	86	103
triadimenol B	8.51	**19**	84	82	98
trichlorfon	2.26	**0**	78	85	**40**
triphenylphosphate (SMC)	10.33	95	94	91	98
uniconazole	9.15	**0**	80	81	86

[a]Spikes were into MeCN-only or squash extract. Recoveries <70% are highlighted in bold type. [c]Mean of isomers A and B. [d]Mean of two peaks observed.

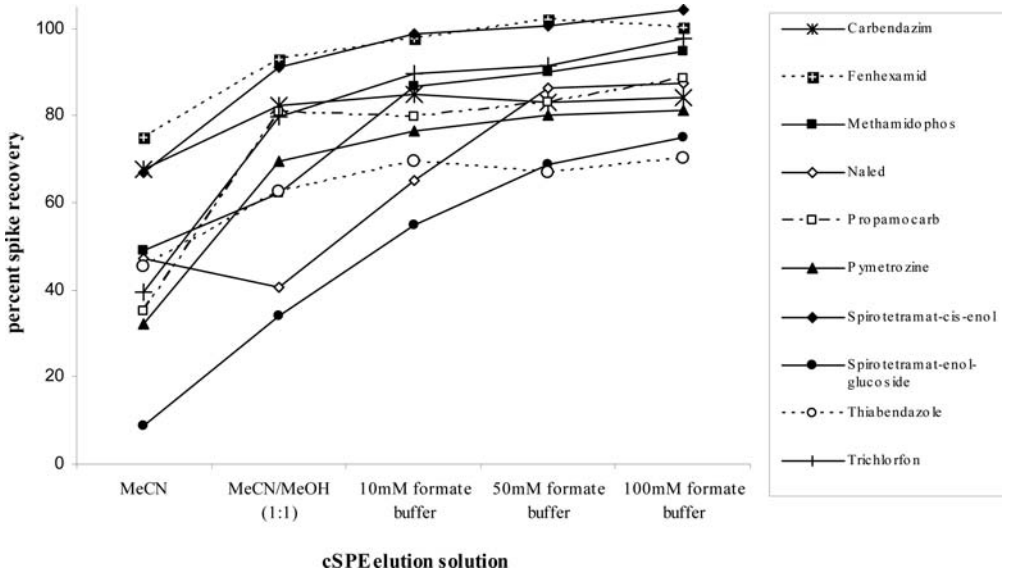

Figure 3. Recoveries from QuEChERS squash extract spiked at 100 μg/L before automated c-SPE using different elution solutions. Buffer solutions were prepared in MeCN/MeOH (1:1). Analyzed by LC-MS/MS.

recoveries were all >70%, as were organophosphates, except for methamidophos (49%), naled (47%), and trichlorfon (40%). Citrate is a stronger Lewis base than formate or acetate and can interact with Zr vacant orbitals through chelation.[5,6] The increased recoveries of macrocyclic lactones, triazoles, and organophosphates with the presence of citrate ions in MeCN indicate that they may be retained by interaction with Z-Sep Zr vacant orbitals and were being displaced by citrate. Consequently, trichlorfon, with a hydroxyl group α- to the phosphate P═O, may bind through chelation more than other organophosphates, giving lower recovery. The basic analytes with amine groups, carbendazim, propamocarb, pymetrozine, and thiabendazole, showed <70% recoveries with MeCN elution of squash extract (Table 3). Recoveries of these compounds improved using MeCN/MeOH (1:1) elution and then improved further with addition of ammonium formate/formic acid buffers (Figure 3). Elution with 10 mM buffer increased the recoveries of pymetrozine from 70 to 76% and of thiabendazole from 62 to 70%, over elution with MeCN/MeOH (1:1). Pymetrozine and thiabendazole, along with carbendazim, also appeared to be retained on CarbonX, limiting their maximum recoveries, as observed in previous studies using graphitized carbon black.[23,27] With increasing buffer strength (10, 50, 100 mM) methamidophos, naled, and trichlorfon recoveries increased (Figure 3). Naled showed the greatest increase, from 41% (MeCN/MeOH (1:1)) to 65% (10 mM buffer), 86% (50 mM buffer), and 87% (100 mM buffer). The spirotetramat metabolite spirotetramat-enol-glucoside had the lowest recovery of the analytes tested, with MeCN/MeOH (1:1) elution (34%); this increased to 55, 69, and 75% as the buffer strength was raised from 10 to 50 and 100 mM, respectively (Figure 3). Consequently, the final method validated used 100 mM buffer (in MeCN/MeOH (1:1)), for elution from Z-Sep/C_{18}/CarbonX cartridges, as this gave >70% recoveries for all 263 analytes in these experiments.

Removal of Di- and Triacylglycerols by Zirconia-Based SPE. LC-HRMS, using a Q-Orbitrap instrument, of crude avocado extract identified six triacylglycerols (TAGs), as their NH_4^+ adducts, with retention times between 13 and 14 min (PLL (*m*/*z* 872.7683; 13.08 min), LLO (*m*/*z* 898.7840; 13.18 min), PLO (*m*/*z* 874.7825; 13.34 min), OOL (*m*/*z* 900.7998;

DOI: 10.1021/jf505539e
J. Agric. Food Chem. 2015, 63, 5107−5119

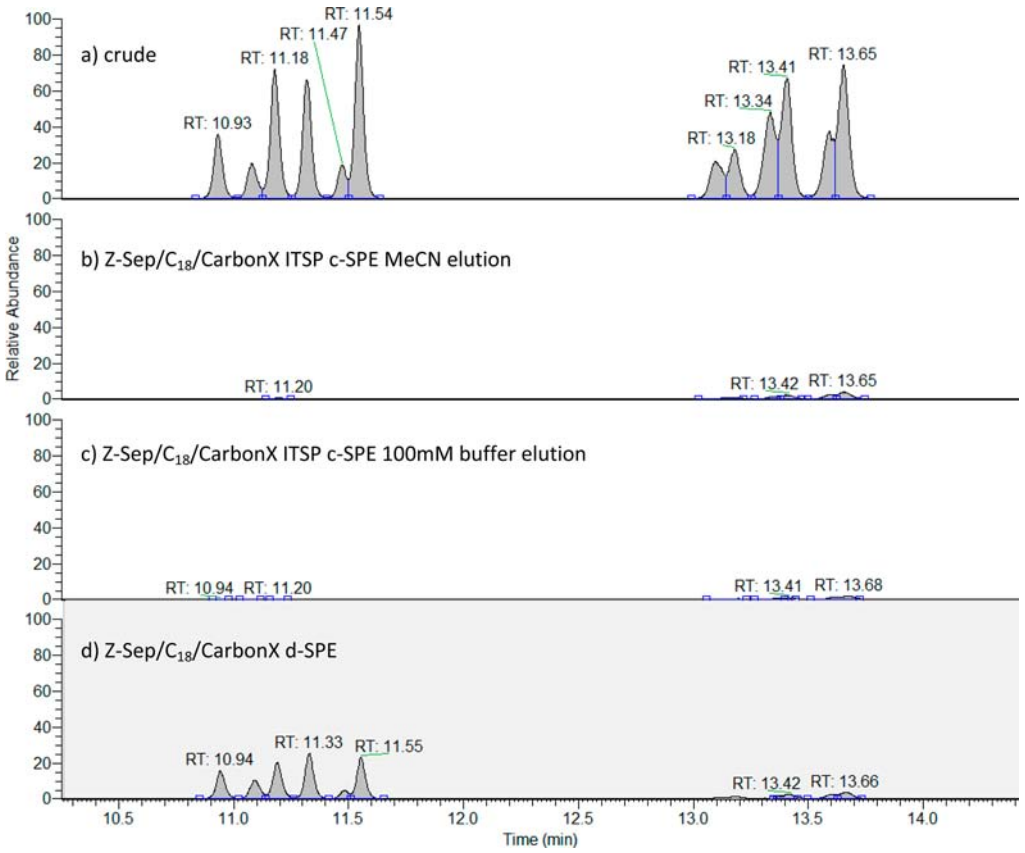

Figure 4. Di- and triacylglycerol recoveries from QuEChERS avocado extract: (a) crude extract; (b) 2-fold dilution and Z-Sep/C_{18}/CarbonX automated c-SPE ITSP eluted with MeCN; (c) 2-fold dilution and Z-Sep/C_{18}/CarbonX automated c-SPE ITSP eluted with 100 mM ammonium formate/formic acid buffer in MeCN/MeOH (1:1); (d) 2-fold dilution and Z-Sep/C_{18}/CarbonX d-SPE. LC-Q-Orbitrap-MS extracted ion chromatograms, with the *y*-axis scale normalized to chromatogram a and the same final dilution for chromatograms a–d.

13.41 min), POO (*m/z* 876.7987; 13.59 min), OOO (*m/z* 902.8160; 13.65 min)), where P = palmitic acid, L = linoleic acid and O = oleic acid (Figure 4). Identities of TAGs were confirmed by reference to the LC-APCI-MS data of Jakab et al.[28] A second group of diacylglycerols (DAGs) and what appeared to be DAG-acetates (based on their accurate masses) was present between 10.9 and 11.6 min, also identified as their NH_4^+ adducts (OL (*m/z* 636.5552; 10.93 min), LL-acetate (*m/z* 676.5508; 11.10 min), OO (*m/z* 638.5704; 11.18 min), OL-acetate (*m/z* 678.5663; 11.32 min), OP-acetate (*m/z* 654.5659; 11.47 min), OO-acetate (*m/z* 680.5819; 11.54 min)).

Comparison of peak areas in chromatograms for avocado crude extract and 2-fold diluted crude extract cleaned up by automated c-SPE on Z-Sep/C_{18}/CarbonX cartridges, eluted with MeCN or 100 mM buffer in MeCN/MeOH (1:1), showed c-SPE removal of >90% of the TAGs and DAGs (Figure 4). Addition of 100 mM buffer and MeOH to the elution solvent showed no observable increase in TAG and DAG recovery, indicating they were not displacing oil from Z-Sep. D-SPE, using the same sorbent mixture (Z-Sep/C_{18}/CarbonX) and ratio of extract to sorbent as c-SPE, with MeCN solvent, resulted in similar removal of TAGs, but poorer retention of DAGs and putative DAG-acetates (24–54% recovery), possibly due to their greater solubility in MeCN. Ismaiel et al.[7] also found that zirconia SPE (using Supelco HybridSPE-PPT well-plates) effectively removed TAGs from blood plasma; however, DAGs were poorly removed.

Method Validation. The method was validated for avocado and citrus, following the Eurachem Method Validation Guide,[29] to provide data on pesticide recoveries and reproducibility through the automated ITSP c-SPE method developed (Table 4). The finalized method used c-SPE cartridges containing 30 mg of Z-Sep/C_{18}/CarbonX, with 150 μL of QuEChERS extract loaded and 150 μL of 100 mM ammonium formate/formic acid buffer in MeCN/MeOH (1:1) used for elution.

Because there appeared to be some matrix suppression of flumethrin, permethrin A, and halfenprox when 2-fold diluted avocado extract was cleaned up using Z-Sep/C_{18}/CarbonX (Table 2), 5-fold dilution before d-SPE was used for avocado validation, with the aim of improving cleanup and reducing ionization suppression while still meeting method detection limits needed to meet the maximum residue limits (MRLs) required, using the Triple Quad 6500 LC-MS/MS.

Avocado was chosen due to its high oil content, up to 30% by weight,[19] which can precipitate on the addition of aqueous buffer for LC-MS/MS analysis, interfere with chromatographic separations by accumulating on C_{18} analytical columns, or elute several injections later and therefore should be removed from extracts before injection.[14,30] During LC-Q-Orbitrap-MS experiments avocado TAGs failed to elute from the C_{18} HPLC column with 95% MeOH, requiring 98% MeOH/isopropanol (1:1), and therefore may accumulate on the column with multiple injections during routine multiresidue analyses. Avocado extracts produce significant matrix suppression for late-eluting compounds, without cleanup.[31] Citrus was selected as "citrus fruits are notoriously difficult matrices for pesticide residue analysis"[2] and can result in high levels of LC-MS/MS matrix ionization suppression,[2,31−33] whereas the high acidity may affect extraction

DOI: 10.1021/jf505539e
J. Agric. Food Chem. 2015, 63, 5107−5119

Table 4. Validation Data for Selected Pesticides from Automated ITSP C-SPE Cleanup of QuEChERS Extracts of Spiked Avocado and Citrus (100 μg/kg), Analyzed by LC-MS/MS, Quantitated against Solvent-Only Calibration Standards (n = 10)[a]

compound	avocado[b]		citrus	
	recovery (%)	RSD (%)	recovery (%)	RSD (%)
acephate	79	5	83	9
aldicarb	90	4	94	6
aldicarb sulfone	93	6	95	9
aldicarb sulfoxide	87	8	90	11
anilazine	**31**	24	**57**	25
atrazine	87	6	96	7
avermectin B1a	93	22	101	9
azaconazole[c]	93	10	95	18
azadirachtin	95	13	110	14
bifenthrin	**58**	16	115	20
bitertanol	92	8	109	16
boscalid	81	7	103	6
bromophos-ethyl	79	21	104	12
bromopropylate	93	23	104	12
cadusafos	90	9	109	6
captafol	74	32	89	35
carbaryl	90	5	87	15
carbendazim	**67**	12	77	5
carboxin	77	8	91	13
chlorantraniliprole	85	10	93	9
chlorfluazuron	82	16	99	10
chlorpyrifos	93	7	107	16
cinerin (i)	96	10	89	37
cinerin (ii)	100	14	107	11
clofentezine	**62**	16	100	9
clothianidin	92	5	**126**	9
coumaphos	100	7	106	9
cyfluthrin	83	28	110	17
cyhalothrin	103	56	103	17
cypermethrin	88	8	111	8
cyproconazole[c]	95	10	102	7
cyprodinil	77	12	105	5
DDAC	93	11	**160**	22
demeton-*S*-methyl	91	11	99	9
diazinon	90	6	104	13
dichlofluanid	91	7	99	11
dichlorvos	87	15	96	9
dicrotophos	92	8	94	4
difenoconazole[c]	91	11	105	8
dimethomorph[c]	95	8	104	13
dodine	102	13	113	13
edifenphos	88	10	99	9
emamectin B1a	85	9	105	13
epoxiconazole	93	12	97	6
fenamiphos	85	8	98	9
fenarimol	87	10	108	13
fenbuconazole	93	12	96	12
fenhexamid	79	12	97	10
fenpropimorph	92	11	98	6
fensulfothion	95	10	102	7
fenvalerate	110	17	112	12
fludioxonil	97	12	108	15
flumethrin	**65**	26	**136**	16
flusilazole	93	6	101	10

Table 4. continued

compound	avocado[b]		citrus	
	recovery (%)	RSD (%)	recovery (%)	RSD (%)
flutriafol	90	12	102	6
fluvalinate	93	17	114	14
forchlorfenuron	**23**	34	**57**	20
halfenprox	**65**	13	118	18
hexaconazole	93	10	100	8
imazalil	92	9	102	5
imidacloprid	91	6	**139**	5
iprodione	94	17	103	10
jasmolin (i)	97	7	105	17
jasmolin (ii)	92	21	116	14
malathion	94	4	100	7
metconazole	79	9	101	8
methabenzthiazuron	70	17	93	8
methamidophos	**42**	9	**64**	4
methomyl	93	4	99	9
methoxyfenozide	84	7	102	8
milbemycin A3	75	19	101	7
milbemycin A4	74	18	100	7
monocrotophos	94	6	98	8
myclobutanil	92	7	106	10
naled	**33**	14	**60**	9
octhilinone	78	17	94	8
omethoate	85	6	88	11
oryzalin	90	18	107	24
oxyfluorfen	82	27	114	14
paclobutrazol	90	5	84	17
parathion-methyl	99	36	117	13
penconazole	92	5	102	10
permethrin[c]	**57**	18	111	14
phosphamidon[c]	93	10	101	9
piperonyl-butoxide	88	13	111	10
prochloraz	90	8	103	15
procymidone	93	18	96	43
propamocarb	85	10	105	8
propiconazole	84	11	100	9
prothiofos	**62**	21	105	14
pymetrozine	**16**	20	74	9
pyraclostrobin	75	18	98	5
pyrethrin (i)	101	11	104	12
pyrethrin (ii)	103	11	108	11
pyrifenox[c]	88	12	98	9
pyrimethanil	81	11	99	10
sethoxydim[d]	71	10	120	22
spinetoram major	74	16	94	11
spinetoram minor	79	9	90	12
spinosyn A	79	13	100	7
spinosyn D	73	13	93	8
spiromesifen	78	7	101	11
spirotetramat	83	9	99	9
spirotetramat-*cis*-enol	71	10	96	8
spirotetramat-*cis*-ketohydroxy	93	9	106	12
spirotetramat-enol-glucoside	**52**	7	76	14
spirotetramat-monohydroxy	93	8	116	10
sulfentrazone	91	7	**182**	18
tebuconazole	82	6	101	6
tebufenozide	86	5	100	7
teflubenzuron	84	21	100	13
terbumeton	91	5	107	7

DOI: 10.1021/jf505539e
J. Agric. Food Chem. 2015, 63, 5107−5119

Table 4. continued

compound	avocado[b] recovery (%)	avocado[b] RSD (%)	citrus recovery (%)	citrus RSD (%)
terbuthylazine	87	6	103	6
terbuthylazine-desethyl	91	5	77	11
tetraconazole	90	10	96	6
thiabendazole	**45**	23	**49**	15
thiacloprid	90	5	85	10
thiophanate-methyl	**65**	14	99	10
tolylfluanid	93	7	101	10
triadimefon	84	9	100	8
triadimenol[c]	87	5	105	7
triazophos	**67**	4	84	13
trichlorfon	88	6	115	9
triphenylphosphate (SMC)	100	6	93	10
uniconazole	82	8	100	9

[a]Recoveries <70% or >120% are highlighted in bold type. [b]Normalized to triphenylphosphate (SMC). [c]Mean of isomers. [d]Mean of two peaks observed.

recoveries of acid labile or basic pesticides, such as acephate and pymetrozine.[2,34] There was also the possibility that the relatively high concentrations of citric acid in citrus fruit, plus the extra trisodium citrate that we added during extraction to bring the pH back into the citrate buffer region (centered on pK_a = 4.76), may have affected cleanup on Z-Sep by displacing matrix.

Validation results for avocado showed recoveries below 70% for 16 of the 269 pesticides tested (including homologues and metabolites, with the 6 pyrethrins considered as one pesticide). Five of the16 analytes at <70% recovery in avocado also fell below 70% recoveries in citrus (Table 4). Recoveries were quantitated against solvent-only calibration standards and therefore include any ESI matrix suppression. Of the compounds falling below 70% recovery, anilazine, carbendazim, forchlorfenuron, methamidophos, pymetrozine, and thiabendazole commonly have poor QuEChERS extraction recoveries,[2,14,15,34,35] due to their basicity or being highly polar. This is in addition to <100% recovery through the c-SPE cleanup (84% for carbendazim, 81% for pymetrozine, 70% for thiabendazole with 100 mM buffer elution, Figure 3). Spirotetramat-enol-glucoside recovery was 52% for avocado, compared with 75% when spiked directly into squash extract before cleanup (Figure 3), and 76% for citrus, indicating some loss, or MS suppression, in the presence of avocado matrix. Naled, clofentezine, and thiophanate-methyl are base sensitive[35] and appeared to be decomposing in aqueous solution, giving low recoveries in avocado (33, 62, and 65%, respectively) and improved recoveries in acidic citrus (60, 100, and 99%, respectively). Matrix suppression was apparent in avocado for the late-eluting analytes bifenthrin (14.21 min), flumethrin (13.97 min), halfenprox (14.51 min), and permethrins A (13.63 min) and B (13.94 min); however, recoveries were >50%, with relative standard deviations (RSDs) <26%, acceptable for screening purposes. Some analytes exhibited >120% recoveries from citrus, with signal enhancement apparent at around 2.30 min affecting clothianidin (2.30 min) and imidacloprid (2.29 min). For the quaternary ammonium compound DDAC, and sulfentrazone, it appeared fewer losses occurred in the instrument injector with high levels of citrate in citrus extracts, giving >120% recoveries (Table 4). RSDs were >20% for 20 compounds but were >30% for only 6 compounds, with mean RSDs of 10% for both matrices, indicating that the automated ITSP c-SPE cleanup was highly reproducible and giving very similar reproducibility to previous studies using d-SPE,[2,33] or no cleanup,[36] and matrix-matched calibration standards. Overall, mean spike recovery for avocado was 87%, and that for citrus was 102%.

The validated method was used to analyze nine avocado and nine orange samples, New Zealand grown, and obtained from local shops in Hamilton, New Zealand. Incurred residues >0.01 mg/kg were detected in eight avocado and eight orange samples. DDAC was present in four avocado samples between 0.23 and 0.42 mg/kg, prochloraz in three samples (0.080–0.15 mg/kg), chlorpyrifos in one sample (0.19 mg/kg), piperonyl butoxide in one sample (0.035 mg/kg), and uniconazole in one sample at 0.010 mg/kg. In the orange samples, diazinon was detected in four samples from 0.014 to 0.24 mg/kg, malathion in three samples, ranging from 0.018 to 0.061 mg/kg, piperonyl butoxide in one sample (1.2 mg/kg), terbuthylazine in one sample (0.010 mg/kg), and the spirotetramat metabolite spirotetramat-*cis*-enol in one sample at 0.019 mg/kg. The oranges with terbuthylazine also showed a trace level of terbuthylazine-desethyl (0.00096 mg/kg), confirming the presence of this herbicide, whereas the sample with spirotetramat-*cis*-enol also contained low levels of spirotetramat-*cis*-ketohydroxy and spirotetramat-enol-glucoside (0.0069 mg/kg for both). The levels of pesticides found were below the New Zealand MRLs,[37] except for chlorpyrifos (MRL = 0.2 mg/kg), taking into account a 7% RSD found for chlorpyrifos recovery in avocado during method validation (Table 4). These results indicate the effectiveness of the method in the detection of incurred pesticide residues in fruits available for purchase by New Zealand consumers.

This is the first investigation into the use of ITSP mini-cartridges for cleanup of QuEChERS extracts for multiresidue pesticide analysis. The zirconia stationary phases Z-Sep and Z-Sep+ have recently been used as d-SPE sorbents to clean up QuEChERS extracts;[9−16] however, this study uses these sorbents in SPE columns, which appear to be more retentive than d-SPE (Table 2). A mixture of Z-Sep, C_{18}, and CarbonX, in mini-column ITSP cartridges, effectively removed oils from QuEChERS extracts of avocado (Figure 4), and elution with formate buffer in MeCN/MeOH gave acceptable recoveries for 269 pesticide analytes (Table 4; Table SI-A). Validation data showed minimal matrix-induced LC-MS/MS ionization suppression for avocado and orange extracts. Automation and miniaturization of c-SPE on an instrument autosampler make this method quick and easy, as well as robust and reproducible.

■ ASSOCIATED CONTENT

Supporting Information

Tables SI-A and SI-B. This material is available free of charge via the Internet at http://pubs.acs.org.

■ AUTHOR INFORMATION

Corresponding Author

*(B.D.M.) Phone: (+64) 78570617. Fax: (+64) 78582001. E-mail: bruce.morris@hill-labs.co.nz.

Notes

The authors declare no competing financial interest.

■ ACKNOWLEDGMENTS

We thank Kim Gamble and Rick Youngblood of ITSP Solutions for gifts of ITSP cartridges and trays and assistance with X-Y-Z autosampler programming. We also thank Ananda

DOI: 10.1021/jf505539e
J. Agric. Food Chem. 2015, 63, 5107−5119

Card (Hill Laboratories) for assistance with LC-Q-Orbitrap analyses and Michael Ye (Supelco) for the gift of Z-Sep and Z-Sep+ sorbents.

■ ABBREVIATIONS USED

QuEChERS, quick, easy, cheap, effective, rugged, and safe; CEN, European Committee for Standardization; d-SPE, dispersive solid phase extraction; c-SPE, column solid phase extraction; LC-MS/MS, liquid chromatography−tandem mass spectrometry; HPLC, high-performance liquid chromatograpy; LC-Q-Orbitrap-MS, liquid chromatography-quadrupole Orbitrap high-resolution mass spectrometry; MRM, multiple reaction monitoring; ESI, electrospray ionization; DP, declustering potential; EP, entrance potential; PSA, primary−secondary amine; C_{18}, octadecyl-functionalized silica; MeOH, methanol; MeCN, acetonitrile; DDAC, didecyldimethylammonium chloride; TAG, triacylglycerol; DAG, diacylglycerol; MRL, maximum residue limit; ITSP, instrument top sample preparation; RSD, relative standard deviation; t_r, retention time; fwhm, full width at half-maximum; GCB, graphitized carbon black; SMC, system monitoring compound

■ REFERENCES

(1) Anastassiades, M.; Lehotay, S. J.; Stajnbaher, D.; Schenck, F. J. Fast and easy multiresidue method employing acetonitrile extraction/partitioning and "dispersive solid-phase extraction" for the determination of pesticide residues in produce. *J. AOAC Int.* **2003**, *86*, 412−431.

(2) Lehotay, S. J.; Ae Son, K.; Kwon, H.; Koesukwiwat, U.; Fu, W.; Maštovská, K.; Hoh, E.; Leepipatpiboon, N. Comparison of QuEChERS sample preparation methods for the analysis of pesticide residues in fruits and vegetables. *J. Chromatogr., A* **2010**, *1217*, 2548−2560.

(3) Lehotay, S. J.; Maštovská, K.; Lightfield, A. R. Use of buffering and other means to improve results of problematic pesticides in fast and easy method for residue analysis in fruits and vegetables. *J. AOAC Int.* **2005**, *88*, 615−629.

(4) Anastassiades, M.; Scherbaum, E.; Tasdelen, B.; Stajnbaher, D. Recent developments in QuEChERS methodology for pesticide multiresidue analysis. In *Crop Protection, Public Health, Environmental Safety*; Ohkanawa, H., Miyagawa, H., Lee, P. W., Eds.; Wiley-VCH: Weinheim, Germany, 2007; pp 439−458.

(5) Aurand, C.; Mi, C.; Lu, X.; Trinh, A.; Ye, M. Troubleshooting analyte recovery when using HybridSPE-precipitation technology. *Supelco Reporter US* **2009**, *27.2*, 17−19; https://www.sigmaaldrich.com/content/dam/sigma-aldrich/docs/Supelco/The_Reporter/t209002.pdf (last accessed Oct 29, 2014).

(6) Ahmad, S.; Kalra, H.; Gupta, A.; Raut, B.; Hussain, A.; Rahman, M. A. HybridSPE: a novel technique to reduce phospholipid-based matrix effect in LC-ESI-MS bioanalysis. *J. Pharm. Bioallied Sci.* **2012**, *4*, 267−275.

(7) Ismaiel, O. A.; Zhang, T.; Jenkins, R. G.; Karnes, H. T. Investigation of endogenous blood plasma phospholipids, cholesterol and glycerides that contribute to matrix effects in bioanalysis by liquid chromatography/mass spectrometry. *J. Chromatogr., B* **2010**, *878*, 3303−3316.

(8) Piatkowska, M.; Jedziniak, P.; Zmudzki, J. Comparison of different sample preparation procedures for multiclass determination of selected veterinary drug, coccidiostat and insecticide residues in eggs by liquid chromatography-tandem mass spectrometry. *Anal. Methods* **2014**, *6*, 3034−3044.

(9) Sapozhnikova, Y. Evalutaion of low-pressure gas chromatography-tandem mass spectrometry method for the analysis of >140 pesticides in fish. *J. Agric. Food Chem.* **2014**, *62*, 3684−3689.

(10) Han, L.; Sapozhnikova, Y.; Lehotay, S. J. Streamlined sample cleanup using combined dispersive solid-phase extraction and in-vial filtration for analysis of pesticides and environmental pollutants in shrimp. *Anal. Chim. Acta* **2014**, *827*, 40−46.

(11) Sapozhnikova, Y.; Lehotay, S. J. Multi-class, multi-residue analysis of pesticides, polychlorinated biphenyls, polycyclic aromatic hydrocarbons, polybrominated diphenyl ethers and novel flame retardants in fish using fast, low-pressure gas chromatography-tandem mass spectrometry. *Anal. Chim. Acta* **2013**, *758*, 80−92.

(12) Lozano, A.; Rajski, L.; Uclés, S.; Belmonte-Valles, N.; Mezcua, M.; Fernandes-Alba, A. R. Evaluation of zirconium dioxide-based sorbents to decrease the matrix effect in avocado and almond multiresidue pesticide analysis followed by gas chromatography tandem mass spectrometry. *Talanta* **2014**, *118*, 68−83.

(13) Stenerson, K. K.; Claus, J. Increase removal of fat and pigment from avocado extracts prior to GC-MS analysis of pesticide and metabolite residues. *Supelco Reporter US* **2013**, *31.2*, 12−13; https://www.sigmaaldrich.com/content/dam/sigma-aldrich/docs/Supelco/The_Reporter/1/T213002_reporter.pdf (last accessed Oct 29, 2014).

(14) Rajski, L.; Lozano, A.; Uclés, A.; Ferrer, C.; Fernández-Alba, A. R. Determination of pesticide residues in high oil vegetal commodoties by using various multi-residue methods and clean-ups followed by liquid chromatography tandem mass spectrometry. *J. Chromatogr., A* **2013**, *1304*, 109−120.

(15) Stenerson, K.; Barrey, E.; Shimelis, O.; Mauney, E. Analysis of pesticides by QuEChERS − application of Z-Sep family of sorbents for cleanup. *Supelco Presentation* **2012**, http://ll1.workcast.net/10311/0279275158671341/Documents/FoodPesticides%20by%20QuEChERS_new%20ZSep%20sorbentT412106H.pdf (last accessed Nov 10, 2014).

(16) Moreno-González, D.; Huertas-Pérez, J. F.; García-Campaña, A. M.; Gámiz-Gracia, L. Determination of carbamates in edible vegetable oils by ultra-high performance liquid chromatography-tandem mass spectrometry using a new clean-up based on zirconia for QuEChERS methodology. *Talanta* **2014**, *128*, 299−304.

(17) Schenck, F. J.; Brown, A. N.; Podhorniak, L. V.; Parker, A.; Reliford, M.; Wong, J. W. A rapid multiresidue method for determination of pesticide residues in fruits and vegetables by using acetonitrile extraction/partitioning and solid-phase extraction column cleanup. *J. AOAC Int.* **2008**, *91*, 422−438.

(18) Eyres, L.; Sherpa, N.; Hendriks, G. Avocado oil: a new edible oil from Australasia. *Lipid Technol.* **2001**, *13*, 84−88.

(19) Yanty, N. A. M.; Marikkar, J. M. N.; Long, K. Effect of varietal differences on composition and characteristics of avocado oil. *J. Am. Oil Chem. Soc.* **2011**, *88*, 1977−2003.

(20) European Committee for Standardization. Technical Committee CEN/TC 275. Foods of plant origin − determination of pesticide residues using GC-MS and /or LC-MS/MS following acetonitrile extraction/partitioning and cleanup by dispersive SPE - QuEChERS method; prEN 15662; European Committee for Standardization: Brussels, Belgium, 2007.

(21) ChemSpider. Royal Society of Chemistry; http://www.chemspider.com (last accessed Nov 7, 2014).

(22) Narong, C.; Ollis, L. W.; Harmon, T.; Lee, S.; Mercer, G. Analysis of 136 pesticides in avocado using a modified QuEChERS method with LC-MS/MS and GC-MS/MS. *J. Agric. Food Chem.* **2013**, *61*, 2315−2329.

(23) Cunha, S. C.; Lehotay, S. J.; Maštovská, K.; Fernandes, J. O.; Beatriz, M.; Oliveira, P. P. Evaluation of the QuEChERS sample preparation approach for the analysis of pesticide residues in olives. *J. Sep. Sci.* **2007**, *30*, 620−632.

(24) Thistlethwaite, P. J.; Gee, M. L.; Wilson, D. Diffuse reflectance infrared fourier transform spectroscopic studies of the adsorption of oleate/oleic acid onto zirconia. *Langmuir* **1996**, *12*, 6487−6491.

(25) Shi, Z.-G.; Feng, Y.-Q.; Xu, L.; Zhang, M.; Da, S.-L. Preparation and evaluation of zirconia-coated silica monolith for capillary electrchromatography. *Talanta* **2004**, *63*, 593−598.

(26) Lehotay, S. J.; Maštovská, K.; Yun, S. J. Evaluation of two fast and easy methods for pesticide residue analysis in fatty food matrixes. *J. AOAC Int.* **2005**, *88*, 630−638.

(27) Rebelo, A. M.; Heller, M.; Dolzan, M. D.; Deschamps, F. C.; Abate, G.; Micke, G. A.; Grassi, M. T. Determination of twenty

DOI: 10.1021/jf505539e
J. Agric. Food Chem. 2015, 63, 5107−5119

pesticides in rice by employing QuEChERS and LC-ESI-MS/MS. *Anal. Methods* **2014**, *6*, 9469−9476.
(28) Jakab, A.; Héberger, K.; Forgács, E. Comparative analysis of different plant oils by high-performance liquid chromatography-atmospheric pressure chemical ionization mass spectrometry. *J. Chromatogr., A* **2002**, *976*, 255−263.
(29) Eurachem Guide. *The Fitness for Purpose of Analytical Methods: A Laboratory Guide to Method Validation and Related topics*, 2nd ed.; 2014; http://www.eurachem.org/images/stories/Guides/pdf/MV_guide_2nd_ed_EN.pdf (last accessed Nov 11, 2014).
(30) García-Reyes, J. F.; Ferrer, C.; Gómez-Ramos, M. J.; Molina-Díaz, A.; Fernández-Alba, A. R. Determination of pesticide residues in olive oil and olives. *TrAC Trends Anal. Chem.* **2007**, *26*, 239−251.
(31) Stahnke, H.; Kittlaus, S.; Kempe, G.; Alder, L. Reduction of matrix effects in liquid chromatography-electrospray ionization-mass spectrometry by dilution of the sample extracts: how much dilution is needed? *Anal. Chem.* **2012**, *84*, 1474−1482.
(32) Kittlaus, S.; Kemp, G.; Speer, K. Evaluation of matrix effects in different multipesticide residue analysis methods using liquid chromatography-tandem mass spectrometry, including an automated two-dimensional cleanup approach. *J. Sep. Sci.* **2013**, *36*, 2185−2195.
(33) Payá, P.; Anastassiades, M.; Mack, D.; Sigalova, I.; Tasdelen, B.; Oliva, J.; Barba, A. Analysis of pesticide residues using the Quick Easy Cheap Effective Rugged and Safe (QuEChERS) pesticide multiresidue method in combination with gas and liquid chromatography and tandem mass spectrometric detection. *Anal. Bioanal. Chem.* **2007**, *389*, 1697−1714.
(34) Lehotay, S. J.; de Kok, A.; Hiemstra, M.; van Bodengraven, P. Validation of a fast and easy method for the determination of residues from 229 pesticides in fruits and vegetables using gas and liquid chromatography and mass spectrometric detection. *J. AOAC Int.* **2005**, *88*, 595−614.
(35) Lacina, O.; Zachariasova, M.; Urbanova, J.; Vaclavikova, M.; Cajka, T.; Hajslova, J. Critical assessment of extraction methods for the simultaneous determination of pesticide residues and mycotoxins in fruits, cereals, spices, and oil seeds employing ultra-high performance liquid chromatography-tandem mass spectrometry. *J. Chromatogr., A* **2012**, *1262*, 8−18.
(36) Pizzutti, I. R.; de Kok, A.; Hiemstra, M.; Wickert, C.; Prestes, O. D. Method validation and comparison of acetonitrile and acetone extraction for the analysis of 169 pesticides in soya grain by liquid chromatography-tandem mass spectrometry. *J. Chromatogr. A* **2009**, *1216*, 4539−4552.
(37) New Zealand (Maximum Residue Limits of Agricultural Compounds) Food Standards 2014; http://www.foodsafety.govt.nz/elibrary/industry/nz-mrl-agricultural-compounds-food-standards-07-2014.pdf (last accessed Jan 23, 2015).

DOI: 10.1021/jf505539e
J. Agric. Food Chem. 2015, 63, 5107−5119

JOURNAL OF AGRICULTURAL AND FOOD CHEMISTRY

Article

pubs.acs.org/JAFC

Characterization of Trisiloxane Surfactants from Agrochemical Adjuvants and Pollinator-Related Matrices Using Liquid Chromatography Coupled to Mass Spectrometry

Jing Chen and Christopher A. Mullin*

Department of Entomology, Center for Pollinator Research, The Pennsylvania State University, University Park, Pennsylvania 16802, United States

Supporting Information

ABSTRACT: Trisiloxane surfactants (TSSs) have been associated with honeybee learning impairment and the ongoing global bee decline. A liquid chromatography−mass spectrometry strategy for the identification of TSSs from agrochemical adjuvants and pollinator-related matrices is introduced here. The strategy incorporates chromatographic retention behavior, isotope ratio, reference to a compiled database of accurate masses, and TSS hydrolysis when necessary. Using this analytical strategy, three TSSs (x = 0, R = H, m = 1, 2, or 3) were identified for the first time from almond flowers of a commercial orchard. The three major purified TSS components in popularly used spray tank adjuvants were identified as TSS (x = 0, m = 0, R = H, CH_3, or $C(O)CH_3$) and their structures confirmed by nuclear magnetic resonance spectroscopy. These monitoring tools allow the assessment of the agricultural residues and potential risks of major TSS contaminants to important nontarget species such as honeybee and other essential pollinators.

KEYWORDS: *trisiloxane surfactant, organosilicone, honeybee decline, LC-MS, adjuvants*

INTRODUCTION

Poor honeybee and other pollinator health continues to be a major threat worldwide since 2006,[1,2] and factors such as parasites, pesticides, pathogens, or their combinations have been implicated in bee decline.[3,4] More recently, the focus has been on the role of pesticide residues in foraging areas or beehives as a primary trigger of bee death.[5] However, no direct correlation has been found between any single pesticide and colony collapse.[3,6,7] Compared to technical grade pesticides, formulated pesticides are usually more toxic to honeybees and other nontarget species.[8] Some formulation additives and solvents are known to be acutely or sublethally toxic to bees, although they are considered and classed as "inerts".[9,10]

Organosilicone surfactants used in agriculture are new-generation adjuvants containing a fully methylated siloxane backbone as the hydrophobic part and mostly one or occasionally more poly(ethylene oxide) (EO)/poly(propylene oxide) (PO) chains as the hydrophilic part. Most often, a propyl group is used to connect the siloxane backbone and EO/PO side chain (Figure 1), but occasionally an alternative alkyl from 1 to 4 carbons or an aryl group can serve as a spacer. According to specific application or the commercial product, the surfactant structure can differ in end group R and the values of x, m, and n,[8,11−13] which are generally not revealed by manufacturers. In agro-ecosystem use, the trisiloxane surfactants (TSSs; x = 0 in Figure 1) dominate and are increasingly applied as spray adjuvants due to their superior spreading and penetrating abilities.[12,13] Recently, high nanograms per gram levels of TSS residues were detected in North American bee hives,[14] and adult bees fed 20 μg of tested TSS adjuvant were strongly impaired in their learning ability to associate a floral odor with an imminent sugar nectar reward.[10] Thus, more attention should be paid to monitoring environmental TSS residues to assess their potential role in the ongoing bee decline.

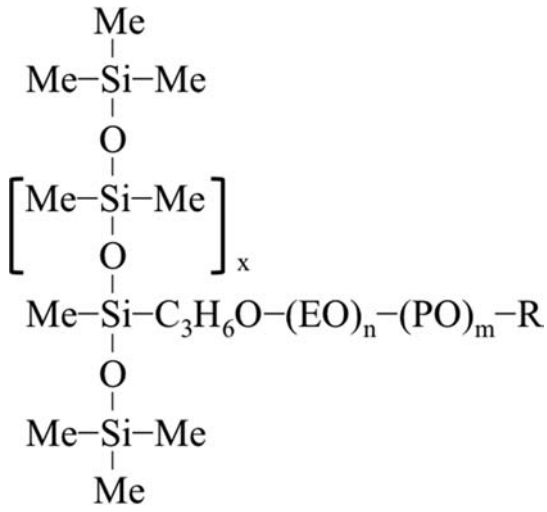

Figure 1. General structure of an organosilicone surfactant. Me, EO, and PO represent methyl, ethylene oxide, and propylene oxide, respectively.

Special Issue: 51st North American Chemical Residue Workshop

Received: November 20, 2014
Revised: February 4, 2015
Accepted: February 5, 2015
Published: February 5, 2015

ACS Publications © 2015 American Chemical Society

DOI: 10.1021/jf505634x
J. Agric. Food Chem. 2015, 63, 5120−5125

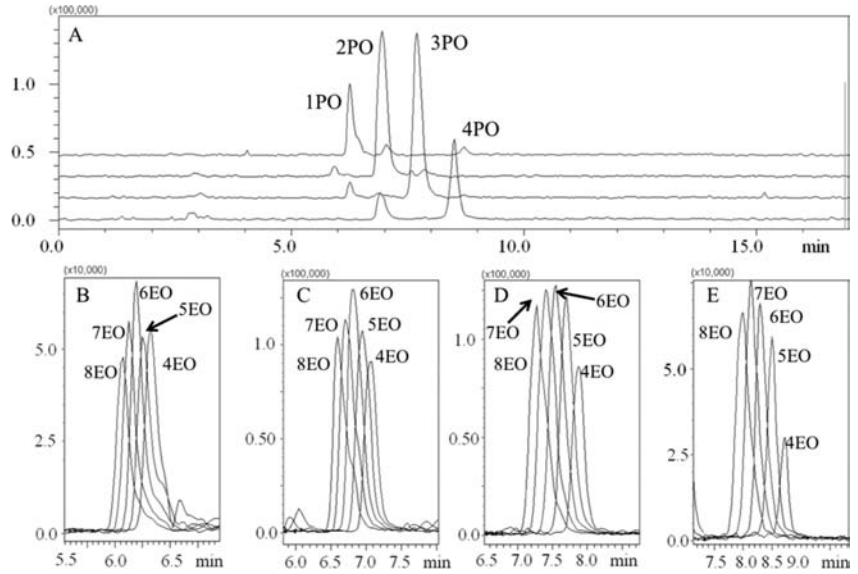

Figure 2. Extracted ion chromatograms of trisiloxane surfactant (R = H) oligomers: (A) oligomers containing 1−4 poly(propylene oxide) (PO) units with 8 poly(ethylene oxide) (EO) units; (B) oligomers of 4−8 EO and 1 PO units; (C−E) oligomers of 4−8 EO and 2−4 PO units, respectively.

Major components of the first commercial TSS, Silwet L-77, were previously identified as primarily methoxy- and some hydroxy-capped TSS (Figure 1; $x = 0$, $m = 0$, R = CH_3 or H; CAS Registry No. 27306-78-1 and 67674-67-3).[15] Subsequently, analytical methods were developed to monitor residues of these TSSs in water,[16] and in addition the acetyl-capped TSS ($x = 0$, $m = 0$, R = $C(O)CH_3$; CAS Registry No. 125997-17-3) in honey, pollen, and beewax.[14] New kinds of TSSs are continually being synthesized and reported,[17−23] and their possible future use in bee environments can be anticipated. It is important to develop an identification strategy for analyzing TSSs and primary degradates in bee-related samples.

Here, a strategy for identifying TSSs and their environmental degradates, based on liquid chromatography coupled to mass spectrometry (LC-MS), is described. Techniques used include low- and high-resolution mass spectrometry (MS), isotope ratio, nuclear magnetic resonance (NMR) spectroscopy, TSS hydrolysis, chromatographic retention behavior, and reference to a compiled database of diagnostic masses. Particular attention was made to distinguishing TSSs from competing polyethoxylate ions in samples. With this strategy, TSSs were identified from almond flower and from commercial high-volume agrochemical adjuvants.

MATERIALS AND METHODS

Chemicals. Acetonitrile (HPLC grade) and formic acid (98%) were purchased from EMD Chemical Inc. (Gibbstown, NJ, USA). Ammonium formate was purchased from Alfa Aesar (Wayne, PA, USA). Magnesium sulfate ($MgSO_4$, anhydrous) and ENVIRO Clean 2 mL dispersed solid phase extraction (SPE) tube (containing 150 mg of $MgSO_4$, 150 mg of CUPSA, and 50 mg of CEC18) were from UCT (Bristol, PA, USA). Sodium acetate (99%, anhydrous) was from Sigma-Aldrich (St. Louis, MO, USA). Chloroform-*d* was from Isotec Inc. (OH, USA). Water used in all experiments was purified using a MilliDI system (Millipore, MA, USA).

LC-MS Conditions. Liquid chromatography coupled to mass spectrometry was performed on an LC-MS 2020 system (Shimadzu, Kyoto, Japan) equipped with an electrospray ionization (ESI) source. A Shim-pack XR-ODS column (100 mm × 2.0 mm) (Shimadzu) was used for LC separation at 50 °C and a flow rate of 0.35 mL/min. Mobile phases A and B were water and acetonitrile, respectively, both containing 2 mM ammonium formate and 0.01% formic acid.

For almond flower analysis, the gradient was started with 15% B and changed to 70% B at 1 min, then changed to 100% B at 9 min and kept at 100% B until 12 min. The gradient was set back to 15% B at 12.1 min and kept for 5 min. In adjuvant analysis, the gradient was set at 5% B and kept for 3 min. It was changed to 50% B at 25 min, changed to 60% B at 40 min, and kept for 20 min. Then, the gradient was changed to 100% B at 62 min and kept for 3 min. Finally, it was set back to 5% B and kept for 5 min.

MS was performed in the positive ion mode. The nebulization gas flow was set to 1.5 L min^{-1}, drying gas flow was set to 10 L min^{-1}, heat block temperature was 300 °C, and DL temperature was set to 250 °C. The interface bias voltage was set to 4500 V.

Accurate mass was determined in the Pennsylvania State University Proteomics and Mass Spectrometry Core Facility on a Waters LCT Premier time-of-flight (TOF) MS (Waters Corp. (Micromass Ltd.), Manchester, UK). The nitrogen drying gas temperature was set to 300 °C, and capillary voltage was 2400 V. The MS was set to scan from m/z 100 to 1000 in positive ion mode, using ESI.

Sample Collection and Preparation. Commercial organosilicone adjuvants analyzed included Dyne-Amic, Kinetic HV, and Silwet L-77 from Helena (Collierville, TX, USA), Sylgard 309 from Dow-Corning (Midland, MI, USA), Syl-Tac from Willbur-Ellis (San Francisco, CA, USA), and Silkin from Agriliance LLC (Inver Grove Heights, MN, USA). All adjuvants were dissolved in acetonitrile at 100 ppm. Almond flowers from Stanislaus county, California, USA, were collected in March 2010 on the same day of a pesticide spray treatment and stored at −20 °C. Floral extracts were prepared as before using a QuEChERS method.[14] One gram of almond flowers was ground in liquid nitrogen before extraction.

TSS Purification. Three TSSs (R = H, CH_3, and $C(O)CH_3$) were purified respectively from the corresponding adjuvants using C18 SPE cartridges (500 mg/6 mL, Supelco, Sigma-Aldrich). Fractions were collected and dried under nitrogen. The purified fractions were analyzed by LC-MS and shown to be >95% pure.

TSS Hydrolysis. Hydrolysis experiments were performed on 100 ppm of purified TSS fractions and sample extracts in 2 mM ammonium formate buffer (pH 2.75) for at least 30 min at room temperature. Hydrolyzed products were analyzed by LC-MS.

NMR Spectroscopy. NMR spectroscopy of the three purified TSS compounds was conducted on a 600 MHz, 14.1 T Bruker AV-III-600 (Bruker-Biospin Corp., Billerica, MA, USA) in the Pennsylvania State

DOI: 10.1021/jf505634x
J. Agric. Food Chem. 2015, 63, 5120−5125

University NMR Facility. Proton nuclear magnetic resonance (^{1}H NMR) and heteronuclear multiple-quantum coherence (HMQC) spectra were collected. Samples were dissolved in chloroform-*d*.

Reference Database. A database was built of accurate masses for TSS oligomers including $[M + H]^+$, $[M + Na]^+$, $[M + K]^+$, and $[M + NH_4]^+$ adducts. TSS oligomers contained 0−20 EO units, 0−10 PO units, end group R = C_aH_{2a+1} (a = 0−18), R = $C(O)C_aH_{2a+1}$ (a = 0−18), or other functional groups. The database is being updated as new TSS structures are published and is available upon request from the authors.

RESULTS AND DISCUSSION

Chromatography and Mass Spectrometry. TSSs can be separated on the basis of the R end group and respective oligomeric array using gradient elution on a C18 reversed phase column.[14] TSS (R = H) oligomers with 8 EO units and 1−4 PO units were eluted in order of increasing number of PO units (Figure 2A). Conversely, oligomers with 4−8 EO and the same PO units increasing from 1 to 4 were eluted in order of decreasing length of EO chain (Figure 2B−E), due to the greater hydrophilic nature of the EO chain.

Protonated ($[M + H]^+$) or deprotonated ($[M - H]^-$) molecular ions are usually produced in the ESI source, but these ions cannot be easily observed for TSSs.[15,24] Instead, $[M + NH_4]^+$, $[M + Na]^+$, or $[M + K]^+$ adducts are usually observed due to a cation trapped in the polyalkylene oxide side chain. The mechanism of forming cation adducts can be explained by the respective chelating effect of the alkali metal.[25]

Peak areas of respective cation adducts for TSSs are displayed in supplementary Figure S1 in the Supporting Information. In the absence of the ammonium buffer in the mobile phase, all $[M + NH_4]^+$, $[M + Na]^+$, and $[M + K]^+$ adduct ions are observed because of trace levels of each cation in glassware and the LC system. Oligomers with longer EO chains show an increased abundance of $[M + K]^+$ adducts (data not shown), which is consistent with results from Bonnington et al.[15] By adding 2 mM ammonium formate to the mobile phase, the incidence of $[M + Na]^+$ and $[M + K]^+$ ions is substantially reduced, and $[M + NH_4]^+$ ions dominate the mass spectrum (supplementary Figure S1). Therefore, inclusion of 2 mM ammonium formate buffer in the mobile phase simplifies spectral identification and provides better sensitivity. However, a higher buffer concentration can result in ion suppression,[26] which reduces LC-MS signal intensity.

TSS Identification Using High-Resolution MS. High-resolution MS enables assignment of elemental compositions based on the measured accurate mass. TSS (m = 0, R = CH_3) at 250 μg/L was prepared in acetonitrile and injected into the TOF-MS. Three silicon ions were found in each oligomer, and a CH_2CH_2O difference was found in all neighboring oligomers (data not shown). The $[M + NH_4]^+$ structure is hard to elucidate due to lack of MS/MS information because the high stability of the adduct does not allow sufficient fragmentation. Because data from TOF-MS only suggest the elemental composition with three silicon atoms and EO/PO duplicates, other structural analysis tools must be included.

Our identification strategy for TSSs is displayed in Figure 3. It can be adapted easily to a low-resolution MS, for example, a single-quadrupole MS, and includes the following steps:

Identifying the EO/PO in the Side Chain. TSS with only EO or an EO/PO combination dominated by EO is mainly used in commercial products. The mass differences of neighboring oligomers are 44.03 and 58.04 amu, respectively, for an EO and PO unit. A TSS oligomer with a longer EO chain has a reduced

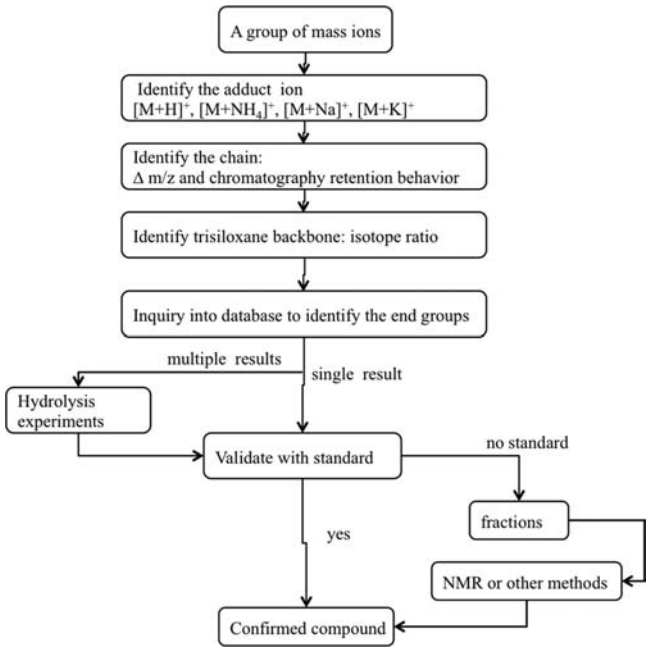

Figure 3. Trisiloxane surfactant identification strategy.

retention time on a reversed phase column (Figure 2B−E), which is similar to other nonionic surfactants.[27] A PO unit further enhances hydrophobicity, and oligomers with increasing PO units have increased retention time (Figure 2A). Combining mass spectral and retention behavior, a prediction for the ratio of EO/PO units in the side chain can be obtained.

Distinguishing TSS from Other Nonionic Surfactants. With a low-resolution MS, accuracy of the determined mass does not support calculating the elemental composition. However, the number of silicon atoms can be determined by isotope ratios. A linear relationship is found with increasing EO chain for TSS between the isotope ratio ($I_{[M+1]}/I_{[M]}$) and m/z (Figure 4A). Surfactants with 0−4 silicon atoms have the same slope values, =0.05, and the intercept value is increased according to the number of silicon atoms. For example, intercept values of nonylphenol ethoxylates (NPEO) and TSSs (m = 0, R = CH_3) are around −1.2 and 12 with 0 or 3 silicon atoms in the structure, so by determining the m/z and $I_{[M+1]}/I_{[M]}$ of an unknown surfactant, its intercept value, B, can be calculated using eq 1.

$$B = 100 \times I_{[M+1]}/I_{[M]} - 0.05 \times m/z \quad (1)$$

By referring to the intercept values in Figure 4 or by comparing those calculated for other similar alkyphenol ethoxylates and alkyl ethoxylates, a putative TSS can be identified and distinguished from other co-occurring nonionic surfactants. Moreover, the relationship of $I_{[M+2]}/I_{[M]}$ ratio and m/z is displayed in Figure 4B. For m/z < 1000, the $I_{[M+2]}/I_{[M]}$ ratios of TSS or higher siloxane surfactant are >13%, whereas they are below 10% in other nonionic surfactants without silicon atoms,[14] the latter attribute confirming that the surfactant is a TSS. A similar strategy can be used to distinguish the TSS (m = 0, R = CH_3) from octylphenol ethoxylates, in which same mass ions were observed.[14,28]

Identifying the End Group. New structural types of TSSs with improved spreading ability and stability have been published recently.[17−23] We have built a reference database that encompasses the mass ions of various TSSs that are used

DOI: 10.1021/jf505634x
J. Agric. Food Chem. 2015, 63, 5120−5125

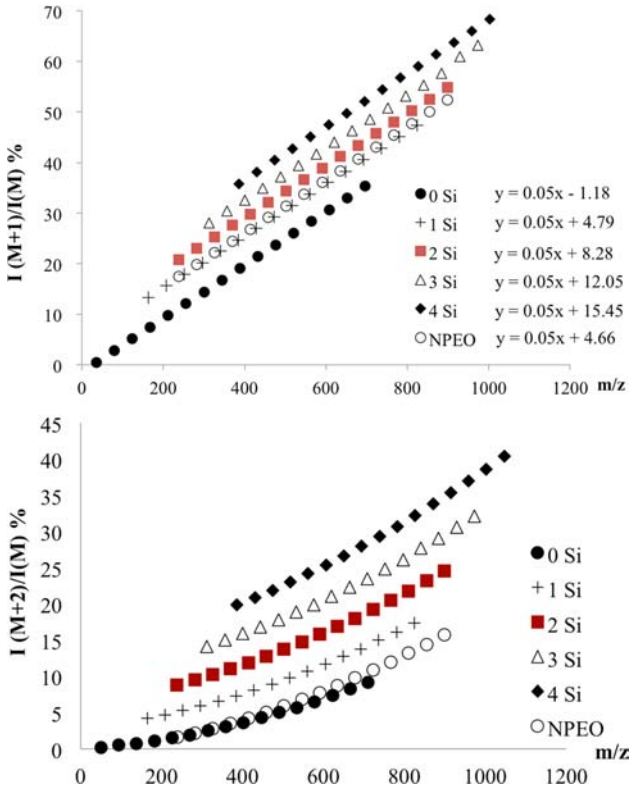

Figure 4. Correlations between (A) m/z and $I_{[M+1]}/I_{[M]}$% and (B) m/z and $I_{[M+2]}/I_{[M]}$% for nonylphenol ethoxylates (NPEO) and siloxane surfactants of various EO chain lengths and siloxanes of increasing methylated silicon atoms (0–4 Si).

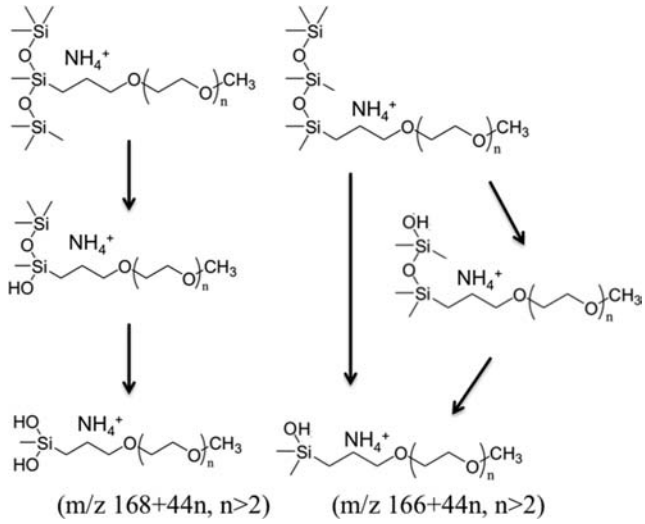

Figure 5. Proposed major hydrolysis pathways of trisiloxane surfactant (m = 0, R = CH_3) in 2 mM ammonium formate buffer, pH 2.75.

or potentially used in bee environments. TSSs with 2–20 EO units, 1–10 PO units, and various end groups (hydroxyl, methyl, acetate, etc.) are included in the database. Entry of the m/z value of an unknown TSS reveals candidate oligomers and their identity.

Identifying Single or Double Side Chains on the TSS Backbone. Most TSSs used in agrichemical formulations have a single hydrophilic side chain to maintain adequate water solubility, but for some product applications requiring increased polarity, a double alkoxylate side chain may be incorporated. Hydrolysis experiments can be used to identify the number of side chains and to which silicon atoms they are attached.

Silicon–oxygen bonds can be hydrolyzed to silanol in acidic or alkaline aqueous solutions.[29,30] In 2 mM ammomiun formate (pH 2.75) buffer, TSS mainly hydrolyzes to silanols with various EO chain lengths (Figure 5). For example, TSS (x = 0, m = 0, R = CH_3) with a single side chain attached to the middle silicon atom hydrolyzes to oligomers of m/z 168 + 44n (n > 2), whereas those with a side chain attached to the terminal silicon atom hydrolyze to oligomers of m/z 166 + 44n (n > 2). If a TSS has two side chains attached to both the middle and end silicons, two oligomer families representing degradation from the either side chain can be detected during LC-MS analysis. If the two side chains are on both terminal silicons, only one degradate of m/z 168 + 44n (n > 2) is produced, but the ratio of "hydrolyzed product/TSS" is double that of the single-chain TSS.

Identifying TSS from Almond Flower Samples. Almond production provides the largest honeybee pollination event in the United States, and agrochemical sprays containing organosilicone adjuvants are applied intensively at bloom, resulting in honeybee exposures to TSS residues.[10] Thus, almond flowers were extracted and analyzed by LC-MS as above, and the total ion chromatogram is displayed in supplementary Figure S2 in the Supporting Information. In the mass range m/z 500–1000, four clusters of oligomers with 44 amu mass differences were found: surfactant 1, m/z 502 + 44n (t_R = 3.5–3.7 min); surfactant 2, m/z 532 + 44n (t_R = 5.8–6.3 min); surfactant 3, m/z 502 + 44n (t_R = 6.3–7.2 min); and surfactant 4, m/z 516 + 44n (t_R = 6.7–8.0 min).

For each cluster, larger m/z mass ions have lower retention times successively separated by 44 amu, indicating these surfactants have EO units. Equivalent mass ions were found in surfactants 1 and 3. By calculating the $I_{[M+1]}/I_{[M]}$ isotope ratios and using eq 1, the calculated intercept value (~5) indicated that surfactant 1 had no silicon atom, and it was further confirmed as NPEO using a standard.

By parallel analysis, surfactants 2, 3, and 4 all had three silicon atoms. Upon hydrolysis in 0.1% formic acid solution at pH 2.6, all three clusters were lost in the LC-MS analysis, indicating the existence of silicon–oxygen bonds. Concomitant LC-MS analysis of respective peaks from the hydrolysis of surfactants 2, 3, and 4 indicated a TSS with a single side chain of EO and possibly PO units. Mass ion m/z 532 from surfactant 2, based on our reference database, indicated a TSS (n = 5, m = 0, R = CH_3) or TSS (n = 4, m = 1, R = H). TSS (n = 5, m = 0, R = CH_3) was previously identified as Silwet L-77.[14,15] Because the longer retention time for m/z 532 from surfactant 2 is not consistent with our standards for Silwet L-77, we assign this m/z 532 to the respective EO side chain with a single PO unit, TSS (n = 4, m = 1, R = H), and surfactant 2 was identified as TSS (m = 1, R = H). Similarly, surfactants 3 and 4 were identified as TSS (m = 2, R = H) and TSS (m = 3, R = H), respectively.

Identifying TSS and Other Nonionic Surfactants from Agrochemical Adjuvants. TSSs in commercial spray adjuvants are often undisclosed and labeled as a "nonionic surfactant", "silicone surfactant", "polyethoxylate", "methylated silicone polyethoxylate", etc. Detailed information about TSS structures and their percentages is rarely revealed. On the basis of pounds of usage on California almonds (primary global site for honeybee pollination) reported from the California Pesticide Information Portal,[10,31] the top-used organosilicone

DOI: 10.1021/jf505634x
J. Agric. Food Chem. 2015, 63, 5120–5125

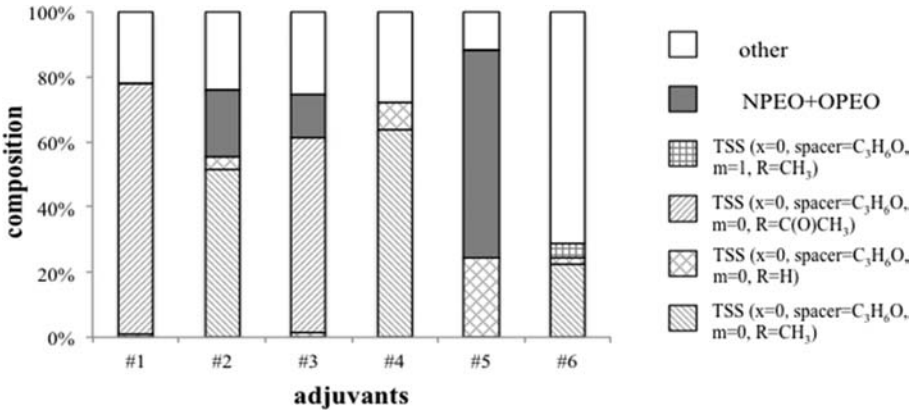

Figure 6. Identification results from top-used spray adjuvants (see text for product details). NPEO and OPEO are nonylphenol ethoxylates and octylphenol ethoxylates, respectively.

surfactant adjuvants were selected and analyzed by LC-MS. On the basis of the identification strategy herein, major TSS and other nonionic surfactants were identified from Dyne-Amic, Kinetic HV, Silkin, Silwet L-77, Sylgard 309, and Syl-Tac (Figure 6). TSS (m = 0, R = H), TSS (m = 0, R = CH_3), and TSS (m = 0, R = $C(O)CH_3$) dominated these popularly used adjuvants. Chemical structures of these TSS were confirmed by ^{1}H NMR and HMQC spectroscopy (Supporting Information, supplementary Figure S3) using purified fractions.

Trisiloxane surfactants were recently detected in every beeswax sample up to 390 ng/g and in 60% of pollen samples up to 39 ng/g.[14] Interest in applications for higher homologues, particularly the tetrasiloxanes (Figure 1, x = 1), is increasing.[32] The prevalence of organosilicone surfactants in agrochemicals including tank adjuvants[13] and other industrial products, along with uncertainty of their environmental fate, advocates more robust efforts for their biomonitoring.

A structural identification strategy for TSSs is described here based on mostly low- and some high-resolution LC-MS. TSSs were identified from a range of commercial spray adjuvants using accurate mass and isotope ratios, a reference database, and hydrolytic experiments. To verify the utility of our protocol, TSS (m = 1, R = H), TSS (m = 2, R = H), and TSS (m = 3, R = H) were identified for the first time from a California almond flower sample. Major TSS components in popularly used spray adjuvants were identified as TSS (m = 0, R = H), TSS (m = 0, R = CH_3), and TSS (m = 0, R = $C(O)CH_3$), and structures were confirmed by NMR. Exploring TSS exposures in bee environments helps us better evaluate this risk factor for honeybees.

■ ASSOCIATED CONTENT

Supporting Information

Supplementary Figures S1−S3. This material is available free of charge via the Internet at http://pubs.acs.org.

■ AUTHOR INFORMATION

Corresponding Author

*(C.A.M.) Phone: (814) 865-2435. Fax: (814) 865-3048. E-mail: camullin@psu.edu.

Notes

The authors declare no competing financial interest.

■ ACKNOWLEDGMENTS

We are grateful to Maryann T. Frazier and Sara A. Ashcraft for providing the almond flower samples used here, and to the USDA-NIFA-AFRI Foundational Award program (nos. 2011-67013-30137 and 2014-67013-21591) for funding this work.

■ ABBREVIATIONS USED

amu, atomic mass unit; CAS, Chemical Abstracts Service; ESI, electrospray ionization; EO, poly(ethylene oxide); HMQC, heteronuclear multiple-quantum coherence; LC-MS, liquid chromatography−mass spectrometry; NMR, nuclear magnetic resonance; NPEO, nonylphenol ethoxylate; PO, poly(propylene oxide); QuEChERS, quick, easy, cheap, effective, rugged, and safe; SPE, solid phase extraction; TOF, time-of-flight; t_R, retention time; TSS, trisiloxane surfactant

■ REFERENCES

(1) Steinhauer, N. A.; Rennich, K.; Wilson, M. E.; Caron, D. M.; Lengerich, E. J.; Pettis, J. S.; Rose, R.; Skinner, J. A.; Tarpy, D. R.; Wilkes, J. T.; vanEngelsdorp, D. A national survey of managed honey bee 2012−2013 annual colony losses in the USA: results from the Bee Informed Partnership. *J. Apic. Res.* **2014**, *53*, 1−18.

(2) Spivak, M.; Mader, E.; Vaughan, M.; Euliss, N. H. The plight of the bees. *Environ. Sci. Technol.* **2011**, *45*, 34−38.

(3) vanEngelsdorp, D.; Evans, J. D.; Saegerman, C.; Mullin, C.; Haubruge, E.; Nguyen, B. K.; Frazier, M.; Frazier, J.; Cox-Foster, D.; Chen, Y. P.; Underwood, R.; Tarpy, D. R.; Pettis, J. S. Colony collapse disorder: a descriptive study. *PLoS One* **2009**, *4*, No. e6481.

(4) Cox-Foster, D. L.; Conlan, S.; Holmes, E. C.; Palacios, G.; Evans, J. D.; Moran, N. A.; Quan, P. L.; Briese, T.; Hornig, M.; Geiser, D. M.; Martinson, V.; vanEngelsdorp, D.; Kalkstein, A. L.; Drysdale, A.; Hui, J.; Zhai, J. H.; Cui, L. W.; Hutchison, S. K.; Simons, J. F.; Egholm, M.; Pettis, J. S.; Lipkin, W. I. A metagenomic survey of microbes in honey bee colony collapse disorder. *Science* **2007**, *318*, 283−287.

(5) Johnson, R. M.; Ellis, M. D.; Mullin, C. A.; Frazier, M. Pesticides and honey bee toxicity − USA. *Apidologie* **2010**, *41*, 312−331.

(6) Mullin, C. A.; Frazier, M.; Frazier, J. L.; Ashcraft, S.; Simonds, R.; vanEngelsdorp, D.; Pettis, J. S. High levels of miticides and agrochemicals in North American apiaries: implications for honey bee health. *PLoS One* **2010**, *5*, No. e9754.

(7) Frazier, J.; Mullin, C.; Frazier, M.; Ashcraft, S. Managed pollinator coordinated agricultural project: Pesticides and their involvement in colony collapse disorder. *Am. Bee J.* **2011**, *151*, 779−784.

(8) Mullin, C. A.; Chen, J.; Fine, J. D.; Frazier, M. T.; Frazier, J. L. The formulation makes the honey bee poison. *Pestic. Biochem. Physiol.* **2015**, in press, DOI: 10.1016/j.pestbp.2014.12.026.

DOI: 10.1021/jf505634x
J. Agric. Food Chem. 2015, 63, 5120−5125

(9) Zhu, W.; Schmehl, D. R.; Mullin, C. A.; Frazier, J. L. Four common pesticides, their mixtures and a formulation solvent in the hive environment have high oral toxicity to honey bee larvae. *PLoS One* **2014**, *9*, No. e77547.
(10) Ciarlo, T. J.; Mullin, C. A.; Frazier, J. L.; Schmehl, D. R. Learning impairment in honey bees caused by agricultural spray adjuvants. *PLoS One* **2012**, *7*, No. e40848.
(11) Vick, S. C. Structure property relationships for silicone polyalkyleneoxide copolymers and their effects on performance in cosmetics. *Soap Cosmet. Chem. Spec.* **1984**, *60*, 36.
(12) Stevens, P. J. G. Organosilicone surfactants as adjuvants for agrochemicals. *Pestic. Sci.* **1993**, *38*, 103−122.
(13) Knoche, M. Organosilicone surfactant performance in agricultural spray application − a review. *Weed Res.* **1994**, *34*, 221−239.
(14) Chen, J.; Mullin, C. A. Quantitative determination of trisiloxane surfactants in beehive environments based on liquid chromatography coupled to mass spectrometry. *Environ. Sci. Technol.* **2013**, *47*, 9317−9323.
(15) Bonnington, L. S.; Henderson, W.; Zabkiewicz, J. A. Characterization of synthetic and commercial trisiloxane surfactant materials. *Appl. Organomet. Chem.* **2004**, *18*, 28−38.
(16) Michel, A.; Brauch, H. J.; Worch, E.; Lange, F. T. Development of a liquid chromatography tandem mass spectrometry method for trace analysis of trisiloxane surfactants in the aqueous environment: an alternative strategy for quantification of ethoxylated surfactants. *J. Chromatogr., A* **2012**, *1245*, 46−54.
(17) Qu, W. S.; Wang, G. Y.; Tao, L. Surface activity and spreading ability of new trisiloxane-tailed dicephalic surfactants. *Colloid J.* **2012**, *74*, 558−563.
(18) Zhang, D. L.; Zhong, G. Y.; Wang, G. Y.; Li, G. J. Synthesis and properties of gluconamide-based trisiloxane surfactant. *J. Disper. Sci. Technol.* **2012**, *33*, 1603−1607.
(19) Zhou, X. Y.; Wang, G. Y.; Lei, T. Self-assembly of trisiloxane-tailed sugar surfactant in aqueous solution. *Phosphorus, Sulfur Silicon* **2013**, *188*, 701−710.
(20) Wang, G. Y.; Li, X.; Du, Z. P.; Li, E. Z.; Li, P. Butynediol-ethoxylate based trisiloxane: structural characterization and physico-chemical properties in water. *J. Mol. Liq.* **2014**, *197*, 197−203.
(21) Han, F.; Liu, Y. L.; Gao, Y. D.; Liang, Y. L.; Zhou, Y. W.; Xu, B. C. Synthesis and characterization of a quaternized glucosamide-based trisiloxane surfactant. *J. Surfactants Deterg.* **2014**, *17*, 733−737.
(22) Peng, Z. L.; Lu, C. F.; Lai, J. X. Synthesis and properties of novel double-tail trisiloxane surfactants. *J. Surfactants Deterg.* **2009**, *12*, 331−336.
(23) Peng, Z. L.; Huang, S. F.; Cao, M. N. Synthesis and properties of novel double-tail trisiloxane surfactants with high spreading ability. *J. Surfactants Deterg.* **2011**, *14*, 521−528.
(24) Evan, K. A.; Dubey, S. T.; Kravetz, L.; Evetts, S. W.; Dzidic, I.; Dooyema, C. C. Quantitation of alcohol ethoxylate surfactants in environmental samples by electrospray mass spectrometry. *J. Am. Oil Chem. Soc.* **1997**, *74*, 765−773.
(25) Okada, T. Complexation of poly(oxyethy1ene) in analytical chemistry − a review. *Analyst* **1993**, *118*, 959−971.
(26) Mallet, C. R.; Lu, Z.; Mazzeo, J. R. A study of ion suppression effects in electrospray ionization from mobile phase additives and solid-phase extracts. *Rapid Commun. Mass Spectrom.* **2004**, *18*, 49−58.
(27) Corbera, M.; Simonet, B. M.; Salvado, V.; Hidalgo, M. Characterisation of alkylamine ethoxylates (ANEOs) in commercial herbicide formulations using liquid chromatography/electrospray ionisation mass spectrometry. *Rapid Commun. Mass Spectrom.* **2010**, *24*, 2931−2937.
(28) Chen, J.; Mullin, C. A. Determination of nonylphenol ethoxylate and octylphenol ethoxylate surfactants in beehive samples by high performance liquid chromatography coupled to mass spectrometry. *Food Chem.* **2014**, *158*, 473−479.
(29) Michel, A.; Brauch, H.; Worch, E.; Lange, F. T. Homologue specific analysis of a polyether trisiloxane surfactant in German surface waters and study on its hydrolysis. *Environ. Pollut.* **2014**, *186*, 126−135.
(30) Laubie, B.; Bonnafous, E.; Desjardin, V.; Germain, P.; Fleury, E. Silicone-based surfactant degradation in aqueous media. *Sci. Total Environ.* **2013**, *454−455*, 194−205.
(31) California Department of Pesticide Regulation, California Pesticide Information Portal; http://calpip.cdpr.ca.gov/main.cfm (accessed June 2012).
(32) Lim, C. H.; Kim, D. W.; Noh, S. T. Thermal and physical properties of oligo-(propylene oxide-block-ethylene oxide) allyl methyl ether containing tetrasiloxane as wetting agent. *J. Ind. Eng. Chem.* **2003**, *9*, 526−536.

DOI: 10.1021/jf505634x
J. Agric. Food Chem. 2015, 63, 5120−5125

JOURNAL OF AGRICULTURAL AND FOOD CHEMISTRY

Article

pubs.acs.org/JAFC

Development of a Liquid Chromatography–Tandem Mass Spectrometry Method for the Determination of Sulfite in Food

Katherine S. Robbins,* Romina Shah, Shaun MacMahon, and Lowri S. de Jager

Center for Food Safety and Applied Nutrition, U.S. Food and Drug Administration, 5100 Paint Branch Parkway, HFS 706, College Park, Maryland 20740, United States

ABSTRACT: Sulfites are widely used food preservatives that can cause severe reactions in sensitive individuals. As a result, the U.S. FDA requires that sulfites be listed on the label of any food product containing >10 mg/kg (ppm) sulfite (measured as sulfur dioxide). Currently, the optimized Monier–Williams (MW) method (AOAC Official Method 990.28) is the most common approach for determining sulfite concentrations in food samples. However, this method is time-consuming and lacks specificity in certain matrices. An improved rapid, sensitive, and selective method has been developed using electrospray ionization (ESI) high-performance liquid chromatography–tandem mass spectrometry (LC-MS/MS) for the determination of sulfite in various food matrices. A total of 12 different types of foods were evaluated. These included dried fruits and vegetables, frozen seafood, sweeteners, and juices. The matrix is extracted with a buffered formaldehyde solution, converting free and reversibly bound sulfite to the stable formaldehyde adduct, hydroxymethylsulfonate (HMS). Extracts are prepared for injection using a C_{18} SPE cartridge to remove any lipophilic compounds. HMS is then separated from other matrix components using hydrophilic interaction chromatography (HILIC) and detected using multiple reaction monitoring (MRM). The method was validated at 5 concentrations in 12 food matrices. Accuracy data showed spiked recoveries ranging from 84 to 115% in representative foods. Six commercially available sulfited products were analyzed using the LC-MS/MS method, as well as the MW method, to determine if differences exist.

KEYWORDS: *LC-MS/MS, sulfites, food additives*

INTRODUCTION

Sulfites are a family of food preservatives that commonly include sulfur dioxide, sodium sulfite, sodium metabisulfite, potassium metabisulfite, sodium bisulfite, and potassium bisulfite. They are used worldwide in a broad range of food and beverage products including dried fruits, dried vegetables, jams, flours, juices, and seafood due to their antioxidant, antimicrobial, and antibrowning properties.[1] Sulfite is present in three forms in food systems: free, reversibly bound, and irreversibly bound. Free sulfite, as its name suggests, is not bound to any other food component and is easily quantified by most existing methods. Reversibly and irreversibly bound sulfites exist when adducts form between sulfite and various food components such as acetaldehyde, sugar monomers, or sugar acids.[2] Through sample preparation steps, such as pH adjustment and heating, sulfite can be released from reversibly bound sulfite and quantified. Irreversibly bound sulfite is very stable, making it difficult to quantify.[1]

Although sulfites contribute beneficial properties to a food system, a small subset of the population has an adverse allergy-like reaction upon consumption. In sensitive individuals, sulfites can produce health effects including skin rashes, nausea, and respiratory distress.[1] In 1986, the U.S. Food and Drug Administration (FDA) began requiring that all sulfite be declared on the label of any product in which the concentration exceeded 10 mg/kg (ppm) (measured as sulfur dioxide (SO_2)) and that no sulfites be added to any food product intended to be served raw or presented fresh to the public such as those items found on a salad bar.[3,4] Similar guidance was adopted by other regulatory agencies including those in Europe, Canada, and Korea.[5−7] The FDA identified AOAC Official Method 990.28,[8] the optimized Monier–Williams (MW) method, as the required method for all regulatory analyses. This method allows for accurate determination of sulfites in most food products and requires readily available glassware and reagents.[9] However, this method includes an extended distillation, displays reduced sensitivity at levels below 10 ppm of SO_2, and lacks specificity in some matrices such as *Allium* and *Brassica* vegetables.[10] Various alternatives to this method have been reported in the literature. These include electrochemical methods,[9,11,12] ion exchange chromatography,[13,14] liquid chromatography,[15] flow injection analysis,[16−18] spectrophotometry,[19] and iodometry.[20] Although these methods have shown promise for sulfite determination, there are still several limitations including lack of sensitivity, specificity, and applicability across multiple food types, making them unsuitable for routine regulatory use.

Sulfite is challenging to analyze in its highly unstable free form, leading to the use of chemical derivatization prior to analysis.[21] Warner et al.[21] found that the addition product of sulfite and formaldehyde, hydroxymethylsulfonate (HMS), is easily formed and more stable than the free form. HMS has been previously determined using ion-pairing high-performance liquid chromatography (HPLC).[22,23] Although this HPLC

Special Issue: 51st North American Chemical Residue Workshop

Received: November 14, 2014
Revised: February 11, 2015
Accepted: February 19, 2015
Published: February 19, 2015

ACS Publications

This article not subject to U.S. Copyright. Published 2015 by the American Chemical Society

DOI: 10.1021/jf505525z
J. Agric. Food Chem. 2015, 63, 5126−5132

Table 1. MS/MS Conditions for Monitored Transitions

Q1 mass (m/z)	Q3 mass (m/z)	ID	dwell time (ms)	DP (V)	EP (V)	CE (V)	CXP (V)
111	81	HMS	170.0	−25.0	−4.00	−15.0	−6.00
111	80	HMS	550.0	−25.0	−4.00	−40.0	−6.00
113	83	HMS (^{34}S)	80.0	−25.0	−4.00	−15.0	−6.00
113	82	HMS (^{34}S)	80.0	−25.0	−4.00	−40.0	−6.00
93	35	chloroacetic acid	25.0	−40.0	−10.0	−12.0	−4.00
95	37	chloroacetic acid	25.0	−40.0	−10.0	−12.0	−4.00
93	93	chloroacetic acid	25.0	−40.0	−10.0	−1.00	−4.00

method is sensitive and selective for sulfite, the postcolumn reaction step requires specialized instrumentation and expertise. Liquid chromatography−tandem mass spectrometry (LC-MS/MS) is a technique that affords high specificity and sensitivity and has become widely used for food analysis. The present study describes the development and validation of an improved LC-MS/MS method for sulfite determination in a variety of food matrices. Sulfite is converted to HMS and then separated using hydrophilic interaction liquid chromatography (HILIC) and quantified by LC-MS/MS. Following method development and optimization for a wide range of food categories, validation was performed at five different concentrations ranging from 0.5 to 100 ppm of SO_2. The LC-MS/MS method was then compared to the MW method using commercially available sulfited products. LC-MS/MS proved to be a more sensitive, selective, and rapid method that will enable improved enforcement of the sulfite labeling requirements protecting sensitive individuals from inadvertently ingesting sulfite.

MATERIALS AND METHODS

Reagents and Materials. Both the internal standard, sodium sulfite-^{34}S ($Na_2{}^{34}SO_3$, 95%), and the surrogate, chloroacetic acid ($ClCH_2CO_2H$, ≥99%), in addition to formaldehyde (37%), ammonium acetate (Sigma Ultra, minimum 98%), and sodium sulfite (Na_2SO_3, ≥ 98%) were acquired from Sigma-Aldrich (St. Louis, MO, USA). LC-MS grade acetonitrile, water, and methanol, in addition to glacial acetic acid, methylene chloride, hydrogen peroxide (30%), sodium hydroxide (certified 0.1 and 0.01 N), and concentrated hydrochloric acid, were purchased from Thermo Fisher Scientific (Pittsburgh, PA, USA). Methyl red from Mallinckrodt Baker (Phillipsburg, NJ, USA) was used in the MW titration. Samples were diluted and extracted using 18 MΩ water obtained from an Aqua Solutions water purification system (Jasper, GA, USA). Unsulfited food samples were purchased online and from grocery stores located in Greenbelt, MD, USA. For comparison of the LC-MS/MS and MW methods, products with sulfite declared on the label were obtained from local grocery stores. All food samples were stored according to the manufacturer's suggested storage conditions.

Standard Preparation. A 2% formaldehyde solution in 0.05 M ammonium acetate was prepared by dissolving 1.925 g of ammonium acetate in 50 mL of 18 MΩ water, adding 27 mL of 37% formaldehyde solution and diluting to 500 mL with 18 MΩ water. The pH of this solution was adjusted to 4.5 by dropwise addition of acetic acid. Working 0.2% formaldehyde extraction solutions were prepared by diluting 2.0% solution 1:10 with 18 MΩ water. The 0.2 and 2% formaldehyde solutions were stable at room temperature for at least 1 week and 3 months, respectively.

Both the chloroacetic acid and $Na_2{}^{34}SO_3$ (IS) solutions were prepared using the formaldehyde extraction solvent. Briefly, a 25 ppm IS stock solution was prepared by dissolving 2.5 mg of $Na_2{}^{34}SO_3$ in 100 mL of 2% formaldehyde solution. This stock was further diluted to form a 5 ppm working solution. The chloroacetic acid stock solution (10 mg/mL) was prepared by weighing 100 mg into a tared 10 mL volumetric flask and diluting to volume with 0.2% formaldehyde solution. Working standards of 2.5 mg/mL, 1 mg/mL, and 5 μg/mL chloroacetic acid were prepared by diluting the stock solution with the appropriate volume of 0.2% formaldehyde. Stock solutions were stored for up to 1 year at 4 °C, and working standards were stored for up to 1 month.

Stock solutions of HMS were prepared by weighing 100 mg of Na_2SO_3 into a tared 10 mL volumetric flask and diluting with 2% formaldehyde solution. On the day of analysis, a 1 mg/mL solution was prepared by diluting the stock solution with 18 MΩ water. Further dilutions with 0.2% formaldehyde solutions were made to give final concentrations of 1, 10, and 100 ppm of Na_2SO_3 working standards. Ten standards (0.01, 0.02, 0.05, 0.1, 0.2, 0.4, 0.8, 1.5, 3.0, and 4.5 μg Na_2SO_3/mL) were prepared in 2 mL glass autosampler vials with a PTFE/red silicone septum cap (Agilent Technologies, Palo Alto, CA, USA) by diluting the 1, 10, or 100 ppm working standards with 0.2% formaldehyde to 100 μL and then adding 100 μL of IS working solution, 100 μL of 5 μg/mL chloroacetic acid, and 700 μL of acetonitrile.

Sample Preparation. Due to the wide variety of food commodities analyzed, both liquid and solid preparation methods were developed. Refrigerated samples were allowed to come to room temperature prior to analysis. For solid samples, the sample (50 ± 1 g) was cut into small $^1/_4$ in. pieces and homogenized with 100 g of 0.2% formaldehyde solution in a variable-speed laboratory blender (Waring Laboratory Science, Torrington, CT, USA) with a 500 mL glass jar. A portion of the homogenate (15.0 ± 0.5 g) was transferred into 50 mL centrifuge tubes, and 20 mL of 0.2% formaldehyde was added along with 50 μL of 2.5 mg/mL chloroacetic acid. The centrifuge tubes were mixed end-over-end on a tube rotator (Glass-Col, Terra Haute, IN, USA) at 70 rpm for 10 min prior to 8 min of sonication (Branson 3510 ultrasonic cleaner, Sigma-Aldrich). The tubes were then centrifuged at 4000 relative centrifugal force (rcf) for 5 min (Marathon 2100R centrifuge, model 120, Thermo Fisher Scientific), and the supernatant was decanted into a 50 mL stoppered graduated cylinder. The extraction steps were repeated on the same sample portion, the supernatant was pooled, and the final volume was brought to 50 mL with the extracting solvent. A 6 mL Bakerbond C_{18} SPE cartridge with a sorbent bed of 500 mg (MG Scientific, Pleasant Prairie, WI, USA) was used to clean up the extract. The cartridges were conditioned by rinsing sequentially with 3 mL portions of methylene chloride, methanol, and 0.2% formaldehyde solution. The extract (2 mL) was passed through the cartridge and the eluent discarded. An additional 2 mL of extract was passed through and collected into a 4 mL clear glass screw cap vial with a solid cap and PTFE liner (Sigma-Aldrich). The vials were heated at 80 °C for 30 min using a DB3 Dri-Block Sample Concentrator from Techne (Staffordshire, UK) and then allowed to cool to room temperature. Samples were prepared for injection by diluting 200 μL of cooled extract with 100 μL of IS working solution (5 ppm) and 700 μL of acetonitrile in a 2 mL glass autosampler vial with a PTFE/red silicone septum cap (Agilent Technologies). After mixing, the vial contents were filtered with a 0.20 μm PTFE filter (17 mm, Thermo Fisher Scientific) into a new vial. Liquid samples were prepared for analysis by weighing 1.00 ± 0.05 g of sample into a 10 mL volumetric flask and diluting to volume with 0.2% formaldehyde solution. The samples were then analyzed in the same manner as the solid samples beginning with the SPE cleanup step and continuing through the heating and filtering steps. For the validation spiking, samples were fortified after grinding but prior to extraction.

LC-MS/MS. An Acquity Ultraperformance LC System (Waters, Milford, MA, USA) equipped with a SeQuant ZIC HILIC analytical

DOI: 10.1021/jf505525z
J. Agric. Food Chem. 2015, 63, 5126−5132

column (150 × 2.1 mm × 5 μm; The Nest Group, Inc., Southborough, MA, USA) was used for separation. The column was thermostated at 30 °C, and a flow rate of 0.30 mL/min was employed. The following 24 min gradient program was used: 6 min hold at 90% mobile phase A (10 mM ammonium acetate in 90:10 ACN/H_2O) and 10% mobile phase B (10 mM ammonium acetate in 50:50 ACN/H_2O), gradient to 50% A in 4 min, 5.75 min hold at 50% A, gradient back to 90% A in 0.25 min, and equilibration at 90% A for 8 min before the next injection. All samples and standards utilized a 5 μL injection volume. An external valve (Valco Instruments Co., Houston, TX, USA) was directed to waste at 0.0, 4.5, and 9.0 min and to the mass spectrometer at 2.0 and 6.5 min.

An AB Sciex 4000 QTRAP mass spectrometer equipped with an electrospray ionization (ESI) source in the negative ion mode was used for analysis. Analyst 1.5.2 (AB Sciex, Foster City, CA, USA) controlled both systems and data analysis. The source parameters were optimized for the HMS transitions. The curtain gas was set to 35 arbitrary units (au), the collisionally activated dissociation (CAD) gas was run at medium, an ion spray voltage of −1200 V was used, the source temperature was 550 °C, gas 1 pressure was 70 au, and gas 2 pressure was 40 au. The MS/MS data were acquired using the MRM mode (unscheduled) with unit resolution of both Q1 and Q3. Table 1 highlights the MS/MS conditions for each monitored transition including the compound ID, dwell time, declustering potential (DP), entrance potential (EP), collision energy (CE), and collision cell exit potential (CXP). There was a 5 ms pause between each transition, and the total scan time was 0.99 s.

Quantitation. A 10-point calibration curve ranging from 0.01 to 4.5 ppm of Na_2SO_3 was generated for the quantitation of sulfite. The curve was created from the MRM ratios of the peak areas of the analyte to the internal standard ($Na_2{}^{34}SO_3$). A quadratic fit with $1/x^2$ weighting was used for the calibration curve due to the 3 orders of magnitude range of standard concentrations. The R^2 values of all curves were >0.990. Concentrations obtained using the calibration curve were adjusted by the appropriate dilution factor (250 for solid samples and 50 for liquid samples) and converted from Na_2SO_3 to SO_2. All values were reported as micrograms of SO_2 per gram of food sample.

Optimized Monier–Williams Method. Six different commercially available sulfited products were analyzed using the optimized MW method (AOAC Method 990.28). Briefly, a volume of 400 mL of 18 MΩ water was added to a 1 L round-bottom flask. A 30% hydrogen peroxide stock solution was diluted 1:10 to give 30 mL of 3% hydrogen peroxide. Three drops of a methyl red indicator were added to the solution, and then 0.01 N NaOH was added dropwise until a yellow end point was reached. This solution was added to a 50 mL graduated cylinder and placed under the bubbler. Nitrogen was bubbled through the entire closed apparatus for 15 min. Fifty grams of sample (both solid and liquid) was added to the round-bottom flask, and the transferring container was rinsed with 100 mL of 5% ethanol. Using the dropping funnel, 90 mL of 4 N HCl was added to the flask. The nitrogen flow was restarted, and the heating mantle (Glas-col, Terre Haute, IN, USA) was turned on to a heating level that produced 80–90 drops/min of condensate from the condenser. The contents of the flask were boiled under these conditions for 105 min. Upon completion of the distillation, the cylinder containing the hydrogen peroxide was removed, and its contents were quantitatively transferred to a 125 mL Erlenmeyer flask. The contents were titrated with either 0.1 or 0.01 N NaOH until the yellow end point was again reached. The volume of titrant needed to reach the end point was recorded. The sulfite content (as μg SO_2/ g food sample) was determined by

$$\text{ppm of } SO_2 = \frac{32.03 \times V_B \times N \times 1000}{w}$$

where 32.03 = milliequivalent weight of SO_2, V_B = volume (mL) of NaOH of normality N required to reach end point, 1000 = factor to convert milliequivalents to microequivalents, and w = weight (g) of sample added to the round-bottom flask.

RESULTS AND DISCUSSION

Method Development. During the early stages of method development, there was no commercially available stable isotopically labeled sulfite, which led to the use of chloroacetic acid as an internal standard. However, chloroacetic acid was not ideal because of its much earlier elution time compared to HMS. During method development, a stable isotope sodium sulfite ($Na_2{}^{34}SO_3$) became commercially available and was added into the method as the internal standard. Although this particular isotopic labeling was not ideal given that approximately 4% of naturally occurring sulfur occurs as the ^{34}S isotope, the calibration curve accounts for this effect, and the use of a true labeled internal standard greatly improved sample quantitation. However, due to the isotope's cost-prohibitive nature, chloroacetic acid remained in the method as a surrogate to identify any significant losses from the extraction process. The chloroacetic acid transitions are not used for quantitation and serve only as a visual check. The chloroacetic acid elutes first at 3.5 min, and HMS elutes at 7.5 min. A sample chromatogram of a 0.4 ppm of Na_2SO_3 (10 ppm of SO_2 in sample) standard is shown in Figure 1.

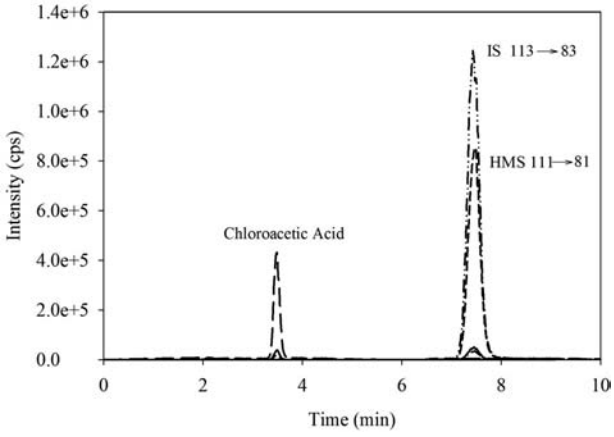

Figure 1. Sample LC-MS/MS chromatogram for a 0.4 ppm of Na_2SO_3 standard with both the chloroacetic acid surrogate and stable isotope internal standard.

Filtration of the extract prior to LC-MS/MS analysis was necessary because a precipitate formed in the autosampler vial for most solid samples after the combination of the cooled extract, IS, and ACN. Initially, an investigation of several types of SPE cartridges was conducted to determine if the precipitation could be prevented. Polystyrene-divinylbenzene, weak anion exchange, strong anion exchange, and primary/secondary amine cartridges from several different manufacturers were examined. Although most resulted in a cleaner extract, none of these cartridges produced consistent sulfite recoveries of >75%. Both the weak anion exchange and strong anion exchange cartridges bound the sulfite too strongly, and no combination of elution solvents could recover the analyte. A mixed-mode cartridge, Isolute HAX (Biotage), yielded high sulfite recovery (>80%) for some matrices, but these results were neither repeatable nor achievable for all required samples. A systematic review of the conditioning and elution solvents did not improve the results. The Bakerbond C_{18} cartridge produced the most consistent and repeatable results and, once coupled with the additional filtering step, produced a clean extract for injection. To determine the best filtering material,

DOI: 10.1021/jf505525z
J. Agric. Food Chem. 2015, 63, 5126–5132

Table 2. Average Percent Recovery for Five Concentration Spikes of Different Food Matrices[a]

matrix	0.5 ppm of SO_2	5 ppm of SO_2	10 ppm of SO_2	20 ppm of SO_2	100 ppm of SO_2
dried apricot	93 (4)	97 (3)	96 (4)	98 (5)	102 (15)
dried coconut	92 (6)	93 (3)	86 (7)	91 (4)	87 (8)
crystallized ginger	96 (9)	95 (6)	103 (5)	99 (7)	109 (13)
dried pineapple	90 (11)	96 (4)	102 (8)	95 (10)	105 (10)
dried potato	88 (5)	87 (12)	89 (17)	94 (5)	93 (16)
dried vegetable mix	92 (11)	89 (5)	89 (7)	91 (7)	87 (13)
bamboo shoots	89 (10)	106 (9)	106 (7)	108 (5)	109 (16)
white grape juice	104 (6)	100 (8)	98 (7)	109 (16)	97 (7)
red wine vinegar	93 (9)	105 (11)	111 (6)	102 (4)	94 (3)
molasses	93 (15)	105 (1)	104 (15)	105 (4)	115 (8)
apricot jam	84 (15)	102 (4)	100 (4)	101 (3)	91 (6)
shrimp	99 (10)	103 (9)	105 (6)	104 (5)	99 (2)

[a] $n = 3$; % RSD is shown in parentheses.

both PTFE and nylon filters (0.20 and 0.45 μm) were evaluated with blank matrix samples, as well as 5 and 10 ppm of Na_2SO_3 spikes. At all three concentrations tested, the PTFE filters resulted in lower sample losses. For this reason, only PTFE filters are used in this method.

Complete conversion of reversibly bound sulfite to free sulfite is necessary for accurate quantitation. Previous studies in wine and apricot have shown that sulfites bind easily with reducing sugars and carbonyls, such as acetaldehyde, galacturonic acid, and glucose.[2,24,25] All of these could potentially be present in the skin and flesh of dried fruits and vegetables. An 8 min sonication step was added in the extraction process to reduce or reverse this binding. The inclusion of this step increased the overall recovery yield in apricot samples. Because there was no indication that its addition would be detrimental to other food matrices, it was permanently added into the method. A heating step was included in the method to ensure that all sulfite−carbonyl adducts remaining after the SPE cleanup were converted to their free form.

On the basis of the large range of samples investigated, slight modifications to the sample preparation method described previously were necessary for a small number of matrices. Solid vegetable samples with low moisture content (i.e., dried potatoes or vegetable mix) formed a thick paste upon the initial addition of extracting solvent making analysis difficult. To avoid paste formation, samples were ground without extracting solvent into a homogeneous powder using the laboratory blender. After grinding, 5 g of the sample was accurately transferred into the 50 mL centrifuge tube, and 30 mL of 0.2% formaldehyde solution was added. The extraction, SPE cleanup, and heating steps were performed in the same manner as described for solid samples. For these matrices, a large amount of precipitate formed with the acetonitrile addition. It was determined that a better cleanup was achieved using a 0.45 μm PTFE filter.

All jam and preserve samples were best analyzed as solid samples. These samples have higher moisture content than the dried fruits and vegetables, so the extracting solvent volume was reduced to 15 mL for both extraction steps. Due to the high lipid content of coconut, after centrifugation three visible layers were present: solid coconut shavings in the bottom of the centrifuge tube, formaldehyde extracting solvent in the middle, and a lipid layer on top. The lipid top layer made pouring off the supernatant difficult. To improve this step, an empty 20 mL reservoir and frit (Agilent) were used to filter the extracting solvent. Additionally, the higher lipid content of the coconut samples necessitated a reduction in SPE extract volume to 1.5 mL. The heating and filtering steps remained the same as detailed previously for the other solid samples.

Two MS/MS transitions were identified for the HMS molecule, but there was some concern as to their validity because the transitions differed by only 1 mass unit. However, previous studies have reported that these two structurally significant product ions are commonly observed during mass spectrometric analysis of sulfonic acids.[26] The MS/MS product ion ratios ranged from 1 to 8% for all of the standards and samples analyzed. For regulatory analyses, all ratios must be within 10% absolute of the value, with a signal-to-noise ratio of >3:1. After several months of analysis with the same column, the peak shape started to degrade and the peaks became extremely broad (>1 min). The column was cleaned using the manufacturer's recommendations: 30 column volumes each of water, 0.5 M NaCl, and water followed by column equilibration. After washing, the peak shape and size returned to their original values.

Initially, a linear regression was used for the calibration curve, but linearity was maintained only over the range from 0.01 to 0.8 μg/mL Na_2SO_3, which equates to a range of 0.25−20 ppm of SO_2 in the food sample. Whereas the 10 ppm of SO_2 regulatory action concentration fits into this range well, there are several foods that commonly contain much more than the 20 ppm of SO_2, which could not be measured with the linear curve. It was found that a quadratic regression maintained a good fit ($r > 0.990$) over the range of 0.25−114 ppm of SO_2, so three additional curve points were added on the upper end. A $1/x^2$ weighting was included to ensure that the lower points on the curve received proper weighting because the curve spanned 3 orders of magnitude.

During analyses of liquid samples, a white powder was observed in the source and on the electrode. The sensitivity also decreased markedly, and the peak shape quickly deteriorated. An external valve was installed to divert the flow to waste when data collection was not necessary. The switching valve was used for all samples, and the white powder was not observed again. Throughout the analysis, the source and the curtain plate were cleaned approximately twice per month during times of heavy analysis.

METHOD VALIDATION

Twelve different matrices representing four commodity categories were selected to determine method accuracy. The four categories investigated included dried fruit (apricot,

DOI: 10.1021/jf505525z
J. Agric. Food Chem. 2015, 63, 5126−5132

coconut, crystallized ginger, and pineapple), dried vegetables (dried potato, dried vegetable mix, and canned bamboo shoots), liquids/sweeteners (white grape juice, red wine vinegar, and molasses), and seafood (shrimp). Each unsulfited matrix was spiked prior to extraction in triplicate at five different SO_2 concentrations (0.5, 5, 10, 20, and 100 ppm of SO_2). Recoveries were determined and are reported in Table 2 along with the relative standard deviation (RSD) for the triplicate measurements. The target values for the percent recovery and the RSD were 80−115 and <16%, respectively. All recoveries in all matrices at all concentrations fell within the desired specifications. The only matrix that did not fall within the target RSD value was the 10 ppm of SO_2 spike with the dried potato. The dried potato and dried vegetable mix samples had among the lowest overall recoveries with 87−94 and 87−92%, respectively. It is believed that these lower values are a result of sample binding, which could produce some irreversibly bound sulfite. The lowest and highest concentration spikes (0.5 and 100 ppm of SO_2) had the largest RSD values on average. At the lowest concentration, the spikes were close to the limit of quantitation for the method, affecting the repeatability. For the 100 ppm of SO_2 spikes, the points lay near the flat portion of the quadratic calibration curve, where small differences in instrument response cause a relatively large variation in the SO_2 value.

One matrix from each category was selected for a stability study. Both the SPE extract and the LC vials were reanalyzed at days 1, 3, and 7. The SPE extract and LC vials were stored at 4 °C and room temperature, respectively. No observable trends or significant differences ($p > 0.05$) were observed for the potatoes or the shrimp. The apricot samples stored in the refrigerator had no significant differences ($p > 0.05$) appear until day 7 of storage, but the samples stored in the autosampler (25 °C) had significant differences for days 1 and 7 ($p < 0.05$). For this reason if any reanalysis needs to be completed, it should be conducted from the cooled SPE extract stored in the refrigerator. The red wine vinegar had no significant differences ($p > 0.05$) except for day 1 with refrigerator storage. Due to these differences in stability, further investigation into other matrices is necessary prior to any attempt to store samples for reanalysis.

Limit of detection (LOD) and limit of quantitation (LOQ) determinations were difficult due to the presence of a blank response in both the matrix and method blanks. The background concentration in the method blanks is due to the presence of sulfite in both the formaldehyde and labeled stable isotope (purity = 95%). Because this background concentration should be consistent for all samples, the standard curve corrects for the increased area. However, all of the samples investigated had an additional concentration of background sulfite. White grape juice had the smallest background with a mean area response of 80 ppb of SO_2. Figure 2 compares the response of a method blank and an apricot blank. An LOD could not be determined for any of the matrices analyzed because sulfite could be detected even in the blank analyses. Because the signal-to-noise ratio is >10 for any injected sample, the LOQ was calculated by analyzing seven blank samples for each matrix studied. The mean (μ_b) and standard deviation (σ_b) of these analyses were calculated, and the LOQ was determined using the following formula: $LOQ = \mu_b + 3.3\sigma_b$. The LOQ was determined for six different matrices to determine the expected range for common sulfite matrices. The matrices selected were white grape juice, molasses, dried potatoes, crystallized ginger, dried apricots, and frozen raw shrimp; results are shown in Table 3. Due to the variation in the mean response (0.08−0.59 ppm), the LOQ varied from 0.12 ppm in white grape juice to 0.75 ppm in dried apricots (Table 3), all of which are >2 orders of magnitude below the Monier−Williams method.

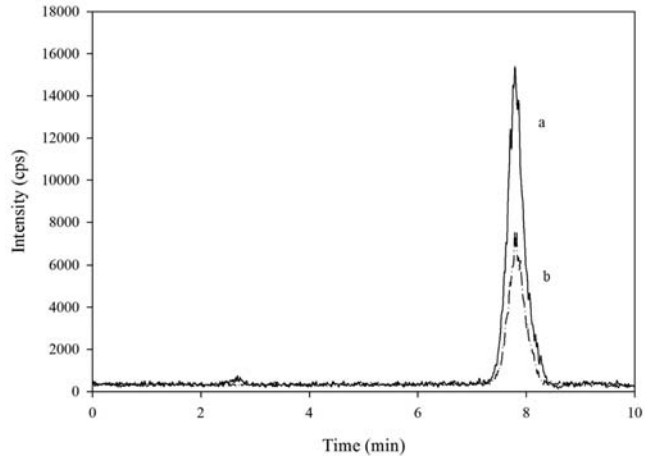

Figure 2. LC-MS/MS HMS transition for (a) a blank apricot sample and (b) a solvent blank sample.

Table 3. Limit of Quantitation (LOQ) in Six Food Matrices

food matrix	blank concentration[a] (ppm of SO_2)	LOQ[b] (ppm of SO_2)
white grape juice	0.08	0.12
molasses	0.36	0.67
dried potatoes	0.17	0.27
crystallized ginger	0.12	0.30
dried apricots	0.40	0.75
frozen raw shrimp	0.59	0.72

[a]Calculated concentration of seven method blanks in food matrix. [b]LOQ was calculated using the following formula: $LOQ = \mu_b + 3.3\sigma_b$, where μ_b is the mean blank concentration for seven method blank replicates and σ_b is the standard deviation for these blanks.

METHOD COMPARISON

Six of the validated matrices (dried pineapple, dried apricot, crystallized ginger, dried potatoes, white grape juice, and raw shrimp) were analyzed in triplicate by both the LC-MS/MS method and the MW distillation to determine differences between the two methods (see Table 4). Dried potato was the only matrix for which there were no significant differences ($p > 0.05$) between the methods. The dried fruit samples (pineapple, apricot, and ginger) tested produced higher values for the MW titration than the LC-MS/MS, whereas the other three matrices investigated produced lower values for the MW titration than the LC-MS/MS. The product labels listed sulfur dioxide as the sulfiting agent for the dried fruit samples, whereas bisulfites and metabisulfites were used in the other products. It is possible that the type of sulfiting agent, along with the physical properties of the food system, may have an effect on the quantitation via the two methods. Further investigation is necessary to determine the cause of this discrepancy.

The relative standard deviations of the analyses for both methods ranged from 1 to 8% for all matrices with the exception of shrimp. The shrimp RSD values were 11 and 28% for the MW and LC-MS/MS methods, respectively. The large

DOI: 10.1021/jf505525z
J. Agric. Food Chem. 2015, 63, 5126−5132

Table 4. Comparison of the Monier−Williams Distillation Method and the LC-MS/MS Method for Sulfite Determination in Six Matrices

food matrix	Monier−Williams titration[a] (ppm of SO_2)	LC-MS/MS (ppm of SO_2)
dried pineapple	266 (4)	207 (8)
dried apricot	2596 (3)	2051 (4)
crystallized ginger	227 (8)	168 (4)
dried potatoes	58 (3)[b]	54 (6)
white grape juice	74 (1)	84 (4)
raw shrimp	50 (28)	94 (11)

[a]n = 3; % RSD is shown in parentheses. [b]Dried potato is the only matrix with no significant differences between methods by a two-sample t test ($p > 0.05$).

variation in sulfite concentration in lots of shrimp may account for the differences observed between the methods. Hardisson et al.[27] investigated the sulfite concentration of frozen prawns from Spain and Venezuela and reported large ranges, values ranging from 12.8 to 546 ppm sulfite. Similar concentration variation was reported by Iammarino et al.[14] for shrimp samples collected over a four year timespan of 2009−2012, and the authors reported that due to the sulfite application process used for shrimp, the residual amount of sulfite present can vary greatly. Therefore, the range found in shrimp in this comparison could be expected.

The LC-MS/MS method presented here can be used in determining sulfite concentrations in a wide range of food and beverage matrices, and the sensitivity limitations of other published sulfite methods have been eliminated. Sulfite concentrations between 0.5 and 1.0 ppm of SO_2 can be detected in most matrices. The sample preparation involves basic extraction techniques and allows for as many as 30 samples to be completed by a single analyst in a single day. This method will be a useful tool for food safety laboratories to monitor sulfite concentrations in foods to ensure compliance with U.S. regulations. Further investigation is needed with this method to determine the rate of false positives in those matrices that contain a high quantity of endogenous sulfur compounds such as *Allium* and *Brassica* vegetables.

AUTHOR INFORMATION

Corresponding Author

*(K.S.R.) Phone: (240) 402-1835. Fax: (301) 436-2634. E-mail: Katherine.robbins@fda.hhs.gov.

Notes

The authors declare no competing financial interest.

REFERENCES

(1) Taylor, S. L.; Higley, N. A.; Bush, R. K. Sulfites in foods: uses, analytical methods, residues, fate, exposure assessment, metabolism, toxicity, and hypersensitivity. *Adv. Food Res.* **1986**, *30*, 1−76.

(2) Jackowetz, J. N.; de Orduna, R. M. Survey of SO_2 binding carbonyls in 237 red and white table wines. *Food Control* **2013**, *32*, 687−692.

(3) U.S. Food and Drug Administration.. *Fed. Regist.* **1986**, *51*, 25012−25020.

(4) U.S. Food and Drug Administration.. *Fed. Regist.* **1986**, *51*, 25021−25026.

(5) Lawrence, J. F.; Chadha, R. K.; Menard, C. Comparison of three liquid chromatographic methods with FDA optimized Monier-Williams method for determination of total sulfite in foods. *J. Assoc. Off. Anal. Chem.* **1990**, *73*, 77−79.

(6) European Commission (EC). Directive 2000/13/EC on the approximation of the laws of the Member States relating to the labeling, presentation, and advertising of foodstuffs; EC, 2000; https://www.fsai.ie/uploadedFiles/Consol_Dir2000_13.pdf (accessed Sept 2, 2014).

(7) Lim, H. S.; Park, S. K.; Kim, S. H.; Song, S. B.; Jang, S. J.; Kim, M. Comparison of four different methods for the determination of sulfites in foods marketed in South Korea. *Food Addit. Contam.: Part A* **2014**, *31*, 187−196.

(8) *Official Methods of Analysis*, 17th ed.; AOAC International: Gaithersburg, MD, USA, 2000.

(9) Isaac, A.; Livingstone, C.; Wain, A. J.; Compton, R. G.; Davis, J. Electroanalytical methods for the determination of sulfite in food and beverages. *TrAC−Trends Anal. Chem.* **2006**, *25*, 589−598.

(10) Perfetti, G. A.; Diachenko, G. W. Determination of sulfite in dried garlic by reversed-phase ion-pairing liquid chromatography with post-column detection. *J. AOAC Int.* **2003**, *86*, 544−550.

(11) Montes, C.; Velez, J. H.; Ramirez, G.; Isaacs, M.; Arce, R.; Aguirre, M. J. Critical comparison between modified Monier-Williams and electrochemical methods to determine sulfite in aqueous solutions. *Sci. World J.* **2012**, 1−6.

(12) Lowinsohn, D.; Bertotti, M. Determination of sulphite in wine by couometric titration. *Food Addit. Contam.* **2001**, *18*, 773−777.

(13) Cooper, P. L.; Marshall, M. R.; Gregory, J. F.; Otwell, W. S. Ion chromatography for determining residual sulfite on shrimp. *J. Food Sci.* **1986**, *51*, 924−928.

(14) Iammarino, M.; Di Taranto, A.; Muscarella, M.; Nardiello, D.; Palermo, C.; Centonze, D. Development of a new analytical method for the determination of sulfites in fresh meats and shrimps by ion-exchange chromatography with conductivity detection. *Anal. Chim. Acta* **2010**, *672*, 61−65.

(15) Theisen, S.; Hansch, R.; Kothe, L.; Leist, U.; Galensa, R. A fast and sensitive HPLC method for sulfite analysis in food based on a plant sulfite oxidase biosensor. *Biosens. Bioelectron.* **2010**, *26*, 175−181.

(16) Araujo, A. N.; Couto, C. M. C. M.; Lima, J. L. F. C.; Montenegro, M. C. B. S. M. Determination of SO_2 in wines using a flow injection analysis system with potentiometric detection. *J. Agric. Food Chem.* **1998**, *46*, 168−172.

(17) Goncalves, L. M.; Pacheco, J. G.; Magalhaes, P. J.; Rodrigues, J. A.; Barros, A. A. Determination of free and total sulfites in wine using an automatic flow injection analysis system with voltammetric detection. *Food Addit. Contam.: Part A−Chem.* **2010**, *27*, 175−180.

(18) Martins, P. R.; Popolim, W. D.; Nagato, L. A. F.; Takemoto, E.; Araki, K.; Toma, H. E.; Angnes, L.; Penteado, M. D. V. C. Fast and reliable analyses of sulphite in fruit juices using a supramolecular amperometric detector encompassing in flow gas diffusion unit. *Food Chem.* **2011**, *127*, 249−255.

(19) Filik, H.; Cetintas, G. Determination of sulfite in water and dried fruit samples by dispersive liquid-liquid microextraction combined with UV-vis fiber optic linear array spectrophotometry. *Food Anal. Methods* **2012**, *5*, 1362−1367.

(20) Vahl, J. M.; Converse, J. E. ripper procedure for determining sulfur-dioxide in wine − collaborative study. *J. Assoc. Off. Anal. Chem.* **1980**, *63*, 194−201.

(21) Warner, C. R.; Daniels, D. H.; Pratt, D. E.; Joe, F. L.; Fazio, T.; Diachenko, G. W. Sulphite stabilization and high-performance liquid chromatographic determination: a reference method for free and reversibly bound sulphite in food. *Food Addit. Contam.* **1987**, *4*, 437−445.

(22) Perfetti, G. A.; Joe, F. L.; Diachenko, G. W. Liquid chromatographic determination of sulfite in grapes and selected grape products. *J. Assoc. Off. Anal. Chem.* **1989**, *72*, 903−906.

(23) Warner, C. R.; Daniels, D. H.; Fitzgerald, M. C.; Joe, F. L.; Diachenko, G. W. Determination of free and reversibly bound sulphite in foods by reverse-phase, ion-pairing high-performance liquid chromatography. *Food Addit. Contam.* **1990**, *7*, 575−581.

DOI: 10.1021/jf505525z
J. Agric. Food Chem. 2015, 63, 5126−5132

(24) Barbe, J. C.; de Revel, G.; Joyeux, A.; Lonvaud-Funel, A.; Bertrand, A. Role of carbonyl compounds in SO_2 binding phenomena in musts and wines from botrytized grapes. *J. Agric. Food Chem.* **2000**, *48*, 3413−3419.
(25) Turkyilmaz, M.; Tagi, S.; Ozkan, M. Changes in chemical and microbial qualities of dried apricots containing sulphur dioxide at different levels during storage. *Food Bioprocess Technol.* **2013**, *6*, 1526−1538.
(26) Jariwala, F. B.; Wood, R. E.; Nishshanka, U.; Attygalle, A. B. Formation of the bisulfite anion (HSO_3^-, m/z 81) upon collision-induced dissociation of anions derived from organic sulfonic acids. *J. Mass Spectrom.* **2012**, *47*, 529−538.
(27) Hardisson, A.; Rubio, C.; Frias, I.; Rodriguez, I.; Reguera, J. I. Content of sulphite in frozen prawns and shrimps. *Food Control* **2002**, *13*, 275−279.

DOI: 10.1021/jf505525z
J. Agric. Food Chem. 2015, 63, 5126−5132

JOURNAL OF AGRICULTURAL AND FOOD CHEMISTRY

Article

pubs.acs.org/JAFC

Rapid and Easy Multiresidue Method for the Analysis of Antibiotics in Meats by Ultrahigh-Performance Liquid Chromatography–Tandem Mass Spectrometry

Takahiro Yamaguchi,[†] Masahiro Okihashi,[†] Kazuo Harada,[*,§,#] Kotaro Uchida,[†] Yoshimasa Konishi,[†] Keiji Kajimura,[†] Kazumasa Hirata,[§,#] and Yoshimasa Yamamoto[†,#]

[†]Osaka Prefectural Institute of Public Health, 1-3-69 Nakamichi, Higashinari-ku, Osaka 537-0025, Japan

[§]Graduate School of Pharmaceutical Sciences, Osaka University, 1-6 Yamadaoka, Suita, Osaka 565-0871, Japan

[#]Global Collaboration Center, Osaka University, 2-7 Yamadaoka, Suita, Osaka 565-0871, Japan

ABSTRACT: This study involved the development of a multiresidue method for the rapid analysis of 43 antibiotics in meats using ultrahigh-performance liquid chromatography–tandem mass spectrometry. This method was performed using dispersive-solid phase extraction, which is able to analyze 20 samples within 2 h. All compounds were determined simultaneously on a C18 separation column with gradient elution. Validation of the analytical method was performed by carrying out linearity, limit of quantification (LOQ), accuracy, precision, and recovery tests in different meat products. The validation criteria were set according to AOAC International and Japanese validation guidelines. The linearity of each compound was almost the coefficient of determination (r^2) > 0.98. The LOQs of all tested antibiotics were <10 μg/kg. The results verify that this method is capable of quantitative analysis of 36, 33, and 37 compounds in beef, pork, and chicken, respectively. This method can be used for rapid and easy multiresidue screening of antibiotics for three meats (pork, beef, and chicken).

KEYWORDS: *antibiotic residues, meat, dispersive solid-phase extraction, ultrahigh-performance liquid chromatography–tandem mass spectrometry*

INTRODUCTION

Antibiotics have been widely used globally for the treatment and prevention of infectious diseases in fishery products to maintain and improve productivity and quality. Some antibiotics are also used as growth-promoting agents in animal feed.[1,2] However, the use of these compounds as feed additives for growth promotion has been banned in the European Union (EU).[3] National agencies and international organizations, such as the Joint Food and Agriculture Organization/World Health Organization Expert Committee on Food Additives, establish limits on the residue levels of veterinary drugs that are allowed to be present in food of animal origin so that consumers are not exposed to unacceptable levels. Levels are set using risk-based assessments from pharmacokinetic, metabolic, toxicity, and carcinogenicity data.[4,5] It is suggested that if incorrect usage and inadequate withdrawal periods are used, then antibiotic residues in food products may become a health hazard in humans.[6,7]

To monitor chemical residues, food products are checked at various steps of the distribution chain, such as farmers, exporters, importers, supermarkets, and governmental intervention. Thus, many analytical laboratories analyze residual antibiotics using various analytical methods: a simple and rapid analysis method is required to not only reduce time, cost, and labor but also to produce a standard analysis procedure enabling direct comparisons between the results of different laboratories. Numerous methods have been published to analyze antibiotics in foodstuff, and these methods usually involve several steps, such as extraction, concentration, separation, and purification.[8−17] We have developed an easy and rapid multiresidue method that can determine a wide range of residual antibiotics in meat samples using ultrahigh-performance liquid chromatography–tandem mass spectrometry (UHPLC-MS/MS).

The objective of our study was to develop a fast, reliable, easy, and robust analytical method to determine residual antibiotics in hundreds of meat samples for use in developing countries, which often do not have adequate fundamental logistical support: basic equipment, such as a vacuum system or glassware with precise graduation, may not be available even though outstanding and expensive instruments have been provided by developed countries. The proposed method was based on our previous study[18] and involved extraction and dispersive solid phase extraction (SPE) using the C18 particle, without liquid–liquid partition and evaporation after clean-up.[19−24]

MATERIALS AND METHODS

Samples. Chicken, pork, and beef muscles were purchased from retail stores in Osaka, Japan. Fat was removed from the samples as much as possible before they were minced using a food processor (MK-K61, Panasonic, Japan) at room temperature and stored in polypropylene bags at −20 °C until analysis. We confirmed the meat samples did not contain any of the antibiotics being analyzed in our study before their use in the validation tests.

Special Issue: 51st North American Chemical Residue Workshop

Received: October 31, 2014
Revised: February 6, 2015
Accepted: February 6, 2015
Published: February 6, 2015

ACS Publications © 2015 American Chemical Society

DOI: 10.1021/acs.jafc.5b00170
J. Agric. Food Chem. 2015, 63, 5133−5140

Table 1. Retention Times and MS/MS Parameters

		quantification			diagnostic		
compound	RT[a] (min)	MRM (m/z)	cone voltage (V)	collision energy (eV)	MRM (m/z)	cone voltage (V)	collision energy (eV)
ampicillin[b]	5.1	350.0→106.0	14	14	350.0→173.9	14	12
aspoxicillin[b]	3.4	494.0→ 250.0	42	16	494.0→114.0	40	34
ciprofloxacin[c]	5.5	332.0→288.0	6	16	332.0→314.0	6	20
cloxacillin[b]	8.7	435.9→276.9	18	12	435.9→159.9	18	12
danofloxacin[c]	5.6	358.0→339.9	6	20	358.0→314.0	30	16
diaveridine	4.8	261.0→245.0	26	26	261.0→122.9	26	20
dicloxacillin[b]	9.2	469.9→159.9	24	10	469.9→310.8	24	12
difloxacin[c]	6.0	400.0→356.0	6	18	400.0→299.0	6	26
enrofloxacin[c]	5.7	360.1→316.0	4	18	360.1→245.0	4	24
erythromycin[d]	7.1	734.2→158.0	34	24	734.2→576.1	34	16
josamycin[d]	8.1	828.2→109.0	76	38	828.2→174.0	76	28
kitasamycin[d]	7.6	772.2→109.0	80	36	772.2→174.0	80	26
lincomycin[d]	4.7	407.1→125.9	58	24	407.1→359.0	58	16
marbofloxacin[c]	5.2	363.0→319.9	14	14	363.0→71.7	22	16
mecillinam[b]	5.7	326.1→167.0	16	18	326.1→139.0	16	28
mirosamicin[d]	6.7	728.2→158.0	54	26	728.2→116.0	54	34
nafcillin[b]	8.8	415.0→198.9	18	10	415.0→170.9	18	32
neospiramycin[d]	5.8	350.2→174.0	12	14	350.2→160.1	12	10
norfloxacin[c]	5.4	320.0→276.0	4	14	320.0→302.0	4	18
ofloxacin[c]	5.4	362.1→260.9	4	24	362.1→318.0	4	16
oleandomycin[d]	7.0	688.2→158.0	44	24	688.2→544.1	44	12
orbifloxacin[c]	5.8	396.1→352.0	2	16	396.1→294.9	2	22
oxacillin[b]	8.3	402.0→159.9	28	10	402.0→242.9	28	8
penicillin G[b]	7.7	335.0→159.9	20	8	335.0→175.9	20	10
penicillin V[b]	8.1	350.9→159.9	18	10	350.9→113.9	18	30
pirlimycin[d]	6.2	411.0→112.0	40	24	411.0→363.0	40	14
sarafloxacin[c]	6.0	386.0→342.0	6	16	386.0→298.9	6	26
spiramycin[d]	6.1	422.2→174.0	28	18	422.2→101.0	28	12
sulfachlorpyridazine[e]	6.4	284.9→91.9	26	24	284.9→155.9	34	14
sulfaclozine[e]	7.2	284.9→91.9	26	24	284.9→155.9	34	14
sulfadimethoxine[e]	7.3	311.0→155.8	40	16	311.0→91.9	40	28
sulfadoxine[e]	6.6	311.0→155.8	40	16	311.0→91.9	40	28
sulfamethazine[e]	5.6	279.0→185.9	44	16	279.0→91.9	44	28
sulfamerazine[e]	5.2	265.0→91.9	4	26	265.0→155.8	4	16
sulfamethoxazole[e]	6.6	254.0→155.9	24	14	254.0→92.0	24	26
sulfamethoxypyridazine[e]	5.9	281.0→155.8	4	16	281.0→91.9	4	28
sulfamonomethoxine[e]	6.2	281.0→155.8	4	16	281.0→91.9	4	28
sulfapyridine[e]	4.9	245.0→155.9	40	14	245.0→91.9	40	24
sulfaquinoxaline[e]	7.3	301.0→155.9	6	14	301.0→91.9	6	28
thiamulin[d]	7.6	494.2→192.0	12	16	494.2→118.9	12	40
tilmicosin[d]	6.6	869.3→88.0	94	76	869.3→174.0	94	40
trimethoprim	5.2	291.0→122.9	42	22	291.0→229.9	42	22
tylosin[d]	7.3	916.3→174.0	60	34	916.3→772.2	60	26

[a]Retention time. [b]β-Lactam group. [c]Quinolone group. [d]Macrolide group. [e]Sulfonamide group.

Chemicals. Kitasamycin (leucomycin hydrate), mecillinam, and oleandomycin phosphate dehydrate were purchased from Dr. Ehrenstorfer GmbH (Augsburg, Germany). Nafcillin sodium salt monohydrate, neospiramycin, and spiramycin were purchased from Hayashi Pure Chemical Industries (Osaka, Japan). Danofloxacin mesylate, penicillin G sodium, sulfamethoxazole, sulfamerazine, sulfamethazine (sulfadimidine), sulfamonomethoxine, sulfamethoxypyridazine, sulfachlorpyridazine, sulfaquinoxaline, sulfadoxine, sulfadimethoxine, and josamycin were purchased from Kanto Chemical (Tokyo, Japan). Ampicillin trihydrate, cloxacillin sodium salt hydrate, dicloxacillin sodium salt hydrate, oxacillin sodium, penicillin V potassium salt, suflapyridine, diaveridine, erythromycin A dehydrate, and lincomycin hydrochloride hydrate were purchased from Riedel-de Haën (St. Louis, MO, USA). Aspoxicillin and orbifloxacin were purchased from Fluka (St. Louis, MO, USA). Norfloxacin and sulfaclozine were purchased from Sigma-Aldrich (St. Louis, MO, USA). Ciprofloxacin, enrofloxacin, ofloxacin, marbofloxacin, sarafloxacin, difloxacin, trimethoprim, and thiamulin fumarate were purchased from Wako Pure Chemicals Industries (Osaka, Japan). Pirlimycin, mirosamicin, tilmicosin, and tylosin were provided by the Japan Scientific Feeds Association (Tokyo, Japan). Acetonitrile and methanol, used in the preparation of test solutions and stock solutions, were of pesticide analytical grade; acetonitrile and formic acid were of LC-MS and LC grade, respectively (Wako Pure Chemicals Industries). Purified water was obtained using a Millipore system (Elix advantage 3 and Milli-Q advantage, Merck Millipore, Billerica, MA, USA). Dispersive SPE BONDESIL-C18 (C18) was purchased from Agilent Technologies (Santa Clara, CA, USA).

Sample Extraction. A 2 g aliquot of each sample was weighed in a 50 mL polypropylene tube. A 10 mL aliquot of acetonitrile/water

DOI: 10.1021/acs.jafc.5b00170
J. Agric. Food Chem. 2015, 63, 5133−5140

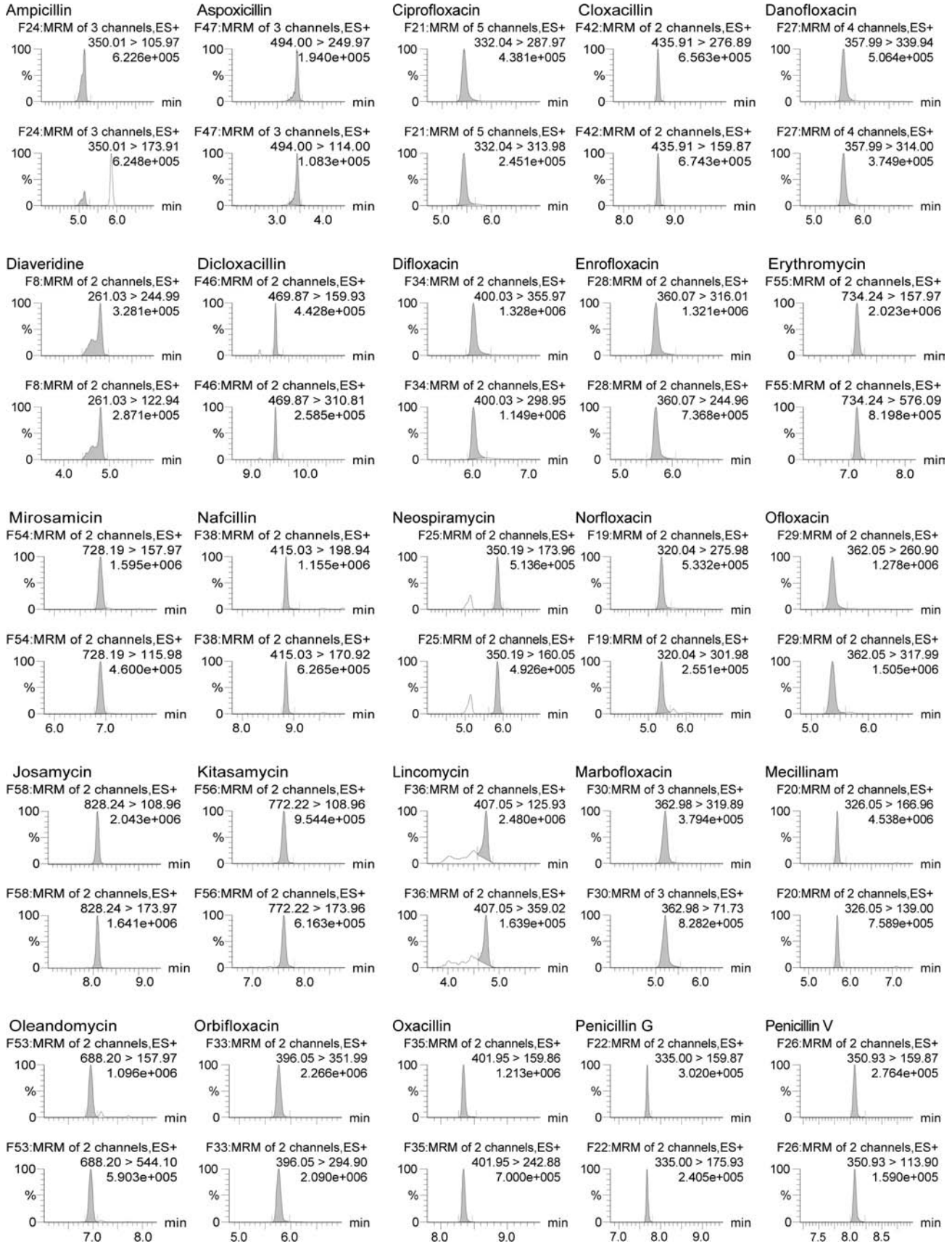

Figure 1. continued

DOI: 10.1021/acs.jafc.5b00170
J. Agric. Food Chem. 2015, 63, 5133−5140

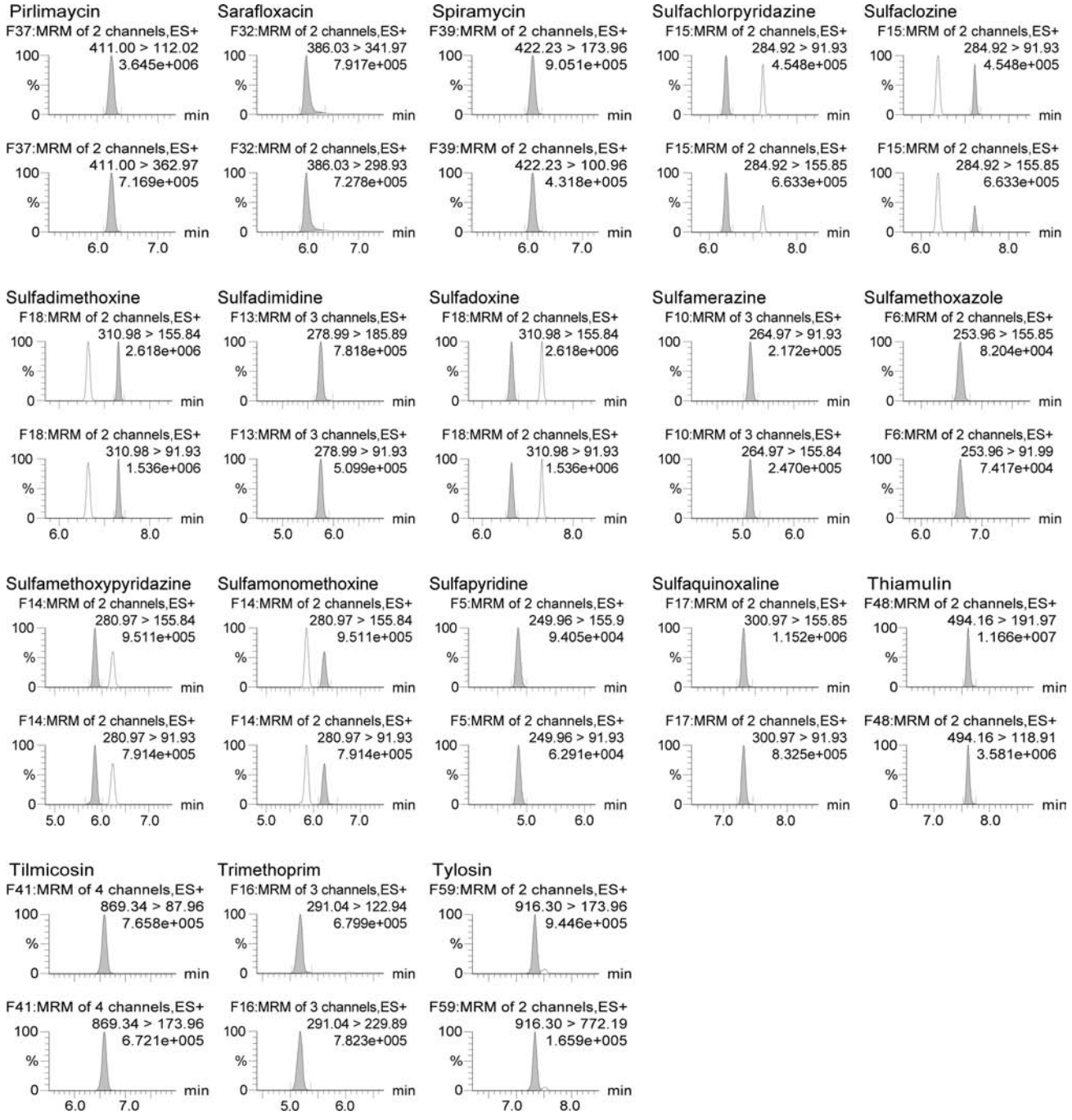

Figure 1. Chromatograms of standard solutions (10 ng/mL).

(4:1) solution was then added and homogenized using a blender (20,000 rpm, 1 min) (PT3100, Kinematica AG, Luzern, Switzerland). The sample was centrifuged using a himac CF7D2 centrifuge (Hitachi Koki, Ibaragi, Japan) at 1500*g* for 5 min, and the supernatant was poured into a 15 mL polypropylene tube containing 0.3 g of dispersive C18. The supernatant was then shaken for 1 min and centrifuged at 1500*g* for 5 min. An aliquot of 1 mL was taken and diluted with 1 mL of distilled water. The extract was filtered through a PTFE membrane filter (Advantec, Tokyo, Japan). This final extract corresponded to 0.1 g/mL sample equivalent.

Determining the Required Amounts of Dispersive SPE. The required amount of C18 particles was examined as follows: 40 g of pork was homogenized with 200 mL of acetonitrile/water (4:1) solution. Ten mililiters of extract solution was then mixed with 0, 0.1, 0.2, 0.3, 0.4, and 0.5 g of C18 particles or 10 mL of hexane, shaken for 1 min, and centrifuged at 1500*g* for 5 min. Each 7 mL of supernatant was placed on an aluminum weighing dish and heated at about 100 °C for 2 h in an incubator; dried residues were weighed after cooling to measure the amount of coextractives.

Instruments and Analytical Methods. UHPLC-MS/MS analysis was performed using a Waters ACQUITY UPLC i-class interfaced with a TQ-S (Milford, MA, USA). Waters Cortecs C18 columns (100 × 2.1 mm i.d., 1.6 μm) with ACQUITY UPLC BEH C18 precolumns (5 × 2.1 mm, 1.7 μm, Waters) were used for chromatography. The column temperature was maintained at 40 °C. Sample injection volume was 2 μL, mobile phases A and B were water with 0.1% formic acid and acetonitrile, respectively. Selected operating parameters were as follows: capillary voltage, 3 kV; desolvation temperature, 400 °C; desolvation gas, 1000 L/h; cone gas, 150/h; and collision gas, 0.15 L/min. Antibiotic analytes were resolved using a gradient program as

DOI: 10.1021/acs.jafc.5b00170
J. Agric. Food Chem. 2015, 63, 5133−5140

follows: 5−10% B (3 min), 10−95% B (9 min), 95% B (3 min), 95−5% B (0.5 min), 5% (3.5 min). The mass spectrometer was operated in the positive electrospray ionization (ESI+) mode. MS/MS detection was selected for multiple reaction monitoring (MRM). Information on the monitored ions and chromatograms is presented in Table 1 and Figure 1.

Stock Standard Solutions. Four milligrams of each standard was weighed in a glass bottle and then transferred to a 20 mL glass volumetric flask and dissolved in methanol. Purified water was used if the standard was insoluble in methanol. Standards, except β-lactam antibiotics, were stored in 15 mL polypropylene tubes at −20 °C until required. β-Lactam antibiotic standards were stored at −80 °C and prepared every 3 months.[25]

Intermediate and Working Standard Solutions. Intermediate standards were prepared from stock standard solutions (200 μg/mL) for each category. Individual intermediate standard solutions (10 μg/mL) for sulfonamides, quinolone, and macrolide antibiotics diaveridine and trimethoprim were prepared using methanol in polypropylene tubes and stored at −20 °C. The same concentration of β-lactam mixture was prepared using distilled water. Working standard solutions were prepared by mixing the intermediate standards to produce concentrations of 0.5, 1, 5, 10, 20, and 50 ng/mL using acetonitrile/water (4:6) and stored at 4 °C before use.

Method Validation. Validation was established according to the guidelines of AOAC International and the Japanese Ministry of Health, Labor and Welfare.[26,27] Method validation was carried out by performing linearity, limit of quantification (LOQ), accuracy, precision, and recovery tests. Repeatability (RSD_r) and within-laboratory reproducibility (RSD_R) precision values for two spiking levels were calculated by one-way analysis of variance (ANOVA).

RESULTS AND DISCUSSION

Method Development. This method intended to provide an easy and rapid multiresidue screening method with the ability to determine a wide range of residual antibiotics in meat samples. Conventional instruments have decreased sensitivity, and sample solutions need to be purified to eliminate interferences before injection and purification steps, such as liquid−liquid partition and column cleanup followed by concentration, which are time-consuming. Novel instruments have very high sensitivity and require very small amounts of sample for analysis,[28] due to less interference and reduced sample purification procedures. Dispersive SPE is a very simple cleanup approach.[29−32] In this study, we used C18 sorbent to remove coextractives. An acetonitrile/water (4:1) solution was chosen for extraction because it efficiently extracts polar components and deproteinizes.[19,33] This solution was convenient for dispersive SPE with C18 and suitable for UHPLC-MS/MS analysis after dilution with water. The entire procedure can be performed without evaporation. In comparison with hexane partitioning, 0.1−0.2 g of C18 produced similar amounts of residue, whereas 0.3−0.5 g of C18 showed a gradual decrease in residue recovery (Figure 2). We also examined recovery of antibiotics in the cleanup steps described above: 10 mL of extract solution was mixed with 0, 0.1, 0.2, 0.3, 0.4, and 0.5 g of C18 particles or 10 mL of hexane, shaken for 1 min, and centrifuged at 1500*g* for 5 min. An aliquot of 1 mL was then diluted with 1 mL of distilled water before UHPLC-MS/MS analysis. Recovery tests for the antibiotics produced similar results: about 40 compounds showed from 70 to 120% recovery at each cleanup step. Considering the cost and interference removal efficiency, 0.3 g of C18 was adopted for the cleanup step.

Validation of Target Compounds. Validation was performed by determining the parameters of a calibration curve, LOQs, precision, and accuracy.

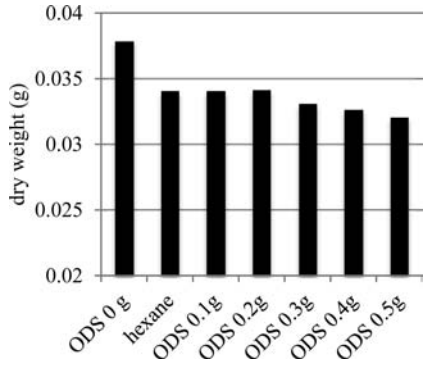

Figure 2. Comparison of the dried weight of extracts after defatting, hexane partitioning, and dispersion with various amounts of C18 particles.

The concentration of the spiked samples was calculated from matrix-matched standards. The resulting coefficient of determination (r^2) values were >0.99 for almost all target compounds, except sulfapyridine and sulfadoxine, which were >0.98. The LOQs were estimated from the signal-to-noise ratio (S/N) (Table 2). S/N was determined at the peak height of beef, pork, and chicken samples spiked with 1 ng/mL target compounds. The background noise was estimated near each analyte peak. Precision and accuracy were performed according to the guidelines of AOAC International and the Japanese Ministry of Health, Labor and Welfare.[26,27] Recovery tests of 43 antibiotic residues from beef, pork, and chicken were performed at two different concentration levels, 10 and 100 μg/kg, in duplicate by three persons on two separate days. No interfering peaks were detected near the retention time of the analytes. The validation data were evaluated on the basis of recoveries of 70−125%, RSD_r of <15%, and RSD_R of <15% for two spiking levels upon recommendation of AOAC International and the Japanese government.[26,27] The results of recovery, RSD_r, and RSD_R precision values are shown in Table 2. All compounds were evaluated at the level of 10 μg/kg LOQs.

The number of compounds that met the criteria were 36, 33, and 37 for beef, pork, and chicken, respectively. Sulfamethoxazole failed to comply with the criteria in all samples. Diaveridine and sulfapyridine complied with the criteria in pork only. Aspoxicillin met with criteria in chicken only. Sarafloxacin and sulfamerazine met with criteria in beef only. Aspoxicillin and sulfaclozine failed to comply with the uniform limit only in beef. Spiramycin failed to comply with the uniform limit only in chicken.

Ciprofloxacin, danofloxacin, difloxacin, enrofloxacin, and sarafloxacin failed to comply with the criteria in pork because the results of the recovery test at a level of 10 μg/kg were <70%; in addition, penicillins G and V failed to comply with the RSD_r criteria standard.

Quinolone was speculated to affect the pork matrix due to the low spiked concentration on recovery.

Our results suggest this method is capable of quantitative analysis of 36, 33, and 37 antibiotic residues in beef, pork, and chicken, respectively. This method is considered to be capable of performing more efficient monitoring of antibiotic residues in meat, and it is possible to simultaneously process a large number of samples without evaporation. This analysis method is specialized for convenient screening, particularly in laboratories with reduced equipment, if they have UHPLC-MS/MS. This method is considered to facilitate contamination

DOI: 10.1021/acs.jafc.5b00170
J. Agric. Food Chem. 2015, 63, 5133−5140

Table 2. Results of Recovery Tests and LOQs

		beef				pork				chicken			
compound	fortification level (μg/kg)	recovery[a] (%)	RSD_r[b] (%)	RSD_R[c] (%)	LOQ (μg/kg)	recovery[a] (%)	RSD_r[b] (%)	RSD_R[c] (%)	LOQ (μg/kg)	recovery[a] (%)	RSD_r[b] (%)	RSD_R[c] (%)	LOQ (μg/kg)
ampicillin	10	75	11	11	4.7	81	8	8	1.2	80	9	9	1.1
	100	75	4	4		81	6	5		79	7	5	
aspoxicillin	10	39	10	9	2.8	71	21	20	7.5	71	14	16	2.8
	100	25	6	7		74	9	8		82	9	10	
ciprofloxacin	10	73	13	13	4.7	69	21	16	4.5	100	10	14	5.8
	100	79	4	3		91	6	5		79	5	5	
cloxacillin	10	83	10	8	3.1	88	8	7	2.0	85	7	9	3.3
	100	79	2	5		86	4	3		81	3	5	
danofloxacin	10	96	12	10	5.2	66	17	21	2.8	99	8	9	2.9
	100	77	5	6		89	7	7		80	5	6	
diaveridine	10	58	11	8	0.3	79	7	6	1.6	63	12	10	0.8
	100	46	9	8		73	4	4		58	6	6	
dicloxacillin	10	79	7	6	1.6	85	3	3	0.5	112	5	3	0.8
	100	76	3	4		86	2	4		104	2	3	
difloxacin	10	70	11	10	2.0	55	10	19	3.7	96	8	17	5.5
	100	75	4	4		81	3	3		78	3	2	
enrofloxacin	10	73	8	7	4.0	59	11	14	2.3	89	11	12	1.9
	100	77	3	3		86	5	4		78	6	5	
erythromycin	10	84	6	6	0.5	92	6	6	0.3	94	2	3	1.1
	100	79	4	5		89	2	4		81	3	4	
josamycin	10	89	5	8	2.4	88	6	5	1.7	99	4	4	1.0
	100	80	2	4		88	4	5		85	3	3	
kitasamycin	10	87	4	6	1.7	81	6	10	4.6	90	7	11	4.4
	100	90	4	4		96	3	4		88	6	5	
lincomycin	10	92	5	7	1.6	85	3	5	1.2	89	5	6	1.1
	100	93	4	4		82	1	1		88	4	3	
marbofloxacin	10	80	14	11	4.8	80	5	8	6.1	93	11	10	3.3
	100	75	7	6		83	4	4		75	5	4	
mecillinam	10	83	7	7	1.0	98	9	8	0.6	88	9	8	0.5
	100	80	4	4		101	6	4		84	4	3	
mirosamicin	10	83	7	6	1.2	88	5	5	0.4	88	4	4	3.2
	100	75	2	6		87	2	5		79	2	4	
nafcillin	10	80	11	10	1.7	83	2	5	7.1	85	9	7	3.7
	100	76	4	4		86	3	3		78	2	3	
neospiramycin	10	90	14	15	5.5	87	6	18	5.4	111	15	20	0.9
	100	90	6	5		111	8	11		86	6	11	
norfloxacin	10	98	17	14	2.6	89	3	5	3.7	98	12	17	3.1
	100	85	12	10		79	3	3		80	10	9	
ofloxacin	10	79	9	8	3.7	84	7	6	2.1	93	5	7	3.1
	100	78	5	5		86	5	5		79	5	4	
oleandomycin	10	88	5	6	1.3	90	5	5	2.0	84	4	5	1.1
	100	76	3	5		85	1	5		78	3	5	
orbifloxacin	10	89	6	7	1.7	80	7	7	1.3	83	6	9	1.2
	100	77	4	4		87	4	4		78	5	4	
oxacillin	10	81	9	7	1.7	84	10	9	1.5	87	9	6	3.0
	100	76	3	4		86	3	4		80	3	3	
penicillin G	10	73	12	10	0.5	89	16	12	3.3	81	14	12	1.4
	100	72	5	7		84	5	5		78	3	3	
penicillin V	10	74	11	13	3.3	92	16	13	3.8	74	8	12	2.2
	100	76	4	5		84	5	8		77	4	8	
pirlimycin	10	74	4	5	0.6	81	8	7	1.2	78	5	7	2.4
	100	70	3	3		81	4	3		75	2	3	
sarafloxacin	10	75	13	13	5.6	55	14	17	5.1	100	16	23	5.3
	100	77	5	5		77	5	4		74	3	3	
spiramycin	10	96	9	12	4.3	82	14	19	0.7	92	21	22	5.2
	100	90	7	6		100	7	7		86	6	9	
sulfachlorpyridazine	10	84	8	14	1.1	102	9	9	3.0	87	6	10	0.8
	100	82	7	7		90	3	4		87	5	4	
sulfaclozine	10	84	12	10	0.8	77	12	15	3.4	86	11	11	1.8
	100	68	2	5		77	3	7		74	4	5	
sulfadimethoxine	10	81	3	6	1.5	87	6	7	0.6	85	4	4	0.8

DOI: 10.1021/acs.jafc.5b00170
J. Agric. Food Chem. 2015, 63, 5133−5140

Table 2. continued

compound	fortification level (μg/kg)	beef recovery[a] (%)	beef RSD_r[b] (%)	beef RSD_R[c] (%)	beef LOQ (μg/kg)	pork recovery[a] (%)	pork RSD_r[b] (%)	pork RSD_R[c] (%)	pork LOQ (μg/kg)	chicken recovery[a] (%)	chicken RSD_r[b] (%)	chicken RSD_R[c] (%)	chicken LOQ (μg/kg)
	100	79	2	5		89	2	6		84	2	5	
sulfadoxine	10	96	11	9	2.1	99	8	9	0.7	94	9	8	0.9
	100	94	5	5		102	4	5		96	5	5	
sulfamethazine	10	84	9	8	0.3	95	5	5	0.5	94	11	9	1.0
	100	83	4	4		88	3	6		94	6	5	
sulfamerazine	10	77	10	9	1.2	78	12	10	3.6	74	13	13	6.3
	100	73	6	7		70	6	9		69	8	10	
sulfamethoxazole	10	79	13	12	2.8	90	15	15	3.5	72	8	19	5.1
	100	51	13	13		63	8	11		60	8	16	
sulfamethoxypyridazine	10	85	5	7	1.0	96	4	4	1.3	94	11	10	0.3
	100	84	5	4		95	2	6		92	6	4	
sulfamonomethoxine	10	84	15	12	2.5	97	8	8	2.3	85	11	13	0.7
	100	82	4	4		93	4	4		88	7	5	
sulfapyridine	10	59	19	16	3.6	80	14	17	7.4	59	15	15	1.2
	100	45	11	15		73	10	14		53	9	11	
sulfaquinoxaline	10	80	3	7	4.0	90	6	8	0.9	85	6	6	0.8
	100	76	2	5		85	4	7		81	3	5	
thiamulin	10	85	7	6	0.6	90	5	5	0.2	90	8	8	0.4
	100	87	5	5		95	2	3		93	5	4	
tilmicosin	10	104	12	10	6.7	110	9	12	9.1	105	14	15	6.4
	100	86	6	6		96	5	4		85	3	3	
trimethoprim	10	93	15	14	4.1	90	6	7	5.0	102	13	13	6.4
	100	95	11	9		76	5	5		99	9	8	
tylosin	10	92	8	8	3.8	87	10	8	3.2	88	5	4	0.8
	100	87	3	5		95	5	6		79	3	3	

[a]Mean recovery $n = 12$. [b]Repeatability. [c]Within-laboratory reproducibility.

surveys of residue antibiotics in foods, which is expected to provide a safer global food chain.

AUTHOR INFORMATION

Corresponding Author

*(K. Harada) Phone: +81-6-6879-8235. Fax: +81-6-6879-8154. E-mail: harada6@phs.osaka-u.ac.jp.

Funding

This work was supported by the Japan Science and Technology Agency (JST)/Japan International Cooperation Agency (JICA) as part of the Science and Technology Research Partnership for Sustainable Development (SATREPS).

Notes

The authors declare no competing financial interest.

REFERENCES

(1) Dibner, J. J.; Richards, J. D. Antibiotic growth promoters in agriculture: history and mode of action. *Poult. Sci.* **2005**, *84*, 634−643.

(2) Castanon, J. I. R. History of the use of antibiotic as growth promoters in European poultry feeds. *Poult. Sci.* **2007**, *86*, 2466−2471.

(3) Council Directive 96/23/EC on measures to monitor certain substances and residues thereof in live animals and animal products and repealing Directives 85/358/EEC and 86/469/EEC and Decisions 89/187/EEC and 91/664/EEC. *Off. J. Eur. Communities* **1996**, *L125*, 10−32.

(4) Council Regulation (EEC) No, 2377/90 laying down a Community procedure for the establishment of maximum residue limits of veterinary medicinal products in foodstuffs of animal origin. *Off. J. Eur. Communities* **1990**, *L224*, 1−8.

(5) Tollefson, L.; Miller, M. A. Antibiotic use in food animals: controlling the human health impact. *J. AOAC Int.* **2000**, *83*, 245−254.

(6) Serratosa, J.; Blass, A.; Rigau, B.; Mongrell, B.; Rigau, T.; Tortadès, M.; Tolosa, E.; Aguilar, C.; Ribó, O.; Balagué, J. Residues from veterinary medicinal products, growth promoters and performance enhancers in food-producing animals: a European Union perspective. *Rev. Sci. Technol.* **2006**, *25*, 637−653.

(7) Van den Bogaard, A. E.; Stobberingh, E. E. Epidemiology of resistance to antibiotics. links between animals and humans. *Int. J. Antimicrob. Agents* **2000**, *14*, 327−335.

(8) Gajda, A.; Posyniak, A.; Zmudzki, J.; Gbylik, M.; Bladek, T. Determination of (fluoro) quinolones in eggs by liquid chromatography with fluorescence detection and confirmation by liquid chromatography−tandem mass spectrometry. *Food Chem.* **2012**, *135*, 430−439.

(9) Toaldo, I. M.; Gamba, G. Z.; Picinin, L. A.; Rubensam, G.; Hoff, R.; Bordignon-Luiz, M. Multiclass analysis of antibacterial residues in milk using RP-liquid chromatography with photodiode array and fluorescence detection and tandem mass spectrometer confirmation. *Talanta* **2012**, *99*, 616−624.

(10) Economou, A.; Petraki, O.; Tsipi, D.; Botitsi, E. Development of a liquid chromatography−tandem mass spectrometry method for the determination of sulfonamides, trimethoprim and dapsone in honey and validation according to Commission Decision 2002/657/EC for banned compounds [corrected]. *Talanta* **2012**, *97*, 32−41.

(11) Pérez-Burgos, R.; Grzelak, E. M.; Gokce, G.; Saurina, J.; Barbosa, J.; Barrón, D. QuEChERS methodologies as an alternative to solid phase extraction (SPE) for the determination and characterization of residues of cephalosporins in beef muscle using LC-MS/MS. *J. Chromatogr., B: Anal. Technol. Biomed. Life Sci.* **2012**, *899*, 57−65.

(12) Bohm, D. A.; Stachel, C. S.; Gowik, P. Validation of a multi-residue method for the determination of several antibiotic groups in honey by LC-MS/MS. *Anal. Bioanal. Chem.* **2012**, *403*, 2943−2953.

(13) Tsai, C. W.; Lin, C. S.; Wang, W. H. Multi-residue determination of sulfonamide and quinolone residues in fish tissues by high performance liquid chromatography-tandem mass spectrometry (LC- MS/MS). *J. Food Drug Anal.* **2012**, *20*, 674−680.

(14) Gaugain-Juhel, M.; Delepine, B.; Gautier, S.; Fourmond, M. P.; Gaudin, V.; Hurtaud-Pessel, D.; Verdon, E.; Sanders, P. Validation of a

DOI: 10.1021/acs.jafc.5b00170
J. Agric. Food Chem. 2015, 63, 5133−5140

liquid chromatography-tandem mass spectrometry screening method to monitor 58 antibiotics in milk: a qualitative approach. *Food Addit. Contam.* **2009**, *26*, 1459−1471.
(15) Granelli, K.; Branzell, C. Rapid multi-residue screening of antibiotics in muscle and kidney by liquid chromatography-electrospray ionization−tandem mass spectrometry. *Anal. Chim. Acta* **2007**, *586*, 289−295.
(16) Biswas, A. K.; Rao, G. S.; Kondaiah, N.; Anjaneyulu, A. S. R.; Malik, J. K. Simple multiresidue method for monitoring of trimethoprim and sulfonamide residues in buffalo meat by high-performance liquid chromatography. *J. Agric. Food Chem.* **2007**, *55*, 8845−8850.
(17) Martos, P. A.; Jayasundara, F.; Dolbeer, J.; Jin, W.; Spilsbury, L.; Mitchell, M.; Varilla, C.; Shurmer, B. Multiclass, multiresidue drug analysis, including aminoglycosides, in animal tissue using liquid chromatography coupled to tandem mass spectrometry. *J. Agric. Food Chem.* **2010**, *58*, 5932−5944.
(18) Yamaguchi, T.; Kakimoto, K.; Nagayoshi, H.; Yamaguchi, M.; Okihashi, M.; Kajimura, K.; Yamamoto, Y. Simultaneous determination of veterinary drugs in livestock products using dispersive and cartridge column solid-phase extraction by LC-MS/MS. *J. Food Hyg. Soc. Jpn.* **2013**, *54*, 290−297.
(19) Lehotay, S. J.; Lightfield, A. R.; Geis-Asteggiante, L.; Schneider, M. J.; Dutko, T.; Ng, C.; Bluhm, L.; Mastovska, K. Development and validation of a streamlined method designed to detect residues of 62 veterinary drugs in bovine kidney using ultra-high performance liquid chromatography-tandem mass spectrometry. *Drug Test Anal.* **2012**, *4* (Suppl. 1), 75−90.
(20) Geis-Asteggiante, L.; Lehotay, S. J.; Lightfield, A. R.; Dutko, T.; Ng, C.; Bluhm, L. Ruggedness testing and validation of a practical analytical method for >100 veterinary drug residues in bovine muscle by ultrahigh performance liquid chromatography-tandem mass spectrometry. *J. Chromatogr., A* **2012**, *1258*, 43−54.
(21) Schneider, M. J.; Mastovska, K.; Lehotay, S. J.; Lightfield, A. R.; Kinsella, B.; Shultz, C. E. Comparison of screening methods for antibiotics in beef kidney juice and serum. *Anal. Chim. Acta* **2009**, *637*, 290−297.
(22) Mastovska, K.; Lightfield, A. R. Streamlining methodology for the multiresidue analysis of beta-lactam antibiotics in bovine kidney using liquid chromatography-tandem mass spectrometry. *J. Chromatogr., A* **2008**, *1202*, 118−123.
(23) Fagerquist, C. K.; Lightfield, A. R.; Lehotay, S. J. Confirmatory and quantitative analysis of beta-lactam antibiotics in bovine kidney tissue by dispersive solid-phase extraction and liquid chromatography-tandem mass spectrometry. *Anal. Chem.* **2005**, *77*, 1473−1482.
(24) Moats, W. A.; Romanowski, R. D. Multiresidue determination of beta-lactam antibiotics in milk and tissues with the aid of high-performance liquid chromatographic fractionation for clean up. *J. Chromatogr., A* **1998**, *812*, 237−247.
(25) Gaugain, M.; Chotard, M.-P.; Verdon, E. Stability study for 53 antibiotics in solution and in fortified biological matrixes by LC/MS/MS. *J. AOAC Int.* **2013**, *96*, 471−480.
(26) AOAC International. *Appendix K: Guidelines for Dietary Supplements and Botanicals*; Rockville, MD, USA, 2012; pp 1−32
(27) Ministry of Health, Labour and Welfare, Japan. *The Guidelines of Method Validation for Pesticide Residues in Food*; 2007; Direction Notification Syoku-An No. 1115001.
(28) Tsai, I.-L.; Sun, H.-Y.; Chen, G.-Y.; Lin, S.-W.; Kuo, C.-H. Simultaneous quantification of antimicrobial agents for multidrug-resistant bacterial infections in human plasma by ultra-high-pressure liquid chromatography-tandem mass spectrometry. *Talanta* **2013**, *116*, 593−603.
(29) Lehotay, S. J.; Stajnbaher, D.; Schenck, F. J.; Anastassiades, M. Fast and easy multiresidue method employing acetonitrile extraction/partitioning and "dispersive solid-phase extraction" for the determination of pesticide residues in produce. *J. AOAC Int.* **2003**, *86*, 412−431.
(30) Junza, A.; Barbosa, S.; Codony, M. R.; Jubert, A.; Barbosa, J.; Barrón, D. Identification of metabolites and thermal transformation products of quinolones in raw cow's milk by liquid chromatography coupled to high-resolution mass spectrometry. *J. Agric. Food Chem.* **2014**, *62*, 2008−2021.
(31) Feng, S.; Chiesa, O. A.; Kijak, P.; Chattopadhaya, C.; Lancaster, V.; Smith, E. A.; Girard, L.; Sklenka, S.; Li, H. Determination of ceftiofur metabolite desfuroylceftiofur cysteine disulfide in bovine tissues using liquid chromatography-tandem mass spectrometry as a surrogate marker residue for ceftiofur. *J. Agric. Food Chem.* **2014**, *62*, 5011−5019.
(32) Van Royen, G.; Dubruel, P.; Daeseleire, E. Development and evaluation of a molecularly imprinted polymer for the detection and cleanup of benzylpenicillin in milk. *J. Agric. Food Chem.* **2014**, *62*, 8814−8821.
(33) Taguchi, S.; Yoshida, S.; Tanaka, Y.; Hori, S. Simple and rapid analysis of trenbolone and zeranol residues in cattle muscle and liver by stack-cartridge solid-phase extraction and HPLC using on-line clean-up with EC and UV detection. *J. Food Hyg. Soc. Jpn.* **2001**, *42*, 226−230.

DOI: 10.1021/acs.jafc.5b00170
J. Agric. Food Chem. 2015, 63, 5133−5140

JOURNAL OF AGRICULTURAL AND FOOD CHEMISTRY

Article

pubs.acs.org/JAFC

Antibiotic Residue Monitoring Results for Pork, Chicken, and Beef Samples in Vietnam in 2012−2013

Takahiro Yamaguchi,[†] Masahiro Okihashi,[†] Kazuo Harada,*[,‡] Yoshimasa Konishi,[†] Kotaro Uchida,[†] Mai Hoang Ngoc Do,[§] Huong Dang Thien Bui,[§] Thinh Duc Nguyen,[§] Phuc Do Nguyen,[§] Vien Van Chau,[#] Khanh Thi Van Dao,[#] Hue Thi Ngoc Nguyen,[#] Keiji Kajimura,[†] Yuko Kumeda,[†] Chien Trong Bui,[#] Mai Quang Vien,[#] Ninh Hoang Le,[§] Kazumasa Hirata,[‡,⊥] and Yoshimasa Yamamoto[†,⊥]

[†]Osaka Prefectural Institute of Public Health, 1-3-69 Nakamichi, Higashinari-ku, Osaka 537-0025, Japan

[‡]Graduate School of Pharmaceutical Sciences, Osaka University, 1-6 Yamadaoka, Suita, Osaka 565-0871, Japan

[§]Institute of Public Health, 159 Hung Phu, District 8, Ward 8, Ho Chi Minh City, Vietnam

[#]Pasteur Institute, 8-10 Pasteur Xuong Huan Ward, Nha Trang City, Vietnam

[⊥]Global Collaboration Center, Osaka University, 1-6 Yamadaoka, Suita, Osaka 565-0871, Japan

ABSTRACT: A monitoring plan of residual antibiotics in food of animal origin was conducted in Vietnam from 2012 to 2013. Meat samples were collected from slaughterhouses and retail stores in Ho Chi Minh City and Nha Trang. A total of 28 antibiotics were analyzed using a LC-MS/MS screening method. Sulfonamides, fluoroquinolones, and tilmicosin were detected in some of the samples. Sulfaclozine and fluoroquinolones were mainly detected in chicken samples, and sulfamethazine was mainly detected in pork samples. High levels of sulfonamide residues, ranging between 2500 and 2700 μg/kg sulfaclozine and between 1300 and 3600 μg/kg sulfamethazine, were present in two chicken and three pork samples, respectively. Tilmicosin was detected at ranges of 150−450 μg/kg in 10 chicken samples. Positive percentages were 17.3, 8.8, and 7.4% for chicken, pork, and beef, respectively, for an average of 11.9%. The results suggest an appropriate withdrawal period after drug administration had not been observed in some livestock.

KEYWORDS: *residual antibiotics, Vietnam, food, liquid chromatography−tandem mass spectrometry*

INTRODUCTION

Antibiotics have been widely used in the treatment and prevention of infectious diseases to maintain and improve quality in livestock and fisheries.[1,2] Advanced nations and national organizations set limits, using risk-based assessments,[3,4] for residual levels of veterinary drugs so that consumers are not exposed to unacceptable levels of residues in foods of animal origin. The European Union (EU) establishes maximum residue limits (MRLs) for antibiotics in food, and the use of these compounds as feed additives for growth promotion is banned.[5] Production of livestock and fisheries is increasing with rapid population growth in developing countries. It is suggested that the management of antibiotics is insufficient in advancing countries.

Vietnam's economic influence in Asia is emerging as its GDP growth has exceeded 5% over the past 25 years.[6] There are nearly 90 million inhabitants, and it is the world's 13th most populated country.[6] The production quantity of indigenous meats (pork, beef, and chicken) increased by 90% from 2002 to 2012.[7] Pork is the main meat food in Vietnam: in 2012, it accounted for about 80% of the production quantity. There is a complex farming style in Vietnam, the so-called "VAC (Vuon, Ao, Chuong = field, pond, stockyard) system" that consists of agriculture, aqua farming, and stockbreeding.[8] In this system, each byproduct of one farming method is used for the other farming methods, such as for feed or fertilizer. This style has promoted many small stockbreeding farms, and it is difficult to regulate the use of antibiotics on the many small farms.

Resistant bacteria carriers are rapidly increasing in Asia,[9,10] particularly in Vietnam, where there are higher carriage ratios compared with other countries. Currently, 42% of the population carry drug-resistant bacteria, which leads to growing concerns over further diffusion.[11] The threat of resistant bacteria has been caused by the abuse of antibiotics in medicines and in stockbreeding and aqua farming.[12−14] Residual antibiotics in food and the spread of resistant bacteria are a cause for concern in human health and the environment.[15,16] Therefore, we investigated residual antibiotics in meats at Ho Chi Minh City (HCM) and Nha Trang (NT). All samples were transferred to the Institute of Public Health, Ho Chi Minh City, for analysis using a liquid chromatography−tandem mass spectrometry (LC-MS/MS) method. We discuss the risk to human health from residual antibiotics in meat from Vietnam.

MATERIALS AND METHODS

Chemicals. Sulfachlorpyridazine, sulfaclozine (sulfachlorpyrazine), sulfadimethoxine, sulfamerazine, sulfamethazine (sulfadimidine), sulfa-

Special Issue: 51st North American Chemical Residue Workshop

Received: October 31, 2014
Revised: January 12, 2015
Accepted: January 20, 2015
Published: January 20, 2015

ACS Publications © 2015 American Chemical Society

DOI: 10.1021/jf505254y
J. Agric. Food Chem. 2015, 63, 5141−5145

Table 1. Retention Times (RT) and MS/MS Parameters

compound	RT (min)	precursor ion (m/z)	product ion (m/z)[a]	DP (V)	CE (V)	CXP (V)
ampicillin[b]	4.7	350	106	51	30	15
			160	51	17	15
aspoxicillin[b]	4.2	494	250	40	20	15
			349	40	20	15
ciprofloxacin[c]	4.9	332	314	46	25	6
			231	46	49	4
danofloxacin[c]	5.0	358	283	56	35	4
			82	56	61	4
difloxacin[c]	5.4	400	356	44	25	4
			299	44	34	4
enrofloxacin[c]	5.1	360	316	44	24	4
			245	44	37	4
marbofloxacin[c]	4.7	363	72	41	43	4
			345	41	25	6
norfloxacin[c]	4.8	320	302	46	25	6
			276	46	21	4
ofloxacin[c]	4.8	362	318	36	23	4
			261	36	36	4
orbifloxacin[c]	5.2	396	352	41	25	4
			295	41	32	4
oxacillin[b]	9.0	402	243	51	19	15
			160	51	21	15
penicillin G[b]	8.2	335	176	61	17	15
			160	61	17	15
penicillin V[b]	8.7	351	160	65	17	15
			114	65	47	15
sarafloxacin[c]	5.4	386	299	52	35	4
			342	52	25	4
spiramycin[d]	5.3	422	174	40	27	15
			101	40	69	15
sulfachlorpyridazine[e]	6.8	285	156	21	19	4
			92	21	39	4
sulfaclozine[e]	7.6	285	92	21	39	4
			156	21	19	4
sulfadimethoxine[e]	7.7	311	156	41	23	4
			92	41	43	4
sulfadoxine[e]	7.0	311	156	41	23	4
			92	41	43	4
sulfamethazine[e]	6.2	279	186	64	24	15
			156	64	44	15
sulfamerazine[e]	5.7	265	108	41	33	4
			92	41	41	4
sulfamethoxazole[e]	7.0	254	156	36	21	4
			92	36	37	4
sulfamethoxypyridazine[e]	6.2	281	156	41	23	4
			92	41	39	4
sulfamonomethoxine[e]	6.6	281	156	46	23	4
			92	46	43	4
sulfapyridine[e]	5.5	250	156	41	21	4
			92	41	37	4
tilmicosin[d]	5.8	435	88	100	47	4
			174	100	47	14
trimethoprim	4.7	291	230	61	31	14
			261	61	33	4
tylosin[d]	6.7	917	174	90	54	15
			83	90	111	15

[a]Upper, quantification ion; lower, identification ion. [b]β-Lactam. [c]Quinolone. [d]Macrolide. [e]Sulfonamide.

doxine, sulfamethoxazole, sulfamethoxypyridazine, sulfamonomethoxine, sulfapyridine, ciprofloxacin, danofloxacin, difloxacin, enrofloxacin, marbofloxacin, norfloxacin, ofloxacin, orbifloxacin, sarafloxacin (Dr. Ehrenstorfer GmbH, Augsburg, Germany), aspoxicillin, ampicillin,

DOI: 10.1021/jf505254y
J. Agric. Food Chem. 2015, 63, 5141−5145

Table 2. Detected Compounds and Percentages at Sampling Sites

		HCM					MRL (μg/kg)	
type	compound	store	slaughterhouse	total	NT	total	EU	Japan
chicken	sulfaclozine	15.6%[a]	12.5%	13.9%	0%	6.4%	100	–[d]
	sulfamonomethoxine	0%	0%	0%	1.2%	0.6%	100	100
	enrofloxacin	3.1%	5.0%	4.2%	1.2%	2.6%	100	50
	difloxacin	3.1%	0%	1.4%	0%	0.6%	300	–[d]
	norfloxacin	0%	0%	0%	3.6%	1.9%	–[d]	20
	tilmicosin	0%	12.5%	6.9%	6.0%	6.4%	75	70
	sub total	7/32[b]	10/40	17/72	10/84	27/156		
		21.9%	25.0%	23.6%	11.9%	17.3%		
pork	sulfamethazine	17.9%	6.7%	14.0%	3.5%	8.8%	100	100
	sub total	10/56	2/30	12/86	3/85	15/171		
		17.9%	6.7%	14.0%	3.5%	8.8%		
beef	sulfamethazine	10.5%	0%	5.9%	–[c]	5.9%	100	100
	difloxacin	5.3%	0%	2.9%	–[c]	2.9%	400	–[d]
	sub total	5/38	0/30	5/68	–[c]	5/68		
		13.2%	0%	7.4%	–[c]	7.4%		
all	total	22/126	12/100	34/226	13/169	47/395		
		17.5%	12.0%	15.0%	7.7%	11.9%		

[a]Detected percentage. [b]Positive/sample number. [c]No data available. [d]No MRL.

oxacillin, penicillin G, penicillin V, spiramycin, tilmicosin, trimethoprim, and tylosin were purchased from Fluka (St. Louis, MO, USA). A dispersive solid-phase extraction (SPE) BONDESIL-C18 (C18) was purchased from Agilent Technologies. (Santa Clara, CA, USA). High-performance liquid chromatography (HPLC) grade acetonitrile was purchased from Scharlau (Barcelona, Spain), and formic acid was from J. T. Baker (Avantor Performance Materials, Center Valley, PA, USA). Membrane filter (PTFE, 3 mm ⌀, 0.2 μm) was obtained from Agilent.

Ultrapure water was made using an EASY pure II system (Thermo Fisher Scientific Inc., Waltham, MA, USA).

Samples. About 50 g–1 kg of samples was obtained from slaughterhouses and retail stores in HCM from October 2012 to December 2013 and a central market of NT, which contained about 400 small shops including over 50 butchers in July 2013. A total of 68 beef samples consisting of 65 meat and 3 internal organs (heart, nerve, stomach), 171 pork samples consisting of 160 meat and 11 liver, and 156 chicken samples consisting of 148 meat and 8 liver were analyzed. Samples were minced, mixed, and stored in polypropylene bags at −20 °C until analysis.

Stock Standard Solutions. Individual stock standard solutions (200 μg/mL) of sulfonamides, fluoroquinolones, and macrolide antibiotics and trimethoprim were prepared in methanol using polypropylene volumetric flasks and stored in the freezer at −20 °C until use. The same concentration of β-lactam antibiotics was prepared using distilled water and stored in the refrigerator at 4 °C for no more than 2 weeks.

Sample Preparation. Samples were prepared according to our method for LC-MS/MS[33] and previous analytical reports.[17,18] A 2 g aliquot of each sample was weighed in a 50 mL polypropylene tube before 10 mL of an acetonitrile/water (4:1) solution was added and homogenized for 30 s at high- speed (20000 rpm) using a blender (PT1300 D, Kinematica AG, Luzern, Switzerland) at room temperature. The sample was centrifuged (Universal 320R, Hettich GmbH & Co. KG, Tuttlingen, Germany) at 1500*g* for 5 min, and the supernatant was poured into a 15 mL polypropylene tube containing 0.3 g of dispersive C18. The supernatant was shaken for 1 min and centrifuged at 1500*g* for 5 min. A 1 mL aliquot was taken and diluted with 1 mL of distilled water. The extract was then filtered through a PTFE membrane filter. This final extract corresponded to a 0.1 g/mL sample equivalent.

Instruments and Analytical Methods. LC-MS/MS analysis was performed using a Prominence UFLC (Shimadzu, Kyoto, Japan) interfaced with an API-5500QTRAP (AB SCIEX, Framingham, CA, USA). The antibiotics were separated in Luna C18 columns (100 × 3 mm i.d., 2.5 μm) (Phenomenex, Torrance, CA, USA) with Alltima HP C18 precolumns (5 × 4.6 mm i.d., 5 μm, Thermo Fisher Scientific Inc.), using a binary gradient system (solvent A, 0.1% formic acid in water; solvent B, acetonitrile), at a flow rate of 0.4 mL/min. Analytes were quantified by multiple reaction monitoring (MRM) using positive electrospray ionization mode. Column temperature was maintained at 40 °C, and the sample injection volume was 5 μL. The antibiotic analytes were resolved using a gradient program, as follows: 5% solvent B at 0.2 mL/min increased to 95% over 10 min and maintained at 95% solvent B for 8 min. Details of the ions monitored are presented in Table 1. LOQs were confirmed to be >10 times the signal-to-noise ratio for the peak intensity of each compound at 10 μg/kg except tilmicosin, which was confirmed to be 10 times more signal-to-noise at 100 μg/kg. The instrument was calibrated every 3 months, and a blank meat sample and six fortified samples were analyzed with every batch of analysis.

RESULTS AND DISCUSSION

Residual antibiotics were detected with an average of 11.9% in the samples analyzed, particularly 17.3, 8.8, and 7.4% in chicken, pork, and beef, respectively (Table 2). Sulfaclozine was detected in chicken samples from HCM but not NT and was not detected in beef or pork samples from either city. Sulfamethazine, enrofloxacin, and tilmicosin were detected in samples from both cities, but difloxacin and norfloxacin were found only in one particular region, suggesting an isolated use of these antibiotics.

In the case of chicken, detected percentages (number of detects/total number of samples analyzed) ranged from 11.9 to 25.0% from each site. The detected percentage of sulfaclozine was comparable between retail stores and slaughterhouses in HCM, and nearly a fourth of chicken samples contained antibiotics. Tilmicosin was detected in 10 samples, 5 each from HCM and NT. Three types of fluoroquinolones were detected in chicken, and its detected percentages were <5%. Only sulfamethazine was detected in pork, and its detected percentages ranged from 3.5 to 17.9% for each site. Samples from HCM stores showed approximately 3 times higher residual

DOI: 10.1021/jf505254y
J. Agric. Food Chem. 2015, 63, 5141–5145

antibiotic percentages compared with samples from slaughterhouses. NT samples had lower residual antibiotic percentages compared with HCM samples. In the case of beef, detected percentages were 0% (slaughterhouse) and 13.2% (stores). In Vietnam, consumption of beef is lower than chicken and pork, and it is not a major import. Beef samples from slaughterhouses contained no antibiotics because they were imported from Australia as live cattle. Some of the samples from stores contained low levels of residual antibiotics, and it was thought that they were domestic.

The concentration of detected antibiotics and their MRLs for the EU and Japan are summarized in Figure 1. Sulfaclozine,

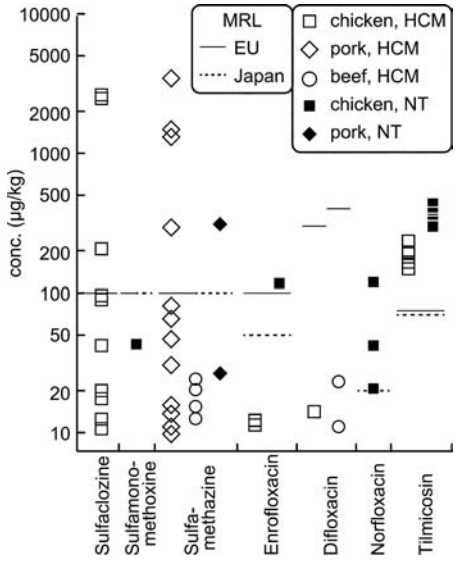

Figure 1. Concentrations of detected antibiotics and their maximum residue limits (MRL) in EU and Japan. Solid and broken lines represent MRLs established by EU and Japan, respectively, and their vertical levels correspond to legislated concentrations.

sulfamonomethoxine, enrofloxacin, norfloxacin, and tilmicosin were detected in chicken, sulfamethazine was detected in pork and beef, and difloxacin was detected in chicken and beef. Although there are no MRLs for these detected antibiotics in each food in Vietnam, 17 chicken samples and 5 pork samples would be illegal if they were found in the EU or Japan.

Chicken samples from HCM were collected on five separate occasions. In March 2013, high amounts of sulfaclozine were detected in 5 of 10 samples, ranging from 93 to 2710 μg/kg. On other occasions, lesser amounts of sulfaclozine were detected in samples collected, ranging from 11 to 44 μg/kg. Sulfamethazine was frequently found in pork samples, especially from HCM. Pork samples were collected seven times from HCM. In August 2013, samples from slaughterhouses and retail stores showed very high amounts of sulfamethazine, ranging from 1350 to 3560 μg/kg. Two samples from HCM and NT also showed high amounts of sulfamethazine, around 300 μg/kg.

We revealed that residues of two sulfonamides were present in meat at high concentrations and high frequency. Sulfaclozine was developed as an antibiotic for poultry coccidiosis and specific bacterial diseases in 1967.[19] Since the first report of sulfamethazine's synthesis in 1941, it has been used in the treatment of bacterial pneumonia, cervical abscesses, and bacterial swine enteritis.[20,21] In addition, sulfamethazine has been detected in water in the Mekong Delta area,[22] suggesting sulfamethazine is a popular antibiotic for Vietnamese farmers. According to reports studying residue depletion, residual levels of sulfaclozine in chicken and turkey were <100 μg/kg after 14 and 21 days, respectively, when a dose of 50 mg/kg body weight/day had been administered orally for 3 days.[23,24] Residual levels of sulfamethazine in pork were <100 μg/kg after 8 days, when a dose of 110 mg/kg feed had been administered orally for 3 days.[25] It is suspected that some farmers do not pay attention to residual antibiotic levels or that there is a lack of understanding about the required withdrawal period after antibiotics have been administered. Sulfaclozine, enrofloxacin, and tilmicosin were also found in a report of chicken jerky dog treats that were imported to the United States from China.[26] It is suggested that these antibiotics are commonly used in Vietnam and China.

The detected percentages of antibiotics in this study were higher than the results presented in the 2008−2012 Osaka, Japan, report, which revealed an 0.8% (1/1183) level,[27] and the 2012 EU monitoring program showing positive sample percentages of 0.13% (60/46905), 0.20% (61/25240), and 0.12% (23/18412) in pork, beef, and poultry, respectively.[28]

Antibiotics are available for use in livestock without prescription, and imported products sometimes lack instructions in local languages. The publicity for careful use of antibiotics is also insufficient in most developing countries.[29] In Vietnam, widespread resistant bacteria may have arisen from abuse of antibiotics during animal husbandry.[30] Coexistence of enteric bacteria in the intestinal tracts of animals and humans facilitates the transfer of antibiotic-resistant genes between commensal and pathogenic bacterial species.[31,32] In this study, residual antibiotics were frequently detected in chicken and pork, and some samples showed high amounts. Pork and chicken are often eaten in Vietnam, suggesting inhabitants will consume low levels of antibiotics, which may increase the occurrence of resistant bacteria. This presents a challenge to reduce exposure and control the use of antibiotics because most agriculture in Vietnam is contributed by small, family farms. We recommend better education and greater regulation of the farmers in Vietnam.

AUTHOR INFORMATION

Corresponding Author

*(K. Harada) Phone: +81-6-6879-8235. Fax: +81-6-6879-8154. E-mail: harada6@phs.osaka-u.ac.jp.

Funding

This work was supported by the Japan Science and Technology Agency (JST)/Japan International Cooperation Agency (JICA) as part of the Science and Technology Research Partnership for Sustainable Development (SATREPS).

Notes

The authors declare no competing financial interest.

ACKNOWLEDGMENTS

We thank Gaijiro Ando for secretarial assistance and Bui Thi Mai Huong, Le Hong Dung, and Dr. Masashi Kanki for their helpful discussions.

REFERENCES

(1) Dibner, J. J.; Richards, J. D. Antibiotic growth promoters in agriculture: history and mode of action. *Poult. Sci.* **2005**, *84*, 634−643.
(2) Castanon, J. I. R. History of the use of antibiotic as growth promoters in European poultry feeds. *Poult. Sci.* **2007**, *86*, 2466−2471.
(3) Council Regulation (EEC) No. 2377/90 laying down a Community procedure for the establishment of maximum residue

DOI: 10.1021/jf505254y
J. Agric. Food Chem. 2015, 63, 5141−5145

limits of veterinary medicinal products in foodstuffs of animal origin. *Off. J. Eur. Communities* **1990**, *L.224*/1−8.
(4) Tollefson, L.; Miller, M. A. Antibiotic use in food animals: controlling the human health impact. *J. AOAC Int.* **2000**, *83*, 245−254.
(5) Conuncil Directive 96/23/EC on measures to monitor certain substances and residues thereof in live animals and animal products and repealing Directives 85/358/EEC and 86/469/EEC and Decisions 89/187/EEC and 91/664/EEC. *Off. J. Eur. Communities* **1996**, *L 125*/10−32.
(6) International Monetary Fund. Vietanam and the IMF; http://www.imf.org/external/country/VNM/index.htm (accessed Oct 21, 2014).
(7) Food and Agriculture Organizaiton of the United Nations. Country Profiles of Vietnam; http://faostat.fao.org/site/339/default.aspx (accessed Sept 16, 2014).
(8) Vu, T. K. V.; Tran, M. T.; Dang, T. T. S. A survey of manure management on pig farms in northern Vietnam. *Livest. Sci.* **2007**, *112*, 288−297.
(9) Hawkey, P. M. Prevalence and clonality of extended-spectrum β-lactamases in Asia. *Clin. Microbiol. Infect.* **2008**, *14*, 159−165.
(10) Thai, T. H.; Yamaguchi, R. Molecular characterization of antibiotic-resistant Salmonella isolates from retail meat from markets in northern Vietnam. *J. Food Prot.* **2012**, *75*, 1709−1714.
(11) Le, T. M. V.; Baker, S.; Le, T. P. T.; Le, T. P. T.; Thuy, C. T.; Nga, T. T. T.; Van Minh Hoang, N.; Campbell, J. I.; Yen, L. M.; Hieu, N. T.; Van Vinh Chau, N.; Farrar, J.; Schultsz, C. High prevalence of plasmid-mediated quinolone resistance determinants in commensal members of the Enterobacteriaceae in Ho Chi Minh City, Vietnam. *J. Med. Microbiol.* **2009**, *58*, 1585−1592.
(12) Serratosa, J.; Blass, A.; Rigau, B.; Mongrell, B.; Rigau, T.; Tortadès, M.; Tolosa, E.; Aguilar, C.; Ribó, O.; Balagué, J. Residues from veterinary medicinal products, growth promoters and performance enhancers in food-producing animals: a European Union perspective. *Rev. Sci. Technol. Off. Int. Epiz.* **2006**, *25*, 637−653.
(13) Van den Bogaard, A. E.; Stobberingh, E. E. Epidemiology of resistance to antibiotics. links between animals and humans. *Int. J. Antimicrob. Agents* **2000**, *14*, 327−335.
(14) Tenhagen, B.-A.; Vossenkuhl, B.; Käsbohrer, A.; Alt, K.; Kraushaar, B.; Guerra, B.; Schroeter, A.; Fetsch, A. Methicillin-resistant *Staphylococcus aureus* in cattle food chains − prevalence, diversity, and antimicrobial resistance in Germany. *J. Anim. Sci.* **2014**, *92*, 2741−2751.
(15) Gullberg, E.; Cao, S.; Berg, O. G.; Ilbäck, C.; Sandegren, L.; Hughes, D.; Andersson, D. I. Selection of resistant bacteria at very low antibiotic concentrations. *PLoS Pathog.* **2011**, *7*, No. e1002158.
(16) Jiang, L.; Hu, X.; Xu, T.; Zhang, H.; Sheng, D.; Yin, D. Prevalence of antibiotic resistance genes and their relationship with antibiotics in the Huangpu River and the drinking water sources, Shanghai, China. *Sci. Total Environ.* **2013**, *458*−*460*, 267−272.
(17) Yamaguchi, T.; Kakimoto, K.; Nagayoshi, H.; Yamaguchi, M.; Okihashi, M.; Kajimura, K.; Yamamoto, Y. Simultaneous determination of veterinary drugs in livestock products using dispersive and cartridge column solid-phase extraction by LC-MS/MS. *J. Food Hyg. Soc. Jpn.* **2013**, *54*, 290−297.
(18) Lehotay, S. J.; Lightfield, A. R.; Geis-Asteggiante, L.; Schneider, M. J.; Dutko, T.; Ng, C.; Bluhm, L.; Mastovska, K. Development and validation of a streamlined method designed to detect residues of 62 veterinary drugs in bovine kidney using ultra-high performance liquid chromatography−tandem mass spectrometry. *Drug Test Anal.* **2012**, *4* (Suppl. 1), 75−90.
(19) Matsuzawa, T.; Kitano, N. Studies on the mode of action of sulfachloropyrazine against Coccidia in chickens. *Jpn. Poult. Sci.* **1974**, *11*, 75−85.
(20) Caldwell, W. T.; Kornfeld, E. C.; Donnell, C. K. Substituted 2-sulfanilamidopyrimidines. *J. Am. Chem. Soc.* **1941**, *63*, 2188−2190.
(21) Buur, J.; Baynes, R.; Smith, G.; Riviere, J. Use of probabilistic modeling within a physiologically based pharmacokinetic model to predict sulfamethazine residue withdrawal times in edible tissues in swine. *Antimicrob. Agents Chemother.* **2006**, *50*, 2344−2351.
(22) Managaki, S.; Murata, A.; Takada, H.; Tuyen, B. C.; Chiem, N. H. Distribution of macrolides, sulfonamides, and trimethoprim in tropical waters: ubiquitous occurrence of veterinary antibiotics in the Mekong Delta. *Environ. Sci. Technol.* **2007**, *41*, 8004−8010.
(23) Łebkowska-Wieruszewska, B.; Kowalski, C. J. Residue depletion of sulfachlorpyrazine in edible tissues of broiler chickens. *Food Addit. Contam. Part A* **2013**, *30*, 272−277.
(24) Łebkowska-Wieruszewska, B. I.; Kowalski, C. J. Sulfachlorpyrazine residues depletion in turkey edible tissues. *J. Vet. Pharmacol. Ther.* **2010**, *33*, 389−395.
(25) Korsrud, G. O.; Papich, M. G.; Fesser, A. C.; Salisbury, C. D.; MacNeil, J. D. Residue depletion in tissues and fluids from swine fed sulfamethazine, chlortetracycline and penicillin G in combination. *Food Addit. Contam.* **1996**, *13*, 287−292.
(26) Sheridan, R.; Mirabile, J.; Hafler, K. Determination of six illegal antibiotics in chicken jerky dog treats. *J. Agric. Food Chem.* **2014**, *62*, 3690−3696.
(27) Osaka Prefectural Institute of Public Health, Japan. Osaka Prefectural Institute of Public Health annual report; http://www.iph.pref.osaka.jp/report/report.html#nenpo (accessed Oct 21, 2014).
(28) Council of the European Union. Commission Staff Working Document on the Implementation of National Residue Monitoring Plans in the Member States in 2012 (Council Directive 96/23/EC).
(29) Duong, V. N.; Paulsen, P.; Suriyasathaporn, W.; Smulders, F. J. M.; Kyule, M. N.; Baumann, M. P. O.; Zessin, K. H.; Pham, H. N. Preliminary analysis of tetracycline residues in marketed pork in Hanoi, Vietnam. *Ann. N. Y. Acad. Sci.* **2006**, *1081*, 534−542.
(30) Thai, T. H.; Hirai, T.; Lan, N. T.; Yamaguchi, R. Antibiotic resistance profiles of *Salmonella* serovars isolated from retail pork and chicken meat in North Vietnam. *Int. J. Food Microbiol.* **2012**, *156*, 147−151.
(31) White, D. G.; Zhao, S.; Simjee, S.; Wagner, D. D.; McDermott, P. F. Antimicrobial resistance of foodborne pathogens. *Microbes Infect.* **2002**, *4*, 405−412.
(32) Aarestrup, F. M.; Wegener, H. C.; Collignon, P. Resistance in bacteria of the food chain: epidemiology and control strategies. *Expert Rev. Anti-Infect Ther.* **2008**, *6*, 733−750.
(33) Yamaguchi, T.; Okihashi, M.; Harada, K.; Uchida, K.; Konishi, Y.; Kajimura, K.; Hirata, K.; Yamamoto, Y. Rapid and easy multiresidue method for analysis of antibiotics in meats by ultrahigh-performance liquid chromatography-tandem mass spectrometry. *J. Agric. Food Chem.* **2015**, submitted for publication.

DOI: 10.1021/jf505254y
J. Agric. Food Chem. 2015, 63, 5141−5145

JOURNAL OF AGRICULTURAL AND FOOD CHEMISTRY

Article

pubs.acs.org/JAFC

Method for the Detection of Desmethylbromethalin in Animal Tissue Samples for the Determination of Bromethalin Exposure

Michael S. Filigenzi,* Adrienne C. Bautista, Linda S. Aston, and Robert H. Poppenga

California Animal Health and Food Safety Laboratory System, Toxicology Laboratory, University of California, Davis, California 95616, United States

ABSTRACT: Bromethalin, a potent neurotoxin, is widely available for use as a rodenticide. As access to other rodenticides is reduced due to regulatory pressure, the use of bromethalin is likely to increase with a concomitant increase in poisonings in nontarget animals. Analytical methods for the detection of bromethalin residues in animals suspected to have been exposed to this rodenticide are needed to support post-mortem diagnosis of toxicosis. This paper describes a novel method for the analysis of desmethylbromethalin (DMB), bromethalin's toxic metabolite, in tissue samples such as liver, brain, and adipose. Samples were extracted with 5% ethanol in ethyl acetate, and an aliquot of the extract was evaporated dry, reconstituted, and analyzed by reverse phase ultrahigh-performance liquid chromatography–mass spectrometry. The mass spectrometer utilized electrospray ionization in negative ion mode with multiple reaction monitoring. This method was qualitatively validated at a level of 1.0 ng/g in liver tissue. The quantitative potential of the method was also evaluated, and a method detection limit of 0.35 ng/g wet weight was determined in fat tissue. DMB was detected in tissue samples from animals suspected to have been poisoned by this compound. To the authors' knowledge, there have been no other methods reported for analysis of DMB in tissue samples using LC-MS/MS.

KEYWORDS: *bromethalin, desmethylbromethalin, electrospray, LC-MS/MS, poisoning*

INTRODUCTION

Bromethalin (Figure 1a) is a substituted diphenylamine used for rodent control. It is widely available to the general public in a variety of formulations. Bromethalin was developed from an analogue that was originally considered for use as a fungicide, but which was determined to be overly toxic for that purpose. Desmethylbromethalin (DMB; Figure 1b) was determined to be an effective rodenticide; however, low palatability in wild rats required the addition of a methyl group to eliminate an acidic proton.[1] This resulted in the commercial product that is used currently.[2]

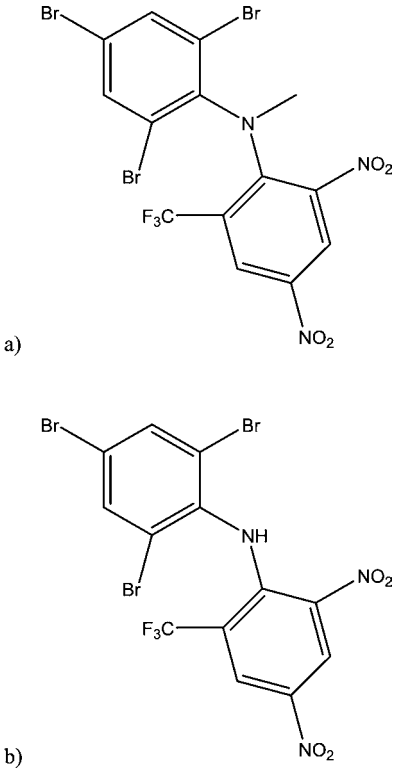

Figure 1. Structures of (a) bromethalin and (b) DMB.

Commercially available as 0.01% bait pellets, bars, and place packs, the rodenticide bromethalin selectively targets the nervous system. Following ingestion, bromethalin is metabolized by the liver to DMB, the active metabolite. Desmethylbromethalin uncouples mitochondrial oxidative phosphorylation leading to decreased cellular adenosine triphosphate production and disruption of sodium–potassium ATPase pumps.[3] With decreased activity of the ATPase pumps, the central nervous system (CNS) no longer maintains a normal sodium–potassium gradient, leading to fluid buildup inside the CNS and subsequently the development of cerebral edema and increased cerebrospinal fluid pressures.

Clinical signs of intoxication, including muscle tremors, hyperthermia, hyperexcitability, and focal or generalized seizures, which have been observed in rodents, cats, dogs, monkeys, and other wildlife such as raccoons, usually develop within 24 h after ingestion of bromethalin at or above the median lethal dose.[2,3] At concentrations below the median

Special Issue: 51st North American Chemical Residue Workshop

Received: October 31, 2014
Revised: January 20, 2015
Accepted: February 17, 2015
Published: February 17, 2015

ACS Publications © 2015 American Chemical Society

DOI: 10.1021/jf5052706
J. Agric. Food Chem. 2015, 63, 5146–5151

lethal dose, lethargy, hind limb weakness, and/or paralysis can develop several days after exposure.[4]

Documented oral median lethal doses range from as low as 1.8 mg/kg in the cat to as high as 13 mg/kg in the rabbit with dogs and monkeys falling in between at around 5 mg/kg.[2] Bromethalin poisonings have been documented in nontarget animals[5−7] and in one fatality in a human.[8]

Recently, the U.S. EPA has canceled the registrations of a number of second-generation anticoagulant rodenticide formulations.[9] There are relatively few alternative commercially available rodenticides, and it is highly likely that bromethalin use will increase along with the attendant nontarget poisonings. Therefore, a reliable method of determination of bromethalin and/or its metabolites in tissue samples is critical for confirmation of bromethalin exposure and toxicosis postmortem. The distribution and accumulation of bromethalin and DMB in adipose tissue are expected on the basis of their octanol−water partition coefficients (log P values) of 6.70 and 4.26, respectively. Consequently, adipose tissue may serve as the best diagnostic sample[7] and could easily be harvested ante- or post-mortem.

Bromethalin rapidly metabolizes to DMB.[2] Thus, the ability to detect DMB would serve as confirmation of exposure to the neurotoxic rodenticide bromethalin. This is particularly important in cases in which there is no history of exposure to the rodenticide.

MATERIALS AND METHODS

HPLC grade methanol, water, acetonitrile, ethyl acetate, and formic acid were obtained from Fisher Scientific (Pittsburgh, PA, USA). Anhydrous USP grade ethanol (Koptec brand) was obtained from VWR (Radnor, PA, USA).

Analytical Standards. Bromethalin (99.3%) was obtained from the U.S. Environmental Protection Agency National Pesticide Standard Repository (Fort Meade, MD, USA). DMB (98%) was obtained from Toronto Research Chemicals (Toronto, ON, Canada).

Control Matrices. Fresh control bovine adipose tissue was obtained from animals submitted to the California Animal Health and Food Safety Laboratory for necropsy. Fresh control liver tissue was purchased from a local market. Control samples were tested to ensure that no detectable DMB was present and were stored at −20 °C.

Extraction of DMB from Tissue. One gram of tissue (adipose or liver) was weighed into a 250 mL French square homogenization jar. Fifty milliliters of 5% ethanol in ethyl acetate was added, and the sample was homogenized using an Ultra-Turrax homogenizer (IKA Works, Inc., Wilmington, NC, USA). The homogenate was centrifuged for 5 min at 52g, and a 5 mL aliquot of the extract was transferred to a clean 15 mL glass tube. The solution was dried under nitrogen using an N-Evap nitrogen evaporator (Organomation, Berlin, MA, USA). The dried extract was reconstituted in 200 μL of methanol and filtered through a 0.45 μm Millex-HV PVDF syringe filter (Millipore, Billerica, MA, USA) into a 2 mL autosampler vial.

Instrument Calibration Standards. Five-point calibration curves for quantification of DMB in adipose tissue samples were prepared by fortifying control bovine adipose tissue and extracting per the method listed above. Calibrators were prepared at levels of 1.0, 5.0, 10, 25, and 50 ng/g.

Quality Control Samples. Each batch of 3−12 diagnostic samples included an appropriate negative control tissue sample and a positive control sample consisting of negative control tissue fortified at a level of 1 ng/g DMB. Fortified samples were prepared by adding an appropriate level of standard solution in methanol to the negative control matrix and allowing it to equilibrate for at least 15 min prior to extraction. Each batch of validation samples included an appropriate negative control tissue sample.

LC-MS/MS Analysis. A model 1290 high-performance liquid chromatograph coupled to a model 6460 triple-stage quadrupole mass spectrometer equipped with a Jetstream electrospray interface (Agilent Corp., Santa Clara, CA, USA) was used for all reported analyses. The chromatograph was fitted with a 100 mm × 2.1 mm i.d., 1.7 μm, Zorbax Eclipse Plus C 18 column fitted with an Eclipse Plus guard column (Agilent Corp.). The mobile phases consisted of 0.1% aqueous formic acid (channel A) and 0.1% formic acid in acetonitrile (channel B). The flow rate was 0.350 mL/min throughout. Gradient elution was used beginning at 20% B, which was held for 1 min and then ramped to 95% B over 8 min. It was held at 95% B for 4 min and then returned to the initial conditions and held for 4 min for re-equilibration. The column was maintained at 35 °C. DMB eluted at approximately 8.5 min under these conditions. Chromatographic flow was diverted to waste for the first 2 min and after 15 min. The injection volume was 10 μL. For diode array detection, an Agilent model 1290 diode array detector was placed in line between the HPLC column and the mass spectrometer. The detector was set to acquire the UV spectrum in the range of 190−400 nm. Agilent's Masshunter software was used for all data acquisition and processing.

The mass spectrometer was tuned and calibrated in negative ion mode using its automated tuning procedure and the provided tuning solution (Agilent Corp.), a proprietary mixture of substituted phosphazines and triazines. DMB was monitored by multiple reaction monitoring (MRM) using a precursor ion of m/z 562 and product ions of m/z 278 and 254. Fragmentation voltage was 135 V, and cell accelerating voltage was 7 V. Collision energies were 25 eV for the m/z 562 → 278 transition and 35 eV for the m/z 562 → 254 transition. Other ion source parameters were as follows: drying gas temperature, 350 °C; drying gas flow, 10 L/min; nebulizer pressure, 45 psi; sheath gas temperature, 300 °C; sheath gas flow, 11 L/min; capillary, 4500 V.

Infusions of bromethalin and DMB were performed by connecting a syringe pump inline with the HPLC, directly ahead of the MS ion source. Separate standards for the two compounds at 1 μg/mL were infused into the MS at 20 μL/min.

Each analytical sequence for qualitative screening began and ended with a 1 ng/mL standard of DMB in methanol. Each sequence for quantitative analysis for method validation began and ended with a five-point calibration curve extracted from fortified negative control matrix.

A sample was considered positive when a peak was detected at a signal-to-noise ratio >3 within 5% of the retention time established for DMB with the ratio of response between the two product ions being within ±15% of that determined by analysis of the standard. These identification criteria are consistent with those defined in the European Commission Health and Consumer Protection Directorate-General guidance document for analytical quality control and validation procedures for pesticides in food and feed (SANCO/12571/2013).[10]

Full Scan LC-MS Analysis. A model 1200 Rapid Resolution HPLC system coupled with an Exactive high-resolution accurate mass spectrometer (Thermo Corp.) was used for full scan LC-MS analysis. The column and HPLC conditions were similar to those used for LC-MS/MS analysis. The mass spectrometer was run in negative ion mode with electrospray ionization. Mass calibration and instrument tuning for negative ion mode were performed <24 h prior to sample analysis. The instrument was tuned and calibrated using the solution provided by the manufacturer, which included sodium dodecyl sulfate, sodium taurocholate, and Ultramark 1621. Spray voltage was 3000 V, capillary temperature was 250 °C, and sheath gas and auxiliary gas were set at 50 and 10, respectively (arbitrary units). Mass resolution was set at 100,000, and the AGC target was 1×10^6.

Method Validation. The method was validated using criteria for qualitative screening methods established in the SANCO/12571/2013 document. Twenty samples each of homogenized liver and homogenized brain tissue were fortified with 1 ng/g of DMB (the screening detection limit) and analyzed. The method was also evaluated by analyzing six replicate control adipose tissue samples fortified at each level of 1.0, 5.0, and 50 ng/g and quantifying the detected DMB against the calibration curve determined by analysis of the extracted calibrators.

DOI: 10.1021/jf5052706
J. Agric. Food Chem. 2015, 63, 5146−5151

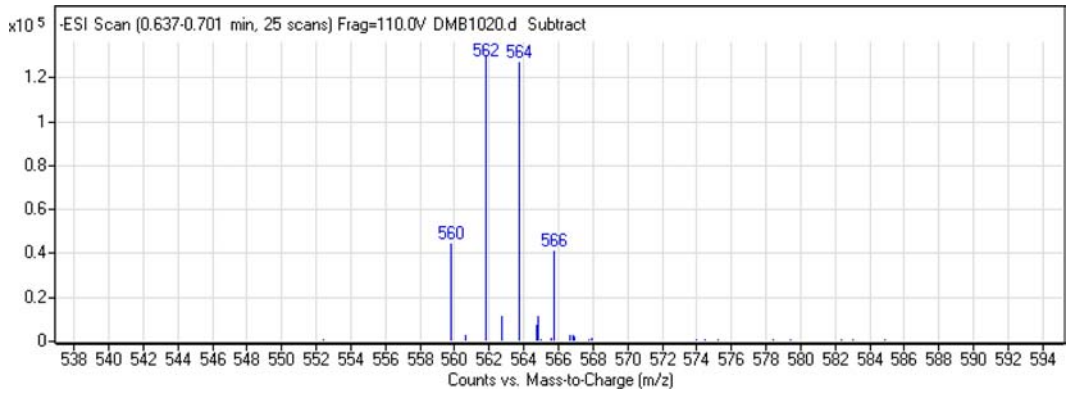

Figure 2. Negative ion electrospray mass spectrum obtained via infusion of a 10 μg/mL standard solution of DMB.

RESULTS AND DISCUSSION

Few methods for the analysis of bromethalin and/or DMB in tissue samples have been reported. These methods have included thin layer chromatography,[11] gas chromatography with electron capture detection,[8] and gas chromatography with negative ion chemical ionization.[8] High-pressure liquid chromatography with diode array and atmospheric pressure chemical ionization mass spectrometry (HPLC-negative ion-APCI-MS)[12] was used for the identification of bromethalin in rodenticide bait formulations. The authors reported that bromethalin gave a broad and intense UV absorbance band between 300 and 415 nm. They also reported that negative ion-APCI-MS did not yield pseudomolecular ions but instead showed extensive fragmentation with a variety of isotopic clusters related to molecular species such as $[M - Br]^-$, $[M - HBr]^-$, and $[M - HBr - NO_2]^-$.

Infusion of a DMB standard solution gave a predominant ion cluster consisting of nominal m/z 560, 562, 564, and 566 in ratios consistent with those expected from its $[M - H]^-$ ions (Figure 2) in negative ion mode. No identifiable signal was detected using positive ion mode. Product ions at m/z 278 and 254 from fragmentation of the precursor at m/z 562 were chosen for MRM acquisition. Analysis by HPLC-MS/MS showed high sensitivity and adequate retention on the reverse phase column.

For qualitative screening method validation, 20 replicate samples of homogenized liver tissue were fortified with DMB at a level of 1 ng/g (the screening detection limit). DMB met detection criteria in all 20 samples, demonstrating that it may be detected reliably at that level. The primary goal of this work was to develop a method suitable for support of post-mortem diagnosis of bromethalin intoxication. Accordingly, it is usually performed on a qualitative, "presence/absence" basis. To provide further support for the screening detection limit and evaluation of the method's quantitative potential, we performed a quantitative method evaluation in fat tissue. Figures of merit for the fat validation data are shown in Table 1. A quadratic model best fit the calibration curve giving a correlation coefficient (r^2) of 0.996. The method detection limit, calculated using Student's t value for five degrees of freedom and the 99% confidence level was determined to be 0.35 ng/g, supporting the 1 ng/g screening detection limit used for qualitative validation. These data indicate that this method is likely to be useful for researchers interested in quantitative analysis for DMB. Figure 3 shows extracted ion chromatograms for a single injection of an extract from an adipose tissue sample fortified with 1 ng/g of DMB. The validation results for fat and liver indicate that this method will provide relevant detection limits for analysis of a variety of tissue types.

Table 1. Figures of Merit for the Quantitative Method Validation

spike level (ppb; n = 6)	mean % recovery	% relative standard deviation
1.0	110	11
5.0	110	15
50	105	24

This method has been used successfully to establish bromethalin exposure in several animals suspected of suffering fatal bromethalin poisoning.[7] Figure 4 shows chromatograms from a single analysis of fat tissue taken from a fox. This animal had displayed signs of severe neurological impairment and was initially suspected of having suffered head trauma. No history of bromethalin exposure or use of the rodenticide in the area inhabited by the animal was noted on the submission form. Upon necropsy, there was no indication of head trauma and the samples taken from the animal were negative for canine distemper and rabies. Results of DMB analysis, along with other case information including clinical signs consistent with bromethalin toxicosis, were considered sufficient to diagnose bromethalin poisoning in this animal. The response of detectable DMB in samples from affected animals has ranged from slightly below that of the associated 1 ng/g spiked negative control sample to approximately 200 times that of the associated spike.

It should be noted that the original goal of this project was the development of an analytical procedure to detect bromethalin rather than the demethylated form, DMB. When a standard of bromethalin was infused into the mass spectrometer, the ions detected were inconsistent with those expected from the $[M - H]^-$ ions for bromethalin (m/z 574, 576, 578, and 580). Instead, the dominant signals were consistent with the cluster of brominated ions at m/z 560, 562, 564, etc., expected for DMB, albeit with poor sensitivity. Initially, it was difficult to determine whether the dominant ion cluster was due to DMB in the standard (as a contaminant or a breakdown product of bromethalin) or to demethylation of bromethalin in the ion source as there was no DMB standard available at the time. LC-MS/MS conditions were developed on the basis of MS/MS of the ions at m/z 562 and 564 from the bromethalin standard, and analysis of liver and fat from some animals suspected of exposure to bromethalin gave positive results. When a DMB standard became available and

DOI: 10.1021/jf5052706
J. Agric. Food Chem. 2015, 63, 5146−5151

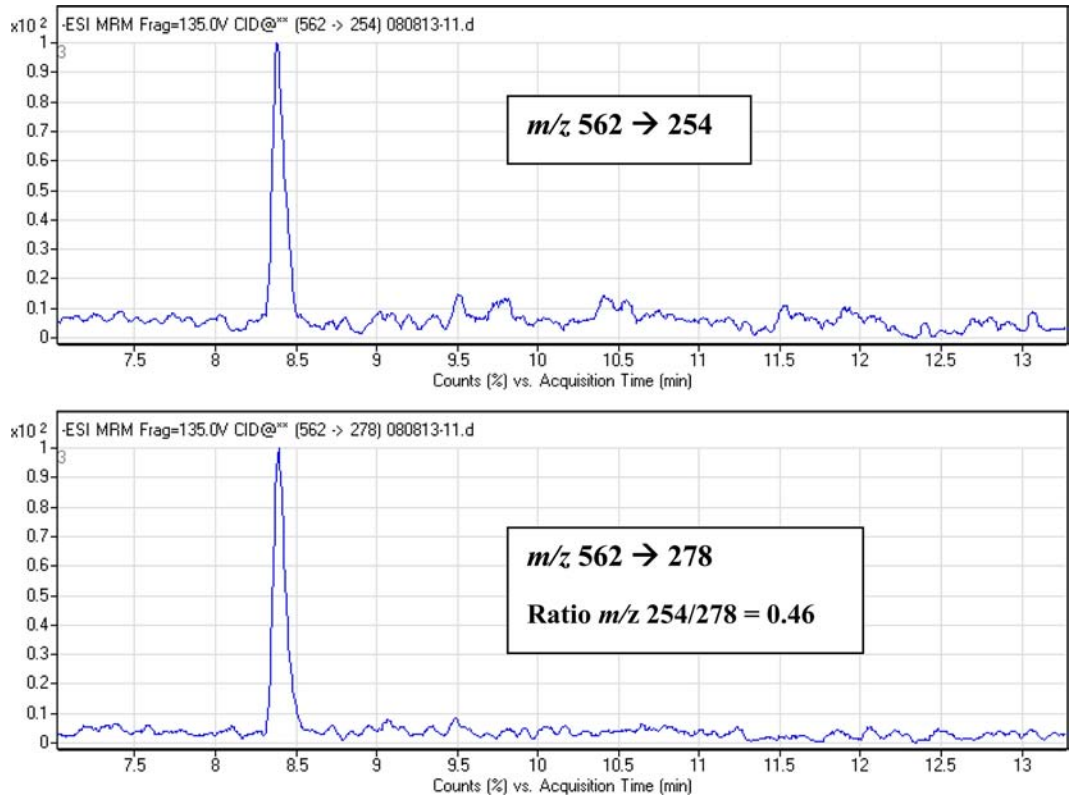

Figure 3. MRM chromatograms from a single analysis of adipose tissue spiked with 1 ng/g DMB.

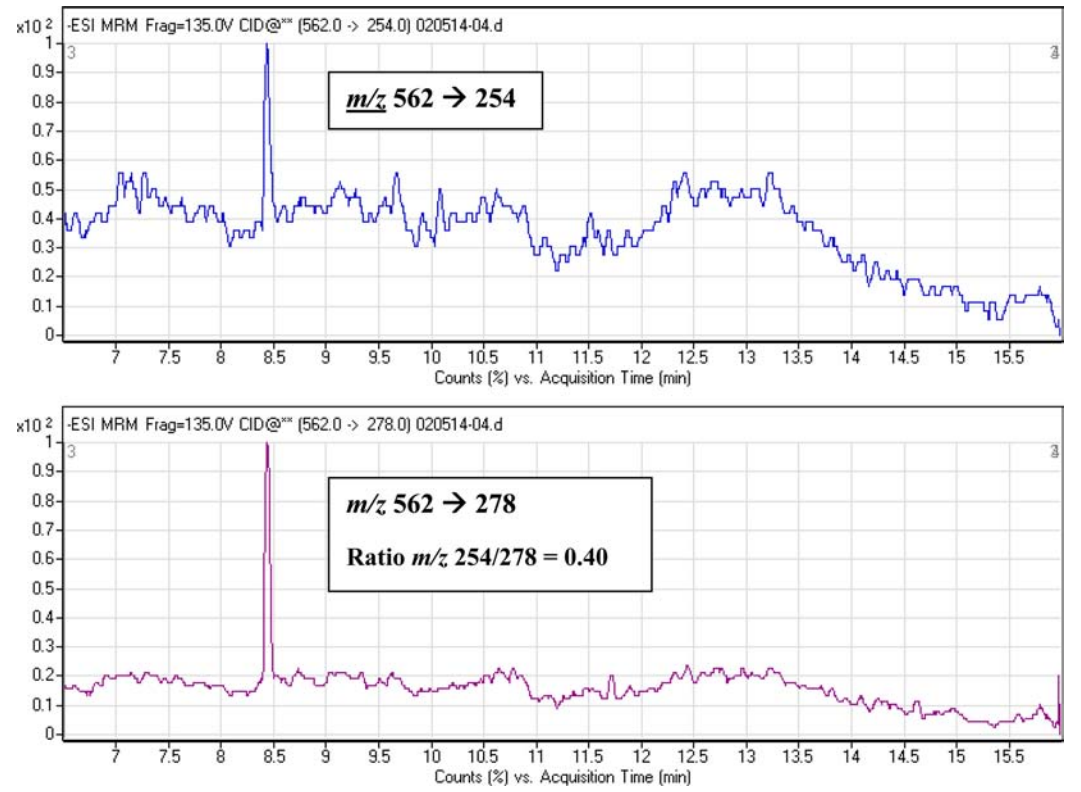

Figure 4. MRM chromatograms from a single analysis of adipose tissue taken from a fox suspected of having been intoxicated by bromethalin.

was analyzed using LC-MS/MS, it was determined that the retention time and ions measured for DMB were identical to those from the bromethalin standard. This raised questions as to the reliability of the bromethalin standard material or the ability to detect bromethalin itself by electrospray LC-MS. To resolve these issues, a highly concentrated bromethalin standard (1000 μg/mL) was analyzed on a system in which a diode array detector was placed ahead of the mass spectrometer

DOI: 10.1021/jf5052706
J. Agric. Food Chem. 2015, 63, 5146−5151

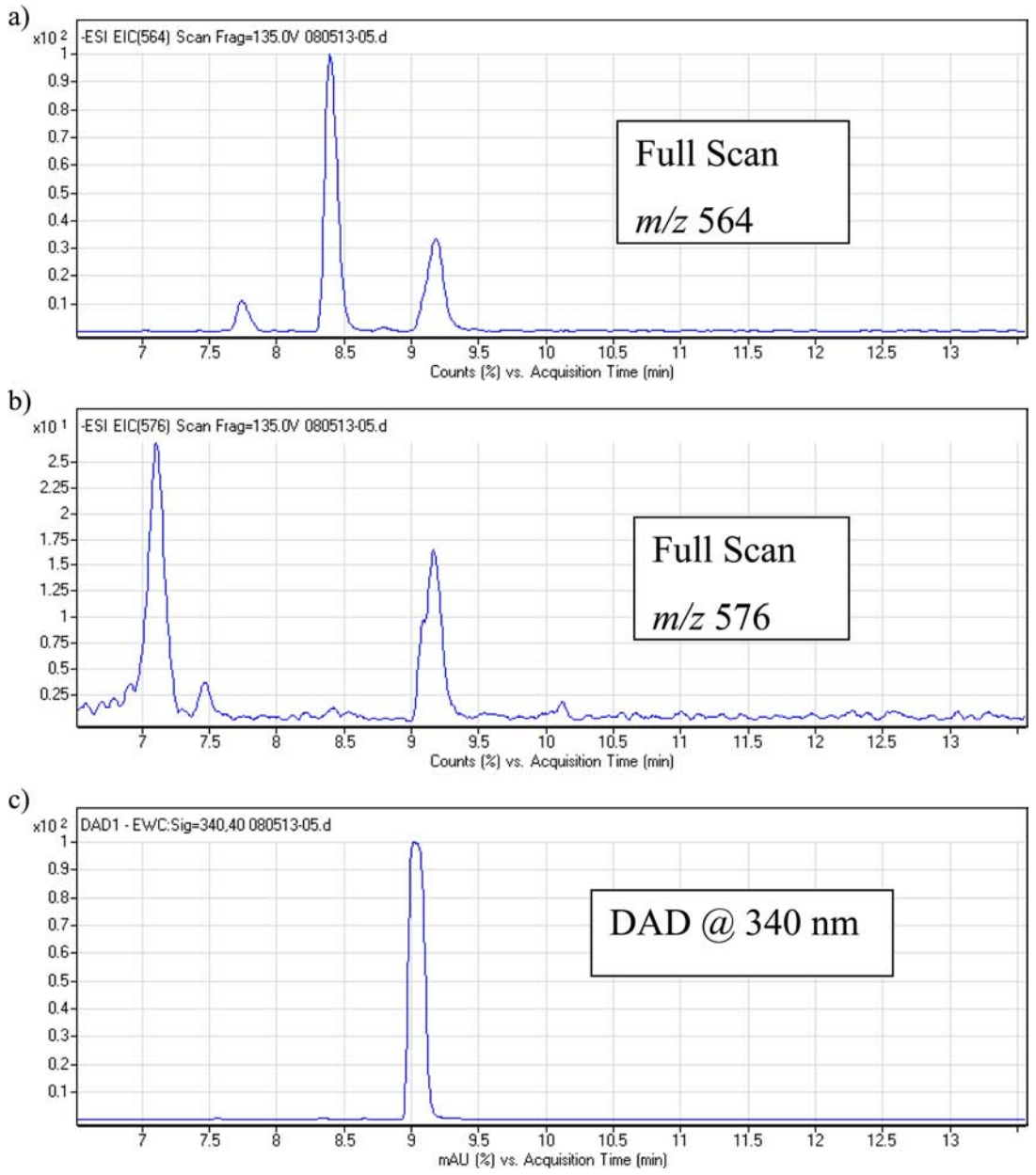

Figure 5. Chromatograms from diode array and MS analysis of a 1 mg/mL bromethalin standard: (a, b) selected ion chromatograms; (c) selected wavelength chromatogram from the diode array detector.

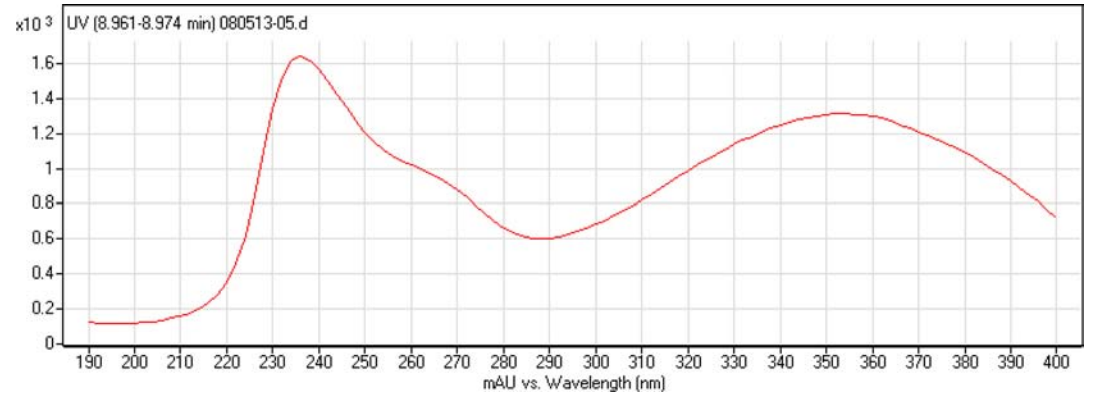

Figure 6. Diode array spectrum of bromethalin.

DOI: 10.1021/jf5052706
J. Agric. Food Chem. 2015, 63, 5146−5151

set to full scan Q1MS mode, with no MS/MS fragmentation. Chromatograms from this analysis are shown in Figure 5. The dominant signal on the MS system was that of DMB at m/z 564 (Figure 5a), corresponding to <0.1% of the bromethalin concentration in the standard based on comparison to a 10 μg/mL DMB standard. This indicated that the detected DMB was likely a low-level impurity present in the bromethalin standard. The diode array detector showed a very intense, saturated peak eluting shortly after DMB (Figure 5c). The UV spectrum of this peak (Figure 6) matched the UV spectrum of bromethalin, which was previously described as "a strong broad absorption band extending from 300 to 415 nm in the mobile phase"[12] and also was nearly identical to the UV spectrum obtained via analysis of DMB under the same conditions (data not shown). No other significant peaks were noted in the UV analysis. This analysis provides compelling evidence that the standard material provided was intact bromethalin. The fact that no other significant peaks were detected by LC-UV despite the saturation in the bromethalin peak indicates that the purity of the bromethalin standard was ≥99%, as reported in the associated certificate of analysis. There were detectable signals in the MS chromatograms for both m/z 564 (DMB, Figure 5a) and m/z 574 (intact bromethalin, Figure 5b) coeluting with bromethalin on the UV detector. These signals may be representative of bromethalin detection by LC-MS/MS, but, if so, they are extremely weak given the concentration of bromethalin injected and indicate that sensitivity using these MS/MS transitions would be well below that necessary for detection in tissue samples. The 1000 μg/mL standard was also analyzed using full scan mode on an Exactive high-resolution LC-MS system in an attempt to determine whether ionization of bromethalin produced ions with m/z ratios other than those from the $[M - H]^-$ ions from bromethalin or those produced by DMB. These systems provide highly sensitive analysis using full scan high-resolution accurate mass analysis of a wide mass range. A 1000 μg/mL concentration would be expected to produce a strong signal for any compound that responds well by this method, but no significant peaks were detected in the range of m/z 100−600 as determined by plotting the total ion chromatogram (TIC) for that range. Analysis of a 100 ng/mL standard of DMB gave a peak that was clearly detectable (S:N > 3) when plotting the TIC from the m/z 100−600 mass range. This finding is in agreement with the detection of bromethalin by APCI because the retention times for diode array and APCI-MS detected coincided. On the basis of the differences between infusion data from our work and that of Mesmer and Flurer, it appears that bromethalin responds differently to the APCI and electrospray ionization processes.

In summary, injection of a 1000 μg/mL bromethalin standard gave a strong response by LC-UV but a barely detectable corresponding response by LC-MS/MS for its $[M - H]^-$ and $[M - CH_3 - H]^-$ ions. Injection of a 1.0 ng/mL standard of DMB consistently gave a peak with >3:1 S:N under the same conditions. A 1000 μg/mL bromethalin standard gave no detectable peak in the TIC of a full scan LC-MS analysis, whereas a 100 ng/mL DMB standard was clearly detectable under those conditions. Together, these results indicate that bromethalin responds very poorly by electrospray LC-MS and that this technique is not suitable for its low-level detection in tissue samples and that diagnostic analysis of tissue samples using electrospray LC-MS should rely on DMB analysis.

To our knowledge, this is the first detailed report of an LC-MS/MS method for the analysis of DMB. The method is fast, efficient, and sufficiently sensitive to detect low, clinically relevant levels of DMB in complex tissue samples and allows for accurate post-mortem diagnosis of bromethalin exposure and intoxication.

AUTHOR INFORMATION

Corresponding Author

*(M.S.F.) Phone: (530) 754-5608. Fax: (530) 752-3361. E-mail: msfiligenzi@ucdavis.edu.

Notes

The authors declare no competing financial interest.

ACKNOWLEDGMENTS

We thank Elizabeth Tor and Dr. Birgit Puschner for their invaluable assistance in reviewing the data and in preparing the manuscript. We also thank Paul Zavitsanos, Steve Royce, and Dr. Jerry Zweigenbaum from Agilent Corp. for their kind assistance in obtaining and operating the LC-MS system used for this work.

REFERENCES

(1) Dreikorn, B. A.; Odoherty, G. O. P. The discovery and development of bromethalin, an acute rodenticide with a unique mode of action. *ACS Symp. Ser.* **1984**, *No. 255*, 45−63.

(2) van Lier, R. B. L.; Cherry, L. D. The toxicity and mechanism of action of bromethalin: a new single-feeding rodenticide. *Fundam. Appl. Toxicol.* **1988**, *11* (4), 664−672.

(3) Dorman, D. C.; Parker, A. J.; Buck, W. B. Bromethalin toxicosis in the dog. Part I: clinical effects. *J. Am. Anim. Hospital Assoc.* **1990**, *26* (6), 589−594.

(4) Dorman, D. C. Bromethalin. In *Small Animal Toxicology*; Peterson, M. E., Talcott, P. A., Eds.; Elsevier: St. Louis, MO, USA, 2006; pp 609−618.

(5) Martin, T.; Johnson, B. A suspected case of bromethalin toxicity in a domestic cat. *Vet. Hum. Toxicol.* **1989**, *31* (3), 239−240.

(6) Gupta, R. C. Non-anticoagulant rodenticides. *Veterinary Toxicology: Basic and Clinical Principles*, 2nd ed.; Elsevier: Amsterdam, The Netherlands, 2012; pp 698−711.

(7) Bautista, A. C.; Woods, L. W.; Filigenzi, M. S.; Puschner, B. Bromethalin poisoning in a raccoon (*Procyon lotor*): diagnostic considerations and relevance to nontarget wildlife. *J. Vet. Diagnostic Invest.* **2014**, *26* (1), 154−157.

(8) Pasquale-Styles, M. A.; Sochaski, M. A.; Dorman, D. C.; Krell, W. S.; Shah, A. K.; Schmidt, C. J. Fatal bromethalin poisoning. *J. Forensic Sci.* **2006**, *51* (5), 1154−1157.

(9) U.S. EPA. *Canceling Some d-CON Mouse and Rat Control Products*; http://www2.epa.gov/rodenticides/canceling-some-d-con-mouse-and-rat-control-products (accessed July 16, 2014).

(10) European Commission Health and Consumer Protection Directorate. *Method Validation and Quality Control Procedures for Pesticide Residues Analysis in Food and Feed*, 2013.

(11) Braselton, W. E.; Johnson, M. Thin layer chromatography convulsant screen extended by gas chromatography-mass spectrometry. *J. Vet. Diagnostic Invest.* **2003**, *15* (1), 42−45.

(12) Mesmer, M. Z.; Flurer, R. A. Determination of bromethalin in commercial rodenticides found in consumer product samples by HPLC-UV-vis spectrophotometry and HPLC-negative-ion APCI-MS. *J. Chromatogr. Sci.* **2001**, *39* (2), 49−53.

DOI: 10.1021/jf5052706
J. Agric. Food Chem. 2015, 63, 5146−5151

JOURNAL OF AGRICULTURAL AND FOOD CHEMISTRY

Article

pubs.acs.org/JAFC

Determination of Neonicotinoid Insecticides and Strobilurin Fungicides in Particle Phase Atmospheric Samples by Liquid Chromatography−Tandem Mass Spectrometry

Renata Raina-Fulton*

Department of Chemistry and Biochemistry, University of Regina, 3737 Wascana Parkway, Regina, Saskatchewan S4S 0A2, Canada

Supporting Information

ABSTRACT: A liquid chromatography−tandem mass spectrometry method has been developed for the determination of neonicotinoids and strobilurin fungicides in the particle phase fraction of atmosphere samples. Filter samples were extracted with pressurized solvent extraction, followed by a cleanup step with solid phase extraction. Method detection limits for the seven neonicotinoid insecticides and six strobilurin fungicides were in the range of 1.0−4.0 pg/m^3. Samples were collected from June to September 2013 at two locations (Osoyoos and Oliver) in the southern Okanagan Valley Agricultural Region of British Columbia, where these insecticides and fungicides are recommended for use on tree fruit crops (apples, pears, cherries, peaches, apricots) and vineyards. This work represents the first detection of acetamiprid, imidacloprid, clothianidin, kresoxim-methyl, pyraclostrobin, and trifloxystrobin in particle phase atmospheric samples collected in the Okanagan Valley in Canada. The highest particle phase atmospheric concentrations were observed for imidacloprid, pyraclostrobin, and trifloxystrobin at 360.0, 655.6, and 1908.2 pg/m^3, respectively.

KEYWORDS: *neonicotinoid insecticides, strobilurin fungicides, atmospheric particle concentrations of pesticides*

INTRODUCTION

In this paper a new method for the simultaneous analysis of neonicotinoid insecticides and strobilurin fungicides in particles in the atmosphere was developed. Table 1 shows that these pesticides have low volatility such that particle transport in the atmosphere may play a role in their movement in the environment. Neither of these classes of pesticides has been previously detected in atmospheric samples (gas or particle phase) in North America, and a suitable method was required to be developed for their analysis in atmospheric samples capable of detection in the low picograms per cubic meter range. The range of volatility of these pesticides and similar solubility in organic solvents that are required to extract pesticides from solid matrices such as particles make development of a simultaneous method for both of these classes of pesticides feasible. Pressurized solvent extraction was used for their extraction as this approach is commonly used in our laboratory and others for the analysis of pesticides and other related contaminants in atmospheric samples.[1−4]

Neonicotinoids are a class of neuroactive insecticides that have high binding affinity to insect acetylcholine receptor.[5] Neonicotinoids registered for use in Canada include acetamiprid, clothianidin, imidacloprid, thiacloprid, and thiamethoxam (see Table 1).[6] They are commonly used on crops within Canada including corn, soybean, canola, sunflower, and a wide variety of fruit tree crops; some as well are used in commercial products such as flea collars for dogs and cats.[6,7] Strobilurin fungicides are a newer class of fungicides of the quinine outside inhibitors (Qol) group or act in a similar way to the natural strobilurin A, produced by the strobilurus tenacellus fungus.[8] This class includes azoxystrobin, fluoxastrobin, kresoxim-methyl, pyraclostrobin, and trifloxystrobin, which are also registered for use in Canada (see Table 1).[6]

In recent years, liquid chromatography−tandem mass spectrometry (LC-MS/MS) methods have been developed for the analysis of selected neonicotinoid insecticides with the number of applications of these methods increasing due to concerns of their harmful effects on honey bees and potential transport in the environment in surface waters due to their higher water solubilities.[7−12] Little attention has been given to studying the presence of neonicotinoids or strobilurin fungicides in the atmosphere. Due to the low volatility and high polarity of neonicotinoids, liquid chromatography is preferred over more complex GC methods. LC with the use of photodiode array or electrochemical detectors has also been used as well as capillary electrophoresis with mass spectrometry.[13−15] However, most recent methods of analysis of selected neonicotinoid insecticides have LC-MS/MS with electrospray ionization in positive ion mode (ESI+) and included their analysis in honey liqueur, bee pollen, fruits, and vegetation.[9,14,16−23] These sample matrices differ significantly from atmospheric samples.

LC-MS/MS methods for neonicotinoids have not included the simultaneous analysis of strobilurin fungicides, nor do the majority of the methods contain as complete a list of individual neonicotinoid insecticides as this study. Strobilurin fungicides can be analyzed by GC or LC methods. GC-MS for analysis of strobilurin fungicides has utilized selected ion monitoring (SIM) mode with electron impact ionization (EI), whereas only selected strobilurin fungicides have been included in multiresidue

Special Issue: 51st North American Chemical Residue Workshop

Received: November 17, 2014
Revised: May 8, 2015
Accepted: May 11, 2015
Published: May 11, 2015

ACS Publications © 2015 American Chemical Society

DOI: 10.1021/acs.jafc.5b01347
J. Agric. Food Chem. 2015, 63, 5152−5162

Table 1. Vapor Pressure, Water Solubility, and Canadian Registration Information for Neonicotinoid Insecticides and Strobilurin Fungicides[a]

compound	vapor pressure, Pa (temperature)	water solubility, g/L (temperature)	currently registered products in Canada (applications to Health Canada for new registration of products) with active ingredient[6]
		Neonicotinoid Insecticides	
dinotefuran	$<1.7 \times 10^{-6}$ (30 °C)	39.83 (20 °C)	0 (11)
nitenpyram	1×10^{-4} (50 °C)	600 (20 °C), pH 7	0 (0) Canadian Patent
thiamethoxam	2.7×10^{-9} (20 °C)	4.1 (25 °C)	25 (17)
	6.6×10^{-9} (25 °C)		
clothianidin	**1.3×10^{-10} (25 °C)**	**0.327 (20 °C)**	**15 (17)**
imidacloprid	**4×10^{-10} (20 °C)**	**0.61 (20 °C)**	**61 (26)**
acetamiprid	**1×10^{-6} (25 °C)**	**4.25 (25 °C)**	**5 (0)**
thiacloprid	8×10^{-10} (25 °C) (extrapolated)	0.185 (20 °C)	2 (0)
		Strobilurin Fungicides	
azoxystrobin	1×10^{-10} (20 °C)	0.0067 (20 °C)	22 (12)
dimoxystrobin	6.0×10^{-9} (25 °C)	0.0043 (20 °C)	0 (0) not listed
fluoxastrobin	5.63×10^{-10} (20 °C)	0.0023 (20 °C)	3 (3)
kresoxim-methyl	**2.3×10^{-6} (20 °C) (extrapolated)**	**0.00200 (20 °C)**	**3 (0)**
		free acid	
		0.091 (20 °C)	
pyraclostrobin	**2.6×10^{-8} (20 °C)**	**0.0019 (20 °C)**	**25 (4)**
trifloxystrobin	**4.5×10^{-4} (25 °C)**	**0.000610 (25 °C)**	**20 (7)**

[a]Boldfaced pesticides were detected in air samples collected from Okanagan Valley. Water solubility and vapor pressures were obtained from manufacturers' MSDS sheets.

LC-MS/MS methods or specific LC-MS/MS methods for individual fungicides.[24−28] Although many of the strobilurin fungicides can be analyzed by GC-MS with EI, confirmation of fungicide identity is limited[29] and atmospheric sample extracts are more prone to MS interference issues with EI as compared to negative chemical ionization GC-MS at low atmospheric concentrations.[30,31] LC-MS/MS methods also provide added confirmation ability with a four-point identification approach (two selected reaction monitoring (SRM) transitions) rather than monitoring of a single ion for each strobilurin fungicide in GC-MS. In addition, the use of LC-MS/MS allows for an opportunity to simultaneously analyze both strobilurin fungicides and neonicotinoids for atmospheric particles where sample extract volume available for chemical analysis is limited.

The sample preparation methods developed for use in LC-MS/MS methods for analysis of neonicotinoids are largely designed for water analysis rather than the solid matrices that are required for collection of atmospheric samples. Extraction of pesticides from these solid matrices used in air sampling has generally utilized pressurized solvent extraction with organic solvents rather than water prior to any cleanup steps such as solid-phase extraction (SPE).[1−4] Selected neonicotinoid insecticides or strobilurin fungicides in solid food product samples have also been extracted with pressurized solvent extraction, and particle phase atmospheric samples have been extracted with microwave-assisted extraction.[17,18,32,33] A variety of other chemical classes of pesticides (organochlorines, organophosphorus pesticides, and azole fungicides) have been extracted from solid matrices used in atmospheric sampling using pressurized solvent extraction.[1−4] Due to the high solubility of these insecticides and fungicides in organic solvents generally ethyl acetate, acetonitrile, or acetone are selected as the extraction solvent or for sample preparation.[14,17−20,24−28,32,33] It should be noted that it is extremely difficult to selectively extract specific chemical classes of pesticides in a specific organic solvent without loss of other target compounds, and thus multiple pressurized solvent extraction steps are generally not preferred. SPE methods are generally used to provide the cleanup of sample extracts (in organic solvents from pressurized solvent extraction) and often designed for specific chemical classes of pesticides due to the large range in polarities of pesticides and solubilities in different organic solvents. Atmospheric sample extract volume is limited with often only 1 mL of final extract available for SPE stages for all chemical classes of pesticides of interest.

Table 1 shows that the vapor pressures of neonicotinoid insecticides and strobilurin fungicides are generally $<10^{-5}$ Pa, and on the basis of the author's experience, if sufficient usage is present, there will be a greater potential for partition into the particle phase. The vapor pressures of these pesticides are also less than those of previously studied organophosphorus pesticides or some azole fungicides, and consequently the focus of the method development was on chemical analysis of the particle phase fraction of atmospheric samples. Sampling locations within the southern Okanagan Valley were selected as there was known current usage of these pesticides on tree fruits or grapes in the region (see Pesticide Usage Information in the Supporting Information). Strobilurin fungicides and neonicotinoid insecticides were targeted for the new method for their simultaneous analysis with pressurized solvent extraction of filters followed by an SPE cleanup stage prior to LC-ESI+/MS/MS. This new analytical method must be capable of detecting low picogram per cubic meter concentrations of pesticides in the atmosphere for future seasonal and annual trend analysis. These pesticide classes have not been previously detected in atmospheric samples in Canada, and this new method allows for the investigation of their occurrence in atmospheric particles at sampling locations in an agricultural region where these pesticides are recommended for use on fruit tree crops and in vineyards.

MATERIALS AND METHODS

Chemicals and Materials. Ethyl acetate, acetonitrile, and methanol were of pesticide grade and supplied by Fisher Scientific. Deionized water (<18 MΩcm resistivity) was from a Nanopure Diamond system (Barnstead International, Dubuque, IA, USA). Aqueous solvents were passed through a 0.45 μm membrane filter

DOI: 10.1021/acs.jafc.5b01347
J. Agric. Food Chem. 2015, 63, 5152−5162

Table 2. Retention Times, SRM Transitions, and Response Ratios for LC-ESI+/MS/MS Analysis of Neonicotinoid Insecticides and Strobilurin Fungicides

compound	MW (g/mol)	t_R (min) MP1 (MP2)	SRM1, SRM2 (optional SRM3 or SRM4)	cone, collision energies (eV)	response ratio SRM2/SRM1 (SRM3/SRM1 SRM4/SRM1) ± % RSD
Neonicotinoid Insecticides					
dinotefuran	202.21	2.53	203.1 → 157.2	15, 7	
			203.1 → 129.2	15, 13	1.19 ± 17.1
			203.1 → 113.0	15, 12	0.665 ± 9.96
nitenpyram	270.72	2.76	271.2 → 56.0	25, 30	
			271.2 → 99.0	25, 17	1.02 ± 10.9
			271.2 → 189.1	25, 10	0.425 ± 20.5
			271.2 → 225.7	25, 11	0.0154 ± 19.8
thiamethoxam	291.72	3.41	292.2 → 211.4	19, 12	
			292.2 → 132.0	19, 20	0.556 ± 22.8
			292.2 → 181.3	19, 27	0.408 ± 14.3
clothianidin	249.68	3.94	250.1 → 169.3	17, 13	
			250.1 → 132.0	17, 15	0.887 ± 6.72
imidacloprid	255.66	4.64	256.1 → 175	20, 15	
			256.1 → 209.5	20, 15	0.261 ± 11.0
acetamiprid	222.68	5.06	223.1 → 126.1	20, 20	
			223.1 → 56.0	20, 15	0.619 ± 14.7
			223.1 → 90.0	20, 30	0.160 ± 22.9
thiacloprid	252.72	7.23	253.1 → 126.0	25, 22	
			253.1 → 186.2	25, 20	0.0350 ± 32.6
Strobilurin Fungicides					
azoxystrobin	403.39	10.95	404.1 → 372.4	20, 13	
			404.1 → 329.4	20, 30	0.152 ± 19.1
dimoxystrobin	326.39	11.27	327.6 → 205.3	15, 10	
			327.6 → 238.5	15, 10	0.0554 ± 21.4
fluoxastrobin	458.83	12.89	459.2 → 427.4	25, 15	
			459.2 → 188.2	25, 30	0.457 ± 9.91
kresoxim-methyl	313.35	12.96	314.1 → 206.3	15, 7	
			314.1 → 116.0	15, 15	0.799 ± 12.3
			314.1 → 267.4	15, 5	0.672 ± 13.4
pyraclostrobin	387.82	14.32	388.1 → 163.5	20, 22	
			388.1 → 194.5	20, 11	0.573 ± 24.8
trifloxystrobin	408.37	15.75	409.1 → 186.4	20, 20	
			409.1 → 206.4	20, 20	0.433 ± 15.7
Deuterated Internal Standards					
imidacloprid-d_4 (IS)	259.66	4.59	260.1 → 213.1[a]	20, 14	
			260.1 → 179.1	20, 14	
diazinon-d_{10} (SURR)	314.35	13.14	315.1 → 170.0	30, 20	
			315.1 → 154.0	30, 22	0.739 ± 3.37
malathion-d_{10} (dilution check std)	340.36	12.51	341.0 → 132.1	20, 14	
			341.0 → 100.0	20, 25	0.524 ± 1.90

[a]SRM transition used for determination of response ratio (area standard/area internal standard).

from Nucleopore (Whatman, Florham Park, NJ, USA). Formic acid (>88.0%) and ammonium acetate (>97.0% purity) were obtained from VWR Scientific (West Chester, PA, USA). Solids or stock solutions at 100 μg/mL in acetonitrile or methanol of strobilurin fungicides (azoxystrobin, dimoxystrobin, fluoxastrobin, kresoxim-methyl, pyraclostrobin, and trifloxystrobin) and neonicotinoid insecticides (acetamiprid, clothianidin, dinotefuran, imidacloprid, nitenpyram, thiamethoxam, and thiacloprid) were supplied by Chem Service Inc. (West Chester, PA, USA). Solid imidacloprid-d_4, diazinon-d_{10}, and malathion-d_{10} were purchased from C/D/N Isotopes Inc. (Pointe-Claire, QC, Canada).

Pesticide Standards. Deuterated internal standard (diazinon-d_{10}) had previously been used as a surrogate standard for other chemical classes in our laboratory[1] and was found to behave with similar retention characteristics as the pesticides under study on C18 SPE sorbent tubes and was used to evaluate recoveries. Diazinon-d_{10} also provides excellent sensitivity with both LC-MS/MS and GC-MS methods and thus can be used as a multiclass surrogate compound. No deuterated strobilurin fungicides were commercially available. The only commercially available deuterated neonicitinoid insecticide at the time of this study was imidacloprid-d_4, which was used as the internal standard for LC-MS/MS analysis. Malathion-d_{10} can also be used as an internal standard and was used to determine the final volume of the dried fraction F1 from the SPE cleanup after the addition of internal standard from the SPE stage, which was ∼1.0 mL.

Solids of individual pesticides (∼1 mg) were dissolved in 1 mL of methanol with further dilution to prepare individual stock solutions at 1.00×10^5 ng/mL in methanol and stored at −4 °C. Suitable calibration standards were prepared by dilution of a standard mixture at 1000 ng/mL and internal standard (IS) with pesticide grade methanol with a final concentration of the internal standard, imidacloprid-d_4, at 20 ng/mL in all standards and samples. All final diluted standards and samples were prepared on the day of analysis. The calibration range

DOI: 10.1021/acs.jafc.5b01347
J. Agric. Food Chem. 2015, 63, 5152−5162

typically examined was MDL−100 ng/mL with lowest standard prepared at 0.5 ng/mL.

Sample Collection and Preparation of Air Extracts. Air samples were collected in the southern Okanagan Valley agricultural region at two field sites (BC Ministry of Environment/Canada Customs Border station in Osoyoos, British Columbia (BC), Canada; and Environment Canada Water Quality Site near Oliver, BC, Canada). The distance between the Osoyoos and Oliver field sites is ∼20 km. Air samples were collected using a polyurethane foam (PUF) high-volume air sampler (Tisch Environmental, Cleves, OH, USA) operated continuously at a flow rate of 225 L/min. The start dates for the samples collected for this study at Osoyoos were June 28, 2013; July 29, 2013; August 6, 2013; August 9, 2013, and August 20, 2013. The last sampling period end date was September 3, 2013. At the Oliver site sampling start dates were the same except no sample was available for the August 6 or 9, 2013, sampling period due to instrument issues. Average duration of samples collected at the Osoyoos sampling location was 13.2 days. Due to restrictions on the use of the sampler at night due to noise concerns from the motor of the air sampler to nearby public homes adjacent to the customs station, the air sampler at Osoyoos was operated continuously from the hours of 7 a.m. to 9 p.m. local time (no operation overnight) with counter time reported for the duration the sample motor was operated. At the Oliver site the air sampler was operated continuously (24 h daily throughout the sampling period).

The sampling module contained the PUF/sorbent cartridge (for gas phase) and a glass fiber filter (for particle fraction) as previously described.[1] The sampling head is equipped with a PM10 cyclone with levels of PM10 (particles <10 μm in diameter) determined from gravimetric analysis of the filters ranging from 13.1×10^6 to 22.8×10^6 pg/m^3 and from 15.3×10^6 to 22.4×10^6 pg/m^3 at Osoyoos and Oliver, respectively. There was a weak relationship of PM10 levels and temperature over the agricultural season; however, for this period under investigation the average temperature during the sampling period ranged from 21.3 to 26.0 °C. Precipitation amounts were low at both sites with rainfall amounts <3 mm.

Particle phase air concentrations of neonicotinoid insecticides and strobilurin fungicides were determined for samples collected between June 28, 2013, and September 3, 2013, at Osoyoos and Oliver and are presented under Results and Discussion.

Extraction and Cleanup. The glass fiber filters were transferred after sampling into 30 mL extraction cells and extracted with ethyl acetate using an ASE100 pressurized solvent extraction system (Dionex, Sunnyvale, CA, USA). Used were the following extraction procedures: temperature, 100 °C; static mode time, 30 min at 1500 psi; two static cycles; 60% flush volume; purge time with nitrogen (UHP) at the end of 600 s. The total extraction volume was approximately 1.5 times the cell volume. A second extraction step with acetonitrile using the same pressurized solvent extraction procedure was performed on the filter samples.

After extraction, samples were dried to ∼5−10 mL, transferred to 15 mL vials, and dried to near dryness. This extract was stored at −4 °C until sample cleanup. The dried extract was redissolved to 1 mL with the addition of 100 μL of 1000 ng/mL diazinon-d_{10} and 900 μL of methanol prior to SPE cleanup. C18 SPE tubes (6 mL, 1000 mg, Canadian Life Science, Peterborough, ON, Canada) were conditioned with 6 mL of methanol and 6 mL of water. Sample extract (250 μL) was loaded onto the preconditioned tubes with 750 μL of water. This was eluted into an F0 fraction. Further rinses of 20:80 v/v% methanol/water were also eluted into the F0 fraction for a total volume of 2 mL. The eluted solvent collected into fraction F0 was observed to contain no insecticides or fungicides of interest. The neonicotinoid insecticides and strobilurin fungicides were eluted with 5 mL of 100% methanol in the next fraction (F1), and the Versiprep drying attachment (Supelco) was used to evaporate and concentrate eluted extracts from SPE (and from ASE) to ∼0.95−1.00 at 0.5 mL/h. To determine the volume of this F1 fraction 10 μL of 1000 ng/mL malathion-d_{10} was added. Internal standard imidacloprid-d_4 (1000 ng/mL) was also added at 20 μL to the these fractions prior to LC-MS/MS analysis such that total volume was ∼1 mL. Surrogate recoveries evaluated with diazinon-d_{10} were 82−105% within batch recoveries of ±10%. A second fraction (F2) was eluted from the SPE tubes with an additional 5 mL of 100% methanol after fraction F1 and showed no presence of pesticides. Particle phase concentrations were determined from the amount of pesticides determined to be in the particle phase extract divided by the total air volume sampled during each collection period. Detection limits could be improved by a factor of 4 by increasing the volume of extract loaded onto the SPE tubes; however, the extract is preserved for future analysis of other chemical classes of pesticides.

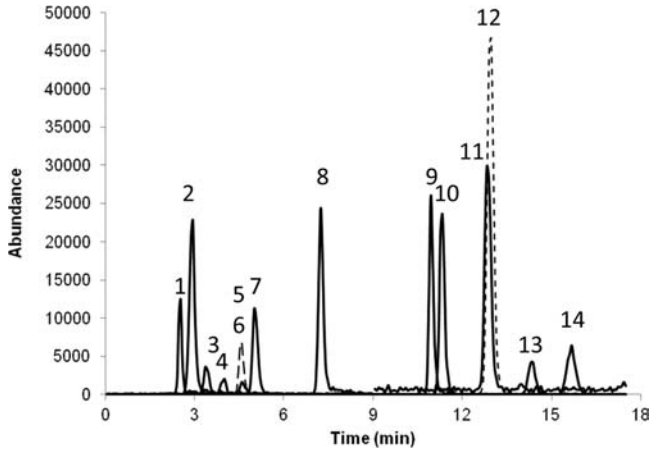

Figure 1. Selected reaction monitoring chromatogram of neonicotinoid insecticides and strobilurin fungicides standard mixture. Analytes (quantitative SRM transition): 1, dinotefuran (203.1 → 157.2); 2, nitenpyram (271.2 → 56); 3, thiamethoxam (292.4 → 211.4); 4, clothiadindin (250.1 → 169.3); 5, internal standard, imidacloprid-d_4 (260.1 → 213.1); 6, imidacloprid (256.1 → 175); 7, acetamiprid (223.1 → 126.1); 8, thiacloprid (253.1 → 126); 9, azoxystrobin (404.1 → 372.4); 10, dimoxystrobin (372.6 → 205.3); 11, fluoxastrobin (459.2 → 427.4); 12, kresoxim-methyl (314.1 → 206.3); 13, pyraclostrobin (388.1 → 163.5); 14, trifloxystrobin (409.1 → 186.4). Standard mixture of neonicotinoid and strobilurin fungicides at 60 ng/mL with internal standard imidacloprid-d_4 at 20 ng/mL (10 μL sample injection).

LC-MS-MS Analysis. LC analysis was performed with a Waters LC system consisting of a 1525 μ binary pump and column heater. A LEAP Technologies autosampler (Carrboro, NC, USA) was used for 10 μL injections at 100 μL/s and two pre- and postcleans with ethyl acetate followed by acetonitrile to minimize sample carry-over. A guard column (4 mm × 2.0 mm, C18 Gemini) was connected to the analytical column, Synergi Polar-RP column, 50 mm × 2.00 mm i.d., 2.5 μm (Phenomenex, Torrance, CA, USA), which was placed in a column heater at 30 °C. Initially the column was equilibrated with 40% acetonitrile containing 0.1% formic acid and 60% aqueous phase containing 0.1% formic acid and 5.0 mM ammonium acetate at a flow rate of 0.10 mL min^{-1}. Mobile phase gradient of acetonitrile with 0.1% formic acid was changed linearly as follows: 0−1.0 min, 40%; 3.0 min, 62.0%, held for 9.0 min; 13.0 min, 85%, then held at 85% for 5 min. All analytes are eluted prior to 18.0 min. The column was then reconditioned with gradient conditions adjusted back to initial mobile phase conditions by 20.0 min and held at initial mobile phase conditions for an additional 10.0 min prior to the next injection (total re-equilibration time of 12.0 min). This gradient program provided reproducibility in retention times within ±0.1 min; carry-over was not observed and was tested with blank injections containing the internal standard approximately every fifth injection. Blank injections were also completed prior to any sample injections.

The Waters LC system was connected to a Quattro Premier (Milford, MA, USA) triple quadrupole, which had electrospray ionization. The temperature of the source was set to 120 °C, desolvation temperature of 300 °C, desolvation gas at 750 L/h, and cone gas at 150 L/h. The optimized settings for ESI were as follows: capillary voltage, 3.50 kV; extractor voltage, 4 V; RF lens, 0.1 V. The collision gas used for SRM was argon (UHP) at 0.15 mL min^{-1} or 9.3×10^{-4}

DOI: 10.1021/acs.jafc.5b01347
J. Agric. Food Chem. 2015, 63, 5152−5162

Table 3. Method Detection Limits (MDLs) for Neonicotinoid Insecticides and Strobilurin Fungicides

compound	SRM1 SRM2 (optional SRM3 or SRM4)	MDL[a] (ng/mL)	MDL[b] (pg/m^3)	$Y = mx + b$ (calibration range MDL-100 ng/mL)	R^2
Neonicotinoid Insecticides					
dinotefuran	203.1 → 157.2	1.0	1.0	$0.0211x + 0.0152$	0.993
	203.1 → 129.2	2.0	2.0	$0.0187x - 0.0005$	0.996
	203.1 → 113.0	1.0	1.0	$0.0134x + 0.0167$	0.997
nitenpyram	271.2 → 56.0	2.0	2.0	$0.0573x - 0.0066$	0.997
	271.2 → 99.0	2.0	2.0	$0.0519x + 0.0028$	0.999
	271.2 → 189.1	2.0	2.0	$0.0207x - 0.0086$	0.995
	271.2 → 225.7	6.0	5.9	$0.00104x - 0.00305$	0.978
thiamethoxam	292.2 → 211.4	1.0	1.0	$0.00941x - 0.00350$	0.999
	292.2 → 132.0	10.0	9.8	$0.00585x + 0.00187$	0.991
	292.2 → 181.3	1.0	1.0	$0.00367x + 0.00053$	0.992
clothianidin	250.1 → 169.3	2.0	2.0	$0.00520x + 0.00510$	0.996
	250.1 → 132.0	1.0	1.0	$0.00475x + 0.00070$	0.998
imidacloprid	256.1 → 175	4.0	3.9	$0.00401x + 0.00230$	0.996
	256.1 → 209.5	4.0	3.9	$0.00110x - 0.00031$	0.982
acetamiprid	223.1 → 126.1	1.0	1.0	$0.0289x - 0.0038$	0.995
	223.1 → 56.0	2.0	2.0	$0.0168x + 0.0025$	0.997
	223.1 → 90.0	4.0	3.9	$0.00487x - 0.00228$	0.982
thiacloprid	253.1 → 126.0	2.0	2.0	$0.0480x + 0.0100$	0.995
	253.1 → 186.2	8.0	7.9	$0.00111x + 0.00614$	0.983
Strobilurin Fungicides					
azoxystrobin	404.1 → 372.4	0.5	0.5	$0.0509x - 0.0092$	0.998
	404.1 → 329.4	8.0	7.9	$0.00729x + 0.00814$	0.995
dimoxystrobin	327.6 → 205.3	2.0	2.0	$0.0612x - 0.045$	0.994
	327.6 → 238.5	4.0	3.9	$0.00347x - 0.00593$	0.998
fluoxastrobin	459.2 → 427.4	4.0	3.9	$0.0855x + 0.0970$	0.998
	459.2 → 188.2	2.0	2.0	$0.0389x + 0.0389$	0.996
kresoxim-methyl	314.1 → 206.3	2.0	2.0	$0.146x - 0.061$	0.999
	314.1 → 116.0	2.0	2.0	$0.109x + 0.0184$	0.998
	314.1 → 267.4	2.0	2.0	$0.0915x - 0.0064$	0.999
pyraclostrobin	388.1 → 163.5	2.0	2.0	$0.0145x + 0.0036$	0.994
	388.1 → 194.5	2.0	2.0	$0.0102x + 0.0013$	0.994
trifloxystrobin	409.1 → 186.4	2.0	2.0	$0.0260x + 0.0184$	0.998
	409.1 → 206.4	2.0	2.0	$0.0123x - 0.0020$	0.995

[a]Based on calibration standards—lowest calibration standard within ≤25% deviation from best-fit regression line. [b]Based on average air volume obtained from samples collected at Osoyoos of 4073 m^3 (average duration of sampling, 13.2 days, continuous air sampling); sample extract volume 1.0 mL with 0.25 mL taken for SPE cleanup stage.

mbar. Cone voltage and collision energy were set up in the MS method and are shown in Table 1. Infusion experiments were conducted for each insecticide or fungicide to determine the SRM conditions in ESI+ with a syringe pump flow rate of 50 μL min^{-1}.

RESULTS AND DISCUSSION

Selection of LC-MS/MS Parameters. Table 2 shows that most neonicotinoid insecticides and strobilurin fungicides have a minimum of two viable SRM transitions that are available for quantitative and confirmation analysis. The most sensitive SRM transition was used for quantitative analysis, and the second most sensitive SRM transition was used for confirmation. Several pesticides including dinotefuran, nitenpyram, thiamethoxam, acetamiprid, and kresoxim-methyl had a third available SRM transition that could be used for additional confirmation analysis when sufficient concentration was available. In general, more background matrix signal was observed for early-eluting compounds such as dinotefuran, nitenpyram, and thiamethoxam. These neonicotinoids were not detected in particle phase atmospheric samples. Dinotefuran has previously been observed to exhibit matrix suppression.[34] The % RSD for the response ratio of SRM2/SRM1 was <25% for all pesticides with the exception of thiacloprid (SRM2/SRM1 ratio of 0.0350 ± 32.6), which was also not detected in any particle phase atmospheric samples.

The column and mobile phase were also selected to achieve the required chromatographic resolution and selectivity and sensitivity in MS detection. All compounds have unique SRMs, and there were no issues of coelution with other target anaytes. Fluoxastrobin, kresoxim-methyl, and diazinon-d_{10} have similar retention times with the optimized gradient program (organic modifier acetonitrile) but can be distinguished by their unique SRMs (see Table 2). When methanol was used as the organic modifier, there was significantly less chromatographic selectivity and much lower resolution obtained for all strobilurin fungicides as compared to when a gradient with acetonitrile as the organic modifier was used. In addition, when the organic modifier in the mobile phase was switched from acetonitrile to methanol, the total analysis time increased by >5 min even under lower chromatographic resolution of the strobilurin fungicides. For example, azoxystrobin, dimoxystrobin, and diazinon-d_{10} had complete coelution with retention times between 20.32 and 20.44 min. Trifloxystrobin and pyraclostrobin also observed significant coelution (retention times 21.63 and

DOI: 10.1021/acs.jafc.5b01347
J. Agric. Food Chem. 2015, 63, 5152−5162

21.87 min) when methanol was used. Prior studies have also shown that better separations of only neonicotinoid insecticides (no strobilurin fungicides) with gradient elution were obtained when acetonitrile rather than methanol was used as the organic modifier in mobile phase.[23,28]

The mobile phase gradient of acetonitrile was required for the separation of all target analytes and provided the best balance between MS sensitivity, selectivity for the separation, and reproducibility of analysis. Previously, higher MS sensitivity has been shown for neonicotinoid insecticides with acetonitrile rather than methanol mobile phases.[22,28] In terms of MS sensitivity under these separation conditions only imidacloprid, imidacloprid-d_4, clothianidin, and thiamethoxam showed significantly higher response (peak area) when a methanol rather than an acetonitrile gradient was used and can be partially attributed to the larger retention times for each analyte when a gradient with methanol is used (corresponding higher percentage of organic modifier in mobile phase at retention times under the same gradient program); however, clothianidin and thiamethoxam also showed poorer reproducibility when methanol was used. Nitenpyram and acetamiprid showed ~3 and 1.5 improvement in sensitivity, respectively, and reductions in % RSD of peak areas from 14 to 8% when acetonitrile rather than methanol was used as the organic modifier in the mobile phase. In general, better consistency in retention times (within ±0.1 min) and smaller % RSD in peak areas were observed when a gradient with acetonitrile containing mobile phase was used. No carry-over effects were observed in the analysis when a gradient with acetonitrile was used and was tested with blank injections.

Synergi Polar-RP stationary phase is an end-capped ether-linked phenyl phase that provides different selectivity from C18 stationary phases. C18 stationary phases can be used for the separation of neonicotinoid insecticides, but require a high percentage of acetonitrile (90−100 v%) at the end of the gradient program.[23,28] The Synergi Polar-RP column provided better selectivity and shorter total analysis times, particularly for the strobilurin fungicides, which elute after the neonicotinoid insecticides, and thus was selected. It is recommended that if a C18 stationary phase is selected, a short column length (e.g., 50 mm) and small particle size (<2 μm) be used to avoid large total analysis times, and the selectivity of the strobilurin fungicides should be further evaluated. With a Synergi Polar-RP column along with the gradient of acetonitrile, the simultaneous analysis of strobilurin fungicides was feasible in the same LC-MS/MS method as required for optimal sensitivity and reproducibility for neonicotinoid insecticides with a total run time <18 min as shown in Figure 1. Under the separation conditions presented herein the strobilurin fungicides eluted later in the separation than the neonicotinoid insecticides, and with the use of acetonitrile in the mobile phase better chromatographic resolution was obtained for the strobilurin fungicides and shorter overall analysis times as compared to when a gradient with methanol was used. Only a few strobilurin fungicides (pyraclostrobin, azoxystrobin, and trifloxystrobin) have been included in LC-MS/MS methods of fungicides, and acetonitrile was the preferred organic modifier in the mobile phase for these methods.[24−26] MS sensitivity for strobilurin fungicides is not significantly different for methanol or acetonitrile containing mobile phases under similar mobile phase gradient conditions.

Calibration, Matrix Effects, and Method Detection Limits (MDLs). Calibration curves showed good linearity with

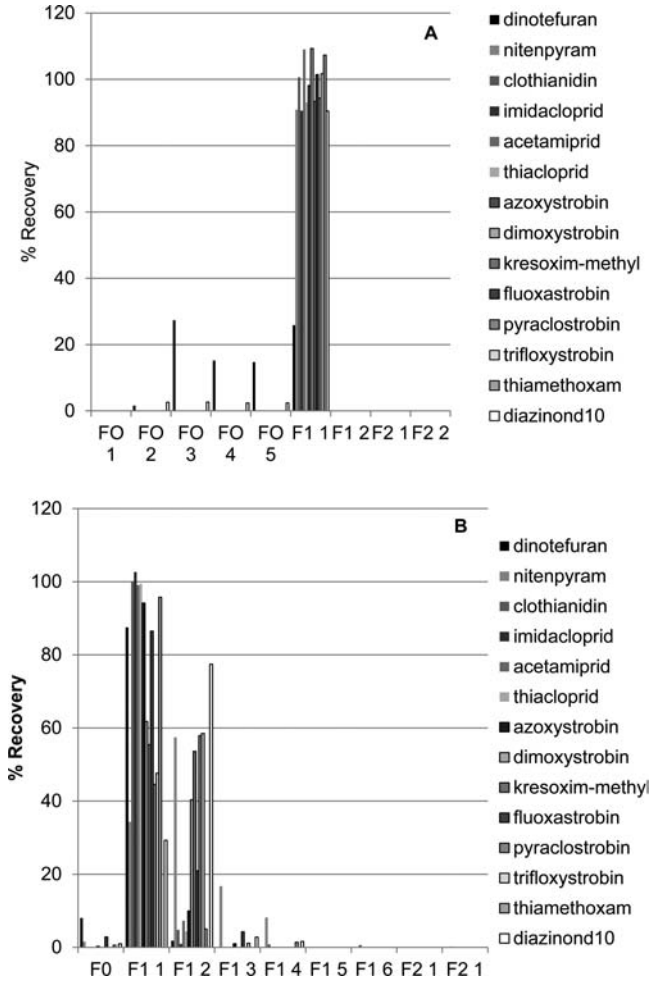

Figure 2. Percent recoveries of neonicotinoid insecticides and strobilurin fungicides from SPE C18 clean-up procedure: (A) F0 solvent 80:20 v/v% water/methanol in 1 mL portions (includes F0 1, F0 2, F0 3, F0 4, and F0 5, where 1−5 represent the 1 mL portions from 1 to 5 mL); F1 fraction is 5 mL of methanol (includes F1 1 as first 5 mL fraction and F1 2 as second 5 mL fraction); F2 fraction is 5 mL of methanol (includes F2 1 as first 5 mL fraction and F2 2 as second 5 mL fraction). (B) F0 fraction 2 mL of 80:20 v/v% water/methanol, F1 1−6 are each 1 mL portions of 100% methanol (for total volume of 6 mL methanol); F2 1 and 2 are each 5 mL portions of methanol. Sample was loaded at 50 ng/mL neonicotinoid insecticides and strobilurin fungicides.

r^2 generally >0.99 as shown in Table 3. MDLs were determined by the lowest standard concentration within 25% deviation of the best-fit line. MDLs generally ranged from 0.98 to 2.0 pg/m^3 except for imidacloprid, thiacloprid, dimoxystrobin, and azoxystrobin, with one SRM showing MDL ≥ 4 pg/m^3. A test for matrix effects was made by comparison of slopes of calibration curves from standards prepared with and without addition of 40 μL of filter extract of a sample collected at Osoyoos. Most pesticides showed a slight reduction in slope of the calibration curve when sample extract was added to standards with difference from −0.7 to −8.3%. Only thiamethoxam, fluoxastrobin, kresoxim-methyl, and pyraclostroin showed a small increase in slope for standards with sample matrix added (1.9−5.7%), which is well within an acceptable range. Reproducibility of samples with matrix added was from 0.8 to 11% and within the range observed for standards with no matrix added.

DOI: 10.1021/acs.jafc.5b01347
J. Agric. Food Chem. 2015, 63, 5152−5162

Table 4. Percent Recoveries of Neonicotinoid Insecticides and Strobilurin Fungicides from Extraction (and Drying)[a]

compound	% recoveries ± relative standard deviation (N = 3)
dinotefuran	97.3 ± 5.8
nitenpyram	<MDL−16.6[b]
thiamethoxam	97.5 ± 12.9
clothianidin	94.9 ± 5.2
imidacloprid	97.0 ± 8.9
acetamiprid	99.5 ± 1.1
thiacloprid	98.2 ± 6.3
azoxystrobin	91.6 ± 12.2
dimoxystrobin	99.9 ± 5.6
fluoxastrobin	100.8 ± 10.4
kresoxim-methyl	101.2 ± 0.2
pyraclostrobin	99.9 ± 0.7
trifloxystrobin	97.7 ± 6.3

[a]Accelerated solvent extraction recoveries from first extraction with solvent selected as ethyl acetate. Drying step is included as it is required for concentration of extracts prior to LC-MS/MS analysis. Particles on filter spiked at pesticide level of 50 ng/mL in final 1 mL extract. [b]Reported as range as 2 replicated <MDL.

SPE Method. SPE was used to clean up the organic extracts obtained from pressurized solvent extraction of filters containing particles from air sampling. Matrix-matched standards are not feasible in atmospheric sampling as the sample matrix changes as a function of time and is often unknown. The matrix is expected to contain hydrocarbons and ammonium sulfate or nitrates on the basis of the fact that both sampling sites are within the vicinity of agricultural and residential activities. For some sampling periods the matrix may also contain other compounds such as polycyclic aromatic hydrocarbons produced from forest fires or residential wood burning. The SPE cleanup method utilizes C18 sorbent, which is commonly used in cleanup of air extracts.[1−4,30] The SPE method is modified from those used for water samples to accommodate the organic solvent used in extraction of the pesticides from the solid particles on filter media and for the small volume of sample extract loaded onto the SPE tubes. Following pressurized solvent extraction a drying step is commonly used in methods for the analysis of air extracts to concentrate the pesticides of interest and also to exchange the solvent from ethyl acetate to methanol (or solvent suitable for subsequent instrumental analysis).[2,3] In this method the dried sample extract is dissolved in methanol to allow for better retention of analytes on SPE C18 sorbent and is suitable for future analysis of other chemical classes of pesticides. In this method an F0 fraction is used to remove potential matrix components that would be more soluble in a higher percentage of water (~80:20 v/v % water/methanol in F0 fraction). The method required the SPE sorbent tubes to be preconditioned in methanol followed by conditioning of the sorbent with water to allow for adequate retention of dinotefuran on the C18 SPE sorbent. Figure 2A shows that most pesticides other than dinotefuran remained retained on the C18 sorbent with up to an elution volume of 5 mL of 80:20 v/v % water/methanol, which was collected in the F0 fractions (F0 1 to F0 5). A final elution volume of 2 mL of 80:20v/v % water/methanol was chosen for the F0 fraction to minimize the loss of dinotefuran. After collection of the F0 fraction, all of the neonicotinoid and strobilurin fungicides were adequately recovered when 5 mL of 100% methanol was used for elution of pesticides in the first F1 fraction as shown in Figure 2A. Methanol was chosen as the elution solvent for pesticides of interest in the F1 fraction to ensure elution of more strongly retained strobilurin fungicides on reversed-phase sorbent. Further investigation (see Figure 2B) of retention of these pesticides with methanol shows that most pesticides were eluted within the first 3 mL of methanol collected in the F1 fraction (F1 1 to F1 3). However, a final volume of 5 mL of methanol for elution of the F1 fraction was chosen as small amounts of clothianidin, thiamethoxam, and diazinon-d_{10} still eluted in the fourth 1 mL portion of methanol (F1 4), and trace levels (but below MDL) were still observed in the fifth 1 mL portion of methanol (F1 5). Figure 2A also showed that overall recoveries of pesticides were excellent when 5 mL of methanol was used for the collection of the F1 fraction. Figure 2B shows that further elution with methanol (in F2 fractions) did not recover any pesticides of interest.

Pressurized Solvent Extraction. The recoveries of neonicotinoid insecticides and strobilurin fungicides were also tested through the pressurized solvent extraction step and subsequent drying step required to concentrate the pesticides of interest. The volume of extract obtained from pressurized solvent extraction is ~45 mL, and after drying the extraction is dissolved with methanol prior to cleanup for LC-MS/MS analysis. Table 4 shows for spiked filter samples all pesticides with the exception of nitenpyram were efficiently extracted with ethyl acetate in the first extraction step (this procedure utilizes two static steps to ensure a more complete extract and contact time with particles). Further evaluation of the low recoveries of nitenpyram showed that nitenpyram was lost during the drying step and that it has a relatively high vapor pressure (vapor pressure = 1×10^{-4} Pa). In earlier experiments it was

Table 5. Particle Phase Atmospheric Concentrations of Neonicotinoid Insecticides and Strobilurin Fungicides Detected at Osoyoos and Oliver, British Columbia, Canada, in 2013[a]

	clothianidin (pg/m^3)		imidacloprid (pg/m^3)		acetamiprid (pg/m^3)		kresoxim-methyl (pg/m^3)		pyraclostrobin (pg/m^3)		trifloxystrobin (pg/m^3)		fluoxastrobin (pg/m^3)
date	Osoyoos	Oliver	Osoyoos	Oliver	Osoyoos	Oliver	Osoyoos	Oliver	Osoyoos	Oliver	Osoyoos	Oliver	Osoyoos
June 28	<MDL	63.7	94.8	360.0	<MDL	6.5	37.4	<MDL	655.6	430.5	11.7	240.8	5.2
July 15		<MDL		10.5		<MDL		<MDL		2.9		<MDL	
July 29	92.1	23.4	14.3	26.5	<MDL	<MDL	<MDL	10.2	88.2	<MDL	12.9	1908.2	<MDL
August 6	55.4		39.7		<MDL		<MDL		39.8		<MDL		<MDL
August 9	11.1		26.2		6.3		<MDL		75.4		6.9		<MDL
August 20	10.3	31.2	13.4	105.0	ND	35.7	<MDL	<MDL	55.3	394.5	22.9	57.0	<MDL

[a]Sampling start dates at Osoyoos: June 28, 2013; July 29, 2013; August 6, 2013; August 9, 2013; and August 20, 2013 (N = 5). Sampling start dates at Oliver: June 28, 2013; July 15, 2013; July 29, 2013; and August 20, 2013 (N = 4). Fluoxastrobin <MDL at Oliver. Empty cells represent no sample collected during this sampling period at specified site.

DOI: 10.1021/acs.jafc.5b01347
J. Agric. Food Chem. 2015, 63, 5152−5162

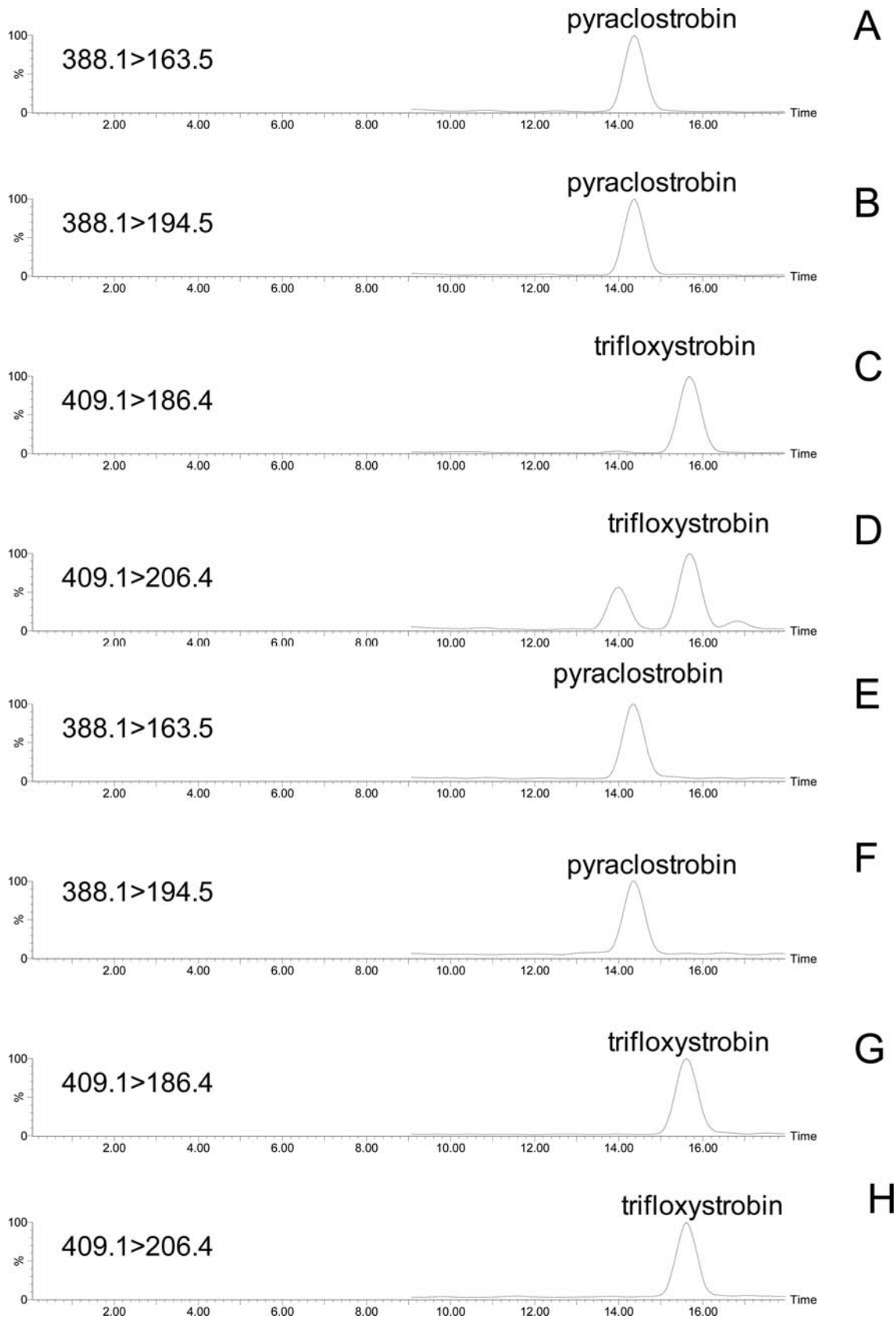

Figure 3. Quantitative and confirmation SRM chromatograms for pyraclostrobin and trifloxystrobin obtained for a particle phase atmospheric sample and 10 ng/mL standard mixture: (A–D) particle phase air extract; (E–H) 10 ng/mL standard mixture containing all neonicotinoid and strobilurin fungicides.

DOI: 10.1021/acs.jafc.5b01347
J. Agric. Food Chem. 2015, 63, 5152–5162

also noted that thiacloprid and azoxystrobin were more susceptible to loss during the drying step but that a drying at a rate of ~0.95−1.00 at 0.5 mL/h provided acceptable recoveries of >85%. A second or third accelerated solvent extraction step of spiked filters (following a first extraction with ethyl acetate) showed no recoveries of pesticides when the solvent was ethyl acetate, acetonitrile, or acetone. For filter samples collected at the two sites in the Okanagan Valley a precautionary second extraction step was included to test if pesticides could be bound more strongly to particles under various field conditions. Although in our spike filter tests we found no difference with choice of organic solvent for the second pressurized extraction step, acetonitrile was selected as the second extraction solvent as nitenpyram and dinotefuran have been shown to have better recoveries with acetonitrile than with acetone or methanol.[22] Particle phase samples with the highest concentrations of pyraclostrobin and trifloxystrobin had <16% of their total concentration detected in the extract obtained from a second pressurized extraction with acetonitrile. Reproducibility of repeat injections (N = 5) of neonicotinoid insecticides and strobilurin fungicides was from 2 to 7%. Most samples had pesticide concentrations <5 pg/m^3 in the second extraction with acetonitrile. Field blank filter samples also showed no presence of pesticides in either the the first or second extraction with ethyl acetate or acetonitrile.

Particle Phase Atmospheric Concentrations of Neonicotinoid and Strobilurin Fungicides. Azoxystrobin, which has a sensitive SRM1 signal, could be detected at trace levels (~2−4 pg/m^3) in two filter samples collected at the Osoyoos sampling site, but could not be confirmed due to the higher MDL for SRM2. Acetamiprid, clothianidin, imidacloprid, kresoxim-methyl, pyraclostrobin, and trifloxystrobin were detected in particle phase samples as shown in Table 5 and represent the first detections of neonicotinoid insecticides and strobilurin fungicides in atmospheric particles in Canada. No prior studies have reported the detection of kresoxim-methyl, clothianidin, pyraclostrobin, or trifloxystrobin in the atmosphere worldwide.

Although there was no detection of thiamethoxam in particle phase atmospheric samples, thiamethoxam may be converted to clothianidin in insects and plants.[35] At this stage of the sampling it is not possible to identify the source of clothianidin in atmospheric particle phase samples collected. The particle phase atmospheric samples collected from the southern Okanagan Valley of British Columbia show the highest reported literature concentrations of neonicotinoid insecticides with particle phase atmospheric concentrations of acetamiprid, clothianidin, and imidacloprid reaching 35.7, 92.1, and 360.0 pg/m^3, respectively (Table 5). Acetamiprid and imidacloprid are the only neonicotinoids that have been detected in the particle phase (particulate matter < 2.5 or 10 μm in diameter (PM2.5 or PM10)) in Spain.[17,32] Particulate (PM10) concentrations of acetamiprid and imidacloprid in the atmosphere at these sites in Spain were 11.9−31.3 and 14.9 pg/m^3, respectively, with a low detection frequency.[32]

The strobilurin fungicides, pyraclostrobin and trifloxystrobin, were observed at the highest concentrations of the pesticides studied with particle phase atmospheric concentrations reaching 655.6 and 1908.2 pg/m^3, respectively. Detection of these strobilurin fungicides in the atmosphere has not been previously reported in the literature, and the concentrations of these pesticides indicate the importance of further studies on their movement in the environment by atmospheric transport. Studies on redistribution of radiolabeled strobilurins on wheat indicate that trifloxystrobin has potential for molecular redistribution by air.[35] These neonicotinoid insecticides and strobilurin fungicides are known to have usage in the southern Okanagan Valley. Further analysis is underway on the gas phase concentrations of these pesticides as gas/particle phase partitioning is expected.

Figure 3 shows the quantitative and confirmation SRM chromatograms for pyraclostrobin and trifloxystrobin in a particle phase air extract obtained from a sample collected at Osoyoos and a 10 ng/mL stanadard mixture. Confirmation of the identity of pesticides in samples included retention time match and a response ratio of SRM2/SRM1 in % RSD range determined on the day of analysis from standards (see Table 2). The particle phase air extract did show some peaks in the chromatogram at different retention times than any of the tested neonicotinoids or strobilurin fungicides such as observed in Figure 3D. The identity of these peaks at retention times of 13.9 and 16.8 min observed in the 409.1 → 206.4 SRM chromatogram is currently unknown. The unknown components in the sample did not have a measurable response at 409.1 → 186.4 and also did not coelute with trifloxystrobin.

In conclusion, a liquid chromatography−tandem mass spectrometry method has been developed for the determination of neonicotinoids and strobilurin fungicides in the particle phase fraction of atmosphere samples. Pyraclostrobin and trifloxystrobin were observed at the highest concentrations of the pesticides studied at the two sites in the Canadian Okanagan Valley agricultural region with this study representing the first reported occurrence of strobilurin fungicides in the atmosphere within Canada. In addition, neonicotinoid insecticides were also detected in the particle phase with maximum concentrations for acetamiprid, clothianidin, and imidacloprid of 35.7, 92.1, and 360.0 pg/m^3, respectively. This study provides support for the occurrence of these compounds in the atmosphere in the particle phase. Further research is required to assess seasonal trends and potential for regional and long-range transport of these neonicotinoids and strobilurin fungicides in the atmosphere.

■ ASSOCIATED CONTENT

Ⓢ Supporting Information

Pesticide sales information for Canada and British Columbia for neonicotinoid insecticides and strobilurin fungicides. The Supporting Information is available free of charge on the ACS Publications website at DOI: 10.1021/acs.jafc.5b01347.

■ AUTHOR INFORMATION

Corresponding Author

*E-mail: renata.raina@uregina.ca.

Funding

I acknowledge funding support for this research from a Natural Sciences and Engineering Research Council of Canada (NSERC) Discovery Grant.

Notes

The authors declare no competing financial interest.

■ ACKNOWLEDGMENTS

I thank the BC Ministry of Environment and Government of Canada for use and access to the Osoyoos and Oliver field sampling locations.

DOI: 10.1021/acs.jafc.5b01347
J. Agric. Food Chem. 2015, 63, 5152−5162

REFERENCES

(1) Raina, R.; Hall, P.; Sun, L. Occurrence and relationship of organophosphorus insecticides and their degradation products in the atmosphere in western Canada agricultural regions. *Environ. Sci. Technol.* **2010**, *44*, 8541−8546.

(2) Raina, R.; Smith, E. Detection of azole fungicides in atmospheric samples collected in the Canadian prairies. *J. AOAC Int.* **2012**, *95*, 1350−1356.

(3) Raina, R.; Sun, L. Trace level determination of selected organophosphorus pesticides and their degradates in environmental air samples by liquid chromatography-positive ion electrospray tandem mass spectrometry. *J. Environ. Sci. Health, Part B* **2008**, *43*, 323−332.

(4) Raina, R.; Hall, P. Field evaluation of solid sorbents for ambient air sampling of pesticides. *Air, Soil Water Res.* **2010**, *3*, 57−66.

(5) Liu, M. Y.; Casida, J. E. High affinity binding of [3H] imidacloprid in the insect acetylcholine receptor. *Pestic. Biochem. Physiol.* **1993**, *46*, 40−46.

(6) Health Canada, Consumer Product Safety, Pesticide and Pest Management, Public Registry, Pesticide Product Information Database available at http://pr-rp.hc-sc.gc.ca/pi-ip/index-eng.php.

(7) Hladik, M. L.; Kolpin, D. W.; Kuivila, K. M. Widespread occurrence of neonicotinoid insecticides in streams in a high corn and soybean producing region, USA. *Environ. Pollut.* **2014**, *193*, 189−196.

(8) Huang, S. W.; Zhao, P.; Liu, C.; Chen, Q.; Liu, Z.; Yang, G. Design, synthesis, and fungicidal activities of new strobilurin derivatives. *J. Agric. Food Chem.* **2007**, *55*, 3004−3010.

(9) Kasiotis, K. M.; Anagnostopoulos, C.; Anastasiadou, P.; Machera, K. Pesticide residues in honeybees, honey and bee pollen by LC-MS/MS screening. Reported death incidents in honeybees. *Sci. Total Environ.* **2014**, *485*−*486*, 633−642.

(10) Barcandritsos, N.; Granato, A.; Budge, G.; Papanastasiou, L.; Roinioti, E.; Caldon, M.; Falcaro, C.; Gallina, A.; Mutinelli, F. Sudden deaths and colony population decline in Greek honey bee colonies. *J. Invertebr. Pathol.* **2010**, *105*, 335−340.

(11) Sanchez-Bayo, F.; Hyne, R. V. Detection and analysis of neonicotinoids in rive waters − development of a passive sampler for three commonly used insecticides. *Chemosphere* **2014**, *99*, 143−151.

(12) Jovanov, P.; Guzsvany, V.; Franko, M.; Lazic, S.; Sakac, M.; Saric, B.; Banjac, V. Multi-residue method for determination of selected neonicotinoid insecticides in honey using optimized dispersive liquid-liquid microextraction combined with liquid chromatography-tandem mass spectrometry. *Talanta* **2013**, *111*, 125−133.

(13) Jovanov, P.; Guzsvany, V.; Lazic, S.; Franko, M.; Sakac, M.; Saric, L.; Kos, J. Development of HPLC-DAD method for determination of neonicotinoids in honey. *J. Food Compos. Anal.* **2015**, *40*, 106−113.

(14) Dankyi, E.; Gordon, C.; Carboo, D.; Fomsgaard, I. S. Quantification of neonicotinoid insecticide residues in soils from cocoa plantations using a QuEChERS extraction procedure and LC-MS/MS. *Sci. Total Environ.* **2014**, *499*, 276−283.

(15) Sanchez-Hernandez, L.; Hernandez-Dominguez, D.; Bernal, J.; Neuseb, C.; Martin, M. T.; Bernal, J. L. Capillary electrophoresis−mass spectrometry as a new approach to analyze neonicotinoid. *J. Chromatogr. A* **2014**, *1359*, 317−324.

(16) Seccia, S.; Fidente, P.; Barbini, D. A.; Morrica, P. Multiresdiue determination of nicotinoid insecticide residues in drinking water by liquid chromatography with electrospray ionization mass spectrometry. *Anal. Chim. Acta* **2005**, *553*, 21−26.

(17) Coscolla, C.; Yusa, V.; Beser, M. I.; Pastor, A. Multi-residue analysis of 30 currently used-pesticides in fine airborne particulate matter (PM2.5) by microwave-assisted extraction and liquid chromatography-tandem mass spectrometry. *J. Chromatogr. A* **2009**, *1216*, 8817−8827.

(18) Kanrar, B.; Mandal, S.; Bhattacharyya, A. Validation and uncertainty analysis of a multiresidue method for 42 pesticides in made tea, tea infusion and spent leaves using ethyl acetate extraction and liquid chromatography-tandem mass spectrometry. *J. Chromatogr. A* **2010**, *1217*, 1926−1933.

(19) Banerjee, K.; Oulkar, D. P.; Dasgupta, S.; Patil, S. B.; Patil, S. H.; Savant, R.; Adsule, P. G. Validation and uncertainty analysis of a multi-residue method for pesticides in grapes using ethyl acetate extraction and liquid chromatography-tandem mass spectrometry. *J. Chromatogr. A* **2007**, *1173*, 98−109.

(20) Giroud, B.; Vauchez, A.; Vulliet, E.; Wiest, L.; Bulete, A. Trace level determination of pyrethroid and neonicotinoid insecticides in beebread using acetontrile-based extraction followed by analysis with ultra-high-performance liquid chromatography-tandem mass spectrometry. *J. Chromatogr. A* **2013**, *1316*, 53−61.

(21) Muccio, A. D.; Fidente, P.; Barbini, D. A.; Dommarco, R.; Seccia, S.; Morrica, P. Application of solid-phase extraction and liquid-chromatography-mass spectrometry to the determination of neonicotinoid pesticide residues in fruit and vegetables. *J. Chromatogr. A* **2006**, *1108*, 1−6.

(22) Wang, P.; Yang, X.; Wang, J.; Cui, J.; Dong, A. J.; Zhao, H. T.; Zhang, L. W.; Wang, Z. Y.; Xu, R. B.; Li, W. J.; Zhang, Y. C.; Zhang, H.; Jing, J. Multi-residue method for determination of seven neonicotinoid insecticides in grains using dispersive solid-phase extraction and dispersive liquid-liquid micro-extraction by high performance liquid chromatography. *Food Chem.* **2012**, *134*, 1691−1698.

(23) Xiao, Z.; Yang, Y.; Li, Y.; Fan, X.; Ding, S. Determination of neonicotinoid insecticides residues in eels using subcritical water extraction and ultra-performance liquid chromatography-tandem mass spectrometry. *Anal. Chim. Acta* **2013**, *777*, 32−40.

(24) Zhang, F.; Wang, L.; Zhou, L.; Pan, H.; Pan, C. Residue dynamics of pyraclostrobin in peanut and field soil by QuEChERS and LC-MS/MS. *Ecotoxicol. Environ. Saf.* **2012**, *78*, 116−122.

(25) Sannino, A.; Bolzoni, L.; Bandini, M. Application of liquid chromatography with electrospray tandem mass spectrometry to the determination of a new generation of pesticides in processed fruits and vegetables. *J. Chromatogr. A* **2004**, *1036*, 161−169.

(26) Dong, F.; Chen, X.; Liu, X.; Xu, J.; Li, Y.; Shan, W.; Zheng, Y. Simultaneous determination of five pyrazole fungicides in cereals, vegetables and fruits using liquid chromatography/tandem mass spectrometry. *J. Chromatogr. A* **2012**, *1262*, 98−106.

(27) Rahman, M. M.; El-Aty, A.M. A.; Choi, J.-H.; Kim, S.-W.; Shin, S. C. Consequences of the matrix effect on recovery of dinotefuran and its metabolites in green tea during tandem mass spectrometry analysis. *Food Chem.* **2015**, *168*, 445−453.

(28) Yamamuro, T.; Ohta, H.; Aoyama, M.; Watanabe, D. Simultaneous determination of neonicotinoid insecticides in human serum and urine using diatomaceous earth-assisted extraction and liquid-chromatography-tandem mass spectrometry. *J. Chromatogr. B: Anal. Technol. Biomed. Life Sci.* **2014**, *969*, 85−94.

(29) Vinas, P.; Martinez-Castillo, N.; Campillo, N.; Hernandez-Cordoda, M. J. Liquid-liquid microextraction methods based on ultrasound-assisted emulsification and single-drop coupled to gas chromatography-mass spectrometry for determining strobilurin and oxazole fungicides in juices and fruits. *J. Chromatogr. A* **2010**, *1217*, 6569−6577.

(30) Bailey, R.; Belzer, W. Large volume cold on-column injection for gas chromatography-negative chemical ionization-mass spectrometry analysis of selected pesticides in air samples. *J. Agric. Food Chem.* **2007**, *55*, 1150−1155.

(31) Raina, R.; Hall, P. Comparison of gas chromatography-mass spectrometry with electron ionization and negative-ion chemical ionization for analyses of pesticides at trace levels in atmospheric samples. *Anal. Chem. Insights* **2008**, *3*, 111−125.

(32) Coscolla, C.; Hart, E.; Pastor, A.; Yusa, V. LC-MS characterization of contemporary pesticides in PM10 of Valencia region, Spain. *Atmos. Environ.* **2013**, *77*, 394−403.

(33) Xiao, Z.; Li, X.; Wang, X.; Shen, J.; Ding, S. Determination of neonicotinoid insecticides residues in bovine tissues by pressurized solvent extraction and liquid chromatography-tandem mass spectrometry. *J. Chromatogr. B: Anal. Technol. Biomed. Life Sci.* **2011**, *879*, 117−122.

DOI: 10.1021/acs.jafc.5b01347
J. Agric. Food Chem. 2015, 63, 5152−5162

(34) Nauen, R.; Ebbinghaus-Kintscher, U.; Salgado, V. L.; Kaussmann, M. Thiamethoxam is a neonicotinoid precursor converted to clothianidin in insects and plants. *Pestic. Biochem. Physiol.* **2003**, *76*, 55−69.
(35) Bartlett, D. W.; Clough, J. M.; Godwin, J. R.; Hall, A. A.; Hamer, M.; Parr-Dobrzanski, B. Review, the strobilurin fungicides. *Pest Manage. Sci.* **2002**, *58*, 649−662.

DOI: 10.1021/acs.jafc.5b01347
J. Agric. Food Chem. 2015, 63, 5152−5162

JOURNAL OF AGRICULTURAL AND FOOD CHEMISTRY

Article

pubs.acs.org/JAFC

Evaluation of Different Parameters in the Extraction of Incurred Pesticides and Environmental Contaminants in Fish

Yelena Sapozhnikova and Steven J. Lehotay*

Eastern Regional Research Center, Agricultural Research Service, U.S. Department of Agriculture, 600 East Mermaid Lane, Wyndmoor, Pennsylvania 19038, United States

Supporting Information

ABSTRACT: Sample processing is often ignored during analytical method development and validation, but accurate results for real samples depend on all aspects of the analytical process. Also, validation is often conducted using only spiked samples, but extraction yields may be lower in incurred samples. In this study, different variables in extraction for incurred pesticides and environmental contaminants in fish were investigated. Among 207 analytes screened using low-pressure gas chromatography−tandem mass spectrometry, consisting of 150 pesticides, 15 polycyclic aromatic hydrocarbons (PAHs), 14 polychlorinated biphenyls (PCBs), 6 polybrominated diphenyl ethers (PBDEs), and 22 other flame retardants (FRs), 35 (16 pesticides, 9 PCBs, 5 PBDEs, and 5 PAHs) were identified for quantification in samples of salmon, croaker, and NIST Standard Reference Material 1947 (Lake Michigan Fish Tissue). Extraction efficiencies using different extraction devices (blending, vortexing, and vibrating) versus time, sample size, and sample/solvent ratio were determined. In comparison to blending results, use of a pulsed-vortexer for 1 min with 1/1 (g/mL) sample/acetonitrile ratio was generally sufficient to extract the incurred contaminants in the homogenized fish tissues. Conversely, extraction with a prototype vibration shaker often took 60 min to achieve 100% extraction efficiency. A main conclusion from this study is that accurate results for real samples can be obtained using batch extraction with a pulsed-vortexer in a simple and efficient method that achieves high sample throughput.

KEYWORDS: *extractability, sample preparation, pesticides, environmental contaminants, fish, residue analysis*

INTRODUCTION

Prior to obtaining regulatory approval of a new pesticide application on crops, the registrant must usually demonstrate that the proposed regulatory method of analysis achieves total extractability of the defined pesticide residues from the crop and soil.[1] Liquid scintillation counting of sample extracts containing radioactive isotopes of the pesticide applied in the field is typically conducted to show if the method meets this total extractability requirement.[2] However, the approved regulatory method is rarely used in practice for monitoring of pesticide residues because it is typically designed only for a single pesticide (including defined metabolites), and it is often unwieldy to perform. Instead, multiclass multiresidue monitoring methods, such as QuEChERS (quick, easy, cheap, effective, rugged, and safe),[3] are employed to provide wide analytical scope with high sample throughput at an affordable cost. In addition, official methods tested for total extractability exist only for registered pesticide/crop combinations, not for unapproved pesticides or environmental contaminants that must also be routinely monitored for food safety, risk assessment, and a range of other purposes.

However, radiotracing to determine total extractability of residues from a diverse range of samples is not feasible for many chemicals of interest. Method development and validation studies involving multiresidue analysis of contaminants in foods and environmental matrices often only involve laboratory-fortified (spiked) samples to assess suitable method performance. Yet, it is common knowledge that analytes are more easily extracted from laboratory-spiked tissues than from real-world incurred samples, which may have stronger analyte−matrix interactions to be overcome. Furthermore, normalization of incurred analytes to a spiked internal standard does not compensate for lower extraction efficiency if incurred recoveries are different from those for spiked samples.

In a search of "extractability" in Scopus, hundreds of papers in the scientific literature were found on the topic, but nearly all of them concerned metals, soils, and food composition studies. Only one paper addressed extractability of chemical contaminants from fish, describing the effect of freeze-drying and how rehydration of samples improves extraction of incurred residues.[4] It is a well-known phenomenon and standard practice to add water to dry samples in pesticide residue analysis.[5] For example, Cajka et al. demonstrated that underestimation of various pesticide concentrations in incurred tea samples was 25−74% when comparing two methods with different degrees of extractability.[6] Also, Anastassiades et al. extensively studied extractability of multiple pesticides from fruits and vegetables by assessing extraction time, temperature, and shaking intensity in QuEChERS.[7]

After method implementation, quality control samples to check ongoing method performance are also typically spiked with the analytes, not incurred.[8] Even in the case of proficiency testing, spiked samples are usually sent to the laboratories for

Special Issue: 51st North American Chemical Residue Workshop

Received: December 29, 2014
Revised: February 10, 2015
Accepted: February 16, 2015
Published: February 16, 2015

ACS Publications

This article not subject to U.S. Copyright. Published 2015 by the American Chemical Society

DOI: 10.1021/jf506256q
J. Agric. Food Chem. 2015, 63, 5163−5168

evaluation, and even if incurred samples are used, the true analyte concentration is seldom known for comparison with the experimental results. Thus, it is conceivable that reported concentrations in real samples are lower than actual because total extractabilities of analyte−matrix combinations are rarely tested for common multiresidue monitoring methods.

Ideally, standard reference materials (SRMs)[9,10] would be used to determine total extractability, but none are available for many common contaminants and food sample types. Despite the known concerns related to spiked-only samples, few chemists validate their methods using incurred samples[6,11,12] because it is often difficult to obtain appropriate samples, and the true concentrations remain unknown. When possible, a bridging study should be conducted in which results from new methods of extraction should be compared with reference methods in side-by-side analysis of the same sample.[13] However, this is not common practice due to the extra time, effort, and cost involved. Thus, many chemists risk inaccurate results in their analyses, even if they follow standard practices for method validation, quality control, and laboratory accreditation (including proficiency testing).

The goal of this study was to investigate variables affecting QuEChERS-based extraction yields of incurred pesticides and environmental contaminants in fish samples (white croaker, salmon, and NIST SRM 1947 − Lake Michigan fish tissue). A diverse range of pesticides, polycyclic aromatic hydrocarbons (PAHs), polychlorinated biphenyls (PCBs), polybrominated diphenyl ethers (PBDEs), and flame retardants (FRs) were chosen for analysis using low-pressure gas chromatography−tandem mass spectrometry (LPGC-MS/MS). We sought to compare extraction efficiencies of different sample sizes, sample/solvent ratio, and extraction time using different shakers and a probe blender as extraction devices.

MATERIALS AND METHODS

Samples, Reagents, and Extraction Devices. Fish samples of salmon and Pacific white croaker (*Genyonemus lineatus*) were from the National Institute of Standards and Technology (NIST) Marine Environmental Specimen Bank in Charleston, SC, USA. The croaker was collected in 2002 from Palos Verdes Shelf Los Angeles Sanitation District Zone 1 EPA Superfund site in Palos Verdes, CA, USA. Croaker samples were received as a frozen, homogenized powder. The salmon of undetermined type collected from an unknown location was contributed to the Specimen Bank by Axys Analytical, Sidney, BC, Canada. The salmon was received frozen as a whole body 81 cm fish weighing 5096 g. It was thawed, filleted into skinless and boneless chunks, refrozen, and then homogenized with dry ice using a Robot Coupe (Ridgeland, MS, USA) RSI 2Y1 chopper and stored in glass containers in a −18 °C freezer until portions were thawed for analysis. Measured moisture contents were 63 and 79% for the salmon and croaker, respectively. Reported average lipid contents are 3−4 and 5−10% for croaker and salmon, respectively.[14] SRM 1947 (Lake Michigan Fish Tissue) was purchased from NIST (Gaithersburg, MD, USA) and contained 73% moisture and 10% fat content.

Pesticide standards were from the Environmental Protection Agency's National Pesticide Repository (Fort Meade, MD, USA), Dr. Ehrenstorfer GmbH (Augsburg, Germany), Chemservice (West Chester, PA, USA), and AccuStandard, Inc. (New Haven, CT, USA). PCB and PBDE congeners and PAHs were purchased from AccuStandard, and standards of FRs were from AccuStandard and Sigma-Aldrich (St. Louis, MO, USA). For use as internal standards (ISTDs), $^{13}C_{12}$-2,2′,4,4′,5,5′-hexachlorobenzene ($^{13}C_{12}$-PCB 153) and $^{13}C_{12}$-*p*,*p*′-DDE, PAH surrogate cocktail containing acenaphthylene-d_8, benzo(*a*)pyrene-d_{12}, benzo(*g*,*h*,*i*)perylene-d_{12}, fluoranthene-d_{10}, naphthalene-d_8, phenanthrene-d_{10}, and pyrene-d_{10}, were purchased from Cambridge Isotope Laboratories (Tewksbury, MA, USA). 5′-Fluoro-2,3′,4,4′,5-pentabromodiphenyl ether (FBDE 126) was purchased from AccuStandard, and atrazine-d_5 (ethyl-d_5) and fenthion-d_6 (*o*,*o*-dimethyl-d_6), were from C/D/N Isotopes (Pointe-Claire, Quebec, Canada). All standards were of ≥98% purity.

All solvents were of HPLC grade. Acetonitrile (MeCN) was from Fisher Scientific (Pittsburgh, PA, USA), and methanol (MeOH) was from VWR International (Radnor, PA, USA). Anhydrous magnesium sulfate (anhydrous $MgSO_4$) and sodium chloride (NaCl) reagent-grade salts and primary−secondary amine (PSA) and C18 sorbents were purchased from UCT (Bristol, PA, USA). Deionized water of 18.2 Ω-cm was prepared with an E-Pure model D4641 from Barnstead/Thermolyne (Dubuque, IA, USA). Zirconium dioxide based sorbent (Z-Sep) was from Supelco (Bellefonte, PA, USA). Ammonium formate was from Sigma-Aldrich. PVDF 0.2 μm filter vials were from Thomson Instrument Co. (Oceanside, CA, USA).

As shown in Figure 1, the extraction devices used in the study consisted of an Ultra-Turrax T25 probe-blending homogenizer (Janke & Kunkel GmbH & Co., IKA Labortechnik, Wilmington, NC, USA), a pulsed-vortexer (Glas-Col, Terre Haute, IN, USA), and a prototype vibration shaker (GL Sciences, Eindhoven, The Netherlands).

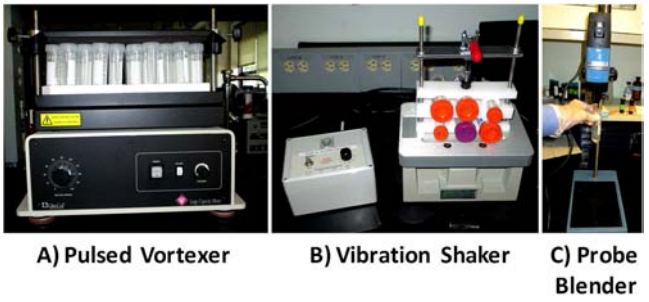

Figure 1. Three types of extraction devices compared in the study.

Sample Preparation. The initial experiments to determine incurred contaminants in fish samples were performed using a QuEChERS sample preparation method described earlier.[9] After addition of internal standards, 10 g of homogenized fish subsamples were extracted by shaking for 1 min with 10 mL of MeCN in triplicate each of salmon and croaker and one replicate for SRM 1947. Anhydrous $MgSO_4$ (4 g) and NaCl (1 g) were added to the initial extracts to induce phase separation, and after centrifugation, a 1 mL portion of the extract was transferred to 2 mL mini-centrifuge tubes containing 150 mg of $MgSO_4$ and 50 mg of Z-Sep for dispersive solid-phase extraction (d-SPE) cleanup. The tubes were centrifuged, and extracts were subjected to LPGC-MS/MS analysis. The final sample preparation method used in experiments described below was updated in accordance with subsequent streamlining improvements already reported.[15]

To determine the optimum extraction time and compare extraction devices, croaker and salmon homogenized tissues (10 g) were weighed into 50 mL polypropylene tubes (5 g was used for SRM 1947) and spiked with the internal standards mixture to achieve 100 ng/g for isotopically labeled pesticides, 50 ng/g for FBDE 126, 20 ng/g for isotopically labeled PAHs, and 2 ng/g for $^{13}C_{12}$ PCB 153. After the addition of 10 mL of MeCN, the tubes were placed into the pulsed-vortexer and shaken at 80% setting with maximum pulsing for 1, 10, 30, and 60 min. Another set of samples was extracted for the same time intervals using the vibration shaker. Four replicates of salmon and croaker and one replicate of SRM 1947 were conducted for each extraction/time parameter. Another four replicates each of croaker, salmon, and SRM 1947 subsamples were extracted using the probe blender for 1 min. After extraction, 5 g of ammonium formate was added to induce phase separation,[16] and the samples were shaken for 1 min on the pulsed-vortexer and centrifuged for 2 min at 3700 rcf. Extracts (0.5 mL) were transferred into the shells (bottom half) of 0.2 μm PVDF filter-vials containing 75 mg of anhydrous $MgSO_4$, 25 mg of PSA, 25 mg of C18, and 25 mg of Z-Sep sorbents. The filter-vial

DOI: 10.1021/jf506256q
J. Agric. Food Chem. 2015, 63, 5163−5168

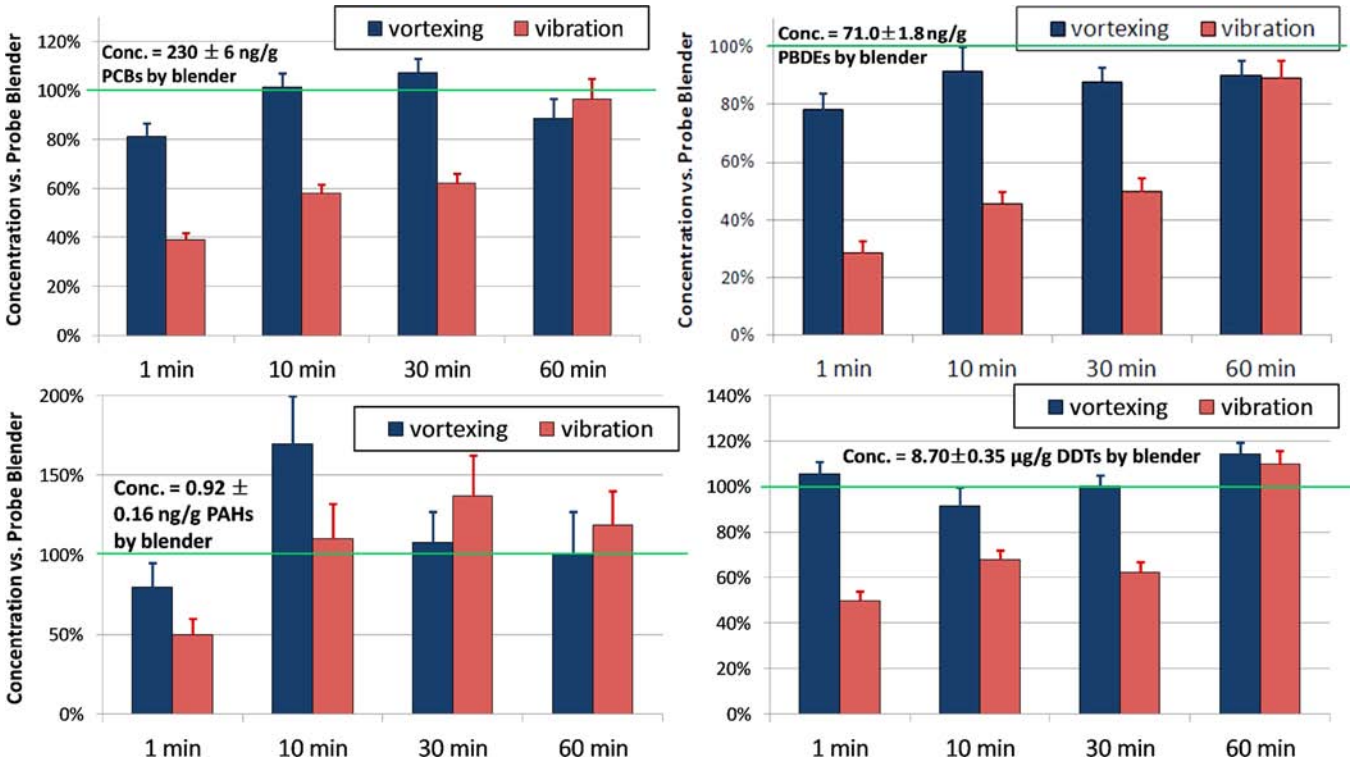

Figure 2. Extraction yields of contaminants in croaker: sum of 9 PCB congeners, sum of 5 PBDE congeners, sum of 5 DDT pesticides, and sum of PAHs (fluorene and anthracene). The pulsed-vortexer and vibrating shaker results are normalized to the probe blender results. Error bars represent standard deviation (n = 4).

plungers (top half) were partially depressed, the extracts were shaken by hand for 30 s in an autosampler vial tray, and then the plungers were fully depressed into the filter-vial shells. A commercial product of this filter-vial d-SPE approach was not yet available; thus, we had to transfer 200 μL of the filtered extracts to glass autosampler vials containing inserts prior to LPGC-MS/MS analysis.

Sample size and solvent ratio were studied in additional experiments using the pulsed-vortexer at 80% setting with maximum pulsing for 10 min and the streamlined filter-vial d-SPE cleanup method. Sample sizes of 2, 4, and 10 g of each fish were extracted with 2, 4, and 10 mL of MeCN for a 1 g/mL sample/solvent ratio, as well as 4 g of each fish was extracted with 8 mL of MeCN to evaluate the 0.5 g/mL sample/solvent ratio. These experiments were also conducted using four replicates at each set of conditions for salmon and croaker and one replicate for the limited amount of SRM 1947.

Rapid LPGC-MS/MS Analysis. An Agilent 7890 GC system with multimode inlet (MMI) interfaced to a 7000B triple-quadrupole MS/MS was used for analysis. The GC instrument was upgraded with a 220 V rapid heating oven device. A restriction capillary of 5 m × 0.18 mm i.d., HydroGuard (Restek, Bellefonte, PA, USA) coupled to 15 m × 0.53 mm i.d. × 1 μm film thickness Rti-5 ms column (Restek) was used for low-pressure (vacuum outlet) GC. High-purity He was the carrier gas at a constant flow rate of 2 mL/min. Injection volume was 5 μL using the MMI initially set at 80 °C for 0.31 min with vent at 50 mL/min, then ramped at 420 °C/min to 320 °C, and held until 9.5 min. The initial oven temperature was at 70 °C for 1.5 min, which was ramped at 80 °C/min to 180 °C and then at 40 °C/min to 250 °C, followed by 70 °C/min to 290 °C, at which it was held until 9.5 min. The transfer line and ion source were set at 280 and 320 °C, respectively, and the quadrupole was at 150 °C. Two MRMs per each analyte were used with a dwell time of 2.5 ms, similar to settings used in previous studies.[9,15,17]

The initial MRM method was divided into 28 time segments totaling 207 analytes and 12 ISTDs (see Supporting Information, Table S1, for the full list, retention times, and MRM transitions). This screen included 150 pesticides, 14 PCB congeners, 15 PAHs, 6 PBDE congeners, and 22 FRs. After nondetected analytes were dropped, the modified method included 35 analytes (16 pesticides, 5 PBDE and 9 PCB congeners, and 5 PAHs) and 9 isotopically labeled ISTDs (atrazine-d_5, fenthion-d_6, $^{13}C_{12}$-p,p'-DDE, pyrene-d_{10}, acenaphthylene-d_8, fluoranthene-d_{10}, phenanthrene-d_{10}, $^{13}C_{12}$-PCB 153, and FBDE 126) divided into 8 time segments. The ISTDs were not used to normalize the results for the analytes, but only as quality control spikes to demonstrate ISTD recoveries.

Due to matrix effects in GC-MS analyses of certain pesticides,[17] we intended to use matrix-matched calibration standards, but we could not find analyte-free salmon or white fish tissues. However, previous studies[9,15,17−19] demonstrated that matrix effects in the GC-MS method were insignificant for the nonpolar analytes determined in the samples, which enabled our use of solvent-based calibration standards to obtain accurate quantification of the final list of monitored contaminants. Calibration points were typically set at 0.1, 1, 5, 10, 50, 100, 250, and 500 ng/g for the analytes and 10 times lower levels for PCB congeners. In the case of croaker, additional points were added for PCB congeners at 100 and 150 ng/g. To quantify the high concentrations of DDE in the croaker, a 1000 ng/g calibration standard of o,p'-DDE was added along with 500, 1000, 2500, 5000, 7500, 10000 and 15000 ng/g of p,p'-DDE. To avoid detector saturation and still achieve linear calibration in the same injected extract as the ultratrace level contaminants, the least intense MRM transitions were selected for DDE, which avoided re-injection of diluted extracts just for this high concentration analyte.

RESULTS AND DISCUSSION

Extraction Devices. Figure 1 displays the three shaking devices employed in the study. A probe blender, or tissue homogenizer, works by inserting the metal probe mixer into a container containing the extraction solvent surrounding the fish tissue, which is ripped to tiny pieces, thus providing effective access of the solvent to the chemicals within the tissue. The pulsed-vortexer, capable of holding two standard trays with 25

DOI: 10.1021/jf506256q
J. Agric. Food Chem. 2015, 63, 5163−5168

tubes of 50 mL each, operates by intensive whirling action in pulsating fashion to thoroughly mix the prehomogenized samples with the extraction solvent. The tubes were placed vertically into the vortexer, although horizontal placement is also possible. The prototype vibration shaker permitted only horizontal placement of the tubes and entailed rapid vibrational motion to conduct extraction. This device was provided by the manufacturer to be evaluated for possible commercialization.

In terms of sample throughput, the pulsed-vortexer was able to process 50 samples at a time, whereas the prototype vibration shaker fits 6 tubes at a time. The probe blender, however, is not well-suited for use to extract a batch of samples because it requires cleaning of the probe between each sample to avoid cross-contamination. Thorough cleaning involved disassembling the probe, scrubbing with soap and water, rinsing with solvent, drying, and reassembly. The probe blender procedure has higher potential for introducing chemical interferences or excess liquid (if drying was not complete) into the sample, and always causes partial loss of extract onto the probe surfaces. The probe is also a safety risk, is very loud, and requires an open vessel that lets possible laboratory contaminants into the tube and sprays extract out of the tube. The sequential operation of the probe blender to extract samples is inconvenient, slow, laborious, and potentially hazardous.

We previously showed that the use of MeCN as an extraction solvent allows for simultaneous extraction of liphophilic nonpolar and relatively polar analytes (such as PAHs and some FRs) in one extraction step, with the added benefit of decreased amount coextracted fat compared to use of nonpolar solvents such as hexane or ethyl acetate.[9] However, even the extensively validated QuEChERS sample preparation method is not exhaustive, and therefore it is not known if total extractability of incurred contaminants is achieved, particularly for lipophilic analytes in fat-containing matrices.

The probe blender extraction method serves as a traditional standard procedure, which entails thorough homogenization of tissues with the solvent to yield total extraction. Table S2 (Supporting Information) lists average determined concentrations of incurred contaminants in croaker and salmon using 1 min extraction with the probe blender, and concentrations measured in SRM 1947 also using the probe blender versus the NIST-certified/reference concentrations. Percent accuracy of results for SRM 1947 was 69−144% with probe-blending extraction, thus demonstrating the degree of total extractability of the analytes in fish tissue with 10% lipid content. The determinations were 100% within typical expected experimental error for ultratrace level analyses. This supports the assertion that the probe blender provided 100% yield of incurred contaminants in the incurred fish samples. Extraction efficiency of contaminants in croaker (Figure 2) and salmon (Table 1) was expressed as relative recovery (%) for concentrations determined in samples extracted using the pulsed-vortexing and vibration-based shakers normalized to the probe blender results.

In terms of extraction efficiency, probe blender extraction for 1 min yielded the same concentrations of nearly all contaminants as maximum concentrations obtained for both types of shakers, which further supports the assertion that total extraction was achieved and true analyte concentrations were determined. As Figure 2 demonstrates, 1 min of shaking with the pulsed-vortexer was enough to yield 80−100% relative recovery of incurred contaminants from all classes in croaker tissues. Meanwhile, the vibration shaker yielded 30−50% extraction efficiency in 1 min and, in most cases, required 60 min of extraction time to achieve ≈100% relative recoveries. This trend also held true for pesticides, PCBs, and PBDEs. With respect to the detected PAHs (anthracene and fluorene), Figure 2 shows that 10 min of extraction with the vibration shaker was enough to yield 100% relative recovery, although <1 ng/g concentrations led to greater uncertainty in the results. This example illustrates how properties of the analytes affect the ease or difficulty of their extractability depending on the sample matrix. The log K_{ow} values of 4.1 and 4.9 for anthracene and fluorene, respectively, are lower compared to the other analyte classes (6.8−7.4 for PCBs, 5.9−7.9 for PBDEs, and 5.4−5.9 for DDT pesticides), and this may explain their faster partitioning into the MeCN extractant.

Table 1. Extraction Efficiency (Relative Recovery ± Standard Deviation) for PCBs, Pesticides, and PAHs in Salmon versus Concentration Determined in Samples Extracted for 1 min with the Probe Blender (100%)

analyte[a]	time (min)	vortexing (%)	vibrating (%)	blending (ng/g)
3 PCBs	1	74 ± 11	75 ± 13	6.68 ± 0.82
	10	153 ± 31	64 ± 14	
	30	129 ± 32	72 ± 15	
	60	132 ± 18	88 ± 14	
7 pesticides	1	79 ± 9	62 ± 7	25.5 ± 2.7
	10	99 ± 14	67 ± 10	
	30	136 ± 19	83 ± 10	
	60	84 ± 10	70 ± 9	
5 PAHs	1	100 ± 9	75 ± 6	3.71 ± 0.27
	10	128 ± 12	94 ± 16	
	30	125 ± 11	133 ± 12	
	60	127 ± 11	145 ± 13	

[a]See Table S2 in the Supporting Information for the specific analytes determined.

High concentrations of PCBs and DDE in croaker are explained by the fish's origin near the EPA Superfund site in Palos Verdes Peninsula, which was a discharge site for production of PCBs and DDTs until ≈1974. Because these contaminants are highly lipophilic and persistent, they accumulate in fish tissues. The Pacific white croaker was collected in 2002 and stored in the Marine Specimen Bank, so it does not reflect the current situation at the collection site. However, a recent study by Venkatesan et al.[20] reported relatively high concentrations of PCBs and DDTs in Santa Monica Bay sediments and suggested that the contaminants could have been transported from the Palos Verdes Shelf area.

Extraction Time. Extraction time for the probe blender was always 1 min, but 1, 10, 30, and 60 min extractions were investigated using the vibration shaker and pulsed-vortexer. Table 1 and Figure 2 show the results for incurred contaminants from salmon and croaker, respectively (individual analyte results are shown in Table S2 in the Supporting Information). The results for individual analytes in NIST SRM 1947 versus extraction time and method are also presented in Figures S1−S4. In salmon tissue, 1 min extraction yielded 62−75 and 74−100% for the vibrating and pulsed-vortexing shakers, respectively, relative to the probe blender results. These yields were greater than those in croaker, suggesting fish composition can play a role in extractability of the

DOI: 10.1021/jf506256q
J. Agric. Food Chem. 2015, 63, 5163−5168

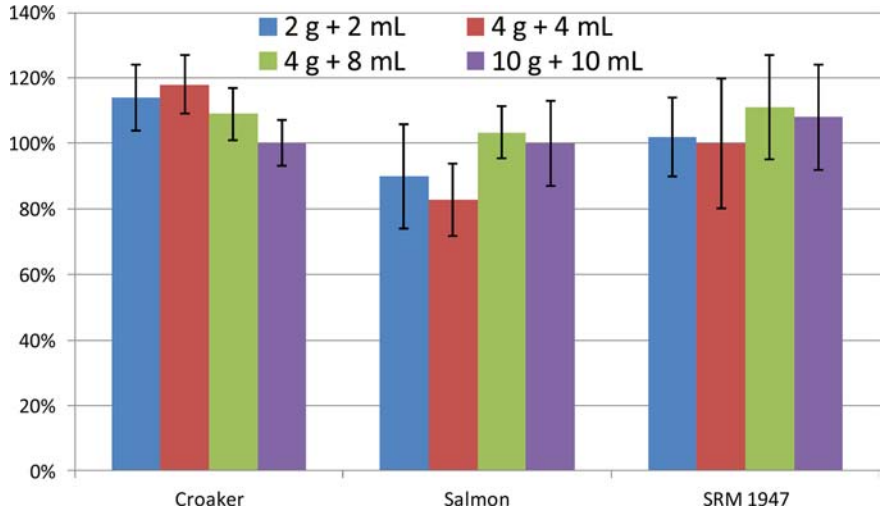

Figure 3. Average recoveries of incurred contaminants from croaker (23 analytes) and salmon (13 analytes), normalized to concentrations measured in samples using 10 g/10 mL (100%) and accuracy of measurements for SRM 1947 versus certified concentrations (27 analytes) for different sample/solvent ratios. See Table S2 in the Supporting Information for the specific analytes determined. Error bars represent standard deviation (n = 4).

contaminants. Lipid content in croaker is reported to be 3−4%, whereas salmon contains 5−10% fat, which often complicates the analysis due to the negative effects of lipids in both sample preparation and analysis. The concentrations of the contaminants in salmon were much lower compared to croaker, and the >100% relative recoveries (high bias) and worse precision in the results were probably due to greater measurement uncertainty at low analyte concentrations, especially in fatty samples.

In our previous study,[18] we observed negative correlations between recoveries of PBDE congeners and their log K_{ow} values. Pearson correlation coefficients were from −0.95 to −0.99, indicating that increased log K_{ow} caused decreased recoveries from lipid-containing samples. PBDE 153 has the highest log K_{ow} value of 7.9 compared to the other congeners determined in SRM 1947. PBDE 153 required 60 min of extraction time with the vibration shaker to reach the same yield as 1 min extraction with the pulsed-vortexer or probe blender (see Supporting Information Figure S5). Clearly, the pulsed-vortexer performed well to fully extract even the most lipophilic analytes in the fish samples containing up to 10% fat, and the prototype vibrational shaker did not adequately meet the need for rapid total extraction.

Sample Size and Solvent Ratio. Another aspect of the study was to determine the effect of sample size and sample/solvent ratio on the results for the incurred fish tissues. Smaller subsample size often translates into faster, easier, and less wasteful methods, provided that the subsample adequately represents the original sample. We used the pulsed-vortexer with 10 min of extraction time in the experiments to assess subsample sizes of 2, 4, and 10 g extracted with 2, 4, and 10 mL of MeCN, respectively (1 g/mL sample/MeCN ratio), and subsamples of 4 g were extracted with 8 mL of MeCN to evaluate 0.5 g/mL ratios. Due to the limited supply and high cost of SRM 1947, only 5/5 g/mL (n = 4) was tested in that case.

For salmon and croaker, the determined concentrations from extractions of 2/2, 4/4, and 4/8 g/mL were compared to concentrations measured using 10/10 g/mL, which was already shown to yield total extractability. As Figure 3 demonstrates, there was no difference in yields for any combination of sample/solvent ratio. This finding suggests that homogeneous subsample size can be minimized as long as it remains representative,[21] thereby requiring less organic solvent and leading to less waste. The same conclusions were drawn for SRM 1947 in the experiment, in which percent accuracy of determined versus certified concentrations did not depend on the subsample amount or sample/solvent ratio. This finding exposes another disadvantage of extraction using the probe blender, which needs at least 5 mL of solvent to work properly.

Fussell et al. evaluated homogeneity of analytical samples homogenized cryogenically versus room temperature, and they concluded that smaller portions of analytical sample can be representative when using cryogenic homogenization for certain matrices.[2] In the case of sample/solvent ratios in QuEChERS, Chamkasem et al. investigated sample/solvent ratios of 3/10, 3/15, 3/20, 3/25, and 3/30 g/mL MeCN for the analysis of lipophilic pesticides in avocado (≈15% fat),[22] and they concluded that 3/25 g/mL was sufficient to yield 100% recoveries from fortified samples. In our study, we did not observe a difference in extraction efficiencies for the same nonpolar pesticides using 1/1 or 1/2 g/mL sample/MeCN ratios in incurred fish. Perhaps the higher fat content in avocado and fat composition differences (salmon contains ≈3.5% of monounsaturated fat vs ≈9.5% in avocado) affected these findings.

In conclusion, we compared extractabilities of 35 incurred contaminants in 3 different types of fish tissues using 3 extraction devices (vibration shaker, pulsed-vortexer, and probe blender) for different lengths of time, subsample size, and solvent ratio. Our results showed that 1 min of extraction with the pulsed-vortexing shaker was sufficient for extraction of many incurred contaminants in the prehomogenized fish tissues, but we chose to use 10 min extractions as a precaution, which still attains 0.2 min/sample equivalent for a batch of 50 samples. The probe blender yielded similar results in 1 min, but cannot come close to approaching the high sample throughput, ease, convenience, safety, versatility, and other practical benefits of the pulsed-vortexer. Extraction with the prototype vibration shaker often took 60 min to achieve total extractability, and the

DOI: 10.1021/jf506256q
J. Agric. Food Chem. 2015, 63, 5163−5168

device is not likely to be commercialized. In other respects, 1 g/mL sample/MeCN was sufficient to achieve full extraction, and 2 g of homogenized subsample gave results equivalent to those with 4 and 10 g subsamples of the cryogenically homogenized fish tissues. This study demonstrated for real-world fish samples up to 10% fat content that a simple QuEChERS method using the pulsed-vortexer for batch extraction of 2 g subsamples with 2 mL of MeCN, followed by a convenient filter-vial d-SPE cleanup, provides complete extraction and high sample throughput. The use of LPGC-MS/MS permitted 10 min quantitative and qualitative analysis of 207 targeted contaminants (pesticides, PCBs, PAHs, PBDEs, and other FRs) at ultratrace concentrations in fish and similar sample types.

■ ASSOCIATED CONTENT

Supporting Information

Figures S1−S5 and Tables S1 and S2. This material is available free of charge via the Internet at http://pubs.acs.org.

■ AUTHOR INFORMATION

Corresponding Author

*(S.J.L.) Phone: (215) 233-6433. Fax: (215) 233-6642. E-mail: Steven.Lehotay@ars.usda.gov.

Notes

Mention of brand or firm names does not constitute an endorsement by the U.S. Department of Agriculture above others of a similar nature not mentioned.

The authors declare no competing financial interest.

■ ACKNOWLEDGMENTS

We thank Rebecca Pugh of NIST Marine Environmental Specimen Bank for providing the croaker and salmon samples, Sam Ellis of Thomson Instrument Co. for d-SPE filter vials, and Mitsuhiro Kurano and Nikolay Gribov of GL Sciences for the prototype vibration shaker. We greatly appreciate the technical assistance of Tawana Simons and Alan Lightfield.

■ REFERENCES

(1) Federal Register 40 CFR Part 158 − Data Requirements for Pesticides, 860. 1340 Residue Analytical Method.

(2) Fussell, R. J.; Hetmanski, M. T.; Macarthur, R.; Findlay, D.; Smith, F.; Ambrus, A.; Brodesser, P. J. Measurement uncertainty associated with sample processing of oranges and tomatoes for pesticide residue analysis. *J. Agric. Food Chem.* **2007**, *55*, 1062−1070.

(3) Anastassiades, M.; Lehotay, S. J.; Stajnbaher, D.; Schenck, F. J. Fast and easy multiresidue method employing acetonitrile extraction/partitioning and "dispersive solid-phase extraction" for the determination of pesticide residues in produce. *J. AOAC Int.* **2003**, *86*, 412−431.

(4) Zhang, Y. Y.; Lin, N.; Su, S.; Shen, G. F.; Chen, Y. C.; Yang, C. L.; Li, W.; Shen, H. Z.; Huang, Y.; Chen, H.; Wang, X. L.; Liu, W. X.; Tao, S. Freeze drying reduces the extractability of organochlorine pesticides in fish muscle tissue by microwave-assisted method. *Environ. Pollut.* **2014**, *191*, 250−252.

(5) *Pesticide Analytical Manual*, 3rd ed.; FDA, U.S. Department of Health and Human Services, Public Health Service: Washington, DC, USA, 1994; Vol. I, Multiresidue Methods.

(6) Cajka, T.; Sandy, C.; Bachanova, V.; Drabova, L.; Kalachova, K.; Pulkrabova, J.; Hajslova, J. Streamlining sample preparation and gas chromatography-tandem mass spectrometry analysis of multiple pesticide residues in tea. *Anal. Chim. Acta* **2012**, *743*, 51−60.

(7) Anastassiades, M.; Barth, A.; Dork, D.; Steffens, T. Studies on the extractability of incurred pesticide residues. Presented at the North America Chemical Residue Workshop, St. Pete Beach, FL, USA, 2013.

(8) SANCO/12571/2013. www.eurl-pesticides.eu/library/docs/allcrl/AqcGuidance_Sanco_2013_12571.pdf.

(9) Sapozhnikova, Y.; Lehotay, S. J. Multi-class, multi-residue analysis of pesticides, polychlorinated biphenyls, polycyclic aromatic hydrocarbons, polybrominated diphenyl ethers and novel flame retardants in fish using fast, low-pressure gas chromatography−tandem mass spectrometry. *Anal. Chim. Acta* **2013**, *758*, 80−92.

(10) Kalachova, K.; Pulkrabova, J.; Drabova, L.; Cajka, T.; Kocourek, V.; Hajslova, J. Simplified and rapid determination of polychlorinated biphenyls, polybrominated diphenyl ethers, and polycyclic aromatic hydrocarbons in fish and shrimps integrated into a single method. *Anal. Chim. Acta* **2011**, *707*, 84−91.

(11) Li, H.; Kijak, P. J.; Turnipseed, S. B.; Cui, W. Analysis of veterinary drug residues in shrimp: a multi-class method by liquid chromatography-quadrupole ion trap mass spectrometry. *J. Chromatogr., B* **2006**, *836*, 22−38.

(12) Guillet, V.; Fave, C.; Montury, M. Microwave/SPME method to quantify pesticide residues in tomato fruits. *J. Environ. Sci. Health B* **2009**, *44*, 415−22.

(13) Feng, S. X.; Chiesa, O. A.; Kijak, P.; Chattopadhaya, C.; Lancaster, V.; Smith, E. A.; Girard, L.; Sklenka, S.; Li, H. Determination of ceftiofur metabolite desfuroylceftiofur cysteine disulfide in bovine tissues using liquid chromatography-tandem mass spectrometry as a surrogate marker residue for ceftiofur. *J. Agric. Food Chem.* **2014**, *62*, 5011−5019.

(14) USDA National Nutrient Database for Standard Reference, http://ndb.nal.usda.gov.

(15) Han, L. J.; Sapozhnikova, Y.; Lehotay, S. J. Streamlined sample cleanup using combined dispersive solid-phase extraction and in-vial filtration for analysis of pesticides and environmental pollutants in shrimp. *Anal. Chim. Acta* **2014**, *827*, 40−46.

(16) González-Curbelo, M. A.; Lehotay, S. J.; Hernández-Borges, J.; Rodríguez-Delgado, M. A. Use of ammonium formate in QuEChERS for high-throughput analysis of pesticides in food by fast, low-pressure gas chromatography and liquid chromatography tandem mass spectrometry. *J. Chromatogr., A* **2014**, *1358*, 75−84.

(17) Kwon, H.; Lehotay, S. J.; Geis-Asteggiante, L. Variability of matrix effects in liquid and gas chromatography-mass spectrometry analysis of pesticide residues after QuEChERS sample preparation of different food crops. *J. Chromatogr., A* **2012**, *1270*, 235−245.

(18) Sapozhnikova, Y. Rapid sample preparation and fast GC-MS/MS for the analysis of pesticides and environmental contaminants in fish. *LCGC North Am.* **2014**, *32*, 878−886.

(19) Sapozhnikova, Y. Evaluation of low-pressure gas chromatography-tandem mass spectrometry method for the analysis of >140 pesticides in fish. *J. Agric. Food Chem.* **2014**, *62*, 3684−3689.

(20) Venkatesan, M. I.; Merino, O.; Baek, J.; Northrup, T.; Sheng, Y.; Shisko, J. Trace organic contaminants and their sources in surface sediments of Santa Monica Bay, California, USA. *Mar. Environ. Res.* **2010**, *69*, 350−362.

(21) Omeroglu, P. Y.; Ambrus, A.; Boyacioglu, D. Estimation of sample processing uncertainty of large-size crops in pesticide residue analysis. *Food Anal. Methods* **2013**, *6*, 238−247.

(22) Chamkasem, N.; Ollis, L. W.; Harmon, T.; Lee, S.; Mercer, G. Analysis of 136 pesticides in avocado using a modified QuEChERS method with LC-MS/MS and GC-MS/MS. *J. Agric. Food Chem.* **2013**, *61*, 2315−2329.

DOI: 10.1021/jf506256q
J. Agric. Food Chem. 2015, 63, 5163−5168

JOURNAL OF AGRICULTURAL AND FOOD CHEMISTRY

Article

pubs.acs.org/JAFC

Effect of Sample Dilution on Matrix Effects in Pesticide Analysis of Several Matrices by Liquid Chromatography−High-Resolution Mass Spectrometry

Paul Yang,*[,†,∥] James S. Chang,[§,∥] Jon W. Wong,[#,∥] Kai Zhang,[#] Alexander J. Krynitsky,[#] Maciej Bromirski,[⊥] and Jian Wang[⊗]

[†]Ontario Ministry of the Environment and Climate Change, Laboratory Services Branch, 125 Resources Road, Etobicoke, Ontario, Canada M9P 3V6

[§]ThermoFisher Scientific, 355 River Oaks Parkway, San Jose, California 95134-1908, United States

[#]U.S. Food and Drug Administration, Center for Food Safety and Applied Nutrition, 5100 Paint Branch Parkway, College Park, Maryland 20740-3835, United States

[⊥]ThermoFisher Scientific, Hanna-Kunath-Strasse 11, 28199 Bremen, Germany

[⊗]Canadian Food Inspection Agency, Calgary Laboratory, Calgary, Alberta, Canada T2L 2L1

Supporting Information

ABSTRACT: This study used two LC columns of different adsorbents and liquid chromatography−electrospray ionization−high-resolution mass spectrometry to study the relationship between matrix effects (ME), the LC separations, and elution patterns of pesticides and those of matrix components. Using calibration standards of 381 pesticides at three dilution levels of 1×, 1/10×, and 1/100×, 108 samples were prepared in solvent and five different sample matrices for the study. Results obtained from principal component analysis and slope ratios of calibration curves provided measurements of the ME and showed the 1/100× sample dilution could minimize suppression ME for most pesticides analyzed. Should a pesticide coeluting with matrix components have a peak intensity of 25 times or higher, the suppression for that pesticide would persist even at 1/100× dilution. The number of pesticides had enhancement ME increased with increasing dilution from 1× to 1/100×, with those early eluting, hydrophilic pesticides affected the most.

KEYWORDS: *matrix effects, multiresidue pesticides analysis, high-performance liquid chromatography (HPLC), Orbitrap mass spectrometry (Orbitrap MS)*

INTRODUCTION

The development and use of liquid chromatography−electrospray ionization−mass spectrometry (LC-ESI-MS) instrumentation have gained tremendous momentum since the turn of the century. Using different LC-MS platforms, analytical methods have been developed for the analysis of organic contaminants such as pesticides,[1−3] antibiotics, pharmaceuticals, personal care products,[4−6] cyanotoxins,[7] and mycotoxins[8−10] in complex environmental and food matrices. These methods are characterized by their superior performance in sensitivity, selectivity, and ability to use rugged sample preparation procedures without requiring the extensive cleanup or derivatization that are commonly required by gas chromatography methods and allow for the development of multiresidue methods capable of analyzing >200 pesticides[11−15] in a single analysis.

LC-MS-based analytical methods suffer from matrix effects (ME)[16−22] that are common in environmental and food analyses and affect the data quality and accuracy of quantitative analyses. Matrix effects are commonly observed as suppression or enhancement of analyte signal in the ESI source and have been studied by many researchers since the mid-1990s. Most of the studies have been focused on the ESI suppression rather than the enhancement. The phenomenon of ESI suppression was first recognized by Kebarle and Tang[23,24] in 1993 with detailed mechanisms explained by Bruins.[25] The upper limit of the effective concentrations (total concentration of the analyte and matrix components) of those ion-emitting droplets in the ESI source was estimated[24] at 1×10^{-5} M (or 6.02×10^{18} charged ions/L). As long as the effective concentration is $<1 \times 10^{-5}$ M, the ESI source should be able to effectively ionize all analytes eluted from the column and no suppression of analyte(s) will be observed. Should the effective concentration become $>1 \times 10^{-5}$ M, the analyte(s) are forced to share the surface of the ion-emitting droplets with matrix components on a competitive basis, resulting in the suppression. Studies to date have been carried out by LC−tandem MS (LC-MS/MS) instrumentation with the sole goal of investigating the ESI suppression of target analytes.

Matrix components are "unknowns" in targeted LC-MS/MS analyses and have not been studied concurrently with the

Special Issue: 51st North American Chemical Residue Workshop

Received: October 26, 2014
Revised: January 12, 2015
Accepted: January 25, 2015
Published: January 25, 2015

ACS Publications © 2015 American Chemical Society

DOI: 10.1021/jf505168v
J. Agric. Food Chem. 2015, 63, 5169−5177

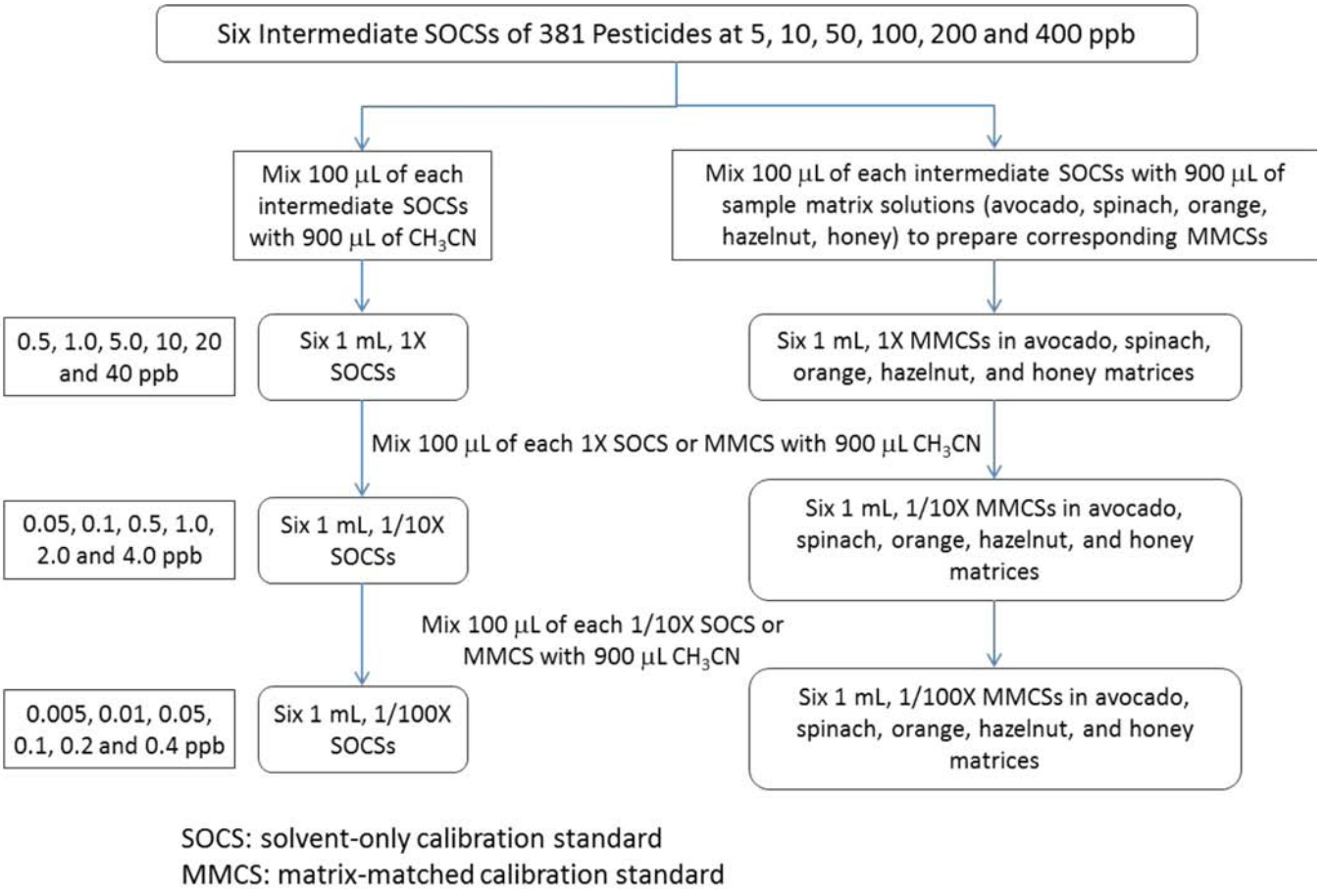

Figure 1. Procedures used in the preparation of 1×, 1/10×, and 1/100× diluted solvent-only calibration standards and matrix-matched calibration standards.

analytes to gain an in-depth understanding of the ME. Consequently, operating strategies have been focused on the analytes without examining the possibility of resolving ME in the context of the matrix components. For example, exhaustive sample cleanup may help remove interfering components, but this is time-consuming and has the risk of losing analytes of interest and of variability of sample results. The use of matrix-matched calibration standards (MMCS) can be an effective approach, but this requires the availability of uncontaminated sample matrix to be used to prepare calibration standards, and this can be a difficult task. The blank matrix may not be identical to the sample matrix and still can cause biases in quantitative analysis. The use of standard addition[18] with which a fixed amount of analytical standards is added to the samples to generate a calibration curve for each sample may be effective but is tedious and impractical for real world sample analysis, where one must deal with a large number of samples and analytes. An effective approach to compensating for ME is the application of isotope dilution MS quantitation using isotopically labeled compound.[10] However, this is an impractical practice for multiresidue analysis with a large number of analytes. At the present time, sample dilution has been demonstrated to be the most effective approach to minimize ME.[20,26] This is performed by serially diluting the final extract such that lesser amounts of matrix components and analytes will be injected into the analytical system. Using post-column infusion and ME versus retention time (RT) plots, Stahnke et al.[26] demonstrated that a dilution factor of 25−40 of extracts would reduce the suppression of total ME to <20% of the initial suppression. This approach, and a similar split of the LC eluent flow before it enters the mass spectrometer, will be limited by the available sensitivity of a specific LC-MS system to reach the desired and required detection limits of the diluted extracts.

The availability of LC-ESI−high-resolution mass spectrometry (LC-ESI-HRMS)[27] systems offers the opportunity to investigate ME with new perspectives. These systems have the ability to acquire high-resolution, full mass spectral data with sensitivity comparable to that of LC-MS/MS systems. Full scan mass spectra not only provide information for the analyte(s) that are affected by sample matrix but also provide an opportunity to investigate other components in the sample that may be responsible for the suppression. These mass spectral data have high mass accuracy and peaks with full width at half-maximum (fwhm) in the 1.5×10^{-3} Da range, allowing for the use of a very narrow mass extraction window (MEW),[28] that is, 5 ppm, to construct extracted ion chromatogram (XIC) for target analyte(s) and matrix components. XICs obtained from these experiments separate pesticides and matrix components in both chromatographic and mass spectrometric domains, provide retention time and area count for the identification and quantization of target pesticides and area counts for the semiquantitative analysis of "unknown", that is, matrix components, and become vital for the concurrent study of ME from the perspective of both target analyte(s) and matrix components. We report in this paper results obtained from LC-ESI-HRMS experiments with an emphasis on the relationship

DOI: 10.1021/jf505168v
J. Agric. Food Chem. 2015, 63, 5169−5177

between ME and pesticides in terms of the LC separations and elution patterns.

EXPERIMENTAL PROCEDURES

Chemicals. The majority of the 381 pesticide standards were obtained from the United States Environmental Protection Agency (U.S. EPA) Pesticide Repository (Ft. Meade, MD, USA), whereas others were obtained through Fluka/Sigma-Aldrich (St. Louis, MO, USA), EQ Laboratories (Dr. Ehrenstofer, Atlanta, GA, USA), and Wako Chemicals USA (Richmond, VA, USA) and are listed in the Supporting Information (SI) (Table S1). HPLC grade water, acetonitrile (CH_3CN), methanol (MeOH), formic acid (HCOOH), ammonium formate (CH_3COONH_4), anhydrous $MgSO_4$, and NaCl were purchased from Fisher Scientific (Pittsburgh, PA, USA). Deuterium-labeled diazinon ($^2H_{10}$-diazinon) was purchased from CDN-Isotopes (Montreal, QC, Canada) and used as internal standard. The QuEChERS product, that is, 4 g of anhydrous magnesium sulfate and 1 g of sodium chloride in 50 mL centrifuge tubes, was purchased from United Chemical Technologies (UCT; Bristol, PA, USA). Five sample matrices consisting of avocado, spinach, honey, orange, and hazelnut were purchased as organic products from commercially available sources. Laboratory nanopure water generated by passing reverse osmosis water through a Thermo Scientific Barnstead Nanopure water purification system was used in the sample preparation and HPLC analysis.

Sample and Standard Preparation. All sample matrices (avocado, orange, spinach, honey, and hazelnut) were prepared using a modified AOAC QuEChERS (quick, easy, cheap, effective, rugged, and safe) method.[1,2] Avocado, orange, and spinach were prepared by weighing 10 ± 0.2 g of cryo-ground sample in 50 mL disposable screw-capped polypropylene centrifuge tubes (Fisher Scientific). Ten milliliters of water was first added to honey (10 ± 0.2 g) and ground hazelnut (5.0 ± 0.02 g) and mixed thoroughly to lessen the viscosity of the honey and to form a homogeneous mixture in the same 50 mL centrifuge tubes. These sample tubes were extracted by the addition of 10 mL of CH_3CN, 4 g of anhydrous $MgSO_4$, and 1 g of anhydrous sodium chloride (UCT). After hand-shaking the sample to prevent clumping of the salts, the sample tubes were placed on a GenoGrinder mechanical shaker (SPEX Sample Prep, LLC, Metuchen, NJ, USA) for 1 min at 1000 strokes/min. Samples were then centrifuged (Labnet Z383, Atlanta, GA, USA) at 4500 rpm for 5 min to separate the sample and extracts. The extracts (~9 mL), which had about 1.0 g/mL of matrix components, were transferred into 12 mL screw-capped polypropylene centrifuge tubes through 0.2 μm PTFE membrane filters (Sun SRi, Rockwood, TN, USA) and used later in the preparation of matrix-matched calibration standard (MMCS).

Six intermediate, solvent-only calibration standards (SOCS) of 381 pesticides were prepared in CH_3CN at six concentration levels of 400, 200, 100, 50, 10, and 5 ng/g (ppb). Using 100 μL of these SOCS with 900 μL of CH_3CN in six separate 1.5 mL autosampler vials resulted in six SOCS at concentration levels of 40, 20, 10, 5, 1, and 0.5 ng/g, which are labeled as 1× SOCS samples (Figure 1). Those 1× MMCS samples were prepared in the same manner by mixing 100 μL of the SOCS and 900 μL of matrix materials in 36 autosampler vials, achieving five MMCS sample sets at six concentrations of 40, 20, 10, 5, 1, and 0.5 ng/g. The 1/10× samples were prepared by diluting 100 μL of the 1× samples using 900 μL of CH_3CN, resulting in 36 samples at pesticide concentrations of 0.05−4 ng/g. Those 1/100× samples were prepared using 100 μL of 1/10× samples and 900 μL of CH_3CN, resulting in concentrations from 0.005 to 0.4 ng/g. After removal of 100 μL of solution from each of the 1/100× sample sets, 20 μL of 2000 ng/g internal standard $^2H_{10}$-diazinon was added to all sample vials to compensate for possible sample volume variation, homogenized on a vortex at 100 rpm, and stored in a freezer at −5 °C until ready for analysis. Matrix components in the 1×, 1/10×, and 1/100× MMCS solutions were about 900, 80, and 7 mg/mL, respectively. Quality control samples prepared with each sample set include matrix blank and system blank (CH_3CN).

LC-Orbitrap MS Analysis. A Thermo Scientific Dionex UltiMateTM 3000 HPLC system consisting of an HRG-3400RS binary pump, a WPS-3000 autosampler, and a TCC-3400 column compartment was used in the HPLC analysis. LC separations were achieved on a Restek Ultra Aqueous non-end-capped C-18 (uAqueous, 3 μm, 100 Å pore size, 15% carbon loading, Bellefonte, PA, USA) and a Thermo Scientific Accucore aQ end-capped C-18 (Accucore, 2.6 μm, 80 Å pore size, 9% carbon loading, San Jose, CA, USA) columns. Both columns had dimensions of 100 × 2.1 mm and had 10 × 2.1 mm guard cartridges. The injection volume used was 15 μL. Mobile phases used were (A) 5 mM $HCOONH_4$ and 0.1% HCOOH in CH_3OH/H_2O = 5:95 v/v and (B) 5 mM $HCOONH_4$ and 0.1% HCOOH in CH_3OH/H_2O = 95:5 v/v. The HPLC separation used an initial equilibration time of 3 min at 5% B. Gradient separation was achieved from 5% B at 0 min, increased to 20% B at 4 min, increased to 40% B at 5.5 min, and increased to 98% B at 10.5 min and maintained at 98% B until the end of the analysis at 15 min. The column temperature used was 35 °C. The flow rates used were 350 μL/min (uAqueous) and 420 μL/min (Accucore).

The HPLC was interfaced to a Thermo Scientific Exactive Plus (Orbitrap MS) using heated ESI (HESI) interfaces. The Orbitrap MS system were tuned and calibrated in positive ion mode by infusion of standard mixtures of MSCAL5 (Sigma-Aldrich). High-purity nitrogen (>99%) was used in the ESI source (35 L/min). The capillary and the HESI temperatures were set at 300 °C. Mass spectrometric data were collected using a spray voltage of 3000 V and a resolving power of 140,000 (full width half-maximum peak width at m/z 200, R_{fwhm}), resulting in a data acquisition rate of 1.5 scans/s when using automatic gain control of 1×10^6 and a C-trap inject time of 50 ms. The R_{fwhm} used meets the minimally required R_{fwhm} of 60,000[29] to carry out multiresidue chemical analysis. The flow rates and analytical columns used in the separation result a chromatographic fwhm of 3−9 s. Therefore, at least nine data points were available to accurately define XIC chromatograms for quantitative analysis. Retention times (RT) from the two LC columns and instrument detection limit (IDL) of the system are listed in Table S1 (SI).

Data Analysis. Analytical data collected were processed offline using Xcalibur 3, TraceFinder 3.2, and SIEVE 2.1 (Thermo Scientific, San Jose, CA, USA) data processing packages. Xcalibur was used to process mass spectral data for graphic presentation. TraceFinder was used to derive area counts, to do quantitative analysis, and to evaluate the ME. A MEW of 5 parts per million (ppm) was used to create XIC chromatograms for quantitative analysis of target analytes and semiquantitative analysis of matrix components. Results were exported to Excel for data compilation, statistical evaluation, and the determination of R_{slope}. Principal component analysis (PCA) and differential expression analysis (DEA) were achieved by SIEVE using Orbitrap mass spectral data sets without further modifications.

RESULTS AND DISCUSSION

Effects of LC Separation and Sample Dilution on ME. Effects of matrix components on the 381 pesticides studied were first examined. Values of slope ratio (R_{slope}) have been used to gauge the extent of ME exerted by different matrices on target pesticides.[2] Different from the post-column infusion approach, which used ME versus RT plots[30] to estimate combined ME at a specific RT, the R_{slope} approach calculated the ratio of slopes of MMCS and SOSC calibration curves for each pesticide to provide ME information for a specific pesticide. In the absence of experimental error, a value of 1.00 for the R_{slope} shows no ME, whereas values deviating from 1.00 indicate the existence of ME as ESI suppression or enhancement. Values of the R_{slope} are listed in Si Tables S2 and S3, respectively, for the uAqueous and Accucore columns. The lowest calibration levels for 1×, 1/10×, and 1/100× samples were 0.5, 0.05, and 0.005 ng/g, equivalent to LC column loadings of 7.5×10^{-12}, 0.75×10^{-12}, and 0.075×10^{-12} g.

DOI: 10.1021/jf505168v
J. Agric. Food Chem. 2015, 63, 5169−5177

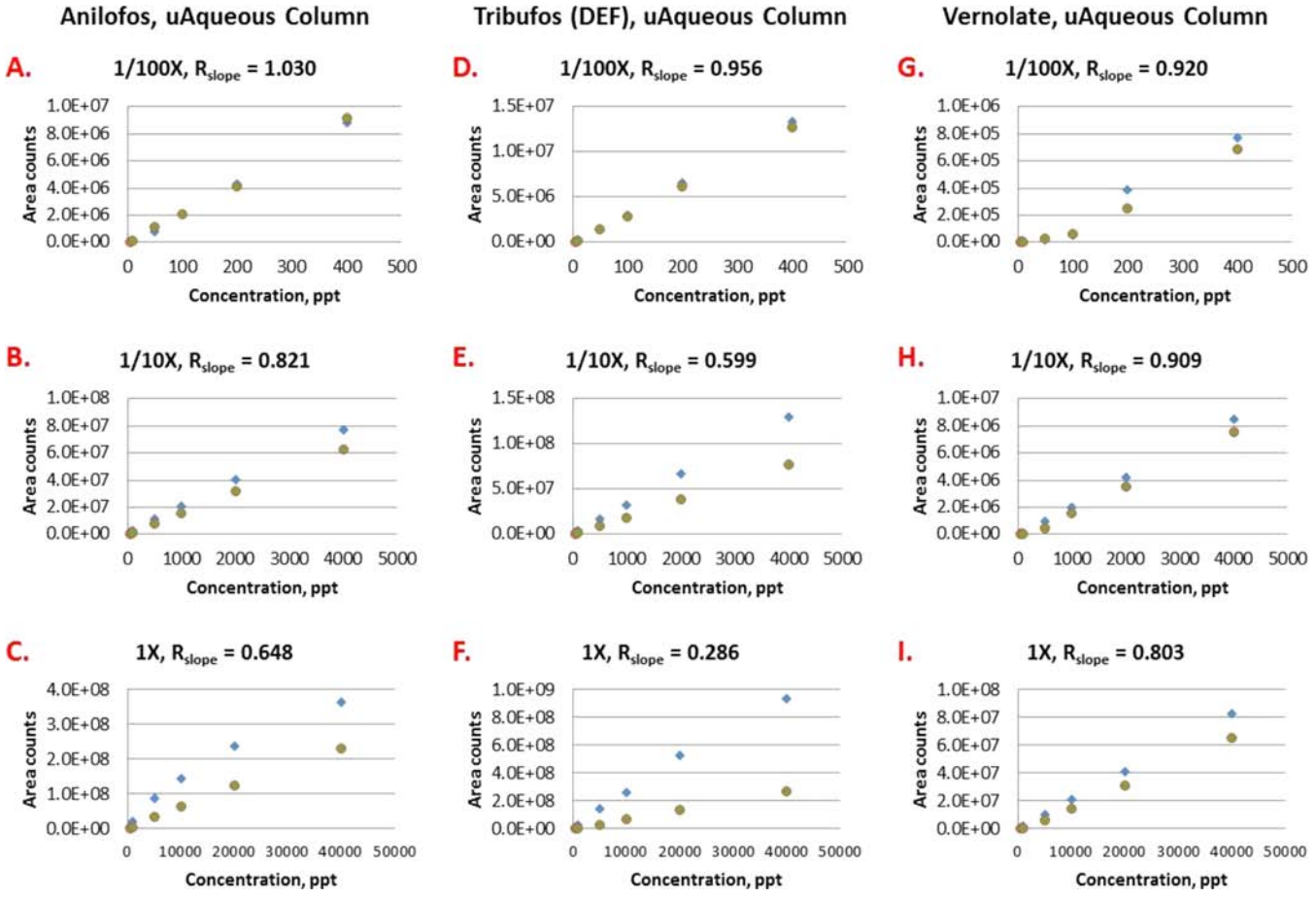

Figure 2. Calibration curves of pesticides anilofos, tribufos and vernolate obtained from SOSC (blue squares) and avocado MMCS (dark green circles) using a uAqueous column at 1×, 1/10×, and 1/100× dilutions.

Table 1. Number of 381 Pesticides Showing Suppression or Enhancement Obtained from the uAqueous and Accucore Analyses in Five Sample Matrices and Different Levels of Sample Dilution[a]

		uAqueous					Accucore				
dilution	R_{slope}	Avo	HzNut	Hon	Org	Spn	Avo	HzNut	Hon	Org	Spn
1×	$0.8 < R_{slope} < 1.2$ (matrix effects free)	88	284	354	191	326	90	98	196	193	252
	$R_{slope} > 1.2$ (enhancement)	12	25	8	12	14	7	14	44	18	90
	$R_{slope} < 0.8$ (suppression)	276	72	19	177	41	272	214	125	157	35
	ND	5	0	0	1	0	12	55	16	13	4
1/10×	$0.8 < R_{slope} < 1.2$ (matrix effects free)	208	328	368	312	359	182	330	352	288	340
	$R_{slope} > 1.2$ (enhancement)	10	34	7	38	11	13	16	11	27	21
	$R_{slope} < 0.8$ (suppression)	157	18	5	29	10	174	28	9	57	12
	ND	6	1	1	2	1	12	7	9	9	8
1/100×	$0.8 < R_{slope} < 1.2$ (matrix effects free)	292	319	330	304	325	286	311	310	298	315
	$R_{slope} > 1.2$ (enhancement)	44	27	14	40	29	23	10	15	30	27
	$R_{slope} < 0.8$ (suppression)	20	11	14	12	3	42	27	29	25	13
	ND	25	24	23	25	24	30	33	27	28	26

[a]Avo, avocado; HzNut, hazelnut; Hon, honey; Org, orange; Spn, spinach; ND, nondetects.

From Table S1, pesticides in low-level calibration solutions may become less than their corresponding IDL and were not detected, labeled as "not detected", and not used for calibration. That pesticide will be marked as "NA" in SI Tables S2 and S3 with more than three calibration levels in a specific sample set failing to meet this criterion. Plots of R_{slope} versus RT for the five sample matrices, three dilutions levels, and two LC columns are shown in SI Figures 1−5. The effect of sample dilutions on suppression is demonstrated in Figure 2 using results obtained from uAqueous column for anilofos, tribufos (DEF), and vernolate, with results obtained from Accucore column shown in SI Figure 6.

From Figure 2 and SI Figure 6, one could observe that suppression is dependent on the LC columns but may not be

DOI: 10.1021/jf505168v
J. Agric. Food Chem. 2015, 63, 5169−5177

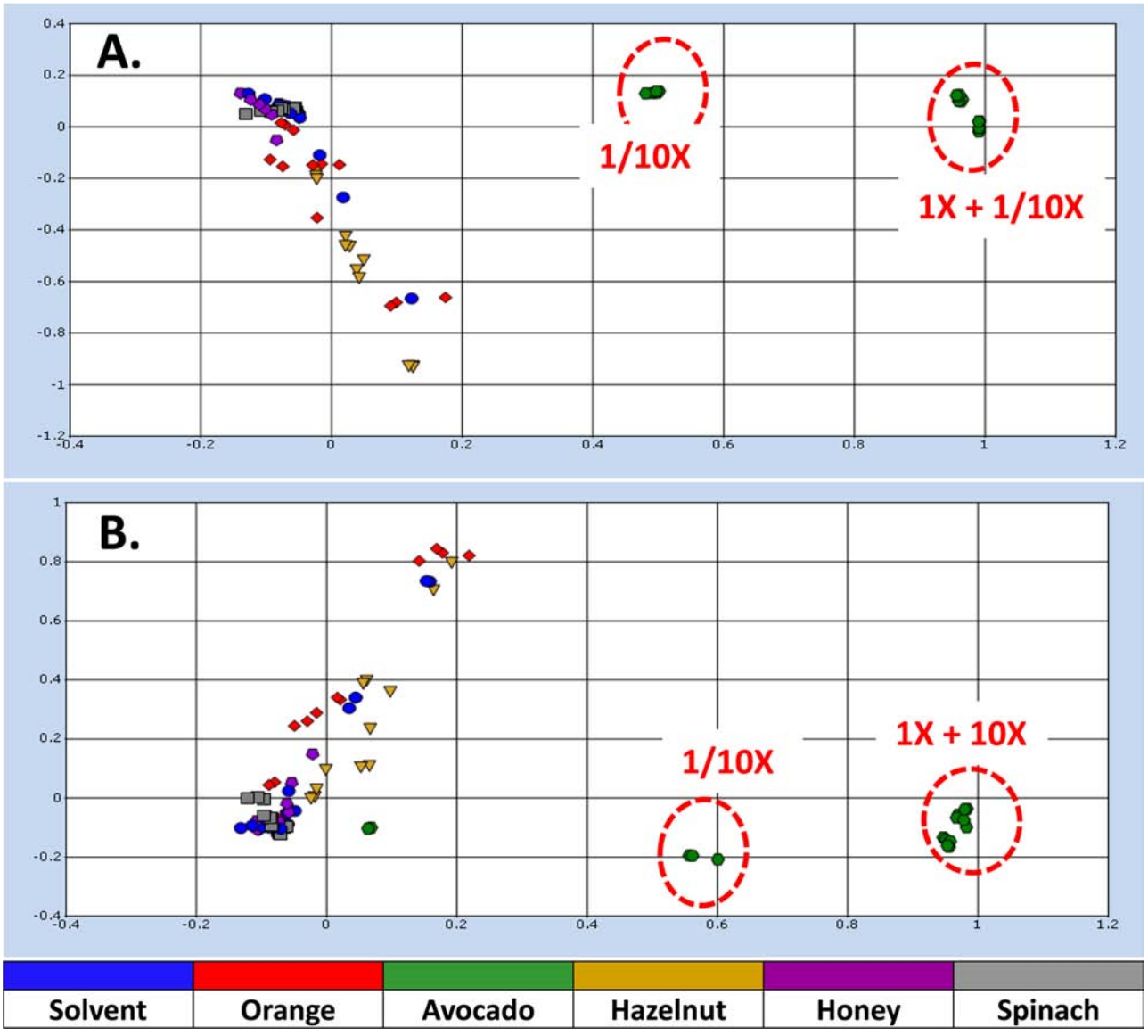

Figure 3. Results of PCA loadings (scores) of SOCS and MMCS samples (denoted by the color chart at the bottom) using uAqueous and Accucore for 1×, 1/10×, and 1/100× diluted samples.

proportional to dilution. Tribufos is the most suppression-affected pesticide and has R_{slope} values of 0.286 and 0.290 from uAqueous and Accucore columns in 1× samples (Figure 2F and SI Figure 6F). Figures 2E and SI Figure 6E show R_{slope} values of tribufos improved by about 100% to 0.599 and 0.574 for the 1× to 1/10× dilution and reached 0.956 and 0.850, respectively, at 1/100× dilution using uAqueous and Accucore columns (Figure 2D and SI Figure 6D). The effect of 1/10× dilution is less for anilofos and is estimated at 27 and 6%, respectively, for uAqueous and Accucore columns (Figure 2B and SI Figure 3B). Minimal suppression can be observed with a 1/100× dilution (Figure 2A,D and SI Figure 6A,D) for anilofos and tribufos using either LC column. In the case of vernolate, minimal suppression is observed using either uAqueous or Accucore columns.

Table 1 summarizes the number of pesticides with values of R_{slope} > 1.2 (enhancement), 1.2 > R_{slope} > 0.8 (minimal ME), and R_{slope} < 0.8 (suppression) for the two columns. Using Table 1 and SI Figures 1−5, one could conclude that suppression decreased with increasing dilutions for all but the honey matrix, which had suppression increased from dilutions 1/10× to 1/100× in both columns. A behavior may be associated with the high sugar contents of honey. One can also observe from SI Figures 1−5 the number of pesticides with R_{slope} > 1.2 increased with dilutions from 1× to 1/10× to 1/100×. In addition, enhancement affected those hydrophilic pesticides more than those less polar ones. The enhancement is more obvious in the uAqueous column than in the Accucore column. There is a minimal understanding of the enhancement ME at the present time, and we cannot explain this phenomenon. As expected, suppression decreases with increasing sample dilution, and the number of pesticides found in the 1.2 > R_{slope} > 0.8 range reached the maximum at 1/100× dilution. The avocado matrix exerted the highest level of suppression on the 381 pesticides compared to the other matrices as only 23% pesticides were ME free at 1× dilution. At 1/100× dilution, >77% of the pesticides became suppression-free in avocado. Honey as an outlier had >96% pesticides ME free at 1/10× dilution. These demonstrate that dilution is an effective approach to alleviate suppression ME in LC-MS analysis.

DOI: 10.1021/jf505168v
J. Agric. Food Chem. 2015, 63, 5169−5177

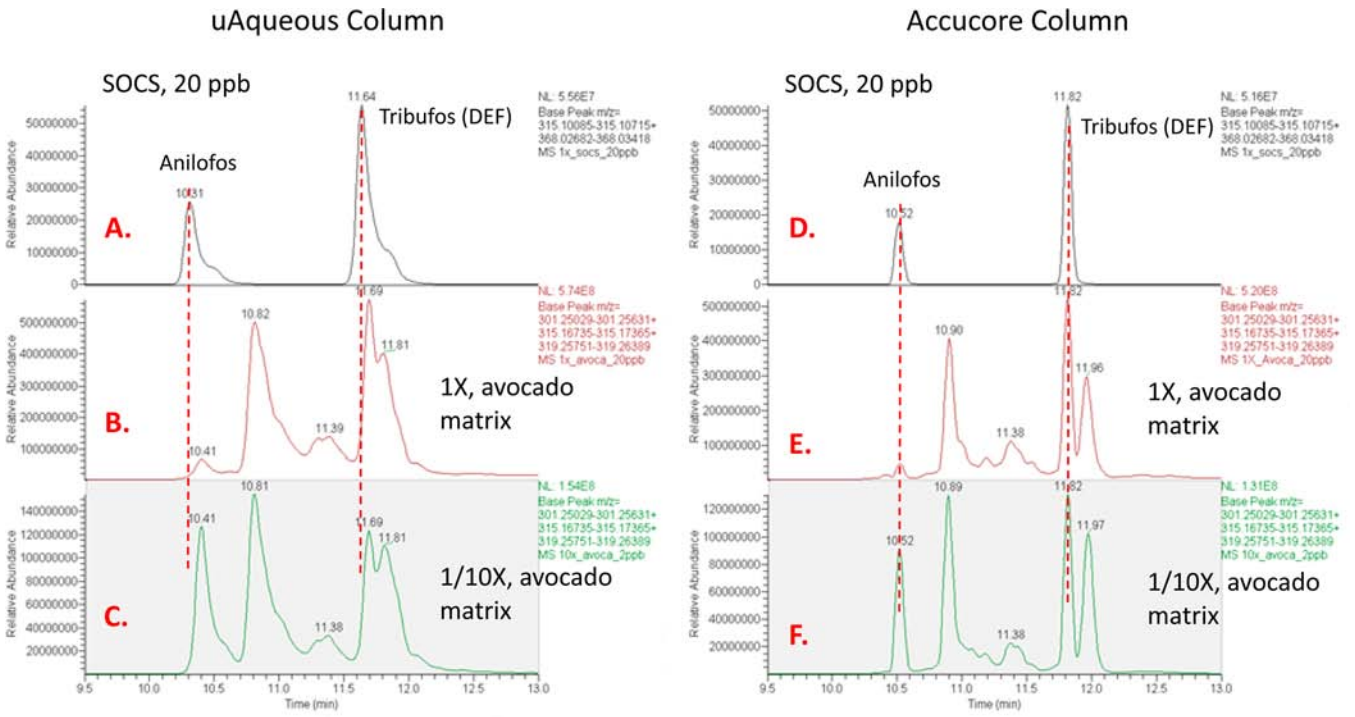

Figure 4. Extracted ion chromatograms (XICs) of pesticides anilofos and tribufos obtained from SOCS (20 ppb) and avocado MMCS samples using uAqueous and Accucore LC columns at 1× and 1/10× dilutions.

At 1/100× dilution, and with the increasing number of pesticides not having a valid R_{slope}, the number of pesticides in the $1.2 > R_{slope} > 0.8$ range was less than expected. For example, 340 and 359 of the 381 pesticides in spinach matrix using uAqueous or Accucore columns at 1/10× dilution were considered as ME free. The number of suppression-free pesticides decreased to 325 and 315 in spinach, whereas the number of those "NA" pesticides increased >20 times to 6.0 and 6.3%, respectively, for uAqueous and Accucore columns. It is clear that higher levels of dilution reduce the overall analytical sensitivity of LC-MS analysis and should be optimized according to the ionization efficiency of each pesticide during the method development and validation stages to ensure a consistent data quality.

Principal Component and Differential Expression Analysis of LC-Orbitrap MS Data. Shown in Figure 3 are results obtained from PCA of the uAqueous and Accucore LC-Orbitrap MS data sets by plotting the sample loadings (scores) of SOCS and MMCS samples collected at the three dilution levels. The PCA used mass spectral data of the 108 samples to form a data set of m/z versus intensities of pesticides and matrix components. Using the first three orthogonal factors (eigenvalues) calculated from the data set, the contribution of each sample to the data set was calculated as a linear combination of weighted values (scores) and plotted along the eigenvectors. Samples with similar contributions to the data set will have similar scores along the eigenvectors and form clusters in the plot. From Figure 3A (uAqueous) and Figure 3B (Accucore), MMCS samples of avocado (green) at 1× and 1/10× dilutions are separated from the other samples in two distinct clusters of 1/10× and ($1x$ + 1/10×) and would have different contributions on the data sets. Other MMCS samples (including those 1/100× avocado samples) have similar contributions to those of SOCS samples, clustered together around the origin, and are considered to have been minimally affected by ME. This observation is supported by the differential expression analysis (DEA) results in which XICs obtained from targeted pesticides (known) and matrix components (unknown) were aligned and shown in SI Figure 7A,B to allow a visual examination of all XICs in one plot. From SI Figure 7, matrix components of avocado (green) and hazelnut (brown) eluted between 10 and 12 min, whereas orange matrix components (red) eluted around 10 min. The avocado matrix components have peak intensities reaching 4×10^9, whereas hazelnut (brown, underneath avocado) and orange (red, around 9−11 min) matrices have peak intensities $<1 \times 10^9$. The XIC base peak intensities of pesticides and other matrix components (i.e., honey and spinach) were much lower than 1×10^9 and were around the baseline area. It is also observed that base peak XICs obtained from the Accucore column (using adsorbent of a 1.75 μM effective core, SI Figure 7B) have, in general, a narrower fwhm chromatographic peak than those from the uAqueous column, which uses 2.6 μm sized particles.

Relationship between Matrix Component Base Peaks and Matrix Effects. Base peak XICs obtained from DEA also provided m/z information on matrix components with significant intensities. Avocado matrix has three major base peaks at m/z 301.2546, 315.1705, and 319.2637, whereas orange matrix has only one base peak at m/z 373.1285. Base peak XICs obtained from m/z 301.2546, 315.1705, and 319.2637 using 1× (1 ng/g) and 1/10× (0.1 ng/g) avocado MMCS samples are shown in Figure 4B,C (uAqueous) and 4E,F (Accucore). Base peak XICs of anilofos and tribufos obtained from corresponding SOCS samples are shown in Figure 4A,D for comparison. Expanded plots of Figure 4A−F are shown in SI Figures 8 and 9. From Figure 4, the avocado XIC peaks had intensities $\approx 5.1 \times 10^8$ in the 1× samples from uAqueous (B) and Accucore (E), decreased by 80% to $(1.2-1.5) \times 10^8$ in the 1/10× samples (C and F), and still have

DOI: 10.1021/jf505168v
J. Agric. Food Chem. 2015, 63, 5169−5177

Table 2. Peak Concentrations Calculated for Seven Pesticides of Different Molecular Weights Eluted at Different Retention Times and Two Different Injection Concentrations

compound	LC column	RT (min)	N_{HETP}	V_{peak} (μL)	peak concentration (M)	
					20 ppb inj	100 ppb inj
acetaprimid (222.0672)	uAqueous C18	7.58	1.02×10^4	28	3.20×10^{-8}	1.60×10^{-7}
	Accucore C18	6.72	5.97×10^4	10	8.74×10^{-8}	4.37×10^{-7}
ametryn (227.1205)	uAqueous C18	9.31	2.87×10^4	21	4.27×10^{-8}	2.14×10^{-7}
	Accucore C18	9.18	1.15×10^5	10	8.68×10^{-8}	4.34×10^{-7}
warfarin (308.1048)	uAqueous C18	9.58	4.37×10^4	17	3.78×10^{-8}	1.89×10^{-7}
	Accucore C18	9.64	1.23×10^5	10	6.30×10^{-8}	3.15×10^{-7}
azinphos-ethyl (345.0371)	uAqueous C18	9.76	3.81×10^4	19	3.09×10^{-8}	1.55×10^{-7}
	Accucore C18	10.12	1.64×10^5	9	6.18×10^{-8}	3.09×10^{-7}
anilofos (367.0232)	uAqueous C18	10.31	4.25×10^4	19	2.91×10^{-8}	1.45×10^{-7}
	Accucore C18	10.50	2.76×10^5	8	7.27×10^{-8}	3.63×10^{-7}
diazinon (304.1010)	uAqueous C18	10.43	5.18×10^4	17	3.83×10^{-8}	1.91×10^{-7}
	Accucore C18	10.55	1.31×10^5	11	6.02×10^{-8}	3.01×10^{-7}
tribufos (315.0961)	uAqueous C18	11.63	8.45×10^4	15	4.25×10^{-8}	2.12×10^{-7}
	Accucore C18	11.82	2.09×10^5	10	6.57×10^{-8}	3.29×10^{-7}

significant ME on the two pesticides. This observation matches well with a prior study[26] that ME correlate linearly with the logarithm of the matrix concentration. The second avocado peak at RT 10.4 and 10.5 min (uAqueous and Accucore, respectively) behaves in an opposite manner with the peak intensity increased by >100% from $\approx 0.5 \times 10^8$ in the 1× (B and E) to $\approx 1.0-1.2 \times 10^8$ (C and F) in the 1/10× MMCS samples.We attribute this to the redistribution of the ESI resource from the 11.7 min to the 10.4 min avocado peaks. It is possible that the 11.7 min peak consumes a majority of the ESI resource and suppresses the ionization of coeluting analyte and other matrix components. With the 11.7 min avocado component diluted 1/10×, both the analyte and other matrix components can be ionized better and, thus, increase peak intensity.

Anilofos and tribufos coeluted separately with the 10.4 and 11.7 min avocado peaks and have peak intensities of $(1.8-2.2) \times 10^6$ and $(2.9-33) \times 10^6$ (Figure 4A,D). The 10.4 min avocado peak has a 20 times higher peak intensity than anilofos, whereas the 11.7 min avocado peak is about 170 times higher than tribufos. As a result, suppression of anilofos (R_{slope} values of 0.648 or 0.745 in uAqueous and Accucore columns) was less than that of tribufos (R_{slope} values of 0.286 or 0.290 in uAqueous and Accucore columns). This supports the suppression ME occurring for a specific pesticide that coelutes with a matrix component with a peak intensity of 25 times or higher. The level of suppression of the pesticide will vary with the close proximity of the RT and relative intensity of the coeluting matrix component. Sample dilution can alleviate or eliminate the level of ME for pesticides with RT different from the coeluting matrix component; however, it will be difficult to reduce ME for pesticides analyzed with matrix component coeluted at the exact RT and a peak intensity of 25 times or higher.

Examination of Matrix Effects in Multiresidue Pesticide Analysis. The discussions above lead to the root cause of ME in LC-MS multiresidue analysis. Kebarle et al.[23,24] determined that suppression of analyte intensity would occur when the total concentration of analytes eluting from a HPLC column is $>10^{-5}$ M. The concentration (C, in units of molar concentration) of an analyte eluted from the HPLC column can be calculated stoichiometrically using the estimated peak volume (V_{peak}) of that specific peak and the column loading (W) such that[31]

$$C = (W/\mathrm{MW})/V_{peak} \quad (1)$$

where MW is the molecular weight of an analyte, W is the weight of a specific pesticide and can be calculated using the injection volume (i.e., 10 μL) and the analyte concentration (i.e., ppb or ng/g), and

$$V_{peak} = 4 \times (V_0 \times (1 + k')/(N_{HETP})^{1/2}) \quad (2)$$

where V_0 is the column void volume used in the analysis, k' is the peak capacity of the peak, and N_{HETP} is the number of height equivalent theoretical plates.

Using eqs 1 and 2, estimated peak concentrations of seven selected pesticides with MW from 222 to 367 and RT from 6.57 to 11.82 min were calculated for the three different LC columns used in this study and are listed in Table 2.

In the case of LC analysis with effective peak concentrations ranging from 2×10^{-7} to 9×10^{-8} M, a matrix component (assuming the same ionization efficiency) with a 100× higher concentration than the coeluting pesticide would bring the total effective peak concentration to approximately 2×10^{-5} M, higher than the 1×10^{-5} M threshold, resulting in ME. Coeluting matrix component(s) have similar chemical properties to target compounds and cannot be removed using nonspecific cleanup procedures. The use of different LC gradients and/or columns, along with the collection of mass spectral data of all eluents, would allow the optimization of LC parameters during the method development and validation stages. This will minimize ME and allow dilute-and-shoot LC-MS analysis without prior cleanup to improve data quality and

DOI: 10.1021/jf505168v
J. Agric. Food Chem. 2015, 63, 5169−5177

operation efficiency in targeted pesticide analysis. It is worth noting from Table 2 that LC peak concentration of pesticides from 20 ppb SOCS ranged from 2×10^{-7} to 9×10^{-8} M, indicating that any ESI source can effectively ionize at least 40 coeluting pesticides (assuming similar ionization efficiency) without causing any concern for ME. This provides a viable solution during the method validation to develop an optimized LC gradient to separate analytes from matrix components and resolve ME in routine LC-MS analysis.

■ ASSOCIATED CONTENT

Supporting Information

Tables S1−S3 and SI Figures 1−9. This material is available free of charge via the Internet at http://pubs.acs.org.

■ AUTHOR INFORMATION

Corresponding Author

*(P.Y.) E-mail: paul.yang@ontario.ca. Phone: (416) 235-6004.

Author Contributions

‖P.Y., J.S.C., and J.W.W. contributed equally to the work.

Notes

The authors declare no competing financial interest.

■ ABBREVIATIONS USED

uAqueous	Restek Ultra Aqueous C-18 column
Accucore	Thermo Fisher Accucore aQ C-18 column
DEA	differential expression analysis
ESI	electrospray ionization
enhancement	electrospray ionization enhancement
suppression	electrospray ionization suppression
fwhm	full width at half-maximum
HESI	heated electrospray ionization
IDL	Instrument detection limit
LC	liquid chromatography
LC-ESI-HRMS	liquid chromatography−electrospray ionization−high-resolution mass spectrometry
LC-ESI-MS	liquid chromatography−electrospray ionization−mass spectrometry
LC-MS/MS	liquid chromatography−tandem mass spectrometry
MEW	mass extraction window
MFLC	microflow liquid chromatography
MMCS	matrix-matched calibration standards
MRLs	maximal residual limits
ND	not detected
Orbitrap MS	Orbitrap mass spectrometry (Exactive Plus)
QuEChERS	quick, easy, cheap, effective, rugged, and safe
R_{fwhm}	mass resolving power at full width at half-maximum
R_{slope}	ratio of slopes of calibration curve obtained from SOCSs and MMCSs
SOCS	solvent only calibration standards
U.S. EPA	United States Environmental Protection Agency
UHPLC	ultrahigh-performance liquid chromatography
XIC	extracted ion chromatogram

■ REFERENCES

(1) Wong, J.; Hao, C. Y.; Zhang, K.; Yang, P.; Banerjee, K.; Hayward, D.; Iftakhar, I.; Schreiber, A.; Tech, K.; Sack, C.; Smoker, M.; Chen, X. R.; Utture, S. G.; Oulkar, D. P. Development and inter-laboratory validation of a QuEChERS based liquid chromatography/tandem mass spectrometry method for multi-residue pesticides analysis. *J. Agric. Food Chem.* **2010**, *58*, 5897−5903.

(2) Zhang, K.; Wong, J.; Yang, P.; Tech, K.; DiBenedetto, A. L.; Lee, N. S.; Hayward, D. G.; Makovi, C. M.; Krynitsky, A. J.; Banerjee, K.; Jao, L.; Dasgupta, S.; Smoker, M. S.; Simonds, R.; Schreiber, A. Multiresidue pesticide analysis of agricultural commodities using acetonitrile salt-out extraction, dispersive solid-phase sample clean-up and high-performance liquid chromatography-tandem mass spectrometry. *J. Agric. Food Chem.* **2011**, *59*, 7636−7646.

(3) Wang, J.; Chow, W.; Leung, D.; Chang, J. Application of ultrahigh-performance liquid chromatography and electrospray ionization quadrupole orbitrap high-resolution mass spectrometry for determination of 166 pesticides in fruits and vegetables. *J. Agric. Food Chem.* **2012**, *60*, 12088−12104.

(4) Turnipseed, S. B.; Clark, S. B.; Storey, J. M.; Carr, J. R. Analysis of veterinary drug residues in frog legs and other aquacultured species using liquid chromatography quadrupole time-of-flight mass spectrometry. *J. Agric. Food Chem.* **2012**, *60*, 4430−4439.

(5) Hao, C.; Zhao, X.; Tabe, S.; Yang, P. Optimization of a multi-residual method for the determination of waterborne emerging organic pollutants using solid phase extraction and liquid chromatography-tandem mass spectrometry and isotope dilution mass spectrometry. *Environ. Sci. Technol.* **2008**, *42*, 4068−4075.

(6) Gros, M.; Petrovic, M.; Barceló, D. Tracing pharmaceutical residues of different therapeutic classes in environmental waters by using liquid chromatography/quadrupole-linear ion trap mass spectrometry and automated library searching. *Anal. Chem.* **2009**, *81*, 898−912.

(7) Dell'Aversano, C.; Eaglesham, G. K.; Quilliam, M. A. Analysis of cyanobacterial toxins by hydrophilic interaction liquid chromatography-mass spectrometry. *J. Chromatogr., A* **2004**, *1028*, 155−164.

(8) Sulyok, M.; Krska, R.; Schuhmacher, R. Development and validation of a (semi-)quantitative UHPLC-MS/MS method for the determination of 191 mycotoxins and other fungal metabolites in almonds, hazelnuts, peanuts and pistachios. *Anal. Bioanal. Chem.* **2007**, *389*, 1509−1523.

(9) Schenzel, J.; Hungerbühler, K.; Bucheli, T. D. Mycotoxins in the environment: II. Occurrence and origin in Swiss river waters. *Environ. Sci. Technol.* **2012**, *46*, 13076−13084.

(10) Zhang, K.; Wong, J. W.; Hayward, D. G.; Vaclavikova, M.; Liao, C. D.; Trucksess, M. W. Determination of mycotoxins in milk-based products and infant formula using stable isotope dilution assay and liquid chromatography tandem mass spectrometry. *J. Agric. Food Chem.* **2013**, *61*, 6265−6273.

(11) Ortelli, D.; Edder, P.; Corvi, C. Multiresidue analysis of 74 pesticides in fruits and vegetables by liquid chromatography-electrospray-tandem mass spectrometry. *Anal. Chim. Acta* **2004**, *520*, 33−45.

(12) Mol, H. G.; Plaza-Bolaños, P.; Zomer, P.; de Rijk, T. C.; Stolker, A. A.; Mulder, P. P. Towards a generic extraction method for simultaneous determination of pesticides, mycotoxins, plant toxins and veterinary drugs in feed and food matrices. *Anal. Chem.* **2008**, *80*, 9450−9459.

(13) Gómez-Pérez, M. L.; Plaza-Bolaños, P.; Romero-González, R.; Martínez-Vidal, J. L.; Garrido-Frenich, A. Comprehensive qualitative and quantitative determination of pesticides and veterinary drugs in honey using liquid chromatography-Orbitrap high resolution mass spectrometry. *J. Chromatogr., A* **2012**, *1248*, 130−138.

(14) Chiaia-Hernandez, A. C.; Krauss, M.; Hollender. Screening of lake sediments for emerging contaminants by liquid chromatography atmospheric pressure photoionization and electrospray ionization coupled to high resolution mass spectrometry. *Environ. Sci. Technol.* **2013**, *47*, 976−986.

(15) Moschet, C.; Piazzoli, A.; Singer, H.; Hollende, J. Alleviating the reference standard dilemma using a systematic exact mass suspect screening approach with liquid chromatography-high resolution mass spectrometry. *Anal. Chem.* **2013**, *85*, 10312−10320.

(16) Souverain, S.; Rudaz, S.; Veuthey, J. L. Matrix effect in LC-ESIMS and LC-APCI-MS with off-line and on-line extraction procedures. *J. Chromatogr., A* **2004**, *1058*, 61−66.

DOI: 10.1021/jf505168v
J. Agric. Food Chem. 2015, 63, 5169−5177

(17) Trufelli, H.; Palma, P.; Famiglini, G.; Cappiello, A. An overview of matrix effects in liquid chromatography−mass spectrometry. *Mass Spectrom. Rev.* **2011**, *30*, 491−509.
(18) Stüber, M.; Reemtsma, T. Evaluation of three calibration methods to compensate matrix effects in environmental analysis with LC−ESI-MS. *Anal. Bioanal. Chem.* **2004**, *378*, 910−916.
(19) Mallet, C. R.; Lum, Z.; Mazzeo, J. R. A study of ion suppression effects in electrospray ionization from mobile phase additives and solid phase extracts. *Rapid Commun. Mass Spectrom.* **2004**, *18*, 49−58.
(20) Ferrer, C.; Lozano, A.; Agüera, A.; Girón, A. J.; Fernández-Alba, A. R. Overcoming matrix effects using the dilution approach in multiresidue methods for fruits and vegetables. *J. Chromatogr., A* **2011**, *1218*, 7634−7639.
(21) Schuhmacher, J.; Zimmer, D.; Tesche, F.; Pickard, V. Matrix effects during analysis of plasma samples by electrospray and atmospheric pressure ionization mass spectrometry: practical approaches to their elimination. *Rapid Commun. Mass Spectrom.* **2003**, *17*, 1950−1957.
(22) Wang, S.; Cyronak, M.; Yang, E. Does a stable isotopically labeled internal standard always correct analyte response? A matrix effect study on a LC/MS/MS method for the determination of carvedilol enantiomers in human plasma. *J. Pharm. Biomed. Anal.* **2007**, *43*, 701−707.
(23) Tang, L.; Kebarle, P. From ions in solution to ions in the gas phase: the mechanism of electrospray mass spectrometry. *Anal. Chem.* **1993**, *65*, 972A−986A.
(24) Tang, L.; Kebarle, P. Dependence of ion intensity in electrospray mass spectrometry on the concentration of the analytes in the electrosprayed solution. *Anal. Chem.* **1993**, *65*, 3654−3668.
(25) Bruins, A. P. Mechanistic aspects of electrospray ionization. *J. Chromatogr., A* **1998**, *794*, 345−357.
(26) Stahnke, H.; Kittlaus, S.; Kempe, G.; Alder, L. Reduction of matrix effects in liquid chromatography−electrospray ionization−mass spectrometry by dilution of the sample extracts: how much dilution is needed? *Anal. Chem.* **2012**, *84*, 1474−1482.
(27) Hu, Q.; Noll, R.; Li, H.; Makarov, A.; Hardman, M.; Cooks, R. G. The Orbitrap: a new mass spectrometer. *J. Mass Spectrom.* **2005**, *40*, 430−443.
(28) Xia, Y. Q.; Lau, J.; Olahl, T.; Jemal, M. Targeted quantitative bioanalysis in plasma using liquid chromatography/high-resolution accurate mass spectrometry: an evaluation of global selectivity as a function of mass resolving power and extraction window, with comparison of centroid and profile modes. *Rapid Commun. Mass Spectrom.* **2011**, *25*, 2863−2878.
(29) van der Heeft, E.; Bolck, Y. J.; Beumer, B.; Nijrolder, A. W.; Stolker, A. A.; Nielen, M. W. Full-scan accurate mass selectivity of ultra-performance liquid chromatography combined with time-of-flight and Orbitrap mass spectrometry in hormone and veterinary drug residue analysis. *J. Am. Soc. Mass Spectrom.* **2009**, *20* (3), 451−463.
(30) Stahnke, H.; Reemtsma, T.; Alder, L. Compensation of matrix effects by postcolumn infusion of a monitor substance in multiresidue analysis with LC−MS/MS. *Anal. Chem.* **2009**, *81* (6), 2185−2192.
(31) Steiner, F. *Applications of Narrow-Bore Columns in HPLC*; Hewlett-Packard: Waldbronn, Germany, 1991.

DOI: 10.1021/jf505168v
J. Agric. Food Chem. 2015, 63, 5169−5177

JOURNAL OF AGRICULTURAL AND FOOD CHEMISTRY

Article

pubs.acs.org/JAFC

Purification, Structural Characterization, and Modification of Organosolv Wheat Straw Lignin

Laurie Mbotchak, Clara Le Morvan, Khanh Linh Duong, Brigitte Rousseau, Martine Tessier, and Alain Fradet*

Sorbonne Universités, UPMC Univ Paris 06, Institut Parisien de Chimie Moléculaire UMR 8232, Chimie des Polymères, F-75005 Paris, France

CNRS, IPCM UMR 8232, F-75005, Paris, France

Supporting Information

ABSTRACT: Biolignin, a wheat straw lignin produced by acetic acid/formic acid/water hydrolysis, was characterized by ^{31}P and ^{13}C−^{1}H 2D NMR spectroscopy and by size-exclusion chromatography. Biolignin is a mixture of low molar mass compounds (M_n = 1660 g/mol) made up of S, G, and H units and of coumaric and ferulic acid units. β-5 and β-O-4 interunit linkages are partially acylated in the γ-position by acetate and *p*-coumarate groups. Deacylated samples with a low content of contaminants were obtained by combining alkaline hydrolysis and solvent extraction. The high phenolic OH content found by ^{31}P NMR reflects the presence of condensed aromatic units, such as 5−5 units. Reaction of purified lignin with ethanol and ethane-1,2-diol yielded esterified lignins much more soluble than Biolignin in common organic solvents. During this reaction, the secondary OH of β-O-4 linkages was simultaneously etherified. Phenol hydroxyethylation by 2-chloroethanol yielded samples containing only aliphatic hydroxyl groups.

KEYWORDS: *wheat straw lignin, NMR, esterification, etherification*

INTRODUCTION

Conversion of lignin to value-added products is one of the challenges for the expanding biobased products industry. In this context, the utilization of lignin from grasses, and especially from crop residues, has attracted increasing research attention.[1,2] Wheat straw lignin is a major industrial crop residue and its separation, purification, and structure have been extensively studied.[3−12] Like lignins from other grasses, wheat straw lignin is a complex polymer formed of three types of aromatic units, syringyl (S), guaiacyl (G), and 4-hydroxyphenyl (H) units, linked to each other by short aliphatic "side chains" of various types through C−C or C−O−C bonds. It presents a relatively high content of acetate and *p*-hydroxycinnamate groups, predominantly bound at the γ-position of side chains.[13] In plants, lignin is linked to polysaccharides, mainly hemicellulose, by ether or ester groups, thus ensuring structural cohesion and rigidity to cell walls. The delignification process, designed to cleave lignin−saccharide bonds, leads to more or less extensive modification of native lignin structure. Therefore, the composition of the resulting technical lignins, for example, the relative abundance of S/G/H units, the nature of side chains, the presence of cinnamate and acetate groups and the content in functional groups (alcohols, phenols, and carboxylic acids), is highly dependent on the delignification process conditions.[14]

Technical lignins are highly functionalized aromatic compounds and, as such, particularly attractive for use as comonomers in polymeric materials.[15] Lignins have thus been used as rigid polyols in polyester,[15−18] polyurethane,[19−21] and epoxy[22−24] thermosetting resins and, after modification, for the synthesis of starlike polystyrene and poly(methyl methacrylate).[25] However, several issues have to be addressed before lignins can find extensive applications in polymeric materials:

(1) Technical lignins are rarely recovered in pure form. While the major portion of hemicelluloses is removed during the fractionation step, the presence of residual carbohydrates in crude lignin fractions (i.e., obtained directly after the delignification process) cannot be excluded. Wax and sugar content in a lignin sample are closely related to the process and to the pre- or posttreatment steps used for lignin isolation. Their presence has to be carefully considered as it may influence lignin reactivity and, therefore, the properties of final materials. Treatment of straw by apolar/polar solvents mixtures prior to the fractionation process is used in some cases to produce dewaxed straw.[3−5] On the other hand, basic hydrolysis is an efficient way to remove residual polysaccharides by cleavage of ester linkages between hemicellulose and lignin, yielding almost polysaccharide-free technical lignins.[4,6,26,27]

(2) As mentioned above, the structure of technical lignins depends heavily on the conditions used in the delignification and purification processes. In order to elaborate materials with controlled properties and to ensure synthesis repeatability, an in-depth knowledge of lignin structure and reactivity is required.

(3) With regard to polymer synthesis, the major drawbacks of technical lignins are their low solubility in organic medium, their functional group heterogeneity, and their relatively poor hydroxyl group accessibility.

Received: February 11, 2015
Revised: May 9, 2015
Accepted: May 10, 2015
Published: May 11, 2015

ACS Publications © 2015 American Chemical Society

DOI: 10.1021/acs.jafc.5b02071
J. Agric. Food Chem. 2015, 63, 5178−5188

To overcome these issues, preliminary purification and chemical modification of technical lignins have been described: for example, esterification of hydroxyl groups by anhydrides,[28] reaction with epichlorhydrin,[22] or reaction with propylene oxide.[29−31] While the characterization of oxypropylated lignin with modern methods has been reported,[31,32] most modified technical lignins, however, have subsequently been used without detailed characterization.

The aim of this study was to evaluate the influence of purification steps and of esterification and etherification chemical modifications of wheat straw lignin on its chemical and structural characteristics. This study was undertaken on wheat straw lignin produced by the CIMV (Compagnie Industrielle de la Matière Végétale) acetic acid/formic acid/water fractionation process,[11,33] available under the trade name Biolignin. Lignin was first purified by hydrolysis and solvent extraction and then modified by esterification with ethanol or ethane-1,2-diol to mask acid groups or by etherification with 2-chloroethanol in alkaline conditions to convert phenol groups into more reactive primary alcohols. The modification reactions were expected to provide samples with enhanced solubility, homogenized functionality in terms of function types, and improved reactivity for future applications as comonomer in polymeric materials. These samples were thoroughly characterized by means of ^{31}P and $^{13}C-^{1}H$ 2D NMR spectroscopy and size-exclusion chromatography (SEC).

MATERIALS AND METHODS

Materials. Absolute ethanol, ethane-1,2-diol (99.8%), 2-chloroethanol (99%), *p*-coumaric acid (98%), ferulic acid (99%), sinapic acid (98%), *p*-toluenesulfonic acid monohydrate (98.5%), sulfuric acid (99%), 2-chloro-4,4,5,5-tetramethyl-1,3,2-dioxaphospholane (95%), anhydrous pyridine (99.8%), chromium(III) acetylacetonate (97%), and acetic anhydride (≥99%) were obtained from Sigma−Aldrich (Saint-Quentin-Fallavier, France). *N*-Hydroxy-6-norbornene-2,3-dicarboximide (>96%) was obtained from Fluka (Saint-Quentin-Fallavier, France). All reagents were used without further purification.

Biolignin (Klason lignin content 89.8%)[34] was obtained from CIMV (Compagnie Industrielle de la Matière Végétale, Neuilly, France). Wheat straw from *Triticum aestivum* L. subsp. *aestivum*, seeded in November 2011, was harvested in Champagne region (France) in July 2012. Biolignin was extracted by the CIMV process with acetic acid/formic acid/water 30:55:15 v/v/v) at 105 °C under atmospheric pressure.[12,33]

Lignin Purification. Biolignin (20.19 g) was hydrolyzed by 1 M aqueous NaOH (300 mL) at 80 °C for 4 h. The reaction mixture was then acidified to pH 2 with 3 M aqueous HCl. The precipitate was filtered and washed thoroughly with deionized water until neutral pH, then dried at 50 °C under reduced pressure for 24 h to give 18.13 g of hydrolyzed Biolignin (Lh; yield 90 wt %). The acidic filtrate was concentrated under reduced pressure to afford a dried hydrolysis residue, Rh.

Lh was further purified by repeated washing steps with CH_2Cl_2 (2×) and ethyl acetate (3×) as follows: Lh (17 g) was poured into 100 mL of solvent, heated to reflux for 1 h, and filtered. After drying under reduced pressure, 13.33 g of purified Biolignin (Lp) was obtained (overall yield from Biolignin 70.5 wt %). Organic phases were evaporated to yield the purification residue, Rp.

Modification of Lignin with Ethanol. Lp (2 g), ethanol (30 mL), and *p*-toluenesulfonic acid monohydrate as a catalyst (200 mg, 0.8 wt %) were heated at 80 °C for 20 h. The insoluble fraction was filtered on sintered glass filter (porosity 5), washed with deionized water until neutral pH, and dried overnight at 50 °C under vacuum to give 1.25 g of ethanol-insoluble modified lignin (i-Lp-Et). The alcohol phase was concentrated under reduced pressure. The residue was precipitated in 200 mL of water, filtered on sintered glass filter (porosity 5), and dried overnight at 50 °C under vacuum to yield 0.75 g of ethanol-soluble modified lignin (s-Lp-Et).

Modification of Lignin with Ethane-1,2-diol. Lp (5 g), ethane-1,2-diol (75 mL) and *p*-toluenesulfonic acid monohydrate as a catalyst (530 mg, 0.6 wt %) were heated at 90 °C for 20 h. The homogeneous mixture was poured into 500 mL of deionized water. The precipitate was filtered on sintered glass filter (porosity 5), washed with deionized water until neutral pH, and dried at 50 °C under vacuum for 24 h to give 4.95 g of ethane-1,2-diol-modified lignin (Lp-EG).

Modification of Lignin with 2-Chloroethanol. Lp (3.1 g) was dissolved in 30 mL of 1 M aqueous NaOH at 90 °C. 2-Chloroethanol (6 mL, 84 mmol) was added dropwise and the mixture was heated at 90 °C for 20 h. The mixture was poured into 300 mL of water and neutralized with 2 M aqueous HCl. The precipitate was filtered on sintered glass filter (porosity 5) and dried at 50 °C under vacuum for 24 h to give 2.80 g of 2-chloroethanol-modified lignin (Lp-CE).

Synthesis of 4-(2-Hydroxyethoxy)cinnamic Acids. 4-(2-Hydroxyethoxy)cinnamic acids were synthesized by reacting the corresponding 4-hydroxycinnamic acids with 2-chloroethanol in alkaline medium according to a procedure described for hydroxyethoxylation of 4-hydroxybenzoic acid.[35]

(2E)-3-[4-(2-Hydroxyethoxy)phenyl]prop-2-enoic Acid, ***20****.* A solution of *p*-coumaric acid (8.2 g, 50 mmol) in 40 mL of 3 M aqueous NaOH was heated to 50 °C. 2-Chloroethanol (5 mL, 75 mmol) was added slowly, and the mixture was heated at 90 °C for 6 h. After cooling, the mixture was poured into 50 mL of deionized water and acidified with 1 M aqueous HCl. The residue was filtered and washed with acetone to remove residual *p*-coumaric acid and ester byproducts. Product **20** was recrystallized from ethanol: yield 6.2 g (60%). ^{1}H NMR (DMSO-d_6) δ, ppm 7.61 (d, J = 8 Hz, H-2, H-6), 7.54 (d, J = 16 Hz, H-α), 6.96 (d, J = 8 Hz, H-3, H-5), 6.36 (d, J = 16 Hz, H-β), 4.02 (t, J = 6 Hz, $-CH_2-$OAr), 3.72 (t, J = 6 Hz, $-CH_2-$OH). ^{13}C NMR (DMSO-d_6) δ, ppm 167.7 (C-γ), 160.3 (C-4), 143.6 (C-α), 129.8 (C-2, C-6), 126.6 (C-1), 116.4 (C-β), 114.8 (C-3, C-5), 69.6 ($-CH_2-$OAr), 59.4 ($-CH_2-$OH).

(2E)-3-[4-(2-Hydroxyethoxy)-3-methoxyphenyl]prop-2-enoic Acid, ***21****.* Compound **21** was synthesized from ferulic acid following the same procedure: yield 5.6 g (47%). ^{1}H NMR (DMSO-d_6) δ, ppm 7.51 (d, J = 16 Hz, H-α), 7.31 (d, J^4 = 2 Hz, H-2), 7.17 (dd, J^4 = 2 Hz, J^3 = 8 Hz, H-6), 6.97 (d, J^3 = 8 Hz, H-5), 6.44 (d, J = 16 Hz, H-β), 4.00 (t, J = 6 Hz, $-CH_2-$OAr), 3.81 (s, $-CH_3$-O−), 3.72 (t, J = 6 Hz, $-CH_2-$OH). ^{13}C NMR (DMSO-d_6) δ, ppm 167.9 (C-γ), 150.1 (C-4), 149.0 (C-3), 144.1 (C-α), 127.0 (C-1), 122.5 (C-6), 116.6 (C-β), 112.5 (C-5), 110.4 (C-2), 70.1 ($-CH_2-$OAr), 59.4 ($-CH_2-$OH), 55.5 (CH_3O−).

(2E)-3-[4-(2-Hydroxyethoxy)-3,5-dimethoxyphenyl]prop-2-enoic Acid, ***22****.* A solution of sinapic acid (0.9 g, 4 mmol) in 5 mL of 3 M aqueous NaOH was heated to 50 °C. 2-Chloroethanol (0.65 mL, 9.5 mmol) was added slowly, and the mixture was heated at 90 °C for 6 h. After cooling, the mixture was poured into 20 mL of deionized water, acidified with 1 M aqueous HCl, and extracted with ethyl acetate (3 × 20 mL). Organic phases were washed with brine and concentrated under reduced pressure. Product **22** was recrystallized from ethyl acetate: yield 0.11 g (10%). ^{1}H NMR (DMSO-d_6) δ, ppm 7.52 (d, J = 16 Hz, H-α), 7.03 (d, J = 2 Hz, H-2, H-6), 6.53 (d, J = 16 Hz, H-β), 3.90 (t, J = 6 Hz, $-CH_2-$OAr), 3.81 (s, CH_3-O−), 3.61 (t, J = 6 Hz, $-CH_2-$OH). ^{13}C NMR (DMSO-d_6) δ, ppm 167.6 (C-γ), 153.0 (C-3, C-5), 144.0 (C-α), 138.4 (C-4), 129.6 (C-1), 118.4 (C-β), 105.8 (C-2, C-6), 74.1 ($-CH_2-$OAr), 60.1 ($-CH_2-$OH), 56.0 (CH_3O−).

Ethyl (2E)-3-[4-(2-Hydroxyethoxy)-3-methoxyphenyl]prop-2-enoate, ***23****.* A mixture of **22** (4.02 g, 16.9 mmol), ethanol (60 mL), and 18 M sulfuric acid as a catalyst (310 mg, 0.6 wt %) was refluxed for 20 h. After cooling, the solution was concentrated under vacuum to yield an orange-colored viscous product. This product was dissolved in 100 mL of diethyl ether, and this solution was washed twice with 30 mL of 0.5 M aqueous solution of $NaHCO_3$, twice with 30 mL of saturated NaCl solution, then twice with 30 mL of deionized water. The organic phase was dried on $MgSO_4$, filtered, and evaporated to dryness under vacuum. The resulting white powder was dried at 60 °C under vacuum for 12 h: yield 3.25 g (72%). ^{1}H NMR (DMSO-d_6) δ, ppm 7.57 (d, J = 16 Hz, H-α), 7.35 (d, J^4 = 2 Hz, H-2), 7.21 (dd, J^4 = 2 Hz, J^3 = 8 Hz, H-6), 6.98 (d, J^3 = 8 Hz, H-5), 6.54 (d, J = 16 Hz, H-β), 4.86 (t, J = 5 Hz,

DOI: 10.1021/acs.jafc.5b02071
J. Agric. Food Chem. 2015, 63, 5178−5188

−O*H*), 4.17 (q, *J* = 7 Hz, −C*H*$_2$−OOC−), 4.01 (t, *J* = 5 Hz, −C*H*$_2$−OAr), 3.81 (s, C*H*$_3$−O−), 3.72 (q, *J* = 5 Hz, −C*H*$_2$−OH), 1.25 (t, *J* = 7 Hz, −C*H*$_3$). ^{13}C NMR (DMSO-d_6) δ, ppm 166.4 (C-γ), 150.3 (C-4), 149.0 (C-3), 144.5 (C-α), 126.8 (C-1), 122.8 (C-6), 115.5 (C-β), 112.4 (C-5), 110.5 (C-2), 70.05 (−CH_2−OAr), 59.7 (−CH_2−OOC−), 59.35 (−CH_2−OH), 55.5 (CH_3O−), 14.1 (−CH_3).

Spectroscopic Methods. One-dimensional (1D) ^{1}H and ^{31}P NMR spectra and two dimensional (2D) ^{13}C−^{1}H NMR correlation spectra were recorded on a Avance 500 spectrometer (Bruker, Karlsruhe, Germany), at 500 MHz (^{1}H NMR), 125 MHz (^{13}C NMR), or 202 MHz (^{31}P NMR) with a 5 mm double-resonance broadband inverse probe (BBI). The 1D ^{13}C NMR spectra were recorded on the same spectrometer at 125 MHz with a 10 mm double-resonance broadband observe probe (BBO). Lignin samples were dissolved in deuterated dimethyl sulfoxide, DMSO-d_6 (^{1}H, ^{13}C, and 2D ^{13}C−^{1}H NMR), or CDCl$_3$/pyridine mixture (^{31}P NMR).

The 2D ^{13}C−^{1}H correlation spectra were recorded through a phase-sensitive gradient-enhanced 2D heteronuclear single quantum coherence (HSQC) with echo−antiecho experiment (HSQCETGP sequence). The 2D ^{13}C−^{1}H long-range correlation heteronuclear multiple bond correlation (HMBC) spectra were recorded via heteronuclear zero and double quantum coherence experiment (HMBCGPLPNDQF sequence). Chemical shifts were referenced to residual DMSO-d_5 (δ = 2.50 ppm) for ^{1}H NMR and to DMSO-d_6 (δ = 39.43 ppm) for ^{13}C NMR.

^{31}P NMR experiments were carried out following a slightly modified previously reported method:[36] Lignin (30 mg) was dissolved in a CDCl$_3$/pyridine mixture (1:1.6 v/v, 0.5 mL). The phosphitylation reagent, 2-chloro-4,4,5,5-tetramethyl-1,3,2-dioxaphospholane (150 μL), and the internal standard, *N*-hydroxy-6-norbornene-2,3-dicarboximide (100 μL of 0.1 M solution in 1:1.6 v/v CDCl$_3$/pyridine mixture)[37] were added successively. Chromium(III) acetylacetonate (100 μL of 0.014 M solution) in the same CDCl$_3$/pyridine mixture was added to the solution in order to homogenize and accelerate phosphorus relaxation. Spectra were recorded with a 25 s relaxation time and an average number of 10 000 scans. The quantitative results shown are the average of duplicate NMR experiments. Chemical shifts are relative to the signal of the phospholane hydrolysis product at 132.2 ppm. The integral value of the internal standard was used for calculations of the absolute amount of each functional group.

Size-Exclusion Chromatography. SEC analyses were performed on a 300 × 7.5 mm i.d., 5 μm Mixed-C (200−(2 × 10^6) Å) PLgel three-column set (Agilent Technologies, Les Ulis, France), connected to a VE5200 automatic injector (Malvern Instruments Ltd., Guyancourt, France) and a model 515 pump and a model 410 differential refractometer (Waters Corp., Guyancourt, France). Tetrahydrofuran (THF) was used as eluent (1 mL/min). Acetylated lignin solution in THF (100 μL, 5 g/L) was injected. Chromatograms were processed by use of OmniSEC software. Polystyrene standards (Polymer Laboratories) were used for the calibration.

Lignin Acetylation. Lignin (220 mg) was reacted with acetic anhydride (5 mL) and pyridine (5 mL) at room temperature for 72 h.[38] The resulting mixture was poured in water (100 mL). The precipitated acetylated lignin was filtered and dissolved in CH_2Cl_2. The solution was dried over $MgSO_4$ and evaporated under reduced pressure to afford acetylated lignin (210 mg, 95% yield).

RESULTS AND DISCUSSION

Purification and Characterization of Biolignin. Biolignin was first hydrolyzed in 1 M aqueous NaOH solution for 4 h at 80 °C, leading to hydrolyzed Biolignin (Lh). This alkaline hydrolysis leads to the cleavage of ester bonds, including those involved in carbohydrate−lignin complexes, and allows the elimination of residual polysaccharides and esters together with some aromatic compounds.[27] Moreover, traces of acetic and formic acids present in the starting material and resulting from the delignification process are also removed. In order to remove water-insoluble impurities, such as low molar mass aromatic compounds and waxes, Lh was then extracted with dichloromethane and ethyl acetate, yielding a final, purified Biolignin (Lp) with highly reduced contaminant content. The purification steps were followed by ^{1}H NMR. Analysis of the hydrolysis and purification residues confirmed the elimination of polysaccharides and of fatty acids, *p*-coumaric acid, and ferulic acid,

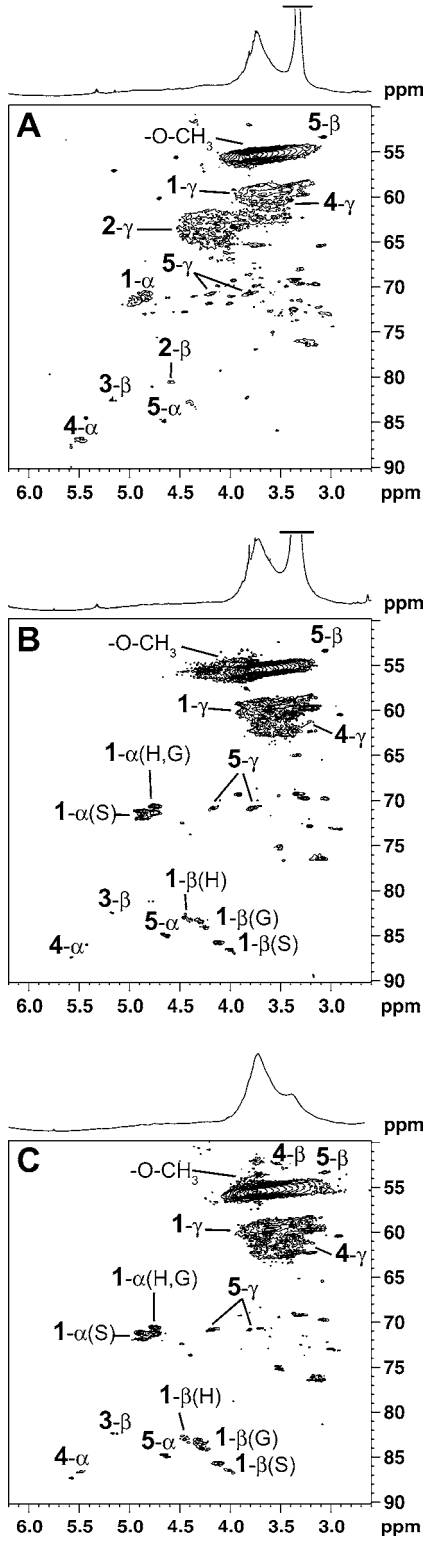

Figure 1. 2D ^{13}C−^{1}H HSQC NMR spectra of (A) Biolignin, (B) Lh, and (C) Lp: expansion of the lignin side-chain domain. Structure notations are given in Figure 3 and discussed in main text.

DOI: 10.1021/acs.jafc.5b02071
J. Agric. Food Chem. 2015, 63, 5178−5188

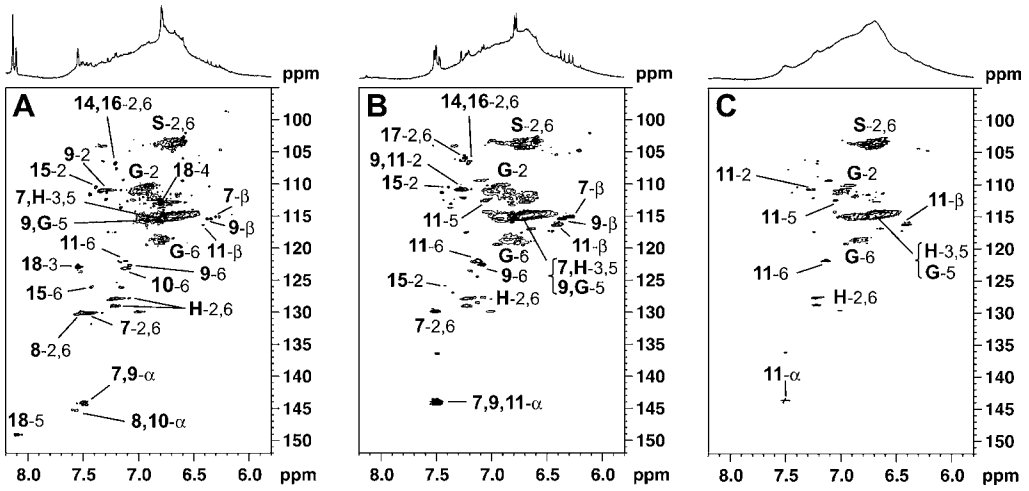

Figure 2. 2D $^{13}C-^{1}H$ HSQC NMR spectra of (A) Biolignin, (B) Lh, and (C) Lp: expansion of the aromatic domain. Structure notations are given in Figure 4 and discussed in main text.

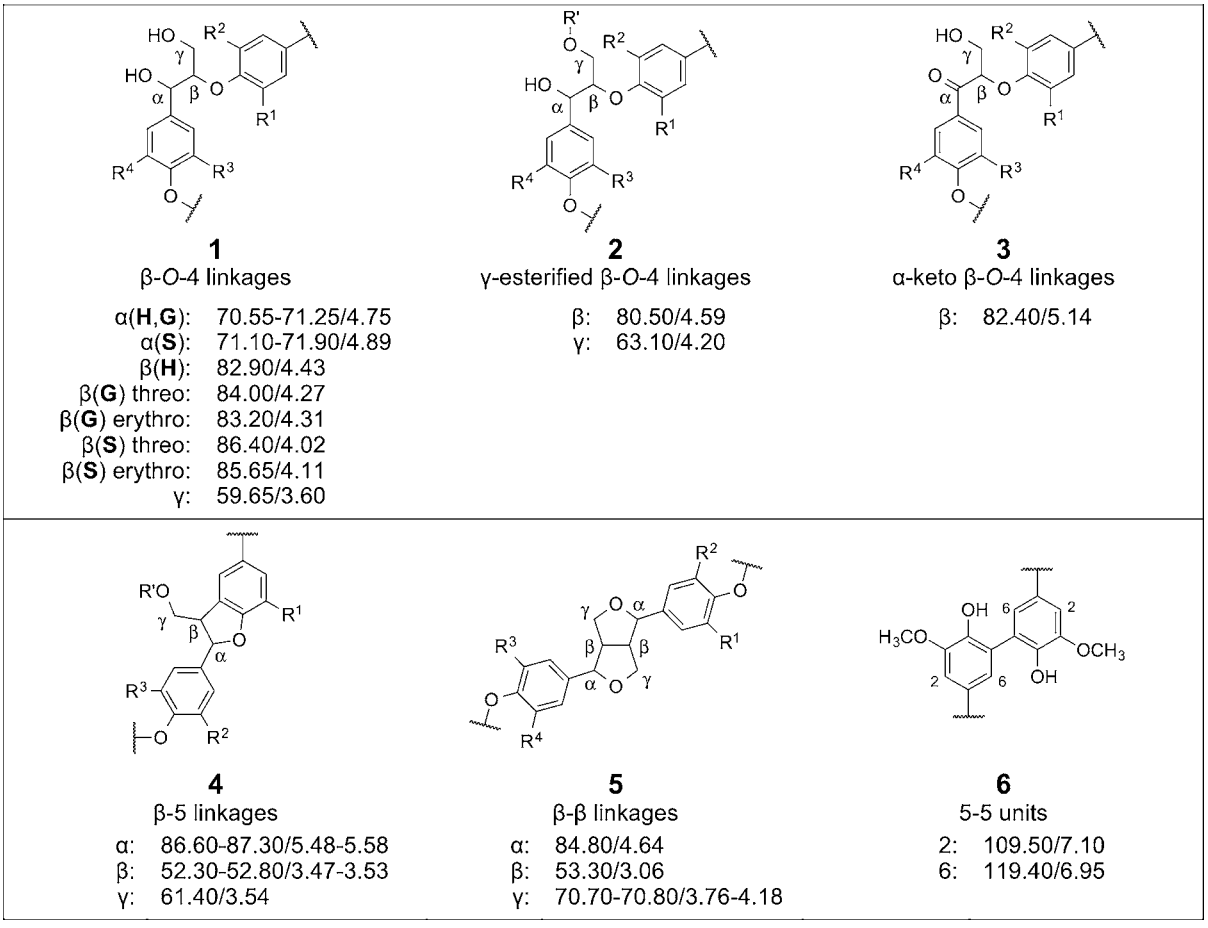

Figure 3. Structures, atom numbering, and HSQC correlations (δ^{C}/δ^{H}, ppm) of interunit linkages found in wheat straw lignin (R^{1-4} = H, CH_3O; R′ = H, CO).

respectively, together with various low molar mass aromatic compounds.

2D $^{13}C-^{1}H$ HSQC NMR Analyses of Biolignin, Lh, and Lp. 2D $^{13}C-^{1}H$ HSQC NMR analyses were performed in DMSO-d_6 (Figures 1 and 2). Correlations were assigned according to literature (Figures 3 and 4).[7,27,38−40] The β-O-4 linkages (alkyl−aryl ether), **1**, of H, G, and S units are easily detected by their α, β, and γ resonances. γ-Esterified β-O-4 linkages, **2**, are also present in Biolignin, as shown by the correlations corresponding to their β- and γ- positions, the latter being more intense (Figure 1A). These two correlations are no longer present after hydrolysis in Lh and Lp spectra (Figure 1B,C). α-Oxidized alkyl−aryl ether structures, **3**, are also detected by a correlation corresponding to the β-position. Correlations corresponding to the α-, β-, and γ-positions of β-5 (phenylcoumaran), **4**, and $\beta-\beta$ (resinol) linkages, **5**, are of much lower intensity as compared to those

DOI: 10.1021/acs.jafc.5b02071
J. Agric. Food Chem. 2015, 63, 5178−5188

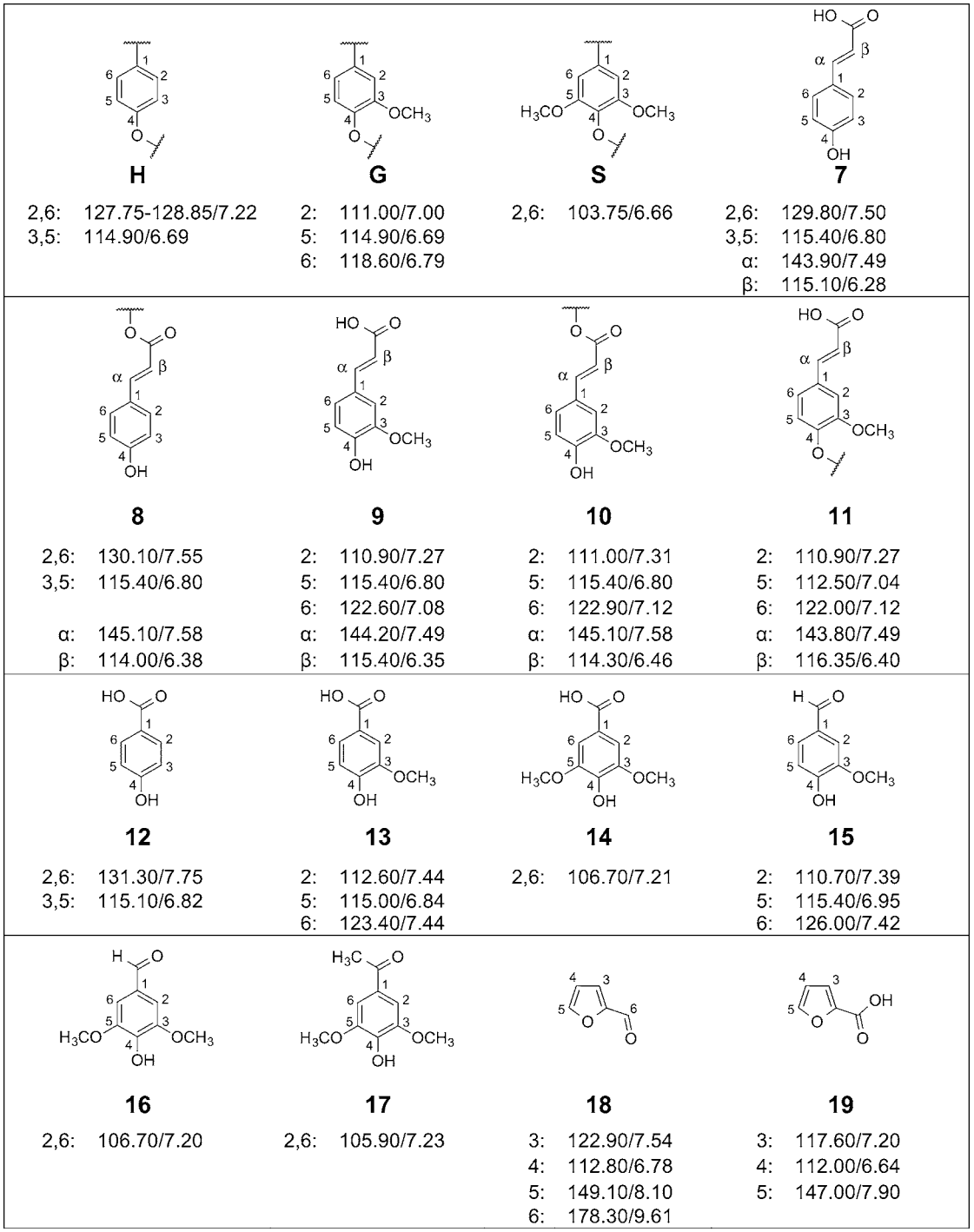

Figure 4. Structures, atom numbering, and 2D $^{13}C-^{1}H$ HSQC NMR correlations (δ^{C}/δ^{H}, ppm) of aromatic units found in wheat straw lignin.

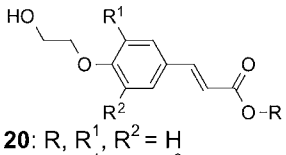

20: R, R^1, R^2 = H
21: R, R^1 = H, R^2 = OCH_3
22: R = H, R^1, R^2 = OCH_3
23: R = CH_2CH_3, R^1 = H, R^2 = OCH_3

Figure 5. Structure of model 4-(2-hydroxyethoxy)cinnamic derivatives.

of *β*-O-**4**, which, therefore, seem to be predominant. However, it is difficult to conclude on their relative abundance, since the NMR sequence used for these analyses does not allow cross-peak quantitation.

In the aromatic domain (Figure 2A), the resonances of H, G, and S units are observed together with moieties derived from *p*-coumaric and ferulic acids. As previously reported in studies on wheat straw lignin,[41] sinapic acid derivatives are not present, since their characteristic signal at 106.1/6.98 ppm (2,6-positions) is not detected. In Biolignin, the presence of free *p*-coumaric and ferulic acids **7** and **9**, and of their esters **8** and **10**, is reflected by their 2,6-, *α*- and *β*-correlations. A cross-peak close to

DOI: 10.1021/acs.jafc.5b02071
J. Agric. Food Chem. 2015, 63, 5178−5188

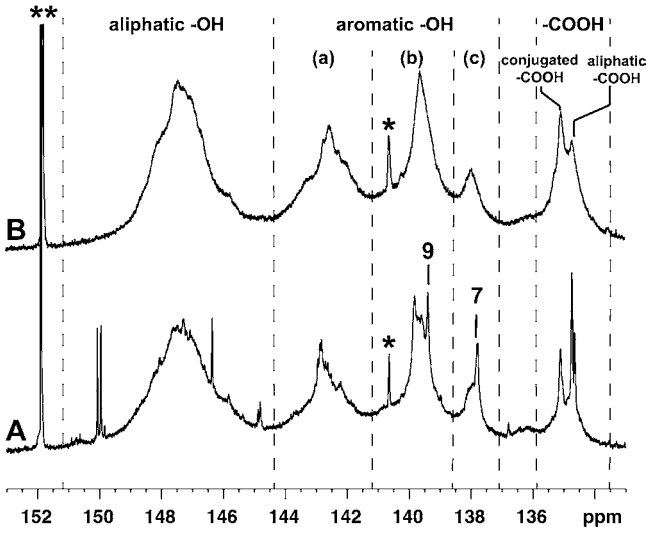

Figure 6. ^{31}P NMR spectra of (A) phosphitylated Biolignin and (B) phosphitylated purified Biolignin Lp. (*) Impurity; (**) internal standard; (a) disubstituted *p*-hydroxyphenyl structure as syringyl and condensed phenolic units; (b) monosubstituted *p*-hydroxyphenyl structure as guaiacyl units; (c) unsubstituted *p*-hydroxyphenyl structure.

the 6-correlation of **9** and **10** was assigned to *p*-etherified ferulic acid **11**, with the help of a model of these moieties, namely, (2*E*)-3-[4-(2-hydroxyethoxy)-3-methoxyphenyl]prop-2-enoic acid **21** (Figure 5). Low molar mass aromatic derivatives are also detected: syringic acid **14**, vanillin **15**, and syringaldehyde **16**. Correlations at 122.9/7.54, 112.8/6.78, and 149.1/8.10 ppm were assigned to the CH groups of furaldehyde **18**, a product of polysaccharide degradation, by comparison with the spectrum of an authentic sample. The CH═O correlation of **18** was also observed at 178.3/9.61 ppm (region not shown).

After hydrolysis (Figure 2B), *p*-coumarates and ferulates **8** and **10** are no longer detected, but free acids **7**, **9**, and **14** and aldehydes **15** and **16** are still present, and a correlation corresponding to acetosyringone **17** appears. These low molar mass compounds are removed during the solvent extraction steps, and the spectrum of Lp (Figure 2C) exhibits a very simplified pattern consisting mainly of signals relative to H, G, and S units and to *p*-etherified ferulic acid (**11**). As found for other lignin types,[13] *p*-etherified ferulates are an integral part of the lignin backbone. These findings were confirmed by the 2D NMR study of hydrolysis and solvent extraction residues.

Milled wood (MW) wheat straw lignin is also reported to contain flavonoids, such as tricin [5,7-dihydroxy-2-(4-hydroxy-3,5-dimethoxyphenyl)-4*H*-chromen-4-one], which presents strong and well-resolved HSQC signals.[7] However, these signals are not detected in Biolignin spectra. The acidic conditions of the CIMV process probably lead to the elimination of this type of compound.

Table 2. Number- and Mass-Average Molar Masses and Molar-Mass Dispersities of Acetylated Lignin Samples[a]

sample	Biolignin	Lp	i-Lp-Et	s-Lp-Et	Lp-EG	Lp-CE
M_w (g/mol)	31890	18400	24270	4160	23520	4633
M_n (g/mol)	1660	1560	2100	1340	1765	1155
$Đ_M$	19.2	11.8	11.6	3.1	13.3	4.0

[a]Determined by size-exclusion chromatography.

^{31}P NMR Spectroscopy. ^{31}P NMR spectroscopy was used to differentiate and quantitate the different types of free hydroxyl groups (aliphatic, phenolic, and carboxylic) in Biolignin and Lp, after phosphitylation by 2-chloro-4,4,5,5-tetramethyl-1,3,2-dioxaphospholane, as described by Argyropoulos and co-workers.[8,36] *N*-Hydroxy-5-norbornene-2,3-dicarboximide was used as internal standard instead of cyclohexanol,[37] as its signal at 151.9 ppm is well separated from those of lignin. It should be noted that the un-, mono-, and disubstituted 4-hydroxyphenyl groups quantitated by this method correspond only to a fraction of the H, G, and S units present in lignin, that is, those bearing free phenol groups. Moreover, the disubstituted 4-hydroxyphenyl structures detected by this method comprise syringyl units with free phenol groups, as well as condensed phenolic units.[36]

There are two main differences between the spectra of Biolignin and Lp (Figure 6): (1) lower relative intensity of unconjugated carboxylic acid resonances with respect to conjugated ones (134.70 and 135.05 ppm,[27] respectively) in the spectrum of Lp, due to the elimination of fatty acids and residual acetic and formic acids during the hydrolysis and purification steps; and (2) disappearance of the sharp peaks emerging from broad signals in the phenolic OH region of Biolignin spectrum (un-, mono-, and disubstituted 4-hydroxyphenyl groups at 137−144 ppm). The well-resolved peaks at 137.80 and 139.40 ppm are assigned to *p*-coumaric and ferulic acids, respectively.[27]

Aliphatic, phenolic, and acidic hydroxyl contents were determined by integration of the corresponding peaks with respect to the internal standard (Table 1). In Biolignin, phenolic OH groups are preponderant, with the aliphatic/phenolic OH ratio r_{OH} being close to 0.8, and acidic OH groups represent about 10% of total OH content. Monosubstituted 4-hydroxyphenyl OH unit content is slightly higher than that of disubstituted units (mono/disubstituted = 1.2), while unsubstituted 4-hydroxyphenyl units represent ca. 15% of total phenolic groups. Hydrolysis and purification lead to a slight increase in total OH content (6.90 vs 5.61 mmol/g) without

Table 1. Hydroxyl Content of Biolignin, Lp, Lp-Et, Lp-EG, and Lp-CE Lignins[a]

	OH content (mmol/g)			OH content (% of total OH + COOH)				
sample	phenolic	aliphatic	COOH	(a)[b]	(b)[b]	(c)[b]	aliphatic	COOH
Biolignin	2.84	2.24	0.53	19.40	23.35	7.85	39.95	9.45
Lp	3.49	2.57	0.84	22.50	21.60	6.50	37.25	12.15
s-Lp-Et[c]	3.12	1.13	0.04	32.40	30.70	9.50	26.30	1.10
Lp-EG	2.08	2.67	0.04	20.0	17.40	6.00	55.70	0.90
Lp-CE[d]				3.30	3.40	0.90	87.80	4.60

[a]Determined by quantitative ^{31}P NMR after phosphitylation with 2-chloro-4,4,5,5-tetramethyl-1,3,2-dioxaphospholane. [b](a) Di-, (b) mono-, and (c) unsubstituted 4-hydroxyphenyl OH, respectively. [c]Ethanol-soluble fraction of Lp-Et. [d]OH content (millimoles per gram) was not determined since Lp-CE is not completely soluble in phosphitylation medium. OH content (percent) was calculated on the soluble fraction.

DOI: 10.1021/acs.jafc.5b02071
J. Agric. Food Chem. 2015, 63, 5178−5188

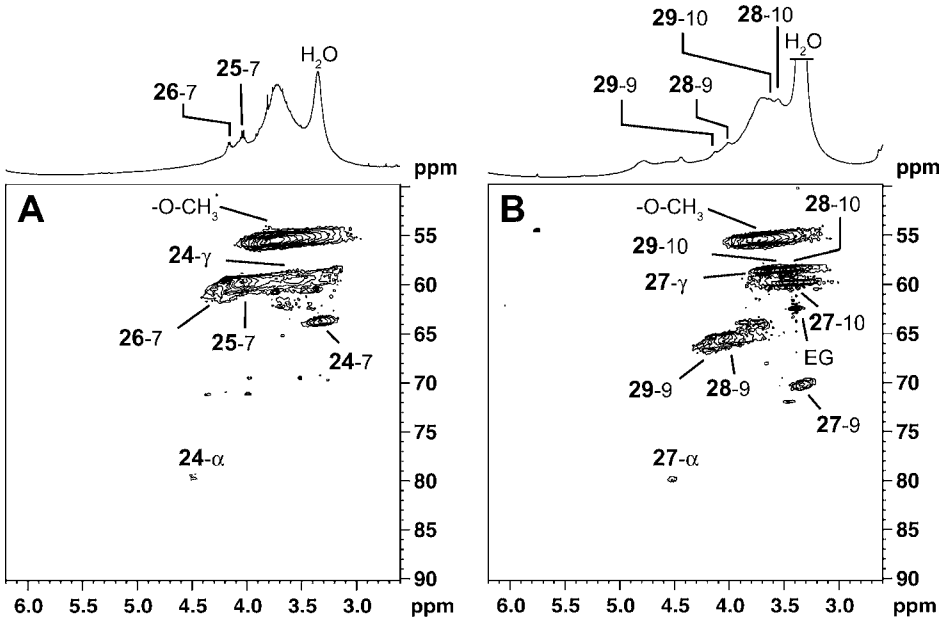

Figure 7. 2D $^{13}C-^{1}H$ HSQC NMR spectra of (A) s-Lp-Et and (B) Lp-EG: expansion of the lignin side-chain domain. Structure notations are given in Figure 8. EG, residual ethane-1,2-diol.

much affecting the aliphatic/phenolic ratio and, therefore, lignin main structure. Although free aliphatic and cinnamic acids were removed by the hydrolysis and purification steps, COOH concentration increases, due to hydrolysis of the ester functions of 4-O-etherified ferulates.

The high total phenolic group content indirectly reflects the presence of condensed phenolic units, such as 5−5 units, **6** (Figure 3). Shoulders at ca. 143 and 142 ppm in the ^{31}P NMR spectra of phosphitylated lignins have been assigned to condensed phenolic structures.[36] However, it is difficult to make any accurate quantitation in this region, even by deconvolution, due to the unknown number and width of signals that overlap in this region. Condensed phenolic units might also be detected in the aromatic region of HSQC spectra. On the basis of NMR literature data on model compounds,[42,43] the 5−5 structure arising from coniferyl alcohol should give two signals (2- and 6-positions), close to the 2- and 6-correlations of G units. Unassigned correlations at 109.5/7.10 and 119.4/6.95 ppm are observed in the HSQC spectrum of Lp (Figure 2C). They could reflect the presence of 5−5 units, but this has yet to be confirmed.

Comparison of ^{31}P NMR literature data on technical wheat straw lignins highlights the importance of the fractionation method on the chemical composition of resulting lignin samples. When either bases, for example, soda wheat straw lignin (GreenValue SA),[32] or organic acids[44] are used, lignins samples exhibit aliphatic/phenolic OH ratio $r_{OH} \leq 1$, close to that found for Biolignin in the present work. On the other hand, r_{OH} is close to 2.4−3 for MW wheat straw lignin[8] and dioxane/HCl lignin[45] samples. The un/mono/disubstituted 4-hydroxyphenyl unit distribution is also process-dependent, with MW samples exhibiting higher unsubstituted unit content as compared to samples obtained by alkaline or acidic processes. Crestini and Argyropoulos[8] studied the effect of 2 M alkaline hydrolysis on MW wheat straw lignin. They observed a strong decrease in unsubstituted 4-hydroxyphenyl unit content, reaching values close to that found above for Biolignin and Lp. They showed that this was mainly due to release of *p*-coumaric acid by the basic hydrolysis of *p*-coumarates present in lignin structure. A similar *p*-coumarate hydrolysis during the acidic CIMV delignification process could also be involved to explain the low unsubstituted 4-hydroxyphenyl unit content of Biolignin.

Size-Exclusion Chromatography. The impact of the hydrolysis and purification steps on average molar masses and molar mass distributions was evaluated by SEC (Table 2). The samples were acetylated, in order to improve their solubility in THF and to avoid the formation of aggregates.[46] Biolignin is a mixture of oligomeric compounds (M_n = 1660 g/mol) exhibiting a very large molar-mass dispersity, close to $Đ_M$ = 19. The hydrolysis and purification steps do not affect molar mass since the M_n of Lp lies in the same range. The molar-mass dispersity of Lp is lower, but still quite high ($Đ_M$ = 11.8). The M_n values previously reported for various technical wheat straw lignins (1000−3780 g/mol)[7,9,12,44] are close to those found for Biolignin in this work, while literature $Đ_M$ values vary between 1.7[9] and 10.6.[44] However, it is difficult to compare these SEC values, since delignification and/or analysis conditions are different from each other. In this work, molar mass values are compared before and after chemical modification, in order to detect potential lignin backbone changes.

Modification of Purified Biolignin. Modification of lignin prior to its use as macromonomer presents many advantages. Besides improving sample solubility in common organic solvents, this could allow selective masking of some functions and homogenizing of reactive group types. Lp was modified by three methods: esterification by (i) ethanol or (ii) ethane-1,2-diol to mask acid groups and (iii) etherification with 2-chloroethanol under alkaline conditions to replace phenol groups by more reactive aliphatic OH groups.

Lignin Modification by Esterification. Both esterification reactions were catalyzed by *p*-toluenesulfonic acid. When esterifications were carried out in ethanol, the reaction mixture remained heterogeneous. After reaction, the insoluble fraction, i-Lp-Et, was isolated from the soluble fraction, s-Lp-Et, by filtration. Both samples were soluble in DMSO-d_6 and were analyzed by ^{1}H and 2D NMR spectroscopy. Spectra with very

DOI: 10.1021/acs.jafc.5b02071
J. Agric. Food Chem. 2015, 63, 5178−5188

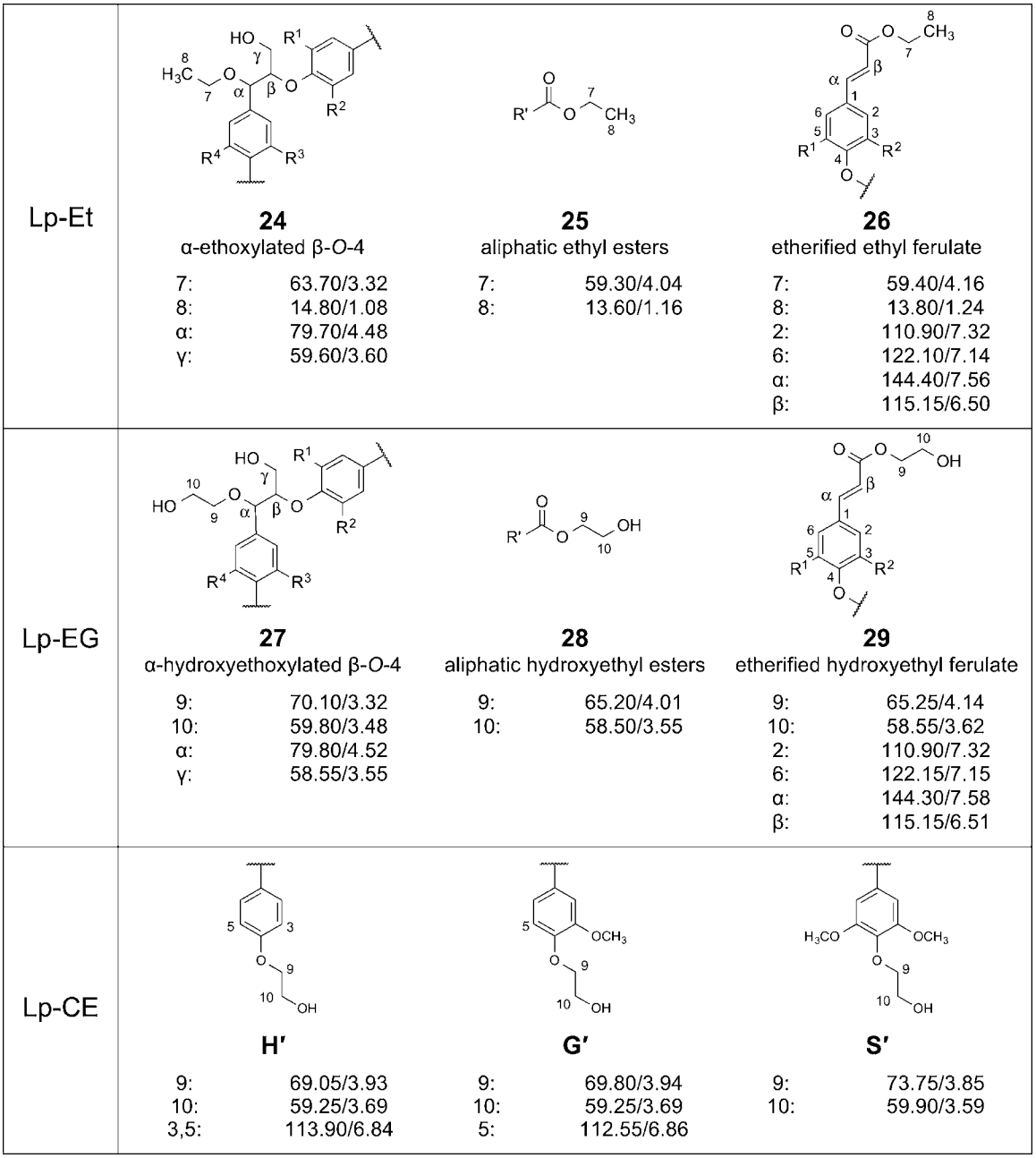

Figure 8. Structures, atom numbering and HSQC correlations (δ^C/δ^H, ppm) of modified lignin units found in Lp-Et, Lp-EG, and Lp-CE (R^{1-4} = H, CH_3O; R′ = aliphatic chain).

similar profiles were obtained, so that only the spectra of s-Lp-Et will be further discussed. On the other hand, esterification with ethane-1,2-diol led very rapidly to a homogeneous reaction mixture and afforded a sample, Lp-EG, that was soluble in common organic solvents such as CH_2Cl_2, THF, and DMSO.

The aliphatic domains of s-Lp-Et and Lp-EG HSQC NMR spectra are presented in Figure 7 with assignments in Figure 8. The spectrum of s-Lp-Et exhibits two distinct signals at 59.3/4.04 and 59.4/4.16 ppm (Figure 7A), assigned to the methylenes of ethyl ester groups of nonlignin aliphatic esters **25**, and of *p*-etherified ethyl ferulate moieties **26**, respectively. This was confirmed by long-range correlations between the corresponding carbonyl carbons and the methylene protons of ethyl esters at 172.45/4.04 and 166.25/4.16 ppm, respectively, observed in the HMBC $^{13}C-^{1}H$ NMR spectrum of s-Lp-Et. These assignments were also confirmed by comparisons with the spectra of ethyl (2*E*)-3-[4-(2-hydroxyethoxy)-3-methoxyphenyl]prop-2-enoate **23**, a model of *p*-etherified ethyl ferulate groups (Figure 5). The HSQC NMR spectrum also reveals that the secondary alcohols of *β*-O-4 structures were simultaneously etherified: The *α*-CH signal of *β*-O-4 linkages (**1**-*α*) is shifted to 79.70/4.48 ppm after reaction (**24**-*α*), that is, in the secondary ether resonance region. Moreover, new correlations are detected at 63.7/3.32 ppm (Figure 7A) and 14.80/1.08 ppm (not shown), which correspond, respectively, to methylene and methyl of the ethyl ether group of **24**. Etherification of the secondary alcohol of *β*-O-4 linkages has already been reported for *Miscanthus giganteus* lignin obtained by the ethanol−water−HCl process.[47]

Similar results were obtained when the reaction was carried out with ethane-1,2-diol. The −COO−CH_2−CH_2−OH meth-

DOI: 10.1021/acs.jafc.5b02071
J. Agric. Food Chem. 2015, 63, 5178−5188

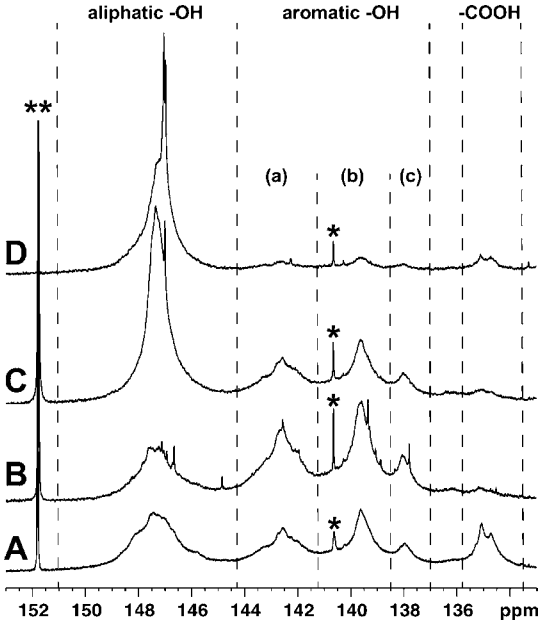

Figure 9. ^{31}P NMR spectra of phosphitylated lignin samples: (A) Lp, (B) s-Lp-Et, (C) Lp-EG, and (D) Lp-CE. (*) Impurity; (**) internal standard; (a) disubstituted *p*-hydroxyphenyl structures as syringyl and condensed phenolic units; (b) monosubstituted *p*-hydroxyphenyl structures as guaiacyl units; (c) unsubstituted *p*-hydroxyphenyl structures.

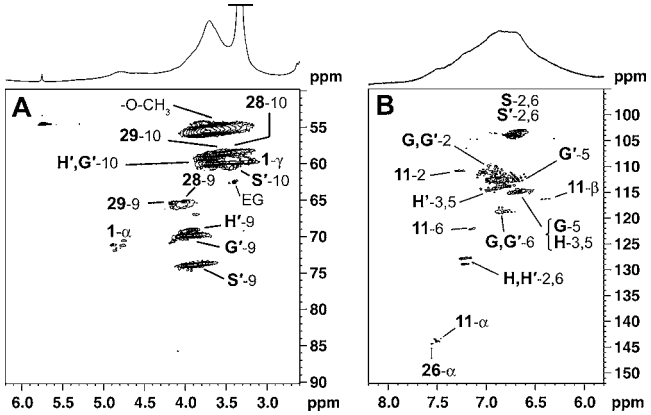

Figure 10. 2D ^{13}C−^{1}H HSQC NMR spectra of Lp-CE: expansion of lignin (A) aliphatic and (B) aromatic domains. Structure notations are given in Figure 8. EG, residual ethane-1,2-diol.

ylenes of non-lignin aliphatic esters **28** and ferulates **29** are clearly identified at 65.20/4.01 and 65.25/4.14 ppm (Figure 7B). As discussed above in the case of modification by ethanol, *α*-etherified *β*-O-4 structures **27** are also observed. No noticeable differences were observed in the aromatic domain, except a slight shift of the *α*- and *β*-resonances of feruloyl moieties after reaction, **29**.

Comparison of Lp, s-Lp-Et, and Lp-EG ^{13}C NMR spectra confirmed the preceding conclusions, in particular with the 2 ppm upfield shift of −COO− resonances (esterification of acids) and the detection of new peaks assigned to $-CH_2-O-$ ether resonances of **24** and **27** at 63.7 and 70.1 ppm, respectively.

The ^{31}P NMR spectra (Figure 9) show that, as expected, carboxylic acid content strongly decreases, from 0.84 mmol/g in Lp to 0.04 mmol/g in s-Lp-Et and in Lp-EG (Table 1). The ratio of un-, mono-, and disubstituted 4-hydroxyphenyl units remains unaffected by the chemical modification. A decrease in the aliphatic/phenolic OH ratio is observed for s-Lp-Et (r_{OH} = 0.36), due to formation of ethyl ethers **24**. In the case of Lp-EG, the aliphatic/aromatic OH ratio increases (r_{OH} = 1.28). In this case, the formation of hydroxyethyl ethers **27** does not change total aliphatic hydroxyl group content, while the hydroxyethylation of **11** leads to etherified hydroxyethyl ferulates **29** and to hydroxyl group concentration increase.

SEC analysis shows that s-Lp-Et exhibits lower M_n (1340 g/mol) and dispersity ($Đ_M$ = 3.1) than Lp, while the M_n of the ethanol-insoluble fraction is slightly higher (2100 g/mol) and dispersity is similar ($Đ_M$ = 11.6). Lp and Lp-EG present very close M_n and molar-mass dispersity (Table 2). Cleavage of lignin *β*-O-4 linkages and their rearrangement into lignin-based polymeric materials was reported for beech MW lignin liquefaction with ethane-1,2-diol.[48] The experimental hydroxyethylation conditions used in the present work (0.6% *p*-toluenesulfonic acid, 90 °C) are significantly milder than those used for wood liquefaction (3% p-toluenesulfonic acid, 150 °C) and appears to leave *β*-O-4 linkages unchanged, with the exception of the *α*-hydroxyethoxylation reaction discussed above.

Lignin Modification by Etherification with 2-Chloroethanol. Etherification of Lp phenol groups with 2-chloroethanol under alkaline conditions yields a modified lignin, Lp-CE, that is insoluble in CH_2Cl_2 and only partially soluble in DMSO. Lp-CE characterization was, therefore, carried out on the soluble fraction. Analysis of the HSQC aliphatic domain (Figure 10A) shows that phenol groups have reacted, since three different signals are observed at 69−74/3.8−4.0 ppm, assigned to the Ar−O−CH_2−CH_2−OH methylene of 2-hydroxyethoxy groups in the 4-position of H, G, and S aromatic rings (Figure 8). Assignments of the resulting etherified units H′, G′, and S′ were made with the help of model compounds **20**, **21**, and **22** (Figure 5) obtained by reaction of coumaric, ferulic, and sinapic acids with 2-chloroethanol in similar conditions. The $-CH_2-$OH methylenes of these groups and of *β*-O-4 linkages (**1**-*γ*) give overlapping cross-peaks. During the reaction, carboxylic acids are partly esterified into hydroxyethyl esters since signals corresponding to ferulate (**29**-9 and **29**-10) and aliphatic esters (**28**-9 and **28**-10) are also detected. On the other hand, *β*-O-4 aliphatic secondary hydroxyl groups remain unchanged, since no signal corresponding to aliphatic ethers (**24**-*α*) is detected at 79.7/4.48 ppm. Etherification of phenol groups by 2-chloroethanol is reflected by new correlations at 112.55/6.86 (G′-5) and 113.90/6.84 ppm (H′-3,5) (Figure 10B).

Lp-CE was also analyzed by ^{31}P NMR (Figure 9). Since the sample was not fully soluble in phosphitylation medium, quantitative determination of OH groups was not possible. The relative aliphatic/aromatic OH content was nevertheless determined on the soluble fraction, showing an almost 7-fold decrease in phenol content, with unchanged ratio of un-, mono-, and disubstituted 4-hydroxyphenyl units. Hydroxyethylation by 2-chloroethanol in basic medium, therefore, appears to be a very efficient modification method of lignin phenol groups.

Since Lp-CE was only partially soluble in THF, even after acetylation, the SEC analyses were performed on the soluble fraction after filtration, leading to lower molar mass (M_n = 1155 g/mol) and dispersity ($Đ_M$ = 4.0) than Lp, as expected for a fractionated polymer sample.

Finally, we can conclude that alkaline hydrolysis (1 M NaOH at 80 °C) and solvent extraction of Biolignin yields a purified, deacylated lignin sample (Lp) with very low content of

DOI: 10.1021/acs.jafc.5b02071
J. Agric. Food Chem. 2015, 63, 5178−5188

contaminants and that the purification does not significantly affect starting lignin main structure and molar masses. Lp contains primary and secondary alcohol groups, carboxylic acid groups, and phenolic OH groups. The large phenolic OH content reflects the existence of condensed aromatic structures, such as units of 5−5 type, which bring two additional phenolic OH groups per lignin molecule.

Modification of Lp by esterification with ethanol or ethane-1,2-diol in the presence of *p*-toluenesulfonic acid catalyst was efficient and, as expected, led to esterified lignin samples (Lp-Et and Lp-EG, respectively) with a very low carboxylic acid content. In these conditions, the secondary alcohols were also totally etherified, but no β-O-4 linkage cleavage was observed, leading to modified lignin containing only primary alcohols and phenols. With ethane-1,2-diol, simultaneous hydroxyethoxylation of secondary OH groups during COOH esterification resulted in an increased aliphatic OH/phenolic OH ratio with respect to Lp-Et. Etherification of phenolic OH groups with 2-chloroethanol yielded lignins containing only aliphatic alcohol groups.

These modification reactions (ethylation, hydroxyethylation, ethoxylation) allow control of the nature and content of OH groups and, therefore, of the chemical functionality of lignins. This is a prerequisite for their use as comonomers in polycondensation reactions, where stoichiometry is a key parameter (e.g., polyesterifications), or as initiators in ring-opening polymerizations and, after further tailored modification, in controlled radical polymerizations. The purified and modified lignins described in this work are, therefore, interesting macromonomers for the preparation of well-defined polymers or polymer blends.

■ ASSOCIATED CONTENT

Supporting Information

^{1}H NMR spectra of Biolignin, Lh, Lp, Rh, and Rp; 2D ^{13}C−^{1}H HSQC NMR spectra of Rh and Rp side-chain and aromatic domains; 2D ^{13}C−^{1}H HMBC NMR spectrum of Rp; 2D ^{13}C−^{1}H HMBC NMR spectrum of s-Lp-Et; and ^{13}C NMR spectra of Lp, s-Lp-Et, and Lp-EG. The Supporting Information is available free of charge on the ACS Publications website at DOI: 10.1021/acs.jafc.5b02071.

■ AUTHOR INFORMATION

Corresponding Author

*Telephone +33-144273804; fax +33-144277089; e-mail alain.fradet@upmc.fr.

Notes

The authors declare no competing financial interest.

■ ACKNOWLEDGMENTS

We thank Dr. Bouchra Benjelloun-Mlayah and Professor Michel Delmas (CIMV) for lignin samples and for helpful discussions.

■ ABBREVIATIONS

Lh, hydrolyzed Biolignin; Lp, purified Biolignin after hydrolysis and solvent extraction; Rh, hydrolysis residue; Rp, solvent extraction residue; Lp-Et, reaction product of purified Biolignin with ethanol; s-Lp-Et, ethanol-soluble fraction of Lp-Et; i-Lp-Et, ethanol-insoluble fraction of Lp-Et; Lp-EG, reaction product of purified Biolignin with ethane-1,2-diol; Lp-CE, reaction product of purified Biolignin with 2-chloroethanol; G, guaiacyl unit; H, 4-hydroxyphenyl unit; S, syringyl unit; G′, 4-(2-hydroxyethoxy)-3-methoxyphenyl unit; H′, 4-(2-hydroxyethoxy)phenyl unit; S′, 4-(2-hydroxyethoxy)-3,5-dimethoxyphenyl unit; MW, milled wood

■ REFERENCES

(1) Buranov, A. U.; Mazza, G. Lignin in straw of herbaceous crops. *Ind. Crops Prod.* **2008**, *28*, 237−259.

(2) Yuan, T.-Q.; Sun, R.-C. Introduction. In *Cereal Straw as a Resource for Sustainable Biomaterials and Biofuels*; Sun, R.-C., Ed.; Elsevier: Amsterdam, 2010; pp 1−7.

(3) Scalbert, A.; Monties, B.; Lallemand, J.-Y.; Guittet, E.; Roland, C. Ether linkage between phenolic acids and lignin fractions from wheat straw. *Phytochemistry* **1985**, *24*, 1359−1362.

(4) Sun, R.; Rowlands, P.; Lawther, J. M. Rapid isolation and physico-chemical characterization of wheat straw lignins. *Recent Res. Dev. Agric. Food Chem.* **2000**, *4*, 1−26.

(5) Xu, F.; Sun, J.-X.; Sun, R.; Fowler, P.; Baird, M. S. Comparative study of organosolv lignins from wheat straw. *Ind. Crops Prod.* **2006**, *23*, 180−193.

(6) Sun, R.; Lawther, J. M.; Banks, W. B. Effects of extraction time and different alkalis on the composition of alkali-soluble wheat straw lignins. *J. Agric. Food Chem.* **1996**, *44*, 3965−3970.

(7) Del Rio, J. C.; Rencoret, J.; Prinsen, P.; Martinez, A. T.; Ralph, J.; Gutierrez, A. Structural characterization of wheat straw lignin as revealed by analytical pyrolysis, 2D-NMR, and reductive cleavage methods. *J. Agric. Food Chem.* **2012**, *60*, 5922−5935.

(8) Crestini, C.; Argyropoulos, D. S. Structural analysis of wheat straw lignin by quantitative ^{31}P and 2D NMR spectroscopy. The occurrence of ester bonds and α-O-4 substructures. *J. Agric. Food Chem.* **1997**, *45*, 1212−1219.

(9) Zeng, J.; Helms, G. L.; Gao, X.; Chen, S. Quantification of wheat straw lignin structure by comprehensive NMR analysis. *J. Agric. Food Chem.* **2013**, *61*, 10848−10857.

(10) Lawther, J. M.; Sun, R.-C.; Banks, W. B. Isolation and characterization of organosolv lignin under alkaline condition from wheat straw. *Int. J. Polym. Anal. Charact.* **1997**, *3*, 159−175.

(11) Delmas, M. Vegetal refining and agrichemistry. *Chem. Eng. Technol.* **2008**, *31*, 792−797.

(12) Delmas, G.-H.; Benjelloun-Mlayah, B.; Le Bigot, Y.; Delmas, M. Functionality of wheat straw lignin extracted in organic acid media. *J. Appl. Polym. Sci.* **2011**, *121*, 491−501.

(13) Ralph, J. Hydroxycinnamates in lignification. *Phytochem. Rev.* **2010**, *9*, 65−83.

(14) Berlin, A.; Balakshin, M. Industrial Lignins: Analysis, Properties, and Applications. In *Bioenergy Research: Advances and Applications*; Gupta, V. K., Kubicek, M. G. T. P., Xu, J. S., Eds.; Elsevier: Amsterdam, 2014; Chapt. 18, pp 315−336.

(15) Gandini, A.; Belgacem, M. N. Lignins as components of macromolecular materials. In *Monomers, Polymers and Composites from Renewable Resources*; Belgacem, M. N., Gandini, A., Eds.; Elsevier: Amsterdam, 2008; pp 243−271.

(16) Matsushita, Y.; Inomata, T.; Takagi, Y.; Hasegawa, T.; Fukushima, K. Conversion of sulfuric acid lignin generated during bioethanol production from lignocellulosic materials into polyesters with ε-caprolactone. *J. Wood Sci.* **2011**, *57*, 214−218.

(17) Chung, Y.-L.; Olsson, J. V.; Li, R. J.; Frank, C. W.; Waymouth, R. M.; Billington, S. L.; Sattely, E. S. A renewable lignin−lactide copolymer and application in biobased composites. *ACS Sustainable Chem. Eng.* **2013**, *1*, 1231−1238.

(18) Laurichesse, S.; Avérous, L. Synthesis, thermal properties, rheological and mechanical behaviors of lignins-grafted-poly(ε-caprolactone). *Polymer* **2013**, *54*, 3882−3890.

(19) Bonini, C.; D'Auria, M.; Emanuele, L.; Ferri, R.; Pucciariello, R.; Sabia, A. R. Polyurethanes and polyesters from lignin. *J. Appl. Polym. Sci.* **2005**, *98*, 1451−1456.

(20) Cateto, C. A.; Barreiro, M. F.; Rodrigues, A. E.; Belgacem, M. N. Kinetic study of the formation of lignin-based polyurethanes in bulk. *React. Funct. Polym.* **2011**, *71*, 863−869.

DOI: 10.1021/acs.jafc.5b02071
J. Agric. Food Chem. 2015, 63, 5178−5188

(21) Cinelli, P.; Anguillesi, I.; Lazzeri, A. Green synthesis of flexible polyurethane foams from liquefied lignin. *Eur. Polym. J.* **2013**, *49*, 1174−1184.
(22) Hofmann, K.; Glasser, W. G. Engineering plastics from lignin. 21. Synthesis and properties of epoxidized lignin-poly(propylene oxide) copolymers. *J. Wood Chem. Technol.* **1993**, *13*, 73−95.
(23) Koike, T. Progress in development of epoxy resin systems based on wood biomass in Japan. *Polym. Eng. Sci.* **2012**, *52*, 701−717.
(24) Delmas, G.-H.; Benjelloun-Mlayah, B.; Le Bigot, Y.; Delmas, M. Biolignin based epoxy resins. *J. Appl. Polym. Sci.* **2013**, *127*, 1863−1872.
(25) Hilburg, S. L.; Elder, A. N.; Chung, H.; Ferebee, R. L.; Bockstaller, M. R.; Washburn, N. R. A universal route towards thermoplastic lignin composites with improved mechanical properties. *Polymer* **2014**, *55*, 995−1003.
(26) Lora, J. Industrial commercial lignins: Sources, properties and applications. In *Monomers, Polymers and Composites from Renewable Resources*; Belgacem, M. N., Gandini, A., Eds.; Elsevier: Amsterdam, 2008; pp 225−241.
(27) Abdelkafi, F.; Ammar, H.; Rousseau, B.; Tessier, M.; El Gharbi, R.; Fradet, A. Structural analysis of alfa grass (*Stipa tenacissima* L.) lignin obtained by acetic acid/formic acid delignification. *Biomacromolecules* **2011**, *12*, 3895−3902.
(28) Glasser, W. G.; Jain, R. K. Lignin derivatives. I. Alkanoates. *Holzforschung* **1993**, *47*, 225−233.
(29) Wu, L. C. F.; Glasser, W. G. Engineering plastics from lignin. I. Synthesis of hydroxypropyl lignin. *J. Appl. Polym. Sci.* **1984**, *29*, 1111−1123.
(30) Cateto, C. A.; Barreiro, M. F.; Rodrigues, A. E.; Belgacem, M. N. Optimization study of lignin oxypropylation in view of the preparation of polyurethane rigid foams. *Ind. Eng. Chem. Res.* **2009**, *48*, 2583−2589.
(31) Sadeghifar, H.; Cui, C.; Argyropoulos, D. S. Toward thermoplastic lignin polymers. Part 1. Selective masking of phenolic hydroxyl groups in Kraft lignins via methylation and oxypropylation chemistries. *Ind. Eng. Chem. Res.* **2012**, *51*, 16713−16720.
(32) Ahvazi, B.; Wojciechowicz, O.; Ton-That, T.-M.; Hawari, J. Preparation of lignopolyols from wheat straw soda lignin. *J. Agric. Food Chem.* **2011**, *59*, 10505−10516.
(33) Avignon, G.; Delmas, M. Method for producing paper pulp, lignins, sugars and acetic acid by fractionation of lignocellulosic vegetable material in formic/acetic acid medium. PCT Int. Appl. WO0068494 (A1), November 16, 2000.
(34) Cachet, N.; Camy, S.; Benjelloun-Mlayah, B.; Condoret, J.-S.; Delmas, M. Esterification of organosolv lignin under supercritical conditions. *Ind. Crops Prod.* **2014**, *58*, 287−297.
(35) Lotti, N.; Siracusa, V.; Finelli, L.; Munari, A.; Manaresi, P. Synthesis and thermal behavior of poly(2-hydroxyethoxybenzoate) and its copolyesters with ε-caprolactone. *J. Therm. Anal. Calorim.* **2001**, *66*, 827−840.
(36) Granata, A.; Argyropoulos, D. S. 2-Chloro-4,4,5,5-tetramethyl-1,3,2-dioxaphospholane, a reagent for the accurate determination of the uncondensed and condensed phenolic moieties in lignins. *J. Agric. Food Chem.* **1995**, *43*, 1538−1544.
(37) Zawadzki, M.; Ragauskas, A. N-Hydroxy compounds as new internal standards for the ^{31}P-NMR determination of lignin hydroxy functional groups. *Holzforschung* **2001**, *55*, 283−285.
(38) Del Rio, J. C.; Rencoret, J.; Marques, G.; Gutierrez, A.; Ibarra, D.; Santos, J. I.; Jimenez-Barbero, J.; Zhang, L.; Martinez, A. T. Highly acylated (acetylated and/or *p*-coumaroylated) native lignins from diverse herbaceous plants. *J. Agric. Food Chem.* **2008**, *56*, 9525−9534.
(39) Martinez, A. T.; Rencoret, J.; Marques, G.; Gutierrez, A.; Ibarra, D.; Jimenez-Barbero, J.; del Rio, J. C. Monolignol acylation and lignin structure in some nonwoody plants: A 2D NMR study. *Phytochemistry* **2008**, *69*, 2831−2843.
(40) Kim, H.; Ralph, J. Solution-state 2D NMR of ball-milled plant cell wall gels in DMSO-d_6/pyridine-d_5. *Org. Biomol. Chem.* **2010**, *8*, 576−591.
(41) Sun, R.; Sun, X. F.; Wang, S. Q.; Zhu, W.; Wang, X. Y. Ester and ether linkages between hydroxycinnamic acids and lignins from wheat, rice, rye, and barley straws, maize stems, and fast-growing poplar wood. *Ind. Crops Prod.* **2002**, *15*, 179−188.
(42) Syrjänen, K.; Brunow, G. Regioselectivity in oxidative cross-coupling of phenols. Application to the synthesis of dimeric neolignans. *Tetrahedron* **2001**, *57*, 365−370.
(43) Yue, F.; Lu, F.; Sun, R.; Ralph, J. Synthesis and characterization of new 5-linked pinoresinol lignin models. *Chem.—Eur. J.* **2012**, *18*, 16402−16410.
(44) Arshanitsa, A.; Ponomarenko, J.; Dizhbite, T.; Andersone, A.; Gosselink, R. J. A.; Van der Putten, J.; Lauberts, M.; Telysheva, G. Fractionation of technical lignins as a tool for improvement of their antioxidant properties. *J. Anal. Appl. Pyrolysis* **2013**, *103*, 78−85.
(45) Salanti, A.; Zoia, L.; Tolppa, E.-L.; Orlandi, M. Chromatographic detection of lignin−carbohydrate complexes in annual plants by derivatization in ionic liquid. *Biomacromolecules* **2012**, *13*, 445−454.
(46) Asikkala, J.; Tamminen, T.; Argyropoulos, D. S. Accurate and reproducible determination of lignin molar mass by acetobromination. *J. Agric. Food Chem.* **2012**, *60*, 8968−8973.
(47) Bauer, S.; Sorek, H.; Mitchell, V. D.; Ibanez, A. B.; Wemmer, D. E. Characterization of *Miscanthus giganteus* lignin isolated by ethanol organosolv process under reflux condition. *J. Agric. Food Chem.* **2012**, *60*, 8203−8212.
(48) Jasiukaityte-Grojzdek, E.; Kunaver, M.; Crestini, C. Lignin structural change during liquefaction in acidified ethylene glycol. *J. Wood Chem. Technol.* **2012**, *32*, 342−360.

DOI: 10.1021/acs.jafc.5b02071
J. Agric. Food Chem. 2015, 63, 5178−5188

JOURNAL OF AGRICULTURAL AND FOOD CHEMISTRY

Article

pubs.acs.org/JAFC

Uptake, Translocation, and Metabolism of Phenols by Submerged Rooted Macrophyte, Water Milfoil (*Myriophyllum elatinoides*)

Daisuke Ando,* Takuo Fujisawa, and Toshiyuki Katagi

Environmental Health Science Laboratory, Sumitomo Chemical Company, Limited, 4-2-1 Takatsukasa, Takarazuka, Hyōgo 665-8555, Japan

ABSTRACT: Shoot and root uptakes of ^{14}C-labeled phenol (**1**), 4-nitrophenol (**2**), 4-cyanophenol (**3**), 4-hydroxybenzamide (**4**), and 4-hydroxybenzoic acid (**5**) by *Myriophyllum elatinoides* were individually examined with water or sediment treatments using the sequestered chamber. Shoot uptake of each ^{14}C-phenol dissolved in water amounted to 21.0% (**1**), 14.3% (**2**), 12.8% (**3**), 4.2% (**4**) and 41.7% (**5**) of the applied radioactivity (AR) after 96 h without significant ^{14}C translocation from shoot to root (≤0.9% AR), and the major metabolite produced was the glucose conjugate. On the other hand, root uptake of ^{14}C-phenols from sediment was much slower/smaller (≤6.6% AR), and ^{14}C transportation from root to shoot was scarcely observed, except for compound **5** (≤1.5% AR). For the water treatment, a kinetic analysis on uptake/metabolism was conducted using the assumed compartment. Good correlation was observed between lipophilicity and shoot uptake rate constants, and the electronic state of the hydroxyl group (σ, σ^-, or $E_{HOMO(OH)}$) and the transformation rate constant of glucosidation.

KEYWORDS: *rooted macrophyte, shoot uptake, root uptake, metabolism, translocation, phenol, kinetics*

INTRODUCTION

Submerged macrophytes are very important aquatic plants for production/circulation of oxygen and nutrient in the water layer and stabilization of the bottom sediment in water bodies, which securely provide precious food and shelter for many aquatic biota.[1−3] Therefore, an adverse effect on the macrophyte community will have serious impact on the overall aquatic ecosystem. Incidentally, herbicides and plant-growth regulators are considered to reach water bodies by spray drift, runoff, drainage, or accidental spills, which may cause substantial damage toward non-target aquatic plant species. In the previous European Union (EU) Directive 91/414/EEC, the acute toxicity data [50% effect concentration (EC_{50})] for two algae and one macrophyte, such as *Lemna* spp., had been required to determine the adverse effect to aquatic plants.[4] However, the assessment with these limited species could underestimate the risk to the sediment-rooted macrophytes because the chemicals may have been taken up not only from the water via shoot but also from the bottom sediment via root.[3,5−7] Hence, in the latest aquatic guidance issued by the European Food Safety Authority (EFSA) on 2013, the risk assessment for submerged-rooted macrophytes, such as *Myriophyllum elatinoides*, a water milfoil, was newly included as additional test species to be evaluated if both algae and *Lemna* are highly susceptible to the chemical or if chronic sediment exposure is to cause concerns.[8]

Despite their importance in the aquatic ecosystem, there are few basic knowledge on the uptake, translocation, and metabolism of pesticides and their degradates by submerged-rooted macrophytes. Therefore, we have studied the behavior of simple phenols, as model compounds, in *M. elatinoides* using a special glass aquarium equipped with a partition board, which enabled separate exposure of the plant by two routes, i.e., water treatment (shoot exposure) and sediment treatment (root exposure).[9] In addition, investigation on the relationship between the uptake/metabolism behavior and various chemical indexes was performed to explain the observed results.

MATERIALS AND METHODS

Chemicals. The ^{14}C compounds uniformly radiolabeled at the phenyl ring were used in the study (Figure 1): phenol (**1**) and 4-nitrophenol (**2**) were purchased from American Radiolabeled Chemicals. Inc., and 4-cyanophenol (**3**), 4-hydroxybenzamide (**4**), and 4-hydroxybenzoic acid (**5**) were prepared in our laboratory according to the reported methods.[10−12] The specific activities were 2.96 GBq/mmol (**1**), 2.85 GBq/mmol (**2**), and 4.37 GBq/mmol (**3**−**5**). Each ^{14}C compound had the radiochemical purity exceeding 98%, as purified by reversed-phase high-performance liquid chromatography (HPLC) prior to use. Non-radiolabeled compounds **1**−**5** with the chemical purity of >95% were purchased from Sigma-Aldrich Co. All

Phenol	R
1	H
2	NO_2
3	CN
4	$CONH_2$
5	COOH

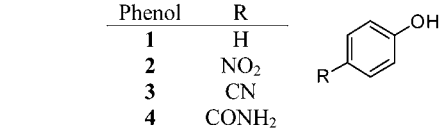

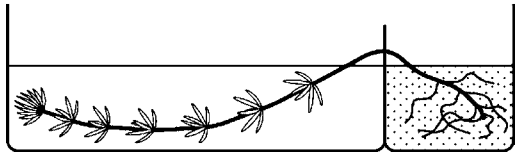

Figure 1. Test materials and the sequestered chamber applied for water and sediment treatments.

Received: March 5, 2015
Revised: May 13, 2015
Accepted: May 18, 2015
Published: May 18, 2015

ACS Publications © 2015 American Chemical Society

DOI: 10.1021/acs.jafc.5b01133
J. Agric. Food Chem. 2015, 63, 5189−5195

of the reagents and solvents used in this experiment were of analytical grade.

Chromatography. A reversed-phase HPLC system to analyze the test phenols and their metabolites consisted of a Hitachi LC module (model L-7000) equipped with a SUMIPAX ODS A-212 column (5 μm, 6 mm inner diameter × 15 cm, Sumika Chemical Analysis Service, Ltd.). The following gradient system was employed to analyze each phenol and its metabolites at a flow rate of 1 mL/min, with 0.1% formic acid (solvent A) and acetonitrile (solvent B): 0 min, 100:0 (% A/% B, v/v); 40 min, 10:90; 40.1 min, 100:0; and 45 min, 100:0. The typical retention times of the corresponding phenols were 18.6 min (**1**), 22.1 min (**2**), 19.8 min (**3**), 6.7 min (**4**), and 12.9 min (**5**). The radioactivity in the column effluent was counted with a flow scintillation analyzer radiomatic 150TR (PerkinElemer Co.) radiodetector equipped with a 500 μL liquid cell using Ultima-Flo AP (PerkinElemer Co.) as a liquid scintillator. The limit of detection (LOD) for the radioactivity in HPLC analysis was 30 dpm. A thin-layer chromatography (TLC) was carried out using precoated silica gel 60F254 thin-layer chromatoplates (20 × 20 cm, 0.25 mm thickness, E. Merck) for the purification of the glucose conjugates of each tested phenol. The TLC solvent used for development was 4:1:1 (v/v/v) butanol/acetic acid/water. The autoradiogram was prepared by exposing the TLC plates to BAS-IIIs Fuji imaging plates (Fuji Photo Film Co., Ltd.) for several hours, and the corresponding radioactive spot transcribed onto the imaging plate was detected by a bioimaging analyzer Typhoon (GE Healthcare).

Spectroscopy. One-dimensional (^{1}H) and two-dimensional [^{1}H−^{1}H, correlation spectroscopy (COSY)] nuclear magnetic resonance (NMR) spectra of the sugar conjugates of compounds **2**, **4**, and **5** were measured in methanol-d_4 with 0.03% tetramethylsilane using a Varian Mercury 400 spectrometer (Varian Technologies, Ltd.) at 400 MHz. Liquid chromatography−electrospray ionization−tandem mass spectrometry (LC−ESI−MS/MS) analysis was conducted for the phenols and their metabolites using a Waters Tandem Quadruple TQD spectrometer equipped with a Waters Separation Module Acquity ultra performance liquid chromatograph (UPLC) and a Waters Acquity photodiode array detector. The following parameters were used for the typical analysis: source temperature, 150 °C; desolvation temperature, 450 °C; capillary voltage, 3.2 kV; cone voltage, 10−40 V; and collision energy, 5−20 V.

Radioanalysis. Radioactivity in water medium and sediment and plant extract was determined by liquid scintillation counting (LSC) with a Packard model 2900TR spectrometer after mixing each aliquot with 10 mL of PerkinElmer Emulsifier Scintillator Plus. The LOD for LSC analysis was 30 dpm. The post-extracted bound residues in plant and sediment were combusted using a PerkinElmer model 307 sample oxidizer. $^{14}CO_2$ produced by the procedure was trapped into 9 mL of a PerkinElmer Carb-CO_2 absorber and mixed with 15 mL of a PerkinElmer Permafluor scintillator. The radioactivity therein was quantified by LSC. The efficiency of the combustion was determined to be greater than 94.4%.

Plant Material and Treatment. *M. elatinoides* purchased from Shimizu Laboratory Suppliers. Co., Ltd. was used in the experiments as previously described.[9] After 10 days of root development in an aquarium filled with an American Academy of Pediatrics (AAP) water medium[13] and Organisation for Economic Co-operation and Development (OECD) synthetic bottom sediment,[14] the plant was sterilized using 0.5% sodium hypochlorite with sonication under reduced pressure for 1 min, washed using sterilized water, and subjected to the exposure experiment. The glass test vessel used for this study had the glass partition board, which completely separates shoot and root chambers, as shown in Figure 1.[9] The growth stage of the plants was as follows: shoot length, 17.1−18.8 cm; root length, 4.2−5.2 cm; root number, 7−11; and fresh body weight, 0.41−0.49 g. The shoot and root chambers were individually filled with 120 mL of the water medium and medium-moistened sediment (20 mL and 35 g), respectively. The medium and sediment were adjusted to pH 7.0 ± 0.1 and autoclaved (1.5 kg cm^{-2} at 120 °C for 20 min) before use. A total of 20−55 μL of the methanol solution containing each ^{14}C-phenol isotopically diluted with the corresponding non-radiolabeled compound was either spiked into the medium in the shoot chamber (water treatment) or the bottom sediment in the root chamber (sediment treatment) and homogeneously mixed to prepare an exposure concentration of 0.1 ppm (0.083 MBq). Approximately 2 cm of the root node was buried into the sediment in the root chamber, and the shoot was gently placed to be immersed under the water in the shoot chamber (Figure 1). To prevent ^{14}C cross-contamination via vaporization/deposition between the chambers, an AAP-moistened cotton was settled on the partition board and each chamber was covered with a polyethylene wrap. Then, the glass vessel was incubated in a climate chamber LH-220S (NK Systems, Ltd.) at 20 ± 2 °C under fluorescence light (8000 lx, 16 h per day) up to 96 h. Each exposure was conducted in triplicate.

Analytical Procedures. The sampling was conducted sequentially after 1, 3, 6, 12, 24, 48, and 96 h of each exposure. The plant sampled from the exposure chamber was surface-washed using 50 mL of a fresh water medium, and the rinsate was combined with the water medium recovered from the corresponding chamber. After measuring its length and wet weight, the plant was further rinsed with 50 mL of acetonitrile (surface rinse). Then, the plant was divided into shoot and root portions, and the total radioactivity in each portion was measured by the combustion analysis, except for the shoots of the water treatment. The corresponding shoot portion was extracted with 20 mL of methanol using a homogenizer AM-8 (Nissei, Ltd.) at 10 000 rpm and 0 °C for 10 min. The homogenate was vacuum-filtered, and the plant residue was further extracted twice in the same manner. The sediment and water medium in the root chamber were separated by vacuum filtration. The sediment was washed once with 100 mL of a fresh water medium, and the combined water was radioassayed. The ^{14}C-treated sediment was further extracted with 30 mL of methanol by 10 min of mechanical shaking with a Taiyo SR-IIw recipro-shaker (Taiyo Chemical Industry Co., Ltd.). The soil residue after vacuum filtration was successively extracted twice in the same manner. Each aliquot of the surface rinses, extracts, and water media was analyzed with LSC and HPLC co-chromatography with authentic standards. The plant/sediment-extracted residues and ^{14}C-unexposed sediment were subjected to the combustion analysis.

Identification of Major Metabolites. The major metabolites were isolated/purified by TLC from the plant samples and subjected to LC−MS and NMR analyses.

Kinetic Analysis. To understand the behavior of the phenols in *M. elatinoides*, kinetic analysis was employed for the samples of the water treatment system using the Model-Maker program (version 4, ModelKinetix). The simulation was conveniently carried out by a compartment model shown in Figure 2. On the basis of the kinetic parameters of compound **1**, the relative rate constants on the uptake and metabolism of each phenol derivative were calculated and their logarithm values were subjected to regression analysis with various physicochemical parameters of the phenols using Microsoft Excel 2010. Physicochemical parameters applied for the analysis are listed in

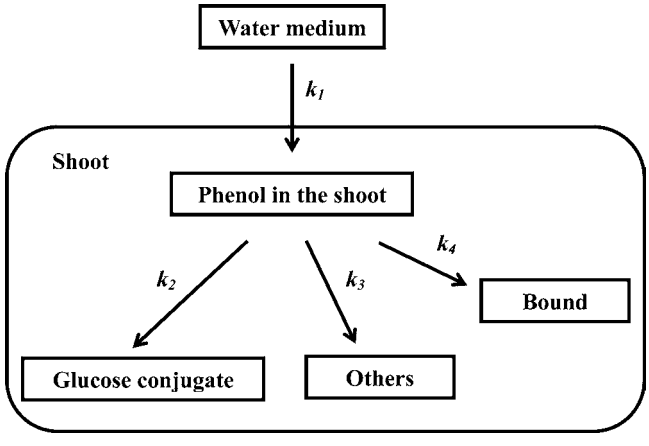

Figure 2. Compartment model employed for the kinetic analysis.

DOI: 10.1021/acs.jafc.5b01133
J. Agric. Food Chem. 2015, 63, 5189−5195

Table 1. Physicochemical Properties of the Phenol Derivatives

phenol	pK_a[a]	$f_{neutral}$[b]	log K_{ow}[c]	log D[d]	σ[e]	σ^-[e]	$E_{HOMO(OH)}$	$E_{HOMO(O^-)}$
1	9.99	0.999	1.47	1.47	0	0	−8.95	−7.31
2	7.15	0.586	1.91	1.68	0.78	1.27	−9.51	−8.27
3	7.77	0.855	1.60	1.53	0.66	1.00	−9.16	−9.90
4	8.18	0.938	0.33	0.30	0.36	0.61	−9.18	−7.60
5	4.58, 9.23	0.004	1.58	−0.83	0.45	0.77	−9.28	−4.49

[a]Calculated from ref 15. [b]$f_{neutral} = [K_a/10^7 + 1]^{-1}$. [c]Calculated from refs 16 and 17. [d]log D values at pH 7.0, calculated using log K_{ow} and pK_a according to ref 18. [e]Calculated from ref 19.

Table 2. ^{14}C Distribution in the Water Treatment System after 96 h[a]

	percentage of the applied radioactivity (%)				
	1	**2**	**3**	**4**	**5**
shoot chamber					
water medium	55.8 ± 4.5	82.9 ± 7.5	80.9 ± 7.9	92.1 ± 8.5	54.5 ± 5.5
root chamber	nd[b]	nd	nd	nd	nd
plant (whole)	25.5 ± 2.2	14.3 ± 1.3	12.8 ± 1.2	4.2 ± 0.5	41.7 ± 4.2
shoot	25.1 ± 1.9	14.3 ± 1.3	12.8 ± 1.2	4.2 ± 0.5	40.8 ± 3.9
roots	0.4 ± 0.1	nd	nd	nd	0.9 ± 0.1
total	81.3 ± 5.2	97.2 ± 2.9	93.7 ± 2.6	96.3 ± 1.8	96.2 ± 2.1

[a]Data are expressed as means ± standard deviation of triplicate samples ($p < 0.05$). [b]nd = values did not exceed 0.1%.

Table 1.[15−19] Because the phase II conjugation reactions of chemicals are considered to be affected by nucleophilicity of the substrates,[20] the energy level of the highest occupied molecular orbital (E_{HOMO}, eV) with its distribution was calculated by SCIGRESS MO Compact program (version 1, standard, Fujitsu, Ltd.) as a potential index to examine the correlation with the transformation rate constant to produce glucoside conjugate of phenols. The molecular geometry of each phenol was optimized by MNDO-PM 3 Hamiltonian with the dielectric constant of $\varepsilon = 78.4$, assuming the water environment, and calculated with a criterion introduced by inputting the PRECISE command. The calculation of each phenol was conducted for the neutral and ionized form at phenoxy oxygen abbreviated as $E_{HOMO(OH)}$ and $E_{HOMO(O^-)}$, respectively. Classical Hammett's constants (σ and σ^-) at the reaction center, i.e., phenolic oxygen, were also examined for the reactivity of phenols.[19] The fraction of the undissociated form of each phenol in the medium at pH 7 was calculated from its acid dissociation constant (K_a) by applying the Henderson−Hasselbalch equation as follows: $f_{neutral} = [K_a/10^{-7} + 1]^{-1}$. Logarithm of the distribution constant (log D), which indicates the hydrophobicity of chemicals adjusted with the dissociation effect was obtained from log K_{ow} and pK_a values according to the method of van der Waterbeemd et al.[18]

RESULTS

Validity Confirmation of the Test System. During the 96 h uptake period, no growth inhibition was observed for the plants exposed to any phenols compared to those acclimated in the control aquarium: increase in length, 0.4−1.1 cm; fresh body weight, 0.04−0.09 g. Cross-contamination of the applied ^{14}C between the shoot and root chambers was considered negligible because extremely little radioactivity [≤0.1% applied radioactivity (AR)] was detected from the ^{14}C-untreated chambers throughout the study. The inner wall of the test vessel was thoroughly washed with methanol after each sampling, and the recovered ^{14}C in the rinsate was below the LOD (<30 dpm), which clarified negligible loss of ^{14}C by adhesion onto the vessel.

^{14}C Distribution in the Water Treatment System. The ^{14}C distribution in the water treatment system after 96 h is summarized in Table 2. The total ^{14}C recovery for compounds **2**−**5** ranged from 93.7 to 97.2% AR with less recovery for compound **1** (81.3% AR). A large amount of the applied radioactivity remained in the water layer for compounds **2**−**4** (>80.9% AR), while a lower amount was observed for compounds **1** (55.8% AR) and **5** (54.5% AR). From the HPLC analysis, the radioactive component in exposure water was clarified to be the unaltered parent only for all of the test materials. The amount of ^{14}C taken up from water via shoot with the incubation period is shown in Figure 3. The ^{14}C uptake by the shoot after 96 h reached 4.2−25.5% AR for compounds **1**−**4**, and 41.7% AR for compound **5**. No detectable radioactivity was recovered from the plant surface wash. For most of the tested phenols, shoot uptake was rapid at the beginning and gradually approached its steady state at the end of exposure. The majority of ^{14}C taken up remained in the shoot, and very minor radioactivity was detected from the root, which amounted to 0.4% AR (**1**), ≤0.1% AR (**2**−**4**), and 0.9% AR (**5**). These results suggest that the basipetal ^{14}C translocation from shoot to root is a minor process.

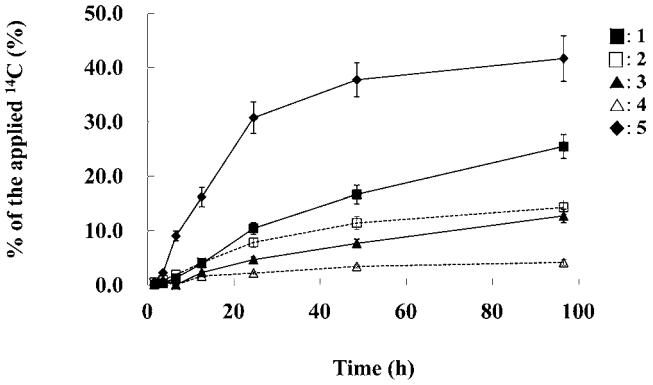

Figure 3. Accumulated ^{14}C by *M. elatinoides* in the water treatment system. The error bars represent mean standard deviation ($n = 3$; $p < 0.05$).

DOI: 10.1021/acs.jafc.5b01133
J. Agric. Food Chem. 2015, 63, 5189−5195

Table 3. ^{14}C Distribution in the Sediment Treatment System after 96 h[a]

	percentage of the applied radioactivity (%)				
	1	2	3	4	5
shoot chamber					
water medium	nd[b]	nd	nd	nd	nd
root chamber					
water medium	47.0 ± 3.1	34.4 ± 3.9	42.2 ± 4.6	85.9 ± 7.8	84.3 ± 8.2
sediment	42.1 ± 3.9	61.0 ± 5.1	51.8 ± 5.3	11.5 ± 1.3	6.5 ± 0.6
plant (whole)	2.4 ± 0.2	1.3 ± 0.1	1.2 ± 0.1	0.8 ± 0.1	6.6 ± 0.7
shoot	nd	nd	nd	nd	1.5 ± 0.1
roots	2.4 ± 0.2	1.3 ± 0.1	1.2 ± 0.1	0.7 ± 0.1	5.1 ± 0.6
total	91.7 ± 3.3	96.7 ± 2.9	95.2 ± 3.0	98.2 ± 3.5	97.4 ± 2.3

[a]Data are expressed as means ± standard deviation of triplicate samples ($p < 0.05$). [b]nd = values did not exceed 0.1%.

^{14}C Distribution in the Sediment Treatment System. The ^{14}C distribution in the test system at 96 h exposure is summarized in Table 3. The total ^{14}C recovery ranged from 91.7 to 98.2% AR. The radioactivity in the sediment is shown as the sum of ^{14}C in the methanol extract and unextractable bound residue, in which the latter amounted to be less than 3.5% AR. For all of the phenols, most of the applied ^{14}C remained in the root chamber (≥89.1% AR) and the radioactivity detected from the untreated water in the shoot chamber was insignificant (≤0.1% AR). In the root chamber, the amount of ^{14}C in water/sediment after 96 h was 47.0% AR/42.1% AR (**1**), 34.4% AR/61.0% AR (**2**), 42.2% AR/51.8% AR (**3**), 85.9% AR/11.5% AR (**4**), and 84.3% AR/6.5% AR (**5**). For both water and sediment fractions in the root chamber, the unchanged phenols were the only radioactive constituent confirmed by HPLC analysis. Root uptake behavior of ^{14}C from the sediment is shown in Figure 4. The ^{14}C taken up after

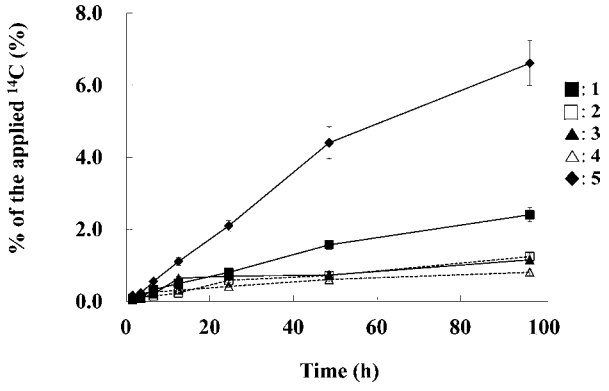

Figure 4. Accumulated ^{14}C by *M. elatinoides* in the sediment treatment system. The error bars represent mean standard deviation ($n = 3$; $p < 0.05$).

96 h reached 0.8−2.4% AR for compounds **1**−**4** and 6.6% AR for compound **5**. No radioactivity was recovered by the plant surface rinse. In comparison to the water treatment, the ^{14}C uptake from sediment via root was much lower and slower than the ^{14}C uptake from water via shoot for all of the test materials. The radioactivity translocated from root to shoot after 96 h was extremely low for compounds **1**−**4** (≤0.1% AR), which suggested that the acropetal ^{14}C translocation from root to shoot was unlikely to occur, whereas compound **5** showed the relatively higher potential of translocation because the radioactivity detected in the shoot was 1.5% AR. For the sediment treatment, the metabolic profiles in root and shoot were not clarified because of their insufficient ^{14}C to be characterized.

Distribution of Metabolites in the Exposed Shoot. The metabolite distribution in the shoot portion of milfoil at 96 h exposure is summarized in Table 4, as representative. In the shoot, 84.4−97.5% of the total radioactive residue (TRR) was extractable and 2.5−6.3% TRR remained as the unextractable bound fraction. In the extracts, the unchanged phenols were quantified to be 14.0−20.5% TRR for compounds **1**−**4**, while the one was only 6.0% TRR for compound **1**, respectively. The glycoside conjugate of each phenol was the main metabolite, which amounted to 72.9% TRR (**6**), 78.8% TRR (**7**), 83.4% TRR (**8**), 63.5% TRR (**9**), and 88.0% TRR (**10**), respectively, after 96 h. For identification, metabolites **6**−**10** were analyzed by LC−MS and LC−MS/MS. The MS analysis of each metabolite gave molecular-related ions, which were identical to the mass number of the monoglucose conjugate of the corresponding phenol. Furthermore, the MS/MS analysis of $[M + H]^+$ or $[M - H]^-$ gave mass fragments suggesting the structure as follows: **6**, m/z 279 $[M + Na]^+$, 257 $[M + H]^+$, and 95 [**1** + H; M − sugar + H]$^+$; **7**, m/z 324 $[M + Na]^+$, 302 $[M + H]^+$, and 140 [**2** + H; M − sugar + H]$^+$; **8**, m/z 322 $[M + Na]^+$, 300 $[M + H]^+$, and 138 [**3** + H; M − sugar + H]$^+$; **9**, m/z 304 $[M + Na]^+$, 282 $[M + H]^+$, and 120 [**4** + H; M − sugar + H]$^+$; and **10**, m/z 299 $[M - H]^-$, 255 $[M - CO_2 - H]^-$, and 137 [**5** − H; M − sugar − H]$^-$. Incidentally, the fragment ion m/z 255 was detected in a negative-ion mode for compound **10**. Because this ion is considered to be produced by decarboxylation during the mass fragmentation similar to compound **5**, compound **10** was concluded to have a free carboxylic acid group and to form an O-glycosidic bond at the phenoxy oxygen. After the tentative identification by LC−MS, the conjugates **7**, **8**, and **10** were subjected to NMR analyses. The chemical shifts of protons were assigned as follows: **7**, δ = 8.36 ppm (2H, d, J = 9.21 Hz, aromatics), 7.34, (2H, d, J = 9.21 Hz, aromatics), 5.16 ppm (1H, d, J = 8.01 Hz, anomeric), and 3.60−4.01 ppm (5H, m, glucose); **8**, δ = 7.80 ppm (2H, d, J = 8.81 Hz, aromatics), 7.27 (2H, d, J = 8.81 Hz, aromatics), 5.14 ppm (1H, d, J = 7.61 Hz, anomeric), and 3.52−3.98 ppm (5H, m, glucose); and **10**, δ = 7.87 ppm (2H, d, J = 8.61 Hz, aromatics), 7.16 (2H, d, J = 8.61 Hz, aromatics), 5.02 ppm (1H, d, J = 6.81 Hz, anomeric), and 3.52−3.98 ppm (5H, m, glucose). The correlation between the anomeric and vicinal protons was distinguishable by the ^{1}H−^{1}H COSY NMR technique for each conjugate, which also indicated the glucoside structure.

Kinetic Analysis. The kinetic analysis was conducted for each phenol in the water treatment. The graph showing the

DOI: 10.1021/acs.jafc.5b01133
J. Agric. Food Chem. 2015, 63, 5189−5195

Table 4. ^{14}C Metabolites in the Shoot Exposed for 96 h in the Water Treatment System[a]

	percentage of the total radioactive residue (%)				
	1	2	3	4	5
extractable					
phenols	20.5 ± 2.9	17.9 ± 1.9	14.0 ± 1.6	19.4 ± 2.0	6.0 ± 0.7
glucose conjugate	72.9 ± 7.3	78.8 ± 7.7	83.4 ± 8.1	63.5 ± 5.9	88.0 ± 8.1
others[b]	0.8 ± 0.1	0.6 ± 0.1	nd[c]	10.8 ± 1.0	2.9 ± 0.2
bound	5.8 ± 0.6	2.7 ± 0.3	2.5 ± 0.2	6.3 ± 0.5	3.1 ± 0.2
total	100.0	100.0	100.0	100.0	100.0

[a]Data are expressed as means ± standard deviation of triplicate samples ($p < 0.05$). [b]Minor degradates amounted to less than 5% TRR, and/or polar degradates were unretained by the HPLC column. [c]nd = values did not exceed 0.1%.

simulated ^{14}C dissipation curves to estimate shoot uptake and metabolic rate constants for compound **5** is given in Figure 5, as

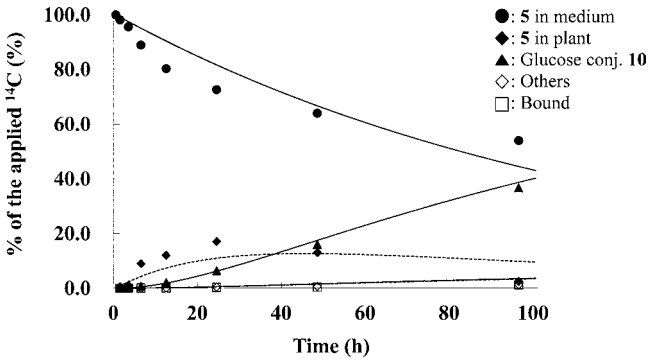

Figure 5. Uptake and metabolism curve of compound **5** by *M. elatinoides* simulated by the Model-Maker program.

representative. The optimization of the rate constants was performed with a good correlation ($r^2 > 0.97$; $p < 0.05$) for all phenols. The relative rate constants of compounds **2**−**5** with respect to compound **1** are summarized in Table 5. The relative rate constants for the production of "others" and "bound" were not obtained because these metabolic processes were insignificant to be compared to those of the most predominant process "glucose conjugation". Successively, the correlation between the physicochemical parameters and the logarithm of the relative rate constants is examined by the regression analysis, as listed in Table 6. The highest correlation for shoot uptake, $\log[k_{1(i)}/k_{1(1)}]$, was observed for log K_{ow} as 0.656 (standard deviation of 0.325), while the other indexes showed a lower correlation (<|0.264|). With respect to the transformation rate to produce a glucose conjugate, $\log[k_{2(i)}/k_{2(1)}]$, better correlations were obtained for the electrochemical parameters σ, σ^-, and $E_{HOMO(OH)}$ because their absolute values exceeded 0.871 with the standard deviation of less than 0.036. The kinetic simulation for the sediment treatment resulted in poor fitting ($r^2 < 0.50$), so that no comparison to the parameters was attempted.

DISCUSSION

In some test systems, the total ^{14}C recovery gradually decreased over the period of incubation. The loss of radioactivity was prominent for compound **1** probably because of the vaporization from the test vessel considering its high vapor pressure at ambient temperature (0.35 mmHg at 25 °C).[21]

In the water treatment, the ^{14}C uptake/accumulation to the plant decreased in the order of compounds **5**, **1**, **2**, **3**, and **4**. With regard to the regression analysis between the relative rate constants and physicochemical parameters, the log K_{ow} index showed the strongest correlation with the shoot uptake rate constants (k_1). Similar to many living organisms, this tendency complies with the observation that uptake of water-dissolved chemicals through the macrophyte surface closely correlates with their lipophilicity. For example, Gobas et al. investigated the uptake of non-ionizable pesticides from water by *M. spicatum* under submergence, and they observed the linear positive correlation between the accumulation factors and log K_{ow} values.[22] The same relationship was also reported on macrophytes by Carvalho et al. but without the linearity at the lower range of log K_{ow}, approximately below 1, which exhibits the minimum uptake potential.[23] Meanwhile, we also compared shoot uptake rate constant and log D, reflecting the actual lipophilicity of an ionizable chemical under dissociation. For example, better positive correlation for log D than log K_{ow} was

Table 5. Kinetic Analysis of Compounds 1−5 in Water Milfoil (Water Exposure)

	1	2	3	4	5
rate constant (h^{-1})					
k_1 (uptake)	5.651×10^{-3}	2.332×10^{-3}	2.818×10^{-3}	9.063×10^{-4}	8.424×10^{-3}
k_2 (conjugation)	3.185×10^{-2}	4.359×10^{-2}	4.044×10^{-2}	4.19×310^{-2}	3.851×10^{-2}
k_3 (others)	6.389×10^{-3}	9.574×10^{-4}	6.346×10^{-3}	1.815×10^{-2}	3.323×10^{-3}
k_4 (bound)	8.284×10^{-3}	2.067×10^{-3}	1.064×10^{-2}	1.741×10^{-2}	3.489×10^{-3}
r^2	0.997	0.989	0.990	0.978	0.989
p^a	3.210×10^{-3}	1.866×10^{-2}	3.731×10^{-4}	4.209×10^{-2}	2.677×10^{-6}
relative rate constant					
$\log[k_{1(i)}/k_{1(1)}]$	0	−0.384	−0.302	−0.795	0.173
$\log[k_{2(i)}/k_{2(1)}]$	0	0.136	0.104	0.119	0.083

[a]Probability in the Levenberg−Marquardt method for nonlinear least-squares curve fitting.

DOI: 10.1021/acs.jafc.5b01133
J. Agric. Food Chem. 2015, 63, 5189−5195

Table 6. Correlation between Logarithm Values of the Relative Rate Constant and Parameters of the Phenols

	pK_a	$f_{neutral}$	log K_{ow}	log D	σ	σ^-	$E_{HOMO(OH)}$	$E_{HOMO(O^-)}$
$\log[k_{1(i)}/k_{1(1)}]$	−0.323	−0.564	0.656	−0.159	−0.263	−0.261	0.178	0.546
$\log[k_{2(i)}/k_{2(1)}]$	−0.467	−0.208	−0.100	−0.033	0.872	0.890	−0.807	−0.265

reported for the accumulation of ionized chemicals by fish.[24] Incidentally, we have obtained a poor correlation, especially because highly dissociated carboxylic acid derivative **5** ($f_{neutral}$ = 0.004 at pH 7) exhibited outstanding accumulation despite its lowest log D value. In general, the ionized chemicals are considered unlikely to bioaccumulate in the leaf/shoot portion of plants because lipophilic materials, such as epicuticular wax, on the plant surface prevent the penetration of ionized compounds. However, Zhang et al. have clarified that many carboxylic compounds, which intensively dissociate in natural water bodies, are largely taken up by macrophytes, irrespective of their extremely low lipophilicity expressed by log D (less than zero).[25] In addition, 3-phenoxybenzoic acid (PBacid), which intensively dissociates in water at pH 7, as indicated by $f_{neutral}$ = 0.001, was largely taken up by *M. elatinoides*.[9] This trend may be explained from the reasons that ions could receive electric attraction/repulsion from electrically charged cell membranes, formation of molecular complex with cations, and as the most crucial process for weak acids, retention of anions at inner cells (ion trap theory), followed by metabolism, which generally increase the solubility of xenobiotics to enhance the trapping.[26]

For the metabolic reaction, glucose conjugation was observed in this study. The conjugation followed by storage into vacuoles is the generally accepted detoxification process in terrestrial plants. This is probably the case for macrophytes, because glucosidation is observed for many aquatic plants. For example, Day and Sounders reported glucose conjugation of halogenated phenols by duckweed, which is one of the major macrophytes.[27] In our kinetic analysis of the transformation rate constants to a glucose conjugate (k_2), high correlations were found for the Hammett constant (σ and σ^-) and $E_{HOMO(OH)}$. These results imply that the electronic distribution at the phenoxy group and/or phenol structure as a whole is important for glucose conjugation at the enzyme active site. Moreover, because the index σ^- also correlated with glucosidation, the inductive effect of the electron-withdrawing substituent on the phenyl ring, such as deprotonation and polarization enhancements, was considered to associate with the conjugation. The key mechanism for glucosidation by glucosyl transferases is generally expressed by the following steps:[28] (1) interaction of histidine at the binding acceptor domain of the enzyme with the hydroxyl group of the sugar-accepting substance to induce deprotonation and (2) nucleophilic attack by the deprotonated acceptor to the C1 anomeric carbon of the donor sugar. Hence, the nucleophilicity expressed by the index, such as σ, σ^-, or $E_{HOMO(OH)}$, likely showed good correlation to k_2. However, with regard to the reaction analysis using the molecular orbital calculation approach, the energy gap between HOMO and lowest unoccupied molecular orbital (LUMO) of the nucleophile and electron acceptor and their transition states are assumed to be important for the bond formation. Furthermore, the conformation rearrangement during interaction with the binding domain followed by HOMO redistribution of the nucleophile at the active site should be taken into account within the specific enzyme to precisely simulate the reaction.[29]

Incidentally, compound **5** possesses both phenoxy and carboxyl groups as the reaction site for glucosidation, but the phenoxy group was the predominant reaction site in *M. elatinoides*. The HOMO coefficients at the carboxylic and phenoxy oxygen were calculated as −0.372 and 0.047, respectively, while the LUMO constant at the anomeric carbon of glucose was −0.241. From deduction of the estimated electronic distribution, the carboxyl group is more likely to be involved in conjugation, but only this may not exclusively explain the selectivity of enzymatic glucosidation. The glucosidation of hydroxybenzoic acids including compound **5** by glucosyl transferases is known to proceed at the hydroxyl or carboxyl group to give glucose ether or ester conjugate, respectively, depending upon the substrate and the gene pattern of the enzymes.[30] Additionally, there are bifunctional glucosyl transferases, which are possible to catalyze either etherification and esterification, and the selectivity is known to be controlled by the reaction pH. For example, the glucosyl transferase in grape can selectively produce the ether glucoside of resveratrol at basic conditions (pH > 7) and the ester glucoside of resveratrol at acidic pH.[31] Because etherifying glucosidation of 3-phenoxybenzoic acid is previously confirmed,[9] *M. elatinoides* is considered to have both types or bifunctional type of glucosyl transferases.

In the sediment treatment, the ^{14}C uptake/accumulation to plant decreased in the order of compounds **5**, **1**, **2**, **3**, and **4**, which was the same trend observed with the water treatment. However, the total amount of radioactivity detected in the plant was much less than that in the water treatment. To estimate the uptake/transport of organic compounds from root to shoot, the transpiration stream concentration factor (TSCF), the concentration ratio of the compound in xylem (transpiration stream), and the solution adjacent to the roots are commonly applied for terrestrial plants. Briggs et al. have reported bell-shaped Gaussian curves for plotting TSCF versus log K_{ow} with the non-ionizable compounds, which imply that significant root uptake and translocation occur for the compound having an intermediate lipophilicity, log K_{ow} of around 1−3, and the maximum uptake is expected at the vertex of 1.8.[32] The similar uptake trend was observed for water milfoils with emergent leaves incubated hydroponically.[33] On the other hand, Dettenmaier et al. have proposed the sigmoidal relationship and suggested that the highly soluble/non-ionizable compound with a very low log K_+ has the highest uptake potential, while that with a high log K_{ow} has the lowest uptake potential.[34] On the basis of Briggs's theory, the amount of radioactivity in the shoot was considered to decrease in the order of compounds **2**, **3**, **5**, **1**, and **4**, but the obtained results were not as expected. One of the reasons for this discrepancy may be explained by the low applicability of the TSCF concept to submerged macrophytes, because their transpiration stream diminishes under submergence. Incidentally, Dettenmaier's theory seems to better elucidate our results, but further accumulation of basic data/knowledge would be necessary to understand precise root uptake profiles of organic chemicals for submerged-rooted macrophytes.

DOI: 10.1021/acs.jafc.5b01133
J. Agric. Food Chem. 2015, 63, 5189−5195

In conclusion, the shoot uptake of phenols by *M. elatinoides* was faster and larger than the root uptake. The carboxylic acid derivative **5** showed the highest accumulation for both shoot and root treatment, which indicated some specific potential for the dissociated ions to be taken up by aquatic plants. Similar to terrestrial plants, the major metabolic pathway was the formation of a glucose conjugate, which was considered as a detoxification strategy. Furthermore, the kinetic analysis had shown high correlations between the shoot uptake rate constant and log K_{ow} and transformation rate constant (glucose conjugation) and Hammett constants or $E_{HOMO(OH)}$ parameter, respectively.

AUTHOR INFORMATION

Corresponding Author

*Telephone: +81-797-74-2116. E-mail: andod@sc.sumitomo-chem.co.jp.

Notes

The authors declare no competing financial interest.

REFERENCES

(1) Scheffer, M. *Ecology of Shallow Lakes*; Chapman and Hall: New York, 1998; p 357.

(2) Fairchild, F. J.; Ruessler, D. S.; Carlson, R. A. Comparative sensitivity of five species of macrophytes and six species of algae to atrazine, metribuzin, alachlor and metolachlor. *Environ. Toxicol. Chem.* **1998**, *17*, 1830−1834.

(3) Lewis, A. L. Use of freshwater plants for phytotoxicity testing: A review. *Environ. Pollut.* **1995**, *87*, 319−336.

(4) European Commission (EC) *Working Document Guidance Document on Aquatic Ecotoxicology in the Context of the Directive 91/414/EEC, Sanco/3268/2001 rev.4 (final)*; EC: Brussels, Belgium, 2002.

(5) Belgers, M. D. J.; Van Lieverloo, J. R.; Van der Pas, T. J. L.; Van den Brink, J. P. Effects of the herbicide 2,4-D on the growth of nine aquatic macrophytes. *Aquat. Bot.* **2007**, *86*, 260−268.

(6) Cedergreen, N.; Streibig, J. C.; Spliid, N. H. Sensitivity of aquatic plants to the herbicide metsulfuron-methyl. *Ecotoxicol. Environ. Saf.* **2004**, *57*, 153−161.

(7) Turgut, C.; Fomin, A. Sensitivity of the rooted macrophyte *Myriophyllum aquaticum* (Vell.) Verdcourt to seventeen pesticides determined on the basis of EC_{50}. *Bull. Environ. Contam. Toxicol.* **2002**, *69*, 601−608.

(8) European Food Safety Authority (EFSA).. Guidance on tiered risk assessment for plant protection products for aquatic organisms in edge-of-field surface waters. *EFSA J.* **2013**, *11* (7), 3290 www.efsa.europa.eu/efsajournal,.

(9) Ando, D.; Fujisawa, T.; Katagi, T. Uptake, translocation and metabolism of 3-phenoxybenzoic acid in the submerged rooted water milfoil (*Myriophyllum elatinoides*). *J. Pestic. Sci.* **2012**, *37*, 342−346.

(10) Yoshitake, A.; Kanamaru, H.; Shono, F.; Nakatsuka, I. Labelled organophosphorus pesticides. III. Synthesis of carbon-14 labelled *o*-(2,6-dichloro-4-methylphenyl) *O*,*O*-dlmethyl phosphorothioate. *J. Labelled Compd. Radiopharm.* **1979**, *16*, 477−482.

(11) Saito, S.; Kawabata, J. Effects of electron-withdrawing substituents on DPPH radical scavenging reactions of protocatechuic acid and its analogues in alcoholic solvents. *Tetrahedron* **2005**, *61*, 8101−8108.

(12) Chen, J.; Zhang, Z.; Stebbins, J.; Zhang, X.; Hoffman, R.; Moore, A.; Pellecchia, M. A fragment-based approach for the discovery of isoform-specific p38α inhibitors. *ACS Chem. Biol.* **2007**, *2*, 329−336.

(13) Organisation for Economic Co-operation and Development (OECD). *OECD Guidelines for the Testing of Chemicals 201, Freshwater Alga and Cyanobacteria, Growth Inhibition Test*; OECD: Paris, France, 2002.

(14) Organisation for Economic Co-operation and Development (OECD). *OECD Guidelines for the Testing of Chemicals 218, Sediment-Water Chironomid Toxicity Test Using Spiked Sediment*; OECD: Paris, France, 2004.

(15) Sugii, A.; Harada, K.; Ogawa, N. Liquid chromatographic characterization of porous vinylpyridine polymer as a weak anion-exchange column packing. *J. Chromatogr. A* **1986**, *354*, 211−217.

(16) Breyer, E. D.; Strasters, J. K.; Khaledi, M. G. Quantitative retention−biological activity relationship study by micellar liquid chromatography. *Anal. Chem.* **1991**, *63*, 828−833.

(17) Cronin, M. T. D.; Schultz, T. W. Development of quantitative structure−activity relationships for the toxicity of aromatic compounds to *Tetrahymena pyriformis*: Comparative assessment of the methodologies. *Chem. Res. Toxicol.* **2001**, *14*, 1284−1295.

(18) van der Waterbeemd, C. H.; Testa, B. The parametrization of lipophilicity and other structural properties in drug design. *Adv. Drug Res.* **1987**, *16*, 85−225.

(19) Hansch, C.; Leo, A. J. *Substituent Constant for Analysis in Chemistry and Biology*; Wiley: New York, 1979; pp 171−319.

(20) Cupid, B. C.; Holmes, E.; Wilson, I. D.; Lindon, J. C.; Nicholson, J. K. Quantitative structure−metabolism relationships (QSMR) using computational chemistry: Pattern recognition analysis and statistical prediction of phase II conjugation reactions of substituted benzoic acids in the rat. *Xenobiotica* **1999**, *29*, 27−42.

(21) Agency for Toxic Substances and Disease Registry (ATSDR). *Toxicological Profile for Phenol (Update)*; ATSDR, Public Health Service, U.S. Department of Health and Human Services: Atlanta, GA, 1998.

(22) Gobas, F. A. P. C.; McNell, E. J.; Lovett-Doust, L.; Haffner, G. D. Bioconcentration of chlorinated aromatic hydrocarbons in aquatic macrophytes. *Environ. Sci. Technol.* **1991**, *25*, 924−929.

(23) de Carvalho, R. F.; Bromilow, R. H.; Greenwood, R. Uptake of pesticides from water by curly waterweed *Lagarosiphon major* and lesser duckweed *Lemna minor*. *Pest Manage. Sci.* **2007**, *63*, 789−797.

(24) Fu, W.; Franco, A.; Trapp, S. Methods for estimating the bioconcentration factor of ionizable organic chemicals. *Environ. Toxicol. Chem.* **2009**, *28*, 1372−1379.

(25) Zhang, D.; Gersberg, R. M.; Ng, W. J.; Tan, S. K. Removal of pharmaceutics and personal care products in aquatic plant-based system: A review. *Environ. Pollut.* **2014**, *184*, 620−639.

(26) Rendal, C.; Kusk, K. O.; Trapp, S. Optimal choice of pH for toxicity and bioaccumulation studies of ionizing organic chemicals. *Environ. Toxicol. Chem.* **2011**, *30*, 2395−2406.

(27) Day, J. A.; Saunders, F. M. Glycosidation of chlorophenols by *Lemna minor*. *Environ. Toxicol. Chem.* **2004**, *23*, 613−620.

(28) Modolo, M.; Li, L.; Pan, H.; Blount, J. W.; Dixon, R. A.; Wang, X. Crystal structure of glycosyltransferase UGT78G1 reveal the molecular basis fot glycosylation and deglycosylation of (iso) flavonoids. *J. Mol. Biol.* **2009**, *392*, 1292−1302.

(29) Siegel, J. B.; Zanghellini, A.; Lovick, H. M.; Kiss, G.; Lambert, A. R.; St. Clair, J. L.; Gallaher, J. L.; Hilvert, D.; Gelb, M. H.; Stoddard, B. L.; Houk, K. N.; Michael, F. E.; Baker, D. Computational design of an enzyme catalyst for a stereoselective bimolecular Diels−Alder reaction. *Science* **2010**, *329*, 309−313.

(30) Lim, E.-K.; Doucet, C. J.; Li, Y.; Elias, L.; Worrall, D.; Spencer, S. P.; Ross, J.; Bowles, D. J. The activity of *Arabidopsis* glycosyltransferases toward salicylic acid, 4-hydroxybenzoic acid, and other benzoates. *J. Biol. Chem.* **2002**, *277*, 586−592.

(31) Hall, D.; Luca, V. D. Mesocarp localization of a bi-functional resveratrol/hydroxycinnamic acid glucosyltransferase of Concord grape (*Vitis labrusca*). *Plant J.* **2007**, *49*, 579−591.

(32) Briggs, G. G.; Bromilow, R. H.; Evans, A. A. Relationships between lipophilicity and root uptake and translocation of non-ionised chemicals by barley. *Pestic. Sci.* **1982**, *13*, 495−504.

(33) de Carvalho, R. F.; Bromilow, R. H.; Greenwood, R. Uptake of pesticides from water by curly waterweed *Lagarosiphon major* and lesser duckweed *Lemna minor*. *Pest Manage. Sci.* **2007**, *63*, 798−802.

(34) Dettenmaier, E. M.; Doucette, W. J.; Bugbee, B. Chemical hydrophobicity and uptake by plant roots. *Environ. Sci. Technol.* **2009**, *43*, 324−329.

DOI: 10.1021/acs.jafc.5b01133
J. Agric. Food Chem. 2015, 63, 5189−5195

JOURNAL OF AGRICULTURAL AND FOOD CHEMISTRY

Article

pubs.acs.org/JAFC

Physicochemical Characteristics and Slow Release Performances of Chlorpyrifos Encapsulated by Poly(butyl acrylate-*co*-styrene) with the Cross-Linker Ethylene Glycol Dimethacrylate

Yu Wang, Zideng Gao, Feng Shen, Yang Li, Sainan Zhang, Xueqin Ren,* and Shuwen Hu*

College of Resources and Environmental Sciences, China Agricultural University, Beijing 100193, China

ABSTRACT: Chlorpyrifos' application and delivery to the target substrate needs to be controlled to improve its use. Herein, poly(butyl acrylate-*co*-styrene) (poly(BA/St)) and poly(BA/St/ethylene glycol dimethacrylate (EGDMA)) microcapsules loaded with chlorpyrifos as a slow release formulation were prepared by emulsion polymerization. The effects of structural characteristics on the chlorpyrifos microcapsule particle size, entrapment rate (ER), pesticide loading (PL), and release behaviors in ethyl alcohol were investigated. Fourier transform infrared and thermogravimetric analysis confirmed the successful entrapment of chlorpyrifos. The ER and PL varied with the BA/St monomer ratio, chlorpyrifos/monomer core-to-shell ratio, and EGDMA cross-linker content with consequence that suitable PL was estimated to be smaller than 3.09% and the highest ER was observed as 96.74%. The microcapsule particle size (88.36−101.8 nm) remained mostly constant. The extent of sustainable release decreased with increasing content of BA, St, or chlorpyrifos in the oil phase. Specifically, an adequate degree of cross-linking with EGMDA (0.5−2.5%) increased the extent of sustainable release considerably. However, higher levels of cross-linking with EGDMA (5−10%) reduced the extent of sustainable release. Chlorpyrifos release from specific microcapsules (monomer ratio 1:2 with 0.5% EGDMA or 5 g chlopyrifos) tended to be a diffusion-controlled process, while for others, the kinetics probably indicated the initial rupture release.

KEYWORDS: *microcapsule, slow release, chlorpyrifos, poly(butyl acrylate-co-styrene), ethylene glycol dimethacrylate, emulsion polymerization*

INTRODUCTION

Chlorpyrifos (*O*,*O*-diethyl *O*-(3,5,6,-trichloro-2-pyridyl phosphorothioate)) is a broad-spectrum, chlorinated organophosphate insecticide, acaricide, and nematicide.[1] It is used worldwide as a moderately toxic organophosphate pesticide against diverse chewing and sucking mouthparts pests on rice, wheat, cotton, fruit, vegetables, and tea trees through the triple effects of stomach action, contact poison, and fumigation. Because of its high volatilization and widespread use, chlorpyrifos represents one of the most significant sources of organophosphate exposure during application, resulting in adverse effects such as pollution of surface/underground water and biological systems. Additionally, its high toxicity to humans can result in severe illnesses, such as prostate cancer[2] and respiratory problems.[3] In China, the high volatilization and easy spreading of chlorpyrifos in the soil and water lead to low utilization efficiencies. As a result, chlorpyrifos needs to be repeatedly applied for effective performance, and that consequently increases the level of adverse health risks to both the environment and humans. Thus, control over the application of chlorpyrifos in the agricultural sector is necessary.

Microcapsule-controlled release technology has been widely used for the delivery of target molecules over the past decades. Microencapsulation offers advantages such as target molecule protection, controlled and triggered release, and the development of new product features.[4] It has been recognized as a new technology and promising solution in the fields of pharmaceuticals, biotechnology, pesticides, environmental engineering, cosmetics, coatings, and food chemistry.[5] Additionally, microcapsule technology has bright prospects in the agriculture sector to prepare controlled release formulation systems for pesticides. It is an effective approach to efficiently increase the performance level of pesticides and reduce human labor and hazard risks to the environment and humans.

In recent years, many papers have reported the preparation of pesticide-based microcapsules. Numerous methods were investigated toward the encapsulation of pesticides namely, interfacial polymerization,[6−9] in situ polymerization[10] and condensation,[11] and solvent evaporation[12−15] methods. Some of these methods successfully achieved the preparation of wall-type material membranes and chlorpyrifos-encapsulating matrices. The materials included synthetic polymers (e.g., polyamide and polyurethane) prepared by interfacial polymerization and natural polymeric membranes (e.g., alginate, chitosan, starch, and cellulose) prepared by condensation methods. However, studies typically focused on the properties of the encapsulating units only rather than on the release profiles of the encapsulated target pesticide.[16−18]

It has been reported that some wall-type materials such as urea formaldehyde, prepared by in situ polymerization,[19] afford short sustainable release profiles, whereas other materials, such as polylactic acid[20,21] and mesoporous silica,[22] afford longer sustainable release profiles. In contrast, emulsion polymerization affords the synthesis of microcapsules with a relatively wide range of sustainable release profiles for the delivery of

Received: March 18, 2015
Revised: May 4, 2015
Accepted: May 6, 2015
Published: May 6, 2015

ACS Publications © 2015 American Chemical Society

DOI: 10.1021/acs.jafc.5b01378
J. Agric. Food Chem. 2015, 63, 5196−5204

active ingredients by varying the contents and ratios of typical monomers including butadiene, styrene, acrylonitrile, acrylate ester, and methacrylate ester.[23−26] Furthermore, the preparation process of emulsion polymerization for chlorpyrifos will not involve any organic solvent, such as toluene, xylene, and cyclohexanone, etc., which might be considered more environmentally friendly. And the chlorpyrifos-loaded microcapsules emulsion can be directly sprayed onto plants following synthesis, thereby not requiring the dispersion of the pesticide microparticles in water before application. The chlorpyrifos-loaded microcapsules prepared by emulsion polymerization have been discussed in several patents and in several research papers.[27−30] However, reports on the effects of the structural characteristics of wall materials on the sustainable release of chlorpyrifos encapsulated in microcapsules are rare.

In the present study, butyl acrylate (BA), styrene (St), and cross-linker ethylene glycol dimethacrylate (EGDMA) were used to synthesize microcapsules by emulsion polymerization. Two series of chlorpyrifos-loaded polyacrylate microencapsulating systems were prepared i.e., microcapsules of chlorpyrifos-loaded poly(BA/St) and chlorpyrifos-loaded poly(BA/St/EGDMA) (poly(BA/St) cross-linked with EGDMA). The glass transition temperature (T_g) of poly(butyl acrylate) is low, and hence, it features an elastomeric state (soft and sticky) at room temperature; whereas, polystyrene features a glassy state (hard and brittle) because of its higher T_g. Hence, it is expected that copolymerization of BA and St whose T_g can be easily designed by the Fox equation may generate microcapsules with the required hardness and viscosity. Furthermore, the addition of cross-linker EGDMA is expected to afford the synthesis of a denser microcapsule wall material or better connections among the microcapsule particles. Thus, copolymerization between BA and St or between BA/St and EGDMA would afford microcapsules with fine characteristics (hardness, viscosity, and dense) to achieve long sustainable release properties as desired. More particularly, the preparation conditions of the chlorpyrifos microcapsules, i.e., the effects of monomer ratio (BA/St), core-to-shell ratio, and content of cross-linker EGDMA in oil phase on the characteristics of the microcapsules (particle size, entrapment rate, and pesticide loading), especially the sustained release performance, were investigated.

MATERIALS AND METHODS

Materials. BA (chemical pure, National Medicine Group Chemical Reagent Co., Ltd.), St (chemical pure, National Medicine Group Chemical Reagent Co., Ltd.), nonylphenol polyoxyethylene (OP-10), sodium dodecyl sulfate (SDS), ammonium persulfate (APS; analytical pure, National Medicine Group Chemical Reagent Co., Ltd.), sodium bisulfite (SBS; analytical pure, Beijing Chemical Reagent Co.), chlorpyrifos (Jiangsu YiJin Agrochemical Co., Ltd.), and EGDMA (99%, J&K Beijing Science and Technology Co., Ltd.) were used in this study.

Preparation of Chlorpyrifos Microcapsules. The chlorpyrifos-loaded poly(BA/St) and chlorpyrifos-loaded poly(BA/St/EGDMA) microcapsules were synthesized by emulsion polymerization in a 250 mL four-neck flask equipped with a mechanical stirrer, a heating mantle with a digital thermometer and a condenser. In a typical synthesis, exact amounts of chlorpyrifos were dissolved in a mixture of BA, St, and EGDMA to form the oil phase. Then, the oil phase was poured into distilled water (30 g) containing OP-10 (0.15 g) and SDS (0.4 g) and emulsified using a homomixer at 1500 rpm for 10 min to form the pre-emulsion. Another solution that was prepared by dissolving OP-10 (0.1 g) and SDS (0.2 g) into distilled water (25 g) was added to the four-neck flask with mechanical stirring at 300 rpm. The initiator solution was prepared by dissolving APS (0.25 g) and SBS (0.25 g) in distilled water (15 g). One-third of the prepared pre-emulsion was added to a four-neck flask under nitrogen gas and maintained at 80 °C. Then, one-third of the initiator was introduced to initiate polymerization. The remainder of the pre-emulsion and initiator solutions was slowly dropped into the reaction mixture over a period of 1 h. The reaction was continued further for 3 h under nitrogen gas. The resulting emulsion was collected after cooling to room temperature for further characterization. The formulations employed for the synthesis of the chlorpyrifos microcapsules are listed in Table 1.

Table 1. Particle Size of the Chlorpyrifos Microcapsules Prepared under Different Conditions

	oil phase			
sample	monomer (BA/St wt/wt)	chlorpyrifos (g)	EGDMA/monomer (mol/mol)	mean diameter (nm)
M1	1:5	1.0	0	88.80 ± 1.47 ef
M2	1:2	1.0	0	95.45 ± 1.96 c
M3	1:1	1.0	0	90.21 ± 1.93 e
M4	2:1	1.0	0	87.40 ± 1.75 ef
M5	5:1	1.0	0	89.21 ± 0.42 ef
E1	1:2	1.0	0.5%	92.82 ± 1.68 d
E2	1:2	1.0	1.0%	88.59 ± 1.71 ef
E3	1:2	1.0	2.5%	89.82 ± 1.66 ef
E4	1:2	1.0	5.0%	88.36 ± 0.89 ef
E5	1:2	1.0	10%	90.66 ± 0.57 de
P1	1:2	5.0	0	97.96 ± 1.10 b
P2	1:2	10.0	0	101.8 ± 1.21 a
P3	1:2	15.0	0	97.17 ± 1.71 bc

Effect of Different Formulations on the Characteristics of Microcapsules. The individual effects of different factors on particle size, entrapment rate, pesticide loading, and slow release behaviors were examined. More specifically, the effects of the monomer ratio, core-to-shell ratio, and EGDMA cross-linker content in the oil phase on the characteristics of the microcapsules were studied. The BA/St monomer ratios (w/w) in the oil phase were 1:5, 1:2, 1:1, 2:1, and 5:1 in the oil phase. The chlorpyrifos/monomer core-to-shell ratios (w/w) in the oil phase were 1:30, 5:26, 10:21, and 15:16. The contents of cross-linker EGDMA in the oil phase (relative to EGDMA/monomer ratio (mol %/mol %)) were 0, 0.5, 1.0, 2.5, 5, and 10%.

Characterization. *Entrapment Rate and Pesticide Loading.* The two parameters entrapment rate (ER, %) and pesticide loading (PL, %) were used to characterize the efficiency of the encapsulation process. ER is defined as the ratio between the weight of encapsulated chlorpyrifos and the theoretical weight of chlorpyrifos during the preparation process

$$\text{ER}\ (\%) = \frac{\text{weight of encapsulated chlorpyrifos}}{\text{theoretical weight of chlorpyrifos}} \times 100\%$$

PL is defined as the weight of encapsulated chlorpyrifos divided by the weight of the corresponding chlorpyrifos-containing microcapsules

$$\text{PL}\ (\%) = \frac{\text{weight of encapsulated chlorpyrifos}}{\text{weight of microcapusles}} \times 100\%$$

Prior to measuring ER and PL of the pesticide microcapsules, the emulsion was demulsified. Typically, the emulsion (2 mL) was added to a 1:1 (w/w) mixture of ethanol and 2% $CaCl_2$ aqueous solution. The demulsified pesticide microcapsule solution was filtered using a mutche filter to obtain aggregates of chlorpyrifos-containing microcapsules. Then, the microcapsules were washed with 50 wt % ethanol/water solution once and distilled water twice to remove any nonencapsulated chlorpyrifos, followed by drying at 45 °C for 24 h.

The microcapsule aggregates (~0.3 g) were introduced into 50 mL centrifuge tubes containing *n*-hexane (20 mL). The encapsulated

DOI: 10.1021/acs.jafc.5b01378
J. Agric. Food Chem. 2015, 63, 5196−5204

chlorpyrifos was extracted into *n*-hexane upon stirring at 150 rpm for 4 h at 25 °C. The concentration of chlorpyrifos in *n*-hexane was analyzed on a WTF UV-2102PC ultraviolet−visible spectrophotometer (UNICO Shanghai Instrument Co., Ltd., China) at 292 nm and the weight of encapsulated chlorpyrifos was calculated.

Particle Size Measurement. The mean diameter of the microcapsule particles was calculated using a HORIBA LA-950 laser particle analyzer (HORIBA Co., Ltd., Japan) at the Beijing Centre for Physical & Chemical Analysis (Beijing, China)

Fourier Transform Infrared (FTIR) Spectroscopy. For sample analysis, the microcapsules obtained from the demulsified solution described above were dried at 40 °C overnight. All the FTIR measurements were conducted on a Nicolet NEXUS-470 spectrometer (Madison, WI, USA).

Thermogravimetric Analysis (TGA). Thermogravimetric analysis for the chlorpyrifos microcapsules was conducted by using a TGA/DSC simultaneous thermal analyzer (Mettler Toledo, Switzerland) at a heating rate of 10 °C/min under a nitrogen atmosphere from 25 to 500 °C.

Transmission Electron Microscopy (TEM). Prior to TEM analysis, the emulsion was diluted 600-fold, followed by negative staining. TEM photographs were taken on a JEM-1230 transmission electron microscope (JEOL Japan Electronics Co., Ltd., Japan) operating at an accelerating voltage of 80 kV at the required magnification (80 000−200 000×) at room temperature.

Slow Release Behaviors of Chlorpyrifos Microcapsules. For the chlorpyrifos release experiments, a chlorpyrifos microcapsule emulsion (5.0 g) was injected into a dialysis bag with molecular weights of 8000−12 000. The dialysis bag was placed in a conical flask (250 mL) containing absolute ethyl alcohol (100 mL) as the release medium under static conditions at 25 °C. The amounts of chlorpyrifos released at different time intervals were measured by recording the absorbance of the release medium at 291 nm on an ultraviolet−visible spectrophotometer (UNICO Shanghai Instrument Co., Ltd., China).

RESULTS AND DISCUSSION

FTIR Spectroscopy Analysis of Chlorpyrifos Microcapsules. To assess the successful encapsulation of chlorpyrifos, the FTIR spectra of the chlorpyrifos, poly(BA/St) microcapsules, and chlorpyrifos-loaded poly(BA/St) microcapsules were recorded (Figure 1). The spectrum of chlorpyrifos (Figure 1a) featured stretching vibration peaks corresponding to pyridine ring C═N, aromatic P−O−C, aliphatic P−O−C, and P═S at 1549.64, 1169.59, 852.84, and 1016.97 cm^{-1}, respectively. These characteristic peaks are typical of chlorpyrifos. The poly(BA/St) microcapsules (Figure 1b) were characterized by the absorption peak at 1727.69 cm^{-1} (corresponding to C═O), which proved the existence of BA/St copolymer. Moreover, the characteristic absorption peak of C═C belonging to monomer BA and St at 1637 cm^{-1} was absent, which proved the successful preparation of the poly(BA/St) wall material. The characteristic peaks observed in both Figure 1a and b were present in the spectrum of the chlorpyrifos-loaded poly(BA/St) microcapsules (Figure 1c), thereby confirming the successful entrapment of chlorpyrifos by poly(BA/St) wall material.

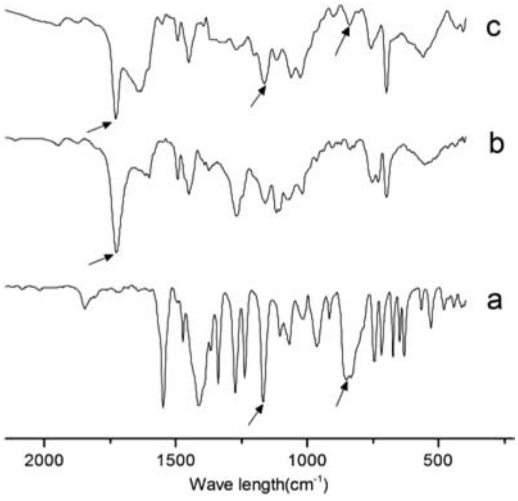

Figure 1. FTIR spectra of (a) chlorpyrifos, (b) poly(BA/St) (1:1, wt/wt) microcapsules, and (c) chlorpyrifos-loaded poly(BA/St) (1:1, wt/wt) microcapsules.

TG Analysis of Chlorpyrifos Microcapsules. Figure 2 demonstrated TGA thermogram of prepared poly(BA/St) chlorpyrifos microcapsules (Figure 2c) comparing with pure chlorpyrifos (Figure 2a), blank poly(BA/St) microcapsules (Figure 2b), and a physical mixture of chlorpyrifos and blank poly(BA/St) microcapsules (Figure 2d). TG curves presented the weight loss of pure chlorpyrifos occurred at 143 °C while that of blank poly(BA/St) microcapsule occurred at 360 °C. TG curves of poly(BA/St) chlorpyrifos microcapsules showed two stage degradation with an initial weight loss from 234 to 301 °C and a second from 360 to 425 °C. Comparing with TG curves of pure chlorpyrifos and blank poly(BA/St) microcapsule, the first stage might result from the gasification of chlorpyrifos and the second one was attributed to the decomposition of poly(BA/St). It also proved that the chlorpyrifos was encapsulated by poly(BA/St) microcapsule successfully. Additionally, TG curves of poly(BA/St) chlorpyrifos microcapsules had the same degradation feature as the TG curves of physical mixture of chlorpyrifos and blank poly(BA/St) microcapsule, which might imply the physical combination between chlorpyrifos and poly(BA/St) wall materials.

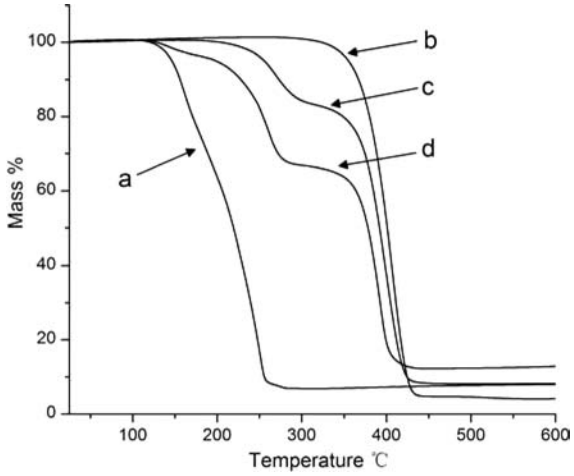

Figure 2. TGA thermogram: (a) chlorpyrifos; (b) blank poly(BA/St) microcapsule; (c) poly(BA/St) microcapsule of chlorpyrifos; (d) physical mixture of chlorpyrifos and blank poly(BA/St) microspheres.

Particle Size of Chlorpyrifos Microcapsules. In order to investigate the diameter feature of microcapsule pesticide sample prepared in this study, particle size distribution analysis was conducted. The particle size distribution of M3 was demonstrated in Figure 3. The diameter presented an approximately normally distribution and the particle size mostly distributed at about 90 nm with the mean diameter of 90.21 nm. For other samples, a similar distribution was

DOI: 10.1021/acs.jafc.5b01378
J. Agric. Food Chem. 2015, 63, 5196−5204

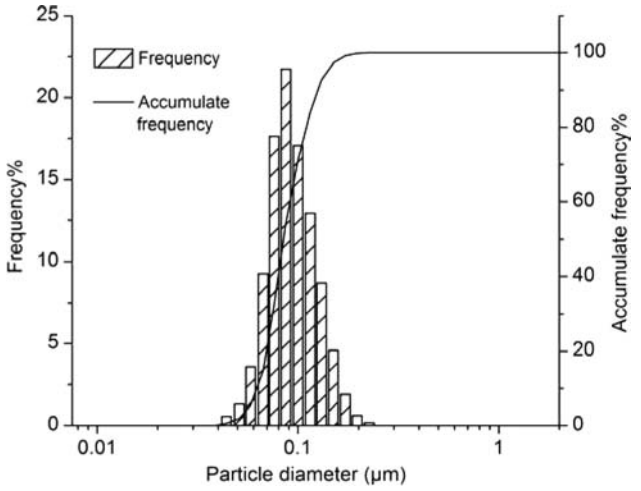

Figure 3. Particle size distribution of chlorpyrifos poly(BA/St) microcapsule with the monomer ratio 1:1 (BA/St wt/wt).

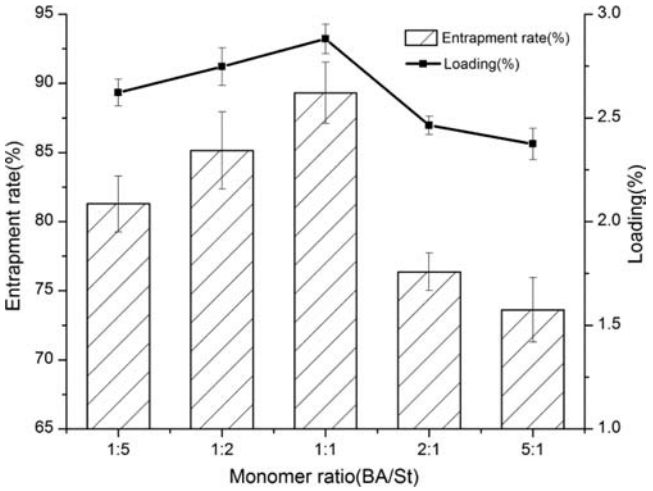

Figure 4. Effect of BA/St monomer ratio in the oil phase on the ER and PL of the microcapsules.

observed. It revealed a narrow and concentrated distribution of the particle size of each sample. As to the mean diameter, presented in Table 1, mean diameters of sample P1−P3 were slightly bigger than others, which probably indicated the influence of chlorpyrifos content on particle mean diameter. When only considering the monomer ratio (M1−M5), M2 is slightly bigger than other formulations (M1, M3, M4, and M5) where no significant difference was observed. Similarly, the mean diameters of E1−E5 were almost the same (about 90 nm), which indicated that the change of EGDMA content had little effect on particle size. These results demonstrated that the content of the monomer, pesticide, and EGDMA minimally influenced the particle size. Consequently, it could be inferred that the release performance of the microcapsules would not be influenced by the diameter of the microcapsules that remained mostly unchanged across the different synthesis conditions studied herein.

Effect of Monomer Ratio on Characteristics of Chlorpyrifos Microcapsules. As observed in Table 2 and Figure 4, when the BA/St monomer ratio changed from 1:5 to 1:1, ER and PL increased from 81.28 to 89.31% and 2.62 to 2.88%, respectively. In contrast, when the BA/St monomer ratio changed from 1:1 to 5:1, ER and PL decreased from 89.31 to 73.62% and 2.88 to 2.37%, respectively. As deduced, excess amounts of BA and St were detrimental to the encapsulation of chlorpyrifos as indicated by the corresponding lower measured ER and PL values when compared with those of other formulations comprising lower amounts of BA and St. At excessive amounts of St (M1), the resulting poly(BA/St) became hard and brittle because of its higher T_g over 55 °C. Hence, the polymer was prone to rupture during the encapsulation of chlorpyrifos. Similarly, when the content of BA in the formulation was high (M4, M5), poly(BA/St) featured soft and sticky characteristics with the lower T_g of about −21 and −39 °C and, hence, was not adequately mechanically stable for the effective entrapment of the pesticide. Therefore, the ER and PL values of the microcapsules were satisfactory at moderate monomer ratios of 1:2 and 1:1 owing to the desirable soft and hard characteristics of poly(BA/St). The monomer ratio of 1:2 was studied further in the subsequent experiments.

Table 2. Characteristics of the Pesticide Microcapsules Prepared under Different BA/St Monomer Ratio Conditions

			characteristic parameter	
sample	monomer (BA/St wt/wt)	designed T_g[a] (°C)	entrapment rate (%)	pesticide loading (%)
M1	1:5	55.13	81.28 ± 2.02 b	2.622 ± 0.07 b
M2	1:2	25.02	85.14 ± 2.80 b	2.747 ± 0.09 b
M3	1:1	−0.023	89.31 ± 2.21 a	2.881 ± 0.07 a
M4	2:1	−21.18	76.37 ± 1.37 c	2.464 ± 0.04 c
M5	5:1	−39.31	73.62 ± 2.34 c	2.375 ± 0.08 c

[a]Calculated by the Fox equation.

Effect of Core-to-Shell Ratio on Characteristics of Chlorpyrifos Microcapsules. The influence of different chlorpyrifos/monomer BA and St core-to-shell ratios on ER and PL was investigated (Table 3, Figure 5). The weight of the oil phase was kept constant and the total weight of chlorpyrifos and monomer BA and St was 31 g. Only the weight of chlorpyrifos was varied from 1 to 15 g to achieve chlorpyrifos/monomer BA and St weight ratios of 1:30, 5:26, 10:21, and 15:16. As observed in Figure 5, PL increased from 2.74 to 29.11% when the loading content of pesticide increased owing to the increased content of pesticides in the oil phase. In contrast, ER decreased from 85.14 to 60.15% when the loading content of chlorpyrifos increased from 1 to 15 g. These results showed that moderate dosages of monomer in the chlorpyrifos emulsion preparation process afforded desirable ER and PL values, whereas similar weight levels of chlorpyrifos and monomer did not result in desirable ER values. However, higher PL values were obtained. This phenomenon was

Table 3. Characteristics of the Pesticide Microcapsules Prepared under Different Content of Chlorpyrifos

			characteristic parameter	
sample	chlorpyrifos (g)	core-to-shell ratio (wt/wt)	entrapment rate (%)	pesticide loading (%)
M2	1.0	1/30	85.14 ± 2.02 a	2.747 ± 0.09 d
P1	5.0	5/26	78.18 ± 1.51 b	12.61 ± 0.24 c
P2	10.0	10/21	67.97 ± 2.87 c	21.93 ± 0.93 b
P3	15.0	15/16	60.15 ± 2.73 d	29.11 ± 1.32 a

DOI: 10.1021/acs.jafc.5b01378
J. Agric. Food Chem. 2015, 63, 5196−5204

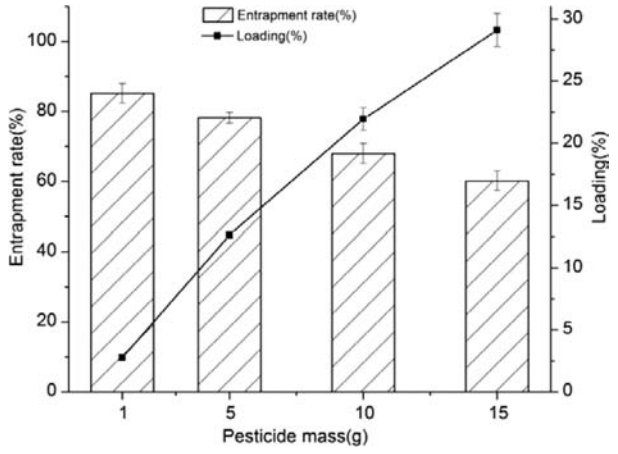

Figure 5. Effect of additive amount of pesticide in the oil phase on the ER and PL of the microcapsules.

attributed to ineffective chlorpyrifos entrapment owing to the inadequately dense polymer obtained in the presence of relatively low monomer dosages. Optimum weight ratios of the pesticide and monomer were determined at 1:30−5:26 for the effective encapsulation of chlorpyrifos into poly(BA/St) microcapsules by emulsion polymerization.

Effect of Content of Cross-Linker EGDMA on Characteristics of Chlorpyrifos Microcapsules. EGDMA, a widely employed cross-linker for emulsion polymerization, will form a dense network within the microcapsule wall material or generate links among the microcapsule particles upon copolymerization with BA and St. In the present study, the effect of EGDMA on the characteristics of the microcapsules was investigated by varying its contents at 0, 0.5, 1.0, 2.5, 5, and 10% (relative to the EGDMA/monomer ratio, mol/mol). The results are shown in Table 4. As observed in Figure 6, ER and

Table 4. Characteristics of the Pesticide Microcapsules Prepared under Different Content of Cross-Linker EGDMA

		characteristic parameter	
sample	EGDMA/monomer (mol/mol)	entrapment rate (%)	pesticide loading (%)
M2	0	85.14 ± 2.02 c	2.747 ± 0.09 c
E1	0.5%	96.74 ± 0.47 a	3.094 ± 0.01 a
E2	1.0%	93.05 ± 1.69 ab	2.951 ± 0.05 b
E3	2.5%	90.02 ± 1.89 b	2.783 ± 0.06 c
E4	5.0%	86.11 ± 3.24 c	2.557 ± 0.10 d
E5	10%	85.78 ± 1.45 c	2.359 ± 0.04 e

PL both reached a maximum when an EGDMA concentration of 0.5% was used, and then decreased with increasing concentrations of cross-linker EGDMA. The observed increase in ER and PL may be attributed to the denser structure of poly(BA/St/EGDMA) relative to that of poly(BA/St) owing to the higher degree of cross-linking. In contrast, the considerable decrease in ER and PL with further increases in the amount of EGDMA may be attributed to the excessively high degrees of cross-linking owing to the higher content of cross-linker. Higher degrees of cross-linking would result in tighter connections among the polymer chains, thereby inhibiting effective encapsulation of the pesticide.

Pesticide Release Study. An important aim of the present study was to study the release performance of chlorpyrifos from

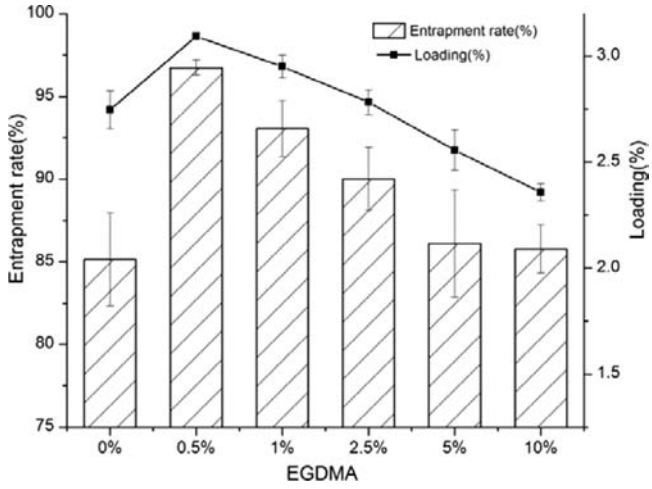

Figure 6. Effect of additive amount of EGDMA in the oil phase on the ER and PL of the microcapsules.

the poly(BA/St) and poly(BA/St/EGDMA) microcapsules. First, the effect of the monomer ratio (BA/St) used in emulsion polymerization on the release profile is discussed. The pesticide microcapsule emulsion was introduced into a dialysis bag and the release of the pesticide from the dialysis bag was monitored over ∼170 h. The results are shown in Figure 7. As observed,

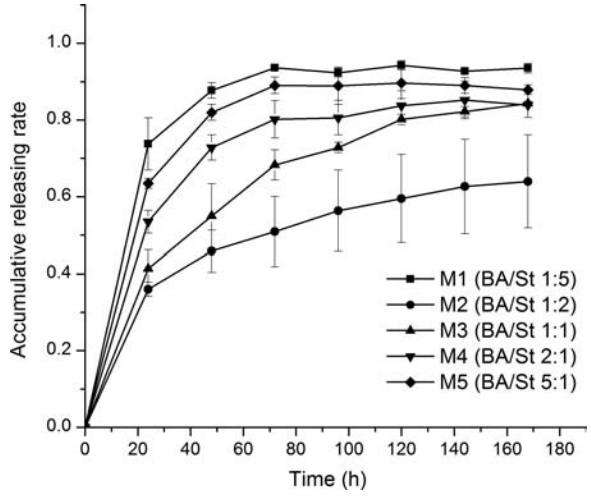

Figure 7. Profiles of chlorpyrifos release from formulations prepared using different ratios of BA/St monomer.

the release of chlorpyrifos from the poly(BA/St) microcapsules M1 and M5 prepared with monomer ratios of 1:5 and 5:1 was fast. A sustainable pesticide release over ∼72 h was observed. A slower release profile was obtained for the chlorpyrifos-loaded poly(BA/St) microcapsules M4 prepared with a monomer ratio of 2:1. The release profile of the microcapsules M2 prepared with a monomer ratio of 1:2 was satisfactory: a lower chlorpyrifos release was observed at the early stages of the release studies that lasted for 168 h. The maximum sustainable release content of the pesticide was 63.9%. These results may be explained by the different chlorpyrifos microcapsule characteristics as a result of the different monomer ratios used in the formulations as observed in Table 2. The ER and PL values of the chlorpyrifos-loaded microcapsules M1 and M5 were relatively lower, which not only led to poor chlorpyrifos encapsulation, but also to a high content of chlorpyrifos

DOI: 10.1021/acs.jafc.5b01378
J. Agric. Food Chem. 2015, 63, 5196−5204

retained on the microcapsule surface or in the water phase. Thus, the fast release profile was caused by the fast dissolution of chlorpyrifos in the external phase at the early stages of the release process and prompt release of the pesticide from the mechanically weak chlorpyrifos-loaded poly(BA/St) microcapsules. Furthermore, the T_g of M1 was much higher than the release temperature of 25 °C while the T_g of M5 was much lower than 25 °C. A relatively large difference between T_g and environmental temperature might lead to a relatively complete polymer state transitions to elastomeric state for M5 and glassy state for M1, which seemed to be conducive to the chlorpyrifos release in the present study. The rapid early release observed for the microcapsules M4 was due to the same phenomena occurring in microcapsules M1 and M5 as discussed previously. However, the slower release profile was due to the stronger mechanical property of the microcapsules. Poly(BA/St) microcapsules M2 and M3 had mechanical properties suited for entrapping the pesticide as well as obtaining high ER and PL values. T_g of M2 and M3 were close to the release temperature, which might let the microcapsule had characteristics of both elastomeric state and glassy state. It seemed to be very suitable for slow release of chlorpyrifos.Therefore, both the early release and sustainable release (>168 h) profiles of these particular pesticide microcapsules were satisfactory. More importantly, our results indicated that the poly(BA/St) microcapsules prepared at a monomer ratio of 1:2 (M2) were the best candidate for achieving sustainable release of chlorpyrifos.

Second, the effect of varying the EGDMA cross-linker content in the microcapsule formulation on the release profile of chlorpyrifos was investigated. The content was varied from 0 to 10%, while the BA/St monomer ratio was fixed at 1:2. The results are depicted in Figure 8. As observed, the sustainable

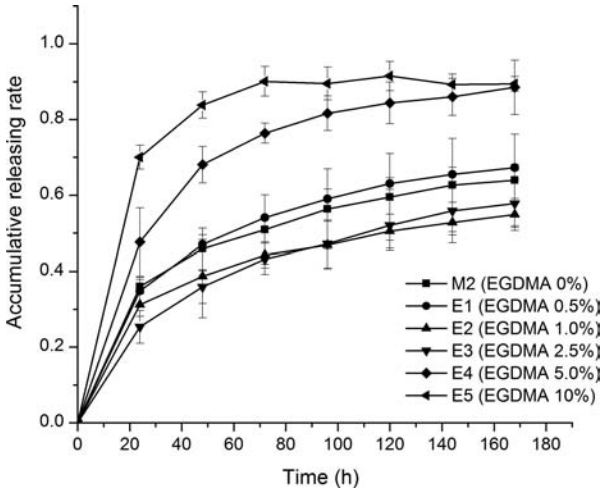

Figure 8. Profiles of chlorpyrifos release from formulations prepared using different contents of EGDMA (The BA/St monomer ratio was 1:2).

release of chlorpyrifos loaded in the microcapsules M2−E3 prepared with increasing EGDMA contents from 0 to 2.5% increased. Further increases in the EGDMA content above 2.5% led to shorter sustainable releases (E4−E5). The reduction in the sustainable release behavior may be due to the dense poly(BA/St/EGDMA) network that prevents effective release of chlorpyrifos from the microcapsule. Moreover, more EGDMA reacted with BA and St, resulting in tighter and denser polymer chains, consequently leading to the decrease in sustainable release. In contrast, increasing the content of EGDMA from 2.5 to 10% resulted in considerably fast release profiles of chlorpyrifos. The fast release profiles may be due to the low mechanical stability of the microcapsules in ethyl alcohol release medium owing to the greater extent of cross-linking by EGDMA. Besides, the relatively lower ER and PL values resulted in a higher level of pesticide retainment on the microcapsule surface or in the water phase that may account for the rapid initial release rate.

To further understand the release profiles of the pesticide-loaded EGDMA-cross-linked microcapsules, TEM analysis was conducted on the pesticide-loaded microcapsules prepared with different cross-linker EGDMA contents. The morphology and dispersion of the microcapsules can be observed in Figure 9. The dark circles of microcapsule from TEM might also represent the relative thin shell polymer forming by the slowly dropped process of monomer, which indicated a core−shell structure of these microcapsules. Figure 9a shows the homogeneous dispersion of the chlorpyrifos-loaded poly(BA/St) microcapsules prepared in the absence of cross-linker EGDMA. In contrast, connections among the pesticide-loaded microcapsules prepared in the presence of 5% EGDMA were obvious (Figure 9b). The external connections among the microcapsules that resulted in denser structures led to slower release of chlorpyrifos when compared with that observed for microcapsules prepared without EGDMA. Unfortunately, excessive connections led to the aggregation of the microcapsules that were prepared in the presence of 10% EGDMA (Figure 9c). Furthermore, the inhomogeneous microcapsule structure may be prone to rupture during the microcapsule synthesis and pesticide release processes. Therefore, poly(BA/St/EGDMA) microcapsules prepared in the presence of 5−10% EGDMA featured fast release profiles, whereas those prepared in the presence of 0.5−2.5% featured slower release characteristics.

Figure 10 shows that the length of sustainable release of chlorpyrifos decreased significantly with increasing loading contents of chlorpyrifos (1−10 g). Accordingly, changes in the loading content of chlorpyrifos altered the chlorpyrifos/monomer BA and St core-to-shell ratio. More specifically, increasing the dosage of pesticide led to decreasing dosages of the monomer at a given combined pesticide and monomer content. The polymer matrix prepared with a lower amount of monomer was not dense enough for chlorpyrifos entrapment. On the basis of the results discussed previously, the lower ER of the microcapsules P1 and P2 loaded with 5 and 10 g pesticide is another reason for the rapid release profile observed. These results indicated that a core-to-shell ratio of 1:30 was optimum to achieving good release profiles, whereas microcapsules loaded with higher contents of chlorpyrifos (5−10 g) featured faster release profiles.

Chlorpyrifos Release Kinetics. All of the slow release profile curves were composed of the gradual release curve followed by constant release curve that implied the fully release of chlorpyrifos. In order to investigated the release mechanism of chlorpyrifos-loaded microcapsule in the present study, data of the gradual release curve from chlorpyrifos release experiments were fitted to the following equation:[31]

$$\frac{M_t}{M_\infty} = kt^n$$

DOI: 10.1021/acs.jafc.5b01378
J. Agric. Food Chem. 2015, 63, 5196−5204

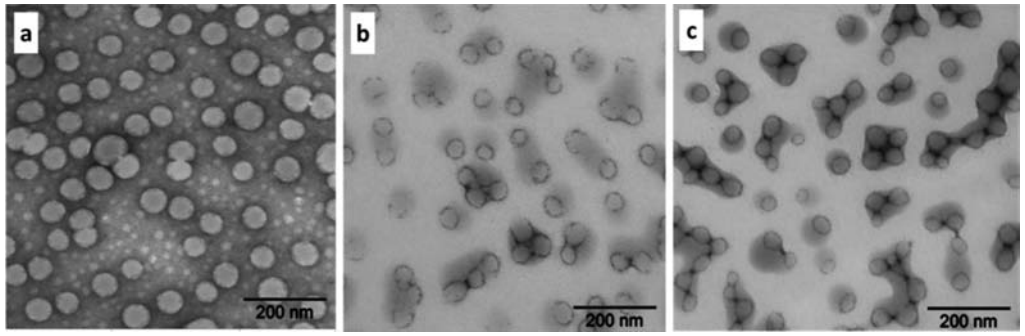

Figure 9. TEM images of the different pesticide microcapsules prepared with (a) 0, (b) 2.5, and (c) 10% EGDMA.

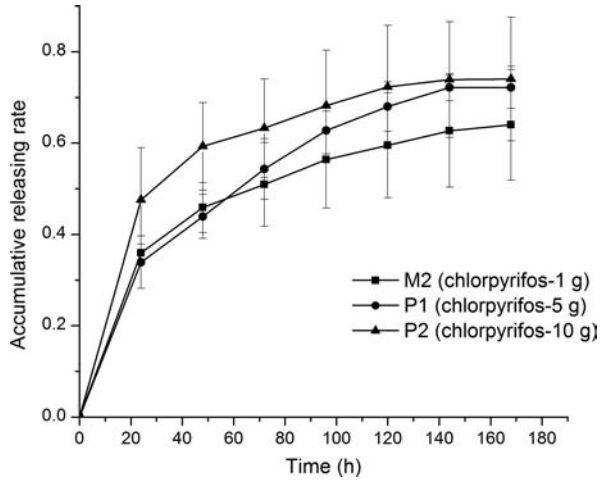

Figure 10. Profiles of chlorpyrifos release from microcapsules prepared with different loading contents of chlorpyrifos (1−10 g).

M_t is the amount of chlorpyrifos released at time t, M_∞ is the total amount of chlorprifos in microcapsules, k is a release constant, and n is a diffusional exponent.

As described in previous study,[20,32,33] the diffusion exponent n was equal to 0.43 for a Fickian diffusion system, when the diffusion of chlorpyrifos was controlled by its concentration difference, and diffusional exponent n was close to 0.85 for a degradation release system, when the release of chlorpyrifos was controlled by the degradation of microcapsules.

Slow release data were fitted with nonlinear regression. The release constant, diffusional exponent and the correlation coefficient R were presented in Table 5.

The release exponent n close to 0.43 of samples M2, M3, E3, and P1 with a high R values that indicated good fitting of exponential equations revealed the release mechanism of these microcapsules to be controlled by diffusion. When the release exponent n values were much lower than 0.43, there might be some other factors that influenced the chlorpyrifos release system, and the rapid initial release profile of these sample probably implied the rupture of microcapsules in the early release stage. All n values were below 0.43, proving that degradation of microcapusle was not the dominant factor of the release.

As to the effects of monomer ratio on the microcapsule, release profiles of M2 and M3 with BA/St ratios of 1:2 and 1:1 fitted well with the equation while profiles of microcapsules of other BA/St monomer ratio did not, which indicated the same conclusion that suitable monomer ratios for chlorpyrifos slow release were 1:2 and 1:1. The n value of E3 with 2.5% EGMDA was 0.428, which represented a good diffusion system of chlorpyrifos. As a result, E3 with 2.5% EGMDA was the finest slow release formulation for controlled chlorpyrifos. For the effects of different core-to-shell ratios, results of slow release kinetics showed that M2 and P1 with core-to-shell ratios of 1:30 and 5:26 basically matched the diffusion system while a ratio of 10:21 might lead to an initial rupture of microcapsule. It might be related to lower ER as a consequence of higher PL.

Table 5. Parameters Characterizing Fitting of the Model Equation on Chlorpyrifos Gradual Release Data

sample	k	n	R
M1	0.433	0.180	0.980
M2	0.132	0.317	0.998
M3	0.120	0.398	0.993
M4	0.161	0.383	0.976
M5	0.234	0.316	0.985
E1	0.167	0.274	0.992
E2	0.126	0.288	0.998
E3	0.067	0.428	0.996
E4	0.187	0.327	0.964
E5	0.337	0.232	0.991
P1	0.086	0.431	0.997
P2	0.230	0.237	0.990

A series of poly(BA/St) and poly(BA/St/EGDMA) microcapsules loaded with various amounts of chlorpyrifos were prepared by emulsion polymerization. All prepared microcapsules featured particles sizes of ∼90 nm with a little difference among each samples. The microcapsules show promise as a carrier for the slow release of pesticide chlorpyrifos. FTIR and TG analysis of the microcapsules confirmed the successful entrapment of chlorpyrifos in the poly(BA/St) wall material. The microcapsule ER varied from 60.15 to 96.74%. The highest ER (96.74%) was observed for microcapsules prepared with a BA/St monomer ratio of 1:2 in the presence of moderate EGDMA cross-linker content of 0.5%. In contrast, lower ERs of 60.15−67.97% were observed for microcapsules prepared with higher contents of chlorpyrifos (5−10 g). Variations in ER were consistent with variations in PL except for the series of microcapsules prepared with different core-to-shell ratios. In this series, maximum PL (29.11%) resulted in the lowest ER (60.15%).

The release performance of chlorpyrifos from the microcapsules was characterized by the medium dialysis method. Microcapsules prepared with a monomer ratio of 1:2 whose T_g was close to the release temperature displayed optimum sustainable release of chlorpyrifos. In contrast, microcapsules prepared with monomer ratios of 1:5 and 5:1 displayed

DOI: 10.1021/acs.jafc.5b01378
J. Agric. Food Chem. 2015, 63, 5196−5204

significantly high pesticide release at the early stages of the release process. Microcapsules featuring adequate degrees of cross-linking by EGDMA (0.5−2.5% EGDMA) displayed prolonged sustainable release profiles, whereas those prepared with higher EGDMA contents of 5−10% displayed enhanced chlorpyrifos release. Additionally, microcapsules prepared with a chlorpyrifos/monomer BA and St core-to-shell ratio of 1:30 displayed optimum release profiles, whereas those prepared at other ratios displayed faster release profiles. Chlorpyrifos release was characterized by nonlinear regression analysis. The diffusion release from microcapsules was found due to having a diffusional exponent n close to 0.43, while for samples that had n values much lower than 0.43, their faster release might be caused by the initial rupture of microcapsule.

The current study investigated the influences of monomer ratio, core-to-shell ratio, and degree of cross-linking on the characteristics and sustainable release behaviors of chlorpyrifos entrapped in poly(BA/St) and poly(BA/St/EGDMA) microcapsules via emulsion polymerization. Moreover, the findings provide a reference for the release profile studies of polyacrylate chlorpyrifos microcapsules.

AUTHOR INFORMATION

Corresponding Authors

*(X.R.) E-mail: renxueqin@cau.edu.cn.
*(S.H.) E-mail: shuwenhu@cau.edu.cn.

Funding

This work was supported by the Special Fund for Agriculture Profession (201303103) from the Ministry of Agriculture of China, the National Key Technology R & D Program (2011BAD11B02) from the Ministry of Science & Technology of China and the Chinese National Scientific Foundation (21375146; 21175150).

Notes

The authors declare no competing financial interest.

REFERENCES

(1) Bending, G. D.; Lincoln, S. D.; Sorensen, S. R.; Morgan, J. A. W.; Aamand, J.; Walker, A. In-field spatial variability in the degradation of the phenyl-urea herbicide isoproturon is the result of interactions between degradative Sphingomonas spp. and soil pH. *Appl. Environ. Microb.* **2003**, *69*, 827−834.

(2) Fleming, L. E.; Bean, J. A.; Rudolph, M.; Hamilton, K. Cancer incidence in a cohort of licensed pesticide applicators in Florida. *J. Occup. Environ. Med.* **1999**, *41*, 279−288.

(3) Salameh, P. R.; Baldi, I.; Brochard, P.; Raherison, C.; Abi Saleh, B.; Salamon, R. Respiratory symptoms in children and exposure to pesticides. *Eur. Respir. J.* **2003**, *22*, 507−512.

(4) Hack, B.; Egger, H.; Uhlemann, J.; Henriet, M.; Wirth, W.; Vermeer, A. W. P.; Duff, D. G. Advanced agrochemical formulations through encapsulation strategies? *Chem. Ing. Tech.* **2012**, *84*, 223−234.

(5) Shim, T. S.; Kim, S. H.; Yang, S. M. Elaborate design strategies toward novel microcarriers for controlled encapsulation and release. *Part. Part. Syst. Char.* **2013**, *30*, 9−45.

(6) Hong, K.; Park, S. Preparation of polyurethane microcapsules with different soft segments and their characteristics. *React. Funct. Polym.* **1999**, *42*, 193−200.

(7) Hashemi, S. A.; Zandi, M. Encapsulation process in synthesizing polyurea microcapsules containing pesticide. *Iran. Polym. J.* **2001**, *10*, 265−270.

(8) Hirech, K.; Payan, S.; Carnelle, G.; Brujes, L.; Legrand, J. Microencapsulation of an insecticide by interfacial polymerisation. *Powder Technol.* **2003**, *130*, 324−330.

(9) Mihou, A. P.; Michaelakis, A.; Krokos, F. D.; Mazomenos, B. E.; Couladouros, E. A. Prolonged slow release of (Z)-11-hexadecenyl acetate employing polyurea microcapsules. *J. Appl. Entomol.* **2007**, *131*, 128−133.

(10) Rochmadi, A. P.; Hasokowati, W. Mechanism of microencapsulation with urea-formaldehyde polymer. *Am. J. Appl. Sci.* **2010**, *7*, 39−45.

(11) Mayya, K. S.; Bhattacharyya, A.; Argillier, J. F. Microencapsulation by complex coacervation: influence of surfactant. *Polym. Int.* **2003**, *52*, 644−647.

(12) Dailey, O. D.; Dowler, C. C. Polymeric microcapsules of cyanazine: preparation and evaluation of efficacy. *J. Agric. Food Chem.* **1998**, *46*, 3823−3827.

(13) P Rez-Mart Nez, J. I.; Morillo, E.; Maqueda, C.; Gin S, J. M. Ethyl cellulose polymer microspheres for controlled release of norfluazon. *Pest Manage. Sci.* **2001**, *57*, 688−694.

(14) El Bahri, Z.; Taverdet, J. L. Elaboration and characterisation of microparticles loaded by pesticide model. *Powder Technol.* **2007**, *172*, 30−40.

(15) Adak, T.; Kumar, J.; Shakil, N. A.; Walia, S. Development of controlled release formulations of imidacloprid employing novel nano-ranged amphiphilic polymers. *J. Environ. Sci. Health, Part B* **2012**, *47*, 217−225.

(16) Zhang, P.; Zhang, Q.; Jiao, Q. Synthesis and characterization of microcapsules with chlorpyrifos cores and polyurea walls. *Chem. Res. Chin. Univ.* **2006**, *22*, 379−382.

(17) Zhu, L.; Wang, Z.; Zhang, S.; Long, X. Fast microencapsulation of chlorpyrifos and bioassay. *J. Pestic. Sci.* **2010**, *35*, 339−343.

(18) Zhang, J.; Li, M.; Fan, T.; Xu, Q.; Wu, Y.; Chen, C.; Huang, Q. Construction of novel amphiphilic chitosan copolymer nanoparticles for chlorpyrifos delivery. *J. Polym. Res.* **2013**, *20*, 107.

(19) Kumbar, S. G.; Kulkarni, A. R.; Dave, A. M.; Aminabhavi, T. M. Encapsulation efficiency and release kinetics of solid and liquid pesticides through urea formaldehyde crosslinked starch, guar gum, and starch +guar gum matrices. *J. Appl. Polym. Sci.* **2001**, *82*, 2863−2866.

(20) Stloukal, P.; Kucharczyk, P.; Sedlarik, V.; Bazant, P.; Koutny, M. Low molecular weight poly(lactic acid) microparticles for controlled release of the herbicide metazachlor: preparation, morphology, and release kinetics. *J. Agric. Food Chem.* **2012**, *60*, 4111−4119.

(21) Zhang, S. F.; Chen, P. H.; Zhang, F.; Yang, Y. F.; Liu, D. K.; Wu, G. Preparation and physicochemical characteristics of polylactide microspheres of emamectin benzoate by modified solvent evaporation/extraction method. *J. Agric. Food Chem.* **2013**, *61*, 12219−12225.

(22) Zhang, W.; He, S.; Liu, Y.; Geng, Q.; Ding, G.; Guo, M.; Deng, Y.; Zhu, J.; Li, J.; Cao, Y. Preparation and characterization of novel functionalized prochloraz microcapsules using silica-alginate-elements as controlled release carrier materials. *ACS Appl. Mater. Interfaces* **2014**, *6*, 11783−11790.

(23) Liu, D.; Ichikawa, H.; Cui, F.; Fukumori, Y. Short-term delayed-release microcapsules spraycoated with acrylic terpolymers. *Int. J. Pharm.* **2006**, *307*, 300−307.

(24) Chen, C.; Chen, Z.; Zeng, X.; Fang, X.; Zhang, Z. Fabrication and characterization of nanocapsules containing n-dodecanol by miniemulsion polymerization using interfacial redox initiation. *Colloid Polym. Sci.* **2012**, *290*, 307−314.

(25) Swamy, B. Y.; Prasad, C. V.; Rao, K. C.; Subha, M. C. S. Preparation and characterization of poly (hydroxyl ethyl methyl acrylate-*co*-acrylic acid) microspheres for drug delivery application. *Int. J. Polym. Mater.* **2013**, *62*, 700−705.

(26) Wu, H.; Xu, Y.; Liu, G.; Ling, J.; Dash, B.; Ruan, J.; Zhang, C. Emulsion cross-linked chitosan/nanohydroxyapatite microspheres for controlled release of alendronate. *J. Mater. Sci.: Mater. Med.* **2014**, *25*, 2649−2658.

(27) Casana, G. V.; Gimeno, S. M.; Gimeno, S. B. Agrochemical formulations containing microcapsules. U.S. Patent 08263530, 2012.

(28) Casana, G. V.; Gimeno, S. M.; Gimeno, S. B. Composition for delivering e.g. pyrethroids comprises microcapsules that each encloses microencapsulated material, where wall of microcapsule is formed by

DOI: 10.1021/acs.jafc.5b01378
J. Agric. Food Chem. 2015, 63, 5196−5204

polymerization of aliphatic/aromatic isocyanate, and acetylene carbamide derivative. U.S. Patent 2012245027-A1, 2012.
(29) Murakami M.; Ogawa M.; Fujinoto, I.; Ohtsubo, T. New pesticidal compositions comprise microcapsules microencapsulating organophosphorus compound e.g. chlorpyrifos, used to control wood-injuring insects, termites and nuisance injurious insects and to produce insect-proof wood. U.S. Patent 5929053-A, 1999.
(30) Yang C.; Pan I. Controlled release pesticidal microcapsule prodn.lby mixing vegetable oil, pesticide and aq.urea-formaldehyde prepolymer, acidifying and cross-linking, giving high encapsulation rate. U.S. Patent 5576008-A, 1996.
(31) Korsmeyer, R. W.; Gurny, R.; Doelker, E.; Buri, P.; Peppas, N. A. Mechanisms of solute release from porous hydrophilic polymers. *Int. J. Pharm.* **1983**, *15*, 25−35.
(32) Zuleger, S.; Lippold, B. C. Polymer particle erosion controlling drug release. I. Factors influencing drug release and characterization of the release mechanism. *Int. J. Pharm.* **2001**, *217*, 139−152.
(33) Asrar, J.; Ding, Y.; La Monica, R. E.; Ness, L. C. Controlled release of tebuconazole from a polymer matrix microparticle: release kinetics and length of efficacy. *J. Agric. Food Chem.* **2004**, *52*, 4814−4820.

DOI: 10.1021/acs.jafc.5b01378
J. Agric. Food Chem. 2015, 63, 5196−5204

JOURNAL OF AGRICULTURAL AND FOOD CHEMISTRY

Article

pubs.acs.org/JAFC

Fate and Stereoselective Behavior of Benalaxyl in a Water−Sediment Microcosm

Mingke Liu,[†] Donghui Liu,[†] Yangguang Xu,[‡] Xu Jing,[†] Zhiqiang Zhou,[†] and Peng Wang*[,†]

[†]Department of Applied Chemistry, China Agricultural University, Beijing 100193, People's Republic of China

[‡]Chinese People's Armed Police Force Academy, Langfang 065000, People's Republic of China

Supporting Information

ABSTRACT: The environmental behavior and stereoselectivity of the chiral fungicide benalaxyl and its chiral metabolite benalaxyl acid in water, sediment, and water−sediment microcosms were studied. The microcosms were incubated at 25 °C with light or under darkness. The influencing factors such as light and microorganism were investigated. The results showed that benalaxyl had half-lives of >21 days in the microcosm system and that the metabolite benalaxyl acid could exist in the microcosm for >70 days. Benalaxyl was mainly transformed through microbial degradation, and thus sediment microorganisms played a major role in the dissipation of benalaxyl in the aquatic microcosm. The stereoselective behavior of benalaxyl and benalaxyl acid was also investigated. (−)-Benalaxyl was preferentially degraded in the microcosm, resulting in an enrichment of the more toxic enantiomer (+)-benalaxyl, which may cause higher risk to the aquatic system. Moreover, (−)-benalaxyl acid was preferentially formed in the microcosm. The enantioselectivity of the enantiomers in the microcosm should be taken into consideration for an accurate risk assessment.

KEYWORDS: *benalaxyl, water−sediment microcosm, stereoselectivity, contamination*

INTRODUCTION

The enantiomers of a chiral compound have identical physical and chemical properties but possibly have different bioactivities, toxicities, metabolisms, and environmental behaviors.[1] Chiral pesticides are widely used in agriculture, and the number is increasing with the development of complex pesticide molecules. It is a common situation that only one of the enantiomers performs the desired effect, whereas the other ineffective enantiomers may be even more toxic to other nontarget organisms or ecosystem and cause environmental problems. For example, of the eight enantiomers of the chiral insecticide deltamethrin, only the (αS,1R,3R)-enantiomer has the desired insecticidal activity, whereas the others are noneffective or less active.[2] The toxicity of the racemate of the herbicide metolachlor to *Daphnia magna* is 100 times higher than that of *S*-metolachlor, and *rac*-metolachlor degraded more slowly than *S*-metolachlor in soil.[3] Therefore, it is necessary to study the environmental behavior of chiral pesticides on an enantiomeric level to evaluate the risks more accurately.

The chiral fungicide benalaxyl (BX) [(±)-methyl *N*-(phenylacetyl)-*N*-(2,6-methylphenyl) alaninate] (Figure 1) has been widely used on cucumber, tomato, tobacco, and many other vegetables and fruit crops to control downy mildew, early blight, late blight, and *Peronospora tabacina* for many years. As a kind of chiral pesticide, BX has two enantiomers, with *R*-(−)-BX more active than *S*-(+)-BX. It has a series of advantages such as high efficiency, low toxicity, and long effective period. Because of its wide usage and relatively long half-life period,[4] BX could be detected in the environment.[5] A number of studies have been conducted to evaluate the enantioselective environmental behaviors on an enantiomeric level in soil,[6,7] animals such as lizards, earthworms, rainbow trout, and rabbits,[8−10] and plants such as cucumber and tomato.[6,11] BX can enter the water system through rainfall, surface runoff, and leaching[12−14] and then cause water pollution and affect aquatic organisms.[15] Unfortunately, few studies have focused on the fate of BX in the aquatic system.

Benalaxyl acid (BX acid) [(±)-*N*-(2,6-xylyl)-*N*-(phenylacetyl)alanine] (Figure 1) is the primary metabolite, which is more water-soluble and persistent than BX in the environment and may be more harmful for aquatic organisms. It also possesses a chiral center to make a couple of enantiomers. There are no published reports for the degradation and stereoselective behavior of the metabolite BX acid.

The impacts of pesticide and metabolite contamination for aquatic ecosystems are tremendous. As a research method for the environmental fate of pesticides, microcosms have been widely used with a series of advantages such as authenticity, flexibility, high performance−price ratio, and security.[16−19] In an artificial microcosm, the incubation conditions can be controlled and the fate of the target compound can be understood clearly.

In this study, the chiral analysis method for the enantiomers of BX and BX acid in water and sediment was set up. The fate and stereoselective behavior of BX and BX acid in water, sediment, and a water−sediment microcosm were studied to evaluate the environmental behavior of BX in the aquatic system. The effect of light and microorganism was also studied following the discussion of the degradation mechanism.

Received: March 21, 2015
Revised: May 12, 2015
Accepted: May 15, 2015
Published: May 26, 2015

ACS Publications © 2015 American Chemical Society

DOI: 10.1021/acs.jafc.5b01448
J. Agric. Food Chem. 2015, 63, 5205−5211

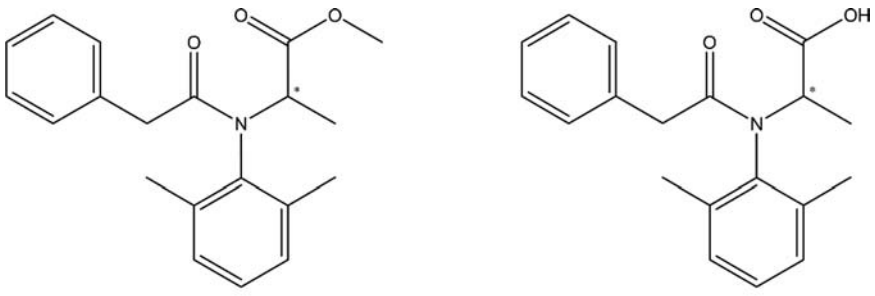

Figure 1. Chemical structures of BX and BX acid.

MATERIALS AND METHODS

Chemicals. BX (>99.0% purity) was obtained from the Institute for the Control of Agrochemicals, Ministry of Agriculture (Beijing, China). Metabolite BX acid (>99.0% purity) was synthesized by the Department of Applied Chemistry, China Agricultural University (Beijing, China). All of the reagents were of analytical grade and obtained from Sinopharm Chemical Reagent Co., Ltd. (Shanghai, China). Mobile phase reagents were distilled and filtered through a 0.22 μm filter membrane before use.

Instrumental Analysis. HPLC analysis in this study was performed by using an Agilent 1200 series HPLC (Agilent Technology) equipped with a G1322A degasser, a G1311A pump, a G1328A injector, a G1314B VWD, and an AT-930 column attemperator (Tianjin Automatic Science Instrument Co. Ltd., China). The signal was received and processed by Agilent Chemstation software.

A Chiralcel OD chiral column (250 mm × 4.6 mm i.d., Daicel Chiral Technology Co., Ltd.) was used to separate the enantiomers of BX and BX acid. Mobile phase was *n*-hexane and 2-propanol (91:9, v/v) with trifluoroacetic acid (1‰, v/v) at the flow rate of 0.8 mL/min. The injection volume was 20 μL, and the UV detection wavelength was 225 nm. The separation was conducted at 20 °C.

The elution order of BX and BX acid enantiomers was determined by a polarimeter detector. The polarimeter detector wavelength was 426 nm. The elution order was as follows: (−)-BX (15.4 min), (+)-BX (18.8 min), (−)-BX acid (21.6 min), and (+)-BX acid (32.0 min).

Assay Validation. The linearity of the instrument for BX (5−1500 mg/L) and BX acid (5−600 mg/L) was investigated by standard solution in 2-propanol (n = 3). The linearity of the method, recovery, limit of detection (LOD), and limit of quantification (LOQ) of the method were investigated. Linearity and recoveries were determined in blank samples (uncontaminated environmental matrix) that were fortified with BX and BX acid at different levels. The linearity of BX (0.2−20 mg/kg) and BX acid (0.2−5 mg/kg) in water samples and of BX (0.2−50 mg/kg) and BX acid (0.2−20 mg/kg) in sediment samples was checked (n = 3). The recoveries of BX enantiomers in water and in sediment (1, 5, and 10 mg/kg) and of BX acid enantiomers in water (0.5, 1, and 2 mg/kg) and in sediment (1, 5, and 10 mg/kg) were investigated (n = 3). The external calibration curves were generated by regression analysis of the peak area against concentrations. Blank sediment and water samples were also analyzed to check the interference from the matrix. LOD and LOQ were defined as concentrations that produced signal-to-noise (S/N) ratios of 3 and 10, respectively.

Degradation in Sediment. The test sediment and water were sampled from Shangzhuang reservoir (Beijing, China) that had not been treated with BX. The sediment was air-dried at room temperature and sieved (2 mm). It took 7 days to activate microorganisms before incubation. Sediment (400 g, moisture content = 25%, m/m) was added in a 500 mL beaker, and BX was fortified at 20 mg/kg. Four variations of incubation were designed: (1) unsterilized, with light (12 h per day); (2) unsterilized, under darkness; (3) sterilized, with light (12 h per day); (4) sterilized, under darkness (experiments S1, S2, S3, and S4, respectively; Table 1). The sediment was sterilized by two periods of autoclaving (2 h per period). The light was provided by fluorescent bulbs in an incubator, and the intensity of light was 2640 lx.

Table 1. Summary of Experiment Designs

system	contamination way	sterilization[a]	light[a]	experiment
sediment	sediment	×	√	S1
		×	×	S2
		√	√	S3
		√	×	S4
water	water	×	√	W1
		×	×	W2
		√	√	W3
		√	×	W4
water−sediment	water	×	√	WS1
		×	×	WS2
	sediment	×	√	SW1
		×	×	SW2

[a]"√" means "yes" and "×" means "no".

Degradation in Water. Water (400 g) was added in a 500 mL beaker, and BX was fortified at 20 mg/kg. Four variations of incubation were designed: (1) unsterilized, with light (12 h per day); (2) unsterilized, under darkness; (3) sterilized, with light; (4) sterilized, under darkness (experiments W1, W2, W3, and W4, respectively; Table 1). The water was sterilized by two periods of autoclaving (1 h per period).

Degradation in Water−Sediment Microcosm. The water−sediment microcosm was made up of 35 g of sediment (moisture content = 25%, m/m) and 150 g of water in a 500 mL beaker. There were two methods of contamination: water contamination and sediment contamination. For water contamination, BX was fortified in water at 20 mg/kg under light (12 h per day) or darkness (experiments WS1 and WS2, respectively; Table 1). For sediment contamination, BX was fortified in sediment at 20 mg/kg under light or darkness (experiments SW1 and SW2, respectively; Table 1).

All experiments were conducted in an incubator at 25 °C, and water was added every 3 days for supplement of evaporation. Sediment and water samples were collected for analysis at 0, 1, 5, 12, 21, 35, 50, 70, and 90 days. Each incubation was carried out in triplicate. The summary of experiment designs is shown in Table 1.

Dissipation curves were defined as $C = C_0\, e^{-kt}$ or $C = at^2 + bt + C_0$, in which C means concentration, C_0 means the highest concentration, k means elimination rate coefficient, and a and b are empirical constants. Half-life ($t_{1/2}$, days) was obtained from the equation $t_{1/2} = \ln 2/k$ or $0 = at^2 + bt + {}^1/_2C_0$ ($t_{1/2} = t$). The enantiomer fraction (EF) was used to evaluate the enantioselective behavior of enantiomers, which was defined by the equation EF = peak areas of the (−)/[(−) +

DOI: 10.1021/acs.jafc.5b01448
J. Agric. Food Chem. 2015, 63, 5205−5211

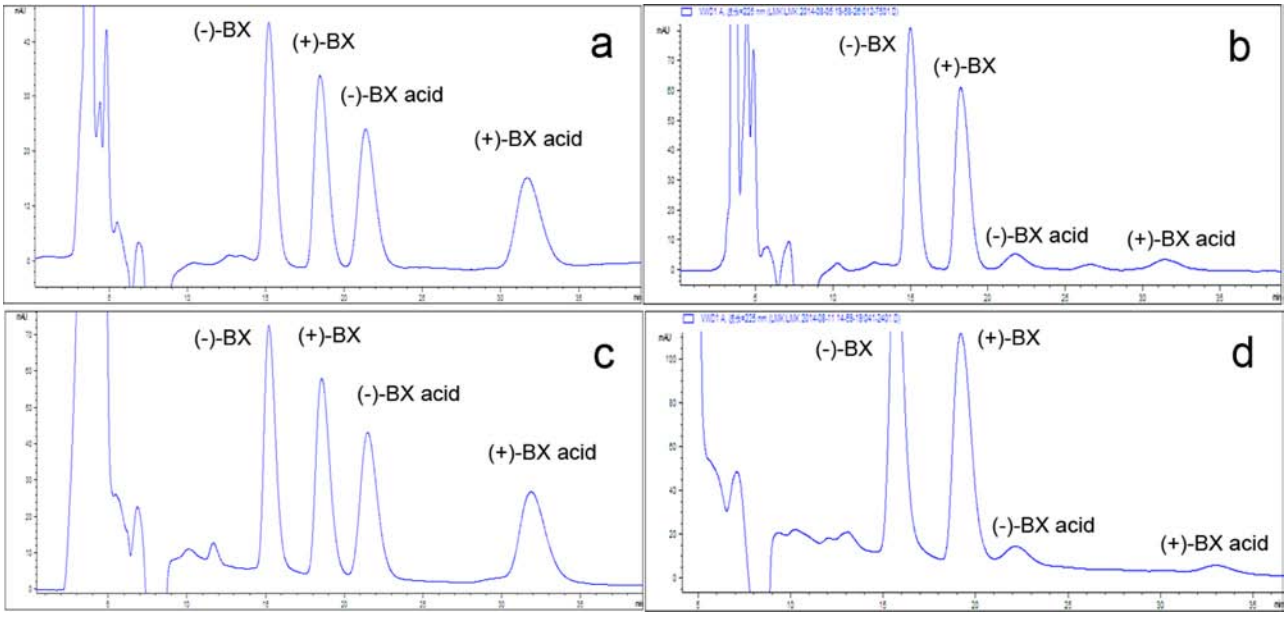

Figure 2. Representative HPLC chromatograms of extract from (a) water fortified with BX (5 mg/kg) and BX acid (5 mg/kg) and (b) incubated water sample of experiment WS1 (35 days) or (c) sediment fortified with BX (5 mg/kg) and BX acid (5 mg/kg) and (d) incubated sediment sample of experiment S3 (35 days).

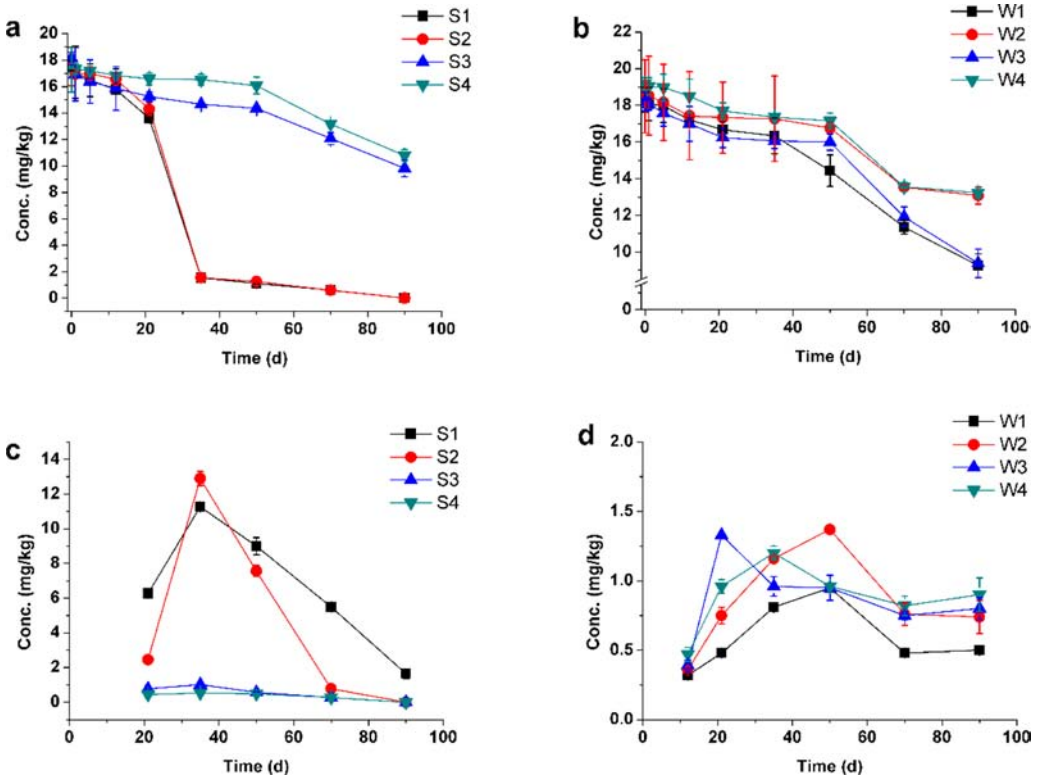

Figure 3. Concentration−time curves of (a) BX in sediment, (b) BX in water, (c) BX acid in sediment, and (d) BX acid in water. (Values represent the mean ± SD.) S1, unsterilized, with light; S2, unsterilized, under darkness; S3, sterilized, with light; S4, sterilized, under darkness.

(+)], in which (−) and (+) indicate the peak areas of the (−)-enantiomer and (+)-enantiomer, respectively. EF values vary from 0 to 1, with EF = 0.5 indicating no enantioselectivity.

Sample Preparation. A solvent extraction method was used for extraction in the experiment. Ethyl acetate (15 mL) and saturated salt water (3 mL) were added to a 50 mL polypropylene centrifuge tube containing 15 g of sediment sample/10 g of water sample (pH was adjusted to 2 by HCl). The centrifuge tube was vortex-mixed for 5 min (sediment) or 3 min (water), exposed to ultrasonic vibration for 15 min, and then centrifuged at 4000 rpm for 7 min (sediment) or 3 min (water). After removing 15 mL of ethyl acetate (extraction solvent), the procedure described above was repeated by adding another 15 mL of ethyl acetate. The combined extraction solvent (30 mL of ethyl acetate) was evaporated to near dryness on a vacuum rotary evaporator at 37 °C and blown to dryness by a gentle stream of

DOI: 10.1021/acs.jafc.5b01448
J. Agric. Food Chem. 2015, 63, 5205−5211

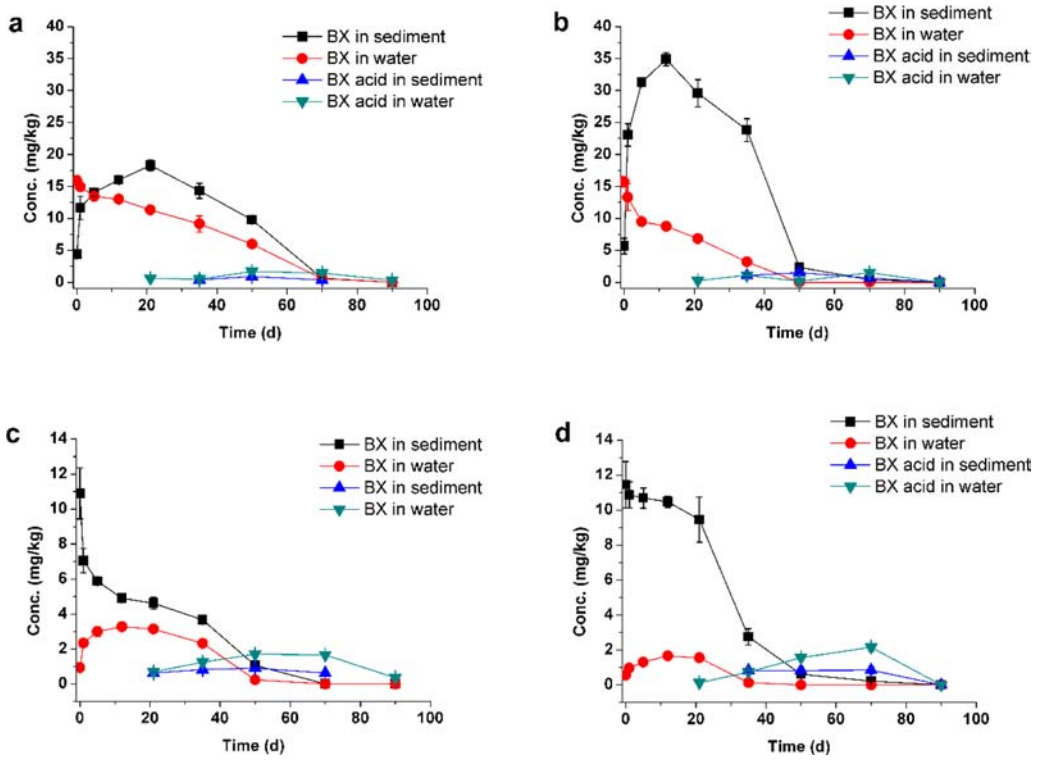

Figure 4. Concentration−time curves of (a) WS1 (with light, water contamination), (b) WS2 (under darkness, water contamination), (c) SW1 (with light, sediment contamination), and (d) SW2 (under darkness, sediment contamination). (Values represent the mean ± SD.)

nitrogen. Finally, the extract was reconstituted with 0.5 mL of 2-propanol and filtered through a 0.22 μm filter membrane.

RESULTS AND DISCUSSION

Assay Validation. The enantiomers of BX and BX acid were baseline separated, and there were no interference peaks from the matrix around the peaks of the four enantiomers (Figure 2). Linearities of the instrument for BX and BX acid in 2-propanol were satisfactory ((−)-BX, $Y = 71.3 + 55.68X$, $R = 0.9993$; (+)-BX, $Y = 62.7 + 90.25X$, $R = 0.9996$; (−)-BX acid, $Y = -66.1 + 35.9X$, $R = 0.9991$; (+)-BX acid, $Y = -79.3 + 61.25X$, $R = 0.9994$). Good linearities of method and recoveries were obtained in water and sediment for BX and BX acid enantiomers (see the Supporting Information, Table S1). Correlation coefficients (R) of linear regression equations were 0.9993−0.9999. In water, the recoveries of BX and BX acid enantiomers were 92.33−118.86 and 91.29−115.96%, respectively; in sediment, the recoveries of BX and BX acid enantiomers were 91.49−113.10 and 79.36−92.48%, respectively. The RSDs were all below 10%. The limits of detection (LODs) for BX and BX acid were 0.013−0.015 mg/kg in water and 0.014−0.016 mg/kg in sediment; the limits of quantitation (LOQs) for BX and BX acid were 0.06−0.08 mg/kg in water and 0.08−0.10 mg/kg in sediment.

Degradation of BX in Sediment. Dissipation equations and half-lives are in the Supporting Information (Table S2). As shown in Figure 3a, the degradation of BX in unsterilized sediment in experiments S1 (unsterilized, with light) and S2 (unsterilized, under darkness) was rapid with half-lives of 26.8 and 28.0 days, but very slow in sterilized sediment in experiments S3 (sterilized, with light) and S4 (sterilized, under darkness) with half-lives of 112.7 and 132.0 days, indicating that microbial degradation played an important role in the degradation of BX and that photolysis affected the degradation slightly.

The trend of metabolite BX acid in sediment is shown in Figure 3c. BX acid in experiments S1 (unsterilized, with light) and S2 (unsterilized, under dark) reached the highest values of 11.3 and 12.9 mg/kg at the 35th day, but in S3 (sterilized, with light) and S4 (sterilized, under dark), very low levels of BX acid were detected, showing microbial degradation was the main factor affecting the formation of BX acid.

Degradation of BX in Water. As shown in Figure 3b, in experiments W1 (unsterilized) and W3 (sterilized) under light, the half-lives of BX were 95.6 and 98.3 days and in experiments W2 (unsterilized) and W4 (sterilized) under darkness, the half-lives were 132.0 and 137.2 days. Obviously, microbial degradation was not a major pathway because water contained fewer microorganisms. Light could accelerate the degradation of BX in water, with a similar result as in sediment, indicating that photolysis was also a pathway for the dissipation of BX. In experiment W4 (sterilized, under darkness), the fact that BX also degraded obviously in unsterilized water under darkness indicated that hydrolysis was the main pathway for the degradation of BX in water.

As shown in Figure 3d, in experiments W1−4, low levels of BX acid (about 0.8 mg/kg) were found from 12 to 90 days in water due to the slow degradation of BX, and further degradation of BX was very slow.

Fate of BX in Water−Sediment Microcosm. Figure 4 shows the concentration−time curves of BX and BX acid in the water and sediment of the microcosm. In experiment WS1 (with light, water contamination), when the water of the microcosm was contaminated (BX was fortified in water), the concentration of BX decreased in water with $t_{1/2}$ = 39.6 days and increased first and then decreased in the sediment because of adsorption and degradation. In WS2 (under darkness, water

DOI: 10.1021/acs.jafc.5b01448
J. Agric. Food Chem. 2015, 63, 5205−5211

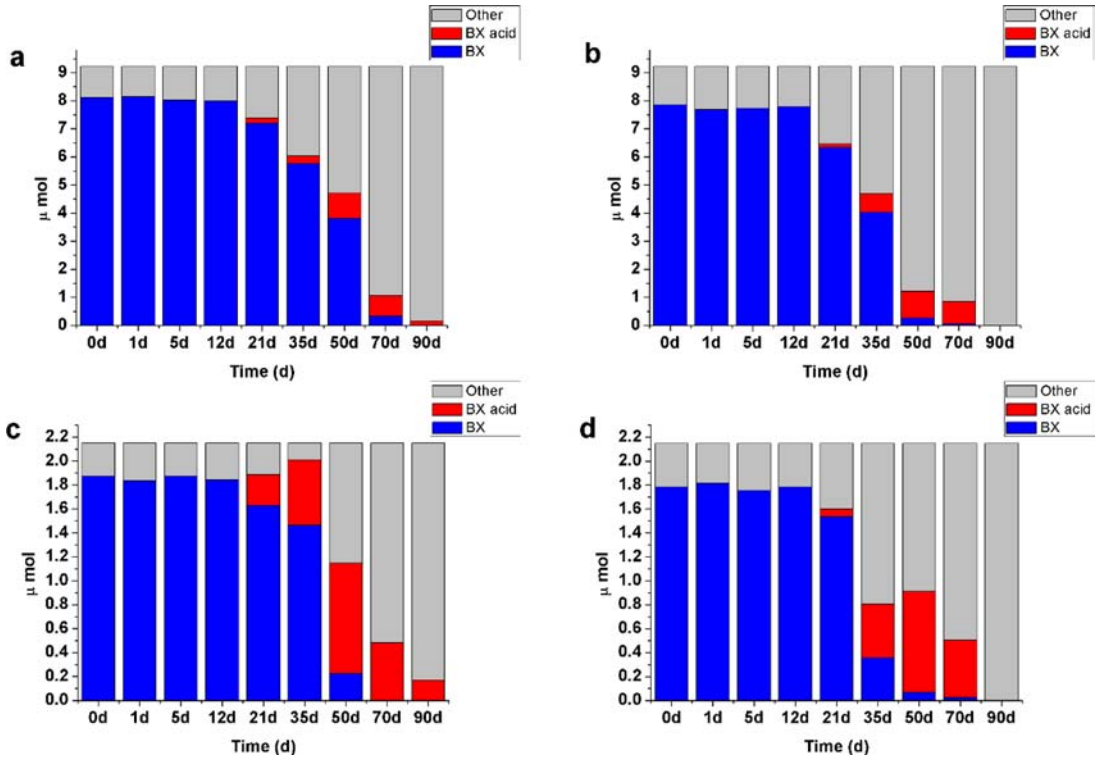

Figure 5. Material balance−time bar chart of (a) WS1 (with light, water contamination), (b) WS2 (under darkness, water contamination), (c) SW1 (with light, sediment contamination), and (d) SW2 (under darkness, sediment contamination). BX, total amount of BX (μmol) in microcosms; BX acid, total amount of BX acid (μmol) in microcosms; other, total amount of other metabolites and nonextractable part in microcosms.

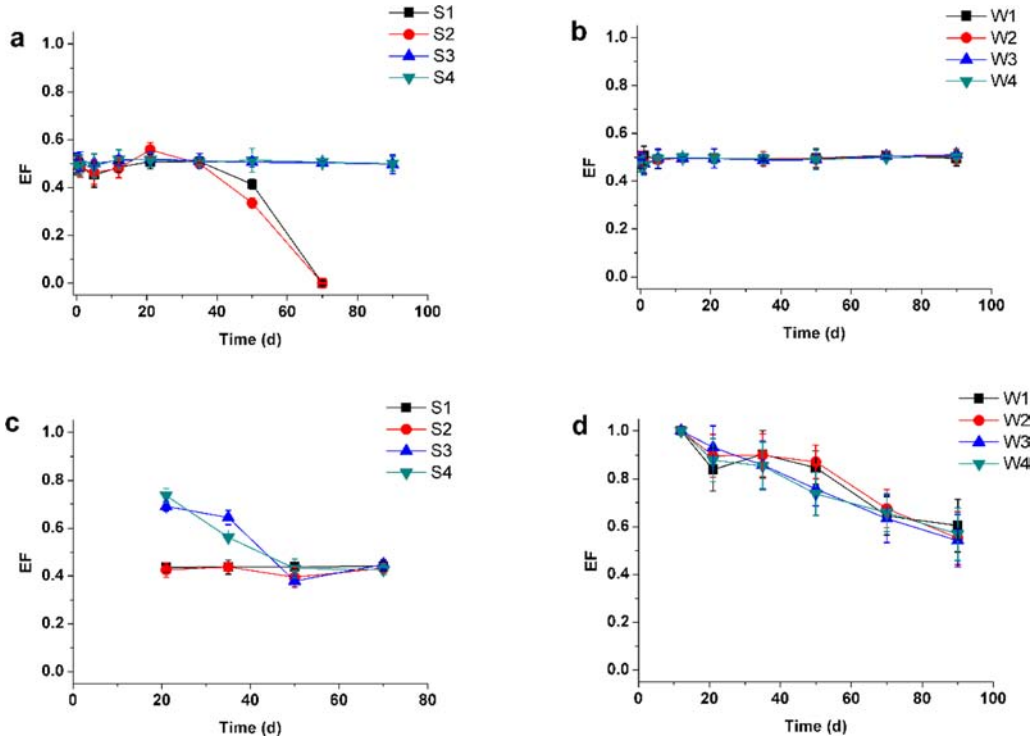

Figure 6. EF−time curves of (a) BX in sediment, (b) BX in water, (c) BX acid in sediment, and (d) BX acid in water. (Values represent the mean ± SD.) S1, unsterilized, with light; S2, unsterilized, under darkness; S3, sterilized, with light; S4, sterilized, under darkness. EF = peak areas of the (−)/[(−) + (+)].

contamination) BX was more easily transferred from water into the sediment with the highest concentration of 34.9 mg/kg at the 12th day (Figure 4b) compared with the result in WS1 (with light). Correspondingly, the decline of BX in water in WS2 (under darkness) was faster ($t_{1/2}$ = 18.4 days) than that in WS1 (with light) ($t_{1/2}$ = 39.6 days). BX acid appeared since the

DOI: 10.1021/acs.jafc.5b01448
J. Agric. Food Chem. 2015, 63, 5205−5211

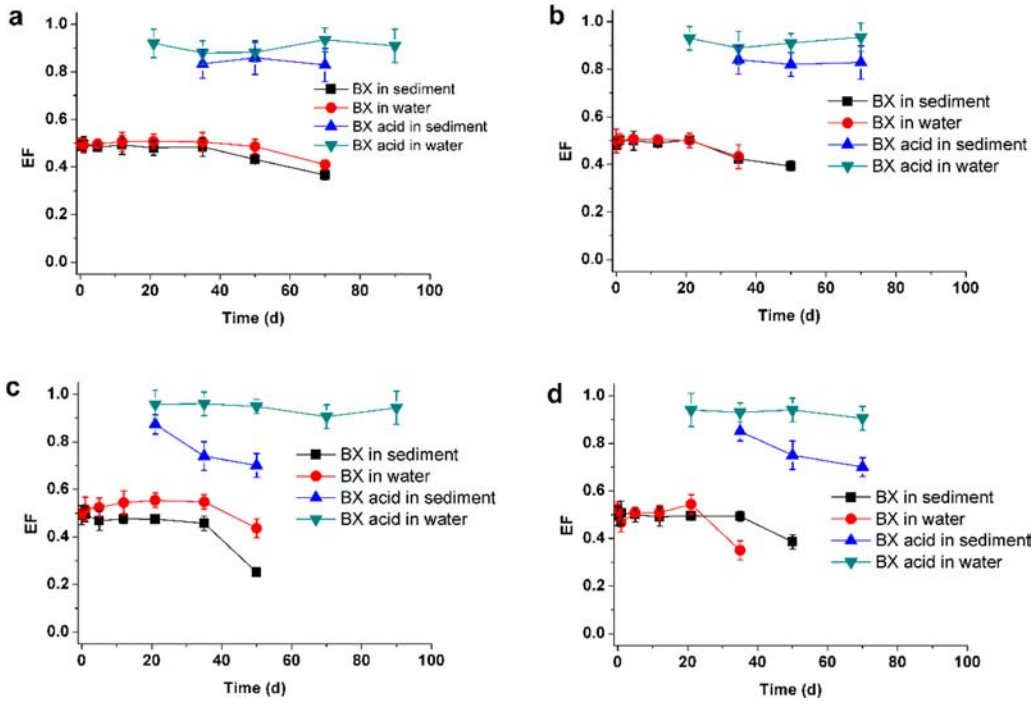

Figure 7. EF−time curves of (a) WS1 (with light, water contamination), (b) WS2 (under darkness, water contamination), (c) SW1 (with light, sediment contamination), and (d) SW2 (under darkness, sediment contamination). (Values represent the mean ± SD.) EF = peak areas of the (−)/[(−) + (+)].

21st day and remained at a relatively low level in both water and sediment. There was no significant difference for BX acid between WS1 (with light) and WS2 (under dark), and the concentrations of BX acid in both experiments WS1 and WS2 were about 0.8 mg/kg.

The result of SW1 (with light, sediment contamination) is shown in Figure 4c. When the sediment of the microcosm was contaminated (BX was fortified in sediment), the concentration of BX in sediment decreased with time, increased to 3.27 mg/kg in water at the 12th day and could not be detected at the 90th day. Compared with SW1 (with light), less BX transferred from sediment into water in SW2 (under darkness, sediment contamination). The concentration of BX in water in SW2 (under darkness) was lower than that in SW1 (with light) at the corresponding time points (Figure 4d). It was found that light could help the distribution of BX in water. There was no significant difference for the formation of BX acid between SW1 (with light) and SW2 (under darkness), and the highest concentrations of BX acid in both experiments SW1 and SW2 were about 2.0 mg/kg. The concentrations of BX acid were always higher in water than in sediment, perhaps because of the high water solubility; for example, in SW2 (under darkness) BX acid could be detected at the 21st day and reached the highest values of 2.16 and 0.85 mg/kg in water and sediment, respectively (Figure 4d).

The material balance in the microcosm during the experiments was also roughly investigated on the basis of the amount of BX/BX acid distributed in water and sediment in the microcosm. The original doses of BX fortified in microcosms were 9.22 μmol (3 mg WS1, WS2, water contamination) and 2.15 μmol (0.7 mg, SW1, SW2, sediment contamination). Considering the nonextractable amount (about 10% of BX and 15% of BX acid) according to the average recoveries, the material balance is shown in Figure 5, from which there was no obvious decline of BX in the first 12 days, showing BX was relatively persistent in the aquatic environment.

Stereoselectivity. *Stereoselectivity of BX Enantiomers.* EF−time curves were plotted (Figure 6 and 7) to characterize enantioselectivity of the enantiomers of BX and BX acid. As shown in experiments S3 (sterilized, with light), S4 (sterilized, under darkness) (Figure 6a) and experiments W1−4 (Figure 6b), the EF values of BX were all approximately 0.5, indicating that both photolysis and hydrolysis did not cause stereoselective degradation. Compared with experiments S3 (sterilized, with light) and S4 (sterilized, under darkness), stereoselectivity of BX enantiomers was found in experiments S1 (unsterilized, with light) and S2 (unsterilized, under darkness) with EF < 0.5. In conclusion, (−)-BX was preferentially degraded in the sediment and microbial degradation played the key role for the stereoselectivity. No stereoselectivity was found in water that contained fewer microorganisms. (−)-BX was also found to be preferentially degraded in the water−sediment microcosm, especially in experiments SW1 (with light, sediment contamination) and SW2 (under darkness, sediment contamination) (Figure 7c,d), which was caused by the microorganisms in the sediment.

Stereoselectivity of BX Acid Enantiomers. (−)-BX acid was preferentially formed in the sterilized sediment in experiments S3 (sterilized, with light) and S4 (sterilized, under darkness) (Figure 6c), and no stereoselectivity was found in the unsterilized sediment (experiments S1 and S2). In water, almost only (−)-BX acid was formed (experiments W1−4, Figure 6d). Figure 7 shows the EF values of BX acid in the water−sediment microcosm. (−)-BX was found to be preferentially degraded in the water−sediment microcosm, and (−)-BX acid was the main form of the primary metabolite. Therefore, it could be inferred that (−)-BX was preferentially transformed to (−)-BX acid.

DOI: 10.1021/acs.jafc.5b01448
J. Agric. Food Chem. 2015, 63, 5205−5211

In this study, the fate and stereoselective behavior of BX and BX acid in a water−sediment microcosm were studied. BX and the metabolite BX acid had long half-lives in the water−sediment microcosm, and it was found that sediment in the microcosm played the most important role in the remediation of BX pollution in the aquatic environment and that microorganism biodegradation and hydrolysis were the major pathways. Significant enantioselective environmental behavior of BX (EF = 0.2−0.4 in microcosm) and the formation of BX acid (EF = 0.7−0.95 in microcosm) were found. It was reported that the toxicity of (+)-benalaxyl for some aquatic organisms was higher than that of *rac*-benalaxyl,[4] so the evaluation of the enantioselective environmental behavior of BX is of significance. Furthermore, there were no published reports on the toxicology information on BX acid, which might be a potential concern to the aquatic environment. The evaluation of the metabolite BX acid should be taken into consideration for an accurate risk assessment, especially on an enantiomeric level.

■ ASSOCIATED CONTENT

Supporting Information

Full validation results of BX and BX acid enantiomers in water and sediment samples for the HPLC-UV assay (Table S1); full dissipation results of BX enantiomers in all experiments (Table S2). The Supporting Information is available free of charge on the ACS Publications website at DOI: 10.1021/acs.jafc.5b01448.

■ AUTHOR INFORMATION

Corresponding Author

*(P.W.) Mail: Department of Applied Chemistry, China Agricultural University, No. 2 Yuanmingyuan West Road, Beijing 100193, China. Phone: +8610-62731294. Fax: +8610-62731294. E-mail: wangpeng@cau.edu.cn.

Funding

This work was supported by the National Natural Science Foundation of China (Contract Grants 21337005, 21277171), supported by the Program for Changjiang Scholars and Innovative Research Team in University, supported by the New-Star of Science and Technology and by Beijing Metropolis Beijing Nova program.

Notes

The authors declare no competing financial interest.

■ REFERENCES

(1) Williams, A. Opportunities for chiral agrochemicals. *Pestic. Sci.* **1996**, *46*, 3−9.

(2) Roussel, C.; Suteu, C.; Shaimi, L.; Soufiaoui, M.; Bonnet, B.; Heitmann, I.; Piras, P. Chiral separation of some 4a-methyl-1,2,3,4,4a,9a-hexahydro-fluoren-9-one derivatives as a probe for difference in solvation by 2-propanol of carbamate moiety in Chiralcel OD-H, Chiralpak AD, and Chiralpak AS chiral stationary phases. *Chirality* **1998**, *10*, 770−777.

(3) Liu, H.; Ye, W.; Zhan, X.; Liu, W. A comparative study of rac- and S-metolachlor toxicity to *Daphnia magna*. *Ecotoxicol. Environ. Saf.* **2006**, *63*, 451−455.

(4) Banasiak, U.; Caldas, E. D.; Funk, S. *Pesticide Residues in Food 2009*; FAO: Rome, Italy, 2009; pp 33−34

(5) Oliveira, F. A.; Reis, L. P.; Soto-Blanco, B.; Melo, M. M. Pesticides residues in the *Prochilodus costatus* (Valenciennes, 1850) fish caught in the Sao Francisco River, Brazil. *J. Environ. Sci. Health, Part B* **2015**, *50*, 398−405.

(6) Wang, X.; Jia, G.; Qiu, J.; Diao, J.; Zhu, W.; Lv, C.; Zhou, Z. Stereoselective degradation of fungicide benalaxyl in soils and cucumber plants. *Chirality* **2007**, *19*, 300−306.

(7) Qin, F.; Gao, Y. X.; Guo, B. Y.; Xu, P.; Li, J. Z.; Wang, H. L. Environmental behavior of benalaxyl and furalaxyl enantiomers in agricultural soils. *J. Environ. Sci. Health, Part B* **2014**, *49*, 738−746.

(8) Wang, Y.; Guo, B.; Gao, Y.; Xu, P.; Zhang, Y.; Li, J.; Wang, H. Stereoselective degradation and toxic effects of benalaxyl on blood and liver of the Chinese lizard *Eremias argus*. *Pestic. Biochem. Physiol.* **2014**, *108*, 34−41.

(9) Xu, P.; Liu, D.; Diao, J.; Lu, D.; Zhou, Z. Enantioselective acute toxicity and bioaccumulation of benalaxyl in earthworm (*Eisenia fedtia*). *J. Agric. Food Chem.* **2009**, *57*, 8545−8549.

(10) Qiu, J.; Wang, Q.; Zhu, W.; Jia, G.; Wang, X.; Zhou, Z. Stereoselective determination of benalaxyl in plasma by chiral high-performance liquid chromatography with diode array detector and application to pharmacokinetic study in rabbits. *Chirality* **2007**, *19*, 51−55.

(11) Gu, X.; Wang, P.; Liu, D.; Lv, C.; Lu, Y.; Zhou, Z. Stereoselective degradation of benalaxyl in tomato, tobacco, sugar beet, capsicum, and soil. *Chirality* **2008**, *20*, 125−129.

(12) Goncalves, C. M.; Esteves da Silva, J. C. G.; Alpendurada, M. F. Evaluation of the pesticide contamination of groundwater sampled over two years from a vulnerable zone in portugal. *J. Agric. Food Chem.* **2007**, *55*, 6227−6235.

(13) Patakioutas, G. I.; Karras, G.; Hela, D.; Albanis, T. A. Pirimiphos-methyl and benalaxyl losses in surface runoff from plots cultivated with potatoes. *Pest Manage. Sci.* **2002**, *58*, 1194−1204.

(14) Guan, Y. F.; Wang, J. Z.; Ni, H. G.; Zeng, E. Y. Organochlorine pesticides and polychlorinated biphenyls in riverine runoff of the Pearl River Delta, China: assessment of mass loading, input source and environmental fate. *Environ. Pollut.* **2009**, *157*, 618−624.

(15) Huang, L.; Lu, D.; Diao, J.; Zhou, Z. Enantioselective toxic effects and biodegradation of benalaxyl in *Scenedesmus obliquus*. *Chemosphere* **2012**, *87*, 7−11.

(16) Laabs, V.; Wehrhan, A.; Pinto, A.; Dores, E.; Amelung, W. Pesticide fate in tropical wetlands of Brazil: an aquatic microcosm study under semi-field conditions. *Chemosphere* **2007**, *67*, 975−989.

(17) Cuppen, J. G. M.; Crum, S. J. H.; Van den Heuvel, H. H.; Smidt, R. A.; Van den Brink, P. J. Effects of a mixture of two insecticides in freshwater microcosms: I. Fate of chlorpyrifos and lindane and responses of macroinvertebrates. *Ecotoxicology* **2002**, *11*, 165−180.

(18) Van den Brink, P. J.; Crum, S. J.; Gylstra, R.; Bransen, F.; Cuppen, J. G.; Brock, T. C. Effects of a herbicide-insecticide mixture in freshwater microcosms: risk assessment and ecological effect chain. *Environ. Pollut.* **2009**, *157*, 237−249.

(19) Colombo, V.; Mohr, S.; Berghahn, R.; Pettigrove, V. J. Structural changes in a macrozoobenthos assemblage after imidacloprid pulses in aquatic field-based microcosms. *Arch. Environ. Contam. Toxicol.* **2013**, *65*, 683−692.

DOI: 10.1021/acs.jafc.5b01448
J. Agric. Food Chem. 2015, 63, 5205−5211

JOURNAL OF AGRICULTURAL AND FOOD CHEMISTRY

Article

pubs.acs.org/JAFC

Effects of Postweaning Administration of Conjugated Linoleic Acid on Development of Obesity in Nescient Basic Helix−Loop−Helix 2 Knockout Mice

Yoo Kim,[†] Daeyoung Kim,[‡] Deborah J. Good,[§] and Yeonhwa Park*[,†]

[†]Department of Food Science and [‡]Department of Mathematics and Statistics, University of Massachusetts, Amherst, Massachusetts 01003, United States

[§]Department of Human Nutrition, Foods and Exercise, Virginia Tech, Blacksburg, Virginia 24061, United States

ABSTRACT: Conjugated linoleic acid (CLA) has been reported to prevent body weight gain and fat accumulation in part by improving physical activity in mice. However, the effects of postweaning administration of CLA on the development of obesity later in life have not yet been demonstrated. The current study investigated the role of postweaning CLA treatment on skeletal muscle energy metabolism in genetically induced inactive adult-onset obese model, nescient basic helix−loop−helix 2 knockout (N2KO) mice. Four-week-old male N2KO and wild type mice were fed either control or a CLA-containing diet (0.5%) for 4 weeks, and then CLA was withdrawn and control diet provided to all mice for the following 8 weeks. Postweaning CLA supplementation in wild type animals, but not N2KO mice, may activate AMP-activated protein kinase (AMPK) and peroxisome proliferator-activated receptor-δ (PPARδ) as well as promote desensitization of phosphatase and tensin homologue (PTEN) and sensitization of protein kinase B (AKT) at threonine 308 in gastrocnemius skeletal muscle, improving voluntary activity and glucose homeostasis. We suggest that postweaning administration of CLA may in part stimulate the underlying molecular targets involved in muscle energy metabolism to reduce weight gain in normal animals, but not in the genetically induced inactive adult-onset animal model.

KEYWORDS: *conjugated linoleic acid, childhood obesity, voluntary activity, glucose homeostasis, AMP-activated protein kinase*

INTRODUCTION

Since 1980, the prevalence of childhood obesity has almost tripled.[1,2] Along with overnutrition, lack of physical activity during the childhood period is one of the significant contributing factors to the development of childhood obesity. Similar to adult obesity, childhood obesity is known to be associated with the increased risk of chronic metabolism diseases.[3,4] Even though early childhood has been considered to be critical for health later in life, most studies in humans and animals have mainly addressed the effects of dietary and exercise regimens rather than focusing on early-onset interventions during critical developmental periods.[5]

Conjugated linoleic acid (CLA) is a term describing a mixture of 18-carbon unsaturated fatty acid isomers with conjugated double bonds. The name, CLA, was first used when its anticancer activities were reported in 1987.[6] Since then, other biological activities of CLA have been reported, including its effects on prevention of atherosclerosis development, modulation of immune responses, promotion of young animal growth, and modulation of body composition, particularly reduction of body fat and improvement of lean and bone masses.[7] It has been suggested that CLA reduces body fat by multiple biochemical mechanisms, including increased energy expenditure, modulated adipogenesis, and/or enhanced fatty acid β-oxidation.[7,8]

The beneficial effects of CLA supplementation during the obesity onset period in nescient basic helix−loop−helix 2 (Nhlh2) knockout mice (N2KO) have been previously reported.[9] Targeted deletion of the Nhlh2 transcription factor expressed in the hypothalamus precedes adult-onset obesity in mice, resulting from a disruption of the hypothalamic−pituitary axis. While N2KO mice have normal levels of food intake, their spontaneous voluntary movement is decreased by more than 50% in both genders.[10] It was suggested that CLA supplementation in young N2KO animals prevented excessive weight gain by improving voluntary activity.[9] However, it is not clear if supplementation of CLA during the preobesity stage would benefit later in life, as was reported in nonobese animals.[11] Thus, the purpose of this study was to determine the effects of CLA supplementation during the early growth period in N2KO animals on the development of obesity and symptoms of type 2 diabetes later in life.

MATERIALS AND METHODS

Materials. CLA was provided by Natural Lipids Ltd. AS (Hovdebygda, Norway). The CLA used consisted of 80.7% CLA (37.8% *cis*-9,*trans*-11, 37.6% *trans*-10,*cis*-12, and 5.3% other CLA isomers) and 13.7% oleic acid, 3.2% stearic acid, 0.4% palmitic acid, 0.2% linoleic acid, and 1.8% unknown. Semipurified powdered diet (TD07518) was obtained from Harlan Laboratories (Madison, WI). Serum triacylglyceride (TG), glucose, and total cholesterol assay kits were purchased from Genzyme Diagnostics (Charlottetown, PE, Canada). A DC protein assay kit (Bio-Rad, Hercules, CA) was used for protein quantitation. Rabbit antibodies for phosphorylated AMP-activated protein kinase α (p-AMPKα), AMPKα, phosphorylated

Received: February 12, 2015
Revised: May 13, 2015
Accepted: May 15, 2015
Published: May 15, 2015

ACS Publications © 2015 American Chemical Society

DOI: 10.1021/acs.jafc.5b00840
J. Agric. Food Chem. 2015, 63, 5212−5223

Table 1. Composition of Experimental Diet

ingredient	amount (g/kg)
casein, "vitamin-free" tested	169.1
L-cystine	2.2
sucrose	100
cornstarch	288.5
maltodextrin	132
cellulose	50
soybean oil	195
CLA or soybean oil	5
mineral mix, AIN-93M-MX (TD 94049)	42.8
vitamin mix, AIN-93-VX (TD 94047)	12.4
choline bitartrate	3
tert-butylhydroquinone	0.04
total	1000

phosphatase and tensin homologue (p-PTEN), phosphorylated phosphoinositide-dependent kinase (p-PDK), phosphorylated protein kinase B at threonine 308 (p-Akt Thr308) and serine 473 (p-Akt Ser473), Akt, and superoxide dismutase 2 (SOD2) were obtained from Cell Signaling (Berberly, MA). Rabbit antibodies for peroxisome proliferator-activated receptor γ coactivator 1α (PGC-1α), sirtuin 1 (SIRT1), peroxisome proliferator-activated receptor-δ (PPARδ), nuclear respiratory factor 1 (NRF-1), mitochondrial transcription factor A (Tfam), cytochrome *c* (Cyt C), cytochrome c oxidase (COX IV), insulin receptor substrate 1 (IRS-1), glucose transporter type 4 (GLUT4), and β-actin were purchased from Santa Cruz Biotechnology, Inc. (Santa Cruz, CA). Horseradish peroxidase-conjugated goat antirabbit IgG antibody was obtained from Boston Bioproducts Inc. (Ashland, MA). Other chemicals used were purchased from either Sigma Chemical Co. (St. Louis, MO) or Fisher Scientific (Pittsburgh, PA).

Animals and Diet. All animal work was conducted in compliance with the Institutional Animal Care and Use Committee at the University of Massachusetts. As described in a previous report,[10] 129 Sv/J male offspring mice were obtained through inbreeding between heterozygous male and female breeders. Litters were housed together with dams until weaning. At 3 weeks old, all male mice were biopsied (0.5 cm tail) for genotyping. Ten wild type and eight N2KO mice were selected for this study and then placed in individual wire-bottomed cages on a 12 h:12 h light:dark cycle in a temperature- and humidity-controlled room. During a 1 week acclimatization period, all mice were fed a semipurified powdered control diet (20 w/w % fat) to induce obesity in rodents[9,12,13] and were subjected to a baseline test for voluntary movement and glucose tolerance in serum. On the basis of body weight, all animals in different genotype groups (wild type and N2KO) were divided into two diet groups and fed either control or 0.5% CLA containing diet for 4 weeks. Then, all animals received the control diet for 8 weeks. Previously it was determined that feeding CLA for 4 weeks in mice was enough to result in changes in body composition as well as changes in activity levels.[14,15] Moreover, it was reported that most CLA remaining in the tissues (liver, adipose tissue, and muscle) returned to levels comparable to that of control animals at 8 weeks postwithdrawal.[14] Thus, we selected 8 weeks post CLA supplementation in the current study. The dose of CLA was determined on the basis of previous reports that supplementing 0.5% CLA for 2−4 weeks in rats led to a serum level range of 23−120 μM and serum levels of CLA after supplementation of 0.8−3.2 g per day for 2 months in humans ranged from 23 to 200 μM.[16,17]

The compositions of diets are shown in Table 1. Diet and water were available ad libitum throughout the experiment and were provided freshly twice per week. Body weight and food intake were monitored weekly. At the end of the study, mice were fasted for 6 h and sacrificed by CO_2 asphyxiation. Blood was immediately collected by cardiac puncture, and the internal organs (liver, heart, kidney, spleen, and white adipose tissues including epididymal, retroperitoneal, and mesenteric fat pads) were weighed at sacrifice.

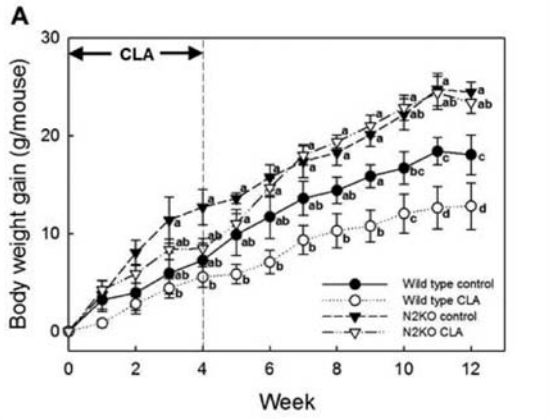

Effect	Genotype (G)	CLA (D)	Time (T)	G x T
Week (0-12)	0.0001	n.s.	< 0.0001	0.0064
Week (0-4)	< 0.0001	0.0047	< 0.0001	n.s.
Week (5-12)	0.0007	n.s.	< 0.0001	n.s.

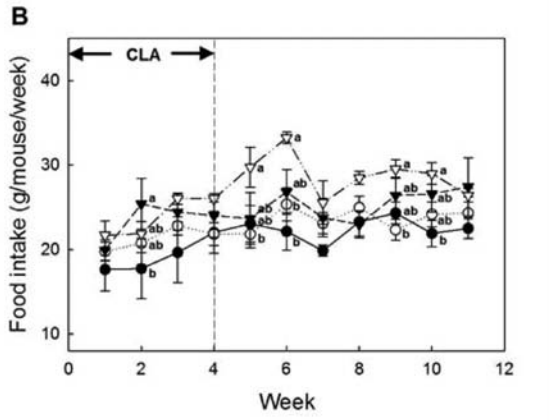

Effect	Genotype (G)	CLA (D)	Time (T)	G x D x T
Week (0-12)	0.0252	n.s.	< 0.0001	0.0048
Week (0-4)	n.s.	n.s.	0.0006	0.0065
Week (5-12)	0.0046	n.s.	0.0002	n.s.

Figure 1. Effect of postweaning administration of conjugated linoleic acid (CLA) on body weight (A) and food intake (B) in wild type and nescient helix−loop−helix knockout (N2KO) mice. Mice were treated with either control or 0.5% CLA diets until 4 weeks and then switched diets from CLA supplementation to control for the following 8 weeks. Values represent means ± SE (n = 3−5). n.s.: not significant. Means with different letters at the same time points are significantly different (P < 0.05). P values in the table are from two-way repeated measures ANOVA with the slice option in the Least Square Means statement to compare the group differences at each week.

Voluntary Movement Measurement (Nonexercise Physical Activity Test). Nonexercise physical activity (voluntary movement) was recorded using LoliTrack Quatro Video Tracking Software Version 1.0 (Loligo Systems, Tjele, Denmark) with a high-resolution infrared camera under dark conditions. This tracking system simultaneously monitored four mice placed in individual cages (30 × 46 × 40 cm) during the dark phase (5:00 pm−5:00 am) once a month with free access to diet and water (provided as HydroGel, Clear H_2O, Portland, ME). Movement data for 8 h (7:00 pm−3:00 am) excluding the first 2 h (5:00 pm−7:00 pm) during the early phase for adapting to environmental change and 2 h (3:00 am−5:00 am) during the late phase due to lack of movement were analyzed.

Serum Parameters. The levels of glucose, total cholesterol, and TG in serum separated by centrifugation at 3000*g* for 20 min at 4 °C were

DOI: 10.1021/acs.jafc.5b00840
J. Agric. Food Chem. 2015, 63, 5212−5223

Table 2. Organ and Adipose Tissue Weights[a]

	body weight (%)						
	wild type		N2KO		effect (P value)		
	control	CLA	control	CLA	genotype	CLA	interaction
			Adipose Tissue				
epididymal fat	6.89 ± 0.37^{ab}	4.56 ± 1.12^{b}	9.39 ± 0.92^{a}	7.89 ± 0.69^{ab}	0.007	(0.0545)	n.s.
retroperitoneal fat	1.47 ± 0.18	1.05 ± 0.18	1.57 ± 0.16	1.39 ± 0.07	n.s.	n.s.	n.s.
mesenteric fat	4.12 ± 0.29	3.82 ± 0.42	4.74 ± 0.86	5.25 ± 0.23	0.0448	n.s.	n.s.
total	12.5 ± 0.30^{ab}	9.43 ± 1.68^{b}	15.7 ± 1.61^{a}	14.5 ± 0.51^{a}	0.007	n.s.	n.s.
			Organ				
liver	3.47 ± 0.24^{bc}	4.37 ± 0.22^{a}	2.80 ± 0.11^{c}	4.21 ± 0.22^{ab}	n.s.	0.0002	n.s.
heart	0.37 ± 0.02	0.41 ± 0.02	0.34 ± 0.01	0.46 ± 0.04	n.s.	0.0234	n.s.
kidney	1.13 ± 0.08^{ab}	1.38 ± 0.08^{a}	0.89 ± 0.05^{b}	1.16 ± 0.11^{ab}	0.0261	0.0118	n.s.
spleen	0.26 ± 0.03	0.23 ± 0.01	0.21 ± 0.03	0.24 ± 0.04	n.s.	n.s.	n.s.

[a]Values represent means ± SE (n = 3–5). Means with different superscripts within the same row are significantly different ($P < 0.05$). P values in the table are from two-way ANOVA. Abbreviations: N2KO, nescient helix–loop–helix knockout mice; CLA, conjugated linoleic acid; n.s., not significant.

determined using commercial kits as specified by the manufacturer's instructions.

Glucose Tolerance. As described previously,[18] intraperitoneal glucose tolerance tests (IGTT) were conducted every 4 weeks. All mice underwent 6 h fasting and then were subjected to baseline measurement of blood glucose levels at 0 min. Blood was collected from the tail vein using a blood glucose meter, Advocate Redi-Code^{+} (Advocate Meters Inc., Dorado, Puerto Rico). Subsequently, 30% glucose solution (2.0 g of glucose/kg of body weight) was administered through intraperitoneal injection and then blood glucose levels were monitored at 15, 30, 60, 90, and 120 min. Collected data were calculated as the areas under the curve (AUC) with SigmaPlot 11.0 (Systat Software, Inc., San Jose, CA).

Western Blot Analysis. The frozen gastrocnemius skeletal muscle tissue was ground, and 50 mg aliquots were prepared and stored at −80 °C until analysis. Each sample was homogenized in premixed lysis radioimmune precipitation assay (RIPA; 50 mM Tris-HCl, 10 mM NaCl, 5 mM $MgCl_2$, and 0.5% NP-40, pH 8.0) buffer (Boston Bioproducts Inc., Ashland, MA), protease inhibitor cocktail (Sigma-Aldrich, St. Louis, MO), and phosphatase inhibitor cocktail (Thermo Scientific, Rockford, IL) and then lysed on ice for 2 h and centrifuged at 12000g for 20 min at 4 °C. The concentration of protein from tissue lysate was determined using the DC protein assay kit. The normalized lysates (37.5 μg/mL of protein) were separated by an 8–15% (w/v) sodium dodecyl sulfate–polyacrylamide gel and transferred to a polyvinylidene fluoride membrane (Millipore, Bedford, MA). After incubation with the appropriate primary rabbit antibodies, membranes were treated with horseradish peroxidase-conjugated goat antirabbit IgG antibody for 1 h at room temperature. Detection was performed using Enhanced Chemiluminescence solution (Bio-Rad, Hercules, CA) with an Image Station 4000MM instrument (Carestream Health, New Heaven, CT). The band density was normalized by β-actin intensity as an internal control. The results were quantified using ImageJ software (U.S. National Institutes of Health).

Statistical Analyses. All data analyses were performed by two-way analysis of variance (ANOVA) followed by the PROC MIXED procedure with Least Squares (LS) Means statement of the SAS software (Version 9.3, SAS Institute Inc., Cary, NC). For data on body weight, food intake, voluntary movement, and glucose tolerance test, two-way repeated measures ANOVA and the slice option in the LS means statement to examine the group differences at each time point with PROC MIXED were used. For internal organ, adipose tissue weight, and serum parameter data, two-way ANOVA with PROC MIXED was conducted. The experimental groups were compared by the multiple comparison basic Tukey–Kramer method in SAS. The Dunnett test in SAS was used for the relative protein expression level. Data are shown as the means ± SE; P values less than 0.05 are reported as statistically significant.

RESULTS

Body Weights and Food Intake. There was significant genotype effect on weight gain; N2KO mice had significantly greater body weight gain over wild type mice (P = 0.0001, Figure 1A). CLA supplementation during the first 4 weeks resulted in no significant different effects on weight gain overall, although the wild type CLA-fed group had the least body weight gain among all treatment groups during the whole experimental period (Figure 1A).

Overall N2KO mice consumed more food than wild type animals during the experimental period (P = 0.0252). No significant differences in food intake were observed between controls and CLA treatment during the preobese period, although the N2KO CLA group temporarily consumed more food right after withdrawal of CLA supplementation for 2 weeks (N2KO control; 50.5 ± 5.6 g vs N2KO CLA; 63.0 ± 2.3 g, the mean ± SE). Although three-way interaction among genotype, CLA, and time was observed, there was no significant two-way interaction in overall food intake (Figure 1B).

Tissue and Organ Weights. Total adipose tissue weights, including epididymal, mesenteric, and retroperitoneal adipose tissue, and internal organ weights (liver, heart, kidney, and spleen) are shown in Table 2. Epididymal, mesenteric, and total adipose tissue weights were significantly increased in N2KO animals in comparison to wild types (all P values were less than 0.05), but no significant effects of genotypes was observed for retroperitoneal fat weights. No significant effects of CLA supplementation for the first 4 weeks were observed for adipose tissue weights.

No differences of genotype effects were observed in the liver, heart, and spleen weights, while significant genotype effects were observed for the kidney weights (P = 0.0261). CLA-fed animals had significantly increased liver, heart, and kidney weights in comparison to control animals. No significant interaction between genotype and CLA was observed in any tissue or organ weight.

Voluntary Movement (Nonexercise Physical Activity). To evaluate the effects of postweaning administration of CLA on physical activity, voluntary movement (nonexercise physical activity) was measured every 4 weeks. Travel distance as total (19:00–03:00) and two time periods, early (19:00–23:00) and late (23:00–03:00), are shown in Figure 2A–C. The changes in total travel distance over time are shown in Figure 2D.

DOI: 10.1021/acs.jafc.5b00840
J. Agric. Food Chem. 2015, 63, 5212–5223

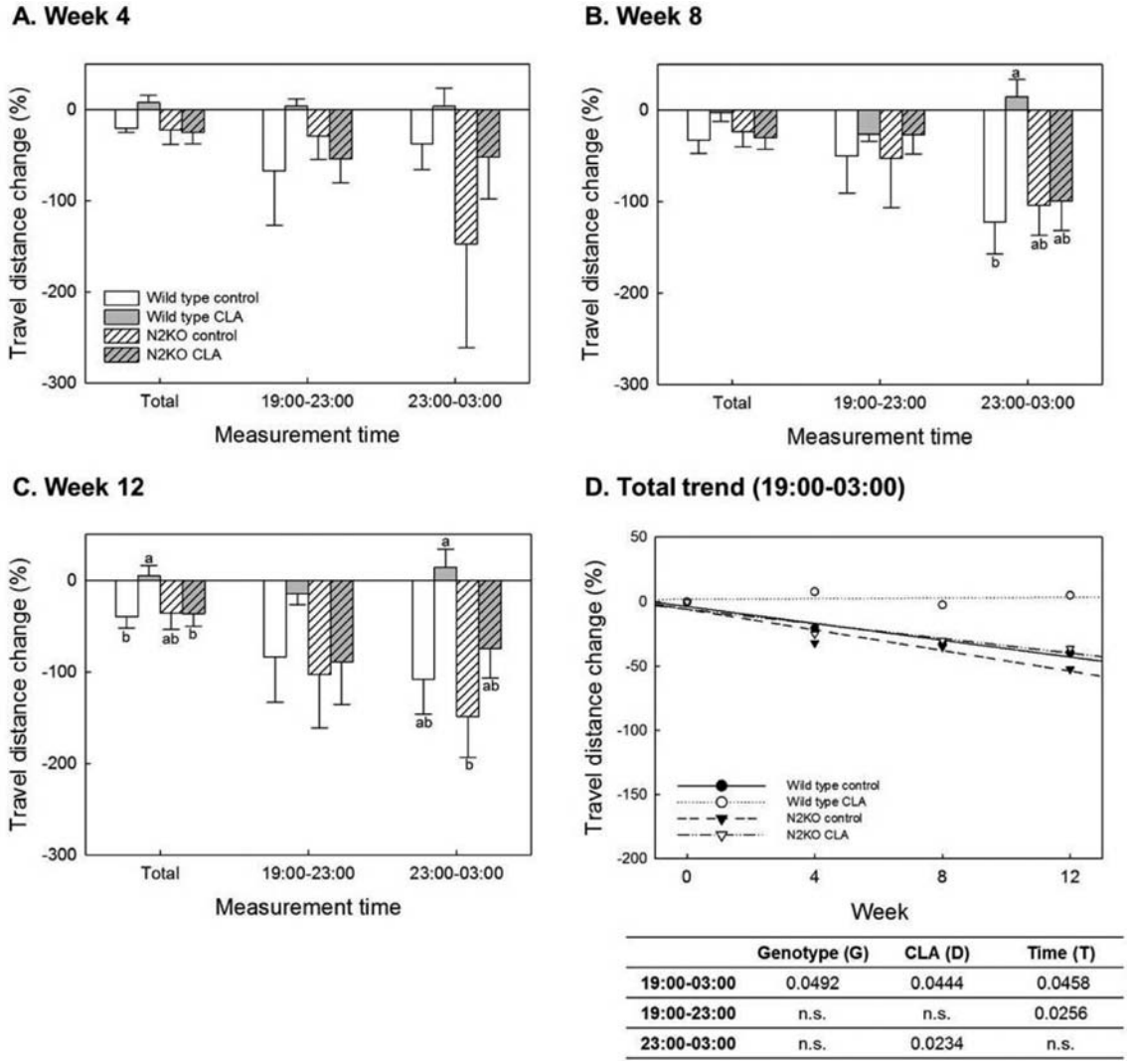

	Genotype (G)	CLA (D)	Time (T)
19:00-03:00	0.0492	0.0444	0.0458
19:00-23:00	n.s.	n.s.	0.0256
23:00-03:00	n.s.	0.0234	n.s.

Figure 2. Effect of postweaning conjugated linoleic acid (CLA) treatment on voluntary movement (nonexercise physical activity) in wild type and nescient helix−loop−helix knockout (N2KO) mice. Mice were fed control or 0.5% CLA diets for 4 weeks (from 4 to 8 weeks old) and then changed diets from CLA-containing to control for the next 8 weeks (from 9 to 17 weeks old). Voluntary movement was recorded during 17:00−05:00 every 4 weeks for 12 weeks (A−C). The data show different time points (total, 19:00−23:00 and 23:00−03:00). Total stands for movement measure during 19:00−03:00, divided into 4 h segments (19:00−23:00 and 23:00−03:00) representing the early or late phase of the dark cycle, respectively. (D) Trend for total travel distances (19:00−03:00). Values represent means ± SE (n = 3−5). n.s.: not significant. Means with different letters at the same time points are significantly different ($P < 0.05$).P values in the tables are from two-way repeated measures ANOVA with the Least Square Means statement to compare the group differences at each time point.

Consistent with the previous reports,[9,19] N2KO mice showed a significantly decreasing tendency of activity in comparison to wild type animals (P = 0.0492). It was evident that all experimental groups except the wild type CLA group showed declining activity over time (Figure 2D), with overall CLA effects being significant (P = 0.0444), particularly during the late period (P = 0.0234). No difference in activity between N2KO groups was observed, while CLA-fed wild types, but not N2KO animals, maintained activity levels throughout the experiment. This suggests that supplementation of CLA during the preobese state prevented reduction of voluntary movement over time in wild types but not in N2KO animals.

Glucose Tolerance Test. To determine the effects of postweaning CLA treatment on glucose homeostasis, glucose tolerance tests were conducted every 4 weeks (Figure 3A−D). N2KO mice showed glucose intolerance in comparison to wild type animals (P = 0.0061). In addition, there was a significant overall time effect (P = 0.0148), suggesting these animals develop glucose intolerance with aging along with the high-fat diet as used in this study. No significant CLA effect was observed; however, the CLA-treated wild type animals showed improved glucose tolerance at week 12 in comparison to wild-type controls, even after CLA withdrawal for 8 weeks (Figure 3E, $P < 0.0001$ for the interaction effect between CLA and time). This suggests that postweaning CLA administration may improve glucose tolerance in wild types but not in N2KOs.

Serum Parameters. The serum levels of TG, glucose, and total cholesterol were analyzed and are shown in Table 3. There were no genotype or CLA effects on these markers in this study, except glucose levels for CLA (P = 0.036). No interactions between genotype and CLA were observed in any of these parameters.

Effects on Muscle Energy Metabolism. To assess whether postweaning administration of CLA contributes to improved

DOI: 10.1021/acs.jafc.5b00840
J. Agric. Food Chem. 2015, 63, 5212−5223

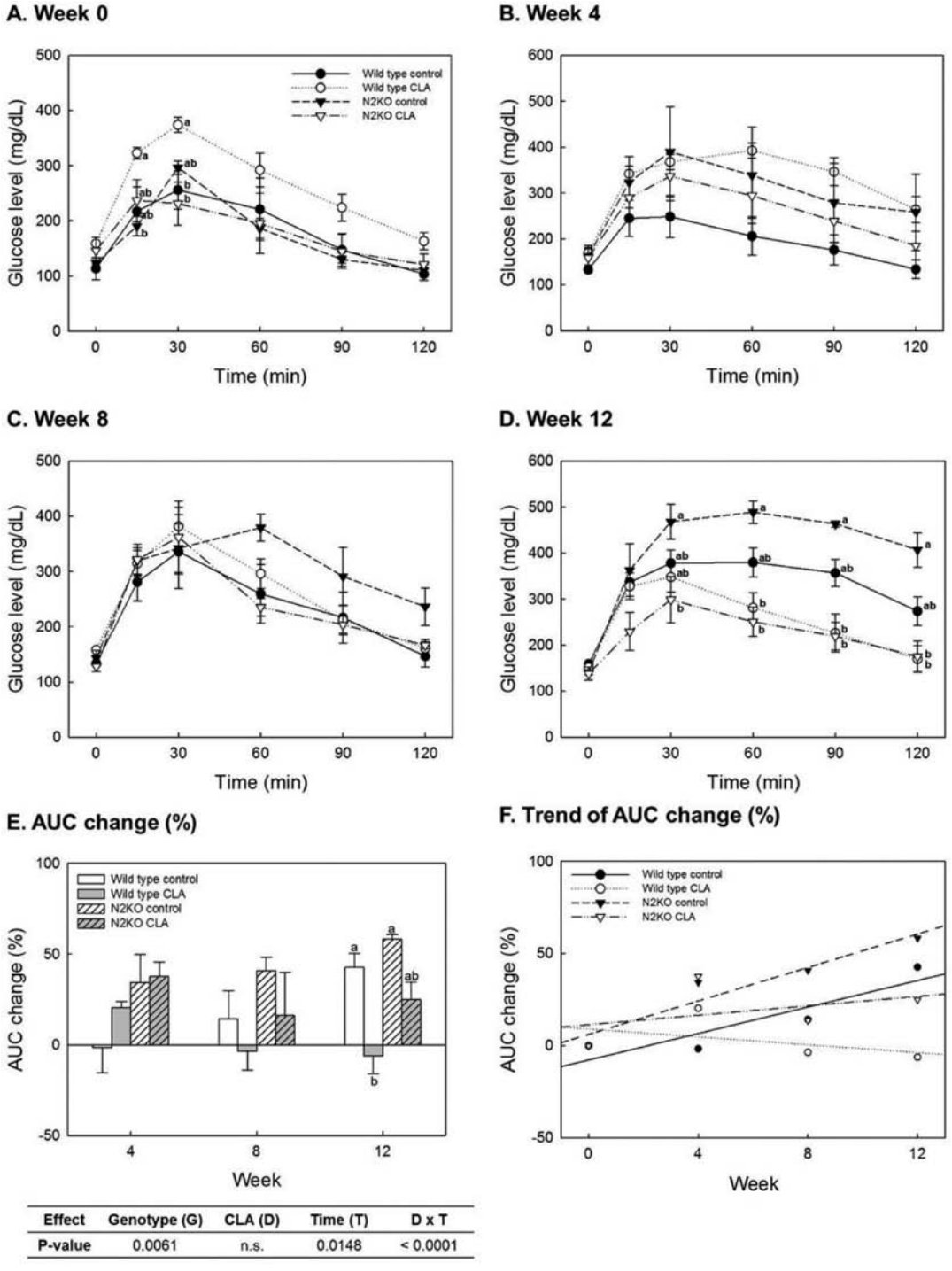

Effect	Genotype (G)	CLA (D)	Time (T)	D x T
P-value	0.0061	n.s.	0.0148	< 0.0001

Figure 3. Effect of time-specific postweaning conjugated linoleic acid (CLA) treatment on glucose levels (A–D), the area under the curve (AUC) change (E), and the overall trend of AUC change (F) in wild type and nescient helix–loop–helix knockout (N2KO) mice. Glucose tolerance was measured every 4 weeks during the whole experimental period. Blood was collected from the tail vein, and glucose levels were determined at 0 min for a baseline. Then glucose solution was administrated by intraperitoneal injection and measured at five different time points (15, 30, 60, 90, and 120 min). The data (E) are changed values of AUC and main effect analysis of AUC change dependent on different time points in the table. Values represent means ± SE (n = 3–5). n.s.: not significant. Means with different letters at the same time points are significantly different ($P < 0.05$). P values in the table are from two-way repeated measures ANOVA with the slice option in the Least Square Means statement to compare the group differences at each time point.

skeletal muscle energy metabolism, we investigated the AMPK signaling pathway, a master sensor to maintain energy homeostasis (Figure 4). Total AMPKα was measured, as it is known that two subunits (α1 and α2) are regulated differentially and overall AMPKα activity is more important.[20] There were no overall effects of any genotype or CLA effects on AMPKα expression, but interaction between them was observed (P = 0.0471) (Figure 4B). For phosphorylated AMPKα (the active form of AMPKα), N2KO animals had significantly lower levels of p-AMPKα in comparison to wild type animals (P = 0.0399). The mice supplemented CLA for the first 4 weeks showed significantly higher expression of phosphorylation of AMPKα in comparison

DOI: 10.1021/acs.jafc.5b00840
J. Agric. Food Chem. 2015, 63, 5212–5223

Table 3. Serum Parameters[a]

	concentration (mg/dL)						
	wild type		N2KO		effect (*P* value)		
	control	CLA	control	CLA	genotype	CLA	interaction
triglyceride	120.3 ± 18.3	99.2 ± 10.6	112.9 ± 2.0	128.4 ± 20.8	n.s.	n.s.	n.s.
glucose	189.8 ± 11.2	169.8 ± 15.9	286.8 ± 55.3	168.5 ± 35.3	n.s.	0.036	n.s.
total cholesterol	267.4 ± 35.0	328.5 ± 25.4	261.9 ± 18.9	232.1 ± 18.2	n.s.	n.s.	n.s.

[a]Values represent means ± SE (n = 3−5). P values in the table are from two-way ANOVA. Abbreviations: N2KO, nescient helix−loop−helix knockout mice; CLA, conjugated linoleic acid; n.s., not significant.

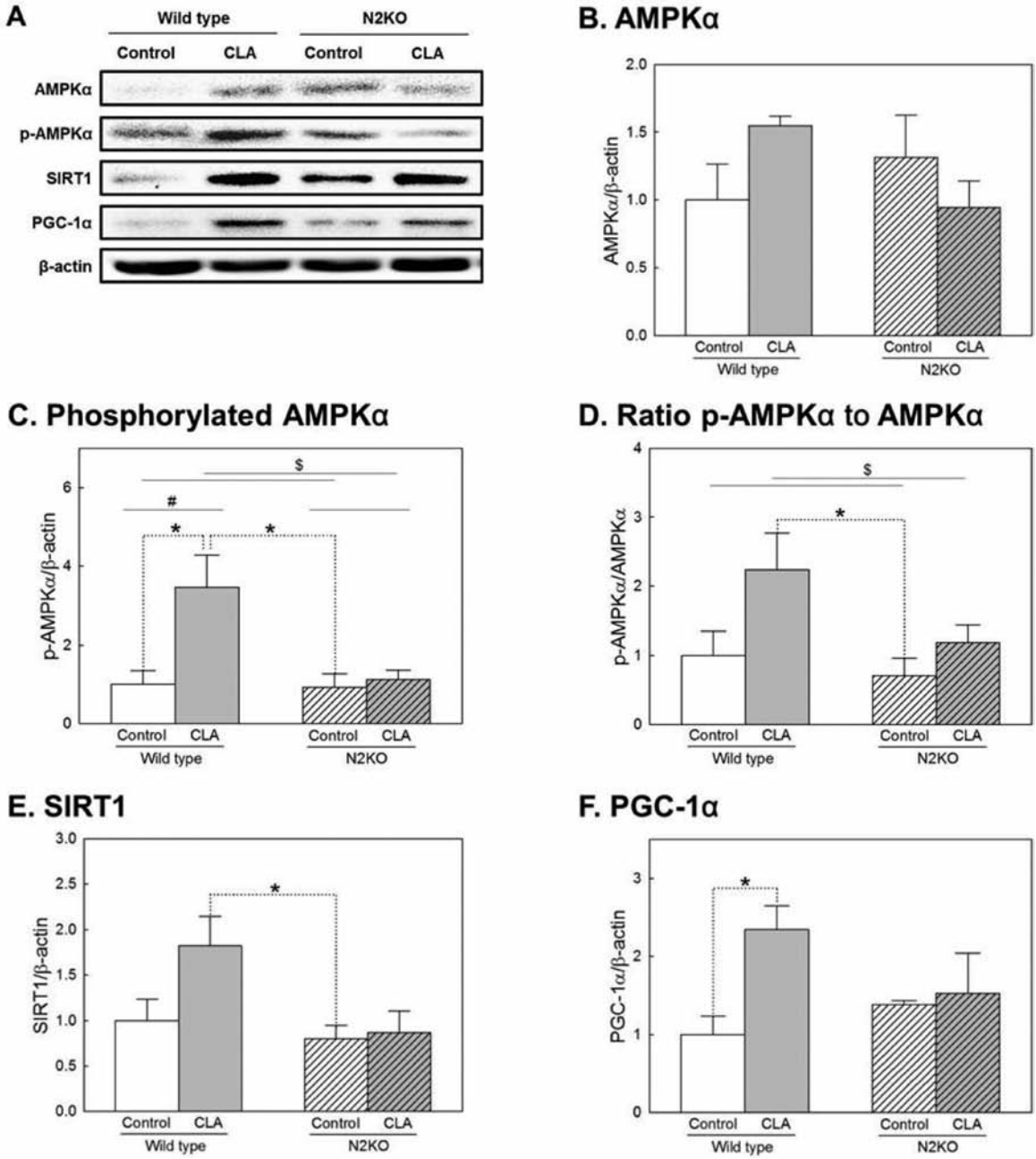

Figure 4. Effect of postweaning treatment of conjugated linoleic acid (CLA) on protein expression of total and phosphorylated AMP-activated protein kinase (AMPK), SIRT1, and PGC-1α from the gastrocnemius muscle. Pictures show representative results (A). The graph expresses the relative expression levels of total AMPKα (B), phosphorylated AMPKα at Threonine 172 (p-AMPKα; C), a ratio of phosphorylated AMPKα to total AMPK expression (D), sirtuin1 (SIRT1; E) and peroxisome proliferator-activated receptor-γ coactivator 1-α (PGC-1α; F). All data were normalized by β-actin. Values represent means ± SE (n = 3−5). # and $ denote significant overall genotype and CLA effect, respectively (P < 0.05). * denotes a significant difference in comparison to the wild type or N2KO control group (P < 0.05). N2KO: nescient helix−loop−helix knockout.

DOI: 10.1021/acs.jafc.5b00840
J. Agric. Food Chem. 2015, 63, 5212−5223

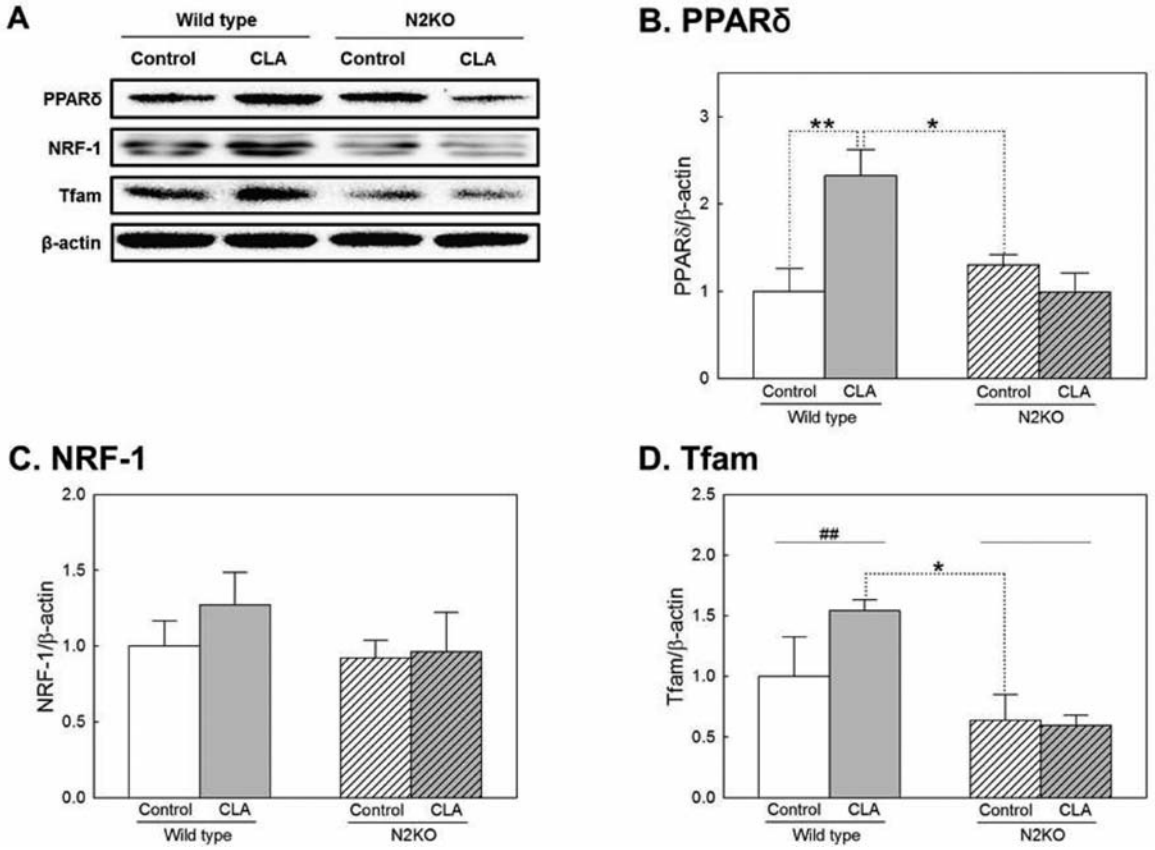

Figure 5. Effect of postweaning treatment of conjugated linoleic acid (CLA) on mitochondrial biogenesis-related factors from the gastrocnemius muscle. Pictures represent results of immunoblotting (A). The relative expression levels of peroxisome proliferator-activated receptor δ (PPARδ; B), nuclear respiratory factor 1 (NRF-1; C), and mitochondrial transcription factor A (Tfam; D) were determined and normalized using β-actin as the internal control. Values represent means ± SE (n = 3−5). ## denotes a significant overall genotype effect ($P < 0.01$). * denotes a significant difference in comparison to the wild type or N2KO control group (*, $P < 0.05$; **, $P < 0.01$). N2KO: nescient helix−loop−helix knockout.

to the control groups (Figure 4C, $P = 0.0264$); in particular, the wild type CLA group in comparison to the respective control (Figure 4C). In addition, an increased ratio of phosphorylated AMPKα to AMPKα by CLA was observed (Figure 4D, P = 0.0471).

Along with AMPKα, SIRT1 (a NAD-dependent deacetylase) is a key activator of PGC-1α (one major downstream marker for AMPKα). There were no significant effects of genotype and CLA on SIRT1 observed, whereas the wild type CLA group showed increased SIRT1 expression level in comparison to the N2KO control (Figure 4E). The expression of PGC-1α, a master regulator of mitochondrial biogenesis, was also not influenced by genotype or CLA (Figure 4F). However, it was evident that CLA treatment had a greater effect on PGC-1α in comparison to the control diet group in wild type animals.

Effects on Mitochondrial Biogenesis-Related Factors. We further determined the effect of postweaning CLA supplementation on mitochondrial biogenesis in the gastrocnemius muscle. Mitochondria are important organelles in determining oxidative capacity and fatigue resistance, resulting in prolonged endurance capacity.[21−23] For mitochondrial biogenesis several nuclear encoded precursor proteins are involved in this metabolic process;[24−26] among them, we selected PPARδ, NRF-1, and Tfam.

PPARδ is a marker involved in mitochondrial biogenesis as well as muscle type transformation from glycolytic to oxidative fiber.[27] No significant overall effects of genotypes or CLA were observed on PPARδ; however, wild type CLA-fed animals showed significantly greater expression levels of PPARδ in comparison to both control diet groups (Figure 5B). No significant difference in NRF-1, a regulator to mediate nuclear-encoding mitochondrial proteins, was observed in any experimental group (Figure 5C). The expression of Tfam, which is the key regulator for mitochondrial DNA replication and transcription, was significantly downregulated in N2KO mice in comparison to wild type mice (P = 0.0062). The CLA supplemented group in wild type animals showed significantly greater Tfam expression over the control group in N2KO mice (Figure 5D).

To estimate overall mitochondrial relative content, we used an indirect method to measure mitochondrial proteins, including cytochrome c and COX IV, located in the inner membrane of mitochondria.[28,29] Additionally, we tested another mitochondrial protein, superoxide dismutase 2 (SOD2) in the inner mitochondrial matrix, to assess mitochondrial function.[30] The expression levels of cytochrome c were significantly decreased in N2KO mice in comparison to wild type animals (P = 0.0496), but no CLA effects were observed (Figure 6B). No genotype or CLA effects were observed in COX IV (Figure 6C). Overall SOD2 protein levels were significantly reduced in N2KO mice (P = 0.0224), while no effects of CLA were observed (Figure 6D).

Effects on Markers of Glucose Metabolism. Along with assessment of postweaning administration of CLA on

DOI: 10.1021/acs.jafc.5b00840
J. Agric. Food Chem. 2015, 63, 5212−5223

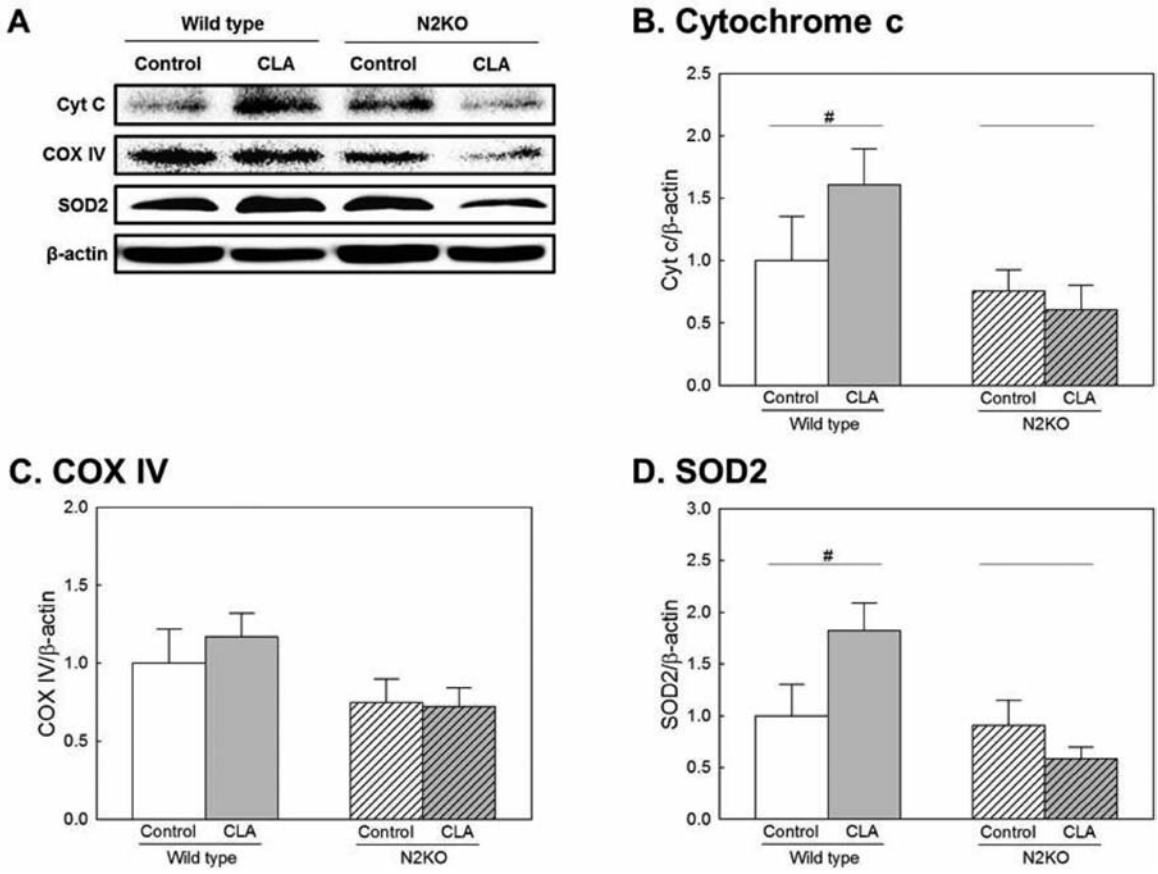

Figure 6. Effect of postweaning treatment of conjugated linoleic acid (CLA) on mitochondrial content and function from the gastrocnemius muscle. Pictures are representative results (A). The relative expression levels of cytochrome *c* (Cyt C, B), cytochrome *c* oxidase (COX IV, C), and superoxide dismutase 2 (SOD2, D) were detected. *β*-Actin was used as the loading control. Data are means ± SE ($n = 3–5$). # denotes a significant overall genotype effect ($P < 0.05$). N2KO: nescient helix–loop–helix knockout. Means with different letters are significantly different ($P < 0.05$).

mitochondrial biogenesis-related factors, we determined the effects of CLA supplementation during the first 4 weeks on markers of glucose metabolism in the gastrocnemius muscle. The expression levels of IRS-1, a member of the IRS family regulating insulin signaling, were significantly decreased in N2KO animals over wild types, while no CLA effects were observed (Figure 7B, overall genotype effect, $P = 0.0335$).

A downstream biomarker of IRS (PTEN, attributed to negatively regulate the AKT signaling pathway) significantly reduced phosphorylation (inactive form of PTEN) in N2KO mice in comparison to wild type animals ($P = 0.0094$). No significant effect of postweaning administration of CLA was observed on PTEN expression in N2KO mice. However, CLA-treated wild type animals significantly upregulated phosphorylated PTEN in comparison to the respective control, while no differences were observed in N2KO animals (Figure 7C).

No difference in protein expression of phosphorylated PDK, a downstream marker of PTEN, was observed for either genotype or CLA (Figure 7D). There were no significant effects of genotypes and CLA on total AKT expressions and phosphorylated AKT (Serine 473) and GLUT4, one of the insulin-regulated glucose transporters (Figure 7E–H). However, we observed marginally increased responses from wild type animals fed CLA on phosphorylated AKT (threonine 308) in comparison to the respective controls ($P = 0.0547$ vs wild-type control and $P = 0.0528$ vs N2KO control, respectively).

DISCUSSION

It was previously reported that supplementation of CLA prevents weight gain and body fat accumulation both during the growth period and in aged N2KO mice.[9,31,32] In particular, CLA increased voluntary activity when supplemented during the growth period.[9,31] Results from the current study suggest that supplementation of CLA in the preobese state may reduce weight gain in normal animals but not in the genetically induced inactive adult-onset animal model, although the stimulation of voluntary activity and improved glucose tolerance remain even after CLA withdrawal in this model.

Previously CLA was reported to be linked with reduced food intake in a number of animal models, although it was not consistent.[14,33,34] Moreover, it was determined that the reduction of food intake by CLA was independent of its effects on body fat reduction.[14,35] Others suggested that CLA reduces food intake by decreasing neuropeptides Y (NPY) and agouti-related protein (AgRP), both of which are known to be related to increased appetite[36] and inducing the storage of glycogen in muscle and liver, which may subsequently serve as satiety signals.[37,38] In the current study, we did not observe any significant differences in food intake during CLA supplementation periods in both genotypes. However, when CLA was withdrawn, apparent compensation of food intake occurred in N2KO animals fed CLA but not in wild type animals, coinciding with greater weight gain during this period (weeks 4–6 in Figure 1A). It is not clear how CLA influenced food intake in these animals; however, these

DOI: 10.1021/acs.jafc.5b00840
J. Agric. Food Chem. 2015, 63, 5212–5223

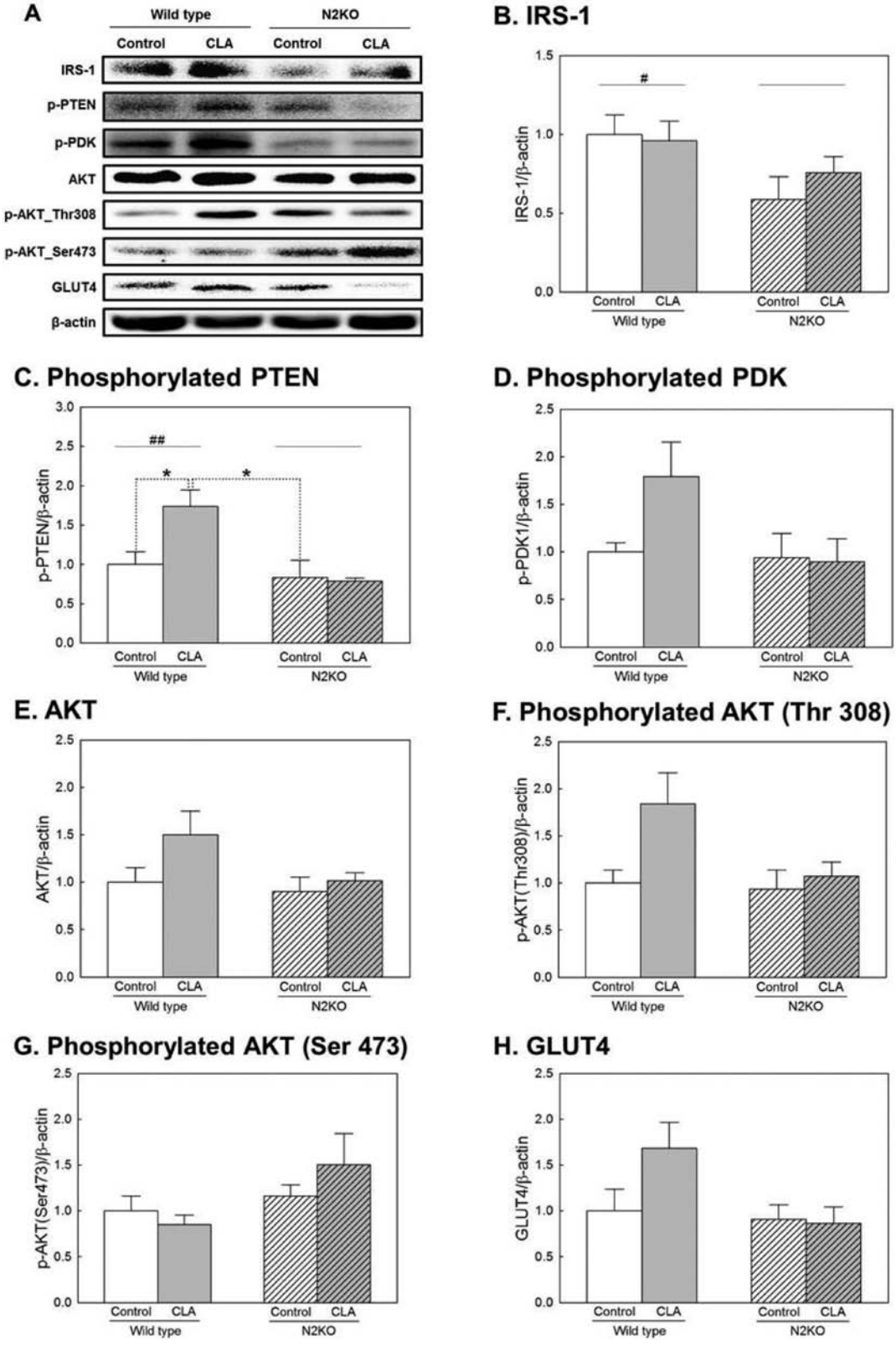

Figure 7. Effect of postweaning treatment of conjugated linoleic acid (CLA) on glucose metabolism from the gastrocnemius muscle. Pictures represent results of Western blotting (A). The graph represents the relative expression levels of insulin receptor substrate 1 (IRS-1; B), phosphorylated phosphatase and tensin homologue (p-PTEN; C), phosphorylated phosphoinositide-dependent kinase (p-PDK; D), protein kinase B (AKT; E), phosphorylated AKT at threonine 308 (p-AKT Thr308; F) and serine 473 (p-AKT Ser473; G), and glucose transporter type 4 (GLUT4; H). All data were normalized by β-actin. Values represent means ± SE ($n = 3–5$). # denotes a significant overall genotype effect (#, $P < 0.05$; ##, $P < 0.01$). * denotes a significant difference in comparison to the wild type or N2KO control group (*, $P < 0.05$). N2KO: nescient helix−loop−helix knockout. P values are from two-way ANOVA.

DOI: 10.1021/acs.jafc.5b00840
J. Agric. Food Chem. 2015, 63, 5212−5223

results suggest that CLA may influence food intake differently in obese animals, which has been previously reported in other animal models.[14,33,34,39]

We observed that N2KO mice had significantly reduced physical activity, consistent with previous reports for N2KO animals.[9,10,40] Overall, postweaning CLA supplementation significantly prevented reduction of voluntary activity levels in comparison to controls, particularly in wild type animals. Intriguingly, our results showed that the effects of CLA on activity during the late phase (23:00−03:00) might remain even after termination of CLA treatment up to 8 weeks, whereas during the early phase (19:00−23:00) there was no significant CLA effect in all experimental groups.

Among various molecular mechanisms to affect increased or maintained physical activity levels, the AMPK signaling pathway has drawn significant attention since the 1990s.[41] An upregulated AMPK signaling pathway is involved in skeletal muscle energy metabolism as well as mitochondrial biogenesis, resulting in enhanced endurance capacity and attenuated exercise intolerance.[42−45] Previously, our group demonstrated the effect of CLA on stimulation of mitochondrial biogenesis through an AMPK signaling pathway.[46] In the same context, our data supported that postweaning administration of CLA might stimulate activation of AMPKα and related factors in wild type but not in N2KO animals.

Wild type animals fed CLA for the first 4 weeks showed improved glucose tolerance over time even after no benefits on weight were observed in comparison to the respective control, suggesting that CLA may have lasting effects on glucose metabolism later in life. On the basis of this observation, we assessed the effects of CLA treatment during the growth period on glucose metabolism through the insulin signaling pathway. Among several measured markers involved in insulin signaling cascades, phosphorylated PTEN and phosphorylated AKT at threonine 308 partially provided evidence regarding how to moderate glucose tolerance in the current study. PTEN and AKT are important effectors of insulin responses mediating glucose uptake and glycogen synthesis in skeletal muscle.[47−50] Our data are consistent with early studies that CLA-specific isomers mediate AKT sensitization.[51,52]

The current results suggest potential benefits of postweaning CLA administration to reduce health risk, as suggested previously.[19,31] This is important, since one potential health concern associated with CLA supplementation is glucose intolerance. We observed a nonsignificant increase in glucose intolerance following CLA supplementation in wild type mice (Figure 3B, week 4); however, when CLA was withdrawn, glucose tolerance improved in the treated groups (week 12 in Figure 3D). As suggested before, this may be due in part to a significant shift of energy metabolism by CLA, such as increased fatty acid β-oxidation associated with reduced glucose utilization.[53,54] However, further studies such as HOMA-IR to better understand glucose and insulin metabolism are needed to determine how postweaning administration of CLA changes energy sources.

As seen in previous studies,[15,55,56] we observed a significant increase in liver weight, as fatty liver, after CLA supplementation. It is unlikely that CLA is directly accumulated in the liver, as levels of CLA in the liver and muscle reached a maximum 1 week for the liver and 2 weeks for muscle after supplementation in mice.[57] Previously it was reported that CLA-fed animals accumulate TG in the liver.[58,59] This is believed to be associated with CLA's dramatic effects on lipid metabolism, particularly in the liver and adipose tissues, increased hepatic lipogenesis, and decreased fat accumulation in adipose tissues.[8,60−62] It is unlikely that an enlarged liver caused by CLA is due to increased glycogen content, as it was previously shown that CLA had no effects on enzyme activities involved in gluconeogenesis.[57] In addition, previous studies reported no pathologically significant observations after 18 months of CLA supplementation or no changes in hepatic gene expressions in lipogenesis from N2KO animals.[9,32,63] Although we provided CLA only during the preobese state and then withdrew CLA, the significant effect of CLA on liver weight still remains. This is consistent with the previous study that withdrawal of CLA did not completely reverse liver enlargement at the end of a 4 week recovery period.[64] Our study might not have enough adaptive time to complete this reversal of CLA's effect. Thus, additional investigation of the relationship between short-term CLA supplementation and changes in hepatic genes should be considered to determine if the liver enlargement caused by CLA is completely reversible or not. Clinical trials with CLA reported no changes or increased markers for liver function, and all were within the normal ranges. In addition, it was reported that a high dose of CLA (14.6 g of *cis*-9,*trans*-11 and 4.7 g of *trans*-10,*cis*-12 CLA per day) for 3 weeks had no changes on markers of liver function in healthy subjects. Thus, it is possible that rodents are more sensitive to CLA's effect in comparison to humans.

In conclusion, CLA supplementation during the preobese state may attenuate reduction of voluntary activity and glucose intolerance after CLA withdrawal in this mouse model. However, it is not sufficient per se to maintain health benefits such as prevention of weight gain and fat accumulation until later life in genetically obese mice. Wild type animals fed CLA may activate AMPKα and PPARδ as well as promote desensitization of PTEN and sensitization of AKT at threonine 308 in gastrocnemius skeletal muscle, improving voluntary activity and glucose homeostasis. We suggest that postweaning administration of CLA may partially stimulate the underlying molecular targets involved in muscle energy metabolism in normal animals but not in the genetically induced inactive adult-onset animal model. The present study should provide a scientific foundation for future trials of targeted application of postweaning CLA intervention in modulating long-term obesity. If further research on genetically predisposed obese mice discovered an appropriate intervention or combination with an additional regime such as exercise, it may be possible to more effectively use it to prevent childhood obesity.

AUTHOR INFORMATION

Corresponding Author

*Y.P.: tel, (413) 545-1018; fax, (413) 545-1262; e-mail, ypark@foodsci.umass.edu.

Funding

This material is based upon work supported by the National Institute of Food and Agriculture, U.S. Department of Agriculture, the Massachusetts Agricultural Experimental Station, and the Department of Food Science under Project No. MAS00998. Y.K. was supported in part by the Charm Sciences scholarship from the Department of Food Science, University of Massachusetts, Amherst.

Notes

The authors declare no competing financial interest.

DOI: 10.1021/acs.jafc.5b00840
J. Agric. Food Chem. 2015, 63, 5212−5223

■ ACKNOWLEDGMENTS

The authors thank Ms. Jayne M. Storkson for help in preparing this paper and Mr. Hyungtaek Cho and Ms. Sunnye Bang for assistance with the experiments. Y.P. is one of the inventors of CLA use patents that are assigned to the Wisconsin Alumni Research Foundation.

■ ABBREVIATIONS USED

Akt, protein kinase B; AMPK, AMP-activated protein kinase; AUC, areas under the curve; CLA, conjugated linoleic acid; COX IV, cytochrome *c* oxidase subunit IV; Cyt C, cytochrome *c*; GAPDH, glyceraldehyde-3-phosphate dehydrogenase; GLUT4, glucose transporter type 4; IRS-1, insulin receptor substrate 1; Nhlh2, nescient basic helix−loop−helix 2; NRF, nuclear respiratory factor; N2KO, nescient basic helix−loop−helix 2 knockout; PDK, phosphorylated phosphoinositide-dependent kinase; PGC-1α, peroxisome proliferator-activated receptor γ coactivator 1α; PPARδ, peroxisome proliferator-activated receptor δ; PTEN, phosphatase and tensin homologue; SIRT1, sirtuin 1; SOD2, superoxide dismutase 2; Tfam, mitochondrial transcription factor A; TG, triacylglyceride

■ REFERENCES

(1) Ogden, C. L.; Carroll, M. D.; Kit, B. K.; Flegal, K. M. Prevalence of Childhood and Adult Obesity in the United States, 2011−2012. *Jama-Journal of the American Medical Association* **2014**, *311*, 806−814.

(2) National Center for Health Statistics (US), 2012.

(3) Daniels, S. R.; Arnett, D. K.; Eckel, R. H.; Gidding, S. S.; Hayman, L. L.; Kumanyika, S.; Robinson, T. N.; Scott, B. J.; St Jeor, S.; Williams, C. L. Overweight in children and adolescents: pathophysiology, consequences, prevention, and treatment. *Circulation* **2005**, *111*, 1999−2012.

(4) Centers for Disease Control and Prevention (CDC) *Centers for Disease Control and Prevention (CDC) National Diabetes Fact Sheet: National Estimates and General Information on Diabetes and Prediabetes in the United States, 2011*. US Department of Health and Human Services, Centers for Disease Control and Prevention, Atlanta, GA, 2011; *201*.

(5) Brown, T.; Avenell, A.; Edmunds, L. D.; Moore, H.; Whittaker, V.; Avery, L.; Summerbell, C. Systematic review of long-term lifestyle interventions to prevent weight gain and morbidity in adults. *Obes. Rev.* **2009**, *10*, 627−638.

(6) Ha, Y. L.; Grimm, N. K.; Pariza, M. W. Anticarcinogens from fried ground beef: heat-altered derivatives of linoleic acid. *Carcinogenesis* **1987**, *8*, 1881−1887.

(7) Dilzer, A.; Park, Y. Implication of Conjugated Linoleic Acid (CLA) in Human Health. *Crit. Rev. Food Sci. Nutr.* **2012**, *52*, 488−513.

(8) Park, Y.; Pariza, M. W. Mechanisms of body fat modulation by conjugated linoleic acid (CLA). *Food Res. Int.* **2007**, *40*, 311−323.

(9) Kim, J. H.; Gilliard, D.; Good, D. J.; Park, Y. Preventive effects of conjugated linoleic acid on obesity by improved physical activity in nescient basic helix-loop-helix 2 knockout mice during growth period. *Food Funct.* **2012**, *3*, 1280−1285.

(10) Coyle, C. A.; Jing, E.; Hosmer, T.; Powers, J. B.; Wade, G.; Good, D. J. Reduced voluntary activity precedes adult-onset obesity in Nhlh2 knockout mice. *Physiol. Behav.* **2002**, *77*, 387−402.

(11) Park, Y.; Storkson, J.; Albright, K.; Liu, W.; Pariza, M. Evidence that the trans-10,cis-12 isomer of conjugated linoleic acid induces body composition changes in mice. *Lipids* **1999**, *34*, 235−241.

(12) Buettner, R.; Parhofer, K. G.; Woenckhaus, M.; Wrede, C. E.; Kunz-Schughart, L. A.; Scholmerich, J.; Bollheimer, L. C. Defining high-fat-diet rat models: metabolic and molecular effects of different fat types. *J. Mol. Endocrinol.* **2006**, *36*, 485−501.

(13) Park, Y.; Park, Y. Conjugated nonadecadienoic acid is more potent than conjugated linoleic acid on body fat reduction. *J. Nutr. Biochem.* **2010**, *21*, 764−773.

(14) Park, Y.; Albright, K. J.; Storkson, J. M.; Liu, W.; Cook, M. E.; Pariza, M. W. Changes in body composition in mice during feeding and withdrawal of conjugated linoleic acid. *Lipids* **1999**, *34*, 243−248.

(15) Park, Y.; Park, Y. Conjugated fatty acids increase energy expenditure in part by increasing voluntary movement in mice. *Food Chem.* **2012**, *133*, 400−409.

(16) Mele, M. C.; Cannelli, G.; Carta, G.; Cordeddu, L.; Melis, M. P.; Murru, E.; Stanton, C.; Banni, S. Metabolism of c9, t11-conjugated linoleic acid (CLA) in humans. *Prostaglandins, Leukotrienes Essent. Fatty Acids* **2013**, *89*, 115−119.

(17) Park, Y.; Albright, K.; Liu, W.; Storkson, J.; Cook, M.; Pariza, M. Effect of conjugated linoleic acid on body composition in mice. *Lipids* **1997**, *32*, 853−858.

(18) Andrikopoulos, S.; Blair, A. R.; Deluca, N.; Fam, B. C.; Proietto, J. Evaluating the glucose tolerance test in mice. *Am. J. Physiol. Endocrinol. Metab.* **2008**, *295*, E1323−E1332.

(19) Kim, J. H.; Park, Y.; Kim, D.; Good, D. J.; Park, Y. Dietary conjugated nonadecadienoic acid prevents adult-onset obesity in nescient basic helix-loop-helix 2 knockout mice. *J. Nutr. Biochem.* **2013**, *24*, 556−566.

(20) Birk, J. B.; Wojtaszewski, J. Predominant $\alpha2/\beta2/\gamma3$ AMPK activation during exercise in human skeletal muscle. *J. Physiol. (Oxford, U. K.)* **2006**, *577*, 1021−1032.

(21) Hock, M. B.; Kralli, A. Transcriptional Control of Mitochondrial Biogenesis and Function. *Annu. Rev. Physiol.* **2009**, *71*, 177−203.

(22) Zierath, J. R.; Hawley, J. A. Skeletal muscle fiber type: influence on contractile and metabolic properties. *PLoS Biol.* **2004**, *2*, e348.

(23) Hoppeler, H.; Fluck, M. Plasticity of skeletal muscle mitochondria: structure and function. *Med. Sci. Sports Exercise* **2003**, *35*, 95−104.

(24) Hood, D. A. Mechanisms of exercise-induced mitochondrial biogenesis in skeletal muscle This paper is one of a selection of papers published in this Special Issue, entitled 14th International Biochemistry of Exercise Conference-Muscles as Molecular and Metabolic Machines, and has undergone the Journal's usual peer review process. *Appl. Physiol., Nutr., Metab.* **2009**, *34*, 465−472.

(25) Hood, D. A.; Irrcher, I.; Ljubicic, V.; Joseph, A. Coordination of metabolic plasticity in skeletal muscle. *J. Exp. Biol.* **2006**, *209*, 2265−2275.

(26) Adhihetty, P. J.; Irrcher, I.; Joseph, A. M.; Ljubicic, V.; Hood, D. A. Plasticity of skeletal muscle mitochondria in response to contractile activity. *Exp. Physiol.* **2003**, *88*, 99−107.

(27) Wang, Y.; Zhang, C.; Yu, R.; Cho, H.; Nelson, M.; Bayuga-Ocampo, C.; Ham, J.; Kang, H.; Evans, R. Regulation of muscle fiber type and running endurance by PPAR delta. *PLoS Biol.* **2004**, *2*, 1532−1539.

(28) Medeiros, D. M. Assessing mitochondria biogenesis. *Methods* **2008**, *46*, 288−294.

(29) Kang, C.; Chung, E.; Diffee, G.; Ji, L. L. Exercise training attenuates aging-associated mitochondrial dysfunction in rat skeletal muscle: role of PGC-1α. *Exp. Gerontol.* **2013**, *48*, 1343−1350.

(30) Spiegelman, B. M. Transcriptional control of mitochondrial energy metabolism through the PGC1 coactivators. In *Mitochondrial Biology: New Perspectives*; Wiley: Hoboken, NJ, 2007 Novartis Foundation symposium *287*, p 60.

(31) Kim, Y.; Good, D.; Park, C.; Park, Y. Molecular mechanisms of conjugated linoleic acid (CLA) on muscle metabolism in adult onset inactivity-induced obese mice (1045.46). *FASEB J.* **2014**, *28*, 1045.46.

(32) Hur, S.; Whitcomb, F.; Rhee, S.; Park, Y.; Good, D. J.; Park, Y. Effects of trans-10, cis-12 conjugated linoleic acid on body composition in genetically obese mice. *J. Med. Food* **2009**, *12*, 56−63.

(33) West, D. B.; Delany, J. P.; Camet, P. M.; Blohm, F.; Truett, A. A.; Scimeca, J. Effects of conjugated linoleic acid on body fat and energy metabolism in the mouse. *Am. J. Physiol.* **1998**, *275*, R667−72.

(34) Sisk, M. B.; Hausman, D. B.; Martin, R. J.; Azain, M. J. Dietary conjugated linoleic acid reduces adiposity in lean but not obese Zucker rats. *J. Nutr.* **2001**, *131*, 1668−1674.

DOI: 10.1021/acs.jafc.5b00840
J. Agric. Food Chem. 2015, 63, 5212−5223

(35) Park, Y.; Albright, K. J.; Storkson, J. M.; Liu, W.; Pariza, M. W. Conjugated linoleic acid (CLA) prevents body fat accumulation and weight gain in an animal model. *J. Food Sci.* **2007**, *72*, S612−7.
(36) Cao, Z.; Wang, F.; Xiang, X.; Cao, R.; Zhang, W.; Gao, S. Intracerebroventricular administration of conjugated linoleic acid (CLA) inhibits food intake by decreasing gene expression of NPY and AgRP. *Neurosci. Lett.* **2007**, *418*, 217−221.
(37) Flatt, J. P. Glycogen levels and obesity. *Int. J. Obes. Relat. Metab. Disord.* **1996**, *20* (Suppl 2), S1−11.
(38) Westerterp-Plantenga, M.; Kovacs, E. SHORT COMMUNICATION The effect of (7)-hydroxycitrate on energy intake and satiety in overweight humans. *Int. J. Obes.* **2002**, *26*, 870−872.
(39) West, D. B.; Blohm, F. Y.; Truett, A. A.; DeLany, J. P. Conjugated linoleic acid persistently increases total energy expenditure in AKR/J mice without increasing uncoupling protein gene expression. *J. Nutr.* **2000**, *130*, 2471−2477.
(40) Good, D. J.; Coyle, C. A.; Fox, D. L. Nhlh2: A basic helix-loop-helix transcription factor controlling physical activity. *Exercise Sport Sci. Rev.* **2008**, *36*, 187−192.
(41) Hardie, D. G.; Sakamoto, K. AMPK: a key sensor of fuel and energy status in skeletal muscle. *Physiology (Bethesda)* **2006**, *21*, 48−60.
(42) Narkar, V. A.; Downes, M.; Yu, R. T.; Embler, E.; Wang, Y.; Banayo, E.; Mihaylova, M. M.; Nelson, M. C.; Zou, Y.; Juguilon, H.; Kang, H.; Shaw, R. J.; Evans, R. M. AMPK and PPAR delta Agonists are exercise mimetics. *Cell* **2008**, *134*, 405−415.
(43) Matsakas, A.; Narkar, V. A. Endurance exercise mimetics in skeletal muscle. *Curr. Sports Med. Rep.* **2010**, *9*, 227−232.
(44) Canto, C.; Auwerx, J. PGC-1alpha, SIRT1 and AMPK, an energy sensing network that controls energy expenditure. *Curr. Opin. Lipidol.* **2009**, *20*, 98−105.
(45) Rockl, K. S. C.; Hirshman, M. F.; Brandauer, J.; Fujii, N.; Witters, L. A.; Goodyear, L. J. Skeletal muscle adaptation to exercise training - AMP-activated protein kinase mediates muscle fiber type shift. *Diabetes* **2007**, *56*, 2062−2069.
(46) Kim, Y.; Park, Y. Conjugated Linoleic Acid (CLA) Stimulates Mitochondrial Biogenesis Signaling by the Upregulation of PPARγ Coactivator 1α (PGC-1α) in C2C12 Cells. *Lipids* **2015**, 1−10.
(47) Downward, J. Mechanisms and consequences of activation of protein kinase B/Akt. *Curr. Opin. Cell Biol.* **1998**, *10*, 262−267.
(48) Wang, Q.; Somwar, R.; Bilan, P. J.; Liu, Z.; Jin, J.; Woodgett, J. R.; Klip, A. Protein kinase B/Akt participates in GLUT4 translocation by insulin in L6 myoblasts. *Mol. Cell. Biol.* **1999**, *19*, 4008−4018.
(49) Jiang, Z. Y.; Zhou, Q. L.; Coleman, K. A.; Chouinard, M.; Boese, Q.; Czech, M. P. Insulin signaling through Akt/protein kinase B analyzed by small interfering RNA-mediated gene silencing. *Proc. Natl. Acad. Sci. U. S. A.* **2003**, *100*, 7569−7574.
(50) Shi, Y.; Wang, J.; Chandarlapaty, S.; Cross, J.; Thompson, C.; Rosen, N.; Jiang, X. PTEN is a protein tyrosine phosphatase for IRS1. *Nat. Struct. Mol. Biol.* **2014**, *21*, 522−527.
(51) Mohankumar, S. K.; Taylor, C. G.; Siemens, L.; Zahradka, P. Activation of phosphatidylinositol-3 kinase, AMP-activated kinase and Akt substrate-160 kDa by trans-10, cis-12 conjugated linoleic acid mediates skeletal muscle glucose uptake. *J. Nutr. Biochem.* **2013**, *24*, 445−456.
(52) Qin, H.; Liu, Y.; Lu, N.; Li, Y.; Sun, C. cis-9,trans-11-Conjugated Linoleic Acid Activates AMP-Activated Protein Kinase in Attenuation of Insulin Resistance in C2C12 Myotubes. *J. Agric. Food Chem.* **2009**, *57*, 4452−4458.
(53) Randle, P. J.; Garland, P. B.; Hales, C. N.; Newsholme, E. A. The glucose fatty-acid cycle its role in insulin sensitivity and the metabolic disturbances of diabetes mellitus. *Lancet* **1963**, *281*, 785−789.
(54) Hue, L.; Taegtmeyer, H. The Randle cycle revisited: a new head for an old hat. *Am. J. Physiol. Endocrinol. Metab.* **2009**, *297*, E578−E591.
(55) Kim, J. H.; Kim, J.; Park, Y. trans-10, cis-12 conjugated linoleic acid enhances endurance capacity by increasing fatty acid oxidation and reducing glycogen utilization in mice. *Lipids* **2012**, *47*, 855−863.
(56) Choi, J. S.; Koh, I.; Jung, M. H.; Song, J. Effects of three different conjugated linoleic acid preparations on insulin signalling, fat oxidation and mitochondrial function in rats fed a high-fat diet. *Br. J. Nutr.* **2007**, *98*, 264−275.
(57) Park, Y. *Regulation of energy metabolism and the catabolic effects of immune stimulation by conjugated linocleic acid*; Ph.D. Dissertation, University of Wisconsin-Madison: Madison, WI, 1996
(58) Koba, K.; Akahoshi, A.; Yamasaki, M.; Tanaka, K.; Yamada, K.; Iwata, T.; Kamegai, T.; Tsutsumi, K.; Sugano, M. Dietary conjugated linolenic acid in relation to CLA differently modifies body fat mass and serum and liver lipid levels in rats. *Lipids* **2002**, *37*, 343−350.
(59) Wendel, A. A.; Purushotham, A.; Liu, L. F.; Belury, M. A. Conjugated linoleic acid fails to worsen insulin resistance but induces hepatic steatosis in the presence of leptin in ob/ob mice. *J. Lipid Res.* **2008**, *49*, 98−106.
(60) Pariza, M. Perspective on the safety and effectiveness of conjugated linoleic acid. *Am. J. Clin. Nutr.* **2004**, *79*, 1132S−1136S.
(61) Clement, L.; Poirier, H.; Niot, I.; Bocher, V.; Guerre-Millo, M.; Krief, S.; Staels, B.; Besnard, P. Dietary trans-10,cis-12 conjugated linoleic acid induces hyperinsulinemia and fatty liver in the mouse. *J. Lipid Res.* **2002**, *43*, 1400−1409.
(62) Poirier, H.; Niot, I.; Clement, L.; Guerre-Millo, M.; Besnard, P. Development of conjugated linoleic acid (CLA)-mediated lipoatrophic syndrome in the mouse. *Biochimie* **2005**, *87*, 73−79.
(63) Park, Y.; Albright, K. J.; Pariza, M. W. Effects of conjugated linoleic acid on long term feeding in Fischer 344 rats. *Food Chem. Toxicol.* **2005**, *43*, 1273−1279.
(64) O'Hagan, S.; Menzel, A. A subchronic 90-day oral rat toxicity study and in vitro genotoxicity studies with a conjugated linoleic acid product. *Food Chem. Toxicol.* **2003**, *41*, 1749−1760.

DOI: 10.1021/acs.jafc.5b00840
J. Agric. Food Chem. 2015, 63, 5212−5223

JOURNAL OF AGRICULTURAL AND FOOD CHEMISTRY

Article

pubs.acs.org/JAFC

Evaluation of Plant Growth Regulatory Activity of Furofuran Lignan Bearing a 7,9′:7′,9-Diepoxy Structure Using Optically Pure (+)- and (−)-Enantiomers

Satoshi Yamauchi,*[,†,§] Hiroaki Ichikawa,[†] Hisashi Nishiwaki,[†] and Yoshihiro Shuto[†]

[†]Faculty of Agriculture, Ehime University, 3-5-7 Tarumi, Matsuyama, Ehime 790-8566, Japan

[§]South Ehime Fisheries Research Center, 1289-1 Funakoshi, Ainan, Ehime 798-4292, Japan

ABSTRACT: The plant growth regulatory activity of furofuran lignan (7,9′:7′,9-diepoxylignan) was evaluated by employing optically pure synthesized (+)- and (−)-enantiomers. (+)-Sesamin possessing a 3,4-methylenedioxy group on the aromatic rings and 7-aryl structure showed growth promotion activity against lettuce roots (EC_{50} = 0.50 mM); on the other hand, growth inhibitory activity was observed against lettuce shoots (EC_{50} = 0.38 mM). Against ryegrass shoots, (−)-sesamolin, which has 3,4-methylenedioxy groups on the aromatic rings and a 7-acetal structure, was effective in showing growth inhibitory activity (EC_{50} = 0.23 mM). Different activity levels were observed between (+)- and (−)-enantiomers. It was assumed that the 3,4-methylenedioxy group on the aromatic ring was more potent for the plant growth regulatory activity.

KEYWORDS: *lignan, furofuran lignan, 7,9′:7′,9-diepoxylignan, sesamin, sesamolin, plant growth regulatory activity*

INTRODUCTION

Furofuran lignans (Figure 1) are a representative group of lignans in food plants,[1,2] possessing a 7,9′:7′,9-diepoxy[3] structure and a wide range of biological activities.[2] Although lignans are biosynthesized by plants, the effect of the main structure and stereochemistry on the plant growth regulatory activity had not been clarified. Recently, we demonstrated the plant growth inhibitory activity of 7,9′-epoxylignan[4,5] and 7,7′-epoxylignan,[6,7] giving information on the favored stereochemistry and substituent for the activity. As for dietary furofuran lignan, we can find some reports on the plant growth regulatory activity using isolated compounds.[8−10] The activity of isolated oxo-type furofuran lignan was also reported.[11] On the other hand, the enantiomeric excess of natural furofuran lignan was estimated as 20−30%,[12,13] suggesting that the effect of stereochemistry on the activity should be examined by employing optically pure synthesized compounds.

In this research, both enantiomers of common dietary furofuran lignans, (+)- and (−)-pinoresinol, **1** and **2**, (+)- and (−)-medioresinol, **3** and **4**, (+)- and (−)-syringaresinol, **5** and **6**, (+)- and (−)-sesamin, **7** and **8**, (+)- and (−)-sesamolin, **9** and **10**, (+)- and (−)-sesamolinol, **11** and **12**, and (+)- and (−)-samin, **13** and **14**, were selected to clarify the plant growth regulatory activity of components of the food plants. With the results of this research, effects of enantiomeric, acetal, and hemiacetal structure on the activity could be compared for the first time. The previously described synthetic methods[14−16] were employed with modification to provide the optically pure furofuran lignans.

MATERIALS AND METHODS

Chemicals. Optical rotation values were measured with a P-2100 instrument (JASCO, Tokyo, Japan). HPLC analysis for compounds was performed with LC-6AD and SPD-6AV instruments (Shimadzu, Kyoto, Japan). The column used for HPLC analyses was a 250 mm × 4.6 mm i.d., 5 μm, CHIRALCEL AD-H and OD-H (DAICEL Chemical Industries, Ltd., Tokyo, Japan).

Furofuran lignans, **1**−**14**, were synthesized by employing a previously described method[14−16] with modification.

(+)-Pinoresinol, **1**: NMR data agreed with those in the literature;[17] $[\alpha]_D^{25}$ +67 (*c* 0.2, $CHCl_3$), $[\alpha]_D^{22}$ +63 (*c* 1.2, $CHCl_3$) in the literature;[18] t_R 51.3 min (OD-H, hexane/isopropyl alcohol = 1:1, v/v, 1 mL/min, detected at 276 nm); >99% ee.

(−)-Pinoresinol, **2**: NMR data agreed with those in the literature;[17] $[\alpha]_D^{25}$ −68 (*c* 0.1, $CHCl_3$), $[\alpha]_D^{25}$ −34.7 ($CHCl_3$) in the litearure;[19] t_R 17.7 min (OD-H, hexane/isopropyl alcohol = 1:1, v/v, 1 mL/min, detected at 276 nm); >99% ee.

(+)-Medioresinol, **3**: NMR data agreed with those in the literature;[20] $[\alpha]_D^{25}$ +68 (*c* 0.2, $CHCl_3$), $[\alpha]_D^{22}$ +54 (*c* 1.0, $CHCl_3$) in the literature;[18] t_R 23.1 min (AD-H, hexane/isopropyl alcohol = 1:4, v/v, 1 mL/min, detected at 280 nm); >99% ee.

(−)-Medioresinol, **4**: NMR data agreed with those in the literature;[20] $[\alpha]_D^{25}$ −69 (*c* 0.3, $CHCl_3$), $[\alpha]_D^{25}$ −17.0 (*c* 0.14, $CHCl_3$) in the literature;[21] t_R 19.8 min (AD-H, hexane/isopropyl alcohol = 1:4, v/v, 1 mL/min, detected at 280 nm); >99% ee.

(+)-Syringaresinol, **5**: NMR data agreed with those in the literature;[20] $[\alpha]_D^{25}$ +38 (*c* 0.4, $CHCl_3$), $[\alpha]_D^{22}$ +23 (*c* 0.7, $CHCl_3$) in the literature;[18] t_R 27.4 min (OD-H, hexane/isopropyl alcohol = 1:4, v/v, 1 mL/min, detected at 273 nm); >99% ee.

(−)-Syringaresinol, **6**: NMR data agreed with those in the literature;[20] $[\alpha]_D^{25}$ −37 (*c* 0.4, $CHCl_3$), $[\alpha]_D$ −28 in the literature;[22] t_R 41.8 min (OD-H, hexane/isopropyl alcohol = 1:4, v/v, 1 mL/min, detected at 273 nm); >99% ee.

(+)-Sesamin, **7**: NMR data agreed with those in the literature;[23] $[\alpha]_D^{25}$ +64 (*c* 0.4, $CHCl_3$), $[\alpha]_D$ +64.8 ($CHCl_3$) in the literature;[24] t_R 14.6 min (AD-H, hexane/isopropyl alcohol = 1:1, v/v, 1 mL/min, detected at 287 nm); >99% ee.

(−)-Sesamin, **8**: NMR data agreed with those in the literature;[23] $[\alpha]_D^{25}$ −65 (*c* 0.4, $CHCl_3$), $[\alpha]_D^{19}$ −68.6 (*c* 0.53, $CHCl_3$) in the

Received: March 1, 2015
Revised: April 30, 2015
Accepted: May 8, 2015
Published: May 8, 2015

ACS Publications © 2015 American Chemical Society

DOI: 10.1021/acs.jafc.5b01099
J. Agric. Food Chem. 2015, 63, 5224−5228

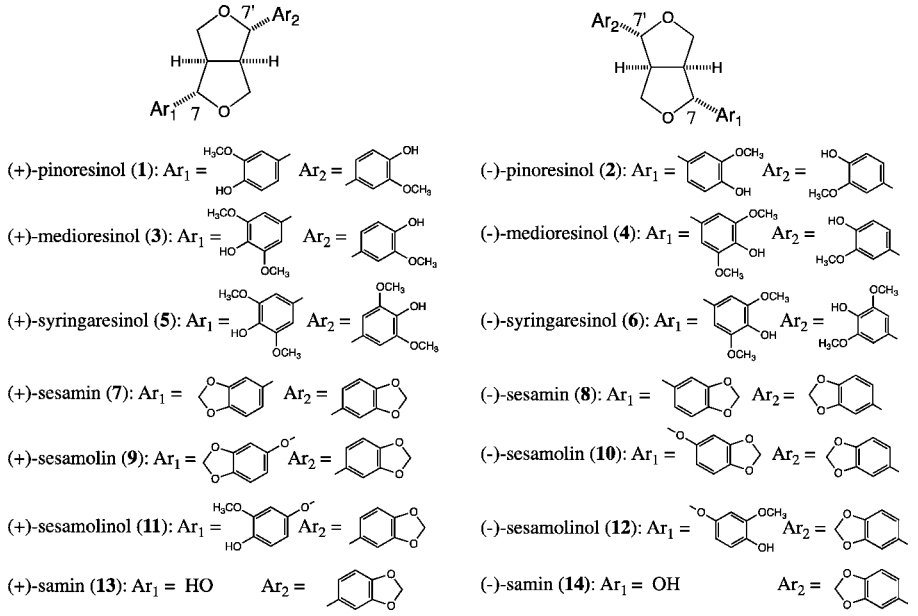

Figure 1. (+)- and (−)-furofuran lignans (7,9′:7′,9-diepoxylignan).

literature;[25] t_R 12.7 min (AD-H, hexane/isopropyl alcohol = 1:1, v/v, 1 mL/min, detected at 287 nm); >99% ee.

(+)-Sesamolin, **9**: NMR data agreed with those in the literature;[26] $[\alpha]_D^{25}$ +198 (*c* 1.2, $CHCl_3$), $[\alpha]_D$ +212 ($CHCl_3$) in the literature;[27] t_R 13.0 min (AD-H, hexane/isopropyl alcohol = 1:1, v/v, 1 mL/min, detected at 287 nm); >99% ee.

(−)-Sesamolin, **10**: NMR data agreed with those in the literature;[26] $[\alpha]_D^{25}$ −195 (*c* 1.1, $CHCl_3$), $[\alpha]_D^{23}$ −216.44 (*c* 0.61, $CHCl_3$) in the literature of synthetic research;[28] t_R 11.3 min (AD-H, hexane/isopropyl alcohol = 1:1, v/v, 1 mL/min, detected at 287 nm); >99% ee.

(+)-Sesamolinol, **11**: NMR data agreed with those in the literature;[29] $[\alpha]_D^{25}$ +179 (*c* 0.8, $CHCl_3$), $[\alpha]_D$ +184 (*c* 1.0, $CHCl_3$) in literature;[29] t_R 11.5 min (AD-H, hexane/isopropyl alcohol = 1:1, v/v, 1 mL/min, detected at 287 nm); >99% ee.

(−)-Sesamolinol, **12**: NMR data agreed with those of (+)-form in the literature;[29] $[\alpha]_D^{25}$ −178 (*c* 1.4, $CHCl_3$); t_R 12.8 min (AD-H, hexane/isopropyl alcohol = 1:1, v/v, 1 mL/min, detected at 287 nm); >99% ee.

(+)-Samin, **13**: diastereomeric mixture of 7*R* and 7*S*; NMR data agreed with those in the literature;[30] $[\alpha]_D^{25}$ +92 (*c* 1.2, $CHCl_3$), $[\alpha]_D$ +81.4 (*c* 0.5, $CHCl_3$) in the literature.[31]

(−)-Samin, **14**: diastereomeric mixture of 7*R* and 7*S*; NMR data agreed with those in the literature;[30] $[\alpha]_D^{25}$ −90 (*c* 2.5, $CHCl_3$), $[\alpha]_D^{24}$ −88.18 (*c* 1.1, $CHCl_3$) in the literature of synthetic research.[28]

Evaluation of Plant Growth Regulatory Activity. The plant growth regulatory activity of all stereoisomers of lariciresinol was evaluated using lettuce (*Lactuca sativa* L. Green-wave (Takii Seed Co. Ltd., Kyoto, Japan)) and Italian ryegrass (*Lolium multiflorum* Lam. Wase-fudo (Takii Seed Co. Ltd.)). A sheet of filter paper (90 mm diameter) was placed in a 90 mm Petri dish and wetted with 500 μL of test sample solution dissolved in acetone at concentrations from 6.0×10^{-3} to 6.0×10^{-8} M. After the filter paper had dried, 3 mL of water was poured into the dish to adjust the final concentration from 1.0×10^{-3} to 1.0×10^{-8} M. Thirty seeds of each plant were placed on the filter paper, and the Petri dishes were sealed with Parafilm. The Petri dishes were then incubated in the dark at 20 °C. The lengths of roots and shoots were measured after 3 days for lettuce and after 5 days for ryegrass by using an ordinary ruler. The roots and shoots lengths of the control were ca. 3 and 1 cm for lettuce and 4 and 3 cm for ryegrass, respectively. Data are presented as percentage differences from the control; positive and negative values represent stimulation and inhibition of plant growth, respectively. Experiments were performed in triplicate or more for each sample (n = 3−7). Statistical analyses were conducted by one-way ANOVA followed by Tukey's multiple-comparison test using PRISM software (Graphpad Software, San Diego, CA, USA), and the values of $p < 0.01$ and 0.05 were considered to be statistically significant.

RESULTS AND DISCUSSION

Optically pure natural furofuran lignans, **1**−**14**, were synthesized by employing a previously described method with modification.[14−16] Although some isolated furofuran lignans, (−)-pinoresinol,[19] (−)-medioresinol,[21] and (−)-syringaresinol,[22] from plants showed lower specific optical rotation in the previous studies, we obtained optically pure samples by organic syntheses for this research. These synthetic results enabled us to evaluate the biological activity of the (−)-form for the first time. In the case of hemiacetal type lignans, (+)- and (−)-samin (**13** and **14**), diastereomeric mixtures of the (7*R*/*S*)-form were employed.

All synthesized furofuran lignans, **1**−**14**, were applied to plant growth regulatory activity test at 1 mM (Figure 2) as a first stage. Against lettuce roots, (+)- and (−)-syringaresinol (**5** and **6**) and (+)- and (−)-sesamin (**7** and **8**) promoted the growth (from 40 to 60% from control) with significant difference, whereas (+)- and (−)-medioresinols (**3** and **4**) had lower activity, suggesting that the 3,5-dimethoxy-4-hydroxyphenyl group or 3,4-methylendioxyphenyl group at both the 7 and 7′ positions is favorable for the growth promotion of lettuce roots. A comparable activity level was shown between the corresponding enantiomers. Even if two 3,4-methylenedioxyphenyl groups are present in the structure, the acetal type compound, (+)- and (−)-sesamolin (**9** and **10**) was inactive, indicating that the 7-aryl structure is more important than the 7-aryloxy group for the growth promotion activity against lettuce roots. No or very weak activities of both enantiomers of pinoresinol (**1** and **2**) medioresinol (**3** and **4**), sesamolinol (**11** and **12**), and samin (**13** and **14**) would be due to the presence of 3-methoxy-4-hydroxy groups and the acetal/hemiacetal structure. On the other hand, growth promotion was not observed, but growth inhibitory activity was exhibited against lettuce shoots for (+)- and (−)-sesamin (**7** and **8**), (+)- and (−)-sesamolin (**9** and **10**), and (+)- and (−)-samin (**13**

DOI: 10.1021/acs.jafc.5b01099
J. Agric. Food Chem. 2015, 63, 5224−5228

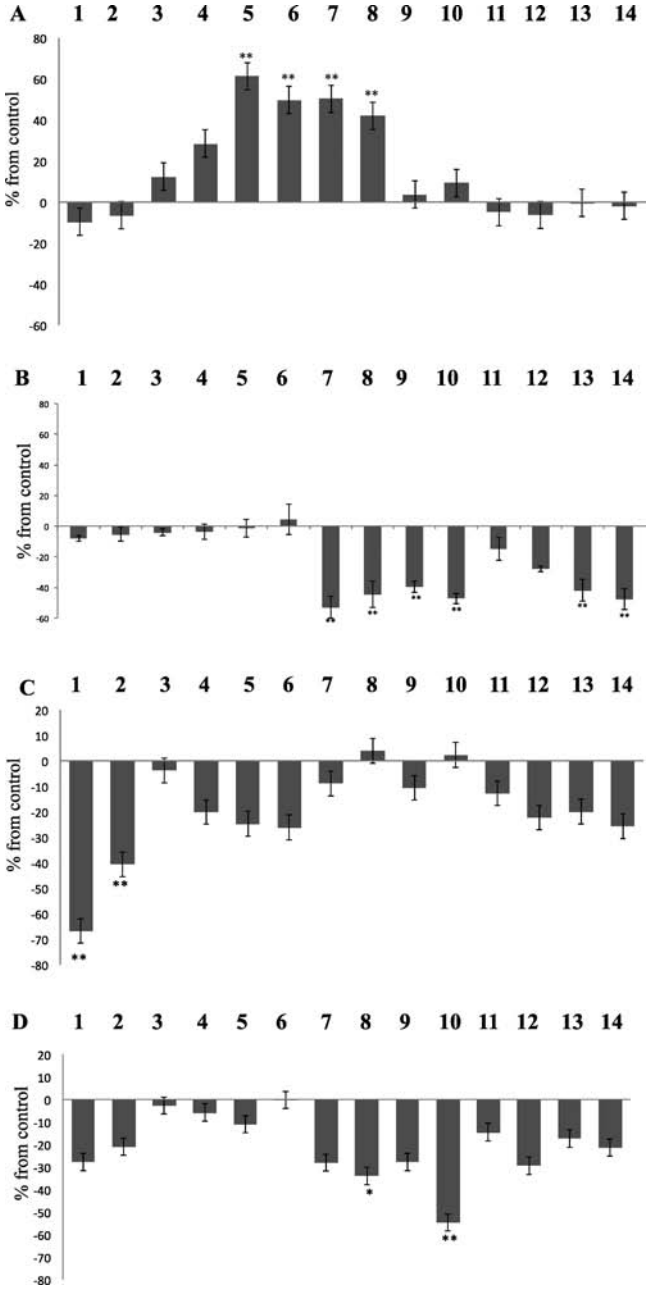

Figure 2. Plant growth regulatory activity of (+)- and (−)-furofuran lignans, **1**−**14**, at 1 mM against (A) lettuce roots, (B) lettuce shoots, (C) ryegrass roots, and (D) ryegrass shoots. (**) $p < 0.01$; (*) $p < 0.05$. (−)-Verrucosin showed −95 and −60% growth inhibition activity against lettuce roots and shoots, respectively. (+)-Verrucosin showed −98 and −63% growth inhibition activity against ryegrass roots and shoots, respectively.[6]

and **14**), showing growth inhibitory activity with significant difference (from −40 to −50% from control). Because the activity level of the 7-aryl structure, **7** and **8**, was similar to that of the 7-acetal structure, **9** and **10**, it could be assumed that the 3,4-methylenedioxy groups on both 7 and 7′ aromatic rings are important for growth inhibitory activity against lettuce shoots. The activity of the 7-hemiacetal structure is also similar to those of the 7-aryl and 7-acetal structures. The enantiomeric structures did not affect the activity. The activities of both enantiomers of pinoresinol (**1** and **2**), medioresinol (**3** and **4**), syringaresinol (**5** and **6**), and sesamolinol (**11** and **12**) were less potent against lettuce shoots. These facts suggest that the substituent on the aromatic ring is a more important factor than the structure of the 7 position and the enantiomeric structure against growth inhibition of lettuce shoots at 1 mM. In our previous study on lignans bearing a 7,9′-epoxy structure[4,5] and a 7,7′-epoxy structure,[6,7] only growth inhibitory activity against lettuce was observed. We found growth promotion activity of furofuran lignan bearing a 7,9′:7′,9-diepoxy structure against lettuce roots in this study. (+)- and (−)-Sesamin showed both growth promotion activity against lettuce roots and growth inhibitory activity against lettuce shoots at 1 mM.

Against ryegrass at 1 mM (Figure 2C,D), we observed only growth inhibitory activity on both roots and shoots elongation. (+)-Pinoresinol (**1**) (−65%) was 1.5-fold more potent than (−)-pinoresinol (**2**) (−40%) against ryegrass roots with significant difference. The activities of other compounds against ryegrass roots were lower (< −25%). (−)-Sesamolin (**10**) exhibited the highest activity of the growth inhibitory activity against ryegrass shoots (−55%) with significant difference at 1 mM; on the other hand, its enantiomer, (+)-sesamolin (**9**), was 2-fold less potent. The activities of other compounds containing pinoresinol, which had the highest activity against ryegrass roots, were < −35%. The higher growth inhibitory activities of shoots against both lettuce and ryegrass at 1 mM were observed in only (−)-sesamolin (**10**), bearing a 3,4-methylenedioxyphenyl group and acetal structure. However, the activity of **10** against roots of lettuce and ryegrass was not observed. In the ryegrass growth experiment, different activity levels between corresponding enantiomers were observed.

As a next step, dilution experiments (from 10^{-4} to 10^{-8} M) of the active compounds at 1 mM were performed (Figure 3). Although significant difference was not observed, (+)-sesamin (**7**) was effective to some extent, exhibiting promotion activity (+40%) against lettuce roots at 10^{-4} M (Figure 3A,B). In the experiment on growth of lettuce shoots, (+)- and (−)-sesamin (**7** and **8**) and (+)- and (−)-sesamolin (**9** and **10**) were proved to show from −40 to −30% inhibitory activity with significant difference at 10^{-4} M. The growth promotion activity of (+)- and (−)-syringaresinol (**5** and **6**) and (−)-sesamin (**8**) against lettuce roots and the growth inhibitory activity of (+)- and (−)-samin (**13** and **14**) against lettuce shoots at 1 mM dramatically disappeared by 10-fold dilution as in our previous experiment employing 7,9′- and 7,7′-epoxylignan possessing a 3-methoxy-4-hydroxyphenyl group.[4,6] Considering these results, 7-(3,4-methylenedioxyphenyl)/(3,4-methylenedioxyphenoxy) and 7′-(3,4-methylenedioxyphenyl) compounds are more advantageous for lettuce growth regulation at diluted concentration. The enantiospecific activity of sesamin was clarified by this dilution experiment; only (+)-sesamin (**7**) showed growth promotion activity (+40%) against lettuce roots at 10^{-4} M. In the dilution experiment on ryegrass (Figure 3C,D), (−)-sesamolin (**10**) showed growth inhibitory activity (−45%) against shoots at 10^{-4} M with significant difference; on the other hand, the higher activities of (+)- and (−)-pinoresinol (**1** and **2**) against roots at 1 mM dramatically disappeared at 10^{-4} M. It could be assumed that the (−)-form, 7-(3,4-methylenedioxyphenoxy) acetal structure, and 7′-(3,4-methylenedioxyphenyl) structure are favorable for the highest ryegrass shoot inhibitory activity at diluted condition. The lower activity of hemiacetal type (−)-samin (**14**), which is converted from **10** by hydrolysis, means that the acetal type (−)-sesamolin (**10**) is an active compound in the plant body.

DOI: 10.1021/acs.jafc.5b01099
J. Agric. Food Chem. 2015, 63, 5224−5228

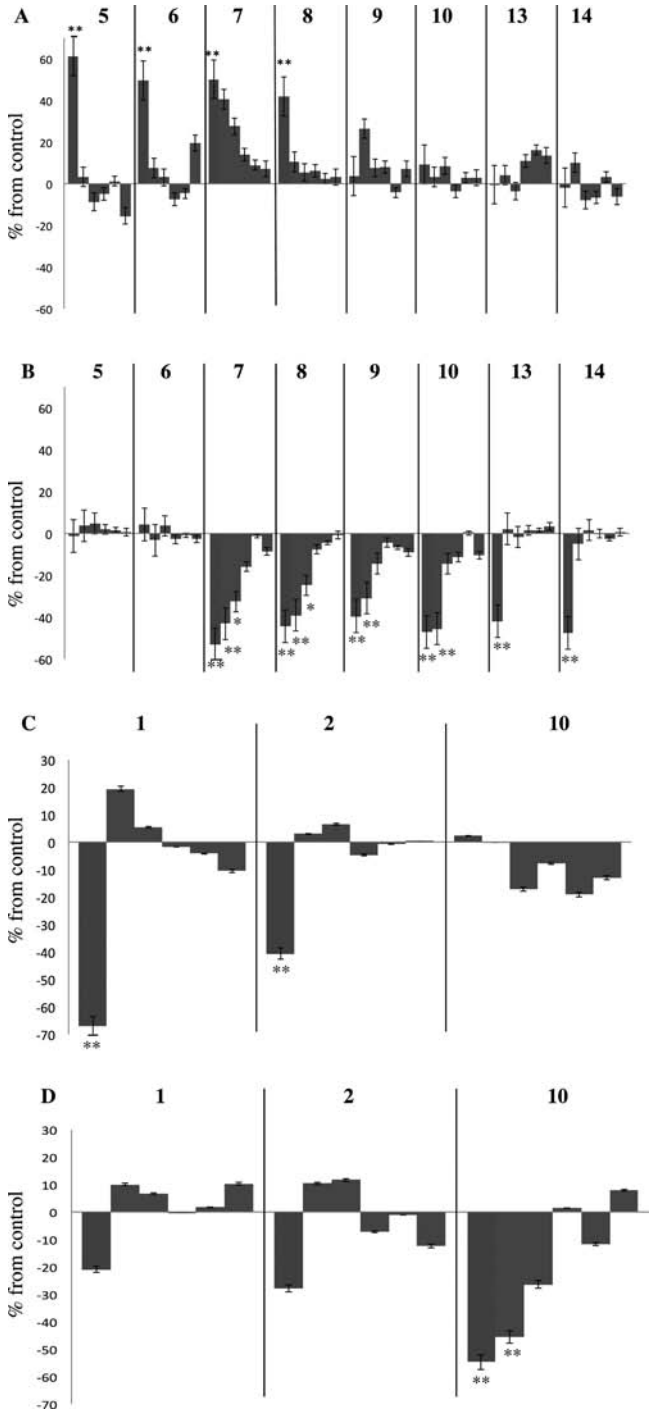

Figure 3. Plant growth regulatory activity of (+)- and (−)-furofuran lignans under diluted conditions against (A) lettuce roots, (B) lettuce shoots, (C) ryegrass roots, and (D) ryegrass shoots. (**) $p < 0.01$; (*) $p < 0.05$.

We evaluated EC_{50} values of furofuran lignans of higher activity (7,9′:7′,9-diepoxylignan) in this experiment (Table 1). The highest active compounds were (+)-sesamin (**7**) against lettuce shoots (growth inhibition, EC_{50} = 0.38 mM) and (−)-sesamolin (**10**) against ryegrass shoots (growth inhibition, EC_{50} = 0.23 mM). The activity of compounds bearing a 3-methoxy-4-hydroxyphenyl group, which is a common phenyl group in the natural lignans, was weak. The highest activity of 7,9′:7′,9-diepoxylignan bearing a 3-methoxy-4-hydroxyphenyl group was shown against ryegrass roots by (+)-pinoresinol (**1**) (growth inhibition, EC_{50} = 0.95 mM). In this experiment, growth promotion activity of lignan was also discovered. The growth promotion activity of (+)-sesamin (**7**) against lettuce roots (EC_{50} = 0.50 mM) was 2-fold higher than that of (+)-syringaresinol (EC_{50} = 1.00 mM). To confirm the growth promotion/inhibitory activities of these compounds, the effects of these compounds on germination were examined, showing 83−101% germination from control. These compounds did not affect much the germination.

This research clarified the plant growth regulatory activity of popular furofuran lignan bearing a 7,9′:7′,9-diepoxy structure using enantiomerically pure synthesized (+)- and (−)-enantiomers for the first time. Compared the activity, the potency of a methylenedioxy group on the aromatic rings and some difference of activity level between enantiomers were more shown. It is evaluated that (+)-sesamin and (−)-sesamolin were more potent in this research. It is noteworthy that (+)-sesamin promotes the growth of lettuce roots and inhibits lettuce shoots. It could be assumed that a 7,9′:7′,9-diepoxy structure is less potent than the 7,9′- and 7,7′-epoxy structures at 1 mM. However, a 7,9′:7′,9-diepoxy structure bearing a 3,4-methylenedioxy group is more potent at lower concentration. Because both enantiomers showed activity, enantiomers seem to have no specific target. Lignans have been focused on their antioxidant activities and medicinal effect.[32] This research showed the plant growth regulatory activity of (+)- and (−)-furofuran lignans. The biosynthetic research of furofuran lignan is now continuing.[33,34] By the combination of structure−activity relationships with the biosynthetic research, new food plants producing higher amounts of growth regulatory lignans could be developed.

AUTHOR INFORMATION

Corresponding Author

*(S.Y.) Phone: +81-89-946-9846. Fax: +81-89-977-4364. E-mail: syamauch@agr.ehime-u.ac.jp.

Funding

We are grateful to Marutomo Co. for financial support.

Notes

The authors declare no competing financial interest.

Table 1. EC_{50} Values[a] of (+)-Pinoresinol, (+)-Syringaresinol, (+)-Sesamin, and (−)-Sesamolin

	lettuce (EC_{50}, mM)		ryegrass (EC_{50}, mM)	
compound	roots	shoots	roots	shoots
(+)-pinoresinol (**1**)	>1.00	>1.00	0.95 ± 0.31 (inhibition)	>1.00
(+)-syringaresinol (**5**)	1.00 ± 0.35 (promotion)	>1.00	>1.00	>1.00
(+)-sesamin (**7**)	0.50 ± 0.26 (promotion)	0.38 ± 0.19 (inhibition)	>1.00	>1.00
(−)-sesamolin (**10**)	>1.00	>1.00	>1.00	0.23 ± 0.04 (inhibition)

[a]EC_{50} values of **1** and **5** were determined by dilution experiment from 1 to 0.2 mM.

DOI: 10.1021/acs.jafc.5b01099
J. Agric. Food Chem. 2015, 63, 5224−5228

■ ACKNOWLEDGMENTS

Part of this study was performed at INCS (Johoku station) of Ehime University.

■ REFERENCES

(1) Penalvo, J. L.; Adlercreutz, H.; Uehara, M.; Ristimaki, A.; Watanabe, S. Lignan content of selected foods from Japan. *J. Agric. Food Chem.* **2008**, *56*, 401−409.
(2) Ayres, D. C.; Loike, J. D. *Lignans*; Cambridge University Press: Cambridge, UK, 1990.
(3) Moss, G. P. Nomenclature of lignans and neolignans (IUPAC recommendations 2000). *Pure Appl. Chem.* **2000**, *72*, 1493−1523.
(4) Nishiwaki, H.; Kumamoto, M.; Shuto, Y.; Yamauchi, S. Stereoselective syntheses of all stereoisomers of lariciresinol and their plant growth inhibitory activities. *J. Agric. Food Chem.* **2011**, *59*, 13089−13095.
(5) Yamauchi, S.; Kumamoto, M.; Ochi, Y.; Nishiwaki, H.; Shuto, Y. Structure-plant growth inhibitory activity relationship of lariciresinol. *J. Agric. Food Chem.* **2013**, *61*, 12297−12306.
(6) Nishiwaki, H.; Nakayama, K.; Shuto, Y.; Yamauchi, S. Synthesis of all stereoisomers of 3,3′-dimethoxy-7,7′-epoxylignane-4,4′-diol and their plant growth inhibitory activity. *J. Agric. Food Chem.* **2014**, *62*, 651−659.
(7) Yamauchi, S.; Nakayama, K.; Nishiwaki, H.; Shuto, Y. Structure-plant phytotoxic activity relationship of 7,7′-epoxylignanes, (+)- and (−)-verrucosin: simplification on the aromatic ring substituents. *Bioorg. Med. Chem. Lett.* **2014**, *24*, 4798−4803.
(8) Cutillo, F.; D'Abrosca, B.; D.Greca, M.; Fiorentino, A.; Zarrelli, A. Lignans and neolignans from *Brassica fruticulosa*: effects on seed germination and plant growth. *J. Agric. Food Chem.* **2003**, *51*, 6165−6172.
(9) Macías, F. A.; López, A.; Varela, R. M.; Torres, A.; Molinillo, J. M. G. Bioactive lignans from a cultivar of *Helianthus annuus*. *J. Agric. Food Chem.* **2004**, *52*, 6443−6447.
(10) DellaGreca, M.; Mancino, A.; Previtera, L.; Zarrelli, A.; Zuppolini, S. Lignans from *Phillyrea angustifolia* L. *Phytochem. Lett.* **2011**, *4*, 118−121.
(11) Kato-Noguchi, H.; Kobayashi, A.; Ohno, O.; Kimura, F.; Fujii, Y.; Suenaga, K. Phytotoxic substances with allelopathic activity may be central to the strong invasive potential of *Brachiaria brizantha*. *J. Plant Physiol.* **2014**, *171*, 525−530.
(12) Suzuki, S.; Umezawa, T.; Shimada, M. Stereochemical diversity in lignan biosynthesis of *Arctium lappa* L. *Biosci., Biotechnol., Biochem.* **2002**, *66*, 1262−1269.
(13) Finefield, J. M.; Sherman, D. H.; Kreitman, M.; Williams, R. M. Enantiomeric natural products; occurrence and biogenesis. *Angew. Chem., Int. Ed.* **2012**, *51*, 4802−4936.
(14) Yamauchi, S.; Sugahara, T.; Matsugi, J.; Someya, T.; Masuda, T.; Kishida, T.; Akiyama, K.; Maruyama, M. Effect of the benzylic structure of lignan on antioxidant activity. *Biosci., Biotechnol., Biochem.* **2007**, *71*, 2283−2290.
(15) Yamauchi, S.; Bando, S.; Kinoshita, Y. Synthesis of 1,2-oxygenated 6-arylfurofuran lignan: stereoselective synthesis of (1*S*,2*S*,5*R*,6S)-1-hydroxysamin. *Biosci., Biotechnol., Biochem.* **2002**, *66*, 1495−1499.
(16) Yamauchi, S.; Ina, T.; Kirikihara, T.; Masuda, T. Synthesis and antioxidant activity of oxygenated furofuran lignans. *Biosci., Biotechnol., Biochem.* **2004**, *68*, 183−192.
(17) Roy, S. C.; Rana, K. K.; Guin, C. (±)-Lariciresinol, (±)-acuminatin, and (±)-lariciresinol monomethyl ether and furofuran lignans (±)-sesamin, (±)-eudesmin, (±)-piperitol methyl ether, (±)-pinoresinol, (±)-piperitol, and (±)-pinoresinol monomethyl ether by radical cyclization of epoxides using a transition-metal radical source. *J. Org. Chem.* **2002**, *67*, 3242−3248.
(18) Kikuchi, T.; Matsuda, S.; Kadota, S.; Tai, T. Studies on the constituents of medicinal and related plants in Sri Lanka. III. Novel sesquilignans from *Hedvotis lawsoniae*. *Chem. Pharm. Bull.* **1985**, *33*, 1444−1451.
(19) Lin-gen, Z.; Seligmann, O.; Jurcic, K.; Wagner, H. Inhaltsstoffe von *Daphne tangutica*. *Planta Med.* **1982**, *45*, 172−176.
(20) Nakasone, Y.; Takara, K.; Wada, K.; Tanaka, J.; Yogi, S.; Nakatani, N. Antioxidant compounds isolated from kokuto, non-centrifugal cane sugar. *Biosci., Biotechnol., Biochem.* **1996**, *60*, 1714−1716.
(21) Badawi, M. M.; Handa, S. S.; Kinghorn, A. D.; Cordell, G. A.; Farnsworth, N. R. Plant anticancer agents. XXVII: antileukemic and cytotoxic constituents of *Dirca occidentalis*. *J. Pharm. Sci.* **1983**, *72*, 1285−1287.
(22) Anjaneyulu, A. S. R.; Murty, S. Chemical examination of heartwood of *Guazuma tomentosa* Kunth. *Indian J. Chem.* **1981**, *20B*, 85−87.
(23) Kim, J.-C.; Kim, K.-H.; Jung, J.-C.; Park, O.-S. An efficient asymmetric synthesis of furofuran lignans: (+)-sesamin and (−)-sesamin. *Tetrahedron: Asymmetry* **2006**, *17*, 3−6.
(24) Rao, E. V.; Sasthry, K. V.; Palanivelu, T. J. Lignan from the stem bark of *Zanthoxylum acanthapodium* DC. *Curr. Sci.* **1975**, *44*, 228−230.
(25) Abe, F.; Yahara, S.; Kubo, K.; Nonaka, G.; Okabe, H.; Nishioka, I. Studies on *Xanthoxylim* spp. II. Constituents of the bark of *Xanthoxylum piperitum* DC. *Chem. Pharm. Bull.* **1974**, *22*, 2650−2655.
(26) Kang, S. S.; Kim, J. S.; Jung, J. H.; Kim, Y. H. NMR assignments of two furofuran lignans from sesame seeds. *Arch. Pharmacal Res.* **1995**, *18*, 361−363.
(27) Haslam, E.; Haworth, R. D. The constituents of natural phenolic resins. Part XXIII. The constitution of sesamolin. *J. Chem. Soc.* **1955**, 827−833.
(28) Takano, S.; Ohkawa, T.; Tamori, S.; Satoh, S.; Ogasawara, K. Enantio-controlled route to the furofuran lignans: the total synthesis of (−)-sesamolin, (−)-sesamin, and (−)-acuminatolide. *J. Chem. Soc., Chem. Commun.* **1988**, 189−191.
(29) Osawa, T.; Nagata, M.; Namiki, M.; Fukuda, Y. Sesamolinol, a novel antioxidant isolated from sesame seeds. *Agric. Biol. Chem.* **1985**, *49*, 3351−3352.
(30) Maiti, G.; Adhikari, S.; Roy, S. G. Stereoselective total synthesis of (±)-samin and the dimethoxy analogue, the general furofuran lignan precursors. *Tetrahedron* **1995**, *51*, 8389−8396.
(31) Fukuda, Y.; Isobe, M.; Nagata, M.; Osawa, T.; Namiki, M. Acidic transformation of sesamolin, the sesame-oil constituent, into an antioxidant bisepoxylignan, sesaminol. *Heterocycles* **1986**, *24*, 923−926.
(32) Saleem, M.; Kim, H. J.; Ali, M. S.; Lee, Y. S. An update on bioactive lignans. *Nat. Prod. Rep.* **2005**, *22*, 696−816.
(33) Satake, H.; Ono, E.; Murata, J. Recent advances in the metabolic engineering of lignan biosynthesis pathway for the production of transgenic plant-based food and supplements. *J. Agric. Food Chem.* **2013**, *61*, 11721−11729.
(34) Renouard, S.; Tribalatc, M.-A.; Lamblin, F.; Mongelard, G.; Fliniaux, O.; Corbin, C.; Marosevic, D.; Pilard, S.; Demailly, H.; Gutierrez, L.; Hano, C.; Mesnard, F.; Lainé, E. RNAi-mediared pinoresinol larisiresinol reductase silencing in flaz (*Linum usitatissimum* L.) seed coat: consequences on lignans and neolignans accumulation. *J. Plant Physiol.* **2014**, *171*, 1372−1377.

DOI: 10.1021/acs.jafc.5b01099
J. Agric. Food Chem. 2015, 63, 5224−5228

JOURNAL OF AGRICULTURAL AND FOOD CHEMISTRY

Article

pubs.acs.org/JAFC

Identification and Quantification of Flavonoids from Two Southern Italian Cultivars of *Allium cepa* L., Tropea (Red Onion) and Montoro (Copper Onion), and Their Capacity to Protect Human Erythrocytes from Oxidative Stress

Idolo Tedesco,[†] Virginia Carbone,[†] Carmela Spagnuolo,[†] Paola Minasi, and Gian Luigi Russo*

Institute of Food Sciences, National Research Council, 83100 Avellino, Italy

ABSTRACT: Onions (*Allium cepa*) are consumed worldwide and represent an important source of dietary phytochemicals with proven antioxidant properties, such as phenolic acids, flavonoids, thiosulfinates, and anthocyanins. Epidemiological and experimental data suggest that regular consumption of onions is associated with a reduced risk of degenerative disorders. Therefore, it is of interest to investigate the biological properties of different varieties of onions. Here, we characterized for the first time a variety of onion, called Ramata di Montoro (coppery onion from Montoro), grown in a niche area in southern Italy, and compared its phenolic profile and antioxidant properties to a commercial ecotype of red onion, Tropea, also present in southern Italy. An analytical method based on high-performance liquid chromatography coupled with UV detection and mass spectrometry was used to separate and characterize the phenolic fraction (anthocyanins and flavonols) extracted from both coppery and red types. The main compounds detected in the two ecotypes were quercetin and quercetin glucosides, isorhamnetin glucosides, kaempferol glucoside, and, among anthocyanins, cyanidin glucosides. Tropea ecotype onion showed a higher content of flavonols (632.82 mg/kg fresh weight) than Montoro type onion (252.91 mg/kg fresh weight). Accordingly, the antioxidant activity of the former was 2.8-fold higher compared to the latter. More pronounced were the differences existing between the four anthocyanins detected in the two ecotypes, with those in the Tropea ecotype onion present at concentrations 20−230-fold higher than in the Montoro type onion. Both extracts reduced LDL oxidation about 6-fold and protected human erythrocytes from oxidative damage induced by HClO by about 40%. In addition, as a consequence of HClO treatment, glutathione concentration in erythrocytes was reduced about 50% and pretreatment with onion extracts induced a recovery of glutathione level by about 15−22%. Qualitative differences highlighted in the chemical composition of the two phenolic extracts, especially the total content of anthocyanins, which was 30-fold higher in Montoro type onion compared to Tropea ecotype, can be associated with the protective effects measured against oxidative damage induced in human erythrocytes.

KEYWORDS: *Allium cepa, Tropea red onion, Montoro copper onion, polyphenols, antioxidants, oxidative stress, HPLC-MS*

INTRODUCTION

Onions are the second most produced vegetable crop after tomatoes, with about 3 642 000 ha grown annually worldwide and a production of 53.6 Mt.[1,2] Their large distribution is probably due to the versatile culinary uses as raw food or in different modes of cooking (baked, boiled, braised, grilled, fried, roasted, etc.). In addition, onions are considered among the healthier vegetables due to the high levels of nonnutrient compounds, such as phenolic acids, flavonoids, thiosulfinates, and anthocyanins. For these reasons, it is of interest to study and characterize the chemical and biological properties of new varieties, including those grown in niche geographical areas, which are produced in limited amounts but may represent a potential source of new biological compounds. Onions are among the richest sources of dietary flavonoids. In bulbs, only compounds belonging to flavonols, anthocyanins, and dihydroflavonols have been detected. As reviewed,[3] yellow onions contain 270−1187 mg/kg fresh weight (FW) flavonols, whereas red onions contain 415−1917 mg/kg FW flavonols. Quercetin derivatives (quercetin 4′-glucoside and quercetin 3,4′-diglucoside) are the predominant flavonols in all onion cultivars. The anthocyanins of red onions (approximately 10% of the total flavonoid content) are mainly cyanidin glucosides acylated with malonic acid or nonacylated.[3] Storage of onions for 6 weeks in different conditions resulted in a decrease of 64−73% of total anthocyanins,which paralleled a reduction in total antioxidant activity of 29−36%.[4] In this regard, it is worthwhile to mention that onions are considered among the major sources of antioxidant compounds,[5] whose level of activity is related to the different cultivars and colors.[6−10]

The scientific literature of the last 20 years or so has been influenced by the syllogism that since free radicals damage cellular structures, their scavenging by antioxidants is health-protective. As a consequence, an increased uptake of antioxidants, such as those deriving from a fruits- and vegetables-rich diet, may increase resistance to reactive-species-induced pathologies. Although this concept probably overestimates the antioxidant capacity of phytochemicals and, possibly, generated misinterpretations in the field,[11,12] biochemical and genetic studies on cellular and animal models on the mechanism(s) of action of phytochemicals provide a

Received: March 8, 2015
Revised: April 26, 2015
Accepted: May 12, 2015
Published: May 12, 2015

ACS Publications © 2015 American Chemical Society

DOI: 10.1021/acs.jafc.5b01206
J. Agric. Food Chem. 2015, 63, 5229−5238

functional explanation of how and why a diet rich in fruits and vegetables can protect against degenerative diseases.[13,14]

Therefore, scientists in this field are constantly in search of novel agronomic species and/or local varieties possessing enhanced protective effects against oxidative damage in cellular and animal models. In the present work, we focused our attention on a local variety of onion, known as Ramata di Montoro (coppery onion from Montoro area; COM), whose cultivation was born and passed down through generations in the area of Montoro Inferiore, a village located in the province of Avellino (southern Italy). We compared the antioxidant properties of polyphenols isolated from COM to a better-characterized commercial ecotype, red Tropea onion (RTO), a variety of red onion grown in a specific area of Calabria, a region in southern Italy.[15]

In the present study, an analytical method based on high-performance liquid chromatography (HPLC) coupled with UV detection and mass spectrometry was used to separate and characterize the phenolic fraction (anthocyanins and flavonols) extracted from cultivated bulbs of COM compared to RTO ecotype. Polyphenolic extracts from the two onions were evaluated for their antioxidant activity. Subsequently, we investigated the protective role of phenolic extracts from RTO and COM against low-density lipoprotein (LDL) oxidation and hypochlorous acid-induced oxidative damage in normal red blood cells (RBCs, erythrocytes) and their interference with the antioxidant defense systems active in erythrocytes. Oxidized LDL contain a diverse set of toxic species, such as aldehydes, oxysterols, and lipid peroxides.[16] They are considered as an important initial step in the development of atherosclerosis; therefore, lowering LDL levels by independent mechanisms is considered protective against the likelihood of atherosclerotic events.[17−19] Previous studies indicated that phytochemicals, such as phenolic acids, flavonoids, and anthocyanins, inhibited LDL oxidation.[20−23] RBCs have been selected as the study model since, for their physiological role, they are exposed to continuous oxidative stress deriving from endogenous[24] or exogenous sources.[25] For these reasons, RBCs have developed efficient enzymatic and nonenzymatic antioxidant defenses to preserve themselves from oxidative damage. In addition, due to their mobility, erythrocytes can be considered as ideal antioxidant scavengers acting throughout the circulation and reducing the damaging mass effect of elevated levels of reactive oxygen species (ROS) on different tissues.[24−26] Therefore, we established a novel in vitro model using RBCs isolated from whole blood, treated with HClO (hypochlorous acid). Millimolar concentrations of HClO generate osmotic fragility and formation of transient membrane pores with the consequent hemolysis of erythrocytes.[27] Treatment with HClO cannot be seen as an experimental adaptation to allow the functionality of our assay on RBCs, but it is very close to physiological processes; in fact, following inflammatory tissue injury and microbial killing, neutrophils and monocytes generate hyperproduction of HClO in the millimolar range.[28]

On the basis of these observations, we first chemically characterized the polyphenolic contents of RTO and COM ecotypes, the latter representing a new variety while the former was used as a reference, being already described and characterized. Subsequently, we compared their protective effect against oxidative damage by taking advantage of two different assays: (i) capacity to reduce LDL oxidation and (ii) protection of human RBCs from healthy subjects from oxidative insult caused by HClO treatment.

MATERIALS AND METHODS

Chemicals. Methanol and formic acid were obtained from Merck (Darmstadt, Germany). Quercetin, Folin−Ciocalteu's reagent, 2,4,6-tris(2-pyridyl)-*s*-triazine (TPTZ), glutathione (GSH), phthaldialdehyde, trichloroacetic acid (TCA), hydrogen peroxide (H_2O_2), low-density lipoprotein (LDL) from human plasma, cupric sulfate anhydrous, xylenol orange, ferrous ammonium sulfate, and butylated hydroxytoluene (BHT) were purchased from Sigma−Aldrich (Milan, Italy). Isoquercitrin (quercetin 3-*O*-glucoside) was obtained from Fluka (Buchs SG, Switzerlandand). Cyanidin 3-*O*-glucoside chloride (kuromanin chloride), delphinidin 3-*O*-glucoside chloride (myrtillin chloride), quercetin 3,4′-di-*O*-glucoside, quercetin 4′-*O*-glucoside (spiraeoside), and kaempferol 3-*O*-glucoside were purchased from Extrasynthese (Genay, France). Ferric chloride, sodium carbonate, and sodium hypochlorite were from Carlo Erba (Milan, Italy). Phosphate-buffered saline (PBS) tablets were purchased from Invitrogen (S. Giuliano Milanese, Milan, Italy). HPLC-grade water (18.2 mΩ) was prepared by use of a Millipore Milli-Q purification system (Millipore Corp., Bedford, MA). All other chemicals used were of research highest purity grade.

Onion Collection and Sample Treatment. Cultivated bulbs of onion, *Allium cepa* L. Tropea ecotype, were collected in Tropea (Calabria, Italy), while cultivated bulbs of brown onion, *Allium cepa* L. Montoro type, were kindly provided by local committee promoters of Cipolla Ramata di Montoro (www.cipollaramatadimontoro.it) located in Montoro (Campania, Italy). The name Cipolla Ramata (coppery onion) derives from the color of the external skin of the bulb. This variety is cultivated in a niche geographical area in southern Italy (17 areas within Avellino and Salerno districts).

For each variety, two bulbs were finely chopped and 10 g was extracted with 20 mL of 80% aqueous methanol, at room temperature, on a horizontal shaker. After 10 min, samples were placed in an ultrasonic bath and sonicated for 15 min and then filtered through filter paper. Extracts were then dried in a rotary evaporator (LaboRota 4000/HB Efficient, Heidolph) and stored at −20 °C until being used.

Analysis of Total Phenolic Content and Antioxidant Capacity. Dry extracts were suspended in PBS to obtain a stock solution of 50 mg/mL (w/v) and kept at 4 °C in the dark. This stock solution was used in all biological assays performed in the present study and for the analysis of total phenolic content and antioxidant capacity. The amount of total phenols was determined according to the Folin−Ciocalteu procedure[29−31] with quercetin as a reference standard. Briefly, 50 μL of Folin−Ciocalteu's reagent and 500 μL of distilled water were added to 10 μL of suitable aqueous dilution of the stock solution (50 mg/mL, w/v). The reaction mixture was mixed and allowed to stand for 2 min. Finally, 0.1 mL of sodium carbonate and 0.34 mL of distilled water were added, and the solution was incubated in the dark for 120 min. The sample's absorbance was measured at 760 nm. The results were expressed as micromolar equivalent of quercetin (QE) in 1 mg/mL onion extracts. All measurements were carried out in triplicate.

The antioxidant capacity of different onion extracts was determined by a ferric reducing antioxidant power (FRAP) assay, as reported,[32] and results were calculated as micromolar QE in 1 mg/mL of the two onion extracts.

Ascorbic acid (AA) content in onion extracts was determined by the ferric reducing ascorbate (FRASC) method.[33] Samples were treated with 10 international units of ascorbate oxidase/mL, diluted in FRAP solution (20 mM $FeCl_3$ and 10 mM TPTZ in acetate buffer, pH 3.5), and finally incubated for 5 min at 37 °C. The absorbance was measured at 595 nm, and micromolar concentrations of AA were calculated by use of a standard curve.

HPLC-UV Analyses. Extracts from cultivated bulbs of the two different onion types were reconstituted in 1% formic acid and analyzed by HPLC-UV/vis on a HP 1110 series HPLC (Agilent, Palo Alto, CA) equipped with a binary pump (G-1312A) and an UV

DOI: 10.1021/acs.jafc.5b01206
J. Agric. Food Chem. 2015, 63, 5229−5238

detector (G-1314A). Individual phenols were separated on a Hypersil BDS C18 column (250 mm × 4.6 mm, 5 μm) (Thermo, Bellefonte, PA) at a flow rate of 1 mL/min; solvent A was 1% formic acid and solvent B was 1% formic acid in methanol and water (50:50, v/v). After a 5 min hold at 20% solvent B, elution was performed according to the following conditions: from 20% B to 80% B in 22 min, isocratic elution (80% B) for the next 13 min, from 80% B to 95% B in 10 min, followed by 15 min of maintenance. Flavonols were monitored at 340 nm and anthocyanins at 520 nm. Standard curves for each flavonol standard were prepared over a concentration range of 1−180 μg/mL with six different concentration levels and triplicate injections at each level. Quantification of anthocyanins was performed with external calibration curves generated by repeated injections of a fixed volume of standard solutions of cyanidin 3-*O*-glucoside over a concentration range of 0.5−20 μg/mL with five different concentration levels and duplicate injections at each level. All samples were prepared and analyzed in duplicate. Results were expressed as millgrams per kilogram fresh weight (FW).

HPLC-ESI-ITMS^n Analysis. Identification of phenolic compounds in the extracts from cultivated bulbs of the two different onion ecotypes was effected by HPLC coupled to electrospray ionization multistage ion trap mass spectrometry (HPLC/ESI-ITMS^n) on a Surveyor MS micro HPLC coupled with a Finnigan LCQ DECA XP Max ion trap mass spectrometer, equipped with Xcalibur system manager data acquisition software (Thermo Finnigan, San Jose, CA). Individual phenols were separated on a Hypersil BDS C18 column (250 mm × 2.1 mm, 5 μm) (Thermo, Bellefonte, PA) at a flow rate of 200 μL/min. The HPLC conditions were as described for the HPLC-UV system. Mass spectra were recorded from mass-to-charge ratio (m/z) 50 to 1200 both in negative and in positive ionization mode. The capillary voltage was set at −13 V, the spray voltage was 4.5 kV, and the tube lens offset was −15 V in negative-ion mode, while in positive-ion mode the capillary voltage was set at 38 V, the spray voltage was 3 kV, and the tube lens offset was 50 V. The capillary temperature was 275 °C. Data were acquired in MS, MS/MS, and MS^n scanning modes.

Low-Density Lipoprotein Oxidation. The assay was performed by incubating 0.1 mL of LDL (200 μg of protein) with or without onion extracts (0.25 mg/mL, w/v) for 15 min, and then oxidation was induced by adding 50 μM $CuSO_4$ at 37 °C for 15 h. Subsequently, 0.9 mL of FOX reagent (1 mM xylenol orange, 2.5 mM ferrous ammonium sulfate, and 4.4 mM BHT in methanol) was added to each sample. After 30 min, samples were centrifuged in a microfuge at maximal speed for 5 min, and absorbance of the supernatants was detected spectrophotometrically at 560 nm. Values were expressed as hydrogen peroxide equivalents.[30,34]

Blood Samples. Whole blood samples were obtained from 16 healthy donors, collected in ethylenediaminetetraacetate (EDTA) -treated tubes and immediately used. All blood samples were obtained after informed consent. Erythrocytes were isolated by centrifugation, 2000*g* for 15 min, to remove plasma, platelets and buffy coat and washed twice in PBS. Erythrocyte pellets were suspended in PBS, and aliquots of 1.2×10^5 cells/μL were used in all experiments presented.

Reaction of Human Erythrocytes with HOCl and Hemolysis Assay. NaOCl was diluted with PBS, and the pH of the solution was adjusted to 7.4 immediately before use. At this pH, the solution contains approximately equimolar amounts of HClO and NaOCl and is referred to hereafter as HClO.[35]

Diluted erythrocytes in PBS (1.2×10^5 cells/μL) were pretreated with onion extracts at the indicated concentrations for 45 min and then 0.3 mM HClO was added for 15 min at 37 °C. After incubation with HClO, samples were centrifuged at 2000*g* for 2 min, and percent hemolysis was determined spectrophotometrically at 540 nm.[24]

Glutathione Measurement and Catalase Assay. In parallel with the hemolysis assay, glutathione (GSH) concentration and catalase enzymatic activity were measured. GSH determination was evaluated by a spectrofluorometric method. Following treatments, erythrocyte pellets were washed with PBS and then proteins were precipitated with TCA (5.0% v/v final concentration in 0.1 M HCl and 10 mM EDTA). Fluorescence of the supernatants was measured at 340 nm (excitation wavelength) and 460 nm (emission wavelength). GSH concentration was calculated from a standard curve and reported as a percentage compared to controls (untreated samples).[24]

To determine catalase activity, after treatment, erythrocytes were diluted with cold distilled water, ethanol, and chloroform (1.5:1:1 v/v/v) to precipitate the hemoglobin. Samples were shaken vigorously and centrifuged at 13000*g* for 3 min, and the water−ethanol layer was used. Catalase activity was evaluated as the first-order kinetic constant of the rate of disappearance of H_2O_2, measured by absorbance at 240 nm, as reported previously.[36] Values were expressed as specific activity of the samples and reported as a percentage of control (untreated sample).

Statistical Analysis. Data are presented as mean values ± standard deviation (SD). For LDL oxidation, hemolysis assay, GSH measurement, catalase assay, and concentration of individual and total polyphenolics determined by HPLC, significance was measured by use of Student's t test. Number of determinations is reported in the figure legends.

RESULTS AND DISCUSSION

Total Polyphenol Content and Antioxidant Activity. Total phenolic content of onion extracts indicate that the highest content of total polyphenols was found in Tropea onion ecotype (29.35 μM QE). They were 2.3-fold higher than those present in Montoro onion (12.68 μM QE) (Table 1). As expected, considering the result of the Folin−Ciocalteu assay, the antioxidant capacity was proportional to the polyphenol content, with RTO showing the highest values, which were about 3-fold higher than COM extract (Table 1).

Table 1. Concentration of Total Polyphenols and Antioxidant Activity of Tropea and Montoro Onion Bulb Extracts[a]

	Tropea red onion (μM QE)	Montoro copper onion (μM QE)	P
total polyphenols[b]	29.35 ± 0.03	12.68 ± 0.02	8.91×10^{-5}
antioxidant activity[c]	4.79 ± 0.02	1.67 ± 0.01	8.67×10^{-5}

[a]With reference to 1 mg/mL (w/v) extract. Results are expressed as average (mean) concentration ± SD of triplicates. [b]By Folin−Ciocalteu method. [c]By ferric reducing antioxidant power (FRAP) assay.

While for COM no previous data were reported in the literature on its total polyphenol content and antioxidant activity to allow a comparison with our results, the information on red onion ecotypes is widely available. Although the use of different extraction protocols complicates the comparison among data from different articles, our determinations are comparable to those reported by others. As an example, Marotti and Piccaglia[37] measured a total amount of flavonoids in the ecotype Tropea rossa tonda of 762.9 mg/kg, not far from 632.82 mg/kg of total flavonols reported in Table 3. In three red ecotypes from Spain, total flavonols ranged between 211.7 and 304.3 mg/kg, lower than Tropea onion but of the same order of magnitude.[2] Comparative evaluation of antioxidant capacity appears more complicated because of the different methods and units used to measure it. However, in general, red onion ecotypes present higher values of antioxidant capacity independently from the scale of color. A good example in this sense is reported by a Turkish group who demonstrated that, in 14 different cultivars differing in color, the red onions had higher antioxidant activities than yellow and white onions although the former had the richest phenolic contents.[15]

DOI: 10.1021/acs.jafc.5b01206
J. Agric. Food Chem. 2015, 63, 5229−5238

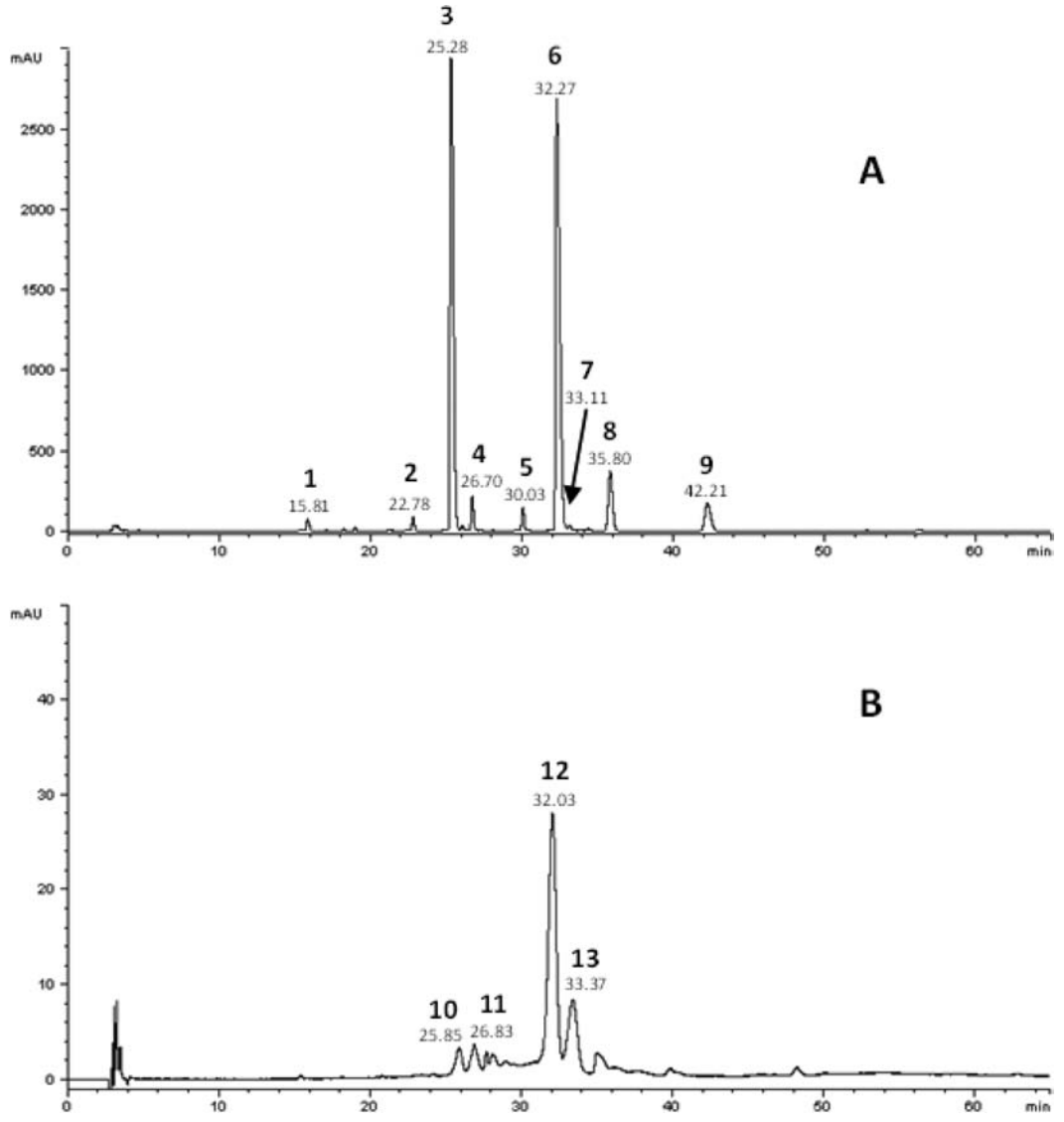

Figure 1. HPLC chromatograms of extract from cultivated bulbs of *Allium cepa* L. Montoro type, recorded at (A) 340 nm and (B) 520 nm. Peaks are labeled according to Table 2.

Identification and Quantification of Polyphenols in the Two Different Onion Extracts. HPLC-UV/vis chromatograms of extract from cultivated bulbs of *Allium cepa* L. Montoro type are shown in Figure 1. Nine flavonols and four anthocyanins were identified and quantified (Tables 2 and 3). The main flavonols found in this onion type were quercetin 3,4′-di-*O*-glucoside and quercetin 4′-*O*-glucoside (spiraeoside), which accounted for ∼85% of the total flavonol content. Results obtained from HPLC-UV/vis and ESI−ITMS^n analyses of Tropea ecotype onion and the total phenolic content measured by HPLC-UV/vis (expressed as mg/kg FW) are also reported in Table 3. RTO showed a higher content of flavonols (632.82 mg/kg FW) than COM (252.91 mg/kg FW). Only kaempferol 3-*O*-glucoside was present in COM and absent in RTO. More pronounced were the differences existing between the four anthocyanins detected in the two ecotypes, with those in RTO present at concentrations between 20-fold (peak 12 in Table 3) and 230-fold (peak 10 in Table 3) higher than in COM. All these differences, including the significant difference in anthocyanin content, may justify the high level of antioxidant capacity measured in RTO (Table 1).

As to anthocyanins, both RTO and COM contained cyanidin glucosides, acylated or not with malonic acid (Tables 2 and 3), which are known to be present in various cultivars of red onions.[3,38,39] The presence of delphinidin and petunidin derivatives has been reported in RTO.[3,4] However, our analyses did not confirm these results. In fact, the HPLC analysis at 340 nm of RTO, specifically used for monitoring flavonols, showed the presence of two very intense peaks at t_R 25.35 and 32.51 min and minor peaks at t_R 26.72 and 36.01 min (data not shown). Compounds present in these fractions produced molecular ions at m/z 627, 465, 641, and 479 respectively, in ESI−ITMS^n analysis carried out in positive-ion mode and were identified as flavonols quercetin 3,4′-diglucoside, quercetin 4-*O*-glucoside, isorhamnetin 3,4′-diglucoside, and isorhamnetin 4′-glucoside. In addition, ESI−ITMS^n analysis of these fractions carried out in negative-ion mode further confirmed the presence of these flavonols (Table 3). In contrast, compounds originating at the same m/z values (m/z 627, 465, 641 and 479) were previously identified as delphinidin and petunidin derivatives.[3,4] It is important to note that quercetin and delphinidin, as well as isorhamnetin and petunidin, displayed

DOI: 10.1021/acs.jafc.5b01206
J. Agric. Food Chem. 2015, 63, 5229−5238

Table 2. List of Compounds Identified in Cultivated Bulbs of *Allium cepa* L. Montoro Extract by HPLC-UV/Vis and HPLC-ESI-ITMS^n

peak	t_R (min)	$[M - H]^-$ (m/z)	MS/MS ions (m/z)	identification
1	15.81	787	625, 463, 301	quercetin 3,7,4′-triglucoside
2	22.78	625	463, 301	quercetin 7,4′-diglucoside
3	25.28	625	463, 301	quercetin 3,4′-diglucoside
4	26.70	639	477, 315	isorhamnetin 3,4′-diglucoside
5	30.03	463	300	quercetin 3-*O*-glucoside[a]
6	32.27	463	301	quercetin 4′-*O*-glucoside
7	33.11	447	285	kaempferol 3-*O*-glucoside
8	35.80	477	315	isorhamnetin 4′-glucoside
9	42.21	301	179, 151	quercetin
peak	t_R (min)	$[M]^+$ (m/z)	MS/MS ions (m/z)	identification
10	25.85	449	287	cyanidin 3-glucoside
11	26.83	611	449, 287	cyanidin 3-laminaribioside[b]
12	32.03	535	449, 287	cyanidin 3-(6″-malonylglucoside)
13	33.37	697	535, 449, 287	cyanidin 3-malonyllaminaribioside[c]

[a]Also known as isoquercitrin. [b]Also known as cyanidin 3-glucosylglucoside. [c]Also known as cyanidin 3-malonylglucosylglucoside.

the same m/z value in the mass spectrum in positive ESI mode (m/z 303 pseudomolecular ion $[M + H]^+$ for quercetin and protonated molecular ion M^+ for delphinidin; m/z 317 pseudomolecular ion $[M + H]^+$ for isorhamnetin and protonated molecular ion M^+ for petunidin). Moreover, quercetin 3,4′-diglucoside, quercetin 4-*O*-glucoside, isorhamnetin 3,4′-diglucoside, and isorhamnetin 4′-glucoside originated MS/MS spectra in positive-ion mode very similar to those of delphinidin (glucosyl glucoside), delphinidin-3-glucoside, petunidin (glucosyl glucoside), and petunidin glucoside, respectively, so that, in this case, tandem mass spectrometry does not lead to a definite discrimination of these compounds and accurate HPLC data are crucial to achieve a conclusive result. In order to rule out the presence of at least delphinidin 3-glucoside, the corresponding standard was analyzed by HPLC-UV/vis under the reported experimental condition. In agreement with the elution order reported by Wu and Prior,[40] the retention time of this compound (t_R 22.64 min) was lower than that of cyanidin 3-glucoside (t_R 25.88) and of any peak in our HPLC chromatogram (Figure 2), thus definitively ruling out the presence of delphinidin-3-glucoside in RTO.

Effect of Onion Extracts on Oxidized Low-Density Lipoprotein. To confirm the antioxidant role of onion extracts and to highlight potential differences between them, we evaluated their ability to reduce the oxidative state of LDL (Figure 3). We incubated commercial LDL with 50 μM Cu^{2+} for 15 h to obtain oxidized LDL. Pretreating isolated LDL for 30 min with 0.25 mg/mL (w/v) onion extracts resulted in a strong and significant reduction in oxidized LDL (Figure 3). The extracts derived from COM and RTO were tested at the same final concentration of 0.25 mg/mL, corresponding to 3.1 and 7.2 μM QE, respectively. Therefore, although the relative polyphenolic amounts of COM was 2.3-fold lower than RTO, they exerted a similar and significant protective effect when compared to oxidized LDL (Cu^{2+} bar in Figure 3), while the difference between RTO + Cu^{2+} and COM + Cu^{2+} time points was not significant. These data suggest that the higher antioxidant capacity of RTO, emerging from Table 1, does not reflect an increased protective activity against LDL oxidation compared to COM.

Protective Effect of Onion Extract against Erythrocyte Oxidative Damage. From the previous results, we hypothesized that the antioxidant activity of the two onion extracts

Table 3. Concentration of Individual and Total Polyphenolics in Extracts of Tropea and Montoro Onions[a]

peak	compd	Tropea ecotype	Montoro ecotype	P
		Flavonols		
1	quercetin 3,7,4′-triglucoside	4.60 ± 0.09	2.44 ± 0.05	0.0011
2	quercetin 7,4′-diglucoside	4.93 ± 0.02	2.18 ± 0.10	0.0007
3	quercetin 3,4′-diglucoside	296.46 ± 0.05	103.70 ± 0.13	<0.0001
4	isorhamnetin 3,4′-diglucoside	21.31 ± 0.07	5.55 ± 0.17	<0.0001
5	quercetin 3-*O*-glucoside ([b])	13.59 ± 0.21	4.22 ± 0.09	0.0003
6	quercetin 4-*O*-glucoside	226.92 ± 0.10	109.76 ± 0.73	<0.0001
7	kaempferol 3-*O*-glucoside		0.75 ± 0.07	
8	isorhamnetin 4′-glucoside	53.98 ± 0.42	16.68 ± 0.66	0.0002
9	quercetin	11.03 ± 0.67	7.63 ± 0.52	0.0298
	total flavonols	632.82 ± 0.89	252.91 ± 2.33	
		Anthocyanins		
10	cyanidin 3-glucoside	4.62 ± 0.25	0.02 ± 0.01	0.0015
11	cyanidin 3-laminaribioside[c]	2.49 ± 0.10	0.04 ± 0.01	0.0008
12	cyanidin 3-(6″-malonylglucoside)	17.18 ± 0.75	0.88 ± 0.21	0.0011
13	cyanidin 3-malonyllaminaribioside[d]	5.83 ± 0.52	0.24 ± 0.07	0.0043
	total anthocyanins	30.12 ± 1.62	1.19 ± 0.29	
	total polyphenols[e]	662.94 ± 2.51	254.10 ± 2.62	

[a]Results were determined by HPLC and are expressed as average (mean) concentration (mg/kg FW) ± SD of triplicate samples. [b]Also known as isoquercitrin. [c]Also known as cyanidin 3-glucosylglucoside. [d]Also known as cyanidin 3-malonylglucosylglucoside. [e]By HPLC method.

DOI: 10.1021/acs.jafc.5b01206
J. Agric. Food Chem. 2015, 63, 5229−5238

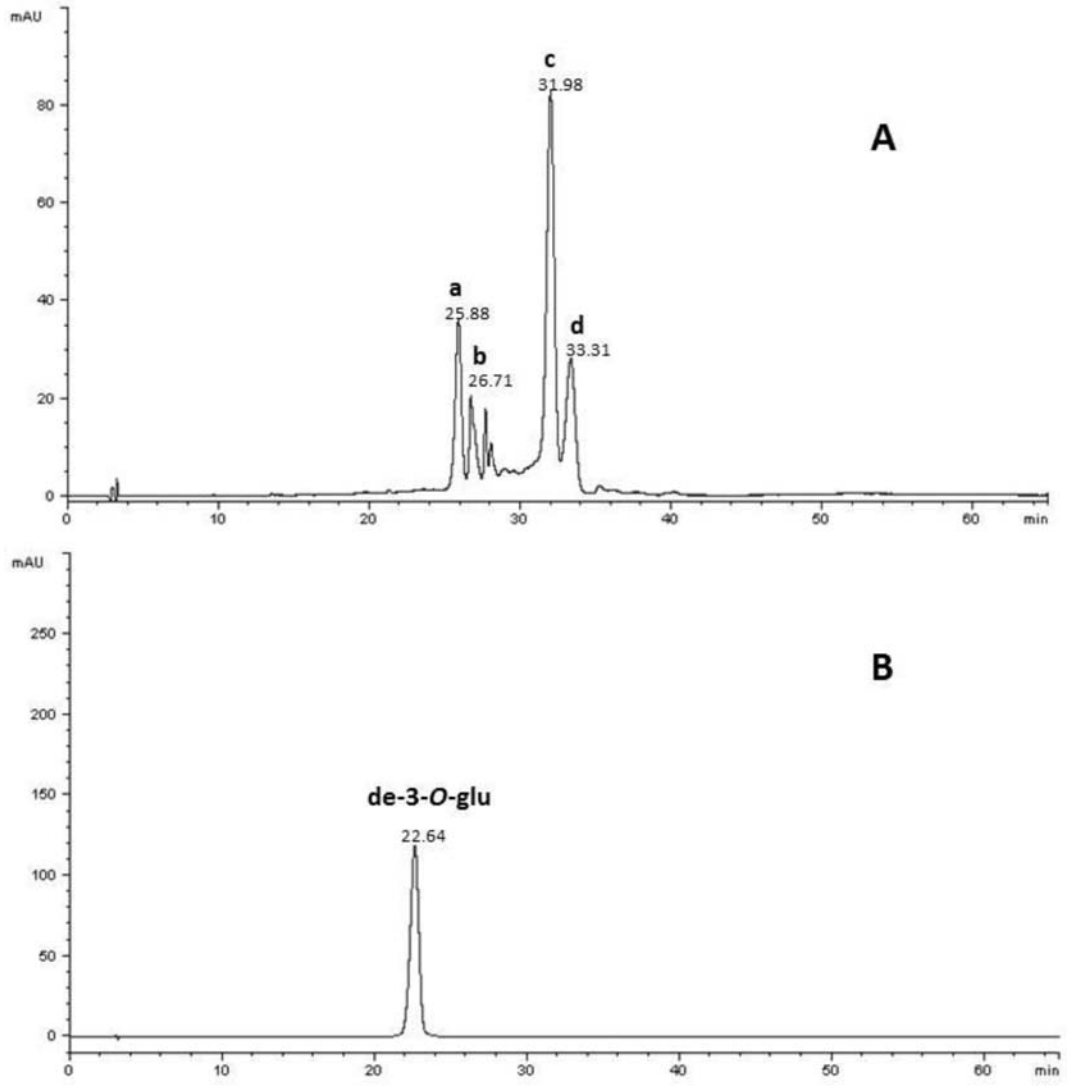

Figure 2. HPLC chromatograms of (A) extract from cultivated bulbs of *Allium cepa* L. Tropea ecotype recorded at 520 nm, with peaks (a) cyanidin 3-glucoside, (b) cyanidin 3-laminaribioside [cyanidin 3-glucosylglucoside], (c) cyanidin 3-(6″-malonylglucoside), and (d) cyanidin 3-malonyllaminaribioside [cyanidin 3-malonylglucosylglucoside]; and of (B) delphinidin 3-*O*-glucoside standard (de-3-*O*-glu).

(Table 1 and Figure 3) could be protective in maintaining redox homeostasis in human erythrocytes. On the basis of this model, we stimulated RBCs isolated from 16 healthy donors, with 0.3 mM HClO to obtain hemolysis of about 25% (Figure 4). Pretreating with 0.25 mg/mL (w/v; corresponding to 3.1 μM QE COM and 7.2 μM QE RTO) of the two onion extracts for 45 min resulted in a significant protective effect against HClO-induced hemolysis of 15% and 17% for RTO and COM, respectively (Figure 4a). The selected concentration applied (e.g., 0.25 mg/mL) was not hemolytic per se; moreover, from previous data we deduce that the total concentration of polyphenols applied in our assay was of the same order of magnitude as that reachable in vivo following ingestion of an amount of onion enough to bring the blood concentration of quercetin near 1 μM.[41−43]

It is worthwhile to note that also in this case, as above for LDL oxidation, the two onion types induced a similar protective effect, despite the 2.31- and 2.86-fold higher amount of polyphenolic content and antioxidant capacity in RTO compared to COM, respectively (Table 1). To better clarify this point, we treated RBCs with equal concentrations of polyphenols (final concentration 2.7 μM QE). In this case, the total amount of polyphenols expressed as QE in our assays was 0.963 μg for RTO and 0.978 μg for COM. As reported in Figure 4b, we observed that COM significantly protected RBCs against HClO-induced hemolysis, while the limited reduction observed for RTO was not significant compared to the control (HClO bar). Mathematical elaboration of data presented in Figure 4 (data not shown) indicates that, to increase by 1% the protective effect of RTO against HClO, 0.208 μg QE of extract is necessary. In the case of COM, only 0.081 μg QE (2.5-fold less) is sufficient. This calculation further demonstrates the higher efficacy of COM extract compared to RTO.

In addition, we can exclude that the presence of AA could contribute to the protection from HClO damage shown in Figure 4. In fact, upon measuring by FRASC assay the AA amount present in 0.25 mg/mL COM and RTO extracts, we observed that AA was null in RTO and present at a concentration of 0.277 μM in COM. When we repeated the assay in the presence of AA in a wide range (0.11−0.55 μM), no reduction of HClO-dependent hemolysis was observed (data not shown).

DOI: 10.1021/acs.jafc.5b01206
J. Agric. Food Chem. 2015, 63, 5229−5238

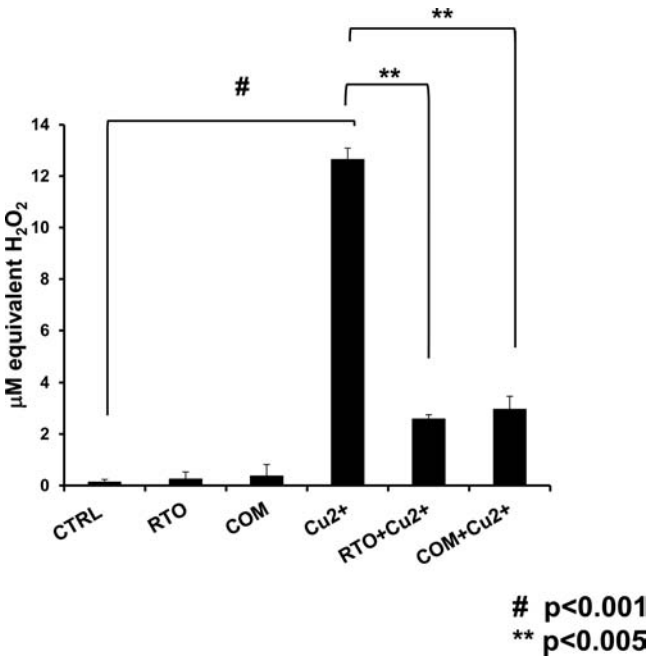

Figure 3. Effect of onion extracts on LDL oxidation. LDL were incubated for 30 min in the presence of 0.25 mg/mL (w/v) of the two different onion extracts before addition of 50 μM Cu^{2+} for 15 h. At the end of treatment, FOX assay was performed to determinate the level of H_2O_2 generated following LDL oxidation. Bar graphs represent the mean ± SD. Experiments were carried out in duplicate. Symbols indicate significance: (#) $p < 0.001$ with respect to untreated LDL (CTRL), (**) $p < 0.005$ with respect to Cu^{2+}-treated samples.

Effects of Onion Extracts on Antioxidant Defenses in Human Erythrocytes. RBCs excellently regulate intracellular oxidative stress; in fact, through the combined activities of GSH peroxidase, catalase, superoxide dismutase (SOD), and shunting of hexose monophosphate, they are able to protect themselves against ROS.[44] We measured GSH level in RBCs isolated from 16 healthy donors, pretreated with 0.25 mg/mL COM and RTO extracts (corresponding to 3.1 and 7.2 μM QE, respectively) for 45 min before HClO addition. As a consequence of HClO treatment, we observed about 50% reduction in GSH concentration present in RBCs. Pretreatment with onion extracts induced a recovery of GSH level of about 22% and 15% for RTO and COM, respectively (Figure 5a). Data were significant for the former, and the trend of increased production of GSH was confirmed in COM. Similarly to diseases associated with increased production of ROS, the presence of a strong electrophile, such as HClO, causes rapid consumption of GSH in RBCs,[24,45] and restoration of the normal erythrocyte GSH concentration has been shown to have a positive therapeutic effects.[45,46] The protective role of onion extracts against oxidative stress was also confirmed by their effect on catalase activity, which increases 2.3-fold compared to basal level after HClO treatment and decreases after pretreatment with the two onion extracts (Figure 5b).

We hypothesized that treatment of whole human blood with a HClO concentration not far from that reachable in vivo following an inflammatory process induces large hemolysis in RBCs, caused by a burst of intracellular ROS. Pretreatment of whole blood with onion extracts generates a protective effect against HClO-induced hemolysis. We postulated that the bioactive compounds in RTO and COM extracts trigger downstream events leading to increased GSH concentration,

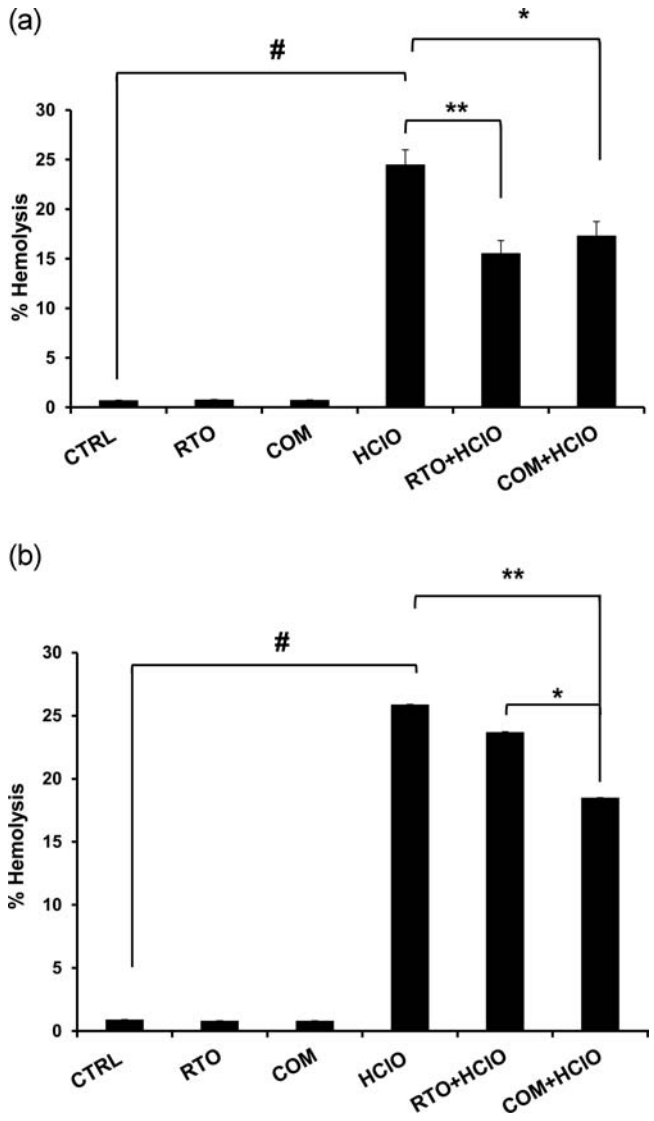

Figure 4. Effect of onion extracts on hemolysis of human erythrocytes. (a) RBCs from 16 healthy donors (in duplicate) were stimulated with 0.25 mg/mL extracts prepared from the two different onion cultivars and incubated for 45 min at 37 °C. (b) RBCs were stimulated with 50 μM QE (final concentration in the assay 2.7 μM QE). Following incubation with the onion extracts, samples were treated with 0.3 mM HClO for 15 min at 37 °C and percentage of hemolysis was measured. Bar graphs represent the mean ± SD. Symbols indicate significance: in panel a, (#) $p < 0.0001$ with respect to untreated RBCs (CTRL) and (*) $p < 0.005$ and (**) $p < 0.0005$ with respect to HClO; in panel B, (#) $p < 0.0001$ with respect to untreated RBCs (CTRL), (*) $p < 0.05$ for RTO + HClO vs COM+HClO, and (**) $p < 0.005$ for COM +HClO vs HClO.

which in turn protects erythrocytes from subsequent oxidative damage caused by HClO (Figure 5). How molecules present in the extracts are responsible for de novo GSH synthesis is actually under investigation in our laboratory. A model for GSH synthesis and turnover in the human erythrocyte has been recently published and represents the starting point for future studies.[47]

We described for the first time to our knowledge the flavonoid composition of a new ecotype of red onion, the coppery onion, cultivated in a well-limited area of about 40 ha within the districts of Avellino and Salerno in southern Italy.

DOI: 10.1021/acs.jafc.5b01206
J. Agric. Food Chem. 2015, 63, 5229−5238

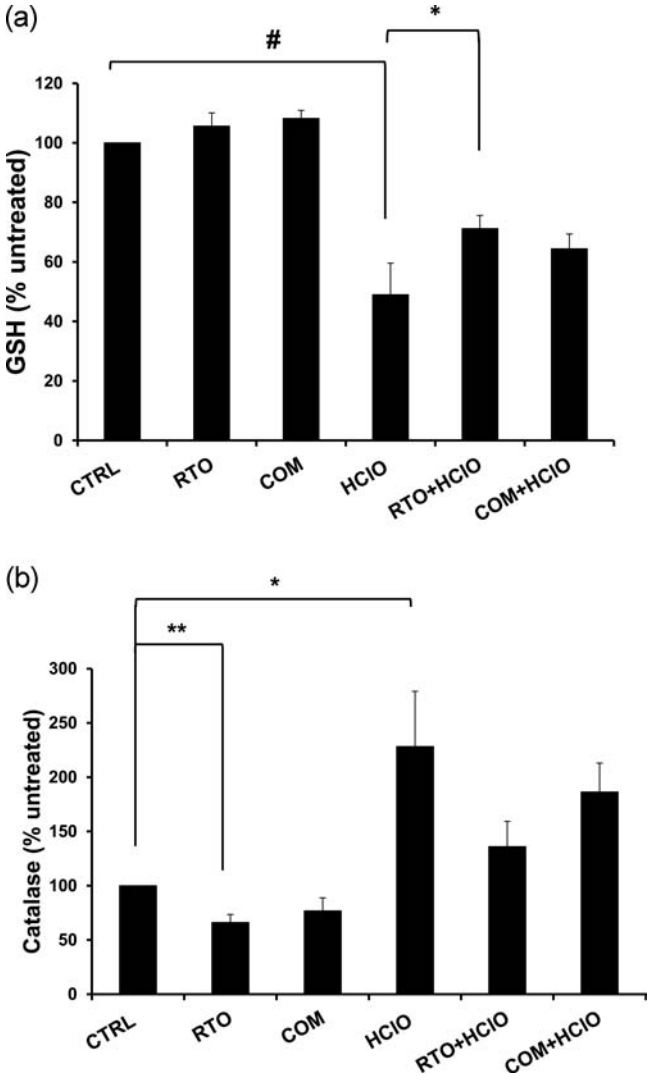

Figure 5. Effects of onion extracts on human erythrocyte antioxidant defense: (a) glutathione (GSH) and (b) catalase levels. (a) GSH content was determined after treatment of RBCs with 0.25 mg/mL extracts prepared from the two different onion cultivars. After 45 min of incubation, samples were treated with 0.3 mM HClO for 15 min at 37 °C. At the end of treatment, RBCs were lysed and phthaldialdehyde was used as a substrate, and GSH levels were measured spectrofluorometrically. (b) Catalase activity was measured in hemolysates prepared from RBCs treated as reported above and compared to untreated samples. Bar graphs represent the mean (expressed as percentage of untreated) ± SD of determinations performed on samples (in duplicate) derived from (a) 16 or (b) 11 healthy donors. Symbols indicate significance: in panel a, (#) $p < 0.0001$ with respect to untreated samples (CTRL) and (*) $p < 0.05$ with respect to HClO treatment; in panel b, (**) $p < 0.005$ and (*) $p < 0.05$ with respect to untreated samples (CTRL).

We also characterize the protective effects of COM against oxidative stress experimentally induced on LDL and RBCs. COM was compared to a red onion variety, RTO, selected for its close geographic origin (southern Italy), high concentration of polyphenols[15,37] and larger commercial distribution. From our study an important observation emerged: although total polyphenol concentration and single flavonoid compounds were both significantly higher in RTO compared to COM, the biological activity was comparable or even more pronounced in COM. This result led us to formulate the following hypotheses: (1) Qualitative compositions differ in the flavonol and anthocyanin families in the two ecotypes. (2) Synergistic associations within the pool of flavonoids in COM result in enhanced antioxidant capacity compared to RTO. (3) Polyphenols in red and coppery onions are not directly responsible for the protective antioxidant effect, which in turn can be attributed to compounds of unknown chemical structure present in relatively comparable amounts in the two extracts. (4) It may be possible that, at least for RBCs, the protective effect of onion extracts, resulting in the reconstitution of depleted intracellular GSH pools, occurs by mechanisms independent from the antioxidant activity of the extracts and involving specific binding to intracellular targets. Hypotheses 3 and 4 require intense experimental efforts, currently in progress, to be verified.

We focused our attention on the different polyphenolic composition between the two ecotypes. Data reported in Tables 2 and 3 indicate that in COM anthocyanins are almost absent (about 0.46% of the total) compared to those present in RTO (4.54%), a difference of about 1 order of magnitude. This may suggest that in Figure 4b, when we assayed comparable amount of QE, the relative abundance of anthocyanins in RTO could counteract the antioxidant effect of the flavonols present. However, initial attempts to identify a cause−effect relationship between the flavonol/anthocyanin ratio and protection from oxidative damage in erythrocytes did not provide conclusive answers.

Perhaps we are facing a situation not totally novel regarding the mechanisms of action of phenolic compounds. In fact, several cases exist in the literature demonstrating that flavonoids may exert their biological activities independently from the capacity to scavenge ROS. Quercetin represents a perfect example in this context, as we largely demonstrated in leukemic cell lines resistant to apoptotic stimuli.[48−50]

In summary, the present work reports for the first time the chemical characterization of polyphenols present in a new variety of onion from southern Italy and suggests that the phenolic-enriched extract prepared from this ecotype exerts a protective effect against oxidative damage in LDL and human erythrocytes. We also highlighted the possibility that synergistic combination of specific phenolic compounds and/or the contribution of uncharacterized molecules may explain the quantitative differences in biological activities measured when extracts derived from different onion varieties are compared.

AUTHOR INFORMATION

Corresponding Author

*Phone +39 0825 299331; fax + 39 0825 781585; e-mail glrusso@isa.cnr.it.

Author Contributions

†I.T., V.C., and C.S. contributed equally.

Funding

This work was partially supported by a grant from the Italian Ministry of Economy and Finance to the National Research Council for the project "Innovazione e Sviluppo del Mezzogiorno - Conoscenze Integrate per Sostenibilità ed Innovazione del Made in Italy Agroalimentare - Legge 191/2009" and by Regione Campania in the framework of the "Rete di Spettrometria di Massa della Campania" (RESMAC).

Notes

The authors declare no competing financial interest.

DOI: 10.1021/acs.jafc.5b01206
J. Agric. Food Chem. 2015, 63, 5229−5238

■ ACKNOWLEDGMENTS

We gratefully thank the committee promoters of Montoro coppery onion (Comitato dei Promotori della IGP Cipolla Ramata di Montoro; www.cipollaramatadimontoro.it) for providing us with Montoro onions.

■ ABBREVIATIONS

ROS, reactive oxygen species; HOCl, hypochlorous acid; RNS, reactive nitrogen species; COM, coppery onion from Montoro; RTO, red Tropea onion; RBCs, red blood cells; LDL, low-density lipoprotein; GSH, glutathione; HPLC, high-performance liquid chromatography; QE, equivalent of quercetin; FW, fresh weight

■ REFERENCES

(1) Griffiths, G.; Trueman, L.; Crowther, T.; Thomas, B.; Smith, B. Onions–a global benefit to health. *Phytother. Res.* **2002**, *16*, 603−615.

(2) Pérez-Gregorio, R. M.; Garcìa-Falcòn, M. S.; Simal-Gàndara, J.; Rodrigues, A. S.; Almeida, D. P. F. Identification and quantification of flavonoids in traditional cultivars of red and white onions at harvest. *J. Food Compos. Anal.* **2010**, *23*, 592−598.

(3) Slimestad, R.; Fossen, T.; Vagen, I. M. Onions: A source of unique dietary flavonoids. *J. Agric. Food Chem.* **2007**, *55*, 10067−10080.

(4) Gennaro, L.; Leonardi, C.; Esposito, F.; Salucci, M.; Maiani, G.; Quaglia, G.; Fogliano, V. Flavonoid and carbohydrate contents in Tropea red onions: Effects of homelike peeling and storage. *J. Agric. Food Chem.* **2002**, *50*, 1904−1910.

(5) Nemeth, K.; Piskula, M. K. Food content, processing, absorption and metabolism of onion flavonoids. *Crit. Rev. Food Sci. Nutr.* **2007**, *47*, 397−409.

(6) Sharma, K.; Assefa, A. D.; Kim, S.; Ko, E. Y.; Lee, E. T.; Park, S. W. Evaluation of total phenolics, flavonoids and antioxidant activity of 18 Korean onion cultivars: A comparative study. *J. Sci. Food Agric.* **2014**, *94*, 1521−1529.

(7) Singh, B. N.; Singh, B. R.; Singh, R. L.; Prakash, D.; Singh, D. P.; Sarma, B. K.; Upadhyay, G.; Singh, H. B. Polyphenolics from various extracts/fractions of red onion (*Allium cepa*) peel with potent antioxidant and antimutagenic activities. *Food Chem. Toxicol.* **2009**, *47*, 1161−1167.

(8) Park, S.; Kim, M. Y.; Lee, D. H.; Lee, S. H.; Baik, E. J.; Moon, C. H.; Park, S. W.; Ko, E. Y.; Oh, S. R.; Jung, Y. S. Methanolic extract of onion (*Allium cepa*) attenuates ischemia/hypoxia-induced apoptosis in cardiomyocytes via antioxidant effect. *Eur. J. Nutr.* **2009**, *48*, 235−242.

(9) Suh, H. J.; Lee, J. M.; Cho, J. S.; Kim, M. H.; Chung, S. H. Radical scavenging compounds in onion skin. *Food Res. Int.* **1999**, *32*, 659−664.

(10) Gökçe, A. F.; Kaya, C.; Serçe, S.; Özgen, M. Effect of scale color on the antioxidant capacity of onions. *Sci. Hortic. (Amsterdam, Neth.)* **2010**, *123*, 431−435.

(11) Halliwell, B. Free radicals and antioxidants: Updating a personal view. *Nutr. Rev.* **2012**, *70*, 257−265.

(12) Forman, H. J.; Davies, K. J.; Ursini, F. How do nutritional antioxidants really work: Nucleophilic tone and para-hormesis versus free radical scavenging in vivo. *Free Radical Biol. Med.* **2014**, *66*, 24−35.

(13) Boffetta, P.; Couto, E.; Wichmann, J.; Ferrari, P.; Trichopoulos, D.; Bueno-de-Mesquita, H. B.; van Duijnhoven, F. J.; Buchner, F. L.; Key, T.; Boeing, H.; Nothlings, U.; Linseisen, J.; Gonzalez, C. A.; Overvad, K.; Nielsen, M. R.; Tjonneland, A.; Olsen, A.; Clavel-Chapelon, F.; Boutron-Ruault, M. C.; Morois, S.; Lagiou, P.; Naska, A.; Benetou, V.; Kaaks, R.; Rohrmann, S.; Panico, S.; Sieri, S.; Vineis, P.; Palli, D.; van Gils, C. H.; Peeters, P. H.; Lund, E.; Brustad, M.; Engeset, D.; Huerta, J. M.; Rodriguez, L.; Sanchez, M. J.; Dorronsoro, M.; Barricarte, A.; Hallmans, G.; Johansson, I.; Manjer, J.; Sonestedt, E.; Allen, N. E.; Bingham, S.; Khaw, K. T.; Slimani, N.; Jenab, M.; Mouw, T.; Norat, T.; Riboli, E.; Trichopoulou, A. Fruit and vegetable intake and overall cancer risk in the European Prospective Investigation into Cancer and Nutrition (EPIC). *J. Natl. Cancer Inst* **2010**, *102*, 529−537.

(14) Crowe, F. L.; Roddam, A. W.; Key, T. J.; Appleby, P. N.; Overvad, K.; Jakobsen, M. U.; Tjonneland, A.; Hansen, L.; Boeing, H.; Weikert, C.; Linseisen, J.; Kaaks, R.; Trichopoulou, A.; Misirli, G.; Lagiou, P.; Sacerdote, C.; Pala, V.; Palli, D.; Tumino, R.; Panico, S.; Bueno-de-Mesquita, H. B.; Boer, J.; van Gils, C. H.; Beulens, J. W.; Barricarte, A.; Rodriguez, L.; Larranaga, N.; Sanchez, M. J.; Tormo, M. J.; Buckland, G.; Lund, E.; Hedblad, B.; Melander, O.; Jansson, J. H.; Wennberg, P.; Wareham, N. J.; Slimani, N.; Romieu, I.; Jenab, M.; Danesh, J.; Gallo, V.; Norat, T.; Riboli, E. Fruit and vegetable intake and mortality from ischaemic heart disease: results from the European Prospective Investigation into Cancer and Nutrition (EPIC)-Heart study. *Eur. Heart J.* **2011**, *32*, 1235−1243.

(15) Dini, I., Red onion (*Allium caepa* L. var. *tropeana*) seeds: Nutritional and functional properties. In *Nuts and Seeds in Health and Disease Prevention*; Preedy, V. R., Watson, R. R., Patel, V. B., Eds.; Academic Press: San Diego, CA, 2011; pp 981−990.

(16) Salvayre, R.; Auge, N.; Benoist, H.; Negre-Salvayre, A. Oxidized low-density lipoprotein-induced apoptosis. *Biochim. Biophys. Acta* **2002**, *1585*, 213−221.

(17) Niki, E.; Noguchi, N. Effects of antioxidants against atherosclerosis. *Mol. Cell. Biochem.* **2002**, *234−235*, 19−25.

(18) Mitra, S.; Deshmukh, A.; Sachdeva, R.; Lu, J.; Mehta, J. L. Oxidized low-density lipoprotein and atherosclerosis implications in antioxidant therapy. *Am. J. Med. Sci.* **2011**, *342*, 135−142.

(19) Poli, G.; Sottero, B.; Gargiulo, S.; Leonarduzzi, G. Cholesterol oxidation products in the vascular remodeling due to atherosclerosis. *Mol. Aspects Med.* **2009**, *30*, 180−189.

(20) Aviram, M.; Kaplan, M.; Rosenblat, M.; Fuhrman, B. Dietary antioxidants and paraoxonases against LDL oxidation and atherosclerosis development. *Handb. Exp. Pharmacol.* **2005**, 263−300.

(21) Fuhrman, B.; Aviram, M. Flavonoids protect LDL from oxidation and attenuate atherosclerosis. *Curr. Opin. Lipidol.* **2001**, *12*, 41−48.

(22) Chu, Y. F.; Liu, R. H. Cranberries inhibit LDL oxidation and induce LDL receptor expression in hepatocytes. *Life Sci.* **2005**, *77*, 1892−1901.

(23) George, T. W.; Waroonphan, S.; Niwat, C.; Gordon, M. H.; Lovegrove, J. A. Effects of acute consumption of a fruit and vegetable puree-based drink on vasodilation and oxidative status. *Br. J. Nutr.* **2013**, *109*, 1442−1452.

(24) Russo, G. L.; Tedesco, I.; Russo, M.; Cioppa, A.; Andreassi, M. G.; Picano, E. Cellular adaptive response to chronic radiation exposure in interventional cardiologists. *Eur. Heart J.* **2012**, *33*, 408−414.

(25) Tedesco, I.; Spagnuolo, C.; Russo, M.; Iannitti, R.; Nappo, A.; Russo, G. L. Protective effect of gamma-irradiation against hypochlorous acid-induced haemolysis in human erythrocytes. *Dose Response* **2012**, *11*, 401−412.

(26) Gong, J. K.; Glomski, C. A.; Guo, Y. A lifelong, wide-range radiation biodosimeter: Erythrocytes with transferrin receptors. *Health Phys.* **1999**, *77*, 713−718.

(27) Zavodnik, L. B.; Zavodnik, I. B.; Lapshyna, E. A.; Buko, V. U.; Bryszewska, M. J. Hypochlorous acid-induced membrane pore formation in red blood cells. *Bioelectrochemistry* **2002**, *58*, 157−161.

(28) Jesaitis, A. J.; Quinn, M. T.; Mukherjee, G.; Ward, P. A.; Dratz, E. A. Death by oxygen: radical views. Presented at *The molecular basis of oxidative damage by leukocytes: a Montana State University/Keystone Symposium*, Big Sky, MT, January 28−February 3, 1991. *New Biol.* **1991**, *3*, 651−655.

(29) Rodriguez Galdon, B.; Rodriguez Rodriguez, E. M.; Diaz Romero, C. Flavonoids in onion cultivars (*Allium cepa* L.). *J. Food Sci.* **2008**, *73*, C599−605.

(30) Tedesco, I.; Nappo, A.; Petitto, F.; Iacomino, G.; Nazzaro, F.; Palumbo, R.; Russo, G. L. Antioxidant and cytotoxic properties of lyophilized beer extracts on HL-60 cell line. *Nutr. Cancer* **2005**, *52*, 74−83.

DOI: 10.1021/acs.jafc.5b01206
J. Agric. Food Chem. 2015, 63, 5229−5238

(31) Singleton, V. L.; Orthofer, R.; Lamuela-Raventos, R. M. Analysis of total phenols and other oxidation substrates and antioxidants by means of Folin-Ciocalteu Reagent. *Methods Enzymol* **1999**, *229*, 152−178.
(32) Firuzi, O.; Lacanna, A.; Petrucci, R.; Marrosu, G.; Saso, L. Evaluation of the antioxidant activity of flavonoids by "ferric reducing antioxidant power" assay and cyclic voltammetry. *Biochim. Biophys. Acta* **2005**, *1721*, 174−184.
(33) Szeto, Y. T.; Tomlinson, B.; Benzie, I. F. Total antioxidant and ascorbic acid content of fresh fruits and vegetables: Implications for dietary planning and food preservation. *Br. J. Nutr.* **2002**, *87*, 55−59.
(34) Jiang, Z. Y.; Hunt, J. V.; Wolff, S. P. Ferrous ion oxidation in the presence of xylenol orange for detection of lipid hydroperoxide in low density lipoprotein. *Anal. Biochem.* **1992**, *202*, 384−389.
(35) Vissers, M. C.; Carr, A. C.; Chapman, A. L. Comparison of human red cell lysis by hypochlorous and hypobromous acids: Insights into the mechanism of lysis. *Biochem. J.* **1998**, *330* (Pt 1), 131−138.
(36) Tedesco, I.; Russo, G. L.; Nazzaro, F.; Russo, M.; Palumbo, R. Antioxidant effect of red wine anthocyanins in normal and catalase-inactive human erythrocytes. *J. Nutr. Biochem.* **2001**, *12*, 505−511.
(37) Marotti, M.; Piccaglia, R. Characterization of flavonoids in different cultivars of onion (*Allium cepa* L.). *J. Food Sci.* **2002**, *67*, 1229−1232.
(38) Fossen, T.; Andersen, Ø. M.; Øvstedal, D. O.; Pedersen, A. T.; Raknes, Å. Characteristic anthocyanin pattern from onions and other *Allium* spp. *J. Food Sci.* **1996**, *61*, 703−706.
(39) Donner, H.; Gao, L.; Mazza, G. Separation and characterization of simple and malonylated anthocyanins in red onions, *Allium cepa* L. *Food Res. Int.* **1997**, *30*, 637−643.
(40) Wu, X.; Prior, R. L. Systematic identification and characterization of anthocyanins by HPLC-ESI-MS/MS in common foods in the United States: Fruits and berries. *J. Agric. Food Chem.* **2005**, *53*, 2589−2599.
(41) Hollman, P. C.; van Trijp, J. M.; Buysman, M. N.; van der Gaag, M. S.; Mengelers, M. J.; de Vries, J. H.; Katan, M. B. Relative bioavailability of the antioxidant flavonoid quercetin from various foods in man. *FEBS Lett.* **1997**, *418*, 152−156.
(42) Manach, C.; Scalbert, A.; Morand, C.; Remesy, C.; Jimenez, L. Polyphenols: Food sources and bioavailability. *Am. J. Clin. Nutr.* **2004**, *79*, 727−747.
(43) Hollman, P. C. H.; Arts, I. C. W. Flavonols, flavones and flavanols − nature, occurrence and dietary burden. *J. Sci. Food Agric.* **2000**, *80*, 1081−1093.
(44) Cimen, M. Y. Free radical metabolism in human erythrocytes. *Clin. Chim. Acta* **2008**, *390*, 1−11.
(45) Foschino Barbaro, M. P.; Serviddio, G.; Resta, O.; Rollo, T.; Tamborra, R.; Elisiana Carpagnano, G.; Vendemiale, G.; Altomare, E. Oxygen therapy at low flow causes oxidative stress in chronic obstructive pulmonary disease: Prevention by N-acetyl cysteine. *Free Radical Res.* **2005**, *39*, 1111−1118.
(46) Pace, B. S.; Shartava, A.; Pack-Mabien, A.; Mulekar, M.; Ardia, A.; Goodman, S. R. Effects of N-acetylcysteine on dense cell formation in sickle cell disease. *Am. J. Hematol.* **2003**, *73*, 26−32.
(47) Raftos, J. E.; Whillier, S.; Kuchel, P. W. Glutathione synthesis and turnover in the human erythrocyte: Alignment of a model based on detailed enzyme kinetics with experimental data. *J. Biol. Chem.* **2010**, *285*, 23557−23567.
(48) Russo, G. L.; Russo, M.; Spagnuolo, C.; Tedesco, I.; Bilotto, S.; Iannitti, R.; Palumbo, R. Quercetin: A pleiotropic kinase inhibitor against cancer. *Cancer Treat Res.* **2014**, *159*, 185−205.
(49) Spagnuolo, C.; Russo, M.; Bilotto, S.; Tedesco, I.; Laratta, B.; Russo, G. L. Dietary polyphenols in cancer prevention: The example of the flavonoid quercetin in leukemia. *Ann. N.Y. Acad. Sci.* **2012**, *1259*, 95−103.
(50) Russo, M.; Nigro, P.; Rosiello, R.; D'Arienzo, R.; Russo, G. L. Quercetin enhances CD95- and TRAIL-induced apoptosis in leukemia cell lines. *Leukemia* **2007**, *21*, 1130−1133.

DOI: 10.1021/acs.jafc.5b01206
J. Agric. Food Chem. 2015, 63, 5229−5238

JOURNAL OF AGRICULTURAL AND FOOD CHEMISTRY

Article

pubs.acs.org/JAFC

Reducing Bacterial Contamination in Fuel Ethanol Fermentations by Ozone Treatment of Uncooked Corn Mash

Mary L. Rasmussen,[†,‡] Jacek A. Koziel,[†,§,∥] Jay-lin Jane,[∥] and Anthony L. Pometto, III*[,⊥]

[†]Department of Civil, Construction, and Environmental Engineering, [‡]Biorenewable Resources and Technology Program, [§]Department of Agricultural and Biosystems Engineering, and [∥]Department of Food Science and Human Nutrition, Iowa State University, Ames, Iowa 50011, United States

[⊥]Department of Food, Nutrition, and Packaging Sciences, Clemson University, Clemson, South Carolina 29634, United States

ABSTRACT: Ozonation of uncooked corn mash from the POET BPX process was investigated as a potential disinfection method for reducing bacterial contamination prior to ethanol fermentation. Corn mash (200 g) was prepared from POET ground corn and POET corn slurry and was ozonated in 250 mL polypropylene bottles. Lactic and acetic acid levels were monitored daily during the fermentation of ozonated, aerated, and nontreated corn mash samples to evaluate bacterial activity. Glycerol and ethanol contents of fermentation samples were checked daily to assess yeast activity. No yeast supplementation, no addition of other antimicrobial agents (such as antibiotics), and spiking with a common lactic acid bacterium found in corn ethanol plants, *Lactobacillus plantarum*, amplified the treatment effects. The laboratory-scale ozone dosages ranged from 26−188 mg/L, with very low estimated costs of $0.0008−0.006/gal ($0.21−1.6/m^3) of ethanol. Ozonation was found to decrease the initial pH of ground corn mash samples, which could reduce the sulfuric acid required to adjust the pH prior to ethanol fermentation. Lactic and acetic acid levels tended to be lower for samples subjected to increasing ozone dosages, indicating less bacterial activity. The lower ozone dosages in the range applied achieved higher ethanol yields. Preliminary experiments on ozonating POET corn slurry at low ozone dosages were not as effective as using POET ground corn, possibly because corn slurry samples contained recycled antimicrobials from the backset. The data suggest additional dissolved and suspended organic materials from the backset consumed the ozone or shielded the bacteria.

KEYWORDS: *ozonation, no-cook, BPX process, corn mash, fuel ethanol, bacteria, dry-grind ethanol, lactic acid*

INTRODUCTION

POET leads the fuel ethanol industry in streamlining corn dry milling to improve ethanol production efficiency, as well as with their feed coproduct, Dakota Gold BPX distiller grains. The efficient BPX, or no-cook, process involves raw starch hydrolysis that, like the conventional process, adds enzymes to convert starch to sugars and adds yeast to ferment sugars to ethanol but without the cooking step.[1] The BPX process is now used by 24 of the 27 POET biorefineries. POET produces over 1.5×10^9 gal (5.7×10^6 m^3) of ethanol annually in a network spanning seven Midwestern states.

The POET BPX process for dry-grind corn ethanol production has important advantages over the conventional process. The energy-intensive liquefaction and cooking steps are omitted, thus reducing plant energy requirements by 8−15%.[1] The BPX process achieves higher ethanol yields by improving starch accessibility, lowers volatile organic carbon (VOC) emissions, cuts cooling water needs, and enhances the nutrient quality, flowability, and anticaking properties of the distillers dried grains with solubles (DDGS) coproduct. Amino acid digestibility in DDGS samples varies considerably among conventional ethanol facilities, attributable to heat damage from corn mash cooking and DDGS drying.[2−5] Heat damage is responsible for lower amino acid digestibility in DDGS than in corn grain.[4,6] Removing the cooking step, therefore, improves the feed quality of Dakota Gold BPX DDGS over conventional DDGS by reducing heat damage of the protein.[7]

Unlike most beverage alcohols, fuel ethanol fermentations are not conducted under pure culture conditions.[8] High-temperature jet cooking (90−165 °C) in the conventional process not only gelatinizes the corn starch but also helps reduce contamination and yield losses caused by unwanted lactic acid bacteria (LAB).[9] Contamination in fuel ethanol fermentations originates from bacteria present on the corn from the fields.[10] Bacteria compete with yeast for nutrients—glucose, trace minerals, vitamins, and free amino nitrogen—and lower ethanol yields by diverting glucose to lactic and acetic acids, which are inhibitory compounds to yeast.[11−13] In addition to yield losses by chronic LAB contamination, acute infections arise unpredictably and can result in plant shutdowns for cleaning, resulting in expensive losses in productivity.[8,13,14]

Gram-positive and Gram-negative bacterial isolates from fuel ethanol production include species of *Pediococcus*, *Enterococcus*, *Acetobacter*, *Gluconobacter*, *Clostridium*, and *Lactobacillus*.[8,15] *Lactobacillus* sp. are the most prevalent in the industry and are ubiquitous in nature. In a study of two commercial dry-grind ethanol plants by Skinner and Leathers,[8] the genus *Lactobacillus* was isolated most frequently, representing 38% and 77% of total bacterial isolates from the first and second plants,

Received: January 30, 2015
Revised: April 9, 2015
Accepted: May 12, 2015
Published: May 12, 2015

ACS Publications © 2015 American Chemical Society

DOI: 10.1021/acs.jafc.5b00563
J. Agric. Food Chem. 2015, 63, 5239−5248

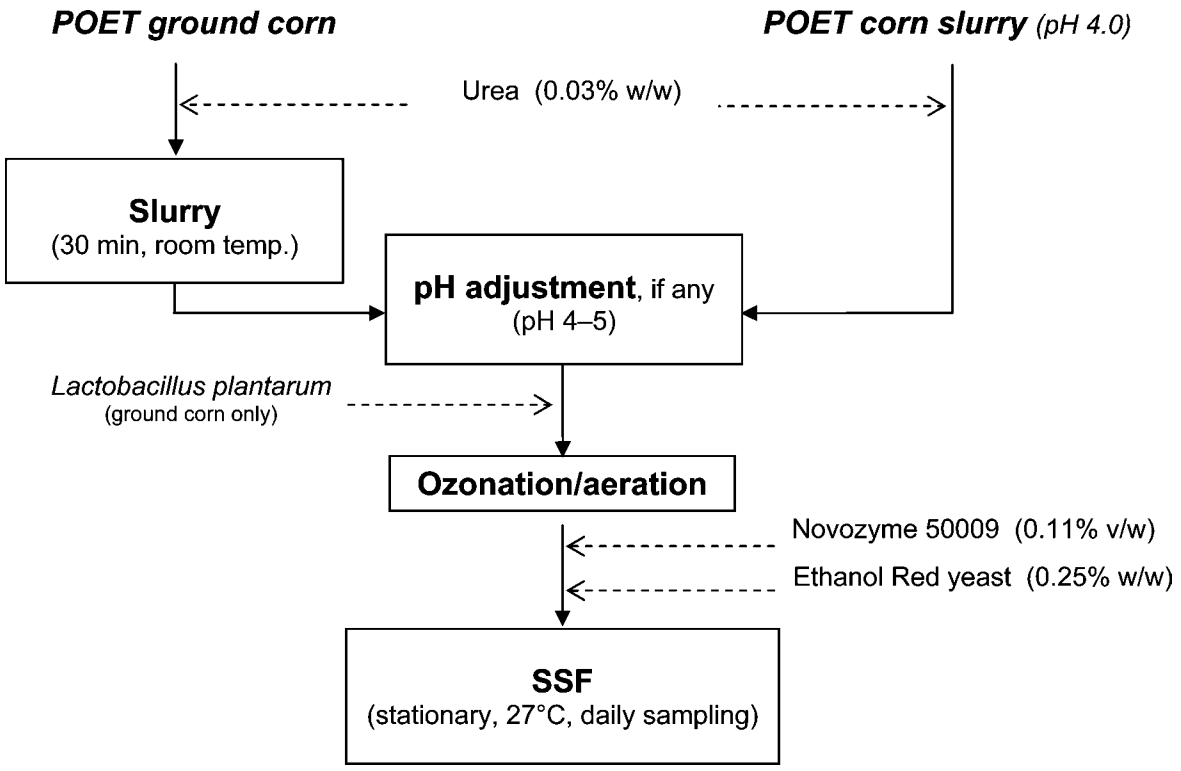

Figure 1. Corn mash preparation, ozonation/aeration, and fermentation with POET ground corn and POET corn slurry.

respectively. Gram-positive LAB are ethanol-tolerant, grow faster than yeast, and produce organic acids that inhibit yeast.

During this research, bacterial growth was controlled at POET biorefineries potentially by dosing with antibiotic and antimicrobial agents and by operation at lower pH levels (pH~ 4.2). Conventional ethanol plants, despite jet cooking, also add antibiotics to fight chronic or acute bacterial infections.[8,16−18] If no antibiotics are used, it is common for a facility to lose 1−5% of its potential ethanol yield.[10] Rising concerns about the use of antibiotics and the emergence of antibiotic-resistant bacteria are creating a demand for alternative methods of controlling bacteria.

Cleaning and sanitation are important microbial control measures in the corn ethanol industry. Infections in process tanks and continuous yeast propagators, as well as resistant biofilms within the process train, can continually reintroduce bacterial contaminants into the fermentors.[8,19] Large yeast inocula (≥2% v/v) help control contamination during fermentations; however, yeast growth and fermentation rates are still reduced by high lactobacilli concentrations.[20]

Penicillin and virginiamycin are the antibiotics available commercially for fuel ethanol production.[15,21] Virginiamycin, produced by *Streptomyces virginiae*, has had limited use in human medicine but extensive use as a growth-promoting additive in animal feed.[22] The recommended dose of virginiamycin in fuel ethanol fermentations is 0.25−2.0 ppm.[23] The use of antibiotics has limitations. Commercial antibiotic applications are essentially selection experiments for resistant microorganisms. Hynes et al.[23] observed reductions in the effectiveness of virginiamycin after extended fermentations, possibly resulting from its breakdown by lactobacilli.[24] *Lactobacillus* sp. with higher tolerance to virginiamycin have been isolated from fuel ethanol plants that dose with virginiamycin. Moreover, bacterial isolates have emerged with resistance to both virginiamycin and penicillin.[15,25]

Hop acids offer a natural alternative to antibiotics for fuel ethanol production.[10] Many of the organic acids found in hops exhibit antimicrobial activities. Hop compounds inhibit growth by disrupting the transmembrane pH gradient of microbes.[26,27] Hops have long been used in the brewing industry to contribute to the flavor of beer, by adding bitterness and aroma, and to improve product shelf life. IsoStab, a liquid hop extract, is a commercially available product for fuel ethanol applications. U.S. producers using IsoStab have obtained higher ethanol yields with less fluctuation.

A variety of disinfectants have been investigated on a laboratory scale for fuel ethanol fermentations, including hydrogen peroxide, chlorine dioxide, potassium metabisulfite, 3,4,4′-trichlorocarbanilide, and lactate with a lactate-tolerant yeast strain.[8,28−33] Bacteria were inhibited over yeast by these agents, but the effectiveness depended on the bacterial strain.[8] Chlorine dioxide and ozonation are common alternatives to chlorination for disinfection of drinking water. Meneghin et al.[30] evaluated the effect of chlorine dioxide against bacteria prevalent in ethanol fermentations (e.g., *Lactobacillus plantarum* and *Lactobacillus fermentum*). The minimum inhibitory concentrations (MIC) for chlorine dioxide on the bacteria and on the yeast inoculum were determined in nutrient media; the effectiveness in nutrient media is likely different from that in the high suspended solids corn mash at fuel ethanol plants. The MICs ranged from 10 to 125 ppm for the bacterial strains tested; *L. plantarum* had the highest MIC of 125 ppm. Yeast growth was also affected at chlorine dioxide concentrations over 50 ppm.

Ozone is a microbial inhibitor that is considered an alternative to chlorine and hydrogen peroxide in food applications.[34] The rate of microbial inactivation is affected

DOI: 10.1021/acs.jafc.5b00563
J. Agric. Food Chem. 2015, 63, 5239−5248

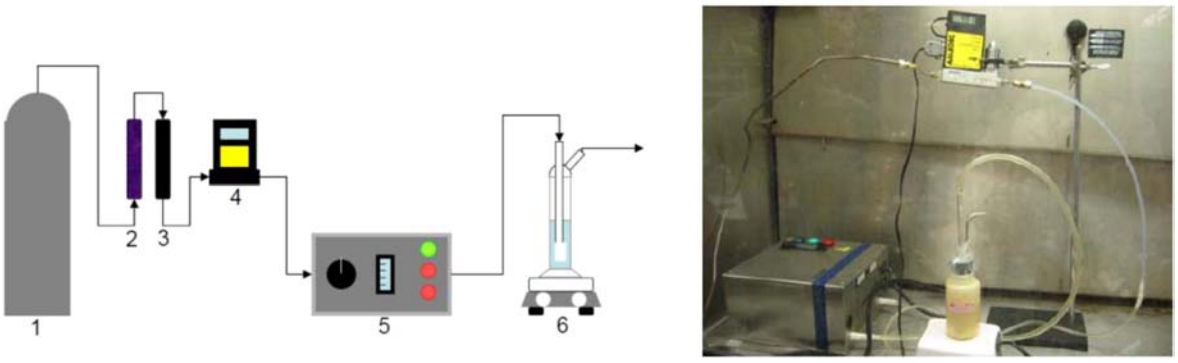

Figure 2. Setup and photo of ozonation of corn mash: (1) compressed air tank, (2) moisture trap, (3) hydrocarbon trap, (4) mass flow controller, (5) corona-discharge ozone generator, and (6) corn mash sample (200 g) in 250 mL PP bottle.

by several environmental factors (concentration of organic compounds, physiological state of the microorganism, pH of the medium, temperature).[35] Thus, ozone has had mixed success in the food industry. García-Cubero et al.[36] illustrated the benefit of pretreatment of straw with ozone, resulting in a reduction in acid-insoluble lignin (Klason lignin) and improved enzymatic hydrolysis of cellulose and hemicelluloses for biofuel production. Freitas-Silva and Venâncio[37] demonstrated mycotoxin degradation by ozone use in corn on the cob, corn kernels, and corn and rice powder. Miller et al.[38] reviewed the advantages and disadvantages of ozonation use for fruits and vegetables preservation, while Gerrity and Snyder[39] review its use in water reuse applications. Thus, the application of ozone in dry-grind corn ethanol production is needed.

Research Objectives. In this research, ozone was used in place of antibiotics (e.g., Lactrol and IsoStab) for control of bacterial contamination in ethanol (yeast) fermentations. Preliminary experiments were subsequently performed on corn slurry to evaluate the effectiveness of ozonation for reducing bacterial contamination under conditions more similar to plant operation, including the contributions of recycled water sources.

MATERIALS AND METHODS

Corn Mash Preparation. Ground corn and corn slurry were obtained from POET Biorefining in Jewell, IA, in the fall and spring of 2007 and 2008. The corn slurry obtained from POET contains the ground corn in a slurry with recycled water streams, such as backset. Figure1 illustrates corn mash preparation, ozone treatment, and simultaneous saccharification and fermentation (SSF) procedures. Corn mash was prepared in 250 mL polypropylene (PP) bottles with 35% (w/w) ground corn (200 g of mash/bottle) and deionized water or with 200 g of corn slurry/bottle. Urea was added (0.03% w/w) as a N source. The final corn mash volume was 186 mL/bottle. Bottles were shaken for 30 min at 250 rpm and room temperature to slurry contents. The pH was adjusted to 5.0 in select experiments. In preliminary work (pH 4.2), all controls with and without Lactrol and/or IsoStab added had similar values for lactic and acetic acids, glycerol, and ethanol, which indicated minimal bacterial contamination even without ozonation (results not shown). Therefore, no antibiotics or other antimicrobials (i.e., Lactrol or IsoStab) were added in these experiments to exemplify treatment effects of ozone. The POET corn slurry experiments, however, potentially contained recycled antimicrobials contributed in the backset from previous fermentations at the plant. Select samples were also LAB-spiked and/or not yeast-supplemented to amplify the differences in treatment effects.

Microorganisms. Select corn mash samples were spiked with *Lactobacillus plantarum*, a lactic acid bacterium, obtained from the American Type Culture Collection (ATCC 14917, Rockville, MD) prior to ozone treatment. Stock cultures of *L. plantarum* were freeze-dried and stored previously in sterile skim milk at 4 °C. Fermentis Ethanol Red (Lesaffre Yeast Corp., Milwaukee, WI), containing the yeast *Saccharomyces cerevisiae*, was added (0.5 g) after ozone treatment for ethanol fermentation.

Ozonation. The laboratory-scale installation used to apply the ozone treatment is shown in Figure 2. Ozone gas was generated from oxygen supplied by a compressed-air gas cylinder by use of a corona-discharge ozone generator (TOG C2B, Trigon, Glasgow, Scotland). Moisture and hydrocarbon traps (Restek, State College, PA) were placed between the ozone generator and compressed-air cylinder to remove impurities in the feed gas. A mass flow controller (GLC17, Aalborg, Orangeburg, NY) was used to control the gas flow rate.

Ozone gas was bubbled into the corn mash samples (200 g) in 250 mL PP bottles at a flow rate of 500 mL/min. The ozone concentration in the gas phase was measured by the potassium iodide titration method.[40] The ozone dose, or consumption, was calculated on the basis of ozone concentrations in the influent and effluent gas from the bottle over time. Corn mash samples were ozonated and residual ozone in off-gas was measured by titration after varying ozonation times. This setup was used to determine the effects of different ozone dosages on ethanol fermentation of corn mash samples prepared from ground corn or corn slurry. Aeration treatment, as a control, was also performed with this equipment. The aeration and ozonation procedures were the same (e.g., similar gas flow rate), but with the ozone generator turned off.

Ethanol Fermentation. Following ozonation, raw starch hydrolyzing enzyme (Novozyme 50009, 0.11% v/w) and Ethanol Red (0.25% w/w) were added to ozonated, aerated, and nontreated corn mash (Figure 1). Bottles were shaken for 2 min at 250 rpm to mix contents and incubated without shaking at 27 °C (POET incubation temperature) until ethanol levels reached a plateau, up to 168 h. SSF samples were HPLC-analyzed on a daily basis.

Sample Analyses. The ethanol, glycerol, lactic acid, and acetic acid contents of corn mash and SSF samples were quantified on a Waters high-pressure liquid chromatograph (HPLC) (Millipore Corp., Milford, MA). The HPLC system was equipped with a Waters model 401 refractive index detector, column heater, automatic sampler, and computer controller. The Aminex HPX-8711 column (300 × 7.8 mm, Bio-Rad Chemical Division, Richmond, CA) separated sample constituents with a mobile phase of 0.012 N sulfuric acid, flow rate of 0.8 mL/min, injection volume of 20 μL, and column temperature of 65 °C.[41]

Experiment Sets. A pH experiment was conducted prior to fermentation. Aeration treatment was included to confirm that ozonation, rather than aeration and mixing, lowered the initial corn mash pH prior to fermentation (0 h).

The ethanol fermentation experiments reported in this publication are divided into three sets, two with POET ground corn and one with POET corn slurry, as outlined in Table 1.

POET Ground Corn (Experiment Sets 1 and 2). Two sets of fermentation experiments with ozone-treated corn mash prepared

DOI: 10.1021/acs.jafc.5b00563
J. Agric. Food Chem. 2015, 63, 5239−5248

Table 1. Experiments Performed with Corn Mash Prepared from POET Ground Corn and POET Corn Slurry[a]

corn mash	treatment	initial pH[b]	LAB spiked	yeast added
	Experiment Set 1			
ground corn	ozone (0−188 mg/L)	5.0	yes	no
ground corn	ozone (0−152 mg/L)	5.0	yes	yes
	Experiment Set 2			
ground corn	none	4.7	no	yes
ground corn	air (60 min)	4.7	no	yes
ground corn	ozone (60 min)	4.7	no	yes
ground corn	none	4.7	yes	yes
ground corn	air (60 min)	4.7	yes	yes
ground corn	ozone (60 min)	4.7	yes	yes
	Experiment Set 3			
corn slurry	none	4.0	no	yes
corn slurry	none	4.0	no	no
corn slurry	none	5.0	no	yes
corn slurry	ozone (60 min)	5.0	no	yes

[a]No antimicrobials were added in these experiments; however, corn slurry obtained from POET contained backset, which potentially has antimicrobials from previous fermentations. [b]Initial pH refers to the pH after adjustment and before treatment. Without adjustment, the pH of corn mash prepared from ground corn was 4.7 and from corn slurry was 4.0.

from ground corn were performed. The first set included spiking with *L. plantarum* before ozone treatment (0−188 mg/L) of corn mash; no yeast and no other antimicrobial agents were added to select bottles to further amplify the treatment effects. The second set included ozonation and aeration treatments of corn mash prior to ethanol fermentation. Select bottles were spiked with *L. plantarum*. Fermentation experiments were conducted with aeration treatment as a control to determine whether lower lactic acid contents in daily samples resulted from ozonation as a disinfect/oxidant or from possible stimulatory effects of aeration on the yeast.

POET Corn Slurry (Experiment Set 3). A preliminary set of fermentation experiments was conducted with POET corn slurry to assess the effectiveness of ozonation for reducing bacterial contamination under conditions more similar to plant operation, including contributions of recycled water streams. The recycled backset potentially contributed other antimicrobials in these experiments. Corn mash samples were prepared with/without addition of yeast, with the slurry initial pH of 4.0 and adjusted to pH 5.0, and with/without ozone treatment, as shown in Table 1.

Statistical Analysis. All treatments were performed in replicates of three. Statistical analysis was carried out with the Statistical Analysis System package (SAS computer program version 9.1.2, SAS Institute Inc., Cary, NC). Student's *t*-test analyses were performed on HPLC data sets to determine statistical significance with a p value of 0.05.

RESULTS AND DISCUSSION

Ozone Dosages. The results of ozonating corn mash samples for various treatment times in order to determine ozone consumption (i.e., ozone dosage) are illustrated in Figure 3. Ozone consumption is the difference between ozone applied to the corn mash, $f(x)$, and unused ozone exiting the headspace of the treated corn mash over time (off-gas), $g(x)$; it equals the green area in Figure 3. The following fitted equations were used to calculate ozone consumption/dosage:

$$\text{applied ozone (mg/min)} = f(x) = 0.996 \quad (1)$$

$$\text{off-gas ozone (mg/min)} = g(x) = 0.00319x + 0.000538x^2 \quad \text{for } 0 \le t \le 37.5 \text{ min} \quad (2)$$

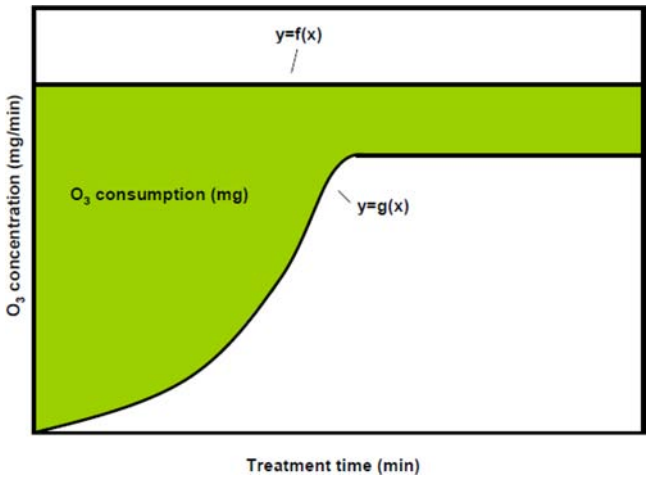

Figure 3. Ozone consumption/dose (green area) as a function of ozonation treatment time for corn mash samples. The curve was fit on the basis of effluent ozone discharge rates, $g(x)$, observed in corn mash over time. The influent ozone application rate was constant, $f(x)$, and $n = 4$.

$$\text{off-gas ozone (mg/min)} = g(x) = 0.884 \quad \text{for } 37.5 \text{ min} \le t \quad (3)$$

$$\int_0^t f(x)\,dx - \int_0^t g(x)\,dx = 0.996t - 0.00159t^2 - 0.000179t^3 \quad \text{for } 0 \le t \le 37.5 \text{ min} \quad (4)$$

$$\int_0^t f(x)\,dx - \int_0^t g(x)\,dx = 0.112(t - 37.5) + 25.7 \quad \text{for } 37.5 \text{ min} \le t \quad (5)$$

The ozone dosages computed for each treatment time are provided in Table 2. In our preliminary work, additional dosages of 26 and 75 mg O_3/L were tested. The higher dosages (127, 152, and 188 mg/L) were chosen for replicate experiments, as reported in this publication.

Table 2. Ozone Dosages Applied to Corn Mash and Estimated Costs in Our Study for Different Ozonation Times

ozonation time (min)	ozone dose[a] (mg of O_3)	ozone dose[b] (mg of O_3/L of corn mash)	est cost[c] ($/1000 gal of ethanol)
5	5	26	0.84
15	14	75	2.39
30	24	127	4.04
60	28	152	4.82
120	35	188	5.97

[a]Ozone dose/consumption was determined by ozonating corn mash samples. The resulting equations used for ozone calculations (milligrams) are $0.996t - 0.00159t^2 - 0.000179t^3$ for $0 \le t \le 37.5$ min and $0.112(t - 37.5) + 25.7$ for $t \ge 37.5$ min. [b]The volume of ozonated corn mash was 0.186 L; ozone dose (milligrams) was divided by this volume. [c]Estimated cost was calculated from ozone dose (milligrams per liter) based on the conversion factor of 3.79 L/gal, an ozone cost of $\$1.68 \times 10^{-6}$/mg, and the assumption of 20% (v/v) final ethanol content (or 1 gal of ethanol to 5 gal of corn mash).

Ozone Cost Estimates. The ozone cost estimates include operating costs to purchase electricity for the ozone generator and to prepare air for the ozonation. The costs of electricity and air are calculated as follows:

DOI: 10.1021/acs.jafc.5b00563
J. Agric. Food Chem. 2015, 63, 5239−5248

electricity consumption of typical ozone generators

$$= 10\ \text{kW·h/kg of ozone} \quad (6)$$

$$\text{electricity} = \$0.07/\text{kW·h} \quad (7)$$

Equation 7represents the 2009 average for industrial consumers.[40]

electricity consumption for air feed drying

$$= \sim 2\ \text{kW·h/kg of ozone} \quad (8)$$

$$\text{total electricity consumption} = 12\ \text{kW·h/kg} \quad (9a)$$

$$\text{total electricity cost} = \$0.84/\text{kg} \quad (9b)$$

Capital costs: since the ozone dosage has not yet been optimized in relation to corn mash formulations in industry, including recycled water sources, the required ozone generator size for a typical plant cannot be determined. As a rough guide, the amortization costs will equal the energy costs. The cost of ozone, therefore, can be expected to amount to roughly $1.68/kg. This cost still needs to be determined to a greater degree of accuracy. Table 2 presents the estimated ozonation costs based on the ozone dosages applied in experiments to date.

Initial pH Experiment. The initial pH of corn mash prepared from ground corn, prior to fermentation (0 h), was adjusted to 4.2 or 5.0. The pH of corn mash samples tended to decrease with increasing ozone treatment times/dosages (Figure 4). The pH of ozonated samples (initial pH 5.0) started to decrease after 15 min of ozonation (75 mg of O_3/L), reaching an average pH of 4.8 in 60 min (152 mg of O_3/L). With an initial pH of 4.2, the corn mash pH was also reduced by 0.2 pH unit to 4.0 after 60 min of ozonation. Aeration with the same procedure, but no ozone generated, did not affect the corn mash pH. This finding shows that the ozone or ozone byproducts, rather than aeration and additional mixing, were responsible for the corn mash pH reductions observed in all experiments with ground corn.

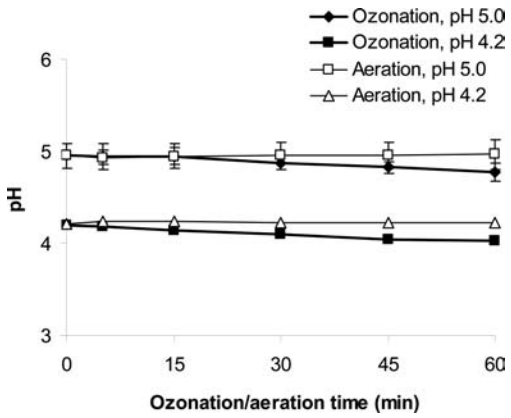

Figure 4. Initial pH experiment: changes in pH observed during ozonation and aeration of corn mash samples prepared from ground corn and adjusted to different initial pH values, 5.0 (n = 3) and 4.2 (n = 1).

Corn mash samples were analyzed by HPLC before and after treatment to detect any changes in concentrations, in particular for organic acids. No consistent changes were observed for ozonated and aerated samples. A slight increase in acetic acid of 0.35 g/L occurred in one ozonated sample but not in replicate samples. There were no changes in acetic acid in aerated samples. No lactic acid was detected in any samples before or after ozonation/aeration.

Ground Corn (Experiment Sets 1 and 2). *Effects of Ozonation on pH and Lactic Acid Contents.* In experiment set 1 (Figure 5), daily pH values of ozonated and nonozonated corn mash samples decreased for the first 24−48 h of fermentation only. The exceptions were samples with higher ozone dosages (152 and 188 mg/L) and no yeast added; the pH of these samples started decreasing after 24−48 h of fermentation and stabilized by 96−120 h. All pH trends corresponded with increases in lactic acid contents. Higher daily pH values, and less lactic acid, were observed in samples subjected to higher ozone dosages.

Statistical analysis was conducted to compare the significance ($p < 0.05$) of 96-h fermentation samples. As expected, lactic acid production in samples without yeast added was higher than in samples with yeast added. Yeast inoculum size affects the ability to compete with bacteria for the same substrate, fermentable sugars.[20] Increasing the ozone dosages from 0 to 127 mg/L and from 127 to 152 mg/L, without yeast added, resulted in significantly lower (p = 0.0004 and p = 0.007, respectively) lactic acid contents; no significant difference (p = 0.4) was observed between 152 and 188 mg ozone/L. These differences were amplified by not supplementing with yeast. With yeast added, the 152 mg/L ozone dosage resulted in significantly lower (p = 0.04) lactic acid contents than the 127 mg/L dosage, indicating less bacterial activity; there was no significant difference (p = 0.9), however, between 0 and 127 mg/L dosages.

In experiment set 2 (Figure 6), daily pH values of ozonated, aerated, and nontreated corn mash samples decreased for the first 24−48 h of fermentation only, without exception. These results agree with experiment set 1 since yeast was added to all samples in this set. Likewise, the daily pH values for all samples corresponded with increases in lactic acid contents.

Nontreated samples tended to have lower daily pH values and higher lactic acid concentrations. Ozonated samples had the highest pH values and least lactic acid throughout the fermentation period, indicating less bacterial and more yeast activity. LAB-spiked, aerated samples had trends similar to those of nontreated samples. Non-LAB-spiked, aerated samples had lower lactic acid values than nontreated samples, which suggest the indigenous LAB populations prefer a reduced oxygen environment. Thus, aeration was effective for reducing lactic acid production only in samples without LAB spiking, but ozonation was still more effective. Statistical comparisons of 96-h fermentation samples showed that all differences in lactic acid contents among ozonated, aerated, and nontreated samples were significant (p values <0.05).

Effects of Ozone on Glycerol Contents. In experiment set 1, glycerol production was lowest in corn mash treated with 127 mg/L of ozone prior to fermentation, compared to nontreated and 152 mg/L ozone-treated samples (Table 3). The 127 mg of O_3/L samples had the highest acetic acid and ethanol contents, which create osmotic stress on the yeast, triggering glycerol production;[42] lactic acid contents, however, were comparable to those of nontreated samples (Figure 5, yeast added). Reduced glycerol contents were also observed in preliminary experiments with increasing ozone dosages, indicating the yeast were less stressed compared to nonozonated samples.

Daily ethanol contents of ozonated and nonozonated corn mash samples began to plateau by 96 h of fermentation (Figure

DOI: 10.1021/acs.jafc.5b00563
J. Agric. Food Chem. 2015, 63, 5239−5248

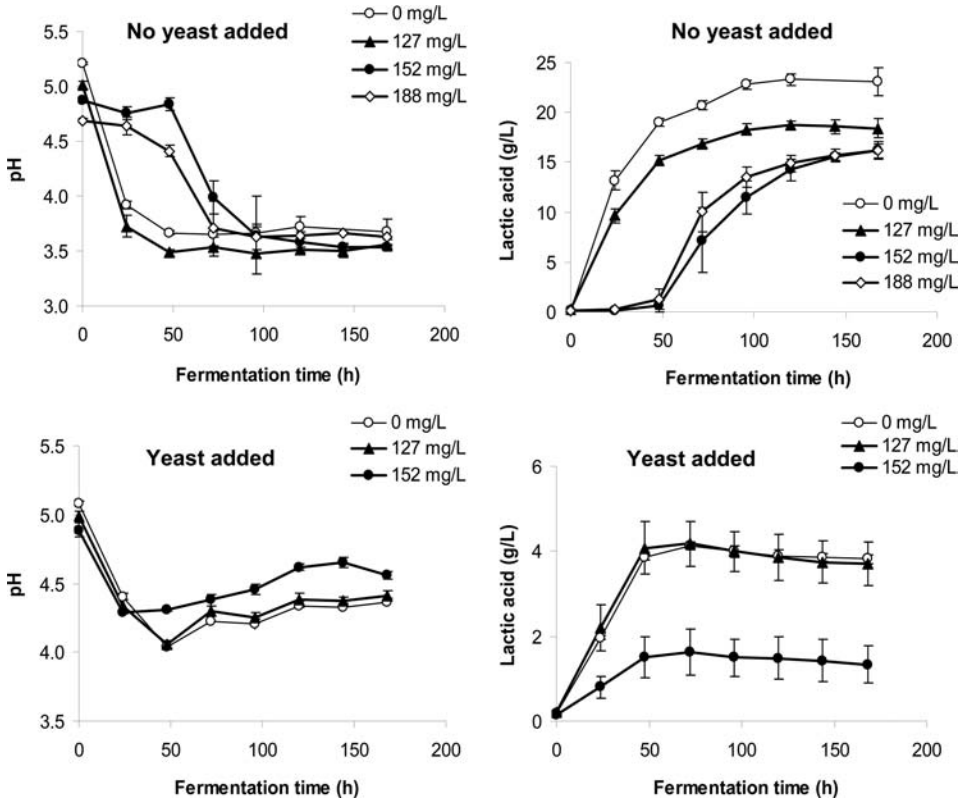

Figure 5. Experiment set 1: samples were spiked with *L. plantarum* and ozonated. Select samples had yeast added. Corn mash pH was adjusted to 5.0 prior to ozonation. No other antimicrobial agents (Lactrol or IsoStab) were added. Daily pH (left) and lactic acid contents (right) of fermentation samples of corn mash prepared from ground corn are shown (n = 3).

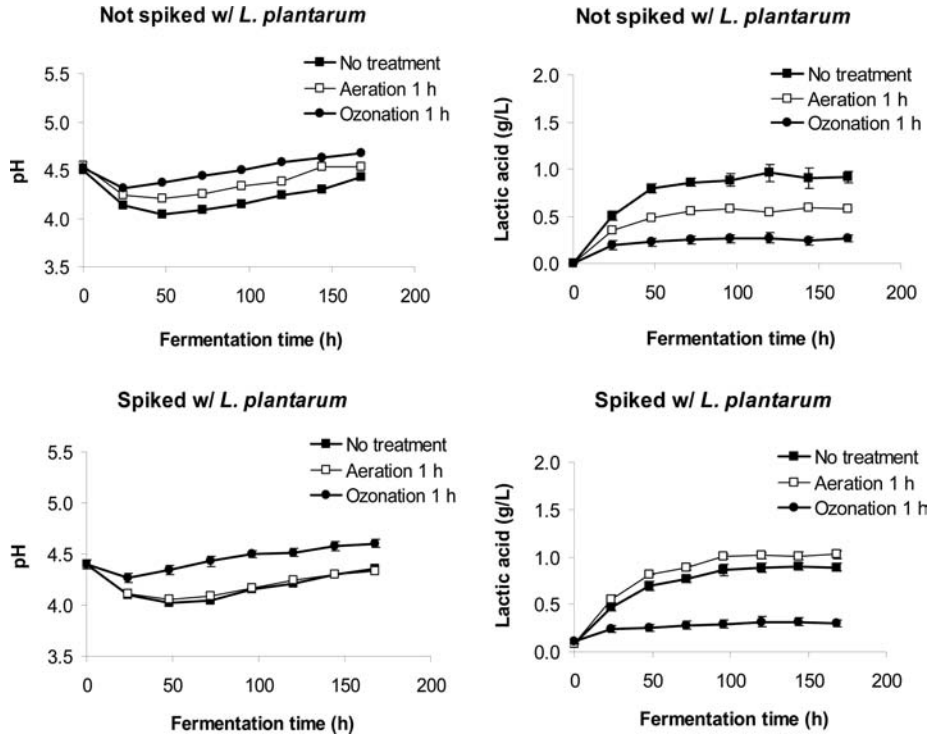

Figure 6. Experiment set 2: select samples were spiked with *L. plantarum* prior to treatment. Samples were ozonated or aerated for 60 min, except for controls with no treatment, and yeast was added. No other antimicrobial agents (Lactrol or IsoStab) were added. Daily pH (left) and lactic acid contents (right) of fermentation samples for corn mash prepared from ground corn are shown (n = 3).

7). With yeast added, the 96-h ethanol concentration ranged from 150 to 154 g/L. The ethanol concentrations in 96-h samples treated with 127 mg/L ozone dosage were significantly higher (p = 0.02) than in samples with no ozone treatment

DOI: 10.1021/acs.jafc.5b00563
J. Agric. Food Chem. 2015, 63, 5239−5248

Table 3. Comparison of Glycerol and Ethanol Contents of 96-h Fermentation Samples from Corn Mash[a]

LAB-spiked	treatment[b]	acetic acid (g/L)	glycerol (g/L)	lactic acid (g/L)	ethanol (g/L)
		Experiment Set 1			
yes	none	0.7	10.2	4.0	150
yes	ozone (127 mg/L)	1.0	9.3	4.0	154
yes	ozone (152 mg/L, 60 min)	0.7	9.8	1.5	152
		Experiment Set 2			
no	none	0.2	10.4	0.9	147
no	aerated (60 min)	0.2	10.7	0.5	147
no	ozone (60 min)	0.4	8.6	0.3	143
yes	none	0.2	10.4	0.9	145
yes	aerated (60 min)	0.3	10.5	1.0	145
yes	ozone (60 min)	0.4	8.8	0.3	143

[a]Prepared from ground corn with yeast addition after ozone treatment (n = 3). No other antimicrobial agents (Lactrol or IsoStab) were added. [b]Initial pH values, prior to ozonation, of experiment sets 1 and 2 were 5.0 and 4.7, respectively. The initial fermentation pH values were 4.8 and 4.5, respectively.

(Table 3). Samples subjected to 152 mg/L ozone dosage had more ethanol than nonozonated samples, but the difference was not significant (p = 0.06). Ethanol production was observed in corn mash samples even without yeast added (up to 61 g/L in 96-h, nonozonated samples); the ground corn used to prepare the corn mash was obtained from POET and presumably contained yeast from exposure during storage at the ethanol biorefinery. Without supplemental yeast, ozone dosage had no significant effect (p values >0.05) on ethanol contents in 96-h samples (Figure 7).

In experiment set 2 (Table 3), daily glycerol trends in corn mash samples were not affected by spiking with *L. plantarum*. Aerated and nontreated samples had similar glycerol production throughout the fermentation period, with slightly more glycerol in the aerated samples. Ozonated samples had the least glycerol after 24 h of fermentation, which coincided with lower daily ethanol production.

The ethanol concentrations in all samples, LAB-spiked and nonspiked, began to plateau by 96 h of fermentation, as observed in experiment set 1. The 96-h ethanol concentration ranged from 143 to 147 g/L. Spiking with *L. plantarum* resulted in somewhat less ethanol than in nonspiked samples (Table 3). The ozonated samples had less ethanol and less lactic acid (Figure 6), than aerated and nontreated samples in this set of experiments, which accounts for less glycerol production. The ethanol findings suggest that higher ozone dosages (152 mg/L) may negatively impact ethanol yields, despite lowering lactic acid contents, depending on the initial pH. The starting pH (posttreatment) for fermentations in the first and second experiment sets was 4.8 and 4.5, respectively.

Corn Slurry (Experiment Set 3). *Yeast Addition.* Corn mash samples were prepared from POET corn slurry (pH 4) by adding urea, enzymes, and yeast. No yeast was added to select samples. As expected, samples without yeast added had higher levels of lactic acid within 24 h and acetic acid within 48 h of fermentation (Figure 8B,C). Higher yeast inoculum size enables the yeast to be more competitive with bacteria. Addition of yeast resulted in significantly (p = 0.002) higher ethanol contents within 24 h of fermentation (Figure 8E); 96-h samples had an average ethanol yield of 146 g/L, with yeast added, as compared to 130 g/L without yeast added.

Initial pH. The initial pH of corn mash prepared with corn slurry from POET was 4.0. This experiment was performed to investigate the effect of increasing the initial corn mash pH to 5.0 on ethanol fermentation with yeast added. Corn mash samples were prepared at slurry pH 4.0 and with pH adjusted to 5.0. The pH of corn mash samples dropped the first 24 h of fermentation (Figure 8A); corn mash with initial pH 4.0 and 5.0 decreased to pH 3.6 and 4.0 in 24 h, respectively. The pH increased gradually to pH 3.8 and 4.2 by the end of the experiment (168 h). The lactic and acetic acid contents increased for the first 24−48 h of fermentation, coinciding with decreasing pH values (Figure 8B,C). Production of lactic/acetic acids and glycerol (Figure 8D) was higher in samples at adjusted pH 5.0 than at slurry pH 4.0, which illustrates an active LAB population. Growth of lactic acid bacteria is reduced at pH less than 4.0. Ethanol production was affected by the increased levels of organic acids; this was demonstrated by higher ethanol concentrations at the slurry pH 4, indicating higher yeast activity.

Ozonation. Corn mash (adjusted pH 5) prepared with POET corn slurry was ozonated to investigate potential reductions in bacterial activity. Lactic acid production in ozonated samples was somewhat lower than in nonozonated

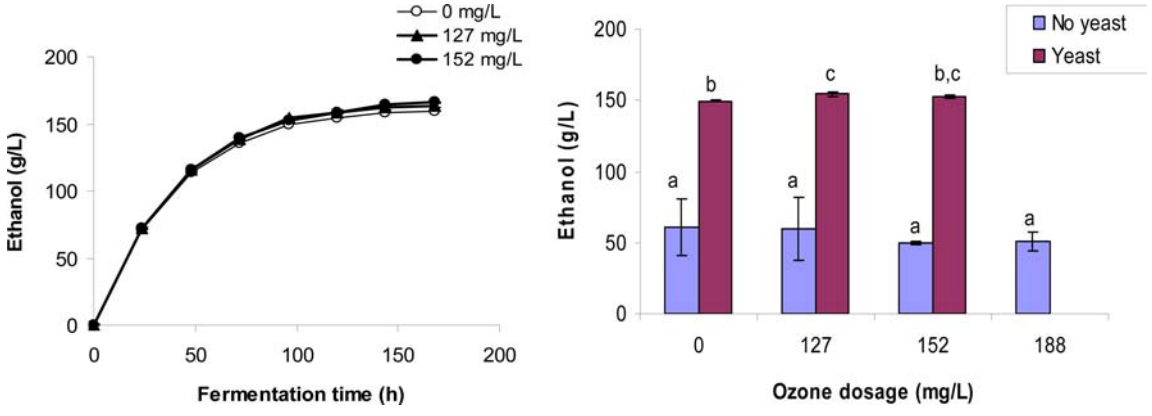

Figure 7. Experiment set 1: (Left) ethanol contents of daily fermentation samples for corn mash prepared from ground corn, spiked with *L. plantarum* and ozonated, with yeast added. No other antimicrobial agents (Lactrol or IsoStab) were added. (Right) Comparison of ethanol contents of 96-h samples (n = 3).

DOI: 10.1021/acs.jafc.5b00563
J. Agric. Food Chem. 2015, 63, 5239−5248

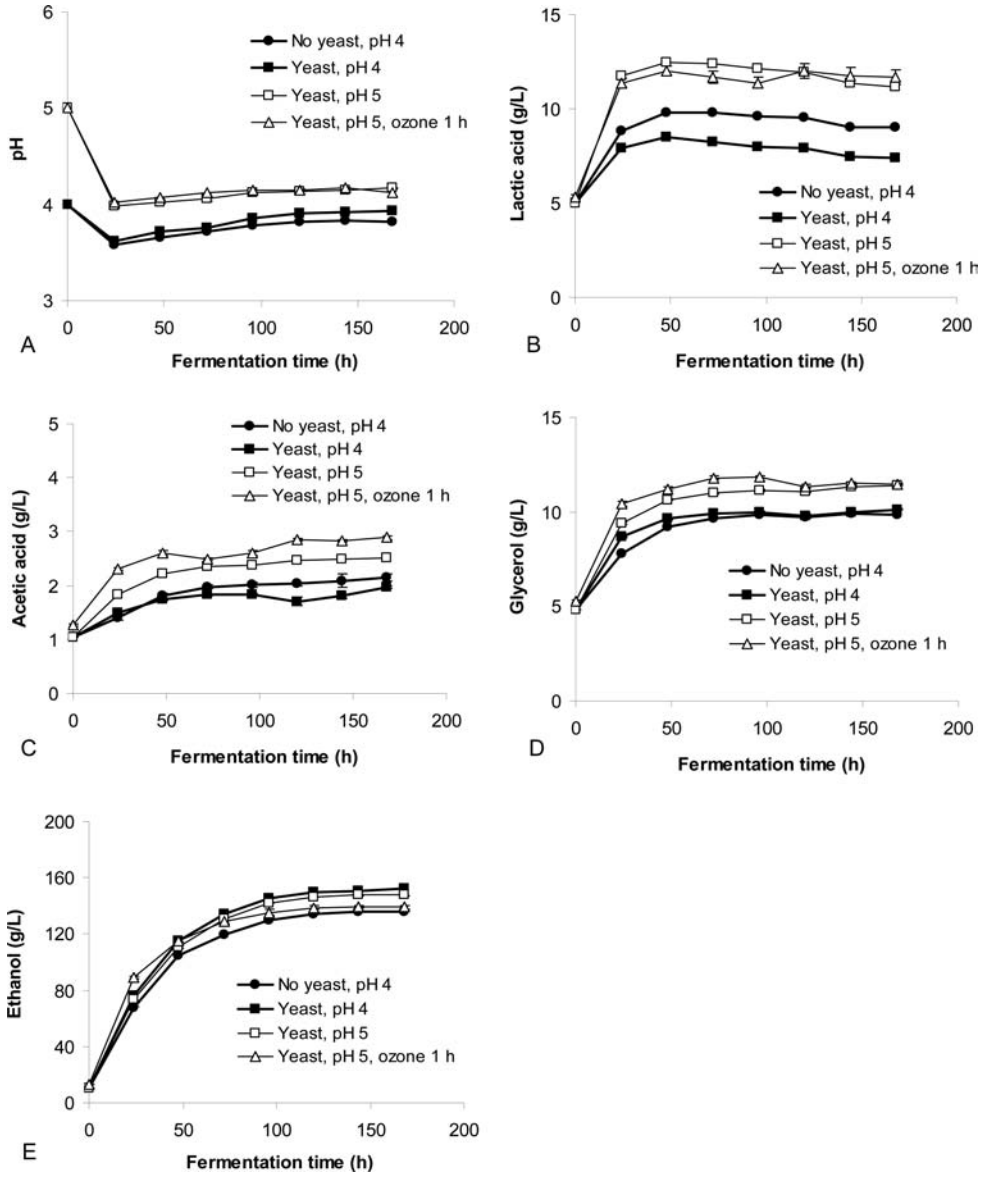

Figure 8. Corn mash prepared from POET corn slurry, which potentially contains recycled antimicrobials in the backset from previous fermentations: (A) pH, (B) lactic acid, (C) acetic acid, (D) glycerol, and (E) ethanol contents of daily fermentation samples from nonozonated/ozonated corn mash samples, with or without yeast added, and initial pH of 4 or 5 (n = 3).

samples (e.g., 12.0 versus 12.5 g/L in 48 h, respectively) up to 120 h (Figure 8B). Acetic acid contents of ozonated samples, however, were higher throughout the fermentation (e.g., 2.6 versus 2.2 g/L in 48 h) (Figure 8C). The initial acetic acid contents, after ozonation, were 0.3 g/L higher in the ozonated samples, which helps explain this finding. These results suggest that ozonation is not as effective in samples prepared from corn slurry in place of ground corn. Additional dissolved and suspended organic materials contributed from the backset may have consumed most of the ozone or shielded the bacteria. Recycled antimicrobial agents, Lactrol and IsoStab, in the corn slurry from the backset may also have reduced the effects of ozonation compared to the nonozonated controls.

Conclusions. Fermentation experiments were conducted with ozone treatment and without the addition of other antimicrobial agents, such as antibiotics. The experiments were performed with POET ground corn and corn slurry.

For POET ground corn we observed the following: (1) Ozonation could be used to lower corn mash pH and, therefore, reduce sulfuric acid requirements to adjust the pH prior to fermentation. (2) Lower lactic acid levels were observed in experiments with ground corn; on this basis, ozonation may reduce bacterial contamination, and thus antibiotic dosages, during fuel ethanol fermentations. (3) The impact of ozonation on ethanol yields, regardless of lowering lactic acid contents, depends on the ozone dosage and initial fermentation pH.

For POET corn slurry, which potentially contained some antimicrobials, we observed the following: (1) Yeast inoculum size affects the ethanol yields and enables the yeast to be more competitive than bacteria, as expected. (2) Ethanol production was higher at initial pH 4.0 than pH 5.0, indicating more yeast activity. (3) Ozone treatment, as applied to ground corn mash, is not as effective in samples prepared from corn slurry.

DOI: 10.1021/acs.jafc.5b00563
J. Agric. Food Chem. 2015, 63, 5239−5248

Additional experiments with POET corn slurry, and the various recycled water streams at a POET ethanol biorefinery, may help clarify the effectiveness of ozonation under fermentation conditions closer to those in plant operation. Higher ozone dosages and use of only recycled water sources that do not contain antimicrobials could be investigated.

AUTHOR INFORMATION

Corresponding Author

*Phone 864-656-4382; fax 864-656-0331; e-mail pometto@clemson.edu.

Notes

The authors declare no competing financial interest.

ACKNOWLEDGMENTS

This research was supported financially by POET and the Grow Iowa Values Fund Grant Program and was assisted by the Center for Crops Utilization Research (CCUR) at Iowa State University. POET Biorefining (Jewell, IA) provided ground corn and corn slurry samples. We thank Dr. Hans van Leeuwen for his assistance in the economic calculations.

REFERENCES

(1) POET. POET Home Page. http://www.poet.com/index.asp (accessed July 25, 2014).

(2) Batal, A.; Dale, N. True metabolizable energy and amino acid digestibility of distillers dried grains with solubles. *J. Appl. Poult. Res.* **2006**, *15*, 89−93.

(3) Fastinger, N.; Latshaw, J.; Mahan, D. Amino acid availability and true metabolizable energy content of corn distillers dried grains with solubles in adult cecectomized roosters. *Poult. Sci.* **2006**, *85*, 1212−1216.

(4) Fontaine, J.; Zimmer, U.; Moughan, P.; Rutherfurd, S. Effect of heat damage in an autoclave on the reactive lysine contents of soy products and corn distillers dried grains with solubles: Use of the results to check on lysine damage in common qualities of these ingredients. *J. Agric. Food Chem.* **2007**, *55*, 10737−10743.

(5) U.S. Grains Council. A Guide to Distiller's Dried Grains with Solubles (DDGS), 3rd ed., 2012, pp 1−406. http://www.ethanolrfa.org/page/-/rfa-association-site/studies/2012_DDGS_Handbook.pdf?nocdn=1 (accessed July 25, 2014).

(6) Stein, H.; Pedersen, C.; Gibson, M.; Boersma, M. Amino acid and energy digestibility in ten samples of distillers dried grain with solubles by growing pigs. *J. Anim. Sci.* **2006**, *84*, 853−860.

(7) POET Nutrition. Dakota Gold BPX − As Fed. Company brochure, July 2009. http://www.dakotagold.com/products/dakotagold.asp (accessed July 25, 2014).

(8) Skinners, K.; Leathers, T. Bacterial contaminants of fuel ethanol production. *J. Ind. Microbiol. Biotechnol.* **2004**, *31*, 401−408.

(9) Kelsall, D.; Lyons, T. Grain dry milling and cooking procedures: extracting sugars in preparation for fermentation. In *Alcohol Textbook: A Reference for the Beverage, Fuel and Industrial Alcohol Industries*, 4th ed.; Jacques, K., Lyons, T., Kelsall, D., Eds.; Nottingham University Press: Nottingham, U.K., 2003; pp 10−21.

(10) Bryan, T. Hopping right into ethanol. *Ethanol Producer Mag.* **2006**, No. February, 98−101.

(11) Barbour, E.; Priest, F. Some effects of *Lactobacillus* contamination in Scotch whisky fermentations. *J. Inst. Brew.* **1988**, *94*, 89−92.

(12) Maiorella, B.; Blanch, H.; Wilke, R. By-product inhibition effects on ethanolic fermentation by *Saccharomyces cerevisiae*. *Biotechnol. Bioeng.* **1983**, *25*, 103−131.

(13) Makanjuola, D.; Tymon, A.; Springham, G. Some effects of lactic acid bacteria on laboratory-scale yeast fermentations. *Enzyme Microb. Technol.* **1992**, *14*, 350−357.

(14) Narendranath, N.; Hynes, S.; Thomas, K.; Ingledew, W. Effects of lactobacilli on yeast-catalyzed ethanol fermentations. *Appl. Environ. Microbiol.* **1997**, *63*, 4158−4163.

(15) Lushia, W.; Heist, P. Antibiotic resistant bacteria in fuel ethanol fermentations. *Ethanol Producer Mag.* **2005**, No. May, 80−82.

(16) Bayrock, D.; Ingledew, W. Changes in steady state on introduction of a *Lactobacillus* contaminant to a continuous culture ethanol fermentation. *J. Ind. Microbiol. Biotechnol.* **2003**, *27*, 39−45.

(17) Narendranath, N.; Power, R. Relationship between pH and medium dissolved solids in terms of growth and metabolism of lactobacilli and *Saccharomyces cerevisiae* during ethanol production. *Appl. Environ. Microbiol.* **2005**, *71*, 2239−2243.

(18) Stroppa, C.; Andrietta, M.; Andrietta, S.; Steckelberg, C.; Serra, G. Use of penicillin and monensin to control bacterial contamination of Brazilian alcohol fermentations. *Int. Sugar J.* **2000**, *102*, 78−82.

(19) Bischoff, K.; Liu, S.; Leathers, T.; Worthington, R.; Rich, J. Modeling bacterial contamination of fuel ethanol fermentation. *Biotechnol. Bioeng.* **2009**, *103*, 117−122.

(20) Thomas, K.; Hynes, S.; Ingledew, W. Effect of lactobacilli on yeast growth, viability and batch and semi-continuous alcoholic fermentation of corn mash. *J. Appl. Microbiol.* **2001**, *90*, 819−828.

(21) Connolly, C. Bacterial contaminants and their effects on alcohol production. In *The Alcohol Textbook*, 3rd ed.; Jacques, K. A., Lyons, T. P., Kelsall, D. R., Eds.; Nottingham University Press: Nottingham, U.K., 1997; pp 317−334.

(22) Cocito, C. Antibiotics of the virginiamycin family, inhibitors which contain synergistic components. *Microbiol. Rev.* **1979**, *43*, 145−198.

(23) Hynes, S.; Kjarsgaard, D.; Thomas, K.; Ingledew, W. Use of virginiamycin to control the growth of lactic acid bacteria during alcohol fermentation. *J. Ind. Microbiol. Biotechnol.* **1997**, *18*, 284−291.

(24) Dutta, G.; Devriese, L. Degradation of macrolide-lincosamide streptogramin antibiotics by *Lactobacillus* strains from animals. *Ann. Microbiol.* **1981**, *132A*, 51−57.

(25) Bischoff, K.; Skinner-Nemec, K.; Leathers, T. Antimicrobial susceptibility of *Lactobacillus* species isolated from commercial ethanol plants. *J. Ind. Microbiol. Biotechnol.* **2007**, *34*, 739−744.

(26) Haakensen, M.; Vickers, D.; Ziola, B. Susceptibility of *Pediococcus* isolates to antimicrobial compounds in relation to hop-resistance and beer-spoilage. *BMC Microbiol.* **2009**, *9*, 190.

(27) Simpson, W. Ionophoric action of *trans*-isohumulone of *Lactobacillus brevis*. *J. Gen. Microbiol.* **1993**, *139*, 1041−1045.

(28) Chang, I.; Kim, B.; Shin, P. Use of sulfite and hydrogen peroxide to control bacterial contamination in ethanol fermentation. *Appl. Environ. Microbiol.* **1997**, *63*, 1−6.

(29) Gibbons, W.; Westby, C. Use of potassium metabisulfite to control bacterial contaminants during fermentation of fodder beet cubes for fuel ethanol. *Biomass* **1986**, *11*, 99−113.

(30) Meneghin, S.; Reis, F.; de Almeida, P.; Ceccato-Antonini, S. Chlorine dioxide against bacteria and yeasts from the alcoholic fermentation. *Braz. J. Microbiol.* **2008**, *39*, 337−343.

(31) Narendranath, N.; Thomas, K.; Ingledew, W. Urea hydrogen peroxide reduces the numbers of lactobacilli, nourishes yeast, and leaves no residues in the ethanol fermentation. *Appl. Environ. Microbiol.* **2000**, *66*, 4187−4192.

(32) Oliva-Neto, P.; Yokoya, F. Effect of 3,4,4′-trichlorocarbanilide on growth of lactic acid bacteria contaminants in alcoholic fermentation. *Bioresour. Technol.* **1998**, *63*, 17−21.

(33) Watanabe, I.; Nakamura, T.; Shima, J. A strategy to prevent the occurrence of *Lactobacillus* strains using lactate-tolerant yeast *Candida glabrata* in bioethanol production. *J. Ind. Microbiol. Biotechnol.* **2008**, *35*, 1117−1122.

(34) Khadre, M. A.; Yousef, A. E.; Kim, J.-G. Microbiological aspects of ozone applications in food: A review. *J. Food Sci.* **2001**, *66*, 1242−1252.

(35) Kim, J.-G.; Yousef, A. E.; Dave, S. Application of ozone for enhancing the microbiological safety and quality of foods: A review. *J. Food Protect.* **1999**, *62*, 1071−1087.

DOI: 10.1021/acs.jafc.5b00563
J. Agric. Food Chem. 2015, 63, 5239−5248

(36) García-Cubero, M. T.; González-Benito, G.; Indacoechea, I.; Coca, M.; Bolado, S. Effect of ozonolysis pretreatment on enzymatic digestibility of wheat and rye straw. *Bioresour. Technol.* **2009**, *100*, 1608−1613.
(37) Freitas-Silva, O.; Venâncio, A. Ozone applications to prevent and degrade mycotoxins: A review. *Drug Metab. Rev.* **2010**, *42*, 612−620.
(38) Miller, F. A.; Silva, C. L. M.; Brandão, T. R. S. A review on ozone-based treatments for fruit and vegetables preservation. *Food Eng. Rev.* **2013**, *5*, 77−106.
(39) Gerrity, D.; Snyder, S. Review of ozone for water reuse applications: toxicity, regulations, and trace organic contaminant oxidation. *Ozone Sci. Eng.* **2011**, *33*, 253−266.
(40) Zhu, W.; Koziel, J.; Cai, L.; Brehm-Stecher, B.; Ozsoy, H.; van Leeuwen, J. Ozonation-based decolorization of food dyes for recovery of fruit leather wastes. *J. Agric. Food Chem.* **2013**, *61*, 8198−8206.
(41) Kunduru, M.; Pometto, A., III. Continuous ethanol production by *Zymomonas mobilis* and *Saccharomyces cerevisiae* in biofilm bioreactors. *J. Ind. Microbiol. Biotechnol.* **1996**, *16*, 249−256.
(42) Walker, G. *Yeast Physiology and Biotechnology*; John Wiley & Sons: Chichester, U.K., 1998.

DOI: 10.1021/acs.jafc.5b00563
J. Agric. Food Chem. 2015, 63, 5239−5248

JOURNAL OF AGRICULTURAL AND FOOD CHEMISTRY

Article

pubs.acs.org/JAFC

Lysine-Based Site-Directed Mutagenesis Increased Rigid β-Sheet Structure and Thermostability of Mesophilic 1,3−1,4-β-Glucanase

Chengtuo Niu,[†,‡,§] Linjiang Zhu,[†,‡,§] Pei Zhu,[†,‡] and Qi Li*[,†,‡]

[†]Key Laboratory of Industrial Biotechnology, Ministry of Education, School of Biotechnology, and [‡]Synergetic Innovation Center of Food Safety and Nutrition, School of Biotechnology, Jiangnan University, Wuxi 214122, China

Supporting Information

ABSTRACT: 1,3−1,4-β-Glucanase is widely applied in the food industry, while its low thermostability often reduces its performance. In a previous study, chemical modification of surface lysine residues was proved to increase the thermostability of β-glucanase. To improve the thermostability, the mesophilic β-glucanase from *Bacillus terquilensis* was rationally engineered through site-directed mutagenesis of the 12 lysines into serines. The results showed that the K20S, K117S, and K165S mutants could both enhance the specific activities and thermostability of β-glucanase. The triple mutant (K20S/K117S/K165S) could increase the optimal temperature and T_{50} value by 15 and 14 °C, respectively. Five percent more structured residues were observed in the mutant, which formed new β-sheet structures in the concave side. Molecular dynamics simulation analysis showed that the flexibility in the mutation regions was decreased, which resulted in the overall rigidity of the β-glucanase. Therefore, the lysine-based site-directed mutagenesis is a simple and effective method for improving the thermostability of β-glucanase.

KEYWORDS: *1,3−1,4-β-glucanase, lysine residues, molecular dynamics simulation, site-directed mutagenesis, thermostability*

INTRODUCTION

1,3−1,4-β-Glucanase (EC 3.2.1.73) is an endo-β-D-glucanase that can hydrolyze 1,3−1,4-β-glucan containing mixed β-1,3 and β-1,4 glycosidic bonds into oligosaccharides.[1] It is widely used in the brewing and animal-feed industries.[2] In the brewing industry, β-glucanase is used to increase the yields of malt extract and the filtration rate of wort and beer, thus enhancing the nonbiological stability of the finished beer.[3] In the animal-feed industry, β-glucanase will increase the digestibility of barley-based diets for animals, especially broiler chickens and piglets.[4] However, these applications often encounter some industrial stresses such as high temperature and low thermostability of β-glucanase, which will reduce its performance. For example, the mashing temperature is elevated from 48 °C to 78 °C[5] and the temperature in animal-feed pelleting is usually between 60 and 90 °C before cooling,[6] whereas the optimal temperatures of 1,3−1,4-β-glucanases from *Bacillus* spp., which are the main sources of β-glucanases, just vary from 45 to 65 °C.[7] The β-glucanases from non-*Bacillus* bacteria and fungi also have similar thermostability.[2] As for thermostable β-glucanases from thermophiles, the optimal temperature can reach 80 °C,[8] but it cannot have a high enzymatic activity under the relatively low-temperature industrial condition of 60−70 °C. Therefore, the thermostability of mesophilic 1,3−1,4-β-glucanase derived from *Bacillus* spp. needs to be improved to meet industrial applications.[2,9]

Enzyme thermostability theoretically involves the maintenance of the balance between overall rigidity of a protein and local flexibility of a catalytic center at a certain temperature.[10] Some amino acid residues located at the protein surface often cause flexible regions at a maladapted high temperature, then reduce the activity, and even lose total activity.[11] Therefore, it is a common strategy for enhancing enzyme thermostability to modify the flexible amino acids on the protein surface.[11,12] As for the mesophilic 1,3−1,4-β-glucanase from *Bacillus* spp., some lysine residues on the protein surface was proved to negatively affect the thermostability, since the chemical modification of five (out of 12) ε-amino groups of lysine residues could significantly enhance its thermostability.[13] Several other researchers also reported that lysine residues on the protein surface influenced the protein thermostability.[14,15] Therefore, some surface lysine residues might induce flexible regions of a protein at a high temperature and reduce protein thermostability. However, there is still a lack of direct evidence about the negative effect of lysine residues on protein thermostability. Considering that chemically modifying some of the 12 ε-amino groups of lysine into hydroxyl groups could simultaneously enhance the catalytic activity and thermal tolerance,[13] the lysine-based site-directed mutagenesis was supposed to improve the overall rigidity and thermostability of 1,3−1,4-β-glucanases from *Bacillus* spp.

In recent years, molecular dynamics (MD) simulation is a common computer-based tool to characterize the detailed dynamical behaviors of protein in different situations, such as high temperature, high pressure, and the presence of detergents,[16] or to identify the flexible regions when temperature is elevated.[17] MD simulation has been applied to compare the unfolding pathways of 12 mesophilic and thermophilic xylanases and predicted the unstable regions at a high temperature.[18] Through MD simulation, the flexibility of 1,4-β-endoglucanase from the GH5 family was found to be highly correlated with their optimal temperatures, and the 1,4-β-endoglucanase was then stabilized by introducing a new

Received: January 27, 2015
Revised: May 6, 2015
Accepted: May 8, 2015
Published: May 8, 2015

ACS Publications © 2015 American Chemical Society

DOI: 10.1021/acs.jafc.5b00480
J. Agric. Food Chem. 2015, 63, 5249−5256

disulfide bond in this flexible region.[19] MD simulation has also been used to study the effect of structural changes on protein properties.[20]

In this study, a new β-glucanase with high enzymatic activity (*bglT*) from *B. terquilensis* CGX 5-1[1] was used. All its 12 lysine residues were mutated into serine residues, which could result in similar structures to those in the previous chemically modified enzyme.[13] The catalytic properties and thermostability properties of the wild-type BglT and the mutant enzymes were determined. Differences in the enzyme dynamical behaviors at high temperatures and the protein structures were also compared.

MATERIALS AND METHODS

Strains, Vectors, and Materials. The recombinant plasmid pET28a(+)-*bglT* was constructed in our previous study.[1] The vector pET28a(+) (Invitrogen, Shanghai, China) was used for construction of the recombinant vector harboring mutant genes. *Escherich coli* JM109 and BL21(DE3) cells were used for plasmid amplification and expression. The *E. coli* cells were incubated at 37 °C in Luria−Bertani media containing ampicillin (50 μg/mL) or kanamycin (100 μg/mL) when necessary. Other reagents of analytical grade were purchased from Sangon (Shanghai, China) or Sinopharm (Shanghai, China).

MD Simulation. The three-dimensional (3D) structures of wild-type BglT and the mutants were homologically modeled in the SWISS-MODEL online server[21] with the reference structure (PDB code: 1GBG).[22] The amino acid sequence identity between BglT and the reference is 92.49% (Online Resource 1, SI). These 3D structures were then submitted to the 2 ns MD simulation processes at 300 K to calculate their total energy values. To further evaluate the thermostability of β-glucanases, the wild-type BglT and triple mutant were subjected to MD simulation processes at 450 K for 20 ns. In the MD, the Gromacs 4.6 package[23] and GROMOS53a6 field force[24] were applied and the structures were put in a cubic box and solvated. Before the final run, the systems were minimized in energy and equilibrated in temperature and pressure using the Berendsen coupling algorithm[25] and the Rahman−Parrinello algorithm,[26] respectively. All bonds were constrained using the LINCS algorithm, and periodic boundary conditions were applied. The long-range electrostatic interactions were calculated by the Particle Mesh Ewald method,[25] while the nonbonded van der Waals interactions were calculated by the L−J model with a cutoff distance of 14 Å. All the MD simulation processes were repeated in triplicate. The root-mean-square deviation (RMSD) and root-mean-square fluctuation (RMSF) analyses were performed using the available Gromacs analysis tools.

Generation of Recombinant 1,3−1,4-β-Glucanase and Its Mutants. The recombinant plasmid pET28a(+)-*bglT*, which was constructed in the previous experiment,[1] was used as a template for site-directed mutagenesis (the gene sequence of *bglT* is shown in Online Resource 2, SI). Mutant β-glucanase gene fragments were obtained by the overlapping extension PCR technique. The primer sequences and the corresponding mutation sites are listed in Online Resource 3, SI. The obtained PCR products were ligated into pET28a(+) and then transformed into *E. coli* BL21(DE3) cells. Positive clones were selected, and the sequences were verified by DNA sequencing (BGI, Shanghai, China).

The expression and purification of recombinant proteins in *E. coli* BL21(DE3) (pET28a-bglT) were as follows. Cells were incubated in optimized TB medium (20 g yeast extract/L; 12.5 g trypton/L; 14.1 mL glycerol/L; 2.17 g KH_2PO_4/L; and 2.74 g K_2HPO_4/L). After incubation at 24 °C for 6 h, 0.06 mM isopropyl β-D-thiogalactoside and 8 mM α-lactose were added. The supernatant was harvested by centrifugation at 9000*g* for 20 min and then loaded into a 5 cm × 1 cm^2 Ni-NTA affinity column (Qiagen, Shanghai, China), which was pre-equilibrated with binding buffer (50 mM NaH_2PO_4, 0.5 M NaCl, and 10 mM imidazole). The column was washed following a step gradient of 50, 100, and 250 mM imidazole solutions as described previously.[13] The obtained liquid was then desalted using a PD-10 desalting column (GE Healthcare, Tianjin, China) and eluted with 20 mM phosphate buffer (pH 6.5). Subsequently, the eluent was concentrated using a Pellicon Cassette concentrator (Millipore, Darmstadt, Germany) with a 10 kDa cutoff membrane. The protein purity was analyzed by sodium dodecyl sulfate-polyacrylamide gel electrophoresis (SDS-PAGE) using 12% (w/v) polyacrylamide gel. The total concentrations of protein samples were estimated according to the Bradford method[27] with bovine serum albumin as the standard protein.

Activity Assay of 1,3−1,4-β-Glucanase. 1,3−1,4-β-Glucanase activity was measured using the improved AZO method[1] with 1% AZO blue barley β-glucan (Megazyme, Wicklow, Ireland) as substrate. The reducing sugar content was measured using the 3,5-dinitrosalicylic acid method.[28] The assay was carried out in a 500 μL volume containing an appropriate amount of diluted enzyme solution and 1% (w/v) substrate at 40 °C for 10 min. Precipitation solution (32.5 g sodium acetate/L, 4 g zinc sulfate/L, and 800 mL methoxy ethanol/L) was added to terminate the reaction, and the OD_{590} was recorded. One unit of enzymatic activity was defined as the amount of enzyme that released 1 μmol of reducing sugar from the substrate per minute at pH 6.5. Each measurement was repeated in triplicate. As for catalytic kinetic properties of wild-type BglT and its mutants, the Lineweaver−Burk double reciprocal method was adopted.[29] The enzyme concentration was set at 100 μg/mL, while the substrate concentration varied from 0 to 10 mg/mL.

Determination of Thermostability Parameters. The optimal temperature of 1,3−1,4-β-glucanase was determined by measuring the enzymatic activity from 35 to 70 °C at 5 °C intervals. For each enzyme, the highest activity measured was designated as 100%. Enzyme thermostability was analyzed by measuring the residual activity as a function of temperature and heating time at elevated temperatures. The enzyme half-inactivation temperature (T_{50}) was evaluated by measuring the enzymatic activity at different temperatures. The enzymes were incubated from 40 to 80 °C for 10 min, followed by 10 min of cooling on ice. The T_{50} value is defined as the temperature that can reduce the enzymatic activity to half after incubation for 10 min. Furthermore, the decay of enzymatic activity over time at 50 and 60 °C was monitored by incubating the enzyme solution at high temperature and measuring the remaining activity at a series of time points. The $t_{(1/2,X°C)}$ value was obtained from the inactivation curve when the β-glucanase lost half of its activity.

Circular Dichroism (CD) Analysis. The far-UV CD spectra of wild-type BglT and the mutant enzymes were measured from 190 to 250 nm by a MOS-450 AF circular dichroism spectrometer (Biologic, Claix, France) with a resolution of 1 nm. The concentration of all enzymes in 20 mM phosphate buffer (pH6.5) was set at 50 μg/mL. The CD spectra of the phosphate buffer were recorded and subtracted from sample spectra. The percentages of secondary structure elements (helix, β-sheet, β-turn, and loop) were predicted using Dichroweb online software.[30]

RESULTS AND DISCUSSION

Enzymatic Properties of 12 Single-Site Mutant β-Glucanases. The 1,3−1,4-β-glucanase from *B. terquilensis* CGX 5-1 is composed of 214 amino acid residues and contains 12 surface lysine residues. All 12 single-site mutants were constructed through the overlapping PCR method, and the recombinant enzymes were expressed in *E. coli* BL21(DE3) through pET28a. The main enzymatic activities of recombinant β-glucanases were detected in the supernatant of the culture media, which were purified by a Ni-NTA column (Online Resource 4, SI). Their specific activities were measured as shown in Table 1. The K20S, K117S, and K165S mutants displayed higher specific activities than the wild-type BglT (2490.1 U/mg), which were increased by 47.6%, 19.4%, and 43.9%, respectively. The other nine mutants showed lower specific activities, which were decreased by 30% to 73.6%.

DOI: 10.1021/acs.jafc.5b00480
J. Agric. Food Chem. 2015, 63, 5249−5256

Table 1. Specific Activity, Total Energy Values, and the Hydrogen Bond (HB) Number of Wild-Type BglT and Its Mutants

protein samples	specific activity (U/mg)	total energy (kJ/mM)	total HB number
WT	2490.1 ± 105.3	−733.200	153
K20S	3675.1 ± 147.0	−733.315	167
K58S	1453.9 ± 36.34	−733.183	150
K80S	1365.4 ± 47.8	−733.194	152
K83S	1742.4 ± 67.9	−733.224	158
K113S	984.6 ± 18.7	−733.270	154
K117S	2973.7 ± 77.3	−733.526	156
K132S	958.4 ± 47.9	−733.571	155
K157S	1265.7 ± 75.9	−733.634	154
K165S	3584.7 ± 113.4	−733.493	156
K178S	812.2 ± 48.7	−733.571	161
K213S	657.2 ± 32.9	−733.834	166
K214S	840.6 ± 54.6	−721.055	161
K20S/K117S/165S	3936.4 ± 122.0	−733.535	165

The effect of lysine-based mutation on the enzyme kinetic parameters was also characterized (Table 2). The K_m value of wild-type BglT was 0.297 mM, while the K_m values of K20S, K117S, and K165S mutants were 0.293, 0.283, and 0.284 mM. This indicated that all three single mutants increased the binding affinity with the substrate of barley β-glucan. Furthermore, the K_{cat} values and K_{cat}/K_m values of K20S, K117S, and K165S mutants were significantly increased. The K20S mutant had the highest K_{cat} value (175.40 s^{-1}) and K_{cat}/K_m value (598.63 $s^{-1}\cdot mM^{-1}$), which were 27.7% and 29.4% higher than those of wild-type BglT, respectively. These results indicated that three out of 12 single-site mutations of lysine residues into serine residues could increase the enzymatic efficiency and the binding affinity of the substrate.

Table 2. Kinetic Parameters of Wild-Type BglT and Various Mutants with Site Mutations of Lysine Residues

protein sample	K_m (mM)	K_{cat} (s^{-1})	K_{cat}/K_m ($s^{-1}\cdot mM^{-1}$)
WT	0.297 ± 0.005	137.36	462.49
K20S	0.293 ± 0.004	175.40	598.63
K117S	0.283 ± 0.004	161.29	569.63
K165S	0.284 ± 0.005	164.89	580.60
K20S/K117S/K165S	0.278 ± 0.004	184.93	665.22

Thermostability Prediction by MD. To predict the enzyme thermostability, changes in the enzyme total energy values induced by mutation of lysine residues were calculated by MD simulation. The total energy values were closely correlated with the entropy values of protein unfolding.[31] Compared with the value of wild-type BglT (−733.200 kJ/mM), nine out of 12 single-site mutants displayed lower total energy values, which means that the nine single-site mutants might have a better thermostability. Furthermore, the number of hydrogen bonds formed in these protein structures was calculated. Compared with the wild-type BglT (153), 10 out of 12 mutants showed an increased number of hydrogen bonds formed in the whole protein structure (Table 1). As for each mutant region, more hydrogen bonds were also observed in seven mutant regions (K20S, K113S, K117S, K132S, K165S, K178S, and K213S), while two mutant regions (K83S and K214S) showed fewer hydrogen bonds (Table 2). Hydrogen bonds can increase protein thermostability in many proteins.[32] Therefore, mutant enzymes with more hydrogen bonds and lower total energy values were predicted to be more thermostable.

Thermostability Parameter Analysis of Three Activity-Improved Mutants. To compare the thermostability of the

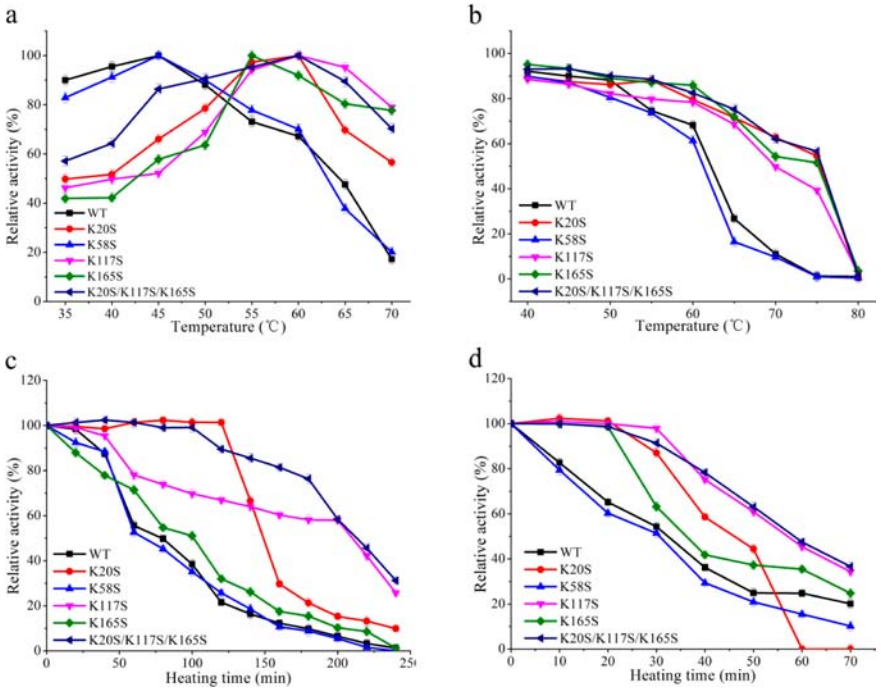

Figure 1. Analysis of thermostability of wild-type BglT and the mutant enzymes. (a) Optimal temperature; (b) kinetic stability curves; (c) inactivation curve at 50 °C; (d) inactivation curve at 60 °C.

DOI: 10.1021/acs.jafc.5b00480
J. Agric. Food Chem. 2015, 63, 5249−5256

mutants, three single-site mutants (K20S, K117S, and K165S) with higher activity and more hydrogen bond formation were subjected to further analysis. One mutant (K58S) with slightly lower enzymatic activity and predicted lower thermostability was also characterized. As shown in Figure 1, the optimal temperatures of K20S, K117S, and K165S mutants were 60, 60, and 55 °C, which were 15, 15, and 10 °C higher than that of wild-type BglT, respectively (Figure 1a). The T_{50} values of wild-type BglT and K20S, K117S, and K165S mutants were determined to be 62, 76, 76, and 75 °C (Figure 1b), respectively, which indicated that the single-site mutations could increase the T_{50} values by 13−14 °C. The comparisons of $t_{(1/2,\ 50°C)}$ and $t_{(1/2,\ 60°C)}$ at 50 and 60 °C are shown in Figure 1c and d, respectively. The $t_{(1/2,\ 50°C)}$ values of K20S, K117S, and K165S mutants reached 149, 210, and 102 min, which were 88.6%, 165.8%, and 29.1% longer than that of wild-type BglT. Especially, the K20S mutant could even maintain 100% of activity after incubation for 125 min. The $t_{(1/2,\ 60°C)}$ values of K20S, K117S, and K165S mutants were 46, 58, and 37 min, which were much higher than that of wide-type BglT (32.5 min). As for the K58S mutant, with a higher predicted total energy value, it showed slightly lower thermostability compared to wild-type BglT. Its optimal temperature and T_{50} value were 45 and 61 °C, while its half-life values at 50 and 60 °C were 77 and 31 min. These results indicated that K20S, K117S, and K165S mutants could significantly enhance the thermostability of β-glucanase, which is in accordance with the above predicated results based on calculations of total energy values.

Analysis of Thermostability in the K20S/K117S/K165S Mutant Enzyme. To further improve the thermostability of 1,3−1,4-β-glucanase, the triple mutant enzyme harboring the K20S, K117S, and K165S mutant sites was constructed and expressed since beneficial substitutions might have an additive effect on protein thermostability.[33] The triple mutant (K20S/K117S/K165S) displayed both higher catalytic activity and better thermostability. Its specific activity reached 3936.4 U/mL, which was almost 2 times higher than that of wild-type BglT. Furthermore, its total energy value was −733.535 kJ/mM (Table 1), which was the lowest among wild-type BglT and all the mutants. The number of hydrogen bonds formed in the triple mutant is 165, more than the wild-type BglT. The optimal temperature and T_{50} value of the triple mutant were 60 and 76 °C, which were 15 and 14 °C higher than those of wild-type BglT, respectively (Figure 1). The half-life values of the triple mutant at 50 and 60 °C were 214 and 59 min, which were 170.9% and 81.5% longer than those of wild-type BglT, respectively. These results indicated that the thermostability of β-glucanase was further improved by combinational mutation of the three lysine sites.

Comparative Analysis of Flexibility between Wild-Type BglT and Triple Mutant Enzyme. To evaluate the effect of lysine mutation on the rigidity of the enzyme structure, the overall and local flexibility of the wild-type BglT and K20S/K117S/K165S mutant was compared using MD simulation. As shown in Table 4, the Cα RMSD value of wild-type BglT stabilized around 0.67 nm at 450 K, while the triple mutant showed an average Cα RMSD value of 0.59 nm. The RMSD values of the backbone, main chain, and side chain also showed a similar trend (Online Resource 5, SI). The flexibility of the three mutant regions was also calculated. Table 4 shows that the average RMSD values of the residues within 5 Å of the three mutant residues in the K20S/K117S/K165S mutant were 0.47, 0.27, and 0.43 nm, which were all slightly lower compared

Table 3. Comparison of the Hydrogen Bond Number in the Mutant Regions (within a 5 Å Distance of the Mutant Sites)

mutant region	wild-type BglT	mutants
K20S	6	7
K58S	5	5
K80S	2	2
K83S	5	4
K113S	1	3
K117S	3	5
K132S	7	8
K157S	5	5
K165S	3	5
K178S	7	8
K213S	0	1
K214S	3	2

Table 4. Comparison of the Global (Cα) and Local (Residues within a Radius of 5 Å of the Mutant Sites) RMSD Values between the Wild-Type BglT and K20S/K117S/K165S Mutant

	average RMSD value	
	WT (nm)	K20S/K117S/K165S (nm)
Cα atoms	0.67 ± 0.03	0.59 ± 0.02
around residue no. 20	0.58 ± 0.05	0.47 ± 0.06
residues within 5 Å of residue no. 117	0.34 ± 0.02	0.27 ± 0.02
residues within 5 Å of residue no. 165	0.47 ± 0.02	0.43 ± 0.03

to the wild-type BglT. The RMSD value is a thermodynamic parameter that reflects the maintenance capability of protein at high temperatures.[34] The lower the RMSD value, the more rigid the protein backbone and the better its thermostability.[35] Therefore, the results indicated that the triple mutant showed more conformational rigidity than the wild-type BglT at high temperature. A more detailed description about residue mobility was described using RMSF values as shown in Figure 2. The triple mutant displayed lower overall RMSF values. The main different regions in the RMSF curves between wild-type BglT and the K20S/K117S/K165S mutant were the lysine-mutation regions. Furthermore, several other regions, such as residues no. 30−40, no. 55−75, no. 80−100, no. 105−115, and

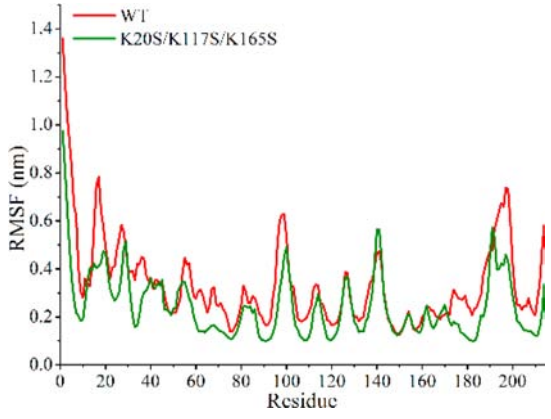

Figure 2. Comparison of Cα RMSF values of wild-type BglT (red line) and K20S/K117S/K165S triple mutant (green line) according to residue numbers after calculation at 450 K for 20 ns.

DOI: 10.1021/acs.jafc.5b00480
J. Agric. Food Chem. 2015, 63, 5249−5256

no. 171−195, also displayed a large decrease in RMSF values in the triple mutant compared to the wild-type BglT. The RMSF value could indicate the flexibility of an atom or a residue. A high RMSF value on the protein surface often means highly flexible regions and large fluctuations of local configuration at a high temperature, which might start the protein unfolding.[11] These results provided the direct evidence that mutation of lysine residues into serine residues could significantly reduce the local RMSF values around lysine-mutation sites, resulting in a higher rigid structure and better thermostability of β-glucanase.

Changes in the Molecular Structure Induced by Mutation of Lysine Residues. Previous reports[34] showed that the increase of RMSF values was always accompanied by the loss of secondary structure. Therefore, to understand the mechanism of the enhanced thermostability, CD analysis was applied to detect the changes in the protein secondary structure. As shown in Figure 3, wild-type BglT and the K20S/K117S/K165S mutant displayed similar CD spectra. Both enzymes were predicted to be composed of mainly β-sheets and β-turns. However, both the positive and negative bands in the CD spectrum were shifted to larger wavelength in the triple mutant compared to the wild-type BglT. The positive band was moved from 193 nm to 196 nm, while the negative band was moved from 210 nm to 217 nm, which means that the proportion of β-sheets in the K20S/K117S/K165S mutant was increased. As shown in Table 5, the percentage of β-sheets was increased from 38% to 46%, while the proportion of helixes, β-turns, and loops decreased. Besides, the percentage of structured residues in the triple mutant was increased from 61% to 66%.

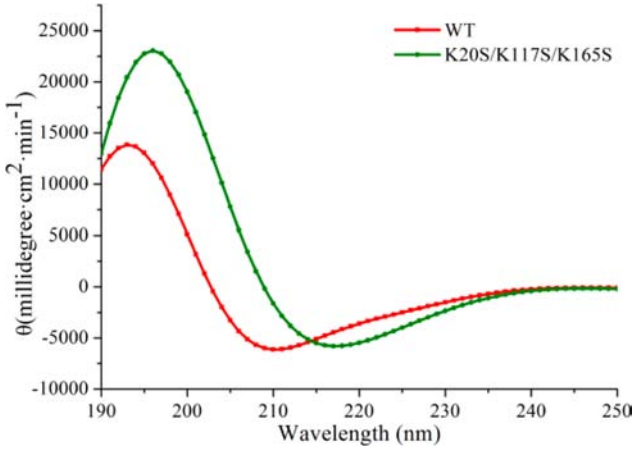

Figure 3. CD spectra of wild-type BglT and K20S/K117S/K165S mutant in 20 mM phosphate buffer (pH 6.5).

Table 5. Comparison of Secondary Structure between Wild-Type BglT and K20S/K117S/K165S Mutant Using Dichroweb Online Software

protein sample	helix (%)	β-sheet (%)	β-turn (%)	loop (%)
WT	11	37	13	39
K20S/K117S/K165S	9	46	11	34

More structured residues usually could result in more rigid secondary structure of the protein,[20] which might be responsible for the increased predicted rigidity of β-glucanase.

To further analyze the structure change induced by lysine mutation, the predicted 3D structures of wild-type BglT and the K20S/K117S/K165S mutant were also compared (Figure 4). The three mutation sites (K20S, K117S, and K165S) were all located on the protein surface. Lys20 was located in the middle of a long loop (loop 2). When the Lys20 was mutated to Ser20, a hydrogen bond between Lys20 and Ala36 was removed, while a new hydrogen bond was formed between Ser20 and Tyr13 (Figure 4a). These two residues were located in the same loop, and the mutation of Tyr13 was reported to have a positive effect on thermostability.[7,36] Therefore, the rigidification of Tyr13 by this hydrogen bond led to a lower RMSF value and more rigidity of the local region. In the wild-type BglT, the mutant sites Lys117 and Lys165 were located within two β-sheets (β7 and β11), respectively. In contrast, although there were no significant changes in conformation around Ser165 in the triple mutant, Ser117 was no longer located in the β7. In the wild-type BglT, there was one hydrogen bond formed between Lys117 and Asp114, while two hydrogen bonds were formed between Ser117 and Asp114 in the mutant enzyme (Figure 4b). This change led to the formation of the β-turn in the Ser117 site instead of the original β-sheet. These two residues were close to the catalytic site, and this change might be the reason for the enhancement of the catalytic properties. In mutant site no. 165, one more hydrogen bond between Ser165 and Trp158 was observed, which linked β10 and β11 (Figure 4c). Besides these, changes in several other regions in the protein structure were also observed. A short helix structure (α2) composed of the residue no. 96−100 in wild-type BglT was lost. As shown in Figure 4d, four hydrogen bonds existed within the helix in the wild-type BglT, while in the triple mutant only one hydrogen bond remained (Figure 4f). Furthermore, several loop regions in the concave side of the wild-type BglT structure turned into β-sheets. The residues no. 88−93 and no. 108−110, which were located in the middle of loop 6 and loop 7, formed two new β-sheets (β14 and β15). The β12 was lengthened by residues no. 179−182. The transformations of loops into β-sheets should be responsible for the lower RMSF values in these regions of the triple mutant. Figure 4e and g showed the hydrogen bond networks within the concave sides of the wild-type BglT and the triple mutant. Three new hydrogen bonds were formed in the mutant. Two hydrogen bonds (Phe110−Ser89 and Thr93−Ile106) were formed between the newly formed β14 and β15, while the third one (Phe92−Met180) was formed between β14 and β12. These three newly formed hydrogen bonds may draw the neighboring residues closer and result in the formation of new β-sheets. Overall, these changes in the predicted enzyme structure induced by the mutation were in accordance with the above results of secondary structure analysis through the CD spectrum.

For the mesophilic β-glucanase BglT, mutations of three out of 12 lysines to serines can increase the thermostability. Interestingly, a recent report showed that a higher percentage of lysine residues was found in some thermophilic enzymes, while mesophilic enzymes tended to contain more serine residues.[37] Moreover, the mutation of lysines to serines was also found in some psychrophilic proteins.[38] In contrast, the positive effects of lysine mutation on BglT thermostability in this study might result from the large-scale changes in the secondary structure of neighboring regions induced by the mutation of the lysine residues. Compared with the wild-type BglT, mutation of lysine residues caused more hydrogen bonds

DOI: 10.1021/acs.jafc.5b00480
J. Agric. Food Chem. 2015, 63, 5249−5256

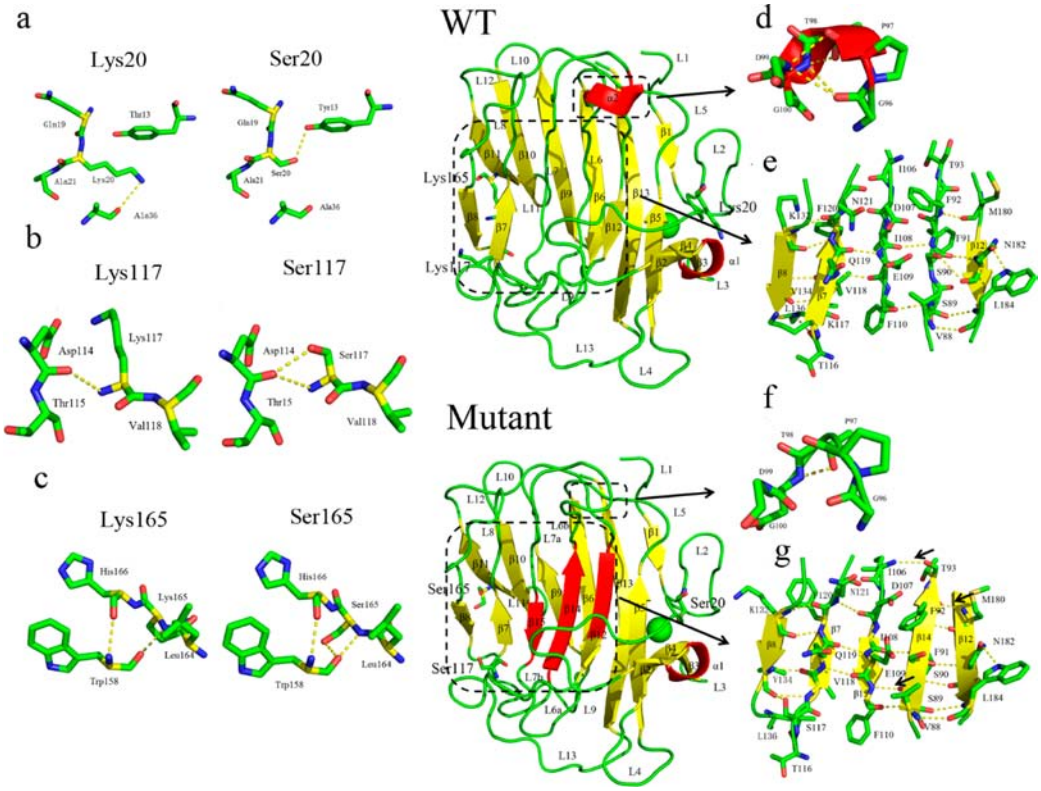

Figure 4. Comparison of the 3D structures of wild-type BglT and the K20S/K117S/K165S mutant (the three mutant sites are shown as sticks): (a) comparison of hydrogen bonds in the K20S mutant region; (b) comparison of hydrogen bonds in the K117S mutant region; (c) comparison of hydrogen bonds in the K165S mutant region; (d) 3D structure of the loop region of no. 96−100 in wild-type BglT; (e) 3D structure of the loop region of no. 96−100 in the triple mutant; (f) hydrogen bond network in the concave side of the structure of wild-type BglT; (g) hydrogen bond network in the concave side of the structure of the triple mutant (the arrows indicate the newly formed hydrogen bonds). The left side shows the interactions between the three mutant sites. The helix, β-sheet, and loop are shown in red, yellow, and green, respectively. The hydrogen bonds are depicted as dashed yellow lines. Structure visualization was performed using the software Pymol 1.7.1.

in both the three local mutant sites and the concave side of the enzyme structure. These changes resulted in more structured amino acids in the triple mutant, especially the formation of new β-sheets in the concave side. This could enhance the rigidity of the local structure, which was confirmed by the lower RMSF values. Rigidifying the local flexible regions in a protein could enhance the protein thermostability.[39] Growing evidence has shown that the loss of the protein thermostability is likely to be directed by some local fluctuation and partial unfolding.[11,40] Therefore, these transformations are thought to rigidify both the global and local structure, thus leading to a better overall thermostability of β-glucanase. Furthermore, the catalytic activity and binding affinity of the substrate in the triple mutant were proved to be increased. As shown by the changes in structure, the concave side of β-glucanase was the region for substrate binding. Several residues related to substrate binding, including Ser90, Glu109, Glu131, and Asn182, were located at these transformed regions. The reason for the enhancement of the catalytic efficiency might be the conformational changes in this region, especially the formation of the hydrogen bond between Phe110 and Ser89, which could influence the catalysis of the substrate.

In conclusion, the site-directed mutagenesis of lysine sites no. 20, no. 117, and no. 165 enhanced both the catalytic properties and the thermostability of β-glucanase BglT. The optimal temperature and T_{50} of the triple mutant were increased by 15 and 14 °C. The half-life values at 50 and 60 °C were also largely extended. New hydrogen bonds were observed in the mutant sites and the concave side of the protein structure, which led to the formation of more β-sheet elements and reduced local flexibility. The large-scale changes in the secondary structure of neighboring regions should be responsible for the increased thermostability and catalytic activity. This study provides a new strategy for improving thermostability by engineering surface lysine residues.

■ ASSOCIATED CONTENT

Supporting Information

Online resource 1 shows the amino acid sequence alignment between the wild-type 1,3−1,4-β-glucanase and the reference enzyme. Online resource 2 shows the gene sequence of the wild-type 1,3−1,4-β-glucanase. Online resource 3 shows the sequences of the primers used in the overlapping PCR. Online resource 4 is the SDS-PAGE image of the purified wild-type and mutant β-glucanases. Online resource 5 is the RMSD curves of the backbone, main chain, and side chain of the wild-type and mutant β-glucanases. Online resource 6 is the RMSD curves of the residues located within 5 Å of the three mutant sites. The Supporting Information is available free of charge on the ACS Publications website at DOI: 10.1021/acs.jafc.5b00480.

■ AUTHOR INFORMATION

Corresponding Author

*E-mail: liqi@jiangnan.edu.cn. Tel: +86-510-85918176. Fax: +86-510-85805219.

DOI: 10.1021/acs.jafc.5b00480
J. Agric. Food Chem. 2015, 63, 5249−5256

Author Contributions

[§]C. Niu and L. Zhu contributed equally to this work.

Funding

This study was financially supported by the program for National Science Foundation (No. 31271919), New Century Excellent Talents in University of China (No. NCET-10-0453), National Basic Research Program of China (973 Program, No. 2010CB735706), the National High Technology Research and Development Program 863 (No. 2012AA021303), the Priority Academic Program Development of Jiangsu Higher Education Institutions (PAPD), Self-determined Research Program of Jiangnan University (JUSRP11218), and Program of Introducing Talents of Discipline to Universities (No. 111-2-06).

Notes

The authors declare no competing financial interest.

■ ABBREVIATIONS USED

3D, three dimensional; CD, circular dichroism; kDa, kilodalton; MD, molecular dynamics; RMSD, root-mean-square deviation; RMSF, root-mean-square fluctuation

■ REFERENCES

(1) Wang, J.; Niu, C.; Liu, X.; Chen, X.; Li, Q. Characterization of a new 1,3−1,4-beta-glucanase gene from *Bacillus tequilensis* CGX5-1. *Appl. Biochem. Biotechnol.* **2014**, *173*, 826−837.

(2) Planas, N. Bacterial 1,3−1,4-beta-glucanases: Structure, function and protein engineering. *Biochim. Biophys. Acta, Protein Struct. Mol. Enzymol.* **2000**, *1543*, 361−382.

(3) Chaari, F.; Belghith-Fendri, L.; Blibech, M.; Driss, D.; Ellouzi, S. Z.; sameh, M.; Ellouz-Chaabouni, S. Biochemical characterization of a lichenase from *Penicillium occitanis* Pol6 and its potential application in the brewing industry. *Process Biochem. (Amsterdam, Neth.)* **2014**, *49*, 1040−1046.

(4) Luo, Z.; Gao, Q.; Li, X.; Bao, J. Cloning of LicB from *Clostridium thermocellum* and its efficient secretive expression of thermostable *β*-1,3−1,4-glucanase. *Appl. Biochem. Biotechnol.* **2014**, *173*, 562−570.

(5) Michael, J. Lewis, T. W. Y. *Brewing*, 2nd ed.; Springer: New York, 2013.

(6) Spring, P.; Newman, K. E.; Wenk, C.; Messkommer, R.; Vranjes, M. V. Effect of pelleting temperature on the activity of different enzymes. *Poult. Sci.* **1996**, *75*, 357−361.

(7) Olsen, O.; Borriss, R.; Simon, O.; Thomsen, K. K. Hybrid bacillus (1−3,1−4)-beta-glucanases - engineering thermostable enzymes by construction of hybrid genes. *Mol. Gen. Genet.* **1991**, *225*, 177−185.

(8) Schimming, S.; Schwarz, W. H.; Staudenbauer, W. L. Properties of a thermoactive beta-1,3−1,4-glucanase (lichenase) from *Clostridium thermocellum* expressed in *Escherichia coli*. *Biochem. Biophys. Res. Commun.* **1991**, *177*, 447−452.

(9) Cheng, Y.-S.; Huang, C.-H.; Chen, C.-C.; Huang, T.-Y.; Ko, T.-P.; Huang, J.-W.; Wu, T.-H.; Liu, J.-R.; Guo, R.-T. Structural and mutagenetic analyses of a 1,3−1,4-*β*-glucanase from *Paecilomyces thermophila*. *BBA-Proteins Proteom.* **2014**, *1844*, 366−373.

(10) Fields, P. A. Review: Protein function at thermal extremes: Balancing stability and flexibility. *Comp. Biochem. Physiol., Part A* **2001**, *129*, 417−431.

(11) Eijsink, V. G. H.; Bjork, A.; Gaseidnes, S.; Sirevag, R.; Synstad, B.; van den Burg, B.; Vriend, G. Rational engineering of enzyme stability. *J. Biotechnol.* **2004**, *113*, 105−120.

(12) Dombkowski, A. A.; Sultana, K. Z.; Craig, D. B. Protein disulfide engineering. *FEBS Lett.* **2014**, *588*, 206−212.

(13) Niu, C. T.; Zhu, L. J.; Wang, J. J.; Li, Q. Simultaneous enhanced catalytic activity and thermostability of a 1,3−1,4-beta-glucanase from *Bacillus amyloliquefaciens* by chemical modification of lysine residues. *Biotechnol. Lett.* **2014**, *36*, 2453−2460.

(14) Khajeh, K.; Naderi-Manesh, H.; Ranjbar, B.; Moosavi-Movahedi, A. A.; Nemat-Gorgani, M. Chemical modification of lysine residues in *Bacillus* alpha-amylases: Effect on activity and stability. *Enzyme Microb. Technol.* **2001**, *28*, 543−549.

(15) Pack, S. P.; Yoo, Y. J. Protein thermostability: Structure-based difference of amino acid between thermophilic and mesophilic proteins. *J. Biotechnol.* **2004**, *111*, 269−277.

(16) Huang, X.; Gao, D.; Zhan, C. G. Computational design of a thermostable mutant of cocaine esterase via molecular dynamics simulations. *Org. Biomol. Chem.* **2011**, *9*, 4138−4143.

(17) Joo, J. C.; Pohkrel, S.; Pack, S. P.; Yoo, Y. J. Thermostabilization of *Bacillus* circulans xylanase via computational design of a flexible surface cavity. *J. Biotechnol.* **2010**, *146*, 31−39.

(18) Purmonen, M.; Valjakka, J.; Takkinen, K.; Laitinen, T.; Rouvinen, J. Molecular dynamics studies on the thermostability of family 11 xylanases. *Protein Eng., Des. Sel.* **2007**, *20*, 551−559.

(19) Badieyan, S.; Bevan, D. R.; Zhang, C. Study and design of stability in GH5 cellulases. *Biotechnol. Bioeng.* **2012**, *109*, 31−44.

(20) Di Marino, D.; Achsel, T.; Lacoux, C.; Falconi, M.; Bagni, C. Molecular dynamics simulations show how the FMRP Ile304Asn mutation destabilizes the KH2 domain structure and affects its function. *J. Biomol. Struct. Dyn.* **2014**, *32*, 337−350.

(21) Biasini, M.; Bienert, S.; Waterhouse, A.; Arnold, K.; Studer, G.; Schmidt, T.; Kiefer, F.; Cassarino, T. G.; Bertoni, M.; Bordoli, L.; Schwede, T. SWISS-MODEL: Modelling protein tertiary and quaternary structure using evolutionary information. *Nucleic Acids Res.* **2014**, *42*, W252−258.

(22) Hahn, M.; Pons, J.; Planas, A.; Querol, E.; Heinemann, U. Crystal structure of *Bacillus licheniformis* 1,3−1,4-beta-D-glucan 4-glucanohydrolase at 1.8 A resolution. *FEBS Lett.* **1995**, *374*, 221−224.

(23) Pronk, S.; Pall, S.; Schulz, R.; Larsson, P.; Bjelkmar, P.; Apostolov, R.; Shirts, M. R.; Smith, J. C.; Kasson, P. M.; van der Spoel, D.; Hess, B.; Lindahl, E. GROMACS 4.5: A high-throughput and highly parallel open source molecular simulation toolkit. *Bioinformatics* **2013**, *29*, 845−854.

(24) Oostenbrink, C.; Villa, A.; Mark, A. E.; Van Gunsteren, W. F. A biomolecular force field based on the free enthalpy of hydration and solvation: The GROMOS force-field parameter sets 53A5 and 53A6. *J. Comput. Chem.* **2004**, *25*, 1656−1676.

(25) Berendsen, H. J.; Postma, J. P. M.; van Gunsteren, W. F.; DiNola, A.; Haak, J. Molecular dynamics with coupling to an external bath. *J. Chem. Phys.* **1984**, *81*, 3684−3690.

(26) Parrinello, M.; Rahman, A. Polymorphic transitions in single crystals: A new molecular dynamics method. *J. Appl. Phys.* **1981**, *52*, 7182−7190.

(27) Bradford, M. M. A rapid and sensitive method for the quantitation of microgram quantities of protein utilizing the principle of protein-dye binding. *Anal. Biochem.* **1976**, *72*, 248−254.

(28) Chen, Y. C.; Chiang, Y. C.; Hsu, F. Y.; Tsai, L. C.; Cheng, H. L. Structural modeling and further improvement in pH stability and activity of a highly-active xylanase from an uncultured rumen fungus. *Bioresour. Technol.* **2012**, *123*, 125−134.

(29) Lineweaver, H.; Burk, D. The determination of enzyme dissociation constants. *J. Am. Chem. Soc.* **1934**, *56*, 658−666.

(30) Whitmore, L.; Wallace, B. A. Protein secondary structure analyses from circular dichroism spectroscopy: Methods and reference databases. *Biopolymers* **2008**, *89*, 392−400.

(31) Quang, A. T. L.; Joo, J. C.; Yoo, Y. J.; Kim, Y. H. Development of thermostable *Candida antarctica* lipase B through novel in silico design of disulfide bridge. *Biotechnol. Bioeng.* **2012**, *109*, 867−876.

(32) Zhang, W.; Mullaney, E. J.; Lei, X. G. Adopting selected hydrogen bonding and ionic interactions from Aspergillus fumigatus phytase structure improves the thermostability of Aspergillus niger PhyA phytase. *Appl. Environ. Microbiol.* **2007**, *73*, 3069−3076.

(33) Zhang, Z. G.; Yi, Z. L.; Pei, X. Q.; Wu, Z. L. Improving the thermostability of Geobacillus stearothermophilus xylanase XT6 by directed evolution and site-directed mutagenesis. *Bioresour. Technol.* **2010**, *101*, 9272−9278.

(34) Paul, M.; Hazra, M.; Barman, A.; Hazra, S. Comparative molecular dynamics simulation studies for determining factors

DOI: 10.1021/acs.jafc.5b00480
J. Agric. Food Chem. 2015, 63, 5249−5256

contributing to the thermostability of chemotaxis protein "CheY". *J. Biomol. Struct. Dyn.* **2014**, *32*, 928−949.
(35) Batista, P. R.; Costa, M. G. D.; Pascutti, P. G.; Bisch, P. M.; de Souza, W. High temperatures enhance cooperative motions between CBM and catalytic domains of a thermostable cellulase: Mechanism insights from essential dynamics. *Phys. Chem. Chem. Phys.* **2011**, *13*, 13709−13720.
(36) Politz, O.; Simon, O.; Olsen, O.; Borriss, R. Determinants for the enhanced thermostability of hybrid (1−3,1−4)-beta-glucanases. *Eur. J. Biochem.* **1993**, *216*, 829−834.
(37) Li, Y. Q.; Middaugh, C. R.; Fang, J. W. A novel scoring function for discriminating hyperthermophilic and mesophilic proteins with application to predicting relative thermostability of protein mutants. *BMC Bioinform.* **2010**, *11*.
(38) Papaleo, E.; Parravicini, F.; Grandori, R.; De Gioia, L.; Brocca, S. Structural investigation of the cold-adapted acylaminoacyl peptidase from Sporosarcina psychrophila by atomistic simulations and biophysical methods. *Biochim. Biophy. Acta, Proteins Proteom.* **2014**, *1844*, 2203−2213.
(39) Yu, H. R.; Huang, H. Engineering proteins for thermostability through rigidifying flexible sites. *Biotechnol. Adv.* **2014**, *32*, 308−315.
(40) Finke, J. M.; Roy, M.; Zimm, B. H.; Jennings, P. A. Aggregation events occur prior to stable intermediate formation during refolding of interleukin 1beta. *Biochemistry* **2000**, *39*, 575−583.

DOI: 10.1021/acs.jafc.5b00480
J. Agric. Food Chem. 2015, 63, 5249−5256

JOURNAL OF AGRICULTURAL AND FOOD CHEMISTRY

Article

pubs.acs.org/JAFC

Comparison of Heat-Induced Aggregation of Globular Proteins

Roy J. B. M. Delahaije,[†] Peter A. Wierenga,[†] Marco L. F. Giuseppin,[§] and Harry Gruppen*[,†]

[†]Laboratory of Food Chemistry, Wageningen University, Bornse Weilanden 9, 6708 WG Wageningen, The Netherlands

[§]AVEBE, Prins Hendrikplein 20, 9641 GK Veendam, The Netherlands

Supporting Information

ABSTRACT: Typically, heat-induced aggregation of proteins is studied using a single protein under various conditions (e.g., temperature). Because different studies use different conditions and methods, a mechanistic relationship between molecular properties and the aggregation behavior of proteins has not been identified. Therefore, this study investigates the kinetics of heat-induced aggregation and the size/density of formed aggregates for three different proteins (ovalbumin, β-lactoglobulin, and patatin) under various conditions (pH, ionic strength, concentration, and temperature). The aggregation rate of β-lactoglobulin was slower (>10 times) than that of ovalbumin and patatin. Moreover, the conditions (pH, ionic strength, and concentration) affected the aggregation kinetics of β-lactoglobulin more strongly than for ovalbumin and patatin. In contrast to the kinetics, for all proteins the aggregate size/density increased with decreasing electrostatic repulsion. By comparing these proteins under these conditions, it became clear that the aggregation behavior cannot easily be correlated to the molecular properties (e.g., charge and exposed hydrophobicity).

KEYWORDS: *β-lactoglobulin, ovalbumin, patatin, pH, ionic strength, concentration*

INTRODUCTION

Heat-induced aggregation of globular proteins is generally described as being caused by the exposure of the internal hydrophobic amino acids due to unfolding.[1,2] After unfolding and exposure of the hydrophobic amino acid residues, the (partially) unfolded protein either refolds or irreversibly aggregates with other (partially) unfolded proteins.[3,4] The likelihood of refolding or aggregation depends on the balance between the increased hydrophobic attraction due to unfolding and the mainly electrostatic barrier for aggregation. Qualitatively, aggregation has been investigated extensively, mainly in terms of (1) aggregation kinetics,[5−7] (2) aggregate size,[8,9] and (3) aggregate structure.[10,11] These studies typically investigate the effect of conditions (e.g., ionic strength) on the aggregation of a single protein (e.g., β-lactoglobulin). A detailed mechanistic comparison of the aggregation of different proteins, on the other hand, is still missing. Exactly such information may advance the understanding of the aggregation process of globular proteins, especially with respect to an overall description of the effect of parameters influencing the aggregation process. Hence, the aim of the present paper is to obtain a mechanistic understanding of the aggregation process and determine the effect of the properties of three proteins on the aggregation behavior under various conditions.

The aggregation kinetics (i.e., order (n) and rate (k)) are generally derived from the decrease of the concentration of nonaggregated protein in time. Therefore, they provide information on the kinetics of protein unfolding and integration of nonaggregated proteins in aggregates, whereas they do not provide information on the size and structure of the formed aggregates.

Aggregation Order. To determine the order of aggregation, two approaches have been described: (A) determination of the concentration dependence of the initial aggregation rate[5−7] and (B) fitting the decrease of the concentration of nonaggregated protein in time with the specific reaction equations. These are eqs 1 and 2 for first- and nth-order kinetics, respectively:[12]

$$C_t = C_0 \times e^{-kt} \text{ for } n = 1 \quad (1)$$

$$C_t = (C_0^{1-n} + (n-1) \times k \times t)^{1/1-n} \text{ for } n \neq 1 \quad (2)$$

C_t and C_0 are the concentrations of nonaggregated protein at time t and at time 0 (g/L), respectively, n is the aggregation order (unitless), and k is the aggregation rate ($(g/L)^{(1-n)}/s$).

The discrepancies between the two approaches are assumed to originate from the fact that the aggregation process becomes more complex at longer heating times. This is due to simultaneous aggregation of nonaggregated protein with other nonaggregated protein, nonaggregated with aggregated proteins, and aggregated proteins with other aggregated proteins.

For ovalbumin, the initial aggregation rate was shown to be concentration independent. Hence, the aggregation process has been described as a first-order reaction.[6] The aggregation rate of β-lactoglobulin, on the other hand, increases with increasing concentration, indicating concentration dependence. This resulted in an aggregation order of 1.5.[5,7,13] In addition, the aggregation orders of ovalbumin and β-lactoglobulin were shown to be independent of temperature,[6,14,15] pH,[8,14] and ionic strength.[6,16]

Aggregation Rate. For proteins, the fraction of unfolded protein and the diffusion rate of the protein molecules typically increase with increasing temperature.[17,18] The fraction unfolded

Received: February 18, 2015
Revised: May 7, 2015
Accepted: May 12, 2015
Published: May 12, 2015

ACS Publications © 2015 American Chemical Society

DOI: 10.1021/acs.jafc.5b00927
J. Agric. Food Chem. 2015, 63, 5257−5265

Table 1. Molecular Protein Properties of β-Lactoglobulin (β-Lg), Ovalbumin (Ova), and Patatin (Pat) As Obtained from the Swiss-Prot Database (http://www.expasy.org)

protein	Expasy code	M_w (kDa)	pI	#COOH/#NH_2[a]	S−S bridges/free SH groups	σ_w[b] (mC/m^2)	rel Q_H[c]
β-Lg	P02754	18.4/36.8[d]	4.83	26/18	2/1	−21.9	1.00
Ova	P01012	44.5	5.19	47/35	1/4	−24.2	0.19
Pat	P07745	40.0	5.25	43/32	0/1	−17.9	0.73

[a]#COOH and #NH_2 are the maximum numbers of negatively charged (aspartic and glutamic acid) and positively charged (arginine and lysine) groups in the primary sequence, respectively. [b]σ_w is the theoretical net surface charge density at pH 7. [c]Rel Q_H is the relative exposed hydrophobicity of the proteins as determined previously.[50] [d]Molecular weight of a β-lactoglobulin dimer (native state under the selected conditions).

proteins depends on the heating temperature relative to the denaturation temperature (T_d). For a more fundamental comparison of the aggregation properties of different proteins, the proteins are studied at a fixed temperature relative to T_d, rather than an absolute temperature. This results in a constant fraction of unfolded protein. An increase of the diffusion rate results in an increased likelihood of the proteins to meet, collide, and aggregate.[19,20] The aggregation rate is also affected by electrostatic repulsion. However, a clear link is difficult to make, because the main factors (i.e., ionic strength and pH) can have several effects. Increasing the electrostatic repulsion increases both the intra- and intermolecular repulsions. The increased intramolecular repulsion decreases the denaturation temperature.[21,22] The increase of intermolecular repulsion, on the other hand, increases the electrostatic barrier for aggregation.[23] Whereas the first effect would (when heating at given temperature) result in an increase of the aggregation rate, the second would decrease the aggregation rate. In addition, a pH change not only affects the electrostatic interactions but also changes the reactivity of the disulfide bonds. Whereas changes in the electrostatic repulsion (i.e., ionic strength and pH) do not affect the aggregation rate of ovalbumin,[6,24] the aggregation rate of β-lactoglobulin increases with increasing ionic strength (<0.1 M)[16] and pH.[8,14] This difference indicates that the electrostatic repulsion affects both proteins differently. The enhancing effect of ionic strength on the aggregation rate of β-lactoglobulin showed that the increase of the denaturation temperature was less important than the decrease of the electrostatic barrier for aggregation.[16] At the same time, a higher denaturation temperature and a decrease of the reactivity of the disulfide bonds were described to reduce the aggregation rate of β-lactoglobulin with decreasing pH.[14]

Aggregate Formation. To describe the aggregate formation, the size and structure of the aggregates are typically determined by scattering techniques (i.e., neutron, X-ray, and light scattering). The structure of the aggregates is described by the fractal dimension. The fractal dimension was found to be independent of the heating temperature.[15,25] As temperature affects only the aggregation kinetics and not the formation of aggregates, the effect of temperature has been described as a purely kinetic effect.[15] Electrostatic repulsion, however, strongly affects the aggregate formation (size as well as structure). A decrease of the electrostatic repulsion, due to an increase of the ionic strength and/or a shift of the pH toward the iso-electric point (pI), resulted in the formation of larger aggregates of ovalbumin,[26,27] β-lactoglobulin,[8,28] BSA,[9] and patatin,[29] as observed via light scattering. At conditions with high electrostatic repulsion (i.e., low ionic strength and pH far from the pI), linear aggregates with a fractal dimension of 1.7 were formed by ovalbumin[30] and β-lactoglobulin.[31,32] When the electrostatic repulsion was decreased (i.e., by increasing the ionic strength from 10 to 100 mM), the β-lactoglobulin and ovalbumin aggregates became more branched. This was indicated by a fractal dimension of 2.0[15,30,33−35] and confirmed by cryo-TEM.[30] When the electrostatic repulsion is minimal (i.e., close to the pI), β-lactoglobulin forms even more compact aggregates with a fractal dimension of 3.0.[36] The effect of electrostatic repulsion on the aggregate size and structure is explained by the electrostatic barrier for aggregation.[30,32,35] Furthermore, the size of β-lactoglobulin and BSA aggregates increased with increasing concentration.[9,15,33,37] This concentration dependence has been postulated to be a result of an increase of the ionic strength due to the counterions of the protein.

Because β-lactoglobulin has most often been used to study the aggregation process, its aggregation behavior is quite well understood. However, little is known of how this knowledge can be extrapolated to describe the aggregation of other proteins. To obtain a more mechanistic understanding of the effect of protein molecular properties on the aggregation of globular proteins, this study compares the aggregation process of different proteins. Hence, the differences in the kinetics and factors influencing the aggregation of three proteins (β-lactoglobulin, ovalbumin, and patatin) under various conditions (pH, ionic strength, temperature, and protein concentration) are studied. The three proteins are selected as their similarities (globular structure, pI, and molecular weight) and differences (surface charge, exposed hydrophobicity, and number of disulfide bridges) (Table 1) enable a comparison of the effects of charge, hydrophobicity, and disulfide bridges on the aggregation behavior.

MATERIALS AND METHODS

Materials. Ovalbumin [A-5503, lot 031M7008 V; pI = 5.19; protein content 92% (N × 6.22)[38] of which ≥98% was ovalbumin (based on agarose gel electrophorese)] and β-lactoglobulin [L-0130, lot SLBC2933 V; pI = 4.83; protein content of 94% (N × 6.38)[38] of which 99% was β-lactoglobulin (based on PAGE)] were purchased from Sigma-Aldrich (St. Louis, MO, USA). Potatoes were provided by AVEBE BA (Veendam, The Netherlands). Patatin was isolated from potato juice as described previously,[39] except that gel filtration was performed on a Superdex 200 column (52 × 10 cm). The obtained patatin fraction [pI = 5.25; purity ≥ 90% based on analytical size exclusion chromatography (SEC)] was dialyzed against demineralized water, freeze-dried, and stored at −20 °C. All other chemicals were of analytical grade and purchased from either Sigma-Aldrich or Merck.

Differential Scanning Calorimetry (DSC). The denaturation temperature of the proteins was determined using a VP-DSC MicroCalorimeter (MicroCal Inc., Northampton, MA, USA). The proteins were dissolved in 10 mM sodium phosphate buffer, pH 7.0, at a concentration of 2 g/L. Subsequently, thermograms were recorded from 20 to 100 °C at a heating rate of 1 °C/min. The denaturation temperatures (T_d) of ovalbumin, β-lactoglobulin, and patatin were found to be 77.5, 75.0, and 60.0 °C, respectively (Supporting Information). This is in close agreement with the denaturation temperatures reported in the literature.[6,21,39]

DOI: 10.1021/acs.jafc.5b00927
J. Agric. Food Chem. 2015, 63, 5257−5265

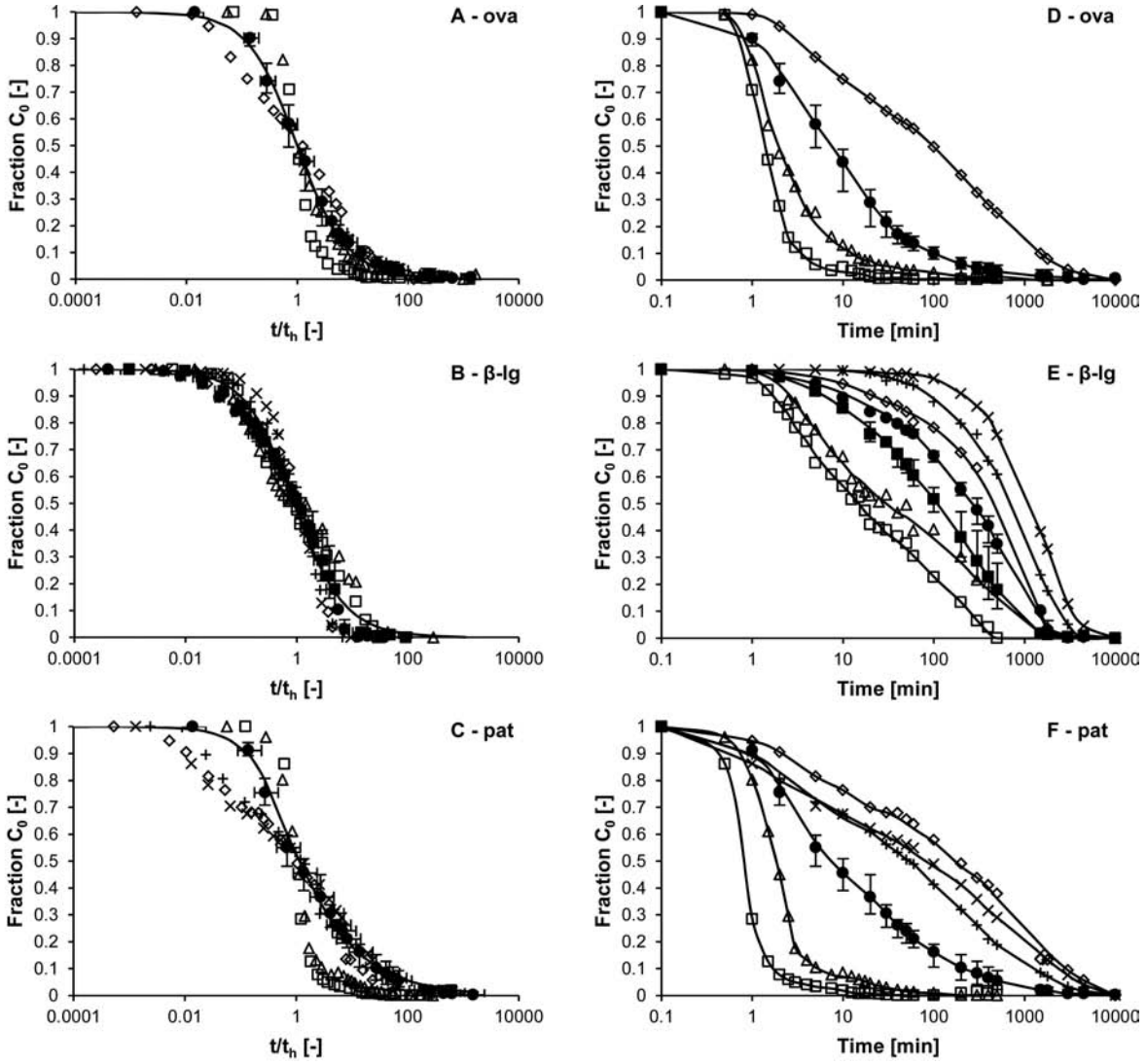

Figure 1. Fraction of nonaggregated protein (C_0) as a function of the time normalized by t_h (A–C) and as a function of the time (D–F) for ovalbumin (A, D), β-lactoglobulin (B, E), and patatin (C, F). The markers represent the different conditions: T_d − 10 °C (◇), T_d (△), T_d + 5 °C (□), pH 5.0 (×), pH 6.0 (+), 5 g/L, 10 g/L, 40 mM NaCl, and 90 mM NaCl (■), and the average of all remaining conditions (T_d − 5 °C, 2 g/L, 10 mM NaCl, and all not indicated by the other markers), with error bars indicating the standard deviation (●). Solid lines in panels D–F are guides to the eye. The solid lines in panels A–C represent the best fits (n = 2.1 for ovalbumin, n = 2.5 for β-lactoglobulin, and n = 2.9 for patatin).

Heat-Induced Aggregation. Heat-induced aggregation was performed in a water bath. Aliquots of 1 mL were heated for different time intervals (0, 1, 2, 5, 10, 20, 30, 40, 50, 60, 100, 200, 300, 400, 500, 1500, 1800, 3000, 4500, and 10080 min) in Kimax tubes. After heating, the samples were cooled on ice–water. Four different sets of experiments were performed.

Effect of Temperature. Proteins were dissolved in 10 mM sodium phosphate buffer, pH 7.0, at a concentration of 2 g/L. Subsequently, these solutions were heated at temperatures at the same distance from the denaturation temperature (T_d): T_d − 10 °C, T_d − 5 °C, T_d, and T_d + 5 °C. This was chosen to ensure as well as possible a similar rate of unfolding for all proteins. The reason is that at T_d, for all proteins, the native and unfolded proteins are present in equal amounts.[12,17] This equilibrium between native and unfolded protein shifts toward the native protein with decreasing and toward unfolded protein with increasing temperature. This equilibrium is, at a certain temperature from T_d (e.g., T_d − 5 °C), assumed to be equal for all proteins. For the incubations at the two highest temperatures, additional time intervals (i.e., 0.5, 1.5, 2.5, 3, 4, 7.5, 12.5, 15, 17.5, and 25 min) were included.

The aggregation rate was determined on the basis of the decrease of the concentration of nonaggregated protein in time using eq 1 or 2. From the temperature dependence of the aggregation rate (k), the activation energy (E_a) was calculated by the Arrhenius equation.

Effect of pH. Proteins were dissolved in 10 mM sodium phosphate buffer, pH 7.0, 6.0, and 5.0, at a concentration of 2 g/L. Subsequently, the solutions were heated at T_d − 5 °C.

Effect of Ionic Strength. Proteins were dissolved in 10 mM sodium phosphate buffer, pH 7.0, in the presence or absence of 10, 40, and 90 mM NaCl at a concentration of 2 g/L. Subsequently, the solutions were heated at T_d − 5 °C.

Effect of Protein Concentration. Proteins were dissolved in 10 mM sodium phosphate buffer, pH 7.0, at concentrations of 1, 2, 5, and 10 g/L. Subsequently, the solutions were heated at T_d − 5 °C.

Size Exclusion Chromatography. The concentration of nonaggregated protein (i.e., monomer concentration for ovalbumin and dimer concentration for β-lactoglobulin and patatin) was determined using SEC on an Äkta Micro equipped with a Superdex 200 PC 3.2/30 column (GE Healthcare, Uppsala, Sweden). Prior to analysis, the samples were centrifuged (16100g, 10 min, 20 °C) to remove insoluble aggregates. Subsequently, samples (20 μL) were injected and eluted with 10 mM sodium phosphate buffer, pH 7.0, at a flow rate of 0.06 mL/min. The elution was monitored at 214 nm. The calibration was performed with globular proteins with a mass range of

DOI: 10.1021/acs.jafc.5b00927
J. Agric. Food Chem. 2015, 63, 5257–5265

13.7−67 kDa (GE Healthcare). The typical experimental error for the determination of the amount of nonaggregated protein was <10% as determined from duplicate time incubations of ovalbumin and patatin, 2 g/L, T_d − 5 °C, 10 mM sodium phosphate buffer, pH 7.0.

Determination of the Aggregation Kinetics. The aggregation kinetics are determined in several ways: (1) concentration dependence of the time required to aggregate half of the protein (i.e., t_h as an indication of the aggregation rate), (2) fitting the decrease of the concentration of nonaggregated protein in time using eqs 1 and 2, and (3) fitting the natural logarithm of concentration (n = 1.0), reciprocal of the square root of concentration (n = 1.5), and the reciprocal of the concentration (n = 2.0) against time with a linear function, fixing the intercept with the y-axis corresponding to the initial concentration (C_0). The first approach includes only the data points $C_t \geq 0.5C_0$, whereas the other two approaches are applied to the regime $C_t \geq 0.05C_0$. For the second approach the data are fitted by minimizing the sum of squares error using the Microsoft Excel solver.

Static Light Scattering (SLS). The scattered light intensity was determined in time using a Malvern Zetasizer Nano ZS (Malvern Instruments, Worcestershire, UK). The protein solutions (as described under Heat-Induced Aggregation) were filtered over a 0.1 μm PTFE filter (Puradisc 13; Whatman, Kent, UK). Subsequently, the filtered solutions were heated at the temperatures described under Heat-Induced Aggregation. The scattered light intensity was measured every 30 s for 7200 s. The intensity of the scattered light is generally described by eq 3[13,40]

$$I(q) \propto K \times C \times M_w \times P(q) \times S(q) \quad (3)$$

in which $I(q)$ is the intensity of the scattered light at angle q (i.e., 173°), K is an optical constant, c is the concentration (g/L), M_w is the molar mass of the particles (g/mol), $P(q)$ is the particle form factor, which describes the shape and size of the particles, and $S(q)$ is the structure factor that describes the spatial arrangement of the particles.

As the concentration (C) and the optical constant (K) are constant during and between the measurements, eq 3 can be simplified to

$$I(q) \propto M_w \times P(q) \times S(q) \quad (4)$$

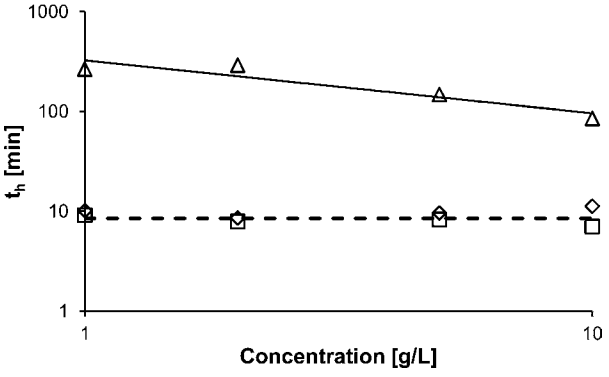

Figure 2. Concentration dependence of the time required to aggregate half of the proteins (t_h) for ovalbumin (□), β-lactoglobulin (△), and patatin (◇) heated at T_d − 5 °C. The solid line has a slope of −0.5. The dashed line is a guide to the eye.

This shows that an increase of the scattered light intensity relates to an increase of the aggregate size and/or a more dense aggregate structure.

RESULTS AND DISCUSSION

Aggregation Order. Generally, the aggregation kinetics are described by the aggregation order and aggregation rate. The first parameter used to compare the aggregation behavior of different proteins is the aggregation order (n). To exclude the effect of aggregation rate and thereby obtain information only on the influence of conditions on the aggregation order, the decrease of the concentration of nonaggregated protein is plotted against the time divided by the time required to aggregate half of the proteins (t_h) (Figure 1A−C). All curves of one protein superimpose onto one master curve, indicating that the aggregation order is not affected by temperature, concentration, pH, or ionic strength. In other words, the general aggregation process of each protein can be described by a single aggregation order under the different conditions studied. The small variations for ovalbumin and patatin at T_d and T_d + 5 °C were ascribed to small inaccuracies as a result of the fast aggregation rate (i.e., indicated by a $t_h \leq 2$ min; Table 3). The observed discrepancies for patatin under conditions with slower aggregation rates (i.e., indicated by a $t_h \geq 50$ min; Table 3) are not completely understood, but could be caused by a stronger tendency to form larger aggregates in the initial stage of the aggregation process.

The aggregation order for each of the three proteins was determined using three approaches. The first approach derives the aggregation order from the concentration dependence of t_h (Figure 2 and Table 2). The t_h is concentration independent for ovalbumin and patatin, indicating a first-order reaction. For ovalbumin, this is in line with previous data,[6] whereas for patatin no previous data are present. For β-lactoglobulin, on the other hand, t_h depends on the concentration. The slope of the concentration dependence of t_h is −0.5. This shows that, within the experimental error, t_h scales with $\sqrt{C}$, implying an order of 1.5.[7] This is in line with the literature.[5,7] The second approach is based on fitting the decrease of the concentration of nonaggregated protein in time using eqs 1 and 2. For all proteins, the order of the aggregation process is higher than second-order kinetics (i.e., n = 2.5, 2.1, and 2.9 for β-lactoglobulin, ovalbumin, and patatin, respectively) (Table 2). This indicates a complex aggregation process, in which nonaggregated proteins, for example, aggregate with other nonaggregated proteins as well as aggregated proteins. The third approach is based on fitting the decrease of ln C_t, $1/\sqrt{C_t}$, or $1/C_t$ in time to a linear function. This resulted in the best fit (i.e., R^2) of an aggregation order of 2.0 for ovalbumin and patatin (R^2 = 0.95 ± 0.04 and 0.97 ± 0.01 for ovalbumin and patatin, respectively) (Table 2). Moreover, it showed that the first-order kinetics for ovalbumin and patatin, as determined by the first approach,

Table 2. Aggregation Order of Ovalbumin (Ova), β-Lactoglobulin (β-Lg), and Patatin (Pat) Determined by Different Methods[a]

determination of the aggregation order	Ova	β-Lg	Pat
(1) concentration dependence of t_h ($C_t \geq 0.5C_0$)	1.0	1.5	1.0
(2) fit concentration in time using eqs 1 and 2 ($C_t \geq 0.05C_0$)	2.1	2.5	2.9
(3.1) linear fit of ln(C_t) in time (n = 1.0) ($C_t \geq 0.05C_0$)	R^2 = 0.28 ± 0.32	R^2 = 0.85 ± 0.13	R^2 = 0.28 ± 0.30
(3.2) linear fit of $1/\sqrt{C}$ in time (n = 1.5) ($C_t \geq 0.05C_0$)	R^2 = 0.80 ± 0.13	R^2 = 0.96 ± 0.04	R^2 = 0.83 ± 0.09
(3.3) linear fit of $1/C$ in time (n = 2.0) ($C_t \geq 0.05C_0$)	R^2 = 0.95 ± 0.04	R^2 = 0.93 ± 0.07	R^2 = 0.97 ± 0.01

[a]The variation reported for methods 3.1−3.3 represents the standard deviation between R^2 values obtained from fitting the individual conditions separately.

DOI: 10.1021/acs.jafc.5b00927
J. Agric. Food Chem. 2015, 63, 5257−5265

Table 3. Half-Times (t_h) and Aggregation Rates (k) of the Ovalbumin (Ova), β-Lactoglobulin (β-Lg), and Patatin (Pat) at Different Heating Conditions

					t_h (min)			k^a (L/g s) (n = 2)		
variable	C (g/L)	pH	I (mM)	T (°C)	Ova	β-Lg	Pat	Ova	β-Lg	Pat
ref	2	7	10	T_d − 5	8.7	223	10.8	9.64×10^{-4}	3.74×10^{-5}	7.71×10^{-4}
T	2	7	10	T_d − 10	81	330	144	1.02×10^{-4}	2.52×10^{-5}	5.78×10^{-5}
	2	7	10	T_d	2.0	29.2	1.5	4.21×10^{-3}	2.85×10^{-4}	5.66×10^{-3}
	2	7	10	T_d + 5	1.1	16.0	0.5	7.87×10^{-3}	5.20×10^{-4}	1.60×10^{-2}
I	2	7	20	T_d − 5	7.8	188	10.7	1.07×10^{-3}	4.42×10^{-5}	7.76×10^{-4}
	2	7	50	T_d − 5	8.7	93	9.9	9.63×10^{-4}	8.94×10^{-5}	8.38×10^{-4}
	2	7	100	T_d − 5	6.8	87	7.2	1.22×10^{-3}	9.63×10^{-5}	1.16×10^{-3}
C	1	7	10	T_d − 5	9.9	255	11.1	1.69×10^{-3}	6.53×10^{-5}	1.50×10^{-3}
	5	7	10	T_d − 5	8.9	128	10.8	3.75×10^{-4}	2.59×10^{-5}	3.07×10^{-4}
	10	7	10	T_d − 5	8.0	84	13.3	2.08×10^{-4}	1.99×10^{-5}	1.26×10^{-4}
pH	2	6	10	T_d − 5	7.1	621	49.1	1.17×10^{-3}	1.34×10^{-5}	1.70×10^{-4}
	2	5	10	T_d − 5	4.8	1052	73	1.72×10^{-3}	7.92×10^{-6}	1.14×10^{-4}

[a]Aggregation rate determined on the basis of n = 2.

with low R^2 (i.e., R^2 = 0.28), disqualifies the first-order kinetics. This discrepancy between the concentration and time fit has been described previously.[41] Because the time fit approaches include all of the data for fitting, it is concluded that the overall aggregation can be well described on the basis of second-order kinetics. The best for β-lactoglobulin was an aggregation order of 1.5 (R^2 = 0.96 ± 0.04). The fit of the data of β-lactoglobulin for a second-order reaction is, however, not significantly different from that of an order of 1.5. Although the aggregation process of β-lactoglobulin can overall be described by an aggregation order of 1.5 or 2.0, the aggregation process at pH 5.0 shows a better fit with first-order kinetics (i.e., R^2 = 0.99 and 0.84 for n = 1.0 and 1.5, respectively).

Summarizing, the aggregation process of all tested proteins, β-lactoglobulin, ovalbumin, and patatin, is described by an order of 2.0 (R^2 > 0.90 for all proteins). The aggregation process of β-lactoglobulin at pH 5.0 is a first-order process.

Aggregation Rate. In the previous section, the reaction order was determined from rescaled data (i.e., t/t_h). The aggregation rate (k) is determined by fitting the decrease of the concentration of nonaggregated protein versus real time (t) with eq 2. To allow quantitative comparison of the aggregation rates, the data of all proteins are fitted with an aggregation order of 2.0 (R^2 > 0.90 for all proteins) (Table 2).

Effect of Temperature (2 g/L in 10 mM Buffer, pH 7.0). Quantitatively, the effect of temperature on the aggregation rate varies significantly between the proteins (Figures 1D-F and Table 3). Whereas the decrease of the concentration of nonaggregated protein for ovalbumin and patatin at T_d − 5 °C (pH 7.0, I = 10 mM, and C = 2 g/L) is in the same order of magnitude (i.e., t_h ∼ 10 min), the decrease of nonaggregated β-lactoglobulin is significantly slower (i.e., t_h ∼ 220 min) (Table 3). In addition, the temperature dependence of the aggregation rate varies significantly between the proteins. This temperature dependence is reflected in the activation energy (E_a), calculated using the Arrhenius equation, which was found to be 343, 293, and 220 kJ/mol for patatin, ovalbumin, and β-lactoglobulin, respectively (Supporting Information). These activation energies are lower than those reported in the literature (i.e., ∼ 260−300 kJ/mol for β-lactoglobulin[42,43] and 338 kJ/mol for ovalbumin[24]) under similar conditions (i.e., pH 6.5−7.0).

Summarizing, the aggregation rate decreases in the order ovalbumin ≥ patatin ≫ β-lactoglobulin. On the basis of the relative exposed hydrophobicity, the order was expected to be β-lactoglobulin > patatin > ovalbumin. On the basis of the net surface charge density, no large differences were expected. Considering the possibility that the free sulfhydryl groups can interchange with disulfide bonds,[44] the expected order is ovalbumin > β-lactoglobulin > patatin. From the preceding, it is concluded that there is no clear unambiguous relationship between one of these protein properties and the determined rate of aggregation. One parameter that has not often been considered is the extent of protein unfolding. The extent of unfolding may be limited by the presence of disulfide bonds. Therefore, patatin and ovalbumin are expected to unfold more completely than β-lactoglobulin, due to the presence of two disulfide bonds in β-lactoglobulin. Consequently, fewer hydrophobic amino acids become exposed for β-lactoglobulin than for the other two proteins, leading to fewer noncovalent interactions.

Effect of pH (2 g/L in 10 mM Buffer Heated at T_d − 5 °C). The aggregation rate of ovalbumin is not affected by the pH in the range from pH 5 to 7 (Figure 1D and Table 3). The aggregation rates of β-lactoglobulin and patatin, on the other hand, are slower at a pH closer to the isoelectric point (pI), with t_h of 223 and 10.8 min at pH 7.0, compared to t_h of 1052 and 73 min at pH 5.0 for β-lactoglobulin and patatin, respectively (Figure 1E,F and Table 3).

For patatin, the effect of pH seems to be due to a difference in the denaturation temperature. When the aggregation rates of patatin at pH 5 and 6 are compared to those at pH 7 at different temperatures, they are similar to those at pH 7 at a temperature between T_d − 5 °C and T_d − 10 °C (Table 3). This corresponds with a theoretical increase of T_d of ∼4 °C, which is in close agreement with the literature, that is, a 3 °C increase of T_d from pH 7 to 6.[45] For β-lactoglobulin, the aggregation rate at pH 5 and 6 is slower than that at pH 7 and T_d − 10 °C (Table 3). The observed decrease of the aggregation rate by shifting the pH toward the pI is in line

DOI: 10.1021/acs.jafc.5b00927
J. Agric. Food Chem. 2015, 63, 5257−5265

with the literature.[5,7,8,14] However, on the basis of the temperature dependence of the aggregation rate (Table 3), the T_d should increase by 7−10 °C to explain the decrease in aggregation rate. Experimentally, the T_d of β-lactoglobulin was reported to increase by only 2 °C when the pH was decreased from pH 7 to 5.[16] Consequently, another factor also has to be influenced by the pH change. The association state of β-lactoglobulin, as measured by SEC, was not affected by the pH changes (data not shown). The thiol groups, on the other hand, become less reactive with decreasing pH.[8] Therefore, the decreased reactivity of the thiol groups can explain the observed differences.

Effect of Ionic Strength (2 g/L in Buffer, pH 7.0, Heated at T_d − 5 °C) and Concentration (10 mM Buffer, pH 7.0, Heated at T_d − 5 °C). For β-lactoglobulin, the aggregation rate increases with increasing ionic strength (i.e., t_h decreases from 223 min at 10 mM to 87 min at 100 mM) and protein concentration (i.e., t_h decreases from 255 min at 1 g/L to 84 min at 10 g/L) (Figure 1E and Table 3). The effect of ionic strength is explained by a decrease of the electrostatic repulsion within and between the protein molecules. This was described to result in an increase of the denaturation temperature (i.e., 2 and 5 °C from 0 to 100 mM for β-lactoglobulin and BSA, respectively).[21,22] In addition, it also results in a decrease of the electrostatic barrier for aggregation.[23] As in this case the aggregation rate increases rather than decreases, the enhancing effect of electrostatics was more important than the observed increase of the denaturation temperature. The effect of concentration on the aggregation rate is in line with previous data.[7] The effect is postulated to be caused by the fact that at higher protein concentrations the absolute number of unfolded protein increases, resulting in an increased likelihood of proteins to meet, collide, and aggregate. In contrast to the observation for β-lactoglobulin, the aggregation rates of ovalbumin and patatin are affected neither by the ionic strength nor by the protein concentration (Figure 1D,F). These results show that it is important to use different proteins, as the behavior of proteins cannot be extrapolated from one protein to another.

Formation of Aggregates. Whereas some protein solutions remained transparent after heating, others became translucent or opaque. These clear visual differences between the heated protein solutions are also reflected in the ionic strength dependence of the aggregated protein in time determined by SEC (Figure 3).

At all ionic strengths, the UV peak area corresponding to the aggregates initially increases and subsequently decreases. This decrease shifted to shorter heating times with increasing ionic strength. This decrease at increased ionic strength and longer times is due to the formation of larger aggregates, which are removed during the centrifugation step prior to SEC analysis.

To obtain insights into the effect of the conditions (e.g., pH) on the formation of aggregates, the scattered light intensity is monitored in time (Figure 4A−C). According to eq 4, an increase in the scattered light intensity is caused by an increase of the aggregate size and/or alterations of the aggregate shape (at a given concentration). On the basis of the aggregation kinetics (Table 3), the time is recalculated into the fraction aggregated protein (Figure 4D−F). This provides insights into the aggregation mechanism (e.g., preference toward the formation of small or large aggregates).

For ovalbumin and β-lactoglobulin, the scattered light intensity does not significantly increase when the proteins are heated at T_d − 5 °C in a concentration of 2 g/L. For patatin, on the other hand, the intensity of the scattered light increases significantly (i.e., I/I_0 = 8 after 7200 s). This indicates that the patatin aggregates are larger and/or denser than the ovalbumin and β-lactoglobulin aggregates. These differences cannot be explained on the basis of the aggregation kinetics (i.e., t_h values of ovalbumin and patatin are similar). This shows that for patatin the formation of fewer, but larger, aggregates is favored over more, smaller aggregates, as is the case for ovalbumin and β-lactoglobulin under these conditions.

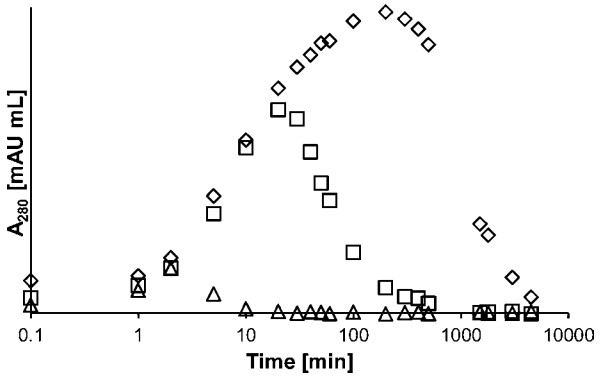

Figure 3. UV peak area of aggregated patatin (10 mM sodium phosphate buffer pH 7.0, 2 g/L, T_d − 5 °C) in time determined by size exclusion chromatography. The markers represent samples heated at different NaCl concentrations: 0 mM NaCl (◇), 10 mM NaCl (□), and 90 mM NaCl (△).

Effect of pH and Ionic Strength. For β-lactoglobulin, a lag phase precedes the intensity increase (Figure 4B). Moreover, the intensity of the scattered light in time increases for all three proteins (i.e., ovalbumin, β-lactoglobulin, and patatin) with increasing ionic strength or a shift of the pH toward the p*I* (Figure 4A−C). The intensity, however, increases more strongly for patatin (i.e., I/I_0 = 47 and 12 after 200 s for pH 5 and 100 mM, respectively) compared to β-lactoglobulin (i.e., I/I_0 = 10 and 22 after 7200 s for pH 5 and 100 mM, respectively) and ovalbumin (i.e., I/I_0 = 12 after 900 s and 8 after 7200 s for pH 5 and 100 mM, respectively). The observed lag phase for β-lactoglobulin has also been reported in the literature, where it is ascribed to the monomer−dimer equilibrium[46] or the formation of small aggregates.[16] Furthermore, it was concluded that a decrease of the electrostatic repulsion results in the formation of larger and/or denser aggregates. This is explained by a lower electrostatic repulsion between the aggregates. Consequently, aggregates can continue to grow to larger sizes and/or the formed aggregates are denser. In the literature, the molecular mass and size of β-lactoglobulin aggregates were also described to increase when the pH shifts toward the p*I* or the ionic strength increases.[8,47,48] However, as shown, this effect is not the same for all proteins. The difference among the proteins indicates that the magnitude by which the aggregate size/structure in time is affected by electrostatics depends on the protein.

Recalculating time into the fraction aggregated protein provides information on the mechanism of aggregation (Figure 4D−F). Close to the p*I* (i.e., pH 5), for patatin and β-lactoglobulin, the intensity increases with the incorporation of even a minor fraction of the protein into the aggregates (i.e., ∼5%) (Figure 4E,F). For ovalbumin, the intensity increased after ∼25% of the protein aggregated (Figure 4D). At a pH away from the p*I* or at lower ionic strength, a larger fraction of aggregated protein is required

DOI: 10.1021/acs.jafc.5b00927
J. Agric. Food Chem. 2015, 63, 5257−5265

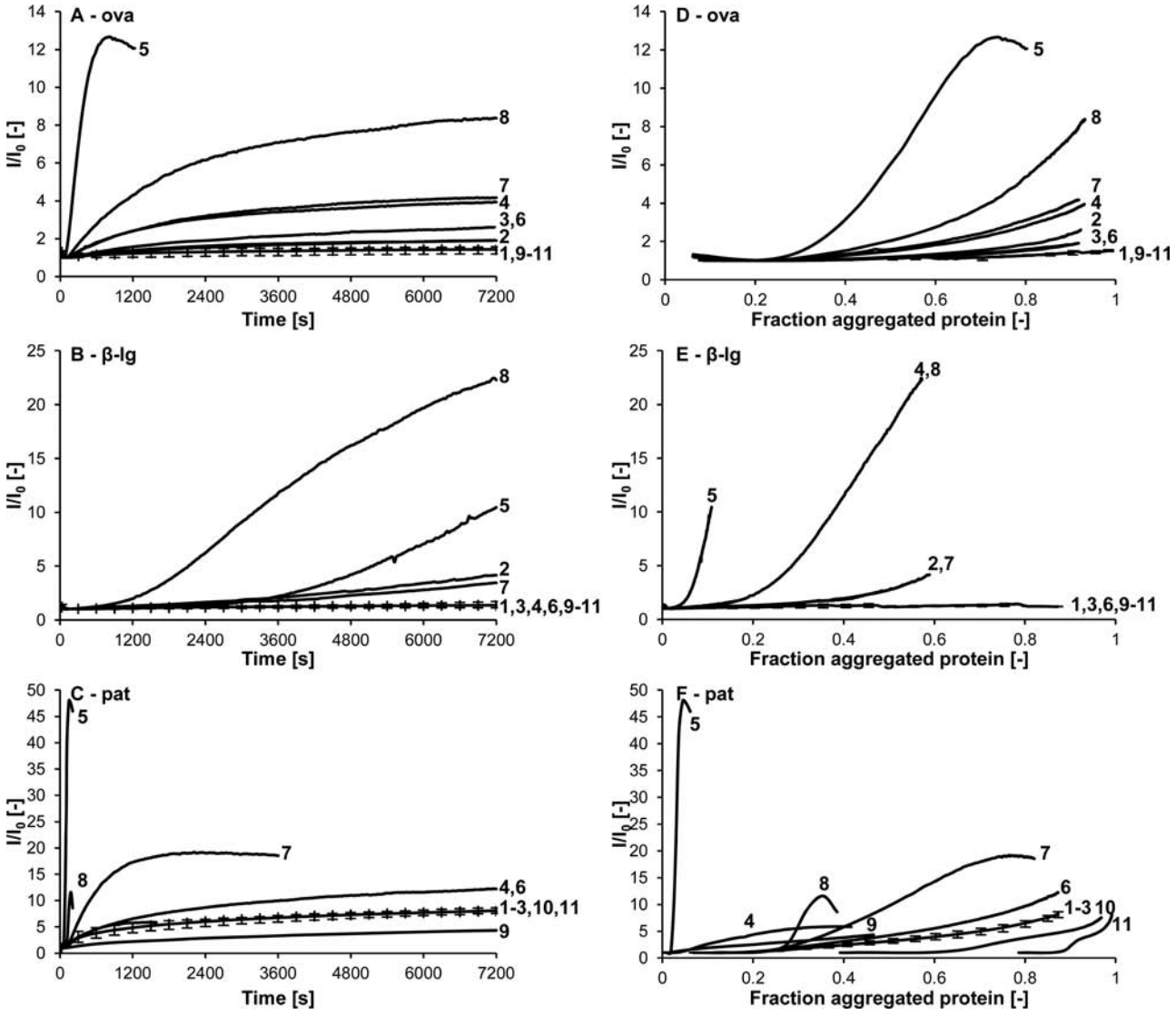

Figure 4. Normalized intensity (I/I_0) of heated ovalbumin (A, D), β-lactoglobulin (B, E), and patatin (C, F) in time (A−C) and as a function of the fraction of aggregated protein (D−F). The numbers represent the different conditions: (1) T_d − 5 °C and 2 g/L; (2) 10 g/L; (3) 5 g/L; (4) pH 6.0; (5) pH 5.0; (6) 10 mM NaCl; (7) 40 mM NaCl; (8) 90 mM NaCl; (9) T_d − 10 °C; (10) T_d; (11) T_d + 5 °C. The error bars indicate the standard deviation between the different conditions with similar behaviors.

for the intensity to increase. These results show that for patatin and β-lactoglobulin at low electrostatic repulsion (i.e., pH 5) even in the initial stages (i.e., <10% aggregated protein) large and/or dense aggregates are formed. For ovalbumin, on the other hand, the lag phase indicates that initially (i.e., <25% aggregated protein) smaller and/or more open aggregates are formed. Subsequently, at a higher fraction of aggregated protein, large and/or denser aggregates are formed. Similarly, also at higher electrostatic repulsion initially smaller and/or more open aggregates are formed, followed by the formation of larger and/or denser aggregates. The differences between the proteins show that patatin has the highest tendency to form larger and/or denser aggregates.

Effect of Concentration and Temperature. In general, changes in temperature or concentration resulted in only minor changes of the light scattering intensity as a function of heating time (Figure 4A−C). This shows that these two parameters do not affect the aggregate formation (i.e., size and structure) as strongly as the ionic strength or pH. For patatin, the intensity increase upon heating is concentration independent, whereas it decreases with decreasing temperature (i.e., $I/I_0 = 4$ after 7200 s) (Figure 4C). For β-lactoglobulin and ovalbumin, the intensity in time increases slightly with increasing concentration (i.e., $I/I_0 =$ 4 and 3 at 10 g/L after 7200 s for β-lactoglobulin and ovalbumin, respectively) (Figure 4A,B). This increase is in line with the literature, as the mass and size of β-lactoglobulin aggregates have been described to increase with concentration (at higher concentrations until 110 g/L).[7,28,49] The effect of temperature on the aggregation of patatin is expected to be purely determined by kinetics, as a consequence the aggregate formation in time is reduced.

From the intensity as a function of the fraction aggregated protein it can be observed that, even at large fractions of aggregated protein, the intensity is not affected by concentration and temperature. This confirms that, also after correcting for the aggregation kinetics, the aggregate size and structure are, within the tested temperature and concentration range, independent of temperature and concentration. Hence, at high electrostatic repulsion (i.e., pH 7.0 and 10 mM), relatively small and/or open aggregates are formed.

DOI: 10.1021/acs.jafc.5b00927
J. Agric. Food Chem. 2015, 63, 5257−5265

In summary, aggregate formation is limited by the electrostatic repulsion between proteins or protein aggregates due to their charge. In the case of charge screening (i.e., increased ionic strength) or a decreased surface charge (i.e., pH closer to p*I*), this electrostatic barrier decreases and larger and/or denser aggregates are formed. Concentration and temperature, on the other hand, did not strongly affect the aggregate size or structure. Although for all proteins aggregate formation was qualitatively similar, quantitatively the behavior was significantly different. This shows that the information on one protein cannot directly be related to another protein. In general, ovalbumin showed to have the least tendency to form larger and/or denser aggregates, followed by β-lactoglobulin. Patatin, on the other hand, directly forms large and/or dense aggregates.

In conclusion, the comparison of different proteins shows that the sensitivity toward system conditions (i.e., pH, ionic strength, and concentration) varies significantly between the proteins. Whereas it was expected that the aggregation behavior relates to the molecular properties of a protein, there is no clear link between the observed aggregation behavior and known protein molecular properties such as surface charge and exposed hydrophobicity. This was, for instance, illustrated by the lower tendency of ovalbumin to form larger, denser aggregates than patatin and β-lactoglobulin, although the surface charges of these proteins are similar. Therefore, the generic relationships commonly assumed in the literature need to be considered with care.

In addition, although the classical reaction rate kinetics are often used to describe the aggregation process of proteins, it was shown to contain little information about the actual size/density of the formed aggregates. Consequently, for a more complete description of the aggregation process, not only the loss of monomers but also a detailed analysis of the aggregates is required.

For a fundamental understanding of the influence of molecular properties on the aggregation process and to exclude factors relating to differences in unfolding behavior, it is important to compare the aggregation behavior at a constant distance from T_d. This is in contrast to the fact that for practical situations a comparison at a constant temperature is more valuable (i.e., realistic).

■ ASSOCIATED CONTENT

Ⓢ Supporting Information

Thermograms of the heat-induced unfolding of ovalbumin, β-lactoglobulin, and patatin (2 g/L, 10 mM sodium phosphate buffer, pH 7.0); Arrhenius plots of ovalbumin, β-lactoglobulin, and patatin (2 g/L, 10 mM sodium phosphate buffer, pH 7.0). The Supporting Information is available free of charge on the ACS Publications website at DOI: 10.1021/acs.jafc.5b00927.

■ AUTHOR INFORMATION

Corresponding Author

*(H.G.) Phone: +31 317 483211. E-mail: harry.gruppen@wur.nl.

Notes

The authors declare no competing financial interest.

■ REFERENCES

(1) Pauling, L. Protein interactions: aggregation of globular proteins. *Discuss. Faraday Soc.* **1953**, *13*, 170−176.

(2) Creighton, T. E. *Proteins: Structure and Molecular Properties*, 2nd ed.; Freeman: New York, 2002.

(3) Lumry, R.; Eyring, H. Conformation changes of proteins. *J. Phys. Chem.* **1954**, *58*, 110−120.

(4) Mahler, H.-C.; Müller, R.; Friebβ, W.; Delille, A.; Matheus, S. Induction and analysis of aggregates in a liquid IgG1-antibody formulation. *Eur. J. Pharm. Biopharm.* **2005**, *59*, 407−417.

(5) Roefs, S. P. F. M.; de Kruif, K. G. A model for the denaturation and aggregation of β-lactoglobulin. *Eur. J. Biochem.* **1994**, *226*, 883−889.

(6) Weijers, M.; Barneveld, P. A.; Cohen Stuart, M. A.; Visschers, R. W. Heat-induced denaturation and aggregation of ovalbumin at neutral pH described by irreversible first-order kinetics. *Protein Sci.* **2003**, *12*, 2693−2703.

(7) Le Bon, C.; Nicolai, T.; Durand, D. Kinetics of aggregation and gelation of globular proteins after heat-induced denaturation. *Macromolecules* **1999**, *32*, 6120−6127.

(8) Hoffmann, M. A. M.; van Mil, P. J. J. M. Heat-induced aggregation of β-lactoglobulin as a function of pH. *J. Agric. Food Chem.* **1999**, *47*, 1898−1905.

(9) Yohannes, G.; Wiedmer, S. K.; Elomaa, M.; Jussila, M.; Aseyev, V.; Riekkola, M.-L. Thermal aggregation of bovine serum albumin studied by asymmetrical flow field-flow fractionation. *Anal. Chim. Acta* **2010**, *675*, 191−198.

(10) Weijers, M.; Visschers, R. W.; Nicolai, T. Influence of the ionic strength on the structure of heat-set globular protein gels at pH 7. Ovalbumin. *Macromolecules* **2004**, *37*, 8709−8714.

(11) Krebs, M. R. H.; Devlin, G. L.; Donald, A. M. Protein particulates: another generic form of protein aggregation? *Biophys. J.* **2007**, *92*, 1336−1342.

(12) van Boekel, M. A. J. S. *Kinetic Modeling of Reactions in Foods*; CRC Press: Boca Raton, FL, USA, 2009.

(13) Hoffmann, M. A. M.; Roefs, S. P. F. M.; Verheul, M.; van Mil, P. J. J. M.; de Kruif, K. G. Aggregation of β-lactoglobulin studied by in situ light scattering. *J. Dairy Res.* **1996**, *63*, 423−440.

(14) Verheul, M.; Roefs, S. P. F. M. Structure of particulate whey protein gels: effect of NaCl, concentration, pH, heating temperature, and protein composition. *J. Agric. Food Chem.* **1998**, *46*, 4909−4916.

(15) Le Bon, C.; Nicolai, T.; Durand, D. Growth and structure of aggregates of heat-denatured β-lactoglobulin. *Int. J. Food Sci. Technol.* **1999**, *34*, 451−465.

(16) Verheul, M.; Roefs, S. P. F. M.; de Kruif, K. G. Kinetics of heat-induced aggregation of β-lactoglobulin. *J. Agric. Food Chem.* **1998**, *46*, 896−903.

(17) Mahler, H.-C.; Friess, W.; Grauschopf, U.; Kiese, S. Protein aggregation: pathways, induction factors and analysis. *J. Pharm. Sci.* **2009**, *98*, 2909−2934.

(18) Wang, W.; Nema, S.; Teagarden, D. Protein aggregation − pathways and influencing factors. *Int. J. Pharm.* **2010**, *390*, 89−99.

(19) Chi, E. Y.; Krishnan, S.; Randolph, T. W.; Carpenter, J. F. Physical stability of proteins in aqueous solution: mechanism and driving forces in nonnative protein aggregation. *Pharm. Res.* **2003**, *20*, 1325−1336.

(20) Speed, M. A.; King, J.; Wang, D. I. C. Polymerization mechanism of polypeptide chain aggregation. *Biotechnol. Bioeng.* **1997**, *54*, 333−343.

(21) Haug, I. J.; Skar, H. M.; Vegarud, G. E.; Langsrud, T.; Draget, K. I. Electrostatic effects on β-lactoglobulin transitions during heat denaturation as studied by differential scanning calorimetry. *Food Hydrocolloids* **2009**, *23*, 2287−2293.

(22) Giancola, C.; De Sena, C.; Fessas, D.; Graziano, G.; Barone, G. DSC studies on bovine serum albumin denaturation. Effects of ionic strength and SDS concentration. *Int. J. Biol. Macromol.* **1997**, *20*, 193−204.

(23) De Young, L. R.; Fink, A. L.; Dill, K. A. Aggregation of globular proteins. *Acc. Chem. Res.* **1993**, *26*, 614−620.

(24) Broersen, K.; Weijers, M.; de Groot, J.; Hamer, R. J.; de Jongh, H. H. J. Effect of protein charge on the generation of aggregation-prone conformers. *Biomacromolecules* **2007**, *8*, 1648−1656.

DOI: 10.1021/acs.jafc.5b00927
J. Agric. Food Chem. 2015, 63, 5257−5265

(25) Mehalebi, S.; Nicolai, T.; Durand, D. The influence of electrostatic interaction on the structure and the shear modulus of heat-set globular protein gels. *Soft Matter* **2008**, *4*, 893−900.
(26) Mine, Y. Laser light scattering study on the heat-induced ovalbumin aggregates related to its gelling property. *J. Agric. Food Chem.* **1996**, *44*, 2086−2090.
(27) Choi, S. J.; Moon, T. W. Influence of sodium chloride and glucose on the aggregation behavior of heat-denatured ovalbumin investigated with a multiangle laser light scattering technique. *J. Food Sci.* **2008**, *73*, C41−C49.
(28) Durand, D.; Gimel, J. C.; Nicolai, T. Aggregation, gelation and phase separation of heat denatured globular proteins. *Phys. A* **2002**, *304*, 253−265.
(29) Pots, A. M.; ten Grotenhuis, E.; Gruppen, H.; Voragen, A. G. J.; de Kruif, K. G. Thermal aggregation of patatin studied in situ. *J. Agric. Food Chem.* **1999**, *47*, 4600−4605.
(30) Weijers, M.; Visschers, R. W.; Nicolai, T. Light scattering study of heat-induced aggregation and gelation of ovalbumin. *Macromolecules* **2002**, *35*, 4753−4762.
(31) Mehalebi, S.; Nicolai, T.; Durand, D. Light scattering study of heat-denatured globular protein aggregates. *Int. J. Biol. Macromol.* **2008**, *43*, 129−135.
(32) Mahmoudi, N.; Mehalebi, S.; Nicolai, T.; Durand, D.; Riaublanc, A. Light-scattering study of the structure of aggregates and gels formed by heat-denatured whey protein isolate and *β*-lactoglobulin at neutral pH. *J. Agric. Food Chem.* **2007**, *55*, 3104−3111.
(33) Baussay, K.; Le Bon, C.; Nicolai, T.; Durand, D.; Busnel, J. P. Influence of the ionic strength on the heat-induced aggregation of the globular protein *β*-lactoglobulin at pH 7. *Int. J. Biol. Macromol.* **2004**, *34*, 21−28.
(34) Gimel, J. C.; Durand, D.; Nicolai, T. Structure and distribution of aggregates formed after heat-induced denaturation of globular proteins. *Macromolecules* **1994**, *27*, 583−589.
(35) Pouzot, M.; Durand, D.; Nicolai, T. Influence of the ionic strength on the structure of heat-set globular protein gels at pH 7. *β*-Lactoglobulin. *Macromolecules* **2004**, *37*, 8703−8708.
(36) Yan, Y.; Seeman, D.; Zheng, B.; Kizilay, E.; Xu, Y.; Dubin, P. L. pH-dependent aggregation and disaggregation of native *β*-lactoglobulin in low salt. *Langmuir* **2013**, *29*, 4584−4593.
(37) Hoffmann, M. A. M.; Sala, G.; Olieman, C.; de Kruif, K. G. Molecular mass distributions of heat-induced *β*-lactoglobulin aggregates. *J. Agric. Food Chem.* **1997**, *45*, 2949−2957.
(38) Creusot, N.; Wierenga, P. A.; Laus, M. C.; Giuseppin, M. L. F.; Gruppen, H. Rheological properties of patatin gels compared with *β*-lactoglobulin, ovalbumin, and glycinin. *J. Sci. Food Agric.* **2011**, *91*, 253−261.
(39) van Koningsveld, G. A.; Gruppen, H.; de Jongh, H. H. J.; Wijngaards, G.; van Boekel, M. A. J. S.; Walstra, P.; Voragen, A. G. J. Effects of pH and heat treatments on the structure and solubility of potato proteins in different preparations. *J. Agric. Food Chem.* **2001**, *49*, 4889−4897.
(40) Podzimek, S. *Light Scattering, Size Exclusion Chromatography and Asymmetric Flow Field Flow Fractionation*; Wiley: Hoboken, NJ, USA, 2011.
(41) Van Boekel, M. A. J. S. Statistical aspects of kinetic modeling for food science problems. *J. Food Sci.* **1996**, *61*, 477−486.
(42) Anema, S. G.; McKenna, A. B. Reaction kinetics of thermal denaturation of whey proteins in heated reconstituted whole milk. *J. Agric. Food Chem.* **1996**, *44*, 422−428.
(43) Dannenberg, F.; Kessler, H.-G. Reaction kinetics of the denaturation of whey proteins in milk. *J. Food Sci.* **1988**, *53*, 258−263.
(44) Mounsey, J. S.; O'Kennedy, B. T. Conditions limiting the influence of thiol−disulphide interchange reactions on the heat-induced aggregation kinetics of *β*-lactoglobulin. *Int. Dairy J.* **2007**, *17*, 1034−1042.
(45) Pots, A. M.; de Jongh, H. H. J.; Gruppen, H.; Hessing, M.; Voragen, A. G. J. The pH dependence of the structural stability of patatin. *J. Agric. Food Chem.* **1998**, *46*, 2546−2553.
(46) Elofsson, U. M.; Dejmek, P.; Paulsson, M. A. Heat-induced aggregation of *β*-lactoglobulin studied by dynamic light scattering. *Int. Dairy J.* **1996**, *6*, 343−357.
(47) Bauer, R.; Carrotta, R.; Rischel, C.; Øgendal, L. Characterization and isolation of intermediates in *β*-lactoglobulin heat aggregation at high pH. *Biophys. J.* **2000**, *79*, 1030−1038.
(48) Zúñiga, R.; Tolkach, A.; Kulozik, U.; Aguilera, J. Kinetics of formation and physicochemical characterization of thermally-induced *β*-lactoglobulin aggregates. *J. Food Sci.* **2010**, *75*, E261−E268.
(49) Ako, K.; Nicolai, T.; Durand, D. Salt-induced gelation of globular protein aggregates: structure and kinetics. *Biomacromolecules* **2010**, *11*, 864−871.
(50) Delahaije, R. J. B. M.; Wierenga, P. A.; van Nieuwenhuijzen, N. H.; Giuseppin, M. L. F.; Gruppen, H. Protein concentration and protein-exposed hydrophobicity as dominant parameters determining flocculation of protein-stabilized oil-in-water emulsions. *Langmuir* **2013**, *29*, 11567−11574.

DOI: 10.1021/acs.jafc.5b00927
J. Agric. Food Chem. 2015, 63, 5257−5265

JOURNAL OF AGRICULTURAL AND FOOD CHEMISTRY

Article

pubs.acs.org/JAFC

Improving Flavonoid Bioaccessibility using an Edible Oil-Based Lipid Nanoparticle for Oral Delivery

Choongjin Ban,[†,$] So Jeong Park,[∥,$] Seokwon Lim,[⊥] Seung Jun Choi,[#] and Young Jin Choi*[,†,‡,§]

[†]Department of Agricultural Biotechnology, [‡]Center for Food and Bioconvergence, and [§]Research Institute of Agriculture and Life Sciences, Seoul National University, 1 Gwanakro, Gwanakgu, Seoul 151-921, Korea

[∥]Dongsuh Foods Corporation, 203 Bupyeongbuk-ro, Bupyeong-gu, Incheon 403-858, Korea

[⊥]Department of Food and Biotechnology, Hoseo University, 79-20 Hoseoro, Asan, Chungnam 336-795, Korea

[#]Department of Food Science and Technology, Seoul National University of Science and Technology, 232 Gongneungro, Nowongu, Seoul 139-743, Korea

Supporting Information

ABSTRACT: To enhance the oral bioaccessibility of flavonoids, including quercetin, naringenin, and hesperetin, we prepared an edible oil-based lipid nanoparticle (LNP) system. Flavonoid-loaded LNPs were similar to the blank LNP in physicochemical characteristics (z average <154.8 nm, polydispersity index <0.17, and ζ potential < −40.8 mV), and their entrapment efficiency was >81% at 0.3 wt % flavonoid concentration of the lipid phase. In the simulated digestion assay (mouth, stomach, and small intestine), LNPs were hydrolyzed under small intestine conditions and protected successfully incorporated flavonoids (≥94%). Moreover, the relative bioaccessibility of flavonoids was >71%, which was otherwise <15%, although flavonoids were released rapidly from LNPs into the medium. In conclusion, since the flavonoids incorporated in LNPs were preserved well during oral digestion and had improved bioaccessibility, the designed LNP system may serve as an encapsulation strategy to enhance the bioavailability of nonbioaccessible nutraceuticals in foods.

KEYWORDS: *flavonoid, lipid nanoparticle, simulated digestion, protectibility, bioaccessibility*

INTRODUCTION

Quercetin is the representative flavonol in various vegetables and fruits such as onion and apple[1] and has antioxidative,[2] anticarcinogenic,[3] anti-inflammatory,[4] antiaggregatory,[5] and vasodilatory[6] effects. Naringenin and hesperetin are the representative flavanones in various fruits, such as orange, lemon, and grape;[7] they have antioxidant[8] and anti-inflammatory[9] activities and influence lipid[10] and sex hormone metabolism.[11] This could imply that quercetin, narigenin, and hesperetin, as the major flavonoids, are easy to take in from foods in the common diet and have crucial roles in human health. Despite their health benefits, the parent forms have low bioavailability because of their low water solubility. Although these compounds can be ingested as their glycosides, such as rutin, naringin, and hesperidin, directly from vegetables and orange/grape juices to increase bioavailability, plasma flavonoid levels are low in comparison to the amount ingested.[12,13] Moreover, as flavonoid glycosides are cleaved by enzymes and microflora before absorption in the small and large intestines, respectively, bioavailability could vary among individuals.[1] Therefore, the bioavailability of the flavonoid parent forms must be improved.

Lipid nanoparticle (LNP) systems have drawn attention for using physiological lipids, protection of core materials, and improvement of the oral bioaccessibility of lipophilic materials; due to their submicron size, they have an increased residence time by adhering to the gastrointestinal wall or entering the intervillar spaces.[14] Some researchers have recently reported that the bioaccessibility of polyphenols such as resveratrol,[15] curcumin, and genistein[16] was enhanced by LNP encapsulation. Despite the benefits of oral administration of bioactive lipophilic molecules such as flavonoids, colloidal stability problems such as aggregation impede food applications. The LNP matrix crystallizes into a β polymorphic form during cooling and can cause morphological changes in individual particles and increase surfactant-depleted areas (hydrophobic patches) of the LNP, resulting in aggregation due to interactions between hydrophobic patches that minimize the uncovered surface area facing the water phase.[17] Additionally, partial coalescence of oil droplets containing crystals during cooling can cause aggregation.[18,19] Thus, methods to enhance stability have been reported, including using a lipid source that prevents or retards β-form crystallization[20] and using an emulsifier that prevents particle aggregation by increasing steric hindrance and electrostatic repulsive forces.[21]

The behavior of flavonoid-loaded LNPs in the oral and gastrointestinal tracts has been described to demonstrate their benefits when the system is adopted to enhance bioaccessibility and protect against physical and biochemical stressors, such as salts, pH, and digestive enzymes.[22] For the same reason, the digestion of LNPs encapsulating bioactive lipophilic components (nutraceuticals) has been evaluated extensively. LNPs mix with saliva in the mouth (neutral pH) after ingestion and

Received: March 24, 2015
Revised: May 14, 2015
Accepted: May 15, 2015
Published: May 15, 2015

ACS Publications © 2015 American Chemical Society

DOI: 10.1021/acs.jafc.5b01495
J. Agric. Food Chem. 2015, 63, 5266−5272

then travel to the stomach (pH 1−3), which provides complex flow and changes the pH, ionic strength, and digestive enzyme levels[23,24] that could promote oxidation of nutraceuticals and particle aggregation due to flocculation and/or coalescence. After it enters the small intestine, the mixture of LNPs, saliva, and gastric juice is blended with duodenal and bile juices containing pancreatic lipase, colipase, bile salts, phospholipids, and bicarbonate, and digestive enzymes convert LNP triglycerides into monoglycerides and free fatty acids. The products of lipid digestion are taken up into bile salt/phospholipid micelles, and the mixed micelles incorporate the nutraceuticals, resulting in transportation of the micelles to the surfaces of enterocytes, where they are absorbed.[21]

Therefore, LNPs encapsulating flavonoids must be resistant to the harsh conditions in the mouth and stomach to improve their bioaccessibility and protect them until they are absorbed into enterocytes. Unfortunately, many studies have investigated the individual digestion process of LNPs under in vivo and in vitro conditions of the mouth, stomach, or small intestine, making it difficult to describe the serial events occurring in an actual digestive system. In this study, the composition of LNPs prepared using food grade materials—including fully hydrogenated canola oil as the solid lipid, liquid oils (liquid soybean oil, squalene, or canola oil) to prevent or retard crystallization, Tween 20 as a nonionic emulsifier to produce a steric effect, and soybean lecithin as an ionic emulsifier providing electrostatic repulsive force—was optimized in terms of colloidal stability. Furthermore, the fates of quercetin-, naringenin-, and hesperetin-loaded LNPs during the serial events of digestion in the mouth, stomach, and small intestine were mimicked in simulated digestive media.

MATERIALS AND METHODS

Chemicals. Lotte Samkang Co. Ltd. (Seoul, Korea) provided fully hydrogenated canola oil (FHCO), which was composed of 79.5 wt % stearic acid, 8.8 wt % palmitic acid, 4.2 wt % oleic acid, 1.8 wt % lauric acid, 1.6 wt % arachidic acid, 1.4 wt % linoleic acid, 0.9 wt % myristic acid, and 1.8 wt % other ingredients. Liquid soybean oil (LSO; 49.3 wt % linoleic acid, 23.2 wt % oleic acid, 10.2 wt % palmitic acid, 4.9 wt % linolenic acid, 3.8 wt % stearic acid, 0.3 wt % arachidic acid, 0.2 wt % lauric acid, 0.2 wt % erucic acid, 0.1 wt % myristic acid, and 7.7 wt % other ingredients) and liquid canola oil (LCO; 58.3 wt % oleic acid, 20.0 wt % linoleic acid, 8.3 wt % linolenic acid, 4.4 wt % palmitic acid, 1.8 wt % stearic acid, 1.3 erucic acid, 0.6 wt % arachidic acid, and 5.3 wt % other ingredients) were obtained from CJ Cheiljedang Co. (Seoul, Korea). Squalene (>98%; SQ) was obtained from Alfa Aesar (Heysham, England). Tween 20 (T20; polyoxyethylene sorbitan monolaurate) and soybean lecithin (SL) were purchased from Sigma-Aldrich Co. (St. Louis, MO, USA) and Fisher Scientific (Pittsburgh, PA, USA), respectively. Quercetin and naringenin were obtained from MP Biomedicals LLC (Solon, OH, USA), and hesperetin was obtained from Sigma-Aldrich Co. All other chemicals were of analytical reagent grade.

Lipid Nanoparticle Production. The LNPs were prepared using an oil-in-water emulsion technique with a high-speed blender and sonication probe as reported previously by us,[17] with a slight modification. First, the lipid (5 wt %) and aqueous (95 wt %) phases were heated to 85 °C, mixed using a high-speed blender (Ultra-Turrax T25D, Ika Werke GmbH & Co., Staufen, Germany) at 8000 rpm for 1 min and then at 11000 rpm for 1 min, and maintained at 85 °C; the lipid phase of the blank LNPs was a mixture of 5−3.5 wt % FHCO (100−70 wt % of the lipid phase) and 0−1.5 wt % of each liquid oil (0−30 wt % of the lipid phase) among LSO, LCO, and SQ;, and the aqueous phase was prepared by adding an emulsifier mixture (one-third of the lipid phase weight) composed of T20 (100−0 wt % of the emulsifier mixture) and SL (0−100 wt % of the mixture) in doubly distilled water (DDW) containing 0.02 wt % sodium azide. After the coarse oil-in-water emulsion was produced, the droplet size was further reduced by sonication (VCX 750, Sonics & Materials Inc., Newtown, CT, USA) for 4 min at 60% amplitude, a duty cycle of 1 s, and 95 °C. After the droplet size was reduced, postsonication for 6 min was applied to the emulsions during cooling to 25 °C in a jacketed beaker, and the samples were maintained at room temperature (25 °C).

The lipid phase was composed of FHCO blended with 30 wt % SQ of the phase to prepare the LNP-loaded flavonoid molecules (quecetin, naringenin, and hesperetin) and the additional flavonoids of 0.1−0.5 wt % concentration in the lipid; a mixture of T20 (32.28 wt % of the mixture) and SL (67.72 wt % of the mixture) was used as an emulsifier in the aqueous phase to optimize system stability. The lipid phase incorporating the flavonoids was stirred gently at 85 °C for 30 min, and the remaining production process was conducted as for the blank LNP.

Quantification of Nonaggregated Lipid Nanoparticles (Yield). LNPs diluted 10-fold with DDW were passed through a 1 μm pore size glass microfiber filter (GF/B, Whatman Ltd., Loughborough, U.K.). The aggregated LNPs remaining on the filter (micrometer scale) were weighed after drying in an oven at 50 °C. The difference in filter weights before and after the procedure, which was the weight of the creamed or aggregated LNPs, was recorded.

Measurements of Lipid Nanoparticle Size and ζ Potential. The prepared LNPs (4.5 mL) were diluted with 40.5 mL of DDW in a vial to separate the layers containing the creamed (creaming layer) and noncreamed LNPs (aqueous layer). The vial containing the diluted samples was sealed tightly with a screw cap and incubated overnight at room temperature. The LNPs in the aqueous layer were collected by filtering with a 1 μm pore size glass microfiber filter (GF/B, Whatman Ltd.) to determine the size of the noncreamed LNP, and their mean particle size (z average) and polydispersity index (PDI) were measured using a Zetasizer instrument (Nano ZS, Malvern Instruments Ltd., Worcestershire, U.K.) operated at a 173° angle with a helium−neon laser (λ 633 nm). In addition, the ζ potential (ZP) was measured using the Zetasizer. The ZP measurement was based on the Smoluchowski equation at 25 °C with an electric field strength of 20 V cm^{-1}.

Entrapment Efficiency of the Flavonoid-Loaded Lipid Nanoparticles. A 1 mL portion of n-butanol was added to 1 mL of each LNP sample encapsulating the flavonoids (quercetin, naringenin, and hesperetin). The sample was vortexed for 10 s and then centrifuged at 10000 RCF for 10 min (Centrifuge Smart 15, Hanil Science Industrial Co., Ltd., Incheon, Korea). After centrifugation, the n-butanol layer was transferred to a microquartz cell, and the absorbance at 377.5 nm (quercetin), 291.5 nm (naringenin), and 289.5 nm (hesperetin) was determined using a spectrophotometer (Pharmaspec UV-170, Shimadzu Corp., Kyoto, Japan). The concentrations of quercetin, naringenin, and hesperetin in the n-butanol layer were calculated using standard curves ranging from 3.125 to 100 μg mL^{-1} for quercetin (R^2 = 0.9975), naringenin (R^2 = 0.9990), and hesperetin (R^2 = 0.9974). Flavonoid entrapment efficiencies (EE) of the LNP samples were determined using the equation

$$\text{EE}\ (\%) = \frac{W_t - W_n}{W_t} \times 100$$

where W_t is the total flavonoid molecule weight in the entire LNP sample system and W_n is the flavonoid molecule weight in the n-butanol layer after centrifugation.

Determining the in Vitro Digestion Patterns of the Lipid Nanoparticles. The simulated in vitro digestion test model was modified from the version described by Hur et al:[25]

(I) preingestion: LNPs were filtered with a 1 μm pore sized filter
(II) mouth (pH 7; 5 min): 5 mL of filtered LNPs was blended with 6 mL simulated salivary medium
(III) stomach (pH 3; 2 h): 12 mL of simulated gastric juice was added
(IV) small intestine (pH 6.5−7; 2 h): simulated duodenal juice (12 mL), bile juice (6 mL), and $NaHCO_3$ solution (2 mL) were added

DOI: 10.1021/acs.jafc.5b01495
J. Agric. Food Chem. 2015, 63, 5266−5272

Table 1. Formulations and Concentrations of the Various Media and Juices for the Simulated in Vitro Digestion Test of Blank Lipid Nanoparticles

	saliva medium	gastric juice	duodenal juice	bile juice
inorganic solution	20 mL $NaHCO_3$, 84.7 g L^{-1}	15.7 mL NaCl, 175.3 g L^{-1}	40 mL NaCl, 175.3 g L^{-1}	30 mL NaCl, 175.3 g L^{-1}
	10 mL KCl, 89.6 g L^{-1}	9.2 mL KCl, 89.6 g L^{-1}	40 mL $NaHCO_3$, 84.7 g L^{-1}	60.3 mL $NaHCO_3$, 84.7 g L^{-1}
	10 mL NaH_2PO_4, 88.8 g L^{-1}	18 mL $CaCl_2{\cdot}2H_2O$, 22.2 g L^{-1}	6.3 mL KCl, 89.6 g L^{-1}	4.2 mL KCl, 89.6 g L^{-1}
	1.7 mL NaCl, 175.3 g L^{-1}	3.0 mL NaH_2PO_4, 88.8 g L^{-1}	9 mL $CaCl_2{\cdot}2H_2O$, 22.2 g L^{-1}	10 mL $CaCl_2{\cdot}2H_2O$, 22.2 g L^{-1}
	10 mL Na_2SO_4 ,57 g L^{-1}	10 mL NH_4Cl, 30.6 g L^{-1}	10 mL KH_2PO_4 ,8 g L^{-1}	150 μL HCl, 35% g L^{-1}
	10 mL KSCN, 20 g L^{-1}	6.5 mL HCl, 35% g g^{-1}	10 mL $MgCl_2$, 5 g L^{-1}	
			180 μL HCl, 35% g g^{-1}	
organic solution	8 mL urea, 25 g L^{-1}	34 mL urea, 25 g L^{-1}	4 mL urea, 25 g L^{-1}	10 mL urea, 25 g L^{-1}
		10 mL glucose, 65 g L^{-1}		
		10 mL glucosamine hydrochloride, 33 g L^{-1}		
		10 mL glucuronic acid, 2 g L^{-1}		
add to mixture inorganic + organic solution	15 mg uric acid	1 g BSA	1 g BSA	1.8 g BSA
	25 mg mucin	3 g mucin	9 g pancreatin	30 g bile
	290 mg α-amylase	2.5 g pepsin	1.5 g lipase	
pH	6.8	1.3	8.1	8.2

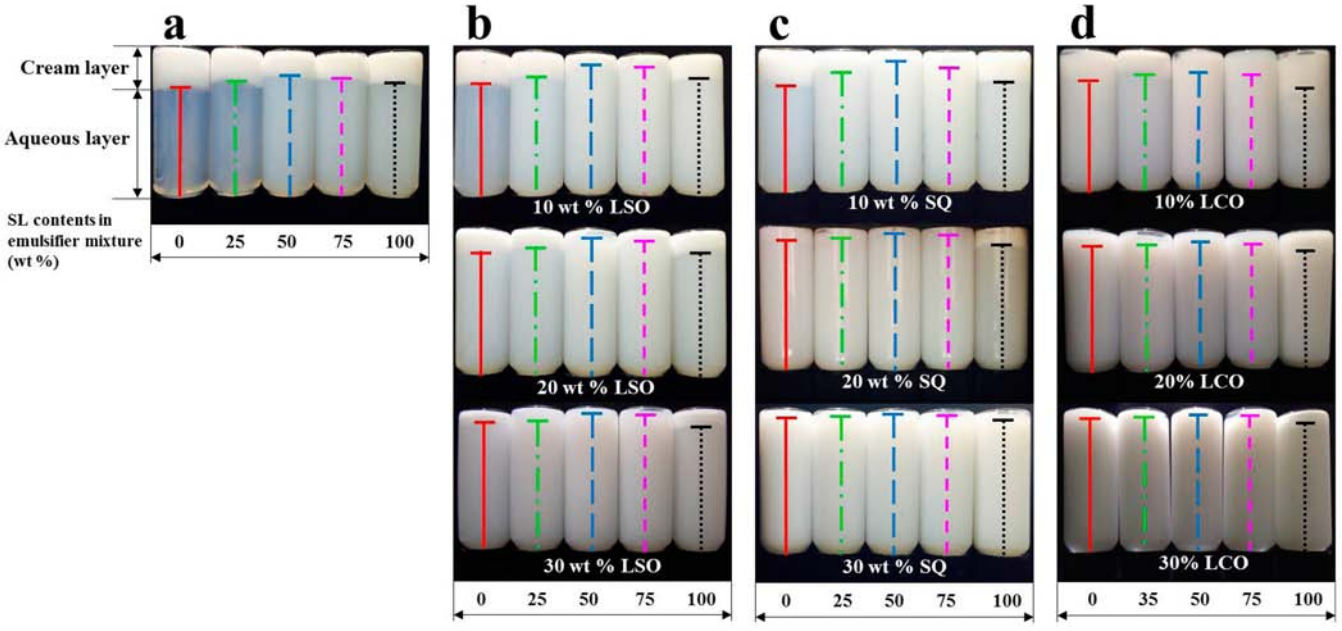

Figure 1. Creaming pattern of the blank lipid nanoparticle dispersion diluted 10-fold: (a) blank lipid nanoparticle dispersions prepared using 100 wt % fully hydrogenated canola oil (FHCO) as the lipid phase; blank lipid nanoparticle dispersions prepared using a mixture of 90–70 wt % FHCO and 10–30 wt % liquid oil, including (b) liquid soybean oil (LSO), (c) squalene (SQ), or (d) liquid canola oil (LCO) as the lipid phase.

The formulations of the simulated saliva medium and gastric, duodenal, and bile juices are shown in Table 1. All samples were stirred (60 rpm) in a shaking water bath (BS-31, JEIO Tech., Seoul, Korea) during the in vitro digestion test and maintained at 37 °C to mimic gastrointestinal tract motility. After each digestion step (I–IV), the size distribution of samples was measured using the Zetasizer.

After 4 h 5 min of digestion, the relative bioaccessibility of the flavonoid (quecetin, naringenin, and hesperetin) was determined as described earlier,[16] with modifications. Briefly, 2 mL of digesta was centrifuged at 1500 RCF for 30 min, and 1 mL of the supernatant was recentrifuged at 16000 RCF for 20 min. A 0.2 mL aliquot of the supernatant was collected and diluted 10-fold with 1.8 mL of methanol, and the solution was centrifuged at 16000 RCF for 20 min. The concentration of flavonoids in the supernatant was quantified using a spectrophotometer and calculated using standard curves ranging from 0.625 to 10 μg mL^{-1} for quercetin (λ 384 nm, R^2 = 0.9971), naringenin (λ 325 nm, R^2 = 0.9990), and hesperetin (λ 324.5 nm, R^2 = 0.9999). The relative bioaccessibility of the flavonoids in the digested micellar fraction was determined using the equation

$$\text{bioaccessibility (\%)} = \frac{W_t - W_s}{W_t} \times 100$$

where W_s is the weight of the flavonoid molecules in the supernatant after digestion and centrifugation. In addition to the flavonoid-encapsulated LNPs, equivalent quantities (150 μg mL^{-1}) of quercetin, naringenin, and hesperetin in their native forms were also investigated.

The protectibility (%) of LNPs for flavonoids against harsh conditions (pH and salt) was determined after each digestion step

DOI: 10.1021/acs.jafc.5b01495
J. Agric. Food Chem. 2015, 63, 5266–5272

Table 2. Nonaggregated Particle Content (Yield), Particle Size, Polydispersity Index (PDI), ζ Potential (ZP), and Entrapment Efficiency (EE) Values of Blank (BLK) and Flavonoid-Loaded Lipid Nanoparticles (LNPs)[a]

	flavonoid concn (wt %)							
code name	Q	N	H	yield (%)	particle size (nm)	PDI	ZP (mV)	EE (%)
BLK LNP				94.4 ± 0.4a	155.7 ± 0.4ab	0.15 ± 0.01a	−41.8 ± 0.5abcd	
0.1Q LNP	0.1			94.7 ± 0.4a	152.7 ± 1.7abcd	0.16 ± 0.02a	−45.1 ± 0.8g	69.7 ± 1.9ef
0.2Q LNP	0.2			94.7 ± 0.1a	153.7 ± 0.8abc	0.19 ± 0.01a	−44.2 ± 0.5fg	74.6 ± 1.3de
0.3Q LNP	0.3			94.5 ± 0.1a	154.7 ± 2.2ab	0.16 ± 0.02a	−43.6 ± 0.4defg	81.0 ± 0.9bc
0.4Q LNP	0.4			94.8 ± 0.2a	148.9 ± 0.9e	0.17 ± 0.03a	−42.8 ± 0.6cdef	71.3 ± 2.9ef
0.5Q LNP	0.5			95.4 ± 0.1a	144.9 ± 0.8f	0.16 ± 0.00a	−43.9 ± 0.6efg	67.9 ± 0.4f
0.1N LNP		0.1		94.1 ± 0.8a	156.2 ± 0.2a	0.14 ± 0.02a	−42.4 ± 0.3bcde	80.0 ± 0.4cd
0.2N LNP		0.2		94.1 ± 0.3a	152.1 ± 0.6bcde	0.16 ± 0.01a	−40.6 ± 0.7ab	89.0 ± 2.0a
0.3N LNP		0.3		94.2 ± 1.1a	149.9 ± 0.4de	0.14 ± 0.03a	−42.1 ± 0.6abcde	90.0 ± 0.5a
0.4N LNP		0.4		94.2 ± 0.9a	148.8 ± 1.8e	0.16 ± 0.02a	−42.3 ± 0.5abcde	85.8 ± 1.4ab
0.5N LNP		0.5		94.1 ± 0.2a	149.1 ± 0.2de	0.17 ± 0.01a	−42.9 ± 0.3cdef	88.0 ± 0.4a
0.1H LNP			0.1	94.9 ± 0.3a	155.2 ± 2.7ab	0.18 ± 0.01a	−40.5 ± 1.0a	72.5 ± 4.0ef
0.2H LNP			0.2	94.8 ± 0.3a	154.7 ± 0.2ab	0.17 ± 0.01a	−42.2 ± 0.5abcde	82.1 ± 1.5bc
0.3H LNP			0.3	94.2 ± 0.4a	154.8 ± 0.2ab	0.17 ± 0.01a	−40.8 ± 0.7ab	90.0 ± 2.5a
0.4H LNP			0.4	94.3 ± 0.9a	150.9 ± 0.8cde	0.16 ± 0.02a	−41.7 ± 0.6abc	88.7 ± 1.2a
0.5H LNP			0.5	94.9 ± 0.8a	149.9 ± 1.2de	0.16 ± 0.02a	−42.1 ± 0.7abcd	89.7 ± 1.1a

[a]Different letters a−g in a column are significantly different at $p < 0.05$. Abbreviations: quercetin, Q; naringenin, N; hesperetin, H.

(II−IV) without enzymes. After each step, 0.2 mL of digesta was collected and diluted 10-fold with 1.8 mL of methanol and centrifuged at 16000 RCF for 20 min. The concentration of flavonoids in the supernatant was quantified using a spectrophotometer and calculated using standard curves ranging from 0.625 to 10 μg mL^{-1}: step II, quercetin (λ 389 nm, R^2 = 0.9999), naringenin (λ 325.5 nm, R^2 = 1.0000), and hesperetin (λ 325.5 nm, R^2 = 0.9999); step III, quercetin (λ 379 nm, R^2 = 1.0000), naringenin (λ 290 nm, R^2 = 0.9998), and hesperetin (λ 287.5 nm, R^2 = 0.9998); step IV, quercetin (λ 389 nm, R^2 = 0.9999), naringenin (λ 325 nm, R^2 = 1.0000), and hesperetin (λ 325 nm, R^2 = 1.0000)). The protectibility of the LNPs incorporating the flavonoids against the enzyme-free digestion medium was determined by the equation

$$\text{protectibilty (\%)} = \frac{W_t - W_s}{W_e} \times 100$$

where W_e is the weight of the flavonoids encapsulated in the LNPs immediately after preparation.

The release patterns of the flavonoids from the LNPs were studied using dialysis bags with a 12 kDa molecular weight cutoff. The bags were immersed in DDW for 12 h before use. They were filled with 1 mL of the flavonoid-loaded LNP sample, tightly sealed, and suspended in 49 mL of 50% (v/v) ethanol to produce a sink condition. The enzyme-free simulated in vitro digestion medium mixture was added, and the bags were rotated at 100 rpm in a 37 °C water bath. At predetermined time intervals, a 1 mL aliquot was withdrawn from the medium mixture, and 1 mL of fresh medium was replaced immediately. Next, the absorbance of the aliquot at the wavelengths for quercetin (377.5 nm), naringenin (291.5 nm), and hesperetin (289.5 nm) was measured with a spectrophotometer. The concentrations of quercetin, naringenin, and hesperetin in the aliquots were calculated using standard curves ranging from 3.125 to 250 μg mL^{-1} for quercetin (R^2 = 0.9996), naringenin (R^2 = 0.9999), and hesperetin (R^2 = 0.9999).

Statistical Analysis. All results were analyzed using Tukey's significant difference test using the IBM SPSS Statistics version 21.0 software (IBM Co., Armonk, NY, USA). Data represent means of at least three independent experiments or measurements. A p value <0.05 was considered to indicate a significant difference.

RESULTS AND DISCUSSION

Stability of the Blank Lipid Nanoparticles. The partially coalesced LNPs and the LNPs with surfactant-depleted patches on the surfaces formed micrometer-sized aggregates.[17] According to Stokes' law, the particle size effect on the creaming rate predominates over the density difference at the same composition. Therefore, the aggregated micrometer-sized particles creamed readily, whereas the stable nanosized LNPs were well-dispersed in aqueous solution.[17]

The creaming phenomenon of the LNP aggregates was observed when blank LNPs prepared with 100 wt % FHCO as the lipid phase were diluted 10-fold with DDW (Figure 1a). The micrometer-sized LNP aggregates and the nanosized LNPs formed creaming and aqueous layers, respectively. The particle size of all blank LNPs prepared with 100 wt % FHCO was 123.2−165.1 nm, indicating that submicron-sized particles comprised the aqueous layer. Thus, the thickness of the aqueous layer reflected the number of LNPs stably produced on a nanosize scale, which was related to the colloidal stability of the LNP system.

The aqueous layers of samples stabilized with a single emulsifier (SL contents: 0 and 100 wt %) were thinner than those emulsified with T20 and SL (SL contents: 25, 50, and 75 wt %). Additionally, the yields of the 25, 50, and 75 wt % SL content samples were larger than those of the 0 and 100 wt % SL content samples (Table S1 in the Supporting Information), suggesting that combined use of T20 and SL enhanced the colloidal stability of the LNP system, which agrees with other studies.[26] This tendency was also applied to the LNP samples fabricated using a lipid mixture with FHCO and liquid oil (LSO, SQ, or LCO) as the lipid phase (Figure 1b−d).

We observed in our previous study that increasing the liquid oil content in the LNP lipid phase improves the colloidal stability of the system,[17] which was confirmed here (Figure 1b−d). Furthermore, the thickness of the aqueous layer differed when the liquid oil type was changed. Therefore, LNP samples with SQ as the liquid oil in the lipid matrix had the thickest aqueous layer at the same liquid oil and SL contents. This result is in agreement with the yield data (Table S1 in the Supporting Information). These results suggest that using SQ as the liquid oil could produce optimum colloidal stability among LSO, SQ, and LCO. Thus, the preparation formula of blank LNP was optimized by using SQ as the liquid oil.

DOI: 10.1021/acs.jafc.5b01495
J. Agric. Food Chem. 2015, 63, 5266−5272

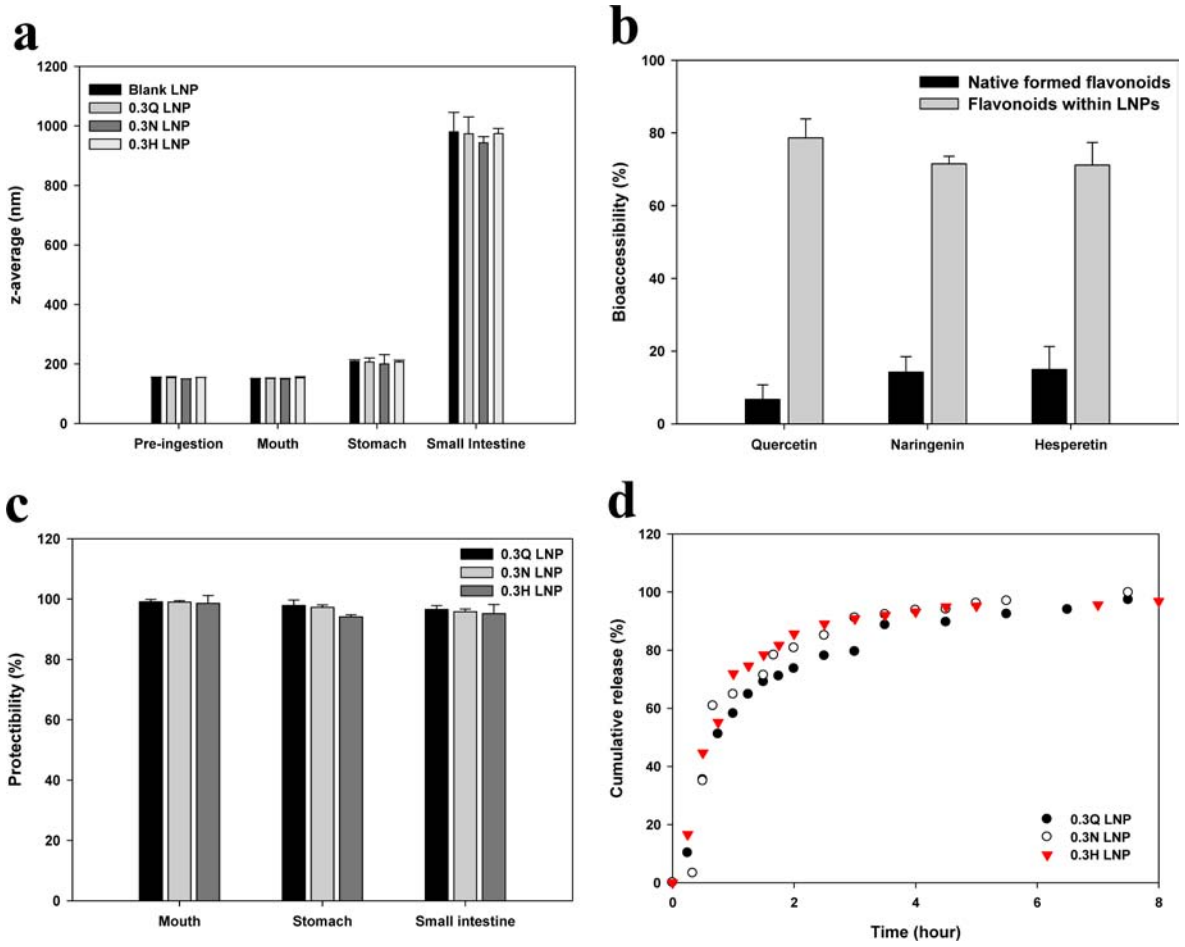

Figure 2. (a) Particle size (*z* average) changes in blank and lipid nanoparticles (LNPs) loaded with 0.3 wt % quercetin (0.3Q), 0.3 wt % naringenin (0.3N), and 0.3 wt % hesperetin (0.3H) after simulated in vitro digestion tests (preingestion, mouth, stomach, and small intestine). (b) Bioaccessibility (%) of Q, N, and H contents in the digested micellar fraction after simulated digestion was completed. (c) Protectibility (%) of flavonoid-loaded LNPs for flavonoids after incubation in an enzyme-free simulated digestion medium. (d) In vitro cumulative release profiles of flavonoid molecules from the lipid matrix in the enzyme-free simulated digestion medium using a dialysis membrane under sink conditions (50% v/v ethanol).

Characteristics of Lipid Nanoparticles. As shown in the previous section, SQ in the lipid phase produced the most stable LNPs, and utilizing the combination of T20 and SL increased the stability. Thus, SQ and SL contents in blank LNPs may be the main factors determining colloidal stability. Consequently, the optimum SQ and SL contents (SQ content, 30 wt %; SL content, 67.72 wt %) for preparing blank LNPs were determined in terms of the stability using RSM (Supporting Information), and the formula was applied also to preparation of the flavonoid-loaded LNPs. Their physicochemical characteristics are shown in Table 2.

All LNP systems had similar yields and PDI values. Moreover, no changes in the particle size (144.9−156.2 nm) or the ZP (−45.1 to −40.5 mV) values were observed, regardless of the concentration and type of flavonoid. In other words, the flavonoid molecules in the LNP did not affect the physicochemical characteristics (yield, particle size, PDI, and ZP). Therefore, an LNP system encapsulating flavonoids at 0.1−0.5 wt % of the lipid phase would have colloidal stability similar to that of the blank system optimized.

Flavonoids are generally water insoluble, and the octanol/water distribution coefficients of quercetin, naringenin, and hesperetin at pH 7.0 (log *P*) were 2.74, 2.30, and 2.59, respectively.[27] Therefore, quercetin, naringenin, and hesperetin in a hydrophobic solvent including oil are more soluble than the flavonoids in water. Even though low oil content (5 wt %) could induce partitioning flavonoids from the oil to the water phase during LNP preparation, flavonoid molecules may have a low concentration in the water phase due to a low concentration of flavonoids in the oil phase (0.1−0.5 wt %).[28] Furthermore, after the preparation, the solid lipid matrix in LNPs could block the migration of flavonoids to the water.[29] Thus, a high flavonoid EE was expected for all LNPs, but it was not detected (Table 2). The EE value was the highest at the 0.3 wt % flavonoid concentration, regardless of the flavonoid type. Hence, the LNPs with a 0.3 wt % flavonoid concentration were chosen for the in vitro digestion assay in terms of their high EE values.

In Vitro Digestion of Lipid Nanoparticles. The purpose of encapsulating flavonoids in nanosized LNPs is to increase their bioaccessibility.[21] Thus, the LNPs incorporating flavonoids must not degrade or aggregate until arrival in the small intestine. The loss of emulsifiers on the particle surface could induce aggregation,[30] or the colloidal particles could aggregate due to the high salt or low pH conditions due to the electrostatic attraction.[22] Fortunately, the initial particle size values of our optimized blank LNPs and all flavonoid-loaded LNPs were maintained under the high-salt conditions of the in

DOI: 10.1021/acs.jafc.5b01495
J. Agric. Food Chem. 2015, 63, 5266−5272

vitro mouth (Figure 2a), indicating nonaggregation of the LNPs due to salts and nondegradation due to α-amylase. Phospholipids consisting of the SL covering the LNPs have a positive charge under basic conditions, whereas the molecules have a negative charge under acidic conditions.[31] Thus, the SL molecules on the LNP surface aggregated the LNPs due to interactions between the phospholipids and the divalent cations in gastric juice. However, despite the low-pH conditions of in vitro gastric juice; i.e., pH 3, the particle size of all LNPs after the 2 h incubation was similar to the initial size (Figure 2a). This result may have been due to the action of T20 as a costabilizer. This nonionic surfactant can sterically stabilize the particles under low-pH conditions,[32] and the emulsion system stabilized with T20 showed good stability under simulated gastric conditions.[16] After 2 h of digestion in the small intestine juice, all particle size values increased ~5-fold over those preingestion due to degradation and aggregation of the particles (Figure 2a). The emulsifiers (T20 and SL) coating the surface were hydrolyzed by lipase, resulting in aggregation of the particles or displacement of the emulsifiers by bile salts, which exposed the LNPs to lipolysis by digestive enzymes.[16] After enzymatic hydrolysis, lipid degradation products such as monoglycerides and fatty acids form mixed micelles with the bile salts, phospholipids in SL, and the degraded T20 fragments. As a result, the particle size of the mixed micelles increased ~5-fold over that preingestion. Thus, these optimum LNP-loaded flavonoids were not degraded in the mouth or stomach and were digested in the small intestine.

Flavonoids have many health benefits but have limited bioavailability due to low permeability across the apical surface of intestinal epithelial cells.[33] We adopted a lipid-based delivery system (LNPs) to overcome this problem. As mentioned previously, the LNP system is degraded in the intestine by bile salts and digestive enzymes, which results in formation of mixed micelles. Flavonoids incorporated into LNPs would solubilize well in these micelles, whereas a native flavonoid would not be easily taken up by intestinal epithelial cells. The micelles amassed at the epithelial surface are absorbed by enterocytes,[16] which would increase the quantity of bioaccessible and bioavailable flavonoids. In this regard, the experimental data could endorse the previous discussion (Figure 2b). The flavonoid bioaccessibilities (%) of the fabricated LNP samples were greater than that of the native flavonoid, regardless of the type (quercetin, ~12-fold; naringenin, ~5-fold; hesperetin, ~5-fold). The high bioaccessibility of the quercetin-loaded LNPs may be due to the considerable hydrophobicity (log P = 2.74).[27] In any case, all LNP systems prepared successfully increased flavonoid bioaccessibility. These results were in agreement with previously reported research in cases of curcumin and genistein.[16]

The antioxidant activity of flavonoids is sensitive to pH[34] and salt,[35] which could decrease the therapeutic benefit due to the dramatic changes in pH and ion concentrations encountered during oral digestion. The LNPs were incubated with in vitro media without enzymes during digestion tests (mouth, stomach, and small intestine) to evaluate the protectibility of flavonoid-loaded LNPs. During the serial digestion test, the protectibility values of quercetin-, naringenin-, and hesperetin-loaded LNPs decreased to 97, 96, and 95%, respectively (Figure 2c), which meant successful protection of the flavonoids by the LNP system against harsh conditions such as low pH and high concentration of salts. In vitro degradation of other bioactive materials (curcumin and genistein) has also been reported at similar levels.[16] Therefore, our LNP system protected the flavonoids from pH and salt changes during digestion, and the protected flavonoids could maintain their antioxidant activity.

The in vitro flavonoid release test from LNPs was conducted in a medium comprising saliva and gastric, duodenal, and bile juices to mimic the small intestine. The reason for using a medium without digestive enzymes was to separate LNP degradation from the flavonoid release effect. Because of the low water solubility of flavonoids, 50% (v/v) ethanol was added to provide a sink condition in the enzyme-free mixture medium. Almost 100% of the flavonoids within the LNPs were released from the matrix into the medium during the 8 h release test, regardless of type (Figure 2d). The quercetin-, naringenin-, and hesperetin-loaded LNPs released ~74% of the quercetin, 81% of the naringenin, and 86% of the hesperetin into the medium, respectively, 2 h (small intestine residence time) after beginning the test. Although the condition was accelerated by 50% ethanol, these values were larger in comparison with those reported in other studies.[16,36] Lipid crystallization was initiated from the LNP core during cooling while the LNPs were prepared, and the core lipid crystals may have pushed flavonoids to the outer shell of the LNP, resulting in a flavonoid-enriched shell and rapid release of the flavonoids.[37] Nevertheless, this burst release did not affect flavonoid solubility in the mixed micelle, bioaccessibility (%), that formed after degradation by digestive enzymes (Figure 2b). Consequently, our LNP system optimized for colloidal stability successfully enhanced the bioaccessibility of quercetin, naringenin, and hesperetin.

The flavonoid-loaded LNP system, which was optimized by controlling the SQ and SL contents, protected the encapsulated flavonoid molecules against the harsh conditions of the in vitro digestion test until arrival in the small intestine. Moreover, flavonoids incorporated in LNPs were solubilized well into micelles mixed with the LNP digesta (fatty acids, monoglycerides, etc.), bile salts, and phospholipids at the end of the simulated digestion. Consequently, our LNP system using edible materials successfully protected flavonoids and improved bioaccessibility of flavonoids. In conclusion, this work may serve as a basis for further studies to develop an oral delivery system for nonbioaccessible molecules, such as flavonoids, for functional foods.

■ ASSOCIATED CONTENT

Supporting Information

Results of optimization of the blank lipid nanoparticle formula using response surface methodology (Tables S1−S4 and Figure S1). The Supporting Information is available free of charge on the ACS Publications website at DOI: 10.1021/acs.jafc.5b01495.

■ AUTHOR INFORMATION

Corresponding Author

*Y.J.C.: tel, +82 2 880 4851; fax, +82 2 873 5095; e-mail, choiyj@snu.ac.kr.

Author Contributions

[$]These authors contributed equally to this work.

Notes

The authors declare no competing financial interest.

DOI: 10.1021/acs.jafc.5b01495
J. Agric. Food Chem. 2015, 63, 5266−5272

■ ACKNOWLEDGMENTS

We thank Professor Pahn-Shick Chang at Seoul National University (Seoul, Korea) for his help in the explanation and discussion of lipid nanoparticle system.

■ REFERENCES

(1) Erlund, I. Review of the flavonoids quercetin, hesperetin, and naringenin. Dietary sources, bioactivities, bioavailability, and epidemiology. *Nutr. Res. (N. Y., NY, U. S.)* **2004**, *24*, 851−874.

(2) Hayek, T.; Fuhrman, B.; Vaya, J.; Rosenblat, M.; Belinky, P.; Coleman, R.; Elis, A.; Aviram, M. Reduced progression of atherosclerosis in apolipoprotein E−deficient mice following consumption of red wine, or its polyphenols quercetin or catechin, is associated with reduced susceptibility of LDL to oxidation and aggregation. *Arterioscler., Thromb., Vasc. Biol.* **1997**, *17*, 2744−2752.

(3) Deschner, E. E.; Ruperto, J.; Wong, G.; Newmark, H. L. Quercetin and rutin as inhibitors of azoxymethanol-induced colonic neoplasia. *Carcinogenesis* **1991**, *12*, 1193−1196.

(4) Ferry, D. R.; Smith, A.; Malkhandi, J.; Fyfe, D. W.; Anderson, D.; Baker, J.; Kerr, D. J. Phase I clinical trial of the flavonoid quercetin: pharmacokinetics and evidence for in vivo tyrosine kinase inhibition. *Clin. Cancer Res.* **1996**, *2*, 659−668.

(5) Pignatelli, P.; Pulcinelli, F. M.; Celestini, A.; Lenti, L.; Ghiselli, A.; Gazzaniga, P. P.; Violi, F. The flavonoids quercetin and catechin synergistically inhibit platelet function by antagonizing the intracellular production of hydrogen peroxide. *Am. J. Clin. Nutr.* **2000**, *72*, 1150−1155.

(6) Pérez-Vizcaíno, F.; Ibarra, M.; Cogolludo, A. L.; Duarte, J.; Zaragozá-Arnáez, F.; Moreno, L.; López-López, G.; Tamargo, J. Endothelium-independent vasodilator effects of the flavonoid quercetin and its methylated metabolites in rat conductance and resistance arteries. *J. Pharmacol. Exp. Ther.* **2002**, *302*, 66−72.

(7) Justesen, U.; Knuthsen, P.; Leth, T. Quantitative analysis of flavonols, flavones, and flavanones in fruits, vegetables and beverages by high-performance liquid chromatography with photo-diode array and mass spectrometric detection. *J. Chromatogr. A* **1998**, *799*, 101−110.

(8) Miyake, Y.; Yamamoto, K.; Tsujihara, N.; Osawa, T. Protective effects of lemon flavonoids on oxidative stress in diabetic rats. *Lipids* **1998**, *33*, 689−695.

(9) Manthey, J. A.; Guthrie, N.; Grohmann, K. Biological properties of citrus flavonoids pertaining to cancer and inflammation. *Curr. Med. Chem.* **2001**, *8*, 135−153.

(10) Kurowska, E. M.; Spence, J. D.; Jordan, J.; Wetmore, S.; Freeman, D. J.; Piché, L. A.; Serratore, P. HDL-cholesterol-raising effect of orange juice in subjects with hypercholesterolemia. *Am. J. Clin. Nutr.* **2000**, *72*, 1095−1100.

(11) Kuiper, G. G. J. M.; Lemmen, J. G.; Carlsson, B. O.; Corton, J. C.; Safe, S. H.; van der Saag, P. T.; van der Burg, B.; Gustafsson, J. Interaction of estrogenic chemicals and phytoestrogens with estrogen receptor β. *Endocrinology* **1998**, *139*, 4252−4263.

(12) Erlund, I.; Silaste, M. L.; Alfthan, G.; Rantala, M.; Kesäniemi, Y. A.; Aro, A. Plasma concentrations of the flavonoids hesperetin, naringenin and quercetin in human subjects following their habitual diets, and diets high or low in fruit and vegetables. *Eur. J. Clin. Nutr.* **2002**, *56*, 891−898.

(13) Erlund, I.; Meririnne, E.; Alfthan, G.; Aro, A. Plasma kinetics and urinary excretion of the flavanones naringenin and hesperetin in humans after ingestion of orange juice and grapefruit juice. *J. Nutr.* **2001**, *131*, 235−241.

(14) Luo, Y.; Chen, D.; Ren, L.; Zhao, X.; Qin, J. Solid lipid nanoparticles for enhancing vinpocetine's oral bioavailability. *J. Controlled Release* **2006**, *114*, 53−59.

(15) Pandita, D.; Kumar, S.; Poonia, N.; Lather, V. Solid lipid nanoparticles enhance oral bioavailability of resveratrol, a natural polyphenol. *Food Res. Int.* **2014**, *62*, 1165−1174.

(16) Aditya, N. P.; Shim, M.; Lee, I.; Lee, Y.; Im, M.; Ko, S. Curcumin and genistein coloaded nanostructured lipid carriers: in vitro digestion and antiprostate cancer activity. *J. Agric. Food Chem.* **2013**, *61*, 1878−1883.

(17) Ban, C.; Lim, S.; Chang, P.; Choi, Y. J. Enhancing the stability of lipid nanoparticle systems by sonication during the cooling step and controlling the liquid oil content. *J. Agric. Food Chem.* **2014**, *62*, 11557−11567.

(18) Boode, K.; Walstra, P. Partial coalescence in oil-in-water emulsions 1. Nature of the aggregation. *Colloids Surf., A* **1993**, *81*, 121−137.

(19) Vanapalli, S. A.; Coupland, J. N. Emulsions under shear—the formation and properties of partially coalesced lipid structures. *Food Hydrocolloids* **2001**, *15*, 507−512.

(20) Helgason, T.; Awad, T. S.; Kristbergsson, K.; McClements, D. J.; Weiss, J. Influence of polymorphic transformations on gelation of tripalmitin solid lipid nanoparticle suspensions. *J. Am. Oil Chem. Soc.* **2008**, *85*, 501−511.

(21) McClements, D. J.; Xiao, H. Potential biological fate of ingested nanoemulsions: influence of particle characteristics. *Food Funct.* **2012**, *3*, 202−220.

(22) Li, Z.; Jiang, H.; Xu, C.; Gu, L. A review: Using nanoparticles to enhance absorption and bioavailability of phenolic phytochemicals. *Food Hydrocolloids* **2015**, *43*, 153−164.

(23) van Aken, G. A. Modelling texture perception by soft epithelial surfaces. *Soft Matter* **2010**, *6*, 826−834.

(24) Kong, F.; Singh, R. Disintegration of solid foods in human stomach. *J. Food Sci.* **2008**, *73*, R67−R80.

(25) Hur, S. J.; Joo, S. T.; Lim, B. O.; Decker, E. A.; McClements, J. D. Impact of salt and lipid type on in vitro digestion of emulsified lipids. *Food Chem.* **2011**, *126*, 1559−1564.

(26) Han, F.; Li, S.; Yin, R.; Liu, H.; Xu, L. Effect of surfactants on the formation and characterization of a new type of colloidal drug delivery system: nanostructured lipid carriers. *Colloids Surf., A* **2008**, *315*, 210−216.

(27) *Flavonoids in Health and Disease*; Rice-Evans, C. A., Packer, L., Eds.; Marcel Dekker: New York, 2010.

(28) McClements, D. J. Crystals and crystallization in oil-in-water emulsions: Implications for emulsion-based delivery systems. *Adv. Colloid Interface Sci.* **2012**, *174*, 1−30.

(29) Müller, R. H.; Petersen, R. D.; Hommoss, A.; Pardeike, J. Nanostructured lipid carriers (NLC) in cosmetic dermal products. *Adv. Drug Delivery Rev.* **2007**, *59*, 522−530.

(30) Müller, R. H.; Rühl, D.; Runge, S. A. Biodegradation of solid lipid nanoparticles as a function of lipase incubation time. *Int. J. Pharm.* **1996**, *144*, 115−121.

(31) Mosqueira, V. C. F.; Legrand, P.; Pinto-Alphandary, H.; Puisieux, F.; Barratt, G. Poly (D, L-lactide) nanocapsules prepared by a solvent displacement process: Influence of the composition on physicochemical and structural properties. *J. Pharm. Sci.* **2000**, *89*, 614−626.

(32) Van Aken, G. A.; Bomhof, E.; Zoet, F. D.; Verbeek, M.; Oosterveld, A. Differences in in vitro gastric behaviour between homogenized milk and emulsions stabilised by Tween 80, whey protein, or whey protein and caseinate. *Food Hydrocolloids* **2011**, *25*, 781−788.

(33) Tian, X.; Yang, X.; Yang, X.; Wang, K. Studies of intestinal permeability of 36 flavonoids using Caco-2 cell monolayer model. *Int. J. Pharm.* **2009**, *367*, 58−64.

(34) Jovanovic, S. V.; Steenken, S.; Tosic, M.; Marjanovic, B.; Simic, M. G. Flavonoids as antioxidants. *J. Am. Chem. Soc.* **1994**, *116*, 4846−4851.

(35) Arora, A.; Nair, M. G.; Strasburg, G. M. Structure−activity relationships for antioxidant activities of a series of flavonoids in a liposomal system. *Free Radical Biol. Med.* **1998**, *24*, 1355−1363.

(36) Li, H.; Zhao, X.; Ma, Y.; Zhai, G.; Li, L.; Lou, H. Enhancement of gastrointestinal absorption of quercetin by solid lipid nanoparticles. *J. Controlled Release* **2009**, *133*, 238−244.

(37) Müller, R. H.; Radtke, M.; Wissing, S. A. Nanostructured lipid matrices for improved microencapsulation of drugs. *Int. J. Pharm.* **2002**, *242*, 121−128.

DOI: 10.1021/acs.jafc.5b01495
J. Agric. Food Chem. 2015, 63, 5266−5272

JOURNAL OF AGRICULTURAL AND FOOD CHEMISTRY

Article

pubs.acs.org/JAFC

4-Hydroxy-2-nonenal (4-HNE) and Its Lipation Product 2-Pentylpyrrole Lysine (2-PPL) in Peanuts

Martin Globisch, Diana Kaden, and Thomas Henle*

Institute of Food Chemistry, Technische Universität Dresden, D-01062 Dresden, Germany

Supporting Information

ABSTRACT: After synthesis of a deuterated 4-hydroxy-2-nonenal (4-HNE) standard, the formation of 4-HNE during heating of peanut oil and whole peanuts, respectively, was measured by GC-MS. Whereas a significant increase in 4-HNE levels was observed for peanut oil, the amount of 4-HNE decreased when whole peanuts were roasted due to lipation reactions with amino acid side chains of the proteins. The ε-amino group of lysine was identified as the favored reaction partner of 4-HNE. After heating N^{α}-acetyl-L-lysine and 4-HNE, a Schiff base, a novel pyridinium derivative, a 2-pentylpyrrol derivative and, following reduction and hydrolysis, a reduced, cyclized Michael adduct were identified. 2-Amino-6-(2-pentyl-1*H*-pyrrol-1-yl)hexanoic acid (2-PPL) was synthesized and quantitated in peanut proteins, which had been incubated with various amounts of 4-HNE by HPLC-ESI-MS/MS after enzymatic hydrolysis. At low 4-HNE concentrations the modification of lysine could be entirely explained by the formation of 2-PPL. Additionally, 2-PPL was quantified for the first time in peanut samples, and an increase depending on the roasting time was observed. 2-PPL represents a suitable marker to evaluate the extent of food protein lipation by 4-HNE.

KEYWORDS: *peanut, peanut oil, lipid peroxidation, lipation, carbonyl protein reaction, 4-hydroxynonenal, 4-hydroxynon-2-enal, 4-hydroxy-2-nonenal, 4-HNE, HNE, 2-pentylpyrrole lysine, 2-PPL, 2-pentylpyrrole*

INTRODUCTION

4-Hydroxynon-2-enal (4-HNE) is a well-known secondary product of lipid peroxidation, which is mainly formed from ω-6 polyunsaturated fatty acids.[1] The formation of secondary lipid peroxidation products during roasting of peanuts, which contain 14% linoleic acid,[2] was shown,[3] and the presence of 4-HNE in commercially available peanuts was recently published, ranging from 0.8 to 3.8 μmol/kg peanut.[4] As a result of roasting peanuts, 30−40% of peptide-bound lysine was modified, but only 10% of this lysine modification could be explained by the formation of Maillard reaction products such as N^{ε}-fructosyllysine, pyrraline, and N^{ε}-carboxymethyllysine.[5] The possibility for a reaction between secondary lipid peroxidation products and amino acid side chains in peanut proteins was recently shown for 2-heptenal, resulting in *cis*- and *trans*-BPP-lysine derivatives. For these protein−carbonyl reactions, the term "lipation" was suggested.[6] Because of its ability to react easily with nucleophilic compounds, the formation of lipation products between 4-HNE and amino acid side chains of peanut proteins during roasting of peanuts is highly likely. Due to the three functional groups of 4-HNE, various reactions are possible. They include the formation of Michael addition products, which are able to undergo secondary reactions involving the carbonyl and the hydroxyl groups,[7] resulting, for example, in stable, cyclic hemiacetals.[8] After the formation of Schiff bases with primary amines, further reactions can lead to the formation of 2-pentylpyrrole residues,[9] which was shown for bovine serum albumin incubated with 4-HNE under physiological conditions.[10] Using ^{13}C NMR spectroscopy, 20% of the protein-bound 4-HNE was found as 2-pentylpyrrole,[10] which was classified as an advanced lipoxidation endproduct (ALE).[8,11] The incubation of RNase A with 4-HNE in sodium phosphate buffer (pH 7.2) at room temperature for 5 h resulted in the formation of a 2-hydroxy-2-pentyl-1,2-dihydropyrrol-3-one iminium fluorophore, accounting for protein cross-linking.[12] The yield of the fluorophore was estimated to account for 1.8% of the lysine residues on the protein. Another possible cross-linking mechanism would be the simultaneous formation of a Michael adduct and a Schiff base at one molecule of 4-HNE.[12,13] Using immunochemical methods, 4-HNE-pyrrole adducts were found to be significantly elevated in the plasma of patients with end-stage renal disease as well as in the plasma of atherosclerotic patients compared to that of healthy volunteers.[14] Furthermore, 4-HNE−pyrrole adducts were detected in collagen fibers of an advanced atherosclerotic lesion. In another study, 4-HNE−lysine adducts in intact apo B and apo B fragments of atherosclerotic lesions were observed by Western blot analysis.[15] Due to the fact that 4-HNE-pyrroles are stable advanced lipoxidation endproducts,[8,11] their quantitative levels in human blood may be an indelible marker of 4-HNE generation in vivo.[14] With regard to 4-HNE−protein adducts in food, only a few studies are available. Using an indirect ELISA, 4-HNE−protein adducts were detected in protein fractions of stored beef.[16] However, the specific proteins and 4-HNE adducts that were detected by the antibodies were not known. In protein extracts prepared from defatted meals of raw and roasted peanuts, 4-HNE−protein adducts were detected by direct ELISA.[17,18] In these studies, no significant differences in 4-HNE adduct levels

Received: March 24, 2015
Revised: May 1, 2015
Accepted: May 6, 2015
Published: May 6, 2015

ACS Publications © 2015 American Chemical Society

DOI: 10.1021/acs.jafc.5b01502
J. Agric. Food Chem. 2015, 63, 5273−5281

between raw and roasted peanuts were detected by observing the UV absorbance. Additionally, the levels of N^{ε}-carboxymethyllysine (CML) did not change either. This is in contrast to a study in which CML was directly quantified in raw and roasted peanuts by GC-MS,[5] clearly showing that CML was not detectable in native peanuts, whereas CML levels increased depending on the roasting conditions.

Up to now, direct and unambiguous quantification of individual, chemically characterized 4-HNE-derived lipation products has not been performed. The aim of this study, therefore, was to develop an HPLC-ESI-MS/MS method for the direct quantification of 4-HNE–lysine adducts in food proteins. For quantification of free 4-HNE in native and heated peanut oil and native and roasted peanuts, a GC-MS (EI) method was developed using synthesized deuterated 4-HNE as internal standard. To identify possible lipation products between 4-HNE and the ε-amino group of lysine, N^{α}-acetyl-L-lysine was incubated with 4-HNE and reaction products were identified by HPLC-ESI-MS/MS. After synthesis of 2-pentylpyrrole lysine, this lipation product was directly quantified in peanuts by HPLC-ESI-MS/MS for the first time.

MATERIALS AND METHODS

Materials. Pepsin (EC 3.4.23.1), Pronase E (EC 3.4.24.4), methanol, γ-nonalactone, ammonium chloride, sodium borohydride, and hydrochloric acid (37%) were obtained from Merck (Darmstadt, Germany). Leucine aminopeptidase (EC 3.4.11.1), prolidase (EC 3.4.13.9), dialysis tubing cellulose membrane (MWCO 14 kDa), tetradeuteromethanol, deuterochloroform, aluminum hydride, 1-octen-3-ol, Hoveyda–Grubbs catalyst second generation, acrolein dimethylacetal, amberlyst 15 (hydrogen form), fumaraldehyde bis(dimethyl acetal), petroleum ether (boiling point 40–60 °C), diethyl ether, *o*-(2,3,4,5,6-pentafluorobenzyl)hydroxylamine hydrochloride, bis-(trimethylsilyl)trifluoroacetamide, triethylamine, pyridinium chlorochromate, and magnesium chips were obtained from Sigma-Aldrich (Taufkirchen, Germany). N^{α}-Acetyl-L-lysine and *N*-benzoylglycyl-L-phenylalanine were obtained from Bachem (Bubendorf, Switzerland). Dichloromethane, hexane, ethyl acetate (pure), and heptafluorobutyric acid were obtained from VWR (Darmstadt, Germany). Acetonitrile, chloroform, tetrahydrofuran, and sulfuric acid were obtained from Fisher Scientific (Schwerte, Germany). Monosodium phosphate, disodium phosphate, sodium sulfate, sodium carbonate, sodium hydroxide, ascorbic acid, sodium tetraborate, and magnesium sulfate were obtained from Grüssing (Filsum, Germany). Tris-(hydroxymethyl)aminomethane was obtained from Serva (Heidelberg, Germany). Thymol and acetone were obtained from Carl Roth (Karlsruhe, Germany). Pentane was from Th. Geyer (Renningen, Germany). Molybdatophosphoric acid was obtained from ChemPUR (Karlsruhe, Germany). 1,1-Dideuterio-1-bromopentane was from Campro Scientific (Berlin, Germany). All chemicals were of the highest purity, except otherwise indicated. For all experiments, ultrapure water was used, prepared by an ELGA LabWater Purelab Plus water system (Celle, Germany). For HPLC-ESI-MS/MS measurements, double-distilled water, prepared in the presence of potassium permanganate, was used. Refined peanut oil and roasted commercial peanuts were obtained from a local market. Raw peanuts were obtained from Veggie's Delight (Düsseldorf, Germany).

Preparation of Samples. Raw peanuts with shell were roasted in a ULM 500 laboratory oven (Memmert, Schwabach, Germany) for 20 and 40 min at 170 °C, respectively. Afterward, the samples were shelled, skinned, and crushed, using a kitchen machine. Commercially available, roasted peanuts were crushed analogously. Protein contents were analyzed by the Kjeldahl method using the factor 5.3 for oilseeds.[19] Fifty grams of refined peanut oil was heated in 250 mL round-bottom flasks for 20 and 40 min at 170 °C, respectively.

Nuclear Magnetic Resonance Spectroscopy (NMR). For nonane-1,4-diol (1,4-ND), 4-oxononanal (4-ON), and 2-pentylpyrrole lysine (2-PPL), ^{1}H NMR spectra were recorded on a Bruker Avance 600 instrument (Rheinstetten, Germany) at 600.16 MHz. 4-Hydroxynonenal dimethyl acetal (4-HNE-DMA) was measured on a Bruker DRX 500 instrument at 500.13 MHz. ^{13}C NMR spectra were recorded on a Bruker DRX 500 instrument at 150.9 MHz, respectively. For fumaraldehyde dimethyl acetal and (*E*)-5,5-dideuterio-1,1-dimethoxynon-2-en-4-ol dimethyl acetal (4-HNE-DMA-d_2), ^{1}H NMR and ^{13}C NMR spectra were recorded on a Bruker Avance 400 instrument (Rheinstetten, Germany) at 400.13 MHz and at 100.61 MHz, respectively. For 4-HNE-DMA, 1,4-ND, 4-ON, fumaraldehyde dimethyl acetal, and 4-HNE-DMA-d_2, deuterochloroform ($CDCl_3$) and for 2-PPL tetradeuteromethanol (MeOH-d_4) were used as solvent. All chemical shifts are given in parts per million (ppm) relative to the solvent signal serving as internal standard. The following 2D-NMR experiments were performed additionally for 4-HNE-DMA, 4-HNE-DMA-d_2 4-ON, 1,4-ND, and 2-PPL: correlation spectroscopy (COSY), nuclear Overhauser enhancement spectroscopy (NOESY), heteronuclear single-quantum coherence (HSQC), and heteronuclear multiple-bond correlation (HMBC).

Elemental Analysis. Elemental analysis was performed using an EuroEA3000 (Eurovector, Milan, Italy) to quantitate the product content in the 2-PPL standard. Therefore, the analyzed percentage of nitrogen was compared to the calculated nitrogen percentage. The purity of 2-PPL is expressed in percent by weight.

Acid and Enzymatic Hydrolysis. For acid hydrolysis, a ratio of 8 mg of protein per 1.0 mL of 6 M hydrochloric acid was used. Samples were hydrolyzed under nitrogen for 23 h at 110 °C. For enzymatic hydrolysis the method published elsewhere was used.[6,20]

Amino Acid Analysis. For measuring of the lysine modification rate and comparison of the release of amino acids after acid and enzymatic hydrolysis, amino acid analyses were performed using a SYKAM S4300 amino acid analyzer (Fürstenfeldbruck, Germany). Amino acids were separated by cationic ion exchange chromatography, derivatized by ninhydrin, and detected using a wavelength of 570 nm.[21] Valine was taken as internal standard, and amino acids were expressed as valine equivalents.

Synthesis of (*E*)-1,1-Dimethoxynon-2-en-4-ol (4-HNE-DMA). For 4-HNE-DMA synthesis, a method published elsewhere was adopted.[22] Therefore, 25 mL of nitrogen-purged dichloromethane, 496 μL of 1-octen-3-ol, 1164 μL of acrolein dimethyl acetal, and 25.9 mg of a Hoveyda–Grubbs catalyst second generation were given in a 50 mL three-neck flask and stirred for 5 h at room temperature under nitrogen. After the addition of another 25.9 mg of catalyst, stirring was continued for 20 h at room temperature under nitrogen. After evaporation of dichloromethane, 4-HNE-DMA was purified by silica gel chromatography using diethyl ether/pentane (50:50, v/v) and 0.1% triethylamine as eluent. Fractions containing 4-HNE-DMA were identified by silica gel thin layer chromatography using the same mobile phase. Detection was realized by spraying a solution of 5% molybdatophosphoric acid in ethanol with 10% sulfuric acid and heating for 5 min in a Memmert laboratory-type drying cabinet (Schwabach, Germany) at 105 °C. Relevant fractions were combined, the solvent was evaporated in vacuo at 40 °C, and the product was lyophilized. ^{1}H NMR (500 MHz, $CDCl_3$) δ 0.86 (t, 3H, J = 7.9 Hz, H-9), 1.23–1.33 (m, 6H, H-6, H-7, H-8), 1.50 (m, 2H, H-5), 3.30 (s, 6H, H-11, H-12), 3.45 (s, 1H, H-10), 4.13 (q, 1H, J = 6.3 Hz, H-4), 4.77 (d, 1H, J = 4.7 Hz, H-1), 5.63 (ddd, 1H, J = 1.3 Hz, J = 4.7 Hz, J = 15.8 Hz, H-2), 5.86 (ddd, 1H, J = 1.3 Hz, J = 6.0 Hz, J = 15.8 Hz, H-3). The compound was found to be pure by observance of a single spot on TLC. Yield = 346 mg (molar yield = 53.7%).

Synthesis of (*E*)-5,5-Dideuterio-1,1-dimethoxynon-2-en-4-ol Dimethyl Acetal (4-HNE-DMA-d_2). The precursors fumaraldehyde dimethyl acetal and deuterated pentylmagnesium bromide were synthesized according to a method published elsewhere.[23] Therefore, 45.9 mL of acetone was given in a 100 mL three-neck flask, and 0.4605 g of amberlyst-15 catalyst and 0.339 mL of water were added. After the addition of 2.084 mL of fumaraldehyde bis(dimethyl acetal), the reaction was continued for 6 min at room temperature with stirring. After filtration through a bed of anhydrous sodium carbonate, the solvent was evaporated in vacuo at 40 °C to yield fumaraldehyde

DOI: 10.1021/acs.jafc.5b01502
J. Agric. Food Chem. 2015, 63, 5273–5281

dimethyl acetal. ^{1}H NMR (400 MHz, $CDCl_3$) δ 3.38 (s, 6H, H-5, H-6), 5.07 (dd, 1H, J = 1.2 Hz, J = 3.9 Hz, H-4), 6.38 (ddd, 1H, J = 1.2 Hz, J = 7.8 Hz, J = 15.9 Hz, H-3), 6.64 (dd, 1H, J = 3.9 Hz, J = 15.9 Hz, H-2), 9.64 (d, 1H, J = 7.8 Hz, H-1). Purity = 93.1% (GC-MS). Yield = 1.2105 g (molar yield = 76.3%). Diethyl ether (0.8 mL) and 0.103 g of magnesium chips were given in a 25 mL three-neck flask. After the addition of 50 μL of 1,1-dideuterio-1-bromopentane, the reaction mixture was heated at 45 °C under reflux with stirring. The emerging white coloration indicated the starting reaction of the formation of the Grignard reagent deuterated pentylmagnesium bromide. Another 5.52 mL of diethyl ether were added followed by 350 μL of 1,1-dideuterio-1-bromopentane in 1.11 mL of diethyl ether, and the reaction mixture was heated under mild reflux at 45 °C for 30 min while the reaction mixture turned dark. After the reaction mixture had been cooled to 0 °C in an ice bath, 280 μL of fumaraldehyde dimethyl acetal in 1.84 mL of diethyl ether were added, and the reaction mixture was stirred for 30 min at 0 °C. By adding 2.76 mL of a solution of saturated ammonium chloride, the reaction was quenched and then extracted four times with 15 mL of diethyl ether, respectively. After drying over anhydrous sodium sulfate, the solvent was removed in vacuo at 40 °C. Purification of 4-HNE-DMA-d_2 was realized as described for the undeuterated 4-HNE-DMA. ^{1}H NMR (400 MHz, $CDCl_3$) δ 0.87 (t, 3H, J = 6.4 Hz, H-9), 1.29 (m, 6 H, H-6, H-7, H-8), 3.31 (s, 6H, H-11, H-12), 3.46 (s, 1H, H-10), 4.13 (d, 1H, J = 6.3 Hz, H-4), 4.78 (d, 1H, J = 4.8 Hz, H-1), 5.64 (ddd, 1H, J = 0.9 Hz, J = 4.8 Hz, J = 15.7 Hz, H-2), 5.87 (ddd, 1H, J = 0.9 Hz, J = 6.0 Hz, J = 15.7 Hz, H-3). The compound was found to be pure by observance of a single spot on TLC. Yield = 154 mg (molar yield = 44.6%).

GC-MS (EI) Quantification of Free 4-HNE in Peanut Oil and Peanut Samples. The developed method is partially comparable to a recently published method.[4] The internal standard 4-HNE-d_2 was obtained by acid hydrolysis of 2 mg of 4-HNE-DMA-d_2 with 0.5 mL of 0.1 mol/L hydrochloric acid with stirring for 1 h in a 5 mL flask at room temperature. Following a 3-fold extraction with hexane (0.5 + 0.3 + 0.3 mL) to prohibit further release of free 4-HNE-d_2 if the reaction was not complete, the concentration was calculated on the basis of the molar extinction coefficient for 4-HNE in hexane,[1] ε = 14400 L mol^{-1} cm^{-1}. To 1.0 g of crushed, shelled, and skinned peanuts or peanut oil were added 20 μL of an internal standard solution containing 95 nmol of 4-HNE-d_2 and 10 mL of a solution of 0.1% ascorbic acid in water. The samples were homogenized using an ultraturrax at 11.200 rpm for 2 min, and the supernatant was collected after centrifugation at 10000g for 10 min at 4 °C. The extraction was repeated analogously, and the combined supernatants were extracted 3-fold with 10 mL of dichloromethane for 1 min, respectively. The organic phases were separated by centrifugation at 10000g for 2 min at 4 °C. After filtration (Whatman, 595 $^1/_2$) the dichloromethane was evaporated at 30 °C with nitrogen. The first derivatization step was realized by adding 200 μL of a o-(2,3,4,5,6-pentafluorobenzyl)-hydroxylamine hydrochloride (PFBHA-HCl) solution (20 mg/mL water) and heating in a water bath for 1 h at 40 °C. Hexane (1.3 mL) was added, and the samples were vortexed, followed by an addition of 100 μL of concentrated sulfuric acid[24] and vortexing again. After centrifugation at 2100g for 3 min at room temperature, the hexane phase was removed, dried over anhydrous sodium sulfate, filtered (0.45 μm), and evaporated at 30 °C under nitrogen. The second derivatization step was performed at room temperature for 3 h by adding 200 μL of N,O-bis(trimethylsilyl)trifluoroacetamide (BSTFA). An aliquot was used for GC-MS (EI) analysis using an Agilent 7890A system, consisting of a 7683 series injector with a sample tray and a 5975C MS detector working in EI mode, all from Agilent (Böblingen, Germany), and a ZB-5 Guardian capillary column (30.0 m plus 5.0 m guard column, inner diameter = 0.25 mm, 0.25 μm film thickness) from Phenomenex (Torrance, CA, USA). Helium was used as carrier gas with a constant flow of 1.0 mL/min. With the injector temperature set to 250 °C, 1 μL of sample was injected by using the pulsed splitless mode. The auxiliary temperature was set to 250 °C, and the ion source and quadrupole were set to 230 and 150 °C, respectively. The initial oven temperature was set to 100 °C and held for 4 min and then raised at 15 °C/min to 300 °C. The post run time was set to 3 min at 300 °C. The mass spectrometer was working in electron impact mode at 70 eV. The solvent delay time was set to 10 min. SIM parameters were as follows: for 4-HNE (syn and anti), quantifier ion m/z 242 and qualifier ion m/z 352; and for 4-HNE-d_2 (syn and anti), quantifier ion m/z 244 and qualifier ion m/z 352. The dwell time was set to 80 ms. Quantification was realized using authentic 4-HNE, being obtained from 4-HNE-DMA as previously described for 4-HNE-DMA-d_2, the addition of 95 nmol of internal standard 4-HNE-d_2, and an analogous derivatization procedure.

Incubation of N^α-Acetyl-L-lysine with 4-HNE. For identification of major amino acid side chain reaction products formed between 4-HNE and N^α-acetyl-L-lysine, 10 mM 4-HNE and 10 mM N^α-acetyl-L-lysine were heated for 4 h at 75 °C in 5 mL of methanol in a 10 mL round-bottom flask under reflux. 4-HNE was obtained by acid hydrolyses as described above, and its concentration in aqueous solution was determined using the molar extinction coefficient[1] ε = 13750 L mol^{-1} cm^{-1}. One milliliter of the reaction mixture was taken for direct HPLC-ESI-MS/MS analysis. For reduction, 1.0 mL of the reaction mixture was evaporated under nitrogen, and 3.0 mL of a 0.2 M sodium tetraborate solution (pH 9.5) and 2.0 mL of a 1.0 M sodium borohydride solution in 0.1 M sodium hydroxide were added. After reduction for 17 h at room temperature, 1.0 mL of 6 M hydrochloric acid and 5 mL of 12 M hydrochloric acid were added, and the samples were hydrolyzed for 23 h at 110 °C. Afterward, the hydrochloric acid was removed by using a waterjet pump at 40 °C. The residue was dissolved in 1.0 mL of methanol and analyzed by HPLC-ESI-MS/MS.

Incubation of Peanut Proteins with 4-HNE. Peanut proteins of raw peanuts were extracted as described elsewhere,[6,25] except for using non-defatted peanuts instead of defatted peanuts. Approximately 50 mg of peanut protein extract was dissolved in 25 mL of 0.1 M phosphate buffer (pH 7.4), and 4-HNE, obtained from 4-HNE-DMA, was added in the following molar ratios related to the sum of relevant reactive amino acids cysteine, histidine, lysine, and arginine:[6] 0.1:1, 0.2:1, 1:1, and 5:1. Additionally, a blank sample consisting of peanut proteins without 4-HNE was prepared. The incubation was carried out under nitrogen for 24 h at 37 °C with stirring, followed by a dialysis (14 kDa MWCO) against deionized water for 24 h at 6 °C. Afterward, the samples were lyophilized and protein contents were analyzed by the Kjeldahl method using the factor 5.3 for oilseeds.[19] For analysis of amino acid modification rates of cysteine, lysine, histidine, and arginine, the samples were hydrolyzed enzymatically. For analysis of 2-PPL, the samples were hydrolyzed enzymatically, freeze-dried, and redissolved in 400 μL of water and 100 μL of methanol. The 0.1:1 sample was diluted 100-fold using water/methanol (80:20, v/v), whereas the other samples were diluted 500-fold including 40 μL of internal standard N-benzoylglycyl-L-phenylalanine in methanol/water (50:50, v/v) with a final concentration of 3.06 pmol/mL sample. The blank sample was used without dilution. After filtration (0.45 μmol), samples were subjected to HPLC-ESI-MS/MS analysis. Quantification was realized using authentic 2-PPL and internal standard N-benzoylglycyl-L-phenylalanine with a final concentration of 3.06 pmol/mL in an enzymatic hydrolysate matrix calibration of the native peanut protein extract, prepared analogously to the samples.

Synthesis of 2-Amino-6-(2-pentyl-1*H*-pyrrol-1-yl)hexanoic Acid (2-PPL). Lithium aluminum hydride (2.6 g) was added to 150 mL of tetrahydrofuran in a 500 mL three-neck flask, and the solution was cooled by an ice bath. γ-Nonalactone (12.5 mL) in 50 mL of tetrahydrofuran was added while cooling continued. After the three-neck flask was allowed to warm to room temperature, the reaction mixture was heated for 3 h under reflux with stirring. After cooling in an ice bath, ice-cold water was added until the formation of hydrogen stopped. After filtration over magnesium sulfate and drying over magnesium sulfate overnight, the tetrahydrofuran was evaporated at 40 °C. ^{1}H NMR of nonane-1,4-diol (600 MHz, $CDCl_3$) δ 0.82 (t, 3H, J = 7.2 Hz, H-9), 1.23 (m, 4 H, H-7, H-8), 1.37 (m, 4H, H-3, H-6), 1.57 (m, 4H, H-2, H-5), 3.52 (m, 2H, H-1), 3.57 (m, 1H, H-4). Purity = 98.2% (GC-MS). Yield = 8.4473 g (molar yield = 67.5%). In a 500 mL three-neck flask 17.0 g of pyridinium chlorochromate was suspended in 100 mL of dichloromethane.[26] Nonane-1,4-diol (8.4473 g) in 50

DOI: 10.1021/acs.jafc.5b01502
J. Agric. Food Chem. 2015, 63, 5273−5281

mL of dichloromethane was added with stirring. The reaction mixture was kept for 2 h at room temperature, resulting in a dark coloration of the reaction mixture. Afterward, 150 mL of diethyl ether were added, and the reaction mixture was filtered over magnesium sulfate. The addition of diethyl ether followed by a filtration step was repeated until no precipitation occurred. After evaporation of the diethyl ether at 40 °C, 4-oxononanal was purified by silica gel chromatography using ethyl acetate/hexane (15:85, v/v) as eluent.[9] Fractions containing 4-oxononanal were detected by GC-MS (EI) and combined, and the solvent was evaporated at 40 °C. ^{1}H NMR of 4-oxononanal (600 MHz, $CDCl_3$) δ 0.85 (m, 6H, H-9), 1.26 (m, 9H, H-7, H-8), 1.55 (m, 3H, H-6), 2.43 (t, 2H, J = 7.5 Hz, H-5), 2.71 (m, 4H, H-2, H-3), 9.77 (s, 1H, H-1). Purity = 49.3% (GC-MS). Yield = 2.3225 g (molar yield = 13.9%). One gram of 4-oxononanal and 2.0 g of N^{α}-acetyl-L-lysine were dissolved in 25 mL of acetonitrile/water (1:1, v/v) in a 50 mL flask under nitrogen and reacted in a Paal–Knorr synthesis at room temperature for 72 h. Afterward, the solvent was evaporated at 40 °C. Hydrolysis of the acetyl group was realized by adding 250 mL of a 2 M sodium hydroxide solution and heating for 23 h under reflux. The solvent was evaporated at 60 °C, and the residue was extracted three times with 10 mL of chloroform, respectively, filtered over magnesium sulfate, and dried over magnesium sulfate overnight. The solvent was evaporated at 40 °C, and 2-PPL was purified using a semipreparative HPLC system. The system consisted of a Smartline solvent manager 5000, a Smartline pump 1000, and a Smartline UV detector 2500 (all from Knauer, Berlin, Germany). Twenty-five milligrams of the unpurified reaction mixture were dissolved in 1.0 mL of methanol and separated after filtration (0.45 μm) using an Eurospher 100-10 C18 column (250 × 16 mm; Knauer, Berlin, Germany) at 23 °C (room temperature), a flow rate of 4.0 mL/min, and a detection wavelength of 227 nm. A gradient was used with solvent A (water) and B (acetonitrile). The gradient program started with 10% solvent B for 2 min, increased to 95% B within 28 min, isocratic elution with 95% B for 10 min, decrease to 10% B within 2 min, followed by an isocratic elution at 10% B for 10 min. 2-PPL eluted between 21 and 23 min. Multiple separations were performed, relevant fractions were combined, and finally the solvent was evaporated at 40 °C prior to HPLC-ESI-MS/MS and one- and two-dimensional NMR analysis. ESI-MS (positive mode), $[M + H]^+$ m/z 267.3; ^{1}H NMR (600 MHz, MeOD) δ 0.99 (m, 6H, H-15), 1.44 (m, 6H, H-14, H-13), 1.51 (m, 5H, H-7), 1.68 (m, 2H, H-12), 1.80 (m, 2H, H-6), 1.98 (m, 2H, H-8a,b), 2.6 (t, 2H, J = 7.5 Hz, H-11), 3.56 (t, 1H, J = 6.0 Hz, H-9), 3.91 (t, 1H, J = 7.5 Hz, H-5), 5.8 (m, 1H, J = 3.0 Hz, H-2), 6.00 (t, 1H, J = 3.0 Hz, H-3), 6.64 (d, 1H, J = 3.0 Hz, H-4). 2-PPL eluted chromatographically pure by HPLC-ESI-MS analysis. Purity based on elemental analysis = 75.1%. Yield = 13.7 mg (molar yield = 4.4%).

Quantitation of 2-PPL in Roasted Peanuts. For quantification of 2-PPL in peanuts, 35 mg of crushed raw, roasted or commercially available peanuts were hydrolyzed enzymatically using the 3-fold amounts of enzymes and solutions as described above. For evaluating amino acid release after enzymatic hydrolysis, the amounts of valine and leucine were compared to those obtained after acid hydrolysis before and after defatting of the samples. Afterward, the samples were freeze-dried and redissolved in 250 μL of water, 80 μL of methanol, and 20 μL of internal standard N-benzoylglycyl-L-phenylalanine in methanol/water (50:50, v/v) with a final concentration of 0.57 pmol/mL. After filtration (0.45 μm), samples were subjected to HPLC-ESI-MS/MS analysis. Quantification was realized using authentic 2-PPL and internal standard N-benzoylglycyl-L-phenylalanine with a final concentration of 0.57 pmol/mL in an enzymatic hydrolyzate matrix calibration of raw peanuts, prepared analogously to the samples.

HPLC-ESI-MS/MS Analysis. The HPLC system consisted of a degasser, a pump, an autosampler, and a diode array detector, all from Agilent Technologies 1200 series (Böblingen, Germany). A triple quad LC-MS 6410 from Agilent Technologies was used for MS/MS measurements. For identification of major reaction products between 4-HNE and N^{α}-acetyl-L-lysine, 10 μL of samples were injected and separated using a Eurospher 100-5 C18 column (250 × 3.0 mm; Knauer) at 30 °C, a flow rate of 0.38 mL/min, and a detection wavelength of 227 nm. A gradient was used with solvent A (water) and B (acetonitrile), each containing 2 mM heptafluorobutyric acid and 11 mM acetic acid. The gradient increased from 2 to 70% B within 50 min and to 90% B within 15 min, isocratic elution at 90% B for 10 min, decreased to 2% B within 3 min, and isocratic elution at 2% for 10 min. First, full scan analyses and then product ion scans were performed. Full scan analyses were performed from 5.1 to 78.0 min in positive mode, scan ranges were from m/z 80 to 1000, scan time was 500 ms, fragmentor voltage was 135 V, gas temperature was 300 °C, gas flow was 11 L/min, and nebulizer pressure was 15 psi. Product ion scans were performed for the unhydrolyzed samples from 15 to 45 min with precursor ions m/z 365.3 for the pyridinium derivative, m/z 327.3 for the Schiff base, m/z 309.2 for the 2-pentylpyrrol-acetyllysine, and m/z 287.2 for the reduced and cyclized Michael adduct after reduction and acid hydrolyses using the same conditions as described above. Product ion scan ranges were from m/z 60 to 400 with a scan time of 200 ms, a fragmentor voltage of 135 V, and collision voltages of 25, 20, 25, and 15 V for the pyridinium derivative, Schiff base, 2-pentylpyrrol-acetyllysine, and the reduced and cyclized Michael adduct, respectively. For quantification of 2-PPL in modified peanut proteins and in peanut samples, 40 and 60 μL of samples, respectively, were separated using a Zorbax SB-C18 column (50 × 2.1 mm) from Agilent Technologies at 30 °C and a flow rate of 0.25 mL/min. A gradient was used with solvent A (water) and B (acetonitrile), each containing 2 mM heptafluorobutyric acid and 11 mM acetic acid. The gradient was as follows: 2% B was held for 5 min, increased to 51% within 17 min, increased to 90% B within 2 min, isocratic elution at 90% B for 6 min, decreased to 2% B within 1 min, and isocratic elution at 2% B for 9 min. Measurements were performed using the multiple reaction monitoring (MRM) mode in positive mode, gas temperature was set to 300 °C, gas flow was set to 11 L/min, and nebulizer pressure was set to 15 psi. Internal standard N-benzoylglycyl-L-phenylalanine was analyzed from 15.5 to 20.6 min with a mass transition from m/z 327.1 to 166.1 for quantification using fragmentor and collision voltages of 90 and 4 V, respectively, and a dwell time of 300 ms. Mass transition from m/z 327.1 to 105.1 was used for qualification using fragmentor and collision voltages of 90 and 34 V, respectively, and a dwell time of 300 ms. 2-PPL was analyzed from 20.6 to 28 min with a mass transition from m/z 267.1 to 204.2 for quantification using fragmentor and collision voltages of 148 and 18 V, respectively, and a dwell time of 100 ms. Mass transition from m/z 267.1 to 84.1 was used for qualification using fragmentor and collision voltages of 148 and 29 V, respectively, and a dwell time of 100 ms.

Statistical Treatment. Results are expressed as mean values ± standard deviations of two separate measurements,[27] except otherwise indicated.

RESULTS AND DISCUSSION

Quantitation of Free 4-HNE in Heated Peanut Oil and Peanut Samples. As reference material for the quantification of free 4-HNE in heated peanut oil and peanut samples, a deuterated 4-HNE-DMA-d_2 standard was synthesized (see Supporting Information Figure I). Figure 1 shows the observed relevant HMBCs of 4 HNE-DMA-d_2. After development of a GC-MS (EI) method, the amounts of 4-HNE were quantified in peanut oil and peanut samples. Figure 2 (left) shows the amounts of free 4-HNE in a native and refined peanut oil as well as in a peanut oil after heating under roasting conditions (20 and 40 min at 170 °C). The amounts were between 0.1 and

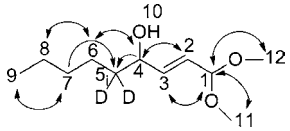

Figure 1. Structure of synthesized 4-HNE-DMA-d_2, showing the observed relevant heteronuclear multiple bond correlations (HMBCs).

DOI: 10.1021/acs.jafc.5b01502
J. Agric. Food Chem. 2015, 63, 5273–5281

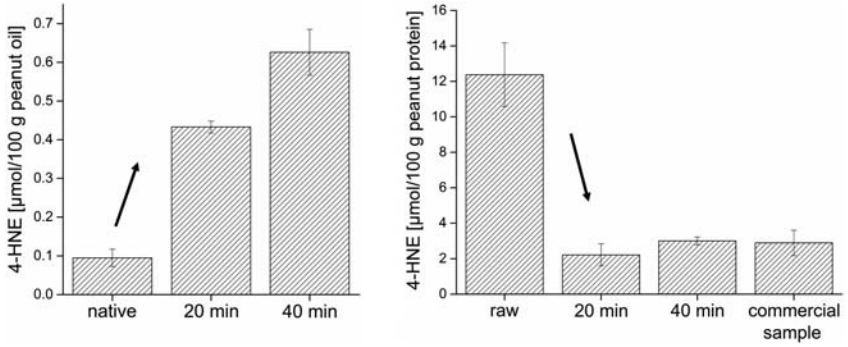

Figure 2. Quantitation of free 4-HNE by GC-MS (EI): (left) amounts of 4-HNE in peanut oil heated at 170 °C; (right) amounts of 4-HNE in peanuts roasted at 170 °C.

0.6 μmol/100 g oil or between 0.2 and 1.0 μg/g oil, clearly indicating an increase in free 4-HNE depending on the heating time. These data are in agreement with published values for 4-HNE in heated soybean oil, butter oil, and corn oil, resulting from HPLC analysis.[28,29] For olive oil (extra virgin), amounts ranging from 0.06 to 0.12 μg 4-HNE/g oil were found using GC-MS.[4] After methyl linoleate had been heated at 185 °C for up to 6 h, it was observed by HPLC analysis that within the first hour of heating, most of the 4-HNE had been formed.[30] The amounts of the precursor linoleic acid in peanut oil and in peanuts are 21.6 and 14%, respectively,[2] indicating that most of the 4-HNE may be formed in the initial stage of heating. This corresponds with the results in Figure 2 (left) and the more pronounced increase in 4-HNE formation during the first 20 min of roasting. Raw peanuts were roasted analogously (20 and 40 min at 170 °C), and the amounts of free 4-HNE are shown in Figure 2 (right). A decrease in free 4-HNE from 12.37 μmol/100 g protein (4.47 mg/kg peanut) in the native to 2.22 μmol/100 g protein (0.82 mg/kg peanut) in the roasted samples was found. The formation of 4-HNE in native peanuts could be a result of drying processes and storage of peanuts after harvesting. Commercially available, roasted peanuts contained 4-HNE in amounts of 2.88 μmol/100 g protein (1.29 mg/kg peanut). No difference between the samples roasted for 20 and 40 min was detectable, indicating that at this stage the formation and degradation of 4-HNE is in equilibrium. This fits with the amount of 4-HNE found in the commercial peanut sample, for which the starting amount is not known. Recently published results for 4-HNE in two commercially available peanut samples were between 0.12 and 0.60 mg/kg peanut sample, analyzed by GC-MS,[4] which is comparable to the amounts of 4-HNE found in this study. Also, 0.14−0.41 mg 4-HNE/kg of sample was found in walnuts and 0.21 mg/kg in an infant formula.[4] In beef and pork, amounts ranging from 2.19 to 21.87 mg/kg and from 0.16 to 23.75 mg/kg, respectively, were found by HPLC analysis,[31] whereupon a correlation between the amounts of 4-HNE and ω-6 fatty acids contents in pork was observed. In fresh blue mackerel, yellowtail, and chicken, amounts of 1.16, 0.50, and 0.04 mg/kg were found, respectively, analyzed by HPLC.[32] A general statement about the toxicology of these levels of 4-HNE is not possible, because data about 4-HNE amounts reaching the small intestine after a gastrointestinal digestion are not available. Due to the fact that in the absence of further peanut constituents heated peanut oil shows an increase of 4-HNE, further reactions with nucleophilic amino acid side chain groups are supposed to be responsible for the loss of 4-HNE when whole peanuts are roasted. These lipation reactions[6] may contribute to the loss of lysine, which cannot be explained by the formation of Maillard reaction products.[5]

Amino Acid Modifications in Modified Peanut Proteins. To investigate the reactions of 4-HNE with nucleophilic amino acid side chains, extracted peanut proteins of raw peanuts were incubated with 4-HNE at 37 °C for 24 h in phosphate buffer (pH 7.4) as previously described for the incubation of other secondary products.[6,33−35] Incubations were performed in different molar ratios between 4-HNE and the sum of the reactive amino acids cysteine, histidine, lysine, and arginine. Samples were hydrolyzed enzymatically because of the instability of certain possible reaction products toward acid hydrolysis. Figure 3 shows the decreases of the amino acids

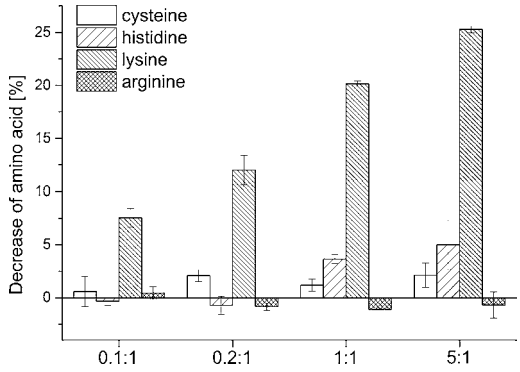

Figure 3. Decreases of amino acids cysteine, histidine, lysine, and arginine in extracted peanut proteins modified by 4-HNE for 24 h at 37 °C in 0.1 M phosphate buffer, analyzed by amino acid analysis. Decreases are presented relative to the amounts of the blank sample.

cysteine, histidine, lysine, and arginine relative to the amounts in the blank sample. Lysine modifications increased from 7.5 to 25.3%, whereas histidine, cysteine, and arginine remained unchanged. Due to the fact that cysteine is able to form disulfide bonds, its accessibility for 4-HNE may be limited, although its reactivity toward 4-HNE is higher than that of lysine.[9]

Identification of Major Reaction Products of 4-HNE and N^{α}-Acetyl-L-lysine. For identification of major reaction products of 4-HNE and the ε-amino group of lysine, 4-HNE and N^{α}-acetyl-L-lysine were incubated in equimolar amounts in methanol for 4 h at 75 °C. Lipation products were identified by HPLC-ESI-MS/MS analysis before hydrolysis (Figure 4). The Michael adduct was identified due to its instability[36] in its reduced, cyclized form after reduction and acid hydrolysis

DOI: 10.1021/acs.jafc.5b01502
J. Agric. Food Chem. 2015, 63, 5273−5281

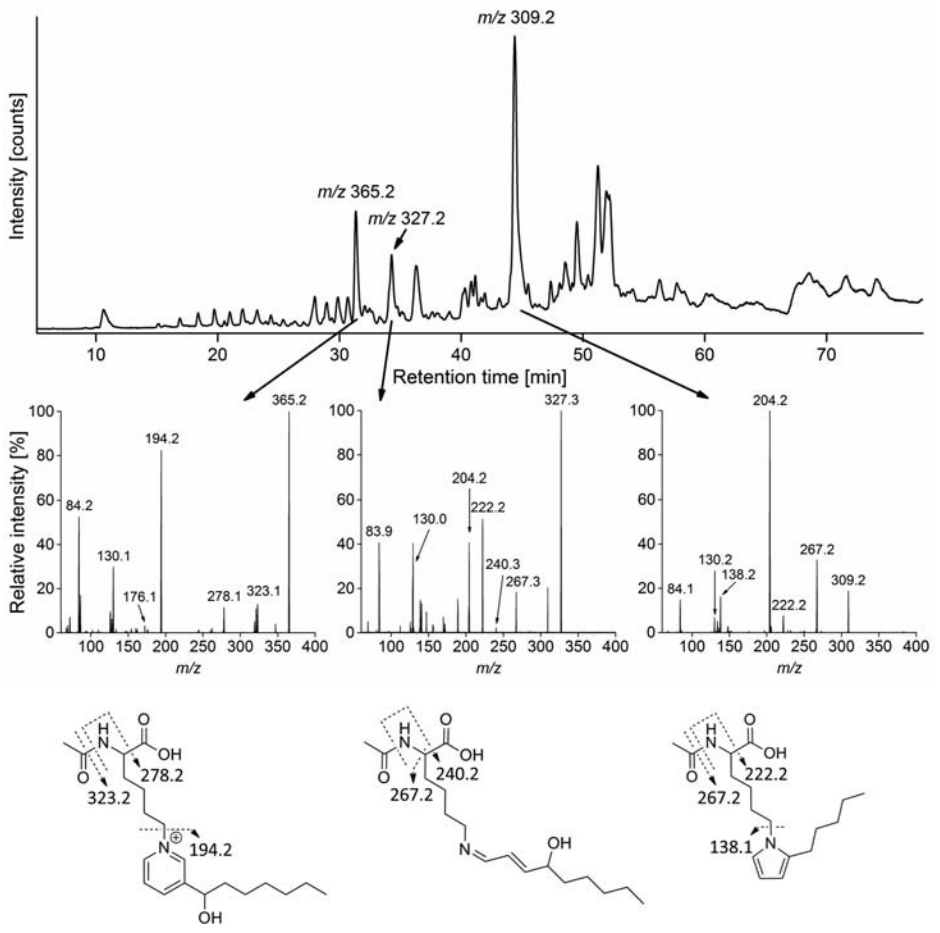

Figure 4. Identification of lipation products by HPLC-ESI-MS/MS after incubation of N^{α}-acetyl-L-lysine and 4-HNE in equimolar amounts in methanol for 4 h at 75 °C. The HPLC-ESI-MS-scan chromatogram (top) shows peaks of N^{α}-acetyl-L-lysine (m/z 189.2), a pyridinium derivative (m/z 365.2), a Schiff base (m/z 327.2), and a 2-pentylpyrrol adduct (m/z 309.2). (Middle) Product ion patterns after fragmentation of the derivatives and selected ions (bottom) resulting from the derivatives, respectively. Detailed explanations of the ions are given in the text.

(Figure II in the Supporting Information). The monoisotopic mass of m/z 365.2 $[M]^+$ and characteristic fragments of the pyridinium moiety (m/z 194.2) after additional loss of water (m/z 176.1) are indicative for a 4-HNE-lysine pyridinium derivative. Furthermore, the fragmentation pattern shows typical lysine fragments (m/z 84.2 and 130.1). Ions with m/z 323.1 and 278.1 are indicative for secessions of the acetyl group and the carboxyl and acetyl groups, respectively. After incubation of 4-hydroxypentenal and glycine, an analogous pyridinium derivative was detected, and a possible reaction pathway was proposed[37] requiring two molecules of 4-hydroxypentenal and one molecule of glycine. To the best of our knowledge, this is the first report of a pyridinium derivative resulting from 4-HNE and the ε-amino group of lysine. Therefore, its formation is also possible in proteins. Further strong hints indicating the presence of a Schiff base were found: a monoisotopic mass of m/z 327.2 $[MH]^+$ and characteristic fragments m/z 240.3 indicating losses of the acetyl and carboxyl groups, m/z 267.3, indicating a secession of the α-amino group with its acetyl moiety, and m/z 222.2, which results after cyclization as analogously postulated for free lysine.[38] The fragment with m/z 204.2 is indicative for loss of water from the cyclized ion. With fragments m/z 267.2 and 222.2, the monoisotopic mass m/z 309.2 $[MH]^+$ shows typical ions of the 2-pentylpyrrole-acetyl lysine (2-PPAcL) indicating losses of the acetyl and carboxyl groups, respectively. The ion m/z 138.2 is indicative for the pyrrol moiety. The characteristic fragment m/z 204.2 might result from a cyclization step analogous to the Schiff base. A possible formation pathway of the characteristic ion with m/z 204.2 is given in Figure III in the Supporting Information, based on the proposed fragmentation of adducts between the ε-amino group of lysine and hexanal.[38]

Formation of the 2-pentylpyrrol derivative occurs initially by the formation of a Schiff base, being in an equilibrium with its enamine, which undergoes keto−enol tautomerism to the 4-oxo-enamine derivative that finally cyclizes to the 2-pentylpyrrol derivative.[9] After reduction and acid hydrolysis, a monoisotopic mass of m/z 287.2 $[MH]^+$ and fragments m/z 242.2 (loss of carboxyl group), m/z 224.2 (losses of carboxyl and amino groups), m/z 158.2 (cleavage between δ carbon and ε nitrogen), and, as typical lysine fragments, m/z 84.1 and 130.1 (Figure II in the Supporting Information) were observed. This points to the presence of the reduced, cyclized Michael adduct.

Due to the fact that 2-PPL is an advanced lipation end product,[8,11] further studies were performed. For synthesis of 2-PPL (for the reaction scheme see Figure IV in the Supporting Information), γ-nonalactone was reduced to nonane-1,4-diol by $LiAlH_4$, which was oxidized to 4-oxononanal by pyridinium chlorochromate. Following a Paal−Knorr synthesis including N^{α}-acetyl-L-lysine, the acetyl group was removed by basic hydrolysis using a 2 M sodium hydroxide solution. Purification

DOI: 10.1021/acs.jafc.5b01502
J. Agric. Food Chem. 2015, 63, 5273−5281

was realized by semipreparative HPLC with UV detection, using an RP-18 column. Identification of 2-PPL was performed by HPLC-ESI-MS/MS measurements and one- and two-dimensional NMR spectroscopy. Figure 5 shows the structure of 2-amino-6-(2-pentyl-1*H*-pyrrol-1-yl)hexanoic acid (2-PPL) and the relevant HMBCs.

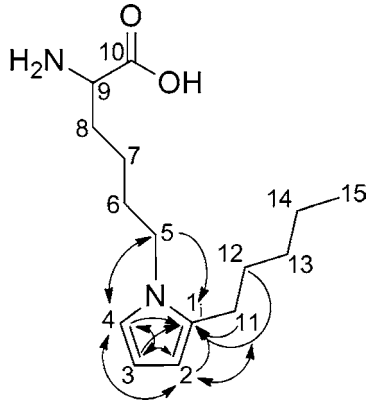

Figure 5. Structure of 2-PPL showing the observed relevant heteronuclear multiple bond correlations (HBMC).

Quantitation of 2-PPL in Modified Peanut Proteins. 2-PPL was quantified after enzymatic hydrolysis by HPLC-ESI-MS/MS. Figure 6 shows the decreases of lysine compared to

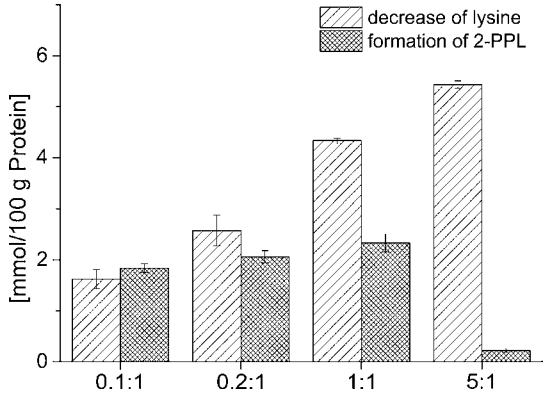

Figure 6. Decrease of lysine due to modification of extracted peanut proteins by 4-HNE after incubation at 37 °C for 24 h in 0.1 M phosphate buffer, analyzed by amino acid analysis compared to the lysine level in the blank sample and amounts of 2-PPL quantitated after enzymatic hydrolysis by HPLC-ESI-MS/MS.

the blank sample analyzed by amino acid analysis and the formation of 2-PPL analyzed by HPLC-ESI-MS/MS, each after enzymatic hydrolysis. In the blank sample, 2-PPL was not detectable. The results indicate that 2-PPL is readily formed when 4-HNE is present and only a slight increase can be observed when the ratio of 4-HNE is increased. In the 5:1 sample, only 12% of the 2-PPL amount compared to the 0.1:1 sample was quantified. These results show that the amounts of 2-PPL as well as the loss of lysine do not increase depending on the amount of 4-HNE. Furthermore, it can be seen that at low concentrations of 4-HNE (0.1:1 and 0.2:1 samples), 2-PPL is the major reaction product, explaining the total loss of lysine, whereas at higher 4-HNE concentrations (1:1 and 5:1 samples), other reaction products must be formed. At higher concentrations of 4-HNE, a polymerization or oxidation of 4-HNE may occur, so that less 4-HNE would be available for the reaction with lysine. In further studies the amounts of free 4-HNE could be measured to check whether the amounts of free 4-HNE are really lowered in the 1:1 and 5:1 samples. Supposing that 2-PPL would be the kinetically preferred reaction product, the reaction pathway could shift at higher concentrations so that, for example, the reaction can remain on the level of the Schiff base, the precursor of 2-PPL.

Quantitation of 2-PPL in Peanuts. Due to its instability during acid hydrolysis, 2-PPL was released from the peanut protein samples enzymatically. To ensure complete enzymatic degradation, results for the amounts of valine and leucine obtained after enzymatic hydrolysis for the native, the two roasted, and the commercial samples were compared to the corresponding values after acid hydrolysis. For valine the enzymatic release ranged from 87.5 to 103.6% and for leucine from 83.4 to 97.0%, indicating complete enzymatic hydrolysis. Quantitation of 2-PPL was realized by HPLC-ESI-MS/MS (MRM mode). Figure 7 shows a representative HPLC-ESI-

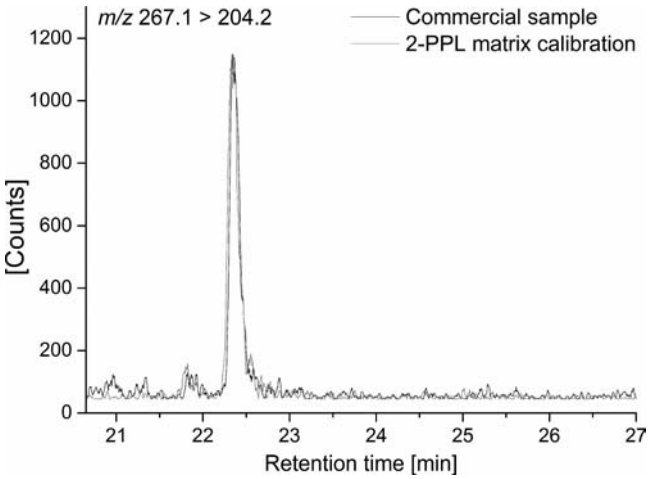

Figure 7. Representative HPLC-ESI-MS/MS chromatogram (MRM mode, transition m/z 267.1 → 204.2) of the enzymatic hydrolysate of the commercial peanut sample (black) and the 2-PPL standard in a raw peanut hydrolyzate matrix (gray).

MS/MS chromatogram (m/z 267.1 → 204.2) of the hydrolyzed commercial peanut sample and the 2-PPL standard in a raw peanut hydrolyzate matrix. The quantitated amounts of 2-PPL in raw, roasted, and commercial peanut samples are given in Figure 8. In raw peanuts, 2-PPL was not detectable, whereas in roasted peanuts, the amounts ranged from 112.1 to 175.1 nmol/100 g protein or from 29.9 to 46.7 μg/100 g protein. In the commercial sample, 144.5 nmol/100 g protein or 38.5 μg/100 g protein was found. These results point to an increase of 2-PPL depending on the roasting conditions. Data obtained for the commercial sample and the samples roasted in laboratory scale were comparable. It should be noted that the formation of 2-PPL would also be possible by a Paal–Knorr reaction if 4-oxononanal was present. Compared to the loss of free 4-HNE as a result of peanut roasting, approximately 1 and 2% of 4-HNE could be recovered, bound to the ε-amino group of lysine as 2-PPL in the peanut samples roasted for 20 and 40 min, respectively. In this estimation, the formation of 4-HNE during the roasting process could not be taken into account. Due to the fact that at low 4-HNE concentrations the total loss of lysine can be explained by the formation of the lipation product

DOI: 10.1021/acs.jafc.5b01502
J. Agric. Food Chem. 2015, 63, 5273–5281

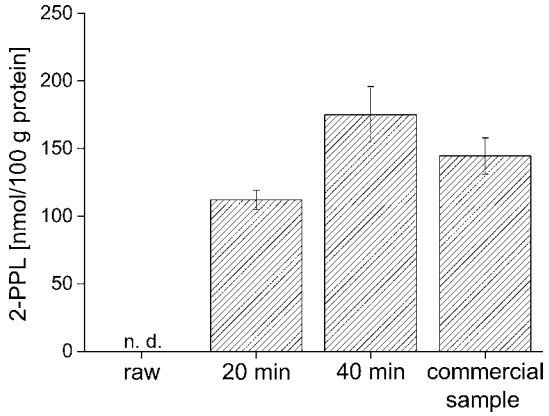

Figure 8. Quantitated amounts of 2-PPL in raw and roasted (170 °C) peanut samples as well as in a commercial peanut sample by HPLC-ESI-MS/MS after enzymatic hydrolysis. n.d., not detectable, (n = 3).

2-PPL (Figure 6), other 4-HNE–lysine adducts should not be of importance. With regard to the loss of amino acids as a result of a modification of raw peanut proteins by 4-HNE (Figure 3), reactions of 4-HNE with other amino acid side chains besides the ε-amino group of lysine seem not to be relevant. A slight decrease in histidine was observed, which might be explained by the formation of Michael adducts or its resulting hemiacetal.[39] Besides the one-to-one 4-HNE–amino acid adducts, cross-linking products may also contribute to the loss of lysine, caused by fluorophores or a Schiff base and Michael adduct at the same molecule of 4-HNE.[12,13] Heating of 4-HNE and primary amines results in only trace amounts of pyrrole and mainly in the condensation product of 4-HNE, 2-pentylfuran.[9] This might, in contrast to peanut oil, contribute to a loss of 4-HNE when proteins are present.

In conclusion, our results show that 4-HNE, a well-known secondary product of the autoxidation of ω-6 polyunsaturated fatty acids,[1] is formed as a result of heating peanut oil depending on the roasting time. Roasting whole peanuts, however, led to a significant decrease in 4-HNE, due to reactions with the amino acid side chains of the peanut proteins as well as a possible degradation of 4-HNE to 2-pentylfuran. As shown, especially lysine derivatives are formed, among which a novel identified pyridinium derivative, Schiff bases, Michael adducts, and 2-pentylpyrrol adducts represent potential lipation products. For a model system, consisting of extracted peanut proteins incubated with 4-HNE at 37 °C for 24 h, the complete decrease of lysine could be explained by the formation of 2-PPL at low concentrations of 4-HNE, indicating that 4-PPL is a good marker for a protein modification by 4-HNE. Furthermore, to the best of our knowledge, a direct quantification of 2-PPL was performed for the first time, showing an increase in 2-PPL depending on the roasting time. This post-translationally formed lipation product contributes to a small percentage of the total loss of lysine observed when peanuts are roasted,[5] showing that lipation products are formed in the course of peanut roasting. Considering the broad spectrum of possible precursors formed when lipid-rich peanuts are roasted, a complex spectrum of lipation products can be formed, accounting for the large modification rate of lysine.[6] Further studies are needed to quantify the amounts of other 4-HNE–lysine adducts and to investigate the influence of these adducts on the allergenic potential of roasted peanuts.

■ ASSOCIATED CONTENT

Supporting Information

Figures I–IV. The Supporting Information is available free of charge on the ACS Publications website at DOI: 10.1021/acs.jafc.5b01502.

■ AUTHOR INFORMATION

Corresponding Author

*(T.H.) Phone: +49-351-463-34647. Fax: +49-351-463-34138. E-mail: Thomas.Henle@chemie.tu-dresden.de.

Notes

Parts of this study were presented as poster contributions to the 43rd Lebensmittelchemikertag, September 22–24, 2014, Gießen, Germany.

The authors declare no competing financial interest.

■ ACKNOWLEDGMENTS

We thank Karla Schlosser, Institute of Food Chemistry, TU Dresden, for performing the amino acid analysis; Anke Peritz, Institute of Organic Chemistry, TU Dresden, for performing the elemental analysis; and Dr. Margit Gruner, Institute of Organic Chemistry, TU Dresden, and Sivathmeehan Yogendra, Institute of Inorganic Chemistry, TU Dresden, for performing the NMR analysis.

■ ABBREVIATIONS USED

4-HNE, 4-hydroxynon-2-enal; MWCO, molecular weight cutoff; GC-MS (EI), gas chromatography with mass spectrometry after electron-impact ionization; HPLC-ESI-MS/MS, high-performance liquid chromatography with electrospray ionization and tandem mass spectrometry; 2-PPL, 2-amino-6-(2-pentyl-1*H*-pyrrol-1-yl)hexanoic acid (2-pentylpyrrole lysine)

■ REFERENCES

(1) Esterbauer, H.; Schaur, R. J.; Zollner, H. Chemistry and biochemistry of 4-hydroxynonenal, malondialdehyde and related aldehydes. *Free Radical Biol. Med.* **1991**, *11*, 81–128.

(2) Souci, S. W., Fachmann, W., Kraut, H., Eds. *Food Composition and Nutrition Tables*, 7th ed.; MedPharm Scientific Publishers: Stuttgart, Germany, 2008.

(3) Liu, X.; Jin, Q.; Liu, Y.; Huang, J.; Wang, X.; Mao, W.; Wang, S. Changes in volatile compounds of peanut oil during the roasting process for production of aromatic roasted peanut oil. *J. Food Sci.* **2011**, *76*, 404–412.

(4) Papastergiadis, A.; Mubiru, E.; Van Langenhove, H.; De Meulenaer, B. Development of a sensitive and accurate stable isotope dilution assay for the simultaneous determination of free 4-hydroxy-2-(*E*)-nonenal and 4-hydroxy-2-(*E*)-hexenal in various food matrices by gas chromatography-mass spectrometry. *Food Anal. Methods* **2014**, *7*, 836–843.

(5) Wellner, A.; Nußpickel, L.; Henle, T. Glycation compounds in peanuts. *Eur. Food Res. Technol.* **2012**, *234*, 423–429.

(6) Globisch, M.; Schindler, M.; Kressler, J.; Henle, T. Studies on the reaction of *trans*-2-heptenal with peanut proteins. *J. Agric. Food Chem.* **2014**, *62*, 8500–8507.

(7) Poli, G.; Schaur, R. J. 4-Hydroxynonenal in the pathomechanisms of oxidative stress. *IUBMB Life* **2000**, *50*, 315–321.

(8) Sayre, L. M.; Lin, D.; Yuan, Q.; Zhu, X.; Tang, X. Protein adducts generated from products of lipid oxidation: focus on HNE and ONE. *Drug Metab. Rev.* **2006**, *38*, 651–675.

(9) Sayre, L. M.; Arora, P. K.; Iyer, R. S.; Salomon, R. G. Pyrrole formation from 4-hydroxynonenal and primary amines. *Chem. Res. Toxicol.* **1993**, *6*, 19–22.

(10) Amarnath, V.; Valentine, W. M.; Montine, T. J.; Patterson, W. H.; Amarnath, K.; Bassett, C. N.; Graham, D. G. Reactions of 4-

DOI: 10.1021/acs.jafc.5b01502
J. Agric. Food Chem. 2015, 63, 5273–5281

hydroxy-2(*E*)-nonenal and related aldehydes with proteins studied by carbon-13 nuclear magnetic resonance spectroscopy. *Chem. Res. Toxicol.* **1998**, *11*, 317−328.
(11) Sayre, L. M.; Sha, W.; Xu, G.; Kaur, K.; Nadkarni, D.; Subbanagounder, G.; Salomon, R. G. Immunochemical evidence supporting 2-pentylpyrrole formation on proteins exposed to 4-hydroxy-2-nonenal. *Chem. Res. Toxicol.* **1996**, *9*, 1194−1201.
(12) Xu, G.; Liu, Y.; Sayre, L. M. Independent synthesis, solution behavior, and studies on the mechanism of formation of a primary amine-derived fluorophore representing cross-linking of proteins by (*E*)-4-hydroxy-2-nonenal. *J. Org. Chem.* **1999**, *64*, 5732−5745.
(13) Uchida, K.; Stadtman, E. R. Covalent attachment of 4-hydroxynonenal to glyceraldehyde-3-phosphate dehydrogenase − a possible involvement of intra- and intermolecular cross-linking reaction. *J. Biol. Chem.* **1993**, *268*, 6388−6393.
(14) Salomon, R. G.; Kaur, K.; Podrez, E.; Hoff, H. F.; Krushinsky, A. V.; Sayre, L. M. HNE-derived 2-pentylpyrroles are generated during oxidation of LDL, are more prevalent in blood plasma from patients with renal disease or atherosclerosis, and are present in atherosclerotic plaques. *Chem. Res. Toxicol.* **2000**, *13*, 557−564.
(15) Ylä-Herttuala, S.; Palinski, W.; Rosenfeld, M. E.; Parthasarathy, S.; Carew, T. E.; Butler, S.; Witztum, J. L.; Steinberg, D. Evidence for the presence of oxidatively modified low density lipoprotein in atherosclerotic lesions of rabbit and man. *J. Clin. Invest.* **1989**, *84*, 1086−1095.
(16) Lynch, M. P.; Faustman, C.; Silbart, L. K.; Rood, D.; Furr, H. C. Detection of lipid-derived aldehydes and aldehyde:protein adducts in vitro and in beef. *J. Food Sci.* **2001**, *66*, 1093−1099.
(17) Chung, S.-Y.; Champagne, E. T. Association of end-product adducts with increased IgE binding of roasted peanuts. *J. Agric. Food Chem.* **2001**, *49*, 3911−3916.
(18) Chung, S.-Y.; Maleki, S.; Champagne, E. T.; Buhr, K. L.; Gorbet, D. W. High-oleic peanuts are not different from normal peanuts in allergenic properties. *J. Agric. Food Chem.* **2002**, *50*, 878−882.
(19) Matissek, R.; Steiner, G.; Fischer, M. *Lebensmittelanalytik*, 4th ed.; Springer-Verlag: Berlin, Germany, 2010.
(20) Henle, T.; Walter, H.; Klostermeyer, H. Evaluation of the extent of the early Maillard-reaction in milk-products by direct measurement of the Amadori-product lactuloselysine. *Z. Lebensm.-Unters. Forsch.* **1991**, *193*, 119−122.
(21) Henle, T.; Walter, H.; Krause, I.; Klostermeyer, H. Efficient determination of individual Maillard compounds in heat-treated milk products by amino acid analysis. *Int. Dairy J.* **1991**, *1*, 125−135.
(22) Soulère, L.; Queneau, Y.; Doutheau, A. An expeditious synthesis of 4-hydroxy-2(*E*)-nonenal (4-HNE), its dimethyl acetal and of related compounds. *Chem. Phys. Lipids* **2007**, *150*, 239−243.
(23) Chandra, A.; Srivastava, S. K. A synthesis of 4-hydroxy-2-*trans*-nonenal and 4-(*H*-3) 4-hydroxy-2-*trans*-nonenal. *Lipids* **1997**, *32*, 779−782.
(24) van Kuijk, F. J. G. M.; Siakotos, A. N.; Fong, L. G.; Stephens, R. J.; Thomas, D. W. Quantitative measurement of 4-hydroxyalkenals in oxidized low-density-lipoprotein by gas-chromatography-mass-spectrometry. *Anal. Biochem.* **1995**, *224*, 420−424.
(25) Chung, S.-Y.; Champagne, E. T. Allergenicity of Maillard reaction products from peanut proteins. *J. Agric. Food Chem.* **1999**, *47*, 5227−5231.
(26) Corey, E. J.; Suggs, J. W. Pyridinium chlorochromate, an efficient reagent for oxidation of primary and secondary alcohols to carbonyl compounds. *Tetrahedron Lett.* **1975**, *31*, 2647−2650.
(27) Funk, W.; Dammann, V.; Donnevert, G. *Qualitätssicherung in der Analytischen Chemie, zweite, vollständig überarbeitete und erweiterte Auflage*; Wiley-VCH Verlag GmbH: Weinheim, Germany, 2005.
(28) Seppanen, C. M.; Csallany, A. S. The effect of intermittent and continuous heating of soybean oil at frying temperature on the formation of 4-hydroxy-2-*trans*-nonenal and other α,β-unsaturated hydroxyaldehydes. *J. Am. Oil Chem. Soc.* **2006**, *83*, 121−127.
(29) Han, I. H.; Csallany, A. S. Temperature dependence of HNE formation in vegetable oils and butter oil. *J. Am. Oil Chem. Soc.* **2008**, *85*, 777−782.
(30) Han, I. H.; Csallany, A. S. Formation of toxic α,β-unsaturated 4-hydroxy-aldehydes in thermally oxidized fatty acid methyl esters. *J. Am. Oil Chem. Soc.* **2009**, *86*, 253−260.
(31) Sakai, T.; Kuwazuru, S.; Yamauchi, K.; Uchida, K. A lipid peroxidation-derived aldehyde, 4-hydroxy-2-nonenal and omega-6 fatty-acids contents in meats. *Biosci., Biotechnol., Biochem.* **1995**, *59*, 1379−1380.
(32) Tanaka, R.; Sugiura, Y.; Matsushita, T. Simultaneous identification of 4-hydroxy-2-hexenal and 4-hydroxy-2-nonenal in foods by pre-column fluorigenic labeling with 1,3-cyclohexanedione and reversed-phase high-performance liquid chromatography with fluorescence detection. *J. Liq. Chromatogr. Relat. Technol.* **2013**, *36*, 881−896.
(33) Ishino, K.; Wakita, C.; Shibata, T.; Toyokuni, S.; Machida, S.; Matsuda, S.; Matsuda, T.; Uchida, K. Lipid peroxidation generates body odor component *trans*-2-nonenal covalently bound to protein in vivo. *J. Biol. Chem.* **2010**, *285*, 15302−15313.
(34) Furuhata, A.; Ishii, T.; Kumazawa, S.; Yamada, T.; Nakayama, T.; Uchida, K. *N*-ε-(3-Methylpyridinium)lysine, a major antigenic adduct generated in acrolein-modified protein. *J. Biol. Chem.* **2003**, *278*, 48658−48665.
(35) Ichihashi, K.; Osawa, T.; Toyokuni, S.; Uchida, K. Endogenous formation of protein adducts with carcinogenic aldehydes − implications for oxidative stress. *J. Biol. Chem.* **2001**, *276*, 23903−23913.
(36) Nadkarni, D. V.; Sayre, L. M. Structural definition of early lysine and histidine adduction chemistry of 4-hydroxynonenal. *Chem. Res. Toxicol.* **1995**, *8*, 284−291.
(37) Napetschnig, S.; Schauenstein, E.; Esterbauer, H. Formation of a pyridinium derivative by reaction of 4-hydroxypentenal with glycine. *Chem.-Biol. Interact.* **1988**, *68*, 165−177.
(38) Fenaille, F.; Tabet, J.-C.; Guy, P. A. Study of peptides containing modified lysine residues by tandem mass spectrometry: precursor ion scanning of hexanal-modified peptides. *Rapid Commun. Mass Spectrom.* **2004**, *18*, 67−76.
(39) Uchida, K.; Stadtman, E. R. Modification of histidine-residues in proteins by reaction with 4-hydroxynonenal. *Proc. Natl. Acad. Sci. U.S.A.* **1992**, *89*, 4544−4548.

NOTE ADDED AFTER ASAP PUBLICATION

Due to a production error, this paper was published on the Web on May 18, 2015, with none of the requested galley corrections implemented. The corrected version was reposted on May 19, 2015.

DOI: 10.1021/acs.jafc.5b01502
J. Agric. Food Chem. 2015, 63, 5273−5281

JOURNAL OF AGRICULTURAL AND FOOD CHEMISTRY

Article

pubs.acs.org/JAFC

Compositional Assessments of Key Maize Populations: B73 Hybrids of the Nested Association Mapping Founder Lines and Diverse Landrace Inbred Lines

Tyamagondlu V. Venkatesh,*[,†] George G. Harrigan,[†] Tim Perez,[†] and Sherry Flint-Garcia*[,§,#]

[†]Monsanto Company, 800 North Lindbergh Boulevard, St. Louis, Missouri 63167, United States

[§]Agricultural Research Service, U.S. Department of Agriculture, Columbia, Missouri 65211, United States

[#]Division of Plant Sciences, University of Missouri, Columbia, Missouri 65211, United States

Supporting Information

ABSTRACT: The present study provides an assessment of the compositional diversity in maize B73 hybrids derived both from the Nested Association Mapping (NAM) founder lines and from a diverse collection of landrace accessions from North and South America. The NAM founders represent a key population of publicly available lines that are used extensively in the maize community to investigate the genetic basis of complex traits. Landraces are also of interest to the maize community as they offer the potential to discover new alleles that could be incorporated into modern maize lines. The compositional analysis of B73 hybrids from the 25 NAM founders and 24 inbred lines derived from landraces included measurements of proximates (protein, fat, ash, and starch), fibers, minerals, amino acids, fatty acids, tocopherols (α-, γ-, and δ-), β-carotene, phytic acid, and raffinose. Grain was harvested from a replicated trial in New York, USA. For each data set (NAM and landrace) canonical discriminant analysis allowed separation of distinct breeding groups (tropical, temperate, flint, mixed/intermediate) within each data set. Overall, results highlighted extensive variation in all composition components assessed for both sets of hybrids. The variation observed for some components within the landraces may therefore be of value for increasing their levels in modern maize lines. The study described here provided significant information on contributions of conventional breeding to crop compositional variation, as well as valuable information on key genetic resources for the maize community in the development of new improved lines.

KEYWORDS: *maize, landraces, Nested Association Mapping (NAM) founder lines, composition analysis*

INTRODUCTION

Maize (*Zea mays* L.) is a key agricultural commodity and a major source of animal food and feed as well as raw material for industrial processes worldwide.[1] Breeding programs committed to improving agronomic, compositional, and nutritional qualities extend globally and include renowned organizations such as the International Maize and Wheat Improvement Center (CIMMYT) headquartered in Mexico. In addition to its commercial significance, maize is also well-established in the scientific community as a model plant for the study of fundamental biological phenomena such as genome evolution and hybrid vigor.[2]

Maize was domesticated from teosinte (*Zea mays* ssp. *parviglumis*) approximately 9000 years in southern Mexico. This domestication and subsequent spread of maize across the Americas resulted in open-pollinated, heterogeneous populations adapted to specific environments called landraces. Although defined by distinct genetic and morphological characteristics, there is often more diversity within a landrace than between landraces.[3] Modern inbred lines developed from landraces through breeding and selection are nearly homozygous; that is, they breed true as additional seed is made by crossing the line with itself (i.e., self-pollinating). Maize hybrids are developed by crossing two distinct inbred lines. Hybridization was initiated in the late 1800s with commercialization of hybrids in the early 1900s.[4]

Today, *Zea* germplasm is defined in terms of teosinte, landraces, and inbred lines. The availability of these distinct germplasm pools has intriguing implications for breeding and the development of new maize hybrids. Although maize inbred lines contain an extraordinary amount of genetic diversity when assessed across all lines, subsets of genes are invariant or have reduced variation due to directional selection and bottlenecks associated with domestication and/or plant breeding.[5] Variation for these genes could be reintroduced into modern maize from landraces and teosinte to support further crop improvement.[6]

Diverse collections of genetically distinct maize inbred lines are now preserved in carefully maintained germplasm banks.[7] The USDA-ARS North Central Regional Plant Introduction Station (NCRPIS), for example, has conserved lines representing almost a century of breeding. The landrace accessions for this study were selected from such a collection representing the geographical diversity of maize adaptation in North and South America and were self-pollinated to generate landrace inbred lines,[8,9] In addition to naturally occurring collections, novel populations are being generated to understand the genetic

Received: January 13, 2015
Revised: April 30, 2015
Accepted: May 12, 2015
Published: May 12, 2015

ACS Publications © 2015 American Chemical Society

DOI: 10.1021/acs.jafc.5b00208
J. Agric. Food Chem. 2015, 63, 5282−5295

complexity of maize. One extensively used population is the Nested Association Mapping (NAM) population. The NAM population[10] was generated by crossing 25 NAM founder lines to B73, an inbred line that has contributed extensively to the pedigree of many important commercial lines[11] and which serves as the source of the high-quality reference genome for maize.[12] The 25 NAM founder lines were chosen solely based on genetic diversity from a collection of 301 maize inbred lines adapted to various climatic regions including tropical, subtropical and temperate regions.[13]

Maize landraces are an extremely heterogeneous germplasm group, in terms of genetic and phenotypic diversity both within a landrace and between landraces.[3] Because any given landrace plant is unique, being heterozygous at a large percentage of loci across the genome, it is very difficult to assess the merit of specific landraces or landraces collections. In addition, landraces often display undesirable traits such as photoperiod sensitivity and unadaptedness to target environments. Thus, genetically stable genetic resources are needed to systematically explore diversity within landraces, just as the NAM population was used to initiate exploration of diversity within maize inbreds. The Seeds of Discovery (SeeD) Project (http://seedsofdiscovery.org) is a large-scale project to explore landrace diversity by sampling a single plant per landrace. Unfortunately, the single plant used for the SeeD project does not allow for follow-up genetic studies. However, a small set of inbred lines was derived by self-pollinating directly out of a set of landraces;[8] thus, these landrace inbred lines are true breeding and can be used for innumerable follow-up studies.

The purpose of the current study was to provide a compositional survey of maize hybrids derived from landraces adapted to diverse geographies and the genetically diverse NAM founder lines. An earlier comparative assessment of teosinte, landrace, and inbred lines revealed key differences in kernel proximates (protein, fat, ash, and starch),[14] but to our knowledge compositional surveys have not extended to diverse hybrids or to a diverse range of kernel components. The NAM population has been utilized to reveal key genetic loci associated with kernel compositional features such as starch, protein, and oil[15] and carotenoids.[16] There has been, however, no systematic compositional evaluation of the NAM founders. Such information could prove beneficial as there are genetic loci known to affect kernel composition such as crtRB1 that influences β-carotene concentration[16] or DGAT 1-2 (acyl-CoA:diacylglycerol acyltransferase) that affects oil content and fatty acid profiles.[17] Similarly, there have been no systematic studies on compositional variation in landrace populations of maize. Understanding the compositional diversity of these lines adapted to local environments could prove significant in improving the nutrient profile of new maize hybrids. Information on compositional diversity of these genetically diverse population is also of interest to researchers involved in compositional evaluation of new crops including genetically modified (GM) crops.[18]

MATERIALS AND METHODS

Biological Materials. The germplasm used in this study was selected to represent a broad diversity within maize landraces and inbred lines. Hybrids were used to decrease the range of maturity and thus decrease environmental effects on the composition data. For example, the inbreds flower over a period of 40−50 days in Missouri, but the B73 hybrids all flower within 22 days (S.F.-G., unpublished data).

The landrace inbred lines were derived from open-pollinated landrace accessions as described in Chia et al.[8] and Hufford et al.[9] The following landrace inbred lines were used in the study: MR01 (Araguito), MR02 (Assiniboine), MR03 (Bolita), MR04 (Canilla), MR05 (Cateto), MR06 (Chapalote), MR07 (Comiteco), MR08 (Costeno), MR09 (Cravo Riogranense), MR10 (Crystalino Norteno), MR11 (Cuban Flint), MR12 (Havasupai), MR13 (Hickory King), MR14 (Longfellow Flint), MR15 (Palomero de Jalisco), MR16 (Pepetilla), MR18 (Reventador), MR19 (Santo Domingo), MR20 (Shoe Peg), MR21 (Tabloncillo), MR22 (Tuxpeno), MR23 (Zapalote Chico), MR25 (Poropo), and MR26 (Pollo). The geographical origins of landrace inbreds are described in Hufford et al.[9] and are indicated in Supplementary Figure 7. On the basis of geographical origin and historical data[19] these inbreds have been classified as tropical/subtropical (Pepetilla, Cateto, Tuxpeno, Araguito, Tabloncillo, Comiteco, Canilla, Poropo, Zapalote Chico, Reventador, Pollo, Cravo Riogranense, Crystalino Norteno, Costeno, Bolita, and Cuban Flint), temperate (Shoe Peg and Hickory King), northern flint (Santo Domingo, Longfellow Flint, Assiniboine, and Havasupai), and intermediate (Palomero de Jalisco and Chapalote). The intermediate group refers to a geographical origin that is less clear, with membership in multiple groups (e.g., Palomero de Jalisco is a flint from a subtropical region).

Modern inbred lines used in the study are the parental lines of the NAM population:[10] B97, CML103, CML228, CML247, CML277, CML322, CML333, CML52, CML69, Hp301, IL14H, Ki11, Ki3, Ky21, M162W, M37W, Mo18W, MS71, NC350, NC358, Oh43, Oh7B, P39, Tx303, and Tzi8. The geographical origin of these inbreds is indicated in Supplementary Figure 7. The inbreds were classified by population structure using genetic marker data as described in Flint-Garcia et al.[13] as tropical/subtropical (NC350, CML103, CML333, Tzi8, Ki11, Ki3, CML69, NC358, CML228, CML247, CML52, CML322, and CML277), nonstiff stalk temperate (MS71, Oh43, B97, Ky21, M162W, and Oh7B), northern flint (P39, Il14H, and HP301), and mixed (Mo18W, M37W, and Tx303). Inbreds classified as mixed group have membership probabilities of <80% in any one of the groups, indicating admixture (shared breeding history) among the tropical and temperate groups. The common parent, B73, is a temperate stiff-stalk inbred and is therefore suitable as a tester for making hybrid seed. In addition, B73 is the reference genome line allowing for downstream genomic and bioinformatic analyses in these materials. Inbred seed material used in the study can be procured from the North Central Regional Plant Introduction Station (NCRPIS).

Production of Hybrid Seed. Hybrid seed of B73 crossed with the landrace inbred lines and the NAM founders was produced over four different seasons: 24 and two entries were produced, respectively, in Columbia, MO and Puerto Rico, USA, in 2008; 18 entries were produced in Puerto Rico in 2009; and six entries were produced in 2010 in Columbia, MO, USA. All hybrids were produced by controlled hand pollination, using B73 as the female for each hybrid.

Field Design. Materials for composition analyses were generated in 2012 near Aurora, NY, USA. The 25 B73 × NAM founder hybrids and 24 B73 × landrace hybrids were planted in a randomized complete block design in 3 m × 0.9 m rows in three replications. Three to five plants were self-pollinated for each row, and selfed ears were hand harvested and dried to 12−13% moisture. Dried ears from each row were bulk-shelled, and grain was stored at room temperature before shipping to Monsanto Co. in St. Louis, MO, USA. Grain samples were homogenized by grinding on dry ice to a fine powder and stored frozen at approximately −20 °C until compositional analysis.

Phenotypic Data. Plant, ear, and kernel traits were evaluated as follows. Anthesis dates were collected on a row basis, when half the plants in the row were shedding pollen, and subsequently converted to days to anthesis by subtracting the planting date from the anthesis date. Plant and ear heights were measured for three plants per plot after flowering from the ground to the collar of the flag leaf and the node of the top ear, respectively. Three self-pollinated ears were harvested per row and used to study the following ear and kernel traits: the number of kernel rows around the ear; the weight of the ear,

DOI: 10.1021/acs.jafc.5b00208
J. Agric. Food Chem. 2015, 63, 5282−5295

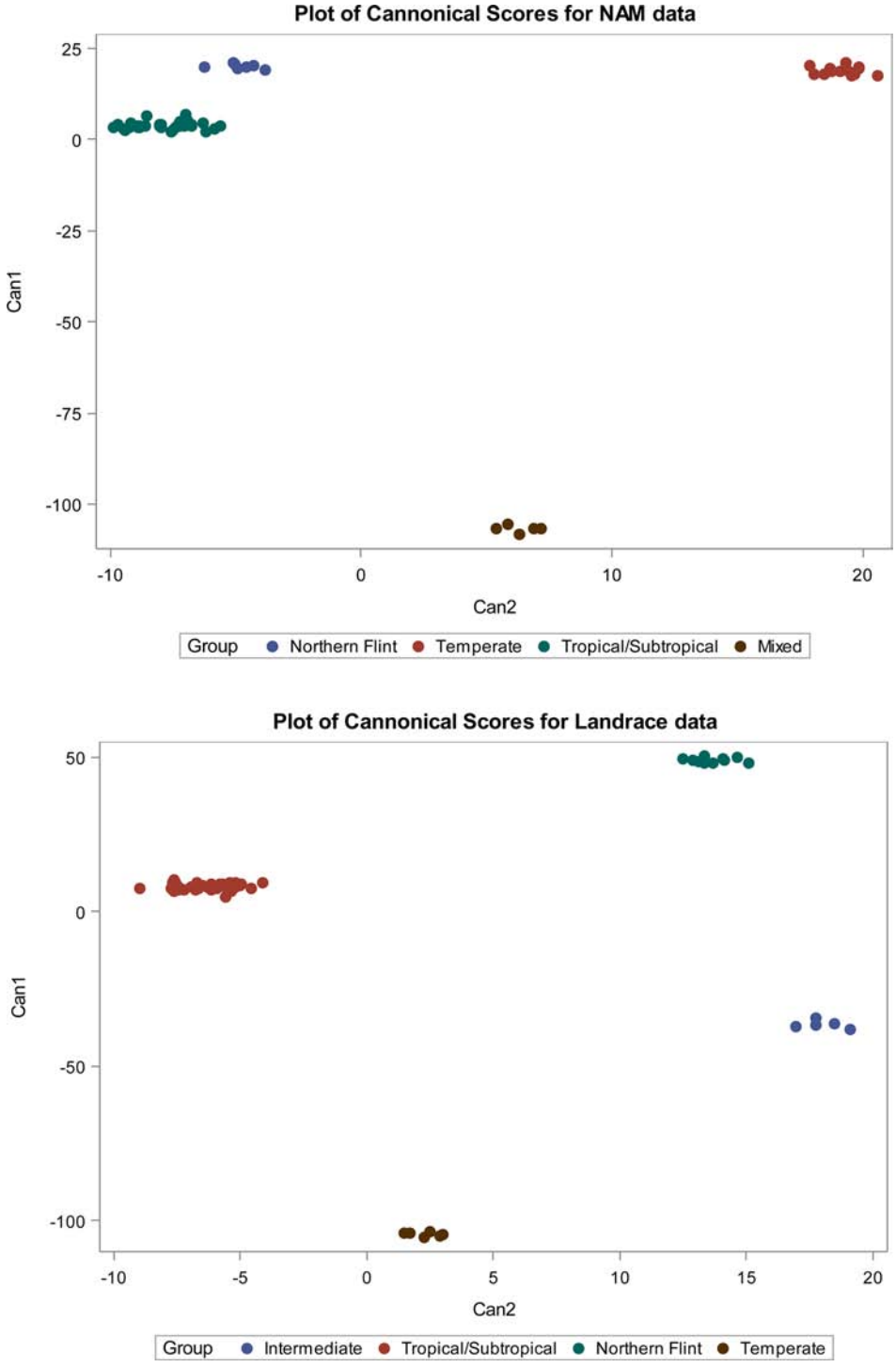

Figure 1. CDA of composiotional data from the NAM hybrids (top) and landrace hybrids (bottom).

the cob, and 50 kernels; the width of the ear and cob; and the length of the ear.

Composition Analysis. Assays for proximates (protein, fat, ash, and starch) except starch have been described before.[20] Starch was based on AOAC[21] protocols. Assays for fatty acids and amino acids,[22] minerals, raffinose, phytic acid, and β-carotene[20] have also been previously reported. Tocopherol analysis was based on a reversed-phase HPLC method using fluorescence detection with excitation at 290 nm and emission at 336 nm.[23] Tocopherols were extracted from ground lyophilized seed with 0.1% pyrogallol in ethanol. The reversed-phase HPLC system comprised a Keystone Aquasil C_{18} column at 40 °C and methanol as the mobile phase. The flow rate was 1 mL/min, and moisture was measured to allow for dry weight conversions. All compositional data are reported as percent dry weight (dwt) and are available in Supporting Information Files S1 and S2.

Three biological replicates were available for all samples except hybrids CML277, M37W, Oh43, and Oh7B, Bolita, Chapalote, Costeno, Cuban Flint, and Tabloncillo (two replicates each), and Canilla and Havasupai (one replicate each). Some assays were not repeated due to sample limitations. Thus, there is only one replicate of the Comiteco hybrid for protein, fat, starch, carbohydrates by calculation, β-carotene, raffinose, ADF, and NDF; one Araguito hybrid replicate for starch and phytic acid; one Tuxpeno hybrid replicate for raffinose; one CML103 hybrid replicate for NDF; and one

DOI: 10.1021/acs.jafc.5b00208
J. Agric. Food Chem. 2015, 63, 5282−5295

Table 1. Mean Proximates and Fiber Values[a] for the NAM Founder Hybrids

group	founder × B73	protein	total fat	starch	carbohydrates[b]	ash	ADF[c]	NDF[d]
tropical	CML69	14.01	4.73	66.97	79.74	1.54	3.56	8.60
tropical	Tzi8	13.78	4.59	64.42	80.00	1.61	3.84	9.93
flint	P39	13.53	7.13	63.81	77.89	1.44	3.50	8.46
tropical	CML333	13.10	4.99	64.23	80.53	1.39	3.98	9.70
temperate	Oh43	12.99	4.54	65.62	81.13	1.33	3.64	9.10
tropical	CML52	12.95	4.27	66.31	81.21	1.54	3.83	10.19
tropical	CML228	12.94	4.96	69.03	80.66	1.48	3.35	8.22
tropical	CML277	12.86	3.87	66.37	81.75	1.50	3.64	9.93
flint	HP301	12.75	4.98	62.98	81.04	1.19	3.88	10.77
mixed	Tx303	12.57	4.60	67.77	81.46	1.35	3.63	9.41
temperate	Ky21	12.54	4.12	69.24	81.89	1.43	3.79	8.71
tropical	CML247	12.51	4.33	64.98	81.80	1.39	3.91	10.70
temperate	Oh7B	12.51	5.21	67.72	81.08	1.21	2.78	8.08
tropical	Ki3	12.32	4.42	64.89	81.76	1.49	3.49	10.06
flint	Il14H	12.25	5.72	66.71	80.59	1.47	4.11	10.39
temperate	B97	12.01	4.33	64.22	82.39	1.24	3.11	8.72
tropical	NC358	11.98	3.85	68.82	82.85	1.34	3.46	9.20
temperate	MS71	11.98	4.92	65.98	81.87	1.29	3.50	9.20
tropical	CML103	11.68	4.11	67.02	82.68	1.55	3.90	9.06
tropical	Ki11	11.48	4.16	67.28	83.06	1.32	3.48	8.76
mixed	Mo18W	11.10	4.97	77.89	82.58	1.37	3.80	9.18
tropical	CML322	11.09	4.83	67.50	82.69	1.37	3.96	10.07
temperate	M162W	11.08	4.40	75.49	83.32	1.21	3.32	9.18
tropical	NC350	10.56	4.73	67.69	83.31	1.42	3.23	9.26
mixed	M37W	10.25	3.97	67.19	84.33	1.44	3.98	10.09
	min	10.25	3.85	62.98	77.89	1.19	2.78	8.08
	mean	12.27	4.67	67.21	81.66	1.40	3.63	9.40
	max	14.01	7.13	77.89	84.33	1.61	4.11	10.77

[a]Values expressed as % dwt. [b]Carbohydrates by calculation. [c]Acid detergent fiber. [d]Neutral detergent fiber. For clarity, only means are presented, individual replicate values are presented in the Supporting Information (File S1).

Ky21 replicate for NDF. Samples with missing data due to sample limitations are noted in Supporting Information Files S1 and S2.

Statistical Analysis. Simple descriptive statistics were employed. Means, minimum replicate values, and maximum values were calculated in JMP 10 (SAS Institute, Cary, NC, USA). Analytes for which 50% of values were below the assay limit of quantitation (LOQ) were not included in the statistical summaries. These analytes included nine fatty acids (C11:0, C12:0, C14:0, C18:4n3, C20:2, C22:0, C22:5, C22:6, and C24:1), as well as sodium. No fatty acid data for one replicate of the M162W hybrid were assessed as one of the major fatty acids (oleic acid, C18:1) was assigned an LOQ during data acquisition. As in typical chemical analysis,[20a,24] analyte values below the LOQ were assigned a value of half of the assay LOQ. This included 54 values of C13:0, 20 values of C17:0, 25 values of C18:3n6, 22 values of C20:1n9, 4 values of C20:5, 24 values of C22:1n9, and 15 values of C24:0 with a value of 0.025% total fatty acid. The five values of β-carotene were assigned a value of 0.02 mg/100 g. All imputed values and associated samples are documented in Supporting Information Files S1 and S2.

We employed canonical discriminant analysis (CDA)[25] to determine if patterns existed in the data that could separate the hybrid groups, using the canonical discriminant CANDISC procedure in SAS. CDA is a dimension reduction technique related to principal component analysis and canonical correlation.[25] CDA analysis finds linear combinations of the quantitative variables that provide maximal separation between classes or groups. Given a classification variable and several quantitative variables, the CANDISC procedure in SAS derives canonical variables, linear combinations of the quantitative variables that summarize between-class variation in much the same way that principal components summarize total variation. The classification variable was hybrid groupings for NAM and landrace inbreds, and the quantitative variables were compositional components/phenotypic observations. Correlations between each of the analyte values and canonical scores 1 and 2 were derived using the multivariate CORR procedure in SAS.

RESULTS AND DISCUSSION

Maize is a highly diverse species, despite the narrow genetic base within U.S. commercial breeding programs.[26] Recently, genetic diversity within inbred lines has been explored to greater depth[7,10b] than ever before. However, systematic exploration of the landraces is lagging behind. In this study, we focus on the phenotypic evaluation of kernel composition traits in B73 hybrids derived from the NAM founders and a set of American landraces. The compositional analysis included quantitative measurement of proximates (protein, fat, ash, and starch), fatty acids, amino acids, minerals, raffinose, phytic acid, tocopherols, and β-carotene levels in mature grain of the two hybrid data sets.

CDA. CDA of the NAM hybrid data set established effective separation of the breeding groups assigned for the NAM hybrids (northern flint, temperate, tropical/subtropical, and mixed). CDA additionally provided effective separation of groups within the landrace hybrid set (northern flint, temperate, tropical/subtropical, and intermediate). Group assignments for each hybrid are provided in all tabulated data sets. The results clearly imply unique compositional characteristics that can distinguish between different sets of maize hybrids (Figure 1). The data also contrast the variation

DOI: 10.1021/acs.jafc.5b00208
J. Agric. Food Chem. 2015, 63, 5282−5295

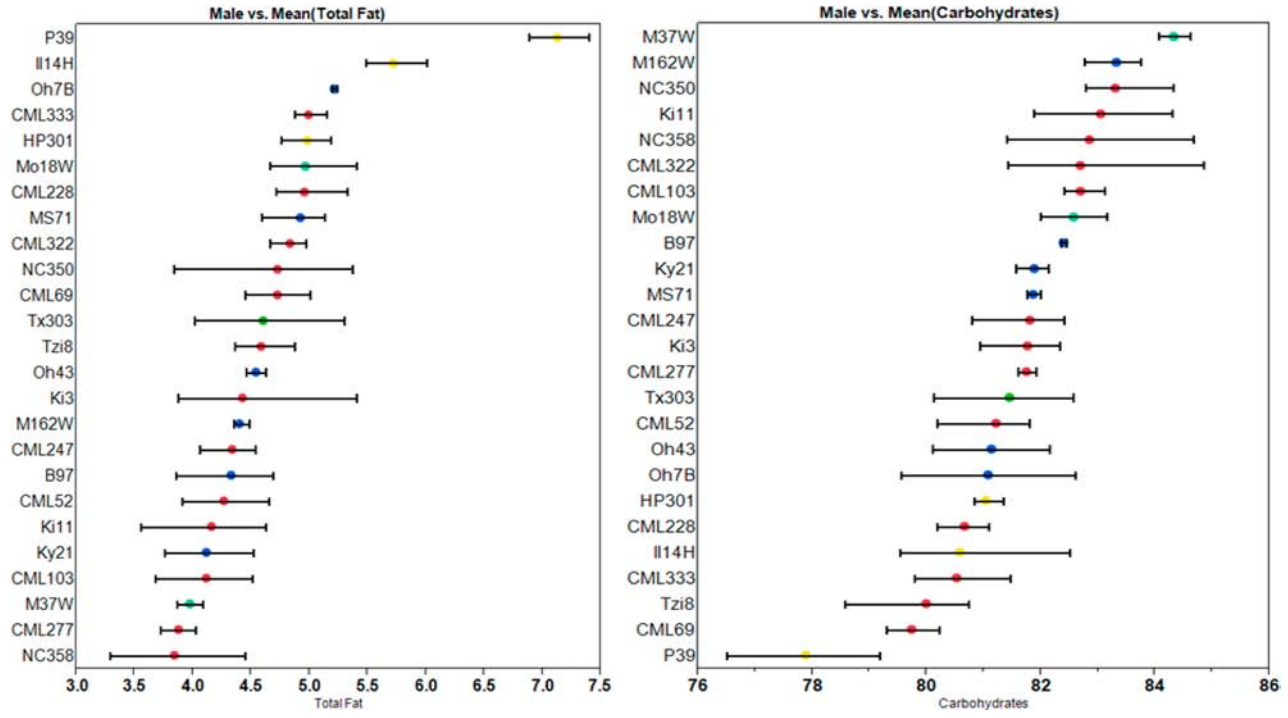

Figure 2. Means and ranges for total fat (left) and carbohydrates (right) of the NAM founder hybrids. Colored circles represent different subgroups: red, tropical; blue, temperate; green, mixed; yellow, flint.

associated with conventional breeding to the relative lack of impact of GM on composition.[18] Overall, however, correlations between the canonical scores (Can1 and Can2; Supplementary Table 1) and individual analytes that provided the separation were generally low (Supporting Information), and no one component was uniquely different in one breeding group versus another. In general, all components were characterized by extensive variation in grain levels, although values were typical for maize hybrids (ILSI, 2014).[27] Variation for individual components and their association with canonical scores is discussed in more detail below.

NAM Founder Hybrid Proximates and Fibers. Results for proximates and fibers are presented in Table 1, where the NAM founder hybrids are tabulated in order of highest to lowest mean protein values. The CML69 × B73 hybrid had the highest mean protein value (14.01% dwt) and M37W × B73 the lowest (10.25% dwt); the corresponding amino acid data are presented in Supplementary Table 2. Overall, all proximates values were variable, and no clear distinctions between the different NAM hybrid subsets were observed. We found that the hybrids with flint ancestry (derived from the sweetcorn lines P39 and Il14H and the popcorn HP301) were characterized by a relatively high-fat, low-carbohydrate profile (see Figure 2). For example, P39 × B73 and Il14H × B73 had the highest mean fat values (7.13 and 5.72% dwt), respectively; P39 × B73 had the lowest mean carbohydrate values (77.89% dwt). These observations are consistent with the abnormal starch content of sweetcorn lines due to the *sugary1* locus.[28] The extensive variation in protein values observed is presented in Supplementary Figure 1. Interestingly, the correlation between the inbred values for the same NAM parents reported by Cook et al.[15] for protein, oil, and starch were $r = -0.02$, 0.58, and 0.38, respectively. It appears that the B73 parent of the hybrids used in this study is contributing strongly to differences in protein content, but not for starch or oil. Correlations between protein, starch, and carbohydrates with canonical score 1 were $r = 0.358$, −0.363, and −0.333, respectively (Supporting Information). These were among the highest correlations observed, and these components are clearly some of the larger contributing factors to the separation of the different breeding groups.

NAM Founder Hybrid Fatty Acids. Results for fatty acids are presented in Table 2. The NAM founder hybrids are tabulated in order of highest to lowest mean linoleic acid (C18:2) values, the major fatty acid in maize. B97 × B73 had the highest mean value (58.92% total FA) and M162W × B73 the lowest mean value (41.68% total FA). The sweetcorn hybrids (derived from P39 and Il14H) and the popcorn HP301 were characterized by a relatively low oleic acid (C18:1) and high linolenic acid (C18:3) profile (see Figure 3), consistent with prior observations that high oil materials have high linolenic acid (C18:3) levels.[15] Correlations of the major individual fatty acids with the canonical scores were generally low; palmitic acid (C16:0) had a value of $r = -0.384$ with canonical score 2, representing the highest correlation for these components.

NAM Founder Hybrid Vitamins and Metabolites. Results for vitamin and metabolites are presented in Table 3. The NAM founder hybrids are tabulated in order of highest to lowest mean α-tocopherol values. Overall, vitamin and metabolite values were highly diverse; values for γ-tocopherol and β-carotene are presented in Figure 4 and for raffinose presented in Supplementary Figure 2. Despite this variation, some of these metabolites represented some of the highest correlations with the canonical scores; for example, raffinose and canonical score 1 ($r = -0.381$), phytic acid and canonical score 2 ($r = -0.418$), and γ-tocopherol and canonical score 2 ($r = 0.353$). Again, none of these components, by themselves, uniquely distinguished any breeding group. The β-carotene values (Table 3) in the hybrids were well correlated with the

DOI: 10.1021/acs.jafc.5b00208
J. Agric. Food Chem. 2015, 63, 5282−5295

Table 2. Mean Fatty Acid Values[a] for the NAM Founder Hybrids

group	founder × B73	C10:0	C13:0	C16:0	C16:1	C17:0	C18:0	C18:1n9	C18:1n7	C18:2n6	C18:3n3	C18:3n6	C20:0	C20:1n9	C20:5	C22:1n9	C24:0
temperate	B97	0.21	0.05	13.19	0.13	0.04	1.82	19.65	0.80	58.92	1.54	0.13	0.32	0.11	0.18	0.23	0.21
flint	HP301	0.11	0.22	11.84	0.13	0.06	1.97	23.28	0.77	54.58	1.32	0.14	0.30	0.10	0.16	0.18	0.16
temperate	Oh43	0.12	0.46	11.84	0.10	0.04	1.37	18.55	0.68	53.87	1.53	0.19	0.17	0.11	0.07	0.23	0.16
tropical	Ki11	0.14	0.16	14.43	0.08	0.05	1.71	22.77	0.71	53.87	1.56	0.06	0.31	0.12	0.21	0.14	0.38
temperate	MS71	0.13	0.10	11.28	0.11	0.05	1.65	26.03	0.77	53.75	1.51	0.13	0.30	0.16	0.19	0.14	0.27
tropical	CML277	0.20	0.14	14.37	0.11	0.05	1.84	21.38	0.74	53.59	1.49	0.21	0.34	0.11	0.20	0.11	0.37
tropical	CML52	0.13	0.12	13.72	0.10	0.07	1.63	25.36	0.74	53.06	1.43	0.15	0.33	0.17	0.16	0.16	0.20
tropical	NC358	0.18	0.08	14.79	0.12	0.07	1.49	23.98	0.84	52.37	1.74	0.08	0.29	0.15	0.14	0.14	0.07
tropical	CML322	0.16	0.11	13.14	0.11	0.08	1.79	25.08	0.77	51.85	1.46	0.11	0.33	0.13	0.24	0.22	0.19
tropical	CML333	0.14	0.07	13.62	0.15	0.07	1.73	26.29	0.87	51.76	1.22	0.16	0.34	0.16	0.22	0.14	0.23
tropical	CML103	0.20	0.04	13.90	0.10	0.08	1.79	27.74	0.77	51.64	1.53	0.17	0.29	0.20	0.29	0.22	0.10
tropical	CML228	0.11	0.31	12.68	0.08	0.06	2.85	23.70	0.58	51.51	1.26	0.11	0.34	0.12	0.18	0.13	0.27
tropical	CML69	0.15	0.07	13.11	0.09	0.06	2.28	26.25	0.67	51.45	1.48	0.06	0.43	0.15	0.23	0.17	0.18
tropical	Tzi8	0.17	0.04	13.44	0.10	0.08	1.81	26.90	0.75	51.02	1.31	0.14	0.35	0.10	0.14	0.12	0.12
temperate	Ky21	0.14	0.19	13.03	0.10	0.04	1.74	26.00	0.77	50.61	1.66	0.21	0.29	0.16	0.19	0.18	0.12
tropical	CML247	0.17	0.08	13.32	0.13	0.07	1.71	26.95	0.82	50.18	1.30	0.11	0.31	0.16	0.28	0.18	0.20
flint	P39	0.14	0.04	11.70	0.11	0.07	2.29	30.77	0.68	50.11	1.12	0.09	0.40	0.16	0.17	0.06	0.15
tropical	NC350	0.16	0.15	13.21	0.13	0.08	1.96	27.09	0.75	49.66	1.56	0.16	0.37	0.15	0.20	0.18	0.21
mixed	Tx303	0.16	0.10	13.81	0.12	0.08	2.17	29.51	0.82	49.26	1.30	0.16	0.37	0.13	0.27	0.16	0.22
mixed	M37W	0.23	0.07	14.96	0.09	0.07	1.54	25.70	0.83	49.03	1.86	0.28	0.34	0.15	0.54	0.11	0.26
tropical	Ki3	0.16	0.07	13.87	0.12	0.07	1.98	29.35	0.73	47.97	1.30	0.14	0.44	0.14	0.15	0.13	0.26
temperate	Oh7B	0.14	0.08	12.75	0.12	0.04	2.07	30.83	0.72	47.89	1.29	0.13	0.36	0.13	0.20	0.12	0.16
mixed	Mo18W	0.11	0.32	12.40	0.11	0.07	1.92	29.12	0.67	46.64	1.20	0.08	0.30	0.12	0.19	0.10	0.28
flint	Il14H	0.18	0.05	12.33	0.11	0.07	2.74	34.44	0.74	42.60	1.25	0.19	0.36	0.21	0.17	0.20	0.05
temperate	M162W	0.12	0.29	12.54	0.13	0.06	1.95	32.37	0.76	41.68	1.44	0.10	0.37	0.11	0.18	0.17	0.20
	min	0.11	0.04	11.28	0.08	0.04	1.37	18.55	0.58	41.68	1.12	0.06	0.17	0.10	0.07	0.06	0.05
	mean	0.15	0.14	13.17	0.11	0.06	1.91	26.36	0.75	50.75	1.43	0.14	0.33	0.14	0.21	0.16	0.20
	max	0.23	0.46	14.96	0.15	0.08	2.85	34.44	0.87	58.92	1.86	0.28	0.44	0.21	0.54	0.23	0.38

[a]Values expressed as % total fatty acid. For clarity only means are presented, individual replicate values are presented in the Supporting Information (File S1).

DOI:10.1021/acs.jafc.5b00208
J. Agric. Food Chem. 2015, 63, 5282−5295

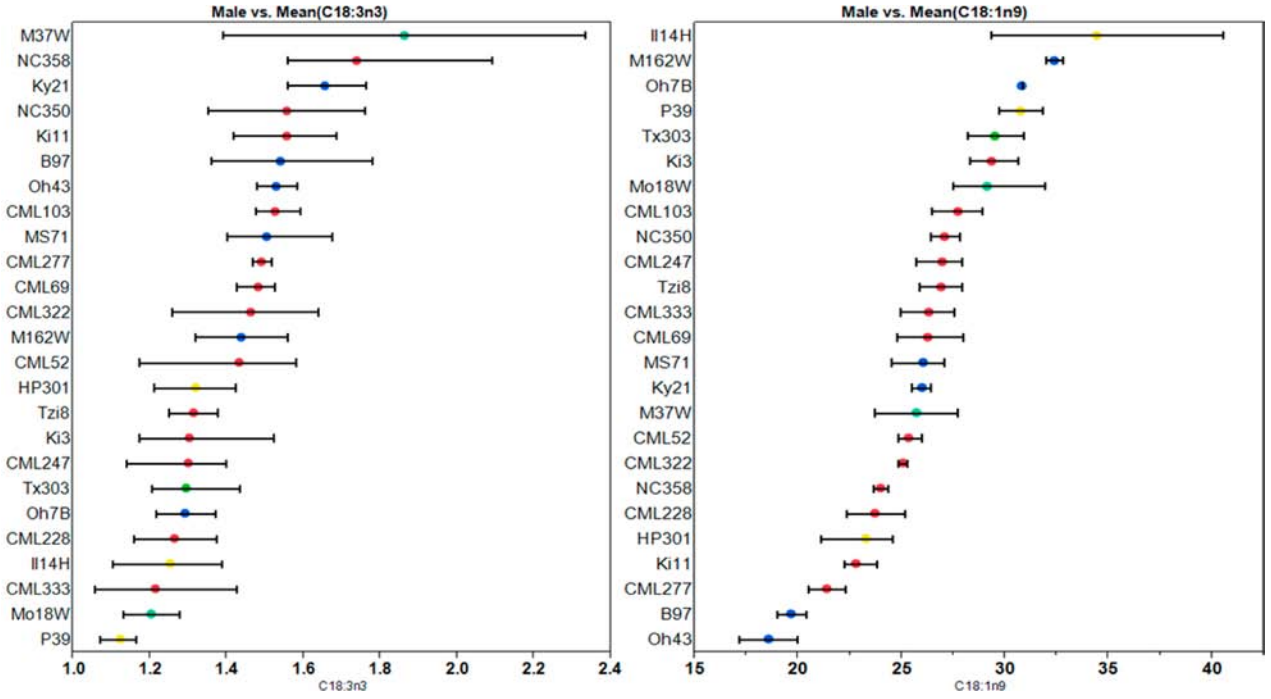

Figure 3. Means and ranges for oleic acid (left) and linolenic acid (right) of the NAM founder hybrids.

Table 3. Mean Vitamin and Metabolite Values[a] for the NAM Founder Hybrids

group	founder × B73	α-tocopherol	γ-tocopherol	δ-tocopherol	β-carotene	raffinose	phytic acid
tropical	NC350	15.33	23.33	1.33	0.13	0.12	1.02
tropical	CML103	13.00	32.67	1.00	0.04	0.13	1.03
tropical	CML333	12.67	26.33	1.33	0.03	0.15	1.11
flint	P39	12.67	39.33	1.33	0.09	0.26	1.10
temperate	MS71	12.00	26.33	1.67	0.10	0.18	1.03
temperate	Oh43	12.00	37.50	1.50	0.16	0.18	0.92
tropical	Tzi8	11.33	25.33	2.67	0.04	0.06	1.13
flint	Il14H	11.00	34.67	3.00	0.02	0.15	1.04
tropical	Ki11	10.67	24.00	1.00	0.23	0.16	0.92
tropical	Ki3	10.67	35.67	2.00	0.18	0.17	1.06
temperate	B97	8.33	35.33	1.67	0.07	0.13	0.91
tropical	CML69	8.33	15.00	1.00	0.14	0.16	1.11
mixed	Mo18W	8.33	34.67	2.67	0.03	0.18	0.87
tropical	NC358	8.33	20.00	0.67	0.09	0.16	1.08
tropical	CML228	8.00	35.33	1.67	0.16	0.18	1.08
tropical	CML247	8.00	19.67	1.00	0.03	0.15	1.07
mixed	M37W	8.00	33.50	1.50	0.07	0.25	1.07
tropical	CML52	7.67	12.00	1.00	0.26	0.12	1.01
temperate	Ky21	7.67	38.33	1.33	0.03	0.13	1.03
temperate	M162W	7.33	22.33	1.67	0.08	0.11	0.85
temperate	Oh7B	7.00	36.50	3.00	0.10	0.11	0.94
mixed	Tx303	6.00	30.67	1.67	0.20	0.21	0.85
tropical	CML322	5.67	27.00	2.33	0.05	0.15	1.00
flint	HP301	5.00	33.33	1.33	0.15	0.21	0.96
tropical	CML277	3.50	25.00	1.50	0.04	0.11	0.95
	min	3.50	12.00	0.67	0.02	0.06	0.85
	mean	9.14	28.95	1.63	0.10	0.16	1.01
	max	15.33	39.33	3.00	0.26	0.26	1.13

[a]Tocopherol values are expressed as mg/kg dwt, β-carotene values are expressed as mg/100 g dwt, raffinose and phytic acid are expressed as % dwt. For clarity only means are presented; individual replicate values are presented in the Supporting Information (File S1).

kernel color (Supplementary Table 7) of the non-B73 parent, with the white parents (Il14H, CML333, Mo18W, CML247, Ky21, CML103, Tzi8, CML277, CML322, M37W, and M162W) having the lowest β-carotene values, the orange

DOI: 10.1021/acs.jafc.5b00208
J. Agric. Food Chem. 2015, 63, 5282−5295

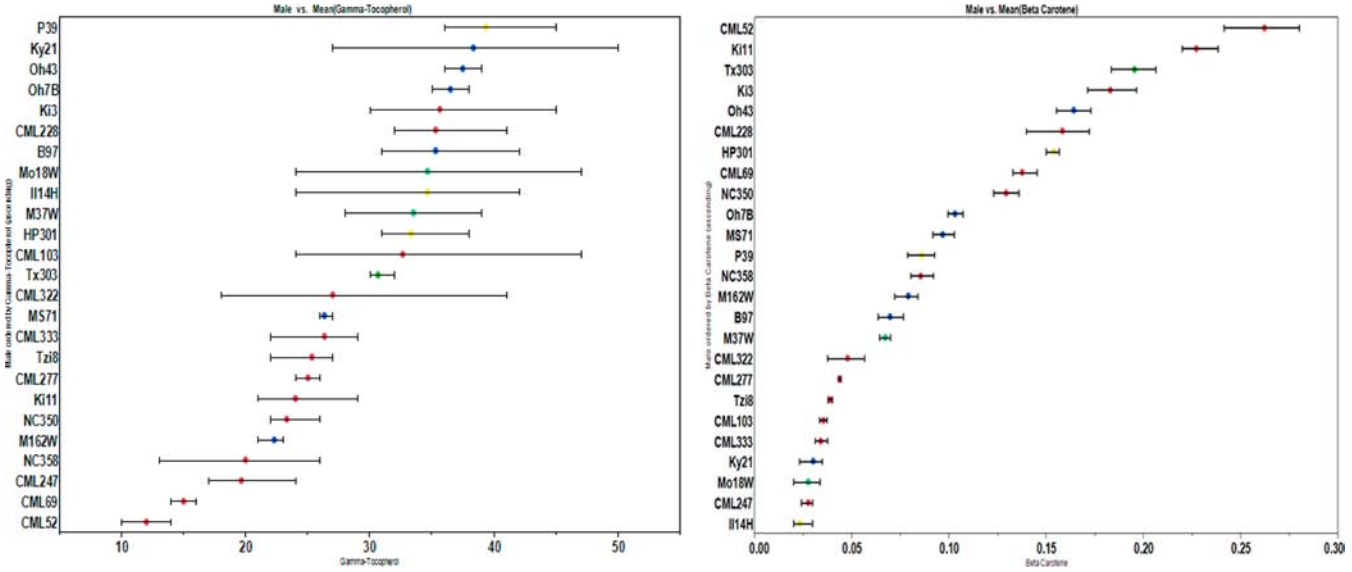

Figure 4. Means and ranges for γ-tocopherol (left) and β-carotene (right) of the NAM founder hybrids.

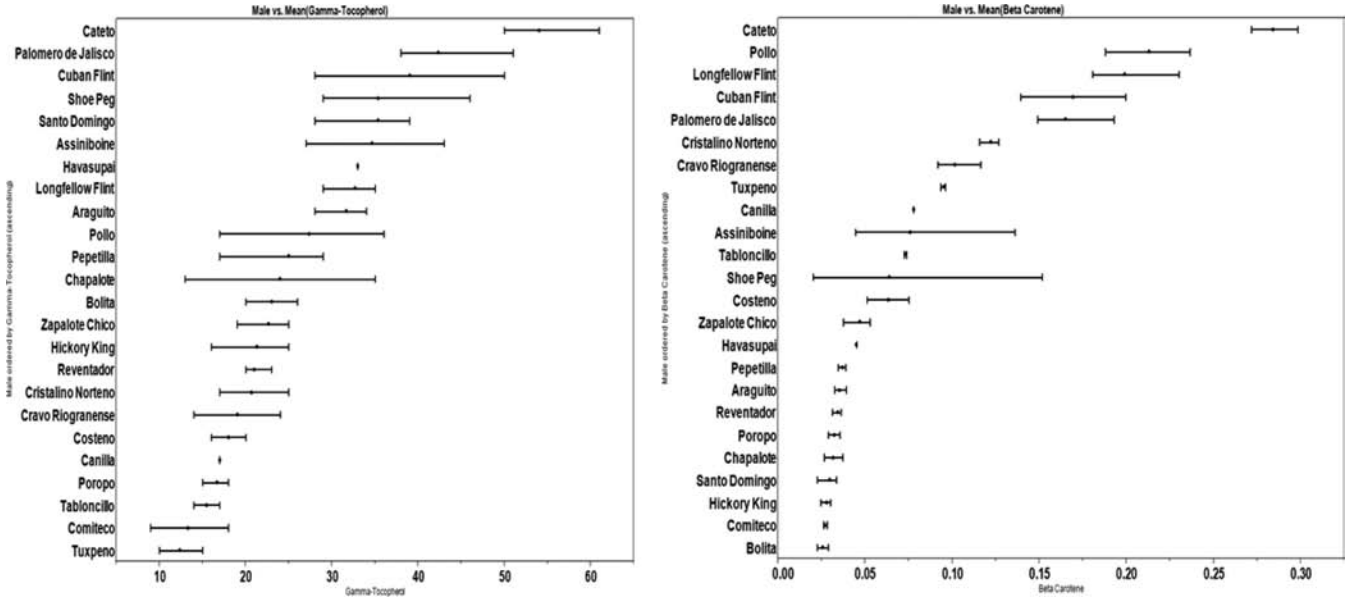

Figure 5. Means and ranges for γ-tocopherol (left) and β-carotene (right) of the landrace hybrids.

parents (P39, NC358, NC350, CML69, HP301, CML228, Ki3, Tx303, Ki11, and CML52) having the highest β-carotene values, and the yellow parents having intermediate values. However, the relationship between kernel color and carotenoid content is not perfect, which is consistent with previous results.[16a] The red kernel color observed for the CML52 hybrid (Figure 6; Supplementary Table 7) originates in the pericarp, the outer layer of the seed, which is derived from maternal tissue. The pericarp does not contain carotenoids, but rather contains other phenolic compounds such as anthocyanins, flavonoids, and phlobaphenes.[29] It is interesting that both the B73 and CML52 inbreds have clear pericarps, but the F1 ear produces red pericarp. This was observed during the development of the NAM population (S.F.-G., unpublished data) and is likely due to independent mutations in the *P1* locus in the two inbred lines that were complemented in the hybrid.

NAM Founder Hybrid Minerals. Mineral values among the NAM founder samples varied within the different subgroups (Supplementary Table 3). Two minerals showed some correlation with the canonical scores (in contrast with the landrace hybrid results shown below). These were manganese and canonical score 1 (r = 0.372) and phosphorus and canonical score 2 (r = −0.535). The phosphorus results are consistent with those of phytic acid (a phosphorus storage compound in maize grain).

Landrace Hybrid Composition Traits. Results for proximates and fibers, minerals, fatty acids, and vitamins and metabolites are presented in Table 4, Supplementary Table 5, Table 5, and Table 6, respectively. Overall, proximates and mineral values were typical for maize hybrids.[27] It is interesting that the hybrid derived from the popcorn Palomero de Jalisco had the highest mean protein value (14.69% dwt) just as was observed for the NAM popcorn parent HP301. Shoe Peg × B73, a landrace that is commonly eaten fresh in the United States, had the lowest protein value (10.12% dwt) (Supplementary Figure 3); the corresponding amino acid data are

DOI: 10.1021/acs.jafc.5b00208
J. Agric. Food Chem. 2015, 63, 5282−5295

Figure 6. Photographs of the B73 × NAM founder ears: (top row) B97, CML103, CML228, CML247, CML277, CML322, CML333, CML52, CML69, Hp301, IL14H, Ki11, Ki3l; (bottom row) Ky21, M162W, M37W, Mo18W, MS71, NC350, NC358, Oh43, Oh7B, P39, Tx303, Tzi8.

Table 4. Mean Proximates and Fiber Values for the Landrace Hybrids[a]

group	landrace × B73	protein	total fat	starch	carbohydrates[b]	ash	ADF[c]	NDF[d]
intermediate	Palomero de Jalisco	14.69	4.11	56.68	79.75	1.46	3.69	8.85
tropical	Pepetilla	14.40	4.62	60.98	79.79	1.18	4.33	10.54
tropical	Cateto	13.82	5.20	64.50	79.56	1.41	3.79	7.81
tropical	Tuxpeno	13.76	4.60	66.62	80.04	1.60	3.68	8.92
intermediate	Chapalote	13.58	5.18	69.90	79.82	1.39	3.40	8.46
tropical	Araguito	13.57	4.85	67.69	80.17	1.42	3.21	8.89
flint	Santo Domingo	13.51	5.24	64.40	79.70	1.55	3.85	10.12
flint	Longfellow Flint	13.49	3.88	67.61	81.25	1.43	3.19	8.65
tropical	Tabloncillo	13.48	5.05	65.53	79.97	1.49	2.84	7.87
tropical	Comiteco	13.41	5.13	58.90	79.90	1.47	3.88	9.51
temperate	Hickory King	13.28	4.00	65.34	81.39	1.31	3.75	10.29
tropical	Canilla	13.26	3.92	65.02	81.52	1.31	3.76	9.13
tropical	Poropo	13.21	5.10	64.09	80.26	1.39	4.00	9.97
tropical	Zapalote Chico	13.19	4.06	63.29	81.07	1.71	3.63	9.45
tropical	Reventador	12.89	4.82	68.09	80.87	1.37	3.45	8.86
tropical	Pollo	12.61	4.95	70.04	81.01	1.40	3.27	7.56
tropical	Cravo Riograneense	12.43	3.93	70.22	82.29	1.41	3.74	9.99
tropical	Crystalino Norteno	12.11	4.76	65.51	81.86	1.28	3.82	8.31
flint	Assiniboine	12.07	4.35	64.59	82.05	1.57	4.34	11.58
tropical	Costeno	11.73	4.65	64.80	82.07	1.53	3.25	8.49
tropical	Bolita	11.40	4.00	65.88	83.25	1.34	3.30	8.95
tropical	Cuban Flint	11.31	4.92	68.36	82.46	1.34	3.57	8.64
flint	Havasupai	10.97	4.20	65.32	83.62	1.20	3.22	9.38
temparate	Shoe Peg	10.12	5.25	71.04	83.32	1.33	3.88	8.64
	min	10.12	3.88	56.68	79.56	1.18	2.84	7.56
	mean	12.85	4.62	65.60	81.12	1.41	3.62	9.12
	max	14.69	5.25	71.04	83.62	1.71	4.34	11.58

[a]Values expressed as % dwt. [b]Carbohydrates by calculation. [c]Acid detergent fiber. [d]Neutral detergent fiber. For clarity only means are presented, individual replicate values are presented in the Supporting Information (File S2).

presented in Supplementary Table 4. Similar variations in mineral levels were reported by Aliu et al.[30] in local populations of maize grown in Kosovo.

Fatty acids were highly variable for the landrace hybrids (Table 5; tabulated in order of highest to lowest mean linoleic acid (C18:2) values. Tuxpeno × B73 had the highest mean value (55.18% total FA) and Zapalote Chico × B73 the lowest (42.11% total FA). The oleic (C18:1) and linolenic (C18:3) fatty acid values are represented in Supplementary Figure 4. Likewise, there were high levels of variability for vitamins and metabolites in the landrace data set, including carotenoids, tocopherols, phytic acid, and raffinose. Values for γ-tocopherol and β-carotene are presented in Figure 5, and those for raffinose are presented in Supplementary Figure 5. Just as in the NAM founders, the carotenoid content of the landrace hybrids closely followed the kernel color. The striking exceptions were the Comiteco and Revenatdor hybrids, where the pink and red

DOI: 10.1021/acs.jafc.5b00208
J. Agric. Food Chem. 2015, 63, 5282−5295

Table 5. Mean Fatty Acid Values[a] for the Landrace Hybrids

group	landrace × B73	C10:0	C13:0	C16:0	C16:1	C17:0	C18:0	C18:1n9	C18:1n7	C18:2n6	C18:3n3	C18:3n6	C20:0	C20:1n9	C20:5	C22:1n9	C24:0
tropical	Tuxpeno	0.18	0.23	13.86	0.12	0.07	1.72	21.68	0.77	55.18	1.50	0.16	0.28	0.20	0.24	0.06	0.31
flint	Longfellow Flint	0.13	0.25	13.53	0.12	0.06	1.60	20.16	0.78	54.50	1.68	0.16	0.22	0.12	0.16	0.19	0.14
tropical	Araguito	0.14	0.16	13.58	0.13	0.03	1.31	23.06	0.90	53.62	1.43	0.12	0.22	0.07	0.13	0.10	0.31
tropical	Canilla	0.13	0.26	14.20	0.15	0.08	1.56	23.39	0.86	51.95	1.56	0.03	0.26	0.15	0.26	0.09	0.12
tropical	Comiteco	0.18	0.07	13.84	0.10	0.07	1.76	26.09	0.76	51.35	1.30	0.17	0.31	0.16	0.18	0.17	0.22
tropical	Cuban Flint	0.14	0.04	13.85	0.10	0.09	2.20	26.12	0.66	51.32	1.36	0.17	0.48	0.12	0.16	0.03	0.16
temperate	Hickory King	0.24	0.10	14.51	0.12	0.04	1.69	27.57	0.86	50.24	1.65	0.18	0.29	0.14	0.33	0.27	0.27
intermediate	Chapalote	0.14	0.19	14.63	0.11	0.04	1.63	27.48	0.71	49.71	1.50	0.14	0.24	0.15	0.21	0.19	0.03
tropical	Pepetilla	0.09	0.25	14.03	0.10	0.05	1.97	24.18	0.70	49.59	1.42	0.11	0.32	0.08	0.11	0.16	0.10
tropical	Cateto	0.12	0.05	12.96	0.13	0.08	1.68	28.26	0.87	49.13	1.35	0.22	0.37	0.15	0.29	0.06	0.13
tropical	Tabloncillo	0.11	0.28	14.08	0.11	0.08	2.23	24.77	0.65	48.90	1.35	0.10	0.34	0.09	0.12	0.03	0.34
flint	Havasupai	0.19	0.03	14.00	0.13	0.08	2.10	30.42	0.77	48.89	1.65	0.20	0.40	0.20	0.38	0.23	0.21
tropical	Pollo	0.16	0.10	14.53	0.12	0.08	2.07	27.52	0.73	48.80	1.32	0.17	0.47	0.15	0.26	0.16	0.21
intermediate	Palomero de Jalisco	0.17	0.16	13.55	0.10	0.07	2.01	28.58	0.74	47.45	1.91	0.13	0.30	0.14	0.20	0.13	0.31
tropical	Crystalino Norteno	0.14	0.03	12.10	0.11	0.09	2.11	32.66	0.80	46.76	1.55	0.11	0.35	0.19	0.19	0.16	0.13
tropical	Bolita	0.13	0.13	13.55	0.12	0.08	2.39	29.20	0.69	46.03	1.37	0.15	0.36	0.13	0.14	0.17	0.23
tropical	Poropo	0.15	0.07	13.37	0.16	0.08	2.10	32.28	0.71	45.67	1.42	0.12	0.35	0.17	0.14	0.09	0.19
tropical	Costeno	0.18	0.03	13.63	0.13	0.07	1.95	31.45	0.83	45.52	1.38	0.22	0.34	0.12	0.54	0.12	0.11
flint	Santo Domingo	0.15	0.12	12.67	0.11	0.07	1.94	31.72	0.71	44.98	1.22	0.07	0.33	0.17	0.37	0.09	0.23
temparate	Shoe Peg	0.19	0.11	12.38	0.12	0.08	1.98	33.23	0.82	44.80	1.27	0.13	0.31	0.20	0.17	0.09	0.29
flint	Assiniboine	0.13	0.08	12.72	0.13	0.08	1.93	33.90	0.76	44.52	1.36	0.18	0.36	0.17	0.19	0.19	0.20
tropical	Cravo Riogranense	0.18	0.06	14.07	0.14	0.06	1.68	32.08	0.91	44.38	1.55	0.27	0.33	0.14	0.32	0.09	0.14
tropical	Reventador	0.09	0.32	13.95	0.14	0.04	2.14	31.32	0.79	42.84	1.36	0.14	0.29	0.12	0.23	0.09	0.27
tropical	Zapalote Chico	0.21	0.11	14.73	0.12	0.06	1.84	32.43	0.79	42.21	1.81	0.25	0.35	0.14	0.21	0.21	0.24
	min	0.09	0.03	12.10	0.10	0.03	1.31	20.16	0.65	42.21	1.22	0.03	0.22	0.07	0.11	0.03	0.03
	mean	0.15	0.13	13.68	0.12	0.07	1.90	28.31	0.77	48.26	1.47	0.15	0.33	0.14	0.23	0.13	0.20
	max	0.24	0.32	14.73	0.16	0.09	2.39	33.90	0.91	55.18	1.91	0.27	0.48	0.20	0.54	0.27	0.31

[a]Values expressed as % total fatty acid. For clarity only means are presented, individual replicate values are presented in the Supporting Information (File S2).

DOI:10.1021/acs.jafc.5b00208
J. Agric. Food Chem. 2015, 63, 5282−5295

Table 6. Mean Vitamin and Metabolite Values[a] for the Landrace Hybrids

group	landrace × B73	α-tocopherol	γ-tocopherol	δ-tocopherol	β-carotene	raffinose	phytic acid
tropical	Cuban Flint	13.00	39.00	1.00	0.17	0.11	1.01
tropical	Cateto	12.67	54.00	3.00	0.28	0.16	1.23
tropical	Cravo Riogranense	11.33	19.00	1.00	0.10	0.13	0.90
intermediate	Palomero de Jalisco	11.33	42.33	3.00	0.16	0.14	1.13
tropical	Crystalino Norteno	11.00	20.67	0.67	0.12	0.20	0.92
tropical	Zapalote Chico	10.67	22.67	0.67	0.05	0.16	1.25
tropical	Pollo	9.00	27.33	1.00	0.21	0.11	0.98
intermediate	Chapalote	8.00	24.00	1.00	0.03	0.12	1.00
flint	Assiniboine	7.67	34.67	2.33	0.08	0.24	1.11
flint	Longfellow Flint	7.67	32.67	2.33	0.20	0.14	0.99
tropical	Bolita	7.50	23.00	1.00	0.03	0.10	0.97
flint	Santo Domingo	7.33	35.33	1.33	0.03	0.15	1.21
tropical	Comiteco	7.00	13.33	0.33	0.03	0.09	1.02
flint	Havasupai	7.00	33.00	1.00	0.04	0.12	0.91
tropical	Tabloncillo	7.00	15.50	1.00	0.07	0.16	1.13
temperate	Hickory King	6.67	21.33	1.33	0.03	0.16	0.89
temparate	Shoe Peg	6.33	35.33	3.67	0.06	0.08	0.82
tropical	Araguito	6.00	31.67	3.00	0.04	0.20	0.96
tropical	Tuxpeno	6.00	12.33	2.33	0.10	0.10	1.06
tropical	Pepetilla	5.67	25.00	1.00	0.04	0.23	0.94
tropical	Reventador	5.67	21.00	1.67	0.03	0.14	1.07
tropical	Poropo	4.67	16.67	1.00	0.03	0.17	1.00
tropical	Costeno	4.50	18.00	1.00	0.06	0.10	0.94
tropical	Canilla	4.00	17.00	1.00	0.08	0.21	1.12
	min	4.00	12.33	0.33	0.03	0.08	0.82
	mean	7.82	26.45	1.53	0.09	0.15	1.02
	max	13.00	54.00	3.67	0.28	0.24	1.25

[a]Tocopherol values are expressed as mg/kg dwt, β-carotene values are expressed as mg/100 g dwt, and raffinose and phytic acid are expressed as % dwt. For clarity only means are presented; individual replicate values are presented in the Supporting Information (File S2).

Figure 7. Photographs of the B73 × landrace ears: (top row) MR01 (Araguito), MR02 (Assiniboine), MR03 (Bolita), MR04 (Canilla), MR05 (Cateto), MR06 (Chapalote), MR07 (Comiteco), MR08 (Costeno), MR09 (Cravo Riogranense), MR10 (Crystalino Norteno), MR11 (Cuban Flint), MR12 (Havasupai); (bottom row) MR13 (Hickory King), MR14 (Longfellow Flint), MR15 (Palomero de Jalisco), MR16 (Pepetilla), MR18 (Reventador), MR19 (Santo Domingo), MR20 (Shoe Peg), MR21 (Tabloncillo), MR22 (Tuxpeno), MR23 (Zapalote Chico), MR25 (Poropo), MR26 (Pollo).

pericarp colors masked white endosperm (Supplementary Table 8; Figure 7).

Correlations with Canonical Scores within Landraces. Correlations between proximates values and the canonical scores showed a pattern different from that for the NAM hybrid data set with, in general, much lower correlations (Supplementary Table 1; Figure 1). The minerals represented some of the highest correlations with canonical score 1; for example, iron, magnesium, manganese, and phosphorus were all >0.4 (Supporting Information). It is therefore probable that these components contribute more so than other components to separation of the breeding groups in the landrace set. This

DOI: 10.1021/acs.jafc.5b00208
J. Agric. Food Chem. 2015, 63, 5282−5295

contrasts slightly with results from the NAM set where minerals (with the possible exceptions of manganese and phosphorus) were less affected. Correlations between fatty acid values and canonical scores were low, suggesting that these components are unlikely to contribute to any separation of the different breeding groups. Of the metabolites, phytic acid showed the highest correlation with canonical score 1 (r = 0.394), whereas γ-tocopherol showed the highest correlation with canonical score 2 (r = 0.384).

Comparison of NAM to Landraces for Composition Traits. Box plots comparing compositional variation of NAM and landrace hybrids for selected analytes discussed above are presented in Supplementary Figure 6 (a−e). Sevaral composition components such as iron, manganese, phosphorus, ash, γ-tocopherol, raffinose, and phytic acid had the highest correlations for both hybrid sets. For most composition traits, the landrace hybrids had either the same or wider ranges of phenotypic variation than the inbred lines. The exceptions were the proximates fat, starch, and carbohydrates (Tables 1 and 4), several of the fatty acids such as palmitic acid (C16:0), stearic acid (C18:0), oleic acid (C18:1), and linoleic acid (C18:2) (Tables 2 and 5), the vitamins and minerals α- and γ-tocopherol and raffinose (Tables 3 and 6), the amino acids methionine and proline (Supplementary Tables 2 and 4), and the minerals copper, manganese, and zinc (Supplementary Tables 3 and 5). Interestingly, for most of these exceptions the lower range for the landrace hybrids did not exceed the lower range of the inbreds, whereas the upper range of the landrace hybrids still exceeded the inbred range, indicating that the landraces may be more valuable for increasing these trait values rather than decreasing them. The wide diversity of phenotypes for all of the kernel composition traits in the landrace hybrids warrants further studies of the genetic architecture underlying composition traits, as well as the exploration of this diversity for maize improvement.

Plant, Ear, and Kernel Phenotypic Data. Results of the CDA on the phenotypic data for both the NAM and landrace hybrid sets are provided in Supplementary Table 6. Positive correlations with canonical scores 1 or 2 were observed for days to anthesis, ear weight, ear width, kernel weight, cob weight, and ear height in the NAM hybrid set. In the landrace hybrid set positive correlations with canonical scores 1 or 2 were observed for days to anthesis, plant height, ear height, ear length, and ear fill length. The majority of the ear/kernel phenotypes showed negative correlations in the landrace hybrid data set. There was wide variability for all plant, ear, and kernel traits in both the NAM and landrace hybrid sets (Supplementary Tables 7 and 8). As with the composition data, the landrace hybrids had wider ranges of plant, ear, and kernel phenotypes. The exceptions were ear and cob weight, which are likely a function of the unadaptedness of the landraces to the temperate environment in which they were evaluated, where the landrace hybrids were not able to produce full-sized ears. These phenotypes have been studied extensively at the genetic level in the NAM population,[31] but as for the composition traits discussed above, they have not been explored in landraces.

The development of modern plant breeding techniques has greatly facilitated wider use of a wealth of genetic diversity from many sources including landraces. Exploitation of genetic diversity in breeding programs has allowed food production to keep up with population growth.[32] The development of improved maize hybrids will require optimization of current resources to guide breeding strategies. The genetic diversity preserved in germplasm banks represents a key current resource. In this study we have provided the maize research community a first survey of kernel composition of hybrids from two important genetic resources: the NAM founder lines and landraces selected from wide geographic areas in the Americas. Multivariate analysis (CDA) showed that subsets within each of the NAM and landrace hybrid data sets could be distinguished by breeding group. Overall, results highlighted extensive variation in all compositional components assessed for both sets of hybrids reflecting the underlying genetic diversity of these lines. Data generated here will be of value to plant breeders and plant biotechnologists involved in the nutritional and agronomic improvement of corn and will be a resource for the wider research community utilizing the NAM founder lines to understand the genetic basis of compositional and other complex traits. The data also contrast the variation associated with conventional breeding to the relative lack of impact of GM on composition.[18b] The natural variability associated with composition observed in these conventional natural populations may therefore also be of interest to regulatory scientists and policy makers involved in safety evaluation of transgenic crops from a food and feed perspective.[33]

■ ASSOCIATED CONTENT

Supporting Information

Additional figures and tables. The Supporting Information is available free of charge on the ACS Publications website at DOI: 10.1021/acs.jafc.5b00208.

■ AUTHOR INFORMATION

Corresponding Authors

*(T.V.) E-mail: t.v.venkatesh@monsanto.com.
*(S.F.-G.) E-mail: Sherry.Flint-Garcia@ars.usda.gov.

Notes

The authors declare no competing financial interest.

■ ACKNOWLEDGMENTS

We are indebted to Nordine Cheikh for his support and encouragement and to Erin Bell for helpful comments on the manuscript. We thank the Buckler laboratory at Cornell University for contributing seed for the analyses.

■ REFERENCES

(1) James, C. Global status of commercialized biotech/GM crops: 2013; International Service for the Acquisition of Agri-Biotech Applications: Ithaca, NY, 2013.

(2) Strable, J.; Scanlon, M. J. Maize (*Zea mays*): a model organism for basic and applied research in plant biology. *Cold Spring Harbor Protocols* **2009**, *2009* (10), pdb.emo132.

(3) Vigouroux, V.; Glaubitz, J. C.; Matsuoka, Y.; Goodman, M. M.; Sánchez, G. J.; Doebley, J. Population structure and genetic diversity of new world maize races assessed by DNA microsatellites. *Am. J. Bot.* **2008**, *95*, 1240.

(4) Crow, J. F. 90 years ago: the beginning of hybrid maize. *Genetics* **1998**, *148* (3), 923−928.

(5) (a) Wright, S. I.; Vroh, B. I.; Schroeder, S. G.; Yamasaki, M.; Doebley, J. F.; McMullen, M. D.; Gaut, B. S. The effects of artificial selection on the maize genome. *Science* **2005**, *308*, 1310. (b) Tenaillon, M. I.; U'Ren, J.; Tenaillon, O.; Gaut, B. S. Selection versus demography: a multilocus investigation of the domestication process in maize. *Mol. Biol. Evol.* **2004**, *21* (7), 1214−1225.

(6) Flint-Garcia, S. A. Genetics and consequences of crop domestication. *J. Agric. Food Chem.* **2013**, *61* (35), 8267−8276.

DOI: 10.1021/acs.jafc.5b00208
J. Agric. Food Chem. 2015, 63, 5282−5295

(7) Romay, M.; Millard, M.; Glaubitz, J.; Peiffer, J.; Swarts, K.; Casstevens, T.; Elshire, R.; Acharya, C.; Mitchell, S.; Flint-Garcia, S.; McMullen, M.; Holland, J.; Buckler, E.; Gardner, C. Comprehensive genotyping of the USA national maize inbred seed bank. *Genome Biology* **2013**, *14* (6), R55.
(8) Chia, J. M.; Song, C.; Bradbury, P. J.; Costich, D.; de Leon, N.; Doebley, J.; Elshire, R. J.; Gaut, B.; Geller, L.; Glaubitz, J. C.; Gore, M.; Guill, K. E.; Holland, J.; Hufford, M. B.; Lai, J.; Li, M.; Liu, X.; Lu, Y.; McCombie, R.; Nelson, R.; Poland, J.; Prasanna, B. M.; Pyhajarvi, T.; Rong, T.; Sekhon, R. S.; Sun, Q.; Tenaillon, M. I.; Tian, F.; Wang, J.; Xu, X.; Zhang, Z.; Kaeppler, S. M.; Ross-Ibarra, J.; McMullen, M. D.; Buckler, E. S.; Zhang, G.; Xu, Y.; Ware, D. Maize HapMap2 identifies extant variation from a genome in flux. *Nat. Genet.* **2012**, *40*, 803.
(9) Hufford, M. B.; Xu, X.; van Heerwaarden, J.; Pyhajarvi, T.; Chia, J.-M.; Cartwright, R. A.; Elshire, R. J.; Glaubitz, J. C.; Guill, K. E.; Kaeppler, S. M.; Lai, J.; Morrell, P. L.; Shannon, L. M.; Song, C.; Springer, N. M.; Swanson-Wagner, R. A.; Tiffin, P.; Wang, J.; Zhang, G.; Doebley, J.; McMullen, M. D.; Ware, D.; Buckler, E. S.; Yang, S.; Ross-Ibarra, J. Comparative population genomics of maize domestication and improvement. *Nat. Genet.* **2012**, *44* (7), 6.
(10) (a) Yu, J.; Holland, J. B.; McMullen, M. D.; Buckler, E. S. Genetic design and statistical power of nested association mapping in maize. *Genetics* **2008**, *178* (1), 539−551. (b) McMullen, M. D.; Kresovich, S.; Villeda, H. S.; Bradbury, P.; Li, H.; Sun, Q.; Flint-Garcia, S.; Thornsberry, J.; Acharya, C.; Bottoms, C.; Brown, P.; Browne, C.; Eller, M.; Guill, K.; Harjes, C.; Kroon, D.; Lepak, N.; Mitchell, S. E.; Peterson, B.; Pressoir, G.; Romero, S.; Rosas, M. O.; Salvo, S.; Yates, H.; Hanson, M.; Jones, E.; Smith, S.; Glaubitz, J. C.; Goodman, M.; Ware, D.; Holland, J. B.; Buckler, E. S. Genetic properties of the maize Nested Association Mapping population. *Science* **2009**, *325* (5941), 737−740.
(11) Mikel, M. A.; Dudley, J. W. Evolution of North American dent corn from public to proprietary germplasm. *Crop Sci.* **2006**, *46* (3), 1193−1205.
(12) Schnable, P. S.; Ware, D.; Fulton, R. S.; Stein, J. C.; Wei, F.; Pasternak, S.; Liang, C.; Zhang, J.; Fulton, L.; Graves, T. A.; Minx, P.; Reily, A. D.; Courtney, L.; Kruchowski, S. S.; Tomlinson, C.; Strong, C.; Delehaunty, K.; Fronick, C.; Courtney, B.; Rock, S. M.; Belter, E.; Du, F.; Kim, K.; Abbott, R. M.; Cotton, M.; Levy, A.; Marchetto, P.; Ochoa, K.; Jackson, S. M.; Gillam, B.; Chen, W.; Yan, L.; Higginbotham, J.; Cardenas, M.; Waligorski, J.; Applebaum, E.; Phelps, L.; Falcone, J.; Kanchi, K.; Thane, T.; Scimone, A.; Thane, N.; Henke, J.; Wang, T.; Ruppert, J.; Shah, N.; Rotter, K.; Hodges, J.; Ingenthron, E.; Cordes, M.; Kohlberg, S.; Sgro, J.; Delgado, B.; Mead, K.; Chinwalla, A.; Leonard, S.; Crouse, K.; Collura, K.; Kudrna, D.; Currie, J.; He, R.; Angelova, A.; Rajasekar, S.; Mueller, T.; Lomeli, R.; Scara, G.; Ko, A.; Delaney, K.; Wissotski, M.; Lopez, G.; Campos, D.; Braidotti, M.; Ashley, E.; Golser, W.; Kim, H.; Lee, S.; Lin, J.; Dujmic, Z.; Kim, W.; Talag, J.; Zuccolo, A.; Fan, C.; Sebastian, A.; Kramer, M.; Spiegel, L.; Nascimento, L.; Zutavern, T.; Miller, B.; Ambroise, C.; Muller, S.; Spooner, W.; Narechania, A.; Ren, L.; Wei, S.; Kumari, S.; Faga, B.; Levy, M. J.; McMahan, L.; Van Buren, P.; Vaughn, M. W.; Ying, K.; Yeh, C.-T.; Emrich, S. J.; Jia, Y.; Kalyanaraman, A.; Hsia, A.-P.; Barbazuk, W. B.; Baucom, R. S.; Brutnell, T. P.; Carpita, N. C.; Chaparro, C.; Chia, J.-M.; Deragon, J.-M.; Estill, J. C.; Fu, Y.; Jeddeloh, J. A.; Han, Y.; Lee, H.; Li, P.; Lisch, D. R.; Liu, S.; Liu, Z.; Nagel, D. H.; McCann, M. C.; SanMiguel, P.; Myers, A. M.; Nettleton, D.; Nguyen, J.; Penning, B. W.; Ponnala, L.; Schneider, K. L.; Schwartz, D. C.; Sharma, A.; Soderlund, C.; Springer, N. M.; Sun, Q.; Wang, H.; Waterman, M.; Westerman, R.; Wolfgruber, T. K.; Yang, L.; Yu, Y.; Zhang, L.; Zhou, S.; Zhu, Q.; Bennetzen, J. L.; Dawe, R. K.; Jiang, J.; Jiang, N.; Presting, G. G.; Wessler, S. R.; Aluru, S.; Martienssen, R. A.; Clifton, S. W.; McCombie, W. R.; Wing, R. A.; Wilson, R. K. The B73 maize genome: complexity, diversity, and dynamics. *Science* **2009**, *326* (5956), 1112−1115.
(13) Flint-Garcia, S. A.; Thuillet, A.-C.; Yu, J.; Pressoir, G.; Romero, S. M.; Mitchell, S. E.; Doebley, J.; Kresovich, S.; Goodman, M. M.; Buckler, E. S. Maize association population: a high-resolution platform for quantitative trait locus dissection. *Plant J.* **2005**, *44* (6), 1054−1064.
(14) Flint-Garcia, S.; Bodnar, A.; Scott, M. Wide variability in kernel composition, seed characteristics, and zein profiles among diverse maize inbreds, landraces, and teosinte. *Theor. Appl. Genet.* **2009**, *119* (6), 1129−1142.
(15) Cook, J. P.; McMullen, M. D.; Holland, J. B.; Tian, F.; Bradbury, P.; Ross-Ibarra, J.; Buckler, E. S.; Flint-Garcia, S. A. Genetic architecture of maize kernel composition in the Nested Association Mapping and Inbred Association panels. *Plant Physiol.* **2012**, *158* (2), 824−834.
(16) (a) Chandler, K.; Lipka, A. E.; Owens, B. F.; Li, H.; Buckler, E. S.; Rocheford, T.; Gore, M. A. Genetic analysis of visually scored orange kernel color in maize. *Crop Sci.* **2013**, *53* (1), 189−200. (b) Yan, J.; Kandianis, C. B.; Harjes, C. E.; Bai, L.; Kim, E.-H.; Yang, X.; Skinner, D. J.; Fu, Z.; Mitchell, S.; Li, Q.; Fernandez, M. G. S.; Zaharieva, M.; Babu, R.; Fu, Y.; Palacios, N.; Li, J.; DellaPenna, D.; Brutnell, T.; Buckler, E. S.; Warburton, M. L.; Rocheford, T. Rare genetic variation at *Zea mays* crtRB1 increases β-carotene in maize grain. *Nat. Genet.* **2010**, *42* (4), 322−327.
(17) Zheng, P.; Allen, W. B.; Roesler, K.; Williams, M. E.; Zhang, S.; Li, J.; Glassman, K.; Ranch, J.; Nubel, D.; Solawetz, W.; Bhattramakki, D.; Llaca, V.; Deschamps, S.; Zhong, G. Y.; Tarczynski, M. C.; Shen, B. A phenylalanine in DGAT is a key determinant of oil content and composition in maize. *Nat. Genet.* **2008**, *40* (3), 367−372.
(18) (a) Herman, R. A.; Price, W. D. Unintended compositional changes in GM crops: 20 years of research. *J. Agric. Food Chem.* **2013**, *61* (48), 11695−11701. (b) Harrigan, G. G.; Lundry, D.; Drury, S.; Berman, K.; Riordan, S. G.; Nemeth, M. A.; Ridley, W. P.; Glenn, K. C. Natural variation in crop composition and the impact of transgenesis. *Nat. Biotechnol.* **2010**, *28* (5), 402−404.
(19) Goodman, M. M.; Brown, W. L. Races of corn. In *Corn and Corn Improvement*, 3rd ed.; Sprague, G. F., Dudley, J. W., Eds.; American Society of Agronomy: Madison, WI, USA, 1988; pp 33−79.
(20) (a) Drury, S. M.; Reynolds, T. L.; Ridley, W. P.; Bogdanova, N.; Riordan, S.; Nemeth, M. A.; Sorbet, R.; Trujillo, W. A.; Breeze, M. L. Composition of forage and grain from second-generation insect-protected corn MON 89034 is equivalent to that of conventional corn (*Zea mays* L.). *J. Agric. Food Chem.* **2008**, *56* (12), 4623−4630. (b) Ridley, W. P.; Sidhu, R. S.; Pyla, P. D.; Nemeth, M. A.; Breeze, M. L.; Astwood, J. D. Comparison of the nutritional profile of glyphosate-tolerant corn event NK603 with that of conventional corn (*Zea mays* L.). *J. Agric. Food Chem.* **2002**, *50* (25), 7235−7243.
(21) AOAC In *Official Methods of Analysis of AOAC International*, 18th ed.; AOAC International: Gaithersburg, MD, USA, 2005; method 996.11.
(22) Harrigan, G. G.; Stork, L. G.; Riordan, S. G.; Reynolds, T. L.; Ridley, W. P.; Masucci, J. D.; MacIsaac, S.; Halls, S. C.; Orth, R.; Smith, R. G.; Wen, L.; Brown, W. E.; Welsch, M.; Riley, R.; McFarland, D.; Pandravada, A.; Glenn, K. C. Impact of genetics and environment on nutritional and metabolite components of maize grain. *J. Agric. Food Chem.* **2007**, *55* (15), 6177−6185.
(23) Hogarty, C. J.; Ang, C.; Eitenmiller, R. R. Tocopherol content of selected foods by HPLC/fluorescence quantitation. *J. Food Compos. Anal.* **1989**, *2* (3), 200−209.
(24) *Assigning Values to Nondetected/Non-quantified Pesticide Residues in Human Health Food Exposure Assessments*; Office of Pesticide Programs, U.S. Environmental Protection Agency: Washington, DC, USA, 2000; p 33.
(25) Johnson, D. E. *Applied Multivariate Methods for Data Analysts*; Duxbury Resource Center: China, 1998.
(26) Goodman, M. M. Broadening the U.S. maize germplasm base. *Maydica* **2005**, *50*, 203−214.
(27) ILSI, International Life Science Institute − Crop Composition Database, v5; www.cropcomposition.org, 2014.
(28) James, M. G.; Robertson, D. S.; Myers, A. M. Characterization of the maize gene sugary1, a determinant of starch composition in kernels. *Plant Cell* **1995**, *7* (4), 417−429.

DOI: 10.1021/acs.jafc.5b00208
J. Agric. Food Chem. 2015, 63, 5282−5295

(29) Morohashi, K.; Casas, M. I.; Ferreyra, L. F.; Mejía-Guerra, M. K.; Pourcel, L.; Yilmaz, A.; Feller, A.; Carvalho, B.; Emiliani, J.; Rodriguez, E.; Pellegrinet, S.; McMullen, M.; Casati, P.; Grotewold, E. A genome-wide regulatory framework identifies maize pericarp color1 controlled genes. *Plant Cell* **2012**, *24* (7), 2745−2764.
(30) Aliu, S.; Rusinovsci, I.; Fetahu, S.; Bisilimi, K. Morpho-physiological traits and mineral composition on local maize population growing in agro ecological conditions in Kosova. *Not. Sci. Biol.* **2013**, *5* (5), 232−237.
(31) (a) Buckler, E. S.; Holland, J. B.; Bradbury, P. J.; Acharya, C. B.; Brown, P. J.; Browne, C.; Ersoz, E.; Flint-Garcia, S.; Garcia, A.; Glaubitz, J. C.; Goodman, M. M.; Harjes, C.; Guill, K.; Kroon, D. E.; Larsson, S.; Lepak, N. K.; Li, H.; Mitchell, S. E.; Pressoir, G.; Peiffer, J. A.; Rosas, M. O.; Rocheford, T. R.; Romay, M. C.; Romero, S.; Salvo, S.; Villeda, H. S.; Sofia da Silva, H.; Sun, Q.; Tian, F.; Upadyayula, N.; Ware, D.; Yates, H.; Yu, J.; Zhang, Z.; Kresovich, S.; McMullen, M. D. The genetic architecture of maize flowering time. *Science* **2009**, *325*, 714. (b) Peiffer, J. A.; Romay, M. C.; Gore, M. A.; Flint-Garcia, S. A.; Zhang, Z.; Millard, M. J.; Gardner, C. A. C.; McMullen, M. D.; Holland, J. B.; Bradbury, P. J.; Buckler, E. S. The genetic architecture of maize height. *Genetics* **2014**, *196* (4), 1337−1356. (c) Brown, P. J.; Upadyayula, N.; Mahone, G. S.; Tian, F.; Bradbury, P. J.; Myles, S.; Holland, J. B.; Flint-Garcia, S.; McMullen, M. D.; Buckler, E. S.; Rocheford, T. R. Distinct genetic architectures for male and female inflorescence traits of maize. *PLoS Genet.* **2011**, *7*, e1002383. (d) Hirsch, C. N.; Flint-Garcia, S. A.; Beissinger, T. M.; Eichten, S. R.; Deshpande, S.; Barry, K.; McMullen, M. D.; Holland, J. B.; Buckler, E. S.; Springer, N.; Buell, C. R.; de Leon, N.; Kaeppler, S. M. Insights into the effects of long-term artificial selection on seed size in maize. *Genetics* **2014**, *198* (1), 409−421.
(32) Wood, D.; Lanne, J. M. *Agrobiodiversity: Characterization, Utilization and Mangement*; CAB Publishing: New York, 1999; p 490.
(33) OECD. *Consensus Document on Compositional Considerations for New Varieties of Maize (Zea mays): Key Food and Feed Nutrients, Anti-nutrients and Secondary Plant Metabolites*; Organisation of Economic Co-Operation and Development: Paris, France, 2002; Vol. OECD ENV/JM/MONO (2002)25.

DOI: 10.1021/acs.jafc.5b00208
J. Agric. Food Chem. 2015, 63, 5282−5295

JOURNAL OF AGRICULTURAL AND FOOD CHEMISTRY

Article

pubs.acs.org/JAFC

Evaluation of Chlorpyrifos Transferred from Contaminated Feed to Duck Commodities and Dietary Risks to Chinese Consumers

Rui Li,[†] Xiaofeng Ji,[†] Liang He,[§] Zhiqiang Liu,[#] Wei Wei,[†] Mingrong Qiang,[†] Qiang Wang,[†] and Yuwei Yuan*[,†]

[†]State Key Laboratory Breeding Base for Zhejiang Sustainable Plant Pest Control, Agricultural Ministry Key Laboratory for Pesticide Residue Detection, Zhejiang Province Key Laboratory for Food Safety, and Institute of Quality and Standard for Agro-products, Zhejiang Academy of Agricultural Sciences, Hangzhou 310021, People's Republic of China

[§]National Shanghai Center for New Drug Safety Evaluation and Research, Shanghai 201203, People's Republic of China

[#]Veterinary Research Institute, Xinjiang Academy of Animal Science, Urumqi 830000, People's Republic of China

ABSTRACT: The present study describes chlorpyrifos residues in duck commodities through the duck food chain, transfer factors, and dietary risks to Chinese consumers. After duck feeding experiments with pellet feed that lasted for 42 days, chlorpyrifos residues found in all samples collected from the ducks on maximum estimated dose group (3.20 mg/kg level) were from <0.0005 to 0.019 mg/kg. The residue levels of the fat, intestine, and tongue were obviously higher than those of the meat and other edible tissues. The transfer factors of all duck commodities were from 0.0001 to 0.0049 among different contamination levels, which indicated that chlorpyrifos had a low persistency in duck meat and metabolism organs. The chronic exposure assessment revealed that only 0.034−0.150% of the acceptable daily intake (ADI; 0−0.01 mg/kg/bw/day) of chlorpyrifos was consumed via the duck commodities for different age and gender groups in China. The acute exposure assessments of different age and gender groups were only 0.019−0.082% of the acute reference dose (ARfD; 0−0.1 mg/kg/bw). The results show that the single dietary exposure risk of chlorpyrifos raised by the intake of duck commodities was quite low in China.

KEYWORDS: *chlorpyrifos, duck commodities, transfer, dietary exposure*

INTRODUCTION

The potential effects of pesticide accumulation along the food chain on human health are of increasing concern to consumers and food safety authorities worldwide.[1−3] Currently, maximum residue limits (MRLs) for various pesticides in products of animal origin were mainly set by international organizations and developed countries, but only a few MRLs (e.g., endosulfan, quintozene) in animal commodities have been set by the Chinese government due to limited research for pesticide transfer along the food chain.[4,5] Evaluations of pesticide transfer from contaminated feed to animal commodities and their potential dietary exposure to consumers are increasingly needed in China.

Chlorpyrifos (*O*,*O*-diethyl *O*-3,5,6-trichloro-2-pyridyl phosphorothioate) is one of the most widely used organophosphorus pesticides in China.[6] Chlorpyrifos kills insects by inhibiting pest acetyl cholinesterase, but the pesticide has potential toxicity to mammals and humans including birth defects, nervous system disorders, and increased rates of leukemia and immune system abnormalities.[7] Therefore, the use of chlorpyrifos in agricultural production has been constantly monitored in many agro-products, mainly including foods of plant origin (e.g., vegetables, fruits, and grain crops).[6,8] However, scant information has been obtained on chlorpyrifos residues in animal commodities. For example, Sun et al. detected the highest concentration of chlorpyrifos residue as 0.46 mg/kg in farmed fish.[9] Kammerbauer et al. found the presence of chlorpyrifos residues (0.011 mg/kg) in the tissues of fish that had been raised near an agricultural field.[10] High chlorpyrifos residues were detected as the one of the main pollutants in raw buffalo's milk in Egypt and cow's milk in Italy.[11,12] Unfortunately, monitoring and controlling chlorpyrifos residues in livestock commodities are still in the early stages, and published data related to pesticide residues and risk assessment of livestock commodities are scattered. Meanwhile, this situation also poses serious problems for the Chinese government and livestock producers to manage chlorpyrifos residues in livestock commodities.

The risk assessment of feed contaminants to humans has often been hampered by a lack of knowledge concerning their behavior after feeding on domestic animals. Several livestock metabolism and feeding studies indicated that organophosphorus pesticide residues (including chlorpyrifos) were rapidly absorbed and excreted mainly through the urine at the test dose of pesticides. Hsu et al. recovered a maximum of 0.14% of chlorpyrifos intake via eggs at a single dose (90 mg) for 8 days, similar to a report by Schenck and Donoghue.[13,14] The levels of chlorpyrifos in milk ranged from <0.01 mg/kg at dietary levels of ≤10 mg/kg to 0.02 mg/kg at 30 mg/kg, and chlorpyrifos residues in cream were approximately 10 times higher than in milk.[15] Chlorpyrifos residues were detected in eggs of laying hens at dietary levels of 0.3−10 mg/kg for 30 days.[15] Currently, little attention has been paid to pesticide residues in farm-raised ducks under realistic dietary burden intake, although duck meat,

Received: January 29, 2015
Accepted: May 6, 2015
Published: May 6, 2015

ACS Publications © 2015 American Chemical Society

DOI: 10.1021/acs.jafc.5b01839
J. Agric. Food Chem. 2015, 63, 5296−5304

Table 1. Chinese Food Consumption Data from Different Age and Gender Groups in Duck Commodities

			meat (fat) consumption (g/day)		egg consumption (g/day)		edible tissue consumption (g/day)	
age group	gender	body wt (kg)	av	97.5th percentile	av	97.5th percentile	av	97.5th percentile
2−3 years	male	13.2	6.3	21.8	20.7	71.6	3.2	11.1
	female	12.3	9.5	32.9	19.3	66.8	2.4	8.3
4−6 years	male	16.8	10.7	37.0	20.0	69.2	2.2	7.6
	female	16.2	9.2	31.8	19.8	68.4	2.7	9.3
7−10 years	male	22.9	12.9	44.6	20.6	71.2	3.5	12.1
	female	21.7	10.9	37.7	17.8	61.6	2.5	8.6
11−13 years	male	34.1	12.2	42.2	21.1	73.0	4.3	14.9
	female	34.0	10.4	36.0	18.0	62.3	3.0	10.4
14−17 years	male	46.7	14.0	48.4	21.6	74.7	5.6	19.4
	female	45.2	14.1	48.8	20.8	72.0	2.7	9.3
18−29 years	male	58.4	15.5	53.6	23.2	80.2	5.7	19.7
	female	52.1	15.9	55.0	22.5	77.8	4.7	16.3
30−44 years	male	64.9	17.5	60.6	24.9	86.2	6.4	22.2
	female	55.7	13.3	46.0	22.4	77.5	4.2	14.5
45−59 years	male	63.1	14.7	50.9	23.2	80.3	5.4	18.7
	female	57.0	11.4	39.4	21.0	72.6	4.3	14.9
60−69 years	male	61.5	11.7	40.5	23.5	81.3	4.5	15.6
	female	54.3	9.9	34.3	20.8	72.1	3.3	11.4
≥70 years	male	58.5	10.3	35.6	22.5	77.8	4.7	16.2
	female	51.0	7.5	26.0	19.9	69.0	3.3	11.4

eggs, and other derived products are among the most popular food items in the Chinese diet.[16]

According to the result of an earlier study in our laboratory, the chlorpyrifos residue determined in the processed duck pellet feed was 3.20 mg/kg.[17] Animal feed is one potential pesticide exposure pathway to transfer pesticides to human foods. We further wondered if chlorpyrifos could contaminate duck commodities through the livestock food chain and influence consumers' health. At present, an obstacle to the evaluation of the risk posed by chlorpyrifos residues in feed is the lack of relevant data related to the transfer of residues from feed to livestock commodities. In the food chain transfer, transfer factors (TFs) are defined as the ratio of the pesticide residue in the tissue or commodity of interest to the pesticide residue in the animal feed. Generally, feeding studies are used to determine transfer factors, which are usually adopted to assist dietary assessment of pesticide intake from animal commodities. Therefore, the objectives of the current study were to investigate the chlorpyrifos residues and transfer in duck commodities (i.e., meat, eggs, and other edible tissues) through feeding trials based on maximum levels in feed contaminated by chlorpyrifos and also to obtain TFs from feed to animal commodities. Finally, the potential dietary exposure risk of chlorpyrifos from consumed duck commodities were further evaluated by using the deterministic approach.

MATERIALS AND METHODS

Materials. Stock solution of chlorpyrifos (100 μg/mL in acetonitrile) was purchased from the Agro-Environmental Protection Institute, Ministry of Agriculture (Tianjin, China). *N*-Propylethylenediamine (PSA) and graphitized carbon black (GCB) were obtained from Bonna-Agela Technologies Inc. (Tianjin, China). Analytical grade acetonitrile, ethyl acetate, $MgSO_4$, and NaCl were obtained from East China Pharmaceutical Group Co., Ltd. (Hangzhou, China). Unless otherwise noted, all reagents used in the study were of HPLC grade. Pure water was generated by a Milli-Q water-purification system (Millipore, Bedford, MA, USA).

Experimental Design and Duck Husbandry. The present study was approved by the Animal Welfare Committee of Zhejiang Academy of Agricultural Sciences. All of the animal studies were conducted in accordance with the guidelines of the Ministry of Public Health of the People's Republic of China. Ducks were raised in cages with plastic-wire floors (60 × 170 × 70 cm^3). The cages were maintained with 24 h of constant light, a relative humidity of 60 ± 10%, and a room temperature of 20 ± 5 °C. The ducks were daily provided commercial pellet feed containing 18.0% protein and water ad libitum throughout the experimental period. All efforts were made to minimize the number of animals used in the study and their suffering.

Randomized Controlled Feeding Trial with Broiler Ducks (Pekin Duck). Pekin duck is the predominant breed used for meat production in China. A total of 30 white Pekin ducks (7 days of age, each weighed 0.09−0.11 kg) were randomly divided into three different groups and were fed duck pellet feed containing chlorpyrifos at levels of 3.20 mg/kg (1×), 9.60 mg/kg (3×), and 32.0 mg/kg (10×) for 42 days, respectively. Three ducks randomly selected from the groups were placed on a pesticide-free diet as a control. After 42 days, all ducks were slaughtered to collect the muscle, fat, heart, stomach, tongue, intestine, liver, and kidney tissues, respectively. All samples were cleaned with deionized water and sealed in plastic bags to minimize the possibility of contamination. All samples were then stored at −20 °C in darkness until analysis.

Randomized Controlled Feeding Trial with Egg-Laying Ducks (Shaoxing Brown Duck). Shaoxing brown duck is a major egg layer breed in southern China. A total of 30 Shaoxing brown ducks (150 days of age, each weighed 1.4−1.6 kg) were randomly divided into three different groups and were fed duck pellet duck containing chlorpyrifos at levels of 3.20 mg/kg (1×), 9.60 mg/kg (3×), and 32.0 mg/kg (10×) in the diet for 42 days. Three ducks randomly selected from the groups were placed on a pesticide-free diet as a control. The eggs from all ducks were collected on days 1, 3, 7, 14, 21, 28, 35, and 42 during the experimental periods. All samples were sealed in plastic tubes and stored at −20 °C in darkness until analysis.

Sample Preparation and Analytical Conditions. Extraction and cleaning procedures of chlorpyrifos from duck samples (meat, eggs, and other edible tissues) were performed according to the method of Li et al. with minor modifications.[18] Briefly, 2.0 g of homogenized sample was transferred to a 50 mL Teflon centrifuge tube with 10 mL of acetonitrile acidified with 1 M HCl (99:1, v/v), along with 2.0 g of $MgSO_4$ and 1.0 g of NaCl. The tube was shaken vigorously for 1 min

DOI: 10.1021/acs.jafc.5b01839
J. Agric. Food Chem. 2015, 63, 5296−5304

followed by centrifugation for 5 min at 966*g*, and the supernatant was transferred to a clean conical tube. The extraction step was repeated again, and all of the supernatant was pooled into a conical tube and frozen at −20 °C (>1 h); the fat layers formed on the sample surface were removed before the next analysis. The remaining liquid extract (10 mL) was concentrated using a rotary vacuum evaporator at 40 °C and dried with a gentle stream of nitrogen. The residue was then redissolved with 1.0 mL of ethyl acetate in a 2.5 mL microcentrifuge tube with a mixture of 150 mg of $MgSO_4$, 25 mg of GCB, and 50 mg of PSA. The tube was shaken vigorously for 1 min and centrifuged for 5 min at 9030*g*. The extract was filtered through a 0.22 μm PVDF filter before analysis by GC-MS/MS.

TSQ Quantum gas chromatography with a GC system TRACE GC Ultra and a triple-quadrupole mass spectrometer Quantum (Thermo Fisher Scientific, USA) were used for the analysis. The Zebron ZB-MultiResidue-2 capillary column (30 m × 0.25 mm i.d., 0.25 μm film thickness; Phenomenex, Torrance, CA, USA) was applied for analyte separation. The injection inlet temperature was 250 °C. The oven temperature was initially at 60 °C for 1 min and then increased in several steps: to 180 °C at a rate of 30 °C/min, to 220 °C at a rate of 10 °C/min, and to 280 °C at a rate of 60 °C/min. The transfer line and ionization source temperatures were set at 260 and 250 °C, respectively. The injection mode was splitless. The mass spectrometer was under the selected reaction monitoring (SRM) mode. The highest intensity ion (m/z 314) was used for parent ions to produce product ions m/z 286 and 258 (quantitative ion) in the GC-MS system.

Pesticide recovery analysis was evaluated by fortified blank samples at four chlorpyrifos concentrations with six replicates. Matrix effects were evaluated by comparing the slopes of solvent and matrix calibration sets. Series 1 was prepared by diluting the stock standard solution in solvent at four concentrations and series 2 by diluting the stock standard solution in matrix extract that was obtained from a pesticide-free sample.

Chinese Food Consumption Data. Chinese food consumption data were derived from the 2002 China National Nutrition and Health Survey (CNNHS) covering residents from 31 areas including provinces, autonomous regions, and metropolises in China (excluding Hong Kong, Taiwan, and Macau).[19] The survey employed a 24 h recall method using a multistage, random cluster process over three consecutive days (two weekdays and 1 weekend day, holidays excluded). In this survey, 23470 families were obtained from a stratified random sample of 68962 individuals including 33551 males and 35411 females. The food types were categorized into 10 groupings, such as rice, flour, coarse cereal, pulses, vegetables, fruits, meat, milk, eggs, and aquatic products. Demographic information on the participants, including age, gender, and body weight, was also gathered in the survey and used for later calculation. Various duck commodities, consumption data in the survey for different age groups (2−3, 4−6, 7−10, 11−13, 14−17, 18−29, 30−34, 45−59, 60−69, and ≥70 years old), and gender (male and female) are presented in Table 1.

Calculation of Pesticide Residue Intakes. Due to the prominent advantages (i.e., simplicity, worldwide use, and acceptance), the deterministic approach is usually selected as the first screening tool to identify the potential risks of pesticides in food.[20] This approach was selected to calculate chlorpyrifos exposure of duck commodities in our study. Here, on the basis of the residue results of the 1× dose in a feeding trial, chlorpyrifos intakes were estimated using STMR and HR to evaluate long- and short-term health risks to consumers on the basis of methods recommended by the WHO.[21]

The data of food consumption and chemical residues are two obligatory factors in the quantification of dietary risk (exposure assessment).[22] The dietary exposure to pesticides was calculated on the basis of consumption data, individual body weights, and residue data from animal feeding studies, usually presented as acute (short-term) and chronic (long-term) exposures. Estimated intakes on a daily basis were expressed as percentages of the ADI (0−0.01 mg/kg/bw/day) and ARfD (0−0.1 mg/kg/bw) values of chlorpyrifos, which were derived from a Joint FAO/WHO Meeting on Pesticide Residues.[23] Chronic intake assessment was calculated by multiplying median residue concentration and the average daily per capita consumption for livestock commodities obtained from the 2002 CNNHS. The estimated daily intake (EDI) and the hazard quotient (HQ) of pesticide residue were calculated by the following the equations: EDI = Σ((Fi × STMR)/(mean body weight)) and HQ = (EDI/ADI) × 100%; Fi is the average food consumption from the 2002 CNNHS, STMR is the median residue level from animal feeding trials, and the mean body weight was obtained from the 2002 CNNHS. For the calculation of acute intake assessment, estimations of short-term intake (ESTI) and acute hazard index (aHI) were calculated by the following equations: ESTI = Σ((F × HR)/(mean body weight)) and aHI = (ESTI/ARfD) × 100%; F is a single-day high-consumption data (at the 97.5th percentile level) from the 2002 CNNHS, and HR was the highest residue obtained from duck commodities. The mean body weight was obtained from the 2002 CNNHS.

Statistical Analysis. Unless otherwise indicated, all tests were performed in three replicates, and of the values are presented as means ± standard deviation (SD). Data were statistically evaluated by one-way ANOVA analysis with SPSS base 11.0 software. Once a significant difference was observed, the least significant difference (LSD) test was applied to validate the differences among means.

Table 2. Chlorpyrifos Analytical Recoveries and RSDs in Different Fortified Duck Samples

matrix	fortification level (mg/kg)	mean recovery (%)	RSD (%)
meat	0.5	96.8	4.7
	0.1	92.6	3.0
	0.01	83.6	7.9
	0.001	76.9	12.1
fat	0.5	106.8	7.4
	0.1	92.2	8.2
	0.01	91.4	9.4
	0.003	82.1	8.6
heart	0.5	91.3	5.1
	0.1	84.9	8.3
	0.01	81.2	10.8
	0.003	75.8	9.9
stomach	0.5	91.7	6.2
	0.1	87.2	5.9
	0.01	81.1	9.3
	0.003	74.2	11.6
liver	0.5	83.2	8.9
	0.1	77.8	11.2
	0.01	73.2	13.4
	0.003	72.9	13.6
intestine	0.5	103.9	6.5
	0.1	91.5	8.8
	0.01	84.2	10.4
	0.003	72.1	13.2
tongue	0.5	89.2	7.8
	0.1	84.3	9.3
	0.01	81.8	11.9
	0.003	82.2	10.2
eggs	0.5	88.3	4.9
	0.1	84.6	6.8
	0.01	75.7	10.1
	0.002	73.8	12.5

DOI: 10.1021/acs.jafc.5b01839
J. Agric. Food Chem. 2015, 63, 5296−5304

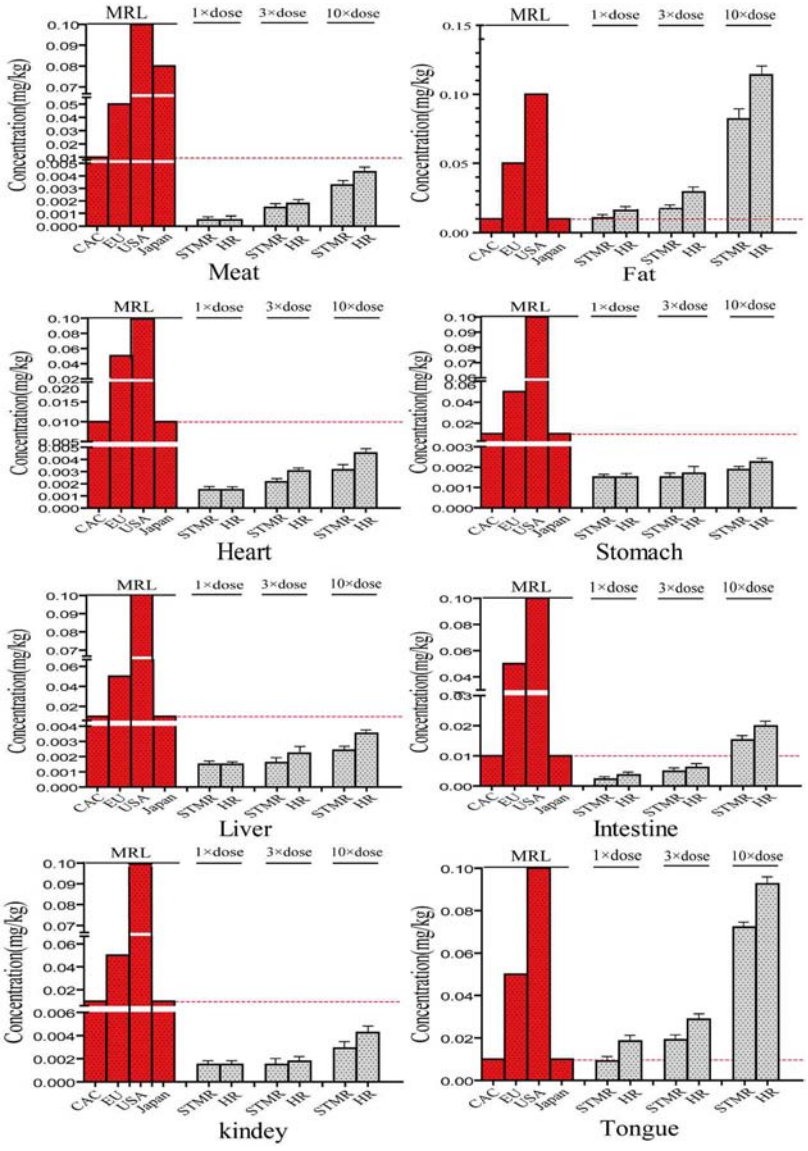

Figure 1. Chlorpyrifos median residue level (STMR) and highest residue level (HR) in meat and edible tissues of Pekin duck at the 1×, 3×, and 10× dose levels in the feed for 42 days.

RESULTS AND DISCUSSION

Analytical Method Validation. The GC-MS analytical results of chlorpyrifos extracted from four fortified concentrations showed that chlorpyrifos recoveries ranged from 72.1 to 106.8% in different matrices (Table 2). All of the relative standard deviations (RSDs) (from 3.0 to 13.6%) were <15%, which indicated good precision and specificity. The LOD (3 × signal-to-noise ratios) and LOQ (10 × signal-to-noise ratios) were 0.0003 and 0.001 mg/kg, respectively, for the duck meat, which were estimated on the basis of signal-to-noise ratio (S/N) of 3 (3:1) and 10 times (10:1) the background chromatographic noise in the present study. As for the substrates of eggs, the LOD and LOQ were 0.0006 and 0.002 mg/kg, respectively. As for the substrates of duck fat and other edible tissues (heart, stomach, liver, intestine, and tongue), the LOD and LOQ were 0.0009 and 0.003 mg/kg, respectively. Matrix effects of chlorpyrifos ranged from 92.4 to 117%, which indicated that the matrix effect was acceptable for quantitative analysis. The validation results based on GC-MS/MS indicated that the analytical method was reliable and efficient for chlorpyrifos determination in different substrates of duck in this study.

Levels and Distribution of Chlorpyrifos Residues in Different Edible Duck Tissues. Animal feeding studies are usually applied by regulators to set MRLs for animal commodities and to assess the dietary risk to consumers.[4] According to the Joint Meeting on Pesticide Residues (JMPR), livestock are typically fed at 1×, 3× (or 5×), and 10× dose level, where 1× is a level based on the maximum estimated dose (highest residue in processed pellet feed) from an earlier study in our laboratory.[17,24] The 10× dose will allow an estimate of what will happen if the normal level is exceeded, which indicates whether residues are proportionate to the intake, and provide additional data when new ways to use the product are introduced.

For the residue values of duck commodities below the LOQs of the analytical method, data were treated with LOQ/2.[25] In the present study, a decrease in body weight was observed in a dose-dependent manner. As compared to the control, the two higher groups of ducks (3× and 10× doses) showed a

DOI: 10.1021/acs.jafc.5b01839
J. Agric. Food Chem. 2015, 63, 5296−5304

significantly decreased body weight at the end of the experiment ($P < 0.05$) and the 1× dose group ducks showed a slightly decreased body weight (data not shown). The loss of body weight could be attributed to oxidative stress induced by chlorpyrifos and the interaction of chlorpyrifos with the enzymes and hormones that are essential for normal metabolic processes.[26]

The market age for meat production ducks is usually 6−8 weeks. Chlorpyrifos residues in various broiler duck tissues are presented in Figure 1. On the basis of this study, China's duck commodities appeared to meet international market standards in good agricultural practice (GAP) conditions. The results showed that chlorpyrifos levels in duck commodities increased with the pesticide levels of daily intake feed, and the chlorpyrifos residues were highest in the 10× dose group.

However, no obvious linear dose−response was observed between chlorpyrifos residues in duck commodities and the dose levels spiked in feed. The above findings could be due to the saturation between absorption and metabolism pathways with increasing dose levels added in the feed. Chlorpyrifos residues (0.0005−0.0045 mg/kg) found in all duck meat, heart, stomach, liver, and kidney samples were below the MRL (0.01 mg/kg) set by the Codex Alimentarius Commission (CAC). These results indicated that chlorpyrifos had a low persistency in the livestock meat and the metabolism organs and that depletion of parent compound residues from the body occurred rapidly, which was different from bioaccumulation of persistent pollutant (e.g., polybrominated diphenyl ether) in ducks.[27] The HR (0.016 mg/kg) in fat of the 1× dose group was slightly higher than the MRL (0.01 mg/kg) set by CAC and Japan and lower than the MRL (0.05 and 0.1 mg/kg) set by the European Union (EU) and the United States, respectively. The HR (0.11 mg/kg) in fat of the 10× dose group was higher than the MRL (0.1 mg/kg) set by the United States. The residues of samples containing fat from all dose groups were obviously higher than those of meat and other edible tissues. This might be attributed to the high fat-soluble characteristic of chlorpyrifos (logarithm of partition coefficient P is 5.1).[28] Chlorpyrifos residues in tongue of each dose group were higher than the MRL (0.01 mg/kg) set by the CAC and Japan. The HRs in tongue in each group were 0.019, 0.029, and 0.093 mg/kg, respectively, which were obviously higher than that of the meat, liver, and stomach. The above findings were probably due to the high level of chlorpyrifos in feed debris and the adhesion property of the tongue structure. The STMR (0.015 mg/kg) and HR (0.020 mg/kg) in the intestine of the 10× dose group were higher than the MRL (0.01 mg/kg) set by the CAC and Japan. Our results showed nondetectable levels or levels close to the quantification limits were observed in the majority of animal foods (e.g., meat and offal) under GAP production conditions. In addition, the findings in our present study were consistent with the results obtained in a market-basket survey of determining residues of organophosphorus pesticides in animal foods in China.[29]

The initial residues in eggs of Shaoxing brown ducks fed diets containing different chlorpyrifos concentrations on day 1 were not detected (Figure 2). However, the chlorpyrifos residues determined in eggs of all treatment groups increased slowly as the feeding time lasted to day 28, which indicated that chlorpyrifos was passed from the feed to the eggs. The STMR (0.012 mg/kg) and HR (0.016 mg/kg) in samples collected at days 28 for the 10× dose group treatment exceeded the MRL (0.01 mg/kg) set by the CAC, EU, United States, and Japan.

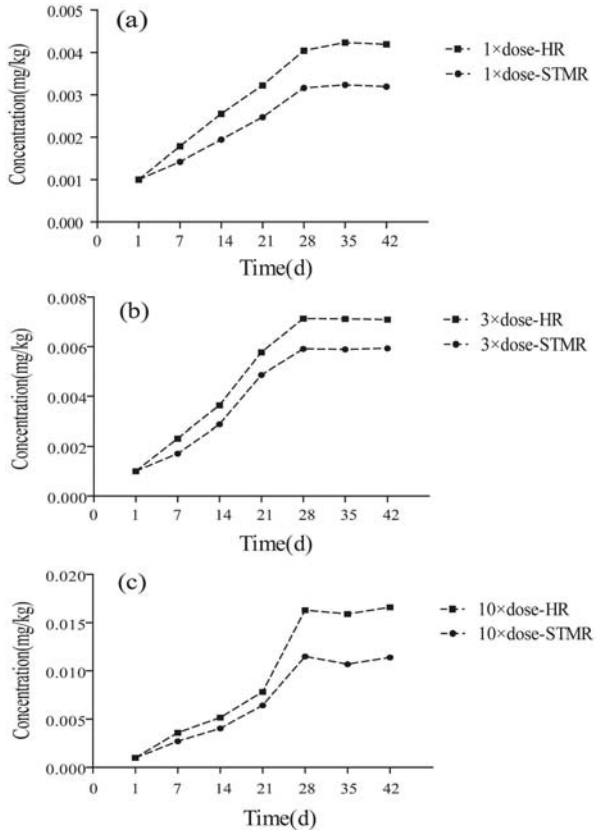

Figure 2. Chlorpyrifos median concentrations (STMR) and highest concentrations (HR) in eggs of Shaoxing brown duck at the 1× dose (a), 3× dose (b), and 10× dose (c) levels in the feed for 42 days.

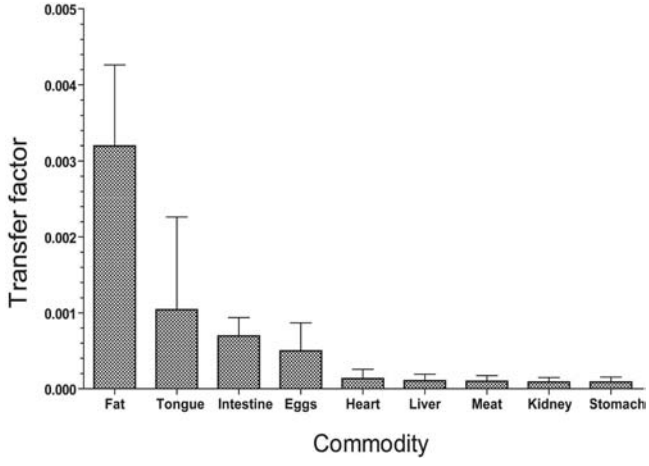

Figure 3. Transfer factors (TFs) of chlorpyrifos feeding trials for ducks.

The chlorpyrifos residues in all samples collected from the 1× and 3× dose groups during 42 days of treatment were not higher than the MRL (0.01 mg/kg), which was similar to the results of eggs from laying hens fed diets containing chlorpyrifos (10 mg/kg in feed) over 28 days.[30] The STMR and HR in all samples collected at days 35 and 42 of treatments were close to the value of day 28, which indicated a 28 day feeding trial was long enough for pesticide residues to reach plateau levels in duck eggs.

Several similar metabolism studies were available for chlorpyrifos in livestock. McKellar et al. fed cattle dairy feed

DOI: 10.1021/acs.jafc.5b01839
J. Agric. Food Chem. 2015, 63, 5296−5304

Table 3. Chronic Intake Assessment Results Evaluated by Median Residue Level of Chlorpyrifos from Duck Feeding Trials

		meat		fat		heart, stomach, liver, kidney		intestine		tongue		eggs	
age group	gender	EDI	HQ (%)	EDI	HQ (%)	EDI	HQ (%)	EDI	HQ (%)	EDI	HQ (%)	EDI	HQ (%)
2−3 years	male	2.4×10^{-7}	2.4×10^{-3}	5.1×10^{-6}	5.1×10^{-2}	3.6×10^{-7}	3.6×10^{-3}	5.9×10^{-7}	5.9×10^{-3}	2.2×10^{-6}	2.2×10^{-2}	3.8×10^{-6}	3.8×10^{-2}
	female	3.9×10^{-7}	3.9×10^{-3}	8.2×10^{-6}	8.2×10^{-2}	2.9×10^{-7}	2.9×10^{-3}	4.8×10^{-7}	4.8×10^{-3}	1.8×10^{-6}	1.8×10^{-2}	3.9×10^{-6}	3.9×10^{-2}
4−6 years	male	3.2×10^{-7}	3.2×10^{-3}	6.8×10^{-6}	6.8×10^{-2}	2.0×10^{-7}	2.0×10^{-3}	3.2×10^{-7}	3.2×10^{-3}	1.2×10^{-6}	1.2×10^{-2}	2.9×10^{-6}	2.9×10^{-2}
	female	2.8×10^{-7}	2.8×10^{-3}	6.0×10^{-6}	6.0×10^{-2}	2.5×10^{-7}	2.5×10^{-3}	4.1×10^{-7}	4.1×10^{-3}	1.5×10^{-6}	1.5×10^{-2}	3.0×10^{-6}	3.0×10^{-2}
7−10 years	male	2.8×10^{-7}	2.8×10^{-3}	6.0×10^{-6}	6.0×10^{-2}	2.3×10^{-7}	2.3×10^{-3}	3.7×10^{-7}	3.7×10^{-3}	1.4×10^{-6}	1.4×10^{-2}	2.2×10^{-6}	2.2×10^{-2}
	female	2.5×10^{-7}	2.5×10^{-3}	5.3×10^{-6}	5.3×10^{-2}	1.7×10^{-7}	1.7×10^{-3}	2.8×10^{-7}	2.8×10^{-3}	1.1×10^{-6}	1.1×10^{-2}	2.0×10^{-6}	2.0×10^{-2}
11−13 years	male	1.8×10^{-7}	1.8×10^{-3}	3.8×10^{-6}	3.8×10^{-2}	1.9×10^{-7}	1.9×10^{-3}	3.1×10^{-7}	3.1×10^{-3}	1.2×10^{-6}	1.2×10^{-2}	1.5×10^{-6}	1.5×10^{-2}
	female	1.5×10^{-7}	1.5×10^{-3}	3.2×10^{-6}	3.2×10^{-2}	1.3×10^{-7}	1.3×10^{-3}	2.2×10^{-7}	2.2×10^{-3}	8.0×10^{-7}	8.0×10^{-3}	1.3×10^{-6}	1.3×10^{-2}
14−17 years	male	1.5×10^{-7}	1.5×10^{-3}	3.2×10^{-6}	3.2×10^{-2}	1.8×10^{-7}	1.8×10^{-3}	2.9×10^{-7}	2.9×10^{-3}	1.1×10^{-6}	1.1×10^{-2}	1.1×10^{-6}	1.1×10^{-2}
	female	1.6×10^{-7}	1.6×10^{-3}	3.3×10^{-6}	3.3×10^{-2}	9.0×10^{-8}	9.0×10^{-4}	1.7×10^{-7}	1.7×10^{-3}	5.4×10^{-7}	5.4×10^{-3}	1.1×10^{-6}	1.1×10^{-2}
18−29 years	male	1.3×10^{-7}	1.3×10^{-3}	2.8×10^{-6}	2.8×10^{-2}	1.7×10^{-7}	1.7×10^{-3}	2.4×10^{-7}	2.4×10^{-3}	8.9×10^{-7}	8.9×10^{-3}	9.8×10^{-7}	9.8×10^{-3}
	female	1.5×10^{-7}	1.5×10^{-3}	3.2×10^{-6}	3.2×10^{-2}	1.4×10^{-7}	1.4×10^{-3}	2.2×10^{-7}	2.2×10^{-3}	8.2×10^{-7}	8.2×10^{-3}	1.1×10^{-6}	1.1×10^{-2}
30−44 years	male	1.4×10^{-7}	1.4×10^{-3}	2.9×10^{-6}	2.9×10^{-2}	1.5×10^{-7}	1.5×10^{-3}	2.4×10^{-7}	2.4×10^{-3}	9.0×10^{-7}	9.0×10^{-3}	9.5×10^{-7}	9.5×10^{-3}
	female	1.2×10^{-7}	1.2×10^{-3}	2.5×10^{-6}	2.5×10^{-2}	1.1×10^{-7}	1.1×10^{-3}	1.8×10^{-7}	1.8×10^{-3}	6.9×10^{-7}	6.9×10^{-3}	9.9×10^{-7}	9.9×10^{-3}
45−59 years	male	1.2×10^{-7}	1.2×10^{-3}	2.5×10^{-6}	2.5×10^{-2}	1.3×10^{-7}	1.3×10^{-3}	2.1×10^{-7}	2.1×10^{-3}	7.8×10^{-7}	7.8×10^{-3}	9.1×10^{-7}	9.1×10^{-3}
	female	1.0×10^{-7}	1.0×10^{-3}	2.1×10^{-6}	2.1×10^{-2}	1.1×10^{-7}	1.1×10^{-3}	1.8×10^{-7}	1.8×10^{-3}	6.9×10^{-7}	6.9×10^{-3}	9.1×10^{-7}	9.1×10^{-3}
60−69 years	male	9.5×10^{-8}	9.5×10^{-4}	2.0×10^{-6}	2.0×10^{-2}	1.1×10^{-7}	1.1×10^{-3}	1.8×10^{-7}	1.8×10^{-3}	6.7×10^{-7}	6.7×10^{-3}	9.5×10^{-7}	9.5×10^{-3}
	female	9.1×10^{-8}	9.1×10^{-4}	1.9×10^{-6}	1.9×10^{-2}	9.1×10^{-8}	9.1×10^{-4}	1.5×10^{-7}	1.5×10^{-3}	5.5×10^{-7}	5.5×10^{-3}	9.5×10^{-7}	9.5×10^{-3}
≥70 years	male	8.8×10^{-8}	8.8×10^{-4}	1.9×10^{-6}	1.9×10^{-2}	1.2×10^{-7}	1.2×10^{-3}	2.0×10^{-7}	2.0×10^{-3}	7.3×10^{-7}	7.3×10^{-3}	9.5×10^{-7}	9.5×10^{-3}
	female	7.4×10^{-8}	7.4×10^{-4}	1.6×10^{-6}	1.6×10^{-2}	9.7×10^{-8}	9.7×10^{-4}	1.6×10^{-7}	1.6×10^{-3}	5.9×10^{-7}	5.9×10^{-3}	9.6×10^{-7}	9.6×10^{-3}

DOI: 10.1021/acs.jafc.5b01839
J. Agric. Food Chem. 2015, 63, 5296−5304

Table 4. Acute Intake Assessment Results Evaluated by the Highest Residue Level of Chlorpyrifos from Duck Feeding Trials

		meat		fat		heart, stomach, liver, kidney		intestine		tongue		eggs	
age group	gender	ESTI	aHI (%)	ESTI	aHI (%)	ESTI	aHI (%)	ESTI	aHI (%)	ESTI	aHI (%)	ESTI	aHI (%)
2−3 years	male	8.3×10^{-7}	8.3×10^{-4}	2.6×10^{-5}	2.6×10^{-2}	4.2×10^{-7}	4.2×10^{-4}	3.1×10^{-6}	3.1×10^{-3}	1.6×10^{-5}	1.6×10^{-2}	2.3×10^{-5}	2.3×10^{-2}
	female	1.3×10^{-6}	1.3×10^{-3}	4.2×10^{-5}	4.2×10^{-2}	3.4×10^{-7}	3.4×10^{-4}	2.5×10^{-6}	2.5×10^{-3}	1.3×10^{-5}	1.3×10^{-2}	2.3×10^{-5}	2.3×10^{-2}
4−6 years	male	1.1×10^{-6}	1.1×10^{-3}	3.5×10^{-5}	3.5×10^{-2}	2.4×10^{-7}	2.4×10^{-4}	1.7×10^{-6}	1.7×10^{-3}	8.4×10^{-6}	8.4×10^{-3}	1.7×10^{-5}	1.7×10^{-2}
	female	9.8×10^{-7}	9.8×10^{-4}	3.1×10^{-5}	3.1×10^{-2}	2.9×10^{-7}	2.9×10^{-4}	2.1×10^{-6}	2.1×10^{-3}	1.1×10^{-5}	1.1×10^{-2}	1.8×10^{-5}	1.8×10^{-2}
7−10 years	male	9.7×10^{-7}	9.7×10^{-4}	3.1×10^{-5}	3.1×10^{-2}	2.6×10^{-7}	2.6×10^{-4}	1.9×10^{-6}	1.9×10^{-3}	9.8×10^{-6}	9.8×10^{-3}	1.3×10^{-5}	1.3×10^{-2}
	female	8.7×10^{-7}	8.7×10^{-4}	2.7×10^{-5}	2.7×10^{-2}	2.0×10^{-7}	2.0×10^{-4}	1.5×10^{-6}	1.5×10^{-3}	7.3×10^{-6}	7.3×10^{-3}	1.2×10^{-5}	1.2×10^{-2}
11−13 years	male	6.2×10^{-7}	6.2×10^{-4}	2.0×10^{-5}	2.0×10^{-2}	2.2×10^{-7}	2.2×10^{-4}	1.6×10^{-6}	1.6×10^{-3}	8.1×10^{-6}	8.1×10^{-3}	9.1×10^{-6}	9.1×10^{-3}
	female	5.3×10^{-7}	5.3×10^{-4}	1.7×10^{-5}	1.7×10^{-2}	1.5×10^{-7}	1.5×10^{-4}	1.1×10^{-6}	1.1×10^{-3}	5.7×10^{-6}	5.7×10^{-3}	7.8×10^{-6}	7.8×10^{-3}
14−17 years	male	5.2×10^{-7}	5.2×10^{-4}	1.6×10^{-5}	1.6×10^{-2}	2.1×10^{-7}	2.1×10^{-4}	1.5×10^{-6}	1.5×10^{-3}	7.7×10^{-6}	7.7×10^{-3}	6.8×10^{-6}	6.8×10^{-3}
	female	5.4×10^{-7}	5.4×10^{-4}	1.7×10^{-5}	1.7×10^{-2}	1.0×10^{-7}	1.0×10^{-4}	7.6×10^{-7}	7.6×10^{-4}	3.8×10^{-6}	3.8×10^{-3}	6.7×10^{-6}	6.7×10^{-3}
18−29 years	male	4.6×10^{-7}	4.6×10^{-4}	1.5×10^{-5}	1.5×10^{-2}	1.7×10^{-7}	1.7×10^{-4}	1.2×10^{-6}	1.2×10^{-3}	6.3×10^{-6}	6.3×10^{-3}	5.8×10^{-6}	5.8×10^{-3}
	female	5.3×10^{-7}	5.3×10^{-4}	1.7×10^{-5}	1.7×10^{-2}	1.6×10^{-7}	1.6×10^{-4}	1.1×10^{-6}	1.1×10^{-3}	5.8×10^{-6}	5.8×10^{-3}	6.3×10^{-6}	6.3×10^{-3}
30−44 years	male	4.7×10^{-7}	4.7×10^{-4}	1.5×10^{-5}	1.5×10^{-2}	1.7×10^{-7}	1.7×10^{-4}	1.3×10^{-6}	1.3×10^{-3}	6.3×10^{-6}	6.3×10^{-3}	5.6×10^{-6}	5.6×10^{-3}
	female	4.1×10^{-7}	4.1×10^{-4}	1.3×10^{-5}	1.3×10^{-2}	1.3×10^{-7}	1.3×10^{-4}	9.6×10^{-7}	9.6×10^{-4}	4.8×10^{-6}	4.8×10^{-3}	5.9×10^{-6}	5.9×10^{-3}
45−59 years	male	4.0×10^{-7}	4.0×10^{-4}	1.3×10^{-5}	1.3×10^{-2}	1.5×10^{-7}	1.5×10^{-4}	1.1×10^{-6}	1.1×10^{-3}	5.5×10^{-6}	5.5×10^{-3}	5.4×10^{-6}	5.4×10^{-3}
	female	3.7×10^{-7}	3.7×10^{-4}	1.1×10^{-5}	1.1×10^{-2}	1.3×10^{-7}	1.3×10^{-4}	9.6×10^{-7}	9.6×10^{-4}	4.8×10^{-6}	4.8×10^{-3}	5.4×10^{-6}	5.4×10^{-3}
60−69 years	male	3.3×10^{-7}	3.3×10^{-4}	1.0×10^{-5}	1.0×10^{-2}	1.3×10^{-7}	1.3×10^{-4}	9.3×10^{-7}	9.3×10^{-4}	4.7×10^{-6}	4.7×10^{-3}	5.6×10^{-6}	5.6×10^{-3}
	female	3.2×10^{-7}	3.2×10^{-4}	1.0×10^{-6}	1.0×10^{-3}	1.1×10^{-7}	1.1×10^{-4}	7.7×10^{-7}	7.7×10^{-4}	3.9×10^{-6}	3.9×10^{-3}	5.6×10^{-6}	5.6×10^{-3}
≥70 years	male	3.0×10^{-7}	3.0×10^{-4}	9.6×10^{-6}	9.6×10^{-3}	1.4×10^{-7}	1.4×10^{-4}	1.0×10^{-6}	1.0×10^{-3}	5.1×10^{-6}	5.1×10^{-3}	5.6×10^{-6}	5.6×10^{-3}
	female	2.6×10^{-7}	2.6×10^{-4}	8.1×10^{-6}	8.1×10^{-3}	1.1×10^{-7}	1.1×10^{-4}	8.2×10^{-7}	8.2×10^{-4}	4.1×10^{-6}	4.1×10^{-3}	5.7×10^{-6}	5.7×10^{-3}

DOI: 10.1021/acs.jafc.5b01839
J. Agric. Food Chem. 2015, 63, 5296−5304

containing chlorpyrifos (0.3−30 mg/kg) for 2 weeks, and low levels (<0.01 mg/kg) of chlorpyrifos were found in milk and cream.[31] Dishburger et al. reported that the average 0.02 mg/kg residue was found predominately in fat tissue of cattle fed 3.0 mg/kg chlorpyrifos in the diet.[32] The above metabolism studies were conducted at experimental dosing levels instead of the realistic dietary burden of livestock. Another limitation was that these livestock feeding studies used Western representative livestock species such as lactating cows and chicken, not traditional Chinese domestic animals. Therefore, it was difficult to obtain correct information about chlorpyrifos residues for a general situation, especially considering possible differences in metabolism, feed concentrations, and exposure periods for each livestock animal by extrapolation. In this study, pesticide residues in livestock commodities were appropriately estimated under simulated duck production in real life.

Chlorpyrifos Transfers from Feed to Commodities. In the present study, the results showed that the differentiation of TFs depended on the potential accumulation of chlorpyrifos in different matrices of duck, feeding levels, and feeding periods (Figure 3). All duck commodity TFs in each group were generally <0.005, and these results were consistent with previous metabolism studies.[4,33] TFs (<0.0001−0.0003) for the meat, heart, stomach, liver, and kidney were generally lower compared with those of fat, tongue, intestine, and eggs (<0.0001−0.0049) among the different feeding levels ranging from 3.20 to 32.0 mg/kg. This result was consistent with chlorpyrifos being rapidly metabolized and excreted through metabolic organs.[33] TFs determined in the duck commodities were in the following order: fat > tongue > intestine > eggs > heart > liver > meat > kidney > stomach. The highest TF found in duck fat was 0.0049, which was similar to the TF (0.005) in chicken fat at a feeding level of 10 mg/kg for 30 days.[30] TFs in animal fat were indeed found to be related to lipophilic compounds, which tended to accumulate in the body fat. It was noted that the fatty tissues (intestine and eggs) had a higher potential accumulation for pesticides when compared to meat and other tissues. This finding was similar to the study of MacLachlan in which the lipophilic pesticides accumulated early in the fat tissue.[34] However, the high TF (0.0028) found in tongue may be attributed to the special structure of duck tongue with numerous lateral brush-like horny lingual papillae. Our results showed that the transfer of chlorpyrifos from the animal feed to the tissues was fairly lower when compared to that of other pesticides (e.g., abamection, emamection, edosulfan, and fipronil).[35−38]

Exposure Assessment and Risk Characterization. Chronic intake assessment revealed that only 0.034−0.150% ADI (HQ) of chlorpyrifos was consumed via the meat, fat, edible tissues, and eggs for different age and gender groups in China (Table 3). Generally, children from 2 to 6 years of age are considered as the most vulnerable group because they tend to eat greater quantities of food commodities on a body weight basis. Our results indicated that the exposure of youths (2−17 years old), especially children, was higher than that of adults (18−59 years old) and seniors (>60 years old). No significant differences were observed in the long-term exposure of gender groups (male and female).The highest EDI (8.2×10^{-6} mg/kg/bw/day) for duck fat tissue was <100 times of ADI, indicating that the dietary risk of chlorpyrifos from duck commodities was fairly low for Chinese consumers. A similar result was obtained from Sun et al., who concluded that only a negligible risk (0.4% of ADI) was observed for chlorpyrifos exposure through consumption of fishery products from Taiwan.[39] Another similar survey from cumulative exposure amount of organophosphorus pesticides to Chinese population accounted for 7.3% of the ADI.[23] The dietary exposure risk of chlorpyrifos raised by the intake of animal foods showed that the products of animal origin contaminated by chlorpyrifos appeared to be safer than products of plant origin in China.[25,40]

The aHIs (0.019−0.082%) for different age and gender groups were far lower than 100% through duck commodity consumption (Table 4). The aHIs of youths (2−17 years old) were significantly higher than those of adults (18−59 years old) and seniors (>60 years old). No significant difference was observed in the short-term exposure of gender groups (male and female). In general, acute dietary risks from the highest residue levels of these duck commodities were still within the safe level in China. Furthermore, the critical intake events identified in the acute risk assessment calculations were considered very unlikely to occur, taking into account the frequency of critical residues and the frequency of extreme consumption events.

It is noteworthy that the intake calculations were conservative because processing factors were not considered here. When processing factors (e.g., boiling and frying) are included, the estimated exposure would be even lower. On the other hand, residual data for dietary risk assessment should be obtained not only from the animal feeding trials but also from other different sources (e.g., market surveys, farms). Furthermore, consumers are usually exposed to various pesticides or toxic chemicals with multiple exposure pathways. Different pesticides or chemicals sometime pose synergized toxicity to organisms; thus, it should be also stated that our results here did not evaluate the total diet exposure but only determined the intake of chlorpyrifos from duck commodities. To the best of our knowledge, this is the first study to evaluate the transfer of chlorpyrifos from contaminated feed to duck commodities and the dietary risk for Chinese consumers through consumption. Results of the study could be considered as a useful reference for the establishment of pesticide MRLs for livestock in China.

AUTHOR INFORMATION

Corresponding Author

*(Y.Y.) Fax: 86-571-86401834. E-mail: ywytea@163.com.

Funding

This work was supported by grants from Zhejiang Provincial Science and Technology Project (2011C12024), the 12th Five-Year Program for Essential Drug Discovery and Development from the Ministry of Science and Technology (2012ZX09505001-003), and Zhejiang Academy of Agricultural Sciences scientific and technological innovation promotion project.

Notes

The authors declare no competing financial interest.

REFERENCES

(1) Dorea, J. G. Fish meal in animal feed and human exposure to persistent bioaccumulative and toxic substances. *J. Food Prot.* **2006**, *69*, 2777−2785.

(2) Pagliuca, G.; Gazzotti, T.; Zironi, E.; Sticca, P. Residue analysis of organophosphorus pesticides in animal matrices by dual column capillary gas chromatography with nitrogen-phosphorus detection. *J. Chromatogr. A* **2005**, *1071*, 67−70.

DOI: 10.1021/acs.jafc.5b01839
J. Agric. Food Chem. 2015, 63, 5296−5304

(3) Yingzi, W.; Paul, K.; Albert, H.; Inge, H.; Wolf-Dieter, R. Pesticide poisoning in domestic animals and livestock in Austria: a 6 years retrospective study. *Forensic Sci. Int.* **2007**, *169*, 157−160.
(4) MacLachlan, D. J.; Bhula, R. Estimating the residue transfer of pesticides in animal feedstuffs to livestock tissues, milk and eggs: a review. *Aust. J. Exp. Agric.* **2008**, *48*, 589−598.
(5) GB 2763-2014 (National Food Safety Standards of China). *National Food Safety Standards: Maximum Residue Limits for Pesticides in Food*; Standard Press of China: Beijing, China, 2014.
(6) Chen, C.; Qian, Y.; Liu, X.; Tao, C.; Liang, Y.; Li, Y. Risk assessment of chlorpyrifos on rice and cabbage in China. *Regul. Toxicol. Pharmacol.* **2012**, *62*, 125−130.
(7) Randhawa, M. A.; Anjum, F. M.; Ahmed, A.; Randhawa, M. S. Field incurred chlorpyrifos and 3,5,6-trichloro-2-pyridinol residues in fresh and processed vegetables. *Food Chem.* **2007**, *103*, 1016−1023.
(8) Ogah, C. O.; Coker, H. A.; Adepoju-Bello, A. A. Pesticide residue levels in maize samples from markets in Lagos State, Nigeria. *Nig. Q. J. Hosp. Med.* **2011**, *21*, 169−174.
(9) Sun, F.; Chen, H. S. Monitoring of pesticide chlorpyrifos residue in farmed fish: investigation of possible sources. *Chemosphere* **2008**, *71*, 1866−1869.
(10) Kammerbauer, J.; Moncada, J. Pesticide residue assessment in three selected agricultural production systems in the Choluteca River Basin of Honduras. *Environ. Pollut.* **1998**, *103*, 171−181.
(11) Shaker, E. M.; Elsharkawy, E. E. Organochlorine and organophosphorus pesticide residues in raw buffalo milk from agroindustrial areas in Assiut, Egypt. *Environ. Toxicol. Pharmacol.* **2015**, *39*, 433−440.
(12) Gazzotti, T.; Sticca, P.; Zironi, E.; Lugoboni, B.; Serraino, A.; Pagliuca, G. Determination of 15 organophosphorus pesticides in Italian raw milk. *Bull. Environ. Contam. Toxicol.* **2009**, *82*, 251−254.
(13) Hsu, S. Y.; Epstein, R. L.; Huei J, C.; Tian F, S. Depletion of pesticides through chicken eggs. *Food Sci. Taiwan* **1995**, *22*, 542−549.
(14) Schenck, F. J.; Donoghue, D. J. Determination of organochlorine and organophosphorus pesticide residues in eggs using a solid phase extraction cleanup. *J. Agric. Food Chem.* **2000**, *48*, 6412−6415.
(15) Draft assessment report on the active substance chlorpyrifos prepared by the rapporteur Member State Spain in the framework of Council Directive 91/414/EEC, February 1999.
(16) Adzitey, F.; Adzitey, S. P. Duck production: has a potential to reduce poverty among rural households in Asian communities − a review. *J. World's Poult. Res.* **2011**, *1*, 7−10.
(17) Li, R.; Wei, W.; He, L.; Hao, L.; Ji, X.; Zhou, Y.; Wang, Q. Chlorpyrifos residual behaviors in field crops and transfers during duck pellet feed processing. *J. Agric. Food Chem.* **2014**, *62*, 10215−10221.
(18) Li, R.; He, L.; Zhou, T.; Ji, X.; Qian, M.; Zhou, Y.; Wang, Q. Simultaneous determination of chlorpyrifos and 3,5,6-trichloro-2-pyridinol in duck muscle by modified QuEChERS coupled to gas chromatography tandem mass spectrometry (GC-MS/MS). *Anal. Bioanal. Chem.* **2014**, *406*, 2899−2907.
(19) Jin, S. *The Tenth Report of Nutrition and Health Status for China Residents: Nutrition and Health Status of Annual 2002*; People's Medical Publishing House: Beijing, China, 2002 (in Chinese).
(20) Claeys, W. L.; Schmit, J. F.; Bragard, C.; Rogister, G. M.; Pussemier, L.; Schiffers, B. Exposure of several Belgian consumer groups to pesticide residues through fresh fruit and vegetable consumption. *Food Control* **2011**, *22*, 508−516.
(21) GEMS/FOOD. *Global Environment Monitoring System − Food Level Monitoring and Assessment Programme, GEMS/Food Cluster Diets*; World Health Organization: Geneva, Switzerland, 2012.
(22) Wendie, L. C.; Jean-François, S.; Claude, B.; Guy, M.-R.; Luc, P.; Bruno, S. Exposure of several Belgian consumer groups to pesticide residues through fresh fruit and vegetable consumption. *Food Control* **2011**, *22*, 508−516.
(23) WHO. *Inventory of ICPS and Rother WHO Pesticides Evaluations and Summary of Toxicological Evaluations Performed by the Joint Meeting on Pesticide Residues (JMPR)*; WHO/PCS/02.3; Geneva, Switzerland, 2003.
(24) FAO/WHO. *Condex Maximum Limits for Pesticides Residues*; Codex Alimentarious Commission, FAO and WHO: Rome, Italy, 2006.
(25) Chen, C.; Li, Y.; Chen, M.; Chen, Z.; Qian, Y. Organophosphorus pesticide residues in milled rice (*Oryza sativa*) on the Chinese market and dietary risk assessment. *Food Addit. Contam. Part A: Chem. Anal. Control Expo. Risk Assess.* **2009**, *26*, 340−347.
(26) Ambali, S. F.; Akanbi, D. O.; Oladipo, O. O.; Yaqu, L. S.; Kawu, M. U. Sub-chronic chlorpyrifos induced clinical hematological and biochemical changes in Swiss albino mice: protective effect of vitamin E. *Int. J. Biol. Med. Res.* **2011**, *2*, 497−503.
(27) Liu, P. Y.; Chen, X. R.; Zhao, Y. X.; Li, Y. Y.; Qin, X. F.; Qin, Z. F. Changes of polybrominated diphenyl ether concentrations in ducks with background exposure level and time. *Chemosphere* **2015**, *118*, 253−260.
(28) Eddleston, M.; Mohamed, F.; Davies, J. O.; Eyer, P.; Worek, F.; Sheriff, M. H.; Buckley, N. A. Respiratory failure in acute organophosphorus pesticide self-poisoning. *QJM* **2006**, *99*, 513−522.
(29) Zhou, R.; Li, H.; Yang, L.; Miao, H.; Zhao, Y.; Wu, Y. Occurrence of organophosphorus pesticides in animal foods and their diet exposure assessment. *Zhonghua Yu Fang Yi Xue Za Zhi* **2014**, *48*, 412−415 (abstract in English) .
(30) FAO/WHO. *Pesticide Residues in Food − 2000 Evaluations − Part I, FAO Plant Production and Protection*; Rome, Italy, 2001; p 165; http://www.fao.org/ag/AGP/AGPP/Pesticid/Default.htm.
(31) McKellar, R. L.; Dishburger, H. J.; Rice, J. R.; Craig, L. F.; Pennington, J. Residues of chlorpyrifos, its oxygen analogue, and 3,5,6-trichloro-2-pyridinol in milk and cream from cows fed chlorpyrifos. *J. Agric. Food Chem.* **1976**, *24*, 283−286.
(32) Dishburger, H. J.; McKellar, R. L.; Pennington, J. Y.; Rice, J. R. Determination of residues of chlorpyrifos, its oxygen analogue, and 3,5,6-trichloro-2-pyridinol in tissues of cattle fed chlorpyrifos. *J. Agric. Food Chem.* **1977**, *25*, 1325−1229.
(33) Kan, C. A.; Meijer, A. L. The risk of level of food with toxic substances present in animal feed. *Anim. Feed Sci. Technol.* **2007**, *133*, 84−108.
(34) MacLachlan, D. J. Transfer of fat-soluble pesticides from contaminated feed to poultry tissues and eggs. *Br. Poult. Sci.* **2008**, *49*, 290−298.
(35) FAO/WHO. *Pesticide Residues in Food − 1992 Evaluations − Part I, Residues, FAO Plant Production and Protection*; Rome, Italy, 1993; p 118; http://www.fao.org/ag/AGP/AGPP/Pesticid/Default.htm.
(36) APVMA Animal Residue Data Sheet − Emamectin, October 2002; http://www.apvma.gov.au/residues/ARDS-emamectin.shtml.
(37) Review of Endosulfan − Interim Report, August 1998; http://www.apvma.gov.au/chemrev/endosulfan.shtml.
(38) FAO/WHO. *Pesticide Residues in Food − 2001 Evaluations − Part I, FAO Plant Production and Protection*; Rome, Italy, 2002; p 171; http://www.fao.org/ag/AGP/AGPP/Pesticid/Default.htm.
(39) Sun, F.; Wong, S. S.; Li, G. C.; Chen, S. N. preliminary assessment of consumes exposure to pesticide residues in fisheries products. *Chemosphere* **2006**, *62*, 674−680.
(40) Yuan, Y. W.; C, C.; Zheng, C. M.; Wang, X. L.; Yang, G. L.; Wang, Q.; Zhang, Z. H. Residue of chlorpyrifos and cypermethrin in vegetables and probabilistic exposure assessment for consumers in Zhejiang Province, China. *Food Control* **2014**, *36*, 63−68.

DOI: 10.1021/acs.jafc.5b01839
J. Agric. Food Chem. 2015, 63, 5296−5304

JOURNAL OF AGRICULTURAL AND FOOD CHEMISTRY

Correspondence/Rebuttal

pubs.acs.org/JAFC

Comment on Authenticity and Traceability of *Vanilla* Flavors by Analysis of Stable Isotopes of Carbon and Hydrogen

Vanilla species are a source of one of the most popular flavors in the world with *Vanilla planifolia* of exceptional importance to the flavor and food industry. In Europe, extract from *Vanilla tahitensis* is much valued in the production of ice cream. Due to an ever-increasing demand and limited sources, the price of *vanilla* has greatly increased over the years, and this has led to adulteration of genuine *vanilla*, in particular by the fraudulent addition of non-natural vanillin to *Vanilla* extracts.

In a recent paper published in this *Journal*, Hansen et al.[1] reported their findings on the assessment of authenticity and traceability of *vanilla* flavor using compound-specific isotope ratio mass spectrometry measuring the carbon and hydrogen stable isotope signatures of vanillin. The analytical procedures employed in the study appear sound, and extracts from 79 natural *vanilla* pods from 12 different regions throughout the world were analyzed. However, the authors have greatly over interpreted their data set and thus the subsequent conclusions drawn now require critical comment and discussion.

Characteristic differences in the $\delta^{13}C$ values of vanillin in extracts from *V. planifolia* ($n = 54$) and *V. tahitensis* ($n = 15$) are reported for samples collected from several regions throughout the world. This finding is in accordance with the literature.[2] *Vanilla* species differentiation is important not only for the quality assessment of the *vanilla* flavor but also for consumer confidence and protection. Hansen et al. attempted to use both the $\delta^{13}C$ and $\delta^{2}H$ values of the vanillin from the *vanilla* extracts not only for species verification but also to determine the geographical origin (traceability) of *vanilla* pods. However, despite what the authors claim, from Figure 4 it is clearly obvious that the values measured for *V. planifolia* from almost all geographical regions overlap one another and thus no inference about geographical origin can be drawn for this species. All that can be deduced from this data set is that it is possible to differentiate the two species investigated and to distinguish between the two geographical origins of *V. tahitensis*.

At this point it is worth emphasizing that from the viewpoint of European Union food law the authenticity of flavors is of considerably more importance than their traceability. Thus, authentic *vanilla* flavor solely comprises vanillin originating from pods of the tropical orchid *Vanilla* species. In terms of European Union food law definitions, natural flavoring substances are flavor active substances formed by biosynthesis.[3] It is irrelevant if these substances are produced in plant or animal tissues or by microorganisms supplemented with natural substrates, for instance, by microbial enzymatic oxidation of naturally occurring 4-hydroxy-3-methoxycinnamic acid (ferulic acid). Because ferulic acid is a natural readily accessible substance in rice bran, the cost of production of natural vanillin microbially from this source is considerably lower when compared with that extracted from *vanilla* pods. This microbially derived flavor compound may be obtained only by authorized preparation processes whereby the biogenic generated structure of the substance remains unaltered during the preparation process. European legislation (EC 178/2002, article 8)[4] requires that vanillin produced by such processes must not be labeled as the popular "Bourbon Vanilla" as this would be fraudulent and also mislead the consumer.

To ensure that the legislation is adhered to and properly policed, new methodologies have recently been developed. For vanillin this has led to position-specific isotope measurements employing site-specific natural isotope fractionation—nuclear magnetic resonance (SNIF-NMR) and gas chromatography isotope ratio mass spectrometry (GC-IRMS).[5−8] Our group developed a procedure for the selective analysis of $\delta^{13}C$ and $\delta^{2}H$ of plant methoxyl groups ($O-CH_3$).[9,10] The procedure is based on the "Zeisel method",[11] whereby methoxyl groups are transformed to methyl iodide using hydriodic acid and isotope measurements are made on the halomethane. In 2010 we adapted and applied the method for selective analysis of the 3-methoxyl group of vanillin.[5]

In the 2010 study we reported the $\delta^{13}C$ and $\delta^{2}H$ values of both vanillin bulk and vanillin methoxyl groups and demonstrated that correlations between these values can be used to fully differentiate between natural vanillin extracted from pods of the tropical orchid *vanilla* and biotechnological vanillin produced from, for example, ferulic acid (from rice bran) by microorganisms or synthetic vanillin of any kind of chemical synthesis.[5] Furthermore, the information gained from two-dimensional plots of the $\delta^{13}C$ and $\delta^{2}H$ values makes it virtually impossible for adulterated vanillin to remain undetected, even when sophisticated adulteration techniques are employed to change the isotopic content of the vanillin. Moreover, we would point out that because the two *vanilla* species, *V. planifolia* and *V. tahitensis*, used in our 2010 study showed much larger isotopic differences in the $\delta^{13}C$ and $\delta^{2}H$ values of their methoxyl values when compared to those observed for their bulk values, we consider the carbon and hydrogen signatures of methoxyl groups to be better suited for studying the geographical origin of *vanilla* species.

It is most unfortunate that even though in their paper Hansen et al. cited several studies, including ours, on vanillin authenticity (references 16−18), they did not use the information contained therein to fully discuss and evaluate their data set. Had they done so, we are certain that despite the evident interesting trends in the carbon and hydrogen δ values of vanillin, the authors would have realized that these values are not sufficient for verification of the authenticity of *vanilla* flavors.

In conclusion, we consider position-specific analysis of vanillin to be the best approach for the authenticity assessment of vanillin because it clearly distinguishes between vanillin from *vanilla*, from biotechnology or chemical synthesis. Moreover, we highly recommend that Hansen et al. consider analyzing the

Received: December 22, 2014
Published: May 7, 2015

ACS Publications © 2015 American Chemical Society

DOI: 10.1021/jf506172q
J. Agric. Food Chem. 2015, 63, 5305−5306

relatively large number of *vanilla* pod samples from different geographical locations using position-specific analysis. From a scientific point of view, these additional data would add significantly to the current database of known stable isotope ratios of natural vanillin and thus be of immense benefit to future authenticity studies and may also assist with the determination of the geographical origin of *vanilla* pods.

Markus Greule[*,†,§]
Armin Mosandl[§]
John T. G. Hamilton[#]
Frank Keppler[†,§]

[†]Institute of Earth Sciences, Ruprecht Karls University Heidelberg, Im Neuenheimer Feld 234-236, D-69120 Heidelberg, Germany

[§]Max Planck Institute for Chemistry, Hahn-Meitner-Weg 1, D-55128 Mainz, Germany

[#]School of Biological Sciences, Queen's University Belfast, 97 Lisburn Road, Belfast BT9 7BL, United Kingdom

AUTHOR INFORMATION

Corresponding Author

*(M.G.) Phone: +49 6221 545228. E-mail: markus.greule@geow.uni-heidelberg.de.

Notes

The authors declare no competing financial interest.

REFERENCES

(1) Hansen, A.-M. S.; Fromberg, A.; Frandsen, H. L. Authenticity and traceability of vanilla flavors by analysis of stable isotopes of carbon and hydrogen. *J. Agric. Food Chem.* **2014**, *62*, 10326−10331.

(2) Scharrer, A.; Mosandl, A. Progress in the Authenticity assessment of vanilla. 2. δ^{13}CV-PDB correlations and methodical optimisations. *Dtsch. Leb. Rundschau* **2002**, *98*, 117−121.

(3) Council Regulation (EC) 1334/2008 of 16 December 2008 on flavourings and certain food ingredients with flavouring properties for use in and on foods and amending Council Regulation (EEC) No. 1601/91, Regulations (EC) No. 2232/96 and (EC) No. 110/2008 and Directive 2000/13/EC [2008] OJ L354/34.

(4) Council Regulation (EC) 178/2002 of 28 January 2002 laying down the general principles and requirements of food Law, establishing the European Food Safety Authority and laying down procedures in matters of food safety [2002] OJ L31/1.

(5) Greule, M.; Tumino, L. D.; Kronewald, T.; Hener, U.; Schleucher, J.; Mosandl, A.; Keppler, F. Improved rapid authentication of vanillin using δ^{13}C and δ^{2}H values. *Eur. Food Res. Technol.* **2010**, *231*, 933−941.

(6) John, T. V.; Jamin, E. Chemical investigation and authenticity of Indian vanilla beans. *J. Agric. Food Chem.* **2004**, *52*, 7644−7650.

(7) Tenailleau, E. J.; Lancelin, P.; Robins, R. J.; Akoka, S. Authentication of the origin of vanillin using quantitative natural abundance ^{13}C NMR. *J. Agric. Food Chem.* **2004**, *52*, 7782−7787.

(8) Remaud, G. S.; Martin, Y. L.; Martin, G. G.; Martin, G. J. Detection of sophisticated adulterations of natural vanilla flavors and extracts: application of the SNIF-NMR method to vanillin and *p*-hydroxybenzaldehyde. *J. Agric. Food Chem.* **1997**, *45*, 859−866.

(9) Greule, M.; Mosandl, A.; Hamilton, J. T. G.; Keppler, F. A simple rapid method to precisely determine ^{13}C/^{12}C ratios of plant methoxyl groups. *Rapid Commun. Mass Spectrom.* **2009**, *23*, 1710−1714.

(10) Greule, M.; Mosandl, A.; Hamilton, J. T. G.; Keppler, F. A rapid and precise method for determination of D/H ratios of plant methoxyl groups. *Rapid Commun. Mass Spectrom.* **2008**, *22*, 3983−3988.

(11) Zeisel, S. Über Ein Verfahren Zum Quantitativen Nachweise von Methoxyl. *Monatsh. Chem.* **1885**, *6*, 989−997.

DOI: 10.1021/jf506172q
J. Agric. Food Chem. 2015, 63, 5305−5306

JOURNAL OF AGRICULTURAL AND FOOD CHEMISTRY

Correspondence/Rebuttal

pubs.acs.org/JAFC

Rebuttal to Comment on Authenticity and Traceability of Vanilla Flavors by Analysis of Stable Isotopes of Carbon and Hydrogen

In Hansen et al.[1], we have published data on $\delta^{13}C$ values and $\delta^{2}H$ values of vanillin extracted from 79 vanilla pods collected from many countries around the world and concluded that "The combined use of results of $\delta^{13}C$ and $\delta^{2}H$ analyses for vanillin, extracted from vanilla pods, shows a relatively close clustering pending upon species as well as geographical location of growth. Analysis of δ values of carbon and hydrogen by compound-specific IRMS is a useful tool in the verification of the authenticity and traceability of vanilla pods".

The goal of previous work by Greule et al.[2] was development of an analytical method to identify vanilla extracted from pods versus vanilla produced synthetically or from a biotechnological process and reported the $\delta^{13}C$ and $\delta^{2}H$ values of both bulk and methoxyl group of vanillin extracted from five vanilla pods. Their $\delta^{13}C$ values for bulk vanillin are very similar to our values for the two different species. The reported values for $\delta^{2}H$ in bulk vanillin show very little variation and are in the range from −47 to −58‰, indicating close geographical origin. We acknowledge that analysis of $\delta^{13}C$ and $\delta^{2}H$ values of both bulk and methoxyl group of vanillin may provide additional information useful in authenticity and traceability studies.

We were interested in the use of δ values of carbon and hydrogen measured on bulk vanilla for authenticity and traceability studies.

The δ values for hydrogen differ around the world primarily as a result of logitudinal and continental effects, and the δ values for hydrogen can therefore differ between countries and even within a single country. Plants take up water from the surroundings, and the ratio of stable hydrogen isotopes in the plant constituents will resemble the ratio of their specific geographical location. Having only information regarding from which country a plant constituent originates, the δ values for hydrogen are expected to show some variation, and also overlap between countries can be expected. We have reported δ values for hydrogen in vanillin together with information on from which country the vanilla pods originate. Information on the specific origin of the vanilla pods was not available. However, information on the δ values for hydrogen is useful in traceability studies as, for example, vanillin with δ values outside the range of −68 to −60‰ is unlikely to originate from Indonesia. Screening of samples against reference datasest enables the possibility to exclude origin possibilities in the verification of label claims. Therefore, we are convinced that our data and results support our discussion and conclusions.

Anne-Mette S. Hansen
Arvid Fromberg
Henrik L. Frandsen*

Division of Food Chemistry, National Food Institute, Technical University of Denmark, Mørkhøj bygade 19, DK-2860 Søborg, Denmark

AUTHOR INFORMATION

Notes

The authors declare no competing financial interest.

REFERENCES

(1) Hansen, A. S.; Fromberg, A.; Frandsen, H. L. Authenticity and traceability of vanilla flavors by analysis of stable isotopes of carbon and hydrogen. *J. Agric. Food Chem.* **2014**, *62*, 10326−10331.

(2) Greule, M.; Tumino, L. D.; Kronewald, T.; Hener, U.; Schleucher, J.; Mosandl, A.; Keppler, F. Improved rapid authentication of vanillin using $\delta^{13}C$ and $\delta^{2}H$ values. *Eur. Food Res. Technol.* **2010**, *231*, 933−941.

Received: March 4, 2015
Published: May 11, 2015

ACS Publications © 2015 American Chemical Society

DOI: 10.1021/acs.jafc.5b01143
J. Agric. Food Chem. 2015, 63, 5307−5307

JOURNAL OF AGRICULTURAL AND FOOD CHEMISTRY

Letter

pubs.acs.org/JAFC

Ethanol in Olive Fruit. Changes during Ripening

ABSTRACT: Ethanol is one of the precursors of ethyl esters, the virgin olive oil quality parameter for the "extra" category recently adopted by the European Union and International Olive Oil Council. Although ethyl ester content has great importance for virgin olive oil classification, the origin of ethanol is not clear. A possible source of ethanol may be the olive fruit itself while it remains on the tree. Variation of fruit ethanol content during ripening was studied for three different olive cultivars: 'Picual', 'Hojiblanca', and 'Arbequina'. Ethanol was measured in fruit homogenates by HS-SPME-GC-FID. The ethanol content varied between 0.56 and 58 mg/kg. 'Hojiblanca' fruits showed the highest ethanol concentration. For all of the cultivars, ethanol content of fruit increased during the ripening process, although a clear cultivar-dependent effect was observed because 'Hojiblanca' fruits showed the most significant raise. Therefore, results indicated that ethanol can be accumulated during fruit maturation on the olive tree.

KEYWORDS: *Olea europaea L., olive fruit, ethanol, ripening, cultivar*

INTRODUCTION

Olive (*Olea europaea* L.) growing has great importance in the Mediterranean basin because is the base of two important food industries, table olives and virgin olive oil production. Although it has great importance, information about the raw material characteristics is scarce, mainly in olives for oil mill use.

In this way, ethanol in olive fruit is a metabolite that has achieved great importance for the past two years because it is one of the precursors of ethyl esters. The level of ethyl esters is a virgin olive oil quality parameter adopted recently by both the European Commission and the International Olive Oil Council[1,2] to discriminate "extra virgin olive oil" produced from healthy and high-quality olive fruits. In fact, for oil classification into "extra virgin" category ethyl ester content must be <40 mg/kg. This limit will be reduced in sequence for the next crop years: 35 mg/kg in 2014/2015 and, finally, 30 mg/kg for the crop year 2015/2016.

Although a close relationship between virgin olive oil quality and ethyl esters was described,[3−5] their biosynthesis and the source of ethanol as ethyl ester precursor are not clear and have to be analyzed.

Conte et al.[6] proposed that ethanol can be solely produced by fermentation during virgin olive oil extraction and storage process. However, a possible source of ethanol may be the synthesis in the olive fruit itself. The production of ethanol in olives may originat on the tree, during fruit collection or transport, and/or in the postharvest treatments until processing. However, to our best of knowledge there are no data for ethanol content in olive fruit and its possible biosynthesis from the olive tree to the oil mill.

Ethanol in fruits is formed by the enzyme alcohol dehydrogenase (ADH; EC 1.1.1.1); it has been described for oranges and pears to increase during maturation.[7,8] Fruits have been described as the source of ethanol, as during ripening on the tree it activates reactions to produce aroma and other components requiring the synthesis of anaerobic metabolites, among them ethanol.[9]

Furthermore, ethanol is accumulated in different fruits that remain for long periods on the tree such as oranges and grapefruits. In these cases the concentration of ethanol showed a fast increase while the fruits were on the tree.[10] Litchi fruits increased ethanol production during maturation on tree.[11] Peaches and nectarines showed increases in aroma volatiles and ethanol during maturation.[12]

Ethanol can be accumulated in over-ripe and senescent fruits than remain on the tree for a long period. In apple cultivars, although a small amount of ethanol can be detected, it can be synthesized at higher concentrations in over-ripe and senescent fruits.[13]

Olive is a nonclimateric fruit that usually remains for long periods on the tree until harvest. This period can oscillate between 5 and 9 months, depending of olive cultivar, including fruit development, ripening, and overmaturation. The mean ripening period described for World Olive Germplasm Bank cultivars varied between 53 and 69 days for the earliest and latest olive cultivars, respectively.[14] However, a considerable part of the olive production can remain on the tree until overmaturation (2−3 months) because of adverse climatic conditions during the harvesting period or high crop yields. Thus, it is of great importance to determine how ethanol content varies in fruit during the ripening process in order to evaluate if ethanol is synthesized on the tree; if so, harvest date may have effect the levels in fruit, olive paste, and finally virgin olive oil of ethanol and ethyl esters.

The objective of this work was to study the ethanol content in olive fruit and its variation during ripeness. To achieve this aim three olive cultivars were selected according to their importance in world olive oil production: 'Picual', 'Hojiblanca', and 'Arbequina'. Acetaldehyde content, as ethanol precursor, was analyzed, too.

MATERIALS AND METHODS

Plant Material. The study was carried out for the crop year 2012/2013. Olive trees of three olive cultivars, 'Picual', 'Hojiblanca', and 'Arbequina', were selected by their crop load homogeneity (3−4). Two trees were selected for each cultivar. The 25-year-old trees were grown in the Wold Olive Germplasm Collection of IFAPA Center Venta del Llano in Mengibar, Jaen, Spain. The trees were spaced 7 × 7 m and grown under irrigation and traditional techniques.

Received: September 3, 2014
Revised: May 22, 2015
Accepted: May 22, 2015
Published: May 22, 2015

ACS Publications © 2015 American Chemical Society

DOI: 10.1021/acs.jafc.5b01453
J. Agric. Food Chem. 2015, 63, 5309−5312

Table 1. Sampling Dates of Olive Fruits from 'Picual', 'Hojiblanca', and 'Arbequina' Olive Cultivars

olive cultivar	Sept 11 (14 WAF[a])	Oct 16[b] (21 WAF)	Oct 24 (22 WAF)	Nov 13[b] (26 WAF)	Dec 20[b] (30 WAF)
'Picual'		0		1.8	2.4
'Hojiblanca'		0		1.5	2.2
'Arbequina'	0	0.3	1.0	2.0	2.4

[a]WAF, weeks after flowering. [b]Harvest dates common for the three olive cultivars.

Olive Samples. Two kilograms of olives was collected from each tree and cultivar at three harvest dates for 'Picual', 'Hojiblanca', and 'Arbequina'. In addition, for 'Arbequina' more harvest dates were included because of the stepped maturation of its fruits. Fruit ripening index was measured according to the method proposed by the Estacion de Olivicultura y Elaiotecnia.[15] The fruit sampling dates and ripening index are shown in Table 1. After harvesting, the fruits were washed using Milli-Q water, dried with filter paper, and processed immediately (15 min) to avoid any alteration.

Fruit Homogenates. To measure the ethanol content, a fruit homogenate approach was followed.[16] For this purpose, 4 g of olive fruit mesocarp, from at least 20 olive fruits, was homogenized with 8 mL of distilled water by means of a homogenizer Ultra-Turrax T-25 at the highest speed (24000 rpm) for 2 min. After an equilibrium period of 5 min at 25 °C, homogenate aliquots of 2 mL were taken into 10 mL vials containing 2 mL of a saturated $CaCl_2$ solution to deactivate the enzyme systems, which were sealed and stored at −18 °C until analysis. Two homogenates were prepared in duplicate for each olive sample.

Analysis of Ethanol and Acetaldehyde. Solid-phase microextraction (SPME) followed by GC-FID was used to analyze the ethanol and acetaldehyde in the samples studied according to the method described by Sanchez-Ortiz et al.[16] Briefly, homogenate samples were conditioned to room temperature and then placed in a 10 mL vial fitted with a silicone septum heater at 40 °C. After 10 min of equilibrium time, ethanol from headspace was adsorbed by exposing the SPME fiber DVB/Carboxen/PDMS 50/30 μm 1 cm (Supelco Co., Bellefonte, PA, USA) for 50 min at 40 °C in the headspace of the sample and then retracting it into the needle, followed by immediate transfer and desorption for 5 min into the injection port of a gas chromatograph equipped with an FID.

Ethanol and acetaldehyde were analyzed using a Varian CP 3800 GC equipped with a Supelcowax 10 capillary column (30 m × 0.25 mm, 0,25 μm, Sigma-Aldrich Co. LLC). Operating conditions were as follows: He was the carrier gas; injector and detector at 250 °C; and column held for 5 min at 40 °C and then programmed at 4 °C min^{-1} to 200 °C. Compound identification was carried out on an ISQ single-quadrupole MS (Thermo Fisher Scientific, Austin, TX, USA) operating in EI mode (70 eV) under identical conditions for GC-FID, matching against the Wiley/NBS Library, and by GC retention time against standard. Quantification was performed using individual calibration curves in the matrix (olive mesocarp homogenate). Results were expressed as milligrams per kilogram of fruit.

Data Analysis. Data for harvest dates are shown as mean value and standard deviation, whereas for cultivar content as mean value and standard error. ANOVA was performed to establish the effect of cultivar and ripening stage considering the three common harvest dates for the three olive cultivars. Tukey's test was applied to establish differences between means, $p = 0.05$. Statistical analyses were performed with Statistix 8.0 software.

RESULTS AND DISCUSSION

ADH activity catalyzes the reversible reduction of aldehydes to alcohols using reduced pyridine nucleotides as cofactors. In previous works ADH activity was measured only in crude extracts prepared from acetone powders of olive mesocarp and seed tissues,[17] whereas it was not detected in crude extracts from fresh tissues.[16] To determine the effect of homogenization process in ethanol synthesis, a previous experiment was carried out. Fruit frozen tissue was ground in a cold blender containing $CaCl_2$ at 0.33 g g^{-1} tissue to inhibit enzyme activities during homogenization compared with the method used in this work. Both methods showed similar contents of ethanol (data not shown).

Ethanol content in fruit varied depending on olive cultivar. For 'Hojiblanca' fruits ethanol concentration varied between 6 and 58 mg/kg, whereas 'Picual' cultivar oscillated from 0.56 to 2.90 mg/kg. 'Arbequina' olives showed an ethanol content that ranged between 1.5 and 11.5 mg/kg.

When ANOVA was performed, the olive cultivar was observed to be mainly responsible for the variability of ethanol concentration, although the harvest date showed similar values (Table 2). Among the olive cultivars analyzed, 'Hojiblanca' showed the highest ethanol content in fruit and 'Picual' achieved the lowest concentration (Table 3). Significant differences between olive cultivars were obtained ($p = 0.05$). These differences in ethanol content between cultivars were described for apples and nectarines previously.[16] There are no previous works describing differences in olive ethanol content between cultivars. The differences observed in this work may be explained by the ADH content/activity in different olive cultivars as described for 'Coratina' and 'Carolea' olive cultivars for C6 volatile alcohols.[18] In our case, the levels of ethanol in fruits of different cultivars corresponded to similar differences for its precursor, acetaldehyde (data not shown).

Harvest date showed a highly significant effect on ethanol content in olive fruits (Table 2). During olive fruit ripening,

Table 2. Partial Mean Squares from Analysis of Variance for the Effect of Cultivar and Harvest Date on Fruit Ethanol Content from the Olive Cultivars 'Picual', 'Hojiblanca', and 'Arbequina'

source	DF[a]	MS[b]	SSTo[c]	p
cultivar	2	942.828	36.36	0.0000
harvest date (HD)	2	938.539	36.20	0.0000
cultivar × HD	4	353.892	27.30	0.0000
error	9	0.805	0.14	
total	17			

[a]DF, degrees of freedom. [b]MS, mean squares. [c]SSTO, partial mean squares for the effect, expressed as percentage, of the total corrected sum of the squares.

Table 3. Mean Ethanol Content of Olive Fruits from 'Picual', 'Hojiblanca', and 'Arbequina' Olive Cultivars

olive cultivar	ethanol (mg/kg)
'Picual'	3.4 ± 1.7 c[a]
'Hojiblanca'	26.1 ± 10.2 a
'Arbequina'	5.7 ± 1.9 b

[a]Different letters indicate significant differences between means for p value of 0.05.

DOI: 10.1021/acs.jafc.5b01453
J. Agric. Food Chem. 2015, 63, 5309−5312

ethanol concentration increased slightly at the beginning of maturation, and then a fast increase was detected (Figure 1).

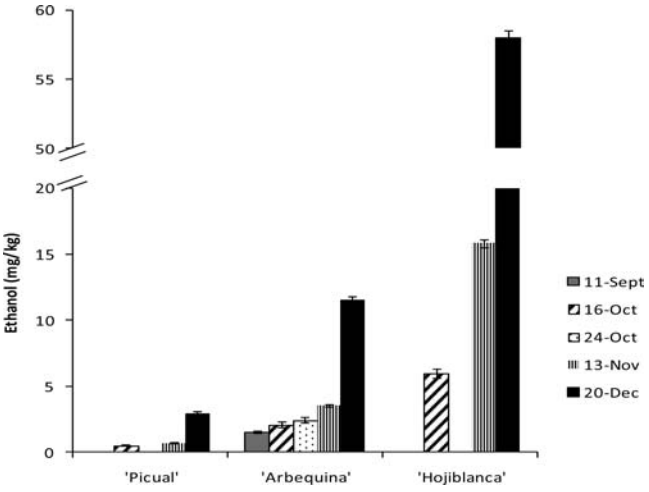

Figure 1. Changes during the ripening process in ethanol concentration of fruits from the olive cultivars 'Picual', 'Hojiblanca', and 'Arbequina'.

Although 'Arbequina' has a fruit stepped maturation and was studied for more harvest dates, the behavior was similar to that of the other cultivars. In the first raise, ethanol showed an increase between 23% for 'Picual' cultivar and 62% for 'Hojiblanca'. For the last harvest date the fastest increases were detected; the increases obtained varied around 70% for the three olive cultivars. Between the first sample collection and the final one, ethanol content rose around 80% for 'Picual' and 'Arbequina', whereas 'Hojiblanca' fruits achieved an increase of 89%. Therefore, 'Hojiblanca' fruits achieved the highest ethanol content during fruit maturation. These differences between cultivars in the biosynthesis of ethanol may be explained by the high significance obtained for the interaction between olive cultivar and harvest date in the ANOVA (Table 2). Ethanol is formed from acetaldehyde by the enzyme ADH. Salas et al.[17] described an increase of ADH activity from 13 weeks after flowering up to 25 weeks after flowering when fruits are still green. After this point ADH activity decreased during the ripening process. Therefore, the increase of fruit ethanol content observed for the three cultivars may not be explained by a higher ADH activity because the period analyzed corresponded to a reduction of ADH activity.

Both acetaldehyde and ethanol have been shown to accumulate in various fruit (both climacteric and non-climacteric) that remain on the tree for long periods.[9] The increase in anaerobic respiration in over-ripen fruit may be explained by a reduction of mithocondrial activity in its tissues. In our case both of them are accumulated in the fruit during maturation, although ethanol showed a faster increase, giving a reduction of the ratio acetaldehyde/ethanol (Figure 2). This ratio can be used as an indicator of fruit anaerobic respiration.

The increase of ethanol content observed for the three cultivars was similar to those described for both climacteric and nonclimateric fruits during the ripening and their residence on the tree for long periods,[10,19] although in our case over-ripening was not achieved.

The results confirm that ethanol is produced naturally in olive fruits while they remain on the tree because for this work their processing was immediate. Ethanol content in olives had a very important genetic component because significant differences were observed between cultivars. 'Hojiblanca' fruits showed the highest ethanol concentration. During fruit ripening ethanol concentration rose, showing a slight increase at the beginning and a fast rise for the last harvest date. Ethanol production during fruit ripening was affected by the cultivar, too. Therefore, ethanol was accumulated in the olive fruit during its residence on the tree as a result of anaerobic respiration. Further works should be focused on the formation of ethanol from olive tree to virgin olive oil and how ethyl esters are synthesized.

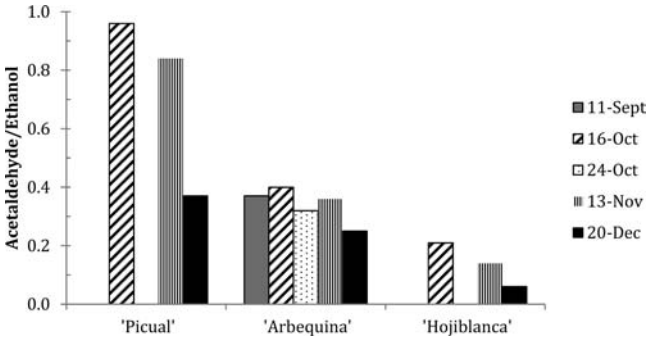

Figure 2. Changes during the ripening process in the ratio of acetaldehyde to ethanol of fruits from the olive cultivars 'Picual', 'Hojiblanca', and 'Arbequina'.

Gabriel Beltrán*
Mohamed A. Bejaoui
Antonio Jimenez
Araceli Sanchez-Ortiz
IFAPA Center Venta del Llano, Junta de Andalucia, P.O. Box 50, 23620 Mengibar Jaén, Spain

AUTHOR INFORMATION

Corresponding Author
*(G.B.) Phone: +34 671 532 213. Fax: +34 953 366 380. E-mail: gabriel.beltran@juntadeandalucia.es.

Funding
This work was supported by the projects FEDER-INIA RTA 2010-00013-C02-01 from the Spanish government and FEDER P10-AGR6099 from Junta de Andalucia.

Notes
The authors declare no competing financial interest.

REFERENCES

(1) European Commission. EU 1348/2013 of 16 December 2013 amending Regulation No 2568/91/EEC on the characteristics of olive oil and olive-residue oil and on the relevant methods of analysis. *Off. J. Eur. Communities* **2013**, *L338*, 31−67.
(2) International Olive Oil Council. Trade standard applying to olive oils and olive-pomace oils. COI 2013/T15/NC No 3/Rev. 17.
(3) Pérez-Camino, M. C.; Cert, A.; Romero-Segura, A.; Cert-Trujillo, R.; Moreda, W. Alkyl esters of fatty acids a useful tool to detect soft deodorized olive oils. *J. Agric. Food Chem.* **2008**, *56*, 6740−6744.
(4) Biedermann, M.; Bongartz, A.; Mariani, C.; Grob, K. Fatty acid methyl and ethyl esters as well as wax esters for evaluating the quality of olive oils. *Eur. Food Res. Technol.* **2008**, *228*, 65−74.
(5) Mariani, C.; Bellan, G. On the possible increase of the alkyl esters in extra virgin olive oil. *Riv. Ital. Sostanze Grasse* **2011**, *88*, 3−10.
(6) Conte, L.; Mariani, C.; Gallina Toschi, T.; Tagliabue, S. Alkyl esters and related compounds in virgin olive oils: their evolution over time. *Riv. Ital. Sostanze Grasse* **2014**, *91*, 21−29.

DOI: 10.1021/acs.jafc.5b01453
J. Agric. Food Chem. 2015, 63, 5309−5312

(7) Bruemmer, J. H.; Roe, B. Pyruvate dehydrogenase activity during ripening of 'Hamlin' oranges. *Phytochemistry* **1985**, *24*, 2105−2106.
(8) Chervin, C.; Truett, J. K. Alcohol dehydrogenase expression and alcohol production during pear ripening. *J. Am. Soc. Hortic. Sci.* **1999**, *124*, 71−75.
(9) Pesis, E. The role of the anaerobic metabolites, acetaldehyde and ethanol, in fruit ripening, enhancement of fruit quality and fruit deterioration. *Postharvest Biol. Technol.* **2005**, *37*, 1−19.
(10) Davis, P. I. Relation of ethanol content of citrus fruits to maturity and storage conditions. *Proc. Fla. State Hort. Soc.* **1970**, *84*, 217−222.
(11) Pesis, E.; Dvir, O.; Feygenberg, O.; Ben-Arie, R.; Ackerman, M.; Lichter, A. Production of acetaldehyde and ethanol during maturation and modified atmosphere storage of litchi fruit. *Postharvest Biol. Technol.* **2002**, *26*, 157−165.
(12) Lavilla, T.; Recasens, I.; Lopez, M. L. Production of volatile aromatic compounds in Big Top nectarines and Royal Glory peaches during maturity. *Acta Hortic.* **2001**, *553*, 233−234.
(13) Nichols, W. C.; Patterson, M. E. Ethanol accumulation and poststorage quality of 'Delicious' apples during short term, low O_2, Ca storage. *Hortscience* **1987**, *33*, 992−994.
(14) Barranco, D.; Rallo, L. Epocas de floracion y maduracion. In *Variedades de Olivo en España*; Rallo, L., Barranco, D., Caballero, J. M., del Rio, C., Martin, A., Trujillo, I., Eds.; Junta de Andalucia-MAPA-Ediciones MundiPrensa: Madrid, Spain, 2005; pp 281−292.
(15) Beltran, G.; Uceda, M.; Hermoso, M.; Frias, L. Maduracion. In *El Cultivo del Olivo*; Barranco, D., Fernandez-Escobar, R., Rallo, L., Eds.; Junta de Andalucia- Ediciones MundiPrensa: Madrid, Spain, 2004; pp 158−183.
(16) Sanchez-Ortiz, A.; Romero-Segura, C.; Gazda, V. E.; Graham, I. A.; Sanz, C.; Perez, A. G. Factors limiting the synthesis of virgin olive oil volatile esters. *J. Agric. Food Chem.* **2012**, *60*, 1300−1307.
(17) Salas, J. J.; Sanchez, J. Alcohol dehydrogenases from olive (*Olea europaea*) fruit. *Phytochemistry* **1998**, *48*, 35−40.
(18) Iara, D. L.; Bruno, L.; Macchione, B.; Tagarelli, A.; Sindona, G.; Giannino, D.; Bitonti, M. B.; Chiapetta, A. The aroma biogenesis-related *Olea europaea* alcohol dehydrogenase gene is developmentally regulated in the fruits of two *O. europaea* L. cultivars. *Food Res. Int.* **2012**, *49*, 720−727.
(19) Zerbini, P. E.; Giudetti, G.; Rizzolo, A.; Grassi, M. Harvest and quality indexes of peach. *Inf. Agrar.* **2001**, *57*, 57−60.

DOI: 10.1021/acs.jafc.5b01453
J. Agric. Food Chem. 2015, 63, 5309−5312

JOURNAL OF AGRICULTURAL AND FOOD CHEMISTRY

Article

pubs.acs.org/JAFC

Postharvest Exogenous Application of Abscisic Acid Reduces Internal Browning in Pineapple

Qin Zhang,[†] Yulong Liu,[†] Congcong He, and Shijiang Zhu*

Guangdong Province Key Laboratory of Postharvest Physiology and Technology of Fruits and Vegetables, College of Horticulture, South China Agricultural University, Guangzhou, Guangdong 510642, China

ABSTRACT: Internal browning (IB) is a postharvest physiological disorder causing economic losses in pineapple, but there is no effective control measure. In this study, postharvest application of 380 μM abscisic acid (ABA) reduced IB incidence by 23.4−86.3% and maintained quality in pineapple fruit. ABA reduced phenolic contents and polyphenol oxidase and phenylalanine ammonia lyase activities; increased catalase and peroxidase activities; and decreased $O_2^{\cdot-}$, H_2O_2, and malondialdehyde levels. This suggests ABA could control IB through inhibiting phenolics biosynthesis and oxidation and enhancing antioxidant capability. Furthermore, the efficacy of IB control by ABA was not obviously affected by tungstate, ABA biosynthesis inhibitor, nor by diphenylene iodonium, NADPH oxidase inhibitor, nor by lanthanum chloride, calcium channel blocker, suggesting that ABA is sufficient for controlling IB. This process might not involve H_2O_2 generation, but could involve the Ca^{2+} channels activation. These results provide potential for developing effective measures for controlling IB in pineapple.

KEYWORDS: *abscisic acid, antioxidant systems, internal browning, pineapple, phenolic compounds, quality*

INTRODUCTION

Internal browning (IB), also referred to as blackheart, is a physiological disorder of pineapple (*Ananas comosus* L.) that often occurs during postharvest processes. The affected fruit develop browning spots or areas mainly in the flesh surrounding the core with no obvious external damage, hence the name. Most cultivars of pineapple are susceptible to internal browning;[1] therefore, the losses due to this disorder are often heavy in production countries.[2,3] For example, it brings about US$1.3 million in annual losses to the Australian pineapple industry,[4] and it could cause even heavier losses to the Chinese pineapple industry, as over 90% of total production in China is from the susceptible cultivar "Comte de Paris". Over the years, various methods have been tried to control IB, including preharvest application of potassium[5] or calcium[6] and postharvest use of calcium,[1,7] strontium chloride,[1] modified atmosphere,[7,8] 1-methylcyclopropene,[9] waxing,[2] and heat treatment.[7,10] However, to date, not a single effective way has been found to be commercially useful, mainly because of their relatively low efficacies. Take the most extensively studied calcium application, for example. Although some contributions reported that calcium was effective in reducing IB incidence, whether applied preharvest[6,11] or postharvst,[1,12] others did not show any effects[7,13] or could not confirm the effects.[14] This implies a complex nature of IB, as harvested pineapple could either develop IB symptoms under low temperature (LT; 10 °C or lower)[1,2,4−6,15] or at ambient temperature (AT; 20 °C or higher).[15,16] The LT-caused IB could be related to chilling injury,[4] while the IB occurred in AT could be the manifestation of senescence. However, the fact plant hormone gibberellins (GAs) are involved in this disorder could make things simpler because exogenous GAs treatment induced IB,[15,17] and this is true for pineapple stored either at LT or AT (20 °C −25 °C).[15] In addition, endogenous GAs levels were found to be positively correlated to IB incidence.[15] It is not known whether abscisic acid (ABA), the antagonist of GAs, can inhibit IB. It is likely that ABA could inhibit IB developed as a result of chilling under LT, as ABA has been widely confirmed to induce chilling tolerance in plants.[18,19] In addition, ABA applied in combination with calcium hydroxide and wax sprays significantly reduced pineapple IB severity under LT.[20] Because LT storage alone can effectively inhibit development of IB for sufficiently long,[16] from the industry point of view, it is not necessary to use ABA to control IB of pineapple stored in LT. On the other hand, pineapple is mostly transported and sold under AT in China and other developing countries that produce it; therefore, it is of great value to develop IB control measures for pineapple stored and shipped under AT. This study investigated effects of application of ABA on IB development in AT, aiming to develop an effective alternative to control IB. In addition, this research investigated the mechanism of ABA in controlling IB to help understand the role of exogenous ABA.

MATERIALS AND METHODS

Plant Materials and Treatment. Pineapple (*Ananas comosus* L. cv "Comte de Paris") fruit of "Queen" group at 70% maturity (commercial maturity in China, with fruit being green with a trace of yellow) were collected from a commercial plantation in Xuwen County, Guangdong Province and transported 300 km to Guangdong Province Key Laboratory of Postharvest Physiology and Technology of Fruits and Vegetables, College of Horticulture, South China Agricultural University, Guangzhou, Guangdong Province. Fruit uniform in size (average weight about 500 g) and free of physical injury or

Received: December 28, 2014
Revised: May 25, 2015
Accepted: May 26, 2015
Published: May 26, 2015

ACS Publications © 2015 American Chemical Society

DOI: 10.1021/jf506279x
J. Agric. Food Chem. 2015, 63, 5313−5320

disease symptoms were selected, with the crown being half-cut and sprayed with a fine mist of solution of diphenylene iodonium (DPI) (5 μM), ABA (95 or 380 μM), tungstate (TS) (50 μM), or lanthanum chloride ($LaCl_3$) (50 μM), each containing 0.01% Tween 80, until runoff and air-dried. For the combination of DPI with ABA, $LaCl_3$ with ABA, and TS with ABA, pineapples were permitted to dry at AT for 6 h before being treated further. The control fruit were sprayed in the same way with distilled water containing 0.01% Tween 80. Each treatment was applied to three replications, each containing 20 fruit. Following treatment, pineapples were wrapped with perforated polyethylene film and kept at 20 °C in the dark at 95% RH. Samples of pulp tissues were collected at 6 h, 12 h, 24 h, 3 days, 6 days, 9 days, and 12 days; frozen in liquid nitrogen; and stored at −80 °C.

Internal Browning Incidence Assessment. Three fruit from each treatment, one from each replicate, were cut every 3 days for monitoring the development of IB. Upon obvious onset of browning in flesh or core of pineapples from any treatment, all the other fruit, 45−60 fruit per treatment, were then cut for observation of IB. IB incidence was calculated as percentage of fruit with symptoms of IB, irrespective of the size of the browning on cut surface. The strict standard is used because fruit with slight or severe browning are all affected fruit in the eyes of consumers. Therefore, the commercial value is lost upon the appearance of the first trace of internal browning.

Determination of Soluble Solids, Titratable Acids, and Ascorbic Acid. Pineapple flesh (100 g) was cut into small pieces, homogenized, and filtered. The filtrate was used for measuring soluble solids concentrations (SSC), titratable acid (TA), and ascorbic acid (AsA) contents according to methods described by Lu et al.[21]

Assay of Enzyme Activity. Polyphenol oxidase (PPO), peroxidase (POD), and catalase (CAT) were extracted and activity was assayed according to the methods we described previously with modification.[22,23] Frozen pineapple flesh (1 g) were ground in liquid nitrogen to fine powder and then homogenized in 4 mL of precooled 0.05 mM potassium phosphate buffer, pH 7.8, containing 5% (w/v) polyvinylpyrrolidone. The homogenate was centrifuged at 15 000*g* for 20 min at 4 °C. The supernatant, referred to as the crude enzyme extract, was used to assay the activity of enzymes. For PPO assay, a 3 mL reaction mixture contained 2 mL of 50 mM phosphate buffer, pH 7.8, 0.9 mL of 10 mM pyrocatechol, and 0.1 mL of crude enzyme extract. PPO activity was expressed as units of grams per fresh weight (FW). One unit was defined as an increase in A_{398} of 0.01 min^{-1}. For POD assay, a 3 mL reaction solution consisted of 0.1 mL of 1% (v/v) guaiacol (1%), 0.1 mL of 0.46% H_2O_2, 2.7 mL of 0.1 M potassium phosphate buffer, pH 7.8, and 0.1 mL of enzyme extract. The enzyme activity was detected by following the change in optical density at 470 nm due to the oxidation of guaiacol. One unit of POD activity was defined as an increase in A_{470} of 0.01 min^{-1}. For CAT assay, a 3 mL reaction mixture contained 2.9 mL of 15 mM H_2O_2 in 0.05 M potassium phosphate buffer, pH 7.8, and 0.1 mL of enzyme extract. Catalase activity was expressed in units of grams per FW, where one unit of CAT activity was defined as causing an increase in A_{240} of 0.01 min^{-1}.

Phenylalanine ammonia lyase (PAL) was extracted and the activity determined according to the method described previously.[23] Frozen pineapple flesh (1 g) was homogenized in 4 mL of precooled 0.05 M sodium borate buffer, pH 7.0, in an ice−water bath. The homogenate was centrifuged at 15 000*g* for 15 min at 4 °C, and the supernatant (enzyme extract) was used for PAL assays. A 3 mL reaction mixture contained 0.4 mL of enzyme extract, 1.6 mL of 0.1 mM sodium borate, pH 8.8, supplemented with 5 mM dithiothreitol and 1 mL of 0.02 M L-phenylalanine as substrate. The mixture was incubated at 38 °C for 3 h. PAL activity was expressed as the difference in optical density at 290 nm before and after incubation. One unit was defined as an increase in A_{290} of 0.01 h^{-1}.

Assay of Total Phenolic Compounds (TPC). The contents of TPC were detected using Folin−Ciocalteu reagent according to the method described previously.[23] The absorbance at 765 nm was measured and used to calculate the phenolic contents using gallic acid (GA) as a standard. Results were calculated and expressed as milligrams of GA equivalent (GAE) per gram of fresh samples.

Determination of $O_2^{\cdot-}$, H_2O_2, and MDA. The contents of superoxide radicals ($O_2^{\cdot-}$), hydrogen peroxide (H_2O_2), and MDA were determined according the method described by Li et al.[24] with modification. First, 0.5 mL of the same supernatant as for measuring PPO, POD, and CAT was reacted with 1 mL of hydroxylamine hydrochloride for 1h, then 1 mL of *p*-aminobenzenesulfonic acid and 1 mL of α-naphthylamine were added, and the solution was kept at 25 °C for 20 min. The absorbance at 530 nm was measured, and the result was expressed as nmol/min·gFW. The H_2O_2 content was determined as a H_2O_2−titanium complex resulting from the reaction of tissue−H_2O_2 with titanium tetrachloride. Absorbance values at 415 nm were calibrated to a standard curve generated using known concentrations of H_2O_2. The MDA content was determined following the method described by Li et al.[24]

Statistical Analyses. The experiments were repeated two or three times with similar results. There were three replications for analysis of each parameter. Data were analyzed by one-way analysis of variance (ANOVA). Mean separations were performed using the least significant difference method (LSD test). Statistically significant differences were assumed when their *P* values were $\leq$0.01.

RESULTS

Effect of ABA on Pineapple IB Incidence. The first experiment conducted in November 2012 showed that ABA at 95 and 380 μM reduced IB incidence by 2.8% and 25%, respectively, with 380 μM ABA treatment being statistically significantly different from the control ($P \leq 0.01$) (Figure 1). Therefore, 380 μM was used in a series of experiments that followed over a period of two years to check whether ABA works for fruit harvested from different seasons. As is shown in Figure 2, exogenous application of ABA at 380 μM obviously inhibited IB development for pineapple harvested in different seasons and different years, with the IB incidence being reduced by 70.83% for the trial in June 2013, 58.00% for September 2013, 23.40% for November 2013, 86.30% for June 2014, and 36.60% for September 2014 (Figure 2). Although there were big variances for fruit from different batches or seasons, the difference between the ABA-treated fruit and the water-treated control reached statistically significant levels for all batches ($P < 0.01$).

Effects of ABA on Quality of Pineapple. The time-course changes of the SSC, TA, and AsA were similar, with the values rising to a peak on day 3 and then declining during the remaining time (Figure 3A). Compared with the control, ABA-treated fruit were almost the same as the control in SSC

DOI: 10.1021/jf506279x
J. Agric. Food Chem. 2015, 63, 5313−5320

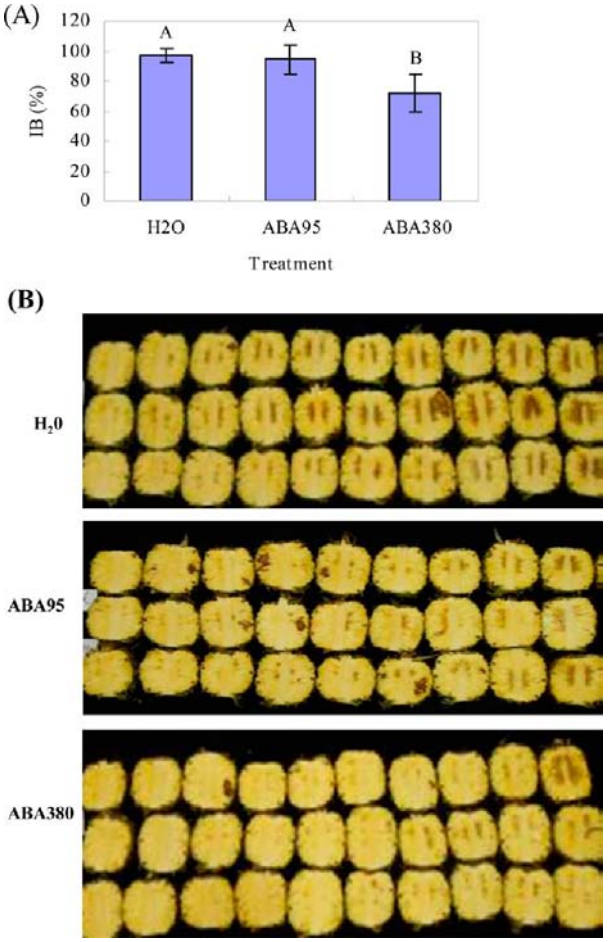

Figure 1. Effect of exogenous ABA at different concentrations on internal browning incidence of harvested pineapple fruit stored at ambient temperature (20 °C). Pineapples were harvested in November 2012 and sprayed with distilled water or ABA solution at 95 μM (ABA95) or 380 μM (ABA380). IB incidence (A) was evaluated and pictures (B) were taken 12 days after treatment. Significance of differences between the control and the treatment is indicated by letters above the bars ($P \leq 0.01$). Standard errors are shown.

contents, while they had 4.5% and 25.7% more contents of TA and AsA, respectively, than the control at the end of storage (Figure 3B,C).

Effect of ABA on TPC Contents and Related Enzymes Activities. The control increased dramatically in contents of TPC and activities of PAL and PPO during the first 9 days, whereas those of the ABA-treated fruit increased much less (Figure 4). As a result, the ABA-treated fruit had much lower TPC contents and enzyme activities during the last 6 days of storage, especially on day 9, when those with ABA treatment were 12.2%, 29.0%, and 32.6% lower than the control in TPC, PAL, and PPO, respectively.

Effects of ABA on Activities of CAT and POD and Levels of ROS and MDA. During storage, CAT activity in pineapple decreases with time, while POD activity first rose to a peak, and then decreased. ABA-treated fruit showed CAT and POD activities higher than that of the control, and they had lower levels of $O_2^{\cdot-}$, H_2O_2, and MDA during the whole storage period (Figure 5).

Role of ROS in ABA-Induced Resistance to IB. To investigate whether ROS plays a role in ABA-induced resistance to IB, DPI, an important ROS generation inhibitor, was applied to pineapple before treatment with ABA. The DPI plus ABA treatment increased IB incidence by only 3.3% compared with treatment with ABA alone, while it significant reduced IB occurrence, by 23.3%, compared with the control ($P \leq 0.01$) (Figure 6).

Effect of $LaCl_3$ on ABA-Induced Resistance to IB. To investigate the effect of blocking of the calcium channel, harvested pineapple fruit were treated with $LaCl_3$ alone or $LaCl_3$ plus ABA. Compared with the control, $LaCl_3$ treatment increased IB incidence by 13.4%, although the difference did not reach a statistically significant level ($P < 0.01$). The combination treatment significantly reduced IB incidence by 20% and 36.4%, compared with the control and $LaCl_3$ treatment, respectively ($P < 0.01$) (Figure 7).

Effects of TS on Efficacy of ABA. To show what role endogenous ABA plays, especially whether it adds to the effects of exogenous ABA, the TS, inhibitor of ABA biosynthesis, was applied before the pineapple was exposed to ABA. When pineapple was treated with TS alone, the IB incidence was only slightly higher than the control (Figure 8). However, the combination of TS and ABA treatment reduced IB incidence by 23% compared with the control ($P < 0.01$), suggesting that exogenous ABA can work alone in controlling IB.

DISCUSSION

Internal browning has been regarded as one of the major problems of the pineapple industry. Over the past 30 years, many researchers have been trying to develop techniques to control it, but they have not found a commercially effective measure. In this study, it was shown that exogenous ABA treatment is effective in inhibiting IB development for storage at 20 °C and that it works well for pineapple harvested in different seasons (Figures 1 and 2). This result is inspiring for two reasons. First, it allows the industry to extend this technique to packing houses because of the decreased ABA production cost as a result of improvement of ABA production methods.[25] Second, it provides a good perspective for studying and unraveling the nature of IB.

In this study, over a period of two years, experiments were conducted with "spring pineapple", pineapple harvested in period from March to June, and "autumn/winter pineapple", the fruit harvested in period from September to February. However, no experiment was conducted in the summer because farmers do not produce pineapple during that period because pineapple is not profitable in the presence of many other fancy fruits produced in the summer. The industry has long noticed that the spring pineapple is less susceptible to IB than autumn/winter pineapple. This study also showed that the efficacy of ABA in controlling IB is obviously higher for spring pineapple than for autumn/winter pineapple (Figure 2). The difference in IB incidence between spring and autumn/winter pineapples could be related to the weather, as the autumn/winter pineapple is exposed to the high temperature and rainfall during development in summer, while the spring pineapple develops in mild temperature and dry season in Xuwen County, Guangdong Province, the major pineapple production area in China. The fact that the fruit develops faster in summer and slower in winter might contribute to the different IB incidences. This could also account for the difference in effects of ABA. How temperature and rainfall during fruit development influence IB incidence and ABA effects remains to be elucidated.

DOI: 10.1021/jf506279x
J. Agric. Food Chem. 2015, 63, 5313−5320

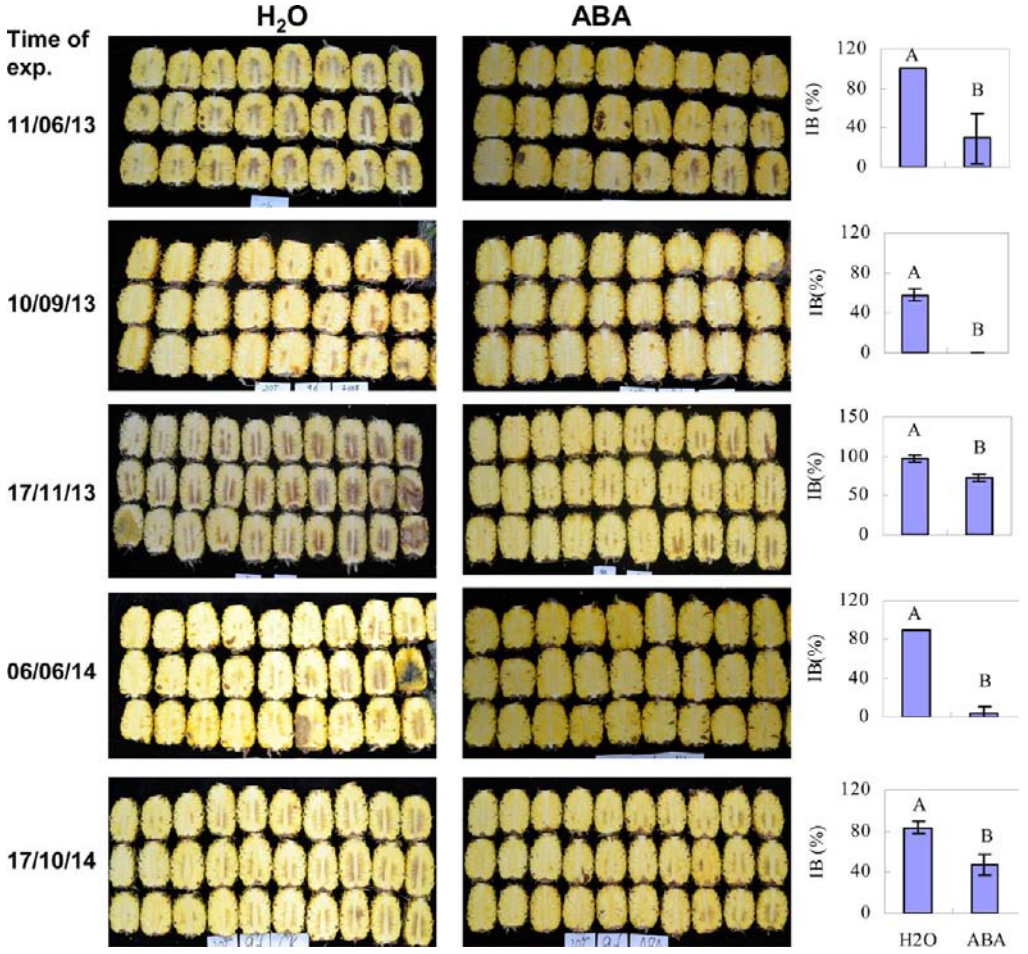

Figure 2. Effects of exogenous ABA treatment on IB incidence of pineapple fruit harvested in different seasons. Fruit were sprayed with distilled water or 380 μM ABA solution before storage at 20 °C. IB incidence was evaluated at 12, 9, 9, 12, and 9 days for trials conducted in June 2013, September 2013, November 2013, June 2014, and October 2014, respectively. Significance of differences between the control and the treatment is indicated by letters above the bars ($P \leq 0.01$). Standard errors are shown.

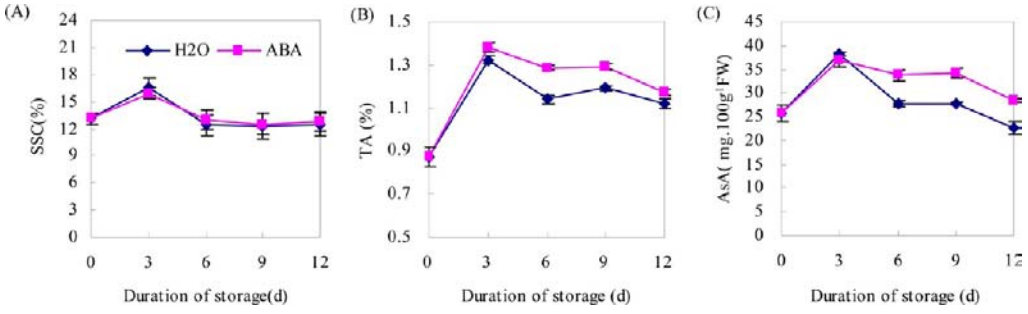

Figure 3. Effects of exogenous ABA treatment on soluble solid concentrations (SSC) (A), TA (B), and AsA (C) contents of harvested pineapple fruit. Fruit were sprayed with distilled water or 380 μM ABA solution before storage at 20 °C. The samples were from experiments conducted in June 2013.

Different studies varied or even conflicted regarding the effects of exogenous ABA on fruit quality such as SSC and TA. Preharvest application of ABA improved color of grapes and increased acidity but reduced SSC contents.[25] ABA application to plants increased tomato fruit soluble sugar, while decreasing organic acid concentrations.[26] ABA treatment at the color-break stage did not affect postharvest quality attributes such as soluble solids and acidity in litchi fruit.[27] In this study, postharvest ABA treatment slowed the decease of TA and AsA levels, while it did not affect SSC contents (Figure 3). These results indicate that ABA maintained the quality of harvested pineapple.

Development of internal browning involves oxidation of phenolic compounds by PPO.[28] In this study, ABA-treatment reduced PPO activity (Figure 4) and inhibited internal browning (Figures 1 and 2), consistent with previous studies that show activities of PPO were positively correlated with severity of IB in pineapple.[15,29] This result suggests that ABA could control IB by inhibiting enzymatic oxidation of phenolic compounds. How ABA inhibited PPO activities remains to be

DOI: 10.1021/jf506279x
J. Agric. Food Chem. 2015, 63, 5313−5320

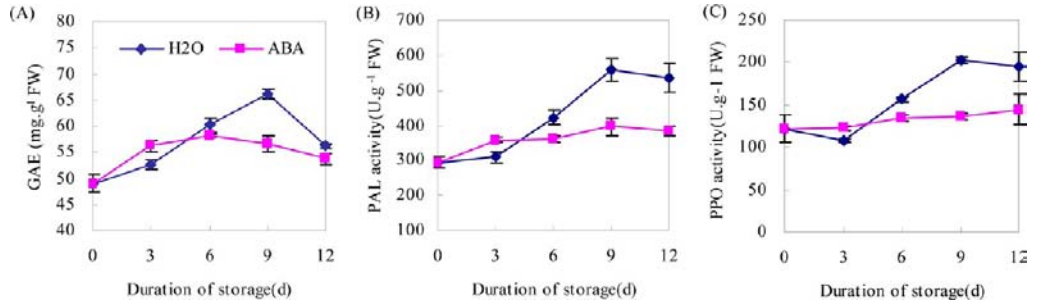

Figure 4. Effects of exogenous ABA treatment on contents of total phenolic compounds (A) and activities of PAL (B) and PPO (C) of harvested pineapple fruit. Fruit were sprayed with distilled water or 380 μM ABA solution before storage at 20 °C. The samples were from experiments conducted in June 2013.

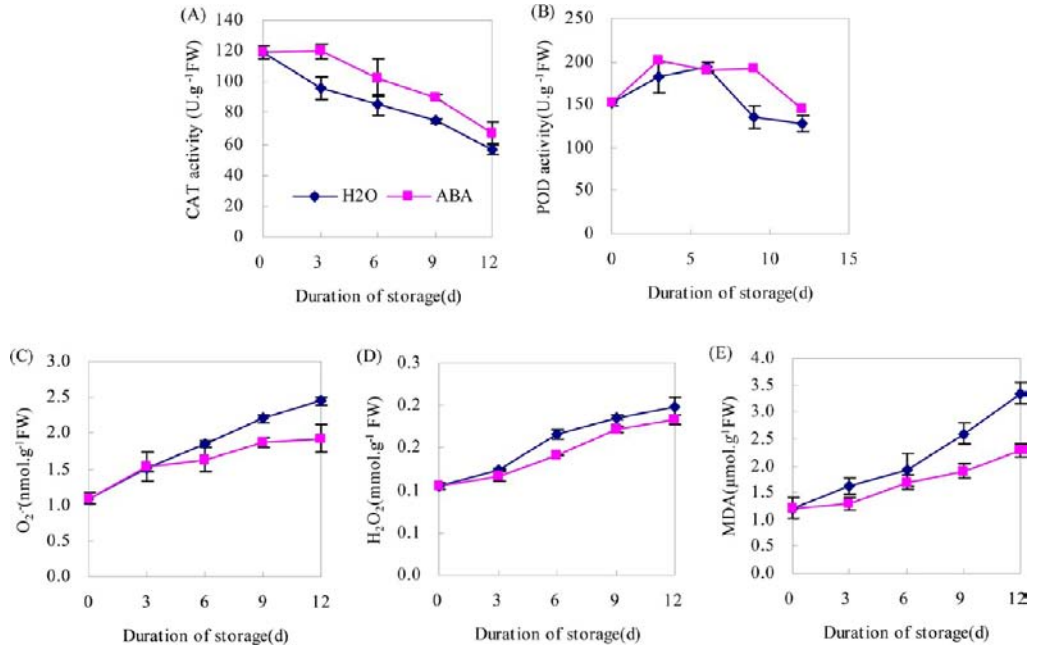

Figure 5. Effects of exogenous ABA treatment on activities of CAT (A) and POD (B) and contents of $O_2^{\cdot-}$ (C), H_2O_2 (D), and MDA (E) of harvested pineapple fruit. Fruit were sprayed with distilled water or 380 μM ABA solution before storage at 20 °C. The samples were from experiments conducted in June 2013.

elucidated. Phenolics are the prerequisite for the PPO enzymatic browning. In eggplant, although both the phenolic content and PPO activity play important roles in browning of stored fruit, the phenolic compounds play a major role, as the cultivar with higher TPC showed higher browning, although the PPO activity was lower.[30] In this study, ABA-treated pineapples had significantly lower TPC, which might be closely related to the lower IB in those fruits. PAL plays an important role in the browning process of fruits and vegetables,[31] as it plays a pivotal role in the biosynthesis of phenolics.[32] In pistachio (*Pistacia vera* L.), there was a high positive correlation between PAL activity and total phenolics contents.[33] In this study, ABA-treated pineapple showed obviously lower PAL activities (Figure 4), suggesting that ABA could reduce biosynthesis of TPC by decreasing PAL activity. How ABA reduces activities of PAL remains to be studied.

The ROS, which include superoxide radicals ($O_2^{\cdot-}$), hydrogen peroxide (H_2O_2), singlet oxygen ($^1O_2$), and perhydroxy radical ($HO_2^{\cdot-}$), affect many cellular functions by damaging nucleic acids, oxidizing proteins, and causing lipid peroxidation.[34] A strong oxidative burst will cause cellular damage and death.[35] Under normal and healthy conditions, the ROS molecules are scavenged by various antioxidative defense mechanisms.[34] These include enzymatic antioxidant systems, such as SOD, POD, glutathionereductase (GR), and CAT, and nonenzymatic low molecular metabolites, such as AsA and reduced glutathione (GSH).[36] Studies with different plants showed ABA increased contents of AsA and activities of CAT and POD.[36,37] In this study, ABA elevated levels of AsA (Figure 3) and enhanced activities of CAT and POD (Figure 5A,B), suggesting that it enhanced antioxidant defense system of pineapples. That ABA-treated pineapple had levels of $O_2^{\cdot-}$ and H_2O_2 lower than those of the control (Figure 5C,D) implies the strengthened defense system efficiently scavenged ROS molecules and thus protected the integrity of cells. This is further confirmed by the reduced MDA contents in ABA-treated fruit (Figure 5E), as MDA is used as an indicator of the severity of cell membrane injury.[36] These results suggest that ABA protected cell membrane systems through activating the antioxidative defense system to reduce ROSs, which greatly contributed to reduced IB.

However, the role of H_2O_2 seems to be complicated. On the one hand, it acts as a cytotoxic molecule. On the other hand, it can function as a signaling molecule.[38] What actual role it plays

DOI: 10.1021/jf506279x
J. Agric. Food Chem. 2015, 63, 5313−5320

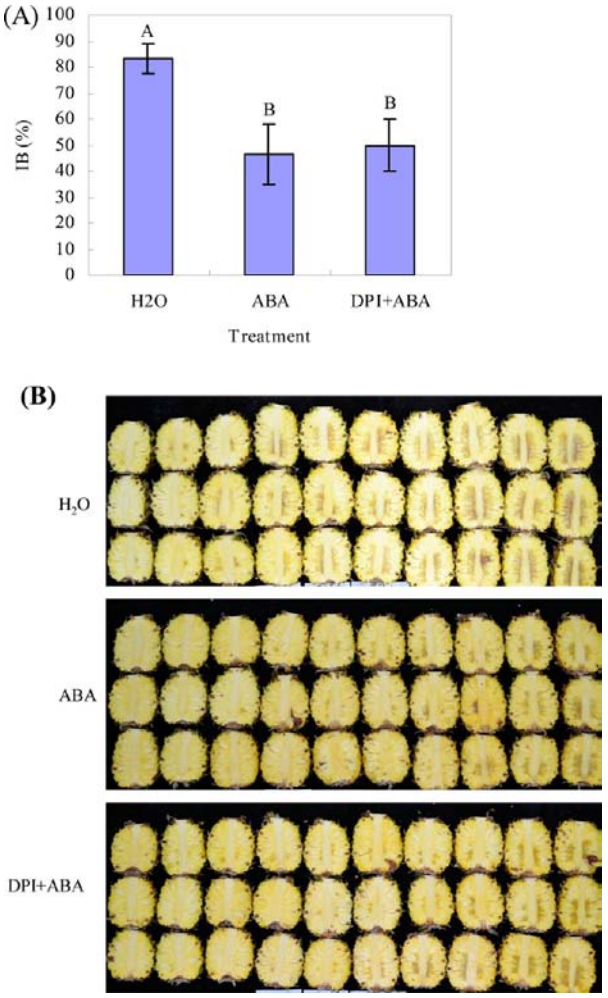

Figure 6. Effect of DPI on ABA induced resistance to internal browning in pineapple fruit stored at 20 °C. Fruit were sprayed with distilled water, 380 μM ABA, or 5 μM DPI before treatment with 380 μM ABA. Incidence (A) was evaluated and pictures (B) were taken 9 days after treatment. Significance of differences between the control and the treatment is indicated by letters above the bars ($P \leq 0.01$). Standard errors are shown. The experiment was conducted in October 2014.

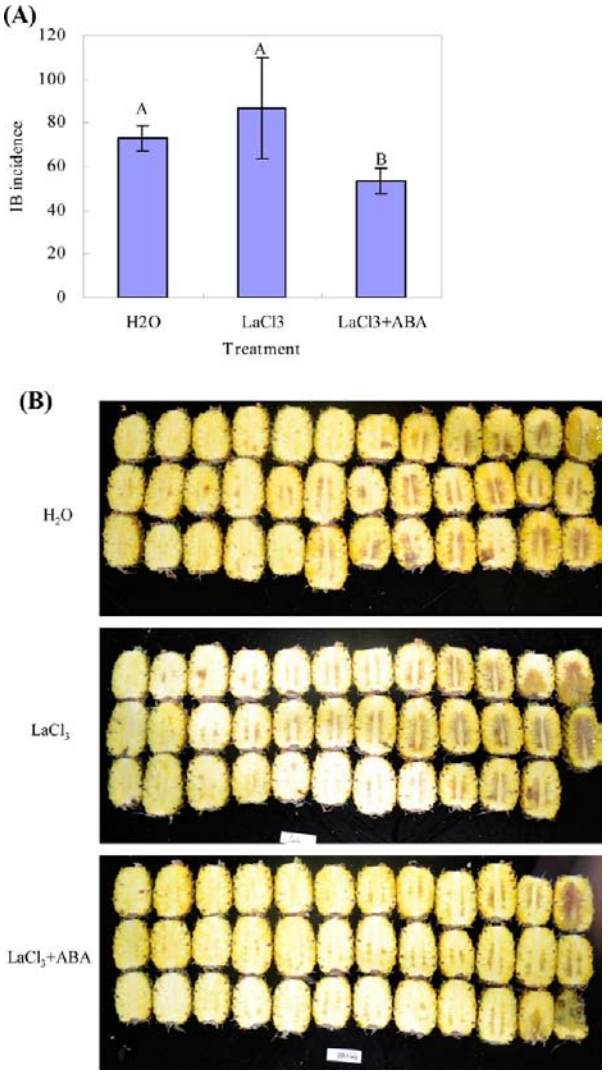

Figure 7. Effects of $LaCl_3$, calcium channel blocker, on IB development in harvested pineapple fruit stored at 20 °C. Fruit were sprayed with distilled water, 50 μM $LaCl_3$, or 380 μM ABA following $LaCl_3$ treatment. Incidence (A) was evaluated and pictures (B) were taken 9 days after treatment. Significance of differences between the control and the treatment is indicated by letters above the bars ($P \leq 0.01$). Standard errors are shown. The experiment was conducted in September 2013.

depends on the delicate equilibrium between ROS production and scavenging at the proper site and time.[39] ABA is a key inducer of H_2O_2 production in maize leaves under water stress.[40] Synthesis of H_2O_2 is essential for ABA-induced stomatal closure in various species.[41] In *Arabidopsis*, ABA-induced stomatal closure was inhibited by DPI, an inhibitor of NADPH oxidase.[42] These suggest that certain functions of ABA depend on H_2O_2 as a signaling molecule. It is worth investigating whether H_2O_2 as a signaling molecule is needed by ABA for activating of the antioxidant system that leads to alleviated internal browning. The result showed that the combination of DPI and ABA treatment did not obviously increase IB severity compared with ABA treatment alone (Figure 6), suggesting that H_2O_2 is not needed by ABA as a signaling molecule to activate the ROS scavenging system and inhibit IB. How ABA activates ROS scavengers, such as POD and CAT, remains to be elucidated.

As a second messenger, cytosolic calcium ($[Ca^{2+}]_{cyt}$) mediates ABA-induced plant's responses to abiotic stresses, such as chilling[43] and heat.[44] ABA functions by activating Ca^{2+}-permeable channels.[45] ABA-induced $[Ca^{2+}]_{cyt}$ increases are mediated by Ca^{2+} influx through plasma membrane Ca^{2+}-permeable (I_{Ca}) channels and Ca^{2+} release from internal stores.[46] If it is the case in harvested pineapple that ABA controls IB by activating Ca^{2+}-permeable channels, what happens when the channels are blocked would be an interesting question. To address this question, $LaCl_3$, a Ca^{2+}-permeable channels blocker, was applied alone or in combination with ABA to harvested pineapple fruit. The results showed the $LaCl_3$ alone increased the IB incidence by 13.7% compared with the control, indicating that blocking calcium channels was unfavorable for control of IB. However, the combination treatment reduced IB by 33.4% compared with $LaCl_3$ treatment alone (Figure 7), indicating that ABA could reactivate the Ca^{2+} channels blocked by $LaCl_3$. These results suggest that control of IB by ABA involves activation of Ca^{2+}-permeable channels.

DOI: 10.1021/jf506279x
J. Agric. Food Chem. 2015, 63, 5313−5320

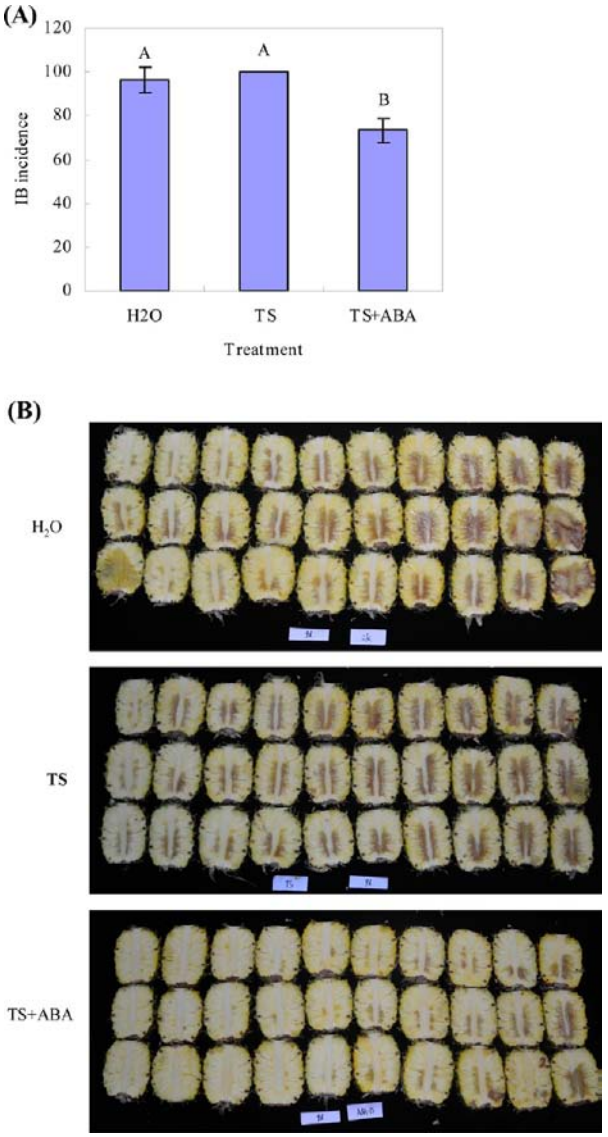

Figure 8. Effects of sodium tungstate dehydrate (TS), inhibitor of ABA biosynthesis, on IB development in harvested pineapple fruit stored at 20 °C. Fruit were sprayed with distilled water, 50 μM TS, or 380 μM ABA following TS treatment. Incidence (A) was evaluated and pictures (B) were taken 9 days after treatment. Significance of differences between the control and the treatment is indicated by letters above the bars ($P \leq 0.01$). Standard errors are shown. The experiment was conducted in November 2013.

To check how important ABA is for pineapple to keep healthy during storage, TS, the inhibitor of ABA biosynthesis, was applied to harvested pineapples. The results showed that TS alone slightly aggravated IB symptoms compared with the control, while the combination of TS and ABA treatment effectively inhibited IB development (Figure 8). This result is consistent with that of Pusittigul et al.[15] which showed that aggravated IB in pineapple coincided with decreased ABA contents. This implies that sufficient ABA content is necessary for controlling IB and that the deficiency or degradation of endogenous ABA during storage process could result in development of IB.

In conclusion, ABA induced resistance to IB and maintained quality of harvested pineapples. ABA reduced IB development by reducing biosynthesis of phenolic substrates, inhibiting enzymatic oxidation of phenolics, and enhancing ROS-scavenging capability to protect cell membranes. ABA-induced resistance to IB is not dependent on synthesis of H_2O_2, but could be through activating the Ca^{2+} channels. ABA is sufficient for controlling IB, and deficiency of ABA in pineapple tissue could induce IB.

AUTHOR INFORMATION

Corresponding Author

*Tel.: +86 20 38902512/13632355208. Fax: +86 2085288280. E-mail: shijiangzhu@yahoo.com.

Author Contributions

†Q.Z. and Y.L.: These authors contributed equally to this work.

Notes

The authors declare no competing financial interest.

ACKNOWLEDGMENTS

This work is supported by Special Fund for Agro-scientific Research in the Public Interest funded by China Ministry of Agriculture (Project 201203021).

ABBREVIATIONS USED

ABA, abscisic acid; GAs, gibberellins; CAT, catalase; PAL, phenylalanine ammonia-lyase; POD, peroxidase; PPO, polyphenol oxidase; SOD, superoxide dismutase; IB, internal browning; MDA, malondialdehyde; TS, tungstate; ROS, reactive oxygen species; AsA, ascorbic acid; TSS, total soluble solids; TA, titratable acids; TPC, total phenolic compounds; FW, fresh weight; $O_2^{\cdot-}$, superoxide radicals; H_2O_2, hydrogen peroxide; LT, low temperature; AT, ambient temperature; OD, optical density; RH, relative humidity; DPI, diphenylene iodonium

REFERENCES

(1) Youryon, P.; Wongs-Aree, C.; McGlasson, W. B.; Glahan, S.; Kanlayanarat, S. Alleviation of internal browning in pineapple fruit by peduncle infiltration with solutions of calcium chloride or strontium chloride under mild chilling storage. *Int. Food Res. J.* **2013**, *20* (1), 239−246.

(2) Rohrbach, K. G.; Paull, R. E. Incidence and severity of chilling induced browning of waxed 'Smooth Cayenne' pineapple. *J. Am. Soc. Hortic. Sci.* **1982**, *107*, 453−457.

(3) Smith, L. G. Cause and development of blackheart in pineapple. *Trop. Agric.* **1983**, *60* (1), 31−35.

(4) Ko, H. L.; Campbell, P. R.; Jobin-Decor, M. P.; Eccleston, K. L.; Graham, M. W.; Smith, M. K. The introduction of transgenes to control blackheart in pineapple (Ananas comosus L.) cv. Smooth cayenne by microprojectile bombardment. *Euphytica* **2006**, *150* (3), 387−395.

(5) Soares, A. G.; Trugo, L. C.; Botrel, N.; Souza, L. F.; da, S. Reduction of internal browning of pineapple fruit (*Ananas comosus* L.) by preharvest soil application of potassium. *Postharvest Biol. Technol.* **2005**, *35* (2), 201−207.

(6) Herath, H. M. I.; Bandara, D. C.; Banda, D. M. G. A. Effect of pre-harvest calcium fertilizer application on the control of internal browning development during the cold storage of pineapple "Mauritius" (*Ananas comosus* L. Merr.). *J. Hortic. Sci. Biotechnol.* **2003**, *78* (6), 762−767.

(7) The, P. M. P; Goncalves, N. B.; Pinto, N. A. V. D. Effect of a combination of calcium chloride, modified atmosphere and hot water treatment on internal browning in pineapple cv. Smooth Cayenne. *Revista Brasileira de Armazenamento* **2005**, *30* (1), 1−7 in Portuguese with English abstract.

DOI: 10.1021/jf506279x
J. Agric. Food Chem. 2015, 63, 5313−5320

(8) Hussain, S. F.; Suntharalingam, S.; Siriwardana, T. D. W. The effect of packaging on the control of internal browning of pineapple. *Tropical Agric.* **1998/1999**, *152*, 53−58.
(9) Selvarajah, S.; Bauchot, A. D.; John, P. Internal browning in cold-stored pineapples is suppressed by a postharvest application of 1-methylcyclopropene. *Postharvest Biol. Technol.* **2001**, *23* (2), 167−170.
(10) Weerahewa, D.; Adikaram, N. K. B. Heat-induced tolerance to internal browning of pineapple (*Ananas comosus* cv. "Mauritius") under cold storage. *J. Hortic. Sci. Biotechnol.* **2005**, *80* (4), 503−509.
(11) Herath, H. M. I.; Bandara, D. C.; Banda, D. M. G. A. Effect of pre-harvest calcium application level for the post-harvest keeping quality in Mauritius pineapple. *Tropical Agric. Res.* **2000**, *12*, 408−411.
(12) Goncalves, N. B.; Carvalho, V. D.; Goncalves, J. R. D. A. Effect of calcium chloride and hot water treatment on enzyme activity and content of phenolic compounds in pineapples. *Pesqui. Agropecu. Bras.* **2000**, *35* (10), 2075−2081.
(13) Youryon, P.; Wongs-Aree, C.; McGlasson, W. B.; Glahan, S.; Kanlayanarat, S. Response of internal browning in pineapple fruit vacuum infiltrated with solutions of calcium chloride or strontium chloride. *Acta Hortic.* **2012**, *943*, 149−154.
(14) Pusittigul, I.; Siriphanich, J.; Juntee, C. Role of calcium on internal browning of pineapples. *Acta Hortic.* **2014**, *1024*, 329−338.
(15) Pusittigul, I.; Kondo, S.; Siriphanich, J. Internal browning of pineapple (Ananas comosus L.) fruit and endogenous concentrations of abscisic acid and gibberellins during low temperature storage. *Sci. Hortic.* **2012**, *146*, 45−51.
(16) Hong, K.; Hu, H.; Wang, J.; Zhang, L.; Hu, H.; Jia, Z.; Gu, H.; He, Q.; Gong, D. Quality changes and internal browning developments of summer pineapple fruit during storage at different temperatures. *Sci. Hortic.* **2013**, *151*, 68−74.
(17) Zhou, Y. C.; O'Hare, T. J.; Jobin-Decor, M.; Underhill, S. J. R.; Wills, R. B. H.; Graham, M. W. Transcriptional regulation of a pineapple polyphenol oxidase gene and its relationship to blackheart. *Plant Biotechnol. J.* **2003**, *1*, 463−478.
(18) Xin, L.; Li, P. H. Relationship between proline and abscisic acid in the induction of chilling tolerance in maize suspension-cultured Cells. *Plant Physiol.* **1993**, *103*, 607−613.
(19) Nayyar, H.; Bains, T.; Kumar, S. Low temperature induced floral abortion in chickpea: relationship to abscisic acid and cryoprotectants in reproductive organs. *Environ. Exp. Bot.* **2005**, *53*, 39−47.
(20) Nanayakkara, K. P. G. A.; Herath, H. M. W.; Senanayake, Y. D. A. Effects of pre-harvest treatments of potassium, post-harvest treatments of calcium, potassium, abscisic acid and light on reducing internal browning in pineapple (*Ananas comosus* (L.) Merr. cv Mauritius) under cold-storage. *Acta Hortic.* **2005**, *666*, 321−327.
(21) Lu, X. H.; Sun, D. Q.; Mo, Y. W.; Xi, J. G.; Sun, G. M. Effects of post-harvest salicylic acid treatment on fruit quality and anti-oxidant metabolism in pineapple during cold storage. *J. Hortic. Sci. Biotechnol.* **2010**, *85*, 454−458.
(22) Zhu, S.; Ma, B. Benzothiadiazole- or methyl jasmonate-induced resistance to *Colletotrichum musae* in harvested banana fruit is related to elevated defense enzyme activities. *J. Hortic. Sci. Biotechnol.* **2007**, *82* (4), 500−506.
(23) Lin, J.; Gong, D.; Zhu, S.; Zhang, L. Expression of *PPO* and *POD* genes and contents of polyphenolic compounds in harvested mango fruits in relation to Benzothiadiazole-induced defense against anthracnose. *Sci. Hortic.* **2011**, *130*, 85−89.
(24) Li, Y.; Zhao, H.; Duan, B.; Korpelainen, H.; Li, C. Effect of drought and ABA on growth, photosynthesis and antioxidant system of *Cotinus coggygria* seedlings under two different light conditions. *Environ. Exp. Bot.* **2011**, *71*, 107−113.
(25) Cantin, C. M.; Fidelibus, M. W.; Crisosto, C. H. Application of abscisic acid (ABA) at veraison advanced red color development and maintained postharvest quality of 'Crimson Seedless' grapes. *Postharvest Biol. Technol.* **2007**, *46*, 237−241.
(26) Barickman, T. C. *Effect of abscisic acid on tomato calcium partitioning and fruit quality*. Ph.D. Dissertation, University of Tennessee, Knoxville, TN, May 2014.http://trace.tennessee.edu/utk_graddiss/2675.
(27) Singha, S. P.; Sainia, M. K.; Singha, J.; Pongenera, A.; Sidhub, G. S. Preharvest application of abscisic acid promotes anthocyanins accumulation in pericarp of litchi fruit without adversely affecting postharvest quality. *Postharvest Biol. Technol.* **2014**, *96*, 14−22.
(28) He, Q.; Luo, Y. Enzymatic browning and its control in fresh-cut produce. *Stewart Postharv. Rev.* **2007**, *6* (3), 1−7.
(29) Raimbault, A. K.; Marie-Alphonsine, P. A.; Horry, J. P.; Francois-Haugrin, M.; Romuald, K.; Soler, A. Polyphenol oxidase and peroxidase expression in four pineapple varieties (*Ananas comosus* L.) after a chilling injury. *J. Agric. Food Chem.* **2011**, *59* (1), 342−348.
(30) Mishra, B. B.; Gautam, S.; Sharma, A. Free phenolics and polyphenol oxidase (PPO): The factors affecting post-cut browning in eggplant (*Solanum melongena*). *Food Chem.* **2013**, *139*, 1−4.
(31) Ke, D.; Saltveit, M. E., Jr. Carbon dioxide-induced brown stain development as related to phenolic metabolism in iceberg lettuce. *J. Am. Soc. Hortic. Sci.* **1989**, *114* (5), 789−794.
(32) Hahlbrock, K.; Scheel, D. Physiology and molecular biology of phenylpropanoid metabolism. *Annu. Rev. Plant Physiol. Plant Mol. Biol.* **1989**, *40*, 347−369.
(33) Nadernejad, N.; Ahmadimoghadam, A.; Hossyinifard, J.; Poorseyedi, S. Effect of different rootstocks on PAL activity and phenolic compounds in flowers, leaves, hulls and kernels of three pistachio (*Pistacia vera* L.) cultivars. *Trees* **2013**, *27*, 1681−1689.
(34) Foyer, C. H.; Noctor, G. Redox homeostis and antioxidant signaling: a metabolic interface between stress perception and physiological responses. *Plant Cell* **2005**, *17*, 1866−1875.
(35) Mittler, R. Oxidative stress, antioxidants and stress tolerance. *Trends Plant Sci.* **2002**, *7*, 405−410.
(36) Guo, W. L.; Chen, R. G.; Gong, Z. H.; Yin, Y. X.; Ahmed, S. S.; He, Y. M. Exogenous abscisic acid increases antioxidant enzymes and related gene expression in pepper (Capsicum annuum) leaves subjected to chilling stress. *GMR, Genet. Mol. Res.* **2012**, *11* (4), 4063−4080.
(37) Jiang, M.-Y.; Zhang, J.-H. Abscisic acid and antioxidant defense in plant cells. *Acta Botanica Sinica* **2004**, *46* (1), 1−9.
(38) Grennan, A. K. A transcriptomic footprint of reactive oxygen species. *Plant Physiol.* **2008**, *148* (3), 1187−1188.
(39) Gratao, P. L.; Polle, A.; Lea, P. J.; Azevedo, R. A. Making the life of heavy metalstressed plants a little easier. *Funct. Plant Biol.* **2005**, *32*, 481−494.
(40) Hu, X.; Zhang, A.; Zhang, J.; Jiang, M. Abscisic acid is a key inducer of hydrogen peroxide production in leaves of maize plants exposed to water stress. *Plant Cell Physiol.* **2006**, *47*, 1484−1495.
(41) Desikan, R.; Cheung, M. K.; Bright, J.; Henson, D.; Hancock, J. T.; Neill, S. J. ABA, hydrogen peroxide and nitric oxide signalling in stomatal guard cells. *J. Exp. Bot.* **2004**, *55*, 205−212.
(42) Cross, A. R.; Jones, O. T. G. The effect of the inhibitor diphenylene iodonium on the superoxide-generating system of neutrophils. *Biochem. J.* **1986**, *237*, 111−116.
(43) Zhou, B.; Guo, Z. Calcium is involved in the abscisic acid-induced ascorbate peroxidase, superoxide dismutase and chilling resistance in *Stylosanthes guianensis*. *Biol. Plant.* **2009**, *53* (1), 63−68.
(44) Jiang, Y. W.; Huang, B. G. Effects of calcium on antioxidant activities and water relations associated with heat tolerance in two cool-season grasses. *J. Exp. Bot.* **2001**, *52*, 341−349.
(45) Murata, Y.; Pei, Z.-M.; Mori, I. C.; Schroeder, J. I. Abscisic acid activation of plasma membrane Ca^{2+} channels in guard cells requires cytosolic NAD(P)H and is differentially disrupted upstream and downstream of reactive oxygen species production in abi1−1 and abi2−1 protein phosphatase 2C mutants. *Plant Cell* **2001**, *13*, 2513−2523.
(46) Kwak, J. M.; Mori, I. C.; Pei, Z. M.; Leonhardt, N.; Torres, M. A.; Dangl, J. L.; Bloom, R. E.; Bodde, S.; Jones, J. D.; Schroeder, J. I. NADPH oxidase AtrbohD and AtrbohF genes function in ROS-dependent ABA signaling in Arabidopsis. *EMBO J.* **2003**, *22*, 2623−2633.

DOI: 10.1021/jf506279x
J. Agric. Food Chem. 2015, 63, 5313−5320

JOURNAL OF AGRICULTURAL AND FOOD CHEMISTRY

Article

pubs.acs.org/JAFC

Genotypic and Environmental Impact on Natural Variation of Nutrient Composition in 50 Non Genetically Modified Commercial Maize Hybrids in North America

Bin Cong,[†] Carl Maxwell,[†] Stanley Luck,[†] Deanne Vespestad,[‡] Keith Richard,[§] James Mickelson,[#] and Cathy Zhong*[,†]

[†]DuPont Pioneer, 200 Powder Mill Road, P.O. Box 8352, Wilmington, Delaware 19803, United States

[‡]Eurofins AgroSciences, Fort Walton Beach, Florida 32547, United States

[§]EPL Bio Analytical Services, 9095 West Harristown Boulevard, Niantic, Illinois 62551, United States

[#]DuPont Pioneer, 8325 N.W. 62nd Avenue, Johnston, Iowa 50131, United States

Supporting Information

ABSTRACT: This study was designed to assess natural variation in composition and metabolites in 50 genetically diverse non genetically modified maize hybrids grown at six locations in North America. Results showed that levels of compositional components in maize forage were affected by environment more than genotype. Crude protein, all amino acids except lysine, manganese, and β-carotene in maize grain were affected by environment more than genotype; however, most proximates and fibers, all fatty acids, lysine, most minerals, vitamins, and secondary metabolites in maize grain were affected by genotype more than environment. A strong interaction between genotype and environment was seen for some analytes. The results could be used as reference values for future nutrient composition studies of genetically modified crops and to expand conventional compositional data sets. These results may be further used as a genetic basis for improvement of the nutritional value of maize grain by molecular breeding and biotechnology approaches.

KEYWORDS: *maize, hybrid, natural variation, nutrient composition, substantial equivalence, compositional analysis*

INTRODUCTION

Maize is a major crop providing not only animal and human nutrition but also raw materials for manufacturing industrial products. World production and consumption of maize were about 989,608 and 953,133 thousand metric tons in 2013/2014, respectively.[1] Maize yield has improved substantially in the past two decades through conventional breeding combined with molecular marker-assisted selection and biotechnology.[2] To feed an expanding world population, projected to reach 9.6 billion in 2050,[3] and to supply feedstock for industrial products, biotechnology is needed to improve crop productivity and sustainability.

Genetically modified (GM) crop varieties were grown on >175.2 million hectares worldwide in 2013.[4] GM crops have been stringently scrutinized by global regulatory agencies in many aspects including agronomic, environmental, toxicological, and nutritional compositional data since the initial application of biotechnology to crops in the 1990s. One of the risk assessments, substantial equivalence evaluation for nutrient composition of GM crops, was first outlined by the Food and Agriculture Organization of the United Nations (FAO)/World Health Organization (WHO) consultation[5,6] and further developed by the Organization for Economic Co-operation and Development (OECD)[7,8] and additional FAO/WHO consultation.[9] Currently, many international organizations including FAO, WHO, and the International Life Sciences Institute (ILSI) have adopted substantial equivalence as an accepted principle in the safety assessment of GM plants.

In substantial equivalence analysis, measurements of analytes representing key nutrients, antinutrients, toxicants, and secondary metabolites from GM crops are compared to data collected from non-GM near-isogenic plants and non-GM conventional hybrids grown under identical conditions and are also compared to historic values from the literature and the ILSI crop composition database.[10,11] This comparative safety assessment approach provides assurance that foods and feeds derived from GM crops are as safe as their conventional counterparts.

Compositional studies of grain as well as forage have been conducted in both non-GM conventional crops and GM crops including maize,[12] soybean,[13] cotton,[14] rice,[15] wheat,[16] potato,[17] and others.[18,19] Many studies have shown that transgenes have less of an effect on nutrient composition than genotypes and environments.[20,21]

Maize was domesticated about 8000 years ago and has undergone extensive human selection for agronomic performance for more than a century. Whereas genetic improvement contributes about 70% of the yield gained in the development of modern hybrids, grain quality and composition also have been changed.[22] This study was designed to assess the degree of genotypic and environmental impact on forage and grain composition in 50 non-GM commercial maize hybrids that

Received: January 22, 2015
Revised: May 12, 2015
Accepted: May 14, 2015
Published: May 14, 2015

ACS Publications © 2015 American Chemical Society

DOI: 10.1021/acs.jafc.5b01764
J. Agric. Food Chem. 2015, 63, 5321−5334

Table 1. Means and Ranges of Proximates, Fibers, and Minerals Measured from Forage across All Six Sites (Percent Dry Weight)

analyte	ON mean range[a]	MN mean range[a]	IL mean range[a]	NE mean range[a]	KS mean range[a]	TX mean range[a]	combined mean range[b]	ILSI range[c]	literature range	% variability		
										genotype	location	G × E
crude protein	7.4	8.6	7.0	7.7	8.8	9.0	8.1			25.5	42.6	30.4
	5.2–9.2	6.5–10.6	5.0–9.2	5.8–9.6	6.6–10.3	7.2–10.8	5.0–10.8	3.14–11.57	3.14–15.9			
crude fat	3.6	3.3	3	3.6	2.3	3.6	3.2			21.2	38.9	33.1
	2.1–4.7	1.9–5.0	1.9–3.9	2.3–4.9	1.4–4.3	2.1–4.7	1.4–5.0	0.296–4.57	0.296–6.7			
ash	3.4	4.5	4.3	6.4	5.8	6.9	5.4			28.1	67.8	34.6
	2.3–4.7	3.2–5.9	2.3–5.5	4.9–9.1	4.4–9.0	4.3–9.5	2.3–9.5	1.53–9.64	1.3–10.5			
carbohydrates	85.6	83.6	85.6	82.3	83.1	80.4	83.3			24	59.2	30.7
	82.2–88.4	80.4–87.1	82.2–89.2	77.5–85.4	79.5–86.0	77.9–83.5	77.5–89.2	76.4–92.1	76.4–92.1			
moisture	5	6.7	5.8	6.2	8.2	5.5	6.3			28.1	57.2	31.3
	3.9–6.3	4.4–9.5	4.4–9.5	4.7–8.3	6.6–10.2	4.0–7.5	3.9–10.2	NA	12.5–46.7			
crude fiber	18.2	19.6	23.7	22.5	25.6	22.5	22.3			38	44	33.5
	12.5–23.6	14.3–24.5	16.0–32.4	17.7–31.6	20.9–30.8	16.4–30.1	12.5–32.4	35.9–62.8	19–62.8			
ADF	24.9	25.7	32.2	30.3	32.1	30.7	29.6			36.4	40.50	34.9
	18.6–31.9	18.8–32.4	23.1–39.9	23.1–41.7	26.6–38.2	23.4–40.4	18.6–41.7	16.1–47.4	16.1–47.4			
NDF	41.5	41.9	50.0	45.6	50.0	46.6	46.2			33	36	31.2
	33.3–51.9	32.9–62.7	39.4–58.6	34.7–57.5	37.9–58.8	32.5–58.1	32.5–62.7	20.3–63.7	20.3–63.7			
calcium	0.24	0.17	0.18	0.21	0.19	0.25	0.21			18.6	28.2	21
	0.12–0.38	0.089–0.27	0.11–0.26	0.12–0.32	0.13–0.29	0.14–0.40	0.089–0.40	0.0714–0.577	0.0714–0.6			
phosphorus	0.24	0.31	0.18	0.31	0.25	0.25	0.26			15.2	61.3	25.8
	0.17–0.30	0.22–0.37	0.12–0.25	0.22–0.40	0.13–0.36	0.16–0.32	0.12–0.40	0.0936–0.37	0.0936–0.55			

[a]The minimum and maximum of sample values for hybrids grown at each location. [b]The combined range for all six sites. [c]ILSI ranges reported in version 3.0.

DOI: 10.1021/acs.jafc.5b01764
J. Agric. Food Chem. 2015, 63, 5321−5334

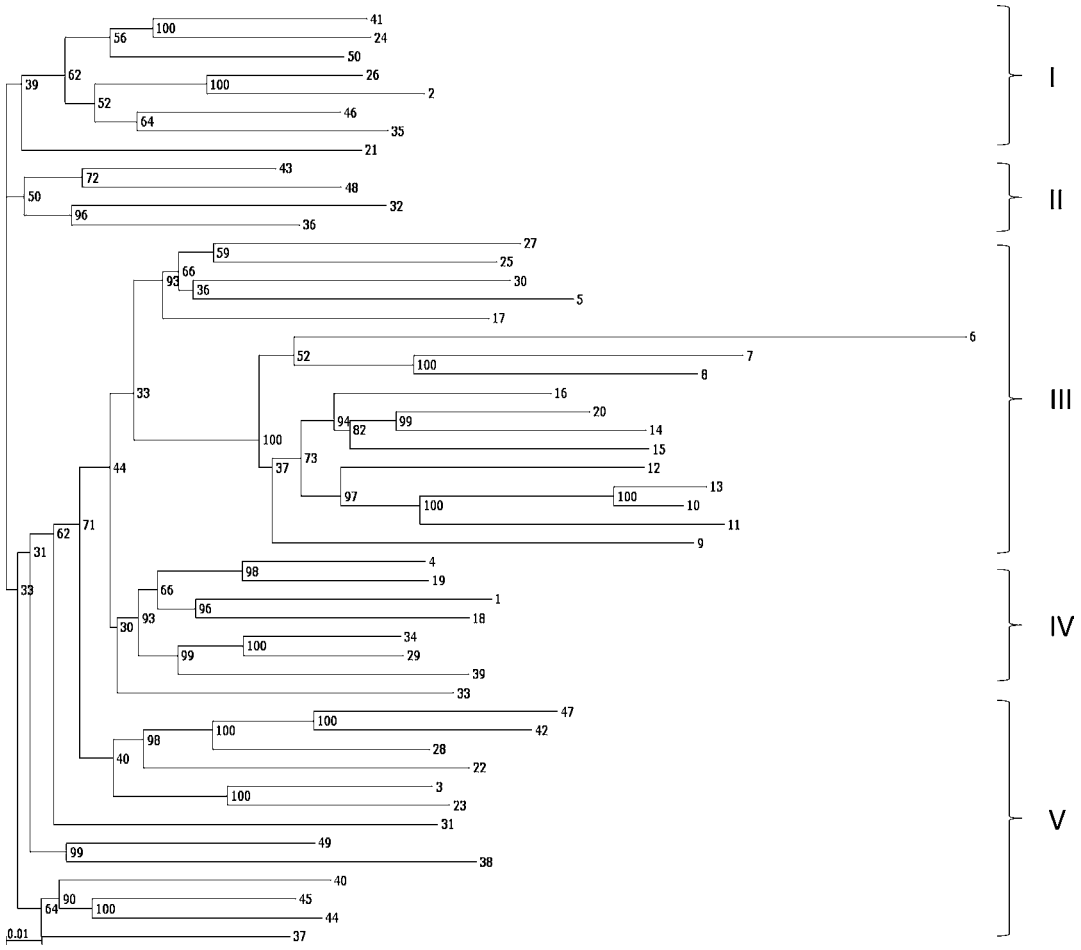

Figure 1. Phylogenetic analysis of 50 hybrids based on SNP genotype data. Fifty hybrids (entry codes 1−50) are clustered in five major distinct groups labeled I, II, III, IV, and V. Five hybrids (entry codes 1−5) were selected to grow at all six sites.

represent different genetic backgrounds and maturity groups. These hybrids were grown in six different geographical regions in North America during the 2010 growing season with each site having 20 unique genotypes. Forage and grain samples collected from the commercial maize hybrids were analyzed for key nutritional components. The genotype data for approximately 3000 single-nucleotide polymorphisms (SNPs) were used in genome-wide association studies (GWAS) for several nutrients. The results for oleic acid are reported here to demonstrate that the genetic variation in the selected hybrids is sufficient in providing an independent confirmation of previous GWAS results for oleic acid. Furthermore, the Pearson correlation matrix was applied to calculate the distance matrix for the analytes. This study provides insights into natural variation in maize nutrient composition by identifying effects of genotype, environment, and their interaction at the analyte level. In addition, the results may offer opportunities for further genetic improvement of maize forage and grain composition.

MATERIALS AND METHODS

Materials. Fifty DuPont Pioneer non-GM commercial maize hybrids (entry codes 1−50) with diverse genetic backgrounds and different maturity groups were grown at six sites in North America (Illinois (IL), Kansas (KS), Minnesota (MN), Nebraska (NE), Texas (TX), and Ontario (ON)). Twenty genotypes were grown at each location as shown in Table 1 of the Supporting Information reported by Asiago et al.[23] At each location, the selected genotypes were planted in three blocks and two replicates per block.

Forage and Grain Sample Collection. One forage sample and one grain sample were collected from each hybrid in each block for compositional analysis. Each forage sample was obtained by cutting the aerial portion of three plants from the root system, approximately 2.5 cm above the soil surface line. The plants were then cut into sections approximately ≤7.5 cm, the cut material was mixed, and one-third of the cut material was collected into a prelabeled, plastic-lined cloth bag and placed on dry ice until transfer to frozen storage (≤ −10 °C).

Each grain sample was obtained by harvesting the grain from five hand-pollinated ears. Grain samples were collected at typical harvest maturity and placed in prelabeled, plastic-lined cloth bags. Samples were kept on dry ice until transfer to frozen storage (≤ −10 °C).

Processing. Grain and forage samples were shipped frozen to EPL Bio Analytical Services (EPL BAS, Niantic, IL, USA) and maintained at approximately −20 °C until processing. Forage samples were dried at 60 °C in a forced-air oven and then ground with a Wiley laboratory mill (model 4, Thomas Scientific, Swedsboro, NJ, USA) to pass a 1 mm screen. Grain samples were not dried prior to grinding in an ultra centrifugal mill fitted with a 0.75 mm distance ring/sieve (ZM 200, Retsch, Newton, PA, USA). Ground samples were stored at −20 °C.

Nutrient Composition Analysis. Compositional analyses were conducted by EPL BAS using GLP validated methods. Both forage and grain were analyzed for crude protein, crude fat, ash, carbohydrates, crude fiber, acid detergent fiber (ADF), neutral detergent fiber (NDF), and minerals (calcium and phosphorus). Grain was further analyzed for fatty acids, amino acids, additional minerals (manganese, iron, magnesium, copper, potassium, sodium, and zinc), vitamins (β-carotene, thiamin, riboflavin, niacin, pantothenic acid, pyridoxine, folic acid, and α-, β-, γ-, and δ-tocopherol), secondary metabolites, and antinutrients (inositol, raffinose, furfural, ferulic acid, *p*-coumaric acid, phytic acid, and

DOI: 10.1021/acs.jafc.5b01764
J. Agric. Food Chem. 2015, 63, 5321−5334

trypsin inhibitor). Most compositional analyses were performed as described by Herman et al.[24] Modified procedures used for measuring fatty acids, minerals, inositol, and raffinose and procedures used for measuring crude fat, niacin, pantothenic acid, and pyridoxine are briefly described below.

Crude Fat. Crude fat content was quantified by an automated hydrolysis method using an ANKOM^{HCl} hydrolysis system (Ankom Technology, Macedon, NY, USA) and an automated extraction method using an ANKOM^{XT15} extraction system.[25−27] Samples were hydrolyzed at 90 °C for 80 and 60 min for forage and grain, respectively, and then extracted using a mixed solvent of petroleum ether/ethyl ether/ethanol (45:45:10). Extracts were evaporated, and the fat residue remaining was determined gravimetrically.

Fatty Acids. Lipid material was extracted from the grain with petroleum ether using a Soxhlet apparatus.[28] Lipids were saponified with 2% methanolic NaOH followed by methylation with 14% BF_3/methanol reagent. The fatty acid methyl esters were extracted with hexane and analyzed by gas chromatography with flame ionization detection (GC-FID).

Minerals. The concentrations of calcium and phosphorus in forage and grain as well as those of copper, iron, magnesium, manganese, potassium, sodium, and zinc in grain were measured by inductively coupled plasma−optical emission spectrometry (ICP-OES) after digestion in 28% aqueous nitric acid with a MarsXpress (CEM Corp., Matthews, NC, USA) microwave.[29,30] Emission intensity at the appropriate wavelength was determined for each element and compared to that of external standards for quantification.

Niacin (Vitamin B3). Grain sample analysis was based on a method from the AACC.[31] Aqueous extracts were prepared of samples and then an aliquot of the extract was mixed with a niacin-free bacterial growth medium. The mixture was inoculated with *Lactobacillus plantarum*. The niacin concentration was determined by measuring the turbidity of the *L. plantarum* growth response in the sample and comparing it with the growth response in standard concentrations of niacin.

Pantothenic Acid (Vitamin B5). Grain sample analysis was based on a method from the AOAC.[32] Panthothenic acid was extracted with a pH 5.65 acetate buffer and autoclaving. The extract was mixed with a pantothenic acid-free bacterial growth medium and then the mixture inoculated with *L. plantarum*. The pantothenic acid concentration was determined by measuring the turbidity of the *L. plantarum* growth response in the sample and comparing it with the growth response in standard concentrations of pantothenic acid.

Pyridoxine, Pyridoxal, and Pyridoxamine (Vitamin B6). Grain sample analysis was based on a method from the AACC.[33] Vitamin B6 was extracted with 0.44 N sulfuric acid and autoclaving. The extract was mixed with a vitamin B6-free microbiological growth medium and then the mixture inoculated with *Saccharomyces cerevisiae*. The vitamin B6 concentration was determined by measuring the turbidity of the *S. cerevisiae* growth response in the sample and comparing it with the growth response in standard concentrations of pyridoxine.

Inositol and Raffinose. Measurement of inositol and raffinose was based on three methods.[34,35] Grain samples were extracted with 50% aqueous ethanol. The ethanol extract was partitioned against chloroform and then split into aliquots and dried. One aliquot was resuspended in 50% aqueous acetonitrile and then analyzed by reverse phase HPLC with refractive index (RI) detection to quantify raffinose. External standards were used to calibrate the HPLC-RI. The other aliquot was treated with butylboronic acid, and butylboronic acid-derivatized inositol was quantified by GC-FID. External standards were used to calibrate the GC-FID.

Statistical Analyses. Statistical analyses were conducted using R[36] and SciPy.[37] For each nutrient composition analyte, the arithmetic means and ranges at each site and across sites were calculated across hybrid maize lines. In each location, measurements were taken for each hybrid with replication in three different blocks. Additive corrections were applied to the data for the replicates to remove the variation between blocks. A two-way ANOVA procedure was used to calculate the explained variance for genotype, location, and genotype by location interaction.

Table 2. Means and Ranges of Proximates and Fibers Measured from Grain across All Six Sites (Percent Dry Weight)

analyte	ON mean range[a]	MN mean range[a]	IL mean range[a]	NE mean range[a]	KS mean range[a]	TX mean range[a]	combined mean range[b]	ILSI range[c]	literature range	% variability		
										genotype	location	G × E
crude protein	8.5	9.7	9.3	9.3	11.6	10.3	9.8			46	58.5	33.4
	6.5−11.8	8.2−11.2	8.5−10.4	7.6−11.0	9.9−13.4	9.1−12.2	6.5−13.4	6.15−17.3	6−17.3			
crude fat	4.5	4.3	4.0	4.5	4.1	4.4	4.3			43.8	13.8	24.4
	3.7−6.9	2.9−5.0	3.2−4.9	3.6−7.7	3.0−5.0	3.3−5.4	2.9−7.7	2.47−5.9	2.47−5.9			
crude fiber	2.6	2.7	2.8	2.8	2.5	2.5	2.6			43.1	27.3	33.1
	2.0−3.1	2.2−3.3	2.2−3.2	2.5−3.4	1.8−3.0	2.0−2.9	1.8−3.4	0.49−3.26	0.49−5.5			
ADF	4.6	3.8	3.9	4.3	3.9	4.1	4.1			36.4	37.2	23.5
	3.7−5.7	3.2−4.5	2.3−4.6	3.7−5.2	3.0−5.1	3.4−4.9	2.3−5.7	1.82−11.3	1.82−11.3			
NDF	10.5	10.5	10.9	11.2	10.5	12	10.9			43.5	9.3	31.2
	8.5−13.5	7.6−12.4	9.2−13.1	9.0−14.8	7.9−12.7	8.2−22.3	7.6−22.3	5.59−22.6	5.59−22.6			
ash	1.3	1.4	1.3	1.4	1.4	1.4	1.4			61.6	19.50	14.1
	1.1−1.7	1.2−1.8	1.1−1.4	1.3−1.6	1.2−1.6	1.3−1.6	1.1−1.8	0.616−6.28	0.616−6.28			
carbohydrates	85.6	84.6	85.4	84.8	82.9	83.8	84.5			52.2	42.1	30.2
	81.5−88.2	82.4−87.1	84.1−87.0	81.8−87.2	80.7−84.7	81.6−85.4	80.7−88.2	77.4−89.5	77.4−89.5			

[a]The minimum and maximum of sample values for hybrids grown at each location. [b]The combined range for all six sites. [c]ILSI ranges reported in version 3.0.

DOI: 10.1021/acs.jafc.5b01764
J. Agric. Food Chem. 2015, 63, 5321−5334

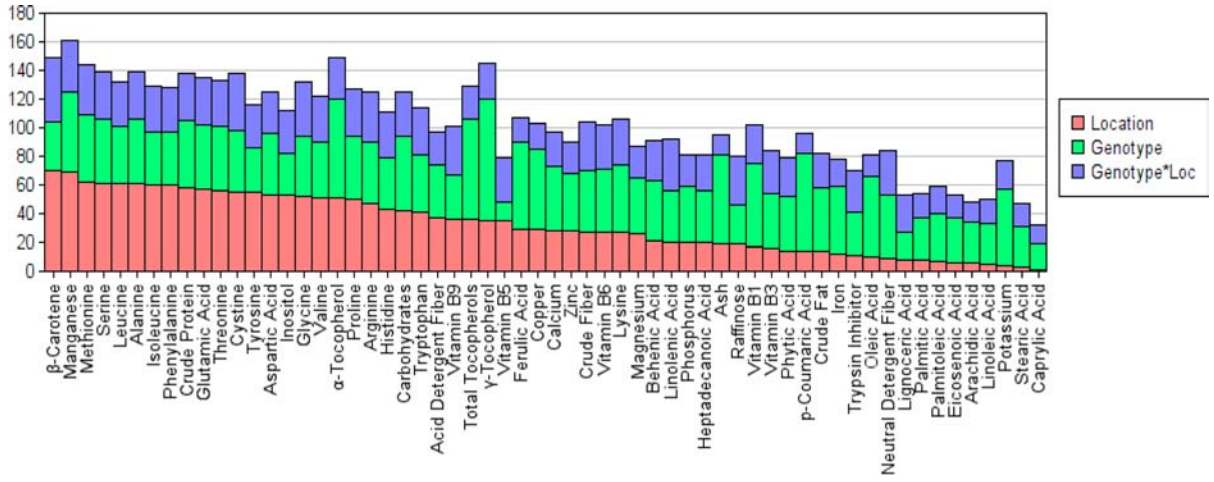

Figure 2. Environmental and genetic impacts on natural variation of analytes. Bar plot of the explained variance from a two-way ANOVA analysis of genotype by environment effects. Variability (from the highest to the lowest) of each analyte explained by location effects was used to order analytes on the *x*-axis.

The inbred parents for the 50 non-GM commercial hybrids were genotyped using Illumina custom bead arrays for 3072 SNPs. Genotypes for the hybrids were inferred from the homozygous base calls for each of the parents, with lexicographic ordering of the base calls. The median for the missing genotype calls was 8%, and the maximum was 32%. Additional genotype data for 2000 SNPs were also included with missing genotype calls up to 78%. The neighbor-joining phylogenetic analysis with 1000 bootstrap iterations was carried out using QuickTree.[38] The phylogeny analysis result file was imported into Archaeopteryx to produce the tree graph.[39]

The genotype data for approximately 3000 SNPs were used in a GWAS for oleic acid. Genotype data for an individual SNP were used as the predictors in a linear statistical model for the phenotype. In the GWAS graph, explained variation, r^2, is plotted versus genetic coordinate for the SNPs. SNPs with minor allele counts of <8 were ignored.

Compositional data for the hybrids in six locations were used to calculate the Pearson correlation matrix for the analytes. A distance matrix was obtained by converting each correlation coefficient to a distance, $1 - r^2$. The distance matrix was used in QuickTree with the neighbor-joining algorithm to calculate the dendrogram.[38] The phylogeny analysis result file was imported into Archaeopteryx to produce the tree graph.[39]

RESULTS AND DISCUSSION

In substantial equivalence analysis, comparative composition analyses have been conducted by measuring and comparing analyte values from GM crops and their non-GM comparators including near-isogenic lines or commercial conventional hybrids. Compositional data generated from comparators have been used as references for biological relevance evaluation because these crops have a long history of safe consumption as food or feed. To shed light on natural variation of compositional components attributable to genetic background, growing location, or the interactions of genetics by environment, evaluation of the composition of commercial hybrids with diverse genetic backgrounds grown at multiple maize production regions is needed. In this study, 50 DuPont Pioneer non-GM commercial hybrids differing in genetic background and maturity group were selected and grown at six sites in commercial maize-growing regions in North America. Associations of the 50 hybrids are shown in a dendrogram based upon marker analysis by using approximately 3000 SNPs across maize genome (Figure 1), suggesting that these 50 hybrids comprise 5 major distinct genetic groups and represent broad genetic diversity of commercial maize hybrids.[40] Mean and range values for each analyte from 20 hybrids grown at each site are reported (Tables 1−7). The composition data collected from this study could expand conventional compositional data sets and be used as reference values for substantial equivalence assessment for GM crops.

In maize breeding programs the standard procedure is to test only the best adopted hybrids in a given location, which are classified into maturity zones. Hybrids with flowering time outside the range for a zone would present a problem for crop management of the field testing and commercial production. This maturity zone constraint resulted in an unbalanced experiment design for this study, but every effort was made to include hybrids across locations that could be adopted to the zones.[21] In the study, five hybrids, representing clades I, III, IV, and V, were grown in all six locations (Figure 1). Data analysis was performed with these 5 hybrids, and the results showed similar trends with the results analyzed from the 50 hybrids (Supplemental Figure 1). Furthermore, two previously published forage and grain metabolomics studies have shown similar results.[23,41] These two studies used samples collected from the same set of non-GM DuPont Pioneer commercial hybrids as reported in this study, with one study focusing on data analysis of metabolites measured from the 50 hybrids and the other one on metabolomics data measured only from the 5 hybrids grown at all locations.[23,41] We regard the hybrids as constituting a representative population for a given location and the data as providing estimates for the population mean and variance for nutrient. Our use of the two-way ANOVA method for the analysis of genotype by environment effects relies on the validity of this approximation. Therefore, our conclusions about genotype by environment interactions are best interpreted as corresponding to elite maize germplasm subject to the maturity zone restriction. The effects of genotype, environment, and their interactions are also reported (Tables 1−7).

Proximate, Fiber, Calcium, and Phosphorus Contents in Forage. Crude protein, fat, carbohydrates, fiber including ADF and NDF, calcium, phosphorus, ash, and moisture were measured and/or calculated for forage from the 50 hybrids across six locations. Statistical analysis demonstrated that natural variation for all components measured in forage was attributed largely to environmental effects rather than genotypic effects (Table 1). The similar results have been previously reported.[23,41]

DOI: 10.1021/acs.jafc.5b01764
J. Agric. Food Chem. 2015, 63, 5321−5334

Table 3. Means and Ranges of Fatty Acids Measured from Grain across All Six Sites (Percent Total Fatty Acids)

analyte	ON mean range[a]	MN mean range[a]	IL mean range[a]	NE mean range[a]	KS mean range[a]	TX mean range[a]	combined mean range[b]	ILSI range[c]	literature range	% variability		
										genotype	location	G × E
caprylic acid	0.097	0.048	0.034	0.11	0.077	0.054	0.07			18.2	0.66	13.3
(C8:0)	0−2.5	0−1.7	0−1.0	0−1.7	0−2.9	0−3.1	0−3.1	0.133−0.34	0.133−0.34			
palmitic acid	12.4	12.1	12.5	12.7	14.9	12.8	12.9			29	7.7	17.6
(C16:0)	9.3−23.9	8.6−27.5	9.5−19.5	9.7−23.1	11.6−34.3	9.5−39.0	8.6−39.0	7.94−20.7	7−20.7			
palmitoleic acid	0.093	0.08	0.12	0.12	0.075	0.14	0.1			32.9	7.3	18.6
(C16:1)	0−0.52	0−0.28	0−0.29	0.0011−0.28	0−0.56	0.072−0.67	0−0.67	0.095−0.447	0−1			
heptadecanoic acid	0.0013	0	0.049	0.032	0.0091	0.032	0.021			36.4	19.8	25.1
(C17:0)	0−0.073	0	0−0.17	0−0.16	0−0.12	0−0.11	0−0.17	0.078−0.111	0−0.111			
stearic acid	1.9	1.7	1.9	1.9	2	1.9	1.9			27.7	3.3	16
(C18:0)	1.2−4.9	1.3−2.6	1.4−3.4	1.4−3.3	0.044−4.9	1.5−4.4	0.044−4.9	1.02−3.4	0−4			
oleic acid	29.2	27.2	28.4	29.8	28.2	31.2	29			55.2	10.40	15.5
(C18:1)	21.2−40.3	21.6−35.2	19.3−38.0	22.8−40.2	21.8−41.6	25.1−39.7	19.3−41.6	17.4−40.2	17.4−50			
linoleic acid	53.8	56.4	53.5	52.8	52.8	51.6	53.5			28	5.1	17
(C18:2)	31.0−64.7	31.5−65.6	32.2−66.5	33.0−61.3	13.9−61.1	13.1−58.8	13.1−66.5	36.2−66.5	34−70			
linolenic acid	1.2	1.2	1.3	1.2	0.9	0.99	1.1			36.4	20.1	35.7
(C18:3)	0.34−1.8	0.60−1.6	0.14−1.9	0.42−1.6	0.080−1.4	0.068−1.3	0.068−1.9	0.57−2.25	0−2.25			
arachidic acid	0.46	0.45	0.51	0.45	0.51	0.45	0.47			28.4	6	13.8
(C20:0)	0.31−1.0	0.31−0.77	0.37−0.89	0.35−0.73	0.35−1.1	0.34−1.2	0.31−1.2	0.279−0.965	0−2			
eicosenoic acid	0.34	0.37	0.32	0.38	0.36	0.35	0.35			30.7	6	16.3
(C20:1)	0.0100−0.52	0.28−0.69	0.22−0.47	0.040−0.83	0.20−1.1	0.014−0.48	0.0100−1.1	0.17−1.92	0−1.92			
behenic acid	0.093	0.1	0.19	0.18	0.022	0.14	0.12			42	21.5	27.7
(C22:0)	0−0.29	0−0.42	0−0.43	0−0.30	0−0.40	0−0.32	0−0.43	0.11−0.349	0−0.5			
lignoceric acid	0.25	0.21	0.3	0.26	0.21	0.2	0.24			18.2	8.4	26.6
(C24:0)	0−0.71	0−0.45	0.018−0.91	0.18−0.44	0−0.43	0−0.41	0−0.91	0.14−0.23	0−0.5			

[a]The minimum and maximum of sample values for hybrids grown at each location. [b]The combined range for all six sites. [c]ILSI ranges reported in version 3.0.

DOI: 10.1021/acs.jafc.5b01764
J. Agric. Food Chem. 2015, 63, 5321−5334

Proximate and Fiber Composition in Maize Grain. Grain quality is determined by its carbohydrate, oil, and protein contents.[42] Some hybrids selected for this study were bred to produce grains with enhanced values of oil, protein, or carbohydrate. Table 2 shows proximate and fiber means and ranges obtained from maize grain at each location. Carbohydrates were the major components (~85%) in corn grain composition; crude protein and NDF were present in similar levels (~10%); crude fat and ADF were present in similar levels (~4%); and ash and crude fiber were present in the lowest amounts (1.4−2.6%).

Values of crude fat varied. Statistical analysis from the 50 hybrids grown in the six locations indicated that variation of crude fat content is mainly contributed by genetic background of the hybrids (Table 2 and Figure 2). Twenty-two oil QTLs were identified including *DGAT1-2* for oil content improvement explaining about 70% of the total variation. The finding in this study agrees with the notion that genetics primarily controls oil content.[43,44]

Protein and carbohydrate are the two components closely associated with maize grain yield. The average content of crude protein is negatively correlated with the average content of carbohydrates ($R^2 = 0.83$, $p = 2.98 \times 10^{-139}$). Crude protein and carbohydrates were genetic traits (46 and 52.2% explained by genotype, respectively), supported by a previous study in which 26 protein and 21 starch QTLs were identified.[44] The quantity of protein and carbohydrates, however, was significantly affected by location, the effects of which account for 58.5 and 42.1% of the total variation with the interaction effects of genotype by location also accounting for 33.4 and 30.2% of the total variation (Table 2 and Figure 2). This is in agreement with the previous findings that protein and carbohydrates in maize grain are mainly influenced by both genotype and environment.[22]

Fatty Acid Composition in Maize Grain. Table 3 shows means and ranges of 12 fatty acids obtained from hybrids at each location. Of the total 29 fatty acids measured, 17 fatty acids were below the low level of quantification (LLOQ) and were excluded from data analysis. Eicosadienoic acid (C20:2) was quantified in three sites in this study, and arachidic acid (C20:0), eicosenoic acid (C20:1), and behenic acid (C22:0) were successfully quantified. The results also showed that palmitic acid (C16:0), oleic acid (C18:1), and linoleic acid (C18:2) constituted the majority of the fatty acid contents. The measurements obtained in the study could be used as reference values in substantial equivalence analysis. Further statistical analysis suggested that genotype and the interaction effects of genotype by environment are primary determinants for levels of all fatty acids measured (Table 3), which was also evident in crude fat content as discussed earlier (Table 2).

Oleic acid is one of the major oil components, and oils with higher oleic acid content are more stable.[45] To meet market demands, some varieties have been developed to increase oleic acid content through long-standing breeding programs. Studies showed that a fatty acid desaturase (*FAD2*) on maize chromosome 4 is responsible for oleic acid content change.[45] To test whether the quantitative trait locus (QTL) *FAD2* is present in the hybrids based on the experimental design reported in this study, the measurements of oleic acid were used in GWAS, and the results show that an association was detected on chromosome 4, at 132 cM, which coincides with the known QTL *FAD2* (Figure 3).[45] This finding not only confirms that oleic acid in maize grain is significantly correlated with genetic effects but also suggests that QTLs underlying other valuable analytes could be mapped or identified in a similar manner. The identified QTLs could be used further for crop improvement by molecular breeding and biotech approaches.

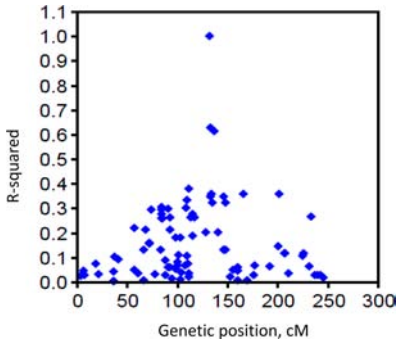

Figure 3. Genome-wide association study for oleic acid for 50 hybrids. For one of the locations (TX), an association is observed on chromosome 4, at 132 cM, which coincides with the known QTL *FAD2*.

Linoleic acid, another major component representing about 50% of the total fatty acid, is a metabolic product downstream of oleic acid. Its content was significantly inversely correlated with oleic acid ($R^2 = 0.70$, $p = 9.85 \times 10^{-95}$). No strong environmental effects were observed for this trait, which is consistent with the findings reported in the literature.[22] In summary, the results from this study confirmed the molecular basis underlying natural variation of oil and oleic acid contents in plants.

Total Amino Acid Composition in Maize Grain. Eighteen amino acids were measured and are summarized in Table 4. Most interestingly, the levels of 17 of 18 total amino acids were strongly correlated with location, which suggests that the variability of these amino acids was mainly due to environmental effects with the exception of lysine, which appears to be more dependent on genotype (Figure 2 and Table 4). The results are similar to a finding in a previous paper that the levels of the 13 amino acids were found to be significantly affected by location.[46]

Mineral Composition in Maize Grain. Minerals including calcium, manganese, phosphorus, iron, magnesium, copper, potassium, sodium, and zinc were analyzed in maize grain samples (Table 5). The range of natural variation in manganese accumulation was significantly associated with sites (68.7%) and genotypes (56.5%). Copper, potassium, iron, calcium, zinc, phosphorus, and magnesium were mainly affected by genotypic effects (Table 5).

Vitamins in Maize Grain. Vitamins were measured from maize grain and are presented in Table 6. There were no previous records for the ranges of vitamins B3 and B5 in the ILSI crop composition database. γ-Tocopherol is the major compound (combined value) followed by B3 and then β-carotene (Table 6). The values could be used as reference values for future substantial equivalence analysis.

β-Carotene, a major dietary source of provitamin A, showed considerable variation across the six sites. Location effects accounted for 69.7% of natural variability (Table 6 and Figure 2). These results indicate strong geographical effects on the level of β-carotene or pro-vitamin A.

Among the four types of tocopherols known as vitamin E, α-tocopherol is a major source of vitamin E in humans and animals and is the most important for human health, whereas γ-tocopherol is the predominant form in the total tocopherols as reported in Table 6 and a previously published paper.[47] Maize grain oil containing a higher concentration of tocopherols has been found to be beneficial in maintaining oil quality in high-oil

DOI: 10.1021/acs.jafc.5b01764
J. Agric. Food Chem. 2015, 63, 5321−5334

Table 4. Means and Ranges of Amino Acids Measured from Grain across All Six Sites (Percent Dry Weight)

analyte	ON mean range[a]	MN mean range[a]	IL mean range[a]	NE mean range[a]	KS mean range[a]	TX mean range[a]	combined mean range[b]	ILSI range[c]	literature range	% variability		
										genotype	location	G × E
alanine	0.62	0.74	0.67	0.68	0.91	0.77	0.73			45.1	60.6	32.9
	0.44−0.90	0.60−0.87	0.57−0.77	0.52−0.84	0.75−1.1	0.67−0.92	0.44−1.1	0.439−1.39	0.439−1.39			
arginine	0.39	0.4	0.44	0.42	0.48	0.44	0.43			43.4	46.6	34.8
	0.31−0.51	0.33−0.47	0.40−0.52	0.35−0.49	0.42−0.56	0.38−0.50	0.31−0.56	0.119−0.639	0.119−0.64			
aspartic acid	0.58	0.69	0.6	0.61	0.75	0.71	0.65			42.6	53.1	29.2
	0.44−0.77	0.60−0.83	0.48−0.70	0.50−0.73	0.62−0.93	0.61−0.91	0.44−0.93	0.335−1.21	0.335−1.21			
cystine	0.16	0.16	0.2	0.19	0.21	0.2	0.19			43	55	40.4
	0.12−0.20	0.12−0.22	0.17−0.24	0.16−0.23	0.17−0.24	0.14−0.26	0.12−0.26	0.125−0.514	0.08−0.514			
glutamic acid	1.6	1.9	1.7	1.8	2.3	2	1.9			44.3	57.5	32.8
	1.1−2.3	1.5−2.2	1.4−2.0	1.3−2.2	1.9−2.8	1.7−2.4	1.1−2.8	0.965−3.54	0.965−3.54			
glycine	0.35	0.35	0.38	0.38	0.42	0.39	0.38			41.5	52.2	38.8
	0.29−0.44	0.31−0.39	0.35−0.44	0.33−0.42	0.36−0.47	0.33−0.44	0.29−0.47	0.184−0.539	0.184−0.539			
histidine	0.26	0.27	0.28	0.28	0.32	0.28	0.28			35.3	43.3	32.5
	0.17−0.34	0.23−0.33	0.24−0.32	0.23−0.32	0.28−0.40	0.24−0.33	0.17−0.40	0.137−0.434	0.137−0.434			
isoleucine	0.29	0.34	0.31	0.32	0.41	0.34	0.33			36.8	60.4	31.4
	0.20−0.40	0.29−0.40	0.27−0.35	0.25−0.39	0.34−0.50	0.28−0.40	0.20−0.50	0.179−0.692	0.179−0.71			
leucine	1	1.3	1.1	1.1	1.6	1.3	1.2			40.4	60.7	31.3
	0.68−1.6	1.0−1.5	0.95−1.3	0.84−1.4	1.3−2.0	1.1−1.7	0.68−2.0	0.642−2.49	0.642−2.49			
lysine	0.25	0.26	0.28	0.27	0.29	0.28	0.27			47.5	26.6	31.6
	0.21−0.38	0.22−0.30	0.22−0.33	0.23−0.31	0.24−0.33	0.24−0.36	0.21−0.38	0.172−0.668	0.05−0.668			
methionine	0.17	0.15	0.22	0.19	0.24	0.19	0.19			46.7	62.3	35.3
	0.12−0.21	0.11−0.25	0.18−0.27	0.15−0.25	0.16−0.29	0.14−0.23	0.11−0.29	0.124−0.468	0.1−0.468			
phenylalanine	0.43	0.54	0.49	0.49	0.66	0.53	0.52			36.6	60.3	31.3
	0.28−0.64	0.45−0.64	0.41−0.58	0.37−0.62	0.50−0.82	0.43−0.68	0.28−0.82	0.244−0.93	0.244−0.93			
proline	0.77	0.84	0.81	0.83	1	0.9	0.86			43.5	50.3	33.3
	0.53−1.1	0.70−0.99	0.68−0.92	0.67−0.99	0.85−1.3	0.80−1.0	0.53−1.3	0.462−1.63	0.462−1.63			
serine	0.44	0.51	0.47	0.47	0.61	0.53	0.5			45.3	60.7	33.3
	0.33−0.62	0.43−0.59	0.41−0.53	0.38−0.56	0.51−0.72	0.46−0.63	0.33−0.72	0.235−0.769	0.235−0.91			
threonine	0.33	0.36	0.34	0.34	0.42	0.38	0.36			44.9	55.9	32.6
	0.23−0.43	0.31−0.41	0.31−0.38	0.29−0.40	0.36−0.48	0.33−0.44	0.23−0.48	0.224−0.666	0.224−0.666			
tryptophan	0.054	0.055	0.063	0.062	0.066	0.06	0.06			40.4	40.6	32.9
	0.042−0.066	0.047−0.064	0.047−0.073	0.050−0.070	0.054−0.074	0.036−0.074	0.036−0.074	0.0271−0.215	0.0271−0.215			
tyrosine	0.24	0.27	0.26	0.24	0.35	0.26	0.27			31.4	54.6	29.8
	0.16−0.36	0.22−0.34	0.19−0.32	0.17−0.32	0.25−0.45	0.19−0.35	0.16−0.45	0.103−0.642	0.103−0.79			
valine	0.4	0.45	0.42	0.43	0.53	0.45	0.45			38.9	51.3	31.4
	0.30−0.54	0.38−0.52	0.38−0.47	0.35−0.50	0.45−0.61	0.38−0.51	0.30−0.61	0.266−0.855	0.21−0.855			

[a]The minimum and maximum of sample values for hybrids grown at each location. [b]The combined range for all six sites. [c]ILSI ranges reported in version 3.0.

J. Agric. Food Chem. 2015, 63, 5321−5334
DOI: 10.1021/acs.jafc.5b01764

Table 5. Means and Ranges of Minerals Measured from Grain across All Six Sites (Percent Dry Weight)

analyte	ON mean range[a]	MN mean range[a]	IL mean range[a]	NE mean range[a]	KS mean range[a]	TX mean range[a]	combined mean range[b]	ILSI range[d]	literature range	% variability		
										genotype	location	G × E
calcium	0.004	0.0037	0.0032	0.0035	0.0044	0.0047	0.0039			45.5	27.9	23.8
	0.0025−0.0081	0.0025−0.0050	0.0024−0.0044	0.0025−0.0046	0−0.0073	0.0034−0.0063	0−0.0081	0.00127−0.0208	0.00127−0.1			
manganese	0.0005	0.0005	0.0008	0.0006	0.0011	0.0007	0.0007			56.5	68.7	36.2
	0.0003−0.0008	0.0004−0.0007	0.0005−0.0011	0.0004−0.0007	3.12×10^{-5}−0.0015	0.0006−0.0010	3.12×10^{-5}−0.0015	0.000169−0.00143	0.00007−0.0054			
phosphorus	0.31	0.33	0.29	0.33	0.3	0.32	0.31			39.2	19.8	21.7
	0.24−0.40	0.29−0.41	0.26−0.32	0.27−0.37	0.010−0.37	0.27−0.36	0.010−0.41	0.147−0.533	0.147−0.75			
iron	0.0019	0.0018	0.0018	0.0016	0.0017	0.0017	0.0018			47.4	11.7	18.7
	0.0014−0.0025	0.0013−0.0023	0.0015−0.0021	0.0013−0.0020	7.12×10^{-5}−0.0042	0.0014−0.0028	7.12×10^{-5}−0.0042	0.00104−0.00491	0.0001−0.01			
magnesium	0.12	0.13	0.11	0.11	0.12	0.12	0.12			39	26.3	22.2
	0.088−0.14	0.11−0.15	0.092−0.13	0.095−0.13	0.0035−0.14	0.096−0.14	0.0035−0.15	0.0594−0.194	0.0594−1			
copper	1.17×10^{-4}	1.03×10^{-4}	1.22×10^{-4}	1.16×10^{-4}	9.32×10^{-5}	1.57×10^{-4}	1.18×10^{-4}			55.9	29.1	18.2
	6.09×10^{-5c}−0.0003	6.21×10^{-5c}−1.73×10^{-4}	7.54×10^{5}−1.93×10^{-4}	6.76×10^{-5c} −1.73×10^{-4}	3.74×10^{-6c}− 1.74×10^{-4}	7.67×10^{-5}−0.0003	3.74×10^{-6c}−0.0003	0.000073−0.00185	0.000073−0.00185			
potassium	0.36	0.36	0.36	0.37	0.35	0.38	0.36			53.1	4.2	19.6
	0.29−0.51	0.29−0.50	0.30−0.43	0.31−0.44	0.020−0.46	0.32−0.45	0.020−0.51	0.181−0.603	0.181−0.72			
sodium	6.89×10^{-5}	6.49×10^{-5}	6.66×10^{-5}	6.81×10^{-5}	1.02×10^{-4}	7.71×10^{-5}	7.45×10^{-5}			13.8	6.6	16.4
	5.45×10^{-5}−0.0003	6.09×10^{-5}− 1.36×10^{-4}	5.85×10^{-5}−0.0002	5.59×10^{-5}−0.0003	2.38×10^{-5}−0.0006	5.44×10^{-5}−0.0003	2.38×10^{-5}−0.0006	0.000017−0.0732	0−0.15			
zinc	0.0021	0.0021	0.0023	0.0023	0.0019	0.0024	0.0022			40.3	27.9	21.6
	0.0016−0.0029	0.0016−0.0024	0.0019−0.0026	0.0020−0.0029	2.83×10^{-5}−0.0025	0.0018−0.0030	2.83×10^{-5}−0.0030	0.00065−0.00372	0.00065−0.00372			

[a]The minimum and maximum of sample values for hybrids grown at each location. [b]The combined range for all six sites. [c]Lower limit of quantification (LLOQ) indicates that the values of the samples were detected below the assay's LLOQ. Sample results that were below the LLOQ are assigned a value equal to the LLOQ for statistical analysis. [d]ILSI ranges reported in version 3.0.

DOI: 10.1021/acs.jafc.5b01764
J. Agric. Food Chem. 2015, 63, 5321−5334

Table 6. Means and Ranges of Vitamins Measured from Grain across All Six Sites (Milligrams per Kilogram Dry Weight)

analyte	ON mean range[a]	MN mean range[a]	IL mean range[a]	NE mean range[a]	KS mean range[a]	TX mean range[a]	combined mean range[b]	ILSI range[d]	literature range	% variability		
										genotype	location	G × E
β-carotene	23.2	15	5.4	7.6	10.6	8.4	11.7			34.2	69.7	45.6
	8.8–33.0	4.8–29.3	3.5–7.7	5.2–13.8	6.4–19.5	3.4–21.6	3.4–33.0	0.19–46.8	0.19–46.8			
vitamin B1	3.4	3.1	2.9	2.8	3	3.5	3.1			57.4	17.4	27
(thiamin)	1.7–5.0	1.7–4.2	1.8–4.3	2.0–3.8	1.7–4.7	2.5–5.2	1.7–5.2	1.26–40	1.26–40			
vitamin B3	17.4	15.5	15.8	18.7	14.6	15.4	16.2			37.3	16.3	30.5
(niacin)	12.9–36.3	11.3–22.0	10.8–22.7	10.0–36.3	12.1–22.4	11.8–20.9	10.0–36.3	NA	9.3–70			
vitamin B5	5.2	3.7	4.4	4.2	4.6	4.1	4.4			13.3	34.6	30.8
(pantothenic acid)	4.7–6.7	3.1–5.3	3.4–6.1	3.0–5.6	3.2–5.8	3.1–5.4	3.0–6.7	NA	3.5–14			
vitamin B6	4.2	4.2	4.9	4.8	4.8	5.8	4.8			44.6	26.9	31
(pyridoxine)	2.2–6.3	2.4–5.5	2.7–8.3	2.9–6.8	2.1–6.9	4.2–7.5	2.1–8.3	3.68–11.3	3.68–11.3			
vitamin B9	1.8	1.1	0.82	0.88	1.1	1.5	1.2			30.7	36.1	33.8
(folic acid)	0.59–3.5	0.29–1.9	0.46–1.5	0.18–1.9	0.71–1.9	0.62–3.4	0.18–3.5	0.147–1.46	0.147–683			
α-tocopherol	4.3	5.8	12.4	12	5.4	10.6	8.4			68.9	50.7	29.6
	1.0–12.3	1.6–12.9	7.0–23.4	6.1–21.8	1.2–13.1	4.4–16.8	1.0–23.4	1.5–68.7	1.5–68.7			
β-tocopherol	<0.50[c]	0.53	0.52	0.51	0.58	0.51	0.53			39.6	14.4	24.4
	<0.50[c]	0.50[c] –0.75	0.5[c]–0.77	0.50[c]–0.74	0.50[c]–0.87	0.50[c]–0.77	0.50[c]–0.87	0.58–22.8	0.58–22.8			
γ-tocopherol	22.6	26.6	12.7	15.6	7.3	19.3	17.4			85.1	34.7	25.7
	4.9–42.9	4.6–49.4	2.4–33.2	2.8–34.9	1.2–19.8	6.2–35.8	1.2–49.4	6.46–61	6.46–61			
δ-tocopherol	0.7	0.91	0.52	0.54	0.54	0.63	0.64			81.1	19.1	20
	0.48–2.0	0.44–2.6	0.48–0.81	0.49–0.88	0.49–0.95	0.48–1.4	0.44–2.6	0.38–16.1	0.38–16.1			
total tocopherols	27.3	33.1	25.3	27.8	13.1	30.3	26.2			70.8	35.6	22.7
	11.0–51.9	10.2–60.2	13.2–45.9	15.1–45.4	3.8–30.5	17.5–47.7	3.8–60.2	8.69–133	8.69–133			

[a]The minimum and maximum of sample values for hybrids grown at each location. [b]The combined range for all six sites. [c]Lower limit of quantification (LLOQ) indicates that the values of the samples were detected below the assay's LLOQ. Sample results that were below the LLOQ are assigned a value equal to the LLOQ for statistical analysis. [d]ILSI ranges reported in version 3.0.

DOI: 10.1021/acs.jafc.5b01764
J. Agric. Food Chem. 2015, 63, 5321−5334

maize. Substantial natural variation (about 3-fold differences) of α- and γ-tocopherols among the sites was evident in this study, and similar substantial natural variation of α- and γ-tocopherols was observed in previous studies.[48,49] Analysis of variance revealed strong genetic and environmental effects for α-tocopherol (68.9 and 50.7%, respectively), which is in accordance with other reports for maize.[49] Statistical analysis also showed that considerably higher heritabilities were found for γ- and δ-tocopherols explaining 85.1 and 81.1% of total variability, respectively, despite the strong genotype by environment interactions and environmental effects that were detected. These results demonstrated that genetic variation was the main contributor to tocopherol variability, implying that breeding efforts may be suitable for improving maize kernel tocopherol composition. Indeed, QTLs for α-, γ-, and δ-tocopherols were identified in previous linkage studies.[50,51] Thus, diverse maize germplasms with broad heritability and wide natural variation for α-, γ-, and δ-tocopherols can be used for breeding to biofortify crops with enhanced levels of tocopherols, with particular emphasis on modulating levels of α-tocopherol by mapping QTLs for tocopherols. This, in turn, can be used to increase the tocopherol concentration by genetic engineering.

Secondary Metabolite and Antinutrient Composition in Maize Grain. Seven analytes of secondary metabolites and antinutrients were measured except furfural, which was below the limit of quantification (Table 7). Levels of the secondary metabolites *p*-coumaric acid and ferulic acid varied from hybrid to hybrid, which demonstrated that their levels were affected mainly by genotype by 68.7 and 60.7%, respectively. Differences for inositol observed among locations implied that location played an important role in the biogenesis of inositol with 53.1% of variability explained by location. Levels of phytic acid were mainly controlled by genotype and the interactions of genotype by location (Table 7). Levels of the antinutrient phytic acid can be decreased by breeding and biotechnology approaches because high levels of phytic acid in grains reduce absorption of minerals. A reduced phytic acid level in maize kernel has been developed by silencing the *lpa1* gene.[52]

Correlations of Analytes Measured from 50 Hybrids. To understand biosynthetic interactions of compositional components from maize grain, the Pearson correlation matrix for the analytes was calculated. Significantly related analytes with the same or related biosynthetic pathways are clustered in groups. Nonsignificantly correlated analytes are in distantly related groups. Such correlations among composition analytes are depicted phylogenetically in Figure 4. For example, all amino acids, correlated to crude protein, appeared in the same clade based on the values of r^2. Significant correlations were observed between carbohydrates and crude protein and between oleic acid and linoleic acid, as described previously in the text, and between fatty acids, etc. Tocopherols were previously known to be synthesized in one pathway and, indeed, the tocopherols were closely clustered (Figure 4). These correlation data suggested that concentrations of the compounds with nonsignificant correlations are influenced by different pathways or regulated by independent genes. Levels of the compounds can be improved simultaneously by molecular breeding. However, the compounds with significant correlations indicate that they are on the same pathway or regulated by a similar set of genes with closely biosynthetic relationships, which need to be bred individually. These results may offer opportunities for further genetic improvement of maize forage and grain composition.

Natural variation of plant metabolites is contributed not only by genetic variation but also by environmental factors.

Table 7. Means and Ranges of Secondary Metabolites and Antinutrient Composition Measured from Grain across All Six Sites (Percent Dry Weight)

										% variability		
analyte	ON mean range[a]	MN mean range[a]	IL mean range[a]	NE mean range[a]	KS mean range[a]	TX mean range[a]	combined mean range[b]	ILSI range[c]	literature range	genotype	location	G × E
p-coumaric acid	0.024	0.022	0.028	0.023	0.025	0.024	0.024			68.7	13.8	13.6
	0.014–0.037	0.015–0.033	0.018–0.039	0.015–0.034	0.014–0.038	0.015–0.039	0.014–0.039	0.00534–0.0576	0.003–0.0576			
inositol	0.035	0.02	0.018	0.022	0.043	0.024	0.027			29.4	53.1	29.8
	0.020–0.065	0.0089–0.039	0.0099–0.027	0.015–0.027	0.011–0.093	0.0063–0.037	0.0063–0.093	0.0089–0.377	0.0089–0.377			
ferulic acid	0.24	0.23	0.25	0.24	0.27	0.21	0.24			60.7	29.3	16.9
	0.19–0.30	0.19–0.29	0.19–0.32	0.18–0.30	0.18–0.38	0.17–0.32	0.17–0.38	0.0292–0.389	0.02–0.389			
phytic acid	0.98	1	0.91	0.93	1	0.89	0.96			37.1	14.5	27.6
	0.72–1.5	0.77–1.4	0.68–1.4	0.69–1.2	0.77–1.3	0.74–1.1	0.68–1.5	0.111–1.57	0.111–1.57			
raffinose	0.1	0.19	0.18	0.14	0.098	0.16	0.15			26.9	19.4	33.8
	0.077–0.24	0.063–0.39	0.071–0.37	0.067–0.40	0.067–0.32	0.078–0.35	0.063–0.40	0.02–0.32	0.02–0.32			
trypsin inhibitor	2.7	2.6	2.6	2.1	2.8	2.6	2.6			29.5	11.2	28.9
	1.5–4.0	0.74–3.9	1.7–3.5	1.1–3.3	1.0–4.7	1.7–3.6	0.74–4.7	1.09–7.18	1.09–7.18			

[a]The minimum and maximum of sample values for hybrids grown at each location. [b]The combined range for all six sites. [c]ILSI ranges reported in version 3.0.

DOI: 10.1021/acs.jafc.5b01764
J. Agric. Food Chem. 2015, 63, 5321−5334

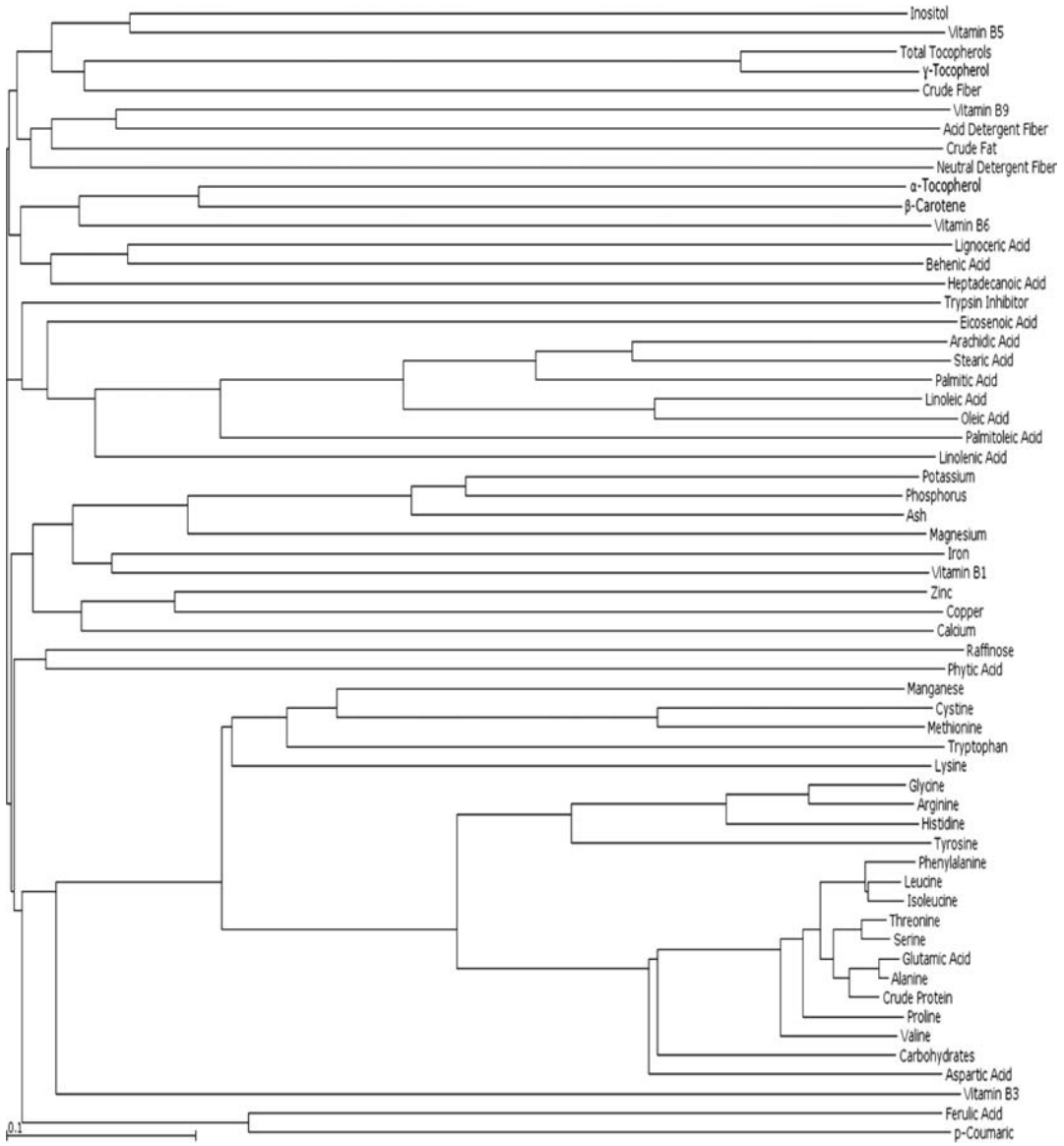

Figure 4. Phylogenetic analysis of analytes for 50 hybrids.

This variability in nutrient composition is important within the context of comparative safety assessments for GM crops. When analytes in GM crops are statistically significant different from those in the isogenic comparators, the Codex guideline states "The statistical significance of any observed differences should be assessed in the context of the range of natural variations" to determine the biological relevance.[53] Understanding the natural variation of conventional crop composition with a history of safe consumption is critical in establishing a baseline for comparison to GM crops. This study documented natural variability of nutrient composition from 50 diverse conventional maize hybrids grown at six commercial maize production locations in North America. All of the composition data were deposited to expand the ILSI crop composition database (version 5) and are ready to be used for GM crop assessment.

■ ASSOCIATED CONTENT

Supporting Information

Supplemental Figure 1, dendrograms and heat maps showing environmental and genetic effects on analytes. The Supporting Information is available free of charge on the ACS Publications website at DOI: 10.1021/acs.jafc.5b01764.

■ AUTHOR INFORMATION

Corresponding Author

*(C.Z.) E-mail: cathy.zhong@cgr.dupont.com. Phone: (302) 695-2169. Fax: (302) 695-3075.

Notes

The authors declare no competing financial interest.

■ ACKNOWLEDGMENTS

We thank Mary Locke, John Duesing, Ian Lamb, Jan Hazebroek, Lee Prochaska, and Bonnie Hong for their help and discussion in designing the experiment and reviewing the study design. We also thank Xiaoxiao Kong for formatting the data, Antoni Rafalski for critically reviewing the manuscript, Jon Artist for handling sample shipments, and Brain Baumbover for managing the study records.

DOI: 10.1021/acs.jafc.5b01764
J. Agric. Food Chem. 2015, 63, 5321−5334

REFERENCES

(1) U.S. Department of Agriculture, Foreign Agricultural Service. *Grain: World Markets and Trade*; USDA: Washington, DC, USA, March 2015.

(2) Fernandez-Cornejo, J. *The Seed Industry in U.S. Agriculture: An Exploration of Data and Information on Crop Seed Markets, Regulation, Industry Structure, and Research and Development*; Agriculture Information Bulletin 786, 2004.

(3) UN News. World population projected to reach 9.6 billion by 2050. Economic and Social Affairs, United Nations, NY, USA, 2013.

(4) James, C. *Global Status of Comercialized Biotech/GM Crops, 2013*; ISAAA Brief 46, 2014.

(5) FAO/WHO. *Strategies for Assessing the Safety of Foods Produced by Biotechnology*; Report of a Joint FAO/WHO Consultation; Geneva, Switzerland, 1991.

(6) WHO. *Application of the Principles of Substantial Equivalence to the Safety Evaluation of Foods or Food Components from Plants Derived by Modern Biotechnology*; Report of a WHO Workshop; Geneva, Switzerland, 1995.

(7) OECD. *Safety Evaluation of Foods Derived by Modern Biotechnology: Concepts and Principles*; Report for OECD; Paris, France, 1993.

(8) OECD. *Consensus Document on Compositional Considerations for New Varieties of Maize (Zea mays): Key Food and Feed Nutrients, Anti-Nutrients and Secondary Plant Metabolites*; Report for OECD; Paris, France, 2002.

(9) FAO/WHO. *Safety Aspects of Genetically Modified Foods of Plant Origin*; Report of a Joint FAO/WHO Expert Consultation; Geneva, Switzerland, 2000.

(10) Ridley, W. P.; Shillito, R. D.; Coats, I.; Steiner, H.-Y.; Shawgo, M.; Phillips, A.; Dussold, P.; Kurtyka, L. Development of the International Life Sciences Institute Crop Composition Database. *J. Food Compos. Anal.* **2004**, *17*, 423−438.

(11) Alba, R.; Phillips, A.; Mackie, S.; Gillikin, N.; Maxwell, C.; Brune, P.; Ridley, W.; Fitzpatrick, J.; Levine, M.; Harris, S. Improvements to the International Life Sciences Institute Crop Composition Database. *J. Food Compos. Anal.* **2010**, *23*, 741−748.

(12) Harrigan, G. G.; Lundry, D.; Drury, S.; Berman, K.; Riordan, S. G.; Nemeth, M. A.; Ridley, W. P.; Glenn, K. C. Natural variation in crop composition and the impact of transgenesis. *Nat. Biotechnol.* **2010**, *28*, 402−404.

(13) Zhou, J.; Harrigan, G. G.; Berman, K. H.; Webb, E. G.; Klusmeyer, T. H.; Nemeth, M. A. Stability in the composition equivalence of grain from insect-protected maize and seed from glyphosate-tolerant soybean to conventional counterparts over multiple seasons, locations, and breeding germplasms. *J. Agric. Food Chem.* **2011**, *59*, 8822−8828.

(14) Harrison, J. M.; Howard, D.; Malven, M.; Halls, S. C.; Culler, A. H.; Harrigan, G. G.; Wolfinger, R. D. Principal variance component analysis of crop composition data: a case study on herbicide-tolerant cotton. *J. Agric. Food Chem.* **2013**, *61*, 6412−6422.

(15) Oberdoerfer, R. B.; Shillito, R. D.; de Beuckeleer, M.; Mitten, D. H. Rice (*Oryza sativa* L.) containing the bar gene is compositionally equivalent to the nontransgenic counterpart. *J. Agric. Food Chem.* **2005**, *53*, 1457−1465.

(16) Obert, J. C.; Ridley, W. P.; Schneider, R. W.; Riordan, S. G.; Nemeth, M. A.; Trujillo, W. A.; Breeze, M. L.; Sorbet, R.; Astwood, J. D. The composition of grain and forage from glyphosate tolerant wheat MON 71800 is equivalent to that of conventional wheat (*Triticum aestivum* L.). *J. Agric. Food Chem.* **2004**, *52*, 1375−1384.

(17) Shepherd, L. V.; McNicol, J. W.; Razzo, R.; Taylor, M. A.; Davies, H. V. Assessing the potential for unintended effects in genetically modified potatoes perturbed in metabolic and developmental processes. Targeted analysis of key nutrients and anti-nutrients. *Transgenic Res.* **2006**, *15*, 409−425.

(18) McCann, M. C.; Rogan, G. J.; Fitzpatrick, S.; Trujillo, W. A.; Sorbet, R.; Hartnell, G. F.; Riodan, S. G.; Nemeth, M. A. Glyphosate-tolerant alfalfa is compositionally equivalent to conventional alfalfa (*Medicago sativa* L.). *J. Agric. Food Chem.* **2006**, *54*, 7187−7192.

(19) Malowicki, S. M.; Martin, R.; Qian, M. C. Comparison of sugar, acids, and volatile composition in raspberry bushy dwarf virus-resistant transgenic raspberries and the wild type 'Mmeeker' (*Rubus idaeus* L.). *J. Agric. Food Chem.* **2008**, *56*, 6648−6655.

(20) Berman, K. H.; Harrigan, G. G.; Riordan, S. G.; Nemeth, M. A.; Hanson, C.; Smith, M.; Sorbet, R.; Zhu, E.; Ridley, W. P. Compositions of forage and seed from second-generation glyphosate-tolerant soybean MON 89788 and insect-protected soybean MON 87701 from Brazil are equivalent to those of conventional soybean (*Glycine max*). *J. Agric. Food Chem.* **2010**, *58*, 6270−6276.

(21) Reynolds, T. L.; Nemeth, M. A.; Glenn, K. C.; Ridley, W. P.; Astwood, J. D. Natural variability of metabolites in maize grain: differences due to genetic background. *J. Agric. Food Chem.* **2005**, *53*, 10061−10067.

(22) Scott, M. P.; Edwards, J. W.; Bell, C. P.; Schussler, J. R.; Smith, J. S. Grain composition and amino acid content in maize cultivars representing 80 years of commercial maize varieties. *Maydica* **2006**, *51*, 417−423.

(23) Asiago, V. M.; Hazebroek, J.; Harp, T.; Zhong, C. Effects of genetics and environment on the metabolome of commercial maize hybrids: a multisite study. *J. Agric. Food Chem.* **2012**, *60*, 11498−11508.

(24) Herman, R. A.; Phillips, A. M.; Collins, R. A.; Tagliani, L. A.; Claussen, F. A.; Graham, C. D.; Bickers, B. L.; Harris, T. A.; Prochaska, L. M. Compositional equivalency of Cry1F corn event TC6275 and conventional corn (*Zea mays* L.). *J. Agric. Food Chem.* **2004**, *52*, 2726−2734.

(25) ANKOM Technology; Hydrolysis Procedure. In *ANKOM^{HCI} Hydrolysis System Operator's Manual*; Macedon, NY, USA, 2014; pp 13−20.

(26) AOCS. Rapid determination of oil/fat utilizing high-temperature solvent extraction. In *Official Methods and Recommended Practices of the AOCS*, 6th ed.; Firestone, D., Ed.; American Oil Chemists' Society: Urbana, IL, USA, 2009; AOCS Standard Procedure Am 5-04.

(27) ANKOM Technology. Fat extraction process. In *ANKOM^{XT15} Extractor Operator's Manual*, Macedon, NY, USA, 2014; pp 10−19.

(28) AOAC. Fat acidity − grains. In *Official Methods of Analysis of AOAC International*, 17th ed.; Horowitz, W., Ed.; Association of Official Analytical Chemists International: Gaithersburg, MD, USA, 2000; AOAC Official Method 939.05, pp 34−35.

(29) AOAC. Determination of lead, cadmium, copper, iron, and zinc in foods. In *Official Methods of Analysis of AOAC International*, 17th ed.; Horowitz, W., Ed.; Association of Official Analytical Chemists International: Gaithersburg, MD, USA, 2000; AOAC Official Method 999.11.

(30) CEM Corp. *ICP Operation Manual*; Matthews, NC, USA, 2004.

(31) AACC. Niacin − microbiological method. In *Approved Methods of the American Association of Cereal Chemists*, 10th ed.; American Association of Cereal Chemists: St. Paul, MN, USA, 2000; AACC Method 86-51.

(32) AOAC. Pantothenic acid in vitamin preparations. In *Official Methods of Analysis of AOAC International*, 17th ed.; Horowitz, W., Ed.; Association of Official Analytical Chemists International: Gaithersburg, MD, USA, 2000; AOAC Official Method 945.74.

(33) AACC. Vitamin B_6 complex − microbiological method. In *Approved Methods of the American Association of Cereal Chemists*, 10th ed.; American Association of Cereal Chemists: St. Paul, MN, USA, 2000; AACC Method 86-31.

(34) AACC. Determination of simple sugars in cereal products − HPLC method. In *Approved Methods of the American Association of Cereal Chemists*, 10th ed.; American Association of Cereal Chemists: St. Paul, MN, USA, 2000; AACC Method 80-04.

(35) Knapp, D. R. *Handbook of Analytical Derivatization Reactions*; Wiley: New York, 1979.

(36) R Development Core Team. *R: A language and Environment for Statistical Computing*; The R Foundation for Statistical Computing: Vienna, Austria, 2011.

(37) Jones, E.; Oliphant, T.; Peterson, P.; et al.*SciPy: Open Source Scientific Tools for Python*; 2001.

(38) Howe, K.; Bateman, A.; Durbin, R. QuickTree: building huge neighbour-joining trees of protein sequences. *Bioinformatics* **2002**, *18*, 1546−1547.

DOI: 10.1021/acs.jafc.5b01764
J. Agric. Food Chem. 2015, 63, 5321−5334

(39) Han, M. V.; Zmasek, C. M. phyloXML: XML for evolutionary biology and comparative genomics. *BMC Bioinf.* **2009**, *10*, 356.
(40) Liu, K.; Goodman, M.; Muse, S.; Smith, J. S.; Buckler, E.; Doebley, J. Genetic structure and diversity among maize inbred lines as inferred from DNA microsatellites. *Genetics* **2003**, *165*, 2117−2128.
(41) Baniasadi, H.; Vlahakis, C.; Hazebroek, J.; Zhong, C.; Asiago, V. Effect of environment and genotype on commercial maize hybrids using LC/MS-based metabolomics. *J. Agric. Food Chem.* **2014**, *62*, 1412−1422.
(42) Mazur, B.; Krebbers, E.; Tingey, S. Gene discovery and product development for grain quality traits. *Science* **1999**, *285*, 372−375.
(43) Zheng, P.; Allen, W. B.; Roesler, K.; Williams, M. E.; Zhang, S.; Li, J.; Glassman, K.; Ranch, J.; Nubel, D.; Solawetz, W.; Bhattramakki, D.; Llaca, V.; Deschamps, S.; Zhong, G. Y.; Tarczynski, M. C.; Shen, B. A phenylalanine in DGAT is a key determinant of oil content and composition in maize. *Nat. Genet.* **2008**, *40*, 367−372.
(44) Cook, J. P.; McMullen, M. D.; Holland, J. B.; Tian, F.; Bradbury, P.; Ross-Ibarra, J.; Buckler, E. S.; Flint-Garcia, S. A. Genetic architecture of maize kernel composition in the nested association mapping and inbred association panels. *Plant Physiol.* **2012**, *158*, 824−834.
(45) Belo, A.; Zheng, P.; Luck, S.; Shen, B.; Meyer, D. J.; Li, B.; Tingey, S.; Rafalski, A. Whole genome scan detects an allelic variant of fad2 associated with increased oleic acid levels in maize. *Mol. Genet. Genomics* **2008**, *279*, 1−10.
(46) Harrigan, G. G.; Stork, L. G.; Riordan, S. G.; Reynolds, T. L.; Ridley, W. P.; Masucci, J. D.; Macisaac, S.; Halls, S. C.; Orth, R.; Smith, R. G.; Wen, L.; Brown, W. E.; Welsch, M.; Riley, R.; McFarland, D.; Pandravada, A.; Glenn, K. C. Impact of genetics and environment on nutritional and metabolite components of maize grain. *J. Agric. Food Chem.* **2007**, *55*, 6177−6185.
(47) Egesel, C. O.; Wong, J. C.; Lambert, R. J.; Rocheford, T. R. Combining ability of maize inbreds for carotenoids and tocopherols. *Crop Sci.* **2003**, *43*, 818−823.
(48) Rocheford, T. R.; Wong, J. C.; Egesel, C. O.; Lambert, R. J. Enhancement of vitamin E levels in corn. *J. Am. Coll. Nutr.* **2002**, *21*, 191S−198S.
(49) Kurilich, A. C.; Juvik, J. A. Quantification of carotenoid and tocopherol antioxidants in *Zea mays*. *J. Agric. Food Chem.* **1999**, *47*, 1948−1955.
(50) Li, Q.; Yang, X.; Xu, S.; Cai, Y.; Zhang, D.; Han, Y.; Li, L.; Zhang, Z.; Gao, S.; Li, J.; Yan, J. Genome-wide association studies identified three independent polymorphisms associated with α-tocopherol content in maize kernels. *PLoS One* **2012**, *7*, No. e36807.
(51) Wong, J. C.; Lambert, R. J.; Tadmor, Y.; Rocheford, T. R. QTL associated with accumulation of tocopherols in maize. *Crop Sci.* **2003**, *43*, 2257−2266.
(52) Shi, J.; Wang, H.; Schellin, K.; Li, B.; Faller, M.; Stoop, J. M.; Meeley, R. B.; Ertl, D. S.; Ranch, J. P.; Glassman, K. Embryo-specific silencing of a transporter reduces phytic acid content of maize and soybean seeds. *Nat. Biotechnol.* **2007**, *25*, 930−937.
(53) Codex Alimentarius. *Foods Derived from Modern Biotechnology*, 2nd ed.; WHO/FAO: Rome, Italy, 2009.

DOI: 10.1021/acs.jafc.5b01764
J. Agric. Food Chem. 2015, 63, 5321−5334

JOURNAL OF AGRICULTURAL AND FOOD CHEMISTRY

Article

pubs.acs.org/JAFC

Proteome of Soybean Seed Exudates Contains Plant Defense-Related Proteins Active against the Root-Knot Nematode *Meloidogyne incognita*

Raquel O. Rocha,[†] Janne K. S. Morais,[†] Jose T. A. Oliveira,[†] Hermogenes D. Oliveira,[†] Daniele O. B. Sousa,[†] Carlos Eduardo A. Souza,[‡] Frederico B. Moreno,[§] Ana Cristina O. Monteiro-Moreira,[§] José Dijair Antonino de Souza Júnior,[∥] Maria F. Grossi de Sá,[∥] and Ilka M. Vasconcelos*[,†]

[†]Department of Biochemistry and Molecular Biology, Federal University of Ceará, Campus do Pici, 60440-900 Fortaleza, Ceará, Brazil

[‡]FANOR Faculty, Devry Brasil, 60191-156 Fortaleza, Ceará, Brazil

[§]School of Pharmacy, University of Fortaleza, 60811-905 Fortaleza, Ceará, Brazil

[∥]Plant−Pest Interaction Laboratory, Embrapa Genetic Resources and Biotechnology, 70770-900 Brasília, Distrito Federal, Brazil

ABSTRACT: Several studies have described the effects of seed exudates against microorganisms, but only few of them have investigated the proteins that have defensive activity particularly against nematode parasites. This study focused on the proteins released in the exudates of soybean seeds and evaluated their nematicidal properties against *Meloidogyne incognita*. A proteomic approach indicated the existence of 63 exuded proteins, including β-1,3-glucanase, chitinase, lectin, trypsin inhibitor, and lipoxygenase, all of which are related to plant defense. The presence of some of these proteins was confirmed by their *in vitro* activity. The soybean exudates were able to reduce the hatching of nematode eggs and to cause 100% mortality of second-stage juveniles (J2). The pretreatment of J2 with these exudates resulted in a 90% reduction of the gall number in tobacco plants. These findings suggest that the exuded proteins are directly involved in plant defense against soil pathogens, including nematodes, during seed germination.

KEYWORDS: *Glycine max, exudation, seed proteins, defense proteins, soil pathogen, Meloidogyne*

INTRODUCTION

Root-knot nematodes (*Meloidogyne* spp.) are obligate endoparasites comprising a major group of plant-parasitic nematodes that affect crop production, causing annual losses of more than one hundred billion U.S. dollars worldwide.[1] Among all *Meloidogyne* species, *Meloidogyne incognita* is the most damaging phytonematode, and it is disseminated throughout the world, particularly in regions with previous plantings of coffee or cotton.[2] Root-knot nematodes have developed a highly specialized and unique way to infect their hosts. The infection takes place when the motile second-stage juvenile (J2), the infective form, is attracted to the root system by the root exudates and enters the elongation zone just behind the root tip.[3] The parasite then moves intra- and intercellularly to reach the primary phloem or the undifferentiated cells of the adjacent parenchyma, where it becomes sedentary and establishes a feeding site.[4]

Currently, the most commonly used procedure in nematode control is the application of synthetic nematicides. However, their high cost and toxicity to the environment and live organisms has encouraged the development of new methods of nematode control.[5] Although transgenic technology, which has offered potential new avenues for crop improvement programs, is useful for designing nematode-resistant crops, this alternative approach has not sufficiently demanded an urgent need for the design of novel management strategies.[6] In this sense, a number of studies have been performed to develop non-chemical and environmentally friendly nematode management practices, including the use of botanicals.[7]

Seed exudates represent a useful source of defense molecules, which are mainly peptides/proteins and secondary metabolites with the capacity to inhibit soil-borne pathogens and, thereby, prevent infection.[8] Although several studies have described the inhibitory effects of seed exudates against microorganisms, only a few of these studies have investigated the proteins that may contribute to the defense activity of the exudates; thus, our knowledge remains essentially incomplete.[9] The present study focused exclusively on the exuded proteins from soybeans [*Glycine max* (L.) Merril]. Soybean seeds stand as an ideal system for the study of the exudates−pathogen interaction because of their great economic value and high protein content.[10] Many seed proteins are usually stored in specialized cellular compartments, preventing their hydrolysis.[11] In addition, it was shown that soybean seeds are capable of exuding large amounts of protease inhibitors along with other proteins in hot water, suggesting their potential role in the defense against pathogens.[12] In this work, the identification and

Received: March 2, 2015
Revised: May 14, 2015
Accepted: May 21, 2015
Published: June 2, 2015

ACS Publications © 2015 American Chemical Society

DOI: 10.1021/acs.jafc.5b01109
J. Agric. Food Chem. 2015, 63, 5335−5343

characterization of some proteins were performed by studying the soybean seed exudates using capillary liquid chromatography/nanoelectrospray ionization tandem mass spectrometry (ESI−LC−MS/MS) in association with data searching for protein identification and by measuring the activity of some classical defense proteins. Moreover, the efficiency of the exuded seed proteins in inhibiting the development of *M. incognita* was investigated. This study was performed to contribute to the understanding of the physiological role of exuded proteins in the defense against soil pathogens, particularly during the germination process as well as to demonstrate the potential of seed exudates as a source of nematicidal compounds.

MATERIALS AND METHODS

Biological Materials and Reagents. Mature soybean seeds cv. BRS Pala, a commercial and conventional soybean cultivar with high protein content (38.8%) and good resistance/tolerance to both biotic and abiotic stresses, were supplied by the Brazilian Agricultural Research Corporation [Empresa Brasileira de Pesquisa Agropecuária (EMBRAPA)] in partnership with the Foundation for ProSeed Research Support, Passo Fundo, Brazil.[13] Rabbit blood was obtained from the animals of colonies maintained at the Federal University of Ceará (Fortaleza, Brazil). *M. incognita* (race 1) eggs were isolated from tomato roots growing in a greenhouse at the Plant−Pest Molecular Interaction Laboratory, Embrapa, Brasília, Brazil. All chemicals used were of analytical grade.

Preparation of the Soybean Seed Exudates. Seed exudates were obtained from 20 whole soybean seeds with no cracks or other injuries. Seeds were surface-sterilized with 30% (v/v) ethanol for 5 min, rinsed exhaustively with distilled water, and soaked in 6 mL of 0.1 M sodium acetate buffer at pH 5.0, 28 °C, and 70% relative humidity. After different time periods of soaking (1, 6, 12, 18, and 24 h), the seeds were removed, the exudates were collected, and the volumes were recorded. The soybean seed exudates were subject to exhaustive dialysis against distilled water to remove organic compounds with a molecular mass below 3500 Da and centrifuged at 8000*g* for 10 min at 4 °C; the supernatant was collected; and its protein content was determined by the Bradford[14] method using bovine serum albumin (BSA) as the standard protein.

Phytochemical Compound Analysis. The presence of phytochemical compounds was assessed[15] in the ethanolic (70%) extract obtained from the lyophilized soybean exudates. To detect phenols and tannins, the extract was mixed with a few drops of alcoholic ferric chloride solution. Color varying between blue and red shows the presence of phenols, and a dark blue or green precipitate denotes tannins. Leucoanthocyanidins were detected by the appearance of red color after acidification of the extract with HCl (pH 1−3), followed by heat treatment for 2−3 min. To identify flavonoids and xanthones, the extract was mixed with magnesium granules in concentrated HCl. The appearance of red color indicates the presence of these compounds. In the test for steroids and triterpenoids, the extract was mixed with chloroform, a few drops of acetic anhydride, and concentrated sulfuric acid. The appearance of blue or green color indicates the presence of steroids, and brown to red color indicates the occurrence of triterpenoids. The test for saponins was performed in the precipitate formed after treatment of the extract with chloroform, followed by the addition of distilled water and vigorous shaking. The appearance of stable froth indicates the presence of saponins. Alkaloids were detected after extraction of the organic bases with diluted HCl, followed by the addition of drops of the Hagger, Mayer, and Dragendorff reagents. The appearance of cream white precipitate indicates the presence of alkaloids.

Sodium Dodecyl Sulfate−Polyacrylamide Gel Electrophoresis (SDS−PAGE) Analysis. SDS−PAGE was performed in a 12.5% discontinuous polyacrylamide gel prepared in 0.025 M Tris−HCl buffer at pH 8.9 containing 1% sodium dodecyl sulfate (SDS).[16] Samples (25 μg) were prepared in 0.5 M Tris-HCl buffer at pH 6.8 containing 1% SDS and heated at 100 °C for 10 min before electrophoresis. Electrophoresis was performed at 20 mA, and the protein bands were visualized after staining with Coomassie Brilliant Blue G-250.[17]

ESI−LC−MS/MS Analysis and Database Searching. The 50 μg aliquots of the dialyzed soybean seed exudates were dissolved in 0.05 M ammonium bicarbonate, denatured in the presence of 0.2% (v/v) RapiGEST SF (Waters, Manchester, U.K.) at 80 °C for 15 min in a dry bath, reduced with 0.1 M dithiothreitol (DTT) at 60 °C for 60 min, and alkylated with 0.3 M iodoacetamide (IAA) for 30 min in the dark at room temperature (23 ± 2 °C). Next, the samples were enzymatically digested overnight, at 37 °C, with the addition of a modified trypsin (Promega, catalog number V5111, Madison, WI) at a 1:100 (w/w) enzyme/protein ratio. To hydrolyze RapiGEST SF and stop digestion, 10 μL of 5% trifluoroacetic acid (TFA) was added, the sample was mixed, incubated for 90 min at 37 °C, and centrifuged (14000*g* for 30 min at 6 °C), and the supernatant was transferred to a Waters Total Recovery vial (Waters, Manchester, U.K.). The nano-ultra-performance liquid chromatography (UPLC) separation of tryptic peptides was performed using a nanoACQUITY UPLC system (Waters, Manchester, U.K.) equipped with a HSS T3 C_{18} reverse-phase column (1.8 μm, 75 μm × 20 mm) equilibrated with the mobile phase A [0.1% (v/v) formic acid in water]. Elution was carried out at 0.35 μL/min flow rate using the mobile phase B [0.1% (v/v) formic acid in acetonitrile] in a gradient mode of 0−40% for 90 min and 40−85% for 5 min. All samples were measured using a data-independent analysis (MS^E, where E represents dynamically variable collision energy), and the tryptic peptides were analyzed using a nano-ESI−LC−MS/MS mass spectrometer (Synapt G1 HDMS, Waters, Manchester, U.K.). The instrument was operated in the electrospray positive-ion mode nano-ESI (+) and in "V" mode, with a precursor double-charge resolution of at least 10 000 full width at half-maximum (fwhm). The mass spectrometer was calibrated by infusion of the standard [Glu1]−fibrinopeptide B human (Glu−Fib) ($[M + 2H]^{2+}$ = 785.2486) into the NanoLockSpray source. Analyses were performed using a Glu−Fib mass channel for every 30 s. The exact mass retention times (EMRTs) of nano-LC−MS^E data were collected in scans alternating between lower (3 eV) and elevated (15−50 eV) collision ramp energy applied to the argon collision cell. The scan time was 1.5 s with a 0.2 s interscan delay for each MS scan at m/z 50−2000. The radio frequency (RF) offset (MS profiles) was adjusted such that LC−MS data were effectively acquired from m/z 300 to 2000, which ensured that any masses observed in the LC−MSE data less than m/z 300 were known to arise from dissociations in the collision cell. The LC−MSE data were processed, and the proteins were identified using Protein Lynx Global Server, version 2.4, software (PLGS) against a reverse *G. max* annotated database, which is accessible on the Universal Protein Knowledgebase (UniProtKB) database. For spectra and database searching, the following default parameters on PLGS were used: a maximum of 1 missed cleavage by trypsin, a fixed modification specified as carbamidomethylation (C), and oxidation (M) as variable modification. The identified proteins were analyzed using AgBase tools.[18] The Plant GOSlimViewer was used to summarize the molecular function and biological process categories using UniProtKB as the reference. The identified proteins were further analyzed by TargetP,[19] iPSORT,[20] and SignalP 3.0,[21] three independent software programs that predict the secreted proteins into the medium via a classical pathway based on their N-terminal signal peptide sequences. In addition, the predictive characterization of proteins secreted via non-conventional pathways was performed using the neural network-based software SecretomeP, version 2.0.[22]

Activity Assay of Plant Defense-Related Proteins. β-1,3-Glucanase (EC 3.2.1.39) was measured by determining the amount of glucose liberated by the action of the enzyme on laminarin (Sigma, St. Louis, MO) used as a substrate. After the addition of the appropriate reagents to the reaction mixture, according to Boller,[23] absorbance readings were taken at 520 nm and the amount of reducing sugars liberated was calculated on the basis of a standard curve created with known amounts (7.5−240.0 mg/L) of commercial glucose (Sigma Chemical Company) dissolved in 0.05 M sodium acetate buffer (pH

DOI: 10.1021/acs.jafc.5b01109
J. Agric. Food Chem. 2015, 63, 5335−5343

5.2) containing 0.5 M NaCl. The activity was expressed as nanokatals per milligram of protein (nkat/mg of protein), with 1 nkat defined as 1.0 nmol of D-glucose released from laminarin per second at 37 °C. Chitinase (EC 3.2.1.14) was assayed using a colorimetric procedure that detects *N*-acetyl-D-glucosamine (NAG) produced by the combined hydrolytic action of chitinases and β-glucuronidase upon the non-radioactive substrate colloidal chitin.[23,24] Colloidal chitin was prepared using non-radioactive acetic anhydride.[25] Absorbance was read at 585 nm, and the amount of NAG produced was calculated on the basis of a standard curve obtained with known concentrations (0.1−0.7 mg/L) of commercial NAG dissolved in 0.05 M sodium acetate buffer (pH 5.2). Chitinase was calculated as nanokatal per milligram of protein (nkat/mg of protein), with 1 nkat defined as 1.0 nmol of NAG produced per second at 37 °C. Peroxidase (EC 1.11.1.7) activity was determined using guaiacol as the proton donor substrate and hydrogen peroxide as the electron donor.[26] Aliquots of 0.02 mL of the dialyzed seed exudates appropriately diluted were mixed with 0.98 mL of 0.05 M sodium acetate buffer at pH 5.2, 0.5 mL of 0.06 M H_2O_2, and 0.5 mL of 0.02 M guaiacol in a total volume of 2.0 mL. The reaction mixture was incubated at 30 °C for 10 min, and the absorbance was measured at 480 nm. The variation of 1 unit of absorbance per minute was defined as 1 unit of peroxidase activity (1 AU) and expressed as activity per milligram of protein (AU/mg of protein). Total proteolytic activity was measured using azocasein as a non-specific substrate.[27] The soybean exudates (500 μL), at different concentrations, dissolved in 0.025 M Na−phosphate buffer at pH 6.0 containing 0.003 M DTT were incubated with 200 μL of 1% (m/v) azocasein for 1 h at 37 °C. The reaction was stopped by the addition of 300 μL of 20% (v/v) trichloroacetic acid (TCA). The tubes were centrifuged (5000*g* for 10 min at 25 °C), and the supernatants obtained were alkalinized with 400 μL of 0.2 N NaOH. The proteolytic activity was expressed as activity unit per milligram of protein per minute (AU mg^{-1} of protein min^{-1}), with 1 AU defined as the change of 0.01 absorbance unit per minute at 420 nm. The trypsin inhibitor assay was carried out by the method originally described by Kakade et al., using N_α-benzoyl-D,L-arginine 4-nitroanilide hydrochloride (L-BAPNA) as the substrate.[28,29] Seed exudates (0.1 mL) at different protein concentrations were mixed with 1.6 mL of 0.05 M Tris−HCl at pH 8.2 containing 0.02 M $CaCl_2$, with 0.1 mL of trypsin (Sigma, type I), from a stock solution of 0.4 mg in 10 mL of 0.001 M HCl, plus 0.1 mL of BAPNA [10 mg/mL in 1% (v/v) dimethyl sulfoxide (DMSO) plus H_2O]. The mixture was incubated for 45 min at 37 °C, and 0.2 mL of 30% (v/v) acetic acid solution was added. The enzymatic hydrolysis of BAPNA was evaluated by recording the absorbance at 410 nm. The amount of trypsin inhibited was calculated from a calibration curve using soybean trypsin inhibitor (Sigma, type I-S). The trypsin inhibitory activity was expressed as the amount of trypsin inhibited per milligram of protein (mg of TI/mg of protein). Papain inhibitory activity was performed as described by Abe et al.[30] using N_α-benzoyl-D,L-arginine-*p*-naphthylamide (BANA) as the substrate. To 20 μL of papain solution (0.1 g/L in 0.025 M sodium phosphate buffer at pH 6.0), 40 μL of an activation solution [containing 0.002 M ethylenediaminetetraacetic acid (EDTA) and 0.003 M DTT at pH 6.0], 100 μL of the dialyzed seed exudates at different concentrations, and 340 μL of 0.025 M sodium phosphate buffer at pH 6.0 were added. The mixture was incubated for 10 min at 37 °C. The reaction was initiated by the addition of 200 μL of 0.001 M BANA solution, prepared in 1% (v/v) DMSO and 0.025 M sodium phosphate buffer at pH 6.0. After 20 min at 37 °C, the reaction was stopped by the addition of 500 μL of 2% HCl in 95% ethanol. The color product was developed by adding 500 μL of 0.06% *p*-dimethylaminocinnamaldehyde in ethanol. Papain inhibitory activity was expressed as inhibition unit per milligram of protein (IU/mg of protein), with 1 IU defined as the amount of inhibitor capable of decreasing the absorbance in 0.01 at 540 nm. Lectin activity was assessed by serial 2-fold dilution of samples, employing native and trypsin-treated rabbit red blood cells.[31,32] The seed exudates were diluted with 0.15 M NaCl in glass tubes and mixed with rabbit erythrocytes (2% suspension prepared in 0.15 M NaCl). The red cell suspensions were enzyme-treated with trypsin (10 mg/L solution prepared in 0.15 M NaCl) for 1 h at room temperature (22 ± 3 °C). Cells were washed 4 times with 0.15 M NaCl, and the suspension final volume was adjusted to attain the original concentration (2%). The degree of agglutination was monitored visually after the tubes had been left to stand at 37 °C for 30 min and at room temperature for a further 30 min. Lectin activity was expressed as hemagglutinating unit per milligram of protein (HU/mg of protein), with 1 HU defined as the reciprocal of the highest dilution giving a visible agglutination to the naked eye.

Nematode Egg Extraction and Production of Juveniles. *M. incognita* (race 1) eggs were extracted from infected tomato roots.[33] These roots were washed with distilled water, cut into 5 cm pieces, and ground in a blender with 0.5% sodium hypochlorite, and the eggs were collected on a 500 mesh sieve (26 μm). Second-stage juveniles (J2s) were hatched from the eggs in distilled water at approximately 28 °C for 48 h. The J2 population was counted and used as the inoculum within 1−2 days of collection.

Attraction Assay. The attraction of *M. incognita* to dialyzed soybean seed exudates was performed following a protocol based on Wang et al.[34] A total of 3 mL of 23% pluronic gel containing 800 freshly hatched J2s was pipetted onto 35 × 10 mm Falcon Easy-Grip Petri dishes (BD Biosciences, San Jose, CA) and kept at room temperature for 24 h. Thereafter, filter paper discs (6 mm diameter) soaked with seed exudates (500 and 1000 mg of protein/L) were added to the center of each dish and then kept at room temperature. The number of nematodes touching the terminal 2 mm of the disc tip was counted at 1, 3, 5, and 24 h time intervals. Distilled water was used as the negative control. The experiment was repeated twice and carried out in triplicate.

***In Vitro* Egg Hatching Test.** Egg suspensions (approximately 500 eggs in distilled water) were incubated at 28 °C in a 12 well culture plate (BD Biosciences, San Jose, CA) with dialyzed seed exudates at a final concentration of 250 and 500 mg of protein/L. The experiment was repeated twice and carried out in triplicate using distilled water as the control. After the incubation time, the number of unhatched eggs was counted under a microscope and the hatch rates were assessed 24 and 48 h after treatment.[35]

***In Vitro* Mortality/Mobility Test of J2s.** A suspension of 50 freshly hatched J2s in distilled water was incubated at 28 °C in a 12-well culture plate with dialyzed seed exudates at final concentrations ranging from 60 to 500 mg of protein/L in a final volume of 0.0005 L. Distilled water was used as the control. After 24 and 48 h of treatment, the mobile and non-mobile J2s were counted under a stereomicroscope. Nematodes were considered dead if they did not move even after the dilution of the exudates to an innocuous concentration.[36] The data were transformed into the percentage mortality [mortality (%) = dead number of J2s/total number of J2s × 100] before the statistical calculations. The experiment was repeated twice and carried out in triplicate.

Root Infection Assay. J2s were kept in contact with the dialyzed seed exudates (125 mg of protein/L) at 28 °C in the dark for 24 h. Thereafter, treated J2s were used in the root inoculation of 1-month-old tobacco seedlings growing in sand/sandy loam (2:1, v/v) in plastic pots. Each seedling received 150 J2s. Tobacco seedlings with J2s exposed to distilled water served as a control. Seedlings inoculated with J2s were maintained in the greenhouse at 28 °C and under a 12/12 h light/dark cycle. At 6 weeks after inoculation, the whole plant was collected and the root system was washed with tap water to remove the soil. The root gall numbers and egg masses were assessed.[35] Seedlings were arranged in a completely randomized block design with 10 individuals per block and three biological replicates.

Statistical Analysis. The experimental design used in all biological assays was completely randomized. The mean of each treatment was compared to its respective control. The data analysis was performed by two ways: (i) when the data were in normal distribution, the analysis was performed using analysis of variation (ANOVA) and Tukey's test to compare means ($p < 0.05$), and (ii) when the data were not in normal distribution, analysis was performed in the JMP 5.1 software using the Wilcoxon/Kruskal−Wallis non-parametric test with a

DOI: 10.1021/acs.jafc.5b01109
J. Agric. Food Chem. 2015, 63, 5335−5343

significance level of 5%. The measurement of dispersion was calculated using standard error.

RESULTS

Protein Content and Molecular Mass of the Exuded Proteins. The type of proteins accumulated in the medium during the imbibition of soybean seeds did not change over time, because the exudates showed similar electrophoretic patterns for the different time periods analyzed. However, the highest amount of protein in the medium was observed 18 h after soaking, which amounted to approximately 3190.00 ± 100.00 mg/L, corresponding to 0.39 ± 0.01 mg/seed. Thus, the exudates obtained under this condition were selected for use in further analyses. Phytochemical compounds were not observed in the dialyzed exudates. SDS−PAGE showed that these exudates contained several proteins ranging in size from 4202 to 97 000 Da, with predominant bands of apparent molecular masses of approximately 28 000 and 45 000 Da (Figure 1).

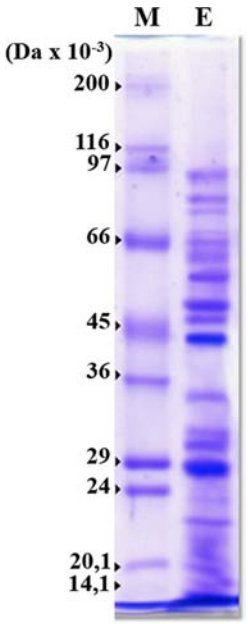

Figure 1. SDS−PAGE of soybean seed exudates: (M) mass markers and (E) soybean seed exudates collected 18 h after soaking in 0.1 M sodium acetate buffer at pH 5.0 and 28 °C. Proteins (25 μg) from seed exudates were loaded in lane E. Protein bands were stained with Coomassie Brilliant Blue G-250.

Identification and Functional Classification of the Exuded Proteins. A gel-free proteomic approach identified 63 protein accessions based on the sequences in the UniProtKB database (Table 1). The distribution of the identified proteins according to their theoretical molecular weights by ESI−LC−MS/MS was corroborated by the results of SDS−PAGE. Among the identified proteins, glycinins, lipoxygenases, proteinase inhibitors, and seed maturation proteins were the most common. Gene ontology annotation allowed for classification of the identified proteins into nine categories: nutrient reservoir activity (14 proteins), DNA binding (1 protein), binding (1 protein), catalytic activity (7 proteins), structural molecule activity (1 protein), hydrolase activity (3 proteins), response to stress (3 proteins), enzyme regulator activity (10 proteins), and carbohydrate binding (1 protein). The 22 remaining proteins were not classified. Interestingly, several proteins identified by ESI−LC−MS/MS are related to plant defense, including β-1,3-glucanase, chitinase class I, lectin, Kunitz and Bowman−Birk trypsin inhibitors, lipoxygenases, late embryogenesis abundant protein, and 7S globulin. In addition, it was observed that most proteins were secreted into the medium via a classical mechanism. However, some of them seem to be secreted via a non-classical, novel fashion pathway (Table 2), because they have scores higher than the threshold value of neural network (NN) > 0.5. One example was the Bowman−Birk protease inhibitor, which was the most highly represented protein.

Activity of Plant Defense-Related Proteins in the Exudates. Specific assays revealed the presence of activities related to some classical defense proteins in the exudates (Table 3). The presence of lectin was evaluated on the basis of the hemagglutinating activity, which was the most pronounced in the seed exudates, particularly when the trypsin-treated rabbit erythrocytes (609.52 HU/mg of protein) were used, reaching up to 4.8 times the value observed for untreated red cells (126.98 HU/mg of protein). To a lesser extent, both β-1,3-glucanase (58.26 nkat/mg of protein) and papain inhibitor (30.48 IU/mg of protein) showed high activities. On the other hand, chitinase activity was not detected, probably because of the low concentration of this protein in the soybean seed exudates.

Biological Effects of Exuded Proteins on Nematodes. A chemotaxis assay showed that the exudates have a repellent effect on the nematode (Figure 2). Indeed, the percentages of J2s of *M. incognita* touching the disc tips immersed in the exudates at 1000 mg of protein/L concentration but not 500 mg of protein/L were significantly ($p < 0.05$) lower compared to the control. This result was particularly true for 1, 3, and 5 h of exposure time. However, at 24 h of exposure, there was no difference between the control and the exudate-treated nematodes.

As demonstrated by the *in vitro* assays, the dialyzed soybean exudates also showed adverse effects on several developmental parameters of *M. incognita*. Indeed, the exudates (500 mg of protein/L) reduced the hatching of the *M. incognita* eggs at 48 h of incubation compared to the control by allowing less than 22% of the eggs to hatch (Figure 3). In addition, the motility of J2s was inhibited by the soybean exudates (60−500 mg of protein/L) compared to the control (Figure 4). The percentage of inactive J2s was approximately 90%, even at the lowest protein concentration (60 mg of protein/L) used. In general, this percentage did not change with the protein concentration of the exudates or the incubation period. Further tests revealed that the exudates were lethal to *M. incognita* J2s (Figure 5). In this case, the percentage of mortality of J2s increased with the incubation period from 24 to 48 h, reaching 100% even in one of the lowest tested protein concentrations (125 mg of protein/L).

The greenhouse experiment using tobacco plants also demonstrated the efficacy of the soybean seed exudates in the *M. incognita* controls. At 6 weeks after inoculation, the pretreatment of J2s with the soybean exudates resulted in around 90 and 94% reduction of the *M. incognita* gall and egg mass number, respectively, in tobacco plants (Figure 6) compared to the control.

DISCUSSION

Plant defense mechanisms have been studied very intensively in vegetative tissues. However, little is known about the strategies

DOI: 10.1021/acs.jafc.5b01109
J. Agric. Food Chem. 2015, 63, 5335−5343

Table 1. Proteins Identified from Soybean Seed Exudates by ESI−LC−MS/MS

protein description[a]	UniProtKB accession number (AC)	molecular weight (MW)[b]	score[c]	coverage (%)[d]
Nutrient Reservoir Activity				
basic 7S globulin	P13917	46393.21	55389.76	58.54
glycinin	P04776	55706.47	32333.35	59.33
2S albumin	P19594	18460.09	14237.19	35.86
β conglycinin β subunit	F7J077	50441.93	8815.38	39.63
7S storage protein α subunit	Q39816	27367.78	3554.79	35.27
DNA Binding				
uncharacterized protein	I1N2Y9	26078.60	138.91	6.03
Binding				
chitinase class I	Q9SDY6	34341.45	1496.48	28.33
Catalytic Activity				
lipoxygenase	B3TDK5	96726.37	3055.39	27.26
Hydrolase Activity				
endo-1,3-β-glucanase	Q6S9W0	36603.47	3032.81	34.70
Response to Stress				
seed maturation protein PM22	Q9XER5	16688.38	5253.49	50.88
protein P21	P25096	21462.86	4481.12	17.57
Enzyme Regulator Activity				
Bowman−Birk type proteinase inhibitor D II	P01064	9467.83	43752.51	72.29
Bowman−Birk type proteinase inhibitor C II	P01063	9201.38	27008.52	65.43
trypsin inhibitor A	P01070	24005.35	17231.35	42
Kunitz trypsin inhibitor 3	Q9LD16	24067.35	11070.21	21.60
Bowman−Birk proteinase inhibitor	Q9SBA9	4530.20	679.02	67.43
trypsin inhibitor B	P01071	20040.66	8585.66	21.17
Enzyme Regulator Activity				
Kunitz type trypsin inhibitor KTI1	P25272	22546.00	603.17	25.12
Carbohydrate Binding				
lectin	P05046	30928.02	5862.31	30.52
Not Classified				
24 kDa protein SC24	Q8W0V9	24569.62	15965.57	39.42
late embryogenesis abundant protein	P93165	11491.34	15633.56	54.92
napin type 2S albumin 1	Q9ZNZ4	17834.76	12450.66	43.44
hydrophobic seed protein	P24337	8358.90	10225.60	38.75
seed maturation protein PM30	Q9XET0	15097.41	7151.64	49.28
uncharacterized protein	I1K6M2	23812.87	11258.69	55.10
uncharacterized protein	C6T0L2	11141.08	8993.93	40.26
uncharacterized protein	I1NGF5	47229.38	8818.34	44.76
uncharacterized protein	I1NGG4	26058.11	2406.17	36.72
dehydrin	Q70EL8	23733.70	1902.39	45.72
P24 oleosin isoform A	P29530	23501.69	1396.25	16.81
seed biotin containing protein SBP65	Q39846	67878.09	616.55	23.74

[a]All proteins were identified in *G. max*. [b]Theoretical molecular mass in daltons. [c]Scores were obtained using an algorithm that includes retention time, ion intensities, charge state, and accurate masses of both precursor and product ions from LC−MS data.[50] [d]Coverage means the percentage (%) of the sequence of the protein represented by the peptides identified in the MS run.

Table 2. Prediction of Non-classical Protein Secretion by SecretomeP

protein description[a]	UniProtKB AC	score[b]
Bowman−Birk type proteinase inhibitor D II	P01064	0.858
uncharacterized protein	C6T0L2	0.778
uncharacterized protein	I1L957	0.521
seed maturation protein	Q9S7N8	0.891
Bowman−Birk proteinase inhibitor	Q9SBA9	0.648
Bowman−Birk type proteinase inhibitor C II	P01063	0.913

[a]All proteins were identified in *G. max*. [b]Neural network (NN) scores of >0.5 are considered to predict extracellular localization.

Table 3. Activities of the Plant Defense-Related Proteins Present in the Soybean Seed Exudates[a]

protein activity	seed exudates
lectin (HU/mg of protein)	
untreated erythrocytes	126.98 ± 4.39
trypsin-treated erythrocytes	609.52 ± 0.01
trypsin inhibitor (mg of TI/mg of protein)	4.81 ± 0.23
papain inhibitor (IU/mg of protein)	30.48 ± 1.83
protease (AU mg^{-1} of protein min^{-1})	1.52 ± 0.05
peroxidase (AU mg^{-1} of protein min^{-1})	0.01 ± 0.00
β-1,3-glucanase (nkat/mg of protein)	58.26 ± 3.02
chitinase (nkat/mg of protein)	ND[b]

[a]Values are the means ± standard deviation (SD) of biological triplicates. [b]ND = not detected.

used by seeds to survive and germinate in substrates densely populated with microorganisms.[37] It is known that the initial infections of seeds and roots by pathogens may be driven by attractive nutritive exudates, which may be hampered by exuded defense-related compounds.[9] Thus, in an attempt to gain better insight into the role of seed exudates in plant defense, the present study focused on the characterization of exuded soybean seed proteins and their effects against the root-knot nematode *M. incognita*.

Proteins with potential roles in plant defense were identified by ESI−LC−MS/MS in soybean seed exudates. Among them, glycinin, lipoxygenase, and protease inhibitors were the predominant exuded proteins (Table 1). Indeed, several storage proteins, of which a majority are globulins, have been identified in soybeans. The plant globulin family can be subdivided into two main classes according to their sedimentation coefficients: glycinin (11S) and β-conglycinin (7S). In addition to their high nutritional value, it has been shown that these proteins exhibit antimicrobial activities against pathogenic bacteria in equivalent or even higher levels than penicillin, suggesting the involvement of these molecules in the innate defense system of soybeans.[38] Along with the traditionally classified storage proteins, plant lipoxygenases are commonly associated with plant defense

DOI: 10.1021/acs.jafc.5b01109
J. Agric. Food Chem. 2015, 63, 5335−5343

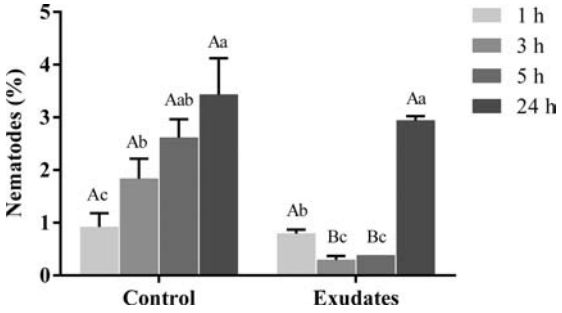

Figure 2. Chemotactic response of the *M. incognita* J2s at 1, 3, 5, and 24 h of exposure to the soybean seed exudates (1000 mg/L). Values represent the means ± SD of triplicates. Significant differences ($p < 0.05$) of the means within the control or within the exudate-treated J2s at different time points are denoted by different lowercase letters. Significant differences ($p < 0.05$) of the means comparing the controls and the exudate-treated J2s at a given time point are denoted by different capital letters ($p < 0.05$).

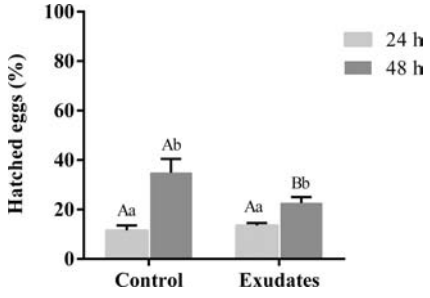

Figure 3. Effect of soybean seed exudates on *M. incognita* eggs at 24 and 48 h of exposure time. Values represent the means ± SD of triplicates. Significant differences ($p < 0.05$) of the means within the control or within the exudate-treated eggs at different time points are denoted by different lowercase letters. Significant differences ($p < 0.05$) of the means comparing the controls and the exudate-treated eggs at a given time point are denoted by different capital letters ($p < 0.05$).

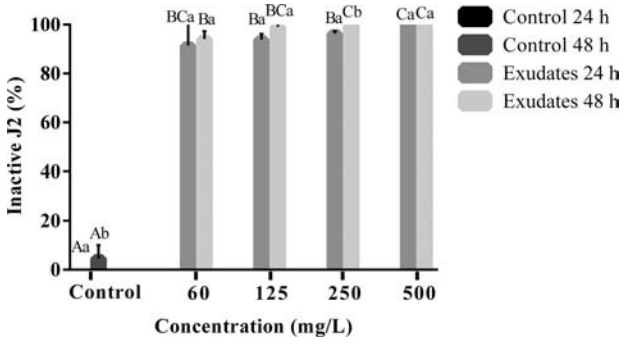

Figure 4. Inactivation of *M. incognita* J2s at 24 and 48 h of exposure to soybean seed exudates. The values represent the means ± SD of triplicates. Significant differences ($p < 0.05$) of the means within the control or within the exudate-treated J2s at different time points are denoted by different lowercase letters. Significant differences ($p < 0.05$) in the means comparing the controls and the exudate-treated J2s at a given time point are denoted by different capital letters ($p < 0.05$).

mechanisms because they are related to the synthesis of a number of different compounds with signaling functions and antimicrobial activity or the development of the hypersensitive response.[39]

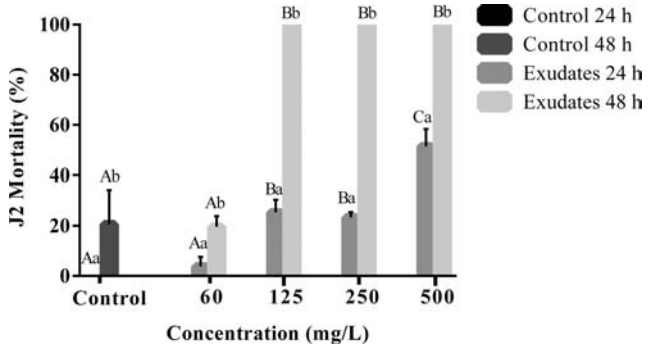

Figure 5. Mortality of *M. incognita* J2s at 24 and 48 h exposure time to soybean seed exudates. The values represent the means ± SD of triplicates. Significant differences ($p < 0.05$) of the means within the control or within the exudate-treated J2s at different time points are denoted by different lowercase letters. Significant differences ($p < 0.05$) of the means comparing the controls and the exudate-treated J2s at a given time point are denoted by different capital letters ($p < 0.05$).

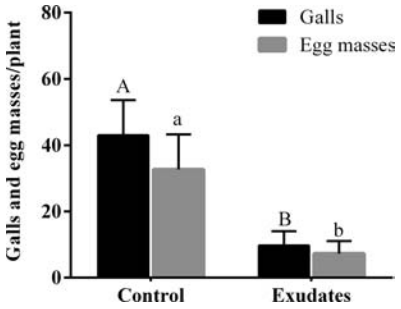

Figure 6. Effect of soybean seed exudates on *M. incognita* virulence. Gall number and egg masses were assessed 6 weeks after inoculation of tobacco roots under greenhouse conditions. Significant differences ($p < 0.05$) of means are denoted by different letters (one-way ANOVA and Tukey test).

Additionally, protease inhibitors can act as storage proteins involved in plant defense. In soybeans, trypsin inhibitors have been reported, which comprise approximately 6% of the total seed proteins. Members of the trypsin inhibitor family inhibit various proteases from plant pathogenic microorganisms and phytophagous insects, suggesting the importance of exudates in the successful seed germination.[40] Other classes of proteins, such as chitinase, β-1,3-glucanase, and lectin, were also released by imbibed soybean seeds. These results agree with those described for legume seed exudates, confirming the complexity of legume proteomes.[9,12]

Most of the exuded soybean proteins appeared to have been released into the germinating medium via a classical mechanism. In contrast, the Bowman−Birk protease inhibitor has been predicted by SecretomeP software to be potentially secreted via a non-conventional pathway. As previously noted, many proteins in soybean exudates undergo secretion via classical mechanisms, with signal peptides targeting the molecules to storage vacuoles.[41] Nevertheless, there is evidence for the existence of plant proteins that are secreted via rough endoplasmic reticulum (RER)−Golgi apparatus-independent routes. The existence of an alternative secretory route can be explained by the need for a rapid and effective defense response to external stress.[42] Accordingly, the Bowman−Birk protease inhibitor might participate in this plant defense process.

DOI: 10.1021/acs.jafc.5b01109
J. Agric. Food Chem. 2015, 63, 5335−5343

To validate the presence of some proteins identified using the gel-free quantitative proteomic approach, the enzymatic and hemagglutinating activities were detected in the soybean exudates. Using these approaches, the presence of proteins, such as lectin, trypsin inhibitor, and β-1,3-glucanase, was confirmed. However, the use of proteomics to identify a certain protein in a sample does not always mean that the *in vitro* assay method is robust enough to detect the activity of that protein, particularly when it is present in low amounts. This can be exemplified by the absence of chitinase activity in the seed exudates, despite the detection of a class I chitinase by ESI−LC−MS/MS. Moreover, the reverse situation was also observed, in which the *in vitro* activity was detected but the corresponding protein was not identified by MS/MS. For instance, our study showed the inhibitory activity of papain in the soybean exudates *in vitro* (Table 3), although the MS/MS analysis did not identify any phytocystatins. Nevertheless, some Kunitz trypsin inhibitors have been reported as bifunctional inhibitors with the ability to inhibit two different enzyme classes (serine and cysteine proteinases).[43] Thus, it is possible that the *in vitro* papain inhibitory activity found in the soybean exudates (Table 3) might be associated with the Kunitz trypsin inhibitors identified through ESI−LC−MS/MS (Table 1).

The *in vitro* inhibitory effect of seed-exuded proteins on the fungal growth has previously been shown.[8] Nonetheless, there have been very few similar studies to date that have addressed plant parasite nematodes. Therefore, after validation of the identities of the exuded proteins involved in plant defense and their corresponding *in vitro* enzymatic activities, our next step was to assess the potential activity of the soybean exudates against *M. incognita*. Indeed, a significant reduction in the mobility and an increase in the mortality of *M. incognita* J2s were observed after treatment with the soybean exudates even at low protein concentrations (60 and 125 mg of protein/L, respectively) (Figures 4 and 5). The nematostatic and nematicidal effects of the exudates on *M. incognita* J2s were also verified using a proteinaceous papain inhibitor purified from *Crotalaria pallida* roots.[7] These effects were found to be lethal, with 95% mortality, when the parasite was exposed to a 50 μg dose of this inhibitor for 48 h.[7] Although the repellent effect of the soybean exudates toward the nematodes was transient (Figure 2), this delay affected their infectivity. This assumption is supported by our experimental findings in which tobacco plants that were inoculated with soybean seed exudate-treated J2s showed around 90 and 94% reductions in the number of galls and egg masses, respectively. The nematicidal activity of the soybean seed exudates is promising because it apparently exerted this effect during more than one stage of the life cycle of the parasite. After 48 h of treatment, the exuded proteins (at 500 mg of protein/L) inhibited the hatching of the nematode eggs by 40% (Figure 3) relative to the controls. This observation is very important because the nematode egg shell has three protective layers, which might complicate the use of chemical agents to control the further development of the nematodes.

Among the various proteins and activities detected in soybean exudates, some can be associated with the nematicidal activity against *M. incognita*, such as the papain inhibitor, which could have impaired the growth rate and fecundity of the nematode. For example, transgenic tomato overexpressing a gene that encodes for the *Colocasia esculenta* cysteine proteinase inhibitor exhibited enhanced resistance to *M. incognita* infection by means of a diminished gall number, decreased proportion of female nematodes, and reduced egg masses.[44] These effects appear to be related, at least in part, to the inhibition of the cysteine proteinase activity present in the nematode intestine.[7] In addition, the hydrolytic enzymes chitinase and protease could have also contributed to the nematicidal activity of the exudates because the *M. incognita* egg shell contains chitin and proteins.[1] This supposition in reinforced by the observation that only 30% of the eggs from transgenic tomato expressing a novel chitinase gene (PjCHI-1) were able to develop to the multi-cell/J1 stage compared to more than 96% from control plants.[45]

Lectin could also be involved in the deleterious activity of the seed exudates against root-knot nematodes. The hemagglutinating properties of lectins have been associated with the protection of plants against roundworms, because these molecules have been shown to impede the penetration of the roots by nematodes, resulting in a reduction in gall development.[46] For example, it has been reported that soybean agglutinin (SBA) interacts with amphids (sensory structures located in the nematode head region) and secretions from J2s, lowering the motility of this parasite and affecting its ability to locate the plant.[47]

In addition, because peroxidase and lipoxygenase are associated with plant responses to pathogens, these proteins may have collaborated with the nematicidal activity of soybean exudates.[26,48] For instance, lipoxygenase activity has been shown to increase in soybean roots upon infection with cyst nematodes.[49]

Taken together, our data indicate that the selective secretion of proteins by soybean seeds may contribute to the defense mechanisms against *M. incognita*. In this context, the present data bring new contributions to the understanding of the physiological role of exuded proteins in the plant defense against soil pathogens and, particularly, against parasite nematodes.

AUTHOR INFORMATION

Corresponding Author

*Telephone: +55-85-3366-9822. Fax: +55-85-3366-9139. E-mail: imvasco@ufc.br.

Notes

The authors declare no competing financial interest.

ACKNOWLEDGMENTS

The authors thank Dr. Sérgio Dotto for assistance with soybean seeds.

REFERENCES

(1) McCarter, J. P. Molecular approaches toward resistance to plant parasitic nematodes. In *Cell Biology of Plant Nematode Parasitism*; Berg, R. H., Taylor, C. G., Eds.; Springer-Verlag Press: Berlin, Germany, 2009; Plant Cell Monographs, Vol. *15*, pp 83−113.

(2) Sasser, N. J. Worldwide dissemination and importance of the root-knot nematodes *Meloidogine* spp. *J. Nematol.* **1977**, *9*, 26−29.

(3) Caillaud, M. C.; Dubreuil, G.; Quentin, M.; Perfus-Barbeoch, L.; Lecomte, P.; de Almeida-Engler, J.; Abad, P.; Rosso, M. N.; Favery, B. Root-knot nematodes manipulates plant cell functions during compatible interaction. *J. Plant Physiol.* **2008**, *165*, 104−113.

(4) Williamson, V. M.; Hussey, R. S. Nematode pathogenesis and resistance in plants. *Plant Cell* **1996**, *8*, 1735−1745.

(5) Noling, J. W.; Becker, J. O. The challenge of research and extension to define and implement alternatives to methyl bromide. *J. Nematol.* **1994**, *26*, 573−586.

DOI: 10.1021/acs.jafc.5b01109
J. Agric. Food Chem. 2015, 63, 5335−5343

(6) Papolu, P. K.; Gantasala, N. P.; Kamaraju, D.; Banakar, P.; Sreevathsa, R.; Rao, U. Utility of host delivered RNAi of two FMRF amide like peptides, *flp-14* and *flp-18*, for the management of root knot nematode, *Meloidogyne incognita*. *PLoS One* **2013**, *8*, No. e80603.
(7) Andrade, L. B. S.; Oliveira, A. S.; Ribeiro, J. K. C.; Kiyota, S.; Vasconcelos, I. M.; Oliveira, J. T. A.; Sales, M. P. Effects of a novel pathogenesis-related class 10 (PR-10) protein from *Crotalaria pallida* roots with papain inhibitory activity against root-knot nematode *Meloidogyne incognita*. *J. Agric. Food Chem.* **2010**, *58*, 4145−4152.
(8) Nelson, E. B. Exudate molecules initiating fungal responses to seed and roots. *Plant Soil* **1990**, *129*, 61−73.
(9) Scarafoni, A.; Ronchi, A.; Prinsi, B.; Espen, L.; Assante, G.; Venturini, G.; Duranti, M. The proteome of exudates from germinating *Lupinus albus* seeds is secreted through a selective dual-step process and contains proteins involved in plant defence. *FEBS J.* **2013**, *280*, 1443−1459.
(10) Morais, J. K. S.; Gomes, V. M.; Oliveira, J. T. A.; Santos, I. S.; Da Cunha, M.; Oliveira, H. D.; Oliveira, H. P.; Sousa, D. O. B.; Vasconcelos, I. M. Soybean toxin (SBTX), a protein from soybeans that inhibits the life cycle of plant and human pathogenic fungi. *J. Agric. Food Chem.* **2010**, *58*, 10356−10363.
(11) Jolliffe, N. A.; Craddock, C. P.; Frigerio, L. Pathways for protein transport to seed storage vacuoles. *Biochem. Soc. Trans.* **2005**, *33*, 1016−1018.
(12) Palavalli, M. H.; Natarajan, S. S.; Wang, T. T.; Krishnan, H. B. Imbibition of soybean seeds in warm water results in the release of copious amounts of Bowman−Birk protease inhibitor, a putative anticarcinogenic agent. *J. Agric. Food Chem.* **2012**, *60*, 3135−3143.
(13) Pro-Seed Foundation. *Licensing of Soybean Cultivars*; http://www.fundacaoprosementes.com.br/cultivares/soja (accessed Sept 27, 2010).
(14) Bradford, M. M. A rapid and sensitive method for the quantification of microgram quantities for proteins utilizing the principle of protein-dye binding. *Anal. Biochem.* **1976**, *72*, 248−254.
(15) Matos, F. J. A. *Introdução à Fitoquímica Experimental (Introduction to Experimental Phytochemistry)*, 2nd ed.; EUFC: Fortaleza, Brazil, 1999.
(16) Laemmli, U. K. Cleavage of structural proteins during the assembly of the bacteriophage T4. *Nature* **1970**, *227*, 680−685.
(17) Candiano, G.; Bruschi, M.; Musante, L.; Santucci, L.; Ghiggeri, G. M.; Carnemolla, B.; Orecchia, P.; Zardi, L.; Righetti, P. G. Blue silver: A very sensitive colloidal Coomassie G-250 staining for proteome analysis. *Electrophoresis* **2004**, *25*, 1327−1333.
(18) Mississippi State University. *AgBase Version 2.00*; http://www.agbase.msstate.edu/cgi-bin/tools/goslimviewer_select.pl (accessed Dec 12, 2014).
(19) Emanuelsson, O.; Nielsen, H.; Brunak, S.; von Heijne, G. Predicting subcellular localization of proteins based on their N-terminal amino acid sequence. *J. Mol. Biol.* **2000**, *300*, 1005−1016.
(20) Bannai, H.; Tamada, Y.; Maruyama, O.; Nakai, K.; Miyano, S. Extensive feature detection of N-terminal protein sorting signals. *Bioinformatics* **2002**, *18*, 298−305.
(21) Bendtsen, J. D.; Nielsen, H.; von Heijne, G.; Brunak, S. Improved prediction of signal peptides: SignalP 3.0. *J. Mol. Biol.* **2004**, *340*, 783−795.
(22) Bendtsen, J. D.; Jensen, J.; Blom, N.; von Heijne, G.; Brunak, S. Feature based prediction of a non-classical and leaderless protein secretion. *Protein Eng., Des. Sel.* **2004**, *17*, 349−356.
(23) Boller, T. Biochemical analysis of chitinase and β-1,3-glucanases. In *Molecular Plant Pathology: A Practical Approach*; Gurr, S. J., McPherson, M. J., Bowles, D. J., Eds.; Oxford University Press: New York, 1992; Vol. *II*, pp 23−30.
(24) Reissig, J. L.; Strominger, J. L.; Leloir, L. F. A modified colorimetric method for the estimation of *N*-acetylamino sugars. *J. Biol. Chem.* **1955**, *217*, 959−966.
(25) Molano, J.; Duran, A.; Cabib, E. A. Rapid and sensitive assay for chitinase using tritiated chitin. *Anal. Biochem.* **1977**, *83*, 648−656.
(26) Urbanek, H.; Kuzniak-Gebarowska, E.; Herka, H. Elicitation of defense responses in bean leaves by *Botrytis cinerea* polygalacturonase. *Acta Physiol. Plant.* **1991**, *13*, 43−50.
(27) Xavier-Filho, J.; Campos, F. A. P.; Ary, M. B.; Silva, C. P.; Carvalho, M. M. M.; Macedo, M. L. R.; Lemos, F. J. A.; Grant, G. Poor correlation between the levels of proteinase inhibitors found in seeds of different cultivars of cowpea (*Vigna unguiculata*) and the resistance/susceptibility to predation by *Callosobruchus maculatus*. *J. Agric. Food Chem.* **1989**, *37*, 1139−1143.
(28) Kakade, M. L.; Simons, N.; Liener, I. E. An evaluation of natural vs. synthetic substrates for measuring the antitryptic activity of soybean sample. *Cereal Chem.* **1969**, *46*, 518−526.
(29) Hamerstrand, G. E.; Black, L. T.; Glover, J. D. Trypsin inhibitor in soy products: Modification of the standard analysis procedure. *Cereal Chem.* **1981**, *58*, 42−45.
(30) Abe, M.; Abe, K.; Kuroda, M.; Arai, S. Corn kernel cysteine proteinase inhibitor as a novel superfamily member of plant origin. Molecular cloning and expression studies. *Eur. J. Biochem.* **1992**, *209*, 933−937.
(31) Moreira, R. A.; Perrone, J. C. Purification and partial characterization of a lectin from *Phaseolus vulgaris*. *Plant Physiol.* **1977**, *59*, 783−787.
(32) Lis, H.; Sharon, N. Soybean (*Glycine max*) agglutinin. *Methods Enzymol.* **1972**, *28*, 360−368.
(33) Hussey, R. S.; Barker, K. R. A comparison of methods of collecting inocula of *Meloidogyne* spp., including a new technique. *Plant Dis. Rep.* **1973**, *57*, 1025−1028.
(34) Wang, C.; Lower, S.; Williamson, V. M. Application of pluronic gel to the study of root-knot nematode behaviour. *Nematology* **2009**, *11*, 453−464.
(35) Campos, H. D.; Campos, V. P.; Coimbra, J. L. Effect of root exudate of *Brachiaria decumbens* and sorgoleone of *Sorghum bicolor* on development of *Meloidogyne javanica*. *Nematol. Bras.* **2006**, *30*, 59−65.
(36) Nelson, E. B. Microbial dynamics and interactions in the spermosphere. *Annu. Rev. Phytopathol.* **2004**, *42*, 271−309.
(37) Terras, F. R. G.; Eggermont, K.; Kovaleva, V.; Raikhel, N. V.; Osborn, R. W.; Kester, A.; Rees, S. B.; Torrekens, S.; Van Leuven, F.; Vanderleyden, J.; Cammue, B. P.A.; Broekaert, W. F. Small cysteine-rich antifungal proteins from radish: Their role in host defense. *Plant Cell* **1995**, *7*, 573−588.
(38) Sitohy, M. Z.; Mahgoub, S. A.; Osman, A. O. *In vitro* and *in situ* antimicrobial action and mechanism of glycinin and its basic subunit. *Int. J. Food Microbiol.* **2012**, *154*, 19−29.
(39) Porta, H.; Rocha-Sosa, M. Plant lipoxygenases, physiological and molecular features. *Plant Physiol.* **2002**, *130*, 15−21.
(40) Cândido, E. S.; Pinto, M. F.; Pelegrini, P. B.; Lima, T. B.; Silva, O. N.; Pogue, R.; Grossi-de-Sá, M. F.; Franco, O. L. Plant storage proteins with antimicrobial activity: Novel insights into plant defense mechanisms. *FASEB J.* **2011**, *25*, 3290−3305.
(41) Cheng, F.; Williamson, J. D. Is there leaderless protein secretion in plants? *Plant Signaling Behav.* **2010**, *5*, 129−131.
(42) Delaunois, B.; Jeandet, P.; Clément, C.; Baillieul, F.; Dorey, S.; Cordelier, S. Uncovering plant−pathogen crosstalk through apoplastic proteomic studies. *Front. Plant Sci.* **2014**, *5*, 249.
(43) Migliolo, L.; Oliveira, A. S.; Santos, E. A.; Franco, O. L.; Sales, M. P. Structural and mechanistic insights into a novel non-competitive Kunitz trypsin inhibitor from *Adenanthera pavonina* L. seeds with double activity toward serine- and cysteine-proteinases. *J. Mol. Graphics Modell.* **2010**, *29*, 148−156.
(44) Chan, Y.-L.; Yang, A.-H.; Chen, J.-T.; Yeh, K.-W.; Chan, M.-T. Heterologous expression of taro cystatin protects transgenic tomato against *Meloidogyne incognita* infection by means of interfering sex determination and suppressing gall formation. *Plant Cell Rep.* **2010**, *29*, 231−238.
(45) Chan, Y.-L.; Cai, D.; Taylor, P. W. J.; Chan, M.-T.; Yeh, K. W. Adverse effect of the chitinolytic enzyme PjCHI-1 in transgenic tomato on egg mass production and embryonic development of *Meloidogyne incognita*. *Plant Pathol.* **2010**, *59*, 922−930.

DOI: 10.1021/acs.jafc.5b01109
J. Agric. Food Chem. 2015, 63, 5335−5343

(46) Marban-Mendonza, N.; Jeyaprakash, A.; Janson, H. B.; Damon, R. A., Jr.; Zuckerman, B. M. Control of root-knot nematodes on tomato by lectins. *J. Nematol.* **1987**, *19*, 31−335.
(47) McClure, M. A.; Stynes, B. S. Lectin binding sites on the amphidial exudates of *Meloidogyne*. *J. Nematol.* **1988**, *20*, 321−326.
(48) Loiseau, J.; Vu, B. L.; Macherel, M.-H.; Le Deunff, Y. Seed lipoxygenases: Occurrence and functions. *Seed Sci. Res.* **2001**, *11*, 199−211.
(49) Alkharouf, N. W.; Klink, V. P.; Chouikha, I. B.; Beard, H. S.; MacDonald, M. H.; Meyer, S.; Knap, H. T.; Khan, R.; Matthews, B. F. Timecourse microarray analyses reveal global changes in gene expression of susceptible *Glycine max* (soybean) roots during infection by *Heterodera glycines* (soybean cyst nematode). *Planta* **2006**, *224*, 838−852.
(50) Li, G. Z.; Vissers, J. P. C.; Silva, J. C.; Golick, D.; Gorenstein, M. V.; Geromanos, S. J. Database searching and accounting of multiplexed precursor and product ion spectra from the data independent analysis of simple and complex peptide mixtures. *Proteomics* **2009**, *9*, 1696−1719.

DOI: 10.1021/acs.jafc.5b01109
J. Agric. Food Chem. 2015, 63, 5335−5343

JOURNAL OF AGRICULTURAL AND FOOD CHEMISTRY

Article

pubs.acs.org/JAFC

Synergistic Effects of [Ile^7]Surfactin Homologues with Bacillomycin D in Suppression of Gray Mold Disease by *Bacillus amyloliquefaciens* Biocontrol Strain SD-32

Keijitsu Tanaka,*[,†] Yusuke Amaki,[†] Atsushi Ishihara,[‡] and Hiromitsu Nakajima[‡]

[†]Tsukuba Research and Technology Center, SDS Biotech K.K., Midorigahara, Tsukuba, Ibaraki 300-2646, Japan

[‡]Department of Agricultural Chemistry, Faculty of Agriculture, Tottori University, Koyama, Tottori 680-8553, Japan

Supporting Information

ABSTRACT: We previously reported that *Bacillus amyloliquefaciens* biocontrol strain SD-32 produces powerful antifungal lipopeptides, C_{17} bacillomycin D homologues. In the course of the investigation we found that the antifungal activity of the culture supernatant of this bacterium was not ascribed exclusively to bacillomycin D. We attempted to identify metabolites other than bacillomycin D to gain insight into the mechanism for the biocontrol by this bacterium. After purifying the fractions of the culture supernatant exhibiting synergistic activity with bacillomycin D, we isolated two new cyclic lipodepsipeptides, *anteiso*-C_{13} and *iso*-C_{13} [Ile^7]surfactins, together with three known [Ile^7]surfactins. Interestingly, [Ile^7]surfactins showed synergistic activities with bacillomycin D to gray mold disease on cucumber leaves but not to *Botrytis cinerea* itself in vitro, suggesting that the synergistic effects might be on infection processes of the fungus. Actually, we observed that they did not show synergistic actions on conidial germination or mycelial growth of *B. cinerea* on the leaves.

KEYWORDS: *Bacillus amyloliquefaciens, Botrytis cinerea, biological control, lipodepsipeptide, surfactin, [Ile^7]surfactin, lipopeptide, bacillomycin D*

INTRODUCTION

Plant pathogenic fungi exhibit a remarkable ability to change and adapt: fungicide-resistant pathogenic strains continually arise and can no longer be controlled by chemicals that were once effective.[1,2] For example, *Botrytis cinerea* Pers., a plant pathogenic fungus, frequently exhibits resistance to, at least, one fungicide or, in the case of many isolates, multiple fungicides.[3] As a result, it is necessary to continue developing novel and effective fungicidal chemicals for control of plant diseases.

Because of the rapid emergence of fungicide resistance and the high cost of discovering, developing, and registering new chemical fungicides, biological control agents (BCAs) have been attracting considerable attention.[4] In fact, many BCA formulations are already available for practical use.[5] Among them, *Bacillus* species-based BCAs are considered to have promising potential due to their safety, ubiquity in nature, and exhibition of high thermal tolerance through the formation of resistant spores. Biological control by *Bacillus* sp. involves a number of mechanisms, such as competitions for space and nutrition, antagonism, and systemic resistance induction. Many strains of *Bacillus* species have been reported to secrete several antimicrobial metabolites.[6] Among these antimicrobial compounds, cyclic lipopeptides (iturins) and cyclic lipodepsipeptides (surfactins and fengycins or plipastatins) have received much attention as key compounds in BCAs because they play an important role in colonization on the plant, show potent activities against a wide variety of microorganisms, and induce plant systemic resistance.[7] Their roles in each biological control system, however, remain to be fully elucidated.

In our previous paper,[8] we reported that *Bacillus amyloliquefaciens* SD-32 was isolated from a soil sample obtained in Japan as a promising and effective agent against gray mold disease, and two new compounds, *anteiso*- and *iso*-C_{17} bacillomycin D, were found in its fermentation broth. Strain SD-32 is quite different from other strains previously reported because it produces C_{17} bacillomycin D homologues as major metabolites. We also showed that the activities of C_{17} bacillomycin D homologues against *B. cinerea* were stronger than those of the known C_{15} and C_{16} homologues both in vitro and in vivo. These data indicate that the strain is a potentially promising resource for the biological control of gray mold disease, and indeed, the culture supernatant of this strain possesses a strong suppressive effect on gray mold disease in vivo. However, we also found that bacillomycin D homologues did not account for all of the activity in the culture supernatant of this strain, suggesting that other factors effective against gray mold disease were also present. The identification of all factors in SD-32 that are effective in controlling gray mold disease could contribute to an understanding of the molecular basis of this biological control system.

To gain insight into the mechanisms responsible for the biological control by *B. amyloliquefaciens* strain SD-32, we attempted in this study to identify the factors that contribute to control gray mold disease, other than bacillomycin D produced by the bacterium, and to clarify the role of these factors in the

Received: March 8, 2015
Revised: May 13, 2015
Accepted: May 15, 2015
Published: May 15, 2015

ACS Publications © 2015 American Chemical Society

DOI: 10.1021/acs.jafc.5b01198
J. Agric. Food Chem. 2015, 63, 5344−5353

biological control system. In the course of purifying the fractions exhibiting synergistic activity with bacillomycin D, two new cyclic lipodepsipeptides (**1** and **2**) were found in the culture supernatant of this strain, together with three known metabolites, *iso*-C_{14}, *anteiso*-C_{15}, and *iso*-C_{15} [Ile^7]surfactins (**3**, **4**, and **5**). Spectroscopic and chemical analyses identified the structures of new compounds **1** and **2** as *anteiso*-C_{13} [Ile^7]surfactin, cyclo[(3*R*)-3-(L-Glu-L-Leu-D-Leu-L-Val-L-Asp-D-Leu-L-Ile-*O*)-10-methyldodecanoyl], and *iso*-C_{13} [Ile^7]surfactin, cyclo[(*R*)-3-(L-Glu-L-Leu-D-Leu-L-Val-L-Asp-D-Leu-L-Ile-*O*)-11-methyldodecanoyl], respectively (Figure 1). Finally, the synergistic effects of compounds **1**−**5** with bacillomycin D in the suppression of gray mold disease were evaluated using an in vivo cucumber leaf-disk assay.

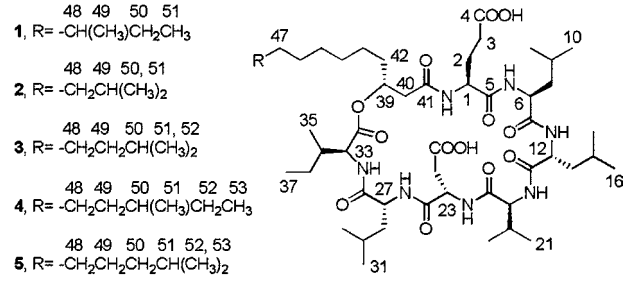

Figure 1. Structures of compounds **1**−**5**.

MATERIALS AND METHODS

General Experimental Procedures. The solvents and reagents used in this study were purchased from Sigma-Aldrich (St. Louis, MO, USA) unless otherwise noted. NMR spectra were measured with Bruker Avance II 600 and Bruker Ascend 400 systems (Bruker Daltonics, Billerica, MA, USA). The spectra for compounds **1**−**5** were acquired in DMSO-d_6 (δ_H 2.49; δ_C 39.5) at room temperature. HR-FAB-MS was obtained with a JEOL JMS-700 spectrometer (JEOL, Tokyo, Japan). Preparative HPLC and HPLC analyses were performed with a Waters Alliance system (Waters, Milford, MA, USA).

Microorganisms. Isolation and identification of the *Bacillus amyloliquefaciens* strain SD-32 were described in our previous paper.[8]

Partial Purification of Factors Effective against Gray Mold Disease. Strain SD-32 was grown at 30 °C with shaking at 150 rpm for 64 h in a 500 mL flask containing 50 mL of liquid medium, composed of maltose (80 g/L), soybean powder (80 g/L; J-OIL MILLS, Tokyo, Japan), yeast extract (10 g/L; Becton, Dickinson and Co., Franklin Lakes, NJ, USA), $MgSO_4{\cdot}7H_2O$ (2 g/L), $CaCl_2$ (2 g/L), K_2HPO_4 (1 g/L), $FeSO_4{\cdot}7H_2O$ (0.1 g/L), $MnSO_4{\cdot}5H_2O$ (0.1 g/L), and H_2O adjusted to pH 7.0 by Na_2CO_3. The culture supernatant (44 mL) was extracted with 50 mL of EtOAc three times after adjustment of the pH (pH 4.0) with HCl. The EtOAc solution was dried over anhydrous Na_2SO_4 and concentrated in vacuo. The dry extract was dissolved in H_2O, and the pH of the solution was adjusted to 7.0. The solution was purified with solid-phase extraction (C18-SPE, Oasis HLB 6g/35 cc LP Extraction Cartridge; Waters) eluted stepwise with 50 mL each of 0, 20, 40, 60, 80, and 100% (v/v) CH_3CN/H_2O containing 0.1% TFA. Each fraction was evaporated in vacuo. The residues of each fraction were dissolved in 40 mL of phosphate buffer (40 mM, pH 7.2), and each solution was evaluated in an in vivo cucumber leaf-disk assay.

HPLC Analyses of Culture Supernatant and C18-SPE Fractions. The amount of bacillomycin D in culture supernatant was determined by HPLC (XBridge C18, 250 × 4.6 mm; Waters), eluted with a linear gradient from 20 to 100% (v/v) CH_3CN/H_2O containing 0.1% TFA for 20 min at a flow rate of 1.0 mL/min at 40 °C, and detected by absorbance at 205 nm. The purified *anteiso*-C_{17} bacillomycin D was used as standard bacillomycin D.[8] The C18-SPE fractions were analyzed under the same condition.

Isolation of Compounds 1−5. Strain SD-32 was grown at 30 °C with shaking at 150 rpm for 64 h in 500 mL flasks containing medium, which was the same as the case of partial purification (50 mL/flask, 1.6 L in total). The metabolites were extracted from the culture supernatant (1.5 L) with 2 L of EtOAc three times after adjustment of the pH (pH 4.0) with HCl. The EtOAc solution was dried over anhydrous Na_2SO_4 and concentrated to dryness to afford a crude extract (4.6 g). This extract was dissolved in H_2O, and the pH of the solution was adjusted to 7.0. The solution was purified by SPE (C18-SPE, Oasis HLB 6g/35 cc LP extraction cartridge) eluted stepwise with 50 mL each of 0, 20, 40, 60, 70, 80, 90, and 100% (v/v) CH_3CN/H_2O containing 0.1% TFA. The fractions eluted with 70−80% CH_3CN/H_2O were combined and concentrated to dryness to afford a residue (0.35 g). The residue was further purified by preparative HPLC (XBridge C18, 250 × 10 mm), eluted with 70% (v/v) CH_3CN/H_2O containing 0.1% TFA at a flow rate of 4.7 mL/min at 40 °C, and detected by absorbance at 205 nm to afford the active compounds **1** (17 mg), **2** (16 mg), **3** (79 mg), **4** (15 mg), and **5** (10 mg). The purified compounds **1**−**5** were analyzed by HPLC (XBridge C18, 250 × 4.6 mm), eluted with 70% (v/v) CH_3CN/H_2O containing 0.1% TFA at a flow rate of 1.0 mL/min at 40 °C, and detected by absorbance at 205 nm.

Amino Acid Analysis. Amino acid analysis of compound **3** was conducted according to the method described in our previous paper.[8]

Matrix-Associated Laser Desorption Ionization Time of Flight (MALDI-TOF) MS/MS Analysis. MALDI-TOF MS/MS analysis of compound **3** was performed according to the method described in our previous paper.[8]

Determination of Lactone Linkage. Determination of the lactone linkage position in compound **3** was conducted according to the method reported by Naruse et al.[9] Compound **3** (10 mg) was treated with $LiBH_4$ (50 mg) in dry THF (5 mL) under reflux for 6 h. The reaction mixture was diluted with H_2O and extracted with EtOAc at pH 2.0. The extract was dried with N_2 and hydrolyzed with 6 N HCl at 110 °C for 20 h. Amino acids in the hydrolysate were analyzed according to the method described in our previous paper.[8]

Absolute Configuration of α-Amino Acids. Absolute configurations of the α-amino acids, except for the three Leu residues, of compound **3** were determined according to Marfey's method.[10] The experimental details were described in our previous paper.[8]

To determine the absolute configurations of Leu^2 and Leu^3, four tripeptides, NH_2-L-Leu-L-Leu-L-Val, NH_2-D-Leu-D-Leu-L-Val, NH_2-D-Leu-L-Leu-L-Val, and NH_2-L-Leu-D-Leu-L-Val, were used as standard peptides (Sigma-Aldrich). Compound **3** (3 mg) was hydrolyzed in 0.5 mL of 12 N HCl/AcOH (2:1, v/v) at 60 °C for 6 h and then dried with N_2. To the hydrolysate was added 150 μL of 25% (v/v) CH_3CN/H_2O, and then the solution was analyzed by LC-MS system (Prominence HPLC system, Shimadzu Corp., Tokyo, Japan; and 3200 QTRAP, AB SCIEX, Framingham, MA, USA) equipped with a reverse-phase column (Zorbax Extend C18, 150 × 2.1 mm; Agilent Technologies, Santa Clara, CA, USA), eluted with a linear gradient of 10−30% (v/v) CH_3CN/H_2O containing 0.1% formic acid in 30 min at a flow rate of 0.2 mL/min and 30 °C. Four standard tripeptides, NH_2-L-Leu-L-Leu-L-Val, NH_2-D-Leu-D-Leu-L-Val, NH_2-D-Leu-L-Leu-L-Val, and NH_2-L-Leu-D-Leu-L-Val, were eluted at 11.4, 15.5, 16.9, and 23.0 min, respectively.

To determine the absolute configuration of Leu^6, two tripeptides, NH_2-L-Asp-L-Leu-L-Ile and NH_2-L-Asp-D-Leu-L-Ile, were used as standard peptides (Sigma-Aldrich). The hydrolysate solution of compound **3** described above was analyzed by LC-MS system (Prominence HPLC system and 3200 QTRAP) equipped with a reverse-phase column (Zorbax Extend C18, 150 × 2.1 mm) and eluted with a linear gradient of 5−95% (v/v) CH_3CN/H_2O containing 0.1% formic acid in 30 min at a flow rate of 0.2 mL/min and 30 °C. Two standard tripeptides, NH_2-L-Asp-L-Leu-L-Ile and NH_2-L-Asp-D-Leu-L-Ile, were eluted at 10.4 and 11.9 min, respectively.

Absolute Configuration of the 3-Hydroxy Fatty Acid. Mosher's method was used to determine the absolute stereochemistry

DOI: 10.1021/acs.jafc.5b01198
J. Agric. Food Chem. 2015, 63, 5344−5353

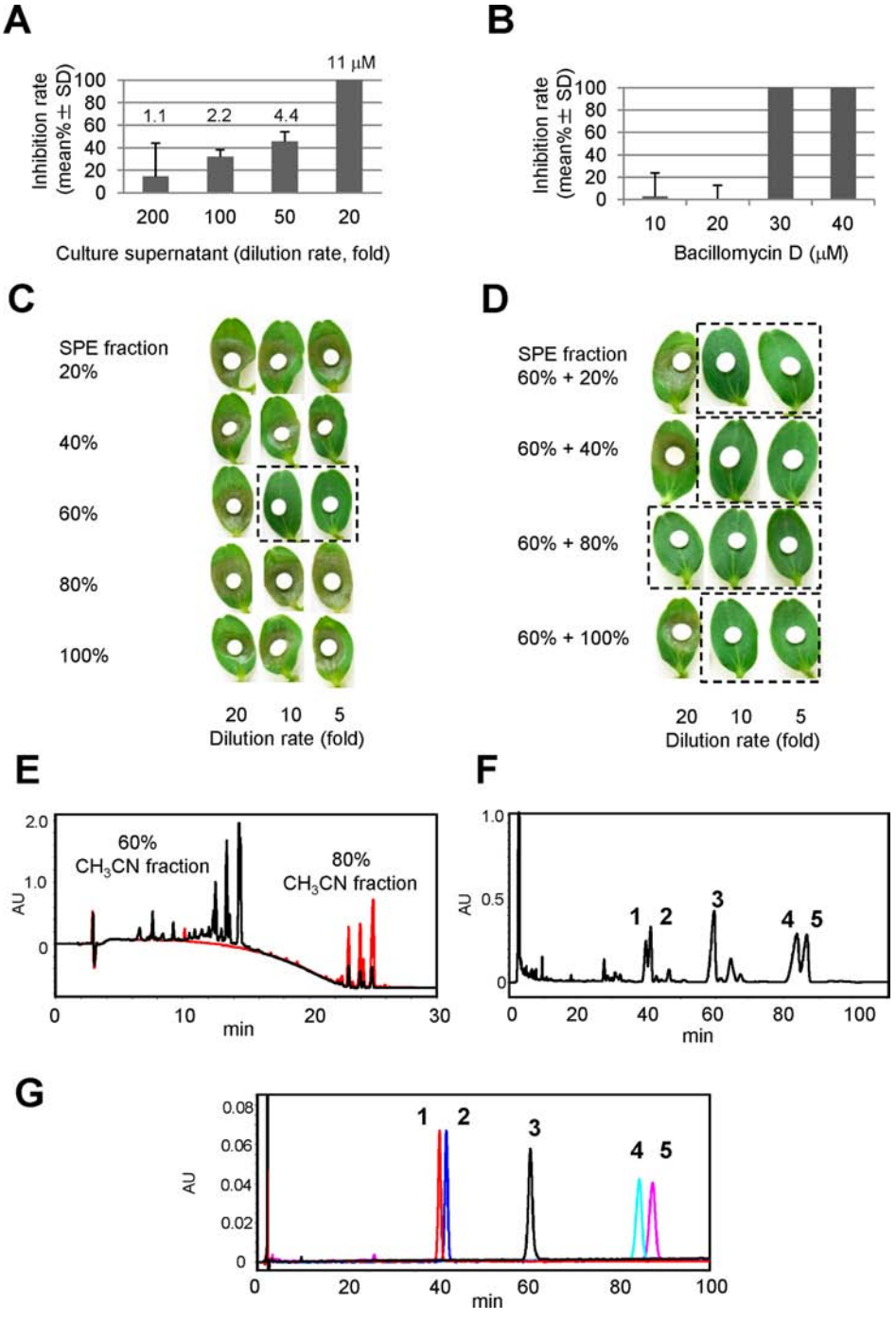

Figure 2. In vivo cucumber leaf-disk assay of the culture supernatant and C18-SPE (Oasis HLB) fractions and HPLC of the metabolites. (A) In vivo cucumber leaf-disk assay of the culture supernatant (n = 4). The values above each bar indicate the bacillomycin D concentrations. (B) In vivo cucumber leaf-disk assay of the purified *anteiso*-C_{17} bacillomycin D (n = 4). (C) In vivo cucumber leaf-disk assay of the SPE fractions. Gray mold disease was completely inhibited on the leaves in the dashed box. (D) In vivo cucumber leaf-disk assay of the SPE fractions combined with a 60% CH_3CN fraction. (E) HPLC analyses of the fractions obtained from partial purification. Chromatograms of the 60 and 80% CH_3CN fractions were overlaid: black line, 60% CH_3CN fraction containing bacillomycin D; red line, 80% CH_3CN fraction containing unknown metabolites. (F) Elution profile at the final HPLC purification step of compounds **1**−**5**. Each peak was fractionated, pooled, and then freeze-dried. (G) HPLC analyses of purified compounds. Each chromatogram was overlaid: red line, compound **1** (0.4 mg/mL); blue line, **2** (0.4 mg/mL); black line, **3** (0.5 mg/mL); sky blue line, **4** (0.5 mg/mL); purple line, **5** (0.5 mg/mL).

of the 3-hydroxy fatty acid residue.[11,12] Compound **3** (10 mg) was hydrolyzed in 1.0 mL of 6 N HCl at 110 °C for 15 h. The hydrolysate was diluted with 5 mL of H_2O, extracted with 5 mL of $CHCl_3$ three times, and dried by N_2. The residue was dissolved with 1 mL of CH_2Cl_2/MeOH (3:1, v/v) and then 0.1 mL of TMS−diazomethane (Tokyo Chemical Industry Co., Ltd., Tokyo, Japan) was added to the solution. The solution was allowed to stand at room temperature for 30 min, and the reaction was terminated by the addition of 10% acetic acid in MeOH. The solution was dried by N_2, and the residue was dissolved in 0.5 mL of dry CH_2Cl_2 and mixed with 5.0 mg of (dimethylamino)pyridine, 2.8 μL of triethylamine, and 3.8 μL of (+)-MTPA chloride (Tokyo Chemical Industry). The solution was

DOI: 10.1021/acs.jafc.5b01198
J. Agric. Food Chem. 2015, 63, 5344−5353

Table 1. ^{1}H NMR Data for Compounds 1−5 in DMSO-d_6[a]

		δ_H (J in Hz)				
moiety	position	1	2	3	4	5
L-Glu	1	4.18m[b]	4.18m[b]	4.18m[b]	4.18m[b]	4.18m[b]
	2	1.92m[c], 1.77m[d]	1.92m[c], 1.76m[d]	1.91m[c], 1.76m	1.91m[c], 1.76m[d]	1.91m[c], 1.76m[d]
	3	2.19m	2.17m	2.19m	2.19m	2.19m
	1-NH	7.84d (6.2)	7.84d (6.4)	7.84d (6.5)	7.84d (6.6)	7.83d (6.6)
L-Leu[2]	6	4.15m[b]	4.15m[b]	4.16m[b]	4.15m[b]	4.15m[b]
	7	1.53m[e]	1.53m[e]	1.53m[d]	1.53m[e]	1.53m[e]
	8	1.50m[e]	1.50m[e]	1.50m[d]	1.50m[e]	1.50m[e]
	9	0.86m	0.86m	0.86m	0.86m	0.86m
	10	0.86m	0.86m	0.86m	0.86m	0.86m
	6-NH	8.00d (5.1)	8.03d (5.3)	8.04d (5.2)	8.03d (5.6)	8.02d (5.4)
D-Leu[3]	12	4.17m[b]	4.16m[b]	4.17m[b]	4.16m[b]	4.17m[b]
	13	1.53m[e]	1.53m[e]	1.53m[d]	1.53m[e]	1.53m[e]
	14	1.50m[e]	1.53m[e]	1.50m[d]	1.50m[e]	1.50m[e]
	15	0.81m[f]	0.82d[f] (6.5)	0.83d[e] (6.5)	0.81m[f]	0.83d[f] (6.6)
	16	0.81m[f]	0.82d[f] (6.5)	0.83d[e] (6.5)	0.81m[f]	0.83d[f] (6.6)
	12-NH	8.29d (7.0)	8.32d (7.0)	8.34d (7.1)	8.32d (7.1)	8.31d (7.3)
L-Val	18	4.07m	4.07m	4.08m	4.07m	4.08m
	19	1.95m[c]	1.95m[c]	1.93m[c]	1.93m[c]	1.94m[c]
	20	0.81m[f]	0.82d[f] (6.5)	0.83d[e] (6.5)	0.81m[f]	0.83d[f] (6.6)
	21	0.75d (6.5)	0.74d (6.5)	0.75d (6.6)	0.74d (6.4)	0.75d (6.6)
	18-NH	7.73d (8.5)	7.75d (8.4)	7.76d (8.3)	7.75d (8.3)	7.75d (8.5)
L-Asp	23	4.49m[g]	4.50m[g]	4.52m[f]	4.50m[g]	4.50m[g]
	24	2.68dd (16.4, 4.3), 2.57dd (16.4, 8.7)	2.68dd (16.6, 4.3), 2.57dd (16.6, 8.7)	2.68dd (16.6, 4.6), 2.58dd (16.6, 8.9)	2.68dd (16.5, 4.2), 2.57dd (16.5, 8.7)	2.69dd (16.6, 4.7), 2.57dd (16.6, 8.6)
	23-NH	8.17d (7.1)	8.18d (7.2)	8.18d (7.1)	8.18d (7.2)	8.17d (7.2)
D-Leu[6]	27	4.51m[g]	4.51m[g]	4.53m[f]	4.51m[g]	4.52m[g]
	28	1.41m[h], 1.38m[h]	1.41m[h], 1.37m[h]	1.43m[g], 1.38m	1.43m[h], 1.38m[h]	1.44m[h], 1.39m[h]
	29	1.50m[e]	1.50m[e]	1.50m[d]	1.50m[e]	1.50m[e]
	30	0.81m[f]	0.82d[f] (6.5)	0.83d[e] (6.5)	0.81m[f]	0.83d[f] (6.6)
	31	0.81m[f]	0.82d[f] (6.5)	0.83d[e] (6.5)	0.81m[f]	0.83d[f] (6.6)
	27-NH	7.66d (8.4)	7.67d (8.5)	7.68d (8.5)	7.67d (8.3)	7.67d (8.5)
L-Ile	33	4.15m[b]	4.15m[b]	4.16m[b]	4.15m[b]	4.15m[b]
	34	1.79m[d]	1.80m[d]	1.81m	1.80m[d]	1.81m[d]
	35	0.81m[f]	0.82d[f] (6.5)	0.83d[e] (6.5)	0.81m[f]	0.83d[f] (6.6)
	36	1.31m, 1.20m[i]	1.31m, 1.20m[i]	1.32m, 1.20m[h]	1.31m, 1.20m[i]	1.32m, 1.20m[i]
	37	0.78m[f]	0.78m[f]	0.79m	0.78m[f]	0.79m[f]
	33-NH	8.23d (7.8)	8.25d (7.8)	8.27d (7.9)	8.25d (7.8)	8.24d (8.0)
(*R*)-3-OH-FA	39	4.98m	4.98m	4.98m	4.98m	4.98m
	40	2.41m	2.40m	2.40m	2.40m	2.41m
	42	1.55m[e]	1.53m[e]	1.56m[d]	1.56m[e]	1.54m[e]
	43	1.20m[i]	1.20m[i]	1.20m[h]	1.20m[i]	1.20m[i]
	44	1.20m[i]	1.20m[i]	1.20m[h]	1.20m[i]	1.20m[i]
	45	1.20m[i]	1.20m[i]	1.20m[h]	1.20m[i]	1.20m[i]
	46	1.20m[i]	1.20m[i]	1.20m[h]	1.20m[i]	1.20m[i]
	47	1.23m[i], 1.07m	1.20m[i]	1.20m[h]	1.20m[i]	1.20m[i]
	48	1.23m[i]	1.11m	1.20m[h]	1.20m[i]	1.20m[i]
	49	0.81m[f]	1.44m[h]	1.11m	1.24m[i], 1.08m	1.20m[i]
	50	1.23m[i]	0.82d[f] (6.5)	1.43m[g]	1.24m[i]	1.11m
	51	0.81m[f]	0.82d[f] (6.5)	0.83d[e] (6.5)	0.81m[f]	1.43m[h]
	52			0.83d[e] (6.5)	1.24m[i]	0.83d[f] (6.6)
	53				0.81m[f]	0.83d[f] (6.6)

[a]Compound **3**, 600 MHz; **1**, **2**, **4**, and **5**, 400 MHz. Superscripts b−i indicate overlapping in each column.

DOI: 10.1021/acs.jafc.5b01198
J. Agric. Food Chem. 2015, 63, 5344−5353

Table 2. ^{13}C NMR Chemical Shifts of Compounds 1−5 in DMSO-d_6[a]

moiety	position	δ_C 1	2	3	4	5
L-Glu	1	52.1	52.1	52.1	52.1	52.1
	2	27.1	27.2	27.1	27.1	27.1
	3	29.8	29.8	29.8	29.8	29.8
	4	174.0	174.0	174.1	174.0	174.0
	5	170.6	170.6	170.6	170.6	170.6
L-Leu[2]	6	51.6	51.6	51.6	51.6	51.6
	7	39.5[b]	39.5[b]	39.5[b]	39.5[b]	39.5[b]
	8	24.2[c]	24.2[c]	24.2[c]	24.2[c]	24.2[c]
	9	23.0	23.0	23.1	23.0	23.0
	10	22.9	22.9	22.9	22.9	22.9
	11	171.8	171.8	171.8	171.8	171.7
D-Leu[3]	12	51.9	51.9	51.9	51.9	51.9
	13	39.5[b]	39.5[b]	39.5[b]	39.5[b]	39.5[b]
	14	24.2[c]	24.2[c]	24.2[c]	24.2[c]	24.2[c]
	15	22.5	22.5	22.5	22.5	22.5
	16	22.1	22.1	22.1	22.1	22.1
	17	172.1[d]	172.1[d]	172.1[d]	172.1[d]	172.1[d]
L-Val	18	58.1	58.1	58.1	58.1	58.1
	19	30.5	30.5	30.5	30.5	30.5
	20	19.1	19.1	19.1	19.1	19.1
	21	18.0	18.0	18.0	17.9	17.9
	22	170.6	170.6	170.6	170.6	170.6
L-Asp	23	49.6	49.6	49.6	49.6	49.6
	24	35.9[f]	36.0	36.0	35.9[f]	36.0
	25	172.1[d]	172.1[d]	172.1[d]	172.1[d]	172.1[d]
	26	169.9	169.9	169.9	169.8	169.8
D-Leu[6]	27	50.5	50.5	50.5	50.5	50.5
	28	41.6	41.6	41.6	41.6	41.6
	29	24.1[c]	24.1[c]	24.1[c]	24.1[c]	24.1[c]
	30	21.9	21.9	21.9	21.8	21.8
	31	21.0	21.0	21.0	21.0	21.0
	32	171.6	171.6	171.6	171.6	171.6
L-Ile	33	56.5	56.5	56.5	56.5	56.5
	34	35.8	35.8	35.8	35.7	35.7
	35	15.5	15.5	15.5	15.4	15.4
	36	24.5[c]	24.5[c]	24.5[c]	24.5[c]	24.5[c]
	37	11.0	11.1	11.1	11.0	11.0
	38	171.0	171.0	171.0	171.0	171.0
(*R*)-3-OH-FA	39	71.6	71.6	71.6	71.6	71.5
	40	40.3	40.4	40.3	40.3	40.6
	41	169.4	169.4	169.4	169.4	169.4
	42	33.1	33.1	33.1	33.1	33.1
	43	24.4[c]	24.4[c]	24.4[c]	24.3[c]	24.3[c]
	44	29.2[e]	29.1[e]	29.3[e]	29.3[e]	29.2[e]
	45	28.9[e]	28.8[e]	28.9[e]	28.9[e]	29.0[e]
	46	28.6[e]	28.5[e]	28.8[e]	28.8[e]	28.8[e]
	47	35.9[f]	26.7	28.5[e]	28.8[e]	28.8[e]
	48	33.7	38.4	26.7	28.5[e]	28.5[e]
	49	19.0	27.3	38.4	35.9[f]	26.7
	50	26.3	22.5[f]	27.4	33.7	38.4
	51	11.2	22.5[f]	22.5[f]	19.0	27.3
	52			22.5[f]	26.4	22.4[f]
	53				11.1	22.4[f]

[a]Compound **3**, 150 MHz; **1**, **2**, **4**, and **5**, 100 MHz. [b]Overlapped with DMSO. [c]Assignments may be interchanged in each column. [d]Overlapped in each column. [e]Assignments may be interchanged in each column. [f]Overlapped in each column.

allowed to stand at room temperature for 4 h. 3-[(Dimethylamino)-propyl]amine (1.9 μL) was added, and after standing for 10 min, the solution was poured into 10 mL of 0.6 N HCl and extracted with 10 mL of EtOAc three times. The EtOAc extract was washed twice with 10 mL of 0.1 M $NaHCO_3$ and evaporated, affording (*R*)-MTPA ester of 3-hydroxy fatty acid methyl ester. The (*S*)-MTPA ester of 3-hydroxy fatty acid methyl ester was prepared according to the same procedure using (−)-MTPA chloride in place of (+)-MTPA chloride.

In Vivo Cucumber Leaf-Disk Assay against *B. cinerea*. Cucumber seeds (*Cucumis stativus* L. Sagami-Hanjiro) were planted in 12 cm pots containing artificial soil and grown in the greenhouse at 16−23 °C without supplemental lighting. The cotyledons were collected from 3-week-old plants. The test compound (or supernatant) was dissolved in an appropriate amount of phosphate buffer (40 mM, pH 7.2), and 50 μL of the solution was applied to a paper disk (8 mm in diameter, thick type, Advantec Toyo Kaisha, Ltd., Tokyo, Japan) on the cucumber cotyledon. For the control, only phosphate buffer was applied. Then the paper disks on the leaves were inoculated with 50 μL of *B. cinerea* spore suspension (2×10^4/mL) containing 0.2% (w/v) yeast extract and 2% (w/v) sucrose. The leaves were kept in a humidity chamber (RH > 95%) at 20 °C for 4 days in darkness. The experiment was repeated four times. The inhibition rate of *B. cinerea* infection was calculated as

$$\text{inhibition rate of infection (\%)} = (1 - D_a/D_b) \times 100$$

where D_a is the diameter of the infection zone in the leaf with a test compound and D_b is the diameter of the infection zone in the control leaf. The results were expressed as inhibition rate (mean % ± SD). The assay was observed under a stereomicroscope SZX7 (Olympus Co., Tokyo, Japan).

In Vitro Mycelial Growth Inhibition Assay. The assay procedure and calculation methods were described in our previous paper.[8] The combined action of two compounds was evaluated using Abbott's formula.[13] The expected efficacy of a mixture of two compounds, expressed as E_{exp}, can be predicted by Abbott's formula:

$$E_{exp} = c + d - (cd/100)$$

c and d are the control levels given by the single compounds. Synergistic interaction was determined to be present in the mixture when the ratio of the experimentally observed efficacy of the mixture (E_{obs}) to the expected one (E_{exp}) was >1.

In Vitro Conidial Germination Inhibition Assay. The compound was dissolved in an appropriate amount of phosphate buffer (40 mM, pH 7.2), and 100 μL of the solution was applied to a tissue culture plate (a 96-well flat-bottom plate with a low evaporation lid; Becton, Dickinson and Co.). For the control, only phosphate buffer was applied. The solution in each well of the tissue culture plate was supplied with 100 μL of *B. cinerea* conidia (2×10^4/mL) containing 0.2% (w/v) yeast extract and 2% (w/v) sucrose. Compound **3** and *anteiso*-C_{14} bacillomycin D were tested at final concentrations of 20 and 4 μM, respectively. The tissue culture plate was kept at 20 °C for 20 h in darkness. The germination of conidia was observed under a light microscope CK2 (Olympus Co.). The assay was done in triplicate.

DOI: 10.1021/acs.jafc.5b01198
J. Agric. Food Chem. 2015, 63, 5344−5353

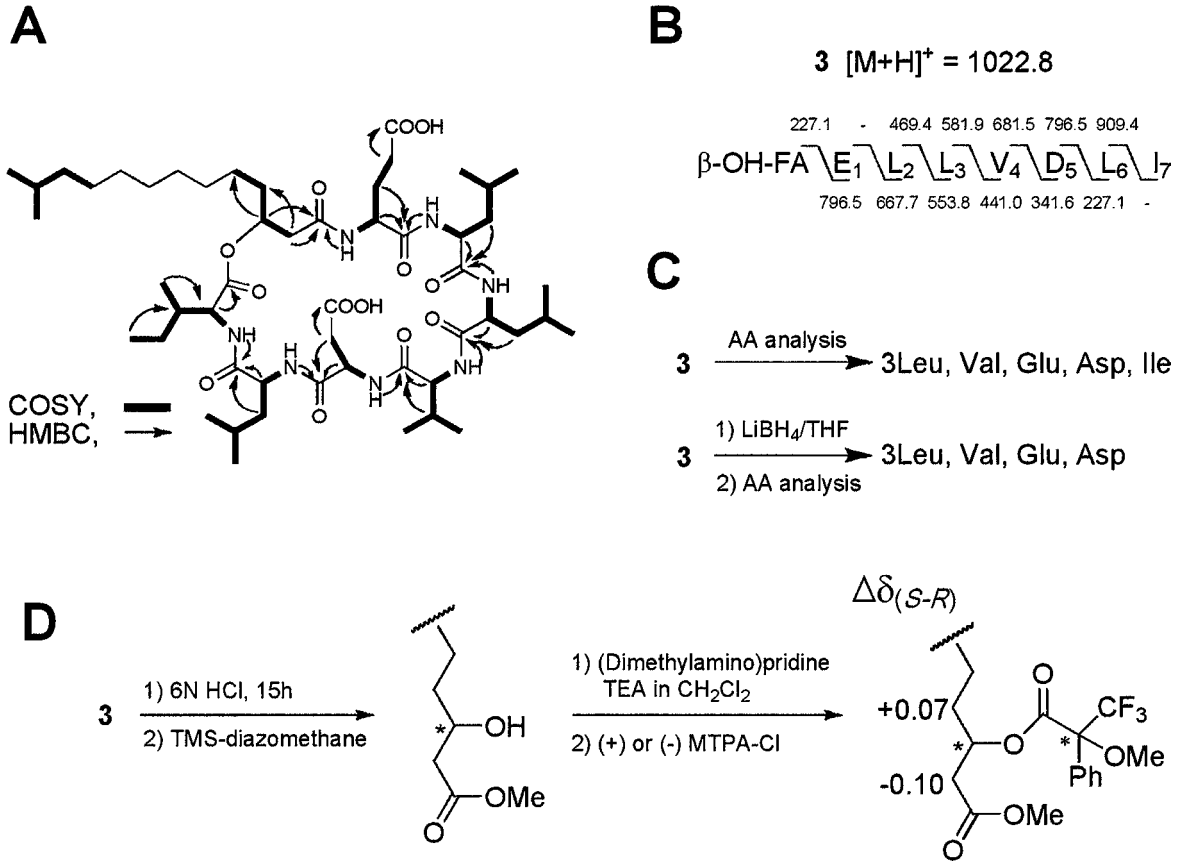

Figure 3. 2D-NMR, MS/MS, and chemical analyses of compound **3**: (A) key COSY and HMBC correlations detected for compound **3**; (B) MALDI-TOF MS/MS analysis of compound **3**; (C) determination of the lactone linkage position of compound **3**; (D) determination of the absolute structure of C-3 in 3-hydroxy fatty acid obtained from compound **3**. $\Delta\delta_{(S\text{-}R)}$ values (in ppm) of derivatives synthesized according to a modified Mosher's method.

RESULTS AND DISCUSSION

Contribution of Bacillomycin D to the Suppressive Activity of the Culture Supernatant against Gray Mold Disease. Strain SD-32 produces C_{15-17} bacillomycin D homologues, which are powerful antifungal lipopeptides.[8] To clarify the actual contribution of bacillomycin D to the suppressive activity of the culture supernatant against gray mold disease, we subjected the culture supernatant to an in vivo cucumber leaf-disk assay and also measured the bacillomycin D concentration in the culture supernatant. A 20-fold dilution of the culture supernatant was sufficient to inhibit the infection of *B. cinerea* completely, and the total concentration of bacillomycin D homologues in this solution was 11 μM (Figure 2A). In this assay, 30 μM bacillomycin D was needed to completely control *B. cinerea* (Figure 2B),[8] suggesting that factors other than bacillomycin D contributed to the effect of the culture supernatant on gray mold disease. These data prompted us to perform the following experiments.

Contribution of Synergistic Factors to the Control of Gray Mold Disease. We partially purified the culture supernatant from SD-32 culture with EtOAc extraction followed by solid-phase extraction (C18-SPE) and evaluated the activities of each fraction. The 60% CH_3CN fraction of C18-SPE showed a suppressive effect against gray mold disease in the in vivo assay (Figure 2C), and this fraction contained bacillomycin D homologues (Figure 2E). Fractions other than the 60% CH_3CN fraction showed no suppressive effects (Figure 2C); interestingly, however, the activity of the 60% fraction was enhanced 2-fold in the presence of the 80% CH_3CN fraction (Figure 2D), suggesting a synergistic effect of the 80% CH_3CN fraction with bacillomycin D homologues. The 80% CH_3CN fraction did not contain bacillomycin D, but did contain several unidentified metabolites (Figure 2E). These data led us to isolate and identify the synergistic factors in the 80% fraction.

Isolation of Compounds 1−5 from *Bacillus amyloliquefaciens* SD-32. SD-32 was cultured in a medium (1.6 L) composed of maltose, soybean powder, yeast extract, and some minerals at 30 °C for 64 h. Synergistic activity-guided purification of the EtOAc extract of the culture supernatant with SPE and preparative HPLC afforded compounds **1** (17 mg), **2** (16 mg), **3** (79 mg), **4** (15 mg), and **5** (10 mg) as white amorphous powders (each purity >90%). The elution profile at the final HPLC purification step is shown in Figure 2F. The chromatograms of each purified compound are shown in Figure 2G.

Structures of Compounds 1−5. Compound **3** was the most abundant in the culture broth, and therefore its structure was elucidated first. Compound **3** gave an $[M + Na]^+$ peak at m/z 1044.6602 (calcd for $C_{52}H_{91}N_7O_{13}Na$, 1044.6573) in HR-FAB-MS. Five α-amino acids, Leu, Glu, Val, Asp, and Ile, were found in a 3:0.9:0.9:0.9:0.7 ratio in an amino acid analysis of the hydrolysate. The ^1H NMR data for compound **3** (Table 1) indicated the presence of seven amide protons (δ_H 8.34−7.68) and seven α-protons (δ_H 4.53−4.08, partially overlapped) of amino acid residues of the peptide. The ^{13}C NMR (Table 2)

DOI: 10.1021/acs.jafc.5b01198
J. Agric. Food Chem. 2015, 63, 5344−5353

and HSQC data for compound **3** exhibited 50 signals (δ_C 172.1 and 22.5; 2C each), including 9 carbonyl (δ_C 174.1−169.4; δ_C 172.1, 2C), 1 methylene (δ_C 41.6−24.5), and 11 methyl carbon signals (δ_C 23.1−11.1; δ_C 22.5, 2C). On the basis of the ^{1}H−^{1}H COSY, HSQC, HMBC, and NOESY data (Figure 3A) and the molecular formula, compound **3** was deduced to be *iso*-C_{14} [Ile^7]surfactin, a cyclic depsipeptide consisting of three Leu residues, one Glu, one Val, one Asp, and one Ile residue and a 3-hydroxy fatty acid with a $-(CH_2)_8CH(CH_3)_2$ group as a side chain. To obtain the sequence information, compound **3** was analyzed by MALDI-TOF MS/MS to afford the sequence shown in Figure 3B, which corresponded with that of *iso*-C_{14} [Ile^7]surfactin. Then, to determine the location of the lactone linkage, compound **3** was reduced with $LiBH_4$ in THF and the amino acid composition of the product was analyzed. The reaction product lacked the Ile residue (Figure 3C; the intact and reduced compound **3** afforded Leu, Val, Glu, Asp, and Ile in the ratios 3:0.9:0.9:0.9:0.7 and 3:1:0.8:0.9:0.03, respectively), indicating that the lactone linkage was between the carboxyl group of Ile and the 3-hydroxy group of the fatty acid. From these results compound **3** was determined to be *iso*-C_{14} [Ile^7]surfactin (Figure 1).

The absolute configurations of α-amino acids in compound **3** were determined by treatment of the hydrolysate with Marfey's reagent[10] and HPLC analyses of the derivatives. The hydrolysate was shown to contain L-Glu, L-Val, L-Asp, L-Ile, L-Leu, and D-Leu. There is no ambiguity in the absolute configuration of the four amino acids other than Leu. The absolute configurations of Leu^2 and Leu^3 were determined by LC-MS comparison of the tripeptide in the products from the partial hydrolysis of compound **3** with four synthesized tripeptides, NH_2-L-Leu-L-Leu-L-Val, NH_2-D-Leu-D-Leu-L-Val, NH_2-D-Leu-L-Leu-L-Val, and NH_2-L-Leu-D-Leu-L-Val. The existence of NH_2-L-Leu-D-Leu-L-Val in the hydrolysate allowed us to determine the absolute configuration of Leu^2 and Leu^3 to be L and D, respectively. The absolute configuration of Leu^6 was also determined by LC-MS comparison of the tripeptide in the products from the partial hydrolysis of compound **3** with two synthesized tripeptides, NH_2-L-Asp-L-Leu-L-Ile and NH_2-L-Asp-D-Leu-L-Ile. The existence of L-Asp-D-Leu-L-Ile in the hydrolysate finally established the amino acid sequence, NH_2-L-Glu-L-Leu^2-D-Leu^3-L-Val-L-Asp-D-Leu^6-L-Ile. The absolute configuration at C-3 of the fatty acid part of compound **3** was determined according to the modified Mosher's method[11,12] as shown in Figure 3D. ^{1}H NMR spectra of the (*R*)-MTPA and (*S*)-MTPA esters of 3-hydroxy fatty acid methyl ester were measured, respectively, and from the $\Delta\delta_{(S-R)}$ values the absolute configuration of C-3 was determined to be *R*.

The HR-FAB-MS of compounds **1** and **2** showed their $[M + H]^+$ ion peaks at *m/z* 1008.6581 (calcd for $C_{51}H_{90}N_7O_{13}$, 1008.6596) and 1008.6575 (calcd for $C_{51}H_{90}N_7O_{13}$, 1008.6596), respectively. The HR-FAB-MS of compounds **4** and **5** showed their $[M + Na]^+$ ion peaks at *m/z* 1058.6741 (calcd for $C_{53}H_{93}N_7O_{13}Na$, 1058.6729) and 1058.6727 (calcd for $C_{53}H_{93}N_7O_{13}Na$, 1058.6729), respectively. A series of NMR spectral analyses revealed that compounds **1**, **2**, **4**, and **5** had the same amino acid sequence as compound **3** but differed from compound **3** with respect to the structure of their 3-hydroxy fatty acids. The ^{1}H NMR and ^{13}C NMR spectra of compounds **1**, **2**, **4**, and **5** showed the presence of the $-(CH_2)_6CH(CH_3)CH_2CH_3$, $-(CH_2)_7CH(CH_3)_2$, $-(CH_2)_8CH(CH_3)CH_2CH_3$, and $-(CH_2)_9CH(CH_3)_2$ groups, respectively. Thus, we concluded that compounds **1**, **2**, **4**, and **5** were *anteiso*-C_{13}, *iso*-C_{13}, *anteiso*-C_{15}, and *iso*-C_{15} [Ile^7]surfactin, respectively (Figure 1).

Compounds **3**, **4**, and **5** are known,[14−18] and **1** and **2** are new. Compounds **1** and **2** have *anteiso*- and *iso*-C_{13} 3-hydroxy fatty acids and seven α-amino acids with the same chiral sequence, LLDLLDL, as the surfactin family. Surfactins are cyclic lipodepsipeptides produced by several strains of *Bacillus* species and contain seven α-amino acids and a 3-hydroxy fatty acid. Standard surfactin possesses a heptapeptide moiety, L-Glu^1-L-Leu^2-D-Leu^3-L-Val^4-L-Asp^5-D-Leu^6-L-Leu^7, linked by an ester bond to an (*R*)-3-hydroxy fatty acid.[19−21] In addition to standard surfactin, [Ala^4]surfactin,[22,23] [Leu^4]surfactin,[24] [Ile^4]-surfactin,[24] [Val^7]surfactin,[14−16,25−27] [Ile^7]surfactin,[14−18] and halobacillin[28,29] (or lichenysins)[30,31] have been reported as main variants. [Ile^7]surfactin homologues have been reported to be produced by *Bacillus subtilis*[14,16−18] and *Bacillus licheniformis*.[15] The present study shows that *B. amyloliquefaciens* strain SD-32 is a producer of [Ile^7]surfactin homologues. Recently, the ^{13}C NMR data (in DMSO) of *anteiso*-C_{15} [Ile^7]surfactin were reported by Tang et al.,[18] and our ^{13}C NMR data for compound **4** were identical to the data in their report, except for the chemical shift of αCH of Ile^7 (δ_C 56.5, present study; δ_C 50.7, reported). The metabolite in the HPLC fraction from *Bacillus subtilis* OKB 105 was characterized from NMR and MS data as C_{13} [Ile^7]surfactin by Kowall et al.,[17] although its chemical structure was not unambiguously determined.

Synergistic Actions of Compounds 1−5 with Bacillomycin D in an in Vivo Cucumber Leaf-Disk Assay against Gray Mold Disease. The effects of compounds **1−5** on the suppressive activity of bacillomycin D were evaluated. The results are shown in Table 3 and Figure 4A. When administered singly, bacillomycin D (10, 15, and 20 μM) did not inhibit the development of gray mold disease on cucumber leaves. Compounds **1−5** (20 and 100 μM) also exhibited no inhibition of gray mold disease in cucumber leaves when administered alone, suggesting that compounds **1−5** (20 and 100 μM) could neither inhibit the growth of *B. cinerea* directly nor induce the resistance of cucumber leaves to gray mold disease. However, the addition of compounds **1−5** (20 and 100 μM) to bacillomycin D (10, 15, and 20 μM) significantly enhanced the effect of bacillomycin D activity in the in vivo assay, indicating that compounds **1−5** have synergistic activities with bacillomycin D under this condition. The inhibition rates of compounds **1−5** (100 μM) with bacillomycin D (10 μM) were 26.8, 51.2, 78.7, 81.7, and 66.5%, indicating that the C_{14} and C_{15} [Ile^7]surfactins were more active than the C_{13} [Ile^7]surfactins. Although these data could not fully explain the suppressive activity gap between the culture supernatant and bacillomycin D in it, they clearly demonstrated that the [Ile^7]surfactin homologues enhance the suppressive activity of bacillomycin D against gray mold disease and can partially close the gap.

To examine the mechanism underlying the synergism of the [Ile^7]surfactin homologues with bacillomycin D, a mycelial growth inhibition assay and a conidial germination inhibition assay using *B. cinerea* were performed in vitro (Figure 4B,C). In the mycelial growth inhibition assay, no significant difference between E_{obs} and E_{exp} was observed, and thus the effect of compound **3** on the activity of bacillomycin D was additive (Figure 4B). In the conidial germination inhibition assay, the addition of 20 μM of compound **3** to 4 μM of bacillomycin D did not enhance the activity of bacillomycin D (Figure 4C).

DOI: 10.1021/acs.jafc.5b01198
J. Agric. Food Chem. 2015, 63, 5344−5353

Table 3. Leaf-Disk Assay of Compounds 1–5 in Combination with Bacillomycin D Using Cucumber Cotyledon and *B. cinerea*[a]

	compd (μM)																	
	none		1			2			3			4			5				
Bac D[b] (μM)	20		100		20	100		20	100		20	100		20	100			
0		−12.5 ± 14.7		11.6 ± 25.1	0 ± 27.0		11.4 ± 6.1		3.1 ± 25.8		14.6 ± 19.9		3.1 ± 27.7		8.5 ± 15.7		6.3 ± 16.1		5.5 ± 20.8
10	−3.1 ± 35.9		21.9 ± 18.8		26.8 ± 26.3	40.6 ± 27.7		51.2 ± 17.2*	18.8 ± 21.7		78.7 ± 25.1**		21.9 ± 15.7		81.7 ± 36.6**		25.0 ± 17.7		66.5 ± 39.0**
15	0 ± 27.0		75.0 ± 35.9**		100**	59.4 ± 21.3**		100**	93.8 ± 12.5**		100**		68.8 ± 21.7**		100**		87.5 ± 17.7**		100**
20	28.1 ± 37.3		100**		100**	96.9 ± 6.3**		100**	100**		100**		100**		100**		100**		100**

[a]Data are expressed as inhibition rate (mean % ± SD, $n = 4$). Groups significantly different (by ANOVA followed by Dunnett's test) from the control group (bac D only) in each row are shown by * ($P < 0.05$) or ** ($P < 0.01$). [b]*ai*-C_{17} Bacillomycin D was used.

Finally, we conducted stereomicroscope observation in the cucumber leaf-disk assay (Figure 4D). The synergistic activity to the disease was observed in the condition 20 μM of compound **3** with 20 μM of bacillomycin D, although mycelial growth of *B. cinerea* was apparently normal in the same condition. These data suggested that the synergistic action of [Ile[7]]surfactin and bacillomycin D does not interfere with the mycelial growth and conidial germination of the gray mold, but rather might inhibit infection processes such as appressorium formation and penetration into the host.

Surfactin family lipodepsipeptides are well-known to act as potent surface-active compounds and antibiotics against a number of bacteria and phytopathogenic fungi.[32] In addition, recent investigations have illustrated a number of other diverse activities for these compounds, including roles in the induction of plant resistance or the mechanism of biofilm formation as part of the biological control system of *Bacillus* species.[7] The present study has shed light on a novel role of [Ile[7]]surfactin homologues in the biological control system of strain SD-32, namely, the compounds were shown to work synergistically with bacillomycin D in controlling gray mold disease under natural conditions, and this synergism may be particularly important for inhibiting the infection process of gray mold in cucumber leaves.

It has been reported that *B. amyloliquefaciens* produces a wide variety of bioactive metabolites such as nonribosomally synthesized polyketides (bacillaenes, difficidin, oxidifficidin, and macrolactins),[33,34] siderophore (bacillibactin),[35] lipopeptide (bacillomycin D),[36] and lipodepsipeptides (surfactins and fengysins or plipastatins)[36] and ribosomally synthesized peptides (plantazolicins).[37] However, to our best knowledge, interactions of each metabolite have not been investigated.

Many *Bacillus* strains have been reported to produce surfactin and bacillomycin D simultaneously,[36,38−41] but the interaction of bacillomycin D and surfactin has not been studied. In contrast, several researchers have focused on the interactions of standard surfactin and iturin A.[42−44] Bacillomycin D belongs to the iturin class lipopeptides, and bacillomycin D (Asn-Tyr-Asn-Pro-Glu-Ser-Thr-β-AA) and iturin A (Asn-Tyr-Asn-Gln-Pro-Asn-Ser-β-AA) have closely related structures.[7] Hiraoka et al.[42] showed that *B. subtilis* RB14 produced both standard surfactin and iturin A and that the standard surfactin could enhance the in vitro activity of iturin A against *Fusarium oxysporum*. They discussed the importance of the structural similarities between surfactin and iturin A in their synergism. Thimon et al.[43] reported that the antifungal activity of iturin A against *Saccharomyces cerevisiae* in vitro was enhanced in the presence of standard surfactin and that this effect was clear at a subinhibitory concentration of iturin A. Their results are in agreement with ours from the point of view of the necessary concentration, although we found their synergism not in vivo but in vitro. A mechanism for the antibiotic action of bacillomycin D and the other lipopeptides has been proposed.[44−46] Lipopeptide molecules penetrate the cytoplasmic membrane of the target cell and form oligomeric structures (lipopeptide aggregates) that are ion-conducting. Maget-Dana et al.[47] stated that the marked surfactant properties of surfactin helped iturin A to reach and disrupt the membrane of the target cells. In our experiment, however, the synergistic action of [Ile[7]]surfactin and bacillomycin D was not observed with respect to in vitro mycelial growth or the conidial germination inhibition assays. These data clearly suggest that the synergistic

DOI: 10.1021/acs.jafc.5b01198
J. Agric. Food Chem. 2015, 63, 5344−5353

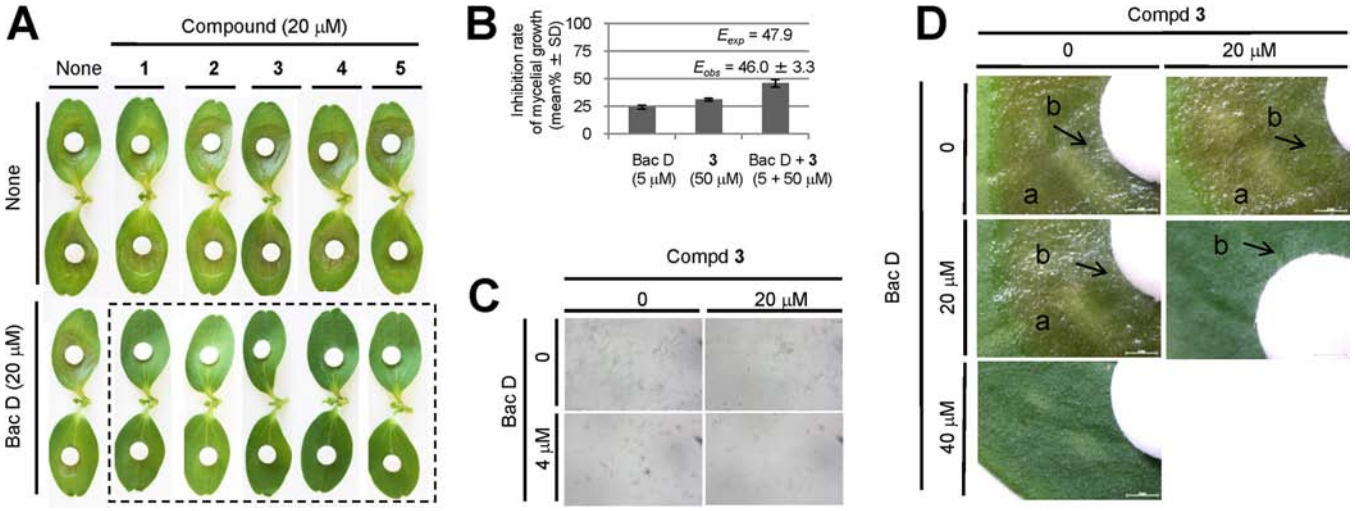

Figure 4. In vivo and in vitro assays of compounds **1**−**5** with bacillomycin D against *B. cinerea*. (A) In vivo assay of compounds **1**−**5** with bacillomycin D using cucumber cotyledon and *B. cinerea* (n = 4). Bac D indicates *anteiso*-C_{17} bacillomycin D. Gray mold disease was completely inhibited on the leaves in the dashed box. (B) Mycelial growth inhibition assay of compound **3** with bacillomycin D in vitro (n = 3). (C) Conidial germination inhibition assay of compound **3** with bacillomycin D in vitro (n = 3). (D) Stereomicroscope observation of in vivo assay of compound **3** with *anteiso*-C_{17} bacillomycin D. Scale bar indicates 2 mm. (a) Infection zone of *B. cinerea*; (b) mycelial growth of *B. cinerea*.

actions of [Ile^7]surfactin and bacillomycin D were different from those of surfactin and iturin A.

The detailed mechanism by which [Ile^7]surfactin homologues enhanced the suppressive effect of bacillomycin D in the cucumber leaf-disk assay is still unknown and remains to be studied. In addition, the data shown in this study could not fully explain the suppressive activity gap between the culture supernatant and bacillomycin D in it. Therefore, to close the gap in the suppression realized by the culture supernatant and bacillomycin D, research to identify relevant factors other than [Ile^7]surfactin and bacillomycin D should be continued.

■ ASSOCIATED CONTENT

Ⓢ Supporting Information

^{1}H NMR, ^{13}C NMR, COSY, HSQC, HMBC, and NOESY spectra of compounds **1**, **2**, and **3**; ^{1}H and ^{13}C NMR spectra of compounds **4** and **5**. The Supporting Information is available free of charge on the ACS Publications website at DOI: 10.1021/acs.jafc.5b01198.

■ AUTHOR INFORMATION

Corresponding Author

*(K.T.) Phone: +81-29-847-0301. Fax: +81-29-847-0501. E-mail: keijitsu_tanaka@sdsbio.co.jp.

Notes

The authors declare no competing financial interest.

■ ACKNOWLEDGMENTS

We thank Dr. Hiroshi Miyazoe and Dr. Takao Nagano for their assistance with NMR measurement and valuable discussion.

■ REFERENCES

(1) Rosslenbroich, H. J.; Stuebler, D. *Botrytis cinerea* − history of chemical control and novel fungicides for its management. *Crop Prot.* **2000**, *19*, 557−561.

(2) van den Bosch, F.; Paveley, N.; Shaw, M.; Hobbelen, P.; Oliver, R. The dose rate debate: does the risk of fungicide resistance increase or decrease with dose? *Plant Pathol.* **2011**, *60*, 597−606.

(3) Leroch, M.; Plesken, C.; Weber, R. W. S.; Kauff, F.; Scalliet, G.; Hahn, M. Gray mold populations in German strawberry fields are resistant to multiple fungicides and dominated by a novel clade closely related to *Botrytis cinerea*. *Appl. Environ. Microbiol.* **2013**, *79*, 159−167.

(4) Glare, T.; Caradus, J.; Gelernter, W.; Jackson, T.; Keyhani, N.; Köhl, J.; Marrone, P.; Morin, L.; Stewart, A. Have biopesticides come of age? *Trends Biotechnol.* **2012**, *30*, 250−258.

(5) Fravel, D. R. Commercialization and implementation of biocontrol. *Annu. Rev. Phytopathol.* **2005**, *43*, 337−359.

(6) Stein, T. *Bacillus subtilis* antibiotics: structures, syntheses and specific functions. *Mol. Microbiol.* **2005**, *56*, 845−857.

(7) Ongena, M.; Jacques, P. *Bacillus* lipopeptides: versatile weapons for plant disease biocontrol. *Trends Microbiol.* **2008**, *16*, 115−125.

(8) Tanaka, K.; Ishihara, A.; Nakajima, H. Isolation of *anteiso*-C_{17}, *iso*-C_{17}, *iso*-C_{16}, and *iso*-C_{15} bacillomycin D from *Bacillus amyloliquefaciens* SD-32 and their antifungal activities against plant pathogens. *J. Agric. Food Chem.* **2014**, *62*, 1469−1476.

(9) Naruse, N.; Tenmyo, O.; Kobaru, S.; Kamei, H.; Miyaki, T.; Konishi, M.; Oki, T. Pumilacidin, a complex of new antiviral antibiotics. Production, isolation, chemical properties, structure and biological activity. *J. Antibiot.* **1990**, *43*, 267−280.

(10) Marfey, P. Determination of D-amino acids. II. Use of a bifunctional reagent, 1, 5-difluoro-2, 4-dinitrobenzene. *Carlsberg Res. Commun.* **1984**, *49*, 591−596.

(11) Dale, J. A.; Mosher, H. S. Nuclear magnetic resonance enantiomer reagents. Configurational correlations *via* nuclear magnetic resonance chemical shifts of diastereomeric mandelate, *o*-methylmandelate, and α-methoxy-α-trifluoromethylphenylacetate (MTPA) esters. *J. Am. Chem. Soc.* **1973**, *95*, 512−519.

(12) Ohtani, I.; Kusumi, T.; Kashman, Y.; Kakisawa, H. High-field FT NMR application of Mosher's method. The absolute configurations of marine terpenoids. *J. Am. Chem. Soc.* **1991**, *113*, 4092−4096.

(13) Gisi, U. Synergistic interaction of fungicides in mixtures. *Phytopathology* **1996**, *86*, 1273−1279.

(14) Baumgart, F.; Kluge, B.; Ullrich, C.; Vater, J.; Ziessow, D. Identification of amino acid substitutions in the lipopeptide surfactin using 2D NMR spectroscopy. *Biochem. Biophys. Res. Commun.* **1991**, *177*, 998−1005.

(15) Jenny, K.; Käppeli, O.; Fiechter, A. Biosurfactants from *Bacillus licheniformis*: structural analysis and characterization. *Appl. Microbiol. Biotechnol.* **1991**, *36*, 5−13.

(16) Itokawa, H.; Miyashita, T.; Morita, H.; Takeya, K.; Hirano, T.; Homma, M.; Oka, K. Structural and conformational studies of [Ile^7]

DOI: 10.1021/acs.jafc.5b01198
J. Agric. Food Chem. 2015, 63, 5344−5353

and [Leu^7]surfactins from *Bacillus subtilis natto*. *Chem. Pharm. Bull.* **1994**, *42*, 604−607.
(17) Kowall, M.; Vater, J.; Kluge, B.; Stein, T.; Franke, P.; Ziessow, D. Separation and characterization of surfactin isoforms produced by *Bacillus subtilis* OKB 105. *J. Colloid Interface Sci.* **1998**, *204*, 1−8.
(18) Tang, J. S.; Gao, H.; Hong, K.; Yu, Y.; Jiang, M. M.; Lin, H. P.; Ye, W. C.; Yao, X. S. Complete assignments of ^{1}H and ^{13}C NMR spectral data of nine surfactin isomers. *Magn. Reson. Chem.* **2007**, *45*, 792−796.
(19) Arima, K.; Kakinuma, A.; Tamura, G. Surfactin, a crystalline peptidelipid surfactant produced by *Bacillus subtilis*: isolation, characterization and its inhibition of fibrin clot formation. *Biochem. Biophys. Res. Commun.* **1968**, *31*, 488−494.
(20) Kakinuma, A.; Hori, M.; Isono, M.; Tamura, G.; Arima, K. Determination of amino acid sequence in surfactin, a crystalline peptidelipid surfactant produced by *Bacillus subtilis*. *Agric. Biol. Chem.* **1969**, *33*, 971−972.
(21) Nagai, S.; Okimura, K.; Kaizawa, N.; Ohki, K.; Kanatomo, S. Study on surfactin, a cyclic depsipeptide. II. Synthesis of surfactin B_2 produced by *Bacillus natto* KMD 2311. *Chem. Pharm. Bull.* **1996**, *44*, 5−10.
(22) Peypoux, F.; Bonmatin, J. M.; Labbé, H.; Grangemard, I.; Das, B. C.; Ptak, M.; Wallach, J.; Michel, G. [Ala4]Surfactin, a novel isoform from *Bacillus subtilis* studied by mass and NMR spectroscopies. *Eur. J. Biochem.* **1994**, *224*, 89−96.
(23) Romano, A.; Vitullo, D.; Pietro, A. D.; Lima, G.; Lanzotti, V. Antifungal lipopeptides from *Bacillus amyloliquefaciens* strain BO7. *J. Nat. Prod.* **2011**, *74*, 145−151.
(24) Bonmatin, J. M.; Labbé, H.; Grangemard, I.; Peypoux, F.; Maget-Dana, R.; Ptak, M.; Michel, G. Production, isolation and characterization of [Leu^4]- and [Ile^4]surfactins from *Bacillus subtilis*. *Lett. Pept. Sci.* **1995**, *2*, 41−47.
(25) Peypoux, F.; Bonmatin, J. M.; Labbé, H.; Das, B. C.; Ptak, M.; Michel, G. Isolation and characterization of a new variant of surfactin, the [Val7]surfactin. *Eur. J. Biochem.* **1991**, *202*, 101−106.
(26) Peypoux, F.; Michel, G. Controlled biosynthesis of Val^7- and Leu^7-surfactins. *Appl. Microbiol. Biotechnol.* **1992**, *36*, 515−517.
(27) Hue, N.; Serani, L.; Laprévote, O. Structural investigation of cyclic peptidolipids from *Bacillus subtilis* by high-energy tandem mass spectrometry. *Rapid Commun. Mass Spectrom.* **2001**, *15*, 203−209.
(28) Trischman, J. A.; Jensen, P. R.; Fenical, W. Halobacillin: a cytotoxic cyclic acylpeptide of the iturin class produced by a marine *Bacillus*. *Tetrahedron Lett.* **1994**, *35*, 5571−5574.
(29) Hasumi, K.; Takizawa, K.; Takahashi, F.; Park, J. K.; Endo, A. Inhibition of acyl-CoA: cholesterol acyltransferase by isohalobacillin, a complex of novel cyclic acylpeptides produced by *Bacillus* sp. A1238. *J. Antibiot.* **1995**, *48*, 1419−1424.
(30) Yakimov, M. M.; Abraham, W. R.; Meyer, H.; Giuliano, L.; Golyshin, P. N. Structural characterization of Lichenysin A components by fast atom bombardment tandem mass spectrometry. *Biochim. Biophys. Acta, Mol. Cell Biol. Lipids* **1999**, *1438*, 273−280.
(31) Grangemard, I.; Bonmatin, J. M.; Bernillon, J.; Das, B. C.; Peypoux, F. Lichenysins G, a novel family of lipopeptide biosurfactants from *Bacillus licheniformis* IM 1307: production, isolation and structural evaluation by NMR and mass spectrometry. *J. Antibiot.* **1999**, *52*, 363−373.
(32) Peypoux, F.; Bonmatin, J. M.; Wallach, J. Recent trends in the biochemistry of surfactin. *Appl. Microbiol. Biotechnol.* **1999**, *51*, 553−563.
(33) Chen, X. H.; Vater, J.; Piel, J.; Franke, P.; Scholz, R.; Schneider, K.; Koumoutsi, A.; Hitzeroth, G.; Grammel, N.; Strittmatter, A. W.; Gottschalk, G.; Süssmuth, R. D.; Borriss, R. Structural and functional characterization of three polyketide synthase gene clusters in *Bacillus amyloliquefaciens* FZB42. *J. Bacteriol.* **2006**, *188*, 4024−4036.
(34) Schneider, K.; Chen, X. H.; Vater, J.; Franke, P.; Nicholson, G.; Borriss, R.; Süssmuth, R. D. Macrolactin is the polyketide biosynthesis product of the pks2 cluster of *Bacillus amyloliquefaciens* FZB42. *J. Nat. Prod.* **2007**, *70*, 1417−1423.
(35) Chen, X. H.; Koumoutsi, A.; Scholz, R.; Eisenreich, A.; Schneider, K.; Heinemeyer, I.; Morgenstern, B.; Voss, B.; Hess, W. R.; Reva, O.; Junge, H.; Voigt, B.; Jungblut, P. R.; Vater, J.; Süssmuth, R.; Liesegang, H.; Strittmatter, A.; Gottschalk, G.; Borriss, R. Comparative analysis of the complete genome sequence of the plant growth-promoting bacterium *Bacillus amyliliquefaciens* FZB42. *Nat. Biotechnol.* **2007**, *25*, 1007−1014.
(36) Koumoutsi, A.; Chen, X. H.; Henne, A.; Liesegang, H.; Hitzeroth, G.; Franke, P.; Vater, J.; Borriss, R. Structural and fanctional characterization of gene clusters directing nonribosomal synthesis of bioactive cyclic lipopetides in *Bacillus amyloliquefaciens* strain FZB42. *J. Bacteriol.* **2004**, *186*, 1084−1096.
(37) Kalyon, B.; Helaly, S. E.; Scholz, R.; Nachtigall, J.; Vater, J.; Borriss, R.; Süssmuth, R. D. Plantazolicin A and B: Structure elucidation of ribosomally synthesized thiazole/oxazole peptides from *Bacillus amyloliquefaciens* FZB42. *Org. Lett.* **2011**, *13*, 2996−2999.
(38) Athukorala, S. N. P.; Fernando, W. G. D.; Rashid, K. Y. Identification of antifungal antibiotics of *Bacillus* species isolated from different microhabitats using polymerase chain reaction and MALDI-TOF-mass spectrometry. *Can. J. Microbiol.* **2009**, *55*, 1021−1032.
(39) Zeriouh, H.; Romero, D.; García-Gutiérrez, L.; Cazorla, F. M.; de Vicente, A.; Pérez-Garcia, A. The iturin-like lipopeptides are essential components in the biological control arsenal of *Bacillus subtilis* against bacterial disease of cucurbits. *Mol. Plant-Microbe Interact.* **2011**, *24*, 1540−1552.
(40) Yuan, B.; Wang, Z.; Qin, S.; Zhao, G. H.; Feng, Y. J.; Wei, L. H.; Jiang, J. H. Study of the anti-Sapstain fungus activity of *Bacillus amyloliquefaciens* CGMCC 5569 associated with *Ginkgo biloba* and identification of its active components. *Bioresour. Technol.* **2012**, *114*, 536−541.
(41) Zhang, R. S.; Liu, Y. F.; Luo, C. P.; Wang, X. Y.; Liu, Y. Z.; Qiao, J. Q.; Yu, J. J.; Chen, Z. Y. *Bacillus amyloliquefaciens* Lx-11, a potential biocontrol agent against rice bacterial leaf streak. *J. Plant Pathol.* **2012**, *94*, 609−619.
(42) Hiraoka, H.; Asaka, O.; Ano, T.; Shoda, M. Characterization of *Bacillus subtilis* RB14, coproducer of peptide antibiotics iturin A and surfactin. *J. Gen. Appl. Microbiol.* **1992**, *38*, 635−640.
(43) Thimon, L.; Peypoux, F.; Maget-Dana, R.; Roux, B.; Michel, G. Interactions of bioactive lipopeptides, iturin A and surfactin from *Bacillus subtilis*. *Biotechnol. Appl. Bioc.* **1992**, *16*, 144−151.
(44) Maget-Dana, R.; Ptak, M. Iturin lipopeptides: interactions of mycosubtilin with lipids in planar membranes and mixed monolayers. *Biochim. Biophys. Acta, Biomembr.* **1990**, *1023*, 34−40.
(45) Maget-Dana, R.; Peypoux, F. Iturins, a special class of pore-forming lipopeptides: biological and physiological properties. *Toxicology* **1994**, *87*, 151−174.
(46) Bonmatin, J. M.; Laprevote, O.; Peypoux, F. Diversity among microbial cyclic lipopeptides: iturins and surfactins. Activity-structure relationships to design new bioactive agents. *Comb. Chem. High Throughput. Screen.* **2003**, *6*, 541−556.
(47) Maget-Dana, R.; Thimon, L.; Peypoux, F.; Ptak, M. Surfactin/iturin A interactions may explain the synergistic effect of surfactin on the biological properties of iturin A. *Biochimie* **1992**, *74*, 1047−1051.

DOI: 10.1021/acs.jafc.5b01198
J. Agric. Food Chem. 2015, 63, 5344−5353

JOURNAL OF AGRICULTURAL AND FOOD CHEMISTRY

Article

pubs.acs.org/JAFC

Emissions of 1,3-Dichloropropene and Chloropicrin after Soil Fumigation under Field Conditions

Scott R. Yates,*[,†] Daniel J. Ashworth,[†,‡] Wei Zheng,[‡,Δ] Qiaoping Zhang,[†] James Knuteson,[§,Π] and Ian J. van Wessenbeeck[§]

[†]U.S. Salinity Laboratory, USDA-ARS, 450 West Big Springs Road, Riverside, California 92507, United States

[‡]Department of Environmental Sciences, University of California, Riverside, California 92521, United States

[§]Dow Agrosciences, Indianapolis, Indiana 46268, United States

Supporting Information

ABSTRACT: Soil fumigation is an important agronomic practice in the production of many high-value vegetable and fruit crops, but the use of chemical fumigants can lead to excessive atmospheric emissions. A large-scale (2.9 ha) field experiment was conducted to obtain volatilization and cumulative emission rates for two commonly used soil fumigants under typical agronomic practices: 1,3-dichloropropene (1,3-D) and chloropicrin. The aerodynamic method and the indirect back-calculation method using ISCST3 and CALPUFF dispersion models were used to estimate flux loss from the treated field. Over the course of the experiment, the daily peak volatilization rates ranged from 12 to 30 μg m^{-2} s^{-1} for 1,3-D and from 0.7 to 2.6 μg m^{-2} s^{-1} for chloropicrin. Depending on the method used for quantification, total emissions of 1,3-D and chloropicrin, respectively, ranged from 16 to 35% and from 0.3 to 1.3% of the applied fumigant. A soil incubation study showed that the low volatilization rates measured for chloropicrin were due to particularly high soil degradation rates observed at this field site. Understanding and quantifying fumigant emissions from agricultural soil will help in developing best management practices to reduce emission losses, reducing adverse impacts to human and ecosystem health, and providing inputs for conducting risk assessments.

KEYWORDS: *soil fumigation, volatilization, emissions, Telone C-35, 1,3-dichloropropene, chloropicrin, bare soil, field experiment, shank injection, Industrial Source Complex Short-Term model (ISCST3), CALPUFF dispersion model, aerodynamic gradient method*

INTRODUCTION

Soil fumigation can significantly affect regional air quality.[1] Soil fumigation can lead to toxic substances entering the regional air stream as well as increasing the concentration of potential precursors for photochemical smog, which is formed by the reaction of volatile organic chemicals with nitrogen oxides in the atmosphere. Photochemical smog has become a problem in California during the summer months, and fumigants have been identified as potential precursors. Monitoring indicates that additional efforts are needed to ensure that U.S. EPA's 8-h ozone standard[2] is attained throughout the state.

The fumigant 1,3-dichloropropene (1,3-D) is an effective nematicide used for preplant soil fumigation; however, it is considered a possible carcinogen and is a Clean Air Act substance.[3] The high volatility (vapor pressure = 4.3 kPa[4]) of 1,3-D facilitates its movement, which increases effectiveness, but may also lead to high atmospheric emissions[3,5] and the potential for worker exposure.[6] In 1990, the detection of high 1,3-D concentrations in ambient air samples at multiple sites in California led to a suspension of 1,3-D as a soil fumigant.[7] The suspension remained in effect until 1995, when approaches to mitigate emissions were developed and tested.

Chloropicrin (trichloronitromethane) is effective for controlling soilborne fungi, diseases, and nematodes and was first registered in the United States in 1975.[8] Significant emissions for chloropicrin are possible after soil fumigation due to its high vapor pressure (2.4 kPa[4]). Chloropicrin has been found to be a reactive compound that promotes tropospheric ozone formation if present with other reactive organic compounds in the atmosphere.[9] Even though chloropicrin has been used in soil fumigation for decades, there is much to learn about its fate and persistence in soil and its volatilization from soil into the atmosphere.[10] More importantly, there is a great need to develop methods to control emissions for all soil fumigants.

There is very little published information on field-scale emissions of 1,3-D or chloropicrin. There have been several reported soil column experiments[11−18] that placed 1,3-D emission losses from bare soil in the range of 20−77% of the applied dosage. These studies also revealed that emission rates obtained using laboratory soil columns can have high variability (i.e., μ = 41%, σ = 16%). Total emission rates have been obtained under field conditions using micrometeorological and flux chamber methods. These studies have shown a similar range in total emissions of 12−80%,[19−25] with the highest estimates obtained using flux chambers (μ = 56%, σ = 22%). Flux chambers offer a relatively simple and cost-effective method for determining emission rates. They are also known to suffer from several practical problems, such as sampling a small surface area and the presence of the chamber affecting the tested surface,[26] which can affect the results. Total emission estimates of chloropicrin based on laboratory soil column

Received: March 19, 2015
Revised: May 13, 2015
Accepted: May 22, 2015
Published: May 22, 2015

ACS Publications © 2015 American Chemical Society

DOI: 10.1021/acs.jafc.5b01309
J. Agric. Food Chem. 2015, 63, 5354−5363

experiments place losses in the range of 7−16% of applied fumigant.[16,18] For measurements utilizing flux chambers,[24] the total losses were reported to be 30%.

It is imperative to better understand emissions from fumigated soil at typical agronomic scales to reduce the adverse impacts from soil fumigation. Large-scale field measurement of fumigant emissions provides information regulators require at the appropriate scale while serving as a reference baseline for the development and testing of new methods to reduce emissions.

Continued use of 1,3-D and chloropicrin will likely require extensive information on their environmental fate and transport collected at agronomic scales. The objective of this study was to conduct a field experiment to obtain needed information on the period-averaged and total emissions of 1,3-D and chloropicrin after shank fumigation in a large-scale agricultural field. Emission information is required by state and federal regulators as inputs into risk assessment models for the development of buffer zones to ensure public safety and also benefits the agricultural community by providing science-based information concerning rates of emission.

EXPERIMENTAL METHODS

The 2007 field experiment was conducted in an agricultural field near Buttonwillow, CA, USA, from September 5 to 21. The field soil was classified as Milham sandy loam (fine-loamy, mixed, thermic Typic Haplargids) and had approximately 1% organic matter content in the upper 10 cm, which decreased with depth. Approximately 2 weeks before the start of the experiment, the field was plowed and disked to break up any large soil aggregates and irrigated so that the soil condition was suitable for fumigation, with a water content of approximately 0.2 (cm^3 cm^{-3}). Telone C-35, a mixture of 1,3-D (68.1%) (CAS Registry No. 542-75-6) and chloropicrin (31.9%) (CAS Registry No. 76-06-2) was provided by Dow Agrosciences (Indianapolis, IN, USA) and applied by a commercial applicator using standard fumigation practices. 1,3-D contains two isomers, *cis*-1,3-D and *trans*-1,3-D, in a 50:50 ratio. The fumigation began at 9:35 a.m. (t = 0.40 day) and was completed within 3 h. The injection rig carried a 450 cm tool bar with nine shanks spaced in 50 cm increments laterally across the tool bar. The target depth of application was 46 cm (18 in.), and the fumigant material was applied to a nearly square 2.9 ha area (162 × 178 m). The target application rate was 240 kg/ha (20 gal/acre), and the actual weight of Telone C-35 applied was determined after fumigation (474.5 kg of 1,3-D and 222.3 kg of chloropicrin).

Measurement of 1,3-D and Chloropicrin Concentration. Atmospheric samples of 1,3-D and chloropicrin were obtained using XAD-4 tubes (SKC 226-175, SKC, Inc., Fullerton, CA, USA) followed by a charcoal backup tube (SKC 226-09, SKC, Inc.) to check for 1,3-D breakthrough both in laboratory and field samples. Ambient air was pulled through the sampling tube at a nominal rate of 150 cm^3/min using a vacuum system.

The 1,3-D and chloropicrin concentrations in the atmosphere were collected at 1.5 m above the soil surface at 12 locations surrounding the field site (see Supporting Information, Figure S1). Sample collection began at 8:00 a.m. (i.e., t = 0.33 day) and consisted of 3-h samples during the daytime and a 12-h sample at night. The daytime sampling intervals were increased to 6 and 12 h beginning on days 4 and 10, respectively. Sampling periods were lengthened to ensure that sufficient mass was collected in the sampling tubes for residue analysis as the experiment progressed.

Additional samples of the 1,3-D and chloropicrin concentrations in the atmosphere were collected at 10, 40, and 80 cm above the ground surface at the center of the treated field for use in a direct method of estimating mass flux because a concentration gradient is required. During days 0−5, the measurement periods were 2 h long during daytime and a single nighttime sample was collected. The daytime sampling intervals were increased to 3, 4, and 6 h beginning on days 5, 9, and 12, respectively.

Meteorological Measurements. Wind speed measurements were obtained at 20, 40, 80, and 160 cm above the ground surface using Windsonic 2-D sonic anemometers (Gill Instruments, Ltd.). Fine-wire thermocouples (FW3, Campbell Scientific, Inc.) were placed at 10, 40, and 80 cm above the ground surface to measure the air temperatures and temperature gradient. Relative humidity and temperature (1.5-m height, CS-215, Campbell Scientific, Inc.), net radiation (1-m height, Q-6, Radiation and Energy Balance Systems, Inc.), and barometric pressure (Vaisala PTA-427, Campbell Scientific, Inc.) measurements were also obtained during the experiment. These sensors were located at field center (see the Supporting Information).

Wind speed, wind direction (Wind Monitor, 5305, R. M. Young, Traverse City, MI, USA), and solar radiation (LI-200S, LI-COR, Inc.) were measured at 10-m height, which was positioned in a nearby field. Hourly averaged solar and net radiation measurements were collected yielding a nominal time series of 384 values (i.e., 24 h × 16 daily values). The average and standard deviation were calculated for each hour of the day to represent a typical daily cycle. This resulted in 24 average solar and net radiations and their standard deviations.

Methods for Measuring the Volatilization Rate. Two regulatory approaches were used to obtain the volatilization rate. A back-calculation method using the Industrial Source Complex Short-Term model (ISCST3),[27,28] has been extensively used for regulatory decisions by the California Department of Pesticide Regulations (CDPR) since the 1990s.[29] A different air dispersion model, CALPUFF,[30] was also used. EPA has recently adopted AERMOD[31] as a replacement for ISCST3. In California, due to the extensive historical use and past decisions based on ISCST3, CDPR has not required or recommended use of AERMOD for determining emission estimates from field application. CDPR evaluated AERMOD and found that the new functionality in AERMOD was not related to the area-source components of the model, and therefore replacement of ISCST3 was not warranted.[29]

The emission rates obtained using the back-calculation method involve comparing observed ambient concentrations in the atmosphere surrounding the field to concentrations calculated using an atmospheric dispersion model (e.g., ISCST3 or CALPUFF). The estimated emission rate is obtained by adjusting the ISCST3 model emission rate to produce the best fit to the measured concentration values (i.e., back-calculating the field emission rate).

The estimated emission rate is based on a linear relationship

$$C_{meas} = b + EC_{ISC} \quad (1)$$

where C_{meas} is the measured ambient concentration, E is the unknown actual emission rate, b is a background concentration that occurs when E = 0, and C_{ISC} is a predicted concentration at the receptor. The model parameters are estimated by linear regression using observed ambient concentrations (C_{meas}) at locations surrounding the treated field and the predicted concentrations (C_{ISC}) at each sampling location obtained using an atmospheric dispersion model with a nominal emission rate (E_{nom}). Because the ISCST3 or CALPUFF concentrations are proportional to the unknown emission rate, E can be estimated from

$$\text{flux} = E = mE_{nom} \quad (2)$$

where the intercept, b, and the slope, m, are obtained from linear regression.

All dispersion model simulations used in back-calculation methods used the regulatory default options, rural dispersion, flat terrain, receptor height of 1.5 m, and meteorological inputs using standard methodology.[30] For CALPUFF simulations, the field was split into four quadrants, and fumigant movement and dispersion were followed from each quadrant to the receptors.

For comparison purposes, the aerodynamic method (ADM)[32] was also used to estimate the volatilization rate based on gradients of wind speed, temperature, and fumigant concentration[32] collected over a relatively large and spatially uniform source area. It is customary to place the instruments at heights that are approximately 1−2% of the upwind fetch distance, which for this experiment would be heights up

DOI: 10.1021/acs.jafc.5b01309
J. Agric. Food Chem. 2015, 63, 5354−5363

to 80 cm. The air concentrations at the 80-cm height were found to be unreliable due to an equipment malfunction; therefore, volatilization rates were calculated using the 10 and 40 cm data. More information is provided in the Supporting Information.

The total fumigant mass lost after application, mass, was calculated using

$$\text{mass} = \text{area} \sum_{n} f_z(t_i)\Delta t_i \quad (3)$$

where $f_z(t_i)$ is the ith period volatilization rate (μg m^{-2} s^{-1}), Δt_i is the time interval for period i, n is the total number of periods, and area is the area (m^2) of the treated region of the field.

Chemical Analysis. Chemical analyses followed the same procedures described in Yates et al.[33] In brief, the concentrations of 1,3-D and chloropicrin in solvent extracts were determined by gas chromatography (GC) using an HP 6890 GC (Agilent Technologies, Palo Alto, CA, USA) equipped with an electron capture detector (ECD). The GC conditions were as follows: use of a 30 m × 0.25 mm × 1.4 μm DB-VRX capillary column (J&W Scientific, Folsom, CA, USA) with 240 °C inlet temperature, 290 °C detector temperature, and 1.6 cm^3 min^{-1} column flow rate (He).

RESULTS

Environmental Conditions. Shown in Figure 1 are hourly means and standard deviations of the solar irradiance (Q_{in}) and net solar radiation (Q_{net}). The maximum and average solar flux densities were 861 and 264 W m^{-2}, respectively. The maximum standard deviation was 72 W m^{-2} and occurred at 5:00 p.m.

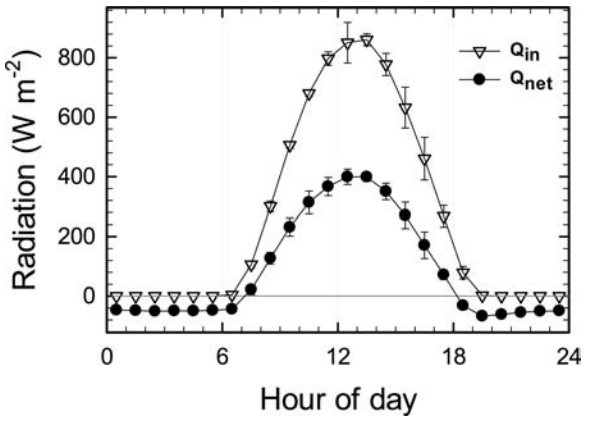

Figure 1. Global solar irradiance (W m^{-2}) and net radiation (W m^{-2}) as a function of time of day. The point values are averages of the hourly radiation over the entire experiment, and the error bars are the standard deviations. Small standard deviations are indicative of relatively uniform clear sky conditions throughout the experiment.

The net radiation was also found to be piecewise smooth during the daytime and was highly uniform at a given time of day during this experiment. The maximum, minimum, and average values were 399 , −67, and 86 W m^{-2}, respectively. The maximum standard deviation for the 24 periods was 44 W m^{-2}.

During the first 8 days of the experiment, the daily maximum temperatures at 1.5 m were similar and ranged from approximately 32 to 35 °C and averaged 33.2 °C (Figure 2A). The daily minimum temperature varied from 15 to 20 °C and averaged 17.3 °C. Starting at day 8, daily maximum temperatures were more variable, ranging from 22 to 31 °C, and averaged 27.3 °C, and the daily minima varied from 12 to 15 °C and averaged 13.1 °C.

The hourly averaged wind speed at 10 m height had a maximum of 5.2 m s^{-1}, and the daily peak 1-h wind speeds had an average and standard deviation of 3.2 ± 0.8 m s^{-1} (Figure 2B). During the nighttime, the daily minimum wind speeds averaged 0.64 m s^{-1} (±0.32), and five values (1.5%) were below 0.5 m s^{-1}, below the starting threshold for the 10-m wind direction sensor.

The wind-rose diagram that summarizes the frequency distribution of the wind speed and direction during the experiment suggests the winds were predominately from the northwest and that there was more variation in wind direction at 10 m compared to measurements taken at the center of the field (1.6 m) (Figure 3). This diagram uses 1- or 2-min averaged wind speed and wind direction data and shows that occasionally winds in excess of 5 m s^{-1} were observed. The length of each wedge provides the frequency that the winds came from that particular direction interval, per unit time. The color sections on each wedge provide frequency information about the wind speed ranges. For example, at 10 m, for approximately 14% of the time during the experiment, the winds were blowing from the north (i.e., 360° ± 11.25°) and about 3.2% of the time the wind speed was within the range of 2.0−2.5 m s^{-1} (i.e., 6.7% − 3.5%). For these short time interval measurements, (i.e., 1−2 min averaging), the maximum observed wind speed was 8.3 m s^{-1}, 1.6% of the measurements exceeded 5 m s^{-1}, and 4.5% were <0.5 m s^{-1}.

Air Concentrations. One air monitoring station was placed 50 m northeast of the field due to a fenced property boundary, and the remaining 11 stations were positioned 30, 90, or 120 m from the field edge. Figure 4 shows the maximum concentrations of *cis*-1,3-D, *trans*-1,3-D, and chloropicrin from the 11 monitoring stations surrounding the field. During periods with steady wind direction, the up-wind air samplers recorded concentrations that were below detectable levels. In general, the highest concentrations occurred during nighttime or early morning hours.

For *cis*-1,3-D, the maximum daily concentrations at the center of the field at height 0.4 m exceeded 1000 μg m^{-3} 14 h after the fumigation was completed. Fumigant labels typically specify a field re-entry period and a buffer setback from the field edge to minimize the potential for bystander exposure. High concentration levels were also observed before sunrise on days 3 (657 μg m^{-3}) and 4 (840 μg m^{-3}). At a distance of 30 m from the field boundary, the daily peak *cis*-1,3-D concentration exceeded 60 μg m^{-3} during the first 2 days after application and the maximum concentrations occurred on days 3−4 (109−112 μg m^{-3}). At greater distances, daily maximum *cis*-1,3-D concentrations were approximately 30 and 35% lower than at 30 m. During the first 24 h after fumigation, the concentrations of *trans*-1,3-D were about 65% less than the *cis*-1,3-D isomer, approximately 20% less than *cis*-1,3-D values for days 3 and 4. After 4 days, *cis*- and *trans*-1,3-D concentrations were similar in magnitude (<10% difference).

Chloropicrin concentrations were generally very low, especially after the first 24 h. The maximum on-field concentration was 60 μg m^{-3} and 15, 13, and 7 μg m^{-3}, respectively, at distances of 30, 90, and 120 m from the field boundary. After approximately 4 days, the maximum chloropicrin concentration levels surrounding the field were low (<1 μg m^{-3}), and after 9.54 days, sampling for chloropicrin ended.

Fumigant Emissions. Transient 1,3-D and chloropicrin volatilization rates using the ISCST3 and CALPUFF methods are shown in Figure 5; the maximum flux rates, the maximum 24-h average flux rates, and the percent total emissions for the

DOI: 10.1021/acs.jafc.5b01309
J. Agric. Food Chem. 2015, 63, 5354−5363

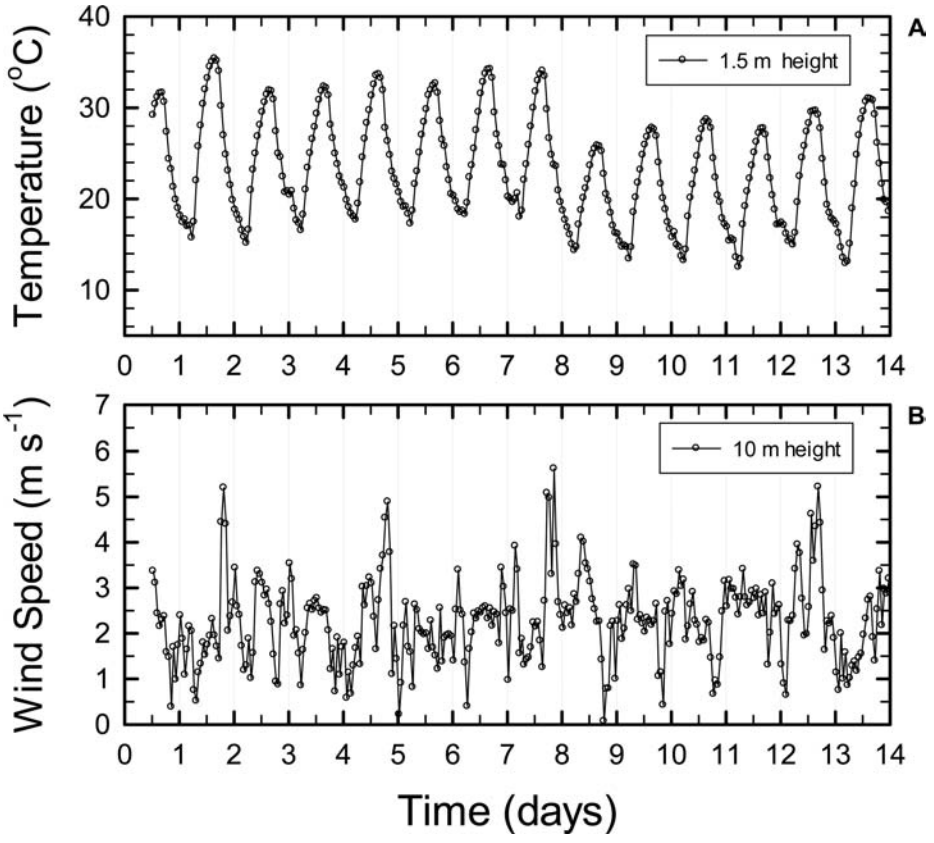

Figure 2. (A) Air temperature (°C) at 1.5 m and (B) wind speed (m s^{-1}) at 10 m above the soil surface during the experiment. Integer values occurred at midnight, and each point is a 1-h sample average.

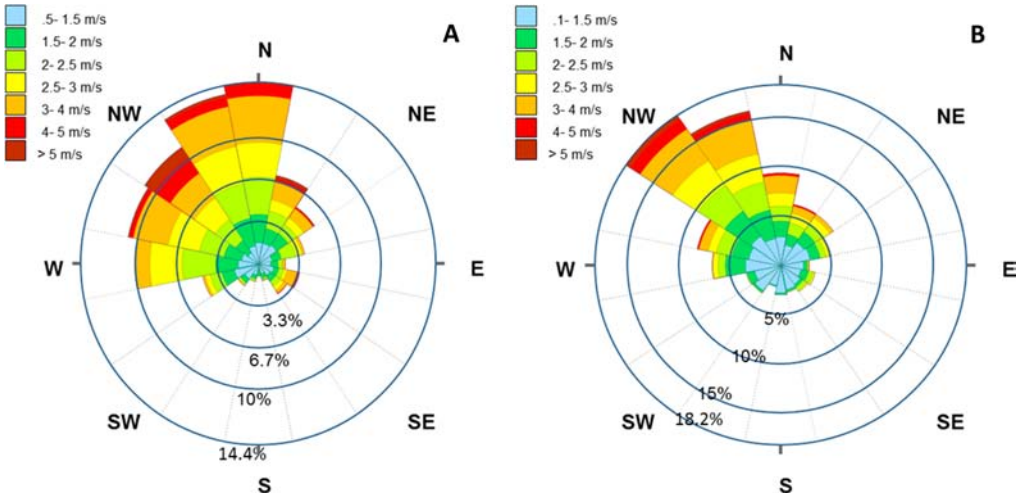

Figure 3. Wind rose diagrams showing the wind direction, wind speed, and frequency that the wind occurred in a specific direction. Two-minute averaged wind speed and direction were used in (A) and 1-min averaged wind speed and direction in (B). In (A), wind measurements at 10 m are shown. In (B), wind measurement at 1.6 m and at field center are shown.

three measurement methods are summarized in Table 1. For CALPUFF and ISCST3, the maximum flux rate for 1,3-D occurred at day 2, and for chloropicrin it occurred during fumigant application. The shaded areas in Figure 5 are the 24-h average flux rates calculated by converting the total mass lost for each day, using CALPUFF, into a flux density. Averaging smooths the short-term fluctuations and more clearly reveals the underlying behavior. The volatilization rates using the ISCST3 model were consistently less than those found using the CALPUFF model. For *cis*-1,3-D and *trans*-1,3-D, the maximum and average ISCST3 flux rates were 59−63% less than CALPUFF rates and for chloropicrin, 74−85% less. For the CALPUFF method, the estimated total volatilization of *cis*-1,3-D, *trans*-1,3-D, and chloropicrin, respectively, was 32, 23, and 0.9% (Table 1). For the ISCST3 model, the estimated total volatilization, respectively, was 19, 13, and 0.3%.

Figure 6 shows time series for 1,3-D and chloropicrin volatilization rates obtained with the aerodynamic method. The maximum emission rates for *cis*-1,3-D, *trans*-1,3-D, and chloropicrin, respectively, were 18, 9.2, and 0.68 μg m^{-2} s^{-1}

DOI: 10.1021/acs.jafc.5b01309
J. Agric. Food Chem. 2015, 63, 5354−5363

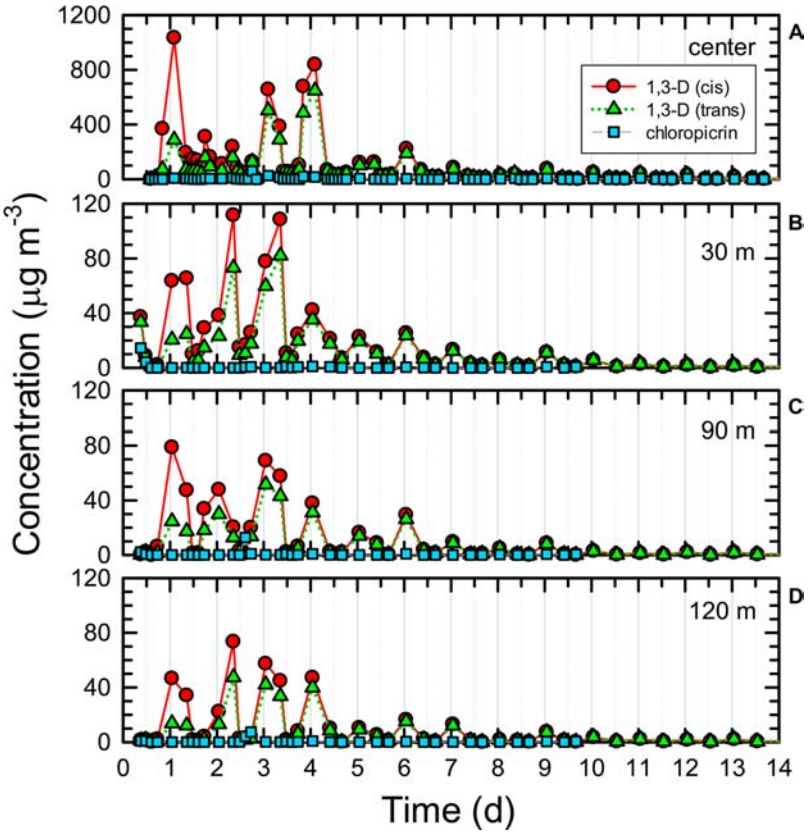

Figure 4. Maximum 1,3-D isomer and chloropicrin concentrations in air at samplers located 30, 90, and 120 m from the edge of field plots (see Supporting Information, Figure S1). Measurements were taken 1.5 m above the soil surface. Time scale begins at midnight September 5, 2007.

(Table 1). For *cis*-1,3-D, the maximum emission rate was within 2% of the back-calculated value using CALPUFF and for *trans*-1,3-D, within 22%. The aerodynamic method yielded total emission estimates of 42, 28, and 1.3% for *cis*-1,3-D, *trans*-1,3-D, and chloropicrin, respectively (Table 1). The aerodynamic method estimates of total emission for *cis*-1,3-D, *trans*-1,3-D, and chloropicrin, respectively, were 33, 25, and 49% higher compared to the back-calculation method using the CALPUFF air dispersion model.

DISCUSSION

Wind Speed, Temperature, and Radiation. Warm temperatures, cloudless conditions, and persistent wind directions are typical weather patterns in the southern San Joaquin Valley in August and September,[33] but wind speeds that produce windblown dust were not observed during the field study. During high wind speeds, windblown dust can reduce visibility and energy inputs, which could affect fumigant emissions. Measurements of solar radiation obtained during a previous experiment that was conducted in late August and early September 2005[33] produced a similar curve as Figure 1, but with slightly lower standard deviations for Q_{in} at 11:00 a.m. and in the early afternoon. The overall low standard deviations shown in Figure 1 indicate that consistent energy inputs were observed during this field experiment and, for comparative purposes, that environmental conditions were similar to a previous experiment conducted in 2005.[33]

Wind speed measurements collected in 2005 in the vicinity of the field experiment using research grade cup anemometers (CWT-1806, C. W. Thornthwaite Associates)[33] indicated that northerly and westerly wind directions are common to this region of California and align with the general orientation of the San Joaquin Valley and surrounding mountains.[33] In 2005, 93% of hourly wind speed measurements during August and September were below 3 m s^{-1} with a maximum of 5.6 m s^{-1} and were predominately from the north-northwest. During this experiment, 78% of the hourly wind speeds were below 3 m s^{-1} and the maximum was 5.6 m s^{-1} (day 8). The average was 2.3 m s^{-1}, the minimum was 0.07 m s^{-1} (day 9), and only six periods were below 0.5 m s^{-1} and only two periods below 0.25 m s^{-1}. Wind direction measured at 1.6 m near the center of the field show similar, but much more consistent, wind direction. This could be partly due to the on-field sensor type, which was a 2-D sonic anemometer consisting of no moving parts and with a threshold measurement of <0.01 m s^{-1}. The mechanical wind direction sensor (10 m) may have been affected by wind buffeting, stalling, and overshoot compared to a high-frequency, nonmechanical device (1.6 m). Even though the field site was flat and had a large uniform surface surrounding the site, near-surface wind directions might also be affected by local topographic effect compared to higher elevation measurements.

Air Concentrations. In general, the highest concentrations occurred during nighttime and early morning hours; this is generally interpreted as a consequence of a stable atmosphere and lower turbulence.[34] The stability of the atmosphere can be estimated from the temperature and wind speed at two heights by calculating the gradient Richardson's number, R_i, and using R_i in an empirical relationship for atmospheric stability, Φ_m (see the Supporting Information). These relationships are described and shown in Figure S2 for a height of 0.6 m. For neutral stability $\Phi_m \approx 1$. Values of $\Phi_m > 1$ indicate a stable atmosphere, which occurred during nighttime and early morning hours of

DOI: 10.1021/acs.jafc.5b01309
J. Agric. Food Chem. 2015, 63, 5354−5363

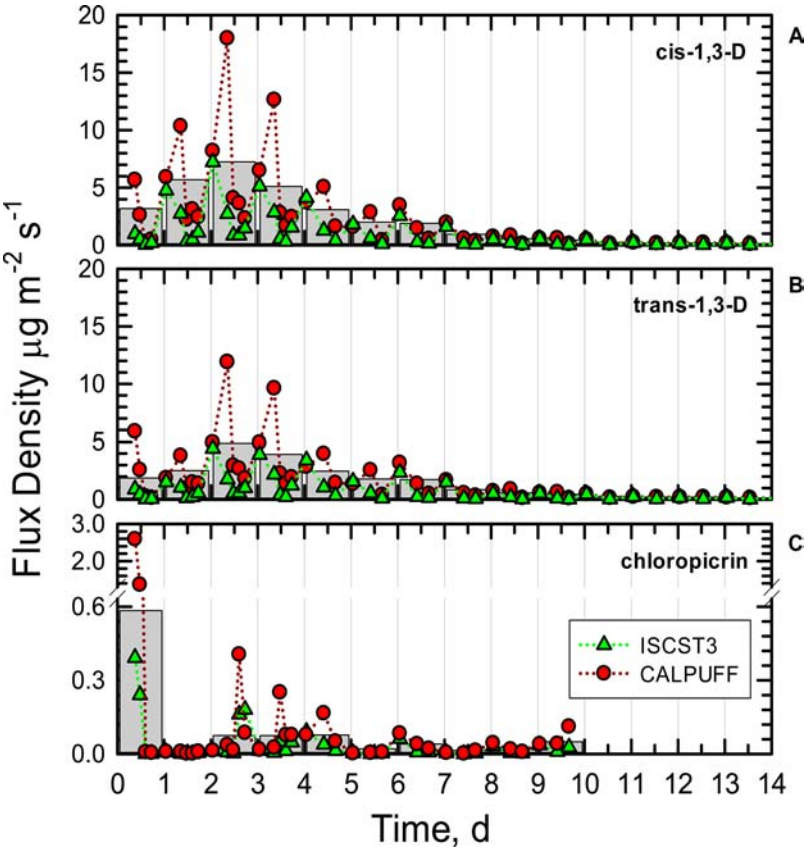

Figure 5. Volatilization rate (i.e., flux density, $\mu g\ m^{-2}\ s^{-1}$) as a function of time (day) after application for the CALPUFF v6 (circles) and ISCST3 (triangles) methods. Shaded areas are mass losses for each day (CALPUFF) converted into daily averaged volatilization rates. For day 0, the shaded area is based on 16 h of available data.

Table 1. Fumigant Mass Applied, Maximum Flux Rate during Experiment, Maximum 24-h Average Flux Rate, and Total Emissions for Several Fumigants and Flux Measurement Methods

		CALPUFF			ISCST3			ADM		
fumigant or formulation	appld mass (kg)	max flux ($\mu g\ m^{-2}\ s^{-1}$)	max 24-h av ($\mu gm^{-2}\ s^{-1}$)	total emissions (%)[a]	max flux ($\mu g\ m^{-2}\ s^{-1}$)	max 24-h av ($\mu gm^{-2}\ s^{-1}$)	total emissions (%)[a]	max flux ($\mu g\ m^{-2}\ s^{-1}$)	max 24-h av ($\mu gm^{-2}\ s^{-1}$)	total emissions (%)[a]
cis-1,3-D	237	18	7.3	32	7.2	3.9	19	18	10	42
trans-1,3-D	237	12	4.9	23	4.4	2.6	13	9.2	6.1	28
chloropicrin	222	2.6	0.58	0.9	0.39	0.1	0.3	0.68	0.43	1.3

[a]Percent of total fumigant mass applied; assumes the flux rate is uniform within the field.

the experiment. During the daytime, the atmosphere was generally unstable (i.e., $\Phi_m < 1$). At night, lower wind speed and weaker buoyancy reduced mixing near the surface, allowing emission of gas to accumulate in concentration.

Fumigant concentrations were largest at the start of the experiment due to the high concentrations in the soil immediately following application, rapid diffusion due to soil fractures caused by the fumigation shanks and large initial gradients, and evaporation of fumigant from the injection rig to the atmosphere during application. This behavior was observed at all sampling distances (Figure 4) but is most easily interpreted for the on-field measurements, which were not influenced by wind direction and sample-station positions.

The off-site samples are particularly useful in determining emissions during the application process, before the on-field sensors could be installed. Application losses can occur when the fumigators lift the shanks from the soil as they turn for the next pass down the field. Although the injection valves are closed to minimize waste and emissions, any residue remaining on the shank injectors and tubing evaporates into the atmosphere, increasing fumigant loadings. This is most noticeable at 30 m, during the first two sampling periods (Figure 4B) that were collected during fumigation and is a combination of application losses and losses from soil. The estimated mass lost during fumigation was <1% of applied.

Shank (i.e., a knife-like blade that cuts through soil with the injection nozzle at the lower end) injections tend to produce a more uniform concentration depth profile and higher concentrations near the soil surface compared to methods that do not produce a fracture,[35] but rapid movement along the shank fracture can lead to higher fumigant emissions. New application technology using a coulter and packer purports to reduce fumigant emissions and increase residue levels in soil,[36] on the basis of measurements collected at a depth of 12 cm. Further research is needed to obtain concentration distributions at other depths.

DOI: 10.1021/acs.jafc.5b01309
J. Agric. Food Chem. 2015, 63, 5354−5363

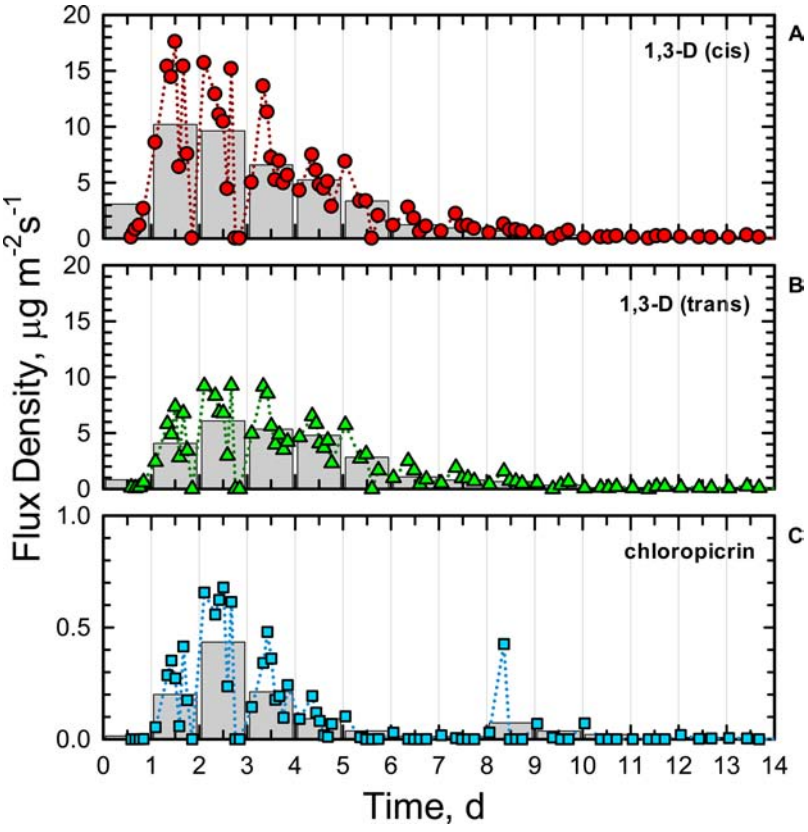

Figure 6. Volatilization rate (i.e., flux density, μg m^{-2} s^{-1}) as a function of time (days) after application for the aerodynamic method. Shaded areas are mass losses for each day converted into daily averaged volatilization rates. For day 0, the shaded area is based on 16 h of available data.

The highest fumigant concentrations were measured near the field center, and progressively lower concentrations were observed at the more distant offsite sample stations. For example, the maximum period-averaged *cis*-1,3-D concentration during the experiment for on-field, 30, 60, and 120 m distances, respectively, were 1035, 112, 79, and 74 μg m^{-3}. The overall behavior of *trans*-1,3-D was similar to that of *cis*-1,3-D, but with slightly lower concentrations (especially at early times). Compared to *cis*-1,3-D, *trans*-1,3-D is known to have an 8.2% higher boiling point (112.6 °C), 6.4% higher solubility (2320 ppm), 33% lower vapor pressure (23 mmHg), and 42% lower dimensionless Henry's law constant (0.037). In concert, these factors may result in a delay in *trans*-1,3-D movement to the soil surface, reduction in peak emission rates, and retardation of the peak emission timing.[13,37] Observed chloropicrin air concentrations were very low for all distances and times after chloropicrin application ended (t > 0.53 day). The higher concentrations during fumigation were most likely due to the application process, as discussed above.

Fumigant Emissions. State and federal regulators are concerned about atmospheric loadings of soil fumigant chemicals, and information on emissions is used to estimate environmental risks and to determine risk related to acute bystander exposure. Information on the total emission rate is useful for determining contributions to regional volatile organic chemicals and for determining risks due to chronic exposure to fumigant chemicals.

The emissions of 1,3-D (*cis* + *trans*) calculated using ISCST3, CALPUFF (Figure 5), and ADM (Figure 6) methods demonstrate a similar overall pattern with higher rates early in the experiment and lower rates about 5−6 days post application. The ISCST3 estimates were found to be consistently lower than estimates obtained using the CALPUFF model (53% lower on average). The largest differences occurred during the morning hours when the ISCST3 emissions were as much as 85% lower than the CALPUFF values. Using ISCST3, the reported total 1,3-D and chloropicrin losses, respectively, were 40 and 64% lower than the CALPUFF values.

During the first 5 days, the short-term volatilization rates follow a consistent cycle where the volatilization rate increases from midnight to midmorning, followed by a steep reduction in the volatilization rate at midday and low values until nighttime. This pattern is consistent with daytime drying of the surface soil, which leads to increased vapor adsorption. Increased adsorption reduces the pesticide vapor density and the vapor gradients,[38−40] which is an important transport mechanism. As water content in soil decreases below a threshold level, the reduction in vapor pressure would cause a reduction in pesticide emissions.[41] Using modeling, the effects of vapor adsorption have been shown to strongly bind volatile pesticides to soil particles in a highly nonlinear process.[42,43]

Whereas the emission measurements vary considerably with time of day, the long-term (e.g., daily averaged) emission rates (shaded areas in Figure 5) show a smoother and more predictable behavior that starts with a steady increase in the emission rate after fumigation, peaks on day 2, and is followed by a long period of decreasing emission rates. In terms of mathematically modeling the emission process, this behavior follows conventional transport theory.[44]

It can be shown that the timing of the maximum emission rate depends on the depth of injection[35] for a shank or point

DOI: 10.1021/acs.jafc.5b01309
J. Agric. Food Chem. 2015, 63, 5354−5363

fumigation (i.e., injection) model. This is due to the time needed for the fumigant to diffuse from the injection depth (46 cm) to the soil surface and volatilize into the atmosphere. For a shank fumigation using *cis*-1,3-D, the model predicts that the peak emission rate would occur at approximately 1−1.3 days after application, assuming a post fumigation soil-disking depth of 15−20 cm. This coincides with the experimental results using the on-field measurements (Figure 6) where the highest daily averaged emissions (shaded area) occur on day 1. For the CALPUFF method (Figure 5), the peak daily averaged emission rate occurs on day 2. It is unclear why the peak flux calculated from CALPUFF occurred at a later time than with the ADM method, but is probably due to differences in the approach for calculating flux values or the temporal nature of wind speed/direction, which are averaged over each sampling duration. For the ADM method, the sampling "footprint" (i.e., area of surface-soil-emissions captured by the sampling equipment) would be a relatively small zone immediately surrounding the sampling equipment, and the time period when the fumigant was injected into this area would have a relatively short duration. For the CALPUFF method, emissions over the entire field and transport from the field boundaries to the surrounding samplers affect the emission rate values. This means that the CALPUFF method could be affected by spatial and temporal averaging of the field emission rates and near-field transport processes.

In Figure 5, the first two flux values were measured during the fumigation period and demonstrate the gas losses occurring during application. Large emission losses during fumigation caused state regulators in California to restrict 1,3-D application from 1990 to 1995[7] to protect people living in fumigation areas. It was not until suitable application guidelines were developed and tested that use of 1,3-D was again allowed in California. During this experiment, losses during application were lower than emissions from soil that occurred later in the experiment and show that current regulations are effectively controlling losses during application.

A laboratory study[45] reported 1,3-D and chloropicrin emissions using Milham sandy loam soil collected from a nearby, nontreated, field in 2005. The stainless steel soil columns (1.5 m long) were placed in a controlled-temperature environment so that the columns were exposed to temperature conditions similar to those observed at the field site. The reported total *cis*-1,3-D emissions 14 days after treatment was 33.1% of applied. The emission rate from the laboratory experiment was within 1% of the CALPUFF *cis*-1,3-D total emission value.

In a follow-up experiment[18] that included 1,3-D and chloropicrin, the total 1,3-D (*cis* + *trans*) and chloropicrin emissions 14 days after injection, respectively, were reported as 40 and 16% of applied. The reported chloropicrin emission losses were much more than observed during this field experiment (e.g., ∼1%). The soil at the field site was found to have relatively high soil degradation rates. Ashworth et al.[18] measured the 1,3-D and chloropicrin half-lives, respectively, as 90 and 2.9 h, at 25 °C. In a subsequent laboratory study Ashworth et al.[46] found that the chloropicrin degradation rate depended on the chloropicrin application rate, with low application rates leading to high degradation rates.

Rapid chloropicrin degradation in soil may have contributed to a reduction in soil concentration levels before sufficient time elapsed to allow significant volatilization, and to test this hypothesis, a mathematical model was used to predict total emissions as a function of soil properties, injection depth, presence of a shank fracture, soil degradation, and surface resistance to volatilization.[35] A feasible explanation for the low chloropicrin emissions observed during the experiment is the soil degradation rate (i.e., $t_{1/2}$ = 2.9 h), which led to predicted total emissions of <1%.

Very few large-scale field measurements of the emissions of 1,3-D and chloropicrin after broadcast application are reported in the literature. There are even fewer reported studies that utilize multiple methods for measuring the emission rate. This is due, in part, because conducting a field campaign is very expensive and requires large investments in time, equipment, and personnel. The current study is unique because it provides a continuous time series of the emissions for 14 days (daytime and nighttime) and involved collection of two independent data sets (i.e., on-field and off-field measurements). These data were then used so that the emission rate was calculated by three methodologies (i.e., ISCST3, CALPUFF, and ADM methods). Comparing the methodologies revealed that the increasing order of the total emissions was ISCST3 < CALPUFF < ADM, and total emissions from CALPUFF are approximately the same as the average of the three methods.

Determining which method provides the most accurate emission rates is not possible with the data currently available, because there is no absolute reference for comparison. Each method encompasses inherent assumptions and/or simplifications that may affect the calculated values under some conditions. For example, ISCST3 is a steady-state atmospheric dispersion model, so results could be compromised for highly variable wind conditions during an hourly time step. CALPUFF is a non-steady-state Lagrangian puff model that tracks chemical movement in a more natural manner, a likely an improvement over ISCST3, but the results depend on the gridding system employed and the representativeness of the meteorological data. The ADM method assumes a well-developed surface layer for measuring gradients (concentration, wind speed, and temperature) and requires evaluation of a correction term for stable and unstable atmospheric conditions, which may introduce uncertainty. It is clear that further research is needed to better understand the accuracy and performance of these methods for calculating fumigant emissions.

Using total emissions from CALPUFF for comparison, the results of this study fall within the range of values reported in the literature for 1,3-D for similar application methodology (25−66%).[24,36,47] The results for chloropicrin were much different from emission values reported in the literature (i.e., 30−60%), which was attributed to the unusually high soil reactivity at the field site.

The results from this study should prove useful for conducting risk assessments. Recent U.S. EPA FIFRA Scientific Advisory Science Panels (SAP) conducted assessments of three fumigant bystander exposure models.[48−50] The SAP and model developers concluded that the availability of appropriate emission rate time series is critical to the effective use of these risk assessment models, because the emission rate defines the source term for fumigants in the airstream that can lead to exposures. Information on emission rates based on multiple and independent estimation methods, and that are applicable to field-scale conditions, provides valuable information for use in risk assessment.

DOI: 10.1021/acs.jafc.5b01309
J. Agric. Food Chem. 2015, 63, 5354−5363

■ ASSOCIATED CONTENT

Supporting Information

Schematic of the field site; description of the micrometeorological methods used in this study including a graph of the temperature difference, gradient Richardson's number, and atmospheric stability parameter; and graph of the soil water content data. The Supporting Information is available free of charge on the ACS Publications website at DOI: 10.1021/acs.jafc.5b01309.

■ AUTHOR INFORMATION

Corresponding Author

*(S.R.Y.) E-mail: scott.yates@ars.usda.gov. Phone: (951) 369-4803. Fax: (951) 342-4964.

Present Addresses

[Δ](W.Z.) Illinois Sustainable Technology Center, University of Illinois at Urbana-Champaign, Champaign, IL 61820, USA.
[Π](J.K.) FluxExperts, LLC, Carmel, IN 46032, USA.

Funding

Part of the research described was supported by the California Air Resources Board (Agreement 05-351).

Notes

The use of trade, firm, or corporation names in this paper is for the information and convenience of the reader. Such use does not constitute an official endorsement or approval by the U.S. Department of Agriculture or the Agricultural Research Service of any product or service to the exclusion of others that may be suitable.

The authors declare no competing financial interest.

■ ACKNOWLEDGMENTS

We are grateful to F. Ernst and J. Jobes for their assistance in preparing and conducting the reported experiment.

■ REFERENCES

(1) van den Berg, F.; Kubiak, R.; Benjey, W.; Majewski, M.; Yates, S. R.; Reeves, G.; Smelt, J.; van der Linden, A. Emission of pesticides into the air. *Water, Air, Soil Pollut.* **1999**, *115*, 195−218.

(2) Neal, R.; Spurlock, F.; Segawa, R. *Annual Report on Volatile Organic Chemical Emissions from Pesticides: Emissions for 1990−2007*; Report EH09-01 (March 2009); California Environmental Protection Agency: Sacramento, CA, USA, 2009; 39 pp.

(3) Baker, L. W.; Fitzell, D. L.; Seiber, J. N.; Parker, T. R.; Shibamoto, T.; Poor, M. W.; Longley, K. E.; Tomlin, R. P.; Propper, R.; Duncan, D. W. Ambient air concentrations of pesticides in California. *Environ. Sci. Technol.* **1996**, *30*, 1365−1368.

(4) Wauchope, R. D.; Buttler, T. M.; Hornsby, A. G.; Augustijn-Beckers, P. W. M.; Burt, J. P. The SCS/ARS/CES Pesticide properties database for environmental decision-making. *Rev. Environ. Contamin. Toxicol.* **1992**, *123*, 1−155.

(5) Yates, S. R.; McConnell, L. L.; Hapeman, C. J.; Papiernik, S. K.; Gao, S.; Trabue, S. L. Managing agricultural emissions to the atmosphere: state of the science, fate and mitigation, and identifying research gaps. *J. Environ. Qual.* **2011**, *40*, 1347−1358.

(6) Albrecht, W. N. Occupational exposure to 1,3-dichloropropene (Telone) in Hawaiian pineapple culture. *Arch. Environ. Health* **1987**, *42*, 286−291.

(7) CDPR (California Department of Pesticides Regulation). California management plan: 1,3-dichloropropene; Department of Pesticide Regulation: Sacramento, CA, USA; http://www.cdpr.ca.gov/docs/emon/methbrom/telone/mgmtplan.pdf.

(8) U.S. EPA. *Reregistration Eligibility Decision (RED) for Chloropicrin*; EPA 738-R-08-009; U.S. EPA Prevention, Pesticide and Toxic Substances: Washington, DC, USA, 2008; 128 pp.

(9) Carter, W. P. L.; Luo, D. M.; Malkina, I. L. Investigation of the atmospheric reactions of chloropicrin. *Atmos. Environ.* **1997**, *31*, 1425−1439.

(10) Wilhelm, S. N.; Shepler, K.; Lawrence, L. J.; Lee, H. Environmental fate of chloropicrin. In Fumigants: Environmental Fate, Exposure, and Analysis. *ACS Symp. Ser.* **1996**, *No. 652*, 79−93.

(11) Basile, M.; Senesi, N.; Lamberti, F. A study of some factors affecting volatilization losses of 1,3-dichloropropene (1,3-D) from soil. *Agric., Ecosyst. Environ.* **1986**, *17*, 269−279.

(12) Gan, J.; Yates, S. R.; Crowley, D.; Becker, J. O. Acceleration of 1,3-dichloropropene degradation by organic amendments and potential application for emissions reduction. *J. Environ. Qual.* **1998**, *27*, 408−414.

(13) Gan, J.; Yates, S. R.; Wang, D.; Ernst, F. F. Effect of application methods on 1,3-dichloropropene volatilization from soil under controlled conditions. *J. Environ. Qual.* **1998**, *27*, 432−438.

(14) Gan, J.; Yates, S. R.; Ernst, F. F.; Jury, W. A. Degradation and volatilization of the fumigant chloropicrin after soil treatment. *J. Environ. Qual.* **2000**, *29*, 1391−1397.

(15) Zheng, W.; Yates, S. R.; Papiernik, S. K.; Wang, Q. Q. Reducing 1,3-dichloropropene emissions from soil columns amended with thiourea. *Environ. Sci. Technol.* **2006**, *40*, 2402−2407.

(16) Gao, S.; Trout, T. J. Surface seals reduce 1,3-dichloropropene and chloropicrin emissions in field tests. *J. Environ. Qual.* **2007**, *36*, 110−119.

(17) McDonald, J. A.; Gao, S.; Qin, R.; Thomas, J. Thiosulfate and manure amendment with water application and tarp on 1,3-dichloropropene emission reductions. *Environ. Sci. Technol.* **2008**, *42*, 398−402.

(18) Ashworth, D. J.; Ernst, F.; Xuan, R.; Yates, S. R. Laboratory assessment of emission reduction strategies for the agricultural fumigants 1,3-dichloropropene and chloropicrin. *Environ. Sci. Technol.* **2009**, *43*, 5073−5078.

(19) van den Berg, F. Measured and computed concentrations of 1,3-dichloropropene in the air around fumigated fields. *Pestic. Sci.* **1992**, *36*, 195−206.

(20) van Wesenbeeck, I.; Knuteson, J. A.; Barnekow, D. E.; Phillips, A. M. Measuring flux of soil fumigants using the aerodynamic and dynamic flux chamber methods. *J. Environ. Qual.* **2007**, *36*, 613−620.

(21) Chellemi, D. O.; Ajwa, A.; Sullivan, D. Atmospheric flux of agricultural fumigants from raised-bed, plastic-mulch crop production systems. *Atmos. Environ.* **2010**, *44*, 5279−5286.

(22) Chen, C.; Green, R. E.; Thomas, D. M.; Knuteson, J. A. Modeling 1,3-dichloropropene vapor-phase advection in the soil profile. *Environ. Sci. Technol.* **1995**, *29*, 1816−1821.

(23) Chen, C.; Green, R. E.; Thomas, D. M.; Knuteson, J. A. Correction To: Modeling 1,3-dichloropropene vapor-phase advection in the soil profile. *Environ. Sci. Technol.* **1996**, *30*, 359.

(24) Gao, S.; Trout, T. J.; Schneider, S. Evaluation of fumigation and surface seal methods on fumigant emissions in an orchard replant field. *J. Environ. Qual.* **2008**, *37*, 369−377.

(25) Gao, S.; Qin, R.; Hanson, B. D.; Tharayil, N.; Trout, T. J.; Wang, D.; Gerik, J. Effects of manure and water applications on 1,3-dichloropropene and chloropicrin emissions in a field trial. *J. Agric. Food Chem.* **2009**, *57*, 5428−5434.

(26) Gao, F.; Yates, S. R.; Yates, M. V.; Gan, J.; Ernst, F. F. Design, fabrication, and application of a dynamic chamber for measuring gas emissions from soil. *Environ. Sci. Technol.* **1997**, *31*, 148−153.

(27) Ross, L. J.; Johnson, B.; Kim, K. D.; Hsu, J. Prediction of methyl bromide flux from area sources using the ISCST3 model. *J. Environ. Qual.* **1996**, *25*, 885−891.

(28) Barry, T. A.; Segawa, R.; Wofford, P.; Ganapathy, C. Off-site air monitoring following methyl bromide chamber and warehouse fumigations and evaluation of the Industrial Source Complex-Short Term 3 air dispersion model. In *Fumigants*; Seiber, J., et al., Eds.; ACS Symposium Series 652; American Chemical Society: Washington, DC, USA, 1996; pp 178−188.

(29) CDPR (California Department of Pesticides Regulation). Memorandum dated Aug 21, 2008 to Randy Segawa, Environmental

DOI: 10.1021/acs.jafc.5b01309
J. Agric. Food Chem. 2015, 63, 5354−5363

Monitoring Branch, Memorandum, Aug 21, 2008; http://www.cdpr.ca.gov/docs/emon/pubs/ehapreps/analysis_memos/2071_segawa.pdf.
(30) Johnson, B.; Barry, T.; Wofford, P. *Workbook for Gaussian Modeling Analysis of Air Concentration Measurements*; Report EH99-03; California Environmental Protection Agency: Sacramento, CA, USA, Sept 1999 (revised May 2010); 61 pp.
(31) U.S. EPA. *User's Guide for the AMS/EPA Regulatory Model − AERMOD*; EPA-454/B-03-001; U.S. Environmental Protection Agency: Research Triangle Park, NC, USA. 2004; 216 pp.
(32) Parmele, L. H.; Lemon, E. R.; Taylor, A. W. Micrometeorological measurement of pesticide vapor flux from bare soil and corn under field conditions. *Water, Air, Soil Pollut.* **1972**, *1*, 433−451.
(33) Yates, S. R.; Knuteson, J.; Ernst, F. F.; Zheng, W.; Wang, Q. The effect of sequential surface irrigations on field-scale emissions of 1,3-dichloropropene. *Environ. Sci. Technol.* **2008**, *42*, 8753−875.
(34) Rosenberg, N. J.; Blad, B. L.; Verma, S. B. *Microclimate, The Biological Environment*; Wiley: New York, 1983; 495 pp.
(35) Yates, S. R. Analytical solution describing pesticide volatilization from soil affected by a change in surface condition. *J. Environ. Qual.* **2009**, *38*, 259−267.
(36) Chellemi, D. O.; Mirusso, J.; Ajwa, H. A.; Sullivan, D. A.; Unruh, J. B. Fumigant persistence and emission from soil under multiple field application scenarios. *Crop Prot.* **2013**, *43*, 94−103.
(37) Kim, J. H.; Mallavarapu, M. Isomeric effects on volatilization of 1,3-dichloropropene fumigant in soil. *J. Environ. Sci. Int.* **2009**, *18* (12), 1325−1330.
(38) Spencer, W. F.; Cliath, M. M.; Farmer, W. J. Vapor density of soil-applied dieldrin as related to soil-water content, temperature, and dieldrin concentration. *Soil Sci. Soc. Am. Proc.* **1969**, *33*, 509−511.
(39) Glotfelty, D. E.; Taylor, A. W.; Turner, B. C.; Zoller, W. H. Volatilization of surface-applied pesticides from fallow soil. *J. Agric. Food Chem.* **1984**, *32*, 638−643.
(40) Reichman, R.; Rolston, D. E.; Yates, S. R.; Skaggs, T. H. Diurnal variation of diazinon volatilization: soil moisture effects. *Environ. Sci. Technol.* **2011**, *45*, 2144−2149.
(41) Spencer, W. F.; Cliath, M. M. Pesticide volatilization as related to water loss from soil. *J. Environ. Qual.* **1973**, *2*, 284−289.
(42) Reichman, R.; Yates, S. R.; Skaggs, T. H.; Rolston, D. E. Effects of soil moisture on the diurnal pattern of pesticide emission: numerical simulation and sensitivity analysis. *Atmos. Environ.* **2013**, *66*, 41−51.
(43) Reichman, R.; Yates, S. R.; Skaggs, T. H.; Rolston, D. E. Effects of soil moisture on the diurnal pattern of pesticide emission: comparison of simulations with field measurements. *Atmos. Environ.* **2013**, *66*, 52−62.
(44) Jury, W. A.; Spencer, W. F.; Farmer, W. J. Behavior assessment model for trace organics in soil: 1. Model description. *J. Environ. Qual.* **1983**, *12*, 558−564.
(45) Ashworth, D. J.; Yates, S. R. Surface irrigation reduces the emission of volatile 1,3-dichloropropene from agricultural soils. *Environ. Sci. Technol.* **2007**, *41*, 2231−2236.
(46) Ashworth, D. J.; Yates, S. R.; van Wesenbeeck, I. J.; Stanghellini, M. Effect of co-formulation of 1,3-dichloropropene and chloropicrin on evaporative emissions from soil. *J. Agric. Food Chem.* **2015**, *63*, 415−421.
(47) Cryer, S. A.; van Wessenbeeck, I. J. Estimating field volatility of soil fumigants using CHAIN_2D: mitigation methods and comparison against chloropicrin and 1,3-dichloropropene field observations. *Environ. Model Assess.* **2010**, *15*, 309−318.
(48) Cryer, S. A. Predicting soil fumigant air concentrations under regional and diverse agronomic conditions. *J. Environ. Qual.* **2005**, *34*, 2197−2207.
(49) Sullivan, D. A.; Holdsworth, M. T.; Hlinka, D. J. Monte Carlo-based dispersion modeling of off-gassing releases from the fumigant metam-sodium for determining distances to exposure endpoints. *Atmos. Environ.* **2004**, *38*, 2471−2481.
(50) Reiss, R.; Griffin, J. A probabilistic model for acute bystander exposure and risk assessment for soil fumigants. *Atmos. Environ.* **2006**, *40*, 3548−3560.

DOI: 10.1021/acs.jafc.5b01309
J. Agric. Food Chem. 2015, 63, 5354−5363

JOURNAL OF AGRICULTURAL AND FOOD CHEMISTRY

Article

pubs.acs.org/JAFC

Influence of Free Amino Acids, Oligopeptides, and Polypeptides on the Formation of Pyrazines in Maillard Model Systems

Gustavo Luis Leonardo Scalone,[†,‡] Tatiana Cucu,[†] Norbert De Kimpe,[‡] and Bruno De Meulenaer*[,†]

[†]Department of Food Safety and Food Quality, nutriFOODchem Group, Member of Food2Know, Faculty of Bioscience Engineering, and [‡]Department of Sustainable Organic Chemistry and Technology, Faculty of Bioscience Engineering, Ghent University, Coupure links 653, B-9000 Ghent, Belgium

ABSTRACT: Pyrazines are specific Maillard reaction compounds known to contribute to the unique aroma of many products. Most studies concerning the generation of pyrazines in the Maillard reaction have focused on amino acids, while little information is available on the impact of peptides and proteins. The present study investigated the generation of pyrazines in model systems containing whey protein, hydrolyzed whey protein, amino acids, and glucose. The impact of thermal conditions, ratio of reagents, and water activity (a_w) on pyrazine formation was measured by headspace solid-phase microextraction with gas chromatography/mass spectrometry (HS-SPME−GC/MS. The presence of oligopeptides from hydrolyzed whey protein contributed significantly to an increased amount of pyrazines, while in contrast free amino acids generated during protein hydrolysis contributed to a lesser extent. The generation of pyrazines was enhanced at low a_w (0.33) and high temperatures (>120 °C). This study showed that the role of peptides in the generation of pyrazines in Maillard reaction systems has been dramatically underestimated.

KEYWORDS: *peptides, Maillard, fractions, pyrazines, flavor, model reactions, HS-SPME−GC/MS*

INTRODUCTION

The Maillard reaction comprises a set of complex chemical reactions, which are initiated when a free amino group of an amino acid, peptide, protein, or amine reacts with the carbonyl group of a reducing sugar. This nonenzymatic browning reaction gives rise to modifications in color, aroma, taste, and nutritional value of thermally treated foods and is influenced by many factors, such as temperature, time, pH, type of buffer, water activity, and reactant concentration.[1] The reaction between free amino acids and carbonyl compounds has been extensively studied,[1] whereas the Maillard reaction between peptides and proteins with carbonyl compounds has been less investigated.[2−4] This in fact is quite surprising, as the amount of free amino acids in food is generally very low as compared to the amounts of peptides and especially proteins.[5]

A limited number of studies have investigated the generation of volatiles in protein−carbohydrate models. Nevertheless, these studies were performed under unrealistically severe thermal conditions.[6−8]

Oligopeptides have been recognized as important flavor enhancers and precursors of the Maillard reaction.[2,9−11] Moreover, peptides can be a flavor enhancer as such (umami taste). In addition, the formation of flavor compounds due to reaction between peptides and carbohydrates has mainly been studied in model systems containing glutathione[12−15] and glycine-derived peptides such as diglycine, triglycine, and tetraglycine.[4] In these studies, pyrazines were indeed the most abundant volatiles.

Substituted and unsubstituted pyrazines are specific Maillard reaction products that are known to contribute significantly to the unique roasted, nutty, meaty, earthy, and popcornlike aroma of many heated food products.[16,17] Oh et al.[4] found that the amount of pyrazines formed from diglycine or tetraglycine was considerably lower compared to that formed from either glycine or triglycine. Van Lancker et al.[18,19] studied the formation of pyrazines from di- and tripeptides with different amino acid sequences. The results of these studies showed significant formation of pyrazines from dipeptides compared to free amino acids and less pyrazine formation in tripeptides compared with dipeptides and free amino acids.

The general mechanism of pyrazine formation via the Maillard reaction implies in the first step the reaction of a dicarbonyl compound **1** produced by sugar degradation and an amino acid **2**, which leads to the formation of Strecker aldehydes **6** and α-aminoketones **7**. A crucial step in this degradation reaction is decarboxylation of the intermediate **4** via a cyclic transition state (Figure 1, part I). The second step in pyrazine formation involves two possible pathways that start with the condensation reaction of two α-aminocarbonyl compounds, **7** and **7′**, forming dihydropyrazine **9**. This dihydropyrazine can react in two distinct ways. The dihydropyrazine can oxidize spontaneously with air to the corresponding pyrazine **11** (pathway A). Alternatively, after deprotonation the dihydropyrazine anion **10** can react with a carbonyl compound **6** in an aldol-type reaction (pathway B). Whenever this reacting carbonyl compound is a Strecker aldehyde **6**, amino-acid-specific pyrazines **15** are formed (Figure 1, part II).

Peptides cannot follow the typical Strecker degradation due to the absence of a free carboxyl group at the α-carbon with respect to the free amino group, making the decarboxylation

Received: March 3, 2015
Revised: May 12, 2015
Accepted: May 14, 2015
Published: May 14, 2015

ACS Publications © 2015 American Chemical Society

DOI: 10.1021/acs.jafc.5b01129
J. Agric. Food Chem. 2015, 63, 5364−5372

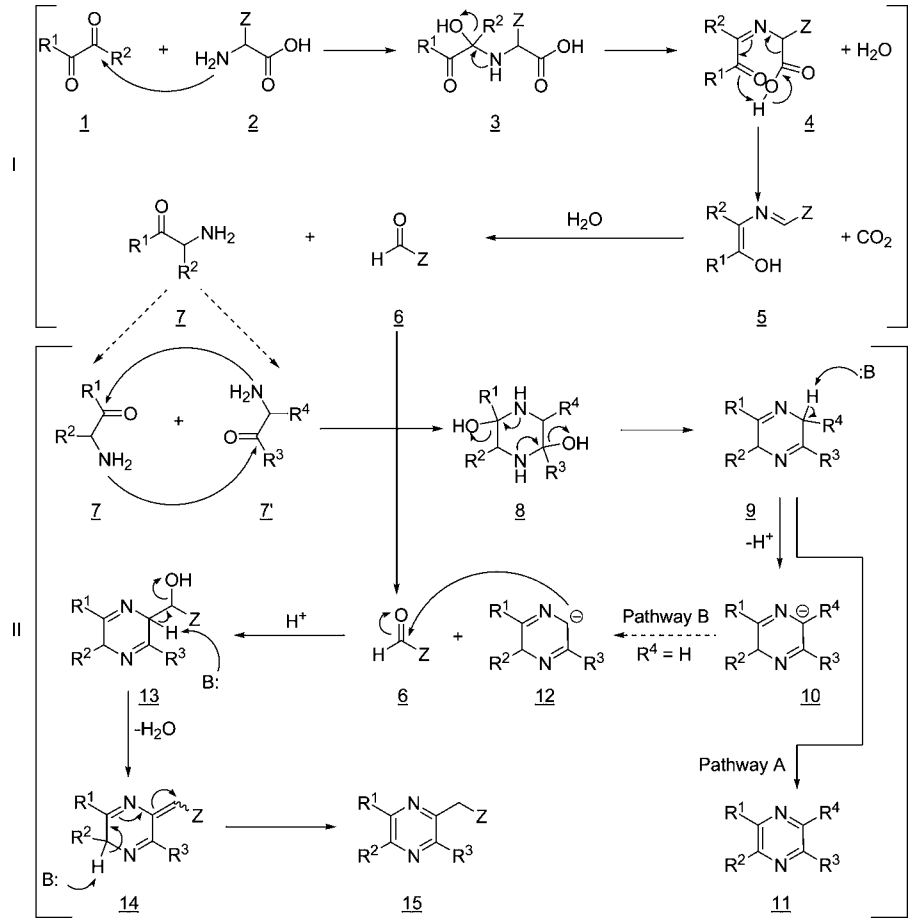

Figure 1. Strecker degradation (part I) and pyrazine formation (part II).

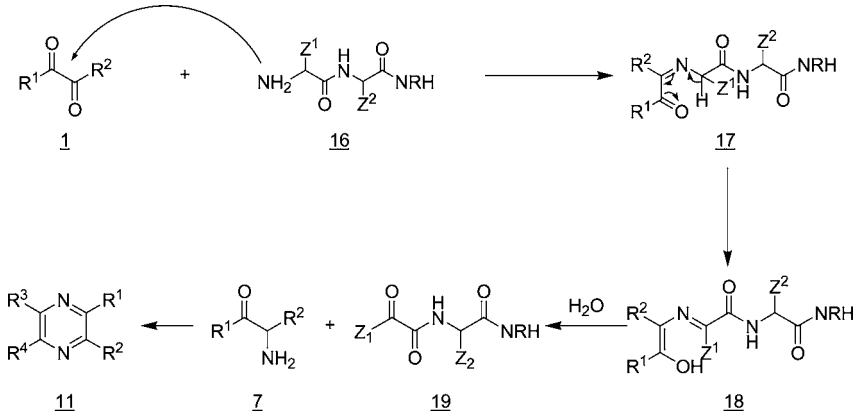

Figure 2. Hypothetical formation mechanism of α-aminoketones from the reaction of peptides with an α-dicarbonyl compound. Adapted from Van Lancker et al.[18]

impossible. Van Lancker et al.[18] have suggested a mechanism of pyrazine formation in model systems containing dipeptides and dicarbonyl compounds as shown in Figure 2. In accordance with the reaction with free amino acids, reaction of α-dicarbonyl compound **1** with the dipeptide starts with formation of an α-ketoimine **17**. Afterward, deprotonation occurs at the α-position of the amide moiety, resulting in a 1,5-H-shift leading to enolization of the carbonyl group of intermediate **17**. Hydrolysis of the imino moiety of 4-hydroxy-2-azadiene **18** produces the α-aminoketone **7**, and instead of forming the Strecker aldehyde, a complex α-ketoamide **19** is formed.[2]

Although it was shown before that peptides may generate pyrazines in the Maillard reaction, their potential contribution to the overall pyrazine formation in food has not been compared to the contribution of amino acids. Therefore, this study aimed to evaluate the impact of trypsinogenic whey hydrolysis products on the formation of pyrazines in a Maillard reaction model, thereby trying to discriminate the role of free amino acids and peptides generated, respectively. In addition the impact of other factors such as heating conditions, ratio of

DOI: 10.1021/acs.jafc.5b01129
J. Agric. Food Chem. 2015, 63, 5364−5372

reagents, and water activity on the formation of pyrazines was investigated.

MATERIALS AND METHODS

Chemicals. DL-Norvaline (99%), L-cysteine (99.5%), L-4-hydroxyproline (99%), DL-valine (99%), DL-alanine (99%), L-tryptophan (99.5%), L-citrulline (99%), sarcosine (99%), DL-histidine (99%), L-isoleucine (99.5%), DL-leucine (99%), and glutamine (99,5%) were purchased from Fluka (Sigma−Aldrich, Bornem, Belgium). DL-Lysine monohydrochloride (98%), DL-methionine (99%), glycine (99.5%), L-arginine hydrochloride (99%), L-phenylalanine (99%), L-glutamic acid (99%), D-(+)-glucose (99.5%), trypsin from porcine pancreas, trypsin−chymotrypsin inhibitor from *Glycine max* (soybean), insulin from bovine pancreas, insulin chain B oxidized from bovine pancreas, cytochrome *c* from equine heart, vitamin B_{12}, Val-Tyr, pyrazine (99%), 2-methylpyrazine (99%), and sodium bromide (99%) were purchased from Sigma−Aldrich (Bornem). L-Lysine (97%), arginine (98%), proline (99%), asparagine monohydrate (99%), 2,5-dimethylpyrazine (99%), 2-ethylpyrazine (98%), 2-ethyl-3-methylpyrazine (99%), 2-ethyl-3,5(6)-dimethylpyrazine (99.5%), and trichloroacetic acid (99%) were purchased from Acros Organics, Thermo-Fisher Scientific (Erembodegem, Belgium). Aspartic acid (99%), DL-threonine (99%), and L-tyrosine (99%) were purchased from Merck (Darmstadt, Germany). DL-Serine, 2,3-dimethylpyrazine (99%), and 2,6-dimethylpyrazine (96%) were purchased from Janssen Chimica (Geel, Belgium). Magnesium chloride hexahydrate (99%), calcium carbonate (99%), potassium iodide (99.5%), and sodium chloride (98%) were purchased from Chemlab Analytical (Zedelgem, Belgium). Whey protein isolate Lacprodan DI-9224 was donated from Arla Foods (Aarhus, Denmark).

Hydrolysis of Whey Protein. Whey protein isolate (84% protein) was dissolved in 0.1 M potassium phosphate buffer, pH 7.8, at a concentration of 5 mg/mL, heated at 95 °C for 5 min, and then cooled down at room temperature. Trypsin was added at a ratio of 1:20 (w/w), and then the mixture was incubated at 37 °C in a water bath for 20 h. The obtained solution was heated at 95 °C for 5 min to inactivate the enzyme and then frozen for later use. The free amino acid content of the hydrolyzed protein was analyzed and reported (Table 1). The nonhydrolyzed whey protein isolate did not contain free amino acids in detectable amounts. The protein hydrolysate was further characterized by gel-permeation chromatography as shown in Figure 3 and outlined below.

Table 1. Free Amino Acid Composition of Native Whey Protein Isolate after Tryptic Hydrolysis

amino acid	content (mg/100 mg of hydrolyzed whey)
lysine	0.9916
leucine	0.1340
valine	0.0960
isoleucine	0.0728
arginine	0.0546
tyrosine	0.0421
threonine	0.0389
tryptophan	0.0359
phenylalanine	0.0297
methionine	0.0218
alanine	0.0104

Size-Exclusion Chromatography. Samples of whey protein and hydrolyzed whey protein were analyzed with an Äkta explorer liquid chromatograph (LC) coupled to a UV detector (GE Healthcare, Zaventem, Belgium) equipped with a Superdex peptide 10/300 GL column (GE Healthcare, Zaventem). Working conditions were as follows: mobile phase, 0.15 M ammonium hydrogen carbonate buffer, pH 7.8; flow, 0.5 mL/min; UV detection, 214 nm.

Free Amino Acid Analysis. Samples of whey protein and hydrolyzed whey protein were treated with a solution of 15% trichloroacetic acid, further centrifuged, filtered, and analyzed by HPLC with fluorescence detection.[20]

Selection of Thermal Reaction Conditions. *Sterilization Conditions.* Samples were mixed in a volumetric flask and the volume was adjusted to 5 mL with 0.1 M potassium phosphate buffer, pH 7.8. Then each sample was transferred to a SPME vial (Gerstel, Mülheim, Germany) and closed with a pressure cap [silicone/poly-(tetrafluoroethylene) (PTFE), 55°, shore A, 1.5 mm, magnetic; Gerstel, Mülheim an der Ruhr, Germany). The vial was heated in a stirring oil bath at 130 °C to obtain an inside temperature of 120 °C, for 2 h, after which the vials were immediately cooled down in an ice bath.

Roasting Conditions. Samples were mixed in a volumetric flask and the volume was adjusted to 5 mL with 0.1 M potassium phosphate buffer pH 7.8. Then each sample was transferred to a SPME vial containing 1.5 g of sand. Subsequently the samples were frozen and freeze-dried in a VaCo5 freeze-dryer (Zirbus Technology, Bad Grund, Germany) to ensure sample homogeneity. Finally, the samples were closed with pressure caps and heated in an oven (Memmert, Fisher Scientific, Erembodegem, Belgium) at 180 °C for 90 min. Preliminary experiments showed that a considerable improvement in reproducibility could be obtained by dissolving, freezing, and freeze-drying instead of dry-mixing the various ingredients.

Reactant Type. Two groups of samples were analyzed to evaluate the yields of pyrazine formation under roasting and sterilization conditions.

Samples containing hydrolyzed whey protein and glucose were prepared at eight different ratios of protein to glucose ranging from 1:1.33 to 1:0.08 (w/w); see Table 2. Samples containing lysine and glucose were prepared at nine different ratios of lysine to glucose ranging from 1:2.53 to 1:0.15 (w/w); see Table 3. Samples were analyzed by headspace solid-phase microextraction with gas chromatography/mass spectrometry (HS-SPME−GC/MS).

Elucidation of the Role of Protein Hydrolysis Products on Formation of Pyrazines. Four groups of model systems were prepared as follows: (1) hydrolyzed whey protein (15 mg) + glucose (7.5 or 15 mg); (2) native whey protein (15 mg) + glucose (7.5 or 15 mg); (3) native whey protein (15 mg) + glucose (7.5 or 15 mg) with addition of a mixture of free amino acids (aa), corresponding to the free amino acid content of the tryptic digestion of whey protein as reported in Table 1; and (4) a mixture of free amino acids (aa), corresponding to the free amino acid content of the tryptic digestion of whey protein as reported in Table 1, and glucose (7.5 or 15 mg).

The reaction mixtures were dissolved in 5 mL of 0.1 M potassium phosphate buffer, pH 7.8, and then transferred to SPME vials containing 1.5 g of sand, freeze-dried, closed with pressure caps, and thermally treated under previously described roasting conditions. Samples were analyzed by HS-SPME−GC/MS.

Impact of Water Activity on Pyrazine Generation from Hydrolyzed Whey Protein. Samples containing 15 mg of hydrolyzed whey protein and 7.5 mg of glucose were dissolved in 5 mL of 0.1 M potassium phosphate buffer, pH 7.8, and transferred to SPME vials containing 1.5 g of sand. Subsequently the vials were freeze-dried and immediately capped. Afterward, the water activity (a_w) values of the samples were determined on a 4TEV dew point water activity meter (Aqualab, Decagon Devices, Pullman, WA) obtaining an initial value of 0.16.

Subsequently, freeze-dried samples were transferred to different hermetic plastic recipients containing saturated solutions of magnesium chloride (32% relative humidity, RH), potassium carbonate (43% RH), sodium bromide (56% RH), potassium chloride (67% RH), and sodium chloride (75% RH). All the samples were incubated in triplicate for 7 days at 30 °C inside an incubator (Memmert, Fisher Scientific, Erembodegem, Belgium) in order to reach the desired water activity in each sample. After reaching equilibrium, all samples were thermally treated under previously described roasting conditions and analyzed by HS-SPME−GC/MS.

Headspace Solid-Phase Microextraction with Gas Chromatography/Mass Spectrometry Analysis. The volatiles produced during the different experimental conditions were extracted by means

DOI: 10.1021/acs.jafc.5b01129
J. Agric. Food Chem. 2015, 63, 5364−5372

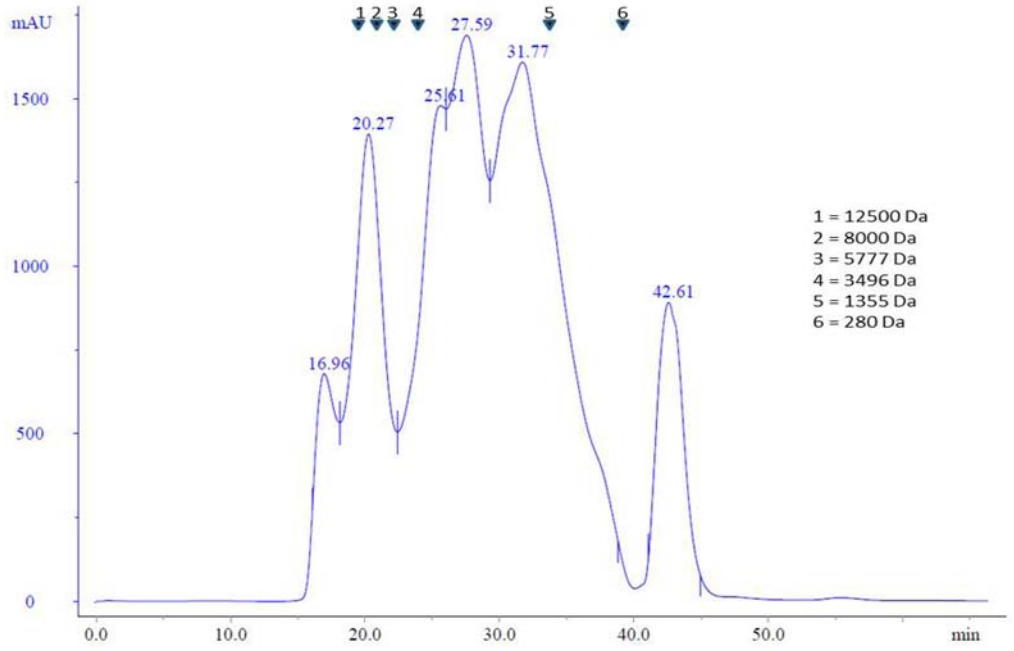

Figure 3. Gel-permeation chromatogram of hydrolyzed whey protein after tryptic hydrolysis. Nonhydrolyzed whey elutes as one unique peak at 16.96 min. Peak position for weight markers are shown on top.

Table 2. Pyrazines Detected in Model Reactions of Glucose and Hydrolyzed Whey[a]

	hydrolyzed whey (15 mg) + glucose as indicated							
	1.25 mg	2.5 mg	5 mg	7.5 mg	10 mg	15 mg	17.5 mg	20 mg
ratio[b]	1:0.08	1:0.17	1:0.33	1:0.5	1:0.67	1:1	1:1.17	1:1.33
				2-Methylpyrazine[d]				
R[c]	4.15 ± 0.12 a	9.46 ± 0.23 b	16.21 ± 0.47 c	23.10 ± 0.36 d	22.54 ± 1.95 cd	20.97 ± 1.20 cd	18.86 ± 1.47 cd	20.87 ± 0.65 d
S	ND[e]	ND	0.94 ± 0.04 a	1.75 ± 0.01 b	3.46 ± 0.24 c	5.45 ± 0.08 de	5.35 ± 0.29 de	6.32 ± 0.39 e
				2,5(6)-Dimethylpyrazine[d]				
R	24.45 ± 1.35 a	35.22 ± 1.88 b	37.81 ± 1.23 bd	42.39 ± 3.04 d	35.25 ± 2.01 b	25.41 ± 1.83 a	22.75 ± 2.22 a	20.22 ± 1.26 a
S	ND	5.65 ± 0.52 a	6.75 ± 0.66 ac	9.64 ± 0.41 be	7.49 ± 0.19 c	11.16 ± 0.04 d	8.32 ± 0.20 e	9.66 ± 0.14 b
				2,3-Dimethylpyrazine[d]				
R	ND	ND	1.13 ± 0.03 a	1.80 ± 0.07 b	2.10 ± 0.15 c	2.16 ± 0.01 c	2.54 ± 0.14 d	2.11 ± 0.03 c
S	ND	ND	ND	ND	ND	ND	ND	ND
				2-Ethylpyrazine[d]				
R	ND	ND	3.45 ± 0.04 a	4.24 ± 0.19 b	4.29 ± 0.16 b	4.73 ± 0.06 c	4.96 ± 0.22 c	4.92 ± 0.12 c
S	ND	ND	ND	ND	ND	ND	ND	ND
				2-Ethyl-3-methylpyrazine[d]				
R	3.79 ± 0.20 a	8.22 ± 0.44 bd	10.84 ± 0.21 c	11.00 ± 0.51 c	9.38 ± 0.48 d	8.80 ± 0.05 bd	9.32 ± 0.50 d	7.92 ± 0.37 b
S	ND	ND	ND	ND	ND	ND	ND	ND
				3-Ethyl-2,5-dimethylpyrazine[d]				
R	3.77 ± 0.18 a	6.70 ± 0.39 b	6.78 ± 0.33 b	5.14 ± 0.13 c	3.59 ± 0.33 a	3.37 ± 0.18 a	3.43 ± 0.21 a	2.42 ± 0.14 da
S	ND	ND	ND	ND	ND	ND	ND	ND
				2-Ethyl-3,5-dimethylpyrazine[f]				
R	ND	ND	2.07 ± 0.04 a	2.28 ± 0.14 a	2.04 ± 0.16 a	1.54 ± 0.08 ba	1.26 ± 0.56 b	1.27 ± 0.09 b
S	ND	ND	ND	ND	ND	ND	ND	ND
				5-Ethyl-2,3-dimethylpyrazine[f]				
R	ND	ND	1.22 ± 0.05 a	1.06 ± 0.06 a	1.03 ± 0.08 a	1.16 ± 0.08 a	1.23 ± 0.11 a	1.12 ± 0.03 a
S	ND	ND	ND	ND	ND	ND	ND	ND

[a]Samples containing hydrolyzed whey protein and glucose were prepared at eight different ratios of protein to glucose, ranging from 1:1.33 to 1:0.08 (w/w), and analyzed by HS-SPME−GC/MS. Data points represent mean values of three independent determinations and are given as GC/MS peak area × 10^6. Values in the same row followed by different letters are significantly different ($p < 0.05$). [b]Protein/glucose ratio (w/w). [c]Model reactions were as follows: R, dry glucose and hydrolyzed whey mixtures under roasting conditions (180 °C/90 min); S, aqueous glucose and hydrolyzed whey solutions under sterilization conditions (120 °C/120 min). [d]Identification confirmed by GC retention index and mass spectra of authentic compounds. [e]ND, not detected. [f]Tentatively identified by matching mass spectra library.

of HS-SPME for 30 min at 35 °C with a DVD/Car/PDMS fiber (Supelco, Bornem) with a multipurpose sampler (MPS-2, Gerstel). GC/MS analyses of the SPME extract were performed with an Agilent 6890 GC Plus apparatus coupled to a quadrupole mass spectrometer

DOI: 10.1021/acs.jafc.5b01129
J. Agric. Food Chem. 2015, 63, 5364−5372

5973 MSD (Agilent Technologies, Diegem, Belgium) and equipped with a DB-5 capillary column (30 m length × 0.25 m i.d; 0.25 μm film thickness) (Agilent Technologies, Diegem). Working conditions were as follows: transfer line to mass-selective detector (MSD) 250 °C, carrier gas (He) 1.0 mL/min; electron ionization (EI) 70 eV; acquisition parameters, scanned m/z 40−200 (2−10 min), 40−300 (10−20 min), and 40−400 (>20 min); oven temperature started at 35 °C, held 5 min, programmed from 35 to 80 °C at 2 °C/min, held 2 min. Pyrazines were identified by comparison of the mass spectrum with mass spectral libraries (Nist 98, Wiley sixth and HPCH2205) and by comparison of the calculated linear retention indices with literature values.

Generation of pyrazines was followed in a semiquantitative way by considering the absolute peak area of each individual pyrazine.[18,21,22] Although this approach does not allow absolute quantitation of each individual pyrazine, it is generally accepted as suitable to evaluate the pyrazine formation in a reliable way.

Statistical Analysis. All analyses were performed with SPSS Statistics version 22 at a significance level of 95% ($p = 0.050$). Data were normally distributed (Kolmogorov−Smirnov test, $p < 0.050$ for all standardized residuals). Therefore, one-way analysis of variance (ANOVA) was selected for statistical analysis. The Games−Howell correction was applied to control the familywise error rate at 5% for all multiple pairwise comparisons.

RESULTS AND DISCUSSION

Selection of Reaction Conditions and Ratio of Model Systems. In a first series of experiments, the impact of reactant ratio (glucose and hydrolyzed whey protein) on the formation of pyrazines was evaluated for both thermal treatments applied.

The results shown in Table 2 indicate that, under roasting conditions (180 °C/90 min), significant quantities of the following pyrazines were produced in model systems containing hydrolyzed whey protein and glucose: 2-methylpyrazine, 2,5(6)-dimethylpyrazine, 2,3-dimethylpyrazine, 2-ethylpyrazine, 2-ethyl-3-methylpyrazine, 3-ethyl-2,5-dimethylpyrazine, 2-ethyl-3,5-dimethylpyrazine, and 5-ethyl-2,3-dimethypyrazine.

The same reactants under sterilization conditions (120 °C/120 min) yielded mainly 2-methylpyrazine and 2,5(6)-dimethylpyrazine. However, the peak areas of the produced pyrazines were considerably lower compared to those observed during roasting conditions. These observations may be due to the fact that indeed a lower amount of pyrazines was produced, which can be explained by the different reaction conditions: temperature and presence of water in the systems. It should be noted as well, however, that by addition of 2 μg of 2-ethyl-3-methylpyrazine to similar amounts of non-thermally-treated samples, a much higher peak area was observed for the dry (107.89×10^6) versus the wet sample (6.68×10^6). This indicated that partitioning of the pyrazines between samples and headspace is totally different for dry and aqueous sample.

The ratio between glucose and hydrolyzed whey protein played a crucial role in the formation of pyrazines. The generation of pyrazines under dry roasting conditions was low in model systems where glucose was present in low amounts (ratio 1:0.08 and 1:0.16). This effect can likely be explained since the amount of dicarbonyl compounds generated from glucose degradation was low, which had an impact on the formation of pyrazines and resulted in lower peak areas. Higher peak areas were detected for ratios up to 1:0.5 and 1:0.67. At higher protein/glucose ratios, a decrease in the formation of pyrazines was again observed. This may be due to excessive formation of different carboxylic acids such as acetic acid from glucose,[23] which might decrease the pH of the model systems. It is generally known that pH has an impact on the generation of pyrazines,[1] hindering their formation at low pH due to the protonation of the amino groups of the amino acids and peptides. Also, under sterilization conditions, the peak area of the formed pyrazines was affected by the protein/glucose ratio although to a lesser extent.

It is broadly known that, in Maillard reaction models, free amino acids have a high reactivity. In order to compare the reactivity of glucose/hydrolyzed whey protein with a glucose/amino acid mixture, lysine was selected. Pyrazine formation at different lysine/glucose ratios was monitored under both heating conditions (see Table 3). Considerably higher amounts of pyrazines were detected in the lysine-containing reaction systems under both heating conditions when compared to hydrolyzed whey. In addition, the detected pyrazines were more diverse, particulary for the roasted samples. Under roasting conditions, the detected amounts of 2-methylpyrazine and 2,5(6)-dimethylpyrazine were considerably less influenced by the lysine/glucose ratio. However, the lysine/glucose ratio did have a considerable effect on the amount of pyrazines detected. At lower lysine/glucose ratios, formation of pyrazines in roasting conditions decreased considerably, while this tendency was not observed under sterilization conditions. These experiments showed that depending upon the amino compounds participating in the reactions, such as free amino acids or peptides involved in the pyrazine formation, the impact of the amino compounds/glucose ratio on the pyrazine formation will be different.

As it was noticed that considerably more pyrazines were detected under roasting conditions (180 °C/90 min) for both glucose/hydrolyzed whey protein and glucose/lysine models, this heat treatment was used in subsequent experiments.

Elucidation of the Role of Protein Hydrolysis Products on Formation of Pyrazines. From the previous experiments, it was obvious that hydrolyzed whey proteins were able to generate pyrazines in Maillard reaction systems. However, it was not clear if the compounds responsible for the pyrazine generation are the free amino acids produced during hydrolysis (Table 1) or the peptidic fraction or both. Therefore, formation of pyrazines by hydrolyzed whey protein was compared with pyrazine generation in a mixture of nonhydrolyzed proteins to which the free amino acids formed upon trypsinogenic hydrolysis were added according to the amounts reported in Table 1. Nonhydrolyzed whey protein was included as a control. In addition, glucose together with the free amino acids generated upon trypsinogenic hydrolysis of whey was considered as well. Experiments were conducted under dry heating conditions at two protein/glucose ratios.

In model systems containing free amino acids as described in Table 1 and glucose, no pyrazines were detected (data not shown). Most likely the amount of reagents was not sufficient to generate sufficient Maillard products. Model systems containing hydrolyzed whey protein and glucose led to formation of the highest amounts of pyrazines (Table 4). In model systems containing native whey protein and glucose, the generation of pyrazines was significantly lower than in samples of hydrolyzed whey. Native whey protein isolate did not contain any free amino acids, suggesting that the limited generation of pyrazines was due to thermal degradation of the protein under the selected reaction conditions, releasing amino compounds that can react with glucose and form pyrazines. Model systems containing native whey with addition of the mixture of free amino acids (Table 1) and glucose produced comparable and statistically similar amounts of pyrazines as the

DOI: 10.1021/acs.jafc.5b01129
J. Agric. Food Chem. 2015, 63, 5364−5372

Table 3. Pyrazines Detected in Model Reactions of Lysine and Glucose[a]

	lysine (14.61 mg) + glucose as indicated								
	2.5 mg	4.5 mg	9 mg	13.5 mg	18 mg	22.5 mg	27 mg	31.5 mg	37 mg
ratio[b]	1:0.17	1:0.3	1:0.61	1:0.92	1:1.23	1:1.54	1:1.84	1:2.15	1:2.53
					2-Methylpyrazine[d]				
R[c]	49.05 ± 0.11 a	36.80 ± 0.15 b	35.96 ± 0.83 b	42.74 ± 0.01 c	48.49 ± 0.87 a	45.16 ± 0.01 d	40.69 ± 1.13 e	43.36 ± 0.18 cd	40.57 ± 0.08 e
S	ND[e]	6.75 ± 0.47 a	13.28 ± 0.19 b	15.11 ± 0.39 bc	16.97 ± 0.40 c	25.45 ± 1.15 d	30.33 ± 1.46 e	34.82 ± 2.04 f	38.87 ± 1.14 g
					2,5(6)-Dimethylpyrazine[d]				
R	430.58 ± 0.01 a	426.55 ± 3.67 a	402.27 ± 1.03 b	450.48 ± 1.28 c	448.55 ± 0.51 c	433.84 ± 3.74 a	392.45 ± 9.19 b	293.06 ± 0.63 d	251.48 ± 1.27 e
S	ND	8.92 ± 0.77 a	19.07 ± 1.37 b	25.24 ± 0.59 dc	20.95 ± 1.74 b	27.52 ± 0.57 c	29.69 ± 1.33 c	25.57 ± 0.45 c	24.37 ± 1.14 d
					2,3-Dimethylpyrazine[d]				
R	2.23 ± 0.03 a	4.12 ± 0.02 b	10.35 ± 0.22 c	13.81 ± 0.11 d	15.11 ± 0.13 e	14.62 ± 0.07 f	12.62 ± 0.27 g	10.62 ± 0.03 c	8.07 ± 0.05 h
S	ND	1.65 ± 0.16 a	2.39 ± 0.06 b	2.86 ± 0.17 bc	2.42 ± 0.03 b	3.17 ± 0.12 c	3.34 ± 0.29 c	3.41 ± 0.29 c	3.20 ± 0.23 c
					2-Ethylpyrazine[d]				
R	ND	ND	8.37 ± 0.12 a	13.44 ± 0.16 b	15.37 ± 0.08 c	15.31 ± 0.33 c	11.81 ± 0.06 d	10.58 ± 0.06 e	8.88 ± 0.02 f
S	ND	ND	ND	ND	ND	ND	ND	ND	ND
					2-Ethyl-3-methylpyrazine[d]				
R	45.50 ± 0.50 a	68.30 ± 0.16 b	211.13 ± 2.29 c	239.29 ± 0.69 d	278.17 ± 0.20 e	263.29 ± 1.66 f	182.96 ± 0.53 g	117.95 ± 2.19 h	75.22 ± 0.04 i
S	ND	ND	ND	1.10 ± 0.05 a	1.56 ± 0.08 b	2.00 ± 0.05 c	2.53 ± 0.05 d	2.75 ± 0.25 d	2.84 ± 0.08 d
					3-Ethyl-2,5-dimethylpyrazine[d]				
R	47.89 ± 0.02 a	67.30 ± 0.57 b	89.62 ± 0.92 c	115.96 ± 2.02 d	121.61 ± 0.80 e	135.47 ± 1.47 f	91.24 ± 0.07 c	48.87 ± 0.56 a	26.95 ± 0.57 g
S	ND	ND	ND	ND	ND	ND	ND	ND	ND
					2-Ethyl-3,5-dimethylpyrazine[f]				
R	4.80 ± 0.10 a	10.58 ± 0.20 b	32.99 ± 0.17 cd	31.58 ± 0.51 d	31.68 ± 0.32 d	32.41 ± 2.70 cd	35.29 ± 0.55 c	17.83 ± 0.43 e	9.96 ± 0.11 b
S	ND	ND	ND	ND	ND	ND	ND	ND	ND
					5-Ethyl-2,3-dimethylpyrazine[f]				
R	7.86 ± 0.09 a	22.07 ± 0.20 b	101.59 ± 3.64 c	191.70 ± 5.51 d	222.19 ± 0.69 e	219.87 ± 6.20 e	85.99 ± 0.39 f	32.70 ± 0.01 b	13.72 ± 0.79 ab
S	ND	ND	ND	ND	ND	ND	ND	ND	ND
					2,5-Diethylpyrazine[f]				
R	N/D	9.69 ± 0.09 a	56.94 ± 0.90 b	89.30 ± 1.28 c	94.04 ± 0.60 c	80.42 ± 4.16 d	23.77 ± 0.10 e	8.07 ± 0.58 a	2.70 ± 0.17 f
S	ND	ND	ND	ND	ND	ND	ND	ND	ND
					2,3-Diethyl-5-methylpyrazine[f]				
R	ND	3.11 ± 0.07 a	7.44 ± 0.07 b	11.18 ± 0.54 c	14.75 ± 0.01 d	16.65 ± 0.54 e	11.59 ± 0.29 c	5.59 ± 0.02 f	2.75 ± 0.07 a
S	ND	ND	ND	ND	ND	ND	ND	ND	ND
					3,5-Diethyl-2-methylpyrazine[f]				
R	N/D	2.95 ± 0.09 a	10.30 ± 0.16 b	14.60 ± 0.32 c	18.20 ± 0.03 d	15.09 ± 0.75 c	8.40 ± 0.15 e	3.36 ± 0.13 a	1.37 ± 0.06 f
S	ND	ND	ND	ND	ND	ND	ND	ND	ND
					2-Ethyl-3,5,6-trimethylpyrazine[f]				
R	ND	3.29 ± 0.06 a	8.43 ± 0.16 b	13.05 ± 0.70 c	19.25 ± 0.11 d	16.99 ± 0.43 e	9.88 ± 0.14 f	4.50 ± 0.02 g	2.38 ± 0.23 a
S	ND	ND	ND	ND	ND	ND	ND	ND	ND
					2-Isopropyl-3,5-dimethylpyrazine[f]				
R	ND	11.11 ± 0.10 a	8.86 ± 0.06 b	9.38 ± 0.10 c	10.72 ± 0.19 d	12.41 ± 0.08 e	9.38 ± 0.11 c	6.59 ± 0.09 f	2.78 ± 0.11 g
S	ND	ND	ND	ND	ND	ND	ND	ND	ND

DOI: 10.1021/acs.jafc.5b01129
J. Agric. Food Chem. 2015, 63, 5364−5372

Table 3. continued

[a]Samples containing lysine and glucose were prepared at nine different ratios of lysine to glucose, ranging from 1:2.53 to 1:0.17 (w/w), and analyzed by HS-SPME−GC/MS. Data points represent mean values of three independent determinations and are given as GC/MS peak area × 10^6. Values in the same row followed by different letters are significantly different ($p < 0.05$). [b]Lysine/glucose ratio (w/w). [c]Model reactions were as follows: R, dry glucose and lysine mixtures under roasting conditions (180 °C/90 min); S, aqueous glucose and lysine solutions under sterilization conditions (120 °C/120 min). [d]Identification confirmed by GC retention index and mass spectra of authentic compounds. [e]ND, not detected. [f]Tentatively identified by matching mass spectra library.

model systems containing native whey protein isolate and glucose.

These results allowed us to conclude that the amount of free amino acids present in the whey hydrolysate was not sufficient to produce pyrazines in measurable amounts under the heating conditions earlier described. Compared to the results from experiments with hydrolyzed whey, it is obvious that the peptides generated upon hydrolysis played an important role in the generation of pyrazines.

Regarding the pathways that involve the peptidic fraction in the generation of α-aminoketones and their posterior condensation into pyrazines, Oh et al.[4] studied model systems with glycine containing di-, tri-, and tetrapeptides. The authors suggested that tetraglycine could be degraded to diglycine and further degraded into glycine to produce pyrazines. Simultaneously, triglycine was suggested to be degraded to diglycine and glycine. However, these results are limited to glycine-containing peptides. Yang et al.[24] studied peptide bond cleavages during the Maillard reaction, and their results show that some peptide bonds can be more resistant or labile depending on the amino acid sequence in the peptide chain. Therefore, the use of di-, tri-, and tetraglycine can only represent some peptides. The mechanism previously depicted in Figure 2 implies the formation of pyrazines in model systems containing dipeptides and dicarbonyl compounds. The alternative mechanism was suggested since dipeptides cannot follow the typical Strecker degradation due to the absence of a free carboxyl group to form α-aminoketones.

It is obvious that a similar mechanism can be responsible for the formation of pyrazine from oligopeptides as well.

Impact of Water Activity on Pyrazine Generation from Hydrolyzed Whey Protein. Lu et al.[25] studied the effects of water content on volatile generation and peptide degradation in the Maillard reaction, using glycerol to limit the water content of the samples. However, Smarrito-Menozzi et al.[26] reported that glycerol is an underestimated flavor precursor in the Maillard reaction. Therefore, the water content of the samples was controlled by equilibrating them in recipients filled with saturated salt solutions, obtaining atmospheres with fixed relative humidities as described by Greenspan et al.[27] Thus, after equilibration, samples with a particular water activity were obtained.

The results presented in Table 5 show that the model systems incubated with a water activity of 0.33 produced the highest amounts and variety of pyrazines. This may be explained by the potential effect of water activity on peptide degradation. Oliyai et al.[28] studied the chemical stability of a hexapeptide under varying conditions of pH, temperature, and moisture content; they found that higher moisture content significantly degraded the hexapeptide, leading to increased reactivity. In addition, water activity has been pointed out to have an impact on reaction rates[29] since water in food often acts as a plasticizer, leading to enhanced mobility and chemical reactivity as well.[30] However, increasing the water activity to values higher than 0.33 lead progressively to a lower generation of pyrazines, which can be explained by the fact that water is a product of several condensation steps in the Maillard reaction.[31]

This is the first paper systematically evaluating the impact of peptides generated by trypsinogenic hydrolysis on the formation of pyrazines via the Maillard reaction. The results suggest that the contribution of peptides to the generation of pyrazines is considerably high, while the role of free amino

DOI: 10.1021/acs.jafc.5b01129
J. Agric. Food Chem. 2015, 63, 5364−5372

Table 4. Pyrazines Detected in Various Model Reactions of Whey and Glucose[a]

	hydrolyzed whey (15 mg) + glucose as indicated		whey (15 mg) + glucose as indicated		whey (15 mg) + aa + glucose as indicated	
compd	7.5 mg	15 mg	7.5 mg	15 mg	7.5 mg	15 mg
2-methylpyrazine[b]	23.10 ± 0.36 a	20.97 ± 1.20 b	8.99 ± 0.62 c	8.53 ± 0.26 c	9.66 ± 1.05 d	8.06 ± 0.66 e
2,5(6)-dimethylpyrazine[b]	42.39 ± 3.04 a	25.41 ± 1.83 b	9.02 ± 0.69 c	9.29 ± 0.82 c	10.99 ± 1.17 d	9.37 ± 0.84 c
2,3-dimethylpyrazine[b]	1.80 ± 0.07 a	2.17 ± 0.01 a	ND[c]	ND	ND	ND
2-ethylpyrazine[b]	4.23 ± 0.19 a	4.73 ± 0.06 a	ND	ND	ND	ND
2-ethyl-3-methylpyrazine[b]	10.70 ± 0.11 a	8.81 ± 0.05 b	1.64 ± 0.05 c	3.50 ± 0.13 d	3.53 ± 0.12 d	3.44 ± 0.42 d
3-ethyl-2,5-dimethylpyrazine[b]	5.14 ± 0.13 a	3.38 ± 0.18 b	ND	ND	ND	ND
2-ethyl-3,5-dimethylpyrazine[d]	2.28 ± 0.14 a	1.54 ± 0.08 b	ND	ND	ND	ND
5-ethyl-2,3-dimethylpyrazine[d]	1.03 ± 0.01 a	1.16 ± 0.08 a	ND	ND	ND	ND

[a]Data points represent mean values of three independent determinations and are given as GC/MS peak area × 10^6. Values in the same row followed by different letters are significantly different ($p < 0.05$). Model reactions were as follows: dry mixtures of glucose + hydrolyzed whey, glucose + whey, or glucose + whey with addition of an amount of free amino acids (aa) as described in Table 1, under roasting conditions (180 °C/90 min). [b]Identification confirmed by GC retention index and mass spectra of authentic compounds. [c]ND, not detected. [d]Tentatively identified by matching mass spectra library.

Table 5. Pyrazines Detected in Model Reactions of Glucose and Hydrolyzed Whey at Different Relative Humidities[a]

	water activity a_w					
compd	0.16	0.33	0.38	0.53	0.62	0.75
2-methylpyrazine[b]	23.10 ± 0.36 a	54.45 ± 4.70 b	37.99 ± 1.23 c	30.40 ± 1.25 d	22.39 ± 0.86 a	19.71 ± 0.89 a
2,5(6)-dimethylpyrazine[b]	42.39 ± 3.04 a	419.99 ± 13.07 b	343.52 ± 16.20 c	327.52 ± 14.63 c	287.13 ± 5.82 d	211.5 ± 12.18 e
2,3-dimethylpyrazine[b]	1.8 ± 0.07 a	5.43 ± 0.26 b	5.73 ± 0.54 b	5.02 ± 0.48 b	4.78 ± 0.37 b	4.59 ± 0.33 b
2-ethylpyrazine[b]	4.24 ± 0.19 a	6.69 ± 0.46 b	5.62 ± 0.40 b	4.84 ± 0.43 ca	5.07 ± 0.28 ca	4.98 ± 0.32 ca
2-ethyl-3-methylpyrazine[b]	11.00 ± 0.51 a	122.23 ± 8.24 b	101.74 ± 6.33 b	97.00 ± 6.95 cd	107.68 ± 6.33 bc	85.2 ± 8.00 d
3-ethyl-2,5-dimethylpyrazine[b]	5.14 ± 0.13 a	262.84 ± 12.30 b	249.39 ± 13.11 b	247.43 ± 12.75 b	254.57 ± 4.56 b	163.00 ± 11.38 c
2-ethyl-3,5-dimethylpyrazine[c]	2.28 ± 0.14 a	30.34 ± 2.08 b	24.82 ± 1.93 c	22.04 ± 2.05 cd	22.26 ± 1.37 c	16.61 ± 1.39 d
5-ethyl-2,3-dimethylpyrazine[c]	1.06 ± 0.06 a	28.34 ± 2.46 b	19.73 ± 1.92 c	22.68 ± 1.15 c	30.82 ± 2.75 b	22.60 ± 1.67 c
2,5-diethylpyrazine[c]	ND[d]	6.78 ± 0.33 a	5.10 ± 0.43 a	5.09 ± 0.45 a	9.92 ± 0.77 b	7.43 ± 0.70 ca
2,3-diethyl-5-methylpyrazine[c]	ND	18.72 ± 0.49 a	16.19 ± 1.05 ab	15.20 ± 0.46 b	18.59 ± 1.21 a	13.49 ± 1.27 b
3,5-diethyl-2-methylpyrazine[c]	ND	20.44 ± 0.37 a	18.07 ± 1.33 a	19.14 ± 1.28 a	26.53 ± 1.77 b	20.04 ± 1.93 a
2-ethyl-3,5,6-trimethylpyrazine[c]	ND	13.03 ± 0.93 a	11.46 ± 0.84 a	10.60 ± 0.72 ab	12.83 ± 1.02 a	8.81 ± 0.65 b
2,5-dimethyl-3-(3-methyl-butyl) pyrazine[c]	ND	47.25 ± 2.70 a	46.88 ± 1.58 a	43.83 ± 1.14 a	42.22 ± 4.01 a	22.55 ± 1.39 b
3-furan-2-ylmethyl-2,5-dimethylpyrazine[c]	ND	11.80 ± 0.95 a	0.39 ± 0.03 b	0.10 ± 0.01 b	0.07 ± 0.01 b	ND

[a]Data points represent mean values of three independent determinations and are given as GC/MS peak area × 10^6. Values in the same row followed by different letters are significantly different ($p < 0.05$). Model reactions were as follows: dry glucose and hydrolyzed whey mixtures were incubated at different relative humidities under roasting conditions (180 °C/90 min). [b]Identification confirmed by GC retention index and mass spectra of authentic compounds. [c]Tentatively identified by matching mass spectra library. [d]ND, not detected.

acids is only minor and more than likely less important. The role of peptides in food on the generation of pyrazines has probably been underestimated and requires more attention.

AUTHOR INFORMATION

Corresponding Author

*Fax 32 9 2646215; e-mail Bruno.DeMeulenaer@UGent.be.

Funding

We thank the Erasmus Mundus program for their financial support of this investigation.

Notes

The authors declare no competing financial interest.

ACKNOWLEDGMENTS

Siele Ceuppens, Monica Ovando Chaves, Laurens De Coen, and Luke Sebastian Scalone are acknowledged for their valuable advice.

REFERENCES

(1) Nursten, H. E. *The Maillard Reaction: Chemistry, Biochemistry, and Implications*; Royal Society of Chemistry: Cambridge, U.K., 2005.

(2) Van Lancker, F.; Adams, A.; De Kimpe, N. Chemical modifications of peptides and their impact on food properties. *Chem. Rev.* **2011**, *111*, 7876−7903.

(3) Ho, C. T.; Oh, Y. C.; Zhang, Y. G.; Shu, C. K. Peptides as flavor precursors in model Maillard reactions. *ACS Symp. Ser.* **1992**, *490*, 193−202.

(4) Oh, Y. C.; Shu, C. K.; Ho, C. T. Some volatile compounds formed from thermal interaction of glucose with glycine, diglycine, triglycine, and tetraglycine. *J. Agric. Food Chem.* **1991**, *39*, 1553−1554.

(5) Arnoldi, A. Thermal processing and nutritional quality. *Nutr. Handb. Food Process.* **2002**, 265−286.

(6) Jing, H.; Kitts, D. D. Chemical and biochemical properties of casein-sugar Maillard reaction products. *Food Chem. Toxicol.* **2002**, *40*, 1007−1015.

(7) Ferretti, A.; Flanagan, V. P.; Ruth, J. M. Nonenzymatic browning in a lactose-casein model system. *J. Agric. Food Chem.* **1970**, *18*, 13−18.

(8) Ferretti, A.; Flanagan, V. P. Lactose-casein (Maillard) browning system: Volatile components. *J. Agric. Food Chem.* **1971**, *19*, 245−249.

DOI: 10.1021/acs.jafc.5b01129
J. Agric. Food Chem. 2015, 63, 5364−5372

(9) Schlichtherle-Cerny, H.; Amado, R. Analysis of taste-active compounds in an enzymatic hydrolysate of deamidated wheat gluten. *J. Agric. Food Chem.* **2002**, *50*, 1515−1522.
(10) Hashiba, H. Glucose-diglycine condensation product participating in oxygen-dependent browning. *J. Agric. Food Chem.* **1975**, *23*, 539−542.
(11) Jiang, Z. M.; Brodkorb, A. Structure and antioxidant activity of Maillard reaction products from alpha-lactalbumin and beta-lactoglobulin with ribose in an aqueous model system. *Food Chem.* **2012**, *133*, 960−968.
(12) Zhang, Y. G.; Chien, M. J.; Ho, C. T. Comparison of the volatile compounds obtained from thermal degradation of cysteine and glutathione in water. *J. Agric. Food Chem.* **1988**, *36*, 992−996.
(13) Zhang, Y. G.; Ho, C. T. Volatile compounds formed from thermal interaction of 2,4-decadienal with cysteine and glutathione. *J. Agric. Food Chem.* **1989**, *37*, 1016−1020.
(14) Zhang, Y. G.; Ho, C. T. Comparison of the volatile compounds formed from the thermal reaction of glucose with cysteine and glutathione. *J. Agric. Food Chem.* **1991**, *39*, 760−763.
(15) Zhang, Y. G.; Ho, C. T. Formation of meatlike aroma compounds from thermal reaction of inosine 5′-monophosphate with cysteine and glutathione. *J. Agric. Food Chem.* **1991**, *39*, 1145−1148.
(16) Maga, J. A. Pyrazine update. *Food Rev. Int.* **1992**, *8*, 479−558.
(17) Adams, A.; De Kimpe, N. Chemistry of 2-acetyl-1-pyrroline, 6-acetyl-1,2,3,4-tetrahydropyridine, 2-acetyl-2-thiazoline, and 5-acetyl-2,3-dihydro-4H-thiazine: Extraordinary Maillard flavor compounds. *Chem. Rev.* **2006**, *106*, 2299−2319.
(18) Van Lancker, F.; Adams, A.; De Kimpe, N. Formation of pyrazines in Maillard model systems of lysine-containing dipeptides. *J. Agric. Food Chem.* **2010**, *58*, 2470−2478.
(19) Van Lancker, F.; Adams, A.; De Kimpe, N. Impact of the N-terminal amino acid on the formation of pyrazines from peptides in Maillard model systems. *J. Agric. Food Chem.* **2012**, *60*, 4697−4708.
(20) Mestdagh, F.; Kerkaert, B.; Cucu, T.; De Meulenaer, B. Interaction between whey proteins and lipids during light-induced oxidation. *Food Chem.* **2011**, *126*, 1190−1197.
(21) Adams, A.; Borrelli, R. C.; Fogliano, V.; De Kimpe, N. Thermal degradation studies of food melanoidins. *J. Agric. Food Chem.* **2005**, *53*, 4136−4142.
(22) Yu, A. N.; Zhang, A. D. The effect of pH on the formation of aroma compounds produced by heating a model system containing L-ascorbic acid with L-threonine/L-serine. *Food Chem.* **2010**, *119*, 214−219.
(23) Davidek, T.; Robert, F.; Devaud, S.; Vera, F. A.; Blank, I. Sugar fragmentation in the Maillard reaction cascade: Formation of short-chain carboxylic acids by a new oxidative alpha-dicarbonyl cleavage pathway. *J. Agric. Food Chem.* **2006**, *54*, 6677−6684.
(24) Yang, C.; Wang, R.; Song, H. L. The mechanism of peptide bonds cleavage and volatile compounds generated from pentapeptide to heptapeptide via Maillard reaction. *Food Chem.* **2012**, *133*, 373−382.
(25) Lu, C. Y.; Hao, Z. G.; Payne, R.; Ho, C. T. Effects of water content on volatile generation and peptide degradation in the Maillard reaction of glycine, diglycine, and triglycine. *J. Agric. Food Chem.* **2005**, *53*, 6443−6447.
(26) Smarrito-Menozzi, C.; Matthey-Doret, W.; Devaud-Goumoens, S.; Viton, F. Glycerol, an underestimated flavor precursor in the Maillard reaction. *J. Agric. Food Chem.* **2013**, *61*, 10225−10230.
(27) Greenspan, L. Humidity fixed-points of binary saturated aqueous-solutions. *J. Res. Natl. Bur. Stand., Sect. A* **1977**, *81*, 89−96.
(28) Oliyai, C.; Borchardt, R. T. Chemical pathways of peptide degradation. VI. Effect of the primary sequence on the pathways of degradation of aspartyl residues in model hexapeptides. *Pharm. Res.* **1994**, *11*, 751−758.
(29) Labuza, T. P. The effect of water activity on reaction kinetics of food deterioration. *Food Technol. (Chicago, IL, U. S.)* **1980**, *34*, 36−40.
(30) Roos, Y. H. Glass transition-related physicochemical changes in foods. *Food Technol. (Chicago, IL, U. S.)* **1995**, *49*, 97−102.
(31) Eichner, K.; Karel, M. Influence of water content and water activity on sugar amino browning reaction in model systems under various conditions. *J. Agric. Food Chem.* **1972**, *20*, 218−223.

DOI: 10.1021/acs.jafc.5b01129
J. Agric. Food Chem. 2015, 63, 5364−5372

JOURNAL OF AGRICULTURAL AND FOOD CHEMISTRY

Article

pubs.acs.org/JAFC

Proanthocyanidins and Their Contribution to Sensory Attributes of Black Currant Juices

Oskar A. Laaksonen,*[,†] Juha-Pekka Salminen,[‡] Leenamaija Mäkilä,[†] Heikki P. Kallio,[†] and Baoru Yang[†]

[†]Food Chemistry and Food Development, Department of Biochemistry, and [‡]Laboratory of Organic Chemistry and Chemical Biology, Department of Chemistry, University of Turku, FI-20014 Turku, Finland

Supporting Information

ABSTRACT: Black currant juices from five different cultivars were analyzed for composition, content, and mean degree of polymerization (mDP) of proanthocyanidins (PA) by UPLC-MS/MS. Juices contained both procyanidins (PC) and prodelphinidins (PD), but the PC-% varied significantly, from 28 to 82% of the total PA. In addition, high PD-% was related to high mDP and total PA content. Enzyme-assisted processing increased significantly total PA (5−14-fold), PD-% (12−65%), and mDP (1.8−6.2-fold) in the juices of all cultivars. Enzymatic treatment increased the contents of large PAs more than those of small PAs. The contents of PA and mDP were positively associated with the mouth-drying and puckering astringent characteristics. However, the PA content did not contribute to the bitter taste. Juices from the most bitter cultivars had the lowest contents of proanthocyanidins regardless of the processing method. This finding indicates the existence of other bitter compounds in black currants in addition to PA.

KEYWORDS: *astringency, bitterness, black currant, juice processing, proanthocyanidins*

INTRODUCTION

Flavonoids are present especially in plant-derived foods and beverages. Proanthocyanidins (PA), often referred to as condensed tannins, form the most common group of tannins in plants. Proanthocyanidins are oligomeric and polymeric tannins composed of different types of flavan-3-ol units. Proanthocyanidins formed from monomeric (+)-catechin and/or (−)-epicatechin units are called procyanidins (PC), whereas the other common group, prodelphinidins (PD), consists of (+)-gallocatechin and/or (−)-epigallocatechin units. Commonly the monomeric units are linked by B-type (C−C; 4α→8 or 4α→6) or A-type (C−O−C) bonds. Proanthocyanidins are generally linked to astringent and bitter sensory properties in foods.

The mechanisms of the astringent sensations have been widely studied, but are not yet well understood.[1−4] A commonly accepted hypothesis is that polymeric tannins binding and precipitating salivary proteins are detected as a drying and rough sensation in the mucous membranes. Astringency is considered as a trigeminal sensation and often dependent on oral movement.[5] The binding to salivary proteins may be affected by the size and molecular flexibility of the tannins tested.[6] Structural characteristics of tannins contribute to different sensory properties. Procyanidins and galloyl glucoses are perceived as more astringent than ellagitannins (hydrolyzable tannins), but the latter have lower thresholds for detection of astringency.[7] Additionally, some astringent compounds do not bind to salivary proteins and thus elicit the sensation by different mechanisms.[8]

The mean degree of polymerization (mDP) of PAs has been associated with astringency.[9−11] However, structural characteristics of the polymeric compounds are more important factors.[12,13] High mDP and high percentage of galloylation in the subfractions activate trigeminal neurons, resulting in high astringency.[5] High galloylation of PA structure may result in a rougher astringent sensation with increased "coarse" attribute.[9] Monomeric flavan-3-ols and low molecular weight PAs have been reported to be more bitter than astringent, whereas higher molecular weight PAs are generally more astringent than bitter.[14,15] The high (−)-epicatechin concentration was significantly more bitter and astringent than the equal concentration of (+)-catechin.[16] In addition to proanthocyanidins, flavonol glycosides and various phenolic acid derivatives have been reported to elicit astringent sensations.[17−22] Compounds belonging to the latter two classes have significantly lower sensory threshold levels for astringency than those of the former.[17,18,20]

Bitter taste is mediated by G protein-coupled receptors of the taste receptor 2 family (TAS2Rs). In general, TAS2Rs are sensitive to several or multiple different bitter compounds. In a recent study, various monomeric flavonoids, including (+)-catechin, (−)-epicatechin, and (−)-epigallocatechin, activated the human bitter taste receptors TAS2R14 and TAS2R39.[23] Soares and co-workers[24] showed that procyanidin trimer C2 (catechin-(4α→8)-catechin-(4α→8)-catechin) and (−)-epicatechin activated TAS2R5 and the latter compound also activated TAS2R4 and TAS2R39. On the other hand, procyanidin dimer B2 (catechin-(4α→8)-catechin) did not activate any receptor in their study.

Black currant (*Ribes nigrum* L.) is used for the production of juices, berry wines, nectars, jams, and nutraceutical ingredients. Pectinolytic enzymes are commonly used in industrial berry processing to increase the juice yield. Simultaneously, the

Received: March 12, 2015
Revised: May 13, 2015
Accepted: May 18, 2015
Published: May 18, 2015

ACS Publications © 2015 American Chemical Society

DOI: 10.1021/acs.jafc.5b01287
J. Agric. Food Chem. 2015, 63, 5373−5380

Table 1. Mean Degree of Polymerization (mDP) and Total Contents of Proanthocyanidins (Milligrams per 100 mL) in the Juices[a]

	Mortti	Ola	Breed15	Marski	Mikael
Nonenzymatic Process					
mDP	2.2	7.0	4.7	4.3	7.7
PC total	8.66 ± 0.6	8.66 ± 0.6	5.58 ± 0.4	5.08 ± 0.4	6.63 ± 0.5
PD total	1.94 ± 0.1	22.1 ± 0.9	8.33 ± 0.3	5.01 ± 0.2	11.8 ± 0.5
PA total	10.6	30.8	13.9	10.1	18.4
PA 1−3	4.4	7.7	5.5	3.3	4.5
PA others	6.2	23.1	8.4	6.8	13.9
PC:PD ratio	82:18	28:72	40:60	50:50	36:64
Enzymatic Process					
mDP*	13.7	16.2	11.0	10.9	14.5
PC total*	16.2 ± 1.1	31.1 ± 2.2	13.2 ± 0.9	11.6 ± 0.8	17.4 ± 1.2
PD total*	136 ± 5.4	151 ± 6.0	70.2 ± 2.8	76.5 ± 3.1	109 ± 4.3
PA total	152	182	83.4	88.1	126
PA 1−3	24.3	21.6	15.2	18.1	17.5
PA others	128	160	68.1	69.9	109
PC:PD ratio	17:83	16:84	14:86	13:87	11:89

[a]Total contents of proanthocyanidins (PA total) is the sum of PC (procyanidins) and PD (prodelphinidins) Total and PC:PD ratio are calculated from the total values; PA 1−3 is the sum of monomers, dimers, and trimers (from Supplementary Tables 1 and 2). PA others is the remainder of PA total and PA 1−3 indicating higher level of polymerization. Values after ± show the maximum deviations by the method.[33] Statistically significant differences between averaged processes are based on Student's *t* test ($p < 0.05$). Differences are presented as * higher contents in enzymatic process.

contents of phenolic compounds of juices increases significantly,[25−27] as do the astringent and bitter sensory properties.[28−30] Moreover, a high content of phenolic compounds in a black currant juice may have a negative impact on liking.[30] We have previously examined the roles of sugars, fruit acids, and smaller phenolic compounds, such as anthocyanins, flavonols, and hydroxycinnamic acids, in the sensory profiles of juices produced from various black currant cultivars.[29] Especially, various flavonol glycosides and hydroxycinnamic acid derivatives contribute to astringency in black currant juices.[28−30] In addition to the aforementioned phenolic compounds, black currants contain also significant amounts of proanthocyanidins.[31,32] The aim of the present study was to investigate the proanthocyanidin profiles and contents in black currant juice samples from our previous study.[29] Enzyme-aided processing was compared with nonenzymatic juice pressing using five different black currant cultivars produced at laboratory scale. The second aim was to investigate the contribution of the compounds to the sensory properties of black currant juices and especially examine the contribution of flavan-3-ols to astringency and bitterness in the juices.

MATERIALS AND METHODS

Black Currant Juice Samples. Juice samples were as introduced by Laaksonen et al.[29] Berries were harvested when optimally ripe in 2010 (four commercial cultivars, 'Mortti', 'Mikael', 'Marski', and 'Ola', and a new breed no. 15, 'Breed15') in southern Finland (MTT Piikkiö, Agrifood Research, Finland). Berries were frozen immediately after harvesting and kept at −20 °C before processing. Two juice-processing methods were applied at laboratory scale from berries of each cultivar. The first process was carried out in 2011 without enzymes and the second in 2012 with the aid of commercial enzymes (Pectinase 714L, Biocatalysts Ltd., Cardiff, UK; dosage = 57 mg of enzyme/380 g of berry mash). All juice samples were frozen at −20 °C for further analyses (sensory evaluations in 2011 for nonenzymatic and in 2012 for enzyme-assisted juices; chemical analyses in 2012).

Proanthocyanidin Analyses. Qualitative and quantitative analyses of proanthocyanidins were carried out according to method of Enström et al.[33] Proanthocyanidins were separated with Sephadex LH-20 gel and analyzed with UPLC-MS/MS (Waters Acquity Xevo UPLC-MS/MS, Waters, MA, USA) including a binary solvent manager, a 96-place sample manager, a PDA detector, and a Xevo TQ triple-quadrupole mass spectrometer equipped with an electrospray interface. The column was a Waters Acquity UPLC BEH Phenyl (1.7 μm, 2.1 × 100 mm).

Purified proanthocyanidins were used as external standards.[33] The standards were obtained from dried black currant leaves with Sephadex LH-20 gel chromatography.[34] The Sephadex fractions were further fractionated by semipreparative HPLC using a Waters Delta 600 system equipped with a Fraction Collector III. The column used was Phenomenex Gemini (150 × 21.2 mm, 10 μm, C18, 110 Å). The purified compounds were used with a Waters XEVO triple-quadrupole mass spectrometer to develop compound-specific multiple reaction monitoring (MRM) methods and quantitative calibration curves.[33]

Sensory Evaluations. The sensory evaluation process using generic descriptive analysis and the sensory characteristics of the juice samples are described by Laaksonen et al.[29] The nonenzymatic and enzymatic juice samples were assessed by two separate trained sensory panels ($n = 14$ and $n = 13$, respectively) in controlled sensory laboratory conditions (according to ISO8589). The data were collected using Compusense-*five* software (Compusense Inc., Guelph, Canada). Of the nine attributes examined by Laaksonen et al.,[29] only taste (sourness, sweetness, and bitterness) and two astringency (mouth-drying and puckering) attributes were selected for this study to examine their correlations with proanthocyanidins.

Statistical Analyses. Differences between the processes were analyzed by Student's *t* test ($p < 0.05$; IBM SPSS Statistics; IBM Corp., Armonk, NY, USA). A partial least-squares regression (PLS) method was applied for standardized data with *X*-variables (predictors) as chemical compounds and/or their ratios and *Y*-variables (responses) as the sensory properties. Full cross-validation was used to estimate the number of factors for a statistically reliable model. Multivariate models were conducted using Unscrambler 10.3 (Camo Process AS, Oslo, Norway).

RESULTS AND DISCUSSION

Proanthocyanidins in Juice Samples. Mean degree of polymerization (mDP in Table 1) indicates the average number of flavan-3-ol monomeric units present in the numerous oligomeric and polymeric condensed tannins present in the juice samples analyzed. The mDP value was significantly higher

DOI: 10.1021/acs.jafc.5b01287
J. Agric. Food Chem. 2015, 63, 5373−5380

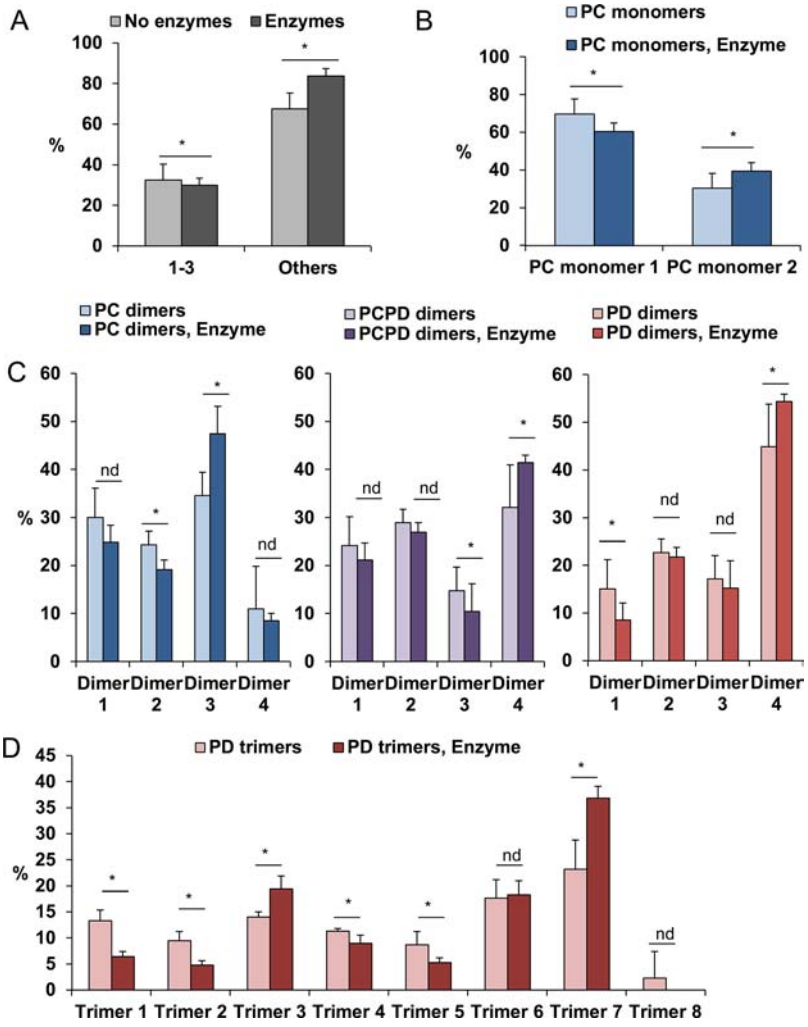

Figure 1. Differences in proanthocyanidin profiles (%; 100% is the sum of PA 1−3 and PA others, two monomers, four dimers, or eight trimers) of the averaged juices: (A) proportions of the sum of monomers, dimers, and trimers (1−3) in comparison to the sum of tetramers or higher level of polymerization (others); (B) monomer profiles; (C) dimer profiles; (D) trimer profiles. Statistical differences between the juice types are marked with ∗ (t test, $p < 0.05$).

in the enzyme-aided juices (3.1-fold higher on average) than in the nonenzymatic juices in all cultivars. Cultivar 'Mortti' had the notably lowest value of mDP among the nonenzymatic; this cultivar had the highest increase in mDP when treated with enzymes. In general, black currants have been reported to have higher mDP than several other small edible berries.[32,35] Freezing of berries can have an impact on their chemical composition. The freezing period between sensory evaluations and the chemical analyses may have had some minor impacts on the mDP values of the juice samples.[36] However, the phenolic compounds of black currants have been reported to be more stable than the compounds of other common berries, such as strawberries or bilberries.[37] Additionally, black currant procyanidin contents remain relatively stable during storage at −20 °C.[38]

Condensed tannins in black currant juices consist of procyanidins (PC) and prodelphinidins (PD). The contents of both were significantly higher in the enzymatic than in the nonenzymatic juices (Table 1). Interestingly, the juice of 'Mortti' from the nonenzymatic process had notably more PC than PD, whereas it was vice versa in the corresponding products of 'Ola', 'Mikael', and 'Breed15', which had more PD than PC. The nonenzymatic juice process represented the original berry pulp without seeds or berry skins. On the other hand, the enzyme released various phenolic compounds from the berry skins to the juice. The PC:PD ratio was very similar in all enzyme-aided juices (average 14:86), which indicated the higher PD contents compared to PC in the berry skins across the five cultivars.

Currently, only a few studies have focused on the analysis of the proanthocyanidin (PA) composition in black currants. In the study of Wu et al.[39] the proanthocyanidins were characterized only by chain length. Liu et al.[40] reported PD monomers, dimers, and trimers in black currant leaves and buds. In the current study, we characterized and quantified the whole PA content, including larger oligomers and polymers as well as monomeric, dimeric, and trimeric PAs, by using a novel group-specific MRM technology.[33] Enzyme-aided juices contained more PAs than the juices without enzymatic assistance (Table 1). The proportions of monomeric, dimeric, and trimeric PAs (from Supplementary Tables Tables 1 and 2) of the total PAs varied between 24 and 41% and between 12 and 21% in the nonenzymatic and enzyme-aided juices, respectively. Thus, the majority of the PAs found in black currant juices had a polymerization degree >3. The contents of these compounds (PA others in Table 1 and Figure 1) were 6.9−20.4 times

DOI: 10.1021/acs.jafc.5b01287
J. Agric. Food Chem. 2015, 63, 5373−5380

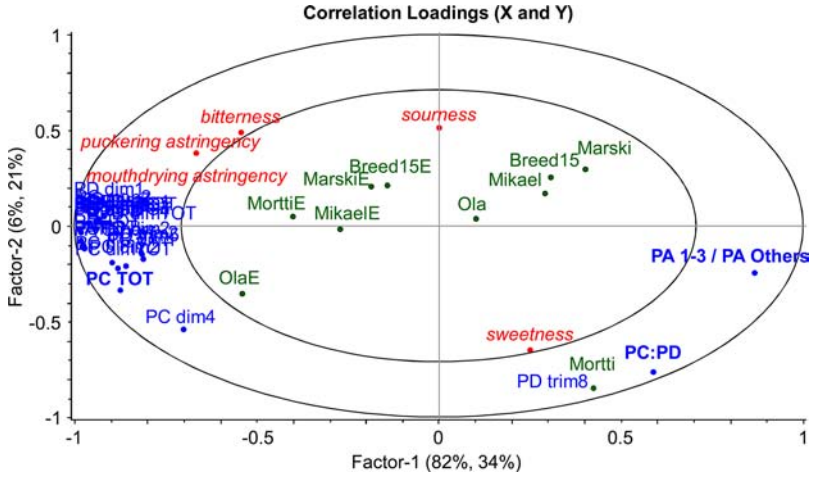

Figure 2. PLS correlation loadings plot of the interaction between taste and astringencies (Y, n = 5) and proanthocyanidin measures (X, n = 35) in all 10 juice samples from both processes. Samples are in green font, sensory attributes are in red italic font, and compounds are in blue. For abbreviations of compounds refer to Table 1 and Supplementary Tables 1 and 2.

higher in enzyme-aided juices than in the juices produced without enzymes.

The individual PAs found in the samples by the compound-specific MRM methods are shown in Supplementary Tables 1 and 2 of the Supporting Information in a fixed order of retention in reverse phase liquid chromatography according to their hydrophilic properties. For example, PC−PC dimer 1 elutes earlier than PC−PC dimer 4. The monomeric PC and PD units of PAs both have two diastereoisomeric configurations ((+)-catechin/(−)-epicatechin and (+)-gallocatechin/(−)-epigallocatechin, respectively) in plants, which results in 12 possible compounds belonging to PC−PC, PC−PD, or PD−PD dimers (Supplementary Table 1). The two PC monomers were identified as (+)-catechin and (−)-epicatechin, respectively. At the same time, PC−PC dimers 1−4 were tentatively identified as catechin-(4α→8)-catechin (trivial name B3), epicatechin-(4α→8)-catechin (B1), catechin-(4α→8)-epicatechin (B4), and epicatechin-(4α→8)-epicatechin (B2), respectively.[41] The same order may be applied for PD−PD dimers, the first being gallocatechin-(4α→8)-gallocatechin, the second epigallocatechin-(4α→8)-gallocatechin, the third gallocatechin-(4α→8)-epigallocatechin, and the fourth epigallocatechin-(4α→8)-epigallocatechin. PD−PD dimers gallocatechin-(4α→8)-gallocatechin and gallocatechin-(4α→8)-epigallocatechin have been previously reported from black currant leaves.[42,43] Additionally, Tits et al.[43] found also a 4α→6 dimer of gallocatechin from the leaves, whereas a 4α→8 bond is more commonly found in edible plants.[35]

In almost all dimers (excluding two PC−PC dimers), the contents were significantly higher in enzyme-aided juices than in nonenzymatic juices (t test, $p < 0.05$; Supplementary Table 1). The PC−PC dimers were less abundant (on average 2.9 and 2.0% of all dimers in nonenzymatic and enzymatic juices, respectively) than the PC−PD (27.3 and 23.3%) and PD−PD dimers (69.8 and 74.8%) in all cultivars and in both processes. Figure 1 shows the abundance of individual monomers, dimers, and trimers in the juices and the comparison of the compound profiles between juice processes. Within PC dimers, compounds 1 (dimer B3) and 3 (B4) were more abundant than compound **2** (B1) or 4 (B2), whereas within PD−PD and PC−PD dimers compounds 2 and 4 were more abundant than compounds 1 or 3 (Figure 1). Within all three dimer types, the proportion of the most abundant dimer (dimer 3 in PC−PC and dimer 4 in PC−PD and PD−PD dimers) was found in significantly higher proportions in enzyme-treated juices. At the same time, the proportion of one dimer (dimer 2 in PC−PC, 3 in PC−PD, and 1 in PD−PD) was higher in nonenzymatic juices than in the enzyme-treated juices. In addition to significant increases in the contents of PAs, the enzyme-assisted juice processing significantly altered the flavan-3-ol composition in the juice by releasing PAs from the berry skins.

Trimers made up of prodelphinidin units only (PD−PD−PD) were found in the juices (Supplementary Table 2). One PD−PD−PD trimer (gallocatechin-(4α→8)-gallocatechin-(4α→8)-gallocatechin) and one PC−PD−PD trimer (catechin-(4α→8)-gallocatechin-(4α→8)-gallocatechin) have earlier been found in black currant leaves.[42,43] The enzyme treatment, again, increased significantly the content of trimeric PAs in the juice. Trimers 3 and 7 were the most abundant in general, and they were significantly more abundant in the juices processed with pectinase. Interestingly, one trimer (PD trimer 8), the most hydrophobic of the PD−PD−PD trimers, was found in the nonenzymatic juice of cultivar 'Mortti' but not in the corresponding enzymatic juice or juices from other cultivars.

Impact of Juice Processing on Sensory Quality. PLS regression model was used to study the interactions between proanthocyanidins and the sensory attributes (Figure 2). PAs in the model are the compounds or compound ratios from Table 1 and Supplementary Tables 1 and 2 (total of 35 X-variables). Three taste attributes (bitterness, sourness, and sweetness) and two astringent qualities (mouth-drying and puckering astringencies) were selected for the model from Laaksonen et al.[29] with a total of five Y-variables. Eighty-eight percent of the variation in X-data explains 55% of the variation in Y with two factors. In the model, proanthocyanidin variation explains 92.4% of the variation (90.0% in validated model) in mouth-drying astringency with one validated factor. Almost all of the X-variables are located on the left side of the plot with the astringency variable. All enzyme-aided juices are located also on the left side of the plot, which indicates that proanthocyanidins have a significant role in the increased mouth-drying astringency in these juices. Especially, a higher degree of polymerization (mDP) and a lower content of PC units in ratio

DOI: 10.1021/acs.jafc.5b01287
J. Agric. Food Chem. 2015, 63, 5373−5380

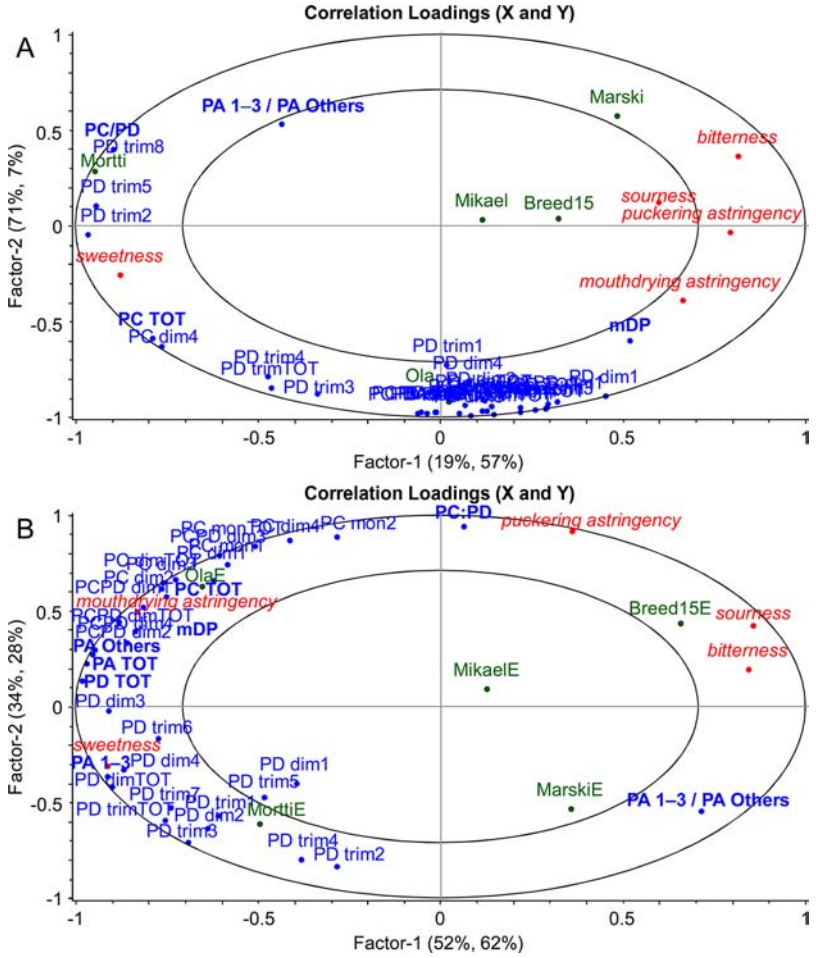

Figure 3. PLS correlation loadings plots of the interaction between taste and astringencies (Y, n = 5) and proanthocyanidin measures (X, n = 35) juice samples from different cultivars within processes: (A) juices without enzymatic assistance; (B) juices with enzymatic (E) assistance. Samples are in green font, sensory attributes are in red italic font, and compounds are in blue. For abbreviations of compounds refer to Table 1 and Supplementary Tables 1 and 2.

to PD contributed to mouth-drying astringency. This suggests that the protein affinity of PAs is enhanced by the increase in PA size, especially if the increase is brought about by a proportionally larger number of phenolic OH units in the additional monomeric building blocks (PDs have 25% more OH units than PCs). In addition, a significant increase in mouth-drying astringent characteristics is caused by the effective breakage of pectin structures in enzyme-aided juice processing.[29] High viscosity and low astringency were observed in our juices without pectinase treatment, which is in agreement with earlier studies.[44,45]

Other sensory attributes were not well explained in the model with the comparison of processes (Figure 2). The X-variables explained only 44.3% (27.9% in the validated model) of variation in puckering astringency with the first factor. However, flavan-3-ols, their dimers and trimers, and polymeric phenolic fractions in red wine have also been reported to have puckering astringent properties.[17,18,46] Besides astringency, the remaining three attributes were poorly explained in the model with the PA contents: only a little of variation in bitterness (10.1%) was explained with the first factor, whereas the variation in sourness or sweetness was not explained at all. The latter findings were as expected; sourness was not different between processes.

Impact of Cultivar on Sensory Quality. Two PLS models were created to examine the sensory contribution of proanthocyanidins in the five juices within processes (Figure 3). Figure 3A presents the model for the samples without pectinase treatment. Ninety percent of the variation in the chemical variable data X explained 64% of the variation in sensory data. However, none of the five sensory attributes was well validated in the full cross-validation. Cultivars 'Mortti' and 'Ola' had the highest contents of proanthocyanidins but were not significantly astringent or bitter in this juice process. Especially nonenzymatic juice from 'Mortti' was the sweetest and the most viscose of the five cultivars.[29] As discussed earlier, the high viscosity due to the high polysaccharide content in these juices masks the astringency of proanthocyanidins. Some correlation can be found between mDP and mouth-drying astringency on the right side of the plot (Figure 3A), which may indicate the role of highly polymerized proanthocyanidins in astringency despite the masking effect of the juice matrix.

A similar model for enzyme-aided juices is shown in Figure 3B with two validated factors. Overall, 86% of the variation in X-data explained 90% of the variation in Y. The best explained Y-variable was mouth-drying astringency with 92.7% (validated 81.1%). Most of the chemical variables, especially variables PA total (total content of proanthocyanidins), PA others (tetramers and larger polymers), and mDP, are located in the

DOI: 10.1021/acs.jafc.5b01287
J. Agric. Food Chem. 2015, 63, 5373−5380

left of the plot with cultivars 'Ola' and 'Mortti' and the mouth-drying astringency. This supports the earlier finding that especially the size of PAs is important in the protein affinity that causes the mouth-drying astringent sensation in the mucosa. In fact, puckering astringency was the second attribute well explained with the model (96.9% explained, but only 56.9% in validated model) in the upper part of the plot. Interestingly, PC−PC and PC−PD dimers are correlated with mouth-drying astringency and cultivar 'Ola', whereas PD dimers and trimers correlate with 'Mortti'. Simultaneously, the PC:PD ratio correlates with the mouth-drying astringency and puckering astringency on factor 2. These findings indicate that variations in the PC:PD ratio may result in different overall astringent properties. The PC:PD ratio being more closely related to puckering astringency suggests that PC-% is more important in causing the puckering sensation, whereas PD-% might be a more important contributor to the mouth-drying sensation together with the size of PA. A high portion of PD in comparison to PC has been previously reported to result in lower "coarse" attribute of astringency.[9] Changes in the PC:PD ratio may result in different overall astringency perception.

Bitterness was poorly explained by the chemical variables in the model (Figure 3B). The compounds studied and their contents did not contribute to bitterness of the juices. These compounds were found in the lowest contents in the bitterest cultivars ('Breed15' and 'Marski'). Additionally, neither total contents of proanthocyanidins, total PD, total PC, nor their ratio contributed to bitterness. However, the ratio between PA 1−3 (sum of monomers, dimer,s and trimers; Table 1) and PA others (degree of polymerization ≥ 4; Table 1) correlated with bitterness on factor 1. In other words, there were more smaller and bitter PAs relative to larger and astringent PAs found in the juice of 'Marski' than in the less bitter juices. As reported by Laaksonen et al.,[29] the flavonols (glycosides or aglycons), hydroxycinnamic acid derivatives, or anthocyanins did not explain the bitterness of the juices. Their contents were the lowest in the bitterest cultivars regardless of the juice production process. All of these compounds, or at least some in each class, activate the human bitter taste receptors.[23,24] These findings suggest that the bitterness in juice of the black currant cultivars may be due to complex interactions among multiple sensory-active compounds. In our previous studies,[29,30] the sugar-to-acid ratio was a more important factor contributing to sweetness than individual sugar components. Similarly, the bitterness of these juices may be due to the ratios between bitter phenolics and sweet sugars and/or sour acids. In our previous study, the bitterest cultivars had high contents of sugars or nonphenolic fruit acids relative to phenolics. Thus, the sugars or acids may affect and mask the astringent properties of the phenolic compounds, but not the bitterness of the juices. On the other hand, bitterness may have been caused by berry components that were not characterized in this study or our earlier investigations.[28−30]

The PC monomers, dimers, and trimers in red wine have been reported to be both bitter and astringent, but the thresholds for bitterness are higher than for astringency.[17,18] According to Hufnagel and Hofmann,[18] the dose-over-threshold (DoT) factors, which indicate the ratio between concentration and taste threshold for the compounds, were <1, indicating their low contribution to bitterness. In the same study,[18] the omission of the PC compounds from a reconstructed wine model resulted in a decrease in bitterness. Therefore, the compounds in subthreshold concentrations may contribute to overall bitterness. By using the same thresholds for the same compounds, PC monomers and PC−PC dimers had also DoT values <1 in this study. However, the contents of PD−PD and PC−PD dimers were notably higher than those of PC−PC dimers.

In conclusion, the proanthocyanidin contents were significantly higher in black currant juices from pectinase-aided processing than in juices without enzyme treatments. The identified compounds contributed to mouth-drying and puckering astringent properties in the juices, especially in juices produced with enzymes. Proanthocyanidin contents did not contribute to bitterness of juices within processes. There may be other bitter-tasting compounds in black currants in addition to PA, flavonols, and hydroxycinnamic acid derivatives. The bitterness may also have been affected by several juice components, especially the ratios between different groups of sensory-active components. Due to the different PA and sensory profiles of the nonenzymatic juices in comparison to enzyme-aided juices, the minimally processed "extra-virgin" type juice processing may have potential in the food industry. Additionally, this study provides important information for farmers and the food industry concerning the interactions between phenolic compounds and sensory characteristics of black currant cultivars.

■ ASSOCIATED CONTENT

Supporting Information

Contents (mg/100 mL) of proanthocyanidin monomers, dimers, and trimers found from the black currant juice samples. The Supporting Information is available free of charge on the ACS Publications website at DOI: 10.1021/acs.jafc.5b01287.

■ AUTHOR INFORMATION

Corresponding Author

*(O.A.L.) E-mail: oskar.laaksonen@utu.fi. Phone: + 358 2 333 6875.

Funding

This study was funded by the Tekes − Finnish Funding Agency for Technology and Innovation together with Finnish food companies on the project "Blackcurrant as Unique Source of Functional Ingredients of Food: Novel Processes and Innovations". Analyses of proanthocyanidins on an ultra-performance liquid chromatography−mass spectrometry system were made possible by a Strategic Research Grant of the University of Turku (Ecological Interactions).

Notes

The authors declare no competing financial interest.

■ ACKNOWLEDGMENTS

We thank Prof. Risto Tahvonen and Jorma Hellsten for their assistance in berry sample collection, Mikael Fabritius for his contributions to sample preparations and sensory evaluations, and Anne Koivuniemi, Piia Koskinen, and Marianne Oraviita for their contribution to chemical analyses.

■ ABBREVIATIONS USED

PA, proanthocyanidin; PC, procyanidin; PD, prodelphinidin; PLS, partial least-squares (regression); mDP, mean degree of polymerization; mon, monomer; dim, dimer; trim, trimer

DOI: 10.1021/acs.jafc.5b01287
J. Agric. Food Chem. 2015, 63, 5373−5380

REFERENCES

(1) Bajec, M. R.; Pickering, G. J. Astringency: mechanisms and perception. *Crit. Rev. Food Sci. Nutr.* **2008**, *48*, 858−875.

(2) McRae, J. M.; Kennedy, J. A. Wine and grape tannin interactions with salivary proteins and their impact on astringency: a review of current research. *Molecules* **2011**, *16*, 2348−2364.

(3) Scollary, G. R.; Pásti, G.; Kállay, M.; Blackman, J.; Clark, A. C. Astringency response of red wines: potential role of molecular assembly. *Trends Food Sci. Technol.* **2012**, *27*, 25−36.

(4) Ma, W.; Guo, A.; Zhang, Y.; Wang, H.; Liu, Y.; Li, H. A review on astringency and bitterness perception of tannins in wine. *Trends Food Sci. Technol.* **2014**, *40*, 6−19.

(5) Schöbel, N.; Radtke, D.; Kyereme, J.; Wollmann, N.; Cichy, A.; Obst, K.; Kallweit, K.; Kletke, O.; Minovi, A.; Dazert, S.; et al. Astringency is a trigeminal sensation that involves the activation of G protein-coupled signaling by phenolic compounds. *Chem. Senses* **2014**, *39*, 471−487.

(6) Dobreva, M. A.; Green, R. J.; Mueller-Harvey, I.; Salminen, J.-P.; Howlin, B. J.; Frazier, R. A. Size and molecular flexibility affect the binding of ellagitannins to bovine serum albumin. *J. Agric. Food Chem.* **2014**, *62*, 9186−9194.

(7) Hofmann, T.; Glabasnia, A.; Schwarz, B.; Wisman, K. N.; Gangwer, K. A.; Hagerman, A. E. Protein binding and astringent taste of a polymeric procyanidin, 1,2,3,4,6-penta-*O*-galloyl-β-D-glucopyranose, castalagin, and grandinin. *J. Agric. Food Chem.* **2006**, *54*, 9503−9509.

(8) Schwarz, B.; Hofmann, T. Is there a direct relationship between oral astringency and human salivary protein binding? *Eur. Food Res. Technol.* **2008**, *227*, 1693−1698.

(9) Vidal, S.; Francis, L.; Guyot, S.; Marnet, N.; Kwiatkowski, M.; Gawel, R.; Cheynier, V.; Waters, E. J. The mouth-feel properties of grape and apple proanthocyanidins in a wine-like medium. *J. Sci. Food Agric.* **2003**, *83*, 564−573.

(10) Chira, K.; Schmauch, G.; Saucier, C.; Fabre, S.; Teissedre, P.-L. Grape variety effect on proanthocyanidin composition and sensory perception of skin and seed tannin extracts from Bordeaux wine grapes (Cabernet Sauvignon and Merlot) for two consecutive vintages (2006 and 2007). *J. Agric. Food Chem.* **2009**, *57*, 545−553.

(11) Chira, K.; Pacella, N.; Jourdes, M.; Teissedre, P.-L. Chemical and sensory evaluation of Bordeaux wines (Cabernet-Sauvignon and Merlot) and correlation with wine age. *Food Chem.* **2011**, *126*, 1971−1977.

(12) Quijada-Morín, N.; Regueiro, J.; Simal-Gándara, J.; Tomás, E.; Rivas-Gonzalo, J. C.; Escribano-Bailón, M. T. Relationship between the sensory-determined astringency and the flavanolic composition of red wines. *J. Agric. Food Chem.* **2012**, *60*, 12355−12361.

(13) Wollmann, N.; Hofmann, T. Compositional and sensory characterization of red wine polymers. *J. Agric. Food Chem.* **2013**, *61*, 2045−2061.

(14) Arnold, R. A.; Noble, A. C.; Singleton, V. L. Bitterness and astringency of phenolic fractions in wine. *J. Agric. Food Chem.* **1980**, *28*, 675−678.

(15) Peleg, H.; Gacon, K.; Schlich, P.; Noble, A. C. Bitterness and astringency of flavan-3-ol monomers, dimers and trimers. *J. Sci. Food Agric.* **1999**, *79*, 1123−1128.

(16) Kallithraka, S.; Bakker, J.; Clifford, M. N. Evaluation of bitterness and astringency of (+)-catechin and (−)-epicatechin in red wine and in model solution. *J. Sens. Stud.* **1997**, *12*, 25−37.

(17) Hufnagel, J. C.; Hofmann, T. Orosensory-directed identification of astringent mouthfeel and bitter-tasting compounds in red wine. *J. Agric. Food Chem.* **2008**, *56*, 1376−1386.

(18) Hufnagel, J. C.; Hofmann, T. Quantitative reconstruction of the nonvolatile sensometabolome of a red wine. *J. Agric. Food Chem.* **2008**, *56*, 9190−9199.

(19) Scharbert, S.; Holzmann, N.; Hofmann, T. Identification of the astringent taste compounds in black tea infusions by combining instrumental analysis and human bioresponse. *J. Agric. Food Chem.* **2004**, *52*, 3498−3508.

(20) Scharbert, S.; Hofmann, T. Molecular definition of black tea taste by means of quantitative studies, taste reconstitution, and omission experiments. *J. Agric. Food Chem.* **2005**, *53*, 5377−5384.

(21) Sáenz-Navajas, M.-P.; Ferreira, V.; Dizy, M.; Fernández-Zurbano, P. Characterization of taste-active fractions in red wine combining HPLC fractionation, sensory analysis and ultra performance liquid chromatography coupled with mass spectrometry detection. *Anal. Chim. Acta* **2010**, *673*, 151−159.

(22) Schwarz, B.; Hofmann, T. Sensory-guided decomposition of red currant juice (*Ribes rubrum*) and structure determination of key astringent compounds. *J. Agric. Food Chem.* **2007**, *55*, 1394−1404.

(23) Roland, W. S. U.; van Buren, L.; Gruppen, H.; Driesse, M.; Gouka, R. J.; Smit, G.; Vincken, J.-P. Bitter taste receptor activation by flavonoids and isoflavonoids: Modeled structural requirements for activation of hTAS2R14 and hTAS2R39. *J. Agric. Food Chem.* **2013**, *61*, 10454−10466.

(24) Soares, S.; Kohl, S.; Thalmann, S.; Mateus, N.; Meyerhof, W.; De Freitas, V. Different phenolic compounds activate distinct human bitter taste receptors. *J. Agric. Food Chem.* **2013**, *61*, 1525−1533.

(25) Buchert, J.; Koponen, J. M.; Suutarinen, M.; Mustranta, A.; Lille, M.; Törrönen, R.; Poutanen, K. Effect of enzyme-aided pressing on anthocyanin yield and profiles in bilberry and blackcurrant juices. *J. Sci. Food Agric.* **2005**, *85*, 2548−2556.

(26) Koponen, J. M.; Buchert, J.; Poutanen, K. S.; Törrönen, A. R. Effect of pectinolytic juice production on the extractability and fate of bilberry and black currant anthocyanins. *Eur. Food Res. Technol.* **2008**, *227*, 485−494.

(27) Koponen, J. M.; Happonen, A. M.; Auriola, S.; Kontkanen, H.; Buchert, J.; Poutanen, K. S.; Törrönen, A. R. Characterization and fate of black currant and bilberry flavonols in enzyme-aided processing. *J. Agric. Food Chem.* **2008**, *56*, 3136−3144.

(28) Laaksonen, O.; Sandell, M.; Nordlund, E.; Heiniö, R.-L.; Malinen, H.-L.; Jaakkola, M.; Kallio, H. The effect of enzymatic treatment on blackcurrant (*Ribes nigrum*) juice flavour and its stability. *Food Chem.* **2012**, *130*, 31−41.

(29) Laaksonen, O.; Mäkilä, L.; Tahvonen, R.; Kallio, H.; Yang, B. Sensory quality and compositional characteristics of blackcurrant juices produced by different processes. *Food Chem.* **2013**, *138*, 2421−2429.

(30) Laaksonen, O. A.; Mäkilä, L.; Sandell, M. A.; Salminen, J.-P.; Liu, P.; Kallio, H. P.; Yang, B. Chemical-sensory characteristics and consumer responses of blackcurrant juices produced by different industrial processes. *Food Bioprocess Technol.* **2014**, *7*, 2877−2888.

(31) Kähkönen, M. P.; Hopia, A. I.; Heinonen, M. Berry phenolics and their antioxidant activity. *J. Agric. Food Chem.* **2001**, *49*, 4076−4082.

(32) Hellström, J. K.; Törrönen, A. R.; Mattila, P. H. Proanthocyanidins in common food products of plant origin. *J. Agric. Food Chem.* **2009**, *57*, 7899−7906.

(33) Engström, M. T.; Pälijärvi, M.; Fryganas, C.; Grabber, J. H.; Mueller-Harvey, I.; Salminen, J.-P. Rapid qualitative and quantitative analyses of proanthocyanidin oligomers and polymers by UPLC-MS/MS. *J. Agric. Food Chem.* **2014**, *62*, 3390−3399.

(34) Salminen, J.-P.; Karonen, M. Chemical ecology of tannins and other phenolics: we need a change in approach. *Funct. Ecol.* **2011**, *25*, 325−338.

(35) Gu, L.; Kelm, M. A.; Hammerstone, J. F.; Beecher, G.; Holden, J.; Haytowitz, D.; Prior, R. L. Screening of foods containing proanthocyanidins and their structural characterization using LC-MS/MS and thiolytic degradation. *J. Agric. Food Chem.* **2003**, *51*, 7513−7521.

(36) Bakowska-Barczak, A. M.; Kolodziejczyk, P. Evaluation of Saskatoon berry (*Amelanchier alnifolia* Nutt.) cultivars for their polyphenol content, antioxidant properties, and storage stability. *J. Agric. Food Chem.* **2008**, *56*, 9933−9940.

(37) Häkkinen, S. H.; Kärenlampi, S. O.; Mykkänen, H. M.; Törrönen, A. R. Influence of domestic processing and storage on flavonol contents in berries. *J. Agric. Food Chem.* **2000**, *48*, 2960−2965.

DOI: 10.1021/acs.jafc.5b01287
J. Agric. Food Chem. 2015, 63, 5373−5380

(38) Bakowska-Barczak, A. M.; Kolodziejczyk, P. P. Black currant polyphenols: their storage stability and microencapsulation. *Ind. Crops Prod.* **2011**, *34*, 1301−1309.
(39) Wu, X.; Gu, L.; Prior, R. L.; McKay, S. Characterization of anthocyanins and proanthocyanidins in some cultivars of *Ribes*, *Aronia*, and *Sambucus* and their antioxidant capacity. *J. Agric. Food Chem.* **2004**, *52*, 7846−7856.
(40) Liu, P.; Kallio, H.; Yang, B. Flavonol glycosides and other phenolic compounds in buds and leaves of different varieties of black currant (*Ribes nigrum* L.) and changes during growing season. *Food Chem.* **2014**, *160*, 180−189.
(41) Escribano-Bailon, T.; Gutierrez-Fernandez, Y.; Rivas-Gonzalo, J. C.; Santos-Buelga, C. Characterization of procyanidins of *Vitis vinifera* variety Tinta del Pais grape seeds. *J. Agric. Food Chem.* **1992**, *40*, 1794−1799.
(42) Tits, M.; Angenot, L.; Poukens, P.; Warin, R.; Dierckxsens, Y. Prodelphinidins from *Ribes nigrum*. *Phytochemistry* **1992**, *31*, 971−973.
(43) Tits, M.; Poukens, P.; Angenot, L.; Dierckxsens, Y. Thin-layer chromatographic analysis of proanthocyanidins from *Ribes nigrum* leaves. *J. Pharm. Biomed. Anal.* **1992**, *10*, 1097−1100.
(44) Smith, A. K.; June, H.; Noble, A. C. Effects of viscosity on the bitterness and astringency of grape seed tannin. *Food Qual. Prefer.* **1996**, *7*, 161−166.
(45) Troszyńska, A.; Narolewska, O.; Robredo, S.; Estrella, I.; Hernández, T.; Lamparski, G.; Amarowicz, R. The effect of polysaccharides on the astringency induced by phenolic compounds. *Food Qual. Prefer.* **2010**, *21*, 463−469.
(46) Gonzalo-Diago, A.; Dizy, M.; Fernández-Zurbano, P. Taste and mouthfeel properties of red wines proanthocyanidins and their relation to the chemical composition. *J. Agric. Food Chem.* **2013**, *61*, 8861−8870.

DOI: 10.1021/acs.jafc.5b01287
J. Agric. Food Chem. 2015, 63, 5373−5380

JOURNAL OF AGRICULTURAL AND FOOD CHEMISTRY

Article

pubs.acs.org/JAFC

Selective One-Dimensional Total Correlation Spectroscopy Nuclear Magnetic Resonance Experiments for a Rapid Identification of Minor Components in the Lipid Fraction of Milk and Dairy Products: Toward Spin Chromatography?

Christina Papaemmanouil,[†] Constantinos G. Tsiafoulis,*[,‡,§] Dimitrios Alivertis,[∥] Ouranios Tzamaloukas,[⊥] Despoina Miltiadou,[⊥] Andreas G. Tzakos,[†] and Ioannis P. Gerothanassis*[,†]

[†]Section of Organic Chemistry and Biochemistry, Department of Chemistry, [‡]NMR Center, [§]Laboratory of Analytical Chemistry, Department of Chemistry, and [∥]Department of Biological Applications and Technology, University of Ioannina, Ioannina GR-451 10, Greece

[⊥]Department of Agricultural Sciences, Biotechnology and Food Sciences, Cyprus University of Technology, Post Office Box 50329, Limassol 3603, Cyprus

Supporting Information

ABSTRACT: We report a rapid, direct, and unequivocal spin-chromatographic separation and identification of minor components in the lipid fraction of milk and common dairy products with the use of selective one-dimensional (1D) total correlation spectroscopy (TOCSY) nuclear magnetic resonance (NMR) experiments. The method allows for the complete backbone spin-coupling network to be elucidated even in strongly overlapped regions and in the presence of major components from 4×10^2 to 3×10^3 stronger NMR signal intensities. The proposed spin-chromatography method does not require any derivatization steps for the lipid fraction, is selective with excellent resolution, is sensitive with quantitation capability, and compares favorably to two-dimensional (2D) TOCSY and gas chromatography−mass spectrometry (GC−MS) methods of analysis. The results of the present study demonstrated that the 1D TOCSY NMR spin-chromatography method can become a procedure of primary interest in food analysis and generally in complex mixture analysis.

KEYWORDS: *lipid fraction, totally correlated NMR spectroscopy (TOCSY), spin chromatography, dairy products*

INTRODUCTION

Separation and identification of components from complex mixtures have occupied a central role in the field of natural products and food chemistry research. The classical protocol for the investigation of complex mixtures has been to apply various chromatographic techniques, to isolate a certain amount of a pure product, and to identify its structure using various spectroscopic techniques[1] and/or the use of specialized hyphenated spectroscopic techniques.[2,3] On the other hand, nuclear magnetic resonance (NMR) spectroscopy is increasingly used as an analytical tool for identification and quantification of low-molecular-weight metabolites on unfractionized biological fluids, natural product extracts, and food samples.[1,4−12]

Milk lipids are very important because they confer distinctive textural, nutritional, and organoleptic properties on dairy products. Recent studies have reported that the consumption of saturated fatty acids has been linked to increased risk of cardiovascular disease, whereas the consumption of milk conjugated linoleic acids (CLAs) has beneficial effects, and this issue is still subject to numerous studies.[13] Accurate analysis, therefore, of minor lipids is important for determining the nutritive value and preparing nutritional labeling materials for particular function or application. The analysis of minor lipids, however, is extremely challenging and complex because it can be very slow and laborious and may require various preparation and analysis steps.[14]

The selective 1D TOCSY experiment has become an important NMR technique for establishing ^{1}H−^{1}H connectivity via scalar coupling in small- and medium-sized molecules[15,16] and in the analysis of mixtures of related compounds.[17] However, the method has found limited application in food matrices; to the best of our knowledge, few studies have, thus far, been published, among them in the metabolomics analysis of amino acids in honey[18] and mango juice.[19] In the present study, we report, for the first time, the direct identification of six minor species: (9-*cis*,11-*trans*) 18:2 and (9-*trans*,11-*trans*) 18:2 CLA isomers, caproleic acid (CA), glycerol in 1,2-diglyceride (1,2-DAG), 1-monoglyceride (1-MAG), and 2-monoglyceride (2-MAG) in the lipid fraction of milk and halloumi cheese, without any derivatization steps, with the use of a spin-chromatography procedure based on the spin diffusion process of selective one-dimensional (1D) total correlation spectroscopy (TOCSY) experiment.

Received: September 13, 2014
Revised: May 14, 2015
Accepted: May 19, 2015
Published: May 19, 2015

ACS Publications © 2015 American Chemical Society

DOI: 10.1021/acs.jafc.5b01335
J. Agric. Food Chem. 2015, 63, 5381−5387

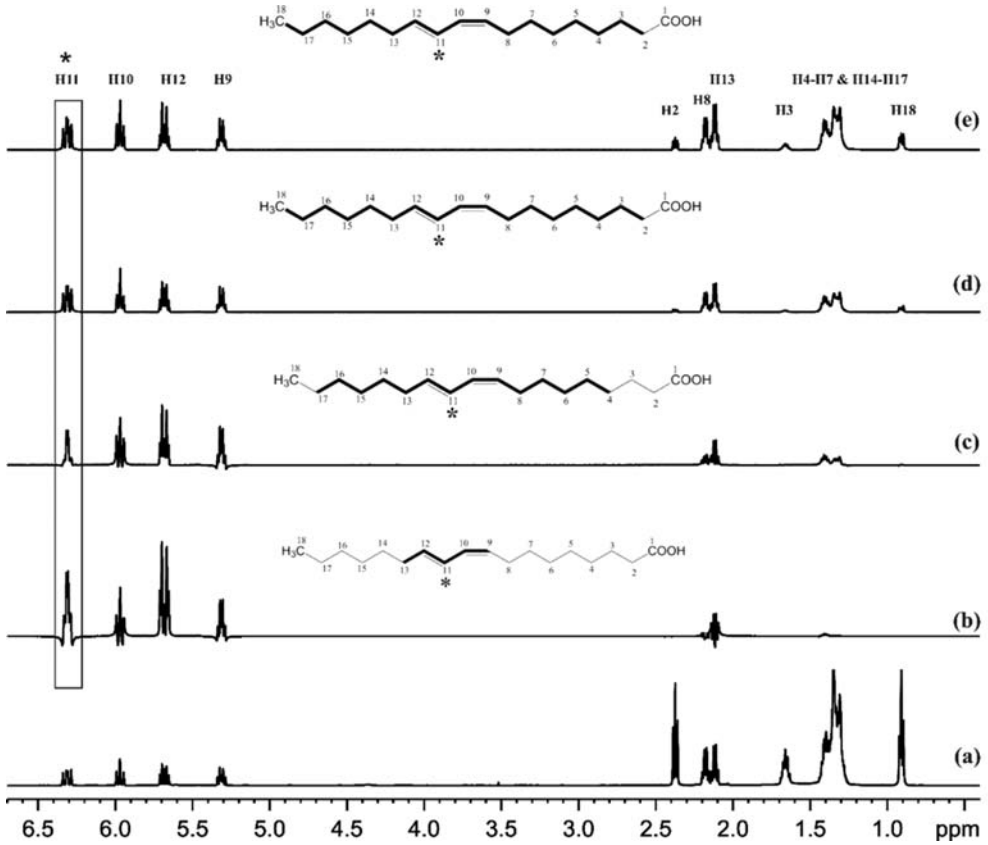

Figure 1. (a) 500 MHz 1D NMR spectrum of 20 mM solution of the (9-*cis*,11-*trans*) 18:2 CLA in $CDCl_3$ (*T*, 298 K; acquisition time, 4.3 s; relaxation delay, 5 s; number of scans, 256; and experimental time, ~25 min). (b–e) Selective 1D TOCSY spectra of the above solution using a mixing time of τ_m = (b) 33 ms, (c) 70 ms, (d) 200 ms, and (e) 400 ms. The asterisk denotes the selected H11 resonance that was excited. For panels b–e, the magnetization transfer network is illustrated.

MATERIALS AND METHODS

Materials. Conjugated (9-*cis*,11-*trans*) 18:2 linoleic acid, purity ≥96% [high-performance liquid chromatography (HPLC) grade], and conjugated (9-*trans*,11-*trans*) 18:2 linoleic acid, purity ≥98% (HPLC grade), were purchased from Fluka. CA, purity ≥96%, was purchased from Sigma-Aldrich. Chloroform and methanol (analytical grade) were obtained from Fisher Scientific (U.K.). $CDCl_3$ (99.8%) was purchased from Deutero (Kastellaun, Germany). The 37 fatty acid methyl ester (FAME) standard mix was purchased from Sigma-Aldrich.

Sample Preparations. The lipid fractions of milk samples were prepared as previously described.[20] The lipid fractions of halloumi cheese were prepared as follows: cheese samples were frozen in liquid N_2 and pulverized in a ceramic mortar. After lyophilization for 2 days, 300 mg of cheese was used for the extraction of the lipid phase, using the Bligh and Dyer method, as previously described.[20]

NMR Instrumentation. NMR experiments were performed on a Bruker AV500 spectrometer (Bruker Biospin, Rheinstetten, Germany) using the Topsin 2.1 suite. The 1D TOCSY experiments were carried out using a standard Bruker pulse program (selmlgp). A shaped pulse length of 20 ms for selective excitation was used, followed by either a MLEV-17 TOCSY spin lock[18] or applying the DIPSI-2 pulse train and incorporating a z filter before acquisition[21] for the suppression of artifacts. The spin lock was adjusted to 7.1 kHz, corresponding to a low power 90° pulse of 35 μs; this allows for safe operation without problems of significant heating of the samples, with spin-lock times up to 400 ms.

Gas Chromatography–Mass Spectrometry (GC–MS) Analysis. FAMEs were prepared by transesterification with methanolic potassium hydroxide according to the ISO 15884:2002 method[22] as previously described.[23] Fatty acid profiles were generated by analyzing the FAME samples on a GC-MS-QP 2010 Plus gas chromatography mass spectrometer (Shimadzu, Duisburg, Germany) equipped with a HT 280 T auto sampler (HTA, Brescia, Italy). Details of the GC–MS analysis are given elsewhere.[20,23]

RESULTS AND DISCUSSION

1D TOCSY of Model Compounds: Effects of Mixing Time. Figure 1 illustrates a series of selective 1D TOCSY spectra of the model (9-*cis*,11-*trans*) 18:2 CLA isomer, where the H11 olefinic proton (δ = 6.27 ppm)[20,24,25] has been selected for excitation using a range of mixing times and, thus, affecting the number of transfers within the spin system.[26] For a mixing time τ_m = 33 ms, the selective 1D TOCSY transfers magnetization to its *J*-coupled partners within the conjugated olefinic protons and the $C(13)H_2$ protons (Figure 1b). Using longer mixing times, the magnetization is transferred throughout the full spin system and, for τ_m values of 200 and 400 ms, resulted in the complete analysis and structure elucidation of the compound (panels d and e of Figure 1). Figure S1 of the Supporting Information illustrates a similar series of selective 1D TOCSY spectra of the (9-*trans*,11-*trans*) 18:2 CLA isomer, where the H10 and H11 (δ = 5.97 ppm) protons have been selected. Again, the 1D TOCSY experiment allows for structural information to be extracted in a time-efficient manner and with high spectral resolution.

Method Application in the Lipid Fraction of Milk and Dairy Products. An important application of the 1D experiment is the selective excitation of a proton sub-spectrum belonging to a single chemical component contained in a complex mixture, thus providing a form of spin chromatography. The selective excitation of a suitable "target" resonance

DOI: 10.1021/acs.jafc.5b01335
J. Agric. Food Chem. 2015, 63, 5381–5387

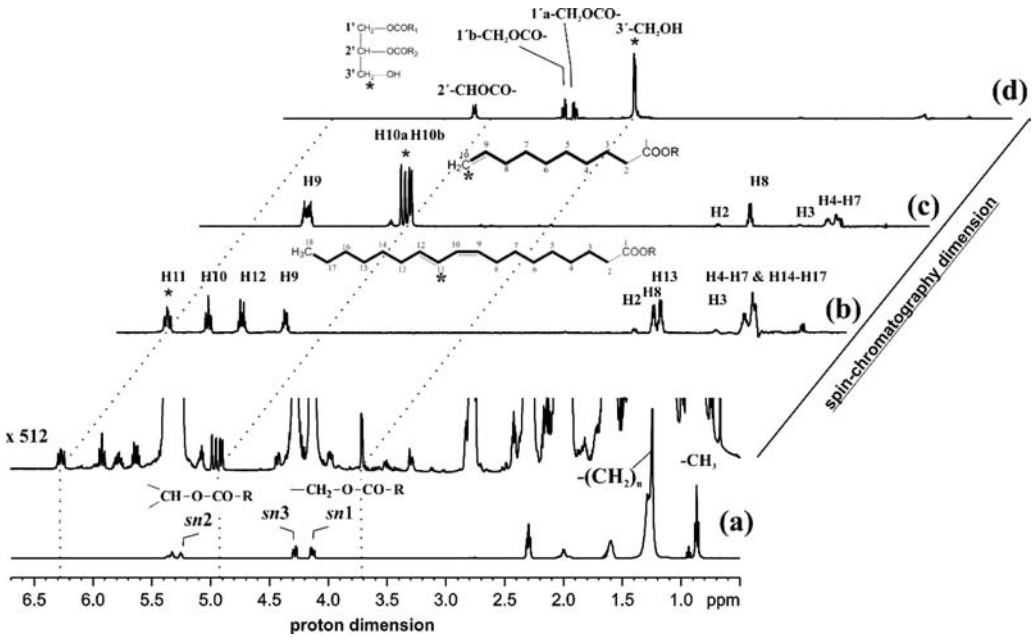

Figure 2. Spin chromatogram of the lipid fraction of a lyophilized cheese sample in $CDCl_3$. (a) 500 MHz ^{1}H NMR spectrum of the lipid fraction of a lyophilized cheese sample in $CDCl_3$ (*T*, 298 K; number of scans, 256; acquisition time, 4.3 s; relaxation delay, 5 s; and total experiment time, ∼25 min). The major lipid resonances are denoted (*sn*1, *sn*2, and *sn*3 indicate the stereospecific numbering of esterified glycerol). The inset shows 512× magnification of the spectrum to display resonances from the 18:2 CLA and other minor species. (b−d) 1D TOCSY spectra of panel a with τ_m = 400 ms (number of scans, 256; and total experiment time, ∼25 min). The asterisks denote the resonances that were excited by the use of a selective pulse.

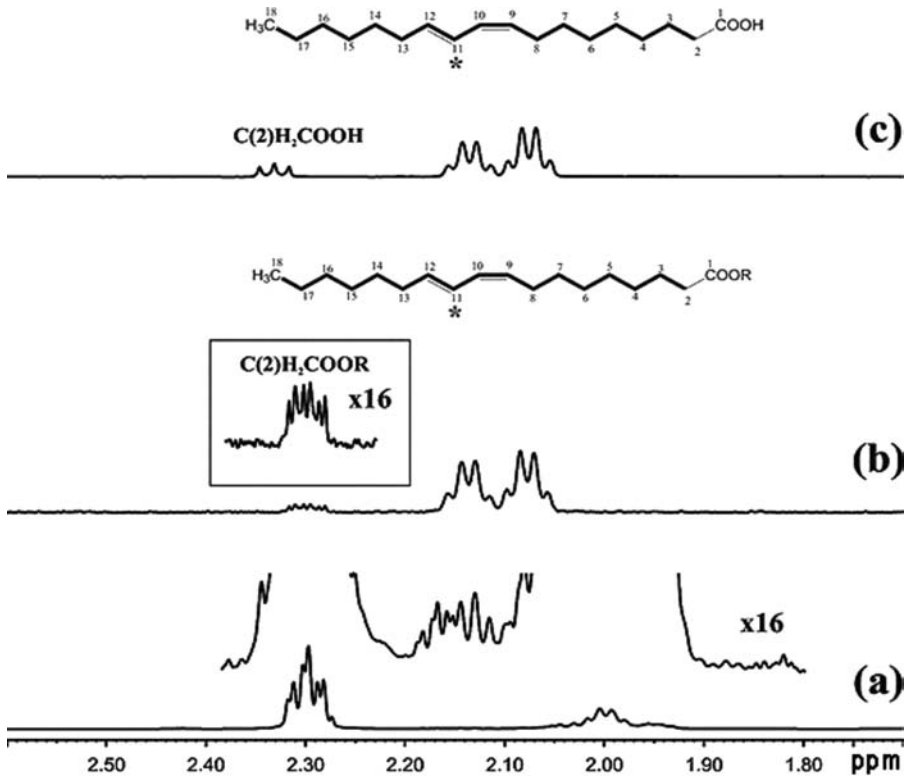

Figure 3. Selected regions of (a) Figure 2a, (b) 1D TOCSY spectrum of Figure 2b, and (c) 1D TOCSY of the model (9-*cis*,11-*trans*) 18:2 CLA isomer. In panels b and c, the selective excitation pulse was set on the H11 proton (δ = 4.92 ppm). The insert in panel b shows 16× magnification of the spectrum to display the C(2)H_2COOR resonances.

of the compound of interest can then reveal the whole spin system, even if the 1D ^{1}H NMR spectrum is heavily overlapped in the region of the other peaks in the selected spin coupling network. Figure 2a illustrates a typical 500 MHz ^{1}H NMR experiment of the lipid fraction of a lyophilized halloumi cheese sample in $CDCl_3$. Selective TOCSY excitation, with 400 ms

DOI: 10.1021/acs.jafc.5b01335
J. Agric. Food Chem. 2015, 63, 5381−5387

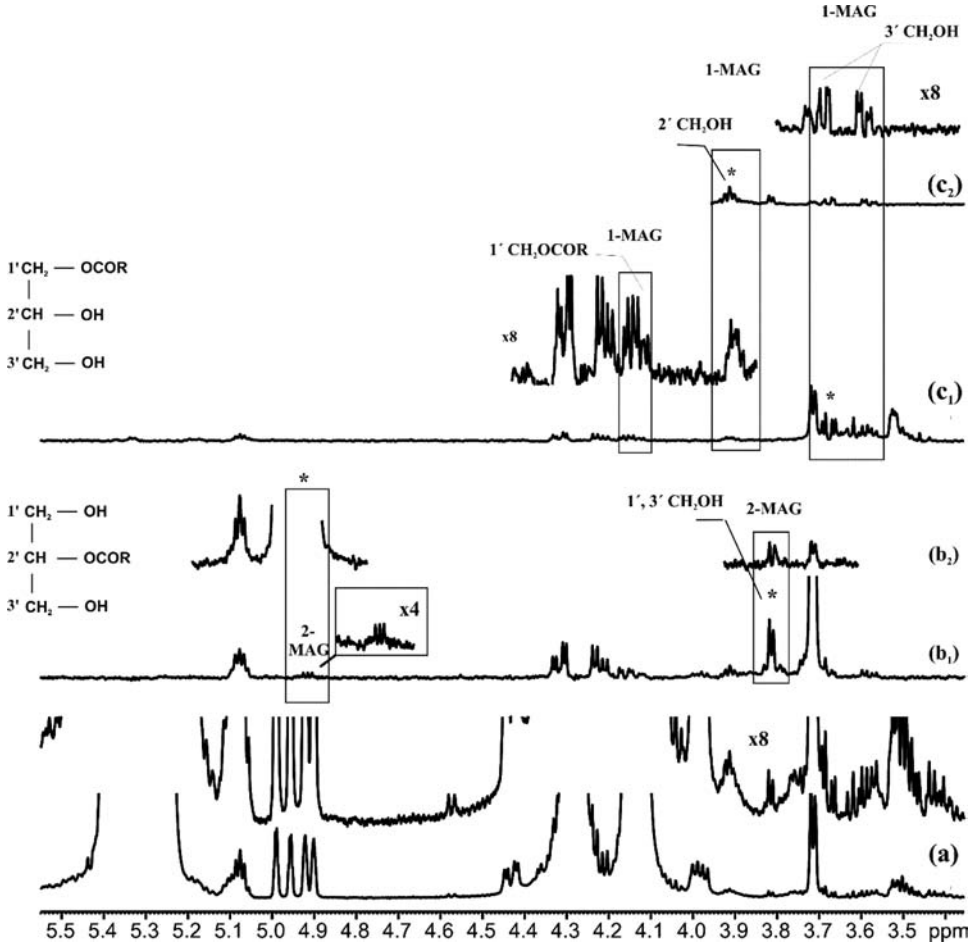

Figure 4. Selected regions of (a) Figure 2a, (b) 1D TOCSY spectrum that demonstrates the spin system of the glycerol moiety in 2-MAG [in panels b_1 and b_2, the selective excitation pulse was set on the 1′,3′-CH_2OH (δ = 3.82 ppm) and 2′-CHOCOR (δ = 4.92 ppm) peaks in 2-MAG, respectively], and (c) 1D TOCSY spectrum of the spin system of the glycerol moiety in 1-MAG [in panels c_1 and c_2, the selective excitation pulse was set on the 3′-CH_2OH (δ = 3.67 ppm) and 2′-CH_2OH (δ = 3.92 ppm) peaks in 1-MAG, respectively].

mixing time, of the H11 proton of the (9-*cis*,11-*trans*) 18:2 CLA isomer (Figure 2b) illustrates effective magnetization transfer from H11 to H2 and from H11 to H18. Therefore, its structure becomes amenable to detailed analysis, although signals from H2 to H8 and from H12 to H18 protons are completely hidden in a conventional 1D ^{1}H NMR spectrum under the resonances of the abundant components from 4 × 10^2 to 3 × 10^3 stronger intensities.

Similar experiments were performed with CA (Figure 2c). Selective TOCSY excitation of the H10a protons at 4.97 ppm with τ_m = 400 ms resulted in the effective magnetization transfer throughout the complete proton spin system, although the signals from H8 to H2 are completely hidden in the conventional 1D ^{1}H NMR spectrum. Selective TOCSY excitation of the doublet at 3.72 ppm reveals the complete spin system of the glycerol moiety in 1,2 DAG at 5.20 ppm (2′-CHOCO), 4.28 ppm, and 4.13 ppm (1′b,1′a-CH_2OCO, respectively) (Figure 2d).

Figure S2 of the Supporting Information illustrates a similar series of selective 1D TOCSY spectra of the lipid fraction of the lyophilized milk sample. Again, the 1D TOCSY allows for the analysis and structure elucidation of minor compounds in a time-efficient manner and with high spectral resolution.

A comparison of the 1D TOCSY spectrum of the model (9-*cis*,11-*trans*) 18:2 CLA isomer to the spectrum obtained from the lipid fraction of the lyophilized halloumi cheese sample illustrates a significant difference of the $C(2)H_2$ spin system (Figure 3). In the model compound, it appears as a triplet (δ = 2.33 ppm, and ^3J = 7.2 Hz) because of coupling with the $C(3)H_2$ protons, while in the spectrum of the extract, it appears at δ = 2.30 ppm with a complex multiplet pattern. This clearly demonstrates that the (9-*cis*,11-*trans*) 18:2 CLA isomer in the extract exists predominantly as an ester and not as a free acid. Because of the asymmetry of the *sn*2 carbon of the glycerol moiety, the $C(3)H_2$ protons become magnetically non-equivalent, thus resulting in a multiplet spin pattern. This result is very important in investigating the hydrolysis products of the ester linkage between an acyl group and the glycerol backbone. The resulting free fatty acids and their catabolic products have been found to be among the primary factors for the aroma of hard cheese, where lipolysis reaches high levels.[24]

Figure 4 illustrates the great potential of the 1D TOCSY experiments in the case of minor species with resonances in overcrowded spectral regions of the 1D ^{1}H NMR spectrum. The spin systems of the glycerol moieties in both 2-MAG (panels b_1 and b_2 of Figure 4) and 1-MAG (panels c_1 and c_2 of Figure 4) were clearly resolved and provided an unequivocal assignment of both species, although the 1-MAG resonances are strongly overlapped in the region of 3.75−3.55 ppm (Figure 4a).

DOI: 10.1021/acs.jafc.5b01335
J. Agric. Food Chem. 2015, 63, 5381−5387

Table 1. Results Obtained Using 1D TOCSY NMR, Conventional 1D ^{1}H NMR, and GC−MS Methods for the Determination of CA in Two Milk Samples

sample	analyte (units)	1D TOCSY[a]	^{1}H NMR[a]	relative deviation[b] (%)	GC−MS	relative deviation[c] (%)
1	CA (mM)	1.02 ± 0.03	0.97 ± 0.02[a]	5.15		
	CA (% of the lipid fraction)		0.26 ± 0.01		0.28	−7.14
2	CA (mM)	1.92 ± 0.06	1.83 ± 0.06[a]	1.75		
	CA (% of the lipid fraction)		0.74 ± 0.01		0.68	8.82

[a]Results are expressed as millimolars of CA [in tube; standard deviation (n = 3)]. [b]Results are expressed as 100[(1D TOCSY$_{value}$) − (1D ^{1}H NMR$_{value}$)]/(1D ^{1}H NMR$_{value}$). [c]Results are expressed as 100[(1D ^{1}H NMR$_{value}$) − (GC−MS$_{value}$)]/(GC−MS$_{value}$).

The excellent selectivity of the 1D TOCSY is demonstrated also in the case of strongly overlapped resonances of the 18:2 CLA geometric isomers. Figure S3 of the Supporting Information illustrates a selected ^{1}H NMR region of the (9,11) 18:2 CLA resonances of the lipid fraction of a lyophilized halloumi cheese sample. The apparent triplet at 5.92 ppm (^3J = 10.9 Hz) has been assigned to the H10 olefinic proton of the (9-*cis*,11-*trans*) 18:2 CLA isomer, and the strongly overlapped minor peak at 5.97 ppm has been assigned to the composite signal of the H10 and H11 protons of the (9-*trans*,11-*trans*) 18:2 CLA isomer. Selective 1D TOCSY of the resonance at 5.97 ppm clearly demonstrates magnetization transfer to H9 and H12 resonances at 5.54 ppm, which are not overlapped with other resonances of the lipid fraction (see Figure S3c of the Supporting Information) and, thus, can be used for the assignment of the (9-*trans*,11-*trans*) 18:2 CLA isomer. A limitation of the method, however, is that, because the identification is based on chemical shifts, the length of the fatty acid and the position of the unsaturation remains ambiguous. For instance, the ^{1}H NMR spectrum of (9-*cis*,11-*trans*) 18:2 has almost identical chemical shifts and J couplings as that from (9-*cis*,11-*trans*) 20:2 and (11-*cis*,13-*trans*) 20:2.

Figure S4 of the Supporting Information illustrates a comparison of the 1D TOCSY spectrum of Figure 2b to the respective extracted column and row in the two-dimensional (2D) TOCSY experiment. It is evident that the 1D TOCSY (i) significantly increases the digital resolution because, in the 2D TOCSY, it is limited by the number of points taken in the indirect dimension, (ii) removes dynamic range issues from the spectrum, (iii) of the whole spin system can be excited even in the region of strong signal overlapping with major components from 4 × 10^2 to 3 × 10^3 stronger NMR signal intensities, and (iv) decreases the experimental time.

Quantification Using 1D TOCSY: Comparison to 1D ^{1}H NMR and GC−MS Methods of Analysis. The excellent sensitivity and digital resolution of the 1D TOCSY experiment allows for the quantification of minor components. The quantitative analysis was based on the standard addition method. Known amounts of CA were added to the sample, and the respective spin chromatograms were recorded with the selective excitation of the H9 proton of the CA. The pulse repetition time (acquisition time + relaxation delay) was set at $5T_1$ (~16 s) of the long relaxation time of the H9 and H10 protons (~3.2 s) of the CA. The results were compared to those obtained by the use of 1D ^{1}H NMR quantitation.

The effect of the mixing time on the quantitation results was studied in detail. Several mixing times were used, more specific 33, 100, and 200 ms (τ_m = 33 ms corresponds to the value of $^1/_2$ ^3J, where ^3J is the coupling of the H9 and H10 protons). The sensitivity of the 1D TOCSY method was higher using smaller mixing time values but at the expense of the quantitation accuracy. Longer mixing times resulted in a moderate decrease of sensitivity, approximately by a factor of 2; however, a significantly improved accuracy of the method was achieved (the relative error was calculated as 31% for τ_m = 33 ms, because of twisted lineshapes,[27] whereas the relative error was calculated as only 2% for τ_m = 200 ms). Moreover, for τ_m = 200 ms, the sensitivity and accuracy of the method were almost equal using either the H9 or the H10 signals (data not shown). It should be pointed out that one of the advantages of the spin-chromatographic procedure is the ability to quantify the analyte of interest using either the excited proton or a nearby proton where the magnetization was transferred.

The 1D TOCSY quantitation was achieved following the procedure described by Sandusky et al.[28] Table 1 provides the quantification data obtained for the milk samples using the 1D TOCSY procedure. A concentration value (in tube) of 1.02 ± 0.03 mmol L^{-1} was determined using the 1D TOCSY and the H9 proton integration (Figure 5 and Figure S5 of the Supporting Information) compared to 0.97 ± 0.02 mmol L^{-1} as determined by using the conventional 1D ^{1}H NMR with an internal standard. For the second milk sample, the respective results were 1.92 ± 0.06 and 1.84 ± 0.06 mmol L^{-1}. The results demonstrate the excellent agreement between the 1D TOCSY method with the conventional 1D ^{1}H NMR method.

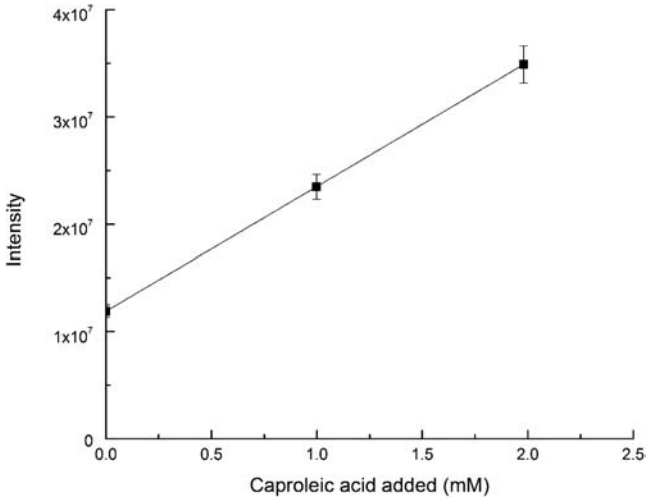

Figure 5. Quantification of CA in the lipid fraction of a lyophilized milk using the 1D TOCSY method (see also Figure S5 of the Supporting Information).

The limit of detection (LOD) for the spin-chromatographic quantitation of CA was calculated by the use of two different methods based on the calibration function[29] or the SNR method.[30,31] By means of the calibration function,[29] a calibration curve of the standard addition method was used; the LOD was found as 0.07 ± 0.01 mmol L^{-1} (in tube) or 0.01

DOI: 10.1021/acs.jafc.5b01335
J. Agric. Food Chem. 2015, 63, 5381−5387

mg g^{-1} for the milk sample. Using the SNR method, the LOD was calculated by applying the 3C/(S/N) equation in a standard sample of CA, where C represents the concentration of the analyte as determined by ^{1}H NMR (data were treated without using a line-broadening exponential function) and the signal-to-noise (S/N) value of the respective 1D TOCSY spectra was calculated. For the concentration levels of 0.97, 2.04, and 2.98 mmol L^{-1} of CA (in tube) the 3C/(S/N) value was calculated as 0.10, 0.11, and 0.08 mmol L^{-1} using the 1D TOCSY spectra and 0.004, 0.007, and 0.010 mmol L^{-1} using the 1D ^{1}H NMR spectra, respectively; thus, the LOD value of CA is 0.10 mmol L^{-1} (in tube) or 0.01 ± 0.001 mg g^{-1} for the milk sample and 0.010 mmol L^{-1} (in tube) or 0.001 ± 0.0001 mg g^{-1} for 1D TOCSY and 1D ^{1}H NMR methods, respectively.

The quantitative results of the spin chromatography and ^{1}H NMR were compared to those obtained with the use of the GC−MS method of analysis (ISO 15884:2002).[22] The results are in accordance with the GC−MS method of analysis; CA was found to be 0.28 and 0.68% of the total lipids when calculated by GC−MS and was measured as 0.26 and 0.74% of the total lipids when calculated by 1D ^{1}H NMR for the first and second milk samples, respectively.

The proposed selective 1D TOCSY spin-chromatographic separation procedure, therefore, is an excellent technique in mixture analysis of minor components, through a careful selection of the spin system to be excited. The method might become of primary interest in food research, including targeting metabolomics[32] because it (i) is rapid, selective, and non-destructive, (ii) allows for the chemical identification of minor components even in strongly overlapped spectral regions, (iii) does not require derivatization steps, and (iv) allows for the quantification of analytes of interest.

■ ASSOCIATED CONTENT

Supporting Information

500 MHz ^{1}H NMR and 1D TOCSY spectra for several mixing times of (9-*trans*,11-*trans*) 18:2 CLA (Figure S1), 500 MHz ^{1}H NMR and 1D TOCSY spectra of the lipid fraction of a lyophilized milk sample (Figure S2), selected regions of 500 MHz ^{1}H NMR and 1D TOCSY spectra for (9-*cis*,11-*trans*) and (9-*trans*,11-*trans*) 18:2 CLAs of the lipid fraction of a lyophilized cheese sample (Figure S3), selected regions of 500 MHz 2D TOCSY and 1D TOCSY spectra of the lipid fraction of a lyophilized cheese sample (Figure S4), and 1D TOCSY quantitation procedure displaying the 1D TOCSY spectra for successive addition of CA in a milk sample (Figure S5) (PDF). The Supporting Information is available free of charge on the ACS Publications website at DOI: 10.1021/acs.jafc.5b01335.

■ AUTHOR INFORMATION

Corresponding Authors

*Telephone: +30-26510-08315. E-mail: ctsiafou@cc.uoi.gr.
*Telephone: +30-26510-08389. E-mail: igeroth@uoi.gr.

Funding

This work was supported by the Cyprus Research Promotion Foundation, the European Regional Development Fund, and the Charalambides Christies, Ltd. dairy industry.

Notes

The authors declare no competing financial interest.

■ ACKNOWLEDGMENTS

Thanks are given to the anonymous reviewers for critical and constructive criticisms.

■ REFERENCES

(1) Novoa-Carballal, R.; Fernandez-Megia, E.; Jimenez, C.; Riguera, R. NMR methods for unravelling the spectra of complex mixtures. *Nat. Prod. Rep.* **2011**, *28*, 78−98.

(2) Albert, K. *On-line LC-NMR and Related Techniques*; John Wiley & Sons: Hoboken, NJ, 2002.

(3) Wolfender, J. L.; Marti, G.; Thomas, A.; Bertrand, S. Current approaches and challenges for the metabolite profiling of complex natural extracts. *J. Chromatogr. A* **2015**, *1382*, 136−164.

(4) Lewis, I. A.; Schommer, S. C.; Hodis, B.; Robb, K. A.; Tonelli, M.; Westler, W. M.; Sussman, M. R.; Markley, J. L. Method for determining molar concentrations of metabolites in complex solutions from two-dimensional ^{1}H−^{13}C NMR spectra. *Anal. Chem.* **2007**, *79*, 9385−9390.

(5) Spyros, A.; Dais, P. ^{31}P NMR spectroscopy in food analysis. *Prog. Nucl. Magn. Reson. Spectrosc.* **2009**, *54*, 195−207.

(6) Charisiadis, P.; Exarchou, V.; Troganis, A. N.; Gerothanassis, I. P. Exploring the "forgotten" −OH NMR spectral region in natural products. *Chem. Commun.* **2010**, *46*, 3589−3591.

(7) Manjunatha Reddy, G. N.; Caldarelli, S. Maximum-quantum (maxQ) NMR for the speciation of mixtures of phenolic molecules. *Chem. Commun.* **2011**, *47*, 4297−4299.

(8) Charisiadis, P.; Primikyri, A.; Exarchou, V.; Tzakos, A.; Gerothanassis, I. P. Unprecedented ultra-high-resolution hydroxy group ^{1}H NMR spectroscopic analysis of plant extracts. *J. Nat. Prod.* **2011**, *74*, 2462−2466.

(9) Charisiadis, P.; Tsiafoulis, C. G.; Exarchou, V.; Tzakos, A.; Gerothanassis, I. P. Rapid and direct low micromolar NMR method for the simultaneous detection of hydrogen peroxide and phenolics in plant extracts. *J. Agric. Food Chem.* **2012**, *60*, 4508−4513.

(10) Robinette, S. L.; Brüschweiler, R.; Schroeder, F. C.; Edison, A. S. NMR in metabolomics and natural products research: Two sides of the same coin. *Acc. Chem. Res.* **2012**, *45*, 288−297.

(11) Mannina, L.; Sobolev, A. P.; Viel, S. Liquid state ^{1}H high field NMR in food analysis. *Prog. Nucl. Magn. Reson. Spectrosc.* **2012**, *66*, 1−39.

(12) Martin-Pastor, M. Experiments for the editing of singlet peaks and simplification of ^{1}H NMR spectra of complex mixtures. *J. Agric. Food Chem.* **2014**, *62*, 1190−1197.

(13) Dilzer, A.; Park, Y. Implication of conjugated linoleic acid (CLA) in human health. *Crit. Rev. Food Sci. Nutr.* **2012**, *52*, 488−513.

(14) Shahidi, F.; Wanasundara, P. K. J. P. D. In *Food Lipids, Chemistry, Nutrition and Biotechnology*; Akoh, C. C., Min, D. B., Eds.; Marcel Decker, Inc.: New York, 2012.

(15) Dalvit, C.; Bovermann, G. Pulsed field gradient one-dimensional NMR selective ROE and TOCSY experiments. *Magn. Reson. Chem.* **1995**, *33*, 156−159.

(16) Parella, T. High-quality 1D spectra by implementing pulsed-field gradients as the coherence pathway selection procedure. *Magn. Reson. Chem.* **1996**, *34*, 329−347.

(17) Sharman, G. J. Development of a selective TOCSY experiment and its use in analysis of a mixture of related compounds. *Chem. Commun.* **1999**, *14*, 1319−1320.

(18) Sandusky, P.; Raftery, D. Use of semiselective TOCSY NMR experiments for quantifying minor components in complex mixtures: Application to the metabonomics of amino acids in honey. *Anal. Chem.* **2005**, *77*, 2455−2463.

(19) Koda, M.; Furihara, K.; Wei, F.; Moyakawa, T. Metabolic discrimination of mango juice from various cultivars by band-selective NMR spectroscopy. *J. Agric. Food Chem.* **2012**, *60*, 1158−1166.

(20) Tsiafoulis, C. G.; Skarlas, T.; Tzamaloukas, O.; Miltiadou, D.; Gerothanassis, I. P. Direct nuclear magnetic resonance identification and quantification of geometric isomers of conjugated linoleic acid in

DOI: 10.1021/acs.jafc.5b01335
J. Agric. Food Chem. 2015, 63, 5381−5387

milk lipid fraction without derivatization steps: Overcoming sensitivity and resolution barriers. *Anal. Chim. Acta* **2014**, *821*, 62−71.
(21) Cavanagh, J.; Rance, M. Supression of cross-relaxation effects in TOCSY spectra via a modified DIPSI-2 mixing sequence. *J. Magn. Reson.* **1992**, *96*, 670−678.
(22) International Organization of Standardization (ISO). *ISO 15884:2002 (IDF 182:2002). Milk Fat—Preparation of Fatty Acid Methyl Esters*; ISO: Geneva, Switzerland, 2002; p 6.
(23) Tzamaloukas, O.; Ordford, M.; Miltiadou, D.; Papachristoforou, C. Partial suckling of lambs reduced the linoleic and conjugated linoleic acid contents of marketable milk in Chios ewes. *J. Dairy Sci.* **2015**, *98*, 1739−1749.
(24) Scano, P.; Anedda, R.; Melis, M. P.; Dessi, M. A.; Lai, A.; Roggio, T. ^{1}H- and ^{13}C-NMR characterization of the molecular components of the lipid fraction of Pecorino Sardo cheese. *J. Am. Oil Chem. Soc.* **2011**, *88*, 1305−1316.
(25) Prema, D.; Pilfold, J. L.; Krauchi, J.; Church, J. S.; Donkor, K. K.; Cinel, B. Rapid determination of total conjugated linoleic acid content in select Canadian cheeses by ^{1}H NMR spectroscopy. *J. Agric. Food Chem.* **2013**, *61*, 9915−9921.
(26) Sachleben, J. R.; Yi, R.; Volden, P. A.; Conzen, S. D. Aliphatic chain length by isotropic mixing (ALCHIM): Determining composition of complex lipid samples by ^{1}H NMR spectroscopy. *J. Biomol. NMR* **2014**, *59*, 161−173.
(27) An effective elimination of the twisted lineshapes (anti-phase components, ZQ artifacts) for short τ_m values can be achieved with the use of the ZQ-filter experiment. Thrippleton, J. M.; Keeler, J. Elimination of zero-quantum interference in two-dimensional NMR spectra. *Angew. Chem., Int. Ed.* **2003**, *42*, 3938−3941.
(28) Sandusky, P.; Amponsah, E. A.; Raftery, D. Use of optimized 1D TOCSY NMR for improved quantitation and metabolomic analysis of biofluids. *J. Biomol. NMR* **2011**, *49*, 281−290.
(29) Danzer, K. *Analytical Chemistry, Theoretical and Metrological Fundamentals*; Springer-Verlag: Berlin, Germany, 2007; p 74, 147.
(30) Tsiafoulis, C. G.; Exarchou, V.; Tziova, P. P.; Bairaktari, E.; Gerothanassis, I. P.; Troganis, A. N. A new method for the determination of free L-carnitine in serum samples based on high field single quantum coherence filtering ^{1}H-NMR spectroscopy. *Anal. Bioanal. Chem.* **2011**, *399*, 2285−2294.
(31) Maniara, G.; Rajamoorthi, K.; Rajan, S.; Stockton, G. Method performance and validation for quantitative analysis by ^{1}H and ^{31}P NMR spectroscopy. Applications to analytical standards and agricultural chemicals. *Anal. Chem.* **1998**, *70*, 4921−4928.
(32) Sundekilde, U. K.; Larsen, L. B.; Bertram, H. C. NMR-based milk metabolomics. *Metabolites* **2013**, *3*, 204−222.

DOI: 10.1021/acs.jafc.5b01335
J. Agric. Food Chem. 2015, 63, 5381−5387

JOURNAL OF AGRICULTURAL AND FOOD CHEMISTRY

Article

pubs.acs.org/JAFC

Classification of Chinese Honeys According to Their Floral Origins Using Elemental and Stable Isotopic Compositions

Zhaobin Wu,[†] Lanzhen Chen,*[,†,§] Liming Wu,[†,§] Xiaofeng Xue,[†,§] Jing Zhao,*[,†] Yi Li,[†,§] Zhihua Ye,[#] and Guanghui Lin[⊥,Δ]

[†]Institute of Apicultural Research, Chinese Academy of Agricultural Sciences, Beijing 100093, China

[§]Risk Assessment Laboratory for Bee Products, Quality and Safety of Ministry of Agriculture, Beijing 100093, China

[#]Institute of Quality Standard and Testing Technology for Agro-products, Chinese Academy of Agricultural Sciences, Beijing 100081, China

[⊥]Center for Earth System Science, Tsinghua University, Beijing 100084, China

[Δ]Graduate School at Shenzhen, Tsinghua University, Shenzhen 518055, China

ABSTRACT: The objective of this study is to test the feasibility of multi-isotopic and elemental analyses combined with chemometric techniques for differentiating the botanical origins of major honey products in China. The stable isotope and elemental compositions of 57 honey samples from four major floral origins in China (i.e., rape honey, acacia honey, vitex honey, and jujube honey) were analyzed using stable isotope ratio mass spectrometry (IRMS) and inductively coupled plasma mass spectrometry (ICP-MS), respectively. The results showed that hydrogen and oxygen isotopes could be more suitable than the carbon isotope for discriminating the floral origins of major honeys in China. There were significant differences in the contents of most elements between or among different floral origins. The combination of IRMS and ICP-MS methods provides the most effective and accurate approach (in most cases close to 100% accuracy) for classifying Chinese honeys according to their floral origins.

KEYWORDS: *honey, chemometric techniques, floral origins, IRMS, ICP-MS*

INTRODUCTION

Honey is known as a natural substance produced by *Apis mellifera* (bees) from the nectar or honeydew of plants and usually contains no additives or preservatives.[1] It can be divided into various types of honey such as acacia, vitex, rape, jujube, and many more according to their sources and constitutions. Honey contains numerous nutrients and may also show biologically active properties (e.g., antimicrobial) depending on its floral origin, which is considered essential to the health-promoting functions of honey for the human body.[2] Because of the large difference in the prices and yields as well as the quantity demand among different varieties of honey, honey products have frequently been the object of fraud in Chinese and international markets. Fraudulent honey products in markets are often manufactured by combining honey resulting from various floral sources where bees forage for different nectars and honeydews, mixing premium and high-grade quality honey with cheaper and lower quality ones, or adding cheaper sweeteners. Thus, the determination and certification of honey according to their floral origins plays an important role in ensuring fairness and equality for beekeepers, producers, distributors, and consumers as well as regulatory agencies.

To guarantee fair play in markets and combat product fraud, we need appropriate and reliable methods to determine the legitimacy of botanical origins of honey in the markets. Melissopalynoloy, the study of pollen components and load within honey, has conventionally been employed to determine floral origin. However, the limitations of this method include unreliability, expertise, time consumption, etc.[3,4] Several new techniques including physicochemical parameters,[5−7] ICP-MS,[8] liquid chromatography−diode array detection−tandem mass spectrometry,[9,10] infrared spectroscopy,[1,11,12] FT-Raman spectroscopy,[13] NMR,[14] gas chromatography,[15] and gas chromatography−mass spectrometry[7,15−17] have been developed to replace the conventional method.

Stable isotope techniques have been successfully applied to detect the adulteration of honey worldwide.[18−21] For instance, Çinar et al.[18] proved the C_4 sugar value was a useful criteria for identifying the distinctiveness and detecting high-fructose corn syrup (HFCS) adulteration of pine honey. Stable isotope technique has also been employed to discriminate honey of differing geographical origins.[20] Schellenberg et al.[20] revealed that the stable isotopic compositions of honey produced in areas with geographical features and diverse climatic conditions could become reliable geographical origin information.

Several previous studies have shown that elemental profiling also provides a good prospect for characterizing geographical origins of honey. As demonstrated by Pellerano et al.,[22] the honey in Argentina could be divided into three producing areas according to their geographical origins by analyzing trace elements in multifloral honey from different geographical locations in combination with instrumental neutron activation analysis. Element profiling, especially using metal contents, has

Received: October 10, 2014
Revised: May 15, 2015
Accepted: May 20, 2015
Published: May 20, 2015

ACS Publications © 2015 American Chemical Society

DOI: 10.1021/acs.jafc.5b01576
J. Agric. Food Chem. 2015, 63, 5388−5394

been used as another chemical profiling method to determine botanical origins of honey. Because metals are stable in honey over a long time, their concentrations should depend on their botanical origins, the type of soils in which nectar-producing plants grow, and the vegetation conditions in the forage area.[23] For example, Chen et al.[24] analyzed 12 elements in Chinese honey samples of diverse types and successfully differentiated Chinese honey through partial least-squares discriminant analysis and back-propagation artificial neural network. Chudzinska et al.[25] also combined multielement concentration analysis and chemometric analysis to forecast the three different types of honey in Poland.

As reported previously, the identification of geographical and botanical origins of agro-products using multistable isotope and multielement combination with chemometric analysis is an expanding field.[26−29] For example, Branch et al.[26] analyzed the contents of Cd, Pb, Se, Sr, and ^{13}C, ^{15}N for the seeds of 20 local *Triticum aestivum* varieties to separate different cultivars or blends using discriminant analysis. To our knowledge, no research has been performed to classify the botanical origins of Chinese honey on the basis of multistable isotope and element compositions. This study thus aimed at testing the feasibility of multi-isotopic and elemental analyses combined with chemometric techniques to differentiate the botanical origins of major honeys in China.

MATERIALS AND METHODS

Sampling and Preparation. A total of 57 honey samples, including those originated from rape (*Brassica campestris* L.), acacia (*Robinia pseudoacacia* L.), vitex (*Vitex negundo* var. *heterophylla* Rehd.), and jujube (*Ziziphus jujuba* Mill. var. *inermis* (Bunge) Rehd.) (n = 16, 16, 12, and 13, respectively), were collected directly from beekeepers during 2012 and 2013 in different regions of China (Table 1). To avoid the effect of variations of bee species, the honey samples for this study were collected only from the bee hives occupied by *Apis mellifera*.

Table 1. Description of Sampling Regions for Four Major Types of Unifloral Honey in China

floral source	geographical origin	characteristics
rape	Yunnan and Sichuan provinces	white color, white crystals
acacia	Beijing and Shanxi provinces	light white color, no crystals
vitex	Beijing and Shanxi provinces	light amber color, crystals
jujube	Beijing and Shanxi provinces	amber color, no crystals

All honey samples were stored in the absence of light in plastic containers that were acid washed before use and maintained at room temperature (about 25 °C) until further analyses. Samples also were separated for stable isotope analysis. A test portion of about 30 g of honey was taken and liquefied at 45 °C and then homogenized in an ultrasonic bath for 0.5 h prior to both stable isotopic and multielemental analyses.

Stable Isotopic Analysis. The stable isotope analyses were carried out using an isotope ratio mass spectrometer (IRMS) (Finnigan Delta V Plus, Thermo Fisher Scientific Corp, Bremen, Germany) in the IRMS Laboratory of Chinese Academy of Forestry, coupled with an elemental analyzer (EA; Flash EA1112, Thermo Scientific) to measure $^{13}C/^{12}C$ ratios and a pyrolyzer (Finnigan TC/EA, High-Temperature Conversion Elemental Analyzer, Thermo Scientific) to measure $^{2}H/^{1}H$ and $^{18}O/^{16}O$ ratios. To separate the gases, the EA was fitted with a Porapack QS GC column (3 m; 6 × 4 mm, o.d./i.d.) and the pyrolyzer with a molecular sieve 5 Å (0.6 m) GC column. The devices were interfaced with the IRMS through a dilutor (Conflo III, Thermo Scientific) for dosing the sample and reference gases and fitted with an autosampler (Finnigan AS2000, Thermo Scientific). An appropriate cover on the pyrolyzer autosampler allowed continuous flushing with helium to guarantee dryness of the samples during measurement. About 1.0 g samples of honey were diluted to 10 mL with ultrapure water, and 3 μL of diluted solution was then placed into a tin capsule for $^{13}C/^{12}C$ measurements.

For hydrogen and oxygen isotopic analyses, about 200 μg of fresh honey of each sample was transferred into a silver capsule in dupluicate as for the 0.2 mg each of two laboratory standards (P1, P2) with known D/H and $^{18}O/^{16}O$ values. All of these silver capsules were not completely sealed so the samples were equilibrated with laboratory vapor with stable isotopic compositions for at least 3 days before the capsules were closed with tweezers and the samples were analyzed in the TC/EA pyrolyzer for D/H and $^{18}O/^{16}O$. The stable isotope compositions were recalculated from the IRMS results using P1 and P2 as QC materials. In this way, only the nonexchangeable hydrogen of honey was tested for D/H.[30]

Carbon, hydrogen, and oxygen isotope ratios were reported in δ notation in units of per mil or parts per thousand (‰) relative to the accepted international standards, $\delta^{13}C$‰ relative to Pee Dee Belimnite (PDB), whereas $\delta^{2}H$ and $\delta^{18}O$ refers to V-SMOW (Vienna Standard Mean Ocean Water). The delta values were calculated as

$$\delta_x = (R_{samp}/R_{ref} - 1) \times 1000$$

where R_{samp} and R_{ref} are the ratios of heavy to light isotope for the sample and reference material, respectively. The quality control standards for the $\delta^{13}C$, $\delta^{2}H$, and $\delta^{18}O$ analyses were IAEA600 ($\delta^{13}C$ = −27.771‰), USGS43 ($\delta^{2}H$ = −50.3‰), EMA P1 ($\delta^{2}H$ = −25.3‰; $\delta^{18}O$ = 20.99‰), EMA P2 ($\delta^{2}H$ = −87.80‰; 26.9‰), and USGS43 ($\delta^{18}O$ = 14.11‰). The analytical precision was 0.2‰ for $\delta^{13}C$, 2‰ for $\delta^{2}H$, and 0.2‰ for $\delta^{18}O$.

Multielement Analyses. The multielement analysis was performed using an Agilent 7500ce ICP-MS (Agilent Technologies Inc., Santa Clara, CA, USA). The honey samples were measured after the hot acid extraction using a heating block digestion system.[31] Briefly, a ∼1.0 g sample of honey was placed into a 50 mL Teflon digestion vessel with 10 mL of HNO_3 (guarantee reagent) and digested at ambient temperature overnight. The sample was placed on a heating block the next day. The combustion procedure was as follows: (1) at 70 °C for 10 min, (2) at 160 °C for 240 min, (3) at 180 °C for 120 min. The digested solution was diluted to a final volume of 50 mL with ultrapure water, decanted into luer-lock syringes, and then filtered through a Pall PVDF 0.45 μm filter into a plastic flask before further analyses. A blank digest was carried out in the same way. All materials were cleaned by soaking for 48 h in diluted HNO_3 (40% v/v) and rinsed three times with ultrapure water prior to use.[32]

The method performances for determination of 20 elements in the honey samples were evaluated by the tests of blank values, limits of detection (LOD), and spiking recovery. The spiking recoveries for these 20 elements in honey samples range from 90.2 to 109.9%, which suggests that the performance of the method allows accurate measurements of the levels of these elements in our honey samples.

Statistical Analysis. Multiple-comparison ANOVA was used to compare the differences among four honey floral origins using the SPSS software (version 17.0). Principal component analysis (PCA) and linear discriminant analysis (LDA) were applied to differentiate the floral origins of the honey samples using Matrix Laboratory (MATLAB) software (version 7.9.0). PCA minimizes the possibility of losses of the information on data matrix by reducing data set dimensionality, which can preserve most of the original variability through complex combination of their variables. The principal component (PC) could account for most of the variability in data grouping. The multivariate method was chosen to assess the stable isotope and multielement data. LDA, as a supervised technique, provided a discriminant model with respect to the descriptors' previously defined botanical origins of honey and found a rule that allocated unknown origins of honey samples to the correct group as well as studied variable discriminate best among the types of honey. To verify the power and the stability of the model, a "leave-one-out"

DOI: 10.1021/acs.jafc.5b01576
J. Agric. Food Chem. 2015, 63, 5388−5394

cross-validation discriminant analysis was carried out. In this test, known samples were used as "unknowns" to validate the model built on the basis of a reduced set of cases. Effectively, one sample was removed from the data set and then classified on the basis of a model constructed from the remainder. This process was then repeated for each sample in turn and the success of the classification recalculated by comparison with the known origin.[33]

RESULTS AND DISCUSSION

Variations in Stable Isotope Ratios of Honey among Floral Origins. The variations in stable isotopic compositions of the honey with different floral origins are presented in Figure 1. The order of the botanical origins according to the honey $\delta^{13}C$ value was vitex > jujube ≈ acacia > rape (Figure 1a). Despite significant difference in the mean $\delta^{13}C$ value among four floral origin by ANOVA test ($P = 0.05$), there were only slight differences in their ranges, resulting in overlapping among the floral origins. In other words, there was no clear differentiation in the $\delta^{13}C$ values among the four Chinese honey types. The nectar sources of Chinese honey are all from C_3 plants, so no big differences in the $\delta^{13}C$ values of honey were expected due to their botanical origins. However, the differences in the $\delta^{13}C$ values could be explained on the basis of the geographical origins and environmental conditions where the honeys were formed, but to much lesser degree on their botanical origins.[20,34] For example, the rape plants tend to grow in southern and central China where the climate is more humid so their honeys have much lower mean $\delta^{13}C$ values because of larger $\delta^{13}C$ discrimination during photosynthesis in a humid environment,[35] whereas the acacia, vitex, and jujube plants grow in drier regions, resulting in slightly higher mean honey $\delta^{13}C$ values (Figure 1a). Thus, stable carbon ratio alone was not suitable for the determination of botanical origins for Chinese honeys.

There were highly significant differences in the mean values of both hydrogen and oxygen isotope ratios according to the floral origins (all $P < 0.01$ from ANOVA and Duncan's LSD tests). The order of floral origin was acacia > jujube > vitex > rape according to the mean $\delta^{2}H$ value of honey samples (Figure 1b), and for the mean $\delta^{18}O$ value the order was jujube > rape > acacia > vitex (Figure 1c). From a two-dimensional plot of stable hydrogen and oxygen isotope ratios (Figure 2), it was obvious that botanical origins of Chinese honeys could be separated in most cases with only these two isotopic parameters. In general, the jujube honey had high $\delta^{2}H$ and $\delta^{18}O$ values, so they appeared at the top right section of the plot, whereas the acacia honey had high $\delta^{2}H$ but low $\delta^{18}O$ values, so they clustered in the top right section, also (Figure 2). With medium $\delta^{18}O$ but low $\delta^{2}H$ values, the rape honeys were positioned to the middle bottom, whereas the vitex honeys were positioned in the left middle section with medium $\delta^{2}H$ but low $\delta^{18}O$ values, which were overlapped with several acacia or vitex honeys (Figure 2). The stable hydrogen compositions in the honey samples are determined by the isotopic compositions of the water to which the plant has assimilated and conserved during photosynthesis,[20,36] whereas the compositions of stable oxygen isotopes in the honey samples were affected not only by waters available for plants but also atmospheric CO_2. Because of different environmental waters and unique plant isotopic interactions with atmospheric CO_2, the honeys with different floral origins could have distinct hydrogen and oxygen isotopic signals, which could be used as biological markers to discriminate the floral origins in China.

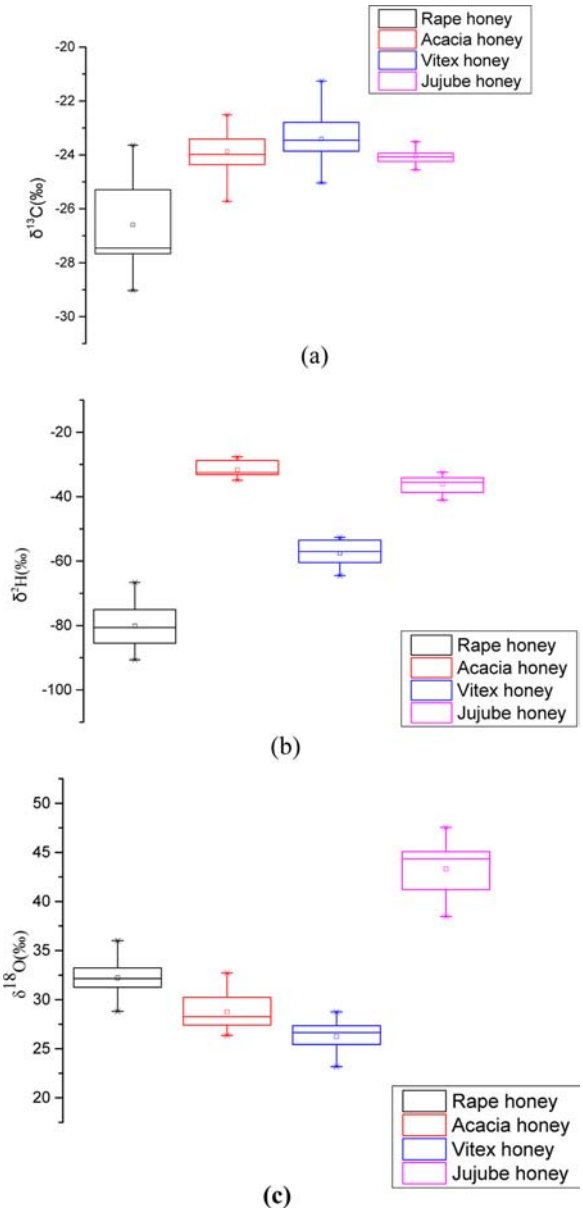

Figure 1. Box plot for carbon isotope ratio ($\delta^{13}C$, a), hydrogen isotope ratio ($\delta^{2}H$, b), and oxygen isotope ratio ($\delta^{18}O$, c) of Chinese honey samples according to floral origins. For each box plot, the boundary of the box closest to zero indicates the 25th percentile, the solid lines within the box mark the mean and median, and the boundary of the box farthest from zero indicates the 75th percentile. Whiskers above and below the box indicate the 90th and 10th percentiles, whereas symbols represent the 5th and 95th percentiles. Significant differences are defined at the 95% confidence level.

Comparisons in Multielement Concentrations of Honey among Floral Origins. As shown in Table 2, there was certain variability of the element compositions in the honey samples tested. Elements grouped as major elements were those having an average concentration of >1 mg/kg in food products.[37] In agreement with previous studies,[23,24,38] K was the most abundant chemical element in Chinese honeys (Table 2). In the honey samples tested, the highest K contents were found in the jujube honey samples, followed by the vitex, acacia, and rape honey samples. Na is the second most common chemical element in honey,[23] and the order of mean Na concentration was jujube honey (46.59 mg/kg) > vitex honey

DOI: 10.1021/acs.jafc.5b01576
J. Agric. Food Chem. 2015, 63, 5388−5394

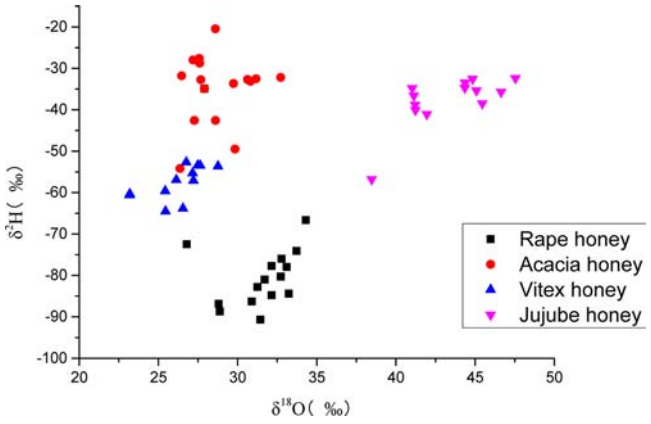

Figure 2. Plot of hydrogen isotope ratio (δ^2H) versus oxygen isotope ratio (δ^{18}O) for Chinese honey samples of four different floral origins.

(31.62 mg/kg) > rape honey (29.71 mg/kg) > acacia honey (22.75 mg/kg). The mineral composition of honey, especially the contents of major elements, correlated with its color. Dark and amber honeys such as the jujube honey contained higher amounts of certain major elements than pale honeys such as the rape and vitex honeys. Indeed, the color of jujube honey was darkest among the four unifloral honey types (Table 1), and the concentrations of K, Na, Ca, and Mg in the jujube honey were exactly the highest among the four botanical origins (Table 2).

The contents of trace elements (usually <1 mg/kg) in Chinese honey samples were quite low (Table 2). The rape honey samples were generally characterized by the highest contents of Ni, Mo, and Ti, but for the acacia honey samples the contents of U were the highest among the four unifloral honey types. The vitex honey samples had higher contents of Cr, As, Se, Ag, and Cd, but in the jujube honey samples none of these trace elements was at high level (Table 2).

Multivariate Analysis of Stable Isotopic and Multielement Compositions. As shown in the above analyses, the compositions of one or two elements either stable isotope ratios or elemental compositions in honey samples provided only an incomplete view with respect to interpretation of honey botanical origins. Thus, it is impossible to assign the botanical origin of an unknown test sample using single-element analysis, and a multivariate evaluation is necessary to improve the overall accuracy of any classification of honey floral origin.

A 3-D plot of first principal component (PC1), second principal component (PC2), and third principal component (PC3) obtained by PCA is shown in Figure 3. The plot

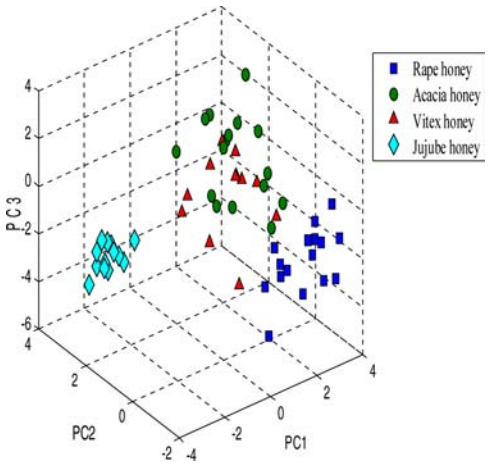

Figure 3. 3-D score plot for the three principal components of Chinese honey samples of four different floral origins.

elucidated the characteristics of four botanical origins of Chinese honeys. The rape honey samples had low values for PC2, the jujube honey samples had low PC1, and both the acacia honey and vitex honey samples had high values for PC2. PC1 explained 30.8% of the variability and high factor loadings on the δ^{18}O, K, Ca, Cu, Sr, Ag, and Ba (Figure 4). Low PC1 values for the jujube honey samples of these components and similar values were found in the rape, vitex, and acacia honey

Table 2. Comparisons of the Contents of Common Elements in Chinese Honeys among Four Floral Origins[a]

element (units)	rape honey (n = 16)	acacia honey (n = 16)	vitex honey (n = 12)	jujube honey (n = 13)
Na (mg/kg)	29.71 ± 16.52a	22.75 ± 30.35a	31.62 ± 38.59ab	46.59 ± 12.71b
Mg (mg/kg)	14.44 ± 2.64b	7.47 ± 3.39a	8.41 ± 2.01a	15.51 ± 1.25b
K (mg/kg)	141.67 ± 46.88a	184.64 ± 46.14b	227.32 ± 98.89c	1749.22 ± 141.3d
Ca (mg/kg)	28.47 ± 12.26a	14.37 ± 8.56b	19.05 ± 6.57c	30.7 ± 14.62a
Fe (mg/kg)	2.41 ± 2.62a	1.22 ± 0.78b	3.43 ± 3.81c	2.19 ± 0.4a
Cr (μg/kg)	12.12 ± 12.07a	16.04 ± 20.45ab	38.12 ± 37.08c	19.57 ± 3.19b
Mn (μg/kg)	351.41 ± 96.89a	184.92 ± 112.95b	134.95 ± 56.57c	493.94 ± 113.37d
Co (μg/kg)	1.45 ± 2.42a	9.25 ± 13.98b	11.82 ± 10.1c	1.49 ± 0.24a
Ni (μg/kg)	38.02 ± 48.66a	35.67 ± 57.22a	17.36 ± 13.31b	11.5 ± 1.47b
Cu (μg/kg)	84.41 ± 65.07a	80.02 ± 24.14a	100.59 ± 27.44b	334.14 ± 42.46c
As (μg/kg)	10.52 ± 7.83a	8.23 ± 5.93b	13.6 ± 19.85c	4.07 ± 1d
Se (μg/kg)	2.32 ± 1.52a	2.25 ± 1.86a	4.35 ± 4.41b	1.46 ± 0.57c
Sr (μg/kg)	102.25 ± 62.28a	78.8 ± 56.8b	94.09 ± 44.63a	3344.13 ± 520.52c
Mo (μg/kg)	14.64 ± 10.27a	10.48 ± 9.02b	9.63 ± 6.48b	5.58 ± 1.45c
Ag (μg/kg)	0.09 ± 0.12a	0.11 ± 0.15a	0.21 ± 0.14b	0.13 ± 0.03a
Cd (μg/kg)	0.62 ± 0.51a	0.71 ± 0.92a	1.18 ± 1.77b	0.41 ± 0.08a
Ba (μg/kg)	71.41 ± 74.83a	61.08 ± 75.25a	86.8 ± 62.65a	295.88 ± 45.87b
Tl (μg/kg)	5.27 ± 2.89a	0.51 ± 0.76b	0.35 ± 0.31b	0.28 ± 0.03b
Th (μg/kg)	0.71 ± 0.99a	1.09 ± 1.66b	1.0 ± 1.99b	0.26 ± 0.07c
U (μg/kg)	0.91 ± 0.90a	1.48 ± 1.77b	1.09 ± 1.45a	1.44 ± 0.57b

[a]The values are means ± SD. For the same element, different letters indicate significant difference between the two floral origins at $P < 0.05$.

DOI: 10.1021/acs.jafc.5b01576
J. Agric. Food Chem. 2015, 63, 5388−5394

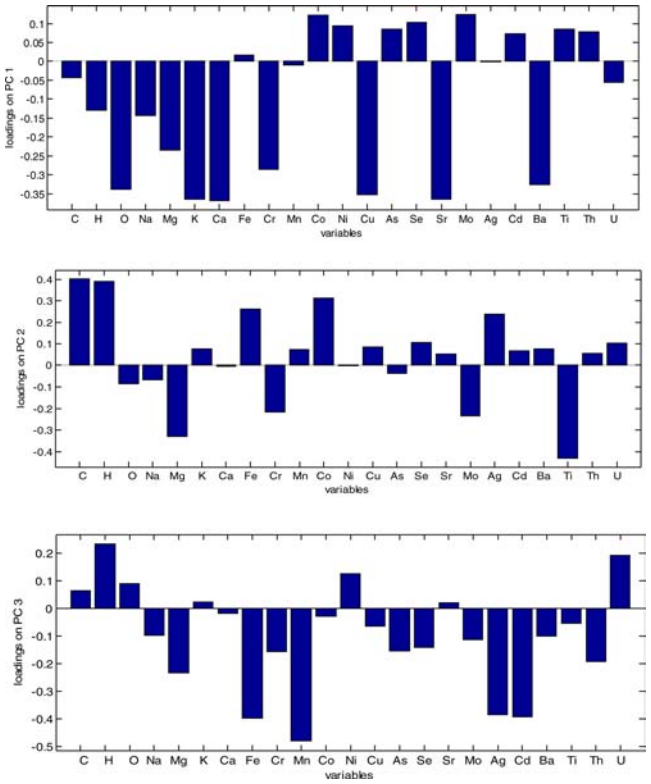

Figure 4. Loadings of the variables on three principal components of PCA analysis (PC1, PC2, and PC3) for Chinese honey samples of four different floral origins.

samples. PC2 explained 14.2% of the variability and high factor loadings on the $\delta^{13}C$, $\delta^{2}H$, Mg, Co, and Ti concentrations (Figure 4). PC3 explained only 9.7% of the variability. Together all three components accounted only for 51.7% of the variation. Intermediate PC2 values were found for the jujube honey samples of these components and low PC2 values for the rape honey samples, but similar PC2 values were found for the vitex and acacia honeys (Figures 3 and 4). Thus, the $\delta^{13}C$, $\delta^{18}O$, $\delta^{2}H$, Mg, K, Ca, Co, Cu, Ag, Sr, Ba, and Ti concentrations were proved to be effective parameters for determining the botanical origins of Chinese honey samples. However, the plot of the PCs for the acacia honey samples overlapped tightly with the vitex honey samples (Figure 3).

For a better analysis of the discriminating botanical origins of honey, LDA was carried out using stable isotope ratios of 3 elements (carbon, oxygen, hydrogen) and contents of all 20 metal elements in 57 Chinese honey samples. LDA was performed as a chemometric technique, and their discrimination models were constructed to classify honey samples according to their botanical origins using the obtained data of $\delta^{13}C$, $\delta^{2}H$, $\delta^{18}O$, Na, Mg, K, Ca, Fe, Cr, Mn, Co, Ni, Cu, As, Se, Sr, Mo, Ag, Cd, Ba, Ti, Th, and U concentrations. The overall correct classification and cross-validation rates from such analysis are shown in Table 3. The LDA with stable isotope data alone gave a reasonable classification rate (ranging from 87.5 to 100%, overall 96.5%) or cross-validation rate (75−100%, overall 87.7%). The LDA using the contents of 20 metal elements resulted in a slightly higher correct classification (91.7−100%, overall 96.5%) but a much lower cross-validation rate (41.7−100%, overall 73.7%). In comparison, the LDA using combination of both isotopic and elemental compositions resulted in the highest successful rates for both correct classification (all cases 100.0%) and cross-validation (100%, except the rape honey samples of 87.5%). Thus, the combination of two analytical techniques performed well, which in most cases could successfully discriminate Chinese honey samples according to their botanical origins. Theoretically, this approach can be applied to other food products, but more feasibility studies are needed.

Table 3. Classification of Chinese Honey Samples with Different Botanical Origins and Percentage of Observations Correctly Classified

	predicted group membership (%)				
	acacia honey	rape honey	vitex honey	jujube honey	overall
Stable Isotope Ratio Only					
original	100	87.5	100	100	96.5
cross-validation	93.8	75	83.3	100	87.7
Element Content Only					
original	100	93.8	91.7	100	96.5
cross-validation	81.3	68.8	41.7	100	73.7
Combination of Stable Isotope Ratios and Elemental Contents					
original	100	100	100	100	100
cross-validation	100	87.5	100	100	96.5

AUTHOR INFORMATION

Corresponding Authors

*(L.C.) Phone/fax: +86 10 62594643. E-mail: chenlanzhen2005@126.com.

*(J.Z.) E-mail: zhaojingjun@sina.com

Funding

The project was supported by the special fund from the Chinese Program of International S&T Cooperation (No. 2012DFA31140), the International Atomic Energy Agency's Coordinated Research Project (CRP) (No. 16567), Chinese Agro-Scientific Research in the Public Interest (No. 201203046), and The Agricultural Science and Technology Innovation Program (CAAS-ASTIP-2015-IAR). G.H.L. was supported by grants from the Shenzhen Commission on Science and Innovation (CXZZ20120831160213590) and Shenzhen Key Laboratory for Coastal Ocean Dynamics and Environment (ZDSY20130402163735964).

Notes

The authors declare no competing financial interest.

ACKNOWLEDGMENTS

We thank the staff at Institute of Apicultural Research, Chinese Academy of Agricultural Sciences, for access to bee hives and providing logistic support during our field honey samplings. We also thank Zhiyong Pang, Yuan Ke, Yan Zhao, and Xuefei Mao for stable isotope and elemental analyses and Jianzhang Chen for honey sample perparations. We are very grateful to Guanghui Lin for improving the English and to the three reviewers and Editor of *Journal of Agricultural and Food Chemistry* for the improvement of the revised manuscript.

ABBREVIATIONS USED

IRMS, stable isotope ratio mass spectrometry; ICP-MS, inductively coupled plasma mass spectrometry; HFCS, high-fructose corn syrup; PC, principal component; PC1, first

DOI: 10.1021/acs.jafc.5b01576
J. Agric. Food Chem. 2015, 63, 5388−5394

principal component; PC2, second principal component; PC3, third principal component; PCA, principal component analysis; LDA, linear discriminant analysis

REFERENCES

(1) Chen, L.; Wang, J.; Ye, Z.; Zhao, J.; Xue, X.; Vander Heyden, Y.; Sun, Q. Classification of Chinese honeys according to their floral origin by near infrared spectroscopy. *Food Chem.* **2012**, *135*, 338−342.

(2) Dezmirean, G. I.; Marghitas, L. A.; Bobis, O.; Dezmirean, D. S.; Bonta, V.; Erler, S. Botanical origin causes changes in nutritional profile and antioxidant activity of fermented products obtained from honey. *J. Agric. Food Chem.* **2012**, *60*, 8028−8035.

(3) Roshan, A. R.; Gad, H. A.; El-Ahmady, S. H.; Khanbash, M. S.; Abou, S. M. I.; Alazizi, M. M. Authentication of monofloral Yemeni Sidr honey using ultraviolet spectroscopy and chemometric analysis. *J. Agric. Food Chem.* **2013**, *61*, 7722−7729.

(4) Molan, P. C. The limitations of the methods of identifying the floral source of honeys. *Bee World* **1998**, *79*, 59−68.

(5) Jandrić, Z.; Haughey, S. A.; Frew, R. D.; McComb, K.; Galvin-King, P.; Elliott, C. T.; Cannavan, A. Discrimination of honey of different floral origins by a combination of various chemical parameters. *Food Chem.* **2015**, DOI: 10.1016/j.foodchem.2014.11.165.

(6) Karabagias, I. K.; Badeka, A. V.; Kontakos, S.; Karabournioti, S.; Kontominas, M. G. Botanical discrimination of Greek unifloral honeys with physico-chemical and chemometric analyses. *Food Chem.* **2014**, *165*, 181−190.

(7) Karabagias, I. K.; Vavoura, M. V.; Nikolaou, C.; Badeka, A. V.; Kontakos, S.; Kontominas, M. G. Floral authentication of Greek unifloral honeys based on the combination of phenolic compounds, physicochemical parameters and chemometrics. *Food Res. Int.* **2014**, *62*, 753−760.

(8) Madejczyk, M.; Baralkiewicz, D. Characterization of Polish rape and honeydew honey according to their mineral contents using ICP-MS and F-AAS/AES. *Anal. Chim. Acta* **2008**, *617*, 11−17.

(9) Zhou, J.; Yao, L.; Li, Y.; Chen, L.; Wu, L.; Zhao, J. Floral classification of honey using liquid chromatography-diode array detection-tandem mass spectrometry and chemometric analysis. *Food Chem.* **2014**, *145*, 941−949.

(10) Jasicka-Misiak, I.; Poliwoda, A.; Deren, M.; Kafarski, P. Phenolic compounds and abscisic acid as potential markers for the floral origin of two Polish unifloral honey. *Food Chem.* **2012**, *131*, 1149−1156.

(11) Bertelli, D.; Plessi, M.; Sabatini, A.; Lolli, M.; Grillenzoni, F. Classification of Italian honeys by mid-infrared diffuse reflectance spectroscopy (DRIFTS). *Food Chem.* **2007**, *101*, 1565−1570.

(12) Kaspar, R.; Werner, L.; Raphael, K.; Mariaa, T. L.; Stefan, B.; Jacques, O. B.; Katharina, V. D. O.; Werner, V. D. O.; Renato, A. Authentication of the botanical and geographical origin of honey by mid-infrared spectroscopy. *J. Agric. Food Chem.* **2006**, *54*, 6873−6880.

(13) Pierna, J. A. F.; Abbas, O.; Dardenne, P.; Baeten, V. Discrimination of Corsican honey by FT-Raman spectroscopy and chemometrics. *Biotechnol. Agron. Soc. Environ.* **2011**, *15*, 75−84.

(14) Schievano, E.; Stocchero, M.; Morelato, E.; Facchin, C.; Mammi, S. An NMR based metabolomic approach to identify the botanical origin of honey. *Metabolomics* **2012**, *8*, 679−690.

(15) Luis, F.; Cuevas, G.; Jorge, A. P.; Santiago, L. S.; Sauri, D. E. A review of volatile analytical methods for determining the botanical origin of honey. *Food Chem.* **2007**, *103*, 1032−1043.

(16) Aliferis, K. A.; Tarantilis, P. A.; Harizanis, P. C.; Alissandrakis, E. Botanical discrimination and classification of honey samples applying gas chromatography/mass spectrometry fingerprinting of headspace volatile compounds. *Food Chem.* **2010**, *121*, 856−862.

(17) Alissandrakis, E.; Tarantilis, P. A.; Harizanis, P. C.; Polissiou, M. Aroma investigation of unifloral Greek citrus honey using solid-phase microextraction coupled to gas chromatographic−mass spectrometric analysis. *Food Chem.* **2007**, *100*, 396−404.

(18) Cinar, S. B.; Eksi, A.; Coskun, I. Carbon isotope ratio ($^{13}C/^{12}C$) of pine honey and detection of HFCS adulteration. *Food Chem.* **2014**, *157*, 10−13.

(19) Simsek, A.; Bilsel, M.; Goren, A. C. $^{13}C/^{12}C$ pattern of honey from Turkey and determination of adulteration in commercially available honey samples using EA-IRMS. *Food Chem.* **2012**, *130*, 1115−1121.

(20) Schellenberg, A.; Chmielus, S.; Schlicht, C.; Camin, F.; Perini, M.; Bontempo, L.; Heinrich, K.; Kelly, S. D.; Rossmann, A.; Thomas, F.; Jamin, E.; Horacek, M. Multielement stable isotope ratios (H, C, N, S) of honey from different European regions. *Food Chem.* **2010**, *121*, 770−777.

(21) Padovan, G. Detection of adulteration of commercial honey samples by the $^{13}C/^{12}C$ isotopic ratio. *Food Chem.* **2003**, *82*, 633−636.

(22) Pellerano, R. G.; Uñates, M. A.; Cantarelli, M. A.; Camiña, J. M.; Marchevsky, E. J. Analysis of trace elements in multifloral Argentine honeys and their classification according to provenance. *Food Chem.* **2012**, *134*, 578−582.

(23) Pohl, P. Determination of metal content in honey by atomic absorption and emission spectrometries. *TrAC, Trends Anal. Chem.* **2009**, *28*, 117−128.

(24) Chen, H.; Fan, C.; Chang, Q.; Pang, G.; Hu, X.; Lu, M.; Wang, W. Chemometric determination of the botanical origin for Chinese honeys on the basis of mineral elements determined by ICP-MS. *J. Agric. Food Chem.* **2014**, *62*, 2443−2448.

(25) Chudzinska, M.; Baralkiewicz, D. Estimation of honey authenticity by multielements characteristics using inductively coupled plasma-mass spectrometry (ICP-MS) combined with chemometrics. *Food Chem. Toxicol.* **2010**, *48*, 284−290.

(26) Branch, S.; Burke, S.; Evans, P.; Fairman, B.; Briche, C. A preliminary study in determining the geographical origin of wheat using isotope ratio inductively coupled plasma mass spectrometry with ^{13}C, ^{15}N mass spectrometry. *J. Anal. At. Spectrom.* **2003**, *18*, 17−22.

(27) Ariyama, K.; Shinozaki, M.; Kawasaki, A. Determination of the geographic origin of rice by chemometrics with strontium and lead isotope ratios and multielement concentrations. *J. Agric. Food Chem.* **2012**, *60*, 1628−1634.

(28) Angelal, P.; Brianw, S.; Andkim, A. A. Stable isotope and trace element profiling combined with classification models to differentiate geographic growing origin for three fruits effects of subregion and variety. *J. Agric. Food Chem.* **2006**, *54*, 4506−4516.

(29) Rummel, S.; Hoelzl, S.; Horn, P.; Rossmann, A.; Schlicht, C. The combination of stable isotope abundance ratios of H, C, N and S with $^{87}Sr/^{86}Sr$ for geographical origin assignment of orange juices. *Food Chem.* **2010**, *118*, 890−900.

(30) Meier-Augenstein, W. *Stable Isotope Forensics: An Introduction to the Forensic Application of Stable Isotope Analysis*; Wiley-Blackwell: Hoboken, NJ, USA, 2011; p 296.

(31) Anderson, K. A.; Hobbie, K. A.; Smith, B. W. Chemical profiling with modeling differentiates wild and farm-raised salmon. *J. Agric. Food Chem.* **2010**, *58*, 11768−11774.

(32) Alda, G. C.; Gallego, P. A.; Bravo, Y. J. C.; Garcinuno, M. R. M.; Fernandez, H. P. Characterization of Spanish honeys with protected designation of origin "Miel de Granada" according to their mineral content. *Food Chem.* **2012**, *135*, 1785−1788.

(33) Heaton, K.; Kelly, S. D.; Hoogewerff, J.; Woolfe, M. Verifying the geographical origin of beef: the application of multi-element isotope and trace element analysis. *Food Chem.* **2008**, *107*, 506−515.

(34) Anderson, K. A.; Smith, B. W. Use of chemical profiling to differentiate geographic growing origin of raw pistachios. *J. Agric. Food Chem.* **2005**, *53*, 410−418.

(35) Farquhar, G. D.; Ehleringer, J. R.; Hubick, K. T. Carbon isotope discrimination and photosynthesis. *Annu. Rev. Plant Physiol. Plant Mol. Biol.* **1989**, *40*, 503−537.

(36) Horacek, M.; Min, J. S.; Heo, S. C.; Soja, G. Discrimination between ginseng from Korea and China by light stable isotope analysis. *Anal. Chim. Acta* **2010**, *682*, 77−81.

(37) Khan, N.; Choi, J. Y.; Nho, E. Y.; Jamila, N.; Habte, G.; Hong, J. H.; Hwang, I. M.; Kim, K. S. Determination of minor and trace elements in aromatic spices by micro-wave assisted digestion and inductively coupled plasma-mass spectrometry. *Food Chem.* **2014**, *158*, 200−206.

DOI: 10.1021/acs.jafc.5b01576
J. Agric. Food Chem. 2015, 63, 5388−5394

(38) Bilandžić, N.; Gačić, M.; Đokić, M.; Sedak, M.; Šipušić, Đ. I.; Končurat, A.; Gajger, I. T. Major and trace elements levels in multifloral and unifloral honeys in Croatia. *J. Food Compos. Anal.* **2014**, *33*, 132−138.

DOI: 10.1021/acs.jafc.5b01576
J. Agric. Food Chem. 2015, 63, 5388−5394

JOURNAL OF AGRICULTURAL AND FOOD CHEMISTRY

Article

pubs.acs.org/JAFC

Microwave-Assisted Extraction of Phenolic Compounds from Almond Skin Byproducts (*Prunus amygdalus*): A Multivariate Analysis Approach

Arantzazu Valdés,* Lorena Vidal, Ana Beltrán, Antonio Canals, and María Carmen Garrigós

Analytical Chemistry, Nutrition & Food Sciences Department, University of Alicante, 03080 Alicante, Spain

Supporting Information

ABSTRACT: A microwave-assisted extraction (MAE) procedure to isolate phenolic compounds from almond skin byproducts was optimized. A three-level, three-factor Box−Behnken design was used to evaluate the effect of almond skin weight, microwave power, and irradiation time on total phenolic content (TPC) and antioxidant activity (DPPH). Almond skin weight was the most important parameter in the studied responses. The best extraction was achieved using 4 g, 60 s, 100 W, and 60 mL of 70% (v/v) ethanol. TPC, antioxidant activity (DPPH, FRAP), and chemical composition (HPLC-DAD-ESI-MS/MS) were determined by using the optimized method from seven different almond cultivars. Successful discrimination was obtained for all cultivars by using multivariate linear discriminant analysis (LDA), suggesting the influence of cultivar type on polyphenol content and antioxidant activity. The results show the potential of almond skin as a natural source of phenolics and the effectiveness of MAE for the reutilization of these byproducts.

KEYWORDS: *microwave-assisted extraction, phenolic compounds, almond skin, HPLC-DAD-ESI-MS/MS, antioxidant activity, linear discriminant analysis*

INTRODUCTION

Almond (*Prunus amygdalus*) production has increased significantly in recent years, with a worldwide production of about 1.9 million tonnes in 2012.[1] Food applications of almonds such as confectionary and bakery items, snack formulations, cereals, and marzipan require the almonds without the seed coats.[2] The external coating of almonds is industrially removed by using a hot water blanching process, with the brown skin contributing around 6.0−8.4% of the seed weight.[3] Almond skin agricultural byproducts are produced during almonds processing in large amounts. Industries are forced to consider ways of treating or using these residues; most are just incinerated or dumped without control, causing several environmental problems, or used as animal feed.[4]

Almond skin contains 50−75% of the total phenols present in the nut, such as aldehydes and hydroxybenzoic acids, flavanones, isoflavones, flavonol glycosides, phenolic acids, flavonol aglycones, flavan-3-ols, flavonone aglycones, flavonone glycosides, and lignans. Flavanol and flavonol glycosides are the most abundant phenolic compounds, particularly epicatechin, catechin, isorhamnetin-3-*O*-glucoside, isorhamnetin-3-*O*-rutinoside, kaempferol-3-*O*-rutinoside, and naringenin-7-*O*-glucoside.[5,6] Polyphenols have been found to decrease the risk of coronary heart disease and function as anti-inflammatory agents due to their high antioxidant capacity.[6] These compounds can function as natural preservatives for meat products, reducing their lipid oxidation.[7,8] Therefore, almond skin byproducts rich in antioxidant compounds could be reused by food industries as natural additives to control the oxidative process, adding value to this residue. It is of economical and ecological significance to find an efficient method to isolate phenolic compounds from these byproducts. However, cultivar differences may affect almond flavonoid concentration.[3]

Extraction of phenolic compounds from food is one of the most important steps prior to their determination by HPLC.[9] Recently, some novel extraction methods of flavonoids such as microwave-assisted extraction (MAE) were developed showing several advantages over the conventional extraction techniques such as the reduction of solvent used for extraction and energy consumption, moderately high recoveries, good reproducibility, shortened extraction time, and minimal sample manipulation for the extraction process.[10−12] This technique has been successfully used with effectively improved flavonoid yield for the extraction of different food matrices, such as honey, peanut skins, sweet potato, and maize.[13−17]

With regard to the extraction of almond skin antioxidants, conventional extraction is usually performed at reflux by using high temperatures for several hours or maceration with solvent for days at room temperature.[18−20] To our knowledge, no MAE application for the extraction of phenolic compounds from almond skin has been found in the literature. Therefore, the objectives of this study were (1) to optimize a new extraction procedure for the extraction of phenolic compounds in almond skin by MAE using an experimental design in terms of highest total phenolic content (TPC) and antioxidant activity (DPPH); (2) to increase the potential added value of almond agricultural byproducts, reducing costs for the food industry; and (3) to select an almond cultivar with higher antioxidant capacity as a

Received: October 18, 2014
Revised: May 24, 2015
Accepted: May 25, 2015
Published: May 25, 2015

ACS Publications © 2015 American Chemical Society

DOI: 10.1021/acs.jafc.5b01011
J. Agric. Food Chem. 2015, 63, 5395−5402

potential antioxidant source. For these purposes, the determinations of TPC, flavonoids (HPLC-UV-ESI-MS/MS), and antioxidant activity (DPPH, FRAP) were performed on seven different almond cultivars, and the presence of different categories within almond skin samples was studied using stepwise linear discriminant analysis (LDA). This characterization is an essential step for the reutilization of these almond skin byproducts.

MATERIALS AND METHODS

Chemicals and Reagents. Water (ultrapure grade) and ethanol (HPLC grade) were acquired from Merck (Madrid, Spain). Quercetin, sodium carbonate, Folin−Ciocalteu reagent (2 N), 2,2-diphenyl-1-picrylhydrazyl (DPPH), (±) 6-hydroxy-2,5,7,8-tetramethylchromane-2-carboxylic acid (Trolox), HPLC grade acetonitrile, and methanol were supplied by Sigma-Aldrich (Madrid, Spain). All other reagents used were of analytical or chromatographic grade and were purchased from Panreac (Barcelona, Spain). Standard compounds such as (+)-catechin, (−)-epicatechin, quercetin-3-*O*-rutinoside, kaempferol-3-*O*-rutinoside, isorhamnetin-3-*O*-glucoside, isorhamnetin-3-*O*-rutinoside, naringenin-7-*O*-glucoside, naringenin, and daidzein (internal standard) were purchased from Extrasynthese (Genay, France).

Sample Preparation. Seven almond cultivars from the 2011 harvest were selected for this study and were supplied by Almendras Llopis (Alicante, Spain): three Spanish (Marcona, Guara, and Planeta) and four American (Butte, Colony, Carmel, and Padre). The blanching process of almonds (100 g) was carried out at 95 °C for 3 min using 150 mL of deionized water to remove the skins from the kernels by hand.[6] Prior to MAE, the obtained skins were oven-dried for 12 h and ground with a ZM 200 high-speed rotary mill (Retsch, Haan, Germany) to increase the extraction efficiency.[12] Particles passing through a 0.5 mm sieve were used to ensure the homogeneity of the residue powder. The almond skin fraction obtained was dried in an oven at 40 °C for 24 h to reduce its moisture content.

Extraction Procedure. MAE was carried out using a modified M1711N domestic microwave oven (Samsung M1711N, Taiwan), with a hole (18 mm diameter) in the top of the oven, at a frequency of 2450 MHz and 800 W maximum power.[21] The sample was stirred at 300 rpm during extraction using a microwave stirrer (Bel-Art Products, Wayne, NJ, USA). The appropriate weight of homogenized almond skin powder was placed in a 100 mL quartz flask, which was connected to a vapor condenser. The system operated as an open-vessel extraction system, where the solvent is heated and refluxed through the sample, allowing a very efficient heating.[22] Ethanol was selected as an effective extraction solvent for phenolic compounds in food samples.[13,23] Ethanol is also recommended by the U.S. Food and Drug Administration as an environmentally nontoxic food grade organic solvent.[24]

MAE was carried out at different extraction times and microwave powers using 60 mL of 70% (v/v) ethanol. The obtained extracts were centrifuged at 4500 rpm for 5 min, filtered through a 0.45 μm PVDF filter (Teknokroma, Barcelona, Spain), made up to 50 mL, and kept at −20 °C until analysis.

Experimental Design. The extraction of phenolic compounds from almond skin was performed under different extraction conditions according to the experimental design shown in Table 1. The parameters considered during MAE optimization were almond skin weight (0.5, 2.0, 3.5 g), microwave power (100, 200, 300 W), and irradiation time (20, 40, 60 s). The Butte cultivar was selected for the optimization of MAE conditions. The range of studied variables was selected on the basis of results obtained in preliminary experiments. In this sense, at increased microwave power level of 300 W in the screening experiment, rapid heating of the extraction medium and bubbling of the substance occurred due to high cavitation, leading to the entry of the extraction medium into the condenser. A Box−Behnken design (BBD), comprising 16 experimental runs, was used, and experiments were carried out in randomized order.[25] The responses obtained from the experimental design were evaluated in terms of TPC and antioxidant activity (DPPH).

Table 1. Box−Behnken Experimental Design and MAE Results

run	almond skin wt (g)	microwave power (W)	irradiation time (s)	TPC (mg QE)	DPPH (% inhibition)
1	0.5	100	40	15.3	13.4
2	3.5	100	40	86.4	77.3
3	0.5	300	40	15.3	14.2
4	3.5	300	40	68.7	70.7
5	0.5	200	20	12.7	11.5
6	3.5	200	20	83.5	77.3
7	0.5	200	60	15.0	13.7
8	3.5	200	60	81.2	67.8
8	2.0	100	20	46.8	44.6
10	2.0	300	20	48.5	51.7
11	2.0	100	60	52.8	46.3
12	2.0	300	60	54.9	60.0
13	2.0	200	40	49.7	53.1
14	2.0	200	40	42.7	43.6
15	2.0	200	40	40.7	43.1
16	2.0	200	40	47.3	54.5

Regression analysis was used for the experimental data and fitted into the following empirical second-order polynomial model:

$$Y = \beta_0 + \Sigma\beta_i X_i + \Sigma\beta_{ii} X_i^2 + \Sigma\Sigma\beta_{ij} X_i X_j$$

Y is the predicted response, X represents the variables of the system, i and j are design variables, β_0 is a constant, β_i is the linear coefficient, β_{ii} is the quadratic coefficient, and β_{ij} is the interaction coefficient of variables i and j.

HPLC Analysis of Flavonoid Compounds. HPLC-DAD-ESI-MS/MS analysis was performed, in triplicate, using an 1100 series HPLC system (Agilent Technologies, Waldbronn, Germany) coupled to a photodiode array UV−vis detector and an LC/MSD Trap SL ion trap mass spectrometer (Agilent, Stuttgart, Germany) via an electrospray ionization (ESI) source. Mass spectra were recorded in the negative ionization mode (m/z 50−900).[26] The electrospray chamber was operated at 3.5 kV with a drying gas temperature of 350 °C, N_2 pressure, and flow rate on the nebulizer at 50 psi and 10 L/min, respectively; MS/MS collision energies were set at 20 V.

The column used for flavonoids separation (10 μL) was a 4.6 mm × 150 mm i.d., 5 μm, Eclipse XDB-C18 (Agilent Technologies) at 25 °C. The mobile phase consisted of 2% acetic acid in ultrapure water (solvent A) and 2% acetic acid in ultrapure water/acetonitrile (73:25, v/v, solvent B) at a flow rate of 1 mL/min. The linear gradient started with 0 min, 40% B; 25 min, 70% B (hold 5 min); 32 min, 100% B (hold 4 min); back to 40% B (hold 5 min). UV detection of flavonoid compounds was carried out at 290 nm. The identification of the most abundant phenolic compounds was made by comparison of retention times and UV−vis and MS/MS spectra with those of commercially standard compounds and available literature.[26] Quantitation was carried out using an MS/MS detector and daidzein as internal standard (20 mg/kg). Final concentrations of flavonoids were expressed in micrograms per gram of dry almond skin.

Total Phenolic Content. The TPC of almond skin extracts was determined, in triplicate, according to the Folin−Ciocalteu colorimetric method, as reported by Singleton and Rossi,[27] using a Biomate-3 UV−vis spectrophotometer (Thermospectronic, Mobile, AL, USA). Deionized water (30 mL) and Folin−Ciocalteu reagent (2.5 mL) were added to 500 μL of almond skin extract. The mixture was vortexed and incubated for 5 min. Then, 7.5 mL of 20% aqueous Na_2CO_3 and 10 mL of deionized water were added and mixed. The absorbance was measured at 760 nm after 90 min of incubation against deionized water as a blank. Quercetin was used as the reference standard (25−1000 mg/kg), and TPC was expressed as milligrams of quercetin equivalent (QE) per gram of dry almond skin.

DOI: 10.1021/acs.jafc.5b01011
J. Agric. Food Chem. 2015, 63, 5395−5402

Determination of Antioxidant Activity. The DPPH assay was used to determine the free radical scavenging activity of almond skin extracts as described by Assimopoulou et al.[29] One hundred microliters of the almond skin ethanolic extract were mixed with 2.7 mL of DPPH solution (10^{-4} M in ethanol). The percentage of free radicals scavenged by DPPH radical was determined at steady state (60 min) at 517 nm.[30,31]

The capacity of almond skin extracts to reduce ferric ions was assessed by using the FRAP method.[32] Two hundred and fifty milliliters of acetic acid buffer (300 mM, pH 3.6), 10 mM 2,4,6-tripyridyl-*s*-triazine (TPTZ) made up in 10 mL of 40 mM HCl, and 10 mL of 20 mM ferric chloride solution were mixed at a 10:1:1 ratio, to make the FRAP reagent. One hundred microliters of the almond skin ethanolic extract was added to 4.9 mL of FRAP reagent. Measurements were performed at 593 nm after 30 min of incubation at 37 °C in darkness. Trolox was used as the reference standard (85−365 mg/kg), and the antioxidant capacity was expressed as micromoles of Trolox equivalent (TE) per gram of dry almond skin.

Both methods were performed in triplicate using a Biomate-3 spectrophotometer (Thermospectronic).

Statistical Analysis. Statgraphics-Plus software 5.1 (Statistical Graphics, Rockville, MD, USA) was employed to generate and analyze the results of the BBD. Graphic analysis of the principal effects and interactions between variables was used for interpretation of results. Response surface methodology (RSM) was used to determine the optimal extraction conditions. Least-squares regression analysis was performed to obtain the coefficients of the quadratic polynomial model previously described. The adequacy of the fitted model was determined by evaluating the lack of fit, the coefficient of determination (R^2), and F test obtained from the analysis of variance (ANOVA). Statistical significance of model parameters was determined at the 5% probability level ($\alpha = 0.05$).

SPSS commercial software, ver. 15.0 (Chicago, IL, USA), was used for statistical analysis of almond cultivar results by means of ANOVA. The Tukey test was used to determine differences between means at a $p \leq 0.05$ significance level. In chemometrics data analysis, pattern recognition methods are a powerful tool in the context of food quality assessment and food composition analysis.[33] The presence of different categories within almond skin cultivars was studied using stepwise LDA as a multidisciplinary approach.[34]

RESULTS AND DISCUSSION

Optimization of Extraction Conditions. A preliminary study was performed to determine the effect of solvent volume and solvent ratio (ethanol in water) on the recovery of TPC and antioxidant activity from almond skin. It was found that 60 mL of 70% (v/v) ethanol provided the maximum TPC and DPPH scavenging activity (data not shown). These conditions were then fixed for further optimization of extraction conditions. The selection of 70% (v/v) ethanol in water was in concordance with results obtained by other authors from the determination of natural phenols in different samples, because extraction efficiency depends on the solubility of the analytes in the extraction solvent.[12,14,22,25] Hughey et al.[5] studied the distribution of polyphenols from almond skin in blanch water as a function of time and temperature, the intrinsic solubility of each polyphenol in water being different depending on its structure. In general, major phenolic compounds present in almond skin are sparingly soluble in hot water. As a consequence, a highest yield extraction of these compounds as the ethanol portion increases can be expected. However, the use of high ethanol contents as solvent extraction could lead to polyphenol degradation and overpressure inside the vessel due to overheating of the sample.[11] In this sense, dipolar rotation and ionic conduction are simultaneously produced during MAE.[26] As the ethanol concentration increases, higher dielectric loss is obtained.[27] As a consequence, the higher capacity of the solvent to absorb microwave energy can lead to a faster rate of solvent heating with respect to the plant material.[12]

With regard to solvent volume, it was found that 60 mL was the more effective volume to be used with a maximum quantity of sample of 3.5 g without the formation of almond skin aggregates in the quartz flask during extraction. In this sense, extraction solvent efficiently absorbs microwave energy and leads to enhanced swelling of food material, which is favorable to increasing the contact surface area between phases.[12] However, a high volume of solvent could decrease the microwave adsorption of material, because more energy was absorbed by the solvent. In this case, the breaking of cell wall material and mass transmission might negatively influence and decrease the phenolics extraction and antioxidant capacity.[28]

There are different factors that can affect the extraction efficiency of MAE, such as microwave power, type and composition of solvent, extraction time, particle size of sample, solvent to solid ratio, soaking time, and extraction cycles.[35] The present study evaluates some of these variables by using a Box−Behnken experimental design. Butte almond skin was used for the experimental design and method optimization assays. The experimental data obtained in terms of TPC and DPPH scavenging activity are presented in Table 1. A statistical analysis of results was performed to estimate the statistical significance of the factors and interactions between them that had the greatest effect on obtaining extracts with high yield of TPC and antioxidant capacity (Figure 1). Among the studied factors, the almond skin weight had the greatest influence on the studied responses, showing a positive effect.

The rest of the investigated parameters had no significant impact on the studied responses. With regard to magnetron power, the increasing microwave energy can favor the penetration of solvent into the food matrix and offer a rapid transfer of energy to the solvent and matrix, increasing

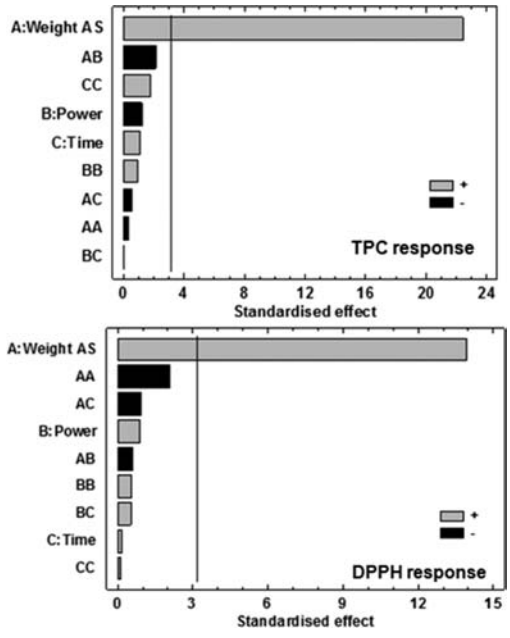

Figure 1. Pareto charts of factors and interactions obtained from the Box−Behnken design for each response: TPC (mg QE/g almond skin) and DPPH scavenging (%). The vertical line indicates the statistical significance at 5% of the effects.

DOI: 10.1021/acs.jafc.5b01011
J. Agric. Food Chem. 2015, 63, 5395−5402

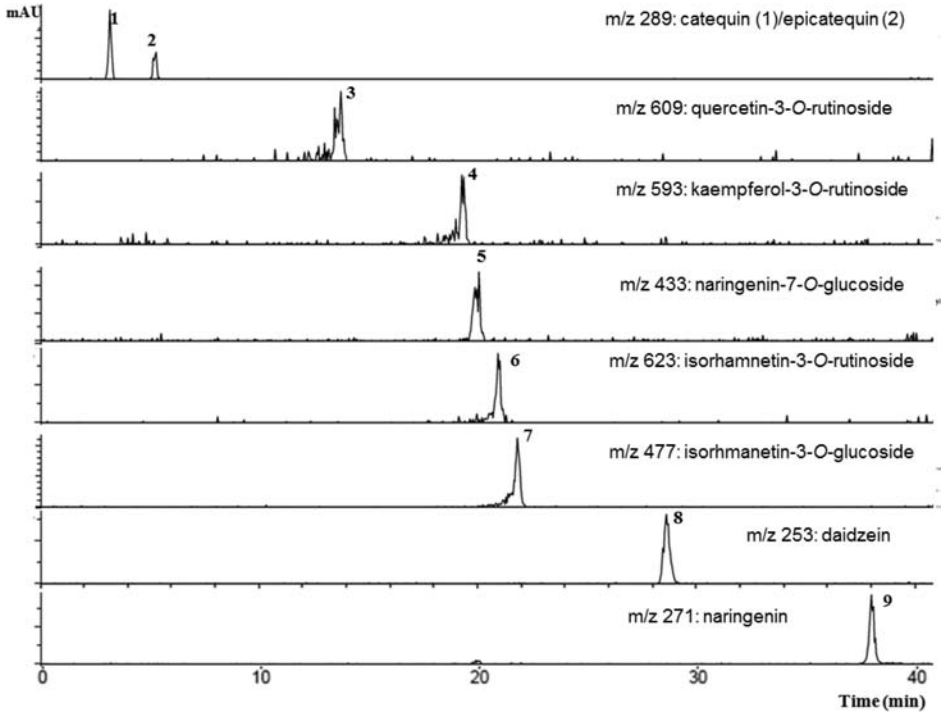

Figure 2. Extracted ion chromatograms of flavonoid standards obtained from $[M - H]^-$ ion by HPLC-ESI-MS/MS analysis (50 mg/kg).

temperature and allowing the dissolution of compounds to be extracted with an increase in the phenolics extraction yield.[26] However, a negative effect with increasing microwave irradiation energy could be observed by thermal degradation of antioxidant compounds and overpressure inside the vessel due to an increase in the extraction temperature.[12] Higher temperatures can also reduce extraction selectivity as matrix materials and nondesired compounds can also be extracted. Microwave power is strongly dependent on time and extraction temperature. In this sense, the increase in microwave power and extraction temperature causes rapid cell rupture, increasing the amount of impurities in extracts, which can affect antioxidant activity. Furthermore, longer exposure with low or moderate power is considered a wiser choice because it results in better purity of the obtained extracts.[11] With regard to irradiation time, this parameter generally has a positive influence on the TPC response.[12] This behavior can be explained by considering that the thermal accumulation within extraction solution due to the absorption of microwave energy promotes the dissolution process of phenolic compounds into the solution.[26] In the present work, the extraction temperature rose to 47 ± 4 °C by using the lower studied power (100 W) and maximum time (60 s). Then, the combination of low microwave power and short extraction time could lead to moderately high temperatures, which could be considered able to extract almond skin antioxidant compounds with high antioxidant activity.

The mathematical models obtained for both studied responses by applying multiple regression analysis on the experimental data were expressed by the following equations:

$$\mathrm{TPC} = 45.10 + 32.70A - 1.73B + 1.55C - 4.41AB - 1.16AC + 0.07BC - 0.69A^2 + 1.99B^2 + 3.65C^2$$

$$\mathrm{DPPH} = 48.57 + 30.045A + 1.87B + 0.34C - 1.84AB + 1.63BC - 2.92AC - 6.35A^2 + 1.71B^2 + 0.36C^2$$

A, B, and C are the coded variables for almond skin weight, microwave power, and irradiation time, respectively.

The computing program showed that the two fitted models were considered satisfactory as the lack of fit was not significant ($p > 0.05$). R^2 is defined as the ratio of the explained variation to the total variation and is a measurement of the degree of fitness.[14] The model can fit well with the actual data when R^2 approaches unity. The R^2 values obtained for TPC and DPPH were 0.9835 and 0.9691, respectively. These values indicated a relatively high degree of correlation between the actual data and predicted values, indicating that both models could be used to predict the studied responses.

Optimal conditions found by prediction of computing program to obtain highest TPC and DPPH values of 89.2 mg CE and 78.4%, respectively, were determined as follows: almond skin weight, 3.5 g; microwave power, 100 W; extraction time, 60 s. As the almond skin weight clearly had a strong significant positive effect, this value was increased until 4 g. The values obtained for TPC and DPPH scavenging after extraction of almond skin under these optimal conditions, in triplicate, were 54 ± 2 mg QE/g almond skin and 90 ± 1%, respectively. As a result, for the extraction of phenolic compounds from almond skin, the best selected extraction conditions were 100 W, 60 s, 4 g, and 60 mL of 70% ethanol.

MAE can be considered a rapid technique showing several advantages compared to conventional extraction methods, which are time-consuming, eventually lead to thermal degradation of antioxidant compounds, and usually require higher quantities of organic solvents, raising process costs and reducing the environmental sustainability. For example, almond skin was extracted during 24 h at 40 °C by using 70% of

DOI: 10.1021/acs.jafc.5b01011
J. Agric. Food Chem. 2015, 63, 5395−5402

Table 2. Flavonoids Content (μg/g Almond Skin) of the Studied Cultivars by HPLC-ESI-MS/MS Analysis[a]

almond cultivar	(+)-catechin	(−)-epicatechin	kaempferol-3-*O*-rutinoside	isorhamnetin-3-*O*-glucoside	isorhamnetin-3-*O*-rutinoside	quercetin-3-*O*-rutinoside	naringenin-7-*O*-glucoside	naringenin
Marcona	13.0 ± 1.1ab	5.8 ± 0.9a	1.6 ± 0.7a	14.1 ± 2.5a	383.8 ± 69.8a	nd	32.8 ± 0.9a	8.5 ± 1.2a
Guara	18.5 ± 4.2ad	23.1 ± 10.4b	238.7 ± 49.6b	32.5 ± 9.0b	752.1 ± 110.9b	58.2 ± 15.6a	33.6 ± 2.0a	5.5 ± 1.8b
Planeta	35.4 ± 5.8c	5.1 ± 3.2a	174.9 ± 32.9c	2.0 ± 0.5c	140.5 ± 30.7c	411.9 ± 99.0b	43.3 ± 3.1b	46.1 ± 6.4c
Butte	14.6 ± 2.5ab	10.3 ± 5.2ab	1.0 ± 0.5a	19.1 ± 9.3a	555.8 ± 12.7a	80.2 ± 18.6a	30.9 ± 1.5a	14.2 ± 4.5a
Colony	7.3 ± 0.4b	9.2 ± 2.4a	32.9 ± 7.6d	27.2 ± 5.4ab	756.5 ± 53.7b	nd	38.4 ± 2.8b	7.9 ± 0.6a
Carmel	25.5 ± 3.2d	1.3 ± 0.4a	95.3 ± 11.4c	2.2 ± 0.1c	495.6 ± 53.7a	nd	32.2 ± 0.6a	0.4 ± 0.2e
Padre	17.6 ± 0.7ad	6.1 ± 0.9a	205.1 ± 10.1b	14.6 ± 2.0a	671.6 ± 6.8b	nd	35.2 ± 1.8ab	15.8 ± 3.1a

[a]Mean ± SD (n = 3). Different letters within the same column indicate statistically significant different values ($p < 0.05$) as obtained by Tukey's test application.

Table 3. Total Flavonoids, TPC, and Antioxidant Activity of Almond Skin Cultivars[a]

almond cultivar	flavonoids (μg/g skin)	TPC (mg QE/g skin)	DPPH (% inhibition)	FRAP (μmol TE/g skin)
Marcona	460 ± 31a	66 ± 1a	93 ± 4a	553 ± 8a
Guara	1162 ± 22b	119 ± 7b	92 ± 1a	556 ± 12a
Planeta	688 ± 20ac	95 ± 3c	93 ± 4a	416 ± 38bc
Butte	900 ± 21bc	54 ± 2d	90 ± 1a	382 ± 35c
Colony	879 ± 32bc	84 ± 8e	93 ± 2a	369 ± 50c
Carmel	653 ± 28ac	80 ± 3e	93 ± 3a	390 ± 7c
Padre	966 ± 25bc	62 ± 1a	92 ± 5a	480 ± 14ab

[a]Mean ± SD, n = 3. Different letters within the same column indicate statistically significant different values ($p < 0.05$) as obtained by Tukey's test application.

aqueous organic solvent (methanol, acetone, or acetonitrile) by Tsujita et al.[36] Also, Hughey et al.[5] extracted almond skin antioxidant compounds during 24 h at 37 °C by using 50% water/methanol with 3.5% (v/v) acetic acid. Finally, Monagas et al.[20] extracted antioxidant compounds from almond skin with 80% (v/v) acetone at a solid to solvent ratio of 1:10 (w/v) during 30 min at 50 °C.

Analysis of Flavonoid Compounds in Almond Skin Cultivars. An adequate separation and good resolution of compounds were obtained for identification and quantitation (Figure 2). According to the unsaturation and oxidation degrees of the three-carbon segment, various families of flavonoids can be distinguished such as flavanones, flavonols, flavones, isoflavones, and anthocyanidins.[9] Peaks 1 and 2 showed a $[M - H]^-$ at m/z 289 and characteristic MS/MS ions at m/z at 245, 205, and 179, respectively, and they were identified as two flavan-3-ols: (+)-catechin and (−)-epicatechin, respectively. Peaks 3, 4, 5, 6, and 7 were identified as five glycosidic compounds: quercetin-3-*O*-rutinoside (m/z 609 with an MS/MS fragment at m/z 300), kaempferol-3-*O*-rutinoside (m/z 593 with an MS/MS fragment at m/z 285), naringenin-7-*O*-glucoside (m/z 433) with an MS/MS fragment at m/z 271, isorhamnetin-3-*O*-rutinoside (m/z 623 with an MS/MS fragment at m/z 315), and isorhamnetin-3-*O*-glucoside (m/z 477 with an MS/MS fragment at m/z 315), respectively. The isoflavone daidzein at m/z 253, with MS/MS fragments at m/z 224 and 135, which was used as internal standard, was identified at peak 8. Finally, peak 9 was identified as the flavanone aglycone naringenin (m/z 271) with MS/MS fragments at m/z 177 and 151. The compounds identified in this work are in agreement with published literature determining the phenolic profile of almond skin.[5,18]

Table 2 summarizes the individual flavonoids content found in the studied almond skin cultivar extracts. Significant differences were obtained among almond skin cultivars regarding their flavonoid profiles. Flavonoids are products of the shikimate pathway from acetate and phenylalanine in plants. The genetic variation in the shikimate pathway of almond cultivars is likely responsible for the different flavonoid profiles between cultivars.[18] For epicatechin, isorhamnetin-3-*O*-glucoside, kaempferol-3-*O*-rutinoside, and isorhamnetin-3-*O*-rutinoside, Guara skin showed the highest content compared to the rest of the studied cultivars. On the other hand, catechin, naringenin-7-*O*-glucoside, quercetin-3-*O*-rutinoside, and naringenin were quantified at higher amounts in Planeta skin.

As has been previously reported, during the blanching process the blanch water will increase in polyphenols, whereas blanched almond skins will decrease in phenolic content.[5,13] The results obtained in this work from the quantitation of flavonoid compounds are in agreement with those found by Hughey et al.[5] As the number of −OH functional groups decreases in the molecule, a higher hydrophobic character and lower solubility in boiling water of the phenolic compound are obtained. As a result, these compounds may present more affinity for an organic phase such as ethanol during MAE.[28] Thus, isorhamnetin-3-*O*-rutinoside, kaempferol-3-*O*-rutinose, isorhamnetin-3-*O*-glucoside, and quercetin-3-*O*-rutinoside, with more than seven −OH groups present in their molecules, were quantified in higher amounts in almond skin cultivars, followed by catechin, epicatechin, and naringenin-7-*O*-glucoside with only five −OH groups. Finally, naringenin was quantified at the lower amount with only three −OH groups in its molecule. Hughey et al.[5] also reported a lower concentration of naringenin in almond skins after blanching. Bolling et al.[37] found the highest and lowest quantities for isorhamnetin-3-*O*-rutinoside and quercetin-3-*O*-rutinoside, respectively, in different almond skin cultivars. Similar results were reported also by Mandalari et al.[4] after lipid removal by almond skin extraction with *n*-hexane and further extraction by sonication. Finally, Garrido et al.[3] reported similar results for the flavonoids quantified in the present work when analyzing almond skin mixtures of Spanish and American cultivars subjected to blanching.

DOI: 10.1021/acs.jafc.5b01011
J. Agric. Food Chem. 2015, 63, 5395−5402

Analysis of Total Flavonoids, TPC, and Antioxidant Activity in Almond Skin Cultivars. The total flavonoids content quantified by HPLC-ESI-MS/MS, TPC results, radical scavenging activity by DPPH, and reducing power by FRAP are shown in Table 3 for all almond skin cultivar extracts. Guara skin showed the highest total flavonoids content (1162 μg/g almond skin), TPC (119 mg QE/g almond skin), and FRAP (556 μmol TE/g almond skin) values. Padre, Butte, and Colony cultivars followed Guara for total flavonoids content and, finally, Planeta, Carmel, and Marcona. With regard to TPC results, Guara was followed by Planeta, Colony, and Carmel and, finally, Marcona, Padre, and Butte. For FRAP, Guara and Marcona did not show statistical differences, with highest antioxidant activity, followed by Padre, Planeta, Carmel, Butte, and, finally, Colony. These results are in accordance with those found in a previous work in which an exhaustive study of the phenolic composition of almond skin was carried out to evaluate their potential application as a functional food ingredient.[38] In this study, TPC and radical scavenging activity results were significantly higher for the almond skin mixture of Spanish varieties than for the American ones. Similar results were also obtained in a previous work in which the polyphenol content and antioxidant activity of seven different almond skin cultivars harvested over three seasons in California were studied.[18] From this work, it was concluded that cultivar had a differential impact on individual polyphenol synthesis, flavonoid content, and antioxidant activity of almonds. With regard to DPPH results, a high radical scavenging activity (>90%) was obtained for all studied cultivars, although no significant differences were obtained among them ($p > 0.05$).

The total flavonoids content found in the present study, which ranged from 46 to 116.2 mg/100 g of almond skin, is higher than the mean value reported for almonds in the USDA flavonoid content database (15.24 mg/100 g almonds), which is based on data from the Food Composition Nutrient Data Laboratory of the USDA.[39] These data were obtained using extracts from whole almonds, whereas in the present study the skin was analyzed, which accounts for 78−98% of the flavonoid content from whole almonds.[19,39,40] On the other hand, differences found in the absolute amount of recovered polyphenols, flavonoid content, and TPC and FRAP results obtained from almond skins between studies may arise from the use of different methods of extraction and analysis.[18,40]

The obtained results clearly showed the efficiency of the optimized MAE method and the high antioxidant potential of almond skin extracts as natural antioxidant sources; Guara skin showed the highest TPC and flavonoids contents. Therefore, it could be concluded that MAE could be considered a potential alternative to conventional extraction methods for the isolation of phenolic compounds from almond skin.

Multivariate Analysis. LDA was applied as a multidisciplinary approach by inserting together all parameters obtained from the determination of TPC, antioxidant activity by FRAP, and individual flavonoid contents quantified by HPLC-ESI-MS/MS as predictors, evaluating the capability of the complete model to discriminate samples according to cultivar. The results obtained for DPPH from almond skin cultivars were not included in the LDA because no significant differences were obtained among samples (Table 3). As a result, 100% of samples were correctly classified, obtaining a λ_w = 0.175, with a good resolution among categories.

Six discriminant functions were obtained, using the variable selection rule for minimizing Wilk's lambda, which account the 61.5, 26.6, 8.1, 3.1, 0.5, and 0.6% of the total variance, respectively. Projections of cultivar scores on the first two determined discriminant functions are shown in Figure 3,

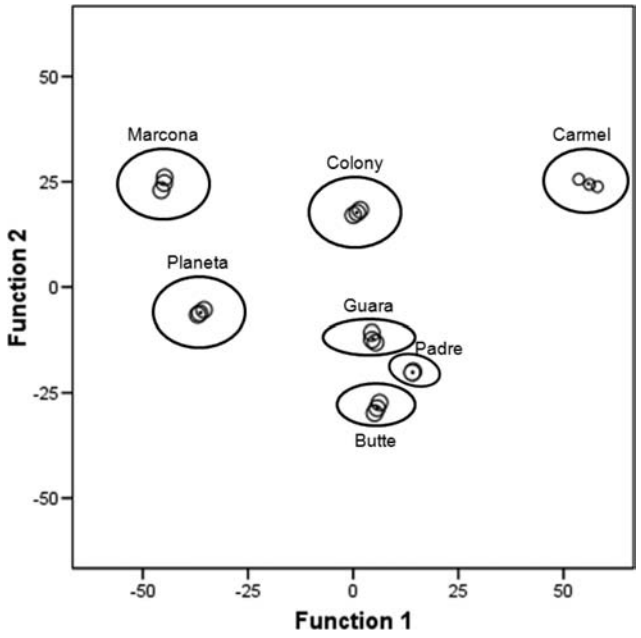

Figure 3. Projections of almond skin cultivar scores on the space determined by the two first discriminant functions obtained by the multidisciplinary approach.

where cultivars appear associated, suggesting seven groups. The first discriminant function showed differences in the discriminant space among the almond skin cultivars. This function was positively affected by TPC and isorhmanetin-3-*O*-rutinoside, kaempferol-3-*O*-rutinoside, and isorhamnetin-3-*O*-glucoside contents. On the other hand, FRAP, quercetin-3-*O*-rutinoside, naringenin-7-*O*-glucoside, naringenin, catechin, and epicatechin predictors negatively affected function 1. With regard to the second discriminant function, it was more affected by TPC, naringenin-7-*O*-glucoside, and isorhamnetin-3-*O*-glucoside contents, whereas the rest of the predictors had a negative influence on it. As a result, the application of the multidisciplinary approach revealed the potential of the obtained model for the discrimination and classification of almond skin cultivars according to the results obtained for TPC, antioxidant capacity (FRAP), and individual flavonoids content (HPLC-ESI-MS/MS). Similarly, Bolling et al.[18] found that canonical discriminant analysis of polyphenols content and antioxidant activity (FRAP) could distinguish almonds from different cultivars harvested in different seasons with 80% confidence. Also, in a previous work, we found that a multidisciplinary LDA approach of structural (FTIR) and thermal parameters (DSC, TGA) could successfully classify and discriminate three different almond cultivars.[34] The obtained results revealed the suitability of the studied techniques combined with LDA for a fast discrimination among different almond skin cultivar residues in food processing.

■ ASSOCIATED CONTENT

Supporting Information

The ANOVA obtained for TPC and DPPH responses is summarized in Table S1. The Supporting Information is

DOI: 10.1021/acs.jafc.5b01011
J. Agric. Food Chem. 2015, 63, 5395−5402

available free of charge on the ACS Publications website at DOI: 10.1021/acs.jafc.5b01011.

AUTHOR INFORMATION

Corresponding Author

*(A.V.) Phone: +34 965903400, ext. 1187. Fax: +34 965903527. E-mail: arancha.valdes@ua.es.

Funding

We acknowledge the Spanish Ministry of Economy and Competitiveness for financial support (MAT-2011-28468-C02-01). A.V. thanks Conselleria de Educación (Spain) for ACIF/2010/172 Predoctoral Research Training Grant.

Notes

The authors declare no competing financial interest.

ACKNOWLEDGMENTS

We acknowledge Almendras Llopis S.A for kindly providing the almond skin byproducts.

REFERENCES

(1) Food and Agriculture Organization of the United Nations. Statistics Division (FAOSTAT); http://faostat.fao.org (last accessed June 11, 2014).

(2) Esfahlan, A. J.; Jamei, R.; Esfahlan, J. R. The importance of almond (*Prunus amygdalus* L.) and its by-products. *Food Chem.* **2010**, *120*, 349−360.

(3) Garrido, I.; Monagas, M.; Gómez-Cordovés, C.; Bartolomé, B. Polyphenols and antioxidant properties of almond skins: influence of industrial processing. *J. Food Sci.* **2008**, *73*, 106−115.

(4) Mandalari, G.; Tomaino, A.; Arcoraci, T.; Martorana, M.; Lo Turco, V.; Cacciola, F.; Rich, G. T.; Bisignano, C.; Saija, A.; Dugo, P.; Cross, K. L.; Parker, M. L.; Waldron, K. W.; Wickham, M. S. J. Characterization of polyphenols, lipids and dietary fibre from almond skins (*Amygdalus communis* L.). *J. Food Compos. Anal.* **2010**, *23*, 166−174.

(5) Hughey, C. A.; Januszewicz, R.; Minardi, C. S.; Phung, J.; Huffman, B. A.; Reyes, L.; Wilcox, B. E.; Prakash, A. Distribution of almond polyphenols in blanch water and skins as a function of blanching time and temperature. *Food Chem.* **2012**, *131*, 1165−1173.

(6) Chen, C.; Lapsley, K.; Blumberg, J. B. A nutrition and health perspective on almonds. *J. Sci. Food Agric.* **2006**, *86*, 2245−2250.

(7) Teets, A. S.; Were, L. M. Inhibition of lipid oxidation in refrigerated and frozen salted raw minced chicken breasts with electron beam irradiated almond skin powder. *Meat Sci.* **2008**, *80*, 1326−1332.

(8) Teets, A. S.; Sundararaman, M.; Were, L. M. Electron beam irradiated almond skin powder inhibition of lipid oxidation in cooked salted ground chicken breast. *Food Chem.* **2008**, *111*, 934−941.

(9) Biesaga, M. Influence of extraction methods on stability of flavonoids. *J. Chromatogr. A* **2011**, *1218*, 2505−2512.

(10) Vagiri, M.; Ekholm, A.; Andersson, S. C.; Johansson, E.; Rumpunen, K. An optimized method for analysis of phenolic compounds in buds, leaves, and fruits of black currant (*Ribes nigrum* L.). *J. Agric. Food Chem.* **2012**, *60*, 10501−10510.

(11) Elez, I. G.; Dragović-Uzelac, V.; Režek, A. J.; Jukić, A. The effect of microwave assisted extraction on the isolation of anthocyanins and phenolic acids from sour cherry Marasca (*Prunus cerasus* var. Marasca). *J. Food Eng.* **2013**, *117*, 437−442.

(12) Routray, W.; Orsat, V. Microwave-assisted extraction of flavonoids: a review. *Food Bioprocess Technol.* **2012**, *5*, 409−424.

(13) Biesaga, M.; Pyrzynska, K. Stability of bioactive polyphenols from honey during different extraction methods. *Food Chem.* **2013**, *136*, 46−54.

(14) Song, J.; Li, D.; Liu, C.; Zhang, Y. Optimized microwave-assisted extraction of total phenolics (TP) from *Ipomoea batatas* leaves and its antioxidant activity. *Innovative Food Sci. Emerging Technol.* **2011**, *12*, 282−287.

(15) Ballard, T. S.; Mallikarjunan, P.; Zhou, K.; O'Keefe, S. Microwave-assisted extraction of phenolic antioxidant compounds from peanut skins. *Food Chem.* **2010**, *120*, 1185−1192.

(16) Gupta, A.; Naraniwal, M.; Kothari, V. Modern extraction methods for preparation of bioactive plant extracts. *Int. J. Appl. Nat. Sci.* **2012**, *1*, 8−26.

(17) Gil-Chávez, G. J.; Villa, J. A.; Ayala-Zavala, J. F.; Heredia, J. B.; Sepúlveda, D.; Yahia, E. M.; González-Aguilar, G. A. Technologies for extraction and production of bioactive compounds to be used as nutraceuticals and food ingredients: an overview. *Compr. Rev. Food Sci. Food Saf.* **2013**, *12*, 5−23.

(18) Bolling, B. W.; Dolnikowski, G.; Blumberg, J. B.; Chen, C.-Y. O. Polyphenol content and antioxidant activity of California almonds depend on cultivar and harvest year. *Food Chem.* **2010**, *122*, 819−825.

(19) Milbury, P. E.; Chen, C.-Y. C.; Dolnikowski, G. G.; Blumberg, J. B. Determination of flavonoids and phenolics and their distribution in almonds. *J. Agric. Food Chem.* **2006**, *54*, 5027−5033.

(20) Monagas, M.; Garrido, I.; Lebrón-Aguilar, R.; Gómez-Cordovés, C. M.; Rybarczyk, A.; Amarowicz, R.; Bartolomé, B. Comparative flavan-3-ol profile and antioxidant capacity of roasted peanut, hazelnut, and almond skins. *J. Agric. Food Chem.* **2009**, *57*, 10590−10599.

(21) Vidal, L.; Domini, C. E.; Grané, N.; Psillakis, E.; Canals, A. Microwave-assisted headspace single-drop microextration of chlorobenzenes from water samples. *Anal. Chim. Acta* **2007**, *592*, 9−15.

(22) Švarc-Gajić, J.; Stojanović, Z.; Segura, A. C.; Arraez, D. R.; Borrás, I.; Vasiljević, I. Development of a microwave-assisted extraction for the analysis of phenolic compounds from *Rosmarinus officinalis*. *J. Food Eng.* **2013**, *119*, 525−532.

(23) Harrison, K.; Were, L. M. Effect of gamma irradiation on total phenolic content yield and antioxidant capacity of almond skin extracts. *Food Chem.* **2007**, *102*, 932−937.

(24) Kamran Khan, M.; E-Huma, Z.; Dangles, O. A comprehensive review on flavanones, the major citrus polyphenols. *J. Food Compos. Anal.* **2014**, *33*, 85−104.

(25) Montgomery, D. C. *Design and Analysis of Experiments*; Wiley: Hoboken, NJ, USA, 2009.

(26) Hughey, C. A.; Wilcox, B.; Minardi, C. S.; Takehara, C. W.; Sundararaman, M.; Were, L. M. Capillary liquid chromatography−mass spectrometry for the rapid identification and quantification of almond flavonoids. *J. Chromatogr. A* **2008**, *1192*, 259−265.

(27) Singleton, V. L.; Rossi, J. A. Colorimetry of total phenolics with phosphomolybdic-phosphotungstic acid reagent. *Am. J. Enol. Vitic.* **1965**, *16*, 147.

(28) Krishnaswamy, K.; Orsat, V.; Gariépy, Y.; Thangavel, K. Optimization of microwave-assisted extraction of phenolic antioxidants from grape seeds (*Vitis vinifera*). *Food Bioprocess Technol.* **2013**, *6*, 441−455.

(29) Assimopoulou, A. N.; Sinakos, Z.; Papageorgiou, V. P. Radical scavenging activity of *Crocus sativus* L. extract and its bioactive constituents. *Phytother. Res.* **2005**, *19*, 997−1000.

(30) Molyneux, P. The use of the stable free radical diphenylpicrylhydrazyl (DPPH) for estimating antioxidant. *J. Sci. Technol.* **2004**, *26*, 211−219.

(31) Mishra, K.; Ojha, H.; Chaudhury, N. K. Estimation of antiradical properties of antioxidants using DPPH assay: a critical review and results. *Food Chem.* **2012**, *130*, 1036−1043.

(32) Farhat, M. B.; Landoulsi, A.; Chaouch-Hamada, R.; Sotomayor, J.; Jordán, M. Characterization and quantification of phenolic compounds andantioxidant properties of *Salvia* species growing in different habitats. *Ind. Crops Prod.* **2013**, *49*, 904−914.

(33) Luiza, A.; Rodrigues, L.; Aráujo, F.; Coelho, M. J.; Bezerra, L. A. Classification of cereal bars using near infrared spectroscopy and linear discriminant analysis. *Food Res. Int.* **2013**, *51*, 924−928.

(34) Valdés, A.; Beltrán, A.; Garrigós, M. C. Characterization and classification of almond cultivars by using spectroscopic and thermal techniques. *J. Food Sci.* **2013**, *78*, C138−C144.

(35) Hayat, K.; Hussain, S.; Abbas, S.; Farooq, U.; Ding, B.; Xia, S.; Jia, C.; Zhang, X.; Xia, W. Optimized microwave-assisted extraction of

phenolic acids from citrus mandarin peels and evaluation of antioxidant activity in vitro. *Sep. Purif. Technol.* **2009**, *70*, 63−70.
(36) Tsujita, T.; Shintani, T.; Sato, H. α-Amylase inhibitory activity from nut seed skin polyphenols. 1. Purification and characterization of almond seed skin polyphenols. *J. Agric. Food Chem.* **2013**, *61*, 4570−4576.
(37) Bolling, B.; Blumberg, J.; Chen, C. Y. The influence of roasting, pasteurisation, and storage on the polyphenol content and antioxidant capacity of California almond skins. *Food Chem.* **2010**, *123*, 1040−1047.
(38) Monagas, M.; Garrido, I.; Lebrón-Aguilar, R.; Bartolome, B.; Gómez-Cordovés, C. Almond (*Prunus dulcis* (Mill.) D.A. Webb) skins as a potential source of bioactive polyphenols. *J. Agric. Food Chem.* **2007**, *55*, 8498−507.
(39) Harnly, J. M.; Doherty, R. F.; Beecher, G. R.; Holden, J. M.; Haytowitz, D. B.; Bhagwat, S.; et al. Flavonoid content of U.S. fruits, vegetables, and nuts. *J. Agric. Food Chem.* **2006**, *54*, 9966−9977.
(40) Bolling, B.; Dolnikowski, G. G.; Blumberg, J.; Chen, C. Y. Quantification of almond skin polyphenols by liquid chromatography−mass spectrometry. *J. Food Sci.* **2009**, *74*, C326−C332.

DOI: 10.1021/acs.jafc.5b01011
J. Agric. Food Chem. 2015, 63, 5395−5402

JOURNAL OF AGRICULTURAL AND FOOD CHEMISTRY

Article

pubs.acs.org/JAFC

Characterization of Antibodies and Development of an Indirect Competitive Immunoassay for Detection of Deamidated Gluten

Olivier Tranquet,* Roberta Lupi, Valerie Echasserieau-Laporte, Manon Pietri, Colette Larré, and Sandra Denery-Papini

INRA, UR1268 Biopolymers, Interactions, Assemblies, rue de la Geraudiere, Nantes cedex 03, France

ABSTRACT: Diversification of gluten applications in the food and cosmetics industries was achieved through the production of water-soluble gluten that can be obtained by deamidation. Current analytical methods dedicated to gluten detection failed to detect deamidated gluten. After immunizing mice with the peptide LQPEEPFPE conjugated to keyhole limpet hemocyanin, five mouse monoclonal antibodies (mAbs) were produced and sequences of bound epitopes were determined as XPXEPFPE, where X is Q or E. The mAbs exhibited high specificity for deamidated gliadins and low molecular weight glutenin subunits. A competitive enzyme-linked immunosorbent assay (ELISA) based on INRA-DG1 mAb was developed with an IC50% of 85 ng/mL and a limit of detection of 25 ng/mL. The intra- and interassay coefficients of variation (CV) were <10% except for the interassay CV of the low-level control (40 ng/mL), which was 20%. This assay was capable of detecting three of the four deamidated gluten samples spiked in rice flour at 20 mg/kg.

KEYWORDS: *deamidated gluten, deamidated gliadins, monoclonal antibodies, ELISA*

INTRODUCTION

Wheat, which is adapted to various climate and agronomic conditions, is consumed worldwide as a major supplier of calories. The gluten protein fraction of flour has unique viscoelastic properties that enable the preparation of bread, pasta, and noodles. These functional properties and its low cost as a byproduct of the starch industry make gluten an ingredient that is now included in numerous foods, feed, and cosmetics far beyond its traditional uses.

Gluten is the causative agent of celiac disease (CD)[1] and is also involved in food allergy to wheat.[2−4] To date, there is no curative treatment for these two pathologies and the only solution for patient is a lifelong gluten-free diet. Codex alimentarius states a threshold of 20 mg of gluten/kg in food as safe for CD patients.[5] Below this content, food can be claimed as "gluten-free". Recently, The VITAL Scientific Expert Panel established that a dose of 1 mg of wheat protein did not trigger symptoms in 95% of people allergic to wheat, suggesting that the 20 mg/kg threshold is also suitable for wheat-allergic patients.[6]

Gluten is a complex network of gliadins and glutenins that interacts by covalent and noncovalent bounds. Gliadins are monomeric proteins classified into α/β-, γ-, ω2-, and ω5-subtypes, while glutenins are polymeric proteins classified in low- and high-molecular weight glutenin subunits (LMW-GS and HMW-GS). Gliadins and GS are insoluble in water and characterized by homologous repetitive domains rich in proline and glutamine.[7] The low water solubility of gluten limits its application as a functional ingredient in the food industry.[8] Diversification of gluten applications has been achieved through the production of gluten samples functionalized by chemical or enzymatic processes.

Deamidation is one of the methods used for this purpose. It may be performed by either chemical or enzymatic treatment, resulting in the conversion of the amide groups of glutamine and asparagine to the corresponding carboxyl groups. By introducing one negative charge at the deamidation site, this reaction affects the physicochemical properties of peptides and proteins.[9] Heating gluten under acidic conditions is an effective and simple method of deamidation used on an industrial scale. Concomitantly to deamidation, partial proteolysis of gluten components may occur at various degrees depending on the acid concentration, temperature and time for treatment. These modified gluten samples exhibit enhanced water solubility, foaming, and emulsifying properties while preserving their nutritional properties.[8,10]

Deamidation has an impact on gluten biological activity. It is known that most of the gluten-derived peptides involved in CD need to be deamidated in vivo by tissue transglutaminase to enhance their T-cell activation potential.[11,12] Gliadin fractions deamidated by chemical treatment (heat/acid treatment) have also been shown to exhibit such activity.[13] Early in the 2000s, severe allergic reactions to deamidated gluten (DG) were reported in individuals otherwise tolerant to native wheat.[14] The allergens and epitopes detected by immunoglobulin E (IgE) from these patients were shown to be different from those from patients allergic to classical wheat products. This allergy to DG was a different entity from wheat allergy specifically elicited by DG.[15] More dramatically, DG has been shown to be involved in a sensitization mechanism enabling both hydrolyzed or native proteins to elicit severe skin reactions and food allergy in more than 1300 individuals.[16] In Japan, almost all of these patients were sensitized by the same soap containing the same ingredient consisting of acid-hydrolyzed gluten (Glupearl 19S).[17]

Received: February 18, 2015
Revised: May 7, 2015
Accepted: May 17, 2015
Published: May 18, 2015

ACS Publications © 2015 American Chemical Society

DOI: 10.1021/acs.jafc.5b00923
J. Agric. Food Chem. 2015, 63, 5403−5409

Gluten detection is mainly based on enzyme-linked immunosorbent assay (ELISA) with antibodies that target epitopes among the repetitive domains of gliadins.[18] Repetition of the recognized epitopes allows the establishment of a sandwich ELISA with a single monoclonal antibody (mAb) and sequence homologies of these domains among gliadins enable the simultaneous detection of several gliadins.[19] However, these repetitive sequences, rich in glutamine, are strongly modified by deamidation and thus mAb recognition is reduced or absent. As a consequence, the concentration of DG detected by these kits is drastically underestimated.[20]

Denery-Papini et al. identified dominant epitopes bound by IgE from DG allergic patients. They corresponded to deamidated repetitive peptides of γ and ω2-gliadins containing two or three Glu residues.[15] As the sequences of these deamidated peptides are absent in native gluten or gliadins, we therefore hypothesized that they would be a good target for the specific detection of DG. In this study, we present the production of mAbs and the development of a competitive ELISA that specifically detects deamidated gluten.

MATERIALS AND METHODS

Gliadin and Glutenin Subunit Purification. Gliadins were extracted from wheat flour (cultivar Hardi) using a sequential procedure.[21] Briefly, the albumins/globulins (water/salt soluble proteins from wheat flour) were extracted from flour with a saline buffer. After three washings, the insoluble components were suspended in 70% (v/v) ethanol for 1 h at room temperature, and after centrifugation, the supernatant, i.e. the total gliadins were collected. The gliadin classes (α, γ, ω2, and ω5) were then prepared by ion-exchange chromatography and reversed-phase HPLC[3,22] and lyophylized. LMW-GS were obtained by the procedure of Verbruggen et al.[23] After pre-extraction of gliadins, glutenin subunits were solubilized from flour at 60 °C with 50% propanol containing 1% dithiothreitol. LMW-GS were then selectively precipitated with a final concentration of 85% propanol. Protein content of the fractions was determined by the Kjeldahl method.

Preparation of Deamidated Wheat Protein Fractions. Purified α-, ω2-, and ω5-gliadins, total gliadins, and LMW-GS were deamidated by acidic treatment as previously described.[24] A set of total gliadin fractions deamidated to different extents was also prepared. Gliadins (10 mg) were solubilized in 1 mL of 50% (v/v) ethanol, 0.1 N hydrochloric acid, and heated at 90 °C for 40, 60, 90, and 120 min. At each time, the reaction was stopped by neutralization with 1 mL 0.1 N NaOH. Solutions were dialyzed by ultrafiltration on AMICON centrifugal units with a MWCO at 3000 Da and centrifuged at 10 000 g, and the supernatant was recovered and freeze-dried. The degree of deamidation was calculated as the ratio of the amount of ammonia released from the deamidated sample to the total ammonia in the native sample and expressed as a percentage. Ammonia release was determined according to manufacturer's instructions (K-AMIAR, Megazyme, Ireland) after complete deamidation (3 h in 2 M HCl at 110 °C) of each sample. The deamidated Gliadins (D-Glia) were analyzed by native-PAGE on 10% acrylamide gels and compared with native gliadins.

Native and Functionalized Industrial Gluten Samples. VITAL Gluten (AIT Ingredients ref M120406) has been used as a native gluten reference. Four functionalized gluten samples (FG) described as wheat protein isolates with enhanced solubility in aqueous solution or with high emulsifying properties were selected for this study, referred to hereafter as FG1 to FG4. FG1 and FG2 were acid hydrolyzed gluten samples, already described by Krogshbo et al.[25] (with a deamidation level of 20−30% and 60%, respectively). FG3 and FG4 have been used in cosmetics. FG3 was provided by ALPOL Cosmétique (France), and FG4 was provided by Prof. Moneret-Vautrin (CH Epinal). No information was available about the processes used for neither their preparation nor their degree of deamidation or hydrolysis. Without any availability of the raw gluten used in these processes, measurement of the percentage of deamidation was not possible. They were characterized by native PAGE.

mAb Generation. Three BALB/c mice were injected subcutaneously twice at two-week intervals with 20 μg of the synthetic peptide LQPEEPFPEQC, conjugated to keyhole limpet hemocyanin (Millegen, France) and emulsified in Titermax Gold Adjuvant (SIGMA, CytRx Corporation, France). Three days after the second immunization, the mice were sacrificed. The popliteal lymph nodes were removed, and the lymphocytes were suspended by perfusion and fused with a SP2/0 myeloma cell line using standard hybridoma preparation and limiting dilution cloning procedures. The hybridoma supernatants from the fusion were screened for the presence of antipeptide antibodies using an indirect ELISA. The five selected hybridomas were cloned by dilution and referred to as INRA-DG1 to INRA-DG5. Crude hybridoma supernatants were used as the source of monoclonal antibodies.

Animal experiments were carried out at the INRA facilities, which are authorized by the Local Veterinary Department (authorization no. 44502). mAb production was approved by the Ethical Comity of Pays de la Loire under the number CEEA-2011.26.

Indirect ELISA. Reactivity of the antibodies to gliadins and LMW-GS, either native or deamidated, was assessed by indirect ELISA as described by Battais et al. for sample preparation and coating.[22] Uncoated sites were blocked with 4% defatted skimmed milk in phosphate-buffered saline (PBS) at pH 7.4 for 1 h. Hybridoma supernatants diluted 250 times in PBS containing 0.1% skimmed milk were then added and incubated for 1 h at room temperature. After washing with PBS 0.05% Tween 20, bound antibodies were detected by incubation with horseradish peroxidase antimouse IgG (Bio-Rad, Marnes-la-Coquette, France, 1:3000 dilution) and orthophenylenediamine as the substrate. Color development was stopped with 100 μL of 2 M H_2SO_4, and the absorbance was read at 492 nm.

Epitope Mapping with Solid-Phase Synthetic Peptides (Pepscan). Impact of the deamidation of the immunogenic peptide on mAb interaction was explored with octapeptides prepared by automated spot synthesis and covalently fixed by their C-terminal end on a cellulose membrane (Abimed, Langenfeld, Germany) as previously described.[15] After washing for 5 min with ethanol and three times for 5 min with Tris 50 mM buffer at pH 8.0 containing 0.05% Tween 20 (v/v) (TBS/T), the membrane was blocked with 2.5% (w/v) skimmed dried milk and 5% (w/v) sucrose in TBS/T for 1 h, washed in TBS-T and incubated overnight with mAb supernatant diluted 4000 times. After further washing, horseradish peroxidase antimouse IgG (170-6516, Bio-Rad) diluted 1/100 000 in blocking buffer was added for 1 h and washed. The membrane was then incubated with a chemiluminescent substrate (SuperSignal West Dura Extended Duration Substrate; Pierce, Rockford, IL). mAb binding was revealed by chemiluminescence with a CCD camera (Luminescent Image Analyzer LAS 3000; Fujifilm, Tokyo, Japan).

Competitive Inhibition ELISA. Microtiter plates (Maxisorp, NUNC, Roskilde, Denmark) were coated with LQPEEPFPEQC conjugated to BSA in 10 mM carbonate-bicarbonate buffer (pH 9.6) and left overnight at 4 °C. D-Glia and FGs were solubilized at 1 mg/mL in water or in PBS, taking into account their protein content. They were further diluted from 20 μg/mL to 8 ng/mL in PBS containing 0.1% skimmed milk prior incubation with INRA-DG1 mAb for 2 h at 37 °C. Then, 100 μL of antibody-sample solution was added to plates coated in BSA-LQPEEPFPEQC and incubated for 1 h. After washing, bound mAbs were revealed as previously described by indirect ELISA. Inhibition of antibody binding was expressed as the percentage of the maximal response obtained with antibody in the absence of the competitor according to the following formula:

$$\%\text{inhibition} = 1 - (\text{sample OD}/\text{blank sample OD})$$

Inhibition curves were obtained and fitted with a four parameter logistic regression. IC50 was defined as the analyte concentration that causes 50% inhibition of antibody binding. Limit of detection (LOD) expressed as a percentage of the inhibition unit was calculated with an

DOI: 10.1021/acs.jafc.5b00923
J. Agric. Food Chem. 2015, 63, 5403−5409

absorbance value equal to the mean value of the blank samples −3.3 × SD.

R5 ELISA kits were purchased from R-Biopharm (RIDASCREEN Gliadin competitive kit, Darmstadt, Germany). Samples were extracted in 60% (v/v) ethanol and analyzed according to the manufacturer's instructions. D-Glia and FGs were analyzed in triplicate in the INRA-DG1 competitive assay and in duplicate in the R5 competitive ELISA. FG2 was used in triplicate when chosen as standard.

Analysis of Wheat and Related Species, Maize, Soya, and Rice Flours. Grains of bread wheat (cv. apache), durum wheat (cv. Neodur), einkorn (cv. pays de sault), spelt (cv. rouquin), rye (cv. caroass), barley (cv. vanessa), oat (cv. evora), and triticale (cv. tremplin) were ground in liquid nitrogen. Maize, rice, and soya flour were purchased in food store. Soluble proteins were extracted by suspending flour at 100 mg/mL in PBS for 1 h, at room temperature under continuous agitation. Supernatants were collected after centrifugation (10 min/2500*g*), diluted at 1:20 in PBS containing 0.1% skimmed milk, and applied in the INRA-DG1 competitive ELISA.

Assay Evaluation. Reproducibility and repeatability were determined with three solutions of FG2 solubilized in water at 1 mg/mL and further diluted at 1000, 200, and 40 ng/mL in PBS containing 0.1% skimmed milk. Each solution was analyzed in quadruplicate on three different days by the same manipulator on freshly coated plates and with three independent standard solutions. We prepared contaminated rice flour samples spiked with 20 mg/kg of each FG. A 5 g portin of rice flour were suspended in 49.9 mL of PBS and 100 μL of FGs at 1 mg/mL (100 μg) and incubated for 1 h at room temperature. After centrifugation (2500 g/10 min), supernatants were collected and diluted at 1:20 in PBS 0.1% skimmed milk before analysis in the competitive ELISA.

Statistical Analysis. Mean and standard deviation were calculated with Excel 2010 (Microsoft) software.

RESULTS

MAbs Production and Specificity. MAbs were produced against the peptide LQPEEPFPEQC containing a dominant epitope QPEEPFPE recognized by patients suffering from an allergy to deamidated gluten.[15] The supernatants of the resulting hybridomas were screened by indirect ELISA for their reactivity to the peptide LQPEEPFPEQC conjugated to BSA. Five of them secreting mAbs specific for the immunogenic peptide were selected. They were denoted as mAbs INRA-DG1 to DG5.

Their substrate specificity was explored by indirect ELISA with native or deamidated α-, γ-, ω2-, and ω5-gliadins and LMW-GS. The five INRA-DG mAbs were specific for deamidated samples. They were divided into two groups according to their profiles of reactivity: the first was represented by INRA-DG1 and the second corresponded to INRA-DG2, -DG3, -DG4, and -DG5, which were represented by INRA-DG2 (Figure 1). mAb INRA-DG1 showed similar binding intensities for all deamidated fractions and it bound weakly to the native ω2-gliadins. mAb INRA-DG2 displayed a more restricted profile of reactivity as it only bound strongly to three deamidated fractions: γ-, ω2-, and ω5-gliadins; it exhibited weak reactivity to deamidated α-gliadins and LMW-GS and no binding to the native gluten proteins. The contribution of the number and the position of Glu residues to the binding of mAbs DG1 and DG2 was then investigated by the pepscan technique on a set of 16 peptides representing all the possible Q/E substitutions of the immunogenic peptide QPEEPFPE (Figure 2, peptide no. 2). Both mAbs recognized four deamidated peptides. All of them were deamidated to at least 50%. The position of the Q/E substitution appeared of importance: at position 1, it did not affect binding to the mAbs;

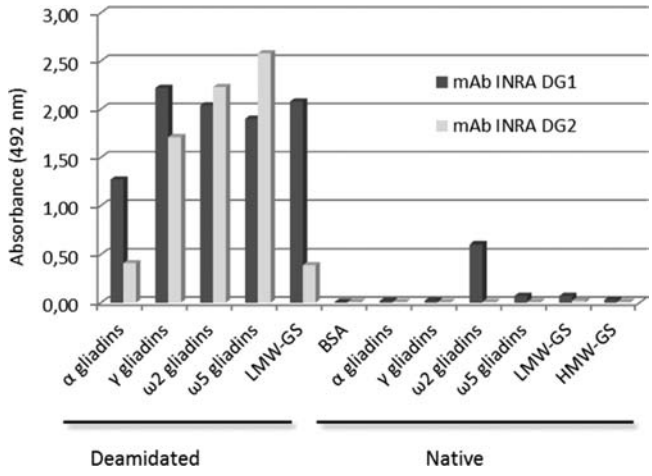

Figure 1. Reactivity of INRA-DG1 and INRA-DG2 mAbs toward native or deamidated gliadins and LMW-GS by indirect ELISA.

Peptide n°	% deamidation	Peptide sequence	INRA-DG1	INRA-DG2
1	100	E P E E P F P E		
2	75	Q P E E P F P E		
3	75	E P E Q P F P E		
4	75	E P Q E P F P E		
5	75	E P E E P F P Q		
6	50	Q P Q E P F P E		
7	50	Q P E Q P F P E		
8	50	Q P E E P F P Q		
9	50	E P Q Q P F P E		
10	50	E P Q E P F P Q		
11	50	E P E Q P F P Q		
12	25	Q P Q Q P F P E		
13	25	Q P Q E P F P Q		
14	25	Q P E Q P F P Q		
15	25	E P Q Q P F P Q		
16	0	Q P Q Q P F P Q		

Figure 2. Reactivity of INRA-DG1 and INRA-DG2 mAbs on octapeptides synthesized on cellulose membrane (Pepscan). Percentages of deamidation were calculated as the ratio number of E/(Q + E).

at position 3, it was not essential, but strongly enhanced the binding intensity; Q/E substitutions at position 4 and 8 were absolutely required for peptide recognition. Thus, epitopic sequences were the same for both MAbs and corresponded to peptides XPXEPFPE, where X is Q or E.

Characterization of Deamidated Gliadins and Functionalized Gluten Samples. Deamidated gliadin fractions with levels of deamidation ranging from 15% to 48% (elsewhere referred to as D-Glia-15% to D-Glia-48%) were produced. Their analysis on native PAGE reveals that the apparent mobility of proteins increased with their deamidation

DOI: 10.1021/acs.jafc.5b00923
J. Agric. Food Chem. 2015, 63, 5403−5409

level under these conditions (Figure 3). Contrarily, native gliadins were almost unable to migrate in these conditions.

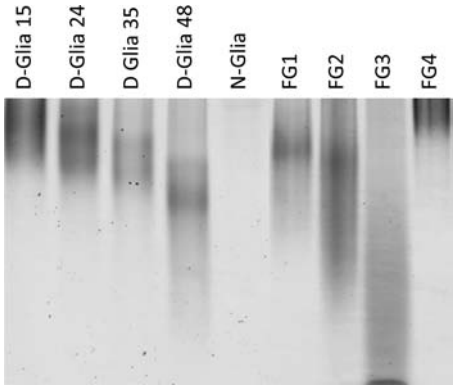

Figure 3. Analysis by native PAGE of deamidated gliadins (D-Glia) at various deamidation levels (15%, 24%, 35%, and 48%), native gliadins (N-Glia), and industrial functionalized gluten samples (FG).

Analysis of these samples illustrated that negative net charge increased proportionally to the duration of acid hydrolysis. Functionalized gluten samples (FG) were subjected to the same analysis by native PAGE. All FG samples were able to migrate along the gel at different distances from the top of the gel revealing that they contained different levels of negative charges. FG1 was very similar to D-Glia-35%. FG2 and FG3 displayed more mobility and a more heterogeneous pattern. The pattern of FG3 suggested that concomitantly with deamidation, strong hydrolysis had occurred. FG4 displayed lower mobility, similar to D-Glia-15%.

Development of Competitive Indirect ELISA. Considering its broad reactivity to deamidated gluten proteins, INRA-DG1 mAb was selected for assay development. Since deamidated gluten may also be cleaved, a competitive format was chosen for the ELISA. Two competitive assays were tested with either deamidated gliadins or the peptide LQPEEPFPEQC conjugated to BSA for coating on the microplates. The similarity of results (data with deamidated gliadins not shown) led us to choose the peptide LQPEEPFPEQC conjugated to BSA for coating the solid phase because it could be easily produced with good reproducibility. Two parameters were then explored to optimize the sensitivity of the ELISA: the concentration for the coating antigen and the antibody dilution. A lower IC50 with D-Glia-48% indicated higher sensitivity. It was reached for a coating performed at 0.75 μg/mL and a dilution of 1:4000 for the DG1 supernatant. Using these conditions, we checked for the reactivity of purified native gliadins and GS. None of them were detected in the competitive assay (data not shown).

Analysis of Samples by Competitive R5 and INRA-DG1 ELISA. Detection of the deamidated gliadin fractions was compared by means of two competitive ELISAs, the first based on the INRA-DG1 mAb, and the second based on the R5 antibody.[26] Increasing percentages of deamidation progressively impaired the detection of gliadins by the competitive R5 assay (Figure 4a). IC50 obtained with D-Glia-15%, −24%, −35%, and −48% were 3, 4, 8, and 50 times lower, respectively, than that of standard in the kit (pepsic/tryptic digest of prolamins from wheat, rye, and barley). The opposite effect of deamidation was observed with the INRA-DG1 assay (Figure 4b) since D-Glia 48% was the better recognized sample while

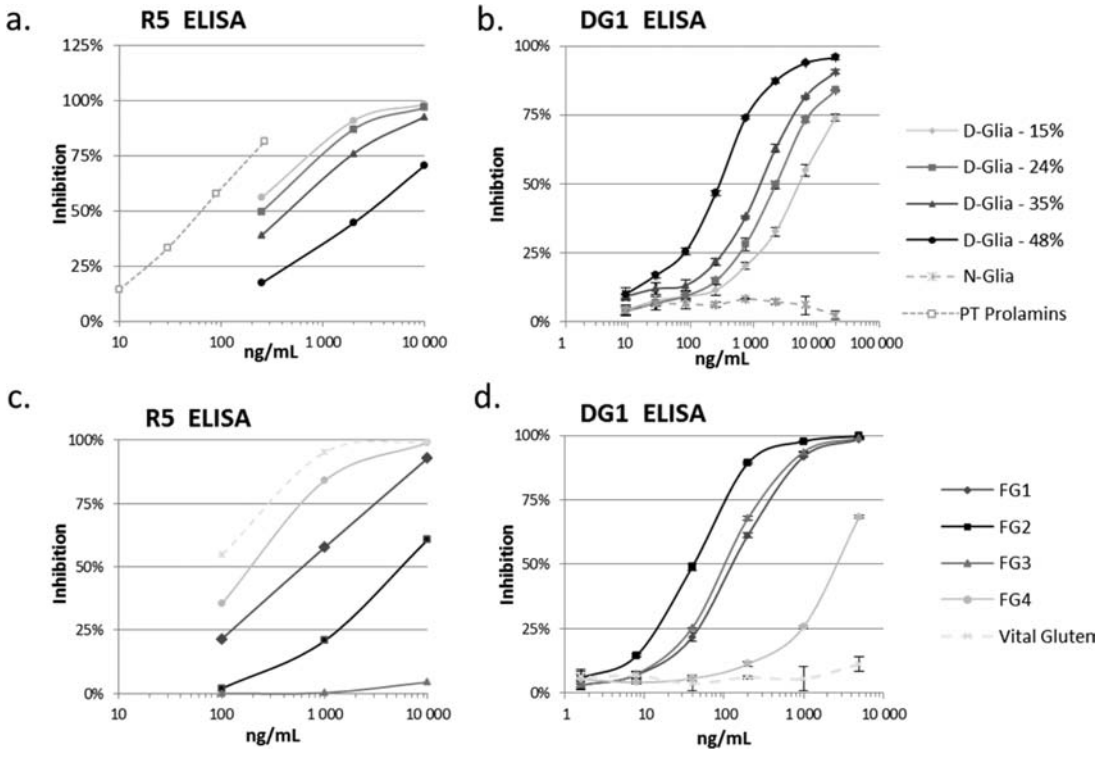

Figure 4. Analysis by indirect competitive ELISA of deamidated gliadins (D-Glia) at various deamidation levels (15%, 24%, 35%, and 48%), native gliadins (N-Glia), industrial functionalized gluten samples (FG), and vital gluten. D-Glia (a) and FG (c) were analyzed by the R5 competitive ELISA. D-Glia (b) and FG (d) were analyzed by the INRA-DG1 Competitive ELISA. Pepsic trypsic digested prolamins from wheat rye and barley (PT-Prolamins).

DOI: 10.1021/acs.jafc.5b00923
J. Agric. Food Chem. 2015, 63, 5403−5409

D-Glia-15% gave the weaker response. Moreover, the absence of response with native gliadins confirmed that deamidation was absolutely required for DG1 binding.

FG samples and vital gluten were then analyzed with both R5 and INRA-DG1 competitive assays. In the competitive R5 ELISA, decreasing responses to FG4, 1, and 2 were observed and were 3, 10, and 100 times lower, respectively, than to vital gluten (Figure 4c). There was no response to FG3. In the competitive INRA-DG1 ELISA vital gluten was not detected while all FG samples were (Figure 4d). In terms of response intensity, FG4, 3, 1, and 2 gave increasing responses in the INRA-DG1 assay. It should be noted that FG3, which was undetected by the R5 assay, was detected similarly to FG1 with the INRA-DG1 competitive ELISA.

Immunoassay Evaluation. Performance evaluation of the competitive ELISA was performed with eight concentrations of FG2 ranging from 3 to 7500 ng/mL in PBS, which were chosen as the standards. A typical standard curve is presented in Figure 5. On the basis of three independent experiments, IC50 and a blank value were calculated as 85 ± 16 and 16 ± 2.8 ng/mL, respectively. Taking into account interassay variation, LOD was set at 25 ng/mL (mean of blank −3.3 × SD), which corresponded to 21% inhibition. Repeatability and reproducibility were assessed with three solutions of FG2 at 40, 200, and 1000 ng/mL in PBS. They were analyzed in quadruplicate in three independent experiments for evaluation of intra- and interassay variations. The intra-assay coefficients of variation (CV) ranged from 2.1% to 6.2%, and the interassay CVs were 7.8%, 5.1%, and 20.3% for the 1000, 200, and 40 ng/mL solutions, respectively (Table 1).

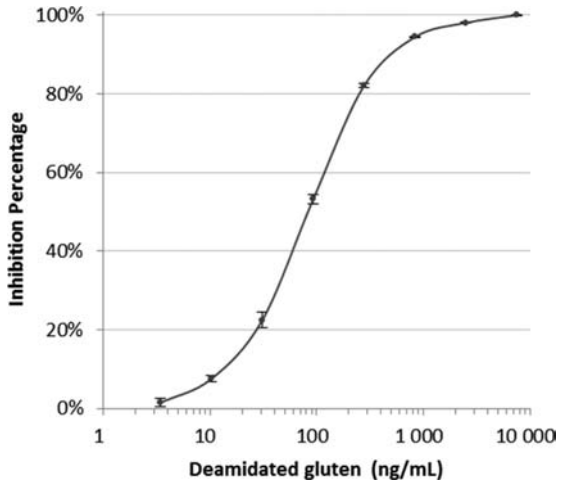

Figure 5. Competitive inhibition curve of FG2.

Soluble proteins extracted from common cereal grains (four wheat species, rye, barley, oat maize, and rice) and from soya seeds were used to check their potential cross reactivity in our assay. None of these extracts caused inhibition over the LOD of the assay (data not shown).

Application to Contaminated Rice Flour (20 mg/kg). Contamination of rice flour was performed with the four FG samples at 20 mg/kg and quantified in the INRA-DG1 ELISA. This level of contamination led to significant percentages of inhibition for FG1, 2, and 3, but not for FG4 (Table 2). Recoveries were then determined using FG2 as standard. Recovery of the FG2 was excellent since it reached 100%. Recoveries of FG1 and FG3 were 42% and 52% respectively.

Table 1. Repeatability and Reproducibility of INRA-DG1 Competitive ELISA Determined at Three FG2 Concentrations

A (ng/mL)	assay	mesured amount (ng/mL)	recovery (%)	intra-assay CV (%)	interassay CV (%)
1000	1	882 ± 54	88	6.1	
	2	1045 ± 31	105	3.0	7.8
	3	1049 ± 62	105	5.9	
200	1	202 ± 12	101	6.2	
	2	222 ± 5	111	2.1	5.1
	3	203 ± 5	101	2.7	
40	1	50 ± 3	124	5.5	
	2	61 ± 4	152	6.1	20.3
	3	64 ± 3	134	4.4	

Table 2. Percentage of Inhibition and Recoveries of FG Samples Spiked at 20 mg/kg in Rice Flour and Analyzed in INRA-DG1 Competitive ELISA

	% inhibition	SD[a]	recovery
FG1	24%	2%	42%
FG2	47%	1%	100%
FG3	29%	2%	52%
FG4	11%	1%	NA

[a]Standard deviation.

These values were expected since FG 1 and FG3 were less recognized than the standard (FG2) by INRA-DG1 mAb.

DISCUSSION

Patients allergic to DG possess IgE specific for peptides derived from the domains containing repetitive sequences of γ- and ω2-gliadins where glutamine has been replaced by glutamic acid. Denery-Papini et al. determined that the peptide QPEEPFPE was a dominant epitope for patients allergic to DG but tolerant to native wheat.[15] Part of this epitope, PEEPFP, has also been found in Japanese patients sensitized by a soap containing DG.[27] After immunizing mice with the synthetic peptide LQPEEPFPEQC, we selected mAbs capable of discriminating between deamidated gluten proteins and their native counterparts. One of them, mAb INRA-DG1, appeared extremely interesting for detection purposes as it bound both deamidated gliadins and deamidated LMW-GS. In accordance with the sequence similarities between the repetitive domains of native gliadins and those of LMW-GS, such cross reactivities are frequent and have already been observed with a large set of mAbs directed toward native domains containing repetitive sequences of gliadins;[28] the same phenomenon was observed after deamidation. We identified four epitopes of mAb INRA-DG1. None of them were present in extenso in all gliadins and LMW-GS. Further exploration is required for complete epitope mapping. When compared to mAbs applied to gluten detection, INRA-DG1 mAb differs from others by its capacity to specifically detect DG with high sensitivity. To date, most of, if not all, commercial kits designed for gluten detection are based on antibodies targeting the repetitive sequences of gliadins.[18] These sequences rich in glutamine are susceptible to deamidation. Kits based on R5, but also on Skerritt's or G12 mAbs[29,30] were incapable of properly detecting deamidated gluten: their binding to gluten deamidated at 52% was abolished for Skerritt's and G12 mAbs or strongly reduced for R5.[20,31] In this study, we demonstrated that the decrease of

DOI: 10.1021/acs.jafc.5b00923
J. Agric. Food Chem. 2015, 63, 5403−5409

R5 binding was a continuous phenomenon directly related to the level of deamidation. Even a low deamidation level, such as 15%, induced a 3-fold decrease for R5 mAb recognition. On the contrary, INRA-DG1 mAb was able to detect gliadins deamidated at levels varying from 15% to 50%. Moreover, the more the gliadins are deamidated, the stronger the binding. The capacity of DG1 to detect weakly deamidated gliadins (15%) added to the fact that the identified epitopes were deamidated at least by 50% suggested that, as a random process, deamidation in acidic condition is heterogeneous and may result in high percentage of deamidation on small portion of the repetitive sequences.

Furthermore, impaired detection by the R5 assay was also observed with the tested FG samples. It should be noted that one of them (FG3) was not even detected. This sample appeared highly hydrolyzed and the remaining fragments should be of smaller length than in the other FG samples. R5 is known to bind sequences as small as the pentapeptide[32] and the competitive format should allow their detection. This absence of detection of FG-3 by R5 might be attributed to the absence of remaining native sequences.

Repetitive sequences of gliadins and GS, which are homologous, are a target of choice for gluten detection. However, these sequences are not identical and are recognized with different affinity by mAbs; therefore, accurate standardization of gluten assays is still a serious issue.[18] Detection of deamidated gluten faces similar difficulties to which possible hydrolysis and heterogeneity in the level of deamidation of the sample are added. The INRA-DG1 competitive assay was capable of detecting contamination as low as 20 mg/kg in rice flour for 3 of 4 of the DGs tested. The particular behavior of FG4 in both assays—low detection by the DG1 assay and good detection by the R5 competitive assay—can be related to a low deamidation level as suggested by weak mobility in native PAGE. In such a case, the R5 and the INRA-DG1 competitive assays appeared fully complementary. With this set of samples with varying degrees of deamidation, we observed that the more a sample is recognized in one assay, the less it would be in the other assay.

In conclusion, the INRA-DG1 mAb assay described here is useful for the detection of deamidated gliadins or gluten with high sensitivity and specificity. Further experiments are required to validate its applicability to incurred processed food and cosmetic samples.

AUTHOR INFORMATION

Corresponding Author

*Tel.: +33 240675027. Fax: +33 240675027. E-mail: olivier.tranquet@nantes.inra.fr.

Funding

This research was supported by INRA Transfert and through the project PREDEXPITOPE funded the French National Research Agency (ANR-08-ALIA-0014).

Notes

The authors declare no competing financial interest.

ACKNOWLEDGMENTS

We thank Julie Le Luhant and Lenaig Guillard for the mAb production and Annabelle Blanchet, Fiona Francini, and Maxime Pecquet for their technical assistance in characterizing the mAbs and developing the competitive ELISA.

ABBREVIATIONS

CD, celiac disease; GS, glutenin subunits; LMW, low molecular weight; DG, deamidated gluten; IgE, immunoglobulin E; mAb, monoclonal antibody; FG, functionalized gluten; D-Glia, deamidated gliadins; PBS, phosphate buffered saline; IC, inhibition concentration; LOD, limit of detection; CV, coefficient of variation

REFERENCES

(1) Sollid, L. M. Coeliac Disease: Dissecting a Complex Inflammatory Disorder. *Nat. Rev. Immunol.* **2002**, *2*, 647−655.

(2) Battais, F.; Richard, C.; Jacquenet, S.; Denery-Papini, S.; Moneret-Vautrin, D. A. Wheat Grain Allergies: An Update on Wheat Allergens. *Eur. Ann. Allergy Clin Immunol* **2008**, *40*, 67−76.

(3) Battais, F.; Courcoux, P.; Popineau, Y.; Kanny, G.; Moneret-Vautrin, D.-A.; Denery-Papini, S. Food Allergy to Wheat: Differences in Immunoglobulin E-Binding Proteins as a Function of Age or Symptoms. *J. Cereal Sci.* **2005**, *42*, 109−117.

(4) Tatham, A. S.; Shewry, P. R. Allergens to Wheat and Related Cereals. *Clin. Exp. Allergy* **2008**, *38*, 1712−1726.

(5) Codex Alimentarius Commission. Codex Standard 118-1979 (revised 2008), *Foods for Special Dietary Use for Persons Intolerant to Gluten*; In FAO/WHO, Rome, 2008.

(6) Taylor, S. L.; Baumert, J. L.; Kruizinga, A. G.; Remington, B. C.; Crevel, R. W. R.; Brooke-Taylor, S.; Allen, K. J.; Houben, G. F. Establishment of Reference Doses for Residues of Allergenic Foods: Report of the VITAL Expert Panel. *Food Chem. Toxicol.* **2014**, *63*, 9−17.

(7) Shewry, P. R.; Tatham, A. S. The Characteristics, Structures and Evolutionary Relationships of Prolamins. In *Seed Proteins*; Shewry, P. R., Casey, R., Eds.; Springer: Dordrecht, The Netherlands, 1999; pp 11−33.

(8) Popineau, Y.; Huchet, B.; Larré, C.; Bérot, S. Foaming and Emulsifying Properties of Fractions of Gluten Peptides Obtained by Limited Enzymatic Hydrolysis and Ultrafiltration. *J. Cereal Sci.* **2002**, *35*, 327−335.

(9) Cui, C.; Hu, Q.; Ren, J.; Zhao, H.; You, L.; Zhao, M. Effect of the Structural Features of Hydrochloric Acid-Deamidated Wheat Gluten on Its Susceptibility to Enzymatic Hydrolysis. *J. Agric. Food Chem.* **2013**, *61*, 5706−5714.

(10) Liao, L.; Zhao, M.; Ren, J.; Zhao, H.; Cui, C.; Hu, X. Effect of Acetic Acid Deamidation-Induced Modification on Functional and Nutritional Properties and Conformation of Wheat Gluten. *J. Sci. Food Agric.* **2010**, *90*, 409−417.

(11) Molberg, Ø.; Mcadam, S. N.; Körner, R.; Quarsten, H.; Kristiansen, C.; Madsen, L.; Fugger, L.; Scott, H.; Norén, O.; Roepstorff, P.; Lundin, K. E. A.; Sjöström, H.; Sollid, L. M. Tissue Transglutaminase Selectively Modifies Gliadin Peptides That Are Recognized by Gut-Derived T Cells in Celiac Disease. *Nat. Med.* **1998**, *4*, 713−717.

(12) Vader, W.; Kooy, Y.; van Veelen, P.; de Ru, A.; Harris, D.; Benckhuijsen, W.; Peña, S.; Mearin, L.; Drijfhout, J. W.; Koning, F. The Gluten Response in Children with Celiac Disease Is Directed toward Multiple Gliadin and Glutenin Peptides. *Gastroenterology* **2002**, *122*, 1729−1737.

(13) Sjöström, H.; Lundin, K. E.; Molberg, O.; Körner, R.; McAdam, S. N.; Anthonsen, D.; Quarsten, H.; Norén, O.; Roepstorff, P.; Thorsby, E.; Sollid, L. M. Identification of a Gliadin T-Cell Epitope in Coeliac Disease: General Importance of Gliadin Deamidation for Intestinal T-Cell Recognition. *Scand. J. Immunol.* **1998**, *48*, 111−115.

(14) Leduc, V.; Moneret-Vautrin, D. A.; Guerin, L.; Morisset, M.; Kanny, G. Anaphylaxis to Wheat Isolates: Immunochemical Study of a Case Proved by Means of Double-Blind, Placebo-Controlled Food Challenge. *J. Allergy Clin. Immunol.* **2003**, *111*, 897−899.

(15) Denery-Papini, S.; Bodinier, M.; Larré, C.; Brossard, C.; Pineau, F.; Triballeau, S.; Pietri, M.; Battais, F.; Mothes, T.; Paty, E.; Moneret-Vautrin, D.-A. Allergy to Deamidated Gluten in Patients Tolerant to

DOI: 10.1021/acs.jafc.5b00923
J. Agric. Food Chem. 2015, 63, 5403−5409

Wheat: Specific Epitopes Linked to Deamidation. *Allergy* **2012**, *67*, 1023−1032.
(16) Chinuki, Y.; Morita, E. Wheat-Dependent Exercise-Induced Anaphylaxis Sensitized with Hydrolyzed Wheat Protein in Soap. *Allergol. Int.* **2012**, *61*, 529−537.
(17) Nakamura, R.; Nakamura, R.; Adachi, R.; Itagaki, Y.; Fukutomi, Y.; Teshima, R. Evaluation of Allergenicity of Acid-Hydrolyzed Wheat Protein Using an in Vitro Elicitation Test. *Int. Arch. Allergy Immunol.* **2013**, *160*, 259−264.
(18) Diaz-Amigo, C.; Popping, B. Accuracy of ELISA Detection Methods for Gluten and Reference Materials: A Realistic Assessment. *J. Agric. Food Chem.* **2013**, *61*, 5681−5688.
(19) Denery-Papini, S.; Nicolas, Y.; Popineau, Y. Efficiency and Limitations of Immunochemical Assays for the Testing of Gluten-Free Foods. *J. Cereal Sci.* **1999**, *30*, 121−131.
(20) Kanerva, P. M.; Brinck, O.; Sontag-Strohm, T. S.; Salovaara, H. O.; Loponen, J. Deamidation of Gluten Proteins and Peptides Decreases the Antibody Affinity in Gluten Analysis Assays. *J. Cereal Sci.* **2011**, *53*, 335−339.
(21) Nicolas, Y.; Martinant, J.; Denery-Papini, S.; Popineau, Y. Analysis of Wheat Storage Proteins by Exhaustive Sequential Extraction Followed by RP-HPLC and Nitrogen Determination. *J. Sci. Food Agric.* **1998**, *96*, 96−102.
(22) Battais, F.; Pineau, F.; Popineau, Y.; Aparicio, C.; Kanny, G.; Guerin, L.; Moneret-Vautrin, D.-A.; Denery-Papini, S. Food Allergy to Wheat: Identification of Immunogloglin E and Immunoglobulin G-Binding Proteins with Sequential Extracts and Purified Proteins from Wheat Flour. *Clin. Exp. Allergy* **2003**, *33*, 962−970.
(23) Verbruggen, I. M.; Veraverbeke, W. S.; Vandamme, a.; Delcour, J. a. Simultaneous Isolation of Wheat High Molecular Weight and Low Molecular Weight Glutenin Subunits. *J. Cereal Sci.* **1998**, *28*, 25−32.
(24) Gourbeyre, P.; Denery-Papini, S.; Larré, C.; Gaudin, J.-C.; Brossard, C.; Bodinier, M. Wheat Gliadins Modified by Deamidation Are More Efficient than Native Gliadins in Inducing a Th2 Response in Balb/c Mice Experimentally Sensitized to Wheat Allergens. *Mol. Nutr. Food Res.* **2012**, *56*, 336−344.
(25) Kroghsbo, S.; Andersen, N. B.; Rasmussen, T. F.; Jacobsen, S.; Madsen, C. B. Acid Hydrolysis of Wheat Gluten Induces Formation of New Epitopes but Does Not Enhance Sensitizing Capacity by the Oral Route: A Study in "Gluten Free" Brown Norway Rats. *PLoS One* **2014**, *9*, e107137.
(26) Valdés, I.; Garcia, E.; Llorente, M.; Mendez, E. Innovative Approach to Low-Level Gluten Determination in Foods Using a Novel Sandwich Enzyme-Linked Immunosorbent Assay Protocol. *Eur. J. Gastroenterol. Hepatol.* **2003**, *15*, 465−474.
(27) Yokooji, T.; Kurihara, S.; Murakami, T.; Chinuki, Y.; Takahashi, H.; Morita, E.; Harada, S.; Ishii, K.; Hiragun, M.; Hide, M.; Matsuo, H. Characterization of Causative Allergens for Wheat-Dependent Exercise-Induced Anaphylaxis Sensitized with Hydrolyzed Wheat Proteins in Facial Soap. *Allergol. Int.* **2013**, *62*, 435−445.
(28) Tranquet, O.; Larré, C.; Denery-Papini, S. Selection of a Monoclonal Antibody for Detection of Gliadins and Glutenins: A Step towards Reliable Gluten Quantification. *J. Cereal Sci.* **2012**, *56*, 760−763.
(29) Skerritt, J. H.; Hill, A. S. Monoclonal Antibody Sandwich Enzyme Immunoassays for Determination of Gluten in Foods. *J. Agric. Food Chem.* **1990**, *38*, 1771−1778.
(30) Morón, B.; Bethune, M. T.; Comino, I.; Manyani, H.; Ferragud, M.; López, M. C.; Cebolla, A.; Khosla, C.; Sousa, C. Toward the Assessment of Food Toxicity for Celiac Patients: Characterization of Monoclonal Antibodies to a Main Immunogenic Gluten Peptide. *PLoS One* **2008**, *3*, e2294.
(31) Kahlenberg, F.; Sanchez, D.; Lachmann, I.; Tuckova, L.; Tlaskalova, H.; Méndez, E.; Mothes, T. Monoclonal Antibody R5 for Detection of Putatively Coeliac-Toxic Gliadin Peptides. *Eur. Food Res. Technol.* **2006**, *222*, 78−82.
(32) Osman, A. A.; Uhlig, H. H.; Valdes, I.; Amin, M.; Mendez, E.; Mothes, T. A Monoclonal Antibody That Recognizes a Potential Coeliac-Toxic Repetitive Pentapeptide Epitope in Gliadins. *Eur. J. Gastroenterol. Hepatol.* **2001**, *13*, 1189−1193.

DOI: 10.1021/acs.jafc.5b00923
J. Agric. Food Chem. 2015, 63, 5403−5409

JOURNAL OF AGRICULTURAL AND FOOD CHEMISTRY

Article

pubs.acs.org/JAFC

Pharmacokinetic Profile of Eight Phenolic Compounds and Their Conjugated Metabolites after Oral Administration of *Rhus verniciflua* Extracts in Rats

Ming Ji Jin,[†] In Sook Kim,[†] Jong Suk Park,[†] Mi-Sook Dong,[§] Chun-Soo Na,[#] and Hye Hyun Yoo*[,†]

[†]Institute of Pharmaceutical Science and Technology and College of Pharmacy, Hanyang University, Ansan, Gyeonggi-do 426-791, Korea

[§]School of Life Sciences and Biotechnology, Korea University, Seoul 136-713, Korea

[#]Lifetree Biotech Company, Ltd., Suwon, Gyeonggi-do 441-350, Korea

ABSTRACT: *Rhus verniciflua* (*Toxicodendron vernicifluum*) is a medicinal tree popularly used in Asian countries such as China, Japan, and Korea as a food additive or herbal medicine because of its beneficial effects. *R. verniciflua* extract (RVE) contains diverse phenolic compounds, such as flavonoids, as its major biological active constituents. In this study, the pharmacokinetic profiles of eight phenolic compounds were investigated following oral administration of RVE to rats. The eight phenolic compounds were 2,4-dihydroxybenzoic acid, 3,4-dihydroxybenzoic acid, fisetin, fustin, butin, sulfuretin, taxifolin, and garbanzol. The plasma concentrations of the eight compounds were determined by using a liquid chromatography−triple-quadrupole mass spectrometer before and after treatment with β-glucuronidase. When 1.5 g/kg RVE was administered, the eight compounds were all detected in plasma, mainly as conjugated forms. These pharmacokinetic data would be useful for understanding the pharmacological effects of RVE.

KEYWORDS: *Rhus verniciflua Stokes, phenolic compounds, bioanalytical method, pharmacokinetics*

INTRODUCTION

Rhus verniciflua (*Toxicodendron vernicifluum*) is a medicinal tree cultivated in Asian countries, including China, Japan, and Korea. It has been traditionally used as a health food, herbal remedy, or food additive.[1,2] *R. verniciflua* contains medicinal ingredients with diaphoretic, cathartic, antiviral, sedative, and antirheumatic activities.[3] There are many reports on the pharmacological activities of *R. verniciflua* extracts (RVE). These include antioxidant activity,[2,4−9] antiproliferative activity with growth of human lymphoma cells,[1] anti-inflammatory activity,[10] antimutagenic activity,[11] apoptotic effects,[12,13] and antimicrobial activity.[14]

These pharmacological activities of RVE are believed to be attributed to its bioactive ingredients, such as phenolic compounds. In previous chemical studies,[15] diverse phenolic compounds, such as caffeic acid, 2,4-dihydroxybenzoic acid (2,4-DHBA), *p*-coumaric acid, chlorogenic acid, protocatechuic acid, garbanzol, fisetin, kaempferol, kaempferol-3-*O*-glucoside, quercetin, butein, butin, gallic acid, fustin, 2,6,3′,4′-tetrahydroxy-2-benzylcoumaran-3-one, and sulfuretin, have been reported as constituents of RVE. These phenolic compounds have been shown to exhibit various beneficial effects.[8,9,15,16] For example, fisetin exhibited anti-inflammatory activity.[17] Fustin exerted neuroprotection on 6-hydroxydopamine-induced cell death.[18] Butin has a protective effect against hydrogen peroxide-induced apoptosis via its antioxidant properties,[19] 2,4-DHBA showed an antioxidative activity for free radical scavenging,[20] and 3,4-DHBA exhibited antioxidant, anti-inflammatory, antihyperglycemic, and anti-apoptotic activities.[21] Sulfuretin exhibited anti-inflammatory activity and therapeutic value in preventing β-cell damage.[22−24] Garbanzol showed anti-inflammatory and antinociceptive effects,[25] and taxifolin inhibited oxidative stress and cell apoptosis to prevent diabetic cardiomyopathy in vivo and in vitro.[26]

However, to our knowledge, pharmacokinetic studies of the bioactive phenolic compounds in RVE have not been performed, although pharmacokinetics is crucial for providing evidence of biological activity in vivo and for understanding the action mechanisms of functional foods. As for analytical methods for RVE, only a few published methods are available, which are high-performance liquid chromatography (HPLC)-based methods.[15] Furthermore, bioanalytical methods for the quantitation of phenolic compounds of RVE in biofluids or tissues have not yet been reported.

In this study, a precise, accurate, and sensitive method based on liquid chromatography−tandem mass spectrometry (LC-MS/MS) for the simultaneous quantitation of eight phenolic compounds of RVE (Figure 1) in rat plasma was developed. Pharmacokinetic profiling of the phenolic compounds was investigated following oral administration of RVE to rats using the developed method. Subsequently, we presented the pharmacokinetic properties of phenolic compounds of RVE as conjugated metabolites as well as parent forms.

MATERIALS AND METHODS

Chemicals. Sulfuretin and fustin were purchased from Extrasynthese (Genay Cedex, France). Chrysin, fisetin, butin, garbanzol,

Received: April 6, 2015
Revised: May 22, 2015
Accepted: May 22, 2015
Published: May 22, 2015

ACS Publications © 2015 American Chemical Society

DOI: 10.1021/acs.jafc.5b01724
J. Agric. Food Chem. 2015, 63, 5410−5416

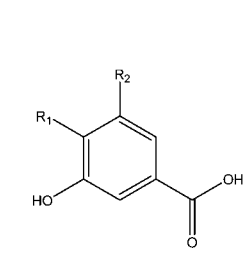

	R1	R2
2,4-dihydroxybenzoic acid	H	OH
3,4-dihydroxybenzoic acid	OH	H

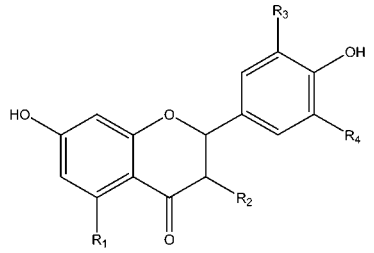

	R1	R2	R3	R4
Butin	H	H	H	OH
Garbanzol	H	OH	H	H
Taxifolin	OH	OH	H	OH
Fustin	H	OH	OH	H

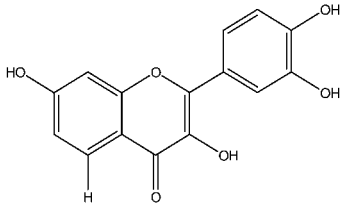

Fisetin

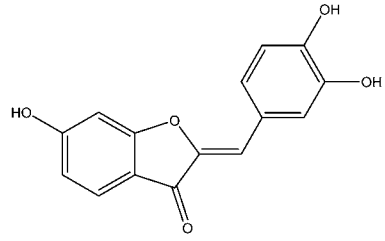

Sulfuretin

Figure 1. Chemical structures of the eight phenolic compounds of *Rhus verniciflua* analyzed in this study.

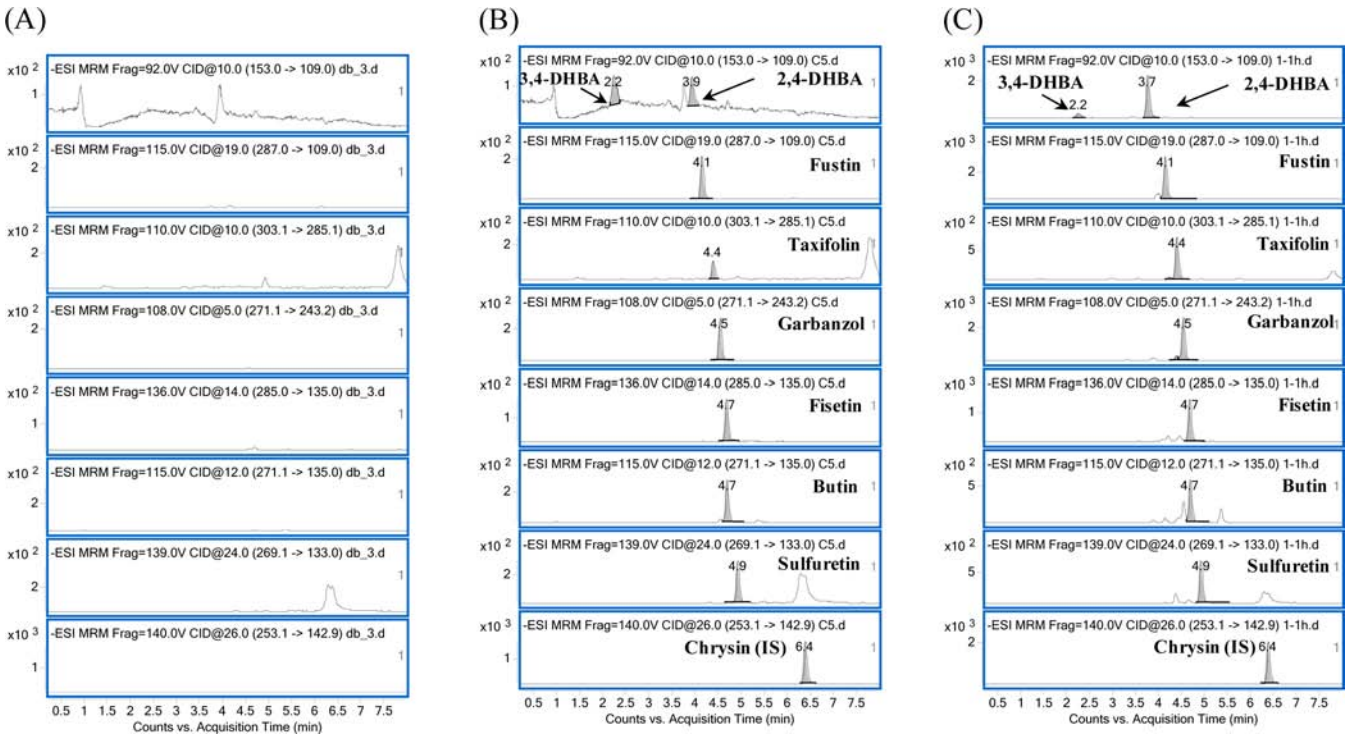

Figure 2. Multiple reaction monitoring chromatograms of (A) blank rat plasma, (B) plasma spiked with standards (100 ng/mL), and (C) plasma taken 1 h after oral administration of *Rhus verniciflua* extracts.

taxifolin, 2,4-DHBA, 3,4-DHBA, ascorbic acid, and formic acid were purchased from Sigma Chemicals (St. Louis, MO, USA). *β*-Glucuronidase (140 U/mL) was purchased from Roche Applied Science (Mannheim, Germany). HPLC grade water, methanol, and acetonitrile were purchased from J. T. Baker (Philipsburg, NJ, USA).

Preparation of RVE. The heartwoods of *R. verniciflua* were cut into small pieces and extracted with a 10-fold volume of water for 3 h

DOI: 10.1021/acs.jafc.5b01724
J. Agric. Food Chem. 2015, 63, 5410−5416

Table 1. Intra- and Interday Assay Results for Accuracy and Precision of the Developed Method

		intraday (n = 5)			interday (n = 3)		
compound	theor concn (ng/mL)	concn found (mean ± SD)	accuracy (%)	CV (%)	concn found (mean ± SD)	accuracy (%)	CV (%)
2,4-DHBA	2	1.8 ± 0.1	91.4	4.4	2.0 ± 0.3	100.7	15.0
	100	101.7 ± 4.4	101.7	4.3	103.7 ± 3.8	103.7	3.7
	1000	979.3 ± 37.6	97.9	3.8	969.0 ± 47.7	96.9	4.9
3,4-DHBA	2	2.2 ± 0.1	108.4	6.5	2.0 ± 0.2	99.6	9.2
	100	98.6 ± 7.9	98.6	8.0	96.8 ± 11.0	96.8	11.3
	1000	1014.5 ± 53.5	101.4	5.3	952.1 ± 64.1	95.2	6.7
butin	2	1.9 ± 0.1	96.2	2.8	1.8 ± 0.2	89.0	11.1
	100	101.5 ± 5.0	101.5	4.9	102.4 ± 6.6	102.4	6.4
	1000	874.6 ± 92.4	87.5	10.6	850.7 ± 101.5	85.0	11.9
fisetin	2	1.9 ± 0.2	96.4	7.9	2.1 ± 0.2	104.4	7.6
	100	98.7 ± 3.8	98.7	3.9	96.2 ± 8.1	96.2	8.4
	1000	967.5 ± 117.4	96.7	12.1	911.5 ± 136.6	91.2	15.0
fustin	2	1.8 ± 0.2	92.4	8.1	1.7 ± 0.2	84.2	11.7
	100	102.5 ± 5.1	102.5	5.0	103.1 ± 6.0	103.1	5.8
	1000	889.0 ± 18.4	88.9	2.1	946.4 ± 55.0	94.6	5.8
garbanzol	2	1.9 ± 0.1	92.5	4.4	1.9 ± 0.1	94.3	4.2
	100	106.0 ± 5.7	106.0	5.4	109.9 ± 6.9	109.9	6.2
	1000	868.9 ± 40.3	86.9	4.6	852.9 ± 39.8	85.3	4.7
sulfuretin	2	1.9 ± 0.2	94.8	9.9	2.1 ± 0.3	106.9	15.4
	100	96.6 ± 4.1	96.6	4.2	93.6 ± 9.1	93.6	9.7
	1000	1066 ± 39.0	106.6	3.7	977.9 ± 144.9	97.8	14.8
taxifolin	2	1.8 ± 0.2	90.3	12.5	1.9 ± 0.0	97.2	1.5
	100	96.6 ± 4.1	96.6	4.3	98.0 ± 5.6	98.0	5.7
	1000	969.7 ± 100.7	97.0	10.4	974.0 ± 93.6	97.4	9.6

at 100 °C and then filtered for removal of impurities. The extract was added to 10% ethanol and 50% dextrin and concentrated through spray-drying. The final desiccated extract was used for the pharmacokinetics experiments.

Calibration and Quality Control (QC) Standards. Each analyte was dissolved in dimethyl sulfoxide at a concentration of 1 mg/mL to make a stock solution. The working standard mixture was prepared by diluting and combining each stock solution with methanol. The internal standard solution (IS; 2.5 μg/mL chrysin) was prepared in methanol. The working standard mixture (50 μL) was spiked into 450 μg/mL of blank rat plasma to prepare calibration (1, 2, 5, 10, 20, 50, 100, 200, 500, and 1000 ng/mL) and QC (2, 100, and 1000 ng/mL) standards. All standard samples were kept in a freezer (−20 °C) until they were analyzed.

Sample Preparation. Fifty microliters of plasma was added to 200 μL of phosphate-buffered saline (PBS; pH 7.2) with IS (5 μL) and 10% ascorbic acid (10 μL) and extracted with 1 mL of ethyl acetate. For β-glucuronidase-treated samples, 50 μL of plasma was added to 200 μL of PBS with β-glucuronidase (1.4 units), and it was incubated for 60 min at 55 °C. After incubation, the mixture was spiked with IS (5 μL) and 10% ascorbic acid (10 μL) and extracted with 1 mL of ethyl acetate. The organic layer was taken and evaporated to dryness. The residue was reconstituted in 70% MeOH (100 μL) and transferred to an LC vial.

LC-MS/MS Analysis. An Agilent 6460 triple-quadrupole mass spectrometer with an Agilent 1260 Infinity HPLC system (Agilent Technologies, Palo Alto, CA, USA) was used for LC-MS/MS analysis. A Poroshell 120 EC-C18 column (50 × 3.0 mm, 5 μm; Agilent) was used, and column temperature was adjusted to 40 °C. The mobile phase was composed of (A) 0.1% formic acid and (B) 90% acetonitrile with 0.1% formic acid. The flow rate was 0.25 mL/min, and gradient elution was used as follows: 10−90% B for 3 min; 90% B for 1 min; and re-equilibrium (10% B) for 4 min. Electrospray ionization was used in negative ion mode. Multiple reaction monitoring (MRM) was employed. The precursor/product ion pairs were m/z 153 → 109 for 3,4-DHBA and 2,4-DHBA; m/z 287 → 109 for fustin; m/z 303 → 285 for taxifolin; m/z 271 → 243 for garbanzol; m/z 285 → 135 for fisetin; m/z 271 → 135 for butin; m/z 269 → 133 for sulfuretin; and m/z 253 → 143 for chrysin (IS). Dwell time for each transition was set at 150 ms.

Method Validation. The analytical method validation was conducted according to the U.S. FDA guideline for bioanalytical method validation (2001).

The calibration curve was generated using eight concentration levels of calibration standards in triplicate. The intraday assay for precision and accuracy was conducted by repeated analyses (n = 5) of QC samples at three concentrations (2, 100, and 1000 ng/mL) for each analyte. The interday assay was performed by repeated analyses on five consecutive days. The precision was presented as percent coefficient of variation (%CV). The accuracy was presented as percentage recoveries to nominal concentration. Freeze-and-thaw stability was tested at three concentrations (20, 100, and 500 ng/mL). The QC samples were frozen at −20 °C for 24 h and thawed completely at room temperature. After this cycle had been repeated two times more, the samples were analyzed. The QC samples were also tested for long-term (−20 °C for 2 weeks) and short-term (room temperature for 4 h) stabilities. Postpreparative stability was tested 24 h after the prepared QC samples had been kept in an autosampler (4 °C).

Animals. Male Sprague−Dawley rats (270−300 g, 8 weeks old) were purchased from NaRa Biotech Co. (Pyungtaksi, Korea). The rats

DOI: 10.1021/acs.jafc.5b01724
J. Agric. Food Chem. 2015, 63, 5410−5416

Table 2. Stability of Eight Phenolic Compounds of RVE in Rat Plasma under Different Storage Conditions (n = 3)

compound	spiked concn (ng/mL)	short-term stability	long-term stability	freeze−thaw stability	autosampler stability
2,4-DHBA	20	100.0 ± 2.5	94.5 ± 1.0	107.4 ± 5.8	106.7 ± 6.8
	100	97.6 ± 0.9	95.6 ± 2.1	99.4 ± 6.8	90.0 ± 13.3
	500	94.8 ± 1.8	87.2 ± 0.3	99.4 ± 6.4	99.4 ± 2.3
3,4-DHBA	20	101.5 ± 1.1	87.3 ± 1.1	106.7 ± 1.5	112.7 ± 6.9
	100	101.1 ± 3.3	94.6 ± 1.3	100.0 ± 5.8	93.7 ± 13.7
	500	102.4 ± 1.6	85.0 ± 0.5	98.1 ± 5.2	102.5 ± 2.1
butin	20	98.8 ± 1.1	95.6 ± 1.0	107.5 ± 4.9	111.7 ± 1.0
	100	102.3 ± 2.6	94.6 ± 2.7	99.8 ± 6.7	96.0 ± 12.7
	500	104.6 ± 2.3	87.4 ± 0.4	101.9 ± 4.5	104.7 ± 1.1
fisetin	20	104.9 ± 4.6	101.2 ± 0.0	96.0 ± 1.8	107.5 ± 5.0
	100	97.1 ± 1.4	92.6 ± 5.1	104.9 ± 1.0	90.0 ± 1.4
	500	94.4 ± 3.8	95.7 ± 3.0	105.1 ± 1.4	88.4 ± 4.5
fustin	20	102.1 ± 2.2	93.6 ± 2.7	109.3 ± 3.2	115.1 ± 1.1
	100	101.2 ± 2.4	91.7 ± 2.8	99.3 ± 6.4	96.3 ± 11.0
	500	101.3 ± 2.2	85.4 ± 0.4	101.1 ± 3.7	103.4 ± 3.2
garbanzol	20	109.0 ± 2.8	94.8 ± 0.9	110.6 ± 2.7	116.7 ± 2.4
	100	106.4 ± 2.4	97.9 ± 2.4	102.0 ± 6.0	99.7 ± 10.1
	500	105.4 ± 1.6	86.4 ± 0.7	103.1 ± 3.7	106.5 ± 2.2
sulfuretin	20	95.0 ± 1.0	95.3 ± 2.0	106.3 ± 4.1	113.6 ± 2.7
	100	91.9 ± 1.9	95.5 ± 0.5	101.2 ± 7.2	95.3 ± 12.0
	500	97.9 ± 0.4	87.0 ± 0.4	102.7 ± 3.9	105.9 ± 1.9
taxifolin	20	87.1 ± 6.3	99.2 ± 6.4	105.0 ± 10.4	104.5 ± 2.9
	100	92.0 ± 4.3	95.8 ± 3.9	91.8 ± 7.4	85.9 ± 1.9
	500	92.6 ± 1.6	102.0 ± 2.0	94.0 ± 5.7	85.5 ± 1.8

were housed in a temperature-controlled (23 ± 2 °C) and moisture-controlled (55 ± 10%) room under a 12 h light/dark cycle and allowed access to food and water. The rats were fasted overnight and until 6 h after dosing. All animal care and experimental procedures were approved by the Institutional Animal Care and Use Committee of Hanyang University (2015-0019).

Pharmacokinetic Experiments. RVE (1.5 g/kg) in 3 mL of water was orally administered to the rats. Whole blood samples were collected by cannulating a polyethylene tube (PE-50) into the carotid artery at intervals of 1, 2, 4, 6, 8, 10, 12, and 24 h after dosing. The collected samples were centrifuged at 15000g for 5 min to obtain plasma. The plasma samples were kept frozen at −20 °C until they were analyzed.

RESULTS AND DISCUSSION

LC-MS/MS Method Development. The quantitative method for eight phenolic compounds of RVE, including fisetin, fustin, butin, sulfuretin, taxifolin, garbanzol, 2,4-DHBA, and 3,4-DHBA, was developed using LC-MS/MS. The LC-MS/MS method covering all of these phenolic compounds is not available, but there are several published papers describing the LC-MS/MS condition for each analyte.[15,27,28] Therefore, we referred to and modified those reported methods to optimize our sample preparation method and LC-MS/MS conditions for sensitive, reproducible, and rapid analysis for all analytes. Eepresentative MRM chromatograms obtained from the optimized method are displayed in Figure 2. Subsequently, the method validation was performed regarding the parameters as follows.

Specificity. The specificity of the method was evaluated by comparing MRM chromatograms of 2,4-DHBA, 3,4-DHBA, fisetin, fustin, garbanzol, taxifolin, butin, sulfuretin, and chrysin for blank plasma, plasma spiked with standards, and plasma obtained 1 h after oral administration of RVE. As shown in Figure 2, there was no interfering peak at the retention time for each analyte in blank matrix.

Matrix Effect. The postextraction method was used to evaluate the matrix effect. The test was performed at three concentrations for all analytes: 20, 100, and 500 ng/mL. The percent recovery was >90% at all concentrations for all analytes (data not shown). This indicated that the ion suppression by matrix effect was negligible in the present method.

Linearity and Lower Limit of Quantitation (LLOQ). Good linearity (R > 0.998) was observed in the calibration curves (1−1000 ng/mL) for all analytes. The back-calculated data for all concentration points except LLOQ showed acceptable accuracy (85−115%) and precision (≤15%). The LLOQ was 1 ng/mL for all analytes as the resulting data met the criteria for accuracy within 80−120% and precision of ≤20%.

Precision and Accuracy. For all QC levels, the intraday precision was <12.1% and the accuracy was 86.9−106.9%. The interday precision was <15.0% and the accuracy was 85.0−109.9% (Table 1). Thus, the intra- and interday assay results met the criteria for analytical method validation on the basis of U.S. FDA guidelines, indicating that the present method is accurate and precise.

DOI: 10.1021/acs.jafc.5b01724
J. Agric. Food Chem. 2015, 63, 5410−5416

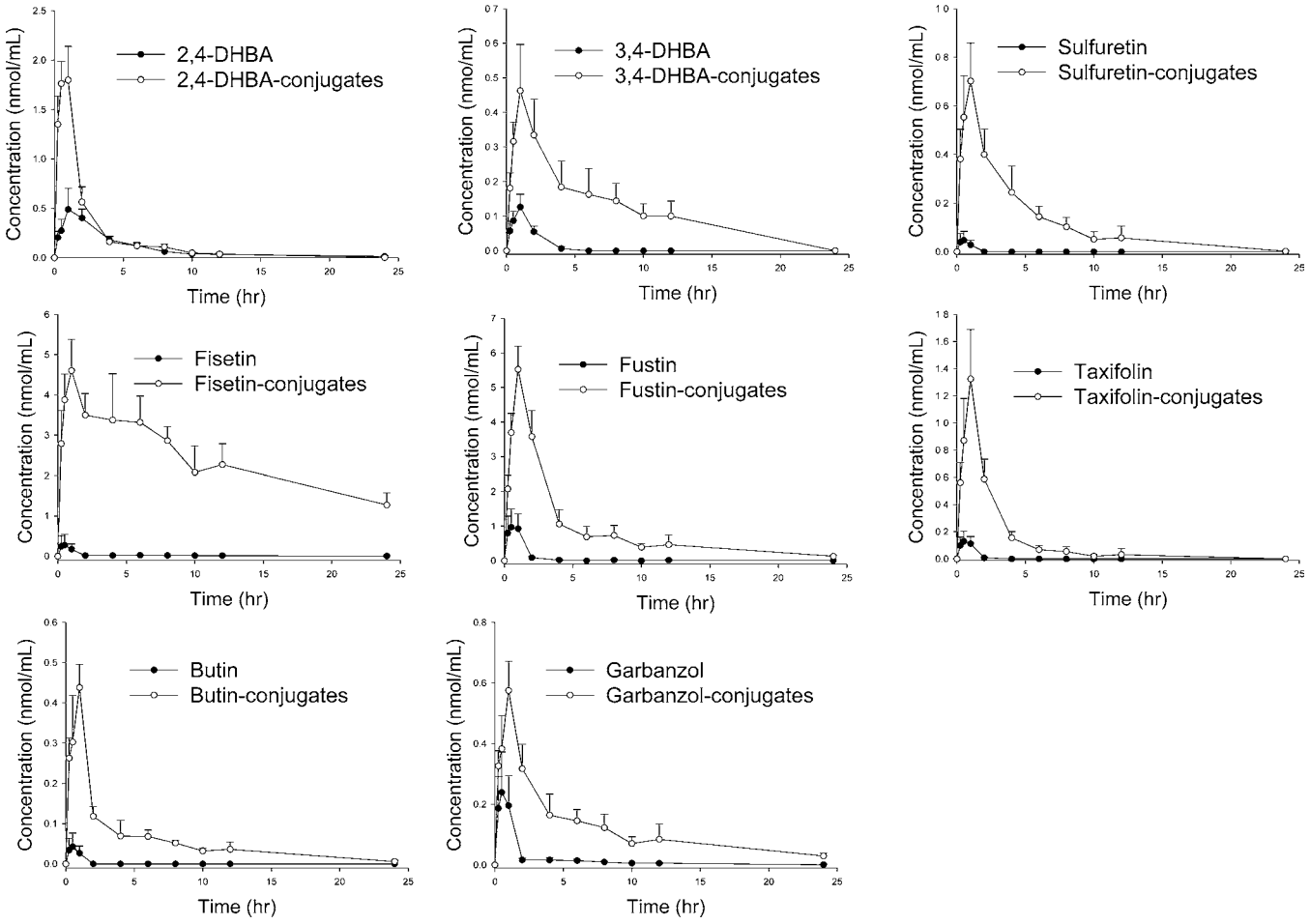

Figure 3. Plasma concentration−time profiles of eight phenolic compounds after oral administration of 1.5 g/kg *Rhus verniciflua* extracts.

Stability. The stability of the eight compounds was evaluated under various storage and process conditions (Table 2). All compounds were stable in rat plasma after three freeze/thaw cycles (91.8−110.6); at room temperature for 4 h (87.1−109.0) and at −20 °C for 2 weeks (85.0−102.0%). In addition, the processed samples were stable in the autosampler for 24 h (85.5−116.7%).

Pharmacokinetic Profile of the Phenolic Compounds and Their Conjugated Metabolites. After oral administration of RVE to rats, the plasma concentrations of the eight phenolic compounds were determined and further analyzed following β-glucuronidase treatment to obtain the plasma concentration profile of the conjugated metabolites. The plasma concentration of the conjugated metabolites was calculated by subtracting that of the free forms from the values of the β-glucuronidase-treated samples. Figure 3 shows the plasma concentration−time curves for the free and conjugated forms of each analyte. The resultant pharmacokinetic parameters are presented in Table 3.

Prior to the pharmacokinetic study, the content of each phenolic compound in RVE was measured by using the developed LC-MS/MS method. The contents of fisetin, fustin, butin, sulfuretin, taxifolin, garbanzol, 2,4-DHBA, and 3,4-DHBA were 4.048, 5.560, 0.457, 0.334, 1.077, 0.769, 0.087, and 0.101 mg/g, respectively. When RVE was orally administered, the plasma concentration level of the free forms was generally low throughout all time points, although the content of each ingredient was different. The C_{max} of the free forms ranged from 0.04 to 1.01 nmol/mL, and the AUC values were between 0.03 and 1.42 nmol·h/mL. In contrast, the plasma concentration level of the conjugated forms was higher than that of the free forms for most of the compounds. The C_{max} of the conjugated forms ranged from 0.44 to 5.53 nmol/mL, and the AUC values were between 1.38 and 57.65 nmol·h/mL. On the basis of the AUC values, the plasma levels of the conjugated forms were approximately 2−100 times greater than that of the corresponding free forms. These results indicate that the phenolic compounds circulate mainly as a conjugated form after being absorbed, which suggests that the conjugated forms might be associated with the biological activity of RVE in vivo.

The pharmacokinetics of phenolic compounds or flavonoids have been extensively investigated. According to the review paper by Manach and Donovan,[29] the pharmacological effects of flavonoids depend on their absorption from the gastrointestinal (GI) tract and subsequent metabolism, and flavonoids show different behaviors in absorption, metabolism, and clearance. Thus, the content of flavonoids in the extracts is not necessarily related to their plasma concentration (or the plasma concentration of their metabolites). In addition, flavonoids undergo extensive first-pass phase II biotransformation processes, such as sulfation, glucuronidation, or methylation, in the small intestine and liver following absorption from the GI tract. Such general pharmacokinetic properties of flavonoids were well observed in our study. In particular, our data indicated that fisetin and fustin were considered the principal bioactive molecules responsible for the pharmacological activity

DOI: 10.1021/acs.jafc.5b01724
J. Agric. Food Chem. 2015, 63, 5410−5416

Table 3. Pharmacokinetic Parameters of Eight Phenolic Compounds and Their Conjugated Metabolites in Rat Plasma

compound	C_{max} (nmol/mL)	AUC (nmol·h/mL)	t_{max} (h)	$t_{1/2}$ (h)	MRT_{0-t} (h)
2,4-DHBA	0.44 ± 0.21	1.95 ± 0.76	1.40 ± 0.55	5.90 ± 2.08	5.56 ± 1.28
2,4-DHBA conjugates	1.83 ± 0.33	4.15 ± 0.74	0.70 ± 0.27	3.52 ± 1.69	2.42 ± 0.30
3,4-DHBA	0.13 ± 0.04	0.21 ± 0.08	1.00 ± 0.00	0.79 ± 0.07	1.22 ± 0.21
3,4-DHBA conjugates	0.46 ± 0.13	3.40 ± 0.99	1.00 ± 0.00	15.37 ± 9.40	8.73 ± 0.29
butin	0.04 ± 0.03	0.03 ± 0.02	0.45 ± 0.11	NA[a]	0.54 ± 0.03
butin conjugates	0.44 ± 0.06	1.38 ± 0.23	1.00 ± 0.00	5.44 ± 1.27	4.99 ± 1.24
fisetin	0.28 ± 0.27	0.55 ± 0.27	0.45 ± 0.11	7.51 ± 2.10	5.28 ± 2.56
fisetin conjugates	4.65 ± 0.75	57.65 ± 3.92	1.60 ± 1.34	16.64 ± 5.80	9.41 ± 0.77
fustin	1.01 ± 0.51	1.42 ± 0.66	0.80 ± 0.27	1.79 ± 2.17	1.12 ± 0.35
fustin conjugates	5.53 ± 0.67	21.10 ± 3.37	1.00 ± 0.00	8.12 ± 3.47	5.09 ± 0.57
garbanzol	0.24 ± 0.13	0.41 ± 0.17	0.60 ± 0.22	5.44 ± 1.22	2.52 ± 0.47
garbanzol conjugates	0.58 ± 0.10	2.91 ± 0.59	0.58 ± 0.10	7.45 ± 2.51	6.58 ± 0.66
sulfuretin	0.05 ± 0.04	0.03 ± 0.03	0.50 ± 0.00	NA	0.54 ± 0.03
sulfuretin conjugates	0.70 ± 0.16	2.68 ± 0.36	1.00 ± 0.00	3.46 ± 1.14	3.84 ± 1.15
taxifolin	0.13 ± 0.07	0.15 ± 0.09	0.70 ± 0.27	0.37 ± 0.03	0.73 ± 0.09
taxifolin conjugates	1.32 ± 0.36	2.96 ± 0.47	1.00 ± 0.00	2.06 ± 0.74	2.25 ± 0.41

[a]NA, not available.

of RVE in terms of pharmacokinetic properties as well as chemical composition.

In conclusion, we developed and validated an accurate, reliable, and sensitive LC-MS/MS method to determine eight phenolic compounds and their conjugate metabolites in rat plasma. The developed method was applied to investigate the pharmacokinetics of the phenolic compounds of RVE and their conjugate metabolites in rat plasma. The present results provided the pharmacokinetic properties of the phenolic compounds of RVE to investigate the underlying pharmacological mechanisms of RVE.

AUTHOR INFORMATION

Corresponding Author

*(H.H.Y.) Phone: +82-31-400-5804. Fax: +82-31-400-5958. E-mail: yoohh@hanyang.ac.kr.

Funding

This research was supported by the Basic Science Research Program through the National Research Foundation of Korea funded by the Ministry of Education, Science and Technology (NRF-2014R1A1A1A05002840).

Notes

The authors declare no competing financial interest.

REFERENCES

(1) Lee, J.-C.; Lee, K.-Y.; Kim, J.; Na, C.-S.; Jung, N.-C.; Chung, G.-H.; Jang, Y.-S. Extract from *Rhus verniciflua* Stokes is capable of inhibiting the growth of human lymphoma cells. *Food Chem. Toxicol.* **2004**, *42*, 1383−1388.

(2) Hong, M. H.; Kim, J. H.; Lee, S. Y.; Go, H. Y.; Kim, J. H.; Shin, Y. C.; Kim, S. H.; Ko, S. G. Early antiallergic inflammatory effects of *Rhus verniciflua* Stokes on human mast cells. *Phytother. Res.* **2010**, *24*, 288−294.

(3) Park, D. K.; Lee, Y. G.; Park, H.-J. Extract of *Rhus verniciflua* bark suppresses 2,4-dinitrofluorobenzene-induced allergic contact dermatitis. *Evidence-Based Complement. Alternat. Med.* **2013**, *2013*, No. 879696.

(4) Lee, J.-C.; Kim, J.; Lim, K.-T.; Yang, M.-S.; Jang, Y.-S. Ethanol eluted extract of *Rhus verniciflua* Stokes showed both antioxidant and cytotoxic effects on mouse thymocytes depending on the dose and time of the treatment. *J. Biochem. Mol. Biol.* **2001**, *34*, 250−258.

(5) Kwak, E.; Jo, I.; Sung, K.; Ha, T. Effect of hot water extracts of roasted *Rhus verniciflua* Stokes on antioxidant activity and cytotoxicity. *J. Korean Soc. Food Sci. Nutr.* **2005**, *34*, 784−789.

(6) Jung, C. H.; Jun, C.-Y.; Lee, S.; Park, C.-H.; Cho, K.; Ko, S.-G. *Rhus verniciflua* Stokes extract: radical scavenging activities and protective effects on H_2O_2-induced cytotoxicity in macrophage RAW 264.7 cell lines. *Biol. Pharm. Bull.* **2006**, *29*, 1603−1607.

(7) Lee, J.-C.; Kim, J.; Jang, Y.-S. Ethanol-eluted extract of *Rhus verniciflua* Stokes inhibits cell growth and induces apoptosis in human lymphoma cells. *J. Biochem. Mol. Biol.* **2003**, *36*, 337−343.

(8) Lim, K.-T.; Hu, C.; Kitts, D. Antioxidant activity of a *Rhus verniciflua* Stokes ethanol extract. *Food Chem. Toxicol.* **2001**, *39*, 229−237.

(9) Lee, J.-C.; Lim, K.-T.; Jang, Y.-S. Identification of *Rhus verniciflua* Stokes compounds that exhibit free radical scavenging and anti-apoptotic properties. *Biochim. Biophys. Acta, Gen. Subj.* **2002**, *1570*, 181−191.

(10) Jung, C. H.; Kim, J. H.; Hong, M. H.; Seog, H. M.; Oh, S. H.; Lee, P. J.; Kim, G. J.; Kim, H. M.; Um, J. Y.; Ko, S.-G. Phenolic-rich fraction from *Rhus verniciflua* Stokes (RVS) suppress inflammatory response via NF-κB and JNK pathway in lipopolysaccharide-induced RAW 264.7 macrophages. *J. Ethnopharmacol.* **2007**, *110*, 490−497.

(11) Park, K.-Y.; Jung, G.-O.; Lee, K.-T.; Choi, J.; Choi, M.-Y.; Kim, G.-T.; Jung, H.-J.; Park, H.-J. Antimutagenic activity of flavonoids from the heartwood of *Rhus verniciflua*. *J. Ethnopharmacol.* **2004**, *90*, 73−79.

(12) Son, Y.-O.; Lee, K.-Y.; Lee, J.-C.; Jang, H.-S.; Kim, J.-G.; Jeon, Y.-M.; Jang, Y.-S. Selective antiproliferative and apoptotic effects of flavonoids purified from *Rhus verniciflua* Stokes on normal versus transformed hepatic cell lines. *Toxicol. Lett.* **2005**, *155*, 115−125.

(13) Sapkota, K.; Kim, S.; Park, S.-E.; Kim, S.-J. Detoxified extract of *Rhus verniciflua* Stokes inhibits rotenone-induced apoptosis in human dopaminergic cells, SH-SY5Y. *Cell. Mol. Neurobiol.* **2011**, *31*, 213−223.

(14) Kim, J.-S.; Yang, J.; Kim, M.-J. α-Glucosidase inhibitory effect, anti-microbial activity and UPLC analysis of *Rhus verniciflua* under various extract conditions. *J. Med. Plants Res.* **2011**, *5*, 778−783.

(15) Kim, S.-A.; Kim, S. H.; Kim, I. S.; Lee, D.; Dong, M.-S.; Na, C.-S.; Nhiem, N. X.; Yoo, H. H. Simultaneous determination of bioactive phenolic compounds in the stem extract of *Rhus verniciflua* Stokes by high performance liquid chromatography. *Food Chem.* **2013**, *141*, 3813−3819.

(16) Park, M. H.; Kim, I. S.; Kim, S.-A.; Na, C.-S.; Hong, C. Y.; Dong, M.-S.; Yoo, H. H. Inhibitory effect of *Rhus verniciflua* Stokes extract on human aromatase activity; butin is its major bioactive component. *Bioorg. Med. Chem. Lett.* **2014**, *24*, 1730−1733.

(17) Lee, J.-D.; Huh, J.-E.; Jeon, G.; Yang, H.-R.; Woo, H.-S.; Choi, D.-Y.; Park, D.-S. Flavonol-rich RVHxR from *Rhus verniciflua* Stokes and its major compound fisetin inhibits inflammation-related cytokines and angiogenic factor in rheumatoid arthritic fibroblast-like synovial cells and in vivo models. *Int. Immunopharmacol.* **2009**, *9*, 268−276.

DOI: 10.1021/acs.jafc.5b01724
J. Agric. Food Chem. 2015, 63, 5410−5416

(18) Park, B. C.; Lee, Y. S.; Park, H.-J.; Kwak, M.-K.; Yoo, B. K.; Kim, J. Y.; Kim, J.-A. Protective effects of fustin, a flavonoid from *Rhus verniciflua* Stokes, on 6-hydroxydopamine-induced neuronal cell death. *Exp. Mol. Med.* **2007**, *39*, 316−326.
(19) Zhang, R.; Chae, S.; Kang, K. A.; Piao, M. J.; Ko, D. O.; Wang, Z. H.; Park, D. B.; Park, J. W.; You, H. J.; Hyun, J. W. Protective effect of butin against hydrogen peroxide-induced apoptosis by scavenging reactive oxygen species and activating antioxidant enzymes. *Mol. Cell. Biochem.* **2008**, *318*, 33−42.
(20) McDonald, S.; Prenzler, P. D.; Antolovich, M.; Robards, K. Phenolic content and antioxidant activity of olive extracts. *Food Chem.* **2001**, *73*, 73−84.
(21) Semaming, Y.; Pannengpetch, P.; Chattipakorn, S. C.; Chattipakorn, N. Pharmacological properties of protocatechuic acid and its potential roles as complementary medicine. *Evidence-Based Complement. Alternat. Med.* **2015**, *2015*, No. 593902.
(22) Lee, D.-S.; Jeong, G.-S.; Li, B.; Park, H.; Kim, Y.-C. Anti-inflammatory effects of sulfuretin from *Rhus verniciflua* Stokes via the induction of heme oxygenase-1 expression in murine macrophages. *Int. Immunopharmacol.* **2010**, *10*, 850−858.
(23) Song, M.-Y.; Jeong, G.-S.; Kwon, K.-B.; Ka, S.-O.; Jang, H.-Y.; Park, J.-W.; Kim, Y.-C.; Park, B.-H. Sulfuretin protects against cytokine-induced β-cell damage and prevents streptozotocin-induced diabetes. *Exp. Mol. Med.* **2010**, *42*, 628−638.
(24) Song, M.-Y.; Jeong, G.-S.; Lee, H.-S.; Kwon, K.-S.; Lee, S.-M.; Park, J.-W.; Kim, Y.-C.; Park, B.-H. Sulfuretin attenuates allergic airway inflammation in mice. *Biochem. Biophys. Res. Commun.* **2010**, *400*, 83−88.
(25) Kim, I.-T.; Park, Y.-M.; Shin, K.-M.; Ha, J.; Choi, J.; Jung, H.-J.; Park, H.-J.; Lee, K.-T. Anti-inflammatory and anti-nociceptive effects of the extract from *Kalopanax pictus*, *Pueraria thunbergiana* and *Rhus verniciflua*. *J. Ethnopharmacol.* **2004**, *94*, 165−173.
(26) Sun, X.; Chen, R.-c.; Yang, Z.-h.; Sun, G.-b.; Wang, M.; Ma, X.-j.; Yang, L.-j.; Sun, X.-b. Taxifolin prevents diabetic cardiomyopathy in vivo and in vitro by inhibition of oxidative stress and cell apoptosis. *Food Chem. Toxicol.* **2014**, *63*, 221−232.
(27) Brinda, B. J.; Zhu, H.-J.; Markowitz, J. S. A sensitive LC−MS/MS assay for the simultaneous analysis of the major active components of silymarin in human plasma. *J. Chromatogr. B: Anal. Technol. Biomed. Life Sci.* **2012**, *902*, 1−9.
(28) Matei, A. O.; Gatea, F.; Radu, G. L. Analysis of phenolic compounds in some medicinal herbs by LC−MS. *J. Chromatogr. Sci.* **2015**, bmu177.
(29) Manach, C.; Donovan, J. L. Pharmacokinetics and metabolism of dietary flavonoids in humans. *Free Radical Res.* **2004**, *38* (8), 771−785.

DOI: 10.1021/acs.jafc.5b01724
J. Agric. Food Chem. 2015, 63, 5410−5416

JOURNAL OF AGRICULTURAL AND FOOD CHEMISTRY

Article

pubs.acs.org/JAFC

Identification of Ellagitannins and Flavonoids from *Eugenia brasilienses* Lam. (Grumixama) by HPLC-ESI-MS/MS

Luciane de Lira Teixeira,[†,‡,#] Fabiano Cleber Bertoldi,[§] Franco Maria Lajolo,[†,‡,#] and Neuza Mariko Aymoto Hassimotto*[,†,‡,#]

[†]Laboratory of Food Chemistry and Biochemistry, Department of Food Science and Experimental Nutrition, FCF, [‡]Food and Nutrition Research Center (NAPAN), FCF, and [#]Food Research Center (FoRC-CEPID), University of São Paulo, Av. Prof Lineu Prestes 580, Bloco 14, 05508-900 São Paulo, SP, Brazil

[§]Laboratory of Pharmacognosy, Experimental Station of Itajai, Empresa de Pesquisa Agropecuária e Extensão Rural de Santa Catarina (Epagri), Rod. Antonio Heil, 6800, 88318-112 Itajaí, SC, Brazil

Supporting Information

ABSTRACT: The grumixama (*Eugenia brasiliensis* Lam.), also known as Brazilian cherry, is a fruit native to Brazil. This study identified the flavonoids in the flesh and seeds and ellagitannin in the flesh of purple and yellow varieties. The physicochemical characteristics and antioxidant capacity of these fruits were also evaluated. Anthocyanins and flavonols were found in high levels in the flesh of purple (32−180 mg 100 g^{-1} FW) and yellow grumixama (13−41 mg 100 g^{-1} FW), respectively. The major flavonoids identified were cyanidin 3-glucoside and quercetin aglycone. Furthermore, ellagitannins were found in high levels in the flesh of purple (82−243 mg ellagic acid equiv 100 g^{-1} FW) and yellow grumixama (92 mg ellagic acid equiv 100 g^{-1} FW) and seeds (2220−2905 mg ellagic acid equiv 100 g^{-1} FW). The ellagitannin profiles of both varieties were first characterized in which pedunculagin isomers, strictinin isomers, and ellagic acid galloyl hexoside were the major ellagitannins identified. In summary, both varieties of the grumixama fruit as well as the seeds could be good sources of bioactive compounds, mainly ellagitannins.

KEYWORDS: *ellagitannins, anthocyanins, grumixama, bioactive compounds*

INTRODUCTION

The grumixama (*Eugenia brasilienses* Lam.) belongs to the Myrtaceae family and is a native fruit of the southern and southeastern regions of the Atlantic Forest of Brazil. It is a fruit similar to a cherry, approximately 2.0 cm in diameter, containing one or many seeds, and is somewhat sweet. Three varieties were recognized by Cambessèdes (1832−1833) according to their fruit colors: The α-variety or purple fruit is the most common and is known as the Brazilian cherry.[1,2] The β-variety has red fruit, and the γ-variety has white fruit, although it was also described by Mattos (1984) as being yellow.[2] Despite belonging to the same species, the yellow and purple varieties show distinct chemotypes with respect to the terpene profiles in the leaves and fruits.[2] Grumixama is rarely consumed as a fresh fruit, but is commonly used to produce fruit juice and frozen pulp, with the pulp frequently containing a mixture of the purple and yellow forms. Although still limited, commercial cultivation has begun in recent years, and this plant represents economic potential due to the attractive sensory attributes and phenolic compounds in its composition, including ellagitannins and flavonoids.[1,4]

In general, fruits belonging to this family are known to be good sources of bioactive compounds.[3−5]The purple grumixama fruit was shown to be rich in anthocyanins, mainly cyanidin-3-glucoside, and carotenoids, mainly monohydroxy carotenoids such as *all-trans*-β-cryptoxanthin.[1,6] High antioxidant capacity[3] and anti-inflammatory activity[1] have been demonstrated. However, no information about phenolic composition, the antioxidant capacity, or other biological activities of the yellow fruit was previously available.

The leaves of grumixama have been used in folk medicine for the treatment of several diseases including arthritis, diabetes, and rheumatism and have showed antidepressant-like[7] and anti-inflammatory activities,[8] which are attributed to their phenolic compounds.

As a member of the Myrtaceae family, in addition to the flavonoids, grumixama would also be expected to be rich in ellagitannins and ellagic acid derivates, another class of phenolic compounds. This class of phenolics is relatively uncommon in dietary fruits and vegetables, although a few berries, such as strawberry, raspberry, blackberry, and pomegranate, have substantial contents of these compounds.[9−11] It has been suggested that ellagitannins as well as flavonoids may prevent chronic diseases such as cancer and cardiovascular diseases. These protective activities are attributed to both classes of phytochemicals, which are thought to provide antiproliferative,[12] anti-inflammatory, and antioxidant activities[11,14−16] and to function as glycemic regulators.[12,13,17]

Therefore, given the importance of bioactive compounds in the promotion of health, the aim of this study was to conduct a systematic analysis of the phenolic compounds, specifically the

Received: October 14, 2014
Revised: May 19, 2015
Accepted: May 20, 2015
Published: May 20, 2015

ACS Publications © 2015 American Chemical Society

DOI: 10.1021/acs.jafc.5b01195
J. Agric. Food Chem. 2015, 63, 5417−5427

ellagitannins and flavonoids, in the purple and yellow grumixama fruits and the seeds of these plants.

MATERIALS AND METHODS

Chemicals. Fluorescein, 2,2′-azobis(2-methyl-propanimidamide) dihydrochloride (AAPH), 2,2-diphenylpicrylhydrazyl (DPPH), trifluoroacetic acid, ytterbium acetate, sucrose, glucose, fructose, catechin, epicatechin, epigallocatechin gallate, gallocatechin gallate, epicatechin gallate, quercetin, gallic acid, ellagic acid, and proanthocyanidin B1 and proanthocyanidin B2 were purchased from Sigma-Aldrich (St. Louis, MO, USA). Quercetin 3-glucoside, myricetin, cyanidin-3-glucoside, cyanidin, and delphinidin were purchased from Extrasynthese (Genay, France). Methanol and acetic acid were purchased from Merck Millipore (Darmstadt, Germany). All other chemicals used were of analytical or HPLC grade.

Plant Materials. The fruits of the yellow and purple grumixama were collected in the southeastern and southern regions of Brazil. Twelve kilograms of purple grumixama was acquired by local producers in the Vale do Paraiba (Sítio do Bello farm) located in São Paulo state, and 4 kg of grumixama was provided by Epagri-Itajaí located in Santa Catarina state. Both samplings were collected in December 2012 and January 2013. Yellow grumixama (4 kg) was acquired by Sitio do Bello farm in December 2012. The fruits of the purple and yellow grumixama were separated into flesh (F) and seed (S) and named F1 and F2 (from São Paulo state), F3 and F4 (from Santa Catarina state), and S1, S2, S3, and S4, respectively. The samples designated F5 and S5 corresponded to the yellow variety. All fruits were harvest at ripening stage and stored at −70 °C until analysis. Samples were thoroughly homogenized by powdering in liquid nitrogen to perform the analysis.

Physicochemical Analyses. The analysis of the protein content was performed according to the Kjedahl method, using the nitrogen conversion factor of 5.75 for vegetable proteins (AOAC, no. 950.48).[18,19] The moisture and lipid contents were analyzed according to the methods described by AOAC (AOAC, no. 925.40 and 948.22, respectively).[18,19] The fiber content was measured according to the method described by AOAC (no. 985.29).[18,19] The soluble solids (°Brix) were determined using a hand-held refractometer (AOAC, no. 932.12).[20]

Soluble Sugars Content. The samples were extracted with 80% ethanol (v/v) at 80 °C for 30 min under stirring. The soluble sugars were analyzed by high-performance liquid chromatography (HPLC) coupled to a pulse amperometric detector (PAD) using a one-Dionex DX500 system (Dionex, Thermo Scientific, Waltham, MA, USA), equipped with a CarboPac PA1 column (4 mm × 250 mm) (Dionex), using a mobile phase consisting of 18 mM NaOH, at a flow rate of 1 mL min^{-1} for 25 min. The quantification was based on an external calibration using sucrose, glucose, and fructose.[21]

Total Phenolic Content, Monomeric Anthocyanins, and Antioxidant Capacity. Three replicate samples (0.5 g) were extracted with 70% methanol containing 5% acetic acid (25 mL) using an ultraturrax (Polytron Kinematica GnbH, Kriens-Luzern, Switzerland), followed by 30 min of stirring at 5 °C and then filtration. These extracts were used to assess total phenolic content, monomeric anthocyanin content, and antioxidant capacity. The assays were carried out in triplicate. The total phenolic content was measured using the Folin−Ciocalteu method, and the absorbance was measured at 763 nm.[22] The results were expressed as gallic acid equivalents per 100 g of sample. The monomeric anthocyanin content was determined using the pH differential method.[23] The monomeric anthocyanin pigment concentration was calculated using the molar absorptivity of cyanidin 3-glucoside (ε = 26900) and expressed as milligrams of cyanidin 3-glucoside equivalents per 100 g of sample. The antioxidant capacity was analyzed using the DPPH[24] and oxygen radical absorbance capacity (ORAC) methods[25] and expressed as millimoles of trolox equivalents per 100 g of sample. All results were expressed as fresh weight.

Ellagitannin Content. The samples were extracted with 80% acetone and dried under nitrogen. An aliquot of the extract was added to 2 M trifluoroacetic acid and hydrolyzed at 120 °C for 120 min, according to the method of Giner-Chávez et al. with a slight modification.[26,27] The hydrolyzed samples were evaporated to dryness under nitrogen, redissolved in methanol, and filtered through a 0.43 μm PTFE filter (Millipore Ltd., Bedford, MA, USA) for HPLC-DAD analysis as described for the phenolic compounds. Ellagic acid (EA) was used to construct the calibration curve, and the results were expressed as milligrams of total EA equivalents per 100 g of sample.

Identification and Quantification of Phenolic Compounds. The samples were extracted with 70% methanol, acidified with 5% acetic acid, using an ultraturrax (Polytron Kinematica GnbH), and filtered. The extract was then concentrated by removal of the methanol under vacuum at 40 °C on a rotary evaporator (Rotavapor RE 120; Buchi, Flawil, Switzerland) prior to application to a solid-phase extraction column. The extract was passed through a polyamide column (1 g) (CC 6, Macherey-Nagel Gmbh and Co., Duren, Germany) previously conditioned with methanol and ultrapure water. The sample was loaded onto the column and washed with ultrapure water. The phenolic compounds were eluted with 0.3% HCl in methanol. The eluates were completely dried using a rotary evaporator under vacuum at 40 °C, resuspended in methanol, and filtered through a 0.45 μm PTFE filter (Millipore Ltd.) for the quantification of flavonoids and phenolic acids by HPLC-DAD analysis.[28]

Analysis of Phenolic Compounds by Reversed-Phase HPLC-DAD. Identification and quantification of the phenolic compounds was performed using a 1260 Infinity Quaternary LC System (Agilent Technologies, USA), with an autosampler and a quaternary pump, coupled to a diode array detector (DAD). The column used was a 5 μm Prodigy ODS3 column (4.60 × 250 mm) (Phenomenex Ltd., UK) with a flow rate of 1 mL/min at 25 °C. The mobile phase consisted of two solvents: solvent A, 0.5% formic acid in water, and solvent B, 0.5% formic acid in acetonitrile. The solvent gradient was applied as follows: 10% B at the beginning, 10% at 5 min, 20% at 15 min, 25% at 25 min, 35% at 33 min, 50% at 38 min, 90% at 43−44 min, and 10% at 45 min. Anthocyanins were detected by monitoring the elution at 525 nm, and other flavonoids were monitored at 270 nm. The phenolic compounds were identified by comparing their retention times, diode array spectral characteristics, and mass spectra, measured using LC-ESI-MS/MS, with the standards and the data available in the literature. The calibration was performed using commercial standards.[28]

Identification of Ellagitannins. Approximately 5 g of sample was extracted with 80% acetone and evaporated to eliminate the acetone. An aliquot of 0.1 M ytterbium acetate was added to the aqueous extract and held overnight at 5 °C. The precipitate (ET-Yb) was centrifuged at 3000*g* for 10 min at 5 °C. The precipitate was washed three times, twice with 80% acetone and once with pure acetone. The precipitate was subsequently dissolved in 10 mM oxalic acid, and the supernatant was dried under nitrogen, resuspended in methanol and filtered using 0.43 μm PTFE membrane filters (Millipore Ltd.) for LC-ESI-MS/MS analysis.[29]

LC-ESI-MS/MS Analysis. The identification of the flavonoids and ellagitannins was performed by LC-ESI-MS/MS using a Prominence liquid chromatograph (Shimadzu, Japan) linked to an ion trap Esquires-LC mass spectrometer (Bruker Daltonics, Billerica, MA, USA) with an electrospray ionization (ESI) interface. The solvent gradient conditions were the same as those used for the HPLC-DAD process. After passing through the DAD, the flow rate was changed to 0.2 mL/min for application to the mass spectrometer. The ESI was used in the positive mode to detect the anthocyanins and in the negative mode for the other classes of flavonoids. The mass spectrometer operating conditions were as follows: collision energies of 4500 and 4000 V were used for the positive and negative mode, respectively, and the capillary temperature was 275 °C. The analysis was carried out using a full scan from m/z 100 to 1500. The compounds were identified according to comparison with the retention times of authentic standards when possible, as well as by absorption spectrum similarity, mass spectral characteristics, and comparison with literature data.[28]

Identification and Quantification of Proanthocyanidin. The freeze-dried samples (0.8 g) were homogeneized with extraction

DOI: 10.1021/acs.jafc.5b01195
J. Agric. Food Chem. 2015, 63, 5417−5427

Table 1. Chemical Composition of the Flesh of *Eugenia brasiliensis* Lam., Purple and Yellow Fruits[a]

	F1	F2	F3	F4	F5
moisture	84.80 (0.18)	88.29 (0.50)	87.60 (0.07)	83.67 (0.33)	85.21 (0.21)
total soluble sugar	2.98 (0.10)	2.69 (0.06)	3.53 (0.22)	2.61 (0.10)	2.97 (0.07)
glucose	2.85 (0.10)	2.55 (0.06)	3.38 (0.23)	2.26 (0.11)	2.84 (0.10)
frutose	0.13 (0.00)	0.12 (0.00)	0.12 (0.00)	0.11 (0.00)	0.12 (0.00)
sucrose	ND	Tr	Tr	0.02 (0.00)	ND
lipid	0.26 (0.01)	0.22 (0.00)	0.16 (0.00)	0.18 (0.01)	0.22 (0.00)
protein[b]	0.66 (0.01)	0.50 (0.00)	0.54 (0.01)	0.61 (0.01)	0.56 (0.02)
total fiber	4.65 (0.24)	3.11 (0.11)	3.10 (0.08)	4.18 (0.10)	3.08 (0.12)
insoluble fiber	1.70 (0.16)	1.07 (0.03)	1.49 (0.08)	2.04 (0.10)	1.45 (0.07)
soluble fiber	2.95 (0.10)	2.04 (0.10)	1.53 (0.03)	2.15 (0.10)	1.75 (0.04)
ash	0.56 (0.01)	0.44 (0.00)	0.31 (0.02)	0.61 (0.01)	0.56 (0.01)
°Brix	1.35 (0.00)	1.35 (0.00)	1.35 (0.00)	1.35 (0.00)	1.35 (0.00)

[a]Results are expressed as g/100 g. ND, not detected; Tr, trace. Values shown are the means (standard deviation). Purple fruit was designated F1, F2, F3, and F4; yellow fruit was designated F5; F1, F2, and F5, from São Paulo state; F3 and F4, from Santa Catarina state. [b]Correction factor for vegetable proteins: 5.75.

solution (acetone/water/acetic acid, 70:29.5:0.5, v/v/v) using an Ultraturrax followed by sonication in an ultrasonic bath for 15 min. The homogenates were centrifuged at 2000*g* for 10 min. The acetone was evaporated under reduced pressure at 35 °C and passed through a Sep-Pack C-18 solid phase extraction cartridge (Waters, Milford, MA, USA) and washed with Milli-Q water. The phenolic compounds were eluted with methanol. The eluates were completely dried using a rotary evaporator under vacuum at 40 °C, resuspended in methanol, and filtered through a 0.45 μm PTFE filter (Millipore Ltd.) for the quantification of proanthocyanidins by HPLC-DAD analysis. For strawberry proanthocyanidin analysis (cv. Camarosa), used to compare proanthocyanidin profile, the same protocols was applied.

Normal Phase HPLC-DAD of Proanthocyanidin Extract. The analysis was carried out as reported previously.[30] The same HPLC equipment described above was used. The column used was a Develosil Diol (4.60 × 250 mm, 5 μm) (Phenomenex Ltd., UK) with a flow rate of 1 mL/min at 25 °C. The mobile phase consisted of two solvents: solvent A, CH_3CN/HOAc (98:2, v/v), and solvent B, CH_3OH/H_2O/HOAc, 95:3:2, v/v/v). The solvent gradient was applied as follows: 0% B at the beginning, 40% at 35 min, and 40% at 45 min. UV detection was set at 280 nm, and fluorescence detection used excitation at 276 nm and emission at 316 nm. The calibration was performed using commercial standards of proanthocyanidin B1 and proanthocyanidin B2.

Statistical Analysis. The results were expressed as the mean values ± standard deviation. Analysis of variance (ANOVA) followed by the Tukey test was performed using Biostat 5.0.

RESULTS AND DISCUSSION

Chemical Composition. Table 1 shows the chemical composition for the flesh of purple grumixama, collected in two different places and times (F1, F2, F3 and F4), and a single sample of the flesh of the rarer yellow variety (F5). According to the °Brix values, all fruits analyzed were at the same ripening stage, but there were slight differences but not significant in the chemical composition among the fruits harvested at different times and places. Glucose was the main sugar found in these fruits, which is compatible with the results for a ripe berry fruit, due to the hydrolysis of sucrose during ripening.[31,32]

Soluble Total Phenolic and Monomeric Anthocyanin Contents and Antioxidant Capacity. Figure 1A shows the results for the soluble total phenolic and monomeric anthocyanin contents for the flesh and seeds. All seeds of purple grumixama, collected in different places and times, presented higher content of total phenolic content (varying from 2.51 ± 0.09 to 3.3 ± 0.12 g 100 g^{-1} fresh weight, FW) than the respective flesh (varying from 0.18 ± 0.01 to 0.75 ± 0.02 g 100 g^{-1} FW). Among the flesh samples, F1 and F4 showed the highest total phenolic, values similar to those found in Brazilian blackberry cultivars (from 0.34 ± 0.01 to 0.50 ± 0.01 g 100 g^{-1} FW).[32] The flesh of purple grumixama contained high contents of the monomeric anthocyanin, varying from 30 to 200 mg 100 g^{-1} FW, where F1 and F4 presented values similar to those founded in Brazilian blackberry cultivar Guarani (*Rubus* sp.) (190 mg 100 g^{-1} FW).[33] Differences in flavonoids and phenolic contents were observed in several vegetables and could be due to agronomic conditions, plant tissue, and varieties. Anthocyanins were not detected in the yellow fruit or in its seeds. The yellow fruit presented the lowest total phenolic content (0.18 ± 0.01 g/100 g FW); however, there was no difference in the phenolic content in the seeds of the two varieties. These results indicate

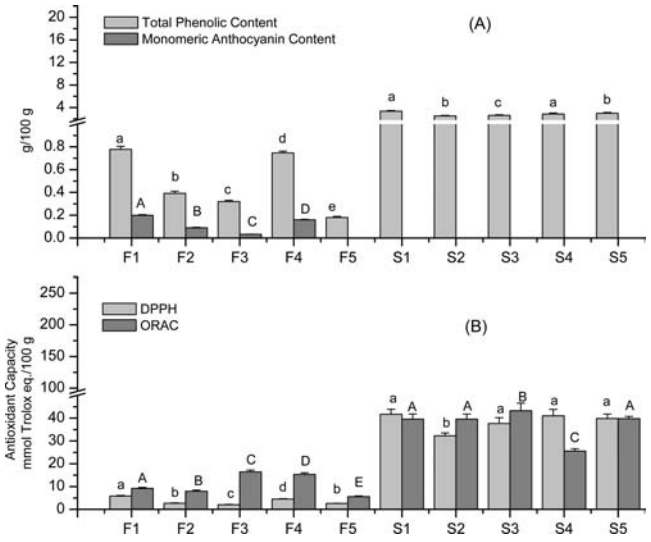

Figure 1. Total phenolic and monomeric anthocyanin contents (A) and antioxidant capacity (B) analyzed by DPPH and ORAC methods for the flesh (F1, F2, F3, F4, and F5) and seeds (S1, S2, S3, S4, and S5) of *Eugenia brasilienses* Lam., purple and yellow fruits. The monomeric anthocyanin and total phenolic contents are expressed as cyanidin-3-glucoside and gallic acid equivalents, respectively. The values are expressed as fresh weight for the flesh. The statistical analyses were performed among the different parts of grumixama. The same letters indicate nonsignificant differences among the samples ($p < 0.05$).

DOI: 10.1021/acs.jafc.5b01195
J. Agric. Food Chem. 2015, 63, 5417−5427

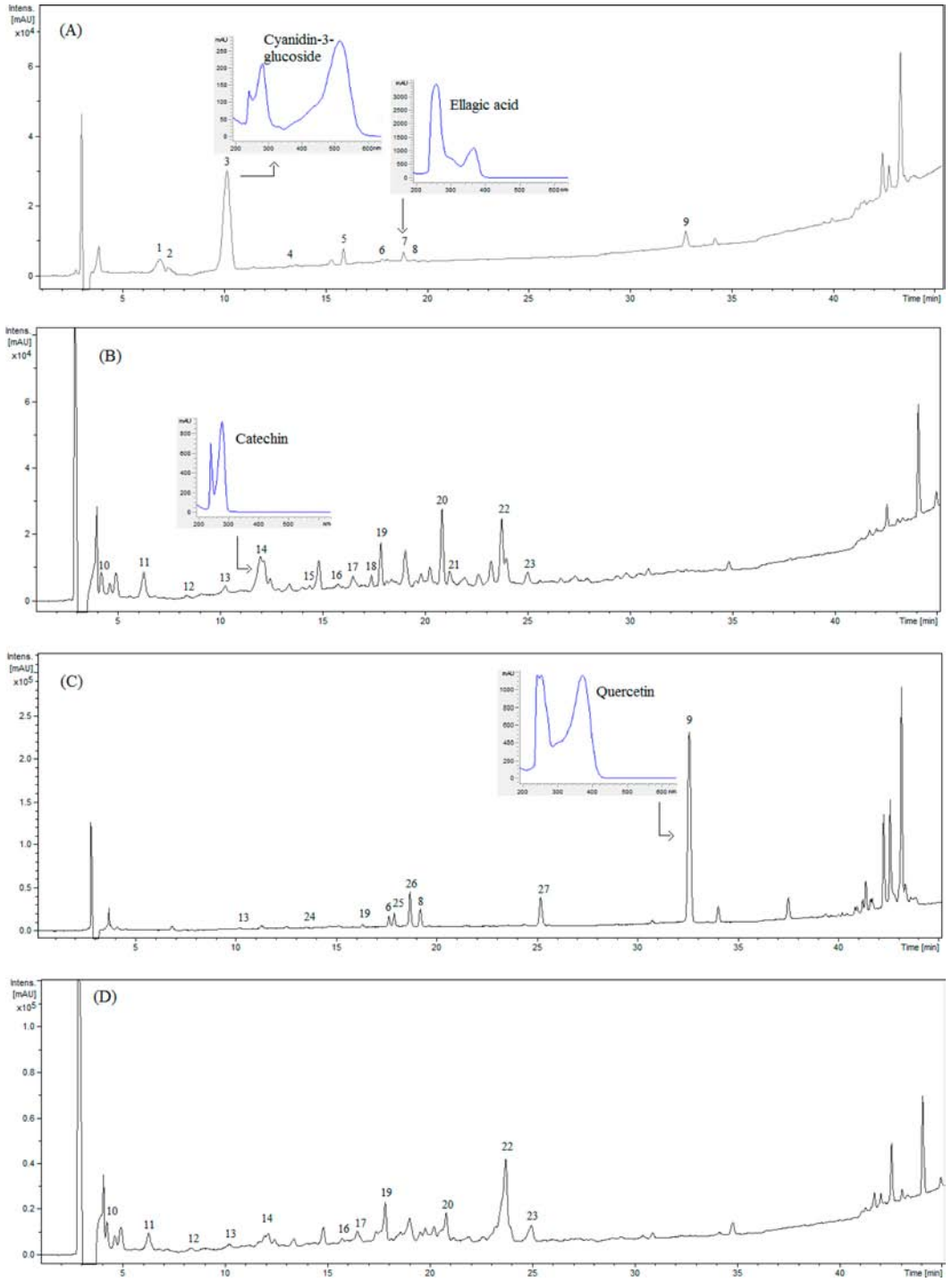

Figure 2. Chromatograms obtained by HPLC-DAD (λ = 270 nm) of the purple (A) and yellow (C) flesh, seeds of purple grumixama (B), and seeds of yellow grumixama (D). The identification of the peaks is given in Table 2.

that the place and time of fruit harvesting do not influence the phenolic or anthocyanin contents of grumixama.

Figure 1B shows the antioxidant capacity evaluated by the DPPH and ORAC methods. The flesh showed the lowest antioxidant capacity values by both methods. No significant differences ($p < 0.05$) with respect to the place or harvest period were observed among the fruits or seeds. Due to their structure, phenolic compounds possess high antioxidant capacities, and these compounds represent one of the main phytochemical classes responsible for the total antioxidant capacity of plant-derived food.[16] Thus, a high correlation (Pearson correlation) was observed between the total phenolic content and the DPPH values (r = 0.93) as well as the ORAC (r = 0.87) values. There was also a strong correlation between the content of monomeric anthocyanins and total phenolic compounds (r = 0.97), suggesting an influence of the phenolic compounds in the antioxidant capacity. In addition, ascorbic acid, an important hydrophilic antioxidant present in fruits, was not detected in the flesh of either the purple or yellow variety.

Identification of Flavonoids and Phenolic Acids. Figure 2 shows the HPLC-DAD chromatograms of the flesh of the purple and yellow grumixama fruits (A and C, respectively) and

DOI: 10.1021/acs.jafc.5b01195
J. Agric. Food Chem. 2015, 63, 5417−5427

Table 2. Phenolic Compounds Identified in the Flesh and Seed of Yellow and Purple Grumixama by HPLC-ESI-MS/MS

compound identified (positive mode)	RT[a] (min)	$[M]^+$ (m/z)	MS/MS (m/z)	peak[b]	purple fruit (%)[c]	yellow fruit (%)[c]	purple seed (%)[c]	yellow seed (%)[c]
anthocyanins								
delphinidin hexoside	6.4	465	303; 229	1	25			
cyanidin 3-galactoside	7.1	449	287; 213	2	6			
cyanidin 3-glycoside[d]	10.0	449	287; 213	3	50			
cyanidin 3-xyloside/ arabinoside	13.4	419	287; 213	4	Tr[e]			
cyanidin aglycone[d]	15.8	287	213	5	2			
compound identified (negative mode)	RT[a] (min)	$[M - H]^-$ (m/z)	MS/MS (m/z)	peak[b]	purple flesh (%)[c]	yellow flesh (%)[c]	purple seed (%)[c]	yellow seed (%)[c]
flavanols								
gallocatechin dimeric ion	6.2	611	305/220	11			11	11
catechin/dimeric ion[d]	12.0	289/579	245/203	14		2	14	14
gallocatechin gallate	14.2	457	305	15			4	
epigallocatechin gallate[d]	15.6	457	305/331/169	16			2	3
(−)-epicatechin gallate[d]	21.2	442	289/245/169	21			3	
epicatechin[d]	13.5	289	245/203	24		3		
proanthocyanidins								
(epi)catechin(epi)catechin	9.2	577	407/289	13			2	2
phenolic acids/derivatives								
free ellagic acid[d]	18.8	301	301	7	5			
ellagic acid dipentoside	17.4	594/593	447/301	18			2	
ellagic acid hexosides	20.7	927	463/301/257	20			24	23
ellagic acetyl rhaminoside/ dimeric ion	23.7	978/489	489/301/257	22			6	11
ellagic acetyl rhaminoside	25.0	489	301	23			7	9
ellagic acid pentoside	17.7	895	447/301	25		14		
ellagic acid derivative	18.7	491	301/257	26		3		
flavonols								
quercetin 3-glucoside[d]	19.2	463	301/151	8	Tr	21		
quercetin aglycone/dimeric ion[d]	32.4	301/603	301/151	9	9	44		
myricetin galloyl hexoside	16.4	633/631	479/316	17			1	1
myricetin hexoside dimeric ion	17.8	959	479/316	19		1	6	8
myricetin aglycone[d]	25.4	317	317/151	27		7		

[a]RT, retention time. [b]Peaks are numbered according to Figure 2A (flesh of the purple grumixama), Figure 2C (flesh of the yellow grumixama), Figure 2B (seeds of the purple grumixama), and Figure 2D (seeds of the yellow grumixama). [c]Percentage was calculated from the total area of the chromatograms at 525 nm for anthocyanins and 270 nm for the other compounds. [d]Compounds were identified by comparison with retention time of standards and mass fragment profile and UV−vis absorption spectra. [e]Tr, traces, <0.01.

seeds (B and D, respectively), and the respective identification of the compounds by LC-ESI-MS/MS is shown in Table 2.

Fruits. Eight compounds were identified in the flesh of each of the two varieties, the purple and yellow grumixama. In the flesh of the purple fruit, two classes of flavonoids (five anthocyanins and two flavonols) and one phenolic acid were identified. In the flesh of the yellow fruit, two classes of flavonoids (four flavonols and two flavanols) and two ellagic acid derivatives were detected. Among these, two flavonoids were common to both fruits (peak 8, quercetin 3-glucoside at m/z 463, and peak 9, quercetin aglycone at m/z 301). As expected, anthocyanins were detected only in purple grumixama. Specifically, this fruit contained two anthocyanidins, cyanidin and delphinidin, with characteristic molecular ions at m/z 287 and 303, respectively. Peaks 6 (at m/z 615), 10, and 12 (at m/z 633) were identified as ellagitannins, and their identification is further discussed below.

The major class of compounds present in the purple grumixama fruit was anthocyanins (82% of total identified compounds), whereas the yellow fruit was dominated by flavonols (74% of total identified compounds). The major anthocyanins present in the purple grumixama were delphinidin hexoside (peak 1, at m/z 465) and cyanidin-3-glucoside (peak 3, at m/z 449), which were responsible for 30 and 61% of total anthocyanins, respectively. In the yellow grumixama, the major flavonols present were quercetin 3-glucoside (peak 8, at m/z 463) and quercetin aglycone (peak 9, at m/z 301), which were responsible for 25 and 53% of total flavonols, respectively.

Peak 1 had a molecular ion at m/z 465 and two MS/MS fragments at m/z 303 $[M - 162]^+$ and at m/z 229, suggesting that this peak represents a delphinidin linked to a hexoside, where the loss of 162 corresponds to a hexose unit. This compound was probably delphinidin-3-glucoside, also identified in purple grumixama.[6] Peaks 2 and 3 had the same molecular ion at m/z 449 and mass fragments at m/z 287 $[M - 162]^+$ and at m/z 213. Peak 3 was identified as cyanidin 3-glucoside, and its identity was confirmed by coelution with the commercial standard. Thus, considering the elution order in relation to cyanidin 3-glucoside, which was consistent with that expected from the reversed phase elution, peak 2 could be cyanidin 3-galactoside, also identified in the purple grumixama.[1,6]

DOI: 10.1021/acs.jafc.5b01195
J. Agric. Food Chem. 2015, 63, 5417−5427

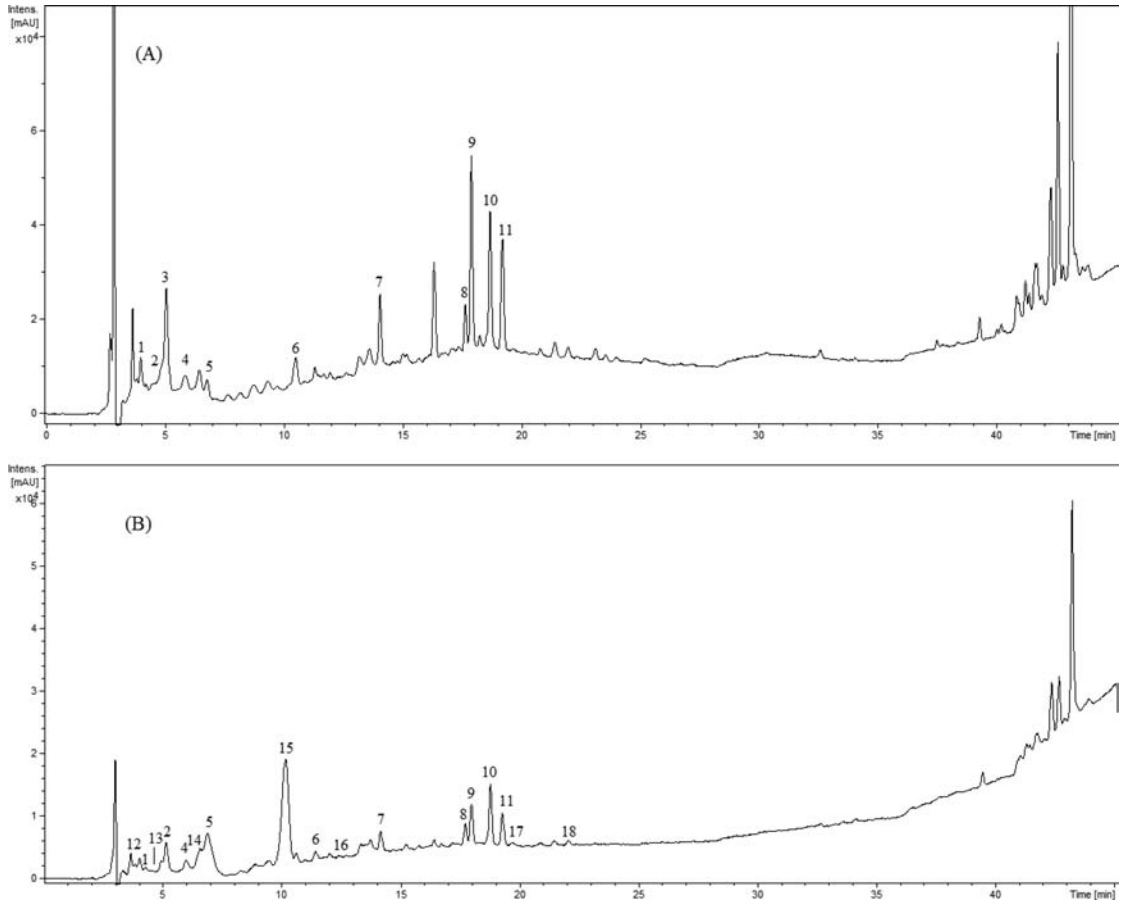

Figure 3. Chromatograms of the ellagitannins extracted using ytterbium acetate obtained by HPLC-DAD (λ = 270 nm) of the flesh of the yellow (A) and purple grumixama (C). The identification of the peaks is given in Table 3.

Peak 4 had a molecular ion at m/z 419 and an MS/MS fragment at m/z 287 $[M - 132]^+$, suggesting that it corresponded to a cyanidin linked to a pentoside: either a xyloside or arabinoside unity.[1] The identity of peak 5 was confirmed by coelution with standard as cyanidin (m/z 287). Peak 7 showed absorption spectra similar to ellagic acid, and its identity was confirmed as ellagic acid (m/z 301) by coelution with commercial standard. Peak 8, identified as quercetin 3-glucoside, had a molecular ion at m/z 463 and one mass fragment at m/z 301, corresponding to quercetin after the loss of a hexose unit (−162 from $[M - H]^-$), and a second fragment at m/z 151. Peak 9, with a molecular ion at m/z 301 and MS/MS fragment at m/z 151, was identified as quercetin aglycone. Quercetin and ellagic acid demonstrated the same characteristic molecular ion at m/z 301. However, on MS/MS analysis, quercetin forms characteristic mass fragments at m/z 179 and 151, whereas the fragments from ellagic acid were observed at m/z 257 and at m/z 229.[34]

In the yellow variety, two flavonols and two flavanols were identified. Peak 27 had a molecular ion at m/z 317, characteristic of myricetin. Peak 19, identified as myricetin hexoside dimeric ion, had a molecular ion at m/z 959 and MS/MS fragments at m/z 479 and at m/z 317 ($[M - H]^- - 162$, corresponding to the loss of a hexose unit).[5,34] Peak 14 showed molecular ions at m/z 579 and at m/z 289 and an MS/MS fragment at m/z 289 ($[M - H]^- - 290$), which suggested it was a catechin dimeric ion. In addition, this compound showed another fragment at m/z 245 (neutral loss of CO_2, 44, from the catechin).[34] A dimeric ion is an ion that is formed by the ionization of a dimer or by the association of an ion with its neutral counterpart such as $[M2]^{\bullet -}$ or $[M - H - M]^-$.[35] Peak 24 had the same molecular ion at m/z 289, characteristic of a catechin isomer, and two mass fragments at m/z 245 and at m/z 203. Peaks 14 and 24 were identified as catechin and epicatechin, respectively, and their identities were confirmed by coelution with the corresponding standards.

The identities of the flavonoids cyanidin-3-glucoside, cyanidin aglycone, quercetin 3-glucoside, quercetin aglycone, and myricetin aglycone, and free ellagic acid were confirmed by coelution with standards and the similarities of the UV−vis absorption spectra and the mass spectral characteristics to those of the standards.

Flavonoids are rarely present in plants as aglycones. Instead, they are usually linked to various sugars.[36,37] It is interesting to observe that high concentrations of the aglycone forms of cyanidin and quercetin were detected in the purple grumixama, and aglycone forms of quercetin and myricetin were detected in the yellow variety of these fruits. No aglycone forms were released when isolated cyanidin-3-glucoside, quercetin-3-glucoside, and quercetin-3-rutinoside were tested in the protocol extraction, excluding the possibility that they were artifacts.

Flores et al.[1] identified nine anthocyanins, of which five were found in the purple grumixama analyzed in this work. In addition, Silva et al.[6] identified three of these and one additional form: cyanidin 3-acetyl-hexoside. However, myricetin, rutin, and kaempferol, also detected by Reynertson et al.[3] in purple grumixama, were not detected in the present study. These differences in the profiles could be due to differences in local

DOI: 10.1021/acs.jafc.5b01195
J. Agric. Food Chem. 2015, 63, 5417−5427

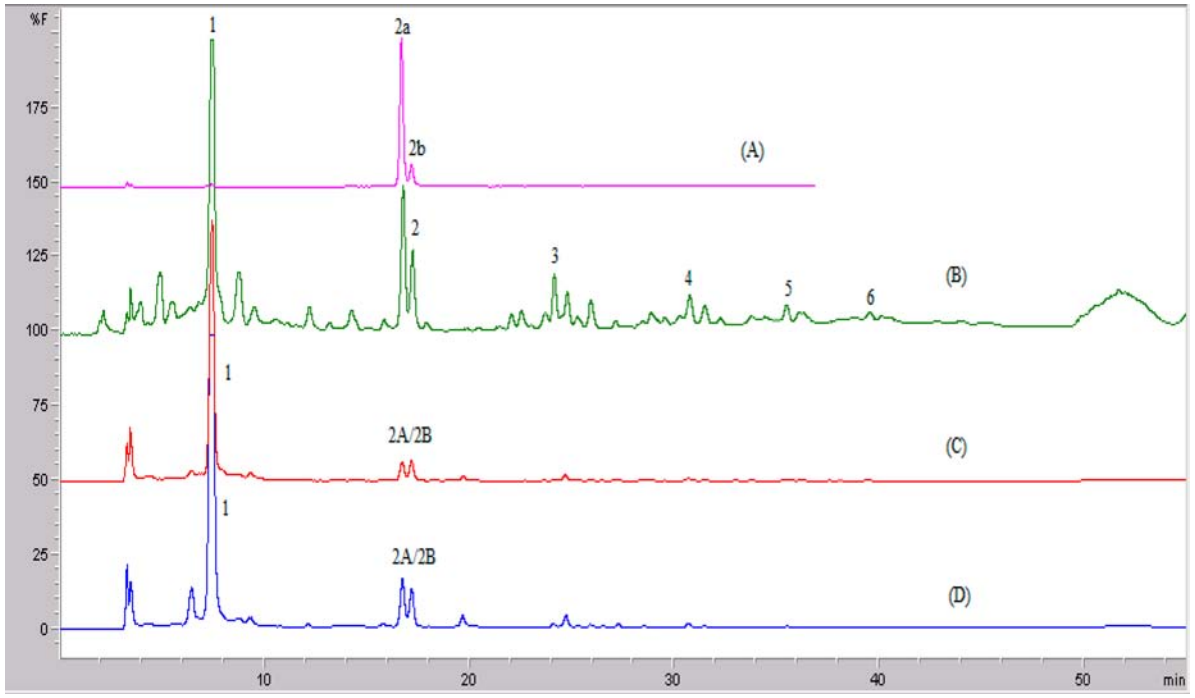

Figure 4. Chromatogram obtained by HPLC-fluorescence of proanthocyanidins in normal phase diol column: (A) proanthocyanidin B1/B2; (B) strawberry extract; (C) yellow grumixama; (D) purple grumixama (cv. Camarosa). The numbers denote the polymerization degree (1, monomers; 2, dimer; 3, timer; etc.). (A) proanthocyanidin B2; (B) proanthocyanidin B1.

plantation and/or agronomic conditions. The phenolic profile of yellow grumixama had not been previously characterized, most likely because this variety is less common than the purple variety. The flavonoid profile of the yellow variety was very different from that of the purple variety. Specifically, the purple and yellow varieties are good sources of anthocyanins and flavonols, respectively.

Seeds. Table 2 presents the compounds identified by LC-ESI-MS/MS in the seeds of the purple and yellow grumixama. The peak numbers in this table refer to the numbered peaks in Figure 2, which identified 12 and 9 phenolic compounds in the seeds of the purple and yellow grumixama, respectively. All compounds identified in the seeds of yellow variety were also found in the purple form. Among the nine compounds present in both seeds, three ellagic acid derivates (peaks 20, 22, and 23, at m/z 927, 489, and 489, respectively), three flavanols (peaks 11, 14, and 16, at m/z 611, 289, and 457, respectively), two flavonols (peaks 17 and 19, at m/z 631 and 959, respectively), and one proanthocyanidin (peak 13, at m/z 577) were identified. In addition to these, in the seed of purple grumixama, four additional compounds were identified: one ellagic acid derivative (peak 18, at m/z 593), two flavanols (peaks 15 and 21, at m/z 457 and 442, respectively), and one flavonol (peak 27, at m/z 317 and 959). Peaks 10 and 12, at m/z 633, were identified as ellagitannins.

The major compounds identified in the seeds of the yellow and purple grumixama were ellagitannins, expressed as total ellagic acid (42 and 38% of the total compounds identified, respectively) and flavanols (28 and 34% of the total compounds identified, respectively).

In addition to myricetin hexoside (at m/z 479), which was also found in the flesh, myricetin galloyl hexoside (peak 17) was identified in seeds of both varieties. Peak 17 showed a molecular ion at m/z 631 and two mass fragments at m/z 479 and 316. The fragment at m/z 479 corresponds to a myricetin hexoside, resulting from the loss of a galloyl group (−152 from $[M - H]^-$).

The phenolic acids or derivatives detected and identified in the grumixama (flesh and seed) have common molecular ions at m/z 301 and 169, which correspond to ellagic acid and gallic acid, respectively. Other structures linked to these phenolic acids included sugars (hexoses and pentoses) and the acetyl group. Examples include ellagic acid hexoside (peak 20, at m/z 463 with an MS/MS fragment at m/z 301) and ellagic acetyl rhaminoside dimeric ion (peak 23, at m/z 489 with an MS/MS fragment at m/z 301), respectively. With the exception of free ellagic acid, all other phenolic acids were identified by comparison with data from the literature.[5,38,39]

Among these compounds (Table 2), catechin, epicatechin, gallocatechin gallate, epigallocatechin gallate, (−)-epicatechin gallate, free ellagic acid, myricetin aglycone, and quercetin aglycone were identified by coelution with the corresponding standards and the similarity of the UV−vis absorption spectra and mass spectra characteristics. The compounds in the seeds had not been previously studied.

Identification of Proanthocyanidin of Fruits. Proanthocyanidin are polymeric flavonoid compounds composed of flavonol-3-ol subunits. Proanthocyandins were the main strawberry phenolics,[30] presenting from dimeric to polymeric forms. Flesh and seed of both grumixama varieties presented dimeric form of proanthocyanidin. None other polymeric form was detected. Peak 13 (Table 2) had a molecular ion at m/z 577 and two MS/MS fragments at m/z 407 and 289, that were identified as proanthocyanidins B1/B2, a dimer of catechin/epicatechin. The identity was confirmed by coelution with the commercial standard (Figure 4).

Identification of Ellagitannins of Fruits. Ellagitannins (ETs) are present in berries and a number of other sources, such as nuts.[10] ETs are hydrolyzable tannins, a class of polyphenols with a structure that consists of esters of

DOI: 10.1021/acs.jafc.5b01195
J. Agric. Food Chem. 2015, 63, 5417−5427

Table 3. Ellagitannins Identified in Flesh of Yellow and Purple Grumixama by HPLC-ESI-MS/MS (Negative Mode)

identified compound	mol wt	RT[a] (min)	$[M - H]^-$ (m/z)	MS/MS (m/z)	peak[b]	yellow flesh (%)[c]	purple flesh (%)[c]
castalagin/vescalagin	934	4.0	933	915/301	1	3	8
pedunculagin	784	4.9	783	301/257	2	6	4
castalagin/vescalagin	934	5.1	933	301	3		17
strictinin	634	5.3	633	301	4	1	3
pedunculagin	784	6.9	783	481/301	5	3	2
potentillin/casuarictin	936	10.7	935	633/301	6	Tr	4
ellagic acid galloyl hexoside	616	17.7	615	463/301	8	6	3
strictinin	634	3.8	633	594/481/301	12	4	
strictinin	634	4.3	633	274/203	13	4	
strictinin	634	6.4	633	301/211	14	4	
tellimagrandin I	786	12.0	785	615/483/301	16	2	

[a]RT, retention time. [b]Peaks are numbered according to Figure 3A (flesh of the yellow fruit) and Figure 3B (flesh of the purple fruit) [c]Percentage was calculated from the total area of the chromatograms at 270 nm.

Table 4. Flavonoid Content in the Flesh and Seeds of *Eugenia brasiliensis* Lam.[a]

sample	quercetin	quercetin-3-glucoside	delphinidin[b]	cyanidin-3-glucoside	cyanidin	total anthocyanin
F1	18.55 (1.44)a	9.49 (0.73)a	15.97 (0.64)a	152.54 (3.77)a	14.71 (3.05)a	179.79 (7.71)a
F2	7.77 (0.77)b	5.45 (0.47)b	10.24 (0.86)b	71.81 (6.66)b	4.88 (0.92)b	86.11 (6.25)b
F3	21.42 (0.44)c	3.71 (0.38)c	2.32 (0.05)c	28.73 (0.55)c	0.86 (0.09)c	31.87 (0.71)c
F4	35.51 (1.77)d	6.22 (0.69)b	8.38 (0.30)d	124.96 (9.46)d	6.71 (0.45)b	138.61 (10.77)d

	quercetin	quercetin 3-glucoside	myricetin	catechin	epicatechin
F5	26.28 (1.20)	13.98 (1.20)	3.46 (0.19)	2.87 (0.41)	2.64 (0.29)

	quercetin	gallotocatechin[c]	myricetin[d]	catechin	epicatechin	epigallocatechin gallate
S1	ND	29.92 (1.59)a	21.32 (1.17)a	36.18 (1.57)a	ND	3.69 (0.22)a
S2	ND	19.31 (1.51)bc	13.60 (2.45)b	19.19 (1.20)b	ND	3.66 (0.51)a
S3	ND	23.97 (1.76)c	13.04 (2.09)b	19.75 (2.10)b	ND	2.73 (0.26)b
S4	ND	21.38 (2.60)b	14.38 (2.13)b	15.34 (1.70)c	ND	1.81 (0.03)c
S5	ND	16.17 (1.19)d	13.28 (1.24)b	20.45 (1.52)d	ND	2.60 (0.18)b

[a]The values shown are the means (standard deviation) expressed as mg/100 g . ND, not detected; Tr, trace. F1 and F2, flesh of the fruit of the purple grumixama from São Paulo; F3 and F4, flesh of the fruit of the purple grumixama from Santa Catarina; F5, flesh of the fruit of the yellow grumixama from São Paulo; S1 and S2, seeds of the purple grumixama from São Paulo; S3 and S4, seeds of the purple grumixama from Santa Catarina; S5, seeds of the yellow grumixama from São Paulo. The same letters indicate nonsignificant differences between samples ($p < 0.05$). [b]Delphinidin hexoside was quantified as delphinidin aglycone. [c]Gallocatechin was quantified as catechin. [d]Myricetin derivatives were quantified as myricetin aglycone.

hexahydroxydiphenoyl (HHDP) groups with a polyol core (usually glucose or quinic acid) that often contains galloyl groups.[12,40,41] An ET-enriched fraction was used to identify the ETs by LC-ESI-MS/MS analysis. The ET-enriched fraction was obtained by the precipitation of ETs using ytterbium acetate, which provided an improved separation from other phenolics such as flavonoids.[29]

Figure 3 shows the chromatograms obtained from the flesh of the yellow and purple grumixama (A and C, respectively). The peak numbers indicate the compounds identified, which are listed in Table 3. Seven ellagic acid derivatives were identified in the ET-enriched fraction, as discussed above.

In the flesh of the purple and yellow varieties, 10 and 7 compounds, respectively, were identified as ETs (Table 3). All of the other numbered peaks in the chromatograms were identified as ellagic acid derivatives and flavonoids and are listed in Table 2. Among these, there were six ellagic acid derivatives and cyanidin 3-glucoside in the purple grumixama and four EA derivatives in the yellow one. All of the ETs detected in the flesh of the yellow fruit were also detected in the purple fruit.

Peaks 1 and 3 were identified as C-glycosidic ellagitannins. The molecular ions for both peaks 1 and 3 were at m/z 933, and both produced two mass fragments at m/z 915 and 301 and identified as castalgin/vescalagin isomers. The fragment at m/z 915 resulted from the neutral loss of water ($[M - H]^- - 18$), and the other, at m/z 301, resulted from the neutral loss of 632 (monogalloyl − glucose).[5,42,43] Castalgin/vescalagin isomers were the major ellagitannins in the flesh of the yellow grumixama, corresponding to approximately 61% of the total ETs identified. Peaks 2 and 5 was identified as peduncunlagin isomers (2,3- or 4,6-dihexahydroxydiphenoyl [HHDP]-glucose) with a molecular ion at m/z 783 and three mass fragments: one at m/z 481 resulting from the neutral loss of an HHDP group ($[M - H]^-$ 302) and two others at m/z 301 ($[M - H]^-$ 482, resulting from the loss of an HHDP (302), a glucosyl group (162) and H_2O (18)) and at m/z 257. The fragment at m/z 301 is characteristic of the ellagitannins, and the one at m/z 257 (loss of CO_2) is a typical fragment of ellagic acid.[42−44]

Peaks 4, 12, 13, and 14, identified as strictinin isomers, all had molecular ions at m/z 633 and mass fragments at m/z 481, resulting from the neutral loss of a galloyl group ($[M - H]^- - 152$) and at m/z 301, resulting from the neutral loss of one hexose unity and one molecule of water ($[M - H]^- - 180$ from the loss of glucosyl (162) groups and water (18)) from the fragment at m/z 481.[45] Among these four isomers, only compound **4** was present in both varieties. Peak 8 showed a molecular ion at m/z 615 and MS/MS fragments at m/z 463,

DOI: 10.1021/acs.jafc.5b01195
J. Agric. Food Chem. 2015, 63, 5417−5427

resulting from the loss of a galloyl group from $[M - H]^-$, and at m/z 301, resulting from the loss of one hexose unit (162). Compound **8** was identified as ellagic acid galloyl hexoside. Pedunculagin isomers, strictinin isomers, and ellagic acid galloyl hexoside were the major ellagitannins in purple grumixama, corresponding to 20, 30, and 19%, respectively, of the total ETs identified. Peak 6 had a molecular ion at m/z 935 and yielded MS/MS fragments at m/z 633 ($[M - H]^- - 302$, resulting from the loss of an HHDP group), and at m/z 301 ($[M - H]^- - 634$, resulting from the loss of HHDP (302), gallic acid (170), and glucosyl (162) groups). On the basis of the mass spectra, this peak was identified as a probable casuarictin (galloyl-bis-HHDP-glucoside), an *O*-glucoside isomer.[46]

Isomeric ions have the same numbers of each isotopic atom, but the positions of these atoms differ.[35] Thus, these molecules have different retention times, but the same mass spectra characteristics.

Ten ellagitannins were identified in the flesh of the fruits. Characterization of the ellagitannins had not previously been studied in grumixama. However, the ellagitannins have been studied in other plants from the Myrtaceae family. Various ellagitannins such as telligramadin, pedunculagin, casuarictin, strictinin, vescalagin and castalagin,[5,43,47] including their monomeric forms, were also identified in these studies. However, dimeric ellagitannin forms such as sanguinin H-6 and sanguinin H-10, which are common in berries,[43,46] were not detected in grumixama. Furthermore, oligomeric forms such as melasquanin A, which are common in other species of the Myrtaceae family, were also not identified here.[48]

Quantification of Flavonoids, Phenolic Acids, Proanthocyanidin, and Ellagitannins. The main constituents of the flesh of the purple grumixama were the anthocyanins (32−180 mg of total anthocyanin equiv 100 g^{-1} FW) and ellagitannins, expressed as total ellagic acid (82−243 mg ellagic acid equiv 100 g^{-1} FW) (Tables 4 and 5, respectively). Ellagitannin quantification is based on hydrolysis of these compounds to yield free ellagic acid (EA), which is detected by HPLC. The cyanidin 3-glucoside contributed 82−89% of the total anthocyanin, of which 3−8% was present as cyanidin aglycone. The amount of the anthocyanins found in the flesh by HPLC-DAD analysis is consistent with the monomeric anthocyanin content (Figure 1A). Thus, the anthocyanin concentrations in purple grumixama vary according to harvest time and local plantation. The lowest concentration was similar to those given for several strawberry cultivars, ranging from 23.5 ± 1.9 mg 100 g^{-1} in cv. Aibión to 46.6 ± 2.9 mg 100 g^{-1} FW in cv. Aguedilla,[30] and cranberry (66.7 mg 100 g^{-1}).[43] Also, the highest concentration was similar to that reported for blackberry cultivars, ranging from 80 to 100 mg 100 g^{-1} FW[32] and blueberry (218 mg 100 g^{-1} FW).[43]

The flesh of the yellow grumixama (Table 4) is rich in flavonols (quercetin and myricetin derivatives), corresponding to 41 mg 100 g^{-1} FW with only small amounts of the flavanols (catechin and epicatechin). However, the major components were the ellagitannins (91.72 mg 100 g^{-1} FW) (Table 5).

The flavonoids identified in the seeds were primarily flavonols and flavanols. The total flavanol amounts in seeds varied from 39 to 70 mg 100 g^{-1} FW, whereas the flavonol amounts varied from 14 to 30 mg 100 g^{-1} FW and consisted mainly of myricetin. However, the major compound in seeds was the ellagitannin, expressed as total ellagic acid, contributing 2.22−2.95 g 100 g^{-1} FW.

The flesh of grumixama presented a low concentration of proanthocyanidins B1/B2 (Table 5). The concentration ranged from 0.41 ± 0.04 to 2.01 ± 0.15 mg/100 g FW in the purple grumixama and to 0.79 ± 0.02 mg/100 g FW in the yellow one. These values were lower than reported for several cultivars of strawberry, ranging from 53.9 to 168.1 mg/100 g FW.[30]

The flesh of purple and yellow grumixama fruits was shown to be a good source of anthocyanins and flavonols, respectively, and both were good sources of ellagitannins. Given the biological activities attributed to these classes of compounds (flavonoids and ellagitannins), the purple and yellow fruits show considerable potential as functional foods. The seeds, although inedible, could be used as sources of bioactive compounds, mainly ellagitannins. However, studies regarding the biological activities of these materials are also necessary to elucidate the mechanisms by which the biological effects attributed to this plant could occur.

Table 5. Total Ellagic Acid and Proanthocyanidin Contents in the Flesh of *Eugenia brasiliensis* Lam.[a]

sample	free ellagic acid	total ellagic acid	total proanthocyanidin
F1	13.76 (2.53)a	201 (12)a	1.99 (0.26)a
F2	9.38 (0.28)b	82 (4)b	0.41 (0.04)b
F3	3.97 (1.16)c	152 (11)c	1.04 (0.11)c
F4	5.14 (0.40)d	243 (9)d	2.01 (0.15)a
F5	13.08 (1.52)	92 (11)	0.79 (0.02)
S1	64.68 (5.53)a	2905 (179)a	na
S2	60.81 (7.28)ab	2734 (152)b	na
S3	37.50 (1.95)c	2225 (126)c	na
S4	69.21 (3.43)a	2240 (113)d	na
S5	53.95 (2.69)b	2323 (105)e	na

[a]The values shown are the means (standard deviation) and are expressed as mg/100 g FW. NA, not analyzed. F1 and F2, flesh of the fruit of the purple grumixama from São Paulo; F3 and F4, flesh of the fruit of the purple grumixama from Santa Catarina; F5, flesh of the fruit of the yellow grumixama from São Paulo; S1 and S2, seeds of the purple grumixama from São Paulo; S3 and S4, seeds of the purple grumixama from Santa Catarina; S5, seeds of the yellow grumixama from São Paulo. The same letters indicate nonsignificant differences between samples (p).

■ ASSOCIATED CONTENT

Supporting Information

Mass spectra of the compounds identified. The Supporting Information is available free of charge on the ACS Publications website at DOI: 10.1021/acs.jafc.5b01195.

■ AUTHOR INFORMATION

Corresponding Author

*(N.M.A.H.) Phone: (+55) 11-30910128. Fax: (+55) 11-3815 4410. E-mail: aymoto@usp.br.

Funding

This research was supported by CNPq (scholarship 153453/2012-5) and FAPESP (2013/07914-8).

Notes

The authors declare no competing financial interest.

■ ACKNOWLEDGMENTS

We thank Eliséo Soprano for collecting the samples in Santa Catarina. We also thank Professor Ernani Pinto and Dr. Felipe Augusto Dörr, Toxicology Laboratory-FCF/USP, who per-

DOI: 10.1021/acs.jafc.5b01195
J. Agric. Food Chem. 2015, 63, 5417−5427

formed the LC-MS/MS analyses. In addition, we thank Bello's farm for providing the photographs used in the TOC graphic.

REFERENCES

(1) Flores, G.; Dastmalchi, K.; Paulino, S.; Whalen, K.; Dabo, A. J.; Reynertson, K. A.; Foronjy, R. F.; D'armiento, J. M.; Kennelly, E. J. Anthocyanins from *Eugenia brasiliensis* edible fruits as potential therapeutics for COPD treatment. *Food Chem.* **2012**, *134*, 1256−1262.

(2) Moreno, P. R. H.; Lima, M. E. L.; Sobral, M.; Young, M. C. M.; Cordeiro, I.; Apel, M. A.; Limberger, R. P.; Henriques, A. T. Essential oil composition of fruit colour varieties of *Eugenia brasiliensis* Lam. *Sci. Agric. (Piracicaba, Braz.)* **2007**, *64*, 428−432.

(3) Reynertson, K. A.; Yang, H.; Jiang, B.; Basile, M. J.; Kennelly, E. J. Quantitative analysis of antiradical phenolic constituents from fourteen edible Myrtaceae fruits. *Food Chem.* **2008**, *109*, 883−890.

(4) Abe, L. T.; Lajolo, F. M.; Genovese, M. I. Potential dietary sources of ellagic acid and other antioxidants among fruits consumed in Brazil: jabuticaba (*Myrciaria jaboticaba* (Vell.) Berg). *J. Sci. Food Agric.* **2012**, *92*, 1679−1687.

(5) Fracassetti, D.; Costa, C.; Moulay, L.; Tomás-Barberán, F. A. Ellagic acid derivatives, ellagitannins, proanthocyanidins and other phenolics, vitamin C and antioxidant capacity of two powder products from camu-camu fruit (*Myrciaria dubia*). *Food Chem.* **2013**, *139*, 578−588.

(6) Silva, N. A.; Rodrigues, E.; Mercadante, A. Z.; Rosso, V. V. Phenolic compounds and carotenoids from four fruits native from the Brazilian atlantic forest. *J. Agric. Food Chem.* **2014**, *62*, 5072−5084.

(7) Colla, A. R. S.; Machado, D. G.; Bettio, L. E. B.; Colla, G.; Magina, M. D. A.; Brighente, I. M. C.; Rodrigues, A. L. S. Involvement of monoaminergic systems in the antidepressant-like effect of *Eugenia brasiliensis* Lam. (Myrtaceae) in the tail suspension test in mice. *J. Ethnopharmacol.* **2012**, *143*, 720−731.

(8) Pietrovski, E. F.; Magina, M. D. A.; Gomig, F.; Pietrovski, C. F.; Micke, G. A.; Barcellos, M.; Pizzolatti, M. G.; Cabrini, D. A.; Brighente, I. M. C.; Otuki, M. Topical anti-inflammatory activity of *Eugenia brasiliensis* Lam. (Myrtaceae) leaves. *J. Pharm. Pharmacol.* **2008**, *60*, 479−487.

(9) Kasimsetty, S. G.; Bialonska, D.; Reddy, M. K.; Ma, G.; Khan, S. I.; Ferreira, D. Colon cancer chemopreventive activities of pomegranate ellagitannins and urolithins. *J. Agric. Food Chem.* **2010**, *58*, 2180−2187.

(10) Landete, J. M. Ellagitannins, ellagic acid and their derived metabolites: a review about source, metabolism, functions and health. *Food Res. Int.* **2011**, *44*, 1150−1160.

(11) Sangiovanni, E.; Vrhovsek, U.; Rossoni, G.; Colombo, E.; Brunelli, C.; Brembati, L.; Trivulzio, S.; Gasperotti, M.; Mattivi, F.; Bosisio, E.; Dell'Agli, M. Ellagitannins from *Rubus* berries for the control of gastric inflammation: in vitro and in vivo studies. *PLoS One* **2013**, *8*, 71762−71774.

(12) Ascacio-Valdés, J. A.; Buenrostro-Figueroa, J. J.; Aguilera-Carbo, A.; Prado-Barragán, A.; Rodríguez-Herrera, R.; Aguilar, C. N. Ellagitannins: biosynthesis, biodegradation and biological properties. *J. Med. Plants Res.* **2011**, *5*, 4696−4703.

(13) Ştefănuţ, M. N.; Căta, A.; Pop, R.; Tănasie, C.; Boc, D.; Ienaşcu, I.; Ordodi, V. Anti-hyperglycemic effect of bilberry, blackberry and mulberry ultrasonic extracts on diabetic rats. *Plant Foods Hum. Nutr.* **2013**, *68*, 378−384.

(14) Morton, L. W.; Abu-Amsha Caccetta, R.; Puddey, I. B.; Croft, K. D. Chemistry and biological effects of dietary phenolic compounds: relevance to cardiovascular disease. *Clin. Exp. Pharmacol. Physiol.* **2000**, *27*, 152−159.

(15) Nijveldt, R. J.; Nood, E. V.; Hoorn, D. E. C. V.; Boelens, P. G.; Norren, K. V.; Leeuwen, P. A. M. V. Flavonoids: a review of probable mechanisms of action and potential applications. *Am. J. Clin. Nutr.* **2001**, *74*, 418−425.

(16) Clifford, M. N.; Brown, J. E. Dietary flavonoids and health — broadening the perspective. In *Flavonoids: Chemistry, Biochemistry, and Applications*; Andersen, O. M., Markham, K. R., Eds.; Taylor and Francis Group: New York, 2006; Vol. 1, pp 320−345.

(17) Sepúlveda, L.; Ascacio, A.; Rodríguez-Herrera, R.; Aguilera-Carbó, A.; Aguilar, C. N. Ellagic acid: biological properties and biotechnological development for production processes. *Afr. J. Biotechnol.* **2011**, *10*, 4518−4523.

(18) AOAC. *Official Methods of Analysis*, 16th ed.; AOAC International: Arlington, VA, USA, 1995.

(19) Venkatachalam, M.; Sathe, S. K. Chemical composition of selected edible nut seeds. *J. Agric. Food Chem.* **2006**, *54*, 4705−4719.

(20) AOAC. *Official Methods of Analysis*, 15th ed.; AOAC International: Arlington, VA, USA, 1990.

(21) Shiga, T.; Soares, C. A.; Nascimento, J. R. O.; Purgatto, E.; Lajolo, F. M.; Cordenunsi, B. R. Ripening-associated changes in the amounts of starch and non-starch polysaccharides and their contributions to fruit softening in three banana cultivars. *J. Sci. Food Agric.* **2011**, *91*, 1511−1516.

(22) Swain, T.; Hillis, W. E. The phenolic constituents of *Prunus domestica*. I. The quantitative analysis of phenolic constituents. *J. Sci. Food Agric.* **1959**, *10*, 63−68.

(23) Lee, J.; Durst, R. W.; Wrolstad, R. E. Determination of total monomeric anthocyanin pigment content of fruit juices, beverages, natural colorants, and wines by the pH differential method: collaborative study. *J. AOAC Int.* **2005**, *88*, 1269−1278.

(24) Brand-Williams, W.; Cuvelier, M. E.; Berset, C. Use of a free radical method to evaluate antioxidant activity. *Lebensm.-Wiss. -Technol.* **1995**, *28*, 25−30.

(25) Prior, R. L.; Hoang, H.; Gu, L.; Wu, X.; Bacchiocca, M.; Howard, L.; Hampsch-Woodill, M.; Huang, D.; Ou, B.; Jacob, R. Assays for hydrophilic and lipophilic antioxidant capacity (oxygen radical absorbance capacity ($ORAC_{FL}$)) of plasma and other biological and food samples. *J. Agric. Food Chem.* **2003**, *51*, 3273−3279.

(26) Giner-Chávez, B. I.; Van Soest, P. J.; Robertson, J. B.; Lascano, C.; Reed, J. D.; Pell, A. N. A method for isolating condensed tannins from crude plant extracts with trivalent ytterbium. *J. Sci. Food Agric.* **1997**, *74*, 359−368.

(27) Pinto, M. S.; Carvalho, J. E.; Lajolo, F. M.; Genovese, M. I.; Shetty, K. Evaluation of antiproliferative, anti-type 2 diabetes, and antihypertension potentials of ellagitannins fro strawberries (*Fragaria* × *ananassa* Duch.) using in vitro models. *J. Med. Food.* **2010**, *13*, 1027−1035.

(28) Sestari, I.; Zsögön, A.; Rehder, G. G.; Teixeira, L. L.; Hassimotto, N. M. A.; Purgatto, E.; Benedito, V. A.; Peres, L. E. P. Near-isogenic lines enhancing ascorbic acid, anthocyanin andcarotenoid content in tomato (*Solanum lycopersicum* L. cv. Micro-Tom) as a tool to produce nutrient-rich fruits. *Sci. Hortic.* **2014**, *175*, 111−120.

(29) Giner-Chavez, B. I.; Soest, P. J. V.; Robertson, J. B.; Lascano, C.; Reed, J. D.; Pell, A. N. A method for isolating condensed tannins from crude plant extracts with trivalent ytterbium. *J. Sci. Food Agric.* **1997**, *74*, 359−368.

(30) Buendia, B.; Gil, M. I.; Tudela, J. A.; Gady, A. L.; Medina, J. J.; Soria, C.; López, J. M.; Tomás-Barberán, F. A. HPLC-MS analysis of proanthocyanidin oligomers and other phenolics in 15 strawberry cultivars. *J. Agric. Food Chem.* **2010**, *58*, 3916−3926.

(31) Wang, C. Y. Maintaining postharvest quality of raspberries with natural volatile compounds. *Int. J. Food Sci. Technol.* **2003**, *38*, 869−875.

(32) Talcott, S. T. Chemical components of berry fruits. In *Berry Fruit: Value-Added Products for Health Promotion*; Zhao, Y., Ed.; Taylor and Francis Group: Boca Raton, FL, USA, 2007; Vol. 1, pp 51−68.

(33) Hassimotto, N. M. A.; Mota, R. V.; Cordenunsi, B. R.; Lajolo, F. M. Physico-chemical characterization and bioactive compounds of blackberry fruits (*Rubus* sp.) grown in Brazil. *Cienc. Tecnol. Aliment.* **2008**, *28*, 702−708.

(34) Gates, P. J.; Lopes, N. P. Characterisation of flavonoid aglycones by negative ion chip-based nanospray tandem mass spectrometry. *Int. J. Anal. Chem.* **2012**, *1*, 1−7.

(35) Murray, K. K.; Boyd, R. K.; Eberlin, M. N.; Langley, G. J.; Li, L.; Naito, Y. Standard definitions of terms relating to mass spectrometry. *J. Am. Soc. Mass Spectrom.* **2006**, *3*, 1−20.

DOI: 10.1021/acs.jafc.5b01195
J. Agric. Food Chem. 2015, 63, 5417−5427

(36) Erlund, I.; Freese, R.; Marniemi, J.; Hakala, P.; Alfthan, G. Bioavailability of quercetin from berries and the diet. *Nutr. Cancer* **2006**, *54*, 13−17.
(37) Wu, X.; Beecher, G. R.; Holden, J. M.; Haytowitz, B. D.; Gebhardt, S. E.; Prior, R. L. Concentrations of anthocyanins in common foods in the united states and estimation of normal consumption. *J. Agric. Food Chem.* **2006**, *54*, 4069−4075.
(38) Scoparo, C. T.; Souza, L. M.; Dartora, N.; Sassaki, G. L.; Gorin, P. A. J.; Iacomini, M. Analysis of *Camellia sinensis* green and black teas via ultra high performance liquid chromatography assisted by liquid−liquid partition and two-dimensional liquid chromatography (size exclusion × reversed phase). *J. Chromatogr. A* **2012**, *1222*, 29−37.
(39) Oliveira, A. L.; Destandau, E.; Fougère, L.; Lafosse, M. Isolation by pressurised fluid extraction (PFE) and identification using CPC and HPLC/ESI/MS of phenolic compounds from Brazilian cherry seeds (*Eugenia uniflora* L.). *Food Chem.* **2014**, *145*, 522−529.
(40) Bakkalbaşi, E.; Menteş, Ö.; Artik, N. Food ellagitannins − occurrence, effects of processing and storage. *Crit. Rev. Food Sci. Nutr.* **2009**, *49*, 283−298.
(41) Clifford, M. N.; Scalbert, A. Ellagitannins − nature, occurrence and dietary burden. *J. Sci. Food Agric.* **2000**, *80*, 1118−1125.
(42) Romani, A.; Campo, M.; Pinelli, P. HPLC/DAD/ESI-MS analyses and anti-radical activity of hydrolyzable tannins from different vegetal species. *Food Chem.* **2012**, *130*, 214−221.
(43) Koponen, J. M.; Happonen, A. M.; Mattila, P. H.; Törrönen, A. R. Contents of anthocyanins and ellagitannins in selected foods consumed in finland. *J. Agric. Food Chem.* **2007**, *55*, 1612−1619.
(44) Mullen, W.; Yokota, T.; Lean, M. E. J.; Crozier, A. Analysis of ellagitannins and conjugates of ellagic acid and quercetin in raspberry fruits by LC−MS*n*. *Phytochemistry* **2003**, *64*, 617−624.
(45) Dou, J.; Lee, V. S. Y.; Tzen, J. T. C.; Lee, M. R. Identification and comparison of phenolic compounds in the preparation of oolong tea manufactured by semifermentation and drying processes. *J. Agric. Food Chem.* **2007**, *55*, 7462−7470.
(46) Zhentian, L.; Jervis, J.; Helm, R. F. C-glycosidic ellagitannins from white oak heartwood and callus tissues. *Phytochemistry* **1999**, *51*, 751−756.
(47) Okuda, T.; Yoshida, T.; Hatano, T.; Yazaki, K.; Ashida, M. Ellagitannins of the Casuarinaceae, Stachyuraceae and Myrtaceae. *Phytochemistry* **1982**, *21*, 2871−2874.
(48) Yoshida, T.; Amakura, Y.; Yoshimura, M. Structural features and biological properties of ellagitannins in some plant families of the order Myrtales. *Int. J. Mol. Sci.* **2010**, *11*, 79−106.

DOI: 10.1021/acs.jafc.5b01195
J. Agric. Food Chem. 2015, 63, 5417−5427

JOURNAL OF AGRICULTURAL AND FOOD CHEMISTRY

Article

pubs.acs.org/JAFC

Youngiasides A and C Isolated from *Youngia denticulatum* Inhibit UVB-Induced MMP Expression and Promote Type I Procollagen Production via Repression of MAPK/AP-1/NF-κB and Activation of AMPK/Nrf2 in HaCaT Cells and Human Dermal Fibroblasts

Myungsuk Kim, Young Gyun Park, Hee-Ju Lee, Sue Ji Lim, and Chu Won Nho*

Natural Products Research Center, Korea Institute of Science and Technology, Gangneung, Gangwon-do 210-340, Republic of Korea

ABSTRACT: This study investigated the effects of youngiaside A (YA), youngiaside C (YC), and *Youngia denticulatum* extract (YDE) on extrinsic aging and assessed its molecular mechanisms in UVB-irradiated HaCaT keratinocytes and human dermal fibroblasts (HDFs). The results showed that YA, YC, and YDE decreased matrix metalloproteinase (MMP) expression and production in HaCaT cell and HDFs and increased collagen expression and production in HDFs. In addition, YA, YC, and YDE significantly increased antioxidant enzyme expression, thereby down-regulating UVB-induced reactive oxygen species (ROS) production and ROS-induced mitogen-activated protein kinase (MAPK) and activator protein-1 (AP-1) signaling in HaCaT cells. Furthermore, YA, YC, and YDE reduced phosphorylation of IκBα and IKKα/β, blocked nuclear factor-κB (NF-κB) p65 nuclear translocation, and strongly suppressed pro-inflammatory mediators. Finally, YA, YC, and YDE augmented UVB-induced adenosine monophosphate activated protein kinase (AMPK) phosphorylation and YA and YC did not inhibit MMP-1 production in AMPK inhibitor or nuclear factor-erythroid 2-related factor-2 (Nrf2) siRNA-treated HaCaT cells. The results suggest that these compounds could be potential therapeutic agents for prevention and treatment of skin photoaging.

KEYWORDS: *youngiaside, Youngia denticulatum, UV, MMPs, type I procollagen*

INTRODUCTION

Skin photoaging is classified into extrinsic aging and intrinsic aging. Extrinsic aging can be triggered by ultraviolet (UV) radiation, stress, or smoking and is characterized by wrinkles, laxity, and dryness.[1] UV radiation consists of three components, UVA, UVB, and UVC. Whereas UVA and UVB reach the Earth in sufficient amounts to damage the skin, UVC is almost completely absorbed by the ozone layer.[2] UVB is particularly damaging, as it penetrates the epidermis and the upper part of the dermis, where it damages keratinocytes and leads to sunburn, photoaging, and skin cancer.[3] UVB radiation activates activator protein-1 (AP-1) and nuclear factor-κB (NF-κB) in the skin, thereby increasing the production of inflammatory cytokines and matrix metalloproteinases (MMPs) in keratinocytes.[4] These cytokines stimulate fibroblasts to promote the production of MMPs, which degrade the extracellular matrix (ECM).[5]

UVB radiation also promotes the generation of intracellular reactive oxygen species (ROS). ROS induce many harmful effects including DNA damage, inflammatory reactions, and damage to ECM integrity.[6] UVB-induced ROS production triggers growth factor receptors, cell surface cytokines, and mitogen-activated protein kinase (MAPK) cascades such as c-Jun N-terminal kinase (JNK), extracellular signal-regulated kinase (ERK), and p38 kinase, which in turn regulate AP-1.[7] Increased AP-1 activity increases MMP-1 production and decreases type I procollagen production.[8] The transcriptional activity of AP-1, a heterodimer composed of c-Jun and c-Fos, is dependent on the degree of c-Jun phosphorylation and c-Fos expression.[8]

The adenosine monophosphate activated protein kinase (AMPK) cascade is a regulator and sensor of cellular energy status. Stresses that consume cellular ATP, such as oxidative stress, hypoxia, nutrient deprivation, and metabolic poisoning, can activate AMPK.[9] Recently, it was reported that AMPK activation plays an important role in MMP-1 expression in human dermal fibroblasts (HDFs) by regulating the upstream and downstream signaling of AMPK.[10] Thus, AMPK activators could be used to prevent UV-induced skin photoaging.

Nuclear factor-erythroid 2-related factor-2 (Nrf2) and Kelch-like ECH associated protein 1 (Keap1) coordinate the transcriptional induction of a large number of antioxidant-metabolizing enzymes, thus affirming the important role of these two proteins.[11] Nrf2 was recently shown to play a central role in protecting cells from UV-induced apoptosis in vitro and acute sunburn reactions in vivo.[12,13] Furthermore, the Nrf2-Keap1 pathway plays an important role in preventing photoaging by maintaining high levels of antioxidants, such as glutathione, in the skin.[14] Thus, Nrf2 activators may also be beneficial for preventing skin photoaging.

Youngia denticulatum is a plant native to Korea, the early sprouts of which have traditionally been eaten as wild vegetables.[15] *Y. denticulatum* contains many phenolic compounds, including chlorogenic acid, dicaffeoylquinic acid, and chicoric acid, all of which exhibit antioxidant activity.[15−18] We recently reported that youngiasides A, B, and C isolated from

Received: January 26, 2015
Revised: May 20, 2015
Accepted: May 21, 2015
Published: May 21, 2015

ACS Publications © 2015 American Chemical Society

DOI: 10.1021/acs.jafc.5b00467
J. Agric. Food Chem. 2015, 63, 5428−5438

Y. denticulatum induce the detoxification enzymes, quinone reductase and CYP1A1, through activation of Nrf2 and the aryl hydrocarbon receptor (AhR).[19] We also reported that *Y. denticulatum* protects liver and retinal cells from oxidative stress-induced damage in vitro and in vivo.[15,20,21] However, it remains unknown whether *Y. denticulatum* and its constituents prevent skin photoaging in HaCaT and HDF cells. Thus, this study was performed to investigate the effects of *Y. denticulatum* extract (YDE) and its active compounds, youngiasides A (YA) and C (YC), on the production of MMPs and type I procollagen in UVB-irradiated HaCaT cells and HDFs and to determine their underlying mechanisms.

MATERIALS AND METHODS

Chemical Reagents. 2′,7′-Dichlorofluorescin diacetate (DCFH-DA) was purchased from Sigma Chemicals (St. Louis, MO, USA). Antibodies against superoxide dismutase (SOD) 1, heme oxygenase (HO)-1, Nrf2, cyclooxygenase (COX)-2, phospho-Akt, phospho-SAPK/JNK (Thr183/Tyr185), SAPK/JNK (Thr183/Tyr185), phospho-p44/42 MAPK (Erk1/2), p44/42 MAPK (Erk1/2), phospho-p38, p38, phospho-IκBα (Ser32/36), IκBα, phospho-NF-κB p65 (Ser536), NF-κB p65, phospho-IκB kinase (IKK) α/β (Ser176/180), IKKα, phospho-c-Jun (Ser243), c-Jun, phospho-c-Fos (Ser32), phospho-AMPKα (Thr172), AMPKα, phospho-acetyl-CoA carboxylase (Ser79), and β-actin were purchased from Cell Signaling Technology (Beverly, MA, USA). Dulbecco's modified Eagle's medium (DMEM) and fetal bovine serum (FBS) were from HyClone Laboratories (Logan, UT, USA). All other chemicals and reagents used were of analytical grade.

Plant Material and Preparation of YA and YC. Whole plants (the aerial component and roots) of *Y. denticulatum* were collected in August 2011 at the Wild Vegetable Experiment Station, Gangwon ARES, Korea, and were identified by one of the authors (C.Y.K.). A voucher specimen (D-043) was deposited at the Natural Product Research Center, KIST Gangneung Institute, Korea. Isolation of chemical constituents (Figure 1A) from *Y. denticulatum* was performed as previously described.[19]

Cell Culture and UVB Irradiation. HaCaT and HDF cells were purchased from the American Type Culture Collection (Manassas, VA, USA). Cells were cultured in DMEM supplemented with penicillin (120 units/mL), streptomycin (75 μg/mL), and 10% FBS in an atmosphere of 5% CO_2 at 37 °C. HaCaT and HDF cells were maintained until 80% confluence and then pretreated with various concentrations of YDE, YA, and YC. After a 1 h incubation, the culture medium was replaced with 1.5 mL of phosphate-buffered saline (PBS). Cells were then exposed to UVB light (15 mJ/cm^2) with a 312 nm UVB light source (VL-6.LM; Vilber Lourmat, Marne-la-Vallée Cedex 1, France). UV strength was measured with a Waldman UV meter (model 585100; Waldman, Wheeling, IL, USA). After UVB irradiation, cells were treated with various concentrations of YDE (5 or 10 μg/mL), YA, and YC (5 or 10 μM) in serum-free medium.

Cell Viability. Cell viability was determined using a 3-(4,5-dimethylthiazol-2-yl)-2,5-diphenyltetrazolium bromide (MTT) (Sigma-Aldrich, St. Louis, MO, USA) colorimetric assay. HaCaT and HDF cells were maintained until 80% confluence and then pretreated with various concentrations of YDE, YA, and YC. After a 1 h incubation, the cells were exposed to UVB (15 mJ/cm^2) and treated with various concentrations of YDE, YA, and YC for 24 h in serum-free medium. Cell medium was replaced with 200 μL of MTT (0.5 mg/mL) and incubated for an additional 3 h. After washing the cells, the insoluble formazan crystals were dissolved in 200 μL of dimethyl sulfoxide. Absorbance at 540 nm was measured by spectrophotometry using a microplate reader (Bio-Tek Instruments, Winooski, VT, USA).

Western Blot Analysis. HaCaT cells were lysed in RIPA buffer containing protease inhibitors and then incubated on ice for 10 min. Protein concentrations of cell lysates were determined by Bradford protein assay (Bio-Rad Laboratories, Hercules, CA, USA). Equal amounts of protein (30 μg) from each sample were loaded and separated by 10% sodium dodecyl sulfate−polyacrylamide gel electrophoresis and then transferred to nitrocellulose membranes (Whatman GmbH, Dassel, Germany). Membranes were initially blocked with 5% skimmed milk in Tris-buffered saline containing 0.1% Tween-20 for 1 h and then incubated with primary antibodies for 16 h at 4 °C. After three washes in Tris-buffered saline containing 0.1% Tween-20, membranes were incubated with horseradish peroxidase-linked secondary antibodies (Santa Cruz Biotechnology, Santa Cruz, CA, USA) for 2 h. Proteins were detected with enhanced chemoluminescence reagents (Amersham Biosciences, Little Chalfont, UK) and visualized using an ECL Advanced system (GE Healthcare, Hatfield, UK).

Enzyme-Linked Immunosorbent Assay (ELISA). HaCaT and HDF cells were cultured in 24-well plates (1×10^5 cells/well) and pretreated with YDE, YA, and YC for 1 h. After washing with PBS, cells were irradiated with UVB (15 mJ/cm^2) through a thin layer of PBS. After UVB irradiation, HaCaT and HDF cells were incubated with serum-free DMEM containing YDE, YA, and YC. Cell culture medium was collected after 24 h, and MMP-1 and type I procollagen productions were quantified using a human MMP-1 ELISA kit (QIA55; Merck & Co. Inc., Whitehouse Station, NJ, USA) and a procollagen type I C-peptide enzyme immunoassay kit (MK101; Takara, Shiga, Japan), respectively.

Reverse Transcription-Polymerase Chain Reaction (RT-PCR). Trizol reagent (Invitrogen, Carlsbad, CA, USA) was used to isolate total RNA from cell pellets. Total RNA was quantified by spectrophotometry at 260 nm. The cDNA was synthesized in a 20 μL reaction containing 2 μg of total RNA, oligo (dT), and Reverse Transcription Premix (ELPIS-Biotech, Daejeon, Korea). PCR amplification of the cDNA products (3 μL) was performed with PCR premix (ELPIS-Biotech, Daejeon, Korea) and the following primer pairs (Bioneer, Daejeon, Korea): MMP-1 forward, 5′-ATT CTA CTG ATA TCG GGG CTT TGA-3′, and MMP-1 reverse, 5′-ATG TCC TTG GGG TAT CCG TGT AG-3′ (409 bp); MMP-2 forward, 5′-ATT CTA CTG ATA TCG GGG CTT TGA-3′, and MMP-2 reverse, 5′-ATG TCC TTG GGG TAT CCG TGT AG-3′ (409 bp); MMP-3 forward, 5′-TGA GGA CAC CAG CAT GAA CC-3′, and MMP-3 reverse, 5′-ACT TCG GGA TGC CAG GAA AG-3′ (248 bp); MMP-9 forward, 5′- GGG CCG CTC CTA CTC TGC CT-3′, and MMP-9 reverse, 5′-TCG AGT CAG CTC GGG TCG GG-3′ (296 bp); collagen, type I, α1 (COL1A1) forward, 5′-CTC GAG GTG GAC ACC ACC CT-3′, and COL1A1 reverse, 5′-CAG CTG GAT GGC CAC ATC GG-3′ (366 bp); collagen, type III, α1 (COL3A1) forward, 5′-TGG TGC CCC TGG TCC TTG CT-3′, and COL3A1 reverse, 5′-TAC GGG GCA AAA CCG CCA GC-3′ (87 bp); tumor necrosis factor α (TNF-α) forward, 5′-AGC CGC ATC GCC GTC TCC TA-3′, and TNF-α reverse, 5′-CAG CGC TGA GTC GGT CAC CC-3′ (163 bp); prostaglandin-endoperoxide synthase 2 (COX-2) forward, 5′-GCC AGC TTT CAC CAA CGG GC-3′, and COX-2 reverse, 5′-CTC CTG CCC CAC AGC AAA CCG-3′ (220 bp); interleukin 6 (IL-6) forward, 5′-TCG AGC CCA CCG GGA ACG AAA-3′, and IL-6 reverse, 5′-AGG CAA CTG GAC CGA AGG CG-3′ (94 bp); p65 forward, 5′-CGC GCC GCT TAG GAG GGA GA-3′, and p65 reverse, 5′-GGG CCA TCT GCT GTT GGC AGT-3′ (197 bp); p50 forward, 5′-AGC AGC GTG GGG ACT ACG AC-3′, and p50 reverse, 5′-GGC TGG GGT CTG CGT AGG GA-3′ (345 bp); superoxide dismutase 1 (SOD1) forward, 5′-ATG GCG ACG AAG GCC GTG TG-3′, and SOD1 reverse, 5′-GAC CAC CAG TGT GCG GCC AA-3′ (360 bp); heme oxygenase 1 (HO-1) forward, 5′-AGG GAA TTC TCT TGG CTG GC-3′, and HO-1 reverse, 5′-GAC AGC TGC CAC ATT AGG GT-3′ (237 bp); Nrf2 forward, 5′-CAG CGA CCT TCG CAA ACA AC-3′, and Nrf2 reverse, 5′-CAT GAT GAG CTG TGG ACC GT-3′ (464 bp); and β-actin forward, 5′-TCA TGT TTG AGA CCT TCA A-3′, and β-actin reverse, 5′-GTC TTT GCG GAT GTC CAC G-3′ (517 bp). Prior to PCR amplification, primers were denatured at 94 °C for 5 min. Amplification consisted of 28 cycles as follows: 30 s denaturation at 94 °C, 1 min annealing at 56 °C, and 1 min extension at 72 °C, followed by a final 5 min extension at 72 °C. PCR was performed on a GeneAmp PCR System 2700

DOI: 10.1021/acs.jafc.5b00467
J. Agric. Food Chem. 2015, 63, 5428−5438

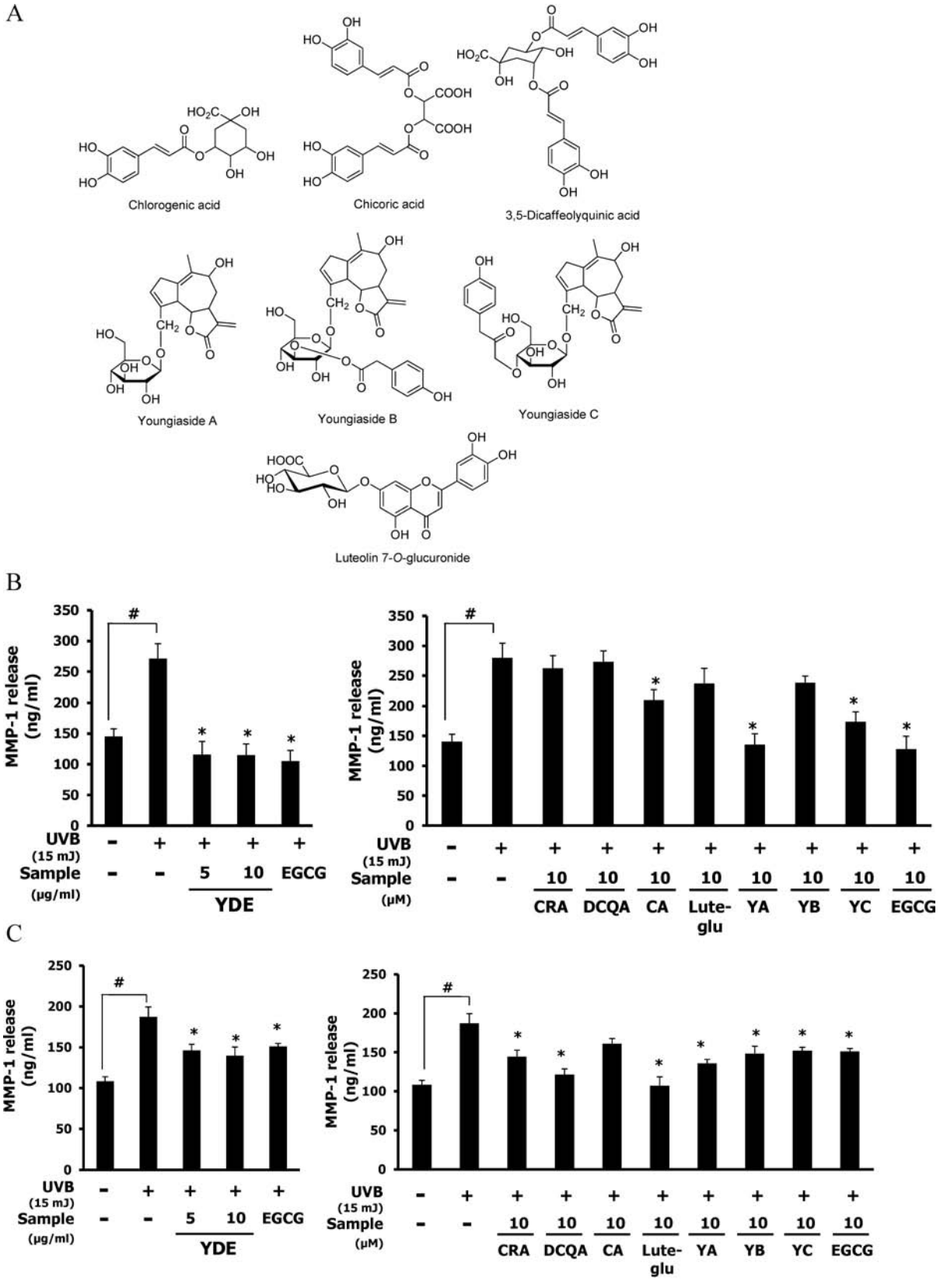

Figure 1. continued

DOI: 10.1021/acs.jafc.5b00467
J. Agric. Food Chem. 2015, 63, 5428−5438

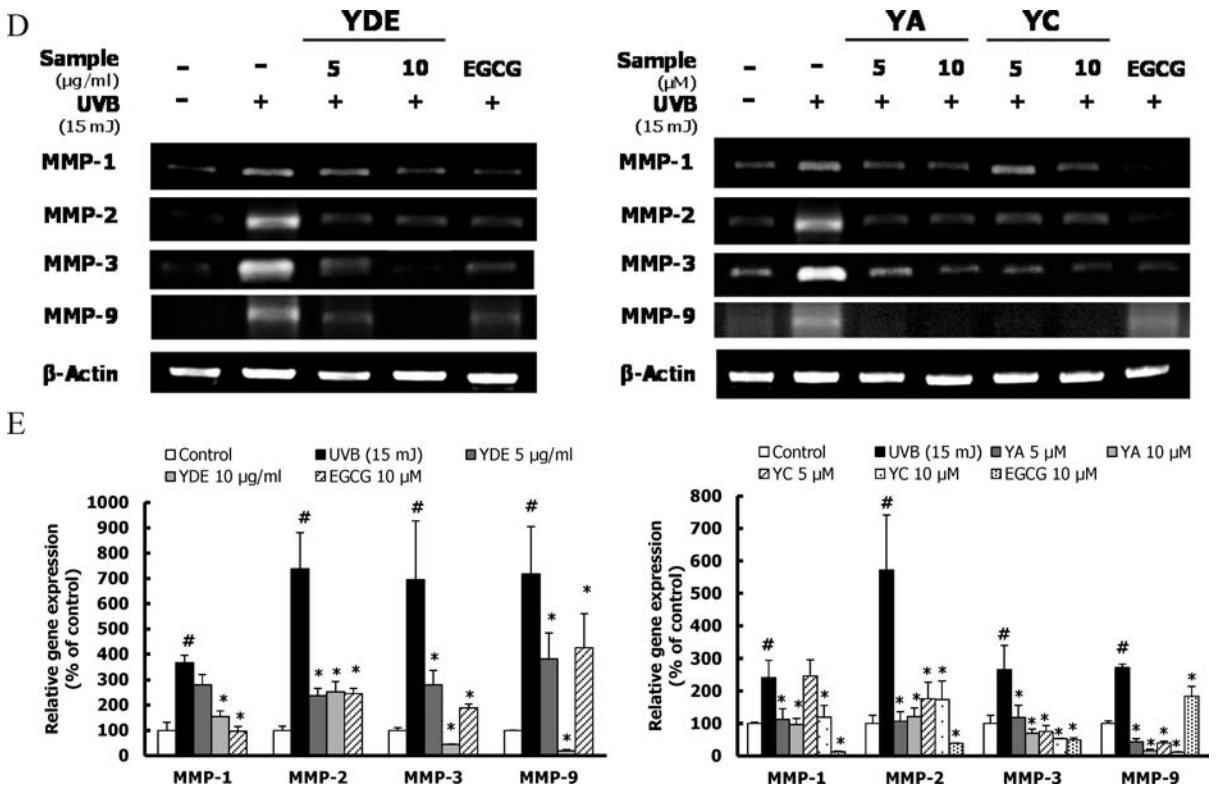

Figure 1. Effects of *Youngia dendiculatum* extract (YDE), youngiaside A (YA), and youngiaside C (YC) on MMP-1 production and MMPs mRNA expression in UVB-irradiated HaCaT cells and human dermal fibroblasts (HDF). (A) Chemical structure of constituents from YDE. HaCaT cells and HDF were treated with different concentrations of YDE and its active compounds, chicoric acid (CRA), 3,5-dicaffeoylquinic acid (DCQA), chlorogenic acid (CA), luteolin 7-*O*-glucuronide (Lute-glu), youngiaside A (YA), youngiaside B (YB), youngiaside C (YC), for 1 h and then exposed to UVB irradiation (15 mJ/cm^2). At 24 h after UVB exposure, (B, C) release of MMP-1 into the culture media was determined by ELISA in HaCaT cell and HDF, respectively. (D, E) mRNA expression of MMP-1, -2 ,-3, and -9 was measured by RT-PCR with regard to YDE, YA, and YC in HaCaT cells. β-Actin was used as an internal control for RT-PCR. Epigallocatechin gallate (EGCG) was used as a positive control. Results are expressed as the mean ± SD (% control) of three independent experiments. (#) $P < 0.05$ compared with vehicle control; (∗) $P < 0.05$ compared with UVB-treated cells.

(Applied Biosystems, Foster City, CA, USA). PCR products were separated by 1.5% agarose gel electrophoresis and visualized with ethidium bromide. β-Actin was used as an internal control. A densitometer was used for RT-PCR on DIG chemiluminescent film (volume of all markers/volume of β-actin).

Measurement of ROS Production. HaCaT cells were pretreated with YDE, YA, and YC for 1 h, washed with PBS, and stained with 40 μM DCFH-DA for 30 min. Cells were then irradiated with UVB (15 mJ/cm^2), and changes in fluorescence intensity were measured using a microplate reader (Bio-Tek Instruments) at excitation and emission wavelengths of 485 and 530 nm, respectively.

siRNA Treatment. The siRNAs targeted against Nrf2 were designed by and purchased from Cell Signaling (Beverly, MA, USA). Transfection of siRNAs (100 pmol) into HaCaT cells was performed with Lipofectamine RNAiMAX (Invitrogen).

Statistical Analysis. All experiments were repeated at least three times, and each experiment was performed in triplicate. Results are presented as the mean ± standard deviation (SD). Statistical analyses were performed using SPSS 12.0 (SPSS Inc., Chicago, IL, USA). Group differences were assessed by one-way analysis of variance (ANOVA), followed by Scheffe's test. A P value of <0.05 was considered statistically significant.

RESULTS

Effects of YDE, YA, and YC on HaCaT and HDF Cell Viability. Potential effects of YDE, YA, and YC on HaCaT and HDF cell viability were evaluated by MTT assay. HaCaT and HDF cells were irradiated with UVB (15 mJ/cm^2) and incubated with YDE, YA, or YC for 24 h. Treatment with YDE (5 or 10 μg/mL), YA, or YC (5 or 10 μM) had no cytotoxic effect on HaCaT and HDF cell viability (data not shown).

Effects of YDE, YA, and YC on MMP-1 Production and MMP mRNA Expression in UVB-Irradiated HaCaT and HDF Cells. Previously we identified and isolated several compounds from YDE.[19] To determine the effect of YDE and these compounds on MMP-1 production, the MMP-1 protein level was examined. YDE inhibited the release of MMP-1 from UVB-irradiated HaCaT cells and HDFs at concentrations of 5 and 10 μg/mL. In addition, we found that YA and YC inhibited MMP-1 production in UVB-irradiated HaCaT cells and HDFs, respectively (Figure 1B,C). Therefore, we selected YA and YC for further study. The results demonstrated that the UV irradiation up-regulated the mRNA levels of collagen-degrading MMPs including MMP-1, MMP-2, MMP-3, and MMP-9. The expression of these genes was down-regulated by treatment with YDE, YA, and YC in UV-irradiated HaCaT cells (Figure 1D,E).

Effects of YDE, YA, and YC on Type I Procollagen Production and COL1A1 and COL3A1 mRNA Expression in UVB-Irradiated HDFs. To investigate the effects of YDE, YA, and YC on type I procollagen production in UVB-irradiated HDFs, cells were exposed to UVB (15 mJ/cm^2), and type I procollagen enzyme activity was measured using a type I procollagen assay kit. Notably, YDE, YA, and YC increased

DOI: 10.1021/acs.jafc.5b00467
J. Agric. Food Chem. 2015, 63, 5428−5438

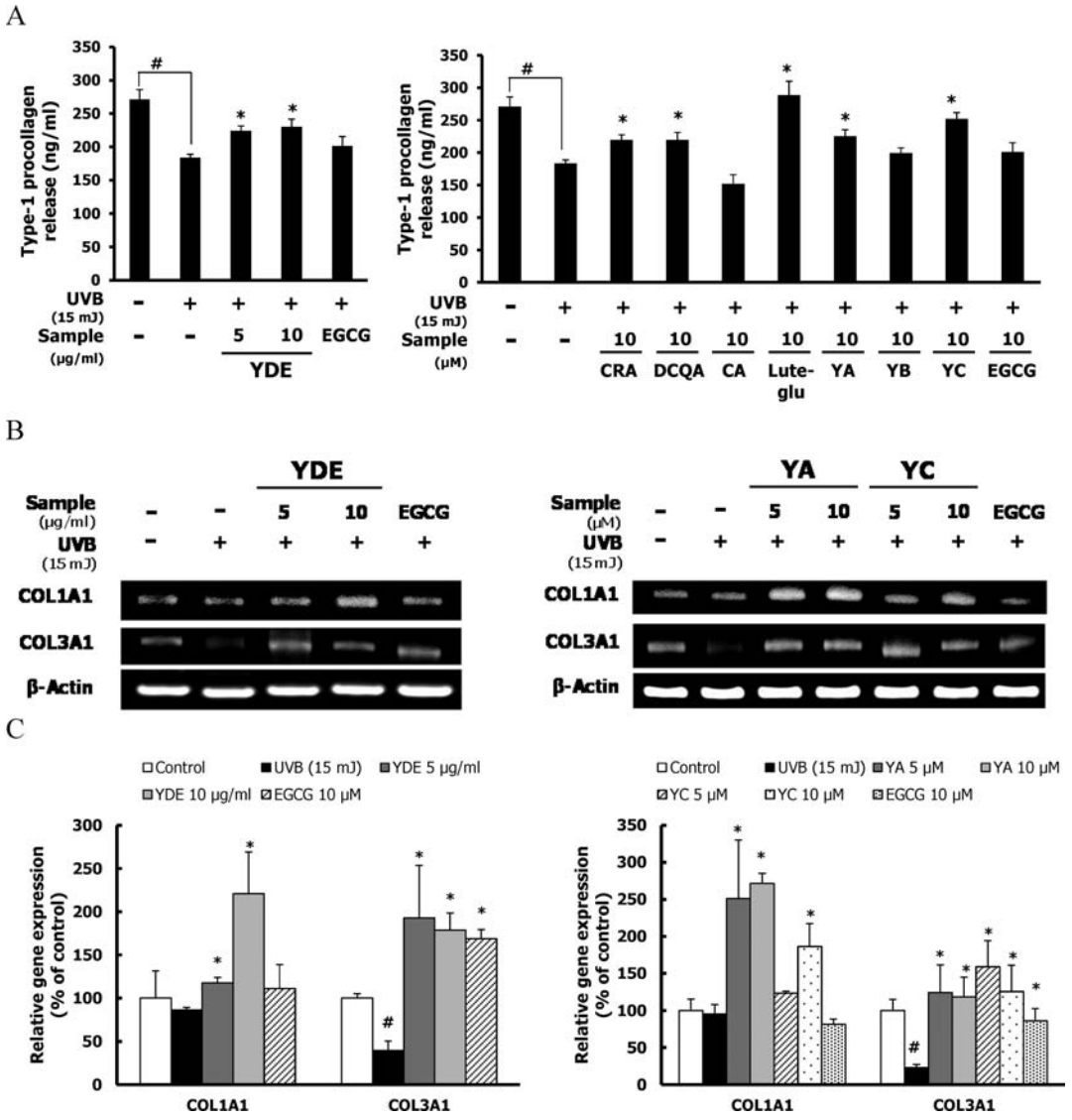

Figure 2. Effects of YDE, YA, and YC on type I procollagen production and COL1A1 and COL3A1 mRNA expression in UVB-irradiated HDF. HDFs were treated with different concentrations of YDE and its active compounds, CRA, CA, DCQA, Lute-glu, YA, YB, and YC, for 1 h and then exposed to UVB irradiation (15 mJ/cm^2). At 24 h after UVB exposure, (A) the amount of type I procollagen secretion into the culture media was determined by ELISA. (B, C) mRNA expression of COL1A1 and COL3A1 was measured by RT-PCR with regard to YDE, YA, and YC. β-Actin was used as an internal control for RT-PCR. EGCG was used as a positive control. Results are expressed as the mean ± SD (% control) of three independent experiments. (#) $P < 0.05$ compared with vehicle control; (*) $P < 0.05$ compared with UVB-treated cells.

type I procollagen protein production and COL1A1 and COL3A1 mRNA levels in HDFs (Figure 2).

Effects of YDE, YA, and YC on UVB-Induced Intracellular ROS Production and Antioxidant Enzyme Expression through Activation of Nrf2 in HaCaT Cells. To study the effects of YDE, YA, and YC on UVB-induced intracellular ROS generation, antioxidant enzyme expression, and Nrf2 activation, we utilized flow cytometry, RT-PCR, and Western blot analyses. Cells treated with YDE, YA, and YC inhibited UVB-induced intracellular ROS levels (Figure 3A) and increased expression of HO-1, SOD1, and Nrf2 (Figure 3B–D) compared to that of the UVB-irradiated control. To further confirm YA- and YC-mediated MMP-1 production through activation of Nrf2, we used Nrf2 RNA interference and treated sulforaphane as an Nrf2 activator. MMP-1 production was inhibited in YA-, YC-, and sulforaphane-treated cells but was not attenuated in Nrf2 siRNA-treated cells (Figure 3E).

Effects of YDE, YA, and YC on UVB-Induced Proinflammatory Mediators and NF-κB Activation in HaCaT Cells. We next investigated the effects of YDE, YA, and YC on UVB-induced expression of inflammatory mediators. Notably, UVB-induced expression of TNF-α, COX-2, IL-6, p65, and p50 was lower in YDE-, YA-, and YC-treated cells than in the UVB-irradiated control (Figure 4A,B).

To examine the mechanism by which YDE, YA, and YC inhibit NF-κB transcriptional activity, we assessed their effects on nuclear translocation and phosphorylation of NF-κB. YDE and YC inhibited UVB-induced nuclear translocation of NF-κB p65 protein (Figure 4C). Furthermore, YDE, YA, and YC inhibited the phosphorylation of IKKα/β and IκB and the degradation of IκB, which regulates nuclear translocation of NF-κB (Figure 4C).

Effects of YDE, YA, and YC on UVB-Induced Phosphorylation/Expression of c-Jun and c-Fos in HaCaT Cells. In this series of experiments, UVB-induced

DOI: 10.1021/acs.jafc.5b00467
J. Agric. Food Chem. 2015, 63, 5428−5438

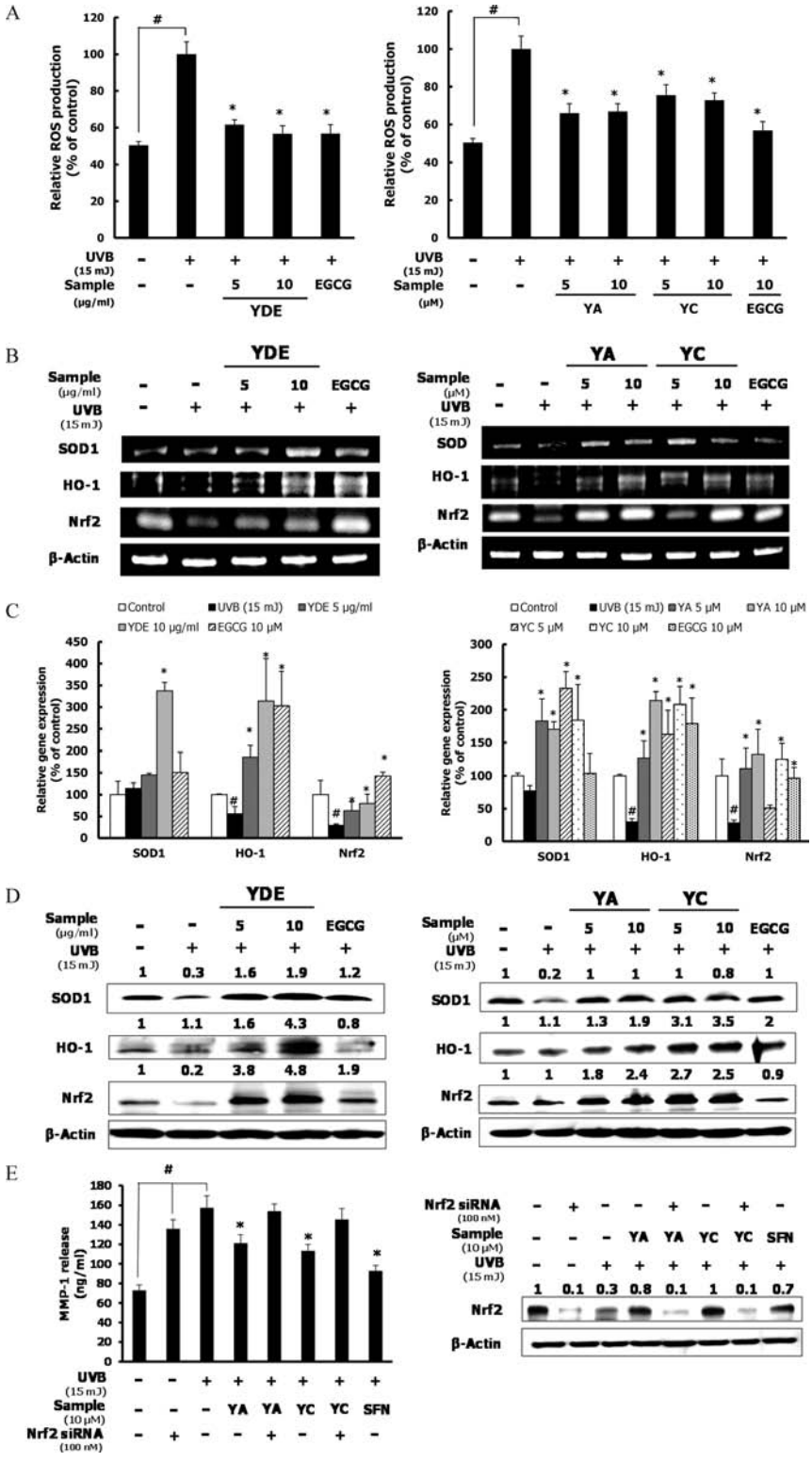

Figure 3. Effects of YDE, YA, and YC on intracellular ROS production, expressions of antioxidant enzymes, and Nrf2-mediated MMP-1 production in UVB-irradiated HaCaT cells. (A) HaCaT cells were pretreated with various concentrations of YDE, YA, and YC for 1 h and then stained with 40 μM 2′,7′-dichlorofluorescein diacetate (DCFH-DA; Sigma-Aldrich) for 30 min. The stained cells were then irradiated with UVB (15 mJ/cm^2). After 30 min, ROS levels were analyzed by flow cytometry. (B−D) HaCaT cells were treated with YDE, YA, and YC for 1 h and then exposed to UVB irradiation (15 mJ/cm^2). At 24 h after UVB exposure, SOD1, HO-1, and Nrf2 expressions were evaluated by RT-PCR and Western blot analysis. (E) HaCaT cells transfected with Nrf2 siRNA were treated with YA and YC for 1 h and then exposed to UVB irradiation (15 mJ/cm^2). At 24 h after UVB exposure, MMP-1 production and Nrf2 expression were measured by ELISA and Western blot analysis, respectively. β-Actin was used as an internal control for RT-PCR and Western blot analysis. EGCG was used as a positive control. Sulforaphane (SFN) was used as a positive control of Nrf2 activator. Results of ROS and MMP-1 production and RT-PCR are expressed as the mean ± SD (% control) of three independent experiments. (#) $P < 0.05$ compared with vehicle control; (∗) $P < 0.05$ compared with UVB-treated cells.

DOI: 10.1021/acs.jafc.5b00467
J. Agric. Food Chem. 2015, 63, 5428−5438

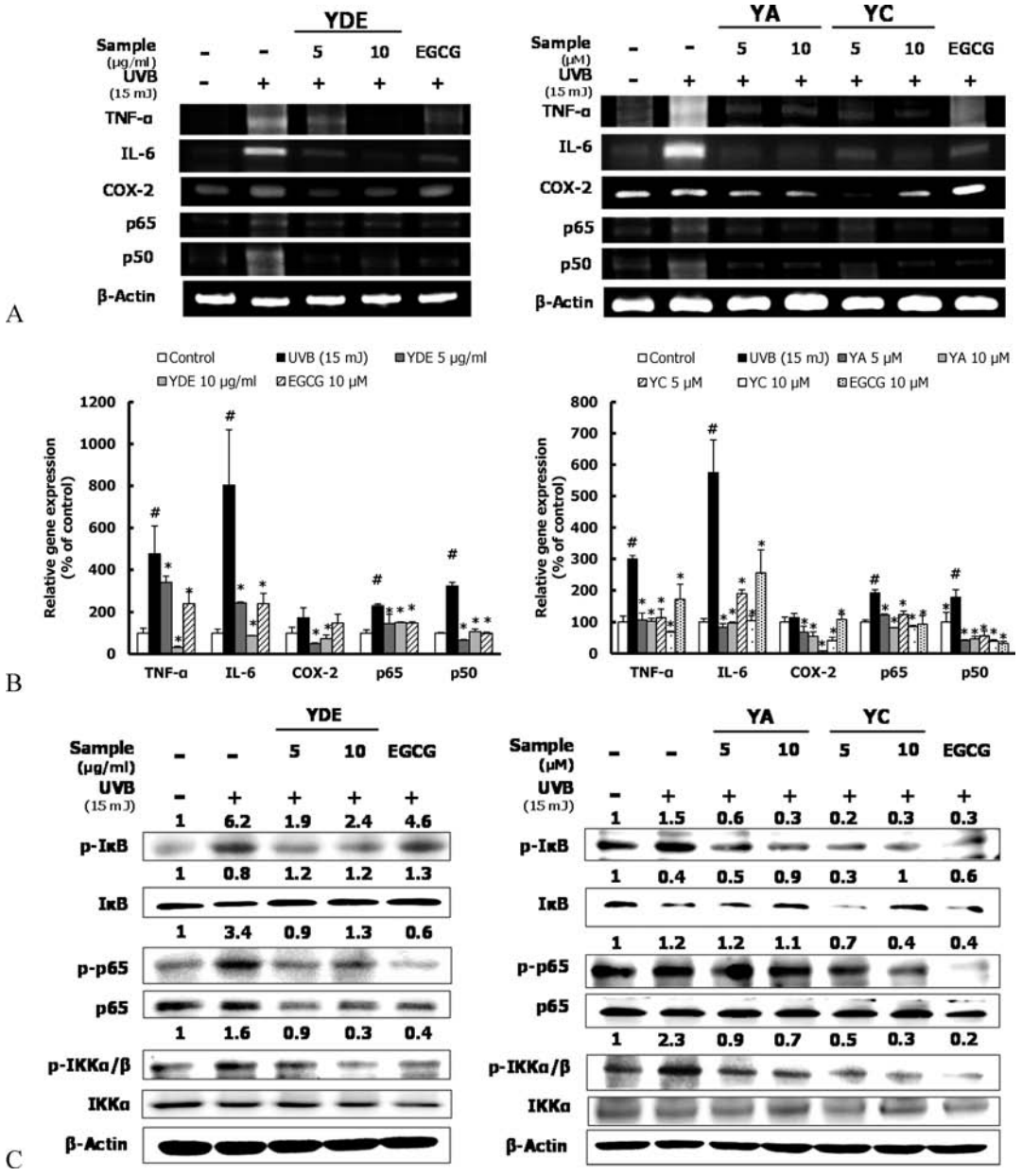

Figure 4. Effects of YDE, YA, and YC on inflammatory mediators and NF-κB activation in UVB-irradiated HaCaT cells. (A, B) HaCaT cells were treated with YDE, YA, and YC for 1 h and then exposed to UVB irradiation (15 mJ/cm^2). At 24 h after UVB exposure, TNF-α, IL-6, COX-2, p65, and p50 were evaluated by RT-PCR. (C) HaCaT cells were treated with YDE, YA, and YC for 1 h and then exposed to UVB irradiation (15 mJ/cm^2). At 30 min after UVB exposure, NF-κB signaling (IκBα, p65, IKKα/β) was assessed by Western blot analysis. β-Actin was used as internal control for Western blot analysis. EGCG was used as a positive control. RT-PCR results are expressed as the mean ± SD (% control) of three independent experiments. (#) $P < 0.05$ compared with vehicle control; (∗) $P < 0.05$ compared with UVB-treated cells.

phosphorylation of Akt, ERK, JNK, and p38 was lower in YDE-treated cells and phosphorylation of Akt and JNK was reduced in YA- and YC-treated cells (Figure 5A), suggesting that YDE, YA, and YC inhibit UVB-induced MMP-1 expression by suppressing MAPK signaling. AP-1 is composed of c-Jun and c-Fos proteins, and increased transcription of AP-1 interferes with the synthesis of the major dermal collagens I and III. Notably, treatment with YDE, YA, and YC inhibited AP-1 transcription (Figure 5B).

Effects of YDE, YA, and YC on AMPK-Mediated MMP-1 Expression. AMPK is known to suppress UVB-induced MMP-1 expression. Therefore, we hypothesized that AMPK activation by YDE, YA, and YC could inhibit UV-induced MMP-1 expression. First, we verified that YDE, YA, and YC increased AMPK phosphorylation in HaCaT cells (Figure 6A). To confirm the role of AMPK activation on UVB-induced MMP-1 expression, we investigated whether YA and YC suppressed MMP-1 production via activation of the AMPK pathway. Treatment with compound **C**, an AMPK inhibitor, and UVB irradiation increased MMP-1 expression. Moreover, MMP-1 expression was inhibited by YA, YC, and AICAR, an activator of AMPK. However, YA and YC did not show inhibitory effects in compound **C**-treated HaCaT cells (Figure 6B).

DISCUSSION

MMPs play an important role in the physiological mechanisms of skin photoaging. UV irradiation alters the connective tissues

DOI: 10.1021/acs.jafc.5b00467
J. Agric. Food Chem. 2015, 63, 5428−5438

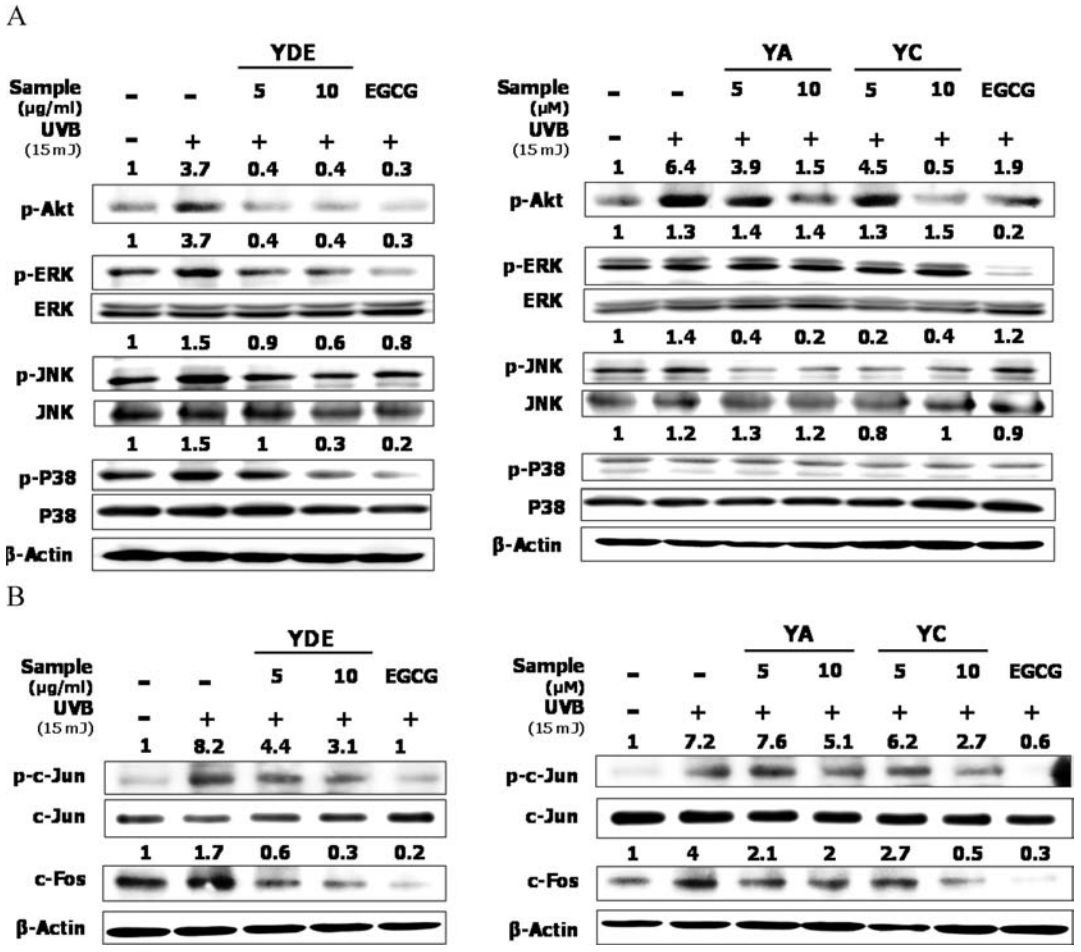

Figure 5. Effects of YDE, YA, and YC on UVB-induced MAPK/AP-1 signaling in UVB-irradiated HaCaT cells. HaCaT cells were treated with YDE, YA, and YC for 1 h and then exposed to UVB irradiation (15 mJ/cm^2). At 30 min after UVB exposure, phosphorylations of (A) Akt, MAPK (ERK, JNK, and p38) and (B) AP-1 (c-Jun and c-Fos) were assessed by Western blot analysis. β-Actin was used as internal control for Western blot analysis. EGCG was used as a positive control.

of the skin by up-regulating the expression of MMPs, which degrade collagen and other ECM proteins.[22−24] MMP-1 is a member of the collagenase subfamily of MMPs. When activated, MMP-1 initiates collagen breakdown by cleaving type I and type III collagen, which are further cleaved by MMP-2 and -9.[25] Latent MMP-1, -2, and -9 derived from dermal fibroblasts or keratinocytes could be greatly activated by MMP-3 and ultimately initiate degradation of type I and III collagens.[25] The gelatinolytic activities of MMP-2 and -9 are the central players in UV-irradiated skin damage and in the formation of wrinkles.[26] One study demonstrated that antioxidants inhibit the activity of UV-induced MMP-9.[27] Therefore, we hypothesized that YDE, YA, and YC, which are known to have antioxidant activities,[15,19−21] affect MMP expression. In the present study, we found that YDE, YA, and YC markedly decreased UV-induced MMP production and expression. Thus, our results clearly show that YDE, YA, and YC down-regulate MMP expression.

Collagens provide resiliency and strength to the skin; therefore, collagen degradation by processes such as photoaging promotes skin aging. Most collagen fibers in the dermis are type I and III collagens.[4] Types I collagen is a fibrillar collagen that is found in extensible connective tissues such as skin, lung, and the vascular system. Type III collagen is a fibrous scleroprotein in bone, cartilage, dentin, tendon, bone marrow stroma, and other connective tissue and yields gelatin on boiling.[4] In this study, YDE, YA, and YC increased type I procollagen protein and mRNA levels of COL1A1 and COL3A1. Because reduced collagen levels in UV-damaged skin may occur via collagen breakdown due to UVB-induced MMPs, the present results indicate that YDE, YA, and YC may prevent or treat UVB-induced ECM damage by inhibiting MMP expression.

In the photoaging process, UV irradiation induces oxidative damage. UV-induced ROS production up-regulates the expression of MMP-1, leading to increased collagen degradation. ROS production also plays an important role in MAPK signaling.[28] Thus, reducing ROS generation is a potentially effective strategy to prevent skin photoaging. Antioxidant agents can mediate decreased ROS production and protect the skin from the effects of UV irradiation. The Nrf2−Keap1 pathway plays a key role in coordinating the transcriptional induction of various antioxidant-metabolizing enzymes that can neutralize the damaging effects of ROS. In a previous study, YDE exhibited antioxidant effects against oxidative stress in hepatocytes and retinal cells by decreasing ROS production and increasing antioxidant enzyme expression.[15,21] In the present study, YDE, YA, and YC significantly reduced intracellular ROS production. Reduced antioxidant enzyme expression in aged and photoaged keratinocytes and fibroblasts can accelerate oxidative damage and promote MAPK signaling to increase the rate of skin aging

DOI: 10.1021/acs.jafc.5b00467
J. Agric. Food Chem. 2015, 63, 5428−5438

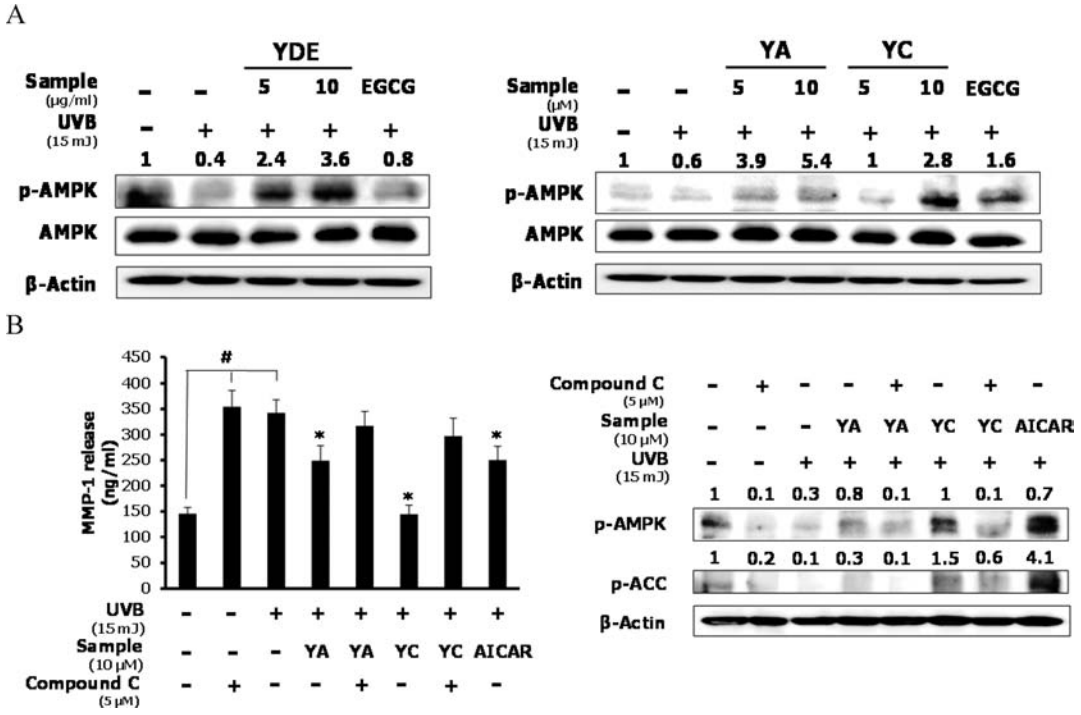

Figure 6. Effects of YDE, YA, and YC on phosphorylation of AMPK and AMPK-mediated MMP-1 production in UVB-irradiated HaCaT cells. HaCaT cells were treated with YDE, YA, and YC for 1 h and then exposed to UVB irradiation (15 mJ/cm^2). At 30 min after UVB exposure, (A) phosphorylation of AMPK and ACC was evaluated by Western blot analysis. HaCaT cells treated with compound **C** were treated with YA and YC for 1 h and then exposed to UVB irradiation (15 mJ/cm^2). At 24 h after UVB exposure, (B) production of MMP-1 and phosphorylation of AMPK and ACC were measured by ELISA and Western blot analyses, respectively. β-Actin was used as an internal control for RT-PCR and Western blot analysis. EGCG was used as a positive control. Compound **C** and AICAR were used as an AMPK inhibitor and activator, respectively. Results of MMP-1 production are expressed as the mean ± SD (% control) of three independent experiments. (#) $P < 0.05$ compared with vehicle control; (∗) $P < 0.05$ compared with UVB-treated cells.

and photoaging.[29] YDE, YA, and YC increased the expression of SOD1, HO-1, and Nrf2 and suppressed MMP-1 production via a Nrf2-dependent pathway. These observed effects indicate that YDE, YA, and YC inhibit UVB-induced alterations in MMP-1 and type I procollagen expression, in part by reducing ROS generation and promoting antioxidant enzyme expression and Nrf2 expression.

MAPK signaling plays a central role in regulating cell proliferation, cell motility, MMP gene expression, and cell survival and death. The three major MAPK subfamilies in mammalian cells include JNK, ERK, and p38.[30] Oxidative stress induced by accumulation of ROS can initiate MAPK signaling by phosphorylation of MAPK proteins.[28] We show in the present study that UVB-induced phosphorylation of ERK, JNK, and p38 was lower in YDE-, YA-, and YC-treated cells. This suggests that YDE, YA, and YC attenuate UVB-induced expression of MMP-1 by inhibiting MAPK signaling. MMP-1 gene expression is regulated by c-Jun and c-Fos, which are components of the AP-1 protein complex. When activated, JNK phosphorylates c-Jun, increasing c-Jun transcriptional activity.[8,31] YDE, YA, and YC inhibited UVB-induced AP-1 activation by reducing c-Jun phosphorylation and c-Fos expression. These results indicate that YDE, YA, and YC reduce UVB-induced c-Jun and c-Fos expression by inhibiting phosphorylation of JNK.

The NF-κB pathway is an important regulator of gene expression associated with immune and inflammatory responses.[32] In addition, NF-κB also increases MMP-1 expression in the dermis.[33] Our results show that YDE, YA, and YC reduced IκBα phosphorylation and NF-κB p65 nuclear translocation.

Pro-inflammatory cytokines and transcription factors, such as TNF-α, COX-2, IL-6, p65, and p50, which affect the aging process, are induced by exposure to UVB radiation. Inflammation, which is mediated by these cytokines, increases the production of ROS, thus amplifying the effects of UV exposure.[34] The antioxidant properties of YDE were confirmed by its ability to increase the antioxidant enzyme activity of hepatocyte and retinal cells under oxidative stress conditions.[15,21] Hence, YDE, YA, and YC may inhibit inflammatory cytokine expression through these factors. Our findings demonstrate that YDE, YA, and YC inhibited TNF-α, COX-2, IL-6, p65, and p50 expression and attenuated UVB-induced expression of pro-inflammatory cytokines.

AMPK regulates UV-induced stabilization of COX-2 mRNA in human keratinocytes.[35] AMPK can also counteract oxidative stress in the vascular endothelium[36] and is a therapeutic target for vascular disease.[37] In a recent study, it was suggested that AMPK activation plays a key role in the suppression of MMP-1.[10] In accordance with these previous studies, we found that treatment with YDE, YA, and YC increases AMPK phosphorylation and inhibits MMP-1 production via AMPK activation. Therefore, we conclude that the AMPK pathway is the major target pathway mediating the effect of YA and YC in HaCaT cells.

The present study is the first to demonstrate that YA, YC, and YDE reduced MMP expression by suppressing UVB-induced oxidative stress and inflammation in HaCaT cells and increased type I procollagen production in HDFs. These

DOI: 10.1021/acs.jafc.5b00467
J. Agric. Food Chem. 2015, 63, 5428−5438

responses may be mediated by inhibition of MAPK, AP-1, and NF-κB and activation of Nrf2 and AMPK pathways in cultured HaCaT cells. Further research using physiologically appropriate skin cell models is needed because keratinocyte cell lines have different biological functions and genetic variations compared with those of primary keratinocytes. These differences may influence cellular responses to UV irradiation such as MMP-1 activation. In addition, it is necessary to elucidate potential anti-aging properties of YA, YC, and YDE in vivo and characterize the underlying mechanisms in animal models.

AUTHOR INFORMATION

Corresponding Author

*(C.W.N.) E-mail: cwnho@kist.re.kr. Phone: +82-33-650-3651. Fax: +82-33-650-3679.

Funding

This work was supported by an intramural grant (2Z043811, 2E25181) from the Korea Institute of Science and Technology, Gangneung Institute.

Notes

The authors declare no competing financial interest.

ABBREVIATIONS USED

MMP, matrix metalloproteinase; AP-1, activator protein-1; MAPK, mitogen-activated protein kinases; NF-κB, nuclear factor-κB; TNF, tumor necrosis factor; HDF, human dermal fibroblasts; AMPK, adenosine monophosphate activated protein kinase; Nrf2, nuclear factor-erythroid 2-related factor-2; ERK, extracellular signal-regulated kinase; JNK, c-Jun N-terminal kinase; UV, ultraviolet; ROS, reactive oxygen species; ECM, extracellular matrix; Keap1, Kelch-like ECH associated protein 1; AhR, aryl hydrocarbon receptor; DCFH-DA, 2′,7′-dichlorofluorescin diacetate; SOD, superoxide dismutase; HO, heme oxygenase; COX, cyclooxygenase; IL, interleukin

REFERENCES

(1) Fisher, G. J.; Kang, S.; Varani, J.; Bata-Sorgo, Z.; Wan, Y.; Datta, S.; Voorhees, J. J. Mechanisms of photoaging and chronological skin aging. *Arch. Dermatol.* **2002**, *138*, 1462−1470.

(2) Madronich, S.; McKenzie, R. L.; Björn, L. O.; Caldwell, M. M. Changes in biologically active ultraviolet radiation reaching the Earth's surface. *J. Photochem. Photobiol., B* **1998**, *46*, 5−19.

(3) Rijken, F.; Kiekens, R. C.; Bruijnzeel, P. L. Skin-infiltrating neutrophils following exposure to solar-simulated radiation could play an important role in photoageing of human skin. *Br. J. Dermatol.* **2005**, *152*, 321−328.

(4) Fisher, G. J.; Datta, S. C.; Talwar, H. S.; Wang, Z. Q.; Varani, J.; Kang, S.; Voorhees, J. J. Molecular basis of sun-induced premature skin ageing and retinoid antagonism. *Nature* **1996**, *379*, 335−339.

(5) Fagot, D.; Asselineau, D.; Bernard, F. Matrix metalloproteinase-1 production observed after solar-simulated radiation exposure is assumed by dermal fibroblasts but involves a paracrine activation through epidermal keratinocytes. *Photochem. Photobiol.* **2004**, *79*, 499−505.

(6) Saito, Y.; Shiga, A.; Yoshida, Y.; Furuhashi, T.; Fujita, Y.; Niki, E. Effects of a novel gaseous antioxidative system containing a rosemary extract on the oxidation induced by nitrogen dioxide and ultraviolet radiation. *Biosci., Biotechnol., Biochem.* **2004**, *68*, 781−786.

(7) Yang, S. H.; Sharrocks, A. D.; Whitmarsh, A. J. Transcriptional regulation by the MAP kinase signaling cascades. *Gene* **2003**, *320*, 3−21.

(8) Xu, Y.; Fisher, G. J. Ultraviolet (UV) light irradiation induced signal transduction in skin photoaging. *J. Dermatol. Sci., Suppl.* **2005**, *1*, S1−S8.

(9) Hardie, D. G. The AMP-activated protein kinase pathway-new players upstream and downstream. *J. Cell Sci.* **2004**, *117*, 5479−5487.

(10) Shin, D. J.; Kim, J. E.; Lim, T. G.; Jeong, E. H.; Park, G.; Kang, N. J.; Park, J. S.; Yeom, M. H.; Oh, D. K.; Bode, A. M.; Dong, Z.; Lee, H. J.; Lee, K. W. 20-*O*-β-D-Glucopyranosyl-20(*S*)-protopanaxadiol suppresses UV-induced MMP-1 expression through AMPK-mediated mTOR inhibition as a downstream of the PKA-LKB1 pathway. *J. Cell. Biochem.* **2014**, *115*, 1702−1711.

(11) Itoh, K.; Chiba, T.; Takahashi, S.; Ishii, T.; Igarashi, K.; Katoh, Y.; Oyake, T.; Hayashi, N.; Satoh, K.; Hatayama, I.; Yamamoto, M.; Nabeshima, Y. An Nrf2/small Maf heterodimer mediates the induction of phase II detoxifying enzyme genes through antioxidant response elements. *Biochem. Biophys. Res. Commun.* **1997**, *236*, 313−322.

(12) Hirota, A.; Kawachi, Y.; Itoh, K.; Nakamura, Y.; Xu, X.; Banno, T.; Takahashi, T.; Yamamoto, M.; Otsuka, F. Ultraviolet A irradiation induces NF-E2-related factor 2 activation in dermal fibroblasts: protective role in UVA-induced apoptosis. *J. Invest. Dermatol.* **2005**, *124*, 825−832.

(13) Kawachi, Y.; Xu, X.; Taguchi, S.; Sakurai, H.; Nakamura, Y.; Ishii, Y.; Fujisawa, Y.; Furuta, J.; Takahashi, T.; Itoh, K.; Yamamoto, M.; Yamazaki, F.; Otsuka, F. Attenuation of UVB-induced sunburn reaction and oxidative DNA damage with no alterations in UVB-induced skin carcinogenesis in Nrf2 gene-deficient mice. *J. Invest. Dermatol.* **2008**, *128*, 1773−1779.

(14) Hirota, A.; Kawachi, Y.; Yamamoto, M.; Koga, T.; Hamada, K.; Otsuka, F.; Hirota, A.; Kawachi, Y.; Yamamoto, M.; Koga, T.; Hamada, K.; Otsuka, F. Acceleration of UVB-induced photoageing in nrf2 gene-deficient mice. *Exp. Dermatol.* **2011**, *20*, 664−668.

(15) Kang, K.; Jho, E. H.; Lee, H. J.; Oidovsambuu, S.; Yun, J. H.; Kim, C. Y.; Yoo, J. H.; Kim, Y. J.; Kim, J. H.; Ahn, S. Y.; Nho, C. W. *Youngia denticulate* protects against oxidative damage induced by *tert*-butylhydroperoxide in HepG2 cells. *J. Med. Food* **2011**, *14*, 1198−1207.

(16) Dalby-Brown, L.; Barsett, H.; Landbo, A. K. R.; Meyer, A. S.; Molgaard, P. Synergistic antioxidative effects of alkamides, caffeic acid derivatives, and polysaccharide fractions from *Echinacea purpurea* on in vitro oxidation of human low-density lipoproteins. *J. Agric. Food Chem.* **2005**, *53*, 9413−9423.

(17) Kim, K. A.; Kang, K. D.; Lee, E. H.; Nho, C. W.; Jung, S. H. Edible wild vegetable, *Gymnaster koraiensis* protects retinal ganglion cells against oxidative stress. *Food Chem. Toxicol.* **2011**, *49*, 2131−2143.

(18) Tsuchiya, T.; Suzuki, O.; Igarashi, K. Protective effects of chlorogenic acid on paraquat-induced oxidative stress in rats. *Biosci., Biotechnol., Biochem.* **1996**, *60*, 765−768.

(19) Yun, J. H.; Lee, S. B.; Lee, H. J.; Kim, C. Y.; Kim, M. A.; Sohn, Y. C.; Nho, C. W. Bi-functional induction of the quinone reductase and cytochrome P450 1A1 by youngiasides via Nrf2-ARE and AhRXRE pathways. *Biol. Pharm. Bull.* **2010**, *33*, 1650−1657.

(20) Yoo, J. H.; Kang, K.; Yun, J. H.; Kim, M. A.; Nho, C. W. *Crepidiastrum denticulatum* extract protects the liver against chronic alcohol-induced damage and fat accumulation in rats. *J. Med. Food* **2014**, *17*, 432−438.

(21) Ahn, H. R.; Lee, H. J.; Kim, K. A.; Kim, C. Y.; Nho, C. W.; Jang, H.; Pan, C. H.; Lee, C. Y.; Jung, S. H. Hydroxycinnamic acids in *Crepidiastrum denticulatum* protect oxidative stress-induced retinal damage. *J. Agric. Food Chem.* **2014**, *62*, 1310−1323.

(22) Stetler-Stevenson, W. G.; Yu, A. E. Proteases in invasion: matrix metalloproteinases. *Semin. Cancer Biol.* **2011**, *11*, 143−152.

(23) Vincenti, M. P.; White, L. A.; Schroen, D. J.; Benbow, U.; Brinckerhoff, C. E. Regulating expression of the gene for matrix metalloproteinase-1 (collagenase): mechanisms that control enzyme activity, transcription, and mRNA stability. *Crit. Rev. Eukaryotic Gene Expression* **1996**, *6*, 391−411.

(24) Kim, S. Y.; Kim, S. J.; Lee, J. Y.; Kim, W. G.; Park, W. S.; Sim, Y. C.; Lee, S. J. Protective effects of dietary soy isoflavones against UV-induced skin-aging in hairless mouse model. *J. Am. Coll. Nutr.* **2004**, *23*, 157−162.

DOI: 10.1021/acs.jafc.5b00467
J. Agric. Food Chem. 2015, 63, 5428−5438

(25) Nagase, H.; Visse, R.; Murphy, G. Structure and function of matrix metalloproteinases and TIMPs. *Cardiovasc. Res.* **2006**, *69*, 562−573.
(26) Steinbrenner, H.; Ramos, M. C.; Stuhlmann, D.; Sies, H.; Brenneisen, P. UVA-mediated downregulation of MMP-2 and MMP-9 in human epidermal keratinocytes. *Biochem. Biophys. Res. Commun.* **2003**, *308*, 486−491.
(27) Vayalil, P. K.; Mittal, A.; Hara, Y.; Elmets, C. A.; Katiyar, S. K. Green tea polyphenols prevent ultraviolet light-induced oxidative damage and matrix metalloproteinases expression in mouse skin. *J. Invest. Dermatol.* **2004**, *122*, 1480−1487.
(28) Rittié, L.; Fisher, G. J. UV-light-induced signal cascades and skin aging. *Ageing Res. Rev.* **2002**, *1*, 705−720.
(29) Heck, D. E.; Shakarjian, M.; Kim, H. D. Mechanisms of oxidant generation by catalase. *Ann. N. Y. Acad. Sci.* **2010**, *1203*, 120−125.
(30) Robinson, M. J.; Cobb, M. H. Mitogen-activated protein kinase pathways. *Curr. Opin. Cell Biol.* **1997**, *9*, 180−186.
(31) Brenneisen, P.; Wenk, J.; Klotz, L. O.; Wlaschek, M.; Briviba, K.; Krieg, T.; Sies, H.; Scharffetter-Kochanek, K. Central role of ferrous/ferric iron in the ultraviolet B irradiation-mediated signaling pathway leading to increased interstitial collagenase (matrix-degrading metalloprotease (MMP)-1) and stromelysin-1 (MMP-3) mRNA levels in cultured human dermal fibroblasts. *J. Biol. Chem.* **1998**, *273*, 5279−5287.
(32) Karin, M.; Greten, F. R. NF-κB: linking inflammation and immunity to cancer development and progression. *Nat. Rev. Immunol.* **2005**, *5*, 749−59.
(33) Bond, M.; Baker, A. H.; Newby, A. C. Nuclear factor kappaB activity is essential for matrix metalloproteinase-1 and -3 upregulation in rabbit dermal fibroblasts. *Biochem. Biophys. Res. Commun.* **1999**, *264*, 561−567.
(34) Pillai, S.; Oresajo, C.; Hayward, J. Ultraviolet radiation and skin aging: roles of reactive oxygen species, inflammation and protease activation, and strategies for prevention of inflammation-induced matrix degradation − a review. *Int. J. Cosmet. Sci.* **2005**, *27*, 17−34.
(35) Zhang, J.; Bowden, G. T. UVB irradiation regulates Cox-2 mRNA stability through AMPK and HuR in human keratinocytes. *Mol. Carcinog.* **2008**, *47*, 974−983.
(36) Colombo, S. L.; Moncada, S. AMPKα1 regulates the antioxidant status of vascular endothelial cells. *Biochem. J.* **2009**, *421*, 163−169.
(37) Nagata, D.; Takeda, R.; Sata, M.; Satonaka, H.; Suzuki, E.; Nagano, T.; Hirata, Y. AMP-activated protein kinase inhibits angiotensin II-stimulated vascular smooth muscle cell proliferation. *Circulation* **2004**, *110*, 444−451.

DOI: 10.1021/acs.jafc.5b00467
J. Agric. Food Chem. 2015, 63, 5428−5438

JOURNAL OF AGRICULTURAL AND FOOD CHEMISTRY

Article

pubs.acs.org/JAFC

Isolation of a Hemagglutinin with Potent Antiproliferative Activity and a Large Antifungal Defensin from *Phaseolus vulgaris* cv. Hokkaido Large Pinto Beans

Cuiming Yin, Jack Ho Wong,* and Tzi Bun Ng*

School of Biomedical Sciences, Faculty of Medicine, The Chinese University of Hong Kong, Shatin, Hong Kong, China

Supporting Information

ABSTRACT: Lectins (hemagglutinins) are defined as sugar-binding proteins or glycoproteins with various biological activities. A 60 kDa dimeric hemagglutinin with a blocked N-terminus was isolated in large yield (190 mg/60 g) from the common edible bean *Phaseolus vulgaris* cv. Hokkaido large pinto bean. Its hemagglutinating, antifungal, and antitumor activities as well as the effects of carbohydrate and metal ions on its hemagglutinating activity were examined. It inhibited the proliferation of nasopharyngeal carcinoma (CNE2), human breast cancer (MCF7), and hepatoma (HepG2) cells. The IC_{50} values toward HepG2, MCF7, and CNE2 cells after treatment for 48 h were 8.1, 6.07, and 7.49 μM, respectively, which were relatively low among lectins of different *P. vulgaris* cultivars. From the pinto beans, a 10888 Da antifungal peptide with similarity to plant defensins as revealed by mass spectroscopic analysis was also isolated with a yield of 3.2 mg of proteins from 60 g of beans. The large defensin was capable of inhibiting mycelial growth in *Mycosphaerella arachidicola*, *Setosphaeria turcica*, *Bipolaris maydis*, and *Fusarium oxysporum* but not in *Valsa mali*.

KEYWORDS: *hemagglutinin, antiproliferative, antifungal, defensin*

INTRODUCTION

From ancient times to the present, pathogen invasion is a health hazard to most of living organisms. During the process of evolution, organisms have developed various defense mechanisms to eliminate these potential life-threatening risks. Lectins and defensins are two types of defense proteins that plants secrete for self-protection.[1]

Lectins (hemagglutinins) are sugar-binding proteins with high carbohydrate selectivity, which exist ubiquitously in diverse species of plants, animals, viruses, bacteria, and fungi.[2] Along with a defensive nature, some of them, such as lectins from edible plants, demonstrate a strong capability of inhibiting cancer cell proliferation. For example, concanavalin A (Con A), a mannose- and glucose-binding lectin isolated from jack bean, was found to have considerable potential in anticancer applications.[3] However, apart from it, currently available lectins may have their own limitations for further development and application. Thus, the discovery of more potential targets is of great significance and a worthwhile undertaking.

Phaseolus vulgaris is a leguminous species that produces common edible beans. Different *P. vulgaris* cultivars share the same characteristic; that is, most of them contain a lectin or a phytohemagglutinin as a storage protein. Even though lectins from various cultivars have similar molecular sizes, they may possess different biological activities and vary in the potency of a particular activity. Antifungal proteins such as defensin may or may not be present in a cultivar. Hence, we set out to isolate a lectin and an antifungal protein from *P. vulgaris* cultivar Hokkaido large pinto bean.

MATERIALS AND METHODS

Purification of Hemagglutinin from Hokkaido Large Pinto Bean. Hokkaido large pinto beans were purchased from a Japanese food supermarket in Hong Kong. After soaking in distilled water overnight, 60 g of beans was homogenized in a Waring blender in 500 mL of 20 mM Tris-HCl buffer (pH 7.6). The homogenate was centrifuged at 16000 rpm for 30 min at 4 °C. The supernatant was filtered by using a piece of filter paper before loading onto an Affi-gel blue gel (Bio-Rad) column (18 cm × 5 cm) that had been pre-equilibrated with 20 mM Tris-HCl buffer (pH 7.6). Then, the column was washed with 1 M NaCl in 20 mM Tris-HCl buffer (pH 7.6) to elute the adsorbed proteins. The adsorbed fraction was dialyzed against double-distilled water overnight at 4 °C and lyophilized into powder form. The powder was resuspended (20 mg/mL buffer) in 20 mM NH_4HCO_3 buffer (pH 9.6) before FPLC-anion exchange chromatography on a Mono Q column (GE Healthcare) using an AKTA Purifier (GE Healthcare). Adsorbed proteins were eluted using a 0−1 M NaCl gradient in 20 mM NH_4HCO_3 buffer (pH 9.6). The first peak containing adsorbed materials was collected, dialyzed, lyophilized, resuspended in 20 mM Tris-HCl buffer (pH 7.6) (5 mg/mL), and then subjected to FPLC-gel filtration on a Superdex 75 HR 10/300 column (GE Healthcare). The first major absorbance peak contained purified Hokkaido large pinto bean lectin.

The three chromatographic steps used for purifying defensin from Hokkaido large pinto beans were the same as described above for the purification of hemagglutinin. In the Mono Q purification step, the unbound fraction was collected and dialyzed against double-distilled water, and buffer was added, resulting in a protein solution in 20 mM Tris-HCl buffer (pH 7.6). Then the sample was subjected to FPLC-gel filtration on a Superdex 75 HR 10/300 column (GE Healthcare). The last major absorbance peak contained purified Hokkaido large pinto bean defensin.

Molecular Mass Determination. Sodium dodecyl sulfate−polyacrylamide gel electrophoresis (SDS-PAGE) was carried out using a 15% separating gel and a 5% stacking gel. The protein sample was

Received: January 26, 2015
Revised: May 7, 2015
Accepted: May 12, 2015
Published: May 12, 2015

ACS Publications © 2015 American Chemical Society

DOI: 10.1021/acs.jafc.5b00475
J. Agric. Food Chem. 2015, 63, 5439−5448

diluted with loading buffer containing β-mercaptoethanol (10% glycerol, 0.4% SDS, 0.005% bromophenol blue, and 20 mM EDTA in 0.5 M Tris-HCl, pH 7.5, 5% β-mercaptoethanol) to reduce disulfide bonds in the proteins. The samples were boiled in water for 5 min. Then, electrophoresis was performed at a constant current of 10 mA and a constant voltage of 120 V for about 75 min. After electrophoresis, the gel was stained with Coomassie brilliant blue, and it was put on a shaker to shake for 1 h and then destained with 10% acetic acid overnight.[4]

Determination of N-Terminal Amino Acid. N-Terminal amino acid sequence analysis was carried out using an HP 1000A Edman degradation unit and an HP 1000 HPLC system (Agilent Technologies, Santa Clara, CA, USA).

Mass Spectrum Analysis. The molecular mass of the antifungal protein was verified by performing matrix-assisted laser desorption ionization time-of-flight mass spectrometry (MALDI-TOF MS), using an Applied Biosystems 4700 Proteomics Analyzer.

Matrix-assisted laser desorption/ionization time-of-flight time-of-flight tandem mass spectrometry (MALDI-TOF-TOF-MS/MS) was utilized to fragment sample proteins by MS/MS, and the fragments were identified by top-down proteomic analysis. The defense protein was identified by analysis of MS and MS/MS data using NCBInr and SwissProt databases (Greenplant).[5]

Assay of Hemagglutinating Activity. A 50 μL test sample was subjected to a 2-fold serial dilution with phosphate-buffered saline (PBS) (pH 7.2) in a 96-well microtiter U-plate. Afterward, 50 μL of a rabbit red blood cell suspension (2%) in PBS was added to each diluted sample. PBS (50 μL) mixed with 50 μL rabbit red blood cell was used as a negative control. The plate was incubated at room temperature until the red blood cells in the negative control formed a red dot at the bottom of the well, which means it had fully sedimented. The hemagglutinating activity of each of the test samples was then recorded. One hemagglutination unit or hemagglutination titer is defined as the reciprocal of the highest dilution of the lectin sample that induces hemagglutination. Specific hemagglutinating activity is the number of hemagglutination units per milligram of protein.[6]

Determination of pH Stability and Temperature Stability of Hemagglutinating Activity. To ascertain the effect of pH, solutions/buffers with different pH values from 0 to 14 were prepared as follows: pH 0−1, HCl; pH 2−5, NH_4OAc; pH 6−10, Tris-HCl; pH 11−12, $NaHCO_3$; and pH 13−14, NaOH. The protein sample was mixed with an equal volume (50 μL) of a solution at a specified pH and incubated at room temperature for 30 min. Then, the mixtures were neutralized and assay of hemagglutinating activity was carried out. The hemagglutinating activity remaining was determined.[7]

To test the effect of temperature, the protein sample was heated at different temperatures from 20 to 100 °C, at 10 °C intervals for 30 min. The sample was immediately cooled on ice for another 30 min to terminate the incubation and then warmed up to room temperature. The assay of hemagglutinating assay was carried out as described above. The hemagglutinating activity of the lectin following incubation at room temperature was considered as 100% activity.

Effects of Carbohydrates and Metal Ions on Hemagglutinating Activity. To investigate the carbohydrate specificity of the purified sample, 200 mM solutions of various kinds of sugars including *N*-acetylglucosamine, L-arabinose, D-fructose, D-fucose, D-galactose, D-glucose, lactose, maltose, D-mannose, raffinose, L-rhamnose, and D-xylose were used to dissolve the lyophilized sample to 0.1 mg/mL. Assay of hemagglutinating activity was carried out using the carbohydrate solutions at their particular concentrations for 2-fold serial dilution instead of PBS. The percentage of hemagglutinating activity remaining was calculated.[8]

On the other hand, the effects of metallic chlorides encompassing calcium chloride, manganese chloride, ferrous chloride, magnesium chloride, copper chloride, and zinc chloride on the hemagglutinating activity of Hokkaido large pinto bean hemagglutinin were also tested. First, the hemagglutinating activity of the original hemagglutinin solution was assessed and the fold number of 2-fold serial dilution that caused the test sample solution to begin to lose its hemagglutining activity was recorded. Then the sample solution was diluted with the recorded fold. Then, 25 μL of a 200 mM solution of a specified metallic salt (in 0.9% NaCl) was subjected to a 2-fold serial dilution with 0.9% NaCl in a 96-well plate. Afterward, 25 μL of diluted sample solution was added to each well, and the mixture was incubated at room temperature for 1 h. In the control group, 25 μL of NaCl was used for 2-fold serial dilution instead of the metallic salt. Fifty microliters of a 2% rabbit erythrocyte suspension were then added to each well for another 2 h incubation at room temperature. Hemagglutination was estimated afterward. A second control experiment containing only the metal salt and red blood cells was run concurrently to ascertain the effect of each metal salt on the red blood cells in the assay.

Assay of Antifungal Activity. Antifungal activity assay was carried out for investigating the antifungal potential of Hokkaido large pinto bean hemagglutinin. Different phytopathogenic fungi including *Mycosphaerella arachidicola*, *Setosphaeria turcica*, *Bipolaris maydis*, *Fusarium oxysporum*, and *Valsa mali* were grown in Petri dishes (90 mm × 15 mm) containing 10 mL of potato dextrose agar. A small amount of each fungal species was planted in the middle of the dish and then incubated at room temperature for a few days until it developed into a mycelial colony. Test samples (2 and 1 mg/mL) were added onto sterile blank round paper disks (0.625 cm in diameter), which were placed 0.5 cm away from the edge of the mycelial colony. Sterile buffer was added as control. After that the plates were incubated at room temperature until the mycelia had grown near the disk of the control group. If the mycelium could not grow near the disk and a clear invagination without mycelium was developed, it indicated that the test sample possessed antifungal activity.[9]

For testing the antifungal activity of the purified proteins against *Candida albicans*, 1×10^7 cells were treated with 2 mg of protein and incubated in Sabouraud dextrose broth (pH 5.5, Sigma). In the control, the protein sample was replaced by autoclaved broth. All eppendorf tubes were placed in an orbital shaker at 37 °C with shaking at a speed of 200 rpm and incubated for 6 h. Ten-fold serial dilution of 50 μL of the mixture containing the test protein and cells was performed in broth. Fifty microliters of the fourth and fifth 10-fold diluted solution were spread on agar plates. Cell counting was implemented after incubation of the plates at 37 °C for 24 h.

The method for testing the antifungal activity of Hokkaido large pinto bean defensin was as previously described. Six species of fungi were tested including *M. arachidicola*, *S. turcica*, *B. maydis*, *F. oxysporum*, *V. mali*, and *C. albicans*. For the assay of antifungal activity toward *C. albicans*, the concentration of defensin used was 0.1 mg/mL.

Assay of Antiproliferative Activity. Nasopharyngeal carcinoma (CNE2), human breast cancer (MCF7 and MDA-MB-231), hepatoma (HepG2) cells, and an immortalized normal nasopharyngeal epithelial cell line NP 69 and human embryo liver (WRL 68) cells, from American Type Culture Collection, were suspended in RPMI medium at a cell density of 5×10^4 cells/mL. A 100 μL aliquot of these cell suspensions was seeded and incubated in the 96-well plates overnight. Then, the protein samples at concentrations of 0.49−125 μM (0.49, 0.98, 1.95, 3.91, 7.81, 15.63, 31.25, 62.5, and 125 μM) in 100 μL of RPMI medium were added to the wells, followed by incubation in a humidified atmosphere of 5% CO_2 at 37 °C. After incubation for 24 and 48 h, the medium was discarded, and the wells were washed with PBS. Then, 25 μL of a 5 mg/mL solution of 3-(4, 5-dimethylthiazol-2-yl)-2,5-diphenyltetrazolium bromide (MTT) in PBS was added into each well, and the plates were incubated at 37 °C for 4 h. After incubation, the plates were centrifuged at 2500 rpm for 5 min. The supernatant was carefully removed, and 150 μL of dimethyl sulfoxide (DMSO) was added into the wells to dissolve the MTT (formazan). OD 590 nm was measured within 10 min by using a microplate reader. Percentage inhibition of the MCF7, HepG2, and CNE2 cells was calculated by using the following formula: [(OD 590 nm of the control (without test protein) − OD 590 nm of the well with test protein at a particular concentration)/OD 590 nm of the control] × 100%.[10]

Results were expressed as means ± standard deviation (SD). The median inhibition concentration (IC_{50}) was determined using SPSS 11.0.1 statistical software (SPSS Inc., Chicago, IL, USA). For between-group comparisons, one-way ANOVA was used. Differences with p values of ≤ 0.05 were considered to be statistically significant.

DOI: 10.1021/acs.jafc.5b00475
J. Agric. Food Chem. 2015, 63, 5439−5448

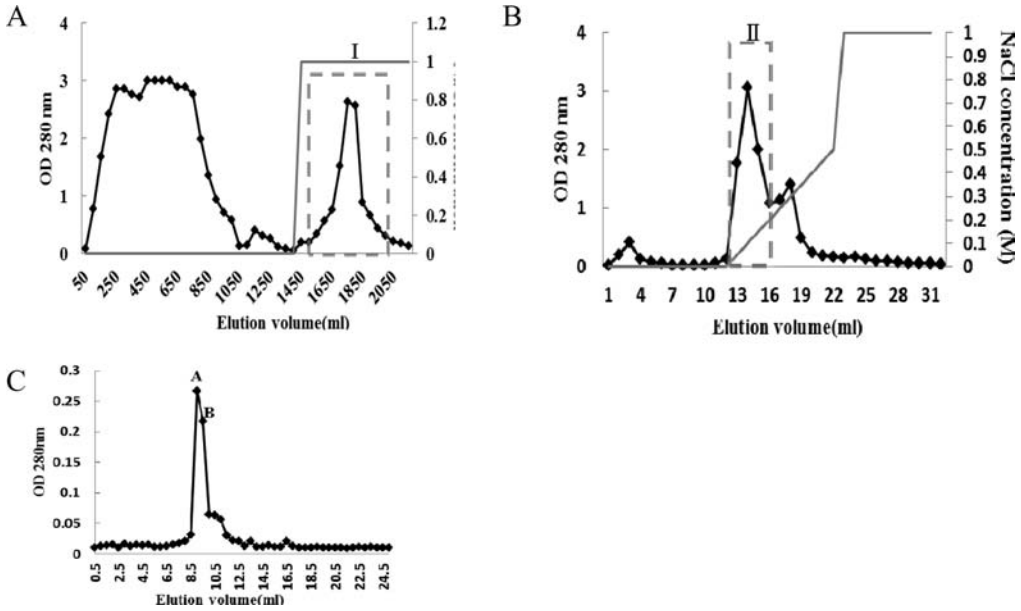

Figure 1. Purification of Hokkaido large pinto bean hemagglutinin: (A) Affi-gel blue gel; (B) Mono Q elution of fraction I; (C) Superdex 75 gel filtration of fraction II. The regions framed with dotted lines signify target fractions with hemagglutinating activity, which were collected and selected for the next step of purification. Peaks A and B represent fractions eluted at the 9th and 9.5th mL, respectively.

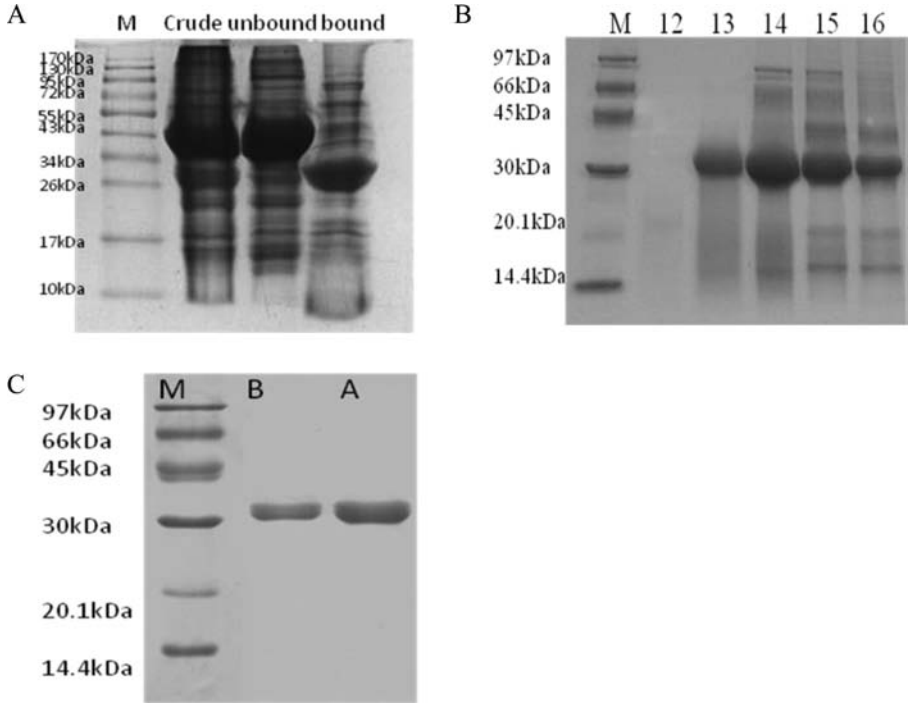

Figure 2. (A) Affi-gel blue gel eluate. Crude, crude extract; unbound, unbound fraction; bound, fraction I. (B) Mono Q eluate: 12, 13, 14, 15, and16, fractions collected at 12th to 16th mL. (C) Fractions A and B eluted from Superdex 75 eluted at the 9th and 9.5th mL, which were labeled in Figure 1C.

RESULTS

Purification of Hemagglutinin from Hokkaido Large Pinto Bean. Three chromatographic steps were utilized for the purification of hemagglutinin from Hokkaido large pinto bean. Hemagglutinins possess at least one noncatalytic domain that reversibly binds to specific carbohydrate structure. This property enables them to aggregate red blood cells. By using the test for hemagglutinating activity to monitor all of the chromatographic fractions, the target chromatographic fraction possessing hemagglutinating activity was identified and selected for further purification

The first chromatographic step on Affi-gel blue gel separated proteins into an unbound fraction that contained most of the proteins of Hokkaido large pinto bean, as shown in Figures 1A and 2A, and a bound fraction, which appeared as a sharper peak. The bound fraction I was obtained by elution with 1 M NaCl solution in the starting buffer. Both unbound and bound fractions were tested by using the test for hemagglutinating activity.

DOI: 10.1021/acs.jafc.5b00475
J. Agric. Food Chem. 2015, 63, 5439−5448

The bound fraction I was identified as the target chromatographic fraction containing hemagglutinating activity. From the SDS-PAGE gel photo shown in Figure 2A, proteins with a size of 30 kDa constituted the bulk of the adsorbed fraction. The second step was FPLC-cation exchange chromatography of bound fraction I from the Affi-gel blue gel column on Mono Q, which yielded one unadsorbed fraction and two major adsorbed peaks (Figure 1B). Hemagglutinating activity was enriched in fraction II. In the third step, fraction II was loaded to an FPLC-gel filtration Superdex 75 column for the purpose of further purification. A major peak was obtained including fractions A and B, which were collected at 9 and 9.5 mL, respectively (Figure 1C). Totally a yield of 190 mg of protein from fractions A and B was obtained from 60 g of Hokkaido large pinto bean (Table 1).

Table 1. Purification of Hemagglutinin from Hokkaido Large Pinto Bean (60 g)

chromatographic fraction	specific hemagglutinating activity (titer mg^{-1})	total protein (mg)	recovery (%)
crude extract	34854	3294	100.00
Affi-gel blue gel	51200	699	31.21
Mono Q	63212	399	22.00
Superdex 75	102400	190	16.95

From the SDS-PAGE gel photo shown in Figure 2C, a single band with a molecular weight around 30 kDa was observed in fractions A and B, indicating that the target hemagglutinin was eluted in the ninth milliliter. On the basis of the standard calibration curve for the Superdex 75 column (data not shown), the molecular mass of Hokkaido large pinto bean hemagglutinin was about 60 kDa. This indicated that the hemagglutinin is a protein with a molecular mass of about 60 kDa and composed of two subunits.

Determination of Temperature Stability, pH Stability, Carbohydrate Selectivity, and Metal Ion Effect. Hokkaido large pinto bean hemagglutinin exhibited moderate thermostability. Its hemagglutinating activity was maintained at temperatures up to 60 °C but dropped dramatically at 70 °C, when only half of the hemagglutinating activity remained. At 80 °C only 0.39% residual activity was detected, and the activity was completely abolished at 90 °C. Testing for pH stability revealed that it retained full activity in the pH range of pH 2−12, indicating fairly high pH stability. The hemagglutinating activity was halved at both pH 1 and 13 and vanished at pH 0 and 14. For investigation of carbohydrate selectivity, none of the carbohydrates at 200 mM concentration interacted with Hokkaido large pinto bean hemagglutinin including D-galactose, D-fructose, D-xylose, D-glucose, D-mannose, L-rhamnose, L-fucose, L-arabinose, xylitol, glucosamine, glucuronic acid, galactonic acid, maltose, α-lactose, and raffinose, as the hemagglutining activity was not attenuated after the addition of various kinds of carbohydrates.

Testing the effect of metal ions on the hemagglutinating activity of Hokkaido large pinto bean hemagglutinin disclosed that 48.8 μM Cu^{2+} or Fe^{2+} ions, 97.7 μM Mn^{2+} ions, 195.3 μM Zn^{2+} ions, and 781.1 μM Ca^{2+} ions enabled the diluted protein sample solution to regain its hemagglutinating activity, indicating an augmenting effect.

Assay of Antifungal Activity. The mycelia of different phytopathogenic fungi all successfully grew near the disks in the presence of Hokkaido large pinto bean hemagglutinin, as in the case of the negative control, and there was no difference in the cell number of *C. albicans* between the hemagglutinin-treated group and the control group. The data suggest that Hokkaido large pinto bean hemagglutinin had no antifungal effect.

Assay for Antiproliferative Activity. The antiproliferative activity of Hokkaido large pinto bean hemagglutinin against HepG2, MDA-MB-231, MCF7, and CNE2 cancer cells was assessed by MTT assay. Results of the assay disclosed that treatment with Hokkaido large pinto bean hemagglutinin for 24 h did not achieve its maximum inhibitory effect (Figure 3A). At concentrations up to 125 μM, the hemagglutinin did not achieve 50% inhibition of each type of cancer cells after 24 h of treatment. The inhibitory effect against MDA-MB 231 metastatic breast cancer cells was minimal. The lectin achieved only 21% inhibition at the highest tested concentration (125 μM), compared with 43, 45, and 47% inhibition of proliferation of HepG2, MCF7, and CNE2 cancer cells, respectively. However, after uninterrupted incubation with Hokkaido large pinto bean hemagglutinin for 48 h, the inhibitory effect against each type of cancer cells was stronger than that observed after 24 h of treatment, with IC_{50} values of 8.135, 6.067, and 7.492 μM toward HepG2, MCF7, and CNE2 cancer cells, respectively. The IC_{50} value for MCF7 cells was smaller than that for CNE2 cancer cells. A further decline in proliferation rate was obtained in CNE2 cells after treatment with 125 μM hemagglutinin, which was 74% compared to 67%. At 125 μM concentration, Hokkaido large pinto bean hemagglutinin inhibited the growth of MDA-MB-231 cancer cells by 28% (Figure 3B). The hemagglutinin did not affect the viability of normal liver cell line WRL68 at 24 h, but

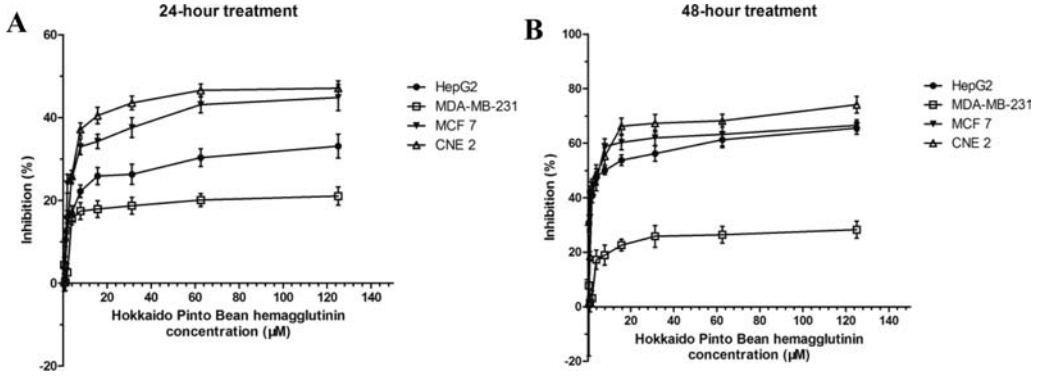

Figure 3. Results of MTT assay for Hokkaido large pinto bean hemagglutinin: MTT assay results after treatment of HepG2, MDA-MB-231, MCF7, and CNE2 cancer cells with different concentrations of Hokkaido large pinto bean hemagglutinin for (A) 24 h and (B) 48 h. Results represent the mean ± SD (n = 3).

DOI: 10.1021/acs.jafc.5b00475
J. Agric. Food Chem. 2015, 63, 5439−5448

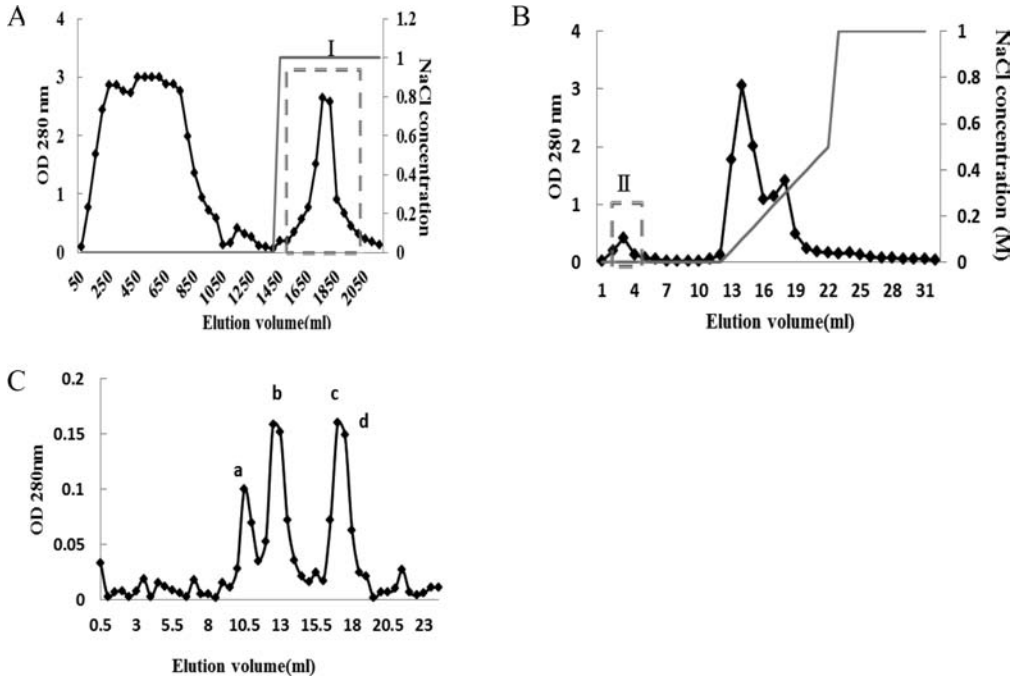

Figure 4. Purification of Hokkaido large pinto bean defensin: (A) affinity chromatography on Affi-gel blue gel; (B) FPLC of Affi-gel blue gel fraction I on Mono Q; (C) gel filtration of Mono Q fraction II on Superdex 75 by FPLC. Fractions a, b, c, and d were collected at elution volumes of 10.5, 12.5, 17, and 17.5 mL, respectively. Regions encircled with dotted lines signify target fractions with antifungal activity, which were collected and selected for the next step of purification.

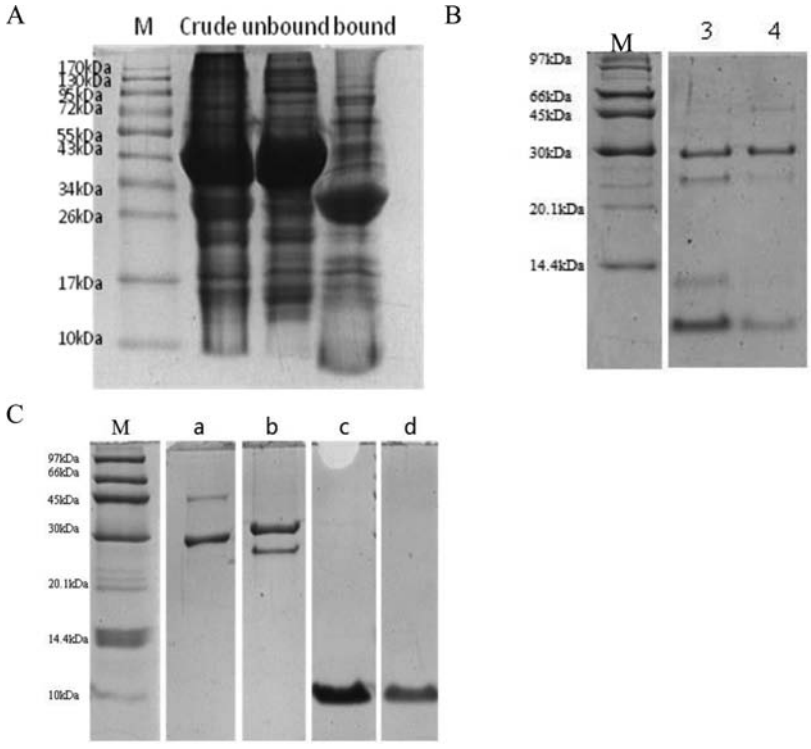

Figure 5. SDS-PAGE results for isolation of Hokkaido large pinto bean defensin: (A) Affi-gel blue gel eluate (crude, crude extract; unbound, unbound fraction; bound, fraction I); (B) Mono Q eluate (M, molecular weight marker; 3 and 4, fraction collected at the 3rd and 4th mL, respectively); (C) M, molecular mass marker; a, b, c, d, fractions collected at elution volumes of 10.5, 12.5, 17, and 17.5 mL, respectively.

caused inhibition when the treatment was lengthened to 48 h (IC_{50} value > 80 μM), and gave rise to an IC_{50} value of 45 μM after treatment for 72 h (Table 3). Yet the effect was much weaker compared with the aforementioned tumor cell lines (IC_{50} values < 10 μM). A comparison of the characteristics of lectins/hemagglutinins from various *P. vulgaris* cultivars is presented in Table 4.

Purification of Hokkaido Large Pinto Bean Defensin. Hokkaido large pinto bean defensin was discovered during the purification of Hokkaido pinto bean hemagglutinin. By

DOI: 10.1021/acs.jafc.5b00475
J. Agric. Food Chem. 2015, 63, 5439−5448

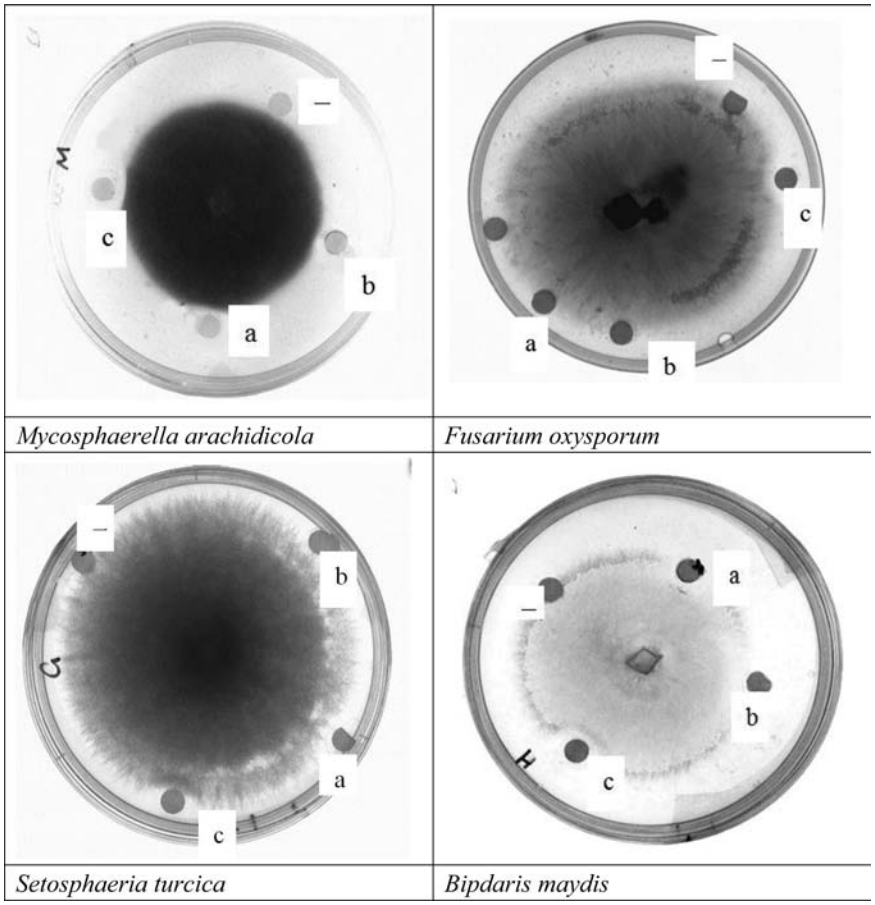

Figure 6. Antifungal activity of Hokkaido large pinto bean defensin toward *Mycosphaerella arachidicola*, *Fusarium oxysporum*, *Setosphaeria turcica*, and *Bipdaris maydis*. (−), negative control (water); a, b, and c refer to fractions a, b, and c, which were collected at elution volumes of 10.5, 12.5, and 17 mL, respectively, during gel filtration on Superdex 75. Antifungal activity was detected only in fraction c.

monitoring the antifungal activity of chromatographic fraction obtained at each purification step with the assay of antifungal activity, it was observed that the crude extract and sample obtained after purification on Affi-gel blue gel (relevant results are shown in Figures 4A and 5A) contained antifungal protein(s), as they both exerted antifungal effect toward *M. arachidicola* (data not shown). In the second chromatographic step using FPLC-cation exchange on Mono Q, the unadsorbed fraction referred to as fraction II in Figure 4B exhibited antifungal activity. The proteins in this fraction (third and fourth milliliter eluted from Mono Q) were checked by SDS-PAGE, as shown in Figure 5B. After further purification of Mono Q fraction II by FPLC-gel filtration on a Superdex 75 column, several main peaks were obtained (Figure 4C). Fractions a, b, c, and d were collected at elution volumes of 10.5th, 12.5th, 17th, and 17.5th mL, respectively. The molecular size and purity of the proteins in the fractions are shown in Figure 5C. After assay of antifungal activity of each fraction, both fractions c and d were found to be effective (Figure 6). Collection of fractions c and d resulted in totally a yield of only 3.2 mg of protein from 60 g of Hokkaido large pinto beans (Table 2).

Mass Spectrum Analysis. The molecular weight of the protein was confirmed by MALDI-TOF MS to be 10888 Da (Supporting Information). An analysis of MS and MS/MS data using NCBInr and SwissProt databases revealed 40% similarity with defensin D1 of *P. vulgaris* protein accession gi|312982410. Hence, the defense protein from fraction c can be regarded as a member of the defensin group.

Table 2. Purification of Defensin from Hokkaido Large Pinto Beans (60 g)

chromatographic fraction	yield (mg)	yield (%)
crude extract	3294	100.0
Affi-gel blue gel fraction I	699	21.22
Mono Q fraction II	20.1	0.61
Superdex 75 fractions c and d	3.2	0.097

Table 3. Percentage Reduction of Viability of WRL68 Normal Liver Cells (Mean ± SD, n = 3) Caused by Hemagglutinin from Hokkaido Large Pinto Bean[a]

hemagglutinin concn (μM)	24 h of incubation	48 h of incubation	72 h of incubation
2.5	6.28 ± 5.35a	6.96 ± 5.88a	14.43 ± 7.38b
5	3.63 ± 1.65a	2.31 ± 1.92a	11.46 ± 8.85b
10	1.84 ± 1.21a	1.22 ± 0.93a	22.55 ± 12.34b
20	4.57 ± 4.22a	17.67 ± 7.82b	40.26 ± 2.76c
40	3.12 ± 2.98a	26.54 ± 3.77b	46.33 ± 7.89c
80	7.03 ± 2.91a	44.71 ± 5.32b	65.51 ± 1.23c

[a]Different letters (a, b, c) next to the data indicate statistically significant difference. The same letter represents no statistically significant difference.

Antifungal Activity of Hokkaido Large Pinto Bean Defensin. Five fungal species were utilized in the assay of antifungal activity, comprising *M. arachidicola*, *S. turcica*, *B.*

DOI: 10.1021/acs.jafc.5b00475
J. Agric. Food Chem. 2015, 63, 5439−5448

maydis, *F. oxysporum*, and *V. mali*. Distilled water was used instead of protein sample as negative control. The antifungal activity of fractions a, b, and c was tested. It was found that fraction b had no antifungal effect on all five types of fungal species, as the mycelial growth extended to the paper disks. Fraction a had only a weak antifungal effect on *M. arachidicola*. Fraction c was capable of inhibiting the growth of *M. arachidicola*, *S. turcica*, *B. maydis*, and *F. oxysporum*, as distinct crescent-like invaginations could be seen around the paper disks. Yet it could not inhibit the growth of the pathogenic fungus *V. mali* (data not shown). Protein in fraction d had a molecular size identical to that of the protein in fraction c, and it also possessed antifungal activity toward the same types of fungi, suggesting they are the same protein (data not shown). Hokkaido large pinto bean defensin exerted strong activities toward *M. arachidicola* and *B.maydis* and a weaker activity toward *S. turcica* and *F. oxysporum*. The defensin had no antifungal effect on *C. albicans* at the concentration of 0.1 mg/mL (data not shown).

DISCUSSION

Nowadays, many lectins from edible plants with potent antitumor activity have been discovered. For instance, legume lectin Con A induced apoptosis in human melanoma A375 cells.[3] *Momordica charantia* lectin exerted an inhibitory action on nasopharyngeal carcinoma cells.[11] Banana lectin demonstrated a suppressive effect on leukemia (L1210) and HepG2 cells.[12] Broccolini lectin[13] and taro lectin[14], etc., are all potential candidates as anticancer agents. *P. vulgaris* merits research efforts because of its relatively inexpensive price, multiple cultivar sources, and high potential in anticancer activity. As Hokkaido large pinto bean has not been investigated before, we selected it for the present study.

By applying affinity chromatography on Affi-gel blue gel and Blue Sepharose, ion exchange chromatography on SP-Sepharose, Mono Q, and Q Sepharose, and FPLC-gel filtration on Superdex 75 and Superdex 200, etc., a variety of lectins with protential were successfully purified from different organisms, such as lectins from jelly fish *Nemopilema nomurai*,[15] bighead carp *Aristichthys nobilis*,[16] coral *Acropora millepora*,[17] *Annona muricata* seeds,[18] and various *P. vulgaris* cultivars including French bean Indian cultivar,[19] Blue Tiger King,[20] jade bean,[21] northeast red bean,[22] and so on. The purification methods adopted in the present study can be used to obtain the target proteins in a fast and simple way. By using fewer purification steps, the loss of the target protein could be minimized. The purification efficiency and the percentage recovery of lectin, which is calculated using the formula percentage recovery = (total hemagglutinating titer of purified sample/total hemagglutinating titer in crude extract) × 100%, showed the yield of Hokkaido large pinto bean hemagglutinin was noteworthy in that 190 mg of hemagglutinin could be purified from 60 g of beans with 17% recovery. It may be due to the abundant occurrence of this storage protein in Hokkaido large pinto beans and the few steps of purification employed. Many lectins isolated from other cultivars of *P. vulgaris* may not have the same advantages. For instance, the yield of lectin from 100 g of French bean cultivar no. 12 was only 4.8 mg with 18.1% recovery;[23] the corresponding values for Anasazi beans were 26 mg and 14% recovery;[24] and the values for French beans (cultivar no. 1) were 96.25 mg and 18.73% recovery.[7] Although larger amounts of lectin from other cultivars have been reported, for example, 428 mg of brown kidney bean lectin from 100 g of beans with about 57% recovery,[25] other advantages such as performance in assays of various biological activities should also be taken into consideration when assessing the utility/value of a protein.

With respect to structure and molecular size, Hokkaido large pinto bean hemagglutinin shared common characteristics with many lectins of *P. vulgaris*, which are dimeric proteins with a molecular mass of about 60 kDa.[21] Yet there are exceptions, for example, a 94 kDa tetrameric lectin purified from the seeds of the Cacahuate cultivar of *P. vulgaris*.[26] Despite these similar characteristics, hemagglutinins or lectins from different cultivars may perform distinctively regarding many biological activities, which may be due to the differences in their sequences. The N-terminal sequence is important for identifying a protein. By examining the N-terminal sequence, a number of *P. vulgaris* lectins have been identified.[23,27−30] However, in this study no peaks were detected after seven sequencing cycles, indicating that the hemagglutinin most likely possessed a blocked N-terminus. This is not a unique case, as lectins of *Castanea crenata*,[31] *Schizophyllum commune*,[32] and *Sclerotium rolfsii*[33] also had a blocked N-terminus.

Lectins or hemagglutinins from *P. vulgaris* possess different thermal and pH stabilities. For instance, lectin from jade bean had modest pH and heat stability: it was stable only at pH 4.5−9.4 and 30−70 °C,[21] whereas lectins purified from Anasazi bean and the Indian cultivar of French bean manifested high pH and heat stability. They were stable at 80 and 90 °C, respectively, and retained their hemagglutinating activity after treatment with solutions at pH 1−14 and 1−13, respectively.[19,27] The high thermal stability may be due to the absence of disulfide linkages, which become unstable at elevated temperatures or attributed to the absence of heat-sensitive tryptophan residues.[34] Some lectins had poor thermostability and pH stability, such as French bean cultivar no. 35, which retained its hemagglutinating activity at an ambient temperature below 50 °C or at a pH within the range of 6−8.[35] Hemagglutinin purified from Hokkaido large pinto bean was characterized by a modest thermostability and pH stability; it was stable at 30−60 °C and at pH values from 2 to 12. Considering its potential for application, it may be utilized as an agent for injection as it is stable at physiological temperature and pH in plasma. As the pH of gastric fluid ranges from 1 to 3, it still has a potential to be employed as a drug for oral administration even though its activity would be halved at pH 1.

With regard to carbohydrate selectivity, selected simple saccharides did not exert any inhibitory effect on the hemagglutinating activity of Hokkaido large pinto bean hemagglutinin. A number of lectins isolated from other *P. vulgaris* cultivars including cultivar 12, cultivar 35, Indian cultivar of French beans, Hokkaido red bean, northeast red bean, etc., also exhibited this common phenomenon.[19,23,34,36] On the other hand, the sugar-binding ability of lectins of some other *P. vulgaris* cultivars has been discovered. For instance, lectin from cultivar no. 1 of French beans bound specifically to glucuronic acid,[22] and lectins from both pinto beans and Extralong Autumn purple beans were galactose-specific.[28] In addition, polysaccharides can also be the binding target of some lectins. For example, lectin isolated from Blue Tiger King bean was polygalacturonic acid-binding specific;[28] meanwhile, the hemagglutinating activity of lectin from red kidney bean was reduced by several glycoproteins.[29]

Lectins are found to be divalent cation-dependent proteins.[20,37] During purification, they may lose ions or become desaturated with ions, which provides a rationale to the assay of the effect of metal ions in this study. Results displayed that metal ions including Ca^{2+}, Zn^{2+}, Mn^{2+}, Cu^{2+}, or Fe^{2+} ions enhanced the hemagglutinating activity of Hokkaido large pinto bean

DOI: 10.1021/acs.jafc.5b00475
J. Agric. Food Chem. 2015, 63, 5439−5448

Table 4. Summary of Properties of some *Phaseolus vulgaris* Lectins

cultivar	yield	mol wt (kDa)	sugar binding	pH stability	thermostability (°C)	ion effect ≤100 μM	IC_{50} (μM) anticancer activity, 48 h	antifungal activity
Hokkaido large pinto bean	190 mg/60 g	60	ND[a]	2−12	up to 60	Cu^{2+}, Fe^{2+}, Mn^{2+}	HepG2 (8.1), MCF7 (6.07), and CNE2 (7.49)	ND
Blue Tiger King[53]	81 mg/350 g	60	polygalacturonic acid	3−10	up to 50	Fe^{3+},Ca^{2+}	HepG2 (7.9 ± 0.5)	N/A[b]
jade bean[54]	162 mg/50 g	60.8	ND	4.5−9.4	30−70	Ca^{2+}	MCF7 (169)	ND
French bean no. 35[35]	1.1 g/100 g	64	ND	6−8	0−50	N/A	HepG2 (100), MCF7 (2)	*Valsa mali*
northeast red bean[55]	292 mg/100 g	64	ND	2−12	up to 65	N/A	CNE1 (1.63), MCF7 (11.66), CNE2 (35) (24 h)	N/A
Chinese pinto bean[56]	110 mg/90 g	58	glucosamine	7−8	up to 60	Mg^{2+}	nasopharyngeal carcinoma (HONE-1) cells (17.3)	*Valsa mali*

[a]ND, not determined. [b]N/A, not applicable.

hemagglutinin at different concentrations, whereas Mg^{2+} ions failed to strengthen the diluted hemagglutinin to regain its hemagglutining capacity. Cu^{2+} or Fe^{2+} ions had the most obvious effect at the minimum concentration, followed by Mn^{2+} and Zn^{2+} ions, whereas Ca^{2+} ions were the least effective. It should be remembered that the effect of metal ion was uncertain. It was demonstrated that Ca^{2+}, Zn^{2+}, Mn^{2+}, and Mg^{2+} had no effect on the hemagglutinating activity of *Grifola frondosa* lectin,[38] whereas they restrained the lectin of *Schizophyllum commune*.[39] This may be due to the change of protein structure in the presence of metal ions.[40] For the *P. vulgaris* species, the effect on lectins varies among different cultivars. The activity of Con A, which is a well-known lectin isolated from jack beans, could be enhanced in the presence of Ca^{2+}, Mg^{2+}, and Mn^{2+} ions.[21] The potentiating effect of Ca^{2+} ions was not very commonly found and has been reported only for a few *Phaseolus* lectins, including *P. coccineus* lectin,[41] *P. lunatus* lectin,[42] and *P. acutifolius* lectin,[43] which was probably because Ca^{2+} ions enable the lectins to resist tryptic proteolysis.

For antifungal activity, Hokkaido large pinto bean hemagglutinin did not affect the growth of the tested fungi. To date, it has been found that some lectins possess antifungal activity. For example, *Aleuria aurantia* lectin inhibited the growth of *Mucor racemosus*.[44] French bean no. 35 lectin exhibited antifungal activity against *V. mali*, *F. oxysporum*, and *Rhizoctonia solani*.[35] However, a number of lectins without antifungal effect have been reported, such as lectin from jade bean,[21] Extralong Autumn purple bean,[28] and ground bean[45] etc.

The proliferation of several kinds of cancer cells encompassing hepatoma (HepG2) cells, breast cancer (MCF7) cells, and nasopharyngeal cancer (CNE2) cells was reduced by Hokkaido large pinto bean hemagglutinin in a time- and dose-dependent manner, whereas its antiproliferative effect on MDA-MB-231 breast cancer cell was only meager. The range of tumors cells found to be sensitive to Hokkaido large pinto bean hemagglutinin was large, compared to that of lectin purified from Blue Tiger King bean, which was specific toward HepG2 cells,[20] as well as lectin from French bean cultivar no. 35, which was active toward MCF7 cells but not toward HepG2 cancer cells.[35]

The anticancer effect of Hokkaido large pinto bean hemagglutinin in vitro was potent among many lectins that have been discovered to date. For instance, its IC_{50} values for HepG2, MCF7, and CNE2 cells after a 48 h exposure were 8.14, 6.07, and 7.49 μM, respectively, which were much smaller in magnitude than that of acaconin from seeds of *Acacia confusa* (IC_{50} = 128 ± 9 μM for MCF7 cells);[10] jade bean lectin (IC_{50} = 169 μM for MCF7 cells);[21] and Chinook salmon roe lectin (IC_{50} = 68 μM for HepG2 cells), etc. Some lectins showed a similar antitumor activity, such as lectin from *Lactarius flavidulus* (IC_{50} = 8.9 μM and 6.81 μM for HepG2 and leukemic L1210 cells, respectively);[10] Nagaimo lectin significantly reduced the growth of MCF7, HepG2, and CNE2 cells after 24 h of treatment, with IC_{50} values of 3.17, 7.12, and 19.79 μM, respectively.[46] With the advantages of pH stability and strong anticancer acitivity, Hokkaido large pinto bean hemagglutinin has the potential to be developed as an antineoplastic agent.

A summary of the properties of some *P. vulgaris* lectins (Table 4) revealed that Hokkaido large pinto bean hemagglutinin manifested the advantageous features of a potent antiproliferative effect toward different types of cancer cells, a wider pH range over which it was stable, and a considerably higher yield, which demonstrate its potential as an anticancer candidate.

Three types of chromatography including affinity chromatography, ion exchange chromatography, and FLPC-gel filtration were utilized for purification of defensin from Hokkaido large pinto beans. The protocol resembles purification procedures for some other defensins.[47,48] It has been reported that plant defensins have been discovered to possess an isoelectric point around 8−9.[49] This facilitates isolation of plant defensins by means of ion exchange chromatography: adsorption on cation exchangers and lack of binding to anion exchangers in neutral buffers (e.g., Tris-HCl, pH 7.6) or acidic buffers (e.g., NH_4OAc, pH 4.6).

The yield of the 10888 Da Hokkaido large pinto bean defensin was only 3.2 mg from 60 g of beans. In other studies on purification of defensin, such as the purification of northeast red bean antifungal peptide, 8 mg of antifungal peptide was extracted from 100 g of beans. Higher yields were observed in the purification of defensin from *Legumi secchi* bean and ground bean, which were 43 and 14 mg from 100 g of beans, respectively. However, a lower yield was also encountered in the purification of cloud bean defensin, which was 1.12 mg per 100 g of seeds.

With regard to its biological activity, Hokkaido large bean defensin displayed antifungal activity on different types of fungi including *M. arachidicola*, *S. turcica*, *F. oxysporum*, and *B. maydis*. However, fungi such as *V. mali* and *C. albicans* were resistant to Hokkaido large pinto bean defensin. In addition, most of the previously reported plant defensins were small proteins with a molecular size ranging from 5 to 9 kDa.[49] With a molecular size of 10.888 kDa, Hokkaido large pinto bean defensin is a big defensin. Defensins with a large size also exist in animals. For instance, a 79-residue defensin, which is responsible for host defense, was found in the Japanese horseshoe crab.[50]

To recapitulate, the pinto bean is an edible bean common in the United States and the Far East. The pH-stable and thermostable hemagglutinin, isolated with a remarkable yield

DOI: 10.1021/acs.jafc.5b00475
J. Agric. Food Chem. 2015, 63, 5439−5448

(190 mg/60 g), has potent antiproliferative activity toward various tumor cells including nasopharyngeal carcinoma (CNE2), human breast cancer (MCF7 cells), and hepatoma (HepG2) cells and thus noteworthy health-promoting activity. Currently there are not many publications reporting the action of lectins against nasopharyngeal cancer cells. The isolated defensin has a larger molecular weight than previously reported defensins and antifungal activity toward various phytopathogenic fungi and could be used in the biological control of agriculturally important fungi. It deserves mention that by comparison some antifungal proteins have activity against only one or two fungal species.[51,52]

■ ASSOCIATED CONTENT

Supporting Information

Supplementary Figure 1. The Supporting Information is available free of charge on the ACS Publications website at DOI: 10.1021/acs.jafc.5b00475.

■ AUTHOR INFORMATION

Corresponding Authors

*(J.H.W.) E-mail: b011590@mailserv.cuhk.edu.hk. Phone: 852-39438031. Fax: 852-26035123.

*(T.B.N.) E-mail: b021770@mailserv.cuhk.edu.hk. Phone: 852-39436872. Fax: 852-26035123.

Notes

The authors declare no competing financial interest.

■ REFERENCES

(1) Wong, J. H.; Ng, T. B.; Cheung, R. C.; Ye, X. J.; Wang, H. X.; Lam, S. K.; Lin, P.; Chan, Y. S.; Fang, E. F.; Ngai, P. H.; Xia, L. X.; Ye, X. Y.; Jiang, Y.; Liu, F. Proteins with antifungal properties and other medicinal applications from plants and mushrooms. *Appl. Microbiol. Biotechnol.* **2010**, *87* (4), 1221−1235.

(2) Li, Y. R.; Liu, Q. H.; Wang, H. X.; Ng, T. B. A novel lectin with potent antitumor, mitogenic and HIV-1 reverse transcriptase inhibitory activities from the edible mushroom *Pleurotus citrinopileatus*. *Biochim. Biophys. Acta, Gen. Subj.* **2008**, *1780* (1), 51−57.

(3) Liu, B.; Li, C. Y.; Bian, H. J.; Min, M. W.; Chen, L. F.; Bao, J. K. Antiproliferative activity and apoptosis-inducing mechanism of voncanavalin A on human melanoma A375 cells. *Arch. Biochem. Biophys.* **2009**, *482* (1−2), 1−6.

(4) Laemmli, U. K.; Johnson, R. A. Maturation of the head of bacteriophage T4. II. Head-related, aberrant tau-particles. *J. Mol. Biol.* **1973**, *80* (4), 601−611.

(5) Fagerquist, C. K.; Sultan, O. Top-down proteomic identification of furin-cleaved α-subunit of Shiga toxin 2 from *Escherichia coli* O157:H7 using MALDI-TOF-TOF-MS/MS. *J. Biomed. Biotechnol.* **2010**, *2010*, 123460.

(6) Wong, J. H.; Ng, T. B. Isolation and characterization of a glucose/mannose-specific lectin with stimulatory effect on nitric oxide production by macrophages from the emperor banana. *Int. J. Biochem. Cell Biol.* **2006**, *38* (2), 234−243.

(7) Chan, Y. S.; Wong, J. H.; Ng, T. B. A glucuronic acid binding leguminous lectin with mitogenic activity toward mouse splenocytes. *Protein Pept. Lett.* **2011**, *18* (2), 194−202.

(8) Koike, T.; Beppu, H.; Kuzuya, H.; Maruta, K.; Shimpo, K.; Suzuki, M.; Titani, K.; Fujita, K. A 35 kDa mannose-binding lectin with hemagglutinating and mitogenic activities from "Kidachi Aloe" (*Aloe arborescens* Miller var. natalensis Berger). *J. Biochem.* **1995**, *118* (6), 1205−1210.

(9) Ye, X. Y.; Wang, H. X.; Ng, T. B. Dolichin, a new chitinase-like antifungal protein isolated from field beans (*Dolichos lablab*). *Biochem. Biophys. Res. Commun.* **2000**, *269* (1), 155−159.

(10) Lam, S. K.; Ng, T. B. Acaconin, a chitinase-like antifungal protein with cytotoxic and anti-HIV-1 reverse transcriptase activities from *Acacia confusa* seeds. *Acta Biochim. Polym.* **2010**, *57* (3), 299−304.

(11) Fang, E. F.; Zhang, C. Z.; Ng, T. B.; Wong, J. H.; Pan, W. L.; Ye, X. J.; Chan, Y. S.; Fong, W. P. *Momordica charantia* lectin, a type II ribosome inactivating protein, exhibits antitumor activity toward human nasopharyngeal carcinoma cells in vitro and in vivo. *Cancer Prev. Res.* **2012**, *5* (1), 109−121.

(12) Cheung, A. H.; Wong, J. H.; Ng, T. B. *Musa acuminata* (Del Monte banana) lectin is a fructose-binding lectin with cytokine-inducing activity. *Phytomedicine* **2009**, *16* (6−7), 594−600.

(13) Xu, P.; Zhang, T.; Guo, X.; Ma, C.; Zhang, X. Purification, characterization, and biological activities of broccolini lectin. *Biotechnol. Prog.* **2015**, March 3. DOI: 10.1002/btpr.2070 [Epub ahead of print].

(14) Chan, Y. S.; Wong, J. H.; Ng, T. B. A cytokine-inducing hemagglutinin from small taros. *Protein Pept. Lett.* **2010**, *17* (7), 823−830.

(15) Imamichi, Y.; Yokoyama, Y. Purification, characterization and cDNA cloning of a novel lectin from the jellyfish *Nemopilema nomurai*. *Comp. Biochem. Physiol., Part B: Biochem. Mol. Biol.* **2010**, *156* (1), 12−18.

(16) Pan, S.; Tang, J.; Gu, X. Isolation and characterization of a novel fucose-binding lectin from the gill of bighead carp (*Aristichthys nobilis*). *Vet. Immunol. Immunopathol.* **2010**, *133* (2−4), 154−164.

(17) Kvennefors, E. C. E.; Leggat, W.; Hoegh-Guldberg, O.; Degnan, B. M.; Barnes, A. C. An ancient and variable mannose-binding lectin from the coral *Acropora millepora* binds both pathogens and symbionts. *Dev. Comp. Immunol.* **2008**, *32* (12), 1582−1592.

(18) Damico, D. C. S.; Freire, M. G. M.; Gomes, V. M.; Toyama, M. H.; Marangoni, S.; Novello, J. C.; Macedo, M. L. R. Isolation and characterization of a lectin from *Annona muricata* seeds. *J. Protein Chem.* **2003**, *22* (7−8), 655−661.

(19) Sharma, A.; Wong, J. H.; Lin, P.; Chan, Y. S.; Ng, T. B. Purification and characterization of a lectin from the Indian cultivar of French bean seeds. *Protein Pept. Lett.* **2010**, *17* (2), 221−227.

(20) Fang, E. F.; Pan, W. L.; Wong, J. H.; Chan, Y. S.; Ye, X. J.; Ng, T. B. A new *Phaseolus vulgaris* lectin induces selective toxicity on human liver carcinoma Hep G2 cells. *Arch. Toxicol.* **2011**, *85* (12), 1551−1563.

(21) Cheung, R. C. F.; Leung, H. H.; Pan, W. L.; Ng, T. B. A calcium ion-dependent dimeric bean lectin with antiproliferative activity toward human breast cancer MCF-7 cells. *Protein J.* **2013**, *32* (3), 208−215.

(22) Chan, Y. S.; Wong, J. H.; Fang, E. F.; Pan, W. L.; Ng, T. B. A hemagglutinin from Northeast red beans with immunomodulatory activity and anti-proliferative and apoptosis-inducing activities toward tumor cells. *Protein Pept. Lett.* **2013**, *20* (10), 1159−1169.

(23) Leung, E. H. W.; Wong, J. H.; Ng, T. B. Concurrent purification of two defense proteins from French bean seeds: a defensin-like antifungal peptide and a hemagglutinin. *J. Pept. Sci.* **2008**, *14* (3), 349−353.

(24) Ang, A. S. W.; Cheung, R. C. F.; Dan, X. L.; Chan, Y. S.; Pan, W. L.; Ng, T. B. Purification and characterization of a glucosamine-binding antifungal lectin from *Phaseolus vulgaris* cv. Chinese pinto beans with antiproliferative activity towards nasopharyngeal carcinoma cells. *Appl. Biochem. Biotechnol.* **2014**, *172* (2), 672−686.

(25) Chan, Y. S.; Zhang, Y. B.; Ng, T. B. Brown kidney bean Bowman-Birk trypsin inhibitor is heat and pH stable and exhibits anti-proliferative activity. *Appl. Biochem. Biotechnol.* **2013**, *169* (4), 1306−1314.

(26) Vargasalbores, F.; Hernandez, J.; Cordoba, F.; Zenteno, E. Isolation of an immunosuppressive lectin from *Phaseolus vulgaris* L cv Cacahuate using stroma. *Prep. Biochem.* **1993**, *23* (4), 473−483.

(27) Sharma, A.; Ng, T. B.; Wong, J. H.; Lin, P. Purification and characterization of a lectin from *Phaseolus vulgaris* cv. (Anasazi beans). *J. Biomed. Biotechnol.* **2009**, *2009*, 929568.

(28) Fang, E. F.; Lin, P.; Wong, J. H.; Tsao, S. W.; Ng, T. B. A lectin with anti-HIV-1 reverse transcriptase, antitumor, and nitric oxide inducing activities from seeds of *Phaseolus vulgaris* cv. Extralong Autumn purple bean. *J. Agric. Food Chem.* **2010**, *58* (4), 2221−2229.

(29) Ye, X. Y.; Ng, T. B.; Tsang, P. W. K.; Wang, J. Isolation of a homodimeric lectin with antifungal and antiviral activities from red kidney bean (*Phaseolus vulgaris*) seeds. *J. Protein Chem.* **2001**, *20* (5), 367−375.

DOI: 10.1021/acs.jafc.5b00475
J. Agric. Food Chem. 2015, 63, 5439−5448

(30) Xia, L. X.; Ng, T. B. A hemagglutinin with mitogenic activity from dark red kidney beans. *J. Chromatogr. B: Anal. Technol. Biomed. Life Sci.* **2006**, *844* (2), 213−216.
(31) Nomura, K.; Ashida, H.; Uemura, N.; Kushibe, S.; Ozaki, T.; Yoshida, M. Purification and characterization of a mannose/glucose-specific lectin from *Castanea crenata*. *Phytochemistry* **1998**, *49* (3), 667−673.
(32) Chumkhunthod, P.; Rodtong, S.; Lambert, S. J.; Fordham-Skelton, A. P.; Rizkallah, P. J.; Wilkinson, M. C.; Reynolds, C. D. Purification and characterization of an *N*-acetyl-D-galactosamine-specific lectin from the edible mushroom *Schizophyllum commune*. *Biochim. Biophys. Acta, Gen. Subj.* **2006**, *1760* (3), 326−332.
(33) Sathisha, G. J.; Prakash, Y. K. S.; Chachadi, V. B.; Nagaraja, N. N.; Inamdar, S. R.; Leonidas, D. D.; Savithri, H. S.; Swamy, B. M. X-ray sequence ambiguities of *Sclerotium rolfsii* lectin resolved by mass spectrometry. *Amino Acids* **2008**, *35* (2), 309−320.
(34) Wong, J. H.; Wan, C. T.; Ng, T. B. Characterisation of a haemagglutinin from Hokkaido red bean (*Phaseolus vulgaris* cv. Hokkaido red bean). *J. Sci. Food Agric.* **2010**, *90* (1), 70−77.
(35) Lam, S. K.; Ng, T. B. Isolation and characterization of a French bean hemagglutinin with antitumor, antifungal, and anti-HIV-1 reverse transcriptase activities and an exceptionally high yield. *Phytomedicine* **2010**, *17* (6), 457−462.
(36) Chan, Y. S.; Ng, T. B. Northeast red beans produce a thermostable and pH-stable defensin-like peptide with potent antifungal activity. *Cell Biochem. Biophys.* **2013**, *66* (3), 637−648.
(37) Neth, O.; Jack, D. L.; Dodds, A. W.; Holzel, H.; Klein, N. J.; Turner, M. W. Mannose-binding lectin binds to a range of clinically relevant microorganisms and promotes complement deposition. *Infect. Immun.* **2000**, *68* (2), 688−693.
(38) Kawagishi, H.; Nomura, A.; Mizuno, T.; Kimura, A.; Chiba, S. Isolation and characterization of a lectin from *Grifola frondosa* fruiting bodies. *Biochim. Biophys. Acta, Gen. Subj.* **1990**, *1034* (3), 247−252.
(39) Han, C. H.; Liu, Q. H.; Ng, T. B.; Wang, H. X. A novel homodimeric lactose-binding lectin from the edible split gill medicinal mushroom *Schizophyllum commune*. *Biochem. Biophys. Res. Commun.* **2005**, *336* (1), 252−257.
(40) Sureshkumar, T.; Priya, S. Purification of a lectin from *M. rubra* leaves using immobilized metal ion affinity chromatography and its characterization. *Appl. Biochem. Biotechnol.* **2012**, *168* (8), 2257−2267.
(41) Feria, M.; PerezSantiago, A.; Cuevas, D.; Martinez, M.; Cordoba, F. Purification and partial characterization of a new anti-A(1) lectin of *Phaseolus coccineus* collected in Oaxaca, Mexico. *Prep. Biochem. Biotechnol.* **1996**, *26* (1), 31−46.
(42) Roberts, D. D.; Goldstein, I. J. Effect of carbohydrate and metal-ion binding on the reactivity of the essential thiol-groups of lima bean lectin. *J. Biol. Chem.* **1984**, *259* (2), 903−908.
(43) Vargasalbores, F.; Delafuente, G.; Agundis, C.; Cordoba, F. Purification and characterization of a lectin from *Phaseolus acutifolius* var Latifolius. *Prep. Biochem.* **1987**, *17* (4), 379−396.
(44) Amano, K.; Katayama, H.; Saito, A.; Ando, A.; Nagata, Y. *Aleuria aurantia* lectin exhibits antifungal activity against *Mucor racemosus*. *Biosci., Biotechnol., Biochem.* **2012**, *76* (5), 967−970.
(45) Wong, J. H.; Ng, T. B. Purification of a trypsin-stable lectin with antiproliferative and HIV-1 reverse transcriptase inhibitory activity. *Biochem. Biophys. Res. Commun.* **2003**, *301* (2), 545−550.
(46) Chan, Y. S.; Ng, T. B. A lectin with highly potent inhibitory activity toward breast cancer cells from edible tubers of *Dioscorea opposita* cv. nagaimo. *PLoS One* **2013**, *8* (1), No. e54212.
(47) Wu, X.; Sun, J.; Zhang, G.; Wang, H.; Ng, T. B. An antifungal defensin from *Phaseolus vulgaris* cv. 'Cloud Bean'. *Phytomedicine* **2011**, *18* (2−3), 104−109.
(48) Lam, S. K.; Ng, T. B. Purification and characterization of an antifungal peptide with potent antifungal activity but devoid of antiproliferative and HIV reverse transcriptase activities from *Legumi secchi* beans. *Appl. Biochem. Biotechnol.* **2013**, *169* (7), 2165−2174.
(49) Carvalho Ade, O.; Gomes, V. M. Plant defensins − prospects for the biological functions and biotechnological properties. *Peptides* **2009**, *30* (5), 1007−1020.
(50) Kouno, T.; Mizuguchi, M.; Aizawa, T.; Shinoda, H.; Demura, M.; Kawabata, S.; Kawano, K. A novel β-defensin structure: big defensin changes its N-terminal structure to associate with the target membrane. *Biochemistry* **2009**, *48* (32), 7629−7635.
(51) Wang, H.; Ng, T. B. Isolation of a novel deoxyribonuclease with antifungal activity from *Asparagus officinalis* seeds. *Biochem. Biophys. Res. Commun.* **2001**, *289* (1), 120−124.
(52) Wang, H. X.; Ng, T. B. Ascalin, a new anti-fungal peptide with human immunodeficiency virus type 1 reverse transcriptase-inhibiting activity from shallot bulbs. *Peptides* **2002**, *23* (6), 1025−1029.
(53) Fang, E. F.; Pan, W. L.; Wong, J. H.; Chan, Y. S.; Ye, X. J.; Ng, T. B. A new *Phaseolus vulgaris* lectin induces selective toxicity on human liver carcinoma Hep G2 cells. *Arch. Toxicol.* **2011**, *85* (12), 1551−1563.
(54) Cheung, R. C.; Leung, H. H.; Pan, W. L.; Ng, T. B. A calcium ion-dependent dimeric bean lectin with antiproliferative activity toward human breast cancer MCF-7 cells. *Protein J.* **2013**, *32* (3), 208−215.
(55) Chan, Y. S.; Wong, J. H.; Fang, E. F.; Pan, W.; Ng, T. B. A hemagglutinin from northeast red beans with immunomodulatory activity and anti-proliferative and apoptosis-inducing activities toward tumor cells. *Protein Pept. Lett.* **2013**, *20* (10), 1159−1169.
(56) Ang, A. S.; Cheung, R. C.; Dan, X.; Chan, Y. S.; Pan, W.; Ng, T. B. Purification and characterization of a glucosamine-binding antifungal lectin from *Phaseolus vulgaris* cv. Chinese pinto beans with antiproliferative activity towards nasopharyngeal carcinoma cells. *Appl. Biochem. Biotechnol.* **2014**, *172* (2), 672−686.

DOI: 10.1021/acs.jafc.5b00475
J. Agric. Food Chem. 2015, 63, 5439−5448

JOURNAL OF AGRICULTURAL AND FOOD CHEMISTRY

Article

pubs.acs.org/JAFC

Metabolomic Analysis Reveals Cyanidins in Black Raspberry as Candidates for Suppression of Lipopolysaccharide-Induced Inflammation in Murine Macrophages

Young-Hee Jo,[†,∥] Hyun-Chang Park,[†,∥] Seulgi Choi,[†,∥] Sugyeong Kim,[†] Cheng Bao,[†] Hyung Woo Kim,[†] Hyung-Kyoon Choi,[‡] Hong Jin Lee,*[,†] and Joong-Hyuck Auh*[,†]

[†]Department of Food Science and Technology, Chung-Ang University, Anseong 456-756, South Korea

[‡]College of Pharmacy, Chung-Ang University, Seoul 156-756, South Korea

Supporting Information

ABSTRACT: The extracts produced by multisolvent extraction and subfractionation with preparative liquid chromatography of black raspberry (*Rubus coreanus* Miquel) cultivated in Gochang, South Korea, were tested for their anti-inflammatory effects. The metabolomic profiling and analysis by orthogonal partial least-squares discriminant analysis (OLPS-DA) suggested that cyanidin, cyanidin-3-glucoside (C3G), and cyanidin-3-rutinoside (C3R) were key components for the anti-inflammatory responses in the most active fraction BF3-1, where they were present at 0.44, 1.26, and 0.56 μg/mg of BF3-1, respectively. Both BF3-1 and mixture of these cyanidins at the same ratio reduced lipopolysaccharide (LPS)-induced protein level of iNOS expression and suppressed mRNA and protein expressions of tumor necrosis factor (TNF)-α, interleukin (IL)-6, and IL-1β through inhibiting the phosphorylation of mitogen-activated protein kinases (MAPKs) and STAT3 in murine macrophage RAW264.7 cells. Overall, the results suggested that co-administration of cyanidin, C3G, and C3R is more effective than that of cyanidin alone and that the coexistence of these anthocyanin components in black raspberry plays a vital role in regulating LPS-induced inflammation even at submicromolar concentrations, making it possible to explain the health beneficial activity of its extracts.

KEYWORDS: *black raspberry, metabolomic profiling, cyanidin, cyanidin-3-glucoside, cyanidin-3-rutinoside*

INTRODUCTION

There are accumulating studies demonstrating the health beneficial efficacy of black raspberry in chronic diseases such as inflammation, metabolic syndrome, atherosclerosis, and cancer.[1−6] Black raspberry supplementation retarded mammary tumorigenesis by inhibiting the expression of estrogen receptor α (ER-α), reducing carcinogen-induced esophageal cancer by regulating pentraxin-3 expression, and suppressing ultraviolet B (UVB)-induced inflammation and skin tumor development.[2,5,7] In addition, a diet containing 5 or 10% of freeze-dried black raspberries suppressed DSS-induced colon injury through inhibiting cyclooxygenase 2 (COX-2) expression and reducing the level of tumor necrosis factor-α (TNF-α) and interleukin 1β (IL-1β).[4] The potential constituents responsible for the health beneficial efficacy of black raspberries have been identified as anthocyanins, simple phenols such as ellagic acid and quercetin, sterols such as β-sitosterol, vitamins, and minerals.[8] Tulio et al. identified five different anthocyanins including cyanidin-3-glucoside and cyanidin-3-rutinoside and demonstrated that cyanidin-3-rutinoside and cyanidin-3-xylosylrutinoside may act as the key components exerting antioxidant activity in black raspberry.[9] Ferulic acid and β-sitosterol were also reported to show antiproliferative activity in oral cancer cell lines without affecting the normal oral epithelial cells.[10] Although the roles of powder or extract of black raspberry in physiological effects and their potent ingredients have been elucidated, there are few studies considering the actual concentrations or interactions of the key phytochemicals in the extracts of black raspberry. To overcome this hurdle, it is meaningful enough to employ a new approach for profiling the whole metabolites and identifying the set of metabolites exerting the health-promoting effects.

Metabolomics is nontargeted identification and quantification of all metabolites within a given set of conditions.[11] It objectively measures all or a substantial fraction of all metabolites within a sample, quantifies each relative to an absolute index of the sample (per gram, milliliter, etc.), and analyzes hundreds to thousands of small molecular weight metabolites comprehensively within samples according to their molecular weights.[12] Metabolomics is a useful tool for the analysis of the phenotype in food science.[13] Currently, metabolite profiling methods have been established including mass spectrometry (MS)-coupled methods, such as LC-MS, ultraperformance LC (UPLC)-MS, and capillary electrophoresis (CE)-MS, which have wide availability in analytical technology.[14] LC-MS methods are often used with electrospray ionization (ESI), atmospheric pressure chemical ionization (APCI), or matrix-assisted laser desorption/ionization (MALDI) to porovide the samples as ionized state. The ionized metabolites pass through linear TOF-MS, single-quadrupole MS, or Q-TOF to detect the ion mass and intensity[15] commonly by MS-MS or MS^n. Following profiling by LC-MS, all data are analyzed by statistical tools to screen out

Received: February 2, 2015
Revised: May 17, 2015
Accepted: May 17, 2015
Published: May 29, 2015

ACS Publications © 2015 American Chemical Society

DOI: 10.1021/acs.jafc.5b00560
J. Agric. Food Chem. 2015, 63, 5449−5458

critical contributors on the significant variations in the target samples.

In our previous study, metabolomic investigation using MS-coupled method was performed between the fractions separated by multistep solvent extraction, and ellagic acid was successfully identified as a key metabolite in the fraction exerting anti-inflammatory activity in strawberry ('Seolhyang').[16] Recently, it was also reported that ^{1}H nuclear magnetic resonance (NMR)-based metabolomic analyses were developed, by which the bioactive contributors in black raspberry against oxidative stress and proliferation of HT-29 colon cancer cells were identified.[17,18] These results suggested that the metabolomic process could be one of the significant approaches to ascertain the constituents responsible for the physiological efficacy of the active food resources. However, comparative demonstration of active components screening with metabolomic approach along with mechanistic evaluation has been tried to date. In this study, black raspberry cultivated in South Korea was separated into several fractions with organic solvents, and then the most active extract in suppressing lipopolysaccharide (LPS)-induced inflammation was further fractionated. The key contributors were discriminated and identified through multivariate statistical analysis, and their anti-inflammatory activity was validated with the underlying mechanism.

MATERIALS AND METHODS

Materials. Black raspberry (*Rubus coreanus* Miquel) cultivated in Gochang, South Korea, was used for the multistep solvent extraction. Fresh black raspberries were freeze-dried and kept in a deep freezer (−80 °C) before use. LPS, cyanidin, cyanidin 3-glucoside chloride, and cyanidin 3-rutinoside chloride were obtained from Sigma-Aldrich Corp. (St. Louis, MO, USA). Ethyl acetate was purchased from DUKSAN (Ansan, South Korea), methanol from SAMCHUN (Pyung-Taek, South Korea), acetonitrile from J. T. Baker (Phillipsburg, NJ, USA), and formic acid from Sigma-Aldrich Corp.

Extraction of Polyphenol Compounds from Black Raspberry. Polyphenols from black raspberry were extracted by multistep solvent extraction method with ethyl acetate and methanol as described previously.[16,19] Black raspberry (2.5 g) was extracted with ethyl acetate (10 mL) for 30 min at room temperature, and the supernatant was evaporated and resuspended with methanol (BF1). The residue was acidified with HCl (2 M, 1 mL) and then extracted with methanol (BF2), and another supernatant portion was hydrolyzed with HCl in MeOH (0.6 M, 5 mL) for 20 h at 60 °C (BF3) and analyzed by LC-MS/MS.

Subfractionation of BF3 Using Preparative LC. BF3 was further fractionated using preparative liquid chromatography (LC-forte/R, YMC, Kyoto, Japan). Separation was carried out using YMC-DispoPack AT ODS (40 g, 25 μm) (YMC). The solvent system was consisted of a gradient mobile phase from 100% B in 3 min, from 100 to 0% in 24 min, held at 0% over 3 min, and finished at 30 min, where solvent A was 0.1% formic acid in water and solvent B was 0.1% formic acid in methanol. The flow rate was set at 25 mL/min, and UV spectra were measured at 280, 360, and 400 nm. The BF3 was separated into three subfractions according to peak shape, which was detected at 280 nm (Figure 2A).

Metabolite Profiling Using LC-MS/MS Analysis. Profiling of the metabolites in each fraction or the extracts was conducted using a LC-MS/MS system consisting of an Accela HPLC system with a PDA detector (Accela 80 Hz PDA detector, Thermo Fisher Scientific, San Jose, CA, USA) and an LTQ-Velos ion trap mass spectrometer fitted with a heat electrospray ionization interface (Thermo Fisher Scientific).[16] Separation was carried out using a UPLC BEH C18 column (1.7 um, 100 × 2.1 mm i.d., Acquity, Waters, Milford, MA, USA) at 35 °C. Solvent A was 0.1% formic acid in water, and solvent B was 0.1% formic acid in acetonitrile. The solvent system consisted of a gradient mobile phase from 5 to 10% B in 5 min, held at 10% B for 5 min, from 10 to 40% B in 20 min, from 40 to 90% B in 10 min, then returned to the initial conditions (5% B) in 5 min and conditioned at 5% B in 10 min, and finished at 55 min. The flow rate was set at 0.3 mL/min, and UV spectra were measured between 180 and 800 nm. Acquisition was performed in the positive and negative ion mode by electrospray ionization (ESI) source, and the m/z range was 100−1000 Da. The capillary temperature was 275 °C, and the source voltage was set to 5 kV for ionization.

Metabolite Identification. The data acquired by LC-MS/MS were processed for peak detection, alignment, and identification by SIEVE software (Thermo Fisher Scientific, Waltham, MA, USA). The acquired LC-MS/MS spectrum was identified after comparison with those proposed by the MASSBANK database (www.massbank.jp), Human Metabolome Database (www.hmdb.ca), METLIN (http://masspec.scripps.edu), KEGG database (www.Kegg.co.jp), and related papers. Identifications of cyanidin, cyanidin 3-glucoside, and cyanidin 3-rutinoside were confirmed with authentic standard compounds.

HPLC Analysis for Quantification of Metabolites. Quantification of anthocyanins and their metabolites was conducted using a standard curve generated from authentic standards of cyanidin, cyanidin 3-glucoside, and cyanidin 3-rutinoside. Analysis was performed by HPLC (Dionex HPLC-3000, Dionex Corp., Sunnyvale, CA, USA) with a UV detector (Ultimate 3000 diode array detector, Dionex Corp.) using an X-bridge C18 column (3.5 μm, 4.6 × 150 mm, Waters) at 35 °C. The solvents were 10% formic acid in water (phase A) and acetonitrile (phase B) at flow rate of 1 mL/mL. The linear gradient profile was as follows: 5−15% B in 15 min, held at 15% B for 5 min, 15−5% B in 5 min, and finished at 25 min. UV spectra were measured at 520 nm.

Cell Culture. RAW264.7 cells were obtained from the Korean Cell Line Bank (Seoul, Korea) and cultured in DMEM supplemented with 10% fetal bovine serum (FBS), 1% penicillin/streptomycin, and 1% HEPES at 37 °C and 5% CO_2.

Cell Proliferation Assay (MTT Assay). The cells were seeded in a 96-well plate and treated with black raspberry extracts for 24 h. The formazan crystals formed from 3-(4,5-dimethylthiazol-2-yl)-2,5-diphenyltetrazolium bromide (MTT, Sigma-Aldrich) were dissolved in DMSO, and the absorbance was measured with an ELISA reader at 570 nm (Molecular Devices, Sunnyvale, CA, USA).

Western Blot Analysis. This analysis was described previously.[16] Briefly, the cells were harvested with radioimmunoprecipitation assay (RIPA) lysis buffer, and the protein extract was separated and transferred to a polyvinylidene difluoride (PVDF) membrane (Millipore, Billerica, MA, USA). The primary antibodies against iNOS (Abcam, Cambridge, MA, USA), COX2, IκBα (Santa Cruz Biotech, Santa Cruz, CA, USA), phospho-ERK, phospho-p38, phospho-JNK, phospho-STAT3 (Cell Signaling Technology, Boston, MA, USA), β-actin (Sigma-Aldrich), and secondary antibodies (Santa Cruz) were used. The expression levels of proteins were visualized with EZ capture MG (ATTO, Tokyo, Japan) and quantified with CS Analyzer (ver. 3.0, ATTO).

RNA Extraction and Quantitative RT-PCR Analysis. The cellular RNA was isolated and reverse-transcribed to cDNA using Trizol reagent (Sigma) and a RevertAid First Strand cDNA Synthesis Kit (Theromo Scientific, Lafayette, CO, USA) in Atlas Thermal Cycler (Astec, Fukuoka, Japan), respectively. The cDNA was amplified using TaqMan primers (iNOS, COX-2, TNF-α, IL-1β, interleukin-6 (IL-6), glyceraldehyde-3-phosphate dehydrogenase (GAPDH); Applied Biosystems, Foster City, CA, USA) in ABI Prism 7500 real-time PCR system (Applied Biosystems) and relatively quantified as described in the previous study.[16]

Enzyme-Linked Immunosorbent Assay (ELISA). Following the instructions from the company, the expression of cytokines (TNF-α, IL-6, IL-1β) in culture supernatants was analyzed using an ELISA kit (Koma Biotech Inc., Seoul, Korea).

Data Processing and Statistical Analysis. SIEVE software (Thermo Fisher Scientific) was used for peak/feature picking and deconvolution of raw data. The SIEVE parameters were as follows: mass range, 100−1000 Da; retention time, 1.5−35 min; frame m/z

DOI: 10.1021/acs.jafc.5b00560
J. Agric. Food Chem. 2015, 63, 5449−5458

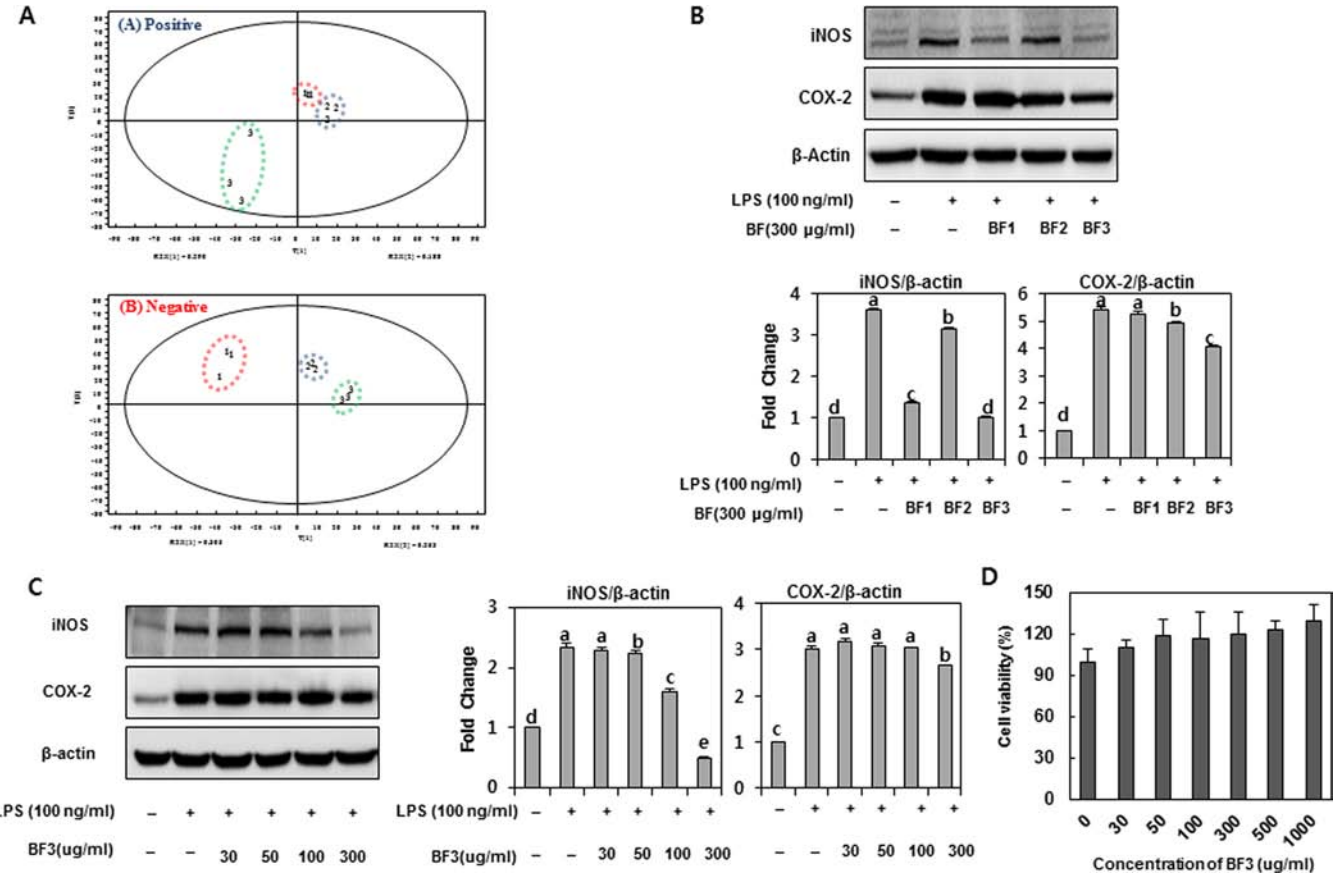

Figure 1. Anti-inflammatory effect of Korean black raspberry fractions in LPS-induced RAW264.7 cells. (A) PCA score plot for the metabolites in each fraction. Fractionation of extract was performed by using multistep solvent extraction and PCA score plot for classifying the distinctive metabolites in extract fractions (1, BF1; 2, BF2; 3, BF3) analyzed by LC-ESI-ion trap MS/MS in positive and negative ion mode. (B) Comparison of anti-inflammatory effects of each fraction. The cells (8×10^5 cells/well in 60 mm dish) were treated with black raspberry fractions (300 μg/mL) together with LPS (100 ng/mL) for 15 h. The protein expression levels of iNOS and COX2 were determined by Western blotting and normalized with β-actin. (C) Anti-inflammatory effect of BF3. The cells (8×10^5 cells/well in 60 mm dish) were treated with BF3 (30, 50, 100, 300 μg/mL) together with LPS (100 ng/mL) for 15 h. iNOS and COX2 protein expression were determined by Western blotting and normalized with β-actin. (D) Effect of BF3 on cell viability. The cells (1×10^4 cells/well in a 96-well plate) were treated with BF3 at the indicated concentrations for 24 h, and cell viability was assessed by MTT assay. Statistical significance was determined by one-way ANOVA with the Duncan test, and differences are indicated with different letters ($p < 0.05$).

width, 0.02 Da; frame time width, 2.5 min. Noise filtering, peak detection, isotope peak removal, alignment of retention time and mass, and peak normalization were conducted. Multivariate statistical analyses, including principal component analysis (PCA) and orthogonal partial least-squares discriminant analysis (OPLS-DA), were performed using SIMCA software (Umetrics, Umea, Sweden). The data sets were mean-centered and pareto-scaled before analysis. For analyzing the data from MTT, Western blot, quantitative RT-PCR, and ELISA assays, one-way ANOVA with Duncan's test was used, and differences were considered statistically significant at $p < 0.05$.

RESULTS

Metabolite Profiling in Fractionated Black Raspberry by LC-ESI-Ion Trap-MS/MS. Black raspberry metabolites were fractionated into three groups (BF1, BF2, BF3) through ethyl acetate and methanol extraction as described under Materials and Methods. PCA clearly indicated that the metabolites in different fractions were separated into different groups as shown in Figure 1A. Differences were mainly contributed by principal component 1 in both negative and positive ion modes. The metabolites in each fraction were analyzed using LC-ESI-MS/MS and summarized (see Supporting Information Table 1). The abundance of all molecular ions was sufficient for further fragmentation into MS^2 and MS^3 analysis for the tentative identification of each metabolite.

Black Raspberry Fraction 1 (BF1). BF1, as ethyl acetate extract, contained *p*-coumaroyl hexose, (epi)catechin-(epi)-catechin, quercetin 3-*O*-rutinoside, quercetin 3-*O*-glucuronide, ellagic acid hexose, kaempferol-deoxyhexose, luteolin 7-glucoside, vanilloyl hexose, myricetin hexose, and hibiscetin tetramethyl ether in positive ion mode. Catechin, ellagic acid, methyl ellagic acid pentose, ellagitannin derivatives, *p*-coumaroylhexose, quercetin, quercetin, quercetin 3-glucoside, quercetin 3-*O*-glucuronide, proanthocyanidin B2 (EC-4,8-C), HHDP-galloyl-glucose, dihydroxybenzoic acid, and hydroxybenzoyl hexose were identified in negative ion mode.

Black Raspberry Fraction 2 (BF2). BF2, as a simple methanol extract, cyanidin 3-glucoside, cyanidin 3-rutinoside, cyanidin 3-sambubioside, cyanidin 3-xylosylrutinoside, (+)-catechin, *p*-coumaroyl hexose, quercetin 3-*O*-glucuronide, quercetin, and pelargonidin 3-rutinoside were identified in positive ion mode. Ellagic acid, ellagic acid-pentose conjugate, quercetin, quercetin glucoside, quercetin 3-*O*-glucuronide, quercetin 3-rutinoside, cyanidin 3-glucoside, malvidin 3-*O*-glucoside, pelargonidin 3-*O*-rutinoside, peonidin glucoside,

DOI: 10.1021/acs.jafc.5b00560
J. Agric. Food Chem. 2015, 63, 5449−5458

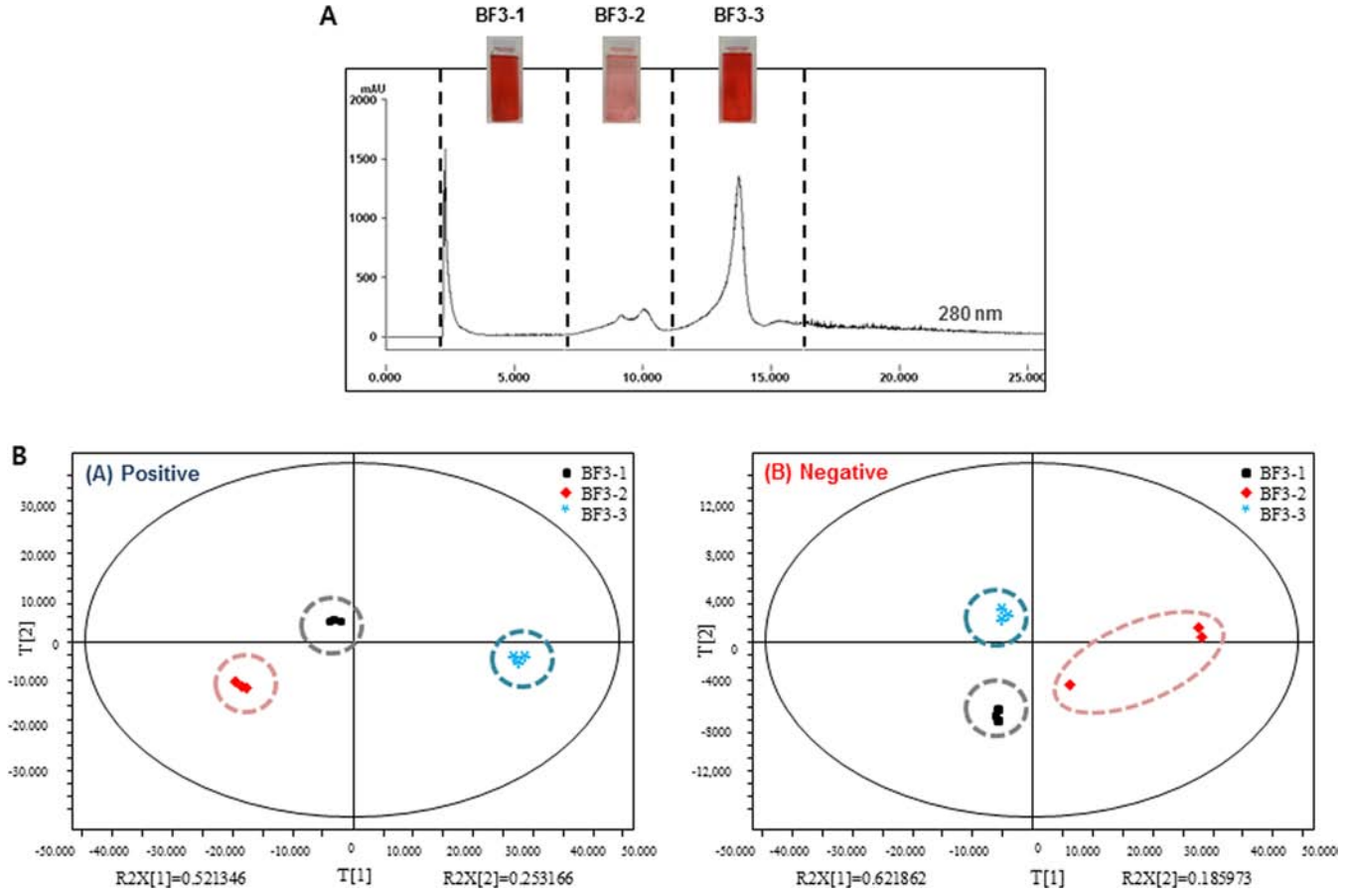

Figure 2. PCA for the metabolites in subfractions of Korean black raspberry extract 3 (BF3). (A) HPLC chromatogram of BF3 by preparative HPLC. BF3 was fractionated into three subfractions (at 280 nm): BF3-1, 2.00−6.84 min; BF3-2, 6.84−10.67 min; BF3-3, 10.67−15.45 min. (B) PCA score plot of Korean black raspberry subfractions analyzed by LC-ESI-ion trap MS/MS in positive (left) and negative ion mode (right).

HHDP-galloyl-glucose, ellagitannin derivatives, galloyl bis-HHDP-glucoside, *p*-coumaroyl hexose, and citric acid were found in negative mode.

Black Raspberry Fraction 3 (BF3). BF3, as the acidic hydrolysate of BF2, cyanidin, cyanidin 3-glucoside, cyanidin 3-rutinoside, cyanidin 3-sambubioside, pelargonidin 3-malonyl-glucoside, pelargonidin 3-rutinoside, and quercetin were found in positive ion mode, whereas cyanidin, cyanidin 3-glucoside, cyanidin 3-rutinoside, isorhamnetin 3-glucuronide, pelargonidin 3-rutinoside, ellagic acid, HHDP-galloyl-glucose, ellagitannin derivatives, kaempferol, and quercetin were identified in negative ion mode.

Black Raspberry Fractions Inhibited LPS-Induced Inflammation in Murine Macrophage Cells. To investigate the effect of black raspberry fractions on regulating inflammation, murine macrophage RAW264.7 cells were treated with extracted fractions (BF1-BF3) at 300 μg/mL concentration, and the protein expression of well-known inflammatory markers iNOS and COX-2 was determined. As shown in Figure 1B, BF3 exerted the most significant inhibition on iNOS expression, followed by BF1, and BF2 did not show suppressive activity. BF3 also reduced the expression of COX-2, but the effect was marginal (Figure 1B). To evaluate the dose dependency of the most potent fraction, RAW264.7 cells were treated with BF3 at different concentrations (30, 50, 100, 300 μg/mL), and we found that BF3 significantly suppressed iNOS expression from 100 μg/mL concentration, with a slight inhibition on COX-2 (Figure 1C). In the MTT assay, BF3 did not affect the cell viability up to 1000 μg/mL, indicating that iNOS inhibition is not derived from the cellular cytotoxicity in the macrophage cells (Figure 1D). On the basis of these results, we chose BF3 for further studies of subfractionation and identification of active metabolites.

Metabolite Phenotyping of Black Raspberry Subfractions. Through prep-LC, BF3 metabolites were fractionated into three subfractions, and then their metabolites were analyzed by LC-ESI-ion trap-MS/MS. PCA indicated that metabolites in subfractions were classified into different groups. In positive ion mode, principal component 1 (explaining 52.1% of the total variance) discriminated the metabolite profiles of subfractions, whereas principal component 2 explained 25.3% of total variance (Figure 2B). In negative ion mode, metabolites in subfractions were discriminated by principal component 1 (explaining 62.2% of total variance), and principal component 2 explained 18.6% of total variance (Figure 2B). The PCA score plots demonstrated the distinctive metabolite phenotypes of subfractions. The metabolites in each subfractions were analyzed using LC-ESI-ion trap-MS/MS and are summarized in the Supporting Information (Table 2). By comparison of retention time and MS^n spectra in positive mode, cyanidin 3-glucoside, cyanidin 3-rutinoside, and cyanidin were identified in BF3-1. Cyanidin 3-glucoside, cyanidin 3-rutioside, pelargonidin 3-rutinoside, quercetin-3-rutinoside, and cyanidin 3-xylosylrutinoside were identified in BF3-3. Cyanidin 3-glucoside, cyanidin 3-rutinoside, cyanidin, and ellagic acid were also identified in BF3-1 in negative mode, and ellagic acid and quercetin were

DOI: 10.1021/acs.jafc.5b00560
J. Agric. Food Chem. 2015, 63, 5449−5458

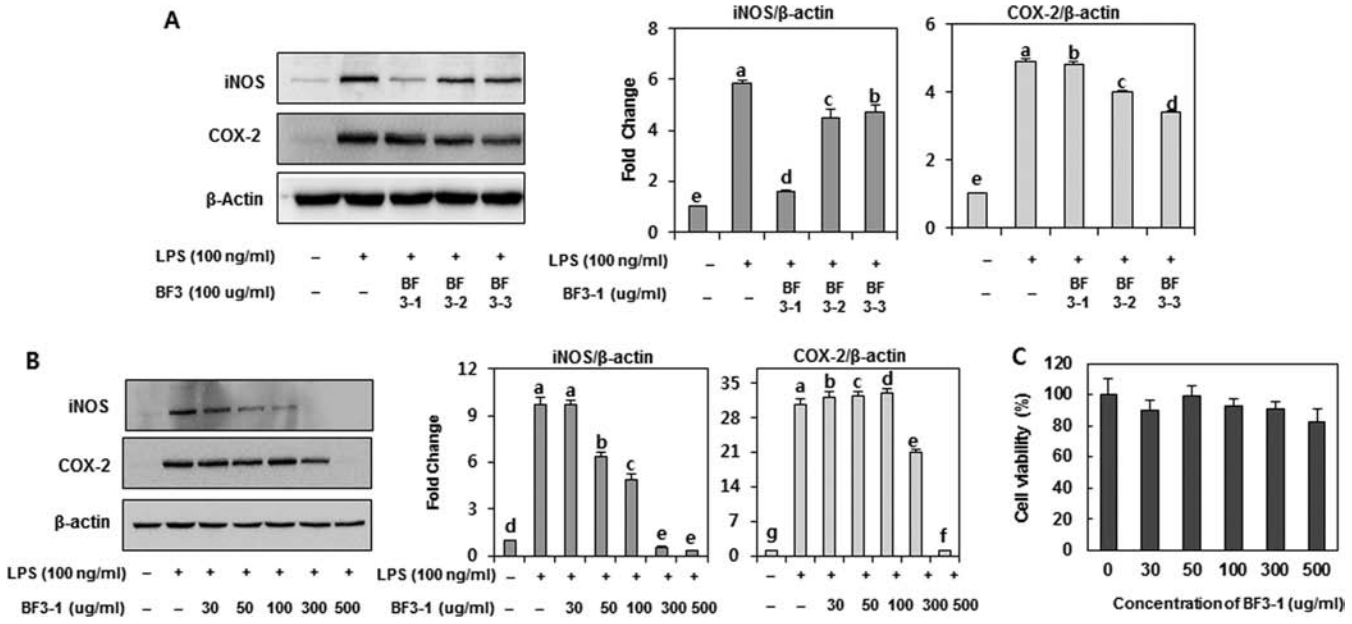

Figure 3. Anti-inflammatory effect of subfractions of BF3 in LPS-induced RAW264.7 cells. (A) Comparison of anti-inflammatory effects of each subfraction. The cells (8×10^5 cells/well in 60 mm dish) were treated with black raspberry subfractions (BF3-1, BF3-2, BF3-3; 100 μg/mL) together with LPS (100 ng/mL) for 15 h. The levels of iNOS and COX2 protein expression were determined by Western blotting and normalized with β-actin. (B) Anti-inflammatory effect of BF3-1. The cells (8×10^5 cells/well in 60 mm dish) were treated with BF3-1 (30, 50, 100, 300, 500 μg/mL) with LPS (100 ng/mL) for 15 h, and iNOS and COX2 protein expressions were determined by Western blotting and normalized with β-actin. (C) Effect of BF3-1 on cell viability. The cells (1×10^4 cells/well in a 96-well plate) were treated with BF3-1 at the indicated concentrations for 24 h, and cell viability was determined by MTT assay. Statistical significance was determined by one-way ANOVA with Duncan's test, and differences are indicated with different letters ($p < 0.05$).

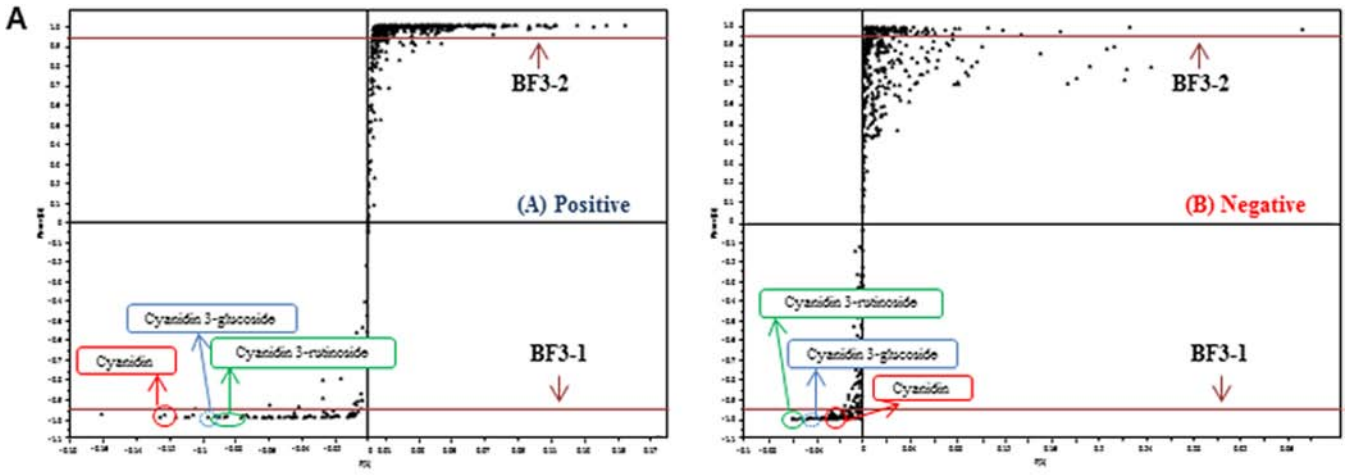

B

No.	Compounds	Quantity (μg/mg of BF3-1)
1	Cyanidin	0.44 ± 0.04
2	Cyanidin 3-glucoside	1.26 ± 0.08
3	Cyanidin 3-rutinoside	0.56 ± 0.06

Figure 4. Analysis for the key compounds in BF3-1. (A) S-plot generated by OPLS-DA for the metabolite in BF3-1 and BF3-2 in positive (left) and negative ion mode (right). (B) Quantification of cyanidin, cyanidin 3-glucoside, and cyanidin 3-rutinoside in BF3-1 by HPLC.

identified in BF3-2 in negative ion mode. Cyanidin 3-glucoside, cyanidin-3-rutinoside, and quercetin-3-rutinoside were found in BF3-3 under negative ion mode of analysis.

Subfractions of BF3 Exerted More Active Efficacy in Regulating Inflammatory Markers in Murine Macrophage Cells. Here, we evaluated the regulatory effects of BF3 subfractions on inflammatory markers iNOS and COX-2 in LPS-induced RAW264.7 macrophage cells. As shown in Figure 3A, BF3-1 (100 μg/mL) strongly inhibited the expression of iNOS induced by LPS treatment, but BF3-2 and BF3-3 exerted

DOI: 10.1021/acs.jafc.5b00560
J. Agric. Food Chem. 2015, 63, 5449−5458

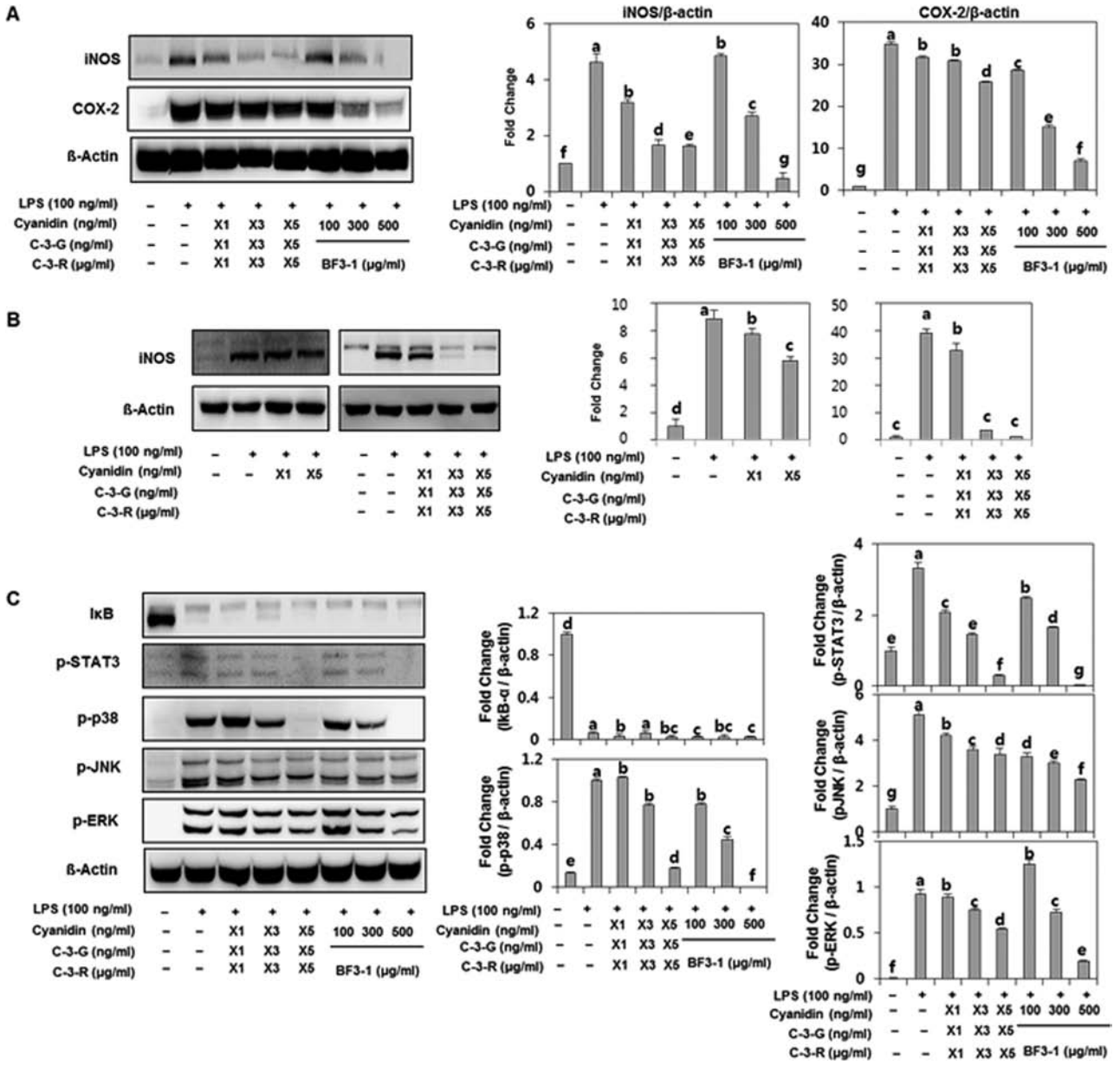

Figure 5. Anti-inflammatory mechanisms of BF3-1 and corresponding key constituents in LPS-induced RAW264.7 cells. (A) The cells (8×10^5 cells/well in 60 mm dish) were treated with the key compounds (cyanidin, C3G, C3R) or BF3-1 (100, 300, 500 μg/mL) with LPS (100 ng/mL) for 15 h. X1 represents 0.15 μM cyanidin, 0.26 μM C3G, and 0.09 μM C3R, respectively, and X3 and X5 represent levels 3 and 5 times higher than X1. The protein expression levels of iNOS and COX2 were determined by Western blotting and normalized with β-actin. (B) The cells (8×10^5 cells/well in 60 mm dish) were treated with cyanidin alone (X1 and X5) and cyanidin mixture (X1, X3, X5) for 15 h. The expression level of iNOS was determined by Western blotting and normalized with β-actin. (C) The cells (8×10^5 cells/well in 60 mm dish) were treated with the key compounds (cyanidin, C3G, C3R) and BF3-1 (100, 300, 500 μg/mL) with LPS (100 ng/mL) for 15 min. The levels of LPS-induced phosphorylation of MAPKs and STAT3 and IκBα degradation were assessed by Western blotting and normalized with β-actin. Statistical significance was determined by one-way ANOVA with Duncan's test, and differences are indicated with different letters ($p < 0.05$).

only slight suppression of iNOS and COX-2. In a concentration dependency test, BF3-1 showed inhibitory efficacy of iNOS from 50 μg/mL and of COX-2 from 300 μg/mL without affecting the cellular viability (Figure 3B,C), suggesting that BF3-1 black raspberry fraction may contain the key components responsible for anti-inflammatory activity.

Screening of Anti-inflammatory Metabolites in BF3-1 and BF3-2 by LC-ESI-Ion Trap MS/MS. All data sets of metabolite profiles of BF3-1 and BF3-2 were analyzed by OLPS-DA. The S-plot visualized the variables that differentiated most in uncoordinated way at the top or bottom in the plot. The variables on the top indicated metabolites in BF3-2, and the ones on the bottom indicated metabolites in BF3-1 in positive and negative ion modes as described in Figure 4A. Cyanidin, cyanidin 3-glucoside (C3G), and cyanidin 3-rutinoside (C3R) were identified as significant variables ($p < 0.05$) specifically found in BF3-1 compared to BF3-2 with regulatory activity on iNOS and COX-2 expression as denoted in Figure 4A. Quantitative analysis on these key molecules revealed that cyanidin, C3G, and C3R were contained in BF3-1 at 0.44, 1.26, and 0.56 μg/mg, respectively (Figure 4B). The critical difference of these compounds in BF3-1 may influence the

DOI: 10.1021/acs.jafc.5b00560
J. Agric. Food Chem. 2015, 63, 5449−5458

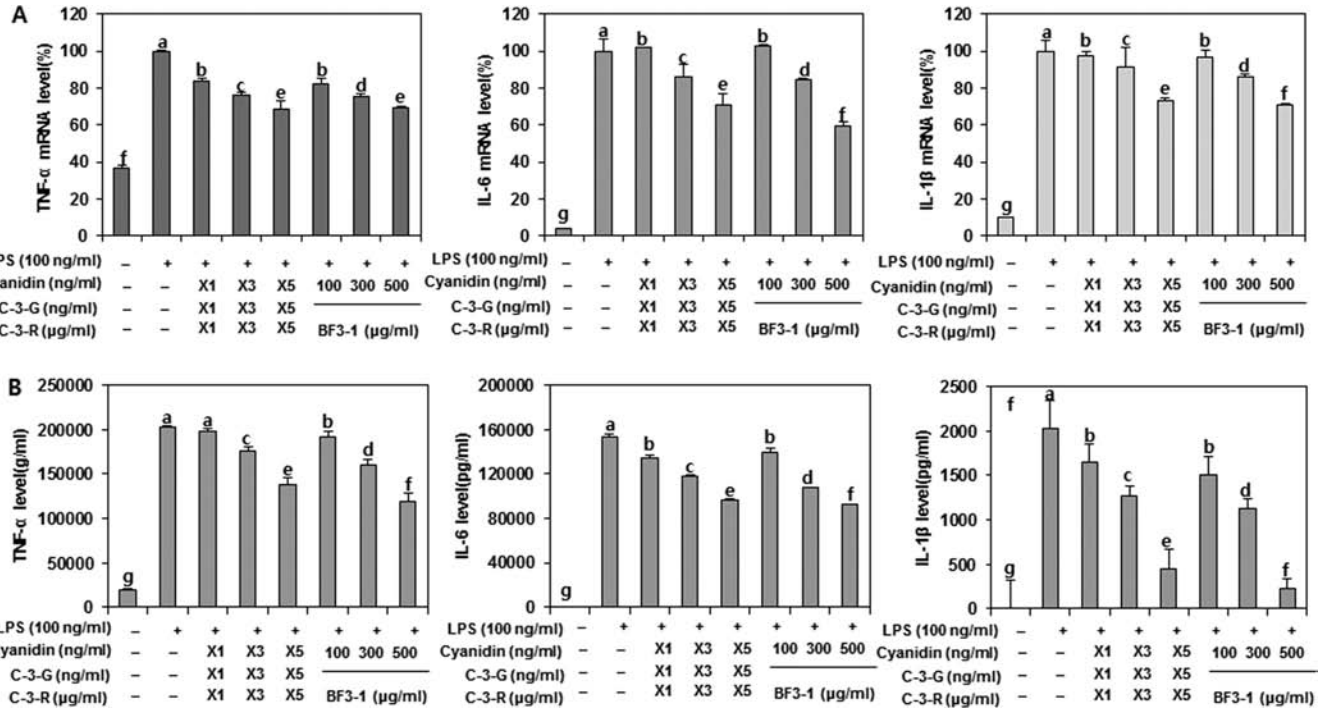

Figure 6. Effect of BF3-1 and key constituents on mRNA and protein expression of cytokines in LPS-induced RAW264.7 cells. The cells (8×10^5 cells/well in 60 mm dish) were treated with the key compounds (cyanidin, C3G, C3R) and BF3-1 (100, 300, 500 μg/mL) with LPS (100 ng/mL) for 15 h. (A) The mRNA levels of cytokines were measured by quantitative RT-PCR. (B) The released cytokine levels in media were measured by ELISA. Statistical significance was determined by one-way ANOVA with Duncan's test, and differences are indicated with different letters ($p < 0.05$).

different anti-inflammatory patterns of BF3-1 and BF3-2 as indicated in Figure 3A.

BF3-1 and Cyanidin Mixture Commonly Suppressed the Inflammatory Markers and Regulated the Same Intracellular Signaling Mediators in Murine Macrophage Cells. Here, we compared the anti-inflammatory activity between the BF3-1 fraction and the cyanidin mixture of the key components, cyanidin, C3G, and C3R, in LPS-induced RAW264.7 cells. On the basis of the quantifications of key components in BF3-1, the actual amounts of cyanidin, C3G, and C3R in BF3-1 at 100 μg/mL were determined as 0.044 μg/mL (~0.15 μM), 0.126 μg/mL (~0.26 μM), and 0.056 μg/mL (~0.09 μM), respectively, which was described as X1 (Figure 5). X3 and X5 represent 3 and 5 times higher amounts of each constituent relative to X1, which are the same amounts present in 300 and 500 μg/mL of BF3-1, respectively. As shown in Figure 5A, the BF3-1 fraction exerted dose-dependent suppression of iNOS expression, and the cyanidin mixture also showed similar activity, although COX-2 inhibition is more significant in BF3-1. In addition, single treatment of cyanidin at the concentrations of X1 (0.044 μg/mL) and X5 (0.22 μg/mL) suppressed LPS-induced iNOS expression only up to 12.8 and 34.7%, respectively, but the treatment of cyanidin mixture exerted iNOS inhibitory activity up to 16.6% and 98.3% (Figure 5B). These results suggest that the regulatory efficacy on iNOS expression by BF3-1 fraction might be derived from the coexistence of cyanidin, C3G, and C3R. To determine whether BF3-1 and the cyanidin mixture share the upstream inflammatory signaling molecules, we tested the expression of inhibitory κB (IκB) and phosphorylation of mitogen-activated protein kinases (MAPKs) and found that the phosphorylations of extracellular signal-related kinase (ERK), c-Jun N-terminal kinase (JNK), and p38 induced by LPS treatment were significantly blocked by both the BF3-1 fraction and cyanidin mixture in a dose-dependent manner (Figure 5B). Interestingly, however, BF3-1 and the cyanidin mixture did not recover the degraded IκB by LPS treatment, indicating that they regulated the LPS-induced inflammation independent of the nuclear factor κB (NF-κB) signaling pathway.

BF3-1 and Cyanidin Mixture Inhibited Expression Level of the Same Cytokines in Murine Macrophage Cells Induced by LPS. Due to critical roles of cytokines during the inflammatory processes,[20] we further investigated the roles of BF3-1 and cyanidin mixture in regulating the expression of well-known cytokines tumor necrosis factor-α (TNF-α), interleukin 1β (IL-1β), and interleukin 6 (IL-6) in RAW264.7 cells. In mRNA expression of cytokines determined by quantitative RT-PCR, both cyanidin mixture and BF3-1 reduced the level of those cytokines most significantly at X5 and 500 μg/mL (Figure 6A). In addition, the amount of the secreted cytokines at protein level was confirmed by ELISA, and it was found to be reduced by cyanidin mixture and BF3-1 treatment, where IL-1β was most strikingly suppressed (Figure 6B). Recently, it was reported that LPS increased the production of cytokines IL-6 and IL-1β through STAT3 activation in murine macrophage cells.[21] Here, we also confirmed that BF3-1 and cyanidin mixture blocked the phosphorylation of STAT3 (Figure 5B), which may lead to reduced LPS-induced expression of IL-6 and IL-1β (Figure 6).

DISCUSSION

Metabolomics is the useful analysis appropriate for profiling a whole set of metabolites and phenotyping the unique metabolome from complicated food and natural resources. This approach has been recently applied to elucidate the relationship between dietary sources and human chronic

DOI: 10.1021/acs.jafc.5b00560
J. Agric. Food Chem. 2015, 63, 5449−5458

diseases and discover new biomarkers by analyzing urine or plasma samples.[22,23] In addition, studies developing the new model system to connect the active metabolites in fruit extracts to bioactivity have been reported.[17,18] Anthocyanin extract from black raspberry was analyzed by NMR spectroscopy and multivariate statistical analysis, and it was found that anthocyanins C3R, cyanidin 3-*O*-xylosylrutinoside (C3X), and C3G were identified as the critical constituents exerting antioxidant activity.[17] Using the same approach, C3R and C3X were also reported to play a predominant role in inhibiting proliferation of human colon cancer cells.[18] In this study, we performed multistep solvent extraction to cover the whole metabolome in black raspberry and further separated the most active fraction inhibiting inflammatory markers with preparative HPLC (Figures 1 and 2). By comparing the metabolites from the fraction with anti-inflammatory effect (BF3-1) to those without the activity (BF3-2) using HPLC-ESI-ion trap MS/MS and OPLS-DA, we successfully identified and quantified the key constituents responsible for the activity, cyanidin, C3G, and C3R (Figures 3 and 4). Most importantly, we validated the mechanistic roles of BF3-1 and the mixture of cyanidin, C3G, and C3R in regulating the same molecular targets during the inflammatory process (Figures 5 and 6).

To investigate the link between the powder or extract of different fruits and vegetables and individual constituents for the prevention of chronic diseases, many studies have evaluated the effects of extracts, identified their components, and finally confirmed the physiological efficacy of several key constituents.[24,25] In some studies, however, a single active component was treated at too high concentration compared to that in the extract,[10,26,27] ranging from 10 to 100 μM in the case of C3G. Here, we quantified the actual concentrations of the cyanidin, C3G, and C3R in the active fraction (BF3-1) and treated the same amount with those in BF3-1, ranging from 0.15 to 0.75 μM cyanidin, from 0.25 to 1.3 μM C3G, and from 0.09 to 0.45 μM C3R, respectively (Figures 5 and 6). The interaction between constituents must also be considered. As many know, it has been reported that synergistic and/or antagonistic effects between different ingredients would influence fatty acid oxidations, antioxidant capacities, tumor cell proliferation, and intracellular molecular target expression.[28−31] In addition, the COX-2 inhibitory activity of the BF3-1 fraction was more dramatic compared to the cyanidin mixture (Figure 5A), which might be explained by the active interactions between other constituents including unknown compounds in BF3-1 fraction.

LPS is known to activate macrophage cells by increasing the pro-inflammatory products including iNOS, COX-2, and cytokines such as TNF-α, IL-6, and IL-1β, and the upstream intracellular signaling by LPS is mediated through the NF-κB pathway regulated by Iκ, and the MAPKs pathway including ERK, JNK, and p38 after binding to Toll-like receptors (TLRs) on the cell membrane.[32−34] Interestingly, a recent finding indicates that LPS led to morphological changes to bigger cell size and increased membrane protein clusters in RAW264.7 cells.[35] Black raspberry powder and extracts have been reported to have regulatory activity of inflammatory markers in different models, for example, iNOS and COX-2 suppression in *N*-nitrosomethylbenzylamine-induced angiogenesis,[36] to inhibit TNF-α, IL-1β, COX-2, and phospho-IκB in dextran solution sulfate-induced ulcerative colitis,[4] and to decrease TNF-α and IL-6 serum levels in patients with metabolic syndrome.[3] Our results in this study also support previous studies in that black raspberry extract regulated LPS-induced phosphorylation of ERK, JNK, p38, and STAT3, resulting in reduction of both mRNA and protein expression of cytokines, TNF-α, IL-6, and IL-1β, in addition to iNOS suppression without cytotoxicity (Figures 5 and 6). The cyanidin mixture containing cyanidin, C3G, and C3R, identified by metabolomic screening and quantified by HPLC analsysis from BF3-1, was validated to have similar efficacy in regulating the inflammatory mediators at submicromolar concentrations (Figures 5 and 6), ascertaining that cyanidin, C3G, and C3R are the critical constituents in black raspberry fraction BF3-1.

The NF-κB, activated by LPS, cytokines (IL-1β or TNF-α), or oxidative stress, is a well-known transcription factor regulating iNOS expression.[37] Berry anthocyanins including cyanidin 3-glucoside have been reported to block the NF-κB activation induced by cytokines and UVB in different models.[27,38,39] In this study, however, neither black raspberry extract (BF3-1) nor corresponding cyanidin mixture induced the recovery of IκB degradation (Figure 5B), which is one of the key events happening during activation of the NF-κB signaling pathway by LSP. This inconsistent result in regulating NF-κB signaling might be from the lower concentration of treated anthocyanins than in other studies. The concentration of the X3 mixture containing cyanidin, cyanidin-3-glucoside, and cyanidin-3-rutinoside in the present study was only 0.678 ug/mL (1.51 μM), whereas other studies used from 8.99 μg/mL (20 μM) to 112.34 μg/mL (250 μM) of cyanidin-3-glucoside.[27,38,39] Instead, BF3-1 and the cyanidin mixture significantly suppressed LPS-induced MAPKs phosphorylation, which can lead to inhibition of the binding of activating protein-1 (AP-1) complex and iNOS expression.[40] These findings suggest that coexistence of anthocyanins even at low concentrations (<1 μM) may exert significant anti-inflammatory activity, although the molecular targets at upstream signaling pathways are different from those at higher concentration treatment.

It is generally known that the bioavailability of anthocyanins is <2%, and their plasma concentrations range from 1 to 100 nM,[41,42] which are relatively lower concentrations compared to that of the cyanidin mixture (0.50−2.52 μM) treated in this study. Interestingly, however, it has been demonstrated that the gastrointestinal tissues absorb the anthocyanins as their intact form, which resulted in higher accumulation of anthocyanins in stomach or intestinal tissues.[43−45] He et al. found that 7.5% of anthocyanins of administered C3G equivalent (27 nmol) were absorbed into intestinal tissues of rat, indicating much more efficient uptake of anthocyanins than those in plasma or urine.[44] In an animal study using a blackberry anthocyanin-enriched diet (14.8 mmol of anthocyanins) for 15 days, the accumulations of C3G equivalent reached 605 nmol/g of tissue in jejunum, whereas the plasma concentration of C3G equivalent was only 0.36 nmol/mL.[45] These studies suggest that the treated concentrations of cyanidin mixture are physiologically relevant to provide a beneficial effect on regulating the local inflammatory processes at least in gastrointestinal tract.

Taken together, we performed a multistep solvent extraction and subfractionation of black raspberry cultivated in South Korea. Metabolomic profiling and OLPS-DA between subfractions determined that cyanidin, C3G, and C3R are the key components responsible for anti-inflammatory activity. We also confirmed that cotreatments of cyanidin, C3G, and C3R at the same concentration with the fraction shared molecular targets, MAPKs and STAT3, which resulted in suppression of iNOS

DOI: 10.1021/acs.jafc.5b00560
J. Agric. Food Chem. 2015, 63, 5449−5458

and cytokines, TNF-α, IL-6, and IL-1β. To our best knowledge, this is the first report to employ a systematic approach using metabolomic analysis to identify and validate the key contributors to anti-inflammatory physiological efficacy. For further study, it is necessary to expand to in vivo studies demonstrating the effect of active compounds on the metabolome in biofluid to clearly elucidate their health beneficial efficacy.

■ ASSOCIATED CONTENT

Supporting Information

Table 1, tentatively identified metabolites in Korean black raspberry extract fractions 1, 2, and 3 (BF1, BF2, and BF3) by LC-ESI-ion trap-MS/MS in positive and negative ion mode; Table 2, tentatively identified metabolites in subfractions (BF3-1, BF3-2, and BF3-3) of Korean black raspberry by LC-ESI-ion trap-MS/MS in positive and negative ion mode. The Supporting Information is available free of charge on the ACS Publications website at DOI: 10.1021/acs.jafc.5b00560.

■ AUTHOR INFORMATION

Corresponding Authors

*(H.J.L.) Phone: +82-31-670-3030. Fax: +82-31-675-4853. E-mail: hongjin@cau.ac.kr.

*(J.-H.A.) Phone: +82-31-670-3079. Fax: +82-31-675-4853. E-mail: jhauh@cau.ac.kr.

Author Contributions

[‖]Y.-H.J., H.-C.P., and S.C. contributed to this work equally.

Funding

This work was carried out with the support of the Cooperative Research Program for Agriculture Science and Technology Development (PJ008550), Rural Development Administration, by the Bio-Synergy Research Project (NRF-2013M3A9C4078156) of the Ministry of Science, ICT and Future Planning through the National Research Foundation, and by a Chung-Ang University Research Grant in 2013.

Notes

The authors declare no competing financial interest.

■ ABBREVIATIONS USED

BF, black raspberry fraction; TNF-α, tumor necrosis factor-α; NF-κB, nuclear factor κB; IκB, inhibitory κB; iNOS, inducible nitric oxide synthase; MAPK, mitogen activated protein kinase; ERK, extracellular signal-regulated kinase; JNK, c-Jun N-terminal kinase; ILs, interleukins; ELISA, enzyme linked immunosorbent assay; LPS, lipopolysaccharide; GAPDH, glyceraldehyde-3-phosphate dehydrogenase; PCA, principal component analysis; OPLS-DA, orthogonal partial least-squares discriminant analysis; ESI, electrospray ionization

■ REFERENCES

(1) Bhandary, B.; Lee, G. H.; So, B. O.; Kim, S. Y.; Kim, M. G.; Kwon, J. W.; Song, J. Y.; Lee, H. K.; Kim, H. R.; Chae, S. W.; Chae, H. J. *Rubus coreanus* inhibits oxidized-LDL uptake by macrophages through regulation of JNK activation. *Am. J. Chin. Med.* **2012**, *40*, 967−978.

(2) Duncan, F. J.; Martin, J. R.; Wulff, B. C.; Stoner, G. D.; Tober, K. L.; Oberyszyn, T. M.; Kusewitt, D. F.; Van Buskirk, A. M. Topical treatment with black raspberry extract reduces cutaneous UVB-induced carcinogenesis and inflammation. *Cancer Prev. Res.* **2009**, *2*, 665−672.

(3) Jeong, H. S.; Hong, S. J.; Lee, T. B.; Kwon, J. W.; Jeong, J. T.; Joo, H. J.; Park, J. H.; Ahn, C. M.; Yu, C. W.; Lim, D. S. Effects of black raspberry on lipid profiles and vascular endothelial function in patients with metabolic syndrome. *Phytother. Res.* **2014**,*28*, 149210.1002/ptr.5154

(4) Montrose, D. C.; Horelik, N. A.; Madigan, J. P.; Stoner, G. D.; Wang, L. S.; Bruno, R. S.; Park, H. J.; Giardina, C.; Rosenberg, D. W. Anti-inflammatory effects of freeze-dried black raspberry powder in ulcerative colitis. *Carcinogenesis* **2011**, *32*, 343−350.

(5) Ravoori, S.; Vadhanam, M. V.; Aqil, F.; Gupta, R. C. Inhibition of estrogen-mediated mammary tumorigenesis by blueberry and black raspberry. *J. Agric. Food Chem.* **2012**, *60*, 5547−5555.

(6) Zhang, Z.; Knobloch, T. J.; Seamon, L. G.; Stoner, G. D.; Cohn, D. E.; Paskett, E. D.; Fowler, J. M.; Weghorst, C. M. A black raspberry extract inhibits proliferation and regulates apoptosis in cervical cancer cells. *Gynecol. Oncol.* **2011**, *123*, 401−406.

(7) Peiffer, D. S.; Zimmerman, N. P.; Wang, L. S.; Ransom, B. W.; Carmella, S. G.; Kuo, C. T.; Siddiqui, J.; Chen, J. H.; Oshima, K.; Huang, Y. W.; Hecht, S. S.; Stoner, G. D. Chemoprevention of esophageal cancer with black raspberries, their component anthocyanins, and a major anthocyanin metabolite, protocatechuic acid. *Cancer Prev. Res.* **2014**, *7*, 574−584.

(8) Stoner, G. D. Foodstuffs for preventing cancer: the preclinical and clinical development of berries. *Cancer Prev. Res.* **2009**, *2*, 187−194.

(9) Tulio, A. Z., Jr.; Reese, R. N.; Wyzgoski, F. J.; Rinaldi, P. L.; Fu, R.; Scheerens, J. C.; Miller, A. R. Cyanidin 3-rutinoside and cyanidin 3-xylosylrutinoside as primary phenolic antioxidants in black raspberry. *J. Agric. Food Chem.* **2008**, *56*, 1880−1888.

(10) Han, C.; Ding, H.; Casto, B.; Stoner, G. D.; D'Ambrosio, S. M. Inhibition of the growth of premalignant and malignant human oral cell lines by extracts and components of black raspberries. *Nutr. Cancer* **2005**, *51*, 207−217.

(11) Bino, R. J.; Hall, R. D.; Fiehn, O.; Kopka, J.; Saito, K.; Draper, J.; Nikolau, B. J.; Mendes, P.; Roessner-Tunali, U.; Beale, M. H.; Trethewey, R. N.; Lange, B. M.; Wurtele, E. S.; Sumner, L. W. Potential of metabolomics as a functional genomics tool. *Trends Plant Sci.* **2004**, *9*, 418−425.

(12) German, J. B.; Hammock, B. D.; Watkins, S. M. Metabolomics: building on a century of biochemistry to guide human health. *Metabolomics* **2005**, *1*, 3−9.

(13) Schauer, N.; Fernie, A. R. Plant metabolomics: towards biological function and mechanism. *Trends Plant Sci.* **2006**, *11*, 508−516.

(14) Theodoridis, G.; Gika, H. G.; Wilson, I. D. LC-MS-based methodology for global metabolite profiling in metabonomics/metabolomics. *TrAC, Trends Anal. Chem.* **2008**, *27*, 251−260.

(15) Gaskell, S. Electrospray: Principles and practice (Vol. 32, pp 677, 1997). *J. Mass Spectrom.* **1997**, *32*, 1378−1378.

(16) Lee, J.; Kim, S.; Namgung, H.; Jo, Y. H.; Bao, C.; Choi, H. K.; Auh, J. H.; Lee, H. J. Ellagic acid identified through metabolomic analysis is an active metabolite in strawberry ('Seolhyang') regulating lipopolysaccharide-induced inflammation. *J. Agric. Food Chem.* **2014**, *62*, 3954−3962.

(17) Wyzgoski, F. J.; Paudel, L.; Rinaldi, P. L.; Reese, R. N.; Ozgen, M.; Tulio, A. Z.; Miller, A. R.; Scheerens, J. C.; Hardy, J. K. Modeling relationships among active components in black raspberry (*Rubus occidentalis* L.) fruit extracts using high-resolution ^{1}H nuclear magnetic resonance (NMR) spectroscopy and multivariate statistical analysis. *J. Agric. Food Chem.* **2010**, *58*, 3407−3414.

(18) Paudel, L.; Wyzgoski, F. J.; Giusti, M. M.; Johnson, J. L.; Rinaldi, P. L.; Scheerens, J. C.; Chanon, A. M.; Bomser, J. A.; Miller, A. R.; Hardy, J. K.; Reese, R. N. NMR-based metabolomic investigation of bioactivity of chemical constituents in black raspberry (*Rubus occidentalis* L.) fruit extracts. *J. Agric. Food Chem.* **2014**, *62*, 1989−1998.

(19) Maatta-Riihinen, K. R.; Kamal-Eldin, A.; Torronen, A. R. Identification and quantification of phenolic compounds in berries of *Fragaria* and *Rubus* species (Family rosaceae). *J. Agric. Food Chem.* **2004**, *52*, 6178−6187.

DOI: 10.1021/acs.jafc.5b00560
J. Agric. Food Chem. 2015, 63, 5449−5458

(20) Fujiwara, N.; Kobayashi, K. Macrophages in inflammation. *Curr. Drug Targets Inflamm. Allergy* **2005**, *4*, 281−286.
(21) Samavati, L.; Rastogi, R.; Du, W.; Huttemann, M.; Fite, A.; Franchi, L. STAT3 tyrosine phosphorylation is critical for interleukin 1β and interleukin-6 production in response to lipopolysaccharide and live bacteria. *Mol. Immunol.* **2009**, *46*, 1867−1877.
(22) Gomez-Casati, D. F.; Zanor, M. I.; Busi, M. V. Metabolomics in plants and humans: applications in the prevention and diagnosis of diseases. *BioMed Res. Int.* **2013**, *2013*, 792527.
(23) Manach, C.; Hubert, J.; Llorach, R.; Scalbert, A. The complex links between dietary phytochemicals and human health deciphered by metabolomics. *Mol. Nutr. Food Res.* **2009**, *53*, 1303−1315.
(24) Mace, T. A.; King, S. A.; Ameen, Z.; Elnaggar, O.; Young, G.; Riedl, K. M.; Schwartz, S. J.; Clinton, S. K.; Knobloch, T. J.; Weghorst, C. M.; Lesinski, G. B. Bioactive compounds or metabolites from black raspberries modulate T lymphocyte proliferation, myeloid cell differentiation and Jak/STAT signaling. *Cancer Immunol. Immunother.* **2014**, *63*, 889−900.
(25) Wang, L. S.; Kuo, C. T.; Cho, S. J.; Seguin, C.; Siddiqui, J.; Stoner, K.; Weng, Y. I.; Huang, T. H.; Tichelaar, J.; Yearsley, M.; Stoner, G. D.; Huang, Y. W. Black raspberry-derived anthocyanins demethylate tumor suppressor genes through the inhibition of DNMT1 and DNMT3B in colon cancer cells. *Nutr. Cancer* **2013**, *65*, 118−125.
(26) Serra, D.; Paixao, J.; Nunes, C.; Dinis, T. C.; Almeida, L. M. Cyanidin-3-glucoside suppresses cytokine-induced inflammatory response in human intestinal cells: comparison with 5-aminosalicylic acid. *PLoS One* **2013**, *8*, e73001.
(27) Speciale, A.; Canali, R.; Chirafisi, J.; Saija, A.; Virgili, F.; Cimino, F. Cyanidin-3-*O*-glucoside protection against TNF-α-induced endothelial dysfunction: involvement of nuclear factor-κB signaling. *J. Agric. Food Chem.* **2010**, *58*, 12048−12054.
(28) Rossetto, M.; Vanzani, P.; Mattivi, F.; Lunelli, M.; Scarpa, M.; Rigo, A. Synergistic antioxidant effect of catechin and malvidin 3-glucoside on free radical-initiated peroxidation of linoleic acid in micelles. *Arch. Biochem. Biophys.* **2002**, *408*, 239−245.
(29) Seeram, N. P.; Adams, L. S.; Hardy, M. L.; Heber, D. Total cranberry extract versus its phytochemical constituents: antiproliferative and synergistic effects against human tumor cell lines. *J. Agric. Food Chem.* **2004**, *52*, 2512−2517.
(30) Shih, P. H.; Hwang, S. L.; Yeh, C. T.; Yen, G. C. Synergistic effect of cyanidin and PPAR agonist against nonalcoholic steatohepatitis-mediated oxidative stress-induced cytotoxicity through MAPK and Nrf2 transduction pathways. *J. Agric. Food Chem.* **2012**, *60*, 2924−2933.
(31) Wang, S.; Meckling, K. A.; Marcone, M. F.; Kakuda, Y.; Tsao, R. Synergistic, additive, and antagonistic effects of food mixtures on total antioxidant capacities. *J. Agric. Food Chem.* **2011**, *59*, 960−968.
(32) Chan, E. D.; Riches, D. W. IFN-gamma + LPS induction of iNOS is modulated by ERK, JNK/SAPK, and p38(mapk) in a mouse macrophage cell line. *Am. J. Physiol. Cell Physiol.* **2001**, *280*, C441−C450.
(33) Karin, M.; Delhase, M. The IκB kinase (IKK) and NF-κB: key elements of proinflammatory signalling. *Semin. Immunol.* **2000**, *12*, 85−98.
(34) Lee, H. N.; Na, H. K.; Surh, Y. J. Resolution of inflammation as a novel chemopreventive strategy. *Semin. Immunopathol.* **2013**, *35*, 151−161.
(35) Pi, J.; Li, T.; Liu, J.; Su, X.; Wang, R.; Yang, F.; Bai, H.; Jin, H.; Cai, J. Detection of lipopolysaccharide induced inflammatory responses in RAW264.7 macrophages using atomic force microscope. *Micron* **2014**, *65*, 1−9.
(36) Chen, T.; Rose, M. E.; Hwang, H.; Nines, R. G.; Stoner, G. D. Black raspberries inhibit *N*-nitrosomethylbenzylamine (NMBA)-induced angiogenesis in rat esophagus parallel to the suppression of COX-2 and iNOS. *Carcinogenesis* **2006**, *27*, 2301−2307.
(37) Kleinert, H.; Pautz, A.; Linker, K.; Schwarz, P. M. Regulation of the expression of inducible nitric oxide synthase. *Eur. J. Pharmacol.* **2004**, *500*, 255−266.
(38) Lee, S. G.; Kim, B.; Yang, Y.; Pham, T. X.; Park, Y. K.; Manatou, J.; Koo, S. I.; Chun, O. K.; Lee, J. Y. Berry anthocyanins suppress the expression and secretion of proinflammatory mediators in macrophages by inhibiting nuclear translocation of NF-κB independent of NRF2-mediated mechanism. *J. Nutr. Biochem.* **2014**, *25*, 404−411.
(39) Pratheeshkumar, P.; Son, Y. O.; Wang, X.; Divya, S. P.; Joseph, B.; Hitron, J. A.; Wang, L.; Kim, D.; Yin, Y.; Roy, R. V.; Lu, J.; Zhang, Z.; Wang, Y.; Shi, X. Cyanidin-3-glucoside inhibits UVB-induced oxidative damage and inflammation by regulating MAP kinase and NF-κB signaling pathways in SKH-1 hairless mice skin. *Toxicol. Appl. Pharmacol.* **2014**, *280*, 127−137.
(40) Kristof, A. S.; Marks-Konczalik, J.; Moss, J. Mitogen-activated protein kinases mediate activator protein-1-dependent human inducible nitric-oxide synthase promoter activation. *J. Biol. Chem.* **2001**, *276*, 8445−8452.
(41) Borges, G.; Mullen, W.; Mullan, A.; Lean, M. E.; Roberts, S. A.; Crozier, A. Bioavailability of multiple components following acute ingestion of a polyphenol-rich juice drink. *Mol. Nutr. Food Res.* **2010**, *54* (Suppl. 2), S268−S277.
(42) Kuntz, S.; Rudloff, S.; Asseburg, H.; Borsch, C.; Frohling, B.; Unger, F.; Dold, S.; Spengler, B.; Rompp, A.; Kunz, C. Uptake and bioavailability of anthocyanins and phenolic acids from grape/blueberry juice and smoothie in vitro and in vivo. *Br. J. Nutr.* **2015**, *113*, 1044−1055.
(43) Fang, J. Bioavailability of anthocyanins. *Drug Metab. Rev.* **2014**, *46*, 508−520.
(44) He, J.; Wallace, T. C.; Keatley, K. E.; Failla, M. L.; Giusti, M. M. Stability of black raspberry anthocyanins in the digestive tract lumen and transport efficiency into gastric and small intestinal tissues in the rat. *J. Agric. Food Chem.* **2009**, *57*, 3141−3148.
(45) Talavera, S.; Felgines, C.; Texier, O.; Besson, C.; Gil-Izquierdo, A.; Lamaison, J. L.; Remesy, C. Anthocyanin metabolism in rats and their distribution to digestive area, kidney, and brain. *J. Agric. Food Chem.* **2005**, *53*, 3902−3908.

DOI: 10.1021/acs.jafc.5b00560
J. Agric. Food Chem. 2015, 63, 5449−5458

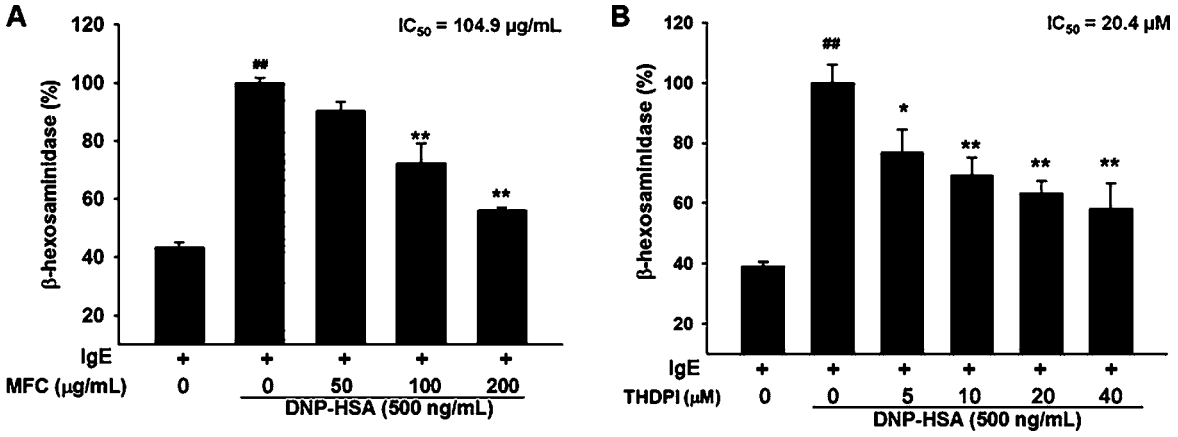

Figure 1. Effect of MFC and THDPI on mast cell degranulation in RBL-2H3 cells. Anti-DNP IgE-sensitized cells were treated with various concentrations of MFC (A) and THDPI (B) for 1 h followed by an antigen stimulation (DNP−HSA) for an additional 1 h. The release of β-hexosaminidase from cells treated with IgE/DNP−HSA was considered to represent 100% degranulation. Data represent the mean ± SD of three independent experiments. (##) $p < 0.01$, compared with IgE-sensitized cells without DNP−HSA; (**) $p < 0.01$, compared with IgE/DNP−HSA-treated cells. THDPI, 5,7,3′,4′-tetrahydroxy-6,8-diprenylisoflavone.

MO, USA). Purified mouse anti-rat FcεRIα-antibody was purchased from BD Biosciences (Franklin Lakes, NJ, USA). *Prime* RT-PCR premix was purchased from Genet Bio (Seoul, Korea), and PRO-PREP protein extraction solution and easy-BLUE total RNA extraction kits were purchased from iNtRON Biotechnology (Kyunggi, Korea). Anti-phospho-Lyn antibody was purchased from Cell Signaling Technology (Danvers, MA, USA). Anti-Lyn, anti-phospho-Syk, anti-Syk, anti-phospho-LAT, and anti-LAT antibody, fluorescent Ca^{2+} probe, Fura 2/AM, FITC-avidin, and FITC-conjugated $F(ab')_2$ goat anti-mouse IgG were purchased from Santa Cruz Biotechnology (Dallas, TX, USA).

Preparation of Methanol Extracts from the Fruits of *C. tricuspidata* (MFC). The fruits of *C. tricuspidata* (Moraceae) were collected from the Korea Forest Research Institute, Southern Forest Research Center (Jinju, Korea). A voucher specimen (accession no. KH1-5-090904) was deposited at the Department of Biosystems and Biotechnology, Korea University (Seoul, Korea). Methanol extract from the fruits of *C. tricuspidata* (MFC) was prepared as follows: The fresh fruits of *C. tricuspidata* (10.7 kg) were sliced and extracted three times with MeOH (10 L × 3) at room temperature. The solvent was evaporated in vacuo to obtain a total MeOH extract (630.95 g).[17]

Ultraperformance Liquid Chromatography (UPLC) Analysis of MFC. The MFC was analyzed using an Acquity UPLC system (Waters, Millford, MA, USA) with an Acquity UPLC BEH C18 column (1.7 μm, 2.1 × 150 mm i.d.). The mobile phase consisted of solvent A (0.05% trifluoroacetic acid in water) and solvent B (acetonitrile). The starting eluent was 40% B at 0 min. The proportion of B was increased linearly to 100% from 0 to 13 min, held constant at 100% until 14 min, returned to the initial composition (40% B) at 14 min, and then held constant for 1 min to re-equilibrate the column. The flow rate was 0.3 mL/min, and the sample injection volume was 2 μL. The column and sample managers were maintained at 35 and 15 °C. The UV detection wavelength was monitored at 280 nm.

Isolation and Identification of Compounds from MFC. The isolation and identification of 10 isoflavones, alpinumisoflavone, 4′-*O*-methylalpinumisoflavone, 5,7,4′-trihydroxy-6,8-diprenylisoflavone, 5,7,3′,4′-tetrahydroxy-6,8-diprenylisoflavone, derrone, erysenegalensein E, isoerysenegalensein E, gancaonin A, warangalone, and osajin, from MFC were described in our previous paper.[17]

Cell Cultures. Rat basophilic leukemia (RBL-2H3) cells (ATCC no. CRL-2256) were cultured at 37 °C and 5% CO_2 in MEM supplemented with 10% (v/v) fetal bovine serum, 100 U/mL penicillin, and 100 μg/mL streptomycin.

Measurement of the Release of β-Hexosaminidase. Mast cell degranulation was determined by β-hexosaminidase release on the basis of a previously described method.[18] Briefly, RBL-2H3 cells (1 × 10^5 cells/100 μL/well) were cultured in 96-well plates and incubated with monoclonal mouse anti-DNP IgE antibody (anti-DNP IgE) (1 μg/mL) for 24 h at 37 °C. The IgE-sensitized RBL-2H3 cells were washed twice with extracellular Hepes buffer (5 mM KCl, 125 mM NaCl, 20 mM Hepes, 1.5 mM $MgCl_2$, 1.5 mM $CaCl_2$). After washing, the cells were treated for 1 h with different concentrations of MFC and isolated compounds in 50 μL of Hepes buffer containing BSA (1%) and glucose (1%) at 37 °C and subsequently stimulated with DNP−HSA (500 ng/mL), a multivalent antigen, for an additional 1 h. Supernatants (40 μL) were transferred to a 96-well plate and incubated with 50 μL of substrate solution (5 mM of 4-nitrophenyl *N*-acetyl-β-D-glucosaminide in 50 mM citric acid buffer, pH 4.5) for 1.5 h at 37 °C. The reactions were stopped by the addition of 50 μL of stop solution (0.5 M Na_2CO_3/$NaHCO_3$, pH 10.0) and the absorbance at 405 nm was measured using a microplate reader (SpectraMax M5, Molecular Devices, Sunnyvale, CA, USA). The activity value measured from cells treated with IgE/DNP−HSA was considered to represent 100% degranulation.

Table 1. Inhibitory Effects of Isolated Compounds from MFC on the Release of β-Hexosaminidase from Mast Cells

compound	β-hexosaminidase release (IC_{50},[a] μM)
(**1**) derrone	>40
(**2**) alpinumisoflavone	>40
(**3**) erysenegalensein E	>40
(**4**) 5,7,3′,4′-tetrahydroxy-6,8-diprenylisoflavone	20.4
(**5**) isoerysenegalensein E	>40
(**6**) gancaonin A	>40
(**7**) 5,7,4′-trihydroxy-6,8-diprenylisoflavone	>40
(**8**) 4′-*O*-methylalpinumisoflavone	>40
(**9**) warangalone	>40
(**10**) osajin	>40
ketotifen (positive control)	23.1

[a]The IC_{50} values were determined in a semilogarithmic graph with four different concentrations of compounds. At least three independent experiments were performed. Ketotifen, a mast cell stabilizer, was used as a positive control compound.

Measurement of Intracellular Ca^{2+}. RBL-2H3 cells (1 × 10^5 cells/100 μL/well) were cultured in black 96-well plates and incubated with anti-DNP IgE (1 μg/mL) for 24 h at 37 °C. Cells were washed with PBS buffer and incubated with Fura 2/AM (20 μM) in 100 μL of Tyrode buffer (5 mM KCl, 130 mM NaCl, 10 mM Hepes, 0.6 mM MgCl, 1 mM $CaCl_2$, 1% BSA, 1% glucose) for 1 h. The cells were washed three times with PBS buffer and treated with different

DOI: 10.1021/acs.jafc.5b00903
J. Agric. Food Chem. 2015, 63, 5459−5467

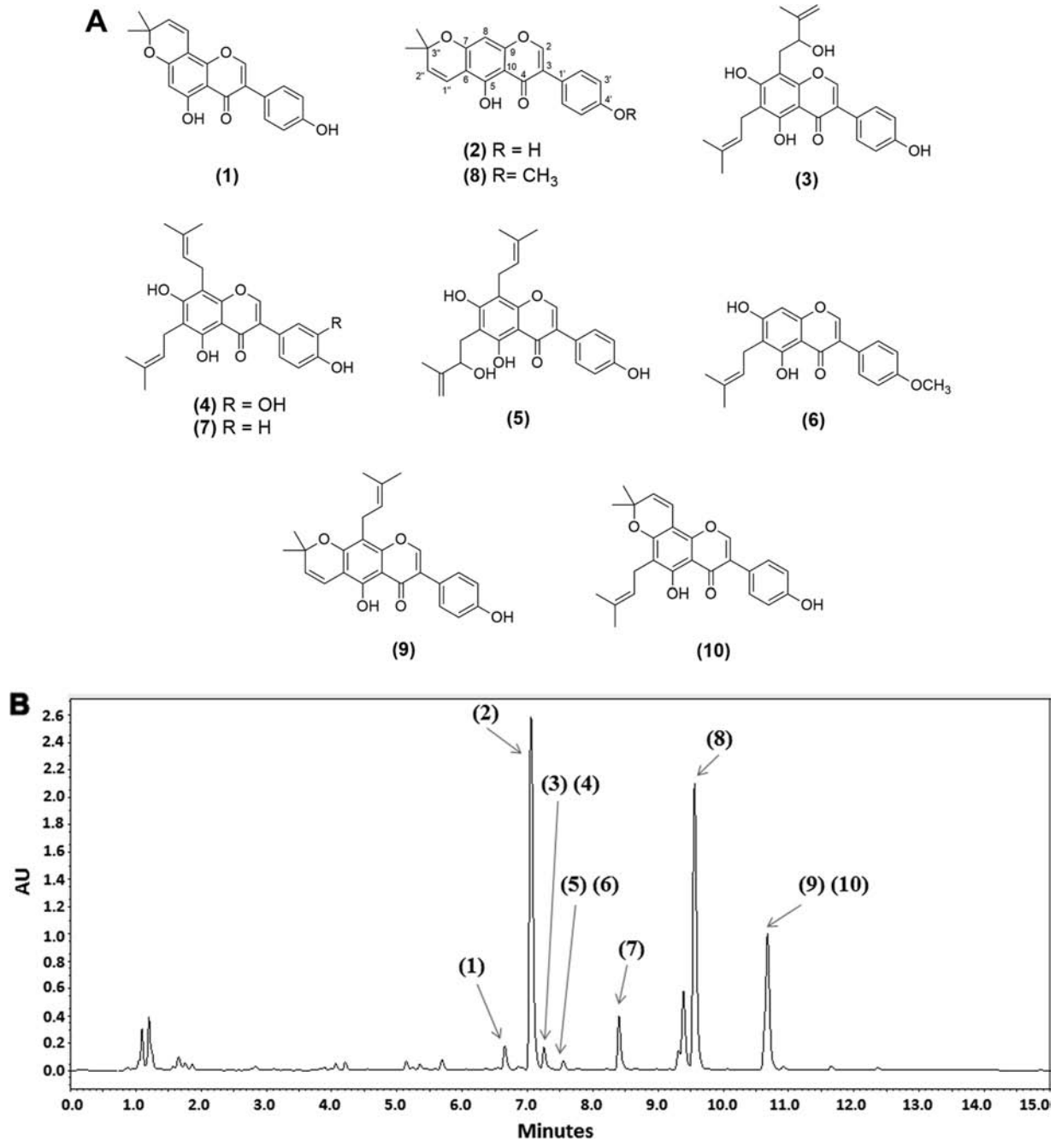

Figure 2. (A) Structures of principal compounds and (B) UPLC chromatogram of MFC. The principal compounds are (**1**) derrone, (**2**) alpinumisoflavone, (**3**) erysenegalensein E, (**4**) 5,7,3′,4′-tetrahydroxy-6,8-diprenylisoflavone, (**5**) isoerysenegalensein E, (**6**) gancaonin A, (**7**) 5,7,4′-trihydroxy-6,8-diprenylisoflavone, (**8**) 4′-*O*-methylalpinumisoflavone, (**9**) warangalone, and (**10**) osajin.

concentrations of MFC and an isolated compound in 100 μL of Tyrode buffer for 15 min and subsequently stimulated with DNP−HSA (500 ng/mL). The fluorescence intensity was recorded for 20 min using a microplate reader (SpectraMax M5, Molecular Devices, Sunnyvale, CA, USA) at an emission of 512 nm and excitation of 340 and 380 nm. The fluorescence ratio (F_{340}/F_{380}) was used as an indication of a rise in the intracellular concentration of Ca^{2+}.[19]

Measurement of Biotinylated IgE Binding to FcεRI. IgE biotinylation (biotinylated IgE) was carried out according to previously reported methods.[20] Briefly, DNP−IgE (0.5 mg) was dissolved in 500 μL of PBS and incubated with 50 μL of 10 mM of succinimidyl-6-(biotinamido) hexanoate (Thermo Fisher Scientific, Waltham, MA, USA) dissolved in DMSO. After 1 h of incubation at 4 °C, 1 mL of Tris (50 mM, pH 8) was added to deactivate residual reactive groups. The biotinylated IgE were dialyzed with PBS at 4 °C, recovered, and stored frozen until use. For binding experiments, RBL-2H3 cells (1×10^6 cells/mL/well) were cultured for 24 h in 12-well plates and washed with PBS containing 0.2% bovine serum albumin. The cells were incubated with biotinylated IgE (2 μg/mL) and MFC and an isolated compound for 1 h at 37 °C, detached by gentle scraping, centrifuged at 4000 rpm for 5 min, suspended in PBS, and stained with 20 μL of FITC-avidin at 4 °C for 30 min. As a background control, untreated cells were stained with FITC-avidin alone. The cells were then washed twice with PBS and subjected to analysis of IgE binding to RBL-2H3 cells using a flow cytometer (FACSCalibur, BD Biosciences, San Jose, CA, USA). Values of florescence intensity were obtained from histogram statistic of CellQuest software (BD Biosciences).

DOI: 10.1021/acs.jafc.5b00903
J. Agric. Food Chem. 2015, 63, 5459−5467

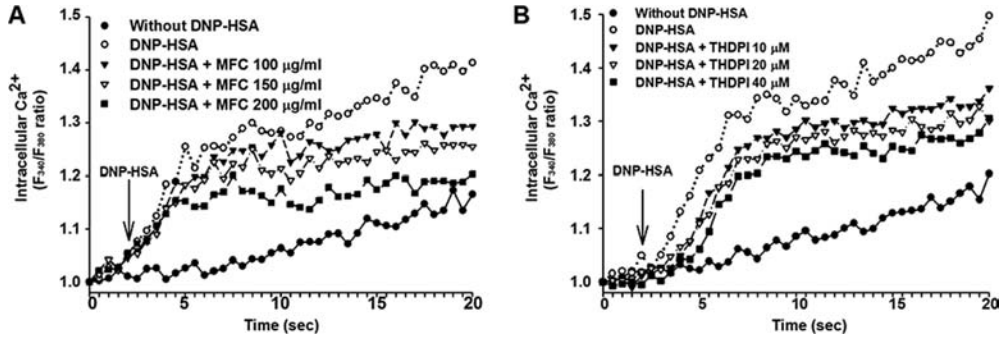

Figure 3. Effect of MFC and THDPI on Ca^{2+} influx in RBL-2H3 cells. Anti-DNP IgE-sensitized cells were incubated with Fura 2/AM for 1 h and thereafter treated with MFC (A) and THDPI (B) for 15 min and subsequently stimulated with an antigen (DNP−HSA, 500 ng/mL). Fluorescence intensity was measured for 20 min (excitation, 340 and 380 nm; emission, 512 nm). Values are expressed as a ratio of the fluorescence at the two excitation wavelengths (F_{340}/F_{380}). The arrow represents the time at which antigen was added.

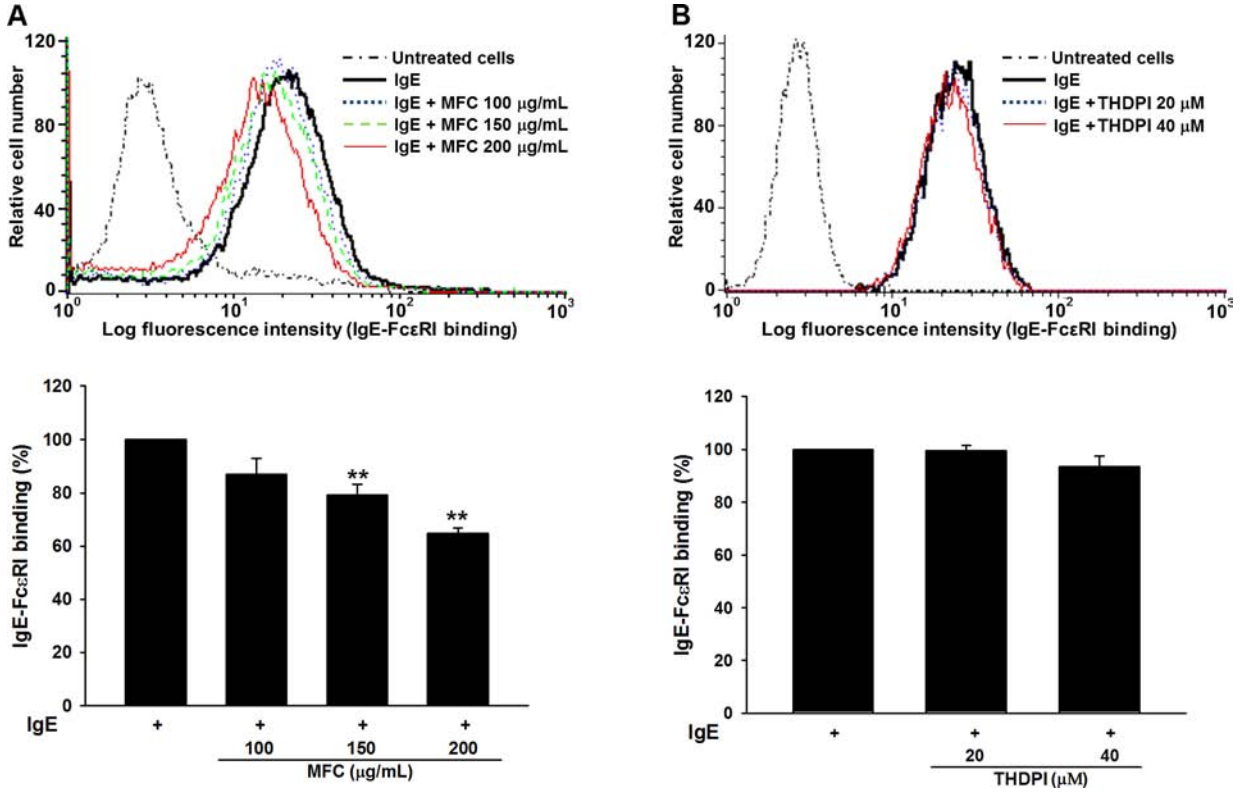

Figure 4. Effect of MFC and THDPI on IgE−FcεRI binding. RBL-2H3 cells were treated with biotinylated IgE (2 μg/mL) and various concentrations of MFC (A) and THDPI (B) for 1 h. The cells were then stained with FITC-avidin for 30 min. IgE bound to FcεRI on RBL-2H3 cells was analyzed by employing flow cytometry. Quantitative comparison of IgE−FcεRI binding between IgE-treated cells and sample-treated cells was made. Values of florescence intensity were obtained from histogram statistic of CellQuest software. Data represent the mean ± SD of three independent experiments. (**) $p < 0.01$, compared with the IgE-treated cells.

Measurement of mRNA Expression. RBL-2H3 cells (5×10^5 cells/500 μL/well) were incubated for 24 h, treated with MFC and an isolated compound for 3, 6, 18, 24 h (time-dependent), and treated with various concentrations of MFC and an isolated compound for 24 h (dose-dependent). The cells were washed twice with PBS, and total RNA was isolated with easy-BLUE (iNtRON Biotechnology, Korea), according to the manufacturer's instruction. cDNA synthesis was performed from 500 ng of total RNA by using a ONE-STEP RT-PCR PreMix kit (iNtRoN Biotechnology, Korea). The following primer pairs were synthesized (Bioneer, Korea):

FcεRIα, 5′-CATTGTGAGTGCCACCATTC-3′, 5′-TTCTTC-CAGCTACGGCATCT-3′;

FcεRIβ, 5′-TTGTCTGCTCCACACTCCAG-3′, 5′-AGGCTG-CCTCTCACCAGATA-3′;

FcεRIγ, 5′-CACCTGTTCTCAGCTGCATT-3′, 5′-GGATCA-GGGAAGGAAAGAGG-3′;

GAPDH, 5′-AGACAGCCGCATCTTCTTGT-3′, 5′-CTTGCC-GTGGGTAGAGTCAT-3′.

The denaturation, annealing, extension, and cycle conditions were performed as follows: 94 °C for 45 s, 62 °C for 45 s, 72 °C for 45 s, and 26 cycles. The PCR reaction was performed with a 2720 Thermal Cycler (Applied Biosystems, USA). Aliquots of the PCR reactions were electrophoresed in 1.5% (w/v) agarose gels and stained with SYBR Safe DNA gel stain (Invitrogen, USA). DNA bands were visualized with LAS 1000plus (FUJIFILM, Japan).

Measurement of p-Lyn, p-Syk, p-LAT, and p-PLCγ Proteins. RBL-2H3 cells (2×10^6 cells/2 mL/well) were cultured in 6-well plates with IgE for 24 h. Cells were then treated with different concentrations

DOI: 10.1021/acs.jafc.5b00903
J. Agric. Food Chem. 2015, 63, 5459−5467

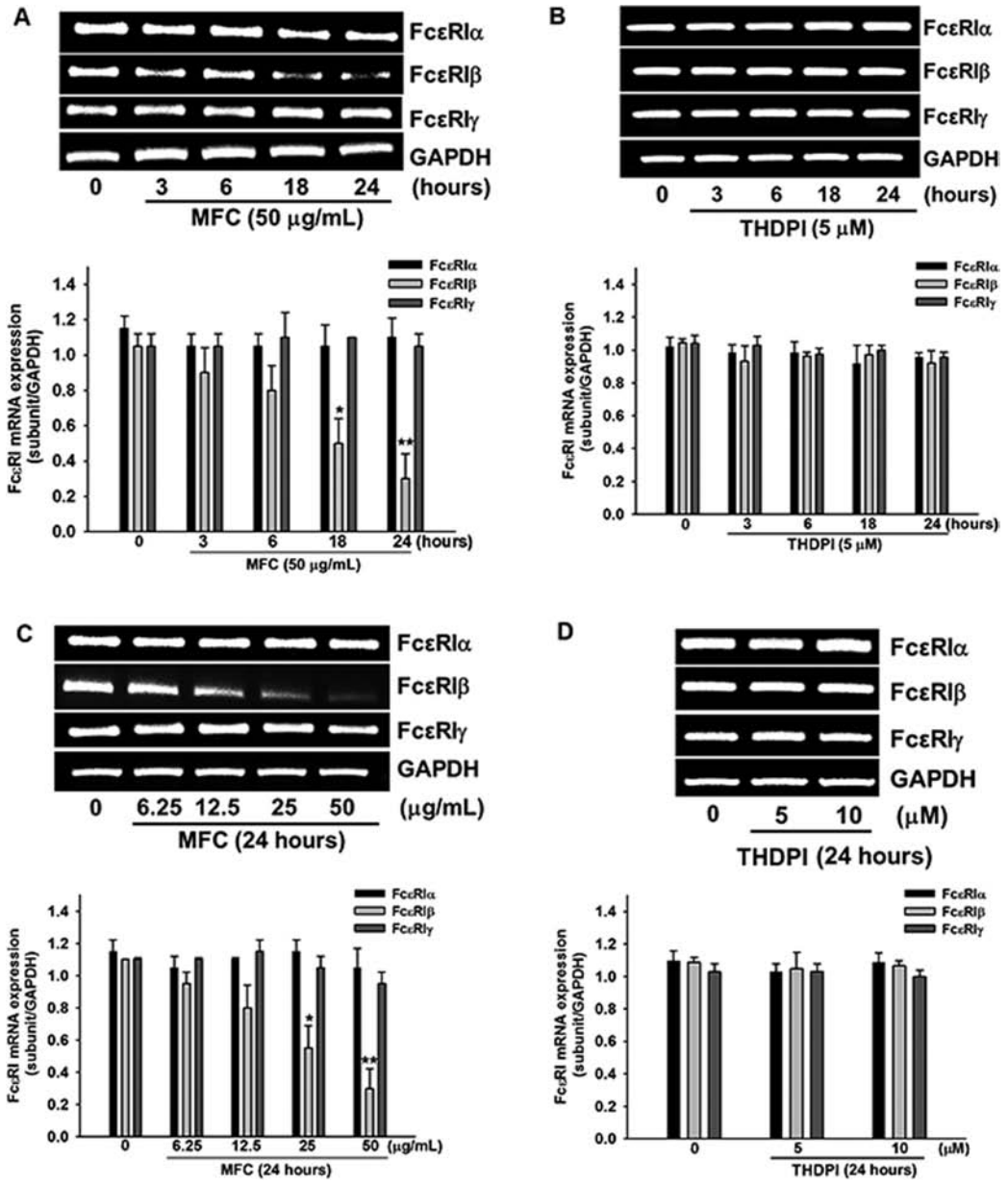

Figure 5. Effect of MFC and THDPI on FcεRI mRNA expression in RBL-2H3 cells. RBL-2H3 cells were treated with MFC and THDPI for different time intervals (0, 3, 6, 18, and 24 h) (A, B). RBL-2H3 cells were treated with various concentrations of MFC and THDPI for 24 h (C, D). The mRNA expression levels of FcεRI-subunit genes, α, β, and γ, were determined by RT-PCR analysis. Quantitative representation of the expression of each subunit of FcεRI and GAPDH mRNA was made using ImageJ software. Data represent the mean ± SD of three independent experiments. (∗) $p < 0.05$ and (∗∗) $p < 0.01$, compared with the non-MFC-treated cells.

of MFC and an isolated compound for 24 h and subsequently stimulated with DNP−HSA (500 ng/mL) for 10 min. Cells were lysed by PRO-PREP protein extraction solution (iNtRON Biotechnology, Korea) for 20 min at −20 °C. After incubation, lysates were centrifuged at 13000 rpm for 10 min at 4 °C for clarification. Approximately 15 μL (30 μg of total protein) of supernatant was subjected to 10% SDS-PAGE and transferred to PVDF membrane (Immobilon-P, Millipore, USA). The membrane was incubated with primary antibodies at 4 °C overnight. After washing, the membranes were probed with secondary antibodies for 1 h and developed with ECL Western blotting detection reagent, WEST-ZOL plus (iNtRON Biotechnology, Korea). Bands were visualized using an image analyzer, LAS 1000plus (FUJIFILM, Japan).

Redistribution of F-Actin Using Confocal Microscopy. RBL-2H3 cells (4×10^4 cells) were cultured in cell culture slides (SPL Lifescience, Korea) and sensitized with IgE (2 μg/mL) for 3 h. Before antigen stimulation, RBL-2H3 cells were treated with different concentrations of MFC, an isolated compound, or piceatannol for 1 h, and then stimulated with DNP−HSA (500 ng/mL) for 15 min. Cell fixation was performed with PBS containing 4% formaldehyde for 30 min and permeabilized twice with PBS containing 0.1% Triton X-100 for 5 min. Staining for F-actin (green) was performed with Alexa Fluor 488 phalloidin (Invitrogen, USA) for 20 min in the dark. 4′,6-Diamidino-2-phenylindole (DAPI) staining was performed to identify all cell nuclei (blue) using a mounting medium containing DAPI (VECTASHIELD Mounting Medium with DAPI, Vector Laboratories, USA) prior to analysis by confocal fluorescent microscopy using a LSM 700 (Carl Zeiss, Germany) and ZEN software for the capture of images (Carl Zeiss, Germany).

Statistical Analysis. Data obtained were expressed as the mean ± standard deviation (SD). Statistical significance was determined using GraphPad Prism (GraphPad Software, USA). The differences among

DOI: 10.1021/acs.jafc.5b00903
J. Agric. Food Chem. 2015, 63, 5459−5467

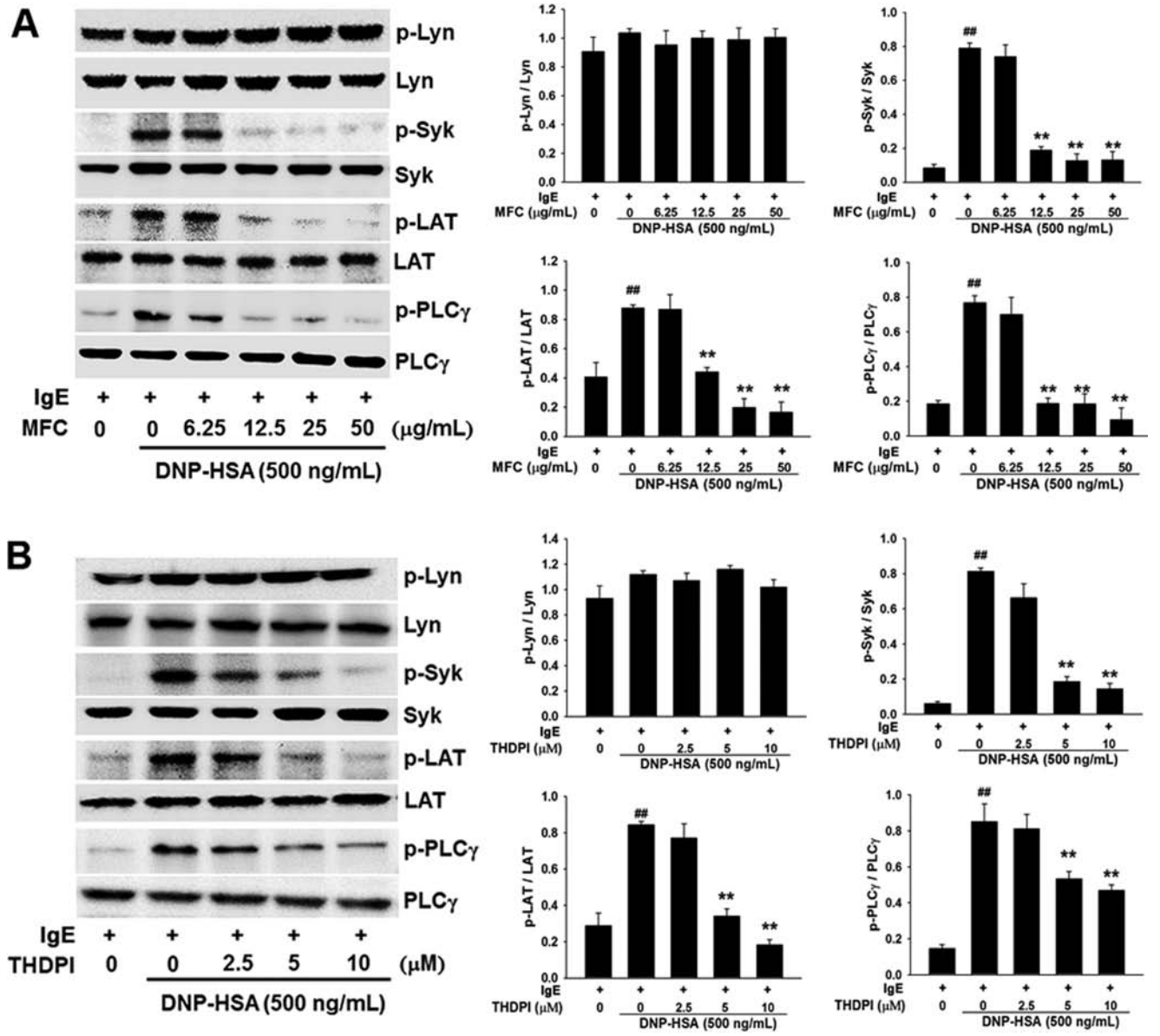

Figure 6. Effect of MFC and THDPI on the FcεRI-mediated phosphorylation of Lyn, Syk, LAT, and PLCγ in RBL-2H3 cells. Anti-DNP IgE-sensitized RBL-2H3 cells were cultured with various concentrations of MFC (A) and THDPI (B) for 24 h followed by antigen stimulation for 10 min. Then, each cell lysate was subjected to immunoblot analysis. p-Lyn, p-Syk, p-LAT, and p-PLCγ represent the phosphorylated Lyn, Syk, LAT, and PLCγ, respectively. Data represent the mean ± SD of three independent experiments. (##) $p < 0.01$, compared with IgE-sensitized cells without DNP-HSA; (**) $p < 0.01$, compared with IgE/DNP-HSA-treated cells.

the groups were evaluated by one-way analysis of variance (ANOVA) with Bonferroni's multiple-comparison method. A p value of <0.05 was considered to be statistically significant. All of the data were obtained from at least three independent experiments.

RESULTS AND DISCUSSION

Mast cells are crucial factors in the regulation of inflammatory and allergic responses due to their ability to produce pro-inflammatory mediators. The major mechanism for the activation of mast cells is the interaction of immunoglobulin E (IgE) with its high-affinity receptor (FcεRI), on the cell surface, which initiates FcεRI signaling through Lyn and Syk to regulate degranulation.[21] In this study, we investigated the inhibitory effects of methanol extract from the fruits of *C. tricuspidata* (MFC) on FcεRI-mediated mast cell activation and identified THDPI as an active compound responsible for the inhibitory action. β-Hexosaminidase has been commonly considered as a useful indicator for the evaluation of the activation of mast cells in various allergic inflammation.[22] As shown in Figure 1A, MFC significantly inhibited the release of β-hexosaminidase in FcεRI-mediated mast cells with an IC_{50} value of 104.9 μg/mL. Major constituents of MFC were identified using UPLC, and 10 compounds were isolated from MFC (Figure 2). Among the 10 isolated compounds from MFC, THDPI attenuated the release of β-hexosaminidase with an IC_{50} value of 20.4 μM, whereas the other compounds revealed no significant effects at concentrations up to 40 μM (Figure 1B and Table 1).

To investigate the mechanism underlying the inhibitory effects of MFC and THDPI on mast cell degranulation, free cytoplasmic calcium levels were examined. The movement of calcium across the membrane into the cytosol, either from an intracellular store such as the endoplasmic reticulum or from the external environment,

DOI: 10.1021/acs.jafc.5b00903
J. Agric. Food Chem. 2015, 63, 5459−5467

plays a crucial role in IgE-mediated mast cell activation and degranulation.[22] Therefore, many antiallergic drugs are known to inhibit calcium influx into the cytosol, resulting in the suppression of the degranulation of mast cells.[23] After the addition of antigen (DNP−HSA) in IgE-sensitized RBL-2H3 cells, the rapid elevation of intracellular calcium influx was observed in the untreated group. However, the treatment of MFC and THDPI decreased the antigen-induced intracellular calcium levels in a dose-dependent manner (Figure 3). These data suggest that MFC and THDPI elicit inhibitory effects on mast cell degranulation at least in part by the inhibition of calcium influx into the cytosol.

Binding of IgE to its receptor, FcεRI, on the surface of mast cells is one of the essential steps to initiate mast cell activation and degranulation. It has been reported that omalizumab, a recombinant DNA-derived humanized IgG1k monoclonal antibody, interferes with the IgE−FcεRI binding and inhibits mast cell degranulation,[24] and it is currently used for the control of allergic asthma and atopic dermatitis.[25] Thus, interfering with IgE binding to FcεRI could be another method to suppress IgE−FcεRI-mediated mast cell activation. When RBL-2H3 cells were treated with MFC at a fixed concentration of IgE, IgE binding levels were decreased to 86.9, 79.3, and 64.7% when treated with MFC at 100, 150, and 200 μg/mL, respectively, compared with control groups treated with IgE alone (Figure 4A). However, the treatment of THDPI showed no significant effects at concentrations up to 40 μM in IgE−FcεRI interaction (Figure 4B).

FcεRI are multimeric immune receptors consisting of one α-subunit, one β-subunit, and two γ-subunits. The α-subunit binds to the Fc portion of IgE, and β- and γ-subunits are thought to account for the cell-activation properties of FcεRI.[26] In FcεRI knockout mice, binding of IgE to mast cells was completely blocked, causing no induction of degranulation following allergic reactions.[27] Therefore, modulation for FcεRI expression could be considered as a therapeutic target for preventing FcεRI-mediated allergic inflammatory diseases. Recently, epigallocatechin gallate (EGCG) has been reported as a possible inhibitor for FcεRI expression by inhibiting mRNA expression of γ-subunit in mast cells.[28] To examine whether MFC and THDPI have an effect on FcεRI expression in mast cells, RBL-2H3 cells were treated with MFC and THDPI for 24 h. MFC inhibited only FcεRI β-subunit mRNA expression significantly; however, mRNA expression of the α- and γ-subunits was not affected (Figure 5A,C). In the group treated with THDPI, however, no inhibitory effect on FcεRI subunits was observed (Figure 5B,D).

Cross-linking of the FcεRI on mast cells activates nonreceptor type protein tyrosine kinases such as Lyn and Syk.[29] Lyn can be constitutively associated with FcεRI and is responsible for the phosphorylation of β- and γ-subunits. These phosphorylation events result in the association of Syk with phosphorylated γ-subunit, thereby promoting the activation of Syk.[30] It has been reported that Syk-deficient mast cells completely abrogated the degranulation, calcium elevation, and activation of the ERK and JNK.[29] LAT is known to be phosphorylated by Syk and is important for activation of PLCγ, which is essential for increasing the intracellular calcium level in the calcium-dependent pathway.[31] In LAT-deficient bone marrow-derived mast cells (BMMCs), tyrosine phosphorylation of FcεRI and Syk was intact following FcεRI engagement; however, activation of PLCγ and calcium mobilization were dramatically reduced.[32] As demonstrated in Figure 6, both MFC and THDPI showed no effect on the phosphorylation of Lyn; however, they suppressed the phosphorylation of Syk as well as its downstream effectors, LAT and PLCγ, in IgE-sensitized RBL-2H3 cells stimulated by antigens. A previous study has reported that piceatannol, a protein kinase inhibitor, reduced the antigen-induced secretion in IgE-sensitized mast cells through the inhibition of phosphorylation of Syk without the inhibition of phosphorylation of Lyn.[33]

The FcεRI-mediated signaling in mast cells leads not only to degranulation and cytokine production but also to actin assembly and various morphological changes in the cells. These morphological changes involve the redistribution of F-actin and are in parallel with degranulation of mast cells.[34] Several studies have demonstrated that these morphological changes are downstream of Syk and are Ca^{2+} dependent.[35,36] It has been also reported that activation of FcεRI induces no or minimal morphological change in $Syk^{-/-}$ cells, but this is reconstituted by stable expression of Syk in these cells.[35] In addition, IgE-mediated redistribution of F-actin is observed only in $Syk^{-/-}$ cells transfected with wild-type Syk.[37] In Figure 7, these morphological changes were observed in RBL-2H3 cells stained with fluorescent phalloidin to visualized F-actin. In unstimulated cells, F-actin (green) was at steady state and concentrated at the cell membrane (Figure 7A). When stimulated with antigen (DNP-HSA), F-actin was redistributed

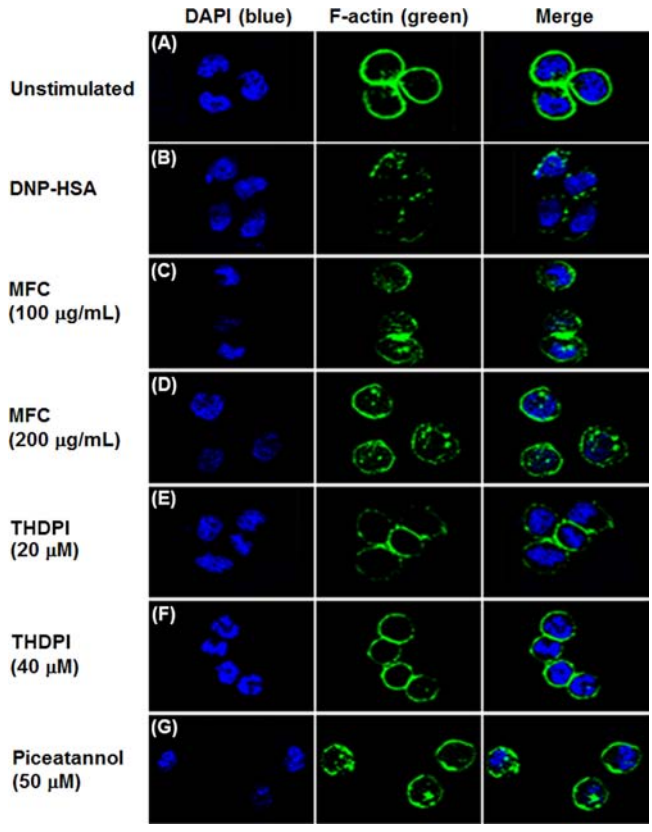

Figure 7. Effect of MFC and THDPI on F-actin assembly in RBL-2H3 cells. IgE-sensitized RBL-2H3 cells were treated with MFC, THDPI, and piceatannol for 1 h followed by antigen stimulation (DNP−HSA, 500 ng/mL) for 15 min. Cells were fixed and then double stained with fluorescent phalloidin for F-actin (green) and DAPI for cell nuclei (blue). Panels show representative images from (A) unstimulated cells, (B) cells stimulated with antigen, (C, D) MFC-treated cells stimulated with antigen, (E, F) THDPI-treated cells stimulated with antigen, and (G) piceatannol-treated cells stimulated with antigen. Original magnification, ×400.

DOI: 10.1021/acs.jafc.5b00903
J. Agric. Food Chem. 2015, 63, 5459−5467

and cells were spread (Figure 7B). However, this redistribution of F-actin was markedly inhibited in MFC-treated cells (Figure 7C,D) and in THDPI-treated cells (Figure 7E,F). These inhibitory effects on F-actin redistribution were compared with those of a Syk inhibitor, piceatannol (Figure 7G), which has been reported to inhibit actin assembly, membrane ruffling, spreading, and degranulation in mast cells.[38]

In conclusion, MFC and its active compound, THDPI, inhibited FcεRI-mediated degranulation and the calcium influx. MFC also interfered with IgE−FcεRI interaction and decreased FcεRIβ mRNA expression. THDPI, however, did not show any significant effects on IgE−FcεRI interaction and FcεRI mRNA expression. It is possible that other minor compounds in MFC may be responsible for the inhibitory effects on the affinity of IgE to the receptors and the expression of FcεRIβ mRNA. Further study is required to identify other compounds in MFC responsible for these inhibitory effects. MFC and THDPI inhibited F-actin redistribution and downstream signaling by suppressing FcεRI-mediated Syk activation in mast cells (Figure 8).

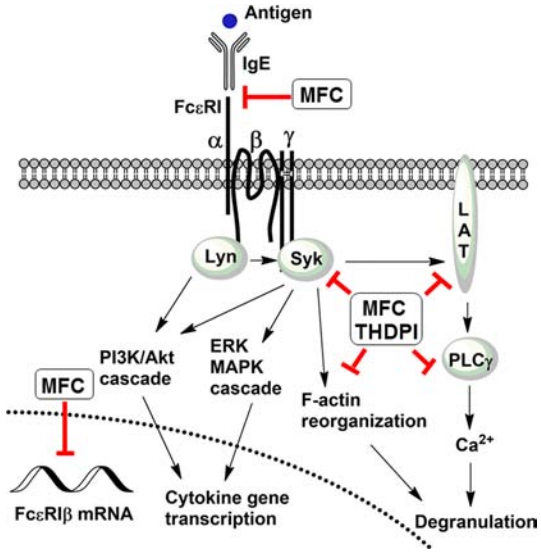

Figure 8. Scheme of the inhibitory effects of MFC and THDPI on FcεRI-mediated signaling in RBL-2H3 cells. MFC and THDPI inhibited mast cell degranulation, calcium influx, and F-actin redistribution. The phosphorylation of Syk, LAT, and PLCγ was inhibited by MFC and THDPI. In addition, MFC inhibited IgE−FcεRI interaction and FcεRIβ subunit mRNA expression.

These findings indicate that MFC and THDPI may have a potential therapeutic benefit for the control of IgE−FcεRI-mediated mast cell activation in inflammatory or allergic processes.

■ ASSOCIATED CONTENT

Supporting Information

Figures S1 and S2. The Supporting Information is available free of charge on the ACS Publications website at DOI: 10.1021/acs.jafc.5b00903.

■ AUTHOR INFORMATION

Corresponding Authors

*(W.M.) Phone: +82-2-880-2473. Fax: +82-2-888-9122. E-mail: mars@snu.ac.kr.

*(D.L.) Phone: +82-2-3290-3017. Fax: +82-2-953-0737. E-mail: dongholee@korea.ac.kr.

Funding

This work was supported by the BK21 plus program in 2015 through the National Research Foundation (NRF) funded by the Ministry of Education of Korea.

Notes

The authors declare no competing financial interest.

■ ACKNOWLEDGMENTS

We appreciate Korea University for supporting plant materials.

■ ABBREVIATIONS USED

THDPI, 5,7,3′,4′-tetrahydroxy-6,8-diprenylisoflavone; DNP, dinitrophenyl; FcεRI, high-affinity IgE receptor; HSA, human serum albumin; IgE, immunoglobulin E; LAT, linker of activated T cells; Syk, spleen tyrosine kinase; MFC, methanol extracts from the fruits of *Cudrania tricuspidata*; PLCγ, phospholipase Cγ; UPLC, ultraperformance liquid chromatography

■ REFERENCES

(1) Plaut, M.; Pierce, J. H.; Watson, C. J.; Hanley-Hyde, J.; Nordan, R. P.; Paul, W. E. Mast cell lines produce lymphokines in response to cross-linkage of Fc epsilon RI or to calcium ionophores. *Nature* **1989**, *339*, 64−67.

(2) Ishida, M.; Nishi, K.; Watanabe, H.; Sugahara, T. Inhibitory effect of aqueous spinach extract on degranulation of RBL-2H3 cells. *Food Chem.* **2013**, *136*, 322−327.

(3) Gu, W.; Han, K. Q.; Su, Y. H.; Huang, X. Q.; Ling, C. Q. Inhibition action of bufalin on human transplanted hepatocellular tumor and its effects on expressions of Bcl-2 and Bax proteins in nude mice. *Zhongxiyi Jiehe Xuebao* **2007**, *5*, 155−159.

(4) Taylor, J. A.; Karas, J. L.; Ram, M. K.; Green, O. M.; Seidel-Dugan, C. Activation of the high-affinity immunoglobulin E receptor Fc epsilon RI in RBL-2H3 cells is inhibited by Syk SH2 domains. *Mol. Cell. Biol.* **1995**, *15*, 4149−4157.

(5) Wong, B. R.; Grossbard, E. B.; Payan, D. G.; Masuda, E. S. Targeting Syk as a treatment for allergic and autoimmune disorders. *Expert Opin. Invest. Drugs* **2004**, *13*, 743−862.

(6) Kim, M.; Lim, S. J.; Kang, S. W.; Um, B. H.; Nho, C. W. Aceriphyllum rossii extract and its active compounds, quercetin and kaempferol inhibit IgE-mediated mast cell activation and passive cutaneous anaphylaxis. *J. Agric. Food Chem.* **2014**, *62*, 3750−3758.

(7) Passante, E.; Frankish, N. The RBL-2H3 cell line: its provenance and suitability as a model for the mast cell. *Inflammation Res.* **2009**, *58*, 737−45.

(8) White, M. Mediators of inflammation and the inflammatory process. *J. Allergy Clin. Immunol.* **1999**, *103*, S378−S381.

(9) Lee, I. K.; Kim, C. J.; Song, K. S.; Kim, H. M.; Koshino, H.; Uramoto, M.; Yoo, I. D. Cytotoxic benzyl dihydroflavonols from *Cudrania tricuspidata*. *Phytochemistry* **1996**, *41*, 213−216.

(10) Park, K. H.; Park, Y. D.; Han, J. M.; Im, K. R.; Lee, B. W.; Jeong, I. Y.; Jeong, T. S.; Lee, W. S. Anti-atherosclerotic and anti-inflammatory activities of catecholic xanthones and flavonoids isolated from *Cudrania tricuspidata*. *Bioorg. Med. Chem. Lett.* **2006**, *16*, 5580−5593.

(11) Tian, Y. H.; Kim, H. C.; Cui, J. M.; Kim, Y. C. Hepatoprotective constituents of *Cudrania tricuspidata*. *Arch. Pharmacal Res.* **2005**, *28*, 44−48.

(12) Han, X. H.; Hong, S. S.; Hwang, J. S.; Jeong, S. H.; Hwang, J. H.; Lee, M. H.; Lee, M. K.; Lee, D.; Ro, J. S.; Hwang, B. Y. Monoamine oxidase inhibitory constituents from the fruits of *Cudrania tricuspidata*. *Arch. Pharmacal Res.* **2005**, *28*, 1324−1327.

(13) Han, X. H.; Hong, S. S.; Jin, Q.; Li, D.; Kim, H. K.; Lee, J.; Kwon, S. H.; Lee, D.; Lee, C. K.; Lee, M. K.; Hwang, B. Y. Prenylated and benzylated flavonoids from the fruits of *Cudrania tricuspidata*. *J. Nat. Prod.* **2009**, *72*, 164−167.

DOI: 10.1021/acs.jafc.5b00903
J. Agric. Food Chem. 2015, 63, 5459−5467

(14) Jeong, C. H.; Choi, G. N.; Kim, J. H.; Kwak, J. H.; Jeong, H. R.; Kim, D. O.; Heo, H. J. Protective effects of aqueous extract from *Cudrania tricuspidata* on oxidative stress-induced neurotoxicity. *Food Sci. Biotechnol.* **2010**, *19*, 1113−1117.
(15) Bajpai, V. K.; Sharma, A.; Baek, K. H. Antibacterial mode of action of *Cudrania tricuspidata* fruit essential oil, affecting membrane permeability and surface characteristics of food-borne pathogens. *Food Control* **2013**, *32*, 582−590.
(16) Lee, H.; Ha, H.; Lee, J. K.; Seo, C. S.; Lee, N. H.; Jung, D. Y.; Park, S. J.; Shin, H. K. The fruits of *Cudrania tricuspidata* suppress development of atopic dermatitis in NC/Nga mice. *Phytother. Res.* **2012**, *26*, 594−599.
(17) Hiep, N. T.; Kwon, J.; Kim, D. W.; Hwang, B. Y.; Lee, H. J.; Mar, W.; Lee, D. Isoflavones with neuroprotective activities from fruits of *Cudrania tricuspidata*. *Phytochemistry* **2014**, *111*, 141.
(18) Lee, T.; Lee, S.; Ho Kim, K.; Oh, K. B.; Shin, J.; Mar, W. Effects of magnolialide isolated from the leaves of *Laurus nobilis* L. (Lauraceae) on immunoglobulin E-mediated type I hypersensitivity in vitro. *J. Ethnopharmacol.* **2013**, *149*, 550−556.
(19) Oh, P. S.; Lim, K. T. Modulatory effects of phytoglycoprotein (75 kDa) on allergic inflammatory cytokines in fi(2-ethylhexyl) phthalate (DEHP)-stimulated RBL-2H3 cells. *J. Cell. Biochem.* **2010**, *109*, 124−231.
(20) Sandomenico, A.; Monti, S. M.; Palumbo, R.; Ruvo, M. A new FcεRI receptor-mimetic peptide (PepE) that blocks IgE binding to its high affinity receptor and prevents mediator release from RBL 2H3 cells. *J. Pept. Sci.* **2011**, *17*, 604−609.
(21) Vial, D.; Oliver, C.; Jamur, M. C.; Pastor, M. V.; da Silva Trindade, E.; Berenstein, E.; Zhang, J.; Siraganian, R. P. Alterations in granule matrix and cell surface of focal adhesion kinase-deficient mast cells. *J. Immunol.* **2003**, *171*, 6178−6186.
(22) Pecht, I.; Corcia, A. Stimulus-secretion coupling mechanisms in mast cells. *Biophys. Chem.* **1987**, *26*, 291−301.
(23) Matsubara, M.; Masaki, S.; Ohmori, K.; Karasawa, A.; Hasegawa, K. Differential regulation of IL-4 expression and degranulation by anti-allergic olopatadine in rat basophilic leukemia (RBL-2H3) cells. *Biochem. Pharmacol.* **2004**, *67*, 1315−1326.
(24) MacGlashan, D. W., Jr.; Bochner, B. S.; Adelman, D. C.; Jardieu, P. M.; Togias, A.; McKenzie-White, J.; Sterbinsky, S. A.; Hamilton, R. G.; Lichtenstein, L. M. Down-regulation of FcεRI expression on human basophils during in vivo treatment of atopic patients with anti-IgE antibody. *J. Immunol.* **1997**, *158*, 1438−1445.
(25) Velling, P.; Skowasch, D.; Pabst, S.; Jansen, E.; Tuleta, I.; Grohe, C. Improvement of quality of life in patients with concomitant allergic asthma and atopic dermatitis: one year follow-up of omalizumab therapy. *Eur. J. Med.Res.* **2011**, *16*, 407−410.
(26) Kraft, S.; Kinet, J. P. New developments in FcεRI regulation, function and inhibition. *Nat. Rev. Immunol.* **2007**, *7*, 365−378.
(27) Dombrowicz, D.; Flamand, V.; Brigman, K. K.; Koller, B. H.; Kinet, J. P. Abolition of anaphylaxis by targeted disruption of the high affinity immunoglobulin E receptor α chain gene. *Cell* **1993**, *75*, 969−976.
(28) Tamura, S.; Yoshihira, K.; Fujiwara, K.; Murakami, N. New inhibitors for expression of IgE receptor on human mast cell. *Bioorg. Med. Chem. Lett.* **2010**, *20*, 2299−2302.
(29) Itoh, T.; Ninomiya, M.; Yasuda, M.; Koshikawa, K.; Deyashiki, Y.; Nozawa, Y.; Akao, Y.; Koketsu, M. Inhibitory effects of flavonoids isolated from *Fragaria ananassa* Duch on IgE-mediated degranulation in rat basophilic leukemia RBL-2H3. *Bioorg. Med. Chem.* **2009**, *17*, 5374−5379.
(30) Knol, E. F. Requirements for effective IgE cross-linking on mast cells and basophils. *Mol. Nutr. Food Res.* **2006**, *50*, 620−624.
(31) Huang, F.; Yamaki, K.; Tong, X.; Fu, L.; Zhang, R.; Cai, Y.; Yanagisawa, R.; Inoue, K.; Takano, H.; Yoshino, S. Inhibition of the antigen-induced activation of RBL-2H3 cells by sinomenine. *Int. Immunopharmacol.* **2008**, *8*, 502−507.
(32) Saitoh, S.; Arudchandran, R.; Manetz, T. S.; Zhang, W.; Sommers, C. L.; Love, P. E.; Rivera, J.; Samelson, L. E. LAT is essential for FcεRI-mediated mast cell activation. *Immunity* **2000**, *12*, 525−535.
(33) Oliver, J. M.; Burg, D. L.; Wilson, B. S.; McLaughlin, J. L.; Geahlen, R. L. Inhibition of mast cell FcεR1-mediated signaling and effector function by the Syk-selective inhibitor, piceatannol. *J. Biol. Chem.* **1994**, *269*, 29697−29703.
(34) Oliver, C.; Sahara, N.; Kitani, S.; Robbins, A. R.; Mertz, L. M.; Siraganian, R. P. Binding of monoclonal antibody AA4 to gangliosides on rat basophilic leukemia cells produces changes similar to those seen with Fcε receptor activation. *J. Cell Biol.* **1992**, *116*, 635−646.
(35) Siraganian, R. P.; de Castro, R. O.; Barbu, E. A.; Zhang, J. Mast cell signaling: the role of protein tyrosine kinase Syk, its activation and screening methods for new pathway participants. *FEBS Lett.* **2010**, *584*, 4933−4940.
(36) Sahara, N.; Siraganian, R. P.; Oliver, C. Morphological changes induced by the calcium ionophore A23187 in rat basophilic leukemia (2H3) cells. *J. Histochem. Cytochem.* **1990**, *38*, 975−983.
(37) de Castro, R. O. Regulation and function of syk tyrosine kinase in mast cell signaling and beyond. *J. Signal Transduction* **2011**, *2011*, No. 507291.
(38) Cox, D.; Chang, P.; Kurosaki, T.; Greenberg, S. Syk tyrosine kinase is required for immunoreceptor tyrosine activation motif-dependent actin assembly. *J. Biol. Chem.* **1996**, *271*, 16597−16602.

DOI: 10.1021/acs.jafc.5b00903
J. Agric. Food Chem. 2015, 63, 5459−5467

JOURNAL OF AGRICULTURAL AND FOOD CHEMISTRY

Article

pubs.acs.org/JAFC

Neohesperidin Dihydrochalcone versus CCl_4-Induced Hepatic Injury through Different Mechanisms: The Implication of Free Radical Scavenging and Nrf2 Activation

Chuanyang Su,[†] Xiaomin Xia,[†] Qiong Shi,[†] Xiufang Song,[†] Juanli Fu,[†] Congxue Xiao,[†] Hongjun Chen,[†] Bin Lu,[†] Zhiyin Sun,[†] Shanmei Wu,[†] Siyu Yang,[†] Xuegang Li,[†] Xiaoli Ye,[‡] Erqun Song,[†] and Yang Song*[,†]

[†]Key Laboratory of Luminescence and Real-Time Analytical Chemistry (Southwest University), Ministry of Education, College of Pharmaceutical Sciences, Southwest University, Chongqing, People's Republic of China, 400715

[‡]College of Life Sciences, Southwest University, Chongqing, People's Republic of China, 400715

ABSTRACT: Neohesperidin dihydrochalcone (NHDC), a sweetener derived from citrus, belongs to the family of bycyclic flavonoids dihydrochalcones. NHDC has been reported to act against CCl_4-induced hepatic injury, but its mechanism is still unclear. We first discovered that NHDC showed a strong ability to scavenge free radicals. In addition, NHDC induces the phase II antioxidant enzymes heme oxygenase 1 (HO-1) and NAD(P)H/quinone oxidoreductase 1 (NQO1) through the activation of the nuclear factor (erythroid-derived 2)-like 2 (Nrf2)/antioxidant response element (ARE) signaling. Further assays demonstrated that NHDC induces accumulation of Nrf2 in the nucleus and augmented Nrf2-ARE binding activity. Moreover, NHDC inhibits the ubiquitination of Nrf2 and suggests the modification of Kelch-like ECH-associated protein 1 (Keap1) and the disruption of the Keap1/Nrf2 complex. c-Jun N-terminal kinase (JNK) and p38 but not extracellular signal-regulated protein kinase (ERK) phosphorylations were up-regulated by NHDC treatment. Taken together, NHDC showed its protective antioxidant effect against CCl_4-induced oxidative damage via the direct free radical scavenging and indirect Nrf2/ARE signaling pathway.

KEYWORDS: *NHDC, Keap1, HO-1, NQO1, MAPK, liver, ubiquitination*

INTRODUCTION

The liver plays an important role in the detoxification of xenobiotics and drugs prior to excretion. However, these toxic substances can lead to hepatic injury. Carbon tetrachloride (CCl_4) has often been used as a common model of acute liver damage. The toxic mechanism of CCl_4 was identified to involve the excessive production of free radicals. CCl_4 is metabolized into $CCl_3^{\bullet}$ and $CCl_3OO^{\bullet}$ radicals with the participation of cytochrome P4502E1, which initiates the process of lipid peroxidation and ultimately resulting necrosis.[1] In the liver, excess free radicals insult may result in liver failure or liver fibrosis.

Previous studies have illustrated that natural compounds with antioxidant activity are effective in protecting the liver from oxidative damage. In this regard, the use of active antioxidants for the prevention and treatment of liver diseases has drawn much attention. Our previous study indicated the protective effects of neohesperidin dihydrochalcone (NHDC) on CCl_4-induced acute hepatic injury in vivo and in vitro.[2] CCl_4-induced acute hepatotoxicity is the most used experiment model. The remarkable restoring of antioxidant enzymes and the amelioration of oxidative biomarkers suggests an antioxidative activity. However, the exact molecular mechanism of NHDC against CCl_4 insult is quite unveiled.

One of the strategies to avoid free radical-mediated damage is to directly increase the radical scavenging capacity. Numerous studies have suggested that polyphenol compounds show antioxidant effects via a scavenging action on both carbon- and oxygen-centered radicals. The second approach is to regulate intrinsic antioxidant defenses at the transcriptional level. Recent reviews have summarized that natural products upregulate a group of cytoprotective genes via nuclear factor erythroid-derived 2-like 2 (Nrf2) signaling.[3,4] Under physiological conditions, Nrf2 was tightly anchored in the cytoplasm by its negative regulator protein Kelch-like ECH-associated protein 1 (Keap1) that binds tightly to Nrf2, which directs Nrf2 to proteasome degradation. Under certain circumstances, Nrf2 activators trigger the dissociation of Nrf2 from Keap1 and facilitate the translocation of Nrf2 into the nucleus. Nucleic Nrf2 binds to the antioxidant-responsive element (ARE) consensus sequence to initiate the transcription of cytoprotective genes.

Thus, the current study was designed to identify the protective mechanisms of NHDC. We discovered that NHDC showed a significant capacity in free radical scavenging. We also illustrated that NHDC potently induces the activation of Nrf2 signaling. These findings revealed the cytoprotective role of Nrf2 against CCl_4 intoxication in in vitro and in vivo models.

MATERIALS AND METHODS

Materials. NHDC (CAS: 20702-77-6, structure shown in Figure 1), ABTS (2,2′-azinobis-3-ethylbenzothiazolin-6-sulfonic

Received: April 7, 2015
Revised: May 14, 2015
Accepted: May 15, 2015
Published: May 15, 2015

ACS Publications © 2015 American Chemical Society

DOI: 10.1021/acs.jafc.5b01750
J. Agric. Food Chem. 2015, 63, 5468−5475

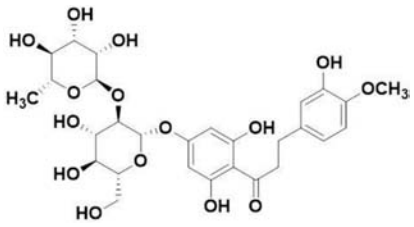

Figure 1. Chemical structure of NHDC.

acid), DPPH (1,1′-diphenyl-2-picryhydrazyl), TPTZ (2,4,6-tripyridyl-*s*-triazine), and luminol were supplied by Aladdin Reagent Database Inc. (Shanghai, China). CCl_4 (≥99.5%) was purchased from Kelong Chemical Co., Ltd. (Chengdu, China). MG132, the proteasome inhibitor, was obtained from Selleck Chemicals (Shanghai, China). The antibodies against Nrf2, heme oxygenase-1 (HO-1), NAD(P)H/quinone oxidoreductase 1 (NQO1), Lamin B, c-Jun N-terminal kinase (JNK), extracellular signal-regulated protein kinase (ERK), and p38 were purchased from Proteintech group, Inc. (Wuhan, China), and antibodies against β-actin, rabbit IgG, the EasyBlot ECL kit, and the nuclear/cytosol fractionation kit were purchased from Sangon Biotech Co., Ltd. (Shanghai, China). The chemiluminescent electrophoretic mobility shift assay (EMSA) kit, Biotin-labeled ARE probe, SP600125 (a JNK inhibitor), PD98059 (an ERK inhibitor), SB203580 (a p38 inhibitor), Western stripping buffer, and protein A agarose beads were obtained from Beyotime Institute of Biotechnology (Nanjing, China). Antibodies against p-JNK, p-ERK, p-p38, and Keap1 were purchased from Biosynthesis Biotechnology Co., Ltd. (Beijing, China). Ubiquitin antibody was from Santa Cruz Biotechnology (Santa Cruz, CA). 3-(4,5-Dimethylthiazol-*z*-yl)-3,5-diphenyltetrazolium bromide (MTT) was purchased from Dingguo Biotechnology Co., Ltd. (Beijing, China). Lipofectamine 2000 transfection reagent was supplied by Promega (Madison, WI). Nrf2 siRNA was synthesized by GenePharma Co., Ltd. (Shanghai, China).

Antioxidant Activity Assays. The free radical scavenging activity of NHDC was determined by ferric-reducing antioxidant power (FRAP), DPPH, ABTS, hydroxyl ($HO^{\bullet}$), and superoxide ($O_2^{\bullet-}$) radical scavenging assays. The FRAP assay is based on the reduction of a ferric 2,4,6-tripyridyl striazine complex (Fe^{3+}-TPTZ) by antioxidants to the ferrous form (Fe^{2+}-TPTZ), which forms a dark blue Fe^{2+}-TPTZ complex with an absorbance maximum at 593 nm.[5] The DPPH assay is based on the reduction of stable radical $DPPH^{\bullet}$ to a yellow product with the incubation of antioxidant. The absorbance was measured at 515 nm.[5] The ABTS assay is based on the ability of an antioxidant to inhibit the generation of a blue-to-green color product, which indicates the reaction of $ABTS^{\bullet+}$ and potassium persulfate. The ABTS radical-scavenging efficiency was measured by spectrophotometry at 750 nm.[5] The superoxide anion scavenging ability was determined by a chemiluminescence method in the pyrogallol−luminol system. The rate of pyrogallol autoxidation was measured at 320 nm.[6] The hydroxyl radical-quenching activity was measured by using the hydroxyl radical generated from Fenton's reaction of $Fe^{2+}-H_2O_2-$luminol chemiluminescence method.[7] All experiments were performed at least three times independently.

Animals, Treatment and Tissue Preparation. Male Kunming mice (22 ± 2 g) were provided by Chongqing Academy of Chinese Materia Medica. All animal studies were approved by the Southwest University Animal Care and Use Committee. Experiments were conducted according to the national institution's guidelines for the care and use of laboratory animals. Animals were kept in an air-conditioned room with a 12 h light and dark cycle with free access to food and water. All animals were adapted in individual plastic cages for a week, then the animals were randomly distributed into four groups with six mice in each group. The control group was administered appropriate vehicles throughout.

The NHDC group was administered NHDC (200 mg/kg body weight/day, dissolved in sodium carboxymethyl cellulose, prepared immediately before use) for 7 continuous days. The CCl_4 group received sodium carboxymethyl cellulose once daily for 7 continuous days. Three hours after the final intragastric administration, the mice were injected with CCl_4 (10 mL/kg body weight, 2% v/v in olive oil). The NHDC + CCl_4 group was treated with NHDC (200 mg/kg body weight/day) for 7 continuous days. Three hours after the final treatment, the mice were injected with CCl_4 (10 mL/kg body weight, 2% v/v dissolved in olive oil). The animals were sacrificed 24 h after the CCl_4 administration. The livers were removed carefully, rinsed twice with ice-cold physiological saline, and then divided into two pieces. One half was prepared for hepatic homogenization, and the others were used for immunohistochemical analysis. All steps were performed at 4 °C.

Cell Culture and Cell Viability Assay. The human hepatoma HepG2 cell line was purchased from the Third Military Medical University (Chongqing, China). HepG2 cells were cultured in DMEM containing 10% (v/v) FBS (HyClone, UT), penicillin (100 U/mL), and streptomycin (100 U/mL) in the humidified incubator at 37 °C under 5% CO_2. HepG2 cells were transferred onto 96-well culture plates at a density of 5×10^3 cells per well. After incubation overnight, the cells were pretreated with various inhibitors for 30 min and replaced with fresh serum-free medium containing NHDC or solvent vehicle for another 1 h. Finally, cells were maintained in 0.5% v/v CCl_4 for 3 h, and then treated with MTT (5 mg/mL final concentration) at 37 °C for 4 h. The supernatant was removed, and 150 μL of DMSO was added, measured spectrophotometrically at 570 nm.

Immunohistochemical Staining. The paraffin-embedded liver sections were deparaffinized and rehydrated; 3% H_2O_2 in methanol was used to block endogenous peroxidase activity for 15 min. Antigen retrieval was measured by 1 mM EDTA buffer (pH = 9.0) in a microwave for 3 min. The nonspecific protein binding was blocked by goat serum for 30 min, then the following steps were followed on the instruction of Histostain-plus and xiaminobenzidine (DAB) substrate kits. The slides were incubated with HO-1, NQO1, or Nrf2 antibodies at 4 °C overnight and incubated with biotin-labeled goat antirabbit IgG for 1 h. 3,3′-DAB solution was used in color development and counterstained with hematoxylin. The images were captured using a light microscope (magnification, 400× , Nikon Eclipse Ti-SR). Representative images are presented.

Preparation of Cytosolic and Nuclear Extracts. Cytosolic and nuclear proteins were extracted by a nuclear/cytosol fractionation kit according to the manufacturer's instructions. The cytosolic and nuclear extractions were stored at −20 and −80 °C, respectively.

EMSA. Nrf2/ARE binding activity was determined by EMSA using the Chemiluminescent EMSA Kit. The double-stranded oligonucleotides were designed according to the sequences of biotin-labeled ARE probe 5′-ACT GAG GGT GAC TCA GCA

DOI: 10.1021/acs.jafc.5b01750
J. Agric. Food Chem. 2015, 63, 5468−5475

Table 1. Free-Radical-Scavenging Activities of NHDC

	NHDC concn (μM)				
	0.05	0.5	5	50	500
FRAP level (μM)	37.3 ± 0.9	83.7 ± 4.2	635.7 ± 17.3	1264.2 ± 43.1	1292.5 ± 56.1
DPPH radical scavenging (%)	7.0 ± 3.6	8.2 ± 4.1	18.2 ± 0.2	59.9 ± 4.6	82.0 ± 3.6
ABTS radical scavenging (%)	9.8 ± 0.1	11.3 ± 0.1	16.1 ± 0.4	66.7 ± 0.1	99.1 ± 0.2
superoxide scavenging (%)	1.0 ± 0.1	1.9 ± 0.2	3.6 ± 0.2	6.3 ± 0.3	30.4 ± 1.2
hydroxyl radical scavenging (%)			6.2 ± 2.7	20.0 ± 2.6	45.7 ± 2.4

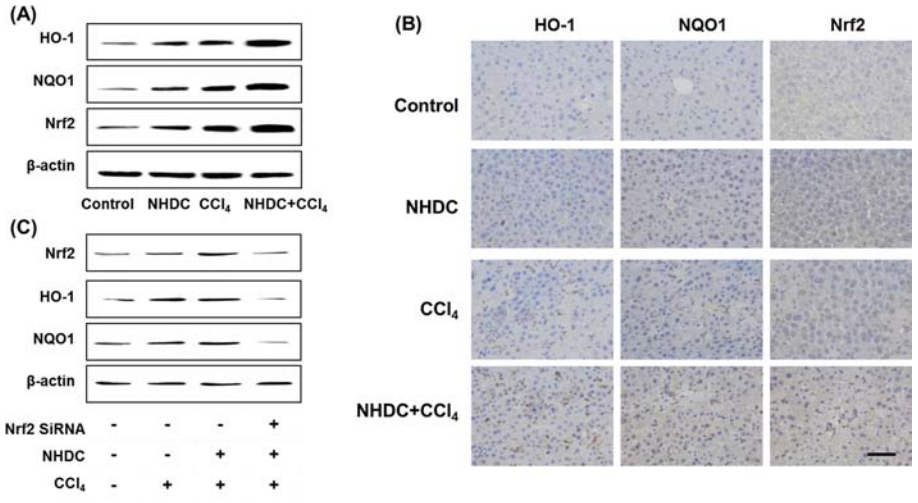

Figure 2. Effects of NHDC on the expression of HO-1, NQO1, and Nrf2. (A) NHDC stimulates HO-1, NQO1, and Nrf2 expressions by Western blot assay. Animals were treated with NHDC or CCl_4 as described in the Materials and Methods section. The test was repeated three times, and representative blots are shown. β-Actin served as a control. (B) Effects of NHDC on the expressions of HO-1, NQO1, and Nrf2 with the immunohistochemical method. Animals were treated with NHDC or CCl_4 as described in the Materials and Methods section. Bar = 50 μM. (C) Nrf2 siRNA down-regulates Nrf2, HO-1, and NQO1 protein expressions. HepG2 cells were transfected with a specific Nrf2 siRNA as described in the Materials and Methods section and pretreated with NHDC (30 μM) for 1 h. The cells were then subjected to a CCl_4 (0.5%, v/v) challenge. After 6 h of CCl_4 treatment, the levels of Nrf2, HO-1, and NQO1 were measured by Western blot analysis. The results are from three independent experiments.

AAA TC-3′ and 3′-TGA CTC CCA CTG AGT CGT TTT AG-5′. Briefly, 5 μg of nuclear protein was incubated with the biotin-labeled ARE probe (10 ng/μL) in the binding buffer at 25 °C for 30 min. The mixtures were fractionated on 6.5% polyacrylamide gels, and then transferred onto a Magmaprobe nylon membrane (Dingguo, Beijing, China). The membrane was incubated with a blocking buffer for 30 min at room temperature and immersed in blocking buffer containing streptavidin-HRP conjugate for 20 min. The membrane was washed four times at room temperature with washing buffer. Western blotting reagents were visualized with the EasyBlot ECL kit (ECL) that showed the gel shifts.

Transfection of Small Interfering RNA (siRNA). Predesigned siRNA against human Nrf2 was purchased from GenePharma Co., Ltd. (Shanghai, China). Transfection of siRNA was performed as previously described.[8] Briefly, HepG2 cells were transferred onto the 6-well culture plates and transfected with 100 nM siRNA against Nrf2 by Lipofectamine 2000. After 6 h of incubation, they were added to the fresh medium, and the cells were cultured for another 24 h. The cells were then pretreated with 30 μM NHDC for 1 h and treated with CCl_4 (0.5% v/v) an additional 6 h for the Western blot assay.

Immunoprecipitation. After treatment with NHDC, the cells were lysed with RIPA lysis buffer (50 mM Tris−HCl, pH = 7.4, 150 mM NaCl, 0.5% sodium deoxycholate, 1% NP-40, 1 mM PMSF, 0.1% SDS, and a proteinase inhibitor cocktail). The lysates were incubated on ice for at least 30 min and homogenized with an ultrasonicator for 10 min. The homogenates were centrifuged at 13 000 rpm at 4 °C for 10 min. The supernatants were collected, the concentrations of proteins were detected using the Bradford Protein Assay Kit. Whole cell lysates were precleared with protein A agarose beads for 10 min. The solutions were incubated with 2 μg of Keap1 or Nrf2 antibody at 4 °C overnight and further incubated with 30 μL of protein A agarose beads at 4 °C for 3 h, then the solution was centrifuged, and the beads were washed five times with lysis buffer. The complexes were mixed with 15 μL of loading buffer, heated at 98 °C for 10 min, and subsequently analyzed by Western blotting.

Western Blotting. The whole cell lysates and the immunoprecipitation products were separated by 8% or 10% SDS-PAGE and transferred onto the PVDF membrane. The membranes were blocked with 5% nonfat milk for 2 h then incubated with different primary antibodies at 4 °C overnight. The membranes were incubated with the secondary antibody for 2 h, followed by visualization using the ECL system. Representative blots were chosen from three or four separate experiments that showed similar results.

Redox Western Blotting. Redox Western blotting for Keap1 was performed on the basis of our previously reported method.[9] Briefly, HepG2 cells were treated with NHDC (0−30 μM) for 6 h. Cells were lysed with lysis buffer containing 50 mM Tris−HCl (pH 7.4), 150 mM NaCl, 0.25% sodium

DOI: 10.1021/acs.jafc.5b01750
J. Agric. Food Chem. 2015, 63, 5468−5475

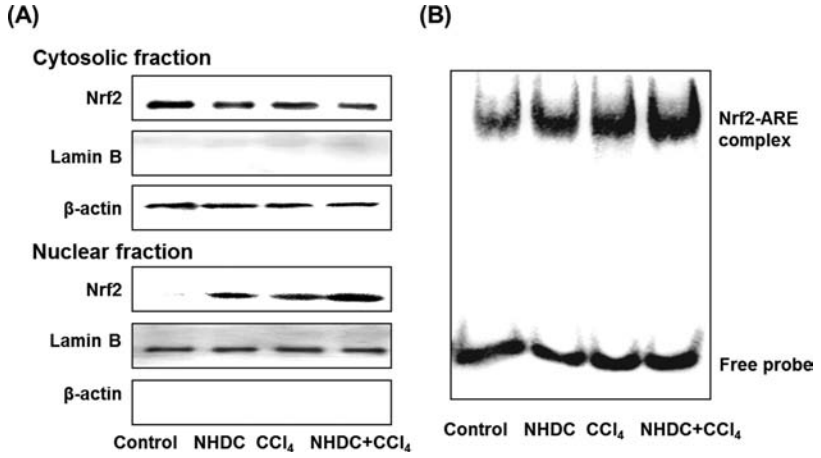

Figure 3. Effects of NHDC on nuclear Nrf2 accumulation and Nrf2-ARE binding activity. (A) Western blot analysis of the Nrf2 protein in cytosol and the nucleus, respectively. β-Actin and Lamin B were tested as loading controls in both the cytosolic and nuclear fractions. (B) EMSA detected for the Nrf2-ARE binding activity. Data were representative of three separate experiments showing similar results.

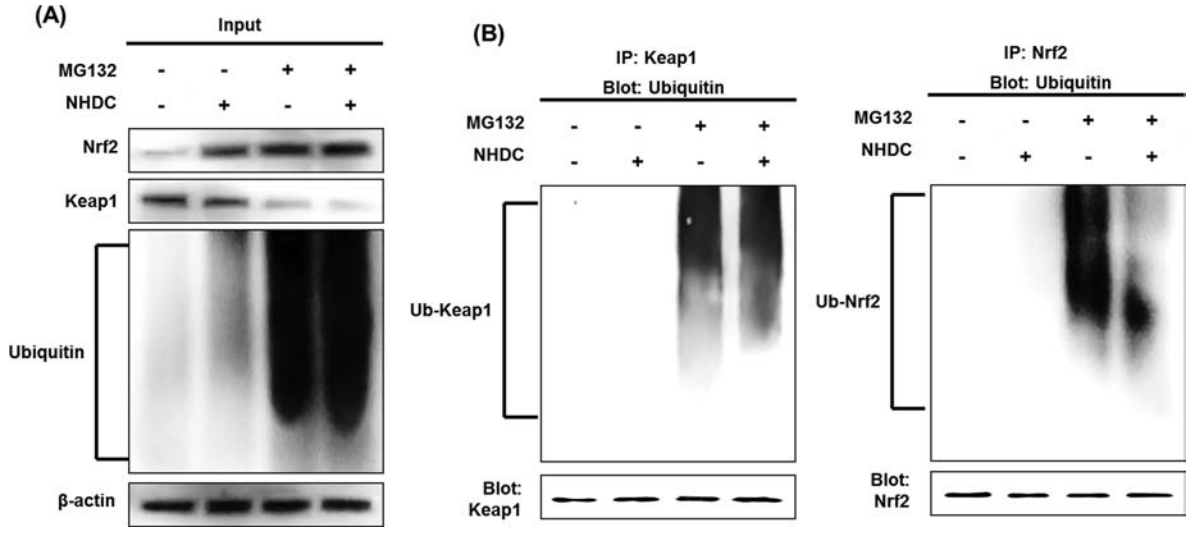

Figure 4. Effects of NHDC on the ubiquitination of Keap1 and Nrf2. (A) Western blot analysis of endogenous Keap1, Nrf2, and ubiquitin. HepG2 cells were treated with MG132 (10 μM) for 1 h and then treated with or without 30 μM NHDC for 6 h. Whole cell lysates were used to investigate Nrf2, Keap1, and ubiquitin with their antibodies. (B) The levels of Keap1 and Nrf2 ubiquitination. The proteins were immunoprecipitated with Keap1 and Nrf2 antibodies, then the precipitated proteins were visualized by Western blot analysis with ubiquitin antibody. Results are representative of three or four experiments.

deoxycholate, 1% NP-40, EDTA, 1 mM PMSF, sodium fluoride, sodium orthovanadate, and leupeptin protease inhibitor. The cell lysates were centrifuged at 12 000 rpm at 4 °C for 10 min, and the supernatant was collected as the redox cell extracts. Half of the extracts were diluted in the buffer containing β-mercaptoethanol (βME). After heat denaturation, the extracts were separated by 8% SDS-PAGE, and then Keap1 was detected by Western blotting.

Statistical Analysis. Values are expressed as the mean ± SD. Statistical analysis was performed using SPSS 18.0. Differences between the means of data were compared by the one-way variance analysis test, and post hoc analysis of group differences was performed by least significant difference test. A P value of <0.05 was considered to be statistically significant.

RESULTS AND DISCUSSION

NHDC Direct Scavenges Free Radicals. As shown in Table 1, NHDC has shown significant free radical scavenging activities in the range of 0.05−500 μM. In the FRAP assay, the

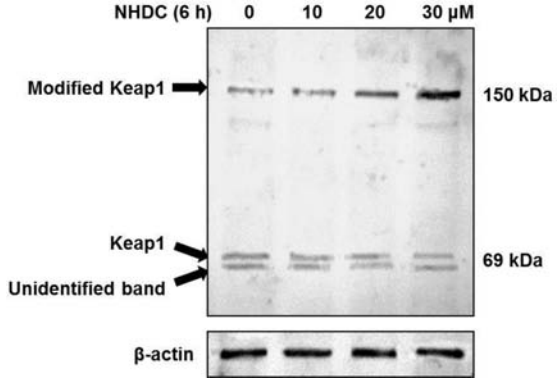

Figure 5. NHDC induces the modification of Keap1. Cells were treated with the indicated concentrations of NHDC for 6 h, analyzed by Western blot with Keap1 antibody and β-actin as a loading control. Data are representative of three separate experiments.

DOI: 10.1021/acs.jafc.5b01750
J. Agric. Food Chem. 2015, 63, 5468−5475

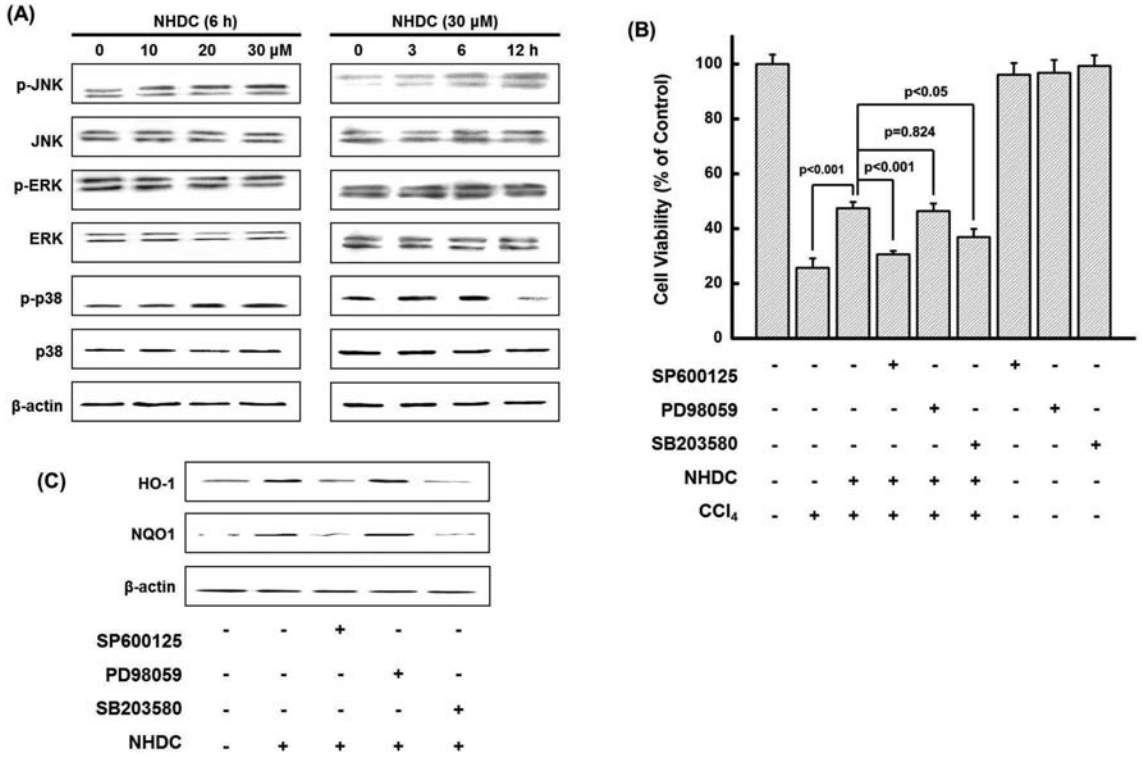

Figure 6. The cytoprotective effect of NHDC involves JNK and p38 MAPK signaling. (A) Concentration and time response of NHDC on the activation of JNK and p38 signaling. HepG2 cells were treated with NHDC at the indicated concentrations or times, and then the proteins were detected by Western blot analysis. (B) The pretreatment of JNK and p38 inhibitors, but not the ERK inhibitor, blocks the cytoprotective effect of NHDC. HepG2 cells were pretreated with 10 μM JNK inhibitor (SP600125), ERK inhibitor (PD98059), or p38 inhibitor (SB203580) for 30 min prior to incubation with 30 μM NHDC for another 1 h, then CCl_4 was introduced to induce cell damage. A MTT assay was performed to investigate the cell viability. Data from three independent experiments are expressed as means ± SD. (C) The pretreatment of JNK and p38 inhibitors, but not the ERK inhibitor, blocks the expressions of HO-1 and NQO1. Cells were treated with 10 μM SP600125, PD98059, or SB203580 for 1 h and then exposed to 30 μM NHDC for another 6 h. Total cell extracts were prepared and analyzed by Western blot analysis for the detection of the levels of HO-1 and NQO1. Data are representative of four separate experiments.

ability of NHDC to reduce Fe^{3+} to Fe^{2+} was increased concentration-dependently. The FRAP values were varied from 37.3 ± 0.9 to 1292.5 ± 56.1 μM at a concentration range of 0.05−500 μM. DPPH is a nitrogen-centered free radical that has been widely used in assessment of free radical quenching capabilities of antioxidants. NHDC possess concentration-dependent scavenging activities against the DPPH radical. According to a previous report, IC_{50} values for butylated hydroxyanisole (BHA), butylated hydroxytoluene (BHT), α-tocopherol, and trolox on the DPPH radical were found to be 61, 220, 31, and 50 μM, respectively.[10] Therefore, the DPPH radical-scavenging efficiency of NHDC is on the same order of magnitude as BHA, α-tocopherol, and trolox and one magnitude higher than BHT. In the ABTS assay, NHDC exhibited a concentration-dependent scavenging activity, and the highest concentration of NHDC (500 μM) scavenged the ABTS radical almost completely (99.1 ± 0.2%). $O_2^{\bullet-}$ is an important oxygen-center radical that can occur during in vivo metabolism, and the basal level of $O_2^{\bullet-}$ may be upregulated under certain pathological conditions.[11] The toxicity of $O_2^{\bullet-}$ has often been identified from neurodegenerative patients or an experimental model, which have relatively low SOD activities.[12] In the current study, pyrogallol was autoxidized to generate $O_2^{\bullet-}$, which can be detected by luminol. $HO^{\bullet}$ is the most reactive oxygen radical, which readily reacts with biomacromolecules and resulting the denaturation of proteins, lipid peroxidation and DNA modification.[13] Here, the generation of $HO^{\bullet}$ was performed by reaction of Fe^{2+} and H_2O_2. The scavenging effects of NHDC on superoxide and the hydroxyl radical are shown in Table 1. Our result indicated 30.4 ± 1.2% of the superoxide generated by a pyrogallol autoxidation system and 45.7 ± 2.4% of the hydroxyl radical generated by a Fenton's reaction were inhibited by 500 μM NHDC, respectively. Together, our results demonstrate that NHDC is a potent antioxidant with high antioxidant capacity, which is consistent with previous investigations.[14,15]

NHDC Enhances the Protein Levels of HO-1, NQO1, and Nrf2 in Mice. Our previous studies have demonstrated that NHDC plays an important role in the attenuation of CCl_4-induced liver injury in vivo and in vitro,[2] but the specific mechanism is still unclear. HO-1 is an endogenous, cytoprotective enzyme, that has both antioxidative and anti-inflammatory effects by catalyzing the first and rate-limiting step in the catabolism of the prooxidant heme to carbon monoxide, biliverdin, and free iron.[16] NQO1 is a cytosolic flavoprotein that catalyzes two-electron reduction and detoxification of quinones and other redox cycling endogenous and exogenous chemicals.[17] Growing evidence indicates that natural antioxidants play important roles in the activation of HO-1 and NQO1.[18] In the present study, the levels of HO-1 and NQO1 expression showed significant increases in the NHDC group (Figure 2A, lane 2 vs 1, lane 4 vs 3). Interestingly, the CCl_4 group also showed the upregulation of these two gene expressions (Figure 2A, lane 3 vs 1), which is consistent with

DOI: 10.1021/acs.jafc.5b01750
J. Agric. Food Chem. 2015, 63, 5468−5475

a previous study;[19] however, controversial results have also been reported. For example, Lee et al. showed that the NQO1 protein level in the CCl_4 group was significantly reduced compared with that in the control group.[20] Although there are disputable effects of CCl_4, it is widely accepted that antioxidants upregulated the expressions of these protective genes.

The activation of Nrf2 signaling and the upregulation of downstream antioxidant/detoxifying enzymes are important to inhibit oxidative stress and maintain the cellular homeostasis.[21] In view of these, we investigated whether NHDC activates HO-1 and NQO1 expression through the Nrf2 pathway. As shown in Figure 2A, the Western blot assay clearly indicated that Nrf2 has markedly increased after treatment with NHDC, which suggested a post-transcriptional regulation mechanism of Nrf2. Furthermore, we investigated the level of HO-1, NQO1, and Nrf2 by immunohistochemical staining. Consistently, HO-1, NQO1, and Nrf2 immunopositive cell numbers were markedly increased in NHDC-treated animals compared with the control or CCl_4 group (Figure 2B).

To further confirm that NHDC-induced HO-1 and NQO1 expression is mediated through Nrf2 activation, HepG2 cells were transfected with Nrf2 siRNA for 6 h, followed by CCl_4 stimulation or NHDC + CCl_4 cotreatment. Transfection of Nrf2 siRNA reduced the expression of Nrf2 as well as NHDC-induced HO-1 and NQO1 expression (Figure 2C). Together, these findings suggest that the protective mechanism of NHDC against CCl_4-induced hepatic injury is associated with the activation of Nrf2 signaling.

NHDC Induces the Translocation of Nrf2 and ARE Binding in HepG2 Cells. Nrf2 is an important transcription factor that is sequestered by the actin-binding protein Keap1 in the cytosol under homeostatic or nonstressed conditions. Cytosolic Nrf2 was subjected to ubiquitination and subsequent proteasomal degradation; thus, Nrf2 is inactive in cytosol.[22] However, once it translocates into the nucleus, Nrf2 heterodimerizes with a small musculo-aponeurotic fibrosarcoma protein and then binds to ARE. We therefore examined whether NHDC facilitates the translocation of Nrf2 from cytosolic into the nucleus. As shown in Figure 3A, Nrf2 in the cytosol fraction was reduced; in contrast, the amounts of nuclear Nrf2 were significantly increased after NHDC, CCl_4, or NHDC + CCl_4 treatment. Housekeeping genes Lamin B and β-actin have not been identified in the cytosolic and nucleus fractions, respectively, indicating the purity of these two fractions. To evaluate the effect of NHDC on Nrf2-ARE binding, EMSA was performed. In Figure 3B, our result suggested that the treatment of NHDC increased the ARE binding activity of Nrf2 in the nuclear fraction. Together, our results suggest that NHDC increased the translocation of Nrf2 and ARE-binding activity.

NHDC Inhibits the Ubiquitination of Nrf2 in HepG2 Cells. Previous studies have revealed that under homeostatic conditions, Nrf2 is rapidly degraded through the ubiquitin-dependent proteasome pathway.[23] To determine whether the up-regulation of Nrf2 by NHDC is due to the inhibition of Nrf2 ubiquitination, we detected the ubiquitination of Nrf2 through immunoprecipitation after treatment with MG132, a proteasome and protease inhibitor that allows the detection of ubiquitinated proteins. The treatment with MG132 also resulted in an increased association of Nrf2 with Keap1 in the cytoplasm.[24] As shown in Figure 4A, the Nrf2 protein level was increased after treatment with NHDC or MG132 alone or in combination; interestingly, the level of Keap1 was reduced by such treatment. Meanwhile, the treatment of MG132 caused an enhancement in the ubiquitin level, whereas NHDC has no effect on the ubiquitin level. Interactions between ubiquitin and Keap1 or Nrf2 were analyzed by immunoprecipitation with anti-Keap1 or anti-Nrf2 antibodies, respectively, followed by blotting with antiubiquitin (Figure 4B). NHDC showed no effect on the level of ubiquitinated Keap1 (left panel, lane 4 vs 3); however, a significant reduction of the ubiquitinated Nrf2 was observed in HepG2 cells cotreated with MG132 and NHDC (right panel, lane 4 vs 3). These results suggest that NHDC-enhanced Nrf2 is, at least partially, due to an inhibitory effect of the ubiquitination of Nrf2. Similarly, quercetin[8] and isothiocyanate sulforaphane[25] inhibit Nrf2 ubiquitination without inducing Keap1 ubiquitination. However, quinone-induced oxidative stress enhances ubiquitination of Keap1, which increases the level of Nrf2 correspondingly.[26,27] Our recent study also demonstrated that halogenated quinone, tetrachlorobenzoquinone, induces an ubiquitination switch from Nrf2 to Keap1.[9] The upregulation of Keap1 ubiquitination may interrupt the ability of Keap1 to assemble into a Cullin-dependent E3 (Cul3) ubiquitin ligase complex, which is critical for the control steady-state levels of Nrf2.[26] Although quinone or oxidative stress-mediated Nrf2 activation is independent of the dissociation of Keap1-Cul3 complex, oxidized fatty acids induces the dissociation of Keap1 from Cullin3, thereby inducing the activation of Nrf2 signaling.[28] These differences in the activation of Nrf2 signaling may suggest a structure−activity relationship between these inducers.

NHDC Induces the Modification of Keap1 in HepG2 Cells. Keap1 contains 25 and 27 cysteine residues in mouse and human homologues, respectively.[23] Because of the high activity of these cysteine residues, inducers are able to binding with Keap1 at different cysteine sites. For example, cysteine 151 is important for the binding of Keap1 to Cul3, and the modification of cysteine 151 causes a conformational change of Keap1, which results in the dissociation of Keap1 from Cul3 and the inhibition of Nrf2 ubiquitination.[27] A number of studies have indicated that some electrophilic compounds induce the formation of Keap1 dimer via S-alkylation[29] or intramolecular disulfide bond formation.[9,30]

To determine whether modification of Keap1 might occur with NHDC, the migrations of Keap1 were evaluated by SDS-PAGE analysis. As shown in Figure 5, Keap1 protein with a molecular mass of 69 kDa has been designated as "normal" Keap1. However, the intensities of the 69 kDa band were slightly decreased in the NHDC groups, whereas a band with slower migration appeared in a concentration-dependent manner. This band, which has an approximate molecular mass of 150 kDa, could be referred to as "modified" Keap1. Hong et al. demonstrated that a typical Nrf2-inducer *tert*-butyl hydroquinone (*t*BHQ) and a thiol-reactive electrophile, *N*-iodoacetyl-*N*-biotinylhexylenediamine (BMCC) generated high-molecular-weight Keap1 forms (>150 kDa), which were identified as K-48-linked polyubiquitin conjugates.[31] However, 1-biotinamido-4-(4′-[maleimidoethyl cyclohexane]-carboxamido)butane (IAB)[31] and sulforaphane[32] have no effect on the ubiquitination of Keap1. Thus, IAB and sulforaphane display a pattern of Keap1 modification different from that of *t*BHQ or BMCC. Combined with the result of unaffected ubiquitination of Keap1 upon NHDC treatment in Figure 4B, we concluded that NHDC may share the same mechanism with IAB and sulforaphane. Interestingly, sulforaphane modified Keap1 most readily in the Kelch domain, but IAB modified

DOI: 10.1021/acs.jafc.5b01750
J. Agric. Food Chem. 2015, 63, 5468−5475

Keap1 in the central linker domain. However, whether NHDC induces Keap1 modification in Kelch or the central linker domain needs further investigation.

The Activation of JNK and p38 Signalings Involved in the Cytoprotective Effect of NHDC. The mitogen-activated protein kinase (MAPK) signaling cascade can be activated by various extracellular signals. Interestingly, previous studies have indicated that Nrf2 inducers have the ability to modulate MAPK activities. For instance, Yu et al. reported *t*BHQ and sulforaphane upregulate the activity of ERK2 and p38 but not JNK1; however, the inhibition of ERK2 or p38 activity blocked the induction of phase II detoxifying enzyme and the ARE-linked reporter gene.[33,34] In our study, NHDC treatment for 6 h up-regulated the phosphorylation of JNK and p38, but not ERK in HepG2 cells, in a concentration-dependent manner, Figure 6A. Time-dependent analysis indicated the phosphorylation of JNK increased time-dependently, but the phosphorylation of p38 reached the maximum at 6 h. To further confirm that the activation of JNK and p38 was involved in the cytoprotective effects related to NHDC, cells were pretreated with the JNK inhibitor (SP600125), ERK inhibitor (PD98059), or p38 inhibitor (SB203580) for 1 h prior to addition of NHDC. We found that JNK and p38 inhibitors, but not ERK inhibitor, attenuated the protective effects of NHDC against CCl_4-induced HepG2 cells damage (Figure 6B). We also detected the expressions of antioxidant enzyme by Western blotting analysis. As expected, the inhibition of JNK and p38, but not ERK, strongly decreased the NHDC-induced expressions of HO-1 and NQO1. These results indicated that JNK and p38 MAPK are involved in Nrf2-mediated expressions of HO-1 and NQO-1, and the cytoprotective function of NHDC possibly link with the activation of JNK and p38 MAPK signaling pathways.

AUTHOR INFORMATION

Corresponding Author

*Phone: +86-23-68251503. Fax: +86-23-68251225. E-mail: ysong@swu.edu.cn.

Funding

This work is supported by National Natural Science Foundation of China (21477098), Science and Technology Talent Cultivation Project of Chongqing (cstc2014kjrc-qnrc00001) and Fundamental Research Funds for the Central Universities (XDJK2014A020, XDJK2015A017).

Notes

The authors declare no competing financial interest.

ABBREVIATIONS USED

ABTS, 2,2′-azinobis-3-ethylbenzothiazolin-6-sulfonic acid; ARE, antioxidant response element; BMCC, 1-biotinamido-4-(4′-[maleimidoethyl cyclohexane]-carboxamido)butane; Cul3, Cullin-dependent E3; DPPH, 1,1′-diphenyl-2-picryhydrazyl; EMSA, electrophoretic mobility shift assay; ERK, extracellular signal-regulated protein kinase; FRAP, ferric-reducing antioxidant power; HO-1, heme oxygenase 1; IAB, *N*-iodoacetyl-*N*-biotinylhexylenediamine; JNK, c-Jun N-terminal kinase; Keap1, Kelch-like ECH-associated protein 1; MAPK, mitogen-activated protein kinase; NQO1, NAD(P)H: quinone oxidoreductase 1; Nrf2, nuclear factor (erythroid-derived 2)-like 2; siRNA, small interfering RNA; *t*BHQ, *tert*-butylhydroquinone; TPTZ, 2,4,6-tripyridyl-*s*-triazine

REFERENCES

(1) Weber, L. W.; Boll, M.; Stampfl, A. Hepatotoxicity and mechanism of action of haloalkanes: carbon tetrachloride as a toxicological model. *Crit. Rev. Toxicol.* **2003**, *33*, 105−36.

(2) Hu, L.; Li, L.; Xu, D.; Xia, X.; Pi, R.; Xu, D.; Wang, W.; Du, H.; Song, E.; Song, Y. Protective effects of neohesperidin dihydrochalcone against carbon tetrachloride-induced oxidative damage in vivo and in vitro. *Chem.-Biol. Interact.* **2014**, *213*, 51−9.

(3) Kumar, H.; Kim, I. S.; More, S. V.; Kim, B. W.; Choi, D. K. Natural product-derived pharmacological modulators of Nrf2/ARE pathway for chronic diseases. *Nat. Prod. Rep.* **2014**, *31*, 109−39.

(4) Jeong, W. S.; Jun, M.; Kong, A. N. Nrf2: a potential molecular target for cancer chemoprevention by natural compounds. *Antioxid. Redox Signaling* **2006**, *8*, 99−106.

(5) Kim, H. J.; Suh, H. J.; Kim, J. H.; Park, S.; Joo, Y. C.; Kim, J. S. Antioxidant activity of glyceollins derived from soybean elicited with Aspergillus sojae. *J. Agric. Food Chem.* **2010**, *58*, 11633−8.

(6) Sun, J.; He, H.; Xie, B. J. Novel antioxidant peptides from fermented mushroom Ganoderma lucidum. *J. Agric. Food Chem.* **2004**, *52*, 6646−52.

(7) Wang, L.; Tu, Y. C.; Lian, T. W.; Hung, J. T.; Yen, J. H.; Wu, M. J. Distinctive antioxidant and antiinflammatory effects of flavonols. *J. Agric. Food Chem.* **2006**, *54*, 9798−804.

(8) Tanigawa, S.; Fujii, M.; Hou, D. X. Action of Nrf2 and Keap1 in ARE-mediated NQO1 expression by quercetin. *Free Radical Biol. Med.* **2007**, *42*, 1690−703.

(9) Su, C.; Zhang, P.; Song, X.; Shi, Q.; Fu, J.; Xia, X.; Bai, H.; Hu, L.; Xu, D.; Song, E.; Song, Y. Tetrachlorobenzoquinone activates nrf2 signaling by keap1 cross-linking and ubiquitin translocation but not keap1-cullin3 complex dissociation. *Chem. Res. Toxicol.* **2015**, *28*, 765−74.

(10) Gulcin, I.; Bursal, E.; Sehitoglu, M. H.; Bilsel, M.; Goren, A. C. Polyphenol contents and antioxidant activity of lyophilized aqueous extract of propolis from Erzurum, Turkey. *Food Chem. Toxicol.* **2010**, *48*, 2227−38.

(11) Kowaltowski, A. J.; Vercesi, A. E. Mitochondrial damage induced by conditions of oxidative stress. *Free Radical Biol. Med.* **1999**, *26*, 463−71.

(12) Shackelford, R. E.; Kaufmann, W. K.; Paules, R. S. Oxidative stress and cell cycle checkpoint function. *Free Radical Biol. Med.* **2000**, *28*, 1387−404.

(13) Sanders, L. H.; Greenamyre, J. T. Oxidative damage to macromolecules in human Parkinson disease and the rotenone model. *Free Radical Biol. Med.* **2013**, *62*, 111−20.

(14) Choi, J. M.; Yoon, B. S.; Lee, S. K.; Hwang, J. K.; Ryang, R. Antioxidant properties of neohesperidin dihydrochalcone: inhibition of hypochlorous acid-induced DNA strand breakage, protein degradation, and cell death. *Biol. Pharm. Bull.* **2007**, *30*, 324−30.

(15) Nakamura, Y.; Watanabe, S.; Miyake, N.; Kohno, H.; Osawa, T. Dihydrochalcones: evaluation as novel radical scavenging antioxidants. *J. Agric. Food Chem.* **2003**, *51*, 3309−12.

(16) Klaassen, C. D.; Reisman, S. A. Nrf2 the rescue: effects of the antioxidative/electrophilic response on the liver. *Toxicol. Appl. Pharmacol.* **2010**, *244*, 57−65.

(17) Vasiliou, V.; Ross, D.; Nebert, D. W. Update of the NAD(P)H:quinone oxidoreductase (NQO) gene family. *Hum. Genomics* **2006**, *2*, 329−35.

(18) Donovan, E. L.; McCord, J. M.; Reuland, D. J.; Miller, B. F.; Hamilton, K. L. Phytochemical activation of Nrf2 protects human coronary artery endothelial cells against an oxidative challenge. *Oxid. Med. Cell. Longevity* **2012**, *2012*, 132931.

(19) Choi, J. H.; Kim, D. W.; Yun, N.; Choi, J. S.; Islam, M. N.; Kim, Y. S.; Lee, S. M. Protective effects of hyperoside against carbon tetrachloride-induced liver damage in mice. *J. Nat. Prod.* **2011**, *74*, 1055−60.

(20) Lee, I. C.; Kim, S. H.; Baek, H. S.; Moon, C.; Kim, S. H.; Kim, Y. B.; Yun, W. K.; Kim, H. C.; Kim, J. C. Protective effects of diallyl disulfide on carbon tetrachloride-induced hepatotoxicity through activation of Nrf2. *Environ. Toxicol.* **2015**, *30*, 538−48.

DOI: 10.1021/acs.jafc.5b01750
J. Agric. Food Chem. 2015, 63, 5468−5475

(21) de Vries, H. E.; Witte, M.; Hondius, D.; Rozemuller, A. J.; Drukarch, B.; Hoozemans, J.; van Horssen, J. Nrf2-induced antioxidant protection: a promising target to counteract ROS-mediated damage in neurodegenerative disease? *Free Radical Biol. Med.* **2008**, *45*, 1375−83.
(22) Kobayashi, A.; Kang, M. I.; Okawa, H.; Ohtsuji, M.; Zenke, Y.; Chiba, T.; Igarashi, K.; Yamamoto, M. Oxidative stress sensor Keap1 functions as an adaptor for Cul3-based E3 ligase to regulate proteasomal degradation of Nrf2. *Mol. Cell. Biol.* **2004**, *24*, 7130−9.
(23) Baird, L.; Dinkova-Kostova, A. T. The cytoprotective role of the Keap1-Nrf2 pathway. *Arch. Toxicol.* **2011**, *85*, 241−72.
(24) He, X.; Chen, M. G.; Lin, G. X.; Ma, Q. Arsenic induces NAD(P)H-quinone oxidoreductase I by disrupting the Nrf2 x Keap1 x Cul3 complex and recruiting Nrf2 x Maf to the antioxidant response element enhancer. *J. Biol. Chem.* **2006**, *281*, 23620−31.
(25) Zhang, D. D.; Lo, S. C.; Sun, Z.; Habib, G. M.; Lieberman, M. W.; Hannink, M. Ubiquitination of Keap1, a BTB-Kelch substrate adaptor protein for Cul3, targets Keap1 for degradation by a proteasome-independent pathway. *J. Biol. Chem.* **2005**, *280*, 30091−9.
(26) Zhang, D. D.; Hannink, M. Distinct cysteine residues in Keap1 are required for Keap1-dependent ubiquitination of Nrf2 and for stabilization of Nrf2 by chemopreventive agents and oxidative stress. *Mol. Cell. Biol.* **2003**, *23*, 8137−51.
(27) Zhang, D. D.; Lo, S. C.; Cross, J. V.; Templeton, D. J.; Hannink, M. Keap1 is a redox-regulated substrate adaptor protein for a Cul3-dependent ubiquitin ligase complex. *Mol. Cell. Biol.* **2004**, *24*, 10941−53.
(28) Gao, L.; Wang, J.; Sekhar, K. R.; Yin, H.; Yared, N. F.; Schneider, S. N.; Sasi, S.; Dalton, T. P.; Anderson, M. E.; Chan, J. Y.; Morrow, J. D.; Freeman, M. L. Novel n-3 fatty acid oxidation products activate Nrf2 by destabilizing the association between Keap1 and Cullin3. *J. Biol. Chem.* **2007**, *282*, 2529−37.
(29) Satoh, T.; Kosaka, K.; Itoh, K.; Kobayashi, A.; Yamamoto, M.; Shimojo, Y.; Kitajima, C.; Cui, J.; Kamins, J.; Okamoto, S.; Izumi, M.; Shirasawa, T.; Lipton, S. A. Carnosic acid, a catechol-type electrophilic compound, protects neurons both in vitro and in vivo through activation of the Keap1/Nrf2 pathway via S-alkylation of targeted cysteines on Keap1. *J. Neurochem.* **2008**, *104*, 1116−31.
(30) Fourquet, S.; Guerois, R.; Biard, D.; Toledano, M. B. Activation of NRF2 by nitrosative agents and H2O2 involves KEAP1 disulfide formation. *J. Biol. Chem.* **2010**, *285*, 8463−71.
(31) Hong, F.; Sekhar, K. R.; Freeman, M. L.; Liebler, D. C. Specific patterns of electrophile adduction trigger Keap1 ubiquitination and Nrf2 activation. *J. Biol. Chem.* **2005**, *280*, 31768−75.
(32) Hong, F.; Freeman, M. L.; Liebler, D. C. Identification of sensor cysteines in human Keap1 modified by the cancer chemopreventive agent sulforaphane. *Chem. Res. Toxicol.* **2005**, *18*, 1917−26.
(33) Yu, R.; Lei, W.; Mandlekar, S.; Weber, M. J.; Der, C. J.; Wu, J.; Kong, A. N. Role of a mitogen-activated protein kinase pathway in the induction of phase II detoxifying enzymes by chemicals. *J. Biol. Chem.* **1999**, *274*, 27545−52.
(34) Yu, R.; Mandlekar, S.; Lei, W.; Fahl, W. E.; Tan, T. H.; Kong, A. N. p38 mitogen-activated protein kinase negatively regulates the induction of phase II drug-metabolizing enzymes that detoxify carcinogens. *J. Biol. Chem.* **2000**, *275*, 2322−7.

DOI: 10.1021/acs.jafc.5b01750
J. Agric. Food Chem. 2015, 63, 5468−5475

JOURNAL OF AGRICULTURAL AND FOOD CHEMISTRY

Article

pubs.acs.org/JAFC

Magnitude Differences in Bioactive Compounds, Chemical Functional Groups, Fatty Acid Profiles, Nutrient Degradation and Digestion, Molecular Structure, and Metabolic Characteristics of Protein in Newly Developed Yellow-Seeded and Black-Seeded Canola Lines

Katerina Theodoridou,[†,⊥] Xuewei Zhang,[†,§] Sally Vail,[#] and Peiqiang Yu*[,†,§]

[†]Department of Animal and Poultry Science, College of Agricultural and Bioresources, University of Saskatchewan, 51 Campus Drive, Saskatoon, Saskatchewan S7N 5A8, Canada

[§]College of Animal Science and Veterinary Medicine, Tianjin Agricultural University, Tianjin 300384, China

[#]Agriculture and Agri-Food Canada, Saskatoon, Saskatchewan S7N 0X2, Canada

[⊥]Institute for Global Food Security, School of Biological Sciences, Queen's University Belfast, BT9 5BN Belfast, Northern Ireland, U.K.

ABSTRACT: Recently, new lines of yellow-seeded (CS-Y) and black-seeded canola (CS-B) have been developed with chemical and structural alteration through modern breeding technology. However, no systematic study was found on the bioactive compounds, chemical functional groups, fatty acid profiles, inherent structure, nutrient degradation and absorption, or metabolic characteristics between the newly developed yellow- and black-seeded canola lines. This study aimed to systematically characterize chemical, structural, and nutritional features in these canola lines. The parameters accessed include bioactive compounds and antinutrition factors, chemical functional groups, detailed chemical and nutrient profiles, energy value, nutrient fractions, protein structure, degradation kinetics, intestinal digestion, true intestinal protein supply, and feed milk value. The results showed that the CS-Y line was lower ($P \leq 0.05$) in neutral detergent fiber (122 vs 154 g/kg DM), acid detergent fiber (61 vs 99 g/kg DM), lignin (58 vs 77 g/kg DM), nonprotein nitrogen (56 vs 68 g/kg DM), and acid detergent insoluble protein (11 vs 35 g/kg DM) than the CS-B line. There was no difference in fatty acid profiles except C20:1 eicosenoic acid content (omega-9) which was in lower in the CS-Y line ($P < 0.05$) compared to the CS-B line. The glucosinolate compounds differed ($P < 0.05$) in terms of 4-pentenyl, phenylethyl, 3-CH_3-indolyl, and 3-butenyl glucosinolates (2.9 vs 1.0 μmol/g) between the CS-Y and CS-B lines. For bioactive compounds, total polyphenols tended to be different (6.3 vs 7.2 g/kg DM), but there were no differences in erucic acid and condensed tannins with averages of 0.3 and 3.1 g/kg DM, respectively. When protein was portioned into five subfractions, significant differences were found in PA, PB1 (65 vs 79 g/kg CP), PB2, and PC fractions (10 vs 33 g/kg CP), indicating protein degradation and supply to small intestine differed between two new lines. In terms of protein structure spectral profile, there were no significant differences in functional groups of amides I and II, α helix, and β-sheet structure as well as their ratio between the two new lines, indicating no difference in protein structure makeup and conformation between the two lines. In terms of energy values, there were significant differences in total digestible nutrient (TDN; 149 vs 133 g/kg DM), metabolizable energy (ME; 58 vs 52 MJ/kg DM), and net energy for lactation (NEL; 42 vs 37 MJ/kg DM) between CS-Y and CS-B lines. For in situ rumen degradation kinetics, the two lines differed in soluble fraction (S; 284 vs 341 g/kg CP), potential degradation fraction (D; 672 vs 590 g/kg CP), and effective degraded organic matter (EDOM; 710 vs 684 g/kg OM), but no difference in degradation rate. CS-Y had higher digestibility of rumen bypass protein in the intestine than CS-B (566 vs 446 g/kg of RUP, $P < 0.05$). Modeling nutrient supply results showed that microbial protein synthesis (MCP; 148 vs 171 g/kg DM) and rumen protein degraded balance (DPB; 108 vs 127 g/kg DM) were lower in the CS-Y line, but there were no differences in total truly digested protein in small intestine (DVE) and feed milk value (FMV) between the two lines. In conclusion, the new yellow line had different nutritional, chemical, and structural features compared to the black line. CS-Y provided better nutrient utilization and availability.

KEYWORDS: *bioactive compounds, nutrition and antinutrition profile, protein structure, fatty acid, energy value, biodegradation and digestion*

INTRODUCTION

Oilseeds and their products are the most valuable agricultural crops in world trade. Nowadays, canola is considered the second most abundant source of edible oil in the world,[1] and canola meal is widely used as a protein source in livestock feeding.[2] Canadian breeders in 1970s developed canola,

Received: March 28, 2015
Revised: May 13, 2015
Accepted: May 21, 2015
Published: May 21, 2015

ACS Publications © 2015 American Chemical Society

DOI: 10.1021/acs.jafc.5b01577
J. Agric. Food Chem. 2015, 63, 5476−5484

containing low "erucic acid" in the oil portion (<2% of total fatty acids in the oil) and "glucosinolates" in the meal portion (<30 μmol of any one or any combination of the four aliphatic glucosinolates in its defatted meal).[3]

The high erucic acid, glucosinolates, and condensed tannins in rapeseed could have adverse effects on animal health. Specifically, erucic acid, a fatty acid with the configuration C22:1 n-9, has been known to cause heart lesions in experimental animals.[4] If animals eat high amounts of this acid, it can result in "fat deposits infiltrating their heart walls".[5] On the other hand, glucosinolates have a negative impact on palatability, feed efficiency, iodine uptake, and weight gain in animals.[6] As to condensed tannins, the high content of condensed tannin affects biological functions such as intake and digestion.

At the same time, the improvement of the quality of canola seed and its byproducts (i.e., canola meal) has been attempted, by increasing the digestibility of the hull and/or reducing the hull proportion in the meal.

Canola varieties consist of yellow-seeded and black (dark brown)-seeded varieties. Hulls from yellow-seeded varieties have lower fiber but higher protein and oil than the black-seeded.[7,8]

Apart from the chemical composition of oilseed crops, their protein secondary structure profiles may also influence the quality and absorption of protein.[9−12] Therefore, to understand a crop's digestive behavior and nutritional value, it is important to look at the protein structure, for example, the secondary structure.[10]

However, studies aiming at evaluating the nutritional value, for ruminants, of *Brassica napus* yellow-seeded varieties, especially their degradation kinetics and protein molecular structure, are scarce. In our study, we hypothesized that these newly developed yellow and black canola seed varieties might be different in terms of their nutritional value and nutrient degradation characteristics as well as their protein's inherent molecular structural makeup.

This study aimed to systematically characterize the chemical, structural, and nutritional features in these yellow- and black-seeded canola lines. The parameters assessed include bioactive compounds and antinutrition factors, functional groups, detailed chemical and nutrient profiles including fatty acid profiles, energy value, nutrient fractions, protein structure, degradation kinetics, intestinal digestion, protein supply, and predicted feed milk value.

MATERIALS AND METHODS

New Lines of Yellow-Seeded and Black-Seeded Canola. Yellow and black canola seeds (*Brassica napus*) were supplied by Agriculture and Agri-Food Canada, Saskatoon Research Center, Canada, and used as feed sources. The yellow-seeded line was called YN01-429, and the black seeded line was a breeding line named N07-1374, which has a contrasting pedigree to YN01-429. Seeds were harvested from plots grown in 2010 and 2011 in adjacent trials about 1500 m apart at the Agriculture and Agri-Food Canada Saskatoon Research Centre in Saskatoon, Canada.

For the black-seeded line, a plot size of 1.9 m^2 had approximately 100 seeds planted mid-May each season. At maturity, seeds were directly combined from the plot. A plot size of 7.4 m^2 was used to grow the yellow-seeded line from approximately 800 seeds planted in mid-May, and plots were combined about 2 weeks after swathing. Seeding dates were 4 and 1 day apart for the two different trials in 2010 and 2011, respectively. For all samples, seeds from two different replications in each experiment of the same line were combined to form the samples used in this study. Adjusted yields ranged from 2200 to 3950 kg/ha for N07-1374 and from 2400 to 2700 kg/ha for YN01-429 in 2010 and 2011, respectively. Agronomically, the lines were very similar with flowering times and maturity ratings ranging from 1 to 3 days and from 2 to 6 days, respectively, with N07-1374 having a slightly later maturity rating.

Rumen in Situ Incubation and Degradation Kinetics. The Animal Care Committee at the University of Saskatchewan approved this trial.[13] The detailed "gradual addition/all out" procedure was reported previously.[14]

In situ degradation kinetics of different nutrients (DM, CP, OM, NDF) were determined.[15−18]

Digestibility of Rumen Bypass Protein in the Small Intestine. The digestibility of rumen bypass crude protein was determined according to the three-step in vitro procedure as described by Calsamiglia and Stern.[19]

Chemical Profiles. The residues of the nylon bags, from both experimental runs, were collected and pooled according to the incubation time, treatment, and run. Samples were analyzed for chemical and nutritional profiles using the methods from AOAC[20] and Van Soest et al.[21]

To prevent inaccurately high NDF value, the samples was incubated in acetone for 2 h to extract fat. The methods for determining the contents of soluble crude protein (SCP) and non-nitrogen protein (NPN) were previously described by Theodoridou and Yu.[22]

Oil and Fatty Acids. Oil content was analyzed using AOAC method 920.39 and fatty acid profile using method 969.33 for preparation and method 996.06 for qualification. Briefly, accurately weighed ground seed samples (0.40g) were put into a labeled Mojonnier flask, and then 110 mg of pyrogallic acid, 2.0 mL of C21:0 (internal standard), 2.0 mL of ethanol, and 10.0 mL of HCl (8.3 M) were added. For complete extraction, the solution was mixed well every 10 min on a vortex mixer and then cooled to room temperature (25 °C). As for the methylation procedure, chloroform (3 mL) and diethyl ether (3 mL) were used to dissolve the extracted fat and then evaporated again in the water bath (40 °C) under a N stream in a glass vial. After dryness was reached, the vial was cooled to room temperature (25 °C), and H_2O (5.0 mL), hexane (1.0 mL), and Na_2SO_4 (1 g) were added to allow layer separation. The top layer was transferred to another vial containing 1 g of Na_2SO_4 for gas chromatography analysis (Agilent 6890, Agilent Technologies Inc., Santa Clara, CA, USA). The column used in this study was a DB 225 capillary column (0.10 mm i.d., 10 min length, and 0.10 μm film thickness). The column temperature program was set up as follows: initial temperature, 35 °C, raised at 25 °C/min to 195 °C, raised at 3 °C/min to 205 °C, and raised at 8 °C/min to 230 °C. The detector temperature was 250 °C. The analysis was repeated if the error was >5% between two replications.

Glucosinolates, Polyphenols, and Condensed Tannins. Glucosinolate profiles in the samples were analyzed using the CGA method.[23,25] Total polyphenols and condensed tannins (CT, HCl-butanol procedure) in samples were determined according to the methods of Slinkard and Singleton[26] and Reed.[27] All samples were analyzed in duplicate; the analysis was repeated if the error was >5%.

Energy Values and Protein Subfractions. Energy values were estimated using a summative approach as suggested by the NRC 2001 dairy.

The Cornell System of CNCPS was applied to partition protein fractions.[28]

Molecular Structure Profile Explored Using Molecular Spectroscopy. Molecular spectroscopic experiments were performed at the Molecular Spectroscopy Lab in the Feed Science Division at APS of the University of Saskatchewan. Attenuated total reflectance-Fourier transformed infrared-vibration spectroscopy (JASCO FT/IR-ATR-4200, Jasco Inc., Easton, MD, USA) was carried out. Samples were placed in the refrigerator to minimize sticking while grinding. Later they were fed slowly into the grinder to further prevent sticking during the grinding process and were finely ground using a fit with a 0.5 mm screen. Five subsamples from each sample were analyzed with 32 scans per sample in the 4000−800 cm^{-1}. The functional spectral

DOI: 10.1021/acs.jafc.5b01577
J. Agric. Food Chem. 2015, 63, 5476−5484

bands and their intensity of ratio calculation (i.e., amide I, II, secondary structures) were according to the previously published study.[29]

Using the Dutch System To Predict Potential Protein Nutrient Supply and Feed Milk Value (FMV). Potential protein nutrient supply was predicted on the basis of the Dutch system[30−33] The FMV was determined on the basis of the metabolizable protein from the NRC 2001 model.

Statistical Analysis. The data were statistically analyzed using the Mixed Model procedure of SAS (version 9.3) (SAS Institute, 1999). For chemical and nutrient data, the model was $Y_{ij} = \mu + V_i + e_{ij}$. The model used for rumen and intestinal data was $Y_{ijk} = \mu + V_i + R_k + e_{ijk}$, where Y_{ijk} is the dependent variable ijk, μ is the population mean, V_i was the fixed effect of canola seed type, R_k was a random effect of the in situ run, and e_{ijk} was the random error. For all statistical analyses, significance was declared at $P < 0.05$ and trends at $P \leq 0.10$.

RESULTS AND DISCUSSION

Chemical Characterization. The results on the chemical profiles of the yellow-type (CS-Y) and black-type (CS-B) canola seeds are presented in Table 1. No significant differences were found between CS-Y and CS-B for the basic nutrients. For carbohydrate profiles, CS-Y was lower in ADF (60.7 vs 98.6 g/kg DM) and ADL (8.1 vs 43.5 g/kg DM) and tended to be lower in NDF (122.1 vs 154.5 g/kg DM) ($P \leq 0.10$) (Table 1). It has been reported that dietary fiber content in yellow-seeded samples was significantly lower than in the black-seeded types, and this is due to "the bigger seed size, the lower contribution of the hull fraction to the total seed mass, and the lower fiber content of the hull fraction for the yellow seeded canola".[7] Moreover, Abraham and Bhatia[34] mentioned that yellow-seeded *Brassica* genotypes "have a thinner and translucent seed coat, resulting in a lower hull proportion with a bigger embryo and consequently greater oil and protein contents in the seeds". Moreover, hulls consist of low molecular weight carbohydrates cellulose, pectin, lignin, and other compounds.[35] Therefore, in this study the significantly notably lower ADL in CS-Y compared to CS-B could be due to the higher digestible hull in the yellow seed.

With regard to the protein profile of the feedstuffs used in this study, CS-Y had lower ($P < 0.05$) NPN (g/kg DM or g/kg SCP) and ADICP (g/kg DM). A trend toward significance was observed when ADICP was expressed as g/kg CP, and in that

Table 1. Chemical Profiles: Comparison between Yellow-Type (CS-Y) and Black-Type (CS-B) Canola Seed (*B. napus*)

item	CS-Y	CS-B	SEM	*P* value
basic chemical				
dry matter	944.7	939.6	1.07	0.078
ash (g/kg DM)	44.8	41.0	6.82	0.735
carbohydrate profile (g/kg DM)				
carbohydrate	314.2	323.8	11.19	0.607
neutral detergent fiber	122.1	154.5	5.40	0.051
acid detergent fiber	60.7	98.6	2.96	0.012
acid detergent lignin	8.1	43.5	1.84	0.005
nitrogen-free neutral detergent fiber	58.2	77.2	7.56	0.218
nitrogen-free acid detergent fiber	50.1	63.3	5.98	0.259
sugars (g/kg DM)	60.1	59.9	8.63	0.987
protein profile				
crude protein (g/kg DM)	207.9	237.5	7.22	0.102
soluble crude protein (g/kg DM)	69.5	84.9	3.13	0.074
soluble crude protein (g/kg CP)	333.9	357.6	5.57	0.095
nonprotein nitrogen (g/kg DM)	55.6	68.0	1.88	0.043
nonprotein nitrogen (g/kg CP)	267.0	218.8	58.59	0.620
nonprotein nitrogen (g/kg SCP)	55.5	68.0	1.87	0.042
neutral detergent insoluble crude protein (g/kg DM)	64.0	77.3	10.08	0.449
acid detergent insoluble crude protein (g/kg DM)	10.6	35.4	3.81	0.044
neutral detergent insoluble crude protein (g/kg CP)	309.6	326.9	56.29	0.848
acid detergent insoluble crude protein (g/kg CP)	50.6	149.4	18.90	0.066

Table 2. Oil Content, Fatty Acids, Glucosinolates, and Bioactive Compounds in Yellow- and Black-Type Canola Seed (*B. napus*)

item	CS-Y	CS-B	SEM	*P* value
chemical compounds				
erucic acid (g/kg DM)	0.2	0.4	0.07	0.184
either extract (EE, g/kg DM)	473.3	441.3	1.98	0.199
fatty acid composition (mg FA/g)				
C12 lauric	0.00	0.2	0.11	0.423
C14 myristic	0.55	0.7	0.05	0.293
C16 palmitic	33.7	39.0	1.58	0.141
C16:1n7 palmitoleic	3.2	3.3	0.21	0.764
C17 margaric	1.2	1.5	0.10	0.168
C18 stearic	16.6	16.0	0.81	0.602
C18:1n9 oleic	534.7	527.1	18.25	0.797
C18:1 octadecenoic	25.3	25.80	3.33	0.918
C18:2 linoleic	187.0	184.9	6.38	0.834
C18:3n3 α-linolenic	74.9	84.0	3.56	0.211
C20 arachidic	5.6	5.8	0.11	0.333
C20:1 eicosenoic	11.3	12.0	0.11	0.049
C20:2n6 eicosadienoic	0.7	0.65	0.08	0.699
C22 behenic	3.0	3.3	0.15	0.293
C22:1n9 erucic	0.2	0.40	0.07	0.184
C24 lignoceric	1.2	1.2	0.04	0.423
C24:1n9 nervonic	1.0	1.50	0.16	0.155
others	2.4	3.9	0.46	0.148
total fatty acids	902.0	910.7	5.17	0.356
total saturates	61.7	67.4	1.88	0.165
total monounsaturates	575.6	570.0	14.45	0.811
total polyunsaturates	262.5	269.5	9.73	0.659
total omega 3	74.9	84.0	3.56	0.211
total omega 6	187.6	185.5	6.45	0.839
total omega 9	547.2	541.0	17.96	0.830
glucosinolates (μmol/g)				
3-butenyl	2.9	1.0	0.08	0.004
4-pentenyl	0.4	0.7	0.05	0.058
2-OH-3-butenyl	2.6	2.4	0.37	0.860
2-OH-4-pentenyl	0.7	0.1	0.05	0.609
CH_3-thiobutenyl	0.1	0.8	0.01	0.292
phenylethyl	0.3	0.8	0.02	0.021
CH_3-thiopentenyl	0.1	0.1	0.02	0.184
3-CH_3-indolyl	0.3	0.2	0.01	0.011
4-OH-3-CH_3-indolyl	3.4	3.2	0.12	0.508
bioactive compounds (g/kg DM)				
total polyphenols	6.3	7.2	1.61	0.056
condensed tannins	3.0	3.2	0.22	0.592

DOI: 10.1021/acs.jafc.5b01577
J. Agric. Food Chem. 2015, 63, 5476−5484

Table 3. Protein and Carbohydrate Fractions Portioned by Cornell Net Carbohydrate and Protein system (CNCPS) in Yellow- and Black-Type Canola Seed (*B. napus*)

item	CS-Y	CS-B	SEM	*P* value
protein fractions (g/kg CP)				
PA[a]	3.9	5.8	0.26	0.036
PB1[b]	65.6	79.2	2.87	0.080
PB2[c]	870.1	842.6	6.37	0.092
PB3[d]	50.4	39.4	11.04	0.555
PC[e]	10.1	33.2	3.60	0.045
true protein[f] (g/kg CP)	986.1	961.1	3.79	0.043
protein fractions (g/kg true protein)				
PB1	66.2	79.9	2.90	0.080
PB2	878.5	850.6	6.43	0.092
PB3	50.8	39.8	11.14	0.555
protein fractions (g/kg DM)				
PA	0.8	1.3	0.08	0.042
PB1	13.0	17.7	0.108	0.090
PB2	171.0	188.0	7.12	0.233
PB3	9.8	8.8	1.92	0.736
PC	2.0	7.4	0.69	0.031

[a]PA, fraction of CP that is instantaneously solubilized at time zero, calculated as NPN. [b]PB1, rapidly degradable protein fraction that is soluble in borate phosphate buffer and precipitated with trichloroacetic acid, calculated as SCP minus NPN. [c]PB2, intermediately degradable protein fraction calculated as total CP minus the sum of fractions PA, PB1, PB3, and PC. [d]PB3, slowly degradable protein fraction, calculated as NDICP minus ADICP. [e]PC, fraction of undegradable protein, calculated as ADICP. It contained the proteins associated with lignin and tannins and/or heat-damaged proteins such as Maillard reaction products. [f]True protein (TP), PB1 (% CP) + PB2 (% CP) + PB3 (% CP).

Table 4. Truly Digestible Nutrients and Estimated Energy Value: Comparison between Yellow- and Black-Type Canola Seed (*B. napus*)

item	CS-Y	CS-B	SEM	*P* value
truly digestible fractions (g/kg DM; NRC 2001)				
digestible nonfiber carbohydrate (tdNFC)	367.1	277.3	11.43	0.031
digestible crude protein (tdCP)	192.4	209.8	6.87	0.215
digestible fatty acid (tdFA)	437.1	404.6	11.72	0.189
digestible neutral detergent fiber (tdNDF)	21.1	7.8	2.54	0.066
total digestible nutrients ($TDN_{1\times}$)[a]	149.4	133.5	1.94	0.029
predicted energy value at production intake level (3×) for dairy cattle (MJ/kg DM; NRC 2001)				
digestible energy ($DE_{3\times}$)[b]	59.9	54.0	0.81	0.037
metabolizable energy ($ME_{3\times}$)[c]	57.9	51.8	0.85	0.037
net energy for lactation ($NE_{L3\times}$)[d]	42.0	37.3	0.71	0.042

[a]$TDN_{1\times}$, total digestible nutrients at maintenance estimated from NRC dairy model 2001. [b]$DE_{3\times}$, digestible energy three times maintenance estimated from the NRC dairy model 2001. [c]$ME_{3\times}$, metabolizable energy at three times maintenance estimated from the NRC dairy model 2001. [d]$NEL_{3\times}$, net energy for lactation at three times maintenance estimated from the NRC dairy model 2001.

Table 5. In Situ Rumen Degradation Characteristics of Dry Matter, Crude Protein, Organic Matter, and Neutral Detergent Fiber: Comparison between Yellow- and Black-Type Canola Seed (*B. napus*)

item	CS-Y	CS-B	SEM	*P* value
in situ rumen dry matter degradation characteristics				
S[a] (g/kg DM)	272.4	297.1	10.65	0.152
D[b] (g/kg DM)	727.6	650.7	13.24	0.006
T_0[c] (/h)	0.9	0.9	0.16	0.958
K_d[d] (/h)	9.0	9.3	0.56	0.743
rumen undegraded dry matter (RUDM, g/kg DM)	291.3	310.9	8.33	0.149
effectively degraded dry matter (EDDM, g/kg DM)	708.7	689.2	8.33	0.149
in situ rumen organic matter degradation characteristics				
S (g/kg OM)	281.1	301.7	11.24	0.242
D (g/kg OM)	799.0	642.8	1.39	0.008
T_0 (/h)	1.0	0.8	0.19	0.589
K_d (/h)	8.91	9.0	0.504	0.914
rumen undegraded organic matter (RUOM, g/kg OM)	289.5	315.3	8.36	0.073
effectively degraded organic matter (EDOM, g/kg OM)	710.4	684.8	8.36	0.073
in situ rumen crude protein degradation characteristics				
S (g/kg CP)	285.9	341.1	12.59	0.021
D (g/kg CP)	672.8	590.2	13.20	0.005
T_0 (/h)	0.4	0.5	0.19	0.765
K_d (/h)	12.2	12.8	1.09	0.684
rumen undegraded crude protein (RUCP, g/kg CP)	257.6	249.9	8.87	0.565
effectively degraded crude protein (EDCP, g/kg CP)	742.5	750.1	8.87	0.565
in situ rumen neutral detergent fiber degradation characteristics				
S (g/kg NDF)	125.2	255.8	7.442	0.283
D (g/kg NDF)	874.8	689.4	7.00	0.134
T_0 (/h)	1.1	1.0	0.21	0.718
K_d (/h)	9.0	8.7	0.64	0.732
rumen undegraded neutral detergent fiber (RUNDF, g/kg NDF)	349.4	336.4	29.47	0.771
effectively degraded neutral detergent fiber (EDNDF, g/kg NDF)	650.6	663.6	29.47	0.771

[a]S, potential soluble fraction in the in situ ruminal incubation. [b]D, potentially degradable fraction in the in situ ruminal incubation. [c]T_0, lag time. [d]K_d, degradation rate.

Table 6. In Vitro Crude Protein Digestibility in the Small Intestine (IVCPD) on the 12 h Residue Determined Using Three Fistulated Dairy Cattle: Comparison between Yellow- and Black-Type Canola Seed (*B. napus*)

item	CS-Y	CS-B	SEM	*P* value
protein digestibility in the small intestine (g/kg CP in ruminally incubated residues)				
IVCPD[a]	565.9	445.6	27.86	0.022

[a]IVCPD, in vitro crude protein digestibility in small intestine.

case the value was lower for the yellow canola compared to the black one (50.6 vs 149.4 g/kg CP). There was no difference in the crude protein as well as the sugar content between the two types of canola seed. The fact that the seed coat color did not result in different CP contents is in accordance with a previous study targeting brown and yellow carinata seeds.[36]

Bioactive Compounds, Anti-nutrition Factors, and Fatty Acid Profiles. Data on the fatty acid profile and the bioactive compounds present in yellow and black canola seeds are summarized in Table 2. Canola oil is recognized for having a relatively low level of saturated fatty acids (≤7%) and

DOI: 10.1021/acs.jafc.5b01577
J. Agric. Food Chem. 2015, 63, 5476−5484

Table 7. Predicted Values of Potential Nutrient Supply to Dairy Cattle from Yellow- and Black-Type Canola Seed (*B. napus*) Using the Dutch DVE/OEB System

item (g/kg DM)	CS-Y	CS-B	SEM	*P* value
absorbable microbial protein synthesis in the rumen ($AMCP^{DVE}$)				
FOM[a]	272.2	297.1	8.46	0.174
MCP_{FOM}[b]	40.8	44.6	1.27	0.174
$MCP_{RDP}{}^{DVE}$[c]	148.45	171.47	3.398	0.041
$AMCP^{DVE}$[d]	26.04	28.41	0.809	0.174
endogenous protein in the small intestine (ENDP)[e]				
ENDP	12.64	12.87	0.595	0.810
truly absorbable rumen undegraded protein in small intestine ($ARUP^{DVE}$)				
RUP^{DVE}[f]	59.45	65.98	4.149	0.382
$ARUP^{DVE}$[g]	33.64	29.74	4.787	0.622
total truly digested protein in small intestine (DVE value)				
DVE[h]	47.05	45.29	3.741	0.770
degraded protein balance (OEB value)				
DPB^{DVE}[i] ($MCP_{FOM} - MCP_{RDP}$)	107.61	126.92	4.504	0.094
feed milk value[j]				
FMV (kg milk per kg feed)	0.96	0.92	0.076	0.769

[a]FOM, organic matter fermented in the rumen. [b]MCP_{FOM}, microbial protein synthesized in the rumen based on available energy. [c]$MCP_{RDP}{}^{DVE}$, microbial protein synthesized in the rumen based on rumen degraded feed crude protein. [d]$AMCP^{DVE}$, truly absorbed rumen synthesized microbial protein in the small intestine. [e]ENDP, endogenous protein losses in the digestive tract. [f]RUP^{DVE}, ruminally undegraded feed CP, calculated according the formula in DVE/OEB system. [g]$ARUP^{DVE}$, truly absorbed bypass feed protein in the small intestine. [h]DVE, truly absorbed protein in the small intestine contributed by (1) feed protein escaping rumen degradation (RUP^{DVE}), (2) microbial protein synthesized in the rumen (MCP_{FOM}), and (3) a correction for endogenous protein losses in the digestive tract (ENDP), DVE = (AMCP + ARUP − ENDP). [i]DPB^{DVE}, reflects the difference between the potential microbial protein synthesis based on rumen degraded feed crude protein (CP) and that based on energy (rumen fermented OM) available for microbial fermentation in the rumen. [j]FMV, reflects the efficiency of use of metabolizable protein for lactation is assumed to be 0.67 (source NRC, 2001) and protein composition in milk is assumed to be 33 g of protein per 1000 g of milk.

Table 8. Protein Molecular Structure Spectral Profiles: Comparison between Yellow- and Black-Type Canola Seeds (*B. napus*)

	endosperm region			
item (IR absorbance)	CS-Y	CS-B	SEM	*P* value
protein molecular structure spectra profiles				
amide I area	4.63	4.87	0.155	0.308
amide II area	1.87	2.00	0.066	0.204
ratio amide I to amide II area	2.48	2.44	0.043	0.501
amide I height	0.06	0.07	0.002	0.246
amide II height	0.04	0.04	0.001	0.409
ratio amide I to amide II height	1.75	1.79	0.027	0.320
protein secondary structure profile				
α-helix (height)	0.06	0.06	0.002	0.421
β-sheet (height)	0.06	0.06	0.002	0.538
ratio α-helix to β-sheet	1.05	1.06	0.011	0.686

significant amounts of essential fatty acids.[37] In this study, there was no difference in the erucic acid level. Among the fatty acids the C20:1 eicosenoic acid content (omega-9) was lower ($P < 0.05$) for the CS-Y than for the CS-B.

There are many studies focusing on the phenolic compounds in crops such as soybean, sunflower, and sorghum; however, knowledge of these compounds in canola remains fragmentary, even though canola contains about 5 times as much phenolic compounds as soybeans.[38] The predominant phenolic groups present in canola seed are phenolic acids and condensed tannins. The last one is present from 150 to 300 g/kg DM, with higher levels in black-seeded varieties.[39,40] In this study, there were no significant differences in the CT content, whereas the total polyphenols tended to be lower for the yellow- than for the black-seeded varieties (6.3 vs 7.2 g/kg DM). According to Shahidi et al.,[41] phenolic compounds (i.e., CT) contribute to the dark color of canola seed and their byproducts.

Glucosinolates are natural antinutritional compounds found in most brassica seeds and plants such as mustard, Brussels sprouts, cabbage, and cauliflower. The presence of relatively high levels of certain glucosinolates in traditional types of rapeseed hindered the use of rapeseed meal as a protein supplement in animal nutrition. The composition of glucosinolates in canola seeds depends on the seed variety.[3,42] Our study found specific glucosinolate compounds present in higher amounts in the yellow than in the black canola seeds. 3-Butenyl, phenylethyl, and 3-CH_3-indolyl exist in a significantly higher amount in CS-Y compared to in CS-B.

Fractionation of Protein. Protein and subfractions are shown in Table 3. Canola yellow type was significantly lower in the PA (3.9 vs 5.8 g/kg CP) and the unavailable PC fraction[24] (10.1 vs 33.2 g/kg CP) compared to the black one. Because the PC fraction in the feed represents the unavailable part of the protein, which cannot be used effectively by the ruminants, our results implied that the yellow canola seeds were expected to show comparatively better protein utilization than the brown seeds.

Energy Values in Newly Developed Lines. Truly digestible nutrients[18] and energy content of yellow and black canola varieties are summarized in Table 4. CS-Y was higher ($P < 0.05$), compared to CS-B, in total digestible nonfiber carbohydrate (367.1 vs 277.3 g/kg DM) and total digestible nutrients (149.4 vs 133.5 g/kg DM). The total digestible NDF tended to be higher for the CS-Y compared to the CS-B (21.1 vs 7.8 g/kg DM).

On the other hand, the energy values ($DE_{1\times}$, $DE_{3\times}$, $ME_{3\times}$, $NE_{L3\times}$) were higher ($P < 0.05$) for the yellow-seeded compared to the black-seeded canola. This result might be due to the

DOI: 10.1021/acs.jafc.5b01577
J. Agric. Food Chem. 2015, 63, 5476−5484

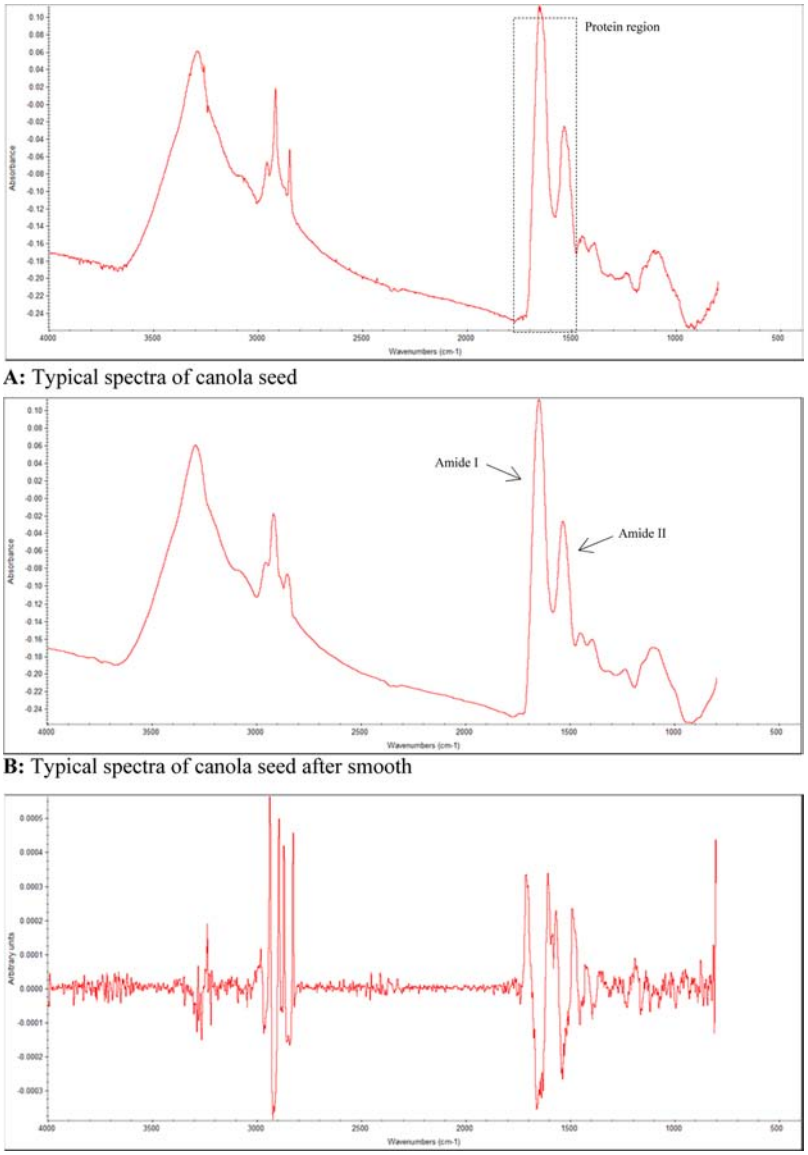

Figure 1. Typical biomolecular spectrum of canola seed in the region from ca. 4000 to 800 cm^{-1}, showing the chemical functional group of protein amides I and II.

tendency for lower fiber content and reduced hull of CS-Y compared to CS-B.

In Situ Rumen Incubation. The effect of canola seed variety on rumen fractions, rate of degradation, and effective degradability of nutrients is presented in Table 5. When CS-Y was compared with CS-B, there were no differences in rumen degradability, soluble fraction, and degradation rate of dry matter. However, the *D* fraction of dry matter in yellow-seeded canola (727.6 g/kg DM) was higher than in the black one (650.7 g/kg DM). The degradable fraction of organic matter (Table 5) was higher for CS-Y compared to CS-B (799.0 vs 642.8 g/kg OM).

The results on the in situ rumen protein degradation study showed that the EDCP (g/kg CP) of CS-Y was similar to that of CS-B. However, the potential soluble fraction was lower ($P < 0.05$) and the degradable fraction was higher ($P < 0.05$) for the yellow-seeded compared to the black-seeded canola.

The NDF degradability depends on the proportion of its main components (i.e., cellulose, hemicellulose, and lignin). Lignin, as well as cellulose and hemicellulose that are associated with it, is known to be highly indigestible.[20] In our study, the lower ($P < 0.05$) ADF and ADL content of yellow-seeded canola and the tendency of the NDF content to be lower, compared to the black one, was expected to be in accordance with a higher EDNDF (g/kg NDF) for CS-Y. However, there was no difference between CS-Y and CS-B concerning the degradation characteristics of neutral detergent fiber.

Intestinal Digestibility of Rumen Undegradated Protein. The in vitro crude protein intestinal digestibility of CS-Y was higher ($P < 0.05$) compared to that of CS-B (565.9 vs 445.6 g/kg CP of rumen undegradable protein) (Table 6). The lower undegradable protein fraction (PC) and the higher intestinal protein digestibility of yellow canola compared to the black-seeded one implies that the yellow type is a better source of intestinally digestible proteins for ruminants.

The absorbance of crude protein in the ruminant's small intestine has been reported to be negatively correlated ($r = -0.81$) with the acid detergent insoluble N content in canola meal.[43] This is in agreement with the results obtained in our study, where the higher protein intestinal digestibility of CS-Y,

DOI: 10.1021/acs.jafc.5b01577
J. Agric. Food Chem. 2015, 63, 5476−5484

compared with the CS-B, was in accordance with its lower ($P < 0.05$) ADICP value.

Protein Metabolic Characteristics and Feed Milk Value. The protein metabolic characteristics and the feed milk value are shown in Table 7. As described before, the microbial protein production is estimated on the FOM basis in the Dutch system. Therefore, similarity in FOM between the yellow and black resulted in similar values of MCP_{FOM} and AMCP.

In comparison with the black-seeded canola, the microbial protein that synthesized in the rumen and was based on the rumen degraded feed protein was significantly lower for the CS-Y in accordance with its trend ($P < 0.10$) for lower OEB value.

In our study, the fact that the OEB value[30] tended to be lower ($P < 0.10$) for the yellow-seeded canola indicates this seed type may result in a better nitrogen availability and utilization by the animals.

The feed milk values for both types of canola seed were not different ($P > 0.05$), so both are expected to have similar efficiencies for milk production.

Protein Molecular Structures of Yellow- and Black-Seeded Canola. The profiles of protein molecular structure of yellow- and black-seeded canola as defined with ATR-FT/IR are presented in Table 8. The research shows that protein secondary structure affects the protein by changing protein quality and biofunctions.[29,44−49] Depending on the α-helix to β-sheet ratios, tissues of the same protein content may differ in their nutritional value.

Figure 1 shows typical spectra, smoothed spectra, and second-derivative spectra of CS-Y and CS-B revealed by ATR-FT/IR molecular spectroscopy. In the present study, no significant differences were observed for the protein's inherent molecular structural makeup between CS-Y and CS-B.

In contrast with our results, Theodoridou et al.[50] concluded that the amide I and II areas, the β-sheet, and the ratio of amide I to amide II were higher ($P < 0.05$) for black-seeded compared to yellow-seeded canola. One possible reason for this variation between the two studies might be the fact that another analytical technique, called synchrotron-based vibrational FTIR microspectroscopy (SR-FTIRM),[51,52] has been employed in their study.

In summary, the results of this study indicated that the yellow-seeded canola was lower in ADF, ADL, NPN, and ADICP content compared to the black one. The yellow-seeded canola had higher values in the total digestible nutrients content, net energy, and digestible and metabolizable energy. There were no differences for the protein's inherent structural spectral characteristics. The findings of the present study show that the breeding of yellow-type canola is a promising route to reducing fiber and hull contents while at the same time increasing the level of oil. The feed protein availability and utilization by the animal might be higher when yellow-type canola is fed to animals, because the in vitro intestinal digestibility was found to be higher for the yellow-seeded canola compared to the black one. On the other hand, the yellow-seeded canola tended to have a lower degraded balance, compared to the black one, which suggests a better nutrient utilization and less output of potentially polluting nitrogen. This needs to be consider because environmentally friendly rations are nowadays very important in animal nutrition.

AUTHOR INFORMATION

Corresponding Author

*(P.Y.) Phone: (306) 966-4150. E-mail: Peiqiang.yu@usask.ca.

Funding

This work was supported by grants from SaskCanola, Natural Sciences and Engineering Research Council of Canada (NSERC-Collaborative Research and Development Grants), and the Ministry of Agriculture Strategic Research Chair. Other financial support for SRP Research Chair Program (P.Y.) from the Natural Sciences and Engineering Research Council of Canada (NSERC-Individual Discovery Grant), the Thousand-Talent People Research Program, University Innovation Team "Veterinary Biotechnology" (TD12-5019, Tianjin), the Saskatchewan Agriculture Development Fund (ADF), the SaskMilk, the Saskatchewan Forage Network (SNK), and Western Grain Research Foundation (WGRF), etc., is acknowledged.

Notes

The authors declare no competing financial interest.

ACKNOWLEDGMENTS

We thank research assistant Zhiyuan Niu in the Department of Animal and Poultry Science, University of Saskatchewan, Canada, for helpful assistance and chemical analysis.

REFERENCES

(1) Rakow, G.; Relf-Eckstein, J. A.; Raney, J. Rapeseed genetic research to improve its agronomic performance and seed quality. *Helia* **2007**, *30*, 199−206.

(2) Heendeniya, R. G.; Christensen, D. A.; Maenz, D. D.; McKinnon, J. J.; Yu, P. Utilization of canola seed fractions for ruminants: effect of canola fibre-protein and can-sugar inclusion in dehydrated alfalfa pellets on palatability and lactation performance of dairy cows. *Can. Vet. J.* **2010**, *90*, 279−283.

(3) Bell, J. M. Factors affecting the nutritional value of canola meal: a review. *Can. Vet. J.* **1993**, *73*, 679−697.

(4) Stringam, G. D.; McGregor, D. I.; Pawlowski, S. H. Chemical and morphological characteristics associated with seed coat color in rapeseed. In *Proceedings of the 4th International Rapeseed Congress*, Giessen, Germany, 1974; pp 99−108.

(5) McDonald, P.; Edwards, R. A.; Greenhalgh, J. F. D.; Morgan, C. A. *Animal Nutrition*; Longman Scientific and Technical: Harlow, Essex, UK, 1995; pp 519−521.

(6) Rashid, A.; Rakow, G.; Downey, R. K. Development of yellow-seeded *Brassica napus* through interspecific crosses. *Plant Breed.* **1994**, *112*, 127−134.

(7) Slominski, B. A.; Campbell, L. D.; Guenter, W. Carbohydrates and dietary fiber components of yellow and brown-seeded canola. *J. Agric. Food Chem.* **1994**, *42*, 704−707.

(8) Simbaya, J.; Slominski, B. A.; Rakow, G.; Campbell, L. D.; Downey, R. K.; Bell, J. M. Quality characteristics of yellow-seeded *Brassica* seed meals: protein, carbohydrates and dietary fiber components. *J. Agric. Food Chem.* **1995**, *43*, 2062−2066.

(9) Yu, P. Protein secondary structures (α-helix and β-sheet) at a cellular level and protein fractions in relation to rumen degradation behaviours of protein: a new approach. *Br. J. Nutr.* **2005**, *94*, 655−665.

(10) Yu, P. New approach in protein research. In *Trends in Dietary Protein Research*; Nova Science: New York, 2006.

(11) Yu, P. Plant-based food and feed protein structure changes induced by gene-transformation, heating and bio-ethanol processing: a synchrotron-based molecular structure and nutrition research program. *Mol. Nutr. Food Res.* **2010**, *54*, 1535−1545.

(12) Abeysekara, S.; Christiensen, D. A.; Niu, Z.; Theodoridou, K.; Yu, P. Molecular structure, chemical and nutrient profiles, and metabolic characteristics of the proteins and energy in new cool-season

DOI: 10.1021/acs.jafc.5b01577
J. Agric. Food Chem. 2015, 63, 5476−5484

corn varieties harvested as fresh forage for dairy cattle. *J. Dairy Sci.* **2013**, *96*, 6631−6643.
(13) Canadian Council on Animal Care. *Guide to the Care and Use of Experimental Animals*, 2nd ed.; CCAC: Ottawa, Canada, 1993; Vol. 1.
(14) Yu, P.; Goelema, J. O.; Tamminga, S. Using the DVE/OEB model to determine optimal conditions of pressure toasting on horse beans (*Vicia faba*) for the dairy feed industry. *Anim. Feed Sci. Technol.* **2000**, *86*, 165−176.
(15) Ørskov, E. R.; McDonald, I. The estimation of protein degradability in the rumen from incubation measurements weighted according to rate of passage. *J. Agric. Sci.* **1979**, *92*, 499−503.
(16) Robinson, P. H.; Fadel, J. G.; Tamminga, S. Evaluation of mathematical models to describe neutral detergent residue in terms of its susceptibility to degradation in the rumen. *Anim. Feed Sci. Technol.* **1986**, *15*, 249−271.
(17) Dhanoa, M. On the analysis of dacron bag data for low degradability feeds. *Grass Forage Sci.* **1998**, *43*, 441−444.
(18) National Research Council. *Nutrient Requirement of Dairy Cattle*, 7th ed.; National Academy Press: Washington, DC, USA, 2001.
(19) Calsamiglia, S.; Stern, M. D. A three-step in vitro procedure for estimating intestinal digestion of protein in ruminants. *J. Anim. Sci.* **1995**, *73*, 1459−1465.
(20) Association of Official Analytical Chemists (AOAC). *Official Methods of Analysis*, 15th ed.; Washington, DC, USA, 1990.
(21) Van Soest, P. J.; Mason, V. C. The influence of the Maillard reaction upon the nutritive value of fibrous feeds. *Anim. Feed Sci. Technol.* **1991**, *32*, 45−53.
(22) Theodoridou, K.; Yu, P. Effect of processing conditions on the nutritive value of canola meal and presscake. Comparison of the yellow and brown-seeded canola meal with the brown-seeded canola presscake. *J. Sci. Food Agric.* **2013**, *93*, 1986−1995.
(23) Licitra, G.; Hernandez, T. M.; Van Soest, P. J. Standardization of procedures for nitrogen fractionation of ruminant feeds. *Anim. Feed Sci. Technol.* **1996**, *57*, 347−358.
(24) Roe, M. B.; Sniffen, C. J.; Chase, L. E. Techniques for measuring protein fractions in feedstuffs. In *Proceedings, Cornell Nutrition Conference*; Department of Animal Science, Cornell University: Ithaca, NY, 1990; pp 81−88.
(25) Daun, J. K.; McGregor, D. I. *Glucosinolate Analysis of Rapeseed (Canola). Methods of the Canadian Grain Commission*; Grain Research Laboratory, Agriculture Canada, Canadian Grain Commission: Winnipeg, Canada, 1983.
(26) Slinkard, K.; Singleto, V. L. Total phenol analysis: automation and comparison with manual methods. *Am. J. Enol. Vitic.* **1996**, *28*, 49−55.
(27) Reed, J. D. Relationships among phenolics, insoluble proanthocyanidins and fiber in East African browse species. *J. Range Manage.* **1986**, *39*, 5−7.
(28) Sniffen, C. J.; O'Connor, J. D.; Van Soest, P. J.; Fox, D. G.; Russell, J. B. A net carbohydrate and protein system for evaluating cattle diets. II. Carbohydrate and protein availability. *J. Anim. Sci.* **1992**, *70*, 3562−3577.
(29) Theodoridou, K.; Yu, P. Application potential of ATR-FT/IR molecular spectroscopy in animal nutrition: Revelation of protein molecular structures of canola meal and presscake, as affected by heat-processing methods, in relationship with their protein digestive behavior and utilisation for dairy cattle. *J. Agric. Food Chem.* **2013**, *61*, 5449−5458.
(30) Tamminga, S.; Van Straalen, W. M.; Subnel, A. P. J.; Meijer, R. G. M.; Steg, A.; Wever, C. J. G.; Blok, M. C. The Dutch protein evaluation system: the DVE/OEB-system. *Livest. Prod. Sci.* **1994**, *40*, 139−155.
(31) Tamminga, S.; Brandsma, G. G.; van Duinkerken, G.; van Vuuren, A. M.; Blok, M. C. *Protein Evaluation for Ruminants: The DVE/OEB 2007-System*; CVB Documentation Report 53; Wageningen University: Wageningen, The Netherlands, 2007.
(32) Yu, P.; Christensen, D. A.; McKinnon, J. J. Comparison of the National Research Council-2001 model with the Dutch system (DVE/OEB) in the prediction of nutrient supply to dairy cows from forages. *J. Dairy Sci.* **2003**, *86*, 2178−2192.
(33) Theodoridou, K.; Yu, P. Metabolic characteristics of the proteins in yellow-seeded and brown-seeded canola meal and presscake in dairy cattle: comparison of three systems (PDI, DVE, and NRC) in nutrient supply and feed milk value (FMV). *J. Agric. Food Chem.* **2013**, *61*, 2820−2830.
(34) Abraham, V.; Bhatia, C. R. Development of strains with yellow seedcoat in Indian mustard (*Brassica juncea* Czern. & Coss.). *Plant Breed.* **1986**, *97*, 86−88.
(35) Naczk, M.; Amarowicz, R.; Sullivan, A. Current research developments on polyphenolics of rapeseed/canola: a review. *Food Chem.* **1998**, *62*, 489−902.
(36) Xin, H.; Falk, K. C.; Yu, P. Studies on *Brassica carinata* seed. 1. Protein molecular structure in relation to protein nutritive values and metabolic characteristics. *J. Agric. Food Chem.* **2013**, *61*, 10118−10126 dx.doi.org/10.1021/jf4020763,.
(37) Oomah, B. D.; Mazza, G. Health benefits of phytochemicals from selected Canadian crops. *Trends Food Sci. Technol.* **1999**, *10*, 193−198.
(38) Zadernowski, R.; Kozlowska, H. Phenolic acids in soybean and rapeseed flours. *Lebensm. Wiss. Technol.* **1983**, *16*, 110−114.
(39) Plahar, W. A.; Annan, N. T.; Nti, C. A. Cultivar and processing effects on the pasting characteristics, tannin content and protein quality and digestibility of cowpea (*Vigna unguiculata*). *Plant Foods Hum. Nutr.* **1997**, *51*, 343−356.
(40) Akhov, L.; Ashe, P.; Tan, Y. F.; Datla, R.; Selvaraj, G. Proanthocyanidin biosynthesis in the seed coat of yellow-seeded, canola quality *Brassica napus* YN01-429 is constrained at the committed step catalyzed by dihydroflavonol 4-reductase. *Botany* **2009**, *87*, 616−625.
(41) Shahidi, F.; Naczk, M. An overview of the phenolics of canola and rapessed: chemical, sensory and nutritional significance. *J. Am. Oil Chem. Soc.* **1992**, *69*, 917−924.
(42) Aider, M.; Barbara, C. Canola proteins: composition, extraction, functional properties, bioactiity, applications as a food ingredient and allergenicity. A practical and critical review. *Trends Food Sci. Technol.* **2011**, *22*, 21−39.
(43) Moshtaghi Nia, S. A.; Ingalls, J. R. Effect of heating on canola meal protein degradation in the rumen and digestion in the lower gastrointestinal tract of steers. *Can. Vet. J.* **1992**, *72*, 83−88.
(44) Dyson, H. J.; Wright, P. E. Peptide conformation and protein folding. *Curr. Opin. Struct. Biol.* **1990**, *3*, 60−65.
(45) Jackson, M.; Mantsch, H. H. The use and misuse of FTIR spectroscopy in the determination of protein structure. *Crit. Rev. Biochem. Mol. Biol.* **1995**, *30*, 95−120.
(46) Carey, F. A. *Organic Chemistry*, 3rd ed.; McGraw-Hill Book Company: New York, 1996.
(47) Samadi, T.; Yu, P. Dry and moist heating-induced changes in protein molecular structure, protein subfraction, and nutrient profiles in soybeans. *J. Dairy Sci.* **2011**, *94*, 6092−6102.
(48) Peng, Q.; Khan, N. A.; Wang, Z.; Yu, P. Moist and dry heating-induced changes in protein molecular structure, protein subfractions, and nutrient profiles in camelina seeds. *J. Dairy Sci.* **2014**, *97*, 1−12.
(49) Yu, P.; Nuez-Ortin, W. G. Relationship of protein molecular structure to metabolisable proteins in different types of dried distillers grains with solubles: a novel approach. *Br. J. Nutr.* **2010**, *104*, 1429−1437.
(50) Theodoridou, K.; Vail, S.; Yu, P. Explore protein molecular structure in endosperm tissues in newly developed black and yellow type canola seeds by using synchrotron-based Fourier transform infrared microspectroscopy. *Spectrochim. Acta, Part A* **2014**, *120*, 421−427.
(51) Miller, L. M.; Dumas, P. From structure to cellular mechanism with infrared microspectroscopy. *Curr. Opin. Struct. Biol.* **2010**, *20*, 649−656.
(52) Marinkovic, N. S.; Huang, R.; Bromberg, P.; Sullivan, M.; Toomey, J.; Miller, L. M.; Sperber, E.; Mosh, S.; Jones, K. W.;

DOI: 10.1021/acs.jafc.5b01577
J. Agric. Food Chem. 2015, 63, 5476−5484

Chouparova, E.; Lappi, S.; Franzen, S.; Chance, M. R. *J. Synchrotron Radiat.* **2012**, *9*, 189−197.

DOI: 10.1021/acs.jafc.5b01577
J. Agric. Food Chem. 2015, 63, 5476−5484

MATERIALS AND METHODS

Plant Materials and Germination Assay. The sweet corn (Yuetian 13) seeds were brought from Guangdong King Zuo Agricultural Science and Technology Company. The seeds were artificially aged under high temperature and humidity (45 °C and 100% relative humidity) conditions. Seeds were surface-sterilized. Seed germination was tested on moist filter paper. In each Petri dish (90 mm diameter), 20 seeds were randomly placed on the filter paper and then 10 mL of deionized water was added. The seeds were germinated for 4 days under dark conditions in a controlled (30 °C) growth chamber. Germination was considered when the coleoptiles were longer than 2 mm. Three replicates were carried out for each treatment.

RNA Isolation. The seeds were artificially aged under high temperature and humidity (45 °C and 100% relative humidity) conditions for 2 days.[29] Seeds that non-artificially aged (0 days) were used as a control (CK). We cut the pericarp and endosperm off the seeds with a knife carefully, and then the samples were immediately frozen in liquid nitrogen and stored at −80 °C. Total RNA was extracted using Trizol reagent (Invitrogen, Carlsbad, CA) following the procedure of the manufacturer.

Small RNA Library Construction, Sequencing, and Sequencing Data Analysis. The total RNA was used for Solexa sequencing. Four libraries were constructed: two sets were from seeds non-artificially aged (CK), the other two sets were from seeds artificially aged for 2 days. According to Illumina's TruSeq Small RNA Sample Preparation Guide, small RNA libraries were constructed using Illumina's TruSeq Small RNA Preparation Kit (Illumina, San Diego, CA).[30] Small RNAs were ligated to a 3′ RNA adapter and a 5′ RNA adapter. The purified cDNAs after reverse transcription and polymerase chain reaction (PCR) were sequenced by the Illumina Hiseq2000 (Illumina, San Diego, CA). Raw sequencing reads were obtained using Illumina's Sequencing Control Studio software, version 2.8 (SCS, version 2.8) (Illumina, San Diego, CA). After quality control using a common pipeline filter, clean reads were directly used for further bioinformatics analysis with ACGT101-miR (LC Sciences, Houston, TX).[31] Then, unique sequences (18−25 nucleotides) were mapped to specific species precursors in the miRNA database (miRBase 20 released) in maize (http://www.mirbase.org) by BLAST search to identify known miRNAs and novel 3p- and 5p-derived miRNAs. New candidate miRNAs were identified by extracting 250 nucleotides of the sequence flanking genome sequence of unique small RNAs using MIREAP (http://sourceforge.net/projects/mireap/), followed by the prediction of secondary structures by the Mfold program. The new candidate miRNA were identified on the basis of the criteria as described.[3]

Degradome Library Construction. The degradome cDNA library was constructed on the basis of the method described previously[32] using sliced ends of polyadenylated transcripts from sweet corn seeds. Identification of the potentially sliced targets of the known and novel miRNA identified by high-throughput sequencing and degradome analysis were processed using the publicly available CleaveLand 3.0 software package and the ACGT301-DGE, version 1.0 program (LC Sciences, Houston, TX).[33]

Quantitative Real-Time (qRT)-PCR. Total RNA was extracted from the sweet corn seeds artificially aged for 0 and 2 days with Trizol reagent (Invitrogen) following the instructions of the manufacturer. These samples were treated under the same conditions as those for miRNA and degradome sequencing. The total RNA (1 μg) was reverse-transcribed using miRNA-specific stem-loop primers. Next, qRT-PCR was performed using Rotor-Gene Q (QIAGEN). The primers used are listed in Table S11 of the Supporting Information. The relative expression ratio was calculated using the $2^{-\Delta\Delta C_t}$ method with 5S rRNA as the reference gene. All of the gene expression data were obtained from three individual biological replicates and processed according to strict statistical methods.

RESULTS AND DISCUSSION

Seed Vigor Changes under Artificial Aging Treatment. Germination percentage reflects seed vigor. With sustained artificial aging under 45 °C and 100% RH conditions, seed vigor decreased gradually. The germination percentage reduced to about 50% after 2 days of aging (Figure 1).

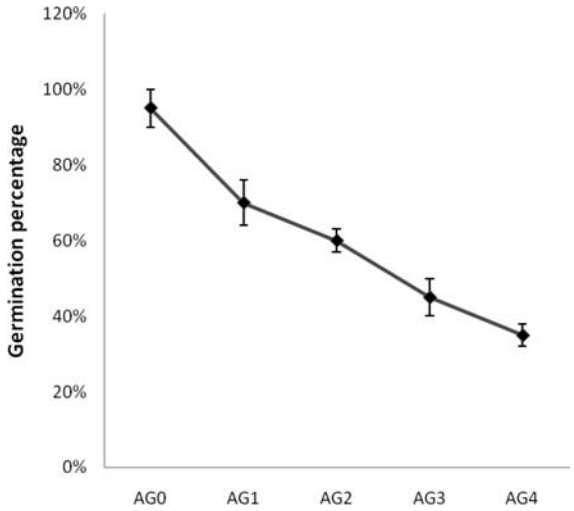

Figure 1. Germination percentage of Yuetian 13 under artificial aging treatment. AG0 means non-artificially aged; AG1 means artificially aged for 1 day; AG2 means artificially aged for 2 days; AG3 means artificially aged for 3 days; and AG4 means artificially aged for 4 days.

Overview over Deep-Sequencing Results. To study the possible miRNAs related with sweet corn seed vigor, we profiled miRNA accumulation during seed artificial aging. We constructed four maize small RNA libraries using mixed RNAs obtained from seeds non-artificially aged (CK) and artificially aged for 2 days. Deep sequencing generated a total number of 9 218 636 and 7 784 067 raw reads from libraries of seeds non-artificially aged named AG0a and AG0b and 7 203 021 and 8 043 385 raw reads from libraries of seeds artificially aged for 2 days named AG2a and AG2b. After removing sequences that 3′ adapter was not found and reads with lengths of <18 and >25 nucleotides, junk reads, there were 6 264 835, 5 943 490, 5 107 877, and 5 791 540 mappable reads obtained for AG0a, AG0b, AG2a, and AG2b libraries, respectively (see Table S1 of the Supporting Information). Most of these miRNAs were 20−24 nucleotides. The length distribution of these small RNA sequences showed that the most abundant sequences were 24 nucleotides long, followed by 22 nucleotides long and 21 nucleotides long (Figure 2). This was consistent with most plant mature small RNAs.[34−36] The mappable reads were then searched against the Rfam (http://rfam.janelia.org), mRNA (ftp.jgi-psf.org/pub/compgen/phytozome/v9.0/Zmays/annotation/), and repeat (http://www.girinst.org/repbase) databases. Finally, after excluding sequences that aligned to those databases, 5 037 856, 4 796 100, 4 269 398, and 4 951 734 sequences remained in the AG0a, AG0b, AG2a, and AG2b libraries, respectively (see Tables S2 and S3 of the Supporting Information).

Identification of Known miRNAs in Seeds of Sweet Corn. To identify the miRNAs in our data set, sRNA sequences identified by deep sequencing were Blastn-searched against the currently known mature plant miRNAs in the miRNA database miRBase. There are currently 172 pre-miRNAs listed that

DOI: 10.1021/acs.jafc.5b00522
J. Agric. Food Chem. 2015, 63, 5485−5491

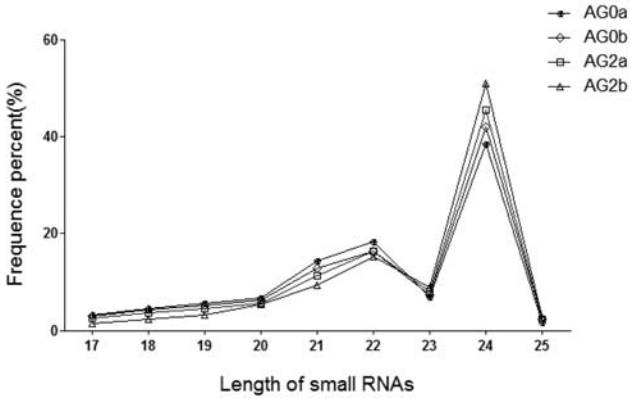

Figure 2. Length distribution of unique sRNAs of sequ-seqs type in four libraries.

correspond to 321 mature miRNAs of *Z. mays* in miRBase. In the present research, there were 146 pre-miRNAs corresponding to 130 mature miRNAs detected, 33 new mature 5′- or 3′-miRNAs corresponding to *Z. mays* pre-miRNAs detected for the first time, and 93 mature miRNAs corresponding to *Z. mays* pre-miRNAs detected confirming miRNA sequences in miRBase but different sequences in our study (see Table S4 of the Supporting Information). Both libraries identified 27 conversed miRNA families, which were 3 conversed miRNA families more than that in dry and imbibed maize seeds, including miR395, miR2118, and miR2275.[4] There were 12 novel pre-miRNAs corresponding to 18 mature miRNAs originating from other species but can be mapped to the *Z. mays* genome. Among the 18 mature miRNAs, 13 new mature 5′- or 3′-miRNAs were detected in *Z. mays* for the first time and 4 mature miRNAs were detected confirming miRNA sequences in miRBase but different sequences in our study (see Table S5 of the Supporting Information). There were 31 novel miRNAs originating from 31 pre-miRNAs that could not be mapped to the *Z. mays* genome; these were mapped to other plant species genomes, and the extended sequences at the mapped positions of the genome potentially form hairpins (see Table S6 of the Supporting Information). Another 4 novel miRNAs identified to originate from pre-miRNAs that could not be mapped to the *Z. mays* genome but were mapped to other plant genomes failed in hairpin structure prediction for extended sequences at the mapped positions (see Table S7 of the Supporting Information).

Identification of New Candidate miRNAs in Seeds of Sweet Corn. Reads that cannot be mapped to the miRBase were used to query the Rfam, the mRNA database, and the repeat Repbase. After removal of mapped reads, the rest of the reads were predicted for potential stem-loop structure. In total, 141 pre-miRNAs corresponding to 137 unique miRNAs were first identified in our study (see Table S8 of the Supporting Information). The 137 candidate miRNAs were 18−24 nucleotides long, with 69.34% of them 24 nucleotides long. Most of the candidate miRNAs were expressed at a low level. However, 6 of the candidate miRNAs were expressed at a high level. Those miRNAs were PC-5p-142680_20, PC-5p-6996_405, PC-3p-144850_17, PC-5p-608_3876, and PC-3p-78961_35; they had more than 20 reads in four libraries.

miRNAs That Related with Sweet Corn Seed Vigor. To identify miRNAs related with sweet corn seed vigor, the reads obtained from the high-throughout sequencing were used for differential expression analysis. With the selection of p value < 0.05, 27 miRNAs were identified to be differentially expressed between the four libraries; 17 miRNAs were upregulated, and 10 miRNAs were downregulated (Table 1). Of the 15 *Z. mays*-specific miRNAs, 9 miRNAs were upregulated and 6 miRNAs were downregulated. Zma-miR319a-3p_R+1, the miRNA that had the highest expression abundance in the four libraries, was upregulated when the sweet corn seed vigor was down. A *Brachypodium distachyon*-specific miRNA, bdi-miR159-3p, was downregulated when the sweet corn seed vigor was down. A total of 11 candidate miRNAs were differentially expressed between the four libraries: 8 were upregulated, and 3 were downregulated. To validate conserved miRNAs identified and novel miRNAs predicted, we selected 10 differential expressed miRNAs for stem-loop qRT-PCR. The expression trends of these miRNAs were consistent with the high-throughout sequencing results. Figure 3 showed that the 10 miRNA expression profiles by qRT-PCR were consistent with those by deep sequencing, indicating the reliability of these methods.

Targets of miRNAs in Seeds of Sweet Corn. To understand the function of the novel miRNAs from seeds of sweet corn, targets of novel miRNAs were predicted using recently developed degradome sequencing technology. In total, 13 621 118 (99.47%) mappable reads were obtained, including 3 986 470 unique mappable reads, while 7 343 113 (99.46%) transcript mapped reads, including 2 282 963 unique transcript mappable reads, were obtained (see Table S9-1 of the Supporting Information). The target transcripts were sorted into five categories according to the relative abundance of the tags at the target mRNA sites. Briefly, category "0" is defined as >1 raw read at the position, with abundance at a position equal to the maximum on the transcript and with only one maximum on the transcript. In category "1", the expected cleavage signature was equal to the maximum on the transcript and more than one maximum position on the transcript. For category "2", abundance at the position was less than the maximum but higher than the median for the transcript. The abundance at the position equal to or less than the median for the transcript was grouped into category "3", and category "4" showed only one raw read at the position. Figure 4 showed the typical five categories of the target transcripts. A total of 1142 targets that were potentially cleaved by 131 miRNAs were identified (see Table S9-2 of the Supporting Information). Meanwhile, 26 genes were identified to be targeted by 9 differentially expressed miRNAs in both degradome analysis and bioinformatics analysis (see Table S9-3 of the Supporting Information). Notably, the targets of miR319, miR156, miR160, and miR167 were identified as transcription factors, such as MYB, TCP, SBP, and ARF, respectively, which have been experimentally validated by the previous studies.[19−21] This demonstrated the high reliability of target identification in the present research.

Gene Ontology (GO) Analysis and Pathway Analysis of Targets. To gain a better understanding of the functional roles of the miRNAs, we did GO and KEGG pathway analysis on putative targets. The targets were annotated using the GO annotations available from B73 RefGen_v2. GO analysis is commonly used to describe the function of genes and gene products, while the KEGG analysis is used to provide the pathway of annotated targets. Figure 5 showed the GO functional classification of novel miRNA targets in the sweet corn seeds. Novel targets covered a broad range of functional categories. Obviously, targets of ATP-binding, regulation of

DOI: 10.1021/acs.jafc.5b00522
J. Agric. Food Chem. 2015, 63, 5485−5491

Table 1. Profiles of the Differentially Expressed miRNAs Related with Sweet Corn Seed Vigor

index	miR_name	miR_seq	AG0a (raw)	AG0b (raw)	AG2a (raw)	AG2b (raw)	AG0a (norm)	AG0b (norm)	AG2a (norm)	AG2b (norm)	log2(fold_change)
1	PC-5p-236947_9	ACTCGTTCCTTGTGTGCCACTGGC	1	1	3	4	0.91	1.09	3.38	3.66	1.82
2	zma-miR398a-3p	TGTGTTCTCAGGTCGCCCCCG	65	62.50	142.50	192.50	59.19	68.03	160.45	176.20	1.40
3	zma-miR398a-3p	TGTGTTCTCAGGTCGCCCCCG	65	62.50	142.50	192.50	59.19	68.03	160.45	176.20	1.40
4	PC-3p-260626_8	TTGTGAGGGGCTGCAAACAGC	3	1.50	7.50	8	2.73	1.63	8.44	7.32	1.85
5	PC-3p-477790_3	TTGATTGCACGCTTGCACCAGGT	0	1	5	5	0	1.09	5.63	4.58	3.23
6	PC-3p-618145_3	ATTCTCTGTCCACCGATCAGCTCT	0	1	5	5	0	1.09	5.63	4.58	3.16
7	PC-5p-670045_3	ATGGAGTGGATTGAGGGGGCTAGA	0	1	5	5	0	1.09	5.63	4.58	3.16
8	zma-miR319a-3p_R+1	TTGGACTGAAGGGTGCTCCCT	2314.08	2210	3095.50	3988.50	2107.33	2405.42	3485.43	3650.83	0.66
9	zma-miR319a-3p_R+1	TTGGACTGAAGGGTGCTCCCT	2314.08	2210	3095.50	3988.50	2107.33	2405.42	3485.43	3650.83	0.66
10	zma-miR319a-3p_R+1	TTGGACTGAAGGGTGCTCCCT	2314.08	2210	3095.50	3988.50	2107.33	2405.42	3485.43	3650.83	0.66
11	zma-miR319a-3p_R+1	TTGGACTGAAGGGTGCTCCCT	2314.08	2210	3095.50	3988.50	2107.33	2405.42	3485.43	3650.83	0.66
12	PC-3p-582028_5	AAATAAGTTTATTTTCGGCGGCCT	2	1	4	6	1.82	1.09	4.50	5.49	1.78
13	zma-MIR319b-p5	AGCTGCCGACTCATTCACCCA	31	26.50	107.50	144.50	28.23	28.84	121.04	132.27	2.15
14	zma-MIR171m-p3	CTTGGATTGAGCCGCGTCAAT	1	1.50	6	6	0.91	1.63	6.76	5.49	2.27
15	zma-MIR319d-p5	AGCTGCCGACTCATTCACCCA	31	26.50	107.50	145.50	28.23	28.84	121.04	133.18	2.16
16	PC-3p-38366_70	ATCCGGAACAACCGAACAGGGCCT	7	7	11	14	6.37	7.62	12.39	12.81	0.85
17	PC-3p-38366_70	ATCCGGAACAACCGAACAGGGCCT	7	7	11	14	6.37	7.62	12.39	12.81	0.85
18	zma-miR156i-3p	GCTCACTGCTCTATCTGTCATC	9.50	8	0.50	1	8.65	8.71	0.56	0.92	−3.55
19	bdi-miR159−3p	CTTGGATTGAAGGGAGCTCT	14	10.50	5	5	12.75	11.43	5.63	4.58	−1.24
20	zma-miR156l-3p	GCTCACTGCTCTATCTGTCACC	116.50	90	40.50	37	106.09	97.96	45.60	33.87	−1.36
21	PC-3p-144850_17	GCCTGCGACGTCGCGAGAA	49	36	7	0	44.62	39.18	7.88	0	−3.41
22	PC-5p-213179_17	ACACCCCAACGTTGACTCCTCT	9	9	2	4	8.20	9.80	2.25	3.66	−1.61
23	zma-miR168b-3p_R+1	CCCGCCTTGCATCAAGTGAAT	739.50	562	54	61.50	673.43	611.69	60.80	56.29	−3.46
24	zma-miR156d-3p_1ss7TG	GCTCACGTCTCTTTCTGTCAGC	2	1.67	0.67	0.67	1.82	1.81	0.75	0.61	−1.42
25	zma-miR156d-3p_1ss7TG	GCTCACGTCTCTTTCTGTCAGC	2	1.67	0.67	0.67	1.82	1.81	0.75	0.61	−1.42
26	zma-miR156d-3p_1ss7TG	GCTCACGTCTCTTTCTGTCAGC	2	1.67	0.67	0.67	1.82	1.81	0.75	0.61	−1.42
27	PC-3p-136373_22	TTTCGGGCTCCCAAACTAGCC	13	10	8	9	11.84	10.88	9.01	8.24	−0.40

J. Agric. Food Chem. 2015, 63, 5485−5491
DOI: 10.1021/acs.jafc.5b00522

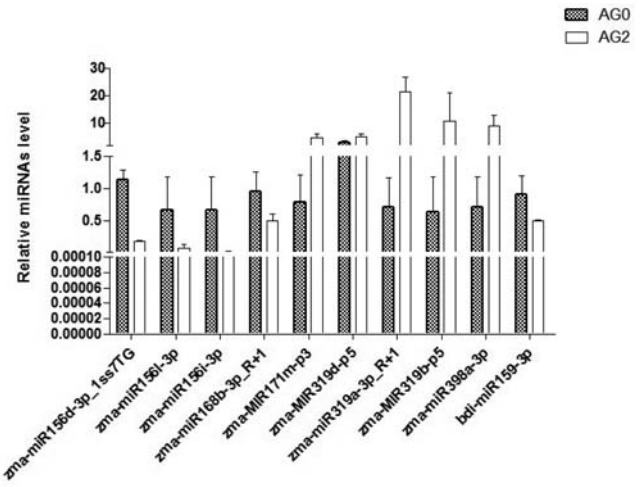

Figure 3. Detection of selected miRNA expression in AG0 and AG2 sweet corn seeds using qRT-PCR. AG0 means non-artificially aged, while AG2 means artificially aged for 2 days. The 5S rRNA was chosen as an endogenous control. The results were obtained from three biological replicates, and the error bars indicate the standard error of the mean.

transcription, DNA-dependent, and nucleus- and membrane-related genes were specifically enriched. This suggested that those genes may play an important role in sweet corn seeds. The pathways of all the miRNAs and targets involved were listed (see Tables S10-1 and S10-2 of the Supporting Information). There were 157 pathways that targets involved, while purine metabolism, cell cycle, and phenylalanine metabolism pathways owned most targets. However, there were only 13 miRNAs found to be involved in pathways, including mitogen-activated protein kinase (MAPK) signaling pathway, endocytosis, spliceosome, and others.

Function of Differentially Expressed miRNAs. Although 27 miRNAs were differentially expressed related with sweet corn seed vigor, only 26 genes targeted by 9 miRNAs were identified in both degradome analysis and bioinformatics analysis, including 10 MYB proteins, 2 TCP family transcription factors, 1 membrane-anchored ubiquitin-fold protein 6 precursor (MUB6), 1 heat stable protein, 3 peroxidase superfamily proteins, 1 selenium-binding protein (SBP), and 6 unknown transcription factors. The function of the MYB protein has been previously identified. MYB proteins are key factors in regulatory networks controlling development, metabolism, and responses to biotic and abiotic stresses.[37] In *Arabidopsis* and rice (*Oryza sativa*), MYB33 and MYB101 targeted by miR159 were ABA-positive regulators, which play a vital role in seed germination. The role of MYB protein in seed vigor is still unknown. In our study, MYB domain proteins 65/33/101 were targeted by bdi-miR159-3p and zma-miR319a-3p_R+1. This suggests that MYB protein may participate in seed vigor regulation through chromatin binding. Loss of seed vigor brings abnormal physiological and biochemical activities in cells, such as free radical lipid peroxidation, chromosome aberration, and non-enzymatic glycosylation (NEG). Peroxidase (POD) is a scavenger of reactive oxygen, which can maintain the stability and integrity of the membrane of the cells. POD superfamily proteins play roles in the oxidation−reduction process and response to oxidative stress, which protect seeds from oxidative damage during artificial aging. This suggests that PC-5p-213179_17 may prevent sweet corn seeds from free-radical lipid peroxidation by participating in the

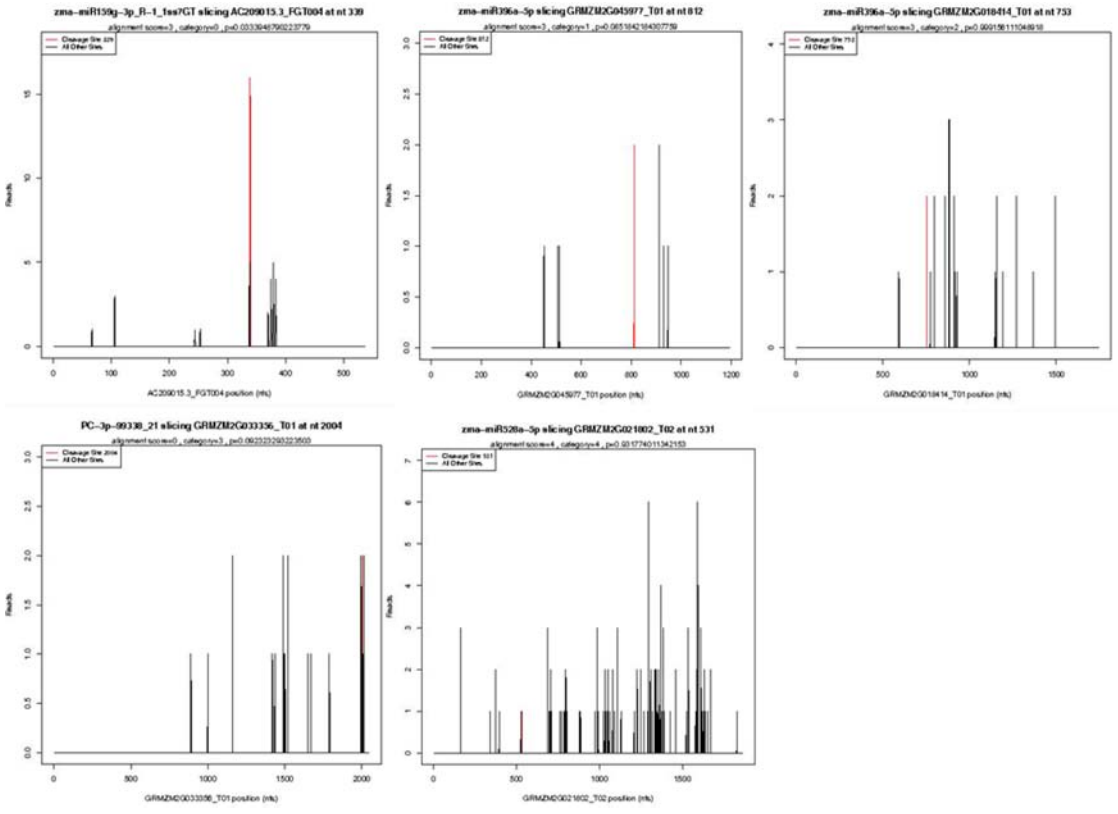

Figure 4. Typical categories of the target transcript according to the relative abundance of the tags at the target mRNA sites.

DOI: 10.1021/acs.jafc.5b00522
J. Agric. Food Chem. 2015, 63, 5485−5491

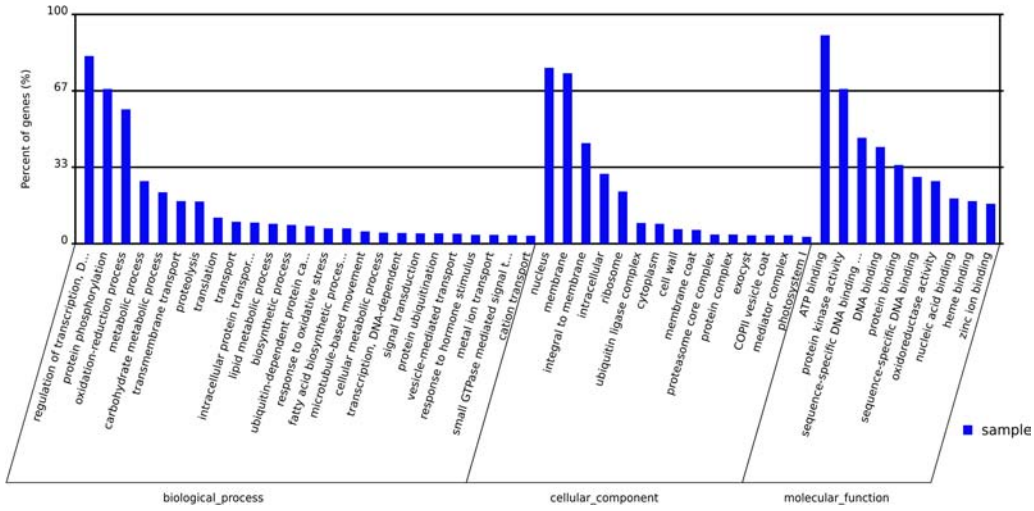

Figure 5. GO functional classification of novel miRNA targets in the sweet corn seeds.

peroxidase activity, oxidation−reduction process, and response to oxidative stress. The function of MUB6 in seed vigor is still unclear, but researchers have proven that MUB6 expressed in seeds associated with plant structure in *Arabidopsis*. Seed aging will destroy the integrity of the membrane. Here, we report a MUB6 in sweet corn seeds regulated by PC-3p-477790_3, which may be a new direction in the research of seed vigor. Heat-stable protein also targeted by PC-3p-477790_3 may be involved in ameliorating the effects of artificial aging on seed vigor by repairing protein damage. Therefore, we propose that miRNAs participate in seed vigor of sweet corn by regulating some genes controlling the process.

■ ASSOCIATED CONTENT

Supporting Information

Distribution of counts of sequ-seqs during standard filtering in four libraries (Table S1), distribution of counts of mappable reads in four libraries (Table S2), length distribution of mappable counts and unique sRNAs of sequ-seqs type in four libraries (Table S3), profile of the known microRNAs in sweet corn seeds referred to *Z. mays* (miRbase20.0) (Table S4), profile of novel microRNAs originating from other plant pre-miRNAs (miRbase 20.0) that can be mapped to the *Z. mays* genome (Table S5), profile of novel microRNAs originating from pre-miRNAs that cannot be mapped to the *Z. mays* genome but novel microRNAs mapped to the genome and extended sequences at the mapped positions of the genome potentially forming hairpins (Table S6), profile of novel microRNAs originating from pre-miRNAs that cannot be mapped to the *Z. mays* genome but novel microRNAs mapped to the genome and extended sequences at the mapped positions of the genome not potentially forming hairpins (Table S7), profile of candidate microRNAs originating from predicted RNA hairpins (Table S8), distribution of counts of mappable reads in the degradome library (Table S9-1), profile of all miRNA targets by degradome sequencing (Table S9-2), profiles of differentially expressed miRNAs targets by degradome sequencing and bioinformatics analysis (Table S9-3), KEGG pathway statistics by degradome sequencing (Table S10-1), KEGG-miRNA gene PLUS expression by degradome sequencing (Table S10-2), and stem-loop primer and qRT-PCR primer of 10 miRNAs (Table S11) (XLS). The Supporting Information is available free of charge on the ACS Publications website at DOI: 10.1021/acs.jafc.5b00522.

■ AUTHOR INFORMATION

Corresponding Author

*Telephone: 86-571-86914510. E-mail: pzhch@cjlu.edu.cn.

Author Contributions

†Shumin Gong and Yanfei Ding are co-first authors.

Funding

This study was supported through funding from the National Natural Science Foundation of China (31401299, 31170251, and 31470368) and the Zhejiang Provincial Natural Science Foundation of China (LZ14C020001 and LY13C020002).

Notes

The authors declare no competing financial interest.

■ REFERENCES

(1) Bennetzen, J. L.; Hake, S. C. *Handbook of Maize: Its Biology*; Springer: New York, 2009.

(2) Gupta, M. L.; George, D. L.; Parwata, I. G. M. A. Effect of harvest time and drying on supersweet corn seed quality. *Seed Sci. Technol.* **2005**, *33*, 167−176.

(3) Zhang, L. F.; Chia, J. M.; Kumari, S.; Stein, J. C.; Liu, Z. J.; Narechania, A.; Maher, C. A.; Guill, K.; McMullen, M. D.; Ware, D. A genome-wide characterization of microRNA genes in maize. *PLoS Genet.* **2009**, *5*, No. e1000716.

(4) Li, D. T.; Wang, L. W.; Liu, X.; Cui, D. Z.; Chen, T. T.; Zhang, H.; Jiang, C.; Xu, C. Y.; Li, P.; Li, S.; Zhao, L.; Chen, H. B. Deep sequencing of maize small RNAs reveals a diverse set of microRNA in dry and imbibed seeds. *PLoS One* **2013**, *8*, No. e55107.

(5) Kang, M. M.; Zhao, Q.; Zhu, D. Y.; Yu, J. J. Characterization of microRNAs expression during maize seed development. *BMC Genomics* **2012**, *13*, 360.

(6) Bartel, D. P. MicroRNAs: Genomics, biogenesis, mechanism, and function. *Cell* **2004**, *116*, 281−297.

(7) Zamore, P. D.; Haley, B. Ribo-gnome: The big world of small RNAs. *Science* **2005**, *309*, 1519−1524.

(8) Park, W.; Li, J.; Song, R.; Messing, J.; Chen, X. M. CARPEL FACTORY, a Dicer homolog, and HEN1, a novel protein, act in microRNA metabolism in *Arabidopsis thaliana*. *Curr. Biol.* **2002**, *12*, 1484−1495.

(9) Jia, L.; Zhang, D. Y.; Qi, X. W.; Ma, B.; Xiang, Z. H.; He, N. J. Identification of the conserved and novel miRNAs in mulberry by high-throughput sequencing. *PLoS One* **2014**, *9*, No. e104409.

DOI: 10.1021/acs.jafc.5b00522
J. Agric. Food Chem. 2015, 63, 5485−5491

(10) Reinhart, B.; Weinstein, E.; Rhoades, M.; Bartel, B.; Bartel, D. MicroRNAs in plants. *Genes Dev.* **2002**, *16*, 1616−1626.
(11) Xie, Z. X.; Allen, E.; Fahlgren, N.; Calamar, A.; Givan, S.; Carrington, J. Expression of *Arabidopsis* MIRNA genes. *Plant Physiol.* **2005**, *138*, 2145−2154.
(12) Yu, B.; Yang, Z. Y.; Li, J. J.; Minakhina, S.; Yang, M.; Padgett, R.; Steward, R.; Chen, X. M. Methylation as a crucial step in plant microRNA biogenesis. *Science* **2005**, *307*, 932−935.
(13) Bollman, K.; Aukerman, M.; Park, M.; Hunter, C.; Berardini, T.; Poethig, R. HASTY, the *Arabidopsis* ortholog of exportin 5/MSN5, regulates phase change and morphogenesis. *Development* **2003**, *130*, 1493−1504.
(14) Park, M.; Wu, G.; Gonzalez-Sulser, A.; Vaucheret, H.; Poethig, R. Nuclear processing and export of microRNAs in *Arabidopsis*. *Proc. Natl. Acad. Sci. U. S. A.* **2005**, *102*, 3691−3696.
(15) Baumberger, N.; Baulcombe, D. *Arabidopsis* ARGONAUTE1 is an RNA slicer that selectively recruits microRNAs and short interfering RNAs. *Proc. Natl. Acad. Sci. U. S. A.* **2005**, *102*, 11928−11933.
(16) Bonnet, E.; Van de Peer, Y.; Rouze, P. The small RNA world of plants. *New Phytol.* **2006**, *171*, 451−468.
(17) Khan, Y.; Yadav, A.; Bonthala, V. S.; Muthamilarasan, M.; Yadav, C. B.; Prasad, M. Comprehensive genome-wide identification and expression profiling of foxtail millet [*Setaria italica* (L.)] miRNAs in response to abiotic stress and development of miRNA database. *Plant Cell, Tissue Organ Cult.* **2014**, *118*, 279−292.
(18) Aukerman, M. J.; Sakai, H. Regulation of flowering time and floral organ identity by a microRNA and its APETALA2-like target genes. *Plant Cell* **2003**, *15*, 2730−2741.
(19) Mallory, A. C.; Vaucheret, H. Functions of microRNAs and related small RNAs in plants. *Nat. Genet.* **2006**, *38*, S31−S36.
(20) Voinnet, O. Origin, biogenesis, and activity of plant microRNAs. *Cell* **2009**, *136*, 669−687.
(21) Carrington, J. C.; Ambros, V. Role of microRNAs in plant and animal development. *Science* **2003**, *301*, 336−338.
(22) Sunkar, R. MicroRNAs with macro-effects on plant stress responses. *Semin. Cell Dev. Biol.* **2010**, *21*, 805−811.
(23) Khraiwesh, B.; Zhu, J. K.; Zhu, J. H. Role of miRNAs and siRNAs in biotic and abiotic stress responses of plants. *Biochim. Biophys. Acta, Gene Regul. Mech.* **2012**, *1819*, 137−148.
(24) Nodine, M.; Bartel, D. MicroRNAs prevent precocious gene expression and enable pattern formation during plant embryogenesis. *Genes Dev.* **2010**, *24*, 2678−2692.
(25) Reyes, J. L.; Chua, N. H. ABA induction of miR159 controls transcript levels of two MYB factors during *Arabidopsis* seed germination. *Plant J.* **2007**, *49*, 592−606.
(26) Gutierrez, L.; Bussell, J. D.; Pacurar, D. I.; Schwambach, J.; Pacurar, M.; Bellini, C. Phenotypic plasticity of adventitious rooting in *Arabidopsis* is controlled by complex regulation of AUXIN RESPONSE FACTOR transcripts and microRNA abundance. *Plant Cell* **2009**, *21*, 3119−3132.
(27) Yang, J. H.; Han, S. J.; Yoon, E. K.; Lee, W. S. Evidence of an auxin signal pathway, microRNA167-ARF8-GH3, and its response to exogenous auxin in cultured rice cells. *Nucleic Acids Res.* **2006**, *34*, 1892−1899.
(28) Cheng, H. L. Study on correlation of miRNA and rice (*Oryza sativa* L.) seed vigor. Master's Thesis, Hunan Normal University, Changsha, Hunan, China, 2011 (in Chinese).
(29) Association of Official Seed Analysts (AOSA). *Seed Vigor Testing Handbook*; AOSA: Washington, D.C., 1983; Contribution Number 32 to the Handbook of Seed Testing.
(30) Tang, Z. H.; Zhang, L. P.; Xu, C. G.; Yuan, S. H.; Zhang, F. T.; Zheng, Y. L.; Zhao, C. P. Uncovering small RNA-mediated responses to cold stress in a wheat thermosensitive genic male-sterile line by deep sequencing. *Plant Physiol.* **2012**, *159*, 721−738.
(31) Li, Y.; Zhang, Q. Q.; Zhang, J. G.; Wu, L.; Qi, Y. J.; Zhou, J. M. Identification of microRNAs involved in pathogen-associated molecular pattern-triggered plant innate immunity. *Plant Physiol.* **2010**, *152*, 2222−2231.
(32) Addo-Quaye, C.; Eshoo, T. W.; Bartel, D. P.; Axtell, M. J. Endogenous siRNA and miRNA targets identified by sequencing of the *Arabidopsis* degradome. *Curr. Biol.* **2008**, *18*, 758−762.
(33) Addo-Quaye, C.; Snyder, J. A.; Park, Y. B.; Li, Y. F.; Sunkar, R.; Axtell, M. J. Sliced microRNA targets and precise loop-first processing of MIR319 hairpins revealed by analysis of the *Physcomitrella patens* degradome. *RNA* **2009**, *15*, 2112−2121.
(34) Jiao, Y. P.; Song, W. B.; Zhang, M.; Lai, J. S. Identification of novel maize miRNAs by measuring the precision of precursor processing. *BMC Plant Biol.* **2011**, *11*, 141.
(35) Szittya, G.; Moxon, S.; Santos, D. M.; Jing, R.; Fevereiro, M. P. S.; Moulton, V.; Dalmay, T. High-throughput sequencing of *Medicago truncatula* short RNAs identifies eight new miRNA families. *BMC Genomics* **2008**, *9*, 593.
(36) Rajagopalan, R.; Vaucheret, H.; Trejo, J.; Bartel, D. P. A diverse and evolutionarily fluid set of microRNAs in *Arabidopsis thaliana*. *Genes Dev.* **2006**, *20*, 3407−3425.
(37) Dubos, C.; Stracke, R.; Grotewold, E.; Weisshaar, B.; Martin, C.; Lepiniec, L. MYB transcription factors in *Arabidopsis*. *Trends Plant Sci.* **2010**, *15*, 573−581.

DOI: 10.1021/acs.jafc.5b00522
J. Agric. Food Chem. 2015, 63, 5485−5491

Table 1. Oligonucleotide Primers Used for PCR in This Study

primer name	sequences (5′-3′)	restriction site
M35-F	CAGCCACTTTTACGCAACGCATAATT	
M35-R	TCAATTACAGATTTTCTTTAACCTACGCAATG	
M10-F	GTATAATTGTTGTCGCGCTGCCGAAAAG	
M10-R	GTTGCGTAAAAGTGGCAGTCAATTACAG	
Mrbs-F	GAAATAAGCATGGCCACGCAGTCCAGAG	
Mrbs-R	CTCCATGCGGTAGGGTGCCGCAC	
PtufB-F	ACTGAGCTCCGATGGTAAGAAATCCACTGC	*Sac*I
PtufB-R	ATATCTAGACCAAAACCCCGCTCCACC	*Xba*I
ga2dh-F	CTATCTAGAGGAGAAACCTGTGCCCCCCATG	*Xba*I
ga2dh-R	GAGGGATCCTTCAGTTCAGTGAGACCGCATCATC	*Bam*HI
qpBBR-F	CGGATTCACCGTTTTTATCAGGCTC	
qpBBR-R	AGTGTGACCGTGTGCTTCTCAAATG	
qpGOX3-F	GTATTGGGCTGCGTTCGT	
qpGOX3-R	AATGGGTTTCATGGTGGC	
q16S−F	GCGGTTGTTACAGTCAGATG	
q16S-R	GCCTCAGCGTCAGTATCG	
qga2dh-F	CCAGAACCTGTCCCAGTCCAC	
qga2dh-R	CAGAAAGGCTGCGAGTTGAC	

at 37 °C and 200 rpm. Gentamicin was added to a final concentration of 25 μg/mL for plasmid maintenance.

General Molecular Biological Techniques. Routine molecular biological techniques were performed according to Sambrook et al.[19] The restriction enzymes and T4 DNA ligase used were purchased from Fermentas (St. Leon-Rot, Germany). Pfu DNA polymerase (Transgen, Beijing, China) was used for PCR amplification of the insets, and Taq PCR MasterMix (Zoman, Beijing, China) was used for the test PCR reactions. The primers used in this study are listed in Table 1. Transformation of *G. oxidans* was performed by triparental mating, essentially as described by Hölscher et al.[20]

Site-Directed Mutagenesis to Construct an Improved pBBR1MCS-5 Series. Site-directed mutagenesis upstream of the gene *rep* in pBBR1MCS-5 was performed, including the −10 and −35 region of the promoter and the ribosome binding site (RBS), using a TOYOBO KOD-Plus-Mutagenesis Kit (Tokyo, Japan) according to the manufacturer's instructions. The primers used for each mutation are listed in Table 1. The pBBR1MCS-5 plasmid was mutated to generate pBBR-10, pBBR-35, pBBR-3510, pBBR-RBS, pBBR-R10, pBBR-R35, and pBBR-R31. Among the resulting plasmids, pBBR-10 was mutated at the −10 region (CATAAT to TATAAT) using the primers M10-F and M10-R. pBBR-35 was mutated at the −35 region (TTGACT to TTGACA) using the primers M35-F and M35-R. pBBR-3510 was created using two rounds of mutagenesis using the primer pairs M35-F and M35-R and M10-F and M10-R consecutively. pBBR-RBS was mutated at the ribosome binding site (GGAGA) of the rep gene (to GGAGGAAA) using the primers Mrbs-F and Mrbs-R. pBBR-R10 was created using two rounds of mutagenesis using the primer pairs M10-F and M10-R and Mrbs-F and Mrbs-R consecutively. pBBR-R35 was created using two rounds of mutagenesis using the primer pairs M35-F and M35-R and Mrbs-F and Mrbs-R consecutively, and pBBR-R31 was created using three rounds of mutagenesis using the primer pairs M35-F and M35-R, M10-F and M10-R, and Mrbs-F and Mrbs-R consecutively.

Construction of Recombinant Plasmids. The fragments of the *G. oxidans tufB* promoter and the *ga2dh* gene were amplified with PCR using the primer pairs PtufB-F and PtufB-R and ga2dh-F and ga2dh-R, respectively, using chromosomal DNA as the template. The resulting fragment of the *tufB* gene was digested using *Sac*I/*Xba*I and was ligated into pBBR1MCS-5 digested with the same enzymes to produce the recombinant plasmid pBBR1MCS-*tufB*. The fragment of *ga2dh* was digested using *Xba*I/*Bam*HI and was cloned into pBBR1MCS-*tufB* digested with the same enzymes to generate pBBR-*ga2dh*. The plasmids pBBR-10-*ga2dh*, pBBR-35-*ga2dh*, pBBR-RBS-*ga2dh*, pBBR-3510-*ga2dh*, pBBR-R10-*ga2dh*, pBBR-R35-*ga2dh*, and pBBR-R31-*ga2dh* were constructed in the same manner. All of the resulting recombinant plasmids were confirmed by sequencing, and these plasmids were transformed into *G. oxidans* DSM 2003 through triparental mating.[20]

Real-Time PCR. The plasmid copy number and level of gene transcription were determined using RT-qPCR. The StepOnePlus Real-Time PCR System (Applied Biosystems, California, United States) was used for qPCR amplification and detection. The qPCR analyses were conducted in a total volume of 20 μL using the CWBIO FastSYBR Mixture (with Rox) (Beijing, China) according to the manufacturer's recommendations. All of the reactions were performed in triplicate.

The recombinant *G. oxidans* cells were cultured at 30 °C and 220 rpm for 22 h. Plasmid DNA was collected from 3 mL cultures according to the Biomiga Plasmid Miniprep Kit protocol (San Diego, CA, United States). The extracted plasmids were used as templates, and the cryptic plasmid pGOX3 was used as the internal single-copy reference. The primer pairs qpBBR-F and qpBBR-R and qpGOX3-F and qpGOX3-R were used in the respective reactions.[21]

Total RNA was isolated from 15 mL cultures using Takara RNAiso Plus (Dalian, China) following the manufacturer's instructions. A 1 μg sample of RNA was reverse transcribed into cDNA using the Takara PrimeScript RT reagent kit including gDNA Eraser (Dalian, China). The relative abundance of the *ga2dh* transcripts in the recombinant strains was analyzed using RT-qPCR with the primers qga2dh-F and qga2dh-R. The 16S rRNA gene was used as the internal standard and detected with the primers q16S-F and q16S-R.

Preparation of Membrane Fractions. The *G. oxidans* cells were harvested by centrifugation at 8 000 rpm for 10 min and washed twice with 20 mM potassium phosphate buffer (pH 7.5). The washed cells were resuspended with the same buffer at a cell wet weight (CWW) concentration of 0.1 g/mL and then disrupted using an ultrasonifier (Xinzhi, Ningbo, China) for 99 cycles (300 W, 5 s sonication, 5 s pause on ice). After centrifugation at 8 000 rpm for 15 min to remove the cell debris, the supernatants were centrifuged at 40 000 rpm for 60 min. The sediments were collected and designated the membrane fractions, which were resuspended into 100 mM NaAc buffer (pH 5.5) on ice subsequently.

Enzyme Activity Assay and Protein Concentration Determination. GA2DH activity was determined at 30 °C by measuring the initial reduction rate of 2,6-dichlorophenolindophenol (2,6-DCIP, Sigma, St. Louis, MO, United States) at 600 nm on a SpectraMax 190 instrument (Molecular Devices, California, United States), and a molar extinction coefficient of 10.8 mM^{-1} cm^{-1} for DCIP was used for the calculation.[22] The basal reaction mixture consisted of 5 mM DCIP and 6.5 mM phenazine methosulfate (PMS, Sigma, St. Louis, MO, United States) in 50 mM potassium phosphate buffer (pH 6.0) and was

DOI: 10.1021/acs.jafc.5b01652
J. Agric. Food Chem. 2015, 63, 5492−5498

prepared just before the assay. The reaction mixtures (200 μL) for enzyme assay containing 80 μL of basal reaction mixture and 0.015 mg of protein in 50 mM potassium phosphate buffer (pH 6.0) was incubated at 30 °C for 5 min, and the reactions were started by adding 50 mM prewarmed GA. One unit of GA2DH activity was defined as the amount of the enzyme that catalyzes the reduction of 1 μM DCIP per min at 30 °C. Protein concentration was determined by the method of Bradford,[23] using bovine serum albumin as a standard.

Relative 2KGA Production by the Different *G. oxidans* Strains. The relative level of 2KGA production was evaluated in the different *G. oxidans* strains by determining the concentration of 2KGA after 2 h of catalysis. The *G. oxidans* strains were cultivated for 22−24 h, after which the cells were collected by centrifugation at 7 000 rpm for 20 min. The reaction system contained 10 g CWW/L resting cells and 40 g/L GA in 50 mL shaking flasks with a working volume of 10 mL. The reactions were performed at 30 °C and 200 rpm using a rotary shaker. All of the experiments were conducted in triplicate.

Biotransformation of GA to 2KGA. Biotransformation of GA to 2KGA was performed in a 7 L fermenter with a working volume of 1.5 L at 30 °C and 600 rpm, with the pH maintained at 5.8 using NaOH. The *G. oxidans* cells were cultivated for 22−24 h, after which the cells were collected by centrifugation at 7 000 rpm for 20 min. The reaction solutions contained 30 g CWW/L resting cells and 320 or 480 g/L GA. Filtered air was injected at a flow rate of 8 L/min to provide dissolved oxygen for the reaction.

Quantification of GA and 2KGA. Quantification of GA and 2KGA was performed using high-performance liquid chromatography (HPLC). The substances were separated using an ICSep COREGEL-87H3 column (Transgenomic, New Haven, CT, United States) at 35 °C, using 0.008 N H_2SO_4 as the mobile phase at a flow rate of 0.35 mL/min, with UV absorption evaluated at 210 nm.

RESULTS AND DISCUSSION

Construction of Mutant Derivatives of Plasmid pBBR1MCS-5. The plasmid used as the template for mutagenesis was the broad-host-range vector pBBR1MCS-5,[18] which has been used to express genes of interest in *Acetobacter* and *Gluconobacter* strains.[24−28]

The replication control region of pBBR-based plasmids is the *rep* gene.[29,30] Tao et al. performed localized random mutagenesis in the replication control region of a pBBR-based plasmid pBHR1 and showed that single amino acid change of serine to leucine at codon 100 of the replication protein and single nucleotide change of C to T at 46 bp upstream of the rep gene caused the increase of plasmid copy number by 3−7 fold.[31] The promoter and the ribosome binding site located in the upstream region of *rep* gene regulate the expression of *rep* gene. Thus, based on the pBBR1MCS-5, the mutant plasmids pBBR-10, pBBR-35, and pBBR-3510 were constructed by mutagenesis of −10 and −35 promoter regions to improve the expression of *rep* (Figure 1). Plasmid pBBR-10 contained a C to T (C1707T) mutation at 86 bp upstream of the *rep* gene, generating a CATAAT to TATAAT mutation in the −10 promoter region. The plasmid pBBR-35 contained a T to A (T1689A) mutation at 104 bp upstream of the *rep* gene, generating a TTGACT to TTGACA mutation in the −35 promoter region. pBBR-3510 contained two mutations, C1707T and T1689A. These mutations made the promoter equipped with conserved −35 and −10 hexamers sequences,[32] thus increasing the promoter activity and the expression level of the *rep* gene. Jacob et al. previously observed that increasing the base complementarity of the ribosomal binding site and the 3′ end of the gene encoding the 16S rRNA enhanced the binding of the mRNA to the ribosome.[33−37] An insertion of GAA (GAA1786ins) at 7 bp upstream of the *rep* gene in pBBR1MCS-5 was generated, yielding the mutant plasmid pBBR-RBS. pBBR-RBS had a GGAGA to GGAGGAAA mutation in the ribosomal binding site of pBBR1MCS-5. A combination of mutations at −10 and −35 of the promoter region and the ribosomal binding site generated the mutant plasmids pBBR-R10, pBBR-R35, and pBBR-R31 (Figure 1). After being transformed into *G. oxidans* DSM 2003, six of the seven mutant plasmids, with the exception of pBBR-R10, were found to be capable of stable replication.

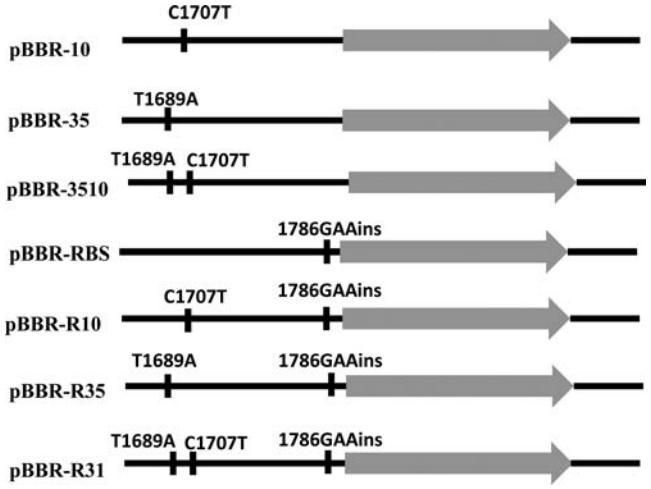

Figure 1. Maps showing the mutations created in the pBBR1MCS-5 plasmid derivatives. The mutations were numbered according to the corresponding base pair positions in pBBR1MCS-5. The nucleotides listed in front of the numbers indicate the wild-type sequences. The nucleotides listed after the numbers indicate the mutated sequences. "GAAins" after the numbers indicates that GAA was inserted at that position.

Determination of the Relative Plasmid Copy Number of the Mutant Plasmids in *G. oxidans*. The relative plasmid copy numbers were determined by qPCR using the total plasmids isolated from recombinant *G. oxidans* DSM 2003 as the templates. The cryptic plasmid pGOX3,[9] which is a low copy-number plasmid in *G. oxidans* with a large size of 14 547 bp, was used as the internal single-copy reference.[21] The relative plasmid copy numbers were calculated from the threshold cycle (C_T) using the $2^{\Delta CT}$ method as described by Zhang et al.[21] The C_T values are calculated automatically by the instrument according to the amplification plot, while ΔC_T is the difference between the C_T value of the single-copy reference and that of the plasmids. The results showed that the relative plasmid copy numbers of pBBR1MCS-5, pBBR-10, pBBR-35, pBBR-RBS, pBBR-R35, pBBR-3510, and pBBR-R31 in *G. oxidans* were 24 ± 6, 37 ± 8, 43 ± 8, 28 ± 8, 59 ± 5, 36 ± 7, and 43 ± 3 greater than that of pGOX3, respectively, demonstrating that the plasmid copy numbers of all the engineered plasmids in *G. oxidans* were higher than that of pBBR1MCS-5 plasmid (Table 2). The copy numbers of the plasmid derivatives with mutations in the −10 or/and −35 region were increased by 50−104% compared to the copy number of the control plasmid. A single insertion of GAA at nucleotide 1786 of pBBR1MCS-5 had little effect on plasmid copy number.

Overexpression of the *ga2dh* Gene in *G. oxidans* Using Different Mutant Vectors. To demonstrate the utility of the mutant plasmids for engineering *G. oxidans*, the key enzyme involved in 2KGA formation, GA2DH, was overexpressed in *G. oxidans* DSM 2003 using the mutant vectors

DOI: 10.1021/acs.jafc.5b01652
J. Agric. Food Chem. 2015, 63, 5492−5498

Table 2. Results of the Quantification of Relative Plasmid Copy Number in *G. oxydans* DSM 2003 Using Real-Time PCR[a]

plasmid	C_T-pGOX3	C_T-pBBR	relative copy number	ratio
pBBR1MCS-5	19.01 ± 0.22	14.42 ± 0.09	24 ± 6	1 ± 0.24
pBBR-10	19.63 ± 0.12	14.44 ± 0.10	37 ± 8	1.54 ± 0.33
pBBR-35	19.22 ± 0.06	13.79 ± 0.17	43 ± 8	1.79 ± 0.33
pBBR-RBS	20.53 ± 0.01	15.73 ± 0.36	28 ± 8	1.17 ± 0.33
pBBR-R35	19.82 ± 0.07	13.94 ± 0.04	59 ± 5	2.50 ± 0.21
pBBR-3510	20.15 ± 0.18	14.98 ± 0.08	36 ± 7	1.50 ± 0.29
pBBR-R31	19.94 ± 0.01	14.53 ± 0.10	43 ± 3	1.79 ± 0.13

[a]The $2^{\Delta CT}$ method was used for quantitation. Plasmid pBBR1MCS-5 was used as the control sample. The relative copy numbers were determined by comparing the value of the plasmids to that of the cryptic plasmid pGOX3. Ratio refers to the ratio of the copy number of plasmids to that of pBBR1MCS-5.

under the control of the *G. oxidans tuf B* promoter, which has been widely used in *G. oxidans*.[25−27] The parental plasmid pBBR1MCS-5 was used as the control for *ga2dh* expression. The relative copy numbers of plasmids harboring *ga2dh* gene in *G. oxidans* were also detected. As shown in Table 3, the

Table 3. Results of the Relative Copy Number of Plasmids Harboring *ga2dh* Gene Using Real-Time PCR[a]

plasmid	C_T-pGOX3	C_T-pBBR	relative copy number	ratio
pBBR-ga2dh	15.91 ± 0.03	11.96 ± 0.05	15 ± 1	1.00 ± 0.07
pBBR-10-ga2dh	15.77 ± 0.34	11.24 ± 0.10	23 ± 8	1.53 ± 0.54
pBBR-35-ga2dh	17.23 ± 0.12	12.14 ± 0.19	34 ± 8	2.27 ± 0.53
pBBR-RBS-ga2dh	15.56 ± 0.06	11.11 ± 0.03	22 ± 1	1.47 ± 0.06
pBBR-R35-ga2dh	15.47 ± 0.13	10.17 ± 0.05	39 ± 6	2.60 ± 0.40
pBBR-3510-ga2dh	15.01 ± 0.03	9.48 ± 0.11	46 ± 5	3.07 ± 0.33
pBBR-R31-ga2dh	15.13 ± 0.14	10.24 ± 0.11	30 ± 5	2.00 ± 0.33

[a]The $2^{\Delta CT}$ method was used for quantitation. Plasmid pBBR-ga2dh was used as the control sample. The relative copy numbers were determined by comparing the value of plasmids to that of the cryptic plasmid pGOX3. Ratio refers to the ratio of the copy number of plasmids to that of pBBR-ga2dh.

plasmids copy numbers were affected by *ga2dh* overexpression, and the relative plasmid copy numbers of mutant plasmids harboring *ga2dh* gene were higher than that of pBBR-ga2dh, which was similar to the result of empty vectors. However, instead of pBBR-R35-ga2dh, the copy number of plasmid pBBR-3510-ga2dh (46 ± 5) was the highest, increased by 207% compared to that of pBBR-ga2dh (15 ± 1).

To validate the relative transcription level of the *ga2dh* gene between the recombinant *G. oxidans* strains harboring the various plasmids, the *ga2dh* mRNA levels were assessed using real-time PCR. Using 16S rRNA as the internal standard, it was clearly demonstrated that the highest abundance of *ga2dh* transcripts was observed in the *G. oxidans*/pBBR-3510-ga2dh strain, which was approximately 22-fold higher than that of the control strain *G. oxidans*/pBBR1MCS and approximately 6-fold higher than that of the *G. oxidans*/pBBR-ga2dh strain (Figure 2).

GA2DH is a membrane-bound protein and is responsible for the oxidation of GA to 2KGA. Membrane fractions of different

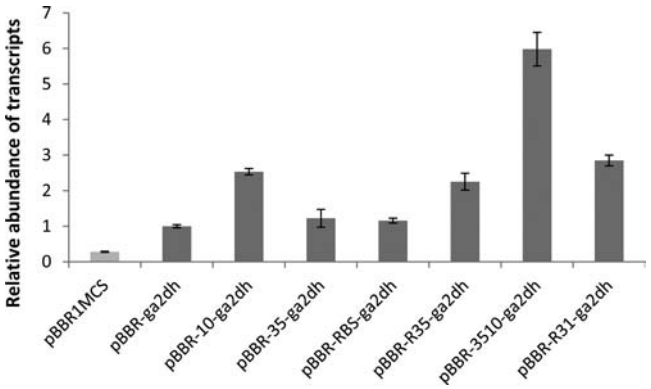

Figure 2. Relative abundance of *ga2dh* transcripts in the different *G. oxidans* strains. All of the cells were cultured in sorbitol-containing medium for 22 h and were harvested for total RNA isolation. The relative transcription levels of the *ga2dh* gene were determined using real-time PCR. The values were compared to that of the strain *G. oxidans*/pBBR-ga2dh.

G.oxidans strains were prepared and used to determine the GA2DH activities toward GA. As shown in Table 4, compared

Table 4. Activities of the Membrane-Bound GA2DH of Different *G. oxydans* Strains[a]

strains	GA2DH activity (U/mg protein)
G. oxidans/pBBR1MCS	0.43 ± 0.06
G. oxidans/pBBR-ga2dh	1.28 ± 0.09
G. oxidans/pBBR-10-ga2dh	1.60 ± 0.11
G. oxidans/pBBR-35-ga2dh	2.10 ± 0.10
G. oxidans/pBBR-3510-ga2dh	3.95 ± 0.07
G. oxidans/pBBR-RBS-ga2dh	1.97 ± 0.28
G. oxidans/pBBR-R35-ga2dh	3.35 ± 0.23
G. oxidans/pBBR-R31-ga2dh	2.90 ± 0.11

[a]Each value represents the average value and standard deviation of three independent experiments.

to the strain *G. oxidans*/pBBR-ga2dh, the GA2DH activities of the obtained constructs using the mutant vectors were increased. Among these strains, *G. oxidans*/pBBR-3510-ga2dh displayed the highest GA2DH activity (3.95 ± 0.07 U/mg protein).

The seven recombinant strains were used to catalyze GA in shaking flasks, and their 2KGA production in 2 h were determined to compare their productivities of 2KGA. The 2KGA concentration achieved by the *G. oxidans* strain containing pBBR1MCS-5 was set as the control value. As shown in Figure 3, all of the *ga2dh*-overexpressing strains

DOI: 10.1021/acs.jafc.5b01652
J. Agric. Food Chem. 2015, 63, 5492−5498

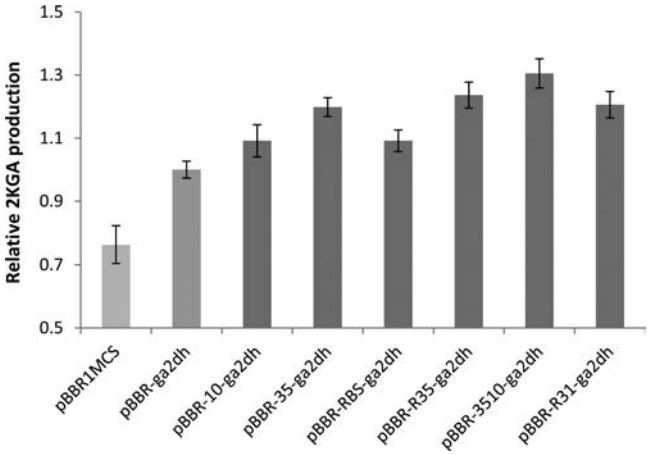

Figure 3. Levels of 2KGA production by *G. oxidans* strains containing various plasmids. The catalytic reactions were performed under the same conditions. The values were compared to that of the strain *G. oxidans*/pBBR-ga2dh.

produced concentrations of 2KGA higher than that of the control strain (*G. oxidans*/pBBR1MCS). More 2KGA was produced by the recombinant strains containing mutant plasmids compared to the 2KGA production of *G. oxidans*/pBBR-ga2dh. Among these strains, *G. oxidans*/pBBR-3510-ga2dh exhibited the highest level of 2KGA production, corresponding to the highest relative transcription level of the *ga2dh* gene and highest GA2DH activity.

Biotransformation of GA to 2KGA by the Recombinant *G. oxidans*/pBBR-3510-ga2dh Strain. To assess the potential industrial use of *G. oxidans*/pBBR-3510-ga2dh, which exhibited the greatest increase in 2KGA production, scaled-up biotransformation of GA was performed in a 7 L fermenter with a continuous air supply. The reaction system contained 30 g CWW/L resting cells and 320 g/L GA. To exclude the effects of the empty vector, *G. oxidans*/pBBR1MCS was also included in the analysis. The level of 2KGA production by the three *G. oxidans* strains harboring pBBR-3510-ga2dh, pBBR-ga2d, or pBBR1MCS-5 is summarized in Figure 4. Time course analysis of GA oxidation by *G. oxidans*/pBBR-3510-ga2dh revealed that approximately 320 g/L 2KGA accumulated from 320 g/L GA in 17 h, generating a productivity of 0.63 g/g CWW/h. In contrast, the *G. oxidans*/pBBR-ga2dh and *G. oxidans*/pBBR1MCS strains required more time to complete this reaction, leading to the productivities of 0.40 g/g CWW/h and 0.22 g/g CWW/h, respectively.

Thus, the overexpression of *ga2dh* in *G. oxidans* with the mutant plasmid pBBR-3510 significantly accelerated the oxidative reaction and resulted in increased 2KGA production, which was enhanced by approximately 58% and 186% compared to that of *ga2dh*-overexpressing *G. oxidans* harboring the control plasmid pBBR1MCS-5 or the parental strain containing the empty vector, respectively.

When the initial GA concentration was increased to 480 g/L, 30 g CWW/L of resting *G. oxidans*/pBBR-3510-ga2dh cells still completely exhausted the supplied GA and produced 474 g/L 2KGA when a continuous air supply was provided, although the conversion time was extended to 96 h, corresponding to a productivity of 0.16 g/g CWW/h (Figure 5). This reaction could not be completed by the *G. oxidans*/pBBR1MCS or the *G. oxidans*/pBBR-ga2dh strain (data not shown). In addition to substrate or product inhibition, we observed that an insufficient

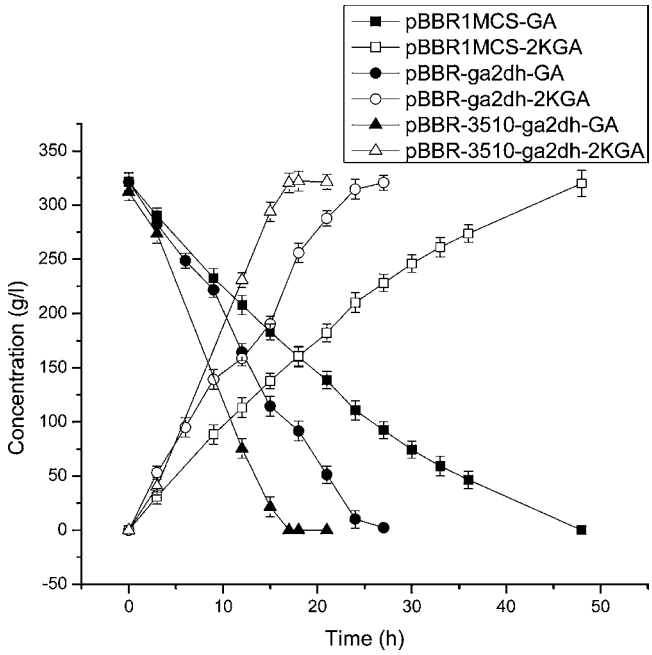

Figure 4. Comparative 2KGA production and GA consumption of *G. oxidans*/pBBR1MCS, *G. oxidans*/pBBR-ga2dh, and *G. oxidans*/pBBR-3510-ga2dh in a 7 L fermenter supplied with 320 g/L GA.

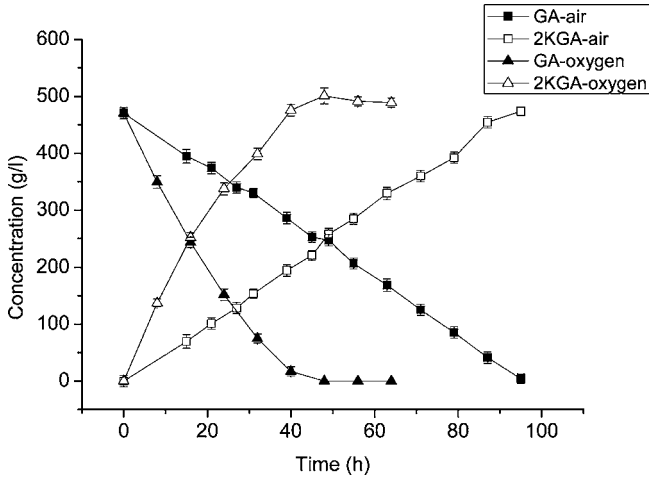

Figure 5. Time course of the oxidation of GA by the engineered strain *G. oxidans*/pBBR-3510-ga2dh.

oxygen supply had a negative impact on the performance of *G. oxidans*/pBBR-3510-ga2dh. During the entire reaction process, the DO level in the fermenter remained less than zero despite the fact that the agitation speed and aeration rate were maintained as high as possible. Thus, oxygen instead of air was supplied continuously to support the oxidation of 480 g/L GA. As expected, 45 h after initiating the reaction, nearly all of the supplied GA had been exhausted by *G. oxidans*/pBBR-3510-ga2dh and approximately 486 g/L 2KGA had been accumulated, corresponding to a productivity of 0.36 g/g CWW/h. Compared to the results of previous studies,[8] the *G. oxidans*/pBBR-3510-ga2dh strain created in this study showed the highest level of 2KGA production and a relatively high productivity level.

DOI: 10.1021/acs.jafc.5b01652
J. Agric. Food Chem. 2015, 63, 5492−5498

AUTHOR INFORMATION

Corresponding Author

*No. 130 Meilong Road, East China University of Science and Technology, Shanghai 200237, China. Tel.: +86-2164252981. Fax: +86-2164250068. E-mail: jplin@ecust.edu.cn.

Author Contributions

‖Y.S. and K.L.: these authors contributed equally.

Funding

This study was financially supported by the National Key Basic Research Development Program of China (Grant 2012CB721003), the Natural Science Foundation of China (Grant 21276084), the Shanghai Natural Science Foundation (Grant 15ZR1408600), the National Major Science and Technology Projects of China (Grant 2012ZX09304009), and the Fundamental Research Funds of the Central Universities.

Notes

The authors declare no competing financial interest.

ABBREVIATIONS

GA, gluconic acid; 2KGA, 2-keto-D-gluconic acid; *ga2dh*, gluconate-2-dehydrogenase; HPLC, high-performance liquid chromatography; CWW, cell wet weight

REFERENCES

(1) Chia, M.; Nguyen, T. B. V.; Choi, W. J. DO-stat fed-batch production of 2-keto-D-gluconic acid from cassava using immobilized *aeruginosa*. *Appl. Microbiol. Biotechnol.* **2008**, *78*, 759−765.

(2) Rehwoldt, R. Tracking the use of antioxidants through industry surveys. *Food Chem. Toxicol.* **1986**, *24*, 1039−1041.

(3) Sun, W.; Yun, Q.; Zhou, Y.; Cui, F.; Yu, S.; Zhou, Q.; Sun, L. Continuous 2-keto-gluconic acid (2KGA) production from corn starch hydrolysate by *Pseudomonas fluorescens* AR4. *Biochem. Eng. J.* **2013**, *77*, 97−102.

(4) Kulka, D.; Hall, A. N.; Walker, T. K. Formation of 2-keto-D-gluconic acid, 5-keto-D-gluconic acid, and tartronic acid by acetobacter species. *Nature* **1951**, *167*, 905−906.

(5) Minisenhermer, T. J.; Anderson, R. F.; Lagoda, A. A.; Tyler, D. Production of 2-ketogluconic acid by *Serratia marcescens*. *Appl. Microbiol.* **1965**, *13*, 393−396.

(6) Wei, D.; Xu, J.; Sun, J.; Shi, J.; Hao, J. 2-Ketogluconic acid production by *Klebsiella pneumonia* CGMCC 1.6366. *J. Ind. Microbiol. Biotechnol.* **2013**, *40*, 561−570.

(7) Teng, W.; Sun, W.; Yu, B.; Cui, F.; Qian, J.; Wang, L.; Qi, X.; Wei, H. Continuous conversion of rice starch hydrolysate to 2-keto-D-gluconic acid by *Arthrobacter globiformis* C224. *Biotechnol. Bioprocess Eng.* **2013**, *18*, 709−714.

(8) Sun, W.; Zhou, Y.; Zhou, Q.; Cui, F.; Yu, S.; Sun, L. Semi-continuous production of 2-keto-gluconic acid by *Pseudomonas fluorescens* AR4 from rice starch hydrolysate. *Bioresour. Technol.* **2012**, *110*, 546−551.

(9) Prust, C.; Hoffmeister, M.; Liesegang, H.; Wiezer, A.; Fricke, W. F.; Ehrenreich, A.; Gottschalk, G.; Deppenmeier, U. Complete genome sequence of the acetic acid bacterium *Gluconobacter oxydans*. *Nat. Biotechnol.* **2005**, *23*, 195−200.

(10) Gupta, A.; Singh, V. K.; Qazi, G. N.; Kumar, A. *Gluconobacter oxydans*: its biotechnological applications. *J. Mol. Microbiol. Biotechnol.* **2001**, *3*, 445−456.

(11) Deppenmeier, U.; Hoffmeister, M.; Prust, C. Biochemistry and biotechnological applications of *Gluconobacter* stains. *Appl. Microbiol. Biotechnol.* **2002**, *60* (3), 233−242.

(12) Macauley, S.; McNeil, B.; Harvey, L. M. The genus *Gluconobacter* and its applications in biotechnology. *Crit. Rev. Biotechnol.* **2001**, *21*, 1−25.

(13) Matsushita, K.; Toyama, H.; Adachi, O. Respiratory chains and bioenergetics of acetic acid bacteria. *Adv. Microb. Physiol.* **1994**, *36*, 247−301.

(14) Hölscher, T.; Schleyer, U.; Merfort, M.; Bringer-Meyer, S.; Görisch, H.; Sahm, H. Glucose oxidation and PQQ-dependent dehydrogenases in *Gluconobacter oxydans*. *J. Mol. Microbiol. Biotechnol.* **2009**, *16*, 6−13.

(15) Chen, H.; Li, K.; Shu, X.; Liu, L.; Lin, J.; Wei, D. High-yield production of 2-keto-D-gluconate by resting cells of *Gluconobacter oxydans*. *Sci. Technol. Food Ind.* **2012**, *19*, 177−181 (in Chinese).

(16) Schleyer, U.; Bringer-Meyer, S.; Sahm, H. An easy cloning and expression vector system for *Gluconobacter oxydans*. *Int. J. Food Microbiol.* **2008**, *125*, 91−95.

(17) Kallnik, V.; Meyer, M.; Deppenmeier, U.; Schweiger, P. Construction of expression vectors for protein production in *Gluconobacter oxydans*. *J. Biotechnol.* **2010**, *150*, 460−465.

(18) Kovach, M. E.; Elzer, P. H.; Hill, D. S.; Robertson, G. T.; Farris, M. A.; Roop, R. M., II; Peterson, K. M. Four new derivatives of the broad-host-range cloing vector pBBR1MCS, carrying different antibiotic-resistance cassettes. *Gene* **1995**, *166*, 175−176.

(19) Sambrook, J.; Fritsch, E. F.; Maniatis, T. *Molecular Cloning: A Laboratory Manual*, 2nd ed.; Cold Spring Harbor Laboratory Press: Cold Spring Harbor, NY. 1989.

(20) Hölscher, T.; Görisch, H. Knockout and overexpression of pyrroloquinoline quinone biosynthetic genes in *Gluconobacter oxydans* 621H. *J. Bacteriol.* **2006**, *188*, 7668−7676.

(21) Zhang, L.; Lin, J.; Ma, Y.; Wei, D.; Sun, M. Construction of a novel shuttle vector for use in *Gluconobacter oxydans*. *Mol. Biotechnol.* **2010**, *46*, 227−233.

(22) Sugisawa, T.; Hoshino, T. Purification and properties of membrane-bound D-sorbitol dehydrogenase from *Gluconobacter suboxydans* IFO 3255. *Biosci., Biotechnol., Biochem.* **2002**, *66*, 57−64.

(23) Bradford, M. M. A rapid and sensitive method for quantitation of microgram quantities of protein utilizing the principle of protein-dye binding. *Anal. Biochem.* **1976**, *72*, 248−254.

(24) Merfort, M.; Herrman, U.; Ha, S. W.; Elfari, M.; Bringer-Meyer, S.; Görisch, H.; Sahm, H. Modification of the membrane-bround glucose oxidation system in *Gluconobacter oxydans* significantly increases gluconate and 5-keto-D-gluconic acid accumulation. *Biotechnol. J.* **2006**, *1*, 556−563.

(25) Merfort, M.; Herrman, U.; Bringer-Meyer, S.; Sahm, H. High-yield 5-keto-D-gluconic acid formation is mediated by soluble and membrane-bound gluconate-5-dehydrogenases of *Gluconobacter oxydans*. *Appl. Microbiol. Biotechnol.* **2006**, *73*, 443−451.

(26) Li, M.; Wu, J.; Liu, X.; Lin, J.; Wei, D. Enhanced production of dihydroxyacetone from glycerol by overexpression of glycerol dehydrogenase in an alcohol dehydrogenase- deficient mutant of *Gluconobacter oxydans*. *Appl. Microbiol. Biotechnol.* **2010**, *101*, 8294−8299.

(27) Zhang, J.; Li, S.; Xu, H.; Zhou, P.; Zhang, L.; Ouyang, P. Purification of xylitol dehydrogenase and improved production of xylitol by increasing XDH activity and NADH supply in *Gluconobacter oxydans*. *J. Agric. Food Chem.* **2013**, *61*, 2861−2867.

(28) Gätgens, C.; Degner, U.; Bringer-Meyer, S.; Herrmann, U. Biotransformation of glycerol to dihydroxyacetone by recombinant *Gluconobacter oxydans* DSM 2343. *Appl. Microbiol. Biotechnol.* **2007**, *76*, 553−559.

(29) Antoine, R.; Locht, C. Isolation and molecular characterization of a novel broad-host-range plasmid from *Bordetalla bronchiseptica* with sequence similarities to plasmids from Gram-positive organisms. *Mol. Microbiol.* **1992**, *6*, 1785−1799.

(30) Kovach, M. E.; Phillips, R. W.; Elzer, P. H.; Roop, R. M., II; Peterson, K. M. pBBR1MCS: a broad-host-range cloning vector. *Biotechniques* **1994**, *16*, 800−802.

(31) Tao, L.; Jackson, R. E.; Cheng, Q. Directed evolution of copy number of a broad host range plasmid for metabolic engineering. *Metab. Eng.* **2005**, *7*, 10−17.

DOI: 10.1021/acs.jafc.5b01652
J. Agric. Food Chem. 2015, 63, 5492−5498

(32) Grana, D.; Youderian, P.; Susskind, M. M. Mutations that improve the *ANT* promoter of Salmonella phage P22. *Genetics* **1985**, *110*, 1−16.
(33) Jacob, W. F.; Santer, M.; Dahlberg, A. E. A single base change in the Shine-Dalgarno region of 16S rRNA of *Escherichia coli* affects translation of many proteins. *Proc. Natl. Acad. Sci. U. S. A.* **1987**, *84*, 4757−4761.
(34) Calogero, R. A.; Pon, C. L.; Canonaco, M. A.; Gualerzi, C. O. Selection of the mRNA translation initiation region by *Escherichia coli* ribosomes. *Proc. Natl. Acad. Sci. U. S. A.* **1988**, *85*, 6427−6431.
(35) Gold, L.; Pribnow, D.; Schneider, T.; Shinedling, S.; Swebillius, S. B.; Stormo, G. D. Translation initiation in prokaryotes. *Annu. Rev. Microbiol.* **1981**, *35*, 365−403.
(36) Thanaraj, T. A.; Pandit, M. W. An additional ribosomal-binding site on mRNA of highly expressed genes and a bifunctional site on the colicin fragment of 16S rRNA from *Escherichia coli*: important determinants of efficiency of translation- initation. *Nucleic Acids Res.* **1989**, *17*, 2973−2985.
(37) Kozak, M. Comparison of initiation of protein synthesis in prokaryotes, eukaryotes, and organelles. *Microbiol. Rev.* **1983**, *47*, 1−45.

DOI: 10.1021/acs.jafc.5b01652
J. Agric. Food Chem. 2015, 63, 5492−5498

list of compounds for which methods of analysis are standardized and authorized by the International Olive Council (IOC).[30] Their response to even some of the most influential sources of variability is practically unknown. Only a few reports studying their intervarietal variability have been published, focusing only on particular major compounds.[27,28,31] No experimental evidence on the effect of ripening on 4-monomethyl- and 4,4′-dimethylsterols in olive oil can be found in available literature; to date, only their behavior in olive fruit has been investigated,[2,3] which can differ significantly. There are no published data on the interdependence and the interactive effect of variety and ripening on 4-monomethyl- and 4,4′-dimethylsterol concentrations. Among the olive oil research and expert community, investigations on indicators of olive oil aging are the focus of interest, mainly because olive oil quality deteriorates with storage, which is directly related to its market categorization and price. Such research is currently in full swing[32] but not a single study to date has addressed the effect of storage temperature and storage in general on the contents of 4-monomethyl- and 4,4′-dimethylsterols in any vegetable oils.

The aim of this study was to investigate the variability of the contents of major 4-monomethyl- and 4,4′-dimethylsterols in olive oil as a result of three key factors, variety, ripening degree, and storage, including the effect of storage temperature. Besides providing new knowledge about the chemistry of olive oil and its important constituents in general, the objective was to assess whether 4-monomethyl- and 4,4′-dimethylsterols have the potential for satisfactory multivariate discrimination and could be used as indicators for each of the mentioned factors of variability. Reliable and stable indicators among these constituents could contribute to the ever-growing scientific area of research on olive oil quality and authenticity and could be used for more reliable characterization, differentiation, authentication, and certification of olive oils of specific origin and attributes. It is expected that the results obtained in this work could have practical application and be useful for producers to optimize individual steps in production to obtain olive oils with targeted 4-monomethyl- and 4,4′-dimethylsterol composition.

MATERIALS AND METHODS

Sampling and Harvesting. Three important autochthonous varieties in the Istria region of Croatia were chosen for the investigation: Buža, Črna, and Rosinjola. In the crop year 2006/2007, nonirrigated trees were identified and carefully marked on different plots located in the corresponding characteristic production zone of each variety. The plots were located in the region of Istria (Croatia) within a radius of approximately 18 km and were characterized by similar pedoclimatic conditions.

Olives were harvested at three ripening degrees denoted as green (RD1), spotted (RD2), and ripe (RD3). For Buža variety, ripening indexes were 1.4, 2.8, and 3.8; for Črna, 1.9, 2.8, and 4.1; and for Rosinjola, 1.5, 3.2, and 3.8, respectively. Each batch of olive fruits giving a single olive sample comprised olives handpicked from three single trees of a given variety at the determined stage of ripeness. Ripening index (RI) was determined from 100 olive fruits, randomly taken from each olive fruit batch. This parameter is a function of fruit color in both skin and pulp and was determined according to Beltrán et al.[33]

Oil Extraction. Each oil sample was extracted from approximately 100 kg of olive fruits transported to the mill immediately after harvest and processed within 24 h. Oils were obtained by the continuous cold automatic olive oil extraction system Oliomio Cultivar 500 (Toscana Enologica Mori Snc., Italy). Olives were washed and crushed with a stainless steel hammer crusher. For each sample, the olive paste was transported to the vertical unit where it was malaxed for 35 ± 2 min at a temperature below 27 °C. Oils were obtained by separation in a horizontal two-phase centrifuge. Oils were filtered through cotton wool to eliminate larger impurities. Samples were stored in amber glass 125 mL bottles. Nine oil samples, representing combinations of three varieties and three ripening degrees, were analyzed within a month of oil extraction (fresh oil samples).

Storage Conditions. In total, 27 oil samples representing each variety/ripening degree combination were stored in the dark for a period of 12 months under three different temperature conditions. Besides variable room temperature (VR, 10−28 °C), which was supposed to simulate common stock and domestic conditions, refrigeration (RE, 4 °C) and freezing (FR, −20 °C) temperatures, which are usually applied for conservation of various other foodstuffs and were recently found to preserve olive oil quality,[34] were also included. Stored samples were analyzed within a month after the 12 month storage period.

Extraction of 4-Monomethylsterols and 4,4′-Dimethylsterols. 4-Monomethylsterol and 4,4′-dimethylsterol analysis was conducted according to the method proposed by IOC[30] and the modified method for the determination of aliphatic alcohols adopted by EEC regulations.[35] Five grams of olive oil was added to 1-eicosanol (5 mg/100 g of olive oil) (Supelco, Bellefonte, PA), used as internal standard, and were saponified with 50 mL of potassium hydroxide ethanolic solution. After the sample was boiled, 50 mL of distilled water was added, the flask was cooled to approximately 30 °C, and the content was quantitatively transferred to a 500 mL separating funnel by use of distilled water portions of a total volume of 50 mL. The extraction of unsaponifiable fraction was carried out with three portions of diethyl ether (80 mL + 70 mL + 70 mL) by vigorous shaking. The ethyl ether extracts were combined in a separating funnel and washed with distilled water (50 mL at a time) until the washing water gave a neutral reaction. Following purification with water and drying over sodium sulfate, diethyl ether was evaporated under vacuum and nitrogen and then completing drying in an oven at 100 °C for 15 min. Unsaponifiable fraction was dissolved in chloroform, and approximately 20 mg was loaded on a basic silica thin-layer chromatography (TLC) plate (Fluka, Buchs, Switzerland). The 4-monomethylsterol and 4,4′-dimethylsterol fraction (the sum of free and esterified forms without glycosides) was separated by elution with a mixture of hexane and diethyl ether (65:35 v/v). The corresponding bands were visualized under UV light after being sprayed with 2′,7′-dichlorofluorescein 0.2% ethanolic solution, then scraped off with a spatula and extracted with chloroform and diethyl ether. After the extract was evaporated to dryness, 4-monomethylsterols and 4,4′-dimethylsterols were converted to trimethylsilyl ethers by addition of pyridine/hexamethyldisilizane/trimethylchlorosilane (9:3:1 v/v/v) (Supelco, Bellefonte, PA), left for 15 min, and then centrifuged at 3500 rpm for 5 min.

Identification of 4-Monomethyl- and 4,4′-Dimethylsterols. Identification of 4-monomethyl- and 4,4′-dimethylsterols as trimethylsilyl ethers was carried out by gas chromatography/mass spectrometry (GC-MS) on a Varian 3900 gas chromatograph coupled with a Varian Saturn 2100T ion trap mass spectrometer (Varian Inc., Harbour City, CA). The fused silica column used was a 30 m × 0.25 mm i.d. × 0.25 μm film thickness Varian VF-5 ms capillary column (5% phenylpolysiloxane/95% dimethylpolysiloxane). Injector temperature was 280 °C. The GC oven parameters were as follows: initial temperature was 180 °C, increased at 2 °C/min to 280 °C, and then kept at 280 °C (total run time approximately 65 min). Transfer line, manifold, and ion trap temperatures were 285, 80, and 220 °C, respectively. Helium was used as a carrier gas with a constant flow of 1.2 mL/min. One microliter of the analytical sample was injected in split mode (1:50). Mass spectra were acquired in the electron impact mode (70 eV) at 1 scan/s, using full scan with a mass acquisition range of 30−650 m/z. Identification of compounds was performed by careful interpretation of retention data and mass spectra and by comparisons with retention and mass spectral data from the literature[1,5,6,8−13,36−39] and NIST05 library when available (trimethylsilyl ethers or acetates).

DOI: 10.1021/acs.jafc.5b01638
J. Agric. Food Chem. 2015, 63, 5499−5508

Table 1. Retention Time and Mass Spectrometric Data[a]

compd	t_R, min	major and characteristic ions, m/z (relative intensity)
		4-Monomethylsterols
obtusifoliol	49.83	41 (32), 67 (25), 69 (30), 73 (38), 75 (30), 81 (30), 95 (38), 109 (32), 189 (43), 227 (36), 393 (100), 394 (29), 483 (33), 498 (14)
gramisterol + cycloeucalenol	51.45	55 (28), 69 (22), 73 (50), 75 (40), 105 (31), 121 (18), 159 (31), 227 (30), 241 (43), 267 (40), 269 (20), 357 (81),, 379 (25), 393 (23), 394 (20), 407 (100), 408 (34), 469 (16), 483 (6), 484 (7), 498 (12), 512 (8)
citrostadienol	55.52	55 (19), 73 (15), 75 (15), 145 (11), 227 (10), 241 (7), 267 (40), 295 (12), 310 (8), 357 (100), 358 (29), 393 (10), 400 (17), 408 (3), 483 (5), 498 (2)
		4,4′-Dimethylsterols
δ-amyrin	49.48	69 (30), 73 (65), 75 (56), 95 (62), 109 (54), 121 (65), 135 (42), 147 (48), 189 (100), 190 (39), 203 (49), 204 (81), 218 (35), 269 (93), 284 (38), 359 (32), 393 (32), 483 (8), 498 (5)
β-amyrin	50.20	73 (23), 75 (17), 95 (15), 119 (14), 135 (10), 147 (14), 189 (41), 190 (17), 203 (100), 204 (17), 218 (40), 393 (4), 483 (2), 498 (1)
butyrospermol	50.88	41 (15), 69 (19), 73 (20), 75 (14), 81 (14), 95 (13), 109 (14), 241 (18), 393 (100), 394 (30), 483 (10), 498 (4)
cycloartenol	52.12	41 (36), 69 (45), 73 (43), 95 (38), 109 (31), 189 (19), 271 (9), 339 (35), 365 (49), 393 (100), 394 (30), 408 (17), 483 (8), 498 (3)
24-methylenecycloartanol	53.94	55 (31), 69 (63), 73 (65), 81 (50), 95 (70), 107 (58), 109 (50), 135 (50), 147 (52), 269 (24), 297 (22), 353 (44), 379 (83), 407 (100), 408 (30), 422 (28), 497 (8), 512 (2)

[a]For trimethylsilyl ethers of 4-monomethylsterols and 4,4′-dimethylsterols identified in olive oils by GC-MS analysis.

The obtained retention time and mass spectrometric data for the corresponding trimethylsilyl ethers are reported in Table 1. Four major 4-monomethylsterols (obtusifoliol, gramisterol + cycloeucalenol, and citrostadienol) and five major 4,4′-dimethylsterols (δ-amyrin, β-amyrin, butyrospermol, cycloartenol, and 24-methylenecycloartanol) were identified. The identity of β-amyrin and cycloartenol was confirmed by comparison of their retention times and mass spectra to those of pure standards [β-amyrin analytical standard, ≥98.5%, Fluka (Buchs, Switzerland); cycloartenol, ≥90.0%, Sigma–Aldrich (St. Louis, MO)], which were the only standards of 4-monomethyl- and 4,4′-dimethylsterols analyzed in this work commercially available.

Quantitative Determination of 4-Monomethyl- and 4,4′-Dimethylsterols. Quantitative determination of 4-monomethyl- and 4,4′-dimethylsterols as trimethylsilyl ethers was carried out by capillary gas chromatography with flame ionization detection (GC-FID) on a Varian 3350 GC (Varian Inc., Harbour City, CA) equipped with the same column described above. Injector and oven were the same as described above, while detector temperature was 290 °C, for approximately 65 min. Helium was used as a carrier gas with a flow rate of 1.27 mL/min. One microliter was injected in split mode (1:50). A typical GC-FID chromatogram of 4-monomethyl- and 4,4′-dimethylsterols as trimethylsilyl ethers is presented in Figure 1. 4-Monomethyl- and 4,4′-dimethylsterol concentrations were expressed as milligrams per 100 g of internal standard, with an assumed response factor equal to 1. Relative amounts of individual compounds were expressed as percentages of total 4-monomethyl- + 4,4′-dimethylsterol peak area (all nine compounds).

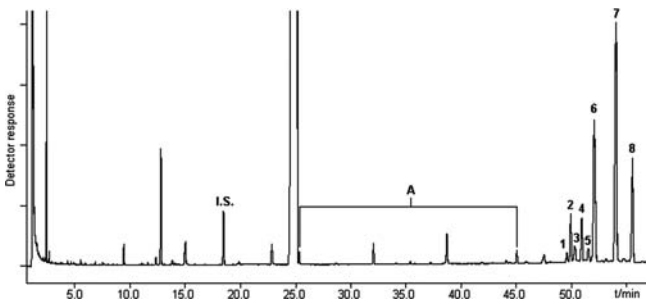

Figure 1. GC-FID chromatogram of trimethylsilyl ethers of 4-monomethyl- and 4,4′-dimethylsterols in Buža olive oil (green olives, RD1). Peak identification: I.S., internal standard (1-eicosanol); A, aliphatic alcohols; 1, δ-amyrin; 2, obtusifoliol; 3, β-amyrin; 4, butyrospermol; 5, gramisterol + cycloeucalenol; 6, cycloartenol; 7, 24-methylenecycloartanol; 8, citrostadienol.

Analyses were performed in duplicate, and average values were used in further data elaboration. The precision of the method was high, with relative standard deviations (n = 2) generally not surpassing 7% and in the case of major compounds, such as citrostadienol, butyrospermol, cycloartenol, and 24-methylenecycloartanol, not surpassing 4%.

To determine linearity, three replicate analyses of a sample spiked with three different concentrations of chemical standards of β-amyrin (2, 5, and 10 mg/100 g of oil) and cycloartenol (10, 30, and 50 mg/100 g of oil) were performed. Correlation coefficients were satisfactory: 0.997 for β-amyrin and 0.993 for cycloartenol. The same data were used for determination of recovery, which ranged from 92% to 103% with an average of 96% for β-amyrin (n = 9) and from 94% to 100% with an average of 98% for cycloartenol (n = 9).

Limits of detection (LOD) were estimated as 3 times the baseline noise and ranged from 0.056 mg/100 g for obtusifoliol to 0.092 mg/100 g for β-amyrin. Limits of quantification (LOQ) were estimated as 10 times the baseline noise and ranged from 0.185 mg/100 g for obtusifoliol to 0.306 mg/100 g for β-amyrin. Since LOD and LOQ for individual compounds change depending on FID sensitivity, average detection limits registered during method validation and analyses were reported.

Analysis of 4-Desmethylsterols. Analysis of 4-desmethylsterols was described in a previous study.[29] Only total concentrations of 4-desmethylsterols (milligrams per 100 g), obtained as the sums of concentrations of individual 4-desmethylsterols, are reported in this work.

Statistical Analysis. Duplicate analysis results were used to calculate average values, which were used in further data elaboration. Variables used for statistical analysis were average values of concentration (milligrams per 100 g) and relative amount (percent) of all analyzed compounds. These data are presented in Tables 3 and 4 without the corresponding deviations. The main-effect three-way analysis of variance (ANOVA) without replication (σ-restricted parametrization, effective hypothesis decomposition)[40] was selected to evaluate the effect of factors variety, ripening degree, and storage temperature on the content of individual and total major 4-monomethyl- and 4,4′-dimethylsterols in olive oil. The results for total 4-desmethylsterols are also presented. Because it was a nonreplicated experiment, the effects of all first- and second-order interactions were treated as random and pooled into error term. The majority of variables exhibited low variability with no statistically significant differences between means for the storage temperature factor (Table 2), so their values were not reported. Mean values for the factors variety and ripening degree are expressed together with the corresponding standard errors. Statistically significant differences were determined by Tukey's honest significant difference (HSD) posthoc analysis. Statistical significance was set at $p < 0.05$ (Tables 3 and 4).

DOI: 10.1021/acs.jafc.5b01638
J. Agric. Food Chem. 2015, 63, 5499−5508

Table 2. Results of Analysis of Variance for Olive Oils[a]

	variable factor					
	variety		ripening degree		storage condition	
compd	*F*-value	*p*-value	*F*-value	*p*-value	*F*-value	*p*-value
4-Monomethylsterols, Concentration (mg/100 g)						
obtusifoliol	13.368	0.000	4.881	0.015	2.998	0.047
gramisterol + cycloeucalenol	8.738	0.001	12.197	0.000	1.366	0.274
citrostadienol	34.851	0.000	3.801	0.035	2.826	0.057
4-Monomethylsterols, Relative Amount (%)						
obtusifoliol	2.270	0.122	39.087	0.000	5.152	0.060
gramisterol + cycloeucalenol	5.751	0.008	7.516	0.002	1.143	0.349
citrostadienol	30.543	0.000	163.903	0.000	1.112	0.361
4,4′-Dimethylsterols, Concentration (mg/100 g)						
δ-amyrin	2.731	0.083	0.684	0.513	0.571	0.638
β-amyrin	41.995	0.000	11.846	0.000	0.482	0.698
butyrospermol	38.423	0.000	0.960	0.395	0.953	0.429
cycloartenol	31.831	0.000	34.209	0.000	1.049	0.386
24-methylenecycloartanol	6.175	0.006	91.930	0.000	0.622	0.607
4,4′-Dimethylsterols, Relative Amount (%)						
δ-amyrin	0.769	0.473	45.623	0.000	0.303	0.823
β-amyrin	109.962	0.000	18.156	0.000	0.795	0.507
butyrospermol	17.361	0.000	26.116	0.000	0.018	0.997
cycloartenol	53.257	0.000	16.817	0.000	0.095	0.962
24-methylenecycloartanol	52.011	0.000	77.235	0.000	0.019	0.996
Total Concentration (mg/100 kg)						
4-monomethylsterols	31.652	0.000	4.067	0.028	1.735	0.183
4,4′-dimethylsterols	0.796	0.461	70.782	0.000	1.012	0.402

[a]Main-effect three-way analysis of variance (ANOVA) without replication for concentrations (milligrams per 100 grams) and relative amounts (percent) of 4-monomethylsterols and 4,4′-dimethylsterols in olive oils, with variety, ripening degree, and storage condition as variable factors. $p < 0.050$ is statistically significant.

Before being subjected to unsupervised (principal component analysis, PCA) and supervised (stepwise linear discriminant analysis, SLDA) multivariate statistical analysis, GC data were standardized (centered) via the autoscale procedure, in which a variable is subtracted from its mean value and the obtained difference is divided by the standard deviation of this variable throughout the data set. For the factors variety and ripening degree, unrotated PCA was carried out by use of variables selected according to their high *F*-statistic values. Kaiser's rule was followed for selection of the number of principal components (PCs), and only factors with eigenvalues higher than 1.00 were retained. PCA models with the best separation capacity are presented. For a valid statistical classification of olive oil samples into categories according to variety or ripening degree, forward SLDA was applied, with Wilk's λ as a selection criterion and an *F*-statistic factor to establish the significance of the changes when a new variable is tested. The value of *F* for a variable to enter the differentiation model was fixed at 1.00, and minimum tolerance was set at 0.01. For presentation of changes as a result of storage by SLDA, variables were previously standardized through all levels of each single subject separately (the same sample fresh and stored at three temperatures) to eliminate the effect of variety and ripening degree. In this way relative changes, expressed as an increase or a decrease, are presented.

Statistical data elaboration was carried out with Statistica v 8.0 software (Stat-Soft Inc., Tulsa, OK).

RESULTS AND DISCUSSION

Results of three-way analysis of variance (ANOVA) for individual (milligrams per 100 g and percent) and total 4-monomethyl- and 4,4′-dimethylsterols in different samples of olive oil, with variety, ripening degree, and storage condition as factors, are presented in Table 2. A significant effect of variety ($p < 0.05$) was determined for the majority of compounds. The highest *F*-statistic values were found for concentrations of *β*-amyrin, butyrospermol, citrostadienol, and cycloartenol, as well as for relative amounts of *β*-amyrin, cycloartenol, and 24-methylenecycloartanol. A significant effect of ripening degree ($p < 0.05$) with the highest *F* values was found for concentrations of 24-methylenecycloartanol and for relative amounts of citrostadienol, 24-methylenecycloartanol, and *δ*-amyrin. Total 4-monomethylsterols were found to be more affected by variety, while total 4,4′-dimethylsterols varied more significantly due to ripening degree. Evidently, variability arising from the effect of storage was much lower than that caused by the other two factors. For this reason, mean values for the storage condition factor are not reported in Tables 3 and 4 together with those for variety and ripening degree.

Variability as a Result of Olive Variety. Buža variety was found to contain the lowest concentrations and relative amounts of 4-monomethylsterols, while Rosinjola had the highest citrostadienol level (Table 3). Among 4,4′-dimethylsterols, Buža was characterized by the highest 24-methylenecycloartanol and the lowest butyrospermol levels. Rosinjola was the most abundant in *β*-amyrin and cycloartenol, and it exhibited the lowest 24-methylenecycloartanol content. The lowest content of *β*-amyrin was found in Črna oils (Table 4). The differences in total 4,4′-dimethylsterols between mean values for the investigated varieties were not significant (Table 2).

When PCA was applied on the data set comprising 36 cases (olive oil samples) and variables with the highest *F* values for the variety factor (Table 2), a model with butyrospermol (milligrams per 100 g), citrostadienol (milligrams per 100 g), *β*-amyrin (percent), and cycloartenol (percent) as variables was found to have the best separation capacity (Figure 2). Two

DOI: 10.1021/acs.jafc.5b01638
J. Agric. Food Chem. 2015, 63, 5499−5508

Table 3. Concentrations and Relative Amounts of 4-Monomethylsterols in Olive Oils[a]

	olive variety												
	Buža				Črna				Rosinjola				
ripening degree	CO	VR	RE	FR	CO	VR	RE	FR	CO	VR	RE	FR	mean (ripening degree)
Obtusifoliol Concentration (mg/100 g)													
green	6.06	6.33	6.30	7.37	8.94	8.74	8.62	10.62	7.33	8.35	9.56	8.31	8.04 ± 0.40 b
spotted	7.02	8.63	8.75	10.13	8.42	8.71	9.40	9.11	9.67	11.41	10.14	8.85	9.19 ± 0.32 a
ripe	7.51	6.88	7.64	7.91	8.33	9.31	9.88	10.97	7.76	9.89	9.48	8.45	8.67 ±0.35 ab
mean (variety)		7.54 ± 0.34 b				9.25 ± 0.24 a				9.10 ± 0.33 a			
Gramisterol + Cycloeucalenol Concentration (mg/100 g)													
green	2.34	2.56	2.37	2.22	3.70	3.84	3.64	3.61	2.08	2.27	2.30	1.89	2.74 ± 0.21 b
spotted	2.71	3.05	2.90	2.80	3.90	3.95	4.08	3.86	5.50	5.85	5.25	4.43	4.02 ± 0.31 a
ripe	3.46	3.35	3.53	2.91	3.82	4.03	3.89	3.62	4.15	5.44	4.38	3.22	3.82 ± 0.19 a
mean (variety)		2.85 ± 0.13 b				3.83 ± 0.05 a				3.90 ± 0.43 a			
Citrostadienol Concentration (mg/100 g)													
green	16.60	14.84	17.40	15.80	22.89	22.24	23.42	22.60	20.64	22.71	23.08	19.74	20.16 ±0.92 ab
spotted	15.91	17.88	17.25	16.87	21.54	21.41	22.75	21.28	25.29	27.58	24.15	20.42	21.03 ± 1.04 a
ripe	15.49	13.67	16.19	12.39	16.89	17.30	17.87	16.22	25.13	27.75	26.03	17.81	18.56 ± 1.43 b
mean (variety)		15.86 ± 0.46 c				20.53 ± 0.77 b				23.36 ± 0.92 a			
Total 4-Monomethylsterol Concentration (mg/100 g)													
green	25.01	23.73	26.08	25.40	35.53	34.82	35.68	36.82	30.04	33.34	34.93	29.94	30.94 ± 1.40 b
spotted	25.63	29.56	28.90	29.80	33.86	34.07	36.24	34.25	40.45	44.84	39.54	33.71	34.24 ± 1.58 a
ripe	26.46	23.90	27.36	23.20	29.04	30.63	31.64	30.81	37.04	43.08	39.88	29.48	31.04 ±1.77 ab
mean (variety)		26.25 ± 0.65 b				33.62 ± 0.72 a				36.36 ± 1.52 a			
Obtusifoliol Relative Amount (%)													
green	5.88	6.78	5.87	7.30	6.38	6.33	6.01	7.42	6.51	6.76	7.55	7.76	6.71 ± 0.19 a
spotted	5.42	5.99	6.20	7.19	5.60	5.78	5.83	6.11	5.38	5.91	5.79	5.82	5.92 ± 0.14 b
ripe	3.65	3.75	3.60	4.28	4.97	5.38	5.44	6.61	3.99	4.86	4.62	4.69	4.65 ± 0.26 c
mean (variety)		5.49 ± 0.39				5.99 ± 0.19				5.80 ± 0.34			
Gramisterol + Cycloeucalenol Relative Amount (%)													
green	2.26	2.75	2.21	2.20	2.64	2.78	2.54	2.52	1.85	1.84	1.81	1.77	2.26 ± 0.11 ab
spotted	2.09	2.12	2.06	1.99	2.59	2.62	2.53	2.59	3.06	3.03	3.00	2.91	2.55 ± 0.12 a
ripe	1.69	1.83	1.66	1.57	2.28	2.33	2.14	2.17	2.13	2.67	2.13	1.79	2.03 ± 0.10 b
mean (variety)		2.04 ± 0.09 b				2.48 ± 0.06 a				2.33 ± 0.16 ab			
Citrostadienol Relative Amount (%)													
green	16.03	15.92	16.20	15.64	16.33	16.10	16.33	15.80	18.34	18.38	18.23	18.45	16.81 ± 0.33 a
spotted	12.29	12.41	12.23	11.97	14.32	14.20	14.11	14.27	14.07	14.28	13.77	13.43	13.45 ± 0.27 b
ripe	7.54	7.45	7.63	6.70	10.08	10.00	9.83	9.77	12.92	13.64	12.68	9.90	9.85 ± 0.66 c
mean (variety)		11.84 ± 1.07 c				13.43 ± 0.79 b				14.84 ± 0.81 a			

[a]Olive oils are Buža, Črna, and Rosinjola varieties obtained from green, spotted, and ripe olives (control, CO) and stored for 12 months at variable room temperature (VR, 10−28 °C), refrigeration (RE, 4 °C), and freezing (FR, −20 °C) temperatures. Different letters within a group represent statistically significant different means at $p < 0.05$ for the variety and ripening degree factors obtained by main-effect three-way ANOVA and Tukey HSD posthoc test. Mean values are reported together with the corresponding standard errors. Mean values for the storage temperature factor are not reported because of low variability with no statistically significant differences for the majority of compounds. Average values of two GC determinations for each variety/degree of ripening/storage temperature combination are represented without standard deviation.

principal components (PCs) were extracted, explaining 86.9% of total variance of the set. Figure 2a shows the projection of olive oil samples along the directions of PC1 and PC2, while the corresponding factor loading plots that establish relative importance of the variables are reported in Figure 2b. Rosinjola oils were differentiated from Buža and Črna along the direction of PC1 by higher percentages of β-amyrin and cycloartenol. Črna oils were associated with higher concentrations of butyrospermol and were differentiated from Buža and Rosinjola oils by PC2.

SLDA was applied on the whole data set (36 cases, 16 variables) and succeeded in classifying oils according to varietal origin correctly. Seven variables were selected according to Wilks' λ criterion. β-Amyrin (percent) entered the model as the first variable and classified 100% of Rosinjola oils correctly. Inclusion of butyrospermol (percent) and δ-amyrin (percent) resulted in 100% correct classification of all 36 oils. Gramisterol + cycloeucalenol (percent), cycloartenol (percent), obtusifoliol (milligrams per 100 g), and citrostadienol (milligrams per 100 g) additionally improved the differentiation capacity of the model.

Single variables (milligrams per 100 g and percent) or their combination, which were found to account for the most variability arising from varietal origin, could be considered as relatively stable indicators of variety, since the intravarietal variability due to ripening degree and storage condition did not compromise their differentiating power. 4-Monomethyl- and 4,4′-dimethylsterols, mostly the major components 24-methylenecycloartanol, cycloartenol, and citrostadienol, were previously found to be useful for characterization and differentiation of monovarietal olive oils, but only in combination

DOI: 10.1021/acs.jafc.5b01638
J. Agric. Food Chem. 2015, 63, 5499−5508

Table 4. Concentrations and Relative Amounts of 4,4′-Dimethylsterols in Olive Oils[a]

ripening degree	olive variety: Buža CO	Buža VR	Buža RE	Buža FR	Črna CO	Črna VR	Črna RE	Črna FR	Rosinjola CO	Rosinjola VR	Rosinjola RE	Rosinjola FR	mean (ripening degree)
						δ-Amyrin Concentration (mg/100 g)							
green	1.47	1.61	1.40	1.38	2.07	2.05	1.96	2.03	2.02	2.01	2.16	1.85	1.83 ± 0.08
spotted	1.60	1.71	1.67	1.71	1.96	1.80	2.02	1.92	1.77	1.80	1.73	1.52	1.77 ± 0.04
ripe	2.18	1.95	2.18	1.96	1.80	1.87	1.88	1.81	1.69	1.81	1.73	1.52	1.86 ± 0.05
mean (variety)		1.73 ± 0.08				1.93 ± 0.03				1.80 ± 0.06			
						β-Amyrin Concentration (mg/100 g)							
green	3.14	2.29	3.25	3.19	3.93	3.90	3.96	4.27	5.12	5.52	5.76	4.89	4.10 ± 0.31 b
spotted	3.68	4.22	4.15	4.43	3.52	3.58	3.91	3.70	6.41	6.96	6.54	5.53	4.72 ± 0.37 b
ripe	5.89	5.42	6.01	5.58	3.45	3.72	3.86	3.82	6.81	7.20	7.36	6.27	5.45 ± 0.41 a
mean (variety)		4.27 ± 0.35 b				3.80 ± 0.07 b				6.20 ± 0.24 a			
						Butyrospermol Concentration (mg/100 g)							
green	5.86	5.13	6.08	5.67	12.02	11.60	12.50	12.29	11.92	12.82	13.01	10.95	9.99 ± 0.93
spotted	6.68	7.45	7.17	7.08	11.51	11.52	12.13	10.89	9.44	9.97	9.37	8.10	9.28 ± 0.56
ripe	9.06	7.87	9.34	8.24	10.77	10.74	11.69	10.33	9.35	10.37	9.82	8.60	9.68 ± 0.33
mean (variety)		7.14 ± 0.39 b				11.50 ± 0.20 a				10.31 ± 0.46 a			
						Cycloartenol Concentration (mg/100 g)							
green	27.66	24.83	28.74	26.61	37.18	36.80	38.46	37.78	42.84	46.96	47.77	40.32	36.33 ± 2.25 b
spotted	31.75	34.93	34.38	33.99	37.15	37.37	40.22	36.74	49.66	53.11	48.84	42.77	40.08 ± 2.02 b
ripe	53.97	49.47	57.20	50.13	39.85	41.00	43.18	38.82	64.44	60.71	67.58	62.05	52.37 ± 2.93 a
mean (variety)		37.81 ± 3.34 b				38.71 ± 0.58 b				52.25 ± 2.67 a			
						24-Methylenecycloartanol Concentration (mg/100 g)							
green	40.37	35.56	41.88	38.77	49.44	48.95	50.86	49.85	20.59	22.93	22.95	19.07	36.37 ± 3.57 c
spotted	60.06	66.27	64.80	63.89	62.39	62.40	66.78	61.59	71.87	76.42	69.28	60.42	65.52 ± 1.43 b
ripe	107.76	94.91	110.00	95.69	82.63	84.97	89.46	80.45	75.22	80.27	78.88	71.96	87.68 ± 3.53 a
mean (variety)		68.33 ± 7.92 a				65.81 ± 4.35 a				55.82 ± 7.49 b			
						Total 4,4′-Dimethylsterol Concentration (mg/100 g)							
green	78.51	69.43	81.36	75.61	104.63	103.30	107.74	106.22	82.48	90.23	91.65	77.09	89.02 ± 3.91 c
spotted	103.76	114.58	112.17	111.09	116.52	116.67	125.07	114.85	139.15	148.26	135.76	118.35	121.35 ± 3.80 b
ripe	178.86	159.62	184.73	161.60	138.50	142.30	150.07	135.22	157.52	160.36	165.37	150.39	157.05 ± 4.34 a
mean (variety)		119.28 ± 12.04				121.76 ± 4.66				126.39 ± 9.49			
						δ-Amyrin Relative Amount (%)							
green	1.42	1.73	1.30	1.36	1.48	1.49	1.36	1.42	1.79	1.63	1.71	1.73	1.54 ± 0.05 a
spotted	1.23	1.19	1.19	1.21	1.30	1.19	1.25	1.29	0.99	0.93	0.99	1.00	1.15 ± 0.04 b
ripe	1.06	1.06	1.03	1.06	1.07	1.08	1.03	1.09	0.87	0.89	0.84	0.85	0.99 ± 0.03 c
mean (variety)		1.24 ± 0.06				1.26 ± 0.05				1.19 ± 0.11			
						β-Amyrin Relative Amount (%)							
green	3.05	2.47	3.03	3.16	2.80	2.83	2.76	2.98	4.55	4.47	4.55	4.57	3.44 ± 0.24 a
spotted	2.85	2.93	2.94	3.14	2.34	2.38	2.42	2.48	3.57	3.60	3.73	3.64	3.00 ± 0.15 b
ripe	2.87	2.95	2.83	3.02	2.06	2.15	2.12	2.30	3.50	3.54	3.59	3.48	2.87 ± 0.17 b
mean (variety)		2.94 ± 0.05 b				2.47 ± 0.09 c				3.90 ± 0.14 a			
						Butyrospermol Relative Amount (%)							
green	5.66	5.51	5.66	5.61	8.58	8.40	8.72	8.59	10.59	10.37	10.28	10.24	8.18 ± 0.59 a
spotted	5.16	5.17	5.08	5.03	7.65	7.65	7.52	7.31	5.25	5.16	5.35	5.33	5.97 ± 0.34 b
ripe	4.41	4.29	4.41	4.46	6.43	6.21	6.43	6.23	4.81	5.10	4.78	4.78	5.20 ± 0.25 b
mean (variety)		5.04 ± 0.15 b				7.48 ± 0.28 a				6.84 ± 0.76 a			
						Cycloartenol Relative Amount (%)							
green	26.72	26.66	26.75	26.35	26.53	26.64	26.82	26.42	38.07	38.00	37.74	37.67	30.36 ± 1.60 a
spotted	24.53	24.23	24.37	24.12	24.70	24.79	24.93	24.65	27.65	27.51	27.87	28.13	25.62 ± 0.47 c
ripe	26.31	26.95	26.97	27.13	23.79	23.71	23.76	23.39	33.12	29.84	32.92	34.50	27.70 ± 1.16 b
mean (variety)		25.93 ± 0.35 b				25.01 ± 0.37 b				32.75 ± 1.28 a			

DOI: 10.1021/acs.jafc.5b01638
J. Agric. Food Chem. 2015, 63, 5499−5508

Table 4. continued

ripening degree	olive variety: Buža CO	Buža VR	Buža RE	Buža FR	Črna CO	Črna VR	Črna RE	Črna FR	Rosinjola CO	Rosinjola VR	Rosinjola RE	Rosinjola FR	mean (ripening degree)
	24-Methylenecycloartanol Relative Amount (%)												
green	38.98	38.18	38.98	38.37	35.27	35.44	35.46	34.85	18.30	18.55	18.13	17.82	30.69 ± 2.70 c
spotted	46.42	45.98	45.94	45.34	41.49	41.39	41.40	41.30	40.02	39.58	39.51	39.74	42.34 ± 0.79 b
ripe	52.47	51.72	51.87	51.77	49.33	49.14	49.24	48.45	38.66	39.46	38.43	40.01	46.71 ± 1.66 a
mean (variety)	45.50 ± 1.65 a				41.90 ± 1.70 b				32.35 ± 3.02 c				

[a]Olive oils are Buža, Črna, and Rosinjola varieties obtained from green, spotted, and ripe olives (control, CO) and stored for 12 months at variable room temperature (VR, 10−28 °C), refrigeration (RE, 4 °C), and freezing (FR, −20 °C) temperatures. Different letters within a group represent statistically significant different means at $p < 0.05$ for the variety and ripening degree factors obtained by main-effect three-way ANOVA and Tukey HSD posthoc test. Mean values are reported together with the corresponding standard errors. Mean values for the storage temperature factor are not reported because of low variability with no statistically significant differences for the majority of compounds. Average values of two GC determinations for each variety/degree of ripening/storage temperature combination are represented without standard deviation.

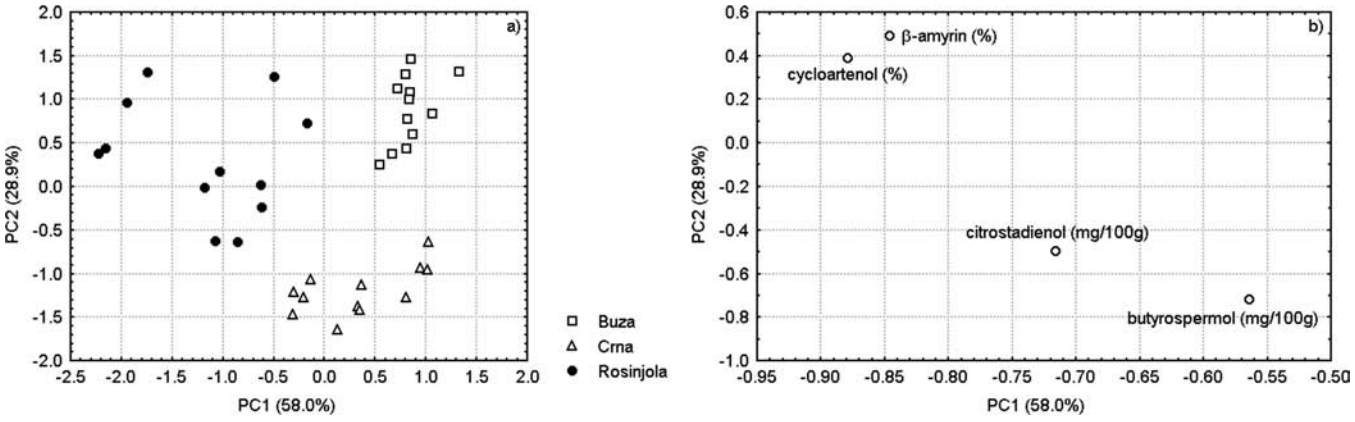

Figure 2. (a) Separation according to variety of olive oils from Buža, Črna, and Rosinjola varieties, harvested at three different ripening degrees and stored for 12 months, along the directions of principal components PC1 and PC2. (b) Factor loadings of selected variables (concentrations in milligrams per 100 g and relative amounts in percent of 4-monomethyl- and 4,4′-dimethylsterols) on PC1 and PC2.

with other constituents and without considering intravarietal variability due to ripening degree and storage.[27,28,31]

Throughout the investigated period of ripening, the major 4-monomethylsterol was citrostadienol, while the most abundant 4,4′-dimethylsterols were 24-methylenecycloartanol and cycloartenol (Tables 3 and 4). The same compounds were also the most abundant in oils from Picholine and Sayali varieties cultivated in Tunisia,[2,41] in Italian varieties Bosana, Coratina, Dritta, Frantoio, Moraiolo, Provenzale, and Leccino,[27,31] and in Spanish olive oils,[4] but with different relative proportions. In two of the most comprehensive and detailed studies on triterpenoids in olive fruit, Stiti and Hartmann[5] and Stiti et al.[3] identified a very large number of major and minor sterol and non-sterol compounds including 4-monomethyl- and 4,4′-dimethylsterols, with triterpenic acids as the most abundant. They used a pattern for the classification of triterpenoids into chemical groups according to their molecular structure which was different from that applied in this work and by other authors. In addition, Stiti et al.[3] did not report quantitative data for all compounds and reported the amounts of free and esterified forms separately. All the aforementioned reasons made these data hard to interpret and compare in terms of olive oil relative composition.

In this work, the level of total 4,4′-dimethylsterols was approximately 4−6 times higher than that of 4-monomethylsterols at different ripening stages, which reasonably corresponds to literature data where Sakouhi et al.[2,41] reported an average ratio of approximately 3:1.

Variability as a Result of Ripening Degree. The average concentrations (milligrams per 100 g) of 4-monomethylsterols, as well as of δ- and β-amyrin and butyrospermol, were found to be stable throughout ripening or slightly increased in oils produced from ripe olives. However, the patterns were not quite uniform for all varieties (Tables 3 and 4). 24-Methylenecycloartanol and cycloartenol increased constantly from RD1 to RD3, which was more pronounced in the case of the latter constituent. Such an increase has caused a significant drop in the relative amounts of other 4-monomethyl- and 4,4′-dimethylsterols in olives produced from spotted (RD2) and especially ripe (RD3) olives (Table 4). The increase in 24-methylenecycloartanol and cycloartenol contributed the most to the increase in total 4,4′-dimethylsterol concentration (Table 4). A constant increase in 4-monomethyl- and 4,4′-dimethylsterols (free + esterified) during olive fruit ontogeny was reported by Stiti et al.[3] The same authors observed a significant rise in 24-methylenecycloartanol and cycloartenol concentration at the moment olive epidermal color began to change from green to spotted, coinciding with the start of the synthesis of anthocyanins and loss of chlorophylls. This phenomenon was explained as a result of a redirection of carbon flux from the triterpenoid toward the sterol pathway, with cycloartenol being a precursor to 24-methylenecycloartanol and a major early

DOI: 10.1021/acs.jafc.5b01638
J. Agric. Food Chem. 2015, 63, 5499−5508

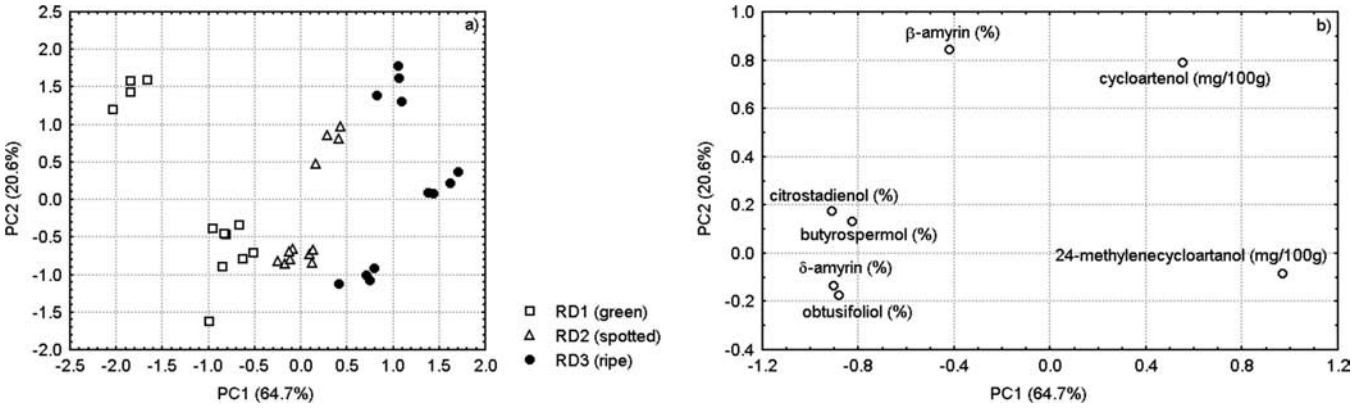

Figure 3. (a) Separation according to ripening degree of olive oils from Buža, Črna, and Rosinjola varieties, harvested at three different ripening degrees (RD1−RD3) and stored for 12 months, along the directions of principal components PC1 and PC2. (b) Factor loadings of selected variables (concentrations in milligrams per 100 g and relative amounts in percent of 4-momomethyl- and 4,4′-dimethylsterols) on PC1 and PC2.

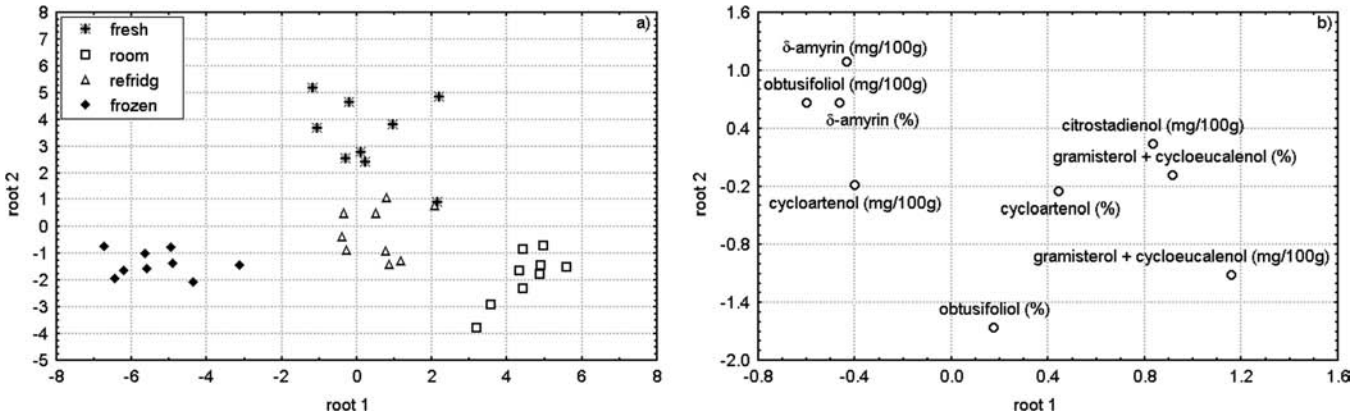

Figure 4. (a) Separation according to storage conditions of olive oils from Buža, Črna, and Rosinjola varieties, harvested at three different ripening degrees and stored for 12 months, along the directions of two discriminant functions. (b) Projection of standardized coefficients of selected variables (concentrations in milligrams per 100 g and relative amounts in percent of 4-methylsterols and 4,4′-dimethylsterols) in two-dimensional space.

biosynthetic intermediate in 4-desmethylsterol synthesis. In this work, the highest average total 4-desmethylsterol concentration was found in oils produced from spotted olives (RD2), which was possibly a result of increased carbon flux toward sterol biosynthesis. The mean values were (in milligrams per 100 g) for Buža, RD1 111.33, RD2 135.65, and RD3 122.16; for Črna, RD1 199.11, RD2 206.61, and RD3 197.16; and for Rosinjola, RD1 135.16, RD2 174.74, and RD3 138.19. Near the end of the olive ripening process, Stiti et al.[3] observed a specific accumulation of 24-methylenecycloartanol, indicating a slowing down of the metabolic flux through the sterol pathway. A sharp increase in 24-methylenecycloartanol concentration (Table 4) together with a drop in total 4-desmethylsterol concentration in RD3 oils were observed in this investigation and are in line with such findings. 4-Monomethyl- and 4,4′-dimethylsterols are components of surface waxes of olive fruit.[5] Therefore, the increase in their concentration in oils made from ripe olives (RD3) is possibly partly a result of a more fragile exocarp that fragments better during milling, as reported by Sánchez Casas et al.[42] Sakouhi et al.[2] noted quite a different behavior of 4-monomethyl- and 4,4′-dimethylsterols during olive ripening, which included much more fluctuation of their content, with the concentrations of cycloartenol and 24-methylenecycloartanol inversely proportional throughout the whole ripening period.

In PCA, the most successful separation between groups of olive oil samples produced at different ripening degrees was achieved by the model that included 36 cases and seven variables: citrostadienol (percent), *δ*-amyrin (percent), *β*-amyrin (percent), obtusifoliol (percent), butyrospermol (percent), 24-methylenecycloartanol (milligrams per 100 g), and cycloartenol (milligrams per 100 g). Two principal components (PCs) were extracted, explaining 85.3% of total variance. The groups were separated along the direction of PC1 (Figure 3). Citrostadienol, *δ*-amyrin, *β*-amyrin, obtusifoliol, and butyrospermol were loaded on the negative side of PC1 and were characteristic for RD1 oils. RD3 oils were associated with higher concentrations of 24-methylenecycloartanol and cycloartenol, which had positive PC1 loadings. RD2 oils were scattered between other two groups in all four quadrants, gravitating toward the intersection of PC1 and PC2. Interestingly, on the scatterplot, three subgroups each comprising four cases/samples could be observed within each of the three groups of oils separated according to ripening degree (Figure 3a). These subgroups corresponded to different varieties, confirming that certain variables can exhibit high variability as a result of both varietal origin and ripening degree.

SLDA, applied on the whole data set (36 cases, 16 variables), classified 97.22% of oil samples correctly according to ripening degree. 24-Methylenecycloartanol (milligrams per 100 g) entered the model as the first variable, which resulted in the

DOI: 10.1021/acs.jafc.5b01638
J. Agric. Food Chem. 2015, 63, 5499−5508

correct classification of 94.44% of all samples. Other variables included were cycloartenol (percent), β-amyrin (milligrams per 100 g), δ-amyrin (percent), and obtusifoliol (percent).

Variability as a Result of Storage Temperature. The results presented in Tables 3 and 4 suggest that 4-monomethyl- and 4,4′-dimethylsterols in oils have undergone certain changes during storage. Among the probable causes are chemical and microbial transformations involving oxidation,[43] cleavage of glycosides into free 4-monomethyl- and 4,4′-dimethylsterol aglycons by acid or enzymatic hydrolysis, and further transformation of reactive sterol precursors such as squalene and (3*S*)-2,3-oxidosqualene.[7] Upon comparison to the magnitude of variability of 4-monomethyl- and 4,4′-dimethylsterols caused by variety and ripening degree, it can be stated that their levels were relatively consistent after the storage period. The concentration of obtusifoliol was the only variable for which a significant effect of storage condition factor was determined by three-way ANOVA. However, certain subtle, and more important, regular patterns were observed after the application of SLDA to the normalized data set (36 cases, 16 variables). The obtained SLDA model classified 100% of all samples according to storage temperature correctly. Nine variables were selected, and 100% correct classification was obtained by the first four variables: gramisterol + cycloeucalenol (percent and milligrams per 100 g), obtusifoliol (percent), and δ-amyrin (milligrams per 100 g). The prediction capacity of the model was evaluated by leave-one-out cross-validation, where each oil sample was removed from the model and classified by the functions derived from all samples other than that sample. Average percentage of correct prediction was 94.44%, with the origin of only two samples not correctly predicted. As seen in Figure 4, very good and clear SLDA differentiation of olive oils was obtained. Fresh oils were discriminated from others along the second discriminant function by higher δ-amyrin (milligrams per 100 g and percent) and obtusifoliol (milligrams per 100 g) and lower gramisterol + cycloeucalenol (milligrams per 100 g) and obtusifoliol (percent) amounts. The first function discriminated samples stored at room temperature and at freezing temperatures from each other as well as from fresh and refrigerated samples, characterizing the former by higher amounts of δ-amyrin (both milligrams per 100 g and percent), obtusifoliol (milligrams per 100 g), and cycloartenol (milligrams per 100 g) and the latter by higher amounts of gramisterol + cycloeucalenol (milligrams per 100 g and percent) and citrostadienol (milligrams per 100 g). It can be said that the composition of oils stored at refrigeration temperature was generally the most similar to that of the fresh oils since Mahalanobis distances between these groups were the shortest (data not shown).

The present investigation demonstrated that olive variety and ripening degree are important sources of variability of 4-monomethyl- and 4,4′-dimethylsterol content in olive oil. Relative amounts of β-amyrin, cycloartenol, and 24-methylenecycloartanol accounted for the most variation due to varietal origin, while the largest influence of ripening degree was observed for relative amounts of citrostadienol and concentrations of 24-methylenecycloartanol. The total concentration of 4,4-dimethylsterols was found to increase during ripening and peak in oils obtained from ripe olives. It should be mentioned that this is the first experimental evidence on the effect of ripening on 4-monomethyl- and 4,4′-dimethylsterols in olive oil. Another novel finding is that the complex interactive effect of variety and ripening degree, which can complicate olive oil characterization, can be overcome by selecting appropriate 4-monomethyl- and 4,4′-dimethylsterols by use of chemometric tools, similarly as recently reported by our group for 4-desmethylsterols[29] and aliphatic alcohols.[22] Successful differentiation of olive oils achieved by multivariate PCA and SLDA models pointed to their potential use as indicators of varietal origin that are independent of ripening degree and vice versa, applicable for both fresh and stored oils. It practically means that there are 4-monomethyl- and 4,4′-dimethylsterols which are more dependent on variety and those which depend more on ripening degree, which is, to our knowledge, the first finding of this type. The presented approach also has practical relevance. It could be especially useful for technical and scientific studies aiming at the authentication and certification of olive oil varietal origin, which often overlook the impact of olive maturity, and vice versa. For example, the approach tested in this work could be utilized for developing more robust olive oil chemical composition specifications for various protected designations, because it considers the interrelationship between three factors of variability and extracts only the most robust and useful indicators. The results obtained in this work could be useful for producers to optimize individual steps in production to obtain olive oils with targeted 4-monomethyl- and 4,4′-dimethylsterol composition.

Variability as a result of storage temperature and storage in general was of a much smaller magnitude. It suggests that olive oil essentially retains its original characteristics and provides health benefits related to 4-monomethyl- and 4,4′-dimethylsterols throughout its shelf life. It also means that, despite the notorious loss of phenols and tocopherols during ripening and storage, oils obtained from ripe olives, even the aged ones, are not inferior with respect to all valuable phytonutrients. Regardless of their small absolute magnitude, relative changes caused by storage were specific for each investigated storage temperature and were found useful in discriminating stored from fresh oils as well, which has not been accomplished by applying the same approach for 4-desmethylsterols[29] and aliphatic alcohols.[22] A clear and regular dependency of 4-monomethyl- and 4,4′-dimethylsterol composition on storage temperature, identified for the first time in our investigation, offers new possibilities for tracking new reliable markers of olive oil age and quality.

■ ASSOCIATED CONTENT

Ⓢ Supporting Information

Eight figures showing mass spectra of 4-monomethyl- and 4,4′-dimethylsterols. The Supporting Information is available free of charge on the ACS Publications website at DOI: 10.1021/acs.jafc.5b01638.

■ AUTHOR INFORMATION

Corresponding Author

*Telephone +385 (0)52 408 342; fax +385 (0)52 431 659; e-mail marina@iptpo.hr.

Notes

The authors declare no competing financial interest.

■ REFERENCES

(1) Damirchi, S. A.; Savage, G. P.; Dutta, P. C. Sterol fractions in hazelnut and virgin olive oils and 4,4′-dimethylsterols as possible markers for detection of adulteration of virgin olive oil. *J. Am. Oil Chem. Soc.* **2005**, *82*, 717−725.

DOI: 10.1021/acs.jafc.5b01638
J. Agric. Food Chem. 2015, 63, 5499−5508

(2) Sakouhi, F.; Absalon, C.; Sebei, K.; Fouquet, E.; Boukhchina, S.; Kallel, H. Gas chromatographic−mass spectrometric characterisation of triterpene alcohols and monomethylsterols in developing *Olea europaea* L. fruits. *Food Chem.* **2009**, *116*, 345−350.
(3) Stiti, N.; Triki, S.; Hartmann, M.-A. Formation of triterpenoids throughout *Olea europaea* fruit ontogeny. *Lipids* **2007**, *42*, 55−67.
(4) Itoh, T.; Yoshida, K.; Yatsu, T.; Tamuta, T.; Matsumoto, T. Triterpene alcohols and sterols of Spanish olive oil. *J. Am. Oil Chem. Soc.* **1981**, *58*, 545−550.
(5) Stiti, N.; Hartmann, M.-A. Nonsterol triterpenoids as major constituents of *Olea europaea*. *J. Lipids* **2012**, 1−13 DOI: 10.1155/2012/476595.
(6) Cherif, A. O.; Ben Messaouda, M. B.; Kaabi, B.; Pellerin, I.; Boukhchina, S.; Kallel, H.; Pepe, C. Characteristics and pathways of bioactive 4-desmethylsterols, triterpene alcohols and 4α-monomethylsterols, from developing Tunisian cultivars and wild peanut (*Arachis hypogaea* L.). *Plant Physiol. Biochem.* **2011**, *49*, 774−781.
(7) Muffler, K.; Leipold, D.; Scheller, M.-C.; Haas, C.; Steingroewer, J.; Bley, T.; Neuhaus, H. E.; Mirata, M. A.; Schrader, J.; Ulber, R. Biotransformation of triterpenes. *Process Biochem.* **2011**, *46*, 1−15.
(8) Bauer, S.; Schulte, E.; Their, H.-P. Composition of the surface wax from tomatoes. I. Identification of the components by GC/MS. *Eur. Food Res. Technol.* **2004**, *219*, 223−228.
(9) Wang, Z.; Guhling, O.; Yao, R.; Li, F.; Yeats, T. H.; Rose, J. K. C.; Jetter, R. Two oxidosqualene cyclases responsible for biosynthesis of tomato fruit cuticular triterpenoids. *Plant Physiol.* **2011**, *155*, 540−552.
(10) Harrabi, S.; Sakouhi, F.; St-Amand, A.; Boukhchina, S.; Kallel, H.; Mayer, P. M. Accumulation of phytosterols, triterpene alcohols and phytostanols in developing *Zea mays* L. kernels. *J. Plant Sci.* **2007**, *2*, 260−272.
(11) Berasategi, I.; Barriuso, B.; Ansorena, D.; Astiasarán, I. Stability of avocado oil during heating: Comparative study to olive oil. *Food Chem.* **2012**, *132*, 439−446.
(12) Li, T. S. C.; Beveridge, T. H. J.; Drover, J. C. G. Phytosterol content of sea buckthorn (*Hippophae rhamnoides* L.) seed oil: Extraction and identification. *Food Chem.* **2007**, *101*, 1633−1639.
(13) Xu, X.; Gao, Y.; Sun, L. Free and esterified triterpene alcohol composition of bee pollen from different botanical origins. *Food Res. Int.* **2012**, *48*, 650−656.
(14) Jurado, J. M.; Jiménez-Lirola, A.; Narváez-Rivas, M.; Gallardo, E.; Pablos, F.; León-Camacho, M. Characterization and quantification of 4-methylsterols and 4,4-dimethylsterols from Iberian pig subcutaneous fat by gas chromatography−mass spectrometry and gas chromatography−flame ionization detector and their use to authenticate the fattening systems. *Talanta* **2013**, *106*, 14−19.
(15) Gordon, M. H.; Magos, P. The effect of sterols on the oxidation of edible oils. *Food Chem.* **1983**, *10*, 141−147.
(16) Boskou, D.; Katsikas, H. Effect of olive oil hydrocarbons and triterpene alcohols on the stability of cotton seed oil. *Acta Aliment.* **1979**, *8*, 317−320.
(17) Benitez-Sánchez, P. L.; León-Camacho, M.; Aparicio, R. A comprehensive study of hazelnut oil composition with comparisons to other vegetable oils, particularly olive oil. *Eur. Food Res. Technol.* **2003**, *218*, 13−19.
(18) Giuffre, A. M. Influence of cultivar and harvest year on triglyceride composition of olive oils produced in Calabria (Southern Italy). *Eur. J. Lipid Sci. Technol.* **2013**, *115*, 928−934.
(19) Sánchez de Medina, V.; El Riachy, M.; Priego-Capote, F.; Luque de Castro, M. D. Mass spectrometry to evaluate the effect of the ripening process on phenols of virgin olive oils. *Eur. J. Lipid Sci. Technol.* **2013**, *115*, 1053−1061.
(20) Matos, L. C.; Cunha, S. C.; Amaral, J. S.; Pereira, J. A.; Andrade, P. B.; Seabra, R. M.; Oliveira, B. P. P. Chemometric characterization of three varietal olive oils (cvs. Cobrançosa, Madural and Verdeal Transmontana) extracted from olives with different maturation indices. *Food Chem.* **2007**, *102*, 406−414.
(21) Giuffre, A. M. Wax ester variation in olive oils produced in Calabria (Southern Italy) during olive ripening. *J. Am. Oil Chem. Soc.* **2014**, *91*, 1355−1366.
(22) Lukić, M.; Lukić, I.; Sladonja, B.; Piližota, V. Policosanol variation in olive oil as a result of variety, ripening, and storage. *Eur. J. Lipid Sci. Technol.* **2015**, DOI: 10.1002/ejlt.201400483.
(23) Stefanoudaki, E.; Williams, M.; Harwood, J. Changes in virgin olive oil characteristics during different storage conditions. *Eur. J. Lipid Sci. Technol.* **2010**, *112*, 906−914.
(24) Issaoui, M.; Mechri, B.; Echbili, A.; Dabbou, S.; Yangui, A.; Belguith, H.; Trigui, A.; Hammami, M. Chemometric characterization of five Tunisian varietals of *Olea europaea* L. olive fruit according to different maturation indices. *J. Food Lipids* **2008**, *15*, 277−296.
(25) Lazzez, A.; Perri, E.; Caravita, M. A.; Khlif, M.; Cossentini, M. Influence of olive maturity stage and geographical origin on some minor components in virgin olive oil of the Chemlali variety. *J. Agric. Food Chem.* **2008**, *56*, 982−988.
(26) Mailer, R. J.; Ayton, J.; Graham, K. The influence of growing region, cultivar and harvest timing on the diversity of Australian olive oil. *J. Am. Oil Chem. Soc.* **2010**, *87*, 877−884.
(27) Bianchi, G.; Giansante, L.; Shaw, A.; Kell, D. B. Chemometric criteria for the characterisation of Italian Protected Denomination of Origin (DOP) olive oils from their metabolic profiles. *Eur. J. Lipid Sci. Technol.* **2001**, *103*, 141−150.
(28) Ranalli, A.; Pollastri, L.; Contento, S.; Di Loreto, G.; lannucci, E.; Lucera, L.; Russi, F. Sterol and alcohol components of seed, pulp and whole olive fruit oils. Their use to characterise olive fruit variety by multivariates. *J. Sci. Food Agric.* **2002**, *82*, 854−859.
(29) Lukić, M.; Lukić, I.; Krapac, M.; Sladonja, B.; Piližota, V. Sterols and triterpene diols in olive oil as indicators of variety and degree of ripening. *Food Chem.* **2013**, *136*, 251−258.
(30) IOC Method of Analysis: Determination of aliphatic and triterpenic alcohols content by capillary gas chromatography. International Olive Council, COI/T.20/Doc. no.26/Rev.1, 2015, pp 1−11.
(31) Giansante, L.; Di Vincenzo, D.; Bianchi, G. Classification of monovarietal Italian olive oils by unsupervised (PCA) and supervised (LDA) chemometrics. *J. Sci. Food Agric.* **2003**, *83*, 905−911.
(32) EEC Agriculture Council. Action plan for the EU Olive oil sector (working paper), 2012. URL http://ec.europa.eu/agriculture/olive-oil/action-plan_en.pdf (accessed August 6, 2014).
(33) Beltrán, G.; del Río, C.; Sánchez, S.; Martínez, L. Seasonal changes in olive fruit characteristics and oil accumulation during ripening process. *J. Sci. Food Agric.* **2004**, *84*, 1783−1790.
(34) Mulinacci, N.; Ieri, F.; Ignesti, G.; Romani, A.; Michelozzi, M.; Creti, D.; Innocenti, M.; Calamai, L. The freezing process helps to preserve the quality of extra virgin olive oil over time: A case study up to 18 months. *Food Res. Int.* **2013**, *54*, 2008−2015.
(35) European Economic Community.. EEC Regulation 2568: On the characteristics of olive oil and olive-residue oil and on the relevant methods of analysis. *EEC Off. Rep.* **1991**, *L248*, 1−48.
(36) Wretensjö, I.; Karlberg, B. Characterization of sterols in refined borage oil by GC-MS. *J. Am. Oil Chem. Soc.* **2002**, *79*, 1069−1074.
(37) Kuroda, N.; Ohnishi, M.; Fujino, Y. Sterol lipids in rice bran. *Cereal Chem.* **1977**, *54*, 997−1006.
(38) Mezghache, M.; Henchiri, S.; Martine, L.; Berdeaux, O.; Aouf, N.; Juaneda, P. Contribution à l'étude de la fraction insaponifiable de trois huiles d'olive issues des variétés Guasto, Rougette et Blanquette plantés dans l'est algérien. *Ol., Corps Gras, Lipides.* **2010**, *17*, 337−344.
(39) Li, J.; Ho, C.; Li, H.; Tao, H.; Liu, L. Separation of sterols and triterpene alcohols from unsaponifiable fractions of three plant seed oils. *J. Food Lipids.* **2000**, *7*, 1−20.
(40) Sokal, R. R.; Rohlf, F. J. *Biometry*, 1st ed.; Freeman: San Francisco, CA, 1981; p 859.
(41) Sakouhi, F.; Absalon, C.; Flamini, G.; Cioni, P. L.; Kallel, H.; Boukhchina, S. Lipid components of olive oil from Tunisian Cv. Sayali: Characterization and authenticity. *C. R. Biol.* **2010**, *333*, 642−648.
(42) Sánchez Casas, J.; Bueno, E. O.; García, A. M. M.; Cano, M. M. Sterol and erythrodiol + uvaol content of virgin olive oils from cultivars of Extremadura (Spain). *Food Chem.* **2004**, *87*, 225−230.
(43) Soupas, L.; Juntunen, L.; Lampi, A.-M.; Piironen, V. Effects of sterol structure, temperature, and lipid medium on phytosterol oxidation. *J. Agric. Food Chem.* **2004**, *52*, 6485−6491.

DOI: 10.1021/acs.jafc.5b01638
J. Agric. Food Chem. 2015, 63, 5499−5508

Table 1. Primers Used in qRT-PCR for *MPK1, MPK2, MPK3* and *UBI3* Genes in Tomato

gene	Solgenomics accession ID	GenBank accession ID	sequence (5′-3′)	product size (base pairs)
SlMPK1	Solyc12g019460.1.1	AJ535702	forward: ATGCGCTTACAGAGGAACAGATG	172
			reverse: CGGACGGAATGCACACATATATAC	
SlMPK2	Solyc08g014420.2.1	AY261513	forward: GCCCTTACCGAGGAACAAATGA	101
			reverse: TCCAACAGCAAACGAGCGAGTA	
SlMPK3	Solyc06g005170.2.1	AY261514	forward: AGCATTAGCTCATCCCTACCTC	107
			reverse: GCTCTTCTCCTATCCCTTGTTG	
SlUBI3	Solyc01g056940.2.1	X58253	forward: TCCATCTCGTGCTCCGTCT	146
			reverse: CTGAACCTTTCCAGTGTCATCAA	

The tomato genome encodes well-defined proteins for the three-layer phospho-relaying MPK cascades and contains 16 SlMPKs (often previously named LeMPKs), 5 SlMPKKs, and 89 SlMPKKKs,[14,15] some of which have been functionally characterized for their possible roles in regulating defense responses against biotic and abiotic stresses. SlMPK1/2/3 could be activated by the wound-signaling peptide systemin, oligosaccharide elicitors, UV−B radiation, and pathogen infections.[16−18] Silencing the *SlMPK1*, *SMPK2*, *SlMPK3*, and *SlMPK4* can reduce the drought tolerance of tomato plants to varying degrees and enhance the susceptibility to *B. cinerea*.[19,20] Furthermore, SlMPK1/2/3 have been reported to be involved in systemin-mediated defense response against herbivorous insects in tomato plants.[21] *SlMKK2* and *SlMKK4* were found to activate *SlMPK1* and *SlMPK2* in vitro and contribute to disease resistance against *B. cinerea*.[22] The *SlMKK2* and *SlMPK2* genes contributed disease resistance to *Xanthomonas campestris pv Vesicatoria* in tomato plant.[23] Although *SlMPK1/2/3* have been associated with the defense response in tomato plants, whether *SlMPK1/2/3* can regulate basal defense in tomato fruit remains to be studied.

MAPK cascades are implicated in multiple defense responses in cooperation with plant hormones and reactive oxygen species (ROS). Recent studies indicate that plant hormones, such as auxin indole acetic acid (IAA), abscisic acid (ABA), gibberellic acid (GA), and methyl jasmonate (MeJA) are implicated in plant defense signaling pathways.[24] IAA, ABA, and GA negatively regulate plant defense against *B. cinerea*.[25−28] Conversely, MeJA plays a positive role in tomato fruit disease resistance against *B. cinerea*.[7] ROS and oxidative enzymes are known to accumulate in response to pathogen attacks,[3,29] and they are involved in MAPKs signaling. Silencing of either *SlMPK1* or *SlMPK2* abolishes brassinosteroid-induced H_2O_2 accumulation in tomato plants.[30] However, whether plant hormones and ROS participate in SlMPK disease response in tomato fruit is still not clear.

To study the function of SlMPK1/2/3 in tomato fruit's innate immunity, we used a specific inhibitor of MAPKK, U0126 (1,4-diamino-2,3-dicyano-1,4-bis(*o*-aminophenylmercapto)butadiene), to treat tomato fruit. The U0126 could bind directly to endogenously active MAPKKs and thus prevent the activation of MAPKs.[31] The results demonstrated that the inhibition of SlMPK1/2/3 in tomato fruit led to increased susceptibility to *B. cinerea*, and that plant hormones and ROS were involved in the immune response of SlMPK1/2/3.

MATERIALS AND METHODS

Fruit Materials and Treatments. Tomato (*Solanum lycopersicum* cv. Lichun) fruit was harvested at the mature green stage from a greenhouse at Xiaotangshan Geothermal Special Vegetable Base, Beijing, China, and immediately transported to the laboratory. The tomato was grown under field conditions. Good cultural practices were followed with adequate and consistent watering. The fruit was tagged at 2 days postanthesis (dpa) and harvested at 45 dpa for mature green fruit. The mature green stage of the fruit was confirmed by the color, size, and texture. Fruit of a uniform size and free of visible blemishes or disease was selected for the experiments. The tomato fruit were then surface-disinfected with 2% (v/v) sodium hypochlorite for 2 min, washed with distilled water, and air-dried. The fruit were then immersed in distilled water containing 0.07 mL/L dimethyl sulfoxide (the control), and 2, 5, 10, or 20 μM U0126 (U0126 was dissolved in 0.07 mL/L dimethyl sulfoxide) solutions. The fruit in the solutions were immediately vacuumed under −35 kPa for 0.5 min, and then kept in the solution under air pressure for 2 min. After being air-dried, the fruit were stored at 25 ± 1 °C with a relative humidity of 85−90%. The fruit were sampled at 0, 0.5, 1, 4, 8, 16, and 24 h and at 2, 3, 4, 5, and 6 d (still at mature green stage) for measurements of *SlMPK1/2/3* gene expression, defense enzyme activities, hormone concentration, H_2O_2 content and antioxidant enzyme activities. Ten tomato fruit pericarps from each treatment were cut (all seed was removed), sliced horizontally from the middle third, diced prior to being frozen in liquid nitrogen, and stored at −80 °C. Before analysis, frozen pericarp tissues were ground to a fine powder in a grinding container (A11 basic, IKA, German), which had been precooled with liquid nitrogen. Each treatment was replicated three times.

Pathogen Inoculation and Measurement of Disease Symptoms. The pathogen *B. cinerea* (ACCC 36028) was purchased from Agricultural Culture Collection of China (Haidian, Beijing) and cultured on potato dextrose agar medium at 25 °C. Spore suspensions (2×10^6 conidia mL^{-1}) were prepared with 10-day-old cultures using sterile, distilled water containing 0.01% Tween-80. Twenty-four hours after treatment, 30 fruits were inoculated with 10 μL of spore suspension of *B. cinerea* into the wound (2 mm wide ×4 mm deep) at two points on the equator of each fruit using a pipet. The fruit were placed in plastic bags without sealing to avoid interaction with other fruit, and stored at 25 ± 1 °C. The relative humidity in the storage room was maintained at 90−95%.

Disease incidence and lesion diameter were recorded daily after inoculation. Disease incidence was calculated as the percentage of fruit showing disease symptoms. The lesion area was calculated as $3.14 \times (\text{lesion diameter}/2)^2$. The inoculated tomato fruit were used only for measurement of disease symptoms.

Quantitative Real-Time PCR (qRT-PCR) Analysis. A 100 mg sample of frozen pericarp tissue in powder form was used to extract the total RNA with *EasyPure* Plant RNA Kit (Beijing Transgen Biotech Co. Ltd., Beijing, China). The total RNA was dissolved in 20 μL of RNase-free water, quantified by microspectrophotometry, and stored at −80 °C. Reverse transcription was completed to synthesize the first strand of cDNA with 1 μg of total RNA, according to the instructions from GoScript Reverse Transcription System (Promega, Madison, WI, USA).

All qRT-PCR was run with GoTag qRT-PCR Master Mix (Promega), 0.2 μM specific primer (Table 1), and 100 ng of cDNA in a 20 μL final volume per reaction. The PCR amplifications were carried out using the Chromo4 Real-Time PCR Detection System (Biorad, Hercules, CA, USA) with the following thermal cycling conditions: 94 °C for 2 min, followed by 40 cycles at 94 °C for 15 s,

DOI: 10.1021/acs.jafc.5b00437
J. Agric. Food Chem. 2015, 63, 5509−5517

Table 2. Effects of U0126 Treatment on the Relative Expressions of *SlMPK1/2/3* in "Lichun" Tomato Fruit[a]

		hours after treatment						
genes	treatments	0	0.5	1	4	8	16	24
SlMPK1	control	1.00 ± 0 a	0.72 ± 0.06 c	1.39 ± 0.0 a	0.78 ± 0.01 ab	0.82 ± 0.07 b	3.46 ± 0.25 a	0.90 ± 0.60 b
	2 μM U0126	0.97 ± 0.04 a	1.03 ± 0.09 a	1.11 ± 0.17 b	0.88 ± 0.06 a	0.96 ± 0.08 a	1.32 ± 0.03 b	1.21 ± 0.07 a
	5 μM U0126	0.98 ± 0.02 a	0.83 ± 0.03 b	0.70 ± 0.05 c	0.69 ± 0.11 c	0.89 ± 0.02 ab	0.77 ± 0.09 c	0.88 ± 0.07 b
	10 μM U0126	0.99 ± 0 a	0.14 ± 0.01 d	0.14 ± 0.04 d	0.50 ± 0.01 d	0.17 ± 0.03 c	0.58 ± 0.01 c	0.25 ± 0.03 c
	20 μM U0126	0.95 ± 0.05 a	0.16 ± 0.01 d	0.07 ± 0.01 d	0.22 ± 0.03 d	0.20 ± 0.01 c	0.19 ± 0.01 d	0.18 ± 0.01 c
SlMPK2	control	1.00 ± 0 a	1.13 ± 0.12 a	1.34 ± 0.31 a	0.99 ± 0.02 a	0.98 ± 0.19 b	3.40 ± 0.03 a	0.67 ± 0.06 b
	2 μM U0126	0.97 ± 0.04 a	1.03 ± 0.11 ab	1.15 ± 0.07 a	1.09 ± 0.04 a	1.35 ± 0.06 a	1.96 ± 0.14 b	1.06 ± 0.10 a
	5 μM U0126	0.98 ± 0.01 a	0.95 ± 0.11 b	0.79 ± 0.04 b	0.88 ± 0.07 b	0.59 ± 0.06 c	0.68 ± 0 c	0.77 ± 0.01 b
	10 μM U0126	0.96 ± 0 a	0.08 ± 0.01 c	0.09 ± 0.01 c	0.69 ± 0.08 c	0.03 ± 0.01 d	0.63 ± 0.01 c	0.35 ± 0 c
	20 μM U0126	0.99 ± 0.01 a	0.10 ± 0.02 c	0.11 ± 0.03 c	0.23 ± 0.01 d	0.18 ± 0.02 e	0.32 ± 0.11 d	0.27 ± 0.04 c
SlMPK3	control	1.00 ± 0 a	0.74 ± 0.03 b	1.11 ± 0.26 a	1.79 ± 0.12 a	1.02 ± 0.14 a	0.96 ± 0.01 a	0.81 ± 0.11 a
	2 μM U0126	1.09 ± 0.04 a	1.07 ± 0.13 a	0.94 ± 0.06 b	1.15 ± 0.06 b	1.26 ± 0.06 b	0.95 ± 0.11 b	0.90 ± 0.07 a
	5 μM U0126	1.03 ± 0.05 a	0.79 ± 0.07 b	0.68 ± 0.07 c	0.76 ± 0.07 c	0.68 ± 0.01 c	0.71 ± 0.08 c	0.66 ± 0.08 b
	10 μM U0126	0.94 ± 0.02 a	0.35 ± 0.06 c	0.1 ± 0.03 d	0.17 ± 0.01 d	0.04 ± 0 d	0.06 ± 0.01 d	0.01 ± 0 c
	20 μM U0126	0.98 ± 0.05 a	0.27 ± 0.02 c	0.18 ± 0.02 e	0.17 ± 0.01 d	0.09 ± 0 d	0.05 ± 0.02 d	0.05 ± 0.01 c

[a]Data are expressed as the mean ± SD of triplicate assays. Values followed by different letters at the same hour indicate a significant difference according to Duncan's multiple range test at $P < 0.05$.

and 60 °C for 20 s. We calculated primer efficiencies using 2-fold cDNA dilutions (1:1, 1:2, 1:4, 1:8, and 1:16) in duplicate, and we checked for amplification in a negative control without cDNA. The efficiencies of the primer sets used in this study were above 90%. The specificity of the primers was checked by analyzing the dissociation curves ranging from 55 to 94 °C. The relative gene expression for each sample was normalized and calibrated to the UBI3 Ct value and calculated using the $2^{-\Delta\Delta Ct}$ method. All experiments were run in triplicate with different cDNAs synthesized from three biological replicates.

Measurement of Phytohormone Concentrations: Indole Acetic Acid, Abscisic Acid, Gibberellic Acid, and Methyl Jasmonate. An indirect competitive enzyme-linked immunosorbent assay (icELISA) was used to quantify the contents of IAA, ABA, GA, and MeJA according to the methods of Yang et al.[32] and Deng et al.[33] with some modifications. A 0.5 g portion of frozen pericarp tissue in powder form was dispersed with 4 mL of extraction buffer (80% methanol, containing 1 mM 2,6-di-*tert*-butyl-4-methylphenol) using an IKA Disperser (T10 basic, IKA, German). The homogenate was centrifuged at 12000*g* for 15 min at 4 °C, and the supernatant was collected for analysis. The supernatant was passed through a C18-SepPak classic cartridge (Waters, Milford, CT, USA), dried by nitrogen, and dissolved with 2 mL of 0.1 mM phosphate buffered saline (PBS, pH 7.5, containing 1% (v/v) Tween-20 and 1% (w/v) gelatin) for hormone determination with icELISA. The absorbance was recorded in the microplate reader at 492 nm.

Assay of Defense Enzymes. To determine activities of β-1,3-glucanases (GLU, EC 3.2.1.39) and Chitinase (CHI, 3.2.1.14), 1 g of frozen pericarp tissue in powder form was extracted with a 5 mL of 100 mM acetic acid buffer (pH 5.2). The powder (1 g) was homogenized with 5 mL of 0.2 mM boric acid buffer (pH 8.8, containing 10% (w/v) polyvinylpyrrolidone and 1 mM EDTA) for phenylalanine ammonia lyase (PAL, EC 4.3.1.5). For polyphenol oxidase (PPO, EC 1.10.3.2) activity, 1 g of frozen pericarp tissue in powder form was extracted with a 5 mL of 100 mM PBS (pH 6.8). All extraction procedures were conducted at 4 °C. The homogenates were centrifuged at 12000*g* for 15 min at 4 °C, and the supernatants were collected. The activities of defense enzymes were determined by a spectrophotometer (Shimadu, Japan) according to Zheng et al.[34]

Assay for H_2O_2 Content and Antioxidant Enzymes. For analysis of H_2O_2, catalase (CAT, EC 1.11.1.6), ascorbate peroxidase (APX, EC 1.11.1.11), and peroxidase (POD, EC 1.11.1.7), frozen pericarp tissue in powder form (3 g) was homogenized with 6 mL of 100 mM PBS (pH 7.0) using an IKA Disperser. All extraction procedures were conducted at 4 °C. The homogenates were centrifuged at 12000*g* for 15 min at 4 °C, and the supernatants were collected. H_2O_2, CAT, and POD assay kits (Nanjing Jiancheng Bioengineering Institute, Jiangsu, China) were used to measure the H_2O_2 content and CAT and POD activities.

The APX activity was determined by the method of Nakano et al.[35] with some modifications. One unit of APX activity was defined as the amount of enzyme that caused a decrease in absorbance of 0.01 min^{-1} at 290 nm.

Statistical Analysis. The data were expressed as the mean ± standard deviation (SD). One-way analysis of variance and Duncan's multiple range tests were used for statistical evaluations by SPSS 18.0 (IBM Corp., Armonk, NY) with differences considered significant if $P < 0.05$. Pearson's regression analysis was performed to determine the correlation between the hormone concentrations, enzyme activities and H_2O_2 accumulation.

RESULTS AND DISCUSSION

Analysis of *SlMPK1/2/3* Relative Expression with qRT-PCR. U0126 is a stong inhibitor of *MAPKK1/2*.[31] Because there is no specific MAPK inhibitor, U0126 is usually used as a MAPK inhibitor. To examine the inhibitory effects of U0126 on the relative expression of *SlMPK1/2/3*, four different concentrations of U0126 were used: 2 μM and 5 μM U0126 partly inhibited the expression of *SlMPK1*, *SlMPK2*, and *SlMPK3*, whereas 10 μM and 20 μM U0126 significantly inhibited the transcript levels of *SlMPK1*, *SlMPK2*, and *SlMPK3* ($P < 0.05$) (Table 2). However, the inhibitory effects between 10 μM U0126 and 20 μM U0126 showed no significant difference in most comparisons. On the basis of these results, we chose 10 μM U0126 for further study.

The expression of *SlMPK1*, *SlMPK2*, and *SlMPK3* reduced rapidly after the 10 μM U0126 treatment (0.5 h), and it remained at low levels until the last sampling time. The expression levels of *SlMPK1* and *SlMPK2* in the control fruit peaked at 16 h. However, the peak values of expression levels for *SlMPK1* and *SlMPK2* in the control fruit were detected 8 h after treatment in our previous report,[34] which might be due to the different tomato cultivars we used in that study. The expression pattern of *SlMPK3* was different from that of *SlMPK1* and *SlMPK2*. The expression of *SlMPK3* reached the peak values at 4 h. The expressions for *SlMPK1* and *SlMPK2* were similar in the control and in the 10 μM U0126-treated tomato fruit. *SlMPK1* and *SlMPK2* show high sequence

DOI: 10.1021/acs.jafc.5b00437
J. Agric. Food Chem. 2015, 63, 5509−5517

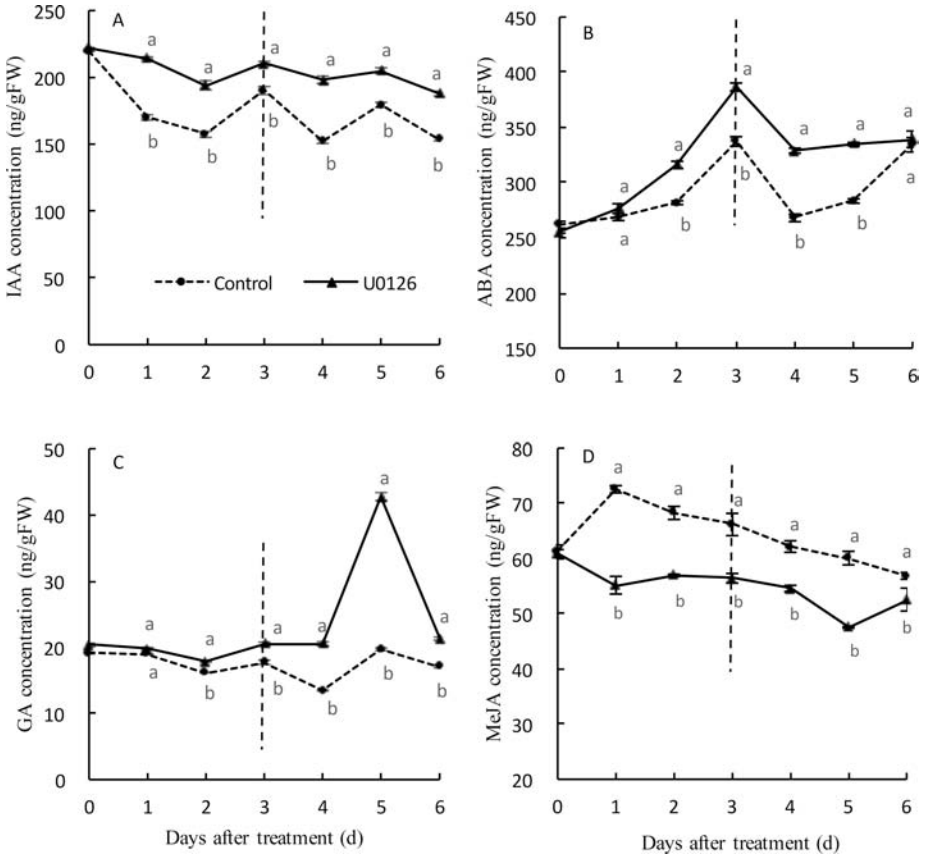

Figure 1. Effects of U0126 (10 μM) treatment on the concentration of the hormones: indole-3-acetic acid (A), abscisci acid (B), gibberellic acid (C), and methyl jasmonate (D). Vertical bars represent the standard errors of the means of triplicate assays. Values followed by different letters on the same day indicate a significant difference, according to Duncan's multiple range test ($P < 0.05$).

homology at the amino acid level, and they could be activated concurrently, which may explain the similar results we obtained. Holley et al.,[17] also reported that *SlMPK1* and *SlMPK2* were activated in response to systemins and to UV−B radiation at the same time. The increased expression of *SlMPK1*, *SlMPK2*, and *SlMPK3* in the control group of tomato fruit may be attributable to the osmotic stress response caused by the vacuum infiltration method. When a vacuum infiltrated, tomato fruit was exposed to a high osmotic stress that could induce the rapid activation of SIPK.[36] SIPK has been shown to exhibit a very high sequence homology to SlMPK1/2.

Effects of U0126 (10 μM) on Plant Hormones: Indole Acetic Aci, Abscisic Acid, Gibberellic Acid, and Methyl Jasmonate. MAPKs' inhibitor increased the concentrations of IAA, ABA, and GA, but decreased the concentration of MeJA (Figure 1). The concentration of IAA showed a fluctuating decrease in both the control and in the U0126-treated fruit. The concentrations of IAA were 26.6%, 21.6%, 10.5%, 30.2%, 14.2%, and 22% higher after the U0126 treatment than that in the controls on days 1, 2, 3, 4, 5, and 6, respectively (Figure 1A). Changes in ABA concentration in response to MAPKs' inhibitor U0126 showed a pattern that was different from that in the IAA concentration (Figure 1B). The concentration of ABA rapidly increased during the first 3 days, and then decreased. Treatment with U0126 showed a higher ABA concentration during the entire storage period. The GA concentration showed a little variation in the control fruit, but in the U0126-treated fruit, the GA concentration rapidly accumulated on day 5 and reached a peak value of 42.76 ng/gFW (Figure 1C). The concentration of MeJA in the control fruit increased on the first day, then decreased slowly through the remaining storage period (Figure 1D). Treatment with U0126 significantly decreased the MeJA concentration compared to that of the control fruit during the entire storage period ($P < 0.05$).

Plant hormones, such as IAA, ABA, GA, and MeJA, have been thoroughly documented to regulate plant development and growth. They have recently emerged as key regulators of plant disease resistance.[37] Pretreatment with IAA enhanced disease caused by *B. cinerea*, suggesting that IAA played a negative role in plant disease resistance.[28] Our study showed that MAPKs' inhibitor increased IAA concentration (Figure 1A) and promoted the susceptibility of tomato fruit to *B. cinerea* (Figure 4). The ABA-deficient mutant *sitiens* could enhance tomato resistance to *B. cinerea*.[25,38] This resistance effect depends on timely production of H_2O_2,[39] changes in cuticle permeability, and pectin composition.[40] The increased ABA level caused by the MAPKs' inhibitor (Figure 1B) increased tomato fruit disease symptoms (Figure 4). GA enhanced the hemibiotroph susceptibility partly by suppressing JA-mediated defenses.[41] MAPKs' inhibitor increased the GA concentration (Figure 1C), resulting in susceptibility to *B. cinerea* (Figure 4). Zhu et al.[7] reported that MeJA promoted the resistance response of tomato fruit to *B. cinerea*, which was consistent with our results that a lower MeJA concentration in U0126-treated fruit (Figure 1D) resulted in a lower resistance to *B. cinerea* (Figure 4). On the basis of these results, we suggest that IAA, ABA, GA, and MeJA may be involved in the

DOI: 10.1021/acs.jafc.5b00437
J. Agric. Food Chem. 2015, 63, 5509−5517

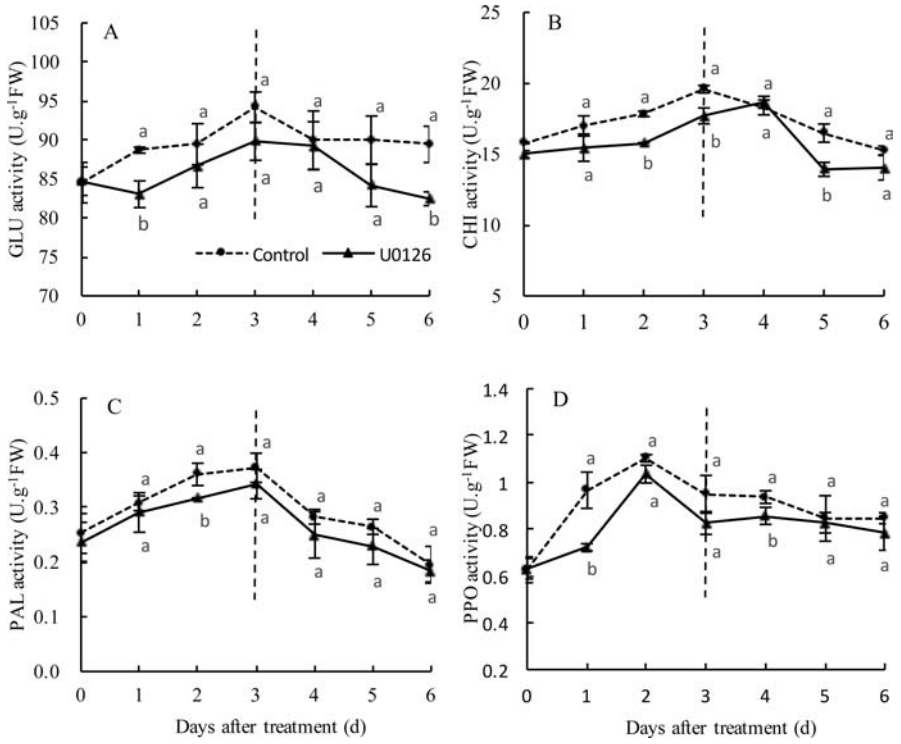

Figure 2. Effects of U0126 (10 μM) treatment on the activities of defense enzymes: β-1,3-glucanase (A), chitinase (B), phenylalanine ammonia lyase (C), and polyphenol oxidase (D). Vertical bars represent the standard errors of the means of triplicate assays. Values followed by different letters on the same day indicate a significant difference, according to Duncan's multiple range test ($P < 0.05$).

defense signaling of SlMPKs that influence tomato resistance to *B. cinerea*.

Effects of U0126 (10 μM) on β-1,3-Glucanases, Chitinase, Polyphenol Oxidase, and Phenylalanine Ammonia Lyase Activities. GLUs are abundant in plants, and they can defend plants against fungal pathogens either alone or in association with CHI and other defense enzymes.[42] GLU activity in U0126-treated tomato fruit was lower than that in the control fruit during the entire storage period (Figure 2A). GLU activity significantly decreased after MAPKs' inhibitor treatment on days 1 and 6 ($P < 0.05$). U0126 treatment decreased the CHI activity, except for day 4 (Figure 2B).

The PAL activity of both the control and U0126-treated fruit increased during the early stage after treatments and then decreased and reached a maximum on day 3; however, PAL activity was inhibited by MAPKs' inhibitor U0126 and showed a significant difference compared with the control on day 2 (Figure 2C).

Changes in PPO activity in response to MAPKs' inhibitor U0126 showed a pattern similar to PAL activity. The PPO activity in both control and U0126-treated fruit increased within 2 days and then decreased. PPO activity reached a maximum on day 2, 1 day earlier than PAL activity (Figure 2D). PPO activity in U0126-treated fruit was lower than that of the control fruit during the entire storage period.

The same trends were observed in GLU, CHI, PAL, and PPO activities in response to MAPKs' inhibitor (Figure 2). Disease enzymes increased during the early stage of storage and then decreased, but they peaked on different days, possibly because different enzymes respond to pathogen attacks at different times. Disease enzymes in the U0126-treated fruit were lower than that in the control fruit, which suggests that there was an intermediate role of SlMPKs in the disease response to *B. cinerea* in postharvest tomato fruit.

Generally, plants have evolved a large variety of defense responses against pathogen infection, including the synthesis of pathogenesis-related (PR) proteins, the enhanced activities of various defense enzymes, and up-regulation of expression of defense genes expression.[3,5,43] CHI and GLU belong to the PR-2 and PR-3 families, respectively. CHI and GLU destroy fungi cell walls by catalyzing the hydrolysis of chitin and β-1,3-glucan.[42] PAL is a key enzyme in the phenylpropanoid pathway of higher plants.[44] Products of the phenylpropanoid pathway are key contributors to disease resistance.[45] Thus, PAL activity can indirectly reflect disease resistance in plants. PPOs are ubiquitous among higher plants, and they are assumed to be involved in plant defense against pathogens. Quinones produced by PPOs may possess direct antibiotic and cytotoxic activities to pathogens. Li et al.[46] found that overexpression of polyphenol oxidase in transgenic tomato plants resulted in enhanced bacterial disease resistance. The effect of U0126 on defense enzymes is possibly a dynamic, unstable process, which has been validated by Melvin et al.[47] They found that pathogen inoculation significantly increased the activities of defense enzymes and that U0126 had no significant influence on the activities of defense enzymes, but U0126 could significantly abolish the activities of defense enzymes induced by pathogen inoculation.[47] So we assume that although there were no large decreases in the activities of GLU, CHI, PAL, and PPO in U0126-treated tomato fruit, when tomato fruit is attacked by pathogens, U0126 may abolish the activities of defense enzymes induced by the pathogen, which leads ultimately to a more serious decay.

Effects of U0126 (10 μM) on H_2O_2, Catalase, Ascorbate Peroxidase, and Peroxidase. The H_2O_2 content peaked on

DOI: 10.1021/acs.jafc.5b00437
J. Agric. Food Chem. 2015, 63, 5509−5517

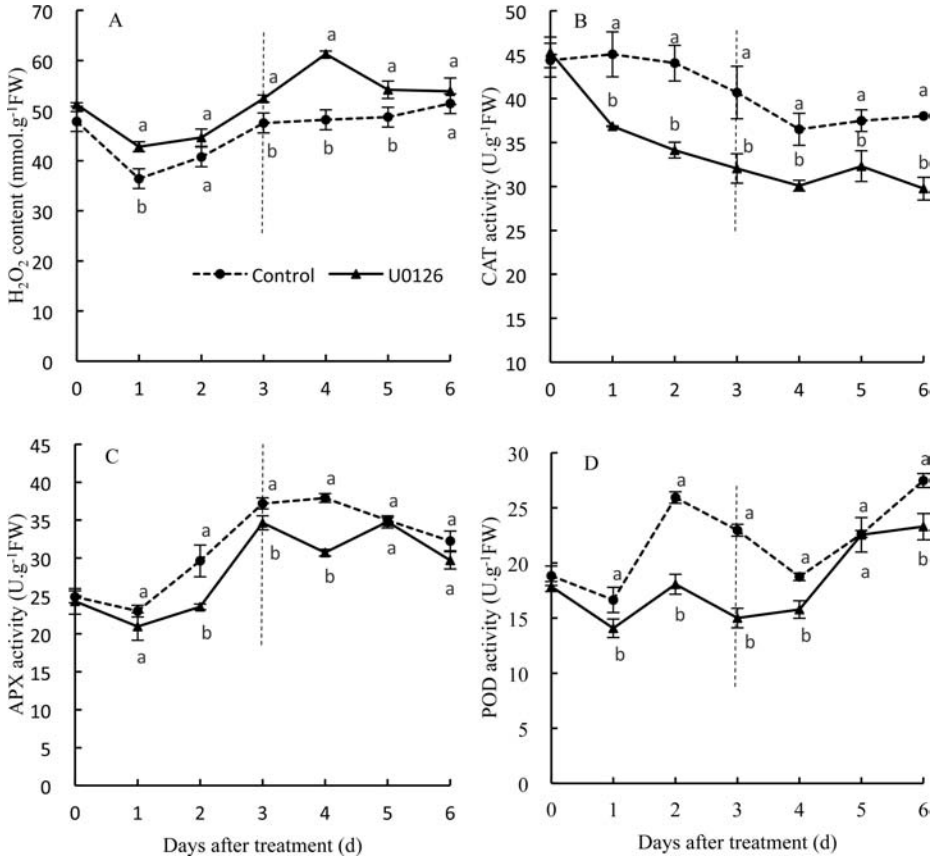

Figure 3. Effects of U0126 (10 μM) treatment on H_2O_2 content (A), catalase (B), ascorbate peroxidase (C), anmd peroxidase (D) in "Lichun" tomato fruit. Vertical bars represent the standard errors of the means of triplicate assays. Values followed by different letters on the same day indicate a significant difference, according to Duncan's multiple range test ($P < 0.05$).

day 4 in the U0126-treated fruit. Treatment with MAPKs' inhibitor U0126 regulated the level of H_2O_2. The H_2O_2 content in the U0126-treated fruit was significantly lower than that of the control at 3−5 days of storage ($P < 0.05$) (Figure 3A).

CAT, APX, and POD activity in U0126-treated fruit were lower than those in control fruit during the entire storage period (Figure 3B, C, and D). CAT activity reached a minimum value on day 4 in the control fruit (Figure 3B), which was consistent with the peak in H_2O_2 content (Figure 3A). CAT activity in U0126-treated fruit showed a fluctuating decrease and was significantly lower than that in the control fruit. Changes in the APX activity (Figure 3C) were different from that of CAT. APX activity in the control fruit increased with some fluctuation during the first 4 days, then decreased. Treatment with U0126 significantly reduced APX activity on days 2, 3, and 4 ($P < 0.05$). POD activity in the U0126-treated fruit significantly decreased compared with the control, except for day 5 ($P < 0.05$). After 6 days, POD activity in the control fruit reached a maximum, with a value of 27.48 U g^{-1} FW, which was 17.9% higher than that of the U0126-treated fruit.

H_2O_2 is one of the most important ROS that have been recorded in the signaling pathway leading to resistance against plant disease.[48] Previous research has indicated that MAPK cascades could mediate the defense response as a downstream component of H_2O_2 signaling, and H_2O_2 was a potent activator of MAPK. Meanwhile, activation of MAPK also enhanced the H_2O_2 content, forming a positive feedback loop.[48,49] Wang et al.[50] found that pretreatment with U0126 could accelerate H_2O_2 production and that it eventually enhanced cell death. We noted a similar change in H_2O_2 production in the U0126-treated tomato fruit, and this finally enhanced the susceptibility to *B. cinerea*.

CAT, APX, and POD, the important antioxidant enzymes downstream of H_2O_2 signaling, serve as efficient scavengers of ROS to avoid oxidative damage. A number of studies have shown that disease resistance to pathogens was accompanied by an increase in CAT, APX, and POD activity.[51] Our results showed that MAPKs' inhibitor (U0126) decreased the activity of CAT, APX, and POD (Figure 3B, C, and D). These results could partly illustrate that H_2O_2, CAT, APX, and POD are involved in the MAPKs pathway, which contributes to the resistance of tomato fruit to invasion and expansion of *B. cinerea*. ABA and H_2O_2 could activate MAPK, enhance the activities of the antioxidant enzymes, and accelerate H_2O_2 production, but U0126 could abolish these effects by ABA and H_2O_2.[48]

Effects of U0126 (10 μM) on Disease Incidence and Lesion Area. *B. cinerea* was used as a model necrotrophic fungal pathogen to investigate whether inhibition of *SlMPK1/2/3* expression in tomato fruit would result in an increased susceptibility to pathogen attacks. The disease incidence and lesion area directly reflected the degree of development of disease symptoms; these measures are used widely in the study of plant defense response.[22] U0126 (10 μM) significantly increased the disease incidence and lesion area in tomato fruit after inoculation with *B. cinerea* when compared with the control ($P < 0.05$). The disease incidence in the U0126-treated fruit increased by 77.3%, 48.0%, 28.2%, and 10.7% on days 1, 2,

DOI: 10.1021/acs.jafc.5b00437
J. Agric. Food Chem. 2015, 63, 5509−5517

3, and 4 after inoculation with *B. cinerea*, respectively (Figure 4A). All fruit in the U0126-treated group showed typical symptoms of *B. cinerea* on the fourth day after inoculation, but 9.67% of the control fruit were still not infected with gray mold disease. The lesion area in the U0126-treated tomato fruit was significantly larger than that of the control fruit. The lesion area in the U0126-treated fruit increased by 189.1%, 145.1%, and 105.1% compared with the control fruit (Figure 4B). Although most of the fruit showed symptoms of decay after inoculation with *B. cinerea*, the symptoms diffused faster in the U0126-treated fruit than in the control fruit. The higher diffusion rate in the treated fruit might result from a disturbance of the fruit's innate system by the MAPKs' inhibitor, which promoted the susceptibility of the tomato fruit to *B. cinerea*. These results indicate that MAPK signaling cascades played a crucial role in the regulation of defense response in the tomato fruit.

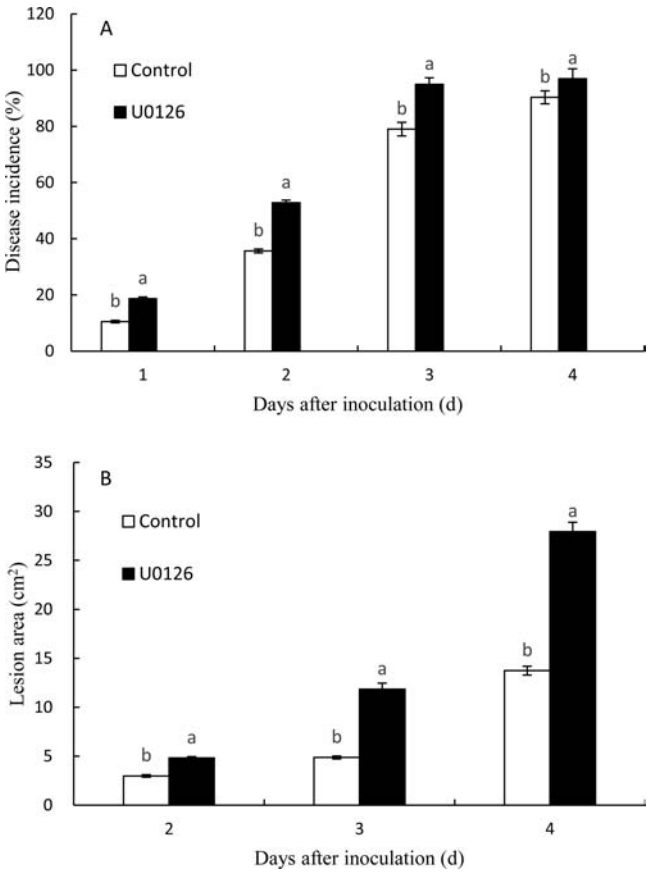

Figure 4. Effects of U0126 (10 μM) treatment on disease incidence (A) and lesion area (B) caused by *B. cinerea* in "Lichun" tomato fruit. Vertical bars represent standard errors of means and different lowercase letters on the same day above the bars are significantly different at $P < 0.05$, according to Duncan's multiple range tests.

Comparison of The Hormone Concentrations, Enzyme Activities and H_2O_2 Accumulation. The correlation coefficients for H_2O_2, POD, CAT, APX, GLU, PAL, CHI, PPO, IAA, GA, ABA, and MeJA are shown in Table 3. Significant correlations were observed among IAA−CAT, ABA−CAT, ABA−APX, GA−MeJA, and GLU−CHI after U0126 treatment ($P < 0.05$); however, no significant correlations were observed between H_2O_2 accumulation and hormone concentrations, and enzyme activities ($P > 0.05$). The significant correlations between ABA−CAT and ABA−APX may be due to that the activities of CAT, and APX could be induced by ABA.[48] The close relationship between GLU and CHI ($R = 0.9$) could possibly be attributed to the fact that both GLU and CHI are PR proteins.

The change profiles of hormone concentrations, enzyme activities, and H_2O_2 content were different between the first 3 days and the last 3 days of treatments. This can be well reflected by the following results: (1) During the first 3 days, the ABA increased rapidly, but decreased during the last 3 days (Figure 1B). (2) GA showed a small variation during the first 3 days, but accumulated sharply during the last 3 days (Figure 1C). (3) The activities of the defense enzymes (GLU, CHI, and PAL) increased during the first 3 days, but decreased during the last 3 days (Figure 2). (4) The H_2O_2 content was higher during the last 3 days than that during the first 3 days (Figure 3A). (5) The activity of CAT rapidly decreased during the first 3 days, but showed a stable and low activity during the last 3 days (Figure 3B). These results illustrate that the effects of U0126 treatment on defense responses were more important during the early stage than the late stage. These may explain why the differences were not large (although significant) in disease symptoms of the control and U0126-treated fruit during the last days of infection.

In conclusion, 10 μM of U0126 significantly inhibited the gene expression of *SlMPK1*, *SlMPK2*, and *SlMPK3*, which resulted in an increase in disease symptoms after inoculation with *B. cinerea*. The balance of hormones (IAA, ABA, GA, and

Table 3. Pearson's correlations (R) between all the hormone concentration, enzyme activities and H_2O_2 content

	H_2O_2	POD	CAT	APX	GLU	PAL	CHI	PPO	IAA	GA	ABA	MeJA
H_2O_2	1	0.251	−0.414	0.716	0.400	−0.462	0.356	−0.061	−0.255	0.265	0.407	−0.291
POD		1	−0.245	0.348	−0.531	−0.740	−0.735	0.061	−0.509	0.568	0.140	−0.574
CAT			1	−0.592	−0.257	0.072	−0.250	−0.586	**0.792**[a]	−0.184	**−0.804**[a]	0.670
APX				1	0.407	−0.135	0.171	0.142	−0.235	0.566	**0.816**[a]	−0.569
GLU					1	0.610	**0.900**[b]	0.421	0.004	−0.245	0.524	0.263
PAL						1	0.548	0.406	0.292	−0.343	0.208	0.394
CHI							1	0.268	0.029	−0.459	0.341	0.334
PPO								1	−0.674	−0.025	0.485	−0.224
IAA									1	0.022	−0.486	0.446
GA										1	0.180	**−0.799**[a]
ABA											1	−0.433
MeJA												1

[a]$P < 0.05$ (two-tail). [b]$P < 0.01$ (two-tail).

DOI: 10.1021/acs.jafc.5b00437
J. Agric. Food Chem. 2015, 63, 5509−5517

MeJA) were interfered by the MAPKs' inhibitor, suggesting that plant hormones were involved in the defense signaling pathway of SlMPKs. In addition, the increase in disease symptoms caused by MAPKs' inhibitor may be due to the decrease in the activity of GLU, CHI, PAL, and PPO, which are the primary defenders against fungal pathogens. Moreover, the H_2O_2 content increased, and CAT, APX, and POD activities decreased in MAPKs' inhibitor-treated fruit compared with that of the control fruit, which suggested that SlMPKs might act as defense signaling molecules, partly through the ROS signal. Thus, recognition of the role of *SlMPK1/2/3* in innate immunity can be useful in culturing *SlMPK1/2/3* overexpression in tomatoes to reduce pathogen losses during tomato plant growth and fruit storage.

AUTHOR INFORMATION

Corresponding Author

*Phone: +86-10-62737620. Fax: +86-10-62737620. E-mail: shen5000@cau.edu.cn.

Funding

This research was supported by the National Natural Science Foundation of China (No. 31371847).

Notes

The authors declare no competing financial interest.

ABBREVIATIONS USED

ABA, abscisic acid; APX, ascorbate peroxidase; *B. cinerea*, *Botrytis cinerea*; CAT, catalase; CHI, chitinase; GA, gibberellic acid; GLU, β-1,3-glucanases; IAA, indole acetic acid; MAPKs, mitogen-activated protein kinases; MeJA, methyl jasmonate; PAL, phenylalanine ammonia lyase; PBS, phosphate buffer saline; POD, peroxidase; PPO, polyphenol oxidase; ROS, reactive oxygen species; SIPK, salicylic acid-induced protein kinase; SlMPKs, *Solanum lycopersicum* mitogen-activated protein kinases; U0126, 1,4-diamino-2,3-dicyano-1,4-bis(*o*-aminophenylmercapto)butadiene; WIPK, wounding-induced protein kinase

REFERENCES

(1) Williamson, B.; Tudzynski, B.; Tudzynski, P.; Kan van, J. A. L. *Botrytis cinerea*: The Cause of Grey Mould Disease. *Mol. Plant Pathol.* **2007**, *8*, 561−580.

(2) Prins, T. W.; Tudzynski, P.; von Tiedemann, A.; Tudzynski, B.; Ten Have, A.; Hansen, M. E.; Tenberge, K.; van Kan, J. A. Infection Strategies of *Botrytis cinerea* and Related Necrotrophic Pathogens. In *Fungal Pathology*; Springer Netherlands: Dordrecht, Netherland, 2000; pp 33−64.

(3) Cantu, D.; Blanco-Ulate, B.; Yang, L.; Labavitch, J. M.; Bennett, A. B.; Powell, A. L. T. Ripening-Regulated Susceptibility of Tomato Fruit to *Botrytis cinerea* Requires nor but Not RIN or Ethylene. *Plant Physiol.* **2009**, *150*, 1434−1449.

(4) Cantu, D.; Vicente, A. R.; Labavitch, J. M.; Bennett, A. B.; Powell, A. L. T. Strangers in the Matrix: Plant Cell Walls and Pathogen Susceptibility. *Trends Plant Sci.* **2008**, *13*, 610−617.

(5) Alkan, N.; Friedlander, G.; Ment, D.; Prusky, D.; Fluhr, R. Simultaneous Transcriptome Analysis of *Colletotrichum Gloeosporioides* Tomato Fruit Pathosystem Reveals Novel Fungal Pathogenicity and Fruit Defense Strategies. *New Phytol.* **2015**, *205*, 801−815.

(6) Cantu, D.; Vicente, A. R.; Greve, L. C.; Dewey, F. M.; Bennett, A. B.; Labavitch, J. M.; Powell, A. L. T. The Intersection Between Cell Wall Disassembly, Ripening, and Fruit Susceptibility to *Botrytis cinerea*. *Proc. Natl. Acad. Sci. U. S. A.* **2008**, *105*, 859−864.

(7) Zhu, Z.; Tian, S. Resistant Responses of Tomato Fruit Treated with Exogenous Methyl Jasmonate to *Botrytis cinerea* Infection. *Sci. Hortic.* **2012**, *142*, 38−43.

(8) Asai, T.; Tena, G.; Plotnikova, J.; Willmann, M. R.; Chiu, W. L.; Gomez-Gomez, L.; Boller, T.; Ausubel, F. M.; Sheen, J. MAP Kinase Signalling Cascade in *Arabidopsis* Innate Immunity. *Nature* **2002**, *415*, 977−983.

(9) Smékalová, V.; Doskočilová, A.; Komis, G.; Šamaj, J. Crosstalk between Secondary Messengers, Hormones and MAPK Modules during Abiotic Stress Signalling in Plants. *Biotechnol. Adv.* **2014**, *32*, 2−11.

(10) Danquah, A.; de Zelicourt, A.; Colcombet, J.; Hirt, H. The Role of ABA and MAPK Signaling Pathways in Plant Abiotic Stress Responses. *Biotechnol. Adv.* **2014**, *32*, 40−52.

(11) Meng, X.; Zhang, S. MAPK Cascades in Plant Disease Resistance Signaling. *Annu. Rev. Phytopathol.* **2013**, *51*, 245−266.

(12) Katou, S.; Asakura, N.; Kojima, T.; Mitsuhara, I.; Seo, S. Transcriptome Analysis of WIPK/SIPK-Suppressed Plants Reveals Induction by Wounding of Disease Resistance-Related Genes Prior to the Accumulation of Salicylic Acid. *Plant Cell Physiol.* **2013**, *54*, 1005−1015.

(13) Xu, J.; Xie, J.; Yan, C.; Zou, X.; Ren, D.; Zhang, S. A Chemical Genetic Approach Demonstrates that MPK3/MPK6 Activation and NADPH Oxidase-Mediated Oxidative Burst Are Two Independent Signaling Events in Plant Immunity. *Plant J.* **2014**, *77*, 222−234.

(14) Kong, F.; Wang, J.; Cheng, L.; Liu, S.; Wu, J.; Peng, Z.; Lu, G. Genome-Wide Analysis of the Mitogen-Activated Protein Kinase Gene Family in *Solanum Lycopersicum*. *Gene* **2012**, *499*, 108−120.

(15) Wu, J.; Wang, J.; Pan, C.; Guan, X.; Wang, Y.; Liu, S.; He, Y.; Chen, J.; Chen, L.; Lu, G. Genome-Wide Identification of MAPKK and MAPKKK Gene Families in Tomato and Transcriptional Profiling Analysis During Development and Stress Response. *PLoS One* **2014**, *9*, e103032.

(16) Higgins, R.; Lockwood, T.; Holley, S.; Yalamanchili, R.; Stratmann, J. W. Changes in Extracellular pH Are Neither Required nor Sufficient for Activation of Mitogen-Activated Protein Kinases (MAPKs) in Response to Systemin and Fusicoccin in Tomato. *Planta* **2007**, *225*, 1535−1546.

(17) Holley, S. R.; Yalamanchili, R. D.; Moura, D. S.; Ryan, C. A.; Stratmann, J. W. Convergence of Signaling Pathways Induced by Systemin, Oligosaccharide Elicitors, and Ultraviolet-B Radiation at the Level of Mitogen-Activated Protein Kinases in *Lycopersicon Peruvianum* Suspension-Cultured Cells. *Plant Physiol.* **2003**, *132*, 1728−1738.

(18) Mayrose, M.; Bonshtien, A.; Sessa, G. LeMPK3 Is a Mitogen-Activated Protein Kinase with Dual Specificity Induced During Tomato Defense and Wounding Responses. *J. Biol. Chem.* **2004**, *279*, 14819−14827.

(19) Li, C.; Yan, J. M.; Li, Y. Z.; Zhang, Z. C.; Wang, Q. L.; Liang, Y. Silencing the SpMPK1, SpMPK2, and SpMPK3 Genes in Tomato Reduces Abscisic Acid-Mediated Drought Tolerance. *Int. J. Mol. Sci.* **2013**, *14*, 21983−21996.

(20) Virk, N.; Liu, B.; Zhang, H.; Li, X.; Zhang, Y.; Li, D.; Song, F.; Tomato SlMPK4, Is Required for Resistance Against *Botrytis cinerea* and Tolerance to Drought Stress. *Acta Physiol. Plant.* **2013**, *35*, 1211−1221.

(21) Kandoth, P. K.; Ranf, S.; Pancholi, S. S.; Jayanty, S.; Walla, M. D.; Miller, W.; Howe, G. A.; Lincoln, D. E.; Stratmann, J. W. Tomato MAPKs LeMPK1, LeMPK2, and LeMPK3 Function in the Systemin-Mediated Defense Response Against Herbivorous Insects. *Proc. Natl. Acad. Sci. U. S. A.* **2007**, *104*, 12205−12210.

(22) Li, X.; Zhang, Y.; Huang, L.; Ouyang, Z.; Hong, Y.; Zhang, H.; Li, D.; Song, F. Tomato SlMKK2 and SlMKK4 Contribute to Disease Resistance Against *Botrytis cinerea*. *BMC Plant Biol.* **2014**, *14*, 166.

(23) Melech-Bonfil, S.; Sessa, G. The SlMKK2 and SlMPK2 Genes Play a Role in Tomato Disease Resistance to *Xanthomonas Campestris Pv.Vesicatoria*. *Plant Signaling Behav.* **2011**, *6*, 154−156.

(24) Bari, R.; Jones, J. D. Role of Plant Hormones in Plant Defence Responses. *Plant Mol. Biol.* **2009**, *69*, 473−488.

DOI: 10.1021/acs.jafc.5b00437
J. Agric. Food Chem. 2015, 63, 5509−5517

(25) Blanco-Ulate, B.; Vincenti, E.; Powell, A. L.; Cantu, D. Tomato Transcriptome and Mutant Analyses Suggest a Role for Plant Stress Hormones in the Interaction Between Fruit and *Botrytis cinerea*. *Front. Plant Sci.* **2013**, *4*, 142.
(26) Navarro, L.; Bari, R.; Achard, P.; Lisón, P.; Nemri, A.; Harberd, N. P.; Jones, J. D. G. DELLAs Control Plant Immune Responses by Modulating the Balance of Jasmonic Acid and Salicylic Acid Signaling. *Curr. Biol.* **2008**, *18*, 650−655.
(27) Audenaert, K.; De Meyer, G. B.; Hofte, M. M. Abscisic Acid Determines Basal Susceptibility of Tomato to *Botrytis cinerea* and Suppresses Salicylic Acid-Dependent Signaling Mechanisms. *Plant Physiol.* **2002**, *128*, 491−501.
(28) Gonzalez-Lamothe, R.; El Oirdi, M.; Brisson, N.; Bouarab, K. The Conjugated Auxin Indole-3-Acetic Acid-Aspartic Acid Promotes Plant Disease Development. *Plant Cell* **2012**, *24*, 762−777.
(29) Asselbergh, B.; Curvers, K.; Franca, S. C.; Audenaert, K.; Vuylsteke, M.; Van Breusegem, F.; Hofte, M. Resistance to *Botrytis cinerea* In Sitiens, an Abscisic Acid-Deficient Tomato Mutant, Involves Timely Production of Hydrogen Peroxide and Cell Wall Modifications in the Epidermis. *Plant Physiol.* **2007**, *144*, 1863−1877.
(30) Nie, W. F.; Wang, M. M.; Xia, X. J.; Zhou, Y. H.; Shi, K.; Chen, Z. X.; Yu, J. Q. Silencing of Tomato RBOH1 and MPK2 Abolishes Brassinosteroid-Induced H_2O_2 Generation and Stress Tolerance. *Plant, Cell Environ.* **2013**, *36*, 789−803.
(31) Duncia, J. V.; Santella, J. B.; Higley, C. A.; Pitts, W. J.; Wityak, J.; Frietze, W. E.; Rankin, F. W.; Sun, J.-H.; Earl, R. A.; Tabaka, A. C. MEK Inhibitors: the Chemistry and Biological Activity of U0126, Its Analogs, and Cyclization Products. *Bioorg. Med. Chem. Lett.* **1998**, *8*, 2839−2844.
(32) You Ming, Y.; Chu Nian, X.; Bao Min, W.; Jun Zhen, J. Effects of Plant Growth Regulators on Secondary Wall Thickening of Cotton Fibres. *Plant Growth Regul.* **2001**, *35*, 233−237.
(33) Deng, A.; Tan, W.; He, S.; Liu, W.; Nan, T.; Li, Z.; Wang, B.; Li, Q. X. Monoclonal Antibody-Based Enzyme Linked Immunosorbent Assay for the Analysis of Jasmonates in Plants. *J. Integr. Plant Biol.* **2008**, *50*, 1046−1052.
(34) Zheng, Y.; Hong, H.; Chen, L.; Li, J.; Sheng, J.; Shen, L. *LeMAPK1*, *LeMAPK2*, And *LeMAPK3* Are Associated with Nitric Oxide-Induced Defense Response Against *Botrytis cinerea* in the *Lycopersicon Esculentum* Fruit. *J. Agric. Food Chem.* **2014**, *62*, 1390−1396.
(35) Nakano, Y.; Asada, K. Hydrogen Peroxide Is Scavenged by Ascorbate-Specific Peroxidase in Spinach Chloroplasts. *Plant Cell Physiol.* **1981**, *22*, 867−880.
(36) Mikołajczyk, M.; Awotunde, O. S.; Muszyńska, G.; Klessig, D. F.; Dobrowolska, G. Osmotic Stress Induces Rapid Activation of a Salicylic Acid-Induced Protein Kinase and a Homolog of Protein Kinase ASK1 in Tobacco Cells. *Plant Cell* **2000**, *12*, 165−178.
(37) Denancé, N.; Sánchez-Vallet, A.; Goffner, D.; Molina, A. Disease Resistance or Growth: the Role of Plant Hormones in Balancing Immune Responses and Fitness Costs. *Front. Plant Sci.* **2013**, *4*, 1−12.
(38) Audenaert, K.; De Meyer, G. B.; Höfte, M. M. Abscisic Acid Determines Basal Susceptibility of Tomato to *Botrytis cinerea* and Suppresses Salicylic Acid-Dependent Signaling Mechanisms. *Plant Physiol.* **2002**, *128*, 491−501.
(39) Asselbergh, B.; Curvers, K.; França, S. C.; Audenaert, K.; Vuylsteke, M.; Van Breusegem, F.; Hofte, M. Resistance to *Botrytis cinerea* in Sitiens, an Abscisic Acid-Deficient Tomato Mutant, Involves Timely Production of Hydrogen Peroxide and Cell Wall Modifications in the Epidermis. *Plant Physiol.* **2007**, *144*, 1863−1877.
(40) Curvers, K.; Seifi, H.; Mouille, G.; De Rycke, R.; Asselbergh, B.; Van Hecke, A.; Vanderschaeghe, D.; Höfte, H.; Callewaert, N.; Van Breusegem, F. Abscisic Acid Deficiency Causes Changes in Cuticle Permeability and Pectin Composition That Influence Tomato Resistance to *Botrytis cinerea*. *Plant Physiol.* **2010**, *154*, 847−860.
(41) Vidhyasekaran, P. Gibberellin Signaling in Plant Innate Immunity. In *Plant Hormone Signaling Systems in Plant Innate Immunity*; Signaling and Communication in Plants; Springer Netherlands: Dordrecht, Netherland, 2015; Vol. 2, pp 383−401.
(42) Cota, I. E.; Troncoso-Rojas, R.; Sotelo-Mundo, R.; Sánchez-Estrada, A.; Tiznado-Hernández, M. E. Chitinase and β-1,3-Glucanase Enzymatic Activities in Response to Infection by *Alternaria Alternata* Evaluated in Two Stages of Development in Different Tomato Fruit Varieties. *Sci. Hortic.* **2007**, *112*, 42−50.
(43) Baysal, Ö.; Soylu, E. M.; Soylu, S. Induction of Defence-Related Enzymes and Resistance by the Plant Activator Acibenzolar-S-Methyl in Tomato Seedlings Against Bacterial Canker Caused by *Clavibacter Michiganensis ssp. Michiganensis*. *Plant Pathol.* **2003**, *52*, 747−753.
(44) Rawal, H. C.; Singh, N. K.; Sharma, T. R. Conservation, Divergence, and Genome-Wide Distribution of PAL and POX a Gene Families in Plants. *Int. J. Genomics* **2013**, *2013*, 1−10.
(45) Vogt, T. Phenylpropanoid Biosynthesis. *Mol. Plant* **2010**, *3*, 2−20.
(46) Li, L.; Steffens, J. C. Overexpression of Polyphenol Oxidase in Transgenic Tomato Plants Results in Enhanced Bacterial Disease Resistance. *Planta* **2002**, *215*, 239−247.
(47) Melvin, P.; Prabhu, S. A.; Anup, C. P.; Shailasree, S.; Shetty, H. S.; Kini, K. R. Involvement of Mitogen-Activated Protein Kinase Signalling in Pearl Millet-Downy Mildew Interaction. *Plant Sci.* **2014**, *214*, 29−37.
(48) Zhang, A. Mitogen-Activated Protein Kinase Is Involved in Abscisic Acid-Induced Antioxidant Defense and Acts Downstream of Reactive Oxygen Species Production in Leaves of Maize Plants. *Plant Physiol.* **2006**, *141*, 475−487.
(49) Li, S. W.; Xue, L. The Interaction Between H_2O_2 and NO, Ca^{2+}, cGMP, and MAPKs During Adventitious Rooting in Mung Bean Seedlings. *In Vitro Cell. Dev. Biol.: Plant* **2010**, *46*, 142−148.
(50) Wang, J.; Li, X.; Liu, Y.; Zhao, X.; Chen, C.; Tian, F. MEK/ERK Inhibitor U0126 Enhanced Salt Stress-Induced Programmed Cell Death in *Thellungiella Halophila* Suspension-Cultured Cells. *Plant Growth Regul.* **2011**, *63*, 207−216.
(51) Su, Y.; Guo, J.; Ling, H.; Chen, S.; Wang, S.; Xu, L.; Allan, A. C.; Que, Y. Isolation of a Novel Peroxisomal Catalase Gene From Sugarcane, Which Is Responsive to Biotic and Abiotic Stresses. *PLoS One* **2014**, *9*, e84426.

DOI: 10.1021/acs.jafc.5b00437
J. Agric. Food Chem. 2015, 63, 5509−5517

The total antioxidant capacity (TAC) of aqueous extracts and the Trolox equivalent antioxidant capacity (TEAC) of the target compounds were assessed using the 2,2-diphenyl-1-picrylhydrazyl radical (DPPH$^{\bullet}$) scavenging and oxygen radical absorbance capacity (ORAC) assays. These assays were selected as they are commonly used by extract manufacturers in South Africa for product specification and quality control of natural plant extracts. The TEAC of the minor benzophenone, maclurin-3-*C*-glucoside, was also calculated to determine the impact of increased B-ring hydroxylation on the antioxidant activity of the benzophenones.

MATERIALS AND METHODS

Chemicals. HPLC gradient-grade methanol was purchased from Merck Millipore (Darmstadt, Germany). Acetonitrile and acetic acid (≥99.8%) were obtained from Riedel-de Haën (Sigma-Aldrich, St. Louis, MO, USA). Analytical grade reagents and chemicals, i.e., 2,2-diphenyl-1-picrylhydrazyl (DPPH), 2,2′-azobis(2-methylpropionamide) dihydrochloride (AAPH), (±)-6-hydroxy-2,5,7,8-tetramethylchromane-2-carboxylic acid (Trolox), potassium dihydrogen phosphate (KH_2PO_4), potassium hydroxide (KOH), and ascorbic acid, were supplied by Sigma-Aldrich. Fluorescein sodium ($C_{20}H_{10}Na_2O_5$) was obtained from Fluka (Sigma-Aldrich). Ethanol was analytical grade (99%) and sourced from Servochem (Cape Town, South Africa). HPLC-grade water was prepared using Elix and Milli-Q Academic (Merck Millipore) water purification systems in series.

Authentic reference standards with purities >95% were supplied by Sigma-Aldrich (mangiferin, hesperidin, iriflophenone-3-*C*-glucoside), Extrasynthese (Genay, France; eriocitrin, narirutin), Chemos GmbH (Regenstauf, Germany; isomangiferin) and Phytolab (Vestenbergsgreuth, Germany; vicenin-2). Maclurin-3-*C*-glucoside (95%) and iriflophenone-3-*C*-glucoside-4-*O*-glucoside (99%) were isolated from *C. genistoides*.[6] Phloretin-3′,5′-di-*C*-glucoside, isolated from *C. subternata* to a purity of 94% (as assessed by liquid chromatography coupled with diode-array and electrospray ionization mass spectrometric detection, LC-DAD-ESI-MS), was unambiguously identified by nuclear magnetic resonance spectroscopy. Stock solutions of the phenolic standards were prepared in dimethyl sulfoxide (DMSO) at concentrations of ca. 1 mg/mL, diluted with water as required, and filtered through 0.22 μm pore size Millex-GV syringe filters (4 mm diameter; Merck Millipore) prior to use.

Thermal Degradation Kinetics Modeling. The levels of the major benzophenones, iriflophenone-3-*C*-glucoside-4-*O*-glucoside and iriflophenone-3-*C*-glucoside, and the major xanthones, mangiferin and isomangiferin, in *Cyclopia genistoides* plant material were monitored during high-temperature oxidation to establish kinetic parameters governing their degradation. Experiments were conducted on a small scale under highly controlled conditions. The two temperature−time combinations investigated, i.e., 80 °C/24 h and 90 °C/16 h, are representative of the optimum temperature−time regiments recommended to the honeybush industry for the production of the oxidized herbal tea product.

The shoots (leaves and fine stems) from a single *C. genistoides* (L.) Vent (Overberg type) bush were harvested from a commercial plantation near Pearly Beach (Western Cape, South Africa; GPS coordinates −34.702, 19.618). The shoots were dried intact in a forced-air laboratory oven at 40 °C to a moisture content of <10%, whereafter the plant material was pulverized using a Retsch rotary mill (Retsch GmbH, Haan, Germany). A subsample was then sieved to obtain the fraction <50 mesh to ensure a homogeneous sample. The sieved plant material (ca. 80 mg) was weighed off into 4 mL clear glass vials (n = 4 for each time point), followed by addition of 130 μL of deionized water to achieve a final moisture content of ca. 65% and water activity (a_w) of ca. 0.97. The a_w value of the wetted plant material was measured using a Labmaster a_w meter (Novasina AG, Lachen, Switzerland). The vial contents were vortexed, the vials were placed in preheated water baths at 80 and 90 °C, and the required number of vials was removed at each time point. Samples were taken hourly until 16 h for both the 80 and 90 °C trials, followed by sampling at 2 h intervals until 24 h for the 80 °C trial. The control samples received no treatment.

The samples were cooled to room temperature, followed by the addition of 4 mL of 40% aqueous ethanol (v/v) and sonication for 30 min (ultrasonic bath, Branson Ultrasonic Corp., Danbury, CT, USA). The extracts were cooled and filtered (0.45 μm pore size, 33 mm diameter Millex-HV syringe filters; Merck Millipore) and an aliquot of each was diluted 10 times with deionized water. Sample extracts were prepared for high-performance liquid chromatographic (HPLC) analysis by adding 100 μL of 10% aqueous ascorbic acid to 1 mL of the diluted extract.

HPLC-DAD analyses were performed in duplicate on an Agilent 1200 series instrument according to the validated method of Beelders et al.[1] The target benzophenones and xanthones in the sample extracts were identified by coelution with the authentic reference standards and were quantified at 280 and 320 nm, respectively. Due to a limited quantity of the isomangiferin standard available, this compound (**5**) was quantified using a previously determined response factor relative to mangiferin (1.1197). Calibration curves for iriflophenone-3-*C*-glucoside-4-*O*-glucoside (**1**), iriflophenone-3-*C*-glucoside (**3**), and mangiferin (**4**) were constructed weekly (R^2 > 0.9999) with on-column levels in the ranges 0.0166−3.3261, 0.0512−1.4906, and 0.0734−2.1173 μg, respectively.

Modeling of benzophenone and xanthone degradation was performed using quantitative data for the period 0−16 h. For each oxidation temperature, a completely randomized experimental design was used with 4 replications for each of the 16 treatment times. Univariate analysis of variance (ANOVA) using SAS, version 9.2 (SAS Institute, Cary, NC, USA), was performed for each oxidation temperature separately, using the General Linear Models Procedure. The Shapiro−Wilk test was performed to test for normality. Outliers were removed when the residual for an observation deviated more than 3 standard deviations from the standardized model value. Fisher's least significant difference was calculated at the 5% level (P < 0.05) to compare treatment means.

Regression analysis with time (h) as independent variable was performed for the data of each temperature treatment to describe the decrease in compound concentration over time. The order of the thermal degradation reaction of the xanthones and benzophenones was predicted using the model

$$\frac{dC}{dt} = -K_D(C)^n \quad (1)$$

where K_D is the degradation rate constant, n is the reaction order, C is the concentration (g of compound/100 g of plant material), and t is the treatment time (h). The order of the degradation reactions was determined by setting component n in eq 1 to 0, 1 and 2, followed by comparing the coefficients of determination (R^2). The integrated forms of zero-, first-, and second-order kinetic models are given in eqs 2−4, with C_0 equal to the initial concentration of the compound (g/100 g plant material) at t = 0 h:

$$\text{zero order:} \quad C = C_0 - K_D t \quad (2)$$

$$\text{first order:} \quad \ln C = \ln C_0 - K_D t \quad (3)$$

$$\text{second order:} \quad \frac{1}{C} - \frac{1}{C_0} = K_D t \quad (4)$$

The temperature dependence of the degradation rate constants was evaluated by calculating the temperature coefficient (Q_{10}) according to[11]

$$Q_{10} = \frac{K_D(T+10\,^{\circ}C)}{K_D(T)} \quad (5)$$

where K_D is the degradation rate constants at temperatures T and T + 10 °C.

Evaluation of the Thermal Degradation Kinetic Model. The developed kinetic model was subsequently applied to predict the levels

DOI: 10.1021/acs.jafc.5b01657
J. Agric. Food Chem. 2015, 63, 5518−5527

of benzophenones and xanthones remaining when coarsely cut plant material (leaves and stems) was oxidized at 90 °C/16 h under upscaled conditions. This tested the robustness of the kinetic model by incorporating additional variation, i.e., heterogeneity of the plant material due to the coarse cut and batch size.

The shoots from 10 individual *C. genistoides* bushes were harvested from the same commercial plantation stated previously. The fresh shoots from each bush were mechanically shredded (≤3 mm), mixed thoroughly, and divided into two sub-batches for the preparation of unoxidized (control) and oxidized plant material to provide content values for 0 and 16 h processing times, respectively. For the latter, the cut plant material (1 kg) was moistened to a moisture content of ca. 65% and oxidized at 90 °C/16 h.[12] Both the control and oxidized samples were dried at 40 °C/6 h and coarsely sieved,[12] followed by the preparation of freeze−dried hot water extracts as described by Beelders et al.[1]

For HPLC analyses, the freeze−dried extracts were reconstituted in deionized water (ca. 6 mg/mL), followed by the addition of 10% aqueous ascorbic acid (v/v, final concentration 9 mg/mL). Samples were filtered using 0.45 μm pore size Millex-HV syringe filters (33 mm diameter; Merck Millipore) and analyzed. The target xanthone and benzophenone constituents were quantified as described in the previous section.

Other phenolic compounds present in the extracts were also quantified to provide further insight into the quantitative changes that occur during high-temperature oxidation, with emphasis on structure−stability relationships. Maclurin-3-*C*-glucoside (**2**), vicenin-2 (**6**), eriocitrin (**7**), phloretin-3′,5′-di-*C*-glucoside (**8**), and hesperidin (**9**) in the sample extracts were identified by coelution with the authentic reference standards. Additionally, compounds **A**−**I** in the sample extracts were identified by taking their characteristic UV−vis spectra and relative elution order into account, in accordance with LC-DAD-MS results presented by Beelders et al.[1] (Table S1, Supporting Information). Maclurin-3-*C*-glucoside and vicenin-2 were quantified at 320 nm, and calibration curves were constructed over the following ranges (μg on-column): 0.0157−0.6905 and 0.0721−0.9008, respectively. The flavanones eriocitrin and hesperidin were quantified at 288 nm, and the ranges for the calibration curves were 0.0200−0.2500 and 0.0776−0.9700 μg on-column, respectively. Due to the limited quantity of the purified phloretin-3′,5′-di-*C*-glucoside standard available, this compound was quantified using a previously determined response factor relative to hesperidin (0.7902). Compounds **A**−**I** were quantified using calibration curves of the most closely related reference standard. For this purpose, an additional calibration curve for narirutin was constructed at 288 nm over a range of 0.0200−0.3340 μg on-column. The correlation coefficients (R^2) of all calibration curves were larger than 0.9999.

Quantitative data generated for extracts prepared from the unoxidized and oxidized plant material (n = 10) were subjected to ANOVA with Fisher's least significant difference calculated at the 5% level to compare treatment means.

Antioxidant Capacity of Selected Xanthones and Benzophenones and the Effect of High-Temperature Oxidation on TAC of Aqueous Extract. The TAC of the reconstituted freeze−dried extracts (n = 10) was determined in triplicate using the DPPH• scavenging[13] and ORAC[14] assays in 96-well microplate format. Corresponding absorbance and fluorescence values were measured using a BioTek SynergyHT microplate reader fitted with a dispenser (BioTek Instruments, Winooski, VT, USA). TAC data were subjected to ANOVA with Fisher's least significant difference calculated at the 5% level to compare treatment means.

Trolox equivalent antioxidant capacity (TEAC) of the target benzophenones and xanthones were determined to calculate their individual contributions to the TAC of aqueous extracts prepared from unoxidized *C. genistoides* and to quantify the impact of their degradation based on the TAC of aqueous extracts prepared from the oxidized plant material. The TEAC value of the minor benzophenone, maclurin-3-*C*-glucoside, was also determined to provide insight into structure−activity relationships.

Dose−response curves were constructed for the aforementioned compounds and Trolox by plotting graphs of concentration (μM) vs percent DPPH• scavenged (DPPH assay) and net area under curve (ORAC assay). The concentration ranges of the standard compounds were selected to ensure that the antioxidant dose−response curves remained linear. TEAC values for each individual compound were then calculated as follows:

$$\mathrm{TEAC}_{\mathrm{compound}} = \mathrm{slope}_{\mathrm{compound}}/\mathrm{slope}_{\mathrm{Trolox}} \quad (6)$$

RESULTS

Thermal Degradation Kinetics Modeling. The high-temperature oxidation process significantly ($P < 0.05$) reduced the mean content values of the target compounds over the evaluated time−temperature combinations, and these losses were more pronounced at 90 than at 80 °C (Table S2, Supporting Information).

The decrease in the contents of these compounds over a 16 h period, as affected by temperature and chemical structure, is depicted in Figure 1. Analysis of the kinetic data at both temperatures indicated first-order degradation reactions ($0.898 < R^2 < 0.970$), with the exception of iriflophenone-3-*C*-glucoside-4-*O*-glucoside at 80 °C ($R^2 = 0.111$) (Table 1). The mean content value of the latter compound did not change significantly over 16 h at 80 °C ($P \geq 0.05$; Table S2, Supporting Information), which explains the poor correlation. Straight lines were obtained for plots of ln C vs t for each of the assessed compounds at each temperature (Figure 2), where the individual slopes are representative of the first-order degradation rate constants (K_D) (Table 1).

Iriflophenone-3-*C*-glucoside-4-*O*-glucoside was the most thermally stable compound, with a K_D(90 °C) value of 0.0061 h^{-1} (Table 1). Isomangiferin was the second most thermally stable compound at 80 °C (K_D(80 °C) = 0.0116 h^{-1}), while its degradation rate was influenced the most by increased temperature (Q_{10} = 2.70, Table 1). Iriflophenone-3-*C*-glucoside and mangiferin had comparable degradation rate constants of 0.0224 and 0.0248 h^{-1}, respectively, at 80 °C (Table 1). The degradation rate constants for these compounds respectively showed 1.40- and 1.72-fold increases with an increase in temperature from 80 to 90 °C (Table 1).

Evaluation of the Thermal Degradation Kinetic Model. Predicted content values for the target benzophenones and xanthones in aqueous extract prepared from oxidized plant material, based on their contents in aqueous extract prepared from the unoxidized plant material and their first-order K_D(90 °C) values, were calculated for comparison with their actual content values in aqueous extract prepared from the oxidized plant material (Table 2).

The first-order kinetic model provided excellent (error <5%) prediction of iriflophenone-3-*C*-glucoside-4-*O*-glucoside and mangiferin degradation, while it was acceptable (error <10%) for isomangiferin (Table 2). However, a poor fit was obtained for iriflophenone-3-*C*-glucoside, as the kinetic model greatly underestimated the degradation of this compound following oxidation at 90 °C for 16 h (Table 2).

Effect of High-Temperature Oxidation on the Levels of Individual Phenolic Compounds in Hot Water Extracts. Oxidation significantly decreased the content values of most phenolic compounds present in *C. genistoides* hot water extracts (refer to Figure 3 for a typical HPLC chromatogram), but some compounds either remained stable or showed a significant increase (Table 3).

DOI: 10.1021/acs.jafc.5b01657
J. Agric. Food Chem. 2015, 63, 5518−5527

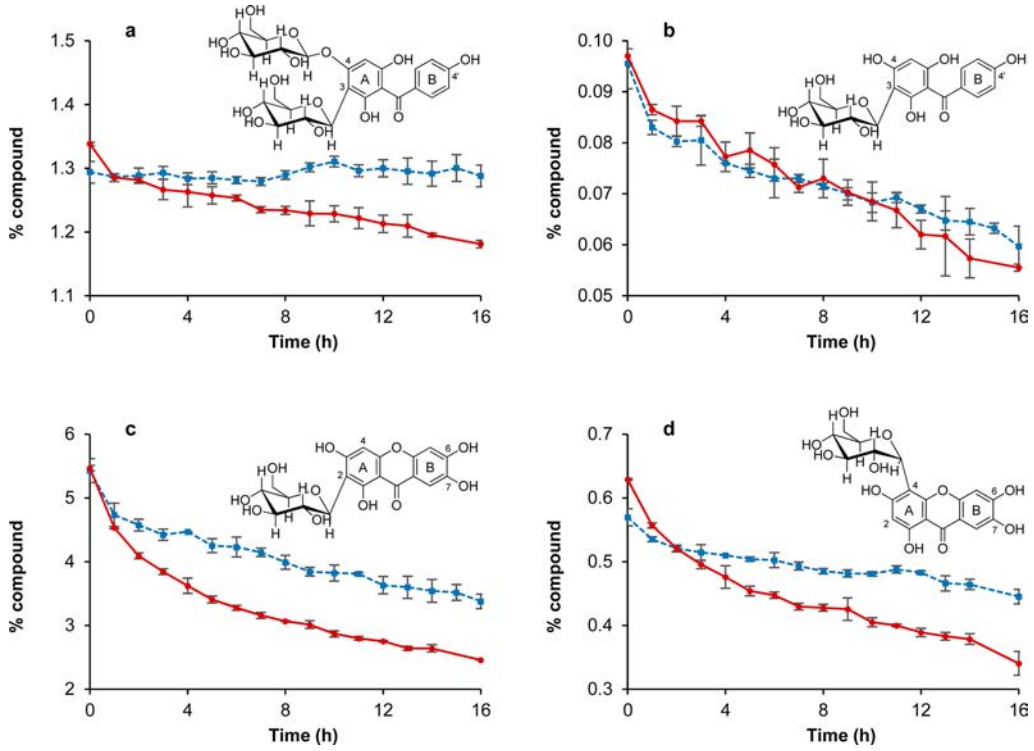

Figure 1. Changes in the mean percentage of compound in *Cyclopia genistoides* (g of compound/100 g of plant material ± standard deviation) for (a) iriflophenone-3-*C*-glucoside-4-*O*-glucoside, (b) iriflophenone-3-*C*-glucoside, (c) mangiferin, and (d) isomangiferin as a function of oxidation temperature over 16 h: (blue dotted curves) 80 °C; (red solid curves) 90 °C.

The *C*-glucosylxanthone mangiferin (**4**) was the major phenolic constituent of freeze-dried hot water extracts prepared from unoxidized (11.80%) and oxidized (6.04%) *C. genistoides* plant material (Table 3). Isomangiferin (**5**) represented the third most abundant phenolic constituent of *C. genistoides* at 1.54% and 0.91% of the unoxidized and oxidized extracts, respectively (Table 3). The mean content values of mangiferin and isomangiferin decreased by 49% and 41%, respectively, with oxidation (Table 3).

The second most abundant phenolic constituent of *C. genistoides* hot water extracts was the novel benzophenone iriflophenone-3-*C*-glucoside-4-*O*-glucoside (**1**), and its mean content value was not significantly affected by processing ($P \geq 0.05$) (Table 3). Iriflophenone-3-*C*-glucoside (**3**) represented the fourth and fifth most abundant phenolic constituent of aqueous extract prepared from the unoxidized (1.12%) and oxidized (0.42%) plant material, respectively. In contrast to the case for compound **1**, the mean content value of iriflophenone-3-*C*-glucoside showed a significant ($P < 0.05$) decrease with oxidation (62%; Table 3).

In addition to these 4 major compounds, 14 additional compounds were also quantified to provide insight into the changes that occur during oxidation (Table 3 and Figure 3). Maclurin-3-*C*-glucoside (**2**) and its glycosylated derivative, maclurin-di-*O*,*C*-hexoside (**A**), were quantified at levels of 0.31% and 0.13%, respectively, in extracts prepared from the unoxidized plant material. The former compound was extremely prone to degradation during the high-temperature oxidation process, exhibiting a decrease of 83%.

A tetrahydroxyxanthone-*C*-hexoside dimer (**C**), a tetrahydroxyxanthone-di-*O*,*C*-hexoside (**D**), and a tetrahydroxyxanthone-*C*-hexoside isomer (**J**) were also quantified as minor constituents of the *C. genistoides* extracts (Table 3). The mean content values of compounds **D** and **J** showed a reduction of 35−40% with oxidation, while the xanthone dimer (compound **C**) was only quantifiable in extracts prepared from the oxidized plant material.

Vicenin-2 (apigenin-6,8-di-*C*-glucoside, compound **6**) represented the sixth and fourth most abundant phenolic constituent of hot water extracts prepared from unoxidized (0.50%) and oxidized (0.45%) *C. genistoides* plant material, respectively. This represents a slight but significant ($P < 0.05$) decrease with oxidation (ca. 10%).

The effect of oxidation on the flavanones was found to differ. The average content of eriocitrin (**7**) in the aqueous extract was not significantly ($P \geq 0.05$) affected by oxidation, while the hesperidin (**9**) and eriodictyol-*O*-hexose-*O*-deoxyhexoside (**E**) contents were significantly ($P < 0.05$) reduced. The average content of naringenin-*O*-hexose-*O*-deoxyhexoside (**G**) also showed a significant ($P < 0.05$) decrease with oxidation (57%), which was accompanied by a significant ($P < 0.05$) increase in the content of another naringenin-*O*-hexose-*O*-deoxyhexoside derivative (compound **F**; 34%).

The mean content values of the dihydrochalcone phloretin-3′,5′-di-*C*-glucoside (**8**) and its hydroxylated derivative, 3-hydroxyphloretin-3′,5′-di-*C*-hexoside (**H**), were both significantly ($P < 0.05$) reduced with oxidation. The former compound presented a decrease of 56%, while the latter was degraded more extensively (84%; Table 3).

Antioxidant Capacity of Selected Xanthones and Benzophenones and the Effect of High-Temperature Oxidation on TAC of Aqueous Extract. Oxidation significantly ($P < 0.05$) lowered the mean TAC of the extracts as assessed using the DPPH$^{\bullet}$ scavenging assay (TAC_{DPPH}; Table 3). Conversely, the TAC_{ORAC} value of extracts was only slightly, but not significantly ($P \geq 0.05$), reduced with oxidation (Table 3).

DOI: 10.1021/acs.jafc.5b01657
J. Agric. Food Chem. 2015, 63, 5518−5527

Table 1. Degradation Rate Constants[a] and Regression Coefficients (R^2) for the Isothermal Degradation of Benzophenones and Xanthones in *Cyclopia genistoides* Plant Material, Estimated by Means of a First-Order Kinetic Model

	80 °C		90 °C		
compound	K_D ± SE (h^{-1})	R^2	K_D ± SE (h^{-1})	R^2	Q_{10}[b]
iriflophenone-3-*C*-glucoside-4-*O*-glucoside	0.0004 ± 0.0003	0.111	0.0061 ± 0.0005	0.921	
iriflophenone-3-*C*-glucoside	0.0224 ± 0.0018	0.914	0.0314 ± 0.0015	0.970	1.40
mangiferin	0.0248 ± 0.0017	0.941	0.0427 ± 0.0037	0.905	1.72
isomangiferin	0.0116 ± 0.0010	0.898	0.0313 ± 0.0023	0.929	2.70

[a]Degradation rate constants ± standard error of regression (K_D ± SE). [b]Temperature coefficient.

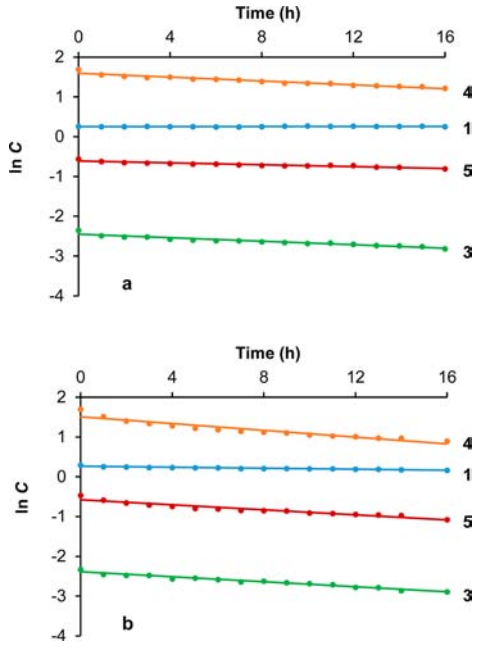

Figure 2. Kinetic degradation data for iriflophenone-3-*C*-glucoside-4-*O*-glucoside (**1**), iriflophenone-3-*C*-glucoside (**3**), mangiferin (**4**), and isomangiferin (**5**) as fitted to a first-order kinetic model at (a) 80 °C and (b) 90 °C.

Table 2. Mean Values[a] for the Major Benzophenones and Xanthones in *Cyclopia genistoides* Plant Material in Relation to the Values Predicted using First-Order Degradation Kinetics

	mean content value (n = 10)			
compound	unoxidized	oxidized[b]	predicted content value oxidized[b]	error (%)
iriflophenone-3-*C*-glucoside-4-*O*-glucoside	1.3579	1.2927	1.2314	4.74
iriflophenone-3-*C*-glucoside	0.2691	0.0952	0.1629	−71.11
mangiferin	2.7965	1.3486	1.4131	−4.78
isomangiferin	0.3672	0.2039	0.2227	−9.22

[a]In units of g of compound/100 g of g plant material (n = 10). [b]Oxidation conditions: 90 °C/16 h.

Assessment of the TEAC of selected benzophenones and xanthones provided some insight into the relative importance of these constituents in terms of the TAC of the extract. $TEAC_{DPPH}$ values for the individual compounds (Table 4) indicated that maclurin-3-*C*-glucoside was the most efficient scavenger of DPPH•. Its $TEAC_{DPPH}$ value (2.19) was ca. 3-fold higher than that of iriflophenone-3-*C*-glucoside (0.65) (Table 4). Despite the low concentration of maclurin-3-*C*-glucoside in the unoxidized *C. genistoides* extract (Table 3), it almost contributed equally to the average TAC of the unoxidized extract in comparison to the much more abundant iriflophenone-3-*C*-glucoside (Table 4). The radical scavenging ability of iriflophenone-3-*C*-glucoside-4-*O*-glucoside toward DPPH• (0.01) was lower than that of its mono-*C*-glucosylated derivative, iriflophenone-3-*C*-glucoside and was also the lowest overall (Table 4).

Both mangiferin and isomangiferin exhibited moderate DPPH• scavenging activity with TEAC values of 1.79 and 1.69, respectively. These xanthones were the major contributors to the TAC of *C. genistoides* hot water extracts, collectively responsible for 41.7% and 25.2% of the TAC_{DPPH} of the extracts prepared from unoxidized and oxidized plant material, respectively (Table 4).

With regard to the ORAC assay, an entirely different ranking of phenolic antioxidants was obtained. The fluorescein fluorescence decay curve of iriflophenone-3-*C*-glucoside-4-*O*-glucoside showed a very different profile in comparison to those of the reference antioxidant, Trolox, and maclurin-3-*C*-glucoside (Figure S1, Supporting Information). Iriflophenone-3-*C*-glucoside-4-*O*-glucoside exhibited the highest $TEAC_{ORAC}$ value (4.76), followed by iriflophenone-3-*C*-glucoside (4.06) (Table 4). Due to both its relative potency and high concentration in the *C. genistoides* extracts (Table 3), iriflophenone-3-*C*-glucoside-4-*O*-glucoside represented a major contributor (>10%) to the average TAC_{ORAC} value of the extracts. Conversely, the contribution of this compound to the TAC_{DPPH} of the extracts was almost negligible (ca. 0.1%) (Table 4). Maclurin-3-*C*-glucoside exhibited a moderate antioxidative effect in the ORAC assay (3.31), comparable to that of isomangiferin (3.38) and notably higher than that of mangiferin (2.80) (Table 4).

DISCUSSION

Thermal Degradation Kinetics Modeling and Evaluation of the Model. The thermal stabilities of iriflophenone-3-*C*-glucoside-4-*O*-glucoside, iriflophenone-3-*C*-glucoside, mangiferin, and isomangiferin were determined, as these compounds represent the major phenolic constituents of *C. genistoides*. Due to the low levels of maclurin-3-*C*-glucoside present in the plant material, its thermal degradation behavior could not be assessed kinetically. An isothermal method was used to estimate reaction kinetics, as the ramp-up time in the thin-walled glass vials was assumed to be negligible in comparison to the length of the holding phase. The kinetic data provided a good fit for first-order degradation reactions, which is in line with the literature on the isothermal degradation of cloudy apple juice phenolic constituents,[15] anthocyanins,[16] and carotenoids,[17] among others.

Addition of an *O*-linked glucopyranosyl moiety at C-4 conferred higher thermal stability to iriflophenone-3-*C*-glucoside-4-*O*-glucoside in comparison to iriflophenone-3-*C*-glucoside during high-temperature oxidation of *C. genistoides* plant

DOI: 10.1021/acs.jafc.5b01657
J. Agric. Food Chem. 2015, 63, 5518−5527

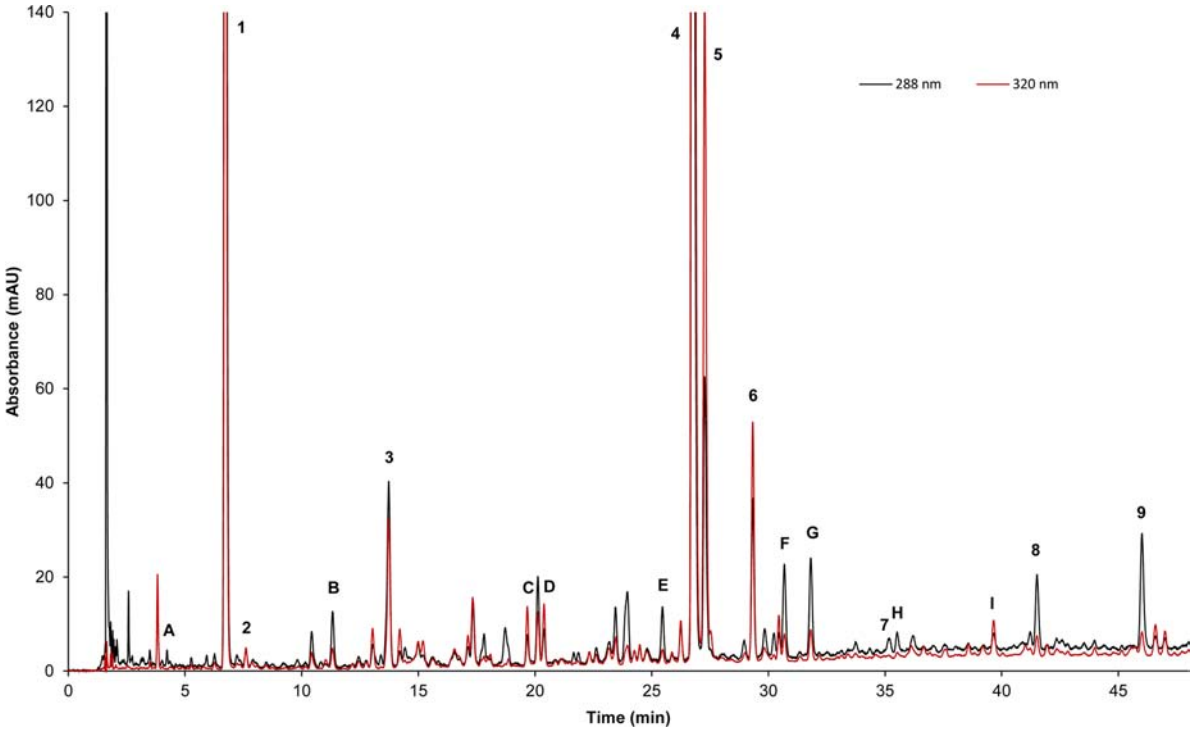

Figure 3. Typical HPLC chromatogram of an aqueous extract prepared from oxidized *Cyclopia genistoides* plant material. Peak labels correspond to Table 3. Refer to Table S1 (Supporting Information) for the identification of compounds **A**–**I**.

Table 3. Mean Values[a] for the Major Phenolic Compounds and TAC of Hot Water Extracts Prepared from Unoxidized and Oxidized[b] *Cyclopia genistoides* Plant Material

peak[c]	compound	unoxidized (n = 10)	oxidized[b] (n = 10)	mean change (%)
A	maclurin-di-*O*,*C*-hexoside[d]	0.1305 ± 0.03a[e]	0.1114 ± 0.02b	−14.64
1	iriflophenone-3-*C*-glucoside-4-*O*-glucoside	5.6950 ± 1.10a	5.7840 ± 1.04a	+1.56
2	maclurin-3-*C*-glucoside	0.3113 ± 0.14a	0.0542 ± 0.03b	−82.59
B	unidentified compound[f]	0.1349 ± 0.03a	0.1102 ± 0.03b	−18.31
3	iriflophenone-3-*C*-glucoside	1.1207 ± 0.67a	0.4236 ± 0.22b	−62.21
C	tetrahydroxyxanthone-*C*-hexoside dimer[g]	nq[h]	0.0523 ± 0.02	
D	tetrahydroxyxanthone-di-*O*,*C*-hexoside[g]	0.1413 ± 0.04a	0.0837 ± 0.02b	−40.76
E	eriodictyol-*O*-hexose-*O*-deoxyhexose[i]	0.1685 ± 0.06a	0.1155 ± 0.04b	−31.45
4	mangiferin	11.7983 ± 1.47a	6.0362 ± 1.40b	−48.84
5	isomangiferin	1.5435 ± 0.24a	0.9131 ± 0.16b	−40.84
6	vicenin-2	0.5014 ± 0.09a	0.4470 ± 0.08b	−10.85
F	naringenin-*O*-hexose-*O*-deoxyhexoside[j]	0.2310 ± 0.08b	0.3086 ± 0.09a	+33.59
G	naringenin-*O*-hexose-*O*-deoxyhexoside[j]	0.6733 ± 0.22a	0.2891 ± 0.06b	−57.06
7	eriocitrin	0.0457 ± 0.01a	0.0495 ± 0.01a	+8.32
H	3-hydroxyphloretin-3′,5′-di-*C*-hexoside[k]	0.2579 ± 0.08a	0.0416 ± 0.02b	−83.87
I	tetrahydroxyxanthone-*C*-hexoside isomer[g]	0.0964 ± 0.02a	0.0620 ± 0.01b	−35.68
8	phloretin-3′,5′-di-*C*-glucoside	0.4049 ± 0.12a	0.1786 ± 0.05b	−55.89
9	hesperidin	0.2984 ± 0.06a	0.2120 ± 0.04b	−28.95
	TAC_{DPPH}[l]	1350 ± 121a	1164 ± 129b	−13.78
	TAC_{ORAC}[l]	4460 ± 423a	4406 ± 463a	−1.21

[a]In units of g of compound/100 g of g dried aqueous extract (DAE) ± standard deviation. [b]Oxidation conditions: 90 °C/16 h. [c]Refer to Table S1 (Supporting Information) for the identification of compounds **A**–**I**. [d]In units of g of maclurin-3-*C*-glucoside equivalents/100 g of DAE. [e]Means in the same row with different letters are significantly different (P < 0.05). [f]In units of g of hesperidin equivalents/100 g of DAE. [g]In units of g of mangiferin equivalents/100 g of DAE. [h]nq = not quantified due to extremely small peak area (<30 mAU), yielding large percentage error associated with difficult integration. [i]In units of g of eriocitrin equivalents/100 g of DAE. [j]In units of g of narirutin equivalents/100 g of DAE. [k]In units of g of phloretin-3′,5′-di-*C*-glucoside equivalents/100 g of DAE. [l]Total antioxidant capacity (TAC) determined according to DPPH radical scavenging and ORAC assays, expressed in units of μmol of Trolox equivalents/g of DAE.

material. Glucosylation at the C-4 position of the dibenzo-γ-pyrone structure, as opposed to the C-2 position, also increased the stability of the tetrahydroxyxanthones.

Previous studies on the thermal degradation of quercetin and rutin in aqueous model systems showed that rutin (quercetin-3-*O*-rutinoside) was more stable than its corresponding

DOI: 10.1021/acs.jafc.5b01657
J. Agric. Food Chem. 2015, 63, 5518−5527

Table 4. Trolox Equivalent Antioxidant Capacity (TEAC)[a] of Benzophenones and Xanthones in the DPPH Radical Scavenging and ORAC Assays with their Concentration Ranges, Slopes, and Correlation Coefficients (R^2), together with their Individual Contributions to the Average Total Antioxidant Capacity (TAC) of *Cyclopia genistoides* Extracts

compound	concentration range (μM)[b]	slope (R^2)	TEAC	contribution to TAC of extracts (%)[c] unoxidized	oxidized[d]
DPPH Assay[e]					
iriflophenone-3-*C*-glucoside-4-*O*-glucoside	260.6−695.0	0.0331 (0.997)	0.0147	0.109	0.128
maclurin-3-*C*-glucoside	3.0−16.3	4.8836 (0.999)	2.1876	1.188	0.240
iriflophenone-3-*C*-glucoside	5.1−21.8	1.4614 (0.993)	0.6547	1.330	0.583
mangiferin	4.1−17.0	4.1673 (0.995)	1.7945	37.117	22.023
isomangiferin	2.9−19.5	3.7808 (0.998)	1.6936	4.583	3.144
contribution of benzophenones				2.627	0.951
contribution of xanthones				41.700	25.167
total contribution				44.327	26.119
ORAC Assay[f]					
iriflophenone-3-*C*-glucoside-4-*O*-glucoside	0.163−0.424	19.9054 (0.987)	4.7623	10.659	10.958
maclurin-3-*C*-glucoside	0.190−0.474	13.7585 (0.996)	3.3149	0.545	0.096
iriflophenone-3-*C*-glucoside	0.101−0.228	18.0819 (0.987)	4.0559	2.496	0.955
mangiferin	0.206−0.463	12.4914 (0.993)	2.8040	17.563	9.096
isomangiferin	0.209−0.470	13.7753 (0.993)	3.3795	2.769	1.658
contribution of benzophenones				13.700	12.009
contribution of xanthones				20.332	10.754
total contribution				34.032	22.763

[a]Activity of compound relative to that of Trolox: i.e., concentration of Trolox solution in μM with equivalent antioxidant activity to a 1 μM concentration of the compound under investigation. [b]The concentration range of a specific compound used in the dose−response curves (final concentrations in the reaction volume). [c]Calculated on the basis of content (Table 3) and TEAC values. [d]Oxidation conditions: 90 °C/16 h. [e]Trolox assessed over a concentration range of 5.0−40.0 μM with an average slope (n = 3) of 2.2670 and R^2 = 0.997. [f]Trolox assessed over a concentration range of 0.6−3.7 μM with an average slope (n = 6) of 4.2240 and R^2 = 0.999. TEAC values for the xanthones and benzophenones were determined in duplicate (% RSDs ≤ 5.6).

aglycone.[18,19] This observation was attributed to the blockage of the 3-hydroxyl group in the C ring by the sugar moiety, which prevents the formation of the carbanion.[18] It is thus possible that the hydroxyl group at C-4 on the diphenyl ketone structure is a key parameter with respect to thermal degradation of benzophenones. Similarly, a study of the thermal stability of quercetin-*O*-glycosides demonstrated that the position of glycosylation and type of sugar determined susceptibility to deglycosylation.[20] Zielinski and co-workers[21] have demonstrated slight differences in the stability of the flavone *C*-glucosides vitexin (apigenin-8-*C*-glucoside; 72% degradation) and isovitexin (apigenin-6-*C*-glucoside; 84% degradation) in buckwheat groats during roasting.

In the current study, an increase in oxidation temperature from 80 to 90 °C increased the rate of degradation for all target compounds, as expected. Of interest is that this effect was more pronounced for iriflophenone-3-*C*-glucoside-4-*O*-glucoside, which was stable under oxidative conditions at 80 °C for 16 h but exhibited a decrease of 11.7% following oxidation at 90 °C after the same time period. The effect of temperature on the degradation rate constants was estimated by calculating the temperature coefficient (Q_{10}). The significance of this value is clear when considering the thermal degradation of isomangiferin. This compound had the lowest degradation rate constant at 80 °C, which by itself would imply that this compound is more stable than mangiferin and iriflophenone-3-*C*-glucoside. However, the degradation rate of isomangiferin showed a 2.7-fold increase with an increase in temperature from 80 to 90 °C, which implies greater susceptibility of this compound toward degradation at elevated temperature than mangiferin and iriflophenone-3-*C*-glucoside.

The kinetic parameters derived for the first-order degradation reactions were subsequently used to predict the amounts of major compounds remaining in *C. genistoides* (n = 10) following oxidation (90 °C/16 h) of the coarsely cut plant material under conditions similar to those used in the industrial oxidation process. In spite of the procedure being less "controlled" than the oxidation process carried out with very small quantities of homogeneous material, the degradation kinetic model provided excellent estimates for the average amounts of iriflophenone-3-*C*-glucoside-4-*O*-glucoside and mangiferin in hot water extracts prepared from the oxidized plant material. The model, however, greatly underestimated the degradation of iriflophenone-3-*C*-glucoside, and the reason for this still has to be established. In light of the apparent bitterness of *C. genistoides* infusions, associated with a high mangiferin content,[22] the model could potentially be used to estimate the processing time needed to decrease the mangiferin content to a level where the infusions are not perceived as bitter, without causing unnecessary losses in bioactivity. Another potential application is to "screen" new *C. genistoides* selections of the ongoing Cultivar Development Programme of the Agricultural Research Council of South Africa for an unacceptable bitter taste by predicting the mangiferin content of the processed herbal tea.

Effect of High-Temperature Oxidation on the Levels of Individual Phenolic Compounds in Hot Water Extracts. It is well-known that the high-temperature oxidation process has a significant impact on the individual phenolic content values of *Cyclopia* extracts. Previous studies have, however, mostly been limited to a small data set of randomly selected or paired-processed samples and/or a limited number

DOI: 10.1021/acs.jafc.5b01657
J. Agric. Food Chem. 2015, 63, 5518−5527

of quantifiable compounds.[1,10,23] In the present study, quantitative data were generated for 9 known compounds and 9 additional compounds in 10 individual batches of *C. genistoides* plant material.

The high-temperature oxidation process (90 °C/16 h), required for the development of the desirable sensory properties of honeybush herbal tea, significantly reduced the mean content values of most phenolic compounds of the aqueous extracts. The thermal stability of a number of minor compounds is worth highlighting. The tetrahydroxyxanthone-*C*-hexoside dimer (compound **C**) could only be quantified in extracts prepared from the oxidized plant material. On the basis of related studies regarding the dihydrochalcone aspalathin,[24,25] it is probable that this xanthone dimer is formed by the nonenzymatic, oxidative coupling of two tetrahydroxyxanthone-*C*-hexoside monomers during high-temperature processing. The dimeric xanthone may be linked through either a rotatable or atropisomeric biaryl C−C bond or a biaryl ether C−O−C linkage.[26] Storage of (−)-epigallocatechin gallate in solid-state samples at elevated temperatures (80 °C) has also been shown to induce auto-oxidation with the formation of B-ring dimers.[27]

Two naringenin derivatives, compounds **F** and **G**, also exhibited interesting behavior during the oxidation process. A significant reduction in the mean content value of compound **G** was accompanied by a significant increase in the mean content value of compound **F**. These flavanones are potential isomers, and it is herein postulated that compound **G** is converted to the more stable structure of compound **F** during the oxidation process. Similar observations have been made with regard to the irreversible conversion of isoorientin to orientin via a Wessely−Moser rearrangement during incubation in phosphate buffer at 37 °C for 48 h.[28]

In this study, phloretin-3′,5′-di-*C*-glucoside (**8**) was more stable than 3-hydroxyphloretin-3′,5′-di-*C*-hexoside (**H**) during oxidation at 90 °C/16 h. The presence of an extra hydroxyl group on the B ring of the basic dihydrochalcone structure therefore decreased thermal stability. This effect was also prominent for iriflophenone-3-*C*-glucoside (**3**; 62% reduction) and its C-3′ hydroxylated derivative, maclurin-3-*C*-glucoside (**2**; 82% reduction). Maini and co-workers[29] found that the stability of flavonols in different cell culture media, and their stability to UVA irradiation, decreased with increasing B-ring substitution. Conversely, De Paepe et al.[15] demonstrated a slight decrease in the K_D value with the presence of an additional hydroxyl group at C-3′ on the A ring of the dihydrochalcone structure. These results therefore suggest that both the degree of hydroxylation and the position of hydroxylation, in particular, are key factors affecting the thermal stability of dihydrochalcones.

Antioxidant Capacity of Selected Xanthones and Benzophenones and Effect of High-Temperature Oxidation on TAC of Aqueous Extract. While a reduction in the contents of mangiferin and isomangiferin, for instance, may be desirable from a sensory perspective, the antioxidant activity of the extracts may also consequently be reduced. Given demonstration of the similar antioxidant capacity of three of these compounds in an online HPLC-ORAC assay,[4] their degradation was expected to have a major impact on the TAC value of hot water extracts of *C. genistoides*. This type of extract is of interest due to its use as an ingredient in food and nutraceutical products.

High-temperature oxidation significantly lowered the average TAC_{DPPH} value of the aqueous extracts, while their average TAC_{ORAC} value was only slightly reduced. These observations are in line with data presented by Joubert et al.,[10] in which oxidation significantly reduced the average antioxidant activity of six paired-processed samples of various *Cyclopia* species (as assessed using the $ABTS^{\bullet+}$ scavenging, ferric reducing antioxidant power (FRAP), and lipid peroxidation assays). The same study showed, however, that the ability of the hot water extract of *C. genistoides* to inhibit lipid peroxidation was not affected.[10] It is therefore possible that unknown degradation products may also possess antioxidant activity and thus could have contributed to the TAC_{ORAC} values of extracts prepared from the oxidized plant material. Buchner et al.[19] and Murakami et al.[30] have previously demonstrated antioxidant activity for flavonol and other polyphenolic degradation products.

The higher $TEAC_{DPPH}$ value of maclurin-3-*C*-glucoside in comparison to that of iriflophenone-3-*C*-glucoside may be attributed to the presence of an extra hydroxyl group at C-3′ on the diphenyl ketone structure, which imparts a catechol-type structure to maclurin-3-*C*-glucoside, one of the structural features responsible for antioxidant activity of polyphenols.[31,32] An increase in the degree of glucosylation was found to reduce the reactivity of the benzophenones toward $DPPH^{\bullet}$, as previously observed for flavonoids.[31] The reduced reactivity of iriflophenone-3-*C*-glucoside-4-*O*-glucoside could possibly be attributed to the substitution of an active phenolic OH group, responsible for free radical scavenging. Furthermore, the additional glucopyranosyl moiety can impede access of the remaining free phenolic OH groups to the hindered radical site of $DPPH^{\bullet}$, thereby reducing reactivity.[33]

While data from the $DPPH^{\bullet}$ scavenging assay inferred that iriflophenone-3-*C*-glucoside-4-*O*-glucoside is ineffective as a radical scavenger, this compound had the highest $TEAC_{ORAC}$ value among the five compounds assessed in this study. The difference in ranking of phenolic antioxidants in the ORAC assay in comparison to the DPPH assay may be related to the differences in the reaction mechanisms of the two assays, which underlines the importance of using more than one assay to assess the antioxidant capacity of natural extracts and/or phenolic compounds. To our knowledge, this is the first report on the antioxidant capacity of iriflophenone-3-*C*-glucoside-4-*O*-glucoside and maclurin-3-*C*-glucoside. Further research is thus required to understand the reaction mechanisms of these benzophenones with free radicals.

Similarly, the effect of glucosylation position on the antioxidant activity of the xanthones differed between the two antioxidant assays. Mangiferin exhibited slightly higher reactivity toward $DPPH^{\bullet}$ than its C-4 regioisomer, isomangiferin, while the $TEAC_{ORAC}$ value of isomangiferin was slightly higher than that of mangiferin. These observations are in line with results presented by Malherbe et al.[4] using online HPLC-DPPH and -ORAC assays. Similar antioxidant activities have also been demonstrated for positional isomers of chlorogenic acid.[34]

Collectively, the four major compounds and maclurin-3-*C*-glucoside contributed 44.3% and 26.1% to the TAC_{DPPH} of extracts prepared from unoxidized and oxidized plant material, respectively. Mangiferin was the major contributor, and this could be ascribed to both its high concentration in the sample extracts and its relatively high scavenging ability toward $DPPH^{\bullet}$. It is also clear that, when the DPPH assay was used, the contribution of the benzophenones to the TAC of the extracts was low and that their degradation during oxidation

DOI: 10.1021/acs.jafc.5b01657
J. Agric. Food Chem. 2015, 63, 5518−5527

would thus have little impact on the TAC_{DPPH} value. Using the ORAC assay, the same five compounds could only explain 34.0% and 22.8% of the TAC of extracts prepared from unoxidized and oxidized *C. genistoides* plant material, respectively. Here, mangiferin and iriflophenone-3-*C*-glucoside-4-*O*-glucoside contributed almost equally to the TAC_{ORAC} of extracts prepared from the oxidized plant material. The remarkable stability of iriflophenone-3-*C*-glucoside-4-*O*-glucoside during high-temperature oxidation was therefore paramount to retaining high TAC_{ORAC} of the extracts, even after processing. A large percentage of the TAC of the hot water honeybush extracts still remains unaccounted for, and this may be ascribed to the antioxidant capacities of other phenolic constituents and other types of compounds present in the extracts (both known and unidentified compounds) which were not assessed in the current study.

In conclusion, the high-temperature oxidation process decreased the antioxidant capacity and individual content values of most phenolic compounds present in *C. genistoides* hot water extracts. Decreases in the individual phenolic contents were compound-specific, with factors such as the degree of hydroxylation and the degree and position of glucosylation playing key roles. Insight into the thermal stability of selected xanthones and benzophenones was obtained for the first time in this study, with the application of thermal degradation kinetics modeling. This includes kinetic data on the novel *Cyclopia* constituent iriflophenone-3-*C*-glucoside-4-*O*-glucoside. Understanding these complex reaction mechanisms is a prerequisite to gain further insights into the chemical pathways during the high-temperature oxidation of *C. genistoides* plant material. Future studies will include assessing the thermal stability of the compounds in model solutions as opposed to the plant material, thereby eliminating matrix effects and interactions between phenolic constituents. Such degradation models will be useful to predict the stability of these compounds during pasteurization/sterilization of ready-to-drink herbal tea beverages, for instance.

■ ASSOCIATED CONTENT

Supporting Information

ORAC curves for the benzophenones iriflophenone-3-*C*-glucoside-4-*O*-glucoside (0.228 μM) and maclurin-3-*C*-glucoside (0.474 μM) in relation to the Trolox reference standard at 0.621 and 3.104 μM (Figure S1), Retention times and UV−vis characteristics of additional phenolic compounds (**A**−**I**) selected for quantification in the current study, based on previously reported data (Table S1), and mean values for the major benzophenones and xanthones in 40% aqueous ethanol extracts of *Cyclopia genistoides* as a function of oxidation time and temperature (Table S2). The Supporting Information is available free of charge on the ACS Publications website at DOI: 10.1021/acs.jafc.5b01657.

■ AUTHOR INFORMATION

Corresponding Author

*E.J.: tel, +27 21 809 3444; fax, +27 21 809 3430; e-mail, joubertL@arc.agric.za.

Funding

This work is based on research supported in part by the South African Department of Science and Technology (DST/CON 0133/2012). Other financial support to E.J. was received through a grant from the Economic Competitive Support Package for Agroprocessing to the ARC by the South African Government. NRF-DST Professional Development Programme Doctoral Scholarship to T.B. is acknowledged.

Notes

The authors declare no competing financial interest.

■ ACKNOWLEDGMENTS

F. Joubert (Koksrivier, Pearly Beach, Western Cape, South Africa) is acknowledged for supplying plant material. M. van der Rijst (Biometry Division, ARC Infruitec-Nietvoorbij) is thanked for statistical data analysis. E. L. Willenburg, an NRF-DST Professional Development Programme Postdoctoral Fellow at the Post-Harvest and Wine Technology Division of ARC Infruitec-Nietvoorbij, is thanked for the isolation of phloretin-3′,5′-di-*C*-glucoside from *C. subternata*.

■ REFERENCES

(1) Beelders, T.; De Beer, D.; Stander, M. A.; Joubert, E. Comprehensive phenolic profiling of *Cyclopia genistoides* (L.) Vent. by LC-DAD-MS and −MS/MS reveals novel xanthone and benzophenone constituents. *Molecules* **2014**, *19*, 11760−11790.

(2) Joubert, E.; Joubert, M. E.; Bester, C.; De Beer, D.; De Lange, J. H. Honeybush (*Cyclopia* spp.): From local cottage industry to global markets − the catalytic and supporting role of research. *S. Afr. J. Bot.* **2011**, *77*, 887−907.

(3) Vyas, A.; Syeda, K.; Ahmad, A.; Padhye, S.; Sarkar, F. H. Perspectives on medicinal properties of mangiferin. *Mini-Rev. Med. Chem.* **2012**, *12*, 412−425.

(4) Malherbe, C. J.; Willenburg, E.; De Beer, D.; Bonnet, S. L.; Van der Westhuizen, J. H.; Joubert, E. Iriflophenone-3-*C*-glucoside from *Cyclopia genistoides*: Isolation and quantitative comparison of antioxidant capacity with mangiferin and isomangiferin using on-line HPLC antioxidant assays. *J. Chromatogr. B: Anal. Technol. Biomed. Life Sci.* **2014**, *951*−*952C*, 164−171.

(5) Kokotkiewicz, A.; Luczkiewicz, M.; Pawlowska, J.; Luczkiewicz, P.; Sowinski, P.; Witkowski, J.; Bryl, E.; Bucinski, A. Isolation of xanthone and benzophenone derivatives from *Cyclopia genistoides* (L.) Vent. (honeybush) and their pro-apoptotic activity on synoviocytes from patients with rheumatoid arthritis. *Fitoterapia* **2013**, *90*, 199−208.

(6) Beelders, T.; Brand, D. J.; De Beer, D.; Malherbe, C. J.; Mazibuko, S. E.; Muller, C. J. F.; Joubert, E. Benzophenone *C*- and *O*-glucosides from *Cyclopia genistoides* (honeybush) inhibit mammalian α-glucosidase. *J. Nat. Prod.* **2014**, *77*, 2694−2699.

(7) Feng, J.; Yang, X.-W.; Wang, R.-F. Bio-assay guided isolation and identification of α-glucosidase inhibitors from the leaves of *Aquilaria sinensis*. *Phytochemistry* **2011**, *72*, 242−247.

(8) Zhang, Y.; Qian, Q.; Ge, D.; Li, Y.; Wang, X.; Chen, Q.; Gao, X.; Wang, T. Identification of benzophenone *C*-glucosides from mango tree leaves and their inhibitory effect on triglyceride accumulation in 3T3-L1 adipocytes. *J. Agric. Food Chem.* **2011**, *59*, 11526−11533.

(9) Zhang, Y.; Liu, X.; Han, L.; Gao, X.; Liu, E.; Wang, T. Regulation of lipid and glucose homeostatis by mango tree leaf extract is mediated by AMPK and PI3K/AKT signaling pathways. *Food Chem.* **2013**, *141*, 2896−2905.

(10) Joubert, E.; Richards, E. S.; Van der Merwe, J. D.; De Beer, D.; Manley, M.; Gelderblom, W. C. A. Effect of species variation and processing on phenolic composition and *in vitro* antioxidant activity of aqueous extracts of *Cyclopia* spp. (honeybush tea). *J. Agric. Food Chem.* **2008**, *56*, 954−963.

(11) Bělehrádek, J. Temperature coefficients in biology. *Biol. Rev.* **1930**, *5*, 30−58.

(12) Le Roux, M.; Cronje, J. C.; Joubert, E.; Burger, B. V. Chemical characterization of the constituents of the aroma of honeybush. *S. Afr. J. Bot.* **2008**, *74*, 139−143.

(13) Arthur, H.; Joubert, E.; De Beer, D.; Malherbe, C. J.; Witthuhn, R. C. Phenylethanoid glycosides as major antioxidants in *Lippia*

multiflora herbal infusion and their stability during steam pasteurisation of plant material. *Food Chem.* **2011**, *127*, 581−588.
(14) Huang, D.; Ou, B.; Hampsch-Woodill, M.; Flanagan, J. A.; Prior, R. L. High-throughput assay of oxygen radical absorbance capacity (ORAC) using a multichannel liquid handling system coupled with a microplate fluorescence reader in 96-well format. *J. Agric. Food Chem.* **2002**, *50*, 4437−4444.
(15) De Paepe, D.; Valkenborg, D.; Coudijzer, K.; Noten, B.; Servaes, K.; De Loose, M.; Voorspoels, S.; Diels, L.; Van Droogenbroeck, B. Thermal degradation of cloudy apple juice phenolic constituents. *Food Chem.* **2014**, *162*, 176−185.
(16) Sui, X.; Dong, X.; Zhou, W. Combined effect of pH and high temperature on the stability and antioxidant capacity of two anthocyanins in aqueous solution. *Food Chem.* **2014**, *163*, 163−170.
(17) Dhuique-Mayer, C.; Tbatou, M.; Carail, M.; Caris-Veyrat, C.; Dornier, M.; Amiot, M. J. Thermal degradation of antioxidant micronutrients in citrus juice: kinetics and newly formed compounds. *J. Agric. Food Chem.* **2007**, *55*, 4209−4216.
(18) Makris, D. P.; Rossiter, J. T. Heat-induced, metal catalyzed oxidative degradation of quercetin and rutin (quercetin-3-*O*-rhamnosylglucoside) in aqueous model systems. *J. Agric. Food Chem.* **2000**, *48*, 3830−3838.
(19) Buchner, N.; Krumbein, A.; Rohn, S.; Kroh, L. W. Effect of thermal processing on the flavonols quercetin and rutin. *Rapid Commun. Mass Spectrom.* **2006**, *20*, 3229−3235.
(20) Rohn, S.; Bucher, N.; Driemel, G.; Rauser, M.; Kroh, L. W. Thermal degradation of onion quercetin glycosides under roasting conditions. *J. Agric. Food Chem.* **2007**, *55*, 1568−1573.
(21) Zielinski, H.; Michalska, A.; Amigo-Benavent, M.; Del Castillo, M. D.; Piskula, M. K. Changes in protein quality and antioxidant properties of buckwheat seeds and groats induced by roasting. *J. Agric. Food Chem.* **2009**, *57*, 4771−4776.
(22) Theron, K. A. *Sensory and phenolic profiling of Cyclopia species (honeybush) and optimization of the fermentation conditions*. MSc (Food Science) Thesis, Stellenbosch University, Stellenbosch, South Africa, 2012.
(23) De Beer, D.; Joubert, E. Development of HPLC method for *Cyclopia subternata* phenolic compound analysis and application to other *Cyclopia* spp. *J. Food Compos. Anal.* **2010**, *23*, 289−297.
(24) Krafczyk, N.; Heinrich, T.; Porzel, A.; Glomb, M. A. Oxidation of the dihydrochalcone aspalathin leads to dimerization. *J. Agric. Food Chem.* **2009**, *57*, 6838−6843.
(25) Heinrich, T.; Willenberg, I.; Glomb, M. A. Chemistry of color formation during rooibos fermentation. *J. Agric. Food Chem.* **2012**, *60*, 5221−5228.
(26) Wezeman, T.; Bräse, S.; Masters, K.-S. Xanthone dimers: a compound family which is both common and privileged. *Nat. Prod. Rep.* **2015**, *32*, 6−28.
(27) Li, N.; Taylor, L. S.; Taylor, L. S.; Ferruzzi, M. G.; Mauer, L. J. Color and chemical stability of tea polyphenol (−)-epigallocatechin-3-gallate in solution and solid states. *Food Res. Int.* **2013**, *53*, 909−921.
(28) Krafczyk, N.; Glomb, M. A. Characterization of phenolic compounds in rooibos tea. *J. Agric. Food Chem.* **2008**, *56*, 3368−3376.
(29) Maini, S.; Hodgson, H. L.; Krol, E. S. The UVA and aqueous stability of flavonoids is dependent on B-ring substitution. *J. Agric. Food Chem.* **2012**, *60*, 6966−6976.
(30) Murakami, M.; Yamaguchi, T.; Takamura, H.; Matoba, T. Effects of thermal treatment on radical-scavenging activity of single and mixed polyphenolic compounds. *J. Food Sci.* **2004**, *69*, FCT7−FCT10.
(31) Rice-Evans, C. A.; Miller, N. J.; Paganga, G. Structure-antioxidant activity relationships of flavonoids and phenolic acids. *Free Radical Biol. Med.* **1996**, *20*, 933−956.
(32) Heim, K. E.; Tagliaferro, A. R.; Bobilya, D. J. Flavonoid antioxidants: chemistry, metabolism and structure-activity relationships. *J. Nutr. Biochem.* **2002**, *13*, 572−584.
(33) Xie, J.; Schaich, K. M. Re-evaluation of the 2,2-diphenyl-1-picrylhydrazyl free radical (DPPH) assay for antioxidant activity. *J. Agric. Food Chem.* **2014**, *62*, 4251−4260.
(34) Nakatani, N.; Kayano, S. I.; Kikuzaki, H.; Sumino, K.; Katagiri, K.; Mitani, T. Identification, quantitative determination, and antioxidative activities of chlorogenic acid isomers in prune (*Prunus domestica* L.). *J. Agric. Food Chem.* **2000**, *48*, 5512−5516.

DOI: 10.1021/acs.jafc.5b01657
J. Agric. Food Chem. 2015, 63, 5518−5527

Table 1. Characteristics of Pigmented Maize Varieties Selected for This Study

henetic hybrid variety	sample ID	color class	growing location/year
LAMA Red R10 × Red Hybrid Ear R3	1	red	Weslaco, TX/2011; College Station, TX/2013
Red Ear R4 × LAMA Red R10	2	red	Weslaco, TX/2011; College Station, TX/2013
Wenwei1 R5 × Red Hybrid Ear R3	3	red	Weslaco, TX/2011; College Station, TX/2013
LH287 R8 × Wenwei1 R5	4	red	College Station, TX/2011; College Station, TX/2013
Wenwei2 R6 × Red Hybrid Ear R3	5	red	College Station, TX/2011; College Station, TX/2013
Red Ear R4 × Wenwei1 R5	6	red	Weslaco, TX/2011; College Station, TX/2013
Wenwei2 R6 × LH287 R8	7	red	Weslaco, TX/2011; College Station, TX/2013
LH195 R7 × Red Hybrid Ear R3	8	red	College Station, TX/2011; College Station, TX/2013
Wenwei2 R6 × Maize Morado R11	9	purple	Weslaco, TX/2011; College Station, TX/2013
Wenwei1 R5 × Maize Morado R11	10	purple	Weslaco, TX/2011; College Station, TX/2013
LH195 R7 × Maize Morado R11	11	purple	Weslaco, TX/2011; College Station, TX/2013
Red Ear R4 × Maize Morado R11	12	purple	Weslaco, TX/2011; College Station, TX/2013
Red Hybrid Ear R3 × Maize Morado R11	13	purple	Weslaco, TX/2011; College Station, TX/2013
Lfy Blue R1 × Maize Morado R11	14	purple	Weslaco, TX/2011; College Station, TX/2013
Lfy Blue R1 × Ethiopia Blue R2	15	blue	Weslaco, TX/2011; College Station, TX/2013
Lfy Blue R1 × Ethiopia Blue2 R9	16	blue	Weslaco, TX/2011; College Station, TX/2013
Ethiopia Blue2 R9 × Ethiopia Blue R2	17	blue	Weslaco, TX/2011
Lfy Blue R1 × Red Ear R4	18	red/blue	Weslaco, TX/2011; College Station, TX/2013
Red Hybrid Ear R3 × Ethiopia Blue2 R9	19	red/blue	College Station, TX/2011, College Station, TX/2013
Wenwei1 R5 × Ethiopia Blue R2	20	red/blue	Weslaco, TX/2011; College Station, TX/2013
Wenwei2 R6 × Lfy Blue R1	21	red/blue	Weslaco, TX/2011; College Station, TX/2013
Red Ear R4 × Ethiopia Blue2 R9	22	red/blue	Weslaco, TX/2011; College Station, TX/2013
Ethiopia Blue2 R9 × Red Ear R4	23	red/blue	Weslaco, TX/2011; College Station, TX/2013
Ethiopia Blue R2 × Red Ear R4	24	red/blue	Weslaco, TX/2011; College Station, TX/2013

on extractable anthocyanin content and changes in the content of these compounds, along with other phenolics, as a way to estimate the composition of bioactives in processed maize.[15−17] However, no studies have yet investigated the potential impact of anthocyanin composition of maize on the stability of color in product (in situ) during thermoalkaline processing. Given that visual color is a primary quality factor for processed foods, identifying pigmented maize varieties that retain their visual appeal during processing is important. In this study, we use a diverse set of genetically distinct pigmented maize hybrids to investigate the effect of pigment composition on color stability during nixtamalization and tortilla chip processing.

MATERIALS AND METHODS

Materials. *Maize Samples.* Twenty-four pigmented maize hybrids with various genetic backgrounds from four different color classes [red, blue, purple (also identified as maiz morado), and red/blue] developed by the Texas A&M University Quantitative Genetics and Maize Breeding Program were used. To create each colored hybrid two corn inbred lines, with one or both parents being colored, were crossed to obtain the experimental hybrid seed. The grain samples used in this study were obtained by self-pollinating plants grown from this hybrid seed in two different environments [College Station, TX, 2013 (CS13), and Weslaco, TX, 2011 (WE11); College Station, TX, 2011, was used instead of WE11 for samples 4, 5, 8, and 19 because of insufficient seed quantity]; self-pollination allowed these grain samples to be genetically pure as would be obtained in a farmer's field. The maize genetic variety, color class, and growing location/year are listed in Table 1, and additional information can be found in Mahan et al. (2013).[18] The pigments in red, purple, and red/blue color classes are located mainly in the pericarp and are maternally inherited, whereas the pigments in the blue color class are in the aleurone layer. Prior to analysis, whole grain samples were preground using a coffee grinder (Cuisinart, model DCG-20N series), ground with a UDY cyclone sample mill equipped with a 0.1 mm screen (model 3010-030, UDY Corp., Fort Collins, CO, USA), and stored in a freezer at −20 °C until extraction. A moisture analyzer (model HB43-S, Mettler-Toledo, LLC, Columbus, OH, USA) was used to determine the moisture contents of the ground samples, which were confirmed using the AACC air-oven method of moisture content determination (method 44-15.02, AACC International, 1999).

Chemicals and Reagents. All reagents used were of analytical grade. Cyanidin chloride and pelargonidin chloride standards were purchased from Extrasynthese Natural Products, Genay, France. Ferulic acid and caffeic acid were purchased from Spectrum Chemical Manufacturing Corp., Gardena, CA, USA; and *p*-coumaric acid was purchased from Sigma-Aldrich Chemicals, St. Louis, MO, USA.

Methods. *Alkaline Processing of Pigmented Maize.* Thirty grams of maize was added to large glass tubes containing 90 mL of distilled water (1:3 w/w, maize/water) and either 0% (control), 0.5%, or 1.0% lime (weight of lime per weight of maize). The samples were cooked in a medium kettle filled with water on a DuxTop induction cooktop (Secura, Appleton, WI, USA) for 50 min at approximately 100 °C. The cooked samples were steeped for 14 h in a covered water bath that was previously heated to 80 °C and shut off prior to sample entry. After steeping, the pH of the cooking liquor (nejayote) was measured, and the liquid was then discarded. The cooked maize (nixtamal) was not washed, as is traditionally done after steeping to remove excess lime and partially remove pericarp, due to the fact that the majority of the anthocyanins are present in the pericarp and aleurone layers, and so pigments would be partially lost through this step. The nixtamal was then ground into masa using a coffee grinder (Cuisinart, model DCG-20N series), and the masa was rehydrated on the basis of moisture content to achieve suitable masa consistency for tortilla production. Pieces of masa (14 g) were then pressed into tortillas using a manual press, and these tortillas were baked on a hot griddle (190 °C) for 30 s on each side for a total of 2 min. The tortillas were left to equilibrate to room temperature and then fried at 198 °C for 50 s using an electric deep fryer (Presto, "Fry Daddy Elite" stock no. 05426). The maize tortilla chips were then stored at −20 °C until further analysis.

Extraction. Ground maize flour (5 g) was extracted in 1% HCl in methanol (10 mL) with continuous shaking for 2 h at room temperature. The samples were then centrifuged at 9900*g* for 8 min (HeraeusMegafuge 11R, Thermo Fisher Scientific, Asheville, NC, USA), and the supernatants were collected. A portion of each supernatant was then passed through a syringe filter with a 0.45 μm

DOI: 10.1021/acs.jafc.5b00798
J. Agric. Food Chem. 2015, 63, 5528−5538

nylon membrane before being injected (3 μL) onto the HPLC column.

The fried maize tortilla chips were ground and defatted using hexanes (1:3, samples/hexanes) for 1.5 h with agitation. This process was repeated five times to remove all residual oil, with the saturated hexanes being discarded and fresh hexanes added each time. Defatted samples were stored open in a fume hood overnight until the hexanes had evaporated. These samples were subsequently extracted as described for grain in the preceding paragraph.

HPLC Analysis. Individual anthocyanins and other phenolics were separated and quantified using an Agilent 1200 HPLC system (Agilent Technologies, Santa Clara, CA, USA) equipped with a ZORBAX Stable Bond Eclipse XDB-C18 column (4.6 × 150 mm, 5 μm; Agilent Technologies), with a guard column (4.6 × 12.5 mm, 5 μm). The mobile phase comprised 2% formic acid in water (A) and 2% formic acid in acetonitrile/methanol (50:50) (B). The elution gradient (B) was 0−2 min, 10% isocratic; 2−4 min, 10−20%; 4−24 min, 20−50%; 24−28 min/ 50% isocratic; 28−30 min, 50−10%; and 30−37 min, 10% isocratic. Separation was achieved at a flow rate of 1 mL/min with the column thermostat held at 40 °C. Compounds were monitored at 280, 320, and 360 nm (for other phenolics) and at 520 nm (for anthocyanins) using a diode array detector.

UPLC-ESI/MS Analysis. Analysis was carried out using a Waters-ACQUITY UPLC/MS system (Waters Corp., Milford, MA, USA), which was equipped with a binary solvent manager, sample manager (autosampler), column heater, and photodiode array eλ detector (PDA). This was interfaced with a mass spectrometer equipped with a tandem quadrupole (TQD) electrospray ionization (ESI) detector. A Kinetex C18 column (150 mm × 2.10 mm, 2.6 μm, Phenomenex, Torrance, CA, USA) was utilized for separation with a column temperature of 50 °C for anthocyanins, which were monitored at 520 nm, and a temperature of 40 °C for other phenolics, which were monitored at 280, 320, and 360 nm. Mass spectrometric data for anthocyanins were acquired in positive mode and in negative mode for other phenolics as previously described.[19] Empower 2 software (Waters Corp.) was employed to obtain and analyze the data. The MS scan was recorded in the range of 100−1000 Da for anthocyanins and other phenolics. Nitrogen was the drying and nebulizing gas used, and argon was used as the collision gas (AOC, Bryan, TX, USA). The nitrogen gas flow conditions were 800 and 50 L/h for desolvation and at the cone, respectively. Source block temperature and desolvation temperature were set at 150 and 400 °C, respectively. The intensity of the mass signals of protonated/deprotonated molecules and aglycone fragments was used for optimization of ionization conditions and was performed for each individual compound/peak detected. Mass parameters were optimized as follows: capillary voltage, 3.5/3.0 kV; and cone voltage, 40/30 V for positive/negative ionization, respectively. The MS/MS scan was optimized as follows: cone voltage, 40/30−55 V; and collision energy, 20/15−35 V for anthocyanins/other phenolics, respectively.

Samples were prepared in identical fashion to those for HPLC analysis, but the final filtration prior to injection was through 0.2 μm PTFE filters, with 1 μL injected onto the LC column for analysis. The solvents used were 2% formic acid in water (solvent A) and acetonitrile (solvent B) for anthocyanin analysis and 0.05% formic acid in water (solvent A) and acetonitrile (solvent B) for the other phenolics. The gradient, at a flow rate of 0.4 mL/min, was as follows: 5% B from 0 to 2 min, 5−75% B from 2 to 27 min, 75% B isocratic from 27 to 30 min, 75−5% B from 30 to 31 min, followed by 5% B isocratic for 5 min to allow for column equilibration before the next injection.

Quantification of Major Anthocyanins and Other Phenolics. Major anthocyanins and other phenolics were quantified on the basis of standard curves calibrated using pure standards. However, when standards were not available, content was determined using a molecular weight correction factor and based on the assumption that derivatives possess molar absorptivities similar to those of their aglycones. Cyanidin and pelargonidin were used to estimate their respective glycosides/acyl-glycosides, whereas cyanidin was used to estimate peonidin derivatives. Phenolic amides were quantified on the basis of molar absorptivities of their respective phenolic acid substituents; their UV profiles were essentially identical to the parent phenolic acid components, as previously demonstrated.[20] Concentrations of identified compounds were expressed as micrograms per gram, dry basis.

Determination of Total Anthocyanin Content and Proportion of Monomeric Anthocyanins. Total anthocyanin content (TAC) and total monomeric anthocyanin content (TMA), as well as proportion of monomeric anthocyanins, were determined using the pH differential method as described by Lee et al.[21] Samples were extracted in 1% HCl in methanol (5 g of sample/10 mL of MeOH) and diluted appropriately to reach A_{520} of around 1.0 using pH 1.0 buffer. Using this determined dilution factor, two dilutions of the sample were prepared (one with pH 1.0 buffer and one with pH 4.5 buffer). Samples were scanned from 800 to 200 nm using a UV−vis spectrophotometer (Shimadzu Scientific Instruments, Columbia, MD, USA), and absorbance data were collected at 520 and 700 nm. The proportion of monomeric anthocyanins was determined for only a subset of purple and red/blue samples. The remaining samples had total pigment contents that were too low, so the proportion monomeric could not be determined. All data were reported in micrograms per gram (dry basis).

Measurement of Visual Color Parameters. Visual color parameters were measured using a Minolta Chroma Meter (model CR-300, Ramsey, NJ, USA). The colorimeter was calibrated prior to each use with a standard white tile. Lightness (L^*), degree of redness (a^*), and degree of yellowness (b^*) were the parameters directly measured by the instrument. Measurements were taken in triplicates. Measurements were taken on masa and tortilla chips for each sample and treatment. These values were then converted into total color difference (ΔE) and chroma (C^*) as follows:

$$\Delta E = ((\Delta L^*)^2 + (\Delta a^*)^2 + (\Delta b^*)^2)^{1/2}$$

$$C^* = ((a^*)^2 + (b^*)^2)^{1/2}$$

These color parameters can assist in relating instrumental data to visual perception. Chroma indicates the strength of chromatic response, essentially the saturation of the color, lightness gives the brilliance of the color, and total color difference/change gives the overall magnitude of change of the sample in relation to the control.[22]

Statistical Analysis. Data analysis was carried out using one-way ANOVA to detect differences among the means, and Fisher's least significant difference was used to separate means with $P < 0.05$. Statistical analysis was done using JMP Pro (version 10.0.0, SAS Institute, Cary, NC, USA).

RESULTS AND DISCUSSION

Anthocyanin Composition of the Different Pigmented Maize Color Classes. The anthocyanins identified in the diverse set of pigmented maize samples analyzed in this study (Figure 1) were generally similar to those previously reported.[11,14] The seven major anthocyanins identified were cyanidin-3-glucoside, pelargonidin-3-glucoside, peonidin-3-glucoside, cyanidin-3-(3″-malonylglucoside), cyanidin-3-(6″-malonylglucoside), pelargonidin-3-malonylglucoside, and peonidin-3-malonylglucoside (Figure 1). The malonylglucoside isomers of cyanidin were distinguished mainly on the basis of LC elution profiles, by comparison to published literature.[12−14] The cyanidin-3-(6″-malonylglucoside) elutes later than cyanidin-3-(3″-malonylglucoside) under conditions used in this study.[13,23] The two dominant anthocyanins in all color classes were cyanidin-3-glucoside (m/z 449, positive mode) and cyanidin-3-(6″-malonylglucoside) (m/z 535). On average, these two major pigments together accounted for approximately 80% of HPLC resolved anthocyanin peaks (Table 2). We did not detect any of the condensed flavonoid−anthocyanin dimers previously reported in some maize

DOI: 10.1021/acs.jafc.5b00798
J. Agric. Food Chem. 2015, 63, 5528−5538

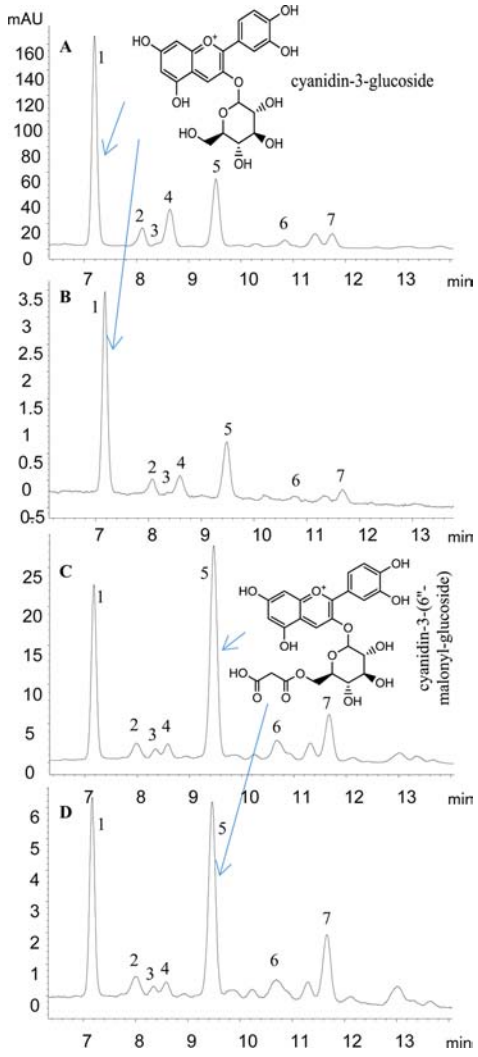

Figure 1. Representative HPLC chromatograms from the Weslaco, TX, 2011, set of samples depicting the differing anthocyanin profiles of a purple maize sample (Wenwei1 R5 × Maize Morado R11) (A) and a red maize sample (Wenwei2 R6 × LH287 R8) (B) versus a red/blue maize sample (Wenwei2 R6 × Lfy Blue R1) (C) and a blue maize sample (Lfy Blue R1 × Ethiopia Blue2 R9) (D) monitored at 520 nm. Numbers identify anthocyanins present: 1 = cyanidin-3-glucoside; 2 = pelargonidin-3-glucoside; 3 = cyanidin-3-(3″-malonylglucoside); 4 = peonidin-3-glucoside; 5 = cyanidin-3-(6″-malonylglucoside); 6 = pelargonidin-3-malonylglucoside; 7 = peonidin-3-malonylglucoside.

varieties[24] in the diverse set of samples we investigated. Such condensed pigments provide far more stable color quality parameters over a wide pH range than their noncondensed analogues.[25] Thus, lines that contain these compounds may provide interesting genetic resources for potential improvement of anthocyanin functionality in maize products.

Major differences in pigment profile were observed between the purple and red color classes, on the one hand, and the red/blue and blue color classes, on the other hand (Figure 1). The main difference between these two groups was the proportion of the two major pigments cyanidin-3-glucoside versus the proportion of cyanidin-3-(6″-malonylglucoside). Overall, the purple and red color classes possessed a higher proportion of monomeric cyanidin-3-glucoside, whereas the red/blue and blue color classes contained a higher proportion of acylated cyanidin-3-(6″-malonylglucoside). The acylated anthocyanins on average accounted for 60% of HPLC resolved pigments in blue and red/blue samples, whereas they accounted for only about 42% of the red and purple sample pigments (Table 2). This is an important observation, because the acylated anthocyanins are more stable to food processing conditions; our findings suggest that color class can be used as one component of a selection criteria for breeding maize to enhance accumulation of stable food colorants.

On the basis of the observed difference in anthocyanin profiles, it was hypothesized that the blue and red/blue color classes would maintain more color through thermoalkaline processing due to the higher proportion of the more stable, malonated derivatives in these color classes. Growth environment had minimal effect on anthocyanin profile within a color class, suggesting that genetic background has the dominant effect on determining anthocyanin composition in pigmented corn.

Color class was also predictive of total anthocyanin content of the maize samples (Table 3). Even though the differences among many hybrids within a color class were significant, a clear pattern based on color class was observed. All samples within the purple color class had significantly higher total anthocyanin content than the other color classes (blue, red/blue, and red). Anthocyanin contents (as cyanidin-3-glucoside equivalents, UV−vis spectroscopy) of purple samples ranged from 890 to 3312 μg/g, whereas the other three color classes had much lower anthocyanin contents (8.9−540 μg/g). Among the nonpurple color classes, the red color class had the lowest pigment content, ranging from 8.9 to 127 μg/g, followed by red/blue (69−368 μg/g) (Table 3). The values were generally within ranges reported for different pigmented maize based on a similar method.[11,14,26]

An interesting observation was that anthocyanin content within each color class appeared to be distinctly influenced by the environment (Table 3). All nonpurple phenotypes (red, red/blue, and blue) had significantly ($p < 0.05$) higher anthocyanin accumulation in Weslaco 2011 than in College Station 2013 samples. In fact, on average, Weslaco 2011

Table 2. Anthocyanin Composition (Range and Mean) of the Two Major Pigments Identified in All Maize Varieties and the Proportion of Acylated Pigments Resolved by HPLC in the Two Growth Environments[a]

	Weslaco 2011				College Station 2013			
color class	Cy-3-glu (mg/g)	Cy-3,6″-MalGlu (mg/g)	av total[b] (mg/g)	% acylated[b]	Cy-3-glu (mg/g)	Cy-3,6″-MalGlu (mg/g)	av total[b] (mg/g)	% acylated[b]
red	0.07−0.16 (0.11)[c]	trace−0.17 (0.08)[c]	0.19	43.4	trace	trace	na	na
purple	4.80−16.4 (10.1)	2.3−10.4 (5.7)	20.8	35.2	4.83−10.1 (8.2)[c]	3.8−10.5 (7.4)[c]	21.9	47.3
blue	0.26−0.64 (0.43)	0.39−0.79 (0.59)	1.18	56.2	0.29−0.38 (0.34)	0.50−0.60 (0.55)	1.08	59.3
red/blue	0.20−0.84 (0.34)	0.14−1.6 (0.55)	1.05	62.3	0.13−0.34 (0.25)	0.18−0.61 (0.44)	0.80	61.1

[a]Cy = cyanidin, Glu = glucoside, Mal = malonyl. [b]Based on resolved anthocyanin peaks monitored at 520 nm. [c]Range (mean).

DOI: 10.1021/acs.jafc.5b00798
J. Agric. Food Chem. 2015, 63, 5528−5538

Table 3. Total Anthocyanin Content of Raw Pigmented Maize Hybrids As Determined by UV−Vis Spectrometry (Mean ± SD, n = 3)

		total anthocyanin content (expressed as Cy-3-glu equiv, μg/g, db)	
sample ID[a]	phenotype	Weslaco 2011	College Station 2013
1	red	59.8 ± 1.7KL	10.8 ± 0.85G
2	red	37.2 ± 6.3L	24.0 ± 0.17G
3	red	126.9 ± 1.8JKL	12.4 ± 0.27G
4	red	44.0 ± 5.3L[b]	12.7 ± 0.74G
5	red	53.1 ± 8.0L[b]	12.2 ± 0.25G
6	red	40.6 ± 3.5L	24.2 ± 0.17G
7	red	57.9 ± 0.78L	12.5 ± 0.63G
8	red	42.9 ± 2.0[b]L	9.0 ± 0.11G
av		57.8 ± 27.8	14.7 ± 5.6
9	purple	1015.4 ± 36.9D	3270.9 ± 46.6A
10	purple	1380.4 ± 9.9C	2473.8 ± 103.9C
11	purple	2257.1 ± 22.8B	1882.1 ± 186.0D
12	purple	2940.0 ± 141.9A	2734.3 ± 86.8B
13	purple	890.5 ± 44.7E	1104.4 ± 37.3E
14	purple	2948.6 ± 15.2A	3312.4 ± 23.8A
av		1905 ± 879	2463 ± 800
15	blue	506.7 ± 10.0F	261.3 ± 16.5F
16	blue	240.0 ± 6.4HI	111.0 ± 1.3FG
17	blue	540.3 ± 3.8F	na[c]
av		429 ± 143	186 ± 92
18	red/blue	264.0 ± 12.4H	112.3 ± 5.4FG
19	red/blue	160.8 ± 0.75IJK[b]	45.8 ± 0.31G
20	red/blue	301.6 ± 1.2GH	136.5 ± 0.67FG
21	red/blue	368.0 ± 5.9G	69.4 ± 1.9G
22	red/blue	205.6 ± 8.5HIJ	83.5 ± 1.0G
23	red/blue	211.4 ± 11.0HIJ	100.1 ± 0.76G
24	red/blue	366.1 ± 0.97G	159.4 ± 0.69FG
av		268 ± 77	101 ± 37

[a]Refer to Table 1 for sample genetic background. Values within the same column with different letters are significantly different ($p < 0.05$). [b]Sample from College Station 2011. [c]na, sample not available.

samples had 2.3−4 times higher anthocyanins than College Station 2013 samples among the three color classes. The average anthocyanin content for red samples from Weslaco 2011 was 57.8 μg/g, whereas for College Station 2013 the average was 14.7 μg/g. The average anthocyanin contents for red/blue samples grown in Weslaco 2011 and College Station 2013 were 268 and 101 μg/g, respectively. For the blue phenotype anthocyanin contents averaged 429 μg/g for Weslaco 2011 and 186 μg/g for College Station 2013. Among the purple phenotype, the College Station 2013 samples generally had higher anthocyanin (average 2463 μg/g) content than Weslaco 2011 samples (1905 μg/g), but the pattern was not as clear-cut as with the other color classes. Whereas the way in which the specific growth environments affect the accumulation of anthocyanins was not a subject of this study, the fact that growth environment can have such a distinct impact on anthocyanin content of maize is important. Growth environments could potentially be selected or optimized to maximize anthocyanin accumulation in maize for various uses.

Major Copigment Composition of the Maize Samples. A question that remains is how much the appearance of pigmented maize is merely a function of the anthocyanin content, given the LC profiles of anthocyanins were fairly similar among the diverse set of samples. UV−vis spectroscopy of crude extracts at pH 1.0 revealed minor differences in visible λ_{max} among the color classes, except for the red color class (average 516 nm); the blue, red/blue, and purple samples had mean λ_{max} values of 528, 527, and 526 nm, respectively (data not shown). Due to the fact that the two dominant anthocyanins in all samples (cyanidin derivatives) (Figure 1) have similar absorbance maxima, the differences in λ_{max} for the various color class crude extracts may be partly attributed to the profile of copigments that coextract with the pigments. Also, in view of the significant overlap in anthocyanin contents among the nonpurple color classes (Table 3), it is apparent that appearance is not affected by merely content but possibly inherent copigment profile, as well as other factors.

To determine the possible effect of extracted copigments on crude anthocyanin color, we characterized the major phenolics that were extracted along with the anthocyanins. The major extractable phenolic compounds identified in all of the maize samples were three phenolic amides; *N*,*N*′-dicoumaroylspermidine, *N*-coumaroyl-*N*′-feruloylputrescine, and *N*,*N*′-diferuloylputrescine (Tables 4 and 5). These phenolic amides have been identified as significant components of methanolic extracts from maize, especially in the bran fraction,[20,27,28] and were suggested to be associated with insect resistance in grain[29] and may have interesting bioactive properties.[30] The concentrations of the phenolic amides in the maize samples were relatively high in comparison to the literature values (Table 5).

Important differences were observed in phenolic amine profiles of the samples (Table 5). The red color class had on

Table 4. Identification of Major (Phenolic Amides) and Minor (Phenolic Acid and Their Glycerides) Extractable Copigments in the Pigmented Maize Samples Based on UPLC Retention Time (t_R), UV−Vis Spectroscopic Characteristics (λ_{max}), and MS and MS/MS Spectroscopic Pattern[a]

t_R (min)	λ_{max} (nm)	$[M - H]^-$ (m/z)	MS/MS fragments (m/z)	identification
7.704	298/308	436	316, 290, 145, 119	*N*,*N*′-dicoumaroylspermidine
10.982	310	409	289, 259, 149, 135, 119	*N*-coumaroyl-*N*′-feruloylputrescine
11.209	318	439	289, 149, 135	*N*,*N*′-diferuloylputrescine
5.568	323	179	135	caffeic acid
7.055	312	237	163, 145, 119	coumaroyl-glycerol
7.793	318	193	178, 134	ferulic acid
12.178	315	399	253, 235, 163, 161, 145, 119	coumaroyl-caffeoylglycerol
12.429	294/327	429	253, 193, 175, 161, 134	feruloyl-caffeoylglycerol

[a]ESI was performed in the negative mode.

DOI: 10.1021/acs.jafc.5b00798
J. Agric. Food Chem. 2015, 63, 5528−5538

Table 5. Major Copigment Content of Pigmented Maize Hybrids As Determined by HPLC-DAD

		N,N′-dicoumaroylspermidine content (μg/g, db)		*N*- coumaroyl-*N′*-feruloylputrescine content (μg/g, db)		*N,N′*-diferuloylputrescine content (μg/g, db)	
sample ID[a]	phenotype	Weslaco 2011	College Station 2013	Weslaco 2011	College Station 2013	Weslaco 2011	College Station 2013
1	red	84.8 ± 20.1K	262 ± 1.2GHIJ	16.2 ± 5.8FG	30.1 ± 0.5IJK	142 ± 41.3FGHIJ	208 ± 7.1IJ
2	red	161 ± 8.0HI	150 ± 2.4K	43.1 ± 0.3EF	62.8 ± 1.2FG	271 ± 1.9DEF	430 ± 4.9DE
3	red	133 ± 58.2IJ	281 ± 13.6FGHI	44.1 ± 20.6EF	67.6 ± 0.6EFG	331 ± 11DEFG	429 ± 4.2DE
4	red	70.4 ± 9.2†,K	138 ± 10.9K	183 ± 27.2†,B	212 ± 4.3A	592 ± 92B[b]	742 ± 14.7A
5	red	169 ± 0.90GHI[b]	239 ± 4.9IJ	35.1 ± 0.2EFG[b]	132 ± 0.0B	193 ± 0.4EFGH	600 ± 6.9C
6	red	260 ± 6.8CDE	209 ± 31.1J	59.4 ± 3.6DE	53.3 ± 16.9GH	282 ± 4.6CDE	345 ± 66.3EF
7	red	169 ± 3.2GHI	118 ± 1.6K	258 ± 20.6A	204 ± 0.3A	606 ± 45.4B	655 ± 1.2BC
8	red	223 ± 12.3EFG[b]	376 ± 47.9CD	154 ± 0.8BC[b]	102 ± 3.7C	936 ± 28.3A[b]	693 ± 38.8AB
mean		159	222	99.1	108	419	520
9	purple	200 ± 2.7EFGH	298 ± 6.8EFGH	11.4 ± 0.3FG	12.4 ± 0.8KL	89.3 ± 0.1HIJ	119 ± 5.4KL
10	purple	289 ± 2.7CD	385 ± 5.4CD	5.7 ± 0.2G	21.8 ± 0.2IJKL	42.2 ± 0.7IJ	174 ± 1.9IJK
11	purple	383 ± 3.9B	338 ± 20.6DEF	17.6 ± 0.6FG	18.4 ± 3.3JKL	178 ± 4.2EFGHI	129 ± 6.6JKL
12	purple	247 ± 1.6CDEF	315 ± 6.7EFG	19.6 ± 0.1FG	12.4 ± 2.6KL	193 ± 2.0EFGH	142 ± 0.1JKL
13	purple	247 ± 5.0DEF	348 ± 3.9DE	8.6 ± 0.3FG	11.7 ± 0.6KL	82.8 ± 1.9HIJ	117 ± 0.9KL
14	purple	294 ± 7.0C	445 ± 3.0B	14.4 ± 0.6FG	9.1 ± 6.2L	104 ± 26.2HIJ	71.7 ± 13.4L
mean		277	355	12.9	14.3	115	125
15	blue	375 ± 5.0B	430 ± 11.4BC	66.7 ± 3.8DE	32.8 ± 0.6IJ	205 ± 9.4DEFGH	122 ± 0.2JKL
16	blue	233 ± 2.9DEF	317 ± 5.2EFG	144 ± 4.4C	94.2 ± 3.0CD	412 ± 9.0C	330 ± 7.0FG
17	blue	374 ± 1.8B	na[c]	43.6 ± 1.1EF	na	90.5 ± 3.3HIJ	na
mean		327	376	84.8	63.5	236	226
18	red/blue	190 ± 1.8FGHI	282 ± 9.3FGHI	129 ± 2.7C	54.1 ± 4.7GH	1045 ± 6.9A	448 ± 13.0D
19	red/blue	257 ± 1.9CDE[b]	380 ± 0.0CD	13.9 ± 1.5FG[b]	80.1 ± 0.6DEF	83.5 ± 0.4HIJ[b]	317 ± 3.0FGH
20	red/blue	161 ± 19.4HI	337 ± 3.7DEF	44.2 ± 5.1EF	55.9 ± 0.4GH	129 ± 16.5GHIJ	234 ± 0.3HI
21	red/blue	786 ± 7.6A	288 ± 4.3FGHI	21.8 ± 0.3FG	84.2 ± 1.3CDE	29.5 ± 0.1J	402 ± 3.7DEF
22	red/blue	168 ± 5.6GHI	349 ± 5.7HIJ	58.9 ± 3.4DE	17.8 ± 0.8JKL	320 ± 9.8CD	98.5 ± 2.0KL
23	red/blue	160 ± 13.84HI	222 ± 7.0J	62.5 ± 2.1D,E	28.5 ± 1.3IJK	305 ± 5.4CDE	135 ± 4.7JKL
24	red/blue	304 ± 10.8C	506 ± 4.1A	91.2 ± 3.5D	39.7 ± 1.0HI	720 ± 28.1B	252 ± 9.5GHI
mean		289	338	60.2	51.5	376	270

[a]Refer to Table 1 for sample genetic background. All data expressed as mean ± SD of duplicates on a dry weight basis. Values within the same column with no letters in common are significantly different ($p < 0.05$). [b]Sample from College Station 2011. [c]na = sample not available.

average much higher content of extractable putrescines (average 574 μg/g) compared to other color classes (average 134−379 μg/g); the red/blue had the second highest content (379 μg/g). On the other hand, the red samples had the lowest average spermidine content (191 μg/g), whereas the blue samples had the highest (351 μg/g). The specific effect of the phenolic amides on anthocyanin color cannot be conclusively determined from these data. However, the different patterns of putrescines (higher in red color) and spermidine (higher in blue color) content in the different color classes suggest that copigments in colored maize likely contribute to shifts in anthocyanin absorption maxima in a way that may influence color appearance of pigmented maize. This is especially important because, as discussed under the thermoalkaline processing section below, the initial color hue has a major impact on visible color changes during processing.

An array of other phenolic compounds, mostly phenolic acids (ferulic, caffeic, and *p*-coumaric) and their glycerol esters (Table 4) were also present in minor quantities in all sample extracts. Interestingly, the glycerol esters of phenolic acids are abundant in sorghum[31,32] but have not been previously reported in maize. No clear pattern was observed for these minor phenolics in the samples; thus, their contribution to anthocyanin color could not be inferred.

Effect of Thermoalkaline Processing on Color Parameters. For processing, samples with yellow endosperm were excluded from tristimulus color analysis to remove this as a confounding variable. Alkaline pH and high temperature are two of the main factors that lead to transformation and degradation of anthocyanins.[33] In the nixtamalization process used in this study, the pH during processing was 4.82 ± 0.34 at 0% lime (control), 9.06 ± 0.52 at 0.5% lime, and 10.74 ± 0.76 at 1% lime (these measurements were taken on the nejayote after cooking and steeping). Additionally, the samples were lime-cooked in a water bath at approximately 100 °C, so the two harsh conditions were combined in nixtamalization and tortilla chip processing, which promoted the degradation of anthocyanins and subsequent color loss/change.

Lightness plays a substantial role in visual color perception. If a sample is too light or too dark, changes in chroma or hue may be imperceptible. The lightness was expected to decrease with an increase in pH due to the fact that in alkaline pH, anthocyanins become blue/purple/black in color from the predominance of quinoidal bases, which produces a dull appearance.[34] This trend was observed in the red/blue, blue, and red color classes (Figure 2; Table 6). Samples from the purple color class appeared and behaved differently from samples of the other three color classes throughout processing

DOI: 10.1021/acs.jafc.5b00798
J. Agric. Food Chem. 2015, 63, 5528−5538

Figure 2. Effect of increasing lime concentration on visual appearance of the four color classes of maize: (A) red/blue; (B) blue; (C) red; (D) purple maize. The left column is 0% lime, 0.5% lime is in the middle, and 1.0% lime is in the far right column.

because they were essentially too dark to detect many differences with the colorimeter. As expected, lightness values of masa were relatively high compared to those of nixtamal (Table 6) due to the exposure of the white endosperm from the grinding step. The red and red/blue color classes generally had the most dramatic change in color of masa as lime concentration increased (Table 6), which was supported by visual appearance of their respective nixtamals (Figure 2). The formation of dark blue quinoidal bases that increase with rising pH at the expense of reddish/yellow hues[33,34] was mostly responsible for this observation. This was confirmed by the large decrease in a^* and b^* color parameters for nixtamal of these two color classes compared to the blue and purple color classes (Table 6). For the tortilla chips, the L^* values did not follow a pattern due to a confounding effect of pillowing or puffing that occurred when frying, which caused the chips to appear brighter, especially at higher lime concentration. More pillowing occurred at higher lime concentrations because the pericarp was more solubilized and thus helped seal the masa surface, trapping moisture and creating pillows when the chips were fried.

In agreement with the visual evidence (Figure 2), the chroma values for red and red/blue sample nixtamal experienced the most dramatic changes, dropping from 27.4 (control) to 12.0 (0.5% lime) and 13.5 (1% lime) for red/blue and from 24.8 (control) to 4.0 (0.5% lime) and 2.3 (1% lime) for red samples (Figure 3) due to the darkening effect of high pH on anthocyanin color. The much larger change in chroma of red compared to red/blue samples can be partly explained by the average loss of anthocyanins to the steep water (nejayote) during nixtamalization. The red sample retained the most pigments at both lime concentrations (Figure 4); the retained pigments contributed to the darker color (and thus lower chroma) at higher pH. The higher pigment retention in the red samples was mostly attributed to the fact that these samples had a visually tougher pericarp, which did not break down as easily

DOI: 10.1021/acs.jafc.5b00798
J. Agric. Food Chem. 2015, 63, 5528−5538

Table 6. Summary of the *L, *a**, *b** Values of Pigmented Maize Varieties from the Four Color Classes (Red/Blue, Blue, Purple, and Red) at Three Stages of Processing (Nixtamal, Masa, and Chip)[a]**

		nixtamal			masa			chip		
color class	lime %	*L*	*a*	*b*	*L*	*a*	*b*	*L*	*a*	*b*
red/blue	0	30.0.2 ± 4.8	17.6 ± 0.83	20.9 ± 0.94	59.8 ± 4.0	4.1 ± 0.22	12.2 ± 0.54	36.6 ± 2.1	9.6 ± 0.45	8.8 ± 0.53
	0.5	22.3 ± 1.4	8.8 ± 1.2	7.2 ± 1.3	54.9 ± 3.2	4.9 ± 0.19	13.7 ± 0.82	35.2 ± 4.3	7.7 ± 0.88	10.1 ± 2.4
	1	21.7 ± 2.3	9.4 ± 0.50	9.0 ± 1.0	48.9 ± 3.0	3.7 ± 0.32	12.8 ± 0.26	34.4 ± 3.6	4.7 ± 0.40	8.0 ± 1.0
blue	0	44.8 ± 2.7	2.2 ± 0.50	8.7 ± 0.65	63.0 ± 1.6	2.6 ± 0.17	5.5 ± 0.61	39.7 ± 3.4	8.4 ± 0.48	3.0 ± 1.1
	0.5	40.4 ± 4.5	3.9 ± 0.77	15.6 ± 3.9	62.3 ± 2.2	2.2 ± 0.14	6.2 ± 0.32	42.9 ± 2.0	5.9 ± 0.92	3.5 ± 0.55
	1	40.4 ± 3.3	3.3 ± 0.43	13.6 ± 1.1	58.4 ± 3.0	0.45 ± 0.12	4.4 ± 1.5	41.9 ± 3.6	1.2 ± 0.71	2.2 ± 0.81
purple	0	17.0 ± 0.67	3.7 ± 0.32	−0.80 ± 0.12	50.5 ± 3.9	7.3 ± 0.22	2.0 ± 0.50	26.7 ± 1.7	4.1 ± 0.43	−0.31 ± 0.10
	0.5	17.9 ± 0.72	1.4 ± 0.17	−0.81 ± 0.17	51.2 ± 3.6	6.3 ± 0.49	2.8 ± 0.08	27.5 ± 1.8	3.5 ± 0.52	−0.13 ± 0.23
	1	17.0 ± 0.58	1.1 ± 0.17	−0.84 ± 0.09	50.5 ± 3.2	5.6 ± 0.53	4.2 ± 0.65	27.9 ± 2.0	3.2 ± 0.55	0.41 ± 0.28
red	0	28.3 ± 2.8	22.1 ± 0.77	10.9 ± 0.42	64.2 ± 2.7	1.9 ± 1.4	16.1 ± 0.62	38.8 ± 1.8	10.5 ± 0.93	12.3 ± 1.4
	0.5	20.2 ± 0.71	3.0 ± 0.98	2.5 ± 0.77	57.0 ± 1.9	1.9 ± 1.6	12.9 ± 0.86	33.6 ± 2.1	7.9 ± 0.51	9.0 ± 2.4
	1	19.8 ± 1.0	1.3 ± 0.56	1.4 ± 0.50	52.0 ± 1.9	2.6 ± 1.8	10.7 ± 0.48	32.6 ± 1.5	7.2 ± 0.76	6.9 ± 0.83

[a]Values are averages within each color class; all data expressed as mean ± SD.

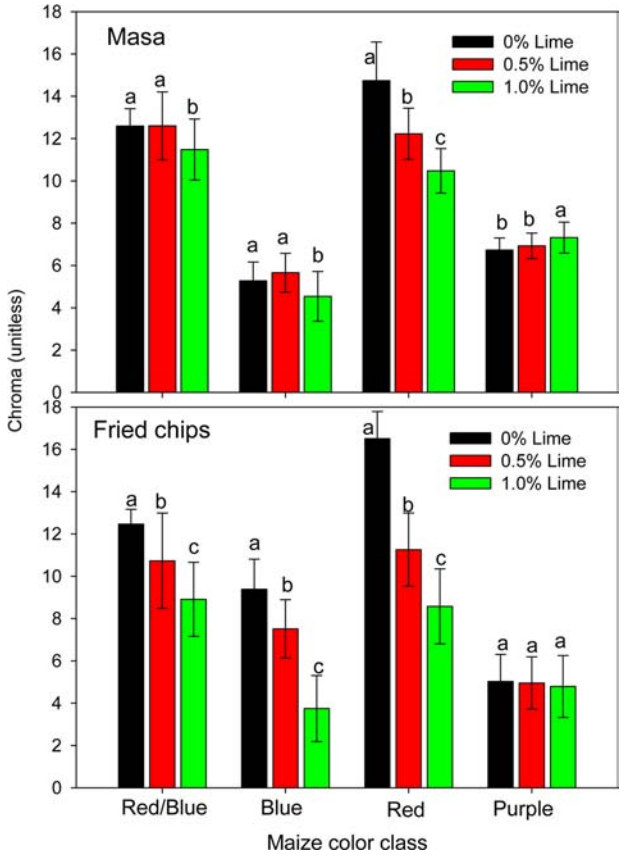

Figure 3. Effect of increasing lime concentration on chroma of red/blue, blue, red, and purple maize samples processed into masa (top) and fried chips (bottom). Data are expressed as mean ± SD; values are averaged for samples from both locations. Columns with different letters within color class are significantly different ($p < 0.05$, Tukey HSD).

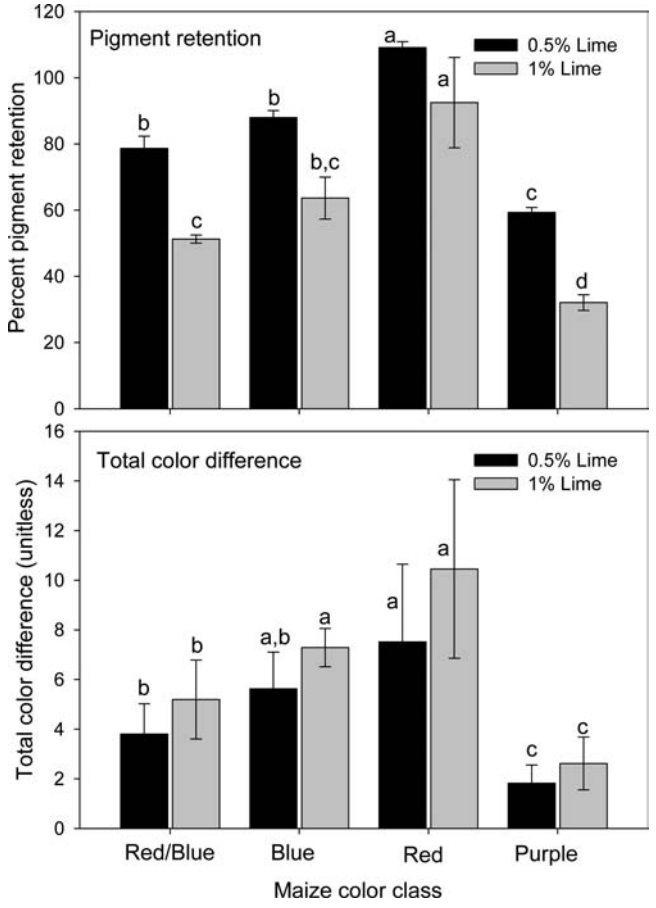

Figure 4. Effect of lime concentration on pigment retention (top) and total color difference (bottom) in processed pigmented maize chips. Values are relative to respective samples processed without any lime. Anthocyanin pigment retention was determined using UV−vis spectrophotometry method; total color differences were calculated from tristimulus color parameters as described under Materials and Methods. Data are expressed as mean ± SD; values are averaged for samples from both locations. Columns with different letters are significantly different ($p < 0.05$, Tukey HSD).

as the other samples during nixtamalization and thus protected most of the pigments from leaching into the nejayote. On the other hand, the blue samples actually showed increasing chroma from 8.1 (control) to 18.8 (0.5% lime) and 14.0 (1% lime). This can be explained by two possible causes; (i) because

DOI: 10.1021/acs.jafc.5b00798
J. Agric. Food Chem. 2015, 63, 5528−5538

Table 7. Major Anthocyanin Retention (Relative to Raw Grain) in the Different Maize Color Classes Processed into Chips, As Measured by HPLC[a]

treatment	Cy-3-glu (mg/g)	Cy-3,6″-MalGlu (mg/g)	total (mg/g)[b]	anthocyanin retention (%)	proportion of monomeric anthocyanins (%)
			Red/Blue		
raw grain	0.35 ± 0.03	0.61 ± 0.03	1.11 ± 0.43		38.7
0% lime	0.39 ± 0.05	0.51 ± 0.02	0.90 ± 0.07	80.9	43.0
0.5% lime	0.42 ± 0.00	0.39 ± 0.01	0.81 ± 0.01	72.9	51.5
1.0% lime	0.26 ± 0.01	0.24 ± 0.00	0.50 ± 0.01	45.3	52.5
			Blue		
raw grain	0.40 ± 0.01	0.60 ± 0.02	1.20 ± 0.04		42.9
0% lime	0.75 ± 0.03	0.40 ± 0.05	1.15 ± 0.02	62.8	65.4
0.5% lime	0.68 ± 0.01	0.40 ± 0.03	1.08 ± 0.02	56.4	62.9
1.0% lime	0.44 ± 0.08	0.30 ± 0.07	0.74 ± 0.16	36.9	59.5
			Purple		
raw grain	8.94 ± 0.02	8.16 ± 0.77	21.6 ± 0.89		51.9
0% lime	7.77 ± 1.37	1.79 ± 0.52	11.6 ± 1.69	53.4	80.1
0.5% lime	1.74 ± 0.53	0.70 ± 0.27	2.98 ± 0.86	13.8	76.4
1.0% lime	0.51 ± 0.22	0.23 ± 0.00	0.74 ± 0.38	3.4	68.8

[a]Cy = cyanidin, Glu = glucoside, Mal = malonyl. Anthocyanin levels in processed red samples were too low to resolve on HPLC. [b]Based on resolved anthocyanin peaks monitored at 520 nm.

the dark blue color hue of these samples closely matches the quinoidal base hues, a darkening effect of alkaline pH was not as apparent, and (ii) partial loss of anthocyanins during the nixtamalization process led to a brighter nixtamal that partially overcame the darkening effect of the rising pH. However, the fact that the blue samples were the only color class without pigments in the pericarp (all pigment in the aleurone layer) may have also contributed to the observations. The aleurone layers may protect the anthocyanin color quality better than the pericarp during alkaline cooking. This is because the alkaline-induced partial solubilization of the pericarp will lead to release of the anthocyanins and other reactive compounds from the cellular matrix. Interactions of the freed anthocyanins with other released compounds would likely contribute to altered anthocyanin color properties.

A clear trend of decreasing chroma was observed in masa from the red color class, but masa from the other three color classes experienced only modest changes in chroma at either lime concentration (Figure 3). Again, because the red samples retained most of their pigments during the nixtamalization process, the darkening effect of high pH on anthocyanins would be most apparent in their masa. In the chips, a trend of decreasing chroma with increasing lime concentration was more easily observed (Figure 3). All color classes (except purple) showed a significant decrease in chroma when the control chip was compared to the lime treatments. Samples from the purple color class had insignificant changes in chroma likely due to the extreme darkness of the chips at all lime concentrations, which made differences not easily distinguishable instrumentally or even visually. Among the nonpurple samples, red and blue chips showed the largest decline in chroma as lime concentration (and pH) increased. The red/blue chips had relatively high chroma values and showed the lowest magnitude of change in chroma as lime concentration increased. These samples produced chips that were more visually appealing because they were less dull compared to all other chips and were closer in appearance to the starting raw material than the red and blue samples.

Effect of Thermoalkaline Processing on Anthocyanin Content and Profile. As hypothesized, samples from the red/blue and blue color classes, which contain higher proportions of cyanidin-3-(6″-malonylglucoside), retained proportionately more anthocyanins than the purple sample at both lime concentrations (Figure 4). HPLC analysis of anthocyanins retained during thermoalkaline processing confirmed the UV–vis data (Table 7). The red and red/blue samples retained 37–81% of measurable anthocyanins, whereas the purple maize retained 3.4–53% of the measurable anthocyanins after processing into chips compared to raw maize (Table 7). Higher lime concentration generally resulted in lower anthocyanin retention in the chips, likely due to adverse effect of higher pH on anthocyanin stability. Anthocyanin retention in the chips was much higher than those previously reported for red and blue maize samples.[17] This is mainly due to the fact that the vast majority of anthocyanin loss during thermoalkaline processing is due to the initial cooking and steeping, which leads to pigments leaching into steep water (usually discarded) as previously demonstrated.[17] In our study, we used just enough water to cook and steep the maize, and thus little steep water was lost. In fact, de la Parra et al.[17] showed (and our data confirm) that the thermal processes involved in baking and frying steps of tortilla chips are too short to result in meaningful anthocyanin degradation. This shows that anthocyanins can be retained much better in pigmented maize during processing by reducing steeping losses.

It was interesting to note that thermoalkaline processing resulted in a higher proportion of monomeric anthocyanins retained compared to acylated anthocyanins in all processed samples, relative to raw maize (Table 7). This was counter to our expectation that the acylated anthocyanins would be retained more. A likely explanation is that the alkaline pH, in combination with heat, resulted in deacylation of some of these anthocyanins into their monomeric forms. Acyl ester bonds are alkaline labile, whereas the glycosidic linkages are more sensitive to acidic pH. Another possible explanation is that the acylated anthocyanins self-associated or polymerized more readily under the conditions used in this study into complexes that did not resolve in HPLC. This may explain why the high-anthocyanin purple maize showed such a dramatic decline in measurable anthocyanins, especially acylated forms, during processing (Table 7), which did not match visual color observations (Figure 2). Anthocyanin self-association and

DOI: 10.1021/acs.jafc.5b00798
J. Agric. Food Chem. 2015, 63, 5528–5538

aggregation increase significantly as their concentration increases,[35] especially at neutral to higher pH.[36] Thus, anthocyanin "retention" in processed samples must be interpreted in the context of the limitations of the detection methods used.

However, it is worth noting that total pigment retention (Figure 4; Table 7), which has been the major target of published investigations in this subject area, was not a good predictor of color performance during processing. How the retained anthocyanins maintain desirable color properties is more important, and this may be a function of anthocyanin structure, content, and composition and copigment profile, as well as the location and interaction of the anthocyanins with nonphenolic constituents in the grain. The total color difference generally agreed with chroma data and supported our own observations. Among the nonpurple samples, the chips from the red/blue samples had the lowest color difference, whereas the red ones had the highest color difference in lime treatments compared to control (Figure 4). Also worth noting is the fact that, even though total color difference generally positively correlated with pigment retention (r = 0.41), this correlation was weak and disappeared when samples were compared within color class (data not shown), indicating that color performance is more complex than mere changes in measurable anthocyanin pigments.

The fact that 2−4 times higher pigments were accumulated in nonpurple maize in one location than the other suggests that specific environmental parameters have a significant nonrandom impact on anthocyanin biosynthesis in maize; this warrants further investigation. Also, the differential color class responses in the two environments suggest that specific genetic traits are more responsive to the environment. Thus, maize with desirable accumulation of high-value pigments and other bioactive compounds for food use could be developed for specific environments. The implications of the high level of phenolic amide in the maize lines used in this study on potential health benefits of the pigmented maize also warrant investigation.

A major concern to food manufacturers when using natural pigments is color predictability in the final product. Often raw materials are selected with the assumption or expectation that they will retain desirable color attributes in the final product. Thus, predictable performance with minimal changes in color during processing, and not just the final product color, is an important advantage in raw material selection. The red/blue samples seem to have an advantage over other color classes for direct thermoalkaline processing into snacks; they retained their appearance and brilliance the best during processing. Even though acylation improves the stability of anthocyanin pigments to color degradation in solution, such stability is not necessarily predictive of performance of the pigments in situ in products. In all, it is apparent that targeted genetic improvement efforts can produce colored maize with improved performance for thermoalkaline processing. This would eventually lead to expanded demand for such products and, perhaps, healthier grain-based snack offerings.

AUTHOR INFORMATION

Corresponding Author

*(J.M.A.) E-mail: jawika@ag.tamu.edu; Phone: (979) 845-2985. Fax: (979) 845-0456.

Funding

Funding was provided by Texas AgriLife Research Monocot Improvement Program.

Notes

The authors declare no competing financial interest.

ACKNOWLEDGMENTS

We thank Adam Mahan of Texas A&M Soil & Crops Science Department for making his research samples available for this study.

REFERENCES

(1) Snack Food Association. *State of the Industry Report: Snack World*; Arlington, VA, USA, 2013; pp 20−21.
(2) Snack Food Association. *State of the Industry Report: Snack World*; Arlington, VA, USA, 2012; pp 22−24.
(3) Long, N.; Suzuki, S.; Sato, S.; Naiki-Ito, A.; Sakatani, K.; Shirai, T.; Takahashi, S. Purple corn color inhibition of prostate carcinogenesis by targeting cell growth pathways. *Cancer Sci.* **2013**, *104*, 298−303.
(4) Song, N. R.; Yang, H.; Park, J.; Kwon, J. Y.; Kang, N. J.; Heo, Y. S.; Lee, K. W.; Lee, H. J. Cyanidin suppresses neoplastic cell transformation by directly targeting phosphatidylinositol 3-kinase. *Food Chem.* **2012**, *133*, 658−664.
(5) Shindo, M.; Kasai, T.; Abe, A.; Kondo, Y. Effects of dietary administration of plant-derived anthocyanin-rich colors to spontaneously hypertensive rats. *J. Nutr. Sci. Vitaminol.* **2007**, *53*, 90−93.
(6) Tsuda, T.; Horio, F.; Uchida, K.; Aoki, H.; Osawa, T. Dietary cyanidin 3-*O*-β-D-glucoside-rich purple corn color prevents obesity and ameliorates hyperglycemia in mice. *J. Nutr.* **2003**, *133*, 2125−2130.
(7) Brouillard, R. Chemical structure of anthocyanins. In *Anthocyanins as Food Colors*; Markakis, P., Ed.; Academic Press: New York, 1982; pp 1−40.
(8) Dangles, O.; Saito, N.; Brouillard, R. Anthocyanin intramolecular copigment effect. *Phytochemistry* **1993**, *34*, 119−124.
(9) Eiro, M. J.; Heinonen, M. Anthocyanin color behavior and stability during storage: effect of intermolecular copigmentation. *J. Agric. Food Chem.* **2002**, *50*, 7461−7466.
(10) Giusti, M. M.; Wrolstad, R. E. Acylated anthocyanins from edible sources and their applications in food systems. *Biochem. Eng. J.* **2003**, *14*, 217−225.
(11) Salinas Moreno, Y.; Sánchez, G. S.; Hernández, D. R.; Lobato, N. R. Characterization of anthocyanin extracts from maize kernels. *J. Chromatogr. Sci.* **2005**, *43*, 483−487.
(12) de Pascual-Teresa, S.; Santos-Buelga, C.; Rivas-Gonzalo, J. C. LC−MS analysis of anthocyanins from purple corn cob. *J. Sci. Food Agric.* **2002**, *82*, 1003−1006.
(13) Aoki, H.; Kuze, N.; Kato, Y.; Gen, S. Anthocyanins isolated from purple corn (*Zea mays* L.). *Foods Food Ingred. J. Jpn.* **2002**, 41−45.
(14) Abdel-Aal, E.-S. M.; Young, J. C.; Rabalski, I. Anthocyanin composition in black, blue, pink, purple, and red cereal grains. *J. Agric. Food Chem.* **2006**, *54*, 4696−4704.
(15) Del Pozo-Insfran, D.; Brenes, C. H.; Serna Saldivar, S. O.; Talcott, S. T. Polyphenolic and antioxidant content of white and blue corn (*Zea mays* L.) products. *Food Res. Int.* **2006**, *39*, 696−703.
(16) Mora-Rochin, S.; Gutiérrez-Uribe, J. A.; Serna-Saldivar, S. O.; Sánchez-Peña, P.; Reyes-Moreno, C.; Milán-Carrillo, J. Phenolic content and antioxidant activity of tortillas produced from pigmented maize processed by conventional nixtamalization or extrusion cooking. *J. Cereal Sci.* **2010**, *52*, 502−508.
(17) de la Parra, C.; Serna Saldivar, S. O.; Liu, R. H. Effect of processing on the phytochemical profiles and antioxidant activity of corn for production of masa, tortillas, and tortilla chips. *J. Agric. Food Chem.* **2007**, *55*, 4177−4183.
(18) Mahan, A. L.; Murray, S. C.; Rooney, L. W.; Crosby, K. M. Combining ability for total phenols and secondary traits in a diverse

DOI: 10.1021/acs.jafc.5b00798
J. Agric. Food Chem. 2015, 63, 5528−5538

set of colored (red, blue, and purple) maize. *Crop Science* **2013**, *53* (4), 1248−1255.
(19) Ojwang, L. O.; Dykes, L.; Awika, J. M. Ultra performance liquid chromatography-tandem quadrupole mass spectrometry profiling of anthocyanins and flavonols in cowpea (*Vigna unguiculata*) of varying genotypes. *J. Agric. Food Chem.* **2012**, *60*, 3735−3744.
(20) Moreau, R. A.; Nuñez, A.; Singh, V. Diferuloylputrescine and *p*-coumaroyl-feruloylputrescine, abundant polyamine conjugates in lipid extracts of maize kernels. *Lipids* **2001**, *36*, 839−844.
(21) Lee, J.; Durst, R. W.; Wrolstad, R. E. Determination of total monomeric anthocyanin pigment content of fruit juices, beverages, natural colorants, and wines by the pH differential method: collaborative study. *J. AOAC Int.* **2005**, *88*, 1269−1278.
(22) Gordillo, B.; Rodríguez-Pulido, F. J.; Escudero-Gilete, M. L.; González-Miret, M. L.; Heredia, F. J. Comprehensive colorimetric study of anthocyanic copigmentation in model solutions. Effects of pH and molar ratio. *J. Agric. Food Chem.* **2012**, *60*, 2896−2905.
(23) Schütz, K.; Persike, M.; Carle, R.; Schieber, A. Characterization and quantification of anthocyanins in selected artichoke (*Cynara scolymus* L.) cultivars by HPLC−DAD−ESI−MS*n*. *Anal. Bioanal. Chem.* **2006**, *384*, 1511−1517.
(24) González-Manzano, S.; Pérez-Alonso, J. J.; Salinas-Moreno, Y.; Mateus, N.; Silva, A. M. S.; de Freitas, V.; Santos-Buelga, C. Flavanol−anthocyanin pigments in corn: NMR characterisation and presence in different purple corn varieties. *J. Food Compos. Anal.* **2008**, *21*, 521−526.
(25) Geera, B.; Ojwang, L. O.; Awika, J. M. New highly stable dimeric 3-deoxyanthocyanidin pigments from *Sorghum bicolor* leaf sheath. *J. Food Sci.* **2012**, *77*, C566−C572.
(26) Lopez-Martinez, L. X.; Oliart-Ros, R. M.; Valerio-Alfaro, G.; Lee, C.-H.; Parkin, K. L.; Garcia, H. S. Antioxidant activity, phenolic compounds and anthocyanins content of eighteen strains of Mexican maize. *LWT − Food Sci. Techno.* **2009**, *42*, 1187−1192.
(27) Choi, S. W.; Lee, S. K.; Kim, E. O.; Oh, J. H.; Yoon, K. S.; Parris, N.; Hicks, K. B.; Moreau, R. A. Antioxidant and antimelanogenic activities of polyamine conjugates from corn bran and related hydroxycinnamic acids. *J. Agric. Food Chem.* **2007**, *55*, 3920−3925.
(28) Sen, A.; Bergvinson, D.; Miller, S. S.; Atkinson, J.; Fulcher, R. G.; Arnason, J. T. Distribution and microchemical detection of phenolic acids, flavonoids, and phenolic acid amides in maize kernels. *J. Agric. Food Chem.* **1994**, *42*, 1879−1883.
(29) Miller, J. D.; Miles, M.; Fielder, D. A. Kernel concentrations of 4-acetylbenzoxazolin-2-one and diferuloylputrescine in maize genotypes and *Gibberella* ear rot. *J. Agric. Food Chem.* **1997**, *45*, 4456−4459.
(30) Kim, E.-O.; Kwon, T.-K.; Choi, S.-W. Diferuloylputrescine, a predominant phenolic amide in corn bran, potently induces apoptosis in human leukemia U937 cells. *J. Med. Food* **2014**, *17*, 519−526.
(31) Svensson, L.; Sekwati-Monang, B.; Lutz, D. L.; Schieber, A.; Gänzle, M. G. Phenolic acids and flavonoids in nonfermented and fermented red sorghum (*Sorghum bicolor* (L.) Moench). *J. Agric. Food Chem.* **2010**, *58*, 9214−9220.
(32) Yang, L.; Allred, K. F.; Geera, B.; Allred, C. D.; Awika, J. M. Sorghum phenolics demonstrate estrogenic action and induce apoptosis in nonmalignant colonocytes. *Nutr. Cancer* **2012**, *64*, 419−427.
(33) Markakis, P. Stability of anthocyanins in foods. In *Anthocyanins as Food Colors*; Markakis, P., Ed.; Academic Press: New York, 1982; pp 163−180.
(34) Fossen, T.; Cabrita, L.; Andersen, O. M. Colour and stability of pure anthocyanins influenced by pH including the alkaline region. *Food Chem.* **1998**, *63*, 435−440.
(35) Asen, S.; Stewart, R. N.; Norris, K. H. Co-pigmentation of anthocyanins in plant tissues and its effect on color. *Phytochemistry* **1972**, *11*, 1139−1144.
(36) Goto, T.; Kondo, T. Structure and molecular stacking of anthocyanins—flower color variation. *Angew. Chem., Int. Ed. Engl.* **1991**, *30*, 17−33.

DOI: 10.1021/acs.jafc.5b00798
J. Agric. Food Chem. 2015, 63, 5528−5538

visceral fat deposition, serum triacylglycerols, and blood glucose in mice and rats.[8]

Sterols oxidize when subjected to heating treatments and/or high temperatures. The effects of culinary processes (such as frying and oven cooking) have been imitated by choosing 180 °C as the heating temperature for most investigations.[14] After 1 h of heating in a conventional oven at this temperature, Menéndez-Carreño et al.[9] found a progressive decrease in stigmasterol content, as well as formation and subsequent degradation of POPs. Xu et al.[15] investigated the oxidative stability of β-sitosterol in a mix with edible oils heated at 180 °C in an oven; after 120 min of heating, a 75% degradation of β-sitosterol was observed. The same research group, Xu et al.,[16] used a mix of β-sitosterol and triacylglycerols with different fatty acid profiles, observing that heating at 180 °C for 120 min led to 85% degradation of β-sitosterol; it seems that the surrounding fatty acids affected sterol oxidation in a time-dependent manner and their effect was unlikely related to their degree of unsaturation. Other studies have shown how the interaction between the conditions used (diverse temperature exposure, heating time, and lipid matrices) can drastically impact PS stability, especially the type of oxidation products, their content and the reaction pathways of oxidation.[17,18]

Among the different cooking techniques, the use of microwave (MW) heating has widely spread in the past two decades at both the domestic and catering levels for cooking, reheating, or thawing food, as it is a fast and easy technique to be employed for the consumption of processed and frozen foods. MW heating of food results from two types of interactions between food components with microwaves: ionic conduction and dipolar rotation.[19] The MW cooking/heating time will thus be greatly influenced by the food dielectric properties (dielectric constant and dielectric loss factor), which are related to the food composition.[20] Despite the large utilization of MW heating, to the best of our knowledge, there are no available data on PS oxidation during microwaving; in fact, only the influence of frying, boiling, and oven heating on sterol oxidation in model systems[14,17,21,22] and food[23−25] has been studied. For a better understanding of how MW heating could impact PS stability, it would therefore be important to first assess PS behavior in a model system during microwaving.

The aim of this study was to evaluate the oxidative stability of PS during MW heating, using two different model systems (a solid film made with a phytosterol mixture (PSF) and a liquid mixture of phytosterols and triolein (PS + TAG (triacylglycerol), 1:100, w/w).

MATERIALS AND METHODS

Reagents and Solvents. All solvents used were of analytical grade. Reagents were supplied by Carlo Erba Reagenti (Rodano, Italy) and Merck (Darmstadt, Germany). β-Sitosterol was purchased from Santa Cruz Biotechnology Inc. (Heidelberg, Germany) (purity 41% β-sitosterol, 23% campesterol, 23% stigmasterol). Triolein was supplied by Nu-Check (Elysian, MN). 5α-Cholestan-3β-ol (dihydrocholesterol, IS; purity 95%), cholest-5-en-3β,19-diol (19-hydroxycholesterol, 19-HC; purity 99%), cholest-5-en-3β,7α-diol (7α-hydroxycholesterol, 7α-HC; purity 99%), cholest-5-en-3β,7β-diol (7β-hydroxycholesterol, 7β-HC; purity 90%), 5α,6α-epoxycholestane-3β-ol (α-epoxycholesterol, α-CE; purity 87%), 5β,6β-epoxycholestan-3β-ol (β-epoxycholesterol, β-CE; purity 80%), cholestane-3β,5α,6β-triol (cholestanetriol, triol; purity 99%), cholest-5-en-3β-ol-7-one (7-KC; purity 99%), and 5-cholestene-3β,25-diol (25-HC; purity 98%) were purchased from Sigma (St. Louis, MO). Glass thin-layer chromatography (TLC) silica plates (20 cm × 20 cm × 0.25 mm film thickness) were supplied by Merck (Darmstadt, Germany). Silica solid-phase extraction (SPE) cartridges (500 mg/3 mL Strata cartridges) from Phenomenex (Torrence, CA) were utilized for POP purification. The silylation mixture was prepared with dried pyridine, hexamethyldisilazane, and trimethylchlorosilane at a ratio of 5:2:1 by volume.

Experimental Design. Two different model systems were used: (a) A phytosterol film (PSF) was prepared with a solution of PS in chloroform (1 mg/mL, composed of 41% β-sitosterol, 23% campesterol, and 23% stigmasterol). An aliquot of 1 mL was transferred to a previously weighed vial (5 mL, 22.00 × 38.25 mm) and taken to dryness under nitrogen flow. (b) A mixture of phytosterols and triolein (PS + TAG) was prepared with a solution of PS in chloroform (1 mg/mL, composed of 41% β-sitosterol, 23% campesterol, and 23% stigmasterol). An aliquot of 1 mL was transferred to a previously weighed vial (5 mL, 22.00 × 38.25 mm), taken to dryness under nitrogen flow, weighed again, added to about 100 mg of triolein, and thoroughly mixed by vortexing.

A domestic multimodal MW oven was used for sample heating (Panasonic NN-CT756, Domestic MW, Bracknell, U.K.). Samples in the opened vials (n = 4 for each model system, 3 of which were for sampling and 1 of which was for temperature control) were placed at the center of the rotatory turntable plate of the oven and exposed (without caps) at a power of 1000 W. Samples were independently heated for 1, 1.5, 3, 6, 12, 20, and 30 min. All heated samples were allowed to cool at room temperature (23 ± 1 °C) after thermal treatment. For each run time, a vial, with triolein or film, was used to measure the temperature of the system. The temperature of the samples was measured immediately after MW exposure, by inserting a thermocouple (K-type; Ni/Al−Ni/Cr) connected to an acquisition system (HI 98804, Hanna Instrument, Villafranca Padovana-PD, Italy) at approximately the geometrical center of the control sample. A 1 mL volume of chloroform was added to each tube, and the tubes were shaken vigorously for 40 s and kept at −20 °C until analysis.

Qualitative TLC of Oxidized Model Systems. Qualitative silica TLC was carried out to verify the formation of polymerization products in the PS + TAG system after oxidation in the MW oven. About 100 mg of the oxidized PS + TAG system was placed in an open vial and heated in the MW oven for 30 min. The sample was then resuspended in 1 mL of chloroform, and an aliquot (0.2 mg/20 μL) was spotted on a 10 cm × 20 cm silica TLC plate. A triolein standard was also loaded as a reference spot (0.2 mg). The mobile phase was a mixture of diethyl ether/n-hexane (35:65, v/v); the TLC plate was developed at 4 °C for 20 min. The TLC bands were visualized by spraying a phosphomolybdic acid solution (20 wt % in ethanol) and then were charred in an oven at 180 °C for 20 min.

Purification and Quantification of PS. PS purification was achieved by using the silica solid-phase extraction (SPE) method described by Bortolomeazzi et al.[26] A known amount of 5α-cholestan-3β-ol (internal standard; 500 μL from a 2 mg/mL solution in n-hexane/2-propanol (3:2, v/v)) was added to 1/10 of the sample for PS quantification. Briefly, apolar lipids were removed by 5 mL of n-hexane/diethyl ether (8:2, v/v), while the polar fraction that contained PS was eluted with an n-hexane/diethyl ether solution (1:1, v/v) and methanol. The eluted fraction was taken to dryness under nitrogen flow, and the PS were silylated at 40 °C for 30 min.[27] The silylated samples were dried under nitrogen flow at 40 °C and dissolved in 1 mL of n-hexane.

The GC determination of sterols was performed with a GC HRGC 5300 (Carlo Erba, Milan, Italy) instrument, equipped with a split−splitless injector, a flame ionization detector (FID), and a computerized data acquisition system (Turbochrom Navigator software, version 6.1.1.0.0:K20, PerkinElmer, Norwalk, CT). The separation of the silylated sterols was performed with a CP-SIL 5CB Low Bleeds/MS column (30 m × 0.32 mm i.d. × 0.25 μm film thickness) (Varian Chrompack, Middelburg, The Netherlands), coated with 100% dimethylpolysiloxane. The oven temperature was programmed from 265 to 280 °C at 0.5 °C/min and then from 280 to 325 °C at 4 °C/min; the injector and detector temperatures were

DOI: 10.1021/acs.jafc.5b00961
J. Agric. Food Chem. 2015, 63, 5539−5547

both set at 325 °C. Helium was used as the carrier gas at a flow of 2.9 mL/min; the split ratio was 1:15. The analysis was run in triplicate.

Sterols were identified by comparing their retention times with those of solutions of silylated sterol standards and further confirmed by injection into a fast gas chromatography−mass spectrometry (Fast GC−MS; same conditions as used for POP analysis) system. Sterols were quantified with the internal standard method, using 5α-cholestan-3β-ol. Their response factors were evaluated with respect to the internal standard.

Purification and Analysis of POPs. Regarding the determination of POPs, the remaining 9/10 of the initial sample solution was purified by silica SPE (Supelclean LC-Si, 500 mg/3 mL) (Supelco, Bellefonte, PA), according to the method suggested by Guardiola et al.[28] A 20 μL volume of internal standard 19-hydroxycholesterol (0.5 mg/mL of *n*-hexane/2-propanol (4:1, v/v)) was added to the sample, dried under nitrogen flow, and redissolved in *n*-hexane/diethyl ether (95:5, v/v) before sample purification. The SPE cartridge was previously activated with 5 mL of *n*-hexane before sample loading and then washed with *n*-hexane (5 mL) and different solvent mixtures of *n*-hexane/diethyl ether (10, 30, and 10 mL of 95:5, 90:10, and 80:20, v/v, mixtures, respectively). The POP fraction was finally eluted with 10 mL of acetone, subjected to silylation, and dissolved in 0.5 mL of *n*-hexane.

POPs were determined and quantified by fast GC−MS. A Shimadzu QP 2010 Plus gas chromatograph (Kyoto, Japan) equipped with a split−splitless injector and coupled to an electron impact (EI) mass spectrometric detector was used. The separation was carried out by a fused-silica capillary column, Restek RTX-5 (10 m × 0.1 mm i.d. × 0.1 μm film thickness; Bellafonte, PA), coated with 95% dimethyl- and 5% diphenylpolysiloxane. A nonsilanized standard split liner (95 mm × 5 mm o.d. × 3.4 mm i.d.) was utilized. The temperature was programmed from 210 to 325 °C at 15 °C/min and kept for 5 min at 325 °C. The injector, the ion source, and the transfer line temperatures were set at 340, 200, and 340 °C, respectively. The injection was performed in the split mode (1:50). Helium was used as the carrier gas at a linear velocity of 47.7 cm/s. The electron energy was 70 eV. A mass range from 40 to 650 *m*/*z* was scanned at a rate of 2500 amu/s. The acquisition and integration modes were full-scan total ion current (TIC) and single ion monitoring (SIM), respectively. Identification of POPs was performed by comparing their retention times and mass spectra with those reported in previous studies.[29−31] POPs were recognized and quantified by their corresponding characteristic ions with a high abundance obtained in the SIM mode (*m*/*z*): IS (19-hydroxycholesterol) (353), 7α-hydroxycampesterol (470), 7α-hydroxystigmasterol (482), 7α-hydroxysitosterol (484), 7β-hydroxycampesterol (470), 7β-hydroxystigmasterol (482), 7β-hydroxysitosterol (484), 6β-hydroxycampesterol (417), 6β-hydroxystigmasterol (429), α-epoxysitosterol (412), β-epoxysitosterol (412), α-epoxystigmasterol (253), β-epoxystigmasterol (253), 7-ketocampesterol (381), 7-ketostigmasterol (386), 6-ketositosterol (473), 7-ketositosterol (500). Considering that most POP standards are not commercially available and assuming that POP fragmentation is similar to that of cholesterol oxidation products (COPs), the quantification of POPs was carried out using calibration curves of oxycholesterols built by quantificator ions with relative abundances similar to those of the ions chosen for oxyphytosterol quantification.[32] Three independent replicates were run per sample.

Statistical Analysis. The mean and standard deviation of each sample's data were calculated. One-way analysis of variance (ANOVA), with Tukey's post hoc multiple comparisons test ($p < 0.05$), was applied to evaluate the significant differences on PS and POP amounts over the MW heating time and between the PSF and PS + TAG models throughout the MW heating process. The SPSS 15.0 program (SPSS, Inc., Chicago, IL) was used for the statistical analysis of the data.

For the kinetic evaluation of PS degradation, a first-order regression analysis of the data was performed using Excel 2008, and the fitting goodness was evaluated on the basis of the regression coefficient (R^2) and the associated *p* value.

RESULTS AND DISCUSSION

Table 1 reports the temperatures reached at each heating time during the two MW experiments, showing that they varied according to the type of model system. The temperature recorded for PSF was lower than that of PS + TAG. This could be mostly attributed to their different compositions and physical status (PSF was a solid film, while PS + TAG was a liquid), as well as the specific heat of triolein, which could have affected their dielectric properties and thus their heating capacities. Another factor that might have partly contributed is the technology of the multimodal domestic MW oven, since the electromagnetic waves enter the cavity, move, and bounce off the walls, generating pockets (called modes) of high and low energy that create a nonuniform microwave field. Moreover, this type of MW oven is unable to deal with power variations and to maintain a constant temperature as unimodal microwave ovens do.

Table 1. Temperature Reached by the Model Systems during Heating in a Multimodal Microwave Oven

	temperature (°C)			temperature (°C)	
time (min)	PSF	PS + TAG	time (min)	PSF	PS + TAG
1.5	43.9	47.5	12	117.05	160.4
3	68.8	61.6	20	140.9	161.9
6	90.5	105.9	30	151.8	159.5

Unreacted PS Trends during MW Heating. The presence of crystals was observed in the PS + TAG model after 20 and 30 min of heating, so silica TLC was performed to verify the occurrence of polymerization products in the mixture, as they could modify the stationary phase of the GC column and affect its peak resolution capacity. Figure 1 shows the TLC plate of the PS + TAG model after 30 min of heating, which qualitatively evidenced a higher degree of polymerization with increasing heating time. Therefore, silica SPE was run for all samples before GC analysis of PS, to remove apolar lipids and polymerization products.

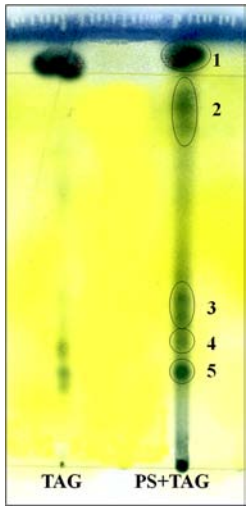

Figure 1. TLC plate of a PS + TAG mixture after 30 min of MW heating. Peak identification: 1, triolein; 2, polymerization products (three bands); 3, free fatty acids; 4, diacylglycerols; 5, phytosterols.

DOI: 10.1021/acs.jafc.5b00961
J. Agric. Food Chem. 2015, 63, 5539−5547

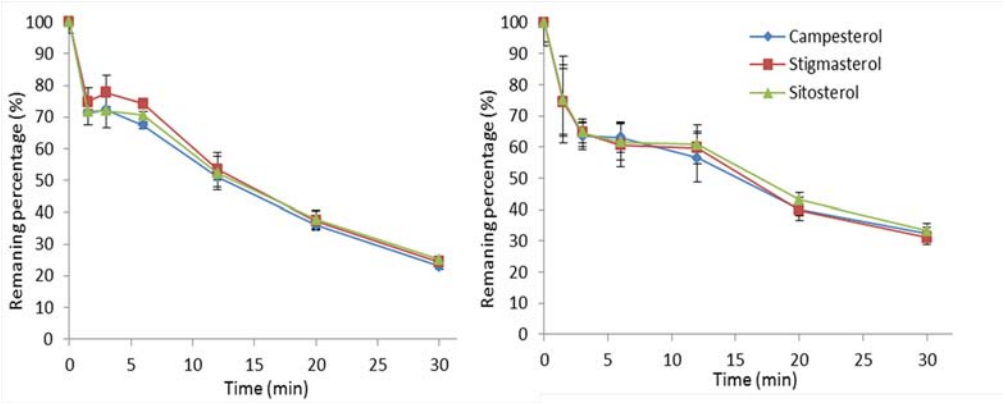

Figure 2. Remaining percentages (%) of phytosterols during microwave heating of PSF and PS + TAG.

Table 2. First-Order Kinetic Parameters (Rate Constant (k) and Corresponding Coefficient of Determination (R^2)) for the Remaining Sterols in Both PSF and PS + TAG Models throughout the MW Heating Process

	PSF			PS + TAG		
	β-sitosterol	campesterol	stigmasterol	β-sitosterol	campesterol	stigmasterol
k	0.042	0.044	0.044	0.031	0.033	0.033
R^2	0.968	0.973	0.979	0.899	0.911	0.910
p^a	<0.001	<0.001	<0.001	<0.01	<0.001	<0.001

[a] p = probability value.

Figure 2 reports the amounts of remaining PS in both model systems after MW heating (0−30 min); the full data with the corresponding statistical treatment are reported in the table in the Supporting Information. In the PSF system, a marked PS degradation (∼30%) was noted in the first 1.5 min of microwaving, which remained almost constant up to 6 min of heating; thereafter, PS showed a continuous, fast drop rate, and at the end of 30 min heating, only about 24% of the initial PS content was observed. The single PS displayed a similar degradation trend, being slightly more pronounced for campesterol than for the other two PS. These results are similar to those obtained by Barriuso et al.,[14] who found the following sterol susceptibility to degradation: campesterol ≈ β-sitosterol ≥ stigmasterol. The authors reported that the experimental heating conditions (temperature/exposure time, modality (e.g., MW, convection, conduction), initial PS amount, sample area/container volume ratio, open/closed container during heating) and PS composition (single PS or mixtures with diverse relative percentages) can differently affect the extent of PS degradation. In PSF, the extent of PS degradation was lower (∼76%) than that observed (∼88%) at 180 °C after 30 min of heating in a thermoblock;[14] such differences could be mainly ascribed to both the diverse temperatures and heating modalities applied (MW vs conduction), as they led to different real sample temperatures. Xu et al.[15] found ∼50% degradation of β-sitosterol when it was heated in a conventional oven at 180 °C for 60 min, being higher than sterol degradation at 150 and 120 °C for 60 min, while Menéndez-Carreño et al.[9] observed ∼38% degradation of the initial stigmasterol at 180 °C after 1 h in a Termaks oven. Derewiaka et al.[33] heated cholesterol at different temperatures (from 120 to 220 °C) and exposure times (from 30 to 180 min); the authors found similar cholesterol concentrations after heating at 150 and 180 °C and the most intense losses at 220 °C, confirming that thermoxidation of cholesterol rapidly increased above its melting point.

Regarding the PS + TAG system, PS also greatly degraded (about 25%) in the first 1.5 min of heating, remaining almost constant up to 12 min. Thereafter, as for the PS + TAG system, a gradual PS drop was noted and about 32% of the initial PS content was detected after 30 min of heating. In this case, all PS exhibited an analogous degradation behavior. However, the extent of PS degradation was much higher (∼68%) than that found (∼21%) when cholesterol + triolein was heated at 180 °C for 30 min in a conventional oven;[21] this distinctive behavior might be attributed to the different heating modalities (MW vs convection), whose influence is more evident in a liquid system than in a solid one. After 30 min of microwaving, only 32% of the PS remained in the PS + TAG system, being in agreement with the amount found in a model system made of stigmasterol, cholesterol, and sunflower oil, and heated at 180 °C for 180 min.[34] This result showed how diverse experimental conditions and temperatures can have a different impact depending on the surrounding matrix. When comparing the two model systems, PS degraded faster when they were microwaved alone than in the presence of TAG, displaying different trends at both the initial and prolonged times of heating. These results are in agreement with those of Soupas et al.,[17] who reported that at high temperature the unsaturated matrix was more quickly oxidized, protecting sterols as observed in the PS + TAG model. In the PS system, the only reactive lipids are phytosterols, so they react more readily following the typical radical chain reaction mechanism of oxidation. Table 2 reports the sterol loss rate throughout the MW heating process in terms of the observed first-order rate constants. All data satisfactorily fit the kinetic model with very high determination coefficients. All sterols in the PS + TAG model exhibited similar degradation rates (k values of 0.03), which were lower than those of the PSF model (0.04), thus confirming that sterol degradations within the same models were similar; furthermore, their degradation was slower in the PS + TAG system.

DOI: 10.1021/acs.jafc.5b00961
J. Agric. Food Chem. 2015, 63, 5539−5547

The behavior described in the previous paragraph could be attributed to the physical/steric protection of TAG toward PS, combined with the dilution effect, which led to a lower air contact, thus hampering oxidation.[35] Moreover, triolein used as the in the model system may have also competed with PS for oxidation. Similar results were found when the influence of the degree of unsaturation of different TAGs on cholesterol oxidation was evaluated at 180 °C in an conventional oven;[21] in this study, both the presence of TAGs and their unsaturation degrees inhibited cholesterol thermoxidation. Other researchers found that the sitosterol oxidation rates in phytosteryl ester- and free phytosterol-enriched rapeseed oils subjected to pan-frying at 160 °C for 10 min were ≤0.4%.[36] However, in our study, 5- and 23-fold higher orders of magnitude of the total phytosterol oxidation rate were noted at 12 min of microwaving for the PS + TAG and PSF systems, respectively. Such differences in sterol oxidation rate could be attributed to the presence of higher unsaturated lipid molecules, which may have exerted a protective effect toward PS through different possible mechanisms (such as competition for oxidation, dilution, and physical protection). When Xu et al.[16] evaluated the interaction of fatty acids with β-sitosterol oxidation, they noted ∼15% degradation of the initial β-sitosterol in the presence of oleic acid if heated at 180 °C for 30 min in an oven. When the heating time increased to 60 min at 180 °C, the four fatty acids (with 18 C atoms and different degrees of unsaturation) accelerated the β-sitosterol degradation (∼70% decrease), and thereafter, their oxidation-promoting effect became weaker or diminished; the authors concluded that the surrounding fatty acids affected the PS oxidation in a time-dependent manner and their effect was unlikely related to their level of unsaturation. This conclusion is in agreement with our study, in which different degradation trends were observed depending on the system considered. In the PS + TAG system, after the drastic PS drop at 3 min of microwaving, no degradation change was noticed between 3 and 12 min, and thereafter, a weak decline occurred.

Another aspect to consider is that, at elevated temperatures (>150 °C), polymerization, dehydration, and formation of midpolar and polar compounds can occur.[9,18,37−40] PS can also generate volatile compounds during oxidation, which may arise from breakdown of the side chain followed by molecular rearrangement.[18] In the present study, PS + TAG reached 161.9 and 159.5 °C after 20 and 30 min of MW heating, respectively, so polymerization could take place, as evinced by TLC fractionation (Figure 1). The proportion of the different polymerization products depends on the conditions used; Dobarganes[37] reported that only dehydrodimers have been found in significant amounts at 150 °C, while mono-, bi-, and tricyclic dimers are mainly generated above 250 °C. Some authors have reported that the average polymerization temperature of polar sterol oxides is approximately 180 °C.[9,40,41]

POP Formation. The trimethylsilyl (TMS) derivatives of POPs were analyzed by Fast GC−MS. The characteristic mass fragmentation pattern produced by EI (Table 3) was used to identify the main POPs, on the basis of those reported in previous studies.[29,30,42] As reported in Table 3, 16 POPs were identified and a specific ion was selected for each POP, on the basis of abundance and specificity. In particular, 7-hydroxysterols (α and β), 6β-hydroxysterols, epoxysterols (α and β), and 7-ketosterols originated from oxidation of the main phytosterols (β-sitosterol, stigmasterol, and campesterol) were formed in both systems.

Table 3. Characteristic Mass Fragmentation Pattern of the Main POPs and the Selected Ions for Their Quantification

phytosterol oxidation product	retention time (min)	m/z[a]	characteristic fragmentation
7α-hydroxycampesterol	8.611	470	129, 233, 455, 470, 471, 472, 560
7α-hydroxystigmasterol	8.805	482	208, 233, 343, 482, 483, 484, 467, 572
6β-hydroxycampesterol	9.224	417	417, 455, 470, 545
7α-hydroxysitosterol	9.381	484	233, 253, 484, 485, 486, 574
6β-hydroxystigmasterol	9.488	429	429, 467, 482, 543, 557, 572
7β-hydroxycampesterol	9.716	470	129, 209, 233, 381, 455, 470, 471, 472, 486, 560
7β-hydroxystigmasterol	9.873	482	209, 233, 482, 483, 484, 572
α-epoxystigmasterol	10.125	253	83, 253, 349, 410, 500
β-epoxystigmasterol	10.313	253	83, 129, 157, 211, 253, 349, 410, 442, 471, 500
7β-hydroxysitosterol	10.476	484	233, 484, 485, 486, 574
α-epoxysitosterol	10.694	412	253, 384, 394, 412, 431, 502, 503, 575
β-epoxysitosterol	10.860	412	253, 384, 394, 412, 474, 502, 503
7-ketocampesterol	11.345	381	129, 381, 396, 469, 486
7-ketostigmasterol	11.685	386	129, 269, 357, 359, 386, 455, 498
6-ketositosterol	12.129	473	473, 474, 487
7-ketositosterol	12.201	500	129, 161, 395, 410, 483, 500, 501, 502

[a]The m/z column reports the ions selected for POP quantification purposes.

All PS examined in this study (campesterol, stigmasterol, and β-sitosterol) produced detectable and quantitative amounts of hydroxy, epoxy, and keto derivatives in the ring structure. The phytosterol oxides found are analogous to the major cholesterol oxidation products obtained by autoxidation and thermoxidation, following similar reaction pathways. The major site of POP formation is at C-7 on the second ring, where hydroperoxides and hydroxy and keto sterols are formed. Other major oxidation products that can be produced in the ring structure are epoxides and triols. The formation of epoxides by autoxidation occurs by a bimolecular mechanism that involves one hydroperoxy radical and one unoxidized sterol molecule.[1]

Table 4 reports the single and total POP contents (expressed as micrograms per milligram of phytosterols) of the PSF and PS + TAG models heated in a multimodal MW oven. The evolution of 16 different POPs was followed in this study. In our experimental conditions, with a time lapse from 6 to 12 min, POP formation in both model systems was observed just after 12 min of MW heating; prior to that time, no detectable amounts of POPs were found, which does not exclude the possibility that POPs might have formed in the time lapse between 6 and 12 min. This result is opposite to that reported by Menéndez-Carreño et al.,[25] since they found that the highest POP level in phytosterol-enriched milk was formed in the first 1.3 min of heating in a microwave oven at 900 W and 69 °C. Such differences between these two studies could be mainly attributed to the high water content of milk (about 87−88%), which can greatly favor heat generation during microwaving by means of the dipolar rotation mechanism, and thus affect phytosterol oxidation; in addition, the manufacturing processes used for dairy products (e.g., high pressures) and their storage

DOI: 10.1021/acs.jafc.5b00961
J. Agric. Food Chem. 2015, 63, 5539−5547

Table 4. Single and Total POP Contents (μg/mg of phytosterols) of the PSF and PS + TAG Models Heated in a Multimodal MW Oven[a]

		time of heating[a] (min)		
		12	20	30
		PSF		
campesterol	7α-OH	2.37 ± 0.50 a	1.73 ± 0.49 a	1.26 ± 0.80 a
	6β-OH	0.22 ± 0.07 a	0.22 ± 0.13 a	0.28 ± 0.09 a
	7β-OH	5.91 ± 0.44 a	5.21 ± 0.60 a	3.54 ± 2.18 a
	7-keto	9.75 ± 1.25 c	12.42 ± 0.24 b	14.92 ± 0.90 a
	total	18.25 ± 1.95 aA	19.58 ± 1.36 aA	20.01 ± 3.96 aB
stigmasterol	7α-OH	1.94 ± 0.26 a	1.54 ± 0.47 a	1.04 ± 0.67 a
	6β-OH	0.19 ± 0.04 a	0.23 ± 0.03 a	0.25 ± 0.08 a
	7β-OH	5.23 ± 0.48 a	4.85 ± 0.54 a	3.25 ± 1.78 a
	5α,6α-epoxy	2.46 ± 0.47 a	2.28 ± 0.28 a	2.80 ± 0.52 a
	5β,6β-epoxy	2.53 ± 0.16 a	3.34 ± 0.69 a	4.44 ± 1.68 a
	7-keto	4.92 ± 1.05 a	6.61 ± 0.28 a	7.83 ± 0.41 a
	total	17.27 ± 1.68 aA	18.85 ± 1.79 aB	19.61 ± 4.52 aB
β-sitosterol	7α-OH	3.77 ± 0.53 a	2.90 ± 1.02a	1.91 ± 1.29a
	7β-OH	10.68 ± 1.25 a	10.02 ± 1.32 a	6.97 ± 4.24 a
	5β,6β-epoxy	4.55 ± 1.19 a	5.84 ± 1.30 a	4.36 ± 2.54 a
	5α,6α-epoxy	5.78 ± 1.56 b	7.75 ± 0.55 a	7.97 ± 2.07 a
	6-keto	1.20 ± 0.27 a	1.87 ± 0.21 a	2.50 ± 0.96 a
	7-keto	29.46 ± 5.64 b	35.76 ± 2.12 ab	43.67 ± 1.56 a
	total	50.89 ± 7.80 aA	58.29 ± 2.88 aA	63.02 ± 6.54 aB
total POPs		90.96 ± 12.46 aA	102.56 ± 6.62 aA	107.00 ± 17.45 aB
oxidation ratio (%)		9.0 aA	10.3 aA	10.7 aB
		PS + TAG		
campesterol	7α-OH	1.53 ± 0.45 c	7.53 ± 0.41 b	9.36 ± 0.20 a
	6β-OH	nd	0.20 ± 0.05 a	0.25 ± 0.08 a
	7β-OH	1.75 ± 0.45 c	7.67 ± 0.18 b	8.73 ± 0.21 a
	7-keto	1.47 ± 0.18 c	8.27 ± 0.67 b	10.62 ± 0.81 a
	total	4.75 ± 1.08 cB	23.67 ± 1.11 bA	28.96 ± 0.87 aA
stigmasterol	7α-OH	1.23 ± 0.29 c	6.21 ± 0.25 b	8.01 ± 0.06 a
	6β-OH	0.09 ± 0.01 b	0.18 ± 0.02 a	0.21 ± 0.03 a
	7β-OH	1.49 ± 0.43 b	6.51 ± 0.27 a	7.23 ± 0.04 a
	5α,6α-epoxy	0.36 ± 0.19 b	4.97 ± 1.54 a	5.80 ± 2.44 a
	5β,6β-epoxy	1.98 ± 0.38 c	10.72 ± 0.91 b	13.61 ± 0.79 a
	7-keto	0.77 ± 0.18 c	3.91 ± 0.59 b	5.59 ± 0.55 a
	total	5.92 ± 1.39 cB	32.49 ± 3.06 bA	40.44 ± 1.77 aA
β-sitosterol	7α-OH	2.22 ± 0.61 c	12.27 ± 0.64 b	14.44 ± 0.89 a
	7β-OH	2.80 ± 0.71 c	12.70 ± 0.51 b	14.19 ± 0.34 a
	5β,6β-epoxy	2.72 ± 0.59 c	17.28 ± 0.97 b	21.55 ± 1.27 a
	5α,6α-epoxy	0.25 ± 0.11 c	5.54 ± 1.54 b	11.34 ± 1.11 a
	6-keto	nd	0.94 ± 0.10 a	1.09 ± 0.32 a
	7-keto	4.47 ± 0.69 c	20.32 ± 1.11 b	27.00 ± 2.73 a
	total	11.99 ± 2.70 cB	69.05 ± 4.63 bA	89.60 ± 5.44 aA
total POPs		22.66 ± 5.16 cB	125.21 ± 8.51 bA	159.00 ± 7.14 aA
oxidation ratio (%)		2.0 cB	12.5 bA	15.9 aA

[a]From 0 to 6 min of heating, no POPs were detected. Each value in the last three columns represents the mean ± standard deviation of three replicates. Different lowercase letters within the same row denote significant differences ($p < 0.05$) among different heating times. For the total of individual oxidized sterols (β-sitosterol, stigmasterol, and campesterol) and total POPs, different capital letters within the same column denote significant differences ($p < 0.05$) for each time among different systems. nd = not detected.

conditions could also influence the initial oxidative status of milk before microwaving, thus impacting POP formation during the heating treatment. However, it must be noted that Menéndez-Carreño et al.[25] found a significant decrease of POP content in phytosterol-enriched milk after 2 min of treatment (304.71 vs 265 μg/mg of fat after 1.5 and 2 min of treatment, respectively).

In our study, an increase of the total amount of POPs was observed at 12 min of treatment, following different trends depending on the model system. In the PSF, the POP content did not significantly change from 12 min until 30 min of heating, remaining around 100 μg/mg of phytosterols. The PS + TAG system displayed a sinusoidal behavior in which a small amount of POPs (22.66 μg/mg of phytosterols) was observed at 12 min of microwaving, and thereafter, an exponential increase was noticed from 20 min of MW heating onward. At 12 min of heating, the POP level in PSF was higher than that in PS + TAG (90.96 vs 22.66 μg/mg of phytosterols), but at 30

DOI: 10.1021/acs.jafc.5b00961
J. Agric. Food Chem. 2015, 63, 5539−5547

min the POP content showed the opposite trend; in fact, the maximum POP levels reached at the end of heating were 107.00 and 159.00 μg/mg of phytosterols for PSF and PS + TAG, respectively. To our knowledge, other studies reported the time course changes of the POP content deriving from thermoxidation of phytosterols with a diverse matrix environment. Xu et al.[16] reported that the fatty acids accelerated β-sitosterol oxidation for the first 60 min of treatment as compared to the control; indeed, changes in the total β-sitosterol oxidation products of >10% and <5% were reported for the system with fatty acids and just β-sitosterol; starting at 90 min and thereafter, their levels were slightly higher in the system with β-sitosterol alone than the sample with fatty acids. This study emphasizes that pure fatty acids might promote the formation of β-sitosterol oxides in an initial phase of oxidation. Another research paper demonstrated that frying oil/fat decreased β-sitosterol oxides up to 50% when heated for 60 min at 180 °C, probably due to antioxidants naturally occurring in the oil.[15] Barriuso et al.[14] reported that the content of sterol oxidation products increases during the first 5−10 min of heating at 180 °C, and subsequently, their degradation rate was higher than their formation one.

As stated before, the MW heating of edible oils, which are commonly used as a heat transfer medium in complex foods, accelerates their oxidation, causing polymerization and thermal oxidative decomposition of sterols in foods.[20] The higher content of POPs in PS + TAG observed between 20 and 30 min of MW treatment could have been affected by the TAG used as the lipid medium. At this temperature (∼160 °C), fatty acids could have undergone oxidation and produced hydroperoxy radicals, which in turn could have accelerated the degradation of phytosterol. It is well-known that MW heating produces fatty acid hydroperoxides at 2−3 times higher rates than conventional heating.[43] On the other hand, the TAG might have exerted a protective effect against phytosterol oxidation for the first 20 min. Ansorena et al.[21] found that cholesterol alone degraded faster than TAG + cholesterol at 180 °C, concluding that the TAG seemed to provide physical protection to the sterol against oxidation. In the present study, it appears that the TAG diluted the PS during heating transfer and exerted physical protection, thus slowing their oxidation as compared to the PSF system, where PS were directly exposed to MW heating. This behavior can be observed in PS degradation (Figure 2), which reflects on the lack of change in the POP levels in the PS + TAG system between 3 and 12 min. In the PSF system, the stable content of total POPs observed from 12 to 30 min could depend on the equilibrium reached between their thermoformation and further degradation into volatile compounds[18] and further evaporation of the oxides formed[44] and/or conversion into high-molecular-weight oxidation compounds (oligomers and/or polymers).[40] Other factors may impact their formation and differences in total POP contents, such as temperature, physical state, and sterol composition.

As for the generation of oxyphytosterols from the different PS, β-sitosterol oxides were the most abundant, followed by those of campesterol and stigmasterol. This is mainly caused by the relative PS concentrations in the original mixture (41% β-sitosterol, 23% campesterol, and 23% stigmasterol). Regarding the total POP content of each sterol, there were no significant modifications during heating of PSF, while a significant difference was observed in PS + TAG between 12 and 20 min of heating. Comparing the time course of total POPs from each sterol between the two systems, the major POP formation observed at 12 min was in the PSF. From 20 to 30 min of heating, contrasting data trends were found, since PS from the PS + TAG system had the highest oxide content. In fact, the behavior of the POPs originated by the single sterols reflects that observed for the total POPs in each model system.

It is generally expected that the main oxidation products of phytosterols and cholesterol are the 7-hydroxy and 7-keto derivatives,[45] at least during the early stages of oxidation. In the PSF system (Table 4), POPs from all phytosterols contained in the mix were found, the 7-keto oxide being the predominant one (42% of total POPs at 30 min of heating), followed by the 7-hydroxy derivative (7% of total POPs).

The content of total POPs generated from β-sitosterol oxidation showed a nonsignificant increasing trend with heating time (50.89, 58.29, and 63.02 μg/mg of phytosterols for 12, 20, and 30 min, respectively). The 7-keto derivative of this sterol was the predominant POP formed during microwaving, which exhibited a significant rise directly correlated with the treatment time (29.46, 35.76, and 43.67 μg/mg of phytosterols for 12, 20, and 30 min, respectively). As illustrated by Rodriguez-Estrada et al.,[10] 7-ketocholesterol is easily formed, and its content could be >30% of the total cholesterol oxidation products; hence, it is often the most representative oxysterol. However, the trend of this oxidation marker could change depending on the time/temperature conditions and interactions with the system (model or food) or with other oxidation compounds.[10,45] According to mathematical predictive models applied to PS oxidation in PS-enriched beverages as a function of the storage time, 7-ketositosterol and 7-ketocampesterol could be used as markers of the PS oxidation level as they showed the highest R^2 value (percentage of variability explained by the model).[45] Other β-sitosterol POPs, such as 7α-OH and 7β-OH, did not significantly change ($p > 0.05$) during heating; between these two epimers, 7β-OH was predominant (about 10 μg/mg of phytosterols). Regarding campesterol and stigmasterol, total POPs formed after 12 min of microwaving, without showing significant differences during the rest of the heat treatment. The total amounts of POPs originated from each sterol were about 20 μg/mg of phytosterols. The individual POPs generated from these phytosterols exhibited the same trend as β-sitosterol's POPs but with different ratios, reflecting the PS concentrations of the original mixture. No epoxy derivatives of campesterol were detected though. Barriuso et al.[14] investigated the formation and degradation pattern of polar POPs during heating at 180 °C for up to 6 h in a conventional oven. The maximum level of POPs was observed between 5 and 10 min of heating, depending on the individual PS, with the highest concentration of total campesterol and β-sitosterol oxides. In particular, at 5−10 min, the 7-keto derivative was the predominant POP, followed by 7α-hydroxy epimers, epoxides, and triol in a lower amount.

In the PS + TAG model (Table 4), different amounts of 7-hydroxy and 7-keto derivatives were found, which accounted for less than 10% and 20% of the total POPs at 30 min of heating, respectively. The content of total POPs generated from degradation of β-sitosterol displayed an increasing tendency with increasing heating time. A significant, rapid change was observed between 12 and 20/30 min of microwaving; this behavior was also observed for single and total campesterol and stigmasterol oxides (Table 4). The total amounts of stigmasterol oxides generated after 30 min of heating were higher compared to those of campesterol oxides; this could be

DOI: 10.1021/acs.jafc.5b00961
J. Agric. Food Chem. 2015, 63, 5539−5547

partly ascribable to the formation of both epoxy derivatives from stigmasterol, which were not found among campesterol's POPs. The epoxidation of the 5,6-double bond of the sterol comes from a bimolecular reaction mechanism between a hydroperoxy radical and an unoxidized sterol. The additional double bond on the side chain of stigmasterol as compared to the other sterols represents a further attack point for free radicals, which can promote hydroperoxide formation at 100 and 180 °C[46] and may thus affect the rate of oxidation of this sterol.[14] Ansorena et al.[21] found that the concentration of COPs in a cholesterol−TAG system model heated in a conventional oven at 180 °C displayed an increasing tendency at different heating times depending on the TAG unsaturation degree.

It must be noted that, in any case, the most abundant POPs were similar in both model systems and that the main differences were due to the relative oxide concentrations. In the PSF system, the concentrations of individual POPs were greatest for the 7-keto derivative, almost twice as much as in the other model system after 30 min of microwaving (43.67 vs 27.00 μg/mg of phytosterols). In PS + TAG, the 7-hydroxy derivatives (α and β) were present in the same proportion, and their contents were higher than in the PSF system, where 7β-hydroxy derivatives were predominant. In both systems, the epoxy derivatives (α and β) from sitosterol and stigmasterol were formed; however, in the presence of a TAG, β-epoxy was more abundant than the corresponding α epimer.

The correlation analysis mainly emphasized the differences between the two systems, PSF and PS + TAG, as related to the temperature reached during microwaving. In the PSF system, the temperature was directly correlated with POP formation (r = 0.999, p = 0.026), while it was inversely correlated with the sterol content (r = −0.933, p = 0.007). Although β-sitosterol was the most abundant in the phytosterol mixture, total POPs were only positively correlated with the total oxidation products of stigmasterol (r = −0.999, p = 0.033) and campesterol (r = 0.999, p = 0.022). In addition, 7-ketostigmasterol formation was inversely correlated with the sterol content (r = −0.999, p = 0.029). In the PS + TAG system, POP formation was not related to the temperature (r = −0.097, p = 0.938), which further confirms the important "protective/dilution" role of the TAG toward PS oxidation, despite the prooxidizing effect of temperature actually detected in PSF.

In conclusion, free phytosterols displayed a different oxidative stability during MW heating which varied according to the model system. Up to 6 min of microwaving, no POPs were detected in both systems; at 12 min of heating, the POP content reached a higher level in PSF (90.96 μg/mg of phytosterols) than in PS + TAG (22.66 μg/mg of phytosterols). However, at the end of the MW treatment (30 min), a trend changed was noted as the POP content was highest in PS + TAG (159 μg/mg of phytosterols). In this case, the presence of the TAG greatly impacted the PS stability in the first heating period, exerting a protective effect through different possible mechanisms (such as dilution, physical protection, and competition for oxidation).[21] Although household MW heating and cooking does not usually require high exposure times and temperatures, these results prove that MW treatment can differently affect the oxidative stability of free sterols according to the medium composition. This aspect should not be disregarded for food products intended to be cooked in a MW for long time periods (>12 min at the power and temperature settings here tested), as it can potentially impact their quality, nutritional value, and safety. Further studies on MW effects are required using more complex systems, including phytosterol esters (largely employed in PS-enriched food), matrices with diverse unsaturation degrees, and natural antioxidants, as they can greatly affect the extent of PS oxidation.

■ ASSOCIATED CONTENT

Supporting Information

Table listing the full data of the remaining percentages of phytosterols during microwave heating of both model systems (PSF and PS + TAG) with the corresponding statistical analysis. The Supporting Information is available free of charge on the ACS Publications website at DOI: 10.1021/acs.jafc.5b00961.

■ AUTHOR INFORMATION

Corresponding Authors

*Phone: +39-051-2096011. Fax: +39-051-2096017. E-mail: maria.rodriguez@unibo.it.

*Phone: 229 934 5701. E-mail: hugosgg@gmail.com.

Notes

The authors declare no competing financial interest.

■ ACKNOWLEDGMENTS

We thank Basic Research Funding (RFO 2013, Alma Mater Studiorum-Università di Bologna, Italy) for financial support. R.I. is grateful for the Ph.D. fellowship granted by the Italian Ministry of Education, University and Research (MIUR). V.C. is grateful for the research fellowship granted by the POR-FESR (2010−2013) Emilia Romagna Program (Italy). The authors thank the National Council of Science and Technology of Mexico (CONACyT) for the graduate fellowship of E.J.L.-C.

■ REFERENCES

(1) García-Llatas, G.; Rodriguez-Estrada, M. T. Current and new insights on phytosterol oxides in plant sterol-enriched food. *Chem. Phys. Lipids* **2011**, *164*, 607−624.

(2) Marangoni, F.; Poli, A. Phytosterols and cardiovascular health. *Pharm. Res.* **2010**, *61*, 193−199.

(3) Escurriol, V.; Cofán, M.; Moreno-Iribas, C.; Larrañaga, N.; Martínez, C.; Navarro, C.; Rodríguez, L.; González, C. A.; Corella, D.; Ros, E. Phytosterol plasma concentrations and coronary heart disease in the prospective Spanish EPIC cohort. *J. Lipid Res.* **2010**, *51*, 618−624.

(4) Hernández, M. A.; Bañuls, C.; Rocha, M.; Morillas, C.; Martínez, T. M. L.; Víctor, V. M.; Lacomba, R.; Alegria, A.; Barbera, R.; Farré, R.; Lagarda, M. J. Effects of phytosterol ester-enriched low-fat milk on serum lipoprotein profile in mildly hypercholesterolaemic patients are not related to dietary cholesterol or saturated fat intake. *Br. J. Nutr.* **2010**, *104*, 1018−1025.

(5) Alemany, C. L.; González, L. M.; García-Llatas, G.; Alegría, A.; Barberá, R.; Sánchez, S. L. M.; Lagarda, M. J. Sterol stability in functional fruit beverages enriched with different plant sterol sources. *Food Res. Int.* **2012**, *48*, 265−270.

(6) Choe, E.; Min, D. B. Mechanisms of antioxidants in the oxidation of foods. *Compr. Rev. Food Sci. Food Saf.* **2009**, *8*, 345−358.

(7) Lengyel, J.; Rimarčík, J.; Vagánek, A.; Fedor, J.; Lukeš, V.; Klein, E. Oxidation of sterols: energetics of C−H and O−H bond cleavage. *Food Chem.* **2012**, *133*, 1435−1440.

(8) Otaegui-Arrazola, A.; Menénde-Carreño, M.; Ansorena, D.; Astiasarán, I. Oxysterols: A world to explore. *Food Chem. Toxicol.* **2010**, *48*, 3289−3303.

(9) Menéndez-Carreño, M.; Ansorena, D.; Astiasarán, I.; Piironen, V.; Lampi, A. M. Determination of non-polar and mid-polar monomeric

DOI: 10.1021/acs.jafc.5b00961
J. Agric. Food Chem. 2015, 63, 5539−5547

oxidation products of stigmasterol during thermo-oxidation. *Food Chem.* **2010**, *122*, 277−284.
(10) Rodríguez-Estrada, M. T.; García-Llatas, G.; Lagarda, M. J. 7-Ketocholesterol as marker of cholesterol oxidation in model and food systems: when and how. *Biochem. Biophys. Res. Commun.* **2014**, *446*, 792−797.
(11) Alemany, L.; Barbera, R.; Alegría, A.; Laparra, J. M. Plant sterols from foods in inflammation and risk of cardiovascular disease: a real threat? *Food Chem. Toxicol.* **2014**, *69*, 140−149.
(12) Gylling, H.; Plat, J.; Turley, S.; Ginsberg, H. N.; Ellegård, L.; Jessup, W.; Jones, P. J.; Lütjohann, D.; Maerz, W.; Masana, L.; Silbernagel, G.; Staels, B.; Borén, J.; Catapano, A. L.; De Backer, G.; Deanfield, J.; Descamps, O. S.; Kovanen, P. T.; Riccardi, G.; Tokgözoglu, L.; Chapman, M. J. Plant sterols and plant stanols in the management of dyslipidaemia and prevention of cardiovascular disease. *Atherosclerosis* **2014**, *232*, 346−360.
(13) O'Callaghan, Y.; McCarthy, F. O.; O'Brien, N. M. Recent advances in phytosterol oxidation products. *Biochem. Biophys. Res. Commun.* **2014**, *446*, 786−791.
(14) Barriuso, B.; Otaegui-Arrazola, A.; Menéndez-Carreño, M.; Astiasarán, I.; Ansorena, D. Sterols heating: degradation and formation of their ring-structure polar oxidation products. *Food Chem.* **2012**, *135*, 706−712.
(15) Xu, G.; Guan, L.; Sun, J.; Chen, Z. Y. Oxidation of cholesterol and β-sitosterol and prevention by natural antioxidants. *J. Agric. Food Chem.* **2009**, *57*, 9284−9292.
(16) Xu, G.; Sun, J.; Liang, Y.; Yang, C.; Chen, Z. Y. Interaction of fatty acids with oxidation of cholesterol and β-sitosterol. *Food Chem.* **2011**, *124*, 162−170.
(17) Soupas, L.; Juntunen, L.; Lampi, A. M.; Piironen, V. Effects of sterol structure, temperature, and lipid medium on phytosterol oxidation. *J. Agric. Food Chem.* **2004**, *52*, 6485−6491.
(18) Rudzinska, M.; Przybylski, R.; Wasowicz, E. Products formed during thermo-oxidative degradation of phytosterols. *J. Am. Oil Chem. Soc.* **2009**, *86*, 651−662.
(19) Malheiro, R.; Casal, S.; Ramalhosa, E.; Pereira, J. A. Microwave heating: a time saving technology or a way to induce vegetable oils oxidation? In *Advances in Induction and Microwave Heating of Mineral and Organic Materials*; Grundas, S., Ed.; Intech: Rijeka, Croatia, 2011; Vol. *26*, pp 597−614.
(20) Inchingolo, R.; Cardenia, V.; Rodriguez-Estrada, M. T. The effects of microwave heating on edible oils and lipid-containing food. *Lipid Technol.* **2013**, *25*, 59−61.
(21) Ansorena, D.; Barriuso, B.; Cardenia, V.; Astiasarán, I.; Lercker, G.; Rodriguez-Estrada, M. T. Thermo-oxidation of cholesterol: effect of the unsaturation degree of the lipid matrix. *Food Chem.* **2013**, *141*, 2757−2764.
(22) Kmiecik, D.; Korczak, J.; Rudzińska, M.; Gramza-Michałowska, A.; Hęś, M.; Kobus-Cisowska, J. Stabilisation of phytosterols by natural and synthetic antioxidants in high temperature conditions. *Food Chem.* **2015**, *173*, 966−971.
(23) Derewiaka, D.; Obiedziński, M. Phytosterol oxides content in selected thermally processed products. *Eur. Food Res. Technol.* **2012**, *234*, 703−712.
(24) Dutta, P. C. Studies on phytosterol oxides. II: content in some vegetable oils and in French fries prepared in these oils. *J. Am. Oil Chem. Soc.* **1997**, *74*, 659−666.
(25) Menéndez-Carreño, M.; Ansorena, D.; Astiasarán, I. Stability of sterols in phytosterol-enriched milk under different heating conditions. *J. Agric. Food Chem.* **2008**, *56*, 9997−10002.
(26) Bortolomeazzi, R.; Frega, N.; Lercker, G. Rapid determination of free and esterified sterols using prepacked silica columns. *Ital. J. Food Sci.* **1990**, *4*, 265−268.
(27) Sweeley, C. C.; Bentley, R.; Makita, M.; Wells, W. W. Gas−liquid chromatography of trimethylsilyl derivatives of sugars and related substances. *J. Am. Chem. Soc.* **1963**, *85*, 2497−2507.
(28) Guardiola, F.; Codony, R.; Rafecas, M.; Boatella, J. Comparison of three methods for the determination of oxysterols in spray-dried egg. *J. Chromatogr. A* **1995**, *705*, 289−304.
(29) Alemany, L.; Cilla, A.; García-Llatas, G.; Rodríguez-Estrada, M. T.; Cardenia, V.; Alegría, A. Effect of simulated gastrointestinal digestion on plant sterols and their oxides in enriched beverages. *Food Res. Int.* **2013**, *52*, 1−7.
(30) Toschi, T. G.; Cardenia, V.; Bonaga, G.; Mandrioli, M.; Rodríguez-Estrada, M. T. Coffee silverskin: characterization, possible uses, and safety aspects. *J. Agric. Food Chem.* **2014**, *62*, 10836−10844.
(31) Grandgirard, A.; Martine, L.; Joffre, C.; Juaneda, P.; Berdeaux, O. Gas chromatographic separation and mass spectrometric identification of mixtures of oxyphytosterol and oxycholesterol derivatives: application to a phytosterol-enriched food. *J. Chromatogr. A* **2004**, *1040*, 239−250.
(32) Cardenia, V.; Rodríguez-Estrada, M. T.; Baldacci, E.; Savioli, S.; Lercker, G. Analysis of cholesterol oxidation products by fast gas chromatography/mass spectrometry. *J. Sep. Sci.* **2012**, *35*, 424−430.
(33) Derewiaka, D.; Molińska, E. Cholesterol transformations during heat treatment. *Food Chem.* **2015**, *171*, 233−240.
(34) Barriuso, B.; Ansorena, D.; Poyato, C.; Astiasarán, I. Cholesterol and stigmasterol within a sunflower oil matrix: thermal degradation and oxysterols formation. *Steroids* **2015**, in press.
(35) Yen, T. Y.; Lu, Y. F.; Inbaraj, B. S.; Chen, B. H. Cholesterol oxidation in lard as affected by CLA during heating—a kinetic approach. *Eur. J. Lipid Sci. Technol.* **2011**, *113*, 214−223.
(36) Soupas, L.; Huikko, L.; Lampi, A. M.; Piironen, V. Pan-frying may induce phytosterol oxidation. *Food Chem.* **2007**, *101*, 286−297.
(37) Dobarganes, M. C. Formation of new compounds during frying—general observations. http://http://lipidlibrary.aocs.org/frying/c-newcpds/index.htm (accessed April 2, 2015).
(38) Lampi, A.; Kemmo, S.; Makela, A.; Heikkinen, S.; Piironen, V. Distribution of monomeric, dimeric and polymeric products of stigmasterol during thermo-oxidation. *Eur. J. Lipid Sci. Technol.* **2009**, *111*, 1027−1034.
(39) Lercker, G.; Rodríguez-Estrada, M. T. Cholesterol oxidation: presence of 7-ketocholesterol in different food products. *J. Food Compos. Anal.* **2000**, *13*, 625−631.
(40) Rudzinska, M.; Przybylski, R.; Zhao, Y. Y.; Curtis, J. M. Sitosterol thermo-oxidative degradation leads to the formation of dimers, trimers and oligomers: a study using combined size exclusion chromatography/mass spectrometry. *Lipids* **2010**, *45*, 549−558.
(41) Soupas, L.; Huikko, L.; Lampi, A. M. Oxidative stability of phytosterols in some food applications. *Eur. Food Res. Technol.* **2006**, *222*, 266−273.
(42) Dutta, P. C. Determination of phytosterol oxidation products in foods and biological samples. In *Cholesterol and Phytosterol Oxidation Products: Analysis, Occurrence and Biological Effects*; Guardiola, F., Dutta, P. C., Codony, R., Savage, G. P., Eds.; AOCS Press: Champaign, IL, 2002; pp 335−374.
(43) Kreps, F.; Vrbiková, L.; Schmidt, Š.; Sekretár, S.; Híreš, O. Chemical changes in microwave heated vegetable oils. *Eur. J. Lipid Sci. Technol.* **2014**, *116*, 1685−1693.
(44) Zhang, X.; Julien-David, D.; Miesch, M.; Geoffroy, P.; Raul, F.; Roussi, S.; Aoudé-Werner, D.; Marchioni, E. Identification and quantitative analysis of beta-sitosterol oxides in vegetable oils by capillary gas chromatography-mass spectrometry. *Steroids* **2005**, *70*, 896−906.
(45) González-Larena, M.; García-Llatas, G.; Clemente, G.; Barberá, R.; Lagarda, M. J. Plant sterol oxides in functional beverages: influence of matrix and storage. *Food Chem.* **2015**, *173*, 881−889.
(46) Kemmo, S.; Soupas, L.; Lampi, A. M.; Piironen, V. Formation and decomposition of stigmasterol hydroperoxides and secondary oxidation products during thermo-oxidation. *Eur. J. Lipid Sci. Technol.* **2005**, *107*, 805−814.

DOI: 10.1021/acs.jafc.5b00961
J. Agric. Food Chem. 2015, 63, 5539−5547

Table 1. Primers and Specific Probes for Hairtail Fish

primer[a]	sequence (5′ to 3′)	target group[b]	reaction type
FP-1	AGAGCTAAGCCAACCAGGCT	G3	multiple
RP-1	AATTATCACGAAGGCATGGG	G3	multiple
FP-2	AGGCACAGCCTTAAGCCTTCT	G2	multiple
RP-2	GCTGTAACGATAACATTGTAAATTTGG	G2	multiple
FP-3	AACTGGCTTATCCCCCTAATGAT	G1	single
RP-3	GCGGAGGAGGCTAGGAGAAG	G1	single
probe 1	[FAM]- CCCTCCTGGGCGATGACCAA -[TAMRA]	G3	multiple
probe 2	[HEX]- CCGCGCAGAGCTAAGCCAGCC-[TAMRA]	G2	multiple
probe 3	[FAM]- CCGACATGGCCTTCCCCCG -[TAMRA]	G1	single

[a]FP, forward primer; RP, reverse primer. [b]Group 1 (G1): Korea, Japan, and China. Group 2 (G2): Senegal and Canada. Group 3 (G3): Thailand.

have unique isotopic fingerprints, stable isotope composition analysis could provide information about ecological and geographical origin of biological products, thereby helping discrimination of food. The utilization of isotope ratio mass spectrometry in distinguishing the geographical origin of food samples has been established. Although this technique is extensively discussed for authenticating food products such as meat, wine, fruit juice, honey, and dairy products,[7] its utility in inferring the geographical origin and authentication of fish, shrimp, and seafood species is scarce.[6] On the other hand, molecular tools, based on protein and DNA biomarkers, have been proposed as suitable strategies for identification of fish and crustacean species. In the case of processed products, due to the lack of stability of the polypeptide targets, electrophoretic and immunological methods are unreliable. However, due to its remarkable stability, DNA analysis circumvents these problems. Among the DNA targets considered for species identification, 12S rRNA, 16S rRNA, tRNAVal, and, to a lesser extent, cytochrome oxidase I (COI) and cytochrome *b* genes have been proposed as useful molecular markers for fish and crustacean species.[4]

Authentication, verification of the geographic origin of a product, and pertinent labeling provide consumers with correct, complete, and transparent information. This enables the consumer to make an informed choice on the type and origin of fish purchased. There has been growing consumer enthusiasm for high-quality food with a clear regional identity. There is also an increased public awareness regarding the means by which it has been produced. This study investigates the applicability of stable isotopic values (δ^{13}C and δ^{15}N) as well as cytochrome *c* oxidase gene I as convergent tools to identify hairtail fish and shrimp and to verify their geographic origin. This would abate counterfeit labeling and help traceability of marketed products.

MATERIALS AND METHODS

Sample Collection. Marketable-sized hairtail fish and shrimp were chosen for the present study. Domestic samples were collected from a seafood market, and their area of catch was confirmed. Imported fishes were obtained from the national seafood quarantine agency after verifying their catchment area and country of origin. In each case, five authentic samples were evaluated.

Stable Isotope Analysis. All samples were brought to the laboratory immediately after collection. They were subsequently separated on the bases of commercial name of the species, country of its origin, body weight, and total length. Dorsal muscle tissue of hairtail fish samples and white muscle tissue of shrimp samples were dissected and stored in the deep freezer (−80 °C). The samples were analyzed according to the method stated by Kim et al.[7] Stable isotope analysis was carried out by use of an elemental analyzer (CHNS-O, Euro Vector) combined with a stable isotope mass spectrometer (Isoprime 100, Isoprime Ltd). The δ^{13}C and δ^{15}N (‰ deviations from Vienna Pee Dee Belemnite, VPDB, and atmospheric N_2, respectively) are expressed as follows:

$$\delta^{13}\mathrm{C}\ (‰) = [(^{13}\mathrm{C}/^{12}\mathrm{C})_{\mathrm{sample}}/(^{13}\mathrm{C}/^{12}\mathrm{C})_{\mathrm{standard}} - 1] \times 1000$$

$$\delta^{15}\mathrm{N}\ (‰) = [(^{15}\mathrm{N}/^{14}\mathrm{N})_{\mathrm{sample}}/(^{15}\mathrm{N}/^{14}\mathrm{N})_{\mathrm{standard}} - 1] \times 1000$$

Two international standards, CH-6 and N-1 of International Atomic Energy Agency (IAEA), were used for calculating the isotope ratios, and the δ^{13}C and δ^{15}N values were reported. In case of both carbon and nitrogen isotope ratios, the analytical precision (standard deviation) was <±0.3‰. An internal standard was run for every 10 samples.

Molecular Analysis. *Genomic DNA Extraction.* Genomic DVA (gDNA) was extracted from muscle tissue by use of the DNeasy blood and tissue kit (Qiagen, Hilden, Germany) as per the protocol described by the manufacturer. The gDNA concentration was measured on a Nanodrop ND-1000 spectrophotometer (Thermo-Fisher Scientific Inc., Waltham, MA). The extracted gDNA was used directly for polymerase chain reaction (PCR) and real-time PCR analysis. Several gDNAs were diluted (1/10), from 10 ng/μL to 0.01 pg/μL, in order to confirm the detection limit of the real-time PCR assay.

DNA Amplification and Sequencing. Mitochondrial cytochrome *c* oxidase I (COI) was selected as the target gene. The COI gene was amplified by use of the following primers, where V indicates vertebrate, F is forward, R is reverse, and In indicates invertebrate:

COI-V-F 5′-TCAACCAACCACAAAGACATTGGCAC-3′
COI-V-R 5′- TAGACTTCTGGGTGGCCAAACAATCA-3′
COI-In-F 5′- GTTCAACAAATCATAAAGATATTGG-3′
COI-In-R 5′- TAAACTTCAGGGTGACCAAAAAATCA-3′

Compatibility of the primer set was confirmed by comparing the full sequence of COI genes of hairtail fish and shrimp with the NCBI database (www.ncbi.nlm.nih.gov). Pre-PCR reaction mixtures were treated in a TaKaRa PCR thermal cycler (TaKaRa Bio Inc., Shiga, Japan), wherein the total volume of 20 μL contained 10 μL of Premix Taq (TaKaRa Bio), 2 μL of primer mix (10 pmol/μL), 1 μL of 5 M betaine, 6 μL of distilled water, and 1 μL of gDNA. Thermal cycling conditions were programmed for initial denaturation at 95 °C for 11 min, followed by a reaction cycle (94 °C for 1 min, 50 °C for 1 min, and 72 °C for 1 min) repeated 35 times, with a final extension step of 72 °C for 5 min. PCR products were analyzed by 1% agarose gel electrophoresis and direct sequencing to identify the sequences accurately (Solgent Inc., Daejeon, Korea).

Primer and Probe Design for Real-Time PCR. Specific primers and probes for the real-time PCR kit were designed from direct sequencing data by use of Primer Express software (Applied Biosystems, Foster City, CA) and web-based software (www.genscript.com, GenScript Inc., Piscataway Township, NJ). Primer and probe sequence information is listed in Tables 1 and 2.

Real-Time Polymerase Chain Reaction and Analysis. Real-time PCR was performed in triplicate in 384-well plates. A 384-well

DOI: 10.1021/acs.jafc.5b01469
J. Agric. Food Chem. 2015, 63, 5548−5556

Table 2. Primers and Specific Probes for Shrimp

primer[a]	sequence (5′ to 3′)	target group[b]	reaction type
FP-1	AACTGGCTTATCCCCCTAATGAT	G1	single
RP-1	GCGGAGGAGGCTAGGAGAAG	G1	single
FP-2	AGGCACAGCCTTAAGCCTTCT	G2	multiple
RP-2	GCTGTAACGATAACATTGTAAATTTGG	G2	multiple
probe 1	[FAM]- CCGACATGGCCTTCCCCCG -[TAMRA]	G1	single
probe 2	[HEX]- CCGCGCAGAGCTAAGCCAGCC-[TAMRA]	G2	multiple

[a]FP, forward primer; RP, reverse primer. [b]Group 1 (G1): Korea (farmed), Malaysia, and Ecuador. Group 2 (G2): India, Netherlands, Thailand, and Indonesia.

high-throughput analysis was performed with the ABI Prism 7900 sequence detection system (Applied Biosystems); here, white-colored 384-well plates (Applied Biosystems) were used to intensify the fluorescent signals by a factor of 3. This system operated with a thermal cycler and a laser that was directed via fiber optics to each of the 384 sample wells. Fluorescence emission from each sample was collected by a charge-coupled device camera. Single real-time PCR reaction mixtures contained 10 μL of TaqMan universal master mix II, no UNG (Applied Biosystems), 1 μL of primer mix (10 pmol/μL), 0.5 μL of probe 3 (10 pmol/μL), 7.5 μL of distilled water, and 1 μL of gDNA. Multiplex real-time PCR reaction mixtures contained 10 μL of TaqMan universal master mix II, no UNG (Applied Biosystems), 2 μL of primer mix (10 pmol/μL), 0.25 μL of probe 1 (10 pmol/μL), 0.5 μL of probe 2 (10 pmol/μL), 6.25 μL of distilled water, and 1 μL of gDNA. Thermal cycling conditions for hairtail fish were an initial denaturation at 95 °C for 10 min, followed by a reaction cycle (95 °C for 15 s and 60 °C for 1 min) repeated 40 times. Thermal cycling conditions for shrimp were an initial denaturation at 95 °C for 10 min, followed by a reaction cycle (95 °C for 15 s and 50 °C for 1 min) repeated 40 times. Data were analyzed by use of SDS software v 2.3 (Applied Biosystems).

Phylogenetic Analysis. Phylogenic and molecular evolutionary analyses were conducted with MEGA version 4.[8] The evolutionary history was inferred by use of the neighbor-joining method.[9] The phylogenetic tree was linearized with the assumption of equal evolutionary rates in all lineages.[10] The tree is drawn to scale, with branch lengths in the same units as those of the evolutionary distances used to infer the phylogenetic tree. The evolutionary distances were computed by the maximum composite likelihood method[11] and are in units of number of base substitutions per site.

Statistical Analysis. Data are presented as mean ± standard deviation (SD). Data were analyzed by one-way analysis of variance (ANOVA), and significant differences were determined by Tukey's posthoc test. Linear discriminant analysis (LDA) was used to calculate the discriminant function that classified each group, while leave-one-out cross-validation (LOOCV) was used to examine data among the test samples.

RESULTS

The mean isotopic values and standard deviation [when the number of authentic samples (n) was ≥5] are provided in Figure 1a. As evidenced in Figure 1a, distinct carbon and nitrogen isotopic values of hairtail fish samples of various geographic origins were obtained; that is, the δ^{13}C and δ^{15}N (‰) values of the fish differed significantly based on their origin.

The δ^{13}C values of the five Korean hairtail fish ranged from −17.16‰ ± 0.56‰ to −18.03‰ ± 0.27‰, whereas the δ^{13}C values of other, non-Korean hairtail fish were −15.55‰ ± 0.46‰ (Canadian), −17.90‰ ± 0.23‰ (Chinese), −15.43‰ ± 0.56‰ (Japanese), −15.73‰ ± 0.32‰ (Senegalese), and −17.80‰ ± 0.14‰ (Thai). On the other hand, nitrogen isotope (δ^{15}N) values of the Korean hairtail fish ranged from 11.66‰ ± 0.16‰ to 13.08‰ ± 0.65‰, while the values for

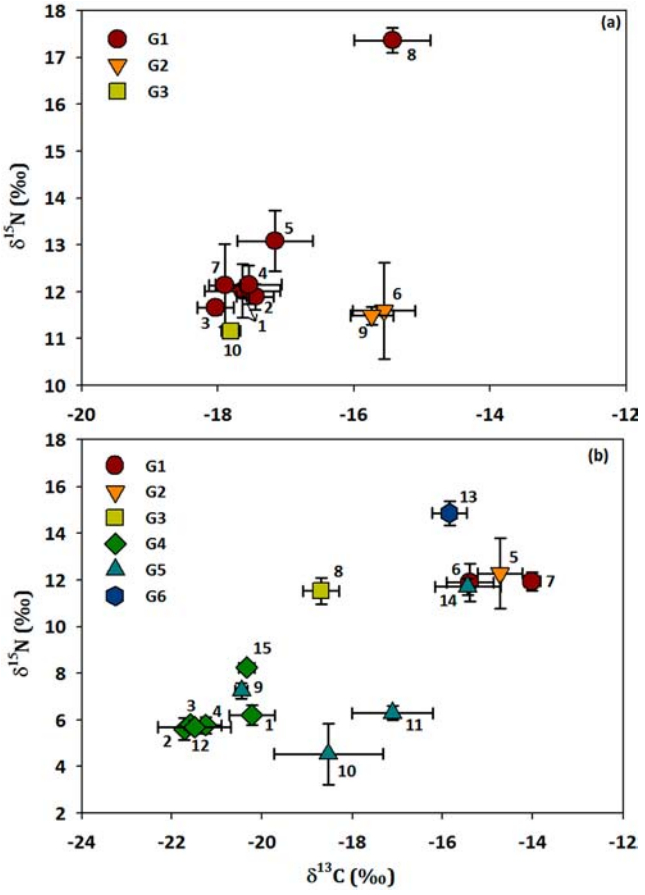

Figure 1. Biplots of δ^{13}C and δ^{15}N values (mean ± SD) of (a) hairtail fish and (b) shrimp based on their geographical origin. Grouping was carried out based on the LDA analysis. Data represent the mean ± SD of five replicates. (a) Group 1 (G1, red circles) represents samples from three countries: Korea [South Sea ID 102 (1), South Sea ID 110 (2), South Sea ID 234 (3), Mokpo (MP) (4), and Gunsan (GS) (5)], China (7), and Japan (8). Group 2 (G2, orange inverted triangles) represents samples from Canada (6) and Senegal (9). Group 3 (G3, yellow squares) represents samples from Thailand (10). (b) Group 1 (G1, red circles) represents wild samples from Korea [Taean (TA) (6) and Gunsan (GS) (7)]. Group 2 (G2, orange inverted triangles) represents wild samples from Korea Guje (GJ) (5). Group 3 (G3, yellow squares) represents wild samples from Yeosu (YS), Korea (8). Group 4 (G4, green diamonds) represents aquacultured samples from Korea [Gunsan (GS) (1), Anmyoendo (AM) (2), Mokpo (MP) (3), and Ansan (AS) (4)] as well as wild samples from Ecuador (12) and Malaysia (15). Group 5 (G5, light blue triangles) represents wild samples from India (9), Indonesia (10), Thailand (11), and Netherlands (14). Group 6 (G6, dark blue hexagons) represents wild samples from Argentina (13).

DOI: 10.1021/acs.jafc.5b01469
J. Agric. Food Chem. 2015, 63, 5548−5556

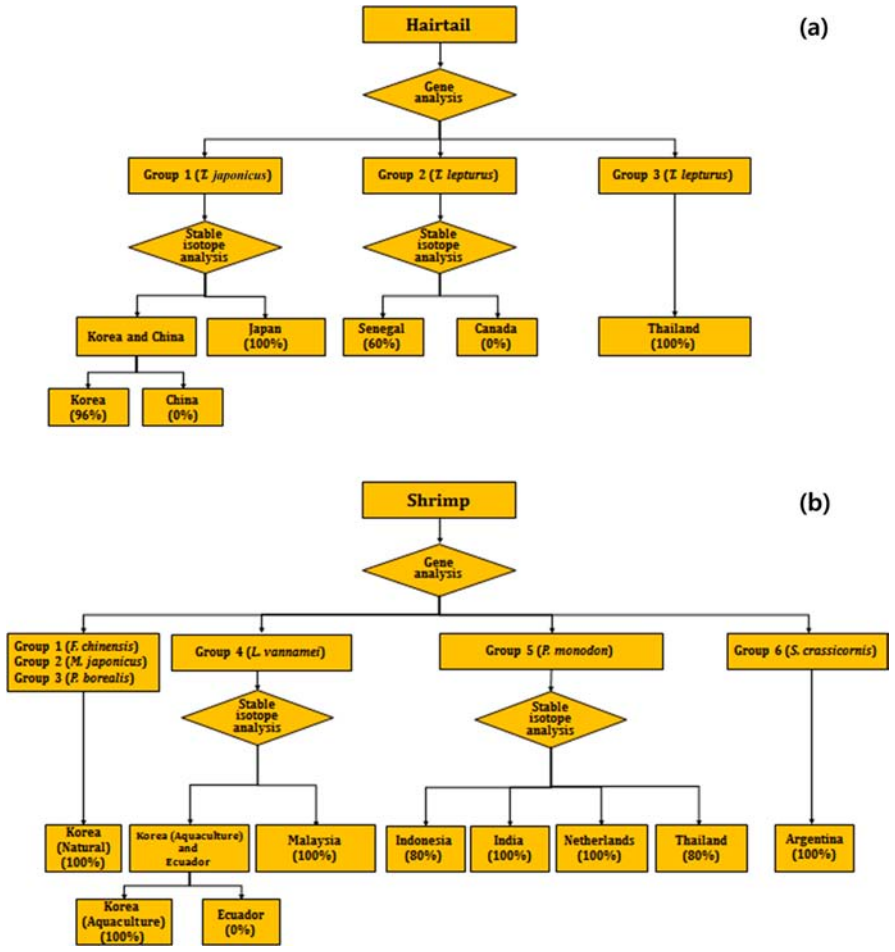

Figure 2. Grouping of (a) hairtail fish and (b) shrimp based on LDA of stable isotopes (δ^{13}C and δ^{15}N). Values in parentheses represent percentage similarity.

other, non-Korean hairtail fish were 11.59‰ ± 1.03‰ (Canadian), 12.14‰ ± 0.88‰ (Chinese), 17.36‰ ± 0.26‰ (Japanese), 11.49‰ ± 0.19‰ (Senegalese), and 11.16‰ ± 0.15‰ (Thai) (Figure 1). LDA of stable isotopes in the hairtail fish samples helped filter the samples into groups (Figure 2a). LOOCV evaluation of the stable isotope data demonstrated approximately 64.7% accuracy in classifying the hairtail fish samples. Here the Korean and Japanese samples were classified with good accuracy (with similarity of 96% and 100% respectively); they varied distinctly from each other.

Aquacultured shrimp samples collected from four different sites in Korea had δ^{13}C values ranging from −20.23‰ ± 0.50‰ to −21.72‰ ± 0.11‰, whereas the δ^{13}C values of wild Korean shrimp ranged from −14.02‰ ± 0.18‰ to −18.69‰ ± 0.40‰. The δ^{15}N (‰) values of aquacultured shrimp ranged from 5.60‰ ± 0.47‰ to 5.80‰ ± 0.14‰, which was quite different from the values for their wild counterparts (from −11.53‰ ± 0.57‰ to −12.82‰ ± 1.51‰). The δ^{13}C values of other, non-Korean shrimp were −20.46‰ ± 0.14‰ (Indian), −18.53‰ ± 1.20‰ (Indonesian), −17.11‰ ± 0.89‰ (Thai), −21.50‰ ± 0.81‰ (Ecuadorian), −15.85‰ ± 0.38‰ (Argentinian), −15.44‰ ± 0.73‰ (Dutch), and −20.3‰ ± 0.18‰ (Malaysian), and their corresponding δ^{15}N values were 7.24‰ ± 0.32‰, 4.54‰ ± 1.31‰, 6.28‰ ± 0.30‰, 5.68‰ ± 0.27‰, 14.87‰ ± 0.51‰, 11.71‰ ± 0.35‰, and 8.23‰ ± 0.21‰, respectively (Figure 1b). The shrimp stable isotope data were filtered to build a LDA model. Model evaluation, carried out via LOOCV, demonstrated an overall accuracy of 75.29% in the case of shrimp. Argentinian and Malaysian shrimp were distinctly classified by this method. Additionally, Indonesian shrimp demonstrated 80% similarity; besides, Thai samples were also classified accurately (80% similarity). All the samples of Korean farmed shrimp resembled each other, and moreover, the Korean natural shrimp also resembled each other; they were classified with 100% accuracy. However, the Korean and natural shrimp distinctly varied from each other (Figure 2b).

PCR amplification was performed by employing mitogenic COI gene primers from isolated total genomic DNA from different samples of hairtail fish and shrimp. PCR products were used for DNA sequencing analysis. Multiple alignments were performed for sequences obtained from DNA sequencing. Here, no insertion, deletion, or stop codons were observed in any sequences. Molecular phylogenetic clustering was undertaken for grouping closely related species or well-identified species enduring on the same clade or sister clades. Phylogenetic analysis revealed identical phylogenetic relationships among the species. Particularly, in the case of hairtail mitochondrial COI sequences, three major clades were obtained (Figure 3a). The first clade, comprising Korean, Japanese, and Chinese hairtail fish samples, formed four clusters. In addition, sequence alignment revealed more similar sequences in hairtail species. From DNA barcoding carried out on the basis of sequencing of a standardized region of the

DOI: 10.1021/acs.jafc.5b01469
J. Agric. Food Chem. 2015, 63, 5548−5556

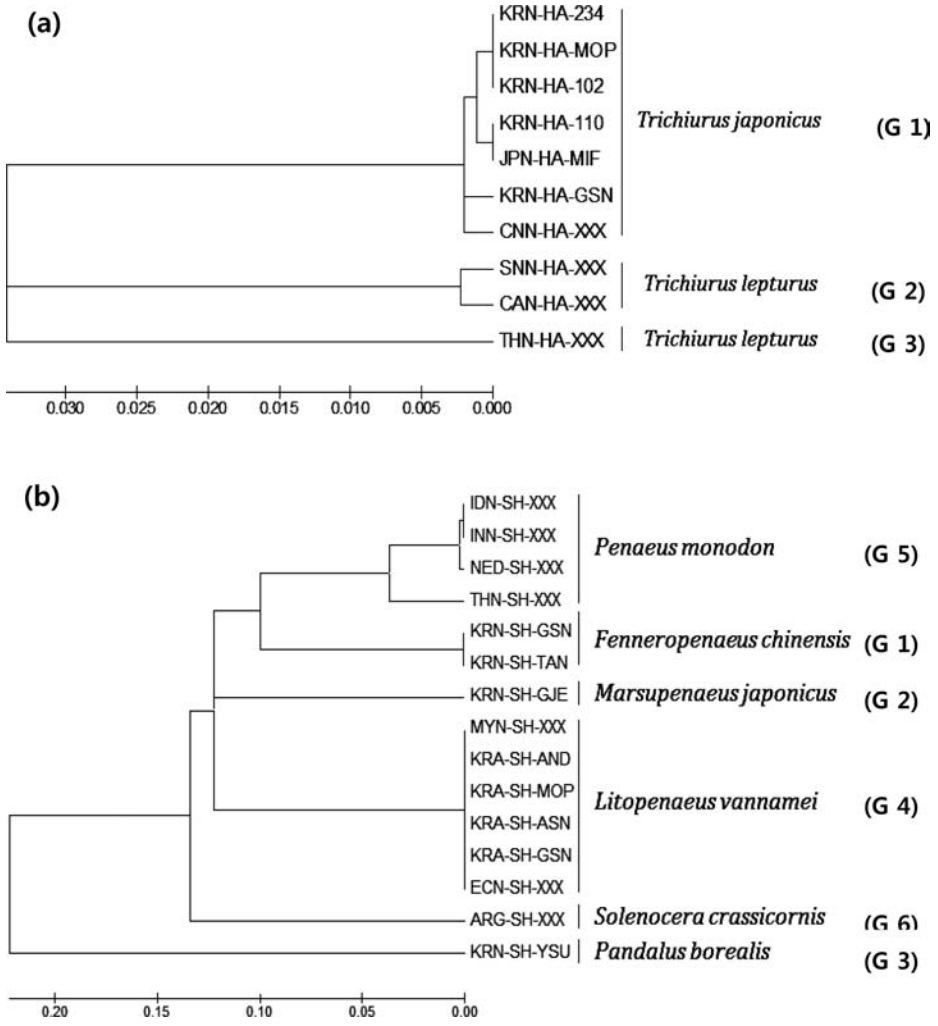

Figure 3. Evolutionary relationships of (a) 10 taxa (linearized) of hairtail fish and (b) 15 taxa (linearized) of shrimp, and neighbor-joining (NJ) phylogenetic trees inferred from DNA sequences of mitochondrial gene COI.

cytochrome *c* oxidase I (COI) gene, the hairtail fish samples from Korea, Japan, and China were identified as *Trichiurus japonicus*, while the hairtail fish samples from Senegal, Canada, and Thailand were identified as *Trichiurus lepturus*.

Phylogenetic analysis of the shrimp samples also displayed identical phylogenetic relationships among the species. Six major clades were obtained from shrimp mitochondrial COI sequences of samples collected from various locations (Figure 3b). In the first clade (G5), two clusters were formed by the species collected from India, Indonesia, and The Netherlands as well as samples from Thailand. The second clade (G1) comprised natural shrimp from Korea. The third phylogenetic clade (G2) (Guje, Korea) was closely related to the second and forth clades. The fourth clade (G4) was formed by the group of shrimp from Korea, Malaysia, and Ecuador. The fifth (G6) and sixth clades (G3) comprised samples from Argentina and Yeosu Korea.

On the basis of DNA barcoding of COI, the shrimp samples from Yeosu and Guje (Korea) were identified as *Pandalus borealis* and *Marsupenaeus japonicus*, respectively, while samples from Gunsan and Taean (Korea) were identified as *Fenneropenaeus chinensis*. The Korean aquacultured shrimp as well as the Malaysian and Ecuadorian shrimp were identified as *Litopenaeus vannamei*, whereas the samples from India, The Netherlands, Thailand, and Indonesia belonged to *Penaeus monodon*. The shrimp from Argentina were *Solenocera crassicornis*.

■ DISCUSSION

Fishery products are considered as a staple food in Korea. In fact, the per capita seafood consumption here is considerably larger than average. In the fish industry, regulations regarding labeling, product quality, and origin have been tightened. Therefore, it is mandatory that fish processing firms must produce proof of origin and traceability. This makes it absolutely essential to formulate an effective traceability system to track fish products throughout the supply chain (harvesting, processing, and marketing). However, identification becomes a rather daunting task in the case of analogous (closely related) fish species. Proper identification of hairtail fishes and their origin is relatively difficult due to their morphological similarities. In Japan, consumer preference for Tachiuo and Tenjikutachi vary with regard to organoleptic characteristics; however, fresh ones are mainly used for raw consumption (sashimi).[12] In addition, most of the morphological characteristicss that are used for species identification (such as head pattern, presence or absence of pectoral fin, dorsal and anal fin ray counts) are lost upon processing; thus, identification of fish species in processed fillets is extremely difficult. This also holds

DOI: 10.1021/acs.jafc.5b01469
J. Agric. Food Chem. 2015, 63, 5548−5556

true for fish sold in parts. Further, shrimp too are often difficult to identify owing to their phenotypic similarities and to the frequent removal of external carapace during processing.[12]

Analytical techniques based on measurement of stable isotopes and DNA-based techniques are suitable for identification of closely related species (both fresh and processed).[5,12] Consequently, they are powerful tools for the detection of counterfeit. This investigation focused on the utility of carbon and nitrogen isotopes, as well as molecular markers, for deriving the geographic origin of hairtail fish and shrimp.

The present study validates the fact that isotopic values of fish vary depending upon the species[13] (Figure 1a). Strikingly distinct δ^{13}C and δ^{15}N values were obtained for hairtail fish of different origin. From a stable δ^{13}C and δ^{15}N biplot for hairtail fish, they could be classified into three groups, wherein samples 1−5, 7, and 10 fell under one group, samples 6 and 9 formed another group, and the remaining sample 8 formed an individual group. Isotopic values (both δ^{13}C and δ^{15}N) of the hairtail fish collected from various sites in Korea differed significantly [$p < 0.05$, Tukey's honestly significant difference (HSD)] from their international counterparts. Moreover, the δ^{13}C and δ^{15}N values of hairtail fish collected from the Asian nations (Korea, China, Japan, and Thailand) were distinctly different ($p < 0.05$, Tukey's HSD) from their Canadian and Senegalese counterparts. Differences in the hydrogeomorphic characteristics between the basins lead to differences in the C signatures of fish.[14] Reports suggest that, in the case of C, isotope ratios of consumers are usually similar to isotope ratios of their diets.[15] On this accord, Gómez-Requeni et al.[16] described that marine fish diets (comprising macroalgae and phytoplankton, which form the lower trophic levels of the marine food web) are isotopically heavier due to their source of carbon (dissolved inorganic carbon pool, δ^{13}C ∼ 0‰), as compared with terrestrial plant photosynthesis from atmospheric CO_2 (δ^{13}C ∼ −7.8‰). Tanaka et al.[17] reported higher (more enriched) δ^{13}C and δ^{15}N ratios in the case of anchovy sampled from inshore habitats as compared to offshore habitats (where lower depleted values were obtained for both). They surmised that higher carbon isotope ratios (in the inshore regions) may reflect a carbon source from benthic primary producers in addition to phytoplankton.[17] Precipitation and temperature variations can also affect the stable isotope ratio of organisms.[18] With respect to the global ocean environment, there is generally a positive correlation between decreasing seawater temperature and lighter δ^{13}C values of particulate organic matter (POM) in cases of high latitude.[19] The geographically classified δ^{13}C values of hairtail fish obtained in this investigation could be attributed to differences in seawater temperature.

The remarkable similarity obtained between the δ^{13}C values of hairtail fish samples collected from various sites within Korea confirm that these values could essentially help traceability of hairtail fish originating from Korea. Nominal variations encountered in the δ^{13}C values of the samples within Korea (in the present investigation) could probably be due to their seasonal and dietary preferences. On this stand, Schell et al.[20] attributed oscillation in carbon isotope ratios of bowhead whale (*Balaene mysticetus*) to seasonal fluctuations of the variety of different zooplankton in the area of study. According to France,[21] the δ^{13}C values of offshore fishes ranged from −20 to −11, while sea grass fishes showed a greater range from −20 to −8. This occurred because a substantial proportion of the fishes collected from sea grass meadows ultimately got their carbon from the plankton-based food web, rather than the benthic-based food web. There are pronounced δ^{13}C isotopic differences between different species. For example, *Geukensia demissa* mussels and *Crassostrea virginica* oysters are isotopically more similar to plankton than to *Spartina* cordgrass, whereas *Orchelimum fidicinium* katydids and *Littorina irrorata* sea snails are isotopically similar to *Spartina*.[22] The δ^{13}C values of the Chinese and Thai hairtail fish (−17.90 and −17.80‰) obtained in this study concurred with the δ^{13}C value of POM reported from China (−19‰).[23] However, the δ^{13}C values obtained for Chinese and Thai samples differed remarkably from those of Canadian, Japanese, and Senegalese hairtail fish (Figure 1a).

During dietary assimilation, nitrogen is more strongly fractionated than carbon, with a mean trophic increase of ∼3‰, as compared to ∼1‰ in carbon.[24] Nitrogen undergoes a 2−4‰ increase in heavier isotope enrichment with each trophic level; it can serve as a tool for determining dietary shifts.[25] Variations in the nitrogen stable isotope ratio reflect not only differences in the trophic level of prey species but also variations in the baseline level of food webs.[17] Measurement of δ^{15}N values allows determination of trophic relationships in complex food webs. These values generally vary with species, diet, and stress. Although the most important application of nitrogen stable isotopes is to determine the trophic level of a species, these values could also indicate an important seasonal change in the marine nitrogen cycle. High anthropogenic inputs on estuarine food webs have also been reported to result in ^{15}N-enriched stable isotope ratios in the community inhabiting the Westerschelde (The Netherlands).[26] In this study, the δ^{15}N value of hairtail fish from China was similar to the report by Wan et al.,[27] who reported δ^{15}N values of 12.9‰ for Chinese hairtail fish. The δ^{15}N values of Japanese hairtail fish in this study were similar to the reports of Shibata et al.[28] and Takai and Mishima;[29] they reported δ^{15}N values of ∼17.5‰ and 17.8‰, respectively, for hairtail fish. Nevertheless, the δ^{13}C and δ^{15}N values of hairtail fish species *T. lepturus* from Brazil (−16.8‰ and 15 ‰)[30] differed from the values obtained for the samples analyzed in this study.

The δ^{13}C values of Korean hairtail fish (−17.16‰ to −18.03‰) were proximate to the δ^{13}C values of POM (−20.2‰) reported by Lee et al.[31] in Korea. The δ^{13}C and δ^{15}N values for Chinese (−17.90‰ and 12.14‰), Japanese (−15.43‰ and 17.36‰), and Thai (−17.80‰ and 11.16‰) hairtail fish were also in compliance with the δ^{13}C and δ^{15}N values of POM in Chinese (−19‰ and 9.8‰), Japanese (−19‰ and 7.3‰), and Thai seawater (−23‰ to −17‰ and 5.7‰ to 8.4 ‰).[23,32,33]

The stable δ^{13}C and δ^{15}N biplot for shrimp classified them into six groups. Here, G1 comprised samples 6 and 7. G2 comprised sample 5, while G3 comprised sample 8. G4 comprised samples 1−4, 12, and 15, while G5 comprised samples 9−11 as well as 14. The remaining sample 13 formed G6 (Figure 2b). Distinct δ^{13}C and δ^{15}N of various species of shrimp collected from different countries showed significant differences. The δ^{13}C and δ^{15}N signatures are known to vary from species to species: for example, the respective δ^{13}C and δ^{15}N values for *Farfantepenaeus indicus* are −16.87‰ and 10.7‰; for *Farfantepenaeus merguiensis*, −16.26‰ and 9.71‰; for *Farfantepenaeus notialis*, −17.15‰ and 9.26‰; for *L. vannamei*, −11.72‰ and 8.9‰; for *P. borealis*, −18.07‰ and 10.78‰; for *P. monodon*, −18.90‰ and 9.66‰; and for *Pleoticus muelleri*, −16.12‰ and 16.86‰).[6] In addition, these

DOI: 10.1021/acs.jafc.5b01469
J. Agric. Food Chem. 2015, 63, 5548−5556

stable isotopic values also vary with the country of origin; for example, the shrimp *P. borealis* from Greenland has different $\delta^{13}C$ and $\delta^{15}N$ values (−18.1‰ and 10.3‰)[34] compared to shrimp from the Mid-Atlantic Ridge (−10.9‰ and 7‰) and Japan (−14.7‰ and 15.8‰).[29,35] Ortea and Gallardo[6] reported unique $\delta^{13}C$ and $\delta^{15}N$ values of shrimp species from Argentina (16.12‰ and 16.86‰), North Atlantic (−18.07‰ and 10.78‰), Mozambique (−16.77‰ and 10.55‰), Nigeria (−17.87‰ and 10.34‰), and Senegal (−16.80‰ and 8.72‰). These reported $\delta^{13}C$ and $\delta^{15}N$ values of various shrimp species from different countries differed significantly from the values of shrimp obtained in our study. This reveals that stable isotopic values could positively indicate the origin of shrimp.

In the present investigation, shrimp from the natural environment showed higher isotopic variability and their mean $\delta^{13}C$ and $\delta^{15}N$ values were statistically different than the farmed ones. The $\delta^{13}C$ values of Korean aquacultured shrimp ranged from −20.23‰ to −21.72‰, whereas the $\delta^{13}C$ values of Korean natural shrimp ranged from −14.02‰ to −18.69‰. In contrast, the $\delta^{15}N$ values of aquacultured shrimp (5.60−6.20‰) were lower than the $\delta^{15}N$ values (11.53−12.28‰) of natural shrimp; this was probably because of differences in diet. Gamboa-Delgado et al.[36] also reported distinct $\delta^{13}C$ and $\delta^{15}N$ values for the shrimp species *L. vannamei* from Ecuador (open sea −16.6‰ and 9.76‰, estuary −18.32‰ and 4.25‰, semi-intensively farmed −19.86‰ and 6.02‰) and *L. vannamei* from the Gulf of Mexico (open sea −17.14‰ and 12.19‰, estuary −18.59‰ and 5.88‰, semi-intensively farmed −19.69‰ and 8.32‰, intensively farmed −21.56‰ and 8.69‰). Aquaculture feeds are frequently formulated with varying dietary levels of plant meals. These plant meals are mostly derived from terrestrial plants having C3 photosynthesis and are less enriched in ^{13}C (mean $\delta^{13}C_{VPDB}$ = −29‰) as compared to C4 plants (mean $\delta^{13}C_{VPDB}$ = −13‰).[36] Also, the C3 plants are less enriched as compared to several marine-derived ingredients such as fish meal ($\delta^{13}C_{VPDB}$ = −17‰). For example, some shrimp feeds used in Mexico have $\delta^{13}C_{VPDB}$ values ranging from −23.6‰ to −22.3‰ and $\delta^{15}N$ values ranging from 5.8‰ to 9.7‰; the $\delta^{13}C_{VPDB}$ values of feed are transferred to the farmed organisms, thereby causing contrasting $\delta^{13}C$ values (more isotopically depleted) as compared to the wild type.[36] Thus, stable isotopic values could help distinguish farmed and natural shrimp.

The unique isotopic values obtained for hairtail fish and shrimp obtained from various regions, viewed through the present study, assert that $\delta^{13}C$ and $\delta^{15}N$ could be used as discriminatory variables to distinguish between various geographic origins.

Although several schematic reports and strategies have been outlined to identify fishery products, determine their geographical origin, and preserve domestic fishery products without adulteration, most of the techniques involved discuss animal meat (beef and lamb). But this study brings forth the applicability of isotopic analysis in the traceability of marine fish products. The identified differences in isotopic patterns of samples from various origins obtained in this study elucidate the potential of stable isotope analysis for validation of geographic authenticity. However, the identified patterns will have to be confirmed in another detailed study comprising a larger number of samples from certified origins and over a time course. Nevertheless, it is a fact that isotopic ratios of fishes are bound to be more stable as compared to other smaller life forms such as phytoplankton. But it is essential to carry out climate, seasonal, and age- and diet-related studies on isotopic ratios in order to derive a better equation. This study positively suggests the reliability of using isotopic ratios of fishes for determining geographic traceability.

DNA barcoding favorably assists identification of seafood species and determination of its origin (i.e., traceability). Here, three gene regions—relatively slowly evolving genes cytochrome *b* (cyt *b*, specified in 72.5% of responses), cytochrome oxidase I (COI, 27.5%), and 16S rDNA (16S, 17.5%)[37]—are proved to be the markers of choice. The COI or *COX1* region demonstrates a good discriminatory power in the identification of fish species. Ward et al.[38] showed 98% of probed marine fish and 93% of freshwater fish were successfully identified from the *COX1* region. DNA barcoding based on partial sequence information from the COI gene has been widely used for species identification of fishes.[39] It provides a paradigm for the development of simple, inexpensive PCR-based assays that can clearly differentiate virtually all fish species. Our results also confirm that the COI barcode is an effective marker for identification of hairtail fish and shrimp; it outright segregates the organisms based on their country of origin (Figure 3).

Investigation of the COI of hairtail fish helped separate the species based on their country of origin. The samples of hairtail fish collected from Korea, Japan, and China were identified as *T. japonicus*, while the samples from Senegal, Canada, and Thailand were identified as *T. lepturus*. Tzeng and Chiu[40] identified 12 cutlass fish species using mitochondrial cytochrome *c* oxidase subunit I (COI) gene of each species and the standard barcode sequences. They illustrated high interspecific differences between the samples of fish, together with high within-species similarities (>95% similarity). These authors explained the degree of interspecific differences was due to the age of phylogenetic origin, and thus, barcode differences were genetically comprehensive.[39] In our study, a clear segregation of patterns of COI was also observed on the basis of geographic origin and species. This validates the effectiveness of the DNA barcoding technique in identifying shrimp as well as hairtail fish and also ascertains its reliability in determining geographic origin. Thus, this particular procedure could be put to use for conservative fisheries management as well as governmental scrutiny of fishery products.

In order to improve the reliability of seafood authentication via statistical analysis, stable isotope ratios as well as the DNA barcoding were combined in this study. The stable isotope data were processed by use of the LDA model. On the basis of this LDA, the hairtail fish (Figure 2a) were segregated into groups. Group 1 consisted of two subgroups; the first clustered together the Korean (with 96% similarity within them) and the Chinese hairtail fish (which had 0% similarity within them), while the second subgroup comprised the Japanese hairtail fish (with 100% match within themselves). LDA of the stable isotope data categorized group 2 as the Senegal (with 60% similarity within them) and Canadian hairtail fish (with 0% similarity within themselves).

The LDA of stable isotopes in shrimp helped subcategorize the Group 4 shrimp into two subgroups. The first subgroup comprised Korean aquacultured shrimp (100% similarity within themselves; 100% accuracy) and natural Ecuador shrimp (0% similarity within themselves), while the second subgroup comprised Malaysian shrimp (having 100% similar profiles). LDA of stable isotopes helped subcategorize group 5 into four subgroups based on the country of origin, wherein the

DOI: 10.1021/acs.jafc.5b01469
J. Agric. Food Chem. 2015, 63, 5548−5556

subgroups comprising Indonesian, Indian, Dutch, and Thai shrimp were identified accurately (as they had 80%, 100%, 100%, and 80% similarity, respectively). Group 6 comprised Argentinian shrimp; the members demonstrated 100% similarity between themselves.

Nowadays, consumers are increasingly interested in validating the reliability of fish products and determining if it is of natural (wild) origin. Nevertheless, international fishery and seafood trade are bound by food safety regulations, which insist on traceability (through all stages of production, processing, and distribution). These regulations aim to promote resource sustainability, quality distinction, and product safety. In fact, the FAO have outlined several analytical approaches for species authentication (NMR analysis, isotope analysis, fingerprints, electrophoresis, peptide mapping, immunological techniques analyzing proteins, target recognition, and blot hybridization), verification of geographic origin (NMR analysis, stable isotope and trace element analysis), and determining if the product is wild or cultivated. This study evaluates two of these techniques: stable isotope analysis and COI sequencing. Both these analyses harmonized in authenticating and tracing the origin of hairtail fish and shrimp from various origins.

Stable isotopes (δ^{13}C and δ^{15}N) and COI gene sequencing have been used to authenticate, discriminate, and trace various food products. But their use in determining the provenance of fish has not been prevalent. On the basis of the present study, we can summarize that COI sequencing helped identify the species of hairtail fish and shrimp. The LDA of stable isotopes helped in further categorizing each species into subgroups, based on the country of origin. Moreover, the stable isotope values distinctly differentiated natural and farmed shrimp from the same country. Thus, this study on hairtail fish and shrimp validates the utility of these tools in identifying these species and establishing their geographical origin.

AUTHOR INFORMATION

Corresponding Author

*Phone +82 31 400 5536; fax +82 31 416 6173; e-mail shinkh@hanyang.ac.kr.

Author Contributions

⊥H.K. and K.S.K. contributed equally.

Funding

This research was a part of the project "Development of integrated techniques for the identification of seafood origin using chemical index and genetic information", funded by the Ministry of Oceans and Fisheries, Korea. It was also supported by a grant from the National Research Foundation (No. 2012012617).

Notes

The authors declare no competing financial interest.

REFERENCES

(1) Ortea, I.; Pascoal, A.; Cañas, B.; Gallardo, J. M.; Barros-Velázquez, J.; Calo-Mata, P. Food authentication of commercially relevant shrimp species: From classical methods to foodomics. *Electrophoresis* **2012**, *33*, 2201−2211.

(2) Tacon, A. G. J.; Metian, M. Fish matters: Importance of aquatic foods in human nutrition and global food supply. *Rev. Fish Sci.* **2013**, *21*, 22−38.

(3) http://www.dpi.nsw.gov.au/__data/assets/pdf_file/0008/375902/Hairtail-and-Frostfish.pdf (accessed on July 27, 2014).

(4) Pascoal, A.; Barros-Velásquez, J.; Ortea, I.; Cepeda, A.; Gallardo, J. M.; Calo-Mata, P. Molecular identification of the black tiger shrimp (*Panaeus monodon*), the white leg shrimp (*Litopenaeus vannamei*) and the Indian white shrimp (*Fenneropenaeus indicus*) by PCR targeted to the 16S rRNA mtDNA. *Food Chem.* **2011**, *125*, 1457−1561.

(5) Lavilla, I.; Costas-Rodríguez, M.; Bendicho, C. Authentication of fishery products. *Comp. Anal. Chem.* **2013**, *60*, 657−717.

(6) Ortea, I.; Gallardo, J. M. Investigation of production method, geographical origin and species authentication in commercially relevant shrimps using stable isotope ratio and/or multi-element analyses combined with chemometrics: An exploratory analysis. *Food Chem.* **2015**, *170*, 145−153.

(7) Kim, H.; Suresh Kumar, K.; Shin, K. H. Applicability of stable C and N isotope analysis in inferring the geographical origin and authentication of commercial fishes (mackerel, yellow croaker and pollock). *Food Chem.* **2015**, *172*, 523−527.

(8) Tamura, K.; Dudley, J.; Nei, M.; Kumar, S. MEGA4: Molecular Evolutionary Genetics Analysis (MEGA) software version 4.0. *Mol. Biol. Evol.* **2007**, *24*, 1596−1599 DOI: 10.1093/molbev/msm092.

(9) Saitou, N.; Nei, M. The neighbor-joining method: A new method for reconstructing phylogenetic trees. *Mol. Biol. Evol.* **1987**, *4*, 406−425.

(10) Takezaki, N.; Rzhetsky, A.; Nei, M. Phylogenetic test of the molecular clock and linearized trees. *Mol. Biol. Evol.* **2004**, *12*, 823−833.

(11) Tamura, K.; Nei, M.; Kumar, S. Prospects for inferring very large phylogenies by using the neighbor-joining method. *Proc. Natl. Acad. Sci. U.S.A.* **2004**, *101*, 11030−11035.

(12) Chakraborty, A.; Aranishi, F.; Iwatsuki, Y. Polymerase chain reaction and restriction fragment length polymorphism analysis for species identification of hairtail fish fillets from supermarkets in Japan. *Fish. Sci. (Tokyo, Jpn.)* **2007**, *73*, 197−201.

(13) Kurle, C. M.; Sinclair, E. H.; Edwards, A. E.; Gudmundson, C. J. Temporal and spatial variation in the δ^{15}N and δ^{13}C values of fish and squid from Alaskan waters. *Mar Biol.* **2011**, *158*, 2389−2404.

(14) Arcagni, M.; Campbell, L. M.; Arribére, M. A.; Kyser, K.; Klassen, K.; Casaux, R.; Miserendino, M. L.; Guevara, S. R. Food web structure in a double-basin ultra-oligotrophic lake in Northwest Patagonia, Argentina, using carbon and nitrogen stable isotopes. *Limnologica* **2013**, *43*, 131−142.

(15) DeNiro, M. J.; Epstein, S. Influence of diet on the distribution of carbon isotopes in animals. *Geochim. Cosmochim. Acta* **1978**, *42*, 495−506.

(16) Gómez-Requeni, P.; Mingarro, M.; Calduch-Giner, J. A.; Médale, F.; Martin, S. A. M.; Houlihan, D. F.; Kaushik, S.; Pérez-Sánchez, J. Protein growth performance, amino acid utilisation and somatotropic axis responsiveness to fish meal replacement by plant protein sources in gilthead sea bream (*Sparus aurata*). *Aquaculture* **2004**, *232*, 493−510.

(17) Tanaka, H.; Ohshimo, S.; Takagi, N.; Ichimaru, T. Investigation of the geographical origin and migration of anchovy *Engraulis japonicus* in Tachibana Bay, Japan: A stable isotope approach. *Fish Res.* **2010**, *102*, 217−220.

(18) Suh, Y. J.; Shin, K. H. Size-related and seasonal diet of the Manila clam (*Ruditapes philippinarum*), as determined using dual stable isotopes. *Estuarine, Coastal Shelf Sci.* **2013**, *135*, 94−105.

(19) Libes, S. M. *An Introduction to Marine Biogeochemistry*; John Wiley and Sons: New York, 1992.

(20) Schell, D. M.; Saupe, S. M.; Haubenstock, N. Bowhead whale (*Balaena mysticetus*) growth and feeding as estimated by δ^{13}C techniques. *Mar. Biol.* **1989**, *103*, 433−443.

(21) France, R. L. Carbon-13 enrichment in benthic compared to planktonic algae: foodweb implications. *Mar. Ecol.: Prog. Ser.* **1995**, *124*, 307−312.

(22) Peterson, B.; Howarth, R. W. Sulfur, carbon and nitrogen isotopes used to trace organic matter flow in the salt-marsh estuaries of Sapelo Island, Georgia. *Limnol. Oceanogr.* **1987**, *32*, 1195−1213.

(23) Wu, Y.; Zhang, J.; Li, D. J.; Wei, H.; Lu, R. X. Isotope variability of particulate organic matter at the PN section in the East China Sea. *Biogeochemistry* **2003**, *65*, 31−49.

DOI: 10.1021/acs.jafc.5b01469
J. Agric. Food Chem. 2015, 63, 5548−5556

(24) MacKenzie, K. M.; Palmer, M. R.; Moore, A.; Ibbotson, A. T.; Beaumont, W. R. C.; Poulter, D. J. S.; Trueman, C. L. Locations of marine animals revealed by carbon isotopes. *Sci. Rep.* **2011**, *1*, 1−6.
(25) Hobson, K. A. Applying isotopic methods to tracking animal movements. In *Tracking Animal Migration Using Stable Isotopes*; Hobson, K. A., Wassenaar, L. I., Eds.; Academic Press: London, 2008; pp 45−78.
(26) Riera, P.; Stal, L. J.; Nieuwenhuize, J. Heavy δ^{15}N in intertidal benthic algae and invertebrates in the Scheldt Estuary (The Netherlands): Effect of river nitrogen inputs. *Estuarine, Coastal Shelf Sci.* **2000**, *51*, 365−372.
(27) Wan, R.; Wu, Y.; Huang, L.; Zhang, J.; Gao, L.; Wang, N. Fatty acids and stable isotopes of a marine ecosystem: study on the Japanese anchovy (*Engraulis japonicus*) food web in the Yellow Sea. *Deep Sea Res. Part II* **2010**, *57*, 1047−1057.
(28) Shibata, J. Y.; Matsumoto, K.; Hamaoka, H.; Sogabe, A.; Nanko, T.; Kunihiro, T.; Onishi, H.; Omori, K. Contribution of pelagic and benthic grazing and detritus food chains to the coastal ecosystem of the Western Seto Inland Sea: A stable isotope and Bayesian mixing model analysis approach. In *Interdisciplinary Studies on Environmental Chemistry—Environmental Pollution and Ecotoxicology*; Kawaguchi, M., Misaki, K., Sato, H., Yokokawa, T., Itai, T., Nguyen, T. M., Ono, J., Tanabe, S., Eds.; Terrapub: Tokyo, 2012; pp 427−435.
(29) Takai, N.; Mishima, Y. Carbon sources for demersal fish in the western Seto Inland Sea, Japan, examined by δ^{13}C and δ^{15}N analyses. *Limnol. Oceanogr.* **2002**, *47*, 730−741.
(30) Di Beneditto, A. P. M.; Bittar, V. T.; de Rezende, C. E.; Camargo, P. B.; Kehrig, H. A. Mercury and stable isotopes (δ^{15}N and δ^{13}C) as tracers during the ontogeny of *Trichiurus lepturus*. *Neotrop. Ichthyol.* **2013**, *11*, 211−216.
(31) Lee, Y.; Hur, J.; Shin, K. H. Characterization and source identification of organic matter in view of land uses and heavy rainfall in Lake Shihwa, Korea. *Mar. Pollut. Bull.* **2014**, *84*, 322−329.
(32) Yokoyama, H.; Tamaki, A.; Harada, K.; Shimoda, K.; Koyama, K.; Ishihi, Y. Variability of diet-tissue isotopic fractionation in estuarine macrobenthos. *Mar. Ecol.: Prog. Ser.* **2005**, *296*, 115−128.
(33) Kuramoto, T.; Minagawa, M. Stable carbon and nitrogen isotopic characterization of organic matter in a mangrove ecosystem on the south-western coast of Thailand. *J. Oceanogr.* **2001**, *57*, 421−431.
(34) Rigét, F.; Møller, P.; Dietz, R.; Nielsen, T. G.; Asmund, G.; Strand, J.; Larsen, M. M.; Hobson, K. A. Transfer of mercury in the marine food web of West Greenland. *J. Environ. Monit.* **2007**, *9*, 877−783.
(35) Vereshchaka, A. L.; Vinogradov, G. M.; Dalton, A. Y. L. S.; Dehairs, F. Carbon and nitrogen isotopic composition of the fauna from the Broken Spur hydrothermal vent field. *Mar. Biol.* **2000**, *136*, 11−17.
(36) Gamboa-Delgado, J.; Molina-Poveda, C.; Godínez-Siordia, D. E.; Villarreal-Cavazos, D.; Ricque-Marie, D.; Cruz-Suárez, L. E. Application of stable isotope analysis to differentiate shrimp extracted by industrial fishing or produced through aquaculture practices. *Can. J. Fish Aquat. Sci.* **2014**, *71*, 1520−1528.
(37) Griffiths, A. M.; Sotelo, C. G.; Mendes, R.; Pérez-Martín, R. I.; Schröder, U.; Shorten, M.; Silva, H. A.; Verrez-Bagnis, V.; Mariani, S. Current methods for seafood authenticity testing in Europe: Is there a need for harmonisation? *Food Control* **2014**, *45*, 95−100.
(38) Ward, R. D.; Hanner, R.; Hebert, P. D. N. The campaign to DNA barcode all fishes, FISH-BOL. *J. Fish Biol.* **2009**, *74*, 329−356.
(39) Spies, I. B.; Gaichas, S.; Stevenson, D. E.; Orr, J. W.; Canino, M. F. DNA based identification of Alaska skates (*Amblyraja*, *Bathyraja* and *Raja*: Rajidae) using cytochrome c oxidase submit (COI) variation. *J. Fish Biol.* **2006**, *69(B)*, 283−292.
(40) Tzeng, C. H.; Chiu, T. S. DNA barcode-based identification of commercially caught cutlassfishes (Family: Trichiuridae) with a phylogenetic assessment. *Fish Res.* **2012**, *127−128*, 176−181.

DOI: 10.1021/acs.jafc.5b01469
J. Agric. Food Chem. 2015, 63, 5548−5556

formed, as well as to investigate the extent of absorption and excretion, tissue distribution and metabolism.[21] Radio-LC-MS is an on-line analytical system that is composed of liquid chromatography (LC), ultraviolet absorbance detection (UV), radioactivity monitoring (RAM), and mass spectrometry (MS). This system, which combines the high separation ability of LC, the structural analysis of MS, and the high sensitivity and specificity of RAM, has become a unique scientific tool for the analysis of radiolabeled drugs.[22−24]

In the present study, the mass balance, metabolism, tissue distribution, and depletion of CYA were investigated in pigs, chickens, carp, and rats following oral administration of ^{3}[H]-CYA using high-performance liquid chromatography combined with radioactivity monitoring and IT/TOF mass spectrometry (LC-RAM-MS-IT-TOF). The comparative in vivo metabolic disposition and tissue depletion of CYA in pigs, chickens, carp, and rats in different organs, tissues, and fluids are reported for the first time. On the basis of these results, the main metabolites, the marker residue, and the target tissue of CYA in animals were identified. This study provides comprehensive information about the disposition and tissue depletion of CYA in animals, which will improve the food safety evaluation of CYA in food animals.

MATERIALS AND METHODS

Chemicals. CYA (≥98%) was synthesized by the Institute of Veterinary Pharmaceuticals of Huazhong Agricultural University (Wuhan, People's Republic of China). 4-[^{3}H]-*O*-nitroaniline ([^{3}H]-ONA) was provided by the Shanghai Institute of Applied Physics, Chinese Academy of Sciences. *O*-Nitroaniline (ONA, ≥99.0%), 10% Pd/C, NaOH, NaClO (5%), pyruvaldehyde dimethylacetal (PDA), and pyrrolidine were purchased from Sinopharm Chemical Reagent Co., Ltd., Shanghai, People's Republic of China. Benzofuroxan (BFO, 99.5%), 2-formylquinoxaline-1,4-dioxide dimethylacetal (FQDDA, 99.7%), and cyanoacetylhydrazine (99.7%) were provided by the Institute of Veterinary Pharmaceuticals (Wuhan, People's Republic of China). Monophase-S was purchased from PerkinElmer Life and Analytical Sciences. ULTIMA GOLD liquid scintillation cocktail and SOLVABLE were purchased from PerkinElmer. StopFlow AD liquid scintillation cocktail was purchased from Aim Research Co. (Hockessin, DE, USA). All chemicals were of reagent grade.

[^{3}H]-CYA was synthesized as previously described.[25] In brief, [^{3}H]-ONA was deoxidized with 2-propanol and NaClO at 25 °C with constant stirring for 2 h to give [^{3}H]-BFO. Next, [^{3}H]-BFO was reacted with PDA and pyrrolidine in an ice bath for 4 h followed by stirring for another 12 h at 17−20 °C and thereafter maintained at 4 °C for 1 h to give [^{3}H]-FQDDA. Finally, [^{3}H]-CYX was obtained by reacting [^{3}H]-FQDDA with cyanoacethlhydrazine in a solution of methanol and concentrated hydrochloric acid at 25 °C with constant stirring for 4 h. The radiochemical purity of the final labeled product was 99.2%. The specific activity of [^{3}H]-CYA was 1.13 mCi/mg by comparing the total radioactivity of 10 mg of [^{3}H]-CYA with the mass (10 mg). The radiochemical purity of [^{3}H]-CYA remained unchanged for 3 months in DMSO solution. A stock solution of [^{3}H]-CYA with a specific activity of 113 mCi/g was prepared 2 weeks before dosing and diluted with 1% aqueous carboxymethyl cellulose to obtain a final dosing suspension of 10 mg/mL with specific activity of 11.3 mCi/g for animal study. When the tritium label compound was used or analyzed during the whole study, the operator was protected with a respirator, gloves, and cottony working clothes to avoid direct contact with tritium.

Animals. Male and female pathogen-free Wistar rats (7 weeks, 200 ± 20 g) were purchased from the Hubei Experimental Animal Research Center (Wuhan, People's Republic of China). Healthy castrated crossbred (Duroc × Large white × Landrace) pigs (weight 15−20 kg) were purchased from the Livestock and Poultry Breeding Center of Hubei Province (Wuhan, People's Republic of China). Cobb 500 chickens (weight 1.0−1.5 kg) were purchased from Wuhan Chai Tai Co., Ltd. (Wuhan, People's Republic of China). Carp (weight 0.4−0.6 kg) were purchased from Wuhan Fish Breeding Farm (Wuhan, People's Republic of China). The animals were fed a basal diet without antimicrobial agents/compounds and acclimatized for 1 week before the experiment. The animals and fish were maintained under standard environmental conditions using the routine methods of animal husbandry and aquaculture. Pigs and broilers were housed singly in all-steel metabolism cages specifically designed for the separate collection of urine and feces in a temperature-controlled room (20 ± 2 °C) with a 12 h light/dark cycle. Carp were held separately in a standalone water tank in the same temperature-controlled room (20 ± 2 °C). Throughout the study period, feed was withheld approximately 12 h before through 4 h after drug administration, while water was available ad libitum. The experimental procedures involving the animals in this study were approved by the Animal Care Center, Hubei Academy of Medical Sciences. All of the in vivo experiments complied with the policy on the care and use of laboratory animals.

Feed. The feed used in this study was purchased from Wuhan Lvhong Bioscience and Technology Co., Ltd. (Wuhan, People's Republic of China). The feed formula was strictly in accordance with the recommended formula of the U.S. National Research Council. Premixed (5%; 3.0 g/kg CYA concentration) and complete feed (150 mg/kg CYA concentration) were initially prepared. The blank feed and the medicated feed were analyzed using the HPLC method described by Wu et al.[22] to determine the drug content. The results indicated that no quinoxaline compound was detected in the blank feed, and only CYA (150 ± 8 mg/kg feed, n = 9) was found in the medicated feed.

Mass Balance Study. Six rats (three male and three female), six chickens, six carp, and four pigs were administered a single oral dose of [^{3}H]-CYA (11.3 mCi/g) by gavage at 20 mg/kg bw (30 mg/kg bw for rats), respectively. Urine and feces samples were collected in preweighed dry ice cooled containers protected from light before dosing at intervals of 0−6, 6−12, and 12−24 h after dose administration and then daily until two consecutive samples from urine and feces had <1% of the total administered radioactivity. At the end of the collection period, the cages were rinsed with water followed by methanol. The cage washings were retained with the excreta. Seven days after the dose administration, all animals were anesthetized and killed, and the pigs were slaughtered using captive bolt stunning equipment and exsanguinated on the basis of guidelines provided by the American Veterinary Medical Association for euthanasia.[26] The samples were stored at −80 °C prior to analyses.

Aliquots of urine (0.2 mL) from the animals at each sampling time were mixed directly with 10 mL of liquid scintillation solution and assayed by liquid scintillation counting (LSC; TriCarb 2900, PerkinElmer Life and Analytical Sciences, Waltham, MA, USA). Aliquots of homogenized feces samples (0.2 g) were first digested with sodium hypochlorite solution (2 mL) for 2 h in a 55 °C water bath. The digested solution was cooled to room temperature and mixed with 0.1 M EDTA (0.2 mL) and 30% H_2O_2 (0.2 mL). The mixture was heated for 30 min in a 55 °C water bath for depigmentation. The efficiency of digestion was confirmed by the digestion of radiochemical standards (^{3}H-Spec-Chec; PerkinElmer Life and Analytical Sciences) for every 10−15 samples and was between 96% and 98%. A correction factor was used accordingly. All of the samples were prepared in 10 mL of scintillation fluid (Ultima Gold) and incubated at room temperature overnight in a dark environment prior to LCS analyses.

Duplicate samples were analyzed by liquid scintillation counting until a statistical error (2σ) of 0.5% was obtained, with a counting time of 5 min, together with representative blank samples. LSC was performed using a Packard Tri-Carb 2900 liquid scintillation analyzer with automatic quench correction using an external method (PerkinElmer Life and Analytical Sciences) to detect the retained [^{3}H] radioactivity.

Metabolism Study. Animals were dosed and sampled as in the mass balance study. In addition to the urine and feces, the blood and bile of the animals were sampled at 6, 12, 24, 48, 72, and 96 h.

DOI: 10.1021/acs.jafc.5b01745
J. Agric. Food Chem. 2015, 63, 5557−5569

Extraction of Radioactive Substances. Urine (2 mL), plasma (2 mL), and bile (1 mL) collected at intervals of 0−6, 6−12, or 12−24 h and then over 24 h periods up to 72 h after dosing were analyzed for each subject. The weight of each aliquot was 0.1% of the total fraction weight (0.25% for urine). Each sample was centrifuged at 4 °C for 5 min at 1500*g*. The supernatant was collected and purified with offline SPE on an Oasis HLB cartridge. The column was activated with methanol (6 mL) and water (6 mL) in sequence and dried by purging the air at a rate of 10 mL/min. Then, the supernatant was loaded onto the SPE column at a flow rate of 1 mL/min, followed by rinsing with 6 mL of water. The analytes were eluted with 6 mL of methanol at a flow rate of 1.0 mL/min. The eluent was evaporated to dryness under a stream of nitrogen at 40 °C. The residues were dissolved with 1 mL of the mobile phase and mixed for 30 s. A fraction of the mixture (0.2 mL) was transferred to a separate tube, and 10 mL of liquid scintillation solution was placed in the tube. The mixture was detected by LSC to quantify the extracted radioactivity. The extraction efficiency of the radioactive substance in the samples was calculated by comparing the extracted radioactivity with the total released radioactivity. The extraction efficiencies of the related compounds in the urine, plasma, and bile were 92.7%, 91.8% and 90.6%, respectively. A portion of the mixture (0.3 mL) was centrifuged at 2000*g* for 5 min. The supernatant was prepared for LC MS ion trap time of flight (LC-MS-IT-TOF) analysis.

Aliquots of the homogenized feces (2 g) were mixed with 5 mL of acetonitrile, sonicated for 2 min, and centrifuged at 4 °C for 5 min at 1500*g*/min. The extraction solution (1) was collected. The residual material was extracted with another 5 mL of ethyl acetate, followed by sonication and centrifugation. The extraction solution (2) was combined with solution (1). Then, the residual precipitate was suspended in 5 mL of NaOH solution (3 mol/L). The mixtures were hydrolyzed in a water bath at 95−100 °C for 30−40 min and then cooled to room temperature. Concentrated HCl (2 mL) was added to the alkaline hydrolysate. The aqueous phase was extracted twice with 10 mL of ethyl acetate by sonicating for 2 min followed by centrifuging for 5 min at 1500*g*/min. The resulting organic phase was combined with solutions (1) and (2). The mixed solutions were evaporated to dryness under a stream of nitrogen in 40−45 °C water baths. The residue was dissolved in 20% MeOH/water (0.5 mL) and analyzed by LC-MS-IT-TOF and a νARC 2.0 Radio-LC assay system with Detector RS232 (AIM Research Co.).

Separation and Identification of Radioactive Substances. The HPLC system (Shimadzu) was equipped with a solvent delivery pump (LC-20AD), an autosampler (SIL-20AC), a DGU-20A3 degasser, a photodiode array detector (PDA; SPD-CY20A), a communication base module (CBM-20A), and a column oven (CTO-20AC). The separation was performed on a Hypersil Gold column (100−2.1 mm i.d.; particle size 5 μm) using a gradient elution consisting of mobile phase A (0.1% formic acid in water) and mobile phase B (acetonitrile). The gradient was as follows: 0−5 min, 8% B; 5−18 min, a linear gradient to 28% B; 18−23 min, a linear gradient to 90% B; 23−26 min, 90% B; 26−26.1 min, a linear gradient back to 8% B. The injection volume was 20 μL, the flow rate was 0.2 mL/min, and PDA detection was performed from 200 to 400 nm. The sample chamber in the autosampler was maintained at 4 °C, while the column was set to 40 °C. The whole analysis lasted for 30 min. Radiochemical detection was performed using the νARC 2.0 Radio-LC system Detector RS232 equipped with a 750 μL detector cell. The instrument was operated in the dynamic liquid scintillation flow mode, and the HPLC eluent was mixed 1/5 with Stop Flow AD scintillation liquid. After radiochemical detection, the total effluent from the detector was transferred directly to the hybrid IT/TOF mass spectrometer without splitting.

The IT-TOF-MS instrument was equipped with an electrospray ionization (ESI) source operated in the positive ionization mode. Mass spectroscopic analyses were carried out on a full-scan mass spectrometer with a mass range of 100−500 Da. Liquid nitrogen was used as the nebulizing gas at a flow rate of 1.5 L/min. The interface and detector voltages were set at 4.5 and 1.6 kV, respectively. The curved desorption line (CDL) and heat block temperatures were both 200 °C. The MS2 spectra were produced by collision-induced dissociation (CID) of the selected precursor ions with Ar as the collision gas. The ion accumulation time and relative collision energy were set at 50 ms and 50%, respectively. Data acquisition and processing were carried out using LCMS solution software version 3.41, supplied with the instrument. The mass numbers corresponding to the particular elemental compositions were also calculated by the formula predictor and generated more than one formula proposed by the software. Therefore, an accuracy error threshold of 5 mDa was set as the limit for the calculation of possible elemental compositions. Hydrogen/deuterium (H/D) exchange was performed to identify the active hydrogen atoms. The extracted samples were dissolved in tritiated water and separated using the mobile phase consisting of acetonitrile and tritiated water.

Distribution and Depletion Study. Each of 30 rats, chickens, and carp and 24 pigs was administered a [^{3}H]-CYA suspension at a single dose of 12 mg/kg bw (rats 16 mg/kg bw) by oral gavage for 7 consecutive days. Four pigs and six rats, chickens, and carp were randomly selected to be slaughtered by exsanguination at 0.25, 1, 3, 7, and 14 days after dosing, respectively. Before slaughter, each animal was anesthetized following the guidelines provided by the American Veterinary Medical Association (AVMA, 2001). The blood, bile, organs, and tissues, including the livers, kidneys, gastrointestinal tracts, hearts, spleens, lungs, muscles, fat, skin, brains, gonads, adrenal glands, and bladders, were collected separately and stored at −80 °C until analysis. Another six rats, pigs, and chickens were administered solvent (1% aqueous carboxymethyl cellulose) at exactly the same amount as the dosed animals. At each time point, one animal was slaughtered and sampled as described for the dosed animals to obtain the blank samples. The weight of each sample was recorded.

All of the samples were homogenized separately and then divided into two parts. One part was prepared and detected by LSC as described in Mass Balance Study for the determination of the total radioactivity. The other part was prepared and analyzed as described in Mass Balance Study for metabolite analysis. The blood and bile were prepared using the same procedure as described for the urine, while organs and tissues were prepared as described for the feces, respectively.

Validation of the Quantitation Methods. All of the samples were quantitated by LSC. The limit of quantitation (LOQ) of LSC was detected by evaluating a series of [^{3}H]-CYA working solutions with different radioactivities; the lowest concentration resulting in a deviation of 5% was designated as the LOQ. The LOQ of [^{3}H]-CYA in the different samples was 10 μg/kg. Two microliters of [^{3}H]-CYA stock solution were diluted 10^9 times with methanol, and then, 20 μL, 40 and 80 μL of diluted [^{3}H]-CYA was added to the blank pig urine, feces, blood and tissues, respectively. The samples were prepared as described above, followed by the determination of the radioactivity of the extracted samples with LSC and LC/LSC. All radioassays were performed in triplicate. On comparison of the extracted radioactivity with the total radioactivity of the diluted solution, the accuracy of [^{3}H]-CYA quantitation in the different samples ranged from 82.6% to 105.2%, with a relative standard deviation of less than 10%. Nine diluted [^{3}H]-CYA stock solutions with different radioactivities were detected by LSC and LC/LSC, and each sample was measured in triplicate. The correlation equation between LSC and LC/LSC was determined to be $y = 4.4579x - 155.87$ ($r = 0.9997$). To calculate the content of volatile radioactivity, such as [^{3}H]-H_2O, another duplicate set of samples was freeze-dried and reconstituted in water ("dry samples") prior to analysis. All radioassays were performed in triplicate. The ^{3}H water exchange in the excretions was between 0.2% and 2.5%.

Data Analysis. The concentrations of radioactive substances were quantitated by reversed-phase HPLC with radiochemical detection. The linear relationship between the cpm (X), which was obtained from the νARC detector, and dpm (Y), which was obtained from the Tricarb 2900TR, was $y = 4.45x - 156$ ($r = 0.9997$). The total residue concentrations and concentrations of the main metabolites were subjected to logarithmic transformation and regressed with the time. The depletion equation and the half-life ($t_{1/2}$) of the total residues and main metabolites were described as $C = C_0e^{-kt}$ and $t_{1/2} = 0.693/k$,

DOI: 10.1021/acs.jafc.5b01745
J. Agric. Food Chem. 2015, 63, 5557−5569

Table 1. Recovery of Total Radioactivity in the Urine and Feces of Pigs, Chickens, Carp, and Rats after Administration of [^{3}H]-CYA at 20 mg/kg bw (30 mg/kg bw for Rats)

	pig		chicken	rat		carp
time (days)	urine (%)	feces (%)	feces + urine (%)	urine (%)	feces (%)	feces + urine (%)
0.5	15.6 ± 2.1	18.3 ± 2.0	34.3 ± 1.1	7.5 ± 2.4	23.8 ± 3.0	43.3 ± 3.2
1	11.3 ± 1.4	28.3 ± 1.7	57.2 ± 1.0	18.8 ± 1.5	40.5 ± 3.7	21.1 ± 1.4
3	16.1 ± 0.3	4.6 ± 0.03	1.5 ± 0.5	1.0 ± 0.2	2.6 ± 0.01	27.8 ± 2.5
12	3.65 ± 0.02	0.9 ± 0.1	2.2 ± 0.8	0.9 ± 0.01	0.3 ± 0.1	5.1 ± 0.2
sum	44.3 ± 3.1	51.6 ± 4.0	95.2 ± 0.8	28.3 ± 5.42	66.2 ± 2.03	97.4 ± 3.6
cage rinse	0.2 ± 0.01		0.2 ± 0.01	0.3 ± 0.05		-
total recovery	96.1 ± 3.8		95.3 ± 0.7	94.8 ± 0.5		97.4 ± 3.7

respectively. The percentages of the individual metabolites within the total residues were calculated as follows:

$$X = \mathrm{AUC_M}/\mathrm{AUC_T} \times 100\%$$

X is the percentage of individual radioactive substances within the total radioactive residues. $\mathrm{AUC_M}$ is the area under the curve of the individual radioactive substances in the specific samples. $\mathrm{AUC_T}$ is the area under the curve of the total radioactive residues in the specific samples.

RESULTS

Radioactivity Excretion. Following a single oral dose of [^{3}H]-CYA, CYA was rapidly excreted in all of the studied animals (Table 1). Nearly 64.4−81.5% of the radioactivity was excreted within 24 h, and more than 90% of the radioactivity was excreted within 72 h in all species after dosing, indicating that CYA could be excreted rapidly by the animals. The mean cumulative recovery of excretion, including that of the cage washings within 12 days, ranged from 95.9% to 98%, indicating that the excretions of CYA in the four animal species were quite similar. For pigs and rats, 51.6% and 66.2% of the total radioactivity was excreted from the feces, respectively, whereas 44.3% and 28.35% was detected in the urine, indicating that the major elimination route of CYA was via feces.

Mass Spectrometric Identification of Radioactive Substances (Metabolites). In addition to the intact parent drug, 15 radioactive peaks in total were characterized by HPLC-νARC and identified by LC-MS-IT-TOF in rats, pigs, chickens, and carp. The detailed LC-MS-MS characterization of seven metabolites, including Cy1, Cy2, Cy4, Cy5, Cy10, Cy13, and Cy14, has been reported previously.[11] Eight new in vivo metabolites of CYA were first characterized as follows. The proposed metabolite structures and supporting spectral data for all matrices are shown in Table 2.

Metabolite Cy3. This radioactive peak indicated that it was a main metabolite in the urine at 6 h. The protonated molecular ion was at m/z 232 (M + H), suggesting that Cy3 is a glycine conjugate of Cy6. The predominant fragment ion at m/z 186 was formed by the loss of a carboxyl from the ion at m/z 232. The fragment ion at m/z 159 was formed by the cleavage of the amide bond and loss of CO to form m/z 131. Exchangeable hydrogen atoms are usually bound to N, O, or S atoms in functional groups, such as OH, NH, NH_2, and COOH. Cy3 has two exchangeable atoms. The m/z of Cy3 should be 235 after H/D exchange. The results were consistent with this speculation. Therefore, Cy3 was identified as 2-(quinoxaline-2-carboxamido) acetic acid (Figure 2).

Metabolite Cy6. The protonated molecular ion was at m/z 175 (M + H), which generated m/z 158 and 129. The retention time and fragment ions were identical with those of synthesized Cy6. The mass spectra of the standard were consistent with the corresponding compounds in the samples. Based on these observations, Cy6 was identified as quinoxaline-2-carboxyl (Figure 2).

Metabolites Cy7 and Cy8. Both compounds were minor metabolites of CYA and were detected in urine but not in tissues. Both metabolites showed a protonated molecular ion at m/z 256, which was consistent with Cy2 and Cy10. However, the MS-MS fragment ions of Cy7 and Cy8 were not identical with those of Cy2 and Cy10. The main fragment ions of Cy7 at m/z 189, 172, and 160 were all 17 Da higher than the fragment ions of Cy2 at m/z 172, 155, and 143. Therefore, it was assumed that Cy7 was hydroxylated on the quinoxaline ring. The fragment ion at m/z 131 was found in the MS-MS of Cy8, suggesting that hydroxyl was not on the quinoxaline ring. Furthermore, Cy7 was eluted before Cy2, near the retention time of Cy16 (only found in vitro). Cy8 was eluted behind Cy2, near the retention time of Cy1. The polarity of Cy16 was higher than that of Cy2 due to the hydroxyl on the quinoxaline ring. The results of H/D exchange showed that the m/z values of Cy7 and Cy8 were 261 and 260, respectively. Cy7 has four exchangeable hydrogen atoms, while Cy8 has three exchangeable hydrogen atoms. Hence, Cy7 was identified as 3-hydroxy-2-formylcyanoacetyl hydrazone quinoxaline, and Cy8 was identified as N'-hydroxy-2-formylcyanoacetyl hydrazone quinoxaline (Figure 2).

Metabolite Cy9. The protonated molecular ion was at m/z 258, 2 Da higher than m/z 256, suggesting that Cy9 may be a hydrogenated product of CYA monoxide. The fragment ion at m/z 174 was formed by the loss of $C_3H_3N_2O$ from that at m/z 258. The loss of CO from the ion at m/z 174 generated an ion at m/z 146. In parallel, the ion at m/z 258 could lose $C_3H_4N_3O$ to give m/z 159, and the loss of CO from the ion at m/z 159 yielded m/z 131, suggesting that the hydrogen atoms were not on the quindoxaline ring, according to the identification of Cy4. Cy9 has four exchangeable hydrogen atoms. The m/z value of Cy9 should be 263 after H/D exchange. The detected results were consistent with this speculation. Therefore, Cy9 was identified as N'-(quinoxaline-N1-oxygen-2-methyl)cyanide acetylhydrazine (Figure 2).

Metabolite Cy11. The protonated molecular ion was at m/z 231. According to the accurate mass measurement, Cy11 was formed by the cleavage of the cyano group after the deoxidation of CYA. The fragment ion at m/z 173 was formed by the loss of $C_2H_2O_2$ from m/z 231. The fragment ion at m/z 231 lost $C_2H_5NO_2$ to form m/z 156. Because Cy11 has one hydrogen exchangeable atom, the m/z of Cy11 should be 233 after H/D exchange. The detected results were consistent with this speculation. Therefore, Cy11 was identified as 2-formylacetylhydrazine-quinoxaline N1-oxide (Figure 2).

DOI: 10.1021/acs.jafc.5b01745
J. Agric. Food Chem. 2015, 63, 5557−5569

Table 2. Metabolite Information of CYA in Pigs, Chickens, Carp, and Rats

Compound	Chemical Name	[M+H] (Da)	Elemental composition	Proposed structure	Major fragment ions
Cy0	2-formyl cyano acetyl hydrazone-quinoxaline N^1,N^4-dioxide	272	$C_{12}H_{10}N_5O_3^+$	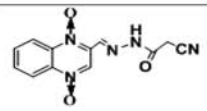	238,225,198,187,174,170,163,146,143,131,116
Cy1	2-formyl cyano acetyl hydrazine-quinoxaline	240	$C_{12}H_{10}N_5O^+$	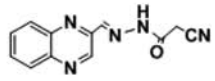	199,173,156,143
Cy2	2-formyl cyano acetyl hydrazine-quinoxaline-N1 -oxide	256	$C_{12}H_{10}N_5O_2^+$	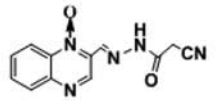	239,215,189,172,171,155,144,143,131,129,116,104,102
Cy3	2-(quinoxaline-2-carboxamido)acetic acid	232	$C_{11}H_{10}N_3O_3^+$	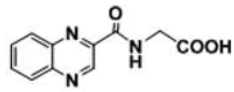	186,159,131
Cy4	N'(quinoceline-2-methyl) cyanide acetyl hydrazine	242	$C_{12}H_{12}N_5O^+$	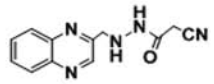	225,158,131
Cy5	2-hydroxy methyl-quinoxaline	161	$C_9H_9N_2O^+$	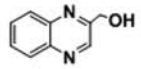	143,132
Cy6	Quinoxaline-2-carboxylic acid	175	$C_9H_7N_2O_2^+$	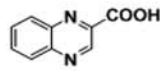	157,129
Cy7	3-hydroxy-2-formyl cyano acetyl hydrazone-quinoxaline	256	$C_{12}H_{10}N_5O_2^+$	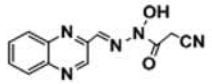	189,172,160
Cy8	N'-Hydroxy-2-formyl cyano acetyl hydrazone-quinoxaline	256	$C_{12}H_{10}N_5O_2^+$	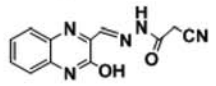	189,172,160,131,
Cy9	N'-(quinoxaline-N1- oxygen-2-methyl)-cyanide acetyl hydrazine	258	$C_{12}H_{12}N_5O_2^+$	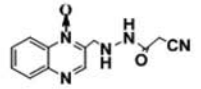	174,159,146,131
Cy10	2-formyl cyano acetyl hydrazine-quinoxaline-N4 -oxide	256	$C_{12}H_{10}N_5O_2^+$	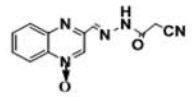	215,189,172,171,155,143,129,117,102
Cy11	2-formyl acetyl hydrazine-quindoxaline-N1-oxide	231	$C_{11}H_{11}N_4O_2^+$	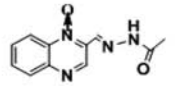	173,156,146
Cy12	2-hydroxymethyl-3-hydroxy quindoxaline	177	$C_9H_9N_2O_2^+$	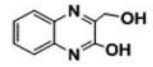	159
Cy13	2-formyl hydrazone-quinoxaline N1,N4-dioxide	205	$C_9H_9N_4O_2^+$	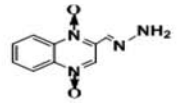	176,159
Cy14	2-formyl hydrazone-quinoxaline N1-oxide	189	$C_9H_9N_4O^+$	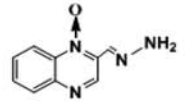	172,144,117
Cy15	N'-(quinoxaline evil morpholine-2-methyl)- acetyl hydrazine	217	$C_{11}H_{13}N_4O^+$	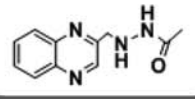	171,144

Metabolite Cy12. The protonated molecular ion was at m/z 177, 16 Da higher than Cy5. There was only one fragment ion at m/z 159, 16 Da higher than m/z 143. The characteristic ions were at m/z 143 and 131, indicating that the hydroxy group was not on the quinoxaline ring. Moreover, the retention time of Cy12 was before that of Cy5, suggesting that the polarity of Cy12 was higher than that of Cy5. Cy12 has two exchangeable hydrogen atoms. The result of H/D exchange showed that the

DOI: 10.1021/acs.jafc.5b01745
J. Agric. Food Chem. 2015, 63, 5557−5569

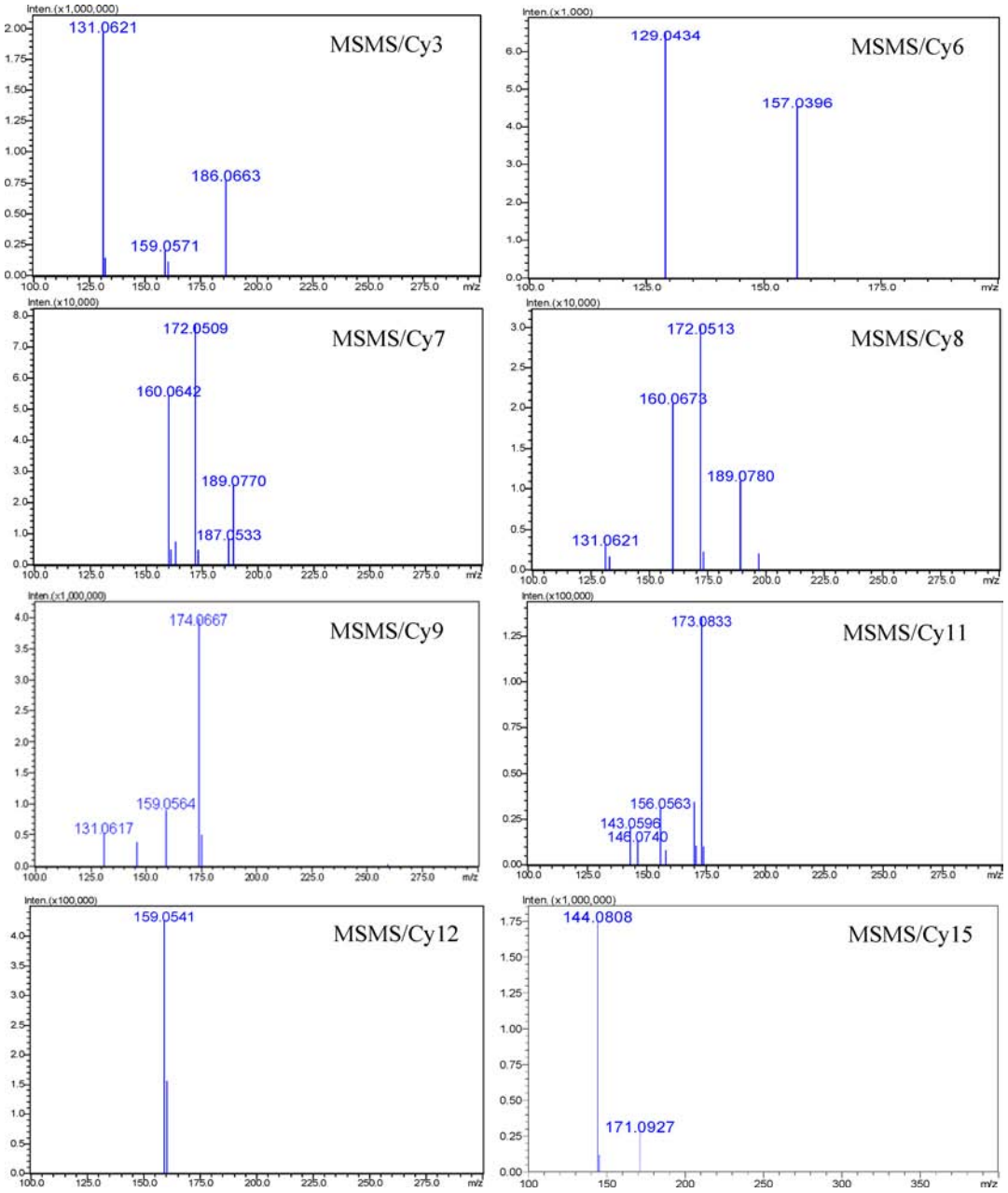

Figure 2. Accurate MS2 spectra of Cy3, Cy6, Cy7, Cy8, Cy9, Cy11, Cy12, and Cy15.

m/*z* value of Cy12 was 180. Hence, Cy12 was identified as 2-hydroxymethyl-3-hydroxyquinoxaline (Figure 2)., and the retention time and mass fragmentation pattern were consistent with those of the synthesized standard.

Metabolite Cy15. The protonated molecular ion was at *m*/*z* 217, 14 Da less than Cy11, suggesting that one oxygen atom was removed from Cy11 and two hydrogen atoms were added to the side chain. The fragmentation ion at *m*/*z* 171 was obtained by the loss of 46 Da from the ion at *m*/*z* 217. Then, the ion at *m*/*z* 144 was formed through the loss of CHN from the ion at *m*/*z* 171. Cy15 has two exchangeable hydrogen atoms. The result of H/D exchange showed that the *m*/*z* value of Cy15 was 220. Therefore, Cy15 was identified as *N*′-(quinoxaline-morpholine-2-methyl)acetyl hydrazine (Figure 2).

Five predominant metabolite standards of CYA were also synthesized and matched the metabolites (Cy1, Cy2, Cy4, Cy10, and Cy12) in the tissues and bodily fluids on the basis of their retention times and mass fragmentation patterns.

Metabolic Profile of CYA in Different Species. Eight metabolites were identified in rats (Table 3). No parent drug could be detected in the urine at any sampling time point, while six metabolites were detected at 12 h after dosing, of which Cy4 and Cy9 represented 29.89% and 32.25%, respectively. Only Cy1 was detected at 48 h, and no metabolites were detected thereafter. The parent drug and seven metabolites were detected in the feces at 12 and 24 h postdosing. Only Cy1 and Cy6 were detected over the 48−72 h time period. No parent drug was detected in the plasma, even at 6 h, but five metabolites could be detected instead.

Thirteen metabolites were observed in pigs (Table 3). The parent drug (Cy0) and 13 metabolites were detected in the urine from 6 to 12 h postdosing, with Cy1, Cy4, and Cy9 being the largest three metabolites, accounting for 11.77%, 26.10%,

DOI: 10.1021/acs.jafc.5b01745
J. Agric. Food Chem. 2015, 63, 5557−5569

Table 3. Summary of Cyadox Metabolites Detected in Extra, Plasma, and Bile of Rats, Pigs, Chickens, and Carp[a]

	rat			pig				chicken			carp		
	urine	feces	plasma	urine	feces	plasma	bile	extra	plasma	bile	extra	plasma	bile
Cy0	ND	√	ND	√	√	ND	ND	√	ND	√	√	ND	√
Cy1	√	√	√	√	√	√	√	√	ND	√	ND	√	√
Cy2	ND	√	ND	√	√	√	√	√	√	√	√	√	√
Cy3	ND	ND	ND	√	√	√	√	ND	ND	ND	ND	ND	ND
Cy4	√	√	√	√	√	√	√	√	√	√	ND	ND	ND
Cy5	√	√	√	√	√	√	√	√	√	√	ND	√	√
Cy6	√	√	√	√	√	√	√	√	√	ND	ND	ND	ND
Cy7	ND	ND	ND	√	√	ND	√	√	ND	ND	ND	ND	ND
Cy8	ND	ND	ND	√	√	ND	√	ND	ND	ND	ND	ND	ND
Cy9	√	ND	ND	√	√	√	√	ND	ND	ND	ND	ND	ND
Cy10	ND	ND	ND	√	ND	ND	ND	ND	ND	√	ND	ND	ND
Cy11	√	√	√	√	√	√	√	ND	ND	√	ND	ND	ND
Cy12	ND	ND	ND	√	ND	√	√	ND	ND	ND	ND	ND	ND
Cy13	ND	ND	ND	√	ND	√	√	ND	ND	√	√	ND	ND
Cy14	ND	ND	ND	ND	ND	√	√	ND	ND	ND	ND	ND	ND
Cy15	ND	√	ND	ND	ND	ND	ND	√	ND	ND	ND	ND	ND

[a]Legend: √, detected; ND: not detected.

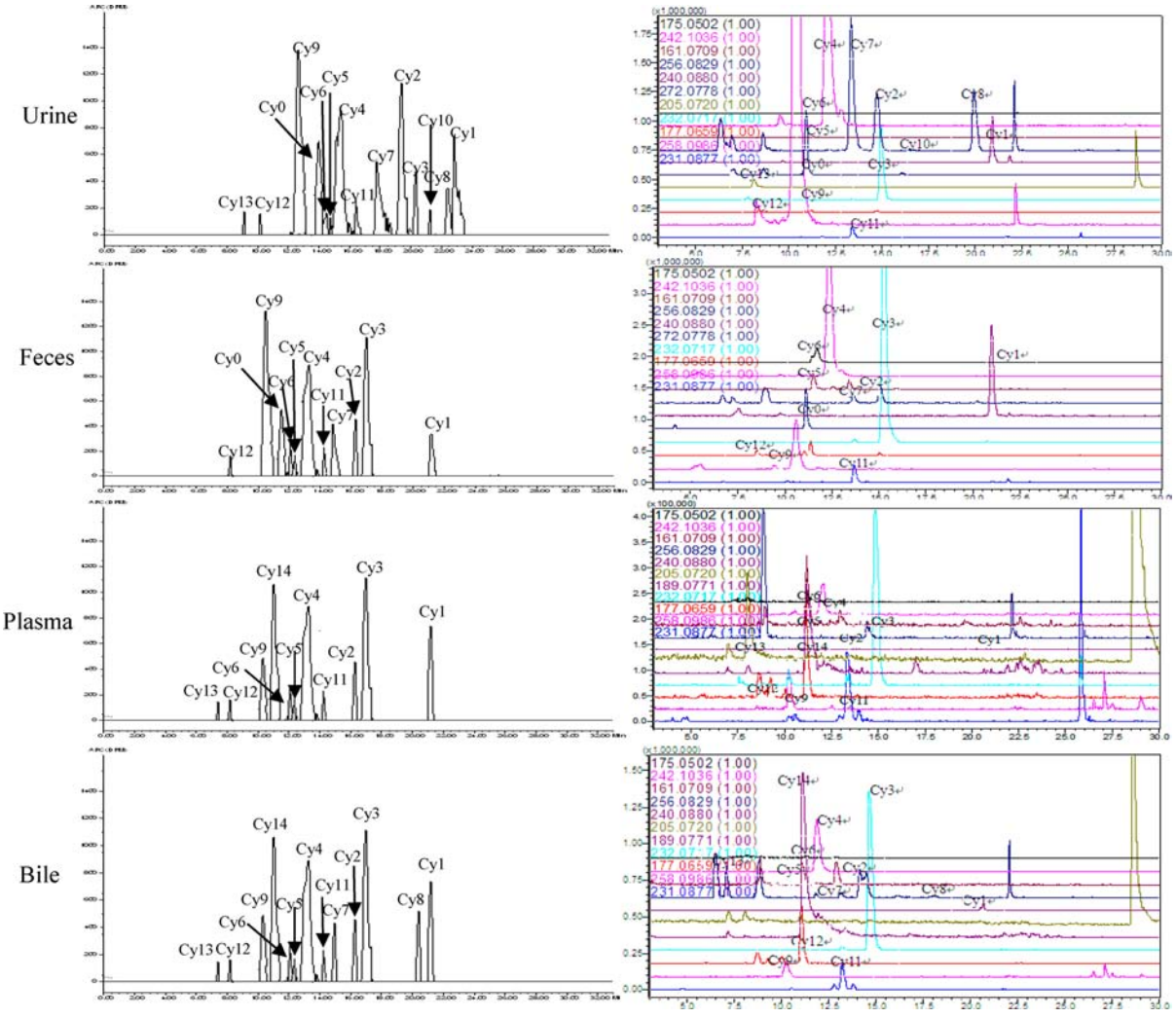

Figure 3. Radioactive chromatography and accurate EIC of CYA and its metabolites in urine, feces, plasma, and bile of pigs after a single oral dose of [^{3}H]-CYA at 20 mg/kg bw.

and 19.78% of the total radioactivity in the urine, respectively. At 24 h, the parent drug and 12 metabolites were still detectable, while only 6 metabolites (Cy1, Cy2, Cy3, Cy12, and Cy9) could be found at 48 h, and Cy1 was the only metabolite

DOI: 10.1021/acs.jafc.5b01745
J. Agric. Food Chem. 2015, 63, 5557−5569

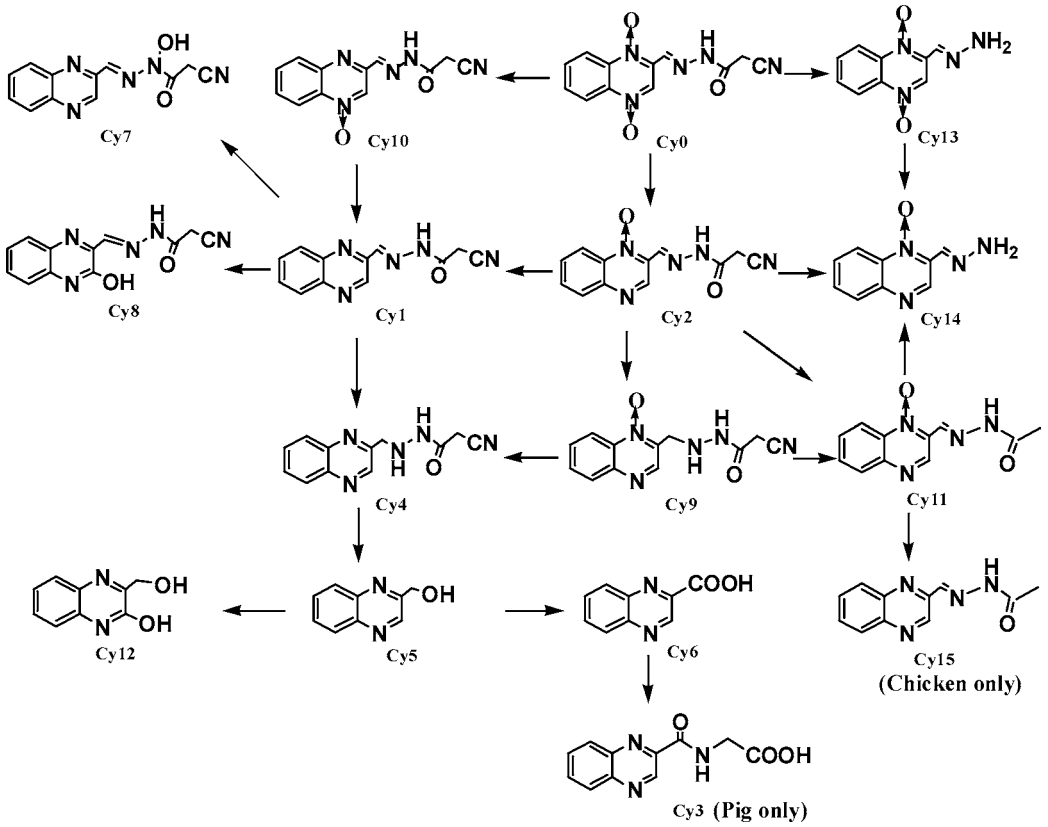

Figure 4. Proposed metabolic pathway of CYA in animals.

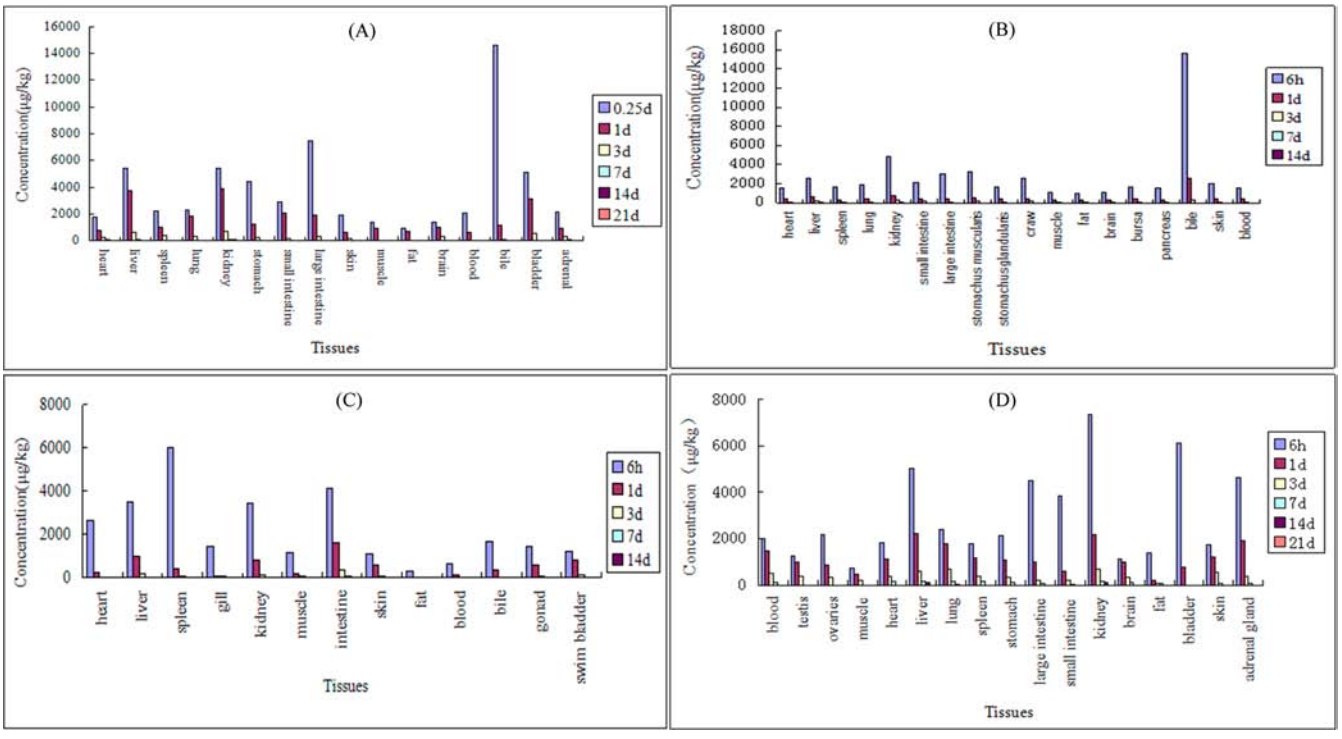

Figure 5. Distribution of [^{3}H]-CYA in pigs (A), chickens (B), carp (C), and rats (D).

detected in the urine up to 72 h. In the feces, the parent drug and 11 metabolites were detected from 0 to 24 h after administration. The amounts of Cy0, Cy1, Cy3, Cy4, and Cy9 were higher than those of the other metabolites. At 48 h, Cy7, Cy8, and Cy11 were undetectable. Thirteen metabolites were found in the bile at 6 h postfinal dosing. At 24 h, Cy7, Cy8, and Cy12 were not detected. At 72 h, no metabolite was characterized in the bile. Eleven metabolites were identified in the blood at 6 h postdosing, but no parent drug was observed (Figure 3).

DOI: 10.1021/acs.jafc.5b01745
J. Agric. Food Chem. 2015, 63, 5557−5569

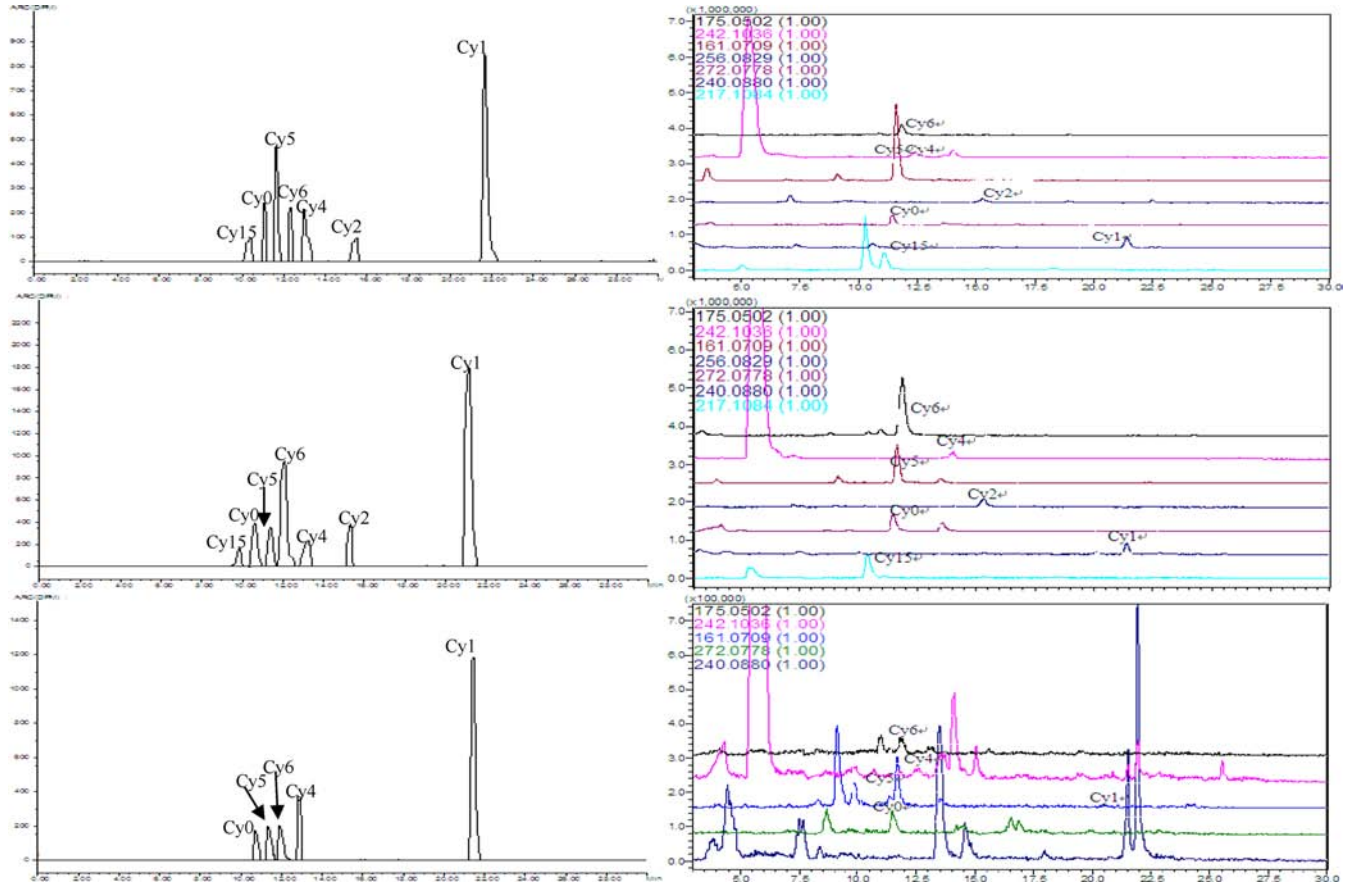

Figure 6. Radioactive chromatography and accurate EIC of CYA and its metabolites in liver, kidney, and muscle of chickens after a single oral dose of [^{3}H]-CYA at 20 mg/kg bw.

Ten metabolites were identified in chickens (Table 3). The parent drug and seven metabolites were detected in the feces at 6 h postdosing, of which Cy0, Cy1, and Cy6 were the main metabolites, with ratios of 29.63%, 23.48%, and 11.49%, respectively. Four metabolites (Cy1, Cy2, Cy5, and Cy6) and the parent drug were found in the feces at 24 h, and Cy0 and Cy1 represented 39.83% and 31.08%, respectively. Only the parent drug and Cy1, Cy2, and Cy6 were detected at 48 h. In the bile, the parent drug and seven metabolites were detected at 12 h postdosing, and Cy13 was not detected in the feces. The parent drug and Cy1, Cy2, and Cy5 were still detectable at 48 h, while only Cy2 and Cy5 were found at 72 h. Four metabolites were identified in the blood at 6 h postdosing.

Four metabolites were identified in carp (Table 3). The parent drug and two metabolites were found in the excreta at 12 h postdosing, and only Cy13 was detected at 24 h. The parent drug and four metabolites were detected in the bile at 6 h, but only Cy0 and Cy2 were found at 24 h. No metabolites were found after 24 h. Three metabolites were detected in the blood at 6 h postdosing.

CYA was metabolized more extensively in pigs than in rats, chickens, and carp because the most metabolites were observed in pigs, and nearly all of the metabolites found in rats, chickens, and carp were observed in pigs, except for Cy15, which was only detected in chickens. Moreover, Cy3 was only observed in pigs and was not observed in the other three species. Carp had a comparatively low metabolic ability for CYA, because only four metabolites were detected in carp during the whole observation. On the basis of the structures and persistence of the metabolites, the metabolic scheme of CYA in animals is proposed in Figure 4.

Tissue Distribution of the Total Radioactivity and Individual Metabolites. Similar trends in the distribution profiles were displayed among the four species (Figure 5). CYA-derived radioactivity underwent a rapid and wide distribution across the various tissues and fluids. Radioactivity was observed in all of the assayed tissues and organs and reached the highest concentration at the first collection time point (6 h) for all of the analyzed matrices after 7 consecutive days of oral exposure to [^{3}H]-CYA. The highest total radioactivity residue (TRR) levels were observed in the bile (14−15 mg/kg) in pigs and chickens and then in the kidneys, livers, and intestines, and the TRR level in the fat was found to be the lowest (less than 1.0 mg/kg) at the withdrawal time of 6 h in the four species. However, the TRR level in the bile of carp was at an extremely low concentration in comparison with that in pigs and chickens.

No parent drug was detected in all of the edible tissues of pigs and rats, even at the earliest withdrawal time of 6 h. The parent drug was detected in the edible tissues of chickens only at the early withdrawal time of 6 h, while it was observed in all of the detected tissues of carp, with a comparably long persistence time of 72 h in the livers and intestines. In rats, five metabolites were detected in the livers, kidneys, and muscles, and Cy11 was additionally detected in the livers at 6 h after final dosing. Cy1, Cy4, and Cy5 persisted for 72−168 h in the livers, kidneys, and muscles of rats, respectively. In pigs, eight metabolites were observed in the livers and kidneys at 6 and 24

DOI: 10.1021/acs.jafc.5b01745
J. Agric. Food Chem. 2015, 63, 5557−5569

Table 4. Percentage of CYA and Its Metabolites (AUC) to Total Residues (AUC) in Tissues of Pigs, Chickens, Carp, and Rats (n = 6)

animal	tissue	Cy0	Cy1	Cy2	Cy3	Cy4	Cy5	Cy6	Cy12
pig	liver	–	32.2	–	22.6	6.4	5.6	20.4	4.3
	kidney	–	33.6	–	18.9	10.4	–	16.1	3.3
	muscle	–	–	–	53.8	–	–	–	–
	fat	–	–	–	54.2	–	–	–	–
chicken	liver	–	60.7	–	–	–	19.1	6.1	–
	kidney	–	58.8	–	–	8.2	–	22.8	–
	muscle	–	64.1	–	–	–	–	–	–
carp	liver	29.0	47.8	–	–	–	7.2	–	–
	kidney	–	31.5	26.0	–	–	–	–	–
	muscle	–	–	–	–	59.6	–	–	–
	intestine	24.9	35.6	19.5		–	–	–	–
rat	liver	–	9.0	–	–	–	64.5	5.2	–
	kidney	–	15.6	–	–	51.6	–	14.3	–
	muscle	–	–	–	–	59.4	26.1	–	–

A dash (–) denotes that the compound depletes too rapidly for calculation of the AUC.

h following the last administration. Most of those metabolites were also detected in the muscle and fat, except for Cy2. Cy1 was the only metabolite that was detected both in the livers and kidneys at 168 h. In chickens, six metabolites were detected in the livers and kidneys (Figure 6), but Cy2 and Cy15 were only detected at 6 h postfinal dosing. Cy1, Cy4, Cy5, and Cy6 were detected in the muscles at 6–24 h, of which Cy1 was still detected at 72 h following the final dosing. In carp, five metabolites were found in the livers, kidneys, and intestines, and Cy6 was detected additionally in the kidneys and intestines at 6 h postfinal dosing. Cy1 and Cy2 persisted for 72–168 h in the livers, kidneys, and intestines.

On the basis of a comparison of the area under the concentration–time curve (AUC) of the metabolites and the TRR (Table 4), Cy1, Cy3, and Cy6 were found to be the predominant metabolites of CYA in the edible tissues of pigs because they composed 32.2–33.6%, 18.9–54.2%, and 16.1–20.4% of the metabolites, respectively. Cy1 was the most predominant metabolite of CYA in chickens, with an extremely high percentage of more than 60% of the total residues. The parent drug occupied 24.9–29.0% of the total residue in the livers and intestines of carp, and Cy1, Cy2, and Cy4 were found to be the main metabolites, with comparatively high percentages ranging from 19.5% to 59.6% in different tissues. In comparison with the food animals, Cy4 and Cy5 were present at an extremely high percentage of 51.6–64.5% in rats. Cy1 and Cy6 were also considered to be the main metabolites, with percentages of more than 10%.

Depletion of the Total Radioactivity and Main Metabolites. The TRR was observed in nearly all of the detected matrices of the four species within 3 days following the withdrawal of the drug and was still detected in most of the matrices of rats and several tissues in pigs, such as the livers, kidneys, hearts, spleens, lungs, and stomachs, at the seventh day following the last dosing. However, TRR was only detected in the livers and kidneys of chickens and carp, at concentrations ranging from 23 to 98 μg/kg at the seventh day after the last administration. In contrast, TRR was still detected in the livers and kidney of pigs and rats even at the 14th day following the last administration. Therefore, TRR underwent a comparatively rapid depletion in the tissues of chickens and carp, with $t_{1/2}$ ranging from 0.63 to 2.38 and from 0.51 to 1.24 days, respectively, in comparison with the slower depletion in the tissues of pigs, with $t_{1/2}$ ranging from 0.57 to 2.83 days. The $t_{1/2}$ values of the TRR in the livers of pigs, chickens, and rats were 2.39, 1.38, and 1.14 days, respectively, whereas the $t_{1/2}$ values of the TRR in the kidneys of pigs, chickens, and rats were 2.83, 2.38, and 0.59 days, respectively (Table 5). These results demonstrate that TRR persists the longest in the kidneys of pigs and chickens and in the livers of carp, suggesting that the

Table 5. Elimination of CYA and Its Main Metabolites in Edible Tissues of Animals

species	tissue	residue	elimination equation	$t_{1/2}$ (days)
pig	liver	TRR	$C = 7.07e^{0.29t}$	2.39
		Cy1	$C = 6.68e^{0.26t}$	2.64
		Cy3	$C = 7.63e^{0.87t}$	0.80
		Cy6	$C = 7.65e^{1.04t}$	0.67
	kidney	TRR	$C = 6.86e^{0.24t}$	2.83
		Cy1	$C = 6.57e^{0.26t}$	2.67
		Cy3	$C = 7.34e^{0.72t}$	0.96
		Cy6	$C = 7.34e^{0.86t}$	0.80
	muscle	TRR	$C = 7.80e^{1.31t}$	0.53
		Cy3	$C = 5.92e^{0.80t}$	0.87
	fat	TRR	$C = 7.41e^{1.21t}$	0.57
		Cy3	$C = 5.57e^{0.72t}$	0.97
chicken	liver	TRR	$C = 6.91e^{0.50t}$	1.38
		Cy1	$C = 6.38e^{0.45t}$	1.54
		Cy5	$C = 6.33e^{0.95t}$	0.73
		Cy6	$C = 4.60e^{0.57t}$	1.21
	kidney	TRR	$C = 6.56e^{0.29t}$	2.38
		Cy1	$C = 5.81e^{0.32t}$	2.17
		Cy4	$C = 5.37e^{0.65t}$	1.07
		Cy6	$C = 7.07e^{1.22t}$	0.57
	muscle	TRR	$C = 7.08e^{1.04t}$	0.67
		Cy1	$C = 6.48e^{0.94t}$	0.74
carp	liver	TRR	$C = 7.27e^{0.61t}$	1.14
		Cy0	$C = 7.16e^{1.15t}$	0.60
		Cy1	$C = 7.16e^{0.83t}$	0.83
		Cy5	$C = 5.68e^{1.12t}$	0.62
	kidney	TRR	$C = 8.21e^{1.17t}$	0.59
		Cy1	$C = 6.73e^{0.84t}$	0.83
		Cy2	$C = 6.72e^{0.99t}$	0.70
	muscle	TRR	$C = 6.79e^{0.84t}$	0.76
		Cy4	$C = 5.40e^{0.43t}$	1.62

DOI: 10.1021/acs.jafc.5b01745
J. Agric. Food Chem. 2015, 63, 5557–5569

residual target tissue of CYA in pigs and chickens could be the kidney and that in carp could be the liver. In comparison with the depletion of TRR in the kidneys of pigs and chickens, the $t_{1/2}$ values of Cy1 in the kidneys of pigs and chickens were 2.67 and 2.17 days, respectively, which were quite similar to that of TRR. Thus, Cy1 could be the marker residue of CYA in food-producing animals.

DISCUSSION

CYA was rapidly excreted in the four species, with more than 90% of the radioactivity recovered in the excreta of the animals within 3 days after dosing. CYA-related compounds were excreted more rapidly in chickens than in the other species, with a high recovery of 91.5% within 24 h due to the shorter intestinal tract, and was excreted relatively slowly in carp, with a low recovery of 64.3% within 24 h due to the lower basic metabolic rate of carp. CYA showed a rapid excretion similar to that of carbadox and olaquindox, the congeners of CYA, in animals, which are recovered at rates of nearly 91% and 95% from the excreta within 72 h when they are fed to pigs.[27,28] Fecal excretion was the primary route of CYA in animals, with a comparatively high percentage of 66.2% and 51.6% for rats and pigs, respectively.

Metabolite profile analysis indicated that CYA underwent extensive metabolic reactions in the four species. Overall, 8, 13, 10, and 7 metabolites were characterized in rats, pigs, chickens, and carp, respectively. Most of the metabolites remained consistent in the four species. The main metabolic pathway for CYA in animals involved a N−O reduction on the benzene ring, C═N cleavage on the side chain, followed by the hydroxylation and oxidation of the side chain, and C═N hydrogenation and hydrolysis of the amido linkage on the side chain. The N−O reduction and cleavage of the side chain were in accordance with the metabolism of quinoxalines in pigs, as previously reported,[27,29] while C═N hydrogenation is a novel and unique metabolic pathway of CYA in animals. On the basis of the in vitro metabolism, abundant deoxidation metabolites (Cy1, Cy2, and Cy10) and hydrolysis metabolites (Cy13 and Cy14) could be detected in both the liver microsomes and the intestines of pigs and chickens,[12,30] indicating that the liver and intestine are the main metabolic organs of CYA in animals. The cytochrome b5 reductase, cytochrome P450, and heme11 in the liver microsomes and the aldehyde oxidase and xanthine oxidase in the cytosol in the livers and intestines, were closely associated with the formation of deoxidation metabolites.[31−33] No hydrogenated metabolites were detected in the liver microsomes of animals, but Cy4, the main hydrogenation product of CYA, was detected in the colon microflora of pigs and chickens with an extremely high percentage of 51.5−73.7%,[12] indicating that the hydrogenation of CYA could be performed in the intestinal microflora. It has been shown that hydrogenase in the intestinal bacteria catalyzes the hydrogenation of the C═N double bond, and hydrazone dehydrogenase in the microflora ruptures the C═N bond of CYA to form 2-hydroxymethylquinoxaline, followed by the formation of carboxylic acid-2-quinoxaline (QCA).[34]

Although the main metabolic pathways of CYA in the four species were the same, several metabolites showed obvious different distribution patterns. First, Cy3 was detected only in pigs and was not observed in the other species. Cy3 is the glycine conjugation of QCA, and its production should be catalyzed by glycine *N*-acyltransferase. Early studies showed that the ratio and activity of glycine *N*-acyltransferase in different species were significantly different, and the glycine *N*-acyltransferase in the livers and bile of pigs were predominantly higher than in the other animals, whereas glycine conjugation was formed in rats only when rats were fed pectin.[35−37] Our results demonstrate that the formation of Cy3 in animals is closely associated with the amount and activity of glycine *N*-acyltransferase in animals. Second, Cy4 and Cy9 were detected in the urine of pigs and rats, with predominantly high percentages ranging from 19.78% to 29.89%, but only a comparatively small amount of Cy4 was detected in chicken feces, while these metabolites were not observed in any excreta or tissues of carp. Both Cy4 and Cy9 are produced by the hydrogenation of desoxycyadox, which is mainly catalyzed by hydrogenase. Hydrogenases are microbial enzymes that catalyze either $_{H}2$ oxidation or production.[38] A high ratio of these two metabolites in pigs and rats indicates that the amounts or activities of hydrogenases in pigs and rats could be higher than those in chickens and carp, which remains to be investigated further. Moreover, Cy4 and Cy9 were not observed in the liver microsomes of pigs and rats,[11] but a large quantity of these metabolites was detected in both the urine and bile, demonstrating that Cy4 and Cy9 could be produced in the intestine by bacteria and then absorbed into systemic circulation.

CYA may be widely distributed in various organs and tissues because the total radioactivity was observed in all of the detected tissues, suggesting that CYA might be effective for systemic infection. The concentrations of the total radioactivity in the pig intestines, livers, and kidneys were comparatively higher than those in the other tissues. The accumulation of CYA in the pig intestines contributes to its excellent antibacterial effects on the harmful microflora in the pig intestines and growth performance[3−5] but also raises concerns about its impact on the human intestinal flora and resistance.[39,40] High radioactivity levels in the livers and kidneys indicated that the livers and kidneys were slow-release depots for CYA and its metabolites, which resulted in obvious organ injury in the livers and kidneys after dosing the rats with a high level of CYA in the feed.[41,42]

Cy1, Cy4, and Cy5 were distributed in nearly all tissues in the four species, suggesting that they were the common metabolites of CYA in edible tissues. Of these, Cy1 was the most common and main metabolite of CYA in the edible tissues of the four different species, with the highest concentration and longest persistence, indicating that it could be the key metabolite for food safety control and toxicology concerns. Cy1 was the *N*-oxide reduction metabolite of CYA by reducing the oxygen atoms on both the N1 and N4 sites on the benzene. Because *N*-oxide reduction is driven by single-electron reductases,[11] while single-electron reduction of quinoxaline *N*,*N*-dioxides leads to DNA damage by radical intermediate production,[43] it could be speculated that the formation of Cy1 may lead to the production of some radical intermediates and then cause QdNO-induced pathological damage.[8,44] Moreover, it has been shown that bisdeoxycarbadox, the bisdeoxy metabolite of carbadox, was positive in the Ames test and cell transformation test, and its tumorigenic potential was apparently greater than that of the parent drug.[27,28] On the basis of the structural similarity with bisdeoxycarbadox and the high proportions in the edible tissues in all species, the toxicology of Cy1 should be a primary concern. Cy4 and Cy5 were the predominant metabolites of CYA in various tissues of rats and the muscle of carp, with high percentages over 50% of

DOI: 10.1021/acs.jafc.5b01745
J. Agric. Food Chem. 2015, 63, 5557−5569

the total residues. Theoretically, the toxicity of Cy4 should be lower than that of Cy1 because Cy4 is the hydrogenated product of Cy1. It has been shown that the hydrogenation of compounds can reduce their toxicity.[45,46] Cy5 is the alcohol form of Cy6 and is formed by the cleavage of the side chain followed by an oxidation reaction. Because no toxic perssad was introduced during this process, it could be speculated that the toxicity of Cy5 is similar to that of Cy6. Nevertheless, because such high proportions of Cy4 and Cy5 were observed in the livers and kidneys of rats, they may have important contributions to the pharmacology and toxicology of CYA in rats. Therefore, further studies on the toxicology of Cy1, Cy4, and Cy5 need to be performed.

Cy3 and Cy6 were found to be the main metabolites in pigs, with an extensive distribution and high proportion of the TRR. Cy6 (quinoxaline-2-carboxylic acid, QCA), the final metabolite of carbadox, has been shown to be negative in various toxicology studies, including those for genotoxicity and carcinogenicity,[27,28] and showed relatively lower oxidative stress toxicity than its parent molecules.[8] Cy3, the glycine conjugate of Cy6, is a phase II metabolite with increased water solubility for easy excretion and thus had a toxicity lower than that of Cy6. Hence, Cy3 and Cy6 pose little threat to the food safety of CYA.

The elimination rate of CYA and its metabolites in food animals was closely related to its food safety. The designation of marker residue and target tissue is essential for the food safety monitoring of CYA. The tissue in which the drug persists for the longest time is considered to be the marker tissue, and the compound that persists for the longest period of time in the target tissue is considered to be the marker residue. That means if the marker residue was depleted to a safe amount in the target tissue, there would be no other drug residues in any of the tissues, and the product would be considered definitely safe for the consumer. Hence, the kidney is suggested as the target residue tissue of CYA in pigs, chickens, and rats in light of the total radioactive depletion rate in all tissues. Cy1, Cy3, Cy4, and Cy6 were the main metabolites in the kidneys at 6 h following the final dose, but only Cy1 persisted for the longest time and showed a depletion similar to that of TRR with a similar elimination half-life. Accordingly, the marker residue of CYA was Cy1 in pigs, chickens, and carp.

In summary, CYA was excreted rapidly from the animals after a consecutive oral dosage, and fecal excretion was the major elimination route of CYA in animals, whereas renal elimination was the minor route. CYA was extensively metabolized in rats, pigs, chickens, and carp, primarily involving N−O group reduction, C═N cleavage, and hydrogenation and hydrolysis on the side chain. The major metabolites of CYA were Cy1, Cy3, and Cy6 in pigs, Cy1, Cy5, and Cy6 in chickens, Cy1, Cy2, and Cy4 in carp, and Cy1, Cy2, Cy4, and Cy5 in rats. Cy1 was suggested to be the marker residue, and the kidney was designated as the target tissue. The toxicity of Cy1, Cy4, and Cy5 needs to be investigated further on the basis of their structures and amounts in the edible tissues of food animals. These results provide significant information on the disposition of CYA in animals, which will improve the understanding of the pharmacology and toxicology of CYA in animals and provide comprehensive evidence for the food safety controls of CYA in animal products.

AUTHOR INFORMATION

Corresponding Author

*Y.Z.: tel, 027-8728 7186; fax, 027-8767 2232; e-mail, yuan5802@mail.hzau.edu.cn.

Funding

This work was financially supported by the National Natural Science Foundation of China (Grant No. 31302143), the Fundamental Research Funds for the Central Universities (2012ZYTS052), and the National Basic Research Program of China (2009CB118800).

Notes

The authors declare no competing financial interest.

ACKNOWLEDGMENTS

The authors thank the senior engineer Dong Mo at the Shanghai Institute of Applied Physics, Chinese Academy of Sciences, for his help with the synthesis of [^{3}H]-CYA and thank postdoctoral fellow Lin Zhoumeng at Kansas State University for his revision of the English language.

ABBREVIATIONS USED

CYA, cyadox; LC-RAM-MS-IT-TOF, high-performance liquid chromatography radioactivity monitor mass spectrometry ion trap time of flight; ONA, *O*-nitroaniline; [^{3}H]-ONA, 4-[^{3}H]-*O*-nitroaniline; PDA, pyruvaldehyde dimethylacetal; BFO, benzofuroxan; FQDDA, 2-formylquinoxaline-1,4-dioxide dimethylacetal; LSC, liquid scintillation counting

REFERENCES

(1) Fan, S. X.; Yuan, Z. H.; Wang, D. J.; Kong, K.; Chen, P.; Ma, J. Z. In vitro antibacterial activity of cyadox. *Journal of Huazhong Agricultural University (Natural Science Edition)* **2000**, *19* (1), 51−4.

(2) Huang, L. L.; Yuan, Z. H.; Fan, S. X.; Liu, D. C.; Chen, P.; Wang, D. J. In vitro antibacterial activity of cyadox on poultry bacteria. *J. South China Agric Univ (Natural Science Edition)* **2003**, *24*, 81.

(3) Wang, Y. L.; Yuan, Z. H.; Zhu, H. L.; Ding, M. X.; Fan, S. X. Effect of cyadox on growth and nutrient digestibility in weanling pigs. *S Afr J. Anim Sci.* **2005**, *35* (2), 117−25.

(4) Ding, M. X.; Wang, Y. L.; Zhu, H. L.; Yuan, Z. H. Effects of cyadox and olaquindox on intestinal mucosal immunity and on fecal shedding of Escherichia coli in piglets. *J. Anim. Sci.* **2006a**, *84* (9), 2367−73.

(5) Ding, M. X.; Yuan, Z. H.; Wang, Y. L.; Zhu, H. L.; Fan, S. X. Olaquindox and cyadox stimulate growth and decrease mucosal immunity in piglets orally inoculated with Escherichia coli. *J. Anim. Physiol. Anim. Nutr.* **2006b**, *90* (5−6), 238−43.

(6) Huang, L. L.; Yuan, Z. H. Prevention effect of cyadox on chickens with Escherichia coli. *Chin J. Vet Med.* **2005**, *41*, 50.

(7) He, Q. H.; Fang, G. J.; Wang, Y. L.; Wei, Z. C.; Wang, D. J.; Zhou, S. Q.; Fan, S. X.; Yuan, Z. H. Experimental evaluation of cyadox phototoxicity to Balb/c mouse skin. *Photodermatol., Photoimmunol. Photomed.* **2006**, *22*, 100−4.

(8) Huang, X. J.; Zhang, H. H.; Wang, X.; Huang, L. L.; Zhang, L. Y.; Yan, C. X.; Liu, Y.; Yuan, Z. H. ROS mediated cytotoxicity of porcine adrenocortical cells induced by QdNOs derivatives in vitro. *Chem.-Biol. Interact.* **2010**, *185*, 227−34.

(9) Wang, X.; Fang, G. J.; Wang, Y. L.; Ihsan, A.; Huang, L. L.; Zhou, W.; Liu, Z. L.; Yuan, Z. H. Two generation reproduction and teratogenicity studies of feeding cyadox in Wistar rats. *Food Chem. Toxicol.* **2011a**, *49* (5), 1068−79.

(10) Ihsan, A.; Wang, X.; Zhang, W.; Tu, H. G.; WangYL; Huang, L. L.; Iqbal, Z.; Cheng, G. Y.; Pan, Y. H.; Liu, Z. L.; Tan, Z. Q.; Zhang, Y. Y.; Yuan, Z. H. Genotoxicity of quinocetone, cyadox and olaquindox in vitro and in vivo. *Food Chem. Toxicol.* **2013**, *59*, 207−14.

DOI: 10.1021/acs.jafc.5b01745
J. Agric. Food Chem. 2015, 63, 5557−5569

(11) Liu, Z. Y.; Huang, L. L.; Dai, M. H.; Chen, D. M.; Tao, Y. F.; Wang, Y. L.; Yuan, Z. H. Metabolism of cyadox in rat, chickens and pig liver microsomes and identification of metabolites by accurate mass measurements using electrospray ionization hybrid ion trap/time-of-flight mass spectrometry. *Rapid Commun. Mass Spectrom.* **2009**, *23* (13), 2026−34.
(12) Xu, N.; Huang, L. L.; Liu, Z. Y.; Pan, Y. H.; Wang, X.; Tao, Y. F.; Chen, D. M.; Wang, Y. L.; Peng, D. P.; Yuan, Z. H. Metabolism of cyadox by the intestinal mucosa microsomes and gut flora of pigs, and identification of metabolites by high-performance liquid chromatography combined with ion trap/time-of-flight mass spectrometry. *Rapid Commun. Mass Spectrom.* **2012**, *25* (16), 2333−44.
(13) Wu, H. X.; Li, L. X.; Shen, J. Z.; Wang, Y.; Liu, K. L.; Zhang, S. X. In vitro metabolism of cyadox in rat, chickens and pigs using ultra-performance liquid chromatography quadrupole time-of-flight mass spectrometry. *J. Pharm. Biomed. Anal.* **2012**, *67- 68*, 175−85.
(14) Huang, L. L.; WangYL; Tao, Y. F.; Chen, D. M.; Yuan, Z. H. Development of high performance liquid chromatographic methods for the determination of cyadox and its metabolites in plasma and tissues of chickens. *J. Chromatogr. B: Anal. Technol. Biomed. Life Sci.* **2008**, *874*, 7−14.
(15) Cheng, L. L.; Wang, Z. H.; Shen, J. Z.; Li, L. X.; Wu, H. X.; Zhang, S. X. A specific UPLC-ESI-MS/MS method for analysis of cyadox and its three main metabolites in fish samples. *Anal. Methods* **2012**, *4*, 217−21.
(16) Yan, D. D.; He, L. M.; Zhang, G. J.; Fang, B. H.; Yong, Y.; Li, Y. Simultaneous Determination of Cyadox and Its Metabolites in Chickens Tissues by LC-MS/MS. *Food Anal Method* **2012**, *5*, 1497−1505.
(17) Zhao, N.; Wang, L.; Lu, X. X.; Jia, H. Q.; Fang, B. H.; Zeng, Z. L.; Ding, H. Z. Pharmacokinetics of cyadox and its major metabolites in pigs after intravenous and oral administration. *J. Integr. Agric.* **2013**, *12* (3), 495−501.
(18) Li, Y. F.; Zhao, N.; Zeng, Z. L.; Gu, X. Y.; Fang, B. H.; Yang, F.; Zhang, B. X.; Ding, H. Z. Tissue deposition and residue depletion of cyadox and its three major metabolites in pigs after Oral Administration. *J. Agric. Food Chem.* **2013**, *61*, 9510−15.
(19) VICH GL46. *Guidance for industry: studies to evaluate the metabolism and residue kinetics of veterinary drugs in food-producing animals: metabolism study to determine the quantity and identify the nature of residues (MRK)*. 2011, *205*, 4−5.
(20) VICH GL47. *Guidance for industry: studies to evaluate the metabolism and residue kinetics of veterinary drugs in food-producing animals: comparative metabolism studies in laboratory animals*. 2011, *206*, 4−5.
(21) Marathe, P. H.; Shyu, W. C.; Humphreys, W. G. The use of radiolabeled compounds for ADME studies in discovery and exploratory development. *Curr. Pharm. Design* **2004**, *10* (24), 2991−3008.
(22) Egnash, L. A.; Ramanathan, R. Comparison of heterogeneous and homogeneous radioactivity flow detectors for simultaneous profiling and LC-MS/MS characterization of metabolites. *J. Pharm. Biomed. Anal.* **2002**, *27* (1−2), 271−84.
(23) Zhang, L.; Jin, Y.; Chen, M.; Huang, M.; Harvey, R. G.; Blair, I. A.; Penning, T. M. Detoxication of structurally diverse polycyclic aromatic hydrocarbon (PAH) o-quinones by human recombinant catechol-O-methyltransferase (COMT) via O-methylation of PAH catechols. *J. Biol. Chem.* **2011**, *286* (29), 25644−54.
(24) Schwen, R. J.; Nguyen, L.; Jackson, R. L. Elucidation of the metabolic pathway of S-equol in rat, monkey and man. *Food Chem. Toxicol.* **2012**, *50* (6), 2074−83.
(25) Yuan Z. H., Pan Y. H., Huang L. L., Yin F. J., Wang Y. L., Tao Y. F., Chen D. M., Liu Z. L., Peng D. P., Dai M. H. The preparation of tritium or deuterium labeled mequindox. China Patent 201210551251.X[P]. Dec 17, 2012.
(26) AVMA.. Panel on Euthanasia 2000 Report of the AVMA panel on euthanasia. *J. Am. Vet. Med. Assoc.* **2001**, *218*, 669.
(27) FAO/WHO. *Thirty-sixth Report of the Joint Export Committee on Food Additives: Evaluation of certain veterinary drug residues in food*; World Health Organization: Geneva, Switzerland, 1990; WHO Food Additive Series 27, World Health Organ Technical Report Series, No. *799*, p 50.
(28) FAO/WHO. *Thirty-sixth Report of the Joint Export Committee on Food Additives: Evaluation of certain veterinary drug residues in food*; World Health Organization: Geneva, Switzerland, 1990; WHO Food Additive Series 27, World Health Organ Technical Report Series, No. *799*, p 45.
(29) Li, J.; Huang, L. L.; Wang, X.; Pan, Y. H.; LiuZY; Chen, D. M.; Tao, Y. F.; Wu, Q. H.; Yuan, Z. H. Metabolic disposition and excretion of quinocetone in rats, pigs, broilers, and carp. *Food Chem. Toxicol.* **2014**, *69*, 109−19.
(30) Liu, Z. Y. Sun ZL.The metabolism of carbadox, olaquindox, mequindox, quinocetone and cyadox: an overview. *Medic Chem.* **2013**, *9* (8), 1017−27.
(31) Chen, C. G.; Cheng, G. Y.; Hao, H. H.; Dai, M. H.; Wang, X.; Huang, L. L.; Liu, Z. L.; Yuan, Z. H. Mechanism of Porcine Liver Xanthine Oxidoreductase Mediated N-Oxide Reduction of Cyadox as Revealed by Docking and Mutagenesis Studies. *PLoS One* **2013**, *8* (9), e73912.
(32) Zheng, M.; Jiang, J.; Wang, J.; Tang, X.; Ouyang, M.; Deng, Y. The mechanism of enzymatic and non-enzymatic N-oxide reductive metabolism of cyadox in pig liver. *Xenobiotica* **2011**, *41* (11), 964−71.
(33) Mu, P.; Zheng, M.; Xu, M.; Zheng, Y.; Tang, X.; Wang, Y.; Wu, K.; Chen, Q.; Wang, L.; Deng, Y. N-oxide reduction of quinoxaline-1,4-dioxides catalyzed by porcine aldehyde oxidase SsAOX1. *Drug Metab. Dispos.* **2014**, *42* (4), 511−19.
(34) Itoh, H.; Suzuta, T.; Hoshino, T.; Takaya, N. Novel dehydrogenase catalyzes oxidative hydrolysis of carbon-nitrogen double bonds for hydrazone degradation. *J. Biol. Chem.* **2008**, *283* (9), 5790−5800.
(35) Ide, T.; Horii, M. Predominant conjugation with glycine of biliary and lumen bile acids in rats fed on pectin. *Br. J. Nutr.* **1989**, *61* (3), 545−57.
(36) Kwakye, J. B.; Johnson, M. R.; Barnes, S.; Diasio, R. B. A comparative study of bile acid CoA:amino acid:N-acyltransferase (BAT) from four mammalian species. *Comp biochem physiol B, Comp biochem* **1991**, *100* (1), 131−6.
(37) Vessey, D. A. The biochemical basis for the conjugation of bile acids with either glycine or taurine. *Biochem. J.* **1978**, *174*, 621−6.
(38) Parkin, A.; Sargent, F. The hows and whys of aerobic H2 metabolism. *Curr. Opin. Chem. Biol.* **2012**, *16*, 26−34.
(39) Hao, H. H.; Guo, W. G.; Iqbal, Z.; Cheng, G. Y.; Wang, X.; Dai, M. H.; Huang, L. L.; Wang, Y. L.; Peng, D. P.; Liu, Z. L.; Yuan, Z. H. Impact of cyadox on human colonic microflora in chemostat models. *Regul. Toxicol. Pharmacol.* **2013**, *67* (3), 335−43.
(40) Guo, W.; Hao, H.; Dai, M.; Wang, Y.; Huang, L.; Peng, D.; Wang, X.; Wang, H.; Yao, M.; Sun, Y.; Liu, Z.; Yuan, Z. Development of quinoxaline 1, 4-dioxides resistance in Escherichia coli and molecular change under resistance selection. *PLoS One* **2012**, *7* (8), e43322.
(41) Fang, G. J.; He, Q. H.; Zhou, S. Q.; Wang, D. J.; Zhang, Y. L.; Yuan, Z. H. Subchronic oral toxicity study with cyadox in Wistar rats. *Food Chem. Toxicol.* **2006**, *44*, 36−41.
(42) Wang, X.; He, Q. H.; Wang, Y. L.; Ihsan, A.; Huang, L. L.; Zhou, W.; Su, S. J.; Liu, Z. L.; Yuan, Z. H. A chronic toxicity study of cyadox in Wistar rats. *Regul. Toxicol. Pharmacol.* **2011**, *59* (2), 324−33.
(43) Badham, H. J.; Winn, L. M. In utero exposure to benzene disrupts fetal hematopoietic progenitor cell growth via reactive oxygen species. *Toxicol. Sci.* **2010**, *113*, 207−15.
(44) Ganley, B.; Chowdury, G.; Bhansali, J.; Scott Daniels, J.; Gates, K. S. Redoxactivated, hypoxia-selective DNA cleavage by quinoxlaine 1,4-di-Noxide. *Bioorg. Med. Chem.* **2001**, *9*, 2395−2401.
(45) Evans, M. A.; Harbison, R. D. Prenatal toxicity of rubratoxin B and its hydrogenated analog. *Toxicol. Appl. Pharmacol.* **1977**, *39* (1), 13−22.
(46) LaFrate, A. L.; Katzenellenbogen, J. A. Improved chemical syntheses of 5,6-dihydro-5-fluorouracil. *J. Org. Chem.* **2007**, *72* (22), 8573−6.

DOI: 10.1021/acs.jafc.5b01745
J. Agric. Food Chem. 2015, 63, 5557−5569

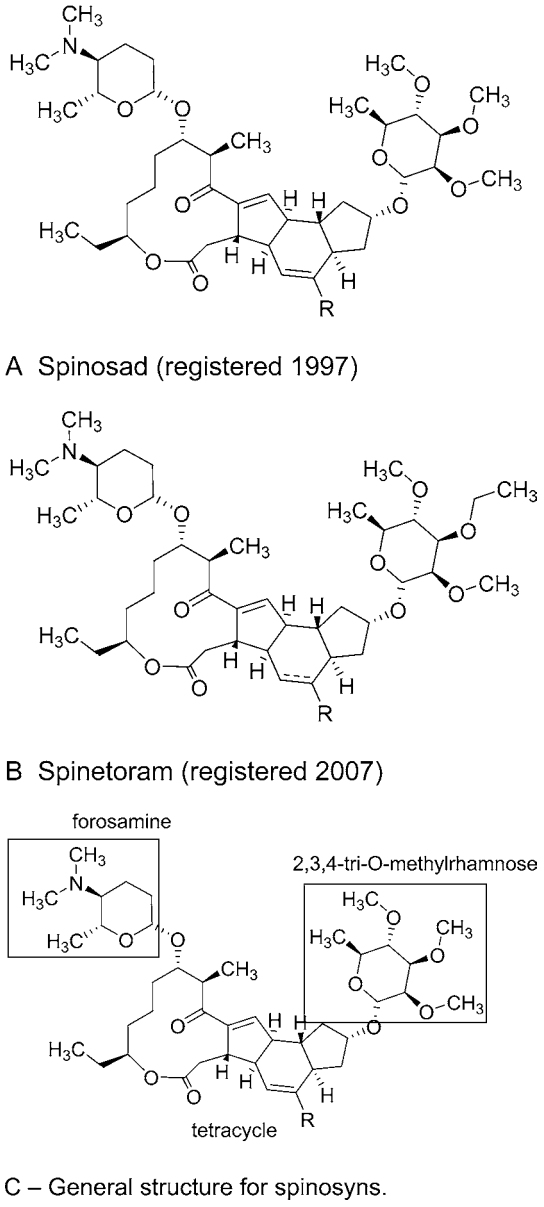

Figure 1. Structures of spinosad, spinetoram, spinosyns: (A) spinosad (primary component spinosyn A (R = H), minor component spinosyn D (R = Me)); (B) spinetoram (primary component 5,6-dihydro-3′-*O*-ethyl spinosyn J (R = H, 5,6 single bond), minor component 3′-*O*-ethyl spinosyn L (R = Me, 5,6-double bond)); (C) general structure of the spinosyns (R = H or Me, boxes highlight the two sugar moieties).

MATERIALS AND METHODS

Synthesis of Spinosyn Analogues. Unless otherwise indicated, all commercial reagents were used without purification. Solvents were of reagent grade. Benzyl alcohol precursors were available commercially or were prepared using published routes. Purity was established as >95% by ^{1}H NMR spectroscopy and LC-MS. Mass spectral data were obtained by electron ionization on one of several systems including a series 1100 mass selective detector (MSD) (Hewlett-Packard, Palo Alto, CA, USA) or a 5890 series II (Hewlett-Packard) with a 5890A mass spectrometer (Hewlett-Packard) or a 6890 series GC system with a 5973 MSD (Hewlett-Packard). Mass spectral data were also obtained by LC-MS analysis using a 215 liquid handler (Gilson, Middleton, WI, USA) for injection coupled to a 1100 chromatography system (Agilent Technologies, Santa Clara, CA, USA) composed of a quaternary pump system and photodiode array detector linked to a 50/50 splitter going simultaneously to a 2000 evaporative light scattering detector (Alltech Associates, Inc., Deerfield, IL, USA) with impactor on and to a ZQ mass spectrometer detector (Waters Corp., Milford, MA, USA) or by a second LC-MS (Waters Corp.) composed of a 2777 autosampler, 1525 μL binary pumps with 100 μL pump heads, and a 2996 photodiode array detector linked to a 50/50 splitter going simultaneously to a 2420 evaporative light scattering detector (Alltech Associates, Inc.) and a ZQ mass spectrometer detector (Waters Corp.). Masses are detected by electrospray ionization (ESI) on both systems. The main method consists of a linear gradient from 5 to 95% organic in 5 min. Solvents are 94.9% H_2O with 5% acetonitrile (aqueous) and 99.9% acetonitrile (organic) both spiked with 0.1% acetic acid. The column used was a 4.6 mm × 50 mm i.d., 5 μm, Sunfire Prep C18 OBD (Waters Corp.). Reverse phase high-performance liquid chromatography (RP HPLC) was conducted on a liquid handler 215 (Gilson) with HPLC grade acetonitrile and water (both with 0.1% acetic acid). ^{1}H NMR spectroscopy data were collected using chloroform-*d* solvent with tetramethylsilane as internal standard.

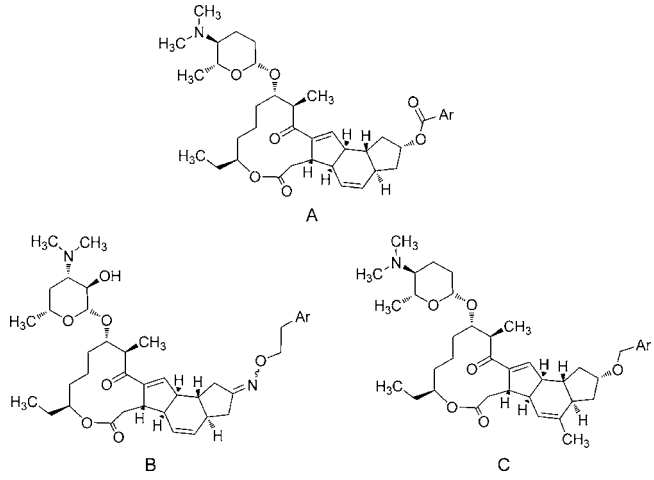

Figure 2. Spinosyn analogues containing rhamnose replacements at C-9: (A) 9-*O*-benzoyl analogues; (B) 9-(*O*-aralkyl) oxime analogues; (C) 9-*O*-benzyl analogues.

Preparation of 3,4,5-Trimethoxybenzyl Bromide. In a 1 dram vial equipped with a magnetic stir bar were added 0.198 g of 3,4,5-trimethoxybenzyl alcohol (1.00 mmol), 1.5 mL of 9:1 dichloromethane/diethyl ether, and hydrogen bromide (40% aqueous solution). The reaction mixture was stirred for 4.5 h. The reaction mixture was poured into a 25 mL vial containing water and ice. This mixture was extracted three times with ethyl acetate, dried over magnesium sulfate, filtered, concentrated under reduced pressure and low heat, and then stored in the freezer.

Preparation of 9-*O*-Benzyl Spinosyn D Analogues. *Method A: Preparation of 9-O-(3,4,5-Tri-O-methylbenzyl)spinosyn D,* ***6q.*** In a 1 dram vial equipped with a magnetic stir bar were added 0.144 g of 3,4,5-trimethoxybenzyl bromide (0.55 mmol), 0.10 g (0.18 mmol) of spinosyn L C-9 pseudoaglycone, 0.150 g of powdered 10:1 potassium hydroxide/tertrabutylammonium hydride (excess), and 3.0 mL of dichloromethane. The reaction mixture was stirred overnight at room temperature. The reaction mixture was diluted with ether and then passed through a 10 mL Celite cartridge. The eluent was concentrated under vacuum. Purification using a Redi Sep 10 g flash column (Isco, Inc., Lincoln, NE, USA), eluting with ethyl acetate/hexanes/dichloromethane/methanol (10:10:10:1, v/v/v/v), yielded 0.066 g (50% yield) of **6q** as a solid foam.

Method B: Preparation of 9-O-(2-Isopropylbenzyl)spinosyn D, ***6d.*** In a 1 dram vial equipped with a magnetic stir bar were added 0.050 g of 1-(bromomethyl)-2-isopropylbenzene (0.21 mmol), 0.020 g (0.036 mmol) of spinosyn L C-9 pseudoaglycone, 0.10 g of powdered 10:1 potassium hydroxide/tertrabutylammonium hydride (excess), and 1.5 mL of dichloromethane. The reaction mixture was stirred overnight at room temperature. The supernatant solution was then

DOI: 10.1021/acs.jafc.5b01987
J. Agric. Food Chem. 2015, 63, 5571−5577

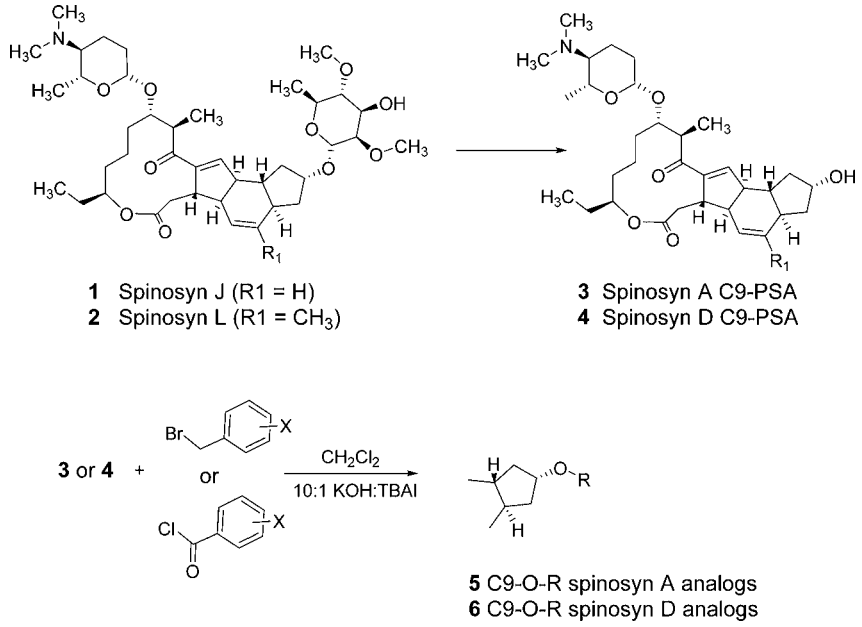

Figure 3. Synthesis of spinosyn D C9 pseudoaglycone and spinosyn D analogues with rhamnose replacements.

added directly to the top of a Redi Sep 2.5 g flash column (Isco, Inc.) and eluted, first with 25 mL of dichloromethane, then with 25 mL of 1% methanol in dichloromethane, and finally with 25 mL of 2% methanol in dichloromethane, which resulted in elution of the desired 9-*O*-benzyl product. Removal of solvent furnished 0.0205 g (79%) of **6d** as a solid foam.

Molecular Modeling Overlays. The spinosyn D and the benzyl and benzoyl structures were built by hand in Sybyl-X 2.1 (Certata, Princeton, NJ, USA) starting from the minimized X-ray structure of spinosyn A. The structures were then minimized and flexibly fit to the minimized X-ray structure of spinosyn A. All of the molecules were initially geometry optimized using the Tripos force field[29] and Gasteiger–Huckel charges[30,31] (Tripos Associates, St. Louis, MO, USA). The shape-based flexible fit of spinosyn D and the benzyl and benzoyl structures was done using Surflex-Sim v2.706 distributed with Sybyl-X 2.1. The top-scoring conformer of each compound from Surflex-Sim was used in the overlay.

Insecticide Bioassays. Dose–response data for each compound against two susceptible laboratory strains of the lepidopteran species *Spodoptera exigua* or *Helicoverpa zea* was determined with a diet-based bioassay using 128-well diet trays (Bio-Serv, Frenchtown, NJ, USA). Three to five second-instar larvae of either lepidopteran were placed in each well (3 mL) of the diet tray that had been previously filled with 1 mL of artificial diet. Selected dosages (12.5, 3.125, 0.78, 0.195, 0.049 μg/cm^2) of the test compound (dissolved in 50 μL of 90:10 acetone/water mixture, v/v) were then applied to the diet in each of 16 wells, allowed to dry, and covered with a clear self-adhesive cover. Controls received solvent only. All treatments were held at 25 °C and 14:10 h light/dark for 6 days. Each well was recorded as a unit (all alive or all dead), the activity across the 16 wells (for each dose) was then averaged. The lethal concentration for 50% of the test population (LC_{50}) and 95% fiducial limits for each compound, with correction for mortality in the controls, were determined using probit analysis.[32]

Bioassays against a susceptible laboratory strain of *Aphis gossypii* (cotton aphid) were conducted as described previously.[33] Briefly, 1-week-old summer crookneck squash seedlings, *Cucurbita pepo*, were pruned to a single cotyledon. A mixed population (immatures and adults) of *A. gossypii* was transferred to the cotyledons 16–24 h prior to the application of test materials. Test compounds were dissolved in 90:10 acetone/ethanol, v/v, to form a stock solution, from which an appropriate amount was diluted in water containing 0.05% Tween 20 to form the spray solution of 50 and 200 ppm. Application was made using a hand-held DeVilbiss airbrush sprayer on aphid-infested plants spraying both leaf surfaces until runoff. There were four replicates (plants) for each treatment, whereas controls consisted of eight replicates treated with a solvent blank. Following treatment, plants were held at 23 °C and 40% RH with a 24 h photoperiod prior to grading. Grading occurred at 72 h post-treatment and consisted of live aphid counts (all nonwinged stages) on each of the replicates compared to the averaged aphid population on the solvent blank controls to estimate a percent mortality.

RESULTS AND DISCUSSION

Synthesis. Rhamnose replacement analogues were made by first deglycosylating spinosyns J, **1**, and L, **2** (Figure 3), to form the pseudoaglycones **3** and **4**, respectively, as described previously.[34] A free C-9 hydroxyl group was then available to prepare benzylated or benzoylated derivatives. Twenty-eight benzyl bromides were selected on the basis of diverse steric and electronic properties. Some of these were available commercially, with the remainder prepared as shown in Figure 3. Commercially available benzyl alcohols were converted into the bromides using hydrogen bromide in dichloromethane/ether. When the benzyl alcohols themselves were unavailable, they were prepared either from the corresponding aldehyde, for **6x**, or acid, for **6l**, by reduction with sodium borohydride or lithium aluminum hydride ($LiAlH_4$), respectively. The substituted aryl methyl bromides were then reacted with **3** or **4**, using individual 1 dram vials with powdered potassium hydroxide/tetra-*n*-butylammonium iodide as the basic catalyst to produce the desired targets **5** and **6** (Figure 3). In addition to exhibiting the expected mass parent ion by LC-MS, the 9-*O*-benzyl products were also characterized by the presence of a $-OC\underline{H}_2-$ signal in the proton NMR between 4.4 and 4.56 ppm, in addition to the expected aromatic signals. This methylene peak was usually a singlet; however, due to its diastereotopic nature, it was sometimes observed as a doublet of doublets. Isolated yields were usually in the range of 50–85%, except when highly electron-rich benzyl bromides such as 2,4-dimethoxy, 2-methoxy, and 4-methoxy were used; in these cases, quaternization of the tertiary amine predominated under the conditions used for this reaction. Structures and selected

DOI: 10.1021/acs.jafc.5b01987
J. Agric. Food Chem. 2015, 63, 5571–5577

physical property data of all final targets are provided in Table 1.

Table 1. Structure of 9-*O*-Benzyl or -*O*-Benzoyl Spinosyn Analogues

analogue	linker	phenyl substitution	MS (ESI) $[M + H]^+$
5a	−CO−	3-OCH_3	678
5b	−CH_2−	3-OCH_3	664
6a	−CO−	3-OCH_3	692
6b	−CH_2−	3-OCH_3	678
6c	−CH_2−	unsubstituted	648
6d	−CH_2−	2-iPr	690
6e	−CH_2−	2-$OCH_2CH_2OCH_3$	722
6f	−CH_2−	2,3-$(CH_3)_2$	676
6g	−CH_2−	2,4-$(CH_3)_2$	676
6h	-CH_2-	2-OCH_3, 4-CO_2CH_3	736
6i	−CH_2−	2-OCH_3, 4-Cl	712
6j	−CH_2−	2-F, 4-CN	691
6k	−CH_2−	2-Cl, 6-CH_3	696
6l	−CH_2−	2,6-$(CH_3)_2$	676
6m	−CH_2−	3-OCF_3	732
6n	−CH_2−	3-$CH_2OC_2H_5$	706
6o	−CH_2−	3-CF_3, 4-OCH_3	746
6p	−CH_2−	3,5-$(OCH_3)_2$	708
6q	−CH_2−	3,4,5-$(OCH_3)_3$	738
6r	−CH_2−	4-Cl	682
6s	−CH_2−	4-CN	673
6t	−CH_2−	4-CH_3	662
6u	−CH_2−	4-CF_3	716
6v	−CH_2−	4-iPr	690
6w	−CH_2−	6-fluoro-4*H*-benzo[1,3]dioxin-8-yl	724
6x	−CH_2−	benzofuran-2-yl	688

Insecticidal Activity. Earlier work using C9-benzoyl derivatives had evaluated 2-, 3-, and 4-methoxy benzoyl analogues,[27] as well as a C9-*O*-methyl. Because of the high reactivity of *o*- and *p*-methoxy-substituted benzyl bromides, which led to the formation of quaternary salts under our reaction conditions, the initial study focused on 3-methoxy analogues of spinosyns A and D, **5b** and **6b**, respectively (Table 2). These compounds were evaluated for insecticidal efficacy against two lepidopteran species, *S. exigua* and *H. zea*. As shown in Table 2, the C9-*O*-(3-methoxybenzyl) derivatives of spinosyns A and D, **5b** and **6b**, were more active than the corresponding C9 pseudoaglycones or the respective C9-*O*-benzoyl derivatives, **5a** and **6a**. However, neither **5b** nor **6b** was as potent as spinosyn A or D (Table 2).

Molecular Modeling Overlay. The 3-methoxybenzoyl, **6a**, and 3-methoxybenzyl, **6b**, derivatives of spinosyn D were overlaid on the structure of spinosyn D. As shown in Figure 4,

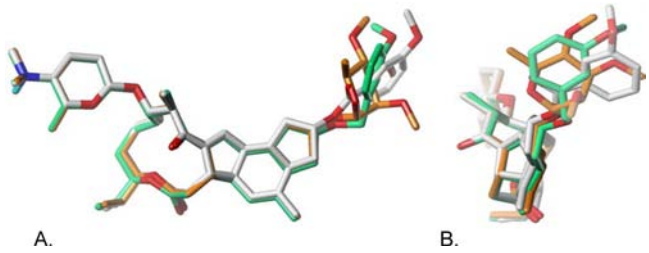

Figure 4. Overlays of C9 3-*O*-methylbenzyl, **6a** (green), and 3-*O*-methylbenzoyl, **6b** (light gray), spinosyn D derivatives, with spinosyn D (orange): (A) side view; (B) end-on view with the C9-benzyl and benzoyl bioisosteres in the foreground.

the benzyl derivative, **6b**, fits into the space of the rhamnose sugar better than the benzoyl derivative, **6a**. The better fit of the benzyl derivatives into the space of the rhamnose (Figure 4) may partially explain their improved insecticidal activity compared to the corresponding benzoyl derivatives (Table 2).

The above results prompted a more comprehensive evaluation of C9-*O*-benzyl analogues. For this study, spinosyn D analogues were prepared due to the availability of gram quantities of the corresponding 9-OH precursor. As noted in Table 2, the relative potencies of A and D analogues are similar. Although the C9-*O*-benzyl analogues displayed a wide range of insecticidal activity (Table 3), all of the analogues were less potent than spinosyn D. A few of the substitutions exhibited insecticidal activity against *S. exigua* that was within 5−15 times that of spinosyn D, whereas most were 20−200-fold less active than spinosyn D. The 2-isopropyl analogue, **6d**, was the most potent against *S. exigua* followed closely by the 3-*O*-methylethoxy, **6n**, 4-methyl, **6t**, 3,5-dimethoxy, **6p**, and benzofuran-2-yl, **6x**, analogues. For larvae of *H. zea*, the most active substitution was only about 3-fold less active than spinosyn D, with the majority being 20− 100-fold less active against *H. zea* than spinosyn D. The most effective substitution against larvae of *H. zea* was the 2-isopropyl, **6d**, followed closely by the 3,5-dimethoxy, **6p**, 4-Cl, **6r**, and 4-CN, **6s** (Table 3). All of the C9-*O*-benzyl analogues were also evaluated against *A. gossypii*. However, no insecticidal activity was observed against *A. gossypii* for any of the analogues at either the 50 or 200 ppm dose (data not shown).

Modifications of the spinosyn structure can greatly alter the insecticidal activity with significant improvements possible over the naturally occurring spinosyns.[13,17,35,36] As such, there has

Table 2. Insecticidal Activity of 9-*O*-Benzyl and 9-*O*-Benzoyl Spinosyns

compound	C9-O substitution	LC_{50}, $\mu g/cm^2$ (95% FL)	
		S. exigua	*H. zea*
spinosyn A	(2′,3′,4′-$(CH_3O)_3$ β-D-rhamnosyl)	0.20 (0.11−0.36)	0.20 (0.18−0.21)
spinosyn D	(2′,3′,4′-$(CH_3O)_3$ β-D-rhamnosyl)	0.044 (0.029−0.049)	0.11 (0.09−0.14)
spinA C9-PsA	H	>12.5	>12.5
spinD C9-PsA	H	7.9 (6.1−12.2)	12.5 (8.6−107)
5a	3-methoxybenzoyl A	4.8 (3.7−9.4)	6.3 (3.6−10.8)
5b	3-methoxybenzyl A	2.0 (1.0−2.7)	4.2 (3.1−8.1)
6a	3-methoxybenzoyl D	>12.5	>12.5
6b	3-methoxybenzyl D	1.4 (0.97−2.0)	5.3 (3.9−10.0)

DOI: 10.1021/acs.jafc.5b01987
J. Agric. Food Chem. 2015, 63, 5571−5577

Table 3. Insecticidal Activity of 9-*O*-Benzyl Spinosyns

compound	C9- phenyl substitution	LC_{50}, $\mu g/cm^2$ (95% FL)	
		S. exigua	*H. zea*
spinosyn D		0.044 (0.029−0.049)	0.11 (0.09−0.14)
6b	3-OCH_3	1.4 (0.97−2.0)	5.3 (3.9−10.0)
6c	unsubstituted	1.6 (1.1−2.3)	1.8 (1.2−2.6)
6d	2-isopropyl	0.2 (0.0003−0.4)	0.3 (0.2−0.6)
6e	2-$OCH_2CH_2OCH_3$	1.7 (1.2−2.4)	10.7 (5.8−16.3)
6f	2,3-$(CH_3)_2$	1.3 (0.9−1.9)	8.2 (8.6−11.2)
6g	2,4-$(CH_3)_2$	1.6 (0.9−1.7)	3.9 (2.8−7.6)
6h	2-OCH_3, 4-CO_2CH_3	3.7 (2.7−7.1)	5.9 (2.09−851)
6i	2-OCH_3, 4-Cl	0.9 (0.5−1.5)	0.9 (0.5−1.5)
6j	2-F, 4-CN	0.9 (0.6−2.8)	1.6 (0.6−3.9)
6k	2-Cl, 6-CH_3	8.5 (4.3−10.7)	6.3 (4.5−9.3)
6l	2,6-$(CH_3)_2$	0.9 (0.5−1.5)	1.2 (0.7−3.4)
6m	3-OCF_3	13.0 (9.4−20.7)	9.6 (5.1−12.2)
6n	3-$OCH_2OC_2H_5$	0.3 (0.01−1.2)	∼17
6o	3-CF_3, 4-OCH_3	1.2 (0.8−1.8)	1.4 (0.8−2.1)
6p	3,5-$(OCH_3)_2$	0.5 (0.3−0.7)	0.5 (0.4−0.7)
6q	3,4,5-$(OCH_3)_3$	8.2 (5.5−12.4)	6.3 (3.6−12.8)
6r	4-Cl	0.7 (0.5−1.1)	0.6 (0.4−0.9)
6s	4-CN	0.7 (0.5−1.2)	0.6 (0.4−0.8)
6t	4-CH_3	0.4 (0.3−0.6)	4.3 (2.3−10.0)
6u	4-CF_3	0.8 (0.4−1.7)	2.4 (0.8−3.9)
6v	4-isopropyl	5.3 (2.7−8.0)	11.1 (7.2−15.5)
6w	6-fluoro-4*H*-benzo[1,3]dioxin-8-yl	0.6 (0.3−0.8)	3.9 (1.8−10.3)
6x	benzofuran-2-yl	0.4 (0.2−12.2)	2.0 (1.4−2.9)
6y	7-(OCH_3)-2-naphthyl	1.4 (0.7−1.7)	1.4 (1.0−2.0)

been interest in exploring further alterations[27,28,33,34,37−41] and especially simplification of some components or the core macrolides tetracycle as a potential means for further exploration of these novel, complex, macrolides.[13,38,41,42] As noted in prior studies, deviation from the 2′,3′,4′-tri-*O*-methyl-*β*-L-rhamnose, whether by removing it, altering the stereochemistry, removing one or more *O*-alkyl groups, or replacing it with D- sugars, furanose sugars, or nonsugars,[13,27,35,36] all result in a large reduction (usually >100-fold) in insecticidal activity. Interestingly, the C9-*O*-benzyl ethers evaluated in the present study retained a significant level of insecticidal potency, demonstrating that, at least to some degree, a substituted benzylic group is better able to mimic the size and placement of the tri-*O*-rhamnosyl group. However, efforts to more closely mimic the shape or electronics of the rhamnose through incorporation of methoxy substituents met with limited success. For example, although the 3,5-dimethoxybenzyl substitution, **6p**, was among the most potent analogues against *S. exigua* larvae, several other simple substitutions, including 4-CN, **6s**, 4-Me, **6t**, 2-isopropyl, **6d**, 4-Cl, **6r**, and 3-methoxyethoxy, **6n**, were equally or more active. Two of the larger moieties, the benzofuran-2-yl, **6x**, and 6-fluoro-4*H*-benzo[1,3]dioxin-8-yl, **6w**, were also insecticidal against *S. exigua* larvae (Table 3), suggesting that to some degree larger moieties can be tolerated as replacements for the 2′,3′,4′-tri-*O*-methyl rhamnose. In general, the analogues showing the greatest potency against *S. exigua* were also among the most active against *H. zea* larvae, with the exception of the larger analogues, **6x** and **6w**.

In contrast to their excellent lepidopteran insecticidal activity, the spinosyns typically are weak against many sap-feeding insects such as aphids.[13,16] For example, spinosyn D is only weakly active (LC_{50} = 50 ppm) against *A. gossypii* compared to commercial aphicides such as imidacloprid (0.06 ppm).[14] None of the C9-*O*-benzyl analogues exhibited any activity against this aphid at the highest dose tested (200 ppm). Thus, the rhamnose bioisosteres were unable to improve on the activity of the spinosyns toward aphids relative to spinosyn D.

Although none of the rhamnose bioisostere-based spinosyns in the present study were as insecticidally active as spinosyn D, several analogues were within 3−15 times, depending on the insect species. Thus, the analogues exhibiting insecticidal activity close to that of spinosyn D demonstrate that an *O*-benzyl moiety can be a reasonable bioisostere for the 2′,3′,4′-tri-*O*-methyl rhamnose. Therefore, as demonstrated by the present and previous studies, the replacement of the sugars on macrolides such as the avermectins, and potentially the spinosyns, with nonsugar bioisoteres is further demonstrated to be a viable approach to developing new insecticidal chemistries.

■ ASSOCIATED CONTENT

Supporting Information

Detailed information on the synthesis of the new spinosyn analogues in this study and supporting NMR data. The Supporting Information is available free of charge on the ACS Publications website at DOI: 10.1021/acs.jafc.5b01987.

■ AUTHOR INFORMATION

Corresponding Author

*(T.C.S.) Phone: (317) 337-3064. Fax: (317) 337-3205. E-mail: tcsparks@dow.com.

Notes

The authors declare no competing financial interest.

DOI: 10.1021/acs.jafc.5b01987
J. Agric. Food Chem. 2015, 63, 5571−5577

■ ACKNOWLEDGMENTS

We thank Cathy Young and James Gifford (Dow AgroSciences) for assistance with the bioassays, Ricky Hunter (Dow AgroSciences) for the insect photograph, and the journal's anonymous reviewers for their very helpful suggestions.

■ ABBREVIATIONS USED

FL, fiducial limits; RH, relative humidity; TBAI, tetra-*n*-butylammonium iodide

■ REFERENCES

(1) Godfray, H. C. J.; Beddington, J. R.; Crute, I. R.; Haddad, L.; Lawrence, D.; Muir, J. F.; Pretty, J.; Robinson, S.; Thomas, S. M.; Toulmin, C. Food security: the challenge of feeding 9 billion people. *Science* **2010**, *327*, 812−818.

(2) Tilman, D.; Balzer, C.; Hill, J.; Befort, B. L. Global food demand and the sustainable intensification of agriculture. *Proc. Natl. Acad. Sci. U. S. A.* **2011**, *108*, 20260−20264.

(3) Popp, J.; Peto, K.; Nagy, J. Pesticide productivity and food security, a review. *Agron. Sustainable Dev.* **2013**, *33*, 243−255.

(4) Whalon, M. E.; Mota-Sanchez, D.; Hollingworth, R. M. Analysis of global pesticide resistance in arthropods. In *Global Pesticide Resistance in Arthropods*; Whalon, M. E., Mota-Sanchez, D., Hollingworth, R. M., Eds.; CAB International: Cambridge, MA, USA, 2008; pp 5−31.

(5) Tabashnik, B. E.; Mota-Sanchez, D.; Whalon, M. E.; Hollingworth, R. M.; Carriere, Y. Defining terms for proactive management of resistance to Bt crops and pesticides. *J. Econ. Entomol.* **2014**, *107*, 496−507.

(6) Sparks, T. C.; Nauen, R. IRAC: Mode of action classification and insecticide resistance management. *Pestic. Biochem. Physiol.* **2015**, *121*, 122−128.

(7) Lamberth, C.; Jeanmart, S.; Luksch, T.; Plant, A. Current challenges and trends in the discovery of agrochemicals. *Science* **2013**, *341*, 742−746.

(8) Sparks, T. C. Insecticide discovery: an evaluation and analysis. *Pestic. Biochem. Physiol.* **2013**, *107*, 8−17.

(9) Cantrell, C. L.; Dayan, F. E.; Duke, S. O. Natural products as sources for new pesticides. *J. Nat. Prod.* **2012**, *75*, 1231−1242.

(10) Gerwick, B. C.; Sparks, T. C. Natural products for pest control: an analysis of their role, value and future. *Pest Manage. Sci.* **2014**, *70*, 1169−1185.

(11) Godfrey, C. R. A., Ed. *Agrochemicals from Natural Products*; Dekker: New York, 1995.

(12) Rimando, A. M.; Duke, S. O. Natural products for pest management. In *Natural Products for Pest Management*; American Chemical Society: Washington, DC, USA, 2006; pp 2−21.

(13) Salgado, V. L.; Sparks, T. C. The spinosyns: chemistry, biochemistry, mode of action, and resistance. In *Insect Control: Biological and Synthetic Agents*; Gilbert, L. I., Gill, S. S., Eds.; Academic Press: New York, 2010; pp 207−243.

(14) Geng, C.; Watson, G. B.; Sparks, T. C. Nicotinic acetylcholine receptors as spinosyn targets for insect pest management. In *Target Receptors in the Control of Insect Pests: Part I, Advances in Insect Physiology*; Cohen, E., Ed.; Academic Press: New York, 2013; Vol. 44, pp 101−210.

(15) Thompson, G. D.; Dutton, R.; Sparks, T. C. Spinosad − a case study: an example from a natural products discovery program. *Pest Manage. Sci.* **2000**, *56*, 696−702.

(16) Dripps, J. E.; Boucher, R. E.; Chloridis, A.; Cleveland, C. B.; DeAmicis, C. V.; Gomez, L. E.; Paroonagian, D. L.; Pavan, L. A.; Sparks, T. C.; Watson, G. B. The spinosyn insecticides. In *Green Trends in Insect Control*; Lopez, O., Fernadez-Bolanos, J. G., Eds.; RSC Publishing: Cambridge, UK, 2011; pp 163−212.

(17) Sparks, T. C.; Crouse, G. D.; Dripps, J. E.; Anzeveno, P.; Martynow, J.; Gifford, J. Artificial neural network-based QSAR and the discovery of spinetoram. *J. Comput.-Aided Mol. Des.* **2008**, *22*, 393−401.

(18) Kornis, G. I. Avermectins and milbemycins. In *Agrochemicals from Natural Products*; Godfery, C. R. A., Ed.; Dekker: New York, 1995; pp 215−255.

(19) Fischer, M. H. Structure-activity relationships of the avermectins and milbemycins. In *Phytochemicals for Pest Control*; Hedin, P. A., Hollingworth, R. M., Masler, E. P., Miyamoto, J., Thompson, D. G., Eds.; American Chemical Society: Washington, DC, USA, 1997; pp 220−238.

(20) Mrozik, H.; Linn, B. O.; Eakola, P.; Lusi, A.; Matzuk, A.; Preiser, F. A.; Ostlind, D. A.; Schaeffer, J. M.; Fisher, M. H. Synthesis and biological activities of 13-substituted avermectin aglycones. *J. Med. Chem.* **1989**, *32*, 375−381.

(21) Pitterna, T. Chloride channel activators/new natural products: avermectins and milbemycins. In *Modern Crop Protection Compounds*, 2nd ed.; Kramer, W., Schirmer, U., Jeschke, P., Witschel, M., Eds.; Wiley-VCH: New York, 2012; Vol. 3, pp 1305−1326, DOI: 10.1002/9783527644179.ch32.

(22) Zhao, J.-H.; Xu, X.-J.; Ji, M.-H.; Cheng, J.-L.; Zhu, G.-N. Design, synthesis, and biological activities of milbemycin analogues. *J. Agric. Food Chem.* **2011**, *59*, 4836−4850.

(23) Xu, X.; Lai, S.; Ji, M.; Zhu, G.; Zhao, J. Synthesis, characterization and insecticidal activity of milbemycin analogues. *Youji Huaxue* **2012**, *32*, 1084−1092.

(24) Sparks, T. C.; Dripps, J. E.; Watson, G. B.; Paroonagian, D. Resistance and cross-resistance to the spinosyns − a review and analysis. *Pestic. Biochem. Physiol.* **2012**, *102*, 1−10.

(25) Tietze, L. F.; Schutzenmeister, N.; Grube, A.; Scheffer, T.; Baag, M. M.; Granitzka, M.; Stalke, D. Synthesis of spinosyn analogues for modern crop protection. *Eur. J. Org. Chem.* **2012**, *29*, 5748−5756.

(26) Tietze, L. F.; Sietz, S.; Schutzenmeister, N.; Biller, S.; Hierold, J.; Scheffer, T.; Baag, M. M. Selective glycosylation with the amino sugar D-forosamine for synthesis of spinosyns and its analogues. *Eur. J. Org. Chem.* **2013**, *2013*, 7305−7312.

(27) Anzeveno, P. B.; Green, F. R., III. Rhamnose replacement analogs of spinosyn A. In *Synthesis and Chemistry of Agrochemicals VI*; Baker, D. R., Fenyes, J. G., Lahm, G. P., Selby, T. P., Stevenson, T. M., Eds.; American Chemical Society: Washington, DC, USA, 2002; pp 262−276.

(28) Jeschke, P.; Velten, R.; Ebbinghaus-Kintscher, U.; Beck, M. E.; Losel, P.; Malsam, O.; Eberz, G.; Mohrle, V.; Frode, R. Synthesis of 9-keto-spinosyn derivatives for use in agriculture as pesticides. Bayer CropScience, Germany, Patent, DE 2003-10301519, Jan 17, 2003; 85 pp.

(29) Clark, M.; Cramer, R. D., III; von Opdenbosch, N. Validation of the general purpose Tripos 5.2 force field. *J. Comput. Chem.* **1989**, *10*, 982−1012.

(30) Gasteiger, J.; Marsili, M. Iterative partial equalization of orbital electronegativity: a rapid access to atomic charges. *Tetrahedron* **1980**, *36*, 3219−3222.

(31) Purcel, W. P.; Singer, J. A. A brief review and table of semiempirical parameters used in the Hückel molecular orbital method. *J. Chem. Eng. Data* **1967**, *12*, 235−246.

(32) Finney, D. J. *Probit Analysis*, 3rd ed; Cambridge University Press: Cambridge, UK, 1971.

(33) Sheehan, L. S.; Lill, R. E.; Wilkinson, B.; Sheridan, R. M.; Vousden, W. A.; Kaja, A. L.; Crouse, G. D.; Gifford, J.; Graupner, P.; Karr, L.; Lewer, L.; Sparks, T. C.; Leadlay, P. F.; Waldron, C.; Martin, C. J. Engineering of the spinosyn PKS: directing starter unit incorporation. *J. Nat. Prod.* **2006**, *69*, 1702−1710.

(34) Creemer, L. C.; Kirst, H. A.; Paschal, J. W. Conversion of spinosyn A and spinosyn D to their respective 9- and 17-pseudoaglycones and their aglycones. *J. Antibiot.* **1998**, *51*, 795−800.

(35) Crouse, G. D.; Sparks, T. C.; Schoonover, J.; Gifford, J. M.; Bruce, T.; Worden, T. V.; Martynow, J. G. Recent advances in the chemistry of the spinosyns. *Pest Manage. Sci.* **2001**, *57*, 177−185.

(36) Sparks, T. C.; Crouse, G. D.; Durst, G. Natural products as insecticides: the biology, biochemistry and quantitative structure

DOI: 10.1021/acs.jafc.5b01987
J. Agric. Food Chem. 2015, 63, 5571−5577

activity relationships of spinosyns and spinosoids. *Pest Manage. Sci.* **2001**, *57*, 896−905.
(37) Crouse, G. D.; Sparks, T. C.; DeAmicis, C. V.; Kirst, H. A.; Martynow, J. G.; Creemer, L. L.; Worden, T. V.; Anzeveno, P. B. Chemistry and insecticidal activity of the spinosyns. In *Pesticide Chemistry and Bioscience: The Food-Environment Challenge*; Brook, G. T., Roberts, T. R., Eds.; Royal Society of Chemistry: Cambridge, UK, 1999; pp155−166.
(38) Kirst, H. A.; Creemer, L. C.; Broughton, M. C; Huber, M. L. B.; Turner, J. R. Chemical and microbial modifications of spinosyn: exploring synergies between fermentation microbiology and organic chemistry. In *Synthesis and Chemistry of Agrochemicals VI*; Baker, D. R., Fenyes, J. G., Lahm, G. P., Selby, T. P., Stevenson, T. M., Eds.; American Chemical Society: Washington, DC, USA, 2002; pp 251−261.
(39) Daeuble, J.; Sparks, T. C.; Johnson, P.; Graupner, P. R. Modification of the butenyl-spinosyns utilizing cross-metathesis. *Bioorg. Med. Chem.* **2009**, *17*, 4197−4205.
(40) Chen, X.; Li, L.; Zhang, X.; Zhao, L. Chemical synthesis of spinosad derivatives. Wuhan University of Light Industry, People;s Republic of China, Patent CN 2013-10613847, Nov 26, 2013; 10 pp.
(41) Shi, D.; Feng, X.; Zhung, X.; Chai, H.; Liu, T.; Zhang, Q.; Li, J. Study of synthesis and biological activities of novel macrolides derivatives. *Youji Huaxue* **2014**, *34*, 2543−2550.
(42) Tietze, L. F.; Brasche, G.; Grube, A.; Boknke, N.; Stradler, C. Synthesis of novel spinosyn analogues by Pd-mediated transformations. *Chem. - Eur. J.* **2007**, *13*, 8543−8563.

DOI: 10.1021/acs.jafc.5b01987
J. Agric. Food Chem. 2015, 63, 5571−5577

Table 1. Treatments, Growing Media, and Applied Fertilizers[a]

treatment	peat	solid fertilizer	liquid fertilizer until 28 DAP (NPK %)	liquid fertilizer after 28 DAP (NPK %)
inorganic (IN)	Pindstrup 2	inorganic already included by company	inorganic vegetative (130 ppm of N)	inorganic generative (90 ppm of N)
Monterra Malt + broad bean (MB)	Pindstrup 0	33 g of Monterra Malt (4−1−5)	broad bean (0.51−0.09−0.41)	broad bean (0.51−0.09−0.41)
Monterra Malt + Pioner (MP)	Pindstrup 0	33 g of Monterra Malt (4−1−5)	Pioner Hi-Fruit (4−1−5)	Pioner K-max (3−1−7)
chicken manure + broad bean (CB)	Pindstrup 0	66 g of chicken manure (2−1−2)	broad bean (0.51−0.09−0.41)	broad bean (0.51−0.09−0.41)
chicken manure + Pioner (CP)	Pindstrup 0	66 g of chicken manure (2−1−2)	Pioner Hi-Fruit (4−1−5)	Pioner K-max (3−1−7)

[a]Solid fertilizers were applied to the peat before planting, and liquid fertilizers were applied via drip fertigation.

Table 2. Nutrient Concentrations, DM Content, and pH of Growing Media before and after Addition of Solid Inorganic and Organic Fertilizer[a]

growing media	NH_4^+-N (mg kg^{-1})	NO_3^--N (mg kg^{-1})	total N (%)	organic C (%)	C:N ratio	total P (mg kg^{-1})	K (mg kg^{-1})	SO_4^{2-} (mg kg^{-1})	DM (%)	pH
peat + inorganic fertilizers	171.3	333.7	0.59	35.0	59	4.03	17.7	3.53	49.3	5.9
peat + chicken manure	752.0	56.5	1.02	36.1	35	11.00	55.0	3.42	50.6	6.9
peat + Monterra Malt	373.2	48.2	1.36	38.8	29	6.37	83.3	20.51	50.3	5.8
peat	104.0	45.2	0.59	34.7	59	0.45	1.7	0.42	47.9	6.0

[a]Values are in mg kg^{-1} DM or % of DM.

Most organic fertilizers contain all essential nutrients required for plant growth and development, but at varying concentrations, and most of them have to be mineralized prior to plant uptake.[5,6] Thus, the availability of nutrients for plant uptake may not be instantaneous and depends on, among other factors, temperature and humidity.[19] Therefore, plants may not necessarily receive adequate amounts of nutrients during the active phases of growth, and an imbalance between nutrient release from organic fertilizers and plant uptake may lead to leaching.[20] With increasing concern for the environment and food safety, fertigation (irrigation with a nutrient solution) is considered a viable option to overcome leaching by synchronizing nutrient demand and supply to the plant. However, optimal nutrient supply through fertigation with organic fertilizers is difficult due to varying rates of mineralization and the lack of organic fertilizers with only one or a few nutrients.[21] Thus, the choice of suitable organic fertilizers for fertigation is imperative to prevent plant nutrient deficiency and to increase the yield and quality of organic strawberries grown in inert growing media.

The effects of organic fertilizers applied via drip irrigation combined with different solid organic fertilizers on the yield, quality, and nutritional status of strawberries are poorly understood as only a very limited amount of research has been conducted within this area. In this context, we hypothesized that fertigation with organic fertilizers results in similar yields and quality of strawberries compared to fertigation with inorganic fertilizers. However, a very limited number of certified organic liquid fertilizers are available in Denmark. The study aimed at elucidating the combined effect of two different solid and two liquid organic fertilizers on the yield, quality, nutrient status, and DM content of leaf tissue and fruit. In addition, the effects on leaf chlorophyll content and pH, electrical conductivity (EC), and nutrient content of drainage water were studied.

MATERIALS AND METHODS

Plant Material and Growth Conditions. The experiment was conducted from early July to late September 2011 in an open plastic tunnel at the Department of Food Science, Aarhus University, Aarslev, Denmark (10°27′ E, 55°18′ N). The mean temperatures outside the tunnel were 16.5, 16, and 14 °C in July, August, and September, respectively. Cold-stored strawberry tray plants (*Fragaria* × *ananassa* Duch. cv. 'Sonata') with 9−15 mm crown diameter were planted in plastic pots (1.4 L) on July 4, 2011. After planting, pots were placed on wooden benches (tabletops) with a distance between benches of 120 cm and a distance between plants of 20 cm, giving 4.2 plants per square meter.

Biological control of aphids, spider mites, and thrips was applied every 2 weeks. In addition, 4 weeks after planting, Nemasys, a biological control agent containing the nematode *Heterorhabditis* spp., was applied against root cutworms. Then, from 5 weeks after planting, plants were sprayed with a 0.3% sulfur solution four times at an interval of 1 week to reduce powdery mildew (*Sphaerotheca macularis*) attack.

Fertilizer Treatments. Pots were filled with peat (Pindstrup substrate 2 standard mix (1 kg m^{-3} 16−6−20 NPK + micronutrients, 0.4 kg m^{-3} powdered superphosphate ($Ca(H_2PO_4)_2$ + $2CaSO_4$), and 0.05 kg m^{-3} Micromax); Pindstrup Mosebrug A/S, Denmark) for the inorganic treatment and the same product without macro- and micronutrients was used for the organic treatments.

Five treatments, one inorganic (IN) and four organic (Table 1), were established in four replicates in a completely randomized layout with four plants per replicate. The organic treatments were combinations of two solid organic fertilizers, composted chicken manure (2−1−2 NPK, Farmergødning, Denmark) and Monterra Malt (4−1−5 NPK, Borregaard BioPlant ApS, Denmark), and two organic liquid fertilizers, broad bean (0.51−0.09−0.41 NPK, Farmergødning, Denmark) and Pioner (Hi-Fruit 4−1−5 NPK or K-Max 3−1−7 NPK, Azelis, Denmark). The broad bean fertilizer was chosen among a very limited number of certified organic fertilizers available in Denmark. Pioner Hi-Fruit and Pioner K-Max are not from organically certified source material but are allowed for organic production. Before planting, either 66 g of chicken manure or 33 g of Monterra Malt was placed into the planting hole just underneath the root system. The nutrient content of the growing media was analyzed by a commercial laboratory (Agrolab, Germany) and is shown in Table 2. Plants were drip fertigated with one dripper per plant. Before the green fruit stage, which occurred 28 days after planting (DAP), plants were supplied with inorganic fertilizer with high N (130 ppm of N) and low K and Ca concentrations, broad bean, or Pioner Hi-Fruit. From 28 DAP plants were fertigated with inorganic fertilizer with low N (90 ppm of

DOI: 10.1021/acs.jafc.5b01366
J. Agric. Food Chem. 2015, 63, 5578−5586

Table 3. Nutrient Concentrations, pH, and EC of Applied Fertigation Solutions

pH, EC (dS m^{-1}), and nutrient content (mg L^{-1})	inorganic (until 28 DAP)	inorganic (after 28 DAP)	broad bean (in both periods)	Pioner Hi-Fruit (until 28 DAP)	Pioner K-Max (after 28 DAP)
pH	5.9	5.7	5.9	5.9	6.9
EC	1.67	1.65	1.44	1.35	1.89
NO_3^--N	112	83	2	2	7
NH_4^+-N	15	8.3	21.4	6.5	11.7
P	31	24	12	19	6
K	142	165	106	171	286
Mg	29	23	18	16	13
Ca	121	179	141	129	153
S	48	90	31	46	54
B	0.24	0.4	0.03	0.04	0.07
Na	20	24	20	33	97
Cl	45	46	66	63	73
Mn	0.37	1.34	0.09	0.12	0.27
Fe	1.33	1.07	1.04	0.68	1.23
Zn	0.44	0.45	0.26	0.41	1.62
Cu	0.13	0.36	0.01	0.05	0.13
Mo	0.03	0.04	<0.01	<0.01	<0.01

N) and high K and Ca concentrations, broad bean, or Pioner K-Max (Tables 1 and 3). All fertigation solutions were made up to contain approximately the same amount of total (organic + inorganic) nitrogen (N) on the basis of the certificates obtained with the fertilizer products along with all other nutrients in nonequimolar concentrations. The actual contents of NO_3^--N, NH_4^+-N, and other nutrient elements in the fertigation solutions were analyzed by a commercial laboratory (Eurofins, Denmark) and are shown in Table 3. Each plant received 105, 210, and 315 mL of fertigation solution daily 0−7, 8−42, and 43−85 DAP, respectively, and each plant received approximately 3 g of N through fertigation during the experiment.

Nutrient Analyses of Drainage Water. EC and pH were measured by a pH and EC meter (HANNA Instruments Inc. model no. HI 9813, Romania) in drainage water from each replicate once a week from 15 to 85 DAP and are referred to as EC_{dw} and pH_{dw}, respectively. Plastic saucers were placed underneath the pots to collect drainage water after fertigation. Samples of drainage water were sent to a commercial laboratory (Eurofins, Denmark) for nutrient analyses 23 and 65 DAP.

Chlorophyll Content of Leaves. The leaf chlorophyll (Chl) content was estimated once a week starting 10 DAP on young fully developed leaves using an SPAD-502 meter (Spectrum Technologies, Inc., Plainfield, IL, USa). SPAD measurements were taken at three different areas per leaf so that major veins did not interfere with the measurement.

Multielement Analysis of Fruits and Leaves. The contents of macronutrients P, K, Ca, Mg, and S and micronutrients B, Cu, Fe, Mn, and Zn in fruit and leaf samples were analyzed by inductively coupled plasma−optical emission spectroscopy (ICP-OES). Fruit was collected 66 DAP, and fully expanded young leaves were collected 24 and 66 DAP and stored at −20 °C. Fruit and leaf samples were freeze-dried for 90 and 48 h, respectively, prior to multielement analysis. Samples were homogenized into a fine powder using a ball mill equipped with containers and balls coated with zirconium to avoid metal contamination (Retsch mm301, Retsch, Haan, Germany). A 250 mg portion of each sample was digested as described by Husted et al.[22] in an open-vessel system. Samples were subsequently diluted to 3.5% v/v HNO_3 with Milli-Q water and analyzed as described by Laursen et al.[23] Data quality was evaluated using two different certified reference materials, namely, apple leaves (NIST 1515, National Institute of Standards and Technology, Gaithersburg, MD, USA) and spinach leaves (NCS ZC73013, China National Analysis Center for Iron and Steel, purchased from LGC Standards, London, UK). Data were rejected if below the limit of detection (LOD). The LOD was determined as 3 times the standard deviation of a minimum of 7 blanks. Furthermore, data were accepted only if the accuracy for each element was >90% of the certified reference value. The concentrations of N and C were measured using IRMS (ANCA-SL elemental analyzer coupled to a 20−20 Tracermass mass spectrometer, Sercon Ltd., Crewe, UK). Quality assurance was performed by analysis of Certified Reference Materials (NIST 1515, NIST 8436, and 141d acetanilide $CH_3CONHC_6H_5$, National Institute of Standards and Technology) as previously described by Laursen et al.[23]

Fruit Harvest, Yield, and Quality. Fruit was harvested two times a week after full color developed, beginning at 43 DAP (in total, 12 times). Fruit of marketable and nonmarketable quality was weighed and counted. Nonmarketable fruit was distinguished from marketable fruit on the basis of size (<20 mm diameter) and surface characteristics. The surface characteristics included signs of decay due to disease or insect incidences and malformations. The total yield and percentage of marketable fruit was calculated.

Total soluble solids (TSS), titratable acid (TA), dry matter (DM), and firmness were measured on fruit of marketable quality two times (56 and 70 DAP) during the experiment. Firmness was measured as maximum penetration force (N) of fruit using a Fruit Texture Analyzer (FTA 264, Guss, South Africa) fitted with a 5 mm diameter convex puncture probe. The metal cylinder was set to a trigger threshold of 1.1 N and run with a forward speed of 30 mm s^{-1}, measuring speed of 10 mm s^{-1}, reverse speed of 30 mm s^{-1}, and measuring distance of 8 mm. The DM content was measured after oven-drying of fruit samples for 72 h at 60 °C. TSS and TA were determined on homogenates. After removal of the calyxes, fruit was liquidized with 50% demineralized water (w/w) until uniform. The samples were then centrifuged at 12000 rpm for 10 min, and the supernatant was poured into glass vials. TSS was measured by a digital refractometer (RFM 712, Bellinghum Stanley, UK) on 1−2 drops and expressed as degrees Brix (°Brix), which is equivalent to TSS (g 100 g^{-1}) of the sample. For TA, 7−9 g of the supernatant was weighed off and titrated with 0.1 N NaOH to an end point of pH 8.1 using an automatic Tritino 719 S titrator (Ω Metrohm, Switzerland). Results were expressed as citric acid equivalents (mg g^{-1}) fresh weight. All measurements were performed in duplicate.

Biomass Distribution. For DM calculation, runners and other plant parts were separated and oven-dried for 24 h at 60 °C. Runners were also cut three times during the experiment, weighed, and oven-dried for calculation of total above-ground biomass.

Statistical Analysis. The statistical data analysis was done using the GLM procedure of SAS (Statistical Analysis System, version 9.2, SAS Institute, Cary, NC, USA). Tukey's studentized range test was applied to determine significant differences between treatments at a $P < 0.05$ level of significance for fruit yield, quality parameters, nutrient

DOI: 10.1021/acs.jafc.5b01366
J. Agric. Food Chem. 2015, 63, 5578−5586

concentrations of leaves and fruit, EC_{dw}, pH_{dw}, and chlorophyll content of leaves.

RESULTS

pH, EC, and Nutrient Concentration of Drainage Water. Throughout the experiment, the pH_{dw} was higher in all organic fertilizer strategies than in the inorganic strategy (Figure 1a). Between 22 and 36 DAP, the pH_{dw} decreased by approximately 1 unit in the organic strategies, but not in the inorganic. Between 43 and 64 DAP, the pH_{dw} increased approximately 1 unit in all treatments, and in the same period the EC_{dw} also increased in all treatments (Figure 1b). Incorporation of Monterra Malt resulted in a slightly higher EC_{dw} than did chicken manure during the first 3 weeks; thereafter, similar or slightly higher EC_{dw} values from chicken manure were measured. From 29 DAP, the EC_{dw} from plants given Pioner High-K/K-max was higher than for plants given broad bean fertigation (Figure 1b). The EC_{dw} for the inorganic fertilizer strategy was between 1.5 and 2 dS m^{-1} for the first 6 weeks, and thereafter it increased in a similar pattern as in the organic strategies.

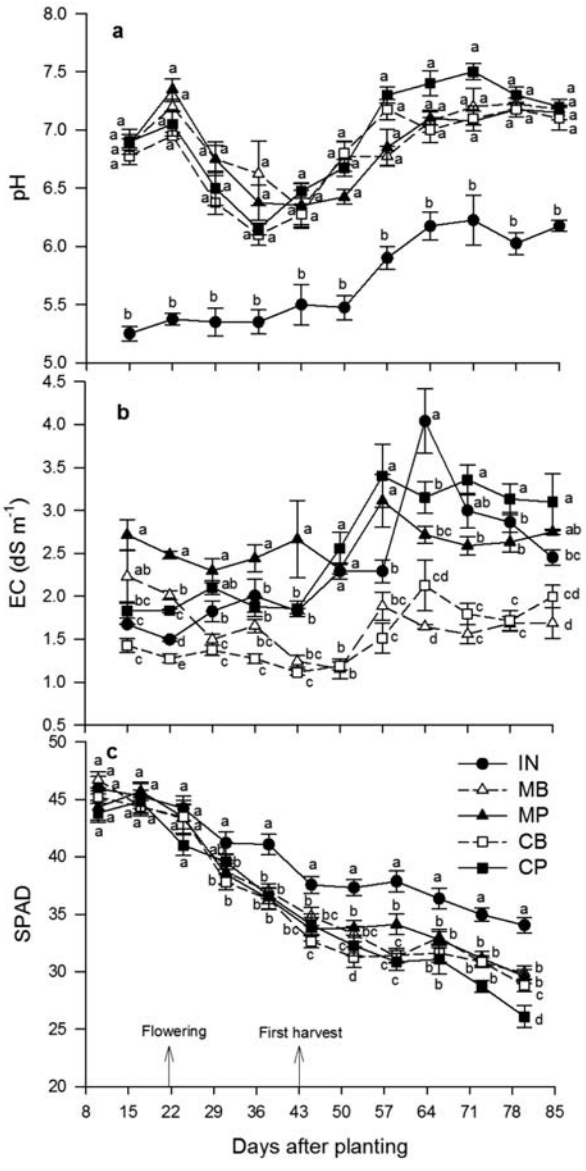

Figure 1. Effect of inorganic (IN) and different organic fertilizer strategies Monterra Malt + broad bean (MB), Monterra Malt + Pioner (MP), chicken manure + broad bean (CB), and chicken manure + Pioner (CP) on (a) pH, (b) EC measured in drainage water 15−85 days after planting, and (c) SPAD measurements on the youngest fully expanded leaves. Bars indicate standard error of the mean (n = 4), and different letters indicate statistically significant differences between strategies within a week (P < 0.05).

Three weeks after planting (23 DAP), almost all nitrogen in the drainage water was in the form of NO_3^- in the inorganic and NH_4^+ in the organic treatments (Table 4). Nine weeks after planting (65 DAP), the NH_4^+ concentration was low in drainage from all treatments, whereas the NO_3^- concentration was high in the inorganic treatment, medium high when fertigated with Pioner K-max, and very low when fertigated with broad bean. The potassium concentration was higher in drainage water from plants fertigated with Pioner Hi-Fruit/K-max compared with broad bean, and 23 DAP more potassium was available from Monterra Malt than from chicken manure. Both potassium and sodium accumulated over time when Pioner Hi-Fruit/K-max was applied, but also to some extent when inorganic fertilizer was given. Concentrations of phosphorus, magnesium, calcium, manganese, zinc, copper, and boron were in general higher in the inorganic treatment.

SPAD. Until 24 DAP, no differences in SPAD values were observed for young fully developed leaves, but after that date the inorganic treatment showed significantly higher SPAD values than the organic treatments (Figure 1c). The observed SPAD values decreased from the beginning of the experiment toward the end in all fertilizer strategies.

DM Distribution. Similar amounts of fruit DM were found in all treatments, whereas more DM was found in leaves and runners of plants receiving inorganic fertilizer (Figure 2a). Therefore, a larger percentage of the accumulated above-ground DM was allocated to fruit in the organic treatments (62−66% of total DM) compared to the inorganic treatment (52% of total DM) (Figure 2b). The total DM per plant was also significantly higher in the inorganic treatment. The biomass of leaves and runners from the different organic treatments was not statistically different. Similar percentages of DM were allocated to leaves (33−39%) in all treatments, but more to runners in plants given inorganic (9%) than in those given organic fertilizer (1−3%).

Nutrient Concentrations in Leaves and Fruits. On day 24 after planting, the leaf concentrations of N, K, Mg, and Ca were within the recommended levels for strawberry growth[14] in all treatments, although for N, K, and Mg relatively high values were found (Table 5). The P concentrations in leaves from the inorganic and chicken manure treatments were in excess of the recommended values at 24 DAP, whereas the P concentration was similar in leaves and fruits given Monterra Malt or chicken manure at 66 DAP. On the other hand, leaf S and Cu levels were deficient in all treatments. In general, the concentrations of all micronutrients were lower in leaves from plants given organic fertilizers compared with the inorganic fertilizer (Table 5). Midway through the picking period (66 DAP) a similar pattern in leaf nutrient concentration was seen as at 24 DAP, but the leaf N levels were slightly lower in all treatments and the N concentration in the inorganic treatment was higher than in the organic treatments. The leaf Ca was highest in the inorganic treatment and low but still within the recommended range in the organic treatments. The S concentration in leaves at 66 DAP was about 3-fold higher than at 24 DAP for all

DOI: 10.1021/acs.jafc.5b01366
J. Agric. Food Chem. 2015, 63, 5578−5586

Table 4. Nutrient Concentration in Drainage Water at 23 and 65 DAP of Strawberry Plants Grown with One Inorganic (IN) and Four Different Organic Fertilizer Strategies, Monterra Malt + Broad Bean (MB), Monterra Malt + Pioner (MP), Chicken Manure + Broad Bean (CB), and Chicken Manure + Pioner (CP)[a]

	23 DAP					65 DAP				
nutrient (mg L^{-1})	IN	MB	MP	CB	CP	IN	MB	MP	CB	CP
NO_3^--N	99a	2b	2b	2b	4b	130a	2c	61b	3c	30b
NH_4^+-N	1e	99b	136a	36d	84c	0	2	1	1	1
P	35bc	18d	34c	38bc	56a	32a	6c	3d	9b	3d
K	143e	259c	321a	218d	283b	257b	192c	472a	176c	492a
Mg	32a	8bc	6c	10b	8bc	68a	25c	17d	33b	27c
Ca	165a	32b	27b	30b	31b	409a	102b	56d	83bc	77cd
S	59b	95a	95a	32c	47bc	371a	45c	62bc	47bc	80b
Na	31d	58b	68a	50c	57b	103b	57c	167a	65c	187a
Cl	53d	98ab	101a	91bc	88c	165ab	141b	165ab	169ab	213a
Mn	0.59a	0.07b	0.07b	0.07b	0.06b	0.06a	0.04b	0.06a	0.02c	0.03bc
Fe	0.88c	1.38ab	1.75a	1.32bc	1.14bc	1.48a	0.20c	0.30b	0.15c	0.20c
Zn	0.45a	0.04b	0.05b	0.06b	0.07bc	0.32a	0.12b	0.15b	0.13b	0.16b
Cu	0.19a	0.03c	0.05b	0.04b	0.04b	0.18a	0.04b	0.01b	0.01b	0.01b
B	0.17a	<LOD	<LOD	0.01b	0.01b	0.11a	0.01b	0.01b	0.01b	0.02b
Mo	<LOD	<LOD	<LOD	<LOD	<LOD	0.01c	0.02b	0.03a	0.02b	0.02ab

[a]Means (n = 4) within each row and development stage followed by different letters are significantly different (P <0.05). <LOD, below limit of detection.

treatments. In fruit, the highest contents of all nutrients were seen in the inorganic treatment, but the magnesium concentration did not differ between treatments at day 66 after planting (Table 6).

Fruit Yield and Quality. The five fertilization strategies influenced fruit weight and total and marketable fruit yield per plant. The inorganic strategy resulted in the highest total yield, marketable yield, and fruit weight, but except for the fruit weight these parameters did not differ significantly from the Monterra Malt combined with broad bean treatment (Table 7). When the organic strategies were compared in a separate statistical analysis, the broad bean fertigation resulted in a higher marketable and total yield than fertigation with Pioner Hi-Fruit/K-max, whereas the two solid fertilizers incorporated in the growing media resulted in similar yields. The fruit weight did not differ among the organic fertilizer strategies. No statistical differences were found in the percentage of marketable fruit among the five treatments (Table 7).

Fruit TSS and TA were generally higher in plants given Pioner Hi-Fruit/K-max compared with broad bean fertilizer (Table 8), but for fruit harvested 56 DAP TSS contents were similar in all treatments. Fertigation with broad bean fertilizer resulted in similar TSS and TA contents as inorganic fertilizer.

In general, fruit from the organic treatments was noticeably firmer than fruit from the inorganic treatment, and plants supplied with chicken manure tended to produce firmer fruit than plants given Monterra Malt. No significant difference was found between treatments with regard to fruit DM content, but fruit from the organic strategies tended to have a higher percentage DM.

DISCUSSION

Fruit Yield and DM Distribution. The fruit yield and quality of strawberries grown under organic conditions may differ from conventional production systems.[4−7] Furthermore, different forms of organic fertilizer may affect the yield, quality, and nutrient content of strawberry fruit differently.[6,24] In our study, differences in fruit yield were primarily due to differences in fruit weight rather than the number of fruits per plant, indicating that deficient or excess levels of nutrients or other growing conditions have not caused flower abortion as fruit number was determined during flower induction the previous year.[25] The observed reductions in fruit yield and fruit weight from organic treatments may be due to a combination of the following conditions in the root zone: (1) high pH and high NH_4^+/NO_3^- ratio; (2) high EC and/or high NaCl concentration; (3) cation imbalance; and (4) nutrient deficiency.

High pH and High NH_4/NO_3 Ratio. In accordance with previous investigations,[26,27] the pH_{dw} from plants supplied with organic fertilizers was higher than for plants receiving inorganic fertilizers. The higher root zone pH could be responsible for the lower fruit yield in the organic treatments because it influences root growth and nutrient solubility/availability and uptake.[6,16] Also, a high pH may cause precipitation of carbonates of Ca^{2+}, Mg^{2+}, and other cations.[28,29] That $CaCO_3$ precipitation took place is supported by the lower Ca concentrations in drainage water and leaves from the organic treatments, although the Ca^{2+} concentrations in the given organic fertigation solution were similar to the inorganic fertigation solution (Table 3). Furthermore, the availability of micronutrients in the root zone may be decreased at a soil pH >6.5, even in nutrient-rich conditions, due to tight binding with organic matter, clay, and other negatively charged particles.[10,15−17]

In addition to high pH, a high concentration of NH_4^+ in the root zone may have reduced the fruit yield from organic treatments. Tabatabaei et al.[30] reported that a high concentration of NH_4^+ inhibited photosynthesis, growth, and yield in strawberry, and a high ratio of NH_4^+ to NO_3^- has been shown to reduce the biomass allocation to vegetative plant parts.[31] In accordance with this, a larger proportion of total plant DM accumulated in fruit from the organic treatments despite a lower fruit yield in three of the four organic combinations compared with inorganic fertigation (Figure 2).

High EC and/or High NaCl. In the present study, the reduced yield and fruit weight from plants receiving Pioner Hi-fruit/K-max could also be due to high EC_{dw} as values were higher than the optimum level recommended for strawberry

DOI: 10.1021/acs.jafc.5b01366
J. Agric. Food Chem. 2015, 63, 5578−5586

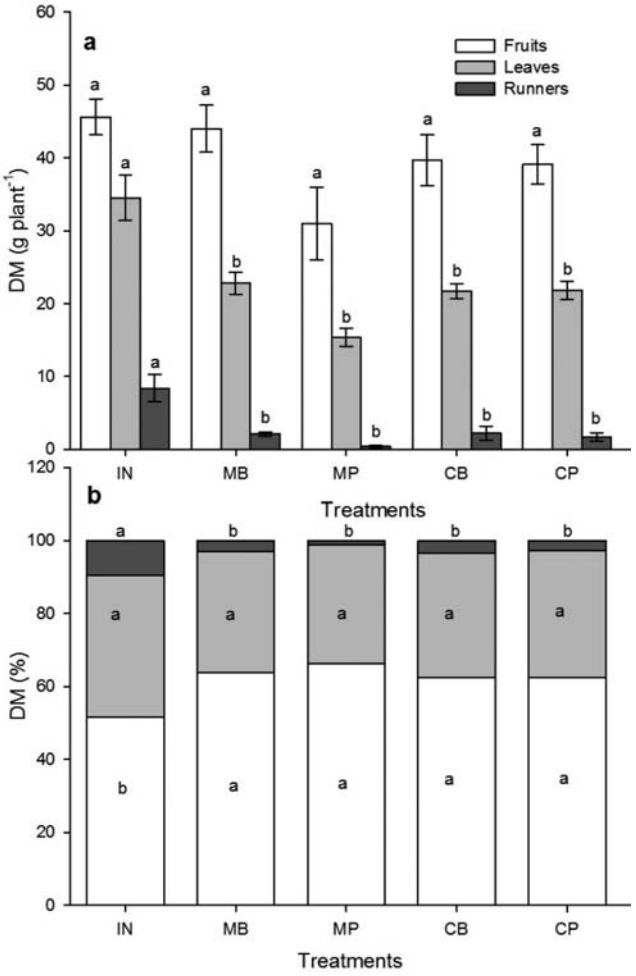

Figure 2. Effect of inorganic (IN) and different organic fertilizer strategies Monterra Malt + broad bean (MB), Monterra Malt + Pioner (MP), chicken manure + broad bean (CB), and chicken manure + Pioner (CP) on (a) dry matter content of fruits, leaves, and runners and (b) percentage of dry mater in fruits, leaves, and runners of *Fragaria ×ananassa* 'Sonata'. Bars are mean values ± standard error of the mean (n = 4). Different letters indicate statistically significant differences within each plant part (P < 0.05).

growth.[32−34] It was shown that EC levels >1.71 dS m^{-1} decreased the fruit yield and fruit weight;[34] however, the sensitivity to high EC depended on cultivar and types of dissolved solutes.[32,34,35] Moreover, the lower yield due to the Pioner fertigation may be the result of high concentrations of Na^+ and Cl^- in the root zone. Strawberry plants are considered sensitive to high concentrations of NaCl, although some cultivars are more tolerant than others.[35,36] Previous studies have reported that NaCl stress can reduce fruit yield in both salt-tolerant and -intolerant strawberry cultivars[36] if the EC value of the nutrient solution is >2.5 dS m^{-1}.[32] In susceptible cultivars leaf symptoms are visible at 6 mM NaCl, but not in tolerant cultivars.[35] In the present study, concentrations of Na^+ and Cl^- in the drainage water reached maximum concentrations of 8.1 and 6.0 mM, respectively, when chicken manure + Pioner fertigation was given; however, visual symptoms were not noticed in leaves (Table 4). Therefore, we cannot exclude a minor negative effect on fruit yield of NaCl, but it is not likely to be the main cause of the lower yield when organic fertilizers were given.

Cation Imbalance. An imbalance between cations in the root zone could also contribute to the reduced fruit yield from organic treatments. It has been shown for several plant species that the concentration ratios of K^+, Ca^{2+}, and Mg^{2+} within the plant are linearly correlated with the corresponding ratios of cation activities (a_K, a_{Ca}, and a_{Mg}) of the soil solution.[37] Nutrient analyses of drainage water revealed very high K^+/Ca^{2+} and K^+/Mg^{2+} ratios in the organic fertilization strategies, especially when Pioner Hi-fruit/K-max was applied (Table 4), and this resulted in decreased concentrations of Ca and Mg in the leaves. High K^+/Ca^{2+} and K^+/Mg^{2+} ratios in the fertigation solution reduce fruit number, fruit weight, and yield in strawberries.[38] Also, the high levels of NH_4^+ in the root zone may have competed with Ca^{2+}, Mg^{2+}, and K^+ during root uptake and resulted in lower leaf concentrations of Ca, Mg, and K and lower fruit concentrations of Ca and K.[31]

Nutrient Deficiency. Low levels of available N and P in the root zone, especially at the end of the fruiting period, could also have caused the reduced fruit yield and fruit weight when plants were supplied with organic fertilizer. Leaf and fruit analyses showed that N and K were the predominant nutrients, which is in agreement with previous findings.[8,31] In all treatments, the leaf N concentrations were between 2.7 and 3.6% of DM, which

Table 5. Effect of Inorganic (IN) and Four Different Organic Fertilizer Strategies, Monterra Malt + Broad Bean (MB), Monterra Malt + Pioner (MP), Chicken Manure + Broad Bean (CB), and Chicken Manure + Pioner (CP), on Nutrient Concentrations in Strawberry Leaves at 24 and 66 DAP[a]

		macronutrients (% of DM)						micronutrients (mg kg^{-1} of DM)				
DAP	treatment	N	P	K	Ca	Mg	S	B	Cu	Fe	Mn	Zn
24	IN	3.6a	0.56a	2.7a	1.14a	0.46a	0.24b	55.4a	3.2a	83.2a	268a	25.9a
	MB	3.5a	0.36c	2.4ab	0.74bc	0.40bc	0.29a	21.7c	2.3b	51.5b	132b	14.1c
	MP	3.6a	0.38c	2.3b	0.65c	0.38c	0.28a	18.7c	2.8b	46.1b	123b	14.8bc
	CB	3.5a	0.48b	2.6ab	0.89b	0.46a	0.27ab	36.3b	2.3b	54.4b	145b	21.2ab
	CP	3.5a	0.50b	2.5ab	0.73bc	0.43ab	0.26ab	29.3c	2.3b	46.9b	151b	18.8bc
66	IN	3.2a	0.48a	2.4a	1.25a	0.36a	0.74a	46.6a	4.0a	82.5a	173a	21.0a
	MB	2.9ab	0.32b	2.1a	0.96b	0.37a	0.76a	10.6c	1.4b	49.3b	169a	20.3ab
	MP	2.8b	0.25b	2.4a	0.74bc	0.27a	0.78a	15.0bc	1.9b	48.0bc	128b	16.7bc
	CB	2.7b	0.30b	2.3a	0.97b	0.34a	0.81a	20.5b	1.6b	50.2b	132b	15.3c
	CP	2.7b	0.26b	2.4a	0.60c	0.31a	0.76a	16.6bc	1.7b	40.5c	103b	17.4abc

[a]Means (n = 4) within each column followed by different letters are significantly different (P <0.05) according to Tukey's studentized range test.

DOI: 10.1021/acs.jafc.5b01366
J. Agric. Food Chem. 2015, 63, 5578−5586

Table 6. Effect of Inorganic (IN) and Four Different Organic Fertilizer Strategies, Monterra Malt + Broad Bean (MB), Monterra Malt + Pioner (MP), Chicken Manure + Broad Bean (CB), and Chicken Manure + Pioner (CP), on Nutrient Concentrations in Strawberry Fruit[a]

	macronutrients (% of DM)						micronutrients (mg kg^{-1} of DM)				
treatment	N	P	K	Ca	Mg	S	B	Cu	Fe	Mn	Zn
IN	1.12a	0.32a	1.87a	0.12a	0.12a	0.089a	13.5a	1.69a	15.5a	36.1a	8.2a
MB	1.03ab	0.23b	1.66ab	0.10ab	0.12a	0.088a	3.5bc	0.38b	9.7b	28.0b	7.3ab
MP	1.03ab	0.19c	1.56b	0.06b	0.11a	0.080ab	3.1c	0.47b	6.4bc	24.6b	5.9b
CB	0.82c	0.21bc	1.57b	0.10ab	0.12a	0.069b	5.3b	0.29b	5.9bc	24.0b	5.4b
CP	0.96bc	0.19bc	1.55b	0.06b	0.12a	0.076ab	4.5bc	0.63b	3.2c	25.0b	5.4b

[a]Means (n = 4) within each column followed by different letters are significantly different (P <0.05) according to Tukey's studentized range test.

Table 7. Effect of Inorganic (IN) and Four Different Organic Fertilizer Strategies, Monterra Malt + Broad Bean (MB), Monterra Malt + Pioner (MP), Chicken Manure + Broad Bean (CB), and Chicken Manure + Pioner (CP), on Individual Fruit Weight, Total and Marketable Fruit Yield, Number of Fruits per Plant, and Percentage of Marketable Yield (± Standard Error of the Mean) of Strawberry Fruit[a]

treatment	fruit yield[b] (g plant^{-1})	fruit wt[b] (g)	no. of fruits per plant[b]	fruit yield (%)[b]	total fruit yield (g plant^{-1})
IN	309 ± 17a	15.0 ± 0.7a	21.6 ± 0.9a	86.8 ± 3.3a	356 ± 15a
MB	265 ± 24ab	13.8 ± 0.5bc	21.0 ± 2.1a	81.6 ± 2.6a	324 ± 22ab
MP	191 ± 15c	11.7 ± 0.4c	16.4 ± 1.1a	83.0 ± 4.3a	231 ± 18c
CB	244 ± 18bc	13.9 ± 0.6b	18.8 ± 1.2a	84.1 ± 2.2a	290 ± 21b
CP	230 ± 12bc	12.7 ± 0.9bc	18.4 ± 0.8a	81.1 ± 1.6a	283 ± 13bc

[a]Means (n = 4) within each column followed by different letters are significantly different (P < 0.05) according to Tukey's studentized range test. [b]Marketable.

Table 8. Effect of Inorganic (IN) and Four Different Organic Fertilizer Strategies, Monterra Malt + Broad Bean (MB), Monterra Malt + Pioner (MP), Chicken Manure + Broad Bean (CB), and Chicken Manure + Pioner (CP), on TSS, TA, Firmness, and DM (± Standard Error of the Mean) of Strawberry Fruits[a]

	56 DAP				70 DAP				
treatment	TSS (°Brix)	TA (g 100 g^{-1})	TSS/TA	firmness (N)	TSS (°Brix)	TA (g 100 g^{-1})	TSS/TA	firmness (N)	DM (%)
IN	5.4 ± 0.2a	0.63 ± 0.01b	8.5 ± 0.2a	2.45 ± 0.1b	6.5 ± 0.1c	0.62 ± 0.01b	10.5 ± 0.1a	2.94 ± 0.1b	11.4 ± 0.6a
MB	5.4 ± 0.1a	0.64 ± 0.01ab	8.5 ± 0.1a	2.93 ± 0.1ab	6.7 ± 0.2bc	0.61 ± 0.02b	11.3 ± 0.4a	3.06 ± 0.4ab	13.1 ± 0.3a
MP	5.8 ± 0.1a	0.64 ± 0.01ab	9.0 ± 0.2a	2.89 ± 0.3ab	8.0 ± 0.1a	0.75 ± 0.01a	10.7 ± 0.1a	3.76 ± 0.3ab	12.7 ± 1.3a
CB	5.5 ± 0.2a	0.63 ± 0.01b	8.8 ± 0.3a	3.02 ± 0.1a	6.8 ± 0.1bc	0.61 ± 0.03b	11.3 ± 0.6a	3.86 ± 0.4a	12.7 ± 0.2a
CP	5.8 ± 0.1a	0.67 ± 0.01a	8.6 ± 0.2a	3.00 ± 0.2a	7.4 ± 0.3ab	0.69 ± 0.02ab	10.9 ± 0.5a	3.82 ± 0.4ab	13.4 ± 0.4a

[a]Means (n = 4) within each column followed by different letters are significantly different (P < 0.05) according to Tukey's studentized range test.

are within the optimum tissue level for strawberry growth (Table 5).[14] When comparing the leaf N concentration in the organic and inorganic treatments, we observed similar concentrations 24 DAP, whereas a lower concentration was found in leaves from the organic treatments 66 DAP. This demonstrates that incorporation of composted chicken manure or Monterra Malt, which increased total N in the growing media considerably, could supply sufficient N in the beginning of the growing period, whereas the organic fertigation solutions were both insufficient in N supply. The N concentration in fruit was also higher in the inorganic than in the organic treatments when composted chicken manure was incorporated prior to planting. Insufficient N supply may have decreased both total plant biomass and total fruit yield due to a reduced chlorophyll content and photosynthesis, which was indicated by lower SPAD values in the organic treatments (Figure 1c). In our study, the K concentration in the Pioner Hi-Fruit fertigation solution was 2 and 2.5 times higher than in the inorganic and broad bean solutions, respectively. However, only minor differences in leaf K were seen, and fruit K concentrations were generally lower in the organic treatments. Also, the leaf Ca concentration was lower in the organic treatments compared with the inorganic treatments, and the level was deficient according to Reuter and Robinson.[14] As previously mentioned, this could be due to $CaCO_3$ precipitation in the alkaline growing medium.[29] Similarly, the low concentrations of Fe, Mn, B, and Zn in the root zone of the organic treatments may be due to complexing with hydroxides, phosphates, and carbonates at the high pH.[39,40] These low levels of micronutrients in the root zone were also reflected by leaf and fruit tissue concentrations in the deficient range of the same micronutrients[14] and may have negatively influenced both the vegetative and generative growth in the organic treatments. Previous studies have also shown that the nutrient concentrations of applied fertilizers are not the only determinant of mineral uptake in strawberry plants and fruits because soil properties such as pH, EC, NaCl, and microbial activity greatly determine nutrient uptake by plants.[6,15]

Fruit Quality. In our study, we considered TSS, TA, firmness, and DM as important parameters for the eating quality of fruits. TSS and firmness were higher in fruit harvested 70 DAP than in fruit harvested 56 DAP, and these differences could be due to the decreasing temperature and the smaller fruit size of secondary and tertiary fruits and thereby an up-concentration of the soluble solids.[41−43] At the last harvest (70 DAP), TSS and TA in fruit supplied with Pioner fertigation

DOI: 10.1021/acs.jafc.5b01366
J. Agric. Food Chem. 2015, 63, 5578−5586

were higher compared with fruit supplied with inorganic fertigation, and fruit from the broad bean treatments were intermediate. Our finding is in agreement with Reganold et al.,[8] and Shehata et al.,[24] as they also observed higher TSS in organically grown fruit than in inorganically grown fruit. Also, the fruit DM content tended to be higher in the organic treatments, indicating that the higher TSS could be due to lower fruit water content as seen in other studies.[8] In our study, plants from the Pioner fertigation were smaller, which may have allowed more light penetration due to less self-shading effect. Hargreaves et al.[6] and Watson et al.[44] reported that plants exposed to a higher light integral contained more sugar in their fruit. The higher availability of nitrogen in the inorganic treatment may also explain the lower TSS in fruit as Cantliffe et al.[12] reported that increasing amounts of nitrogen fertilizer reduced fruit TSS. The fruit firmness and DM content tended to be higher in the organic fertilization strategies, which is in agreement with the findings of Reganold et al.,[8] and may be due to a higher proportion of cell wall content in the small-sized organic fruits compared to the large-sized inorganic fruits[45] as a result of the lower N level in organic fruit.[46]

In conclusion, incorporation of Monterra Malt in a limed peat-based growing medium combined with broad bean fertigation resulted in similar marketable fruit yield and quality, except for slightly smaller fruits, compared to an inorganic fertilizer strategy. A minor increase in quality parameters of fruits (firmness, TSS, and TA) was seen at the end of the fruiting period when plants were fertigated with Pioner High Fruit/K-max, which was probably due to reduced fruit size. Organic fertilizer combinations resulted in high pH, EC, and/or NaCl concentration and NH_4^+/NO_3^- ratio, cation imbalance, and nutrient deficiency in the root zone, which may be responsible for the lower fruit yield and fruit weight relative to organic treatments.

AUTHOR INFORMATION

Corresponding Author

*(B.P.) E-mail: bhaniswor.pokhrel@food.au.dk. Phone: +45 87158316.

Notes

The authors declare no competing financial interest.

ABBREVIATIONS USED

IN, inorganic; DAP/F, days after planting/fertigation; TSS, total soluble solids; TA, titratable acid; DM, dry matter; EC_{dw}, electrical conductivity of drainage water; pH_{dw}, pH of drainage water

REFERENCES

(1) FAOSTAT. *Annual Production Report*; United Nations: Rome, Italy, 2015.

(2) Bourn, D.; Prescott, J. A comparison of the nutritional value, sensory qualities and food safety of organically and conventionally produced food. *Crit. Rev. Food Sci. Nutr.* **2002**, *42*, 1−34.

(3) Brandt, K. Organic agriculture and food utilization. *Issues Paper for the International Conference on Organic Agriculture and Food Security*; FAO: Rome, Italy, May 3−5, 2007.

(4) Cayuela, A.; Vidueira, M.; Albi, M. A.; Gutie, F. Influence of the ecological cultivation of strawberries (*Fragaria ×ananassa* cv. Chandler) on the quality of the fruit and on their capacity for conservation. *J. Agric. Food Chem.* **1997**, *45*, 1736−1740.

(5) Wang, S. Y.; Lin, S. Compost as soil supplement enhanced plant growth and fruit quality of strawberry. *J. Plant Nutr.* **2002**, *25*, 2243−2259.

(6) Hargreaves, J. C.; Adl, M. S.; Warman, P. R.; Vasanta Rupasinghe, H. P. The effects of organic and conventional nutrient amendments on strawberry cultivation: fruit yield and quality. *J. Sci. Food Agric.* **2008**, *88*, 2669−2675.

(7) Arancon, N. Q.; Edwards, C. A.; Bierman, P.; Welch, C.; Metzger, J. D. Infuences of vermicomposts on field strawberries: effect on growth and yield. *Bioresour. Technol.* **2004**, *93*, 145−153.

(8) Reganold, J. P.; Andrews, P. K.; Reeve, J. R.; Carpenter-Boggs, L.; Schadt, W. C.; Alldredge, J. R.; Ross, C. F.; Davies, N. M.; Zhou, J. Fruit and soil quality of organic and conventional strawberry agroecosystems. *PLoS One* **2010**, *5*, e12346.

(9) Brandt, K.; Leifert, C.; Sanderson, R.; Seal, C. J. Agroecosystem management and nutritional quality of plant food: the case of organic fruit and vegetables. *Crit. Rev. Plant Sci.* **2011**, *30*, 177−197.

(10) Hochmuth, G. J.; Maynard, D.; Vavrina, C.; Hanlon, E. A.; Simonne, E. H. *Plant Tissue Analysis and Interpretation for Vegetable Crops in Florida*; HS964; UF-IFAS: Gainesville, FL, USA, Feb 2004.

(11) Yavari, S.; Eshghi, S.; Tafazoli, E.; Karimian, N. Mineral elements uptake and growth of strawberry as influenced by organic substrates. *J. Plant Nutr.* **2009**, *32*, 1498−1512.

(12) Cantliffe, D. J.; Castellanos, J. Z.; Paranjpe, A. V. Yield and quality of greenhouse-grown strawberries as affected by nitrogen level in coco coir and pine mark media. *Proc. Fla. St. Hortic. Soc.* **2007**, *120*, 157−161.

(13) Hochmuth, G. J.; Albregts, E. E.; Chandler, C. C.; Cornell, J.; Harrison, J. Nitrogen fertigation requirements of drip-irrigated strawberries. *J. Am. Soc. Hortic. Sci.* **1996**, *121*, 660−665.

(14) Reuter, D. J.; Robinson, J. B. *Plant Analysis: An Interpretation Manual*; CSIRO Publishing: Clayton, VIC, Australia, 1997; pp 376−377.

(15) Milosevic, T. M.; Milosevic, N. T.; Glisic, I. P. Strawberry (*Fragaria ×ananassa* Duch.) yield as affected by the soil pH. *An. Acad. Bras. Cienc.* **2009**, *81*, 265−269.

(16) Wright, A. L.; Hanlon, E. A.; Sui, D.; Rice, R. *Soil pH Effects on Nutrient Availability in the Everglades Agricultural Area*; HS287; UF-IFAS: Gainesville, FL, USA, April 2009.

(17) Jett, L. W. *Growing Strawberries in High Tunnels in Missouri*; University of Missouri: Columbia, MO, USA, 2007; Hight Tunnels Web site, http://hightunnels.org/wp-content/uploads/2013/06/Growing_Strawberries_in_High_Tunnels.pdf (accessed July 10, 2012.

(18) Gavriloaiei, T. The Influence of electrolyte solutions on soil pH measurements. *Rev. Chim. Bucharest* **2012**, *63*, 396−400.

(19) Sommer, S. G.; Hutchings, N. J. Ammonia emission from field applied manure and its reduction − invited paper. *Eur. J. Agron.* **2001**, *15*, 1−15.

(20) Pang, X. P.; Letey, J. Organic farming: challenge of timing nitrogen availability to crop nitrogen requirements. *Soil Sci. Soc. Am. J.* **2000**, *64*, 247−253.

(21) Miles, J.; Peet, M. *Maintaining Nutrient Balances in Systems Utilizing Soluble Organic Fertilizers*; Organic Farming Research Foundation Project Report; Santa Cruz, CA, USA, 2002; pp 00−23.

(22) Husted, S.; Mikkelsen, B. F.; Jensen, J.; Nielsen, N. E. Elemental fingerprint analysis of barley (*Hordeum vulgare*) using inductively coupled plasma mass spectrometry, isotope-ratio mass spectrometry, and multivariate statistics. *Anal. Bioanal. Chem.* **2004**, *378*, 171−182.

(23) Laursen, K. H.; Schjoerring, J. K.; Olesen, J. E.; Askegaard, M.; Halekoh, U.; Husted, S. Multielemental fingerprinting as a tool for authentication of organic wheat, barley, faba bean and potato. *J. Agric. Food Chem.* **2011**, *59*, 4385−4396.

(24) Shehata, S. A.; Gharib, A. A.; El-mogy, M. M.; Gawad, A.; Shalaby, E. A. Influence of compost, amino and humic acids on the growth, yield and chemical parameters of strawberries. *J. Med. Plants Res.* **2011**, *5*, 2304−2308.

(25) Le Miére, P.; Hadley, P.; Darby, J.; Battey, N. H. The effect of temperature and photoperiod on the rate of flower induction and the onset of dormancy in strawberry (*Fragaria ×ananassa* Duch.). *J. Hortic. Sci.* **1996**, *71*, 361−371.

(26) Moore, A. D.; Alva, A. K.; Collins, H. P.; Boydston, R. A. Mineralization of nitrogen from biofuel by-products and animal

DOI: 10.1021/acs.jafc.5b01366
J. Agric. Food Chem. 2015, 63, 5578−5586

manures amended to a sandy soil. *Commun. Soil Sci. Plant Anal.* **2010**, *41*, 1315−1326.
(27) Baitilwake, M.; De Bolle, S.; Salomez, J.; Mrema, J. P.; De Neve, S. Effect of organic fertilizers on nitrate accumulation in vegetables and mineral nitrogen in tropical soils of Morogoro, Tanzania. *Exp. Agric.* **2012**, *48*, 111−126.
(28) Nakayama, F. S. Calcium activity, complex and ion-pair in saturated $CaCO_3$ solution. *Soil Sci.* **1968**, *106*, 429−434.
(29) Coto, B.; Martos, C.; Peña, J. L.; Rodríguez, R.; Pastor, G. Effects in the solubility of $CaCO_3$: experimental study and model description. *Fluid Phase Equilib.* **2012**, *324*, 1−7.
(30) Tabatabaei, S. J.; Yusefi, M.; Hajiloo, J. Effects of shading and NO_3:NH_4 ratio on the yield, quality and N metabolism in strawberry. *Sci. Hortic.* **2008**, *116*, 264−272.
(31) Choi, J. M.; Latigui, A.; Lee, C. W. Growth and nutrient uptake responses of 'Seolhyang' strawberry to various ratios of ammonium to nitrate nitrogen in nutrient solution culture using inert media. *Afr. J. Biotechnol.* **2011**, *10*, 12567−12574.
(32) D'Anna, F.; Incalcaterra, G.; Moncada, A.; Miceli, A. Effects of different electrical conductivity levels on strawberry grown in soilless cultures. *Acta Hortic.* **2003**, *609*, 355−360.
(33) Khayyat, M.; Tafazoli, E.; Eshghi, S.; Rahemi, M.; Rajaee, S. Salinity, supplementary calcium and potassium effects on fruit yield and quality of strawberry (*Fragaria ×ananassa* Duch.). *Am.-Eurasian J. Agric. Environ. Sci.* **2007**, *2*, 539−544.
(34) Suarez, D. L.; Grieve, C. M. Growth, yield and ion relations of strawberry in response to irrigation with chloride-dominated waters. *J. Plant Nutr.* **2013**, *36*, 1963−1981.
(35) Martinez Barroso, M. C.; Alvarez, C. E. Toxicity symptoms and tolerance of strawberry to salinity in the irrigation water. *Sci. Hortic.* **1997**, *71*, 177−188.
(36) Saied, A. S.; Keutgen, A. J.; Noga, G. The influence of NaCl salinity on growth, yield and fruit quality of strawberry cvs. Elsanta and Korana. *Sci. Hortic.* **2005**, *103*, 289−303.
(37) Nielsen, N. E.; Hansen, E. M. Macronutrient cation uptake by plant. II. Effects of plant species, nitrogen concentration in plant, cation concentration, activity and activity ratio in solution. *Plant Soil* **1984**, *77*, 347−365.
(38) Lieten, P. Effect of K:Ca:Mg ratio on performance of Elsanta strawberry grown on peat. *Acta Hortic.* **2006**, *708*, 397−400.
(39) Silveira, M. L. A.; Alleoni, L. R. F.; Guilherme, L. R. G. Biosolids and heavy metals in soils. *Sci. Agric.* **2003**, *60*, 793−806.
(40) Park, J. H.; Lamb, D.; Panneerselvam, P.; Choppala, G.; Bolan, N. Role of organic amendments on enhanced bioremediation of heavy metal (loid) contaminated soils. *J. Hazard. Mater.* **2011**, *185*, 549−574.
(41) Wang, S. Y.; Camp, M. J. Temperatures after bloom affect plant growth and fruit quality of strawberry. *Sci. Hortic.* **2000**, *85*, 183−199.
(42) Hoppula, K. B.; Karhu, S. T. Strawberry fruit quality responses to the production environment. *J. Food Agric. Environ.* **2006**, *4*, 166−170.
(43) Ferreyra, R. M.; Vina, S. Z.; Mugridge, A.; Chaves, A. R. Growth and ripening season effects on antioxidant capacity of strawberry cultivar Selva. *Sci. Hortic.* **2007**, *112*, 27−32.
(44) Watson, R.; Wright, C. J.; Mcburney, T.; Taylor, A. J.; Linforth, R. S. T. Influence of harvest date and light integral on the development of strawberry flavour compounds. *J. Exp. Bot.* **2002**, *53*, 2121−2129.
(45) Amarante, C. V. T.; Steffens, C. A.; LuizMafra, A.; Albuquerque, J. A. Yield and fruit quality of apple from conventional and organic production system. *Pesqui. Agropecu. Bras.* **2008**, *43*, 333−340.
(46) Miner, G. S.; Poling, E. B.; Carroll, D. E.; Nelson, L. A.; Campbell, C. R. Influence of fall nitrogen and spring nitrogen-potassium applications on yield and fruit quality of 'Chandler' strawberry. *J. Am. Soc. Hortic. Sci.* **1997**, *122*, 290−295.

DOI: 10.1021/acs.jafc.5b01366
J. Agric. Food Chem. 2015, 63, 5578−5586

sized compounds displayed nanomolar potency toward *At*HPPD. In addition, some compounds exhibited promising and broad-spectrum herbicidal activity at the rate of 150 g ai/ha as well as selectivity to several crops, such as maize, wheat, or rice.

MATERIALS AND METHODS

Detailed information for the synthesis of compounds **I**–**VI** is shown in Figures 1–4.

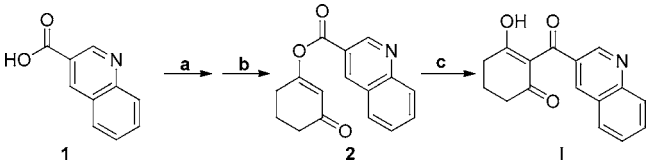

Figure 1. Synthetic route for lead compound **I**. Reagents and conditions: (a) $(COCl)_2$, CH_2Cl_2, −5 °C; (b) 1,3-cyclohexanedione, CH_2Cl_2, 0 °C; (c) acetone cyanohydrin, Et_3N, CH_2Cl_2, room temperature.

X-ray Diffraction. Compound **III-d** was recrystallized from a mixture of acetone and *n*-hexane to afford a suitable single crystal. Light brown crystals of **III-d** (0.20 mm × 0.20 mm × 0.20 mm) were mounted on a quartz fiber with protection oil. Cell dimensions and intensities were measured at 298 K on a Bruker SMART APEX DUO area detector diffractometer (Bruker AXS, Madison, WI, USA) with graphite monochromated Mo Kα radiation (λ = 0.71073 Å); θ_{max} = 28.00; 14889 measured reflections; 4658 independent reflections (R_{int} = 0.0484). The data sets were integrated and reduced using the SAINT Plus program.[24] Data were corrected for Lorentz and polarization effects and for absorption (T_{max} = 0.9821; T_{min} = 0.9821). The structure was solved by direct method using SHELXS97 and refined with SHELXL970.[25] Full-matrix least-squares refinement based on F^2 using the weight of $1/[\sigma^2(F_0^2) + (0.0976P)^2 + 0.2989P]$ gave final values of R_1 = 0.0690, ωR_2 = 0.1652, and GOF(F) = 1.128 for 265 variables, 265 parameters, and 4658 contributing reflections. Maximum shift/error = 0.000, and maximum/minimum residual electron density = 0.614 per −0.329 e Å^{-3}. Hydrogen atoms were observed and placed at their ideal positions with a fixed value of their isotropic displacement parameter.

Compound **III-f** was recrystallized from a mixture of acetone and *n*-hexane to afford a suitable single crystal. Light yellow crystals of **III-f** (0.12 mm × 0.10 mm × 0.10 mm) were mounted on a quartz fiber with protection oil. Cell dimensions and intensities were measured at 298 K on a Bruker SMART APEX DUO area detector diffractometer with graphite monochromated Mo Kα radiation (λ = 0.71073 Å); θ_{max} = 30.00; 15593 measured reflections; 4396 independent reflections (R_{int} = 0.1064). The data sets were integrated and reduced using the SAINT Plus program.[24] Data were corrected for Lorentz and polarization effects and for absorption (T_{max} = 0.9904; T_{min} = 0.9885). The structure was solved by direct method using SHELXS97 and refined with SHELXL970.[25] Full-matrix least-squares refinement based on F^2 using the weight of $1/[\sigma^2(F_0^2) + (0.0886P)^2 + 0.2528P]$ gave final values of R_1 = 0.0514, ωR_2 = 0.1438, and GOF(F) = 1.067 for 211 variables, 211 parameters, and 4396 contributing reflections. Maximum shift/error = 0.000, and maximum/minimum residual electron density = 0.869 per −0.369 e Å^{-3}. Hydrogen atoms were observed and placed at their ideal positions with a fixed value of their isotropic displacement parameter.

Crystallographic data for compounds **III-d** and **III-f** have been deposited with the Cambridge Crystallographic Data Centre as a supplementary publication with the deposition no. 1040193 and 977357, respectively. These data can be obtained free of charge from http://www.ccdc.cam.ac.uk/.

Plasmid Construction, Protein Expression and Purification, Activity Assays, and Kinetic Inhibition Studies. *At*HPPD was constructed by PCR using cDNA of HPPD in pMD19-T Simple (Hangzhou BIOSCI Biotechnology Company, Hangzhou, China) as the template. The primers used here were 5′-CATGCCATGGGCC-ACCAAAACGCCGC-3′ (Nco*I*) and 5′- CGCGGATCCTCAGTG-GTGGTGGTGGTGGTCCCACTAACTGTTT-3′ (*Bam*HI). PCR conditions were 35 cycles at 94 °C for 30 s, 55 °C for 30 s, and 68 °C for 1.5 min. The amplion was introduced into the expression vector pET-15b and subsequently transformed into *Escherichia coli* BL-21(DE3). The DNA sequences of the positive clones were confirmed by DNA sequencing with Shanghai SANGON Company.

Recombinant *At*HPPD was overexpressed in *E. coli* BL-21 (DE3) cells with pET-15b-HPPD plasmid. Recombinant homogentisate 1,2-dioxygenase (HGD) from human was overexpressed in *E. coli* BL-21 (DE3) cells with pET-28a-HGD plasmid. The cells were grown at 37 °C in Luria–Bertani broth supplemented with 50 μg/mL kanamycin (pET-28a plasmid) or 100 μg/mL antimycin (pET-15b plasmid) according to a previous publication.[26] Expression of the *At*HPPD plasmid was incubated at 37 °C for 12 h. HGD was induced by 0.5 mM isopropyl β-D-1-thiogalactopyranoside (IPTG) when bacterial grown reached an A_{600} of 0.6, and then the cells were incubated for another 40 h at 15 °C. After harvesting by centrifugation (5000*g*, 30 min), the pellet was resuspended in buffer (20 mM HEPES, 20 mM NaCl, pH 7.0) and washed twice, followed by sonication using a cell

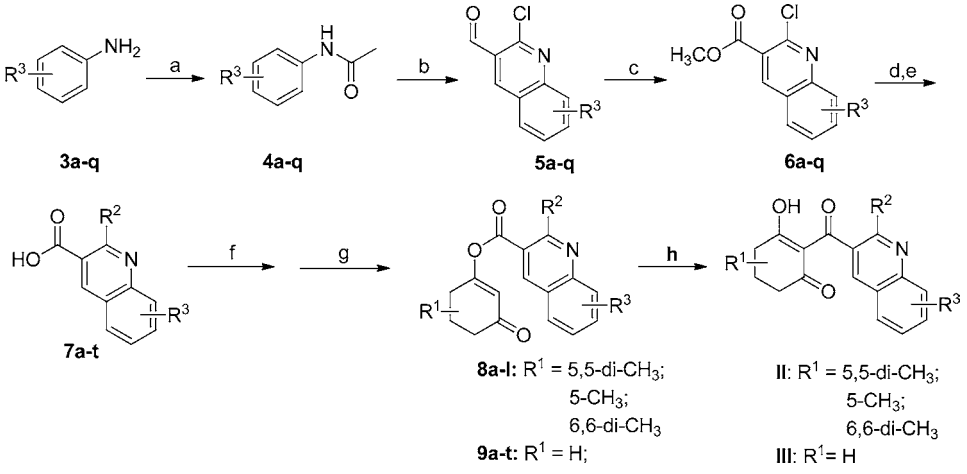

Figure 2. Synthetic route for compounds **II** and **III**. Reagents and conditions: (a) $(CH_3C)_2O$, Et_3N, CH_2Cl_2, 0 °C–room temperature; (b) DMF, $POCl_3$, 0–80 °C; (c) K_2CO_3, CH_3OH, I_2, reflux; (d) Na, alcohols, reflux; (e) H_2O, citric acid; (f) $(COCl)_2$, CH_2Cl_2, −5 °C; (g) (substituted) 1,3-cyclohexanedione, CH_2Cl_2, 0 °C; (h) acetone cyanohydrin, Et_3N, CH_2Cl_2, room temperature.

DOI: 10.1021/acs.jafc.5b01530
J. Agric. Food Chem. 2015, 63, 5587–5596

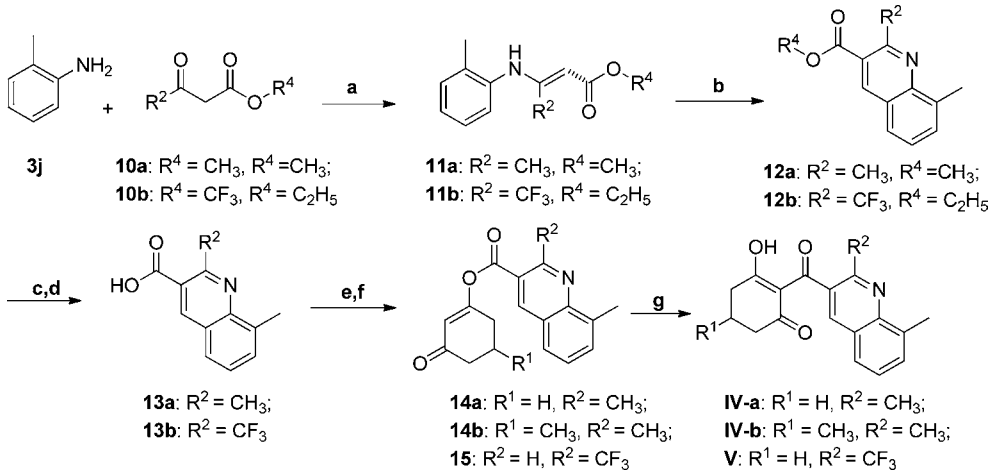

Figure 3. Synthetic route for target compounds **IV** and **V**. Reagents and conditions: (a) *p*-toluenesulfonic acid (*p*-TSA), cyclohexane, reflux; (b) DMF, $POCl_3$, DCE, 70−80 °C; (c) $LiOH{\cdot}H_2O$, methanol, H_2O, reflux; (d) citric acid; (e) $(COCl)_2$, CH_2Cl_2, 0 °C; (g) (substituted) 1,3-cyclohexanedione, Et_3N, CH_2Cl_2, 0 °C; (h) acetone cyanohydrin, Et_3N, CH_2Cl_2, room temperature.

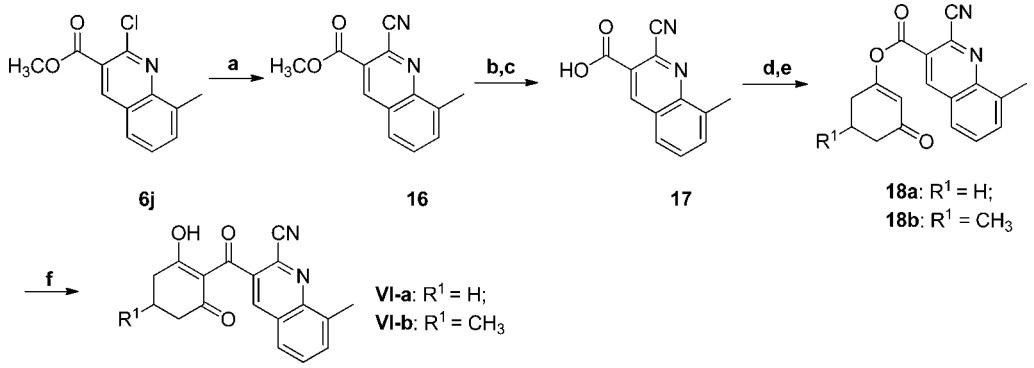

Figure 4. Synthetic route for target compounds **VI**. Reagents and conditions: (a) CuCN, DMF, reflux; (b) $LiOH{\cdot}H_2O$, methanol, H_2O, reflux; (c) citric acid; (d) $(COCl)_2$, CH_2Cl_2, 0 °C; (e) (substituted) 1,3-cyclohexanedione, Et_3N, CH_2Cl_2, 0 °C; (f) acetone cyanohydrin, Et_3N, CH_2Cl_2, room temperature.

disruptor. A crude cell-free supernatant was obtained by centrifugation at 20000 *g* for 30 min.

*At*HPPD was purified in two chromatographic steps. The crude cell-free supernatant was loaded onto a Ni-NTA column (Qiagen, Canada), equilibrated with 20 mM HEPES, pH 7.0. Then, HPPD was eluted with 20 mM HEPES, pH 7.0, 150 mM NaCl, and 250 mM imidazole. The fractions containing HPPD were concentrated, and the buffer was exchanged for 20 mM HEPES, pH 7.0, by ultrafiltration in Ultrafree filter devices (Millipore, Bedford, MA, USA). To further purify the recombinant HPPD, anion exchange chromatography was carried out on Q resin (Amersham-Pharmacia Biotech, Germany) in 20 mM HEPES, pH 7.0. Elution of the recombinant HPPD was carried out in a linear gradient from 0 to 250 mM NaCl. Again, the HPPD-containing fractions were collected and the buffer was exchanged to 20 mM HEPES, pH 7.0.

The in vitro activity and inhibition of *At*HPPD were measured by a modification of coupled enzyme assay methods previously reported in the literature.[27] Assays were performed in 96-well plates at 30 °C using a UV−visible plate reader (Biotech, Winooski, VT, USA) to monitor the formation of maleylacetoacetate at 318 nm (ε_{330} = 13500/M/cm). The reaction mixture in a total assay volume of 200 μL contained appropriate amounts of HPPA, 100 μM $FeSO_4$, 2 mM sodium ascorbate, 20 mM HEPES buffer (pH 7.0), HPPD, and HGD. Before assays were conducted, all reaction components were pre-equilibrated at 30 °C for at least 10 min. The amount of HGD activity was predetermined to be in large excess of the HPPD activity to ensure that the reaction was tightly coupled (the K_m of HGD for HGA was 25 μM). Each experiment was repeated in at least three duplicates, and the values were averaged. HPPD inhibitors were dissolved in dimethyl sulfoxide (DMSO) for stock solution and diluted to various concentrations with reaction buffer just before use. The inhibition constant (K_i), the indication of an inhibitor's potency, was obtained from the Dixon plot of plotting $1/v$ against concentration of inhibitor at certain concentrations of substrate. Bovine serum albumin is usually added up to 0.5% of the total reaction volume for coating of the target enzyme during the incubation. In our assay, no obvious effect from bovine serum albumin on the activity of the compounds has been found, which indicated that the new compounds selectively inhibited the target enzyme but did not interact with bovine serum albumin.

Computational Modeling and CoMSIA Analysis. The crystal structure of *At*HPPD was taken from the PDB data bank (PDB ID 1TFZ). Compounds were constructed and optimized by using SYBYL 7.0 (Tripos Inc.), and Gasteiger−Huckel charges were calculated for them. Docking calculations were performed on the two molecules by using AutoDock 4.0. The protein and ligand structures were prepared with AutoDock Tools. A total of 256 runs was launched for each molecule. Each docked structure was scored by the built-in scoring function and was clustered by 0.8 Å of RMSD criterions. The best binding modes were determined by docking scores and also the comparison with available complex crystal structure of DAS645 with *At*HPPD (PDB entry 1TG5) as reference.[28] Standard Amber ff99 force field parameters were assigned to protein, and general AMBER force field (gaff) was assigned to ligands. The partial atomic charges of ligands were calculated using the AM1-BCC method, and the system was solvated in an octahedral box of TIP3P water with the crystallographic water molecules kept. The edge of the box was at

DOI: 10.1021/acs.jafc.5b01530
J. Agric. Food Chem. 2015, 63, 5587−5596

Table 1. Chemical Structure and Postemergent Herbicidal Activity[a] of Compounds I–IV and Their Inhibitory Activities against *At*HPPD

				% inhibition						*At*HPPD inhibition
compd	R^1	R^2	R^3	EC[b]	SF[b]	DS[b]	AR[b]	EP[b]	AJ[b]	K_i[c] (μM)
I	H	H	H	0	0	0	0	0	0	0.075 ± 0.001
II-a	5,5-diCH_3	OCH_3	6-OCH_3	0	0	0	0	0	0	0.055 ± 0.005
II-b	5,5-diCH_3	OCH_3	7-OCH_3	0	0	0	30	0	30	0.304 ± 0.008
II-c	5,5-diCH_3	OCH_3	6-Cl	0	0	0	0	0	0	0.055 ± 0.001
II-d	5,5-diCH_3	OCH_3	7-SH_3	30	0	75	70	80	80	0.341 ± 0.005
II-e	5,5-diCH_3	OCH_3	8-CH_2CH_3	0	0	0	40	40	15	0.222 ± 0.009
II-f	5,5-diCH_3	OCH_3	8-$CH(CH_3)_2$	50	40	45	0	45	30	0.132 ± 0.009
II-g	5,5-diCH_3	OCH_3	7-F-8-CH_3	0	0	0	0	70	0	0.626 ± 0.210
II-h	5,5-diCH_3	OCH_3	7-Cl-8-CH_3	0	0	0	0	0	0	0.291 ± 0.015
II-i	5,5-diCH_3	OCH_3	7-Br-8-CH_3	0	0	0	0	0	0	0.041 ± 0.004
II-j	5,5-diCH_3	OCH_3	8-CH_3	0	0	0	0	50	0	0.298 ± 0.007
II-k	5-CH_3	OCH_3	8-CH_3	0	0	0	50	50	50	0.099 ± 0.003
II-l	6,6-diCH_3	OCH_3	8-CH_3	0	0	0	30	30	50	0.074 ± 0.009
III-a	H	OCH_3	8-CH_3	0	0	0	40	20	80	0.009 ± 0.001
III-b	H	OCH_2H_3	8-CH_3	0	0	0	0	30	0	0.025 ± 0.002
III-c	H	O-*n*-Pr	8-CH_3	0	0	0	0	30	0	0.171 ± 0.008
III-d	H	OCH_2Ph	8-CH_3	0	0	0	0	0	0	0.213 ± 0.006
III-e	H	OCH_3	H	15	0	0	30	20	100	0.062 ± 0.003
III-f	H	OCH_3	6-CH_3	0	0	0	0	0	0	0.030 ± 0.002
III-g	H	OCH_3	7-CH_3	0	0	0	60	60	80	0.024 ± 0.001
III-h	H	OCH_3	6-OCH_3	0	0	0	0	0	0	0.076 ± 0.005
III-i	H	OCH_3	7-OCH_3	30	0	0	80	50	30	0.029 ± 0.005
III-j	H	OCH_3	6-Cl	0	0	0	0	0	95	0.072 ± 0.008
III-k	H	OCH_3	7-Cl	0	0	0	80	55	95	0.011 ± 0.001
III-l	H	OCH_3	7-SCH_3	90	85	90	90	90	100	0.009 ± 0.001
III-m	H	OCH_3	8-CH_2CH_3	75	80	60	80	90	100	0.017 ± 0.001
III-n	H	OCH_3	8-$CH(CH_3)_2$	85	75	70	90	100	100	0.035 ± 0.007
III-o	H	OCH_3	5,8-diCH_3	0	0	0	30	0	0	0.039 ± 0.001
III-p	H	OCH_3	6,8-diCH_3	0	0	0	0	0	0	0.028 ± 0.002
III-q	H	OCH_3	7,8-diCH_3	0	0	0	0	0	0	0.016 ± 0.001
III-r	H	OCH_3	7-F-8-CH_3	40	50	0	80	80	90	0.011 ± 0.001
III-s	H	OCH_3	7-Cl-8-CH_3	70	60	0	90	80	80	0.014 ± 0.001
III-t	H	OCH_3	7-Br-8-CH_3	0	0	0	70	30	70	0.021 ± 0.001
IV-a	H	CH_3	8-CH_3	75	60	0	60	90	80	0.007 ± 0.001
IV-b	5-CH_3	CH_3	8-CH_3	80	85	80	90	90	95	0.007 ± 0.001
V	H	CF_3	8-CH_3	50	30	0	60	50	80	0.020 ± 0.003
VI-a	H	CN	8-CH_3	0	0	0	0	30	30	0.007 ± 0.001
VI-b	5-CH_3	CN	8-CH_3	0	0	0	0	0	0	0.008 ± 0.001
mesotrione				85	50	75	95	95	95	0.013 ± 0.001

[a]Herbicidal activity was tested at the rate of 150 g ai/ha. [b]Abbreviations: EC, *Echinochloa crus-galli*; SF, *Setaria faberii*; DS, *Digitaria sanguinalis*; AR, *Amaranthus retroflexus*; EP, *Eclipta prostrata*; AJ, *Abutilon juncea*. [c]Inhibition constant of the enzyme reaction.

least 8 Å from the solute, and appropriate counterions were added to the system to preserve neutrality. In each step, energy minimization was first performed by using the steepest descent algorithm for 1000 steps and then the conjugated gradient algorithm for another 2000 steps.

We selected the majority of the new molecules that show different activities to perform 3D-QSAR. All molecular modeling and 3D-QSAR studies were performed using SYBYL7.3 with TRIPOS Force Field. The 3D structures of all compounds were built by using default setting of SYBYL, and the molecules were subjected for energy minimization at a gradient of 1.0 kcal/mol with delta energy change of 0.05 cal/mol. The CoMFA descriptors and steric and electrostatic field energies were calculated using the SYBYL default parameters: 2.0 Å rid points spacing, an sp^3 carbon probe atom with +1 charge, a minimum σ (column filting) of 2.0 kcal/mol, and an energy cutoff of 30.0 kcal/mol.

Herbicidal Activities. The postemergent herbicidal activities of compounds **I–VI** against *Echinochloa crus-galli* (EC), *Setaria faberi* (SF), *Digitaria sanguinalis* (DS), *Amaranthus retroflexus* (AR), *Eclipta prostrata* (EP), and *Abutilon juncea* (AJ) were evaluated according to the previously reported procedure;[14−16,29] the commercial triketone herbicide mesotrione was selected as a positive control. All test compounds were formulated as 100 g/L emulsified concentrates by using DMF as solvent and Tween-80 as emulsification reagent. The concentrates were diluted with water to the required concentration and applied to pot-grown plants in a greenhouse. The soil used was a clay soil, pH 6.5, 1.6% organic matter, 37.3% clay particles, and CEC 12.1 mol/kg. The rate of application (g ai/ha) was calculated by the total amount of active ingredient in the formulation divided by the surface area of the pot. Plastic pots with a diameter of 9 cm were filled with soil to a depth of 8 cm. Approximately 20 seeds of the tested weeds were sown in the soil at the depth of 1−3 cm and grown at a temperature of 15−30 °C in a greenhouse. The air relative humidity was 50%. The diluted formulation solutions were applied for postemergence treatment. Broadleaf weeds were treated at the two-leaf stage, and monocotyledon weeds were treated at the one-leaf

DOI: 10.1021/acs.jafc.5b01530
J. Agric. Food Chem. 2015, 63, 5587−5596

stage. The postemergence application rate was 150 g ai/ha. Untreated seedlings were used as the control group, and the solvent (DMF + Tween-80)-treated seedlings were used as the solvent control group. Herbicidal activity was evaluated visually at 15 days post-treatment (Tables 1 and 2), with three replicates per treatment.

Table 2. Postemergent Herbicidal Activity of Compounds III-l−III-n and IV-b

		% inhibition					
compd	dosage (g ai/ha)	EC[a]	SF[a]	DS[a]	AR[a]	EP[a]	AJ[a]
III-l	75	80	80	80	80	80	90
	37.5	70	65	70	80	80	85
III-m	75	70	65	40	80	80	90
	37.5	60	45	30	80	80	80
III-n	75	80	60	60	80	90	85
	37.5	70	45	30	80	80	80
IV-b	75	80	75	70	85	80	80
	37.5	60	50	30	75	75	70
mesotrione	75	80	30	70	80	90	90
	37.5	50	30	55	80	90	85

[a]Abbreviations: EC, *Echinochloa crus-galli*; SF, *Setaria faberii*; DS, *Digitaria sanguinalis*; AR, *Amaranthus retroflexus*; EP, *Eclipta prostrata*; AJ, *Abutilon juncea*.

Crop Selectivity. The conventional rice, soybean, cotton, wheat, canola, and maize were planted separately in pots (12 cm diameter) containing test soil and grown in a greenhouse at 20−25 °C.[23] After the plants had reached the four-leaf stage, the spraying treatment was conducted at the dosage of 150 g ai/ha. The visual injury and growth state of the individual plants were observed at regular intervals. After 15 days, the final results of crop safety were determined (Table 3), using three replicates per treatment.

Table 3. Crop Selectivity of Selected Compounds Postemergence[a]

	% injury					
compd	maize	rice	wheat	soybean	cotton	canola
III-l	5	40	30	30	40	80
III-m	0	0	0	25	20	55
III-n	0	30	20	30	40	80
mesotrione	10	50	40	55	70	100

[a]The experiments were conducted at the rate of 150 g ai/ha.

RESULTS AND DISCUSSION

Chemistry. According to the substituents at R^2, the target compounds **I**−**VI** were prepared by four different synthetic routes. When R^2 is a hydrogen atom, the synthetic details for compound **I** are shown in Figure 1; when R^2 is an alkoxy or aryloxy group, the synthetic routes for compounds **II** and **III** are outlined in Figure 2; when R^2 is a methyl or trifluoromethyl group, the detailed synthetic routes for compounds **IV** and **V** are shown in Figure 3; when R^2 is a cyano group, the detailed synthetic route for compounds **VI** is outlined in Figure 4. The lead compound **I** can be obtained by a three-step synthetic route using the commercially available quinoline-3-carboxylic acid **1** as the starting material (Figure 1). The carboxylic acid **1** was very sensitive to $SOCl_2$, $POCl_3$, PCl_5, and PCl_3 because of the high reactivity of the hydrogen at the 2-position on the quinoline ring. To our delight, by using 1.2 equiv of oxalyl chloride as the chloroformylation reagent and CH_2Cl_2 as the reaction solvent, the corresponding acid chloride can be successfully synthesized. The acid chloride thus obtained was very unstable, so it was used in the next step without further purification. Subsequently, the acid chloride reacted with 1,3-cyclohexanedione, and the enol ester **2** can be obtained in a yield of 78%. Finally, by using acetone cyanohydrin as the Fries catalyst, lead compound **I** was synthesized in a yield of 66%.

Because no carboxylic acids **7a**−**q** are commercially available, the reported methods were applied to synthesize them.[30−32] As seen in Figure 2, the target compounds **II** and **III** were synthesized by an eight-step synthetic route using (substituted) anilines **3a**−**q** as the starting materials. After reaction with acetic anhydride, the corresponding (substituted) *N*-phenylacetamides **4a**−**q** can be synthesized in high yields. Subsequently, the corresponding intermediates **5a**−**q** were obtained in yields of 30−80% via the Vilsmeier−Haack reaction. It was found that the substitutions of R^3 have a big impact on reactivity at this reaction step; if R^3 was an electron-withdrawing group, the reaction yields were very low or there was no reaction at all. **5a**−**q** were then oxidized by iodine in methanol, and compounds **6a**−**q** were synthesized in yields of 70−98%. Various carboxylic acids **7a**−**q** were prepared by a three-step one-pot method. More specifically, **6a**−**q** first reacted with sodium alkoxides or aryloxides, and then water was added to the reaction solution to hydrolyze the methoxycarbonyl group. After treating the residue with citric acid, the corresponding **7a**−**q** were obtained in yields of 64−98%. Followed by chloroformylation and esterification reactions, the enol esters **8a**−**l** and **9a**−**t** were obtained in yields of 42−90%. Finally, by using the same method as the synthesis of **I**, the title compounds **II** and **III** can be afforded in yields of 52−84%.

The key intermediates **11a** and **11b** were prepared by reaction of methyl acetoacetate **10a** or ethyl trifluoroacetoacetate **10b** with *o*-toluidine **3j** in the presence of 4-methylbenzenesulfonic acid as the catalyst (Figure 3). Then, **11a** and **11b** reacted with *N*,*N*-dimethylformamide (DMF) and $POCl_3$ in dichloroethane (DCE), and the corresponding **12a** and **12b** were obtained in yields of 90 and 50%, respectively. Alkaline hydrolysis of **12a** and **12b** with $LiOH{\cdot}H_2O$ in the presence of methanol and water furnished the hydroxyacids **13a** and **13b**. The syntheses of the target compounds **IV** and **V** from **13a** and **13b** were the same as the preparation of compound **I**. Similarly, compounds **VI** can be obtained by a six-step reaction route using methyl 2-chloro-8-methylquinoline-3-carboxylate **6j** as the starting material; after cyanation reaction with CuCN, the key intermediate **16** was synthesized in a yield of 88%. Then followed by hydrolysis, chloroformylation, enol esterification, and rearrangement reactions, the target compounds **VI** can be successfully obtained.

The chemical structures of all of the synthetic triketone−quinoline hybrids (**I**−**VI**) were confirmed by ^1H NMR and ^{13}C NMR spectroscopic and HRMS spectrometric data. Furthermore, the structures of compounds **III-d** and **III-f** were verified by X-ray analysis (Figure 5).

HPPD Inhibition and SAR. The K_i value of the designed lead compound **I** against *At*HPPD was about 0.075 μM, suitable for further optimization (Table 1). Molecular modeling was performed to guide us in rational structural optimization. Because no crystal structure of compound **I** with *At*HPPD was available, we used the reported binding mode of DAS645 with *At*HPPD (PDB entry 1TG5) as reference.[33] There were two major interactions of compound **I** with the *At*HPPD active site (Figure 6). The triketone part of compound **I** can form a

DOI: 10.1021/acs.jafc.5b01530
J. Agric. Food Chem. 2015, 63, 5587−5596

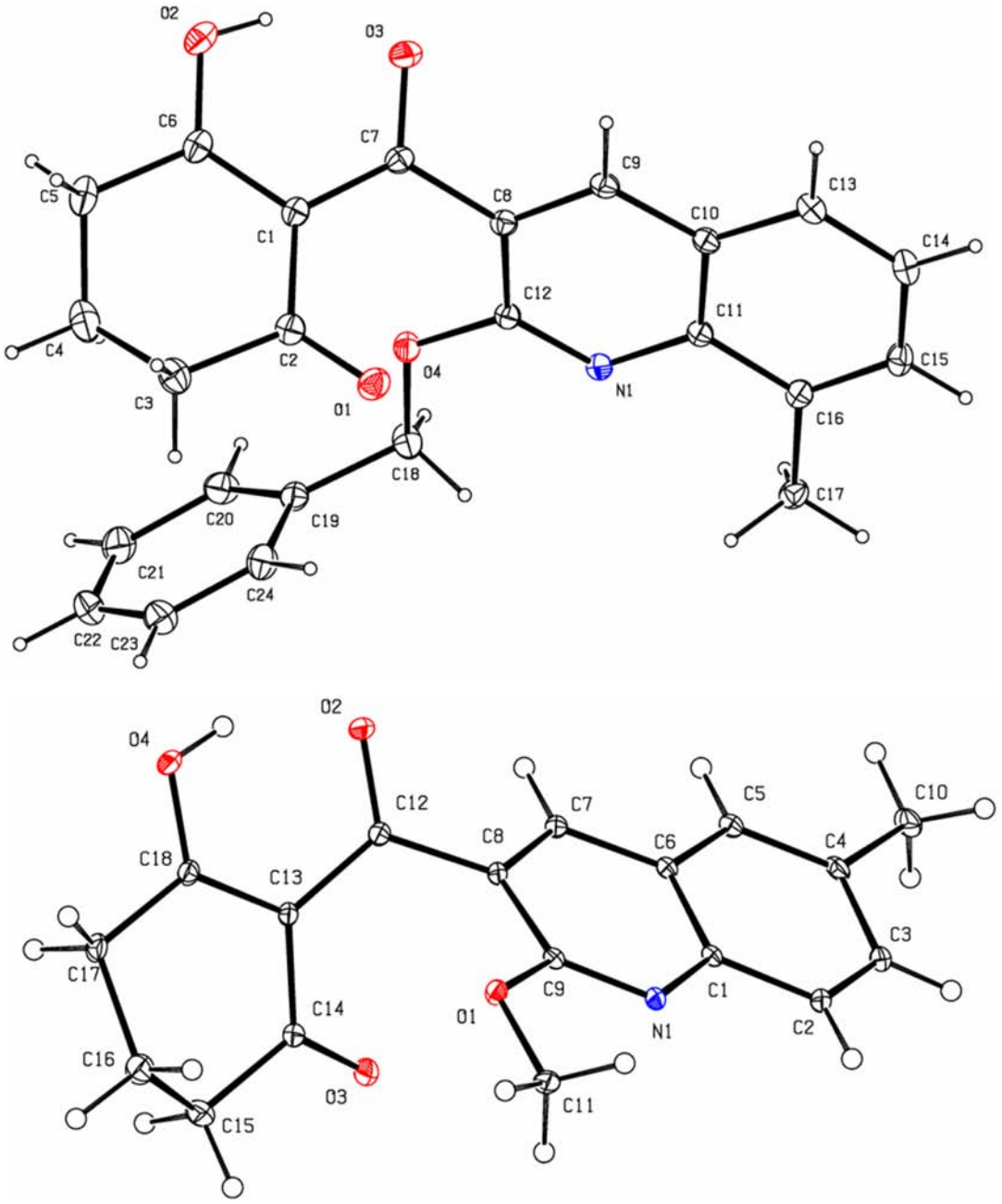

Figure 5. X-ray crystal structures for compounds **III-d** and **III-f**.

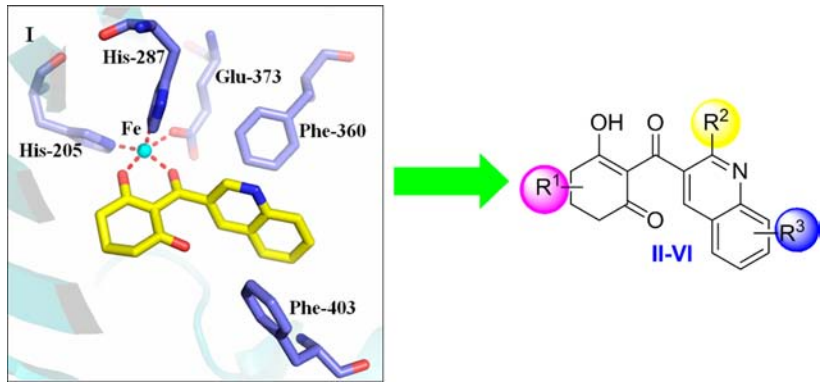

Figure 6. Simulated binding mode of lead compound **I** with *At*HPPD and the designed compounds **II** and **III**. The ferrous iron is shown as a cyan sphere, the structure of compound **I** is shown in yellow sticks, and the key residues surrounding the active site are shown in light blue.

DOI: 10.1021/acs.jafc.5b01530
J. Agric. Food Chem. 2015, 63, 5587−5596

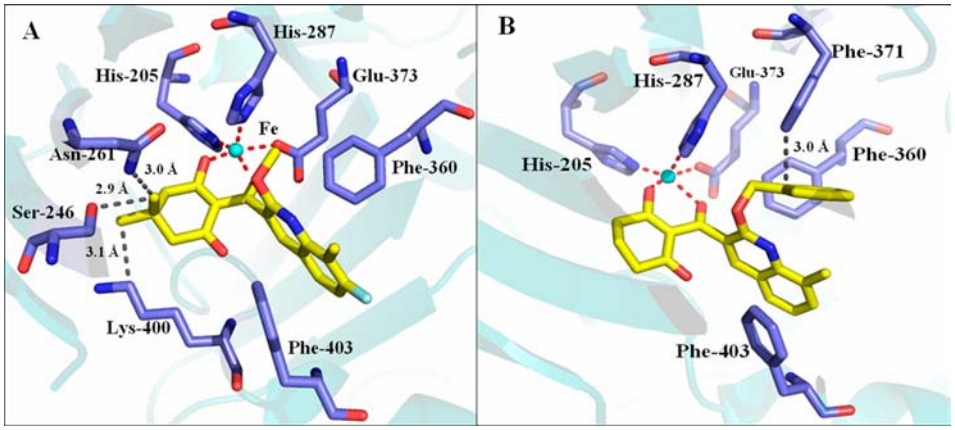

Figure 7. Simulated binding mode of compounds **II-g** (A) and **III-t** (B) with *At*HPPD. The ferrous iron is shown as a cyan sphere, the structures of compounds **II-g** and **III-t** are shown in yellow sticks, and the key residues surrounding the active site are shown in light blue.

bidentate interaction with the active site iron^{II}, whereas the quinoline motif can form $\pi-\pi$ interaction with Phe360 and Phe403. Furthermore, there was no significant interaction of compound **I** with the active site of *At*HPPD (around 4 Å residues), which indicated that a variety of substituent groups might be introduced to compound **I** to increase its interaction with the enzyme. To obtain new compounds with improved *At*HPPD inhibitory activity, we then designed compounds **II**−**VI** on the basis of the core structure on lead compound **I**.

The substituents at R^1 have a significant impact on the activity (Table 1). In most cases, compounds with a 5,5-di-CH_3 at R^1 had decreased HPPD inhibitory activity compared to lead compound **I**. Although the K_i value of compound **II-i** was 0.041 μM, it showed a slightly more potent activity than compound **I**; however, its activity is still far from sufficient when compared with that of mesotrione. For further optimization, compound **II-g** was chosen as a representative to investigate the binding modes. The trikeone part of compound **II-g** can form a bidentate association with the ferrous iron active site, and the quinoline ring can form $\pi-\pi$ interaction with Phe360 and Phe403, respectively (Figure 7A). When the two methyl groups were introduced to the 5-position of the 1,3-cyclohexane ring, the distances between the methyl groups and the surrounding residues would be reduced to lead to steric hindrance. The distances from the two methyl groups on the cyclohexanedione ring of compound **II-g** to residues Asn261, Ser246, and Lys400 are 3.0, 2.9, and 3.1 Å, respectively (Figure 7A). The loss of activity might due to the spatial repellence caused by the methyl groups at the 5-position of the 1,3-cyclohexane ring. Therefore, we proposed that the removal of steric hindrance at this position may be favorable to activity. After one methyl group was removed from this position, the activity of compound **II-k** was greatly improved compared with that of its parent compound **II-j**; however, its activity was still inadequate. This suggests that removing the remaining methyl group would further improve the activity of these molecules.

On the basis of the above analysis, another methyl group was also removed from the 5-position of the 1,3-cyclohexane ring of compound **II-j**. The K_i value of compound **III-a** was as low as 0.009 μM, about 10 times more potent than its parent compound **II-k** and slightly more potent than the commercial mesotrione (K_i = 0.013 μM). Encouraged by these results, we further optimized the structure and studied the activity of this series of compounds. As the steric effects at R^1 had a big impact on activity, compounds **III-b**—**III-d** were synthesized to test the contribution of R^2 to activity. The sterically bulk groups at R^2 were also detrimental to activity; for example, compound **III-a** with a methoxy group at R^2 displayed enhanced activity relative to compounds **III-b**—**III-d** (**III-a** > **III-b** > **III-c** > **III-d**). To understand the structural basis, compound **III-d** was used as a representative for further binding mode investigation. The distance of the benzyl group between Phe371 is 3.0 Å, showing strong steric repulsion effect (Figure 7B).

On the basis of above observation, the methoxy group at R^2 was retained and another set of compounds **III-e**−**III-t** were synthesized to further investigate their HPPD inhibitory activity (Figure 2). All newly synthesized compounds displayed inhibitory constants at the nanomolar range, some of them even showing slightly more potential than mesotrione (Table 1). The position of a single group at R^3 has a big influence on activity. For example, when a methyl group was introduced at the 6-position (**III-f**), the 7-position (**III-g**), or the 8-position (**III-a**) on the quinoline ring, compound **III-a** would have better activity than compounds **III-g** and **III-f** (**III-a** > **III-g** > **III-f**). A similar SAR can also be applied to those with methoxy-substituted analogues (**III-i** > **III-h**) and chloro-substituted analogues (**III-k** > **III-j**). It appeared that the steric bulky groups at R^3 were also detrimental to activity (**III-a** > **III-m** > **III-n**). As to the multisubstituted analogues, compounds with substituents at the 7,8-positions showed improved activity relative to those equivalent substitutions at the 5,8- and 6,8-positions (**III-q** > **III-p** > **III-o**). It seemed that the electron-withdrawing groups at R^3 would produce enhanced effects compared to those with electron-donating groups, although there may be a few exceptions.

Herbicidal Activity and SAR. The postemergence herbicidal activities of the newly prepared compounds were tested against monocotyledon weeds (*E. crus-galli*, *S. faberii*, and *D. sanguinalis*) and broadleaf weeds (*A. retroflexus*, *E. prostrata*, and *A. juncea*) in the greenhouse experiments. The commercial herbicide mesotrione was used as a control; the results are listed in Tables 1 and 2. The treated weeds had developed unique whitening symptoms in light, which indicated that these compounds inhibited HPPD in planta. Some of the synthesized compounds displayed promising and broad-spectrum herbicidal activities at the rate of 150 g ai/ha. Compound **III-l** even exhibited a broader spectrum of weed control (inhibition > 80%) than mesotrione at the rate of 75 g ai/ha.

In most cases, introducing substitutions at R^1 was detrimental to herbicidal activity (Table 1). Notably,

DOI: 10.1021/acs.jafc.5b01530
J. Agric. Food Chem. 2015, 63, 5587−5596

compounds with sterically bulky groups at R^2 also displayed decreased herbicidal activity effects (**III-a** > **III-6b** > **III-c** > **III-d**). These results were consistent with in vitro HPPD inhibitory activity. Furthermore, an interesting structure−activity relationship was observed with respect to the R^3 substitution. For example, when a single substitution was introduced at different positions on the quinoline ring, compounds with substituents at the 7-position would have a broader spectrum of weed control than compounds with substituents at the 8- and 6- positions (**III-g** > **III-a** > **III-f**). It seemed that bulky groups on the quinoline ring were favorable to herbicidal activity (**III-n** > **III-m** > **III-a**). In most case, compounds with electron-withdrawing groups at R^3 were found to exhibit higher herbicidal activity than those with electron-donating groups (**III-k** > **III-g**). Surprisingly, compounds **II-d** and **III-l** with methylthio group at R^3 also displayed excellent herbicidal activity at the rate of 150 ai/ha; even at a dosage as low as 37.5 g ai/ha compound **III-1** still showed >80% control against tested broadleaf weeds and >65% inhibition against monocotyledon weeds (Table 2). A possible explanation for the enhanced herbicidal activity of compounds **II-d** and **III-l** is that the unique properties of the methylthio group make compounds more easily absorbed by plants.[33]

In this work, some of the synthesized compounds had good HPPD-inhibiting activity; however, their herbicidal activities were not satisfactory. For example, compound **III-a** (K_i = 0.009 μM) showed a slightly higher HPPD inhibitory activity than mesotrione (K_i = 0.013 μM); however, its herbicidal activity still could not compete with that of mesotrione. As far as we know, there are many reasons for a compound to have good in vitro inhibitory activity without displaying promising herbicidal activity, such as the absorption, distribution, metabolism, and excretion (ADME) properties. As there is a methoxy group at the 2-position on the quinoline ring of compound **III-a**, we inferred that the methoxy group of compound **III-a** might be easily metabolized by plants.[34] This is because the unique chemical properties of quinoline make its 2-position very active compared with other positions. Therefore, a series of compounds with different metabolism blocking groups were synthesized to verify this hypothesis (Figures 3 and 4). As indicated in Table 1, among the newly prepared compounds **IV** and **VI**, compounds with an electron-withdrawing group at R^2 were found to be detrimental to herbicidal activity. Promisingly, compounds **IV-a** and **IV-b** displayed significantly enhanced herbicidal activity relative to their parent compounds **III-a** and **II-k**, respectively. Therefore, the SAR of R^2 can be summarized as follows: CH_3 > CF_3> OCH_3 > CN > OCH_2H_3, $OCH_2CH_2H_3$ > OCH_2Ph.

Crop Selectivity. As mentioned in the Introduction, crop selectivity is one of the main concerns in herbicide discovery. Compounds **III-l**, **III-m**, and **III-n** with promising herbicidal activity were chose as representatives for further crop selectivity studies. Maize displayed high tolerance to compound **III-l** after postemergence application at the rate of 150 g ai/ha (Table 3). The promising results indicated that compound **III-l** might be developed as a potential herbicidal for maize fields. Most promisingly, compound **III-m** was found to be "selective" to maize, rice, and wheat at the dosage of 150 g ai/ha; however, the commercial mesotrione was found to be "nonseletive" to rice and wheat at the same rate. These results showed that there is a great potential for **III-m** to be developed as a herbicide for weed control in maize, rice, and wheat fields. Furthermore, compound **III-n** was safe for maize at the dosage of 150 g ai/ha, indicating that **III-n** might be developed as a potential herbicide for maize fields.

CoMFA analysis. To further understand the substituent effects on *At*HPPD inhibition, we performed a brief CoMFA analysis of 31 representative compounds with SYBYL.[29] The predicted CoMFA model was established with the conventional coefficient r^2 = 0.974, the cross-validated coefficient q^2 = 0.806, and the predicted non-cross-validated coefficient r^2(pred) = 0.854. The calculated activity values and the plots of the predicted versus the actual activity values for the selected compounds are shown (Table 4). The contour map of the steric contributions was marked in green and yellow areas (Figure 8A). The yellow contour means a bulky substituent in this area is unfavorable for the inhibition activity of *At*HPPD. For example, the compound **II-b** (R^1 = 5,5-diCH_3, K_i = 0.304 μM) is less active than compound **III-i** (R^1 = H, K_i = 0.029 μM), although they have the same R^2 and R^3 groups, which is similar to **II-e** and **III-m**, **II-f** and **III-n**, and **II-j** and **II-k**. On the contrary, the green region highlights positions where a bulky group would be favorable for HPPD inhibition activity. The electrostatic contour map is shown in Figure 8B. The blue color represents that the electro-positive group will be advantageous to the bioactivity of HPPD inhibitors. The electro-negative groups is marked by a red area, which is closed

Table 4. Comparison of Experimental pK_i and Calculated pK_i Values

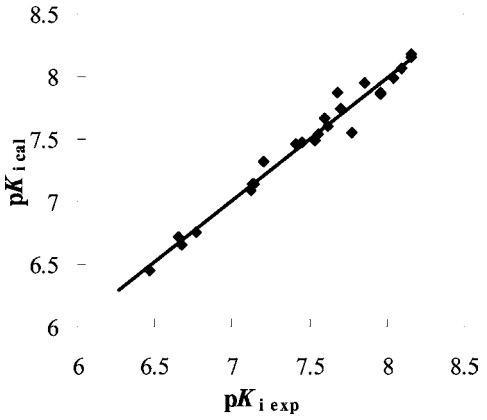

	pK_i[a]			pK_i[a]	
compd	exptl	calcd	compd	exptl	calcd
II-b	6.517	6.528	**III-i**	7.538	7.483
II-d	6.467	6.446	**III-j**	7.143	7.143
II-e	6.654	6.719	**III-k**	7.959	7.862
II-f	6.879	6.593	**III-l**	8.046	7.989
II-i	7.387	7.048	**III-m**	7.770	7.552
II-j	6.526	6.642	**III-n**	7.456	7.481
II-k	7.004	7.363	**III-o**	7.409	7.456
II-l	7.131	7.137	**III-p**	7.553	7.543
III-b	7.602	7.670	**III-q**	7.796	7.927
III-c	6.767	6.762	**III-r**	7.959	7.871
III-d	6.672	6.649	**III-s**	7.854	7.948
III-e	7.208	7.317	**III-t**	7.678	7.875
III-f	7.523	7.377	**IV-b**	8.097	8.061
III-g	7.620	7.596	**V**	7.699	7.738
III-h	7.119	7.089	**VI-a**	8.155	8.174
III-i	7.538	7.483	**VI-b**	8.097	8.061

[a] pK_i = -logK_i.

DOI: 10.1021/acs.jafc.5b01530
J. Agric. Food Chem. 2015, 63, 5587−5596

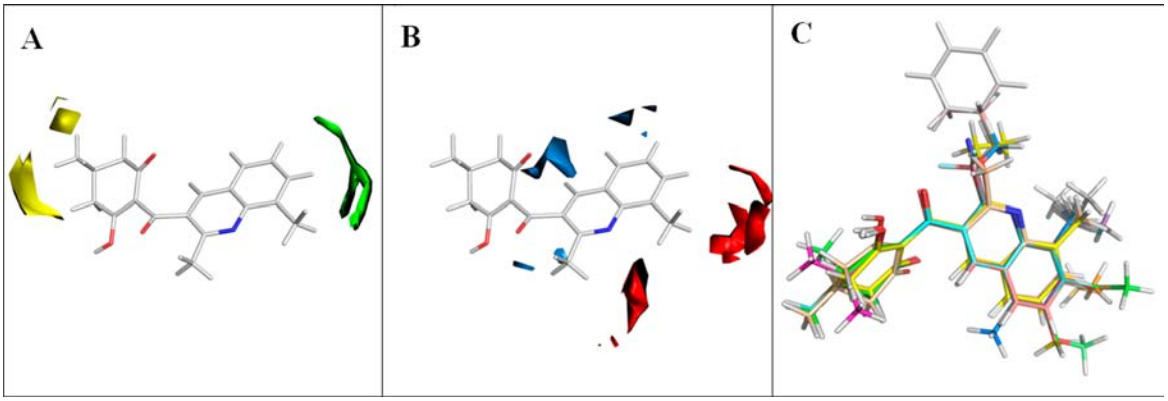

Figure 8. (A) CoMFA map for steric contribution. Compound **IV-b** is shown inside the field. Green polyhedra represents the sterically favored areas where bulkier substituents favor activity, and yellow polyhedra represents the disfavored areas where less bulky substituents favor activity. (B) CoMFA map for electrostatic contribution. Compound **IV-b** is shown inside the field. Blue contours mean the increase of positive charge in these areas will promote the activity; on the contrary, it will enhance the activity if we increase negative charges in the red contour areas. (C) Alignment of 24 compounds of the training set.

to the region of R^2 group and the 7,8-positions on the quinoline ring. Therefore, we can infer that the compound which bears an electron-withdrawing group at R^2 and R^3 (7- and 8-positions) will show higher activity. The experimental values are consistent with our calculation results; for example, the activities of **III-r** (R^3 = 7-F-8-CH_3, K_i = 0.011 μM) > **III-s** (R^3 = 7-Cl-8-CH_3, K_i = 0.014 μM) > **III-t** (R^3 = 7-Cl-8-CH_3, K_i = 0.014 μM), **III-b** (R^3 = OCH_2H_3, K_i = 0.025 μM) > **III-c** (R^3 = O-*n*-Pr, K_i = 0.171 μM) > **III-d** (R^3 = OCH_2Ph, K_i = 0.213 μM) and the activities of compounds **VI-a** and **VI-b** are higher than those of most of other compounds in Table 4 because of the cyano group at the R^2 position.

In conclusion, a series of novel triketone−quinoline hybrids were rationally designed and identified as potent HPPD inhibitors for herbicide discovery. Most of the synthesized compounds displayed excellent HPPD inhibitory activity, and some of them were even superior to the commercial herbicide mesotrione. To our delight, compounds **III-l**, **III-m**, and **III-n** displayed promising herbicidal activity at the rate of 37.5−150 g ai/ha. Especially, compound **III-l** displayed a broader spectrum of weed control than mesotrione. In addition, compounds **III-l** and **III-n** were highly "selective" to maize, and **III-m** was safe for maize, rice, and wheat by postemergence application at the rate of 150 g ai/ha. These results indicated that triketone−quinoline hybrids could be novel lead compounds for novel herbicide discovery. Further field trials and structure optimization of compounds **III-l**, **III-m**, and **III-n** are underway.

■ ASSOCIATED CONTENT

Supporting Information

Detailed information for the preparation and the analytical data of compounds **I**−**VI**. The Supporting Information is available free of charge on the ACS Publications website at DOI: 10.1021/acs.jafc.5b01530.

■ AUTHOR INFORMATION

Corresponding Author

*(Q.C.) E-mail: qchen@mail.ccnu.edu.cn. Phone: +86-27-67867800. Fax: +86-27-67867141.

Funding

We are very grateful to the National Key Technologies R&D Program of China (No. 2011BAE06B03) and National Natural Science Foundation of China (No.21332004 and 21372093).

Notes

The authors declare no competing financial interest.

■ REFERENCES

(1) Duke, S. O. Why have no new herbicide modes of action appeared in recent years? *Pest Manage. Sci.* **2012**, *68*, 505−512.
(2) Green, J. M. Current state of herbicides in herbicide-resistant crops. *Pest Manage. Sci.* **2014**, *70*, 1351−1357.
(3) Ahrens, H.; Lange, G.; Müller, T.; Rosinger, C.; Willms, L.; van Almsick, A. 4-Hydroxyphenylpyruvate dioxygenase inhibitors in combination with safeners: solutions for modern and sustainable agriculture. *Angew. Chem., Int. Ed.* **2013**, *52*, 9388−9398.
(4) Beaudegnies, R.; Edmunds, A. J.; Fraser, T. E.; Hall, R. G.; Hawkes, T. R.; Mitchell, G.; Schaetzer, J.; Wendeborn, S.; Wibley, J. Herbicidal 4-hydroxyphenylpyruvate dioxygenase inhibitors − a review of the triketone chemistry story from a Syngenta perspective. *Bioorg. Med. Chem.* **2009**, *17*, 4134−4152.
(5) Xu, Y. L.; Lin, H. Y.; Cao, R. J.; Ming, Z. Z.; Yang, W. C.; Yang, G. F. Pyrazolone−quinazolone hybrids: a novel class of human 4-hydroxyphenylpyruvate dioxygenase inhibitors. *Bioorg. Med. Chem.* **2014**, *22*, 5194−5211.
(6) Wójcik, A.; Broclawik, E.; Siegbahn, P. E. M.; Lundberg, M.; Moran, G.; Borowski, T. Role of substrate positioning in the catalytic reaction of 4-hydroxyphenylpyruvate dioxygenase − A QM/MM study. *J. Am. Chem. Soc.* **2014**, *136*, 14472−14485.
(7) Mitchell, G.; Bartlett, D. W.; Fraser, T. E.; Hawkes, T. R.; Holt, D. C.; Townson, J. K.; Wichert, R. A. Mesotrione: a new selective herbicide for use in maize. *Pest Manage. Sci.* **2001**, *57*, 120−128.
(8) Moran, G. R. 4-Hydroxyphenylpyruvate dioxygenase. *Arch. Biochem. Biophys.* **2005**, *433*, 117−128.
(9) Lee, D. L.; Prisbylla, M. P.; Cromartie, T. H.; Dagarin, D. P.; Howard, S. W.; Provan, W. M.; Ellis, M. K.; Fraser, T.; Mutter, L. C. The discovery and structural requirements of inhibitors of *p*-hydroxyphenylpyruvate dioxygenase. *Weed Sci.* **1997**, *45*, 601−609.
(10) Wu, C. S.; Huang, J. L.; Sun, Y. S.; Yang, D. Y. Mode of action of 4-hydroxyphenylpyruvate dioxygenase inhibition by triketone-type inhibitors. *J. Med. Chem.* **2002**, *45*, 2222−2228.
(11) Witschel, M. Design, synthesis and herbicidal activity of new iron chelating motifs for HPPD-inhibitors. *Bioorg. Med. Chem.* **2009**, *17*, 4221−4229.
(12) Dayan, F. E.; Duke, S. O.; Sauldubois, A.; Singh, N.; Mccurdy, C.; Cantrell, C. L. *p*-Hydroxyphenylpyruvate dioxygenase is a

DOI: 10.1021/acs.jafc.5b01530
J. Agric. Food Chem. 2015, 63, 5587−5596

herbicidal target site for β-triketones from *Leptospermum scoparium*. *Phytochemistry* **2007**, *68*, 2004−2014.
(13) Dayan, F. E.; Singh, N.; McCurdy, C.; Godfrey, C. A.; Larsen, L.; Weavers, R. T.; Van Klink, J. W.; Perry, N. B. β-triketone inhibitors of plant *p*-hydroxyphenylpyruvate dioxygenase: modeling and comparative molecular field analysis of their interactions. *J. Agric. Food Chem.* **2009**, *57*, 5194−5200.
(14) Wang, D. W.; Lin, H. Y.; Cao, R. J.; Yang, S. G.; Chen, Q.; Hao, G. F.; Yang, W. C.; Yang, G. F. Synthesis and herbicidal evaluation of triketone-containing quinazoline-2,4-diones. *J. Agric. Food Chem.* **2014**, *62*, 11786−11796.
(15) Wang, D. W.; Lin, H. Y.; Cao, R. J.; Ming, Z. Z.; Chen, T.; Hao, G. F.; Yang, W. C.; Yang, G. F. Design, synthesis and herbicidal activity of novel quinazoline-2,4-diones as 4-hydroxyphenylpyruvate dioxygenase inhibitors. *Pest Manage. Sci.* **2014**, n/a.
(16) Wang, D. W.; Lin, H. Y.; Cao, R. J.; Yang, S. G.; Chen, T.; He, B.; Chen, Q.; Yang, W. C.; Yang, G. F. Synthesis and bioactivity studies of triketone-containing quinazoline-2,4-dione derivatives. *Huaxue Xuebao* **2015**, *73*, 29−35.
(17) Elban, M. A.; Sun, W.; Eisenhauer, B. M.; Gao, R.; Hecht, S. M. Synthesis and biological evaluation of 10,11-methylenedioxy-14-azacamptothecin. *Org. Lett.* **2006**, *8*, 3513−3516.
(18) Patel, R. V.; Park, S. W. Access to a new class of biologically active quinoline based 1,2,4-triazoles. *Eur. J. Med. Chem.* **2014**, *71*, 24−30.
(19) Singh, K.; Kaur, H.; Smith, P.; de Kock, C.; Chibale, K.; Balzarini, J. Quinoline−pyrimidine hybrids: synthesis, antiplasmodial activity, SAR, and mode of action studies. *J. Med. Chem.* **2014**, *57*, 435−448.
(20) Hendrickx, R.; Johansson, J. G.; Lohmann, C.; Jenvert, R.; Blomgren, A.; Börjesson, L.; Gustavsson, L. Identification of novel substrates and structure−activity relationship of cellular uptake mediated by human organic cation transporters 1 and 2. *J. Med. Chem.* **2013**, *56*, 7232−7242.
(21) Zhao, Q. Q.; Liu, S. H.; Li, Y. H.; Wang, Q. M. Design, synthesis, and biological activities of novel 2-cyanoacrylates containing oxazole, oxadiazole, or quinoline moieties. *J. Agric. Food Chem.* **2009**, *57*, 2849−2855.
(22) Xu, M.; Wagerle, T.; Long, J. K.; Lahm, G. P.; Barry, J. D.; Smith, R. M. Insecticidal quinoline and isoquinoline isoxazolines. *Bioorg. Med. Chem. Lett.* **2014**, *24*, 4026−4030.
(23) Abdel-Gawad, S. M.; El-Gaby, M. S. A.; Heiba, H. I.; Aly, H. M.; Ghorab, M. M. Synthesis and radiation stability of some new biologically active hydroquinoline and pyrimido[4,5-*b*]quinoline derivatives. *J. Chin. Chem. Soc.* **2005**, *52*, 1227−1236.
(24) *SAINT and SMART*; Bruker AXS: Madison, WI, USA, 2003.
(25) Sheldrick, G. M. *SHELXS97*; University of Gottingen: Gottingen, Germany, 1997.
(26) Meazza, G.; Scheffler, B. E.; Tellez, M. R.; Rimando, A. M.; Romagni, J. G.; Duke, S. O.; Nanayakkara, D.; Khan, I. A.; Abourashed, E. A.; Dayan, F. E. The inhibitory activity of natural products on plant *p*-hydroxyphenylpyruvate dioxygenase. *Phytochemistry* **2002**, *60*, 281−288.
(27) Schmidt, S. R.; Müller, C. R.; Kress, W. Murine liver homogentisate 1,2-dioxygenase. Purification to homogeneity and novel biochemical properties. *Eur. J. Biochem.* **1995**, *228*, 425−430.
(28) Yang, C.; Pflugrath, J. W.; Camper, D. L.; Foster, M. L.; Pernich, D. J.; Walsh, T. A. Structural basis for herbicidal inhibitor selectivity revealed by comparison of crystal structures of plant and mammalian 4-hydroxyphenylpyruvate dioxygenases. *Biochemistry* **2004**, *43*, 10414−10423.
(29) Jiang, L. L.; Tan, Y.; Zhu, X. L.; Wang, Z. F.; Zuo, Y.; Chen, Q.; Xi, Z.; Yang, G. F. Design, synthesis, and 3D-QSAR analysis of novel 1,3,4-oxadiazol-2(3*H*)-ones as protoporphyrinogen oxidase inhibitors. *J. Agric. Food Chem.* **2010**, *58*, 2643−2651.
(30) Srivastava, A.; Singh, R. M. Vilsmeier-Haack reagent: a facile synthesis of 2-chloro-3-formylquinolines from *N*-arylacetamides and transformation into different functionalities. *Indian J. Chem.* **2005**, *44B*, 1868−1875.
(31) Verma, A. K.; Rustagi, V.; Aggarwal, T.; Singh, A. P. Iodine-mediated solvent-controlled selective electrophilic cyclization and oxidative esterification of *o*-alkynyl aldehydes: an easy access to pyranoquinolines, pyranoquinolinones, and isocumarins. *J. Org. Chem.* **2010**, *75*, 7691−7703.
(32) Suzuki, M.; Iwasaki, H.; Fujikawa, Y.; Kitahara, M.; Sakashita, M.; Sakoda, R. Synthesis and biological evaluations of quinoline-based HMG-CoA reductase inhibitors. *Bioorg. Med. Chem.* **2001**, *9*, 2727−2743.
(33) Pauly, J.; Spiteller, D.; Linz, J.; Jacobs, J.; Allen, C.; Nett, M.; Hoffmeister, D. Ralfuranone thioether production by the plant pathogen *Ralstonia solanacearum*. *ChemBioChem* **2013**, *14*, 2169−2178.
(34) Hu, Y. C.; Zhang, Z.; Shi, W. G.; Mi, T. Y.; Zhou, L. X.; Huang, N.; Hoptroff, M.; Lu, Y. H. 2′,4′-Dihydroxy-6′-methoxy-3′,5′-dimethylchalcone promoted glucose uptake and imposed a paradoxical effect on adipocyte differentiation in 3T3-L1 cells. *J. Agric. Food Chem.* **2014**, *62*, 1898−1904.

DOI: 10.1021/acs.jafc.5b01530
J. Agric. Food Chem. 2015, 63, 5587−5596

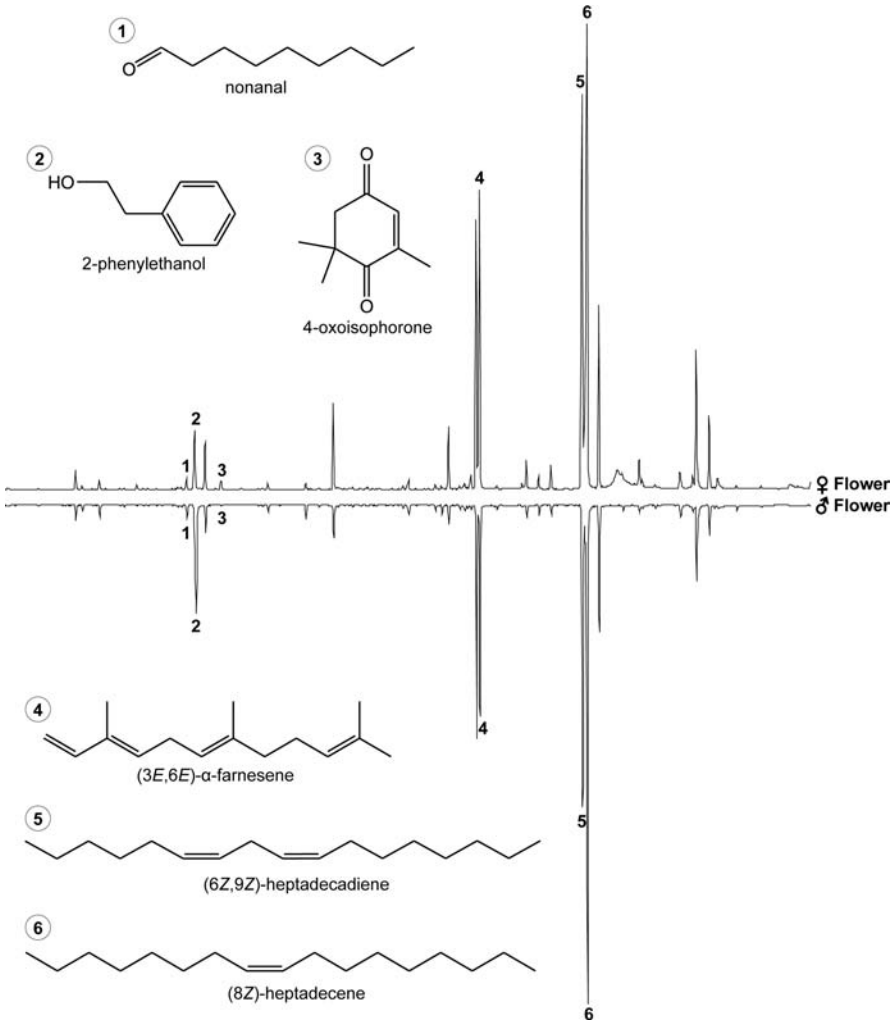

Figure 1. GC-MS chromatograms of kiwifruit floral volatiles from pooled male flower and pooled female flower headspace. The numbered peaks correspond to the antennally active compounds.

from apple skins, obtaining 98% chemical purity. (6Z,9Z)-Heptadecadiene was also not commercially available, so we synthesized it from linoleic acid (99%) using reductive radical decarboxylation.[27] (8Z)-Heptadecene was also synthesized from oleic acid (99%) according to this method to give 94% isomeric purity by GC.

Headspace Sampling of Kiwifruit Flowers. *Actinidia deliciosa* flowers from male (n = 6) and female (n = 10) 'Hayward' vines were individually encased in situ on the vine using custom-made two-piece cylindrical glass chambers (radius = 20 mm, length = 60 mm). The glassware was conditioned in a hot air oven at 150 °C overnight before use. The chamber was joined around the flower, with the stem passing through a small groove in the glass that was then gently sealed with polytetrafluoroethylene tape to avoid any damage to plant tissue. A constant flow rate of 500 mL/min was used, with air entering the chamber through a charcoal filter and leaving the chamber by passing through 60 mg of Tenax#-GR 35/60 (Grace Davison Discovery Sciences, VIC, Australia). The Tenax was conditioned at 250 °C for 3 h under nitrogen before use. Controls were an empty chamber (n = 2) and a chamber containing a leaf (n = 2) set up as outlined above for male and female flowers. Two-hour volatile collections were made between 11:00 a.m. and 1:00 p.m. in a Waikato NZ kiwifruit orchard (37°44′38.12″ S, 175°38′45.49″ E) when large numbers of bee foragers were flying. The Tenax was then eluted with 1 mL of hexane and stored at −80 °C until analysis.

Gas Chromatography–Electroantennogram Detection (GC-EAD). Honey bee antennal depolarizations in response to kiwifruit floral volatiles were recorded using GC-EAD. Honey bees were collected as they left the hives at Plant & Food Research's Lincoln (NZ) apiary (43°38′20.99″ S, 172°28′19.53″ E) with whole head mounts (or alternatively excised antenna) used for recordings. The freshly excised head (or antenna) of an anesthetized honey bee (n = 10 for female flower, n = 8 for male flower) was mounted between silver electrodes containing either salt solution or Spectra 360 electrode gel (Parker Laboratories Inc., Fairfield, NJ, USA). One hundred microliters of each female flower extract was taken, pooled, and then concentrated 10 times under a stream of argon; this was then repeated for the male flowers. The concentrated, pooled sample was then injected into a Varian 3800 GC (Varian, Walnut Creek, CA, USA) coupled to a Syntech EAD recording unit (Syntech Research and Equipment, Hilversum, The Netherlands). Injections were splitless for 0.6 min, and helium was used as a carrier gas with a constant flow of 1 mL/min. A 1:1 split of the column effluent to the antenna and flame ionization detector (FID) was maintained for the duration of the experiment. The GC was equipped with a DB-5 ms column (J&W Scientific, Folsom, CA, USA), 30 m × 0.25 mm i.d. × 0.25 μm film thickness. The injector temperature was 250 °C, and the column oven was programmed from 40 °C (held for 2 min) to 280 °C at 10 °C/min. The transfer line to the antennal preparation was maintained at 250 °C.

Gas Chromatography–Mass Spectrometry (GC-MS). Volatile collections, reaction products, and synthetic compounds were analyzed using a Varian 3800 GC coupled to a Saturn 2200 MS (Varian). Injections were splitless for 0.6 min, and a constant flow of 1 mL/min

DOI: 10.1021/acs.jafc.5b01165
J. Agric. Food Chem. 2015, 63, 5597–5602

Table 1. Summary of Honey Bee Electroantennogram Responses to Volatiles Released from Male and Female Kiwifruit Flowers

compound showing antennal activity	Kovats index DB-5 ms (DB-wax)	response to male flowers (mV)	response to female flowers (mV)	male flower extract (ng)[a]	female flower extract (ng)[a]
nonanal	1105 (1404)	−1.8 ± 1.0	−1.7 ± 0.2	4	4
2-phenylethanol	1111 (1927)	−2.7 ± 0.6	−3.0 ± 0.4	62	25
4-oxoisophorone	1144 (1708)		−1.5 ± 0.3	tr[b]	3
(3*E*,6*E*)-α-farnesene	1503 (1758)	−1.2 ± 0.5	−1.5 ± 0.4	79	111
(6*Z*,9*Z*)-heptadecadiene	1669 (1765)	−1.4 ± 0.3	−3.4 ± 0.9	104	142
(8*Z*)-heptadecene	1678 (1722)	−1.6 ± 0.2	−3.1 ± 0.7	155	169

[a]Estimation of quantity of volatile perceived at the antenna based on comparison with external standards. [b]tr, trace.

of helium was used as the carrier gas. The GC oven was equipped with two columns: a DB-5 ms and a DB-wax, both with dimensions of 30 m × 0.25 mm i.d. × 0.25 μm film thickness. The GC oven temperature programs were 40 °C (held for 2 min) to 280 °C at 10 °C/min for the DB-5 ms column and 40 °C (held for 2 min) to 240 °C at 10 °C/min for the DB-wax column. The injector temperatures were 250 and 220 °C, whereas the transfer line was maintained at 280 and 250 °C for the DB-5 ms and DB-wax columns, respectively. All MS analysis was carried out in electron impact mode at 70 eV and a mass range of m/z 29−399.

Microchemical Derivatization. Hydrogenation of the extract was carried out using 150 μL of the volatile collection solution in combination with 1 mg of 10% Pd/C under a hydrogen atmosphere. The solution was filtered before analysis by GC-MS. For location of the double bond in the heptadecene, dimethyl disulfide (DMDS) derivatization[28] was used. Twenty microliters of the extract was blown down under argon and reacted with DMDS and iodine in diethyl ether for 2 h at 40 °C. The reaction was quenched with a $Na_2S_2O_3$ solution, extracted with pentane, and dried over $MgSO_4$. For identification of the heptadecadiene double-bond locations, the extract was subjected to partial reduction and DMDS derivatization. The partial reduction followed the method of Jham et al.[29] using hydrazine and hydrogen peroxide. Fifty microliters of the extract was concentrated under a stream of argon and then reacted with 150 μL of 10% N_2H_4 in methanol and 150 μL of 4% H_2O_2 in methanol for 2 h at 60 °C. The reaction was quenched with 100 μL of 30% HCl solution, and the organics were then extracted with pentane, washed with water, and dried over $MgSO_4$. The organic products of this partial reduction were subject to reaction with DMDS as outlined above. The extract was also reacted with 4-methyl-1,2,4-triazoline-3,5-dione (MTAD)[30] to test for conjugation. Twenty microliters of the extract was blown down to dryness under a stream of argon and then dissolved in a solution of MTAD, 1.2 mg/mL, in dichloromethane. This solution was injected directly into the GC-MS for analysis.

Synthesis of (6*Z*,9*Z*)-Heptadecadiene. For acid chloride formation, 280 mg of linoleic acid (1.00 mmol) was dissolved in 5 mL of chloroform, and a drop of dimethylformamide was added. Oxalyl chloride (94 μL, 1.09 mmol) dissolved in 1 mL of chloroform was added to the acid solution dropwise at room temperature under argon. After 1 h, the reaction mix was heated and refluxed for 3 h. For Barton decarboxylation, 179 mg of 2-mercaptopyridine *N*-oxide, sodium salt (1.2 mmol), and 1 mg of 4-(dimethylamino)pyridine (0.008 mmol) were dissolved in 5 mL of chloroform. The mixture was heated to reflux, and the crude acid chloride was added dropwise from above with simultaneous irradiation by a tungsten lamp (240 V, 500 W). After 2 h, the reaction mix was cooled to room temperature and added to a separatory funnel containing 20 mL of 1 M HCl and 20 mL of dichloromethane. The organic layer was washed with brine and dried over $MgSO_4$. The solvent was removed, and the crude product was purified by column chromatography (SiO_2, pentane) to give 86 mg of the diene (0.36 mmol, 36% yield, 99% chemical purity, 89% isomeric purity by GC) as a clear, colorless oil: ^{1}H NMR (500 MHz, $CDCl_3$) δ 5.37 (m, 4H, $-CH_2C\underline{H}{=}C\underline{H}CH_2C\underline{H}{=}C\underline{H}CH_2-$), 2.78 (t, 2H, J = 6.56 Hz, $=CHC\underline{H}_2CH=$), 2.05 (q, 4H, J = 6.89 Hz, $=CHC\underline{H}_2CH_2CH_2CH_2CH_3$, $=CHC\underline{H}_2CH_2CH_2CH_2CH_2CH_2CH_3$), 1.40−1.25 (br m, 16H, $=CHCH_2C\underline{H}_2C\underline{H}_2C\underline{H}_2CH_3$, $=CHCH_2C\underline{H}_2C\underline{H}_2C\underline{H}_2C\underline{H}_2C\underline{H}_2CH_3$), 0.89 (t, 3H, J = 6.97 Hz, $-CH_3$), 0.88 (t, 3H, J = 7.13 Hz, $-CH_3$); ^{13}C NMR (125.8 MHz, $CDCl_3$) δ 130.20 (C6 and C10), 127.96 (C7 and C9), 31.88 (C3), 31.54 (C15), 29.70 (C12), 29.36 (C4), 29.30 (C13), 29.23 (C14), 27.25 (C5 or C11), 27.21 (C11 or C5), 25.64 (C8), 22.68 (C2), 22.58 (C16), 14.10 (C1 or C17), and 14.06 (C17 or C1); MS data 70 eV, m/z (relative intensity) 236 (9, M^+), 152 (3), 138 (7), 124 (11), 109 (25), 95 (55), 81 (78), 67 (100), 55 (26), and 41 (37).

Proboscis Extension Response (PER). The general methodology based on Pavlovian conditioning and reviewed by Matsumoto et al.[25] was followed. The synthetic flower mixtures used for PER were made up of the six antennally active compounds at the ratios present in the natural flower extracts (Figure 1). 1-Nonanol was chosen as the untrained control compound as it is readily detected by honey bees over a range of concentrations[31] (from ng to mg) and is a standard control compound for PER experiments.[25]

Honey bees were collected in the morning and harnessed in small cylindrical tubes of 8 mm i.d. Bees were then fed 4 μL of 50% sucrose solution and left for 3 h before training. Bees were set 5 cm in front of a syringe containing 1 μg of a synthetic mixture from either male or female kiwifruit flowers deposited on filter paper. Bees had a 15 s settling time before being exposed to 30 mL of air containing the odor over 4 s. This corresponds to the conditioned stimulus (CS+). After 3 s of odor exposure, bees' antennae were gently touched with a toothpick soaked in 50% sucrose solution and once the proboscis was extended in response, a sugar reward was given corresponding to the unconditioned stimulus (US).

The association in time of the CS+ with the US is expected to trigger the formation of a memory of the odor cues with the presence of the reward. Each bee was trained four times, with 10 min intervals between training. Bees were rested for 1 h before testing in a random order to three odor blends: 1 μg of the synthetic flower mix on which they were trained, 1 μg of the correspondingly sexed flower extract, and an untrained control compound, 100 μg of 1-nonanol. In the absence of sugar reward, bees' responses to the presentation of each odor were recorded as 1 if they showed a PER or as 0 if they did not show a PER. If bees responded positively to the synthetic flower mix as well as the natural extract, we considered that this was a demonstration that the synthetic flower mix was perceived as similar to the natural flower extract. The ability of bees to discriminate between the male or female flower extract when trained on the synthetic mix of either sex was also tested.

Statistical Analysis. In total, 75 bees were trained with the PER. Thirty-seven bees were trained and tested with the kiwifruit female flower synthetic mix, and 38 bees were trained and tested with the kiwifruit male flower synthetic mix. Among those, seven bees were excluded from the final analysis because of death or lack of hunger. A chi-square test was used to compare the observed proportions of bees responding or not to the odors for each test to the calculated expected values if the null hypothesis of independency was assumed. p values of <0.05 reject the hypothesis of independence of proportions and therefore suggest that proportions are similar.

RESULTS

Honey Bee Response to Floral Volatiles with GC-EAD.

Honey bees gave consistent antennal responses to six compounds in the kiwifruit flower headspace, marked in Figure

DOI: 10.1021/acs.jafc.5b01165
J. Agric. Food Chem. 2015, 63, 5597−5602

1. Only compounds to which ≥80% of the bees responded were counted as provoking active responses in the antenna. Quantities of each compound and average antennal responses are shown in Table 1. For female flowers 100% of the foragers responded to nonanal, 2-phenylethanol, 4-oxoisophorone, and (8*Z*)-heptadecene, whereas 90% responded to (3*E*,6*E*)-α-farnesene and (6*Z*,9*Z*)-heptadecadiene. For male flowers, 100% of honey bee foragers responded to 2-phenylethanol, (3*E*,6*E*)-α-farnesene, and (6*Z*,9*Z*)-heptadecadiene, 88% responded to (8*Z*)-heptadecene, and 63% responded to nonanal. Nonanal was included for the male flower as a positive response because of the 100% response in the female extract, which had a similar quantity of nonanal. The 4-oxoisophorone evoked no responses in the male extract as it was thought to be below the detection threshold of the bee.

Analysis of Kiwifruit Flower Volatiles. Pooled samples of male and female flower volatiles of *Actinidia deliciosa* showed no qualitative differences by GC analysis, but there were some quantitative differences, as shown in Table 1. Of the six antennally active compounds in Figure 1, three have previously been identified in kiwifruit flowers:[9] nonanal, 2-phenylethanol, and (3*E*,6*E*)-α-farnesene. These were confirmed with synthetic and isolated standards. 4-Oxoisophorone was identified by mass spectra library match and confirmed by comparison with a synthetic standard. Heptadecene and heptadecadiene were first tentatively identified by their mass spectra, before other confirmatory tests. The double-bond location for the heptadecene was confirmed as the 8-position via DMDS reaction, with the pooled sample giving an adduct with a molecular ion at *m*/*z* 332 and diagnostic ions at *m*/*z* 159 and 173. The geometry of the double bond was confirmed as *Z* using a synthetic standard of 8-heptadecene containing 85% of the *Z* isomer and 15% of the *E* isomer. For identification of the double-bond positions in the diene, the pooled sample was first partially reduced to give the corresponding monoenes, which were then reacted with DMDS. The DMDS adducts both had molecular ions at *m*/*z* 332, with diagnostic ions at *m*/*z* 159, 173, and *m*/*z* 131, 201, corresponding to a double-bond position of 8 or 9 and 6 or 11, respectively. To rule out the possibility of the double bonds being conjugated, an MTAD test was done. Because the pooled extract did not react with the MTAD solution, the double bonds could not be conjugated, meaning the positions had to be 6 and 9. The geometry of the double bonds in the diene was confirmed as (6*Z*,9*Z*)-heptadecadiene via synthesis of the molecule, co-injection with the pooled sample on both DB-5 ms and DB-wax columns, comparison with literature ^{13}C NMR,[32] and electroantennogram testing of the synthetic material with the insect.

Training and Response of Honey Bees with Synthetic Floral Odors. After four training sessions, 85% of bees consistently extended their proboscis in expectation of the reward when the odor was presented. When the bees' memories were tested 1 h after training to the synthetic floral mix, 98 and 93% of bees responded to the male and female synthetic floral mixes, respectively (Figure 2). When presented with the natural extract of the corresponding male and female flowers, bees were also highly responsive, with 97 and 90% PER. However, when bees were presented with a new compound, 1-nonanol, only 28 and 44%, respectively, exhibited PER. For both sexes, the PER responses of bees between the synthetic floral mixtures and the natural extract were similar (chi-square = 21.17, df = 1, $p < 0.0001$, null hypothesis of independence rejected), whereas bees' responses to the synthetic floral mixtures were independent from their responses to the new compound, 1-nonanol (chi-square = 0.22, df = 1, $p = 0.63$). When bees were trained to the synthetic floral mix of either sex (male or female), they responded similarly to the natural extract of both sexes (70%, chi-square = 26.17, df = 1, $p < 0.001$).

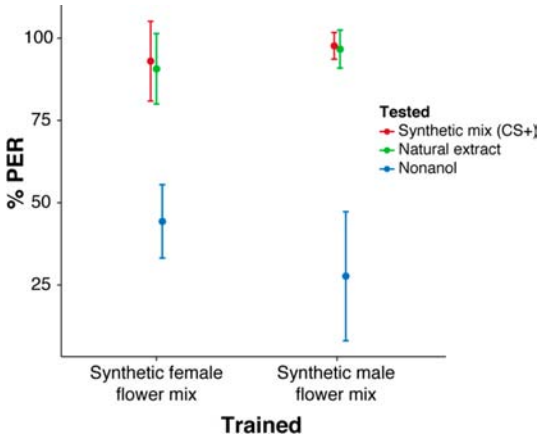

Figure 2. Mean percentage (±SD) of honey bee showing the proboscis extension response (PER) after being trained to synthetic mixes of volatiles from male (n = 37) or female (n = 38) kiwifruit flowers.

DISCUSSION

Our volatile profile for the flowers showed some differences from those previously reported for kiwifruit species.[9−12] The major peaks were the hydrocarbons (6*Z*,9*Z*)-heptadecadiene and (8*Z*)-heptadecene and the sesquiterpene (3*E*,6*E*)-α-farnesene shown in Figure 1. Earlier work on floral volatiles from kiwifruit flowers by Tatsuka et al.[9] found that (3*E*,6*E*)-α-farnesene was the most abundant, whereas hydrocarbons with Kovats indices similar to the ones we identified were in lower abundance and remained unidentified.[9] Others have reported high concentrations of terpenes and their derivatives in the headspace of kiwifruit flower species.[10−12] All aforementioned work has used cut flowers for volatile analysis,[9−12] which provides the benefit of having large concentrated samples but adds plant-wounding volatiles. When plants are cut or wounded, volatile compounds released by the plant change.[33] This can be part of a defense mechanism to deter herbivory by insects[34] or attack by microbes or simply as a result of cellular material being released as a result of the wounding. To avoid this complication, we sampled undamaged flowers in situ on the vine, collecting real-time volatile emissions when the bees were foraging.

Honey bees consistently detected six floral odor compounds from the headspace of the intact kiwifruit flowers. Previous publications on kiwifruit flower headspace report up to 70 floral volatiles.[9−12] This suggests honey bees are using only a few volatiles from the floral mixture for olfactory recognition of the flower. These results are similar to those reported for sunflower extracts collected by Thiery et al.,[13] which contained >100 volatile components, with up to 24 compounds giving EAD response but only 4 compounds were detected by 100% of the bees.[13] The seven Brassicaceae crops tested by Kobayashi et al.[15] contained 52 compounds across the species, but only 14 compounds were physiologically active. Blight et al.[16] found 16 behaviorally active compounds in *Brassica napus*. Of these active compounds, kiwifruit shared 2-phenylethanol and

DOI: 10.1021/acs.jafc.5b01165
J. Agric. Food Chem. 2015, 63, 5597−5602

(3*E*,6*E*)-α-farnesene with some of the Brassicaceae species and none with the sunflower, whereas sunflower and Brassicaceae shared 1,8-cineole and β-elemene as bee-active compounds.

Honey bees have evolved over millions of years alongside angiosperms, acting as generalist pollinators for a multitude of flowers in many different environments. It does not come as a surprise to find that they are cueing in on only some of the floral compounds in a particular flower species and that there are common cues between plant species.[35] Nonanal, 2-phenylethanol, 4-oxoisophorone, and (3*E*,6*E*)-α-farnesene are all well-reported plant volatiles and insect attractants.[35] (8*Z*)-Heptadecene is reported as a plant volatile for boronias[36] and blue roses[37] as well as an attractant across many insect orders.[35] To our knowledge this is the first report of (6*Z*,9*Z*)-heptadecadiene as a floral compound, but it is previously reported as a VOC from astigmatid mites, oribatid mites, and geometrid moths.[35]

The large EAD response by honey bees to (8*Z*)-heptadecene and (6*Z*,9*Z*)-heptadecadiene may not be adapted from a floral origin. (8*Z*)-Heptadecene has been reported as a compound associated with bee larvae,[38] nurse bees,[39] and pollen foragers,[40] but its behavioral function is not yet known. (6*Z*,9*Z*)-Heptadecadiene may also be a honey bee-produced compound, but remains to be identified as such for *Apis mellifera*. Nonetheless, (6*Z*,9*Z*)-heptadecadiene provides an excellent species-specific floral odor for training bees to kiwifruit flowers.

Honey bees trained to the synthetic floral mix responded similarly to the natural extract, indicating that recognition of kiwifruit flower odor may be reliant on only a few key odor compounds of the floral headspace. This is in line with the work of Reinhard et al.,[17] who showed that honey bees learn a few key compounds in recognition of complex volatile mixtures. In addition, honey bees did not seem to discriminate between male and female flower extracts when trained to either floral sex synthetic mix. Differences in visitation rate between male and female flowers reported by Goodwin and Steven[7] cannot be explained by odor cues, but instead may be based on visual cues potentially including the abundance of pollen in the male flower.

Several field trials have been carried out to encourage honey bees to visit more kiwifruit flowers, but with little success.[41,42] In NZ kiwifruit orchards, Goodwin et al.[43] have shown that providing in-hive feeders of sugar solution during the flowering period increases the amount of kiwifruit pollen collected by those hives. However, kiwifruit still need high hive densities to achieve sufficient pollination rates, and further behavioral manipulations at the colony level will be required for more efficient pollination.

This study has highlighted that only a few odors from kiwifruit flowers are likely to be implicated in bee foraging behavior. A better understanding of how honey bees perceive and respond to floral odors at the hive level will be needed before any behavioral manipulation to improve pollination can be undertaken, but this study has enabled the next step in this process.

AUTHOR INFORMATION

Corresponding Author

*(A.M.T.) E-mail: andrew.twidle@plantandfood.co.nz. Phone: +64-3-9777347. Fax: +64-3-3252074.

Funding

This work was funded by the New Zealand Ministry of Business Innovation and Employment (CONT-33481-BTR-PFR).

Notes

The authors declare no competing financial interest.

ACKNOWLEDGMENTS

We thank Barry Bunn for running NMR on the diene. We also thank Mark Goodwin and Rikard Unelius for their valuable comments on the manuscript.

REFERENCES

(1) FAO. FAOSTAT. http://faostat.fao.org/site/567/DesktopDefault.aspx?PageID=567#ancor (accessed Dec 11, 2014).

(2) Craig, J. L.; Stewart, A. M.; Pomeroy, N.; Heath, A. C. G.; Goodwin, R. M. A review of kiwifruit pollination: where to next? *N. Z. J. Exp. Agric.* **1988**, *16*, 385−399.

(3) Costa, G.; Testolin, R.; Vizzotto, G. Kiwifruit pollination − an unbiased estimate of wind and bee contribution. *N. Z. J. Crop Hortic. Sci.* **1993**, *21*, 189−195.

(4) Goodwin, M.; Haine, H. How many bee visits to fully pollinate kiwifruit? *N. Z. Kiwifruit* **1995**, *111*, 5.

(5) Delaplane, K. S.; Mayer, D. F. *Crop Pollination by Bees*; CABI: Cambridge, UK, 2000.

(6) Palmer-Jones, T.; Clinch, P. G.; Briscoe, D. A. Effect of honey bee saturation on the pollination of Chinese gooseberries variety 'Hayward'. *N. Z. J. Exp. Agric.* **1976**, *4*, 255−256.

(7) Goodwin, R. M.; Steven, D. Behavior of honey-bees visiting kiwifruit flowers. *N. Z. J. Crop Hortic. Sci.* **1993**, *21*, 17−24.

(8) Clinch, P. G. Kiwifruit pollination by honey bees. 1. Tauranga observations, 1978−81. *N. Z. J. Exp. Agric.* **1984**, *12*, 29−38.

(9) Tatsuka, K.; Suekane, S.; Sakai, Y.; Sumitani, H. Volatile constituents of kiwifruit flowers: simultaneous distillation and extraction versus headspace sampling. *J. Agric. Food Chem.* **1990**, *38*, 2176−2180.

(10) Matich, A. J.; Young, H.; Allen, J. M.; Wang, M. Y.; Fielder, S.; McNeilage, M. A.; MacRae, E. A. *Actinidia arguta*: volatile compounds in fruit and flowers. *Phytochemistry* **2003**, *63*, 285−301.

(11) Nieuwenhuizen, N. J.; Wang, M. Y.; Matich, A. J.; Green, S. A.; Chen, X. Y.; Yauk, Y. K.; Beuning, L. L.; Nagegowda, D. A.; Dudareva, N.; Atkinson, R. G. Two terpene synthases are responsible for the major sesquiterpenes emitted from the flowers of kiwifruit (*Actinidia deliciosa*). *J. Exp. Bot.* **2009**, *60*, 3203−3219.

(12) Samadi-Maybodi, A.; Shariat, M. R.; Zarei, M.; Rezai, M. B. Headspace analysis of the male and female flowers of kiwifruit grown in Iran. *J. Essent. Oil Res.* **2002**, *14*, 414−415.

(13) Thiery, D.; Bluet, J. M.; Pham-Delegue, M. H.; Etievant, P.; Masson, C. Sunflower aroma detection by the honeybee. Study by coupling gas chromatography and electroantennography. *J. Chem. Ecol.* **1990**, *16*, 701−711.

(14) Henning, J. A.; Teuber, L. R. Combined gas chromatography-electroantennogram characterization of alfalfa floral volatiles recognized by honey bees (Hymenoptera: Apidae). *J. Econ. Entomol.* **1992**, *85*, 226−232.

(15) Kobayashi, K.; Arai, M.; Tanaka, A.; Matsuyama, S.; Honda, H.; Ohsawa, R. Variation in floral scent compounds recognized by honeybees in Brassicaceae crop species. *Breed. Sci.* **2012**, *62*, 293−302.

(16) Blight, M. M.; LeMetayer, M.; Delegue, M. H. P.; Pickett, J. A.; Marion-Poll, F.; Wadhams, L. J. Identification of floral volatiles involved in recognition of oilseed rape flowers, *Brassica napus* by honeybees, *Apis mellifera*. *J. Chem. Ecol.* **1997**, *23*, 1715−1727.

(17) Reinhard, J.; Sinclair, M.; Srinivasan, M. V.; Claudianos, C. Honeybees learn odour mixtures via a selection of key odorants. *PLoS One* **2010**, *5*, e9110.

DOI: 10.1021/acs.jafc.5b01165
J. Agric. Food Chem. 2015, 63, 5597−5602

(18) Wenner, A. M.; Wells, P. H.; Johnson, D. L. Honey bee recruitment to food sources: olfaction or language? *Science (Washington, DC, U. S.)* **1969**, *164*, 84−86.
(19) von Frisch, K. Decoding the language of the bee. *Science (Washington, DC, U.S.)* **1974**, *185*, 663−668.
(20) Farina, W. M.; Gruter, C.; Diaz, P. C. Social learning of floral odours inside the honeybee hive. *Proc. R. Soc. London, Ser. B* **2005**, *272*, 1923−1928.
(21) Gil, M.; De Marco, R. J. Olfactory learning by means of trophallaxis in *Apis mellifera*. *J. Exp. Biol.* **2005**, *208*, 671−680.
(22) Farina, W. M.; Gruter, C.; Acosta, L.; McCabe, S. Honeybees learn floral odors while receiving nectar from foragers within the hive. *Naturwissenschaften* **2007**, *94*, 55−60.
(23) Díaz, P.; Grüter, C.; Farina, W. Floral scents affect the distribution of hive bees around dancers. *Behav. Ecol. Sociobiol.* **2007**, *61*, 1589−1597.
(24) Giurfa, M.; Sandoz, J. C. Invertebrate learning and memory: fifty years of olfactory conditioning of the proboscis extension response in honeybees. *Learn. Mem.* **2012**, *19*, 54−66.
(25) Matsumoto, Y.; Menzel, R.; Sandoz, J. C.; Giurfa, M. Revisiting olfactory classical conditioning of the proboscis extension response in honey bees: a step toward standardized procedures. *J. Neurosci. Methods* **2012**, *211*, 159−167.
(26) Murray, K. α-Farnesene: isolation from the natural coating of apples. *Aust. J. Chem.* **1969**, *22*, 197−204.
(27) Ko, E. J.; Savage, G. P.; Williams, C. M.; Tsanaktsidis, J. Reducing the cost, smell, and toxicity of the barton reductive decarboxylation: chloroform as the hydrogen atom source. *Org. Lett.* **2011**, *13*, 1944−1947.
(28) Carlson, D. A.; Roan, C. S.; Yost, R. A.; Hector, J. Dimethyl disulfide derivatives of long-chain alkenes, alkadienes, and alkatrienes for gas-chromatography mass-spectrometry. *Anal. Chem.* **1989**, *61*, 1564−1571.
(29) Jham, G. N.; Attygalle, A. B.; Meinwald, J. Location of double bonds in diene and triene acetates by partial reduction followed by methylthiolation. *J. Chromatogr.* **2005**, *1077*, 57−67.
(30) McElfresh, J. S.; Millar, J. G. Sex pheromone of the common sheep moth, *Hemileuca eglanterina*, from the San Gabriel Mountains of California. *J. Chem. Ecol.* **1999**, *25*, 687−709.
(31) Sachse, S.; Galizia, C. G. The coding of odour-intensity in the honeybee antennal lobe: local computation optimizes odour representation. *Eur. J. Neurosci.* **2003**, *18*, 2119−2132.
(32) Shimizu, N.; Naito, M.; Mori, N.; Kuwahara, Y. De novo biosynthesis of linoleic acid and its conversion to the hydrocarbon (*Z,Z*)-6,9-heptadecadiene in the astigmatid mite, *Carpoglyphus lactis*: incorporation experiments with C-13-labeled glucose. *Insect Biochem. Mol. Biol.* **2014**, *45*, 51−57.
(33) Beck, J. J.; Smith, L.; Baig, N. An overview of plant volatile metabolomics, sample treatment and reporting considerations with emphasis on mechanical damage and biological control of weeds. *Phytochem. Anal.* **2014**, *25*, 331−341.
(34) Pare, P. W.; Tumlinson, J. H. Plant volatiles as a defense against insect herbivores. *Plant Physiol.* **1999**, *121*, 325−331.
(35) El-Sayed, A. M. The Pherobase: Database of Insect Pheromones and Semiochemicals, http://www.pherobase.com, Ashraf M. El-Sayed, 2015.
(36) MacTavish, H. S.; Davies, N. W.; Menary, R. C. Emission of volatiles from brown boronia flowers: some comparative observations. *Ann. Bot.* **2000**, *86*, 347−354.
(37) Joichi, A.; Nakamura, Y.; Haze, S.; Ishikawa, T.; Atoji, H.; Nishida, T.; Sakurai, K. Volatile constituents of blue-coloured hybrid tea rose flowers. *Flavour Fragrance J.* **2013**, *28*, 180−187.
(38) Nazzi, F.; Milani, N.; Vedova, G. D. (*Z*)-8-Heptadecene from infested cells reduces the reproduction of Varroa destructor under laboratory conditions. *J. Chem. Ecol.* **2002**, *28*, 2181−2190.
(39) Pernal, S. F.; Baird, D. S.; Birmingham, A. L.; Higo, H. A.; Slessor, K. N.; Winston, M. L. Semiochemicals influencing the host-finding behaviour of Varroa destructor. *Exp. Appl. Acarol.* **2005**, *37*, 1−26.
(40) Del Piccolo, F.; Nazzi, F.; Della Vedova, G.; Milani, N. Selection of Apis mellifera workers by the parasitic mite Varroa destructor using host cuticular hydrocarbons. *Parasitology* **2010**, *137*, 967−973.
(41) Tsirakoglou, V.; Thrasyvoulou, A.; Hatjina, F. Techniques to increase the attractiveness of kiwi flowers to honey bees. In *Third International Symposium on Kiwifruit*; Sfakiotakis, E., Porlingis, J., Eds.; 1997; Vol. 1 and 2, pp 439−443.
(42) Pinzauti, M. Kiwi pollination: several ways of increasing the activity of honeybees. *Acta Hortic.* **1990**, 149−150.
(43) Goodwin, R. M.; Houten, A. T.; Perry, J. H. Feeding sugar syrup to honey bee colonies to improve kiwifruit pollen collection: a review. *Acta Hortic.* **1991**, 265−269.

DOI: 10.1021/acs.jafc.5b01165
J. Agric. Food Chem. 2015, 63, 5597−5602

δ-zein, with a minor fraction of 10 kDa; and (iv) γ-zein (5−10%), with a MW of 27 kDa.[19,20] Zein is an amphiphilic protein, possessing high percentages of hydrophobic amino acids such as leucine (20%), proline (10%), and alanine (10%).[19,20] Due to this amino acid composition, zein is insoluble in water, and, thus, the resulting devices (e.g., films, nanoparticles) display a hydrophobic character with interesting properties that control the release of the loaded compound.[20,21] In addition, as for other nanocarriers of protein origin, these devices are biodegradable and can accommodate a great variety of compounds in a nonspecific way.[22]

Therefore, the aim of this work was to prepare, characterize, and evaluate a resveratrol nanoparticulate formulation based on zein and to study its oral bioavailability and anti-inflammatory effects in a mouse model of induced endotoxic shock.

MATERIALS AND METHODS

Chemicals. Zein, resveratrol, lysine, mannitol, sodium ascorbate, poly(ethylene glycol) 400 (PEG 400), and Tween 20 were purchased from Sigma-Aldrich (Steinheim, Germany). Resveratrol-3-*O*-D-glucuronide (Rsv-O-glu) was from @rtMolecule (Poitiers, France). Ethanol, methanol, acetic acid, and acetonitrile of HLPC grade were obtained from Merck (Darmastadt, Germany). Lipopolysaccharide (LPS) from Salmonella *enterica* serovar Minnesota was purchased from Sigma, (St. Louis, MO, USA). Deionized reagent water (18.2 MO resistivity) was prepared using a water purification system (Wasserlab, Spain). All reagents and chemicals used were of analytical grade.

Preparation of Resveratrol-Loaded Nanoparticles (Rsv-NP-Z). Nanoparticles were prepared by a desolvation method followed by an ultrafiltration purification step and subsequent drying in a spray-dryer apparatus. Briefly, 600 mg of zein and 100 mg of lysine were dissolved in 60 mL of an ethanol/water mixture (65% ethanol by vol). In parallel, 100 mg of resveratrol was dissolved in 10 mL of ethanol, and 6 mL of this solution was transferred to the zein solution. In addition, 6 mg of sodium ascorbate was added to minimize the oxidation of the polyphenol. The mixture was magnetically stirred in the dark for 10 min at room temperature. Nanoparticles were obtained by the continuous addition of 60 mL of purified water. The suspension was purified and concentrated by ultrafiltration using a membrane cartridge with a 50 kDa pore size polysulfone (Medica SPA, Italy). Then, 15 mL of purified water containing 1.2 g of mannitol was added to the resulting suspension of nanoparticles to prevent aggregation and irreversible interactions among the nanoparticles during the drying process. Finally, the suspension was dried in a Büchi Mini Spray Dryer B-290 apparatus (Büchi Labortechnik AG, Flawil, Switzerland) under the following experimental conditions: (i) inlet temperature, 90 °C; (ii) outlet temperature, 45−50 °C; (iii) air pressure, 4−6 bar; (iv) pumping rate, 5 mL/min; (v) aspirator, 100%; and (vi) air flow, 400−500 L/h.

Control formulations (NP-Z) were prepared as described above but in the absence of resveratrol.

Preparation of Resveratrol Conventional Formulations. Two different formulations of resveratrol were also prepared. The first one, a solution of the polyphenol in a mixture of PEG400 and water (1:1 by vol), was prepared by dissolving 37.5 mg of resveratrol in 5 mL of PEG400 under magnetic stirring. Then 5 mL of purified water was added, and the final mixture was agitated in the dark for 10 min. This formulation was named Rsv-sol.

The second one was an extemporary suspension of resveratrol in purified water (Rsv-susp). Briefly, 37.5 mg of resveratrol was dispersed in 10 mL of purified water under magnetic agitation for 10 min. The size of the resulting suspension was 21.4 ± 9.2 μm. The suspension was used after inspection for the absence of aggregates.

Characterization of Nanoparticles. *Size, Zeta Potential, and Morphology.* The mean hydrodynamic diameter and the zeta potential of the nanoparticles were determined by photon correlation spectroscopy (PCS) and electrophoretic laser Doppler anemometry, respectively, using a Zetamaster analyzer system (Malvern Instruments Ltd., Worcestershire, UK). The diameter of the nanoparticles was determined after dispersion in ultrapure water (1:10) and was measured at 25 °C with a scattering angle of 90 °C. The zeta potential was measured after dispersion of the dried nanoparticles in 1 mM KCl solution.

The morphology of the nanoparticles was studied by field-emission scanning electron microscopy (SEM) using a Zeiss DSM940 digital scanning electron microscope (Oberkochen, Germany) coupled with a digital imaging system (Point Electronic GmBh, Germany). The yield of the process was calculated by gravimetry as described previously.[22]

Resveratrol Analysis. The amount of resveratrol loaded into the nanoparticles was quantified by HPLC-UV using a previously described analytical method[23] with minor modifications. Analyses were carried out in an Agilent 1100 series LC system coupled to a diode array detector set at 306 nm. The data were analyzed using ChemStation G2171 v. B.01.03 software (Agilent, USA). The chromatographic system was equipped with a reverse C18 Alltima column (150 mm × 2.1 mm, particle size = 5 μm; Alltech, USA) and a Gemini AJO-7596 C18 precolumn. The mobile phase, pumped at 0.25 mL/min, was a mixture of water/methanol/acetic acid under gradient conditions. The column was heated to 40 °C, and the injection volume was 10 μL. Under these conditions, the retention time for resveratrol was 22.8 ± 0.5 min. Calibration curves in 75% ethanol were designed over the range of 1−100 μg/mL ($R^2 \geq 0.999$). Under these experimental conditions, the limit of quantitation was calculated to be 200 ng/mL.

For analysis, 10 mg of nanoparticles was dispersed in 1 mL of water and centrifuged at 30500*g* for 20 min. The amount of encapsulated resveratrol was calculated by dissolution of the pellets in 1 mL of 75% ethanol. Each sample was assayed in triplicate, and the results are expressed as the amount of resveratrol (μg) per milligram of nanoparticles.

The encapsulation efficiency (EE) was calculated as

$$\mathrm{EE}\ (\%) = \frac{\mathrm{Rsv_p}}{\mathrm{Rsv_t}} \times 100 \quad (1)$$

where $\mathrm{Rsv_t}$ is the total amount of resveratrol in the formulations and $\mathrm{Rsv_p}$, the amount of resveratrol quantified in the pellet.

In Vitro Release Study. Release experiments were conducted under sink conditions at 37 °C using simulated gastric fluid (SGF; pH 1.2) and intestinal fluid (SIF; pH 6.8),[22] containing 0.5% Tween 20 as a surfactant to increase the aqueous solubility of resveratrol. The studies were performed under agitation in a Slide-A-Lyzer Dialysis Cassete with a 10000 MWCO (Thermo Scientific, Rockford, IL, USA). For this purpose, the cassette was filled with 3 mg of resveratrol nanoparticles previously dispersed in 5 mL of water and then introduced into a vessel containing 500 mL of SGF (pH 1.2; 37 °C) under magnetic stirring. After 2 h in the SGF, the cassette was introduced into another vessel containing 500 mL of thermostated SIF (pH 6.8; 37 °C, under agitation). At different time points, samples were collected and filtered through filters with a 0.45 μm pore size (Thermo Scientific) before quantification by HPLC. Calibration curves for resveratrol in SGF and SIF (0.05−6 μg/mL; $R^2 \geq 0.999$ in both cases) were generated.

To ascertain the resveratrol release mechanism, the obtained data were fitted to the Korsmeyer−Peppas and Peppas−Sahlin models. The Korsmeyer−Peppas model is a simple semiempirical approach, which exponentially relates drug release with the elapsed time as expressed in the equation[24]

$$\frac{M_t}{M_\infty} = K_{\mathrm{KP}} \times t^n \quad (2)$$

where M_t/M_∞ is the drug release fraction at time t, K_{KP} is a constant incorporating the structural and geometric characteristics of the matrix, and n is the release exponent indicative of the drug release mechanism.[25] Values close to 0.5 indicate a case I (Fickian) diffusion mechanism, and values between 0.5 and 0.89 indicate anomalous (non-Fickian) diffusion. Values of n between 0.89 and 1 indicate case II transport, erosion of the matrix.

DOI: 10.1021/jf505694e
J. Agric. Food Chem. 2015, 63, 5603−5611

The contributions of Fickian and non-Fickian release were also evaluated by using the Peppas–Sahlin model equation[26]

$$\frac{M_t}{M_\infty} = K_D \times t^{1/2} + K_E \times t \quad (3)$$

where the first term of the right-hand side is the Fickian contribution (K_D is the diffusional constant) and the second term is the case II erosional contribution (K_E is the erosional constant). K_D and K_E values were used to calculate the contribution percentage of diffusion (D) and erosion (E) as follows:[26]

$$D = \frac{1}{1 + \frac{K_E}{K_D} \times t^{0.5}} \quad (4)$$

$$\frac{E}{D} = \frac{K_E}{K_D} \times t^{0.5} \quad (5)$$

Only one portion of the release profile ($M_t/M_\infty \leq 0.6$) was used to fit the experimental data to the previous equation.

In Vivo Pharmacokinetic Studies in Wistar Rats. *Pharmacokinetic Studies.* Pharmacokinetic studies were performed in male Wistar rats (200–250 g) obtained from Harlan (Barcelona, Spain). The studies were approved by the Ethical Committee for Animal Experimentation of the University of Navarra (protocol 028-11) in accordance with European legislation on animal experiments.

Prior to the oral administration of the formulations, animals were fasted overnight to avoid interference with absorption, but were allowed free access to water. For the pharmacokinetic studies, rats were randomly divided into four groups of six animals each. The three experimental groups were (i) aqueous resveratrol suspension (Rsv-susp), (ii) resveratrol in a PEG400/water mixture (Rsv-sol), and (iii) resveratrol-loaded zein nanoparticles (Rsv-NP-Z). As a control, a group of animals was treated intravenously with the PEG400/water (1:1 by vol) solution of resveratrol. Each animal received the equivalent amount of resveratrol at a dose of 15 mg/kg body weight either by oral gavage or intravenously via the tail vein.

Blood samples were collected at set times after administration (0, 10, and 30 min and 1, 2, 4, 6, 8, 24, and 48 h) in specific plasma tubes (Microvette 500 K3E, SARSTEDT, Germany). Samples were immediately centrifuged at 9400*g* for 10 min, and plasma aliquots were kept frozen at −80 °C until HPLC analysis of both resveratrol and resveratrol-3-*O*-D-glucuronide.

Determination of Resveratrol and Resveratrol-3-O-D-glucuronide Plasma Concentration by HPLC. The amount of resveratrol was determined by HPLC-UV using a previously reported analytical method[27] with minor modifications. Analyses were carried out using an Agilent 1100 series LC and a diode array detector set at 306 nm. The data were analyzed in a ChemStation G2171 program (B.01.03). The chromatographic system was equipped with a reverse-phase Kromasil C18 column (250 mm × 2.1 mm, particle size = 5 μm) and a Gemini AJO-7596 C18 precolumn. The mobile phase, pumped at 0.5 mL/min, was a mixture of water, methanol, and acetic acid (50:45:5 by vol) under isocratic conditions. The column was thermostated at 30 °C, and the injection volume was 30 μL. Under these conditions, the retention times for resveratrol-3-*O*-D-glucuronide and resveratrol were 6.2 ± 0.5 and 12.6 ± 0.5 min, respectively.

For analysis, a 100 μL aliquot of plasma was mixed with 50 μL of 0.1 N HCl and 500 μL of acetonitrile (for protein precipitation) followed by vigorous shaking. The samples were then centrifuged at 4000 rpm for 10 min, and the obtained supernatants were evaporated under vacuum in a Speed Vac system (Holbrook, NY, USA) at 25 °C for 30 min. Finally, 100 μL of a mixture of acetonitrile and water (1:1 by vol) was added and vigorously stirred by vortexing for 10 min. The samples were then filtered through a 0.45 μm filter (Thermo Scientific) prior to injection.

For quantification, calibration curves were prepared over the ranges of 2–70 μg/mL for the metabolite and 50–3000 ng/mL for resveratrol ($R^2 \geq 0.99$). All of the calibration standards were obtained by adding either resveratrol or resveratrol-3-*O*-D-glucuronide in acetonitrile (500 μL) to 100 μL of plasma from nontreated animals. The polyphenol or its metabolite was then extracted using the same protocol as described above.

Under these experimental conditions, the limits of quantification were calculated to be 70 ng/mL for resveratrol and 4 μg/mL for the metabolite. Linearity, accuracy, and precision values on the same day (intraday assay) at low, medium, and high concentrations of both resveratrol and the metabolite were always within the acceptable limits (relative error and coefficient of variation of <15%).

Pharmacokinetic Data Analysis. The resveratrol plasma concentration was plotted against time, and the pharmacokinetic analysis was performed using a noncompartmental model within WinNonlin 5.2 software (Pharsight Corp., USA). The following parameters were estimated: the maximal serum concentration (C_{max}), the time in which C_{max} is reached (t_{max}), the area under the concentration–time curve from time 0 to the last sampling time point (48 h) (AUC), the mean residence time (MRT), the clearance (Cl), the volume of distribution (V), and the half-life in the terminal phase ($t_{1/2}$). Furthermore, the relative bioavailability (Fr, %) of resveratrol was estimated by the equation

$$\text{Fr}\ (\%) = \frac{\text{AUC}_{oral}}{\text{AUC}_{iv}} \times 100 \quad (6)$$

where AUC_{iv} and AUC_{oral} are the areas under the curve for the iv and oral administrations, respectively.

In Vitro/in vivo Correlation (INVIC). The eventual correlation between the in vitro and in vivo results was determined by point-to-point plotting of the amount of resveratrol released from the nanoparticles versus the fraction of resveratrol absorbed (FRA), calculated from the mean plasma concentration–time inputs using the Wagner–Nelson equation[28]

$$\text{FRA} = \frac{C_t + k \times \text{AUC}_{0-t}}{k \times \text{AUC}_{0-\infty}} \quad (7)$$

where C_t is the plasma concentration of resveratrol at time t, k is the elimination rate constant of the polyphenol, AUC_{0-t} is the area under the resveratrol concentration versus time curve from 0 to time t, and $AUC_{0-\infty}$ is the area under the curve from 0 to infinity.

Linear regression analysis was applied to the in vitro/in vivo correlation plot, and the coefficient of determination (R^2) was calculated.

Anti-inflammatory Efficacy Study. *Animal Model.* Four-week-old (20–22 g) C57BL/6J female mice were purchased from Harlan (Barcelona, Spain) and housed in standard animal facilities (six animals per cage with free access to food and drinking water). Housing conditions were maintained with controlled temperature and humidity and with 12 h on/off light cycles. Animals were allowed to acclimate for 1 week before the experiment.

In vivo anti-inflammatory studies were evaluated in an endotoxic shock model set up by intraperitoneal (ip) administration of LPS at a dose of 40 μg per mouse.[29] Before administration, the LPS was dissolved in PBS and vortexed for 30 min to complete homogenization.

On day 1, mice were randomly distributed into four groups. The first group of animals received an oral dose of 15 mg/kg resveratrol daily as an oral solution (Rsv-sol) for 7 days. The second group of animals received the same posology of polyphenol (15 mg/kg resveratrol daily for 7 days) but within the zein nanoparticle formulation (Rsv-NP-Z). As controls, a group of animals received LPS treatment (positive-control group), and another group received neither LPS nor resveratrol (negative-control group).

Twenty-four hours after the last dose of resveratrol (day 8), the animals were challenged with 40 μg of LPS by the ip route. Throughout the study, the rectal temperature of the mice was measured until 24 h after challenge. Clinical anaphylactic reactions were scored 6 h postchallenge by two independent observers. Piloerection was scored as follows: (−) normal mouse, (+) weak reaction and/or scratching of the nose and head, (++) moderate piloerection, and (+++) strong piloerection. Depending on the activity

DOI: 10.1021/jf505694e
J. Agric. Food Chem. 2015, 63, 5603–5611

Table 1. Physicochemical Characteristics of Empty and Resveratrol-Loaded Nanoparticles[a]

	size[b] (nm)	PDI	zeta potential (mV)	Rsv loading[c] (μg/mg NP)	EE[d] (%)
NP-Z	264 ± 2	0.07 ± 0.01	−46.2 ± 2.15		
Rsv-NP-Z	307 ± 3	0.10 ± 0.01	−51.1 ± 1.55	80.2 ± 3.26	82.1 ± 4.12

[a]NP-Z, empty zein nanoparticles; Rsv-NP-Z, resveratrol-loaded zein nanoparticles; PDI, polydispersity index. The data are expressed as the mean ± SD (n = 6). [b]Determination of volume mean diameter by photon correlation spectroscopy. [c]Determination of resveratrol content by HPLC-UV. [d]Encapsulation efficiency (%).

of the animals, their mobility was classified as very low (no reaction after pushing), low (arched back and low movements) or normal.

In addition, 90 min after challenge, blood samples were collected into EDTA-K vials (Microvette 500 K3E, SARSTEDT, Germany) from the retro-orbital cavity, centrifuged at 8000g for 10 min for serum collection, and stored at −20 °C until use.

Measurement of Plasma TNF-α. The concentration of circulating TNF-α in the serum was determined using an enzyme-linked immunosorbent assay kit (Mouse TNF-alpha Quantikine ELISA Kit, MTA00B, R&D Systems, Minneapolis, MN, USA) according to the manufacturer's instructions.

Statistical Analysis. The data are expressed as the mean ± standard deviation (SD) of at least three experiments. The nonparametric Kruskal−Wallis test followed by the Mann−Whitney U test with Bonferroni correction was used to investigate significant differences. In all cases, $p < 0.05$ was considered to be statistically significant. All data processing was performed using GraphPad Prism statistical software.

RESULTS

Preparation and Characterization of Nanoparticles. Table 1 shows the physicochemical characteristics of the nanoparticles used in this study. Overall, the mean diameter of empty nanoparticles was smaller than that of nanoparticles loaded with resveratrol. When resveratrol was encapsulated, zein nanoparticles displayed a mean size of approximately 310 nm, whereas the polydispersity index (PDI) was found to be <0.2, indicating a homogeneous nanoparticle formulation. Furthermore, the zeta potential of the nanoparticles was negative (−51 mV); however, when resveratrol was encapsulated, the resulting nanoparticles were slightly more negative than empty ones were (Table 1). Additionally, the resveratrol loading was calculated to be approximately 80 μg/mg nanoparticles, with an encapsulation efficiency close to 82%.

Figure 1 shows the morphology and shape of the resveratrol-loaded nanoparticles. In all cases, the nanoparticles consisted of homogeneous populations of spherical particles with a smooth surface. In addition, the size of the nanoparticles, as observed by SEM, was slightly smaller than the value determined by PCS (Table 1). This observation is related to the fact that nanoparticles composed of macromolecules (such as proteins or polysaccharides) tend to swell when they are dispersed in an aqueous medium.

In Vitro Release Profile. Figure 2A represents the profile of resveratrol release from nanoparticles, expressed as the cumulative percentage of drug released versus time. In all cases, the release of resveratrol from zein-based nanoparticles was found to be independent of the pH conditions. During the first 2 h, under SGF conditions (pH 1.2), approximately 20% of the loaded resveratrol was released from the zein nanoparticles. Then, 6 h later (during incubation under SIF conditions), the amount released was close to 60% of the total resveratrol content. After 48 h, all of the loaded resveratrol had been released from the nanoparticles.

The profile of resveratrol release from the nanoparticles was fitted to different mathematical release models. Using the Korsmeyer−Peppas equation, R^2 values were high ($R^2 > 0.96$),

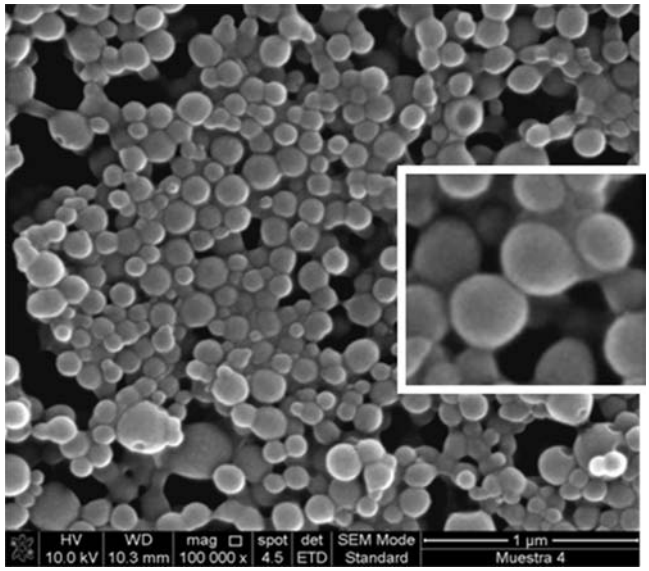

Figure 1. Scanning electron microscopy (SEM) microphotograph of resveratrol-loaded zein nanoparticles. The bar indicates the resolution (1 μm). The white box delimits a magnified area.

and the exponent n value was 0.75 ± 0.06. All of these results suggest that the release of resveratrol from the nanoparticles was due to a combination of Fickian diffusion and erosion of the nanoparticle matrix. Under these circumstances, the Peppas−Sahlin model was applied, and the erosion (K_E) and diffusion (K_D) constants were calculated (K_D = 0.08 ± 0.02 $h^{-1/2}$; K_E = 0.04 ± 0.01 h^{-1}). Figure 2B displays the contributions of both the diffusion and the erosion mechanisms to the release of resveratrol from zein nanoparticles. The time at which the two mechanisms (diffusion and erosion) similarly contributed to the release of resveratrol was calculated to be 3.5 h.

In Vivo Pharmacokinetics. Figure 3A shows the plasma concentration−time profile of a resveratrol solution in PEG400/water (1:1 by vol) after intravenous (iv) administration of a single dose of 15 mg/kg to rats. The data were adjusted to a noncompartmental model. The resveratrol plasma concentration decreased rapidly, in a biphasic way, during the first 8 h of postadministration. The peak plasma concentration (C_{max}) of resveratrol was 15.2 μg/mL, whereas the AUC and half-life ($t_{1/2}$) were calculated to be 11.4 μg h/mL and 2.04 h, respectively. The clearance and volume of distribution of resveratrol were 199 mL/h and 569 mL, respectively (Table 2).

Figure 3B shows the plasma concentration levels of resveratrol when administered orally to rats as a single dose of 15 mg/kg. Interestingly, when resveratrol was formulated as a suspension, no quantifiable levels of the polyphenol were detected in the plasma. In contrast, when resveratrol was administered as a solution (Rsv-sol), the polyphenol plasma levels displayed a maximum concentration (C_{max}), or 0.20 μg/

DOI: 10.1021/jf505694e
J. Agric. Food Chem. 2015, 63, 5603−5611

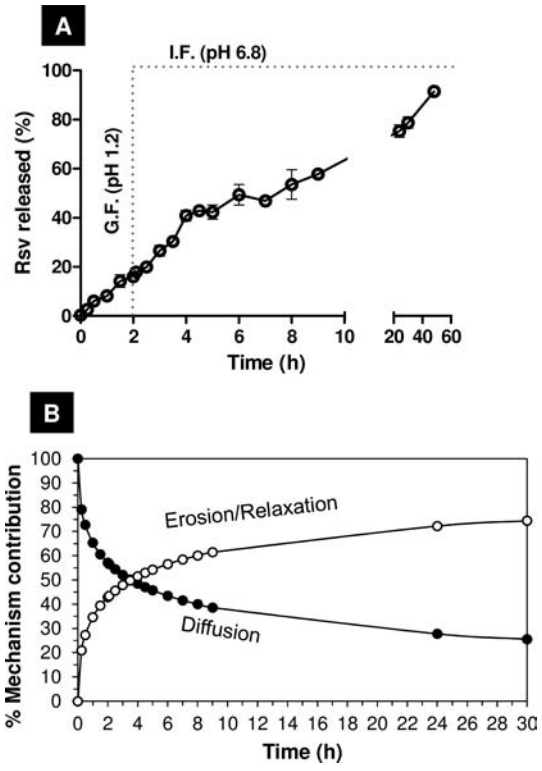

Figure 2. Resveratrol release from zein-based nanoparticles (Rsv-NP-Z). (A) Resveratrol release profile when incubated in simulated gastric fluid (SGF, pH 1.2; 0−2 h) and simulated intestinal fluid (SIF, pH 6.8; 2−48 h) under sink conditions. The data represent the mean ± standard deviation (SD) (n = 3). (B) Fractional contributions of the Fickian diffusion (●) and the erosion/relaxation (○) mechanisms to resveratrol release from zein nanoparticles (Rsv-NP-Z).

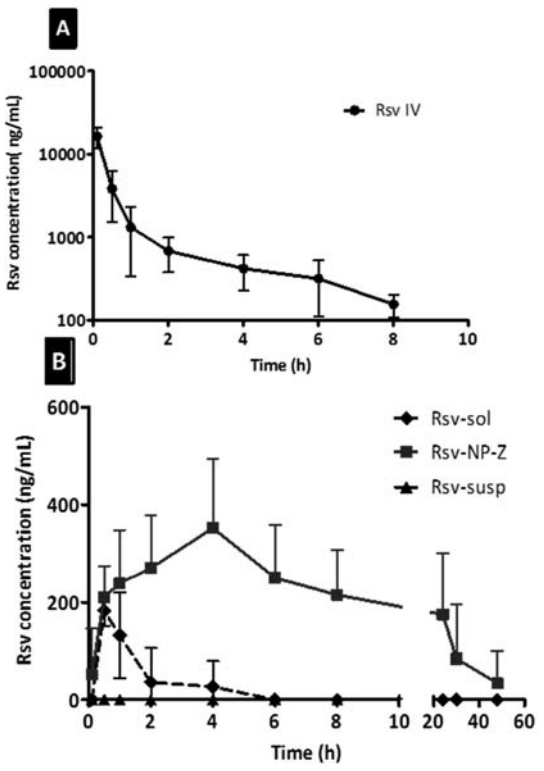

Figure 3. Resveratrol plasma concentration versus time after a single administration of the polyphenol at a dose of 15 mg/kg. (A) Intravenous (iv) administration of the resveratrol solution in the PEG400/water mixture. (B) Oral administration of the following resveratrol formulations: (i) resveratrol suspension (Rsv-susp, ▲), (ii) resveratrol solution (Rsv-sol, ◆), and (iii) resveratrol-loaded zein nanoparticles (Rsv-NP-Z, ■). Data are expressed as the mean ± SD (n = 6).

mL, 30 min after administration. The plasma levels of resveratrol then decreased rapidly, and quantifiable levels were detected only during the first 4 h postadministration.

For resveratrol loaded in zein nanoparticles (Rsv-NP-Z), the amount of the polyphenol in the plasma increased during the first 4 h after administration until reaching a maximum. The resveratrol plasma levels then decreased slowly for the following 20 h. Forty-eight hours postadministration, the amount of resveratrol in the plasma was very close to the quantitation limit of the analytical technique.

Table 2 summarizes the main pharmacokinetic parameters estimated via a noncompartmental analysis of the experimental data obtained after administration of the different formulations to rats. The resveratrol AUC values for the zein nanoparticle formulation were significantly higher ($p < 0.05$) than those observed for the polyphenol solution. Similarly, the MRT of resveratrol was 13 times higher when resveratrol was administered in the form of zein nanoparticles than when solubilized in the PEG400/water mixture and administered orally. Finally, the relative oral bioavailability of resveratrol when incorporated in zein nanoparticles was calculated to be 50%. This value was significantly higher than the bioavailability obtained with the PEG400/water solution (2.64%).

Figure 4 shows the plasma concentration versus time profile of the main resveratrol metabolite (resveratrol-*O*-3-glucuronide) after a single administration of the polyphenol in the formulations tested. Interestingly, the profiles of the plasma curves for resveratrol and its metabolite were similar; however, the metabolite levels were always higher than the levels of the polyphenol. When resveratrol was administered intravenously, the metabolite concentration reached 41.9 μg/mL (C_{max}), and then the metabolite levels decreased sharply. The AUC value was calculated to be 197 μg h/mL.

For the orally administered solution of resveratrol, the C_{max} of the metabolite in the plasma was found to be 2 times lower (22.1 μg/mL) than when resveratrol was administered by the iv route. In this case, the metabolite was only quantified in the plasma during the first 8 h postadministration. The AUC value was calculated to be 104 μg h/mL, which was approximately half of that for the iv solution.

For the nanoparticles, the metabolite was quantified during the first 24 h after administration. In addition, the metabolite AUC was approximately 342 μg h/mL for Rsv-NP-Z. This value was approximately 3 times higher than that for the resveratrol administered as an oral solution or intravenously.

In Vitro/in Vivo Correlations. Figure 5 represents the relationship between the in vitro dissolution data (expressed as the cumulative percentage of the polyphenol released) and the fraction of resveratrol absorbed during the first 8 h postadministration. An acceptable linear regression was observed between the two types of data (R^2 = 0.83 for Rsv-NP-Z).

Anti-inflammatory Efficacy Study. Figure 6A shows the rectal temperatures of the mice for 24 h after ip administration of 40 μg of LPS. Before challenge, all of the animals displayed similar rectal temperatures (data not shown). However, 6 h after challenge, important differences were observed between

DOI: 10.1021/jf505694e
J. Agric. Food Chem. 2015, 63, 5603−5611

Table 2. Pharmacokinetic Parameters of Resveratrol Obtained after the Administration of the Different Formulations Tested at a Dose of 15 mg/kg to Wistar Male Rats[a]

	route	C_{max} (μg/mL)	t_{max} (h)	AUC (μg h/mL)	$t_{1/2}$ (h)	Cl (mL/h)	V (mL)	MRT (h)	Fr (%)
Rsv-iv	iv	15.2 ± 5.18	0.05 ± 0.0	10.4 ± 3.80	2.04 ± 0.51	199 ± 89.8	569 ± 221	2.44 ± 1.01	100
Rsv-sol	oral	0.20 ± 0.02*	0.60 ± 0.22	0.28 ± 0.13*	0.28 ± 0.24	387 ± 225	112 ± 104	1.34 ± 0.77	2.64
Rsv-susp	oral	ND	ND	ND	ND	ND	ND	ND	ND
Rsv-NP-Z	oral	0.39 ± 0.11*†	4.94 ± 3.10	5.17 ± 2.61†	5.45 ± 1.70	125 ± 41.2	909 ± 184	17.1 ± 7.18*†	50.0

[a](i) Resveratrol intravenous (Rsv-iv); (ii) Rsv solution (Rsv-sol); (iii) resveratrol suspension (Rsv-susp); (iv) resveratrol loaded in zein nanoparticles (Rsv-NP-Z). Data are expressed as the mean ± SD (n = 6). *, significant differences vs Rsv-Sol (p < 0.05) Mann–Whitney U; †, significant differences vs Rsv-iv (p < 0.01) Mann–Whitney U. C_{max}, peak plasma concentration; T_{max}, time to reach plasma concentration; AUC, area under the curve; $t_{1/2}$, half-life of the terminal phase; Cl, clearance; MRT, mean residence time; Fr, relative oral bioavailability.

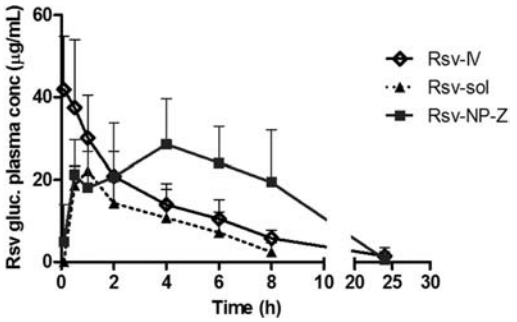

Figure 4. Resveratrol-*O*-3-glucuronide concentration versus time after a single administration (iv or oral) of the different formulations at a dose of 15 mg/kg: iv resveratrol (Rsv-IV, ◇); orally administered resveratrol solution (Rsv-Sol, ▲); orally administered resveratrol-loaded zein nanoparticles (Rsv-NP-Z, ■). Data are expressed as the mean ± SD (n = 6).

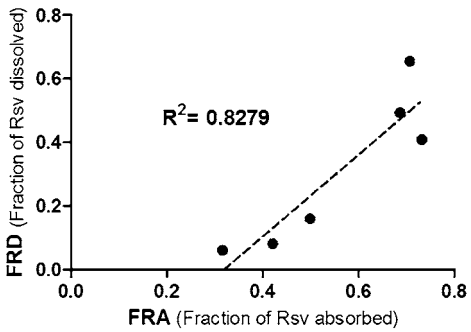

Figure 5. Relationship between fractions dissolved in vitro versus fractions absorbed in vivo for resveratrol loaded into zein nanoparticles (Rsv-NP-Z). FRD, fraction of resveratrol dissolved; FRA, fraction of resveratrol absorbed.

the groups. Positive-control animals (without any resveratrol treatment) displayed a body temperature of approximately 4 °C below the basal normal levels. For animals treated with Rsv-sol, their body temperature was 3 °C lower than before challenge. In contrast, the rectal temperature of the animals treated with resveratrol loaded in zein nanoparticles decreased by only 0.5–1 °C. No variations were observed in the negative-control group. Twenty-four hours after challenge, the animals treated with free resveratrol or encapsulated resveratrol returned to their normal temperature.

Table 3 shows the overall endotoxic symptom score, including the number of animals displaying a temperature 2 °C lower than the basal temperature 6 h postchallenge. Positive-control animals displayed low mobility and signs of bristly hair and respiratory distress. In contrast, animals treated with Rsv-NP-Z displayed nearly normal behavior and evidently

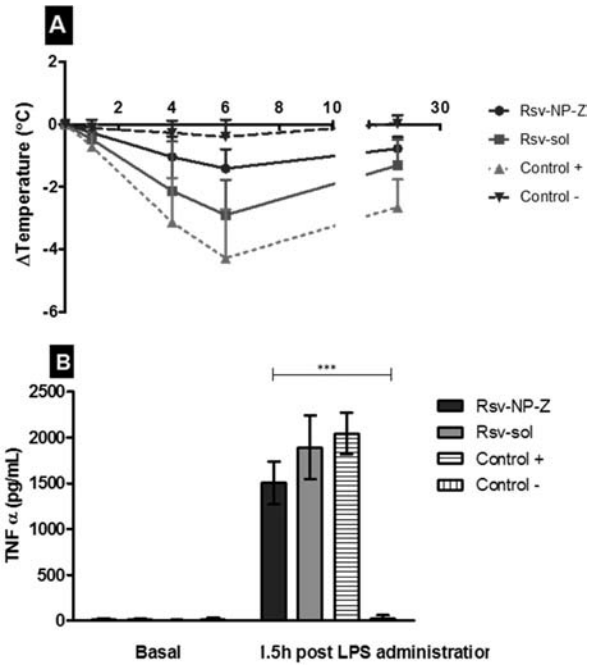

Figure 6. Anti-inflammatory activity of resveratrol. (A) Comparatively decreased rectal temperature of mice after intraperitoneal (ip) administration of LPS (40 μg) over time. (B) TNF-α serum levels before and 1.5 h after LPS (40 μg) administration. Mice were orally pretreated with resveratrol loaded in zein nanoparticles (Rsv-NP-Z) or resveratrol solubilized in PEG400/water (Rsv-sol) (1:1 by vol) daily for 7 days. Controls not pretreated with resveratrol (positive control) and negative controls (no pretreatment with resveratrol and no treatment with LPS) were also included. Results are expressed as the mean ± SD (n = 6). (***) p < 0.01, Kruskal–Wallis test.

Table 3. Endotoxic Symptoms in the Resveratrol-Treated versus Nontreated LPS-Inoculated Mice[a]

treatment[a]	body temperature[b] > 2 °C	piloerection[c]	mobility
control −	0/6	−	normal
control +	6/6	+++	very low
Rsv-sol	4/6	++	very low
Rsv-NP-Z	1/6	+	low

[a]Control −, nontreated, no LPS; control +, nontreated but inoculated with LPS; Rsv-sol, administration of resveratrol solution daily for 7 days, LPS; Rsv-NP-Z, administration of resveratrol-loaded zein nanoparticles daily for 7 days, LPS. n = 6. [b]Number of animals displaying a temperature 2 °C lower than the basal temperature 6 h postchallenge. [c]Severity of symptoms: (−) none; (+) weak; (++) moderate; (+++) strong.

DOI: 10.1021/jf505694e
J. Agric. Food Chem. 2015, 63, 5603–5611

better symptomatology than those animals receiving resveratrol as an oral solution, which appeared to be immobile or had great difficulty in coordinating any simple movement.

Figure 6B shows the serum levels of TNF-α, as measured by ELISA before and 90 min after LPS challenge. Negligible levels of TNF-α were observed before LPS administration. The oral administration of Rsv-NP-Z induced a decrease in the levels of TNF-α with respect to mice pretreated with resveratrol solution and the positive-control group; however, the differences were not statistically significant. Significant differences ($p < 0.01$) were observed between the negative control and the rest of the groups.

DISCUSSION

In the past, zein was proposed as material for the preparation of nanoparticles due to its hydrophobic character, degradability, adherence properties, and versatile processability.[19,20] However, as zein possesses abundant nonpolar amino acids, dispersibility of the resulting nanoparticles in an aqueous medium (and therefore their potential applications) is a challenge.[30] Recently, the use of citrate and phosphate salts was proposed to minimize this problem.[31] In our case, lysine was added during the process of preparing the nanoparticles. In this way, the resulting dry powder of zein nanoparticles was easily redispersed, yielding a homogeneous, fine suspension (Table 1) after the addition of water and simple manual agitation.

Resveratrol-loaded zein nanoparticles displayed a mean size close to 300 nm and a negative zeta potential. The resveratrol loading was 80 μg/mg nanoparticles, with an encapsulation efficiency of 80%. This payload is in line with values previously reported using solid lipid nanoparticles,[17] PLGA nanoparticles,[18] or nanoemulsions.[32] The release of resveratrol from zein nanoparticles was found to be pH independent. In fact, this phenomenon combined Fickian diffusion and erosion of the nanoparticle matrix (Peppas−Sahlin model). During the first hours of the release process, resveratrol molecules likely mainly diffused from the nanoparticles and into the aqueous medium by Fickian diffusion. Later (3.5 h), the release of resveratrol would be mainly due to erosion and/or relaxation of the nanoparticle matrix. Interestingly, as a consequence of both phenomena, the amount of resveratrol released (at least during the first 8 h) was constant and approached zero-order kinetics.

Pharmacokinetic studies were carried out at a single dose of 15 mg/kg, which is comparable to doses used in previous studies.[33,34] The oral administration of a single dose of resveratrol to rats as an aqueous suspension (Rsv-susp) did not produce quantifiable levels of the polyphenol in the plasma (Figure 3B). For the solution formulation in a PEG400/water mixture (Rsv-sol), the plasma levels of the polyphenol were higher than for the suspension, but the levels rapidly decreased, and 6 h postadministration, only traces of resveratrol were detected in the plasma. These findings are directly related to the extensive metabolism of resveratrol.[35] In fact, when administered orally, resveratrol (due to its lipophilic character) can rapidly enter enterocytes by passive diffusion.[36] However, resveratrol is highly metabolized to glucuronide and sulfate derivatives, which may be secreted back into the intestinal lumen through multidrug resistance proteins (MRP) and breast cancer resistance protein (BCRP).[37,38] This extensive biotransformation of resveratrol decreases the circulating levels of free resveratrol and facilitates its excretion (in the form of conjugates) by the kidneys via the urine.[14] Controversy remains about the physiological activity of the metabolites and whether they can act as resveratrol prodrugs. There is evidence that at sufficient concentrations, resveratrol metabolites have biological activity in various tissues.[36] Nevertheless, there is also evidence that these compounds have no effects in certain tissues.[39]

However, when resveratrol was administered after its encapsulation in zein nanoparticles in the current study, sustained plasma levels of the polyphenol were observed for at least 24 h (Figure 3B), and its relative oral bioavailability was approximately 50% (Table 3), which is 19-fold higher than the value observed for Rsv-sol (approximately 2.6%). This increased capability to promote the absorption and bioavailability of resveratrol by using zein nanoparticles is related to the highly hydrophobic character of zein, which offers greater stability in vivo, and to the capability of this corn protein to develop mucoadhesive interactions within the gut mucus layer.[40] Thus, this characteristic may provide a longer time in close contact with the intestinal epithelium and may facilitate the establishment of a concentration gradient from the nanoparticulate matrix until the absorptive membrane. Interestingly, the fraction of resveratrol absorbed from zein nanoparticles correlated well with the percentage of the polyphenol released in vitro (see Figure 5).

In some previous studies, it has been reported that the oral bioavailability of resveratrol and some of its derivatives is negligible.[34,41] To improve its absorption, different strategies have been proposed, such as the use of oral absorption enhancers (e.g., Tween 80, cyclodextrins) or the employment of resveratrol derivatives. In this way, Kapetanovic and coworkers reported an oral bioavailability of close to 30% for resveratrol (formulated as an aqueous solution containing methylcellulose and Tween 80) after the administration of a single dose of 50 mg/kg in rats. In the same work, administration of the same resveratrol formulation at a dose of 150 mg/kg produced an oral bioavailability of 19%.[42] In another study, resveratrol trimethyl ether administered orally in a solution formulated with randomly methylated β-cyclodextrin (15 mg/kg) yielded a bioavailability of approximately 47%. More recently, the use of nanocarriers has also been proposed. In mice, using a dose of 50 mg/kg, the oral bioavailability of resveratrol when loaded in either Eudragit or chitosan/lecithin nanoparticles was calculated to be 39 and 61%, respectively.[43] For solid lipid nanoparticles, the oral bioavailability of the polyphenol was found to be 8-fold higher than for a conventional solution of resveratrol.[44] In our case, the bioavailability of resveratrol was 19.2-fold higher when resveratrol was loaded in zein nanoparticles than when it was dissolved in the PEG400/water solution. Furthermore, zein nanoparticles offering sustained and prolonged levels of resveratrol in the plasma provide a supplementary advantage compared with other strategies.

With regard to the presence of the main metabolite (resveratrol-*O*-3-glucuronide[13]) in the plasma of animals, the levels of this compound (measured as AUC values) were higher when resveratrol was administered via encapsulation in zein nanoparticles than when administered in the conventional solution by the iv route (approximately 1.7 times) or orally (approximately 3.3 times). This result could be related to the slow release of the polyphenol from the nanoparticles (where it was protected from degradation) and the prolonged residence of nanoparticles in the gut mucosa due to their mucoadhesive properties. In other words, by using nanoparticles, more resveratrol would reach the circulation during a longer period,

DOI: 10.1021/jf505694e
J. Agric. Food Chem. 2015, 63, 5603−5611

counterbalancing the rapid natural metabolism of the polyphenol.

Finally, we studied the anti-inflammatory activity of resveratrol when loaded in zein nanoparticles. Several in vitro and in vivo studies have suggested that resveratrol inhibits the inflammatory response mediated by microbial stimuli[45] by inhibiting the transcription factor NF-κB.[10,11] Therefore, we tested the protective effect of encapsulated resveratrol against inoculation with LPS in mice. LPS is present exclusively on the outer membrane of Gram-negative bacteria, and consequently, it is one of the strongest alarm signals for the innate immune system, inducing a pathophysiological syndrome known as endotoxic shock in animals. This syndrome is similar to septic shock syndrome that progresses to multiple organ failure,[29,46] causing piloerection, hypothermia, shivering, tachycardia, and lethargy. These symptoms are related to the large amounts of inflammatory mediators released, such as TNF-α, NO, and prostaglandin E2 (PGE2), with TNF-α playing a central role as the first one to be released.[10] Under our experimental conditions, untreated mice challenged with LPS (positive control) displayed the greatest decrease in rectal temperature and the highest TNF-α serum level. In contrast, Rsv-NP-Z administered daily for 7 days diminished endotoxic symptoms, such as hypothermia or piloerection, and increased the movement of mice compared with resveratrol solution administered on a daily basis (Figure 6; Table 3). Moreover, for animals treated with Rsv-NP-Z, TNF-α levels were lower than for controls, although the high variability of the values abolished the statistical significance ($p < 0.05$). These results appear to indicate that the presence of sustained high levels of resveratrol in the plasma could be efficient in reducing the levels of inflammatory mediators in endotoxic shock induced by LPS.

In summary, zein nanoparticles appear to be interesting carriers for the oral delivery of resveratrol. The polyphenol is released from this carrier by a combination of both diffusion and erosion of the nanoparticle matrix, providing higher and more prolonged plasma levels of resveratrol up to 48 h. Consequently, these nanocarriers significantly increase the oral bioavailability of resveratrol, reaching a value close to 50%. Weeklong oral administration of these nanoparticles to mice challenged with LPS protected the mice from the inflammatory symptoms and mediators of endotoxic shock. Future studies should be performed to ascertain how this treatment modulates TNF-α production to explore the potential use of Rsv-NP-Z as an anti-inflammatory treatment.

AUTHOR INFORMATION

Corresponding Author

*(J.M.I.) Phone: +34 948 42 56 00. Fax: +34 948 42 56 19. E-mail: jmirache@unav.es.

Funding

This work was supported by the Regional Government of Navarra (Alimentos funcionales, Euroinnova call) and the Spanish Ministry of Science and Innovation and Gobierno de Navarra (ADICAP; ref IPT-2011-1717-900000). R.P. acknowledges the Asociación de Amigos Universidad de Navarra for financial support.

Notes

The authors declare no competing financial interest.

ABBREVIATIONS USED

Rsv	resveratrol
SIRT1	sirtuin 1
LPS	lipopolysaccharide from Salmonella *enterica* serovar. Minnesota
Rsv-NP-Z	resveratrol-loaded zein nanoparticles
NP-Z	empty zein nanoparticles
Rsv-sol	resveratrol solution in a PEG 400/water mixture
Rsv-susp	suspension of resveratrol in purified water
PCS	photon correlation spectroscopy
SEM	scanning electron microscopy
EE	encapsulation efficiency
iv	intravenous
C_{max}	maximal serum concentration
T_{max}	time in which C_{max} is reached
AUC	area under the concentration−time curve from time 0 to last time
MRT	mean residence time
Cl	clearance
V	volume of distribution
$t_{1/2}$	half-life in the terminal phase
Fr	relative bioavailability
FRD	fraction of resveratrol dissolved
FRA	fraction of resveratrol absorbed
ip	intraperitoneal
PGE2	prostaglandin E2
PDI	polydispersity index
MRP	multidrug resistance proteins
BCRP	breast cancer resistance protein

REFERENCES

(1) Baur, J. A.; Sinclair, D. A. Therapeutic potential of resveratrol: the in vivo evidence. *Nat. Rev. Drug Discovery* **2006**, *5*, 493−506.

(2) Amri, A.; Chaumeil, J. C.; Sfar, S.; Charrueau, C. Administration of resveratrol: what formulation solutions to bioavailability limitations? *J. Controlled Release* **2012**, *158*, 182−193.

(3) Kasiotis, K. M.; Pratsinis, H.; Kletsas, D.; Haroutounian, S. A. Resveratrol and related stilbenes: their anti-aging and anti-angiogenic properties. *Food Chem. Toxicol.* **2013**, *61*, 112−120.

(4) Orallo, F.; Alvarez, E.; Camina, M.; Leiro, J. M.; Gomez, E.; Fernandez, P. The possible implication of trans-Resveratrol in the cardioprotective effects of long-term moderate wine consumption. *Mol. Pharmacol.* **2002**, *61*, 294−302.

(5) Li, S.; Wang, X.; Kong, L. Design, synthesis and biological evaluation of imine resveratrol derivatives as multi-targeted agents against Alzheimer's disease. *Eur. J. Med. Chem.* **2014**, *71*, 36−45.

(6) Singh, G.; Pai, R. S. Recent advances of resveratrol in nanostructured based delivery systems and in the management of HIV/AIDS. *J. Controlled Release* **2014**, *194*, 178−188.

(7) Palsamy, P.; Subramanian, S. Resveratrol protects diabetic kidney by attenuating hyperglycemia-mediated oxidative stress and renal inflammatory cytokines via Nrf2−Keap1 signaling. *Biochim. Biophys. Acta, Mol. Basis Dis.* **2011**, *1812*, 719−731.

(8) Timmers, S.; Konings, E.; Bilet, L.; Houtkooper, R. H.; van de Weijer, T.; Goossens, G. H.; Hoeks, J.; van der Krieken, S.; Ryu, D.; Kersten, S. Calorie restriction-like effects of 30 days of resveratrol supplementation on energy metabolism and metabolic profile in obese humans. *Cell Metab.* **2011**, *14*, 612−622.

(9) Gillum, M. P.; Kotas, M. E.; Erion, D. M.; Kursawe, R.; Chatterjee, P.; Nead, K. T.; Muise, E. S.; Hsiao, J. J.; Frederick, D. W.; Yonemitsu, S.; Banks, A. S.; Qiang, L.; Bhanot, S.; Olefsky, J. M.; Sears, D. D.; Caprio, S.; Shulman, G. I. SirT1 regulates adipose tissue inflammation. *Diabetes* **2011**, *60*, 3235−3245.

(10) Farghali, H.; Černý, D.; Kameníková, L.; Martínek, J.; Hořínek, A.; Kmoníčková, E.; Zídek, Z. Resveratrol attenuates lipopolysacchar-

DOI: 10.1021/jf505694e
J. Agric. Food Chem. 2015, 63, 5603−5611

ide-induced hepatitis in D-galactosamine sensitized rats: role of nitric oxide synthase 2 and heme oxygenase-1. *Nitric Oxide* **2009**, *21*, 216−225.
(11) de la Lastra, C. A.; Villegas, I. Resveratrol as an anti-inflammatory and anti-aging agent: Mechanisms and clinical implications. *Mol. Nutr. Food Res.* **2005**, *49*, 405−430.
(12) Walle, T. Absorption and metabolism of flavonoids. *Free Radical Biol. Med.* **2004**, *36*, 829−837.
(13) Kuhnle, G.; Spencer, J. P.; Chowrimootoo, G.; Schroeter, H.; Debnam, E. S.; Srai, S. K. S.; Rice-Evans, C.; Hahn, U. Resveratrol is absorbed in the small intestine as resveratrol glucuronide. *Biochem. Biophys. Res. Commun.* **2000**, *272*, 212−217.
(14) Walle, T.; Hsieh, F.; DeLegge, M. H.; Oatis, J. E., Jr.; Walle, U. K. High absorption but very low bioavailability of oral resveratrol in humans. *Drug Metab. Dispos.* **2004**, *32*, 1377−1382.
(15) Planas, J. M.; Alfaras, I.; Colom, H.; Juan, M. E. The bioavailability and distribution of *trans*-resveratrol are constrained by ABC transporters. *Arch. Biochem. Biophys.* **2012**, *527*, 67−73.
(16) Bolko, K.; Zvonar, A.; Gašperlin, M. Mixed lipid phase SMEDDS as an innovative approach to enhance resveratrol solubility. *Drug Dev. Ind. Pharm.* **2013**, *40*, 102−109.
(17) Teskač, K.; Kristl, J. The evidence for solid lipid nanoparticles mediated cell uptake of resveratrol. *Int. J. Pharm.* **2010**, *390*, 61−69.
(18) Singh, G.; Pai, R. S. Optimized PLGA nanoparticle platform for orally dosed trans-resveratrol with enhanced bioavailability potential. *Expert Opin. Drug Delivery* **2014**, *11*, 647−659.
(19) Anderson, T. J.; Lamsal, B. P. Zein extraction from corn, corn products, and coproducts and modifications for various applications: a review. *Cereal Chem.* **2011**, *88*, 159−173.
(20) Paliwal, R.; Palakurthi, S. Zein in controlled drug delivery and tissue engineering. *J. Controlled Release* **2014**, *189*, 108−122.
(21) Shi, K.; Kokini, J. L.; Huang, Q. Engineering zein films with controlled surface morphology and hydrophilicity. *J. Agric. Food Chem.* **2009**, *57*, 2186−2192.
(22) Penalva, R.; Esparza, I.; Agüeros, M.; Gonzalez-Navarro, C. J.; Gonzalez-Ferrero, C.; Irache, J. M. Casein nanoparticles as carriers for the oral delivery of folic acid. *Food Hydrocolloids* **2015**, *44*, 399−406.
(23) Iacopini, P.; Baldi, M.; Storchi, P.; Sebastiani, L. Catechin, epicatechin, quercetin, rutin and resveratrol in red grape: content, in vitro antioxidant activity and interactions. *J. Food Compos. Anal.* **2008**, *21*, 589−598.
(24) Ritger, P. L.; Peppas, N. A. A simple equation for description of solute release I. Fickian and non-Fickian release from non-swellable devices in the form of slabs, spheres, cylinders or discs. *J. Controlled Release* **1987**, *5*, 23−36.
(25) Sujja-areevath, J.; Munday, D. L.; Cox, P. J.; Khan, K. A. Relationship between swelling, erosion and drug release in hydrophillic natural gum mini-matrix formulations. *Eur. J. Pharm. Sci.* **1998**, *6*, 207−217.
(26) Peppas, N. A.; Sahlin, J. J. A simple equation for the description of solute release. III. Coupling of diffusion and relaxation. *Int. J. Pharm.* **1989**, *57*, 169−172.
(27) Boocock, D. J.; Patel, K. R.; Faust, G. E. S.; Normolle, D. P.; Marczylo, T. H.; Crowell, J. A.; Brenner, D. E.; Booth, T. D.; Gescher, A.; Steward, W. P. Quantitation of *trans*-resveratrol and detection of its metabolites in human plasma and urine by high performance liquid chromatography. *J. Chromatogr. B: Anal. Technol. Biomed. Life Sci.* **2007**, *848*, 182−187.
(28) Kassem, M. A.; ElMeshad, A. N.; Fares, A. R. Enhanced bioavailability of buspirone hydrochloride via cup and core buccal tablets: formulation and in vitro/in vivo evaluation. *Int. J. Pharm.* **2014**, *463*, 68−80.
(29) Nemzek, J. A.; Hugunin, K. M. S.; Opp, M. R. Modeling sepsis in the laboratory: merging sound science with animal well-being. *Comp. Med.* **2008**, *58*, 120−128.
(30) Chen, H.; Zhong, Q. Processes improving the dispersibility of spray-dried zein nanoparticles using sodium caseinate. *Food Hydrocolloids* **2014**, *35*, 358−366.
(31) Molina, M. I.; Wagner, J. R. The effects of divalent cations in the presence of phosphate, citrate and chloride on the aggregation of soy protein isolate. *Food Res. Int.* **1999**, *32*, 135−143.
(32) Sessa, M.; Balestrieri, M. L.; Ferrari, G.; Servillo, L.; Castaldo, D.; D'Onofrio, N.; Donsì, F.; Tsao, R. Bioavailability of encapsulated resveratrol into nanoemulsion-based delivery systems. *Food Chem.* **2014**, *147*, 42−50.
(33) Colom, H.; Alfaras, I.; Maijó, M.; Juan, M. E.; Planas, J. M. Population pharmacokinetic modeling of trans-resveratrol and its glucuronide and sulfate conjugates after oral and intravenous administration in rats. *Pharm. Res.* **2011**, *28*, 1606−1621.
(34) Lin, H. S.; Ho, P. C. Preclinical pharmacokinetic evaluation of resveratrol trimethyl ether in Sprague-Dawley rats: the impacts of aqueous solubility, dose escalation, food and repeated dosing on oral bioavailability. *J. Pharm. Sci.* **2011**, *100*, 4491−4500.
(35) Wenzel, E.; Soldo, T.; Erbersdobler, H.; Somoza, V. Bioactivity and metabolism of *trans*-resveratrol orally administered to Wistar rats. *Mol. Nutr. Food Res.* **2005**, *49*, 482−494.
(36) Smoliga, M.; Blanchard, O. Enhancing the delivery of resveratrol in humans: if low bioavailability is the problem, what is the solution? *Molecules* **2014**, *19*, 17154−17172.
(37) Juan, M. E.; Gonzalez-Pons, E.; Planas, J. M. Multidrug resistance proteins restrain the intestinal absorption of *trans*-resveratrol in rats. *J. Nutr.* **2010**, *140*, 489−495.
(38) Alfaras, I.; Pérez, M.; Juan, M. E.; Merino, G.; Prieto, J. G.; Planas, J. M.; Alvarez, A. I. Involvement of breast cancer resistance protein (BCRP1/ABCG2) in the bioavailability and tissue distribution of *trans*-resveratrol in knockout mice. *J. Agric. Food Chem.* **2010**, *58*, 4523−4528.
(39) Kenealey, J. D.; Subramanian, L.; van Ginkel, P. R.; Darjatmoko, S.; Lindstrom, M. J.; Somoza, V.; Ghosh, S. K.; Song, Z.; Hsung, R. P.; Kwon, G. S.; Eliceiri, K. W.; Albert, D. M.; Polans, A. S. Resveratrol metabolites do not elicit early pro-apoptotic mechanisms in neuroblastoma cells. *J. Agric. Food Chem.* **2011**, *59*, 4979−4986.
(40) Yin, Y.; Yin, S.; Yang, X.; Tang, C.; Wen, S.; Chen, Z.; Xiao, B.; Wu, L. Surface modification of sodium caseinate films by zein coatings. *Food Hydrocolloids* **2014**, *36*, 1−8.
(41) Wenzel, E.; Somoza, V. Metabolism and bioavailability of *trans*-resveratrol. *Mol. Nutr. Food Res.* **2005**, *49*, 472−481.
(42) Kapetanovic, I. M.; Muzzio, M.; Huang, Z.; Thompson, T. N.; McCormick, D. L. Pharmacokinetics, oral bioavailability, and metabolic profile of resveratrol and its dimethylether analog, pterostilbene, in rats. *Cancer Chemother. Pharmacol.* **2011**, *68*, 593−601.
(43) Oganesyan, E.; Miroshnichenko, I.; Vikhrieva, N.; Lyashenko, A.; Leshkov, S. Y. Use of nanoparticles to increase the systemic bioavailability of trans-resveratrol. *Pharm. Chem. J.* **2010**, *44*, 74−76.
(44) Pandita, D.; Kumar, S.; Poonia, N.; Lather, V. Solid lipid nanoparticles enhance oral bioavailability of resveratrol, a natural polyphenol. *Food Res. Int.* **2014**, *62*, 1165−1174.
(45) Youn, H. S.; Lee, J. Y.; Fitzgerald, K. A.; Young, H. A.; Akira, S.; Hwang, D. H. Specific inhibition of MyD88-independent signaling pathways of TLR3 and TLR4 by resveratrol: molecular targets are TBK1 and RIP1 in TRIF complex. *J. Immunol.* **2005**, *175*, 3339−3346.
(46) Yang, Y.; Li, S.; Yang, Q.; Shi, Y.; Zheng, M.; Liu, Y.; Chen, F.; Song, G.; Xu, H.; Wan, T.; He, J.; Chen, Z. Resveratrol reduces the proinflammatory effects and lipopolysaccharide-induced expression of HMGB1 and TLR4 in RAW264.7 cells. *Cell. Physiol. Biochem.* **2014**, *33*, 1283−1292.

DOI: 10.1021/jf505694e
J. Agric. Food Chem. 2015, 63, 5603−5611

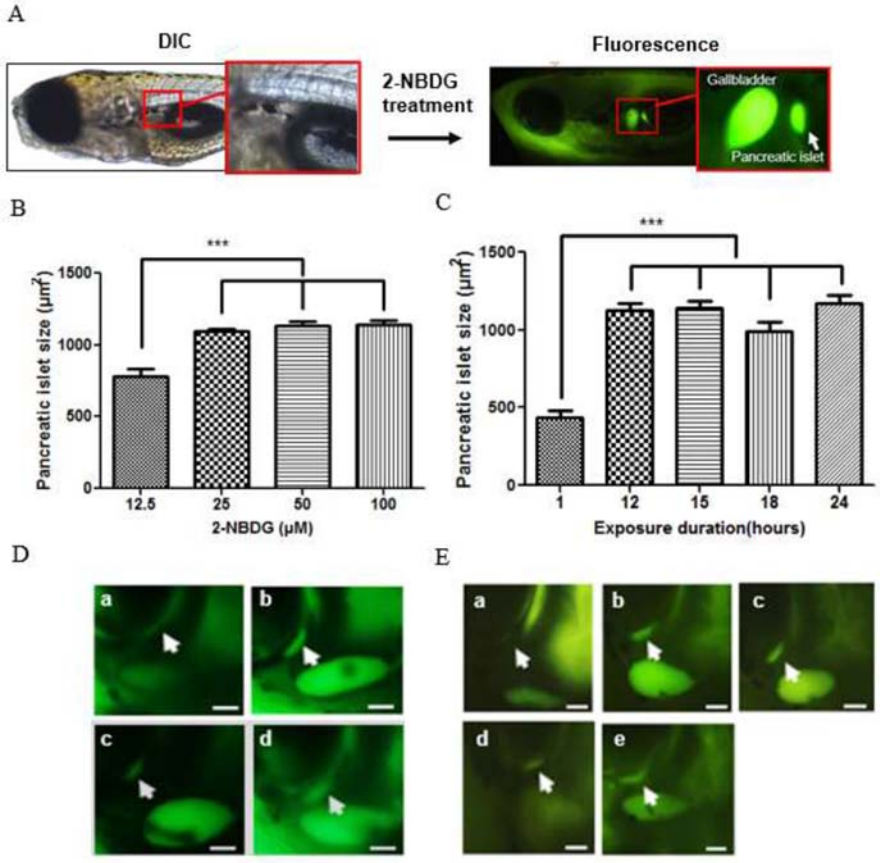

Figure 1. Changes in pancreatic islet (PI) area and fluorescence intensity caused by 2-NBDG. (A) PIs in wild-type zebrafish and zebrafish larva at 5 days postfertilization (dpf) were evaluated by differential interference contrast (DIC) and fluorescence microscopy. (B) Dose-dependent changes in PI size caused by 2-NBDG were analyzed using Focus Lite software. (***) $p < 0.001$. (C) Treatment over 24 h demonstrated a time-dependent uptake, which was visualized by fluorescent microscopy. The PI area demonstrated dose-dependent uptake. (***) $p < 0.001$. (D) Fluorescent microscopic images of PI following treatment with 2-NBDG at a concentration of (a) 12.5 μM, (b) 25 μM, (c) 50 μM, or (d) 100 μM. Scale bar = 100 μm. (E) Fluorescent microscopic images of PI at (a) 1 h, (b) 12 h, (c) 15 h, (d) 18 h, and (e) 24 h. Scale bar = 100 μm.

Sigma Chemical Co. (St. Louis, MO, USA). Trigonelline (TRG) hydrochloride was purchased from Tokyo Chemical Industry Co., Ltd. (Tokyo, Japan). 2-(*N*-(7-Nitrobenz-2-oxa-1,3-diazol-4-yl)amino)-2-deoxyglucose (2-NBDG) was purchased from Invitrogen (Life Technologies, Grand Island, NY, USA). Glimepiride (GLM) was obtained from Cayman Chemical Co. (Ann Arbor, MI, USA). Diazoxide (DZ) was purchased from Santa Cruz Biotechnology Inc. (Dallas, TX, USA). A Shimadzu LC-20A HPLC instrument was used for HPLC (Shimadzu, Japan). An Olympus 1X70 microscope was used for fluorescence microscopy (Olympus, Japan). Focus Lite (Focus Co, Daejeon, Korea) and ImageJ software (National Institutes of Health) were used for image analysis.

Zebrafish Maintenance and Egg Collection. Adult zebrafish were maintained in an S type zebrafish system (1500 mm (W) × 400 mm (D) × 2050 mm (H)) (Daejeon, Korea). To obtain ZFL, three pairs of zebrafish were placed in a spawning box overnight. The next day, zebrafish began spawning after a 30 min light period. Zebrafish eggs were collected 3 h postfertilization (hpf) for experiments and incubated in a Petri dish in a 0.03% sea salt solution. Embryos were maintained on a 14 h light/10 h dark cycle in a 28.5 °C incubator. Fish were cared for in accordance with standard zebrafish protocols approved by the Animal Care and Use Committee of Kyung Hee University (KHUASP(SE)-15-10).

Validation of 2-NBDG and AX in ZFL. Staining for PI visualization was evaluated according to a previously reported method.[17] First, 5 day postfertilization (dpf) zebrafish were placed into 96-well plates. Next, the ZFL were treated with various concentrations of 2-NBDG (12.5, 25, 50, and 100 μM, final volume = 100 μL) for various lengths of time (1, 12, 15, 18, and 24 h). Following treatment, ZFL were rinsed with a 0.03% sea salt solution and observed by fluorescence microscopy. To obtain AX-induced PI-damaged zebrafish larvae (AIPD-ZFL), ZFL were treated with 100 μL of AX solution at various concentrations (50, 100, and 300 μM) for 15 min. The AX solution was then changed to the 0.03% sea salt solution, and ZFL were observed every 2 h thereafter. To capture images, ZFL were restained for 1 h with 25 μM 2-NBDG. PI images were then captured using fluorescence microscopy and analyzed using Focus Lite and ImageJ software.

Survival Rates. Zebrafish survival rates were evaluated according to a previously reported method.[18] Briefly, at 6 hpf, zebrafish eggs were placed into 24-well plates. The zebrafish eggs were then divided into the following six groups: normal, 100 μM AX, 10 μM GLM, 300 μg/mL CE, 100 μM AX + 10 μM GLM, and 100 μM AX + 300 μg/mL CE. Next, each well in the 24-well plates was filled with 1 mL of AX, GLM, and/or CE solution or 0.03% sea salt solution. The survival rates of ZFL were calculated using the percentage of fish that remained alive after treatment for 48 h. The solutions were replaced daily with fresh solutions.

Efficacy of Coffee and Coffee Components on PIs. We measured the efficacy of CE and the coffee components CFI, TRG, and CGA in AIPD-ZFL. Wild-type ZFL at 5 dpf were treated with 25 μM 2-NBDG in 96-well plates for 12 h. After PI damage was induced using 100 μM AX, the sizes of ZFL PIs were measured using fluorescence microscopy. To determine the efficacy of CE, CFI, TRG, and CGA, ZFL were treated with 100 μL of CE (50, 100, and 300 μg/mL), coffee components (CFI, TRG, or CGA 10 μg/mL each), or GLM (10 μM) for 1 h. Next, the ZFL were treated with 25 μM 2-NBDG (100 μL) for 1 h, and images were captured using

DOI: 10.1021/acs.jafc.5b00027
J. Agric. Food Chem. 2015, 63, 5612−5621

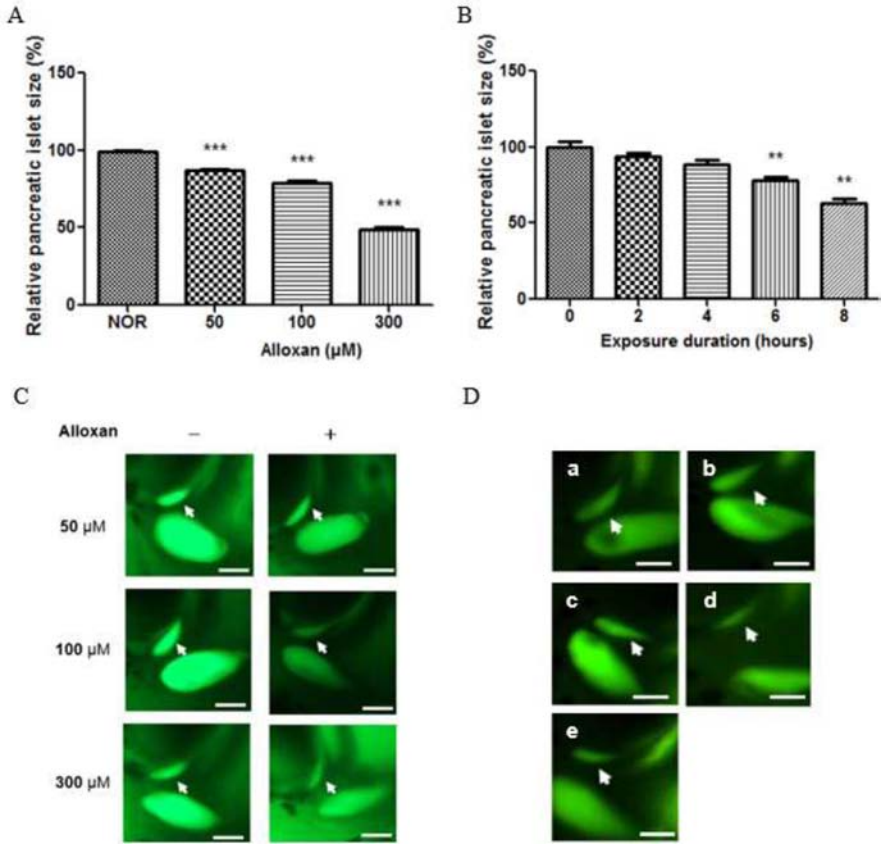

Figure 2. Dose- and time-dependent changes in pancreatic islet (PI) size following alloxan treatment (AX). (A) Dose-dependent changes in PI size after treatment with AX at 50, 100, or 300 μM after exposure to 25 μM 2-NBDG. (***) $p < 0.001$, compared to normal. (B) Time-dependent effects of 100 μM AX were quantified using image analysis of PI size. (**) $p < 0.01$ and (***) $p < 0.001$, compared to normal. (C) Fluorescent microscopic image of treatment with AX at doses of 50, 100, and 300 μM after exposure to 25 μM 2-NBDG. Scale bar = 100 μm. (D) Fluorescent microscopic image of the time dependency of 100 μM AX effects. Scale bar = 100 μm.

fluorescence microscopy. For normal group treatments, solutions including AX were replaced with the sea salt solution to compare treated groups with normal PI size and fluorescence intensity. To measure changes in PI size and intensity, images were analyzed using Focus Lite and ImageJ software, respectively. We analyzed PI size and fluorescence intensity via images before and after treatment, and all values were expressed as size change values and percent intensity change according to the following equations, respectively: size change value = PI size after treatment − PI size before treatment; percent change in fluorescence intensity value = [(PI intensity after treatment/PI intensity before treatment) × 100] − [(PI intensity before treatment/PI intensity before treatment) × 100].

Efficacy of Coffee on Islet β-Cells of ins:GFP Zebrafish. Transgenic zebrafish lines expressing GFP specifically in β-cells were obtained from the Zebrafish Organogenesis Mutant Bank (ZOMB). The GFP-tagged line was ins:GFP, which expresses GFP in the pancreas.[19] Experiments were performed using 5 dpf larvae. Transgenic ZFL were first imaged in the no-treatment state and then after exposed to 100 μM AX. Following AX treatment, transgenic ZFL were treated with 100 μg/mL of CE for 1 h and then imaged. Treatments for the normal group including AX consisted of a sea salt solution to compare treated groups with normal β-cells size and fluorescence intensity. To measure changes in β-cells, the size and intensity of all images were analyzed using Focus Lite and ImageJ software, respectively.

HPLC Analysis of Coffee Components. *CFI Analysis.* HPLC analysis of CFI was based on a modification of a previous study.[20] Briefly, chromatographic separation was performed using a Bischoff Chromatography ProntoSIL C18 column (250 × 4.6 mm, 5 μm). The mobile phase consisted of a mixture of water (80%) and acetonitrile (20%) at a flow rate of 0.7 mL/min. The column temperature was set at 40 °C, the sample injection volume was 10 μL, and the detection wavelength was set at 265 nm. The calibration curve was generated using three replicated points of CFI at 50, 100, and 200 μg/mL. CE (2 mg/mL) was injected after filtration. The analytical method was validated for the limits of detection and quantitation (LOD and LOQ, respectively).

TRG Analysis. HPLC analysis of TRG was performed using a Knauer 25XE184E2J C18 column (250 × 3 mm, 5 μm). The mobile phase consisted of a mixture of water (15%) and acetonitrile (85%) at a flow rate of 0.6 mL/min. The column temperature was set at 40 °C, the sample injection volume was 10 μL, and the detection wavelength was set to 265 nm. The calibration curve was generated using three replicated points of TRG at 10, 30, and 50 μg/mL. CE (1 mg/mL) was injected after filtration. The analytical method was validated for the LOD and LOQ.

CGA Analysis. HPLC analysis condition of CGA was performed using a Bischoff Chromatography ProntoSIL C18 column (250 × 4.6 mm, 5 μm). The mobile phase consisted of a mixture of water (70%) and 1% acetic acid in methanol (30%) at a flow rate of 0.7 mL/min. The column temperature was set at 40 °C, the sample injection volume was 10 μL, and the detection wavelength was set at 265 nm. The calibration curve was generated using three replicated points of CGA at 30, 50, and 100 μg/mL. CE (1 mg/mL) was injected after filtration. The analytical method was validated for the LOD and LOQ.

TRG and CGA Interaction in AIPD-ZFL. The interaction between TRG and CGA was analyzed using an isobologram based on 50% effect concentration (EC_{50}) data. EC_{50} data were obtained through nonlinear regression using GraphPad Prism software (version 5). To determine EC_{50} values, we measured the effects of TRG and CGA on AIPD in ZFL at concentrations ranging from 0.4 to 10 μM. TRG and

DOI: 10.1021/acs.jafc.5b00027
J. Agric. Food Chem. 2015, 63, 5612−5621

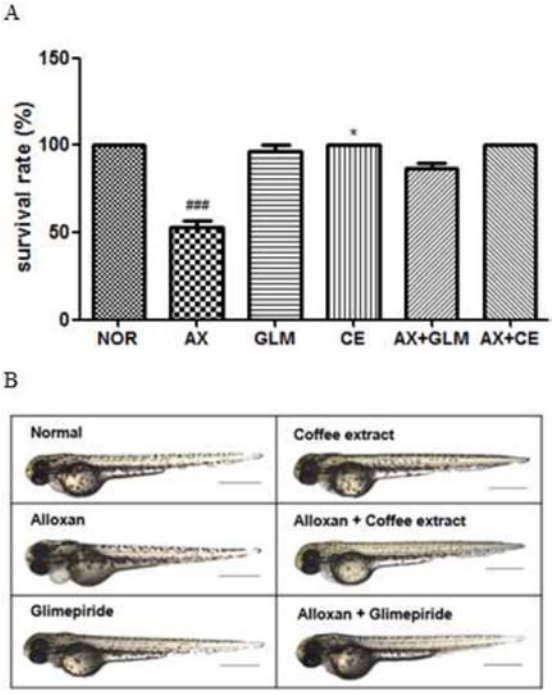

Figure 3. Survival rate of zebrafish embryos. (A) Survival rate of zebrafish embryos treated with 100 μM alloxan (AX), 10 μM glimepiride (GLM), 300 μg/mL coffee extract (CE), 100 μM AX + 10 μM GLM, or 100 μM AX + 300 μg/mL CE for different time points. Survival rates were determined at 48 h. (*) $p < 0.05$, compared to AX; (###) $p < 0.001$, compared to normal. (B) Microscopic images after 48 h of treatment. Scale bar = 1 mm.

CGA were combined at three points: $EC_{25}/EC_{12.5}$ (TRG + CGA, point 1), $EC_{25}/EC_{16.7}$ (TRG + CGA, point 2), and EC_{25}/EC_{25} (TRG + CGA, point 3). To assess synergy, experimental data were plotted on an isobologram, and a combination index (CI) was generated using CompuSyn software.[21]

Action of DZ on AIPD-ZFL. ZFL were divided into the following 12 groups: normal, normal treated with DZ or AX, AIPD-ZFL treated with DZ, and AIPD-ZFL treated with GLM, GLM+DZ, CE, CE+DZ, TRG, TRG+DZ, CGA, and CGA+DZ. The following dosages were used: GLM, TRG, and CGA at 10 μg/mL each, DZ at 25 μM, and CE at 100 μg/mL. Prior to capturing images, ZFL were treated with 25 μM 2-NBDG for 1 h. All images were analyzed using Focus Lite software.

Statistical Analyses. Statistical analyses were performed using GraphPad Prism software (version 5). Data were expressed as the mean ± standard error of the mean (SEM). Statistical significance was determined using repeated one-way ANOVA followed by Tukey's post test. The probability level for statistical significance was set at $p < 0.05$.

RESULTS

Optimization of 2-NBDG. PI sizes were significantly different ($p = 0.0005$) between groups treated with 12.5 and 25 μM 2-NBDG. Additionally, PI size remained stable at concentrations of >25 μM. Validation of 2-NBDG exposure revealed that PI sizes were stable for >12 h. Therefore, the optimal concentration and exposure time of 2-NBDG were established as 25 μM and 12 h, respectively (Figure 1).

Optimization of AX Dosage. PI sizes were significantly decreased at doses of 50, 100, and 300 μM AX in a dose-dependent manner. The 100 μM dose of AX was selected as the optimal concentration for induction of PI damage, as it resulted in a PI size decrease of approximately 20%, $p = 0.0001$.

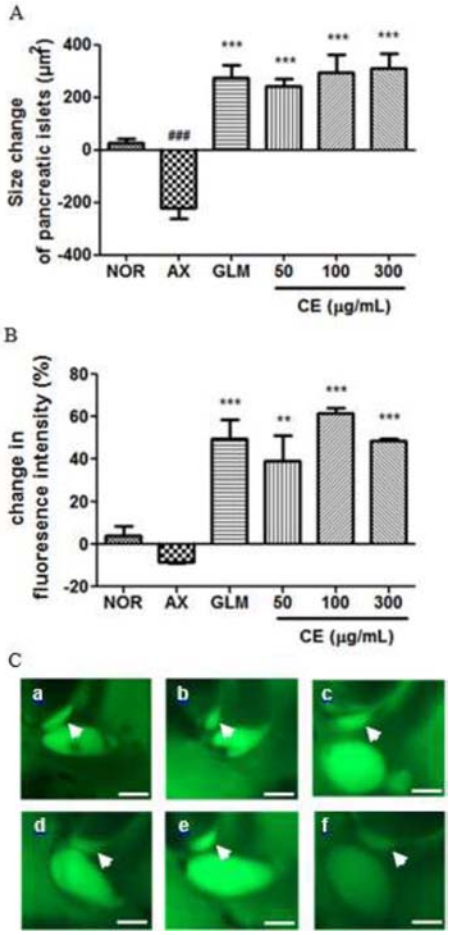

Figure 4. Dose-dependent effects of coffee extract (CE) on alloxan-induced pancreatic islet-damaged zebrafish larvae (AIPD ZFL). (A) Change in pancreatic islet (PI) size caused by CE and glimepiride (GLM). (***) $p < 0.001$, compared to alloxan (AX); (###) $p < 0.001$, compared to normal. (B) Change in PI fluorescence intensity evaluated using image analysis. (**) $p < 0.01$ and (***) $p < 0.001$, compared to alloxan (AX). (C) Fluorescent microscopic image of PI in (a) the normal group, (b) 100 μM alloxan (AX) group, (c) 10 μM GLM group, (d) 50 μg/mL CE group, (e) 100 μg/mL CE group, and (f) 300 μg/mL CE group. Scale bar = 100 μm.

PI sizes were decreased at 2, 4, 6, and 8 h of exposure in a time-dependent manner. PI size was significantly decreased at 6 h ($p = 0.0078$) and 8 h ($p = 0.0016$). An AX dose of 100 μM for 6 h was selected because an 8 h exposure caused severe damage (Figure 2).

Survival Rate. The survival rate was 100% in the normal, 10 μM GLM, 300 μg/mL CE, and 100 μM AX + 300 μg/mL CE treatment groups. However, the survival rate was 60% in the 100 μM AX group and 90% in the 100 μM AX + 10 μM GLM cotreatment group (Figure 3A). In addition, the 100 μM AX group showed toxicity-related characteristics of pericardial edema, unlike the normal group (Figure 3B).

Effect of CE on PIs. The normal group was used as the basis for comparison in the determination of the effects of AX with respect to induction of PI damage as determined by PI size and fluorescence intensity. The PI size in the AX-treated group was significantly decreased (9.8-fold, $p < 0.0001$) relative to the normal group. A 2.24-fold ($p < 0.0001$) increase in PI size was observed in the GLM-treated group. Likewise, the 50, 100, and 300 μg/mL CE-treated groups showed significantly increased

DOI: 10.1021/acs.jafc.5b00027
J. Agric. Food Chem. 2015, 63, 5612−5621

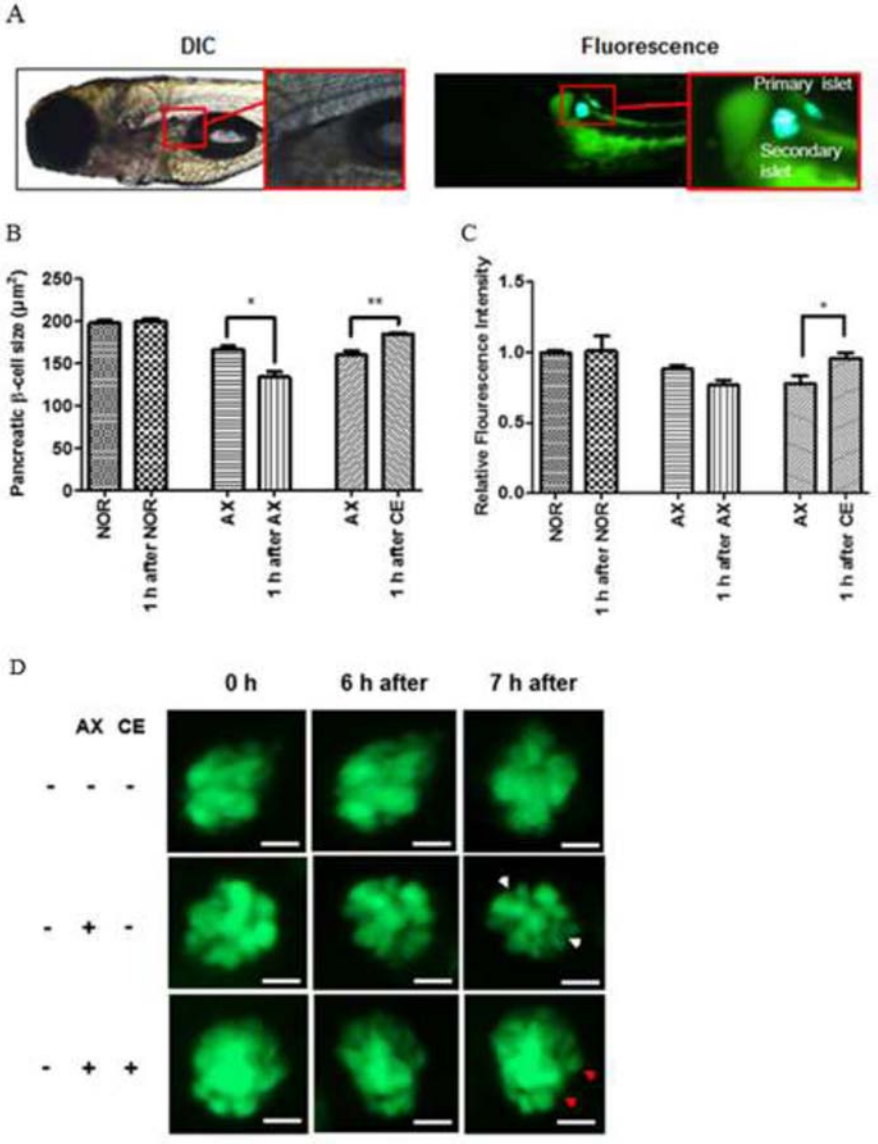

Figure 5. Effect of 100 μg/mL coffee extract (CE) on pancreatic β-cell regeneration. (A) Whole transgenic ins:GFP zebrafish and PIs were imaged by differential interference contrast (DIC), and zebrafish larva at 5 days postfertilization (dpf) were imaged by fluorescence microscopy. (B) Change in pancreatic β-cell size due to 100 μg/mL CE. (*) $p < 0.05$; (**) $p < 0.01$). (C) Relative fluorescence intensity of pancreatic β-cells due to 100 μg/mL CE. (*) $p < 0.05$. (D) Pancreatic β-cell image of each group. Damage is indicated in white and regeneration in red. Scale bar = 100 μm.

PI sizes (2.1-fold, $p < 0.0001$; 2.31-fold, $p < 0.0001$; and 2.39-fold, $p < 0.0001$, respectively; Figure 4A). We measured PI fluorescence using ImageJ software and found that the fluorescence intensity ratio in the AX group decreased (8.58 ± 0.15%) relative to the normal group (3.89 ± 7.81%) but was significantly increased in the GLM-treated (49.49 ± 16.15%, $p = 0.0034$) and 50, 100, and 300 μg/mL CE-treated groups (39.27 ± 20.18%, $p = 0.0148$; 61.75 ± 3.69%, $p < 0.0001$; and 48.58 ± 2.05%, $p < 0.0001$, respectively) relative to the AX-treated group (Figure 4B).

Efficacy of Coffee on Islet β-Cells of ins:GFP Zebrafish. Treatment of zebrafish with 2-NBDG is useful for staining PIs in tissue in their entirety. On the other hand, transgenic ins:GFP zebrafish express a fluorescent protein specifically in β-cells, allowing for specific visualization of primary and secondary islets. Using ins:GFP transgenic animals, we focused on secondary islets. The pancreatic β-cell size of the AX-treated group decreased by 33% ($p = 0.0006$) compared to the normal group. The decreased pancreatic β-cell size caused by AX treatment was increased by 16% ($p = 0.0062$) after treatment with 100 μg/mL CE (Figure 5A). The pancreatic β-cell fluorescence intensity in the AX-treated group decreased by 24% compared to the normal group. Following AX treatment, the pancreatic β-cell fluorescence intensity decreased due to damage, but was significantly increased by 18% ($p = 0.0449$) after exposure to 100 μg/mL CE (Figure 5B). We also observed pancreatic β-cell regeneration following treatment with CE in transgenic ins:GFP ZFL.

HPLC Analysis of CFI, TRG, and CGA in CE (Figure 6). A water/acetonitrile (80:20, v/v) CFI mobile phase was successfully used in the C18 column. The CFI content in 1 mg/mL CE was 60.6 μg/mL (Figure 6A, B). Likewise, a water/acetonitrile (15:85, v/v) phase was used for TRG analysis on a C18 column and showed that CE contains

DOI: 10.1021/acs.jafc.5b00027
J. Agric. Food Chem. 2015, 63, 5612−5621

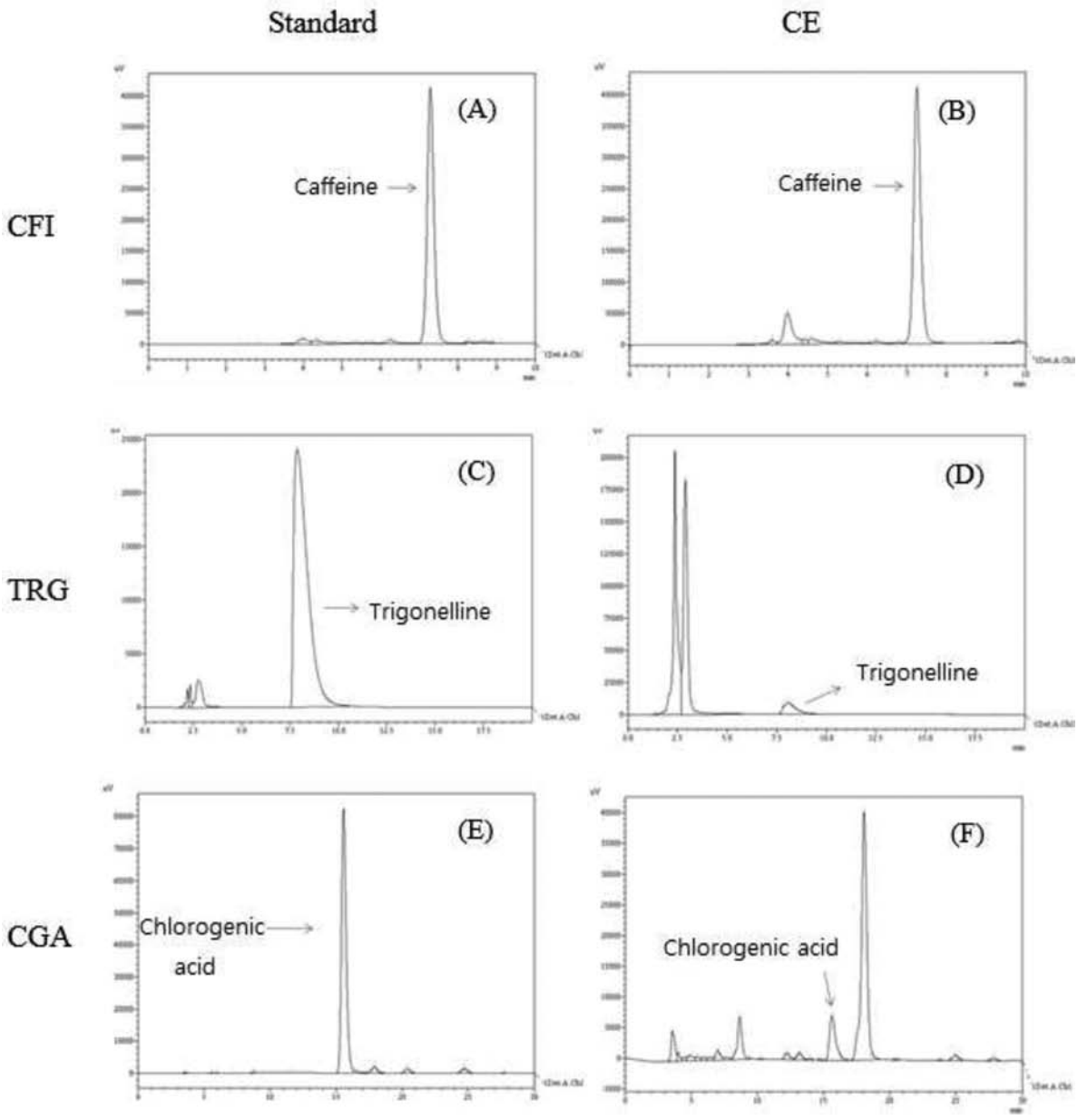

Figure 6. Chromatograms of caffeine (CFI), trigonelline (TRG), chlorogenic acid (CGA), and coffee extract (CE): (A) 100 μg/mL CFI; (B) 2 mg/mL CE; (C) 50 μg/mL TRG; (D) 1 mg/mL CE; (E) 100 μg/mL CGA; (F) 1 mg/mL CE.

11.85 μg/mL of TRG (Figure 6C, D). Lastly, CGA was analyzed using a mobile phase of water and 1% acetic acid in methanol (70:30, v/v) on a C18 column. The analysis showed that 1 mg/mL CE contains 34.1 μg/mL CGA (Figure 6E, F). Calibration curve equations, LOD, LOQ, and the CFI, TRG, and CGA concentrations are shown in Table 1.

Effects of CFI, TRG, and CGA on AIPD ZFL. The TRG- and CGA-treated groups had significantly increased PI sizes (2.16-fold, $p < 0.0001$; and 1.91-fold, $p < 0.0001$, respectively) compared to the AX-treated group. Additionally, PI size increased 0.75-fold in the CFI-treated group (Figure 7A). We next assessed PI fluorescence intensities and found that compared with the AX-treated group (8.58 $\pm$ 0.15%), the groups treated with GLM, CFI, TRG, and CGA had significantly increased fluorescence intensities (49.47 $\pm$ 16.15%, $p = 0.0034$; 44.81 $\pm$ 5.91%, $p < 0.0001$; 43.24 $\pm$ 5.44%, $p < 0.0001$; and 57.93 $\pm$ 1.88%, $p < 0.0001$, respectively; Figure 7B).

Synergy of TRG and CGA in AIPD ZFL. The 50% effect concentration (EC_{50}) was determined using nonlinear regression analysis of the logistic dose response curves with the GraphPad Prism 5 software suite. The EC_{50} values of TRG and CGA were 1.13 and 1.96 μg/mL, respectively. We determined the dose−response curves of combined TRG/CGA, TRG alone, and CGA alone in AIPD ZFL (Figure 8A). Using a CI plot of TRG/CGA combination we found that the synergistic effect had a CI value <1. Specifically, the CI values were 0.68, 0.51, and 0.47 for TRG/CGA points 1, 2, and 3, respectively (Figure 8B), indicating a synergistic effect. This synergistic effect was confirmed using an isobologram (Figure 8C).

Action of Diazoxide (DZ) on AIPD ZFL. To study the involvement of pancreatic β-cell K_{ATP} channel stimulation activity, we next evaluated PI size in response to diazoxide (DZ) treatment to open K^+ channels. We used the normal group as a baseline against which to determine significant differences in the

DOI: 10.1021/acs.jafc.5b00027
J. Agric. Food Chem. 2015, 63, 5612−5621

Table 1. Calibration Curve Equations, LOD,[a] LOQ,[b] and Concentrations of Caffeine, Trigonelline, and Chlorogenic Acid in Coffee Extract

sample	equation	R^2	LOD (μg/mL)	LOQ (μg/mL)	concentration of coffee extract (%)
caffeine	$y = 31032x + 1789355$	0.9941	0.279	0.777	6.0
trigonelline	$y = 21354x + 157253$	0.9909	0.186	0.563	1.2
chlorogenic acid	$y = 6200x + 23229$	0.9997	0.277	0.840	3.4

[a]LOD, limit of detection. [b]LOQ, limit of quantitation.

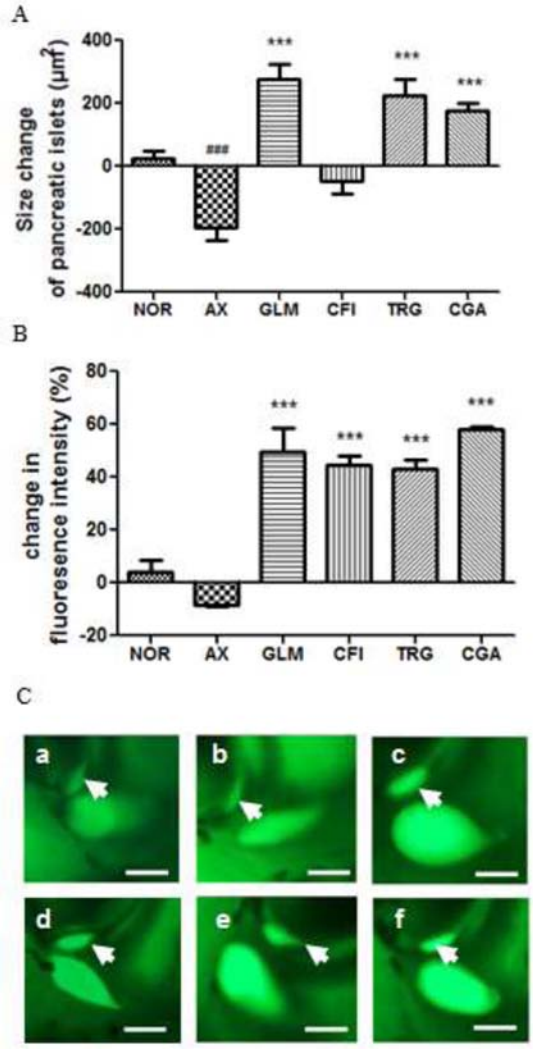

Figure 7. Effects of 10 μM caffeine (CFI), 10 μM trigonelline (TRG), and 10 μM chlorogenic acid (CGA) on alloxan-induced PI-damaged zebrafish larvae (AIPD ZFL). (A) Changes in pancreatic islet (PI) size caused by 10 μM CFI, 10 μM TRG, 10 μM CGA, and 10 μM glimepiride (GLM). (***) $p < 0.001$, compared to alloxan, AX; (###) $p < 0.001$, compared to normal. (B) Change in PI fluorescence intensity determined by image analysis. (***) $p < 0.001$, compared to alloxan, AX. (C) Fluorescent microscopic image of PIs in (a) the normal group, (b) 100 μM alloxan (AX) group, (c) 10 μM GLM group, (d) 10 μM CFI group, (e) 10 μM TRG group, and (f) 10 μM CGA group. Scale bar = 100 μm.

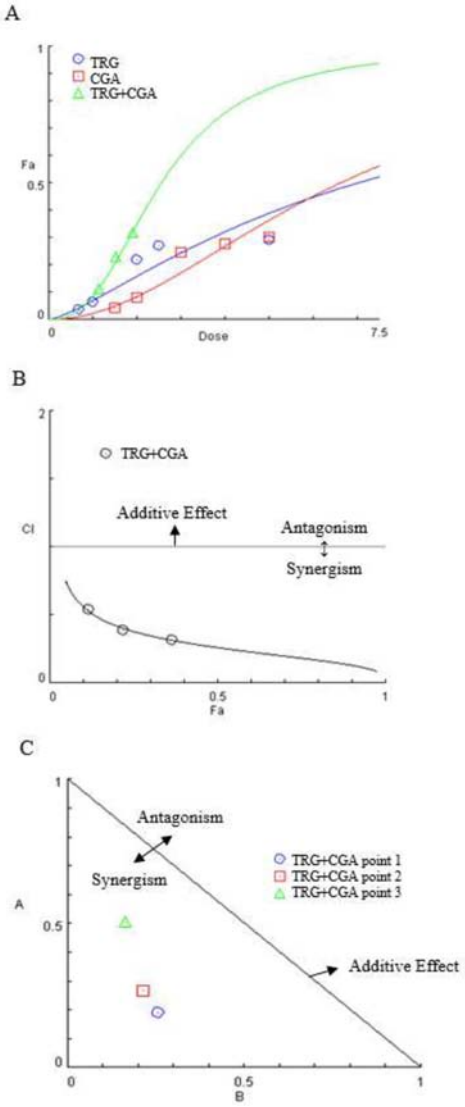

Figure 8. Combination of trigonelline (TRG) and chlorogenic acid (CGA). (A) Dose−effect curves of TRG, CGA, and combined TRG/CGA. (B) Combination index (CI)−fractional effect (Fa) plot of combined TRG/CGA. (C) Normalized isobologram constructed by connecting the EC_{50} value of TRG with the EC_{50} of CGA. The black line indicates the combined effect of TRG/CGA at points 1, 2, and 3.

AX-treated groups with or without DZ. The values of the AX-treated groups were below zero. The size of PIs in the DZ-treated normal group was significantly decreased (3.28-fold, $p = 0.0184$) relative to the no-DZ normal group. Furthermore, the AX-treated group showed no significant differences after treatment with 25 μM DZ. We next compared the GLM-, CE-, TRG-, and CCA-treated groups to the AX-treated groups, with or without DZ, as well as each DZ-treated group with the corresponding no-DZ treatment control group. The PI sizes in the 10 μM GLM with 25 μM DZ cotreatment groups were significantly decreased (0.61-fold, $p = 0.0437$) compared to the group treated with 10 μM GLM alone. Similarly, after cotreatment with 25 μM DZ, the PI sizes in the 100 μg/mL CE-treated, 10 μg/mL TRG-treated, and 10 μg/mL CGA-treated groups were significantly decreased (0.40-fold, $p = 0.0493$; 0.38-fold, $p = 0.0376$; and 0.33-fold, $p = 0.0228$, respectively; Figure 9).

DOI: 10.1021/acs.jafc.5b00027
J. Agric. Food Chem. 2015, 63, 5612−5621

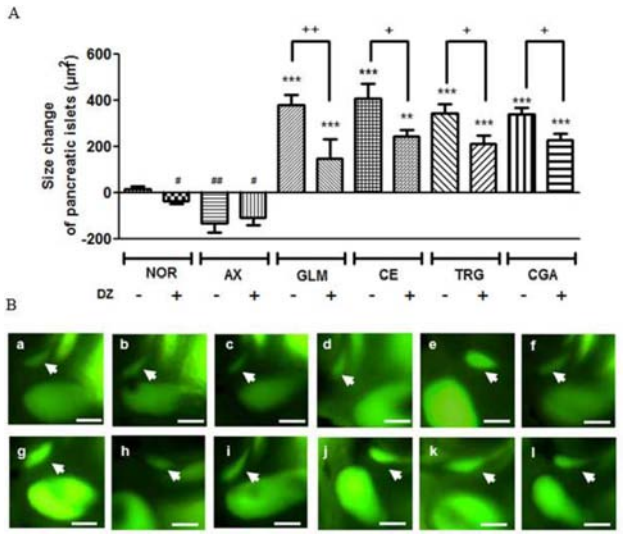

Figure 9. Effects of 10 μM glimepiride (GLM), 100 μg/mL coffee extract (CE), 10 μg/mL trigonelline (TRG), or 10 μg/mL chlorogenic acid (CGA) with 25 μM diazoxide (DZ) on alloxan-induced PI-damaged zebrafish larvae (AIPD ZFL). (A) Changes in PI size caused by 10 μM GLM, 100 μg/mL CE, 10 μg/mL TRG, and 10 μg/mL CGA with 25 μM DZ. (**) $p < 0.01$ and (***) $p < 0.001$, compared to alloxan, AX; (#) $p < 0.05$ and (##) $p < 0.01$, compared to normal; (+) $p < 0.05$ and (+2) $p < 0.01$. (a) Fluorescent macroscopic image of PI in (a) the normal group, (b) normal + 25 μM DZ group, (c) 100 μM AX group, (d) 100 μM AX + 25 μM DZ group, (e) 10 μM GLM group, (f) 10 μM GLM + 25 μM DZ group, (g) 100 μg/mL CE group, (h) 100 μg/mL CE group + 25 μM DZ group, (i) 10 μM TRG group, (j) 10 μM TRG + 25 μM DZ group, (k) 10 μM CGA group, and (l) 10 μM CGA + 25 μM DZ group. Scale bar = 100 μm.

DISCUSSION

Although immune-mediated processes are the main cause of type 1 diabetes, we used an AX-induced experimental diabetes model in this study. AX is a cytotoxic agent that acts as a diabetogenic chemical to induce experimental diabetes. Indeed, AX treatment has been widely utilized as an animal model of type 1 (insulin-dependent) diabetes mellitus.[9,13,39] AX-induced experimental diabetes decreases β-cells present in PIs, damages extra-pancreatic tissues, and consequently induces insulin deficiency.[9,40] Consistent with this model, type 1 diabetes is associated with a significant reduction of pancreas size in children.[6] In addition, type 1 diabetes mellitus adult patients have decreased pancreatic volume according to helical computed tomography (CT).[41] Consistent with these findings, we observed PI morphological changes following AX-induced diabetes mellitus in zebrafish model.

The ability to observe cells absorb glucose is a mainstay of diabetes studies. In this study, we used 2-NBDG, which is a fluorescent molecule derived from glucose that contains a 2-(*N*-(7-nitrobenz-2-oxa-1,3-diazol-4-yl)amino group at the C-2 position[22] and allows for experimental visualization of PIs. This approach was successfully employed by Lee et al.,[23] who introduced a new assay for discovering antidiabetic drugs by determining 2-NBDG uptake in the eyes of ZFL, thereby allowing for simple, economical, and rapid screening. Distinct staining of the pancreas and PI of zebrafish, unlike in humans, was reported by Wallace and Pack.[28] Mature α-, β-, and δ-cells and PP cells are located within fish PIs,[33,34] and in this study, due to the presence of insulin in PI β-cells,[32] we focused on PI observation using 2-NBDG. On the basis of preliminary experiments, we determined that the optimal treatment time and dose of 2-NBDG for PI observation were 12 h and 25 μM, respectively.

As described above, we used AX to induce PI damage in this study and first determined the optimal treatment time and dose for AX. As expected, AX significantly decreased PI size in the treated group compared to the normal group. To demonstrate the beneficial effects of diabetes therapy in AIPD ZFL, we used GLM as a positive control, as it promotes insulin secretion by closing K^+_{ATP} channels.[24,25] In the GLM-treated group, both PI size and fluorescence intensity were significantly increased compared to the AX-treated group.

We next determined the regenerative effects of CE on damaged PIs. Our results showed that CE significantly increased the size and fluorescence signal of PIs in AIPD ZFL. In addition, pancreatic β-cells damaged by AX showed improvement after treatment with CE. 2-NBDG-stained PIs and β-cells expressing GFP in zebrafish showed a similar pattern: PI staining with 2-NBDG was decreased in AX-induced damage and increased in response to CE.

To investigate the efficacy of the components of coffee together or in combination, we treated PIs with CFI, TRG, and CGA. We focused on CFI, TRG, and CGA as they are well-known major compounds in coffee and because they have been reported to have beneficial effects for diabetes.[29] First, the concentrations of CFI, TRG, and CGA in CE were determined using HPLC followed by efficacy testing in PIs. The amounts of TRG (1.2 μg/mL) and CGA (3.4 μg/mL) in CE (100 μg/mL) were lower than those used in individual TRG or CGA treatments, but the efficiency of 100 μg/mL of CE was superior to that of 10 μg/mL of TRG or CGA. Specifically, our data indicated a positive efficacy and synergistic effect of TRG and CGA in PIs, which was consistent with both previous studies and our observation that TRG and CGA have significant regenerative effects when tested individually. When we investigated the synergistic effect of TRG/CGA in CE using CI values and an isobologram, we found that the combination of TRG/CGA at three different concentrations resulted in CI values of 0.47, 0.51 and 0.68, where a CI value <1 indicates a synergistic effect. Taken together, our findings were consistent with the report by Zhou et al.,[30] who showed that organic degeneration of pancreatic β-cells in diabetes is normalized by TRG, which also preserves β-cell mass, and is associated with recovery of PI damage. CGA has also been reported to stimulate glucose transport, thereby enabling greater glucose absorption.[31]

The metabolism of glucose in pancreatic β-cells is the key step in glucose-stimulated insulin secretion.[42] Therefore, we also used 2-NBDG to observe glucose uptake in PIs and investigated the mechanism of insulin secretion by modulating K_{ATP} channels. Closure of K_{ATP} channels leads to membrane depolarization, opening of voltage-gated Ca^{2+} channels, and Ca^{2+} influx and rise and then induces insulin secretion.[43] To confirm the effects of CE and its active components on K_{ATP} channels, we performed cotreatments with DZ after inducing hyperglycemia.[26,27] DZ opens K_{ATP} channels in pancreatic β-cells, which has been shown to inhibit the secretion of insulin in AX-induced diabetic mice.[44] Furthermore, Kappel et al.[38] reported that DZ significantly decreases Ca^{2+} uptake in isolated rat pancreatic islets. Our results showed that cotreatment with DZ decreased the beneficial effects of CE and reduced the increase in PI size in response to TRG and CGA treatment. These results suggested that CE might stimulate insulin secretion by Ca^{2+} influx via closure of K_{ATP} channels in β-cells.

DOI: 10.1021/acs.jafc.5b00027
J. Agric. Food Chem. 2015, 63, 5612−5621

This study had several limitations. First, we did not measure blood glucose levels as a main marker of diabetes, nor did we investigate the relationship between increased or decreased PI and blood glucose levels. Thus, additional studies that include blood glucose level measurements will be required. In addition, although we investigated the effect of CE on K_{ATP} channels and pancreatic β-cells, specific evaluation of the effects of CE on insulin secretion will require further investigation.

In conclusion, we showed that CE significantly increases the size of PIs in AIPD ZFL. Furthermore, we determined that recovery of damaged pancreatic β-cells and restoration of insulin secretion are possible using CE, TRG, and CGA to block K_{ATP} channels in ZFL. Combined TRG/CGA treatment exhibited synergistic effects compared to treatment with TRG or CGA alone. Taken together, the results of our study demonstrate that coffee confers a regenerative effect on PIs injured by diabetes, which can increase insulin secretion by blocking K_{ATP} channels. Lastly, the synergistic effects of TRG and CGA may be primarily responsible for the beneficial effects of coffee.

AUTHOR INFORMATION

Corresponding Author

*(T.H.K.) E-mail: panjae@khu.ac.kr. Fax: +82-303-0300-0030.

Funding

This study was supported by the Basic Science Research Program through the National Research Foundation of Korea (NRF) funded by the Ministry of Science, ICT & Future Planning (2012R1A1A2041525).

Notes

The authors declare no competing financial interest.

REFERENCES

(1) Cavaghan, M. K.; Ehrmann, D. A.; Polonsky, K. S. Interactions between insulin resistance and insulin secretion in the development of glucose intolerance. *J. Clin. Invest.* **2000**, *106* (3), 329.

(2) Van Belle, T. L.; Coppieters, K. T.; Von Herrath, M. G. Type 1 diabetes: etiology, immunology, and therapeutic strategies. *Physiol. Rev.* **2011**, *91* (1), 79−118.

(3) Kim, S. K.; Hebrok, M. Intercellular signals regulating pancreas development and function. *Genes Dev.* **2001**, *15* (2), 111−127.

(4) Rorsman, P.; Renström, E. Insulin granule dynamics in pancreatic beta cells. *Diabetologia* **2003**, *46* (8), 1029−1045.

(5) Rhodes, C. J.; White, M. F. Molecular insights into insulin action and secretion. *Eur. J. Clin. Invest.* **2002**, *32* (s3), 3−13.

(6) Altobelli, E.; Blasetti, A.; Verrotti, A.; Di Giandomenico, V.; Bonomo, L.; Chiarelli, F. Size of pancreas in children and adolescents with type I (insulin-dependent) diabetes. *J. Clin. Ultrasound.* **1998**, *26* (8), 391−395.

(7) Rhodes, C. J. Type 2 diabetes − a matter of β-cell life and death? *Science* **2005**, *307* (5708), 380−384.

(8) Alzaid, A.; Aideyan, O.; Nawaz, S. The size of the pancreas in diabetes mellitus. *Diabetic Med.* **1993**, *10* (8), 759−763.

(9) Desgraz, R.; Bonal, C.; Herrera, P. L. β-Cell regeneration: the pancreatic intrinsic faculty. *Trends Endocrinol. Metab.* **2011**, *22* (1), 34−43.

(10) Pick, A.; Clark, J.; Kubstrup, C.; Levisetti, M.; Pugh, W.; Bonner-Weir, S.; Polonsky, K. S. Role of apoptosis in failure of β-cell mass compensation for insulin resistance and β-cell defects in the male Zucker diabetic fatty rat. *Diabetes* **1998**, *47* (3), 358−364.

(11) Van Dam, R. M.; Hu, F. B. Coffee consumption and risk of type 2 diabetes: a systematic review. *JAMA* **2005**, *294* (1), 97−104.

(12) Atanasov, A. G.; Dzyakanchuk, A. A.; Schweizer, R. A.; Nashev, L. G.; Maurer, E. M.; Odermatt, A. Coffee inhibits the reactivation of glucocorticoids by 11β-hydroxysteroid dehydrogenase type 1: a glucocorticoid connection in the anti-diabetic action of coffee? *FEBS Lett.* **2006**, *580* (17), 4081−4085.

(13) Shaw Dunn, J.; McLetchie, N. G. B. Experimental alloxan diabetes in the rat. *Lancet* **1943**, *242* (6265), 384−387.

(14) Soto, C.; Del Razo, L. M.; Neri, L. Alloxan decreases intracellular potassium content of the isolated frog skin epithelium. *Comp. Biochem. Physiol., Part C: Toxicol. Pharmacol.* **2001**, *130* (1), 19−27.

(15) Carroll, P. B.; Moura, A. S.; Rojas, E.; Atwater, I. The diabetogenic agent alloxan increases K+ permeability by a mechanism involving activation of ATP-sensitive K^+-channels in mouse pancreatic β-cells. *Mol. Cell. Biochem.* **1994**, *140* (2), 127−136.

(16) Rohilla, A.; Ali, S. Alloxan induced diabetes: mechanisms and effects. *Int. J. Res. Pharm. Biomed. Sci.* **2012**, *3*, 819−21.

(17) Shin, E. J. *Validation of Diabetic Zebrafish Model.* M.S. thesis, Kyung Hee University, Seoul, Korea, Feb 2012.

(18) Zhang, J.; Qian, J.; Tong, J.; Zhang, D.; Hu, C. Toxic effects of cephalosporins with specific functional groups as indicated by zebrafish embryo toxicity testing. *Chem. Res. Toxicol.* **2013**, *26* (8), 1168−1181.

(19) Kinkel, M. D.; Prince, V. E. On the diabetic menu: zebrafish as a model for pancreas development and function. *BioEssays* **2009**, *31* (2), 139−152.

(20) El-Shahawi, M. S.; Hamza, A.; Bahaffi, S. O.; Al-Sibaai, A. A.; Abduljabbar, T. N. Analysis of some selected catechins and caffeine in green tea by high performance liquid chromatography. *Food Chem.* **2012**, *134* (4), 2268−2275.

(21) Chou, T. C. Preclinical versus clinical drug combination studies. *Leuk. Lymphoma* **2008**, *49* (11), 2059−2080.

(22) Yoshioka, K.; Saito, M.; Oh, K. B.; Nemoto, Y.; Matsuoka, H.; Natsume, M.; Abe, H. Intracellular fate of 2-NBDG, a fluorescent probe for glucose uptake activity in *Escherichia coli* cells. *Biosci., Biotechnol., Biochem.* **1996**, *60* (11), 1899−1901.

(23) Lee, J.; Jung, D. W.; Kim, W. H.; Um, J. I.; Yim, S. H.; Oh, W. K.; Williams, D. R. Development of a highly visual, simple, and rapid test for the discovery of novel insulin mimetics in living vertebrates. *ACS Chem. Biol.* **2013**, *8* (8), 1803−1814.

(24) Mowl, A.; Alauddin, M.; Rahman, M.; Ahmed, K. Antihyperglycemic effect of *Trigonella foenum-graecum* (fenugreek) seed extract in alloxan-induced diabetic rats and its use in diabetes mellitus: a brief qualitative phytochemical and acute toxicity test on the extract. *Afr. J. Tradit., Complementary Altern. Med.* **2009**, *6* (3).10.4314/ajtcam.v6i3.57165

(25) Phadatare, P. D.; Chandrashekhar, V. M. Influence of esomeprazole on hypoglycemic activity of oral antidiabetic agents in rats and rabbits. *Mol. Cell. Biochem.* **2011**, *354* (1−2), 135−140.

(26) Sturgess, N. C.; Kozlowski, R. Z.; Carrington, C. A.; Hales, C. N.; Ashford, M. L. J. Effects of sulphonylureas and diazoxide on insulin secretion and nucleotide-sensitive channels in an insulin-secreting cell line. *Br. J. Pharmacol.* **1988**, *95* (1), 83−94.

(27) Milner, R. D. G.; Hales, C. N. The interaction of various inhibitors and stimuli of insulin release studied with rabbit pancreas in vitro. *Biochem. J.* **1969**, *113*, 473−479.

(28) Wallace, K. N.; Pack, M. Unique and conserved aspects of gut development in zebrafish. *Dev. Biol.* **2003**, *255* (1), 12−29.

(29) Van Dijk, A. E.; Olthof, M. R.; Meeuse, J. C.; Seebus, E.; Heine, R. J.; Van Dam, R. M. Acute effects of decaffeinated coffee and the major coffee components chlorogenic acid and trigonelline on glucose tolerance. *Diabetes Care* **2009**, *32* (6), 1023−1025.

(30) Zhou, J.; Zhou, S.; Zeng, S. Experimental diabetes treated with trigonelline: effect on β cell and pancreatic oxidative parameters. *Fundam. Clin. Pharmacol.* **2013**, *27* (3), 279−287.

(31) Ong, K. W.; Hsu, A.; Tan, B. K. H. Anti-diabetic and anti-lipidemic effects of chlorogenic acid are mediated by ampk activation. *Biochem. Pharmacol.* **2013**, *85* (9), 1341−1351.

(32) Rutter, G. A. Insulin secretion: feed-forward control of insulin biosynthesis? *Curr. Biol.* **1999**, *9* (12), R443−R445.

(33) Parsons, M. J.; Pisharath, H.; Yusuff, S.; Moore, J. C.; Siekmann, A. F.; Lawson, N.; Leach, S. D. Notch-responsive cells initiate the

DOI: 10.1021/acs.jafc.5b00027
J. Agric. Food Chem. 2015, 63, 5612−5621

secondary transition in larval zebrafish pancreas. *Mech. Dev.* **2009**, *126* (10), 898−912.
(34) Wilfinger, A.; Arkhipova, V.; Meyer, D. Cell type and tissue specific function of islet genes in zebrafish pancreas development. *Dev. Biol.* **2013**, *378* (1), 25−37.
(35) Vascotto, S. G.; Beckham, Y.; Kelly, G. M. The zebrafish's swim to fame as an experimental model in biology. *Biochem. Cell Biol.* **1997**, *75* (5), 479−485.
(36) Parng, C.; Seng, W. L.; Semino, C.; McGrath, P. Zebrafish: a preclinical model for drug screening. *Assay Drug Dev. Technol.* **2002**, *1* (1), 41−48.
(37) Lin, S.; Lai, T. C.; Chen, L.; Kwok, H. F.; Lau, C. B. S.; Cheung, P. C. Antioxidant and antiangiogenic properties of phenolic extract from *Pleurotus tuber-regium*. *J. Agric. Food Chem.* **2014**, *62* (39), 9488−9498.
(38) Kappel, V. D.; Frederico, M. J.; Postal, B. G.; Mendes, C. P.; Cazarolli, L. H.; Silva, F. R. The role of calcium in intracellular pathways of rutin in rat pancreatic islets: potential insulin secretagogue effect. *Eur. J. Pharmacol.* **2013**, *702* (1), 264−268.
(39) Szkudelski, T. The mechanism of alloxan and streptozotocin action in B cells of the rat pancreas. *Physiol. Res.* **2001**, *50* (6), 537−546.
(40) Lenzen, S. The mechanisms of alloxan-and streptozotocin-induced diabetes. *Diabetologia* **2008**, *51* (2), 216−226.
(41) Goda, K.; Sasaki, E.; Nagata, K.; Fukai, M.; Ohsawa, N.; Hahafusa, T. Pancreatic volume in type 1 und type 2 diabetes mellitus. *Acta Diabetol.* **2001**, *38* (3), 145−149.
(42) Miki, T.; Nagashima, K.; Seino, S. The structure and function of the ATP-sensitive K^+ channel in insulin-secreting pancreatic β-cells. *J. Mol. Endocrinol.* **1999**, *22* (2), 113−123.
(43) Henquin, J. C. Triggering and amplifying pathways of regulation of insulin secretion by glucose. *Diabetes* **2000**, *49* (11), 1751−1760.
(44) Tabachnick, I. I. A.; Gulbenkian, A.; Seidman, F. The effect of a benzothiadiazine, diazoxide, on carbohydrate metabolism. *Diabetes* **1964**, *13* (4), 408−418.

DOI: 10.1021/acs.jafc.5b00027
J. Agric. Food Chem. 2015, 63, 5612−5621

to D-mannose, rather than sucrose or fructose.[10] Previously, pectic oligosaccharides were reported to inhibit the adhesion of enterohemorrhagic and enteropathogenic strains of *E. coli* to HT29 cells.[11] This establishes a precedent for plant cell wall oligosaccharides that have anti-adhesive properties for *E. coli* binding to epithelial cell receptors. The cranberry plant cell wall structure consists of parenchyma cellulose, hemicellulose, and pectin rich in arabinan.[12]

Xyloglucan is a well-known hemicellulose that cross-links type 1 plant cell walls found in dicotyledonous and non-commelinoid monocotyledonous plants.[13] Xyloglucan, which has a β-(1−4)-glucan backbone, is able to hydrogen bond to the surface of cellulose microfibrils, forming a network that connects adjacent microfibrils in cell walls. The xyloglucan network is intermeshed with the pectin network of cell wall matrix polysaccharides.[14] This makes xyloglucan an important polysaccharide in the growth and development of primary cell walls.[14] There is a block-like structure in xyloglucan in which a 6-11 sugar sequence is repeated throughout the polysaccharide. Carbohydrate characterization of xyloglucan oligosaccharide fragments has been used to describe polysaccharide structures specific for plant taxonomic groups.[15−18] Three types of xyloglucan structure have been described, with fucogalacto-xyloglucan the most commonly distributed in about half of the monocot taxonomic orders and all dicot orders except for the Solanales, Laminales, Gentianales, and Ericales.[14,18] Xyloglucan from these later orders contains arabino-xyloglucan structure. Small amounts of a third xyloglucan structure are also present in commelinoid monocots (grasses, bromeliads, palms, and cypresses) as randomly distributed single-xylose substituents on a cellulosic backbone.[14] A single-letter nomenclature was developed to describe xyloglucan substituent sequences.[19] We investigated cranberry xyloglucan structure and detected arabino-xyloglucan (SSGG) oligosaccharide fractions with anti-*E. coli* adhesion activity for epithelial cell receptors.

MATERIALS AND METHODS

Materials. The following were obtained from Sigma-Aldrich (St. Louis, MO, USA): phosphate-buffered saline tablets (PBS; pH 7.4 ± 0.2, 0.1 mol/L), nonessential amino acid solution, trypsin−EDTA solution, Dulbecco's modified Eagle medium with GlutaMAX-1 (DMEM), tryptic soy agar, and 2,5-dihydroxybenzoic acid. Fetal bovine serum was obtained from the American Type Culture Collection (ATCC, Manassas, VA, USA). PBS was filter sterilized with a 0.2 μm syringe filter prior to use.

Xyloglucan-oligosaccharides with a degree of polymerization (DP) of 7−9 were purchased from Megazyme (Bray, Ireland). Commercial juices were purchased from a local grocery store.

Oligosaccharide Isolation. A cranberry (*Vaccinium macrocarpon*, mainly Stevens variety harvested in Massachusetts during 2009) hull enzyme-treated concentrate fraction (A1) was produced using Klerzyme 150 pectinase (DSM Food Specialties, South Bend, IN, USA) during cranberry depectinization. Fractionation of A1 was accomplished by utilizing a FLASH-40 system (Biotage, Charlotte, NC, USA), converted to accept Biotage SNAP KP-C18-HS 120 g cartridges. A1 (20 g) was dissolved in 200 mL of deionized (DI) water, and 50 mL of the solution was loaded onto the preconditioned (300 mL of methanol, 300 mL of DI water) C18 column cartridge. The C18 column cartridge was eluted first with 500 mL of DI water, followed by 500 mL of a 15% methanol/water mixture (35 mL/min flow rate). The remaining phenolic content was washed from the column with 500 mL of methanol. The column was reconditioned before loading it again with the next 50 mL of A1 solution. After the C18 separation, the 15% methanol/water fractions were combined and dried to produce the A2 fraction (4.97 g of a pink colored powder). An unknown peak was observed in A2 chromatograms at approximately 6.7 min during high-pressure liquid chromatography (HPLC) analysis of fraction A2 using an 1100 series (Agilent Technologies, Santa Clara, CA, USA) system equipped with a refractive index detector and HPX-87C HPLC column (Bio-Rad Laboratories, Inc., Hercules, CA, USA). Fraction A2 was further purified by Sephadex LH20 (Sigma-Aldrich) chromatography to eliminate phenolic pigments. Fraction A2 (4.8 g) was dissolved in 60 mL of DI water, and the mixture was loaded on a 300 × 45 mm Sephadex LH20 column (preconditioned with 500 mL of DI water). The column was eluted with 500 mL of DI water using a Masterflex L/S pump (Cole-Parmer, Vernon Hill, IL, USA) at a flow rate of 2.5 mL/min, followed by lyophilization to produce 4.32 g of a slightly pink, off-white powder A6 fraction.

Carbohydrate Analysis. The neutral sugar content (NS), uronic acid content (UA), degree of methyl esterification (DE), and degree of acetylation (DA) were determined as reported previously[20] except that the NS (glucose standard) was used as the basis for DE and DA instead of the UA. Monosaccharide analysis by high-performance anion-exchange chromatography with pulsed amperometric detection (HPAEC-PAD) following methanolysis was performed according to the procedure reported previously.[21] Unhydrolyzed oligosaccharides were also separated by HPAEC-PAD according to the procedure reported previously.[11]

High-Performance Size Exclusion Chromatography. Cranberry samples (10−20 mg/mL) were dissolved in 0.05 M $NaNO_3$ and 0.01% NaN_3 mobile phase by stirring at room temperature, centrifuged at 50000*g* for 10 min, and filtered through a 0.22 or 0.45 μm Millex HV filter (Millipore Corp., Bedford, MA, USA). The model 1200 series solvent delivery system included a degasser, pump, and autosampler (Agilent Corp.) with flow rate set at 0.7 mL/min. The injection volume was 200 μL. Samples were run in triplicate. The column set consisted of three 300 mm × 7.8 mm i.d., 13 μm, TSK $GMPW_{XL}$ size exclusion columns in series and two 40 mm × 6.0 mm i.d., 12 μm, guard columns of the same material (Tosoh Bioscience, Tokyo, Japan) with one guard column placed before the separatory columns and the other prior to the detectors. The column temperature was controlled in a water bath set at 35 °C. Column effluent was detected with a HELEOS II multiangle laser light scattering photometer (Wyatt Technology, Santa Barbara, CA, USA) in series with a model Viscostar II differential pressure viscometer (Wyatt Technology) and an differential refractive index interferometer (Wyatt Technology). Electronic outputs from these three detectors were processed with ASTRA software version 6.1.1.17 (Wyatt Technology).

Mass Spectrometry. Matrix-assisted laser desorption ionization mass spectrometry with tandem time-of-flight mass spectrometry (MALDI-TOF/TOF MS/MS) utilized a 4700 Proteomics Analyzer mass spectrometer (Applied Biosystems, Framingham, MA, USA) in the positive reflectron mode. Spectra were obtained by averaging 1000 and 2500 acquired spectra in the MS and MS/MS modes, respectively. Collision-induced dissociation (CID) with air at approximately 1×10^{-6} Torr and 1 keV acceleration voltage was used for obtaining the MS/MS spectra for selected oligosaccharides. Conversion of TOF to mass (Da) for the monoisotopic ions, $[M + Na]^+$, was based on calibration of the instrument with a peptide standard calibration kit (Applied Biosystems). Oligosaccharide samples (3−5 mg) were dissolved in 1 mL of water and cleaned with CarboPrep 90 graphitized carbon cartridges, 3 mL, 250 mg (Restek, Bellefonte, PA, USA). The cartridges were first conditioned by passing 3 mL of acetonitrile/water (50:50) and then washed four times with 3 mL of water. After conditioning, the oligosaccharide solution was passed through the graphitized carbon cartridge and washed three times with 3 mL of water, and the water wash was discarded. The oligosaccharides were eluted with 1 mL of acetonitrile/water (30:70, v/v) containing 0.1% TFA. From this solution, 2 μL was mixed with 10 μL of a solution of 2,5-dihydroxybenzoic acid (10 mg/mL in acetonitrile/water (50:50), 0.1% TFA), and spotted onto a MALDI plate for analysis.

Nuclear Magnetic Resonance Spectroscopy. Cranberry fraction A6 was dissolved in ^2H_2O (99.6% ^2H, Cambridge Isotope Laboratories, Tewksbury, MA, USA), lyophilized and redissolved in 0.6 mL of 99.96% enriched ^2H_2O, and transferred to a 5 mm NMR tube. Spectra were recorded at 40 °C on either a Bruker Avance-II 700

DOI: 10.1021/acs.jafc.5b00730
J. Agric. Food Chem. 2015, 63, 5622−5633

MHz spectrometer (Billerica, MA, USA) using a 5 mm *xyz*-PFG QXI HCNP probe or a Varian INOVA 500 MHz spectrometer (Santa Clara, CA, USA) equipped with a *z*-PFG PentaProbe. Data processing was performed using NMR-Pipe[22] and analyzed using SPARKY.[23] All spectra were referenced to the internal ^{1}H and ^{13}C resonances of either 4,4-dimethyl-4-silapentane-1-sulfonic acid (DSS) or 3-(trimethylsilyl)-2,2′,3,3′-tetradeuteropropionic acid (TMSP-d_4). One-dimensional ^{1}H NMR spectra were acquired at 700 MHz using a spectral width of 5000 Hz, 32768 points, a 70° pulse width, and a recycle time of 2.5 s. One-dimensional ^{13}C NMR spectra were acquired at 176 MHz using 65536 data points, a 70° pulse width, and a recycle delay of 2.5 s. Gradient enhanced versions of the following experiments were run: three 2D TOCSY (10, 120, and 300 ms using the DIPSI-2 sequence[24] for a spin-lock), 2D ROESY (200 ms mixing time), two $^{1}H-^{13}C$-HSQC, long-range $^{1}H-^{13}C$ HSQC, J_{H-C}-coupled HSQC, $^{1}H-^{13}C$ HMBC ($J_{nC\text{-}H}$ = 6 Hz), and two HMQC TOCSY (50 and 300 ms spin-lock). The 2D homonuclear experiments were recorded with spectral widths of 5K−7K Hz in both dimensions, using 8192−16384 points in the directly detected dimension, 512 increments in the second dimension, 32 or 64 transients per acquisition depending on signal intensity, and a 2.5 s delay between scans. The heteronuclear experiments were acquired with a range of parameter values depending on the specific experiment, the instrument, and the digital resolution needed. These parameter values were 2097 or 7000 Hz spectral width in the ^{1}H dimension and 10K or 19K Hz in the ^{13}C dimension (or in the HMBC 25K Hz), using 1024−8192 points in the directly detected dimension, 512 increments in the second dimension, 32 or 64 transients per acquisition depending on signal intensity, and a 2.5 s delay between scans. These experiments were run on several batches of the sample and enabled the assignment of resonances and measurement of coupling constants to determine the sugar residue identities, their anomeric configuration, and connectivity as well as the local structure.

Anti-adhesive Activity. A bacterial adhesion assay was carried out with human bladder epithelial cells T24 (ATCC HTB-4 UEC) and *E. coli* CFT073 (ATCC 700928) and UTI89 strains.[25,26] Cranberry extracts A1 and A6 were diluted in PBS to concentrations of 0−5 mg/mL. A cranberry-enriched proanthocyanidin (PAC) fraction (55% total PAC analyzed by 4-dimethylaminocinnamaldehyde colorimetric method with purified cranberry PACs as a reference standard)[27] was used as positive control in the CFT073 assay and was diluted in PBS to concentrations of 0−0.5 mg/mL (pH 7). α-D-Mannose was used as positive control in the UTI89 assay and was diluted in PBS to concentrations of 0−2 mg/mL. PBS was used as a negative control. Briefly, fluorescent-labeled uropathogenic *E. coli* strains CFT073 and UTI89 were subcultured using colonizing factor agar (CFA) and Luria−Bertani (LB) broth, respectively. CFA was used to promote p-fimbriae growth in CFT073, whereas UTI89 only expresses type 1 fimbriae. Bacteria were pre-incubated with A1 and A6 fractions and control samples for 30 min at 35 °C before being added to T24 cells in 96-well plates at an *E. coli*/T24 ratio of 400:1. *E. coli* and T24 co-cultures were incubated in a 5% CO_2 humidified atmosphere for 1 h at 37 °C. Following the incubation, bacteria not adhering to the T24 cells were removed by washing with PBS. The fluorescence intensity (FI) was measured in a microplate reader at 480 nm excitation/516 nm emission (Synergy H1 Hybrid, Biotek Instruments, Winooski, VT, USA). All samples were tested in triplicate.

The effect of A6 on bacterial adhesion was also determined with *E. coli* O157:H7 (ATCC BAA-1883) and human colonic epithelial cells HT29 (ATCC HTB-38) using a standard assay reported earlier.[11] Working cultures of *E. coli* were prepared by inoculating slopes of agar in universal bottles and incubating the agar for 18−24 h at 37 °C. *E. coli* broth cultures for adhesion assays were grown in DMEM supplemented with 5% (v/v) fetal bovine serum and 1% (v/v) nonessential amino acid solution (SDMEM). The broth was inoculated from a slope culture and incubated anaerobically at 37 °C for 18−24 h. The overnight culture was then inoculated 1% (v/v) into fresh SDMEM and incubated for a further 18−24 h under the same conditions. This was repeated. On the day of the assay, a 10% (v/v) inoculum was again inoculated into prewarmed SDMEM and incubated for 4 h aerobically at 37 °C.

HT29 human intestinal epithelial cells were grown in 25 cm^2 tissue culture flasks in SDMEM at 37 °C in 5% CO_2 until approximately 90% confluent, split according to the method recommended by the European Collection of Cell Cultures, and stored in aliquots over liquid nitrogen. These aliquots were used to seed 25 cm^2 flasks, which after growth were split into 12-well tissue culture plates. The 12-well plates were grown to approximately 95% confluence before being used for the adhesion assays.

A culture of the *E. coli* strain was prepared as described above and then diluted 1:500 in PBS. The viable count of the diluted suspension was determined by spread plating onto plate count agar, with decimal dilution being carried out in PBS buffer as appropriate. A6 was dissolved in PBS (5 mg/mL) and sterilized by passing through a 0.2 μm syringe filter. The carbohydrate solution was further diluted in sterile PBS as required. The SDMEM was aspirated into a 12-well tissue culture plate with near-confluent monolayers of HT29 cells, prepared as described above. The monolayers were washed by pipetting in 1 mL of sterile PBS per well, swirling by hand, and then aspirating. A 0.5 mL aliquot of the A6 solution was added to the well, followed by 0.5 mL of bacterial suspension in PBS. Control wells contained unsupplemented PBS substituted for the A6 solution. All assays were performed in triplicates. The plates were swirled by hand to mix and then incubated at 37 °C aerobically for 2 h.

After incubation, the bacterial suspension was aspirated from the wells. A 1 mL aliquot of PBS was added to each well, the plate swirled briefly by hand, and the PBS removed. The washing step was repeated two more times. A 70 μL aliquot of trypsin−EDTA solution was added to each well, the plate was rocked to ensure even coverage, and then it was incubated at 37 °C for 5 min. A 1 mL aliquot of PBS was then pipetted into each well and pipet-mixed until the monolayer was completely dislodged and clumps were dissolved (as determined visually). Bacteria in cell suspension were then enumerated by plate counting on plate count agar plates with decimal dilutions performed in PBS as required. All plates were incubated at 37 °C for 18−24 h before colonies were enumerated. Viable counts were calculated for all wells and the inoculum and are expressed as colony-forming units (CFU) per milliliter. For each test the mean and the standard error of the triplicate wells were calculated. Statistical significance was determined by one-way analysis of variance, using ANOVA software.

RESULTS AND DISCUSSION

Carbohydrate Analysis. The A1 fraction produced by commercial pectinase treatment of cranberry hulls contained pectin fragments and significant amounts of neutral sugar-rich material (Table 1). The A2 fraction was neutral sugar-rich and had relatively low amounts of uronic acid, indicating little pectin was present. The most purified of the cranberry fractions (A6) consisted of a neutral sugar-rich polysaccharide with a weight-average molar mass of 2750 Da compared to 3410 Da for A2 and 5510 Da for A1. The *z*-average hydrodynamic radius and weight-average intrinsic viscosity were consistent with low-molecular-weight and low-viscosity polysaccharides. Fraction A6 had no absorption at 230 and 280 nm, indicating the lack of aromatic structures present in proanthocyanidins (PACs).

Table 1. Carbohydrate Analysis of Cranberry Fractions[a]

	UA (mol % (SD))	DE (mol % (SD))	DA (mol % (SD))	NS (mol % (SD))
A1	35.6 (3.5)	7.0 (0.9)	1.7 (0.3)	53.8 (2.7)
A2	5.3 (0.1)	4.9 (0.2)	1.5 (0.0)	86.0 (2.2)
A6	13.0 (0.6)	7.5 (0.1)	1.7 (0.0)	81.3 (0.5)

[a]UA, uronic acid; DE, degree of methyl esterification; DA, degree of acetylation; NS, neutral sugar.

DOI: 10.1021/acs.jafc.5b00730
J. Agric. Food Chem. 2015, 63, 5622−5633

Table 2. Monosaccharide Composition of Cranberry Fractions[a]

	Glc (mol %)	Ara (mol %)	Gal (mol %)	Xyl (mol %)	Rha (mol %)	Fuc (mol %)	GalA (mol %)	GlcA (mol %)
A1	25.4	10.7	7.4	6.6	0.3	0.2	49.4	0.1
A2	46.0	28.5	4.6	17.0	0.5	0.4	3.2	0.0
A6	50.3	25.7	4.4	14.8	0.5	0.4	3.7	0.2

[a]Glc, glucose; Ara, arabinose; Gal, galactose; Xyl, xylose; Rha, rhamnose; Fuc, fucose; GalA, galacturonic acid; GlcA, glucuronic acid.

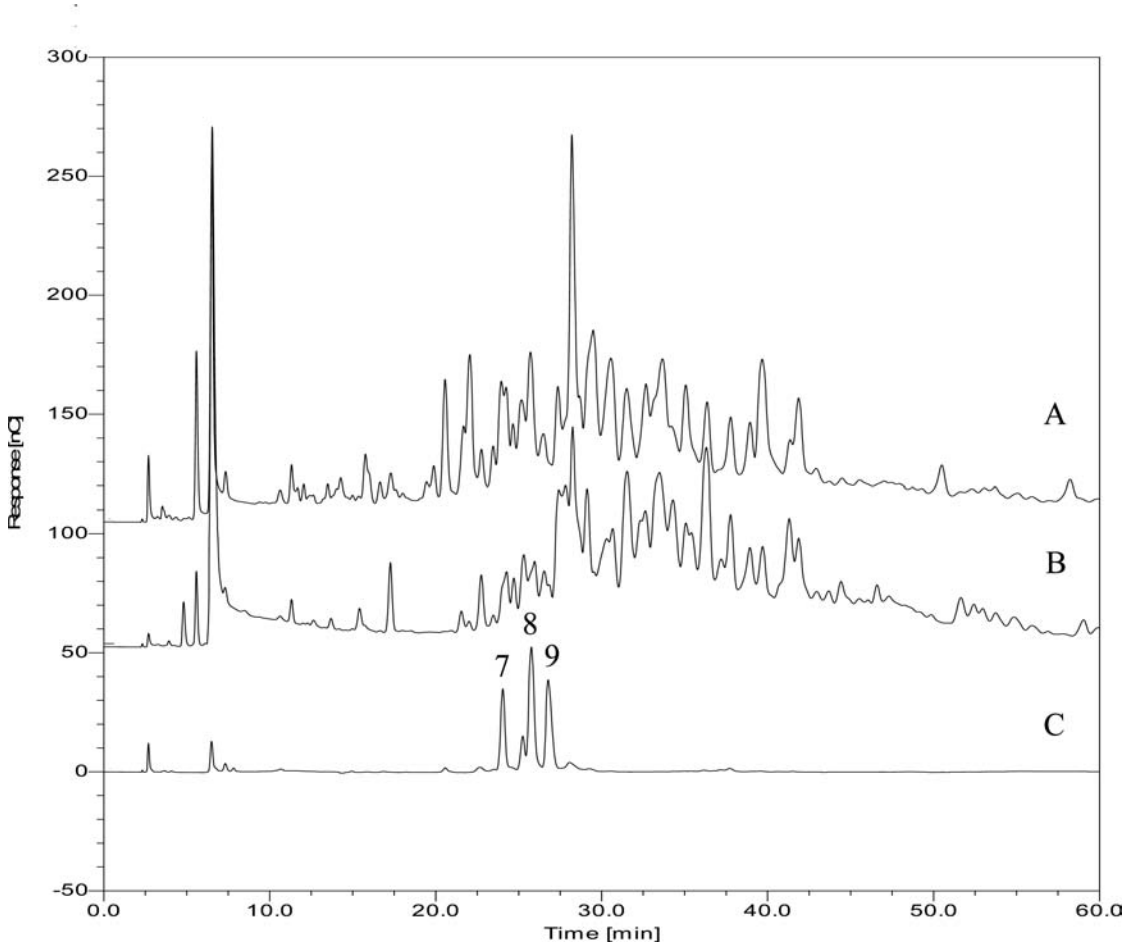

Figure 1. HPAEC-PAD oligosaccharide analysis of cranberry fractions A6 (A) and A2 (B) compared with xyloglucan oligosaccharide standards (C, degree of polymerization indicated above each peak).

The monosaccharide compositions of the A2 and A6 cranberry fractions were dominated by glucose, arabinose, and xylose with very little galacturonic acid and rhamnose present (Table 2). This indicated that the A2 and A6 polysaccharide fragments were possibly a xyloglucan. The A1 fraction contained a significant amount of galacturonic acid, but the low levels of rhamnose detected indicated that little rhamnogalacturonan was present. Therefore, A1 contained homogalacturonan-rich pectin and other polysaccharides released from the pectinase treatment of cranberry hulls.

Series of oligosaccharide peaks were present in A2 and A6 cranberry fraction HPAEC-PAD chromatograms that were consistent with the retention times of xyloglucan standard oligosaccharides (Figure 1). However, the structure of the Megazyme standard xyloglucan oligosaccharides was galacto-xyloglucan. For example, the DP 7 xyloglucan oligosaccharide consisted of a cellotetraose backbone and three single xylose substituents attached to three of the glucose residues. The DP 8 and DP 9 xyloglucan standards had one or two of the xylose residues substituted with a galactose residue, respectively. This xyloglucan structure is typical of fucogalacto-xyloglucan without fucose. However, relatively low amounts of galactose were detected in the A2 and A6 monosaccharide composition, which indicated that the cranberry xyloglucan structure might differ from fucogalacto-xyloglucan.

Mass Spectrometry. MALDI-TOF mass spectrometry of the A6 fraction produced a series of $[M + Na]^+$ ions (Figure 2) that were consistent with xyloglucan structure (Table 3). No $[M + Na]^+$ ions were observed corresponding to PACs.[9] The ions at m/z 1085, 1217, 1379, and 1525 were reported for argan tree (Sapotaceae) xyloglucan with Hex_4Pent_3, Hex_4Pent_4, Hex_5Pent_4, and Hex_5Pent_4dHex compositions, respectively, and described as fucogalacto-xyloglucan structure.[17] Ions at m/z 791 and 923 were previously reported in tobacco suspension culture xyloglucan with SGG and/or XXG and SXG and/or XSG structure, respectively.[15] The very abundant m/z 1217 ion in cranberry A6 (Figure 2) was previously reported to have XXSG structure in oleander and olive fruit xyloglucan.[16,18]

DOI: 10.1021/acs.jafc.5b00730
J. Agric. Food Chem. 2015, 63, 5622−5633

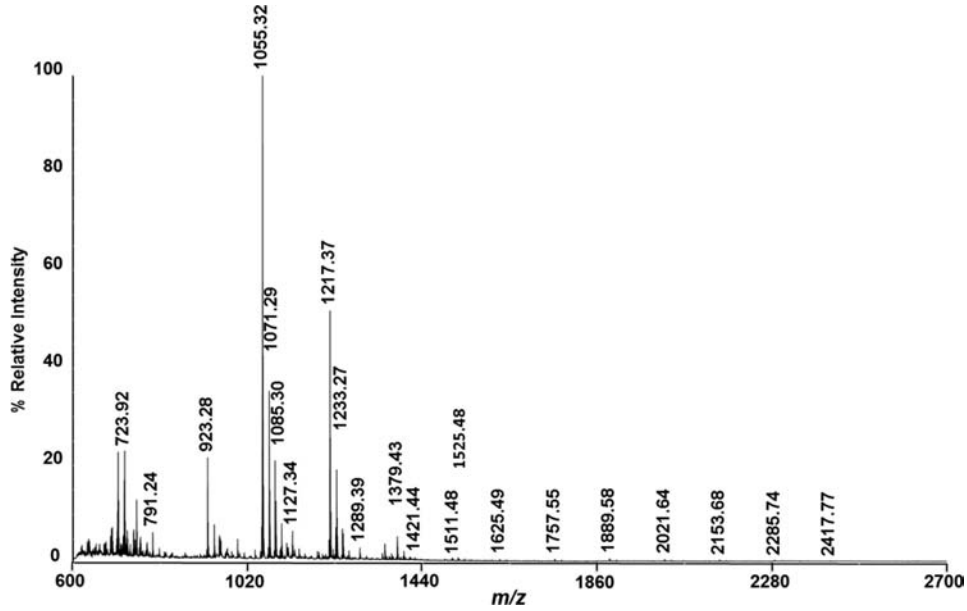

Figure 2. MALDI-TOF MS of fraction A6.

Table 3. MALDI-TOF Mass Spectrometry of A6[a]

$[M + Na]^+$	composition	assigned structure	$[M + Na]^+$	composition	assigned structure
791.24	Hex_3Pent_2	SGG, XXG	1421.44	Hex_5Pent_4-Ac	GSSGG-Ac
821.26	Hex_4Pent	XGGG	1493.47	$Hex_2Pent_6dHexHexAMe$	
833.25	$Hex_2PentdHexHexAMe$		1511.48	Hex_5Pent_5	SSXGG
923.28	Hex_3Pent_3	SXG, XSG	1525.48	Hex_5Pent_4dHex	XUFG
953.30	Hex_4Pent_2	SGGG	1625.49	$Hex_2Pent_7dHexHexAMe$	
965.29	$Hex_2Pent_2dHexHexAMe$		1757.55	$Hex_2Pent_8dHexHexAMe$	
1055.32	Hex_3Pent_4	SSG, GSS	1889.58	$Hex_2Pent_9dHexHexAMe$	
1085.33	Hex_4Pent_3	GSXG	2021.64	$Hex_2Pent_{10}dHexHexAMe$	
1097.34	$Hex_2Pent_3dHexHexAMe$		2153.68	$Hex_2Pent_{11}dHexHexAMe$	
1127.34	Hex_4Pent_3-Ac	XSGG-Ac	2285.74	$Hex_2Pent_{12}dHexHexAMe$	
1217.37	Hex_4Pent_4	SSGG	2417.77	$Hex_2Pent_{13}dHexHexAMe$	
1229.38	$Hex_2Pent_4dHexHexAMe$				
1259.36	Hex_4Pent_4-Ac	SSGG-Ac			
1289.39	Hex_5Pent_3-Ac	XSGGG-Ac			
1331.37	Hex_5Pent_3-Ac_2	XSGGG-Ac_2			
1379.43	Hex_5Pent_4	SSGGG			

[a]Hex, hexose; Pent, pentose; dHex, deoxyhexose (rhamnose or fucose); Ac, *O*-acetyl; G, β-D-glucose; X, β-D-glucose with a terminal α-D-xylose substituent at the O-6 position; S, β-D-glucose with α-L-Ara*f*-(1−2)-α-D-Xyl*p* at the O-6 position; L, β-D-glucose with β-D-Gal*p*-(1−2)-α-D-Xyl*p* at the O-6 position; F, β-D-glucose with α-L-Fuc*p*-(1−2)-β-D-Gal*p*-(1−2)-α-D-Xyl*p* at the O-6 position; U, β-D-glucose with β-D-Xyl*p*-(1−2)-Xyl*p* with the O-6 position.

However, the diagnostic XXSG MS/MS fragments[16] were not present in the cranberry MALDI-TOF/TOF MS/MS spectrum for the *m*/*z* 1217.37 ion shown in Figure 3B. Therefore, the SSGG xyloglucan structure appeared to be the predominant cranberry xyloglucan structure as was reported for *m*/*z* 1217 in tobacco.[15] Ions at *m*/*z* 1127, 1259, 1289, 1331, and 1421 ions were previously reported as acetylated xyloglucan oligosaccharides in tobacco.[15] The *m*/*z* 1289 and 1331 ions were assigned previously as XLXG and/or XXLG and UXGGG and/or XUGGG structure, respectively.[15] However, in cranberry xyloglucan, these ions are more likely to represent an alternative structure due to the relatively low amount of galactose present in the monosaccharide composition. Therefore, XSGGG-Ac and XSGGG-Ac_2 cranberry xyloglucan structures appear to be more appropriate. The $Hex_4Pent_ndHexHexA_2Me_3$ xyloglucan composition series has never been reported before, but these structures are similar to the *m*/*z* 1525 XUFG structure reported for the argan tree (Ericales) xyloglucan and the xylan oligosaccharides containing two 4-*O*-methylglucuronic acids from the same source.[17] Another very abundant cranberry ion, *m*/*z* 1055, also has never been reported previously for a xyloglucan structure and was used for further MS/MS structural elucidation. The cranberry *m*/*z* 1055 and 1217 ions also were detected as their potassiated forms ($[M + K]^+$) at *m*/*z* 1071 and 1233, respectively. The most abundant cranberry MALDI-TOF MS ions were *m*/*z* 1055, 1085, and 1217 depending on batch-to-batch variation in A6.

The MS/MS spectra of oligosaccharides by MALDI-TOF/TOF produced a set of ions that provides the essential information for carbohydrate structural characterization.[28] The MS/MS spectrum represents two types of ions corresponding to cross-ring fragmentation between two bonds on the same

DOI: 10.1021/acs.jafc.5b00730
J. Agric. Food Chem. 2015, 63, 5622−5633

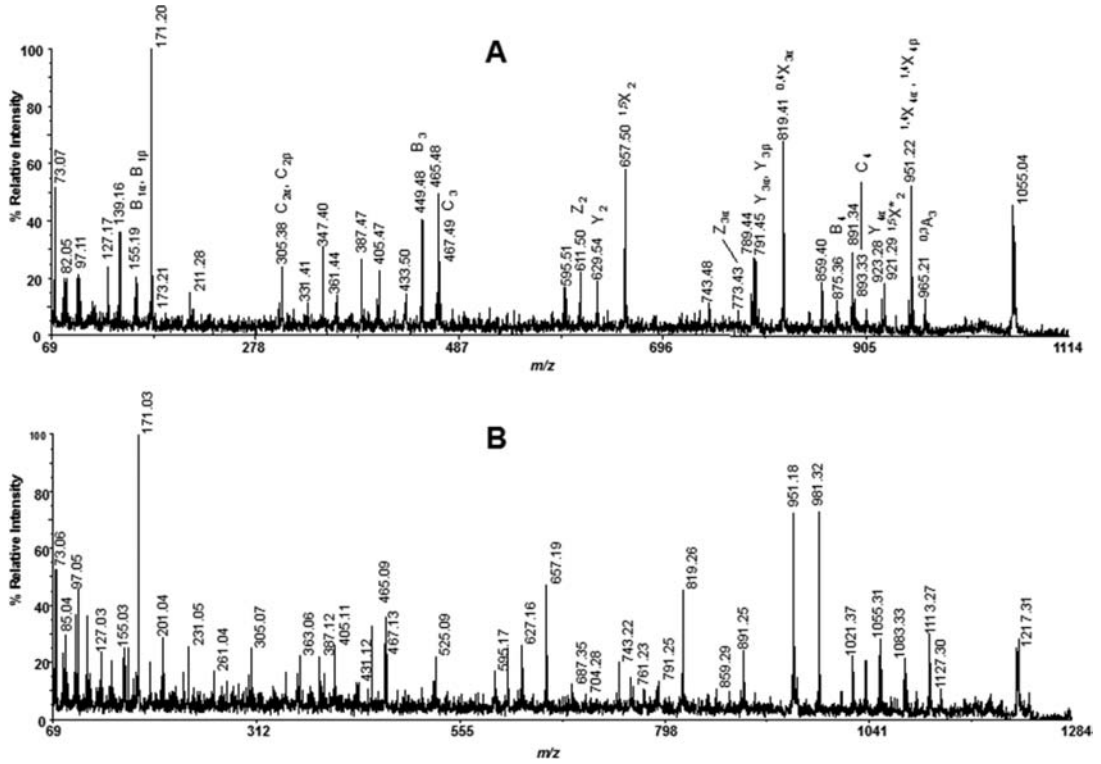

Figure 3. MALDI-TOF/TOF MS/MS of (A) m/z 1055.32 and (B) m/z 1217.37.

sugar residue and glycosidic bond cleavage between two sugar residues. When the charge of the resulting fragment is located toward the reducing end of the oligosaccharide, then the ions are designated as X ions for cross-ring fragmentation and as Y and Z ions for the glycosidic bond fragments. If the charge is located at the nonreducing end, then the ions are designated as A for cross-ring fragmentation and B and C for the glycosidic bond fragments. The fragmented bond site is indicated with the corresponding letter, a subscript number, and a Greek letter to designate the branched chain involved. Superscript numbers preceding the ions X or A indicate the cleaved bonds in the sugar ring.

The MS/MS spectrum in Figure 3A corresponds to the sodiated oligosaccharide, $[M + Na]^+$, with m/z 1055.32 (Figure 2). This precursor ion is consistent with an oligosaccharide structure formed by four pentoses and three hexoses. The ion at m/z 305.3 in the MS/MS spectrum (Figure 3A) suggests that two pentoses are present as a side chain, labeled as fragments $C_{2\alpha}$ and $C_{2\beta}$ in structure 1 (Figure 4). No ion corresponding to a side antenna with one, three, or four pentoses is observed in the spectrum. The ion at m/z 893 indicates the loss of a hexose from the precursor ion (1055−162) (cleavage C_4) (Figure 4). This suggests that one of the hexoses is not linked to a side chain. The spectrum is not dominated by Y or B ions but with ions that are consistent with cross-ring fragmentation as indicated in structure 1. As the spectrum shows, the cross-ring cleavage (loss 104 Da) at the pentose-end produces the ion at 951 ($^{1,4}X_{4\alpha}$ or $^{1,4}X_{3\beta}$ fragment) that further loses a pentose to generate the ion at 819 and a hexose to generate the ion at m/z 657. However, these two ions can also correspond to the $^{1,5}X_{3\alpha}$ and $^{1,2}X_2$ fragments, respectively. Some of the ions are generated from subsequent fragmentation of the 951 fragment, such as the ion at m/z 891 (951 − 60). The significant ion at m/z 465 could also be explained by subsequent cleavages of the ion at 951 after losing one hexose, two pentoses, and a cross-ring fragment (951 − 162 − 132 − 132 − 60 = 465). Therefore, several ions in Figure 3A could be produced by multiple fragmentation patterns. Further analysis of the fragmentation pattern suggests that the isobaric structure 2 (Figure 4) is also present. The evidence supporting structure 2 is found in the ion at m/z 921, which corresponds to the cross-ring cleavage $^{1,5}X^*_2$ of the hexose at the nonreducing terminus. Therefore, both SSG and GSS structures were present and assigned (Table 3). The spectrum in Figure 3B is consistent with the structures in Figure 4 but with an extra hexose. The cross-ring cleavage of the end terminus pentose produces the ion at m/z 1113 (1217 − 104), but also the loss of a hexose from the precursor ion, generates the ion at m/z 1055, and that fragment is consistent with the spectrum and structures in Figure 3A.

Nuclear Magnetic Resonance Spectroscopy. NMR analysis of the anomeric region in the 1D-^{1}H spectrum (Figure 5) reveals that the resonances near 4.5 ppm have H1−H2 coupling constants of $J_{H1-H2} \sim 7-9$ Hz, indicating that the H1 and H2 are in axial−axial orientation. Therefore, they were assigned as β-D-Glc and β-D-Gal. The resonances at 4.94, 5.24, 5.21, 5.15, 5.31, and 5.28 ppm have $J_{H1-H2} \sim 3.8-4.7$ Hz and denote that H1 and H2 have an axial−equatorial orientation. Likewise, the peak at 5.08 ppm has a shoulder that is also 3.5 Hz from the main peak. These chemical shifts and coupling constants are characteristic of pyranoses, such as rhamnose, fucose, and xylose. Several peaks in the region of ∼5.1−5.2 ppm have very small or indiscernible coupling in the 1D-^{1}H spectra. These attributes support an assignment of α-L-Ara$f$, and there is no evidence for β-L-Ara$f$ in the sample. Furanoses such as these undergo rapid repuckering of their rings, resulting in an averaging of the coupling constants. The absence of aromatic resonances in the 1D-^{1}H NMR spectra supported the absence

DOI: 10.1021/acs.jafc.5b00730
J. Agric. Food Chem. 2015, 63, 5622−5633

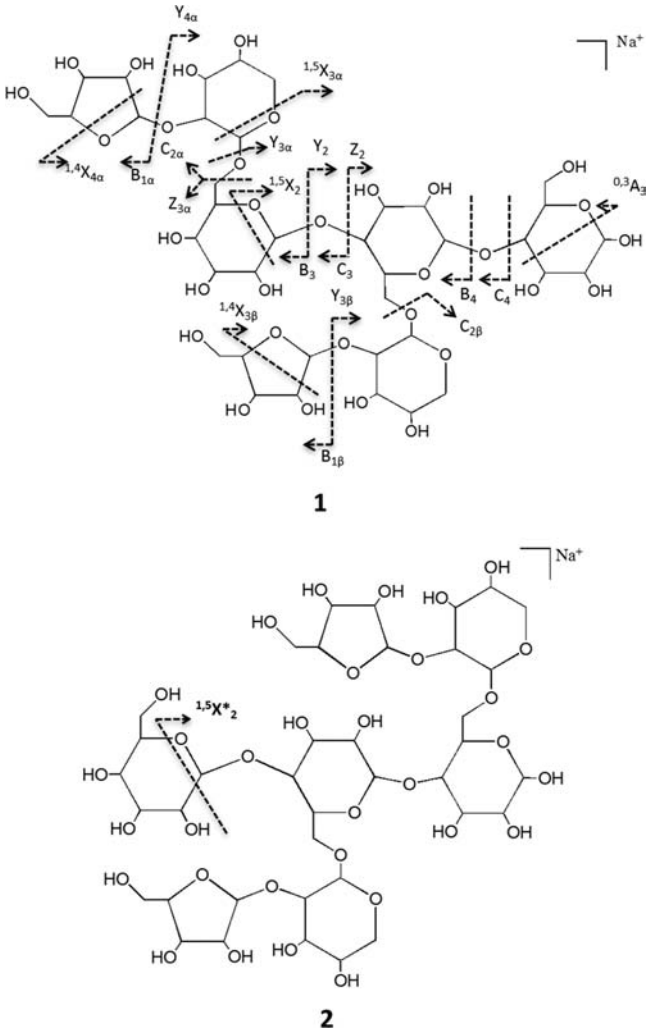

Figure 4. Xyloglucan structure (1) based on MALDI-TOF/TOF MS/MS of m/z 1055.32. An alternate structure (2) is also consistent with MALDI-TOF/TOF MS/MS xyloglucan fragmentation.

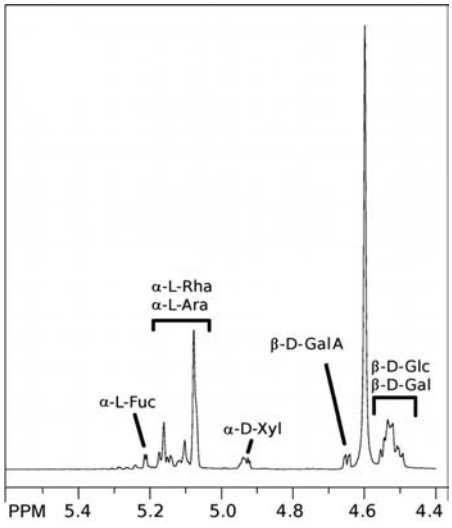

Figure 5. Anomeric region of 1D ^{1}H NMR spectrum of fraction A6.

of PACs and other phenolic compounds in cranberry fraction A6.

Analysis of the 2D HSQC (Figure 6) confirms β-Glc, α-Xyl*p*, and α-Ara*f* are present, as well as other residues expected from

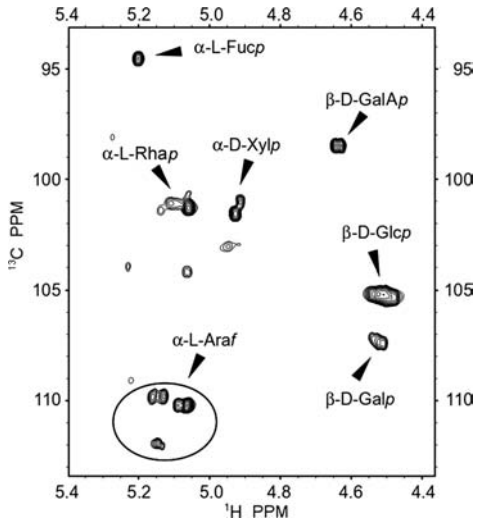

Figure 6. NMR HSQC of anomeric region showing primary assignments.

the monosaccharide composition and 1D-^{1}H spectrum. The HSQC reveals that the proton resonances at 4.48−4.57 ppm are separated into two main clusters on the basis of their ^{13}C resonances. One is centered at a ^{13}C frequency of ∼105 ppm and corresponds to β-D-Glc*p*, whereas the other cluster is at ∼107 ppm and corresponds to β-D-Gal*p*. Such β-D-Glc*p* resonances are commonly found in S and G structures in SG or GS environments.[29] Whereas the β-D-Gal*p* resonance can be found in xyloglucan F and L structures,[29] it is also present in rhamnogalacturonan pectin, and this monosaccharide is less abundant in the cranberry fractions. Therefore, it is unclear what structure includes the galactose in cranberry A6.

The HMBC and long-range HSQC experiments provide evidence for α-D-Xyl*p* -C1 → β-D-Glc*p*-H6 correlations, confirming xyloglucan structure. In addition, there are two sets of through-bond α-L-Ara*f*-C1→ α-D-Xyl*p*-H2 correlations, which are consistent with S-type structures (Figure 7). One of these xylose residues also has an HMBC correlation to a glucose H6 and thus proves an entire S-type structure of α-L-Ara*f* (1→2) α-D-Xyl*p* (1→6) β-D-Glc*p*. The fact that there are two sets of α-L-Ara*f* (1→2) α-D-Xyl*p* correlations suggests that the S structures are in slightly different environments, as would be expected from GSS and SSG sequences. Although additional arabinose and xylose residues were observed in the NMR spectra, their sequential connectivity could not be determined due to spectral congestion and overlapping resonances.

There is also evidence of acetylation of some of the sugars in the fraction. Analysis of the HSQC, HMBC, long-range HSQC, and HMQC-TOCSY experiments revealed the presence of methyl groups (∼2.2 ppm in ^{1}H and ∼20 ppm in ^{13}C) that have HMBC correlations to carbonyl carbons (∼175 ppm), and these in turn have correlations for the H2 resonances (∼4.3 ppm) of several α-L-Ara*f* residues. Whereas each sample batch demonstrated acetylation correlations, we noted that there was batch-to-batch variation in the specific arabinose residue involved in these correlations. However, acetylation was never observed for those arabinose residues identified as being in the S-type xyloglucan structure.

DOI: 10.1021/acs.jafc.5b00730
J. Agric. Food Chem. 2015, 63, 5622−5633

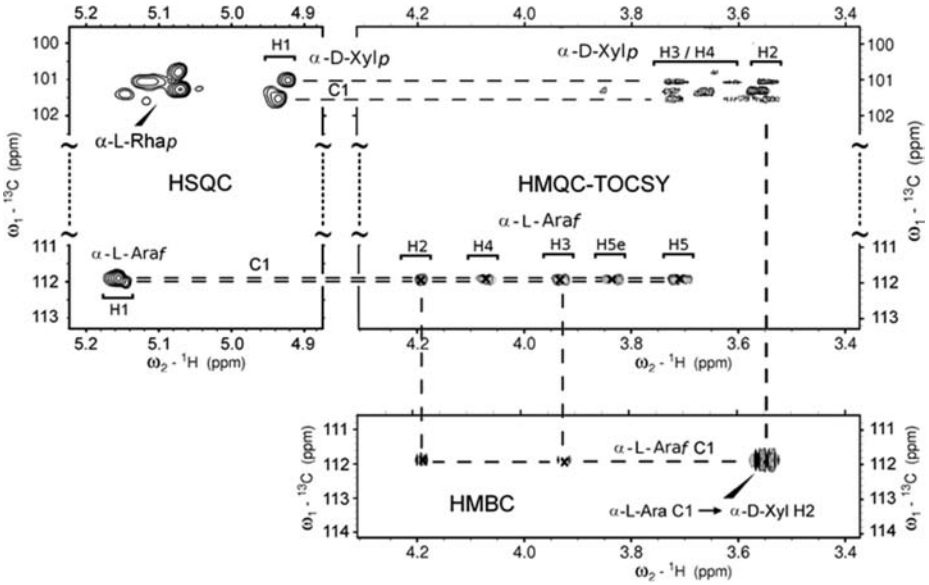

Figure 7. Correlations between α-L-Araf-C1→ α-D-Xylp-H2 were observed consistent with S structures.

The NMR data also indicate the presence of secondary components consisting of β-D-GalpA, α-L-Rhap, and α-L-Fucp in addition to the β-D-Galp discussed above. The β-D-GalpA is indicated by through-bond correlations in the HMBC spectrum between the C6 in the carboxylic acid group and the H5 in its sugar ring. The presence of α-L-Fucp is indicated by H6 methyl resonances (1.26 ppm) that have TOCSY correlations to H5 protons on the directly attached sugar rings (3.44−4.74 ppm and have J_{H5-H6} = 6−7 Hz). These α-L-Fuc correlations can be followed in the HMBC, long-range HSQC, and HMQC-TOCSY experiments from the methyl resonances to corresponding anomeric resonances (data not shown). Additional methyl resonances exist (1.10−1.20 ppm), which are consistent with α-L-Rhap. Spectral congestion does not allow through-bond correlations of these α-L-Rhap methyl protons to their anomeric resonances. Therefore, the α-L-Rhap assignment is likely but cannot be verified due to the lack of through-bond correlations.

The anomeric proton orientations (α or β) were confirmed by means of their C−H coupling constants, J_{C1-H1}, as derived from the C−H coupled HSQC and HMBC experiments. This determination helps to confirm resonance assignments and utilizes the fact that axially oriented H-1 has J_{C1-H1} ∼ 160 Hz and those with an equatorial H-1 have values ∼170 Hz.[28] A summary of the anomeric chemical shifts, their assignments, and likely substructures can be found in Table 4 and are annotated in Figure 6. These assignments are based on coupling constants and through-bond correlations and are consistent with literature values of both the ^{1}H and ^{13}C chemical shifts.[16,18,30−35] The same xyloglucan oligosaccharides with SSGG structure (*m*/*z* 1217 most abundant ion) were also detected in commercial cranberry juice with the MALDI-TOF MS ion intensity directly proportional to the amount of cranberry juice present (data not shown). No xyloglucan oligosaccharides were detected in commercial apple, grape, or pomegranate juices using the same graphitized carbon extraction method detailed above for cranberry fractions.

Anti-adhesive Activity of Cranberry Fractions. The anti-adhesive activity of cranberry xyloglucan-rich fractions was determined by bacterial adhesion to epithelial cell assays using both uropathogenic and enterohemorrhagic *E. coli* strains to identify binding to type 1 (UTI89) or p- (CFT073) fimbriae and those produced by enterohemorrhagic *E. coli* (O157:H7). Fimbriae are important bacterial virulence factors required for binding to epithelial cells in the urinary tract; type 1 fimbriae are typically associated with cystitis and p-fimbriae with pyelonephritis infections. Specific binding of p-fimbriated *E. coli* to uroepithelial cells decreased with increasing concentrations (0−5 mg/mL) of cranberry extract A6 in a dose-dependent manner (Figure 8). The half-maximal inhibitory concentration of A6 was 0.82 mg/mL. As previously reported by Kimble et al.,[25] a cranberry polyphenol extract enriched in anthocyanidins, polyphenolic acids, flavonols, and PACs was used as a positive control in the p-fimbriated *E. coli* assay and exhibited a specific binding reduction between 0 and 1.25 mg/mL with a half-maximal inhibitory concentration of 0.12 mg/mL. Therefore, the oligosaccharide enriched extract A6 showed 6.8 times lower binding affinity to the p-fimbriated *E. coli* compared to the cranberry polyphenolic enriched standard. Cranberry extract A1 showed a slightly higher inhibitory effect compared to A6 (0−30 mg/mL A1) with a half-maximal inhibitory concentration of 0.64 mg/mL (data not shown), possibly due to the presence of phenolic compounds, especially PACs in extract A1.

A concentration-dependent (0−5 mg/mL A6) reduction of binding was also observed in the type 1 *E. coli* assay (Figure 9). The half-maximal inhibitory concentration of A6 was 0.66 mg/mL. These results are comparable to the half-maximal inhibitory concentration of α-D-mannose (0.9 mg/mL) standard, a natural ligand for type 1 fimbriae. Cranberry A1 exhibited a half-maximal inhibitory concentration of 4.3 mg/mL and therefore was less effective at preventing bacterial adhesion compared to A6 for type 1 fimbriated *E. coli*. The cranberry extract A1 was enriched in pectic oligosaccharides and contained polyphenolic compounds compared to the xyloglucan oligosaccharide-enriched A6 fraction. Thus, the higher levels of xyloglucan oligosaccharides correlated with the higher anti-adhesion activity for type 1 fimbriated *E. coli*. From these results, purified cranberry A6 xyloglucan oligosaccharides have

DOI: 10.1021/acs.jafc.5b00730
J. Agric. Food Chem. 2015, 63, 5622−5633

Table 4. Chemical Shift Assignments (Parts per Million) of Identified Sugar Resonances

residue	C1	C2	C	C4	C5	C6	C6(Me)	C=O	C(Acyl-Me)	H1	H2	H3	H4	H5	H5e	H6	H6e	H6(Me)	H(Acyl-Me)	possible structure	possible structure environment
a-L-Fuc*p*	94.53	74.00	74.75		72.73		19.34			5.21	3.58	3.84	3.85	3.94				1.29			
α-D-Gal*p*	98.10									5.28	3.76	3.84	3.94	4.08							
β-D-Gal*p*	107.40	78.37								4.53	3.68		3.94	3.60			3.80				
β-D-Gal*p*	107.30									4.53	3.66	3.83	3.94	3.64			3.80				
β-D-Gal*p*	107.20									4.54	3.40			3.61							
β-D-Gal*p*	107.10									4.53	3.66	3.67	3.93	3.65		3.91	3.92				
β-D-Gal*p*A	97.7	77.05				62.77		173.7		4.65	3.28	3.62	3.94	3.81							
β-D-Glc*p*	105.10	75.49								4.53	3.40		3.68							**G**, **S**, or **X**	
β-D-Glc*p*	105.00	75.54								4.52	3.38		3.65								
β-D-Glc*p*	105.20	75.48								4.51	3.35	3.50	3.67	3.83		3.93	3.93				
β-D-Glc*p*	105.40	75.78								4.51	3.32										
α-L-Ara*f*	110.23	85.21	79.48		69.58			174.13	19.51	5.07	4.12	4.00	4.20	3.79	3.88				2.07		
α-L-Ara*f*	110.20									5.07	4.12	4.03	3.95	3.71	3.89						
α-L-Ara*f*	110.20	81.95			69.53			176.70	23.03	5.10	4.27	3.92	4.10	3.72	3.82				2.12		
α-L-Ara*f*	109.90	86.51		86.68						5.14	4.11	3.97	4.13	3.72							
α-L-Ara*f*	109.80	82.43	86.25	85.28				176.70	22.90	5.17	4.35	3.96	4.14	3.73	3.82				2.20		
α-L-Ara*f*	111.91	83.85		86.52						5.16	4.19	3.93	4.07	3.71	3.83					**S**	X**S**G, G**S**G, S**S**G,G**S**S
α-L-Ara*f*	111.92									5.19	4.19	3.92	4.08	3.71	3.8						
α-L-Rha*p*	101.20	74.62/74.70[a]						5.11	3.61				3.87								
α-L-Rha*p*	101.07									5.13	3.68			3.53							
α-L-Rha*p*	100.80	74.64/72.21[a]						5.07	3.58	3.77	3.72	3.66	3.70								
α-L-Rha*p*	101.60									5.12	3.83										
α-D-Xyl*p*	101.56	77.88	75.80							4.94	3.53	3.71	3.72	3.58	3.70					**S** or **X**	**GSS**, **SSG**
α-D-Xyl*p*	101.10	81.47	75.75		64.49					4.93	3.54	3.69	3.66	3.70	3.86						
α-D-Xyl*p*	101.40	83.06	72.24							4.95	3.58	3.65	3.72	3.56	3.88						

[a]Two resonances were observed, but assignment as C2, C3, and/or C4 could not be determined.

DOI: 10.1021/acs.jafc.5b00730
J. Agric. Food Chem. 2015, 63, 5622−5633

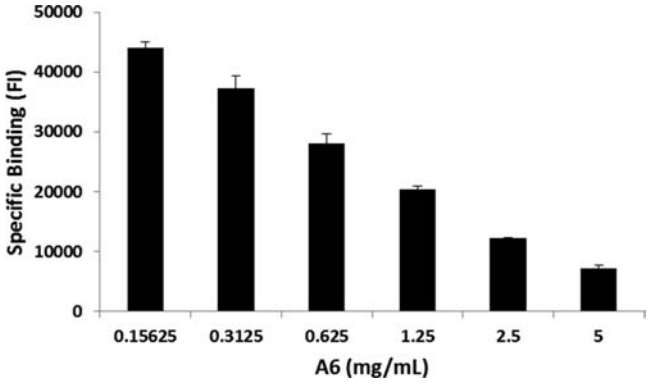

Figure 8. Adhesion of *E. coli* CFT073 to uroepithelial T24 cells in the presence of cranberry A6 fraction.

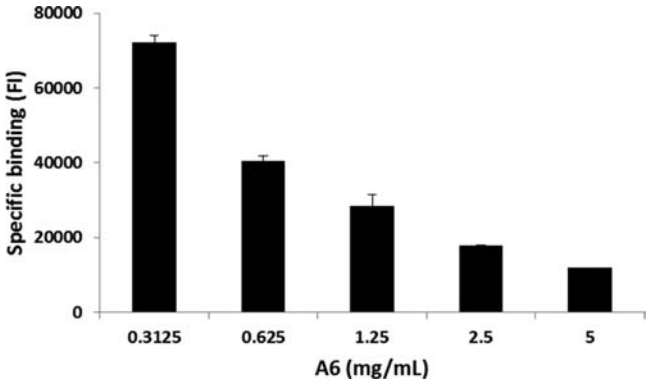

Figure 9. Adhesion of *E. coli* UTI89 to T24 cells in the presence of cranberry A6 fraction.

a higher binding affinity toward type 1 fimbriated *E. coli* compared to p-fimbriated strains.

A non-dose-dependent response was observed for the anti-adhesive activity of A6 in the bacterial adhesion assay reported earlier.[11] The adhesion of *E.coli* O157:H7 to human colonic epithelial HT29 cells was blocked by A6 at low concentrations (0.001−0.1 mg/mL) relative to the unsupplemented PBS control (Figure 10). At higher concentrations, the cranberry A6 fraction was not able to inhibit *E. coli* O157:H7 adhesion to HT29 cells. Enterohemorrhagic *E. coli* produces several adhesive structures including the *E. coli* common pilus and type IV pilli.[36,37] Prebiotic oligosaccharides (galacto-oligosaccharides and pectic-oligosaccharides) were also reported to have dose-dependent anti-adhesive properties against enterohemorrhagic and enteropathogenic *E. coli* strains.[11,38] P-fimbriated *E. coli* and verocytotoxins produced by enterohemorrhagic strains of *E. coli* utilize the same α-Gal-(1−4)-β-Gal terminal oligosaccharide receptor for adhesion to epithelial cells, whereas type 1 fimbriae utilize a α-Man-(1−2)-Man receptor.[39] It is unlikely that xyloglucan, pectic-, and galacto-oligosaccharides prevent *E. coli* adhesion through receptor mimicry because α-Man-(1−2)-Man or α-Gal-(1−4)-β-Gal have not been detected in cranberry or citrus fractions or prebiotic products. However, these data indicate that cranberry xyloglucan oligosaccharides have a higher affinity for type 1 fimbriae, whereas pectic- and galacto-oligosaccharides have higher affinity for p-fimbriae and those produced by enterohemorrhagic and enteropathogenic *E. coli* strains.

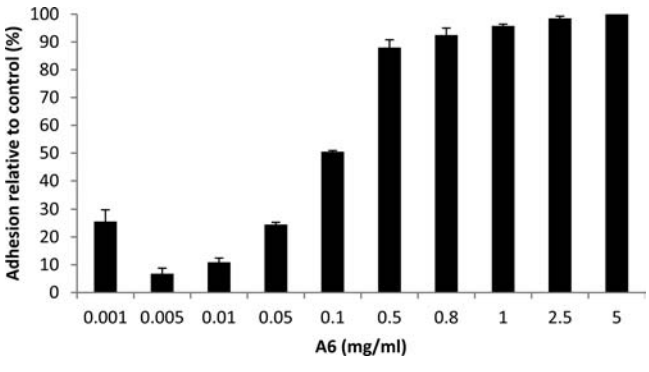

Figure 10. Adhesion of *E. coli* O157:H7 to HT29 cells in the presence of cranberry A6 fraction.

In conclusion, the cranberry xyloglucan structure was characterized for the first time as an arabino-xyloglucan with SSGG structure. This is the first member of the Ericales with this type of xyloglucan structure, but only the second plant in the order to have the xyloglucan characterized. A new xyloglucan heptasaccharide from cranberry was characterized by MALDI-TOF/TOF MS/MS and NMR with SSG and GSS oligosaccharide structure. NMR data, including through-bond correlations, coupling constants, and chemical shift values, enabled the assignment of α and β linkages and the sugar residues and confirmed the structural sequence. NMR provided direct through-bond correlation evidence for α-L-Ara*f* (1→2) α-D-Xyl*p* linkages and α-D-Xyl*p* (1→6) β-D-Glc*p* linkages, as found in xyloglucans with S-type structures. There appear to be two cranberry xyloglucan S structures with slightly different physical environments, which can be attributed to SSG and GSS sequences. The cranberry A6 fraction that included SSGG-type xyloglucan oligosaccharides prevented adhesion of both p-fimbriated and type 1 uropathogenic *E. coli* strains to human uroepithelial cells and veritoxigenic *E. coli* to colonic epithelial cells in vitro using three independent assays. In addition to proanthocyanidins, SSGG-type xyloglucan oligosaccharides are new bioactive cranberry juice ingredients with potential to control urinary tract infections. However, more research is needed to determine the exact mechanism of xyloglucan oligosaccharide anti-adhesion activity against pathogenic *E. coli*.

■ ASSOCIATED CONTENT

Supporting Information

SI 1, molar mass, intrinsic viscosity, and hydrodynamic radius of cranberry fractions; SI 2, NMR data for α-D-Xyl*p* -C1 → β-D-Glc*p*-H6 correlations; SI 3, 2D NMR data for acetylation of Ara*f* residues; SI 4, 2D NMR data for GalA*p* residues. The Supporting Information is available free of charge on the ACS Publications website at DOI: 10.1021/acs.jafc.5b00730.

■ AUTHOR INFORMATION

Corresponding Author

*(A.T.H.) E-mail: arland.hotchkiss@ars.usda.gov. Phone: (215) 233-6448. Fax: (215) 233-6795.

Funding

This work was supported by a Cooperative Research and Development Agreement with Ocean Spray Cranberries, Inc. (58-3K95-1-1503). Mention of brand or firm name does not constitute an endorsement of the U.S. Department of Agriculture above others of a similar nature not mentioned.

Notes

The authors declare no competing financial interest.

DOI: 10.1021/acs.jafc.5b00730
J. Agric. Food Chem. 2015, 63, 5622−5633

■ ACKNOWLEDGMENTS

We acknowledge helpful discussions with Drs. Darón Freedberg (FDA), Eugene Mazzola (FDA), and Bruce Coxon (The Eunice Kennedy Shriver National Institute of Child Health and Human Development, NIH) for interpretation of NMR data.

■ REFERENCES

(1) Zopf, D.; Roth, S. Oligosaccharide anti-infective agents. *Lancet* **1996**, *347*, 1017−1021.

(2) Holmes, A.; Starr, M. Cranberry juice. In *Fruit Juice Processing Technology*; Nagy, S., Chen, C. S., Shaw, P. E., Eds.; AGSCIENCE: Auburndale, FL, USA, 1993; pp 515−531.

(3) Clifford, M.; Gibson, G.; Hu, H.; Rodig-Penman, A. Prebiotic use of fruits and fruit juices in the promotion of beneficial gut microflora. U.S. Patent Application D.N. 20090022849, Jan 22, 2009.

(4) Ofek, I.; Goldhar, J.; Zafriri, D.; Lis, H.; Adar, R.; Sharon, N. Anti-*Escherichia coli* adhesin activity of cranberry and blueberry juices. *N. Engl. J. Med.* **1991**, *324*, 1599.

(5) Ofek I.; Goldhar, J.; Sharon, N. Anti-*Escherichia coli* adhesin activity of cranberry and blueberry juices. In *Toward Anti-Adhesion Therapy for Microbial Diseases, Advances in Experimental Medicine and Biology*; Kahane, I., Ofek, I., Eds.; 1996; Vol. 408, pp 179−183.

(6) Lavigne, J.-P.; Bourg, G.; Combescure, C.; Botto, H.; Sotto, A. In-vitro and in-vivo evidence of dose-dependent decrease of uropathogenic Escherichia coli virulence after consumption of commercial *Vaccinium macrocarpon* (cranberry) capsules. *Clin. Microbiol. Infect.* **2008**, *14*, 350−355.

(7) Urpi-Sarda, M.; Monagas, M.; Khan, N.; Lamuela-Raventos, R. M.; Santos-Buelga, C.; Sacanella, E.; Castell, M.; Permanyer, J.; Andres-Lacueva, C. Epicatechin, procyanidins, and phenolic microbial metabolites after cocoa intake in humans and rats. *Anal. Bioanal. Chem.* **2009**, *394*, 1545−1556.

(8) Yan, X.; Murphy, B. T.; Hammond, G. B.; Vinson, J. A.; Neto, C. C. Antioxidant activities and antitumor screening of extracts from cranberry fruit (*Vaccinium macrocarpon*). *J. Agric. Food Chem.* **2002**, *50*, 5844−5849.

(9) Howell, A. B.; Reed, J. D.; Krueger, C. G.; Winterbottom, R.; Cunningham, D. G.; Leahy, M. A-type cranberry proanthocyanidins and uropathogenic bacterial anti-adhesion activity. *Phytochemistry* **2005**, *66*, 2281−2291.

(10) Minatelli, J. A.; Hill, W. S. Method of preventing, controlling and ameliorating urinary tract infections using a synergistic cranberry derivative and D-mannose composition. U.S. Patent Application D.N. 20090226548 A1, Sept 10, 2009.

(11) Rhoades, J.; Manderson, K.; Wells, A.; Hotchkiss, A. T.; Gibson, G. R.; Formentin, K.; Beer, M.; Rastall, R. A. Oligosaccharide-mediated inhibition of the adhesion of pathogenic *Escherichia coli* strains to human gut epithelial cells in vitro. *J. Food Prot.* **2008**, *71*, 2272−2277.

(12) Holmes, A. B.; Rha, C. Structure and chemical composition of cranberry cell wall material. *J. Food Sci.* **1978**, *43*, 112−120.

(13) Carpita, N. C.; Gibeaut, D. M. Structural models of primary cell wall in flowering plants: consistency of molecular structure with the physical properties of the walls during growth. *Plant J.* **1993**, *3*, 1−30.

(14) Carpita, N.; McCann, M. The cell wall. In *Biochemistry and Molecular Biology of Plants*; Buchanan, B. B., Gruissem, W., Jones, R. L., Eds.; American Society of Plant Physiologists: Rockville, MD, USA, 2000; pp 52−108.

(15) Sims, I. M.; Munro, S. L. A.; Currie, G.; Craik, D.; Bacic, A. Structural characterization of xyloglucan secreted by suspension-cultured cells of *Nicotiana plumbaginifolia*. *Carbohydr. Res.* **1996**, *293*, 147−172.

(16) Vierhuis, E.; York, W. S.; Kolli, V. S. K.; Vincken, J.-P.; Schols, H. A.; Van Albeek, G.-J.W.M.; Voragen, A. G. J. Structural analyses of two arabinose containing oligosaccharides derived from olive fruit xyloglucan: XXSG and XLSG. *Carbohydr. Res.* **2001**, *332*, 285−297.

(17) Ray, B.; Loutelier-Bourhis, C.; Lange, C.; Condamine, E.; Driouich, A.; Lerouge, P. Structural investigation of hemicellulosic polysaccharides from *Argania spinosa*: characterization of a novel xyloglucan motif. *Carbohydr. Res.* **2004**, *339*, 201−208.

(18) Hoffman, M.; Jia, Z.; Pena, M. J.; Cash, M.; Harper, A.; Blackburn, A. R.; Darvill, A.; York, W. S. Structural analysis of xyloglucans in the primary cell walls of plants in the subclass Asteridae. *Carbohydr. Res.* **2005**, *340*, 1826−1840.

(19) Fry, S. C.; York, W. S.; Albersheim, P.; Darvill, A. G.; Hayashi, T.; Joseleau, J.-P.; Kato, Y.; Lorences, E. P.; Maclachlan, G. A.; McNeil, M.; Mort, A. J.; Reid, J. S. G.; Seitz, H. U.; Selvendran, R. R.; Voragen, A. G. J.; White, A. R. An unambiguous nomenclature for xyloglucan-derived oligosaccharides. *Physiol. Plant.* **1993**, *89*, 1−3.

(20) Fishman, M. L.; Chau, H. K.; Cooke, P. H.; Hotchkiss, A. T. Global structure of microwave-assisted flash-extracted sugar beet pectin. *J. Agric. Food Chem.* **2008**, *56*, 1471−1478.

(21) Zhao, Z. Y.; Liang, L.; Fan, X.; Yu, Z.; Hotchkiss, A. T.; Wilk, B. J.; Eliaz, I. The role of modified citrus pectin as an effective chelator of lead in children hospitalized with toxic lead levels. *Alternat. Ther.* **2008**, *14*, 34−38.

(22) Delaglio, F.; Grzesiek, S.; Vuister, G. W.; Zhu, G.; Pfeifer, J.; Bax, A. NMR Pipe: a multidimensional spectral processing system based on UNIX pipes. *J. Biomol. NMR* **1995**, *6*, 277−293.

(23) Goddard, T. D.; Kneller, D. G. SPARKY 3, University of California, San Francisco. http://www.cgl.ucsf.edu/home/sparky/ (accessed Oct 15, 2014).

(24) Shaka, A. J.; Lee, C. J.; Pines, A. Iterative schemes for bilinear operators; application to spin decoupling. *J. Magn. Reson.* **1988**, *77*, 274−293.

(25) Kimble, L. L.; Mathison, B. D.; Kaspar, K. L.; Khoo, C.; Chew, B. P. Development of a fluorometric microplate antiadhesion assay using uropathogenic *Escherichia coli* and human uroepithelial cells. *J. Nat. Prod.* **2014**, *77*, 1102−1110.

(26) Mulvey, M. A.; Schilling, J. D.; Hultgren, S. J. Establishment of a persistent *Escherichia coli* reservoir during the acute phase of a bladder infection. *Infect. Immun.* **2001**, *69*, 4572−4579.

(27) Martín, M. A.; Ramos, S.; Mateos, R.; Marais, J. P. J.; Bravo-Clemente, L.; Khoo, C.; Goya, L. Chemical characterization and chemo-protective activity of cranberry phenolic powders in a model cell culture. Response of the antioxidant defenses and regulation of signaling pathways. *Food Res. Int.* **2015**, *71*, 68−82.

(28) Mechref, Y.; Novotny, M. V. Structural characterization of oligosaccharides using MALDI-TOF/TOF tandem mass spectrometry. *Anal. Chem.* **2003**, *75*, 4895−4903.

(29) CCRC NMR Database. The Xyloglucan NMR Database, The Complex Carbohydrate Research Center and Department of Biochemistry and Molecular Biology, The University of Georgia, Athens GA, USA; http://www.ccrc.uga.edu/world/xgnmr/ (accessed Nov 12, 2014).

(30) Bock, K.; Lundt, I.; Pedersen, C. Assignment of anomeric structure to carbohydrates through geminal ^{13}C-H coupling constants. *Tetrahedron Lett.* **1973**, *13*, 1037−1040.

(31) Bock, K.; Pedersen, C. Carbon-13 nuclear magnetic resonance data of monosaccharides. *Adv. Carbohydr. Chem. Biochem.* **1983**, *41*, 27−66.

(32) Bock, K.; Pedersen, C.; Pedersen, H. Carbon-13 nuclear magnetic resonance data for oligosaccharides. *Adv. Carbohydr. Chem. Biochem.* **1984**, *42*, 193−225.

(33) Hanniffy, O. M.; Shashkov, A. S.; Moran, A. P.; Prendergast, M. M.; Senchenkova, S. N.; Knirel, Y. A.; Savage, A. V. Chemical structure of a polysaccharide from *Campylobacter jejuni* 176.83 (serotype O:41) containing only furanose sugars. *Carbohydr. Res.* **1999**, *319*, 124−132.

(34) Jansson, P. E.; Stenutz, R.; Widmalm, G. Sequence determination of oligosaccharides and regular polysaccharides using NMR spectroscopy and a novel Web-based version of the computer program casper. *Carbohydr. Res.* **2006**, *341*, 1003−1010.

(35) Mazzola, E. P.; Parkinson, A.; Kennelly, E. J.; Coxon, B.; Einbond, L. S.; Freedberg, D. I. Utility of coupled-HSQC experiments in the intact structural elucidation of three complex saponins from *Blighia sapida*. *Carbohydr. Res.* **2011**, *346*, 759−768.

DOI: 10.1021/acs.jafc.5b00730
J. Agric. Food Chem. 2015, 63, 5622−5633

(36) Rendon, M. A.; Saldana, Z.; Erdem, A. L.; Monteiro-Neto, V.; Vazquez, A.; Kaper, J. B. Commensal and pathogenic *Escherichia coli* use a common pilus adherence factor for epithelial cell colonization. *Proc. Natl. Acad. Sci. U. S. A.* **2007**, *104*, 10637−10642.
(37) Xicohtencati-Cortes, J.; Monteiro-Neto, V.; Ledesma, M. A.; Jordan, D. M.; Francetic, O.; Kaper, J. B.; Puente, J. L.; Giron, J. A. Intestinal adherence associated with type IV pili of enterohemorrhagic *Escherichia coli* O157:H7. *J. Clin. Invest.* **2007**, *117*, 3519−3129.
(38) Shoaf, K.; Mulvey, G. L.; Armstrong, G. D.; Hutkins, R. W. Prebiotic galactooligosaccharides reduce adherence of enteropathogenic *Escherichia coli* to tissue culture cells. *Infect. Immun.* **2006**, *74*, 6920−6928.
(39) Hotchkiss, A. T.; Buddington, R. K. Intestinal infections and prebiotics: the role of oligosaccharides in promoting health. *Funct. Food Rev.* **2011**, *3*, 119−134.

DOI: 10.1021/acs.jafc.5b00730
J. Agric. Food Chem. 2015, 63, 5622−5633

Neferine, **6**, a benzylisoquinoline alkaloid (Figure 1), isolated from the seed embryo of *N. nucifera* has been reported to block

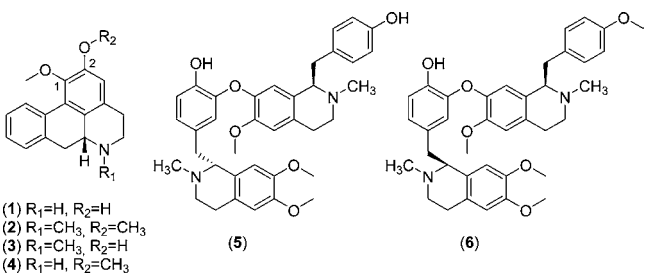

Figure 1. Chemical structures of lotus alkaloids: (−)-asimilobine, **1**, nuciferine, **2**, *O*-nornuciferine, **3**, *N*-nornuciferine, **4**, liensinine, **5**, and neferine, **6**.

hERG channels stably expressed in human embryonic kidney (HEK293) cells. In whole-cell patch clamp studies, this compound induced a concentration-dependent decrease in hERG current amplitude with an IC_{50} of 7.42 μM.[19] Moreover, Western blot analysis and immunofluorescence experiments gave insights into the effect of compound **6** on hERG protein levels in HEK293 cells. Liensinine, **5**, a structurally similar benzylisoquinoline alkaloid (Figure 1) from *N. nucifera* seed embryos, was also described to be a hERG blocker, however, at concentrations below 10 μM in much lower potency than its more hydrophobic derivative, **6**.[20]

The aim of the present study was to evaluate the hERG-blocking activity of alkaloids present in *N. nucifera* leaves and to quantitatively analyze their content in commonly consumed herbal supplements for weight loss including a critical discussion of the potential cardiotoxic risk caused by these products.

MATERIALS AND METHODS

General Experimental Procedures. Optical rotations were measured on a model 341 polarimeter (PerkinElmer, Waltham, MA, USA) at 25 °C. 1D- and 2D-NMR experiments were performed by using DRX300 and TXI600 NMR spectrometers (Bruker, Billerica, MA, USA) operating at 300 and 600 MHz, respectively. The samples were measured in $CDCl_3$ (calibrated to the residual nondeuterated solvent signals). MS analysis was performed on an Esquire 3000 plus ion-trap mass spectrometer (Bruker Daltonics, Billerica, MA, USA) equipped with electrospray ionization (ESI) in the positive and negative modes: spray voltage, 4.5 kV; sheath gas, N_2, 30 psi; dry gas, N_2, 6 L/min, 350 °C; scanning range, m/z 50−1000. Column chromatography was performed using silica gel 60 (40−63 μm) from Merck (Darmstadt, Germany) and Sephadex LH-20 (20−100 μm) from Pharmacia (Stockholm, Sweden). Fast centrifugal partition chromatography was carried out on a FCPC A200 instrument from Kromaton (Annonay, France). Fractions obtained from all chromatographic steps were analyzed by TLC (mobile phase, acetone/CH_3Cl/EtOH/NH_3 (4:3:1:0.1, v/v/v/v); stationary phase, Merck silica gel 60 PF_{254}, sprayed with Dragendorff reagent at Vis, UV_{254}, and UV_{366}). HPLC was performed on an Agilent 1200 LC system (Santa Clara, CA, USA) with a photodiode array detector (DAD). LC parameters were as follows: stationary phase, 150 × 3.0 mm i.d., 5 μm, Phenomenex Gemini NX-C18; temperature, 35 °C; mobile phase, A = 95% ammonium acetate 50 mM/5% CH_3CN (pH of mixture 6.8); B = 25% ammonium acetate 50 mM/75% CH_3CN (pH of mixture 7.6); flow rate, 0.4 mL/min; DAD detection wavelength, 270 nm; injection volume, 10 μL. Separations were performed by gradient elution (80:20 A/B in 25 min to 30/70 A/B, then within 1 min to 2/98 A/B), followed by a 4 min column wash (2A:98B) and a re-equilibration period of 10 min. All chemicals and solvents used were of analytical grade.

Plant Material. The leaves of *N. nucifera* Gaertn. (Nymphaeaceae) were obtained from Plantasia (MMag. E.A. Stöger, Oberndorf/Salzburg, Austria). A voucher specimen (JR-20100922_A1) is deposited in the Herbarium of the Department of Pharmacognosy, University of Vienna, Austria.

Extraction, Isolation, and Identification of Pure Compounds. The dried ground leaves of *N. nucifera* (712 g) were macerated with 6 L of CH_2Cl_2/MeOH (1:1) (at 22 °C, three times for 72 h each). After removal of the solvent under vacuum, 56 g of extract was obtained. This extract was then redissolved in CH_2Cl_2 and aqueous MeOH (1:1) and separated via liquid−liquid partition using petroleum ether followed by CH_2Cl_2. After removal of MeOH from the aqueous phase under vacuum, it was alkalized to a pH of 10 to extract alkaloids with CH_2Cl_2 to obtain 885 mg of an enriched alkaloid fraction (NN-A).

For the isolation of the alkaloids, NN-A was subjected in pilot scale (50 mg) to fast centrifugal partition chromatography (FCPC) using a biphasic solvent system of petroleum ether/ethyl acetate/methanol/water (1:5:1:5, v/v/v/v). The FCPC instrument was operated in descending mode (lower phase as mobile phase). The sample was dissolved in a mixture of mobile and stationary phase (1:1, v/v). After filling the stationary phase into the system, the mobile phase was pumped in while equilibrating at 800 rpm (column volume = 200 mL). Finally, the sample solution was injected, and separation was carried out at a flow rate of 1.8 mL/min and a rotation speed of 1200 rpm in a counterclockwise direction. Resulting fractions were monitored and combined according to their TLC pattern to give nine fractions (A1−A9). A7 was identified as pure compound **3** (9.96 mg).

In a large-scale approach, another 882 mg of NN-A was fractionated by FCPC applying the same parameters and conditions as described above for the small-scale separation (column volume = 200 mL). In sum, 18 fractions were obtained (B1−B18). Fractions B9 (14.35 mg) and B10 (42.24 mg) were purified via silica gel column chromatography (Merck silica gel 60 PF_{254}, 43 cm × 2 cm) by applying an isocratic system of acetone/CH_2Cl_2/EtOH/NH_3 (4:3:1:0.1, v/v/v/v) to yield compound **4** (5.41 mg) and compound **5** (8.75 mg). B7 (18.35 mg) and B17 (28.56 mg) were purified via Sephadex LH-20 column chromatography (mobile phase, MeOH), yielding compounds **1** (4.10 mg) and **2** (7.03 mg).

All isolated compounds (**1**−**5**) could be identified by using HPLC, MS analysis, optical rotation, and 1D- and 2D-NMR experiments. The physical and spectroscopic data of compounds **1**−**5** agreed with those published previously for (−)-asimilobine, **1**, nuciferine, **2**, *O*-nornuciferine, **3**, *N*-nornuciferine, **4**, and liensinine, **5**.[21−24] Their purity was checked using TLC and LC-MS and revealed to be >98% in all cases.

Expression of hERG Channels in *Xenopus* Oocytes and Voltage Clamp Studies. Preparation of stage V−VI oocytes from *X. laevis* (NASCO), synthesis of capped runoff complementary RNA (cRNA) transcripts from linearized complementary DNA (cDNA) templates, and injection of cRNA were performed as described previously.[25] cDNA of hERG (accession no. NP000229) was kindly provided by Dr. Sanguinetti (University of Utah). Currents through hERG channels were studied 1−4 days after microinjection of the cRNA by the two-microelectrode voltage clamp technique making use of a TURBO TEC-03X amplifier (npi electronic GmbH, Tamm, Germany). The bath solution contained 96 mM NaCl, 2 mM KCl, 1 mM $MgCl_2{\cdot}6H_2O$, 1.8 mM $CaCl_2{\cdot}2H_2O$, and 5 mM HEPES (all Sigma, pH 7.4). Voltage-recording and current-injecting microelectrodes (Harvard Apparatus) were filled with 3 M KCl and pulled to have resistances between 0.5 and 2 MΩ. Oocytes with maximal current amplitudes >3 μA were discarded to avoid voltage clamp errors. The pClamp software package v.10.0 (Molecular Devices, Inc.) was used for data acquisition.

Unless otherwise stated, the following voltage protocol was used: from a holding potential of −80 mV, the cell membrane was initially depolarized to +20 mV (300 ms) to achieve channel activation and subsequent rapid inactivation. During the following repolarization to −50 mV (300 ms) channels recover from inactivation and elicit the

DOI: 10.1021/acs.jafc.5b01901
J. Agric. Food Chem. 2015, 63, 5634−5639

hERG current (I_{hERG}). A final step to the holding potential ensured that channels returned to the closed state. The protocol was applied in 1 s intervals (1 Hz pulse frequency).

Drug Application and Data Analysis of Voltage Clamp Studies. Drugs were applied to *Xenopus* oocytes by means of a screening tool fast perfusion technique (npi electronic GmbH).[26] Data were analyzed using Origin software 7.0 (OriginLab Corp., Northampton, MA, USA). Each data point represents the mean ± SE from at least three oocytes and two oocyte batches.

Whole-Cell Patch Clamp Assay Using HEK293 Cells. Measurements were performed using the automated patch clamp device CytoPatch 2 Instrument.[27] Whole-cell patch clamp recordings were applied to examine the effects of the selected lotus leaf alkaloids on the hERG ion channel. To elicit hERG-mediated currents, cells were clamped for 200 ms to −80 mV and then shifted for 200 ms to −50 mV. The voltage step to −50 mV was used to determine the leak current of the cell. Thereafter, the cell was depolarized for 2 s at +40 mV. By stepping back to −50 mV for 2 s, the hERG tail current was activated. At the end of the pulse protocol, the cells were clamped again to holding potential. This voltage protocol was repeated at a frequency of 0.1 Hz. The membrane resistance, R_m, was monitored during the complete recording time. Recordings during which R_m decreased to <500 MΩ without recovery were stopped and repeated. Experiments were carried out at room temperature.

hERG tail current amplitudes were monitored before and during test compound application. The amplitude of the hERG tail current was calculated by subtraction of the leak current (determined during the −50 mV depolarization step prior to the activation of the hERG current) from the maximal current peak amplitude during the tail phase. The current inhibition for each test concentration was calculated by dividing the mean peak current of the last five current amplitudes at the end of each application phase by the respective control values. Results from the individual experiment were averaged to give the mean inhibition (±SD).

Human Embryonic Kidney (HEK293) Cells. HEK293 cells stably transfected with hERG were used in this study. These cells were frozen instant cells produced by the Cytocentrics Bioscience GmbH, Rostock, Germany.[27] They were stored in liquid nitrogen and were ready-to-use directly after thawing without any cultivation. After thawing, the cells were kept in the Cytocentrics Cells Reservoir as a cell suspension at a density of ∼2.0 million cells/mL in extracellular buffer at room temperature.

Buffers Used for Whole-Cell Patch Clamp Assay. The extracellular buffer (EC) was used for cell preparation and cell storage as well as for the dilution of compounds and patch clamp recordings.

The EC contained 140 mM NaCl, 2.5 mM KCl, 2 mM $MgCl_2$, 2 mM $CaCl_2$, 10 mM HEPES, 10 mM glucose, and 15 mM sucrose; pH adjusted to 7.4 (±0.1; NaOH), osmolality adjusted to 310−320 mOsm/L (saccharose), storage at 4 °C. Before use, the required EC was heated to room temperature and degassed. The intracellular buffer (IC) was used to fill the patch pipets. The intracellular buffer (IC) contained 100 mM K-gluconat, 20 mM KCl, 1 mM $CaCl_2$, 1 mM $MgCl_2$, 10 mM HEPES, 11 mM EGTA-KOH, 4 mM Mg ATP, 3 mM Na_2 phosphocreatine hydrate, and 9 mM sucrose; pH was adjusted to 7.2 ± 0.1; osmolality to 295 ± 5 mOsm/L, storage at −20 °C. After thawing, the IC was used for up to 4 h.

Curve Fitting. The concentration dependence of drug effects was modeled with a standard four-parameter logistic equation:

$$\text{effect} = \min + \left[\max / \left(1 + 10^{(\log IC_{50} - \log X)\cdot nH}\right)\right]$$

The parameters were minimal and maximal effects (min, max), half-maximal inhibitory drug concentration (IC_{50}), drug concentration (X), and Hill slope (nH). Minimal and maximal effects were treated as constants (max = 100 and min = 0) and IC_{50} and nH as variables (GraphPad Prism 4).

Test and Reference Compounds. To prepare working solutions, the stock solutions of the test alkaloids were diluted in DMSO and then 1:1000 in extracellular buffer, yielding the correct compound concentration in 0.1% DMSO. Work solutions were used immediately after thawing for up to 4 h and disposed of afterward. As reference compound for the hERG recordings, 100 nM cisapride was applied to three cells (positive control). To prove that the compound vehicle DMSO does not affect hERG-mediated currents, the vehicle (extracellular buffer containing 0.1% DMSO) was applied to three cells (negative control). When a stable whole-cell recording configuration was established, the cell was initially perfused with extracellular buffer to ensure stable recording conditions (control phase). Up to three increasing concentrations of the same test compound were applied to the same cell for 5 min each.

Quantitative Analysis of hERG-Blocking Alkaloids in Dietary Supplements. Five randomly selected commercially available dietary supplements (products 1−5) were analyzed according to a previously reported validated method using solid phase extraction (SPE) in combination with HPLC-DAD.[28] Briefly, the contents of three to four capsules (between 0.7 and 1.5 g) of each product were weighed and extracted with 8 mL of acidified MeOH (1% hydrochloric acid aqueous solution/MeOH; 50:50, v/v) on the ultrasonic bath for 15 min. Then the samples were centrifuged at room temperature at 5000 rpm for 5 min. This extraction was repeated twice for each sample, the resulting supernatants were combined in a volumetric flask, and the volume was filled to 25 mL with acidified MeOH.

Furthermore, an aliquot of each solution was subjected to SPE to clean up and enrich the sample. Oasis MCX (60 mg/3 mL) SPE cartridges were activated under vacuum with 4 mL of alkalized MeOH (5% ammonia in MeOH, w/w) and washed with 4 mL of H_2O. Then, 3 mL of alkaloid solution was passed through the cartridges without using vacuum. This was followed by three washing steps with 3 mL of 20% aqueous MeOH each time. Prior to HPLC analysis, the alkaloids were eluted with 4 mL of alkalized MeOH (5% ammonia in MeOH, w/w).

In Silico Screening of hERG Blocking Compounds. The pharmacophore-based hERG-blocking predictions on compounds **1**−**6** were conducted within Discovery Studio version 4.0 (Biovia, CA, USA). For each compound, up to 255 conformations were calculated in BEST quality. The compound fitting was performed using the Ligand Pharmacophore Mapping protocol and the flexible fitting option, allowing the ligand conformation to be energetically minimized within the pharmacophore model during the screening.

RESULTS AND DISCUSSION

Discovery of hERG-Blocking Natural Material. Using an automated two-microelectrode voltage clamp assay on *Xenopus* ooctyes, an in vitro screening for hERG channel blocking natural materials was performed. As a result, an enriched alkaloid fraction of *N. nucifera* leaves (NN-A; Figure 2) was found to cause strong hERG current inhibition, that is, 50.4 ± 10.3% (n = 3, data not shown), at a concentration of 100 μg/mL.

Isolation and Identification of hERG Blocking Compounds in NN-A. Separation and purification techniques including FCPC as well as silica gel and Sephadex column chromatography were applied to isolate five lotus leaf alkaloids from an enriched extract (NN-A). By using LC-MS analysis and 1D- and 2D-NMR experiments as well as by comparison with published data,[21−24] the constituents (Figure 1) were identified as (−)-asimilobine, **1**, nuciferine, **2**, *O*-nornuciferine, **3**, *N*-nornuciferine, **4**, and liensinine, **5**. Compounds **1**−**4** can be classified as aporphine-type alkaloids, whereas compound **5** belongs to the class of benzylisoquinoline alkaloids.

To evaluate the hERG channel blocking properties of the isolated compounds, we applied them to *Xenopus* oocytes making use of the automated two-microelectrode voltage clamp technique. All five isolated and identified lotus leaf constituents induced hERG current inhibition between 5.8% (compound **5**) and 81.9% (compound **2**) at 100 μM (Table 1).

DOI: 10.1021/acs.jafc.5b01901
J. Agric. Food Chem. 2015, 63, 5634−5639

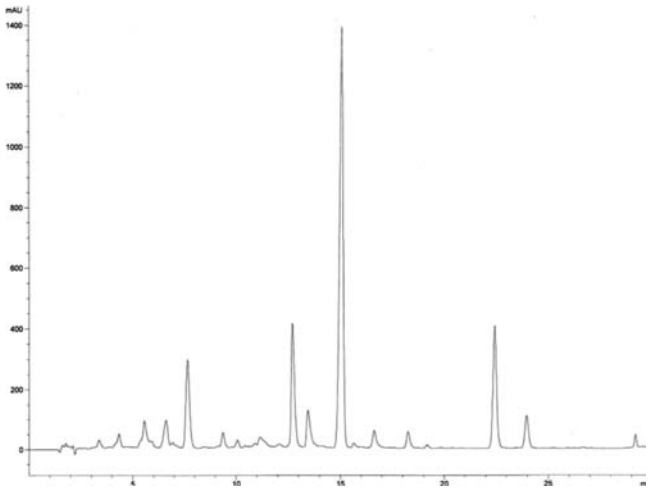

Figure 2. HPL chromatogram of NN-A recorded at 270 nm.

Table 1. Percentage of hERG Current Inhibition in *Xenopus* Oocytes by Lotus Alkaloids at 100 μM (n = 3)

compound	% hERG channel inhibition at 100 μM
1	24.3 ± 1.7
2	81.9 ± 5.6
3	47.0 ± 0.3
4	44.2 ± 0.2
5	5.80 ± 1.5

Evaluation of hERG Blockage in HEK293 Cells. To further investigate hERG-blocking properties of the isolated *N. nucifera* leaf alkaloids, a whole-cell patch clamp assay was performed with the three most potent inhibitors, that is, compounds **2**, **3**, and **4**. All three alkaloids induced a concentration-dependent decrease in current amplitude of the hERG channel stably expressed in HEK293 cells with IC_{50} values of 2.89, 7.91, and 9.75 μM, respectively. In our system the hERG blocker cisapride (positive control) showed an IC_{50} of 56 nM.

Corresponding dose–response curves of the three lotus alkaloids and current traces are shown in Figure 3. The less pronounced channel block on *Xenopus* oocytes is likely due to the presence of a large amount of yolk particles inside the oocyte membrane, which may absorb the compounds, thereby reducing the effective intracellular free drug concentration.[29,30]

Pharmacophore Model Predicting hERG-Blocking Constituents. Recently, several ligand-based pharmacophore models were established to predict hERG-blocking properties.[7] The model showing the best performance, when validated with synthetic compounds, consists of a positively ionizable, two hydrophobic, and one hydrophobic aromatic feature. To test the reliability of the model (Catalyst hERG model) toward natural products and to get a rough insight into ligand–target interactions, the five isolated compounds and the already known hERG blocker from lotus seeds, that is, compound **6**, were virtually screened. As a result, compounds **2**, **4**, **5**, and **6** were predicted as virtual hits (VHs). Among them, **2**, **4**, and **6** were predicted correctly as hERG-blocking constituents. A feature overlay of these compounds mapping the pharmacophore is shown in Figure 4. The hERG-blocking compound **3** was not predicted because it contains a hydroxyl instead of a methoxy group in position 2. Hence, the methoxy group in position 1 is fitted to the hydrophobic feature of the model with the result that no other required hydrophobic feature can be mapped. Furthermore, compound **5** was predicted to be a hERG blocker. In our experimental evaluation this could not be confirmed. However, in an earlier study,[20] this compound was identified as a weak hERG blocker with much lower potency than its hydrophobic derivative **6**.

Quantitation of hERG-Blocking Lotus Alkaloids in Dietary Supplements. Lotus leaf products are widely advertised as weight loss dietary supplements. Moreover, nuciferine, **2**, is known to block fat absorption and fat accumulation and thus to have strong antiobesity effects.[31] In our study this compound was identified as the most potent hERG blocker in HEK293 cells, indicating potential cardiac liabilities. To investigate the relevance and significance of these findings, five randomly selected lotus leaf dietary supplements for weight loss (products 1–5) were quantitatively analyzed focusing on the identified hERG-blocking alkaloids, that is, **2**, **3**, and **4**.

A previously published method using SPE in combination with HPLC-DAD[28] was adapted for quantitation. The method was validated for linearity, limit of detection (LOD), and limit of quantitation (LOQ). The calibration curves were obtained by injecting a series of compound solutions at increasing concentrations. For all three compounds there was good linearity (correlation coefficient = 0.99998) over a wide concentration range, with the LOQ between 0.42 and 0.62 mg/mL and the LOD between 1.43 and 2.11 mg/mL.

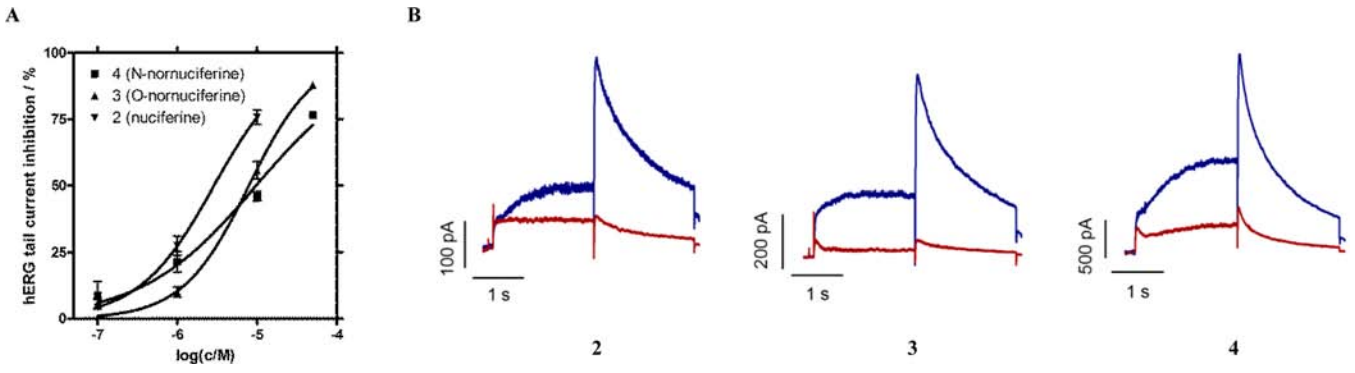

Figure 3. (A) Concentration-dependent inhibition of hERG tail current in HEK293 cells, induced by lotus alkaloids (**2**, **3**, and **4**). (B) Representative whole-cell current traces in control conditions (blue) and after wash-in of the test compounds (red): **2** at 10 μM; **3** and **4** at 50 μM.

DOI: 10.1021/acs.jafc.5b01901
J. Agric. Food Chem. 2015, 63, 5634–5639

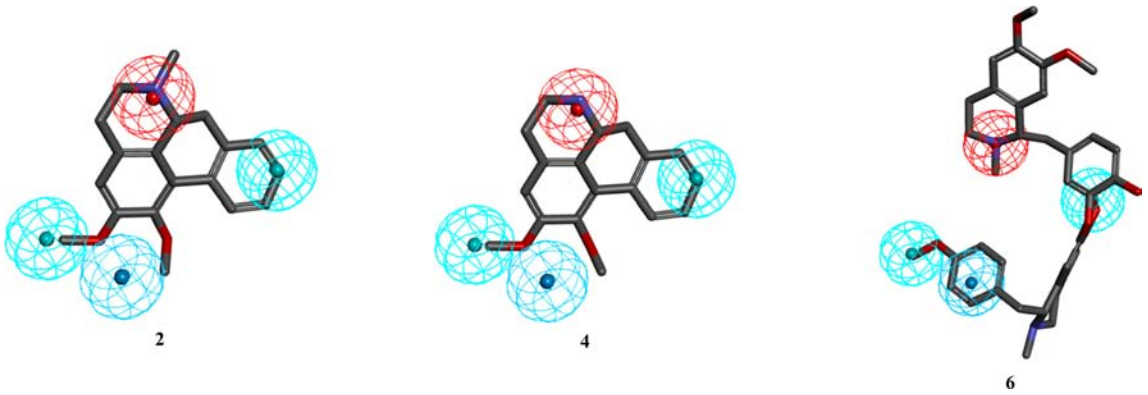

Figure 4. Feature overlay of hERG-blocking lotus alkaloids (**2**, **4**, and **6**) with Catalyst hERG pharmacophore model. The chemical features are color-coded: positively ionizable, red; hydrophobic, cyan; aromatic hydrophobic, blue.

Table 2. Percentage of Alkaloids (n = 3) in Selected Lotus Dietary Supplements[a]

compound	product 1	product 2	product 3	product 4	product 5
2	0.066 ± 0.07 (992.39)	0.011 ± 0.01 (318.54–637.08)	0.010 ± 0.01 (100.52)	n.d.[b]	0.004 ± 0.01 (57.94–77.25)
3	0.064 ± 0.12 (957.27)	0.010 ± 0.09 (283.39–566.77)	0.009 ± 0.08 (90.31)	n.d.	n.d.
4	n.d.	n.d.	n.d.	n.d.	n.d.

[a]The calculated amounts of alkaloids (μg) consumed in the recommended daily dose(s) of selected lotus dietary supplements are given in parentheses. [b]n.d. = not detectable.

The quantitative composition of the three focused alkaloids in the five commercial products varied significantly (Table 2). For instance, the highest percentages of compounds **2** and **3** were found in product 2 (0.066 and 0.064%, respectively), whereas none of the three focused alkaloids could be detected in product 4. Moreover, compound **4** was not found in any of the investigated products. With the recommended daily dose given on each package of the investigated dietary supplements taken into account, the amount of daily intake of hERG-blocking lotus leaf alkaloids was calculated (Table 2). The highest daily intake of alkaloids **2** and **3** was found for product 1, with almost up to 1 mg each. In the other three products (products 2, 3, and 5) the amount of hERG-blocking alkaloids is considerably lower (up to 637 μg per day). In sum, **2** was found as the predominant alkaloid of the selected leaf products, whereas **3** was found in lesser content and **4** was not detected in any product.

Because *N. nucifera* leaves and commercially available lotus leaf products are taken in the form of teas or capsules containing lotus extracts or powdered leaves, it is of high relevance to have knowledge on the oral bioavailability of the main hERG-blocking alkaloids. To date, first pharmacokinetic data are already available for **2**, which we identified as a hERG-blocking natural compound with an IC_{50} of 2.89 μM in HEK293 cells. Compound **2** was quantitated in rat plasma after oral and iv administration.[32,33] It was observed that there is a rapid distribution and a poor absorption into the systemic circulation, but an extensive tissue uptake. The absolute bioavailability is around 4%. Moreover, **2** is distributed into brain, liver, and adipose tissues.[32,33]

Supported by in silico ligand–target predictions, three major lotus leaf alkaloids, that is, compounds **2**, **3**, and **4**, were identified as hERG-blocking constituents. With regard to the possibility of severe cardiotoxic events combined with vague or nonexistent legislation concerning the licensing of herbal dietary supplements, it is of high relevance to screen commonly consumed botanicals for their hERG-interacting properties. The quantitative analysis of the three identified hERG-blocking alkaloids **2**, **3**, and **4** in five lotus leaf slimming products revealed that their content and thus their daily dose vary significantly. However, without complete data on the pharmacokinetics and pharmacodynamics of these compounds, a full risk estimation concerning safety is not feasible. Notably, especially in Asian countries, lotus leaves have been used in traditional medicines for thousands of years, and they have stood the test of time without a notable increase of sudden cardiac deaths. Nevertheless, if nonstandardized weight loss products are consumed in excess or taken by patients with already existing cardiac problems, the identified hERG toxic lotus alkaloids might increase health risks. Especially if taken in addition to medication with potentially cardiotoxic drug substances or in combination with lotus leaf containing food products, an accumulation of hERG-interacting compounds may increase the risk of cardiotoxic side effects.

■ ASSOCIATED CONTENT

Supporting Information

Table S1, validation data for alkaloid quantitation; Figure S1, HPLC of quantitated alkaloids (compounds **3**, **4**, and **2**); Figure S2, HPLC of commercial products 1–5. The Supporting Information is available free of charge on the ACS Publications website at DOI: 10.1021/acs.jafc.5b01901.

■ AUTHOR INFORMATION

Corresponding Author

*(J.M.R.) Phone: +43-1-4277-55255. Fax: +43-1-4277-855255. E-mail: judith.rollinger@univie.ac.at.

Funding

This study was supported by a Marie Curie International Research Staff Exchange Scheme Fellowship within the seventh European Community Framework Programme (hERGscreen, 295174). D.S. is supported by the Erika Cremer Habilitation Program of the University of Innsbruck.

DOI: 10.1021/acs.jafc.5b01901
J. Agric. Food Chem. 2015, 63, 5634–5639

Notes

The authors declare no competing financial interest.

■ ACKNOWLEDGMENTS

Technical support by S. J. Lehmann and C. Bachmair (Institute of Pharmacy/Pharmacognosy, University of Innsbruck, Austria) is gratefully acknowledged.

■ ABBREVIATIONS USED

HEK293, human embryonic kidney cells; hERG, human ether-à-go-go-related gene; TdP, Torsades de Pointes

■ REFERENCES

(1) Raschi, E.; Vasina, V.; Poluzzi, E.; De Ponti, F. The hERG K+ channel: target and antitarget strategies in drug development. *Pharmacol. Res.* **2008**, *57*, 181−195.

(2) Sanguinetti, M. C.; Tristani-Firouzi, M. hERG potassium channels and cardiac arrhythmia. *Nature* **2006**, *440*, 463−469.

(3) Vandenberg, J. I.; Perry, M. D.; Perrin, M. J.; Mann, S. A.; Ke, Y.; Hill, A. P. hERG K(+) channels: structure, function, and clinical significance. *Physiol. Rev.* **2012**, *92*, 1393−1478.

(4) Killeen, M. J. Drug-induced arrhythmias and sudden cardiac death: implications for the pharmaceutical industry. *Drug Discovery Today* **2009**, *14*, 589−597.

(5) ICH International conference on harmonization of technical requirements for registration of pharmaceuticals for human use. *The Non-Clinical Evaluation of the Potential for Delayed Ventricular Repolarization (QT Interval Prolongation) By Human Pharmaceuticals. S7B (Step 4)*; ICH Harmonized Tripartite Guideline; EMA: London, UK, 2005.

(6) Aronov, A. M. Predictive *in silico* modeling for hERG channel blockers. *Drug Discovery Today* **2005**, *10*, 149−155.

(7) Kratz, J. M.; Schuster, D.; Edtbauer, M.; Saxena, P.; Mair, C. E.; Kirchebner, J.; Matuszczak, B.; Baburin, I.; Hering, S.; Rollinger, J. M. Experimentally validated hERG pharmacophore models as cardiotoxicity prediction tools. *J. Chem. Inf. Model.* **2014**, *54*, 2887−2901.

(8) Sanguinetti, M. C.; Mitcheson, J. S. Predicting drug−hERG channel interactions that cause acquired long QT syndrome. *Trends Pharmacol. Sci.* **2005**, *26*, 119−124.

(9) Wang, S.; Li, Y.; Xu, L.; Li, D.; Hou, T. Recent developments in computational prediction of hERG blockage. *Curr. Trends Med. Chem.* **2013**, *13*, 1317−1326.

(10) Schramm, A.; Saxena, P.; Chlebek, J.; Cahlikova, L.; Baburin, I.; Hering, S. Hamburger, M. Natural products as potential human ether-a-go-go-related gene channel inhibitors − screening of plant-derived alkaloids. *Planta Med.* **2014**, *80*, 740−746.

(11) Alper, K.; Bai, R.; Liu, N.; Fowler, S. J.; Huang, X.-P.; Priori, S. G.; Ruan, Y. hERG blockade by iboga alkaloids. *Cardiovasc. Toxicol.* **2015**, 1−9.

(12) Koenig, X.; Kovar, M.; Boehm, S.; Sandtner, W.; Hilber, K. Anti-addiction drug ibogaine inhibits hERG channels: a cardiac arrhythmia risk. *Addict. Biol.* **2014**, *19*, 237−239.

(13) Koenig, X.; Kovar, M.; Rubi, L.; Mike, A. K.; Lukacs, P.; Gawali, V. S.; Todt, H.; Hilber, K.; Sandtner, W. Anti-addiction drug ibogaine inhibits voltage-gated ionic currents: a study to assess the drug's cardiac ion channel profile. *Toxicol. Appl. Pharmacol.* **2013**, *273*, 259−268.

(14) Jenks, C. Extraction studies of *Tabernanthe iboga* and *Voacanga africana*. *Nat. Prod. Lett.* **2002**, *16*, 71−76.

(15) Schramm, A.; Baburin, I.; Hering, S.; Hamburger, M. hERG channel inhibitors in extracts of *Coptidis rhizoma*. *Planta Med.* **2011**, *77*, 692−697.

(16) Camp, D.; Davis, R. A.; Campitelli, M.; Ebdon, J.; Quinn, R. J. Drug-like properties: guiding principles for the design of natural product libraries. *J. Nat. Prod.* **2012**, *75*, 72−81.

(17) Baburin, I.; Beyl, S.; Hering, S. Automated fast perfusion of *Xenopus oocytes* for drug screening. *Pfluegers Arch.* **2006**, *453*, 117−123.

(18) Mukherjee, P. K.; Mukherjee, D.; Maji, A. K.; Rai, S.; Heinrich, M. The sacred lotus (*Nelumbo nucifera*) − phytochemical and therapeutic profile. *J. Pharm. Pharmacol.* **2009**, *61*, 407−422.

(19) Gu, D. F.; Li, X. L.; Qi, Z. P.; Shi, S. S.; Hu, M. Q.; Liu, D. M.; She, C. B.; Lv, Y. J.; Li, B. X.; Yang, B. F. Blockade of hERG K+ channel by isoquinoline alkaloid neferine in the stable transfected HEK293 cells. *Naunyn-Schmiedeberg's Arch. Pharmacol.* **2009**, *380*, 143−151.

(20) Dong, Z. X.; Zhao, X.; Gu, D. F.; Shi, Y. Q.; Zhang, J.; Hu, X. X.; Hu, M. Q.; Yang, B. F.; Li, B. X. Comparative effects of liensinine and neferine on the human ether-a-go-go-related gene potassium channel and pharmacological activity analysis. *Cell. Physiol. Biochem.* **2012**, *29*, 431−442.

(21) Han, B.; Park, M.; Han, Y. Aporphine and tetrahydrobenzylisoquinoline alkaloids from the seeds of *Zizyphus vulgaris* var. *spinosus*. *Arch. Pharmacal Res.* **1989**, *12*, 263−268.

(22) Zheng, Z.; Wang, M.; Wang, D.; Duan, W.; Wang, X.; Zheng, C. Preparative separation of alkaloids from *Nelumbo nucifera* leaves by conventional and pH-zone-refining counter-current chromatography. *J. Chromatogr. B: Anal. Technol. Biomed. Life Sci.* **2010**, *878*, 1647−1651.

(23) Itoh, A.; Saitoh, T.; Tani, K.; Uchigaki, M.; Sugimoto, Y.; Yamada, J.; Nakajima, H.; Ohshiro, H.; Sun, S.; Tanahashi, T. Bisbenzylisoquinoline alkaloids from *Nelumbo nucifera*. *Chem. Pharm. Bull.* **2011**, *59*, 947−951.

(24) Lo, W. L.; Huang, L. Y.; Wang, H. M.; Chen, C. Y. Chemical constituents from the stems of *Michelia alba*. *Chem. Nat. Compd.* **2010**, *46*, 664−665.

(25) Stork, D.; Timin, E. N.; Berjukow, S.; Huber, C.; Hohaus, A.; Auer, M.; Hering, S. State dependent dissociation of HERG channel inhibitors. *Br. J. Pharmacol.* **2007**, *151*, 1368−1376.

(26) Windisch, A.; Timin, E.; Schwarz, T.; Stork-Riedler, D.; Erker, T.; Ecker, G.; Hering, S. Trapping and dissociation of propafenone derivatives in HERG channels. *Br. J. Pharmacol.* **2011**, *162*, 1542−1552.

(27) Scheel, O.; Himmel, H.; Rascher-Eggstein, G.; Knott, T. Introduction of a modular automated voltage-clamp platform and its correlation with manual human ether-a-go-go related gene voltage-clamp data. *Assay Drug Dev. Technol.* **2011**, *9*, 600−607.

(28) Chen, S.; Zhang, H. H.; Liu, Y. L.; Fang, J. B.; Li, S. H. Determination of lotus leaf alkaloids by solid phase extraction combined with high performance liquid chromatography with diode array and tandem mass spectrometry detection. *Anal. Lett.* **2013**, *46*, 2846−2859.

(29) Goldin, A. L. Expression of ion channels in *Xenopus* oocytes. In *Expression and Analysis of Recombinant Ion Channels*; Clare, J. J., Trezise, D. J., Eds.; Wiley-VCH Verlag: Weinheim, Germany, 2006; pp 1−25.

(30) Witchel, H. J.; Milnes, J. T.; Mitcheson, J. S.; Hancox, J. C. Troubleshooting problems with *in vitro* screening of drugs for QT interval prolongation using HERG K^+ channels expressed in mammalian cell lines and *Xenopus* oocytes. *J. Pharmacol. Toxicol. Methods* **2002**, *48*, 65−80.

(31) Ahn, J. H.; Kim, E. S.; Lee, C.; Kim, S.; Cho, S. H.; Hwang, B. Y.; Lee, M. K. Chemical constituents from *Nelumbo nucifera* leaves and their anti-obesity effects. *Bioorg. Med. Chem. Lett.* **2013**, *23*, 3604−3608.

(32) Gu, S. Y.; Zhu, G. H.; Wang, Y. Z.; Li, Q.; Wu, X.; Zhang, J. G.; Liu, G. L.; Li, X. Y. A sensitive liquid chromatography-tandem mass spectrometry method for pharmacokinetics and tissue distribution of nuciferine in rats. *J. Chromatogr. B: Anal. Technol. Biomed. Life Sci.* **2014**, *961*, 20−28.

(33) Liu, H.; Hao, Y.; Zhu, X. Y.; Wang, M.; Zhang, D. Q. Determination of nuciferine in rat plasma by HPLC and its application to pharmacokinetic study. *Chin. J. Exp. Tradit. Med. Formulae* **2010**, *16*, 165−168.

DOI: 10.1021/acs.jafc.5b01901
J. Agric. Food Chem. 2015, 63, 5634−5639

been reported that antioxidants, such as vitamin C, hydrogen sulfide, ginsenoside, and sesamol, have great potential to enhance the proliferation capacity of a broad range of cells, likely due to their high ability to scavenge intracellular reactive oxygen species (ROS).[20−22] Sesamol (3,4-methylenedioxyphenol) is a natural phenolic compound found in sesame oil. In addition to its potent antioxidation activity, sesamol is able to inhibit malic enzyme, which is a major source of NADPH in many oleaginous microorganisms.[23,24]

C. cohnii synthesizes saturated and monounsaturated fatty acids via a NADPH-dependent fatty acid synthase complex of enzymes. The application of sesamol attenuates the intracellular production of NADPH by inhibiting malic enzyme and thus may decrease the accumulation of these de novo synthesized fatty acids leading to the buildup of fatty acid precursors in *C. cohnii*. The precursors, on the other hand, maybe redirected to the biosynthesis of DHA via the desaturase-independent PKS pathway, resulting in the possible increase in DHA content. To validate this hypothesis for improved DHA production by *C. cohnii*, a set of sesamol concentrations were tested. Our work represents, to the best of our knowledge, the first effort to utilize the natural phenolic compound sesamol for enhanced DHA production by *C. cohnii* and may provide alternative directions to lower the production cost in future industrial applications.

MATERIALS AND METHODS

Microalga and Culture Conditions. *C. cohnii* (ATCC 30556) was maintained heterotrophically in liquid By+ medium (pH 6.5) with 5 g/L glucose at 16 °C and subcultured every month. By+ medium contained (per liter) 15 g of sea salt (Sigma), 1 g of yeast extract (Oxoid), and 1 g of tryptone (Oxoid). The inocula were prepared by culturing the microalga in 500 mL Erlenmeyer flasks with 100 mL of By+ medium at 25 °C for 48 h with orbital shaking at 150 rpm in the dark. The seed of *C. cohnii* was inoculated to 100 mL of fresh modified By+ medium (containing, per liter, 15 g of sea salt, 0.5 g of yeast extract, 0.5 g of tryptone, and 20 g of glucose) for batch culture in 500 mL Erlenmeyer flasks. The media of all fermentations were supplemented with various concentrations of sesamol (0−2 mM), and each concentration was carried out in triplicate. The pH of By+ medium was adjusted to 6.5 prior to autoclaving. After inoculation, the flasks were incubated at 25 °C in an orbital shaker at 150 rpm in the dark for 96 h.

Determination of Residual Glucose Concentration, Cell Dry Weight, and Specific Growth Rate. The cells were centrifuged at 3000*g* for 5 min. The concentration of glucose in the supernatant was determined according to the method of Miller.[25] The pellet was washed with deionized water twice and filtered through a predried filter paper (Whatman GF/C). Then the cells on the disks were dried to constant weight in a vacuum oven at 80 °C. The specific growth rate (μ) in the log phase was calculated by using the equation $\mu = (\ln X_2 - \ln X_1)/(t_2 - t_1)$, where X_1 and X_2 are the cell dry weight concentrations (g/L) at time t_1 and t_2, respectively.

Fatty Acid Analysis. Twenty milligrams of lyophilized algal cells was incubated in a solvent mixture (1 mL of toluene, 2 mL of 1% sulfuric aicd in methanol (v/v), and 0.8 mg of heptadecanoic acid in 0.8 mL of hexane as the internal standard) overnight at 50 °C. The formed fatty acid methyl esters (FAMEs) were then extracted three times with hexane in a reciprocating shaker. The FAMEs were analyzed by using a GC-MS-QP 2010 SE (electron ionization type) gas chromatograph−mass spectrometer (Shimadzu, Japan) and a Stabilwax-DA capillary column (30 m × 0.25 mm × 0.25 μm) (Shimadzu, Japan). Helium was used as the carrier gas. The injection temperature, ion temperature, and interface temperature were set at 250, 200, and 260 °C, respectively. The initial column temperature was set at 150 °C. The column temperature subsequently rose to 200 °C by 10 °C/min and then to 250 °C by 15 °C/min, followed by a hold at 250 °C for 3 min. FAMEs were identified by NIST 11 mass spectral library (NIST/EPA/NIH mass spectral library, 2011 edition). FAMEs were quantified by using a standard FAMEs mix (Sigma-Aldrich) with heptadecanoic acid as the internal standard. The response factors of representative fatty acids related to the internal standard are shown in Table S1 of the Supporting Information.

Determination of Enzyme Activities. The cells were harvested by centrifugation at 3000*g* for 5 min. The pellet was resuspended in extraction buffer (containing 100 mM KH_2PO_4/KOH (pH 7.5), 20% (v/v) glycerol, 1 mM benzamidine·HCl, and 1 mM DTT) and ground with liquid nitrogen. The disrupted cell suspension was centrifuged at 12000*g* for 10 min at 4 °C, and the supernatant was used for enzyme analysis. The activities of $NADP^+$-dependent malic enzyme (ME), $NADP^+$-dependent isocitrate dehydrogenase (ICDH), and glucose-6-phosphate dehydrogenase (G-6-PDH) were determined using continuous spectrophotometric assays following the increase of NADPH at 340 nm. All assays were carried out at 25 °C. ME, ICDH, and G-6-PDH were assayed as described by Hsu and Lardy,[26] Wynn and Ratledge,[24] and Langdon,[27] respectively. The enzyme activity was defined as the reducing amount of $NADP^+$ (nmol) catalyzed by the enzyme solution with 1 mg of protein in 1 min (nmol min^{-1} (mg protein)$^{-1}$). The protein concentrations of enzyme solutions were determined according to the method of Bradford,[28] with BSA as a standard.

Determination of Intracellular Reactive Oxygen Species. The intracellular ROS levels in collected cells were determined using the ROS assay kit (Beyotime Institute of Biotechnology, China) according to the instructions. The 2′,7′-dichlorofluorescein (DCF) fluorescence intensity of 10^6 cells/mL was detected by the fluorescent microplate reader Fluoroskan Ascent (Thermo Fisher, USA) with the excitation and emission wavelengths at 485 and 535 nm, respectively.

Statistical Analysis. The data of all the measurements were obtained from three repetitions and analyzed using a one-way analysis of variance (ANOVA) with subsequent post hoc multiple-comparison LSD tests, which were calculated by using SPSS Statistics 20 software. Statistically significant values were defined as $P < 0.05$.

RESULTS AND DISCUSSION

Effect of Sesamol on Cell Growth. In the present study, several sesamol concentrations of 0, 0.5, 1, 1.5, and 2 mM were tested to examine the effect of sesamol on the cell growth of *C. cohnii*. Compared with the control group (0 mM), the addition of 0.5 mM sesamol in the medium significantly enhanced the growth of *C. cohnii*, leading to an increase in biomass concentration by 44.20% (Figure 2A). No significant difference in biomass accumulation of *C. cohnii* was observed when the concentration of sesamol was increased from 0.5 to 1 mM (Figure 2A). Further increase in sesamol concentration to 2 mM, however, severely inhibited algal growth with a biomass concentration of only 0.06 g/L, indicating that high sesamol concentration (>2 mM) is lethal to the growth of *C. cohnii* (Figure 2A). Our results were in accordance with previous studies in which phenolic compounds promoted cell growth at appropriate concentrations and caused cell apoptosis at higher concentrations (>1 mM).[29,30]

Notably, in the presence of 1 mM sesamol, there was an obvious growth lag within the first 24 h of cultivation, as evident by the much lower amount of biomass accumulated (Figure 2B). Thereafter, sesamol induced a significantly greater specific growth rate (from 0.041 to 0.067 h^{-1}), leading to a higher final cell density (Figure 2B). Microorganisms tend to accumulate ROS under certain conditions, such as nitrogen depletion.[31] The buildup of ROS may have an adverse effect on cell growth and cause oxidative damage to cellular components.[32] As indicated by Figure 3B, the intracellular ROS level in *C. cohnii* supplemented with sesamol was reduced by 63.5%

DOI: 10.1021/acs.jafc.5b01441
J. Agric. Food Chem. 2015, 63, 5640−5645

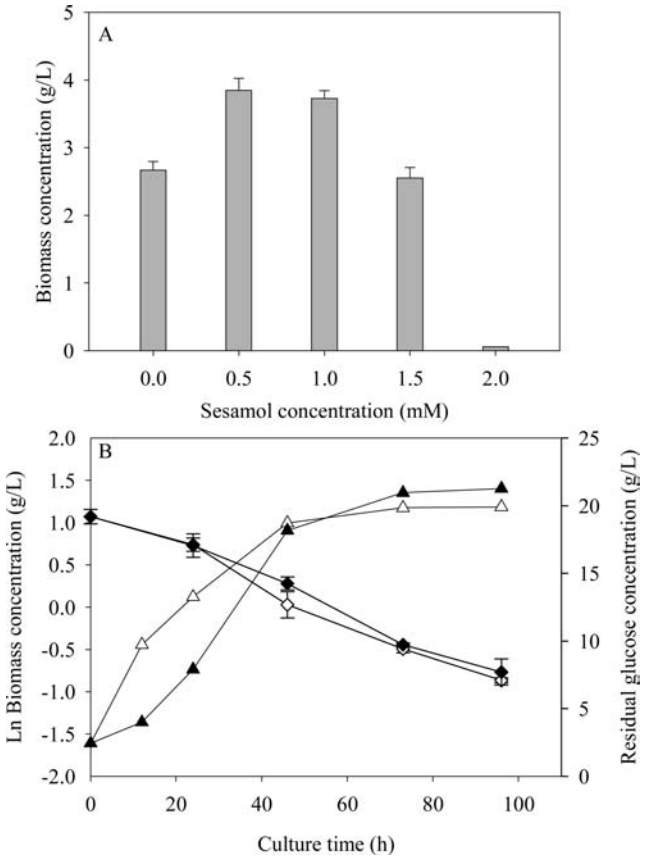

Figure 2. Effect of sesamol on the growth of *C. cohnii*: (A) biomass concentration at 96 h of growth with different concentrations of sesamol; (B) cell growth curves (triangles) of *C. cohnii* and residual glucose concentration (diamonds) in medium growing with (solid) or without (open) 1 mM sesamol.

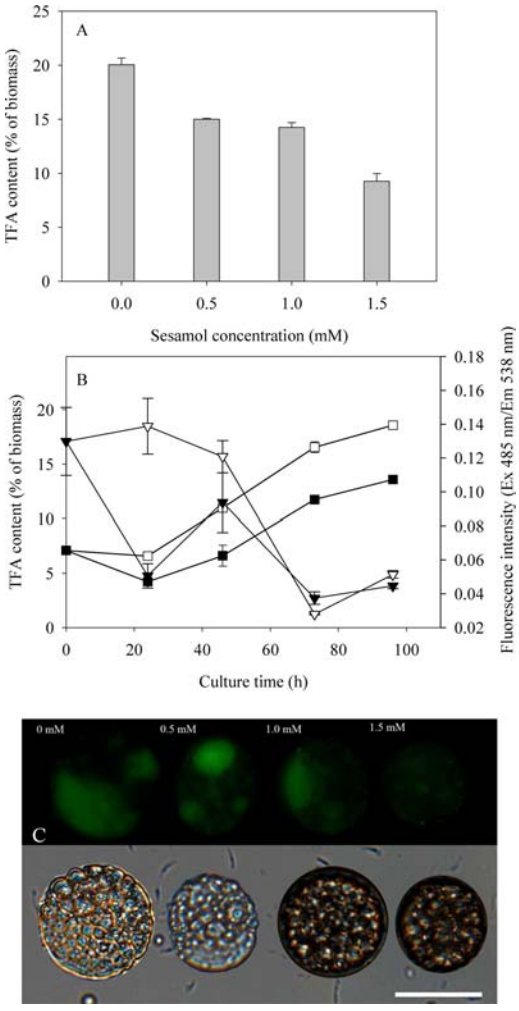

Figure 3. Effect of sesamol on TFA accumulation ROS levels and TFA accumulation in *C. cohnii*: (A) TFA content as affected by different concentrations of sesamol; (B) time course of TFA accumulation (squares) and intracellular ROS levels (triangles) in *C. cohnii* growing with (solid) or without 1 mM sesamol (open); (C) cells growing in different concentrations of sesamol stained by Nile red under fluorescence (upper) and white light (lower). Lipids in *C. cohnii* can be stained by Nile red, and there is a positive correlation between the fluorescence intensity and lipid contents. The scale bar represents 20 μm.

at 24 h of cultivation and remained significantly lower at 48 h, as compared to the sesamol-free cultures. This result is in line with previous works that showed sesamol or other antioxidants have the potential to attenuate intracellular ROS levels, thereby enhancing cell growth.[20,21]

To check if the increase in the final cell density is related to the consumption of glucose, the residual glucose in the culture medium supplemented or not with sesamol was monitored, and the results are shown in Figure 2B. During the whole culture period of 96 h, no significant difference in glucose concentration was observed between the sesamol-containing and sesamol-free cultures, suggesting that the presence of sesamol had little effect on the glucose consumption rate by *C. cohnii*. Likely, in the presence of sesamol, the alga may possess a higher growth coefficient based on glucose (0.35 g/g versus 0.27 g/g) and transform more carbon per glucose to algal biomass.

Effect of Sesamol on Fatty Acid Accumulation. In contrast to the enhanced biomass production, sesamol exhibited an adverse effect on the accumulation of fatty acids (Figure 3). The total fatty acids (TFA) content per cell dry weight was decreased by 25.24% in the presence of 0.5 mM sesamol. No significant difference was observed in the TFA content between the cultures with 0.5 and 1 mM sesamol; however, the further increase of sesamol concentration to 1.5 mM inhibited TFA accumulation remarkably, and the TFA content accounted for only 46.29% of the control cultures without sesamol (Figure 3A,C). After staining with the lipophilic stain Nile red, the fluorescence intensity of *C. cohnii* also showed a decrease in response to sesamol in a concentration-dependent manner (Figure 3C). This decrease in fatty acid content was accompanied by the attenuation of ROS level in *C. cohnii* (Figure 3B), indicating that sesamol may inhibit fatty acid biosynthesis by the sequestration of the intracellular ROS, which is thought to be positively linked to lipid accumulation.[33]

Effect of Sesamol on Docosahexaenoic Acid Production. Sesamol exhibited significant effects on not only TFA accumulation but also fatty acid composition (Table 1). The fatty acids in *C. cohnii* consisted mainly of C14:0, C16:0, C18:0, C18:1, and C22:6, with C22:6 being the most abundant (36.97% of TFA). The addition of sesamol showed little influence on the percentage of saturated fatty acids (C14:0, C16:0, and C18:0). In contrast, there was a significant decrease in C18:1, which was sesamol concentration dependent and

DOI: 10.1021/acs.jafc.5b01441
J. Agric. Food Chem. 2015, 63, 5640−5645

Table 1. Effect of Sesamol Concentration on the Fatty Acids Content of *C. cohnii* ATCC 30556[a]

	sesamol concentration			
fatty acid	0 mM	0.5 mM	1 mM	1.5 mM
	Fatty Acid Proportion (% of TFA)			
C14:0	24.36 ± 0.35	21.32 ± 0.23	21.23 ± 0.66	22.01 ± 0.36
C16:0	25.75 ± 0.16	25.24 ± 0.27	26.16 ± 1.27	28.4 ± 0.07
C18:0	2.92 ± 0.06	2.84 ± 0.38	3.62 ± 1.43	3.71 ± 0.08
C18:1	10.00 ± 0.14	9.48 ± 0.21*	8.97 ± 0.28**	8.52 ± 0.07***
DHA	36.97 ± 0.38	41.13 ± 0.23**	40.02 ± 2.27*	37.36 ± 0.44
	Fatty Acid Content (mg/g Cell Dry Weight)			
C14:0	48.83 ± 2.20	31.96 ± 0.50	30.28 ± 1.85	20.42 ± 1.88
C16:0	51.6 ± 1.82	37.83 ± 0.39	37.26 ± 1.33	26.33 ± 1.92
C18:0	5.85 ± 0.29	4.25 ± 0.55	5.13 ± 1.91	3.44 ± 0.33
C18:1	20.04 ± 0.37	14.21 ± 0.34	12.79 ± 0.77	7.90 ± 0.67
DHA	74.07 ± 1.60	61.66 ± 0.69	57.05 ± 4.14	34.62 ± 2.21
TFA	200.38 ± 6.23	149.92 ± 0.85	142.52 ± 4.20	92.70 ± 7.01
TSF	53.03	49.40	51.01	54.12
Δ/mol	2.32	2.56	2.49	2.33

[a]Cells of *C. cohnii* were collected at 96 h for FA analysis. TSF, total saturated fatty acids; Δ/mol, degree of unsaturation. Values were calculated according to ref 36. Δ/mol = [1.0 (% monoene) + 2.0 (% diene) + 3.0 (% triene)]/100. *, $P < 0.05$; **, $P < 0.01$; ***, $P < 0.001$.

dropped from 10.00 to 8.50% in the presence of 1.5 mM sesamol (Table 1). On the other hand, DHA percentage of TFA was increased significantly by sesamol and reached 41.13% in the presence of 0.5 mM sesamol, which was 11.25% higher than the control cultures without sesamol. Notably, the sesamol-mediated enhancement in DHA percentage was observed during the whole culture period (Figure 4B). Our results were in good agreement with those found in cultures of *Mucor circinelloides* and *Nannochloropsis* sp. that the C18:1 content (%TFA) decreased significantly in the presence of sesamol.[23,34] From the weight content point of view, the presence of sesamol attenuated the content of all fatty acids, but DHA was much less affected as compared to other fatty acids (Table 1). Notably, because of the considerable increase in biomass, a final DHA yield of 0.23 g/L was obtained in the presence of 1 mM sesamol, still significantly higher than the control cultures (Figure 4B). In terms of DHA productivity, it was enhanced significantly by sesamol at concentrations of 0.5−1 mM, but dropped remarkably when sesamol reached 1.5 mM (Figure 4A).

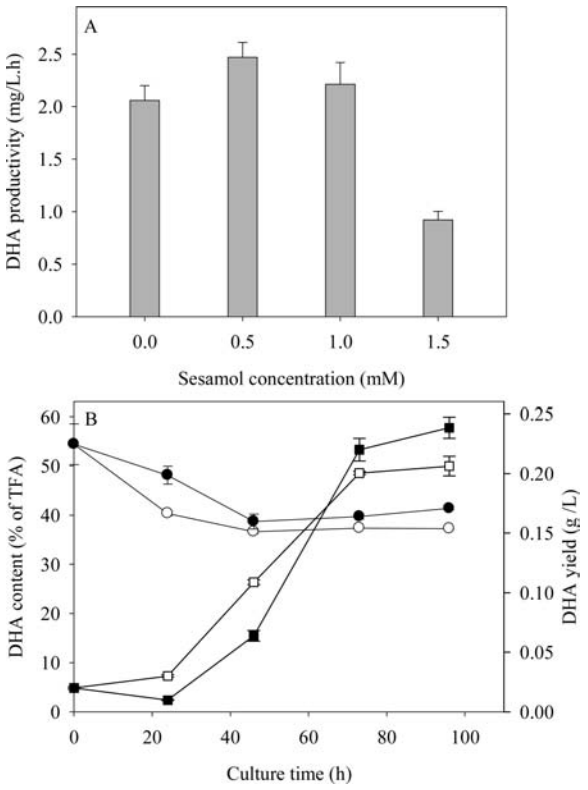

Figure 4. Effect of sesamol on DHA accumulation in *C. cohnii*: (A) DHA productivity under different concentrations of sesamol; (B) time course of DHA percentage per TFA (circles) and volumetric DHA yield (squares) in *C. cohnii* with (solid) or without (open) 1 mM sesamol supplementation.

Effects of Sesamol on the Activities of Key Enzymes Related to Fatty Acid Biosynthesis. It is well-known that the supply of reducing power in the form of NADPH plays an important role in fatty acid biosynthesis in oil-rich microorganisms.[15] NADPH is mainly used for acyl chain growth and desaturation of fatty acids, and its supply is thought to be positively linked to fatty acid biosynthesis and accumulation.[35] Efforts remain to be made to overcome the provision limitation of NADPH for enhancing lipid synthesis in oleaginous microorganisms.[13] There are several intracellular enzymes involved in the generation of NADPH, including malic enzyme (ME), isocitrate dehydrogenase ICDH, and glucose-6-phosphate dehydrogenase (G-6-PDH).

In *C. cohnii*, regardless of sesamol supplementation, the activity of ME increased as the culture time went and reached its maximum at 72 h, followed by a slight decline (Figure 5A). However, sesamol inhibited ME activity during the whole culture period, for example, 174.9 nmol min^{-1} (mg protein)$^{-1}$ at 72 h, which is 37% less as compared to the control cultures. In contrast, there was no significant difference in ICDH activity between the cultures with and without sesamol, except at 72 h, when sesamol attenuated the activity of ICDH (Figure 5B). Interestingly, unlike *Thraustochytrium* sp., in which a high level of G-6-PDH activity was observed, we detected no G-6-PDH activity in all samples of *C. cohnii*. G-6-PDH is a key enzyme involved in the pentose phosphate pathway (PPP) and serves as the prime alternative for producing NADPH.[13] Our results suggested that *C. cohnii* might utilize ME and ICDH rather than

DOI: 10.1021/acs.jafc.5b01441
J. Agric. Food Chem. 2015, 63, 5640−5645

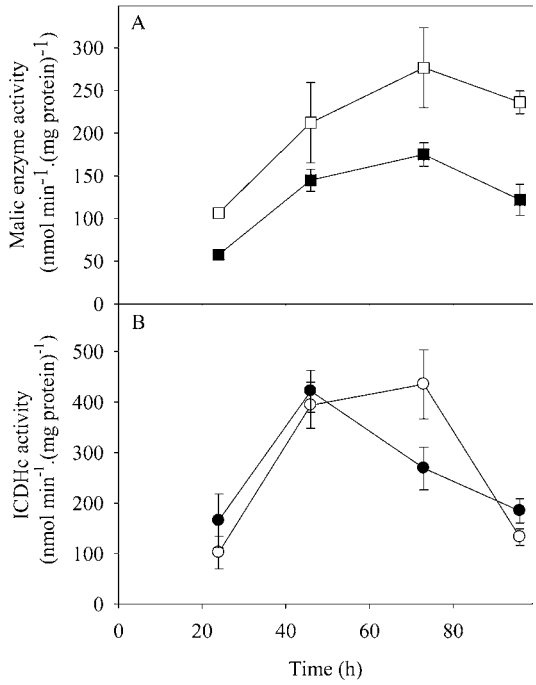

Figure 5. Effect of sesamol on the activities of ME (A) and ICDHC (B) of *C. cohnii* growing with 1 mM (solid) or without sesamol (open).

G-6-PDH to produce NADPH and that sesamol attenuated the intracellular NADPH level, to a large degree, by inhibiting ME activity instead of ICDH or G-6-PDH.

So far, the DHA biosynthetic pathway is not completely defined in *C. cohnii*.[11] DHA can be synthesized via the conventional route, which involves a series of aerobic NADPH-dependent desaturation reactions (Figure 1). Alternatively, DHA biosynthesis can utilize the PKS route, which is thought to be anaerobic and desaturase-free and present in *Schizochytrium* sp. and certain related thraustochytrid marine protists.[15] In our work, accompanied by the sesamol-mediated decrease in NADPH level, *C. cohnii* showed a drop in TFA content but an increase in DHA proportion per TFA (Figure 3A and Table 1). These results may suggest that *C. cohnii* is likely to employ, at least partially, the PKS pathway for DHA biosynthesis. In the presence of sesamol, NADPH production is attenuated due to the inhibition of malic enzyme, leading to a decrease in the accumulation of these de novo synthesized saturated and monounsaturated fatty acids and thus the buildup of fatty acid precursors in *C. cohnii*. The precursors, on the other hand, may be redirected to the biosynthesis of DHA via the desaturase-free PKS pathway, which required much less NADPH, resulting in the possible increase in the relative DHA content.

Sesamol is well-known as a potent antioxidant and inhibitor of malic enzyme. In the present study, sesamol was used to improve DHA production by the marine microalga *C. cohnii* for the first time. Sesamol attenuated the intracelluar ROS level and promoted cell density, DHA proportion per TFA, and DHA productivity of *C. cohnii*, with concomitant decreases in NADPH level and TFA content. Our results suggest that *C. cohnii*, to a large degree, utilizes ME rather than ICDH or G-6-PDH to produce NADPH for the de novo fatty acid biosynthesis. DHA, on the other hand, is likely synthesized, at least partially, via the alternative PKS pathway, which involves no oxygen or NADPH-dependent desaturases. The finding that sesamol has the potential to enhance DHA production by *C. cohnii* is scientifically interesting and provides valuable future directions for lowering production costs in industrial applications.

■ ASSOCIATED CONTENT

Ⓢ Supporting Information

Response factors of the representative fatty acids related to the internal standard of C17:0 (Table S1). The Supporting Information is available free of charge on the ACS Publications website at DOI: 10.1021/acs.jafc.5b01441.

■ AUTHOR INFORMATION

Corresponding Author

*(F.C.) Phone: +86-10-62745356. Fax: +86-10-62757427. E-mail: sfchencoe@pku.edu.cn.

Funding

This study was supported by a 985 Project of Peking University, the 863 Plan of Ministry of Science and Technology of China (Grant 2012AA023107), Public Science and Technology Research Funds Projects of Ocean (Grant 201505032), and the National Natural Science Foundation of China (Grant 31471717).

Notes

The authors declare no competing financial interest.

■ REFERENCES

(1) Mayurasakorn, K.; Williams, J. J.; Ten, V. S.; Deckelbaum, R. J. Docosahexaenoic acid: brain accretion and roles in neuroprotection after brain hypoxia and ischemia. *Curr. Opin. Clin. Nutr. Metab. Care* **2011**, *14*, 158−167.

(2) Karr, J. E.; Alexander, J. E.; Winningham, R. G. Omega-3 polyunsaturated fatty acids and cognition throughout the lifespan: a review. *Nutr. Neurosci.* **2011**, *14*, 216−225.

(3) Gogus, U.; Smith, C. n-3 Omega fatty acids: a review of current knowledge. *Int. J. Food Sci. Technol.* **2010**, *45*, 417−436.

(4) Chitranjali, T.; Anoop, P. A.; Kurup, G. M. Omega-3 fatty acid concentrate from *Dunaliella salina* possesses anti-inflammatory properties including blockade of NF-κB nuclear translocation. *Immunopharmacol. Immunotoxicol.* **2015**, *37*, 81−89.

(5) Liu, J.; Sommerfeld, M.; Hu, Q. Screening and characterization of *Isochrysis* strains and optimization of culture conditions for docosahexaenoic acid production. *Appl. Microbiol. Biotechnol.* **2013**, *97*, 4785−4798.

(6) Ganuza, E.; Anderson, A. J.; Ratledge, C. High-cell-density cultivation of *Schizochytrium* sp. in an ammonium/pH-auxostat fed-batch system. *Biotechnol. Lett.* **2008**, *30*, 1559−1564.

(7) Lian, M.; Huang, H.; Ren, L. J.; Ji, X. J.; Zhu, J. Y.; Jin, L. J. Increase of docosahexaenoic acid production by *Schizochytrium* sp. through mutagenesis and enzyme assay. *Appl. Biochem. Biotechnol.* **2010**, *162*, 935−941.

(8) Pleissner, D.; Eriksen, N. T. Effects of phosphorous, nitrogen, and carbon limitation on biomass composition in batch and continuous flow cultures of the heterotrophic dinoflagellate *Crypthecodinium cohnii*. *Biotechnol. Bioeng.* **2012**, *109*, 2005−2016.

(9) Kuratko, C. N.; Salem, N. Docosahexaenoic acid from algal oil. *Eur. J. Lipid Sci. Technol.* **2013**, *115*, 965−976.

(10) Mendes, A.; Reis, A.; Vasconcelos, R.; Guerra, P.; da Silva, T. L. *Crypthecodinium cohnii* with emphasis on DHA production: a review. *J. Appl. Phycol.* **2009**, *21*, 199−214.

(11) de Swaaf, M. E.; de Rijk, T. C.; van der Meer, P.; Eggink, G.; Sijtsma, L. Analysis of docosahexaenoic acid biosynthesis in *Crypthecodinium cohnii* by C-13 labelling and desaturase inhibitor experiments. *J. Biotechnol.* **2003**, *103*, 21−29.

(12) Song, X. J.; Tan, Y. Z.; Liu, Y. J.; Zhang, J. T.; Liu, G. L.; Feng, Y. G.; Cui, Q. Different impacts of short-chain fatty acids on saturated

DOI: 10.1021/acs.jafc.5b01441
J. Agric. Food Chem. 2015, 63, 5640−5645

and polyunsaturated fatty acid biosynthesis in *Aurantiochytrium* sp. SD116. *J. Agric. Food Chem.* **2013**, *61*, 9876−9881.
(13) Ratledge, C. The role of malic enzyme as the provider of NADPH in oleaginous microorganisms: a reappraisal and unsolved problems. *Biotechnol. Lett.* **2014**, *36*, 1−12.
(14) Metz, J. G.; Roessler, P.; Facciotti, D.; Levering, C.; Dittrich, F.; Lassner, M.; Valentine, R.; Lardizabal, K.; Domergue, F.; Yamada, A. Production of polyunsaturated fatty acids by polyketide synthases in both prokaryotes and eukaryotes. *Science* **2001**, *293*, 290−293.
(15) Ratledge, C. Fatty acid biosynthesis in microorganisms being used for single cell oil production. *Biochimie* **2004**, *86*, 807−815.
(16) Hillig, F.; Porscha, N.; Junne, S.; Neubauer, P. Growth and docosahexaenoic acid production performance of the heterotrophic marine microalgae *Crypthecodinium cohnii* in the wave-mixed single-use reactor CELL-tainer. *Eng. Life Sci.* **2014**, *14*, 254−263.
(17) da Silva, T. L.; Mendes, A.; Mendes, R. L.; Calado, V.; Alves, S. S.; Vasconcelos, J. M. T.; Reis, A. Effect of *n*-dodecane on *Crypthecodinium cohnii* fermentations and DHA production. *J. Ind. Microbiol. Biotechnol.* **2006**, *33*, 408−416.
(18) de Swaaf, M. E.; Sijtsma, L.; Pronk, J. T. High-cell-density fed-batch cultivation of the docosahexaenoic acid producing marine alga *Crypthecodinium cohnii*. *Biotechnol. Bioeng.* **2003**, *81*, 666−672.
(19) de Swaaf, M. E.; Pronk, J. T.; Sijtsma, L. Fed-batch cultivation of the docosahexaenoic-acid-producing marine alga *Crypthecodinium cohnii* on ethanol. *Appl. Microbiol. Biotechnol.* **2003**, *61*, 40−43.
(20) Huang, Q.; Gao, B.; Jie, Q.; Wei, B. Y.; Fan, J.; Zhang, H. Y.; Zhang, J. K.; Li, X. J.; Shi, J.; Luo, Z. J.; Yang, L.; Liu, J. Ginsenoside-Rb2 displays anti-osteoporosis effects through reducing oxidative damage and bone-resorbing cytokines during osteogenesis. *Bone* **2014**, *66*, 306−314.
(21) Kiss, L.; Csizmazia, A.; Benko, Z.; Marosi, G.; Schumacher, U.; Dongo, E. P341Hydrogen sulphide treatment of human adipose derived stem cells increases their proliferation, decreases their mitochondrial activity and enhances their antioxidant defenses. *Cardiovasc. Res.* **2014**, *103* (Suppl. 1), S62.
(22) Molina, N.; Morandi, A. C.; Bolin, A. P.; Otton, R. Comparative effect of fucoxanthin and vitamin C on oxidative and functional parameters of human lymphocytes. *Int. Immunopharmacol.* **2014**, *22*, 41−50.
(23) Wynn, J. P.; Kendrick, A.; Ratledge, C. Sesamol as an inhibitor of growth and lipid metabolism in *Mucor circinelloides* via its action on malic enzyme. *Lipids* **1997**, *32*, 605−610.
(24) Wynn, J. P.; Ratledge, C. Malic enzyme is a major source of NADPH for lipid accumulation by *Aspergillus nidulans*. *Microbiology* **1997**, *143*, 253−257.
(25) Miller, G. L. Use of dinitrosalicylic acid reagent for determination of reducing sugar. *Anal. Chem.* **1959**, *31*, 426−428.
(26) Hsu, R.; Lardy, H. Malic enzyme. *Methods Enzymol.* **1969**, *13*, 230−235.
(27) Langdon, R. G. Glucose 6-phosphate dehydrogenase from erythrocytes. *Methods Enzymol.* **1966**, *9*, 126−131.
(28) Bradford, M. M. A rapid and sensitive method for the quantitation of microgram quantities of protein utilizing the principle of protein-dye binding. *Anal. Biochem.* **1976**, *72*, 248−254.
(29) Yuan, Z. H.; Yao, F.; Hu, Z. Y.; Sun, S. M.; Wu, B. Y. Quercetin inhibits the migration and proliferation of astrocytes in wound healing. *NeuroReport* **2015**, *26*, 387−393.
(30) Thushara, R. M.; Hemshekhar, M.; Sunitha, K.; Kumar, M. S.; Naveen, S.; Kemparaju, K.; Girish, K. S. Sesamol induces apoptosis in human platelets via reactive oxygen species-mediated mitochondrial damage. *Biochimie* **2013**, *95*, 2060−2068.
(31) Liu, J.; Sun, Z.; Zhong, Y. J.; Huang, J. C.; Hu, Q.; Chen, F. Stearoyl-acyl carrier protein desaturase gene from the oleaginous microalga *Chlorella zofingiensis*: cloning, characterization and transcriptional analysis. *Planta* **2012**, *236*, 1665−1676.
(32) Valentine, J. S.; Wertz, D. L.; Lyons, T. J.; Liou, L.-L.; Goto, J. J.; Gralla, E. B. The dark side of dioxygen biochemistry. *Curr. Opin. Chem. Biol.* **1998**, *2*, 253−262.
(33) Menon, K. R.; Balan, R.; Suraishkumar, G. K. Stress induced lipid production in *Chlorella vulgaris*: relationship with specific intracellular reactive species levels. *Biotechnol. Bioeng.* **2013**, *110*, 1627−1636.
(34) Recht, L.; Zarka, A.; Boussiba, S. Patterns of carbohydrate and fatty acid changes under nitrogen starvation in the microalgae *Haematococcus pluvialis* and *Nannochloropsis* sp. *Appl. Microbiol. Biotechnol.* **2012**, *94*, 1495−1503.
(35) Guay, C.; Madiraju, S. R. M.; Aumais, A.; Joly, E.; Prentki, M. A role for ATP-citrate lyase, malic enzyme, and pyruvate/citrate cycling in glucose-induced insulin secretion. *J. Biol. Chem.* **2007**, *282*, 35657−35665.
(36) Jiang, Y.; Chen, F. Effects of temperature and temperature shift on docosahexaenoic acid production by the marine microalga *Crypthecodinium cohnii*. *J. Am. Oil Chem. Soc.* **2000**, *77*, 613−617.

DOI: 10.1021/acs.jafc.5b01441
J. Agric. Food Chem. 2015, 63, 5640−5645

to carry out numerous tasks in the olive oil field.[23,24] In this case, a two-layer backpropagation neural network (BNN) was designed using the absorption information as input data to attain a fast and competent adulterant identifier as well as an EVOO of the Picual varietal quantifying system.

MATERIALS AND METHODS

Visible Spectroscopy. A Varian Cary 1E UV−vis spectrophotometer operating between 440 and 800 nm was used to obtain the absorption spectra of the binary mixtures (EVOO and adulterant). The samples were analyzed in a transparent cell of 1 cm path length.

Adulterated EVOO Samples. To accomplish this work, EVOO of the Picual varietal was mixed with different known concentrations of one of the following adulterants: corn oil (CO), sunflower oil (SO), orujo olive oil (OOO), or refined olive oil (ROO).

Twenty samples of 2 mL of EVOO with one of the adulterants were prepared within the EVOO volume percentage range of 80−100%, making a total of 81 samples (counting the pure Picual sample). No additional solvents were used apart from the oils, enabling this method to be used online. The oils used are listed in Table 1.

Table 1. Oils Used for Sample Preparation

type	supplier
Picual varietal EVOO	Borges Pont SAU Oil
corn oil (CO)	KOIPE, SOS Cuétara SA
sunflower oil (SO)	KOIPE, SOS Cuétara SA
orujo olive oil (OOO)	DIA
refined olive oil (ROO)	KOIPE, SOS Cuétara SA

The spectra obtained when the mixtures were measured were used to create two types of data sets: the maximum absorption peaks (profile descriptors) and areas under the curve (AUC). For the first type, the five maximum intensity values of the different absorption bands of the spectra were selected. For the second one, the AUC of those same five bands were calculated, avoiding overlaps as done by Díaz-Rodríguez et al. for the quantification of ionic liquids in mixtures.[25]

Mathematical Modeling. *Partial Least Squares.* PLS regression is a classic statistical modeling approach that is used to create a linear regression by the projection of both predicted and observed variables into a new space (somewhat related to principal components analysis).[21]

The resulting linear models possess the structure (eq 1)

$$y = c + \sum_n a_n x_n \tag{1}$$

where c is the constant of the model (regression coefficient for the intercept), x and y represent the independent and dependent variables, respectively, and a_n is the regression coefficient for the independent variables.

In the present context, five independent PLS equations will be obtained after the design of the PLS model using the spectroscopic information as independent variables (same variables as the BNN). A first equation will be used to estimate the EVOO content, and four others will be employed to determine the adulterating oil, which is comparable to the five outputs from the BNN. These last four equations act as discriminators, in other words, forming a PLS discriminant analysis, as the results are categorical, and, moreover, a PLS-2 model, because there are more than two groups (four adulterants) to be classified.[26]

The PLS models have been carried out through the software Statgraphics Centurion XVI.

Artificial Neural Networks. ANNs were chosen for this task due to their ability to find and adequately interpret nonlinear relationships between different variables in databases. This principal characteristic and also advantage of ANNs enables them to work with different oil mixtures at the same time, providing a versatility and flexibility that classic lineal models do not offer.[27] In addition, these algorithms have been employed by the authors in the past to achieve other olive oil adulteration-related tools and applications.[23,24]

In the present scenario, multilayer perceptron (MLP)-based ANNs have been employed. MLPs are one of the most used ANNs thanks to their notable results in many fields such as food technology,[24] chemistry,[25,27,28] and nanochemistry.[29]. The specific MLP used was a BNN.

These tools are composed by three different layers as can be seen in Figure 1: the input layer, the hidden layer, and the output layer. The

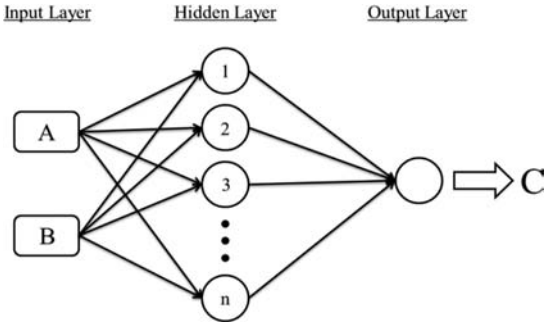

Figure 1. Multilayer perceptron scheme, where *A* and *B* are independent input variables and *C* is the dependent output variable.

first one is made of nodes in charge of introducing all of the data into the BNN, and the other two layers are formed by neurons, which are the calculation centers responsible of transforming the input signals into processed output responses, and in the present case, they all employed a sigmoid transfer function to carry out the nonlinear calculations.[30]

The signals that enter a neuron can come from another neuron or have an external origin and are modulated by weights. These weights control the connection between emitting nodes or neurons and receiving neurons. Therefore, their optimization is essential for the correct functioning of the network.[31] The way this optimization is carried out is further explained in the Supporting Information.

The learning process of a supervised neural network, such as BNNs, is carried out entering paired input−output values into the network, or, in other words, labeled data. It is based on a series of iterative calculations that minimize the difference between the real value and the one estimated by the network, therefore lowering the prediction error of the model. During this learning process, the network adjusts its parameters until obtaining weight values capable of representing the studied sample. However, the training of the network must be controlled; otherwise, "underachieving" or "over-fit" models can result. The first type takes place when the given input values are not representative or the model has not been correctly designed, and the network is incapable of defining nonlinear trends. The second undesired phenomenon is caused by excessive training, and the obtained relationships do not correspond to the wanted properties or characteristics, but to intrinsic characteristics of specific data points such as noise or experimental error.

To avoid these undesirable effects, the database used to optimize the weights is divided into two parts; training data and verification data. The training data are used to modify and optimize the weights and the verification data to analyze the applicability or generalizing capacity of the model. The goal of this second step is to stop the training cycles when the error in the estimation of these verification data points starts to increase, thus avoiding overtrained systems.[32] While the iterative process takes place, using the training data, the prediction error is reduced progressively. Meanwhile, with the verification data the weights are not modified, so the prediction error decreases until it reaches its minimum value for certain specific weights, and after that it begins to increase if the weights continue optimizing for the training data. In that precise moment the model is

DOI: 10.1021/acs.jafc.5b01700
J. Agric. Food Chem. 2015, 63, 5646−5652

considered to be optimized and the iterative calculations come to an end.[27,33]

Once the learning is completed, a representative algorithm that can interpret the relationship between the input and the output is obtained, enabling the network to generate adequate outputs for new inputs, not comprised in the learning process.[25] It is important to highlight that these mathematical tools are designed to carry out very precise interpolations, but they do not give satisfactory results when the provided data points are outside the operation range of the network.[31] In other words, ANNs are not made for extrapolating.

All of the BNN calculations have been developed through Matlab version 7.0.1.24704 (R14).[34]

Optimization of the BNN. The used BNN was designed to estimate five variables (five output neurons), four of them (CO, SO, OOO, and ROO) with a classifying purpose to identify the specific adulteration, and the fifth one (EVOO %) to quantify the volume percentage of EVOO in the mixture. The adulterants were detected with an identification vector composed by four outputs, one per adulterant, being [1, 0, 0, 0] for CO, [0, 1, 0, 0] for SO, [0, 0, 1, 0] for OOO, and [0, 0, 0, 1] for ROO.

The numbers of input nodes and output neurons are defined according to the available information and to the specific task required, respectively. In this case, visible absorption data of the adulterated EVOO samples were employed for the posterior detection of adulterants and quantification of Picual EVOO in the mixtures.

Another relevant process is the selection of an adequate training function as it controls the algorithms in the learning process of the model. Therefore, it is very important to choose a function that generates low estimative errors, thus ensuring the correct functioning of the BNN.[35] Between all of the analyzed training functions, the Levenberg−Marquardt algorithm (TrainLM) and the Bayesian regularization algorythm (TrainBR) offered a correct performance, so they were both further studied and the better one was selected for the final model. When working with medium size networks as in the present work, TrainLM is the fastest, and it also has a memory reduction feature for large training sets. On the other hand, TrainBR is a modification of the before-mentioned algorithm, and it reduces the difficulty of finding the optimum network topology as well as creating networks that generalize well.[35]

Besides the already mentioned optimization steps, to achieve a functional model, the hidden neuron number (HNN), the learning coefficient (L_c), and its own controlling parameters were also optimized.[34] The HNN must be modified until optimum performance of the model is achieved, and the chosen strategy was a heuristic approach,[32] considering that the number of neurons or weights to be optimized should not be higher than half of the amount of samples to avoid overfitting effects. On the other hand, L_c and its decreasing (L_{cd}) and increasing (L_{ci}) factors were optimized using a thorough experimental design based on the Box−Wilson Central Composite Design 2^3 + start points.[32] The experimental design has been done using Statgraphics Centurion 16.1.18.

Validation of the BNN. Once the BNN was adequately trained or optimized, an internal validation procedure was carried out to evaluate the performance of the BNN[36] in terms of adulterant identification and Picual EVOO quantification. This validation process consists of dividing randomly the database into three different groups of data: training, verification, and simulation, containing 70, 20, and 10% of the data, respectively. Three individual and randomized internal validations were carried out.

RESULTS AND DISCUSSION

Visible Spectroscopy. Different spectra of samples of the pure oils (Picual EVOO and four adulterants) were taken as a preliminary analysis of the compounds prior to their study in mixtures. According to the studies of Mínguez-Mosquera et al., chlorophyll (420 and 670 nm) and carotenoids (470 and 495 nm) present in oils are responsible for their absorption bands in the visible spectra.[37] The visible spectra of the pure Picual EVOO (Figure 2) and the four adulterants (Figure 3) are shown. Absorption between 400 and 500 nm can be observed for all five of them, whereas around 650−700 nm, only EVOO, ROO, and OOO present an absorption band.

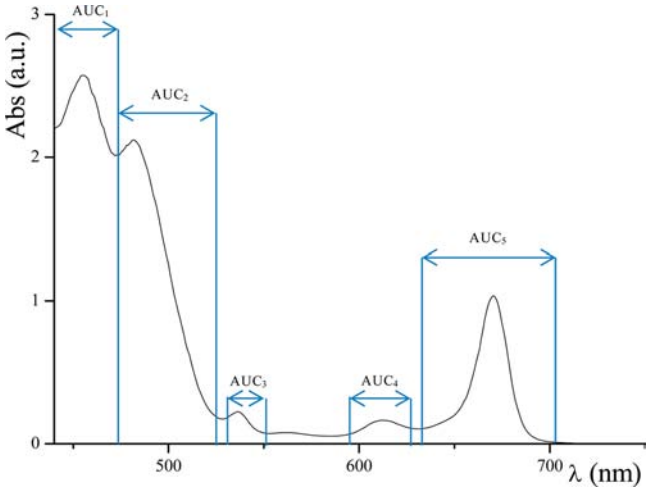

Figure 2. Visible spectrum of the pure Picual varietal EVOO used. The range of the AUC is shown.

Following this, absorption spectra of adulterated samples of Picual EVOO were analyzed. In Figure 4, examples can be found of EVOO being adulterated with ROO. The intensity of the band between 650 and 700 nm is highlighted to show how the absorption intensity decreases with greater concentrations of ROO.

The same procedure was followed for the other three adulterants (total 81 samples; data shown in the Supporting Information), and they all followed the same tendency: a lower yet specific intensity of the representative absorption bands for the samples with higher adulterant concentrations. For example, adulterants such as CO and SO originate a faster decrease in the absorption of the peak at AUC_5, compared to the effects of OOO or ROO. The reason behind this phenomenon is that neither CO nor SO presents that absorption band at that wavelength, and as absorption values are additive, this results in the mentioned quicker decline.

Even though the relationship is linear when a single binary system is analyzed, the ANN is capable of identifying four different but similar adulterants at the same time, which provides a great adaptability to the mathematical tool. This is possible due to the fact that the absorption spectra of the pure adulterants are different (Figure 3), which leads to dissimilar resulting spectra of the samples mixed with particular amounts of distinct adulterants, enabling the mathematical modeling of the system via ANNs.

Mathematical Analysis. In this subsection, two different mathematical approaches will be compared to fulfill the EVOO amount estimation and adulterant identification. First, a BNN model and all of the necessary steps to optimize it as well as to evaluate its performance will be presented, followed by a linear PLS-2 model and its validation with the same data as the BNN to achieve a controlled experiment, which enables their comparison.

Artificial Neural Networks. (a) Data Analysis for Input Selection and BNN Optimization. The information used as input in the BNN has a major influence on the correct functioning of the model. Therefore, the way in which it is presented will greatly determine the precision of the final results.

DOI: 10.1021/acs.jafc.5b01700
J. Agric. Food Chem. 2015, 63, 5646−5652

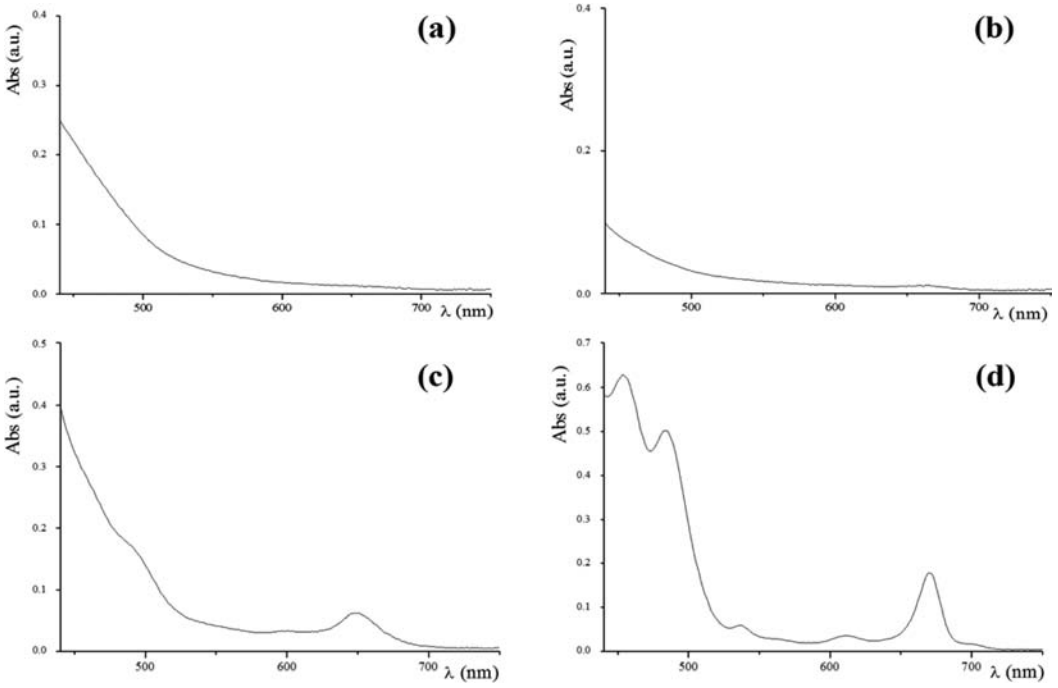

Figure 3. Absorption spectra of the four adulterants: (a) corn oil; (b) sunflower oil; (c) orujo olive oil; (d) refined olive oil.

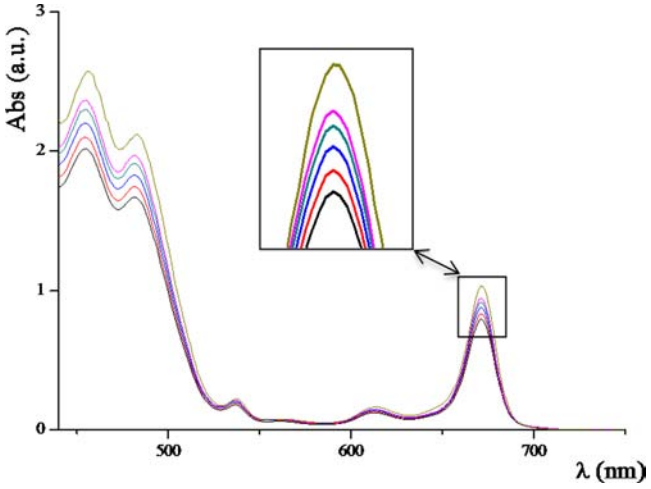

Figure 4. Absorption spectra of six samples of Picual EVOO adulterated with ROO: 100% EVOO (green), 99% EVOO (pink), 95% EVOO (greenish blue), 90% EVOO (blue), 85% EVOO (red), and 80% of EVOO (black). The absorption band centered at 670 nm is amplified to facilitate understanding the trend (same for all bands).

If all of the information contained in the absorption spectra (every wavelength−absorption pair) was used for the models, it may translate into an overfit system that would use redundant and noninformative data. Therefore, certain representative features of the obtained spectra were selected. The two types of data sets (vide supra) that were chosen as input data to simplify the calculations of the ANN were (a) five maximum absorption peaks at wavelengths 456, 483, 536, 612, and 670 nm and (b) the AUC of the previous bands, ranging from 440 to 472 nm for AUC_1, from 473 to 526 nm for AUC_2, from 529 to 551 nm for AUC_3, from 593 to 630 nm for AUC_4, and, finally, from 632 to 703 nm for AUC_5 (shown in Figure 2), which were calculated through peak integration.[32] These two sets of five inputs were used to create two BNN models.

Comparison of the results from the models that used the two different input sets is shown in Table 2. The statistical performance was much better when using the AUCs, so the maximum absorption peaks were discarded and further optimization of the model continued using only AUCs as input data. This performance was quantified through two tests, the first one being an adulterant identification rate (ideally 100%) and the second one the mean prediction error (MPE) of the estimated versus real Picual EVOO volume percentage (ideally 0%). To determine the identification rate, the four identifying outputs provided by the BNN are transformed into vectors containing a single "1" and three "0" (greatest value converted into "1"). The resulting estimated vectors are compared with the real ones to determine the final identification rate. On the other hand, to assess the Picual EVOO amount estimation, the MPE was calculated according to eq 2

Table 2. Results Obtained for the Different Input Sets, the Different Training Functions Assessed, and the HNN Study[a]

parameter optimized	option or amount	identification rate (%)	MPE of the volume percentage of EVOO (%)
input set	Abs_{max}	83	1.3
	AUC	**100**	**0.6**
training function	**TrainLM**	**100**	**0.6**
	TrainBR	100	1.0
HNN	3	100	1.3
	4	100	1.0
	5	**100**	**0.6**

[a] L_c, L_{cd}, and L_{ci} parameters kept the default values of the software (0.001, 0.1, and 10, respectively) during these three steps (best and selected choices in bold).

DOI: 10.1021/acs.jafc.5b01700
J. Agric. Food Chem. 2015, 63, 5646−5652

$$\mathrm{MPE} = \frac{1}{N}\sum_{k=1}^{N}\frac{|r_k - y_k|}{r_k} \times 100 \quad (2)$$

where N represents the number of data evaluated, r_k is the real value and y_k is the value estimated by the network (vide supra).

Once the input data that provided the best results had been selected, the selection of the training function was performed. In Table 2 the results of the two functions used, TrainBR and TrainLM, are shown. The TrainLM function gave the lowest MPE, thus eliminating TrainBR from the next step of optimization of the model.

Next, considering the amount of data points, the range of HNN was studied between three and five, so that the number of weights stayed below or near half the number of data points and, therefore, avoiding the mentioned overfitting models. The results can be seen in Table 2, and they show that the network is more accurate when it contains five hidden neurons.

As said before, the parameters L_c, L_{cd}, and L_{ci} are optimized following an experimental design based on the Box−Wilson Central Composite Design 2^3+star points". L_c and L_{cd} were analyzed between 0.001 and 1, whereas L_{ci} was studied between 2 and 100. The combination of these three parameters that provided the lowest errors was employed in the final optimized version of the nonlinear model (Table 3).

Table 3. Optimized Parameters of the Final BNN Model

parameter	results
input variables	AUC
training function	TrainLM
HNN	5
L_c	0.51
L_{cd}	0.002
L_{ci}	98

Finally, in Table 3 all of the selected and optimized parameters for the final BNN model are shown. The combination of these parameters enables the design of an ANN that is capable of accurately detecting adulterants in binary mixtures and quantifying the volume percentage of Picual EVOO within the range of the studied samples.

(b) BNN Validation. The results of the three independent internal validation tests performed for the optimized BNN are shown in Table 4.

Table 4. Results of the Internal Validation of the BNN Model (n = 8 per Validation)

internal validation	identification rate (%)	MPE of the volume percentage of EVOO (%)
1	100.0	0.9
2	87.5	1.8
3	100.0	0.9
mean value	**95.8**	**1.2**

The final results demonstrate that the designed model is able to determine the type of adulterant present in a contaminated sample of EVOO with high precision, giving an identification rate of 96% (23/24 correctly classified). It can also estimate the volume percentage of the pure EVOO in the mixture with a low mean prediction error of 1.2%.

Linear Models To Compare with BNN. A PLS-2 model was designed to compare the results with those attained through the BNN. The resulting five equations were used to estimate each of the five outputs defined for the nonlinear MLP. This was carried out three times independently, using the same data and independent variables (five AUCs) contained in the training and verification data sets of the internal validations of the BNN to make the results comparable. The final statistical performance is evaluated by testing the resulting PLS models with the 10% of the data not employed during their construction (same as simulation data sets from the BNNs; vide supra). The regression coefficients for all the PLS models are shown in the Supporting Information (Tables S1−S3). In Table 5, the results for each PLS model are shown, which are comparable to those shown in Table 4.

Table 5. Results of the Tests of the Different PLS Models Using the Same Data from the Internal Validations of the BNN (n = 8 per Validation)

PLS model (comparable to internal validations)	identification rate (%)	MPE of the volume percentage of EVOO (%)
1	100.0	1.2
2	75.0	1.8
3	87.5	1.6
mean value	**87.5**	**1.5**

The results offered by the linear PLS models are accurate in terms of both EVOO amount estimation (1.5% MPE) and adulteration identification (87.5%; 21/24 correctly classified). Nevertheless, these results are worse when compared with the BNN model optimized, showing one of the advantages of the nonlinear alternative. In contrast, the PLS models are much easier and faster to develop, as they do not present the amount of optimization steps that neural networks do.

In this work, we have successfully estimated the amount of EVOO in contaminated samples (MPE = 1.2%), as well as accurately identified the presence of four different adulterants (96% accuracy) using a nonlinear BNN and visible absorption spectroscopy. In comparison to other techniques of adulterant determination and authentication of EVOO, such as GC-MS used by Yang et al., we can observe that their identification rate is of 88.5%.[38] On the other hand, HPLC used by De la Mata-Espinosa et al. gave a root-mean-square error of prediction of 10% for the adulterant determination,[21] whereas that same error calculated with the results here obtained is of 9.5%. This is very interesting considering that our technique is much cheaper and less time-consuming than GC-MS or HPLC.

In terms of being user-friendly and requiring a low sample treatment, FT-IR spectroscopy is close to vis spectroscopy. It was employed by Oussama et al., who combined it with a lineal mathematical model (PLSs together with variable importance in projection), which resulted in a relative prediction error of 3% for the oil composition and an identification rate of 100% for two types of adulterant,[39] in contrast to the four adulterants analyzed here with a single and adaptable nonlinear MLP.

These notable results enable our flexible and updatable nonlinear model to compete with techniques such as FT-IR,[39] GC-MS,[38,40] NMR,[41] or HPLC,[21] simply by employing absorption information. Furthermore, some of the advantages of the proposed methodology are its speed and straightforwardness due to minor necessary sample treatments. The employment of the equipment is noncomplicated, and additionally it is nondestructive (samples do not suffer any alteration). The use of solvents is low, which decreases the cost of the already

DOI: 10.1021/acs.jafc.5b01700
J. Agric. Food Chem. 2015, 63, 5646−5652

inexpensive approach. Finally, it offers the possibility of applying this method for real-time applications such as EVOO online monitoring and control, which is useful for both producers and distributors.

■ ASSOCIATED CONTENT

Supporting Information

Description of the weight optimization process, the absorption spectra registered, and the PLS coefficients. The Supporting Information is available free of charge on the ACS Publications website at DOI: 10.1021/acs.jafc.5b01700.

■ AUTHOR INFORMATION

Corresponding Author

*(J.S.T.) Phone: +34 91 394 42 44. Fax: +34 91 394 42 43. E-mail: jstorre@ucm.es.

Notes

The authors declare no competing financial interest.

■ REFERENCES

(1) Stark, A. H.; Madar, Z. Olive oil as a functional food: epidemiology and nutritional approaches. *Nutr. Rev.* **2002**, *60*, 170−176.

(2) Visioli, F.; Galli, C. The effect of minor constituents of olive oil on cardiovascular disease: new findings. *Nutr. Rev.* **1998**, *56*, 142−147.

(3) Menéndez, J. A.; Vázquez-Martín, A.; Colomer, R.; Brunet, J.; Carrasco-Pancorbo, A.; García-Villalba, R.; Fernández-Gutiérrez, A.; Segura-Carretero, A. Olive oil's bitter principle reverses acquired autoresistance to trastuzumab (Herceptin) in HER2-overexpressing breast cancer cells. *BMC Cancer* **2007**, *7*, 80−98.

(4) Martín Lagos, J. A. *Estudio de los índices de calidad en aceites de oliva de la provincial de Granada*; Ph.D. thesis, 2007.

(5) Civantos Lopez, L. *Obtención del Aceite De Oliva Virgen*; Agrícola Española S.A.: Madrid, Spain, 1999.

(6) Boskou, D. Sources of natural phenolic antioxidants. *Trends Food Sci. Technol.* **2006**, *17*, 505−512.

(7) Torrecilla, J. S. *The Olive. Its Processing and Waste Management*; Nova Science Publishers: Hauppauge, NY, USA, 2010, ISBN: 978-1-60876-719-9.

(8) Tay, A.; Sink, R. K.; Krishnan, S. S.; Gone, J. P. Authentication of olive oil adulterated with vegetable oils using fourier transform infrared spectroscopy. *Lebensm. Wiss. Technol.* **2002**, *35*, 99−103.

(9) Maggio, R. M.; Cerretani, L.; Chiavaro, E.; Kaufman, T. S.; Bendin, A. A novel chemometric strategy for the estimation of extra virgin olive oil adulteration with edible oils. *Food Control* **2010**, *21*, 890−895.

(10) García-González, D. L.; Luna, G.; Morales, M. T.; Aparicio, R. Stepwise geographical traceability of virgin olive oils by chemical profiles using artificial neural network models. *Eur. J. Lipid Sci. Technol.* **2009**, *111*, 1003−1013.

(11) Sacchi, R.; Patumi, M.; Fontanazza, G.; Barone, P.; Fiordiponti, P.; Mannina, L.; Rossi, E.; Segne, A. L. A high-field-^{1}H nuclear magnetic resonance study of the minor components in virgin olive oils. *J. Am. Oil Chem. Soc.* **1996**, *73*, 747−758.

(12) Rezzi, S.; Axelson, D. E.; Héberger, K.; Reniero, F.; Mariani, C.; Guillou, C. Classification of olive oils using high throughput flow $_1$H NMR fingerprinting with principal component analysis, linear discriminant analysis and probabilistic neural networks. *Anal. Chim. Acta* **2005**, *552*, 13−24.

(13) Concha-Herrera, V.; Lerma-García, M. J.; Herrero-Martínez, J. M.; Simó-Alfonso, E. F. Classification of vegetable oils according to their botanical origin using amino acid profiles established by high performance liquid chromatography with UV-vis detection: a first approach. *Food Chem.* **2010**, *120*, 1149−1154.

(14) Fasciotti, M.; Netto, P. Optimization and application of methods of triacylglycerol evaluation for characterization of olive oil adulteration by soybean oil with HPLC−APCI−MS−MS. *Talanta* **2010**, *81*, 1116−1125.

(15) Arslan, D.; Özcan, M. M. Phenolic profile and antioxidant activity of olive fruits of the Turkish variety 'Sariulak' from different locations. *Grasas Aceites* **2011**, *62*, 453−461.

(16) Guimet, F.; Boqué, R.; Ferré, J. Application of non-negative matrix factorization combined with Fisher's linear discriminant analysis for classification of olive oil excitation−emission fluorescence spectra. *Chemom. Intell. Lab. Syst.* **2006**, *81*, 94−106.

(17) Poulli, K. I.; Mousdis, G. A.; Georgiou, C. A. Synchronous fluorescence spectroscopy for quantitative determination of virgin olive oil adulteration with sunflower oil. *Anal. Bioanal. Chem.* **2006**, *86*, 1571−1575.

(18) Poulli, K. I.; Mousdis, G. A.; Georgiou, C. A. Classification of edible and lampante virgin olive oil based on synchronous fluorescence and total luminescence spectroscopy. *Anal. Chim. Acta* **2005**, *542*, 151−156.

(19) Dankowska, A.; Malecka, M.; Kowalewski, W. Discrimination of edible olive oils by means of synchronous fluorescence spectroscopy with multivariate data analysis. *Grasas Aceites* **2013**, *64*, 425−431.

(20) Pizarro, C.; Rodríguez-Tecedor, S.; Pérez del Notario, N.; Esteban-Díez, I.; González Sáiz, J. M. Classification of Spanish extra virgin olive oils by data fusion of visible spectroscopic fingerprints and chemical descriptors. *Food Chem.* **2012**, *138*, 915−922.

(21) De la Mata-Espinosa, P.; Bosque-Sendra, J. M.; Bro, R.; Cuadros-Rodríguez, L. Olive oil quantification of edible vegetable oil blends using triacylglycerols chromatographic fingerprints and chemometric tools. *Talanta* **2011**, *85*, 177−182.

(22) Jain, A. K.; Mao, J. C.; Mohiuddin, K. M. Artificial neural networks: a tutorial. *Computer* **1996**, *29*, 31−44.

(23) Torrecilla, J. S.; Cancilla, J. C.; Matute, G.; Díaz-Rodríguez, P.; Flores, A. I. Self-organizing maps based on chaotic parameters to detect adulterations of extra virgin olive oil with inferior edible oils. *J. Food Eng.* **2013**, *118*, 400−405.

(24) Torrecilla, J. S.; Cancilla, J. C.; Matute, G.; Díaz-Rodríguez, P. Neural network models to classify olive oils within the protected denomination of origin framework. *Int. J. Food Sci. Technol.* **2013**, *48*, 2528−2534.

(25) Díaz-Rodríguez, P.; Cancilla, J. C.; Wierzchós, K.; Torrecilla, J. S. Non-linear models applied to experimental spectroscopical quantitative analysis of aqueous ternary mixtures of imidazolium and pyridinium-based ionic liquids. *Sens. Actuators, B* **2015**, *206*, 139−145.

(26) De Almeida, M. R.; Correa, D. N.; Rocha, W. F. C.; Scafi, F. J. O.; Poppi, R. J. Discrimination between authentic and counterfeit banknotes using Raman spectroscopy and PLS-DA with uncertainty estimation. *Microchem. J.* **2013**, *109*, 170−177.

(27) Díaz-Rodríguez, P.; Cancilla, J. C.; Plechkova, N. V.; Matute, G.; Seddon, K. R.; Torrecilla, J. S. Estimation of the refractive indices of imidazolium-based ionic liquids using their polarisability values. *Phys. Chem. Chem. Phys.* **2014**, *16* (1), 128−134.

(28) Curteanu, S.; Cartwright, H. Neural networks applied in chemistry. I. Determination of the optimal topology of multilayer perceptron neural networks. *J. Chemom.* **2011**, *25*, 527−549.

(29) Wang, B.; Cancilla, J. C.; Torrecilla, J. S.; Haick, H. Artificial sensing intelligence with silicon nanowines for ultraselective detection in the gas phase. *Nano Lett.* **2014**, *14*, 933−938.

(30) Torrecilla, J. S.; Tortuero, C.; Cancilla, J. C.; Díaz-Rodríguez, P. Estimation with neural networks of the water content in imidazolium-based ionic liquids using their experimental density and viscosity values. *Talanta* **2013**, *113*, 93−98.

(31) Cancilla, J. C.; Torrecilla, J. S.; Matute, G. Current applications of artificial neural networks in biochemistry with emphasis on cancer research. *Curr. Biochem. Eng.* **2014**, *1*, 25−34.

(32) Cancilla, J. C.; Díaz-Rodríguez, P.; Izquierdo, J. G.; Bañares, L.; Torrecilla, J. S. Artificial neural networks applied to fluorescence studies for accurate determination of N-butylpyridinium chloride concentration in aqueous solution. *Sens. Actuators, B* **2014**, *198*, 173−179.

DOI: 10.1021/acs.jafc.5b01700
J. Agric. Food Chem. 2015, 63, 5646−5652

(33) Torrecilla, J. S.; Mena, M. L.; Yáñez-Sedeño, P.; García, J. Application of artificial neural network to the determination of phenolic compounds in olive oil mill wastewater. *J. Food Eng.* **2007**, *81*, 544−552.
(34) Demuth, H.; Beale, M.; Hagan, M. *Neural Network Toolbox for Use with Matlab® User's Guide*, version 4.0.6, ninth printing revised for version 4.0.6 (release 14SP3); Natick, MA, USA, 2005.
(35) Torrecilla, J. S.; Aragón, J. M.; Palancar, M. C. Optimization of an artificial neural network by selecting the training function. Application to olive oil mills waste. *Ind. Eng. Chem. Res.* **2008**, *47*, 7072−7080.
(36) Cancilla, J. C.; Wang, S. C.; Díaz-Rodríguez, P.; Matute, G.; Cancilla, J. D.; Torrecilla, J. S. Linking chemical parameters to sensory panel results through neural networks to distinguish olive oil quality. *J. Agric. Food Chem.* **2014**, *62*, 10661−10665.
(37) Mínguez-Mosquera, I.; Rejano-Navarro, L.; Gandul-Rojas, B.; Sanchez-Gomez, A. H.; Garrido-Fernandez, J. Color-pigment correlation in virgin olive oil. *J. Am. Oil Chem. Soc.* **1991**, *68* (5), 332−336.
(38) Yang, Y.; Duarte-Ferro, M.; Cavaco, I.; Liang, Y. Detection and identification of extra virgin olive oil adulteration by GC-MS combined with chemometrics. *J. Agric. Food Chem.* **2013**, *61*, 3693−3702.
(39) Oussama, A.; Elabadi, F.; Platikanov, S.; KzaiBer, F.; Tauler, R. Detection of olive oil adulteration using FT-IR spectroscopy and PLS with variable importance of projection scores. *J. Am. Oil Chem. Soc.* **2012**, *89*, 1807−1812.
(40) Jabeur, H.; Zribi, A.; Makni, J.; Rebai, A.; Abdelhedi, R.; Bouaziz, M. Detection of chemlali extra-virgin olive oil adulteration mixed with soybean oil, corn oil, and sunflower oil by using GC and HPLC. *J. Agric. Food Chem.* **2014**, *62*, 4893−4904.
(41) Xu, Z.; Morris, R. H.; Bencsik, M.; Newton, M. I. Detection of virgin olive oil adulteration using low field unilateral NMR. *Sensors* **2014**, *14*, 2028−2035.

DOI: 10.1021/acs.jafc.5b01700
J. Agric. Food Chem. 2015, 63, 5646−5652

Three commercially available elderberry genotypes (Adams II, Bob Gordon, and Wyldewood) were used. These three genotypes have widely disparate geographic origins, originating from wild genetic material in New York, Missouri, and Oklahoma, respectively. Phenotypically, they behave differently when cultivated side-by-side, suggesting that there are inherent genetic differences among them.[19] Experimental plots contained four plants of the same genotype, planted 1.2 m apart. Forty-eight plots were established in four rows, with plots separated 2.4 m within and 3.1 m between rows. The three genotypes were assigned to 16 of the 48 plots in a completely randomized manner. The total number of plants was 192, and the site covered 0.10 ha. The site was prepared by killing existing vegetation in the planting rows with glyphosate herbicide prior to planting, and alleyways of mixed grasses were maintained and mowed during the study. Throughout the study, plants were irrigated via drip lines to provide 2.5−4.0 cm water per week when rainfall was lacking. Weeds were managed with mulch, hand weeding, and herbicides (glyphosate, clethodim); no insecticides or fungicides were used.

For this study, fresh ripe fruit was harvested from 39 of the 48 plots on August 26−27, 2013, promptly refrigerated, transported under refrigeration to the laboratory on August 28 for analysis, and stored at −80 °C for 1 week. Elderberry samples were then thawed, destemmed, and hand pressed into juice. All other debris, pulp, and seeds were discarded. The juice obtained was filtered through a nylon filter (0.22 μm), and 1.5 mL of each replicate was individually aliquotted into 1.5 mL microcentrifuge tubes and stored at −20 °C The samples were screened for TP, TMA, and IAC initially and after 3, 6, and 9 months of frozen storage. Samples were thawed, an aliquot was removed for analysis, and then the samples were refrozen for future analysis. The number of independent juice samples ranged from 11 to 14 for each of the three genotypes for all assays conducted.

Chemicals. Cyanidin 3-*O*-glucoside chloride analytical standard (≥95%), Folin−Ciocalteu's phenol reagent, sodium acetate trihydrate (≥99.0%), and gallic acid (97.5−102.5%) were purchased from Sigma-Aldrich (St. Louis, MO, USA). Ammonium hydroxide (Optima), sodium carbonate anhydrous (certified ACS powder), potassium chloride (certified ACS crystalline), hydrochloric acid (Optima), water (HPLC grade), formic acid (HPLC grade), and acetonitrile (HPLC grade) were purchased from Fisher Scientific (Fair Lawn, NJ, USA). Trifluoroacetic acid (TFA; 99%) used for acidifying solid phase extraction (SPE) mobile phase was purchased from Acros Organics (Morris Plains, NJ, USA).

Total Phenolic. Folin−Ciocalteu's method was used with slight modifications.[20] Juice samples were initially diluted 100-fold with water, then 0.5 mL of Folin−Cicoalteu's phenol reagent (diluted 10-fold) was added, followed by 0.4 mL of sodium carbonate (75 g/L) after 30 s, but before 8 min. Samples equilibrated at room temperature, in the absence of light, for 2 h. Absorbance measurements were taken in triplicate at a wavelength of 760 nm with a PerkinElmer Enspire 2300 multimode plate reader. Five gallic acid standards of 25, 50, 100, 200, and 400 μg/mL were prepared in the same manner as the samples. The TP concentrations are expressed as gallic acid equivalents (mg GAE/mL).

Total Monomeric Anthocyanin. The TMA content of elderberry juice was measured utilizing the pH-differential method.[21] Elderberry juice samples were diluted 200-fold in potassium chloride (pH 1.0) and sodium acetate (pH 4.5) buffers and equilibrated for 60 min at room temperature. Five cyanidin 3-*O*-glucoside standards of 2, 4, 6, 8, and 10 μg/mL were prepared in the same manner as the samples. Absorbance measurements were taken in triplicate at wavelengths of 520 and 700 nm in each buffer solution. Equation 1 shows how the final absorbance values were obtained. TMA concentrations were determined using a standard curve and are expressed as cyanidin 3-*O*-glucoside equivalents (mg C3GE/mL). The standard solution concentrations were verified using the molar extinction coefficient of cyanidin 3-*O*-glucoside (MW 449.2 g/mol, ε = 26900 M^{-1} cm, λ = 520 nm).[22]

$$A = (A_{520} - A_{700})_{pH1.0} - (A_{520} - A_{700})_{pH4.5} \quad (1)$$

Solid Phase Extraction. Mixed-mode cation-exchange chromatography was employed to isolate the anthocyanins from the other potentially interfering compounds in the juice matrix.[4] Oasis MCX 3 cm^3 (60 mg) extraction cartridges were used with a Supelco Visiprep SPE vacuum manifold, operated at 10 ± 2 in.Hg. Columns were initially conditioned with 2 mL of acidified water (0.01% TFA). After conditioning, 50 μL of juice was added, followed by an additional 2 mL of water (0.01% TFA) and 2 mL of methanol (0.01% TFA). Then 1 mL of methanol (1% NH_4OH) and 1 mL of 40:60 water/methanol (1% NH_4OH) were added, and these two eluates were combined for analysis. Ten microliters of formic acid was added to reacidify the solution. The solvent was evaporated with a constant flow of nitrogen gas. Dry samples were redissolved in 1 mL of water (4.5% formic acid) and refrigerated until analysis.

Juice samples were spiked with three concentrations of cyanidin 3-*O*-glucoside standard before the extraction step to assess the overall recovery rate of the SPE procedure. The cyanidin 3-*O*-glucoside concentration of the spiked juice sample was compared to that of a control juice sample. The percent recovery was calculated using eq 2.

$$\frac{\text{spiked sample concn} - \text{control sample concn}}{\text{concn of standard added}} \times 100\% \quad (2)$$

The average SPE recovery of cyanidin 3-*O*-glucoside ranged from 94 to 107% (Table 1). Three different volumes of cyanidin 3-*O*-glucoside standard spiking solution were used to analyze recovery over a range of concentrations. Acceptable recovery was seen for all volumes of concentrations added.

Table 1. Average Recovery of Elderberry Juice Spiked with Three Different Cyanidin 3-*O*-Glucoside Concentrations before SPE[a]

	av response	C3GE (ng/mL)	C3GE added (ng/mL)	av recovery (%)
control	220,956	525.2		
2 μL spike	340,669	808.3	298.4	94.9 ± 0.8
3 μL spike	395,931	938.0	439.2	94 ± 1
5 μL spike	539,214	1,277.8	705.5	107 ± 1

[a]Three independent samples were tested for each spike concentration. Concentrations were measured using UPLC-MS/MS and are represented as C3GE (ng/mL). Concentrations of the spiked juice sample are compared to the concentration of the control juice sample. Recoveries are represented as a percentage ± the standard error of the mean (n = 3).

Ultraperformance Liquid Chromatography−Tandem Quadrupole Mass Spectrometry (UPLC-MS/MS). A previously described UPLC-MS/MS method was followed for anthocyanin quantification.[23] A Waters Acquity ultraperformance liquid chromatograph with a quaternary solvent manager was used. A C18 column (Acquity BEH, 1.7 μm, 50 mm × 2.1 mm, Waters, Milford, MA, USA) was selected to separate anthocyanins. The mobile phases used were water A (4.5% formic acid) and acetonitrile B (0.01% formic acid). The gradient used was 95% A at 0 min, 91% A at 2.5 min, 85% A at 3.5 min, 5% A at 4 min, and 95% A at 4.8 min. The flow rate was 400 μL/min, and the sample injection volume was 10 μL in full loop mode. The column and sample chamber were kept at ambient temperature.

A Waters Xevo TQ-S triple-quadrupole mass spectrometer with electrospray ionization (ESI) in the positive ion mode was used. Multiple reaction monitoring scans were conducted by selecting the parent and daughter ion masses of the anthocyanins. A desolvation temperature of 350 °C and a source temperature of 150 °C were used. A capillary voltage of 2.0 kV and cone voltage of 20 V were used, and the nebulizer gas rate was 500 L N_2/h. Individual collision energies were manually optimized. MassLynx software (version 4.1, Waters) was used for all data acquisition. Six cyanidin 3-*O*-glucoside external standards of 1, 10, 100, 200, 500, and 1000 ng/mL were prepared and used to quantitate IAC. Samples were measured in triplicate, and concentrations were determined on the basis of their ion chromato-

DOI: 10.1021/acs.jafc.5b01702
J. Agric. Food Chem. 2015, 63, 5653−5659

graphic peak areas. Individual anthocyanin concentrations are expressed as μg C3GE/mL. Nine individual anthocyanin compounds were monitored during the experiment. Information regarding their parent and daughter ion mass-to-charge ratios (m/z) and retention times (t_R) is listed in Table 2 and is representative of the anthocyanin compounds in the juice samples.

Table 2. Parent and Daughter Ion Mass-to-Charge Ratios (m/z) of Each Individual Anthocyanin Monitored, along with the Retention Time (t_R) of Each Ion Chromatographic Peak

anthocyanin	parent ion (m/z)	daughter ion (m/z)	t_R (min)
cyanidin 3-*O*-coumaroyl-sambubioside-5-glucoside	889.4	287.1	4.61
cyanidin 3-*O*-sambubioside-5-glucoside	743.2	287.1	2.47
cyanidin 3-*O*-coumaroyl-sambubioside	727.4	287.1	4.67
cyanidin 3-*O*-sophoroside	611.1	287.1	2.37
cyanidin 3-*O*-rutinoside	595.1	287.1	4.63
cyanidin 3-*O*-sambubioside	581.0	287.1	3.78
cyanidin 3-*O*-galactoside	449.1	287.1	2.41
cyanidin 3-*O*-glucoside	449.1	287.1	3.66
cyanidin-based anthocyanin	785.3	287.1	4.45

Statistical Analysis. Data analysis was carried out in Matlab, version 8.3 (Mathworks, Natick, MA, USA). One-way ANOVA was performed to compare the effects of frozen storage on the TP and TMA contents of the elderberry juice samples. The Tukey honestly significant difference (hsd) test was conducted to compare the TP and TMA values of the same genotype at different time points during long-term frozen storage and also to compare the TP and TMA values of the three genotypes at the same time points, both done at the 95% confidence interval. Two-way t tests were performed at the 95% confidence interval to analyze the difference in IAC during frozen storage.

RESULTS AND DISCUSSION

Freeze–Thaw Analysis. The TMA content of juice samples was tested to determine if sample degradation occurs by repeated freeze–thaw cycles. Samples were initially thawed and analyzed for TMA content, frozen overnight (−20 °C), and tested each day for 4 days. Each genotype included seven independent samples (n = 7). The TMA content of the juice did not have a significant difference between any of the freeze–thaw cycles ($p > 0.05$). This was true for all three genotypes over the course of all freeze–thaw cycles.

Total Phenolic Content. The TP content was significantly different among all three genotypes initially ($p < 0.05$), suggesting genotype plays a role in TP content of elderberry fruit juice, as also shown in other papers.[14,15] Bob Gordon contained the highest TP content initially (8.1 ± 0.3 mg GAE/mL) followed by Wyldewood (6.7 ± 0.1 mg GAE/mL) and Adams II (5.6 ± 0.3 mg GAE/mL) (Figure 1). After 3 months of frozen storage, Bob Gordon had a significantly higher TP content compared with Adams II and Wyldewood; however, the latter two genotypes were not significantly different. Each genotype displayed the same trend of losing a statistically significant ($p < 0.05$) amount of polyphenols during the first 3 months of storage (Figure 1) and then remained rather stable for the course of the storage study. By the end of 9 months of frozen storage, all of the genotypes still had at least 72% of their initial polyphenol content. Some of this TP loss can be attributed to anthocyanin degradation, which is discussed further below. Therefore, the other nonanthocyanin polyphenols in elderberry fruit juice exhibited greater stability during long-term frozen storage.

Total Monomeric Anthocyanin Content. The initial TMA content of the Bob Gordon juice was also significantly different from the Adams II and Wyldewood juices ($p < 0.05$), suggesting that the genetics of the elderberry fruit is one factor that influences the anthocyanin content of the juice (Figure 2). Once again, Bob Gordon had the highest concentration initially (3.8 ± 0.2 mg C3GE/mL) followed by Wyldewood (2.4 ± 0.2 mg C3GE/mL) and Adams II (1.8 ± 0.2 mg C3GE/mL). However, after 3 and 6 months of frozen storage, the three genotypes possessed significantly different TMA contents from each other (Figure 2). Not only did the Bob Gordon genotype have the highest TMA content, but it also had the highest anthocyanin percentage of the TP content at 47% anthocyanin, followed by 36 and 32% for Wyldewood and Adams II, respectively. In another study involving American elderberry

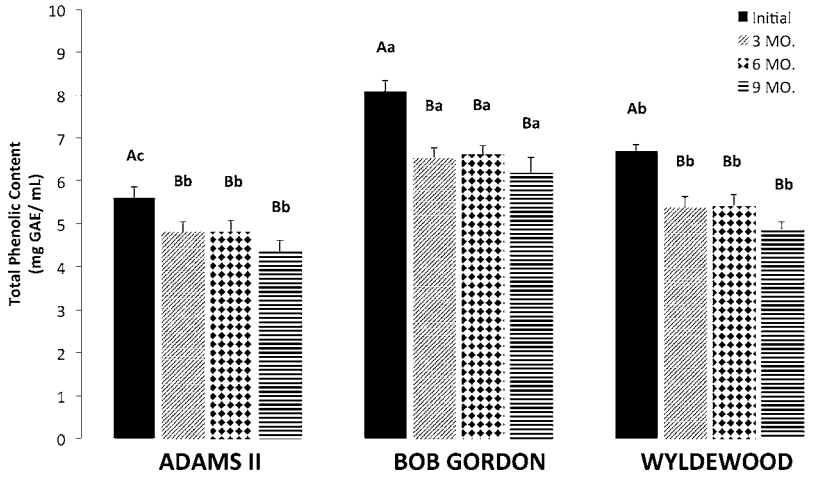

Figure 1. Total phenolic (TP) content of Adams II, Bob Gordon, and Wyldewood genotypes. The data are represented as the mean ± the standard error of the mean (n = 11–14). Each bar indicates the time period of testing, starting with the initial test, 3 months, 6 months, and 9 months (left to right). Significant differences ($p < 0.05$) between TP content of frozen storage periods are represented by different letters (A is significantly different from B, but AB is equivalent to both A and B groups, for example), according to Tukey's honest significance test. Significant differences ($p < 0.05$) between TP content between each genotype during the same time periods are indicated by different lower case letters.

DOI: 10.1021/acs.jafc.5b01702
J. Agric. Food Chem. 2015, 63, 5653–5659

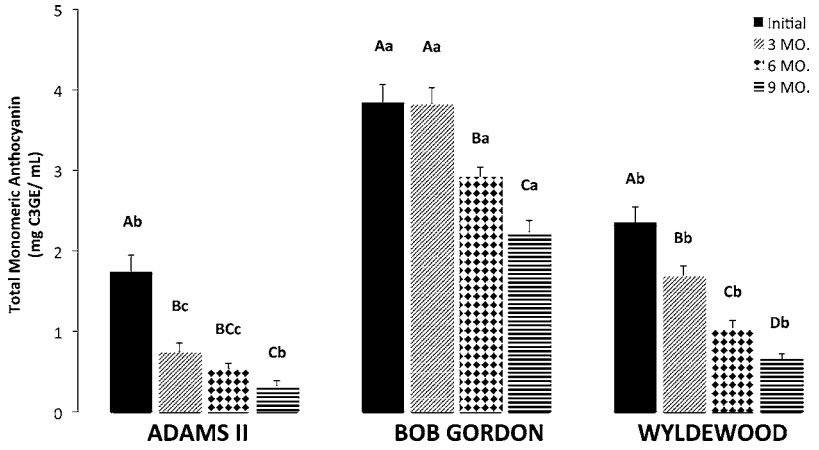

Figure 2. Total monomeric anthocyanin (TMA) content of Adams II, Bob Gordon, and Wyldewood genotypes. The data are represented as the mean ± the standard error of the mean (n = 11−14). Each column indicates the time period of testing, starting with the initial test, 3 months, 6 months, and 9 months (left to right). Significant differences ($p < 0.05$) between TMA content of frozen storage periods are represented by different letters (A is significantly different from B, but AB is equivalent to both A and B groups, for example), according to Tukey's honest significance test. Significant differences ($p < 0.05$) between TMA content between each genotype during the same time periods are indicated by different lower case letters.

fruit, the TMA content of 14 different elderberry fruit accessions varied highly (37.5%), which was much more than the 14.4% TP variance among accessions.[10] This suggests that the anthocyanin content is more susceptible to changes than other polyphenols based on the genotype, growing conditions, location, year, and other factors, which is in good agreement with our results. Future studies investigating these parameters would be helpful to understand how to optimize and preserve anthocyanins in elderberry fruit.

There were large differences in the stability of the anthocyanins during frozen storage among genotypes. Bob Gordon showed the best TMA stability during the first 3 months of frozen storage (Figure 2), whereas the other two genotypes saw a significant decline in TMA content during this time. All three genotypes saw a significant and relatively similar decline in TMA content from 3 to 6 months and also from 6 to 9 months of frozen storage. Bob Gordon retained 99, 76, and 58% of its initial anthocyanins during 3, 6, and 9 months of storage, respectively. Wyldewood retained 72, 44, and 28% and Adams II 42, 30, and 18% of their initial anthocyanins during 3, 6, and 9 months of storage, respectively. These large differences during frozen storage suggest that the genetics of the fruit also influence the stability of anthocyanins in the juice matrix, with an increase in storage time adversely affecting the TMA content of the juice.

Thomas et al. tested elderberry fruit for TMA and included the same three genotypes as in this study.[14] The TMA contents of their samples are in good agreement with the values obtained from this study, showing that Bob Gordon was more concentrated in anthocyanins than Wyldewood and Adams II, strengthening the hypothesis that the genotype of elderberry is a primary factor influencing the anthocyanin composition of the berry.

There are a variety of processes that could cause a decrease in the TMA content of the juice during frozen storage. For instance, enzymatic degradation could have contributed to anthocyanin loss, especially because the juice samples were not heated during processing. During the study, the same samples were thawed and refrozen every 3 months for analysis. Reactivation of enzymes upon repeated thawing could possibly cause anthocyanin degradation or polymerization. Nonenzymatic polymerization is also possible due to condensation reactions between anthocyanins and proanthocyanidins. To explore the role of sample degradation due to repeated freeze−thaw cycles, juice samples were tested for their integrity over multiple cycles to ensure any anthocyanin loss was due to long-term frozen storage and not another cause. During this test, there were no significant differences ($p > 0.05$) in TMA content of any of the genotypes of juice during the initial testing and after 4 days of daily freeze−thaw cycles, strengthening the theory that long-term frozen storage contributes to anthocyanin loss in elderberry juice.

Individual Anthocyanin Content. Three main individual anthocyanin compounds, among all three genotypes, were identified using SPE coupled with UPLC-MS/MS: cyanidin 3-*O*-coumaroyl-sambubioside-5-glucoside, cyanidin 3-*O*-sambubioside-5-glucoside, and cyanidin 3-*O*-sophoroside (Table 3). Six other cyanidin-based anthocyanins were also present in the juice samples in smaller quantities, including cyanidin 3-*O*-coumaroyl-sambubioside, cyanidin 3-*O*-rutinoside, cyanidin 3-*O*-sambubioside, cyanidin 3-*O*-galactoside, cyanidin 3-*O*-glucoside, and a cyanidin-based anthocyanin with a tentative identification (Table 3). These nine anthocyanins were the ones present in highest concentration after SPE and represent a cross section of the anthocyanins present in elderberry juice. An example of one MRM ion channel chromatogram of cyanidin 3-*O*-coumaroyl-sambubioside-5-glucoside of a Wyldewood juice sample is presented in Figure 3. The integrated ion signal listed under the retention time indicated in the figure is used to quantitate IAC. Four chromatograms, one for each test period, are presented, and a decrease in ion signal over time was seen. A continual decrease in concentration of this particular individual anthocyanin occurs as a function of increased frozen storage time, because the area under the chromatographic peak decreases over time.

Lee and Finn showed that individual anthocyanin profiles vary dramatically between *Sambucus nigra* subsp. *canadensis* and subsp. *nigra*.[24] Cyanidin 3-coumaroyl-sambubioside-5-glucoside and cyanidin 3-sambubioside-5-glucoside were identified as the major individual anthocyanin components in subsp. *canadensis* in their study and are also two of the three main individual anthocyanins found in the three subsp. *canadensis* genotypes in

DOI: 10.1021/acs.jafc.5b01702
J. Agric. Food Chem. 2015, 63, 5653−5659

Table 3. Individual Anthocyanin Content (IAC) of Adams II, Bob Gordon, and Wyldewood Genotypes during Different Durations of Frozen Storage[a]

	Coum-samb-5-glc[b]	Samb-5-glc[c]	Coum-samb[d]	Sophor[e]	rutin[f]	Samb[g]	Galact[h]	Glc[i]	Based-2[j]
				Adams II					
initial	28 ± 1	18.47 ± 0.07	4.4 ± 0.4	15.9 ± 0.2	0.97 ± 0.02	3.9 ± 0.3	2.46 ± 0.01	2.1 ± 0.1	2.05 ± 0.05
3 months	8.8 ± 0.2**	5.5 ± 0.5**	0.95 ± 0.03**	3.6 ± 0.2**	1.03 ± 0.01	nd[k]	0.86 ± 0.01**	0.97 ± 0.03**	1.01 ± 0.01**
6 months	1.39 ± 0.06**	0.9 ± 0.1**	0.66 ± 0.01**	0.83 ± 0.07**	nd	nd	nd	nd	nd
9 months	nd	nd	nd	nd	nd	nd	nd	nd	nd
				Bob Gordon					
initial	56 ± 3	41 ± 4	7.8 ± 0.4	69 ± 7	1.28 ± 0.04	8.1 ± 0.7	6.7 ± 0.6	4.7 ± 0.3	3.8 ± 0.3
3 months	47 ± 4*	32 ± 3*	1.04 ± 0.05**	38 ± 5**	nd	3.2 ± 0.3**	2.8 ± 0.3*	1.8 ± 0.2*	3.1 ± 0.3
6 months	12.2 ± 0.9**	7.4 ± 0.9**	1.2 ± 0.3**	18 ± 3**	nd	nd	3.0 ± 0.5*	1.6 ± 0.1*	0.85 ± 0.07*
9 months	0.49 ± 0.03**	nd	1.04 ± 0.06**	0.28 ± 0.04**	nd	nd	nd	1.5 ± 0.2*	nd
				Wyldewood					
initial	32 ± 3	22 ± 2	4.0 ± 0.3	16 ± 1	1.01 ± 0.04	2.6 ± 0.2	2.6 ± 0.1	1.54 ± 0.06	2.2 ± 0.2
3 months	24 ± 2*	15 ± 1*	1.5 ± 0.1*	8.5 ± 0.9*	nd	1.22 ± 0.08*	1.29 ± 0.05*	1.26 ± 0.06*	1.7 ± 0.1
6 months	4.7 ± 0.3**	2.64 ± 0.09**	1.4 ± 0.1*	nd	nd	nd	nd	nd	nd
9 months	0.21 ± 0.01**	nd	0.45 ± 0.02**	nd	nd	nd	nd	nd	nd

[a]Data are represented as mean ± standard rrror of the mean as μg C3GE/mL (n = 11−14). Significant differences between the IAC of samples during frozen storage compared to the initial IAC are represented with asterisks ($p < 0.05$ = *, $p < 0.01$ = **) according to two-sample mean t test. [b]Coum-samb-5-glc = cyanidin 3-*O*-coumaroyl-sambubioside-5-glucoside. [c]Samb-5-glc = cyanidin 3-*O*-sambubioside-5-glucoside. [d]Coum-samb = cyanidin 3-*O*-coumaroyl-sambubioside. [e]Sophor = cyanidin 3-*O*-sophoroside. [f]Rutin = cyanidin 3-*O*-rutinoside. [g]Samb = cyanidin 3-*O*-sambubioside. [h]Galact = cyanidin 3-*O*-galactoside. [i]Glc = cyanidin 3-*O*-glucoside. [j]Based-2 = cyanidin-based anthocyanin. [k]nd = not detected. Limit of detection (0.3 ng/mL).

DOI: 10.1021/acs.jafc.5b01702
J. Agric. Food Chem. 2015, 63, 5653−5659

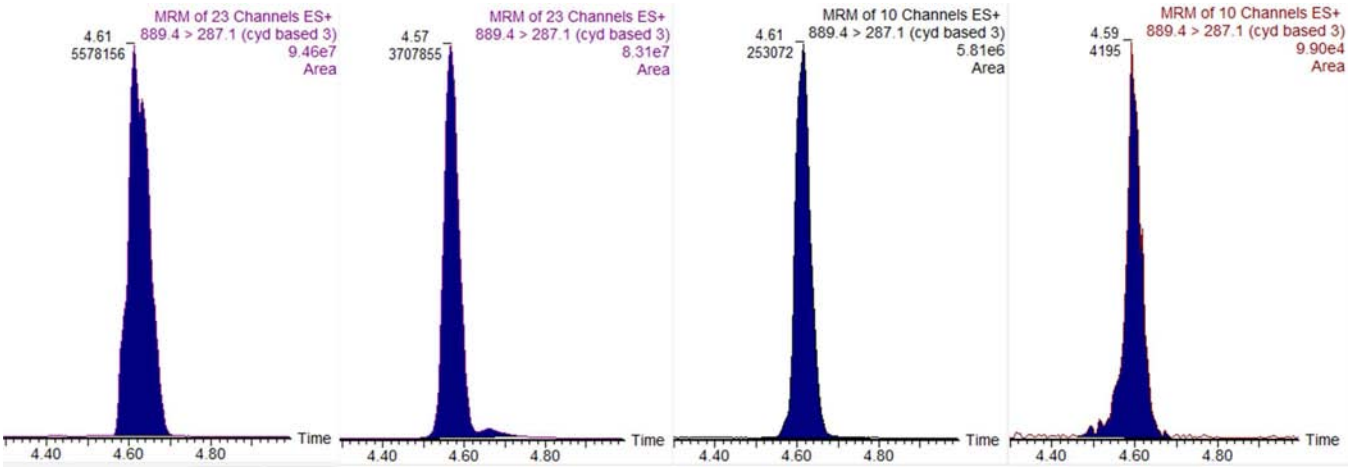

Figure 3. Ion chromatograms for cyanidin 3-*O*-coumaroyl-sambubioside-5-glucoside anthocyanin initially and after 3, 6, and 9 months of frozen storage (left to right). The retention time (min) and integrated area used for quantitation are listed at the top of each peak.

the present study. Most of the prior work analyzing the anthocyanin content of elderberry involves subsp. *nigra*[1] and identifies cyanidin 3-*O*-glucoside as a major individual anthocyanin. Cyanidin 3-*O*-glucoside is present in subsp. *canadensis*, but in much smaller quantities (Table 3), which agrees well with Lee and Finn, who tested both subspecies for IAC.[23] Although the magnitudes of IAC were different initially among the three genotypes, the relative compositions or contributions of each individual anthocyanin to the total IAC were extremely similar, especially between Adams II and Wyldewood. Bob Gordon also had a similar relative composition, except the cyanidin 3-*O*-sophoroside content was almost 2-fold higher than those of the other two genotypes. This could have relevance in future biochemical studies. Kamonpatana et al. showed that the structure of the anthocyanin affects the stability of the molecule in the human oral cavity, and some anthocyanins are more readily available for uptake by the buccal cells, whereas others degrade quickly in the mouth.[25] Between their different stabilities in vivo and during storage, anthocyanins do not interact equally. This information regarding higher levels of certain anthocyanins in different genotypes underscores the importance of developing new cultivars of fruit with different anthocyanin profiles.

Bob Gordon (198 μg C3GE/mL) had the highest IAC, followed by Wyldewood (84 μg C3GE/mL) and Adams II (78 μg C3GE/mL), respectively (Table 3). A large decline in IAC in the Adams II genotype is seen after 3 months of frozen storage, and although there is a statistical difference between Bob Gordon and Wyldewood IAC after 3 months of frozen storage, the anthocyanins are much more stable in these two genotypes during long-term frozen storage (Table 3). This trend is seen in both the cyanidin 3-*O*-coumaroyl-sambubioside-5-glucoside and cyanidin 3-*O*-sambubioside-5-glucoside anthocyanins. It is also interesting to note that cyanidin 3-*O*-sophoroside content varies highly between the genotypes initially (Table 3).

The individual anthocyanins in elderberry juice are less stable during frozen storage compared to the monomeric anthocyanins. Bob Gordon retained 65, 22, and 2% of its total IAC during 3, 6, and 9 month of frozen storage, respectively (Table 3). Wyldewood and Adams II retained 65, 10, <1% and 29, 10, and 0% of their IAC during 3, 6, and 9 months of frozen storage, respectively. These results suggest that prolonged frozen storage has a significant impact on the anthocyanin content of elderberry fruit juice. The different sugar-containing moieties may play a role in the stability of the anthocyanins during storage. It is difficult to identify a trend in the individual anthocyanins with a very small contribution because a majority fall below the detection limit after 3 months of frozen storage. Cyanidin 3-*O*-coumaroyl-sambubioside was the least stable during storage among all three genotypes, retaining <38% IAC in all three genotypes after 3 months of frozen storage. Cyanidin 3-*O*-coumaroyl-sambubioside-5-glucoside and cyanidin 3-*O*-sambubioside-5-glucoside showed much better stability in Bob Gordon with 84 and 78% anthocyanin retention, respectively, and Wyldewood with 75 and 69% anthocyanin retention, respectively.

Individual anthocyanins also displayed different stabilities between genotypes. Cyanidin 3-*O*-sophoroside had very poor stability (23% retention) in Adams II, but >53% retention in both Bob Gordon and Wyldewood after 3 months of frozen storage. Cyanidin 3-*O*-sambubioside-5-glucoside displayed a very similar trend. Adams II once again had very poor stability (30%), whereas Bob Gordon (78%) and Wyldewood (68%) showed much higher anthocyanin stability after 3 months of frozen storage. Cyanidin 3-*O*-coumaroyl-sambubioside-5-glucoside had the best stability in all three genotypes during the first 3 months of frozen storage. Bob Gordon saw 84% anthocyanin retention, and Wyldewood and Adams II had 75 and 31% retention, respectively. Cyanidin 3-*O*-coumaroyl-sambubioside had the worst stability of the individual anthocyanins tested, with all genotypes having <38% of their IAC after 3 months of frozen storage. Further exploration of the juice matrix of different genotypes of elderberry fruit juice could provide insight into which compounds may contribute to increased anthocyanin stability and degradation.

We have shown that individual anthocyanin concentrations in elderberry fruit juice can vary during frozen storage, and the UPLC-MS/MS method used here yields important information that is not obtained by commonly used TP and TMA testing methods. By conducting extensive sample cleanup, potentially interfering juice matrix compounds were removed, allowing for more accurate anthocyanin quantification. More information was gathered regarding the stability of individual anthocyanins in three genotypes of elderberry juice. The TP, TMA, and IAC contents of elderberry juice varied with genotype.

DOI: 10.1021/acs.jafc.5b01702
J. Agric. Food Chem. 2015, 63, 5653−5659

AUTHOR INFORMATION

Corresponding Author

*(C.M.G.) Phone: (573) 882-3288. Fax: (573) 882-2754. E-mail: greenliefm@missouri.edu.

Funding

This project was made possible by Grant P50AT006273 from the National Center for Complementary and Alternative Medicines (NCCAM), the Office of Dietary Supplements (ODS), and the National Cancer Institute (NCI). Its contents are solely the responsibility of the authors and do not necessarily represent the official views of the NCCAM, ODS, NCI, or the National Institutes of Health.

Notes

The authors declare no competing financial interest.

ABBREVIATIONS USED

alt, altitude; BEH, ethylene-bridged hybrid; C18, octadecyl carbon chain; ESI, electrospray ionization; ha, hectare; hsd, honestly significant difference; HPLC, high-performance liquid chromatography; IAC, individual anthocyanin content; MCX, mixed-mode cation-exchange; mequiv, milliequivalent; SPE, solid phase extraction; TFA, trifluoroacetic acid; TMA, total monomeric anthocyanin; TP, total phenolic; UPLC-MS/MS, ultraperformance liquid chromatography−tandem mass spectrometry

REFERENCES

(1) Ulbricht, C.; Basch, E.; Cheung, L.; Goldberg, H.; Hammerness, P.; Isaac, R.; Khalsa, K. P.; Romm, A.; Rychlik, I.; Varghese, M.; Weissner, W.; Windsor, R. C.; Wortley, J. An evidence-based systematic review of elderberry and elderflower (*Sambucus nigra*) by the natural standard research collaboration. *J. Diet. Suppl.* **2014**, *11*, 80−120.

(2) Del Rio, D.; Borges, G.; Crozier, A. Berry flavonoids and phenolics: bioavailability and evidence of protective effects. *Br. J. Nutr.* **2010**, *104*, S67−S90.

(3) González-Gallego, J.; García-Mediavilla, M. V.; Sánchez-Campos, S.; Tuñón, M. J. Fruit polyphenols, immunity and inflammation. *Br. J. Nutr.* **2010**, *104*, S15−S27.

(4) He, J.; Giusti, M. M. High-purity isolation of anthocyanins mixtures from fruits and vegetables − a novel solid-phase extraction method using mixed mode cation-exchange chromatography. *J. Chromatogr., A* **2011**, *1218*, 7914−7922.

(5) Tuñón, M. J.; García-Mediavilla, M. V.; Sánchez-Campos, S.; González-Gallego, J. Potential of flavonoids as anti-inflammatory agents: modulation of pro-inflammatory gene expression and signal transduction pathways. *Curr. Drug Metab.* **2009**, *10*, 256−271.

(6) Kinoshita, E.; Hayashi, K.; Katayama, H.; Hayashi, T.; Obata, A. Anti-influenza virus effects of elderberry juice and its fractions. *Biosci., Biotechnol., Biochem.* **2012**, *76*, 1633−1638.

(7) Yao, L. H.; Jiang, Y. M.; Shi, J.; Tomás-Barberán, F. A.; Datta, N.; Singanusong, R.; Chen, S. S. Flavonoids in food and their health benefits. *Plant Foods Hum. Nutr.* **2004**, *59*, 113−122.

(8) Knekt, P.; Järvinen, R.; Seppänen, R.; Heliövaara, M.; Teppo, L.; Pukkala, E.; Aromaa, A. Dietary flavonoids and the risk of lung cancer and other malignant neoplasms. *Am. J. Epidemiol.* **1997**, *146*, 223−230.

(9) Bosetti, C.; Rossi, M.; McLaughlin, J. K.; Negri, E.; Talamini, R.; Lagiou, P.; Montella, M.; Ramazotti, V.; Franceshi, S.; LaVecchia, C. Flavonoids and the risk of renal cell carcinoma. *Cancer Epidemiol., Biomarkers Prev.* **2007**, *16*, 98−101.

(10) Ozgen, M.; Scheerens, J. C.; Reese, R. N.; Miller, R. A. Total phenolic, anthocyanin contents and antioxidant capacity of selected elderberry (*Sambucus canadensis L.*) accessions. *Pharmacogn. Mag.* **2010**, *6*, 198−203.

(11) Plaza, M.; Kariuki, J.; Turner, C. Quantification of individual phenolic compounds' contribution to antioxidant capacity in apple: a novel analytical tool based on liquid chromatography with diode array, electrochemical, and charged aerosol detection. *J. Agric. Food Chem.* **2014**, *62*, 409−418.

(12) Tian, Q.; Giusti, M. M.; Stoner, G. D.; Schwartz, S. J. Screening for anthocyanins using high-performance liquid chromatography coupled to electrospray ionization tandem mass spectrometry with precursor-ion analysis, product-ion analysis, common-neutral-loss analysis, and selected reaction monitoring. *J. Chromatogr., A* **2005**, *1091*, 72−82.

(13) Veberic, R.; Stampar, F.; Schmitzer, V.; Cunja, V.; Zupan, A.; Koron, D.; Mikulic-Petkovsek, M. Changes in the contents of anthocyanins and other compounds in blackberry fruits due to freezing and long-term frozen storage. *J. Agric. Food Chem.* **2014**, *62*, 6926−6935.

(14) Thomas, A. L.; Veazie, P. P.; Beyers, P. L.; Finn, C. E.; Lee, J. A comparison of fruit characteristics among diverse elderberry genotypes grown in Missouri and Oregon. *J. Berry Res.* **2013**, *3*, 159−168.

(15) Thomas, A. L.; Byers, P.L.; Gu, S.; Avery, J. D., Jr.; Kaps, M.; Datta, A.; Fernando, L.; Grossi, P.; Rottinghaus, G. E. Occurrence of polyphenols, organic acids, and sugars among diverse elderberry genotypes grown in three Missouri (USA) locations. *Acta Hortic.* **2015**, *1061*, 147−154.

(16) Wilkes, K.; Howard, L. R.; Brownmiller, C.; Prior, R. L. Changes in chokeberry (*Aronia melanocarpa* L.) polyphenols during juice processing and storage. *J. Agric. Food Chem.* **2014**, *62*, 4018−4025.

(17) Hager, A.; Howard, L. R.; Prior, R. L.; Brownmiller, C. Processing and storage effects on monomeric anthocyanins, percent polymeric color, and antioxidant capacity of processed black raspberry products. *J. Food Sci.* **2008**, *73*, H134−H140.

(18) Brownmiller, C.; Howard, L. R.; Prior, R. L. Processing and storage effects on procyanidin composition and concentration of processed blueberry products. *J. Agric. Food Chem.* **2009**, *57*, 1896−1902.

(19) Finn, C. E.; Thomas, A. L.; Byers, P. L.; Serce, S. Evaluation of American (*Sambucus canadensis*) and European (*S. nigra*) elderberry genotypes grown in diverse environments and implications for cultivar development. *HortScience* **2008**, *43*, 1385−1391.

(20) Singelton, V. L.; Rossi, J. J. A. Colorimetry of total phenolics with phosphomolybdic-phosphotungstic acid reagents. *Am. J. Enol. Vitic.* **1965**, *16*, 144−158.

(21) Giusti, M.; Wrolstad, R. E. Characterization and measurement of anthocyanins by UV-visible spectroscopy. In *Current Protocols in Food Analytical Chemistry*; Wiley: Hoboken, NJ, USA, 2001; pp F1.2.1−F1.2.6.

(22) Jurd, L.; Asen, S. The formation of metal and "co-pigment" complexes of cyanidin 3-glucoside. *Phytochemistry* **1966**, *5*, 1263−1271.

(23) Wu, H.; Johnson, M. C.; Lu, P.; Fritsche, K. L.; Thomas, A. L.; Cai, Z.; Greenlief, C. M. Determination of anthocyanins and total polyphenols in a variety of elderberry juices by UPLC/MS and other methods. *Acta Hortic.* **2015**, *1061*, 43−51.

(24) Lee, J.; Finn, C. E. Anthocyanins and other polyphenolics in American elderberry (*Sambucus canadensis*) and European elderberry (*S. nigra*) cultivars. *J. Sci. Food Agric.* **2007**, *87*, 2665−2675.

(25) Kamonpatana, K.; Failla, M. L.; Kumar, P. S.; Giusti, M. M. Anthocyanin structure determines susceptibility to microbial degradation and bioavailability to the buccal mucosa. *J. Agric. Food Chem.* **2014**, *62*, 6903−6910.

DOI: 10.1021/acs.jafc.5b01702
J. Agric. Food Chem. 2015, 63, 5653−5659

every stage of pathogenesis, and apoptosis is now recognized as an integral process during the spread of atherosclerotic plaques to neighboring healthy tissue.[19] Oxidative stress and apoptosis are even more apparent in vascular tissue following an acute ischemia-reperfusion (IR) event, such as a myocardial infarct after a lesion ruptures in a coronary artery.[20,21] The lack of waste removal and uncoupling of the electron transport chain during ischemia, combined with the oxidative burst during reperfusion, lead to large amounts of reactive oxygen species (ROS) being produced in cells. Oxidative stress can trigger apoptosis by activating the mitochondrial pathway, caspases, and mitogen-activated protein kinases (MAPK).[22] High levels of oxidative stress and apoptosis therefore characterize IR-induced myocardial damage. We hypothesized that antioxidant and anthocyanin-rich Manitoba lingonberry would have a protective effect against apoptosis induced by ischemia-reperfusion.

In this study, we aimed to extract the phenolic and anthocyanic compounds found in wild lingonberry clones collected from Newfoundland and Labrador and in a composite of two wild populations of Manitoba and to examine the anti-apoptotic effects of Manitoba lingonberry extracts by measuring caspase-3 activation, nuclear condensation, and MAPK signaling in H9c2 myoblasts undergoing simulated IR injury.

MATERIALS AND METHODS

Chemicals and Materials. Optima grade methanol, acetonitrile, HPLC grade phosphoric acid, and 2,2′-azobis(2-amidinopropane) dihydrochloride (AAPH) from Wako Chemicals (Richmond, VA, USA) and all other chemicals of at least ACS reagent grade, including the selective JNK inhibitor SP600125, were acquired from Sigma-Aldrich (St. Louis, MO, USA). Reference compounds cyanidin-3-glucoside (95%) and cyanidin-3-galactoside (95%) were purchased from Chromadex (Irvine, CA, USA) whereas cyanidin-3-arabinoside chloride (>95%) was from Cerilliant Corp. (Round Rock, TX, USA).

Plastic pots were purchased from East-Chem Inc. (Mount Pearl, NL, Canada), Acrodisc syringe filters and BioTrace Nitrocellulose Transfer Membrane were acquired from Pall Corp. (Ann Arbor, MI, USA), SepPak tC18 columns were acquired from Waters Corp. (Milford, MA, USA), SensoLyte Homogeneous AFC Caspase-3/7 Assay Kits were acquired from Anaspec (Fremont, CA, USA), and cleaved poly-ADP ribose polymerase (PARP) antibody (rat specific) was purchased from Cell Signaling (Danvers, MA, USA). HRP-conjugated goat anti-rabbit IgG and western immunoblotting equipment and reagents were purchased from Bio-Rad Laboratories (Hercules, CA, USA). Personal protective equipment and laboratory safety guidelines were implemented for all experiments.

Apparatus and Software. A Milli-Q Synthesis A10 water purification system was acquired from Millipore Corp. (Billerica, MA, USA), and the SpectraMax M5 microplate reader and SoftMax Pro (version 6.2) software were acquired from Molecular Devices (Sunnyvale, CA, USA). ACQUITY ultraperformance liquid chromatography (UPLC) equipment and Empower 3 software were acquired from Waters Corp., and the AlphaInnotech FluorChemQ system was purchased from Fisher Scientific (Fair Lawn, NJ, USA). A Billups-Rothenberg modular incubator chamber was purchased from Stem Cell Technologies (Vancouver, BC, Canada), and a Sector Imager 2400 and electrochemiluminescent assay kits were purchased from Meso Scale Discovery (Rockville, MD, USA).

Berry Collection. *Eastern Canada and European Berries.* Five wild lingonberry clones, designated L3, L10, L16, L20, and L23, collected from Newfoundland and Labrador, Canada, and the European (Polish) cultivar Mesovia (L24) have been grown and maintained at the Atlantic Cool Climate Crop Research Centre, St. John's, NL, Canada, for over 10 years. Each clone represents a single plant selected from the wild on the basis of vigor, berry color, size, and yield per plant and apparent freedom from disease and insects. GPS locations of the collection sites are shown in Table 1. All genotypes were grown in a greenhouse in plastic pots (25 cm in diameter and 18 cm deep, equivalent to 6 L) containing 2 peat:1 perlite (v/v), under natural light conditions at a maximum photosynthetic photon flux of 90 μmol m^{-2} s^{-1} at 20 ± 2 °C and 85% relative humidity. Fully ripe berries were collected and were shipped to our laboratory in Winnipeg, MB, Canada, for analysis and stored at −80 °C until use.

Table 1. GPS Locations for Collection Sites of Wild Lingonberry Clones from Newfoundland and Labrador (NL) and Harvest Sites of Wild Lingonberries (Not Clones) from Manitoba (MB) and Saskatchewan (SK)

clone	province	community	latitude (N)	longitude (W)
L3	NL	Colinet	47°13′	53°32′
L10	NL	L'anse aux Meadows	51°36′	55°32′
L16	NL	Logy Bay	47°37′	52°40′
L20	NL	Gunner's Cove	51°31′	55°27′
L23	NL	Lords Cove/Pump Cove	46°52′	55°40′
not clones	MB	Sherridon Lake	55°7′	101°5′
not clones	SK	Deschambault Lake	54°55′	103°21′

Manitoba Berries. Berries from two wild populations were hand-picked by local berry pickers at Deschambault Lake, SK, Canada, and Sherridon Lake, MB, Canada, in September 2011 and immediately frozen. GPS locations of harvest sites are shown in Table 1.

Extraction. Frozen berries were ground roughly in a coffee grinder, freeze-dried, and ground to a fine powder with a mortar and pestle. Methanol, ethanol, water, acetonitrile, acetone, and ethyl acetate were tested in aqueous and acidified solutions for their ability to extract phenolic compounds from lyophilized lingonberry. Acidified methanol was selected as the extraction solvent due to its ability to extract high amounts of phenolic compounds and anthocyanins while also being a compatible solvent for other analyses, such as HPLC. Extraction conditions were optimized by testing several temperatures and sonication times to maximize total phenolic and anthocyanin extraction (data not shown). Half a gram of lyophilized berry powder was extracted twice in 6 mL of methanol (2% formic acid) with 15 min of sonication at 37 °C followed by centrifugation for 15 min at 3000*g*. The supernatants from the two extractions were combined and filtered with a 0.2 μm syringe filter and stored at −20 °C. Methanol was then removed by rotary evaporation, and the remaining extract was brought back up to the original volume with ultrapure water so it could be loaded onto the SepPak columns.

Separation of Anthocyanin-Rich and Phenolic-Rich Fractions. The filtered aqueous Manitoba lingonberry extract was named the "complete extract" (CE). Eight milliliters was removed and separated into two fractions, one named the "anthocyanin-rich fraction" (ARF) and the other named the "phenolic-rich fraction" (PRF), using a protocol modified from that of Rodriguez-Saona and Wrolstad.[23] Briefly, a SepPak tC18 column (plus long cartridge, 900 mg of silica per cartridge, 37−55 μm particle size) was conditioned using methanol (0.5% formic acid), washed with ultrapure water (0.5% formic acid), loaded with 8 mL of CE, and washed again with ultrapure water (0.5% formic acid) to remove sugars and acids. Ten milliliters of ethyl acetate was used to collect polyphenolic compounds (PRF), and 5 mL of methanol (0.5% formic acid) was used to collect anthocyanins (ARF). The ethyl acetate and acidified methanol fractions were collected in separate flasks, and solvents were removed by rotary evaporation to near dryness. Both fractions were resuspended in methanol (0.2% formic acid) to one-fifth the original loaded volume. Both fractions were filtered with a 0.2 μm syringe filter and stored at 4 °C until analysis. Fractions were standardized on the basis of ORAC and total anthocyanin content.

Determination of Total Phenolics. Total phenolic contents of the complete extract and fractions were determined colorimetrically using Folin−Ciocalteu (F-C) reagent, following a protocol modified from that of Ainsworth and Gillespie.[24] Briefly, 40 μL of 25% F-C reagent and 20 μL of sample were added to a 96-well plate. After 5 min of incubation, 140 μL of an aqueous 700 mM sodium carbonate solution was added to

DOI: 10.1021/acs.jafc.5b00797
J. Agric. Food Chem. 2015, 63, 5660−5669

each well. This was followed by 2 h of incubation at room temperature, and the developed color was measured at 765 nm using a SpectraMax M5 microplate reader; data were analyzed using SoftMax Pro (version 6.2) software. All samples and standards were tested in triplicate. Results were expressed as milligram gallic acid equiv per 100 g DW of lyophilized berries using gallic acid as a standard.

Oxygen Radical Absorbance Capacity (ORAC) Assay. The oxygen radical absorbance capacities of all samples were determined fluorescently using AAPH as a peroxyl generator to oxidize fluorescein, following a method modified from that of Gillespie, Chae, and Ainsworth.[25] Briefly, 25 μL of sample or standard was incubated with 75 μL of a 0.2 μM fluorescein solution for 10 min with agitation at 37 °C. After incubation, 100 μL of a 37 mM AAPH solution was added to each well. Loss of fluorescence intensity was measured kinetically at 1.5 min intervals over 60 min using a SpectraMax M5 microplate reader, and data were analyzed using SoftMax Pro (version 6.2) software. All samples and standards were tested in triplicate. Results were expressed as micromole Trolox equiv per 100 g DW of lyophilized berries using Trolox as a standard.

Determination of Total Anthocyanins. The total anthocyanins of the complete extract and fractions were determined using the pH differential method from Lee, Durst, and Wrolstad.[26] Briefly, samples were diluted in each of 0.025 M potassium chloride (pH 1.0) and 0.4 M sodium acetate (pH 4.5) at an appropriate dilution factor. Within 15 min, absorption was measured at both 520 and 700 nm using a SpectraMax M5 microplate reader. Data were analyzed using SoftMax Pro (version 6.2) software. Anthocyanin concentration was calculated as

$$\text{mg cyanidin-3-glucoside equiv/L sample} = \frac{A \times \text{MW} \times \text{DF} \times 10^3}{\varepsilon \times \text{PL}}$$

where $A = (A_{520} - A_{700})_{\text{pH1.0}} - (A_{520} - A_{700})_{\text{pH4.5}}$; MW = 449.2 g/mol for cyanidin-3-glucoside; DF = dilution factor; PL = path length in cm; ε = 26900 molar extinction coefficient; and 10^3 = conversion factor from g to mg. All samples were tested in quadruplicate, and results were expressed as milligram cyanidin-3-glucoside equivalents per 100 g DW of lyophilized berries.

UPLC Conditions and Analysis. Chromatography was performed using a Waters ACQUITY UPLC system. For each sample and standard, 1 μL was injected onto a 2.1 × 100 mm, 1.7 μm, ACQUITY UPLC BEH C18 column with the flow rate set at 0.6 mL min^{-1}. The column temperature was maintained at 42 °C using an ACQUITY UPLC Column Manager, and spectral data (210−600 nm) were collected with an ACQUITY UPLC photodiode array (PDA) eλ detector. The mobile phases used were (A) 0.3% phosphoric acid, 5% methanol in 18.2 MΩ·cm water and (B) acetonitrile. The gradient condition was 0 min, 1% B; 0.5 min, 1% B; 2.25 min, 8% B; 3 min, 9% B; 4.5 min, 12% B; 5 min, 15% B; 6.5 min, 16% B; 10 min, 30% B; 11 min, 95% B; 11.65 min, 95% B; 11.7 min, 1% B; and 15 min, 1% B. The system was controlled and data were collected and analyzed using Empower 3 software. Peak identification was achieved by comparing retention time and spectral data with those of standards listed under Chemicals and Materials.

Cell Culture and Cytotoxicity Assay. H9c2 rat myoblasts were purchased from ATCC (Manassas, VA, USA). H9c2 cells were cultured in high-glucose (4500 mg/L) Dulbecco's modified Eagle's medium (DMEM) supplemented with 10% fetal bovine serum. To assess the cytotoxicity of the lingonberry samples, cells were seeded into black 96-well plates (1.0 × 10^4 cells per well). After allowing cells to adhere, medium was aspirated and replaced with medium supplemented with berry samples. After 24 h, AlamarBlue cell viability reagent was added to each well, and plates were incubated for 2 h at 37 °C. Fluorescence was measured (excitation = 570 nm, emission = 585 nm) using a SpectraMax M5 microplate reader, and data were analyzed using SoftMax Pro (version 6.2) software. All samples and controls were tested in quadruplicate, and results were expressed as percentage of control (control = 100%).

Simulated Ischemia-Reperfusion (IR). After 24 h of pretreatment with berry sampless, medium was aspirated and cells were washed twice with phosphate-buffered saline (PBS), and IR was simulated using the method established in our previous studies.[27] Medium was replaced with ischemic buffer (137 mM sodium chloride 15.8 mM potassium chloride, 0.49 mM magnesium chloride, 0.9 mM calcium chloride, 4 mM HEPES, 10 mM deoxyglucose, 20 mM sodium lactate, 1 mM sodium dithionate, pH 6.4), and cells were placed in a modular incubator chamber. Oxygen was removed by flushing the chamber with a mixture of 95% N_2 and 5% CO_2 gas for 5 min at 25 L per minute. The chamber was sealed and incubated for 1 h at 37 °C to simulate ischemia. After 1 h, ischemic buffer was aspirated, cells were washed twice with PBS, and cells were incubated in medium for 30 min under normoxic conditions to simulate reperfusion. For treatment groups, both ischemic buffer and reperfusion media were supplemented with berry extract, fractions, or anthocyanins. For control cells (no ischemia reperfusion), medium was aspirated, cells were washed twice with PBS, fresh medium was added, and cells were incubated for 90 min.

Determination of Apoptosis. *Hoechst Stain.* Cells were seeded into 6-well plates (1.2 × 10^5 cells per well) and incubated in cell culture medium (control and IR groups) or cell culture medium pretreated with berry samples (IR treatment groups) for 24 h. Similarly, in place of the berry samples, the selective JNK inhibitor SP600125 was also tested at 5 and 10 μM. IR was simulated while control plates were incubated for 90 min. After 1 h of ischemia and 10 min of reperfusion, 7 μL of Hoechst 33258 was added to each well, and plates were returned to the incubator for the final 20 min of reperfusion. Cells were then fixed with 10% formalin and viewed at 200× magnification with an Olympus IX81 microscope equipped with X-CITE Fluorescence Illumination Series 120Q. Each sample was tested on 3 wells, and 34 random fields were photographed per well, for a total of 102 fields per treatment. Photos were analyzed using ImageJ software to count the numbers of apoptotic nuclei and nonapoptotic nuclei.[28] Results were expressed as percentage of nuclei that were apoptotic compared to the IR group (IR = 100%).

Caspase-3 Activity Assay. Caspase-3 assays were performed using SensoLyte Homogeneous AFC Caspase-3/7 Assay Kits. Cells were seeded into 100 mm plates (4 × 10^5 cells per well) and incubated in cell culture medium (control and IR groups) or cell culture medium pretreated with berry samples (IR treatment groups) for 24 h. IR was simulated while control plates were incubated for 90 min. Cells were washed twice with ice-cold PBS, covered with 1 mL of ice cold lysis buffer, and scraped into microfuge tubes. Tubes were shaken for 30 min at 4 °C and centrifuged for 10 min at 2500g at 4 °C, and the supernatant was collected. Protein was determined using a Bradford protein assay.[29] Supernatant and caspase-3 tetrapeptide substrate (DEVD) solution were added to each well of a black 96-well plate, using lysis buffer for blank wells. The plate was shaken at 100−200 rpm for 30−60 min at room temperature, fluorescent intensity was measured (excitation = 380 nm, emission =5 00 nm) using a SpectraMax M5 microplate reader, and data were analyzed using SoftMax Pro (version 6.2) software. All samples were tested in quadruplicate, and results were expressed as percentage of the IR group (IR = 100%).

Assays for Total and Phosphorylated JNK and c-Jun. Cells were seeded into 100 mm plates (4 × 10^5 cells per well) and incubated in cell culture medium (control and IR groups) or cell culture medium pretreated with berry samples or anthocyanins (IR treatment groups) for 24 h. IR was simulated while control plates were incubated for 90 min. Control cells, IR cells, and IR cells treated with berry samples or pure anthocyanins (cyanidin-3-galactoside, cyanidin-3-glucoside, and cyanidin-3-arabinoside at 0.1, 1, and 5 μg/mL) were collected and frozen as whole cells at −80 °C until use. On the day of the assay, cells were lysed, supernatants were collected, and assays were performed according to Meso Scale Discovery protocols. One set of electrochemiluminescent multiplex microplates was spotted with c-Jun N-terminal kinase (JNK) and phospho-JNK antibodies, and one set of microplates wsd spotted with c-Jun and phospho-c-Jun antibodies. Briefly, multiplex microplates were blocked with blocking solution, washed three times, incubated with cell lysates, washed another three times, incubated with detection antibodies, and analyzed using a Sector Imager 2400. Samples were tested in triplicate, and percent phosphoprotein was calculated as (phospho-signal/total signal) × 100. Protein was determined using a Bradford protein assay.[29] Results were expressed as percentage of IR group (IR = 100%).

DOI: 10.1021/acs.jafc.5b00797
J. Agric. Food Chem. 2015, 63, 5660−5669

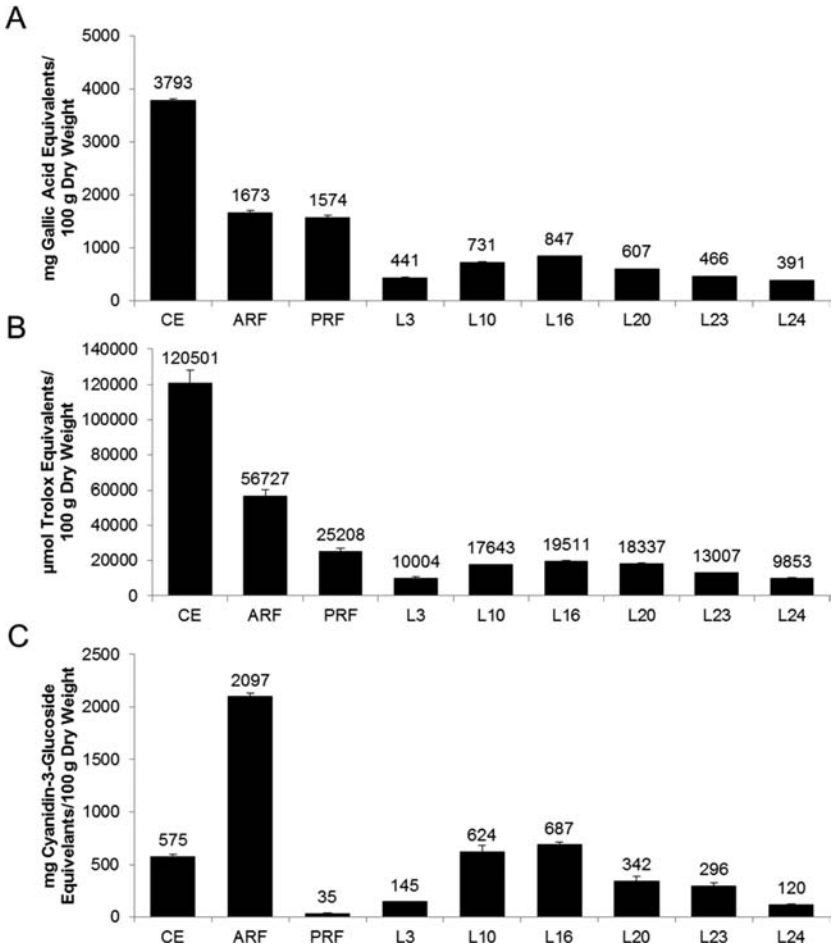

Figure 1. Phenolic content in milligram gallic acid equiv (A), antioxidant capacity in micromole Trolox equiv (B), and anthocyanin content in milligram cyanidin-3-glucoside equiv (C) per 100 g DW of lingonberry genotypes measured by total phenolics assay, oxygen radical absorbance assay, and total anthocyanins assay, respectively.

Western Immunoblotting Analysis. Cells were seeded into 100 mm plates (4×10^5 cells per well) and incubated in cell culture media (control and IR groups) or cell culture media pretreated with berry samples (IR treatment groups) for 24 h. IR was simulated while control plates were incubated for 90 min. Cleaved PARP levels were measured in control cells, IR cells, and IR cells treated with lingonberry samples using Western immunoblotting analysis. Whole cell lysate proteins (40 μg) were separated by electrophoresis on an 8% SDS-polyacrylamide gel,[30] transferred to a nitrocellulose membrane (Pall BioTrace, pore size = 0.2 μm),[31] and probed with rabbit polyclonal anticleaved PARP antibody (1:1000). Subsequent to incubation with HRP-conjugated goat anti-rabbit IgG secondary antibody (1:2000), bands were visualized using enhanced chemiluminescence reagent (Millipore Corp.) and the Alpha Innotech FluorChem Q imaging system. β-Actin was used as an internal control for equal loading of samples in the gel.

Statistical Analysis. Data are presented as means ± SE of at least three independent experiments. Results were analyzed using one-way ANOVA followed by Student−Newman−Keuls multiple-comparison test. P values <0.05 were considered statistically significant. For all data, groups specified by the same letter are not significantly different. All statistical analyses were performed using PASW Statistics 18 software (SPSS, New York, NY, USA).

RESULTS

Antioxidant Capacity and Anthocyanin Content of Lingonberry Extract and Fractions. In Figure 1, the antioxidant capacity (Figure 1A) and total phenolic content (Figure 1B) of the five eastern Canada lingonberry clones, the European cultivar, CE, ARF, and PRF, and anthocyanin content (Figure 1C) of CE, ARF, and PRF are shown; all values are shown per 100 g DW. The undiluted CE contained 240 μg cyanidin-3-glucoside equiv and 1580 μg gallic acid equiv per milliliter, the undiluted ARF contained 874 μg cyanidin-3-glucoside equiv per milliliter, and the undiluted PRF contained 656 μg gallic acid equiv per milliliter. On the basis of these results, for subsequent experiments four concentrations of each sample were used, corresponding to 1:100, 1:500, 1:1000, and 1:2000 dilutions with cell culture medium.

Overall, on the basis of the methods used in this study, the Manitoba lingonberry had high antioxidant capacity. It should be noted that the antioxidant capacities of ARF and PRF add up to only two-thirds of the antioxidant capacity of CE. This may be due to the fact that small phenolic compounds such as gallic acid are washed out of the column during the initial wash steps of the fractionation process. These compounds likely account for a significant proportion of the antioxidant capacity of CE.

UPLC Profiles of Extract and Fractions. UPLC chromatograms detected at 525 nm showed that lingonberry extract contained three main anthocyanin peaks. We identified the smallest peak as cyanidin-3-glucoside, the next smallest peak as cyanidin-3-arabinoside, and the largest peak as cyanidin-3-galactoside by comparing retention times and spectral maximums with available standards (Figure 2A). The structures of these anthocyanins are shown in Figure 3. We confirmed the

DOI: 10.1021/acs.jafc.5b00797
J. Agric. Food Chem. 2015, 63, 5660−5669

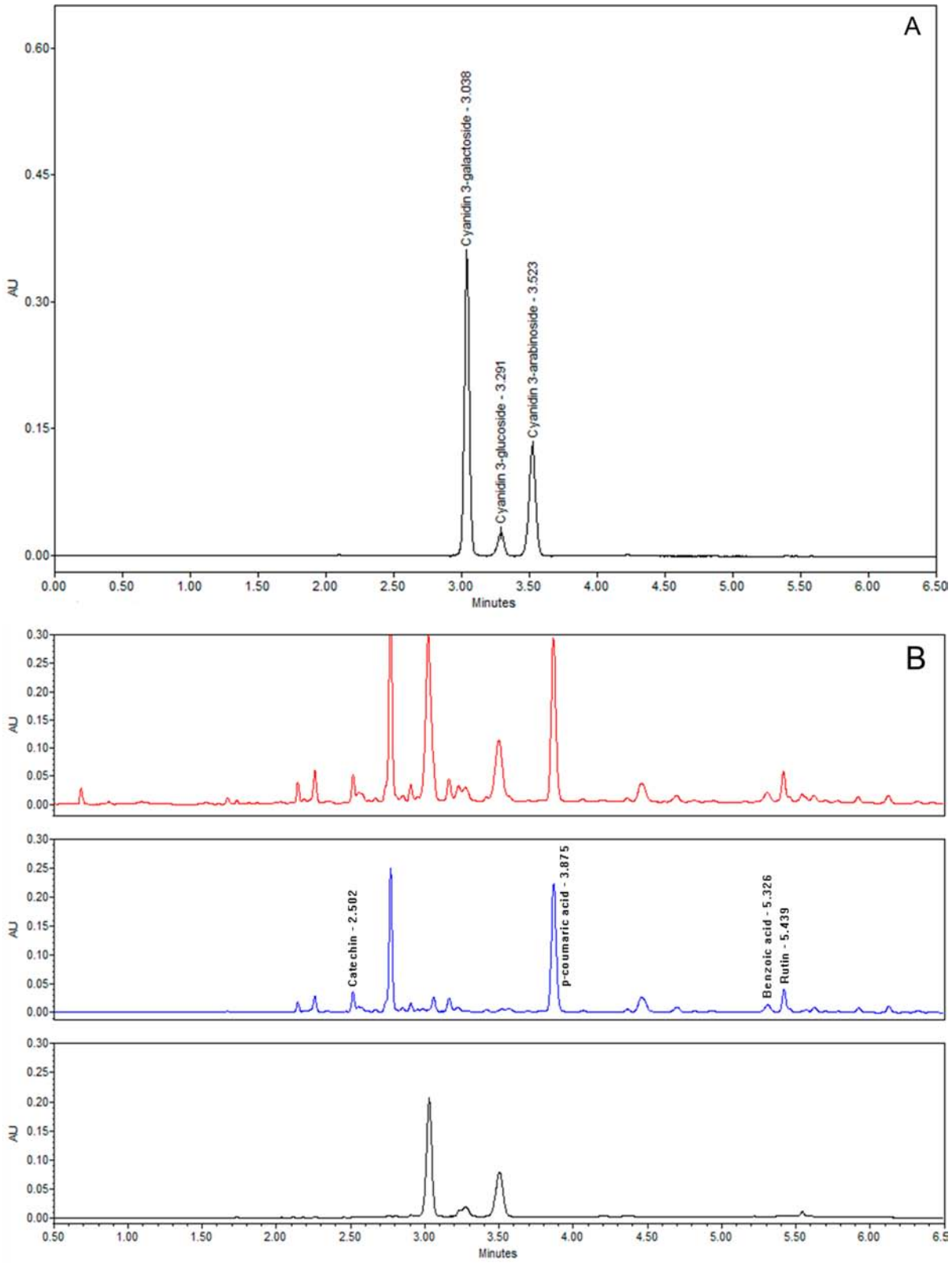

Figure 2. UPLC chromatograms of CE detected at 525 nm (A) and CE (red), PRF (blue), and ARF (black) detected at full scanning range (B). Note, in (B), ARF contains only the three anthocyanin peaks, anthocyanin peaks are absent from PRF, and CE contains all peaks present in ARF and PRF.

effectiveness of our fractionation technique by observing the chromatograms detected at 525 and maximum plots of the CE, ARF, and PRF. As expected, the chromatogram of ARF was devoid of peaks other than the three anthocyanin peaks, whereas the PRF chromatogram contained many peaks identified as phenolic compounds but did not contain any of the three anthocyanin peaks (Figure 2B).

Characterization of Apoptosis and Cytoprotection. *Inhibition of Nuclei Condensation.* All samples were tested at the high concentrations for cytotoxicity prior to subsequent

DOI: 10.1021/acs.jafc.5b00797
J. Agric. Food Chem. 2015, 63, 5660−5669

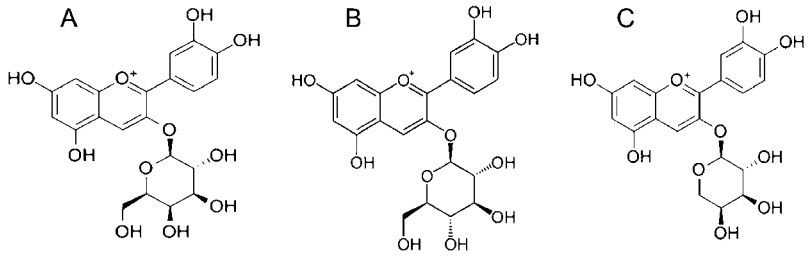

Figure 3. Structures of the major anthocyanins found in lingonberry: cyanidin-3-galactoside (A), cyanidin-3-glucoside (B), and cyanidin-3-arabinoside (C).

experiments. None of the concentrations tested affected cell viability, as indicated in Figure 4. Our model of IR induced a 25-

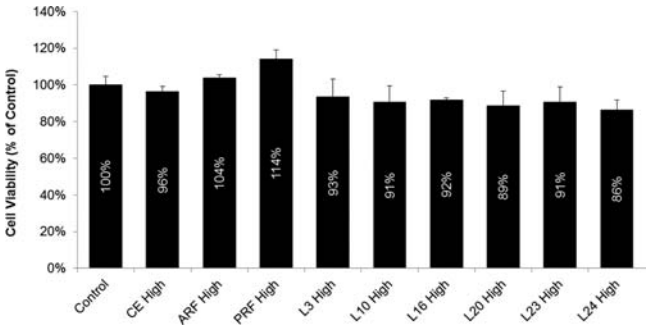

Figure 4. Cell viability of H9c2 cells treated with lingonberry extracts (1:100) as measured fluorescently using AlamarBlue cell viability reagent. None of the treatments reduced cell viability.

fold increase in nuclei condensation (an indicator of apoptosis) compared to H9c2 cells not exposed to IR (Figure 5A,B). Addition of CE (Figure 5C), ARF (Figure 5D), and PRF (Figure 5E) to the cell culture medium prevented IR-induced nuclei condensation as measured by the Hoechst stain. The ratio of condensed to normal nuclei in the IR group without treatment was set to 100%, and CE, ARF, and PRF treatment groups and controls were compared to this ratio (Figure 6). For Manitoba lingonberry, even at the lowest concentrations tested, all three samples inhibited nuclei condensation by at least 50% when compared to the IR group. Each sample exhibited a dose-dependent inhibition of nuclei condensation, which is indicative of apoptosis.

The selective JNK inhibitor SP600125 was also tested for its ability to inhibit nuclei condensation in H9c2 cells to demonstrate the role of JNK in the apoptotic mechanism induced by our model of IR (Figure 6). SP600125 was able to inhibit nuclei condensation by 75% at a concentration of 5 μM, indicating that JNK activation plays a role in apoptosis in this setting.

Inhibition of Caspase-3 Activity and Cleaved PARP Expression. In our model, IR induced a >2-fold increase in caspase-3 activity compared to control cells. The effects of all lingonberry samples on caspase-3 activity are shown in Figure 7. In the case of Manitoba lingonberry, CE exhibited stronger inhibition of caspase-3 activity than PRF and ARF, and PRF was slightly more effective than ARF at inhibiting caspase-3 activity. All three samples significantly inhibited caspase-3 activation. IR induced a 2-fold increase in levels of cleaved PARP, a target of caspase-3 in IR-injured cells, and CE prevented this increase (Figure 8).

Inhibition of JNK Activity. Using electrochemiluminescent multiplex assays, it was determined that IR induced a 20-fold increase in phosphorylated JNK and a 7-fold increase in c-Jun phosphorylation. Treatment with CE, ARF, and PRF had no effect on JNK or c-Jun phosphorylation in control cells. The effects of treatment with CE, ARF, and PRF on JNK phosphorylation are shown in Figure 9A, and the effects on c-Jun phosphorylation are shown in Figure 9B. All three samples significantly inhibited JNK activity in a concentration-dependent manner. ARF provided the strongest inhibitory effect on IR-induced JNK activation. The effects of treatment with cyanidin-3-glucoside, cyanidin-3-galactoside, and cyanidin-3-arabinoside on JNK phosphorylation are shown in Figure 10. All three anthocyanins showed an inhibitory effect on JNK phosphorylation, an indication of their protective effect against IR-induced JNK activation. Cyanidin-3-glucoside provided the highest level of protection, but all three anthocyanins effectively protected against JNK activation at physiologically relevant doses.

DISCUSSION

The novel findings of this study are that (1) Manitoba lingonberry, analyzed for the first time in the scientific literature, has high in vitro antioxidant capacity and contains large quantities of anthocyanins including three main anthocyanins in agreement with European varieties and (2) the significant protection against nuclear condensation, caspase-3 activation, and JNK phosphorylation is provided by Manitoba lingonberry samples and pure anthocyanins in a model of IR in H9c2 cells.

The antioxidant capacity of the Manitoba lingonberry CE was higher than many reported ORAC values for commonly consumed berries[7,12] and the ORAC values of eastern Canada and European lingonberry. However, from this study, it is not possible to compare the antioxidant activity among different genotypes and the Manitoba populations. The Manitoba lingonberries consist of two populations containing a number of genotypes. They were collected from the wild in 2011, but the Newfoundland clones and the cultivar Mesovia were being grown in a greenhouse under controlled conditions for more than 10 years. There is evidence that berries grown in colder temperatures and at higher latitudes produce more anthocyanins and polyphenolic compounds.[32] It is possible that the colder climate of Manitoba may be responsible for the increase in antioxidant capacity in Manitoba lingonberry. Anthocyanin and total phenolic content were strongly correlated (Pearson correlation coefficient = 0.97, data not shown) for the Newfoundland and European clones grown in-house; however, the ratio of anthocyanin content to total phenolic content in wild Manitoba lingonberry was much higher than that of the lingonberries grown in-house due to the exceptionally high levels of total phenolics. Further research will investigate whether

DOI: 10.1021/acs.jafc.5b00797
J. Agric. Food Chem. 2015, 63, 5660−5669

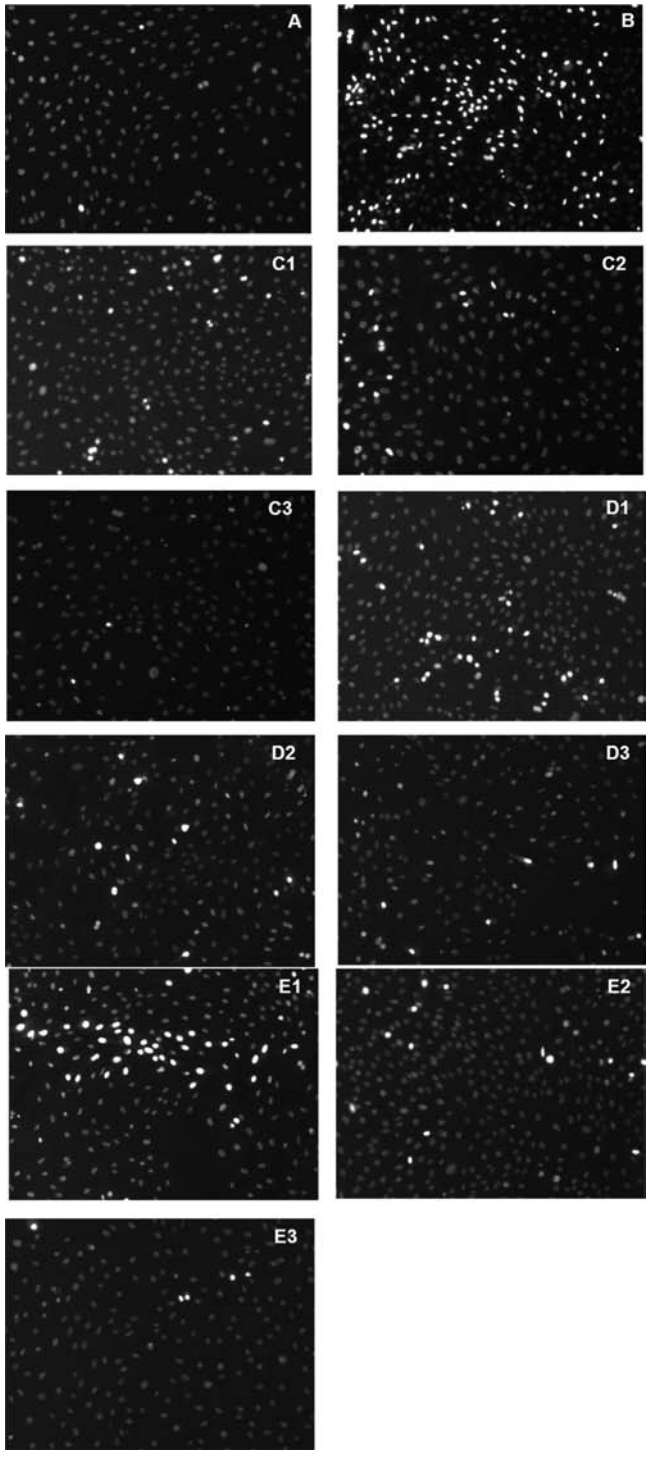

Figure 5. Hoechst staining of H9c2 cells (A) under normoxic conditions, (B) after 1 h of simulated ischemia and 30 min of simulated reperfusion (IR), (C) after 1 h of simulated ischemia and 30 min of simulated reperfusion with CE treatment at three concentrations (1, very low; 2, low; 3, medium), (D) after 1 h of simulated ischemia and 30 min of simulated reperfusion with ARF treatment at three concentrations, and (E) after 1 h of simulated ischemia and 30 min of simulated reperfusion with PRF treatment at three concentrations.

the change in ratio is due to genetic variability or growing conditions.

The identified anthocyanin peaks are in agreement with results from studies on North American and European lingonberry.[2,33]

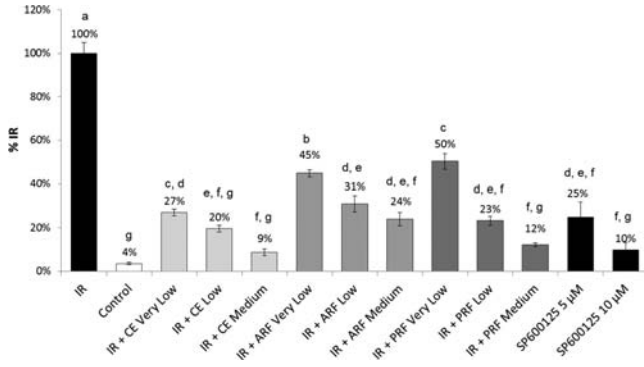

Figure 6. Effect of CE, ARF, and PRF (medium dose = 1:500 dilution in cell culture media, low dose = 1:1000 dilution, very low dose = 1:2000 dilution) on ratio of condensed to normal nuclei as measured by Hoechst stain in control cells and cells subjected to 1 h of simulated ischemia and 30 min of simulated reperfusion (IR), with IR set to 100%. Results are expressed as the mean ± SEM (n = 3). Groups specified by the same letter are not significantly different at $P < 0.05$.

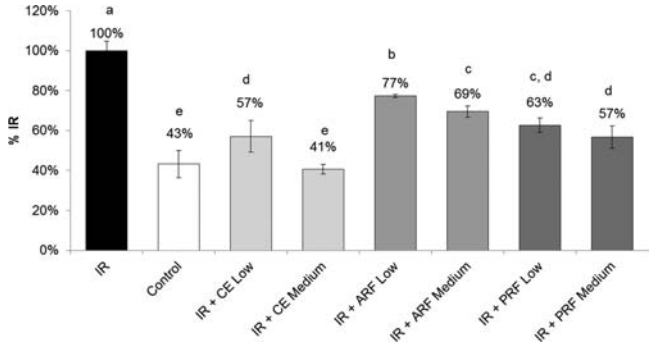

Figure 7. Effect of CE, ARF, and PRF (medium dose = 1:500 dilution in cell culture media, low dose = 1:1000 dilution) on caspase-3 activity in control cells and cells subjected to 1 h of simulated ischemia and 30 min of simulated reperfusion (IR), with IR set to 100%. Enzyme activity was measured fluorescently, and results are expressed as the mean ± SEM (n = 3). Groups specified by the same letter are not significantly different at $P < 0.05$.

Brown et al. confirmed that wild lingonberry from British Columbia, Canada, contained 300 mg of anthocyanins per 100 g DW and identified cyanidin-3-glucoside, cyanidin-3-galactoside, and cyanidin-3-arabinoside as the three major anthocyanins.[34] Using the results for the ORAC, total phenolics, and total anthocyanins assays of CE, ARF, and PRF, the doses used for the subsequent cell studies were selected on the basis of a literature review of other cellular studies on lingonberry as well as reported plasma concentrations of anthocyanins and antioxidants achieved following oral dosing.[35,36] Future studies will need to standardize berry cultivation and collection to account for these differences and also test the year-to-year variability of wild lingonberry extracts to confirm the exceptionally high anthocyanin and antioxidant content of Manitoba lingonberry.

IR injury in H9c2 cells is well-described in the literature. In these cells, IR has been shown to induce JNK and ERK activation,[37−42] nuclei condensation,[27] caspase-3 activation,[38] and pro-apoptotic protein activation.[40−42] Because reactive oxygen species accumulate rapidly during reperfusion, polyphenolic compounds with high in vitro antioxidant capacity have been hypothesized as potential therapeutic treatments for IR injury. Indeed, the polyphenols tyrosol,[27] curcumin,[38] danshensu,[40] resveratrol,[41] and others have been shown to be

DOI: 10.1021/acs.jafc.5b00797
J. Agric. Food Chem. 2015, 63, 5660−5669

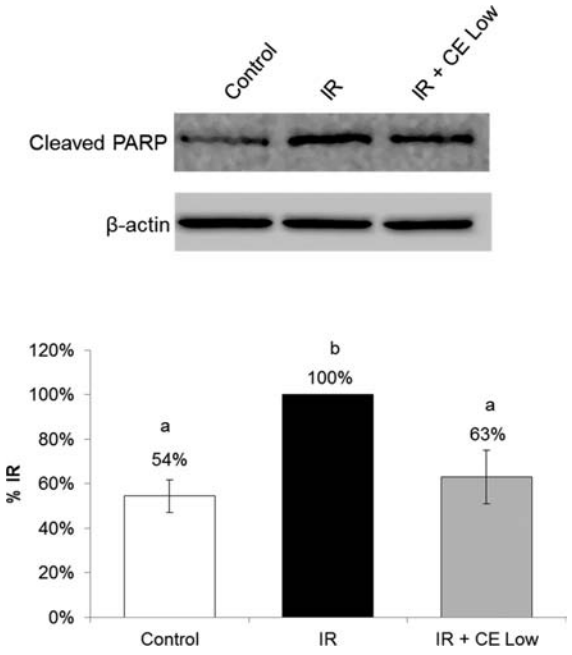

Figure 8. Effect of CE (medium dose = 1:500 dilution in cell culture media) on levels of cleaved PARP in cells subjected to 1 h of simulated ischemia and 30 min of simulated reperfusion (IR) as compared to untreated normoxic cells and untreated IR cells. Protein was determined by Western immunoblotting analysis (40 μg of protein). Results are expressed as the mean ± SEM (n = 3). Groups specified by the same letter are not significantly different at $P < 0.05$.

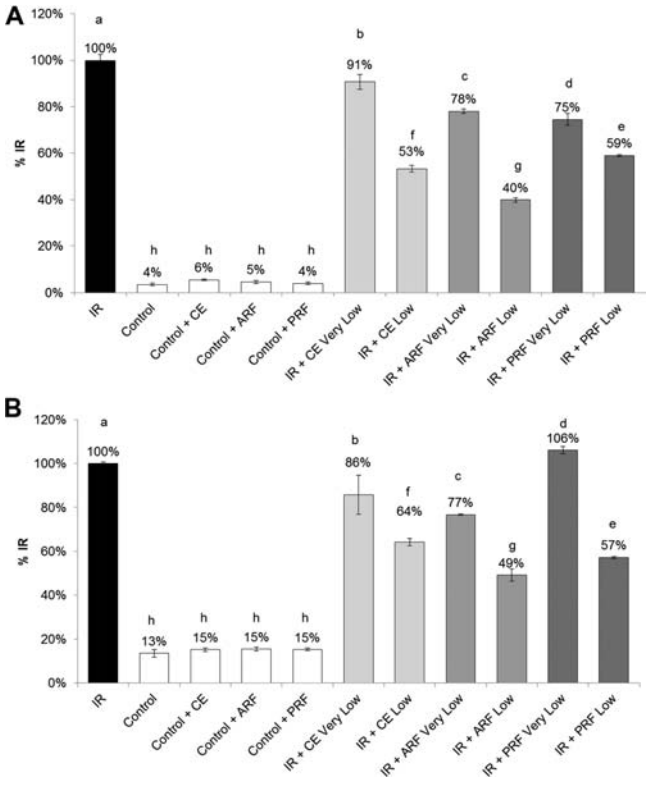

Figure 9. Effect of CE, ARF, and PRF (low dose = 1:1000 dilution in cell culture media, very low dose = 1:2000 dilution) on JNK activation (A) and c-Jun phosphorylation (B) in control cells and cells subjected to 1 h of simulated ischemia and 30 min of simulated reperfusion (IR), with IR set to 100%. Percent protein phosphorylation was measured electrochemiluminescently with Meso Scale Discovery multiplex assay kits. Results are expressed as the mean ± SEM (n = 3). Groups specified by the same letter are not significantly different at $P < 0.05$.

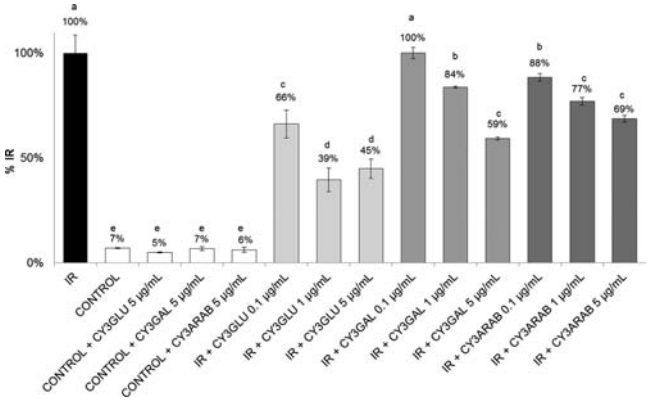

Figure 10. Effects of individual anthocyanins cyanidin-3-glucoside (CY3GLU), cyanidin-3-galactoside (CY3GAL), and cyanidin-3-arabinoside (CY3ARAB) at 5, 1, and 0.1 μg/mL on JNK activation in control cells and cells subjected to 1 h of simulated ischemia and 30 min of simulated reperfusion (IR), with IR set to 100%. Percent protein phosphorylation was measured electrochemiluminescently with Meso Scale Discovery multiplex assay kits. Results are expressed as the mean ± SEM (n = 3). Groups specified by the same letter are not significantly different at $P < 0.05$.

protective in cardiomyocyte IR injury. Polyphenols may act as direct intracellular antioxidants, because intracellular ROS accumulation is generally inhibited with these treatments. An NADPH oxidase inhibitor has been shown to simultaneously reduce intracellular ROS and JNK phosphorylation in H9c2 cells,[37] so perhaps antioxidants may inhibit apoptosis by reducing ROS production. Recently, Bhullar and Rupasinghe demonstrated that lingonberry extracts could protect fibroblasts against peroxyl radical-induced stress by scavenging reactive oxygen species and activating the Nrf2 pathway, indicating that lingonberry polyphenols may be potent intracellular antioxidants.[43]

Several lines of evidence in this study demonstrated the anti-apoptotic effects of Manitoba lingonberry compounds. First, our results indicated that Manitoba lingonberry was efficient at preventing nuclei condensation in a model of IR. Nuclei condensation is an indicator of apoptosis because as the cell dismantles its nucleus and fragments its DNA, nuclei become small and stain brightly with Hoechst 33528. Second, Manitoba lingonberry also inhibited caspase-3 activation significantly in this model and reduced levels of cleaved PARP. Caspase-3, an executioner caspase, has numerous cellular targets, the cleavage of which is essential for apoptosis, including PARP.[44] The fact that Manitoba lingonberry treatment inhibited nuclei condensation and caspase-3 activation simultaneously suggested that apoptosis, rather than necrosis, was the primary mode of cell death in our model of IR. Third, we observed that Manitoba lingonberry inhibited JNK and c-Jun phosphorylation concurrently with inhibiting apoptosis. We used the selective JNK inhibitor, SP600125[45] to show the relevance of this MAPK signaling pathway in our model. JNK inhibition was associated with a marked decrease in apoptosis, indicating that JNK activation is relevant to apoptosis in this setting. Importantly, pure anthocyanins also inhibited JNK activation in IR-injured H9c2 cells. These results are significant because several reports have confirmed the presence of pure anthocyanins in plasma and physiologically relevant doses were used.[37] However, future

DOI: 10.1021/acs.jafc.5b00797
J. Agric. Food Chem. 2015, 63, 5660−5669

studies are needed to examine the bioactivities of lingonberry metabolites because these compounds certainly have bioactivities themselves and may be formed in cell culture studies.[46,47] MAP kinases include JNK and extracellular signal-regulated kinase (ERK) and are involved in critical signaling pathways needed for cell proliferation, differentiation, and apoptosis. In the MAPK signaling cascades, many different signals may converge on JNK at once, and the balance between the pro- and anti-apoptotic signals will decide whether JNK will be activated or not. Once activated via phosphorylation, JNK may translocate to the nucleus, where it phosphorylates specific pro-apoptotic transcription factors, or to the mitochondria, where it modulates the activity of mitochondrial proteins by phosphorylation. An important nuclear target of JNK is c-Jun, a component of the activator protein-1 pro-apoptotic transcription factor complex. JNK inhibitors have been shown to be protective against apoptosis in several cell types in vitro, and a JNK inhibitor decreased myocardial apoptosis and reduced infarct size after myocardial IR in rats.[48]

In conclusion, our study provides the first analysis of Manitoba lingonberry and demonstrates the protective effects of lingonberry in a model of IR injury, which is a clinically relevant phenomenon in many diseases. Lingonberry fruits can be safely consumed at low cost and, due to their high content of various bioactive compounds, may constitute part of a healthy diet. Future research will allow further mechanistic insight into the role of lingonberry phytochemicals in human health.

AUTHOR INFORMATION

Corresponding Author

*E-mail: Chris.Siow@agr.gc.ca. Phone: (204) 235-3457.

Funding

C.K.I. is supported in part by a BMO Financial Group Research Scholarship for Excellence, a studentship from the Manitoba Health Research Council, and the estate of Margurite Jermaine Gerome (deceased).

Notes

The authors declare no competing financial interest.

ABBREVIATIONS USED

AAPH, 2,2′-azobis(2-amidinopropane) dihydrochloride; ARF, anthocyanin-rich fraction; CE, complete extract; DMEM, Dulbecco's modified Eagle's medium; DW, dry weight; ERK, extracellular signal-regulated kinase; FW, fresh weight; IR, ischemia-reperfusion; JNK, cJun N-terminal kinase; MAPK, mitogen-activated protein kinases; ORAC, oxygen radical absorbance capacity; PARP, poly-ADP ribose polymerase; PBS, phosphate-buffered saline; PRF, phenolic-rich fraction; UPLC, ultraperformance liquid chromatography; ROS, reactive oxygen species

REFERENCES

(1) Hulten, E. On the races in the Scandinavian flora. *Svensk. Botanisk. Tidskrift. Bd.* **1949**, *43*, 383−406.

(2) Ek, S.; Kartimo, H.; Mattila, S.; Tolonen, A. Characterization of phenolic compounds from lingonberry (*Vaccinium vitis-idaea*). *J. Agric. Food Chem.* **2006**, *54*, 9834−9842.

(3) Bere, E. Wild berries: a good source of omega-3. *Eur. J. Clin. Nutr.* **2007**, *61*, 431−433.

(4) Szakiel, A.; Paczkowski, C.; Koivuniemi, H.; Huttunen, S. Comparison of the triterpenoid content of berries and leaves of lingonberry *Vaccinium vitis-idaea* from Finland and Poland. *J. Agric. Food Chem.* **2012**, *60*, 4994−5002.

(5) Hakkinen, S. H.; Karenlampi, S. O.; et al. Heinonen, et al. Content of the flavonols quercetin, myricetin, and kaempferol in 25 edible berries. *J. Agric. Food Chem.* **1999**, *47*, 2274−2279.

(6) Erlund, I.; Marniemi, J.; Hakala, P.; et al. Consumption of black currants, lingonberries, and bilberries increases serum quercetin concentrations. *Eur. J. Clin. Nutr.* **2003**, *57*, 37−42.

(7) Bakowska-Barczak, A. M.; Marianchuk, M.; Kolodziejczyk, P. Survey of bioactive components in Western Canadian berries. *Can. J. Physiol. Pharmacol.* **2007**, *85*, 1139−1152.

(8) Lee, J.; Finn, C. E. Lingonberry (*Vaccinium vitis-idaea* L.) grown in the Pacific Northwest of North America: anthocyanin and free amino acid composition. *J. Funct. Foods* **2012**, *4*, 213−218.

(9) Kylli, P.; Nohynek, L.; Puupponen-Pimia, R.; et al. Lingonberry (*Vaccinium vitis-idaea*) and European cranberry (*Vaccinium microcarpon*) proanthocyanidins: isolation, identification, and bioactivities. *J. Agric. Food Chem.* **2011**, *59*, 3373−3384.

(10) Rimando, A. M.; Kalt, W.; Magee, J. B.; et al. Resveratrol, pterostilbene, and piceatannol in *Vaccinium* berries. *J. Agric. Food Chem.* **2004**, *52*, 4713−4719.

(11) Del Rio, D.; Borges, G.; Crozier, A. Berry flavonoids and phenolics: bioavailability and evidence of protective effects. *Br. J. Nutr.* **2010**, *104*, S67−S90.

(12) Zheng, W.; Wang, S. Y. Oxygen radical absorbing capacity in blueberries, cranberries, chokeberries, and lingonberries. *J. Agric. Food Chem.* **2003**, *51*, 502−509.

(13) Mane, C.; Loonis, M.; Juhel, C.; Dufour, C.; Malien-Aubert, C. Food grade lingonberry extract: polyphenolic composition and in vivo protective effect against oxidative stress. *J. Agric. Food Chem.* **2011**, *59* (7), 3330−3339.

(14) Kivimaki, A. S.; Ehlers, P. I.; Turpeinen, A. M.; Vapaatalo, H.; Korpela, R. Lingonberry juice improves endothelium-dependent vasodilation of mesenteric arteries in spontaneously hypertensive rats in a long-term intervention. *J. Funct. Foods* **2011**, *3*, 267−274.

(15) Kivimaki, A. S.; Siltari, A.; Ehlers, P. I.; Korpela, R.; Vapaatalo, H. Lingonberry juice lowers blood pressure of spontaneously hypertensive rats (SHR). *J. Funct. Foods* **2013**, *5*, 1432−1440.

(16) Torronen, R.; Kolehmainen, M.; Sarkkinen, E.; Mykkanen, H.; Niskanen, L. Postprandial glucose, insulin, and free fatty acid responses to sucrose consumed with blackcurrants and lingonberries in health women. *Am. J. Clin. Nutr.* **2012**, *96*, 527−533.

(17) Zamora-Ros, R.; Knaze, V.; Lujan-Barroso, L.; et al. Estimation of the intake of anthocyanidins and their food sources in the European Prospective Investigation into Cancer and Nutrition (EPIC) Study. *Br. J. Nutr.* **2011**, *106*, 1090−1099.

(18) Government of Canada. Leading causes of death, 2011 (updated 11/01); available at http://www40.statcan.gc.ca/l01/cst01/hlth36a-eng.htm.

(19) Kavurma, M. M.; Bhindi, R.; Lowe, H. C.; Chesterman, C.; Khachigian, L. M. Vessel wall apoptosis and atherosclerotic plaque instability. *J. Thromb. Haemostasis* **2005**, *3* (3), 465−472.

(20) Dorweiler, B.; Pruefer, D.; Andrasi, T.; et al. Ischemia-reperfusion injury. *Eur. J. Trauma Emerg. Surg.* **2007**, *33* (6), 600−612.

(21) Powers, S. K.; Zsolt, M.; Wu, M.; Kavazis, A. N. Ischemia-reperfusion-induced cardiac injury: a brief review. *Med. Sci. Sports Exercise* **2007**, *39* (9), 1539−1539.

(22) Kumar, D.; Lou, H.; Singal, P. K. Oxidative stress and apoptosis in heart dysfunction. *Herz.* **2002**, *27* (7), 662−668.

(23) Rodriguez-Saona, L. E.; Wrolstad, R. E. Extraction, isolation, and purification of anthocyanins. *Curr. Protoc. Food Anal. Chem.* **2001**, F1.1.1−F1.1.11.

(24) Ainsworth, E. A.; Gillespie, K. M. Estimation of total phenolic content and other oxidation substrates in plant tissues using Folin-Ciocalteu reagent. *Nat. Protoc.* **2007**, *2* (4), 875−877.

(25) Gillespie, K. M.; Chae, J. M.; Ainsworth, E. A. Rapid measurement of total antioxidant capacity in plants. *Nat. Protoc.* **2007**, *2* (4), 867−870.

(26) Lee, J.; Durst, R. W.; Wrolstad, R. E. Determination of total monomeric anthocyanin pigment content of fruit juices, beverages, natural colorants, and wines by the pH differential method: a collaborative study. *J. AOAC Int.* **2005**, *88* (5), 1269−1278.

DOI: 10.1021/acs.jafc.5b00797
J. Agric. Food Chem. 2015, 63, 5660−5669

(27) Sun, L.; Isaak, C. K.; Zhou, Y.; et al. Salidroside and tyrosol from *Rhodiola* protect H9c2 cells from ischemia/reperfusion-induced apoptosis. *Life Sci.* **2012**, *91*, 151−158.
(28) Abramoff, M. D.; Magalhaes, P. J.; Ram, S. J. Image processing with ImageJ. *Biophotonics Int.* **2004**, *11*, 36−42.
(29) Bradford, M. M. Rapid and sensitive method for the quantitation of microgram quantities of protein utilizing the principle of protein-dye binding. *Anal. Biochem.* **1976**, *72*, 248−254.
(30) Laemmli, U. K. Cleavage of structural proteins during the assembly of the head of bacteriophage T4. *Nature* **1970**, *227*, 680−685.
(31) Towbin, H.; Staehelin, T.; Gordon, J. Electrophoretic transfer of proteins from polyacrylamide gel to nitrocellulose sheets: procedure and some applications. *Proc. Natl. Acad. Sci. U. S. A.* **1979***76*, 4350−4354.10.1073/pnas.76.9.4350
(32) Uleberg, E.; Rohloff, J.; Trost, K.; Junttila, O.; Haggman, H.; Martinussen, I. Effects of temperature and photoperiod on yield and chemical composition of northern and southern clones of bilberry (*Vaccinium myrtillus* L.). *J. Agric. Food Chem.* **2012**, *60*, 10406−10414.
(33) Lee, J.; Finn, C. E. Lingonberry (*Vaccinium vitis-idaea* L.) grown in the Pacific Northwest of Northwest of North America: anthocyanin and free amino acid composition. *J. Funct. Foods* **2012**, *4*, 213−218.
(34) Brown, P. N.; Turi, C. E.; Shipley, P. R.; Murch, S. J. Comparisons of large (*Vaccinium macrocarpon* Ait.) and small (*Vaccinium oxycoccos* L., *Vaccinium vitis-idaea* L.) cranberry in British Columbia by phytochemical determination, antioxidant potential, and metabolomics profiling with chemometric analysis. *Planta Med.* **2012**, *78*, 630−640.
(35) Wang, S. Y.; Feng, R.; Bowman, L.; Penhallegon, R.; Ding, M.; Lu, Y. Antioxidant activitiy in lingonberries (*Vaccinium vitis-idaea* L.) and its inhibitory effect on activator protein-1, nuclear factor-κB, and mitogen-activated protein kinases activation. *J. Agric. Food Chem.* **2005**, *53*, 3156−3166.
(36) McGhie, T. K.; Walton, M. C. The bioavailability and absorption of anthocyanins: towards a better understanding. *Mol. Nutr. Food Res.* **2007**, *51*, 702−713.
(37) Borchi, E.; Parri, M.; Papucci, L.; et al. Role of NADPH oxidase in H9c2 cardiac muscle cells exposed to simulated ischaemia-reperfusion. *J. Cell. Mol. Med.* **2009**, *13* (8B), 2724−2735.
(38) Fiorillo, C.; Becatti, M.; Pensalfini, A.; et al. Curcumin protects cardiac cells against ischemia-reperfusion injury: effects on oxidative stress, NFκB, and JNK pathways. *Free Radical Biol. Med.* **2008**, *45*, 839−846.
(39) Xu, B.; Zhou, Y.; O, K.; Choy, P. C.; Pierce, G. N.; Siow, Y. L. Regulation of stress-associated scaffold proteins JIP1 and JIP3 on the c-Jun NH_2-terminal kinase in ischemia-reperfusion. *Can. J. Physiol. Pharmacol.* **2010**, *88*, 1084−1092.
(40) Yin, Y.; Guan, Y.; Duan, J.; et al. Cardioprotective effect of Danshensu against myocardial ischemia/reperfusion injury and inhibits apoptosis of H9c2 cardiomyocytes via Akt and ERK1/2 phosphorylation. *Eur. J. Pharmacol.* **2013**, *699*, 219−226.
(41) Becatti, M.; Taddei, N.; Cecchi, C.; Nassi, N.; Nassi, P. A.; Fiorillo, C. SIRT1 modulates MAPK pathways in ischemic-reperfused cardiomyocytes. *Cell. Mol. Life Sci.* **2012**, *69*, 2245−2260.
(42) Pechtelidou, A.; Beis, I.; Gaitanaki, C. Transient and sustained oxidative stress differentially activate the JNK1/2 pathway and apoptotic phenotype in H9c2 cells. *Mol. Cell. Biochem.* **2008**, *309*, 177−189.
(43) Bhullar, K. S.; Rupasinghe, H. P. V. Antioxidant and cytoprotective properties of partridgeberry polyphenols. *Food Chem.* **2015**, *168*, 595−605.
(44) Chowdhury, I.; Tharakan, B.; Bhat, G. K. Caspases − an update. *Comp. Biochem. Physiol., Part B: Biochem. Mol. Biol.* **2008**, *151*, 10−27.
(45) Bennett, B. L.; Sasaki, D. T.; Murray, B. W.; et al. SP600125, an anthrapyrazolone inhibitor of Jun N-terminal kinase. *Proc. Natl. Acad. Sci. U. S. A.* **2001**, *98* (24), 13681−13686.
(46) Vitaglione, P.; Donnarumma, G.; Napolitano, A.; et al. Protocatechuic acid is the major human metabolite of cyanidin-glucosides. *J. Nutr.* **2007**, *137*, 2043−2048.
(47) Nurmi, T.; Mursu, J.; Heinonen, M.; Nurmi, A.; Hiltunen, R.; Voutilainen, S. Metabolism of berry anthocyanins to phenolic acids in human. *J. Agric. Food Chem.* **2009**, *57*, 2274−2281.
(48) Ferrandi, C.; Ballerio, R.; Gaillard, P.; et al. Inhibition of c-Jun N-terminal kinase decreases cardiomyocyte apoptosis and infarct size after myocardial ischemia and reperfusion in anaesthetized rats. *Br. J. Pharmacol.* **2004**, *142*, 953−960.

DOI: 10.1021/acs.jafc.5b00797
J. Agric. Food Chem. 2015, 63, 5660−5669

Table 1. Characteristics of the Commercial Dry Yeast Products Used in the Elaboration of White and Rosé Sparkling Wines and Doses Applied

product added	commercial supplier	dose (g/L)	expected effect (information provided by the manufacturer)	characteristics
DYA-1[a]	Agrovin	0.30	increase the volume of the lees, increase mouthfeel and foam persistence	product with autolysated yeast enriched in polysaccharides
DYA-2	Agrovin	0.30	increase the volume of the lees; increase mouthfeel and foam persistence	cell wall autolysated yeast enriched in polysaccharides and with 20−22% of soluble mannoproteins
DYA-3	Sepsa-Enartis	0.15	aromatic protection; increase freshness and prevent browning; increase colloidal stability, mouthfeel, and roundness sensations; improve foam stability	inactivate yeast with high content in parietal polysaccharides
DYA-4	Sepsa-Enartis	0.15	aromatic protection, increase freshness and prevent browning; increase colloidal stability, mouthfeel, and roundness sensations; improve foam stability; protect stability and aromatic persistence	product with polysaccharides from the yeast cell walls, highly purified and with high content in free mannoproteins

[a]DYA, commercial dry yeast autolysates.

lees for 9 months. For this purpose, four commercial dry yeast products with different compositions were used.

MATERIALS AND METHODS

Chemicals. The volatile compound standards were purchased from Fluka (Buchs, Switzerland), Sigma-Aldrich (Steinheim, Germany), and Lancaster (Strasbourg, France), as can be seen in Table 3.

L-Cysteine, L-leucine, L-phenylalanine, L-lysine, L-histidine, cadaverine, L-arginine, histamine, L-alanine, spermidine, glycine, β-alanine, L-aspartic acid, L-glutamic acid, L-tyrosine, L-serine, L-phenylethylamine, D-(+)-galacturonic acid, D-glucuronic acid, *myo*-inositol, trifluoroacetic acid, and HPLC grade orthophosphoric 85% acid were purchased from Fluka (Buchs, Switzerland). Isoamylamine, L-proline, diethyl ethoxymethylenemalonate (DEEMM), putrescine, tyramine, tryptamine, *trans*-4-hydroxy-L-proline, L-2-aminoadipic acid, L-ornithine monohydrochloride, L-tryptophan, L-asparagine, L-threonine, γ-aminobutyric acid (GABA), L-isoleucine, L-glutamine, L-methionine, sodium azide, D-(+)-fucose, L-rhamnose, 2-*O*-methyl-D-xylose, L-(+)-arabinose, D-(+)-galactose, D-(+)-glucose, D-(+)-mannose, 2-keto-3-deoxyoctonate ammonium salt (Kdo), hexane, dried methanol, pyridine, hexamethyldisilazane, trimethylchlorosilane, and D-apiose solution were purchased from Sigma-Aldrich (Steinheim, Germany).

The phenolic compounds were purchased from Extrasynthèse (Lyon, France), and Toyopearl gel HW-50F was obtained from Tosoh Corp. (Tokyo, Japan).

HPLC grade reagents, ethanol, methanol, acetonitrile, acetyl chloride, ethanol 96% (v/v), acetone, acetic acid glacial, and sodium acetate were provided by Scharlab (Barcelona, Spain). Dichloromethane (HPLC grade) was provided by Merck (Darmstadt, Germany), and the remaining reagents were supplied by Panreac (Madrid, Spain). Milli-Q water was obtained via a Millipore system (Bedford, MA, USA).

Polysaccharide Commercial Dry Yeast Products. Table 1 shows the information provided by the commercial manufacturers regarding the commercial dry yeast autolysates (DYA) used in this study as well as the doses applied. These products were selected because they were more specifically developed for sparkling wine elaboration according to the manufacturers' information. Considering this information, the maximum doses recommended by the manufacturers were assayed.

Winemaking Process. All sparkling wine production was carried out in the experimental winery of the Enological Station (ITACyL) sited in Rueda (Valladolid, Spain), following the traditional or *champenoise* method. White monovarietal base wines were elaborated with *Vitis vinifera* cv. Verdejo grapes from the Rueda Denomination of Origin (D.O.), and *V. vinifera* cv. Godello grapes from the Bierzo D.O. Rosé monovarietal base wines were obtained with *V. vinifera* cv. Tempranillo and Garnacha grapes from the Cigales D.O. Godello and Garnacha grape varieties were harvested in 2010 and Verdejo and Tempranillo in 2011.

The base wines were elaborated following the traditional white or rosé winemaking process in stainless steel tanks of 2000 and 2600 L, respectively. After cold stabilization and clarification of base wines, the tirage liquor was added and the wines were bottled. The tirage liquor was formed by yeast *S. cerevisiae* var. *bayanus* (0.30 g/L, IOC 18-2007, Oenologique Institut de Champagne, Epernay, France), sucrose (23 g/L), bentonite calcium activated (0.10 g/L) (Laffort, France), and the different commercial dry yeast products in the doses indicated in Table 1. Previously, a starter was prepared with 10% of the base wine, 180 g/L sucrose, and 0.30 g/L yeast. The experiments carried out were the control wines (C), without the addition of any product, and the sparkling wines made with the addition of the four different commercial dry yeast autolysates (DYA-1, DYA-2, DYA-3, and DYA-4). After that, the bottles were kept in a cellar at controlled a temperature (11−13 °C) and relative humidity (75−85%) for 9 months. The pressure and residual sugars were measured periodically to control the second fermentation. The pressure was measured by an aphrometer, and the sugars were measured by using an enzymatic method.

Wines were analyzed after 3, 6, and 9 months of aging on lees. Wines were riddled and disgorged, and no expedition liqueur was added. Because the second fermentation takes place in individual bottles, three bottles of each varietal sparkling wine at each sampling time were analyzed.

Analysis of Polysaccharide Composition of Commercial Dry Yeast Products and Sparkling Wine Samples. To characterize the different dry yeast preparations, the monosaccharide composition and their polysaccharide molecular weight distribution were analyzed. The monosaccharide composition of the commercial preparations was determined by GC-MS of their trimethylsilyl ester *O*-methyl glycosyl residues obtained after acidic methanolysis and derivatization.[29] GC was controlled by ChemStation software and equipped with a 7653B automatic injector consisting of an Agilent 7890A gas chromatograph (Agilent Technologies, Waldbronn, Germany) coupled to a 5975C VL quadrupole mass detector (MS). A high-resolution size exclusion chromatography (HRSEC) system (1100 Agilent Technologies) connected to a refractive index detector (RID) was used to obtain the molecular weight distributions of the polysaccharides. Two serial Shodex OHpack KB-803 and KB-805 columns (0.8 × 30 cm, Showa Denko, Japan) equilibrated at 1 mL/min in 0.1 M $LiNO_3$ were used, and calibration was performed with narrow pullulan molecular weight standards as previously described.[29] All analyses were performed in triplicate.

Wine polysaccharides were recovered by precipitation after ethanolic dehydration, and their monosaccharide composition was determined by GC-MS as commented before. The content of mannoproteins was estimated from the content of mannose as described by Guadalupe et al.[29] The content of glucans was estimated from the content of glucose.

Analysis of Phenolic Compounds. Anthocyanins, hydroxycinnamic acids, flavonols, and flavan-3-ols were analyzed by HPLC in an 1100 Agilent liquid chromatograph (Agilent Technologies) equipped with a photodiode array detector (DAD). Separation was achieved in an ACE HPLC column (Teknokroma, Barcelona, Spain) (250 mm × 4.6 mm, particle size = 5 μm), according to the methodology previously described.[30]

For analyzing proanthocyanidins, wine samples were fractionated by gel permeation chromatography (GPC) on a Toyopearl gel HP-50 F column (Tosohaas, Montgomeryville, PA, USA) as described by

DOI: 10.1021/acs.jafc.5b01336
J. Agric. Food Chem. 2015, 63, 5670−5681

Table 2. Monosaccharide Composition, Polysaccharide Purity, and Polysaccharide Composition of the Different Commercial Products[a]

	commercial product			
	DYA-1	DYA-2	DYA-3	DYA-4
mannose (%)	52.9 ± 5.1a	85.9 ± 6.1d	77.1 ± 4.5cd	62.3 ± 6.8ab
glucose (%)	47.1 ± 3.2b	14.1 ± 1.7a	22.9 ± 4.3a	37.7 ± 4.6b
polysaccharide purity[b] (%)	71.3 ± 6.2a	88.8 ± 10.2b	63.2 ± 2.8a	73.6 ± 4.3ab
∑ (P400−P50)[c] (%)	52.5 ± 4.0a	100.0 ± 0.0b	100.0 ± 7.2b	100.0 ± 7.1b
P10[c] (%)	47.5 ± 3.0			

[a]Data shown are the average and standard deviation of three analyses of each product. Values with different letters indicate statistically significant differences at $p < 0.05$. [b]Polysaccharide purity expressed as the total amount of monosaccharides in relation to the dry weight of the product analyzed. [c]∑ (P400−P50), polysaccharides with an average molecular weight between 47.3 and 404 kDa; P10, polysaccharides with an average molecular weight of 11.8 kDa. Polysaccharide fractions estimated by HRSEC as described in the text.

Guadalupe et al.[31] A first fraction was eluted with ethanol/water/trifluoroacetic acid; a second fraction containing proanthocyanidins was recovered by elution with acetone/water. Phloroglucinol adducts in the second fraction were analyzed by reversed-phase HPLC-DAD.[32] The column was an ACE HPLC (Teknokroma) (250 mm × 4.6 mm, particle size = 5 μm) protected by a guard column containing the same material. Total proanthocyanidin content was calculated as the sum of all the subunits: extension subunits (phloroglucinol adducts) and terminal subunits (catechin, epicatechin, and epicatechin gallate).

Analysis of Amino Acids and Biogenic Amines. Amino acid and biogenic amine content was determined simultaneously using the method described by Gómez-Alonso et al.[33] HPLC was performed using an 1100 Agilent liquid chromatograph (Agilent Technologies) equipped with a DAD. Chromatographic separation was performed in an ACE HPLC column (Teknokroma) (250 mm × 4.6 mm, particle size = 5 μm), thermostated at 16 °C.

Analysis of Volatile Compounds. The volatile compounds were extracted by liquid−liquid extraction following the method developed by Rodríguez-Bencomo et al.[7] Two hundred and fifty milliliters of wine, 5 mL of dichloromethane, and 75 μL of a mixture of two internal standards (550 mg/L of methyl octanoate from Sigma-Aldrich and 450 mg/L of 3,4-dimethylphenol from Lancaster) were added to a flask. The extraction was carried out for 3 h with continuous stirring (150 rpm) in an orbital shaker. The organic phase was then separated and concentrated until 400 μL. The chromatographic analyses were performed with an HP-6890N GC coupled to an HP-5973 inert MS detector equipped with a Quadrex 007CWBTR capillary column (60 m length, 0.25 mm i.d., and 0.25 μm film thickness), following the chromatographic conditions established by Rodríguez-Bencomo et al.[7]

Quantification was carried out following the internal standard quantification method. Quantitative data of the relative areas (absolute areas/internal standard area) were subsequently interpolated in the calibration graphs built from results of pure reference compounds. Quantification ions and internal standard used for each compound studied are indicated in Pérez-Magariño et al.[34]

Measurement of Foaming Properties by Instrumental Method. Foam properties of sparkling wines were evaluated using Mosalux equipment (Station Oenotechnique de Champagne, Cormontreuil, France) according to the Mosalux procedure.[35] This equipment consists of a glass cylinder with a glass frit in the bottom. This cylinder was filled with 100 mL of wine, and CO_2 was injected through the glass frit at a rate of 7 L/h under a constant pressure of 1 bar for 15 min. Then the gas injection was stopped.

Three parameters were measured: (1) maximum height reached by foam after CO_2 injection through the glass frit (HM, expressed in mm), which represents the foamability; (2) foam stability height during CO_2 injection (HS, expressed in mm), which represents the wine's ability to produce stable foam persistence of foam collar; and (3) foam stability time (TS, expressed in s), evaluated as the time until all bubbles collapsed when CO_2 injection was interrupted, which could represent the foam stability time once effervescence has decreased. Three bottles of each varietal sparkling wine at each sampling time were analyzed, and three measurements for each bottle were carried out.

Sensory Analyses. The sensory analysis was performed in a designed test room in accordance with ISO 8589 Standard (2010) and was carried out by 12 expert tasters from the Regulatory Councils of different Spanish D.O. and wineries (eight males and four females between 30 and 55 years old). These tasters defined the descriptors used in this sensory analysis, according to the methodology described in González-Sanjosé et al.,[36] and were trained to quantify them using structured numerical scales. This training was carried out in accordance with UNE-87-020-93 Standard (ISO 4121:1987).

Samples were presented in standard glasses in random order, and a structured numerical scale of seven points was used (1 representing no intensity and 7 the highest intensity). This work has focused on olfactory attributes: olfactory intensity, varietal, vegetal, yeasty, fruity, exotic fruit, citrus fruit, and floral notes were evaluated in the white sparkling wines, and olfactory intensity, varietal, vegetal, yeasty, fruity, oxidized, and reduced notes in the rose sparkling wines.

Sensory foam properties were valuated using the descriptors defined by Gallart et al.:[37] initial foam, foam area, foam collar, bubble size, and effervescence speed with scores from 1 to 3.

The sparkling wines were tasted after 9 months of aging on lees.

Statistical Analyses. The data were treated by applying the variance analysis (ANOVA), the least significant difference test at a significance level of $p < 0.05$, and multifactor analyses of variance. Factor analysis was applied to study the association of variables and to determine similarities or differences between wines by aging time or by treatment. Varimax rotation criterion was performed, and only factors with eigenvalues >1 were selected. Stepwise discriminant analysis is a supervised method that consists of finding a linear combination of the variables that characterizes or separates two or more classes of objects. The forward method was used to select the variables most useful for differentiating the wines according to treatment. The F statistical function was used as the criterion for variable selection. These statistical analyses were carried out using the Statgraphics Plus 5.0 statistical package.

Generalized Procrusters analysis (GPA) was applied on the mean ratings for olfactory attributes by using the Senstools 3.3.2. program (Utrecht, The Netherlands).

RESULTS AND DISCUSSION

Monosaccharide and Polysaccharide Contents in the Commercial Dry Yeast Products. Table 2 shows the monosaccharide composition, polysaccharide purity, and polysaccharide composition of the commercial dry yeast products. The monosaccharides from grape polysaccharides and from other vegetables (such as gum arabic) were not detected. Only mannose and glucose could be quantified in the commercial products. The percentage of mannose in these preparations, which is used to estimate the content of mannoproteins, was between 53 and 86%. The percentage of glucose, used to estimate the glucan content, was between 14 and 47%, which indicated

DOI: 10.1021/acs.jafc.5b01336
J. Agric. Food Chem. 2015, 63, 5670−5681

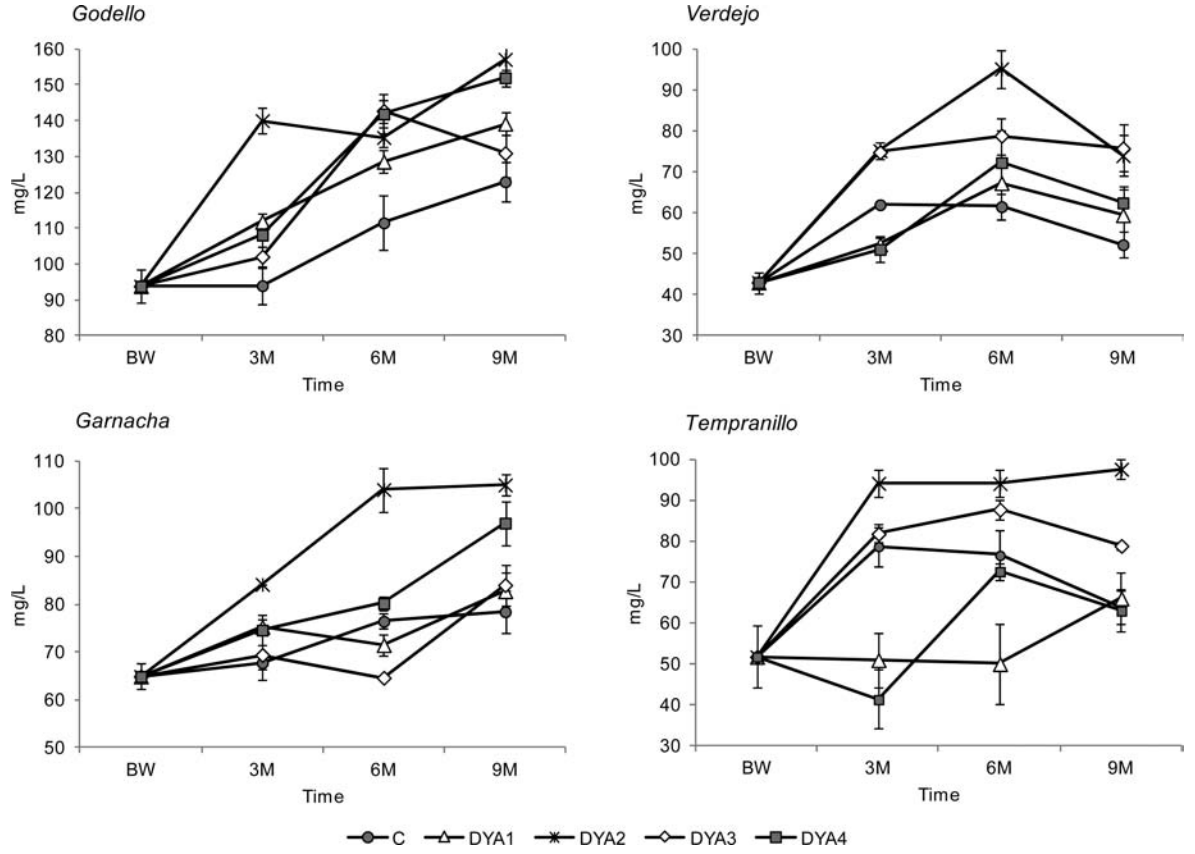

Figure 1. Concentration (mg/L) of mannoproteins during the different stages of aging on lees of the sparkling wines. C, control wines; DYA, wines treated with the commercial dry yeast autolysates; BW, base wine; 3M, 6M, 9M, 3, 6, and 9 months of aging on lees, respectively.

that during the process to obtain these products more mannoproteins were extracted than glucans. DYA-2 was the product with the highest percentage of mannoproteins, and it showed the highest mannoprotein/glucan relationship (6.1). The other mannoprotein/glucan values were 1.1 for DYA-1, 1.65 for DYA-4, and 3.3 for DYA-3.

Table 2 also shows the polysaccharide purity of the commercial products evaluated, expressed as the total amount of monosaccharides in relation to the weight of the product analyzed. Although all products showed values of purity above 60%, it is important to point out that the DYA-2 product showed significantly the highest value, showing a polysaccharide purity of 88.8%. With the exception of DYA-1, the commercial products were composed of only large polysaccharides with an average molecular weight of 47.3 kDa. In contrast, DYA-1 showed a similar content of low molecular weight polysaccharides (average molecular weight of 11.8 kDa) and high molecular weight polysaccharides.

Effect of the Addition of the Commercial Dry Yeast Products on the Phenolic Compounds, Amino Acids, and Biogenic Amines and Mannoprotein Content. In any of the varieties analyzed, no significant differences were found between control and sparkling wines treated with DYA in nonacylated, acetyl-glucoside, coumaryl-glucoside, and total monomeric anthocyanins, free, esterified, and total hydroxycinnamic acids, and total flavonols ($p < 0.05$). Other authors such as Morata et al.[38] and Guadalupe et al.[1] showed a reduction of some phenolic compounds and anthocyanins in red wines aged on lees and in red wines treated with yeast mannoproteins, respectively. The different results obtained in our work could be due to the quantitative differences in phenolic compounds shown between the red and the rosé and white wines.

No significant differences were observed either in the content of amino acids and biogenic amines ($p < 0.05$) or in the amount of total proanthocyanidins ($p < 0.05$) between control and treated sparkling wines. Therefore, it could be concluded that the added products did not have any effect on phenolic compounds, amino acids, or biogenic amines.

Contrary to that was observed with these chemical compounds, significant differences were observed in the content of mannoproteins (Figure 1). To determine the effectiveness of the addition of the commercial products, the content of mannoproteins was assessed in control and treated sparkling wines before and after the addition of the product. Except for Verdejo sparkling wines, the samples treated with the DYA-2 preparation showed significantly the highest concentrations of mannoproteins after 3 months of aging. In the same way, Garnacha, Tempranillo, and Verdejo treated with DYA-2 showed the highest content of mannoproteins after 6 months of aging. A decrease in the mannoprotein content was observed in some of the wines of Verdejo, Godello, and Tempranillo after 6 months of aging. As reported in other works, this fact could be attributed to mannoprotein precipitation phenomena as a result of their interaction with other wine components to form unstable colloids.[13]

At the end of the aging, all of the wines treated with DYA-2 showed the highest concentrations of mannoproteins, showing 21−34% more mannoproteins than their respective controls. These results were attributed to the fact that DYA-2 was the commercial product with both the highest polysaccharide purity

DOI: 10.1021/acs.jafc.5b01336
J. Agric. Food Chem. 2015, 63, 5670−5681

Table 3. Multifactor Analysis of Variance Carried out Considering All Volatile Compounds of All Sparkling Wines Studied

		grape variety		treatment		aging time	
	supplier[a]	*F* ratio	*p* value[b]	*F* ratio	*p* value	*F* ratio	*p* value[b]
ethyl butyrate	1	45.5	**0.000**	2.23	0.069	35.9	**0.000**
1-propanol	1	2566	**0.000**	1.93	0.109	48.4	**0.000**
ethyl 2-methylbutyrate	2	369	**0.000**	1.10	0.357	142	**0.000**
ethyl isovalerate	1	538	**0.000**	1.38	0.242	86.6	**0.000**
isobutanol	1	392	**0.000**	1.14	0.339	58.0	**0.000**
isoamyl acetate	2	657	**0.000**	0.52	0.721	406	**0.000**
isoamyl alcohols	1	330	**0.000**	2.19	0.073	77.2	**0.000**
ethyl hexanoate	1	84.2	**0.000**	5.73	**0.000**	181	**0.000**
hexyl acetate	1	225	**0.000**	1.62	0.173	526	**0.000**
ethyl lactate	1	248	**0.000**	11.3	**0.000**	317	**0.000**
1-hexanol	1	2028	**0.000**	4.78	**0.001**	39.3	**0.000**
trans-3-hexen-1-ol	2	1387	**0.000**	2.04	0.092	14.6	**0.000**
cis-3-hexen-1-ol	1	1290	**0.000**	2.69	**0.033**	20.3	**0.000**
ethyl octanoate	1	124	**0.000**	10.0	**0.000**	229	**0.000**
linalool	2	1170	**0.000**	11.2	**0.000**	132	**0.000**
γ-butyrolactone	1	299	**0.000**	4.15	**0.003**	37.5	**0.000**
ethyl decanoate	2	36.9	**0.000**	98.1	**0.000**	194	**0.000**
isovaleric acid	1	436	**0.000**	4.55	**0.002**	41.3	**0.000**
α-terpineol	1	1791	**0.000**	16.5	**0.000**	306	**0.000**
citronellol	1	560	**0.000**	10.9	**0.000**	137	**0.000**
2-phenylethyl acetate	1	452	**0.000**	10.1	**0.000**	542	**0.000**
hexanoic acid	1	36.7	**0.000**	4.53	**0.002**	120	**0.000**
benzyl alcohol	1	536	**0.000**	9.13	**0.000**	53.1	**0.000**
2-phenylethanol	1	811	**0.000**	4.93	**0.001**	100	**0.000**
γ-nonalactone	2	10651	**0.000**	15.9	**0.000**	24.2	**0.000**
octanoic acid	1	303	**0.000**	5.35	**0.001**	103	**0.000**
4-vinylguaiacol	3	1878	**0.000**	5.46	**0.000**	81.8	**0.000**
decanoic acid	1	398	**0.000**	109	**0.000**	391	0.142
methyl vanillate	3	1180	**0.000**	2.67	**0.034**	16.9	**0.000**
acetovanillone	2	3602	**0.000**	2.63	**0.037**	46.5	**0.000**

[a]1, Fluka (Buchs, Switzerland); 2, Sigma-Aldrich (Steinheim, Germany); 3, Lancaster (Strasbourg, France). [b]Values in bold showed statistically significant differences in each compound and factor considered (p values < 0.05).

and mannoprotein content. Therefore, the content of mannoproteins added to the wine was higher with the addition of DYA-2 than with the rest of the products.

Effect of the Addition of Commercial Dry Yeast Products on Volatile Composition. Due to the high number of data, initially, multifactor analysis was carried out with all of the volatile compound data. Table 3 shows the effects of grape variety, treatment, and aging time for each compound. All of the wines were included in this analysis (60 wines: 4 varieties × 5 treatments × 3 aging times). It can be observed that there are strong grape variety and aging time effects on all volatile compounds evaluated. Despite these effects, treatment with DYA also showed effects on most of the compounds. Therefore, the volatile data were treated by grape variety separately due to the great influence of this factor.

Factorial analyses were performed to see whether the information given by these compounds would allow differentiating the sparkling wines by the treatment with DYA.

The four factorial analyses (one for each grape variety) selected five factors with an eigenvalue >1, which explained between 85 and 91% of the total variance.

Figure 2 shows the distribution of the different sparkling wines studied in the plane defined by the first two factors and the percentage of the total variance explained by each factor. In general, the variables associated with factor 1 mainly permit differentiation of the sparkling wines by aging time. These changes were due to the increase in ethyl esters of branched-chain fatty acids, ethyl lactate, and 2-phenylethanol and the decrease in ethyl esters of straight-chain fatty acids, alcohol acetates, and terpenes (mainly citronellol and linalool). These results are in agreement with those obtained in a previous work with several grape varieties[34] and with those obtained by other authors in white and rosé sparkling wines.[39−41] Therefore, it seems that the grape variety does not affect the changes in volatile composition that occur during the aging time on lees of the sparkling wines.

The aging time is an important factor in the volatile composition of the sparkling wines, and it does not allow observing clear differences by the addition of different DYAs. Therefore, discriminant analyses were carried out to see if volatile compounds would allow differentiating the sparkling wines treated with the different commercial products.

These discriminant analyses were carried out with all of the wines by each grape variety, and therefore four different models were obtained. Forward stepwise discriminant analysis was applied to determine the volatile compounds most useful for differentiating the sparkling wines according to treatment.

The final model for Godello sparkling wines selected 20 volatile compounds. The variables with the greatest discriminating power were decanoic acid, ethyl hexanoate, ethyl decanoate, citronellol, ethyl butyrate, and methyl vanillate. Figure 3A shows the distribution of the Godello sparkling wines in the plane

DOI: 10.1021/acs.jafc.5b01336
J. Agric. Food Chem. 2015, 63, 5670−5681

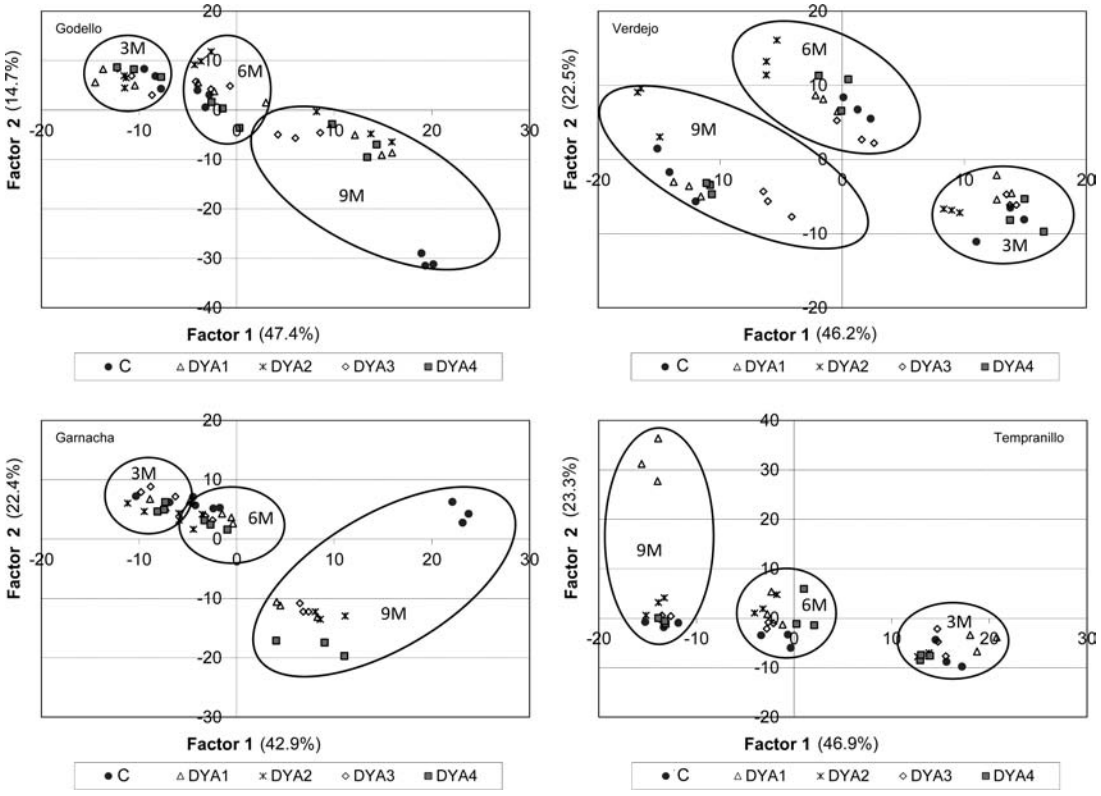

Figure 2. Distribution of sparkling wines from the four grape varieties in the plane defined by factors 1 and 2. C, control wines; DYA, wines treated with the commercial dry yeast autolysates; 3M, 6M, 9M, 3, 6, and 9 months of aging on lees, respectively.

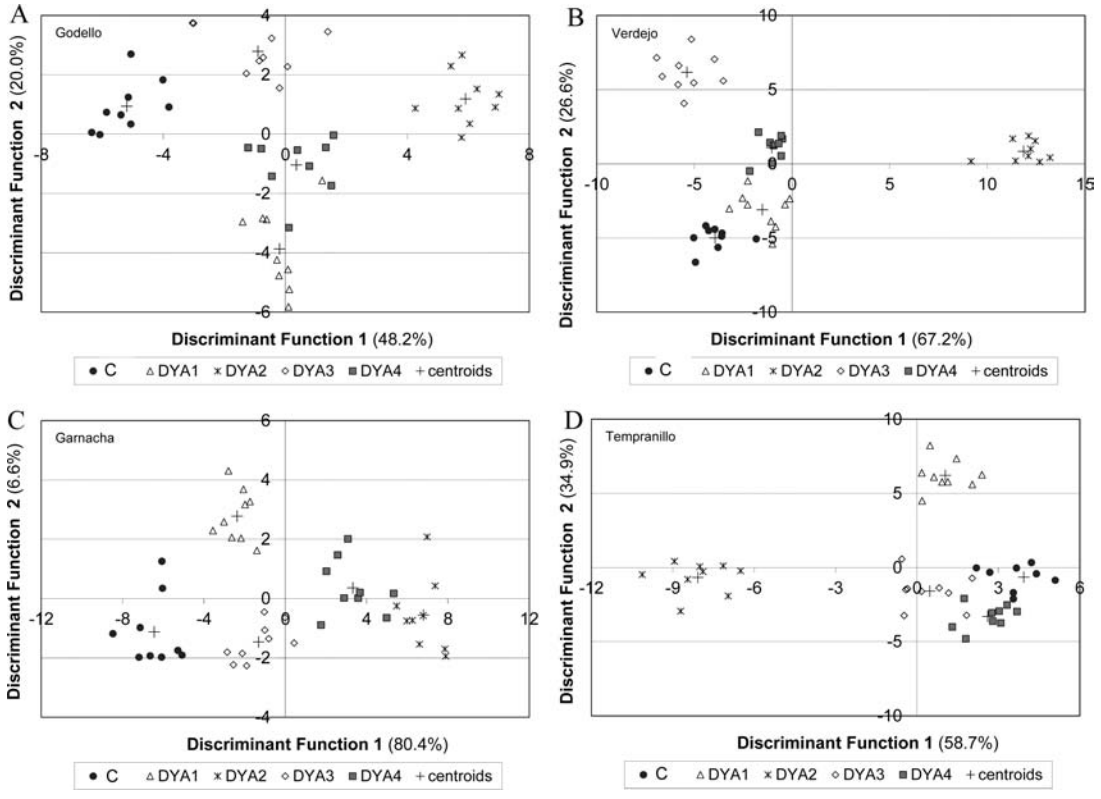

Figure 3. Distribution of sparkling wines from the four grape varieties in the plane defined by the first two discriminant functions of the stepwise model. C, control wines; DYA, wines treated with the commercial dry yeast autolysates.

defined by the first two discriminant functions, which explained 68.2% of the total variance. The wines treated with the different commercial products were well separated, and taking into account that the distance between centroids is proportional to

DOI: 10.1021/acs.jafc.5b01336
J. Agric. Food Chem. 2015, 63, 5670−5681

Table 4. Volatile Compounds of Sparkling Wines Aged on Lees for 9 Months after Tirage[a]

	Godello					Verdejo				
	C[b]	DYA-1	DYA-2	DYA-3	DYA-4	C	DYA-1	DYA-2	DYA-3	DYA-4
ethyl butyrate	0.293 b	0.329 c	0.372 d	0.181 a	0.373 d	0.096 a	0.116 a	0.234 b	0.251 b	0.243 b
1-propanol	16.5 a	18.7 ab	21.0 b	21.1 b	19.3 b	23.0 ab	22.9 a	24.1 c	23.6 b	22.8 a
ethyl 2-methylbutyrate	0.020 b	0.021 b	0.021 b	0.015 a	0.021 b	0.005 a	0.006 b	0.008 c	0.010 d	0.008 c
ethyl isovalerate	0.031 a	0.038 b	0.038 b	0.028 a	0.037 b	0.012 a	0.014 a	0.018 b	0.018 b	0.018 b
isobutanol	11.6 a	12.5 ab	13.2 b	13.5 b	13.1 b	12.5	12.8	13.0	13.2	13.4
isoamyl acetate	0.826 b	0.881 b	0.853 b	0.723 a	0.915 b	0.590	0.599	0.905	0.811	0.681
isoamyl alcohols	158 a	169 ab	176 b	178 b	168 ab	139	140	139	140	142
ethyl hexanoate	1.226 b	1.311 c	1.208 b	0.954 a	1.190 b	0.555 a	0.563 a	0.776 c	0.770 c	0.638 b
hexyl acetate	0.052 a	0.074 d	0.066 bc	0.060 b	0.070 cd	0.049	0.053	0.071	0.087	0.066
ethyl lactate	18.6 b	15.8 a	14.7 a	14.5 a	14.7 a	11.6	11.1	12.7	10.4	10.7
1-hexanol	2.294	2.109	2.084	2.086	2.013	1.081 a	1.057 a	1.195 b	1.020 a	0.984 a
trans-3-hexen-1-ol	0.162 c	0.138 b	0.129 ab	0.123 a	0.132 ab	0.117 a	0.112 a	0.132 b	0.111 a	0.111 a
cis-3-hexen-1-ol	0.227	0.235	0.229	0.224	0.231	0.125	0.117	0.134	0.115	0.117
ethyl octanoate	1.237 d	1.222 cd	1.007 b	0.851 a	1.137 c	0.575 a	0.582 a	0.848 c	0.899 c	0.707 b
linalool*	2.66 a	4.96 b	5.07 b	4.78 b	5.01 b	2.10 a	2.36 b	2.17 ab	2.82 c	2.29 ab
γ-butyrolactone	10.5 b	8.5 a	8.9 a	8.2 a	8.6 a	5.4 b	5.5 b	6.8 c	5.0 a	5.3 ab
ethyl decanoate	0.081 a	0.126 b	0.077 a	0.154 c	0.117 b	0.077 b	0.076 b	0.062 a	0.119 d	0.094 c
isovaleric acid	1.220 b	1.086 a	1.042 a	1.041 a	1.059 a	0.647	0.641	0.695	0.645	0.634
α-terpineol*	4.04 a	5.36 c	6.03 d	4.49 b	5.78 cd	1.10 a	1.10 a	1.49 c	1.29 b	1.05 a
citronellol*	1.63 a	2.33 b	2.33 b	2.36 b	2.24 b	1.58 a	1.89 b	1.61 a	2.31 c	1.72 ab
2-phenylethyl acetate	0.111 a	0.178 b	0.182 b	0.177 b	0.179 b	0.119	0.127	0.119	0.132	0.123
hexanoic acid	10.46 b	8.38 a	8.09 a	8.00 a	7.99 a	7.89 a	7.67 a	10.13 b	7.57 a	7.92 a
benzyl alcohol	0.074	0.082	0.079	0.077	0.082	0.073 a	0.075 a	0.086 b	0.069 a	0.073 a
2-phenylethanol	40.5	41.7	39.8	38.5	39.0	28.4 a	27.0 a	40.7 b	25.7 a	26.9 a
γ-nonalactone*	2.18 a	2.92 b	2.89 b	2.71 b	2.71 b	nq[c]	nq	nq	nq	nq
octanoic acid	14.29d	10.31 b	10.05 ab	9.47 a	11.90 c	12.53 c	11.87 bc	10.82 b	9.69 a	10.60 ab
4-vinylguaiacol	0.167 a	0.434 b	0.433 b	0.413 b	0.448 b	0.184 a	0.209 b	0.235 c	0.237 c	0.195 ab
decanoic acid	1.432 b	1.353 b	1.138 a	1.383 b	1.428 b	1.944 c	1.716 b	1.107 a	1.537 b	1.657 b
methyl vanillate*	2.20 a	4.51 c	6.17 d	3.22 b	4.07 c	8.4 d	8.1 cd	5.0 a	7.5 b	7.8 bc
acetovanillone*	6.1 a	7.1 bc	6.7 ab	7.3 bc	7.7 c	16.6 b	16.5 b	18.7 c	15.1 a	16.7 b
	Garnacha					Tempranillo				
	C	DYA-1	DYA-2	DYA-3	DYA-4	C	DYA-1	DYA-2	DYA-3	DYA-4
ethyl butyrate	0.376 c	0.179 b	0.164 b	0.162 b	0.092 a	0.289 a	0.364 c	0.324 b	0.319 b	0.281 a
1-propanol	19.2	22.2	21.1	21.0	20.6	43.2	45.1	43.3	43.7	44.8
ethyl 2-methylbutyrate	0.013 c	0.006 b	0.006 b	0.007 b	0.003 a	0.009 ab	0.010 c	0.009 a	0.010 bc	0.009 bc
ethyl isovalerate	0.018 d	0.010 b	0.009 b	0.011 c	0.005 a	0.016	0.019	0.019	0.018	0.017
isobutanol	16.8	18.0	17.2	17.6	17.5	16.6	17.5	17.1	16.4	17.5
isoamyl acetate	1.914 d	0.796 b	0.753 b	0.964 c	0.403 a	1.273 a	1.630 d	1.421 bc	1.561 cd	1.375 ab
isoamyl alcohols	171 a	188 b	184 b	186 b	179 ab	164 ab	174 d	170 cd	161 a	168 bc
ethyl hexanoate	1.239 c	0.560 b	0.542 b	0.520 b	0.306 a	0.728 ab	0.777 b	0.684 a	0.731 ab	0.700 a
hexyl acetate	0.067 c	0.036 b	0.035 b	0.034 b	0.019 a	0.042	0.044	0.044	0.044	0.044

J. Agric. Food Chem. 2015, 63, 5670−5681
DOI: 10.1021/acs.jafc.5b01336

Table 4. continued

	Garnacha					Tempranillo				
	C	DYA-1	DYA-2	DYA-3	DYA-4	C	DYA-1	DYA-2	DYA-3	DYA-4
ethyl lactate	18.6 c	15.5 ab	16.5 b	14.8 a	15.6 ab	17.6 c	18.5 d	16.3 a	16.9 b	17.5 c
1-hexanol	2.041 b	1.693 a	1.682 a	1.731 a	1.714 a	0.617 a	0.692 b	0.582 a	0.620 a	0.614 a
trans-3-hexen-1-ol	0.057 b	0.046 a	0.046 a	0.048 a	0.049 a	0.194 a	0.278 b	0.189 a	0.189 a	0.189 a
cis-3-hexen-1-ol	0.439	0.416	0.441	0.413	0.415	0.285 a	0.440 b	0.283 a	0.282 a	0.284 a
ethyl octanoate	1.137 c	0.459 b	0.449 b	0.444 b	0.320 a	0.875 a	0.990 b	0.811 a	0.820 a	0.860 a
linalool*	3.59 a	5.04 c	4.79 b	5.13 d	4.78 b	2.29	2.65	2.56	2.42	2.27
γ-butyrolactone	9.1	9.1	10.2	10.0	9.6	6.3	6.5	6.5	6.4	6.4
ethyl decanoate	0.078 a	0.161 c	0.092 a	0.152 bc	0.138 b	0.127 b	0.129 b	0.093 a	0.121 b	0.129 b
isovaleric acid	1.044 b	0.959 ab	1.036 b	0.940 a	0.934 a	0.634 a	0.660 b	0.642 a	0.643 a	0.646 a
α-terpineol*	3.18 a	4.03 c	3.54 b	3.91 c	3.28 a	1.14 ab	2.33 d	1.75 c	1.26 b	0.97 a
citronellol*	2.99 a	3.19 ab	2.98 a	3.50 b	3.19 ab	1.25 a	1.86 d	1.48 c	1.39 b	1.25 a
2-phenylethyl acetate	0.197 a	0.245 c	0.219 b	0.261 c	0.224 b	0.117 a	0.126 b	0.127 b	0.121 ab	0.116 a
hexanoic acid	10.49 b	8.43 a	8.75 a	8.55 a	8.48 a	6.87	7.30	7.44	7.26	7.34
benzyl alcohol	0.078 a	0.089 b	0.092 bc	0.088 b	0.098 c	0.045 a	0.073 b	0.043 a	0.043 a	0.044 a
2-phenylethanol	45.3 b	40.2 a	43.0 ab	40.9 a	42.2 a	16.4 a	16.9 ab	17.5 c	16.8 ab	17.0 b
γ-nonalactone*	3.3 a	4.4 c	4.1 bc	4.1 bc	4.0 b	nq	nq	nq	nq	nq
octanoic acid	13.15 c	8.79 ab	7.97 a	9.03 b	8.32 ab	10.55 a	13.37 c	12.13 b	10.88 a	11.36 ab
4-vinylguaiacol	0.028 a	0.045 c	0.039 b	0.042bc	0.040 b	0.005 a	0.008 c	0.006 b	0.005 a	0.005 a
decanoic acid	1.267 b	1.407 c	1.017 a	1.258 b	1.186 b	1.984 cd	2.161 d	1.351 a	1.780 b	1.967 c
methyl vanillate*	9.0 a	12.6 c	10.6 b	11.9 c	10.3 b	1.5 c	1.0 a	1.2 b	1.3 bc	1.3 bc
acetovanillone*	22.8 a	24.7 ab	26.9 bc	27.0 bc	30.2c	13.1	12.9	13.2	13.1	13.1

[a]Data expressed in mg/L except those marked with an asterisk (*), which are expressed in μg/L. Values with different letters in each compound and grape variety indicate statistically significant differences at $p < 0.05$, and values without letters indicate no statistically significant differences. [b]C, control wine; DYA, sparkling wines treated with the different dry yeast autolysates. [c]nq, below the quantification limit (<1.2 μg/L).

DOI: 10.1021/acs.jafc.5b01336
J. Agric. Food Chem. 2015, 63, 5670−5681

Table 5. Mosalux Foam Parameters and Sensory Foam Attributes of Sparkling Wines Aged on Lees for 9 Months after Tirage[a]

	Godello					Verdejo				
	C[b]	DYA-1	DYA-2	DYA-3	DYA-4	C	DYA-1	DYA-2	DYA-3	DYA-4
HM[c]	111	124	121	121	119	119	121	114	110	115
HS[c]	22.0d	20.0c	13.7a	17.4b	13.8a	17.8b	20.8c	20.2c	21.0c	15.5a
initial foam	2.5	2.7	2.4	2.5	2.6	1.7	2.3	2.3	2.2	1.5
foam area	2.0	1.9	1.8	2.0	1.9	1.2a	1.8b	2.2b	2.2b	2.0b
foam collar	2.1	2.2	1.7	2.1	2.3	1.7a	2.3b	2.7b	2.7b	2.2b
bubble size	2.1	2.2	2.3	1.9	2.3	2.3	2.5	2.3	2.2	2.0
effervescence	2.3	2.2	2.2	2.2	2.1	1.8	2.2	2.0	2.5	1.8
	Garnacha					Tempranillo				
	C[b]	DYA-1	DYA-2	DYA-3	DYA-4	C	DYA-1	DYA-2	DYA-3	DYA-4
HM[c]	115a	132b	121ab	122ab	108a	161b	161b	118a	154b	129a
HS[c]	24.2	21.7	24.8	23.7	22.4	35.8a	34.7a	34.3a	36.7a	49.2b
initial foam	2.3	2.5	2.2	2.3	2.4	2.3	2.7	2.5	2.5	2.5
foam area	2.1	2.2	2.1	2.1	2.1	2.3	2.5	2.7	2.3	2.3
foam collar	2.2	2.4	2.4	2.4	2.6	2.7	2.7	2.7	2.7	2.7
bubble size	2.5	2.4	2.3	2.1	2.3	2.8	2.5	2.5	2.5	2.3
effervescence	1.9	2.3	2.2	2.3	2.1	2.7	2.3	2.2	2.7	2.2

[a]Values with different letters in each attribute and grape variety indicate statistically significant differences at $p < 0.05$, and values without letters indicate no statistically significant differences. [b]C, control wine; DYA, sparkling wines treated with the different dry yeast autolysates. [c]HM, foam maximum height (mm); HS, foam stability height (mm).

the similarity between groups, the wines treated with DYA-2 were more different from control wines. The final model for Verdejo sparkling wines selected 16 volatile compounds, the first variables selected with the greatest discriminating power being ethyl butyrate, decanoic acid, methyl vanillate, terpineol, acetovanillone, and ethyl decanoate. Figure 3B shows the distribution of the Verdejo sparkling wines in the plane defined by the first two discriminant functions, which explained 93.2% of the total variance. In these wines, the treatment with DYA-2 showed also major differences compared to the control wines.

The final model for Garnacha rosé sparkling wines selected 13 volatile compounds. The variables with the greatest discriminating power were decanoic acid, acetovanillone, 2-phenylethyl acetate, ethyl butyrate, ethyl decanoate, and isoamyl acetate. Figure 3C shows the distribution of these sparkling wines in the plane defined by the first two discriminant functions, which explained 87.0% of the total variance. The final model for Tempranillo rosé sparkling wines selected 13 volatile compounds, the first variables selected with the greatest discriminating power being ethyl decanoate, ethyl lactate, octanoic acid, decanoic acid, isovaleric acid, and isobutanol. Figure 3D shows the distribution of these sparkling wines in the plane defined by the first two discriminant functions, which explained 93.6% of the total variance. In both rosé sparkling wines, treatment with DYA-2 showed also major differences compared to the control wines, as observed in white sparkling wines.

On the other hand, the differences observed between the control wines and those treated with the rest of the DYAs depended on the varietal wine.

All of the models were satisfactory with a global classification of 100% of the wines.

As indicated, the final models for each grape variety were slightly different, and the selected variables were not exactly the same for each model. However, in general, the main variables responsible for the observed distribution of wines were some ethyl esters, terpenes (mainly terpineol), decanoic acid, and some alcohols.

Considering the results obtained with the factorial and discriminant analyses, the data of the volatile compounds of sparkling wines aged on lees for 9 months were studied to see the effect of the addition of DYAs in the sparkling wines, focusing on the more discriminating compounds. Table 4 shows the mean values by treatment and the ANOVA results. Differences depending on the varietal wine and commercial product used were observed. In general, it was observed that the sparkling wines treated with DYAs had a lower content of the ethyl esters of fatty acids than the control wines, with the exception of Verdejo wines. These differences could be due to the sorption phenomenon onto the yeast lees and/or DYAs being a reversible process, and several factors can influence these interactions.[6,7,42] In addition, all of the sparkling wines treated with DYA-2 showed the lowest content mainly in ethyl decanoate. This compound has a high hydrophobicity,[43] and therefore it can be retained by the yeast cell walls and mannoproteins.[16,17]

With regard to the fatty acids, decanoic acid presented lower levels in wines treated with DYA-2 than in control wines, which indicated possible adsorption on the DYA surface. This fact could be due to the high hydrophobicity of this compound and to the high content of mannoproteins of the DYA-2.

In general, the addition of DYAs in the tirage phase of sparkling wine elaboration maintained higher concentrations of terpenes in the treated wines compared with their respective control wines and mainly of α-terpineol in white sparkling wines treated with DYA-2. Therefore, these products reduced the losses of these compounds occurring during aging in the bottle.[34]

Therefore, it can be said that the commercial product with the highest mannoprotein content (DYA-2) modified the volatile composition of the sparkling wines to a great extent. However, these changes did not affect their aging evolution or their varietal identity.

Effect of the Addition of the Commercial Dry Yeast Products on Foam Parameters. Table 5 shows the data of the different Mosalux parameters of the four grape variety sparkling wines and the ANOVA and LSD results.

DOI: 10.1021/acs.jafc.5b01336
J. Agric. Food Chem. 2015, 63, 5670−5681

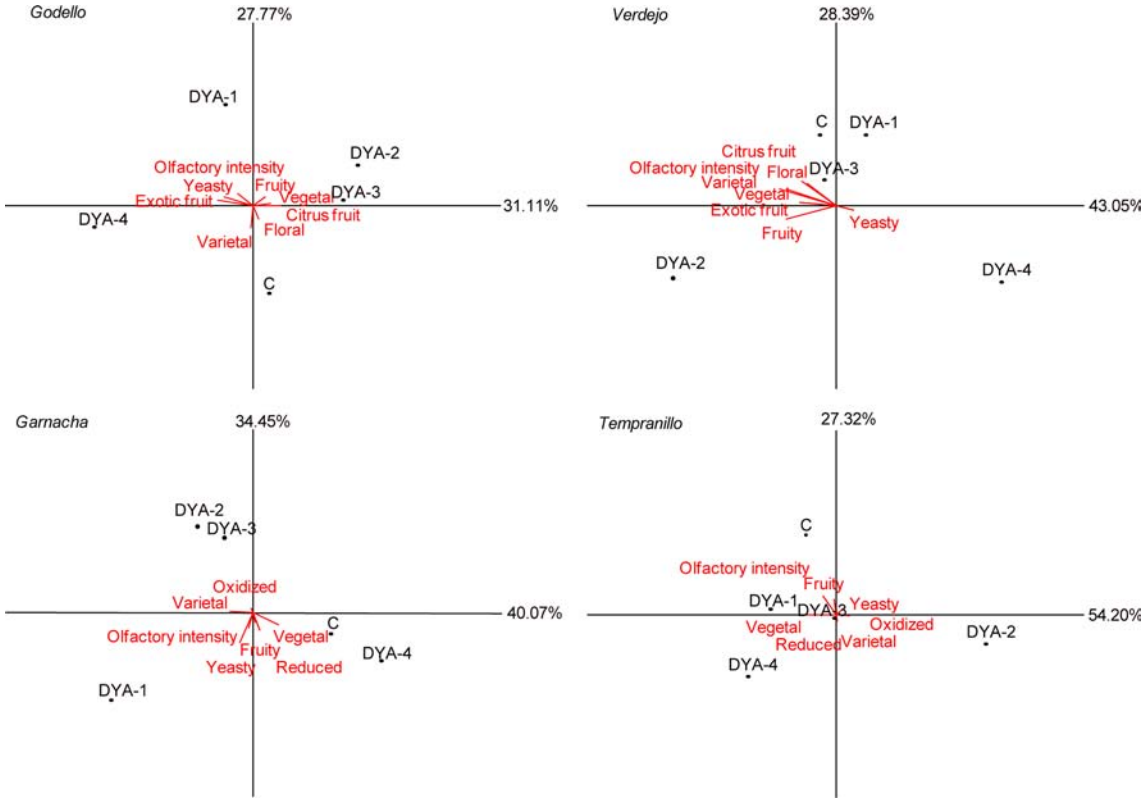

Figure 4. Generalized Procrustes analysis of the mean ratings for olfactory phase in the different sparkling wines after 9 months of aging on lees. C, control wines; DYA, wines treated with the commercial dry yeast autolysates.

The DYA addition did not modify the foam maximum height (HM) in white sparkling wines, and only slight differences were observed in rosé sparkling wines. The average values of HM were higher than those obtained in other vintages,[44] which can be due to their different composition in amino acids and in phenolic compounds in the case of rosé sparkling wines.[45]

Slight differences were found in the foam stability (HS) of the white sparkling wines, the addition of the DYA being positive in the Verdejo sparkling wines. In the rosé sparkling wines, only the Tempranillo wines treated with DYA-4 showed statistically significant higher HS values than the rest of the wines.

Nuñez et al.[19] showed a positive effect of one mannoprotein thermal extract to the foaming properties of sparkling wines. These different results could be due to the fact that they used this type of product in final sparkling wines, not during the aging time on lees.

The measurements of time stability (TS) did not show good repeatability, and therefore no conclusion of the effect of DYA addition in the sparkling wines can be drawn.

Therefore, although some differences were detected in the foam parameters of the different sparkling wines depending on the DYA treatment, it can be pointed out that, in general, these commercial products did not modify the foam properties of sparkling wines, and the few differences detected were not justified.

Effect of the Addition of the Commercial Dry Yeast Products on the Sensory Properties of the Sparkling Wines. The sensory foam properties evaluated using the descriptors defined by Gallart et al.[37] are shown in Table 5. No differences were found in the foam attributes of the different sparkling wines by treatment with DYA. Only the foam area and foam collar of Verdejo sparkling wines showed statistically significant differences.

GPA was applied to the olfactory data to provide information about the relationships between sparkling wines and olfactory attributes (Figure 4). The effects produced on the aroma by the addition of the commercial products were different in the white and rosé sparkling wines. Therefore, the addition of the DYA-2 product enhanced the fruity aromas in both the Verdejo and Godello sparkling wines. On the contrary, the increment in the fruity aromas was not observed in the sparkling rosé wines of Tempranillo or Garnacha. In summary, the addition of the DYAs used in this study in the tirage phase for sparkling wine elaboration can modify the volatile profile of these wines. However, this effect appears to be associated with the content in mannoproteins of these products, because the volatile changes were mainly observed in DYA-2, which has the highest mannoprotein content and the highest purity. In addition, the fruity aromas of white sparkling wines were enhanced by the addition of DYA-2. On the other hand, the addition of these products did not have any effect on phenolic compounds, amino acids, or biogenic amines or on foam properties.

■ ASSOCIATED CONTENT

Supporting Information

Data of total phenolic compounds, hydroxycinnamic acids, flavan-3-ols, flavonols, total proanthocyanidins, total amino acids, acid amino acids, neutral amino acids, basic amino acids and total biogenic amines of the sparkling wines (Supplementary Table 1); factor loadings after varimax rotation of the sparkling wines by grape variety (Supplementary Table 2). The Supporting Information is available free of charge on the ACS Publications website at DOI: 10.1021/acs.jafc.5b01336.

DOI: 10.1021/acs.jafc.5b01336
J. Agric. Food Chem. 2015, 63, 5670−5681

AUTHOR INFORMATION

Corresponding Author

*(S.P.-M.) Phone: +34 983 415245. E-mail: permagsi@itacyl.es.

Present Address

#(M.O.-H.) Dpto. Biotecnología y Ciencia de los Alimentos, Universidad de Burgos, Burgos, Spain.

Funding

We thank the Instituto Nacional de Investigación y Tecnología Agraria y Alimentaria (INIA) for the funding provided for this study through Project RTA2009-029-C02 (with FEDER funds). L.M.-L. also thanks La Rioja Government for the financing of her predoctoral fellowship.

Notes

The authors declare no competing financial interest.

REFERENCES

(1) Guadalupe, Z.; Martínez, L.; Ayestarán, B. Yeast mannoproteins in red winemaking: effect on polysaccharide, polyphenolic, and color composition. *Am. J. Enol. Vitic.* **2010**, *61*, 191−200.

(2) Vidal, S.; Williams, P.; Doco, T.; Moutounet, M.; Pellerin, P. The polysaccharides of red wine: total fractionation and characterization. *Carbohydr. Polym.* **2003**, *54*, 439−447.

(3) Doco, T.; Vuchot, P.; Cheynier, V.; Moutounet, M. Structural modification of wine arabinogalactans during aging on lees. *Am. J. Enol. Vitic.* **2003**, *54*, 150−157.

(4) Alexandre, H.; Guilloux-Benatier, M. Yeast autolysis in sparkling wine. A review. *Aust. J. Grape Wine Res.* **2006**, *12*, 119−127.

(5) Bautista, R.; Fernández, E.; Falqué, E. Effect of the contact with fermentation lees or comercial-lees on the volatile composition of white wines. *Eur. Food Res. Technol.* **2007**, *224*, 405−413.

(6) Chalier, P.; Angot, B.; Delteil, D.; Doco, T.; Gunata, Z. Interactions between aroma compounds and whole mannoprotein isolated from Saccharomyces cerevisiae strains. *Food Chem.* **2007**, *100*, 22−30.

(7) Rodríguez-Bencomo, J. J.; Ortega-Heras, M.; Pérez-Magariño, S. Effect of alternative techniques to ageing on lees and use of non-toasted oak chips in alcoholic fermentation on the aromatic composition of a red wine. *Eur. Food Res. Technol.* **2010**, *230*, 485−496.

(8) Del Barrio-Galán, R.; Ortega-Heras, M.; Sánchez-Iglesias, M.; Pérez-Magariño, S. Interactions of phenolic and volatile compounds with yeast lees, commercial yeast derivatives and non toasted chips in model solutions and young red wines. *Eur. Food Res. Technol.* **2012**, *234*, 231−244.

(9) Escot, S.; Feuillat, M.; Dulau, L.; Charpentier, C. Release of polysaccharides by yeasts and the influence of released polysaccharides on colour stability and wine astringency. *Aust. J. Grape Wine Res.* **2001**, *7*, 153−159.

(10) Vidal, S.; Courcoux, P.; Francis, L.; Kwiatkowski, M.; Gawel, R.; Williams, P.; Waters, E.; Cheynier, V. Use of an experimental design approach for evaluation of key wine components on mouth-feel perception. *Food Qual. Prefer.* **2004**, *15*, 209−217.

(11) Vidal, S.; Francis, L.; Williams, P.; Kwiatkowski, M.; Gawel, R.; Cheynier, V.; Waters, E. The mouth-feel properties of polysaccharides and anthocyanins in a wine like medium. *Food Chem.* **2004**, *85*, 519−525.

(12) Poncet-Legrand, C.; Doco, T.; Williams, P.; Vernhet, A. Inhibition of grape seed tannin aggregation by wine mannoproteins: effect of polysaccharide molecular weight. *Am. J. Enol. Vitic.* **2007**, *58*, 87−91.

(13) Guadalupe, Z.; Palacios, A.; Ayestarán, B. Maceration enzymes and mannoproteins: a possible strategy to increase colloidal stability and color extraction in red wines. *J. Agric. Food Chem.* **2007**, *55*, 4854−4862.

(14) Pozo-Bayón, M. A.; Martínez-Rodríguez, A.; Pueyo, E.; Moreno-Arribas, M. V. Chemical and biochemical features involved in sparkling wine production: from a traditional to an improved winemaking technology. *Trends Food Sci. Technol.* **2009**, *20*, 289−299.

(15) Torresi, S.; Frangipane, M. T.; Anelli, G. Biotechnologies in sparkling wine production. Interesting approaches for quality improvement: a review. *Food Chem.* **2011**, *129*, 1232−1241.

(16) Gallardo-Chacón, J.; Vichi, S.; López-Tamames, E.; Buxaderas, S. Analysis of sparkling wine lees surface volatiles by optimized headspace solid-phase microextraction. *J. Agric. Food Chem.* **2009**, *57*, 3279−3285.

(17) Gallardo-Chacón, J. J.; Vichi, S.; López-Tamames, E.; Buxaderas, S. Changes in the sorption of diverse volatiles by *Saccharomyces cerevisiae* lees during sparkling wine aging. *J. Agric. Food Chem.* **2010**, *58*, 12426−12430.

(18) Núñez, Y. P.; Carrascosa, A. V.; González, R.; Polo, M. C.; Martínez-Rodríguez, A. Effect of accelerated autolysis of yeast on the composition and foaming properties of sparkling wines elaborated by a champenoise method. *J. Agric. Food Chem.* **2005**, *53*, 7232−7237.

(19) Núñez, Y. P.; Carrascosa, A. V.; González, R.; Polo, M. C.; Martínez-Rodríguez, A. Isolation and characterization of a thermally extracted yeast cell wall fraction potentially useful for improving the foaming properties of sparkling wines. *J. Agric. Food Chem.* **2006**, *54*, 7898−7903.

(20) Abdallah, Z.; Aguié-Béghin, V.; Abou-Saleh, K.; Douillard, R.; Bliard, C. Isolation and analysis of macromolecular fractions responsible for the surface properties in native Champagne wines. *Food Res. Int.* **2010**, *43*, 982−987.

(21) Coelho, E.; Reis, A.; Domingues, M. R. M.; Rocha, S. M.; Coimbra, M. A. Synergistic effect of high and low molecular weight molecules in the foamability and foam stability of sparkling wines. *J. Agric. Food Chem.* **2011**, *59*, 3168−3179.

(22) Coelho, E.; Rocha, S. M.; Coimbra, M. A. Foamability and foam stability of molecular reconstituted model sparkling wines. *J. Agric. Food Chem.* **2011**, *59*, 8770−8778.

(23) Vincenzi, S.; Crapisi, A.; Curioni, A. Foamability of Prosecco wine: cooperative effects of high molecular weight glycocompounds and wine PR-proteins. *Food Hydrocolloids* **2014**, *34*, 202−207.

(24) Blasco, L.; Viñas, M.; Villa, T. G. Proteins influencing foam formation in wine and beer: the role of yeast. *Int. Microbiol.* **2011**, *14*, 61−71.

(25) Pérez-Serradilla, J. A.; Luque de Castro, M. D. Role of lees in wine production: a review. *Food Chem.* **2008**, *111*, 447−456.

(26) Pozo-Bayón, M. A.; Andújar-Ortiz, I.; Moreno-Arribas, M. V. Scientific evidences beyond the application of inactive dry yeast preparations in winemaking. *Food Res. Int.* **2009**, *42*, 754−761.

(27) Del Barrio-Galán, R.; Pérez-Magariño, S.; Ortega-Heras, M.; Guadalupe, Z.; Ayestarán, B. Polysaccharide characterization of commercial dry yeast preparations and their effect on white and red wine composition. *LWT−Food Sci. Technol.* **2012**, *48*, 215−223.

(28) Rodríguez-Nogales, J. M.; Fernández-Fernández, E.; Vila-Crespo, J. Effect of the addition of β-glucanases and yeast commercial preparations on the chemical and sensorial characteristics of traditional sparkling wine. *Eur. Food Res. Technol.* **2012**, *235*, 729−744.

(29) Guadalupe, Z.; Martínez-Pinilla, O.; Garrido, A.; Carrillo, J. D.; Ayestarán, B. Quantitative determination of wine polysaccharides by gas chromatography−mass spectrometry (GC−MS) and size exclusion chromatography (SEC). *Food Chem.* **2012**, *131*, 367−374.

(30) Gómez-Alonso, S.; García-Romero, E.; Hermosín-Gutiérrez, I. HPLC analysis of diverse grape and wine phenolics using direct injection and multidetection by DAD and fluorescence. *J. Food Compos. Anal.* **2007**, *20*, 618−626.

(31) Guadalupe, Z.; Soldevilla, A.; Sáenz-Navajas, M. P.; Ayestarán, B. Analysis of polymeric phenolics in red wines using different techniques combined with gel permeation chromatography fractionation. *J. Chromatogr. A* **2006**, *1112*, 112−120.

(32) Kennedy, J. A.; Jones, G. P. Analysis of proanthocyanidin cleavage products following acid-catalysis in the presence of excess phloroglucinol. *J. Agric. Food Chem.* **2001**, *49*, 1740−1746.

(33) Gómez-Alonso, S.; Hermosín-Gutiérrez, I.; García-Romero, E. Simultaneous HPLC analysis of biogenic amines, amino acids, and ammonium ion as aminoenone derivatives in wine and beer samples. *J. Agric. Food Chem.* **2007**, *55*, 608−613.

DOI: 10.1021/acs.jafc.5b01336
J. Agric. Food Chem. 2015, 63, 5670−5681

(34) Pérez-Magariño, S.; Ortega-Heras, M.; Martínez-Lapuente, L.; Guadalupe, Z.; Ayestarán, B. Multivariate analysis for the differentiation of sparkling wines elaborated from autochthonous Spanish grape varieties: volatile compounds, amino acids and biogenic amines. *Eur. Food Res. Technol.* **2013**, *236*, 827−841.
(35) Maujean, A.; Poinsaut, P.; Dantan, H.; Brissonnet, F.; Cossiez, E. Etude de la tenue et de la qualité de mousse des vins effervescents. II. Mise au point d'une technique de mesure de la moussabilité de la tenue et de la stabilité de la mousse des vins effervescents. *Bull. O.I.V.* **1990**, *63*, 405−427.
(36) González-Sanjosé, M. L.; Ortega-Heras, M.; Pérez-Magariño, S. Micro-oxygenation treatment and sensory properties of young red wines. *Food Sci. Technol. Int.* **2008**, *14*, 123−130.
(37) Gallart, M.; Tomás, X.; Suberbiola, G.; López-Tamames, E.; Buxaderas, S. Relationship between foam parameters obtained by sparging method and sensory evaluation of sparkling wines. *J. Sci. Food Agric.* **2004**, *84*, 127−133.
(38) Morata, A.; Gómez-Cordovés, M. C.; Suberviola, J.; Bartolomé, B.; Colomo, B.; Suárez, J. A. Adsorption of anthocyanins by yeast cell walls during the fermentation of red wines. *J. Agric. Food Chem.* **2003**, *51*, 4084−4088.
(39) Hidalgo, P.; Pueyo, E.; Pozo-Bayón, M. A.; Martínez-Rodríguez, A. J.; Martín-Álvarez, P.; Polo, M. C. Sensory and analytical study of rosé sparkling wines manufactured by second fermentation in the bottle. *J. Agric. Food Chem.* **2004**, *52*, 6640−6645.
(40) Pozo-Bayón, M. A.; Pueyo, E.; Martín-Álvarez, P. J.; Martínez-Rodríguez, A. J.; Polo, M. C. Influence of yeast strain, bentonite addition, and aging time on volatile compounds of sparkling wines. *Am. J. Enol. Vitic.* **2003**, *54*, 273−278.
(41) Riu-Aumatell, M.; Bosch-Fuste, J.; Lopez-Tamames, E.; Buxaderas, S. Development of volatile compounds of cava (Spanish sparkling wine) during long ageing time in contact with lees. *Food Chem.* **2006**, *95*, 237−242.
(42) Lubbers, S.; Voilley, A.; Feuillat, M.; Charpentier, C. Influence of mannoproteins from yeast on the aroma intensity of a model wine. *LWT−Food Sci. Technol.* **1994**, *27*, 108−114.
(43) Rodríguez-Bencomo, J. J.; Muñoz-González, C.; Andújar-Ortiz, I.; Martín-Álvarez, P. J.; Moreno-Arribas, M. V.; Pozo-Bayón, M. A. Assessment of the effect of the non-volatile wine matrix on the volatility of typical wine aroma compounds by headspace solid phase micro-extraction/gas chromatography analysis. *J. Sci. Food Agric.* **2011**, *91*, 2484−2494.
(44) Pérez-Magariño, S.; Ortega-Heras, M.; Bueno-Herrera, M.; Martínez-Lapuente, L.; Guadalupe, Z.; Ayestarán, B. Grape variety, aging on lees and aging in bottle after disgorging influence on volatile composition and foamability of sparkling wines. *LWT−Food Sci. Technol.* **2015**, *61*, 47−55.
(45) Martínez-Lapuente, L.; Guadalupe, Z.; Ayestarán, B.; Pérez-Magariño, S. Role of major wine constituents in the foam properties of white and rosé sparkling wines. *Food Chem.* **2015**, *174*, 330−338.

DOI: 10.1021/acs.jafc.5b01336
J. Agric. Food Chem. 2015, 63, 5670−5681

Sigma-Aldrich (Taufkirchen, Germany). All other chemicals were of analytical grade and were obtained from Applichem (Darmstadt, Germany), Carl Roth (Karlsruhe, Germany), or Sigma-Aldrich (Taufkirchen, Germany). Protein purification columns and resins were purchased from GE (Munich, Germany) or were a friendly gift from Knauer Wissenschaftliche Geräte GmbH (Berlin, Germany).

Endopeptidase Activity Assay. The azocasein assay was performed according to the method of Iversen and Jørgensen,[24] with some modifications. The substrate azocasein (5 g/L) was dissolved in double-distilled water (H_2O_{dd}), and the assay was performed as follows: The substrate solution (125 μL) was preincubated with 125 μL of the respective buffer solution at the respective temperature for 5 min. The reaction was started with the addition of enzyme solution (50 μL), stopped by the addition of trichloroacetic acid (1.5 M, 50 μL), and subsequently centrifuged (20000*g*, 4 °C, 5 min). A volume of 195 μL of the supernatant was transferred into a microtiter plate, 65 μL of NaOH (1 M) was added, and the absorbance at 450 nm was measured using a microtiter plate reader (Multiskan FC, Thermo Scientific, Braunschweig, Germany). One azocasein unit (ACU) was defined as the increase of 1 absorbance unit per minute at 450 nm in 0.25 M NaOH.

Aminopeptidase and Dipeptidylpeptidase Activity Assay. Aminopeptidase and dipeptidylpeptidase activities were measured according to the method of Chrispeels and Boulter,[25] with some modifications.[26] The assay contained 177 μL of the respective buffer solution and 50 μL of enzyme solution. After 5 min of preincubation at the respective temperature, the reaction was started by the addition of 12.5 μL of the corresponding substrate stock solution [*p*NA derivative dissolved in dimethylformamide (DMF)]. The substrate concentration in the final reaction volume was 3.7 mM except for Lys-Ala-*p*NA (1 mM). The reaction was stopped by the addition of 50% (v/v) acetic acid (50 μL) and was centrifuged afterward (20000*g*, 4 °C, 5 min). The supernatant (240 μL) was transferred into a microtiter plate, and the absorbance at 405 nm was measured using a microtiter plate reader (Multiskan FC). One katal (kat) of aminopeptidase or dipeptidylpeptidase activity was defined as the release of 1 mol *p*NA per second.

Amylase Activity Assay. The amylase activity was measured according to the Somogyi–Nelson method,[27,28] with some modifications. The following two reagents were prepared: Reagent A consisted of $Na_2HPO_4{\cdot}2H_2O$ (35.2 g/L), $KNaC_4H_4O_6{\cdot}4H_2O$ (40 g/L), $CuSO_4{\cdot}5H_2O$ (8 g/L), and NaOH (4 g/L) dissolved in H_2O_{dd}. Reagent B consisted of $(NH_4)_6Mo_7O_{24}{\cdot}4H_2O$ (50 g/L), H_2SO_4 (42 g/L), and $Na_2HAsO_4{\cdot}7H_2O$ (6 g/L) dissolved in H_2O_{dd}.

The substrate starch (10 g/L) was dissolved at 70 °C for 60 min in H_2O_{dd}, and the assay was performed as follows. The substrate solution (125 μL) was preincubated with 75 μL of citrate phosphate buffer at the respective temperature for 5 min. The reaction was started with the addition of enzyme solution (50 μL). After the reaction, a volume of 125 μL was transferred into 125 μL of citrate phosphate buffer (100 mM, pH 7.5). Afterward, reagent A (100 μL) was added and the reaction mixture was subsequently incubated at 98 °C for 10 min (water bath). Finally, a volume of 100 μL of reagent B and 800 μL of H_2O_{dd} were added. The mixture was incubated at 20 °C for 30 min and then centrifuged (13000*g*, 20 °C, 1 min). The supernatant (200 μL) was transferred into a microtiter plate, and the absorbance at 450 nm was measured using a microtiter plate reader (Multiskan FC). The calibration was performed using glucose as a reference. One katal (kat) of amylase activity was defined as the release of 1 mol of glucose equivalents per second.

Mass Spectrometric Investigations. The respective bands from the Coomassie-stained SDS gel (see below) were eluted from the gel and hydrolyzed tryptically by the Life Science Center (University of Hohenheim) using a modified method according to Shevchenko et al.[29] The protein spots were excised from the gel and incubated in 200 μL of H_2O_{dd} for 5 min at 1000 rpm. Afterward, the supernatant was replaced by 150 μL of acetonitrile and shaken at 1000 rpm. After 10 min, the supernatant was discarded and 100 μL of 100 mM NH_4HCO_3 containing 10 mM DTT was added and incubated for 30 min at 56 °C at 1000 rpm. The supernatant was subsequently replaced by 150 μL of acetonitrile and 85 μL of 100 mM NH_4HCO_3 containing 55 mM iodoacetamide. After incubation for 20 min in the dark, the gel piece was washed in 150 μL of 100 mM NH_4HCO_3 for 10 min at 1000 rpm and dehydrated by the addition of 150 μL of acetonitrile for 10 min at 1000 rpm. Afterward, the supernatant was discarded and 25 μL of trypsin solution (10 ng/μL in 40 mM NH_4HCO_3) was added. After 30 min on ice, a further 40 mM NH_4HCO_3 was added if needed. The digestion was carried out overnight at 37 °C. The sample was centrifuged after the addition of 2 μL of 50% (v/v) formic acid, and the supernatant was used for mass spectrometric analysis (MALDI-TOF-MS). The sample was analyzed by liquid chromatography electrospray ionization–mass spectrometry (LC-ESI-MS^2) using a nano-HPLC system (Aquity Waters, Milford, MA, USA) connected to an LTQ-Orbitrap XL hybrid mass spectrometer (Thermo Fisher Scientific, Waltham, MA, USA). A gradient from 1 to 50% (v/v) acetonitrile in 0.1% (v/v) formic acid over 30 min was used for separation (Life Science Center, University of Hohenheim). The data were treated by XCalibur software version 2.0.7, and *m*/*z* spectral data were transformed to spectra representing mass values. All MS^2 samples were analyzed using Mascot (Matrix Science, London, UK; version 2.3.02). Mascot was set up to search the NCBI database no. 20131117 (selected for Other Fungi, unknown version, 2111786 entries), assuming the digestion enzyme trypsin. Mascot was searched with a fragment ion mass tolerance of 0.60 Da and a parent ion tolerance of 15 ppm. Carbamidomethyl of cysteine was specified in Mascot as a fixed modification. Oxidation of methionine was specified in Mascot as a variable modification. Scaffold (version Scaffold 4.2.1, Proteome Software Inc., Portland, OR, USA) was used to validate MS^2-based peptide and protein identifications. Peptide identifications were accepted if they could be established at >95% probability by the Peptide Prophet algorithm,[30] with Scaffold delta-mass correction. Protein identifications were accepted if they could be established at >99% probability and contained at least five identified peptides. Protein probabilities were assigned by the Protein Prophet algorithm.[31] Proteins that contained similar peptides and could not be differentiated on the basis of MS^2 analysis alone were grouped to satisfy the principles of parsimony.

Sodium Dodecyl Sulfate–Polyacrylamide Gel Electrophoresis (SDS-PAGE) and Native PAGE. Respective samples were analyzed by SDS-PAGE (12.5%) according to the method of Laemmli.[32] The molecular weight protein standard mixture was obtained from New England Biolabs (NEB, broad range, 2–212 kDa; Frankfurt, Germany) and was used as a reference. The protein bands of the SDS gel were located by staining with Coomassie Brilliant Blue R-250.[33] The protein load was 5 μg per lane for the Flavourzyme mixture and 1 μg per lane for the purified enzyme samples. The protein content was determined by using the method of Bradford[34] and bovine serum albumin as a standard.

A native molecular weight protein standard mixture (SERVA native marker, liquid mix; SERVA, Heidelberg, Germany) was used as the reference for the native PAGE (8%). The native gel was activity stained (see below) to visualize aminopeptidase and dipeptidylpeptidase activity and to determine specific marker substrates for the automated purification protocol. Samples were diluted depending on the activity toward their particular substrate for further activity staining. An enzyme activity of approximately 50 μkat was applied per lane.

Aminopeptidase and Dipeptidylpeptidase Activity Staining of Polyacrylamide Gels. After electrophoresis, the native PAGE gels were washed with Tris-HCl buffer (50 mM, pH 7.5). An amount of 5 mg of the corresponding *p*NA derivative was solved in 25 μL of DMF and filled to 5 mL with Tris-HCl buffer (50 mM, pH 7.5) for the activity staining. In total, 13 X-*p*NA derivatives were tested (X = Ala, Ala-Pro, Arg, Glu, Gly, His, Ile, Leu, Lys, Lys-Ala, Phe, Pro, and Val). The gels were incubated in the buffer containing the respective *p*NA substrate until a yellow band appeared and were then washed with H_2O_{dd}. The bands were redyed, according to the method of Božić and Vujčić,[35] for improved visibility. Therefore, the gels were incubated in 1 g/L $NaNO_2$ (dissolved in 1 M HCl) for 120 s and washed in urea buffer (10 g/L) for 30 s. The gels were incubated in 0.25 g/L *N*-(1-naphthyl)-ethylenediamine dihydrochloride dissolved in 22% (v/v) EtOH for 10 min for staining.

Zymography. Native gels were supplemented with casein to a final concentration of 0.1% (w/v). An enzyme activity of 5×10^{-4} ACU was applied per lane. The separation of the proteins was performed in an ice

DOI: 10.1021/acs.jafc.5b01665
J. Agric. Food Chem. 2015, 63, 5682–5693

bath to prevent a hydrolysis of the casein during the enzyme migration. After electrophoresis, the gel was incubated in 0.1% (w/v) Triton X-100 at 7 °C for 1 h and subsequently incubated in Tris-HCl buffer (50 mM, pH 7.5) at 20 °C for 16 h. Afterward, the gel was Coomassie-stained[33] to visualize endopeptidase activity.

Automated Nine-Step Purification of Flavourzyme Peptidases. Flavourzyme enzymes were purified using a Bioline chromatography system (Knauer, Berlin, Germany). The system was equipped with a pump (S 1000), a UV detector (S 2520), a conductivity meter (S 2900), a manual injection six-port/three-channel injection valve, two seven-port/one-channel switching valves, and two six-port/three-channel injection valves. The eluting purified enzymes were detected at 280 nm and were collected using a fraction collector (Frac 3050). The fraction collector was cooled at 10 °C. The Bioline chromatography system was controlled by ChromGate Data System V.3.3.1. The fast protein liquid chromatography system and valve position setup were the same as previously reported.[36] Modifications to the system described[36] were the columns used and that a 5 mL sample loop was used for protein parking instead of a Superloop (GE Healthcare, Munich, Germany). Valves 1 and 2 were responsible for directing the flow to the columns. Three different modes could be operated with the positions of valves 3 and 4. The first mode (V3, inject; V4, load) was used for the standard chromatography. In the second mode (V3, load; V4, load), a protein fraction was parked in the sample loop. In the third mode (V3, inject; V4, inject), the parked protein fraction was applied to the next column. The three modes and the valve configuration are shown in the Supporting Information (Figure S1). The buffers and columns used for the automated purification protocol are listed in Tables 1 and 2.

Table 1. Buffer Compositions Used during the Automated Nine-Step Purification Protocol

buffer	composition	pH
A	10 mM sodium acetate, 0.1 mM $ZnCl_2$, 0.1 mM $CaCl_2$	4.85
B	10 mM sodium acetate, 0.1 mM $ZnCl_2$, 0.1 mM $CaCl_2$, 100 mM NaCl	4.9
C	1 M NaCl	
D	20 mM Tris-HCl	7.5
E	20 mM Tris-HCl, 1.5 M $(NH_4)_2SO_4$	7.5
F	35 mM sodium acetate, 0.1 mM $ZnCl_2$, 1 mM $CaCl_2$	4.5

Table 2. Purification Stages and Columns That Were Used during the Automated Nine-Step Purification Protocol

stage	column	chromatographic principle
I	MonoS 5/50 GL (CV = 1 mL; GE Healthcare, Munich, Germany)	ion exchange
II, IV, VI	HiTrap desalting column (3 × 5 mL; GE Healthcare, Munich, Germany)	size exclusion
III, VIII	BioFox 17/1200 Q (CV = 4.3 mL; Knauer; Berlin, Germany)	ion exchange
V	RESOURCE PHE (CV = 1 mL; GE Healthcare, Munich, Germany)	hydrophobic interaction
VII	MonoQ 5/50 GL (CV = 1 mL; GE Healthcare, Munich, Germany)	ion exchange
IX	Superdex 200 10/300 GL (CV = 24 mL; GE, Munich, Germany)	size exclusion

The column temperatures were 20 °C. A schematic representation of the automated purification protocol is shown in Figure 1. Prior to the purification, Flavourzyme was diluted in H_2O_{dd} and, subsequently, buffer was exchanged for the first buffer in the purification protocol (buffer A, Table 1) using a PD10 column (GE Healthcare). A final Flavourzyme solution of 10% (v/v) was obtained, resulting in a protein content of 7.3 g/L.

A volume of 2 mL of the Flavourzyme solution was injected at a flow rate of 0.5 mL/min into a strong cation exchange chromatography (CEX) column (stage I, Table 2) with 100% buffer A. The unbound protein was washed out using 10 column volumes (CV) at a flow rate of

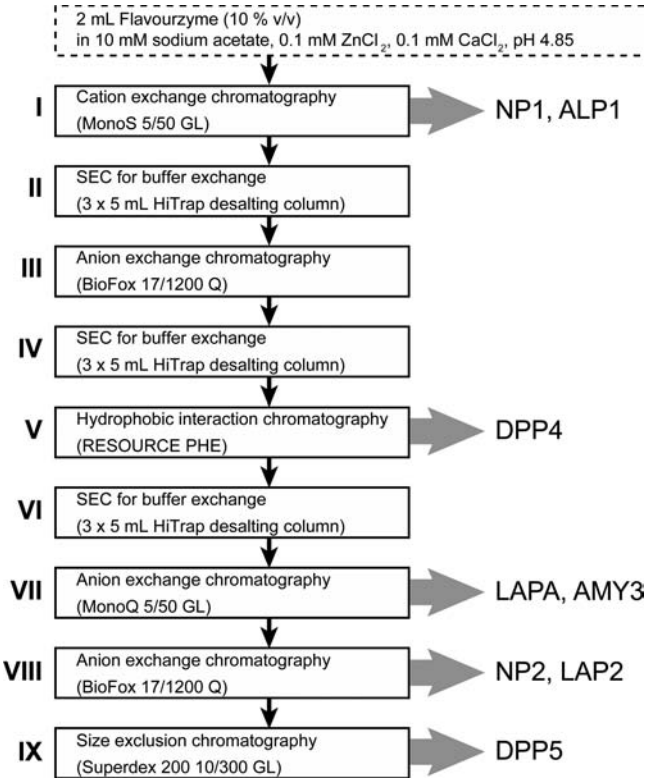

Figure 1. Schematic representation of the automated purification protocol for the Flavourzyme enzymes. Stages I–IX are in accordance with Table 2. Protein fractions, which were injected into the next purification stage, were always parked in a 5 mL sample loop. ALP1, alkaline protease 1; AMY3, α-amylase A type 3; DPP4, dipeptidyl peptidase 4; DPP5, dipeptidyl peptidase 5; LAPA, leucine aminopeptidase A; LAP2, leucine aminopeptidase 2; NP1, neutral protease 1; NP2, neutral protease 2.

0.5 mL/min. The flow-through volume (4.25 mL) was collected and automatically parked in the 5 mL sample loop. The column-bound protein was eluted using a one-step gradient and two linear gradients at a flow rate of 0.75 mL/min. The protein eluted from the step gradient (80% buffer A, 20% buffer B) was discarded. The proteins eluted from the first linear gradient (10 CV; 65% buffer A, 35% buffer B) and the second linear gradient (16 CV; 80% buffer A, 20% buffer C) were collected individually from 27.5 to 32.5 min (3.75 mL) and from 45.3 to 48.3 min (2.25 mL), respectively. Afterward, the parked protein was injected into three lined-up size exclusion chromatography (SEC) columns (stage II, Table 2) for a buffer exchange to 100% buffer D at a flow rate of 2 mL/min and, subsequently, parked (5 mL) again. Then, the desalted protein solution was injected into a strong anion exchange chromatography (AEX) column (stage III, Table 2) with 100% buffer D at 0.5 mL/min. No flow-through was collected here. One bound protein fraction was eluted using a step gradient (21% buffer C, 79% buffer D) at a flow rate of 1 mL/min. The protein eluted (3.8 mL) was automatically parked. Additional bound protein remained on the column until further notice. Again, the parked protein was injected into three lined-up SEC columns (stage IV, Table 2) for a buffer exchange to 100% buffer E at a flow rate of 2 mL/min and, subsequently, parked (5 mL) again. The parked protein was then injected into a hydrophobic interaction chromatography (HIC) column (stage V, Table 2) with 100% buffer E at 0.5 mL/min. The unbound protein was washed out using 10 CV, and no flow-through was collected at this point. The elution was performed at a flow rate of 1 mL/min. The first bound protein fraction was eluted using a linear gradient (3.75 CV; 12% buffer D, 88% buffer E) and was discarded. The second bound protein fraction (3.5 mL) was eluted with a step gradient (55% buffer D, 45% buffer E) and was automatically parked. The third bound protein fraction was eluted by linear gradient

DOI: 10.1021/acs.jafc.5b01665
J. Agric. Food Chem. 2015, 63, 5682−5693

Table 3. Identification of Flavourzyme Enzymes by Mass Spectrometric Analysis and Assignment to the Corresponding UniProtKB Entry

no.	enzyme	abbrev	UniProtKB ID	size[a] (kDa)	EC no.
1	leucine aminopeptidase A	LAPA	Q2U1F3	32.5	3.4.11
2	leucine aminopeptidase 2	LAP2	Q2ULM2	51.9	3.4.11
3	dipeptidyl peptidase 4	DPP4	Q2UH35	85.1	3.4.14.5
4	dipeptidyl peptidase 5	DPP5	Q9Y8E3	78.6	3.4.14
5	neutral protease 1	NP1	Q2U1G7	42.4	3.4.24
6	neutral protease 2	NP2	P46076	19.0	3.4.24.39
7	alkaline protease 1	ALP1	P12547	29.0	3.4.21.63
8	α-amylase A type 3	AMY3	P0C1B4	52.5	3.2.1.1

[a]Molecular masses calculated from the respective UniProtKB entry (mature monomer).

(8 CV; 100% buffer D) and collected from 194 to 197 min (3 mL). Next, the parked protein fraction from stage V (Table 2) was injected into three lined-up SEC columns (stage VI, Table 2) for a buffer exchange to 100% buffer D at a flow rate of 2 mL/min and, subsequently, parked (5 mL) again. The parked protein fraction was injected into a strong AEX column (stage, VII Table 2) with 100% buffer D at 0.5 mL/min. The unbound protein was washed out using 20 CV, and no flow-through was collected here. The elution was performed at a flow rate of 1 mL/min. The first bound protein fraction was eluted using a linear gradient (4 CV; 35% buffer D, 65% buffer F), and the fraction was collected from 273.5 to 277.5 min (4 mL). The second bound protein fraction was eluted with a step gradient (30% buffer C, 70% buffer D), and the fraction was collected from 281.3 to 283.3 min (2 mL). Afterward, the remaining protein fractions on the column from stage III (Table 2) were eluted at a flow rate of 1 mL/min (stage VIII, Table 2). The first bound fraction was obtained after linear gradient elution (1.2 CV; 20% buffer C, 80% buffer D) from 312 to 315 min (3 mL). The gradient was kept for 2.4 CV, and then 100% buffer D was used for 0.7 CV. A second fraction was obtained by a subsequent linear gradient elution (1.9 CV; 50% buffer D, 50% buffer F) from 325.5 to 327.5 min (2 mL). A third fraction (1.15 mL) was automatically collected and parked after a step gradient (35% buffer C, 65% buffer D). The parked protein fraction was then injected directly into a SEC column (stage IX, Table 2) with 20% buffer C and 80% buffer D at a flow rate of 0.75 mL/min. A last protein fraction was obtained by isocratic elution for 1 CV from 384.8 to 387.8 min (2.25 mL). The total run time for the automated nine-step purification protocol of the Flavourzyme enzymes was 420 min (7 h). A detailed overview of the particular purification steps, including valve positions, is summarized in Table S2 (Supporting Information).

Characterization of the Purified Flavourzyme Enzymes. Protein fractions from the automated purification protocol were taken, and the buffer was exchanged using PD10 desalting columns (GE Healthcare). The exchange buffer was 10 mM Tris-HCl (pH 7.5) containing 0.1 mM $ZnCl_2$ and 0.1 mM $CaCl_2$. Formulated purified enzymes were stored at −20 °C. The enzyme samples were conveniently diluted in corresponding assay buffers for the following characterization.

Effect of pH on the Enzyme Activity. The pH profiles of the purified enzymes were determined with citrate phosphate buffer (50 mM; pH 3.0−7.5), Bis-Tris-propane buffer (50 mM; pH 7.5−10.0), CHES buffer (50 mM; pH 9.0−10.0), or glycine-NaOH buffer (50 mM; pH 10.0−12.0) at 37 °C. As an exception, the pH profile of the AMY3 was measured in the presence of 5 mM of the corresponding buffer.

Effect of Temperature on the Enzyme Activity. The temperature profiles of the purified enzymes were determined at the optimum pH in the corresponding buffer system (determined before). The assay temperatures ranged from 20 to 75 °C.

Determination of the Native Molecular Size by HPLC-SEC. The native molecular size of the purified enzymes was evaluated by SEC on an UHPLC system (PLATINblue; Knauer, Berlin, Germany). Therefore, 5 μL of the purified enzyme solution was loaded into a Yarra SEC-2000 column (Phenomenex, Aschaffenburg, Germany). The flow rate was 1 mL/min, and the mobile phase was 50 mM sodium phosphate buffer, pH 6.5, supplemented with 300 mM NaCl. Eluted proteins were detected at 280 nm. The sizes were calculated, on the basis of the retention time obtained, using a calibration curve determined with standard proteins (gel filtration LMW/HMW calibration kits; GE Healthcare). All samples were taken from the fractions of the automated purification protocol without any further preparation. Only the DPP4 fraction was concentrated 60-fold, using a vacuum centrifuge (RVC 2-33 IR, Christ, Osterode, Germany; 1 mbar, 40 °C, 4 h), due to the low protein content of the fraction.

Statistical Analysis. The standard deviation was used for data evaluation and calculated with Excel (Microsoft, Redmond, WA, USA). All trials were conducted at least in duplicate, with two independent measurements. The automated purification protocol was carried out five times to check the reproducibility of the system.

RESULTS AND DISCUSSION

Identification of Key Flavourzyme Enzymes. A comprehensive and comparative study was carried out to identify the key enzyme activities in the Flavourzyme preparation. The approach was as follows: First, relevant proteins from Flavourzyme were identified by mass spectrometric investigations (LC-ESI-MS^2). Second, a substrate screening using various aminopeptidase and dipeptidyl peptidase substrates was carried out. Third, if possible, the activities of the substrate screening were assigned to particular proteins by activity staining of native polyacrylamide gels or by zymography.

In total, eight enzymes were identified in the Flavourzyme mixture (Table 3). The table also includes the UniProtKB identifier of the particular enzyme and the molecular mass calculated from the respective UniProtKB entry (mature monomer). All enzymes identified originated from *A. oryzae* (strain ATCC 42149/RIB 40), also known as yellow koji mold. In summary, three endopeptidases (neutral protease 1, NP1; neutral protease 2, NP2; alkaline protease 1, ALP1), two aminopeptidases (leucine aminopeptidase A, LAPA; leucine aminopeptidase 2, LAP2), two dipeptidyl peptidases (dipeptidyl peptidase 4, DPP4; dipeptidyl peptidase 5, DPP5), and one amylase (α-amylase A type 3, AMY3) were identified. ALP1, NP1, and NP2 are also known as oryzin, fungalysin, and deuterolysin, respectively. LAPA is also known as leucine aminopeptidase 1. The sequence coverages (MS analysis) were 28, 30, 46, 60, 73, 7, 52, and 45% for NP1, NP2, ALP1, LAPA, LAP2, DPP4, DPP5, and AMY3, respectively.

All peptidase activities could be verified either by activity staining of native polyacrylamide gels or by zymography. Three endopeptidase activities were determined by zymography (data not shown). Four specific marker substrates were revealed for the aminopeptidases and dipeptidyl peptidases after the *p*NA substrate screening and by activity staining of native gels (Figure 2). Here, the Flavourzyme preparation was applied on a native PAGE and activity stained with different *p*NA substrates. It can be concluded that four different aminopeptidases and dipeptidyl peptidases are present in Flavourzyme due to the

DOI: 10.1021/acs.jafc.5b01665
J. Agric. Food Chem. 2015, 63, 5682−5693

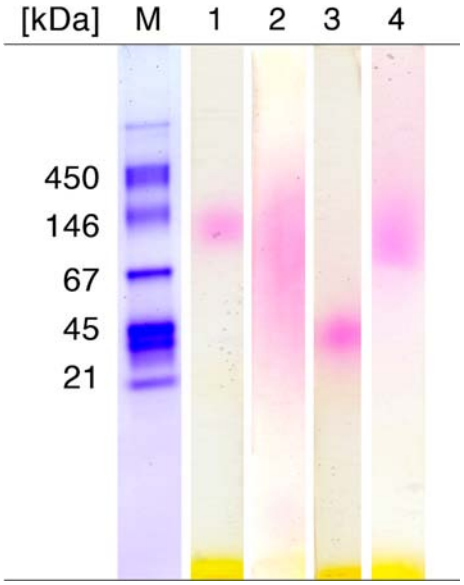

Figure 2. Native PAGE with activity staining of Flavourzyme preparation with different *p*NA substrates. Lanes: 1, Ala-Pro-*p*NA; 2, Lys-Ala-*p*NA; 3, Ile-*p*NA; 4, Pro-*p*NA. M indicates the protein marker (SERVA native marker, liquid mix; SERVA, Heidelberg, Germany). An enzyme activity of 50 μkat on the corresponding substrate was loaded per lane.

different activity staining patterns (Figure 2). Later, it was confirmed for the purified peptidases that the substrate Ile-*p*NA was hydrolyzed only by LAPA, Pro-*p*NA was hydrolyzed only by LAP2, Ala-Pro-*p*NA was hydrolyzed only by DPP4, and Lys-Ala-*p*NA was hydrolyzed only by DPP5. With these marker substrates, a distinction between these four enzymes was possible and advantageous for a later assessment of the purification of the Flavourzyme enzymes.

All marker substrates, which were used for the indication of the enzymes during the automated purification, are summarized in Table 4. Because specific marker substrates could not be determined for the endopeptidases (NP1, NP2, ALP1), the same substrate (azocasein) was used for the evaluation of the purification. Starch was used as the substrate for AMY3.

Because Flavouryzme is an industrial enzyme preparation from *A. oryzae*, the proteomic analysis of extracellular proteins from *A. oryzae* gives an indication of the enzymes present in the preparation. Oda et al.[18] evaluated the production of extracellular proteins from *A. oryzae* RIB40 under submerged and solid-state culture conditions. The cultures were cultivated on wheat bran (solid-state and submerged). The proteins were identified by MALDI-TOF-MS. A functionality (enzyme activity) of a specific protein was not determined. The authors found that mainly glucosidases were secreted during the cultivation.[18] Oryzin (ALP1) and DPP5 were expressed under solid-state conditions. Oryzin (ALP1) was also expressed under submerged conditions.[18] Because wheat bran contains around 80% carbohydrates,[37] a preferred expression of glucosidases over peptidases seems convincing. Liang et al.[19] analyzed the extracellular proteins of *A. oryzae* AS 3.951 and RIB40 grown on soy sauce koji (soybeans) by MALDI-TOF-MS. Again, functionality (enzyme activity) was not determined. Here, an ALP1, an NP1, an NP2, a DPP5, an X-prolyl aminopeptidase, a leucine aminopeptidase, and an α-amylase were found.[19] In conclusion, an impact of the cultivation medium (wheat bran or soy sauce koji) on the expression of the enzyme set can be assumed. Nakadai and Nasuno[38] also showed that the production of peptidases from *A. oryzae* ATCC 20386 varied, depending on the culture conditions. The conclusion was that submerged cultivation was preferable to solid-state cultivation for the production of peptidases.[38] In this study,[38] casein and the aminopeptidase substrate (Leu-βNA) were used to determine the particular peptidase activity. On the other hand, solid-state cultivation was preferable for the production of glucosidases.[38] The study of Sriranganadane et al.[20] showed that different sets of peptidases are expressed and secreted depending on the pH of the culture medium. The authors detected peptidases from *Aspergillus fumigatus* by MALDI-TOF-MS. The fungus was grown on a malt agar including collagen at pH 3.5 and 7.0. The authors concluded that neutral pH favors the secretion of neutral and alkaline endopeptidases and leucine aminopeptidases (LAP2, DPP4, DPP5), whereas acidic pH promotes the secretion of endopeptidases of the pepsin family and carboxypeptidases.[20] Taking these results together, *A. oryzae* ATCC 42149/RIB 40, which is used for the production of Flavourzyme, was most probably cultivated under neutral culture conditions.

Various enzyme activities in Flavourzyme were determined using an API-ZYM test system in the study of Kilcawley et al.[6] The authors used a solid preparation (Flavourzyme MG/A) and did not correlate a certain enzyme activity to a specific protein. They identified various esterase, peptidase, lipase, and glycosidase activities with the API-ZYM test.[6] In addition, various aminopeptidase activities were detected, whereas endopeptidase activity and carboxypeptidase activity could not be ascertained.[6]

Automated Nine-Step Purification of Flavourzyme Enzymes. An automated purification protocol was developed

Table 4. Purified Enzymes from Flavourzyme That Were Obtained from the Automated Nine-Step Purification Protocol[a]

no.	enzyme[b]	marker substrate	apparent purity[c] (%)	total enzyme activity	specific enzyme activity	recovery (%)	purification fold
1	LAPA	Ile-*p*NA	90	9.5 nkat	10.7 nkat/mg	42	7.5
2	LAP2	Pro-*p*NA	88	1.5 nkat	6.6 nkat/mg	42	29.5
3	DPP4	Ala-Pro-*p*NA	40	1.8 nkat	603 nkat/mg	36	1898
4	DPP5	Lys-Ala-*p*NA	94	30.1 nkat	133 nkat/mg	475	328
5	NP1	azocasein	>95	450 ACU	775 ACU/mg		na[d]
6	NP2	azocasein	89	9.0 ACU	6.3 ACU/mg	23[e]	na
7	ALP1	azocasein	>95	151 ACU	495 ACU/mg		na
8	AMY3	starch	>95	2950 nkat	2190 nkat/mg	54	6.3

[a]The total enzyme activity is calculated per purification batch (200 μL of Flavourzyme) at 37 °C and pH 7.5. Specific enzyme activity is calculated per mg of protein, determined with Bradford. [b]ALP1, alkaline protease 1; AMY3, α-amylase A type 3; DPP4, dipeptidyl peptidase 4; DPP5, dipeptidyl peptidase 5; LAPA, leucine aminopeptidase A; LAP2, leucine aminopeptidase 2; NP1, neutral protease 1; NP2, neutral protease 2. [c]Apparent purity was estimated by integration of the SEC chromatograms (see Supporting Information Figures S3−S10). [d]na, not applicable. [e]Total recovery of NP1, NP2, ALP1.

DOI: 10.1021/acs.jafc.5b01665
J. Agric. Food Chem. 2015, 63, 5682−5693

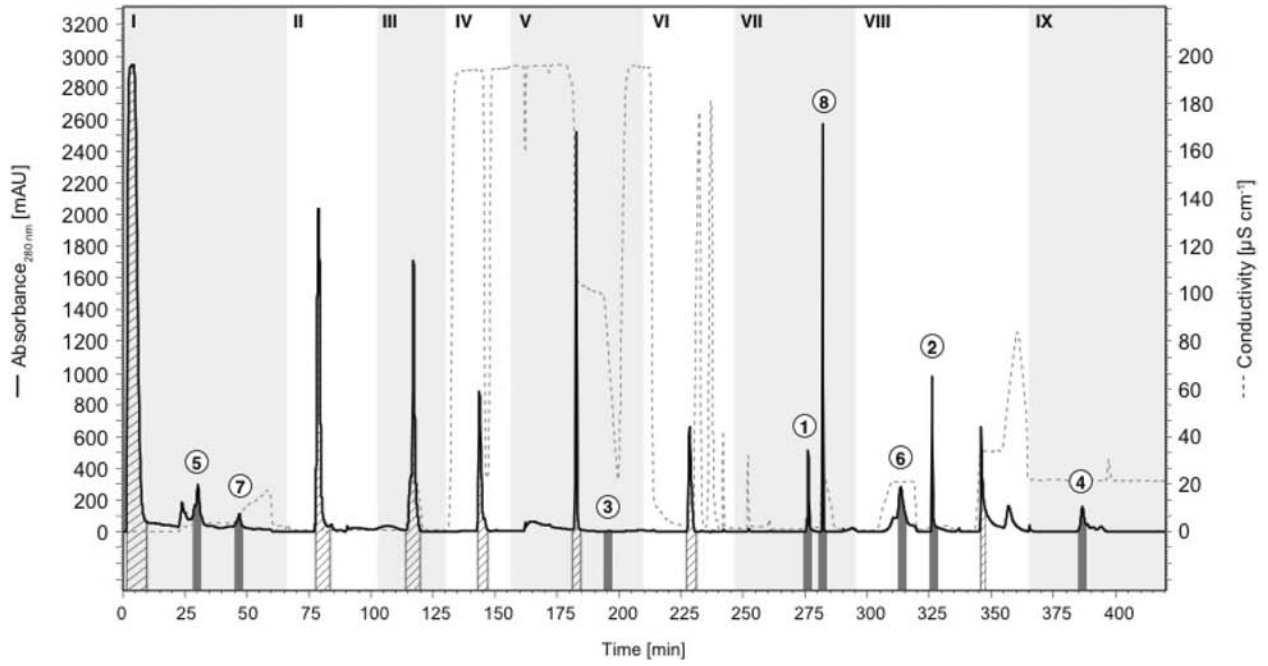

Figure 3. Automated nine-step purification of eight Flavourzyme key enzymes. The purification stages comply with Table 2 and Figure 1: I, CEX (Mono S 5/50 GL, 1 mL); II, IV, VI, buffer exchange (HiTrap desalting column, 3 × 5 mL); III, AEX (Biofox 17Q, 4.3 mL); V, HIC (ResourcePhe, 1 mL); VII, AEX (Mono Q 5/50 GL, 1 mL); VIII, AEX (Biofox 17Q, 4.3 mL); IX, SEC (Superdex 200 10/300 GL, 24 mL). Fractions of interest (isolated enzymes) are indicated with gray bars, and the encircled numbers comply with the consecutive numbering in Tables 3 and 4. Fractions that were automatically injected to the next chromatography step are indicated by hatched areas.

to purify the eight enzymes of Flavourzyme simultaneously in a semipreparative scale. All fractions collected were tested for endopeptidase, aminopeptidase, dipeptidylpeptidase, and α-amylase activity. In addition, all active fractions were investigated by MALDI-TOF-MS. The final chromatogram of the automated nine-step purification protocol is displayed in Figure 3. The different stages (I–IX) of the purification protocol correspond to Table 2. Encircled numbers in Figure 3 represent the fractions of interest (gray areas indicate the purified enzymes) and are in accordance with the consecutive numbering in Tables 3 and 4. The purified enzymes collected were immediately chilled on ice and desalted to 10 mM Tris-HCl, pH 7.5, containing 0.1 mM $ZnCl_2$ and 0.1 mM $CaCl_2$ before the enzyme activity was determined. The hatched areas in Figure 3 indicate fractions that were parked and, subsequently, injected into the next chromatography step.

We observed a loss of the LAPA activity after the CEX in preliminary experiments (data not shown). The LAPA is a zinc-dependent metallopeptidase (UniProtKB annotation) and, thus, the removal of the cation from the enzyme by the chromatography resin could be an explanation. Because most other enzymes identified are also metal-dependent (zinc, NP1, NP2, LAP2; calcium, AMY3), buffers A, B, and F (Table 1) were supplemented with zinc and calcium chloride. With these additions, the recovery of the LAPA activity was about 5-fold higher (data not shown). The other enzymes were not affected by the supplementation.

As mentioned before, a schematic representation of the automated purification protocol is shown in Figure 1. Two protein fractions were eluted from 27.5 to 32.5 min (3.75 mL) and from 45.3 to 48.3 min (2.25 mL), respectively. The proteins eluted were identified by LC-ESI-MS^2 as NP1 (⑤; Figure 3) and ALP1 (⑦; Figure 3). A total activity of 450 ACU with a specific activity of 775 ACU/mg was obtained for NP1. A total activity of 151 ACU with a specific activity of 495 ACU/mg was obtained for ALP1 (see Table 4). The next fraction of interest was eluted in stage V (Figure 3) from 194 to 197 min (3 mL) and was identified by LC-ESI-MS^2 as DPP4 (③; Figure 3). A total enzyme activity of 1.8 $nkat_{H\text{-}Ala\text{-}Pro\text{-}pNA}$ was obtained. In comparison to the Flavourzyme preparation, the specific activity increased 1898-fold to 603 $nkat_{H\text{-}Ala\text{-}Pro\text{-}pNA}$/mg for the purified peptidase. The recovery was 36% (Table 4). The next two fractions of interest were eluted in stage VII (Figure 3) from 273.5 to 277.5 min (4 mL) and from 281.3 to 283.3 min (2 mL) and were identified by LC-ESI-MS^2 as LAPA (①; Figure 3) and AMY3 (⑧; Figure 3), respectively. A total enzyme activity of 9.5 $nkat_{H\text{-}Ile\text{-}pNA}$ was obtained for LAPA. The specific activity increased 7.5-fold to 10.7 $nkat_{H\text{-}Ile\text{-}pNA}$/mg for the purified peptidase. The recovery was 42% (Table 4). A total enzyme activity of 2950 $nkat_{Starch}$ was obtained for AMY3. The specific activity increased 6.3-fold to 2190 $nkat_{Starch}$/mg for the purified amylase (recovery, 54%; Table 4). Another two protein fractions were obtained in stage VIII (Figure 3) from 312 to 315 min (3 mL) and from 325.5 to 327.5 min (2 mL) and were identified by LC-ESI-MS^2 as NP2 (⑥; Figure 3) and LAP2 (②; Figure 3), respectively. A total activity of 9 ACU with a specific activity of 6.3 ACU/mg was obtained for NP2 (Table 4). Because all endopeptidases investigated use the same substrate (azocasein), it was not possible to assign a specific recovery and a purification factor for a particular endopeptidase. In total, a recovery of 23% of the three endopeptidases was achieved. A total enzyme activity of 1.5 $nkat_{H\text{-}Pro\text{-}pNA}$ was obtained for the aminopeptidase LAP2. The specific activity of LAP2 increased 29.5-fold to 6.6 $nkat_{H\text{-}Pro\text{-}pNA}$/mg for the purified peptidase. The recovery was 42% (Table 4). The last protein fraction of interest was obtained in stage IX (Figure 3) from 384.8 to 387.8 min (2.25 mL) and was identified by LC-ESI-MS^2 as DPP5 (④; Figure 3). A total enzyme activity of 30.1 $nkat_{H\text{-}Lys\text{-}Ala\text{-}pNA}$ was obtained for DPP5.

DOI: 10.1021/acs.jafc.5b01665
J. Agric. Food Chem. 2015, 63, 5682–5693

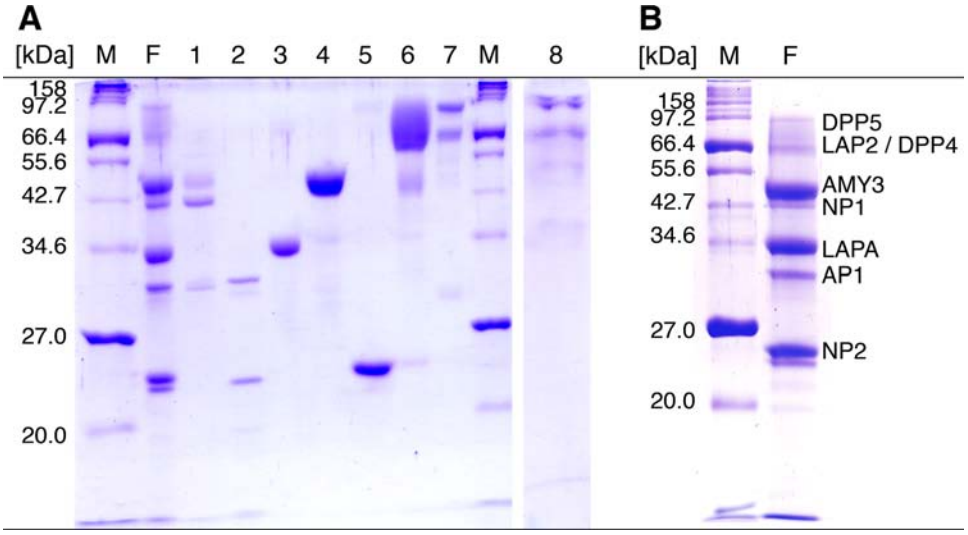

Figure 4. SDS-PAGE with Coomassie staining of protein fractions from the automated purification protocol (A) and Flavourzyme (B). M indicates the protein marker (broad range, 2−212 kDa; NEB, Frankfurt, Germany). Protein load was 1 μg per lane for the purified protein fractions (lanes 1−8) and 5 μg for the Flavourzyme samples (F). Lanes: 1, neutral protease 1; 2, alkaline protease 1; 3, leucine aminopeptidase A; 4, α-amylase A type 3; 5, neutral protease 2; 6, leucine aminopeptidase 2; 7, dipeptidyl peptidase 5; 8, dipeptidyl peptidase 4.

The specific activity increased 328-fold to 133 $nkat_{H\text{-}Lys\text{-}Ala\text{-}pNA}$/mg for the purified peptidase. The recovery was 475% (Table 4).

The reproducibility of the automated purification was tested with five independent trials. The deviation of the five purification trials was <5% concerning purification factors, yields of the enzymes, and alteration of the retention times.

The automated purification of proteins with a comparable setup was shown by Eisele et al.[36] and Stressler et al.[39] Eisele et al.[36] purified angiotensin-converting enzyme from a mammalian tissue (pig lung) with a yield of 23.6% and a 308-fold increase of the specific activity. The automated six-step purification protocol took 8 h. Stressler et al.[39] purified a prolyl-specific aminopeptidase (PepX) from *Lactobacillus helveticus* from a crude cell extract. They achieved a yield of 56% with a purification factor of 162-fold. The automated four-step purification protocol took 6 h. In contrast to the literature presented, eight proteins of interests were simultaneously purified here from a complex industrial fungal enzyme preparation.

Characterization of Purified Flavourzyme Enzymes. Purified and formulated enzymes were conveniently diluted in the appropriate buffer system. The effect of the pH and the temperature on the enzyme activity was tested using the purified enzymes and is described below. Additionally, the purified enzymes were analyzed by HPLC-SEC and SDS-PAGE to determine the native sizes and the sizes under denaturing conditions, respectively. The apparent purity (Table 4) of the particular enzyme was estimated by integration of the HPLC-SEC chromatogram (Figures S3−S10 in the Supporting Information). The extinction coefficients of the respective proteins were not considered because some areas from the HPLC-SEC chromatogram could not be assigned to a specific protein from the LC-ESI-MS^2 analysis. The major impurities in the purified fractions, found by LC-ESI-MS^2 analysis, were a β-glucosidase A, a *N*-acetylglucosaminidase, a IgE-binding protein and a glucoamylase.

All purified enzyme fractions exhibited <5% activity toward the other marker substrates (data not shown).

Leucine Aminopeptidase A (LAPA). The calculated size of LAPA is 32.5 kDa (UniProtKB). Under denaturing conditions (SDS-PAGE; Figure 4A, lane 3), a protein band at approximately 34 kDa was observed. A native size of 36.2 kDa was determined by HPLC-SEC. These results indicate a monomeric structure for the active enzyme. The apparent purity of the isolated enzyme was 90% (Table 4). The pH profile of the purified LAPA is displayed in Figure 5(1) and shows an optimum pH of 9.0 with reasonable activity between pH 6.5 and 10.0. The effect of the temperature on the activity is shown in Figure 6(1). The highest activity was measured at 65 °C. An extracellular leucine aminopeptidase from *A. oryzae* RIB40 was described previously by Matsushita et al.[40] Here, the aminopeptidase exhibited the highest activity at pH 8.5 and 60 °C and showed a molecular weight of 33 kDa by SDS-PAGE analysis.[40] A leucine aminopeptidase 1 from *A. oryzae* ATCC 20386 was purified and characterized by Nakadai et al.[41] Again, the enzyme exhibited the highest enzyme activity at pH 8.5 and 60 °C. However, in contrast to our observations, the native size determined was 26.5 kDa by SEC analysis. In the current study, the enzyme activity at optimum pH and temperature was 75.1 $nkat_{H\text{-}Ile\text{-}pNA}$/mg.

Leucine Aminopeptidase 2 (LAP2). A monomeric molecular weight of 51.9 kDa was calculated (UniProtKB) for LAP2. No discrete protein band could be detected under denaturing conditions (SDS-PAGE; Figure 4A, lane 6). A broad protein band from approximately 60 to 100 kDa was observed, and a native size of 105.7 kDa was determined by HPLC-SEC. These results indicate a seemingly dimeric structure for the active enzyme. The smeared band observed on the SDS-PAGE and the native size of 105.7 kDa can be explained by the high glycosylation of the enzyme (computed glycosylation at amino acid positions 224, 307, 341, 402, 424, and 458; UniProtKB). This observation was also described by Blinkovsky et al.[42] for aminopeptidase 2 from *A. oryzae* ATCC 20386. After deglycosylation of the N-linked sugars, the protein band was sharp at 56 kDa.[42] Thus, a heterogeneous glycosylation pattern could lead to higher and variable molecular masses for a monomer. The apparent purity of the isolated enzyme was 88% (Table 4). The pH profile of the purified LAP2 is displayed in Figure 5(2) and shows an optimum pH of 9.5 with about 50% relative activity at pH 8.5 and 10.5. An optimum pH of 8.0 was determined by Nakadai et al.,[43] and an optimum pH of 9.5 was

DOI: 10.1021/acs.jafc.5b01665
J. Agric. Food Chem. 2015, 63, 5682−5693

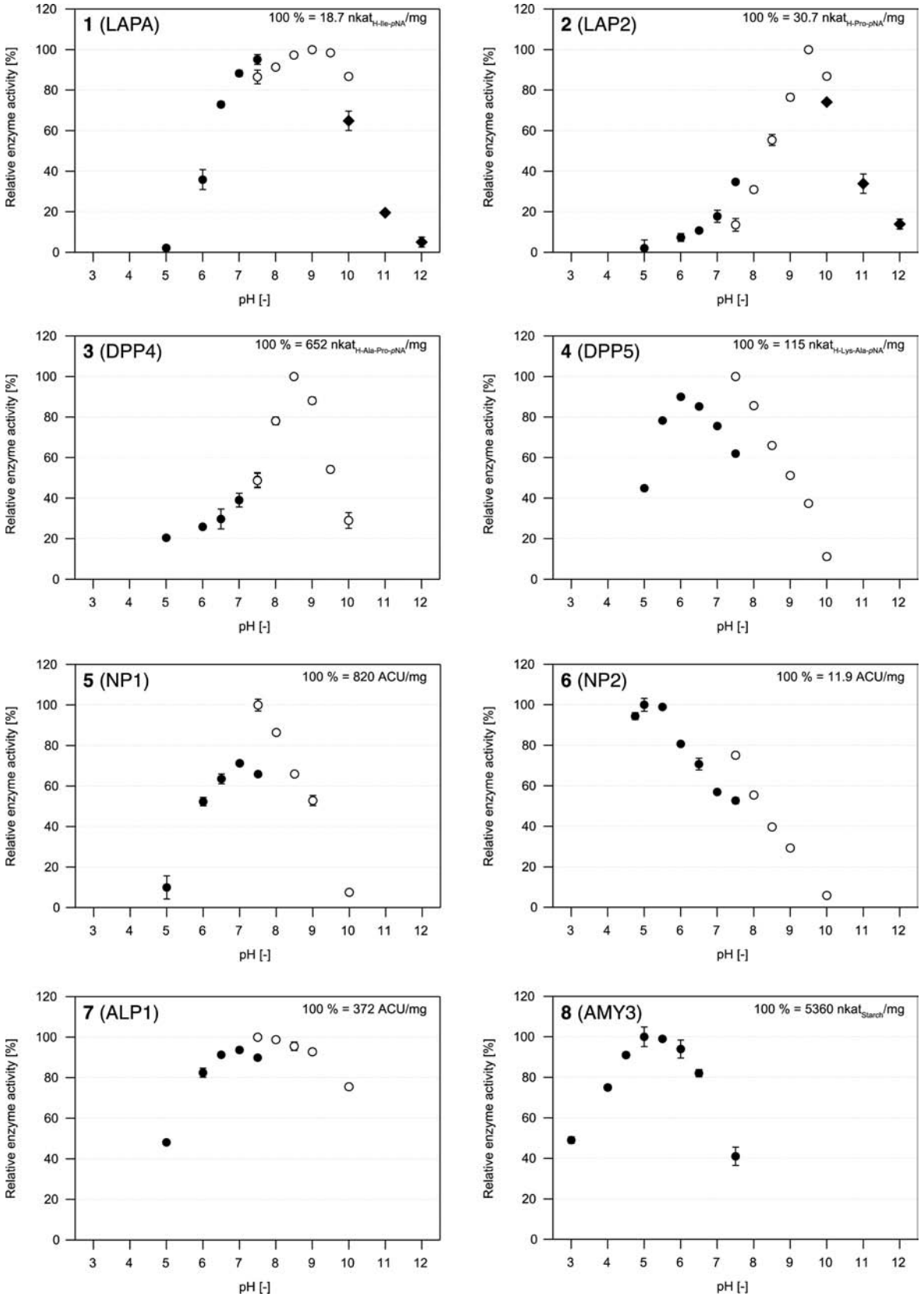

Figure 5. Influence of pH value on enzyme activity of purified Flavourzyme enzymes at 37 °C. Buffers: solid circles, 50 mM citrate phosphate; open circles, 50 mM Bis-Tris-propane; solid diamonds, 50 mM glycine-NaOH. AMY3 was incubated in 5 mM corresponding buffer.

determined by Blinkovsky et al.[42] for leucine aminopeptidase 2 from *A. oryzae* ATCC 20386, respectively. The effect of the temperature on the activity of LAP2 is shown in Figure 6(2). The highest activity was measured at 50 °C. This is in accordance with the literature.[43] The enzyme activity of LAP2 at optimum pH and temperature was 54.2 $nkat_{H\text{-}Pro\text{-}pNA}/mg$.

DOI: 10.1021/acs.jafc.5b01665
J. Agric. Food Chem. 2015, 63, 5682−5693

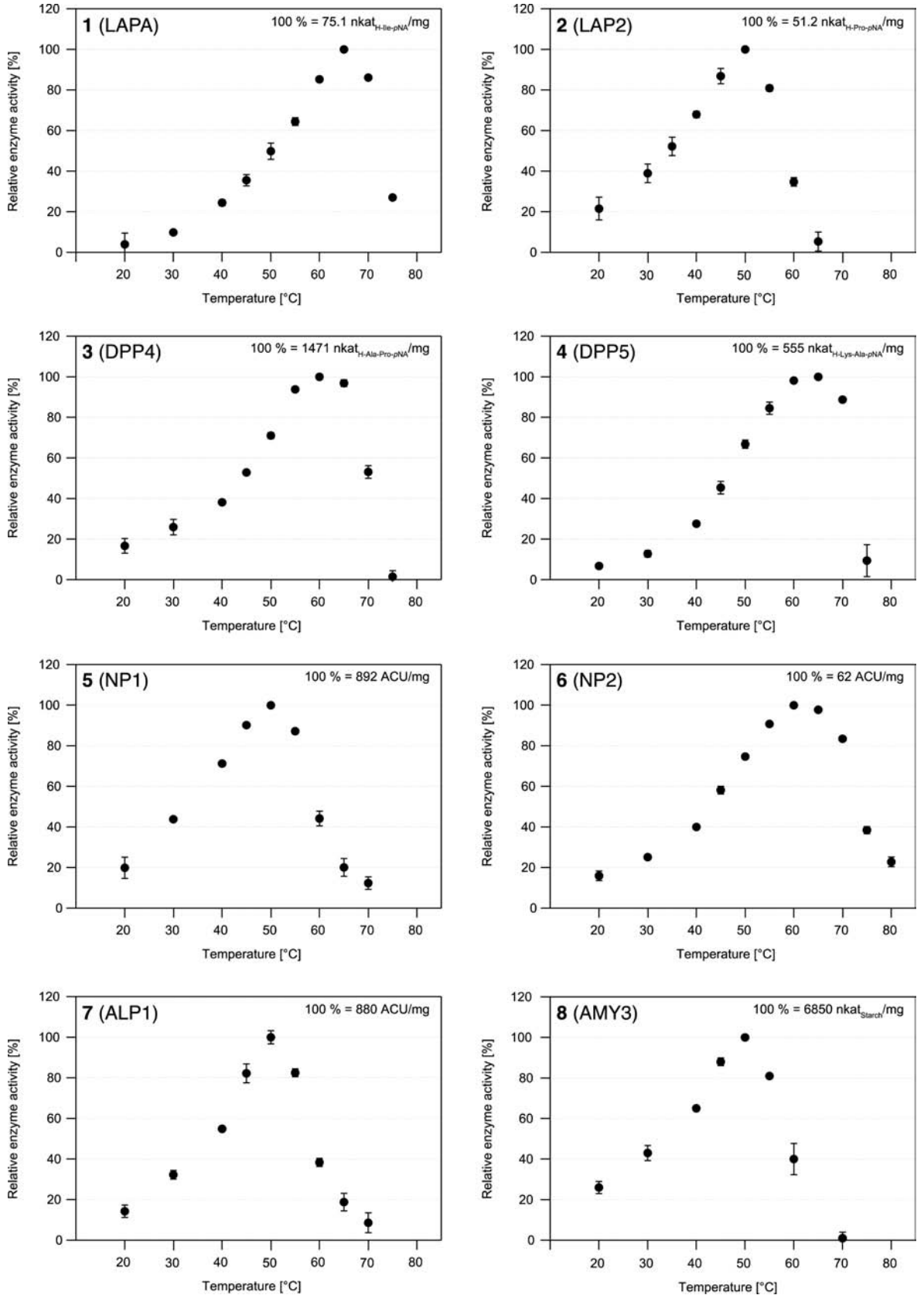

Figure 6. Influence of temperature on enzyme activity of purified Flavourzyme enzymes at the respective optimum pH (50 mM of the corresponding buffer). AMY3 was incubated in 5 mM corresponding buffer.

Dipeptidyl Peptidase 4 (DPP4). The size of DPP4 calculated was 85.1 kDa (UniProtKB). A single protein band could not be obtained on a SDS-PAGE (Figure 4A, lane 8). The presence of DPP in this fraction was ascertained by LC-ESI-MS[2]

DOI: 10.1021/acs.jafc.5b01665
J. Agric. Food Chem. 2015, 63, 5682−5693

analysis. The apparent purity of DPP4 was approximately 40% (Table 4) by HPLC-SEC. The native size (HPLC-SEC) of DPP4 was 206.6 kDa, which most probably indicates a dimeric form of the enzyme. The results are in accordance with the literature. The existence of DPP4, which was expressed as a 95 kDa glycoprotein, from *A. oryzae* has been shown.[44] Tachi et al.[45] also showed that DPP4 from *A. oryzae* existed as a homodimer. The pH profile of the purified DPP4 is shown in Figure 5(3). The optimum pH was 8.5 with about 50% relative activity at pH 7.5 and 9.5. Tachi et al.[45] determined an optimum pH of 7.0−7.5 with the substrate H-Gly-Pro-*p*NA. The effect of the temperature on the activity is shown in Figure 6(3). The highest activity was measured at 60 °C. The enzyme activity at optimum pH and temperature was 1471 $nkat_{H\text{-}Ala\text{-}Pro\text{-}pNA}$/mg.

Dipeptidyl Peptidase 5 (DPP5). To the best of our knowledge, there has been no detailed biochemical characterization of DPP5 from *A. oryzae* so far. In contrast to other dipeptidyl peptidases, DPP5 is not able to cleave X−prolyl bonds (tested with Ala-Pro-*p*NA, Gly-Pro-*p*NA, and Arg-Pro-*p*NA). This difference makes a distinction between DPP5 and DPP4 possible. Beauvais et al.[46] described a fungal DPP5 from *A. fumigatus*. They observed a monomeric size (SDS-PAGE analysis) of 79 kDa after deglycosylation (88 kDa as glycosylated protein). In our study, we determined a native size of 220.3 kDa (HPLC-SEC), which indicates a dimeric or trimeric form when considering the size of 78.6 kDa calculated (UniProtKB). In addition, the HPLC-SEC analysis showed a single and distinct peak (94% apparent purity, Table 4). In contrast to the latter, three distinct protein bands were obtained on a SDS-PAGE (Figure 4A, lane 7). All three bands were independently identified as DPP5 by LC-ESI-MS^2. The protein bands at approximately 66 and 90 kDa showed sequence coverages of 45 and 46%, respectively. The protein band at approximately 30 kDa showed a sequence coverage of 19%. The reason for the three bands on the SDS-PAGE is not clear. The presence of fractions after electrophoresis can probably explain the broad staining of the native PAGE (Figure 2, lane 2). The pH profile of the purified DPP5 is shown in Figure 5(4). The optimum pH was determined to be 6.0 with about 50% relative activity at pH 5.0 and about 80% relative activity at pH 7.0, respectively. The highest activity was measured in Bis-Tris-propane buffer at pH 7.5. A strong inactivation (buffer effect) was observed using citrate phosphate buffer. The effect of the temperature on the activity is shown in Figure 6(4). The highest activity was measured at 65 °C. The enzyme activity at optimum pH and temperature was 555 $nkat_{H\text{-}Lys\text{-}Ala\text{-}pNA}$/mg.

Neutral Protease 1 (NP1). The purified NP1 showed two distinct protein bands at approximately 29 and 42 kDa (SDS-PAGE analysis; Figure 4A, lane 1). The LC-ESI-MS^2 measurements identified both bands as NP1. Only two distinct proteins with 41.3 and 58.5 kDa were detected for the native size of the NP1 determined by HPLC-SEC. The mass calculated (UniProtKB) for the NP1 was 42.4 kDa (Table 3). The two proteins were obtained in different fractions during the automated purification. Therefore, the 41.3 and 58.5 kDa proteins were separately characterized. We observed the same properties regarding pH and temperature profiles and specific enzyme activity. Thus, the respective protein fractions of the NP1 were pooled. A proteolysis during the storage of the Flavourzyme preparation seems to be a plausible explanation for two NP1 fragments. The optimum pH was determined at pH 7.0 in citrate phosphate buffer, as shown in Figure 5(5). However, the highest activity was measured in Bis-Tris-propane buffer at pH 7.5, due to a strong inactivation (buffer effect) caused by the citrate phosphate buffer. This result complies with a characterization of a neutral protease 1 from *A. oryzae* ATCC 20386 previously described.[47] The authors determined a native size of 41 kDa and an optimum pH of 7.0 with about 50% relative enzyme activity in phosphate buffer compared to Tris-HCl buffer.[47] The effect of the temperature on the activity is shown in Figure 6(5). The highest activity was measured at 50 °C. The enzyme activity at optimum pH and temperature was 892 ACU/mg.

Neutral Protease 2 (NP2). NP2 showed a distinct band at approximately 25 kDa (SDS-PAGE analysis; Figure 4A, lane 5). A distinct peak was also obtained by HPLC-SEC analysis, which corresponds to a native size of 24.4 kDa (89% apparent purity, Table 4). The size calculated was 19.0 kDa (UniProtKB). Therefore, a monomeric state of the peptidase can be assumed. The highest activity was determined at pH 5−5.5 [Figure 5(6)] and 60 °C [Figure 6(6)]. A moderate influence of the buffer system was also observed. The NP2 activity was lower in the citrate phosphate buffer. The enzyme activity at optimum pH and temperature was 62 ACU/mg. Tatsumi et al.[48] expressed a neutral protease 2 from *A. oryzae* ATCC 20386 and determined a molecular size of 26 kDa (SDS). Nakadai et al.[49] also described a neutral protease 2 from *A. oryzae* ATCC 20386 and determined a native size of 19 kDa (SEC) with the highest activity at pH 5.5−6.

Alkaline Protease 1 (ALP1). As described for NP1, the purified ALP1 fraction also showed two distinct proteins, with approximately 25 and 30 kDa (SDS-PAGE analysis; Figure 4A, lane 2). Both proteins were identified as ALP1 by LC-ESI-MS^2. The native size (HPLC-SEC) was determined at 19.5 and 41.1 kDa, respectively. The theoretical mass for the ALP1 was 29.0 kDa (UniProtKB, Table 3). Again, the two proteins were obtained in different fractions during purification. The 19.5 and 41.1 kDa proteins were separately characterized. As described for NP1, we observed the same properties (pH profile, temperature profile, and specific enzyme activity) for both protein fractions. Therefore, we pooled the respective protein fractions of the ALP1 for further investigation. The pH profile of the ALP1 is shown in Figures 5 and 6. The optimum pH was measured at pH 7.0 with reasonable activities from pH 6.0 to 10.0. The highest activity was measured in Bis-Tris-Propane buffer at pH 7.5 due to a slight inactivation caused by the citrate phosphate buffer. The optimum temperature [Figure 6(7)] was 50 °C. The enzyme activity at optimum pH and temperature was 880 ACU/mg. In contrast to our result, Guo and Ma[50] characterized an alkaline protease from *A. oryzae* Y2942 and determined a molecular size of 34 kDa (SDS-PAGE) and the highest activity at 40 °C and pH 9.0. Nakadai and Nasuno[51] described an alkaline protease 1 from *A. oryzae* ATCC 20386 and determined a native size of 23 kDa (SEC) and the highest activity at pH 10.5.

α-Amylase A Type 3 (AMY3). The AMY3 fraction from the purification protocol showed a protein band at approximately 48 kDa (SDS-PAGE: Figure 4A, lane 4). A native size of 54.9 kDa was determined by HPLC-SEC and is in accordance with the molecular mass of 52.5 kDa calculated (UniProtKB). The pH profile of the purified AMY3 is shown in Figure 5(8). An optimum pH of 5.0−5.5 with about 50% relative activity at pH 3.0 and 7.0 was determined. The effect of the temperature on the activity is shown in Figure 6(8). The highest activity was measured at 50 °C. The enzyme activity at optimum pH and temperature was 6850 $nkat_{Starch}$/mg. The optimum conditions determined (50 °C, pH 5.0) were also described for α-amylases

DOI: 10.1021/acs.jafc.5b01665
J. Agric. Food Chem. 2015, 63, 5682−5693

from *A. oryzae* ATCC 76080[52] and *A. oryzae* IFO-30103.[53] The activity of the purified amylase of the current study was compared with a commercial amylase preparation from *A. oryzae* (Fungamyl 2500G, Novozymes, Bagsværd, Denmark). Almost the same specific enzyme activity was determined for both enzymes. The purified Flavourzyme amylase exhibited 2190 $nkat_{Starch}$/mg, whereas Fungamyl 2500G exhibited 2240 $nkat_{Starch}$/mg. The same molecular mass was also determined for both samples on SDS-PAGE (data not shown).

In summary, we could identify eight active key enzymes in Flavourzyme 1000L. Due to the results presented, the enzymes identified can be assigned to the different protein bands of a SDS-PAGE of Flavourzyme (Figure 4B). Flavourzyme 1000L is sold as an aminopeptidase preparation with at least 1000 LAPU/g (leucine aminopeptidase units/g determined with Leu-*p*NA). However, it has to be mentioned that the substrate Leu-*p*NA is only converted by the LAPA and LAP2 in the Flavourzyme complex, of which the LAPA makes around 90% of the Leu-*p*NA activity (data not shown). We showed that six proposed marker substrates [azocasein (endopeptidases NP1, NP2, ALP1), H-Ile-*p*NA (LAPA), H-Pro-*p*NA (LAP2), H-Ala-Pro-*p*NA (DPP4), H-Lys-Ala-*p*NA (DPP5), and starch (AMY3)] could be used for the characterization of the Flavourzyme enzymes. It will now be possible to distinguish between respective enzyme activities in any Flavourzyme protein hydrolysis processes. This is helpful to provide a better understanding of the enzymatic complex and to allow its improved use on different substrates. Furthermore, we realized a time-saving fully automated nine-step purification of the eight Flavourzyme enzymes.

■ ASSOCIATED CONTENT

Supporting Information

Table S2 and Figures S1 and S3−S10. The Supporting Information is available free of charge on the ACS Publications website at DOI: 10.1021/acs.jafc.5b01665.

■ AUTHOR INFORMATION

Corresponding Author

*(L.F.) E-mail: Lutz.Fischer@uni-hohenheim.de.

Notes

The authors declare no competing financial interest.

■ ACKNOWLEDGMENTS

We thank Knauer Wissenschaftliche Geräte GmbH for technical support and assistance. We gratefully acknowledge the cooperation with the Nestlé Product Technology Centre at Singen, Germany.

■ ABBREVIATIONS USED

ACU, azocasein unit; AEX, anion exchange chromatography; ALP1, alkaline protease 1; AMY3, α-amylase A type 3; CEX, cation exchange chromatography; CV, column volume; DPP4, dipeptidyl peptidase 4; DPP5, dipeptidyl peptidase 5; H_2O_{dd}, double-distilled water; DMF, dimethylformamide; HIC, hydrophobic interaction chromatography; LAPA, leucine aminopeptidase A; LAP2, leucine aminopeptidase 2; NP1, neutral protease 1; NP2, neutral protease 2; *p*NA, *p*-nitroanilide; SEC, size exclusion chromatography

■ REFERENCES

(1) Anwar, A.; Saleemuddin, M. Alkaline proteases: a review. *Bioresour. Technol.* **1998**, *64*, 175−183.

(2) Jian, S.; Wenyi, T.; Wuyong, C. Kinetics of enzymatic unhairing by protease in leather industry. *J. Cleaner Prod.* **2011**, *19*, 325−331.

(3) Sprössler, B. G. Enzymanwendung in Der Lebensmittelindustrie Und Entwicklungstrends. In *Lebensmitteltechnologie: Biotechnologische, Chemische, Mechanische Und Thermische Verfahren Der Lebensmittelverarbeitung*; Heiss, R., Ed.; Springer: Berlin, Germany, 2004; pp 484−485.

(4) Clemente, A. Enzymatic protein hydrolysates in human nutrition. *Trends Food Sci. Technol.* **2000**, *11*, 254−262.

(5) Maldonado, J.; Gil, A.; Narbona, E.; Molina, J. A. Special formulas in infant nutrition: a review. *Early Hum. Dev.* **1998**, *53* (Suppl.), S23−S32.

(6) Kilcawley, K. N.; Wilkinson, M. G.; Fox, P. F. Determination of key enzyme activities in commercial peptidase and lipase preparations from microbial or animal sources. *Enzyme Microb. Technol.* **2002**, *31*, 310−320.

(7) Merz, M.; Eisele, T.; Claaßen, W.; Appel, D.; Rabe, S.; Stressler, T.; Fischer, L. Continuous long-term hydrolysis of wheat gluten using a principally food-grade enzyme membrane reactor system. *Biochem. Eng. J.* **2015**, *99*, 114−123.

(8) Giesler, L.; Linke, D.; Rabe, S.; Appel, D.; Berger, R. G. Hydrolysis of wheat gluten by combining peptidases of *Flammulina velutipes* and electrodialysis. *J. Agric. Food Chem.* **2013**, *61*, 8641−8649.

(9) Berends, P.; Appel, D.; Eisele, T.; Rabe, S.; Fischer, L. Performance of enzymatic wheat gluten hydrolysis in batch and continuous processes using Flavourzyme. *LWT−Food Sci. Technol.* **2014**, *58*, 534−540.

(10) Aaslyng, M. D.; Elmore, J. S.; Mottram, D. S. Comparison of the aroma characteristics of acid-hydrolyzed and enzyme-hydrolyzed vegetable proteins produced from soy. *J. Agric. Food Chem.* **1998**, *46*, 5225−5231.

(11) Imm, J. Y.; Lee, C. M. Production of seafood flavor from red hake (*Urophycis chuss*) by enzymatic hydrolysis. *J. Agric. Food Chem.* **1999**, *47*, 2360−2366.

(12) Parris, N.; Moreau, R. A.; Johnston, D. B.; Dickey, L. C.; Aluko, R. E. Angiotensin I converting enzyme-inhibitory peptides from commercial wet- and dry-milled corn germ. *J. Agric. Food Chem.* **2008**, *56*, 2620−2623.

(13) Boschin, G.; Scigliuolo, G. M.; Resta, D.; Arnoldi, A. Optimization of the Enzymatic hydrolysis of lupin (*Lupinus*) proteins for producing ACE-inhibitory peptides. *J. Agric. Food Chem.* **2014**, *62*, 1846−1851.

(14) Wanasundara, P. K. J. P. D.; Ross, A. R. S.; Amarowicz, R.; Ambrose, S. J.; Pegg, R. B.; Shand, P. J. Peptides with angiotensin I-converting enzyme (ACE) inhibitory activity from defibrinated, hydrolyzed bovine plasma. *J. Agric. Food Chem.* **2002**, *50*, 6981−6988.

(15) Xue, Z.; Yu, W.; Liu, Z.; Wu, M.; Kou, X.; Wang, J. Preparation and antioxidative properties of a rapeseed (*Brassica napus*) protein hydrolysate and three peptide fractions. *J. Agric. Food Chem.* **2009**, *57*, 5287−5293.

(16) Raghavan, S.; Kristinsson, H. G.; Leeuwenburgh, C. Radical scavenging and reducing ability of tilapia (*Oreochromis niloticus*) protein hydrolysates. *J. Agric. Food Chem.* **2008**, *56*, 10359−10367.

(17) Celus, I.; Brijs, K.; Delcour, J. A. Enzymatic hydrolysis of brewers' spent grain proteins and technofunctional properties of the resulting hydrolysates. *J. Agric. Food Chem.* **2007**, *55*, 8703−8710.

(18) Oda, K.; Kakizono, D.; Yamada, O.; Iefuji, H.; Akita, O.; Iwashita, K. Proteomic analysis of extracellular proteins from *Aspergillus oryzae* grown under submerged and solid-state culture conditions. *Appl. Environ. Microbiol.* **2006**, *72*, 3448−3457.

(19) Liang, Y.; Pan, L.; Lin, Y. Analysis of extracellular proteins of *Aspergillus oryzae* grown on soy sauce koji. *Biosci., Biotechnol., Biochem.* **2009**, *73*, 192−195.

(20) Sriranganadane, D.; Waridel, P.; Salamin, K.; Reichard, U.; Grouzmann, E.; Neuhaus, J.-M.; Quadroni, M.; Monod, M. *Aspergillus* protein degradation pathways with different secreted protease sets at neutral and acidic pH. *J. Proteome Res.* **2010**, *9*, 3511−3519.

(21) Camper, D. V.; Viola, R. E. Fully automated protein purification. *Anal. Biochem.* **2009**, *393*, 176−181.

(22) Bhikhabhai, R.; Sjöberg, A.; Hedkvist, L.; Galin, M.; Liljedahl, P.; Frigård, T.; Pettersson, N.; Nilsson, M.; Sigrell-Simon, J. A.; Markeland-Johansson, C. Production of milligram quantities of affinity tagged-

DOI: 10.1021/acs.jafc.5b01665
J. Agric. Food Chem. 2015, 63, 5682−5693

proteins using automated multistep chromatographic purification. *J. Chromatogr. A* **2005**, *1080*, 83−92.
(23) Kong, Y.; Li, X.; Bai, G.; Ma, G.; Su, Z. An automatic system for multidimensional integrated protein chromatography. *J. Chromatogr. A* **2010**, *1217*, 6898−6904.
(24) Iversen, S. L.; Jørgensen, M. H. Azocasein assay for alkaline protease in complex fermentation broth. *Biotechnol. Tech.* **1995**, *9*, 573−576.
(25) Chrispeels, M. J.; Boulter, D. Control of storage protein metabolism in the cotyledons of germinating mung beans: role of endopeptidase. *Plant Physiol.* **1975**, *55*, 1031−1037.
(26) Stressler, T.; Eisele, T.; Schlayer, M.; Lutz-Wahl, S.; Fischer, L. Characterization of the recombinant exopeptidases PepX and PepN from *Lactobacillus helveticus* ATCC 12046 important for food protein hydrolysis. *PLoS One* **2013**, *8*, No. e70055.
(27) Somogyi, M. Notes on sugar determination. *J. Biol. Chem.* **1952**, *195*, 19−23.
(28) Nelson, N. A photometric adaptation of the Somogyi method for the determination of glucose. *J. Biol. Chem.* **1944**, *153*, 375−379.
(29) Shevchenko, A.; Wilm, M.; Vorm, O.; Mann, M. Mass spectrometric sequencing of proteins from silver-stained polyacrylamide gels. *Anal. Chem.* **1996**, *68*, 850−858.
(30) Keller, A.; Nesvizhskii, A. I.; Kolker, E.; Aebersold, R. Empirical statistical model to estimate the accuracy of peptide identifications made by MS/MS and database search. *Anal. Chem.* **2002**, *74*, 5383−5392.
(31) Nesvizhskii, A. I.; Keller, A.; Kolker, E.; Aebersold, R. A statistical model for identifying proteins by tandem mass spectrometry. *Anal. Chem.* **2003**, *75*, 4646−4658.
(32) Laemmli, U. K. Cleavage of structural proteins during the assembly of the head of bacteriophage T4. *Nature* **1970**, *227*, 680−685.
(33) Wong, C.; Sridhara, S.; Bardwell, J. C.; Jakob, U. Heating greatly speeds Coomassie blue staining and destaining. *Biotechniques* **2000**, *28*, 426−428, 430, 432.
(34) Bradford, M. M. A rapid and sensitive method for the quantitation of microgram quantities of protein utilizing the principle of protein-dye binding. *Anal. Biochem.* **1976**, *72*, 248−254.
(35) Božić, N.; Vujčić, Z. Detection and quantification of leucyl aminopeptidase after native electrophoresis using leucine-p-nitroanilide. *Electrophoresis* **2005**, *26*, 2476−2480.
(36) Eisele, T.; Stressler, T.; Kranz, B.; Fischer, L. Automated multi-step purification protocol for angiotensin-I-converting-enzyme (ACE). *J. Chromatogr. B: Anal. Technol. Biomed. Life Sci.* **2012**, *911*, 64−70.
(37) Nandini, C. D.; Salimath, P. V. Carbohydrate composition of wheat, wheat bran, sorghum and bajra with good chapati/roti (Indian flat bread) making quality. *Food Chem.* **2001**, *73*, 197−203.
(38) Nakadai, T.; Nasuno, S. Culture conditions of *Aspergillus oryzae* for production of enzyme preparation. *J. Ferment. Technol.* **1988**, *66*, 525−533.
(39) Stressler, T.; Eisele, T.; Kranz, B.; Fischer, L. PepX from *Lactobacillus helveticus*: automated multi-step purification and determination of kinetic parameters with original tripeptide substrates. *J. Mol. Catal. B: Enzym.* **2014**, *108*, 103−110.
(40) Matsushita-Morita, M.; Tada, S.; Suzuki, S.; Hattori, R.; Marui, J.; Furukawa, I.; Yamagata, Y.; Amano, H.; Ishida, H.; Takeuchi, M.; et al. Overexpression and characterization of an extracellular leucine aminopeptidase from *Aspergillus oryzae*. *Curr. Microbiol.* **2011**, *62*, 557−564.
(41) Nakadai, T.; Nasuno, S.; Iguchi, N. Purification and properties of leucine aminopeptidase I from *Aspergillus oryzae*. *Agric. Biol. Chem.* **1973**, *37*, 757−765.
(42) Blinkovsky, A. M.; Byun, T.; Brown, K. M.; Golightly, E. J.; Klotz, A. V. A non-specific aminopeptidase from *Aspergillus*. *Biochim. Biophys. Acta, Protein Struct. Mol. Enzymol.* **2000**, *1480*, 171−181.
(43) Nakadai, T.; Nasuno, S.; Iguchi, N. Purification and properties of leucine aminopeptidase II from *Aspergillus oryzae*. *Agric. Biol. Chem.* **1973**, *37*, 767−774.
(44) Doumas, A.; van den Broek, P.; Affolter, M.; Monod, M. Characterization of the prolyl dipeptidyl peptidase gene (dppIV) from the koji mold *Aspergillus oryzae*. *Appl. Environ. Microbiol.* **1998**, *64*, 4809−4815.
(45) Tachi, H.; Ito, H.; Ichishima, E. An X-prolyl dipeptidyl-aminopeptidase from *Aspergillus oryzae*. *Phytochemistry* **1992**, *31*, 3707−3709.
(46) Beauvais, A.; Monod, M.; Debeaupuis, J.-P.; Diaquin, M.; Kobayashi, H.; Latgé, J.-P. Biochemical and antigenic characterization of a new dipeptidyl-peptidase isolated from *Aspergillus fumigatus*. *J. Biol. Chem.* **1997**, *272*, 6238−6244.
(47) Nakadai, T.; Nasuno, S.; Iguchi, N. Purification and properties of neutral proteinase I from *Aspergillus oryzae*. *Agric. Biol. Chem.* **1973**, *37*, 2695−2701.
(48) Tatsumi, H.; Murakami, S.; Tsuji, R.; Ishida, Y.; Murakami, K.; Masaki, A.; Kawabe, H.; Arimura, H.; Nakano, E.; Motaf, H. Cloning and expression in yeast of a cDNA clone encoding *Aspergillus oryzae* neutral protease II, a unique metalloprotease. *Mol. Gen. Genet.* **1991**, *228*, 97−103.
(49) Nakadai, T.; Nasuno, S.; Iguchi, N. Purification and properties of neutral proteinase II from *Aspergillus oryzae*. *Agric. Biol. Chem.* **1973**, *37*, 2703−2708.
(50) Guo, J.-P.; Ma, Y. High-level expression, purification and characterization of recombinant *Aspergillus oryzae* alkaline protease in *Pichia pastoris*. *Protein Expression Purif.* **2008**, *58*, 301−308.
(51) Nakadai, T.; Nasuno, S. Purification and properties of alkaline proteinase from *Aspergillus oryzae*. *Agric. Biol. Chem.* **1973**, *37*, 2685−2694.
(52) Chang, C.-T.; Tang, M.-S.; Lin, C.-F. Purification and properties of α-amylase from *Aspergillus oryzae* ATCC 76080. *Biochem. Mol. Biol. Int.* **1995**, *36*, 185−193.
(53) Ramachandran, S.; Patel, A. K.; Nampoothiri, K. M.; Chandran, S.; Szakacs, G.; Soccol, C. R.; Pandey, A. α-Amylase from a fungal culture grown on oil cakes and its properties. *Braz. Arch. Biol. Technol.* **2004**, *47*, 309−317.

DOI: 10.1021/acs.jafc.5b01665
J. Agric. Food Chem. 2015, 63, 5682−5693

MATERIALS AND METHODS

Materials. Fully hydrogenated coconut oil (melting point, 33.3 °C) was kindly provided by Cargill Refined Oils Europe (Izegem, Belgium) and glycerol triheptanoate oil from Eigenmann & Veronelli (Rho, Italy). Dowex 50WX8, lysozyme from chicken egg white, sodium azide, Tween 20, thiobarbituric acid (TBA), and 1,1,3,3-tetraethoxypropane (TEP) were purchased from Sigma-Aldrich (Diegem, Belgium). Whey proteins isolate (85% pure) was acquired from Acatris Food Belgium NV (Londerzeel, Belgium). KH_2PO_4, K_2HPO_4, NaOH, sodium acetate, and glacial acetic acid of analytical grade were purchased from Chem-Lab (Zedelgem, Belgium). Trichloroacetic acid (TCA) was purchased from Acros Organics (Geel, Belgium). Acetone analytical grade, methanol, and acetonitrile high-performance liquid chromatography (HPLC) grade was provided by Fisher Scientific (Aalst, Belgium).

Preparation of NaMDA. NaMDA was prepared according to a procedure previously reported with slight modifications.[15] TEP (10 mmol) was suspended in 10 mL of distilled water, mixed with 10 g of Dowex 50W-X8 resin, and shaken at room temperature for 40 min. The resin was filtered off, and the filtrate was neutralized to pH 7 with NaOH. Then the solution was rotary evaporated (Laborato 4000, VWR, Leuven) at 30 °C to approximately 3 mL and the residue was crystallized by addition of acetone. After the mixture was allowed to stand overnight at 7 °C, the crystalline NaMDA was collected by filtration, washed with a small amount of acetone, and recrystallized twice from water-acetone. ^{1}H NMR (D_2O) δ: 8.57 (2H, d), 5.23 (1H, t). ^{13}C NMR (D_2O) δ: 192.92, 109.53. The spectrum coincided with that of NaMDA reported by Cighetti et al.[16] The crystalline NaMDA was stored at −20 °C under nitrogen.

Self-Condensation and Cleavage of NaMDA in an Aqueous Buffer and Oil (Cases 1 and 2). The aldol condensation reaction and degradation of NaMDA was examined in 0.1 M potassium phosphate buffer pH 6.8 (cf. case 1) and in glycerol triheptanoate oil (cf. case 2), as shown in Figure 1. Glycerol triheptanoate oil was chosen because it is completely saturated similar to fully hydrogenated coconut oil. Therefore, it cannot oxidize and produce lipid oxidation products. This was confirmed by performing a blank analysis. In addition, because of the low melting point (−40 °C) of glycerol triheptanoate oil, the reactivity of MDA at 4 °C could be measured in a saturated oil. An aliquot of 100 μL of NaMDA in buffer solution (initial concentration, 0.7 mM) was added to 10 mL of phosphate buffer (pH 6.8) or glycerol triheptanoate oil. The samples were vortexed (VWR, Leuven, Belgium) for 2 min and incubated for 24 h at 4 and 40 °C. After mixing, the glycerol triheptanoate oil samples were turbid. No phase separation was observed during incubation. The MDA content was determined after extraction by HPLC. Each case was performed in triplicate.

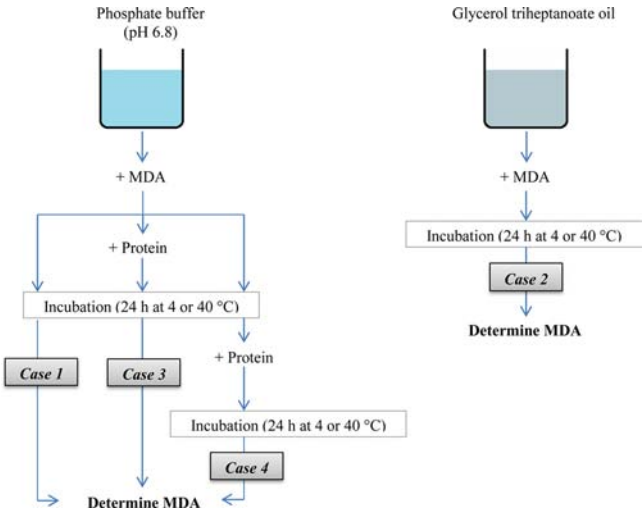

Figure 1. Model systems considered to determine the reactivity of MDA in aqueous buffer and oil. In cases 1 and 2, the condensation and cleavage of MDA was examined in phosphate buffer (pH 6.8) and glycerol triheptanoate oil, respectively. In cases 3 and 4, the interaction between MDA and food proteins (lysozyme or whey proteins) was analyzed after adding MDA and proteins together (cf. case 3) or separately (cf. case 4) to phosphate buffer. After incubation, the MDA content was determined by HPLC.

Interaction between Proteins and NaMDA in an Aqueous Buffer (Cases 3 and 4). The reactivity of NaMDA toward proteins was examined in phosphate buffer pH 6.8 (Figure 1). Two model systems were distinguished: cases 3 and 4. In case 3, 100 μL of a NaMDA solution (initial concentration, 0.7 mM) was added to 10 mL of phosphate buffer. Simultaneously, 1 mL of lysozyme (0.1 g/mL in phosphate buffer) or 2 mL of whey proteins (0.05 g/mL in phosphate buffer) solution was added to the same buffer. After 24 h at 4 or 40 °C, the MDA content was determined. In case 4, NaMDA was added to phosphate buffer and an incubation step of 24 h at 4 or 40 °C was applied. After incubation, the protein solutions were supplemented as before. Again, a 24 h incubation step was performed. Afterward the MDA content was determined by HPLC. Each case was performed in triplicate.

Preparation of Coconut O/W Emulsions. Tween 20- and whey proteins-stabilized coconut O/W emulsions were considered in this study. An aqueous solution of 1 wt % Tween 20 was prepared by dispersing the surfactant in 0.1 M potassium phosphate buffer (pH 6.8). A solution of 0.6 wt % whey proteins isolate was prepared by dissolving powdered protein in the same buffer at room temperature and subsequent stirring with a magnetic stirrer for more than 2 h to ensure complete hydration and dispersion of the whey proteins prior to homogenization. Sodium azide (0.02 wt %) was included in our solutions to prevent microbial growth. Coarse emulsions, consisting of 10 wt % fully hydrogenated coconut oil and 90 wt % emulsifier solution (Tween 20 or whey proteins), were blended using an Ultra turrax (Janke and Kunkel, IKA-Werk, Staufeb, Germany) for 10 min at 10 000 rpm. These pre-emulsions were then homogenized seven times at 250 bar/30 bar through a high-pressure valve, two-stage APV Lab 1000 homogenizer (APV Benelux NV/SA, Erpe Mere, Belgium). All procedures were carried out at 60 °C so that the crystallization of the fully hydrogenated coconut oil (melting point, 33.3 °C) was prevented during the process. After homogenization, the emulsions were cooled fast to 4 or 40 °C according to the studied model system.

Emulsified Model Systems (Cases 5−12). *Tween 20-Stabilized Coconut O/W Emulsions.* A 10 mL sample was spiked at various moments with 100 μL of NaMDA buffer solution (initial concentration, 0.7 mM) and food protein solution (1 mL of lysozyme (0.1 g/mL) or 2 mL of whey proteins (0.05 g/mL)). Figure 2 represents the different model systems studied (cases 5−10). Two scenarios were differentiated: scenario A and B. The main difference between the two scenarios is that for scenario B a preincubation step (rest period) of 24 h at 4 or 40 °C after homogenization of the emulsion was applied, while in scenario A, the reactivity of MDA was studied immediately after preparing the emulsion. In both scenarios coconut O/W emulsions were examined 24 h (at 4 or 40 °C) after supplementing MDA in the absence (cf. cases 5 and 6) or presence of proteins (cf. cases 7 and 9). Proteins were also added 24 h (at 4 or 40 °C) after the addition of MDA to the emulsions in both scenarios after which again a 24 h incubation step was applied (cf. cases 8 and 10).

Whey Proteins-Stabilized Coconut O/W Emulsions. A 10 mL sample was spiked immediately after homogenization (cf. case 11) or after a 24 h preincubation step (cf. case 12) with 100 μL of NaMDA solution (initial concentration, 0.7 mM), as shown in Figure 3.

The various model systems were incubated at 4 and 40 °C and were performed in triplicate. The MDA content was determined by HPLC.

MDA Extraction and Determination. Depending on the nature of the sample, different extraction techniques were applied, as described below.

Phosphate Buffer or Protein Solution (Cases 1, 3, and 4). Exactly 3 mL of solution was brought in a Falcon tube of 15 mL and was

DOI: 10.1021/acs.jafc.5b01780
J. Agric. Food Chem. 2015, 63, 5694−5701

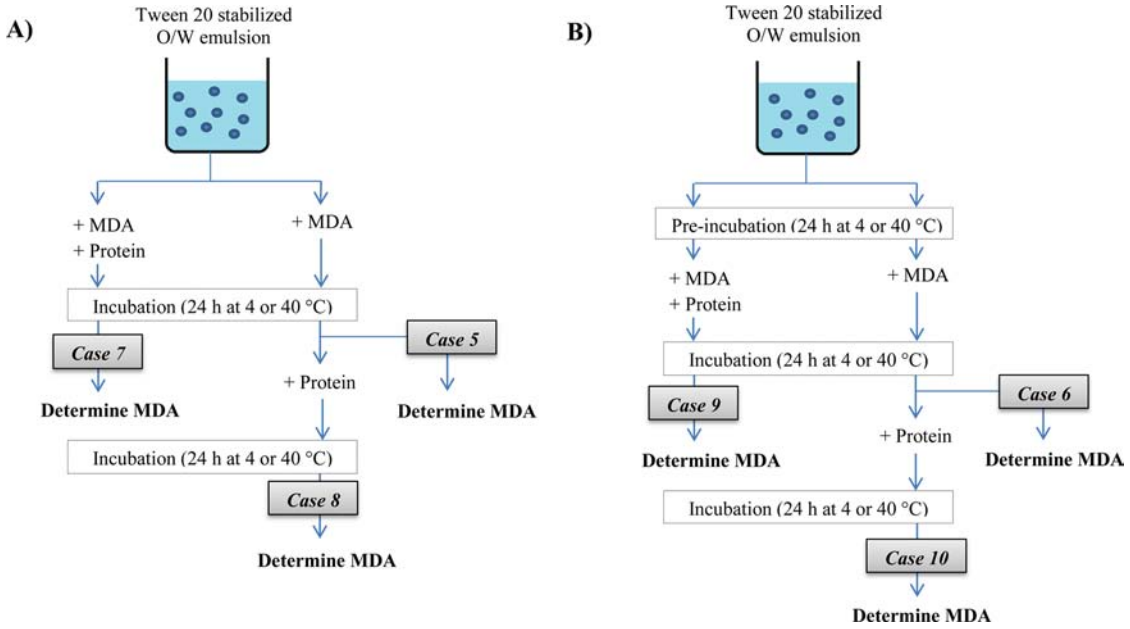

Figure 2. Summary of the various model systems studied for Tween 20-stabilized coconut O/W emulsions. In scenario B, a preincubation step (rest period) was performed before MDA (and proteins) were added. The MDA content was determined by HPLC.

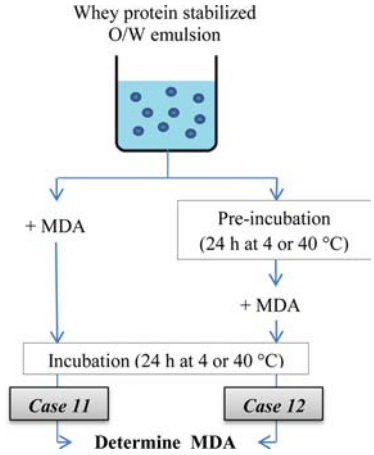

Figure 3. Overview of the different model systems studied for whey proteins-stabilized coconut O/W emulsions. In case 11, an extra incubation step was applied before adding MDA. After incubation, the MDA content was determined.

diluted with 3 mL 30% TCA. The mixture was vortexed for 1 min and was put on ice for 15 min.

Glycerol Triheptanoate Oil (Case 2). Approximately 3 g of oil was weighed in a 15 mL falcon tube. A total of 3 mL of distilled water was added. The mixture was vortexed for 2 min and centrifuged (Sigma 4K15, Sartorius, Goettingen, Germany) at 9 000*g* for 15 min.

Emulsions (Cases 5−12). A total of 3 mL of emulsion was brought in a 15 mL Falcon tube to which 3 mL of 30% TCA was added. After being vortexed for 1 min, the mixture was put on ice for 15 min.

Subsequently for all samples, the aqueous layer was collected by filtration over a paper filter (Schleicher & Schuell, Germany). The MDA content of the extract was determined after TBA derivatization by a HPLC method as described by Papastergiadis et al.[17] For quantification, standard solutions of MDA in 7.5% TCA were prepared from TEP and calibration curves were constructed at concentrations ranging from 0.6 to 10 μM.

Statistical Analyses. Initially the homogeneity of variances was determined by the Levene test. Thereafter, one-way analysis of variance (ANOVA) were applied to detect the significant differences ($p < 0.05$) between samples. When differences were detected, multiple comparisons were performed by the Tukey-b test. The analyses were carried out with the SPSS 22 statistics package (IBM, SPSS, Inc.).

RESULTS AND DISCUSSION

Reactivity of MDA in Aqueous Buffer (in Presence or Absence of Proteins) and Saturated Oil at 40 °C (Cases 1−4). As mentioned above, MDA can undergo self-condensation and cleavage in aqueous solution under physiological conditions.[6,13,14] In order to know how much MDA condensates and degrades in both phases of O/W emulsions in the absence of proteins, the reactivity of MDA in phosphate buffer (pH 6.8) and glycerol triheptanoate oil was initially examined (cf. case 1 versus 2). As shown in Table 1, a major significant difference in MDA recovery was observed between the two model systems after 24 h at 40 °C. Approximately 8% MDA reacted by means of aldol condensation and/or cleavage in the aqueous solution. When the solution was incubated for 48 h, the same recovery was found. Yet surprisingly only 15.5% recovery was found when MDA was added to oil, which indicates that the condensation and/or cleavage of MDA happens more readily in oil. These findings are quite contradictory with the multitude of reports found in the literature on the increasing MDA levels in foods upon progressive oxidation. Of course, in those cases, in contrast to in this study, MDA was continuously produced as a result of the oxidation process. However, it is shown from this experiment that a major portion of the formed MDA is further reacting in a lipid medium. Thus, the cumulative amount of MDA found is not reflecting the actual amount of MDA in a particular oil or food produced during oxidation.

In cases 3 and 4, the interaction between MDA and food proteins (lysozyme and whey proteins) in aqueous solution was examined. Because of the presence of proteins, the recoveries in both cases were significantly lower than in case 1 and moreover were protein-dependent. Although the supplemented concentration of whey proteins was lower, less MDA was measured when whey proteins were added instead of lysozyme. Hence,

DOI: 10.1021/acs.jafc.5b01780
J. Agric. Food Chem. 2015, 63, 5694−5701

Table 1. Recovery of MDA (Initial Concentration, 7 μM) in Cases 1−12 after Incubating at 40 °C (Figures 1−3)[a]

case	model description	recovery of MDA (%)		
		no protein	lysozyme	whey proteins
1	MDA in phosphate buffer (pH 6.8)	91.77 ± 0.57a	n.a.	n.a.
2	MDA in glycerol triheptanoate oil	15.46 ± 0.32b	n.a.	n.a.
3	MDA in phosphate buffer (pH 6.8) directly supplemented with protein	n.a.	58.58 ± 0.81c	30.36 ± 0.87d
4	MDA in phosphate buffer (pH 6.8), protein added after 24 h	n.a.	49.51 ± 0.10e	27.33 ± 0.98f
5	MDA in coconut O/W emulsion stabilized by Tween 20 in absence of proteins	61.06 ± 0.69g	n.a.	n.a.
6	MDA in coconut O/W emulsion stabilized by Tween 20 after preincubation in absence of proteins	66.85 ± 1.18h	n.a.	n.a.
7	coconut O/W emulsion stabilized by Tween 20: MDA added along with proteins after homogenization	n.a.	34.76 ± 1.03i	23.40 ± 0.07j
8	coconut O/W emulsion stabilized by Tween 20: MDA added after homogenization; proteins added after 24 h	n.a.	46.38 ± 1.12k	33.81 ± 0.99i
9	coconut O/W emulsion stabilized by Tween 20: MDA added along with proteins after preincubation	n.a.	28.02 ± 0.80f,n	17.43 ± 0.41l
10	coconut O/W emulsion stabilized by Tween 20: MDA added after preincubation, proteins added 24 h later	n.a.	43.63 ± 1.29m	29.61 ± 0.55d,n
11	coconut O/W emulsion stabilized by whey proteins: MDA added after homogenization	n.a.	n.a.	43.19 ± 0.46m
12	coconut O/W emulsion stabilized by whey proteins: MDA added after preincubation	n.a.	n.a.	48.28 ± 0.93k

[a]Values are the average of three replications ± the standard deviation. Different letters indicate statistically significant differences ($p < 0.05$) in the recovery of MDA. "n.a." indicates not applicable.

whey proteins were shown to be more prone to interact with MDA, probably because it contains more reactive lysine groups, as shown in Table 2.[18−20]

Table 2. Number of MDA-Reactive Groups in Lysozyme and Whey Proteins in Cases 3, 4, and 7−10[19]

reactive amino acids	lysozyme (μmol/mL)	whey proteins (μmol/mL)
lysine	3.8	6.2
arginine	7.6	1.4
histidine	0.6	1.3
cysteine	5.7	3.2

Furthermore, a significant impact of supplementing the proteins separately (after 24 h) or together with NaMDA was observed (cf. case 3 versus 4). In case 4, MDA underwent condensation and/or cleavage in aqueous solution during the first 24 h, prior to protein addition. After incubation, food proteins were added which could interact with MDA, the condensation products, and/or acetaldehyde (Figure 4).

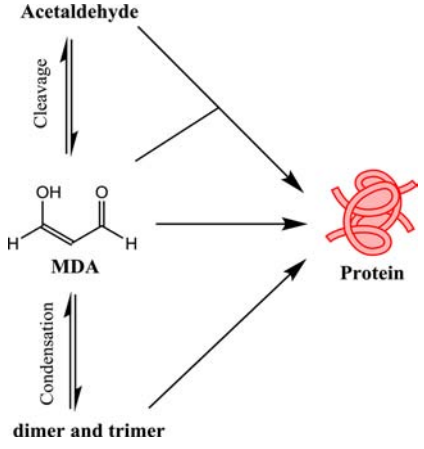

Figure 4. Possible mechanisms of interaction between MDA and proteins in aqueous buffer (pH 6.8). In aqueous solution MDA can undergo reversible condensation and cleavage reactions. The products formed from these reactions can also interact with proteins.

However, if MDA and proteins were added together (cf. case 3), there was a competition for MDA to form condensation and degradation products and protein−MDA adducts. On the basis of the results and because of the high reactivity of MDA, we assume that the interaction between MDA and proteins was favored. This is corroborated by the fact that the experimentally obtained recoveries of both proteins in case 4 corresponded quite well to the theoretically predicted recoveries considering a 91.8% recovery of MDA after 24 h of incubation in aqueous buffer, followed by an additional recovery of 58.6 and 30.4%, respectively, after incubation with lysozyme and whey proteins.

Reactivity of MDA in Coconut O/W Emulsions Stabilized by Tween 20 at 40 °C in Absence of Proteins (Cases 5 and 6). In order to investigate the condensation and/or cleavage of MDA in a coconut O/W emulsion at 40 °C, the recovery of MDA was determined upon addition of MDA directly after preparation of the emulsion (cf. case 5) or after a rest period of 24 h (cf. case 6). In both cases the recovery of MDA was significantly lower than that of case 1. Nevertheless, the recovery was still much higher than when MDA was added to a pure oil (cf. case 2). In case 2, it was shown that MDA is particularly prone to condensate and/or degrade in a lipophilic environment. As no other degradation routes are possible, these results indicate that in an emulsion a part of the supplemented MDA was translocated to the oil phase and/or interface of the oil droplets, which can be explained by its amphipathic nature.[21,22]

Furthermore, a statistically significant but limited effect of the preincubation (rest period) on the recovery of MDA was observed (cf. case 5 versus 6). Tween 20, a nonionic surfactant, stabilizes O/W emulsions against flocculation and coalescence by forming a protective membrane around the oil droplets. Nevertheless, after homogenization, there are significant quantities of nonadsorbed surfactant molecules present in the aqueous phase of emulsions.[23,24] Above the critical micelle concentration (CMC), the nonadsorbed surfactant molecules form micelles. On the other hand, adsorbed Tween 20 molecules in the O/W interface at a lower coverage can self-organize to give a denser adsorbed phase, thus opening up more surface sites for further adsorption of Tween 20[25] and making the oil droplet less permeable for MDA later. During

DOI: 10.1021/acs.jafc.5b01780
J. Agric. Food Chem. 2015, 63, 5694−5701

the rest period, the interface had probably time to undergo these rearrangements and as such to stabilize itself. In addition, Tween 20 micelles were most likely formed in the aqueous phase of O/W emulsions in view of the low CMC of the surfactant (0.007% w/v).[26] On the basis of the results in Table 1, MDA was still able to shift to the apolar phases of the emulsion, i.e., oil droplets, interfaces, and surfactant micelles, but to a lesser extent than when no stabilization period was performed. Therefore, more MDA remained in the aqueous phase, leading to a slightly higher recovery of MDA.

Reactivity of MDA in Coconut O/W Emulsions Stabilized by Tween 20 at 40 °C in the Presence of Proteins (Cases 7−10). The reactivity of MDA was further evaluated in coconut O/W emulsions in the presence of proteins (lysozyme or whey proteins) at 40 °C (cf. case 7−10). On the basis of the observations with respect to the previous set of experiments, again the impact of stabilizing the emulsion after preparation was considered (cf. case 7/8 versus 9/10). As shown in Table 1, the presence of proteins had an explicit effect on the recovery of MDA (cf. case 5 versus 7/8; case 6 versus 9/10). Less MDA was found when proteins were present, and similar to the results of cases 3 and 4, a lower recovery was observed when whey proteins were supplemented instead of lysozyme. Hence, in protein-supplemented coconut O/W emulsions, a protein-dependent interaction between MDA and proteins could be observed.

Moreover, a significant difference was observed when MDA and proteins were supplemented simultaneously (cf. cases 7 and 9) or 24 h after the MDA was added (cf. cases 8 and 10). In cases 8 and 10, MDA had 24 h to shift toward the apolar phases (i.e., oil droplets, interfaces, and micelles) of the emulsion. Based on the results obtained in view of the amphipathic character of MDA and its enolate, it is speculated that MDA present at the interfaces is less prone to react with proteins and is also more stable toward aldol condensation and degradation compared to MDA in oil. Furthermore, the impact of the stabilization period (cf. case 8 versus 10) was quite restricted for both proteins considered because the interface of the emulsion had in both cases at least 24 h to reorganize and stabilize. However, if proteins were supplemented together with MDA (cf. cases 7 and 9), there was a competition for MDA (1) to interact with proteins, (2) to shift to the apolar phases (i.e., oil droplets and interfaces), (3) to undergo condensation and/or cleavage in the aqueous phase and oil phase. Again we assume that the interaction between MDA and proteins was favored as in case 3. In addition, the stabilization period had also an effect on the recovery of MDA (cf. case 7 versus 9). As mentioned before, after homogenization, there are still free surfactant molecules present in the aqueous phase, searching for their most optimal condition. It has been reported that nonionic surfactants, such as Tween 20, are also able to interact with proteins present in the aqueous phase.[24,27,28] Thus, they could protect proteins against MDA by binding to the hydrophobic regions of the surface of proteins, decreasing the molecular interactions.[29,30] In addition, they may act as a chemical chaperone, favoring refolding by binding transiently with partially folded protein molecules and thus sterically hindering interaction with MDA.[28] Therfore, if proteins were added after stabilization of the interface, together with MDA (cf. case 9), less surfactant molecules were available to interact with the proteins and thus protected them from interacting with MDA.

Figure 5 represents an overview of the potential reaction mechanisms of MDA in coconut O/W emulsions in the presence of proteins when no stabilization period was applied, as discussed above (cf. case 7).

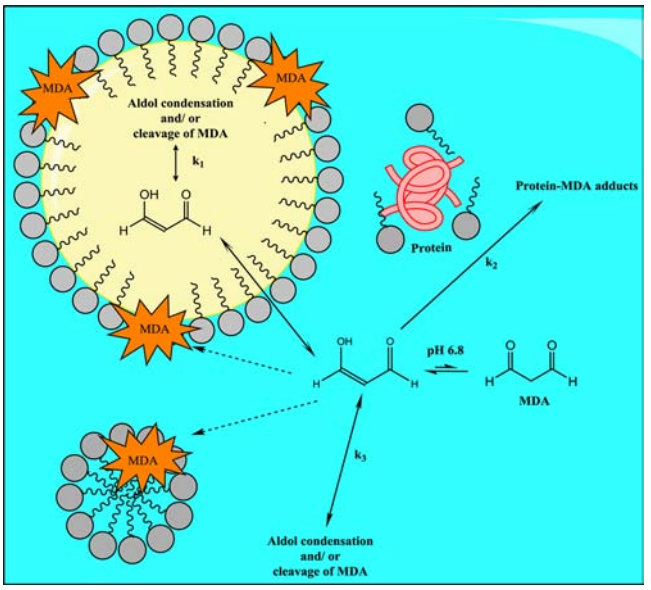

Figure 5. Potential reaction mechanisms of MDA in coconut O/W emulsions stabilized by Tween 20 in the presence of proteins when no stabilization period was applied (cf. case 7). MDA can exist in various forms depending on pH. At neutral conditions, the predominant (>99%) form is the enolate anion.[11] A competition for MDA takes place (1) to shift to the apolar phases of the emulsion (i.e., oil droplets, interfaces and micelles), (2) to interact with proteins, and (3) to condensate and/or degrade in the aqueous phase with corresponding reaction rates k_1, k_2, and k_3.

Effect of Temperature on the Reactivity of MDA in the Various Model Systems (4 versus 40 °C). In parallel to the experiments at 40 °C, a similar set of experiments was conducted at 4 °C. Obviously, temperature will affect the reactivity of MDA itself, but it will also have an impact on the physical state of the interface and the crystallization of the oil droplets (in the case of fully hydrogenated coconut oil). As shown in Table 3, no significant difference in aldol condensation and/or cleavage of MDA was observed between phosphate buffer and glycerol triheptanoate oil (cf. case 1 versus 2). Compared to 40 °C, the condensation and/or cleavage of MDA was the same for the aqueous buffer but excessively lower in the case of glycerol triheptanoate oil. This suggests that temperature has a major impact on the condensation and/or degradation of MDA in a pure oil. Consequently, when the MDA content of a particular oil is determined, the measured content will greatly depend on the storage and operating temperature of the oil.

In cases 3 and 4, proteins were supplemented in the aqueous phase together with MDA or after 24 h, respectively. Similar to the case at 40 °C, less MDA was measured in case 4, but compared to the experiments at 40 °C, the MDA content was now higher. Thus, the reactivity toward proteins was severely reduced at 4 °C. Again a lower recovery was observed when whey proteins where added instead of lysozyme, confirming the higher reactivity of whey proteins toward MDA.

In Tween 20-stabilized coconut O/W emulsions in the absence of proteins (cf. cases 5 and 6), again a considerably

DOI: 10.1021/acs.jafc.5b01780
J. Agric. Food Chem. 2015, 63, 5694−5701

Table 3. Recovery of MDA (Initial Concentration, 7 μM) in Cases 1−12 after Incubating at 4 °C (Figures 1−3)[a]

case	model description	recovery of MDA (%)		
		no protein	lysozyme	whey proteins
1	MDA in phosphate buffer (pH 6.8)	92.39 ± 0.26a	n.a.	n.a.
2	MDA in glycerol triheptanoate oil	92.87 ± 1.25a	n.a.	n.a.
3	MDA in phosphate buffer (pH 6.8) directly supplemented with protein	n.a.	88.67 ± 1.01c	79.53 ± 0.47e
4	MDA in phosphate buffer (pH 6.8), protein added after 24 h	n.a.	83.00 ± 0.78d	76.90 ± 0.53f
5	MDA in coconut O/W emulsion stabilized by Tween 20 in absence of proteins	91.41 ± 0.73a,b	n.a.	n.a.
6	MDA in coconut O/W emulsion stabilized by Tween 20 after preincubation in absence of proteins	91.52 ± 0.66a,b	n.a.	n.a.
7	coconut O/W emulsion stabilized by Tween 20: MDA added along with proteins after homogenization	n.a.	89.74 ± 0.41b,c	89.89 ± 0.85b,c
8	coconut O/W emulsion stabilized by Tween 20: MDA added after homogenization; proteins added after 24 h	n.a.	90.71 ± 0.20a,b,c	84.79 ± 1.17d,g
9	coconut O/W emulsion stabilized by Tween 20: MDA added along with proteins after preincubation	n.a.	91.20 ± 0.88a,b	91.50 ± 0.94a,b
10	coconut O/W emulsion stabilized by Tween 20: MDA added after preincubation; proteins added 24 h later	n.a.	91.46 ± 0.93a,b	88.99 ± 0.37c
11	coconut O/W emulsion stabilized by whey proteins: MDA added after homogenization	n.a.	n.a.	83.18 ± 0.44d
12	coconut O/W emulsion stabilized by whey proteins: MDA added after preincubation	n.a.	n.a.	86.62 ± 0.95g

[a]Values are the average of three replications ± the standard deviation. Different letters indicate statistically significant differences ($p < 0.05$) in the recovery of MDA. "n.a." indicates not applicable.

lower reactivity of MDA was observed at 4 °C compared to that at 40 °C. MDA showed moreover a higher reactivity toward proteins (cf. case 5/6 versus 3/4), similar to that observed at 40 °C. In addition, no effect of stabilizing the interface was found (cf. case 5 versus 6). In view of the high melting point of the fully hydrogenated coconut oil (33.3 °C) and the low temperature at which this set of experiments was conducted, fat crystallization in the oil droplets most likely occurred. This was also corroborated by the observed slightly higher apparent viscosity of the emulsions. It should be noted, however, that the emulsions remained stable at 4 °C. As MDA losses at 4 °C in the aqueous and oil phase (cf. case 1 and 2) were similar, in contrast to the behavior observed at 40 °C, it seems logical that no impact of the stabilization of the interface and its permeability toward MDA could be expected. However, we do assume that the oil phase became less receptive for MDA in view of its higher crystallinities; therefore, MDA remained more present in the aqueous phase or the interfaces of the emulsion.

Upon supplementing proteins to the Tween 20-stabilized emulsions at 4 °C (cf. cases 7−10), also no additional effect could be observed, except when whey proteins were added 24 h after MDA was added (cf. case 8). In view of the observed reactivity between MDA and proteins (cf. cases 3 and 4), these results seem to suggest that MDA is especially present in the interface of the emulsion where it is then protected from reaction with proteins. This would be in line with our earlier observations with respect to the experiments at 40 °C related to cases 7/9 versus 8/10. It remains unclear, however, why MDA showed the highest reactivity when whey proteins were added 24 h after MDA addition to freshly prepared emulsion (cf. case 8), especially as this was not observed at 40 °C.

Reactivity of MDA in Coconut O/W Emulsions Stabilized by Whey Proteins at 4 and 40 °C (Cases 11 and 12). In the following set of experiments, Tween 20 as the interfacial molecule was replaced by a protein itself. Whey proteins, in contrast to lysozyme, were able to stabilize the coconut O/W emulsions both at 4 and 40 °C. Tables 1 and 3 represent the recovery of MDA in whey proteins-stabilized coconut O/W emulsions incubated at 40 and 4 °C, respectively (cf. cases 11 and 12). In contrast to Tween 20-stabilized emulsions supplemented with whey proteins (cf. case 7−10), more MDA was recovered at 40 °C. It should be noted, however, that the concentration of whey proteins in these emulsions was lower than those stabilized by Tween 20: 0.5 and 0.8 wt %, respectively. However, when the same concentration of whey proteins was added to Tween 20-stabilized coconut emulsions (similar as case 7), the recovery was still significantly lower (36.97 ± 0.36%) compared to whey proteins-stabilized coconut emulsions. This indicates that whey proteins adsorbed at the interface of the oil droplets showed a lower reactivity toward MDA. When whey proteins adsorb to O/W interfaces, they may undergo substantial conformational changes and interactions due to the change in its molecular environment. The time required for these conformational changes to occur depends on the molecular flexibility and packing of the adsorbed molecules and can take even hours for whey proteins as these are rigid globular proteins. For many globular proteins including whey proteins, these conformational changes lead surprisingly to an increased exposure of nonpolar and sulfhydryl-containing amino acids to the aqueous phase.[31,32] Therefore, polar reactive amino acids such as lysine, arginine, and histidine are less accessible for MDA present in the aqueous phase, explaining the higher recovery of MDA in these type of emulsions compared to Tween 20-stabilized coconut emulsions. Additionally, a significant effect was found when a 24 h stabilization step (cf. case 12) was applied before MDA was added at both storage temperatures. During this step, whey proteins, adsorbed at the interface, had 24 h to undergo conformational rearrangement, reducing further the accessibility of the polar amino acids for MDA and resulting in a higher recovery in case 12.

However, at 4 °C, MDA was shown to be more reactive in the whey proteins-stabilized coconut emulsions compared to the Tween 20-stabilized coconut emulsions to which whey proteins were added (cf. cases 7 and 9). However, we assume this is not likely because of the higher interaction between MDA and whey proteins at the interface, but because of a lower extent of fat crystallization in the whey proteins-stabilized coconut emulsions. It has been reported that the onset temperature for fat crystallization within the oil droplets

DOI: 10.1021/acs.jafc.5b01780
J. Agric. Food Chem. 2015, 63, 5694−5701

depends on emulsifier type and is substantially lower for whey proteins than for Tween 20.[33] Therefore, at 4 °C, the solid fat content of the oil droplets was likely to be considerably lower in whey proteins-stabilized emulsions. Hence, the translocation of MDA toward the apolar phases (i.e., oil droplets and interfaces) happened more readily. Thus, an additional degradation route of MDA was favored (degradation in oil phase), apart from the other routes already available (degradation in aqueous phase and reaction with proteins), explaining the lower recovery of MDA in whey proteins-stabilized coconut emulsions at 4 °C.

In Figure 6, an overview of the potential reaction mechanisms of MDA in whey proteins-stabilized coconut O/W emulsions (cf. cases 11 and 12) at 40 °C is given.

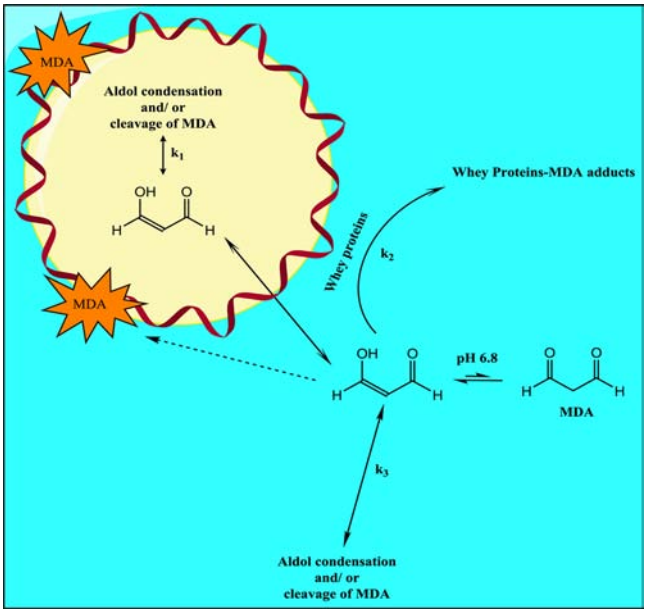

Figure 6. Potential reaction mechanisms of MDA in whey proteins-stabilized coconut O/W emulsions at 40 °C (cf. cases 11 and 12). MDA can (1) shift to the apolar phases (i.e., oil droplets and interfaces) of the emulsion to undergo condensation and/or cleavage, (2) interact with whey proteins at the interface, and (3) condensate and/or degrade in the aqueous phase with corresponding reaction rates k_1, k_2 and k_3.

From this study it can be concluded that the behavior of MDA in O/W emulsions is influenced by many factors and thus depends greatly on the model system parameters. At the one hand, degradation of MDA itself was shown to be considerable in both the aqueous and oil phases. With respect to the oil phase, especially at higher temperatures, the MDA degradation proved to be quite significant. Second, the reactivity of MDA toward proteins should be considered. Finally, it seems that MDA is present in the interface of the emulsion as well in which it is likely to be protected from the various degradation routes considered. Therefore, when a model system is selected to study the interaction between proteins and MDA in foods, it is advisible to choose the model system parameters wisely because the applied parameters can favor or even inhibit the interaction. Further research is necessary to elucidate the interactions between MDA and food proteins in O/W emulsions, keeping in mind the influences of the model parameters.

AUTHOR INFORMATION

Corresponding Author

*Phone: +32 9 264 61 66. Fax: +32 9 264 62 15. E-mail: Bruno.DeMeulenaer@UGent.be.

Notes

The authors declare no competing financial interest.

ACKNOWLEDGMENTS

We thank Cargill Refined Oils Europe for kindly delivering the fully hydrogenated coconut oil.

REFERENCES

(1) McClements, D. J. Context and background. In *Food Emulsions: Principles, Practices, and Techniques*, 2nd ed.; CRC Press: Boco Raton, FL, 2005; pp 1−26.

(2) Narayan, K. A.; Kummerow, F. A. Factors influencing the formation of complexes between oxidized lipids and proteins. *J. Am. Oil Chem. Soc.* **1963**, *40*, 339−342.

(3) Buttkus, H. The reaction of Myosin with Malonaldehyde. *J. Food Sci.* **1967**, *32*, 432−434.

(4) Berton, C.; Ropers, M. H.; Guibert, D.; Solé, V.; Genot, C. Modifications of interfacial proteins in oil-in-water emulsions prior to and during lipid oxidation. *J. Agric. Food Chem.* **2012**, *60*, 8659−8671.

(5) Slatter, D. A.; Bolton, D. H.; Bailey, A. J. The importance of lipid-derived malondialdehyde in diabetes mellitus. *Diabetologia* **2000**, *43*, 550−557.

(6) Janero, D. R. Malondialdehyde and thiobarbituric acid-reactivity as diagnostic indices of lipid peroxidation and peroxidative tissue injury. *Free Radical Biol. Med.* **1990**, *9*, 515−540.

(7) Uchida, K.; Sakai, K.; Itakura, K.; Osawa, T.; Toyokuni, S. Protein modification by lipid peroxidation products: formation of malondialdehyde-derived N-(2-propenal)lysine in proteins. *Arch. Biochem. Biophys.* **1997**, *346*, 45−52.

(8) Refsgaard, H. F.; Tsai, L.; Stadtman, E. R. Modifications of proteins by polyunsaturated fatty acid peroxidation products. *Proc. Natl. Acad. Sci. U. S. A.* **2000**, *97*, 611−616.

(9) Domingues, R. M.; Domingues, P.; Melo, T.; Pérez-Sala, D.; Reis, A.; Spickett, C. M. Lipoxidation adducts with peptides and proteins: deleterious modifications or signaling mechanisms? *J. Proteomics* **2013**, *92*, 110−131.

(10) Ishii, T.; Ito, S.; Kumazawa, S.; Sakurai, T.; Yamaguchi, S.; Mori, T.; Nakayama, T.; Uchida, K. Site-specific modification of positively-charged surfaces on human serum albumin by malondialdehyde. *Biochem. Biophys. Res. Commun.* **2008**, *371*, 28−32.

(11) Wei, Z. J.; Li, X. H.; Thushara, D.; Liu, Y. X. Determination and removal of malondialdehyde and other 2-thiobarbituric acid reactive substances in waste cooking oil. *J. Food Eng.* **2011**, *107*, 379−384.

(12) Traverso, N.; Menini, S.; Maineri, E. P.; Patriarca, S.; Odetti, P.; Cottalasso, D.; Marinari, U. M.; Pronzato, M. A. Malondialdehyde, a lipoperoxidation-derived aldehyde, can bring about secondary oxidative damage to proteins. *J. Gerontol., Ser. A* **2004**, *59A*, 890−895.

(13) Esterbauer, H.; Schaur, R. J.; Zollner, H. Chemistry and biochemistry of 4-hydroxynonenal, malondialdehyde and related aldehydes. *Free Radical Biol. Med.* **1991**, *11*, 81−128.

(14) Gómez-Sánchez, A.; Hermosin, I.; Lassaletta, J. M.; Maya, I. Cleavage and oligomerization of malondialdehyde. *Tetrahedron* **1993**, *49*, 1237−1250.

(15) Slatter, D. A.; Murray, M.; Bailey, A. J. Formation of a dihydropyridine derivative as a potential cross-link derived from malondialdehyde in physiological systems. *FEBS Lett.* **1998**, *421*, 180−184.

(16) Cighetti, G.; Debiasi, S.; Ciuffreda, P.; Allevi, P. *β*-ethoxyacrolein contamination increases malondialdehyde inhibition of milk xanthine oxidase activity. *Free Radical Biol. Med.* **1998**, *25* (7), 818−825.

(17) Papastergiadis, A.; Mubiru, E.; Van Langenhove, H.; De Meulenaer, B. Malondialdehyde measurement in oxidized foods:

DOI: 10.1021/acs.jafc.5b01780
J. Agric. Food Chem. 2015, 63, 5694−5701

evaluation of the spectrophotometric thiobarbituric acid reactive substances (TBARS) test in various foods. *J. Agric. Food Chem.* **2012**, *60*, 9589−9594.
(18) Kerkaert, B.; Mestdagh, F.; Cucu, T.; Aedo, P. R.; Ling, Y. S.; De Meulenaer, B. Hypochlorous and peracetic acid induced oxidation of dairy proteins. *J. Agric. Food Chem.* **2011**, *59*, 907−914.
(19) Kerkaert, B.; Mestdagh, F.; Obando, M.; Cucu, T.; De Meulenaer, B. Identification of modified lysozyme peptides upon photo-oxidation by LC-TOF-MS. *J. Agric. Food Chem.* **2013**, *61*, 12727−12726.
(20) Universal Protein Resource. Uniprot. http://www.uniprot.org (accessed December 2014).
(21) Cheng, Y.; Chen, J.; Xiong, Y. L. Interfacial Adsorption of peptides in oil-in-water emulsions costabilized by Tween 20 and antioxidative potato peptides. *J. Agric. Food Chem.* **2014**, *62*, 11575−11581.
(22) Nuchi, C. D.; Hernandez, P.; McClements, D. J.; Decker, E. A. Ability of lipid hydroperoxides to partition into surfactant micelles and alter lipid oxidation rates in emulsions. *J. Agric. Food Chem.* **2002**, *50*, 5445−5449.
(23) Waraho, T.; McClements, D. J.; Decker, E. A. Mechanisms of lipid oxidation in food dispersions. *Trends Food Sci. Technol.* **2011**, *22*, 3−13.
(24) McClements, D. J.; Decker, E. A. Lipid oxidation in oil-in-water emulsions; impact of molecular environment on chemical reactions in heterogeneous food systems. *J. Food Sci.* **2000**, *65* (8), 1270−1282.
(25) Shen, L.; Guo, A.; Zhu, X. Tween surfactants: adsorption, self-organization, and protein resistance. *Surf. Sci.* **2011**, *605*, 494−499.
(26) Kerwin, B. A. Polysorbates 20 and 80 used in the formulation of protein biotherapeutics: structure and degradation pathways. *J. Pharm. Sci.* **2008**, *97* (8), 2924−2935.
(27) Demetriades, K.; McClements, D. J. Influence of pH and heating on physicochemical properties of whey protein-stabilized emulsions containing a nonionic surfactant. *J. Agric. Food Chem.* **1998**, *46*, 3936−3942.
(28) Chou, D. K.; Krishnamurthy, R.; Randolph, T. W.; Carpenter, J. F.; Manning, M. C. Effects of Tween 20 and Tween 80 on the stability of albutropin during agitation. *J. Pharm. Sci.* **2005**, *94*, 1368−1381.
(29) Thanasukarn, P.; Pongsawatmanit, R.; McClements, D. J. Impact of fat and water crystallization on the stability of hydrogenated palm oil-in-water emulsions stabilized by whey protein isolate. *Colloids Surf., A* **2004**, *246*, 49−59.
(30) Boode, K.; Walstra, P.; De Groot-Mostert, A. E. A. Partial coalescence in oil-in-water emulsions 2: influence of the properties of the fat. *Colloids Surf., A* **1993**, *81*, 139−151.
(31) McClements, D. J. Protein-stabilized emulsions. *Curr. Opin. Colloid Interface Sci.* **2004**, *9*, 305−313.
(32) Kim, H. J.; Decker, E. A.; McClements, D. J. Impact of protein surface denaturation on droplet flocculation in hexadecane oil-in-water emulsions stabilized by β-lactoglobulin. *J. Agric. Food Chem.* **2002**, *50*, 7131−7137.
(33) Thanasukarn, P.; Pongsawatmanit, R.; McClements, D. J. Influence of emulsifier type on freeze-thaw stability of hydrogenated palm oil-in-water emulsions. *Food Hydrocolloids* **2004**, *18*, 1033−1043.

DOI: 10.1021/acs.jafc.5b01780
J. Agric. Food Chem. 2015, 63, 5694−5701

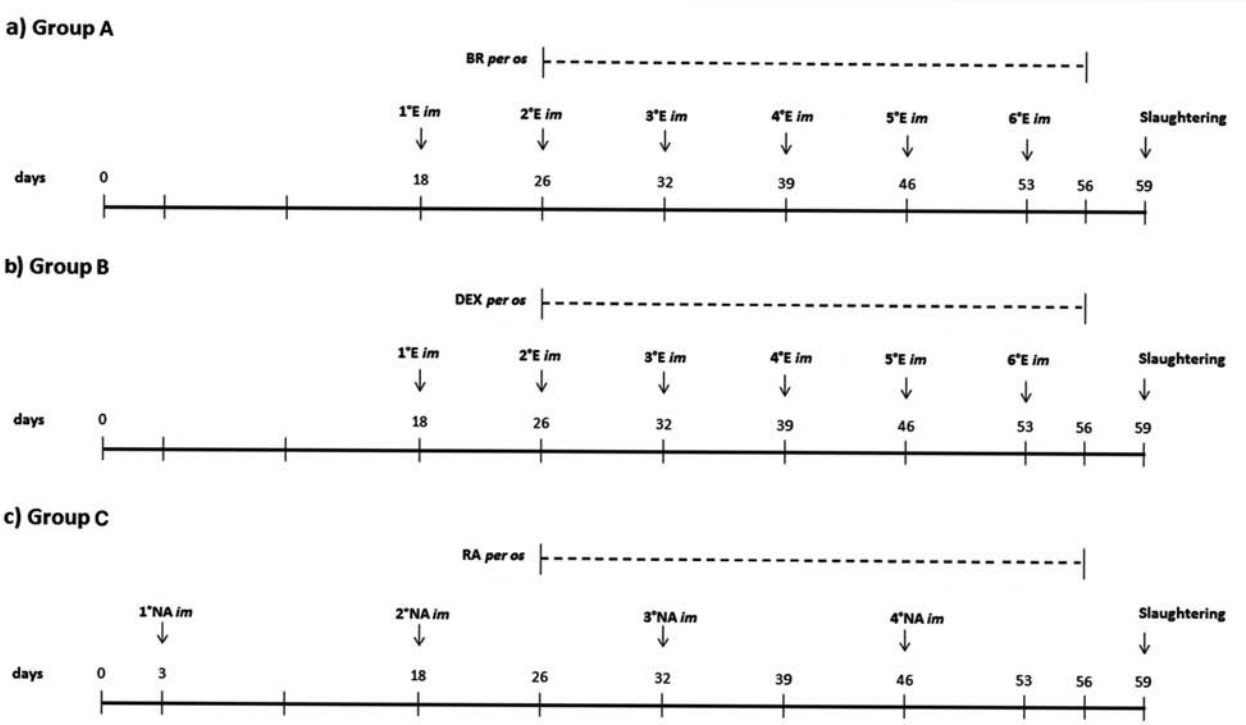

Figure 1. Treatment schedule of veal calves. Group A was weekly administered 5 mg/animal of estradiol benzoate (E) intramuscularly for 6 weeks in combination with 0.25 mg/animal/day of brotizolam (BR) per os for the last 31 days of treatment (a); group B was weekly administered 5 mg/animal of estradiol benzoate intramuscularly for 6 weeks in combination with 0.40 mg/animal/day of dexamethasone (DEX) per os for the last 31 days of treatment (b); group C was administered 150 mg/animal of Nandrosol (NA) every 2 weeks four times in combination with 80 mg/animal/day of ractopamine (RA) per os for the last 31 days of treatment (c). The calves were slaughtered 3 days after the last treatment.

intramuscularly for 6 weeks in combination with 0.25 mg/animal/day of brotizolam per os for the last 31 days of treatment; group B (n = 6) was weekly administered 5 mg/animal of estradiol benzoate intramuscularly for 6 weeks in combination with 0.40 mg/animal/day of dexamethasone (DEX) per os for the last 31 days of treatment; group C (n = 8) was administered 150 mg/animal of Nandrosol (17β-19-nortestosterone phenylpropionate) every 2 weeks for four times in combination with 80 mg/animal/day of ractopamine per os for the last 31 days of treatment; group K (n = 8) served as control (Figure 1). The calves were slaughtered 3 days after the last treatment. The hormone dosages were selected according to previous studies.[2,21,22]

The animals were healthy upon intravitam and post-mortem examinations. The experiments were authorized through the Italian Ministry of Health and the Ethical Committee of the University of Turin. The carcasses of the treated animals were appropriately destroyed (2003/74/CE-DL 16 March 2006, No. 158).

Tissue Sampling and Processing. Samples of bulbo-urethral glands, prostate and testis tissues were obtained from each animal at slaughter. The samples were immediately frozen in liquid nitrogen and then stored at −80 °C for molecular and Western blot (WB) analyses.

RNA Extraction, Reverse Transcription, and qPCR. Several milligrams of each tissue sample were disrupted using a TissueLyser II (Qiagen, Hilden, Germany) using stainless steel beads in 1 mL of TRIzol reagent (Ambion, Life Technologies, Carlsbad, CA, USA) according to the manufacturer's protocol. The RNA concentration was spectrophotometrically determined, and the RNA integrity was evaluated using an automated electrophoresis station (Experion Instrument, Bio-Rad, Hercules, CA, USA). cDNA was synthesized from 1 μg of total RNA using the QuantiTect Reverse Transcription Kit (Qiagen).

The effect of sex steroid hormones on RGN mRNA expression in the bulbo-urethral glands, prostate, and testis of veal calves was evaluated through quantitative polymerase chain reaction (qPCR). To determine the relative amounts of specific RGN transcripts, the cDNA obtained from retrotranscription was subjected to qPCR[23] using the IQ5 detection system (Bio-Rad) and respective gene primers in an IQ SYBR Green Supermix (Bio-Rad). Primer sequences of RGN were designed using Primer3 (vers. 0.4.0), as previously described.[20] The cyclophilin A (PPIA) gene was used as a housekeeping gene, as previously described.[20] The levels of gene expression were calculated using a relative quantification assay based on the comparative Cq method (ΔΔCq method),[24] previously verifying that efficiencies of target and housekeeping gene amplification were similar. Subsequently, the relative abundances of each transcript, normalized to the endogenous housekeeping gene (PPIA) and relative to the control sample, were calculated as $2^{-\Delta\Delta Cq}$ (fold increase).[25]

Western Blot Analysis. The effect of sex steroid hormones on RGN protein expression in the bulbo-urethral glands, prostate, and testis of veal calves was evaluated through WB analysis. Total protein was isolated from veal calves' bulbo-urethral glands, prostate, and testis using RIPA buffer (50 mM Tris, pH 8.0, 150 mM NaCl, 1.0% IGEPAL CA-630, 0.5% sodium deoxycholate, 0.1% SDS, 2 mM EDTA) supplemented with protease inhibitor cocktail (Sigma). Protein concentration was determined using the Bio-Rad DC Protein Assay. Twenty micrograms of total protein were resolved through 12.5% SDS-PAGE. The proteins were blotted onto Trans-Blot Turbo Mini Nitrocellulose Transfer membrane (Bio-Rad) using a Trans-Blot Turbo Blotting System (Bio-Rad). The blotted membranes were blocked with 5% BSA in TBS-0.1% Tween for 1 h at room temperature, followed by overnight incubation with an anti-RGN rabbit polyclonal antibody (1:200; Sigma, St. Louis, MO, USA). The membranes were subsequently incubated with secondary anti-rabbit horseradish peroxidase (HRP)-conjugated antibody (1:1000), developed using the SuperSignal West Pico IgG Detection Kit (Thermo Fisher Scientific, Waltham, MA, USA), and recorded on CL-XPosure X-ray film (Thermo Fisher Scientific).

α-tubulin (1:10000; clone B-5-1-2; Sigma) was used as a total protein loading control.

DOI: 10.1021/acs.jafc.5b01337
J. Agric. Food Chem. 2015, 63, 5702−5706

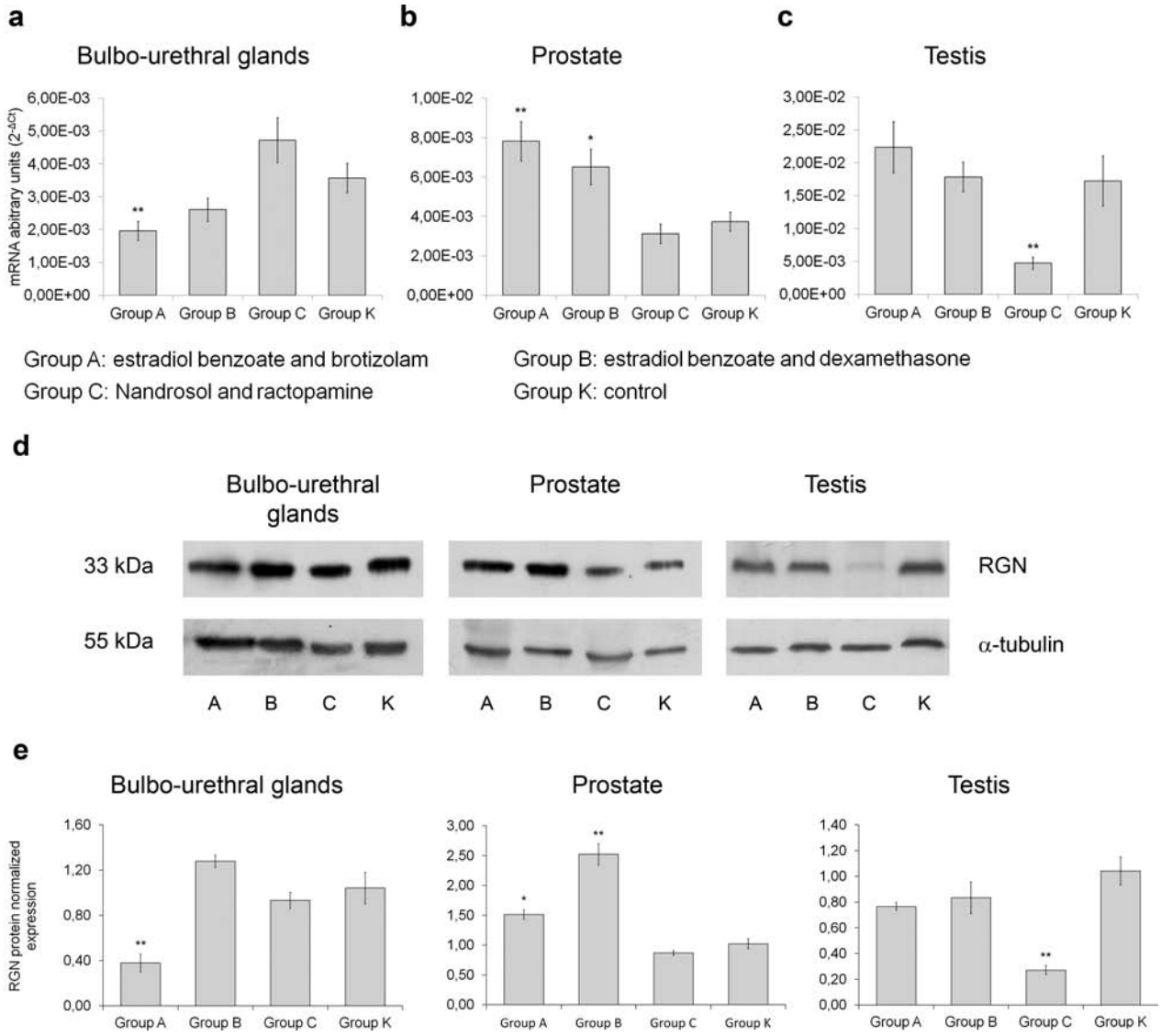

Figure 2. Effects of estradiol benzoate combined with brotizolam (group A), estradiol benzoate combined with dexamethasone (group B), and Nandrosol combined with ractopamine (group C) on *RGN* gene expression compared with the control group K in the bulbo-urethral glands (a), prostate (b), and testis (c) of veal calves. The results are presented as the means ± SEM. The *y*-axes show arbitrary units representing mRNA relative expression levels. A representative Western blot showing RGN protein expression in the bulbo-urethral glands, prostate, and testis (d) of veal calves using an anti-RGN polyclonal antibody (1:200). α-Tubulin (1:10000) was used as loading control. The relative expression levels of RGN protein in the bulbo-urethral glands, prostate, and testis (e) of veal calves were determined and normalized using α-tubulin. The results are presented as the means ± SEM. (∗) $P < 0.05$ and (∗∗) $P < 0.01$ versus the control group K.

Band densities were obtained according to standard methods using ImageJ software (U.S. National Institutes of Health) and normalized by division with the respective α-tubulin band density.

Statistical Analysis. Statistical analyses were performed using Graph-Pad InStat (vers. 3.05) statistical software (GraphPad Inc., San Diego, CA, USA). The analysis of RGN expression was performed using one-way analysis of variance (ANOVA), followed by Dunnett's post-test versus the control group K. The Grubbs test was used to reveal potential outliers. A P value of <0.05 was considered statistically significant. The data obtained by qPCR are shown as the mean arbitrary units ($2^{-\Delta Cq}$) ± standard error of the mean (SEM).

RESULTS

Effect of Sex Steroid Hormones on RGN Gene Expression in the Accessory Sex Glands of Veal Calves. *RGN* gene expression decreased in the bulbo-urethral glands of group A (mean of mRNA arbitrary units ± SEM, $1.96 \times 10^{-3} \pm 2.94 \times 10^{-4}$) compared with the control group K ($3.57 \times 10^{-3} \pm 4.45 \times 10^{-4}$) ($P < 0.01$) (Figure 2a). The RGN expression increased in the prostate of group A ($7.82 \times 10^{-3} \pm 9.88 \times 10^{-4}$) ($P < 0.01$) and group B ($6.51 \times 10^{-3} \pm 9.05 \times 10^{-4}$) ($P < 0.05$) compared with the control group K ($3.73 \times 10^{-3} \pm 4.84 \times 10^{-4}$) (Figure 2b). The RGN expression decreased in the testis of group C ($4.73 \times 10^{-3} \pm 8.88 \times 10^{-4}$) ($P < 0.01$) compared with the control group K ($1.72 \times 10^{-2} \pm 3.80 \times 10^{-3}$) (Figure 2c).

Western Blot Analysis. RGN protein expression was down-regulated in the bulbo-urethral glands of group A compared with control group K ($P < 0.01$) (Figure 2d,e) and up-regulated in the prostate of groups A and B compared with control group K ($P < 0.05$ and $P < 0.01$, respectively) (Figure 2d,e). RGN protein expression decreased only in the testis of

DOI: 10.1021/acs.jafc.5b01337
J. Agric. Food Chem. 2015, 63, 5702−5706

group C compared with the control group K ($P < 0.01$) (Figure 2d,e).

DISCUSSION

The European Union bans the use of sex steroid hormones in bovine husbandry to preserve consumers' health. Indeed, measurable levels of these molecules have been found in muscle, fat, liver, kidney, and other organs in meat products.[26] The potential effects of estrogen residues include, among others, impaired fertility,[27] increased incidence of hormone-related cancers,[28] and congenital malformations[29] in humans.

In bovine livestock, in addition to the desired effects, such as the increase of live weight and reduced fat deposits, the anabolic agents cause severe changes and alterations in target organs.[24,30,31] Estrogenic hormones induce characteristic lesions such as hyperplasia and squamous metaplasia in the prostate and bulbo-urethral glands of male animals and in the Bartholin's glands of females.[24,32,33] This histological method can identify the illicit E_2 treatment up to 15 days after the last drug administration in veal calves[2,34] and in adult male animals.[3] This screening method is officially adopted by the Italian National Program for Residue Surveillance (PNR) for the detection of illicit hormone treatment (PNR 2014). However, low-dosage cocktails often elude the preliminary screening and official tests. Therefore, in this context novel methods of detection, as transcriptomic techniques, have been employed. *RGN* gene expression is clearly estrogen-regulated in several reproductive and nonreproductive organs.[6,16−20] Recently, down-regulation of *RGN* gene expression in the accessory sex glands of veal calves following E_2 administration was demonstrated.[20] In the present study low doses of estradiol benzoate combined with the benzodiazepine brotizolam down-regulated RGN expression in the bulbo-urethral glands. Moreover, *RGN* gene expression was up-regulated by the combination of estradiol benzoate with brotizolam or DEX in the prostate.

The expression of RGN mRNA is regulated by several factors, including Ca^{2+}.[35,36] Several studies have demonstrated that E_2 can induce an increase of intracellular Ca^{2+} in the prostate cells,[37−39] and these effects have been suggested to be associated with rapid nongenomic mechanisms, through a membrane-bound estrogen receptor (mER).[6,40] RGN up-regulation in the prostate following estrogen administration could be sustained through this mechanism. In this context further studies are needed to better understand this relationship.

In addition, *RGN* gene expression is also under androgen control. The presence of numerous androgen response elements consensus sequences in the promoter region of the *RGN* gene has been demonstrated.[6] Testosterone administration greatly decreased RGN mRNA expression only in the testis of veal calves.[20] In the present study, even low doses of Nandrosol induced a significant decrease of RGN mRNA levels in the testis of group C animals compared with the control group. Moreover, RGN protein expression was dramatically decreased by Nandrosol administration in the testis. Conversely, this treatment induced no change of RGN expression in the bulbo-urethral glands and prostate. Therefore, the down-regulation of RGN expression following androgen treatment seems to be a specific response of testis.

A tightly regulated equilibrium between germ cell apoptosis and proliferation is required for a successful spermatogenesis,[41] as approximately 75% of testicular germ cells undergo apoptosis.[42] RGN inhibits apoptosis through the up-regulation of Akt-1 and Bcl-2 expression and the down-regulation of caspase-3.[43] The reduction of RGN expression via androgen administration could inhibit normal spermatogenesis through the stimulation of abnormal apoptosis and the termination of germ cell line maturation, as previously described.[20]

In conclusion, these results confirm that sex steroid hormones, even at low doses and in combination with other GPs, specifically affect RGN expression in the accessory sex glands and testis of veal calves. Interestingly, *RGN* gene expression in the testis changes only following androgen administration. This finding could allow the application of RGN expression as a first indirect biomarker in a low-cost screening test to detect the illicit treatment of veal calves with androgens in the official residue-monitoring programs. Therefore, the detection of androgen abuse by RGN down-regulation is a promising tool to further ensure food safety and quality, considering that changes of the expression of this gene may persist for up to some days after the suspension of androgen treatment.

AUTHOR INFORMATION

Corresponding Author

*(F.T.C.) Phone: +39 011 670 9032. Fax: +39 011 670 9031. E-mail: tiziana.cannizzo@unito.it.

Funding

This work was partially funded by SAFORISK project "Prevenzione dell'uso di anabolizzanti in zootecnia. Creazione di un Marchio a difesa degli allevamenti italiani" (D.M. 2089/09, January 29, 2009).

Notes

The authors declare no competing financial interest.

ACKNOWLEDGMENTS

We thank the Centro di Referenza di Patologia Comparata "Bruno Maria Zaini" (Torino, Italy).

REFERENCES

(1) De Brabander, H. F.; Antignac, J. P.; Courtheyn, D.; Pinel, G.; Verheyden, K.; Le Bizec, B.; Mortier, V.; Noppe, H. Past, present and future of mass spectrometry in the analysis of residues of banned substances in meat producing animals. *J. Mass Spectrom.* **2007**, *42*, 983−998.

(2) De Maria, R.; Divari, S.; Spada, F.; Oggero, C.; Mulasso, C.; Maniscalco, L.; Cannizzo, F. T.; Bianchi, M.; Barbarino, G.; Brina, N.; Biolatti, B. Progesterone receptor gene expression in the accessory sex glands of veal calves. *Vet. Rec.* **2010**, *167*, 291−296.

(3) Divari, S.; Mulasso, C.; Uslenghi, F.; Cannizzo, F. T.; Spada, F.; De Maria, R.; Brina, N.; Biolatti, B. Progesterone receptor up-regulation: a diagnostic tool for the illicit use of oestrogens in adult beef cattle. *Food Addit. Contam., Part A* **2011**, *28*, 1677−1686.

(4) Uslenghi, F.; Divari, S.; Cannizzo, F. T.; De Maria, R.; Spada, F.; Mulasso, C.; Pezzolato, M.; Bozzetta, E.; Attucci, A.; Giorgi, P.; Biolatti, B. Application of absolute qPCR as a screening method to detect illicit 17β-oestradiol administration in male cattle. *Food Addit. Contam., Part A* **2013**, *30*, 253−263.

(5) Divari, S.; Cannizzo, F. T.; Starvaggi Cucuzza, L.; Brina, N.; De Maria, R.; Biolatti, B. Oxytocin precursor gene expression in bovine skeletal muscle is regulated by 17β-oestradiol and dexamethasone. *Food Chem.* **2013**, *144*, 4358−4366.

(6) Maia, C.; Santos, C.; Schmitt, F.; Socorro, S. Regucalcin is under-expressed in human breast and prostate cancers: effect of sex steroid hormones. *J. Cell. Biochem.* **2009**, *107*, 667−676.

DOI: 10.1021/acs.jafc.5b01337
J. Agric. Food Chem. 2015, 63, 5702−5706

(7) Yamaguchi, M.; Yamamoto, T. Purification of calcium binding substance from soluble fraction of normal rat liver. *Chem. Pharm. Bull.* **1978**, *26*, 1915−1918.
(8) Takahashi, H.; Yamaguchi, M. Role of regucalcin as an activator of Ca^{2+}-ATPase activity in rat liver microsomes. *J. Cell. Biochem.* **1999**, *74*, 663−669.
(9) Fukaya, Y.; Yamaguchi, M. Characterization of protein tyrosine phosphatase activity in rat liver microsomes: suppressive effect of endogenous regucalcin in transgenic rats. *Int. J. Mol. Med.* **2004**, *14*, 427−432.
(10) Yamaguchi, M. Role of regucalcin in maintaining cell homeostasis and function. *Int. J. Mol. Med.* **2005**, *15*, 371−389.
(11) Yamaguchi, M. Role of regucalcin in brain calcium signaling: involvement in aging. *Integr. Biol. (Cambridge)* **2012**, *4*, 825−837.
(12) Ishigami, A.; Fujita, T.; Handa, S.; Shirasawa, T.; Koseki, H.; Kitamura, T.; Enomoto, N.; Sato, N.; Shimosawa, T.; Maruyama, N. Senescence marker protein-30 knockout mouse liver is highly susceptible to tumor necrosis factor-α- and Fas-mediated apoptosis. *Am. J. Pathol.* **2002**, *161*, 1273−1281.
(13) Matsuyama, S.; Kitamura, T.; Enomoto, N.; Fujita, T.; Ishigami, A.; Handa, S.; Maruyama, N.; Zheng, D.; Ikejima, K.; Takei, Y.; Sato, N. Senescence marker protein-30 regulates Akt activity and contributes to cell survival in Hep G2 cells. *Biochem. Biophys. Res. Commun.* **2004**, *321*, 386−390.
(14) Nakagawa, T.; Sawada, N.; Yamaguchi, M. Overexpression of regucalcin suppresses cell proliferation of cloned normal rat kidney proximal tubular epithelial NRK52E cells. *Int. J. Mol. Med.* **2005**, *16*, 637−643.
(15) Jeong, D. H.; Goo, M. J.; Hong, I. H.; Yang, H. J.; Ki, M. R.; DO, S. H.; Ha, J. H.; Lee, S. S.; Park, J. K.; Jeong, K. S. Inhibition of radiation-induced apoptosis via overexpression of SMP30 in Smad3-knockout mice liver. *J. Radiat. Res.* **2008**, *49*, 653−660.
(16) Yamaguchi, M.; Oishi, K. 17β-Estradiol stimulates the expression of hepatic calcium-binding protein regucalcin mRNA in rats. *Mol. Cell. Biochem.* **1995**, *143*, 137−141.
(17) Kurota, H.; Yamaguchi, M. Steroid hormonal regulation of calcium-binding protein regucalcin mRNA expression in the kidney cortex of rats. *Mol. Cell. Biochem.* **1996**, *155*, 105−111.
(18) Laurentino, S. S.; Correia, S.; Cavaco, J. E.; Oliveira, P. F.; Rato, L.; Sousa, M.; Barros, A.; Socorro, S. Regucalcin is broadly expressed in male reproductive tissues and is a new androgen-target gene in mammalian testis. *Reproduction* **2011**, *142*, 447−456.
(19) Maia, C. J.; Santos, C. R.; Schmitt, F.; Socorro, S. Regucalcin is expressed in rat mammary gland and prostate and down-regulated by 17β-estradiol. *Mol. Cell. Biochem.* **2008**, *311*, 81−86.
(20) Starvaggi Cucuzza, L.; Divari, S.; Mulasso, C.; Biolatti, B.; Cannizzo, F. T. Regucalcin expression in bovine tissues and its regulation by sex steroid hormones in accessory sex glands. *PLoS One* **2014**, *9* (11), No. e113950.
(21) Meyer, H. H. Biochemistry and physiology of anabolic hormones used for improvement of meat production. *APMIS* **2001**, *109*, 1−8.
(22) Cannizzo, F. T.; Miniscalco, B.; Riondato, F.; Bollo, E.; Barbarino, G.; Giorgi, P.; Mazzini, C.; Biolatti, B. Effects of anabolic and therapeutic doses of dexamethasone on thymus morphology and apoptosis in veal calves. *Vet. Rec.* **2008**, *163*, 448−452.
(23) Kubista, M.; Andrade, J. M.; Bengtsson, M.; Forootan, A.; Jonàk, J.; Lind, K.; Sindelka, R.; Sjöback, R.; Sjögreen, B.; Strömbom, L.; Ståhlberg, A.; Zoric, N. The real-time polymerase chain reaction. *Mol. Aspects Med.* **2006**, *27*, 95−125.
(24) Bustin, S. A.; Benes, V.; Garson, J. A.; Hellemans, J.; Hugget, J.; Kubista, M.; Mueller, R.; Nolan, T.; Pfaffl, M. W.; Shipley, G. L.; Vandesompele, J.; Wittwer, C. T. The MIQE guidelines: Minimum information for publication of quantitative real-time PCR experiments. *Clin. Chem.* **2009**, *55*, 611−622.
(25) Wong, M. L.; Medrano, J. F. Real-time PCR for mRNA quantitation. *BioTechniques* **2005**, *39*, 75−85.
(26) Henricks, D. M.; Gray, S. L.; Owenby, J. J.; Lackey, B. R. Residues from anabolic preparations after good veterinary practice. *APMIS* **2001**, *109*, 273−283.
(27) Skakkebaek, N. E. Testicular dysgenesis syndrome. *Horm. Res.* **2003**, *60* (Suppl. 3), 49.
(28) Miller, W. R.; Sharpe, R. M. Environmental oestrogens and human reproductive cancers. *Endocr.-Relat. Cancer* **1998**, *5*, 69−96.
(29) Sharpe, R. M.; Skakkebaek, N. E. Are oestrogens involved in falling sperm counts and disorders of the male reproductive tract? *Lancet* **1993**, *341*, 1392−1395.
(30) Biolatti, B.; Cabassi, E.; Rosmini, R.; Groot, M.; Castagnaro, M.; Benevelli, R.; Gilioli, G.; Ghizzinardi, A.; Giorgi, P.; Mazzini, C.; Comellini, F.; Alberghini, L.; Zancanaro, G.; Cannizzo, F. T.; Amedeo, S.; Poppi, L.; Cantoni, A. Lo screening istologico nella prevenzione dell'uso di anabolizzanti nel bovino. *Large Anim. Rev.* **2003**, *9*, 9−19.
(31) Groot, M. J.; Schilt, R.; Ossenkoppele, J. S.; Berende, P. L. M.; Haasnoot, W. Combinations of growth promoters in veal calves: consequences for screening and confirmation methods. *J. Vet. Med., A* **1998**, *45*, 425−440.
(32) Groot, M. J.; Ossenkoppele, J. S.; Bakker, R. Changes in cytokeratin expression in accessory sex glands of growth promoter treated veal calves: influences of treatment schedule and combination of drugs. *Eur. J. Vet. Pathol.* **2000**, *6*, 19−24.
(33) Schilt, R.; Groot, M. J.; Berende, P. L.; Ramazza, V.; Ossenkoppele, J. S.; Haasnoot, W.; van Bennekom, E. O.; Brouwer, L.; Hooijerink, H. Pour on application of growth promoters in veal calves: analytical and histological results. *Analyst* **1998**, *123*, 2665−2670.
(34) Pezzolato, M.; Maurella, C.; Varello, K.; Meloni, D.; Bellino, C.; Borlatto, L.; Di Corcia, D.; Capra, P.; Caramelli, M.; Bozzetta, E. High sensitivity of a histological method in the detection of low-dosage illicit treatment with 17β-estradiol in male calves. *Food Control* **2011**, *22*, 1668−1673.
(35) Isogai, M.; Yamaguchi, M. Calcium administration increases calcium-binding protein regucalcin concentration in the liver of rats. *Mol. Cell. Biochem.* **1995**, *143*, 53−58.
(36) Yamaguchi, M.; Kurota, H. Expression of calcium-binding protein regucalcin mRNA in the kidney cortex of rats: the stimulation by calcium administration. *Mol. Cell. Biochem.* **1995**, *146*, 71−77.
(37) Audy, M. C.; Vacher, P.; Duly, B. 17β-Estradiol stimulates a rapid Ca^{2+} influx in LNCaP human prostate cancer cells. *Eur. J. Endocrinol.* **1996**, *135*, 367−373.
(38) Huang, J. K.; Jan, C. R. Mechanism of estrogens-induced increases in intracellular Ca^{2+} in PC3 human prostate cancer cells. *Prostate* **2001**, *47*, 141−148.
(39) Rouayrenc, J. F.; Vignon, F.; Bringer, J.; Pujol, P. Non-genomic steroid effects: estrogen action revisited. *Ann. Endocrinol. (Paris)* **2000**, *61*, 517−523.
(40) Govind, A. P.; Thampan, R. V. Membrane associated estrogen receptors and related proteins: localization at the plasma membrane and the endoplasmic reticulum. *Mol. Cell. Biochem.* **2003**, *253*, 233−240.
(41) Print, C. G.; Loveland, K. L. Germ cell suicide: new insights into apoptosis during spermatogenesis. *BioEssays* **2000**, *22*, 423−430.
(42) Giampietri, C.; Petrungaro, S.; Coluccia, P.; D'Alessio, A.; Starace, D.; Riccioli, A.; Padula, F.; Palombi, F.; Ziparo, E.; Filippini, A.; De Cesaris, P. Germ cell apoptosis control during spermatogenesis. *Contraception* **2005**, *72*, 298−302.
(43) Nakagawa, T.; Yamaguchi, M. Overexpression of regucalcin suppresses apoptotic cell death in cloned normal rat kidney proximal tubular epithelial NRK52E cells: change in apoptosis-related gene expression. *J. Cell. Biochem.* **2005**, *96*, 1274−1285.

DOI: 10.1021/acs.jafc.5b01337
J. Agric. Food Chem. 2015, 63, 5702−5706

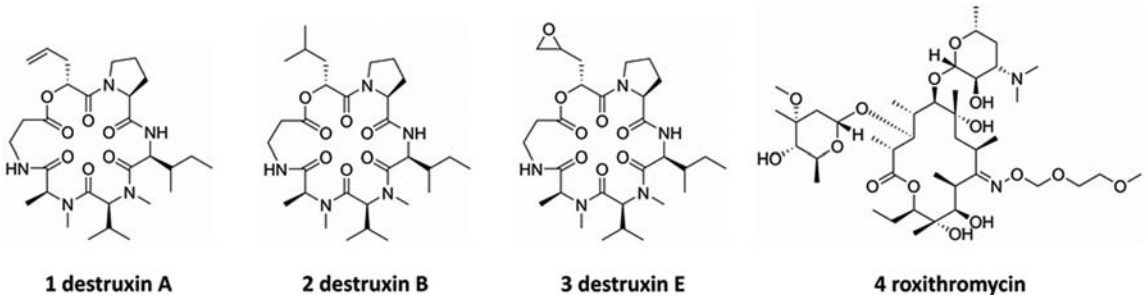

Figure 1. Structural formulas of the main destruxin congeners **1**, **2**, and **3** and the internal standard roxithromycin **4**.

decided to use this reference extraction procedure for our approach because no appropriate method for the analysis of destruxins in crop matrices is currently available. A novel QuEChERS-based sample preparation protocol for the extraction of destruxins from different crop matrices was developed and combined with a quantitative UHPLC-QTOF-MS method with an anticipated sensitivity in the lower parts per billion range. The destruxin isolation and purification protocol from strawberry and maize as well as the chromatographic separation and mass spectrometric detection method for the quantitative determination of three major congeners, namely, destruxin A, **1**, destruxin B, **2**, and destruxin E, **3**, are now reported. These plants have been chosen as model crops due to the application of *M. brunneum* as BCA in such cultivation settings.

MATERIALS AND METHODS

Materials and Chemicals. Destruxin reference materials with a NMR purity ≥98% (**1**−**3**) were isolated from *M. brunneum* strain BIPESCO 5 as previously described.[34] Matrix samples were harvested products from untreated field plots; strawberry samples (without calyx) were obtained from Martell (South Tyrol, Italy) and maize samples from Dietzen (Styria, Austria). Any harvested material was frozen as soon as possible to avoid rotting or molding during transport and storage. Gradient grade acetonitrile, Sabouraud−2% dextrose (SD) broth, and anhydrous sodium sulfate for analysis were purchased from Merck (Darmstadt, Germany); technical grade dichloromethane was from VWR International (Rue Carnot, France); water free glucose was from Roth (Karlsruhe, Germany); agar was from Kottas Pharma (Vienna, Austria); ammonium formate for mass spectrometry ≥99.0% and HPLC grade roxithromycin ≥90% (**4**) were from Sigma-Aldrich (Vienna, Austria); and Clerol FBA antifoam agent was from Cognis (Monheim, Germany). Nitrogen for mass spectrometry was produced on site by a nitrogen generator (PeakScientific Instruments, Fountain Crescent, UK). HPLC grade water was prepared on site.

Cultivation of *Metarhizium brunneum*, Preparation of Crude Extract, and Isolation of Reference Materials. *M. brunneum* strain BIPESCO 5 from the Innsbruck culture collection was cultivated in a D304 stirred tank bioreactor (NLF Bioengineering, Wald, Switzerland) containing SD medium supplemented with 2% glucose as previously described.[25] Destruxin enrichment was achieved by extraction of the culture filtrate with dichloromethane.[34] Aliquots of the culture filtrate were extracted five times with dichloromethane at a ratio of 3 volumes per volume culture filtrate. Combined organic layers were washed twice with 50 mL of water, dried with sodium sulfate, and evaporated to dryness. The obtained crude extract was stored at −20 °C until needed. Reference materials were isolated from this crude extract as described previously.[34]

Preparation of Stock Solutions and Standards. Calibration curves were obtained for a dilution series of **1**−**3** in acetonitrile as well as in strawberry and maize serving as matrix models. Starting from two stock solutions in acetonitrile containing a combination of **1**−**3**, a series of nine spike solutions for strawberries was prepared at the following concentrations: 0.1, 0.25, 0.5, 0.75, 1.0, 2.5, 5.0 7.5, and 10.0 μg/mL, each fortified with 1 μg/mL internal standard (IS) roxithromycin, **4**. On the basis of these spike solutions a second series for the maize samples was prepared by a 1:1 dilution in acetonitrile. Final calibration levels were obtained by adding 100 μL of the appropriate standard solution to 10 g of strawberry or 5 g of maize sample. Calibration levels in acetonitrile were obtained by a 1:100 dilution in acetonitrile of the spike solutions for strawberry samples.

For the production of quality control (QC) materials (assessment of precision and accuracy) a third stock solution in acetonitrile containing **1**−**3** was prepared. Four spike solutions for strawberry samples with concentration levels of **1**−**3** of 0.5, 1.0, 5.0, and 7.5 μg/mL were generated. A second series for maize samples was obtained by a 1:1 dilution of those spike solutions. Final QC materials were obtained by adding 100 μL of the appropriate spike solution to either strawberry or maize. For additional spike experiments a *M. brunneum* (BIPESCO 5) crude extract stock solution (100 μg extract/mL acetonitrile fortified with 1 μg/mL internal standard) was prepared. This stock was used without further dilution to spike the strawberry matrix; for maize samples it was further diluted 1:1 with acetonitrile.

QuEChERS-Based Sample Preparation Protocol. Sample preparation was based on a commercially available QuEChERS protocol (EN method 15662, buffered extraction tubes) (Agilent, Waldbronn, Germany). All crop materials were stored at −20 °C until used. Frozen strawberries were defrosted, mixed with a hand blender, and weighed (10 g ± 0.1 g) into a 50 mL extraction tube. Dry and frozen maize samples were ground in an MF10 basic mill (IKA Labortechnik, Staufen, Germany) and weighed (5 ± 0.1 g) into an extraction tube, and 10 mL of water was added. Samples for calibration curves and quality control material were prepared by spiking the appropriate amounts of spike solutions as described above. Real samples were imitated by spiking crude extract and internal standard solution (IS) into strawberry and maize samples. Ten milliliters of acetonitrile was added to the samples and vigorously shaken for 1 min, and the partitioning buffer salts (6 g of magnesium sulfate, 1 g of sodium chloride, 1 g of sodium citrate, 0.5 g of disodium citrate sesquihydrate) were added. The mixture was vigorously shaken for 1 min and subsequently centrifuged for 5 min at 1547*g*. An aliquot of 6 mL of the organic supernatant was transferred into a 15 mL centrifuge tube containing 150 mg of PSA, 45 mg of GCB, and 855 mg of $MgSO_4$ ("QuEChERS Dispersive Kit for HIGHLY Pigmented Fruits and Vegetables") (Agilent), vigorously shaken for 1 min, and centrifuged for 5 min at 1547*g*. An aliquot of 1 mL of the purified sample was transferred to an HPLC vial and either directly analyzed by UHPLC-QTOF-MS (strawberry samples) or evaporated to dryness, reconstituted in 500 μL of acetonitrile, and filtered through a 0.45 μm membrane filter prior to analysis (maize samples).

UHPLC-DAD Conditions. Chromatographic analyses were performed on the basis of a previously published method, which was slightly modified for the needs of this project.[25] A model 1200 UHPLC liquid chromatograph (Agilent) equipped with a diode array detector (DAD), an autosampler set at 10 °C, an automatic injector, and a column oven was used for all measurements. As stationary phase a 50 mm × 2.1 mm i.d., 1.8 μm particle size column, Zorbax Eclipse XDB-C18, guarded with an 0.2 μm pore size frit, 2.1 mm diameter in-line filter (Agilent), kept in a column oven at 40 °C, was applied.

DOI: 10.1021/acs.jafc.5b01562
J. Agric. Food Chem. 2015, 63, 5707−5713

Analyses were performed at a flow rate of 0.3 mL/min using a mobile phase consisting of water (A) and 95% acetonitrile (v/v) (B), each containing 10 mM ammonium formate, with the following gradient: 0 min, 75% A; 0.5 min, 75% A; 3.5 min, 60% A; 4.5 min, 50% A; 5.5 min, 35% A; 6.5 min, 5% A; 7.0 min, 2% A; 12 min, 2% A. Between runs the column was equilibrated with 75% A for 12 min. The injection volume was 2.5 μL, and chromatograms were recorded at 210 nm.

UHPLC-QTOF-MS Conditions. For the quantitative analysis of **1**−**3** UHPLC-QTOF-MS experiments were carried out using a micrOTOF-QII mass spectrometer (Bruker Daltonics, Bremen, Germany) hyphenated to the UHPLC-DAD instrument described above. Experiments were performed in positive ESI mode with the following ionizer and transfer parameters: capillary energy, 4500 V; nebulizer gas, 23.2 psi; dry gas, 6.0 L/min at a temperature of 200 °C; scan range, m/z 400−1000 with a scan rate of 2 Hz; quadrupole, ion energy 5 eV; low mass m/z 300.00; collision cell, collision energy 10 eV; transfer time, 40 μs; collision RF, 916.7 Vpp; prepulse storage, 16 μs; transfer, funnel 1 RF 200.0 Vpp, funnel 2 RF 395.2 Vpp, hexapole RF 500.0 Vpp. High-resolution mass calibration was facilitated by injecting 10 mM NaOH in isopropanol/water (1:1, v/v) fortified with 0.1% formic acid at the beginning of each analysis. The exact mass of the sodium formate clusters was used as calibrant. Destruxins were monitored by using the $[M + H]^+$ as quantifier ion and $[M + Na]^+$ as qualifier; for both ions the mass error had to better than 5 ppm.

Assay Validation for the Quantitative Analysis of Destruxins from Strawberry and Maize Samples. Calibration functions were obtained for a dilution series containing **1**−**3** and the internal standard roxithromycin, **4**, in acetonitrile as well as for a dilution series spiked in strawberry and maize matrix. Sample preparation of the matrix calibration levels was carried out using the QuEChERS protocol described above, and acetonitrile reference standards were used without further preparation steps. All calibration levels were analyzed in triplicates. Validation results were evaluated using the Bruker analysis software (QuantAnalysis version 2.0 SP4), and calibration functions were obtained for all three models. The limit of detection (LOD) and the limit of quantitation (LOQ) were calculated from the regression models including only the lowest four dilution levels. From the obtained regression equation data the LOD was calculated as 3 times the standard deviation (STD) of the y-intercept divided by the slope, whereas the LOQ was calculated as 10 times the STD of the y-intercept divided by the slope.[14,25,35]

The precision and accuracy of the method were assessed at four different concentration levels (covering the range of the calibration curve) by using spiked strawberry and maize matrix samples. All samples were prepared in triplicates; sample preparation was carried out using the QuEChERS protocol described above. For intra- and interday repeatability, samples were measured on three different days in triplicate. Precision was determined as the relative standard deviation (RSD) of the respective replicate measurements of the different levels; accuracy was expressed as percentage of recovery of the measured analyte concentration in relation to the spiked concentration.

RESULTS AND DISCUSSION

Internal Standard. As internal standards everolimus, cyclosporin A (both immunosuppressant), rifampicin (antibiotic drug of the rifamycin group), azithromycin (an azalide, a subclass of macrolide antibiotics), roxithromycin, and clarithromycin (both semisynthetic macrolide antibiotics) have been tested. All of them with the exception of roxithromycin showed either a loss of analyte during the sample preparation procedure, instability in the extraction solvent, elution in the wash phase of the method, or broad distorted peaks during chromatography. Finally, roxithromycin was chosen as internal standard, which showed a good recovery and was eluting in the retention time window between **1** and **2**.

Optimization of the Sample Preparation Protocol. Different sample preparation procedures to extract destruxin congeners from the crop matrices such as liquid−liquid extraction or solid phase extraction (SPE) protocols with various organic solvents were tested. For example, SPE over C18 materials, Supel Tox AflaZea, or Tricho SPE cartridges (Sigma-Aldrich, Vienna, Austria) has been evaluated. However, none of those procedures was suitable for destruxin analysis due to a loss of either analytes or the internal standard. Therefore, a QuEChERS-based protocol was chosen for sample preparation. Using this procedure achieved good recovery for the targeted analytes **1**−**3**, as well as for the chosen internal standard **4**.

Mixed strawberry (10 g) or ground maize (5 g) samples were weighed into the QuEChERS extraction tube and spiked with the internal standard. Depending on the matrix and its own water content, a specific volume of water had to be added to the sample to guarantee entire extraction of the analytes. In contrast to strawberry, which has a typical water content of approximately 90%, maize has a water content of only 10%. Therefore, homogenized maize samples were diluted with 2 mL water/g sample and mixed by vigorous shaking before the subsequent sample preparation. Extraction was carried out using 10 mL of acetonitrile followed by a partitioning step after the addition of a salt mixture. An aliquot of the organic layer was then purified by dispersive solid phase extraction (d-SPE) using the QuEChERS Dispersive Kit for HIGHLY Pigmented Fruits and Vegetables, which removes polar organic acids, some sugars and lipids, carotenoids, and chlorophyll.

UHPLC-QTOF-MS Assay Optimization. Analyses were performed using an Agilent 1200 UHPLC liquid chromatograph coupled to a micrOTOF-QII mass spectrometer with an electrospray ionization (ESI) interface operating in positive mode. For the initial method setup the MS was equipped with a syringe pump to enable experiments for the optimization of ionization parameters of the main metabolites **1**−**3**. Therefore, a destruxin standard solution of **1**−**3**, each at a concentration of 0.1 μg/mL, was directly infused into the mass spectrometer using a 500 μL syringe operating the syringe pump at a flow rate of 300 μL/h. UHPLC was operated at a flow rate of 0.1 mL/min with a solvent mixture of 20% water (A). To improve the ionization of analytes, the binary solvent system consisting of water (A) and acetonitrile (B) was modified while mass spectrometric parameters kept constant. Different concentrations of acetic acid, formic acid, ammonium formate, ammonium acetate, and mixtures were added to the mobile phase. Depending on the concentration of ammonium acetate and ammonium formate, it was necessary to add 2−5% water to completely dissolve the salt. Optimal conditions for ionization of analytes were obtained using water (A) and 95% acetonitrile (v/v) (B), each containing 10 mM ammonium formate, as mobile phase. This chromatographic setup was used for optimization of ion source parameters such as capillary voltage (3−5 kV), nebulizer gas (10−30 psi), dry gas flow (4−10 mL/min), and temperature (180−250 °C) as well as for optimization of further mass spectrometric parameters such as voltages of funnels (50−400 Vpp), of hexapole (50−800 Vpp), or collision cell (5−16 eV), as well as transfer (20−120 μs) and prepulse storage time (6−18 μs). Figure 2 shows the extracted ion chromatograms of destruxins, **1**−**3**, and the internal standard roxithromycin, **4**, under optimized chromatographic and mass spectrometric conditions.

Assay Validation for the Quantitative Analysis of Destruxins from Strawberry and Maize Samples. Assay

DOI: 10.1021/acs.jafc.5b01562
J. Agric. Food Chem. 2015, 63, 5707−5713

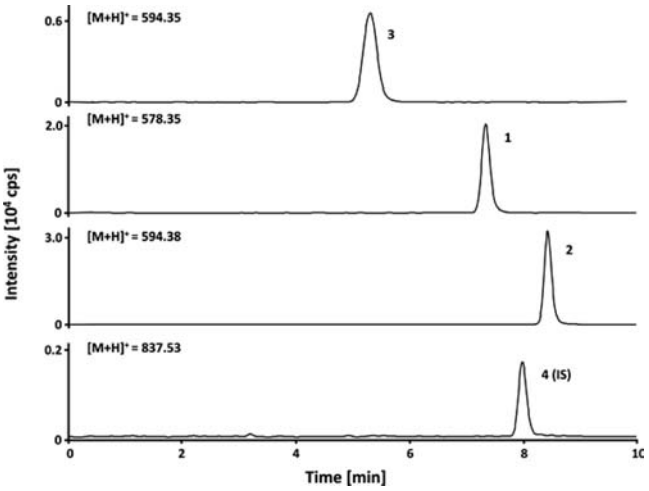

Figure 2. UHPLC-QTOF-MS extracted ion chromatograms of the main metabolites **1**−**3** (each 50 ng/mL) and the internal standard roxithromycin (10 ng/mL) in acetonitrile under optimized chromatographic and mass spectrometric conditions.

validation was performed with a dilution series containing destruxins, **1**−**3**, and the internal standard roxithromycin, **4**, in acetonitrile as well as with a dilution series spiked in strawberry and maize matrix. Calibration levels in acetonitrile were analyzed without further treatment, whereas matrix samples were prepared using the described QuEChERS-based extraction protocol. All solutions were measured in triplicates. During sample workup sample dilution was chosen such that nanogram per milliliter concentrations in solution correspond to parts per billion (ppb; μg analyte/kg matrix) concentrations in the matrix. Calibration curve equations were generated resulting in quadratic functions with correlation coefficient values (R^2) exceeding 0.999. Calibration ranges were found to be valid from 1.0 to 100.0 ng/mL (corresponding to ppb in spiked matrix) for destruxins, **1**−**3**, for all three matrices with the exception of destruxin E in maize ranging from 2.5 to 100.0 ng/mL (ppb). LOD and LOQ ranged from <1.0 to 1.4 ng/mL and from 1.7 to 4.3 ng/mL, respectively, for the analytical assay, with nanograms per milliliter corresponding to parts per billion. Precision and accuracy of the method were assessed using spiked matrix samples of four different concentration levels, each in triplicates. Intraday and interday assay precisions of all levels of destruxins, **1**−**3**, in strawberry samples were found to be <11.2% RSD and <10.7% RSD, respectively. Accuracy of strawberry samples was found to be between 82.3 and 105.0% for destruxins A and B and between 83.2 and 97.7% for destruxin E, independent of the calibrator matrix used for quantitative analysis (Table 1).

For all but the lowest fortification level, intraday RSDs for destruxins A and B in maize ranged between 4.0 and 15.3% and interday RSDs between 8.6 and 12.8%, whereas precision of the measurement was lowered for the fortification level close to the LOQ with intraday and interday RSDs better than 24%. In the case of destruxin E, assay precision for all fortification levels was found to be between 7.3 and 26.7% for intraday RSD and <23.9% for interday RSD, which indicated a loss of the

Table 1. Results for Assay Accuracy and Intraday and Interday Precision Using Spiked Strawberry Matrix Samples[a]

			RSD (%)				accuracy (%)			
analyte	matrix	level[b] (ng/mL)	day 1	day 2	day 3	days 1−3	day 1	day 2	day 3	days 1−3
destruxin A	acetonitrile	5	4.5	9.1	11.2	10.7	89.8	104.0	92.9	95.7
		10	4.4	10.2	7.2	7.9	97.5	104.0	103.5	101.4
		50	4.0	8.3	8.1	7.7	89.7	97.4	94.6	93.9
		75	4.2	7.1	6.6	6.1	101.6	105.0	101.4	102.7
destruxin B	acetonitrile	5	4.0	5.9	6.2	7.6	94.0	103.2	90.8	96.2
		10	3.6	10.3	9.2	8.1	97.5	101.2	96.9	98.6
		50	3.2	8.3	6.0	6.8	94.9	99.2	92.1	95.4
		75	3.6	7.1	9.4	7.3	104.7	101.0	97.5	101.1
destruxin E	acetonitrile	5	5.1	5.3	2.2	4.7	84.9	86.7	83.2	85.1
		10	6.3	6.2	9.4	7.1	93.1	91.9	92.8	92.6
		50	3.9	4.2	7.0	5.1	87.5	88.9	89.0	88.5
		75	4.4	5.2	11.1	7.3	93.4	91.4	92.5	92.4
destruxin A	strawberry	5	0.6	9.3	5.6	7.9	82.3	92.0	86.4	86.9
		10	4.6	10.8	8.0	9.1	88.0	96.9	93.7	92.8
		50	3.5	7.8	7.6	7.2	82.9	89.7	86.8	86.5
		75	5.0	7.1	10.0	7.5	92.6	95.5	94.8	94.3
destruxin B	strawberry	5	5.3	5.9	5.0	7.8	87.6	97.6	86.2	90.6
		10	4.6	10.9	10.3	8.8	95.0	98.5	95.2	96.3
		50	2.8	7.8	5.8	6.6	93.3	97.0	89.6	93.3
		75	4.0	7.0	8.3	7.1	101.2	97.1	93.8	97.4
destruxin E	strawberry	5	5.4	5.0	4.1	5.5	87.1	89.9	85.3	87.5
		10	7.0	5.8	6.3	6.2	97.7	96.9	95.7	96.8
		50	3.3	4.1	6.4	4.7	92.6	93.5	93.5	93.2
		75	5.1	4.9	5.3	5.2	97.6	95.3	93.6	95.6

[a]Three samples were prepared for each fortification level (n = 12), and each sample was measured 3-fold on three different days (n = 9). Precision and accuracy were calculated using the calibration curve in either acetonitrile or crop matrix. [b]Analyte concentration in the final sample solution. It corresponds to ppb analyte in matrix.

DOI: 10.1021/acs.jafc.5b01562
J. Agric. Food Chem. 2015, 63, 5707−5713

Table 2. Results for Assay Accuracy and Intraday and Interday Precision Using Spiked Maize Matrix Samples[a]

			RSD (%)				accuracy (%)			
analyte	matrix	level[b] (ng/mL)	day 1	day 2	day 3	days 1−3	day 1	day 2	day 3	days 1−3
destruxin A	acetonitrile	5	11.7	11.3	20.7	14.7	90.1	83.3	82.4	85.4
		10	4.6	12.1	9.1	8.6	88.2	87.3	87.5	87.7
		50	11.0	11.9	6.0	10.6	85.8	86.2	78.9	83.6
		75	6.8	12.9	13.6	12.1	88.4	87.4	97.0	90.7
destruxin B	acetonitrile	5	9.1	13.3	23.6	17.1	102.6	93.6	82.9	93.1
		10	10.3	11.2	8.5	10.6	98.2	93.8	87.8	93.6
		50	9.8	9.0	5.0	9.9	90.0	87.5	78.7	85.4
		75	8.4	13.8	15.3	12.8	89.8	86.6	94.7	90.2
destruxin E	acetonitrile	5	14.6	11.1	21.1	16.7	29.8	27.8	25.2	27.6
		10	26.7	22.7	24.2	23.9	32.0	29.9	27.9	30.0
		50	13.4	12.6	8.8	12.5	32.9	31.3	29.1	31.1
		75	12.6	9.2	23.2	18.0	43.1	40.4	48.0	43.8
destruxin A	maize	5	12.8	11.2	14.2	13.3	93.2	87.7	81.2	87.8
		10	5.0	12.6	10.0	9.1	96.3	95.9	95.1	95.8
		50	10.5	10.6	4.4	9.7	91.2	92.0	84.3	89.2
		75	5.9	12.0	12.2	10.9	91.4	90.0	99.2	93.3
destruxin B	maize	5	15.6	18.2	20.3	19.0	115.4	103.2	94.6	104.8
		10	10.5	11.9	10.0	11.5	111.2	105.9	97.6	105.3
		50	9.8	9.0	4.0	9.8	97.9	95.1	85.6	92.9
		75	8.4	14.1	15.3	12.7	96.8	92.1	99.5	96.0
destruxin E	maize	5	9.8	7.4	14.9	13.0	75.2	68.3	62.3	68.6
		10	21.6	19.9	18.9	19.6	69.9	66.2	63.0	66.6
		50	12.4	11.2	7.3	11.2	61.4	59.4	55.3	58.7
		75	10.6	7.9	19.2	14.8	74.8	70.7	81.7	75.7

[a]Three samples were prepared for each fortification level (n = 12), and each sample was measured 3-fold on three different days (n = 9). Precision and accuracy were calculated using the calibration curve in either acetonitrile or crop matrix. [b]Analyte concentration in the final sample solution. It corresponds to ppb analyte in matrix.

respective metabolite. Accuracy of destruxins A and B in maize samples ranged from 78.7 to 115.4%, but was strongly reduced for destruxin E (Table 2). Depending on the calibration curve used for calculation, destruxin E accuracy ranged from 25.2 to 48.0% (calibration in acetonitrile) and from 55.3 to 81.7% (calibration in spiked matrix samples); destruxin E is underestimated up to approximately 45% even if the quantitative analysis is based on matrix-matched calibrators. In summary, it can be stated that accuracy and precision data proved the internal standard fortified assay design to be matrix independent with the exception of destruxin E in maize matrix, for which severe analyte loss was observed. For all analytes except destruxin E in maize, the analytical sensitivity (slope of the calibration function) in standard solution (acetonitrile) was identical to the matrix materials. This as well as validation results proves that the QuEChERS-based extraction protocol is suitable for the application in strawberry and (with some limitations) maize. This was additionally proved by spike experiments using a stock solution of a dichloromethane crude extract (BIPESCO 5) and the internal standard. Samples were prepared in both matrices and as reference in acetonitrile. Even if the complete removal of more polar maize constituents was not achieved (Figure 3), destruxin congeners were completely extracted from all matrices.

Because recoveries of the structurally similar destruxins A and B from maize were satisfying, the loss of destruxin E (Figure 44) in this matrix may be explained with either the obvious structural differences of this congener featuring a chemically highly reactive epoxide moiety in the variable side chain or the presence of additional polar constituents in this crop leading to a matrix-related detection problem (e.g., an ion yield attenuation effect). Consequently, in maize the quantitative analysis of destruxin congeners has to be limited to destruxins A and B, which are, however, major metabolites of

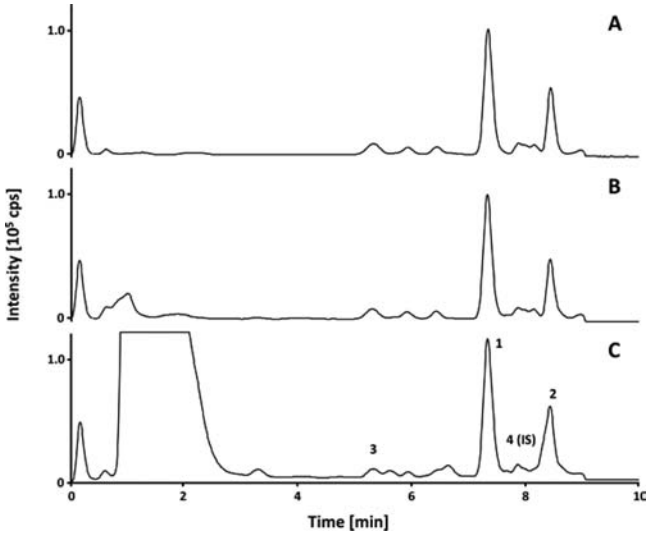

Figure 3. Representative UHPLC-QTOF-MS base peak chromatogram of spike experiments using a stock solution of crude extract (BIPESCO 5) and the internal standard roxithromycin, **4** (IS): (A) reference of crude extract stock solution and IS in acetonitrile; (B) spiked strawberry sample; (C) spiked maize sample. Final concentrations of crude extract and **4** in matrix samples were 1000 and 10 ppb, respectively (corresponding to ng/mL in the analysis solution).

DOI: 10.1021/acs.jafc.5b01562
J. Agric. Food Chem. 2015, 63, 5707−5713

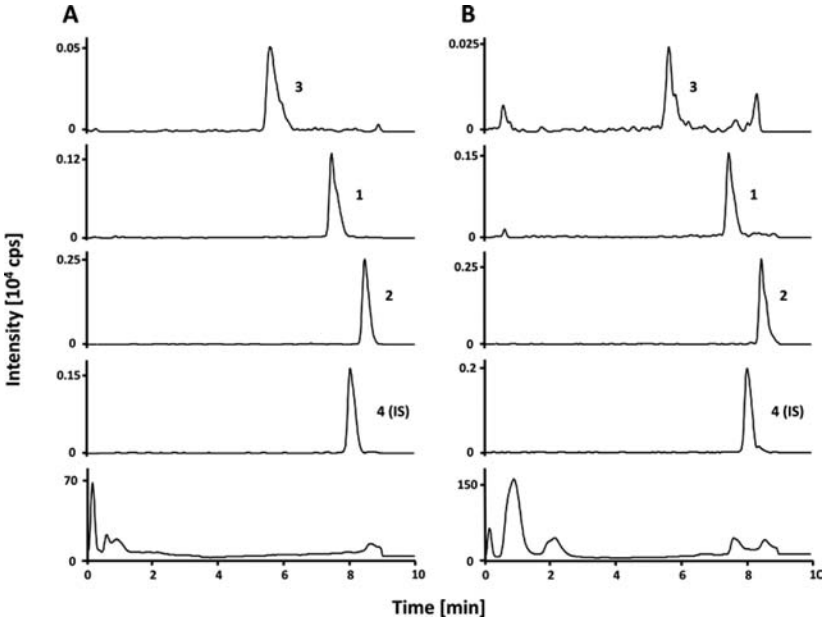

Figure 4. Representative UHPLC-QTOF-MS ion trace (top rows) and base peak (bottom rows) chromatograms of a 5 ppb (destruxins **1**−**3**) spike experiment into (A) strawberry and (B) maize matrices (ppb corresponds to ng/mL in the analysis solution).

the investigated *M. brunneum* strains and therefore can be used as surrogate markers for the presence of this fungus or its secondary metabolites in the investigated matrices.[14,19,22,25,34]

Consequently, we consider this platform as a new sensitive, precise, accurate, and stable method for routine risk assessment of the use of *M. brunneum* as BCA in food production. It allows monitoring the presence of destruxins in crop products in the lower parts per billion range.

■ ASSOCIATED CONTENT

Supporting Information

Supplemental Table S1. The Supporting Information is available free of charge on the ACS Publications website at DOI: 10.1021/acs.jafc.5b01562.

■ AUTHOR INFORMATION

Corresponding Author

*(S.S.) Phone: 0043 512 507 58408. Fax: 0043 512 507 58499. E-mail: sonja.sturm@uibk.ac.at.

Funding

This research has been supported by the European Community's Seventh Framework Programme Grant FP7_ENV.2011.3.1.9-1 ECO-INNOVATION, INBIOSOIL (Grant Agreement 282767).

Notes

The authors declare no competing financial interest.

■ REFERENCES

(1) Bischoff, J. F.; Rehner, S. A.; Humber, R. A. A multilocus phylogeny of the *Metarhizium anisopliae* lineage. *Mycologia* **2009**, *101*, 512−530.

(2) Kepler, R. M.; Rehner, S. A. Genome-assisted development of nuclear intergenic sequence markers for entomopathogenic fungi of the *Metarhizium anisopliae* species complex. *Mol. Ecol. Resour.* **2013**, *13*, 210−217.

(3) Petzold-Maxwell, J. L.; Jaronski, S. T.; Clifton, E. H.; Dunbar, M. W.; Jackson, M. A.; Gassmann, A. J. Interactions among Bt maize, entomopathogens, and rootworm species (Coleoptera: Chrysomelidae) in the field: effects on survival, yield, and root injury. *J. Econ. Entomol.* **2013**, *106*, 622−632.

(4) N.N. (2011) Commission implementing regulation (EU) No. 540/2011 of 25 May 2011 implementing Regulation (EC) No. 1107/2009 of the European Parliament and of the Council as regards the list of approved active substances, OJEU, L 153/1-186. URL (http://eur-lex.europa.eu/LexUriServ/LexUriServ.do?uri=OJ:L:2011:153:0001:0186:EN:PDF) (accessed Jan 23, 2015).

(5) Zimmermann, G. Review on safety of the entomopathogenic fungus *Metarhizium anisopliae*. *Biocontrol Sci. Technol.* **2007**, *17*, 879−920.

(6) Dornetshuber-Fleiss, R.; Heffeter, P.; Mohr, T.; Hazemi, P.; Kryeziu, K.; Seger, C.; Berger, W.; Lemmens-Gruber, R. Destruxins: fungal-derived cyclohexadepsipeptides with multifaceted anticancer and antiangiogenic activities. *Biochem. Pharmacol.* **2013**, *86*, 361−377.

(7) Dumas, C.; Matha, V.; Quiot, J. M.; Vey, A. Effects of destruxins, cyclic depsipeptide mycotoxins, on calcium balance and phosphorylation of intracellular proteins in lepidopteran cell lines. *Comp. Biochem. Physiol., Part C: Pharmacol., Toxicol. Endocrinol.* **1996**, *114*, 213−219.

(8) Hinaje, M.; Ford, M.; Banting, L.; Arkle, S.; Khambay, B. An investigation of the ionophoric characteristics of destruxin A. *Arch. Biochem. Biophys.* **2002**, *405*, 73−77.

(9) Nakagawa, H.; Takami, M.; Udagawa, N.; Sawae, Y.; Suda, K.; Sasaki, T.; Takahashi, N.; Wachi, M.; Nagai, K.; Woo, J. T. Destruxins, cyclodepsipeptides, block the formation of actin rings and prominent clear zones and ruffled borders in osteoclasts. *Bone* **2003**, *33*, 443−455.

(10) Pedras, M. S. C.; Irina Zaharia, L.; Ward, D. E. The destruxins: synthesis, biosynthesis, biotransformation, and biological activity. *Phytochemistry* **2002**, *59*, 579−596.

(11) Tsunoo, A.; Kamijo, M. Non-cyclic AMP-dependent, positive inotropic cyclodepsipeptides with negative chronotropy. *J. Pharmacol. Exp. Ther.* **1999**, *290*, 1006−1012.

(12) Strasser, H.; Hutwimmer, S.; Burgstaller, W. Metabolite toxicology of fungal biocontrol agents. In *Regulation of Biological Control Agents*; Ehlers, R.-U., Ed.; Springer: Dordrecht, The Netherlands, 2011; pp 191−213.

(13) Strauch, O.; Strasser, H.; Hauschild, R.; Ehlers, R.-U. Proposals for bacterial and fungal biocontrol agents. In *Regulation of Biological Control Agents*; Ehlers, R.-U., Ed.; Springer: Dordrecht, The Netherlands, 2011; pp 267−288.

DOI: 10.1021/acs.jafc.5b01562
J. Agric. Food Chem. 2015, 63, 5707−5713

(14) Seger, C.; Sturm, S.; Stuppner, H.; Butt, T. M.; Strasser, H. Combination of a new sample preparation strategy with an accelerated high-performance liquid chromatography assay with photodiode array and mass spectrometric detection for the determination of destruxins from *Metarhizium anisopliae* culture broth. *J. Chromatogr. A* **2004**, *1061*, 35−43.
(15) Buchwaldt, L.; Jensen, J. HPLC purification of destruxins produced by *Alternaria brassicae* in culture and leaves of *Brassica napus*. *Phytochemistry* **1991**, *30*, 2311−2316.
(16) Jegorov, A.; Havlícek, V.; Sedmera, P. Rapid screening of destruxins by liquid chromatography/mass spectrometry. *J. Mass Spectrom.* **1998**, *33*, 274−280.
(17) Jegorov, A.; Paizs, B.; Zabka, M.; Kuzma, M.; Havlícek, V.; Giannakopulos, A. E.; Derrick, P. J. Profiling of cyclic hexadepsipeptides roseotoxins synthesized in vitro and in vivo: a combined tandem mass spectrometry and quantum chemical study. *Eur. Mass Spectrom.* **2003**, *9*, 105−116.
(18) Kershaw, M. J.; Moorhouse, E. R.; Bateman, R.; Reynolds, S. E.; Charnley, A. K. The role of destruxins in the pathogenicity of *Metarhizium anisopliae* for three species of insect. *J. Invertebr. Pathol.* **1999**, *74*, 213−223.
(19) Loutelier, C.; Cherton, J.-C.; Lange, C.; Traris, M.; Vey, A. Studies on the dynamics of the production of destruxins by *Metarhizium anisopliae* Direct high-performance liquid Chromatographic and fast atom bombardment mass spectrometric analysis correlated with biological activity tests. *J. Chromatogr. A* **1996**, *738*, 181−189.
(20) Potterat, O.; Wagner, K.; Haag, H. Liquid chromatography−electrospray time-of-flight mass spectrometry for on-line accurate mass determination and identification of cyclodepsipeptides in a crude extract of the fungus *Metarhizium anisopliae*. *J. Chromatogr. A* **2000**, *872*, 85−90.
(21) Wang, C.; Skrobek, A.; Butt, T. M. Concurrence of losing a chromosome and the ability to produce destruxins in a mutant of *Metarhizium anisopliae*. *FEMS Microbiol. Lett.* **2003**, *226*, 373−378.
(22) Wang, C.; Skrobek, A.; Butt, T. M. Investigations on the destruxin production of the entomopathogenic fungus *Metarhizium anisopliae*. *J. Invertebr. Pathol.* **2004**, *85*, 168−174.
(23) Morais, R. P.; Lira, S. P.; Seleghim, M. H. R.; Berlinck, R. G. S. A method for dextruxin analysis by HPLC-PDA-ELSD-MS. *J. Braz. Chem. Soc.* **2010**, *21*, 2262−2271.
(24) Hsiao, Y.; Ko, J. Determination of destruxins, cyclic peptide toxins, produced by different strains of *Metarhizium anisopliae* and their mutants induced by ethyl methane sulfonate and ultraviolet using HPLC method. *Toxicon* **2001**, *39*, 837−841.
(25) Taibon, J.; Sturm, S.; Seger, C.; Parth, M.; Strasser, H.; Stuppner, H. Development of a fast and selective UHPLC-DAD-QTOF-MS/MS method for the qualitative and quantitative assessment of destruxin profiles. *Anal. Bioanal. Chem.* **2014**, *406*, 7623−7632.
(26) Liu, C.-M.; Huang, S.-S.; Tzeng, Y.-M. Analysis of destruxins produced from *Metarhizium anisopliae* by capillary electrophoresis. *J. Chromatogr. Sci.* **2004**, *42*, 140−144.
(27) Skrobek, A.; Shah, F. A.; Butt, T. M. Destruxin production by the entomogenous fungus *Metarhizium anisopliae* in insects and factors influencing their degradation. *BioControl* **2008**, *53*, 361−373.
(28) Anastassiades, M.; Lehotay, S. J.; Stajnbaher, D.; Schenck, F. J. Fast and easy multiresidue method employing acetonitrile extraction/partitioning and "dispersive solid-phase extraction" for the determination of pesticide residues in produce. *J. AOAC Int.* **2003**, *86*, 412−431.
(29) Lehotay, S. J.; Son, K. A.; Kwon, H.; Koesukwiwat, U.; Fu, W.; Mastovska, K.; Hoh, E.; Leepipatpiboon, N. Comparison of QuEChERS sample preparation methods for the analysis of pesticide residues in fruits and vegetables. *J. Chromatogr. A* **2010**, *1217*, 2548−2560.
(30) Lehotay, S. J. QuEChERS sample preparation approach for mass spectrometric analysis of pesticide residues in foods. *Methods Mol. Biol.* **2011**, *747*, 65−91.
(31) Lehotay, S. J.; Mastovská, K.; Yun, S. J. Evaluation of two fast and easy methods for pesticide residue analysis in fatty food matrixes. *J. AOAC Int.* **2005**, *88*, 630−638.
(32) Lehotay, S. J.; Mastovská, K.; Lightfield, A. R. Use of buffering and other means to improve results of problematic pesticides in a fast and easy method for residue analysis of fruits and vegetables. *J. AOAC Int.* **2005**, *88*, 615−629.
(33) AOAC Official Method 2007.01. Pesticide residues in foods by acetonitrile extraction and partitioning with magnesium sulfate. Gas chromatography /mass spectrometry and liquid chromatography/tandem mass spectrometry; http://www.weber.hu/PDFs/QuEChERS/AOAC_2007_01.pdf (accessed Jan 23, 2015).
(34) Seger, C.; Eberhart, K.; Sturm, S.; Strasser, H.; Stuppner, H. Apolar chromatography on Sephadex LH-20 combined with high-speed counter-current chromatography. High yield strategy for structurally closely related analytes-Destruxin derivatives from *Metarhizium anisopliae* as a case study. *J. Chromatogr. A* **2006**, *1117*, 67−73.
(35) N.N. (2006) ICH Harmonized Tripartite Guideline Validation of Analytical Procedures: Text and Methodology *Q2(R1)*; http://www.ich.org/fileadmin/Public_Web_Site/ICH_Products/Guidelines/Quality/Q2_R1/Step4/Q2_R1__Guideline.pdf) (accessed March 23, 2015).

DOI: 10.1021/acs.jafc.5b01562
J. Agric. Food Chem. 2015, 63, 5707−5713

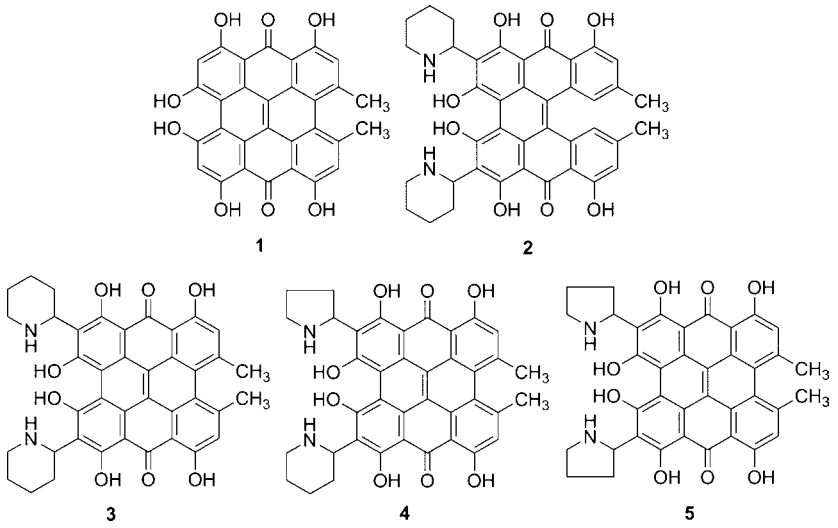

Figure 1. Structures of hypericin (**1**), protofagopyrin (**2**), fagopyrin A (**3**), fagopyrin E (**4**), and fagopyrin F (**5**).

Figure 1 are currently known, five yet remaining to be elucidated.

Melting Point. The melting points of two isolated, incompletely purified, and unidentified fagopyrins were tested. One of them did not melt at 375 °C, whereas the other melted at 375 °C, but did not melt sharply, suggesting that the product was impure.[19]

Chemical Reactivity. Many contradictions on the chemical reactivity of fagopyrins exist among different studies. Chick[21] reported that the extracts became inactive in the terms of phototoxicity, tested on rats, after treatment of the extracts with heat and alkaline solvents such as sodium bicarbonate, diethylene glycol, enzymatic digestion with trypsin, boiling ethyl alcohol, and, to our surprise, even ethanol, which is not entirely in accordance with other data, where fagopyrins were not soluble in or sensitive to ethanol. The findings by Chick were later confirmed only in part, when the alkaline hydrolysis of fagopyrins to hypericin-like compounds was observed in ammonia and pyridine solutions. In contrast, acidic conditions slowed the conversion of protofagopyrins to fagopyrins but did not affect the short-term stability of fagopyrins.[20] On the basis of thin-layer chromatography (TLC), fagopyrins hydrolyze to a compound that is similar to hypericin when heated with pyridinium chloride at 220 °C.[22,23] Bromination of fagopyrin and hypericin resulted in the same product, from which it can be suggested that during bromination, fagopyrins are hydrolyzed.[24]

IR Spectrum. The IR spectrum of fagopyrins exhibited a broad band at 3350−3450 cm^{-1} (OH groups) and strong bands at 2850 and 2925 cm^{-1} (CH_2 groups from the piperidine side chain) and at 1600 cm^{-1} (carbonyl groups associated through hydrogen bonding).[23]

UV−Visible Spectrum. In the UV−visible spectrum, the absorption maxima of all eight fagopyrins occur at 284, 329, 545, and 590 nm.[20,25]

Fluorescence. Fagopyrins fluoresce orange to red under UV light at 366 nm. Fluorescence detection using an excitation wavelength of 330 nm and an emission wavelength of 590 nm is more sensitive than UV−vis detection.[20]

Protofagopyrin Transformation. Many authors observed the transformation of "invisible" molecular forms, termed protofagopyrins (Figure 1), to "visible" fagopyrins upon excitation with light.[20,22,26] They declared that protofagopyrins do not fluoresce and exhibit low absorption. Although the structural elucidation of protofagopyrins has not yet been performed, substantial evidence supports their existence. There are two theories about the presence of fagopyrins and their protoforms in buckwheat plant. The first is that fagopyrins and their protoforms are both present in the plant, analogously to hypericin and protohypericin. The second is that the compounds convert only after solubilization in the extraction solvent and that protofagopyrins are the only genuine plant products. We believe there is more evidence for the second theory, which we prove in the following section.

The second theory is supported by the experiment where protofagopyrins were observed in a light-protected extract sample using an HPLC-DAD instrument as a weak signal at 590 nm; they showed retention times similar, but not equal, to those of fagopyrins from an identical but light-exposed sample. Before light exposure, there were no fagopyrin peaks in the sample. In the UV−vis spectra, a strong absorbance maximum at 590 nm was observed upon exposure to light, indicating the formation of fagopyrins. Simultaneously, the compounds began to fluoresce (excitation at 330 nm and emission at 590 nm). The reaction was not reversible under normal light−darkness conditions. In another study it was deduced that the reactivity of protofagopyrins could be decreased because of piperidine rings and the esterification or etherification of para-hydroxyl groups with phenols, naphthols, anthranols, or other molecules.[22] Due to the ease of acid hydrolysis, 7,7′-hydroxy glycoside esters were postulated to be present in the plant. These moieties could in fact affect the solubility of the substances, which was observed in one of the experiments: The extraction of fagopyrins with acetone resulted in fagopyrin-rich extracts, but, when dry, the fagopyrins became insoluble in the same solvent.[22] The fact that other buckwheat moieties may help to solubilize fagopyrins was further supported by animal studies, in which buckwheat extract exhibited more activity than the purified pigment, which appeared to be insoluble.[21]

In contrast to the second theory, Samel[23] did not observe the transformation of protofagopyrins to fagopyrins in the UV−vis absorption spectra of an irradiated purified extract. Their experiment seemed to disprove the occurrence of chemical conversions from protofagopyrins to fagopyrins. However, from

DOI: 10.1021/acs.jafc.5b01163
J. Agric. Food Chem. 2015, 63, 5715−5724

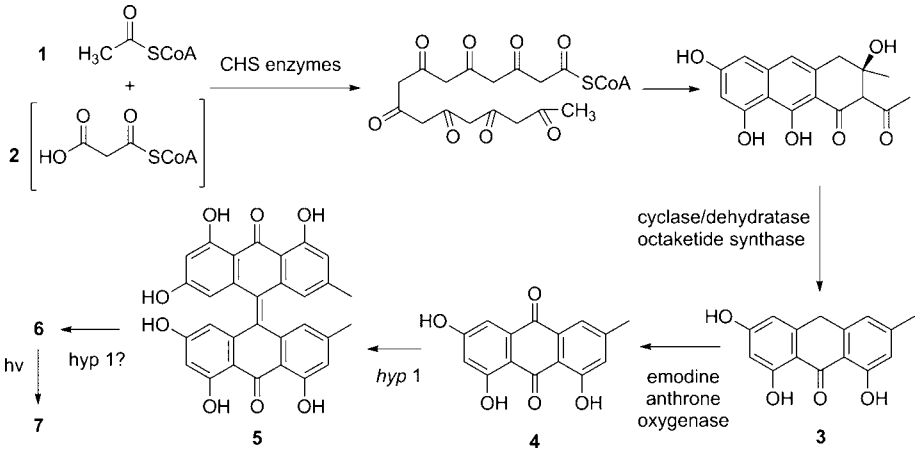

Figure 2. Possible route of fagopyrin biosynthesis:[28] acetyl coenzyme A (1), malonyl coenzyme A (2), emodianthrone (3), emodine (4), emodine dianthrone (5), protofagopyrin (6), and fagopyrin (7).

his description, we can deduce that the initial unpurified extract changed from yellow to red over a period of 2 days. We believe that the majority of the substance had already been converted at that point, which resulted in the false conclusions of a later experiment.[23]

To conclude, many comparisons between protohypericins and protofagopyrins have been made, but we believe that the conversions of these two compound classes do not occur in the same manner. We conclude that the OH groups of hypericin are not shielded with piperidine rings, whereas those of fagopyrins are, so the more reactive protohypericin readily transforms to hypericin in plants, whereas fagopyrins develop only after solubilization, upon light exposure.[27]

Biosynthesis. By analogy with the biosynthesis of other phenolic compounds, the chalcone synthase- and benzophenone synthase-related polyketide pathway (type III PKS) was predicted to be the most probable fagopyrin synthesis pathway (Figure 2). The polyketide chain that generates aromatic ring compounds is formed from acetate and malonate units by an enzyme complex, known as polyketide synthase. The precursor to protofagopyrin is emodin anthrone, which is generated by the condensation of one acetyl coenzyme A molecule and seven malonyl coenzyme A molecules. Emodin anthrone is further oxidized to emodin by emodin anthrone oxygenase and is condensed to dianthrone. The last conversion from protofagopyrin to fagopyrin occurs during extraction from the herb upon exposure to light.[28] Similar findings were confirmed for hypericin.[29] Unfortunately, the authors did not discuss the biosynthetic processes from which the structural differences between fagopyrin and hypericin (e.g., attachment of piperidine rings) arise. This information might be useful for the design of fagopyrin synthesis on the basis of hypericin synthesis.[30,31]

Solubility and Extraction Solvents. A variety of different extraction solvents was tested with fagopyrins, as summarized in Table 5. Previous authors agree that fagopyrins are insoluble in polar solvents and in organic solvents that possess no hydroxyl groups. Most authors reported efficient solubility in protic organic solvents, mixtures of aprotic solvents with water, pyridine, and dimethylformamide. As shown in Table 1, the results of different investigators are not always in agreement. For example, Tavčar Benković et al.[20] could not confirm the solubility of fagopyrins in ether or chloroform as indicated by Wender et al.[19] These contradictions confirm that the effective solubility of fagopyrins in a certain solvent is highly influenced by other parameters, such as light exposure, temperature, and the presence of chlorophylls, polyphenols, or presumed esters and ethers of fagopyrins. The analytical methods used to determine the fagopyrin content were also different and not always appropriate, a consideration that is discussed in detail in other sections of this paper

Structural Elucidation. Many authors observed three different fagopyrin pigments and speculated that (as for hypericin, isohypericin, and pseudohypericin) these pigments could represent fagopyrin, isofagopyrin, and pseudofagopyrin. A molecular structure of fagopyrin with two piperidine groups was first elucidated through chromatographic separation and by the NMR spectral analysis of fagopyrins that were acetylated with acetic anhydride and pyridine.[24] The structure was later confirmed by analyzing the pure compound, which was termed fagopyrin F. Two additional novel structures were elucidated (fagopyrins A and E) by using UV−vis absorption, NMR spectroscopy, and mass spectrometry. The aforementioned isofagopyrin and pseudofagopyrin forms were not confirmed, but at least five additional structures are reported to be in need of elucidation.[20]

Mass Spectrometric Analyses. The following fragments were observed in positive spectra of LC-MS TOF ESI analysis:[20,25] fagopyrin A, *m/z* 643, 626, 625, 609, 574, 70; fagopyrin E, *m/z* 657, 640, 639, 622, 588, 84, 70; fagopyrin F, *m/z* 671, 654, 653, 636, 588, 84.

NMR Analyses. The signals that were observed in the NMR spectrum of fagopyrins F, E, and A are presented in Table 2.

■ ISOLATION ATTEMPTS

The first isolation of fagopyrins was performed using an alcohol extraction; subsequent precipitation of chlorophyll with lead acetate and boiling with lead oxide yielded a fluorescent substance that was not further evaluated.[32] Many further attempts to isolate the red pigment have been undertaken, as described in Table 3.

Although the isolation of pure fagopyrins had already been reported in 1943, the product did not melt sharply, which indicated the presence of impurities.[19] The most promising isolation approach appears to be reported by Samel,[23] but our unpublished reproduction of their procedure was unsuccessful, as we were unable to elute a fluorescent fraction from silica gel 60 with any solvent.[23] In all reported isolation attempts, effective extraction solvents for fagopyrins are evidently highly

DOI: 10.1021/acs.jafc.5b01163
J. Agric. Food Chem. 2015, 63, 5715−5724

Table 1. Solubility of Fagopyrins in Different Solvents

							Wender[59] very ++++, quite +++, somewhat ++, slightly +		
solvent	Chick[21]	Brockmann[22]	Hinneburg[33]	Eguchi[25]	Hagels[58]	Tavčar Benković[20]	fagopyrin A	fagopyrin B	fagopyrin C
acetone	−				+	−		+++	++++
acetone/pyridine (9:1)						+			
acetone/water (9:1) and (4:1)						+			
acetone/water/acetic acid (8:1:1)		+		+		+			
acetonitrile						−			
acetonitrile/water (2:1)						+			
amyl alcohol								+++	
benzene	−							++	
butanol		+							
chloroform	−					−	+	++	
dimethyl sulfoxide						+			
dimethyl sulfoxide/methanol (1:1)						+			
dimethylformamide						+			
dioxane	−								
EDTA									
ethanol (>70%)	−		+			+			+
ether	−	−				−		++	++++
ethyl acetate						−		++	
ethylene glycol	−								
formic acid								+++	
glacial acetic acid	−						+	++++	++++
glycerol	−								
glycol with 10% acetic acid	+								
hydrochloric acid	+								
isopropanol						−			
light petroleum	−								
methanol		+ −	+	+		+ −	−	++	+
methanol with 10% acetic acid	+								
methylglycol		+							
olive oil							++		
pepsin	+								
phenol		+							
piperidine		+							
pyridine		+				+	+++		
pyroboric acetate		+							
sodium hydroxide, alcoholic 10%		+					+	+	
sodium hydroxide, water		−							
sulfuric acid (strong acidic solutions)		+							
tetrahydrofuran		+				−			
toluene						−			
water	−					−			

Table 2. Signals of Fagopyrins in the NMR (d-DMSO) Spectrum[20,24]

^{1}H NMR	^{13}C NMR	group	fagopyrins
sharp singlet at δ 2.7	23.5 ppm	methyl groups bound to C3 and C4	F, E, A
singlet at δ 7.543	119.4 ppm	H2, C2; and H5, C5	F, E, A
multiplet at 4.89 ppm	52 ppm	methine protons of piperidine units connected to C9 and C12 of the aromatic core of the molecule	F, E
1.7−2.1 ppm		part of piperidine spin system	F, E
5.32 ppm		methine protons of pyrrolidines on C9 and C12	E, A

unspecific and are difficult to evaporate due to their high boiling points. Given the need to evaporate the solvent, we conclude that the best extraction solvent is acetone/water (9:1). A higher temperature (60 °C) and the use of ultrasound can significantly accelerate the extraction procedure. Protofagopyrins are probably extractable with many organic solvents (methanol, acetone) before transformation, but no analytical method is available to examine this process due to the "invisibility" of the compounds. Besides fagopyrins, buckwheat contains high amounts of chlorophyll (especially in the leaves and flowers), anthocyanins, and other polyphenols. Hence, yellow, red, and green fractions were difficult to remove in most studies. The best solvent for chlorophyll removal is dichloromethane, and some flavonoids can be removed with 30% ethanol. Flowers are a superior extraction material compared to other plant parts due to their higher fagopyrin content and lower chlorophyll levels. Currently, the most efficient isolation method is an HPLC method, which enables the full separation

DOI: 10.1021/acs.jafc.5b01163
J. Agric. Food Chem. 2015, 63, 5715−5724

Table 3. Isolation and Extraction Attempts

reference	extraction, purification, or isolation procedure	result
Chick[21]	90% ethylene glycol or methanol with 10% glacial acetic acid	the entire photosensitizing material was successfully extracted along with all other extractable constituents
Wender[59]	substance A: 80% acetone extract extracted by ether; sodium sulfate and talc were subjected to chromatography in an acetone solution; elution of substance from sodium sulfate with warm water and glacial acetic acid solution, followed by precipitation with ether yielded substance A substance B: talc extraction with ethanol; eluent was transferred to ether and extracted with 15% hydrochloric acid substance C: ether, after extraction with hydrochloric acid to obtain B, was extracted with 5% sodium carbonate solution and purified with methanol	not entirely pure substances were obtained with no quantification data
Brockmann[22]	extraction: pre-extraction with ether; extraction of fagopyrin fraction with acetone/water/acetic acid (86:10:4) purification: column chromatography with silica gel pretreated with 2% hydrochloric acid; elution with tetrahydrofuran, ethanol with 5% sulfuric acid, and methanol with 20% sulfuric acid, followed by solubilization in 2-methoxyethanol, ethyl acetate, and 5% butanol. countercurrent distribution with ethyl acetate, methylglycol, water, and *n*-butanol	up to 270 mg of partially purified fagopyrins per kilogram of dried flowers
Samel[23]	pre-extraction with dichloromethane; residual drug macerated in acetone/acetic acid/water (8:1:1); treated with water to remove water-soluble impurities, precipitate extracted with tetrahydrofuran purification: column chromatography with silica gel 60; elution with ethyl acetate/acetone and acetone/methanol mixtures; final elution with acetone/methanol (1:9) with 0.5% acetic acid was further purified using styrene divinylbenzene copolymer CC with water/methanol gradients; fagopyrins were eluted using methanol with 0.5% acetic acid and further purified on Sephadex LH 20 CC that was eluted with dichloromethane/acetone/methanol (5:3:2); yellow fractions that comigrated with the red fluorescent compounds in the silica gel were successfully removed using Dianion	from 8.3 kg of dried plant material, 10 mg of pure TLC extract was obtained
Theurer[34]	• ethanol/water (1:1) • boililng aqueous extract, lyophilized	extracts were used in in vitro phototoxicity tests
Hinneburg[35]	silica gel 60 F240 plate, developed twice with toluene/ethyl acetate/acetic acid; the red fagopyrin band was scratched out and dissolved in 70 and 30% ethanol solutions	from 0.25 mg of dried buckwheat herb, approximately 0.1 ng of fagopyrins was obtained
Ožbolt[36]	herbal material extracted with 80% tetrahydrofuran in water at 65 °C for 30 min; extract was evaporated and redissolved in methanol in an ultrasonic bath	partially purified extract, used for spectrophotometric determination
Eguchi[25]	freeze-dried sample was macerated in dichloromethane, dried, and then macerated in acetone/acetic acid/water (8:1:1) for TLC; the authors extracted the spots with methanol	mixture of fagopyrins; no other impurities can be seen on the HPLC chromatogram
Tavčar Benković[20]	prior removal of chlorophylls with dichloromethane, then extraction at 60 °C by ultrasound in acetone/water (9:1); HPLC separation and fraction collection according to the method described underAnalytical Methods	isolation of individual fagopyrin, with impurities of other fagopyrins

DOI: 10.1021/acs.jafc.5b01163
J. Agric. Food Chem. 2015, 63, 5715−5724

Table 4. Fagopyrin Content in Different Parts of Three Species of Buckwheat, As Calculated by Comparison with a Standard Solution of Hypericin

reference	source	common (mg g^{-1})	tartary (mg g^{-1})	cymosum (mg g^{-1})
Chick[21]	young flowers	positive		
	mature flowers and husks	less than in young flowers		
	leaves, stems, and flowers	none		
Hagels[58]	inflorescences	0.8 fagopyrin, 0.3 pseudofagopyrin		
	leaves	0.5 fagopyrin, 0.2 pseudofagopyrin		
Ožbolt[36]	leaves	0.4−0.6		
	stems	0.04−0.12		
Eguchi[25]	leaves	0.39	1.06	
	flowers	0.64	1.84	
	stems	0.04	0.11	
	hulls	0.02	0.04	
	groats			
Kreft[37]	sprouts	0.0025−0.041	0.10−0.12	
Stojilkovski[38]	leaves	0.3−2.3	0.512[1]	0.9
	leaves and flowers	1.6		
	herbs	3.7−4.8		
	seed		0.068	
	stems			0.3
	leaves and thin stems			1.9
	flowers			20.8
HagerROM[60]		0.01		

of fagopyrins from other compounds. However, an analytical system was used, which did not allow a sufficient quantity of fagopyrins to be obtained for weight determination.[20] We therefore recommend that the method be scaled up to allow preparative quantities of product to be isolated and to improve the resolution of the method. Many authors have reported difficulties in the solubilization of their dried, purified extracts. We conclude that solvents allowing efficient extraction are not necessarily also able to solubilize isolated fagopyrins, as the presence of other compounds may influence their solubility.

The task of eliminating fagopyrins from extracts is much easier. To obtain polyphenol-rich buckwheat extract with no risk of phototoxicity, a 30% ethanol in water solution is adequate for extracting phenols while simultaneously avoiding fagopyrins.[33]

■ ANALYTICAL METHODS

Fagopyrins and their acetylated derivatives were first analyzed by chromatography on silica gel with chloroform/methanol (97:3). The compounds with the highest retention times were hexa-acetylated fagopyrins. Fagopyrin and the hydrolyzed products of acetates did not migrate with the mobile phase. Fagopyrins were separated into several red spots using a $CaSO_4$ stationary phase.[24]

A successful method to separate three fagopyrin spots used silica gel 60 F_{254} with a mobile phase of toluene/ethyl formate/formic acid/pyridine (5:4:1:2).[23,34] This method was successfully used for preparative purposes, starting with 50 μL of extract.[35] Eguchi[25] used the same method but analyzed the plate at 302 nm and observed two spots.[25]

For spectrophotometric determination of fagopyrin content, several modifications of the pharmacopoeial method for the determination of hypericin have been used. Samples of dry buckwheat extracts were suspended in tetrahydrofuran; the supernatant was evaporated, and the residue was extracted again with methanol. Some authors used methanol directly as an extraction solvent and then centrifuged the sample. The absorbance of the supernatant was measured at 590 nm. The authors calculated the fagopyrin concentration compared with a standard solution of hypericin.[25,33,36,37]

The first HPLC method for fagopyrin isolation was developed with water/methanol/trifluoroacetic acid/tetrahydrofuran (3:40:1:1) as a mobile phase. The authors monitored the absorbance at 590 nm and observed three barely resolved peaks.[25] This method was improved with the use of an acetonitrile/water gradient with 0.1% trifluoroacetic acid, employing fluorescent detection (excitation at 330 nm, emission at 590 nm). Eight peaks of fagopyrins were partially separated.[20]

We must emphasize the fact that, to date, no quantitative isolation and characterization of entirely pure fagopyrins to use as a reference standard has been reported.

■ CONTENT

The fagopyrin contents in different materials and determined in different studies are summarized in Table 4.

All parts of tartary buckwheat contain at least 2 times more fagopyrin than the corresponding part of common buckwheat.[25,37,38] The fagopyrin content was influenced by the cultivation method.[37] Illumination and cultivation in sprouters increased the fagopyrin content by 2-fold. The fagopyrin

DOI: 10.1021/acs.jafc.5b01163
J. Agric. Food Chem. 2015, 63, 5715−5724

content was independent of whether the seeds were soaked in different solutions of selenium or the level of UV-B radiation.[36] Similarly to hypericin, a nitrogen-limited environment was postulated to favor fagopyrin production in a highly sensitive manner.[28]

In quantitative evaluations of fagopyrin content, none of the authors reported using a fagopyrin reference standard, which would be necessary to obtain genuine results. Therefore, all values from Table 4 can be considered only as estimates. The authors mainly expressed the fagopyrin content by using hypericin equivalents. Parameters such as absorbance or fluorescence depend on complex molecular characteristics and thus cannot be directly compared between two different compounds such as hypericin and fagopyrin, despite their similarity. A justification of these statements can be found in the next section.

Photodynamic Properties of Fagopyrins. Fagopyrin is a photodynamic agent, which is a molecule that absorbs light and transforms itself into an excited state. Two paths are possible for emitting the absorbed energy: the first is through a photochemical reaction, which releases orange to red fluorescence in the case of fagopyrins, and the second is a transfer of the absorbed energy to an acceptor molecule. In the latter case, the photodynamic molecule transforms from a singlet to a triplet state. When returning to the singlet state in the presence of triplet oxygen as an acceptor molecule, singlet oxygen forms. Singlet oxygen further oxidizes cell lipids, proteins, and nucleic acids, which leads to inflammation.[39] The formation of superoxide radical instead of singlet oxygen is also possible but was not observed in a study of the photoexcited forms of hypericin.[17] Hypericin underwent a one-electron transfer to singlet oxygen in egg yolk lecithin liposomes at pH 7.0. However, at a higher pH of 9.7, superoxide radical production proceeded mainly via electron transfer between excited hypericin and its ground state with little participation of singlet oxygen.[40] Energy transfer paths are therefore highly dependent on the environment. Efficient cell death has been demonstrated to occur when light, oxygen, and the evaluated photosensitizer are not limited,[41] and reports of the phototoxicity and fluorescence of fagopyrins are consistent with this idea. In our unpublished work, we found that the fluorescence of solubilized fagopyrins depends greatly on the solvent conditions, especially pH. This phenomenon should be considered in all experiments that evaluate fagopyrin content. Solution pH apparently influences the energy emission pathways of fagopyrin molecules. Excitation also undoubtedly depends on the light source. Amber glass did not stop the photosensitization process, but blue glass did.[42] In vivo, fagopyrins have demonstrated excitation at wavelengths of visible light between 530 and 690 nm, which is important information for the occurrence of fagopyrism and for the potential therapeutic use of fagopyrins.[21]

Fagopyrism. The first reports about fagopyrism are epidemiological observations of its manifestation in stock animals, feeding on pastures rich in buckwheat. As early as 1843, Fuchs correlated the symptoms of buckwheat sensitivity with the level of exposed light necessary for their expression. Chick[21] was the first to conduct controlled experiments. He observed the lesions on animals after feeding with buckwheat and compared them with animals kept in the dark. He also compared covered and uncovered areas of the skin. In the beginning of the 20th century, many reports were published on fagopyrism that confirmed the effect and its symptoms. The whole plant was observed to be more effective than the seeds alone for inducing the condition. The symptoms in guinea pigs persisted for 36 months after feeding with a buckwheat diet. Several attempts at isolation and pharmacological testing on animals were also made. Öhmke successfully sensitized mice, guinea pigs, and rabbits by feeding them buckwheat seeds and hulls, which should not contain very high amounts of fagopyrins.[21,32,43−45] The characteristic absorption bands of fagopyrins were observed in swine serum, which demonstrated that these compounds can be absorbed through the walls of the digestive system.[42] The safety of commercially available Fagorutin tablets with powdered buckwheat herb was also investigated in a randomized, double-blind placebo-controlled study. The influence of UV-A and UV-B on skin after a single dose and after 14 days of application (3 × 2 tablets daily, 500 mg of buckwheat herb each) was tested. No differences relative to the placebo were observed. We can thus conclude that the evaluated doses were below the phototoxicity-causing threshold.[46]

The typical symptoms of fagopyrism are similar in all observed in vivo systems, as indicated in Table 5. They occur in sunlight-exposed areas of the skin after the ingestion of fagopyrin-rich buckwheat products. These reactions do not primarily involve immune system responses, and so fagopyrism cannot be correctly described as a buckwheat allergy. Other possible symptoms that are not directly connected to photosensitivity include hyperemia, swelling of the intestinal canal, and gastrointestinal hemorrhage.[45,47]

Table 5. Symptoms of Fagopyrism[21,42,49,61]

livestock (sheep, horses, cattle, swine, goats, chickens)	rats, mice, guinea pigs	humans
erythema	erythema of the naked parts of the skin	burns
swelling	uncovered portions of the skin becoming swollen and inflamed	tingling and numbness in the hands
skin lesions	dilation of the veins but not capillaries	cold sensitivity
skin irritation	hair loss	
inflammation	scratching	
blindness	irritable, uncomfortable behavior	
sensory disturbances	temporary loss of appetite and weight	
intestinal disturbances	conjunctivitis	
	diarrhea	
	convulsions	

Information about the minimum toxic doses of fagopyrin is scarce. The safe consumption limits of buckwheat were estimated by comparison to hypericin toxic doses. For sprouts, the safe limit was 0.14 g of dry sprout mass (corresponding to 40 sprouts) per kg body mass per day; a severe phototoxic dose would correspond to the consumption of 10 g of dry mass per person.[37] However, the findings of Theurer[34] are not in accordance with these results. The authors examined the effect of an ethanol buckwheat extract, irradiated with artificial sunlight, on 3T3 fibroblasts and found that fagopyrin is 10 times less phototoxic than hypericin (6 μg/mL). An aqueous extract demonstrated no activity.[34] Epidermal growth factor receptor- and insulin receptor-associated protein kinases were inhibited with purified buckwheat extract to a similar extent as

DOI: 10.1021/acs.jafc.5b01163
J. Agric. Food Chem. 2015, 63, 5715−5724

hypericin. They both inhibited serine/threonine kinases and cytosolic protein kinases (Lyn, Fgr, CSK) to a lesser extent. In the case of casein kinase 2, hypericin was found to be a much more potent inhibitor.[23] From both studies, we can conclude that comparison with hypericin is not an appropriate benchmark from which to obtain quantitative results. Similarly, pseudohypericin was a much less efficient photosensitizer in biological systems than hypericin due to its high adsorption to serum components. This discrepancy can serve as further proof of the high dependence of photodynamic effects on the structural features of individual molecules.[48] Unfortunately, no fagopyrin reference standard is currently available, so only buckwheat extracts with unknown fagopyrin contents were tested. In experiments on rats, the minimal activating dose of dried flowers was 0.25 g/100 g animal.[21] Maximal reactions were observed between the fourth and eighth day and could take up to 4 weeks. After several days, local irradiation produced a general effect, with inflammation occurring on exposed but non-irradiated parts of the body. The duration of the symptoms was proportional to the size of the dose and worsened after light exposure. Fagopyrins were not detected in urine or feces. A second relevant study is a retrospective report about one author's personal encounter with fagopyrism as a consequence of the daily consumption of "healthful" juice that contained buckwheat herb. Unfortunately, accurate records of the amount of buckwheat consumed are not provided. From the author's description, we can infer that he drank one glass of buckwheat juice per day, but it is uncertain as to whether the juice was diluted with water. His personal experience was followed by an inquiry, which revealed that many other people reported similar experiences. Their symptoms always appeared after an extended-duration diet, which suggests that fagopyrins require accumulation over time.[49] Like hypericins, fagopyrins are presumably largely unable to cross the blood−brain barrier in animals, so the neurological symptoms described in several cases are probably consequences of oxidative stress from inflammation.[50] Notably, porphyrin derivatives that are present in buckwheat herbs, such as phylloerythrin, an anaerobic fermentation product of chlorophyll molecules, can also induce phototoxicity, but at different wavelengths.[42,47,51] Other components of buckwheat extract, such as quercetin, may also contribute to the formation of reactive oxygen species, which are involved in photosensitizing activity; however, their contribution is likely negligible.[35] No reports can be found about fagopyrins in milk during lactation. Considering hypericin, the compound is poorly excreted into human milk. The only report is about a mother that was on a postnatal depression therapy, taking 900 mg of St. John's wort extract (3−6:1) per day; the plasma of the breast-fed infant was analyzed. Hypericin was found to be in concentrations below the quantification limit (0.20 ng/mL).[52,53]

We can summarize from all available pharmacological data that acute poisoning of humans with any parts of the whole buckwheat plant is not probable, as the amounts required would be too large given the ratios with other buckwheat compounds. From solubility studies, we can conclude that aqueous extracts such as tea should not threaten human health. The most problematic consumption method is an extended-term diet, lasting more than a few days, of buckwheat herbs, especially flowers, or of protic lipophilic buckwheat extracts.

Pharmacotherapeutic Potential. The phenomenon of photosensitization described above can be exploited in photodynamic therapy, in which initiation of the photochemical formation of singlet oxygen in a restricted area is deliberate and limited in extent. Photosensitizers can be applied locally or systemically, and a selected area is irradiated with laser light of chosen wavelengths to induce oxidation of the biological tissue.[39] Hypericin has been widely tested as a therapeutic agent in recent years, mainly for tumor treatment.[54] Hypericin exhibits several advantages over common photosensitizers, including substantial quantum yield, intense absorption in the visible region, low photobleaching, and a large excitation range. The delivery of hypericin by most pharmaceutically suitable vehicles is limited due to its hydrophobicity.[55] Nevertheless, its hydrophobicity could favor local application and higher selectivity for certain tissues. In the present paper, we show that fagopyrin is even more specific in its solvation environment, so it may serve as a potential photodynamic agent with even greater selectivity.

Hypericin also exhibits antiviral activity. Interestingly, its potential for photo-oxidation plays only a minor role in this observed activity. Instead, the antiviral activity is primarily mediated by other mechanisms, which are potential avenues for the investigation of fagopyrins.[56] Molecules with anthrone skeletons are also often used as topical antipsoriatic treatments.[57]

To summarize, the long-term consumption and study of buckwheat have provided only rough information about the safety of phototoxic fagopyrins. Unfortunately, reliable quantitative data on their toxicity are not yet available. Buckwheat seeds, flour, or teas are safe in normal amounts. However, an extensive diet that includes buckwheat sprouts or herbs and particularly flowers or fagopyrin-rich buckwheat extracts may cause fagopyrism on parts of the skin upon simultaneous exposure to visible light. Fagopyrins were discovered more than 100 years ago but remain poorly characterized substances. The main difficulty lies in their unique molecular characteristics, which hinder their isolation. Consequently, no reference standard is currently available; a reference standard would enable proper fagopyrin content evaluation in buckwheat products and proper testing of their undiscovered characteristics, biosynthetic pathways, and biological activities. Many methods remain to be established. Nevertheless, fagopyrins are not only health-threatening compounds but also potent photodynamic agents that warrant further research.

AUTHOR INFORMATION

Notes

The authors declare no competing financial interest.

REFERENCES

(1) Nešković, M.; Srejović, V.; Vujičić, R. Buckwheat (*Fagopyrum esculentum* Moench.). In *Crops I*; Bajaj, P. D. Y. P. S., Ed.; Biotechnology in Agriculture and Forestry; Springer: Berlin, Germany, 1986; pp 579−602.

(2) Zhou, X.; Wen, L.; Li, Z.; Zhou, Y.; Chen, Y.; Lu, Y. Advance on the benefits of bioactive peptides from buckwheat. *Phytochem. Rev.* **2015**, *14*, 1−8.

(3) Merendino, N.; Molinari, R.; Costantini, L.; Mazzucato, A.; Pucci, A.; Bonafaccia, F.; Esti, M.; Ceccantoni, B.; Papeschi, C.; Bonafaccia, G. A new "functional" pasta containing tartary buckwheat sprouts as an ingredient improves the oxidative status and normalizes some blood pressure parameters in spontaneously hypertensive rats. *Food Funct.* **2014**, *5*, 1017−1026.

(4) Li, S.; Zhang, Q. H. Advances in the development of functional foods from buckwheat. *Crit. Rev. Food Sci. Nutr.* **2001**, *41*, 451−464.

DOI: 10.1021/acs.jafc.5b01163
J. Agric. Food Chem. 2015, 63, 5715−5724

(5) Zhao, J.-L.; Zou, L.; Zhang, C.-Q.; Li, Y.-Y.; Peng, L.-X.; Xiang, D.-B.; Zhao, G. Efficient production of flavonoids in *Fagopyrum tataricum* hairy root cultures with yeast polysaccharide elicitation and medium renewal process. *Pharmacogn. Mag.* **2014**, *10*, 234−240.
(6) Kalinova, J.; Vrchotova, N. Level of catechin, myricetin, quercetin and isoquercitrin in buckwheat (*Fagopyrum esculentum* Moench), changes of their levels during vegetation and their effect on the growth of selected weeds. *J. Agric. Food Chem.* **2009**, *57*, 2719−2725.
(7) Lee, C.-C.; Hsu, W.-H.; Shen, S.-R.; Cheng, Y.-H.; Wu, S.-C. *Fagopyrum tataricum* (buckwheat) improved high-glucose-induced insulin resistance in mouse hepatocytes and diabetes in fructose-rich diet-induced mice. *Exp. Diabetes Res.* **2012**, *2012*, 375673.
(8) Skrabanja, V.; Kreft, I.; Golob, T.; Modic, M.; Ikeda, S.; Ikeda, K.; Kreft, S. Nutrient content in buckwheat milling fractions. *Cereal Chem.* **2004**, *81*, 172−176.
(9) Hur, S.-J.; Park, S.-J.; Jeong, C.-H. Effect of buckwheat extract on the antioxidant activity of lipid in mouse brain and its structural change during in vitro human digestion. *J. Agric. Food Chem.* **2011**, *59*, 10699−10704.
(10) Jiang, P.; Burczynski, F.; Campbell, C.; Pierce, G.; Austria, J. A.; Briggs, C. J. Rutin and flavonoid contents in three buckwheat species *Fagopyrum esculentum*, *F. tataricum*, and *F. homotropicum* and their protective effects against lipid peroxidation. *Food Res. Int.* **2007**, *40*, 356−364.
(11) Kreft, I.; Fabjan, N.; Yasumoto, K. Rutin content in buckwheat (*Fagopyrum esculentum* Moench) food materials and products. *Food Chem.* **2006**, *98*, 508−512.
(12) Li, X.; Thwe, A. A.; Park, N. I.; Suzuki, T.; Kim, S. J.; Park, S. U. Accumulation of phenylpropanoids and correlated gene expression during the development of tartary buckwheat sprouts. *J. Agric. Food Chem.* **2012**, *60*, 5629−5635.
(13) Hinneburg, I.; Kempe, S.; Rüttinger, H.-H.; Neubert, R. H. H. Antioxidant and photoprotective properties of an extract from buckwheat herb (*Fagopyrum esculentum* Moench). *Pharmazie−Int. J. Pharm. Sci.* **2006**, *61*, 237−240.
(14) Kreft, S.; Strukelj, B.; Gaberscik, A.; Kreft, I. Rutin in buckwheat herbs grown at different UV-B radiation levels: comparison of two UV spectrophotometric and an HPLC method. *J. Exp. Bot.* **2002**, *53*, 1801−1804.
(15) Kreft, S.; Knapp, M.; Kreft, I. Extraction of rutin from buckwheat (*Fagopyrum esculentum* Moench) seeds and determination by capillary electrophoresis. *J. Agric. Food Chem.* **1999**, *47*, 4649−4652.
(16) Yang, F.; Yu, S.; Wang, Y.; Wang, R.; Jing, F. Prospective induction of peripheral neuropathy by the use of tartarian buckwheat. *J. Neurol. Sci.* **2014**, *347*, 155−158.
(17) Dumas, S.; Leprêtre, J.-C.; Lepellec, A.; Darmanyan, A.; Jardon, P. Reactivity of the photo excited forms of hypericin, hypocrellin A, hypocrellin B and methylated hypericin towards molecular oxygen: the role of charge transfer interaction. *J. Photochem. Photobiol., A* **2004**, *163*, 297−306.
(18) Duráan, N.; Song, P.-S. Hypericin and its photodynamic action. *Photochem. Photobiol.* **1986**, *43*, 677−680.
(19) Wender, S. H.; Gortner, R. A.; Inman, O. L. The isolation of photosensitizing agents from buckwheat. *J. Am. Chem. Soc.* **1943**, *65*, 1733−1735.
(20) Tavčar Benković, E.; Žigon, D.; Friedrich, M.; Plavec, J.; Kreft, S. Isolation, analysis and structures of phototoxic fagopyrins from buckwheat. *Food Chem.* **2014**, *143*, 432−439.
(21) Chick, H.; Ellinger, P. The photosensitizing action of buckwheat (*Fagopyrum esculentum*). *J. Physiol.* **1941**, *100*, 212−230.
(22) Brockmann, H.; Weber, E.; Pampus, G. Protofagopyrin und Fagopyrin, die photodynamisch wirksamen Farbstoffe des Buchweizens (*Fagopyrum esculentum*). *Justus Liebigs Ann. Chem.* **1952**, *575*, 53−83.
(23) Samel, A. D.-D. The effect of purified extract of *Fagopyrum esculentum* (buckwheat) on protein kinases involved in signal transduction pathways. *Planta Med.* **1996**, *62*, 106−110.
(24) Brockmann, H.; Lackner, H. Zur konstitution des fagopyrins. *Tetrahedron Lett.* **1979**, *20*, 1575−1578.
(25) Eguchi, K.; Anase, T.; Osuga, H. Development of a high-performance liquid chromatography method to determine the fagopyrin content of tartary buckwheat (*Fagopyrum tartaricum* Gaertn.) and common buckwheat (*F. esculentum* Moench). *Plant Prod. Sci.* **2009**, *12*, 475−480.
(26) Habermann, B. Protofagopyrin or fagopyrin, what is genuine? *Arch Farm Farm Med. Chem.* **2000**, *333*, Suppl. 2.
(27) Baugh, S. F. Simultaneous determination of protopseudohypericin, pseudohypericin, protohypericin, and hypericin without light exposure. *J. AOAC Int.* **2005**, *88*, 1607−1612.
(28) Oksana Sytar, M. B. Possible ways of fagopyrin biosynthesis and production in buckwheat plants. *Fitoterapia* **2013**, *84*, 72−79.
(29) Huang, L.-F.; Wang, Z.-H.; Chen, S.-L. Hypericin: chemical synthesis and biosynthesis. *Chin. J. Nat. Med.* **2014**, *12*, 81−88.
(30) Brockmann, H.; Kluge, F.; Muxfeldt, H. Totalsynthese des Hypericins. *Chem. Ber.* **1957**, *90*, 230210.1002/cber.19570901027.
(31) Motoyoshiya, J.; Masue, Y.; Nishi, Y.; Aoyama, H. Synthesis of hypericin via emodin anthrone derived from a two-fold Diels-Alder reaction of 1,4-benzoquinone. *Nat. Prod. Commun.* **2007**, *2*, 67−70.
(32) Blum, H. F. *Photodynamic Action and Diseases Caused by Light*; Reinhold Publishing: New York, 1941.
(33) Hinneburg, I.; Neubert, R. H. H. Influence of extraction parameters on the phytochemical characteristics of extracts from buckwheat (*Fagopyrum esculentum*) herb. *J. Agric. Food Chem.* **2004**, *53*, 3−7.
(34) Theurer, C.; Gruetzner, K.; Freeman, S. J.; Koetter, U. In vitro phototoxicity of hypericin, fagopyrin rich, and fagopyrin free buckwheat herb extracts. *Pharm. Pharmacol. Lett.* **1997**, *7*, 113−115.
(35) Hinneburg, I.; Kempe, S.; Rüttinger, H.-H.; Neubert, R. H. H. A CE method for measuring phototoxicity in vitro. *Chromatographia* **2005**, *62*, 325−329.
(36) Ožbolt, L.; Kreft, S.; Kreft, I.; Germ, M.; Stibilj, V. Distribution of selenium and phenolics in buckwheat plants grown from seeds soaked in Se solution and under different levels of UV-B radiation. *Food Chem.* **2008**, *110*, 691−696.
(37) Kreft, S.; Janeš, D.; Kreft, I. The content of fagopyrin and polyphenols in common and tartary buckwheat sprouts. *Acta Pharm.* **2013**, *63*, 553−560.
(38) Stojilkovski, K.; Glavač, N. K.; Kreft, S.; Kreft, I. Fagopyrin and flavonoid contents in common, Tartary, and cymosum buckwheat. *J. Food Compos. Anal.* **2013**, *32*, 126−130.
(39) Pečar, S.; Mravljak, J. *Šumi življenja ali Radikali in druge reaktivne snovi v telesu*; Slovensko farmacevtsko društvo: Ljubljana, 2015 (in press).
(40) Hadjur, C.; Jardon, P. Quantitative analysis of superoxide anion radicals photosensitized by hypericin in a model membrane using the cytochrome c reduction method. *J. Photochem. Photobiol., B* **1995**, *29*, 147−156.
(41) Piette, J.; Volanti, C.; Vantieghem, A.; Matroule, J.-Y.; Habraken, Y.; Agostinis, P. Cell death and growth arrest in response to photodynamic therapy with membrane-bound photosensitizers. *Biochem. Pharmacol.* **2003**, *66*, 1651−1659.
(42) Sheard, C.; Caylor, H. D.; Schlotthauer, C. Photosensitization of animals after the ingestion of buckwheat. *J. Exp. Med.* **1928**, *47*, 1013−1028.
(43) Foster, E. M. *Toxicants Occurring Naturally in Foods*; National Academies: Washington, DC, USA, 1973.
(44) Hockberger, P. E. A history of ultraviolet photobiology for humans, animals and microorganisms. *Photochem. Photobiol.* **2002**, *76*, 561−579.
(45) Giese, A. C. *Photophysiology: Current Topics in Photobiology and Photochemistry*; Elsevier: Amsterdam, The Netherlands, 2013.
(46) Diefenbach, K.; Donath, F.; Bauer, S.; Arold, G.; Maurer, A.; Patz, B.; Theurer, C.; Roots, I. Einschätzung eines phototoxischen Risikos bei Buchweizenkraut. In *Phytopharmaka VII*; Schulz, P. D. V., Rietbrock, P. D. N., Roots, P. D. I., Loew, P. D. D. D., Eds.; Steinkopff: Berlin, Germany, 2002; pp 181−187.
(47) Keeler, R. F.; Tu, A. T. *Handbook of Natural Toxins*; CRC Press: Boca Raton, FL, USA, 1983.

DOI: 10.1021/acs.jafc.5b01163
J. Agric. Food Chem. 2015, 63, 5715−5724

(48) Vandenbogaerde, A. L.; Kamuhabwa, A.; Delaey, E.; Himpens, B. E.; Merlevede, W. J.; de Witte, P. A. Photocytotoxic effect of pseudohypericin versus hypericin. *J. Photochem. Photobiol., B* **1998**, *45*, 87−94.
(49) Arbour, G. Are buckwheat greens toxic? *Townsend Lett. Doctors Patients* **2004** (December).
(50) Caccia, S.; Gobbi, M. St. John's wort components and the brain: uptake, concentrations reached and the mechanisms underlying pharmacological effects. *Curr. Drug Metab.* **2009**, *10*, 1055−1065.
(51) Ebermann, R.; Alth, G.; Kreitner, M.; Kubin, A. Natural products derived from plants as potential drugs for the photodynamic destruction of tumor cells. *J. Photochem. Photobiol., B* **1996**, *36*, 95−97.
(52) Briggs, G. G.; Freeman, R. K.; Yaffe, S. J. *Drugs in Pregnancy and Lactation: A Reference Guide to Fetal and Neonatal Risk*; Lippincott Williams & Wilkins: Baltimore, MD, USA, 2011.
(53) Klier, C. M.; Schäfer, M. R.; Schmid-Siegel, B.; Lenz, G.; Mannel, M. St. John's wort (*Hypericum perforatum*) is it safe during breastfeeding? *Pharmacopsychiatry* **2002**, *35*, 29−30.
(54) Kiesslich, T.; Krammer, B.; Plaetzer, K. Cellular mechanisms and prospective applications of hypericin in photodynamic therapy. *Curr. Med. Chem.* **2006**, *13*, 2189−2204.
(55) Lima, A. M.; Pizzol, C. D.; Monteiro, F. B. F.; Creczynski-Pasa, T. B.; Andrade, G. P.; Ribeiro, A. O.; Perussi, J. R. Hypericin encapsulated in solid lipid nanoparticles: phototoxicity and photodynamic efficiency. *J. Photochem. Photobiol., B* **2013**, *125*, 146−154.
(56) Fehr, M. J.; Carpenter, S. L.; Petrich, J. W. The role of oxygen in the photoinduced antiviral activity of hypericin. *Bioorg. Med. Chem. Lett.* **1994**, *4*, 1339−1344.
(57) Müller, K. Antipsoriatic anthrones: aspects of oxygen radical formation, challenges and prospects. *Gen. Pharmacol.* **1996**, *27*, 1325−1335.
(58) Hagels, H.; Wagenbreth, D.; Schilcher, H. Phenolic compounds of buckwheat herb and influence of plant and agricultural factors (*Fagopyrum esculentum* Moench) and *Fagopyrum tataricum* Gartner). *Curr. Adv. Buckwheat Res.* **1995**, *115*, 801−809.
(59) Wender, S. H. The action of photosensitizing agents isolated from buckwheat. *Am. J. Vet. Res.* **1946**, *7*, 486−489.
(60) *HagerROM 2010. Hagers Enzyklopädie der Arzneistoffe und Drogen*; Springer: Berlin, Germany, 2010
(61) Brockmann, H. Photodynamisch wirksame Pflanzenfarbstoffe. In Fortschritte der Chemie Organischer Naturstoffe/Progress in the Chemistry of Organic Natural Products/Progrès dans la Chimie des Substances Organiques NaturellesZechmeister, L., Ed.; *Fortschritte der Chemie Organischer Naturstoffe/Progress in the Chemistry of Organic Natural Products/Progrès dans la Chimie des Substances Organiques Naturelles*; Springer: Vienna, Austria, 1957; pp 141−185.

DOI: 10.1021/acs.jafc.5b01163
J. Agric. Food Chem. 2015, 63, 5715−5724

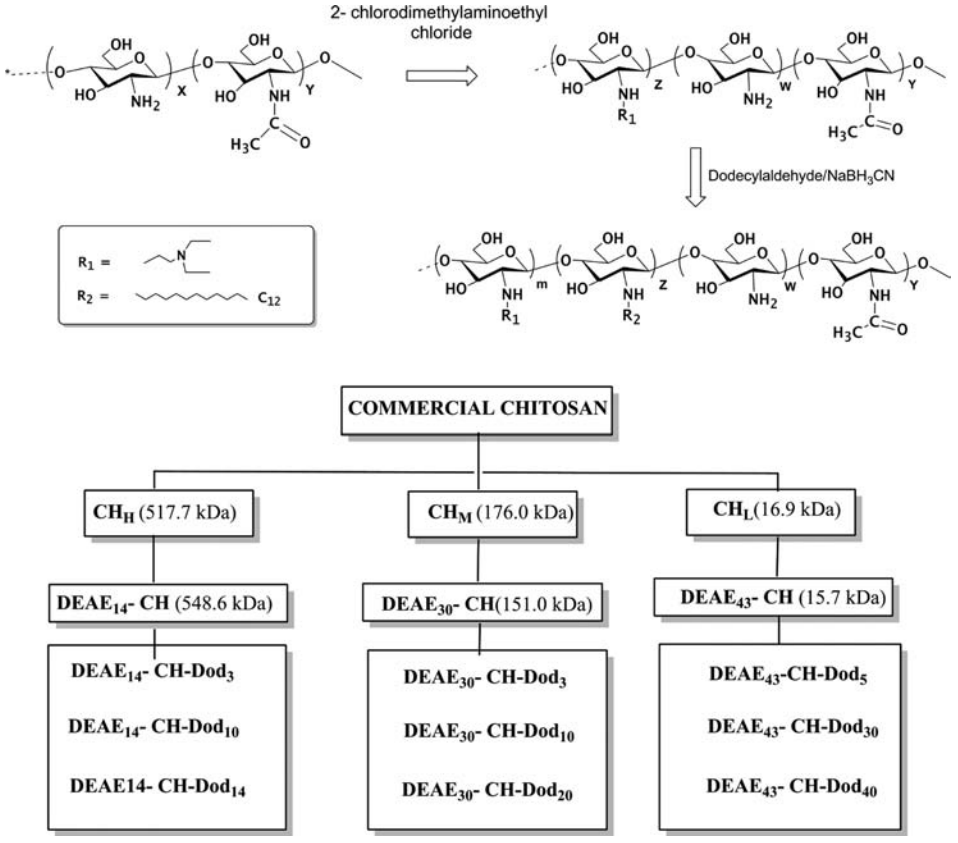

Figure 1. Synthesis of amphiphilic derivatives of diethylaminoethyl chitosan.

Table 1. Molar Ratios of Dodecyl/NH_2 and Degrees of Substitution with Dodecyl Groups

polymer	molar ratio dodecyl/NH_2	DS_{DEAE} (%)	DS_{Dod} (%)	M_w (kDa)	M_w/M_n	CAC (g/L) pH 5.0	I_1/I_3 (at 0.2 g/L)
CCH (DDA 86.0%)				1068	4.8		
CH_H (DDA = 98%)				517.7	3.4		
$DEAE_{14}$-CH		14.0		**548.6**	3,9		
$DEAE_{14}$-CH-Dod_3	0.05	14.0	2.6				1.50
$DEAE_{14}$-CH-Dod_{10}	0.15	14.0	10.0			7.0×10^{-3}	1.22
$DEAE_{14}$-CH-Dod_{14}	0.36	14.0	14.0			6.0×10^{-3}	1.13
CH_M (DDA = 98.0%)				176.0	3.35		
$DEAE_{30}$-CH		30.0		**151.0**	2.90		
$DEAE_{30}$-CH-Dod_3	0.05	30.0	2.7				1.80
$DEAE_{30}$-CH-Dod_{10}	0.15	30.0	10			1.14×10^{-2}	1.21
$DEAE_{30}$-CH-Dod_{20}	0.37	30.0	19			7.0×10^{-3}	1.18
CH_L (DDA = 98.0%)				16.9	2.50		
$DEAE_{43}$-CH		43.0		**15.7**	2.25		
$DEAE_{43}$-CH-Dod_5	0.06	43.0	5				1.79
$DEAE_{43}$-CH-Dod_{30}	0.45	43.0	28			9.0×10^{-3}	1.24
$DEAE_{43}$-CH-Dod_{40}	0.65	43.0	39			6.2×10^{-3}	1.15

(Fortaleza, Ceará, Brazil). Tween 80, sodium acetate, acetic acid, and sodium hydroxide were purchased from Synth (Diadema, São Paulo, Brazil). DEAE chloride, deuterium chloride (35%) in deuterium oxide, and deuterium oxide were purchased from Sigma-Aldrich Chemical Co. (São Paulo, Brazil). Potato dextrose agar (PDA) was purchased from Acumedia Manufacturers, Inc. (Lansing, MI, USA). Water was deionized using a Gehaka water purification system. Spectra/Pore membranes (Spectrum) were employed for dialysis. All solvents were of reagent grade and were used as received.

Instrumentation. ^1H NMR spectra were recorded using a Bruker ARX-500 500 MHz spectrometer (Bruker, Germany). UV−vis spectra were measured using a Cary 100 spectrophotometer equipped with a Peltier system. pH was measured using a DM-23 Digimed pH meter (Digimed, Campo Grande, Brazil).

Synthesis of Amphiphilic Derivatives of DEAE-CH. CH derivatives were synthesized using deacetylated CH samples, prepared as previously described by Tiera et al.[20] CH derivatives were obtained by reacting DEAE chloride with CH of different M_w values (517.7, 176, and 16.7 kDa) in aqueous media at pH 8.0 under an N_2 atmosphere.[21] The resulting derivatives (DEAE-CH) were purified by dialysis against water for 4 days and were then lyophilized. Subsequently, the derivatives were subjected to hydrophobic modifications through reductive amination with dodecylaldehyde, as shown in Figure 1. The procedure for generating $DEAE_{30}$-CH-Dod_{10} with a sample containing 30% DEAE groups and 10% Dod groups is

DOI: 10.1021/acs.jafc.5b00278
J. Agric. Food Chem. 2015, 63, 5725−5731

described below. Deacetylated CH (0.8 g, 176 kDa) was solubilized in a mixture of 90 mL of 2% acetic acid and 50 mL of ethanol. The pH was adjusted to 5.0, and while the reaction mixture was stirred, 0.12 mL of dodecylaldehyde dissolved in 10 mL of ethanol was added to it in a dropwise manner. The reaction mixture was continuously stirred for 25 h at room temperature, and sodium cyanoborohydride (3:1, $NaCNBH_3/NH_2$, mol/mol) was added after the first hour. Thereafter, the reaction mixture was dialyzed (using a membrane with a MWCO of 6000−8000 g/mol), first against water for 2 days, then against aqueous NaOH (0.05 M) for 1 day, and finally against water for 3 days. The derivative $DEAE_{30}$-CH-Dod_{10} was lyophilized. Other DEAE-CH-Dod derivatives were prepared under identical conditions using different initial NH_2/dodecylaldehyde molar ratios (Table 1). The derivatives were subsequently purified with a Soxhlet system using chloroform to remove nonreacted dodecylaldehyde. The derivatives were characterized by ^{1}H NMR, FTIR and gel permeation chromatography (GPC) measurements.

GPC Analysis. GPC measurements were performed using an LC-20 Shimadzu liquid chromatograph (Shimadzu, Japan) equipped with a refractive index detector (model RID-10) using OHpak SB-803 HQ and OHpak SB-805 HQ columns (Shodex) and pullulan standards from 805 to 6.2 kDa (Supporting Information, Supplementary Figure S1). A mixture of acetic acid (0.3 M)/sodium acetate (0.2 M) (pH 4.5) was used as the mobile phase at a flow rate of 0.8 mL/min at 35 °C. Solutions were prepared for GPC analysis by dissolving the polymer in an acetic acid (0.3 M)/sodium acetate (0.2 M) buffer to achieve concentrations of between 0.5 and 1.0 mg/mL. The polymer solutions were stirred for 3 days and then filtered through 0.45 μm membranes before analysis.

Self-Association Study: Determination of Critical Aggregation Concentrations (CACs). The self-association of the amphiphilic derivatives was evaluated at 25.0 ± 0.1 °C using a Hitachi 4500 fluorescence spectrometer (Hitachi, Japan). The temperature of the water-jacketed cell holder was controlled using a circulating bath. Pyrene fluorescence was assessed to monitor the solution properties of the modified CHs. One microliter of a stock solution of pyrene (1 mM) in methanol was added to quartz cuvettes, and the solvent was removed by blowing N_2. To each of these pyrene-containing cuvettes was added 2 mL of an acetic acid/sodium acetate buffer, pH 5.0, followed by sonication for 4−5 min. Measured amounts (5 μL) of concentrated stock solutions of the derivatives (2.0 g/L) were added to buffered aqueous solutions of pyrene (5.0×10^{-7} M) under magnetic stirring, and fluorescence spectra were recorded after each addition. The ratio between the fluorescence intensities of peaks I (372.4 nm) and III (384 nm) of the emission spectrum of pyrene (I_1/I_3 ratio) was used to evaluate the polarity of the local environment[22] and to determine the CAC. Pyrene was excited at 310 nm, and its emission was recorded from 350 to 650 nm.

Fungal Strains and Culture Conditions. The antifungal activities of CH and its derivatives were tested against *A. flavus* and *Aspergillus parasiticus*. The strains used were kindly provided by the Brazilian Collection of Microorganisms from the Environment and Industry (CBMAI; Campinas, São Paulo, Brazil) and were maintained on PDA (200 g/L potato infusion, 20 g/L dextrose, and 15 g/L agar) in the dark at 25 ± 2 °C.

Effects of CH Derivatives on Mycelial Growth of *Aspergillus flavus*. To compare the antifungal potentials of deacetylated and commercial CH to those of the synthesized amphiphilic DEAE-CH-Dod derivatives, an in vitro mycelial growth inhibition assay was conducted. The different CH solutions were previously prepared in an aqueous solution of acetic acid (1% m/m) and adjusted to pH 5.5. Next, 10 mL of the derivatives was added aseptically to 10 mL of sterile melted culture medium (PDA, 10%) to obtain 20 mL of culture medium at the desired polymer concentration (0−1.0 g L^{-1}), which was then transferred to Petri dishes. After solidification, the mixtures were inoculated with fragments of *A. flavus* mycelium (1 mm in diameter), which were placed at the center of the Petri dishes. The plates were then incubated in an oven for 7 days at 25 ± 2 °C. The inhibition index, which is a measure of the inhibition of the fungus by the derivatives, was determined on the basis of the radial growth of the colony, as measured using a caliper on the third, fifth, and seventh days of cultivation. The results obtained on the seventh day were used for comparative purposes.

The antifungal index was calculated as

$$\text{antifungal index (\%)} = [1 - (D_a/D_b)] \times 100$$

where D_a is the diameter of the growth zone on the test plates and D_b is the growth zone on the control plate.[23]

All experiments were performed in quadruplicate, and the data were averaged. Student's t test and the Kruskal−Wallis test with Dunn's multiple-comparison test were used to evaluate differences in the antifungal index obtained using the antifungal tests. Results with $P < 0.05$ were considered statistically significant.

RESULTS AND DISCUSSION

Synthesis and Characterization of Amphiphilic Derivatives. Deacetylation was carried out under continuous nitrogen bubbling to prevent degradation of the polymer. The degrees of deacetylation, expressed as $-NH_2$ mol %, and determined on the basis of the ^{1}H NMR spectra of commercial chitosan (CCH) and the deacetylated samples (CH), were 86.0 and 98.0 mol %, respectively. These values were calculated on the basis of the area of the singlet at 3.7 ppm, which was assigned to the proton linked to carbon 2 of the glucosamine ring (H2), and on the singlet at 2.5 ppm, which was assigned to the acetamido methyl protons (Support Information, Supplementary Figure S2a). The degrees of substitution by DEAE groups (DS) were calculated on the basis of the areas (I_{CH_3}) of the signal at 1.72 ppm, which were assigned to the methyl protons NH−$(CH_2-\boldsymbol{CH_3})_2$, and on the signals at 5.1−5.35 ppm, which were assigned to the anomeric protons of substituted and unsubstituted glucosamine residues, H_{1s} and H_1, respectively (Figure S2b). The degrees of substitution were calculated using eq 1:

$$DS_{DEAE} = \frac{I_{CH_3}/6}{(I_{H_1} + I_{H_{1s}})} \quad (1)$$

Derivatives substituted with DEAE ($DEAE_{30}$-CH and $DEAE_{43}$-CH) were subsequently grafted with increasing proportions of Dod groups. The ^{1}H NMR spectra of the derivatives $DEAE_{43}$-CH and $DEAE_{43}$-CH-Dod_{30} are shown in the Support Information (Supplementary Figures S2b and S2c, respectively). The ^{1}H NMR spectra of the amphiphilic derivatives exhibited three new signals after substitution with Dod, including a singlet at 1.47 ppm, corresponding to the protons of the methyl group on the Dod chain, and signals at 1.94 and 2.35 ppm (Supplementary Figures S3−S5). The latter signals corresponded to protons in the hydrocarbon chain and the methylene protons of the carbon atom linked to the amino group of CH, respectively. The attachment of Dod groups to the DEAE-CH framework further altered the ^{1}H NMR spectrum of $DEAE_{43}$-CH, most notably with respect to the resonances of the methyl protons of the DEAE groups and the anomeric protons of substituted and unsubstituted glucosamine units. The former underwent a downfield shift from 1.72 to 1.88 ppm, and the latter underwent a shift from 5.15 to 5.3 to 5.5−5.7 ppm, which might have resulted from aggregation of the amphiphilic chains (Supplementary Figures S2b and S2c). The integrated areas of the signal at 1.47 ppm and those assigned to the anomeric protons of CH chains at 5.5−5.7 ppm were used to calculate the degree of substitution by Dod (DS_{Dod}) using eq 2:[24]

DOI: 10.1021/acs.jafc.5b00278
J. Agric. Food Chem. 2015, 63, 5725−5731

$$DS_{Dod} = \frac{I_{CH_3}}{I_{H_1} + I_{H_{1s}}} \quad (2)$$

The DEAE-CH derivatives were synthesized at pH 8.0 under an N_2 atmosphere. As shown in Table 1, GPC analysis confirmed that the molecular masses of the DEAE derivatives ($DEAE_{14}$-CH, $DEAE_{30}$-CH, and $DEAE_{43}$-CH) did not significantly differ from those of the starting CHs (CH_H, CH_M, and CH_L). Although degradation can occur during the first step of the reaction, the M_w values of the $DEAE_x$-CH derivatives remained similar to those of the starting CHs (Table 1). However, the obtained M_w values of the DEAE-CH derivatives may be rationalized by considering that the attachment of DEAE can induce conformational changes, thus affecting retention time. Moreover, the M_w distribution is also affected by extensive dialysis. Thus, the polydispersities (M_w/M_n) of the DEAE derivatives were smaller than those of the starting CHs. The reductive amination reaction carried out during the second synthesis step was performed at a low temperature and pH 5.0; thus, significant degradation was not expected to have occurred during the reaction.

Amphiphilic Properties. The self-association of the amphiphilic derivatives was studied in aqueous buffered solutions at pH 5.0. At this pH, CH is positively charged, and medium-M_w samples might aggregate at concentrations >3.0 g/L.[25] Hence, it is expected that at low concentrations, hydrophobically modified CHs will self-associate in aqueous solutions to form intra- and intermolecular aggregates. This intrinsic property might affect not only the conformation of the polymer chains but also their interactions with the cell wall. Hydrophobic modifications might strengthen the interaction with the cell membrane but could also introduce intra- and intermolecular interactions that affect antimicrobial activity. Therefore, amphiphilic polycations, such as small amphiphilic molecules, may be active as aggregate assemblies rather than as discrete polymer chains.[26]

The CAC values were determined on the basis of fluorescence experiments using pyrene as a probe. Figure 2 shows typical graphs of I_1/I_3 based on the emission spectra of pyrene in the presence of increasing concentrations of CH and its derivatives. The obtained I_1/I_3 ratios reflect the microenvironments probed by pyrene and indicate the concentration range at which self-association begins. The less substituted derivatives, $DEAE_{30}$-CH-Dod_3 and $DEAE_{43}$-CH-Dod_5, exhibited no clear breaks in the curves (I_1/I_3 vs concentration) at concentrations of >0.2 g/L, and the I_1/I_3 ratio values remained at approximately 1.7−2.0, indicating that the derivatives were of hydrophilic character. Electrostatic repulsion between positively charged chains overcame the hydrophobic effects of Dod groups, hindering intermolecular aggregation at this concentration range (Figure 2).

The more substituted derivatives exhibited clear decreases in the I_1/I_3 ratios in the range from 5.0×10^{-3} to 1.2×10^{-2} g/L, indicating that aggregates were formed due to intermolecular interactions. The CACs decreased modestly with the degree of substitution with Dod groups (Table 1); however, the CAC values indicate the onset of aggregation in the polydisperse samples. The amphiphilic derivatives prepared from $DEAE_{14}$-CH (M_w = 548.6 kDa), the highest M_w derivative, exhibited a more gradual decrease in the I_1/I_3 ratio (Support Information, Supplementary Figure S6), which might have resulted from the concurrent formation of inter- and intramolecular aggregates. Overall, amphiphilic derivatives of increasing hydrophobicity

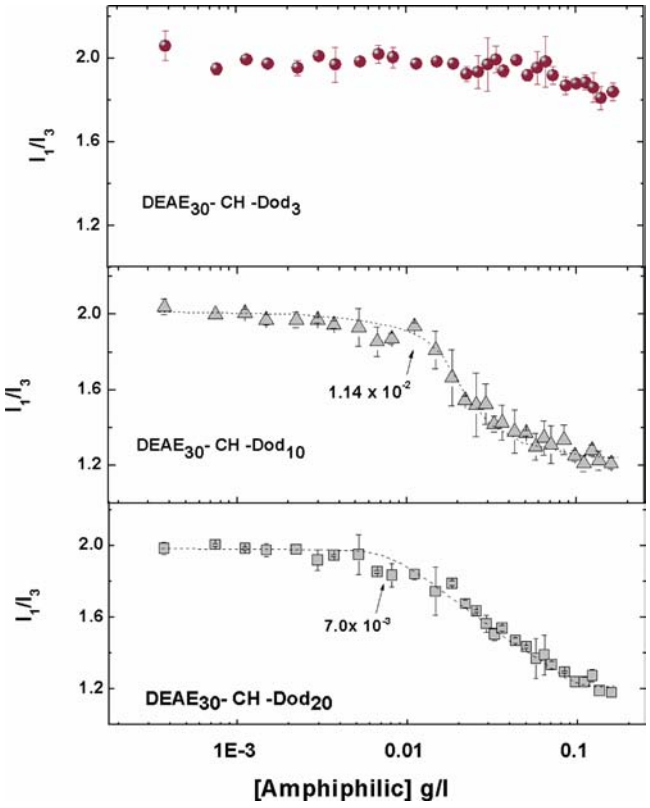

Figure 2. I_1/I_3 ratio versus $DEAE_{30}$-CH-Dod_x concentration at pH 5.0.

may be obtained by increasing the proportion of dodecylaldehyde in the feed.

In Vitro Antifungal Activity against *A. flavus*. The antimicrobial activity of CH has been mainly attributed to its cationic nature in acidic media, which enables its interaction with fungal cell walls and triggers its mechanisms of action. To evaluate the effect of M_w on antifungal activity, we tested three highly deacetylated CHs (16.9, 176, and 517.7 kDa). Figure 3a shows the effects of deacetylated and commercial CHs at various polymer concentrations (0.1 to 1.0 g/L) on the mycelial growth of *A. flavus* after an incubation period of 7 days at 25 ± 2 °C. As can be inferred from Figure 3a, the inhibitory effects of both the deacetylated and commercial samples increased with increasing polymer concentrations and M_w values (16.9 kDa < 176 kDa < 517.7 kDa). The effect of M_w on the antifungal activity of CH has been reported to depend on the type of fungus; for example, fungal growth has been reported to decrease with increasing M_w for *Fusarium oxysporum* and with decreasing DA for *Alternaria solani*, but no dependence on MW or DA has been observed for A*spergillus niger*.[27] Seyfarth et al. reported that antifungal activity against *Candida* species decreases with declining molecular mass;[28] however, oligochitosans with M_w values ranging from 2 to 20 kDa have been recently reported to efficiently inhibit the growth of *Candida* species and clinical isolates of *Candida albicans*.[13] Although the mechanism of antifungal activity remains controversial, reports of cell wall alterations and membrane damage have been shown for oligochitosans against *Candida* species.[13] In the case of *A. parasiticus*, the mechanism has been reported to be mainly fungistatic and has been attributed to the high M_w values (170−300 kDa) of the CH samples employed.[29] Therefore, the increase in activity with increasing M_w may be due to improved fungistatic activity because higher M_w CHs do not permeate the

DOI: 10.1021/acs.jafc.5b00278
J. Agric. Food Chem. 2015, 63, 5725−5731

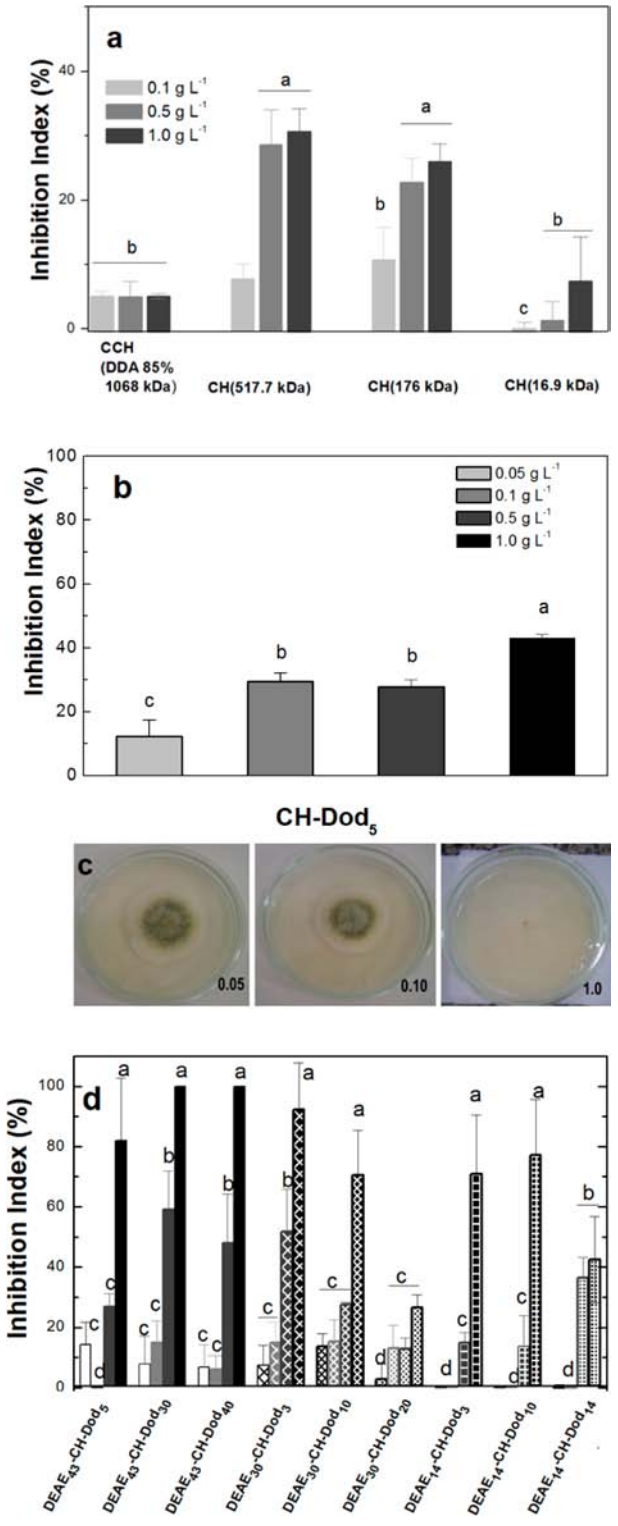

Figure 3. (a) Effect of chitosan molecular weight (CH_H, CH_M, and CH_L) on the mycelial growth of *A. flavus*. (b) Effect of CH-Dod_5 concentration on the inhibition index of *A. flavus*. (c) Effect of $DEAE_{43}$-CH-Dod_{30} concentration on the radial growth of *A. flavus* on the seventh day after inoculation. From left to right: 0.05, 0.1, and 1.0 g/L. (d) Effect of $DEAE_x$-CH-Dod_y derivative concentration on the inhibition index of *A. flavus*. From left to right: 0.05, 0.1, 0.5, and 1.0 g/L. Vertical bars with different letters indicate significant differences according to the Kruskal–Wallis test ($P < 0.05$).

hypha but may affect nutrition through the cell wall.[11] CCH exhibited a lower level of activity (5% at 1.0 g/L), possibly due to the lower availability of amino groups (DDA 85%). The greater antifungal activities exhibited by the CH_H and CH_M samples compared with CCH is attributed to stronger interactions with the cell membrane.

The hydrophobic modification of CH has been reported to effectively enhance antibacterial[15] and antifungal activities by strengthening its interaction with the cell wall.[16,29,30] To investigate the effect of the hydrophobic modification itself, 517.7 kDa deacetylated chitosan (CH_H) was grafted with only Dod (5.0%) (Figure 3b). At a concentration of 1.0 g/L, the inhibition produced was 43%, which was higher than that provided by CH_H (30%). A similar result has also been obtained against *A. parasiticus* in a previous study showing 32% inhibition of radial growth, indicating the importance of hydrophobic interactions in causing further activity.[17]

Conversely, the attachments of both groups (DEAE and Dod) appeared to be synergistic, and a marked increase in antifungal activity was noted. A representative experiment comparing the effect of $DEAE_{43}$-CH-Dod_5 concentration on the radial growth of *A. flavus* after the seventh day of inoculation is shown in Figure 3c, revealing that at a concentration of 1.0 g/L, fungal growth was completely inhibited. At 0.5 g/L, the inhibition indices obtained for the less substituted derivatives of the three series ($DEAE_{14}$-CH-$Dod_{2.5}$, $DEAE_{30}$-CH-Dod_3, and $DEAE_{43}$-CH-Dod_5) were 15, 51, and 27%, respectively. Overall, amphiphilic compounds synthesized from $DEAE_{43}$-CH (M_w = 15.7 kDa) exhibited the highest activities; however, complete inhibition of *A. flavus* was achieved with the most hydrophobic derivatives ($DEAE_{43}$-CH-Dod_{28} and $DEAE_{43}$-CH-Dod_{39}; Figure 3d). Despite their different degrees of substitution, all amphiphilic derivatives exhibited higher activities than those of the starting CHs and their hydrophilic DEAE-CH derivatives. At 1.0 g/L, the most substituted derivatives of the three series ($DEAE_{43}$-CH-Dod_{39}, $DEAE_{30}$-CH-Dod_{19}, and $DEAE_{14}$-CH-Dod_{14}) were able to reduce the mycelial growth of *A. flavus* by 100, 29, and 34%, respectively, indicating that the antifungal activities decreased with the increasing M_w values of the starting DEAE-CH derivatives (15.7, 176.0, and 548.6 kDa, respectively).

The importance of hydrophobic effects on the antimicrobial activities of CH derivatives has been recently reported by our group[16,17] and by others.[15,31] The improved activities of hydrophobized CH derivatives have been attributed to the reinforcement of hydrophobic interactions with the cell membrane.[16,32] Therefore, the attachment of Dod groups is considered important for the antifungal activities of these derivatives. However, the lower inhibition indices observed for the most substituted derivatives of this series indicate that the hydrophilic/hydrophobic balance must be adjusted to obtain higher antifungal activities. As shown in Figure 4a, the attachment of increasing numbers of Dod groups initially increased antifungal activity, but it was decreased for the more substituted derivatives ($DEAE_{14}$-CH-Dod_{14} and $DEAE_{30}$-CH-Dod_{20}).

To confirm this trend, we tested the $DEAE_{14}$-CH-Dod derivatives against *A. parasiticus* and found that inhibition increased with increasing derivative concentration; however, less substituted derivatives were again more effective in inhibiting fungal growth (Figure 4b). It is postulated that the discrete amphiphilic chains of less substituted derivatives might interact with cell membranes more effectively than aggregates

DOI: 10.1021/acs.jafc.5b00278
J. Agric. Food Chem. 2015, 63, 5725–5731

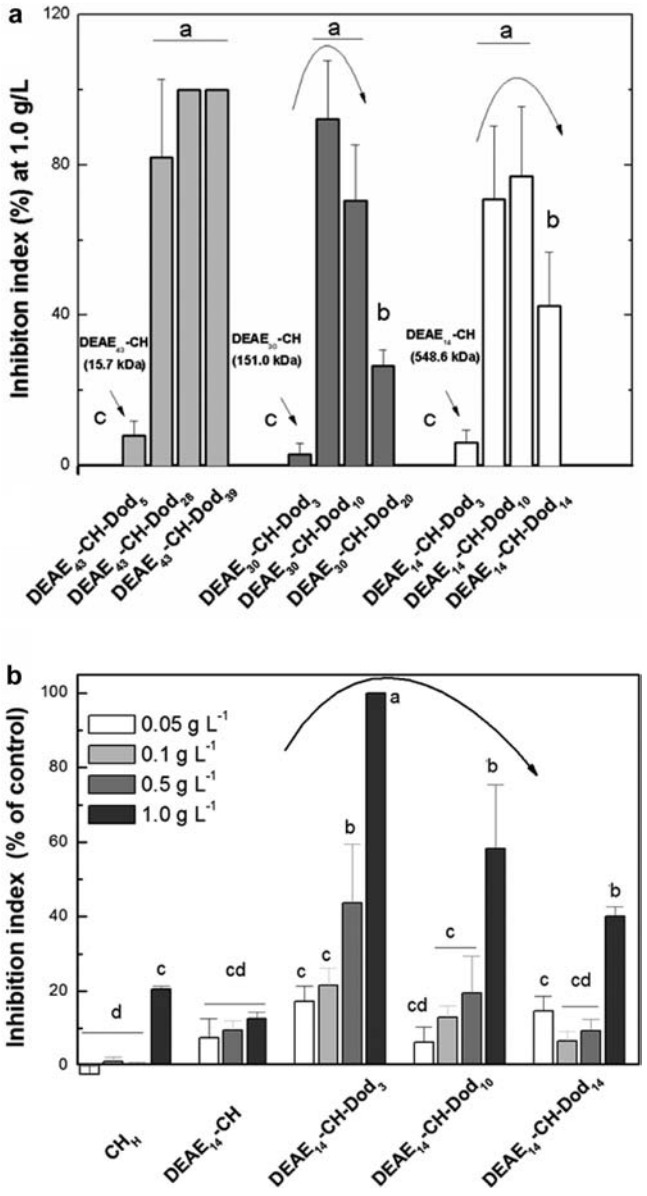

Figure 4. (a) Effects of changes in hydrophobicity: inhibitory effects of $DEAE_x$-CH-Dod_y derivatives (1.0 g/L) on the mycelial fungal growth of *A. flavus*. (b) Inhibition of in vitro growth of *A. parasiticus* in the presence of various concentrations of $DEAE_{14}$-CH-Dod_x derivatives. Vertical bars with different letters indicate significant differences according to the Kruskal–Wallis test ($P < 0.05$). The arrows on the top indicate the trend for inhibition indices with increasing hydrophobe content.

that are formed due to the self-association of more hydrophobic derivatives, thus decreasing the antifungal activities of these two types of derivatives. Overall, the results confirm the importance of hydrophobic groups for the antifungal activities of CH derivatives and may enable the development of more effective biofungicides based on natural polysaccharides.

Conclusions. Novel amphiphilic derivatives of CH were synthesized and characterized, and their antifungal activities against *A. flavus* were tested. Our results showed that deacetylated, medium-M_w (200–500 kDa) CHs were the most effective in inhibiting the mycelial growth of *A. flavus*, achieving an inhibition index of >25%. Attaching DEAE groups increased the solubilities of these derivatives at a neutral pH; however, no significant reduction in the mycelial growth of *A. flavus* was observed as a result of these modifications, indicating that small changes in the polymer structure may significantly affect activity. Hydrophobic modifications with Dod groups strengthened the interaction with the fungal cell wall and markedly increased the antifungal activity of CH against *A. flavus*. These results clearly show that M_w and hydrophobicity must both be controlled to increase antifungal activity. Overall, higher inhibition can be achieved using amphiphilic compounds with high M_w values and low hydrophobicities or using compounds with low M_w values and high hydrophobicities. The synthesis and characterization of new derivatives containing an appropriate hydrophilic/hydrophobic balance are ongoing in our laboratory to optimize their antifungal activities.

■ ASSOCIATED CONTENT

Supporting Information

Figures S1–S9. The Supporting Information is available free of charge on the ACS Publications website at DOI: 10.1021/acs.jafc.5b00278.

■ AUTHOR INFORMATION

Corresponding Author

*(V.A.O.T.) E-mail: verapoli@ibilce.unesp.br. Phone: +55 17 32212358. Fax: +55 17 32248692.

Funding

We thank FAPESP (Grant 2012/03619-9) for their financial support. J.S.G. thanks FAPESP (2010/13942-6) for providing an undergraduate fellowship.

Notes

The authors declare no competing financial interest.

■ REFERENCES

(1) Satpathy, G.; Tyagi, Y. K.; Gupta, R. K. A novel optimized and validated method for analysis of multi-residues of pesticides in fruits and vegetables by microwave-assisted extraction (MAE)-dispersive solid-phase extraction (d-SPE)-retention time locked (RTL)-gas chromatography-mass spectrometry with deconvolution reporting software (DRS). *Food Chem.* **2011**, *127* (3), 1300–1308.

(2) Ymele-Leki, P.; Cao, S.; Sharp, J.; Lambert, K. G.; McAdam, A. J.; Husson, R. N.; Tamayo, G.; Clardy, J.; Watnick, P. I. A high-throughput screen Identifies a new natural product with broad-spectrum antibacterial activity. *PLoS One* **2012**, 7 (2), No. e31307.

(3) Tian, J.; Huang, B.; Luo, X.; Zeng, H.; Ban, X.; He, J.; Wang, Y. The control of Aspergillus flavus with Cinnamomum jensenianum Hand.-Mazz essential oil and its potential use as a food preservative. *Food Chem.* **2012**, *130* (3), 520–527.

(4) Kong, M.; Chen, X. G.; Xing, K.; Park, H. J. Antimicrobial properties of chitosan and mode of action: a state of the art review. *Int. J. Food Microbiol.* **2010**, *144* (1), 51–63.

(5) Zhang, H. Y.; Li, R. P.; Liu, W. M. Effects of chitin and its derivative chitosan on postharvest decay of fruits: a review. *Int. J. Mol. Sci.* **2011**, *12* (2), 917–934.

(6) Jayakumar, R.; Prabaharan, M.; Sudheesh Kumar, P. T.; Nair, S. V.; Tamura, H. Biomaterials based on chitin and chitosan in wound dressing applications. *Biotechnol. Adv.* **2011**, *29* (3), 322–337.

(7) Alburquenque, C.; Bucarey, S. A.; Neira-Carrillo, A.; Urzúa, B.; Hermosilla, G.; Tapia, C. V. Antifungal activity of low molecular weight chitosan against clinical isolates of *Candida* spp. *Med. Mycol.* **2010**, *48* (8), 1018–1023.

(8) Liu, X.; Xia, W.; Jiang, Q.; Xu, Y.; Yu, P. Synthesis, characterization, and antimicrobial activity of kojio acid grafted chitosan oligossaccharide. *J. Agric. Food Chem.* **2014**, *62*, 297–303.

DOI: 10.1021/acs.jafc.5b00278
J. Agric. Food Chem. 2015, 63, 5725–5731

(9) Rabea, E. A.; Badawy, M. E. T.; Stevens, C. V.; Smagghe, G.; Steurbaut, W. Chitosan as antimicrobial agent: applications and mode of action. *Biomacromolecules* **2003**, *4*, 1457−1465.
(10) El Ghaouth, A.; Aru, l. J.; Asselin, A.; Benhamou, N. Antifungal activity of chitosan on post-harvest pathogens: induction of morphological and cytological alterations in *Rhizopus stolonifer*. *Mycol. Res.* **1992**, *96* (9), 769−779.
(11) Li, M. Q.; Chen, X. G.; Liu, J. M.; Zhang, W. F.; Tang, X. X. Molecular weight-dependent antifungal activity and action mode of chitosan against *Fulvia fulva* (Cooke) Ciffrri. *J. Appl. Polym. Sci.* **2011**, *119* (6), 3127−3135.
(12) Geisberger, G.; Gyenge, E. B.; Hinger, D.; Kach, A.; Maake, C.; Patzke, G. R. Chitosan-thioglycolic acid as a versatile antimicrobial agent. *Biomacromolecules* **2013**, *14*, 1010−1017.
(13) Kulikov, S. N.; Lisovskaya, S. A.; Zelenikin, P. V.; Bezrodnykh, E. A.; Shakirova, D. R.; Blagodatskikh, I. V.; Tikhonov, V. E. Antifungal activity of oligochitosans (short chain chitosans) against some *Candida* species and clinical isolates of *Candida albicans*: molecular weight-activity relationship. *Eur. J. Med. Chem.* **2014**, *74*, 169−178.
(14) Mohamed, N. A.; Mohamed, R. R.; Seoudi, R. S. Synthesis and characterization of some novel antimicrobial thiosemicarbazone *O*-carboxymethyl chitosan derivatives. *Int. J. Biol. Macromol.* **2014**, *63*, 163−169.
(15) Rúnarsson, Ö. V.; Holappa, J.; Malainer, C.; Steinsson, H.; Hjálmarsdóttir, M.; Nevalainen, T.; Másson, M. Antibacterial activity of N-quaternary chitosan derivatives: synthesis, characterization and structure activity relationship (SAR) investigations. *Eur. Polym. J.* **2010**, *46*, 1251−1267.
(16) Pedro, R. O.; Takaki, M.; Gorayeb, T. C. C.; Del Bianchi, V. L.; Thomeo, J. C.; Tiera, M. J.; Tiera, V. A. O. Synthesis, characterization and antifungal activity of quaternary derivatives of chitosan on *Aspergillus flavus*. *Microbiol. Res.* **2013**, *168*, 50−55.
(17) Souza, R. H. F. V.; Takaki, M.; Pedro, R. O.; Gabriel, J. S.; Tiera, M. J.; Tiera, V. A. O. Hydrophobic effect of amphiphilic derivatives of chitosan on the antifungal activity against *Aspergillus flavus* and *Aspergillus parasiticus*. *Molecules* **2013**, *18* (4), 4437−4450.
(18) Jiang, X. Z.; Ge, Z. Z.; Xu, J.; Liu, H.; Liu, S. Y. Fabrication of multiresponsive shell cross-linked micelles possessing pH-controllable core swellability and thermo-tunable corona permeability. *Biomacromolecules* **2007**, *8*, 3184−3192.
(19) Syntor Fine Chemicals home page, http://www.syntor.co.uk/diethylaminoethyl-chloride-hydrochloride (accessed April 2, 2015).
(20) Tiera, M. J.; Qiu, X. P.; Bechaouch, S.; Shi, Q.; Fernandes, J. C.; Winnik, F. M. Synthesis and characterization of phosphorylcholine-substituted chitosans soluble in physiological pH conditions. *Biomacromolecules* **2006**, *7* (11), 3151−3156.
(21) Oliveira, F. P. P.; Picola, I. P. D.; Fernandes, J.; Tiera, V. A. O.; SHI, Q.; Barbosa, H. F. G.; Tiera, M. J. Synthesis and evaluation of diethylethylamine-chitosan for gene delivery. *Nanotechnology* **2013**, *24*, 055101−055106.
(22) Vieira, N. A. B.; Moscardini, M. S.; Tiera, V. A. D. O.; Tiera, M. J. Aggregation behavior of hydrophobically modified dextran in aqueous solution: a fluorescence probe study. *Carbohydr. Polym.* **2003**, *53*, 137−143.
(23) Guo, Z. Y.; Chen, R.; Xing, R.; Liu, S.; Yu, H.; Wang, P.; Li, C.; Li, P. Novel derivatives of chitosan and their antifungal activities in vitro. *Carbohydr. Res.* **2006**, *341* (3), 351−354.
(24) Desbrieres, J.; Martinez, C.; Rinaudo, M. Hydrophobic derivatives of chitosan: Characterization and rheological behaviour. *Int. J. Biol. Macromol.* **1996**, *19*, 21−28.
(25) Philippova, O. E.; Volkov, E. V.; Sitnikova, N. L.; Khokhlov, A. R.; Desbrieres, J.; Rinaudo, M. . Two types of hydrophobic aggregates in aqueous solutions of chitosan and its hydrophobic derivative. *Biomacromolecules* **2001**, *2*, 483−490.
(26) Fukushima, K.; Liu, S.; Wu, H.; Engler, A. C.; Coady, D. J.; Maune, H.; Pitera, J.; Nelson, A.; Wiradharma, N.; Venkataraman, S.; Huang, Y.; Fan, W.; Ying, J. Y.; Yang, Y. Y.; Hedrick, J. L. Supramolecular high-aspect ratio assemblies with strong antifungal activity. *Nat. Commun.* **2013**, *4*, 2861.
(27) Younes, I.; Sellimi, S.; Rinaudo, M.; Jellouli, K.; Nasri, M. Influence of acetylation degree and molecular weight of homogeneous chitosans on antibacterial and antifungal activities. *Int. J. Food Microbiol.* **2014**, *185* (18), 57−63.
(28) Seyfarth, F.; Schliemann, S.; Elsner, P.; Hipler, U.-C. Antifungal effect of high- and low-molecular-weight chitosan hydrochloride, carboxymethyl chitosan, chitosan oligosaccharide and *N*-acetyl-D-glucosamine against *Candida albicans*, *Candida krusei* and *Candida glabrata*. *Int. J. Pharm.* **2008**, *353*, 139−148.
(29) Cota-Arriola, O.; Cortez-Rocha, M. O.; Rosas-Burgos, E. C.; Burgos-Hernández, A.; López-Franco, Y. L.; Plascencia-Jatomea, M. Antifungal effect of chitosan on the growth of *Aspergillus parasiticus* and production of aflatoxin B1. *Polym. Int.* **2011**, *60*, 937−944.
(30) Jagadish, R. S.; Divyashree, K. N.; Viswanath, P.; Srinivas, P.; Raj, B. Preparation of *N*-vanillyl chitosan and 4-hydroxybenzyl chitosan and their physico-mechanical, optical, barrier, and antimicrobial properties. *Carbohydr. Polym.* **2012**, *87*, 110−116.
(31) Sajomsang, W.; Gonil, P.; Saesoo, S.; Ovatlarnporn, C. Antifungal property of quaternized chitosan and its derivatives. *Int. J. Biol. Macromol.* **2012**, *50*, 263−269.
(32) Sajomsang, W.; Tantayanon, S.; Tangpasuthadol, V.; Daly, W. H. Quaternization of *N*-aryl chitosan derivatives: synthesis, characterization and antibacterial activity. *Carbohydr. Res.* **2009**, *344*, 2502−2511.

DOI: 10.1021/acs.jafc.5b00278
J. Agric. Food Chem. 2015, 63, 5725−5731

Table 1. Optimization of the Glucosylation of Benzoic Acids[a]

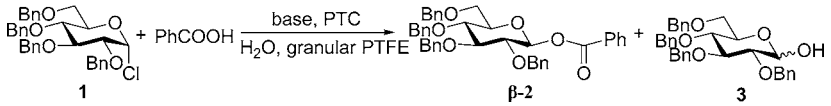

entry	base	H_2O (equiv)	T (°C)	PTC (equiv)	t (h)	.yield[b] (%) (**1**:***β*-2**:**3**)
1	Li_2CO_3	310	40	Aliquat 336 (0.15)	2	0:18:82
2	Li_2CO_3	20	40	Aliquat 336 (0.15)	6	74:17:9
3	Li_2CO_3	15	40	Aliquat 336 (0.15)	12	62:23:15
4	Li_2CO_3	10	40	Aliquat 336 (0.15)	12	37:34:29
5	Na_2CO_3	10	40	Aliquat 336 (0.15)	12	49:36:15
6	K_2CO_3	10	40	Aliquat 336 (0.15)	9	41:49:10
7	TBAOH	30	40	Aliquat 336 (0.15)	1	43:38:19
8	Cs_2CO_3	10	40	Aliquat 336 (0.15)	6	0:67:33
9	Cs_2CO_3	10	25	Aliquat 336 (0.15)	12	42:36:22
10	Cs_2CO_3	10	60	Aliquat 336 (0.15)	2	0:84:16
11	Cs_2CO_3	10	80	Aliquat 336 (0.15)	0.33	>99 only (***β*-2**)
12	Cs_2CO_3	10	80	Aliquat 336 (0.05)	0.67	>99 only (***β*-2**)
13	Li_2CO_3	10	80	TBAB (0.05)	0.67	23:22:55
14	Na_2CO_3	10	80	TBAB (0.05)	0.67	31:51:18
15	K_2CO_3	10	80	TBAB (0.05)	0.67	27:63:10
16	Cs_2CO_3	10	80	TBAB (0.05)	0.67	>99 only (***β*-2**)
17	Cs_2CO_3	310	80	TBAB (0.05)	6.6	0:29:71
18	Cs_2CO_3	20	80	TBAB (0.05)	0.83	0:74:26
19	Cs_2CO_3	15	80	TBAB (0.05)	0.75	>99 only (***β*-2**)
20	Cs_2CO_3	5	80	TBAB (0.05)	1.5	>99 only (***β*-2**)
21	Cs_2CO_3	10	80	TBAB (0.01)	2	>99 only (***β*-2**)
22	Cs_2CO_3	10	80	TBAB (0.1)	0.58	>99 only (***β*-2**)
23[c]		10	80	TBAB (1.05)	0.67	32:0:68
24	Cs_2CO_3	10	80	SDS (0.05)	2	NR[d]

[a]Reaction conditions: 2,3,4,6-tetra-*O*-benzyl-*α*-D-glucopyranosyl chloride (300 mg, 0.54 mmol), benzoic acid (1.05 equiv), base, water, PTC, granular PTFE (5 g), mechanical stirring (400 rpm). [b]Determined by ^{1}H NMR. [c]Reaction conditions: 2,3,4,6-tetra-*O*-benzyl-*α*-D-glucopyranosyl chloride (300 mg, 0.54 mmol), TBAB (182 mg, 0.56 mmol), water (97 mg, 5.38 mmol), granular PTFE (5 g), mechanical stirring (400 rpm). [d]No reaction.

mechanically stirred (400 rpm) at 80 °C for 2 min followed by the addition of water (10 equiv, 97 mg, 5.38 mmol). Initially, the reaction media appeared as thick milk, and it gradually turned to a semisolid, which adhered to the glass. After thin-layer chromatography (TLC) indicated completion of the reaction, ethyl acetate (2 × 10 mL) was added to extract the crude product, which was washed with 5% aqueous Na_2CO_3 (1 × 10 mL) and water (1 × 10 mL) and dried over Na_2SO_4. Concentration under reduced pressure gave benzoic acid 1-*O*-[2,3,4,6-tetra-*O*-benzyl-*β*-D-glucopyranosyl] ester: (351 mg, >99%).

Typical 5−12 g Scale Glycosylation Procedure Using Glucosylation of Benzoic Acid at an 11.7 g Scale as an Example. A mixture of 2,3,4,6-tetra-*O*-benzyl-*α*-D-glucopyranosyl chloride (10 g, 17.89 mmol), benzoic acid (1.05 equiv, 2.29 g, 18.75 mmol), Cs_2CO_3 (0.51 equiv, 2.97 g, 9.12 mmol), TBAB (0.05 equiv, 288 mg, 0.89 mmol), and granular PTFE (5 g) was mechanically stirred (400 rpm) at 80 °C for 2 min, followed by the addition of water (10 equiv, 3.22 g, 178.69 mmol). Initially, the reaction mixture appeared as thick milk and had good fluidity. After completion of the reactions as detected by TLC and removing the oil bath, the products started to solidify and eventually became fine granules. The product was filtered after the addition of water (3 × 15 mL) to wash the reaction flask, and the filtrates were washed with 5% aqueous Na_2CO_3 (3 × 10 mL) and water (3 × 10 mL) and air-dried to give benzoic acid 1-*O*-[2,3,4,6-tetra-*O*-benzyl-*β*-D-glucopyranosyl] ester (11.7 g, > 99%).

Benzoic acid 1-*O*-[2,3,4,6-tetra-*O*-benzyl-*β*-D-glucopyranosyl] ester,[9] *p*-nitrobenzoic acid 1-*O*-[2,3,4,6-tetra-*O*-benzyl-*β*-D-glucopyranosyl] ester,[9] 2-acetyloxybenzoic acid 1-*O*-[2,3,4,6-tetra-*O*-benzyl-*β*-D-glucopyranosyl] ester,[26] palmitic acid 1-*O*-[2,3,4,6-tetra-*O*-benzyl-*β*-D-glucopyranosyl] ester,[27] bile acid 24-*O*-[2,3,4,6-tetra-*O*-benzyl-*β*-D-glucopyranosyl] ester,[28] benzoic acid 1-*O*-[2,3,4,6-tetra-*O*-benzyl-*β*-D-galactopyranosyl] ester,[29] *p*-nitrobenzoic acid 1-*O*-[2,3,4,6-tetra-*O*-benzyl-*β*-D-galactopyranosyl] ester,[30] and *p*-nitrobenzoic acid 1-*O*-[2,3,4-tri-*O*-benzyl-*β*-D-xylopyranosyl] ester[31] are known compounds.

2-(Benzyloxycarbonylamino)-3-phenylpropanoic acid 1-*O*-[2,3,4,6-tetra-*O*-benzyl-*β*-D-glucopyranosyl] ester: 410 mg, 93% yield; white solid, mp 108−109 °C; ^{1}H NMR (600 MHz, $CDCl_3$) *δ* 7.35−7.14 (m, 30H) 5.65 (d, *J* = 8.1 Hz, 1H, H-1), 5.13 (d, *J* = 8.3 Hz, 1H), 5.09 (q, *J* = 12.3 Hz, 1H), 4.90 (d, *J* = 11.0 Hz, 1H), 4.84 (m, 2H), 4.71 (s, 1H), 4.58 (m, 3H), 4.53 (d, *J* = 12.0 Hz, 1H), 3.75 (dt, *J* = 17.8, 9.1 Hz, 5H), 3.60 (dd, *J* = 18.4, 9.7 Hz, 3H), 3.12 (dd, *J* = 20.7, 5.5 Hz, 2H); ^{13}C NMR (151 MHz, $CDCl_3$) *δ* 170.20, 137.86, 135.23, 129.74, 128.58, 128.48, 128.26, 128.17, 127.98, 127.95, 127.89, 127.80, 127.14, 94.85 (C-1), 84.79, 80.40, 75.74, 75.58, 75.09, 74.98, 73.68, 67.02, 54.57, 37.54; IR (KBr) *ν* 3327, 3030, 3897, 1765, 1695, 1537, 1453, 1265, 1157, 1079, 751, 696; HRMS calcd for $C_{51}H_{51}NO_9Na$ [M + Na]$^+$, 844.3456, found, 844.3454.

4-{[(1,1-Dimethylethyl)dimethylsilyl]oxy}-1-[(4-methylphenyl)-sulfonyl]-L-proline 6-*O*-[2,3,4,6-tetra-*O*-benzyl-*β*-D-glucopyranosyl] ester: 480 mg, 97% yield; white solid; mp 117−118 °C; ^{1}H NMR (600 MHz, $CDCl_3$) *δ* 7.79 (d, *J* = 8.0 Hz, 2H), 7.45 (d, *J* = 7.2 Hz, 2H), 7.40−7.28 (m, 18H), 7.22 (d, *J* = 6.6 Hz, 2H), 5.78 (d, *J* = 8.0 Hz, 1H, H-1), 5.01 (d, *J* = 11.0 Hz, 1H), 4.96 (d, *J* = 10.9 Hz, 1H), 4.88 (t, *J* = 10.4 Hz, 2H), 4.80 (d, *J* = 11.0 Hz, 1H), 4.67 (d, *J* = 12.1 Hz, 1H), 4.62 (d, *J* = 10.7 Hz, 1H), 4.56 (d, *J* = 12.1 Hz, 1H), 4.49 (t, *J* = 7.7 Hz, 1H), 4.41 (s, 1H), 3.85−3.75 (m, 4H), 3.71 (t, *J* = 8.2 Hz, 1H), 3.67−3.60 (m, 2H), 3.31 (d, *J* = 10.3 Hz, 1H), 2.44 (s, 3H), 2.25−2.04 (m, 2H), 0.81 (s, 9H), −0.00 (d, *J* = 2.6 Hz, 6H); ^{13}C NMR (151 MHz, $CDCl_3$) *δ* 171.09, 143.60, 143.55, 138.45, 138.07, 129.69, 128.48, 128.42, 127.97, 127.95, 127.86, 127.76, 95.05 (C-1), 84.70, 80.59, 75.68, 75.05, 74.86, 73.51, 70.57, 59.63, 56.43, 40.12, 25.67, 21.58, 17.94, −4.88, −5.01; IR (KBr) *ν* 3060, 2931, 2860, 1769,

DOI: 10.1021/acs.jafc.5b02534
J. Agric. Food Chem. 2015, 63, 5732−5739

1596, 1453, 1348, 1411, 1170, 1090, 777, 698; HRMS calcd for $C_{52}H_{63}NO_{10}SSiNa$ $[M + Na]^+$, 944.3834, found, 944.3834.

4-Pentenoic acid 1-*O*-[2,3,4,6-tetra-*O*-benzyl-*β*-D-glucopyranosyl] ester: 338 mg, >99% yield; white solid; mp 74−75 °C; ^{1}H NMR (600 MHz, $CDCl_3$) δ 7.40−7.25 (m, 18H), 7.14 (d, J = 5.5 Hz, 2H), 5.80 (dd, J = 13.9, 7.4 Hz, 1H), 5.63 (d, J = 8.0 Hz, 1H, H-1), 5.05 (d, J = 17.1 Hz, 1H), 4.99 (d, J = 10.1 Hz, 1H), 4.89 (d, J = 10.8 Hz, 1H), 4.86−4.80 (m, 2H), 4.76 (q, J = 11.4 Hz, 2H), 4.63 (d, J = 12.1 Hz, 1H), 4.53 (d, J = 10.6 Hz, 1H), 4.48 (d, J = 12.1 Hz, 1H), 3.82−3.67 (m, 4H), 3.59 (dd, J = 18.8, 9.6 Hz, 2H), 2.45 (dd, J = 18.3, 9.5 Hz, 1H), 2.36 (s, 3H); ^{13}C NMR (151 MHz, $CDCl_3$) δ 171.47, 138.43, 138.16, 138.08, 137.98, 136.37, 128.49, 128.45, 128.03, 127.97, 127.94, 127.85, 127.78, 115.85, 94.11 (C-1), 84.88, 81.10, 77.28, 75.80, 75.57, 75.08, 73.57, 68.10, 33.50, 28.44; IR (KBr) ν 3063, 3030, 2917, 2864, 1751, 1495, 1453, 1359, 1155, 1081,916, 748, 698; HRMS calcd for $C_{39}H_{42}O_7Na$ $[M + Na]^+$, 645.2823, found, 645.2828.

Ursolic acid 28-*O*-[2,3,4,6-tetra-*O*-benzyl-*β*-D-glucopyranosyl] ester: 483 mg, 92% yield; white solid; mp 79−80 °C; ^{1}H NMR (600 MHz, $CDCl_3$) δ 7.39−7.21 (m, 18H), 7.17 (s, 2H), 5.49 (d, J = 8.1 Hz, 1H, H-1), 5.26 (s, 1H), 4.84 (d, J = 33.2 Hz, 5H), 4.61 (dd, J = 20.3, 10.7 Hz, 2H), 4.50 (d, J = 10.2 Hz, 1H), 3.81−3.65 (m, 4H), 3.64−3.48 (m, 2H), 3.20 (s, 1H), 2.24 (s, 1H), 2.03 (s, 1H), 1.87 (s, 3H), 1.71 (d, J = 8.9 Hz, 2H), 1.55 (d, J = 59.8 Hz, 4H), 1.45−1.14 (m, 10H), 1.03 (d, J = 9.4 Hz, 3H), 0.97 (dd, J = 19.9, 9.6 Hz, 9H), 0.86 (d, J = 8.8 Hz, 6H), 0.77 (d, J = 9.4 Hz, 3H), 0.69 (t, J = 14.4 Hz, 3H); ^{13}C NMR (101 MHz, $CDCl_3$) δ 175.93, 138.47, 138.28, 138.19, 137.50, 128.39, 128.34, 128.31, 127.93, 127.81, 127.63, 127.58, 127.46, 127.13, 125.95, 94.21 (C-1), 85.10, 80.70, 79.05, 77.53, 75.61, 74.96, 74.66, 73.46, 68.29, 55.27, 52.83, 48.12, 47.63, 42.10, 39.50, 39.18, 38.92, 38.75, 36.97, 36.20, 32.73, 30.72, 29.73, 28.32, 28.21, 27.28, 24.43, 23.29, 21.21, 18.31, 17.08, 16.94, 15.68, 15.53; IR (KBr) ν 2923, 2866, 1747, 1496, 1454, 1360, 1308, 1072, 739, 696; HRMS calcd for $C_{64}H_{82}O_8Na$ $[M + Na]^+$, 1001.5902, found, 1001.5901.

Stearic acid 1-*O*-[2,3,4,6-tetra-*O*-benzyl-*β*-D-glucopyranosyl] ester: 435 mg, >99% yield; syrup; ^{1}H NMR (600 MHz, $CDCl_3$) δ 7.30 (m, 18H), 7.13 (m, 2H), 5.62 (d, J = 8.2 Hz, 1H, H-1), 4.89 (d, J = 10.9 Hz, 1H), 4.82 (dd, J = 10.5, 8.7 Hz, 2H), 4.77 (s, 2H), 4.63 (d, J = 12.1 Hz, 1H), 4.50 (dd, J = 23.6, 11.4 Hz, 2H), 3.74 (m, 4H), 3.59 (m, 2H), 2.34 (dd, J = 15.6, 7.8 Hz, 1H), 2.28 (t, J = 7.7 Hz, 1H), 1.61 (m, 2H), 1.27 (dd, J = 27.3, 9.0 Hz, 28H), 0.88 (t, J = 7.0 Hz, 3H); ^{13}C NMR (151 MHz, $CDCl_3$) δ 172.26, 138.46, 138.18, 138.09, 137.98, 128.52, 128.50, 128.46, 128.08, 128.00, 127.98, 127.86, 127.80, 94.04 (C-1), 84.88, 81.13, 77.30, 75.84, 75.56, 75.11, 75.09, 73.58, 68.08, 34.36, 32.05, 29.83, 29.81, 29.79, 29.74, 29.56, 29.50, 29.39, 29.23, 29.18, 24.91, 24.65, 22.83, 14.29; IR (KBr) ν 2924, 2853, 1756, 1458, 1359, 1081, 910, 737, 698; HRMS calcd for $C_{52}H_{70}O_7Na$ $[M + Na]^+$, 829.5014, found, 829.5015.

4-[[(1,1-Dimethylethyl)dimethylsilyl]oxy]-3-methoxybenzoic acid 1-*O*-[2,3,4-tri-*O*-benzyl-*β*-D-xylopyranosyl] ester: 433 mg, 92% yield; syrup; ^{1}H NMR (600 MHz, $CDCl_3$) δ 7.39 (dd, J = 8.3, 1.8 Hz, 1H), 7.35 (d, J = 1.7 Hz, 1H), 7.18−7.14 (m, 10H), 7.08 (s, 1H), 7.04 (s, 4H), 6.68 (d, J = 8.3 Hz, 1H), 5.65 (d, J = 7.6 Hz, 1H, H-1), 4.70 (dd, J = 21.6, 10.9 Hz, 2H), 4.61 (t, J = 6.5 Hz, 1H), 4.57 (d, J = 11.7 Hz, 1H), 4.48 (d, J = 11.6 Hz, 1H), 3.81 (dt, J = 14.1, 7.1 Hz, 1H), 3.68 (s, 1H), 3.64 (s, 2H), 3.52 (ddd, J = 19.5, 16.3, 8.5 Hz, 4H), 3.30−3.25 (m, 1H), 0.82 (d, J = 7.6 Hz, 9H), 0.01 (d, J = 8.0 Hz, 6H); ^{13}C NMR (151 MHz, $CDCl_3$) δ 164.79, 150.81, 150.33, 138.44, 137.98, 137.86, 128.58, 128.48, 128.43, 128.06, 127.95, 127.85, 127.81, 123.92, 122.50, 120.61, 113.20, 95.03 (C-1), 83.45, 80.19, 77.33, 77.12, 76.91, 75.63, 75.05, 73.35, 64.54, 55.52, 25.67, 18.57, −4.52; IR (KBr) ν 2931, 2859, 1729, 1596, 1511, 1460, 1287, 1215, 1079, 890, 698; HRMS calcd for $C_{40}H_{48}O_8SiNa$ $[M + Na]^+$, 707.3011, found, 707.3013.

RESULTS AND DISCUSSION

Initially, a mixture of benzoic acid with acetobromoglucose or acetochloroglucose in the presence of a carbonate, a PTC, water, and granular PTFE was stirred mechanically at various temperatures using the modified stirring rod.[22,23] Various carbonates including lithium, sodium, potassium, and cesium were used; the PTC was Aliquat 336 or TBAB, the amount of water was varied from 10 to 310 equiv, and the reaction temperature ranged from 25 to 80 °C. For all reaction combinations, the desired product, *β*-glucosyl ester, was contaminated with a substantial amount of the partially hydrolyzed products. Therefore, 2,3,4,6-tetra-*O*-benzyl-*α*-D-glucopyranosyl chloride (**1**, Table 1) was used as the starting material. When Li_2CO_3, Na_2CO_3, K_2CO_3, or tetrabutylammonium hydroxide ($TBAOH{\cdot}30H_2O$) was used as the base and Aliquat 336 (0.15 equiv) as the catalyst, the amount of undesired hydrolysis product, 2,3,4,6-tetra-*O*-benzyl-D-glucose (**3**) varied from 29 to 19% (Table 1, entries 4−7). However, the amount of **3** was affected by the amount of water, and 10 equiv of water was found to be optimal in reducing the amount of side product **3** (Table 1, entries 1−6 and 8).

When Li_2CO_3 was replaced with Cs_2CO_3 and the reactions were performed at 40 and 25 °C, the yields of the desired product ***β*-2** were 67 and 36% (Table 1, entries 8 and 9), respectively. Thus, raising the reaction temperature could improve the reaction yield. When the temperature was increased to 60 °C, the yield of ***β*-2** increased to 84% and only 16% of **3** was formed (Table 1, entry 10). Further raising the temperature to 80 °C completely avoided the side reaction (the hydrolysis of **1** to **3**) and gave ***β*-2** in quantitative yield (Table 1, entry 11). When the amount of Aliquat 336 was reduced to 0.05 equiv, the yields were similar, but the reaction time increased from 0.33 to 0.67 h (Table 1, entries 11 and 12).

The only problem associated with this new synthesis is that Aliquat 336 is water-insoluble and contaminates the product. Replacing 0.05 equiv of Aliquat 336 with 0.05 equiv of TBAB led to the quantitative and stereospecific synthesis of ***β*-2** (Table 1, entry 16). Increasing the amount of water to 20 or 310 equiv yielded a mixture of ***β*-2**:**3** in ratios of 74:26 and 29:71 (Table 1, entries 18 and 17), respectively. Decreasing the amount of water to 5 equiv increased the reaction time (1.5 h) (Table 1, entry 20). The reaction rates were altered by variation of the amounts of TBAB (0.01 equiv, 2 h; 0.05 equiv, 0.67 h; and 0.1 equiv, 0.58 h) (Table 1, entries 21, 16, and 22). The reaction rates and yields became worse after using Li_2CO_3, Na_2CO_3, and K_2CO_3 to replace Cs_2CO_3 (Table 1, entries 13−15). The fact that Cs_2CO_3 is much better than the other bases for this glucosylation (Table 1, entries 1−6 vs 8 and 13−15 vs 16) is probably due to the cesium effect.[26,32] It has been reported by Lemieux et al.[33−35] that the anomerizations of tetra-*O*-acetyl-*β*-D-glucopyranosyl chloride took place in the presence of tetraethylammonium chloride, TBAB, or tetrabutylammonium iodide in organic solvents. However, no anomerization was observed when **1** was treated with 1.05 equiv of TBAB (Table 1, entry 23) in this aqueous reaction. The only detected products were **3** and **1** (68:32). This indicated that the reaction rates of **1** with carboxylates were fast enough to avoid the possible hydrolysis of **1** in these aqueous conditions. Using sodium dodecyl sulfate (SDS) (0.05 equiv) instead of TBAB did not produce ***β*-2** (Table 1, entry 24). On the basis of all these results, the optimized conditions are 2,3,4,6-tetra-*O*-benzyl-*α*-D-glucopyranosyl chloride (1.0 equiv), benzoic acid (1.05 equiv), TBAB (0.05 equiv), Cs_2CO_3 (0.51 equiv), water (10 equiv), and granular PTFE (5 g) at 80 °C with mechanical agitation at 400 rpm (Table 1, entry 16).

We believe that this reaction system is probably micelle-catalyzed,[36,37] which is based on the following observations. First, the reaction mixture was milky at the beginning of the reaction and then turned to a semisolid, which adhered to the

DOI: 10.1021/acs.jafc.5b02534
J. Agric. Food Chem. 2015, 63, 5732−5739

Table 2. β-Glycosylation of a Series of Carboxylic Acids[a]

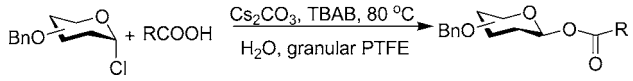

Entry	RCOOH	t (h)	Yield of Glycoside[b]
1	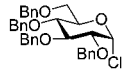	1	94%
2	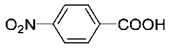	1	97%
3	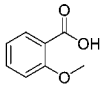	0.83	96%
4	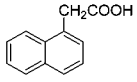	1.2	> 99%
5	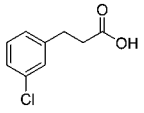	1.3	94%
6	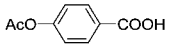	0.75	92%
7	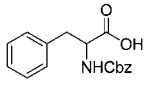	1.5	93%
8	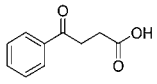	1	97%
9	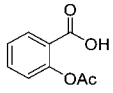	0.67	94%
10	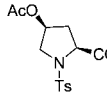	1.6	96%
11	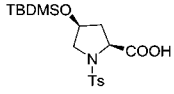	0.83	97%
12	$CH_2{=}CHCH_2CH_2COOH$	0.5	>99%
13	$CH_3(CH_2)_3COOH$	1.2	98%
14	$H_3C(H_2C)_7HC{=}CH(CH_2)_7COOH$	0.67	>99%
15	$CH_3(CH_2)_{14}COOH$	1	>99%
16	$CH_3(CH_2)_{16}COOH$	1.2	>99%
17	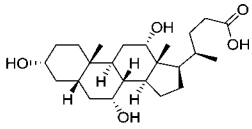	1.5	83%
18	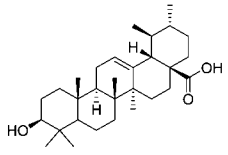	0.8	92%
19	PhCOOH	1	93%
20	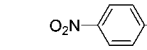	1.2	97%
21	$CH_3(CH_2)_{14}COOH$	0.83	> 99%
22	$CH_3(CH_2)_{16}COOH$	1	> 99%
23	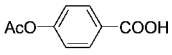	1.4	94%
24	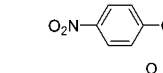	1.5	96%
25	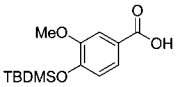	1.4	92%
26	$CH_3(CH_2)_{14}COOH$	1	98%
27	$CH_3(CH_2)_{16}COOH$	1	96%

[a]Reaction conditions: glycosyl chloride (300 mg, 0.54 mmol), acid (1.05 equiv), water (10 equiv), Cs_2CO_3 (0.51 equiv), TBAB (0.05 equiv), granular PTFE (5 g), mechanical stirring (400 rpm) at 80 °C. [b]All conversions were 100%, and all yields are isolated yields.

flask walls and the stirrer after the completion of the reaction. Second, in our previous research in which Aliquat 336 was used as both a solvent and a catalyst,[21−25] the amount of water used was not important. In contrast, the amount of water was critical for this reaction (Table 1, entries 20, 18, and 17 vs entry 16). Third, the reaction temperature had to be raised to 80 °C to reduce the amount of side product **3**. This can be attributed to the efficient formation of micelles at this temperature. All of these facts support the reaction being micelle-catalyzed.

One of the reasons for the stereospecificity of the β-glycosylation is the closer contact between the carboxylates and the glucosyl chlorides in the micelles than in conventional organic solvents. Although it is commonly believed that the negatively charged head of the carboxylates is oriented toward the aqueous phase, it is possible that certain amounts of the carboxylates are oriented toward the glycosyl chlorides because of the geometry or charge demands in the micelles.

Water-soluble TBAB can form ionic pairs with carboxylic acids under basic conditions, which are lipophilic enough to replace Aliquat 336 to form micelles with glycosyl chloride. In the literature, surfactants containing 8−18 carbon atoms in straight alkyl chains are often used in micelle-catalyzed reactions, but there have been no reports of using TBAB in these types of reactions.[38]

Next a series of β-glycosyl esters were synthesized under the optimized conditions. Most of the reaction yields were >90%,

DOI: 10.1021/acs.jafc.5b02534
J. Agric. Food Chem. 2015, 63, 5732−5739

with some being quantitative, and all of the reaction times were short (0.67−2.5 h) (Table 2). In all cases, only the β-glycosyl esters were obtained. The reactions were compatible with a series of functional groups including alkenes (Table 2, entries 1, 12, 14, and 18), nitro groups (Table 2, entries 2, 20, and 24), ethers (Table 2, entries 3 and 25), halide (Table 2, entry 5), aliphatic esters (Table 2, entry 10), phenolic esters (Table 2, entries 6, 9, and 23), benzyloxycarbonylamino group (Table 2, entry 7), ketone (Table 2, entry 8), silyl ethers (Table 2, entries 11 and 25), and hydroxyl groups (Table 2, entries 17 and 18). The ^{1}H NMR and ^{13}C NMR data for the β-glycosyl esters are 5.49−5.92 ppm (1H, J = 7.1−8.2 Hz, H-1) and 94.01−95.48 ppm (C-1), respectively, which are in agreement with the data from the literature.[9,26−31]

It has been reported that glycosylation can improve the properties of peptide biopharmaceuticals.[2,39,40] Therefore, three amino acid derivatives were subjected to the glucosylation conditions, and the yields were excellent (Table 2, entries 7, 10, and 11). However, the yields for carbohydrate−peptide conjugations are around 30% in the literature.[39] Bile acid glycoside, which has been identified in biological materials, has been synthesized as a mixture of α- and β-anomers (ratio of α:β = 1:3) in <30% yields, and it had to be purified via HPLC.[28] However, under our reaction conditions, the β-glycoside was obtained stereospecifically in 83% yield with no chromatography (Table 2, entry 17). Similar results were obtained starting from carboxylic acids and 2,3,4,6-tetra-*O*-benzyl-α-D-galactopyranosyl chloride (Table 2, entries 19−23) or 2,3,4-tri-*O*-benzyl-α-D-xylopyranosyl chloride (Table 2, entries 24−27) in terms of reaction yields, rates, and stereoselectivities.

An additional advantage of the reaction is the simplicity of the workup. In the synthesis of glycosyl esters starting from 300 mg of glycosyl chloride, some of the products adhered to the wall of the flask. These were recovered after in-flask extraction with ethyl acetate and were concentrated to yield pure products without chromatography. In the enlarged scale synthesis of benzoic acid 1-*O*-[2,3,4,6-tetra-*O*-benzyl-β-D-glucopyranosyl] ester using 5 or 10 g of glucosyl chloride, the reaction phenomena were different. The reaction mixture resembled thick milk and had good fluidity at 80 °C. When the oil bath was removed after completion of the reaction, the product gradually became fine granules, which could be filtered with the aid of additional water. The product was quantitative and pure.

In this way, five β-glucosyl esters (Figure 1, ***β*-2**, **4**, **5**, **6**, and **7**) were synthesized quantitatively and stereospecifically in quantities from 5.8 to 12.3 g without using any organic solvents in the entire process. In the 300 mg scale synthesis of **5** and **6**, the yields were not quantitative and organic solvents were used for in-flask extractions. After the scale had been enlarged, the adhesion of the products on the glass was avoided and organic solvent extraction was not needed.

Among the five products, β-glucosyl ester **4** is a useful glucosyl donor.[26,41,42] The advantages of β-glucosyl esters as glucosyl donors over their α-isomers in glucosylations have been reported.[26] Previously it has been prepared as an unspecified stereoisomer mixture in 90−95% yields using 4-pentenoic acid and 1-hydroxyl sugar in organic solvents.[41,42] Glucosyl ester **5** is a precursor of an aspirin prodrug.[43,44] Glucosyl ester **5** has previously been obtained in 67% yield from the reaction of 2,3,4,6-tetra-*O*-benzyl-α-D-glucopyranosyl chloride, aspirin, and Cs_2CO_3.[26] Ursolic acid occurs in various fruits such as apples, basil, bilberries, and cranberries and plants.[45] Glucosyl ester **6** is a key intermediate for ursolic acid

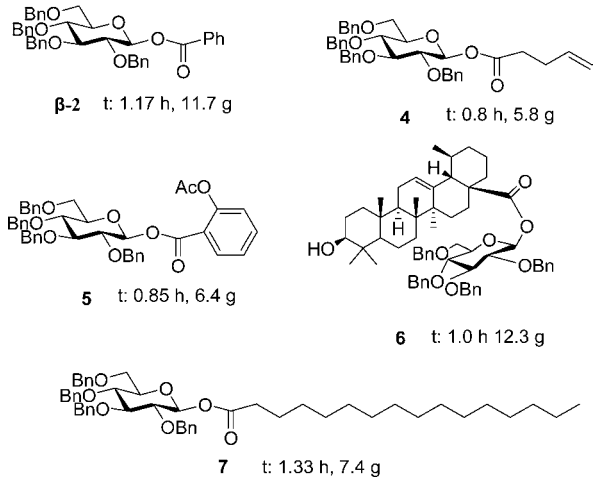

Figure 1. Quantitative synthesis of β-glucosyl esters in 5−12 g scales.

28-*O*-(β-D-glucopyranosyl) ester, an antitumor reagent.[3,46] In previous synthetic routes, the hydroxyl group of the ursolic acid had to be protected in some cases, but this was not necessary for our method.[46,47] It is well-documented in the literature that deprotection of the benzyl group can be achieved using H_2 and Pd/C, in which the olefin double bond can even survive.[48−51] Glycosyl ester ***β*-2** was debenzylated to produce benzoic acid 1-*O*-β-D-glucopyranosyl ester in 97% yield through H_2 and Pd/C hydrogenolysis.

Six experiments were carried out to demonstrate the acceleration effects of the granular PTFE. A mixture of **1** (300 or 1000 mg), benzoic acid (1.05 equiv), Cs_2CO_3 (0.51 equiv), H_2O (10 equiv), and TBAB (0.05 equiv) was mechanically stirred (400 rpm) with granular PTFE (5000 or 0 mg) at 80 °C. For both reaction scales (300 and 1000 mg of **1**), quantitative and stereospecific β-glycoside ***β*-2** was formed (Table 3, entries 1 and 3) when granular PTFE (5000 mg) was used. Without granular PTFE, both reactions ended in a mixture of glucosyl ester and aldosyl hemiacetal **3**, with the latter being the major product of the reaction (81 and 55%) (Table 3, entries 2 and 4). In the 1000 mg scale, both anomers ***α*-2** and ***β*-2** were produced without granular PTFE (Table 3, entry 4). Varying the reactions scaled from 300 to 5000 mg of **1** while keeping the two ratios of granular PTFE to **1** equal to 1:1, we noted that the reaction rate at 300 mg scale was worse than the one at 5000 mg scale (Table 3, entries 5 and 6). This clearly indicated that this type of glycosylation would be more efficient for large-scale preparations and that granular PTFE is critical for this method.

In our previous studies of the synthesis of high-melting-point water-insoluble organic compounds, the granular PTFE functioned as hundreds of individual stirrers, which dispersed the solid materials.[21−25] In this case, the starting glycosyl chlorides are syrups, and the carboxylates are partially or completely water-soluble, giving thick-milk-like reaction mixtures. Most likely the role of the granular PTFE is to promote ion exchange between TBAB and the carboxylates, which facilitates the formation of the micelles.

To demonstrate the advantages of water as a solvent, reactions in water and in organic solvents were compared. A mixture of 2,3,4,6-tetra-*O*-benzyl-α-D-glucopyranosyl chloride (1.0 equiv), benzoic acid (1.05 equiv), TBAB (0.05 equiv), and Cs_2CO_3 (0.51 equiv) was heated in DMF, AcOEt, THF, toluene, or $CHCl_3$, respectively, and the results are shown in

DOI: 10.1021/acs.jafc.5b02534
J. Agric. Food Chem. 2015, 63, 5732−5739

Table 3. Effects of Granular PTFE on the Reaction Rates[a]

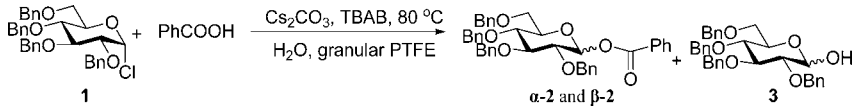

entry	reaction scale **1**:granular PTFE (mg)	recovered **1** (%)	yield[b] (***β*-2**:***α*-2**) (%)	**3** (%)	yield[b] (***β*-2**:***α*-2**) (%)	**3** (%)
			t = 0.67 h		t = 1.50 h	
1	300:5000		>99 (only ***β*-2**)			
2	300:0	9	60 (38:22)	31	19 (only ***β*-2**)	81
			t = 1.10 h		t = 3.30 h	
3	1000:5000		>99 (only ***β*-2**)			
4	1000:0	46	17 (9:8)	37	45 (26:19)	55
			t = 0.85 h		t = 2.5 h	
5	5000:5000		>99 (only ***β*-2**)			
6	300:300	43	34 (only ***β*-2**)	23	64 (only ***β*-2**)	36

[a]Reaction conditions: 2,3,4,6-tetra-*O*-benzyl-*α*-D-glucopyranosyl chloride (300 mg, 0.54 mmol), benzoic acid (1.05 equiv), Cs_2CO_3 (0.51 equiv), water (10 equiv), TBAB (0.05 equiv), granular PTFE, mechanical stirring (400 rpm) at 80 °C. [b]Determined by ^{1}H NMR.

Table 4. Control Experiments in Water and in Organic Solvents

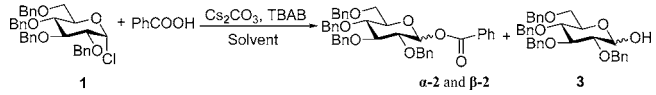

		t = 40 min			t = 6 h		
entry	solvent	recovered **1** (%)	yield[a] (***β*-2**:***α*-2**) (%)	**3** (%)	recovered **1** (%)	yield[a] (***β*-2**:***α*-2**) (%)	**3** (%)
1[b]	H_2O		>99 (only ***β*-2**)				
2[c]	DMF	12	69 (54:15)	19		59 (only ***β*-2**)	41
3[c]	AcOEt	15	21(12:9)	64	3	27 (19:8)	70
4[c]	THF		NR[d]		66	21 (only ***β*-2**)	13
5[c]	toluene		NR[d]		28	55 (42:13)	17
6[c]	$CHCl_3$		NR[d]			NR[d]	

[a]Determined by ^{1}H NMR, [b]Reaction conditions: 2,3,4,6-tetra-*O*-benzyl-*α*-D-glucopyranosyl chloride (300 mg, 0.54 mmol), benzoic acid (1.05 equiv), Cs_2CO_3 (0.51 equiv), water (10 equiv), TBAB (0.05 equiv), granular PTFE (5 g), mechanical stirring (400 rpm) at 80 °C. [c]Reaction conditions: 2,3,4,6-tetra-*O*-benzyl-*α*-D-glucopyranosyl chloride (100 mg, 0.18 mmol), benzoic acid (1.05 equiv), Cs_2CO_3 (0.51 equiv) in DMF or toluene (1 mL) at 80 °C or AcOEt, THF or $CHCl_3$ (1 mL) at refluxing temperatures. [d]No reaction.

Table 4. In DMF and AcOEt, a mixture of ***α*-2** and ***β*-2** (***β*-2**:***α*-**2** = 54:15 and 12:9, respectively) and byproduct **3** (19 and 64%, respectively) was obtained in 40 min (Table 4, entries 2 and 3). When the reaction time was prolonged to 6 h, the product distributions were 59% (***β*-2** only) and 41% (**3**) in DMF and 27% (***β*-2**:***α*-2** = 19:8) and 70% (**3**) in AcOEt (Table 4, entries 2 and 3). No reactions occurred in THF and toluene after 40 min, and after 6 h, yields of only 21% of ***β*-2** and 55% of ***β*-2**/***α*-2** (42:13) were obtained, respectively (Table 4, entries 4 and 5). The reaction did not take place in $CHCl_3$ after 6 h (Table 4, entry 6). Only in water could the *β*-glycosyl esters be synthesized with excellent yields and high stereoselectivities.

In conclusion, a simple, efficient, and green method for synthesizing *β*-glycosyl esters has been developed. The glycosylation is stereospecific and produces excellent yields. The micelle-catalyzed reactions used water-soluble TBAB as the surfactant and water as the medium. Therefore, the workup was simple with no need for chromatography. Five *β*-glucosyl esters were scaled up to 5−12 g, and all of the yields were quantitative. No organic solvents were used in the entire processes. The indispensable roles of granular PTFE and the correct amount of water in these reactions have also been demonstrated. This procedure should be assumed to be particularly useful in synthesizing food additives and modifying the properties of bioactive molecules through glycosylation.

■ ASSOCIATED CONTENT

Ⓢ Supporting Information

Pictures of glucosylations at different scales, general information, typical glycosylation procedures for different scales, analytic data of the products, procedure for the debenzylation of benzoic acid 1-*O*-[2,3,4,6-tetra-*O*-benzyl-*β*-D-glucopyranosyl] ester, ^{1}H NMR and ^{13}C NMR spectra for all compounds, mass spectra for new compounds, and references. The Supporting Information is available free of charge on the ACS Publications website at DOI: 10.1021/acs.jafc.5b02534.

■ AUTHOR INFORMATION

Corresponding Author

*(C.L.) Phone: +86-022-27892351. Fax: +86-022-27403475. E-mail: lichunbao@tju.edu.cn.

Notes

The authors declare no competing financial interest.

DOI: 10.1021/acs.jafc.5b02534
J. Agric. Food Chem. 2015, 63, 5732−5739

REFERENCES

(1) Gruner, S. A. W.; Locardi, E.; Lohof, E.; Kessler, H. Carbohydrate-based mimetics in drug design: sugar amino acids and carbohydrate scaffolds. *Chem. Rev.* **2002**, *102*, 491−514.

(2) Kahne, D.; Leimkuhler, C.; Lu, W.; Walsh, C. Glycopeptide and lipoglycopeptide antibiotics. *Chem. Rev.* **2005**, *105*, 425−448.

(3) Li, J. F.; Chen, S. J.; Zhao, Y.; Li, J. X. Glycoside modification of oleanolic acid derivatives as a novel class of anti-osteoclast formation agents. *Carbohydr. Res.* **2009**, *344*, 599−605.

(4) Michihata, N.; Kaneko, Y.; Kasai, Y.; Tanigawa, K.; Hirokane, T.; Higasa, S.; Yamada, H. High-yield total synthesis of (−)-strictinin through intramolecular coupling of gallates. *J. Org. Chem.* **2013**, *78*, 4319−4328.

(5) Shimotori, Y.; Tsutano, K.; Soga, K.; Osawa, Y.; Aoyama, M.; Miyakoshi, T. Synthesis of glycosyl ferulate derivatives by amine-promoted glycosylation with regioselective hydrolysis using Novozym 435 and evaluation of their antioxidant properties. *Carbohydr. Res.* **2012**, *359*, 11−17.

(6) Shimotori, Y.; Hoshi, M.; Soga, K.; Osawa, Y.; Miyakoshi, T. Synthesis of hydroxycinnamoyl β-D-xylopyranosides and evaluation of their antioxidant properties. *Carbohydr. Res.* **2014**, *388*, 138−146.

(7) Calvaresi, E. C.; Hergenrother, P. J. Glucose conjugation for the specific targeting and treatment of cancer. *Chem. Sci.* **2013**, *4*, 2319−2333.

(8) Ceunen, S.; Geuns, J. M. C. Steviol glycosides: chemical diversity, metabolism, and function. *J. Nat. Prod.* **2013**, *76*, 1201−1228.

(9) Gould, N. D.; Liana Allen, C.; Nam, B. C.; Schepartz, A.; Miller, S. J. Combined Lewis acid and Bronsted acid-mediated reactivity of glycosyl trichloroacetimidate donors. *Carbohydr. Res.* **2013**, *382*, 36−42.

(10) Su, X.; Surry, D. S.; Spandl, R. J.; Spring, D. R. Total synthesis of sanguiin H-5. *Org. Lett.* **2008**, *10*, 2593−2596.

(11) Smith, A. B.; Hale, K. J.; Vaccaro, H. A.; Rivero, R. A. Phyllanthoside-phyllanthostatin synthetic studies. 9. Total syntheses of (−)-phyllanthostatin 1, (+)-phyllanthostatin 2, and (+)-phyllanthostatin 3. *J. Am. Chem. Soc.* **1991**, *113*, 2112−2122.

(12) Kenny, J. R.; Maggs, J. L.; Meng, X.; Sinnott, D.; Clarke, S. E.; Park, B. K.; Stachulski, A. V. Syntheses and characterization of the acyl glucuronide and hydroxy metabolites of diclofenac. *J. Med. Chem.* **2004**, *47*, 2816−2825.

(13) Smith, A. B.; Rivero, R. A.; Hale, K. J.; Vaccaro, H. A. Phyllanthoside-phyllanthostatin synthetic studies. 8. Total synthesis of (+)-phyllanthoside. Development of the Mitsunobu glycosyl ester protocol. *J. Am. Chem. Soc.* **1991**, *113*, 2092−2112.

(14) Vallinayagam, R.; Schmitt, F.; Barge, J.; Wagnieres, G.; Wenger, V.; Neier, R.; Juillerat-Jeanneret, L. Glycoside esters of 5-amino-levulinic acid for photodynamic therapy of cancer. *Bioconjugate Chem.* **2008**, *19*, 821−839.

(15) Hsu, M. C.; Lee, J.; Kishi, Y. Synthetic 3-*O*-methylmannose-containing polysaccharides (sMMPs): design and synthesis. *J. Org. Chem.* **2007**, *72*, 1931−1940.

(16) Zhang, Y.; Wang, P.; Song, N.; Li, M. Bromodimethylsulfonium bromide/silver triflate-promoted glycosylations using glycosyl allenoates as donors. *Carbohydr. Res.* **2013**, *381*, 101−111.

(17) Mei, X.; Heng, L.; Fu, M.; Li, Z.; Ning, J. Synthesis of β-D-Glcp-(1→3)-[β-D-Glcp-(1→6)]-β-D-Glcp-(1→3)-β-D-Glcp-(1→6)-[β-D-Galp-(1→4)-β-D-Glcp-(1→3)]-β-D-GlcpOLauryl, an oligosaccharide with anti-tumor activity. *Carbohydr. Res.* **2005**, *340*, 2345−2351.

(18) Chervin, S. M.; Lowe, J. B.; Koreeda, M. Synthesis and biological evaluation of a new sialyl Lewis X mimetic derived from lactose. *J. Org. Chem.* **2002**, *67*, 5654−5662.

(19) Shimizu, H.; Kitahara, T. Synthesis of the glycosidic precursor of isomeric marmelo lactones, volatile components of the quince fruit *Cydonia oblonga*. *Biosci., Biotechnol., Biochem.* **2002**, *66*, 743−748.

(20) Akin, A.; Curran, T. T. Preparation of CI-1027 glucuronide: metabolite of a remarkable lipid-modulating agent. *Synth. Commun.* **2005**, *35*, 1649−1661.

(21) Cui, X.; Li, B.; Liu, T.; Li, C. A practical solution for aqueous reactions of water-insoluble high-melting-point organic substrates. *Green Chem.* **2012**, *14*, 668−672.

(22) Li, B.; Li, C. Neighboring heteroatom effect unique to aqueous aldol reactions of water-insoluble substrates. *J. Org. Chem.* **2014**, *79*, 2242−2254.

(23) Li, B.; Li, C. Darzens reaction rate enhancement using aqueous media leading to a high level of kinetically controlled diastereoselective synthesis of steroidal epoxyketones. *J. Org. Chem.* **2014**, *79*, 8271−8277.

(24) Li, T.; Cui, X.; Sun, L.; Li, C. Economical and efficient aqueous reductions of high-melting-point imines and nitroarenes to amines: promotion effects of granular PTFE. *RSC Adv.* **2014**, *4*, 33599−33606.

(25) He, G.; Li, B.; Li, C. Quantitative "on water" ring-opening of steroidal epoxides accelerated by sand: a green procedure. *J. Agric. Food Chem.* **2013**, *61*, 2913−2918.

(26) Kunz, H.; Kullmann, R.; Wernig, P.; Zimmer, J. Stereoselective synthesis of β-1-*O*-acyl derivatives of carbohydrates: an application of the cesium effect. *Tetrahedron Lett.* **1992**, *33*, 1969−1972.

(27) Pfeffer, P. E., Moore, G. G. Preparation of 1-α- and 1-β-glucose esters by stereoselective acylation of metalated 2,3,4,6-tetra-*O*-benzyl-D-glucopyranose. US4107425, Aug 15, 1978.

(28) Iida, T.; Nakamori, R.; Yabuta, R.; Yada, S.; Takagi, Y.; Mano, N.; Ikegawa, S.; Goto, J.; Nambara, T. Potential bile acid metabolites. 24. An efficient synthesis of carboxyl-linked glucosides and their chemical properties. *Lipids* **2002**, *37*, 101−110.

(29) Mao, J.; Chen, H.; Zhang, J.; Cai, M. Studies on glycosides XIV. stereoselectivity and reactivity of new C1 leaving group trichloroacetoxyl in glycosylation reaction. *Synth. Commun.* **1995**, *25*, 1563−1565.

(30) Ané, A.; Josse, S.; Naud, S.; Lacône, V.; Vidot, S.; Fournial, A.; Kar, A.; Pipelier, M.; Dubreuil, D. Unusual anomeric rearrangement of *p*-nitrobenzoylxanthate D-glycosides: a new direct stereoselective access to α-thioglycosides from pyranose sugars. *Tetrahedron* **2006**, *62*, 4784−4794.

(31) Bar-Guilloux, É.; Defaye, J.; Driguez, H.; Robic, D. Synthèse, conformation et affinité tréhalasique des α-D-glucopyranosyl-α-D-xylopyranoside, α-D-glucopyranosyl-α-D-mannopyranoside et α-D-allopyranosyl-α-D-glucopyranoside. *Carbohydr. Res.* **1975**, *45*, 217−236.

(32) Gisin, B. F. The preparation of Merrifield-resins through total esterification with cesium salts. *Helv. Chim. Acta* **1973**, *56*, 1476−1482.

(33) Lemieux, R. U.; Levine, S. Synthesis of alkyl 2-deoxy-α-D-glycopyranoside and their 2-deuterio derivative. *Can. J. Chem.* **1964**, *42*, 1473−1480.

(34) Lemieux, R. U.; Hayami, J. The mechanism of the anomerization of the tetra-*O*-acetyl-D-glucopyranosyl chlorides. *Can. J. Chem.* **1965**, *43*, 2161−2173.

(35) Lemieux, R. U.; Lineback, D. R. The mechanism of the dehydrobromination of tetra-*O*-acetyl-α-D-glucopyranosyl bromide. *Can. J. Chem.* **1965**, *43*, 94−105.

(36) Gawande, M. B.; Bonifacio, V. D.; Luque, R.; Branco, P. S.; Varma, R. S. Benign by design: catalyst-free in-water, on-water green chemical methodologies in organic synthesis. *Chem. Soc. Rev.* **2013**, *42*, 5522−5551.

(37) La Sorella, G.; Strukul, G.; Scarso, A. Recent advances in catalysis in micellar media. *Green Chem.* **2015**, *17*, 644−683.

(38) Tehrani-Bagha, A.; Holmberg, K. Solubilization of hydrophobic dyes in surfactant solutions. *Materials* **2013**, *6*, 580−608.

(39) Jerić, I.; Horvat, Š. Novel ester-linked carbohydrate−peptide adducts: effect of the peptide substituent on the pathways of intramolecular reactions. *Eur. J. Org. Chem.* **2001**, *2001*, 1533−1539.

(40) Brimble, M. A.; Edwards, P. J.; Harris, P. W. R.; Norris, G. E.; Patchett, M. L.; Wright, T. H.; Yang, S.-H.; Carley, S. E. Synthesis of the antimicrobial S-linked glycopeptide, glycocin F. *Chem.−Eur. J.* **2015**, *21*, 3556−3561.

(41) Choi, T. J.; Baek, J. Y.; Jeon, H. B.; Kim, K. S. A new efficient glycosylation method employing glycosyl pentenoates and PhSeOTf. *Tetrahedron Lett.* **2006**, *47*, 9191−9194.

DOI: 10.1021/acs.jafc.5b02534
J. Agric. Food Chem. 2015, 63, 5732−5739

(42) Baek, J. Y.; Choi, T. J.; Jeon, H. B.; Kim, K. S. A highly reactive and stereoselective β-mannopyranosylation system: mannosyl 4-pentenoate/PhSeOTf. *Angew. Chem., Int. Ed.* **2006**, *45*, 7436−7440.
(43) Truelove, J. E.; Hussain, A. A.; Kostenbauder, H. B. Synthesis of 1-*O*-(2′-acetoxy) benzoyl-α-D-2-deoxyglucopyranose, a novel aspirin prodrug. *J. Pharm. Sci.* **1980**, *69*, 231−232.
(44) Hanessian, S.; Mascitti, V.; Lu, P.-P.; Ishida, H. One-step stereocontrolled synthesis of α-anomeric carboxylic acid esters from unprotected glycosyl donors: a water-soluble aspirin pro-drug analogue. *Synthesis* **2002**, *2002*, 1959−1968.
(45) Sultana, N. Clinically useful anticancer, antitumor, and antiwrinkle agent, ursolic acid and related derivatives as medicinally important natural product. *J. Enzyme Inhib. Med. Chem.* **2011**, *26*, 616−642.
(46) Wang, P.; Li, C.; Zang, J.; Song, N.; Zhang, X.; Li, Y. Synthesis of two bidesmosidic ursolic acid saponins bearing a 2,3-branched trisaccharide residue. *Carbohydr. Res.* **2005**, *340*, 2086−2096.
(47) Bliard, C.; Massiot, G.; Nazabadioko, S. Glycosylation of acids under phase transfer conditions. Partial synthesis of saponins. *Tetrahedron Lett.* **1994**, *35*, 6107−6108.
(48) Schmidt, R. R.; Michel, J. *O*-(α-D-Glucopyranosyl)-trichloroacetimidate as a glucosyl donor. *J. Carbohydr. Chem.* **1985**, *4*, 141−169.
(49) Kai, K.; Horita, J.; Wakasa, K.; Miyagawa, H. Three oxidative metabolites of indole-3-acetic acid from *Arabidopsis thaliana*. *Phytochemistry* **2007**, *68*, 1651−1663.
(50) Schimmel, J.; Passos Eleutério, M. I.; Ritter, G.; Schmidt, R. R. Synthesis of saponins with cholestanol, cholesterol, and friedelanol as aglycones. *Eur. J. Org. Chem.* **2006**, *2006*, 1701−1721.
(51) Shimoda, K.; Hamada, H.; Hamada, H. Chemo-enzymatic synthesis of ester-linked taxol−oligosaccharide conjugates as potential prodrugs. *Tetrahedron Lett.* **2008**, *49*, 601−604.

DOI: 10.1021/acs.jafc.5b02534
J. Agric. Food Chem. 2015, 63, 5732−5739

agricultural soil, and their chemical structures and physical properties are listed in Table 1.

Table 1. Chemical Structures and Physical Properties of Herbicides

common name	acetochlor	metribuzin
Chemical structure	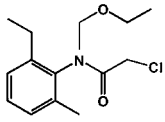	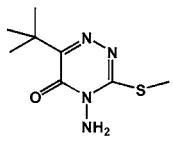
Mol wt (g mol^{-1})	269.77	214.28
Density (g cm^{-3})[a]	1.10	1.28
Solubility in water (mg L^{-1})[a]	223 (25 °C)	1200 (20 °C)
logK_{ow}[a]	3.03	1.70

[a]Data from http://www.guidechem.com.

Treatment of Biochars with Soil Minerals. The biochars obtained after thermal treatment (at 400 and 600 °C) were treated in an aqueous suspension of alumina or Ca-mont at a ratio of 10 g of mineral per gram of biochar sample. First, 1 g of biochar sample was mixed with mineral powder and then soaked in 100 mL of deionized pure water. The suspension was mixed with gentle stirring at room temperature for 24 h and placed in a thermostatic bath at 25 ± 0.1 °C with shaking for an additional 6 days at a rotation speed of 125 rpm. The pH during the treatment was monitored, and final pH values in the suspension close to neutral (7.0–7.8) were observed. The biochar pieces were separated by filtration through a sieve with a pore diameter of 0.15 mm, and the pieces caught on the sieve were washed with deionized pure water to remove the surface-adhered minerals. Finally, the treated biochar products were oven-dried at 70 °C and are referred to hereafter as Al-BC400, Al-BC600, Mo-BC400, and Mo-BC600, according to the fresh biochars (BC400 or BC600) that were treated with either alumina (Al-) or Ca-mont (Mo-). All of the biochar samples were ground to <0.15 mm in size for use in the following characterization and sorption experiments.

Biochar Sample Characterization. The elemental (C, H, O, N) compositions of the biochars were determined in an EA3000 elemental analyzer (Euro Vector) with an average of triplicate experiments. Specifically, the oxygen content was directly measured with the oxygen analysis model in the same analyzer at the set furnace temperature of 1080 °C. The ash content of biochars was determined by heating the samples at 800 °C for 4 h. The surface characteristics of the biochars and two minerals (alumina and Ca-mont) were obtained from nitrogen adsorption isotherms at 77 K (Figure S1 in the Supporting Information) in a Tristar II 3020 surface area and porosity analyzer (Micromeritics) after degassing at 473 K. The specific surface area (SA_{BET}) was determined using the Brunauer–Emmett–Teller (BET) method, and the micropore area (SA_{micro}) was obtained with the *t*-plot method. The pore size distribution, average pore diameter (PD), cumulative surface area, and cumulative volume of the pores between diameters of 17 and 500 Å ($SA_{17-500\ Å}$ and $PV_{17-500\ Å}$) were established by analyzing the N_2 adsorption data using the Barrett–Joyner–Halenda (BJH) method. Infrared spectra (IR) were recorded in the 4000–400 cm^{-1} region on a Nexus FT-IR spectrophotometer (Nicolet) using a KBr pellet. A JSM-6360LV scanning electron microscope (SEM) (JEOL) equipped with an X-act energy-dispersive X-ray spectrometer (EDX) (Oxford) was used for the morphological survey and elemental identification of the surface of the biochars.

Sorption Experiments. The sorption isotherms of two herbicides on the biochar samples were determined by batch equilibration of the solid biochars (0.10 g for sorption of acetochlor and 0.20 g for sorption of metribuzin) in 25 mL of aqueous solutions of various initial herbicide concentrations (C_0, μmol L^{-1}), which ranged from 100 to 700 μmol L^{-1} for acetochlor (the saturated concentration C_s = 827 μmol L^{-1} (25 °C)) and from 700 to 4200 μmol L^{-1} for metribuzin (C_s = 5600 μmol L^{-1} (20 °C)), respectively. For comparison, the sorption of herbicides to the two minerals was carried at the same range of initial herbicide concentrations, but with different doses of solid minerals (0.10 and 0.20 g for sorption of acetochlor to alumina and Ca-mont and 2.0 g for sorption of metribuzin to alumina, respectively). The sorption experiment was carried out in a thermostatic shaker bath at 25 ± 0.1 °C for 24 h according to a previous method,[24] and the preliminary kinetic studies (Figure S2 in the Supporting Information) indicated that the sorption equilibrium had been reached before 24 h. The analysis of the supernatant solution was conducted in an LC-20A HPLC system (Shimadzu) equipped with an ultraviolet detector. The herbicides, acetochlor and metribuzin, were analyzed at 225 and 228 nm, respectively, with a detection limit of 0.2 μmol L^{-1} for both herbicides. The amount adsorbed (Q_e, μmol g^{-1}) was calculated from the difference in concentration between the initial (C_0, μmol L^{-1}) and the equilibrium (C_e, μmol L^{-1}) solutions. Blanks without herbicide and duplicates of each sorption point were used in every experiment series.

RESULTS AND DISCUSSION

Influence of Soil Minerals on Biochars' Properties. Elemental compositions of biochars before and after treatment with soil minerals are listed in Table 2. The total amount of measured elements (C, H, and O) accounted for 99.0% (weight) and 94.5% for the untreated BC400 and BC600 biochars, respectively. The very low ash contents indicated few intrinsic minerals in these two biochars. However, much lower percentages of C, H, and O elements were measured for the mineral-treated biochars (Al-BC400, Al-BC600, Mo-BC400, and Mo-BC600). This difference is attributed to the residual minerals (accounting for 10.4–18.1% in weight) in these treated biochars, which was confirmed by SEM/EDX analysis as shown in Figure 1. In this figure, Si and Al elements of Ca-mont were observed on the surface of the Mo-BC600 biochar, and Al element of alumina on the surface of the Al-BC600 biochar (more details can be found in Figures S4 and S5 in the Supporting Information). The increased H/C and O/C ratios

Table 2. Elemental Composition of Biochar Samples

biochar	C[a] (%)	H[a] (%)	O[a] (%)	C + H + O (%)	H/C[b]	O/C[b]	mineral[c] (%)	ash (%)
BC400	73.8	2.89	22.3	99.0	0.471	0.226		0.9
Al-BC400	59.2	2.52	19.2	80.9	0.511	0.244	18.1	16.1
Mo-BC400	59.4	2.56	20.4	82.3	0.516	0.257	16.7	13.5
BC600	81.7	1.89	10.8	94.5	0.278	0.0994		1.6
Al-BC600	62.7	1.83	12.6	77.1	0.351	0.151	17.4	16.6
Mo-BC600	70.8	1.81	11.5	84.1	0.307	0.122	10.4	10.1

[a]Elemental content in weight presented as the average of triplicates. [b]Atomic ratios. [c]The content of mineral (alumina or Ca-mont) was estimated from the difference of total elements measured (C + H + O) between the original biochars and the mineral-treated biochars.

DOI: 10.1021/acs.jafc.5b01654
J. Agric. Food Chem. 2015, 63, 5740–5746

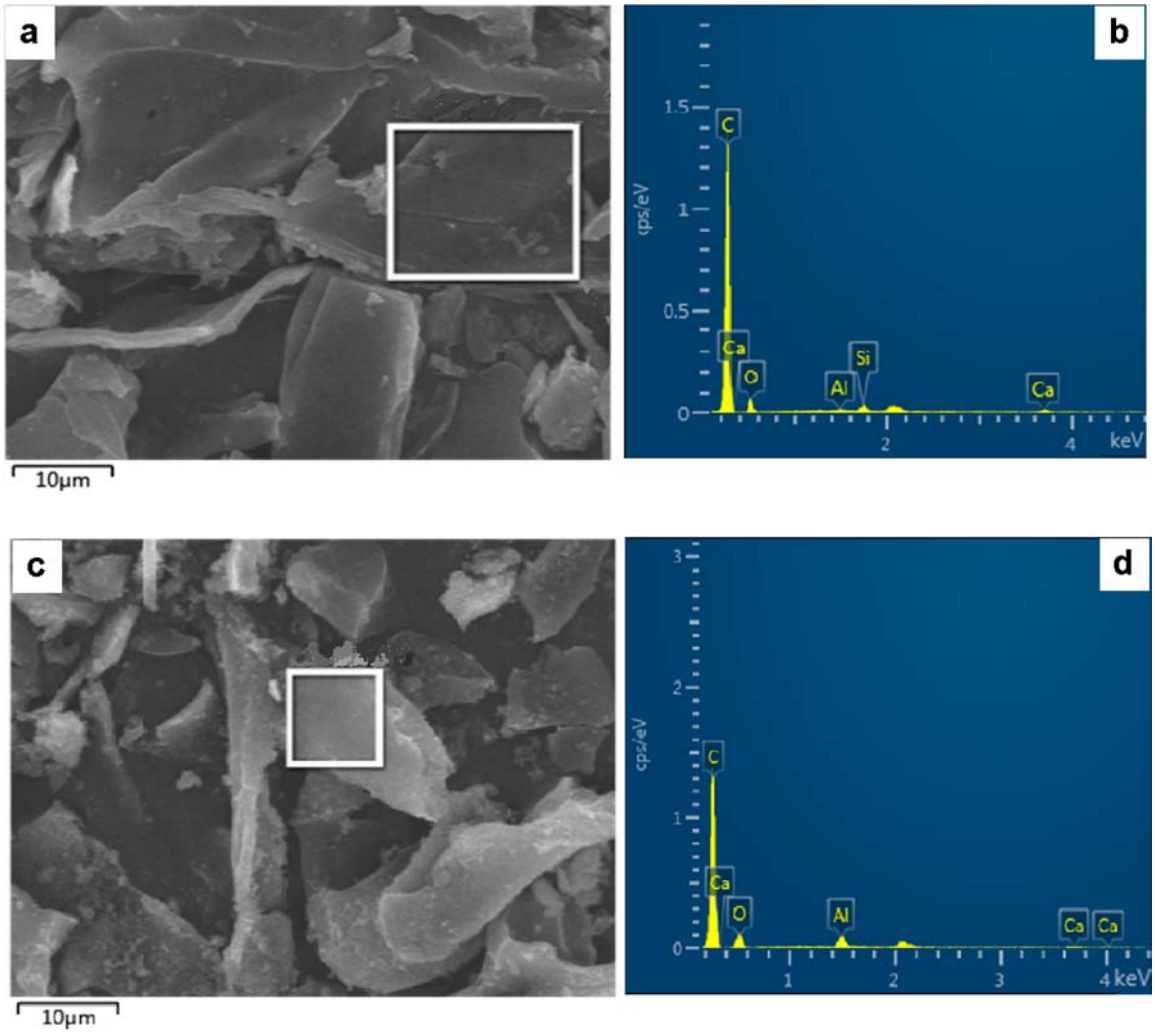

Figure 1. SEM/EDX analysis of mineral-treated biochars: (a) SEM image of Mo-BC600 biochar, (b) EDX spectrum of square region inside image (a), (c) SEM image of Al-BC600 biochar, and (d) EDX spectrum of square region inside image (c).

Table 3. Porous Structure of Biochar Samples

sample	SA_{BET}[a] ($m^2\ g^{-1}$)	PD (Å)	SA_{micro} ($m^2\ g^{-1}$)	$SA_{17-500\ Å}$ ($m^2\ g^{-1}$)	$PV_{17-500\ Å}$ ($cm^3\ g^{-1}$)	$SA_{17-500\ Å}/SA_{micro}$
BC400	121	33.4	77.3	29.0	0.0212	0.375
Al-BC400	235 (273)[b]	67.2	159 (189)	56.7 (59.9)	0.0644	(0.316)
Mo-BC400	127 (142)[b]	49.4	87.0 (99.5)	30.2 (29.9)	0.0288	(0.300)
BC600	430	27.2	316	97.6	0.0647	0.309
Al-BC600	441 (527)[b]	49.9	278 (336)	161 (189)	0.163	(0.562)
Mo-BC600	416 (461)[b]	33.4	298 (332)	111 (121)	0.0864	(0.366)
alumina	64.4	279	23.0	42.9	0.173	1.87
Ca-mont	55.1	153	25.8	32.1	0.0716	1.24

[a]SA_{BET}, BET specific surface area; PD, BJH adsorption average pore diameter; SA_{micro}, *t*-plot micropore area; $SA_{17-500\ Å}$, BJH adsorption cumulative surface area of pores between 17 and 500 Å diameter; $PV_{17-500\ Å}$, BJH adsorption cumulative volume of pores between 17 and 500 Å diameter. [b]Data in parentheses are corrected values obtained by deducting the contribution of residual minerals in the treated biochar samples.

for the mineral-treated biochars are likely related to the water bonded in the residual minerals. The mineral-bonded water was evaporated in measurement of ash content, which resulted in the lower value of ash content than the estimated mineral content in the same mineral-treated biochar.

Significant changes of surface characteristics were obtained for both biochars after treatment with soil minerals, as shown in Table 3. Both the surface area (SA_{BET}) and the average pore diameter (PD) of the BC400 biochar were increased after treatment with minerals ($p < 0.05$). Additionally, the average PD of the BC600 biochar was increased ($p < 0.10$), although no obvious enhancement of its surface area was observed. The residual minerals in the treated biochar samples should be considered before we discuss these enhancements, because both alumina and clay are materials containing porous structures (Table 3 and Figure S6 in the Supporting Information). If their porous structure was assumed to not be changed during the mixing with the biochars, the surface

DOI: 10.1021/acs.jafc.5b01654
J. Agric. Food Chem. 2015, 63, 5740−5746

characteristics of the treated biochars may be corrected by deducting the fractions that should be attributed to the residual minerals. We observe from the corrected data (as shown in parentheses) that the micropore area (SA_{micro}) of the BC400 biochar was enhanced by 2.4 times after treatment with alumina, and its mesopore area ($SA_{17-500\ Å}$) was doubled ($p < 0.05$). In our treatment of the biochars with alumina, neither thermal nor chemical processes were involved, so the porous structure would have been produced during the pyrolysis of the wood biomass. During the cooling process after thermal treatment, some micropores should be blocked by condensed noncarbonized organic matter, the byproducts of wood pyrolysis at relatively low temperature.[26−28] Most likely, the alumina removed some of these organic blocks from the biochar pores during the mineral treatment.

However, only a slight increase in the micropore area (SA_{micro}) was observed after alumina treatment for the higher temperature biochar (BC600 vs Al-BC600) ($p < 0.10$), and the increased surface area was mainly attributed to the mesopores, as suggested in the corrected data in parentheses in Table 3 and pore size distribution shown in Figure 2. In contrast to the

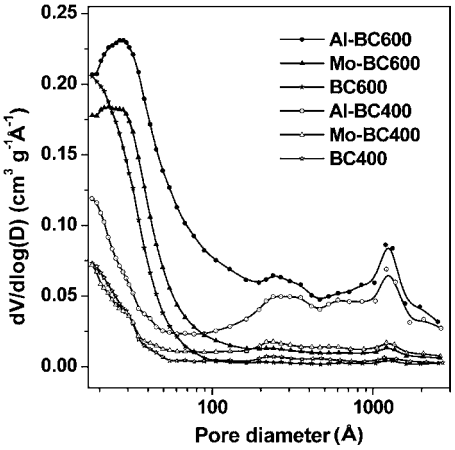

Figure 2. BJH pore size distribution (17−3000 Å diameter) of various biochars.

biochar obtained at lower temperature (400 °C), the microporous structures were well developed during pyrolysis at the higher temperature (600 °C), and the alumina further expanded some micropores into mesopores by digging the condensed organic matter out from the micropores. The decrease of micropore area after pore expansion should be compensated by the new opening of some blocked micropores by alumna treatment, resulting in the lesser increase of SA_{micro} for the higher temperature biochar. According to the pore size distribution shown in Figure 2 and Figure S6 in the Supporting Information, the fraction of macropores (>500 Å) for the alumina-treated biochars (Al-BC400 and Al-BC600) should be attributed to the residual alumina. In conclusion, the alumina expanded the pores, and the contribution of mesopores (17−500 Å) to the total pore volume and pore area was increased for the higher temperature biochar (BC600), whereas both micropores and mesopores contributed to the enlarged pore volume and pore area for the lower temperature biochar (BC400).

The pore-expanding effect was also observed in the clay-treated biochars (Mo-BC400 and Mo-BC600). For the lower temperature (BC400) biochar, expansion of the surface area by the Ca-mont was due to the increased micropore area ($p < 0.10$), whereas the pore expansion of the BC600 biochar was mainly due to the increased mesopore area ($p < 0.10$). Specifically, the clay expanded the pores in the biochars in a similar manner as alumina expanded them, despite the smaller pore area in comparison to the alumina-treated biochars.

Potential Role of Soil Minerals on Expanding the Pore of Biochars. The pore expansion of the biochars after mineral treatment may be explained by the adsorption of biochars' authigentic organic matter by soil minerals. Previous studies showed that alumina and its hydrated form (Al-OOH) are both good adsorbents for natural organic matter,[22,25] and such adsorption is believed to be an important method of retention of organic matter in soils and sediments.[29] Montmorillonite clay is also a well-known adsorbent for organic matter. Lin et al.[30] investigated recently the water-extractable organic carbon (WEOC) in biochars and found that the dominant fractions of WEOC in the low-temperature biochar are humic acids and low-molecular-weight neutrals (alcohols, aldehydes, ketones, sugars, etc.). Despite their trace amount (e.g., 93.4 $\mu g\ g^{-1}$ in a wood biochar by slow pyrolysis at 450 °C),[30] these dissolved organic matters may affect the sorption of herbicides and influence the herbicides' mobility in biochar-amended soil.[31,32] In addition, solvent-extractable hydrocarbons (e.g., polycyclic aromatic hydrocarbons, PAHs) have been detected in biochars, with maximum PAH content of 26.6 $\mu g\ g^{-1}$ in a wood biochar produced at 400 °C.[26,33] If these solvent-extractable matters were removed from the wood biochar, the obviously enhanced surface area and pore volume were observed by Nguyen et al.[34] Therefore, it is reasonable to propose that the biochars prepared at moderate temperatures (400−600 °C) have a porous structure, and the pore surface is coated by some organic matter removable by soil minerals. The FT-IR spectra (Figure S7 in the Supporting Information) show apparent attenuation of absorption at 1640 cm^{-1} (C═O) and 1040 cm^{-1} (C—O—C) for both the Al-BC400 and Mo-BC400 biochars in comparison with the BC400 biochar, which suggests the removal of some oxygen-containing organic matter from the biochar surface. Thus, the removal may involve the interaction with surface functional groups of minerals. Specifically, at a pH close to neutral (7.0−8.5, as shown in Figure S8 in the Supporting Information) but below the point of zero charge for alumina,[22] there exists on the mineral surface some crystallographically bound $>Al-OH_2^+$ groups,[25] which probably interact with those oxygen-containing organic matter by the reaction

$$>Al-OH_2^+ + HO-R \rightarrow >Al-OH_2-O-R + H^+ \quad (1)$$

The release of hydrogen protons is confirmed by the falling pH during the treatment of biochars with alumina and Ca-mont, specifically in the first 3 days (Figure S8 in the Supporting Information). The latter mineral may possibly interact with biochars in a similar way as alumina, as surface bound $>Al-OH_2^+$ groups might also exist on the clay if its high content of aluminum oxide were considered.

The pore-expanding effect of soil minerals on the biochars may explain the change in surface properties of biochars with soil applications, particularly the increased surface area during aging in soil.[35,36] Trigo et al.[35] suggested that the increase resulted from the elimination of the organic film from the biochar surface, which is in good agreement with our research results.

DOI: 10.1021/acs.jafc.5b01654
J. Agric. Food Chem. 2015, 63, 5740−5746

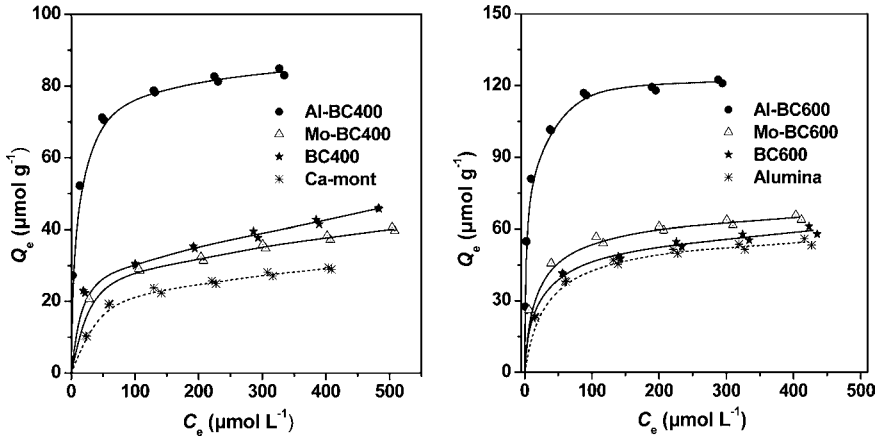

Figure 3. Sorption isotherms of acetochlor to various biochars, alumina, and clay at 25 °C.

Table 4. Fitting Results of the Sorption Data with the Combined Adsorption/Partition Model

biochar/herbicide	Q_A (μmol g^{-1})	K_P(L g^{-1})	R	Q_A/Q_e at C_e/C_s = 0.3 (%)	Q_A/SA_{BET} (μmol m^{-2})	$Q_A/SA_{17-500\ Å}$ (μmol m^{-2})
BC400/Atl[a]	26.8	0.0399	0.994	73.0	0.221	0.924
Al-BC400/Atl	75.2 (81.8)[b]	0.0273	0.985	91.7	(0.299)	(1.36)
Mo-BC400/Atl	26.0 (27.3)	0.0286	0.996	78.6	(0.193)	(0.914)
BC600/Atl	43.7	0.0380	0.979	82.3	0.102	0.448
Al-BC600/Atl	114 (130)	0.0262	0.995	94.6	(0.246)	(0.687)
Mo-BC600/Atl	52.9 (57.1)	0.0306	0.973	87.5	(0.124)	(0.470)
alumina/Atl	46.5	0.0282	0.972		0.722	1.08
Ca-mont/Atl	20.1	0.0230	0.994		0.364	0.625
BC400/Mtb[a]	63.2	0.0165	0.992	69.5	0.522	2.18
Al-BC400/Mtb	153 (187)	0.0196	0.974	82.3	(0.684)	(3.12)
BC600/Mtb	90.8	0.0120	0.982	81.8	0.211	0.930
Al-BC600/Mtb	184 (224)	0.0233	0.989	82.4	(0.426)	(1.19)
alumina/Mtb	3.70	0.00165	0.998		0.0575	0.0862

[a]Atl and Mtb refer to acetochlor and metribuzin, respectively. [b]Data in parentheses are corrected values by deducting the contribution of residual minerals in the treated biochars.

Changed Sorption of Herbicides to Mineral-Treated Biochars. Alumina-treated biochars (Al-BC600 and Al-BC400) exhibit an increase in sorption for the herbicide acetochlor as shown in Figure 3. For the same equilibrium concentration of the acetochlor solution, the amount of herbicide that adsorbed on both alumina-treated biochars was 2 times higher than on the untreated biochars (BC600 and BC400). In contrast, sorption of the acetochlor in the clay-treated biochar (Mo-BC600) was slightly increased, and the sorption even decreased for the clay-treated lower temperature biochar (Mo-BC400). To understand why there was a difference, the sorption data for various biochars were analyzed with the combined adsorption and partition model (eq 2)[2,37] in which Q_A represents the amount of surface adsorption and K_P is the partition coefficient. On the basis of the isotherm shape shown in Figure 3, a linear regression was conducted at a concentration of $C_e/C_s > 0.1$, and the fitting results with correlation coefficients $R > 0.97$ are shown in Table 4. Thus, the relative contribution of surface adsorption (Q_A/Q_e, %) to the total sorption at each equilibrium concentration was calculated, and Q_A/Q_e (%) values at $C_e/C_s = 0.3$ (a middle concentration) for various biochars are shown in Table 4.

$$Q_{total} = Q_e = Q_A + K_P C_e \quad (2)$$

According to the data in Table 4, both surface adsorption (Q_A) and its contribution to the total sorption (Q_A/Q_e) of acetochlor to the alumina-treated biochars (Al-BC400 and Al-BC600) were increased in comparison to the untreated biochars, which resulted from the expanded pore areas of the alumina-treated biochars (Table 3). As acetochlor is a pesticide composed of aromatic structure, the $\pi-\pi$ interactions between herbicide molecules and turbostratic graphene crystallites in biochars may play an important role for the surface adsorption.[38,39] The removal of oxygen-containing organic matter away from the biochar makes it easier for acetochlor molecules to access these adsorption sites in the expanded pores. Therefore, it is understandable that the surface adsorption (Q_A) to the Ca-mont-treated BC600 biochar (Mo-BC600) was also improved, corresponding to its expanded mesopore area. However, the Ca-mont treatment did not increase the surface adsorption of acetochlor to the BC400 biochar, although the BC400 biochar's micropore area was enlarged. This may be related to the inaccessibility of micropores to the herbicide molecules to allow surface adsorption. According to previous studies,[40,41] the pore size of the carbons should be large enough (with diameter >1.7 times the molecule's second widest dimension) for adsorption to occur, and most herbicides have a molecular weight >200 g mol^{-1} and an estimated length >10 Å.[42] Therefore, a significant fraction of micropores (<17 Å in diameter) in biochars may be inaccessible for the acetochlor molecules (with a molecular weight of 269.77 g mol^{-1}). The residual minerals in the treated biochars may play a potential role in herbicide adsorption, because aluminol (═AlOH) and silanol (═SiOH) groups on

DOI: 10.1021/acs.jafc.5b01654
J. Agric. Food Chem. 2015, 63, 5740−5746

the mineral surface can form H-bonding with −O− groups in acetochlor molecules.[43] However, the low surface area of these minerals (Table 3) restricts their adsorption sites available for herbicide molecules, so the limited adsorption capability of a small amount of residual minerals in treated biochars should not contribute much to the dramatic increment of herbicide adsorption particularly observed on the alumina-treated biochars. In other words, the enhanced acetochlor sorption to the mineral-treated biochars is predominantly related to their enlarged mesopore (17−500 Å in diameter) areas. This is particularly true for the higher temperature biochar (BC600), the micropore area of which did not change significantly after treatment with the soil minerals. The significant increase in surface adsorption of the herbicide can be attributed only to the magnified mesopore areas.

A similar enhancement in sorption of metribuzin by alumina-treated biochars was observed as shown in Figure 4. In contrast

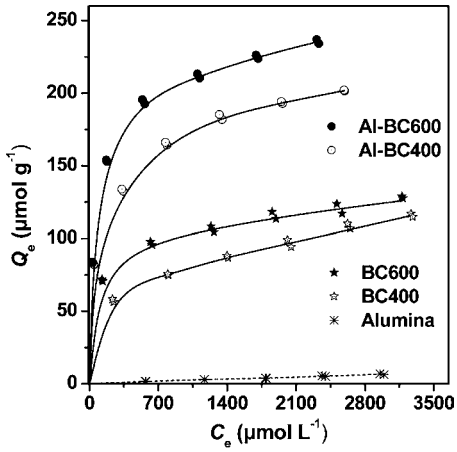

Figure 4. Sorption isotherms of metribuzin to biochars and alumina at 25 °C.

to acetochlor, the sorption of metribuzin by alumina is almost negligible, which should be related to the higher hydrophilicity of metribuzin (as indicated by its lower logK_{ow} and higher water solubility) and its weak affinity to the aluminol surface sites.[43] Thus, the enhanced sorption can be attributed only to the change in porous structure of the biochars after alumina treatment, because the residual alumina in the treated biochar will not do any favor for the sorption of metribuzin. The fitting results of the sorption data of metribuzin with the above-mentioned combined adsorption and partition model are listed in Table 4, and an increase in surface adsorption (Q_A) and contribution of Q_A to the total sorption (Q_A/Q_e) for this herbicide were also observed.

Relationship of Enhanced Sorption and Expanded Pore of Biochars. Further comparisons were made with the corrected values of adsorption capacity (Q_A) (data in parentheses in Table 4) by deducting the contribution of the residual minerals, and surface-normalized adsorptions (Q_A/SA_{BET} and $Q_A/SA_{17-500\ Å}$) were calculated by dividing Q_A with the corrected SA_{BET} and $SA_{17-500\ Å}$ values. When the reported size of the metribuzin molecule (10.43 Å in length and 4.43 Å in width)[42] was used, the theoretical value of maximal monolayer adsorption was calculated to be 3.60 μmol m^{-2}, which is much closer to the $Q_A/SA_{17-500\ Å}$ values for the lower temperature biochar (BC400 and Al-BC400) than to the Q_A/SA_{BET} values. The results showed again the dominant contribution of the mesopores (17−500 Å) on the surface adsorption of the herbicides.

When all of the $Q_A/SA_{17-500\ Å}$ values for both acetochlor and metribuzin were considered, the lower $Q_A/SA_{17-500\ Å}$ values were obtained for the higher temperature biochars (BC600, Al-BC600, and Mo-BC600), suggesting that part of the mesopores in these biochars act only as a passageway for the herbicides' entry into the adsorption sites. In addition, on the same biochar sorbent, the surface-normalized adsorption ($Q_A/SA_{17-500\ Å}$) is obviously larger for metribuzin than for acetochlor, which may be partially due to the smaller molecular size of metribuzin.

Our results are useful for understanding the change in the sorption properties of the biochars with soil applications. Thus, soil minerals may transport some authigenic organic matters from biochars and expand their porous structure, leading to enlarged surface area and enhanced sorption for herbicides. This can explain the enhancement of sorption to biochars after aging in soil[35] and also suggests that the sorption property of biochars may change quickly in soil without experiencing long biological processes, especially in infertile croplands poor in natural organic matter. Furthermore, the increased surface adsorption with mesopore area of mineral-treated biochars implied that more herbicide molecules were entrapped in these mesopores, which will affect the availability of herbicides for both plant uptake and utilization by soil microorganisms. Therefore, the efficacy and environmental fate of soil-applied pesticides will be influenced by the interaction of biochars with soil minerals, which needs further investigation by considering more environmental factors such as pH and coexisting matter.

■ ASSOCIATED CONTENT

Ⓢ Supporting Information

N_2 adsorption isotherms of biochars, kinetics of herbicide sorption to biochars, detailed SEM/EDX reports of biochar samples, pore size distribution of two minerals, FT-IR spectra of some biochar samples, and pH change during the mineral treatment of biochars. The Supporting Information is available free of charge on the ACS Publications website at DOI: 10.1021/acs.jafc.5b01654.

■ AUTHOR INFORMATION

Corresponding Authors

*(J.L.) Mail: Huancheng West Road, Zhejiang, Shaoxing 312000, China. Phone: +86 575 8834 1524. Fax: +86 575 8834 1521. E-mail: ljf@usx.edu.cn.

*(Y.L.) E-mail: liym@usx.edu.cn.

Funding

Funding was provided by the National Natural Science Foundation of China (41271475).

Notes

The authors declare no competing financial interest.

■ REFERENCES

(1) Yang, Y.; Sheng, G. Enhanced pesticide sorption by soils containing particulate matter from crop residue burns. *Environ. Sci. Technol.* **2003**, *37*, 3635−3639.

(2) Chen, B.; Zhou, D.; Zhu, L. Transitional adsorption and partition of nonpolar and polar aromatic contaminants by biochars of pine needles with different pyrolytic temperatures. *Environ. Sci. Technol.* **2008**, *42*, 5137−5143.

(3) Cao, X.; Ma, L.; Gao, B.; Harris, W. Dairy-manure derived biochar effectively sorbs lead and atrazine. *Environ. Sci. Technol.* **2009**, *43*, 3285−3291.

DOI: 10.1021/acs.jafc.5b01654
J. Agric. Food Chem. 2015, 63, 5740−5746

(4) Kookana, R. S. The role of biochar in modifying the environmental fate, bioavailability, and efficacy of pesticides in soils: a review. *Aust. J. Soil Res.* **2010**, *48*, 627−637.
(5) Yu, X.; Ying, G.; Kookana, R. S. Sorption and desorption behaviors of diuron in soils amended with charcoal. *J. Agric. Food Chem.* **2006**, *54*, 8545−8550.
(6) Si, Y.; Wang, M.; Tian, C.; Zhou, J.; Zhou, D. Effect of charcoal amendment on adsorption, leaching and degradation of isoproturon in soils. *J. Contam. Hydrol.* **2011**, *123*, 75−81.
(7) Spokas, K. A.; Koskinen, W. C.; Baker, J. M.; Reicosky, D. C. Impacts of woodchip biochar additions on greenhouse gas production and sorption/degradation of two herbicides in a Minnesota soil. *Chemosphere* **2009**, *77*, 574−581.
(8) Sun, K.; Gao, B.; Ro, K. S.; Novak, J. M.; Wang, Z.; Herbert, S.; Xing, B. Assessment of herbicide sorption by biochars and organic matter associated with soil and sediment. *Environ. Pollut.* **2012**, *163*, 167−173.
(9) Jones, D. L.; Edwards-Jones, G.; Murphy, D. V. Biochar mediated alterations in herbicide breakdown and leaching in soil. *Soil Biol. Biochem.* **2011**, *43*, 804−813.
(10) Uchimiya, M.; Wartelle, L. H.; Boddu, V. M. Sorption of triazine and organophosphorus pesticides on soil and biochar. *J. Agric. Food Chem.* **2012**, *60*, 2989−2997.
(11) Larsbo, M.; Löfstrand, E.; de Veer, D. A.; Ulén, B. Pesticide leaching from two Swedish topsoils of contrasting texture amended with biochar. *J. Contam. Hydrol.* **2013**, *147*, 73−81.
(12) Li, J.; Li, Y.; Wu, M.; Zhang, Z.; Lü, J. Effectiveness of low-temperature biochar in controlling the release and leaching of herbicides in soil. *Plant Soil* **2013**, *370*, 333−344.
(13) Cheng, C.-H.; Lehmann, J. Ageing of black carbon along a temperature gradient. *Chemosphere* **1999**, *75*, 1021−1027.
(14) Hale, S. E.; Hanley, K.; Lehmann, J.; Zimmerman, A. R.; Cornelissen, G. Effects of chemical, biological, and physical aging as well as soil addition on the sorption of pyrene to activated carbon and biochar. *Environ. Sci. Technol.* **2011**, *45*, 10445−10453.
(15) Martin, S. M.; Kookana, R. S.; Van Zwieten, L.; Krull, E. Marked changes in herbicide sorption-desorption upon ageing of biochars in soil. *J. Hazard. Mater.* **2012**, *231*−*232*, 70−78.
(16) Yang, Y.; Sheng, G. Pesticide adsorptivity of aged particulate matter arising from crop residue burns. *J. Agric. Food Chem.* **2003**, *51*, 5047−5051.
(17) Qiu, Y.; Xiao, X.; Cheng, H.; Zhou, Z.; Sheng, D. Influence of environmental factors on pesticide adsorption by black carbon: pH and model dissolved organic matter. *Environ. Sci. Technol.* **2009**, *43*, 4973−4978.
(18) Kasozi, G. N.; Zimmerman, A. R.; Nkedi-kizza, P.; Gao, B. Catechol and humic acid sorption onto a range of laboratory-produced black carbons (biochars). *Environ. Sci. Technol.* **2010**, *44*, 6189−6195.
(19) Pignatello, J. J.; Kwon, S.; Lu, Y. Effect of natural organic substances on the surface and adsorptive properties of environmental black carbon (char): attenuation of surface activity by humic and fulvic acids. *Environ. Sci. Technol.* **2006**, *40*, 7757−7763.
(20) Lin, Y.; Munroe, P.; Joseph, S.; Kimber, S.; Van Zwieten, L. Nanoscale organo-mineral reactions of biochars in ferrosol: an investigation using microscopy. *Plant Soil* **2012**, *357*, 369−380.
(21) Qian, L.; Chen, B. Interactions of aluminum with biochars and oxidized biochars: Implications for the biochar aging process. *J. Agric. Food Chem.* **2014**, *62*, 373−380.
(22) Janot, N.; Reiller, P. E.; Zheng, X.; Croué, J.-P.; Benedetti, M. F. Characterization of humic acid reactivity modifications due to adsorption onto α-Al_2O_3. *Water Res.* **2012**, *46*, 731−740.
(23) Li, H.; Sheng, G.; Teppen, B. J.; Johnston, C. T.; Boyd, S. A. Sorption and desorption of pesticides by clay minerals and humic acid-clay complexes. *Soil Sci. Soc. Am. J.* **2003**, *67*, 122−131.
(24) Lü, J.; Li, J.; Li, Y.; Chen, B.; Bao, Z. Use of rice straw biochar simultaneously as the sustained release carrier of herbicides and soil amendment for their reduced leaching. *J. Agric. Food Chem.* **2012**, *60*, 6463−6470.
(25) Fein, J. B.; Boily, J.-F.; Güçlü, K.; Kaulbach, E. Experimental study of humic acid adsorption onto bacteria and Al-oxide mineral surfaces. *Chem. Geol.* **1999**, *162*, 33−45.
(26) Keiluweit, M.; Kleber, M.; Sparrow, M. A.; Simoneit, B. R. T.; Prahl, F. G. Solvent-extractable polycyclic aromatic hydrocarbons in biochar: Influence of pyrolysis temperature and feedstock. *Environ. Sci. Technol.* **2012**, *46*, 9333−9341.
(27) Zhao, L.; Cao, X.; Mašek, O.; Zimmerman, A. Heterogeneity of biochar properties as a function of feedstock sources and production temperatures. *J. Hazard. Mater.* **2013**, *256*−*257*, 1−9.
(28) Li, J.; Li, Y.; Wu, Y.; Zheng, M. A comparison of biochars from lignin, cellulose and wood as the sorbent to an aromatic pollutant. *J. Hazard. Mater.* **2014**, *280*, 450−457.
(29) Kaiser, K.; Guggenberger, G. The role of DOM sorption to mineral surfaces in the preservation of organic matter in soils. *Org. Geochem.* **2000**, *31*, 711−725.
(30) Lin, Y.; Munroe, P.; Joseph, S.; Henderson, R.; Ziolkowski, A. Water extractable organic carbon in untreated and chemical treated biochars. *Chemosphere* **2012**, *87*, 151−157.
(31) Cabrera, A.; Cox, L.; Spokas, K. A.; Celis, R.; Hermosín, M. C.; Cornejo, J.; Koskinen, W. C. Comparative sorption and leaching study of the herbicides fluometuron and 4-chloro-2-methylphenoxyacetic acid (MCPA) in a soil amended with biochars and other sorbents. *J. Agric. Food Chem.* **2011**, *59*, 12550−12560.
(32) Cabrera, A.; Cox, L.; Spokas, K.; Hermosín, M. C.; Cornejo, J.; Koskinen, W. C. Influence of biochar amendments on the sorption−desorption of aminocyclopyrachlor, bentazone and pyraclostrobin pesticides to an agricultural soil. *Sci. Total Environ.* **2014**, *470*−*471*, 438−443.
(33) Hilber, I.; Blum, F.; Leifeld, J.; Schmidt, H.-P.; Bucheli, T. D. Quantitative determination of PAHs in biochar: a prerequisite to ensure its quality and safe application. *J. Agric. Food Chem.* **2012**, *60*, 3042−3050.
(34) Nguyen, T. H.; Cho, H.-H.; Poster, D. L.; Ball, W. P. Evidence for a pore-filling mechanism in the adsorption of aromatic hydrocarbons to a natural wood char. *Environ. Sci. Technol.* **2007**, *41*, 1212−1217.
(35) Trigo, C.; Spokas, K. A.; Cox, L.; Koskinen, W. C. Influence of soil biochar aging on sorption of the herbicides MCPA, nicosulfuron, terbuthylazine, indaziflam, and fluoroethyldiaminotriazine. *J. Agric. Food Chem.* **2014**, *62*, 10855−10860.
(36) Heitkötter, J.; Marschner, B. Interactive effects of biochar ageing in soils related to feedstock, pyrolysis temperature, and historic charcoal production. *Geoderma* **2015**, *245*−*246*, 56−64.
(37) Chen, B.; Chen, Z.; Lv, S. A novel magnetic biochar efficiently sorbs organic pollutants and phosphate. *Bioresour. Technol.* **2011**, *102*, 716−723.
(38) Sun, K.; Keiluweit, M.; Kleber, M.; Pan, Z.; Xing, B. Sorption of fluorinated herbicides to plant biomass-derived biochars as a function of molecular structure. *Bioresour. Technol.* **2011**, *102*, 9897−9903.
(39) Qiu, Y.; Zheng, Z.; Zhou, Z.; Sheng, G. D. Effectiveness and mechanisms of dye adsorption on a straw-based biochar. *Bioresour. Technol.* **2009**, *100*, 5348−5351.
(40) Kasaoka, S.; Sakata, Y.; Tanaka, E.; Naitoh, R. Design of molecular-sieve carbon: studies on the adsorption of various dyes in the liquid phase. *Int. Chem. Eng.* **1989**, *29*, 734−742.
(41) Pelekani, C.; Snoeyink, V. L. Competitive adsorption in natural water: role of activated carbon pore size. *Water Res.* **1999**, *33*, 1209−1219.
(42) Chen, S.-S.; Taylor, J. S.; Mulford, L. A.; Norris, C. D. Influences of molecular weight, molecular size, flux, and recovery for aromatic pesticide removal by nanofiltration membranes. *Desalination* **2004**, *16*, 103−111.
(43) Clausen, L.; Fabricius, I.; Madsen, L. Adsorption of pesticides onto quartz, calcite, kaolinite, and α-alumina. *J. Environ. Qual.* **2001**, *30*, 846−857.

DOI: 10.1021/acs.jafc.5b01654
J. Agric. Food Chem. 2015, 63, 5740−5746

Table 1. Nutrient Composition and Carbohydrate Ingredients of the Syrups per 100 g[a]

classification of processed food	energy (kcal)	protein (g)	fat (g)	carbohydrate (g)	nondigestible oligosaccharide (g)		
					FOS	GOS	raffinose
food for specified health use	207	0.0	0.0	72.5	40.0		
food for specified health use	276	0.0	0.0	73.9		44.4	
so-called healthy food	282	0.0	0.0	78.0			9.4

[a]FOS, fructooligosaccharide; GOS, galactooligosaccharide.

enzyme instead of amyloglucosidase (improved method).[27] The contents of FOS, GOS, and raffinose were accurately determined as nondigestible oligosaccharides by the improved method, whereas sucrose, isomaltulose, panose, and maltotriose were completely hydrolyzed and did not affect the determination of nondigestible oligosaccharides.[27] Although the improved method was superior to the existing AOAC method in terms of determining oligosaccharides, its application in nondigestible oligosaccharide in marketed processed foods remains untested.

In the present study, we applied the improved method to measure nondigestible oligosaccharides in processed foods and made comparisons with the existing AOAC method. Here, we show that the improved method using porcine small intestinal enzyme, instead of amyloglucosidase, accurately determined nondigestible oligosaccharide contents in currently marketed food products.

MATERIALS AND METHODS

Test Samples and Preparation. We analyzed two types of test samples by the improved method and the existing AOAC method.

In the first, we prepared five different cookies with added oligosaccharides. Cookies (Morinaga & Co. Ltd., Tokyo, Japan) were chosen as test sample without nondigestible oligosaccharide by evidence based on our previous experiments.[29,30] Cookies were crushed using a mortar and pestle and were passed through a mesh sieve of 500 μm. Each oligosaccharide (1.000 g) and cookie (9.000 g) were accurately weighed and mixed using a mortar. Added oligosaccharides were FOS, GOS, or raffinose as nondigestible oligosaccharides as well as isomaltooligosaccharide (IMO) or sucrose as digestible oligosaccharides. FOS (purity > 98%) was donated by Meiji Co., Ltd. (Tokyo, Japan). GOS (purity > 90%) was donated by Nissin Sugar Manufacturing Co., Ltd. (Tokyo, Japan). IMO (purity > 90.8%) was donated by Showa Sangyo Co. (Tokyo, Japan). Raffinose (purity > 98.0%) and sucrose (purity > 99.5%) were purchased from Wako Pure Chemical Industries Ltd. (Osaka, Japan).

In the second analytical experiment, we employed three commercially available syrups containing nondigestible oligosaccharide. In Japan, two syrups approved as "food for specified health uses" and one so-called healthy food was used. Nutrient compositions of three syrups containing nondigestible oligosaccharide are shown in Table 1. Syrup samples were purchased over the internet.

Analytical Method. *AOAC Method 2009.01 (Existing AOAC Method). (a) Chemicals.* All chemicals were of analytical grade or of the highest grade available. The Integrated Total Dietary Fiber kit specified in the existing AOAC method was purchased from Megazyme International Ireland, Ltd. (Wicklow, Ireland). The kit contains pancreatic α-amylase from swine, amyloglucosidase from *Aspergillus niger*, and protease from *Bacillus licheniformis*. Ion-exchange resin (Amberlite MB-4), diatomaceous earth, and Trizma base were purchased from Japan Organo Co., Ltd. (Tokyo, Japan), Kishida Chemical Co., Ltd. (Osaka, Japan), and Sigma-Aldrich Japan Co. LLC (Tokyo, Japan), respectively.

(b) Procedure. Nondigestible oligosaccharide contents in test samples were determined using the existing AOAC method.[26] The apparatus for the existing AOAC method was used. HPLC analyses were performed using a liquid chromatography system (LC-20AD, Shimadzu Corp., Kyoto, Japan) with a refractive index detector (RID-10A, Shimadzu Corp.) and a Shodex SUGAR KS-802 column (8.0 φ × 300 mm, Showa Denko Co., Tokyo, Japan), and analyses were conducted at a column temperature of 40 °C. Samples were eluted with deionized distilled water at a flow rate of 0.5 mL/min. The limit of detection for glucose was 10 μg/mL in HPLC analysis.

Improved AOAC Method 2009.01 (Improved Method). (a) Chemicals. Chemicals used were the same as for the existing AOAC method.

(b) Preparation of Porcine Small Intestinal Brush Border Membrane Vesicles (PSIBBMVs). PSIBBMVs were prepared using the method described by Kessler et al.[31] with modifications. Small intestine from the pylorus to the ileocecal junction with the mesentery of an adult swine was obtained from the Isahaya Prefectural Office of Meat Inspection (Isahaya, Japan). PSIBBMVs were suspended in sufficient volumes of 50 mM sodium maleate buffer containing 2 mM $CaCl_2$ and 0.02% sodium azide (pH 6.0) and were stored at −80 °C until assay.

(c) Determination of α-Glucosidase and Disaccharidase Activities. The α-glucosidase activity (units/mg protein) was determined using the method described by Robertson and Halvorson with *p*-nitrophenyl-α-D-methyl-glucopyranoside as a substrate.[32] One unit of α-glucosidase activity per milligram of protein was defined as the amount of enzyme that produced 1 μmol of glucose from *p*-nitrophenyl-α-D-methyl glucopyranoside per minute.

Assays of disaccharidase activity in PSIBBMVs were performed according to the methods described by Oku et al.,[33] which were modified from the method described by Dahlqvist et al.[34] Sucrose, maltose, trehalose, lactose, and isomaltulose used substrates included. Specific activity (SA) per milligram of protein was defined as the activity of enzyme that hydrolyzed 1 μmol of glucose from substrate per hour (μmol substrate hydrolyzed/mg protein/h). Concentrations of protein were determined using the Bradford assay with bovine serum albumin as a standard.[35]

(d) Procedure. Nondigestible oligosaccharide contents of test samples were determined according to the method of Tanabe et al.[27] Digestible saccharides were hydrolyzed using an enzyme mixture containing pancreatic α-amylase (50 units/mL) and PSIBBMVs (2720 units/mL as α-glucosidase; SA, sucrase, 125.8; maltase, 453.2; trehalase, 35.3; lactase, 8.7; isomaltulase, 14.4) for 16 h at 37 °C. Test samples were added to enzyme mixtures, and nondigestible oligosaccharide contents were determined using the method described by Tanabe et al.[27]

Calculation of the Recovery of Nondigestible Oligosaccharides in Processed Food. Each nondigestible oligosaccharide in added oligosaccharides in processed food was assayed once in duplicate. On the other hand, each nondigestible oligosaccharide in commercially available processed food was assessed five times, and it was expressed the mean ± standard deviation (SD). Nondigestible oligosaccharide contents were measured according to the calculation for nonprecipitable soluble dietary fiber using the existing AOAC method.[26] Nondigestible oligosaccharides were defined as saccharides with degrees of polymerization (DP) of ≥2, according to the definition of "luminacoid", which is a comprehensive concept of nondigestible component from the Japanese Association for Dietary Fiber Research, suggesting[36] nondigestible oligosaccharide was defined as saccharide with DP 2 or more than DP 2. The margin of error was accepted as ±20% on the contents of nondigestible oligosaccharides in processed foods for Japanese nutrition labeling;[37] accurate determination thus

DOI: 10.1021/jf505844y
J. Agric. Food Chem. 2015, 63, 5747−5752

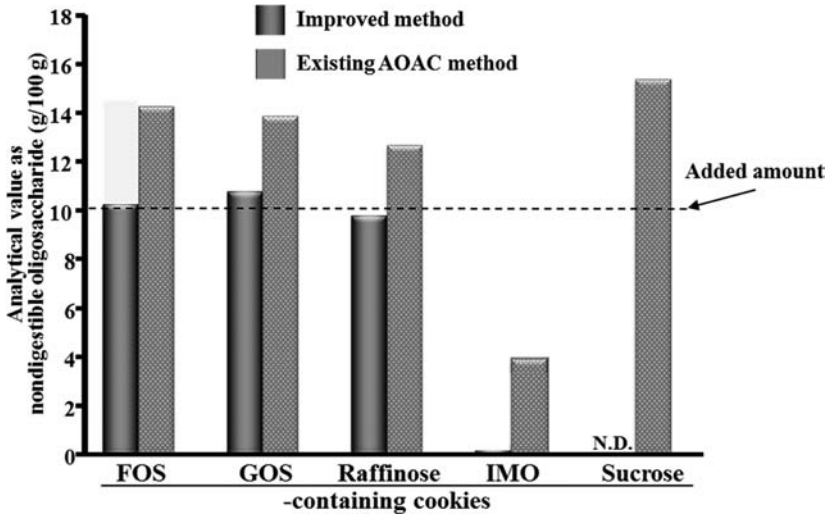

Figure 1. Comparison of nondigestible oligosaccharides in cookies using the improved method and the existing AOAC method. Data was expressed average of duplicate analysis. The nondigestible oligosaccharide fractions were DP ≥ 2. N.D., not detected.

was accepted as ±20% on the contents of nondigestible oligosaccharides in processed foods on the label.

Ethics. Porcine experiments were performed according to the guidelines for the care and use of laboratory animals of the University of Nagasaki, Siebold. All experiments were performed at the Laboratory of Public Health Nutrition, University of Nagasaki, Siebold.

RESULTS

Quantification of Oligosaccharides Added to Processed Foods by the Improved Method and the Existing AOAC Method. Nondigestible oligosaccharide fractions were recovered from cookies using the improved method and the existing AOAC method (Figure 1). After the treatment of cookies containing 10% of FOS, GOS, and raffinose by hydrolyzing enzymes in the improved method, recoveries of these nondigestible oligosaccharides were 10.1, 10.7, and 9.7%, respectively. When IMO and sucrose were hydrolyzed by enzymes in the improved method, the content of IMO that was recovered as nondigestible oligosaccharide fraction was only 0.1%, and sucrose was not detected. It was reported that IMO with α-1,4- and α-1,6-glucosidic linkages was digested readily by human intestinal disaccharidases.[38] This suggests that the improved method is able to measure accurately the quantity of nondigestible oligosaccharide in foods.

In contrast, when oligosaccharides in the same samples were determined by the existing AOAC method, the recoveries as nondigestible oligosaccharide were 14.2% for FOS, 13.8% for GOS, 12.6% for raffinose, and 15.3% for sucrose. Especially, the recovery of IMO was only 4.0%. Thus, the results demonstrate that the existing AOAC method overestimates more than the quantity of nondigestible oligosaccharide in foods.

Quantification of Nondigestible Oligosaccharide in the Syrups by the Improved Method and the Existing AOAC Method. Nondigestible oligosaccharides were determined in the syrups using the improved method and the existing AOAC method (Table 2). The improved method provided the concentrations of FOS and raffinose in the syrups similar to those stated on the label, but the level of GOS was lower than that stated on the food label. In contrast, treatment with hydrolyzing enzymes in the existing AOAC method gave approximately 30% greater than values of FOS, GOS, and raffinose on the label.

Table 2. Analyses of Nondigestible Oligosaccharides in the Syrups Using the Improved Method and the Existing AOAC Method and Comparison with Nutritional Label Values[a]

	nondigestible oligosaccharide value/100 g (%)		
	improved method	existing AO AC method	labeled value
syrup containing FOS (/100 g)	41.2 ± 1.8 (103.0%)	54.8 ± 1.3 (137.0%)	40.0
syrup containing GOS (/100 g)	37.2 ± 2.5 (83.8%)	58.9 ± 1.6 (132.7%)	44.4
syrup containing raffinose (/100 g)	9.6 ± 0.5 (102.1%)	50.1 ± 0.2 (533.0%)	9.4

[a]The values in parentheses show relative ratio of nondigestible oligosaccharide determined by each method and that on the label. Analytical values are expressed as the mean ± SD in duplicate experiments. Nondigestible fractions, ≥DP 2; FOS, fructooligosaccharide; GOS, galactooligosaccharide.

DISCUSSION

In the previous study on the improved method, PSIBBMVs completely hydrolyzed digestible oligosaccharide and distinguished nondigestible oligosaccharide from digestible oligosaccharide.[27] Although the improved method was superior to the existing AOAC method in terms of determining oligosaccharides, its application to nondigestible oligosaccharides in marketed processed foods remains untested. We previously have confirmed that cookies used in the present study do not contain nondigestible oligosaccharides.[29,30] Here, cookies were added digestible (sucrose or IMO) or nondigestible oligosaccharides (FOS, GOS or raffinose) at the level of 10%. As shown Figure 1, the improved method hydrolyzed digestible oligosaccharides such as sucrose and IMO in cookies and gave almost complete recovery of added nondigestible oligosaccharides such as FOS, GOS, and raffinose.

Next, the improved method was applied to marketed syrups, and contents of FOS and raffinose were shown to be similar to those indicated on the food label (Table 2). According to the improved method, the concentration of GOS in the syrups was lower than that stated on the food label (Table 2). This discrepancy may reflect the accepted ±20% margin of error for Japanese nutrition labeling;[37] the content of GOS in the syrup would be between 35.5 and 53.2 g in case of 44.4 g of GOS in

DOI: 10.1021/jf505844y
J. Agric. Food Chem. 2015, 63, 5747−5752

the product. The value (37.2 ± 2.5) by the improved method was within the value accepted by Japanese nutrition labeling. Although porcine small intestinal disaccharidases may hydrolyze GOS with low efficiency, GOS added to cookies was not hydrolyzed (Figure 1), indicating that the improved method accurately measured GOS. Therefore, it is concluded that the improved method is proper to determine GOS in processed foods.

When commercially available processed foods and cookies with added oligosaccharides were treated with the hydrolyzing enzyme amyloglucosidase, of the existing AOAC method, nondigestible oligosaccharide contents were overestimated (Figure 1 and Table 2). These results indicate that the existing AOAC method cannot hydrolyze digestible saccharides such as sucrose and starch-decomposed products and maltodextrin in processed foods, consequently quantifying digestible saccharides as nondigestible oligosaccharides. In agreement, Brunt and Sanders showed that the existing AOAC method does not fully convert digestible starch and maltooligosaccharide fractions into glucose, leading to an erroneous quantification of partially hydrolyzed digestible starch as dietary fiber.[39] Our previous study showed that digestible oligosaccharides are barely hydrolyzed by either AOAC method 2001.03 or 2009.01 using amyloglucosidase,[27,40] which also failed to hydrolyze digestible saccharides.[41] Taken together, these studies show that the hydrolyzing activity of enzymes from bacteria does not reflect the hydrolyzing activities of enzymes of the human gastrointestinal tract.

Pigs are omnivorous with physiological characteristics that allow their use as a model of human digestive functions.[42] Many studies have characterized hydrolyzing specificity of small intestinal disaccharidases in pigs.[43−45] In particular, pigs have been used as models in studies of dietary fiber and nondigestible oligosaccharide digestion.[46−48] Porcine small intestinal disaccharidases could substitute for those in humans. Moreover, pigs are common low-cost domestic animals. Therefore, porcine small intestinal disaccharidases may be suitable for determining nondigestible oligosaccharides in foods for human consumption.

Prebiotic agents are not digested in the human gastrointestinal tract, and their effectiveness is dependent on the quantity of fermentable nondigestible saccharides in the large intestine.[49] Therefore, a precise quantification of nondigestible oligosaccharides in food is necessary to find good sources of prebiotic agents and to accurately label the content of nondigestible oligosaccharides in food.

In conclusion, we developed the improved method for the accurate quantification of nondigestible oligosaccharides in processed foods using porcine small intestinal disaccharidases. The present improved method may be used to comprehensively determine nondigestible oligosaccharides in commercially available processed foods. An appropriate quantification of nondigestible oligosaccharides in foods is essential to estimate health benefits. Moreover, an accurate determination method for newly developed nondigestible oligosaccharides is imperative for nutrition labeling, which indicates prebiotic contents to help consumers chose healthy foods. Improved AOAC method 2009.01 could be the determination method for nondigestible oligosaccharide dietary fiber. Furthermore, the partially purified enzymes isolated from PSIBBMVs and a stable supply of these enzymes should be required to make the improved method as a commercial dietary fiber assay kit.

AUTHOR INFORMATION

Corresponding Author

*(K.T.) Mail: Department of Food Science and Nutrition, Nagoya Women's University, 3-40 Shioji, Mizuho-ku, Nagoya 4678610, Japan. Phone/fax: +81 52 852 1499. E-mail: ktanabe@nagoya-wu.ac.jp.

Funding

This study was supported in part by a Grant-in-Aid for Challenging Exploratory Research, 24650498.

Notes

The authors declare no competing financial interest.

ACKNOWLEDGMENTS

We thank Meiji Co., Ltd. (ex-Meiji Seika Kaisha, Ltd., Tokyo, Japan), for providing FOS, Nissin Sugar Manufacturing Co., Ltd. (Tokyo, Japan), for providing GOS, and Showa Sangyo Co. (Tokyo, Japan) for providing IMO. We thank the Isahaya Prefectural Office of Meat Inspection (Nagasaki, Japan) for supplying porcine intestines.

ABBREVIATIONS USED

AOAC, Association of Official Analytical Chemists; CAC, Codex Alimentarius Commission; DP, degree of polymerization; FOS, fructooligosaccharide; GOS, galactooligosaccharide; IMO, isomaltooligosaccharide; PSIBBMVs, porcine small intestinal brush border membrane vesicles; SA, specific activity; SD, standard deviation

REFERENCES

(1) Rastall, R. A. Functional oligosaccharides: application and manufacture. *Annu. Rev. Food Sci. Technol.* **2010**, *1*, 305−339.

(2) Bornet, F. R.; Brouns, F.; Tashiro, Y.; Duvillier, V. Nutritional aspects of short-chain fructooligosaccharides: natural occurrence, chemistry, physiology and health implications. *Dig. Liver Dis.* **2002**, *34* (Suppl. 2), S111−S120.

(3) Depeint, F.; Tzortzis, G.; Vulevic, J.; l'Anson, K.; Gibson, G. R. Prebiotic evaluation of a novel galactooligosaccharide mixture produced by the enzymatic activity of Bifidobacterium bifidum NCIMB 41171, in healthy humans: a randomized, double-blind, crossover, placebo-controlled intervention study. *Am. J. Clin. Nutr.* **2008**, *87*, 785−791.

(4) Martínez-Villaluenga, C.; Frías, J.; Vidal-Valverde, C.; Gómez, R. Raffinose family of oligosaccharides from lupin seeds as prebiotics: application in dairy products. *J. Food Prot.* **2005**, *68*, 1246−1252.

(5) Terada, A.; Hara, H.; Kataoka, M.; Mitsuoka, T. Effect of lactulose on the composition and metabolic activity of the human faecal flora. *Microb. Ecol. Health Dis.* **1992**, *5*, 43−50.

(6) Aachary, A. A.; Prapulla, S. G. Xylooligosaccharides (XOS) as an emerging prebiotic: microbial synthesis, utilization, structural characterization, bioactive properties, and applications. *Compr. Rev. Food Sci. Food Saf.* **2011**, *10*, 2−16.

(7) Gibson, G. R.; Roberfroid, M. B. Dietary modulation of the human colonic microbiota: introducing the concept of prebiotics. *J. Nutr.* **1995**, *125*, 1401−1412.

(8) Oku, T.; Nakamura, S. Digestion, absorption and fermentation of newly developed sugar substitutes and their available energy. *Pure Appl. Chem.* **2002**, *74*, 1253−1261.

(9) Roberfroid, M. B. Prebiotics: the concept revisited. *J. Nutr.* **2007**, *137*, 830S−837S.

(10) Sanders, M. E.; Lenoir-Wijnkoop, I.; Salminen, S.; Merenstein, D. J.; Gibson, G. R.; Petschow, B. W.; Nieuwdorp, M.; Tancredi, D. J.; Cifelli, C. J.; Jacques, P.; Pot, B. Probiotics and prebiotics: prospects for public health and nutritional recommendations. *Ann. N.Y. Acad. Sci.* **2014**, *1309*, 19−29.

DOI: 10.1021/jf505844y
J. Agric. Food Chem. 2015, 63, 5747−5752

(11) Kellow, N. J.; Coughlan, M. T.; Reid, C. M. Metabolic benefits of dietary prebiotics in human subjects: a systematic review of randomised controlled trials. *Br. J. Nutr.* **2014**, *111*, 1147−1161.
(12) Chung, H.; Kasper, D. L. Microbiota-stimulated immune mechanisms to maintain gut homeostasis. *Curr. Opin. Immunol.* **2010**, *22*, 455−460.
(13) Ding, S.; Chi, M. M.; Scull, B. P.; Rigby, R.; Schwerbrock, N. M.; Magness, S.; Jobin, C.; Lund, P. K. High-fat diet: bacteria interactions promote intestinal inflammation which precedes and correlates with obesity and insulin resistance in mouse. *PLoS One* **2010**, *5*, No. e12191.
(14) Bäckhed, F.; Manchester, J. K.; Semenkovich, C. F.; Gordon, J. I. Mechanisms underlying the resistance to diet-induced obesity in germ-free mice. *Proc. Natl. Acad. Sci. U.S.A.* **2007**, *104*, 979−984.
(15) Havenaar, R. Intestinal health functions of colonic microbial metabolites: a review. *Benefic. Microbes* **2011**, *2*, 103−114.
(16) Cani, P. D.; Neyrinck, A. M.; Fava, F.; Knauf, C.; Burcelin, R. G.; Tuohy, K. M.; Gibson, G. R.; Delzenne, N. M. Selective increases of bifidobacteria in gut microflora improve high-fat-diet-induced diabetes in mice through a mechanism associated with endotoxaemia. *Diabetologia* **2007**, *50*, 2374−2383.
(17) Cani, P. D.; Possemiers, S.; Van de Wiele, T.; Guiot, Y.; Everard, A.; Rottier, O.; Geurts, L.; Naslain, D.; Neyrinck, A.; Lambert, D. M.; Muccioli, G. G.; Delzenne, N. M. Changes in gut microbiota control inflammation in obese mice through a mechanism involving GLP-2-driven improvement of gut permeability. *Gut* **2009**, *58*, 1091−1103.
(18) Hill, M. J. Intestinal flora and endogenous vitamin synthesis. *Eur. J. Cancer Prev.* **1997**, *6* (Suppl. 1), S43−S45.
(19) Scholz-Ahrens, K. E.; Ade, P.; Marten, B.; Weber, P.; Timm, W.; Açil, Y.; Glüer, C. C.; Schrezenmeir, J. Prebiotics, probiotics, and synbiotics affect mineral absorption, bone mineral content, and bone structure. *J. Nutr.* **2007**, *137*, 838S−846S.
(20) Blumberg, R.; Powrie, F. Microbiota, disease, and back to health: a metastable journey. *Sci. Transl. Med.* **2012**, *4*, 137rv7.
(21) Bäckhed, F.; Fraser, C. M.; Ringel, Y.; Sanders, M. E.; Sartor, R. B.; Sherman, P. M.; Versalovic, J.; Young, V.; Finlay, B. B. Defining a healthy human gut microbiome: current concepts, future directions, and clinical applications. *Cell Host Microbe* **2012**, *12*, 611−622.
(22) Prosky, L.; Asp, N. G.; Furda, I.; DeVries, J. W.; Schweizer, T. F.; Harland, B. F. Determination of total dietary fiber in foods and food products: collaborative study. *J. Assoc. Off. Anal. Chem.* **1985**, *68*, 677−679.
(23) Prosky, L.; Asp, N. G.; Schweizer, T. F.; DeVries, J. W.; Furda, I.; Lee, S. C. Determination of soluble dietary fiber in foods and food products: collaborative study. *J. AOAC Int.* **1994**, *77*, 690−694.
(24) Ohkuma, K.; Matsuda, I.; Katta, Y.; Tsuji, K. New method for determining total dietary fiber by liquid chromatography. *J. AOAC Int.* **2000**, *83*, 1013−1019.
(25) McCleary, B. V. An integrated procedure for the measurement of total dietary fibre (including resistant starch), non-digestible oligosaccharides and available carbohydrates. *Anal. Bioanal. Chem.* **2007**, *389*, 291−308.
(26) McCleary, B. V.; DeVries, J. W.; Rader, J. I.; Cohen, G.; Prosky, L.; Mugford, D. C.; Ohkuma, K. Determination of total dietary fiber (CODEX definition) by enzymatic-gravimetric method and liquid chromatography: collaborative study. *J. AOAC Int.* **2010**, *93*, 221−233.
(27) Tanabe, K.; Nakamura, S.; Oku, T. Inaccuracy of AOAC method 2009.01 with amyloglucosidase for measuring non-digestible oligosaccharides and proposal for an improvement of the method. *Food Chem.* **2014**, *151*, 539−546.
(28) Joint FAO/WHO Food Standards Programme, Codex Committee on Nutrition and Foods for Special Dietary Uses 32th Session (2010) Draft table of Conditions for Methods of Analysis for Dietary Fibre. REP11/NFSDU 2 and Appendix IV.
(29) Oku, T.; Nakamura, S. Evaluation of the relative available energy of several dietary fiber preparations using breath hydrogen evolution in healthy humans. *J. Nutr. Sci. Vitaminol.* **2014**, *60*, 246−254.
(30) Oku, T.; Nakamura, M.; Hashiguchi-Ishiguro, M.; Tanabe, K.; Nakamura, S. Bioavailability and laxative threshold of 1-kestose in human adults. *Dyn. Biochem. Process Biotechnol. Mol. Biol.* **2009**, *3* (Special Issue 1), 90−95.
(31) Kessler, M.; Acuto, O.; Storelli, C.; Murer, H.; Müller, M.; Semenza, G. A modified procedure for the rapid preparation of efficiently transporting vesicles from small intestinal brush border membranes. Their use in investigating some properties of D-glucose and choline transport systems. *Biochim. Biophys. Acta, Biomembr.* **1978**, *506*, 136−154.
(32) Robertson, J. J.; Halvorson, H. O. The components of maltozymase in yeast, and their behavior during deadaptation. *J. Bacteriol.* **1957**, *73*, 186−198.
(33) Oku, T.; Konishi, F.; Hosoya, N. Mechanism of inhibitory effect of unavailable carbohydrate on intestinal calcium absorption. *J. Nutr.* **1982**, *112*, 410−415.
(34) Dahlqvist, A. Method for assay of intestinal dissacharidases. *Anal. Biochem.* **1964**, *7*, 18−25.
(35) Bradford, M. M. A rapid and sensitive method for the quantitation of microgram quantities of protein utilizing the principle of protein-dye binding. *Anal. Biochem.* **1976**, *72*, 248−258.
(36) Kiriyama, S.; Ebihara, K.; Ikegami, S.; Innami, S.; Sugawa-Katayama, Y.; Takehisa, F. Searching for definition, terminology and classification of dietary fiber and the new proposal from Japan. *J. Jpn. Assoc. Dietary Fiber Res.* **2006**, *10*, 11−24.
(37) Consumer Affairs Agency, Government of Japan. Nutrition Label (in Japanese); http://www.caa.go.jp/foods/pdf/syokuhin685.pdf (accessed Nov 8, 2014).
(38) Kohmoto, T.; Tsuji, K.; Kaneko, T.; Shiota, M.; Fukui, F.; Takaku, H.; Nakagawa, Y.; Ichikawa, T.; Kobayashi, S. Metabolism of ^{13}C-isomaltooligosaccharides in healthy men. *Biosci., Biotechnol., Biochem.* **1992**, *56*, 937−940.
(39) Brunt, K.; Sanders, P. Improvement of the AOAC 2009.01 total dietary fiber method for bread and other high starch containing matrices. *Food Chem.* **2013**, *140*, 574−580.
(40) Tanabe, K.; Nakamura, S.; Oku, T. Fatal imperfection of enzymatic-HPLC quantitative method for non-digestible oligosaccharides and its proposed solution strategy newly quantitative method for non-digestible oligosaccharides. *Curr. Nutr. Food Sci.* **2011**, *7*, 209−215.
(41) Manjunath, P.; Shenoy, B. C.; Raghavendra; Rao, M. R. Fungal glucoamylases. *J. Appl. Biochem.* **1983**, *5*, 235−260.
(42) Miller, E. R.; Ullrey, D. E. The pig as a model for human nutrition. *Annu. Rev. Nutr.* **1987**, *7*, 361−382.
(43) Taravel, F. R.; Datema, R.; Woloszczuk, W.; Marshall, J. J.; Whelan, W. J. Purification and characterization of a pig intestinal α-limit dextrinase. *Eur. J. Biochem.* **1983**, *130*, 147−153.
(44) Sørensen, S. H.; Norén, O.; Sjöström, H.; Danielsen, E. M. Amphiphilic pig intestinal microvillus maltase/glucoamylase. Structure and specificity. *Eur. J. Biochem.* **1982**, *126*, 559−568.
(45) Sjöström, H.; Norén, O.; Christiansen, L.; Wacker, H.; Semenza, G. A fully active, two-active-site, single-chain sucrase isomaltase from pig small intestine. Implications for the biosynthesis of a mammalian integral stalked membrane protein. *J. Biol. Chem.* **1980**, *255*, 11332−11338.
(46) Houdijk, J. G.; Bosch, M. W.; Tamminga, S.; Verstegen, M. W.; Berenpas, E. B.; Knoop, H. Apparent ileal and total-tract nutrient digestion by pigs as affected by dietary nondigestible oligosaccharides. *J. Anim. Sci.* **1999**, *77*, 148−158.
(47) Smiricky-Tjardes, M. R.; Grieshop, C. M.; Flickinger, E. A.; Bauer, L. L.; Fahey, G. C., Jr. Dietary galactooligosaccharides affect ileal and total-tract nutrient digestibility, ileal and fecal bacterial concentrations, and ileal fermentative characteristics of growing pigs. *J. Anim. Sci.* **2003**, *81*, 2535−2545.
(48) Urriola, P. E.; Stein, H. H. Effects of distillers dried grains with solubles on amino acid, energy, and fiber digestibility and on hindgut fermentation of dietary fiber in a corn-soybean meal diet fed to growing pigs. *J. Anim. Sci.* **2010**, *88*, 1454−1462.
(49) Oku, T.; Tanabe, K.; Watanabe, Y.; Ono, H.; Naruse, M.; Nakamura, S. Effects of non-digestible oligosaccharides with different

DOI: 10.1021/jf505844y
J. Agric. Food Chem. 2015, 63, 5747−5752

properties on Ca and Mg metabolism in rats. *J. Jpn. Soc. Nutr. Food Sci.* **2007**, *60*, 233−240 (in Japanese). .

DOI: 10.1021/jf505844y
J. Agric. Food Chem. 2015, 63, 5747−5752

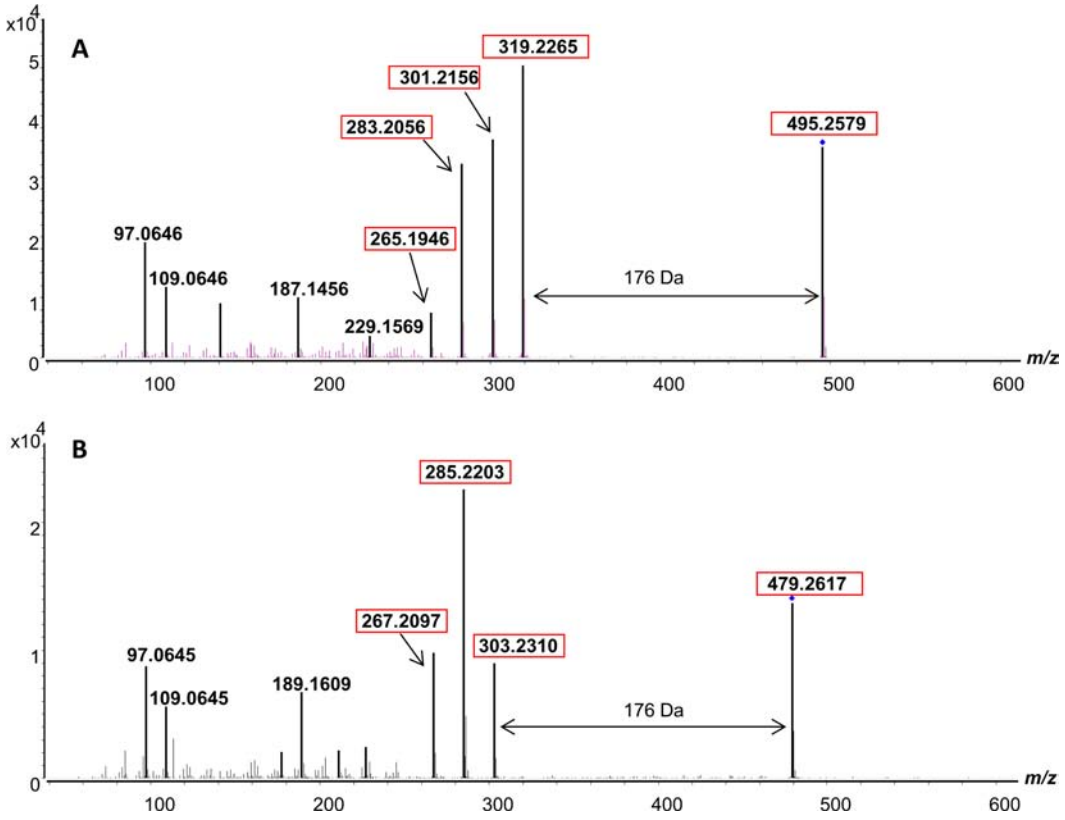

Figure 2. MS/MS of OHMT-glu (A) and MS/MS of MT-glu (B), CE 30.

acetate (EtOAc) were of high-performance liquid chromatography (HPLC) grade (Burdick & Jackson, Muskegon, MI). Ammonium Hydroxide (NH_4OH), potassium dihydrogen phosphate (KH_2PO_4), dipotassium hydrogen phosphate (K_2HPO_4), and formic acid were of reagent grade supplied by Fisher Scientific (Pittsburgh, PA). Oasis MAX strong anion exchange (3 mL, 60 mg) solid-phase extraction (SPE) cartridges were obtained from Waters Corp. (Milford, MA). The lyophilized enzyme β-glucuronidase type VII A from *Escherichia coli* (20 000U) was purchased from Sigma Chemical Co. (St. Louis, MO).

Fish Dosing. Fish were dosed with MT at the Center for Veterinary Medicine aquaculture facility. Tilapia (*Oreochromis* species, not sex reversed) was obtained from Aquasafra Inc. (Bradenton, FL) as ∼1 g fry. Fish were raised in freshwater recirculating systems consisting of two 500 gal tanks at a temperature range of 20−30 °C until they reached a suitable size for dosing (400−700 g). Tilapia were given a single oral dose of 60 mg/kg body weight MT and sacrificed at 1, 3, 7, and 14 days after the dose. One fish was used for each time point. Bile samples were removed and stored at −80 °C until analysis. Control bile was also removed from a fish that was not fed with MT. The experimental protocol was approved by the Animal Care and Use Committee at the Office of Research, Center for Veterinary Medicine, U.S. Food and Drug Administration, and all procedures were conducted in accordance with the principles stated in the Guide for the Care and Use of Laboratory Animals (2011) and the Animal Welfare Act of 1966 (P.L. 89-544), as amended.

Sample Preparation. Bile from dosed and control fish were weighed (∼100 mg each) into 15 mL polypropylene centrifuge tubes. A 1 mL sample of 5% aqueous ammonium hydroxide solution was added to each sample and vortexed for 30 s. The extracts were subjected to SPE cleanup by an automated SPE system (RapidTrace workstation by Caliper Life Science, Hopkinton, MA). Waters Oasis MAX, SPE cartridges were preconditioned with 2.5 mL of MeOH (42 mL/min) followed by 2.5 mL of water (42 mL/min). After the samples were loaded (1 mL/min), cartridges were rinsed successively with 2 mL of 0.5 M NH_4OH in 5% MeOH (42 mL/min) followed by 2 mL of 20% MeOH (42 mL/min). Cartridges were dried by passing 6 mL of air (42 mL/min). Glucuronides were eluted with 2 mL of freshly prepared 2% formic acid in MeOH (1 mL/min). The eluents were evaporated to dryness by blowing N_2 at 40 °C. Samples were reconstituted to 200 μL with MeOH/water (60/40 v/v) and transferred to autosampler vials for mass spectral analysis after filtering through a 0.2 μm nylon syringe filter.

Enzymatic Hydrolysis of Bile from Dosed Fish with β-Glucuronidase from *E. coli*. Glucuronide enriched fraction from SPE of control and dosed fish bile (3 days) was evaporated to dryness and dissolved in 200 μL of 0.25 M potassium phosphate buffer (pH ∼ 6.8). A 40 μL (1000U) of β-glucuronidase enzyme from *E. coli* in 0.25 M phosphate buffer was added. The phosphate buffer was prepared by mixing 55 mL of 0.5 M dipotassium hydrogen phosphate and 45 mL of 0.5 M potassium dihydrogen phosphate. The sample was incubated overnight in a shaking water bath at 37 °C and was extracted twice with 300 μL of ethyl acetate. The combined ethyl acetate extract was evaporated to dryness under nitrogen in a TurboVap evaporator at 40 °C. The residue was reconstituted in 200 μL of 60:40 methanol:water. The sample was transferred to autosampler vial after filtering through a 0.2 μm nylon syringe filter for mass spectral analysis.

Liquid Chromatography−Quadrupole Time-of-Flight Mass Spectrometry (LC-QTOFMS) Analysis. Chromatographic separation was carried out using a HPLC system (Agilent Series 1100 or 1290 Palo Alto, CA) equipped with a reversed phase C18 analytical column of 150 × 2.0 mm, 3 μm particle size (Phenomenex Luna C18) with a guard column of the same packing. The column oven was held at 40 °C, and the autosampler tray was maintained at 20 °C. The injection volume was 5 or 10 μL. Mobile phase A and B were 0.1% aqueous formic acid and ACN with 0.1% formic acid, respectively. The optimized chromatographic method on the Agilent 1290 pump was a linear gradient of 40−90% ACN in 10 min, hold at 90% ACN for 2 min, linear gradient of 90-40% ACN in 1 min, followed by equilibration at 40% ACN for 12 min before the next injection. The optimized method for Agilent 1100 pump was a linear gradient of 30−90% ACN in 10 min, hold at 90% ACN for 5 min, linear gradient of 90−30% ACN in 1 min, followed by equilibration at 30% ACN for 9 min before the next injection. Flow rate was 0.2 mL/min for both gradients. The HPLC system was connected to a

DOI: 10.1021/jf506151g
J. Agric. Food Chem. 2015, 63, 5753−5760

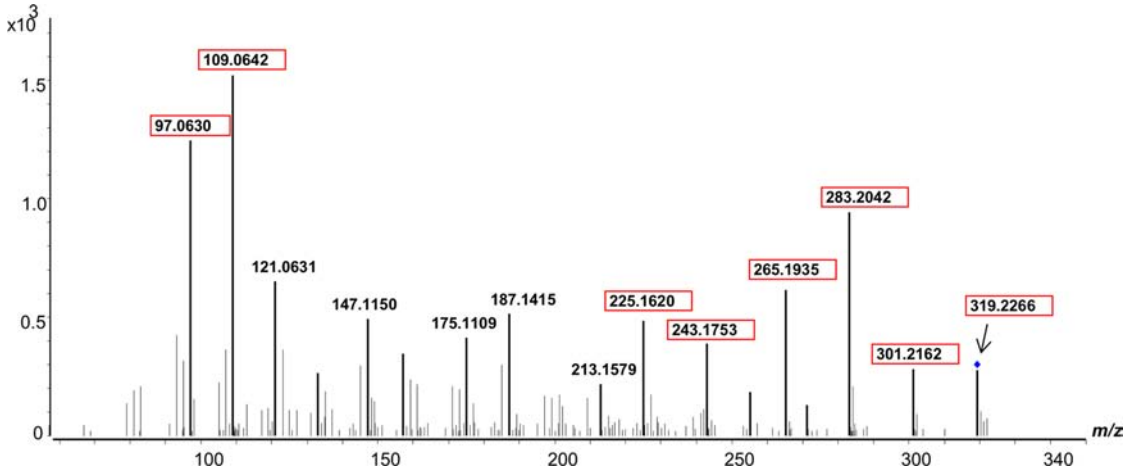

Figure 3. MS/MS of OHMT (in-source generated 319).

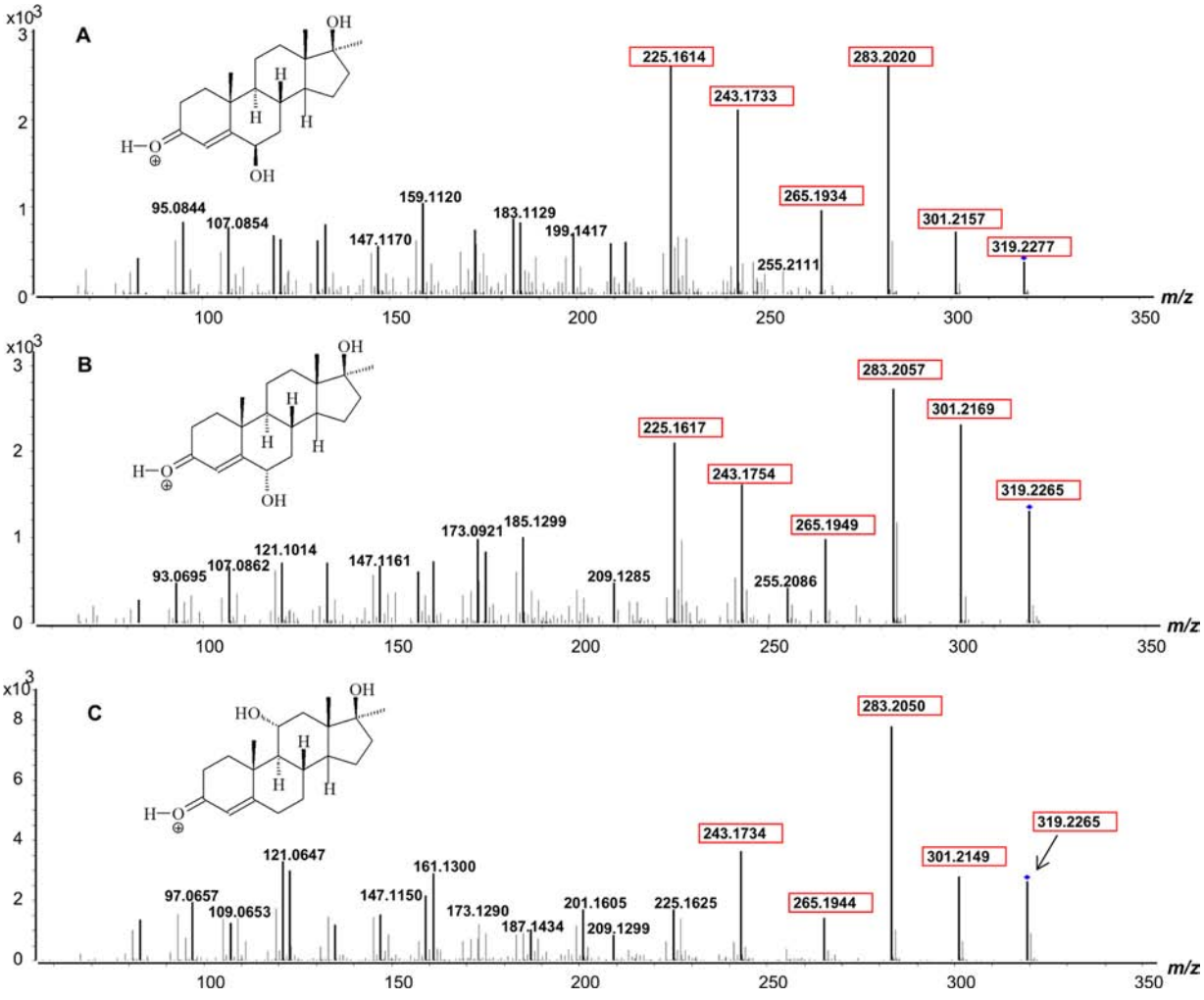

Figure 4. MS/MS spectra of C-6α (A), C-6β (B), and C-11α (C) hydroxy-MT standards.

quadrupole time-of-flight mass spectrometer model 6530 from Agilent (Agilent Technologies, Palo Alto, CA) equipped with electrospray jet stream technology operating in the positive ion mode, using the following operation parameters: capillary voltage 3500 V; nebulizer pressure, 50 psi; drying gas, 12 L/min; gas temperature, 325 °C; nozzle voltage, 1000 V; fragmentor voltage, 165 V; skimmer voltage, 65 V; and octapole RF, 750 V. LC/MS accurate mass spectra were recorded across the range of m/z 50−1000 at 4 GHz high resolution. Data were collected in both centroid and profile formats and processed with Mass Hunter software. Accurate mass measurements of each peak from the extracted ion chromatograms were obtained by means of a calibrant solution delivered by an external isocratic pump. This solution contains the internal reference masses of purine ($C_5H_4N_4$) at m/z 121.0509 and HP-921 [hexakis-(1H, 1H, 3H-tetrafluoro-pentoxy) phosphazene] ($C_{18}H_{18}O_6N_3P_3F_{24}$) at m/z 922.009. The OHMT-glu ion at calculated exact mass of m/z 495.2589 was extracted from the total ion

DOI: 10.1021/jf506151g
J. Agric. Food Chem. 2015, 63, 5753−5760

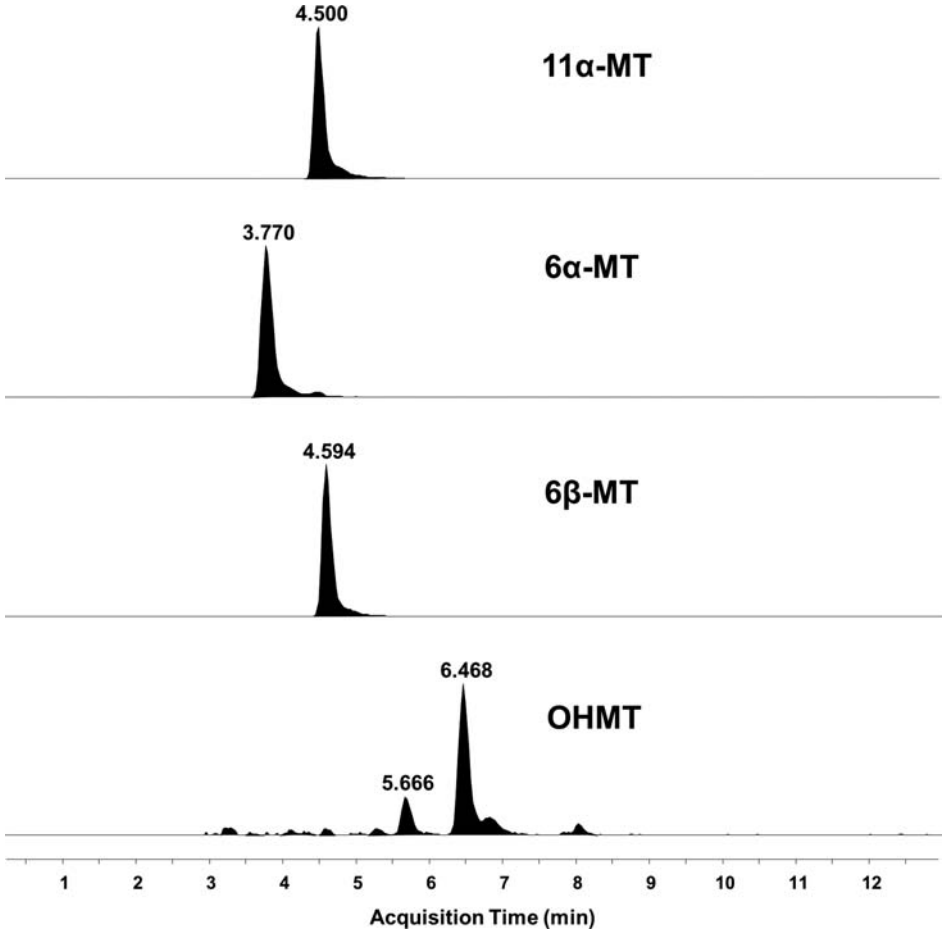

Figure 5. Extracted ion (m/z 319.2268) chromatograms of hydroxylated MT standards (6α, 6β, and 11α) and hydrolyzed bile (OHMT).

chromatogram and selected as the precursor ion for collision-induced dissociation (CID) experiment. For targeted tandem mass spectrometry (MS/MS) analysis, product ion scan range was 50−500 Da. A retention time window was set at ±0.5 min, and the isolation width was set at medium (~4 m/z). Collision energy of 30 eV was used for MS/MS experiments to obtain maximum intensity of fragments at m/z 319.2265, 301.2156, and 283.2056.

RESULTS AND DISCUSSION

We utilized the MFE algorithm in the Q-TOF Mass Hunter qualitative analysis software to detect the molecular features in the glucuronide-rich extract of dosed tilapia bile. For the extraction of molecular features, we used a peak height filter of >15 000 in the compounds filter tab. The charge state was limited to 1. Ion species were limited to the positive ions H^+ and Na^+. The 523 molecular features extracted under these criteria were then searched against our in-house database of MT metabolites. We used the criteria of mass and a mass accuracy tolerance of 5 ppm for the library search to identify OHMT-glu of the correct formula $C_{26}H_{38}O_9$ at m/z 495.2579 with a mass accuracy of 2 ppm. The in-house MT metabolite database was constructed to include the exact masses and the molecular formulas of mono-, di-, and tri-hydroxylated MT and their glucuronides.

According to the formula $C_{26}H_{38}O_9$, OHMT-glu has an additional hydroxyl function. The QTOF high-resolution mass spectrometry (HRMS) approach utilized provided us with exact masses of good mass accuracy to determine the chemical formula of OHMT-glu as well as its fragment ions. The correct formula generated for the fragment ions enabled us to propose structures for them. We took advantage of published literature of steroid fragmentation pathways and compared them with our experimental observations. This is a difficult strategy because small differences in chemical structure such as additional double bonds and methyl groups can result in a significantly different fragmentation pathway of steroids.[10]

The MS/MS analysis of OHMT-glu at a collision energy (CE) of 30 eV (Figure 2A) showed an abundant peak at m/z 319.2265 ($C_{20}H_{31}O_3$) $[M + H - 176\ Da]^+$ due to the loss of a dehydrated glucuronide molecule (176 Da). Successive losses of water from m/z 319 were observed at m/z 301.2156 ($C_{20}H_{29}O_2$), 283.2056 ($C_{20}H_{27}O$), and 265.1946 ($C_{20}H_{25}$) for $[M + H - glu - H_2O]^+$, $[M + H - glu - 2H_2O]^+$, and $[M + H - glu - 3H_2O]^+$, respectively, indicating three oxygens in OHMT-glu structure. The MS/MS spectrum of our previously synthesized MT-glu showed corresponding losses of dehydrated glucuronide molecule followed by only two consecutive water losses (Figure 2B). This further confirms that OHMT-glu bears an additional hydroxyl group in the aglycone in comparison to MT-glu. We designate the aglycone of OHMT-glu as OHMT. Our challenge was to place the additional hydroxyl group in OHMT.

Hydroxylation is a common metabolic pathway of anabolic steroids. Therefore, an understanding of fragmentation of hydroxylated steroids is very important in their structure elucidation. Also, an in-depth comparison of fragmentation of known related hydroxylated MT analogs with that of OHMT is a useful strategy for structure elucidation. The hydroxylation can be at any of the ring carbons or one of the three methyl groups. Hydroxylation has been reported previously at C6, 7, 11, 15, and

DOI: 10.1021/jf506151g
J. Agric. Food Chem. 2015, 63, 5753−5760

Scheme 1. Proposed Mechanism for the Formation of *m/z* 243 and 225

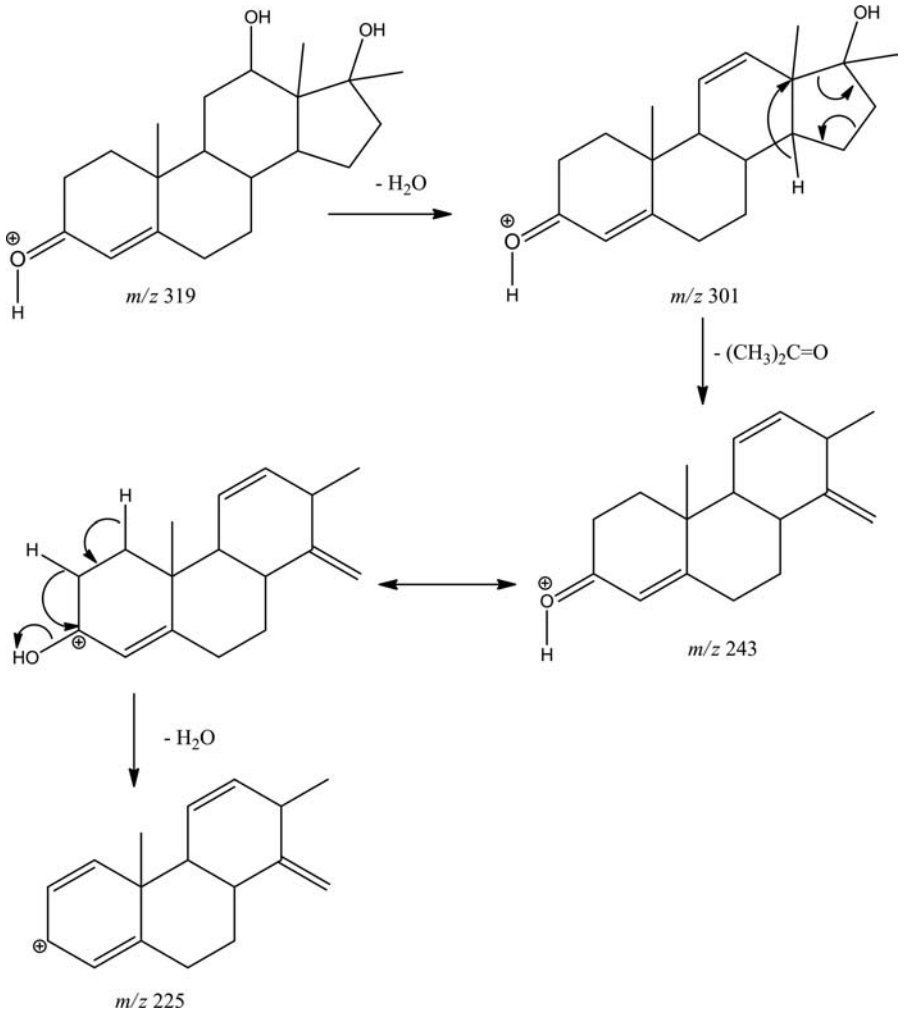

16 of MT and related compounds.[7,11−13] To simplify the discussion, the nominal masses are sometimes used in this paper.

To find further structural information on OHMT, we optimized the fragmentation voltage at 200 V in the MS1 experiment to produce in-source generated fragment ion at *m/z* 319 (protonated OHMT) from precursor ion at *m/z* 495 (the protonated OHMT-Glu). We then recorded the MS/MS spectrum of the in-source generated OHMT (*m/z* 319) (Figure 3) and compared it with those generated from the three commercially available standards C-6*α*, -6*β*, and -11*α* hydroxy-MT (Figure 4).

Mass spectra of hydroxylated MT standards and OHMT showed significant ions at *m/z* 301, 283, and 265 indicating three sequential losses of water (Figures 3 and 4). In addition, two other common ions were observed at *m/z* 243 and 225. These can be attributed to the loss of 58 Da (acetone) from fragment ions at *m/z* 301 and 283, respectively.[14]

However, the lower *m/z* region of product ion spectra of the three standards looked quite different from that of OHMT. We observed very prominent ions at *m/z* 97.0630 (C_6H_9O) and 109.0642 (C_7H_9O) in the MS/MS spectra of OHMT (Figure 3). In fact, these two ions were the most abundant ions in its MS/MS spectrum. However, these ions were either absent or of very low abundance in the MS/MS spectra of the 3 hydroxylated MT standards (Figure 4).

Williams et al.[15] extensively studied the abundance of *m/z* 97 and 109 ions in monohydroxylated testosterones. According to their study, the hydroxylation of testosterone at C-2, C-6, C-7, C-11, and C-19 positions greatly reduces the relative abundances of the *m/z* 97 and 109 ions. Therefore, the presence of intense fragment ions at *m/z* 97 and 109 in the MS/MS spectra of OHMT provides strong support to rule out hydroxylation at C-2, C-6, C-7, C-11, and C-19 positions.

In an attempt to characterize the aglycone OHMT further, the glucuronide extract from the anion exchange SPE of bile was successfully hydrolyzed by *β*-glucuronidase enzyme from *E. coli* in 0.25 M phosphate buffer (pH ∼6.8) to produce hydroxylated MT analogs. One major and a few other minor isomeric hydroxylated MT analogs were detected in the hydrolysis reaction (Figure 5). They were less polar, and their retention times did not match with that of commercially available hydroxy MT standards C-6*α*, C-6*β*, and C-11*α* (Figure 5). Therefore, the additional hydroxyl group cannot be on either C-6 or C-11*α* of the OHMT.

Moreover, hydroxylation of methyl groups at C-17, C-18, and C-19 can also be ruled out because of the absence of a characteristic 30 Da (formaldehyde) loss in the spectrum of OHMT.[14,16]

As reported previously, 17-alkyl steroids (MT, ethisterone, oxymestrone, and mibolerone) show a neutral loss of 58 Da corresponding to a loss of acetone molecule due to

DOI: 10.1021/jf506151g
J. Agric. Food Chem. 2015, 63, 5753−5760

Scheme 2. Proposed Alternative Mechanism for the Formation of *m/z* 225

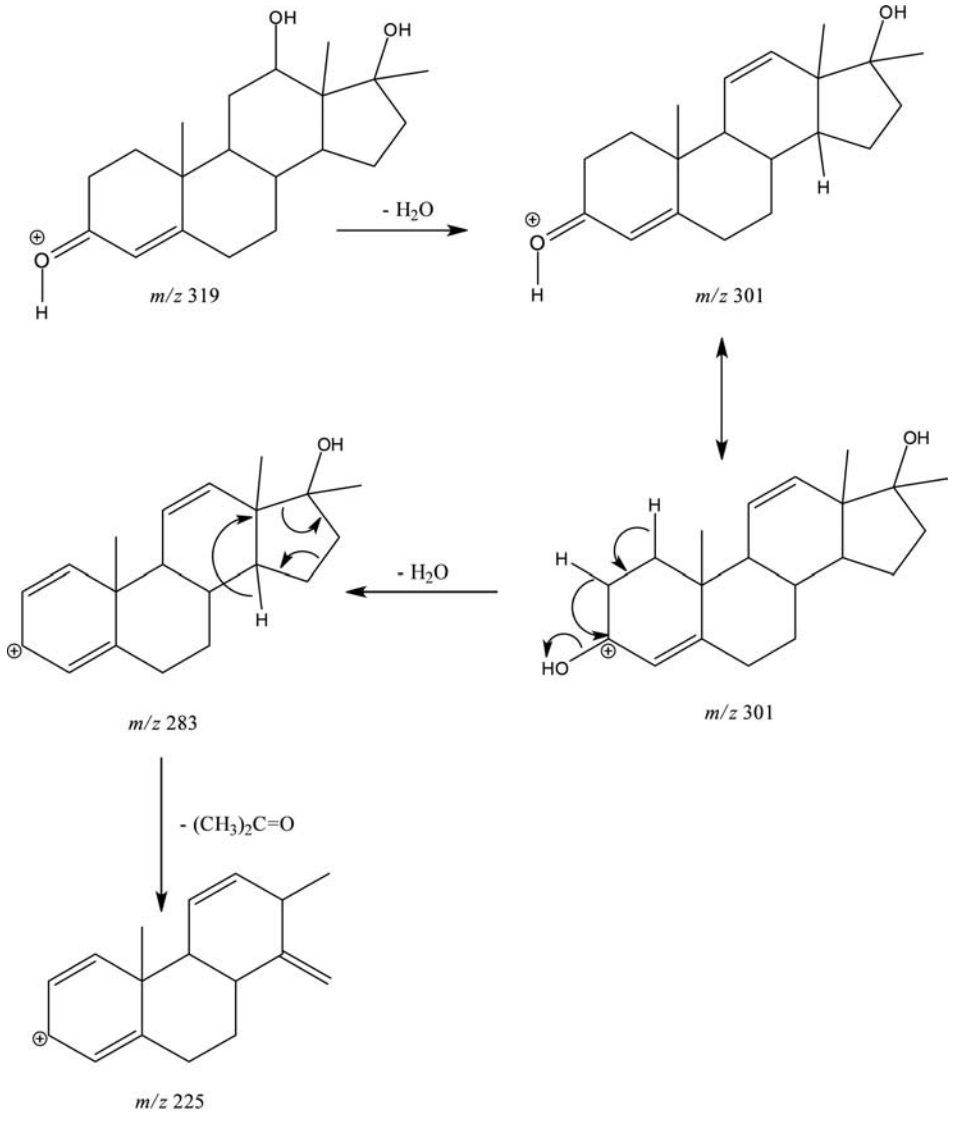

fragmentation of the D ring. Also, it has been stated that this neutral loss can be seen after losing a water molecule from the molecular ion.[14] According to the proposed mechanism (Schemes 1 and 2), the molecular ion at *m/z* 319 loses a water molecule to generate an ion at *m/z* 301 followed by a loss of a neutral acetone molecule to generate the ion at *m/z* 243. On the basis of this mechanism, C-16 cannot be substituted with a hydroxyl group because we see a significant D ring fragment at *m/z* 243 in OHMT.

A careful in-depth analysis and comparison of our mass spectrometric data against published literature has enabled us to eliminate hydroxylation of most of the carbons in OHMT except for the 15 and 12 positions of the nucleus. As postulated in the proposed pathways (Schemes 1 and 2), formation of the two ions we observe at *m/z* 243 and 225 can be better explained by locating the new hydroxyl group at C-12 than at C-15 in OHMT. Similar mechanisms have been proposed by Pozo et al. in a study to elucidate urinary metabolites of fluoxymesterone.[14] The *m/z* 225 ion can originate from *m/z* 243 (Scheme 1) or the ion at *m/z* 283 (Scheme 2). Therefore, we are proposing C-12 as the most probable position for the hydroxyl group in OHMT (Figure 1). The glucuronidation can be at C-17 or on the new hydroxyl moiety, which generates ambiguity about positioning of the glucuronide in OHMT-glu. To confirm the structure of OHMT-glu we need to compare the mass spectrometric and LC data (retention time) with a standard. Unfortunately, there are no commercial standards available for OHMT-glu or OH-MT for comparison purposes. The multistep procedure to synthesize OHMT-glu was beyond the scope of our study. We were also limited by the minute amount of OHMT-glu present in the bile to purify sufficient quantity to get NMR data to support the structure elucidation. However, by a careful study of the steroid fragmentation pathways, we were able to propose a tentative structure for OHMT-glu to best fit all our experimental data. This is a useful strategy in cases in which a chemical standard is not available.

Typical extracted ion chromatograms of the parent ion at *m/z* 495.2589 for $[M + H]^+$ in bile of dosed fish over a 14 day period are shown in Figure 6. All bile samples from dosed fish contained OHMT-glu. The control bile was confirmed negative. A rough estimate of the OHMT-glu concentrations in bile as compared to a MT-glu standard over 14 days are reported in Table 1.

The previously reported MT-Glu is not detected 7 days after administration.[9] However, the OHMT-glu stays in the bile for at

DOI: 10.1021/jf506151g
J. Agric. Food Chem. 2015, 63, 5753−5760

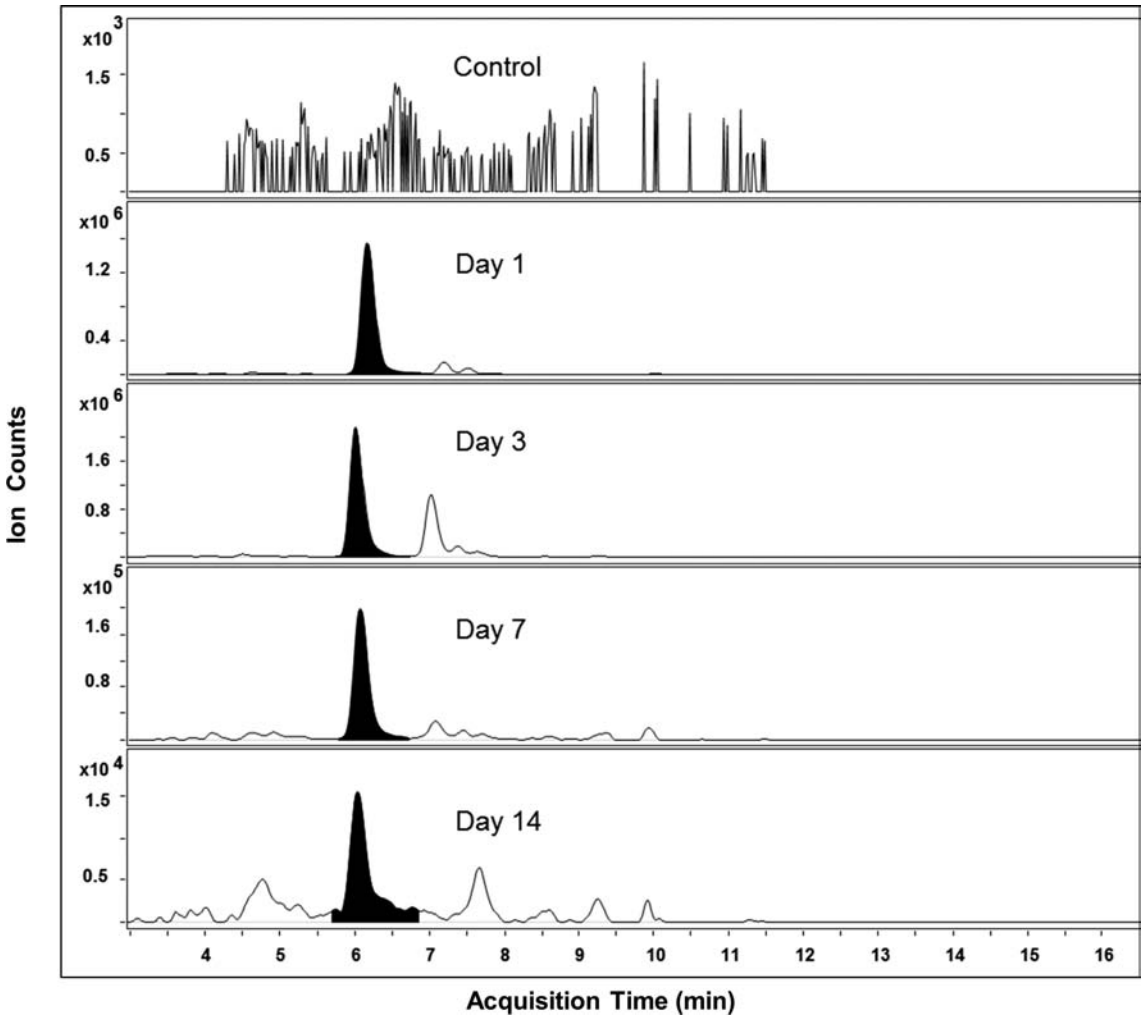

Figure 6. Extracted ion (m/z 495.2579) chromatograms of OHMT-glu in bile of control and dosed fish. Note that the y-scales for each extracted ion chromatogram are different.

Table 1. Levels of OHMT-glu in Dosed Tilapia

days after dosing	concentration of OHMT-glu (μg/mL)
1	2.2
3	2.7
7	0.2
14	0.07

least up to 14 days after administration. Because it persists in bile longer, OHMT-Glu is a better metabolite to monitor in bile than the previously reported MT-glu. MT is not approved for use in aquaculture in the United States. Therefore, this method can be used for monitoring its illegal use and for surveillance purposes.

In this paper we have attempted to show the strength of HRMS in providing the exact mass of OHMT-glu with high mass accuracy to arrive at the correct molecular formula for structure elucidation purposes. In addition, utilization of retrospective analysis of data generated in the past to discover other unknown metabolites is also highlighted.

AUTHOR INFORMATION

Corresponding Author

*Phone: 240 402 6688. Fax (240) 264-8401. E-mail: hiranthi.jayasuriya@fda.hhs.gov.

Notes

The authors declare no competing financial interest.

REFERENCES

(1) Gale, W. L.; Fitzpatrick, M. S.; Lucero, M.; Contreras-Sanchez, W. M.; Schreck, C. B. Masculinization of Nile tilapia (Oreochromis niloticus) by immersion in androgens. *Aquaculture* **1999**, *178* (3−4), 349−357.

(2) Kuwaye, T. T.; Okimoto, D. K.; Shimoda, S. K.; Howerton, R. D.; Lin, H. R.; Pang, P. T. K.; Grau, E. G. Effect of 17α-methyltestosterone on the growth of the euryhaline tilapia, *Oreochromis mossambicus*, in fresh water and in sea water. *Aquaculture* **1993**, *113* (1−2), 137−152.

(3) Pandian, T. J.; Sheela, S. G. Hormonal induction of sex reversal in fish. *Aquaculture* **1995**, *138* (1−4), 1−22.

(4) Cravedi, J. P.; Delous, G.; Rao, D. Disposition and Elimination Routes of 17-α-Methyltestosterone in Rainbow Trout (*Salmo gairdneri*). *Can. J. Fish. Aquat. Sci.* **1989**, *46*, 159−165.

(5) Stanley, S. M. R.; Smith, L.; Rodgers, J. P. Biotransformation of 17-alkylsteroids in the equine: gas chromatographic-mass spectral identification of ten intermediate metabolites of methyltestosterone. *J. Chromatogr., Biomed. Appl.* **1997**, *690*, 55−64.

(6) Dumasis, M. C. In vivo biotransformation of 17-α-Methyltestosterone in the horse revisited: identification of 17- hydroxymethyl metabolites in equine urine by capillary gas chromatography/mass spectrometry. *Rapid Commun. Mass Spectrom.* **2003**, *17*, 320−329.

(7) Clarke, D. J.; George, S. G.; Burchell, B. Glucuronidation in fish. *Aquat. Toxicol.* **1991**, *20* (1−2), 35−56.

DOI: 10.1021/jf506151g
J. Agric. Food Chem. 2015, 63, 5753−5760

(8) Hintikka, L.; Kuuranne, T.; Leinonen, A.; Thevis, M.; Schanzer, W.; Halket, J.; Cowan, D.; Grosse, J.; Hemmersbach, P.; Nielen, M. W. F.; Kostiainen, R. Liquid chromatographic-mass spectrometric analysis of glucuronide-conjugated anabolic steroid metabolites: method validation and interlaboratory comparison. *J. Mass Spectrom.* **2008**, *43* (7), 965−973.
(9) Amarasinghe, K.; Chu, P. S.; Evans, E.; Reimschuessel, R.; Hasbrouck, N.; Jayasuriya, H. Development of a Fast Screening and Confirmatory Method by Liquid Chromatography−Quadrupole-Time-of-Flight Mass Spectrometry for Glucuronide-Conjugated Methyltestosterone Metabolite in Tilapia. *J. Agric. Food Chem.* **2012**, *60* (20), 5084−5088.
(10) Guan, F.; Soma, L. R.; Luo, Y.; Uboh, C. E.; Peterman, S. Collision-Induced Dissociation pathways of Anabolic Steroids by Electrospray Ionization Tandem Mass Spectrometry. *J. Am. Soc. Mass Spectrom.* **2005**, *17*, 477−489.
(11) Biddle, S. T. B.; O'Donnell, A.; Houghton, E.; Creaser, C. Metabolism of methyltestosterone in the greyhound. *Rapid Commun. Mass Spectrom.* **2009**, *23*, 713−721.
(12) Gauthier, J.; Goudreault, D.; Poirier, D.; Ayotte, C. Identification of drostanolone and 17-methyldrostanolone metabolites produced by cryopreserved human hepatocytes. *Steroids* **2009**, *74*, 306−314.
(13) Musharraf, S. G.; Ali, A.; Khan, N. T.; Yousuf, M.; Choudhary, M. I.; Rahman, A. Tandem mass spectrometry approach for the investigation of the steroidal metabolism: Structure-fragmentaion relationship (SFR) in anabolic steroids and their metabolites by ESI-MS/MS analysis. *Steroids* **2013**, *78*, 171−181.
(14) Pozo, O. J.; Van, W.; Deventer, K.; Van, E.; Delbeke, F. T. Elucidation of urinary metabolites of fluoxymesterone by liquid chromatography−tandem mass spectrometry and gas chromatography−mass spectrometry. *J. Mass Spectrom.* **2008**, *43* (3), 394−408.
(15) Williams, T. M.; Kind, A. J.; Houghton, E.; Hill, D. W. Electrospray collision-induced dissociation of testosterone and testosterone hydroxy analogs. *J. Mass Spectrom.* **1999**, *34*, 206−216.
(16) Pozo, O. J.; Van, E.; Deventer, K.; Hernandez, F.; Delbeke, F. T. Detection and characterization of anabolic steroids in doping analysis by LC-MS. *TrAC, Trends Anal. Chem.* **2008**, *27* (8), 657−671.

DOI: 10.1021/jf506151g
J. Agric. Food Chem. 2015, 63, 5753−5760

chemistry move toward the simplification and miniaturization of sample preparation. This can be simply achieved by scaling down the size of previous systems or by developing new setups and techniques.[21] Different extraction methods to accelerate and miniaturize the process (sample size and organic solvent volumes) in the search for cost-effective solutions have been evaluated.[22] Despite these benefits, few protocols[23] have been developed in human milk matrices to cover this demand.

With regard to TAG determination in milk, several techniques such as thin-layer chromatography (TLC),[7,24] silver ion adsorption−TLC,[25] RP-HPLC,[16,23,26−28] or with silver ions (Ag-HPLC),[14,29] two-dimensional LC,[30] gas chromatography (GC),[25] and tandem MS with ammonia negative ion chemical ionization[31] have been employed. From all of these techniques, RP-HPLC has been widely used, because it provides a better resolution of individual TAG molecules. Thus, these compounds are separated according to both chain length and degree of unsaturation of the FAs.[32] However, RP-HPLC for TAGs separation has been usually performed using a binary gradient of acetonitrile (ACN)−isopropanol[14,27] or a linear ternary gradient of ACN−dichloromethane−acetone.[16,23,28] These latter gradients led to low resolution of TAGs peaks, and the first-mentioned gave a long analysis time (90 min).

To improve chromatographic performance in terms of throughput and/or resolution, particularly when numerous complex food extracts have to be analyzed, recent advances in LC instrumentation could be beneficial.[33] In this context several analytical strategies related to column technology have been developed in HPLC, including the use of monolithic supports packed columns with sub-2-μm particles operating at ultrahigh pressure (UHPLC) or with core−shell or fused-core particles. These latter core−shell particle columns are capable of maintaining high efficiencies at increasing flow rates with the subsequent reduction of analysis time. Also, these columns operate comfortably within the pressure limits of conventional LC instruments, rivaling the performance obtained with sub-2-μm columns on UHPLC instruments. However, the use of these columns in conventional LC systems for TAG separation in human milk samples has not been reported to date.

Multivariate data analysis can be used to obtain more information on major, minor, and trace components in foods.[34,35] Within these statistical tools, linear discriminant analysis (LDA) is probably one of the best known methods, and it has been successfully used for the identification/differentiation of several foods, such as dairy products, oils, wines, and others.[36,37]

In this work, the development of analytical conditions for the extraction and RP-HPLC separation of milk fat TAGs is described. For this purpose, a small-scale fat extraction protocol (with reduced consumption of reagents and processing time, consistent with the recent trends in green chemistry) and in combination with the use of a fused-core HPLC column is presented and compared. In addition, on the basis of TAG profiles of milk samples from different mammalian species (human, bovine, caprine, and ovine), a LDA model is applied to differentiate these matrices according to their species origin.

MATERIALS AND METHODS

Chemicals. TAG standards including trilaurin (LaLaLa), trimyristin (MMM), tripalmitin (PPP), tripalmitolein (PaPaPa), and triolein (OOO) from Sigma (St. Louis, MO, USA) were employed. The following analytical grade reagents were also used: HPLC grade ACN and methanol (MeOH) were purchased from VWR Chemicals (Barcelona, Spain); reagent grade dichloromethane, *n*-pentanol, and *n*-hexane, HPLC grade 2-propanol and *n*-butanol, and anhydrous sodium sulfate were supplied by Scharlau (Barcelona, Spain). Butylhydroxytoluene (BHT) was purchased from Fluka (Buchs SG, Switzerland).

Samples. Human milk samples (n = 15) were kindly donated by healthy well-nourished mothers in different stages of lactation (3 colostrum (1−5 days); 5 transitional milk (6−15 days); 7 mature milk (after 16 days)). All mothers, who were Caucasian, middle-class, and lived within the urban area of Valencia, consumed an unrestricted omnivorous diet. The samples were collected between the baby's feed by manual expression using a Medela Harmony Breastpump (Zug, Switzerland).

Bulk raw milk samples of Holstein-Friesian cows (n = 20) were collected by milking machines, whereas milk samples of Cartera goats (n = 20) and Murciano-Granadina sheep (n = 20) were collected by manual expression from animals in midlactation stage. All of these samples were kindly donated by different farms located at La Comunitat Valenciana, Spain. All animals were free from mastitis or any other inflammatory diseases. They were grazed in the morning and in the afternoon were reared in stables and fed hay, fodder grass, and vegetables. After collection, milk samples were rapidly heated to 80 °C and held at this temperature for 1.5 min to inactivate the lipases and to avoid TAG hydrolysis.[38]

Sample Preparation. A lipid extraction method (method I) was developed in this study. It consisted of a modification of the traditional gravimetric method.[16] Briefly, a well-mixed milk aliquot (150 μL) was placed in a centrifuge tube and 2.5 mL of a dichloromethane−MeOH solution (2:1, v/v), containing 5 μg mL^{-1} BHT to prevent lipid oxidation,[24] was added. The mixture was sonicated for 10 min, vortexed for 1 min, placed in the refrigerator (4 °C) for 15 min, and centrifuged at 10000 rpm for 8 min. Then, 800 μL of distilled water was added, sonicated for 10 min, mixed for 1 min in the vortex, and centrifuged at 10000 rpm for 8 min. The organic layer was washed with 800 μL of a saturated solution of sodium chloride, sonicated for 10 min, vortexed for 1 min, and centrifuged 8 min at 10000 rpm. The organic fraction was dried with anhydrous sodium sulfate, and the fat solution was then filtered with a syringe through a 0.45 μm filter, collected in a preweighed HPLC vial, and dried under a nitrogen stream. The fat was dissolved in a 2:2:1 ACN/2-propanol/*n*-hexane (v/v/v) ternary mixture and injected in the LC system. This method was compared with that described by Morera et al.[16] (method II).

High-Performance Liquid Chromatography and Mass Spectrometry. An 1100 series liquid chromatograph (Agilent Technologies, Waldbronn, Germany) provided with a quaternary pump, a degasser, a thermostated column compartment, an automatic sampler, and a UV−vis diode array detector online coupled to an Agilent 385-ELSD was employed. Separation was carried out with a Kinetex C18 100 Å column (150 mm × 4.6 mm, 2.6 μm; Phenomenex, Torrance, CA, USA). The optimized separation conditions were as follows: isocratic elution with an 80:20 ACN/*n*-pentanol mixture for 45 min, followed by a gradient of ACN/*n*-pentanol up to ratio of 60:40 in 20 min; column temperature, 10 °C; flow rate, 1.0 mL min^{-1}; and injection volume, 10 μL. UV detection was performed at 205 ± 10 nm (360 ± 60 nm as reference). The ELSD parameters were as follows: evaporation and nebulization temperature, 55 °C; gas flow rate, 1.2 standard liters per minute (SLM); gain factor, 1.

For TAG identification, a UPLC binary pump system (Acquity, Waters, Milford, MA, USA) was interfaced to a triple-quadrupole mass spectrometer (TQD, Waters, Manchester, UK) through an atmospheric pressure chemical ionization (APCI) source. The MS working conditions were as follows: probe temperature, 600 °C; corona discharge current, 20 μA; source temperature, 120 °C; desolvation gas flow, 800 L h^{-1}; cone gas flow, 60 L h^{-1}. Drying as well as nebulizing gas was nitrogen (Praxair, Valencia, Spain). The mass spectrometer scanned within the m/z 150−1000 range in the positive ionization mode at one scan per second.

Data Treatment and Statistical Analysis. The area of selected TAG peaks was measured from the ELSD detector, and a data matrix

DOI: 10.1021/acs.jafc.5b01158
J. Agric. Food Chem. 2015, 63, 5761−5770

was constructed (see Results and Discussion). After normalization of the variables, statistical data treatment was performed using SPSS (v. 15.0, Statistical Package for the Social Sciences, Chicago, IL, USA). Using a stepwise algorithm, the predictors to be included in the LDA model were selected. According to this algorithm, a predictor is considered eligible for its inclusion in the model if the significance of its F test exceeds the specified probability level given by the entrance threshold, F_{in}. However, the entrance of a new predictor modifies the significance of those predictors that are already present in the model. For this reason, after the inclusion of a new predictor, a rejection threshold, F_{out}, is used to decide if one of the other predictors should be removed from the model. This sequential process continues until no more predictors are eligible for entrance or removal from the model. The default probability values of F_{in} and F_{out}, 0.05 and 0.10, respectively, were adopted.

RESULTS AND DISCUSSION

Optimization of the Separation of TAGs. The initial separation conditions were adapted from a previous work for TAG separation in vegetable oils.[39] The optimization study was performed using human milk samples. Using a flow rate of 1.5 mL min^{-1} and a column temperature of 10 °C, a similar optimization study of mobile phase, including several binary mixtures of ACN with different alcohols (2-propanol, *n*-butanol, and *n*-pentanol) at 70:30 ratio, was conducted. Using 2-propanol, poor resolution and relatively long analysis times (ca. 50 min) were obtained. Using *n*-butanol and *n*-pentanol, analysis time and resolution improved significantly, although most peaks still overlapped. Despite this overlapping, the ACN/*n*-pentanol mixture gave shorter analysis time with respect to *n*-butanol and, therefore, *n*-pentanol was selected for the following studies.

Next, the influence of the content of *n*-pentanol in the 20−30% range on TAGs separation was studied. As shown in Figure S1 (see the Supporting Information), resolution was improved with decreasing *n*-pentanol content. Broad peaks with separation times longer than 45 min were obtained with <20% *n*-pentanol. Thus, an 80:20 (v/v) ACN/*n*-pentanol mixture was selected. This mobile phase also provided a satisfactory response in ELSD. Then, the effect of column temperature on TAG separation and detection response of UV (Figure S2, left) and ELSD (Figure S2, right) detectors was performed under isocratic conditions. As it can be seen, the TAG resolution increased when the temperature decreased, with a concomitant increase in both backpressure (from 22.4 to 25.4 MPa along the 5−20 °C range) and analysis time. Within the studied temperature interval, the TAG peaks showed satisfactory peak widths (measured at 50% peak height) ranging between 6.3 and 53.0 s (Figure S2, left) and 6.2−42.2 s (Figure S2, right). With regard to detector response, neither UV nor ELSD detection showed significant changes in the response (measured as peak area) over the temperature range investigated. These observations in ELSD response were different from those reported in the literature, where a positive[40] or negative[41] correlation with column temperature for peak area could be found. This behavior could be explained by the narrow temperature interval (5−20 °C) considered in this study. Thus, a column temperature of 10 °C provided the highest number of resolved peaks (30) (with peak widths ranging between 5.4 and 29.1 s) in <50 min with a reasonable backpressure (24.1 MPa), being selected for further studies.

Next, the influence of flow rate on TAG separation was also studied. A flow rate decrease from 1.5 to 1.0 mL min^{-1} led to an improvement in the resolution at the expense of an increase of analysis time. Lower flow rates (<1.0 mL min^{-1}) provided a significant peak broadening (peak widths ranged between 10.2 and 80.3 s and asymmetry factors comprised between 0.85 and 1.60) at very long separation time (>100 min). In addition, a decrease of the ELSD response with increasing flow rate was found, which was consistent with findings reported by several authors.[40,42] As a result, a flow rate of 1.0 mL min^{-1} was selected for further studies. Under these conditions, the late-eluting compounds were barely distinguished from baseline. To decrease the retention time and improve detection (peak shape), a solvent gradient step was established. Thus, the *n*-pentanol content was increased from 20 to 40% in 20 min after the first 45 min of isocratic elution with 80:20 ACN/*n*-pentanol. Figure 1 shows the ELSD chromatogram obtained under these conditions, where satisfactory peak shapes for highly retained TAGs were obtained.

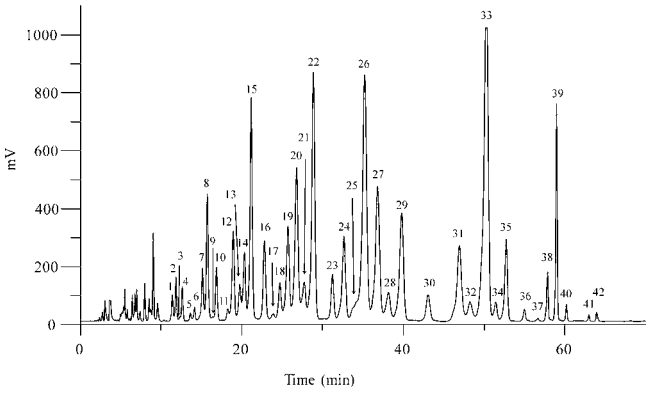

Figure 1. TAG profile of mature human milk. Chromatographic conditions: isocratic elution for 45 min at 80:20 ACN/*n*-pentanol followed by a linear gradient to 60:40 ACN/*n*-pentanol in 20 min; column temperature, 10 °C; flow rate, 1.0 mL min^{-1}.

The performance of the developed RPLC method was compared to those previously reported for analysis of TAGs in human milk. Most of these studies were usually conducted using conventional microparticulate columns packed with 5 μm silica particles;[23,27,28] however, it should be mentioned that data of efficiency or other analytical parameters were not provided. In any case, an estimation of the number of resolved peaks of some of these works was done. These values were between 17 and 22,[23,27,28] which were significantly lower than those obtained in this work (35). Also, packed columns of sub-2-μm particles operating at UPLC conditions have been applied to these samples.[43,44] To our knowledge, the work of Beccaria et al.[43] is the only one that has reported performance data (peak capacities values up to 170 for 114 min gradient) using three serially coupled core−shell type C18 columns. However, the number of resolved peaks was similar to our method, which is accomplished in shorter analysis (<65 min) using a RP column in a conventional high-pressure system.

Identification of TAGs. Generally, the elution of TAGs in RP-HPLC occurs according to the partition number (PN).[32,45] The PN for each individual TAG can be calculated as follows: PN = CN − 2ND, where CN is the number of carbon atoms and ND is the number of double bonds in the FAs attached to the glycerol molecule (see Table 1). However, the procedure for identifying the TAGs based on the PN is complicated due to the large number of FA constituents and rather limited to the coincidence of this parameter for several TAGs. For this reason,

DOI: 10.1021/acs.jafc.5b01158
J. Agric. Food Chem. 2015, 63, 5761−5770

Table 1. TAGs Identified by APCI-HPLC-MS Analysis of Mature Human Milk

peak[a]	TAGs[b]	PN	$[M + H]^+$	$[M + H - R_1COOH]^+$	$[M + H - R_2COOH]^+$	$[M + H - R_3COOH]^+$
1	CaML + LaLaL	38	719.62	LaLa 439.40	LaL 519.44	
				CaM 439.40	CaL 491.41	ML 547.47
2	CaLaO	38	693.60	CaLa 411.34	CaO 493.42	LaO 521.45
3	ni					
4	CaMM + LaLaM	38	667.59	CaM 439.40		MM 495.44
				LaLa 439.40	LaM 467.41	
5	LaLL	40	799.68	LaL 519.44		LL 599.50
6	CaOL	40	773.67	CaO 493.42	CaL 491.41	OL 601.52
7	CaPL + LaML	40	747.65	CaP 467.41	CaL 491.41	PL 575.50
				LaM 467.41	LaL 519.44	ML 547.47
8	CaMO + LaLaO	40	721.63	CaM 439.40	CaO 493.42	MO 549.48
				LaLa 439.40	LaO 521.45	
9	ni					
10	CaLaS + CaMP + LaLaP + LaMM	40	695.61	CaLa 411.34	CaS 495.44	LaS 523.47
				CaM 439.40	CaP 467.41	MP 523.47
				LaLa 439.40	LaP 495.44	
				LaM 467.41		MM 495.44
11	MLL/PaPaETE + MPaETE + PLLn	42	827.71	ML 547.47		LL 599.50
			853.73	PaPa 547.47	PaETE 599.50	
			827.71	MPa 521.45	METE 573.48	PaETE 599.50
			853.73	PL 575.50	PLn 573.48	LLn 597.50
12	LaOL	42	801.70	LaO 521.45	LaL 519.44	OL 601.52
13	CaOO	42	775.68	CaO 493.42		OO 603.53
14	LaPL + MML	42	775.68	LaP 495.44	LaL 519.44	PL 575.50
				MM 495.44	ML 547.47	
15	CaPO + LaMO	42	749.67	CaP 467.41	CaO 493.42	PO 577.52
				LaM 467.41	LaO 521.45	MO 549.48
16	CaMS + CaPP + LaLaS + LaMP + MMM + OLL	42	723.65	CaM 439.40	CaS 495.44	MS 551.50
				CaP 467.41		PP 551.50
				LaLa 439.40	LaS 523.47	
				LaM 467.41	LaP 495.44	MP 523.47
				MM 495.44		
		44	881.76	OL 601.52		LL 599.50
17	PaOL	44	855.74	PaO 575.50	PaL 573.48	OL 601.52
18	PLL	44	855.74	PL 575.50		LL 599.50
19	MOL	44	829.73	MO 549.48	ML 547.47	OL 601.52
20	LaOO	44	803.71	LaO 521.45		OO 603.53
21	MPL	44	803.71	MP 523.47	ML 547.47	PL 575.50
22	LaPO + MMO	44	777.70	LaP 495.44	LaO 521.45	PO 577.52
				MM 495.44	MO 549.48	
23	CaPS + LaMS + LaPP + MMP	44	751.68	CaP 467.41	CaS 495.44	PS 579.53
				LaM 467.41	LaS 523.47	MS 551.50
				LaP 495.44		PP 551.50
				MM 495.44	MP 523.47	
24	OOL	46	883.76	OO 603.53	OL 601.52	
25	PaOO	46	857.76	PaO 575.50		OO 603.53
26	POL	46	857.76	PO 577.52	PL 575.50	OL 601.52
27	MOO + PPaO	46	831.74	MO 549.48		OO 603.53
				PPa 549.48	PO 577.52	PaO 575.50
28	PPL	46	831.74	PP 551.50	PL 575.50	
29	LaSO + MPO	46	805.73	LaS 523.47	LaO 521.45	SO 605.55

DOI: 10.1021/acs.jafc.5b01158
J. Agric. Food Chem. 2015, 63, 5761−5770

Table 1. continued

peak[a]	TAGs[b]	PN	$[M + H]^+$	$[M + H - R_1COOH]^+$	$[M + H - R_2COOH]^+$	$[M + H - R_3COOH]^+$
				MP 523.47	MO 549.48	PO 577.52
30	LaPS + MMS + MPP	46	779.71	LaP 495.44	LaS 523.47	PS 579.53
				MM 495.44	MS 551.50	
				MP 523.47		PP 551.50
31	OOO	48	885.76	OO 603.53		
32	SOL	48	885.76	SO 605.55	SL 603.53	OL 601.52
33	POO	48	859.77	PO 577.52		OO 603.53
34	PSL	48	859.77	PS 579.53	PL 575.50	SL 603.53
35	MSO + PPO	48	833.76	MS 551.50	MO 549.48	SO 605.55
				PP 551.50	PO 577.52	
36	LaSS + MPS + PPP	48	807.74	LaS 523.47	-	SS 607.56
				MP 523.47	MS 551.50	PS 579.53
				PP 551.50		
37	ni					
38	SSL + SOO	50	887.81	SS 607.56	SL 603.53	
				SO 605.55		OO 603.53
39	PSO	50	861.79	PS 579.53	PO 577.52	SO 605.55
40	PPS	50	835.76	PP 551.50	PS 579.53	
41	POAra + SSO	52	889.82	PO 577.52	PAra 607.57	OAra 633.58
				SS 607.56	SO 605.55	
42	PSS	52	863.81	PS 579.53		SS 607.56

[a]Peak identification number according to Figure 2; TAGs identified according to protonated molecule ($[M + H]^+$) and diacylglycerol ions ($[M + H - R_{1,2,3}COOH]^+$) observed in the APCI mass spectrum and to the relative order of PN. [b]Structure indicated by FA composition (e.g., OOO for triolein) using the following abbreviations: Ca, capric acid (C10.0); La, lauric acid (C12:0); M, myristic acid (C14:0); P, palmitic acid (C16.0); Pa, palmitoleic acid (C16:1); S, stearic acid (C18:0); O, oleic acid (C18:1); L, linoleic acid (C18:2); Ln, linolenic acid (C18:3); Ara, arachidic acid (C20:0); ETE, eicosatrienoic acid (C20:3).

to achieve a reliable TAG identification, a fragmentation study resulting from the APCI-MS analysis of TAGs in the positive ionization mode was performed.[46,47] The APCI mass spectra of TAGs exhibited a protonated molecule, $[M + H]^+$, the intensity of which depends on the degree of unsaturation of the TAG molecule, and $[M + H - R_{1,2,3}COOH]^+$ ions resulting from the loss of fatty acyl moieties (diacylglycerol (DAG) ions). The intensities of the protonated molecules $[M + H]^+$ formed from saturated TAGs were low or even undetected (for fully saturated TAGs), and their identification was performed according to their respective DAG ions. These results were consistent with those previously reported.[45,48] Table 1 shows the m/z values of the protonated molecules and DAG ions found in the human milk samples studied. No distinction was made between the *sn*-1, *sn*-2, and *sn*-3 positions in the TAG species identified. It should be noted that despite the satisfactory resolution achieved in this work, some cases of coelution of TAGs were observed (see Table 1 and Figure 1).

With regard to the number of TAGs here identified, this can be favorably compared to that reported in previous human milk studies. For example, in the work of Morera et al.[16] up to 43 different TAGs were reported, whereas in recent studies of Linderborg et al.[44] and Mondello's group,[43] 37 and 51 different TAGs, respectively, were positively identified. However, these values were lower than those reported by Haddad et al.;[49] where up to 98 TAGs were identified by using two serially coupled C18 columns in combination with tandem ESI-MS and subsequently confirmed by GC-MS.

Small-Scale Extraction Method and Quantification. First, the evaluation of fat content using the proposed small-scale extraction method was performed. To evaluate the efficiency of fat extraction, the method developed here (method I) was compared to the conventional protocol (method II). Thus, fat was extracted and gravimetrically determined[25,26,41,42] from 12 mature human milk aliquots, 6 by method I and 6 by method II. The fat content obtained by methods I and II ranged between 0.021 and 0.029 g mL^{-1} and between 0.025 and 0.029 g mL^{-1}, respectively. Table 2 shows the fat content

Table 2. Fat Content in Human Milk Obtained Gravimetrically by Methods I and II

	fat (g mL^{-1})	
human milk aliquot	method I	method II
1	0.0231	0.0270
2	0.0246	0.0249
3	0.0294	0.0258
4	0.0252	0.0256
5	0.0258	0.0279
6	0.0207	0.0291
mean ± SD	0.0248 ± 0.0029	0.0267 ± 0.0016

(expressed as mean ± SD) obtained for both methods. No significant differences in the fat milk content between both extraction procedures were observed ($p > 0.05$, Student's t test), and the results found were consistent with those described in the literature.[3,23] After these results had been obtained, the evaluation of TAG content was next considered.

When performing quantification in ELSD, several authors have established that its response is linear for a wide range of

DOI: 10.1021/acs.jafc.5b01158
J. Agric. Food Chem. 2015, 63, 5761−5770

Table 3. Calibration Equation Coefficients (Linear Regression and Power Curve Fittings), LODs and LOQs, and RRF Values for TAG Standards in the Assayed LC-ELSD Method

	linear regression[a] ($y = ax + b$)			power curve[a] ($y = bx$)					
TAG[b]	a	b	r^2	b	a	r^2	LOD (ng)	LOQ (ng)	RRF[c]
LaLaLa	859.59	−856.49	0.9798	253.51	1.50	0.9995	9.2	30.6	1.0067
PaPaPa	806.75	−929.79	0.9638	198.47	1.56	0.9991	12.4	41.1	1.0475
MMM	711.87	−768.68	0.9646	186.91	1.54	0.9992	13.1	43.3	1.0357
OOO	738.15	−830.13	0.9703	208.15	1.49	0.9976	10.9	36.0	1.0000
PPP	412.05	−246.41	0.9885	217.27	1.26	0.9986	9.4	31.1	0.8471

[a] x = μg injected; y = peak area in mV. [b] For abbreviations see Table 1. [c] RRF values are given in relation to OOO.

concentrations.[38,50] However, some studies[51,52] have demonstrated that the response from HPLC-ELSD follows a nonlinear empirical model: $A = am^b$, where A is the area of chromatographic peak, m the mass of analyte, and a and b two experimental parameters related to the ELSD configuration. Thus, each change in the instrumental working conditions would require a new estimation of these parameters. This equation can be easily linearized as follows: $\log A = b \log m + \log a$. However, the application of this equation requires the availability of each TAG identified in the target sample, which is not commercially feasible. To overcome this limitation, Heron et al.[52] have developed an empirical methodology to evaluate the TAG content in vegetable oils based on the previous equation using a reduced number of standards. However, the method provided a high variability (between 1 and 40%) with respect to the real mass percentage. Another approach proposed by several authors[28,51] is based on the application of the internal normalization method as measurement of mass percentage, where a similarity in the response factors of TAGs (relative response factors, RRF) with respect to triolein (OOO) ranged between 0.83 and 1.21) was assumed. To confirm this assumption, calibration curves of homologous TAG standards were performed and fitting equations of both linear and power models to detector response (area) versus mass of lipid injected were obtained. As shown in Table 3, the peak areas were well-fitted by power model equations in the mass range studied (0.5−100 μg). The limits of detection (LOD) and limits of quantification (LOQ) were also estimated for signal-to-noise ratios of 3 and 10, respectively. The results obtained for homogeneous TAG standards were LOD (9.2−13.1) ng and LOQ (30.6−43.3) ng (see Table 3). Then, the RRF calculated for pure homogeneous TAG standards in relation to OOO were obtained, giving values close to unity, which allows a quantitative estimation of TAGs on the basis of the percentage peak area. The relative content of each TAG (expressed as mean ± SD) obtained is given in Table 4. As shown in Table 4, no significant differences ($p > 0.05$, Student's t test) were observed between results obtained with both methods for >85% of the TAGs. From this study, it can be derived that method I provided satisfactory results, both in the total fat content and in the quantitative analysis of representative TAGs. Moreover, method I has several advantages over method II. Table 5 summarizes the essential features of both sample preparation methods. Method I uses much smaller volumes of the sample and chemical solutions (90% reduction); thus, the expense and chemical hazards are greatly reduced. Although other operational steps for both methods were quite similar, the small-scale protocol requires the use of materials such as micropipets or small syringes, which simplifies the handling of more samples simultaneously and speeds the isolation process of fat. In particular, method I allowed processing 120 samples per day (in an 8 h working day), whereas a rate of 30 samples per day could be achieved with method II. A comparison between our method and the traditional Folch method for milk samples[43,49] was also done. In this protocol, the extraction step employs larger volumes of solvents (40−180 mL of chloroform/methanol (2:1, v/v), followed by several re-extractions and washings, which results in larger experimental effort, longer time, and greater amounts of residues of harmful solvents generated than the developed protocol. Consequently, the present procedure is suitable to be applied to systematic and routine characterization of lipid composition in human milk samples. Additionally, due to the small sample volume required, the proposed method offers the possibility of analyzing separate individual milk sample portions from within one feeding, allowing the characterization of possible fluctuations in the TAG composition.

As shown in Table 4, from 69 TAG molecular species identified, the major TAGs found in the lipid fraction in both protocols were POO, POL, LaPO + MMO, MOO, and PSO (see Table 1 for abbreviations) at 20, 10, 7, 6, and 5%, respectively. The amounts of these most abundant TAGs were similar to those obtained in the literature.[16,27,49] For example, the studies of Zou et al.,[27] in milk from Danish women pointed out that the TAGs were mainly composed of POO (21.52%) and POL (16.93%). These small discrepancies can be attributed to natural factors such as randomization in human milk, the physiological stage,[16] and the susceptibility of human milk TAGs to dietary habits.[5,44] It is also important to remark that the molecular weight distribution of TAGs (expressed as CN:ND groups[44]) in human milk reported in this work (see Figure S3) is in agreement with the findings of studies previously reported.[44,49]

Taking into account the advantages described above for method I, it was extended to the milk of other mammalian species (cow, sheep, and goat). Thus, the total fat content varied within the ranges 0.023−0.046, 0.046−0.057, and 0.034−0.076 g mL^{-1} for cow, sheep, and goat milks, respectively. These milk samples were also analyzed using the developed LC method with an excellent resolution/elution time ratio compared to those previously reported[14,16,23,27,28] (Figure 2). TAG profiles (particularly for the main TAG peaks) similar to those reported in the literature were found for these samples.[14] From these profiles, 22 common peaks, which could be easily integrated, were selected for the four mammalian species and used for statistical treatment.

Classification of Mammalian Milks Using TAG Profiles with LDA Model. First, to reduce the variability associated with total amount of TAGs recovered from milk samples and to minimize the sources of variance also affecting the sum of the areas of all peaks, normalized rather than absolute peak area

DOI: 10.1021/acs.jafc.5b01158
J. Agric. Food Chem. 2015, 63, 5761−5770

Table 4. Relative Content of Each TAG in Mature Human Milk Obtained by Methods I and II[a]

peak[b]	TAGs[b]	method I (n = 3), mean ± SD	method II (n = 3), mean ± SD	p
1	CaML + LaLaL	0.385 ± 0.005	0.371 ± 0.019	0.057
2	CaLaO	0.612 ± 0.007	0.649 ± 0.017	0.173
3	ni	0.066 ± 0.003	0.091 ± 0.019	0.149
4	CaMM + LaLaM	0.508 ± 0.007	0.51 ± 0.02	0.359
5	LaLL	0.140 ± 0.003	0.146 ± 0.014	0.568
6	CaOL	0.242 ± 0.007	0.241 ± 0.006	0.866
7	CaPL + LaML	1.034 ± 0.006	0.977 ± 0.003	0.0001
8	CaMO + LaLaO	2.33 ± 0.02	2.134 ± 0.008	0.0001
9	ni	0.092 ± 0.007	0.10 ± 0.02	0.710
10	CaLaS + CaMP + LaLaP + LaMM	0.915 ± 0.017	0.896 ± 0.019	0.266
11	MLL/PaPaETE + MPaETE + PLLn	0.232 ± 0.009	0.243 ± 0.005	0.124
12	LaOL	2.09 ± 0.04	1.98 ± 0.06	0.055
13	CaOO	0.86 ± 0.05	0.82 ± 0.02	0.309
14	LaPL + MML	1.58 ± 0.04	1.55 ± 0.05	0.362
15	CaPO + LaMO	5.04 ± 0.07	4.86 ± 0.07	0.031
16	CaMS + CaPP + LaLaS + LaMP + MMM + OLL	1.95 ± 0.12	2.03 ± 0.04	0.302
17	PaOL	0.17 ± 0.03	0.18 ± 0.04	0.768
18	PLL	0.96 ± 0.07	0.96 ± 0.07	0.991
19	MOL	2.77 ± 0.06	2.760 ± 0.08	0.875
20	LaOO	4.74 ± 0.12	4.68 ± 0.07	0.507
21	MPL	1.29 ± 0.05	1.278 ± 0.015	0.795
22	LaPO + MMO	7.39 ± 0.14	7.30 ± 0.10	0.412
23	CaPS + LaMS + LaPP + MMP	1.18 ± 0.03	1.25 ± 0.02	0.051
24	OOL	2.75 ± 0.04	2.82 ± 0.12	0.445
25	PaOO	0.91 ± 0.17	0.9 ± 0.2	0.748
26	POL	9.88 ± 0.21	10.1 ± 0.3	0.335
27	MOO + PPaO	5.410 ± 0.016	5.55 ± 0.05	0.010
28	PPL	1.220 ± 0.014	1.22 ± 0.05	0.947
29	LaSO + MPO	4.27 ± 0.07	4.44 ± 0.03	0.013
30	LaPS + MMS + MPP	1.036 ± 0.006	1.06 ± 0.04	0.402
31	OOO	3.65 ± 0.06	3.7 ± 0.2	0.551
32	SOL	0.97 ± 0.02	1.03 ± 0.03	0.118
33	POO	20.3 ± 0.6	20.21 ± 0.19	0.914
34	PSL	1.117 ± 0.010	1.14 ± 0.08	0.680
35	MSO + PPO	4.09 ± 0.07	4.17 ± 0.16	0.480
36	LaSS + MPS + PPP	0.55 ± 0.03	0.56 ± 0.04	0.946
37	ni	0.15 ± 0.02	0.117 ± 0.009	0.068
38	SSL + SOO	1.48 ± 0.04	1.43 ± 0.05	0.246
39	PSO	5.06 ± 0.13	4.9 ± 0.2	0.425
40	PPS	0.34 ± 0.03	0.35 ± 0.03	0.833
41	POAra + SSO	0.133 ± 0.006	0.139 ± 0.011	0.448
42	PSS	0.145 ± 0.002	0.157 ± 0.014	0.282

[a]Data obtained from three extractions performed the same day for each extraction method. [b]Peak identification number, TAG information, and abbreviations as indicated in Table 1.

Table 5. Comparison of Sample Preparation Protocols

	method I (small scale)	method II[16]
sample volume (mL)	0.15	1.5
extraction		
(i) CH_2Cl_2/MeOH (2:1, v/v) (mL)	2.5	25
(ii) water (mL)	0.8	8
(iii) saline solution (mL)	0.8	8
material required	10 mL centrifuge tubes, syringes, syringe filters, micropipets	Falcon 50 mL conical centrifuge tubes, separating funnels, filter funnels, filter paper, pipettes, Pasteur pipets
samples per day	120	30

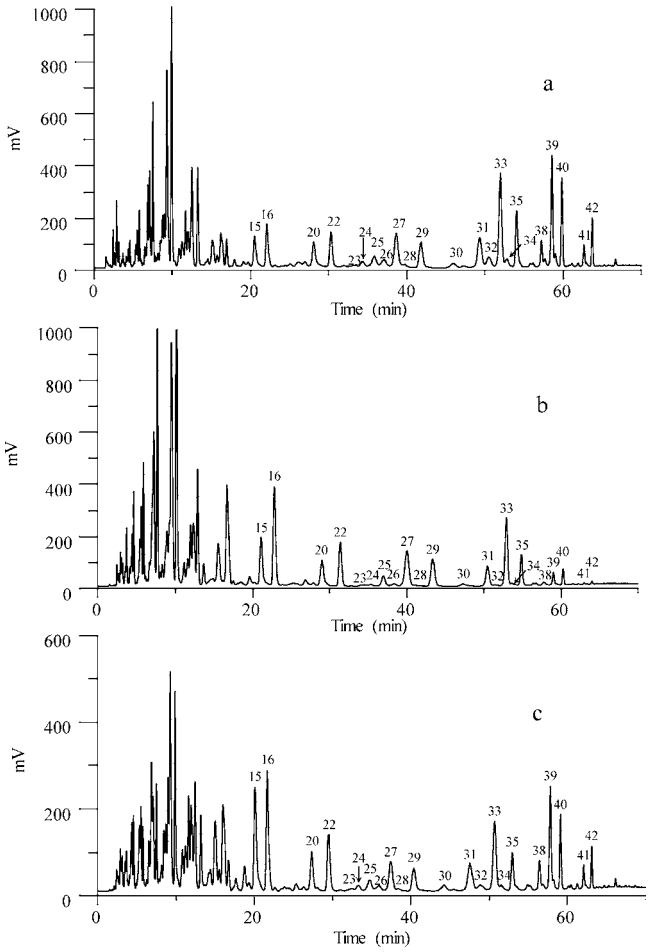

Figure 2. TAG profile of milk from different mammalian species: cow (a); sheep (b); goat (c). Chromatographic conditions were as in Figure 1.

was used. To normalize the variables, the area of each peak was divided by each of the areas of the other 21 peaks; in this way, and taking into account that each pair of peaks should be considered only once, (22 × 21)/2 = 231 non-redundant peak area ratios were obtained to be used as predictors. Using the normalized variables, an LDA model capable of classifying the milk samples according to their respective mammalian species was constructed. A matrix containing 75 objects that corresponded to all of the milk samples analyzed was constructed. Thus, this matrix was divided into two groups of objects to constitute the training and evaluation sets. The training set was composed by 67 objects (18 milks × 3 animal mammalian species + 13 human milk samples), whereas the evaluation set was constituted by the remaining samples (8 objects). A response column, containing the categories corresponding to the four mammalian species, was added to these matrices. When the LDA model was constructed, an excellent resolution between all of the category pairs was

DOI: 10.1021/acs.jafc.5b01158
J. Agric. Food Chem. 2015, 63, 5761−5770

achieved (Wilks' lambda, $\lambda_w < 0.01$). The variables selected by the SPSS stepwise algorithm, and the corresponding standardized coefficients of the model, showing the predictors with large discriminant capabilities, are given in Table 6. As shown in Figure 3a, a large resolution between the human milk from the other mammalian milks was achieved along the first discriminant function (df). As deduced from Table 6, the first df was mainly constructed with the peak area ratios OOL/PaOO and POO/(POAra + SSO) (peaks labeled 24/25 and 33/41, respectively). The projection on the second df shows a lack of capability to resolve between cow and goat milks. However, both milks were clearly distinguished from sheep and human milks. In this case, the second df was mainly constructed with the peak area ratios (CaMS + CaPP + LaLaS + LaMP + MMM + OLL)/(MOO + PPaO) and (LaPO + MMO)/PSO (peaks labeled 16/27 and 22/39, respectively). According to Figure 3b, along the third df, it is not possible to distinguish between sheep and human milk, but both were markedly differentiated from cow and goat milks. As shown in Table 6, the third df was mainly constituted with the peak area ratios (CaPO + LaMO)/(CaPS + LaMS + LaPP + MMP) and (CaMS + CaPP + LaLaS + LaMP + MMM + OLL) (peaks labeled 15/23 and 16/24, respectively). Finally, as illustrated in Figure 3c, by using a plane oblique to the three first discriminant functions, all of the possible pairs of categories were very well resolved from each other.

Table 6. Predictors Selected and Corresponding Standardized Coefficients of the LDA Model Constructed To Discriminate between Milks Obtained from Different Mammalian Species

predictor[a]	first df	second df	third df
peak 15/peak 23	−0.466	0.219	2.275
peak 16/peak 24	0.700	−0.302	−2.742
peak 16/peak 27	0.075	−2.114	2.020
peak 16/peak 35	−0.262	0.126	1.306
peak 16/peak 41	−0.395	1.559	0.128
peak 22/peak 39	−0.284	2.067	0.067
peak 23/peak 41	−0.230	−1.282	0.055
peak 24/peak 25	2.748	0.463	−0.143
peak 26/peak 40	0.949	0.263	0.243
peak 30/peak 33	−0.115	0.693	1.016
peak 33/peak 41	1.662	0.724	0.812

[a]See Table 1 for peak identification.

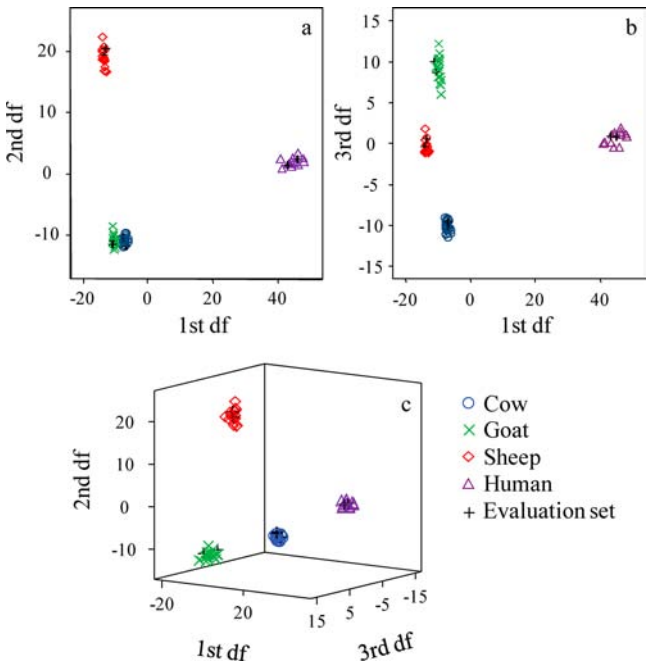

Figure 3. Score plots on the planes of the first and second (a) and second and third discriminant functions (df) (b) and on an oblique plane of the 3-D space defined by the three discriminant functions (c) of the LDA model constructed to discriminate between different mammalian milk species. Evaluation set samples are labeled as indicated in the legend.

Using this model and leave-one-out validation, all of the objects of the training set were correctly classified. On the other hand, the prediction capability of the model was evaluated using the evaluation set. In this case, all of the objects (represented with a cross symbol in Figure 3) were correctly assigned within 95% probability level. It should be pointed out that in the case of human milk samples, different periods of lactation were taken, and in all cases, an excellent classification within this category was accomplished, which supports the robustness of the developed LDA model.

In summary, a highly efficient RP-HPLC-UV-ELSD method of TAGs in human milk samples has been developed. Also, a small-scale sample preparation method has been established, being particularly important for human milk samples. The combination of this sample extraction protocol with HPLC-UV-ELSD technique could provide a methodology highly recommended in studies on breastfeeding and its contribution to infant growth and development. Finally, the possibility of classifying milks according to their mammalian origin by using TAG profiles obtained by HPLC-ELSD has been successfully demonstrated.

■ ASSOCIATED CONTENT

Supporting Information

Figures S1-S3. The Supporting Information is available free of charge on the ACS Publications website at DOI: 10.1021/acs.jafc.5b01158.

■ AUTHOR INFORMATION

Corresponding Author

*(J.M.H.M.) E-mail: jmherrer@uv.es. Phone: +34 963 54 40 62. Fax: +34 963 54 44 36.

Funding

Project CTQ2014-52765-R (MINECO of Spain and FEDER). I.T.-D. thanks the MINECO for an FPU grant for Ph.D. studies.

Notes

The authors declare no competing financial interest.

■ REFERENCES

(1) Picciano, M. F. Nutrient composition of human milk. *Pediatr. Clin. North Am.* **2001**, *48*, 53−67.

(2) Jensen, R. G. Lipids in human milk. *Lipids* **1999**, *34*, 1243−1271.

(3) Salamon, S.; Csapó, J. Composition of the mother's milk II. Fat contents, fatty acid composition. A review. *Acta Univ. Sapientiae, Aliment.* **2009**, *2*, 196−234.

DOI: 10.1021/acs.jafc.5b01158
J. Agric. Food Chem. 2015, 63, 5761−5770

(4) Koletzko, B.; Rodriguez-Palmero, M.; Demmelmair, H.; Fidler, N.; Jensen, R.; Sauerwald, T. Physiological aspects of human milk lipids. *Early Hum. Dev.* **2001**, *65* (Suppl.), S3−S18.
(5) Rocquelin, G.; Tapsoba, S.; Dop, M.; Mbemba, F.; Traissac, P.; Martin-Prével, Y. Lipid content and essential fatty acid (EFA) composition of mature Congolese breast milk are influenced by mothers' nutritional status: impact on infants' EFA supply. *Eur. J. Clin. Nutr.* **1998**, *52*, 164−171.
(6) Mandel, D.; Lubetzky, R.; Dollberg, S.; Barak, S.; Mimouni, F. B. Fat and energy contents of expressed human breast milk in prolonged lactation. *Pediatrics* **2005**, *116*, 432−435.
(7) Sala-Vila, A.; Castellote, A. I.; Rodriguez-Palmero, M.; Campoy, C.; López-Sabater, M. C. Lipid composition in human breast milk from Granada (Spain): changes during lactation. *Nutrition* **2005**, *21*, 467−473.
(8) Hytten, F. E. Clinical and chemicals studies in human lactation. *Br. Med. J.* **1954**, *2*, 176−179.
(9) Khan, S.; Hepworth, A.; Prime, D.; Lai, C.; Trengove, N.; Hartmann, P. Variation in fat, lactose, and protein composition in breast milk over 24 h: associations with infant feeding patterns. *J. Hum. Lact.* **2013**, *29*, 81−89.
(10) Kent, J. C.; Mitoulas, L. R.; Cregan, M. D.; Ramsay, D. T.; Doherty, D. A.; Hartmann, P. E. Volume and frequency of breastfeedings and fat content of breast milk throughout the day. *Pediatrics* **2006**, *117*, e387−e395.
(11) Harzer, G.; Haug, M.; Dieterich, I.; Gentner, P. Changing patterns of human milk lipids in the course of the lactation and during the day. *Am. J. Clin. Nutr.* **1983**, *37*, 612−621.
(12) Harzer, G.; Haug, M. Dependency of human milk lipids on length of the lactation period, time of day, nursing and maternal diet. *Z. Ernaehrungswiss.* **1984**, *23*, 113−125.
(13) D'Auria, E.; Agostoni, C.; Giovannini, M.; Riva, E.; Zetterström, R.; Fortin, R.; Greppi, G. F.; Bonizzi, L.; Roncada, P. Proteomic evaluation of milk from different mammalian species as a substitute for breast milk. *Acta Paediatr.* **2005**, *94*, 1708−1713.
(14) Zou, X.-Q.; Huang, J.-H.; Jin, Q.-Z.; Guo, Z.; Liu, Y.-F.; Cheong, L.-Z.; Xu, X.-B.; Wang, X.-G. Model for human milk fat substitute evaluation based on triacylglycerol composition profile. *J. Agric. Food Chem.* **2013**, *61*, 167−175.
(15) El-Agamy, E. I. The challenge of cow milk protein allergy. *Small Rumin. Res.* **2007**, *68*, 64−72.
(16) Morera, S.; Castellote, A. I.; Jauregui, O.; Casals, I.; López-Sabater, M. C. Triacylglycerol markers of mature human milk. *Eur. J. Clin. Nutr.* **2003**, *57*, 1621−1626.
(17) Folch, J.; Lees, M.; Sloane Stantley, G. H. A simple method for the isolation and purification of total lipides from animal tissues. *J. Biol. Chem.* **1957**, *266*, 497−509.
(18) Chen, I. S.; Shen, C.-S. J.; Sheppard, A. J. Comparison of methylene chloride and chloroform for the extraction of fats from food products. *J. Am. Oil Chem. Soc.* **1981**, *58*, 599−601.
(19) AOAC International.. *AOAC Official Method 989.05 Fat in Milk* **1992**, *21*, 5−6.
(20) Barbano, D. M.; Clark, J. L.; Dunham, C. E. Comparison of Babcock and ether extraction methods for determination of fat content of milk: collaborative study. *J. Assoc. Off. Anal. Chem.* **1988**, *71*, 898−914.
(21) Ramos, L.; Ramos, J. J.; Brinkman, U. A. T. Miniaturization in sample treatment for environmental analysis. *Anal. Bioanal. Chem.* **2005**, *381*, 119−140.
(22) Jánská, M.; Tomaniová, M.; Hajšlová, J.; Kocourek, V. Appraisal of "classic" and "novel" extraction procedure efficiencies for the isolation of polycyclic aromatic hydrocarbons and their derivatives from biotic matrices. *Anal. Chim. Acta* **2004**, *520*, 93−103.
(23) Romeu-Nadal, M.; Morera-Pons, S.; Castellote, A. I.; López-Sabater, M. C. Comparison of two methods for the extraction of fat from human milk. *Anal. Chim. Acta* **2004**, *513*, 457−461.
(24) Bitman, J.; Wood, L.; Hamosh, M.; Hamosh, P.; Mehta, N. R. Comparison of the lipid composition of breast milk from mothers of term and preterm infants. *Am. J. Clin. Nutr.* **1983**, *38*, 300−312.
(25) Fontecha, J.; Goudjil, H.; Ríos, J. J.; Fraga, M. J.; Juárez, M. Identity of the major triacylglycerols in ovine milk fat. *Int. Dairy J.* **2005**, *15*, 1217−1224.
(26) Gastaldi, D.; Medana, C.; Giancotti, V.; Aigotti, R.; Dal Bello, F.; Baiocchi, C. HPLC-APCI analysis of triacylglycerols in milk fat from different sources. *Eur. J. Lipid Sci. Technol.* **2011**, *113*, 197−207.
(27) Zou, X.; Huang, J.; Jin, Q.; Guo, Z.; Liu, Y.; Cheong, L.; Xu, X.; Wang, X. Lipid composition analysis of milk fats from different mammalian species: potential for use as human milk fat substitutes. *J. Agric. Food Chem.* **2013**, *61*, 7070−7080.
(28) Morera Pons, S.; Castellote Bargalló, A. I.; López Sabater, M. C. Analysis of human milk triacylglycerols by high-performance liquid chromatography with light-scattering detection. *J. Chromatogr. A* **1998**, *823*, 475−482.
(29) Dugo, P.; Kumm, T.; Lo Presti, M.; Chiofalo, B.; Salimei, E.; Fazio, A.; Cotroneo, A.; Mondello, L. Determination of triacylglycerols in donkey milk by using high performance liquid chromatography coupled with atmospheric pressure chemical ionization mass spectrometry. *J. Sep. Sci.* **2005**, *28*, 1023−1030.
(30) Dugo, P.; Kumm, T.; Chiofalo, B.; Cotroneo, A.; Mondello, L. Separation of triacylglycerols in a complex lipidic matrix by using comprehensive two-dimensional liquid chromatography coupled with atmospheric pressure chemical ionization mass spectrometric detection. *J. Sep. Sci.* **2006**, *29*, 1146−1154.
(31) Kallio, H.; Rua, P. Distribution os the major fatty acids of human milk between sn-2 and sn-3 positions of triacylglycerols. *J. Am. Oil Chem. Soc.* **1994**, *71*, 985−992.
(32) Ruíz-Gutiérrez, V.; Barron, L.-J. Methods for the analysis of triacylglycerols. *J. Chromatogr., Biomed. Appl.* **1995**, *671*, 133−168.
(33) Núñez, O.; Gallart-Ayala, H.; Martins, C. P. B.; Lucci, P. New trends in fast liquid chromatography for food and environmental analysis. *J. Chromatogr. A* **2012**, *1228*, 298−323.
(34) Pripp, A. H. Application of multivariate analysis: benefits and pitfalls. In *Statistics in Food Science and Nutrition*; Hartel, R. W., Ed.; Springer: New York, 2013; pp 53−64.
(35) Wehrens, R. Linear discriminant analysis. In *Chemometrics with R. Multivariate Data Analysis in the Natural Sciences and Life Sciences*; Gentleman, R., Hornik, K., Parmigiani, G., Eds.; Springer: Berlin, Germany, 2011; pp 105−109.
(36) Karoui, R.; De Baerdemaeker, J. A review of the analytical methods coupled with chemometric tools for the determination of the quality and identity of dairy products. *Food Chem.* **2007**, *102*, 621−640.
(37) Lerma-García, M. J.; Simó-Alfonso, E. F.; Méndez, a.; Lliberia, J. L.; Herrero-Martínez, J. M. Classification of extra virgin olive oils according to their genetic variety using linear discriminant analysis of sterol profiles established by ultra-performance liquid chromatography with mass spectrometry detection. *Food Res. Int.* **2011**, *44*, 103−108.
(38) Morera Pons, S.; Castellote Bargalló, A. I.; López Sabater, M. C. Evaluation by high-performance liquid chromatography of the hydrolysis of human milk triacylglycerides during storage at low temperatures. *J. Chromatogr. A* **1998**, *823*, 467−474.
(39) Lerma-García, M. J.; Lusardi, R.; Chiavaro, E.; Cerretani, L.; Bendini, A.; Ramis-Ramos, G.; Simó-Alfonso, E. F. Use of triacylglycerol profiles established by high performance liquid chromatography with ultraviolet-visible detection to predict the botanical origin of vegetable oils. *J. Chromatogr. A* **2011**, *1218*, 7521−7527.
(40) Khandagale, M. M.; Hutchinson, J. P.; Dicinoski, G. W.; Haddad, P. R. Effects of eluent temperature and elution bandwidth on detection response for aerosol-based detectors. *J. Chromatogr. A* **2013**, *1308*, 96−103.
(41) Hazotte, A.; Libong, D.; Matoga, M.; Chaminade, P. Comparison of universal detectors for high-temperature micro liquid chromatography. *J. Chromatogr. A* **2007**, *1170*, 52−61.
(42) Hutchinson, J. P.; Li, J.; Farrell, W.; Groeber, E.; Szucs, R.; Dicinoski, G.; Haddad, P. R. Comparison of the response of four aerosol detectors used with ultra high pressure liquid chromatography. *J. Chromatogr. A* **2011**, *1218*, 1646−1655.

DOI: 10.1021/acs.jafc.5b01158
J. Agric. Food Chem. 2015, 63, 5761−5770

(43) Beccaria, M.; Sullini, G.; Cacciola, F.; Donato, P.; Dugo, P.; Mondello, L. High performance characterization of triacylglycerols in milk and milk-related samples by liquid chromatography and mass spectrometry. *J. Chromatogr. A* **2014**, *1360*, 172−187.
(44) Linderborg, K. M.; Kalpio, M.; Mäkelä, J.; Niinikoski, H.; Kallio, H. P.; Lagström, H. Tandem mass spectrometric analysis of human milk Triacylglycerols from normal weight and overweight mothers on different diets. *Food Chem.* **2014**, *146*, 583−590.
(45) Sandra, P.; Medvedovici, A.; Zhao, Y.; David, F. Characterization of triglycerides in vegetable oils by silver-ion packed-column supercritical fluid chromatography coupled to mass spectroscopy with atmospheric pressure chemical ionization and coordination ion spray. *J. Chromatogr. A* **2002**, *974*, 231−241.
(46) Mottram, H. R.; Crossman, Z. M.; Evershed, R. P. Regiospecific characterisation of the triacylglycerols in animal fats using high performance liquid chromatography-atmospheric pressure chemical ionisation mass spectrometry. *Analyst* **2001**, *126*, 1018−1024.
(47) Mottram, H. R.; Woodbury, S. E.; Evershed, R. P. Identification of triacylglycerol positional isomers present in vegetable oils by high performance liquid chromatography/atmospheric pressure chemical ionization mass spectrometry. *Rapid Commun. Mass Spectrom.* **1997**, *11*, 1240−1252.
(48) Separation and Identification of Triacylglycerols of Peanut Oil by APCI LC/MS, Application Note AMD 31; www.waters.com (accessed Sept 5, 2014).
(49) Haddad, I.; Mozzon, M.; Strabbioli, R.; Frega, N. G. A comparative study of the composition of triacylglycerol molecular species in equine and human milks. *Dairy Sci. Technol.* **2012**, *92*, 37−56.
(50) Stolyhwo, A.; Colin, H.; Martin, M.; Guiochon, G. Study of the qualitative and quantitative properties of the light-scattering detector. *J. Chromatogr. A* **1984**, *288*, 253−275.
(51) Cunha, S.; Oliveira, M. Discrimination of vegetable oils by triacylglycerols evaluation of profile using HPLC/ELSD. *Food Chem.* **2006**, *95*, 518−524.
(52) Heron, S.; Maloumbi, M.-G.; Dreux, M.; Verette, E.; Tchapla, A. Method development for a quantitative analysis performed without any standard using an evaporative light-scattering detector. *J. Chromatogr. A* **2007**, *1161*, 152−156.

DOI: 10.1021/acs.jafc.5b01158
J. Agric. Food Chem. 2015, 63, 5761−5770

Table 1. Summary of the Coffees Analyzed in This Survey

ID	country	region[a]	supplier	description	beans[b]	style
1	Ethiopia	A	Blackstar	Yiracheffe	*arabica*	beans
2	Ethiopia	A	The Coffee Roaster	Yiracheffe	*arabica*	beans
3	Ethiopia	A	Di Bella	single origin	*arabica*	beans
4	Ethiopia	A	Elixer	Smado org	*arabica*	beans
5	Ethiopia	A	The Coffee Roaster	Yiracheffe	*arabica*	beans
6	Ethiopia	A	The Coffee Roaster	Yiracheffe	*arabica*	beans
7	Ethiopia	A	Coles	Ethiopian	*arabica*	ground
8	Kenya	A	Expressi	Kenya	*arabica*	ground
9	Kenya	A	Blue Sky	single origin	*arabica*	beans
10	Kenya	A	The Coffee Roaster	AA lena	*arabica*	beans
11	Rwanda	A	The Coffee Roaster		*arabica*	beans
12	Uganda	A	The Coffee Roaster		blend	beans
13	Australia	Au	Cairns Highland	highland pearls	*arabica*	beans
14	Australia	Au	Cairns Highland	black mountain	*arabica*	beans
15	Australia	Au	Cairns Highland	Queensland blue	*arabica*	beans
16	Australia	Au	The Coffee Roaster	Nats organic	*arabica*	beans
17	PNG	Au/PNG	The Coffee Roaster	Kimel estate	blend	beans
18	Costa Rica	CA	The Coffee Roaster	Colibri tarrazu	*arabica*	beans
19	Costa Rica	CA	Sexie	Tarrazy	*arabica*	beans
20	El Salvador	CA	Cleanskin	La Calandria	*arabica*	beans
21	Guatemala	CA	Blackstar	Anekos	blend	bean
22	Guatemala	CA	The Coffee Roaster	Los Volcanoes	blend	beans
23	Guatemala	CA	Sexie	Huehuetenango	blend	beans
24	Honduras	CA	Di Bella	single origin	*arabica*	beans
25	Jamaica	CA	The Coffee Roaster	blue mountain	*arabica*	beans
26	Mexico	CA	The Coffee Roaster		*arabica*	beans
27	Mexico	CA	Di Bella	single origin	*arabica*	beans
28	Nicaragua	CA	The Coffee Roaster	La Bastilla	*arabica*	beans
29	Indonesia	Ind	Expressi	Sumatra	blend	ground
30	Indonesia	Ind	Blackstar	Aceh	blend	beans
31	Indonesia	Ind	Cleanskin	Aceh	blend	beans
32	Indonesia	Ind	The Coffee Roaster	Kuda mas	*arabica*	beans
33	Indonesia	Ind	Coles	Sumatran	blend	ground
34	India	In	The Coffee Roaster		*arabica*	beans
35	India	In	Sexie	Monsoon Malabar	*arabica*	beans
36	Bolivia	SA	Blue Sky	single origin	*arabica*	beans
37	Brazil	SA	Cleanskin	Pedro redona	blend	beans
38	Brazil	SA	Di Bella	single origin	blend	beans
39	Brazil	SA	The Coffee Roaster	Toffee Cerrado	blend	beans
40	Brazil	SA	The Coffee Roaster	Sao Marcos	blend	beans
41	Brazil	SA	Coles	Brazilian	blend	ground
42	Colombia	SA	Expressi	Colombia	*arabica*	ground
43	Colombia	SA	Blackstar	Excelso	*arabica*	bean
44	Colombia	SA	The Coffee Roaster	Supremo Bachue	*arabica*	beans
45	Colombia	SA	Sexie	Colombia	*arabica*	beans
46[c]	Colombia	SA	Coles	Colombian (decaff)	*arabica*	ground
47	Colombia	SA	Woolworths Select	espresso	*arabica*	ground
48	Ecuador	SA	Cleanskin	Yambura	blend	beans
49	Ecuador	SA	Blue Sky	single origin	blend	beans
50	Peru	SA	Woolworths Macro	ground coffee	*arabica*	ground
51[c]	Peru	SA	Blackstar	Peruvian (decaf)	*arabica*	ground
52	Peru	SA	Di Bella	single origin	*arabica*	beans
53	Peru	SA	The Coffee Roaster		*arabica*	beans
54	Peru	SA	Woolworths Macro	Peru	*arabica*	ground

[a]Samples were classified by region (A, Africa; AU, Australia; PNG, Papua New Guinea; CA, Central America; Ind, Indonesia; In, India; SA, South America). [b]Samples were classified according to bean cultivar (*Coffea arabica*) or blend, a mixture of *Coffea arabica* and *Caffea robusta*. [c]Coffee sold as decaffeinated.

and 51) were decaffeinated. Samples were stored frozen at −20 °C and opened immediately prior to analysis.

Samples of beans were initially ground in a domestic coffee mill to a particle size typical of filter coffee. Previous work within the authors'

DOI: 10.1021/acs.jafc.5b01526
J. Agric. Food Chem. 2015, 63, 5771−5779

Table 2. Results from a Preliminary Study of the Effects of Extracting Ground Coffee Beans with Water or with Hexane

			Δ ^{13}C			
		$\delta^{13}C_{VPDB} \times 10^3$	aqueous extract		solvent extract	
sample	country	whole beans	beans	extract	beans	extract
1	Ethiopia	−26.86	−0.02	0.60	−0.84	3.72
10	Kenya	−25.96	0.17	0.72	−1.33	4.00
27	Mexico	−29.30	−0.11	1.15	−1.07	3.74
33	Indonesia	−27.59	−0.14	0.16	−0.69	3.92
35	India	−28.65	−0.23	−0.07	−0.43	4.35
50	Peru	−28.80	−0.51	0.75	−0.45	4.26
	average		−0.14	0.55	−0.80	4.00
	median		−0.13	0.66	−0.77	3.96

		$\delta^{15}N_{AIR} \times 10^3$	Δ^{15}N aqueous extract	
sample	country	whole beans	beans	extract
1	Ethiopia	4.39	−0.17	3.04
10	Kenya	3.99	−0.02	3.10
27	Mexico	2.51	−0.22	2.76
33	Indonesia	2.85	−0.05	2.04
35	India	2.52	−0.13	2.30
50	Peru	4.89	−0.12	2.05
	average		−0.12	1.29
	median		−0.13	0.81

laboratory has demonstrated that this process did not introduce significant metal contamination, and all subsequent stages of handling were performed using metal-free materials. Approximately 10−15 g of coarsely ground coffee was taken for a pretreatment study and for caffeine extraction. The remainder was ground with a zirconium oxide ball mill (Fritsch, Idar-Oberstein, Germany) to produce a fine, visibly homogeneous powder. This sample was divided between two sterile, acid-washed containers for stable isotope and elemental analysis.

Sample Pretreatment. As an initial study, six samples (samples 1, 10, 27, 33, 35, and 50), from diverse geographical origins, were extracted with water and with hexane to determine whether these pretreatments could increase the discrimination of isotopic analysis by removing some complexity from the analyte. Approximately 5 g of coarsely ground samples was extracted with approximately 150 mL of high-purity water or hexane using conventional Soxhlet apparatus for 5 h. Aqueous extracts were heated in wide beakers at 102 °C until visibly dry. Hexane extracts were dried by rotary evaporation. The dried extracts were analyzed by FT-infrared spectroscopy to determine the chemical composition, and both the extracted samples and the dried extracts were analyzed to determine the carbon and nitrogen isotopic composition.

Extraction of the samples with water or hexane were considered to represent the extremes of what might be removed or recovered from the coffee beans, that is, by polar, aqueous, or nonpolar, organic, solvents. The aqueous extracts of the coffee were found to have infrared spectra consistent with mixtures of sugars and proteins, whereas the solvent extracts were found to have infrared spectra consistent with vegetable oil. The results of the isotopic analysis of the extracts and residues are summarized in Table 2. Extraction with water was found to have a negligible effect on either the δ^{13}C or δ^{15}N composition of the residual coffee, whereas the aqueous extracts were somewhat enriched in both isotopes. In contrast, extraction with organic solvent produced a significant depletion in the δ^{13}C composition of the residual coffee with a concomitant large enrichment in the extract. The solvent extracts did not contain sufficient nitrogen to permit δ^{15}N determination, and the extracted coffee was not significantly changed in nitrogen isotopic composition (data not shown).

When considering the patterns and relationships within these data, it was concluded that the pretreatments did not enhance the discriminatory power of isotopic analysis (based on δ^{13}C and δ^{15}N measurements), and all subsequent analyses were performed on untreated samples.

Stable Isotope Analysis. All isotope ratio measurements were performed using a Thermo Scientific (Bremen, Germany) Delta V^{Plus} isotope ratio mass spectrometer (IRMS) coupled to a ConFlo IV interface for working gas introduction and sample dilution.

Carbon and nitrogen isotopic compositions were determined using a Thermo Scientific Flash 2000 HT elemental analyzer (EA) configured for flash combustion at 950 °C with a helium flow of 100 mL/min. The reactor comprised a single quartz tube containing chrome oxide, reduced copper, and silver/cobaltous oxide. A chemical trap containing magnesium perchlorate was inserted between the reactor and the IRMS. Each sample was analyzed in triplicate with median standard deviations of 0.09 and 0.13‰ for carbon and nitrogen measurements, respectively.

Hydrogen and oxygen isotopic compositions were determined using a Thermo Scientific Flash 2000 HT EA configured for thermal conversion (TC/EA) operating at 1400 °C with a helium flow of 100 mL/min introduced via a bottom-feed adaptor. Samples were measured into silver capsules (4 × 3.2 mm, IVA Analysentechnik, Meerbursch, Germany) and equilibrated with purified Brisbane tap water (with a well-characterized isotopic composition) for 3 days. Samples were then dried over phosphorus pentoxide for 3 days, under vacuum. Encapsulated samples were introduced into the reactor via a Zero blank autosampler (Costech Analytical Technologies Inc., Valencia, CA, USA). Each sample was analyzed in triplicate with median standard deviations of 1.3 and 0.10‰ for hydrogen and oxygen measurements, respectively.

Data were normalized to the international isotope scales (VPDB-LSVEC or VSMOW-SLAP) by two-point calibration; a list of the reference materials and quality control (QC) materials used is given in the Supporting Information (supplement 1).

The δ values of the nonexchangeable hydrogen content were estimated from the measured values of the sample and the equilibration water by mass balance:

DOI: 10.1021/acs.jafc.5b01526
J. Agric. Food Chem. 2015, 63, 5771−5779

$$R_{nex} = R_{meas} - (R_{water} \times \alpha \times f_{ex})/(1 - f_{ex})$$

R_{nex} is the nonexchangable H isotope ratio, R_{meas} is the measured H isotope ratio, and R_{water} is the equilibration water H isotope ratio.

The fraction of exchangeable H atoms (f_{ex}) was taken as 0.25,[22] and the fractionation factor (α) between H atoms in the equilibration water and samples was taken as 1. This estimate of nonexchangeable hydrogen was considered appropriate for a comparative study.

Caffeine Extraction. Caffeine was isolated from an aqueous extract of coffee by supported liquid−liquid extraction using a method previously described to isolate active pharmaceutical ingredients.[21] This method was reported to have no significant effect on isotopic composition. Coarsely ground coffee was extracted with high-purity water as described above. When cooled, 0.6 mL of the extracts was loaded onto ChemElute 1 mL unbuffered liquid extraction cartridges (Agilent Australia, Victoria, Australia) and allowed to permeate for 15 min. The cartridges were then eluted with 3.5 mL of high-purity chloroform, yielding 1.5 mL of extract directly into a 2 mL autosampler vial. The method was shown to recover >98% of the caffeine present in the sample.

Caffeine Analysis. Extracted caffeine was characterized using a 7819A (Agilent Australia) gas chromatograph (GC) coupled to a Thermo Scientific ISQ MS. The injector was maintained at 280 °C with a constant helium flow of 1 mL/min and a split ratio of 10:1. Caffeine was separated using a DB-5 column (30 m × 0.25 mm × 0.25 μm) (Agilent Australia) with the following temperature program: 120 °C (2 min) raised at 15 °C/min to 280 °C (2 min). The carbon isotopic composition of extracted caffeine was determined using the analytical conditions above, with the GC column coupled to a Thermo Scientific GC-IsoLink interface with the combustion reactor operated at 1030 °C. Data were normalized to the VPDB-LSVEC scale using a certified sample of natural caffeine (IAEA-600; $\delta^{13}C_{VPDB}$ −27.77 ‰) and a sample of synthetic caffeine ($\delta^{13}C_{VPDB}$ −38.40 ‰) calibrated in-house using the methodology described above.

Elemental Analysis. The methods of analysis have been previously described.[23,24] In summary, approximately 0.3 g samples were accurately weighed into PTFE vessels and digested with high-purity nitric acid (69% Seastar Chemicals, Canada) using a Mars Xpress microwave digestion system (CEM Corp., Matthews, NC, USA).

Digested samples were analyzed using a Vista Pro ICP-OES (Varian Australia) and a 7700 ICP-MS (Agilent Australia) with autosampler and Integrated Sample Introduction System (ISIS). Appropriate reference materials were used for quality control (Supporting Information supplement 1).

Data Pretreatment. All elemental concentration data that were below the limit of detection (LoD) for more than 50% of the samples were removed from the overall data. Any of the remaining data that were below the LoD were replaced with the numerical value of the LoD for a given element and are presented as such. Data are reported for 13 elements (Ca, K, P, Mg, Al, Ti, Mn, Fe, Ni, Cu, Zn, Sr, Ba), together with the δ^2H, δ^{13}C, δ^{15}N, and δ^{18}O compositions (Supporting Information supplement 2).

To constrain the data further, the median and interquartile range (IRQ) were calculated for each measured parameter, and data were considered to be outliers if an individual value fell beyond

$$\text{median} - (1.5 \times \text{IQR}) \text{ or } \text{median} + (1.5 \times \text{IQR})$$

Outliers were substituted with the median value for the measured parameter and are presented in the Supporting Information (supplement 2, highlighted in green). In total approximately 6% of the elemental concentration data were substituted by this process, although notably, 22% of the aluminum concentration data and 33% of the nickel concentration data were considered to be outliers. These elevated metal concentrations did not appear to be associated with particular countries of origin, suppliers, or style of coffee (beans vs ground) and may have resulted from contact with metal surfaces during storage. None of the isotopic data were classified as outliers.

None of the measured parameters showed significant differences between coffees purchased ground or as beans or between *arabica* and blends of *arabica* and *robusta*.

Statistical Analysis. Data were analyzed and plotted using the R 3.0.1 software environment for statistical computing and graphics.[25] Two-tailed *t* tests were used to compare coffees purchased ground versus beans and *arabica* versus blends of *arabica* and *robusta*. Least absolute deviation (LAD) regression was applied to the data to determine the equation of robust fit and the correlation, R^2 (observed vs predicted). Principal component analysis (PCA) was performed on the elemental data to determine which parameters accounted for the largest differences between samples. This was performed using the L_1-norm to increase robustness to outliers compared to traditional PCA.[26] Discriminant analysis (DA) was applied to both elemental and isotopic data to determine to what extent these parameters distinguished between the different regions or countries of origin. Stepwise DA, using the Mahalanobis distance, was used to find the optimum set of discriminant functions (DFs), and once these parameters were established, the classifications were calculated using jackknife tests. The results of conventional DA represent the recognition ability based on the samples used to generate the model, whereas the jackknife approach assesses the external validity and is considered a good approach when, as in this case, sample sizes are small. In these tests, one case is eliminated from the original data set and the DFs are computed using the remaining observations. This procedure is repeated with each individual observation in turn omitted, and the values are averaged to provide a *jackknifed* estimate of the DFs.

RESULTS AND DISCUSSION

Samples were grouped according to their region of origin: Africa (A), Australia (Au), Central America (CA), Indonesia (Ind), India (In), Papua New Guinea (PNG), and South America (SA), as shown in Table 1. When discriminant analysis was performed, the data for PNG were grouped with the close geographical neighbor Australia, so as not to include a group with a single member. Because of wide geographical differences, Indonesia and India were treated as separate entities rather than as a single "Asia" grouping.

Correlation. A Pearson correlation matrix was calculated for all measured parameters in which few significant relationships were observed. Strong correlations were observed between δ^2H and δ^{18}O compositions and between δ^{18}O composition and the δ^{13}C compositions of both the coffee and the extracted caffeine (see below). The only strong correlation observed within the elemental concentration data was between the concentrations of strontium and barium, both group II metals.

Principal Component and Discriminant Analysis. PCA was applied to the elemental concentration data to determine which parameters accounted for the largest differences between samples. The loading factors for PC1 were dominated by potassium concentration, the loading factors for PC2 by the concentrations of calcium and magnesium, and the loading factors of PC3 by phosphorus. PCA did not provide clear discrimination between the regions of origin.

Stepwise DA reduced the elemental concentration data to 5 variables (Ca, Ti, Fe, Ni, Zn) from the original 13, the major contributions to the DFs being the concentrations of calcium and titanium. Stepwise DA reduced the isotopic data to three variables, (δ^2H, δ^{13}C, δ^{18}O) from the original five, δ^{13}C and δ^{18}O being the major contributors to the DFs. This reduced data set can be explained by the strong covariance between δ^2H and δ^{18}O and between $\delta^{13}C_{coffee}$ and $\delta^{13}C_{caffeine}$. Combining the elemental and isotopic data, stepwise DA identified eight variables, consistent with the results above (δ^2H, δ^{13}C, δ^{18}O,

DOI: 10.1021/acs.jafc.5b01526
J. Agric. Food Chem. 2015, 63, 5771−5779

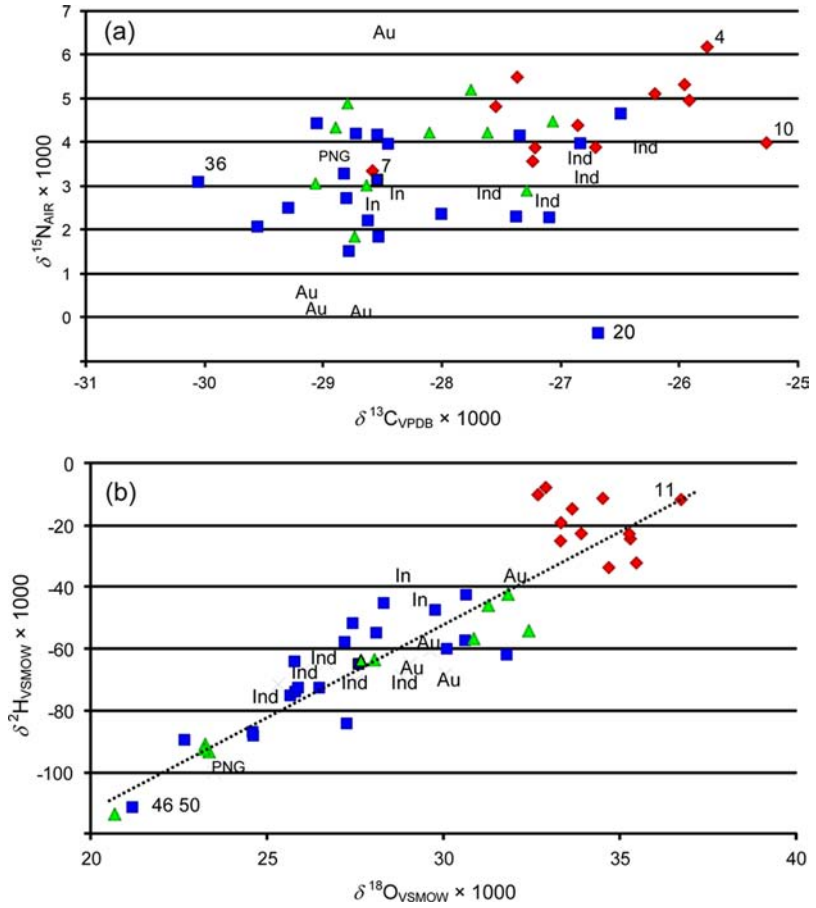

Figure 1. Plots of (a) carbon versus nitrogen isotopic composition and (b) hydrogen versus oxygen isotopic composition of roasted coffee beans: Africa (diamonds, red), Central America (squares, blue), South America (triangles, green); other countries are identified by letters (see Table 1). Dashed line shows the LAD regression ($Y = 5.93X - 229$; $R^2 = 0.83$).

Ca, P, Ti, Ni, Zn) with the major contributions to the DFs being the isotopic data.

Stepwise DA was also applied to distinguish between countries within Central/Douth America. Both the elemental concentrations (Ca, K, Ti, Fe, Ni, Cu, Zn, Ba) and isotopic compositions (δ^2H, δ^{13}C, δ^{15}N) identified as major contributors to the DFs were different from those that contributed to global variations. When elemental concentration and isotopic data were combined, stepwise DA removed only the concentrations of strontium and barium from the data, confirming that climatic and geological variations are more subtle on a regional scale than globally.

The same approach was applied to distinguish between countries within the African continent. Stepwise DA identified variables within the isotopic data (δ^2H/δ^{18}O) and within the elemental concentration data (Ca, K, Mg, P, Al, Mn, Fe), which were quite different from those selected for global data or for the Central/South America region. Again, this finding suggests that regional variations are driven by different factors from global variations and from variations within other regions.

Carbon and Nitrogen Isotopes. Figure 1a shows an $X-Y$ scatter plot of δ^{15}N versus δ^{13}C compositions of the coffee samples. Overall, the δ^{13}C data spanned a wide range (from −30.0 to −25.2‰); the most enriched samples originated from Ethiopia or Kenya (samples 4 and 10) and the most depleted sample (sample 36) from Bolivia. The δ^{15}N compositions spanned a similar range (from −0.3 to +6.4‰); the most enriched samples originated in Australia (sample 16) or Ethiopia (sample 4) and the most depleted samples originated from Australia (samples 13−15) or El Salvador (sample 20).

The variation in δ^{13}C composition of roasted coffees measured in this study (from −30.0 to −25.2‰) was in agreement with those determined in earlier studies of green coffee beans: from −29.9 to −24.6 to‰[17] and from −28.1 to −23.8‰.[18] The variation in δ^{15}N composition spanned a slightly wider range (from −0.3 to +6.4‰) than reported in these earlier studies: from +1.5 to +3.3[17] and from +1.2 to +5.6.[18] These findings suggest that, akin to elemental composition, there was little change in the isotopic composition of green and roasted coffee with respect to δ^{13}C and δ^{15}N.

The large variation in the data presented in Figure 1 suggested that many factors influence the isotopic composition such as water and nutrient availability, light intensity, and temperature.[27] Despite the large number of environmental factors that may control these data, some trends were apparent. In general, the samples most enriched in both ^{13}C and ^{15}N came from Africa and the most depleted samples came from Central/South America. The one exception to this trend was sample 7, which was purchased as ground coffee from a large supermarket chain and claimed to be a product of Ethiopia. Coffees from Indonesia formed a cluster with little variation in carbon and nitrogen composition. Coffees from Australia, Papua New Guinea, and India had similar δ^{13}C compositions, typical of C_3 plants (approximately −28.7‰), but had δ^{15}N compositions that spanned the entire range observed in this study.

DOI: 10.1021/acs.jafc.5b01526
J. Agric. Food Chem. 2015, 63, 5771−5779

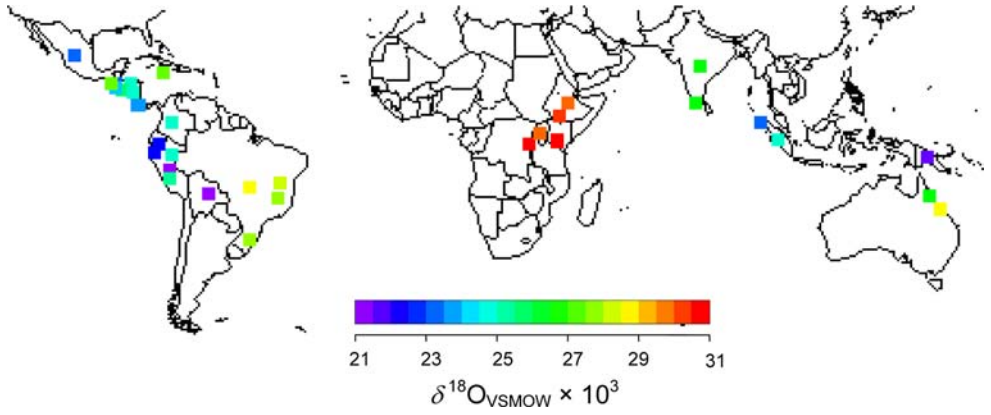

Figure 2. Isoscape of the oxygen isotopic composition of coffee samples.

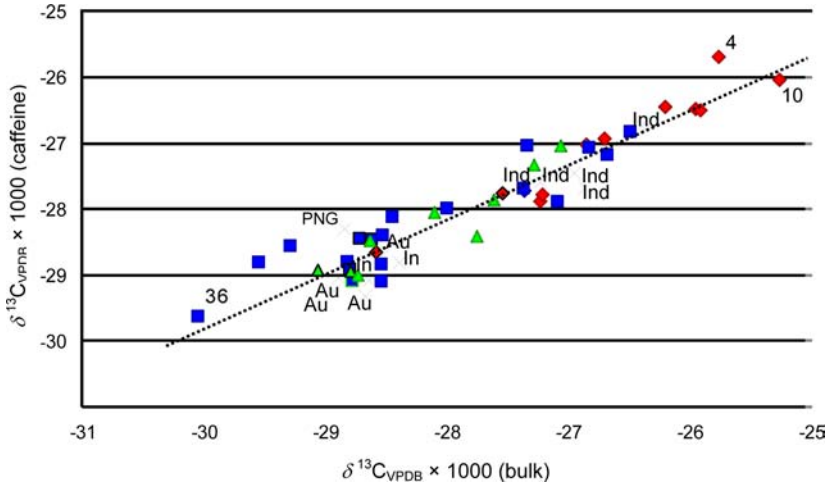

Figure 3. Carbon isotopic composition of extracted caffeine versus carbon isotopic composition of roasted beans: Africa (diamonds, red), Central America (squares, blue), South America (triangles, green); other countries are identified by letters (see Table 1). Dashed line shows the LAD regression ($Y = 0.81X - 5.3$; $R^2 = 0.81$).

In common with earlier studies of green coffee beans[18] it was apparent that a combination of carbon and nitrogen isotopic composition allowed some degree of discrimination between Africa, Asia, and Central/South America regions but not intracontinent.

Three Australian coffees had $\delta^{15}N$ compositions close to that of atmospheric nitrogen (0‰), whereas the fourth (sample 16) was the most enriched sample in this study (+6.4‰), claiming to be organic, as did sample **4**. Nitrogen stable isotopic composition has been used to distinguish organic and conventional cultivation methods for a range of fruits[28−31] on the basis that inorganic fertilizers have $\delta^{15}N$ compositions close to atmospheric nitrogen (from −6 to +6‰), whereas manure and other organic fertilizers can be greatly enriched (from +1 to +37‰). From the limited data available in this study it appeared that $\delta^{15}N$ composition may be extended to the authentication of organic coffee beans. This principle would also support the fact that African countries, in which natural fertilizers predominate, are typically enriched in ^{15}N with respect to countries that favor the use of inorganic fertilizers.

Hydrogen and Oxygen Isotopes. Figure 1b shows an $X-Y$ scatter plot of the δ^2H versus $\delta^{18}O$ compositions of the coffee samples with a relationship defined by

$$\delta^2H = \delta^{18}O \times 5.9 - 229$$

The hydrogen isotopic composition spanned a range from −113 to −8‰, and the oxygen isotopic composition spanned a range from +20.6 to +36.7‰. The most enriched sample (sample 11) originated from Rwanda and the most depleted samples (samples 46 and 50) from Colombia and Peru. The range of $\delta^{18}O$ compositions (from +20.6 to +32.4‰) was somewhat smaller than previously reported for green coffee beans (from +18.7 to +34.8‰).[17] Although the $\delta^{18}O$ composition of plant material is attributed mainly to precipitation at different latitudes and altitudes,[32] the data in this study showed no correlation with latitude. This may reflect little variation, as a majority of coffee is grown between latitudes 23°26′ north and south of the equator.

The relationship between δ^2H and $\delta^{18}O$ was characterized by a slope that was typical neither of meteoric water (typical slope 8)[33] or of evaporation-enriched water in fruits (typical slope 4).[34] It is likely that the observed relationship contained contributions from both of these processes and/or water loss through roasting. During roasting, green coffee beans are progressively heated to 230 °C, losing approximately 13% of their weight,[35] the majority of which is likely to be water.

The pattern of data presented in Figure 1b for $\delta^2H/\delta^{18}O$ broadly reflected those observed from $\delta^{13}C/\delta^{15}N$, samples from Africa being the most isotopically enriched and samples from Central/South America being the most depleted. For $\delta^2H/\delta^{18}O$

DOI: 10.1021/acs.jafc.5b01526
J. Agric. Food Chem. 2015, 63, 5771−5779

data there was a clear delineation of African countries, including sample 7, which had ambiguous $\delta^{13}C/\delta^{15}N$ characteristics. Samples from low-coffee-producing nations (Australia, India, and Indonesia) formed discrete groupings within the data, with the exception of Australian sample 16, which was an organic product. On the basis of Figure 1b it is likely that $\delta^{2}H/\delta^{18}O$ composition was also characteristic of organic production methods, organic and African samples being the most enriched.

Figure 2 presents a simple geo-spatial map (*isoscape*) showing the distribution of $\delta^{18}O$ of the coffee samples from this study. The isotopic data were ranked into 20 groups, assigned a color according to the palette shown in Figure 3, and plotted on a global map using the longitude and latitude of each sample (Supporting Information supplement 2). Very similar patterns were observed for plots of $\delta^{2}H$ and $\delta^{13}C$ as might be expected given the strong correlations between these variables. Although the data shown in Figure 2 were relatively sparse, there was a marked similarity to isoscapes predicting plant $\delta^{18}O$ composition derived from global precipitation.[36] By plotting data in this way it becomes possible to answer the question, "is the isotopic composition consistent with the claimed geographical origin?", removing the need for comparative samples.

Caffeine. Figure 3 shows an $X-Y$ scatter plot of the $\delta^{13}C$ composition of the extracted caffeine versus that of the whole coffee with a relationship defined by

$$\delta^{13}C_{caffeine} = \delta^{13}C_{coffee} \times 0.8 - 5.3$$

The isotopic compositions of the extracted caffeine spanned a slightly smaller range (from −29.6 to −25.7‰) than previously reported (from −29.9 to −25.1‰),[20] and there was a strong correlation between $\delta^{13}C_{caffeine}$ and $\delta^{13}C_{coffee}$ (R^2 = 0.81). The small difference between $\delta^{13}C_{caffeine}$ and $\delta^{13}C_{coffee}$ (median difference = −0.22‰; range from −0.80 to +0.77‰) was in agreement with a study of the biosynthesis of purine alkaloids (specifically caffeine), which predicted a small depletion in the carbon isotopic composition of caffeine with respect to cellulose.[37]

The general trends observed in Figure 1 were also apparent in Figure 3, African samples being the most isotopically enriched, Central/South American samples being the most depleted, and low-coffee-producing regions (Australia, India, and Indonesia) forming discrete groupings within the data. The strong correlation between $\delta^{13}C_{caffeine}$ and $\delta^{13}C_{coffee}$ may provide a limited means to determine the authenticity of caffeinated beverages by reference to Figure 3. However, such an approach may be limited by the technical complexity of GC-IRMS measurements for elements other than carbon.

Country of Origin. Table 3 summarizes the results of DA applied to the analytical data obtained in this study. A reduced data set of elemental concentrations (Ca, Ti, Fe, Ni, Zn) provided a reasonable basis to discriminate between regions of production (63% overall correct). A reduced data set of isotopic composition ($\delta^{2}H$, $\delta^{13}C$, $\delta^{18}O$) provided somewhat better discrimination for some regions but misclassified samples from Central/South America and India, leading to similar overall success (65% correct). Combining elemental and isotopic data improved the discrimination between Central and South America and the overall correct classification (77% correct). Although the degree of correct classification was lower than reported by previous studies,[16−19] we find that the current results represent a realistic estimate of what is possible with a limited number of samples.

Table 3. Results of Discriminant Analysis Applied to Regions and Countries of Origin Showing the Percentage Correct Classification Obtained by Jackknifed and Conventional (Non-jackknifed) Methods

	percentage correct classification		
region/country	elemental	isotopic	combined
A	83	92	100
AU	60	80	60
CA	43	27	64
Ind	40	80	80
In	50	50	100
SA	68	65	71
total, jackknifed	63	65	77
total, conventional	74	73	88
Bolivia	0	0	0
Brazil	20	40	0
Colombia	50	0	0
Costa Rica	0	50	50
Ecuador	50	0	0
El Salvador	0	0	0
Guatemala	100	33	0
Honduras	0	0	100
Jamaica	0	0	0
Mexico	0	0	0
Nicaragua	0	0	0
Peru	40	50	25
total, jackknifed	33	21	11
total, conventional	97	57	100
Kenya	0	33	0
Ethiopia	0	57	0
Rwanda	100	0	100
Uganda	100	0	100
total, jackknifed	17	42	17
total, conventional	100	83	100

DA was also applied independently to data from Central/South America and from Africa (Table 3). These tests failed to correctly classify coffee from any of the countries, with the possible exceptions of Guatemala/Honduras and Rwanda/Uganda. As only a single sample from each country was analyzed, it is not possible to conclude if this finding reflects that these countries were characterized by a unique elemental composition.

DA results can be explained with reference to Figures 1 and 2; countries from Africa were clearly delineated by enriched isotopic compositions, whereas data for Central/South America and low-coffee-producing countries (Australia, India, and Indonesia) were encompassed in a broad band of values. Isotopic composition appeared to be driven by factors such as precipitation, more than national or continental boundaries. Consequently, in South America there was a distinction between the ^{18}O compositions of coffees from the east and west coasts, which was more pronounced than any difference between Central/South America; that is, intraregion differences were similar to, or greater than, inter-region differences. For this reason, assigning countries to broad, man-made groupings such as "Asia" as a basis for DA may not be appropriate.

DOI: 10.1021/acs.jafc.5b01526
J. Agric. Food Chem. 2015, 63, 5771−5779

Although DA was successfully applied to assess numerically the region of origin, it was apparent (Table 3) that the level of discrimination provided by DA was greatly overestimated when compared to the results obtained using a jackknifed approach. We recommend caution in the haphazard use of DA; specifically, the number of observations must be significantly greater than the number of independent variables (>5:1), and the number of observations in the smallest group must be greater than the number of independent variables. In the absence of such large sample sets, simpler $X-Y$ and geo-spatial plots (Figures 1−2) provide a simple and robust approach to narrow the range of possible origins.

The isotopic composition of a coffee can be compared against the data presented in Figure 1 to determine if the combinations of both $\delta^{13}C/\delta^{15}N$ and $\delta^{2}H/\delta^{18}O$ are consistent with a single geographical origin in Africa, Australia, India, Indonesia, or Papua New Guinea. The elemental composition of a sample can then act as a further point of comparison, and an analyst may have reasonable confidence in reporting such a result. The use of kernel density estimation (kde) has been applied to stable isotope data to calculate a quantitative weight of evidence that a sample belongs to one group rather than another.[38] This approach may be extended to food forensic applications but is beyond the scope of the current work. The wide spread and overlap of isotopic data for Central and South American coffees may preclude such comparisons but, as noted above, the presentation of isotopic data in the form of a geo-spatial map or isoscape (Figure 2) provides a means by which to consider whether the isotopic composition of a sample is consistent with the proposed region of origin. Increasing the value of such comparisons will require large data sets and/or models linking our data to existing databases such as global precipitation.[36]

■ ASSOCIATED CONTENT

Supporting Information

Measured and assigned values of quality control materials used for isotopic or elemental analysis and the δ values assigned to reference materials for the normalization and quality control of IRMS data (Supplement 1); sample details and analytical data for all of the coffees analyzed in this study (Supplement 2). The Supporting Information is available free of charge on the ACS Publications website at DOI: 10.1021/acs.jafc.5b01526.

■ AUTHOR INFORMATION

Corresponding Author

*(J.F.C.) Phone: +61 (07) 3274 9228. Fax: +61 (07) 3274 9196. E-mail: Jim.Carter@health.qld.gov.au.

Notes

The authors declare no competing financial interest.

■ ACKNOWLEDGMENTS

We are grateful to the editorial staff for their patience and to the reviewers for identifying a number of flaws in the original drafts of the manuscript. We acknowledge the support of Queensland Health Forensic and Scientific Services in completing this work. We are also grateful to and apologize to the specialty coffee roasters of Brisbane who enthusiastically sold us their finest single-origin coffee without realizing that it would never be drunk. We extend special thanks to Prof. Brian Fry of Griffith University for many mutually valuable discussions on the appropriate use of discriminant analysis.

■ REFERENCES

(1) http://www.ico.org (accessed March 2015).
(2) Lewin, B.; Giovannucci, D.; Varangis, P. In *Coffee Markets: New Paradigms in Global Supply and Demand, Agriculture and Rural Development*; The World Bank: Washington, DC, USA, 2004.
(3) Ahmed, Z. U.; Johnson, J. P.; X Yang, X.; Fatt, C. K.; H.S. Teng, H. S.; Boon, L. C. Does country of origin matter for low-involvement products? *Int. Marketing Rev.* **2004**, *102*, 1.
(4) Accum, F. *There Is Death in the Pot*, 2nd ed.; Longman: London, UK, 1820.
(5) Alonso-Salces, R. M.; Serra, F.; Reniero, F.; Héberger, K. Botanical and geographical characterization of green coffee (*Coffea arabica* and *Coffea canephora*): chemometric evaluation of phenolic and methylxanthine contents. *J. Agric. Food Chem.* **2009**, *57*, 4224−4235.
(6) Anderson, K. A.; Smith, B. W. Chemical profiling to differentiate geographic growing origins of coffee. *J. Agric. Food Chem.* **2002**, *50*, 2068−2075.
(7) Bertrand, B.; Villarreal, D.; Laffargue, A.; Posada, H.; Lashermes, P.; Dussert, S. Comparison of the effectiveness of fatty acids, chlorogenic acids, and elements for the chemometric discrimination of coffee (*Coffea arabica* L.) varieties and growing origins. *J. Agric. Food Chem.* **2008**, *56*, 2273−2280.
(8) Choi, M.-Y.; Choi, W.; Park, J. H.; Lim, J.; Kwon, S. W. Determination of coffee origins by integrated metabolomic approach of combining multiple analytical data. *Food Chem.* **2010**, *121*, 1260−1268.
(9) Arana, V. A.; Medina, J.; Alarcon, R.; Moreno, E.; Heintz, L.; Schäfer, H.; Wist, J. Coffee's country of origin determined by NMR: the Colombian case. *Food Chem.* **2015**, *175*, 500−506.
(10) Briandet, R.; Kemsley, E. K.; Wilson, R. H. Discrimination of Arabica and Robusta in instant coffee by Fourier transform infrared spectroscopy and chemometrics. *J. Agric. Food Chem.* **1996**, *44*, 170−174.
(11) Charlton, A. J.; Farrington, W. H. H.; Brereton, P. Application of ^{1}H NMR and multivariate statistics for screening complex mixtures: quality control and authenticity of instant coffee. *J. Agric. Food Chem.* **2002**, *50*, 3098−3103.
(12) Downey, G.; Briandet, R.; Wilson, R. H.; Kemsley, E. K. Near- and mid-infrared spectroscopies in food authentication: coffee varietal identification. *J. Agric. Food Chem.* **1997**, *45*, 4357−4361.
(13) Monakhova, Y. B.; Ruge, W.; Kuballa, T.; Ilse, M.; Winkelmann, O.; Diehl, B.; Thomas, F.; Lachenmeier, D. W. Rapid approach to identify the presence of Arabica and Robusta species in coffee using ^{1}H NMR spectroscopy. *Food Chem.* **2015**, *182*, 178−184.
(14) Wei, F.; Furihata, K.; Koda, M.; Hu, F.; Kato, R.; Miyakawa, T.; Tanokura, M. ^{13}C NMR-based metabolomics for the classification of green coffee beans according to variety and origin. *J. Agric. Food Chem.* **2012**, *60*, 10118−10125.
(15) Liu, H.-C.; You, C.-F.; Chen, C.-Y.; Liu, Y.-C.; Chung, M.-T. Geographic determination of coffee beans using multi-element analysis and isotope ratios of boron and strontium. *Food Chem.* **2014**, *142*, 439−445.
(16) Rodrigues, C.; Brunner, M.; Steiman, S.; Bowen, G. J.; Nogueira, J. M. F.; Gautz, L.; Prohaska, T.; Máguas, C. Isotopes as tracers of the Hawaiian coffee-producing regions. *J. Agric. Food Chem.* **2011**, *59*, 10239−10246.
(17) Rodrigues, C. I.; Maia, R.; Miranda, M.; Ribeirinho, M.; Nogueira, J. M. F.; Máguas, C. Stable isotope analysis for green coffee bean: a possible method for geographic origin discrimination. *J. Food Compos. Anal.* **2009**, *22*, 463−471.
(18) Serra, F.; Guillou, C. G.; Reniero, F.; Ballarin, L.; Cantagallo, M. I.; Wieser, M.; Iyer, S. S.; Héberger, K.; Vanhaecke, F. Determination of the geographical origin of green coffee by principal component analysis of carbon, nitrogen and boron stable isotope ratios. *Rapid Commun. Mass Spectrom.* **2005**, *19*, 2111−2115.
(19) Valentin, J. L.; Watling, R. J. Provenance establishment of coffee using solution ICP-MS and ICP-AES. *Food Chem.* **2013**, *141*, 98−104.

DOI: 10.1021/acs.jafc.5b01526
J. Agric. Food Chem. 2015, 63, 5771−5779

(20) Weckerle, B.; Richling, E.; Heinrich, S.; Schreier, P. Origin assessment of green coffee (*Coffea arabica*) by multi-element stable isotope analysis of caffeine. *Anal. Bioanal. Chem.* **2002**, *374*, 886−890.
(21) de Korompay, A.; Hill, J. C.; Carter, J. F.; NicDaeid, N.; Sleeman, R. Supported liquid-liquid extraction of the active ingredient (3,4-methylenedioxymethylamphetamine) from ecstasy tablets for isotopic analysis. *J. Chromatogr. A* **2008**, *1178*, 1−8.
(22) Chesson, L. A.; Podlesak, D. W.; Cerling, T. E.; Ehleringer, J. R. Evaluating uncertainty in the calculation of non-exchangeable hydrogen fractions within organic materials. *Rapid Commun. Mass Spectrom.* **2009**, *23*, 1275−1280.
(23) Carter, J. F.; Tinggi, U.; Yang, X.; Fry, B. Stable isotope and trace metal compositions of Australian prawns as a guide to authenticity and wholesomeness. *Food Chem.* **2015**, *170*, 241−248.
(24) Carter, J. F.; Yates, H. S. A.; Tinggi, U. Stable isotope and chemical compositions of European and Australasian ciders as a guide to authenticity. *J. Agric. Food Chem.* **2015**, *63*, 975−982.
(25) R Core Team. *R: A Language and Environment for Statistical Computing*; R Foundation for Statistical Computing: Vienna, Austria, 2010.
(26) Brooks, J. P.; Dulá, J. H.; Boone, E. L. A pure-norm principal component analysis. *Comput. Stat. Data Anal.* **2013**, *61*, 83−98.
(27) Vogel, J. C. Variability of carbon isotope fractionation during photosynthesis. In *Stable Isotopes and Plant Carbon-Water Relations*; Saugier, B., Ehleringer, J. R., Hall, A. E., Farquhar, G. D., Eds.; Academic Press: San Diego, CA, USA, 1993; pp 29−46.
(28) Bateman, A. S.; Kelly, S. D. Fertilizer nitrogen isotope signatures. *Isot. Environ. Health Stud.* **2007**, *43*, 237−247.
(29) Bateman, A. S.; Kelly, S. D.; Jickells, T. D. Nitrogen isotope relationships between crops and fertilizer: implications for using nitrogen isotope analysis as an indicator of agricultural regime. *J. Agric. Food Chem.* **2005**, *53*, 5760−5765.
(30) Bateman, A. S.; Kelly, S. D.; Woolfe, M. Nitrogen isotope composition of organically and conventionally grown crops. *J. Agric. Food Chem.* **2007**, *55*, 2664−2670.
(31) Camin, F.; Perini, M.; Bontempo, L.; Fabroni, S.; Faedi, W.; Magnani, S.; Baruzzi, G.; Bonoli, M.; Tabilio, M. R.; Musmeci, S.; Rossmann, A.; Kelly, S. D.; Rapisarda, P. Potential isotopic and chemical markers for characterising organic fruits. *Food Chem.* **2011**, *125*, 1072−1082.
(32) Flanagan, L. B. Environmental and biological influences on the stable oxygen and hydrogen isotopic composition of leaf water. In *Stable Isotopes and Plant Carbon-water Relations*; Saugier, B., Ehleringer, J. R., Hall, A. E., Farquhar, G. D., Eds.; Academic Press: San Diego, CA, USA, 1993; pp 71−90.
(33) Craig, H. Isotopic variation in meteoric waters. *Science* **1961**, *133*, 1702−1703.
(34) Dunbar, J.; Wilson, A. T. Oxygen and hydrogen isotopes in fruit and vegetable juices. *Plant Physiol.* **1983**, *72*, 725−727.
(35) http://www.coffeeresearch.org/coffee/roasting.htm (accessed March 2015).
(36) West, J. B.; Sobek, A.; Ehleringer, J. R. A simplified GIS approach to modelling global leaf water isoscapes. *PLoS One* **2008**, *13*, No. e2447.
(37) Weilacher, T.; Gleixner, G.; Schmidt, H. L. Carbon isotope pattern in purine alkaloids a key to isotope discriminations in C1 compounds. *Phytochemistry* **1996**, *41*, 1073−1077.
(38) Carter, J. F.; Doyle, S.; Phasumane, B.-L.; NicDaeid, N. The role of isotope ratio mass spectrometry as a tool for the comparison of physical evidence. *Sci. Justice* **2014**, *54*, 327−335.

DOI: 10.1021/acs.jafc.5b01526
J. Agric. Food Chem. 2015, 63, 5771−5779

epoxide groups, where a variety of internal standards were used.[13,14] In one of these studies,[13] the nondeuterated chloroform present in the deuterated chloroform was used as an internal reference for quantitative purposes. Generally, the main benefit of using the residual solvent signal as an internal standard is that it allows the sample to be recovered because the solvents are volatile and therefore easy to remove. However, the residual solvent content was found to vary from batch to batch, and its use for quantitative purposes requires external calibrants to determine its content in the deuterated solvent.[15] Therefore, frequent calibrations are required when using the deuterated solvent as an internal standard. Moreover, because chloroform is easily evaporated, when it is used as an internal standard for quantification, special care must be taken in handling the samples and the solvents. In the other study,[14] signals from methyl groups were used as the internal standard for quantification, but the applicability of this method to oxidized oils needs to be verified, because alkanes can be formed when oils undergo lipid oxidation,[16] especially at high temperatures. Glycerol protons were found to be constant during oxidation in the absence of water;[17] therefore, they can be used as alternative internal standards for ^{1}H NMR quantification, which will allow rapid sample preparation and easy handling.

In this study, a quantitative NMR method of measuring epoxides was developed and validated using soybean oil. This method represents significant improvement over other methods[12−14] in that partially epoxidized oils are synthesized and used for quantification, instead of using epoxy fatty acid standards, so that signals are generated to mimic those that would be encountered in oxidized oils. Specifically, synthetic epoxidized soybean oils were made to establish a calibration curve, and used to validate the proposed method. The one-step sample preparation allowed rapid determination of epoxides at low levels without any addition of external references. As the objective of this study was to develop a method to monitor epoxides during lipid oxidation, the application of the proposed method to thermally oxidized soybean oils was also verified by conducting an accelerated study of oxidative stability.

MATERIALS AND METHODS

Materials. Commercial soybean oil was obtained from Clic International Inc. (Montreal, Canada). Hydrogen bromide−acetic acid solution (33 wt % in acetic acid) and deuterated chloroform were purchased from Sigma-Aldrich Co. (St. Louis, MO, USA). Hydrogen peroxide (50%) was from Fisher Scientific (Ottawa, Canada). All chemicals were of analytical grade.

GC Analysis of Fresh Soybean Oil. The fatty acid profile of soybean oil was analyzed using gas chromatography with flame ionization detection (GC-FID). A modified version of the Global Organization for EPA and DHA Voluntary Monograph for Omega-3 was followed to convert triacylglycerols to fatty acid methyl esters (FAME).[18] FAME were separated on a DB-23 column ((50%-cyanopropyl)methylpolysiloxane, 30 m, 0.25 mm i.d., 0.25 μm thickness) using helium as the carrier gas. The GC conditions were as follows: the initial temperature of the oven was held at 153 °C for 2 min and increased to 205 °C at 2.3 °C/min and held for 8.3 min; the FID was set to 270 °C, whereas the injector was operated in split mode (100:1) at 250 °C.[19] The fatty acid profile was reported as percent of total mass.

Epoxidation. The fatty acid profile of the commercial soybean oil was obtained by GC-FID and the concentration of double bonds was therefore calculated using fatty acid proportional data. To prepare epoxidized soybean oil for characterization of epoxides, a molar ratio of 1:0.5:1.5 double bonds/formic acid/hydrogen peroxide was used for epoxidation. The mixture of formic acid, hydrogen peroxide, and soybean oil was heated at 38 °C for 6 h.[20,21]

To establish a calibration curve, epoxidized soybean oils with a range of different concentrations of epoxides were prepared by reducing the amount of the reagents (formic acid and hydrogen peroxide) used for epoxidation while maintaining the molar ratios of formic acid and hydrogen peroxide at 0.5:1.5 (1:3). As the amount of epoxides generated from lipid oxidation is usually small, much lower amounts (<10% of the original amount) of epoxidation reagents were used. For converting <2% double bonds in soybean oils to epoxy groups, 2 h instead of 6 h was used with heating at 38 °C. Ethyl acetate was used to recover the epoxidized oil, following the procedures in a previous study,[22] and was then dried with anhydrous sodium sulfate. The solvent in the oil layer was evaporated under nitrogen, and the remaining oil was collected as the epoxidized soybean oil.

^{1}H NMR Analysis. The ^{1}H NMR spectra were recorded on a Bruker Avance 500 MHz spectrometer. All of the oil samples were prepared for ^{1}H NMR analysis by dissolving 0.1 g of sample in 2.0 mL of deuterated chloroform and placing 750 μL of the solution in a NMR tube (5 mm diameter, 8 in. in length, Wilmad-LabGlass, Vineland, NJ, USA). The acquisition parameters were modified from a previous study:[23] spectral width, 10080 Hz; relaxation delay, 3 s; number of scans, 64; acquisition time, 3.25 s; with a total acquisition time of 6.9 min for each sample. The signal of nondeuterated chloroform present in the deuterated chloroform was used as a reference for chemical shifts, and the signals associated with the *sn*-1,3 glycerol protons (4.18, 4.33 ppm) on the glycerol backbone were taken as an internal standard for quantification. All of the integrations for quantitative NMR were conducted using Topspin 2.1.

Epoxide Content Determined by the HBr Method. The concentration of epoxides in synthetic epoxidized soybean oil was determined by a modified AOCS Method Cd 9-57 using hydrogen bromide (HBr).[2] To accurately determine the low epoxide concentrations, diluted HBr−acetic acid solution and increased sample size were used. As HBr is sensitive to air and light, the HBr−acetic acid solution was standardized each time before use. Crystal violet solution (0.001 g/mL in acetic acid) was used as the indicator, and the samples were titrated to a blue-green end point. This determination was performed in triplicate for each sample.

To facilitate comparison with PV, the concentration of epoxides was reported as millimoles of epoxy groups per kilogram of oil (mmol/kg)

$$\text{epoxide content (mmol/kg)} = (V \times N \times 1000)/M$$

where V is the volume of HBr to titrate the sample in mL, N is the normality of the HBr solution in mol/L, and M is the mass of sample in g.

Characterization of Epoxides by ^{1}H NMR. The fresh and the epoxidized soybean oils were analyzed by ^{1}H NMR for characterization of epoxides. The signals were assigned by taking into account the descriptions of the chemical shifts from the previous work.[13]

Quantification of Epoxides by ^{1}H NMR. A standard curve is usually established by analyzing a series of standard solutions and plotting the signal responses versus the concentrations. However, when using NMR, this may contribute to large deviations from a linear relationship over a variety of concentration, as observed in previous work.[24] Therefore, rather than establishing a standard curve by making serial dilutions of a stock solution, a calibration curve method was used to keep the NMR samples at the same total lipid concentration of ∼50 mM but with various epoxide contents.

A set of 20 synthetic epoxidized soybean oil samples were analyzed by ^{1}H NMR. The signals of the *sn*-1 and *sn*-3 glycerol protons (4.18, 4.33 ppm) were taken as an internal standard for quantification because they were well separated from other signals and remained constant during both epoxidation and oxidation. The area of the signal of epoxides was obtained by calibrating the area of the internal standard as 4.0000. The integrations were performed in triplicate. A calibration curve was established by plotting the epoxide area versus the epoxide concentration determined by using the modified AOCS Method Cd 9-57 described.[2]

DOI: 10.1021/acs.jafc.5b01719
J. Agric. Food Chem. 2015, 63, 5780−5786

Table 1. Test of Accuracy and Precision of the Proposed Method, Evaluated by the *p* Values of the Two-Sample *t* Test and the Acceptable Horwitz %RSDs, Respectively

	epoxide content (HBr method)		epoxide content (^{1}H NMR)			
sample	mean ± SD (mmol/kg)	%RSD	mean ± SD (mmol/kg)	%RSD	two-sample *t* test *p* value	acceptable Horwitz %RSD
1	666.1 ± 4.7	0.71	660.7 ± 8.8	1.33	>0.10	2.65
2	325.9 ± 5.4	1.66	320.8 ± 5.8	1.81	>0.10	2.96
3	54.6 ± 0.8	1.49	55.6 ± 1.4	2.61	>0.10	3.87
4	11.7 ± 0.3	2.26	12.2 ± 0.5	3.73	>0.05	4.88

The validation of this quantitative NMR technique included the testing of linearity, parameters of accuracy, and repeatability.[25] Thus, the validation process was conducted following the guidelines previously addressed by the International Union of Pure and Applied Chemistry (IUPAC).[26] The statistical tests were conducted by Minitab 17. For the test of linearity, the regression and the residuals of the calibration curve were analyzed. For the estimation of accuracy and precision, four epoxidized samples were analyzed by ^{1}H NMR in five replicates. The average epoxide content of each sample was compared to the value determined according to AOCS Method Cd 9-57 for the test of trueness or bias, using a two-sample *t* test (Table 1). The precision was described by the relative standard deviation (%RSD) of the quintuplet results (Table 1) and characterized by the Horwitz equation.[27] According to the Horwitz equation, an acceptable Horwitz %RSD was calculated as

$$\%\mathrm{RSD} = \frac{2}{3} \times 2^{(1-0.5 \log C)}$$

where *C* was the mass concentration of epoxides in decimal fraction. % RSD falling below this level indicated sufficient precision.[27]

To assess precision using the Horwitz equation,[27] the epoxide content was calculated as mass fraction of the oxirane oxygen in the oil[2]

$$\text{epoxide content} = (V \times N \times 0.016)/M$$

where *V* is the volume of HBr to titrate the sample in mL, *N* is the normality of the HBr solution in mol/L, and *M* is the mass of sample in g.

The precision of the method was also evaluated using thermally oxidized soybean oils. Five soybean oil samples were incubated in open test tubes at 100 °C for 4, 8, 12, 16, and 20 days. Each sample was tested for its PV (AOCS Method Cd 8-53)[2] and epoxide content (the proposed method). The tests were conducted for each sample in triplicate (Table 2). The precision was described by the %RSD of the triplicate results.

Table 2. Peroxide Value and Epoxide Content Measured for Soybean Oil Heated at 100 °C for the Test of Repeatability, Expressed by %RSD

	peroxide value		epoxide content	
sample	mean ± SD (mmol/kg)	%RSD	mean ± SD (mmol/kg)	%RSD
1	47.2 ± 0.3	0.61	8.4 ± 0.4	4.15
2	48.3 ± 1.4	2.80	17.2 ± 0.6	3.58
3	89.1 ± 0.7	0.79	29.2 ± 1.1	3.85
4	87.6 ± 0.6	0.64	55.7 ± 1.5	2.69
5	60.0 ± 0.6	1.02	90.7 ± 2.0	2.20

Stability Studies of Soybean Oil. A stability study of soybean oil was conducted to monitor the changes in PV and epoxide content over the course of oxidation. Three open amber containers (125 mL) were used for incubations at 100 °C with each initially containing 30 g of soybean oil. Every 2 days, 2.5 g of oil was sampled from each container for analysis of its PV (AOCS Method Cd 8-53)[2] and epoxides (the proposed method). The tests of each oil sample were performed in triplicate. PV and epoxide content were plotted over time for comparison.

RESULTS AND DISCUSSION

Characterization of Epoxides Derived from Soybean Oil. The initial soybean oil contained 10.2 ± 0.1% palmitic acid (16:0), 21.9 ± 0.3% oleic acid (18:1n-9), 52.5 ± 0.8% linoleic acid (18:2n-6), and 7.7 ± 0.2% linolenic acid (18:3n-3). Therefore, the total unsaturation was estimated to be 5.46 mol of double bonds per kilogram of oil. The signals of epoxides derived from soybean oil were between 2.90 and 3.24 ppm; as the size of those signals increased, the size of the signals due to double bonds (~5.40 ppm) decreased correspondingly (Figure 1; Supplementary Table 1 in the Supporting Information). Thus, the epoxidation method used here was successful in epoxidizing the commercial soybean oil, generating obvious signals of epoxides in the ^{1}H NMR spectra.

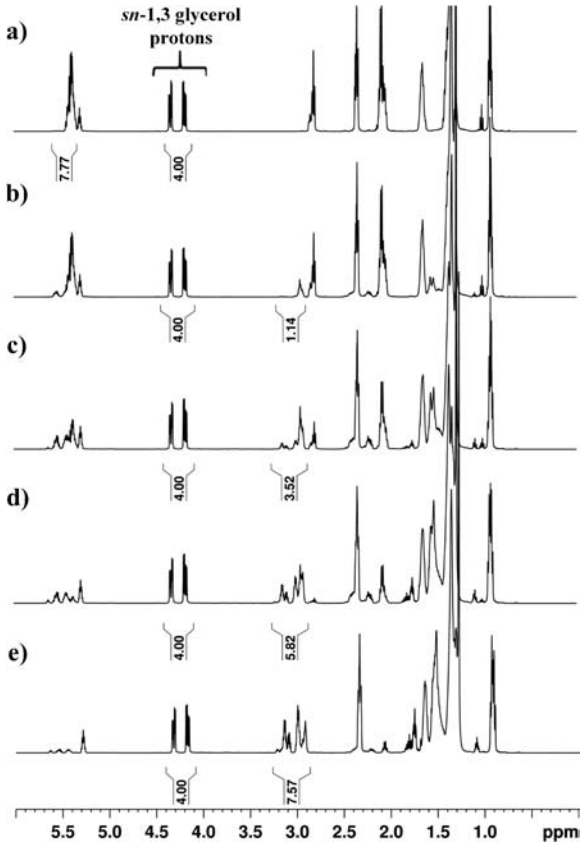

Figure 1. ^{1}H NMR spectrum of (a) fresh soybean oil and epoxidized soybean oils with epoxide contents of (b) 0.70 mol/kg, (c) 2.06 mol/kg, (d) 3.41 mol/kg, and (e) 4.16 mol/kg. The integrations of the double bonds (5.40−5.60 ppm in (a)) and the epoxides (2.90−3.24 ppm in (b−e)) were made by taking the signals of *sn*-1 and *sn*-3 glycerol protons (4.18 and 4.33 ppm) as internal standards. The area of the internal standard was calibrated as 4.00 as the number of *sn*-1 and *sn*-3 glycerol protons is 4.

DOI: 10.1021/acs.jafc.5b01719
J. Agric. Food Chem. 2015, 63, 5780−5786

On the basis of previous publications[13,14] and our observation of the ^{1}H NMR spectra in Figure 1, we made the assignments as follows, where −CHOCH− represents an epoxy group: δ 1.45−1.60 (−C**H**$_2$—CHOCH−), 1.70−1.85 (−CHOCH—C**H**$_2$—CHOCH−), 2.00−2.10 (−C**H**$_2$—CH═CH−), 2.80−2.85 (−CH═CH—C**H**$_2$—CH═CH−), 2.90−2.95 (−C**H**OC**H**−), 2.90−2.95 (−C**H**OC**H**−CH$_2$−CH═CH−), 3.00 (−C**H**OCH−CH$_2$−CHOC**H**−), 3.06−3.24 (−CHOC**H**−CH$_2$−C**H**OCH−), 5.35−5.45 (−C**H**═C**H**−), 5.40−5.60 (−C**H**═C**H**—CH$_2$—CHOCH−), 5.60−5.65 (−CHOCH—CH$_2$—C**H**═C**H**—CH$_2$—CHOCH−) (Supplementary Table 1). The range of chemical shifts of epoxides increased with the concentration of epoxides in the oil (Figure 1). For oils with a low epoxide content (Figure 1b), the signals of epoxides appeared around 2.90−2.95 ppm, which was likely related to the formation of the partially epoxidized linoleic acid and linolenic acid (−C**H**OC**H**—CH$_2$—CH═CH−), and overlapped with the less intense signal of epoxy oleic acid at 2.90−2.95 ppm (−CH$_2$—C**H**OC**H**—CH$_2$−). For oil samples with higher epoxide content (Figure 1c), the signals associated with diepoxides appeared at ∼3.00 ppm (−C**H**OCH—CH$_2$—CHOC**H**−) and 3.09 and 3.16 ppm (−CHOC**H**—CH$_2$—C**H**OCH−), and their intensities increased with increasing concentration. The signal that indicated the presence of triepoxides appeared at 3.20 ppm, when ∼62% of the original double bonds had been converted into epoxy groups (Figure 1d). In Figure 1e, the epoxidized soybean oil gave five signals between 2.90 and 3.24 ppm, with small signals due to double bonds remaining between 5.40 and 5.60 ppm, which indicated that ∼76% of the double bonds were converted into epoxy groups.

Lipid oxidation is a relatively complex autoxidation process, so the structure of epoxy products may vary with the conditions of oxidation. Although the chromatography method employs common GC-FID instrumentation,[28] making it an accessible technique to many analysts, it does rely on the use of epoxy fatty acid methyl ester (FAME) standards for identification of the signals on the chromatograms. Any epoxide structures that vary from the standards may be overlooked during identification and cause underestimations of epoxide concentration. Moreover, the selectivity of quantitative NMR did not depend on the structure of epoxides, and therefore it gave an overview of all the epoxy groups formed in the oil. The chemical shifts of epoxides (2.90−3.24 ppm) were distinct from other oxidation products including alcohols (3.43−3.62 ppm), conjugated dienes (5.40−6.58 ppm), double bonds conjugated with carbonyls (6.08−6.82 ppm), hydroperoxides (8.30−8.90 ppm), and aldehydes (9.49−9.79 ppm).[29] In summary, ^{1}H NMR can be used to detect epoxides in oxidized soybean oils with superior selectivity, which is a major advantage over the chromatography method.

Quantification of Epoxides. Although fully epoxidized soybean oil gave signals between 2.90 and 3.24 ppm, oxidized oils, with relatively low epoxide content, gave signals between 2.90 and 3.10 ppm, mostly due to monoepoxides with or without adjacent double bonds (Supplementary Table 1). The epoxy protons were monitored for quantitative purposes because the size of the signals between 2.90 and 3.24 ppm was proportional to the amount of epoxy groups generated in the oil, regardless of the presence of saturated/unsaturated mono- and diepoxides. Although the signals at 1.45−1.60 ppm (−C**H**$_2$—CHOCH−) and 2.00−2.10 ppm (−C**H**$_2$—CH═CH−) were related to the generation of epoxides (Figure 1), the change in size of the signals was not proportional to the amount of epoxy groups; therefore, the epoxy protons were the best indicators of formation of epoxides.

When signal response versus concentration was plotted, a calibration curve was established for epoxides in soybean oil with a good linear relationship. The regression equation was $y = 0.0151 + 0.0016x$ with an R^2 of 99.96%, where y represented the signal response and x was the concentration of epoxides (Figure 2). To our knowledge, this is the first demonstration of

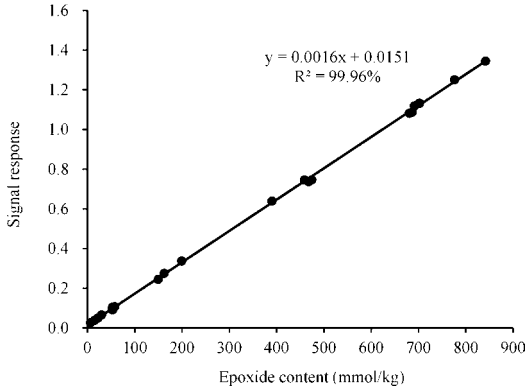

Figure 2. Fitted linear relationship by plotting signal response (y) versus the epoxide concentration (x) measured by the HBr method. Each point represents a single epoxidized soybean oil sample.

agreement between the ^{1}H NMR method and the HBr method for low epoxide concentrations. Residual analysis of all calibration points did not reveal any trends relating to the concentration of epoxides. The residuals passed the Anderson−Darling test and followed a normal distribution with a p value of 0.148. Thus, the linear relationship between the signal response and the epoxide content did not depend on the concentration of epoxides in the experimental range of concentrations (6.7−841.6 mmol/kg). A linear fit was found for the calibration curve ($F = 7.63$, $p < 0.001$). Therefore, the area ratio of the signals of epoxides/internal reference increased linearly with the epoxide content. Because epoxides were not found in the fresh soybean oil using the HBr method, the fresh soybean oil was considered a blank. The limit of quantification (LOQ) was therefore determined to be 6.3 mmol/kg by taking into account the standard deviation (σ) of the blank and the slope (s) of the calibration curve (LOQ = $10\sigma/s$).[30]

Accuracy testing was conducted on four epoxidized samples with different concentrations. As shown in Table 1, the proposed method gave results similar to those measured by AOCS Method Cd 9-57 (HBr method), with little bias and two-sample t tests showing no difference between the mean values determined by the HBr method and the proposed method for each sample (p value > 0.05). The precision of the proposed method (%RSD 1.33−3.73) was slightly poorer than that of the HBr method (%RSD 0.71−2.26), which was likely due to the errors introduced by manual integration of the ^{1}H NMR signals. The precision of both methods varied with concentration. Compared to the acceptable Horwitz %RSD values (2.65−4.88), the proposed method provided good precision (%RSD 1.33−3.73). Thus, quantitative NMR was shown to provide reliable results.

The objective of this work was to develop a quantitative method to determine epoxide content in oxidized oils for the study of lipid oxidation. Therefore, it was important to verify

DOI: 10.1021/acs.jafc.5b01719
J. Agric. Food Chem. 2015, 63, 5780−5786

the applicability of this method to thermally oxidized oils. The test of repeatability of the method was performed on five thermally oxidized soybean oil samples, which were heated at 100 °C for 4, 8, 12, 16, and 20 days (Table 2). There were contrasting patterns of PV and epoxide content with samples 1 and 2 (Table 2) having similar PVs (47.2 and 48.3 mmol/kg) but different epoxide contents (8.4 and 17.2 mmol/kg). Similarly, samples 3 and 4 (Table 2) had comparable PVs (89.1 and 87.6 mmol/kg) but very different epoxide contents (29.2 and 55.7 mmol/kg). The differing epoxide concentrations indicate that the two samples had undergone different oxidation processes, an observation that would be overlooked with just examination of PV. Thus, epoxide content provided a different evaluation of the extent of lipid oxidation compared to PV.

Compared to the HBr method,[2] the proposed method overcomes the problem of the interferences caused by other lipid oxidation products (α- or β-unsaturated carbonyls and conjugated dienes) when using the HBr method. Additionally, much less organic solvent is required for NMR analysis, because standardization of HBr solution is required before use of the reagent; the HBr method is also time-consuming. Compared to the previous methods of measuring epoxides, such as the NBP,[10] DTC,[11] and transmethylation[31] methods, the major advantage of quantitative NMR is its convenience. No derivatization is needed for analysis of epoxy compounds, and the preparation of an NMR sample is simple and rapid, making NMR a competitive approach to determine epoxides.

In this study, the *sn*-1,3 glycerol protons were taken as the internal standards instead of using the signals due to the residual chloroform[13] or the methyl protons.[14] As described earlier, methyl protons have limited applications as internal standards for oxidized oils, whereas the use of the residual solvent as standard may require external calibrants and special handling of the samples. Therefore, taking the signals related to the structure of triacylglycerol as internal standards can overcome these problems and still allow the sample to be recovered in its pure form, because no extra standard material is added. Unfortunately, information describing LOQ, accuracy, or precision was not provided in those previous studies,[13,14] so it is impossible to compare the performance of the proposed method with the previous methods in those aspects.

The method described here is an original approach; rather than spiking fully epoxidized soybean oil or epoxy fatty acid standards into samples, synthetic partially epoxidized oils (<10% double bonds were converted into epoxy groups) were used to establish a calibration curve. The synthetic epoxidized oils with low epoxide levels gave signals (2.90−3.10 ppm) similar to those derived from the oxidation process, making it possible to establish a calibration curve mimicking the real situation. The use of synthetic epoxidized oils as calibration standards has a number of advantages. First, commercial unsaturated epoxy fatty acid standards and diepoxide standards are only available as a limited number of structures. The proposed method utilizes commonly used reagents, hydrogen peroxide and formic acid, to synthesize partially epoxidized oils with remaining double bonds, which avoids the limitation of the commercially available standards. Second, the extent of epoxidation can be controlled by the amount of reagents used; therefore, the range of the concentrations encompassed by the calibration curve is adjustable. When epoxides are expected at a relatively low level, epoxy groups are likely surrounded by double bonds, and only a small amount of reagents is needed. When epoxides are expected at a high level, diepoxides can be synthesized by increasing the amount of epoxidation reagents. Third, the current epoxidation method can be easily applied to other kinds of oils,[20,22] so this method will have a wide range of applications.

Stability Study of Soybean Oil. To further study the formation of epoxides during lipid oxidation, a stability study of soybean oil was performed at 100 °C for 12 days. The curves representing PV and epoxide content showed different patterns over time, although deviations were observed between the three samples determined at each test point (RSD between 1.62 and 10.63% for PV and between 0.61 and 8.69% for epoxide content; Figure 3). PV increased quickly in the first 8 days and

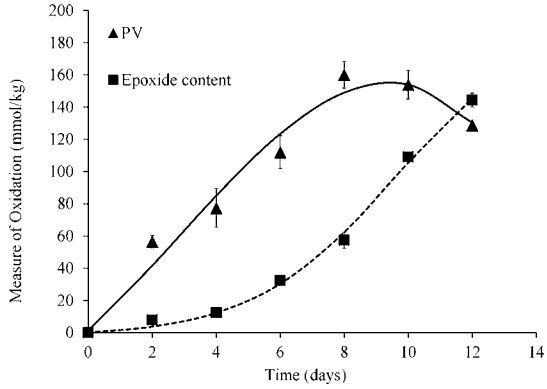

Figure 3. Peroxide value (PV) and epoxide content (mean ± standard deviation, n = 3 for each point) in the stability study of soybean oil performed at 100 °C with model 2 shown for PV and with model 3 for the epoxide content. See Table 3 for model parameters.

then reached a peak, followed by a slow decline. However, no significant increase was found for the epoxide content in the first 4 days. Epoxide content increased drastically after the lag time (days 0−4) and was not observed to decrease in the experimental period. Compared to the stability study of sunflower oil at 100 °C in the previous study,[13] lower amounts of epoxides were found in the soybean oil in this work. The two oils would have had different fatty acid compositions, which are well-known to influence the rate of formation and structure of lipid oxidation products. The surface area of oil during oxidation was also much greater in the previous work,[13] likely leading to a faster oxidation process.[32]

The PV and epoxide content were fitted by three selected models using the least-squares method (Table 3), including a second-order polynomial function, a third-order polynomial function, and a phenomenological model,[9] all in the variable t, which represented the days of thermal oxidation. The polynomial functions were selected because PV showed a significant decrease after the peak value. The phenomenological model was previously introduced for modeling PV because hydroperoxides are known as intermediates, forming and decomposing at the same time. The parameters of the phenomenological model, $a(T)$, $k_f(T)$, and $t_{cf}(T)$, were temperature dependent, related to the formation and decomposition of hydroperoxides as intermediate products of lipid oxidation.[9] In this work, this model was extensively fitted to the epoxide data because epoxides have also been considered as important intermediates.[7] The mean square error (MSE) of each regression was used as a measure of the goodness of fit (Table 3). Specifically, PV was fitted by the second-order model $y(t) = -1.44t^2 + 28.83t + 1.32$ with an MSE of 163.94,

DOI: 10.1021/acs.jafc.5b01719
J. Agric. Food Chem. 2015, 63, 5780−5786

Table 3. Fit of the Selected Mdels to PV and Epoxide Content Observed in the Stability Study of the Soybean Oil

model 1:	$y(t) = at^2 + bt + c$			
	a	b	c^a	MSE
PV	−1.44	28.83	1.32	163.94
epoxide content	1.10	−0.93	0.00	23.86
model 2:	$y(t) = at^3 + bt^2 + ct + d$			
	a	b	c	d^a	MSE
PV	−0.16	1.35	18.12	1.32	88.26
epoxide content	0.00[b]	1.08	−0.84	0.00	23.86
model 3:[c]	$y(t) = y_0 + [a(T) - y_0] \times \left\{\frac{1}{1+\exp\{k_f(T)[t_{cf}(T)-t]\}} - \frac{1}{1+\exp[k_f(T)t_{cf}(T)]}\right\}$			
	$a(T)$	$k_f(T)$	$t_{cf}(T)$	MSE
PV	204.15	0.47	2.17	220.47
epoxide content	199.37	0.45	9.62	10.31

[a]This constant was determined by the PV or epoxide content measured on the initial day (day 0). [b]The value was 0.0014 in four

whereas the epoxide content was fitted by $y = 1.10t^2 - 0.93t$ with an MSE of 23.86. Increased order of polynomial function contributed to the lowest MSE for PV (MSE of 88.26 for the third-order model) but resulted in the same MSE for epoxide content (MSE of 23.86 for the third-order model) so a third-order model was not necessary for epoxides. In addition, PV and epoxide content were fitted by the phenomenological model (model 3 in Table 3), where the fit of PV gave a large MSE (MSE of 220.47), but the best fit was observed for the epoxide content (MSE of 10.31). Therefore, model 2, employing a third-order polynomial, was suggested for PV, whereas model 3, the phenomenological model, was best for epoxides (Figure 3). Further studies can be conducted to allow the model to be adapted to the formation of epoxides at different temperatures.

Although the physical meanings of these models are not discussed here, it is obvious that the curves of epoxide concentrations and PV show very different trends, indicating that the rearrangement of radicals is an important reaction during lipid oxidation and should be taken into consideration when monitoring the oxidation process. Epoxides are important lipid oxidation products, produced in large concentrations under the condition of this study, and their formation has a lag time in the initial period of lipid oxidation. As an additional indicator of oxidation, epoxide content provided more information about the extent of the process, which may enable a more comprehensive understanding of the mechanisms of lipid oxidation. With appropriate validation, this ^{1}H NMR technique should be easily applied to other oils.

■ ASSOCIATED CONTENT

Supporting Information

Integrals of the relevant signals in Figure 1 by taking the *sn*-1,3 glycerol protons as the internal standard (4.00), where overlapped peaks are deconvolved with Lorentzian line shapes. The Supporting Information is available free of charge on the ACS Publications website at DOI: 10.1021/acs.jafc.5b01719.

■ AUTHOR INFORMATION

Corresponding Author

*(W.X.) Mail: Department of Process Engineering and Applied Science, Dalhousie University, 1360 Barrington Street, Halifax, NS B3H 4R2, Canada. E-mail: wei.xia@dal.ca. Phone: (902) 494-6015.

Funding

This work was supported by a Natural Sciences and Engineering Research Council of Canada Discovery Grant to S.M.B.

Notes

The authors declare no competing financial interest.

■ REFERENCES

(1) Barriuso, B.; Astiasarán, I.; Ansorena, D. A review of analytical methods measuring lipid oxidation status in foods: a challenging task. *Eur. Food Res. Technol.* **2013**, *236*, 1−15.

(2) American Oil Chemists' Society. *Official Methods and Recommended Practices of the AOCS*, 6th ed.; Firestone, D., Ed.; American Oil Chemists' Society Press: Urbana, IL, USA, 2009.

(3) Shahidi, F.; Zhong, Y. Lipid oxidation and improving the oxidative stability. *Chem. Soc. Rev.* **2010**, *39*, 4067.

(4) Belingheri, C.; Giussani, B.; Rodriguez-Estrada, M. T.; Ferrillo, A.; Vittadini, E. Oxidative stability of high-oleic sunflower oil in a porous starch carrier. *Food Chem.* **2015**, *166*, 346−351.

(5) Frankel, E. N. Chemistry of free radical and singlet oxidation of lipids. *Prog. Lipid Res.* **1984**, *23*, 197−221.

(6) Yin, H.; Xu, L.; Porter, N. A. Free radical lipid peroxidation: mechanisms and analysis. *Chem. Rev.* **2011**, *111*, 5944−5972.

(7) Schaich, K. M. Thinking outside the classical chain reaction box of lipid oxidation. *Lipid Technol.* **2012**, *24*, 55−58.

(8) Calligaris, S.; Manzocco, L.; Conte, L. S.; Nicoli, M. C. Application of a modified Arrhenius equation for the evaluation of oxidation rate of sunflower oil at subzero temperatures. *J. Food Sci.* **2004**, *69*, E361−E366.

(9) Aragao, G. M. F.; Corradini, M. G.; Peleg, M. A phenomenological model of the peroxide value's rise and fall during lipid oxidation. *J. Am. Oil Chem. Soc.* **2008**, *85*, 1143−1153.

(10) Hammock, L. G.; Hammock, B. D.; Casida, J. E. Detection and analysis of epoxides with 4-(*p*-nitrobenzyl)-pyridine. *Bull. Environ. Contam. Toxicol.* **1974**, *12*, 759−764.

(11) Dupard-Julien, C. L.; Kandlakunta, B.; Uppu, R. M. Determination of epoxides by high-performance liquid chromatography following derivatization with *N*,*N*-diethyldithiocarbamate. *Anal. Bioanal. Chem.* **2007**, *387*, 1027−1032.

(12) Velasco, J.; Marmesat, S.; Bordeaux, O.; Márquez-Ruiz, G.; Dobarganes, C. Formation and evolution of monoepoxy fatty acids in thermoxidized olive and sunflower oils and quantitation in used frying oils from restaurants and fried-food outlets. *J. Agric. Food Chem.* **2004**, *52*, 4438−4443.

(13) Goicoechea, E.; Guillen, M. D. Analysis of hydroperoxides, aldehydes and epoxides by ^{1}H nuclear magnetic resonance in sunflower oil oxidized at 70 and 100 °C. *J. Agric. Food Chem.* **2010**, *58*, 6234−6245.

(14) Aerts, H. A. J.; Jacobs, P. A. Epoxide yield determination of oils and fatty acid methyl esters using ^{1}H NMR. *J. Am. Oil Chem. Soc.* **2004**, *81*, 841−846.

(15) Pauli, G. F.; Gödecke, T.; Jaki, B. U.; Lankin, D. C. Quantitative ^{1}H NMR. Development and potential of an analytical method: an update. *J. Nat. Prod.* **2012**, *75*, 834−851.

(16) Schaich, K. M. Lipid oxidation: theoretical aspects. In *Bailey's Industrial Oil and Fat Products*; Wiley: New York, 2005.

(17) Guillén, M. D.; Uriarte, P. S. Contribution to further understanding of the evolution of sunflower oil submitted to frying temperature in a domestic fryer: study by ^{1}H nuclear magnetic resonance. *J. Agric. Food Chem.* **2009**, *57*, 7790−7799.

DOI: 10.1021/acs.jafc.5b01719
J. Agric. Food Chem. 2015, 63, 5780−5786

(18) Global Organization for EPA and DHA Omega-3s. GOED Voluntary Monograph (v. 4); http://www.goedomega3.com/index.php/files/download/155 (accessed April 2, 2015).
(19) Sullivan, J. C.; Budge, S. M.; St-Onge, M. Modeling the primary oxidation in commercial fish oil preparations. *Lipids* **2011**, *46*, 87−93.
(20) Dinda, S.; Patwardhan, A. V.; Goud, V. V.; Pradhan, N. C. Epoxidation of cottonseed oil by aqueous hydrogen peroxide catalysed by liquid inorganic acids. *Bioresour. Technol.* **2008**, *99*, 3737−3744.
(21) Mudhaffar, B.; Salimon, J. Epoxidation of vegetable oils and fatty acids: catalysts, methods and advantages. *J. Appl. Sci.* **2010**, *10*, 1545−1553.
(22) Anuar, S. T.; Zhao, Y. Y.; Mugo, S. M.; Curtis, J. M. Monitoring the epoxidation of canola oil by non-aqueous reversed phase liquid chromatography/mass spectrometry for process optimization and control. *J. Am. Oil Chem. Soc.* **2012**, *89*, 1951−1960.
(23) Guillén, M. D.; Ruiz, A. Study of the oxidative stability of salted and unsalted salmon fillets by ^{1}H nuclear magnetic resonance. *Food Chem.* **2004**, *86*, 297−304.
(24) Mo, H.; Harwood, J. S.; Raftery, D. Receiver gain function: the actual NMR receiver gain. *Magn. Reson. Chem.* **2010**, *48*, 235−238.
(25) Malz, F.; Jancke, H. Validation of quantitative NMR. *J. Pharm. Biomed. Anal.* **2005**, *38*, 813−823.
(26) Thompson, M.; Ellison, S. L. R.; Wood, R. Harmonized guidelines for single-laboratory validation of methods of analysis (IUPAC Technical Report). *Pure Appl. Chem.* **2002**, *74*, 835−855.
(27) Boyer, K. W.; Horwitz, W.; Albert, R. Interlaboratory variability in trace element analysis. *Anal. Chem.* **1985**, *57*, 454−459.
(28) Mubiru, E.; Shrestha, K.; Papastergiadis, A.; De Meulenaer, B. Development and validation of a gas chromatography−flame ionization detection method for the determination of epoxy fatty acids in food matrices. *J. Agric. Food Chem.* **2014**, *62*, 2982−2988.
(29) Martínez-Yusta, A.; Goicoechea, E.; Guillén, M. D. A review of thermo-oxidative degradation of food lipids studied by ^{1}H NMR spectroscopy: influence of degradative conditions and food lipid nature. *Compr. Rev. Food Sci. Food Saf.* **2014**, *13*, 838−859.
(30) Shrivastava, A.; Gupta, V. Methods for the determination of limit of detection and limit of quantitation of the analytical methods. *Chron. Young Sci.* **2011**, *2*, 21−25.
(31) Mubiru, E.; Shrestha, K.; Papastergiadis, A.; De Meulenaer, B. Improved gas chromatography-flame ionization detector analytical method for the analysis of epoxy fatty acids. *J. Chromatogr., A* **2013**, *1318*, 217−225.
(32) Damodaran, S.; Parkin, K.; Fennema, O. R. *Fennema's Food Chemistry*, 4th ed.; CRC Press/Taylor & Francis: Boca Raton, FL, USA, 2008.

DOI: 10.1021/acs.jafc.5b01719
J. Agric. Food Chem. 2015, 63, 5780−5786

oxide could be detected in areca nut extract (ANE)-treated oral cells. We therefore chemically synthesized arecoline *N*-oxide and investigated its effects on normal human cells and immunodeficient NOD/SCID mice. Our study unearthed clues about how areca nut induces OMPD. This study also increases our understanding of the mechanism by which betel chewing may lead to tumorigenesis.

MATERIALS AND METHODS

Cell Culture and Treatment. Normal human gingival fibroblast cells (HGF-1, CRL-2014) were obtained from American Type Culture Collection (ATCC, Manassas, VA, USA)/Bioresource Collection and Research Center (BCRC, Taipei, Taiwan). Cells were grown and maintained in Dulbecco's modified Eagle's medium (DMEM), supplemented with 10% fetal bovine serum, at 37 °C in a 5% CO_2 incubator. Normal human oral keratinocyte HOK cells purchased from ScienCell Research Laboratories (Carlsbad, CA, USA) were cultured in the oral keratinocyte growth medium (ScienCell Research Laboratories). For identifying the protein adducts of the areca nut in HOK cells, equal amounts of cells were treated with 200 μg/mL ANE or saliva-contained ANE for 24 h. For determination of DNA damage or fibrotic related genes, equal amounts of HGF-1 cells were seeded and grown until confluent for chemical treatment, avoiding strong cytotoxicity via arecoline or arecoline *N*-oxide. Cells were then treated with arecoline or arecoline *N*-oxide for 7 days. The culture medium was refreshed every 2 days during the experiment.

Chemicals. ANE or saliva-contained ANE were prepared as previously described.[11] Arecoline hydrobromide was purchased from Sigma-Aldrich (St. Louis, MO, USA). Arecoline *N*-oxide was synthesized as previously described.[10a] In brief, a solution of arecoline in ether was treated with aqueous 3 M peroxyacetic acid (1.95 g in 13 mL of H_2O) dropwise during 30 min at 0 °C. After 2 h, the oily lower layer was separated and then precipitated three times by the addition of ether, which concentrated under reduced pressure to afford arecoline *N*-oxide as a pale yellow viscous oil. The synthesized chemical has been confirmed by high-resolution mass spectrometry and NMR analysis. The used arecoline *N*-oxide was dissolved in 0.1% DMSO/deionized water.

Identification of Protein Adducts in HOK Cells. Protein adducts from ANE-exposed cells were identified using the LC-MS/MS system (LTQ Orbitrap Discovery hybrid Fourier transform mass spectrometer; Thermo Fisher Scientific Inc., Germany) as previously described.[12] The raw data files from each treated cell were processed with Proteome Discoverer 1.1 software (Thermo Scientific) to gain the file of peak lists. Protein identification was analyzed by an in-house Mascot server.

Cytotoxicity Detection. To measure the cytotoxicity, 10^4 HGF-1 cells were seeded into 96-well culture plates and cultured for 24 h for arecoline or arecoline *N*-oxide treatment. The released lactate dehydrogenase (LDH) in the culture medium was assessed using a LDH assay (CytoTox-ONE Homogeneous Membrane Integrity Assay, Promega, Madison, WI, USA).

Animals and Experimental Protocol. In this study, the experimental animals used were 10-week-old NOD.CB17-*Prkdc*^{scid}/NcrCrl (NOD SCID Mouse) animals purchased from LASCO Charles River Technology (Taiwan) and then maintained in a specific pathogen-free environment. In the present study, animal procedures conformed to the guidelines published by the National Institutes of Health (NIH Publication No. 85-23) and were approved by the Institutional Animal Care and Use Committee (IACUC) of China Medical University (CMU). The mice (each weighing approximately 28 g) were randomly divided into two groups. Group 1 (the control group, $n = 8$) was treated with 0.1% DMSO/deionized water by cotton swab smearing the oral cavity once daily, 5 days per week. Group 2 ($n = 12$) was treated with 500 μg/mL arecoline *N*-oxide dissolved in 0.1% DMSO/deionized water in the same manner. During treatment, a standard laboratory diet and water were offered to all mice.

Real-Time Quantitative PCR (RT-qPCR). Total RNA was isolated from treated cells using TRIzol reagent (Invitrogen Corp., Carlsbad, CA, USA) according to the manufacturer's protocol. The cDNA templates were produced by reverse transcription of the total RNA with random primer and a high-capacity cDNA reverse transcription kit (Applied Biosystems, Foster City, CA, USA). The products were then subjected to RT-qPCR analysis with the specific primer pairs using the ABI StepOnePlus Real-Time PCR Systems (Applied Biosystems) with Power SYBR Green PCR Master Mix (Invitrogen Corp.). The primer sequences are listed in Table S1.

Western Blotting. To detect H2A.X phosphorylation, the cells were lysed in lysis buffer A (50 mM Tris-HCl, pH 7.4, 100 mM NaCl, 1 mM EDTA, 10 mM magnesium acetate, and 1% NP-40) containing a cocktail of protease inhibitors (Roche, Germany) on ice for 10 min. The extracts were centrifuged at 15600*g* for 5 min at 4 °C to sediment the insoluble fraction. The pellet was resuspended in lysis buffer A and mixed with an equal volume of 4× Laemmli's sample buffer. Sample loading of the insoluble fraction was normalized by protein concentration of the soluble fraction. Protein samples from both the soluble (for GAPDH) and insoluble (for H2A.X phosphorylation) fractions were separated by SDS−polyacrylamide gel and electro-transferred to polyvinylidene fluoride membranes (Millipore, Bedford, MA, USA). The membranes were incubated with primary antibodies as indicated and peroxidase-conjugated secondary antibodies, and protein signals were detected by enhanced chemiluminescence reagent (Millipore). For detection of collagen 1, cell lysates were prepared in lysis buffer B (50 mM Tris-HCl, pH 7.4, 100 mM NaCl, 1 mM EDTA, 10 mM magnesium acetate, 1% Triton X-100, and protease inhibitors cocktail). Monomeric collagen 1 was detected using a denaturing polyacrylamide gel electrophoresis (PAGE). To ensure equal loading, Western blotting was performed by using a denatured PAGE with double layers (6 and 9%) for separation. For detection of polymeric collagen, total protein (120 μg) was separated by nonreducing PAGE. The primary antibodies used were antiphospho-histone H2A.X (Ser139; Cell Signaling Technology), anticollagen 1 (St. John's Laboratories, United Kingdom), and anti-GAPDH (GeneTex Inc., Taiwan).

Immunohistochemistry Analysis. Tongue tissue samples from all 20 treated mice of 21 weeks were fixed with 4% paraformaldehyde for 3 days, embedded in paraffin. The 3−5 μm sections were stained with hematoxylin and eosin (H&E), specific antibodies, and Masson's trichrome for histological evaluation and scoring. Immunohistochemical detection of mouse H2A.X phosphorylation (gamma-H2A.X) was performed using the antiphospho-histone H2A.X (Ser139; Cell Signaling Technology) antibody. The protein signal was detected using the appropriate primary antibody amplifier, horseradish peroxidase (HRP)-conjugated polymer, and DAB chromogen/substrate. The positive signals of gamma-H2A.X were counted in a high-power field (200× magnification) in five mice from each group. The results were averaged, the numbers from 60 cells per fS randomly selected sublingual positions each mouse. A trichrome stain for assessment of fibrosis was performed by using a Trichrome Modified Masson's Stain Kit (Scytek Laboratories, Logan, UT, USA) according to the manufacturer's instructions. Tongue fibrosis sections were counted and scored under 50× magnification of five separated fields of three mice per group. The quantification was used by the Fovea Pro 3.0 and OptiPix 2.0 free Wide Histogram Photoshop plug-in software. In this study, results of all immunohistochemical were interpreted by two pathologists.

RESULTS

Detection of Arecoline *N*-Oxide Protein Adduct in Cultured Oral Keratinocytes. Diseases caused by chemical exposure have been demonstrated through the metabolism of chemically bound products, such as DNA or protein adducts.[9a] To confirm the possibility of arecoline *N*-oxide presence in oral cells exposed to areca nuts, normal HOK cells were stimulated with ANE or saliva-contained ANE, and protein samples from the cell lysate were assayed to identify protein adducts (Table 1). The protein adduct of arecoline *N*-oxide-bound annexin A1

DOI: 10.1021/acs.jafc.5b01351
J. Agric. Food Chem. 2015, 63, 5787−5794

Table 1. Identification of Areca Nut Related Protein Adduct in HOK Cells by LTQ Orbitrap

treatment	protein name (accession no.)	peptide sequence[a]
ANE	myosin gil531138	arecaidine **I**VEANPLLEAFGNAK
	S100a6 gil20664042	arecaidine *N*-oxide **A** EPLDQAIGLLVAIFHK
	beta-actin gil62897625	arecaidine *N*-oxide **LC**YVALDFEQEMATAASSSSLEK[b]
saliva-ANE	myosin gil531138	arecaidine **I**VEANPLLEAFGNAK
	S100a6 gil20664042	arecaidine *N*-oxide **A**EPLDQAIGLLVAIFHK
	annexin A1 gil4502101	arecoline *N*-oxide **D**LAKDITSDTSGDFR

[a]Chemically bound amino acids are shown in bold and underlined. [b]Both arecaidine *N*-oxide bound leucine 215 and cysteine 216 of beta-actin were identified.

was identified in the saliva-contained ANE-treated HOK cells. Products of arecaidine and arecaidine *N*-oxide bound proteins were also detected. These results indicated the presence of arecoline *N*-oxide in oral cells exposed to areca nuts.

Arecoline *N*-Oxide Increased Oral Collagen Deposition in Mice. Protein or DNA targets of arecoline *N*-oxide remain uncharacterized. Because the effects of arecoline *N*-oxide might result from multiple DNA or protein adducts in vivo, we investigated its effects by treating it directly. Commercial arecoline *N*-oxide is rarely obtained. Hence, we produced arecoline *N*-oxide chemically. We tested whether arecoline *N*-oxide can cause oral pathological changes in NOD/SCID mice. The immunodeficiency NOD/SCID mice were used as a model to avoid antitumor immune response.

The average body weight of the mice, in both arecoline *N*-oxide and control groups, slightly increased during the 21 weeks of treatment. The average increases in body weight in the control and arecoline *N*-oxide-treated mice were 1.08 and 1.1%, respectively. No tumor formation was observed in the exterior alimentary canal. An increase in collagen synthesis is a main cause of OSF.[13] To assess whether arecoline *N*-oxide enhanced collagen expression, tongue specimens were examined, and collagen deposition was found to be significantly higher in arecoline *N*-oxide-treated mice than in control mice with obvious observation in sublingual tongue (Figure 1A,B and Figure S1). Quantitative analysis of staining intensity and percentage indicated that arecoline *N*-oxide-treated mice showed a 1.97-fold increase in collagen deposition on the tongue. These results suggest that oral fibrotic potential is shown in arecoline *N*-oxide-treated mice.

Pathologic changes in all mouse tongues were observed by H&E staining (Figure 1C,D). The arecoline *N*-oxide-treated group showed significant pathologic hyperplastic lesions in the epithelium of the sublingual tongue (Figure 1D). In contrast, control groups showed mild pathologic change of hyperplasia (Figure 1C), which might be due to long-term exposure to a low concentration of DMSO. No pathologic changes were observed in the upper surface of the tongue in both groups. These results indicate that arecoline *N*-oxide increased the severity of squamous hyperplasia in the sublingual tongue.

Arecoline *N*-Oxide Increased Expression of Collagen 1. Our mouse experiment indicated that arecoline *N*-oxide induced oral collagen deposition, which implies that arecoline *N*-oxide has fibrotic potential.[7a] Next, we tested the fibrotic related effects of arecoline *N*-oxide in cultured HGF-1 cells. During betel chewing, the concentration of arecoline in saliva can reach as much as 97.39 μg/mL (about 600 μM).[14] First, we compared the cytotoxicity between arecoline and arecoline *N*-oxide by determining the LDH release in cells treated with various concentrations of arecoline or arecoline *N*-oxide. Indeed, cytotoxicity was induced in both treatment groups (Figure 2A). Arecoline *N*-oxide induced higher LDH release than arecoline, with a significant effect observed at a concentration of 400 μM (1.44-fold, $p < 0.05$, vs arecoline). Taken together, these results indicate that arecoline *N*-oxide induced stronger cytotoxicity than arecoline.

To ascertain if arecoline *N*-oxide stimulation increases collagen 1 production, confluent HGF-1 cells were treated with arecoline *N*-oxide for 7 days and then analyzed for levels of collagen 1 mRNA (Figure 2B) and protein (Figure 2C,D). Arecoline *N*-oxide significantly increased the expression of collagen 1 mRNA and protein, and significant induction was observed at both 200 and 400 μM concentrations, respectively. These results indicate that arecoline *N*-oxide increased collagen 1 production in HGF-1 cells, which corresponded to the observations of our mouse study.

Arecoline *N*-Oxide Increases the Expression of Oral Fibrotic Related Genes. TGF-beta 1 is a well-known fibrotic signaling molecule that is increased in OSF tissues.[15] The effects of arecoline *N*-oxide on *TGF-beta1* induction in HGF-1 cells were estimated by RT-qPCR. Both arecoline and arecoline *N*-oxide significantly increased the mRNA of *TGF-beta1* (Figure 3 **A**). The effect of arecoline *N*-oxide was significantly higher than that of arecoline (at both 200 and 400 μM, $p < 0.05$). A series of oral precancerous related gene transcripts were also examined. These genes included *S100A4*,[16] *matrix metalloproteinase-9* (*MMP-9*),[17] *interleukin-6* (*IL-6*),[18] *fibronectin*,[19] *E-cadherin*,[20] and *alpha-smooth muscle actin* (*alpha-SMA*)[21] (Figure 3B−F and Figure S3). Arecoline *N*-oxide significantly stimulated increased expression of *S100A4, MMP-9, IL-6, fibronectin*, and *alpha-SMA*. It also reduced the level of *E-cadherin* mRNA. These results correlate with previous observations of genetic regulation in OSF. Arecoline *N*-oxide showed higher activity than arecoline in its effects on the expression of these genes expect *alpha-SMA* (at 400 μM, $p < 0.05$, vs arecoline). Thus, arecoline *N*-oxide may be a causative agent of OSF.

Arecoline *N*-Oxide Increased H2A.X Phosphorylation. DNA damage is triggered early in tumorigenesis. To compare the effect on DNA damage, phosphorylation of histone H2A.X at serine (Ser) 139 (also called gamma-H2A.X), a marker of DNA double-strand breaks,[22] was determined in confluent cells after 7 days of treatment. Whereas a slight effect of arecoline was observed, arecoline *N*-oxide significantly induced gamma-H2A.X (Figure 4A,B). At arecoline *N*-oxide concentrations of 200 and 400 μM, levels of gamma-H2A.X increased 4.32- and 5.13-fold, respectively, as compared with the control. Arecoline *N*-oxide showed higher activity than arecoline at an equal concentration (at both 200 and 400 μM, $p < 0.05$). Similar results were shown when we measured 8-OHdG, another

DOI: 10.1021/acs.jafc.5b01351
J. Agric. Food Chem. 2015, 63, 5787−5794

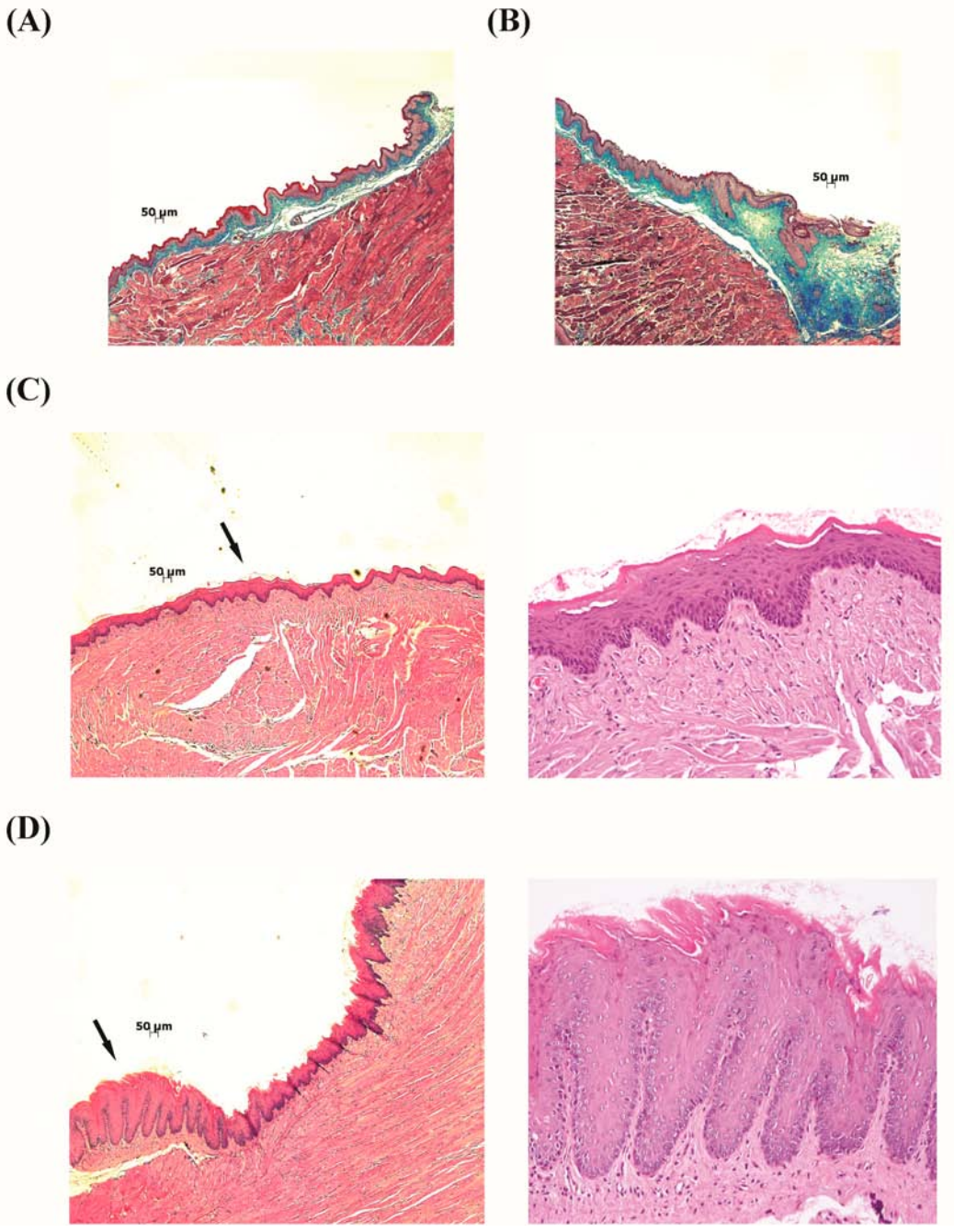

Figure 1. Arecoline *N*-oxide increased collagen deposition and severity of squamous hyperplasia in mouse tongue. Mice were consecutively treated with arecoline *N*-oxide (500 μg/mL) for 21 weeks. Tongues were stained with Masson's trichrome staining in control (A) and arecoline *N*-oxide groups (B). Sublingual tongues are shown (magnification, 50×; scale bar, 50 μm). Pathological changes of sublingual tongue samples from the control (C) and arecoline *N*-oxide groups (D) were visualized by H&E staining. Indicated areas in left panels (black arrowheads, magnification, 50×) were observed under higher magnification (200×). Scale bar, 50 μm.

marker for oxidative stress and DNA damage (Figure S2). Our data indicated that arecoline *N*-oxide induced gamma-H2A.X in HGF-1 cells. Therefore, immunostaining of tongue sections from each mouse group using the anti-gamma-H2A.X antibody was performed (Figure 4C,D). Significant expression of gamma-H2A.X was detected in the cells of the sublingual tongue in the arecoline *N*-oxide group (10.93-fold, $p < 0.05$, vs the control group), indicating that DNA damage occurred in this region. Taken together, these data indicate that arecoline *N*-oxide induced DNA damage response in vitro and in vivo.

DISCUSSION

Arecoline *N*-oxide was first identified as a metabolite of arecoline in rat urine in 1971.[10a] A later study also identified it in mouse urine, which indicates that it is a major metabolite of arecoline.[23] The metabolic interconversion between arecoline, arecaidine, arecoline *N*-oxide, and arecaidine *N*-oxide has been suggested.[10b,23] Previous study showed that arecoline was converted to arecoline *N*-oxide by the human flavin-containing monooxygenases FMO1 and FMO3.[10b] The FMO1 and FMO3 are predominantly expressed in kidney or liver.[24] In the present study, we identified arecoline *N*-oxide in ANE-treated human

DOI: 10.1021/acs.jafc.5b01351
J. Agric. Food Chem. 2015, 63, 5787−5794

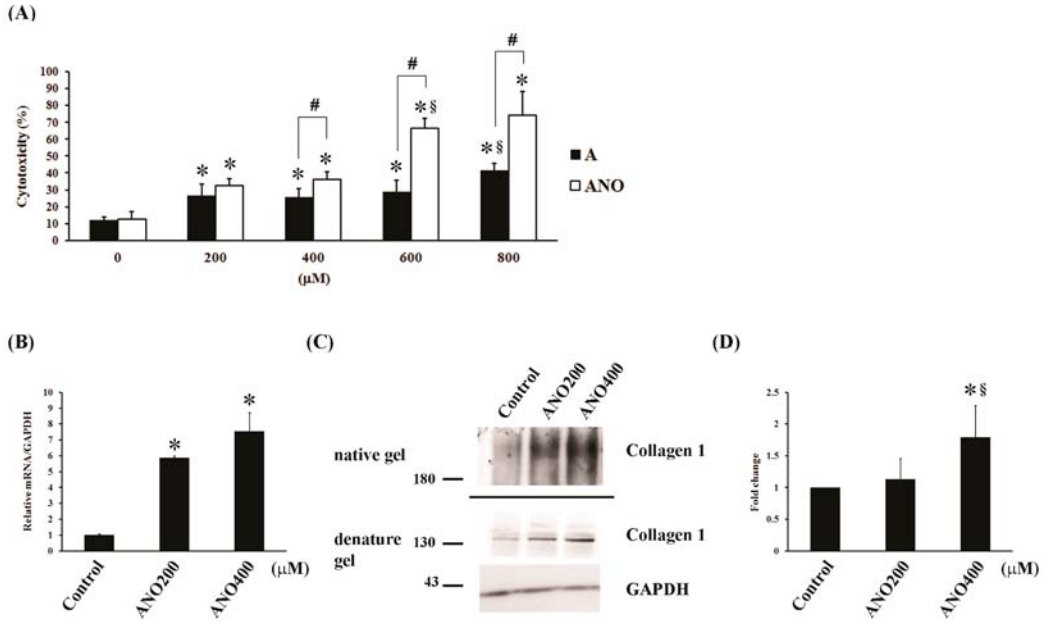

Figure 2. Arecoline *N*-oxide increased the expressions of collagen 1. (A) Arecoline *N*-oxide induced cytotoxicity in HGF-1 cells. HGF-1 cells (10^4) in a 96-well plate were exposed to arecoline (abbreviated A) or arecoline *N*-oxide (abbreviated ANO) for 24 h. Cytotoxicity was measured by LDH assay. (B–D) Arecoline *N*-oxide increased the expression of collagen 1. Confluent cells were treated with arecoline *N*-oxide for 7 days. (B) Transcripts of collagen 1 were measured by qRT-PCR. (C) Protein expression of collagen 1 was confirmed by Western blotting of collagen 1 in native (for polymer, upper panel) and denatured (for monomer, lower panel) PAGE gels. (D) An increased effect on collagen 1 is plotted on a bar graph. Signals of collagen 1 were quantified by densitometry analysis. For panels A, B, and D, the graphs represent mean (±SD) values of three or more independent experiments. (∗) $p < 0.05$ compared with cells without arecoline or arecoline *N*-oxide stimulation; (#) $p < 0.05$, arecoline *N*-oxide group compared to arecoline; (§) $p < 0.05$, compared to the last dose of the same chemical.

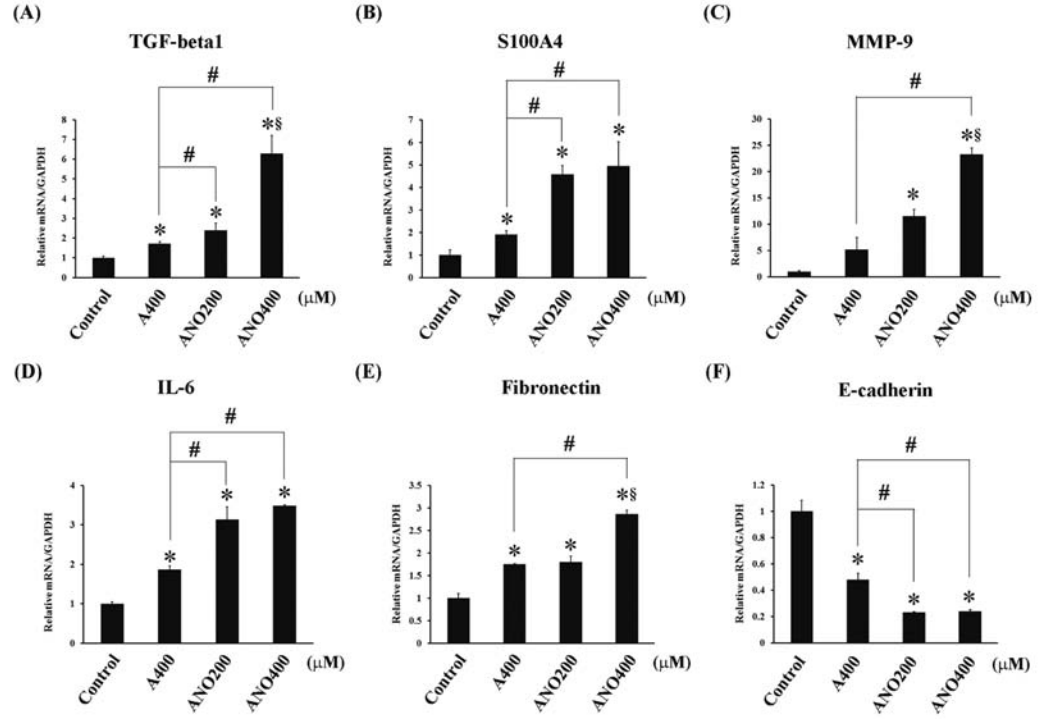

Figure 3. Arecoline *N*-oxide increased the levels of oral fibrotic related gene transcripts. Confluent HGF-1 cells were treated with arecoline (abbreviated A) or arecoline *N*-oxide (abbreviated ANO) for 7 days. Transcripts of *TGF-beta1* (A), *S100A4* (B), *MMP-9* (C), *IL-6* (D), *fibronectin* (E), and *E-cadherin* (F) were measured by qRT-PCR. The graphs represent mean (±SD) values, and each experiment was performed more than three times in triplicate. (∗) $p < 0.05$ compared with control cells; (#) $p < 0.05$, arecoline *N*-oxide group versus arecoline; (§) $p < 0.05$, arecoline *N*-oxide 400 μM versus arecoline *N*-oxide 200 μM.

DOI: 10.1021/acs.jafc.5b01351
J. Agric. Food Chem. 2015, 63, 5787–5794

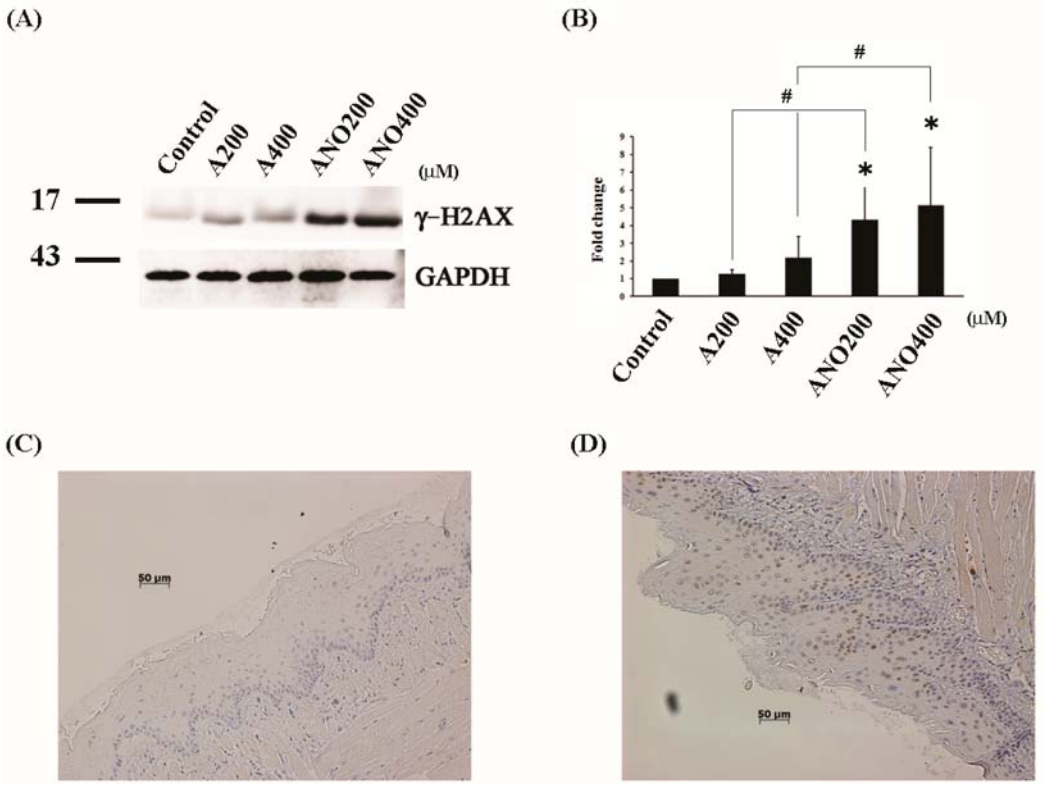

Figure 4. Arecoline *N*-oxide induced gamma-H2A.X in HGF-1 cells and mice. (A) Gamma-H2A.X (γ-H2AX) protein expression was detected by Western blotting in confluent cells treated with arecoline or arecoline *N*-oxide for 7 days. (B) Induction effect on gamma-H2A.X is plotted on a bar graph. Signals of gamma-H2A.X were quantified by densitometry analysis and expressed as average percentage of respective control cells. Results depict mean (±SD) of three independent experiments. (∗) $p < 0.05$ compared with cells without arecoline or arecoline *N*-oxide stimulation; (#) $p < 0.05$, arecoline *N*-oxide group versus arecoline. Arecoline *N*-oxide induced expression of gamma-H2A.X in mice. Immunohistochemical expression of gamma-H2A.X in sublingual tongue samples from the control (C) and arecoline *N*-oxide groups (D). Magnification, 200×.

oral cells. Our data indicated effective cytotoxicity, genotoxicity, and fibrotic gene regulation and increased pathological changes induced by arecoline *N*-oxide. Because arecoline *N*-oxide showed a potential influence on tumorigenesis, it is reasonable to suspect that the toxicity of the areca nut on oral tumorigenesis might be dependent on the cellular amount of its metabolites. Hence, cellular conditions affecting the metabolism of areca nut might play a key role in the occurrence of oral carcinogenesis via betel chewing.

To test whether the constituents of the areca nut enhance oral tumorigenesis or cause precancerous lesions in vivo, numerous studies have treated experimental animals with areca nut or arecoline through diet, drinking water, or intraperitoneal injection. Mice treated with areca nut or arecoline showed higher gene mutation frequency and mutations in *BRCA1*.[25] Lung adenocarcinoma, stomach squamous cell carcinoma, testicular lymphoma, and liver hemeangioma induced in areca nut-stimulated animals have also been studied.[26] In one study focused on the induction of oral lesions or tumor formation, cotreatment with arecoline and 4-NQO of tobacco-related carcinogen induced tongue tumors in mice; however, arecoline alone did not induce any oral pathological lesions.[27] In addition, 3-(methymitrosamino)propionitriIe (MNPN) and *N*-(nitrosomethylamino)propionitrile (NMAP), lime-enhancing synthesized derivatives from the areca nut in saliva, showed lower effects on tumor induction in the oral cavity of rats.[28] Although a strong association between oral precancer or cancer and betel chewing has been demonstrated,[3] the results from multiple animal studies have not proven that there is a link. Differences affecting the metabolism of areca nut, such as oral condition or genetic background, might lead to different outcomes in humans and other experimental animals during areca nut exposure. Areca nut might show a higher potential for oral tumorigenesis in humans than in other experimental animals.

It has been reported that *N*-oxide derivatives of various chemicals show DNA binding activity or reaction with cellular ion containing enzymes. Formation of DNA and protein adducts is central to tumorigenesis via environmental chemicals, such as tobacco or alcohol.[29] Recently, we established a screening platform for identifying protein adducts in samples exposed to arecoline and arecaidine.[12] In this study, protein adducts of ANE in culture keratinocytes were identified (Table 1). Myosin and beta-actin are abundantly expressed in most types of cells, which might be easy binding targets for chemicals. In contrast, they are important cell regulators. It has been shown that some adducts to abundantly expressed proteins, such as antibodies or tubulins, are involved in the immune response or drug sensitivity.[30] Most importantly, the *N*-oxide derivatives from the areca nut, arecoline *N*-oxide and arecaidine *N*-oxide, exist in areca nut exposed oral cells. The influence of those metabolites on diseases requires further investigation.

Both the areca nut and arecoline have been reported to induce DNA damage. Both of these molecules have been suggested as a cause of oral cell carcinogenesis.[6c] In this study, we used gamma-H2A.X as a marker to determine genotoxicity via arecoline *N*-oxide (Figure 4). When DNA damage occurs,

DOI: 10.1021/acs.jafc.5b01351
J. Agric. Food Chem. 2015, 63, 5787−5794

the histone H2AX is rapidly phosphorylated at Ser 139 (gamma-H2A.X). This process is involved in the DNA double-strand break repair pathway.[22b] Oxidative stress via the areca nut and arecoline is the main pathway causing DNA damage.[6c] Therefore, *N*-oxide derivatives of the areca nut might induce strong oxidative stress. Gamma-H2A.X was reported as an independent prognostic marker in oral squamous cell carcinoma, which is associated with reduced overall survival time.[22a] Here, we suggest that it might be a marker of the incidence of malignant transformation in OPMD. To avoid strong side effects via other solvents, we used a lower concentration (0.1%) of DMSO to dissolve the arecoline *N*-oxide. However, our results suggested that arecoline *N*-oxide increased the severity of hyperplasia (Figure 1), which is based on the observation of mild hyperplasia in the 0.1% DMSO treated group (the control group). DMSO induced the proliferation of human gingival fibroblasts[31] and sebaceous hyperplasia.[32] Thus, the trace of hyperplasia in the control group is most likely due to DMSO. OSF is a precancerous condition with high collagen expression in oral carcinogenesis. It is a chronically insidious oral mucosal condition, with submucosal fibrosis affecting the oral cavity, pharynx, and esophagus.[13] TGF-beta is well-known as a potent stimulator of the production and deposition of collagen.[33] The areca nut increases collagen accumulation and activates the TGF-beta signaling pathway. Our data also showed an increase in collagen and TGF-beta production by arecoline *N*-oxide, which suggests that arecoline *N*-oxide may be an inducer of OSF. Interestingly, most of the effects of arecoline *N*-oxide were observed in the regions located in the sublingual space below the tongue, possibly due to longer chemical exposure time in that area than in other areas of mouth. In addition, these chemicals might also react with saliva for longer periods of time, which implies that there are more toxic derivatives being produced.

The presence of arecoline *N*-oxide in saliva during betel chewing has not been studied to our knowledge. Arecoline concentration in the saliva can reach around 600 μM.[14] Although the cellular concentration of arecoline *N*-oxide is unclear, our results indicate that fibrotic gene regulation was induced by 200 μM arecoline *N*-oxide (Figure 3). In addition to arecoline, other alkaloids of the areca nut might also metabolically convert to *N*-oxide products, which can also induce oral fibrosis or tumorigenesis. The inhibitory effects on mutagenicity of arecoline *N*-oxide by sulfhydryl compounds and titanium trichloride in bacteria were cited by Lin et al.[6b] Therefore, uptake of inhibitors against those chemicals during betel chewing might be a way to prevent related oral diseases.

Although oral tumors were not induced by arecoline *N*-oxide in our study, this compound may still enhance tumorigenicity. Exposure to arecoline *N*-oxide in an increasing frequency for longer periods might be required for tumor formation. Because the immunodeficient mice are prone to spontaneous cancer and other diseases, further study using wild-type mice is required. Further investigation is also necessary to reveal arecoline *N*-oxide-targeted DNA or protein adducts that lead to tumorigenicity. In conclusion, our study showed the oral fibrotic potential of arecoline *N*-oxide in vitro and in vivo. Our findings provide new insights into the mechanism of carcinogenesis of the areca nut.

■ ASSOCIATED CONTENT

Supporting Information

Table S1 and Figures S1−S3. Experimental procedures for determination of 8-OHdG. The Supporting Information is available free of charge on the ACS Publications website at DOI: 10.1021/acs.jafc.5b01351.

■ AUTHOR INFORMATION

Corresponding Author

*(Y.-C.K.) E-mail: ycko0406@gmail.com, ycko@mail.cmu.edu.tw. Phone: 886-4-2205-2121, ext. 7621. Mail: China Medical University Hospital, 2 Yude Road, Taichung, Taiwan 40447, Taiwan.

Funding

This study was supported by the Health and Welfare surcharge of tobacco products, the China Medical University Hospital Cancer Research Center of Excellence (MOHW104-TDU-B-212-124-002), the National Science Council (NSC 101-2314-B-037-051-MY3, MOST 103-2314-B-039-002), and research projects (DMR-103-113, DMR-103-114, DMR103-120), China Medical University Hospital, Taiwan.

Notes

The authors declare no competing financial interest.

■ ABBREVIATIONS USED

ANE, areca nut extract; ANO, arecoline *N*-oxide; HGF-1, human gingival fibroblast; HOK, human oral keratinocyte; IL-6, interleukin-6; OPMD, oral potentially malignant disorders; OSF, oral submucous fibrosis; TGF-beta1, transforming growth factor-beta 1

■ REFERENCES

(1) Gupta, P. C.; Ray, C. S. Epidemiology of betel quid usage. *Ann. Acad. Med., Singapore* **2004**, *33* (4 Suppl.), 31−36.

(2) (a) Yardimci, G.; Kutlubay, Z.; Engin, B.; Tuzun, Y. Precancerous lesions of oral mucosa. *World J. Clin. Cases* **2014**, *2* (12), 866−872. (b) Dionne, K. R.; Warnakulasuriya, S.; Zain, R. B.; Cheong, S. C. Potentially malignant disorders of the oral cavity: current practice and future directions in the clinic and laboratory. *Int. J. Cancer* **2015**, *136* (3), 503−515.

(3) (a) Lee, C. H.; Ko, Y. C.; Huang, H. L.; Chao, Y. Y.; Tsai, C. C.; Shieh, T. Y.; Lin, L. M. The precancer risk of betel quid chewing, tobacco use and alcohol consumption in oral leukoplakia and oral submucous fibrosis in southern Taiwan. *Br. J. Cancer* **2003**, *88* (3), 366−372. (b) Ko, Y. C.; Huang, Y. L.; Lee, C. H.; Chen, M. J.; Lin, L. M.; Tsai, C. C. Betel quid chewing, cigarette smoking and alcohol consumption related to oral cancer in Taiwan. *J. Oral Pathol. Med.* **1995**, *24* (10), 450−453.

(4) *Betel-Quid and Areca-Nut Chewing and Some Areca-Nut Derived Nitrosamines*; IARC monographs on the evaluation of carcinogenic risks to humans; World Health Organization, International Agency for Research on Cancer: Lyon, France, 2004; Vol. 85, pp 1−334.

(5) Sen, S.; Talukder, G.; Sharma, A. Betel cytotoxicity. *J. Ethnopharmacol.* **1989**, *26* (3), 217−247.

(6) (a) Chiang, S. L.; Jiang, S. S.; Wang, Y. J.; Chiang, H. C.; Chen, P. H.; Tu, H. P.; Ho, K. Y.; Tsai, Y. S.; Chang, I. S.; Ko, Y. C. Characterization of arecoline-induced effects on cytotoxicity in normal human gingival fibroblasts by global gene expression profiling. *Toxicol. Sci.* **2007**, *100* (1), 66−74. (b) Lin, K. H.; Lin, C. Y.; Liu, C. C.; Chou, M. Y.; Lin, J. K. Arecoline *N*-oxide: its mutagenicity and possible role as ultimate carcinogen in areca oral carcinogenesis. *J. Agric. Food Chem.* **2011**, *59* (7), 3420−3428. (c) Sundqvist, K.; Liu, Y.; Nair, J.; Bartsch, H.; Arvidson, K.; Grafstrom, R. C. Cytotoxic and genotoxic effects of areca nut-related compounds in cultured human buccal epithelial cells. *Cancer Res.* **1989**, *49* (19), 5294−5298.

DOI: 10.1021/acs.jafc.5b01351
J. Agric. Food Chem. 2015, 63, 5787−5794

(7) (a) Chang, M. C.; Lin, L. D.; Wu, H. L.; Ho, Y. S.; Hsien, H. C.; Wang, T. M.; Jeng, P. Y.; Cheng, R. H.; Hahn, L. J.; Jeng, J. H. Areca nut-induced buccal mucosa fibroblast contraction and its signaling: a potential role in oral submucous fibrosis − a precancer condition. *Carcinogenesis* **2013**, *34* (5), 1096−1104. (b) Khan, I.; Kumar, N.; Pant, I.; Narra, S.; Kondaiah, P. Activation of TGF-beta pathway by areca nut constituents: a possible cause of oral submucous fibrosis. *PLoS One* **2012**, *7* (12), No. e51806.

(8) Sharan, R. N.; Mehrotra, R.; Choudhury, Y.; Asotra, K. Association of betel nut with carcinogenesis: revisit with a clinical perspective. *PLoS One* **2012**, *7* (8), No. e42759.

(9) (a) Guengerich, F. P. Metabolism of chemical carcinogens. *Carcinogenesis* **2000**, *21* (3), 345−351. (b) Cohen, S. M.; Arnold, L. L. Chemical carcinogenesis. *Toxicol. Sci.* **2011**, *120* (Suppl. 1), S76−S92.

(10) (a) Nery, R. The metabolic interconversion of arecoline and arecoline 1-oxide in the rat. *Biochem. J.* **1971**, *122* (4), 503−508. (b) Giri, S.; Krausz, K. W.; Idle, J. R.; Gonzalez, F. J. The metabolomics of (±)-arecoline 1-oxide in the mouse and its formation by human flavin-containing monooxygenases. *Biochem. Pharmacol.* **2007**, *73* (4), 561−573.

(11) Chiang, S. L.; Chen, P. H.; Lee, C. H.; Ko, A. M.; Lee, K. W.; Lin, Y. C.; Ho, P. S.; Tu, H. P.; Wu, D. C.; Shieh, T. Y.; Ko, Y. C. Up-regulation of inflammatory signalings by areca nut extract and role of cyclooxygenase-2 −1195G > a polymorphism reveal risk of oral cancer. *Cancer Res.* **2008**, *68* (20), 8489−8498.

(12) Chou, C. H.; Chuang, L. Y.; Tseng, W. L.; Lu, C. Y. Characterization of protein adducts formed by toxic alkaloids by nano-scale liquid chromatography with mass spectrometry. *J. Mass Spectrom.* **2012**, *47* (10), 1303−1312.

(13) Angadi, P. V.; Rao, S. Management of oral submucous fibrosis: an overview. *Oral Maxillofacial Surg.* **2010**, *14* (3), 133−142.

(14) Cox, S.; Vickers, E. R.; Ghu, S.; Zoellner, H. Salivary arecoline levels during areca nut chewing in human volunteers. *J. Oral Pathol. Med.* **2010**, *39* (6), 465−469.

(15) (a) Haque, M. F.; Meghji, S.; Khitab, U.; Harris, M. Oral submucous fibrosis patients have altered levels of cytokine production. *J. Oral Pathol. Med.* **2000**, *29* (3), 123−128. (b) Khan, I.; Agarwal, P.; Thangjam, G. S.; Radhesh, R.; Rao, S. G.; Kondaiah, P. Role of TGF-beta and BMP7 in the pathogenesis of oral submucous fibrosis. *Growth Factors* **2011**, *29* (4), 119−127. (c) Wenghoefer, M.; Pantelis, A.; Najafi, T.; Deschner, J.; Allam, J. P.; Novak, N.; Reich, R.; Martini, M.; Berge, S.; Fischer, H. P.; Jepsen, S.; Winter, J. Gene expression of oncogenes, antimicrobial peptides, and cytokines in the development of oral leukoplakia. *Oral Surg., Oral Med., Oral Pathol., Oral Radiol., Endodontics* **2010**, *110* (3), 351−356.

(16) Yu, C. C.; Tsai, C. H.; Hsu, H. I.; Chang, Y. C. Elevation of S100A4 expression in buccal mucosal fibroblasts by arecoline: involvement in the pathogenesis of oral submucous fibrosis. *PLoS One* **2013**, *8* (1), No. e55122.

(17) Rajendran, R.; Rajeesh, M. P.; Shaikh, S.; Shanthi; Pillai, M. R. Expression of matrix metalloproteinases (MMP-1, MMP-2 and MMP-9) and their inhibitors (TIMP-1 and TIMP-2) in oral submucous fibrosis. *Indian J. Dental Res.* **2006**, *17* (4), 161−166.

(18) Tsai, C. H.; Yang, S. F.; Chen, Y. J.; Chu, S. C.; Hsieh, Y. S.; Chang, Y. C. Regulation of interleukin-6 expression by arecoline in human buccal mucosal fibroblasts is related to intracellular glutathione levels. *Oral Dis.* **2004**, *10* (6), 360−364.

(19) Utsunomiya, H.; Tilakaratne, W. M.; Oshiro, K.; Maruyama, S.; Suzuki, M.; Ida-Yonemochi, H.; Cheng, J.; Saku, T. Extracellular matrix remodeling in oral submucous fibrosis: its stage-specific modes revealed by immunohistochemistry and in situ hybridization. *J. Oral Pathol. Med.* **2005**, *34* (8), 498−507.

(20) Anura, A.; Das, R. K.; Pal, M.; Paul, R. R.; Ray, A. K.; Chatterjee, J. Correlated analysis of semi-quantitative immunohistochemical features of E-cadherin, VEGF and CD105 in assessing malignant potentiality of oral submucous fibrosis. *Pathol., Res. Pract.* **2014**, *210* (12), 1054−1063.

(21) Chang, Y. C.; Tsai, C. H.; Lai, Y. L.; Yu, C. C.; Chi, W. Y.; Li, J. J.; Chang, W. W. Arecoline-induced myofibroblast transdifferentiation from human buccal mucosal fibroblasts is mediated by ZEB1. *J. Cell. Mol. Med.* **2014**, *18* (4), 698−708.

(22) (a) Oliveira-Costa, J. P.; Oliveira, L. R.; Zanetti, R.; Zanetti, J. S.; da Silveira, G. G.; Chavichiolli Buim, M. E.; Zucoloto, S.; Ribeiro-Silva, A.; Soares, F. A. BRCA1 and gammaH2AX as independent prognostic markers in oral squamous cell carcinoma. *Oncoscience* **2014**, *1* (5), 383−391. (b) Paull, T. T.; Rogakou, E. P.; Yamazaki, V.; Kirchgessner, C. U.; Gellert, M.; Bonner, W. M. A critical role for histone H2AX in recruitment of repair factors to nuclear foci after DNA damage. *Curr. Biol.* **2000**, *10* (15), 886−895.

(23) Giri, S.; Idle, J. R.; Chen, C.; Zabriskie, T. M.; Krausz, K. W.; Gonzalez, F. J. A metabolomic approach to the metabolism of the areca nut alkaloids arecoline and arecaidine in the mouse. *Chem. Res. Toxicol.* **2006**, *19* (6), 818−827.

(24) Zhang, J.; Cashman, J. R. Quantitative analysis of FMO gene mRNA levels in human tissues. *Drug Metab. Dispos.* **2006**, *34* (1), 19−26.

(25) (a) Wu, M.; Xing, G.; Qi, X.; Feng, C.; Liu, M.; Gong, L.; Luan, Y.; Ren, J. Assessment of the mutagenic potential of arecoline in gpt delta transgenic mice. *Mutat. Res., Genet. Toxicol. Environ. Mutagen.* **2012**, *748* (1−2), 65−69. (b) Choudhury, Y.; Sharan, R. N. Altered BRCA1 and BRCA2 responses and mutation of BRCA1 gene in mice exposed chronically and transgenerationally to aqueous extract of betel nut (AEBN). *Environ. Toxicol. Pharmacol.* **2011**, *31* (1), 57−69.

(26) (a) Bhide, S. V.; Shivapurkar, N. M.; Gothoskar, S. V.; Ranadive, K. J. Carcinogenicity of betel quid ingredients: feeding mice with aqueous extract and the polyphenol fraction of betel nut. *Br. J. Cancer* **1979**, *40* (6), 922−926. (b) Bhisey, R. A.; Ramchandani, A. G.; D'Souza, A. V.; Borges, A. M.; Notani, P. N. Long-term carcinogenicity of pan masala in Swiss mice. *Int. J. Cancer* **1999**, *83* (5), 679−684. (c) Kurkalang, S.; Banerjee, A.; Ghoshal, N.; Dkhar, H.; Chatterjee, A. Induction of chromosome instability and stomach cancer by altering the expression pattern of mitotic checkpoint genes in mice exposed to areca-nut. *BMC Cancer* **2013**, *13*, 315.

(27) Chang, N. W.; Pei, R. J.; Tseng, H. C.; Yeh, K. T.; Chan, H. C.; Lee, M. R.; Lin, C.; Hsieh, W. T.; Kao, M. C.; Tsai, M. H.; Lin, C. F. Co-treating with arecoline and 4-nitroquinoline 1-oxide to establish a mouse model mimicking oral tumorigenesis. *Chem.−Biol. Interact.* **2010**, *183* (1), 231−237.

(28) (a) Prokopczyk, B.; Brunnemann, K. D.; Bertinato, P.; Hoffmann, D. The role of *N*-(nitrosomethylamino)propionitrile in betel-quid carcinogenesis. *IARC Sci. Publ.* **1987**, *No. 84*, 470−473. (b) Wenke, G.; Rivenson, A.; Hoffmann, D. A study of betel quid carcinogenesis. 3. 3-(Methylnitrosamino)-propionitrile, a powerful carcinogen in F344 rats. *Carcinogenesis* **1984**, *5* (9), 1137−1140. (c) Prokopczyk, B.; Rivenson, A.; Bertinato, P.; Brunnemann, K. D.; Hoffmann, D. 3-(Methylnitrosamino)propionitrile: occurrence in saliva of betel quid chewers, carcinogenicity, and DNA methylation in F344 rats. *Cancer Res.* **1987**, *47* (2), 467−471.

(29) Wogan, G. N.; Hecht, S. S.; Felton, J. S.; Conney, A. H.; Loeb, L. A. Environmental and chemical carcinogenesis. *Semin. Cancer Biol.* **2004**, *14* (6), 473−486.

(30) (a) Wang, Y.; Yin, S.; Blade, K.; Cooper, G.; Menick, D. R.; Cabral, F. Mutations at leucine 215 of beta-tubulin affect paclitaxel sensitivity by two distinct mechanisms. *Biochemistry* **2006**, *45* (1), 185−194. (b) Yokoyama, H.; Ishii, H.; Nagata, S.; Kato, S.; Kamegaya, K.; Tsuchiya, M. Experimental hepatitis induced by ethanol after immunization with acetaldehyde adducts. *Hepatology* **1993**, *17* (1), 14−19.

(31) Guo, F.; Carter, D. E.; Leask, A. Mechanical tension increases CCN2/CTGF expression and proliferation in gingival fibroblasts via a TGFbeta-dependent mechanism. *PLoS One* **2011**, *6* (5), No. e19756.

(32) Ito, M.; Ikeda, K.; Yokoyama, H.; Motoyoshi, K.; Sato, Y.; Hashimoto, K. Stereographic and stereometric study of sebaceous gland hyperplasia in rabbit pinnas induced by topically applied substances. *J. Invest. Dermatol.* **1991**, *97* (1), 85−90.

(33) Rajalalitha, P.; Vali, S. Molecular pathogenesis of oral submucous fibrosis − a collagen metabolic disorder. *J. Oral Pathol. Med.* **2005**, *34* (6), 321−328.

DOI: 10.1021/acs.jafc.5b01351
J. Agric. Food Chem. 2015, 63, 5787−5794

gastrointestinal tract, its bioavailability tends to be highly variable and low.[21]

A possible way of slowing osteoporosis is to increase the absorption and bioavailability of calcium by using absorption enhancers or reducing the size of the compounds from microscale to nanoscale. The surface area of the nanoparticles increases, and the properties of the more reactive surface molecules lead to the new properties of the nanoparticles.[22] Whereas nanodelivery systems can increase the absorption and bioavailability of nutrients, they also can change the distribution of the substances in the body.[23] Previous studies by Mohanty et al.[24] and Thakkar et al.[25] on the effect of nanoparticle size, delivery system, and bioavailability revealed that particle size reduction is one of the most important factors to enhance absorption and bioavailability. These combined effects, namely, using suitable composition and nano-size reduction, can help to protect against the development of osteoporosis.

There are different experimental techniques for measuring calcium bioavailability. One of these techniques is the use of in vivo assay. Particularly, small animals such as rats are used as their bones respond quickly to changes, in a human-like fashion, and they are easy to use and inexpensive. The ovariectomized (OVX) rat model is a widely used animal model to simulate estrogen deficiency induced bone loss and is commonly used to test calcium bioavailability for the treatment of postmenopausal osteoporosis.

The current study developed a fortified milk powder containing calcium citrate and some calcium bioavailability enhancers (i.e., inulin, water-soluble and fat-soluble vitamins including B_6, K_1, and D_3, and DHA as well as EPA). To improve the absorption and bioavailability of dietary calcium, two types of fortified milk powder have been developed and compared in vivo by OVX and OVX-OS rats as a model of menopause and menopause-OS women, respectively. It has been hypothesized that the fortified milk with specific composition and optimum preparation condition improves the absorption and bioavailability of calcium in OVX and OVX-OS rats. It is accepted that adequate amounts of calcium, vitamins D_3, K_1, B_6, inulin, DHA, and EPA are key elements for healthy bone development, maintenance of bone density and bone strength, and prevention of osteoporosis, but fortification with micro calcium particles results in lower absorption efficiency than nano calcium particles. Among various sources of fortified foods, little information is available about nanoparticles. Therefore, for the purpose of finding another type of fortified food, we have compared nanofortified milk powder with micro- and non-fortified milk on calcium absorption and bioavailability in OVX and OVX-OS rats as a model of menopause and menopause-OS women, respectively.

MATERIALS AND METHODS

Chemicals and Materials. Skim milk powder (T1) was provided by Fonterra (Kuala Lumpur, Malaysia). Food grade calcium citrate, inulin, vitamins D_3, K_1, and B_6, EPA, and DHA were procured from Finuco (Sankyo Seifun Co, Ltd., Chugoku/Okayama, Japan). A Sartorius stedim biotech system (GmbH, 37070 Gottingen, Germany) was used to obtain deionized water for all procedures.

Milk Fortification. The fortified milk powder contained calcium citrate, EPA and DHA (1:1), vitamins D_3, K_1, and B_6, and inulin based on the North American and Western European recommended dietary allowance (Table 1).[10] These compounds were added to skim milk powder and mixed for 5 min with a mixer (Bachiller, Barcelona, Spain) (Table 1). The samples were kept in airtight glass bottles and stored in a refrigerator.

Table 1. Specification of Experimental Diets

	content (%)		
specification	basal diet[a]	skim milk[b]	fortified milk[c]
protein	22	36.25	25.8
fiber	5.0		
fat	3.0	0.9	11.5
moisture	13.0	3.9	3.9
ash	8.0	8.3	18.8
lactose		49.8	34.8
nitrogen-free extract	49.0		
inulin			5
calcium	1.0	0.85	13
phosphorus	0.8	0.6	0.5
EPA and DHA			11
K_1			0.00055
D_3			0.0001
B_6		0.001	0.015

[a]Gold Coin Animal Feed (702P-Pellet). [b]T1. [c]T2 and T2-nano.

Phase 1: Optimization of Preparation Condition of Calcium Nanofortified Milk Powder. *High-Pressure Homogenization.* Sample preparation was achieved by dispersing milk powder in deionized water (20% w/v). A mixer (Silverson L4R, Buckinghamshire, UK) was used for 5 min at 1000 rpm as prehomogenizer to prepare coarse sample. Then, the sample passed through a high-pressure homogenizer (APV, Crawley, UK) with different homogenization condition (i.e. cycle, 3−5; pressure, 200−400 bar) to produce calcium citrate nanofortified milk sample (T2-nano).

Polydispersity Index (PDI) and Average Particle Size (APS). A dynamic light-scattering particle analyzer (Malvern Series ZEN 1600, Malvern Instruments Ltd., Worcester, UK) was used to analyze APS and PDI of fortified milk powder. A laser ray passed through the sample and was scattered by the particles in a distinctive pattern. A photodiode array detector measured the APS. The measurement scale of APS was reported in micrometers. The experiment was carried out in triplicate for each diluted sample. The system reported a measure of particle size distribution as PDI. PDI values range from 0, for a completely monodisperse system, to 1.0, for a polydisperse particle dispersion.

Response Surface Analysis. Response surface methodology (RSM) evaluated the effect of two independent variables, namely, x_1 (cycle (3, 4, and 5)) and x_2 (pressure (200, 300, and 400 bar)), on the response variables, Y_1 (PDI) and Y_2 (particle size (nm)). A central composite design (CCD) consisting of 14 treatments, including 6 center points, was created to optimize the preparation condition of nano calcium citrate fortified milk powder prepared by high-pressure homogenization and simultaneously study the main, interaction, and quadratic effects of independent variables on the dependent variables.[26]

Optimization and Validation Procedure. To determine the optimum level of preparation parameters leading to minimum particle size and minimum PDI, graphical (three-dimensional response surface) and numerical optimization[27] were carried out (Minitab v.16, Minitab Inc., State College, PA, USA). To predict the exact optimum level of independent variables, response optimizer (Minitab v. 16) was used for numerical optimization leading to the desired response goals. The adequacy of RSM (model validation) was evaluated using the t test.

Particle Morphology. The nanoparticle structure and morphology were examined using energy filtered transmission electron microscopy (EFTEM; LEO 912 AB Omega, LEO Electron Optics, Oberkochen, Germany). Air-dried samples on a copper grid were negatively stained with 2% phosphotungstic acid solution (2 min) and air-dried before being observed under EFTEM.[27] The diameters of the particles were determined using the scale bar on the electron micrographs. Reproducibility of the EFTEM images was assured by taking at least four pictures of each sample.

DOI: 10.1021/acs.jafc.5b01468
J. Agric. Food Chem. 2015, 63, 5795−5804

Phase 2: In Vivo Study. The ultimate test of success of a formula depends on its in vivo performance, which was conducted in a suitable animal model (refer to graphical abstract). Approval to carry out in vivo study was obtained from the Animal Care and Use Committee of Faculty of Veterinary Medicine of Universiti Putra Malaysia (UPM, Selangor, Malaysia). The animals used for in vivo experiments were female Sprague–Dawley rats (n = 96, 7 weeks old) weighing ∼250 g obtained from UPM veterinary hospital (Serdang, Selangor, Malaysia). The animals were kept under standard laboratory condition at a temperature of 22 ± 2 °C and relative humidity of 50 ± 5%. The animals were housed in metabolic cages (a conventional, circular metabolic cage made of clear plastic was used), one per cage, with free access to standard laboratory feed (Gold Coin animal feed, Kuala Lumpur, Malaysia) (Table 1) and distilled water ad libitum.

The experimental diets contained the nonfortified milk powder (T1, 850 mg/100 g) as the main protein source. Ovariectomy was performed by excising the ovaries. The animals were anesthetized with a combination of ketamine (80 mg/kg) and xylazine (10 mg/kg), intraperitoneally.[28] Briefly, hair was cut over the surgical area and scrubbed with iodine. A small incision (∼1.0 cm) was made in the skin between the middle of the back, starting at the last rib. The skin was moved to one lateral side, and a small incision was made through the peritoneal lining. The entire ovary was removed with a single cut between the uterine horn and oviduct on each side. The skin was then recovered with a surgical staple.[29] Sham surgery consisted of the skin incision and staple procedures only.[30] After 1 week postsurgery treatment, the rats were randomly assigned to three main groups (sham, OVX, and OVX-OS). Each group of rats was randomized into four different subgroups including eight rats each and maintained for a period of 8 weeks as an experimental period.

The first and second groups included sham and OVX rats that were fed treatment diets (1, basal diet, standard rat chow diet as a control diet; 2: T1; 3, T2; and 4, T2-nano). The third group included OVX rats that were fed a low-calcium diet for 6 weeks prior to experimental diets. The idea was to induce osteoporosis in the OVX rats and change them to OVX-OS rats. To ensure all groups were fed treatment diets similarly, during that 6 week period the other two groups (sham and OVX rats) were kept on basal diet. After 6 weeks of low-calcium diet feeding, the OVX-OS rats were randomly divided into four subgroups. Then they received experimental diets for 8 weeks the same as sham and OVX rats. During the 8 week experimental period, the treatment diets were given (5 mL) orally by gavage twice daily.

Sample Collection. After an 8 week feeding period, following overnight fasting, rats were anesthetized with a 1:2 (v/v) mixture of ketamine (10 mg/kg) and xylazine (25 mg/kg) and sacrificed.[31] Blood collected by cardiac puncture was centrifuged (Hettich EBA 20 centrifuge, Andreas Hettich GmbH & Co. KG, Tuttlingen, Germany) at 5000 rpm (2850g) for 8 min at 4 °C to separate serum that was maintained at −20 °C for further chemical analysis. Feces were collected for each individual rat in the last 6 days of the experiment. Then, the feces were air-dried, finely ground, stored in a plastic tube, and kept at 4 °C until further use for calcium analysis. The bones (femurs) were cleaned by eliminating the soft tissue. However, they were initially soaked in saline solution prior to sealing in plastic bags and storing at −20 °C.[32] They were saved for calcium determination, bone strength (maximum load) measurement, and bone morphology.

Experimental Analysis. *Mechanical Assays.* Femurs were subjected to an Instron universal testing instrument (5kN model 3365, Norwood, MA, USA) for evaluation of biomechanical function of bones. Femurs were brought to room temperature before breaking in the exact center of the bones. To analyze the maximum load, the bone was placed on two supporting bars (2 mm in diameter) with a span of 15 mm, and an upper crosshead roller (6 mm diameter) was applied in the middle of the bone and advanced at 0.5 mm/min until the rupture was automatically determined by the apparatus. The midpoints of the femurs were determined by measuring the length of each bone and dividing the length using a Vernier caliper. The crosshead compressed the middle of the femur with linearly increasing force, until fracture occurred. The load deformation curve was recorded. The test results provided values for maximum load (N).[32]

Calcium Analysis. To measure serum calcium, an automatic blood chemical analyzer with Roche testing kits (Roche COBAS MIRA PLUS, Basel, Switzerland) was used. Total concentration of calcium in the diet, feces, and bone calcium contents were measured by an atomic absorption spectrophotometry (Thermo Scientific, S series, Waltham, MA, USA) using a standard procedure.[32]

Morphology Structure. Fractured surfaces of the femurs obtained from the mechanical strength test were processed for scanning electron microscopy (SEM) (LEO 1455VPSEM, London, UK). Briefly, bone was fixed (2.5% glutaraldehyde for 72 h and postfixation

Table 2. Matrix of Central Composite Design (CCD), Independent Variables and Their Level, and the Responses for the Processing of T2-Nano

	independent variables		dependent variables[a]	
run	x_1	x_2	Y_1 (mean ± SD)	Y_2 (mean ± SD)
1	−1	−1	0.514 ± 0.002	0.497 ± 0.005
2[b]	0	0	0.452 ± 0.004	0.350 ± 0.003
3[b]	0	0	0.439 ± 0.005	0.327 ± 0.004
4	−1	+1	0.480 ± 0.003	0.259 ± 0.001
5	+1	+1	0.560 ± 0.002	0.341 ± 0.001
6[b]	0	0	0.491 ± 0.004	0.326 ± 0.007
7	+1	−1	0.320 ± 0.001	0.368 ± 0.003
8[b]	0	0	0.450 ± 0.003	0.344 ± 0.002
9	0	+1.414	0.480 ± 0.005	0.341 ± 0.005
10[b]	0	0	0.440 ± 0.002	0.360 ± 0.006
11	0	−1.414	0.370 ± 0.004	0.483 ± 0.008
12	−1.414	0	0.544 ± 0.003	0.369 ± 0.005
13[b]	0	0	0.470 ± 0.006	0.340 ± 0.004
14	+1.414	0	0.468 ± 0.007	0.319 ± 0.003

	level used, actual (coded)		
independent variable	low (−1)	medium (0)	high (+1)
x_1 = cycle	3	4	5
x_2 = pressure (bar)	200	300	400

[a] Y_1, PDI (polydispersity index); Y_2, APS (average particle size) (nm). [b] Center point of the design.

Table 3. Regression Coefficients, R^2, p Value, Lack of Fit Test, and Significance Probability of Independent Variable Effects in the Reduced Response Surface Models[a]

regression coefficient		PDI	APS
b_0		1.5209	1.4756
b_1		−0.4351	−0.1608
b_2		−0.0013	−0.0046
b_{12}		0.0006	0.0005
b_{11}		0.0252	−0.0015
b_{22}		−0.0001	0.000
R^2		0.953	0.965
regression (p value)		0.000[b]	0.000[b]
lack of fit (p value)		0.162[c]	0.128[c]

		main effects		interaction effects	quadratic effects	
variable		x_1	x_2	x_1x_2	x_1^2	x_2^2
PDI (Y_1)	p value	0.00	0.00	0.00		
	F ratio	148.23	83.27	124.93		
APS (Y_2)	p value	0.18	0.00	0.00	0.01	0.00
	F ratio	2.21	711.98	52.19	15.99	679.85

[a] PDI, polydispersity index; APS, average particle size; x_1, cycle; x_2, pressure. Only terms with statistical significance are included. [b] Significant ($p < 0.05$). [c] Insignificant ($p > 0.05$)

DOI: 10.1021/acs.jafc.5b01468
J. Agric. Food Chem. 2015, 63, 5795−5804

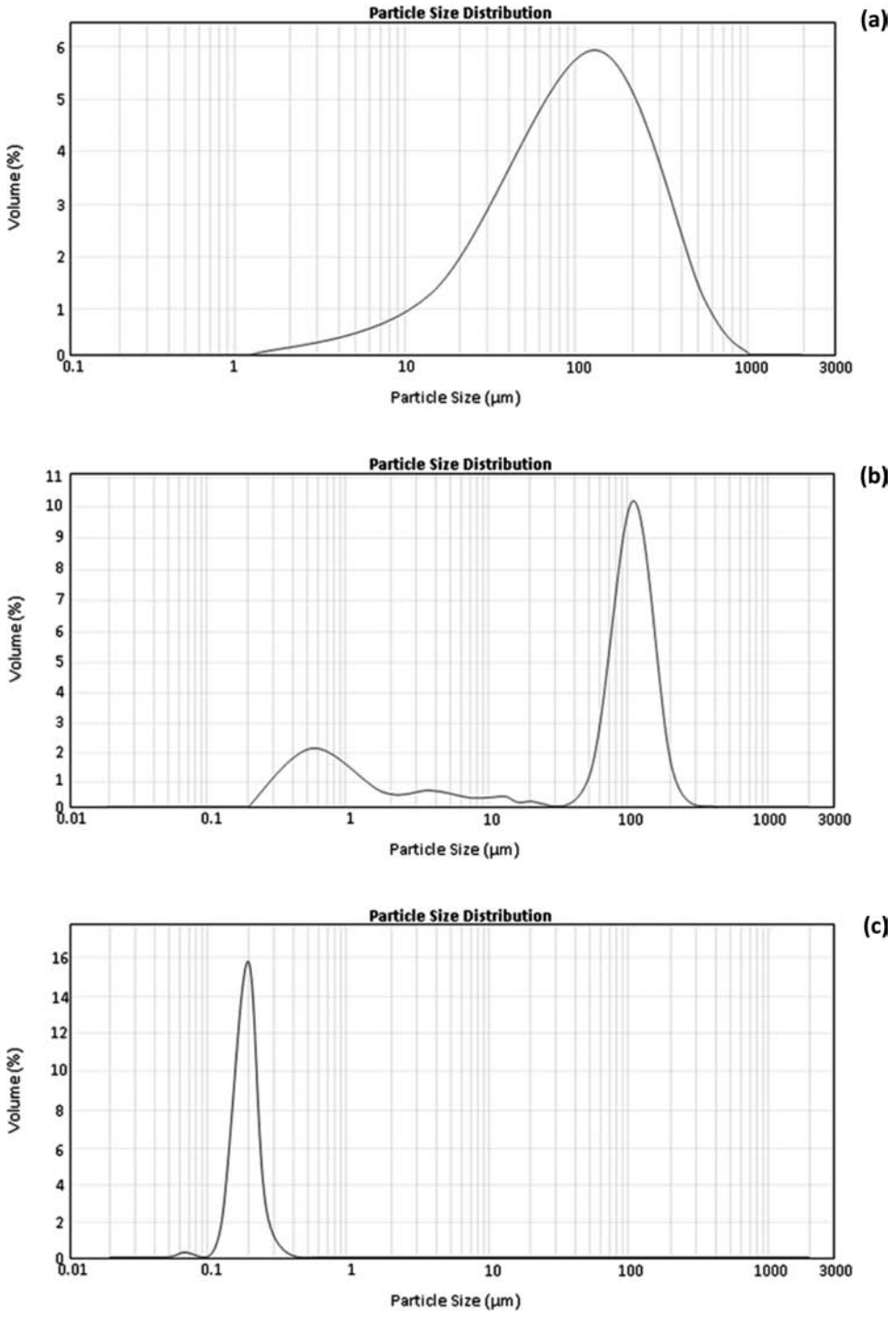

Figure 1. Particle size distribution of (a) skim milk powder (T1), (b) calcium citrate fortified milk powder (T2), and (c) calcium citrate nanofortified milk powder (T2-nano).

in 1% osmium tetroxide for 24 h), then dehydrated in ethanol, and dried with CO_2 at critical point. Finally, it was attached to aluminum specimen holders with colloidal silver. This process provided a conducting path to remove charges that would result from the incident electron beam of SEM striking the specimen. The mounting stubs were placed in an oven at 70 °C for 15 min to allow evaporation of volatile solvents from the carbon element and silver paint. Then sputter was coated with palladium−gold using a sputter coater. Finally, the processed bone was analyzed at 25 kV accelerating voltage by SEM.[32] Three micrographs at final magnifications (×450) were taken from each animal.

Absorption and Bioavailability. Apparent calcium absorption and relative bioavailability values were calculated using consumed calcium in the diets, fecal calcium, and total calcium in bones as explained previously.[20]

Statistical Analysis. Data analysis was carried out using Minitab software (version 16, Minitab Inc., State College, PA, USA). A completely randomized design was employed to generate all treatments. In each experiment, a comparison was made using one-way ANOVA within and between groups receiving the same diets. Significant ($p < 0.05$) differences were determined among treatment groups with Tukey's multiple-range tests.

DOI: 10.1021/acs.jafc.5b01468
J. Agric. Food Chem. 2015, 63, 5795−5804

RESULTS

Response Surface Analysis. RSM is an experimental design method useful in optimization processes. The ability to experimentally explore the main and interaction effects and the relationship between several independent and dependent variables are the advantages of RSM over the conventional optimization process, where one factor is varied while the others remain constant. Using RSM reveals that just a few experimental runs are required to generate a vast amount of information for optimization, which reduces the time and cost required to obtain the optimized parameters. According to Table 2, the arrangement of CCD permits the progress of the suitable empirical equations.[26]

The estimated regression coefficients of two high-pressure variables, along with the corresponding R^2, p values, lack of fit test, significant probability of each parameter, and their F ratios, are shown in Table 3. The final reduced models (FRMs) fitted for PDI and APS showed high coefficients of determination (0.953 and 0.965, respectively), which indicated the satisfactory adjustment of the reduced response surface models employed for describing the variation of dependent variables as a function of the main preparation parameters.[33]

The analyses of PDI and APS of T2-nano were significantly ($p < 0.05$) influenced by cycle and pressure (Table 3). Both response variables were significantly ($p < 0.05$) fitted by a second-order regression equation. In fact, the variability of PDI was significantly ($p < 0.05$) defined as a function of linear and interaction effects of both homogenization variables (Table 3). In addition, the variability of APS was significantly ($p < 0.05$) defined as a function of linear effects of pressure variable ($p = 0.00$) and interaction as well as quadratic effects of both homogenization variables (Table 3).

In the present study, both high-pressure variables had the same negative (b_1 and b_2) significant ($p < 0.05$) effect on APS and PDI (Table 3). It was concluded that the APS and PDI of the fortified milk powder were significantly ($p < 0.05$) decreased with increasing pressure and cycle (Table 3).

Effect of Homogenization Condition on Characteristics of Fortified Milk Powder. Figure 1 demonstrates the APS of T1, T2, and T2-nano. Lower PDI values for T2-nano compared with T2 and T1 are clearly presented in the figure. Figure 2 exhibits the significant ($p = 0.00$) interaction effects of high-pressure variables on APS and PDI of the fortified milk powder. The interaction effect of cycle and pressure decreased the APS of the fortified milk powder. This observation confirmed that the presence of the interaction effects improved the fitness of the FRM to the experimental data for the APS. The interaction between cycle and pressure had equal significant ($p = 0.00$) effects on the APS and PDI of the fortified milk powder (Table 3).

Optimization and Validation of Homogenization Process. The multiple response optimizations leading to the minimum APS and PDI of the T2-nano were carried out. The overall optimal condition leading to the minimum PDI and APS was predicted to be obtained at the combined level of four cycles and ~300 bar pressure (Figure 3). The average cycle and pressure led to the minimum PDI. Moreover, the region resulting in the smallest average size was predicted to be obtained by the average cycle and pressure. Under corresponding optimum condition, the desirable fortified milk powder with the predicted optimum PDI and APS was prepared to verify the accuracy of the reduced models. Thus, PDI and APS of the

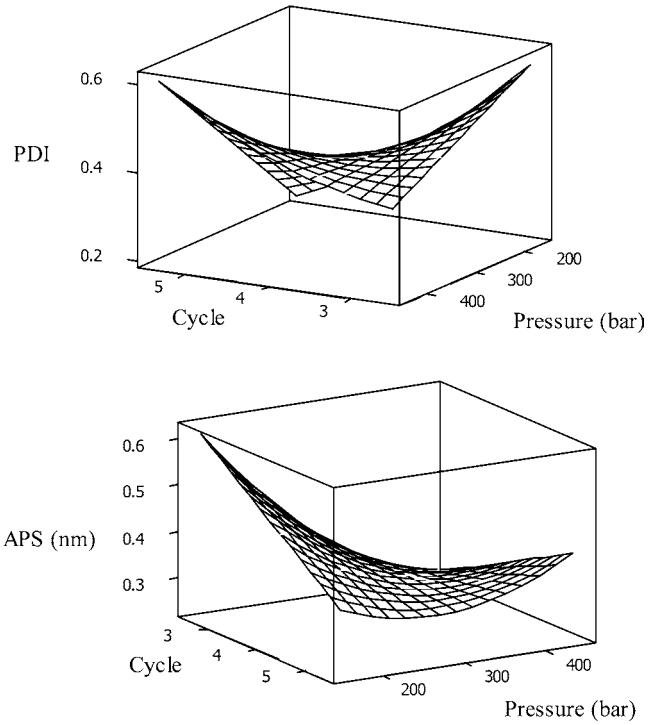

Figure 2. Response surface plots showing the interaction effect of independent variables on polydispersity index (PDI) and average particle size (APS) of the fortified milk powder.

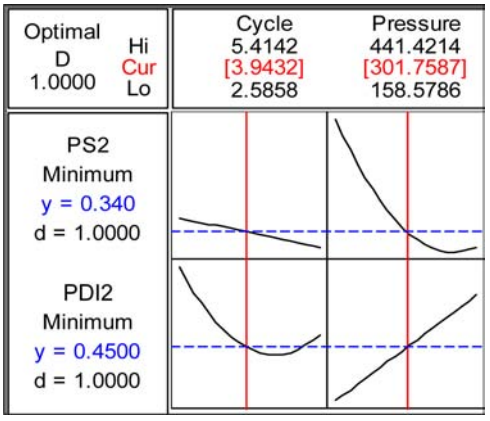

Figure 3. Response optimization, parameters, predicted responses (y), and desirability (d). PS, particle size; PDI, polydispersity index.

prepared fortified milk powder were determined and subsequently compared with the predicted values. The corresponding response values obtained from the experimental data and the ones predicted by the reduced models were observed to be close together (Table 4), and no significant ($p = 0.63$) difference was observed between the experimental and predicted values (Table 4), thus indicating the adequacy of the FRMs fitted by RSM. Briefly, the optimization of high-pressure homogenization of the calcium citrate fortified milk powder resulting in nanoparticles (100−1000 nm) was targeted. In this study, either increase or decrease of the pressure from 300 to 200 bar or from 300 to 400 bar resulted in the larger particle size and higher PDI. The same undesirable particle size and PDI were obtained with the application of more or fewer than four cycles.

DOI: 10.1021/acs.jafc.5b01468
J. Agric. Food Chem. 2015, 63, 5795−5804

Table 4. Comparison between Experimental and Predicted Values Based on Final Reduced Models[a]

	APS[b]			PDI[b]		
run	Y_0	Y_i	$Y_0 - Y_i$	Y_0	Y_i	$Y_0 - Y_i$
1	0.497	0.498	−0.001	0.514	0.518	−0.004
2	0.350	0.341	0.009	0.452	0.457	−0.005
3	0.327	0.341	−0.014	0.439	0.457	−0.018
4	0.259	0.276	−0.017	0.480	0.471	−0.462
5	0.341	0.352	−0.011	0.560	0.553	0.007
6	0.326	0.341	−0.356	0.491	0.457	0.034
7	0.368	0.363	−0.358	0.320	0.326	−0.006
8	0.344	0.341	0.003	0.450	0.457	−0.007
9	0.341	0.324	0.017	0.480	0.490	−0.010
10	0.360	0.341	0.019	0.440	0.457	−0.017
11	0.483	0.488	−0.005	0.370	0.363	0.007
12	0.369	0.359	0.010	0.544	0.547	−0.003
13	0.340	0.341	−0.001	0.470	0.457	0.013
14	0.319	0.317	0.002	0.468	0.468	0.000

[a]APS, average particle size; PDI, polydispersity index; Y_0, experimental value; Y_i, predicted value; $Y_0 - Y_i$, residue. [b]No significant difference ($p > 0.05$) between Y_0 and Y_i.

Particle Morphology. The transmission electron microscopy (TEM) images of T1, T2, and T2-nano are shown in Figure 4. Nanoparticles are generally characterized by their size and morphology using such advanced microscopic techniques as TEM. As Figure 4 shows, the size of particles was significantly reduced in nanofortified milk powder (C) compared with fortified milk (B) and skim milk (A) powders. The results of TEM were in agreement with particle size analyzer for all milk powders.

Effect of Experimental Diets on Serum Calcium in Sham, OVX, and OVX-OS Rats. Blood was collected at the beginning of the experiment showing the serum calcium content of 2.54 mmol/L. Table 5 compares the experimental data on total serum calcium concentration of sham, OVX, and OVX-OS rats at the end of experiments. It is apparent from this table that, although the highest amount of total serum calcium was fournd for T2-nano, regardless of treatments, no significant ($p = 0.21$) difference was found among the experimental diets and between the groups (sham, OVX, and OVX-OS).

Effect of Experimental Diets on Bone Calcium in Sham, OVX, and OVX-OS Rats. The results obtained from the analysis of bone calcium are shown in Table 5. To assess calcium bioavailability, bone calcium content was tested. In Table 5 there is a clear trend of decreasing bone calcium in T2-nano, T2, T1, and basal diet in both OVX and OVX-OS rats. Indeed, bone calcium content was significantly ($p = 0.00$) higher in both OVX and OVX-OS groups fed T2 compared to those in basal diets and T1. Moreover, significant difference ($p = 0.00$) was observed between T1 and basal diet in OVX rats. On the other hand, there was no significant ($p = 0.18$) difference between T1 and basal diet in OVX-OS rats. It is apparent from this table that the T2-nano group had the greatest femur calcium content compared with other groups in both OVX and OVX-OS rats. Furthermore, the femoral calcium in OVX rats was significantly ($p = 0.00$) higher than in OVX-OS rats (Table 5), therefore indicating higher femoral bone mineral density. Moreover, the results in Table 5 show that the amount of bone calcium in the sham group was significantly ($p = 0.00$) higher than in OVX and OVX-OS rats.

Effect of Experimental Diets on Mechanical Properties of Bones in Sham, OVX, and OVX-OS Rats. Maximum load (bone strength) was used to evaluate calcium bioavailability. Table 5 presents the results of maximum load in sham, OVX, and OVX-OS rats. The strength test revealed a significant ($p = 0.02$) positive effect for the fortified diet on the rat femurs. As the results show, the T2 intake in sham, OVX, and OVX-OS rats significantly ($p = 0.02$) enhanced the maximum load in femurs compared with basal diet and T1 groups. In the mechanical testing, the maximum load of T1 groups slightly increased in comparison with basal diet groups. However, there was no significant ($p = 0.09$) difference in maximum load between these groups after 8 weeks of feeding in sham and OVX rats, whereas there was a significant ($p = 0.00$) difference between T1 and basal diet groups in OVX-OS rats. There was no significant difference ($p = 0.08$) between the bone strength of OVX and OVX-OS rats receiving T2 during the experiment, but the present results (Table 5) demonstrated significant improvement in bone strength and maximum load in the sham group fed with fortified milk powder compared to the rest. The results obtained from this study indicated that fortified milk powder may have a preventive effect on bone loss in rats.

In addition, rats in the T2-nano groups had significantly ($p = 0.01$) higher bone stiffness and bone strength compared with other groups in all sham, OVX, and OVX-OS rats (Table 5). Therefore, particle size reduction in the diets could increase maximum load and affect bone strength. As shown in Table 5, it was found that the bone strength of OVX rats receiving T2-nano significantly ($p = 0.01$) increased compared with OVX-OS rats. Interestingly, it was found that OVX rats fed T2-nano had similar maximum load with T2-nano sham group with no significant difference ($p = 0.23$).

Effect of Experimental Diets on Bone Morphology of Sham, OVX, and OVX-OS Rats. Alterations of bone morphology can be compared among all experimental diets in Figure 5. The SEM images of basal diet groups (as control diet) of sham, OVX, and OVX-OS rats clearly showed severe reduction of bone mass in the femurs (Figure 5A,E,I). SEM of

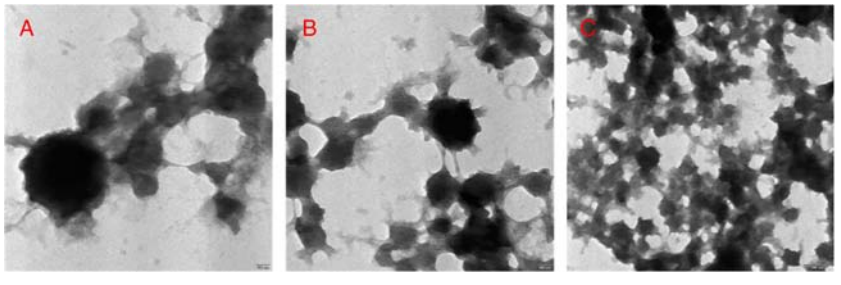

Figure 4. Transmission electron micrographs (TEM) of the milk powder particles: T1 (A); T2 (B); T2-nano (C).

DOI: 10.1021/acs.jafc.5b01468
J. Agric. Food Chem. 2015, 63, 5795−5804

Table 5. Serum Calcium Content, Bone Calcium Content, and Maximum Load in Sham, Ovariectomized (OVX), and OVX-Osteoporosis (OS) Rats (Mean ± SD; n =8)[a]

diet	serum calcium (mmol/L)			bone calcium (mmol/g)			maximum load (N)		
	sham	OVX	OVX-OS	sham	OVX	OVX-OS	sham	OVX	OVX-OS
basal diet	2.84 ± 0.05aA	2.86 ± 0.06aA	2.73 ± 0.08aA	5.26 ± 0.12bA	1.71 ± 0.03dB	0.65 ± 0.03cC	68.77 ± 0.47cA	62.53 ± 1.32cB	56.40 ± 0.21dC
T1	2.95 ± 0.09aA	2.89 ± 0.12aA	2.85 ± 0.01aA	5.31 ± 0.18bA	2.28 ± 0.04cB	0.77 ± 0.01cC	69.17 ± 0.34cA	63.59 ± 1.31cB	59.70 ± 1.30cC
T2	3.01 ± 0.07aA	2.96 ± 0.04aA	2.89 ± 0.36aA	5.40 ± 0.06bA	4.54 ± 0.08bB	1.40 ± 0.11bC	72.07 ± 0.70bA	68.93 ± 0.91bB	65.99 ± 0.57bB
T2-nano	3.04 ± 0.19aA	3.05 ± 0.18aA	3.05 ± 0.16aA	6.42 ± 0.04aA	5.56 ± 0.07aB	2.79 ± 0.08aC	90.06 ± 1.21aA	87.37 ± 1.62aA	70.28 ± 0.21aB

[a]Means with different lower case letters (a−d) in a column are significantly ($p < 0.05$) different. Means with different upper case letters (A−C) in a row are significantly ($p < 0.05$) different. T1, skim milk; T2, fortified milk powder containing calcium citrate + vitamins (D_3 + K_1 + B_6) + EPA and DHA + inulin.

rat femurs receiving T1 illustrated no immense cracks resulting from increasing bone mass (Figure 5B,F,J). It was found that the bone morphology of T1 groups had an improvement compared to basal diet in sham, OVX, and OVX-OS rats. Treatment with T2 restored the morphological abnormalities (Figure 5C,G,K) in the groups. As compared with T2, treatment with T2-nano demonstrated better status of bones. It can be seen from Figure 5D,H,L that femur morphology and canal openings had a great improvement in T2-nano groups. After 8 weeks of feeding with experimental diets, the SEM images of the rat femurs showed that bone morphology was better improved in the OVX groups compared with the OVX-OS groups. In all sham, OVX, and OVX-OS rats, T2-nano showed better bone morphology than the rest of the diet groups.

Effect of Experimental Diets on Absorption and Bioavailability of Calcium in Sham, OVX, and OVX-OS Rats. The results obtained from the calcium absorption and bioavailability analysis of sham, OVX, and OVX-OS rats are shown in Figure 6. It can be seen from the data in Figure 6a that the T2 groups had significantly (p = 0.00) more absorption than the T1 groups in both OVX and OVX-OS rats; however, the difference between T2 and T1 was not significant (p = 0.11) in the sham group. In addition, calcium absorption in T2-nano was significantly (p = 0.00) higher than T2 in all groups. As a result, the percentage of calcium absorption in the T2-nano group was at the highest level compared with the other groups for sham, OVX, and OVX-OS rats. Under experimental conditions, the absorption of calcium for T2-nano had a significant (p = 0.00) increase in sham and OVX rats compared to OVX-OS rats. On the other hand, the opposite trend was observed in calcium absorption for T2 (Figure 6a).

From the data in Figure 6b, the same trends as calcium absorption were observed for the bioavailability of calcium with significant differences (p = 0.00) among the groups in sham, OVX, and OVX-OS rats. Similar to the calcium absorption, in all groups of rats, calcium bioavailability of T2 was higher than T1. Moreover, the percentage of calcium bioavailability in T2-nano was significantly (p = 0.00) higher than in T2. As clearly displayed in Figure 6b, the amount of calcium bioavailability had a positive significant (p = 0.00) impact in sham and OVX compared with OVX-OS rats.

■ DISCUSSION

This study set out with the aim of assessing the importance of suitable formula and reducing particle size in improving calcium absorption and calcium bioavailability. With respect to calcium, the average intakes among postmenopausal women are below the current recommended value. Some researchers[34,35] have mainly been interested in calcium fortification, which is an important source of dietary calcium and a basic defense against osteoporosis. The results of the present study showed that fortification with calcium and suitable enhancers had a positive effect on femur morphology, bone strength, and bone calcium. Results of SEM are in agreement with previous findings,[36] which showed that improved calcium absorption could decrease the occurrence of bone fracture and osteoporosis.

The current study developed a calcium citrate fortified milk powder to improve the calcium absorption and bioavailability and to decrease the occurrences of bone fracture as well as osteoporosis. For instance, researchers have previously demonstrated that calcium absorption is determined by the chemical form of the calcium compound, other components of

DOI: 10.1021/acs.jafc.5b01468
J. Agric. Food Chem. 2015, 63, 5795−5804

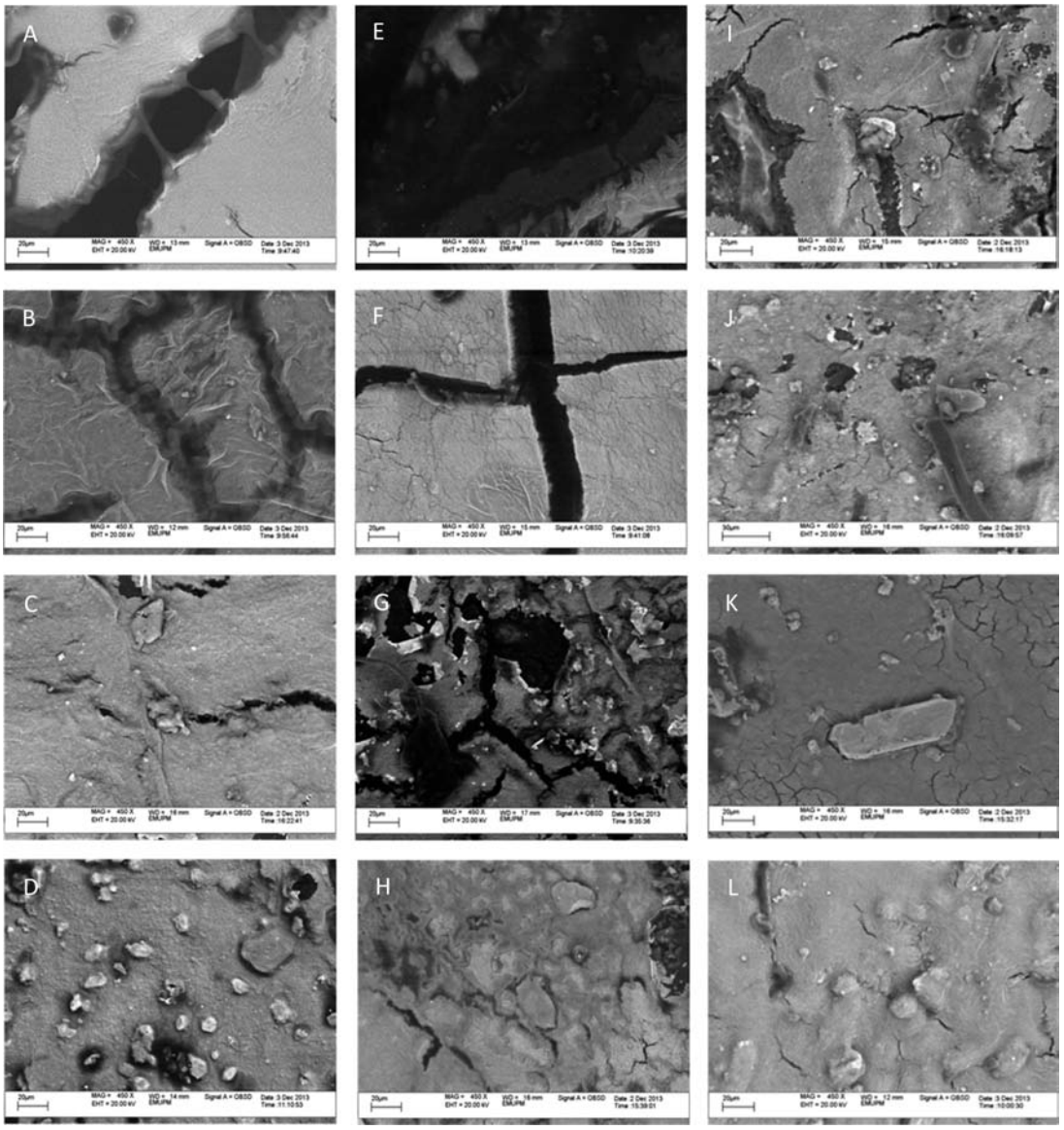

Figure 5. Bone SEM images of OVX rats (A–D), OVX-OS rats (E–H), and sham (I–L): basal diet (A, E, and I), T1 (B, F, and J), T2 (C, G, and K); calcium citrate + vitamins (D_3 + K_1 + B_6) + EPA + DHA + inulin and T2-nano (D, H, and L).

the diet, and the absorption capacity of the intestines.[37] The first important mentioned factor was the chemical form of the calcium compound. Calcium citrate with 21% of elemental calcium is widely used in calcium supplements and fortified foods.[38] In addition, calcium citrate is absorbed equally well when taken with or without food.[39] It is also the best choice for people with inflammatory bowel disease and other conditions that hamper calcium absorption.[40] Therefore, it was chosen as the preferred source for fortification of skim milk powder.

It has also been reported that there was difference in the bioavailability of calcium from milk and that from calcium salts.[16] In the present study, observations showed that the fortified milk powder had more absorption and bioavailability compared to the skim milk powder. These differences might be due to the added absorption enhancers as the components of the diet. In fact, mineral bioavailability could be influenced by several factors in the diet. The magnitude of this influence depends on inhibitors and promoters contained in meal and the diet composition.

Some researchers observed positive effects of inulin and the other compounds (omega-3, vitamins D_3, K_1, and B_6) on calcium absorption and bioavailability.[41−45] The present results indicated that when calcium absorption enhancers were used in combination, absorption and bioavailability of calcium increased (Figure 6). These observations confirmed that bone loss caused via osteoporosis is preventable by effective calcium absorption enhancers.

Furthermore, some researchers concluded that hormonal status and an adequate intake of calcium are major factors in determining calcium and bone status, whereas the particle size of the calcium supplement is not significant in this relation.[46] On the other hand, Cho et al.[47] demonstrated that nanoparticles had higher absorption and more extensive organ distribution when administered orally. Furthermore, Wegmüller et al.[48] stated that decreasing the particle size of elemental iron powders increases iron absorption. Moreover, Singh et al.[49] studied the effect of different-sized cerium oxide nanoparticles on the decomposition and hydrogen absorption kinetics of magnesium hydride. Their results showed nanoparticles had 1.5 times better absorption kinetics with respect to pure

DOI: 10.1021/acs.jafc.5b01468
J. Agric. Food Chem. 2015, 63, 5795−5804

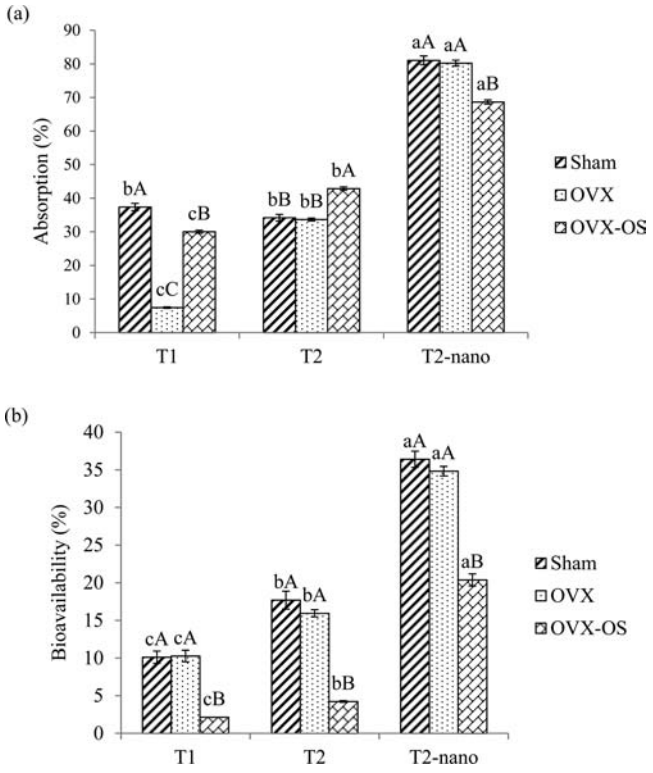

Figure 6. (a) Absorption and (b) bioavailability of calcium for sham, OVX rats, and OVX-OS rats. Different lower case letters show significant difference ($p < 0.05$) between rats fed different diets. Different upper case letters show significant difference ($p < 0.05$) among rats fed the same diet.

magnesium hydride. Similarly, the results of the present study revealed that using a suitable composition and particle size reduction to nanoscale may induce high intestinal calcium absorption and decrease bone loss by ovariectomy and osteoporosis.

The findings of the current study are also consistent with those of Kruger et al.,[43] who indicated that improved calcium absorption could decrease the occurrences of bone fracture and osteoporosis. Thus, the data on the absorption and bioavailability indicated the importance of suitable formulation and preparation conditions in high intestinal absorption and high bioavailability of calcium in rats. Although, the current findings demonstrate the efficacy of nutrients and reducing particle size in the treatment of osteoporosis in rats, further experimental investigations are required to clarify the mechanism of this system in the human body.

AUTHOR INFORMATION

Corresponding Author

*(M.Y.A.M.) Phone: +603 8947 1952. Fax: +603 8943 9745. E-mail: myazid@upm.edu.my.

Notes

The authors declare no competing financial interest.

ABBREVIATIONS USED

ANOVA, analysis of variance; APS, average particle size; CCD, central composite design; DHA, docosahexaenoic acid; EFTEM, energy filtered transmission electron microscopy; EPA, eicosapentaenoic acid; FRM, final reduced model; OS, osteoporosis; OVX, ovariectomized; PDI, polydispersity index; RSM, response surface methodology; SEM, scanning electron microscopy; TEM, transmission electron microscopy

REFERENCES

(1) Badaruddoza; Hundal, M. K. Comparison of anthropometric characteristics and blood pressure phenotypes between pre-and post-menopausal Punjabi women. *Anthropologist* **2009**, *11*, 271−275.
(2) Shapiro, R.; Heaney, R. Co-dependence of calcium and phosphorus for growth and bone development under conditions of varying deficiency. *Bone* **2003**, *32*, 532−540.
(3) O'Brien, K.; Abrams, S.; Liang, L.; Ellis, K.; Gagel, R. Increased efficiency of calcium absorption during short periods of inadequate calcium intake in girls. *Am. J. Clin. Nutr.* **1996**, *63*, 579−583.
(4) Miller, G. D.; Jarvis, J. K.; McBean, L. D. The importance of meeting calcium needs with foods. *J. Am. Coll. Nutr.* **2001**, *20*, 168S−185S.
(5) Hasling, C.; Charles, P.; Jensen, F. T.; Mosekilde, L. Calcium metabolism in postmenopausal osteoporosis: the influence of dietary calcium and net absorbed calcium. *J. Bone Miner. Res.* **1990**, *5*, 939−946.
(6) Hunt, C. D.; Johnson, L. K. Calcium requirements: New estimations for men and women by cross-sectional statistical analyses of calcium balance data from metabolic studies. *Am. J. Clin. Nutr.* **2007**, *86*, 1054−1063.
(7) Ma, J.; Johns, R. A.; Stafford, R. S. Americans are not meeting current calcium recommendations. *Am. J. Clin. Nutr.* **2007**, *85*, 1361−1366.
(8) Straub, D. Calcium supplementation in clinical practice: a review of forms, doses and indications. *Nutr. Clin. Pract.* **2007**, *22*, 286−296.
(9) Soto, A. M.; Morales, P.; Haza, A. I.; Garcia, M. L.; Selgas, M. D. Bioavailability of calcium from enriched meat products using Caco-2 cells. *Food Res. Int.* **2014**, *55*, 263−270.
(10) World Health Organization. *Human Vitamin and Mineral Requirements*; Joint FAO/WHO Expert Consultation, Bangkok, Thailand; WHO: Geneva, Switzerland, 2001; pp 48−197.
(11) Ministry of Health and Family Welfare Government of India. *Guidelines for Control of Iron Deficiency Anaemia, Adolescent Division*; 2013; pp 16−18.
(12) Heaney, R. P. Dietary protein and phosphorus do not affect calcium absorption. *Am. J. Clin. Nutr.* **2000**, *72*, 675−676.
(13) Mekmene, O.; Le Graët, Y.; Gaucheron, F. A model for predicting salt equilibria in milk and mineral-enriched milks. *Food Chem.* **2009**, *116*, 233−239.
(14) Van den Hee, R. M.; Regin, E. M.; Miret, S.; Slettenaar, M.; Duchateau, G. S.; Rietveld, A. G.; Wilkinson, J. E.; Teucher, B. Calcium absorption from fortified ice cream formulations compared with calcium absorption from milk. *J. Am. Diet. Assoc.* **2009**, *109*, 830−835.
(15) Singh, G.; Arora, S.; Sharma, G. S.; Sindhu, J. S.; Kansal, V. K.; Sangwan, R. B. Heat stability and calcium bioavailability of calcium-fortified milk. *LWT−Food Sci. Technol.* **2007**, *40*, 625−631.
(16) Costa, F. F.; Resende, J. V.; Abreu, L. R.; Goff, H. D. Effect of calcium chloride addition on ice cream structure and quality. *J. Dairy Sci.* **2008**, *91*, 2165−2174.
(17) Daengprok, W.; Garnjanagoonchorna, W.; Mine, Y. Fermented pork sausage fortified with commercial or hen eggshell calcium lactate. *Meat Sci.* **2002**, *62*, 199−204.
(18) Cáceres, E.; García, M. L.; Selgas, M. D. Design of a new cooked meat sausage enriched with calcium. *Meat Sci.* **2006**, *73*, 368−377.
(19) Heaney, R. P.; Bilezikian, J. P.; Holick, M. F.; Nieves, J. W.; Weaver, C. M. The role of calcium in peri- and postmenopausal women: 2006 position statement of The North American Menopause Society. *Menopause* **2006**, *13*, 862−877.
(20) Ayed, M. A.; Thannoun, A. M. Calcium bioavailability of calcium carbonate based diets formale growing rats. *Mesopotamia J. Agric.* **2006**, *34*, 1−14.
(21) Waterbeemd, H. V.; Lennernäs, H.; Artursson, P. The importance of gut wall metabolism in determining drug bioavailability. In *Drug Bioavailability-Estimation of Solubility Permeability, Absorption and Bioavailability*; WaterBeemd, H., Testa, B., Eds.; Wiley-VCH: Weinheim, Germany, 2009; 321 pp.

DOI: 10.1021/acs.jafc.5b01468
J. Agric. Food Chem. 2015, 63, 5795−5804

(22) Shimomura, M.; Sawadaishi, T. Bottom-up strategy of materials fabrication: a new trend in nanotechnology of soft materials. *Curr. Opin. Colloid Interface Sci.* **2001**, *6*, 11−16.
(23) Whitesides, G. M.; Grzybowski, B. Self-assembly at all scales. *Science* **2002**, *295*, 2418−2421.
(24) Mohanty, A. K.; Dilnawaz, F.; Mohanty, C.; Sahoo, S. K. Etoposide-loaded biodegradable amphiphilicmethoxy (polyethylene glycol) and poly(ε-caprolactone) copolymeric micelles as drug delivery vehicle for cancer therapy. *Drug Delivery* **2010**, *17*, 330−342.
(25) Thakkar, K. N.; Snehit, S.; Mhatre, M. S.; Rasesh, Y.; Parikh, M. S. Biological synthesis of metallic nanoparticles. *Nanomedicine* **2010**, *6*, 257−262.
(26) Montgomery, D. C. *Design and Analysis of Experiments*; Wiley: New York, 2001.
(27) Rasti, B.; Jinap, S.; Mozafari, M. R.; Abd-Manap, M. Y. Optimization on preparation condition of polyunsaturated fatty acids nanoliposome prepared by Mozafari method. *J. Liposome Res.* **2014**, *24*, 99−105.
(28) Shirke, S. S.; Jadhav, S. R.; Jagtap, A. G. Methanolic extract of *Cuminum cyminum* inhibits ovariectomy-induced bone loss in rats. *Exp. Biol. Med.* **2008**, *233*, 1403−1410.
(29) Park, H.; Jeon, B.; Ahn, J.; Kwak, H. Effects of nano calcium supplemented milk on bone calcium metabolism in ovariectomized rats. *Asian−Australas. J. Anim. Sci.* **2007**, *20*, 12−66.
(30) Bimonte-Nelson, H. A.; Singleton, R. S.; Hunter, C. L.; Price, K. L.; Moore, A. B.; Granholm, A. E. Ovarian hormones and cognition in the aged female rat: I. Long-term, but not short-term, ovariectomy enhances spatial performance. *Behav. Neurosci.* **2003**, *117*, 1395−1406.
(31) Ken, K.; Yasuhiro, T.; Hiroaki, M.; Jun-Ichi, Y.; Yasuhiro, M.; Hiroshi, K.; Akira, I.; Masayoshi, K.; Seiichiro, A.; Yukihiro, T. Milk basic protein enhances the bone strength in ovariectomized rats. *J. Food Biochem.* **2000**, *24*, 467−476.
(32) Erfanian, A.; Mirhosseini, H.; AbdManap, M. H.; Rasti, B.; Hair Bejo, M. Influence of nano-size reduction on absorption and bioavailability of calcium from fortified milk powder in rats. *Food Res. Int.* **2014**, *66*, 1−11.
(33) Joglekar, A.; May, A. Product excellence through design of experiments. *Cereal Foods World* **1987**, *32*, 857−868.
(34) Chen, Y. C.; Chen, T. C. Mineral utilization in layers as influenced by dietary oligofructose and inulin. *Int. J. Poult. Sci.* **2004**, *3*, 442−445.
(35) Kaushik, R.; Sachdeva, B.; Arora, S.; Kapila, S.; Wadhwa, B. K. Bioavailability of vitamin D_2 and calcium from fortified milk. *Food Chem.* **2014**, *147*, 307−311.
(36) Sunyecz, J. A. The use of calcium and vitamin D in the management of osteoporosis. *Ther. Clin. Risk Manage.* **2008**, *4*, 827−836.
(37) Deroisy, R.; Zartarian, M.; Meurmans, L.; Nelissenne, N.; Micheletti, M.; Albert, A.; Reginster, J. Acute changes in serum calcium and parathyroid hormone circulating levels induced by the oral intake of five currently available calcium salts in healthy male volunteers. *Clin. Rheumatol.* **1997**, *16*, 249−253.
(38) National Institutes of Health. *Optimal Calcium Intake*; NIH Consensus Statement; Bethesda, MD, USA, 1994; Vol. 12, pp 1−31.
(39) Straub, D. A. Calcium supplementation in clinical practice: a review of forms, doses, and indications. *Nutr. Clin. Pract.* **2007**, *22*, 286−296.
(40) Committee to review dietary reference intakes for vitamin D and calcium, food and nutrition board, institute of medicine. *Dietary Reference Intakes for Calcium and Vitamin D*; National Academy Press: Washington, DC, USA, 2010.
(41) Hunt, J. R.; Hunt, C. D.; Zito, C. A.; Idso, J. P.; Johnson, L. K. Calcium requirements of growing rats based on bone mass, structure, or biomechanical strength are similar. *J. Nutr.* **2008**, *138*, 1462−1468.
(42) Probst-Hensch, N. M.; Imboden, M.; Dietrich, D. F.; Barthélemy, J. C.; Ackermann-Liebrich, U.; Berger, W.; Gaspoz, J. M.; Schwartz, J. Glutathione s-transferasepolymorphisms, passive smoking, obesity, and heart rate variability in nonsmokers. *Environ. Health Perspect.* **2008**, *116*, 1494−1499.
(43) Kruger, M. C.; Gallaher, B. W.; Schollum, L. M. The effects of fructooligosaccharides with various degrees of polymerization on calcium bioavailability in the growing rat. *Exp. Biol. Med.* **2003**, *228*, 683−688.
(44) Sun, D.; Krishnan, A.; Zaman, K.; Lawrence, R.; Bhattacharya, A.; Fernandes, G. Dietary n-3 fatty acids decrease osteoclastogenesis and loss of bone mass in ovariectomized mice. *J. Bone Miner. Res.* **2003**, *18*, 1206−1216.
(45) Watkins, B. A.; Reinwald, S.; Li, Y.; Seifert, M. F. Protective actions of soy isoflavones and n-3 PUFAs on bone mass in ovariectomized rats. *J. Nutr. Biochem.* **2005**, *16*, 479−88.
(46) Shahnazari, M.; Martin, B. R.; Legette, L. L.; Lachcik, P. J.; Welch, J.; Weaver, C. M. Diet calcium level but not calcium supplement particle size affects bone density and mechanical properties in ovariectomized rats. *J. Nutr.* **2009**, *139*, 1308−1314.
(47) Cho, W. S.; Kang, B. C.; Lee, J. K.; Jeong, J.; Che, J. H.; Seok, S. H. Comparative absorption, distribution, and excretion of titanium dioxide and zinc oxide nano particles after repeated oral administration. *Part. Fibre Toxicol.* **2013**, *10*, 9−19.
(48) Wegmüller, R.; Zimmermann, M. B.; Moretti, D.; Arnold, M.; Langhans, W.; Hurrell, R. F. Particle size reduction and encapsulation affect the bioavailability of ferric pyrophosphate in rats. *J. Nutr.* **2004**, *134*, 3301−3304.
(49) Singh, R. K.; Sadhasivam, T.; Sheeja, G. I.; Singh, P.; Srivastava, O. N. Effect of different sized CeO_2 nano particles on decomposition and hydrogen absorption kinetics of magnesium hydride. *Int. J. Hydrogen Energy* **2013**, *38*, 1−5.

DOI: 10.1021/acs.jafc.5b01468
J. Agric. Food Chem. 2015, 63, 5795−5804

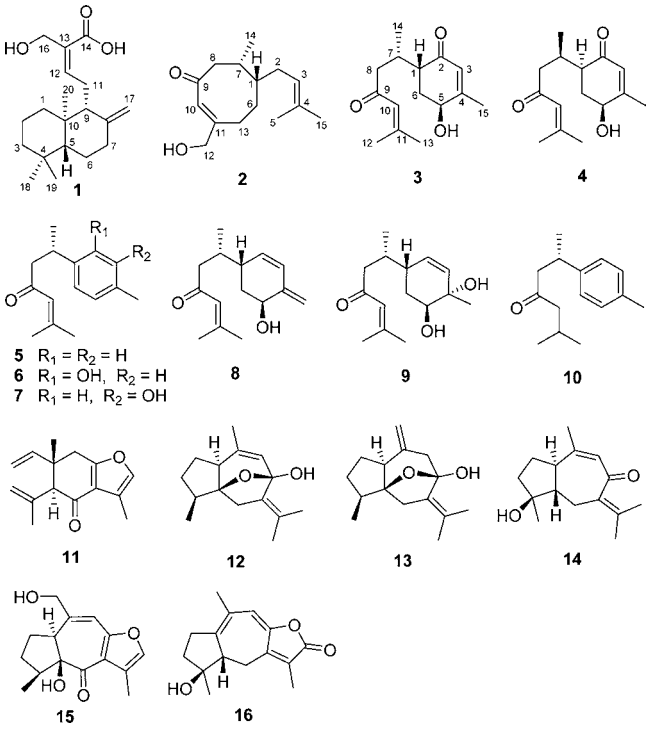

Figure 1. Structures of compounds **1**–**16** from *C. longa*.

Ltd., Kyoto, Japan). The flow rate of HPLC was 5.5 mL/min. Silica gel (100–200 mesh) was used for column chromatography (Qingdao Haiyang Chemical Group Co. Ltd., Qingdao, People's Republic of China). Chemical reagents for isolation were of analytical grade and purchased from Tianjin Chemical Reagent Co. (Tianjin, People's Republic of China). Biological reagents were from Sigma Chemical Co. The murine microglial BV-2 cell line was from Shanghai Institutes for Biological Sciences, Chinese Academy of Sciences (Shanghai, People's Republic of China).

Plant Material. The rhizomes of *C. longa* were purchased in July 2009 from Anguo Materia Medica Market, Hebei province, People's Republic of China. The plant material was identified by one of the authors (Dr. Yuanqiang Guo), and a voucher specimen (no. 20090871) was deposited at the laboratory of the Research Department of Natural Medicine, College of Pharmacy, Nankai University.

Extraction and Isolation. The air-dried rhizomes of *C. longa* (6.0 kg) were powdered and extracted with MeOH (3 × 48 L) under reflux. The organic solvent was removed to give a crude residue (750 g). This residue was suspended in H_2O (0.8 L) and partitioned with EtOAc (3 × 0.8 L). The EtOAc-soluble portion (245.0 g) was fractionated by silica gel column chromatography (silica gel, 1.0 kg; column, 9 × 70 cm), using a gradient solvent system of petroleum ether/acetone (100:0, 100:1, 100:2, 100:3, 100:5, 100:8, 100:11, 100:16, 100:23, and 100:30; 21 L for each gradient elution), to yield eight fractions (F_1–F_8) based on TLC analyses. Fraction F_7 was subjected to MPLC over ODS eluting with a step gradient from 73–93% MeOH in H_2O to give four subfractions ($F_{7\text{-}1}$–$F_{7\text{-}4}$). Subfraction $F_{7\text{-}3}$ was further isolated by preparative HPLC (78% MeOH in H_2O) to give compound **1** (t_R = 27 min, 16.9 mg). The purification of subfraction $F_{7\text{-}2}$ with the same HPLC (74% MeOH in H_2O) yielded compound **9** (t_R = 24 min, 13.7 mg). Fraction F_5, with the same procedures as for F_7, gave four subfractions $F_{5\text{-}1}$–$F_{5\text{-}4}$, and compounds **2** (t_R = 26 min, 13.2 mg) and **14** (t_R = 21 min, 13.1 mg) were obtained from $F_{5\text{-}2}$ (82% MeOH in H_2O) with the same HPLC system. Fraction F_6 was fractionated by the above MPLC to yield three subfractions $F_{6\text{-}1}$–$F_{6\text{-}3}$, and the purification of subfraction $F_{6\text{-}1}$ (80% MeOH in H_2O) with the same HPLC system afforded compounds **3** (t_R = 21 min, 11.9 mg), **4** (t_R = 23 min, 9.9 mg), **15** (t_R = 35 min, 14.1 mg), and **16** (t_R = 39 min, 13.7 mg). Using the same MPLC system as for the above fractions, F_2, F_3, and F_4 afforded their subfractions $F_{2\text{-}1}$–$F_{2\text{-}5}$, $F_{3\text{-}1}$–$F_{3\text{-}4}$, and $F_{4\text{-}1}$–$F_{4\text{-}6}$, respectively. The following purification of subfractions $F_{2\text{-}5}$ (88% MeOH in H_2O), $F_{2\text{-}1}$ (85% MeOH in H_2O), and $F_{2\text{-}3}$ (86% MeOH in H_2O) yielded compounds **5** (t_R = 25 min, 15.0 mg), **6** (t_R = 26 min, 18.1 mg), and **11** (t_R = 29 min, 10.1 mg), respectively. Compounds **7** (t_R = 41 min, 20.9 mg) and **8** (t_R = 33 min, 14.6 mg) were obtained from subfraction $F_{4\text{-}3}$ with the same HPLC system (80% MeOH in H_2O). Compounds **10** (t_R = 36 min, 8.9 mg) and **12** (t_R = 28 min, 12.7 mg) were isolated from $F_{3\text{-}2}$ (82% MeOH in H_2O) and the purification of $F_{3\text{-}4}$ (84% MeOH in H_2O) to afford compound **13** (t_R = 29 min, 19.2 mg).

Table 1. ^{13}C NMR Data for Compounds 1–4[a]

position	1		2		3		4	
1	39.2	CH_2	50.8	CH	45.7	CH	49.8	CH
2	19.3	CH_2	26.0	CH_2	200.6	C	199.6	C
3	42.0	CH_2	124.4	CH	127.0	CH	127.3	CH
4	33.6	C	131.5	C	159.9	C	163.9	C
5	55.4	CH	25.7	CH_3	66.8	CH	70.2	CH
6	24.1	CH_2	22.2	CH_2	32.0	CH_2	34.8	CH_2
7	37.9	CH_2	30.3	CH	27.8	CH	28.8	CH
8	148.0	C	34.6	CH_2	48.9	CH_2	48.1	CH_2
9	56.7	CH	201.1	C	200.8	C	201.1	C
10	39.6	C	123.8	CH	123.7	CH	123.8	CH
11	23.8	CH_2	162.6	C	156.1	C	155.7	C
12	150.1	CH	26.0	CH_2	20.8	CH_3	20.8	CH_3
13	129.5	C	64.9	CH_2	27.7	CH_3	27.7	CH_3
14	172.2	C	15.6	CH_3	17.0	CH_3	16.6	CH_3
15			17.7	CH_3	21.2	CH_3	19.6	CH_3
16	57.2	CH_2						
17	107.9	CH_2						
18	33.6	CH_3						
19	21.7	CH_3						
20	14.4	CH_3						

[a] δ in ppm, 100 MHz, in $CDCl_3$. Assignments of ^{13}C NMR data are based on DEPT, HMQC, and HMBC experiments.

DOI: 10.1021/acs.jafc.5b01584
J. Agric. Food Chem. 2015, 63, 5805–5812

Table 2. ^{1}H NMR Data for Compounds 1−4[a]

position	1	position	2	3	4
1	α 1.74 m	1	2.21 m	β 2.49 m	α 2.31 m
	β 1.09 m	2	a 1.81 m		
2	α 1.59 m		b 2.01 m		
	β 1.51 m	3	5.11 m	5.74 d (1.2)	5.80 s
3	α 1.42 m	5	1.68 s	α 4.32 t (4.5)	α 4.48 dd (11.9, 4.4)
	β 1.19 m	6	a 1.76 m	α 2.07 m	α 1.75 m
5	1.14 m		b 1.98 m	β 2.01 m	β 2.27 m
6	α 1.74 m	7	2.34 m	β 2.68 m	α 2.66 m
	β 1.34 dd (12.8, 4.5)	8	a 1.31 d (15.4)	a 2.39 dd (15.4, 6.2)	a 2.56 dd (15.1, 4.4)
7	α 2.00 ddd		b 1.29 dd (15.4, 8.1)	b 2.29 dd (15.4, 8.1)	b 2.22 dd (15.1, 9.6)
	(17.5, 12.8, 4.2)	10	6.11 s	6.06 d (1.1)	6.15 s
	β 2.40 m	12	4.24 s	2.07 s	2.13 s
9	1.87 d (10.4)	13	a 2.35 m	1.84 s	1.89 s
11	a 2.53 m		b 2.29 m		
	b 2.31 m	14	0.81 d (6.8)	0.85 d (6.8)	0.94 d (7.0)
12	6.97 t (6.7)	15	1.60 s	1.99 s	2.04 s
16	4.39 s				
17	a 4.42 s; b 4.84 s				
18	0.89 s				
19	0.83 s				
20	0.74 s				

[a]δ in ppm, J in Hz, 400 MHz, in $CDCl_3$. Assignments of ^{1}H NMR data are based on ^{1}H−^{1}H COSY, HMQC, and HMBC experiments.

*Longpene A, **1**:* colorless oil; $[\alpha]_D^{27}$ +6.8 (c 0.20, CH_2Cl_2); CD (0.5 mg/mL, CH_3CN) 194 ($\Delta\varepsilon$ −25.2) and 224 ($\Delta\varepsilon$ +6.6) nm; IR (KBr) ν_{max} 3432, 2927, 2851, 1693, 1643, 1492, 1440, 1386, 1201, and 1016 cm^{-1}; ^{13}C NMR (100 MHz, $CDCl_3$) and ^{1}H NMR (400 MHz, $CDCl_3$) data, see Tables 1 and 2; ESIMS m/z 305 $[M - H]^-$; HR-ESIMS m/z 305.2121 $[M - H]^-$, calcd for $C_{19}H_{29}O_3$, 305.2117.

*Longpene B, **2**:* colorless oil; $[\alpha]_D^{20}$ −10.8 (c 0.24, CH_2Cl_2); CD (0.5 mg/mL, CH_3CN) 201 ($\Delta\varepsilon$ −17.2), 234 ($\Delta\varepsilon$ +2.9), and 341 ($\Delta\varepsilon$ −2.3) nm; IR (KBr) ν_{max} 3400, 2961, 2925, 2856, 1658, 1452, 1378, 1208, and 1065 cm^{-1}; ^{13}C NMR (100 MHz, $CDCl_3$) and ^{1}H NMR (400 MHz, $CDCl_3$) data, see Tables 1 and 2; ESIMS m/z 259 $[M + Na]^+$; HR-ESIMS m/z 259.1671 $[M + Na]^+$, calcd for $C_{15}H_{24}NaO_2$, 259.1674.

*Longpene C, **3**:* colorless oil; $[\alpha]_D^{27}$ −9.0 (c 0.20, CH_2Cl_2); CD (0.5 mg/mL, CH_3CN) 207 ($\Delta\varepsilon$ +11.4), 230 ($\Delta\varepsilon$ −12.6), and 316 ($\Delta\varepsilon$ +0.9) nm; IR (KBr) ν_{max} 3422, 2926, 2874, 1671, 1618, 1457, 1383, 1248, and 1081 cm^{-1}; ^{13}C NMR (100 MHz, $CDCl_3$) and ^{1}H NMR (400 MHz, $CDCl_3$) data, see Tables 1 and 2; ESIMS m/z 273 $[M + Na]^+$; HR-ESIMS m/z 273.1460 $[M + Na]^+$, calcd for $C_{15}H_{22}NaO_3$, 273.1467.

*Longpene D, **4**:* colorless oil; $[\alpha]_D^{27}$ +69.2 (c 0.09, CH_2Cl_2); CD (0.5 mg/mL, CH_3CN) 208 ($\Delta\varepsilon$ +13.1), 229 ($\Delta\varepsilon$ −4.1), 248 ($\Delta\varepsilon$ +1.6), and 342 ($\Delta\varepsilon$ +1.7) nm; IR (KBr) ν_{max} 3425, 2957, 2925, 2856, 1668, 1620, 1452, 1382, 1261, and 1082 cm^{-1}; ^{13}C NMR (100 MHz, $CDCl_3$) and ^{1}H NMR (400 MHz, $CDCl_3$) data, see Tables 1 and 2; ESIMS m/z 273 $[M + Na]^+$; HR-ESIMS m/z 273.1464 $[M + Na]^+$, calcd for $C_{15}H_{22}NaO_3$, 273.1467.

Computational Methods. Starting from the conformation of every compound deduced from NOESY spectrum and Chem3D modeling, conformational searches were performed first using MOE software[17] and conformers were selected for geometry optimizations. Geometry optimizations and reoptimizations on the B3LYP/6-31+G(d,p) level were finished by the Gaussian 09 package.[18] TDDFT ECD calculations[19−21] for the optimized conformers were performed at the CAM-B3LYP/SVP level with a CPCM solvent model in acetonitrile, and the calculated ECD spectra of different conformers were simulated with a half bandwidth of ∼0.4 eV. The CD curves were extracted by SpecDis 1.62 software.[22] The overall ECD curves of all the compounds were weighted by Boltzmann distribution after UV correction.

Bioassay for NO production. The bioassay for NO production was performed according to the reported method.[16]

RESULTS AND DISCUSSION

The ethyl acetate-soluble part of the methanol extract of the rhizomes of *C. longa* was fractionated by silica gel column chromatography and MPLC and further purified by HPLC to afford 2 new and 14 known terpenoids, **1**−**16**.

Compound **1** was obtained as a colorless oil. Its HR-ESIMS provided the molecular formula $C_{19}H_{30}O_3$, which was supported by the NMR data (Tables 1 and 2). The molecular formula suggested five unsaturation degrees for **1**. The ^{1}H NMR spectrum of **1** indicated three methyl groups [δ_H 0.89 (3H, H_3-18), 0.83 (3H, s, H_3-19), and 0.74 (3H, s, H_3-20)], three olefinic protons [δ_H 6.97 (1H, t, J = 6.7 Hz, H-12), 4.42 (1H, s, H-17a), and 4.84 (1H, s, H-17b)], and two hydroxymethyl protons [δ_H 4.39 (2H, s, H_2-16)]. The ^{13}C NMR spectrum of **1** showed 19 carbon signals, which were sorted as three methyls [δ_C 33.6 (C-18), 21.7 (C-19), and 14.4 (C-20)], eight methylenes [δ_C 39.2 (C-1), 19.3 (C-2), 42.0 (C-3), 24.1 (C-6), 37.9 (C-7), 23.8 (C-11), 57.2 (C-16), and 107.9 (C-17)], three methines [δ_C 55.4 (C-5), 56.7 (C-9), and 150.1 (C-12)], and five quaternary carbons [δ_C 33.6 (C-4), 148.0 (C-8), 39.6 (C-10), 129.5 (C-13), and 172.2 (C-14)] with the aid of DEPT and HMQC spectra. On the basis of the total unsaturation degrees, the aforementioned spectroscopic features, and the reported terpenoids from the genus *Curcuma*,[23−26] compound **1** might be a norditerpene with two rings. Comparison of the chemical shifts of C-1−C-10, and C-17−C-20 of compound **1** with those of reported labdane-type diterpenes[23−25] showed the occurrence of a structural fragment, two fused six-membered rings. To corroborate the above deductions and elucidate the structure, HMBC and ^{1}H−^{1}H COSY experiments were performed. The following interpretation of HMQC, HMBC, and ^{1}H−^{1}H COSY spectra (Figure 2) resulted in the confirmation of the above structural moiety of two fused six-membered rings, where the olefinic

DOI: 10.1021/acs.jafc.5b01584
J. Agric. Food Chem. 2015, 63, 5805−5812

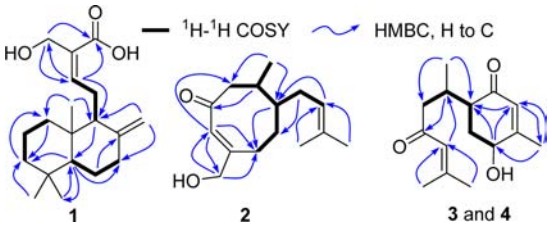

Figure 2. ^{1}H−^{1}H COSY and key HMBC correlations of compounds **1**−**4**.

carbons of the terminal double bond at δ_C 148.0 and 107.9 were assigned to C-8 and C-17, and the three methyls (C-18, C-19, and C-20) were demonstrated to be attached at C-4, C-4, and C-10, respectively. The residual five carbons at δ_C 23.8, 150.1, 129.5, 172.2, and 57.2 were assigned to C-11−C-16 by the HMBC correlations of H-12 to C-9, C-11, C-13, C-14, and C-16 and H_2-16 to C-12, C-13, and C-14. On the basis of the above evidence and further detailed analyses of HMQC, HMBC, and ^{1}H−^{1}H COSY spectra, the planar structure of compound **1** was elucidated as a 15-nor labdane diterpene.[23,24]

The relative configuration of compound **1** was deduced from NOESY spectrum and Chem3D modeling (Figure 3). NOESY correlations observed for H-1β/H-3β, H-1β/H-5, H-1β/H-9, H-3β/H_3-19 H-3β/H-5, H-2α/H_3-18, H_3-18/H_3-20, H_3-18/H-6α, H_3-20/H-7α, H-7α/H-11b, H-9/H-17a, H-9/H-12, H-17a/H-12, H-12/H_2-16, H-17b/H-7β, and H-11a/H-1α, together with Chem3D modeling, implied a conformation for compound **1** as shown in Figure 3, where the two six-membered rings A and B were *trans*-fused and existed in a chair and a twisted boat conformation, respectively, the H-5 proton was found to be β-axially oriented, the methyl groups Me-18 and Me-20 were both in an α-axial position, and the double bond of C-12 and C-13 was *Z*-configuration. After finishing the elucidation of the relative configuration, the absolute configuration of **1** was established by comparing the experimental and calculated ECD spectra.[19] The calculated ECD spectra were obtained as follows. Starting from the conformation of **1** deduced from NOESY correlations and Chem3D modeling, conformational searches by MOE software[17] and the final geometry optimization on the B3LYP/6-31+G(d,p) level by the Gaussian 09 package[18] were performed. Then, the ECD spectra were calculated at the CAM-B3LYP/SVP level with the CPCM model in acetonitrile. The obtained ECD spectrum of **1a** (Figure 4) matched the experimental

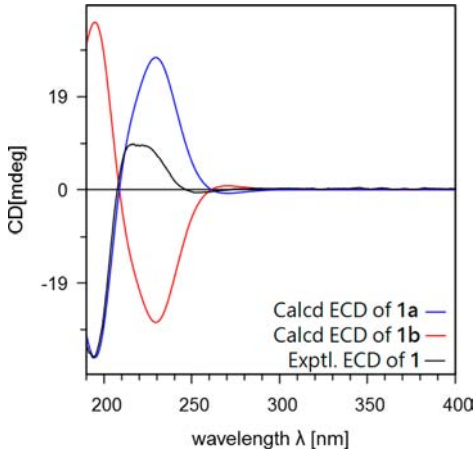

Figure 4. Calculated ECD spectra of **1a** (5*R*,9*R*,10*R*)-isomer and **1b** (5*S*,9*S*,10*S*)-isomer and the experimental ECD spectrum of **1** in acetonitrile.

results closely. All of the above evidence allowed the structure of **1** to be elucidated as (5*R*,9*R*,10*R*,12*Z*)-15-norlabda-8(17),11-diene-14-oic acid, which has been named longpene A.

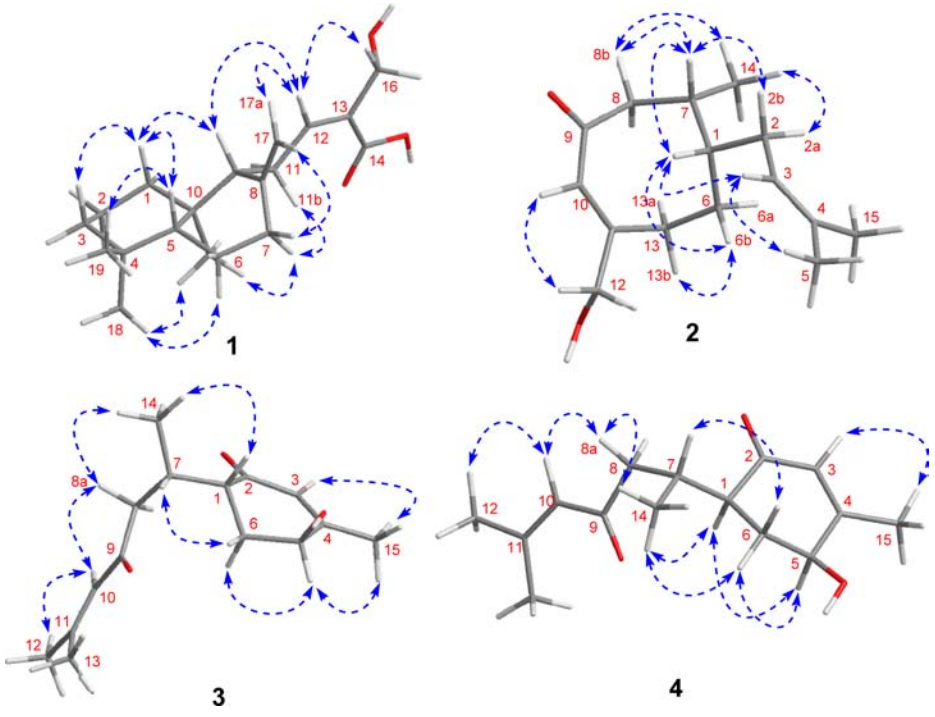

Figure 3. Conformations and key NOESY correlations of compounds **1**−**4**.

DOI: 10.1021/acs.jafc.5b01584
J. Agric. Food Chem. 2015, 63, 5805−5812

The molecular formula of compound **2** was determined as $C_{15}H_{24}O_2$ on the basis of the HR-ESIMS. The IR spectrum showed an absorption band (1658 cm^{-1}) of an α,β-unsaturated ketone moiety. From the ^1H NMR spectrum of **2**, the typical signals of three methyl groups, two olefinic protons, and two methylene protons were observed (Table 2). The ^{13}C NMR spectrum of **2** exhibited 15 carbon resonances, comprising three quaternary carbons (C-4, C-9, and C-11), four methines (C-1, C-3, C-7, and C-10), five methylenes (C-2, C-6, C-8, C-12, and C-13), and three methyls (C-5, C-14, and C-15) indicated by DEPT and HMQC spectra. On the basis of the unsaturation degrees from the molecular formula and the above spectroscopic characteristics, compound **2** might be a monocyclic sesquiterpene. To verify this deduction, the following HMBC and $^1H-^1H$ COSY experiments were performed. In the HMBC spectrum, the correlations of the olefinic proton H-10 with the carbons C-8, C-9, C-11, C-12, and C-13, the methyl protons H_3-14 with the carbons C-1, C-7, and C-8, and the methylene protons H_2-12 with the carbons C-10, C-11, and C-13 disclosed the presence of an eight-membered ring, which was supported by the cross signals in the $^1H-^1H$ COSY spectrum. In addition to this eight-membered ring, a 3-methyl-2-butenyl fragment was also disclosed by interpretation of the HMBC spectrum, which showed the long-range couplings of the olefinic proton H-3 to the carbons C-1, C-2, C-4, C-5, and C-15 and the methyl protons H_3-5 (H_3-15) to the carbons C-4 and C-3. This 3-methyl-2-butenyl moiety was demonstrated to be linked to C-1 of the eight-membered ring by the corresponding HMBC and $^1H-^1H$ COSY correlations (Figure 2). Further analyses of the HMQC, HMBC, and $^1H-^1H$ COSY spectroscopic data resulted in the assignments of all the protons and carbons. Hence, the planar structure for **2** could be established, which possesses an eight-membered ring.

The stereochemistry of **2** was elucidated by interpretation of the NOESY spectrum. NOESY correlations observed for H-1/H-7, H-1/H-3, H-1/H-6b, H-2b/H-7, H-2a/H_3-14, H-3/H_3-5, H-7/H-8b, H_3-14/H-8b, H-8a/H-13a, and H-10/H_2-12, together with Chem3D modeling, implied a molecular arrangement for compound **2** as shown in Figure 3, in which the C-14 methyl group was in an α-position, the H-1 proton was in a β-position, and the double bond between C-10 and C-11 was found to be in *E*-configuration. After definition of the relative configuration, the same energy minimization, geometry optimizations, and TDDFT ECD calculations as for compound **1** were performed to confirm the absolute configuration. The obtained ECD spectra calculated at the CAM-B3LYP/SVP level with the CPCM model in acetonitrile for **2a** (1*S*,7*S*) and **2b** (1*R*,7*R*) are shown in Figure 5. By comparison of the experimental and calculated ECD spectra, the absolute configuration of **2** was determined to be 1*S* and 7*S*. Thus, compound **2** (longpene B) was elucidated as a skeletally novel sesquiterpene with an eight-membered ring, which may be derived from bisabolane sesquiterpenes through the cleavage of C-6 and C-5 and the cyclization of C-6 and C-13.

Compound **3**, a colorless oil, possessed a molecular formula of $C_{15}H_{22}O_3$ as supported by the HR-ESIMS. From the ^1H NMR spectrum of **3**, four methyl groups, two olefinic protons, and one oxygenated methine proton were displayed (Table 2). The ^{13}C NMR spectrum of **3** exhibited 15 carbon resonances. With the aid of DEPT and HMQC spectra, these 15 carbons were sorted as 4 methyls, 5 methines, 2 methylenes, and 4 quaternary carbons including 2 ketone carbonyl carbons

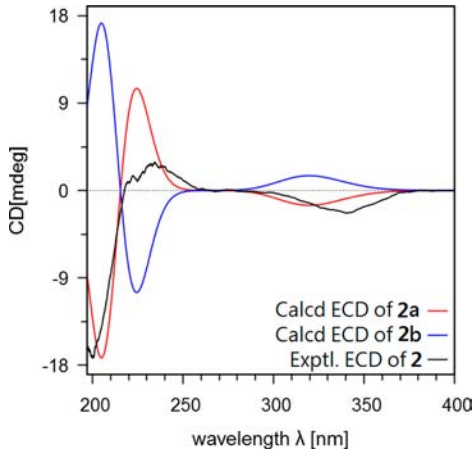

Figure 5. Calculated ECD spectra of **2a** (1*S*,7*S*)-isomer and **2b** (1*R*,7*R*)-isomer and the experimental ECD spectrum of **2** in acetonitrile.

conjugated with double bonds. The above spectroscopic features disclosed compound **3** should be a sesquiterpne with two ketone carbonyls.[3,5,26−28] To elucidate the sesquiterpene skeleton and accomplish the assignments of proton and carbon signals, an HMBC experiment was carried out. From the HMBC spectrum, the long-range correlations of the olefinic H-3 proton [δ_H 5.74 (1H, d, J = 1.2 Hz)] with carbons C-1, C-2, C-4, C-5, and C-15 and of the oxygenated H-5 proton [δ_H 4.32 (1H, t, J = 4.5 Hz)] with carbons C-1, C-3, C-4, C-6, and C-15 revealed the presence of a six-membered ring, which was supported by the $^1H-^1H$ COSY correlations (Figure 2). Furthermore, the side chain comprising C-7−C-14 was deduced from the HMBC correlations of H_3-14 to C-1, C-7, and C-8, H-10 to C-8, C-9, C-11, C-12, and C-13, and the corresponding $^1H-^1H$ COSY correlations. The linkage of the six-membered ring and the side chain allowed the establishment of planar structure for compound **3**, which was a bisabolane-type sesquiterpene.[26,27] This planar structure of **3** was the same as that of 5α-hydroxyl-1β-bisabolon-9-one reported in the literature,[29] and the NMR data for these two compounds were almost identical. However, the orientation of C-14 methyl in 5α-hydroxyl-1β-bisabolon-9-one was not assigned, and the absolute configuration of this compound was also unknown. To elucidate the configuration of **3**, a NOESY experiment and TDDFT ECD calculations were performed.

The NOESY correlations of H-1/H_3-14, H-3/H_3-15, H-5/H_3-15, H-5/H-6α, H-6β/H-7, H-8a/H_3-14, H-8b/H-10, and H-8a/H-10 and a Chem3D modeling revealed a conformation as shown in Figure 3. In this arrangement for compound **3**, the unsaturated six-membered ring was found to be a twist-chair preferential conformation, the side chain C-7−C-10 was α-equatorially oriented, and the hydroxy group at C-5 was β-axially oriented, which was supported by a triplet peak for H-5 and the coupling constant ($J_{5,6\alpha/6\beta}$ = 4.5 Hz). According to this arrangement inferred from the NOESY spectrum, the C-14 methyl group was determined to be in an α-position. The relative configuration of compound **3** was therefore characterized. On the basis of the relative configuration of **3** deduced from the above analyses, an energy minimization of this conformation was performed. Furthermore, the geometry optimizations were carried out and the calculated ECD spectra at the CAM-B3LYP/SVP level were obtained. A comparison of these ECD spectra revealed that the calculated ECD spectrum

DOI: 10.1021/acs.jafc.5b01584
J. Agric. Food Chem. 2015, 63, 5805−5812

of (1*R*,5*S*,7*S*)-**3** (Figure 6) was in good agreement with the experimental spectrum. Therefore, the absolute configuration of

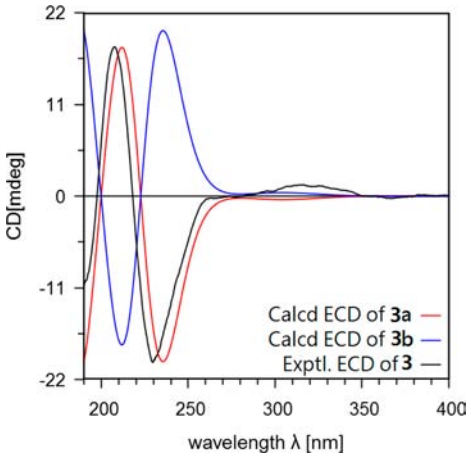

Figure 6. Calculated ECD spectra of **3a** (1*R*,5*S*,7*S*)-isomer and **3b** (1*S*,5*R*,7*R*)-isomer and the experimental ECD spectrum of **3** in acetonitrile.

3 was assigned as 1*R*, 5*S*, and 7*S*. Thus, the structure of **3** was assigned as shown and given the trivial name longpene C.

Compound **4** had the same molecular formula of $C_{15}H_{22}O_3$ as **3** on the basis of their HR-ESIMS data. The ^{13}C and ^{1}H NMR spectra (Tables 1 and 2) of compound **4** were almost identical with those of **3**, which implied that **4** should also be a similar bisabolane-type sesquiterpene. This bisabolane-type sesquiterpene structure was verified by the following HMQC, HMBC, and $^{1}H-^{1}H$ COSY experiments, and the two carbonyl carbons at δ_C 199.6 and 201.1, four olefinic carbons at δ_C 127.3, 163.9, 123.8, and 155.7, and one oxygenated carbon at δ_C 70.2 were attributed to C-2, C-9, C-3, C-4, C-10, C-11, and C-5, respectively. By further analyses of 2D NMR spectra, the planar structure of **4** was established, which was the same as that of **3**, whereas compound **4** was also found to almost have the same NMR data as 5β-hydroxyl-1β-bisabolon-9-one reported in the above-mentioned literature,[29] where the relative configuration of C-14 methyl and the absolute configuration were not determined. Using the same NOESY experiment and TDDFT ECD calculations, the configuration of **4** was elucidated as follows. NOESY correlations observed for H-1/H-5, H-1/H_3-14, H-3/H_3-15, H-5/H-6α, H-6β/H-7, H-8a/H_3-14, and H-8a/H-10, together with Chem3D modeling, implied a conformation for **4** as shown in Figure 3, where the protons H-1 and H-5 were both in an α-position with an axial orientation, and the C-14 methyl group was found to be in a β-position. On the basis of the relative configuration of **4**, the calculated ECD spectra were obtained using TDDFT method, of which the calculated ECD spectrum for (1*S*,5*S*,7*R*)-**4** (Figure 7) matched the experimental spectrum closely. The absolute configuration of **4** was therefore determined as 1*S*, 5*S*, and 7*R*, and compound **4** was given the trivial name longpene D.

By analyses of the NMR spectroscopic data and comparison with the literature, the remaining known compounds were elucidated as *ar*-tumerone, **5**;[27] turmeronol B, **6**;[28] turmeronol A, **7**;[28] intermedin B, **8**;[30] bisacurone, **9**;[31] *ar*-dihydroturmerone, **10**;[27] curzerenone, **11**;[32] curcumenol, **12**;[33] isocurcumenol, **13**;[34] procurcumenol, **14**;[35] zedoardiol, **15**;[36,37] and zedoalactone F, **16**.[38]

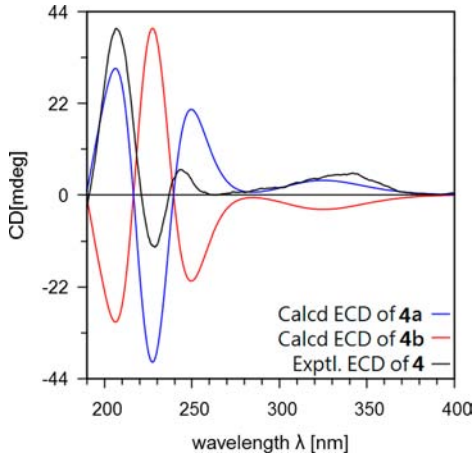

Figure 7. Calculated ECD spectra of **4a** (1*S*,5*S*,7*R*)-isomer and **4b** (1*R*,5*R*,7*S*)-isomer and the experimental ECD spectrum of **4** in acetonitrile.

To explore the potential pharmacological activities of these terpenoids and search for NO inhibitors as candidates for inflammatory diseases,[39] terpenoids **1**−**16** isolated from the rhizomes of *C. longa* were assayed for their NO inhibitory effects in murine microglial BV-2 cells according to a method previously reported.[40] 2-Methyl-2-thiopseudourea sulfate (SMT) was used as a positive control (IC_{50} = 2.8 μM). All of the isolated terpenoids exhibited inhibitory activities on LPS-induced NO production, and the IC_{50} values are shown in Table 3. The (3-(4,5-dimethylthiazol-2-yl)-2,5-diphenyltetrazolium bromide (MTT) assay showed that these compounds had no significant cytotoxicity to the BV-2 cells at their effective concentrations for the inhibition of NO production (data not shown).

Table 3. IC_{50} Values of Compounds 1−16 Inhibiting NO Production in BV-2 Cells

compound	IC_{50} (μM)	compound	IC_{50} (μM)
1	74.0	**10**	>100
2	>100	**11**	>100
3	87.3	**12**	>100
4	98.1	**13**	23.6
5	92.1	**14**	97.0
6	49.0	**15**	37.1
7	>100	**16**	95.4
8	30.0	SMT[a]	2.8
9	29.8		

[a]SMT (2-methyl-2-thiopseudourea, sulfate) was used as a positive control. Data are presented on the basis of three experiments.

In conclusion, the present phytochemical investigation on *C. longa* has led to the isolation and characterization of 2 new and 14 known terpenoids, **1**−**16**. Their structures, especially the absolute configurations of **1**−**4**, were elucidated by analyses of their NMR spectroscopic data and comparison of their calculated and experimental ECD spectra. Among them, compound **1** is a rare norditerpene with an *ent*-labdane skeleton, and **2** is a skeletally novel sesquiterpene having an eight-membered ring. In the biological screening executed, all of the isolated terpenoids displayed NO inhibitory effects, and compound **13** exerted the most inhibition against LPS-induced NO production in BV-2 cells. The discovery of two new

DOI: 10.1021/acs.jafc.5b01584
J. Agric. Food Chem. 2015, 63, 5805−5812

compounds further elucidated the chemical components of *C. longa* used a food spice, and these bioactive terpenoids with NO inhibitory activities implied that the natural spice *C. longa* may be potentially promotive to human health.[39]

■ ASSOCIATED CONTENT

Supporting Information

1D and 2D NMR and HR-ESIMS spectra of compounds **1**−**4**. The Supporting Information is available free of charge on the ACS Publications website at DOI: 10.1021/acs.jafc.5b01584.

■ AUTHOR INFORMATION

Corresponding Author

*(Y.G.) Phone/fax: +86-22-23502595. E-mail: victgyq@nankai.edu.cn.

Funding

This work was supported in part by the National Natural Science Foundation of China (No. 21372125).

Notes

The authors declare no competing financial interest.

■ REFERENCES

(1) Nanjing University of Chinese Medicine. *Dictionary of Chinese Herb Medicines*, 2nd ed.; Shanghai Scientific and Technologic Press: Shanghai, China, 2006; pp 2404−2406.

(2) Liao, K. K.; Wu, M. J.; Chen, P. Y.; Huang, S. W.; Chiu, S. J.; Ho, C. T.; Yen, J. H. Curcuminoids promote neurite outgrowth in PC12 cells through MAPK/ERK- and PKC-dependent pathways. *J. Agric. Food Chem.* **2012**, *60*, 433−443.

(3) Chen, J. J.; Tsai, C. S.; Hwang, T. L.; Shieh, P. C.; Chen, J. F.; Sung, P. J. Sesquiterpenes from the rhizome of *Curcuma longa* with inhibitory activity on superoxide generation and elastase release by neutrophils. *Food Chem.* **2010**, *119*, 974−980.

(4) Dao, T. T.; Nguyen, P. H.; Won, H. K.; Kim, E. H.; Park, J.; Won, B. Y.; Oh, W. K. Curcuminoids from *Curcuma longa* and their inhibitory activities on influenza A neuraminidases. *Food Chem.* **2012**, *134*, 21−28.

(5) Nishiyama, T.; Mae, T.; Kishida, H.; Tsukagawa, M.; Mimaki, Y.; Kuroda, M.; Sashida, Y.; Takahashi, K.; Kawada, T.; Nakagawa, K.; Kitahara, M. Curcuminoids and sesquiterpenoids in turmeric (*Curcuma longa* L.) suppress an increase in blood glucose level in type 2 diabetic KK-Ay mice. *J. Agric. Food Chem.* **2005**, *53*, 959−963.

(6) Lin, X.; Ji, S.; Li, R.; Dong, Y.; Qiao, X.; Hu, H.; Yang, W.; Guo, D.; Tu, P.; Ye, M. Terpecurcumins A-I from the rhizomes of *Curcuma longa*: absolute configuration and cytotoxic activity. *J. Nat. Prod.* **2012**, *75*, 2121−2131.

(7) Lin, X.; Ji, S.; Qiao, X.; Hu, H.; Chen, N.; Dong, Y.; Huang, Y.; Guo, D.; Tu, P.; Ye, M. Density functional theory calculations in stereochemical determination of terpecurcumins J-W, cytotoxic terpene-conjugated curcuminoids from *Curcuma longa* L. *J. Org. Chem.* **2013**, *78*, 11835−11848.

(8) Wright, L. E.; Frye, J. B.; Timmermann, B. N.; Funk, J. L. Protection of trabecular bone in ovariectomized rats by turmeric (*Curcuma longa* L.) is dependent on extract composition. *J. Agric. Food Chem.* **2010**, *58*, 9498−9504.

(9) Funk, J. L.; Frye, J. B.; Oyarzo, J. N.; Zhang, H.; Timmermann, B. N. Anti-arthritic effects and toxicity of the essential oils of turmeric (*Curcuma longa* L.). *J. Agric. Food Chem.* **2010**, *58*, 842−849.

(10) Park, S. Y.; Kim, D. S. Discovery of natural products from *Curcuma longa* that protect cells from beta-amyloid insult: a drug discovery effort against Alzheimer's disease. *J. Nat. Prod.* **2002**, *65*, 1227−1231.

(11) Simon, A.; Allais, D. P.; Duroux, J. L.; Basly, J. P.; Durand-Fontanier, S.; Delage, C. Inhibitory effect of curcuminoids on MCF-7 cell proliferation and structure-activity relationships. *Cancer Lett.* **1998**, *129*, 111−116.

(12) Miriyala, S.; Panchatcharam, M.; Rengarajulu, P. Cardioprotective effects of curcumin. *Adv. Exp. Med. Biol.* **2007**, *595*, 359−377.

(13) Park, B. S.; Kim, J. G.; Kim, M. R.; Lee, S. E.; Takeoka, G. R.; Oh, K. B.; Kim, J. H. *Curcuma longa* L. constituents inhibit sortase A and *Staphylococcus aureus* cell adhesion to fibronectin. *J. Agric. Food Chem.* **2005**, *53*, 9005−9009.

(14) Wang, M.; Zhang, Q.; Ren, Q.; Kong, X.; Wang, L.; Wang, H.; Xu, J.; Guo, Y. Isolation and characterization of sesquiterpenes from *Celastrus orbiculatus* and their antifungal activities against phytopathogenic fungi. *J. Agric. Food Chem.* **2014**, *62*, 10945−10953.

(15) Xu, J.; Zhang, Q.; Wang, M.; Ren, Q.; Sun, Y.; Jin, D. Q.; Xie, C.; Chen, H.; Ohizumi, Y.; Guo, Y. Bioactive clerodane diterpenoids from the twigs of *Casearia balansae*. *J. Nat. Prod.* **2014**, *77*, 2182−2189.

(16) Wang, M.; Zhang, Q.; Wang, H.; Ren, Q.; Sun, Y.; Xie, C.; Xu, J.; Jin, D. Q.; Ohizumi, Y.; Guo, Y. Characterization and NO inhibitory activities of chemical constituents from an edible plant *Petasites tatewakianus*. *J. Agric. Food Chem.* **2014**, *62*, 9362−9367.

(17) MOE 2013.08; Chemical Computing Group Inc., www.chemcomp.com.

(18) *Gaussian 09*, revision B, 01; Gaussian Inc.: Wallingford, CT, USA, 2010.

(19) Autschbach, J.; Nitsch-Velasquez, L.; Rudolph, M. Time dependent density functional response theory for electronic chiroptical properties of chiral molecules. *Top. Curr. Chem.* **2011**, *298*, 1−98.

(20) Zhang, Q.; Xiao, J.; Sun, Q. Q.; Qin, J. C.; Pescitelli, G.; Gao, J. M. Characterization of cytochalasins from the endophytic *Xylaria* sp. and their biological functions. *J. Agric. Food Chem.* **2014**, *62*, 10962−10969.

(21) Wang, K. B.; Di, Y. T.; Bao, Y.; Yuan, C. M.; Chen, G.; Li, D. H.; Bai, J.; He, H. P.; Hao, X. J.; Pei, Y. H.; Jing, Y. K.; Li, Z. L.; Hua, H. M. Peganumine A, a β-carboline dimer with a new octacyclic scaffold from *Peganum harmala*. *Org. Lett.* **2014**, *16*, 4028−4031.

(22) Bruhn, T.; Schaumlöffel, A.; Hemberger, Y.; Bringmann, G. *SpecDis*, version 1.62; University of Wuerzburg: Germany, 2014.

(23) Roth, G. N.; Chandra, A.; Nair, M. G. Novel bioactivities of *Curcuma longa* constituents. *J. Nat. Prod.* **1998**, *61*, 542−545.

(24) Liu, Y.; Nair, M. G. *Curcuma longa* and *Curcuma mangga* leaves exhibit functional food property. *Food Chem.* **2012**, *135*, 634−640.

(25) Xu, J.; Liu, C.; Guo, P.; Guo, Y.; Jin, D. Q.; Song, X.; Sun, Z.; Gui, L.; Ma, Y. Neuroprotective labdane diterpenes from *Fritillaria ebeiensis*. *Fitoterapia* **2011**, *82*, 772−776.

(26) Zeng, Y.; Qiu, F.; Takahashi, K.; Liang, J.; Qu, G.; Yao, X. New sesquiterpenes and calebin derivatives from *Curcuma longa*. *Chem. Pharm. Bull.* **2007**, *55*, 940−943.

(27) Fujiwara, M.; Yagi, N.; Miyazawa, M. Acetylcholinesterase inhibitory activity of volatile oil from *Peltophorum dasyrachis* Kurz ex Bakar (yellow batai) and bisabolane-type sesquiterpenoids. *J. Agric. Food Chem.* **2010**, *58*, 2824−2829.

(28) Imai, S.; Morikiyo, M.; Furihata, K.; Hayakawa, Y.; Seto, H. Turmeronol A and turmeronol B, new inhibitors of soybean lipoxygenase. *Agric. Biol. Chem.* **1990**, *54*, 2367−2371.

(29) Zhang, W. Y.; Wang, H. F.; Cheng, G.; Zhang, O.; Bai, S.; Pei, Y. H. Two new bisabolane sesquiterpenoids from *Curcuma longa*. *J. Asian Nat. Prod. Res.* **2014**, *16*, 271−274.

(30) Li, H. M.; Lei, C.; Luo, Y. M.; Li, X. N.; Li, X. L.; Pu, J. X.; Zhou, S. Y.; Li, R. T.; Sun, H. D. Intermedins A and B; new metabolites from *Schisandra propinqua* var. *intermedia*. *Arch. Pharmacal Res.* **2008**, *31*, 684−687.

(31) Uehara, S.; Yasuda, I.; Takeya, K.; Itokawa, H.; Iitaka, Y. New bisabolane sesquiterpenoids from the rhizomes of *Curcuma xanthorrhiza* (Zingiberaceae) II. *Chem. Pharm. Bull.* **1990**, *38*, 261−263.

(32) Zhu, N.; Kikuzaki, H.; Sheng, S.; Sang, S.; Rafi, M. M.; Wang, M.; Nakatani, N.; DiPaola, R. S.; Rosen, R. T.; Ho, C. T. Furanosesquiterpenoids of *Commiphora myrrha*. *J. Nat. Prod.* **2001**, *64*, 1460−1462.

(33) Hikino, H.; Sakurai, Y.; Numabe, S.; Takemoto, T. Structure of curcumenol. *Chem. Pharm. Bull.* **1968**, *16*, 39−42.

(34) Firman, K.; Kinoshita, T.; Itai, A.; Sankawa, U. Terpenoids from *Curcuma heyneana*. *Phytochemistry* **1988**, *27*, 3887−3891.

(35) Ohshiro, M.; Kuroyanagi, M.; Ueno, A. Structures of sesquiterpenes from *Curcuma longa*. *Phytochemistry* **1990**, *29*, 2201−2205.
(36) Yin, G. P.; Li, L. C.; Zhang, Q. Z.; An, Y. W.; Zhu, J. J.; Wang, Z. M.; Chou, G. X.; Wang, Z. T. iNOS inhibitory activity of sesquiterpenoids and a monoterpenoid from the rhizomes of *Curcuma wenyujin*. *J. Nat. Prod.* **2014**, *77*, 2161−2169.
(37) Zhang, C. M.; Fan, P. H.; Li, M.; Lou, H. X. Two new sesquiterpenoids from the rhizomes of *Curcuma xanthorrhiza*. *Helv. Chim. Acta* **2014**, *97*, 1295−1300.
(38) Lou, Y.; Zhao, F.; He, H.; Peng, K. F.; Zhou, X. H.; Chen, L. X.; Qiu, F. Guaiane-type sesquiterpenes from *Curcuma wenyujin* and their inhibitory effects on nitric oxide production. *J. Asian Nat. Prod. Res.* **2009**, *11*, 736−746.
(39) Chen, H.; Xie, C.; Wang, H.; Jin, D. Q.; Li, S.; Wang, M.; Ren, Q.; Xu, J.; Ohizumi, Y.; Guo, Y. Sesquiterpenes inhibiting the microglial activation from *Laurus nobilis*. *J. Agric. Food Chem.* **2014**, *62*, 4784−4788.
(40) Xu, J.; Jin, D. Q.; Liu, C.; Xie, C.; Guo, Y.; Fang, L. Isolation, characterization, and NO inhibitory activities of sesquiterpenes from *Blumea balsamifera*. *J. Agric. Food Chem.* **2012**, *60*, 8051−8058.

DOI: 10.1021/acs.jafc.5b01584
J. Agric. Food Chem. 2015, 63, 5805−5812

Table 1. Composition of the *P. emblica* SDF

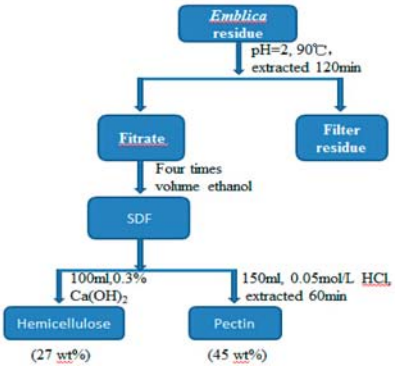

The monosaccharide compositions and contents of PESDF

Retention Time(min)	Mass Charge Ratio	Chemical Compound	Relatice Amount
22.81	217	Ribose	14.2%
22.95	217	Arabinose	27.8%
23.40	204	Rhamnose	7.0%
24.03	217	Xylose	29.8%
26.16	204	Mannose	5.6%
30.45	217	Galactose	5.6%
31.74	204	Glucose	10.0%

monosaccharide compositions and contents of PESDF

retention time (min)	mass/charge ratio	chemical compd	rel amount (%)
22.81	217	ribose	14.2
22.95	217	arabinose	27.8
23.40	204	rhamnose	7.0
24.03	217	xylose	29.8
26.16	204	mannose	5.6
30.45	217	galactose	5.6
31.74	204	glucose	10.0

new way to apply the polyphenols and soluble polysaccharide fibers for biomedical or food preservation based on their medical function,[12] excellent film-forming potential, and homogeneous dispersion in water.[27,28]

MATERIALS AND METHODS

Materials and Reagent. *Phyllanthus emblica* residues were obtained from South Subtropical Experimental Station (Jingdong), Research Institute of Resource Insects, Chinese Academy of Forestry, located in Yunnan. Hydrochloric acid and 95% ethanol were purchased from Guanghua Technologies Co. Ltd. (Guangzhou, Guangdong, China). Tannin, anhydrous calcium chloride, and gelatin were from Crystal Pure Industrial Co. Ltd. (Shanghai, China).

Fabrication of SDF. SDF was extracted according to the modified previous method.[29,30] The residue of *P. emblica* was dried in a vacuum drying oven (VOS-300VD, Tokyo Chemical Equipment, Tokyo, Japan) at 105 °C and smashed into an 80 mesh sieve. SDF was extracted from 30 g of residue of *P. emblica*, and then residue was digested with 500 mL of hydrochloric acid (5%, volume fraction) at 80 °C for 8 h to extract SDF. After these treatments, the sample was filtered to remove solid. Remaining liquid was suspended in 4 times volumes of 95% ethanol to precipitate SDF. The precipitate was allowed to form at room temperature for 0.5 h, followed by centrifugation at 8000 rpm for 15 min. The residue was washed twice with 78% ethanol and 95% ethanol, respectively, and was dried in a vacuum drying oven to constant weight at 60 °C. Then, SDF was stored at 4 °C for further use.

Fabrication of SDF−Tannin Self-Assembled Film. At first, the SDF−tannin self-assembled nanoscale clusters were prepared by dissolving 1 g of SDF in 50 mL of deionized water at 60 °C. The solid of tannin (1, 2, 3, and 4 g) and $CaCl_2$ were put in SDF solution to be stirred for 1 h before cooling to room temperature, followed by centrifugation at 8000 rpm for 30 min. The residue cluster was washed several times with deionized water to take away unchelated component and dried at 60 °C for further use.[31,32] Ten grams of gelatin was placed in a 150 mL beaker, followed by the addition of 100 mL of deionized water at 60 °C for 2 h. The gelatin solution was not stirred and allowed to cool to room temperature to form a hydrogel. A certain amount of the SDF−tannin self-assembled nanoscale clusters was dispersed in deionized water after sonication for 30 min and then added in this beaker to observe the phenomenon of gelatin hydrogel surface.

Characterizations. *Fiber Quality Analysis of SDF.* The size distribution analysis of individual SDFs was performed using a fiber quality analyzer (FQA) (Lda02, Optest, Ontario, Canada).[33] The quantity of SDF was maintained from 25 to 40 roots per second. Equal fiber length and width were measured.

Zeta Potential Analysis. Zeta potential was measured with a Lazer Zee microelectrophoresis analyzer from Mutek. Dilute SDF suspensions of interest were placed into the chambers of the capillary cell of this device. Looking through a microscope, the voltage was adjusted until the SDF particles appeared stationary.

Gel Point Determination. Gel point was determined according to viscosity change. One gram of SDF and 4 g of tannin were dissolved in 100 mL of deionized water. Then the viscosity value was recorded while calcium ion was gradually added. To equilibrate the solution, each sample was allowed to settle at room temperature for 30 min. The measurement was done using a rheometer (N1000, Eyela, Tokyo, Japan) at 20 °C.

Fourier Transfer Infrared Spectroscopy (FT-IR). The sample was placed in FT-IR (Tenson 27, Brook, MI, USA), with the scanning range set from 4000 to 400 cm^{-1} with a resolution ratio of 4 cm^{-1} to observe typical functional absorption peak.

Wide-Angle X-ray Diffraction (WAXD). WAXD measurements were carried out on a WAXD diffractometer (D8-Advance, Bruker, Madison, WI, USA) in reflection mode. The X-ray used was Ni-filtered Cu Kα radiation with a wavelength of 1.5418 Å. The voltage was set at 40 kV and the current was set at 40 mA. Measurement was done by 2θ = 2° min^{-1} scan over a 2θ range of 8−40°.[16]

Differential Scanning Calorimetry (DSC). The samples were investigated by DSC instrument (DSC200, Netzsch, Bavaria, Germany) under the protection of nitrogen. The test temperature ranged from 35 to 500 °C, with a heating rate of 10 °C/min, under which condition the endothermic peak of the DSC curve was observed.

Transmission Electron Microscope (TEM). TEM observations were performed using a Philips CM30 operated at 100 kV. A droplet of sample suspension was placed on a copper grid covered by a thin SDF film and allowed to dry at 80 °C overnight.

Scanning Electron Microscope (SEM). The sample was evenly dispersed on conducting paper, to separate the superficial and

DOI: 10.1021/acs.jafc.5b00192
J. Agric. Food Chem. 2015, 63, 5813−5820

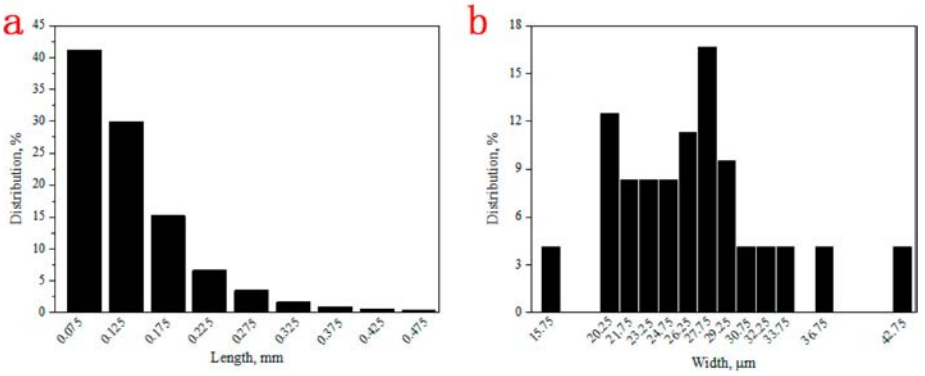

Figure 1. Length distribution of SDF (a); width distribution of SDF (b).

nonadherent part. The sample was placed in the SEM (IGMA, Zeiss, Oberkochen, Germany) for observation of its appearance.

Controllable Film Thickness. Film thickness was determined by using a thin film measurement system. The samples for microscope (VHX-1000, Keyence, Tokyo, Japan) observation were scraped by using a sharp razor blade and placed on a glass slide.[17] The proportion of SDF to tannin ranged from 1:1 to 1:4, all of which were applied to the same amount of calcium ion. The film thickness was measured by image-processing software.

In Vitro Cytotoxicity Test. The MTT method was used to test the in vitro cytotoxicity. In brief, 1×10^4 cells per well were seeded in 96-well plates and exposed to different types of film. After the exposure was complete, the culture medium was removed from each well and replaced with 100 mL of new medium containing MTT (0.5 mg/mL) and incubated for 3 h at 37 °C. The resulting formation product was dissolved by adding an equal amount of acidified isopropanol. Ninety-six-well plates were centrifuged at 2500 rpm for 10 min. Then, a 100 mL supernatant was transferred to other fresh wells of a mictotiter plate and absorbance was measured at 570 nm by using a microplate reader (Varioskan Flash, ThermoFisher, Foster City, CA, USA). This value corresponds to a 0% decrease in MTT conversion activity and represents 100% cell viability.

Antibacterial Activity Test. The antibacterial activity of film against Gram-positive bacteria including *Staphylococcus aureus*, flavobacterium, *Bacillus subtilis*, and Gram-negative bacteria involving *Pseudomonas aeruginosa* was determined using the modified disk diffusion method. Bacteria were incubated at 37 °C for 36 h before films were pasted onto agar plates. The surface of self-assembled films was observed and recorded.[34]

Alcohol Insulation Test. Alcohol solution (60 wt %) dyed by melanin was poured onto SDF−tannin self-assembled film to observe if the alcohol infiltrated into the gelatin hydrogel. The optical microscope (VHX-1000, Keyence) and SEM (IGMA, Zeiss) were employed to observe changes of the film (SDF/tannin = 1:2) after soaking in a 60 wt % alcohol solution.

RESULTS AND DISCUSSION

Determination of SDF. As we know, comprehensive utilization of residue resource has potent economic value and exploitation prospects. Preparation of SDF could realize *P. emblica* residue value. *P. emblica* SDF properties were not found in existing papers, so it was necessary for us to characterize the physical and chemical properties of SDF extracted from *P. emblica* residue. As Table 1 shows, the main components of the SDF was pectin, representing approximately 45 wt %. There was 27 wt % hemicellulose and other water-soluble polysaccharides in the SDF exacted from *P. emblica* residue. The high pectin content may be attributed to the high pulp content of the *P. emblica* residue. The monosaccharide composition of SDF was determined by our previous experiment.[35] The monosaccharide composition was determined by GC-MS and is shown in Table 1; SDF was mainly composed of ribose, arabinose, rhamnose, xylose, mannose, galactose, and glucose, which bears a certain similarity to hemicellulose.[36] Hemicellulose could be easily incorporated with physical or chemical cross-linking in forming special property clusters, film, and hydrogel, and so did SDF.[37] FT-IR spectra of the SDF showed strong adsorption peaks at 1744 and 3418 cm^{-1}, which were attributed to the −CO− of the carboxyl group and the ionizable −OH group due to the high pectin content of the SDF. Meanwhile, the value of the zeta potential test was −14.2 mV, which was an important factor to estimate sample stability and to judge opposite charge. It can indicate that the SDF aggregates are negatively charged and relatively stably dispered in aqueous solution. Fiber length and width distribution of SDF were determined by fiber quality analyzer as shown in Figure 1. The length distribution of SDF ranged from 0.075 to 0.475 mm. The lengths of the main distributions at 0.075 and 0.125 mm were 41.20 and 29.89%, respectively. In the present investigation, the length of SDF was much bigger compared to rod-like hemicellulose.[38] The main width distribution was 20.25−29.25 μm. These SDF showed good properties of film-forming ability due to their large geometrical size. The result of the dietary fiber analysis indicated that the SDF extracted from *P. emblica* residue could fairly stably disperse in water by the ionized carboxyl groups of the different kinds of monosaccharide.[8] In addition, reagent labels of hydrolyzable tannins show its formula is $C_{76}H_{52}O_{46}$, corresponding to a combination of 10 mol of gallic acid and 1 mol of glucose. All molecules were connected by ester bonds. A large number of phenolic hydroxyl groups are exposed on the surface of the molecule.

Preparation and Characteristics of Nanoclusters. Figure 2 shows the system viscosity at the gelation point as a function of the weight of calcium ion. The curve of viscosity of the SDF−tannin complex system showed the gel−sol transition behavior. With the increase of calcium ion, the viscosity of the system increased first. The cross-linked clusters were prepared with calcium ion, which functioned as contact phenolic hydroxyl group (tannin) and carboxylic group (SDF) by coordinate bond.[39] The complex system changed from solution to dispersed nanoparticle at the gel point (calcium ion, 19.2 mg) as the TEM images of Figure 3 show. Subsequently, the cross-linked clusters formed with calcium ion increased while the value of viscosity declined until constant. Major differences in the shape distribution and the internal structure of sample were visualized in the TEM images (Figure 3). Without calcium ion, the sample SDF−tannin mixture, which remained clear,

DOI: 10.1021/acs.jafc.5b00192
J. Agric. Food Chem. 2015, 63, 5813−5820

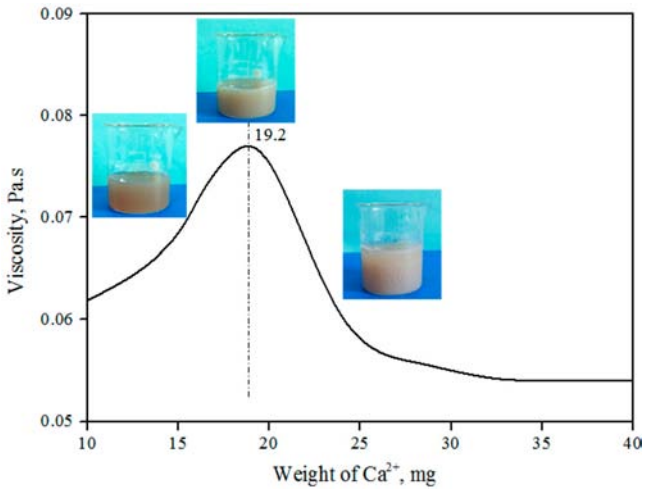

Figure 2. Weight of calcium ion dependence of SDF−tannin complex system viscosity.

could form a micrometer-scale film on the surface of the copper grid. On the contrary, the structure of SDF−tannin clusters after cross-linking was a series of nanoscale sphere (d < 50 nm), which could homogeneously disperse in solution. This proved that tannin and SDF were aggregated by cross-linking to form nanoscale particles.

We employed the FT-IR, XRD, and DSC tests to investigate the interaction between the SDF and tannins before and after cross-linking induced by calcium ion. FT-IR is used as an analytical tool to characterize the chemical change of the functional groups. The nanoclusters showed a wider hydroxyl association peak than SDF, and narrower than that of tannin. Because tannin contained a large number of phenolic hydroxyls, only a part of phenolic groups were coordinated by calcium ion, whereas the remaining part was involved in hydrogen bond formation with itself and hydrogel of SDF.[40] Figure 4 shows the adsorption intensity of SDF−tannin nanoclusters decreased obviously at approximately 2930 cm^{-1}, which belonged to sugar C−H stretching vibration; therefore, the configuration of SDF and tannin was changed after chelating with tannin and calcium ion.[41] Meanwhile, because the carboxyl group of the carbohydrate was mainly calcium cross-linked, the shift of these peaks from 1744 to 1736 cm^{-1} was likely to result from the electrostatic interaction between SDF and divalent cations. The peaks at 1708, 1536, and 1200 cm^{-1} belonged to the C═O stretch of esters, the stretch of aromatic rings, and C—OH stretches of phenols, respectively, the intensity of which decreased remarkably.[42] This can be attributed to the metal−ligand coordination restricting the movement of the tannin molecule.

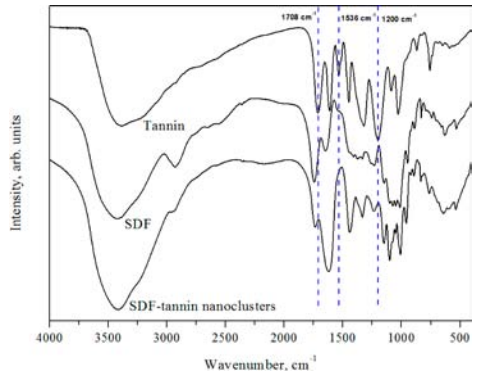

Figure 4. FT-IR spectra of tannin, SDF, and SDF−tannin nanoclusters.

Figure 5 shows the XRD patterns of the tannin, SDF, and SDF−tannin nanoclusters. XRD was used to determine the crystallinity changes to detect the aggregation state of the molecule. On the basis of multipeak fitting, the noncrystallinity peak of tannin was at 25°. SDF had two noncrystallinity peaks and crystallinity peaks at 13°, 21°, and 34°, respectively. Remarkably, there was no obvious peak at the curve of SDF−tannin nanoclusters. The characteristic peak of SDF disappeared. Its features demonstrated that crystallization of the SDF was severely restricted by the interaction between SDF and calcium ion.

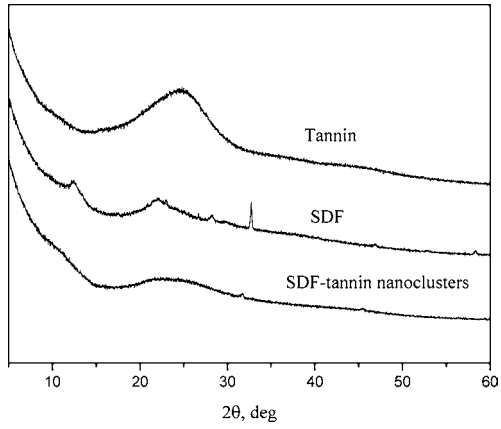

Figure 5. XRD patterns of the tannin, SDF, and SDF−tannin nanoclusters.

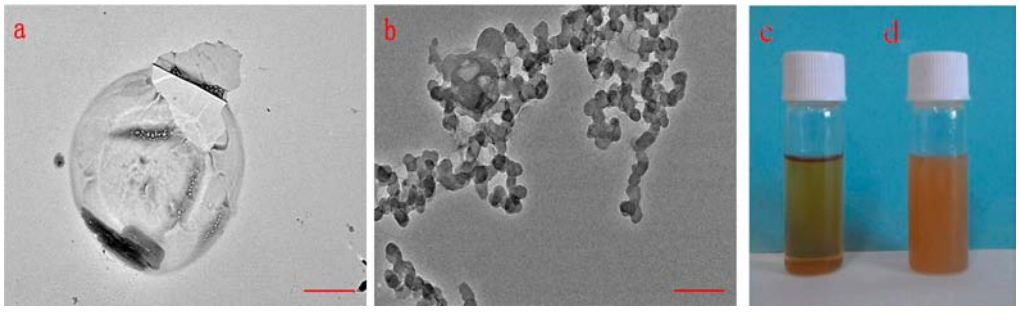

Figure 3. TEM images of the mixture (tannin and SDF) (a) and SDF−tannin nanoclusters (b) (bar = 200 nm); photograph of the simple tannin−SDF mixture (c) and SDF−tannin nanoclusters (d).

DOI: 10.1021/acs.jafc.5b00192
J. Agric. Food Chem. 2015, 63, 5813−5820

Following the literature studied, we used DSC to elucidate the effect of chelation on the thermal transition. Figure 6 shows

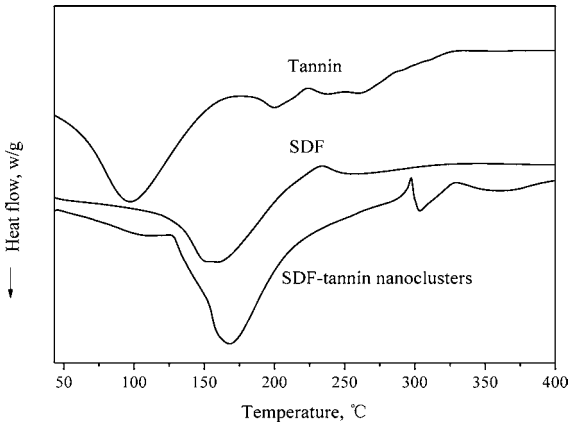

Figure 6. DSC thermograms of the tannin, SDF, and SDF−tannin nanoclusters.

the DSC curves of tannin, SDF, and SDF−tannin nanoclusters. There were two obviously endothermic peaks of tannin, SDF, and SDF−tannin nanoclusters. The low-temperature peak was ascribed to endotherm and the high-temperature one to restricted decomposition or melting state. The endotherm of SDF−tannin nanoclusters (168.2 °C) was significantly higher than that of SDF (157.5 °C) or tannin (96.8 °C). SDF−tannin nanoclusters showed the highest melting state temperature (303.4 °C) followed by SDF (250.9 °C) and tannin (157.5 °C). Compared to SDF, the endothermic peak of SDF−tannin nanoclusters was increased by 11.3 °C and decomposition temperature was elevated by 52.5 °C. The exothermic transition was shifted to the high temperature. From the above analysis, this behavior is another demonstration of the strong interaction between calcium and SDF−tannin aqueous dispersion.

Self-Assembly Behavior of SDF−Tannin Nanoclusters on the Protein Surface. Four kinds of film are shown in Figure 7. When the weight proportion of SDF to tannin was 1:1, the film was thin and uneven. The appearance of the other three (1:2, 1:3, and 1:4) films was more homogeneous and dense. This demonstrated that the amount of tannin would affect its ability to adhere to gelatin. As the proportion of tannin

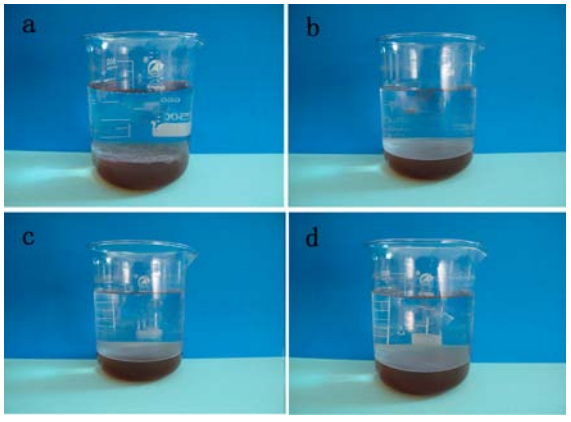

Figure 7. Films prepared at different tannin and SDF proportions: ratios 1:1 (a), 1:2 (b), 1:3 (c), and 1:4 (d).

increased, more uncovered phenolic hydroxyl groups were retained to form more hydrogen bonds with the protein on the surface of gelatin. The attractive force between SDF−tannin nanoclusters and gelatin was enhanced, and the formed film was more stable. The thickness of the SDF−tannin self-assembled films could be controlled by changing the tannin concentration. In Figure 8, the thickness of the film was 144 μm

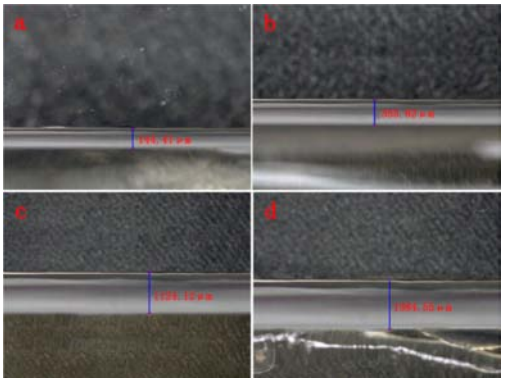

Figure 8. Photographs of SDF−tannin self-assembled films with different proportion of SDF to tannin: ratios 1:1 (a), 1:2 (b), 1:3 (c), and 1:4 (d).

at the ratio of 1:1. It increased as the proportion of tannin rose, with the maximum reaching 1384 μm at a ratio of 1:4. It is quite evident that film thickness could be changed by controlling the proportion of tannin.

Figure 9 shows SEM recorded for SDF and SDF−tannin self-assembled film specimens. The SDF micrograph depicted

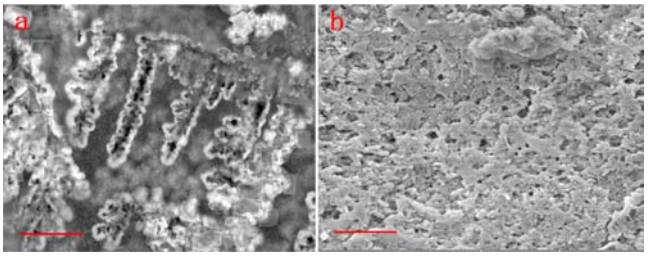

Figure 9. SEM images of SDF (a) (bar = 30 μm) and SDF−tannin self-assembled film (b). (Bar = 200 nm.)

apparent features of rod-like microscale. According to the TEM and SEM results, the formation process of self-assembly film was evidently confirmed. First, the nanoclusters were fabricated by the electrostatic interaction between calcium ion and SDF−tannin mixed system. Calcium ion as an initiator was an ionic compound that could combine with SDF and tannin through metal−ligand coordination. Then, SDF and tannin were cross-linked to gel and aggregated to form nanoclusters. These nanoclusters had phenolic hydroxyl groups and showed properties of tannins, which could adhere to the surface of protein.[43] Finally, the smooth film was formed by the hydrogen-bonding actions of −OH (tannin) and $-NH_2$ (the protein surface of gelatin hydrogel).[15] The process mechanism is given in Figure 10.

Properties of the Self-Assembled Film. Similar to other biomedical materials, the toxicity of film should be evaluated. Figure 11 shows the cell tended to grow more rapidly on the surface of the film. Of the four types of film, the toxicity was

DOI: 10.1021/acs.jafc.5b00192
J. Agric. Food Chem. 2015, 63, 5813−5820

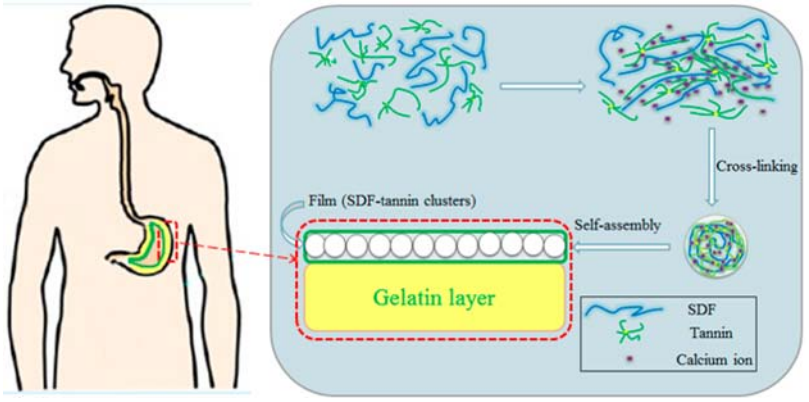

Figure 10. Schematic illustration of nanoclusters and self-assembly film preparation process, and design concept of gastric mucosa protection.

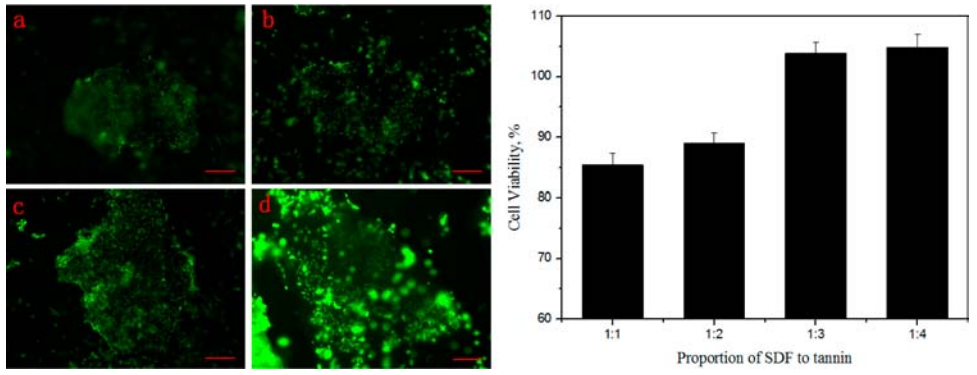

Figure 11. Photographs of cell growth on the surface of the films with different proportions of SDF to tannin: ratios 1:1 (a), 1:2 (b), 1:3 (c), and 1:4 (d). (Bar = 100 μm.) Histogram shows the cell viability of the films.

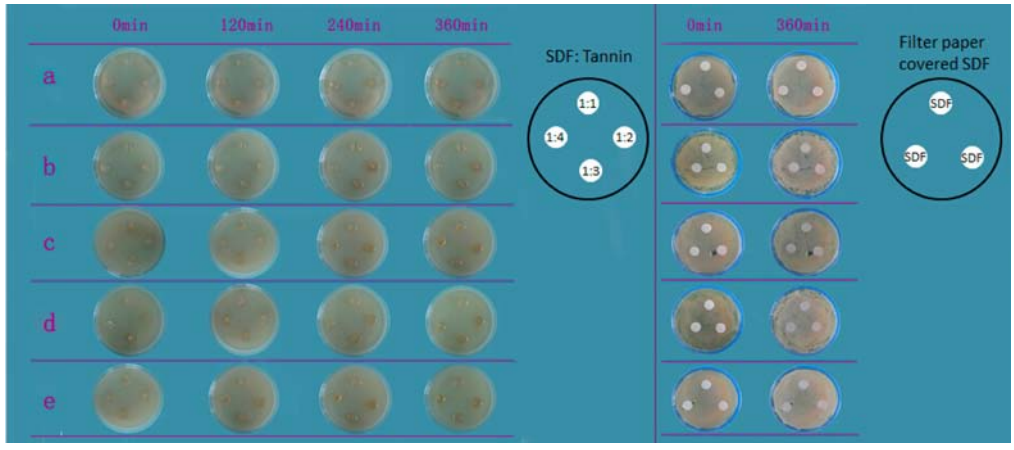

Figure 12. Antimicrobial activity of SDF−tannin self-assembled film and the filter paper covered SDF at different reaction times against *Staphylococcus aureus* (a), flavobacterium (b), *Bacillus subtilis* (c), *Pseudomonas aeruginosa* (d), and *Escherichia coli* (e).

decreased as tannin increased. Film a showed the cell viability value was 85.40% followed by film b (89.04%), film c (103.90%), and film d (104.90%). It could be assumed that the SDF−tannin self-assembled film could be considered to be safe under normal conditions. All of the films exhibited great cell viability and adhesion, which could be attributed to the protein attachment properties of tannin. The results showed that SDF−tannin self-assembled film had good biocompatibility as well as application potential for wound recovery. Figure 12 shows the antibacterial activity of the film against flavobacterium, *Bacillus subtilis*, Gram *Pseudomonas aeruginosa*, and *Escherichia coli*. Five types of bacteria could not grow on the surface of four films with the proportion of SDF to tannin ranging from 1:1 to 1:4. The broad-spectrum antibacterial property of SDF−tannin self-assembled film was mainly attributed to the tannin component. The result also indicates that the activity of tannins as natural antimicrobials for food preservation are also retained after the cross-linking process.[44] In addition, there was no inhibition zone because tannin was fastened to the film. This demonstrated that the SDF−tannin self-assembled film could be applied in the field of food preservation and biomedical wound dressing to inhibit bacterial growth.

DOI: 10.1021/acs.jafc.5b00192
J. Agric. Food Chem. 2015, 63, 5813−5820

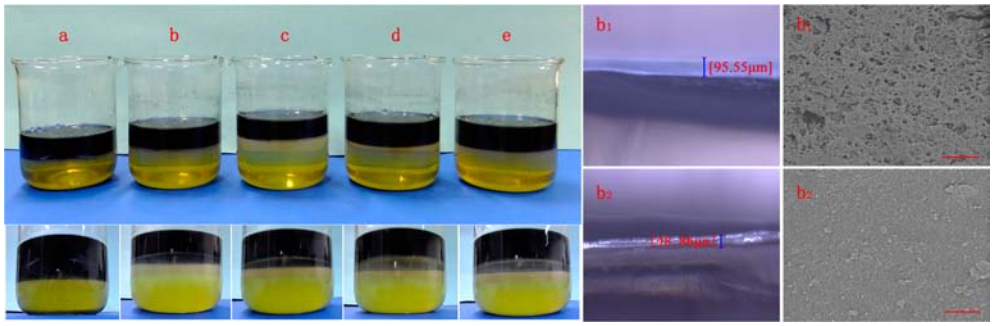

Figure 13. Films with different proportions of SDF to tannin (a, 0:1; b, 1:1; c, 1:2; d, 1:3; e, 1:4) were used to defend alcohol; cross-section image and SEM image of the film (SDF/tannin = 1:2) before (b1) and after (b2) soaking in 60 wt % alcohol solution. (Bar = 10 μm.)

Gelatin was used to imitate human gastric mucosa in this experiment, which helped evaluate if SDF−tannin self-assembled film could prevent alcohol passing to reduce gastric mucosa damage from alcohol. Alcohol (50 mL) was added into the system to simulate drinking to test if it had any impact on the film-covered gelation surface. It turned out that the film was well attached at gelatin and maintained stability even in the presence of high concentrations of alcohol (Figure 13). We have tested the four kinds of proportion of SDF to tannin film as the alcohol insulation. Simple SDF could not be tested because they cannot form membrane structure by themselves. The film containing only tannin cannot prevent alcohol passing. In contrast, tannin film with any proportion of SDF added could served as an alcohol barrier. This can be attributed to the special alcohol insolubility of SDF. In Figure 13, we find that film thickness shrank from 95.5 to 48.8 μm after soaking in alcohol solution for 12 h. As the film shrank, a dense structure without holes was formed that can prevent alcohol passing, as the SEM images showed. Thus, SDF−tannin self-assembled film could prevent gastric mucosa damage from alcohol and is applicable in the pharmaceutical area.[45]

In this work, we successfully developed a facile route to prepare SDF−tannin nanoclusters by using calcium ion as a bridging cross-linking agent. The appearance of SDF−tannin nanoclusters was a series of nanoscale microspheres. Meanwhile, we found there was a strong hydrogen interaction between the tannin component of nanoclusters and protein, through which the SDF−tannin nanoclusters could self-assemble on the surface of the protein to form a dense film. The SDF−tannin self-assembled film, the thickness of which could be controlled by the concentration of tannin, showed nontoxic and broad-spectrum antimicrobial properties. It is worth noting that the SDF−tannin self-assembled film could well attach to gelatin and prevent damage to gastric mucosa from alcohol because the film shrank due to the special alcohol insolubility of SDF. In conclusion, this work provided a novel strategy to develop the application of SDF and tannin for the food preservation and biomedical wound-dressing fields.

AUTHOR INFORMATION

Corresponding Authors

*(Hong Zheng) E-mail: kmzhh@hotmail.com. Phone: +86-871-63860021.

*(Kai Li) E-mail: lkjnkmwh@hotmail.com. Phone: +86-871-63861466.

Funding

This study was financially supported by the National Key Technology R&D Program, China (2012BAD36B03-03).

Notes

The authors declare no competing financial interest.

ACKNOWLEDGMENTS

We express our sincere gratitude to all staff members of the department for their kind assistance.

REFERENCES

(1) Guo, Y.; Zhao, J.; Yin, X.; Gao, X.; Tian, Y. Electrochemistry investigation on protein protection by alkanethiol self-assembled monolayers against urea impact. *J. Phys. Chem. C* **2008**, *112* (15), 6013−6021.

(2) Augustyniak, A.; Skrzydlewska, E. L-Carnitine in the lipid and protein protection against ethanol-induced oxidative stress. *Alcohol* **2009**, *43* (3), 217−223.

(3) Carpenter, J. F.; Izutsu, K.-i.; Randolph, T. W. Freezing-and drying-induced perturbations of protein structure and mechanisms of protein protection by stabilizing additives. *Drugs Pharm. Sci.* **2004**, *137*, 147−186.

(4) Mohammed Fayaz, A.; Balaji, K.; Girilal, M.; Kalaichelvan, P. T.; Venkatesan, R. Mycobased synthesis of silver nanoparticles and their incorporation into sodium alginate films for vegetable and fruit preservation. *J. Agric. Food Chem.* **2009**, *57* (14), 6246−6252.

(5) Jhong, J.-F.; Venault, A.; Liu, L.; Zheng, J.; Chen, S.-H.; Higuchi, A.; Huang, J.; Chang, Y. Introducing mixed-charge copolymers as wound dressing biomaterials. *ACS Appl. Mater. Interfaces* **2014**, *6* (12), 9858−9870.

(6) Lutz, A.; van den Berg, O.; Van Damme, J.; Verheyen, K.; Bauters, E.; De Graeve, I.; Du Prez, F. E.; Terryn, H. A shape-recovery polymer coating for the corrosion protection of metallic surfaces. *ACS Appl. Mater. Interfaces* **2015**, *7* (1), 175−183.

(7) Li, Y.; McClements, D. J. Modulating lipid droplet intestinal lipolysis by electrostatic complexation with anionic polysaccharides: Influence of cosurfactants. *Food Hydrocolloids* **2014**, *35* (0), 367−374.

(8) Elleuch, M.; Bedigian, D.; Roiseux, O.; Besbes, S.; Blecker, C.; Attia, H. Dietary fibre and fibre-rich by-products of food processing: characterisation, technological functionality and commercial applications: a review. *Food Chem.* **2011**, *124* (2), 411−421.

(9) Sun-Waterhouse, D.; Melton, L. D.; O'Connor, C. J.; Kilmartin, P. A.; Smith, B. G. Effect of apple cell walls and their extracts on the activity of dietary antioxidants. *J. Agric. Food Chem.* **2008**, *56* (1), 289−295.

(10) Ramulu, P.; Udayasekhara Rao, P. Total, insoluble and soluble dietary fiber contents of Indian fruits. *J. Food Compos. Anal.* **2003**, *16* (6), 677−685.

(11) Bindon, K. A.; Madani, S. H.; Pendleton, P.; Smith, P. A.; Kennedy, J. A. Factors affecting skin tannin extractability in ripening grapes. *J. Agric. Food Chem.* **2014**, *62* (5), 1130−1141.

(12) Manach, C.; Scalbert, A.; Morand, C.; Rémésy, C.; Jiménez, L. Polyphenols: food sources and bioavailability. *Am. J. Clin. Nutr.* **2004**, *79* (5), 727−747.

DOI: 10.1021/acs.jafc.5b00192
J. Agric. Food Chem. 2015, 63, 5813−5820

(13) De Freitas, V.; Carvalho, E.; Mateus, N. Study of carbohydrate influence on protein−tannin aggregation by nephelometry. *Food Chem.* **2003**, *81* (4), 503−509.
(14) De Freitas, V.; Mateus, N. Nephelometric study of salivary protein−tannin aggregates. *J. Sci. Food Agric.* **2002**, *82* (1), 113−119.
(15) Obreque-Slíer, E. A.; Peña-Neira, A. L.; Lopez-Solis, R. Enhancement of both salivary protein− enological tannin interactions and astringency perception by ethanol. *J. Agric. Food Chem.* **2010**, *58* (6), 3729−3735.
(16) You, J.; Luo, Y.; Wu, J. Conjugation of ovotransferrin with catechin shows improved antioxidant activity. *J. Agric. Food Chem.* **2014**, *62* (12), 2581−2587.
(17) Xu, L.; Yang, L.; Lei, S. Self-assembly of conjugated oligomers and polymers at the interface: structure and properties. *Nanoscale* **2012**, *4* (15), 4399−4415.
(18) Ward, M. D.; Raithby, P. R. Functional behaviour from controlled self-assembly: challenges and prospects. *Chem. Soc. Rev.* **2013**, *42* (4), 1619−1636.
(19) Appel, E. A.; del Barrio, J.; Loh, X. J.; Scherman, O. A. Supramolecular polymeric hydrogels. *Chem. Soc. Rev.* **2012**, *41* (18), 6195−6214.
(20) van der Boom, M. E.; Richter, A. G.; Malinsky, J. E.; Lee, P. A.; Armstrong, N. R.; Dutta, P.; Marks, T. J. Single reactor route to polar superlattices. Layer-by-layer self-assembly of large-response molecular electrooptic materials by protection-deprotection. *Chem. Mater.* **2001**, *13* (1), 15−17.
(21) Whitesides, G. M.; Grzybowski, B. Self-assembly at all scales. *Science* **2002**, *295* (5564), 2418−2421.
(22) Bazin, G.; Zhu, X. Crystalline colloidal arrays from the self-assembly of polymer microspheres. *Prog. Polym. Sci.* **2013**, *38* (2), 406−419.
(23) Khong, T. T.; Aarstad, O. A.; Skjåk-Bræk, G.; Draget, K. I.; Vårum, K. M. Gelling concept combining chitosan and alginate—proof of principle. *Biomacromolecules* **2013**, *14* (8), 2765−2771.
(24) Thompson, A. B.; Calhoun, A. K.; Smagghe, B. J.; Stevens, M. D.; Wotkowicz, M. T.; Hatziioannou, V. M.; Bamdad, C. A gold nanoparticle platform for protein−protein interactions and drug discovery. *ACS Appl. Mater. Interfaces* **2011**, *3* (8), 2979−2987.
(25) Hnilova, M.; Liu, X.; Yuca, E.; Jia, C.; Wilson, B.; Karatas, A. Y.; Gresswell, C.; Ohuchi, F.; Kitamura, K.; Tamerler, C. Multifunctional protein-enabled patterning on arrayed ferroelectric materials. *ACS Appl. Mater. Interfaces* **2012**, *4* (4), 1865−1871.
(26) Darder, M.; Aranda, P.; Ruiz-Hitzky, E. Bionanocomposites: a new concept of ecological, bioinspired, and functional hybrid materials. *Adv. Mater.* **2007**, *19* (10), 1309−1319.
(27) Zhang, M.; Bai, X.; Zhang, Z. Extrusion process improves the functionality of soluble dietary fiber in oat bran. *J. Cereal Sci.* **2011**, *54* (1), 98−103.
(28) Fukudome, I.; Kobayashi, M.; Dabanaka, K.; Maeda, H.; Okamoto, K.; Okabayashi, T.; Baba, R.; Kumagai, N.; Oba, K.; Fujita, M. Diamine oxidase as a marker of intestinal mucosal injury and the effect of soluble dietary fiber on gastrointestinal tract toxicity after intravenous 5-fluorouracil treatment in rats. *Med. Mol. Morphol.* **2014**, *47*, 1−8.
(29) Li, J.; Liu, F.; Fan, F.; Chen, S.; Qin, Y.; Li, W. Response surface methodology as an approach to optimize the extraction of soluble dietary fiber from Chinese gooseberry skin [J]. *Food Sci.* **2009**, *14*, No. 027.
(30) O'Toole, D. K. Characteristics and use of okara, the soybean residue from soy milk production a review. *J. Agric. Food Chem.* **1999**, *47* (2), 363−371.
(31) Bierhalz, A. C.; da Silva, M. A.; Braga, M. E.; Sousa, H. J.; Kieckbusch, T. G. Effect of calcium and/or barium crosslinking on the physical and antimicrobial properties of natamycin-loaded alginate films. *LWT−Food Sci. Technol.* **2014**, *57* (2), 494−501.
(32) Ji, S.; Peng, B.; Lin, M.; Li, M.; Wu, Z. Study on gelation of polyacrylamide/aluminum citrate colloidal dispersion gel by measurement of viscosity. *Acta Polym. Sin.* **2000**, *1*, 013.
(33) Shi, Y.; Belosinschi, D.; Brouillette, F.; Belfkira, A.; Chabot, B. Phosphorylation of Kraft fibers with phosphate esters. *Carbohydr. Polym.* **2014**, *106*, 121−127.
(34) Wu, S.; Du, Y.; Hu, Y.; Shi, X.; Zhang, L. Antioxidant and antimicrobial activity of xylan−chitooligomer−zinc complex. *Food Chem.* **2013**, *138* (2), 1312−1319.
(35) Maisuthisakul, P.; Pasuk, S.; Ritthiruangdej, P. Relationship between antioxidant properties and chemical composition of some Thai plants. *J. Food Compos. Anal.* **2008**, *21* (3), 229−240.
(36) Nigam, P. S. Microbial enzymes with special characteristics for biotechnological applications. *Biomolecules* **2013**, *3* (3), 597−611.
(37) Hartman, J.; Albertsson, A.-C.; Sjöberg, J. Surface-and bulk-modified galactoglucomannan hemicellulose films and film laminates for versatile oxygen barriers. *Biomacromolecules* **2006**, *7* (6), 1983−1989.
(38) Zdunek, A.; Kozioł, A.; Pieczywek, P.; Cybulska, J. Evaluation of the nanostructure of pectin, hemicellulose and cellulose in the cell walls of pears of different texture and firmness. *Food Bioprocess Technol.* **2014**, *7* (12), 3525−3535.
(39) Abulateefeh, S. R.; Taha, M. O. Enhanced drug encapsulation and extended release profiles of calcium−alginate nanoparticles by using tannic acid as a bridging cross-linking agent. *J. Microencapsulation* **2014**, 1−10.
(40) Torres, E.; Mata, Y.; Blazquez, M.; Munoz, J.; Gonzalez, F.; Ballester, A. Gold and silver uptake and nanoprecipitation on calcium alginate beads. *Langmuir* **2005**, *21* (17), 7951−7958.
(41) Guerrero, P.; Kerry, J. P.; de la Caba, K. FTIR characterization of protein−polysaccharide interactions in extruded blends. *Carbohydr. Polym.* **2014**, *111* (0), 598−605.
(42) Jensen, J. S.; Egebo, M.; Meyer, A. S. Identification of spectral regions for the quantification of red wine tannins with Fourier transform mid-infrared spectroscopy. *J. Agric. Food Chem.* **2008**, *56* (10), 3493−3499.
(43) Marek, W. U. Recent advances in film formation from colloidal particles: synthesis of non-spherical colloidal shapes with stimuli-responsive characteristics. In *Film Formation*; American Chemical Society: Washington, DC, USA, 2006; Chapter 8, pp 105−122.
(44) Widsten, P.; Cruz, C. D.; Fletcher, G. C.; Pajak, M. A.; McGhie, T. K. Tannins and extracts of fruit byproducts: antibacterial activity against foodborne bacteria and antioxidant capacity. *J. Agric. Food Chem.* **2014**, *62* (46), 11146−11156.
(45) Sosnik, A.; das Neves, J.; Sarmento, B. Mucoadhesive polymers in the design of nano-drug delivery systems for administration by non-parenteral routes: a review. *Prog. Polym. Sci.* **2014**, *39* (12), 2030−2075.

DOI: 10.1021/acs.jafc.5b00192
J. Agric. Food Chem. 2015, 63, 5813−5820

and aqueous phases to see if the mode of addition affected AOX efficacy in a low-moisture system. The AOX efficacy was related to cracker structure and AOX partitioning via imaging with confocal microscopy. Commercial AOX of varying hydrophobicities were also used to evaluate the relationship between hydrophobicity and AOX efficacy.

Improving our understanding of AOX mechanisms has broad and long-lasting implications. Development of new, tailored AOX that can extend product quality, thereby reducing industry loss and supporting development of foods with extended shelf life, can have benefits to consumers as well as meals for space and military programs. Improved AOX technologies will also improve the health and wellness of the food supply by allowing greater utilization of heart-healthy polyunsaturated fats and other bioactive lipids susceptible to oxidation.

MATERIALS AND METHODS

Materials. Baking soda (Arm & Hammer), iodized table salt (Morton), and all-purpose flour (Gold Medal) were purchased from local grocery stores. Interesterified soybean oil 762420 (henceforth referred to as ISO) was provided by Archer Daniels Midland Co. (Decatur, IL, USA). Dry goods were stored in closeable freezer bags to prevent moisture sorption; ISO was kept frozen (−20 °C) until use. Dodecyl and eicosyl rosmarinate esters were prepared as described previously (structures in original publication).[11] Rosmarinic acid, the fluorescent probe Nile Red, and all other chemicals were purchased from Sigma-Aldrich (St. Louis, MO, USA). All solutions were prepared using double-distilled water.

General Sample Manufacture and Preparation. Crackers were prepared as previously described[12] by premixing dry ingredients (sifted flour, baking soda, and salt) and then blending with the ISO until the fat was homogeneously cut into the flour; all mixing was done with a KitchenAid model KSM95 (Mississauga, ON, Canada) and associated attachments. Water was then added to form a dough, which was briefly kneaded by hand until all flour was visibly incorporated (∼30 s). Ten grams of additional flour was sprinkled on the surface of a baking mat to prevent sticking; all of this flour was incorporated during kneading. The dough was flattened by twice sheeting it through a pasta roller (KitchenAid KPSA attachment; thickness setting 2). Crackers (2.5 cm × 2.5 cm) were cut from the dough with a pizza cutter and baked on an ungreased cookie sheet at 163 °C for 21 min in an electric oven (General Electric model JB350DFWW; Fairfield, CT, USA). After baking, crackers were coarsely crushed using a mortar and pestle, and 0.5 g was placed into acid-washed, 10 mL glass GC vials (Supelco Analytical, Bellefonte, PA, USA). The vials were closed with aluminum caps containing PTFE/silicone septa (Supelco Analytical) and stored at 55 °C in the dark for 30−75 days depending upon lag phase. Crackers for confocal image analysis were stored in closeable freezer bags in the dark at ∼4 °C and imaged within 3 days of manufacture.

AOX and Dye Incorporation into the Crackers. One hundred and fifty-nine micromoles of rosmarinic acid (R0) or its 12- (R12) and 20- (R20) carbon esters (henceforth collectively referred to as "rosemary AOX") or 344 μmol of synthetic antioxidants [propyl gallate (PG), *tert*-butylhydroquinone (TBHQ), and butylhydroxy toluene (BHT)] were dissolved in 1.0 mL of ethanol and mixed with ISO in the KitchenAid mixer (model KSM95) for 1 min before the dry ingredients were added. Alternatively, rosmarininc acid esters in 1.0 mL of ethanol were mixed with water before dough formation in some experiments. In all cases, the same volume of ethanol was added to control (no AOX) treatments. Nile Red in ethanol (0.5 mL) was added to the ISO prior to mixing in the rosemary AOX and control treatments.

Measurement of Lipid Oxidation. Lipid hydroperoxides, the primary oxidation products, were measured in triplicate using a modified version of the International Dairy Federation method as previously described by Shantha and Decker.[13] In short, coarsely crushed crackers (0.105 g) were pulverized using a mortar and pestle and added to a mixture of chloroform and methanol (5 mL; 2:1 v/v), vortexed briefly, and centrifuged (3400*g*) for 10 min to extract the hydroperoxide-containing lipid fraction. This extract (200 μL) was mixed with (1) 16.7 μL of a 50:50 solution of ferrous sulfate (66 mM in double-distilled water) and barium chloride (38 mM in 0.4 N HCl) and (2) 16.7 μL of ammonium thiocyanate (3.9 M in double-distilled water). The final mixture was vortexed, covered to prevent evaporation, and incubated 20 min at ambient temperature as color developed. Absorbance was measured at 500 nm on a Genesys 20 spectrophotometer (ThermoSpectronic, Waltham, MA, USA). The concentration of hydroperoxides was calculated from a cumene hydroperoxide standard curve.

Headspace hexanal, the secondary oxidation product, was measured in triplicate with a GC-2014 Shimadzu gas chromatograph equipped with an AOC-5000 autosampler (Shimadzu, Kyoto, Japan) based on the solid phase microextraction (SPME) method of Panya et al.[8] Specifically, a 50/30 μm divinylbenzene/carboxen/polydimethylsiloxane (DVB/Carboxen/PDMS) SPME fiber (Supelco, Bellefonte, PA, USA) was inserted through the vial septum and exposed to the sample headspace for 10 min at 55 °C. The SPME fiber was desorbed at 250 °C for 3 min in the gas chromatograph detector at a split ratio of 1:7. The temperatures of the oven, injector, and flame ionization detector were 65, 250, and 250 °C, respectively, and samples ran for 6 min. Volatile aldehydes were separated on a fused-silica capillary column (30 m × 0.32 mm i.d. × 1 μm) coated with 100% poly(dimethylsiloxane) (Equity-1, Supelco), and peak integration was calculated using Shimadzu EZstart (version 7.4) software. A standard curve made from crushed cracker spiked with known hexanal concentrations (hexanal was diluted in methanol with a range from 0 to 136 mmol hexanal per kilogram of cracker) was used to determine hexanal concentrations in the samples.

Measurement of Rosemary AOX. To prepare samples for high-performance liquid chromatography (HPLC), 0.150 ± 0.005 g of pulverized crushed cracker was mixed with 1 mL of methanol, sonicated for 30 min, and filtered (0.45 μm syringe filter Millex-FH, Millipore Corp., Bedford, MA, USA) into amber vials with polyethylene snap caps (Waters, Milford, MA, USA). HPLC determination of rosmarinic acid and its esters was carried out with a Hypersil gold C18 reversed phase column (250 mm × 4.6 mm, 5 μm) equipped with a Hypersil gold guard column (10 mm × 4 mm, 5 μm) (Thermo Scientific, USA) using an LC-10ATvp HPLC system (Shimadzu, USA). Samples were injected into the HPLC at a flow rate of 1 mL/min at room temperature using a mobile phase of either methanol (to detect rosemary antioxidants) or acetonitrile (to detect caffeic acid). Pure rosmarinic acid and its alkyl esters and caffeic acid were dissolved in methanol and used as standards. R0 and its esters were detected with a photodiode array detector (SPD-M10Avp, Shimadzu, USA) at 328 nm. Peak integration was performed using Shimadzu EZstart (version 7.4).

Confocal Microscopy. A Nikon confocal microscope (C1 Digital Eclipse, Tokyo, Japan) with a PL FLUOTAR ELWD 20.0 × 0.45 objective lens was used to capture the confocal images. Whole crackers were glued to a slide and imaged by quadrants, with at least four images taken in each quadrant. A 408 nm laser was used to excite the R0 and esters, and a 488 nm laser was used to excite Nile Red. Emission spectra were collected from 415 to 485 nm for the R0 and esters and from 485 to 545 nm for the Nile Red, and the resulting images were overlaid. Detector pinhole size was 150 μm. All resulting images consisted of 512 × 512 pixels, with a pixel size of 414 nm, and a pixel dwell time of 10.40 μs. Images were analyzed using EZ-CS1 (version 3.8) software (Nikon, Melville, NY, USA).

Statistical Analysis. Differences between treatments were determined by differences in the laboratory phase of lipid hydroperoxide and hexanal formation. The cutoff for the end of the oxidation lag phase was marked by the first datum point that was significantly greater than the time-zero value with all subsequent data points also being significantly greater than the time-zero value. Means were compared using analysis of variance (General Linear Model with Tukey's Honestly Significant Difference test as a post hoc test for multiple comparisons). Statistical difference was set at $p < 0.05$. All

DOI: 10.1021/acs.jafc.5b01085
J. Agric. Food Chem. 2015, 63, 5821−5827

calculations were performed using XLSTAT statistical software (version 2006.3, Addinsoft, New York, NY, USA).

RESULTS

Sample Quality. To ensure consistent production, all crackers were made by one individual, trained for >8 h before experimentation, and all samples were consistent both visually and in final moisture content. To ensure reproducibility, cracker production steps were carefully controlled; two batches were freshly prepared for every treatment, and all treatments presented in a single figure were prepared the same day, including fresh control treatments.

Homologous AOX Series. R0 and its alkyl esters were selected as a means of varying hydrophobicity while keeping the AOX portion of the molecule constant.[11] The activity of each antioxidant was tested at 159 μmol because it corresponded to 500 ppm of R0, a concentration typically used by industry for AOX applications. R0 and its alkyl esters naturally fluoresce (blue region of Figure 1), allowing their location to be determined with confocal microscopy without the use of additional probes. Nile Red was used as a lipid-soluble confocal probe to view the lipids (green region of Figure 1) in the cracker. In all treatments, the ISO formed a continuous lipid phase surrounding the starch granules (data not shown), as was seen in a previous study.[12] AOX were first added by incorporating them in the lipid prior to dough formation.

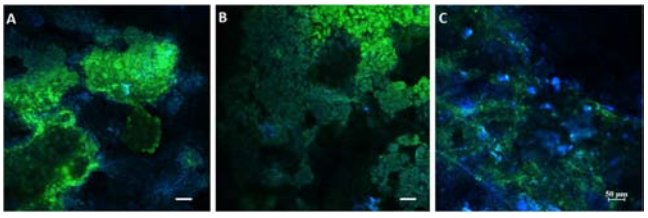

Figure 1. Fluorescence of Nile Red dye (green) and either (A) rosmarinic acid, (B) dodecyl (R12) rosmarinate ester, or eicosyl (R20) rosmarinate ester (blue) in crackers at day 0. Antioxidants were incorporated by mixing with the lipid phase prior to dough formation. Scale bars: 20 μm in panels A and B; 50 μm in panel C.

Confocal microscopy can provide useful information about the location of different components in foods, but it does have its limitations due to limits in resolutions and variations in focusing depths in foods with rough textures. Therefore, we attempted to keep our discussion of the confocal results as general and conservative as possible and realize that the images can be difficult to interpret. Figure 1A shows crackers containing free R0. In this system, the blue R0 tended to partition separately from the green lipid region. This is likely due to the low lipid solubility of R0, which agrees with findings by Panya et al.[8] in which <15% of R0 was found in the lipid phase of oil-in-water emulsions. In contrast, Figure 1B shows that the R12 ester of rosmarinic acid tended to overlap with the lipid, thereby creating more regions of turquoise areas in the confocal images and suggesting that the R12 ester was associated with the lipid more than R0. This would also be in agreement with Panya et al.,[8] who found that >90% of R12 was in the lipid phase of oil-in-water emulsions. The partitioning behavior of R20 is shown in Figure 1C. It differs from R0 and R12 in that it formed distinct regions of blue scattered throughout the cracker. It is unclear why this would occur because R20 is the most hydrophobic and would be soluble in the lipid. However, these images suggest that instead of forming a homogeneous mixture with the ISO, some of the R20 is self-aggregating apart from the ISO. This could occur if the concentration of the R20 used in these experiments exceeded its solubility in the ISO.

The difference in AOX partitioning observed via confocal microscopy was compared to the actual AOX efficacy. The esterified rosemary esters, which showed greater overlap with the lipid in the confocal images, significantly extended the lag phase of both hydroperoxide (Figure 2A) and hexanal (Figure 2B) development when the AOX was incorporated into the lipid phase prior to dough formation. R0 was the least effective. It extended the hydroperoxide lag phase only a few days compared to the control, but it actually increased the formation of headspace hexanal compared to the control, decreasing the hexanal headspace lag phase from 40 days (control) to 21 days (R0) (Figure 2B). This suggests the polar R0 destabilized hydroperoxides, perhaps by binding and solubilizing prooxidant metals or by reducing metals to their more reactive state, causing increased lipid hydroperoxide decomposition into secondary lipid oxidation products such as hexanal. In contrast, R20 and R12 both delayed hydroperoxide generation and extended the headspace hexanal lag phase, for R12 to 48 days and for R20 to 55 days.

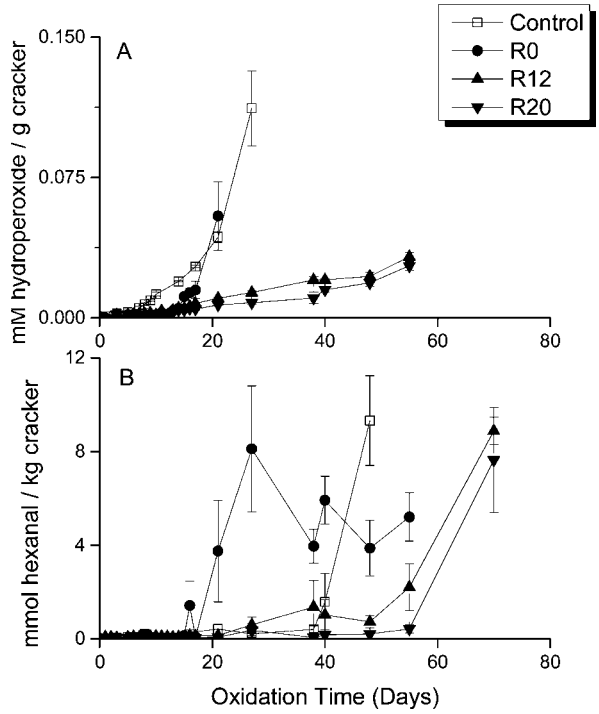

Figure 2. (A) Lipid hydroperoxides and (B) headspace hexanal in crackers with rosmarinic and its esters (chain lengths = 0, 12, or 20 carbons) incorporated into the lipid prior to dough formation. Crackers were stored in the dark at 55 °C. Standard error bars are smaller than data points in some instances.

To determine how AOX partitioning and efficacy were affected by the mode of incorporation, R0 and its alkyl esters (R12 and R20) were also dissolved in ethanol and added to the water phase prior to formation of the dough (Figure 3). Addition of the AOXs to the water altered AOX activity because none of the treatments extended the hydroperoxide lag phase compared to the control, although hydroperoxide

DOI: 10.1021/acs.jafc.5b01085
J. Agric. Food Chem. 2015, 63, 5821−5827

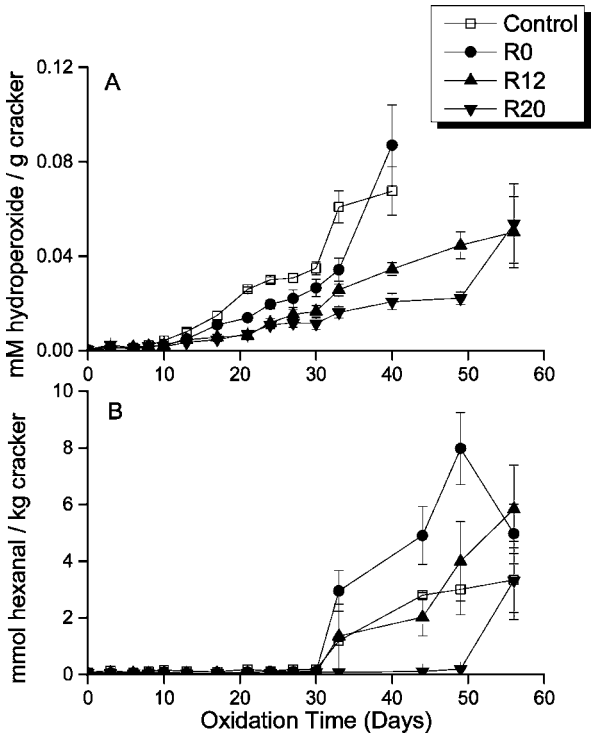

Figure 3. (A) Lipid hydroperoxide and (B) headspace hexanal formation in crackers made by incorporating rosmarinic ester antioxidants (chain lengths = 0, 12, or 20 carbons) into the aqueous phase prior to dough formation. Crackers were stored in the dark at 55 °C. Standard error bars are smaller than data points in some instances.

generation was slower in all three rosemary treatments (Figure 3A). However, R20 was considerably more effective than R12 at inhibiting hexanal formation by extending the lag phase almost 20 days (Figure 3B). That means R12 increased the lag phase of hexanal formation when added to the lipid phase but was ineffective compared to the control when added to the aqueous phase. R20 produced similar hexanal lag phases when added to the lipid (54 days) or aqueous (49 days) phases. Finally, R0 did not increase hexanal formation when added to the water phase, again suggesting that AOX activity was altered by mode of addition.

Lipid oxidation data (Figure 3) were again related to physical structure. Confocal images of the crackers where the AOX were added to the water suggested that R20 still formed distinct regions of blue scattered throughout the lipid regions as it did when added to the lipid, which likely explains its continued efficacy (Figure 4C). Previously (Figure 1A), we showed that

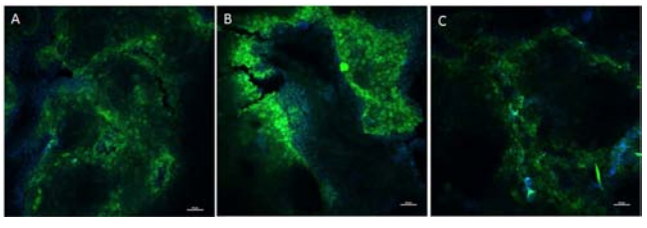

Figure 4. Fluorescence of Nile Red dye (green) and either (A) rosmarinic acid, (B) dodecyl (R12) rosmarinate ester, or (R20) eicosyl rosmarinate ester (blue) phase partitioning of lipid and antioxidant, respectively, in crackers at day 0. Antioxidants were incorporated by mixing with the aqueous phase. Scale bars: 50 μm.

R0, when added to the lipid phase, was not highly associated with the lipid phase. This trend also occurred when the R0 was added to the aqueous phase (Figure 4A). When R12 was added to the lipid phase, areas of AOX overlapped with the lipid created turquoise zones (Figure 1B). However, fewer of these types of overlap were observed when R12 was added to the aqueous phase (Figure 4B). Few differences were observed in the confocal images between R0 and R20 when they were added to the water, which could help explain why their AOX activity was similar (Figure 3). The change in R12 partitioning could be due to its inability to solubilize in the solid fat when added to the water phase. It is also theoretically possible that R12 uniquely interacted with starch and that these interactions were increased when it was added to the water phase. The unbranched $\alpha(1\rightarrow4)$ glucan chains of starch are known to form a helical structure with a hydrophobic interior that interacts with other nonpolar molecules and residues.[14] Many published studies show that lauric acid (C12:0) is commonly complexed with starch.[15−17] The 12-carbon alkyl chain of R12 may have behaved like lauric acid, readily forming complexes with the helical starch. In either case, this would partition R12 away from the lipid, thereby decreasing its ability to inhibit lipid oxidation.

Free radical scavenging AOX are degraded during lipid oxidation reactions, so their concentrations during storage can be used as a measure of oxidation reactions. HPLC was used to monitor the loss of R0 and its esters during storage when they were added to the lipid phase. The loss was in the order R0 > R12 > R20 (Figure 5). In all cases, the rosmarinic acid

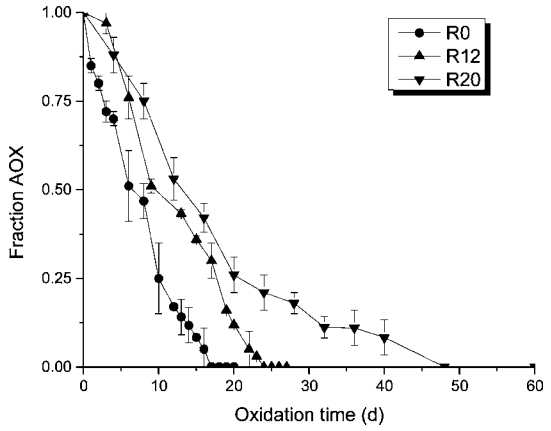

Figure 5. Loss of rosmarinic ester antioxidants (chain lengths = 0, 12, or 20 carbons) added to the lipid phase during storage at 55 °C in the dark as determined by HPLC. Vertical lines indicate standard error for each point.

homologues were completely lost prior to the formation of hexanal (Figure 2B). HPLC was also used to monitor the loss of R0 and its esters during storage when they were added to the water. In that case, loss was in the order R0 ≅ R12 > R20 (Figure 6). Again, the rosmarinic acid homologues were completely lost prior to formation of hexanal (Figure 3B). The similarity of R0 and R12 degradation rates when they were added to the aqueous phase again supports the observation that these two AOX were behaving similarly.

It is unclear what made the R20 ester oxidize more slowly. Previous research has shown that the rosmarinate esters in oil-in-water emulsions degraded into caffeic acid in the presence of α-tocopherol. Because caffeic acid also has AOX activity, its

DOI: 10.1021/acs.jafc.5b01085
J. Agric. Food Chem. 2015, 63, 5821−5827

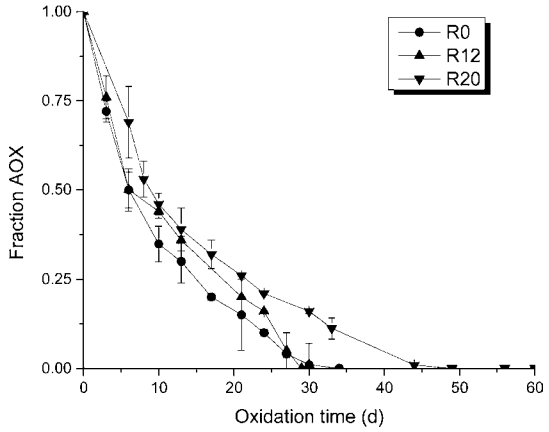

Figure 6. Loss of rosmarinic ester antioxidants (chain lengths = 0, 12, or 20 carbons) added to the aqueous phase during storage at 55 °C in the dark as determined by HPLC. Vertical lines indicate standard error for each point.

formation decreased the rate of R20 degradation and further decreased lipid oxidation.[10] The formation of caffeic acid in the crackers was determined by HPLC as described by Panya et al.[10] In the cracker systems, no quantifiable caffeic acid was measured by HPLC regardless of alkyl chain length. This could be because the crackers contained no quantifiable amounts of tocopherols from the ISO.

Another possibility for the decreased degradation rate of R20 compared to R0 and R12 could be due to interactions with other food components. Phenolic AOX can interact with transition metals, resulting in the reduction of the metal and the degradation of the antioxidant.[18] Therefore, it is possible that the R0 and R12 could interact with metal more when they partition separately from the lipid, thereby causing them to degrade more quickly. The R20, which partitioned in the lipid and formed concentrated pockets outside the lipid, could have fewer interactions with metals and thus degrade more slowly, leaving more R20 for scavenging free radicals. Finally, it is important to note that AOX efficacy is linked to concentration: as the concentrations of AOX such as tocopherols are increased, their effectiveness can decrease.[19] Therefore, a third possibility is that the R20 concentration in the lipid phase produced optimal AOX activity. As the R20 decomposed during oxidation, it is possible it moved from its discrete pockets outside the lipid back into the lipid phase. This could keep R20 concentrations in the ISO at optimal levels, thus enhancing efficacy.

Commercial AOX. The homologous series of rosmarinate esters are an excellent research tool to study AOX properties because they vary in hydrophobicity and yet their AOX functionalities are very similar.[11] However, rosmarinate esters are not approved food grade ingredients. Hence, the activity of approved food additives with various hydrophobicities was also investigated. This study tested the efficacy of PG (least hydrophobic), TBHQ, and BHT (most hydrophobic) in the model cracker system by incorporating the AOX into the lipid phase; all were added at a molar equivalent to 500 ppm of TBHQ. PG was prooxidative as determined by both lipid hydroperoxides and headspace hexanal (Figure 7). This is similar to what was observed with the hydrophilic R0, which had little effect on lipid hydroperoxide formation and accelerated headspace hexanal formation when added to the lipid phase (Figure 2). TBHQ and BHT are both more

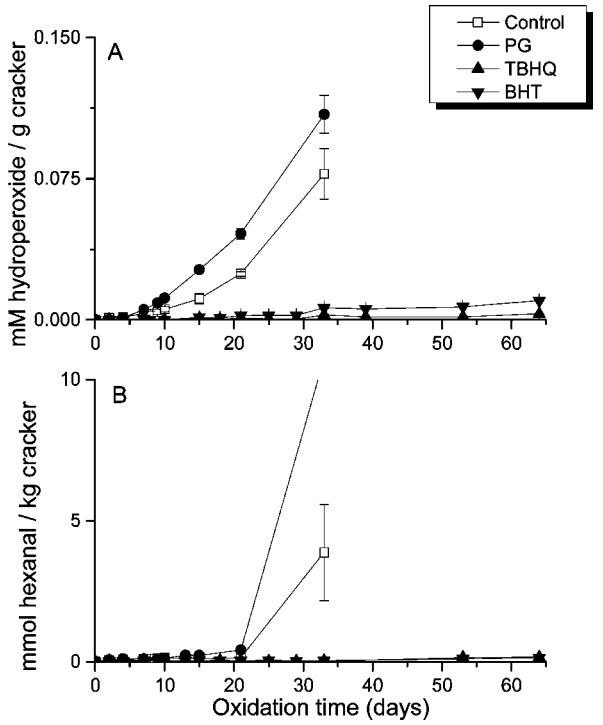

Figure 7. (A) Lipid hydroperoxide and (B) headspace hexanal in crackers made by incorporating propyl gallate (PG), *tert*-butylhydroquinone (TBHQ), or butylhydroxytoluene (BHT) into the lipid phase. Crackers were stored at 55 °C in darkness. Standard error bars are smaller than data points in some instances.

hydrophobic than PG and exhibited greater antioxidant efficacy. Figure 7A shows that, after 33 days, both TBHQ and BHT treatments were still in the lag phase of hydroperoxide formation. Analysis of headspace hexanal formation led to the same conclusion: the hydrophobic antioxidants BHT and TBHQ were more effective than PG treatments and similar to each other at limiting lipid oxidation. This again agrees with the rosmarinate ester experiments in that AOX efficacy increases with increasing hydrophobicity. However, it should also be noted that unlike the rosmarinic acid esters, the free radical scavenging effects of PG, BHT, and TBHQ are not equal, and thus the observed differences would also be due to differences in chemical reactivity. Both BHT and TBHQ (at 344 μmol) were more effective than the R20 rosmarinate esters (at 159 μmol).

DISCUSSION

These results suggest that AOX efficacy in crackers increases with increasing hydrophobicity, meaning that crackers follow markedly different trends from bulk oils and oil-in-water emulsions.[3,4,6,8−10,18,20] Much of this likely relates to the unique physical structure of low-moisture foods, which affects the physical location of the AOX. AOX should be most effective when they partition at the site of oxidation, which in both oil-in-water emulsions and bulk oils containing association colloids is oil−water interfaces.[3,19] The ISO used in the model crackers formed a continuous lipid phase that surrounds starch granules (Figure 1). In addition, the crackers are very low in water and, as in other low-moisture foods, the water that is in the crackers is likely associated with molecules such as starch and proteins and therefore does not exist as dispersed droplets.[21,22] This means that that there will be very few water−lipid interfaces

DOI: 10.1021/acs.jafc.5b01085
J. Agric. Food Chem. 2015, 63, 5821−5827

where lipids and water-soluble prooxidant would interact as would be seen in oil-in-water emulsions and bulk oils with association colloids.

The inability of highly polar R0 to inhibit lipid oxidation could be due to its exclusion from the lipid phase, meaning it is physically separated from lipid oxidation reactions, as suggested by the confocal microscopy. The R12 ester had inconsistent activity given that it was effective when added to the lipid phase prior to dough formation but ineffective when added to the aqueous phase. R12 has intermediate solubility characteristics of the three rosmarinates tested,[8] suggesting that the method of introduction into dough could impact its partitioning. For example, when added to the ISO, it might be better retained in the lipid phase compared to when it is added to the aqueous phase, where it might interact with other molecules in the flour, thereby preventing it from partitioning into the lipid phase. The consistent ability of R20 to inhibit lipid oxidation suggests that it partitions at the site of lipid oxidation regardless of the method used to introduce it into the dough.

Overall, the ability of AOX to inhibit lipid oxidation in low-moisture crackers is very different from bulk oils and oil-in-water emulsions. R0 is effective in bulk oils[23] but was prooxidative in the crackers. In oil-in-water emulsions, rosmarinate esters follow the "cutoff effect" in which the activity of AOX esters increases with increasing hydrophobicity up to 8−12 carbon alkyl chain length, after which AOX activity decreases dramatically with increasing chain length, with R20 having essentially no activity.[6−11] In the crackers, R20, the most hydrophobic ester, had the most activity. In addition, results with the synthetic AOX support the notion that highly hydrophobic AOX are the most effective in the crackers. Thus, the physical properties of low-moisture crackers have a much different impact on the activity of AOX from bulk oils and oil-in-water emulsions, and they therefore may require a different class of AOX than other types of foods.

Extending the lag phase of lipid oxidation correlates directly to extended shelf life and maximizing nutritional benefits by inhibiting the degradation of vitamins susceptible to oxidation. This research suggests that the lag phase of lipid oxidation can be extended in low-moisture crackers by using the most hydrophobic AOX option available. Such an AOX selection is unique to low-moisture foods compared to oil-in-water emulsions and bulk oils. These AOX could be used in combination with other AOX strategies such as control of transition metals and elimination of oxygen and light exposure to maximize the shelf life of low-moisture foods.

AUTHOR INFORMATION

Corresponding Author

*(E.D.) Mail: Department of Food Science, University of Massachusetts, Amherst, 228 Chenoweth Laboratory, 102 Holdsworth Way, Amherst, MA 01003, USA. Phone: (413) 545-2276. Fax: (413) 545-1262. E-mail: edecker@foodsci.umass.edu.

Funding

This work was supported by a USDA NIFA National Needs grant.

Notes

The authors declare no competing financial interest.

ABBREVIATIONS USED

AOX, antioxidant(s); BHT, butylhydroxytoluene; ISO, interesterified soybean oil; PG, propyl gallate; R0, rosmarinic acid; R12, dodecyl rosmarinate ester; R20, eicosyl rosmarinate ester; TBHQ, *tert*-butylhydroquinone

REFERENCES

(1) Porter, W. L. Recent trends in food applications of antioxidants. In *Autoxidation in Food and Biological Systems*; Simic, M. G., Karel, M., Eds.; Plenum Press: New York, 1980; pp 295−365.

(2) Porter, W. L.; Black, E. D.; Drolet, A. M. Use of polyamide oxidative fluorescence test on lipid emulsions: contrast in relative effectiveness of antioxidants in bulk versus dispersed systems. *J. Agric. Food Chem.* **1989**, *37*, 615−624.

(3) Frankel, E. N.; Huang, S.; Kanner, J.; German, J. B. Interfacial phenomena in the evaluation of antioxidants: bulk oils vs emulsions. *J. Agric. Food Chem.* **1994**, *42*, 1054−1059.

(4) Laguerre, M.; López Giraldo, L. J.; Lecomte, J.; Figueroa-Espinoza, M.; Baréa, B.; Weiss, J.; Decker, E. A.; Villeneuve, P. Chain length affects antioxidant properties of chlorogenate esters in emulsion: the cutoff theory behind the polar paradox. *J. Agric. Food Chem.* **2009**, *57*, 11335−11342.

(5) Sasaki, K.; Alamed, J.; Weiss, J.; Villeneuve, P.; Lopez Giraldo, L.J.; Lecomte, J.; Figueroa-Espinoza, M. C.; Decker, E. A. Relationship between the physical properties of chlorogenic acid esters and their ability to inhibit lipid oxidation in oil-in-water emulsions. *Food Chem.* **2010**, *118*, 830−835.

(6) Laguerre, M.; López Giraldo, L. J.; Lecomte, J.; Figueroa-Espinoza, M.; Baréa, B.; Weiss, J.; Decker, E. A.; Villeneuve, P. Relationship between hydrophobicity and antioxidant ability of phenolipids in emulsion: a parabolic effect of the chain length of rosmarinate esters. *J. Agric. Food Chem.* **2010**, *58*, 2869−2876.

(7) Panya, A.; Laguerre, M.; Lecomte, J.; Villeneuve, P.; Weiss, J.; McClements, D. J.; Decker, E. A. Effects of chitosan and rosmarinate esters on the physical and oxidative stability of liposomes. *J. Agric. Food Chem.* **2010**, *58*, 5679−5684.

(8) Panya, A.; Laguerre, M.; Bayrasy, C.; Lecomte, J.; Villeneuve, P.; McClements, D. J.; Decker, E. A. An investigation of the versatile antioxidant mechanisms of action of rosmarinate alkyl esters in oil-in-water emulsions. *J. Agric. Food Chem.* **2012**, *60*, 2692−2700.

(9) Lee, J. H.; Panya, A.; Laguerre, M.; Bayrasy, C.; Lecomte, J.; Villeneuve, P.; Decker, E. A. Comparison of antioxidant capacities of rosmarinate alkyl esters in riboflavin photosensitized oil-in-water emulsions. *J. Am. Oil Chem. Soc.* **2013**, *90*, 225−232.

(10) Panya, A.; Kittipongpittaya, K.; Laguerre, M.; Bayrasy, C.; Lecomte, J.; Villeneuve, P.; McClements, D. J.; Decker, E. A. Interactions between α-tocopherol and rosmarinic acid and its alkyl esters in emulsions: synergistic, additive, or antagonistic effect? *J. Agric. Food Chem.* **2012**, *60*, 10320−30.

(11) Lecomte, J.; Laguerre, M.; Barea, B.; Villeneuve, P.; Giraldo, L. J. L. Synthesis, characterization and free radical scavenging properties of rosmarinic acid fatty esters. *J. Am. Oil Chem. Soc.* **2010**, *87*, 615−620.

(12) Barden, L.; Vollmer, D.; Johnson, D.; Decker, E. Impact of iron, chelators and free fatty acids on lipid oxidation in low-moisture crackers. *J. Agric. Food Chem.* **2015**, *63*, 1812−1818.

(13) Shantha, N. C.; Decker, E. A. Rapid, sensitive, iron-based spectrophotometric methods for determination of peroxide values of food lipids. *J. AOAC Int.* **1994**, *77*, 421−424.

(14) Putseys, J. A.; Lamberts, L.; Delcour, J. A. Amylose-inclusion complexes: formation, identity and physico-chemical properties. *J. Cereal Sci.* **2010**, *51*, 238−247.

(15) Chang, F.; He, X.; Huang, Q. The physicochemical properties of swelled maize starch granules complexed with lauric acid. *Food Hydrocolloids* **2015**, *32*, 365−372.

(16) Gujral, H. S.; Rosell, C. M. Modification of pasting properties of wheat starch by cyclodextrin glycosyltransferase. *J. Sci. Food Agric.* **2004**, *84*, 1685−1690.

DOI: 10.1021/acs.jafc.5b01085
J. Agric. Food Chem. 2015, 63, 5821−5827

(17) Tang, M. C. Analysis of complexes between lipids and wheat starch. *Carbohydr. Polym.* **2007**, *67*, 80−85.
(18) Chen, B.; Panya, A.; McClements, D. J.; Decker, E. A. New insights into the role of iron in the promotion of lipid oxidation in bulk oils containing reverse micelles. *J. Agric. Food Chem.* **2012**, *60*, 3524−3532.
(19) Frankel, E. N. *Antioxidants in Food and Biology: Facts and Fiction*; Woodhead Publishing: Philadelphia, PA, USA, 2012; Vol. 20.
(20) Chen, B.; Han, A.; McClements, D. J.; Decker, E. A. Physical structures in soybean oil and their impact on lipid oxidation. *J. Agric. Food Chem.* **2010**, *58*, 11993−11999.
(21) Haynes, L. C.; Locke, J. P. Microwave permittivities of cracker dough, starch and gluten. *J. Microwave Power Electromagn. Energy* **1995**, *30*, 124−131.
(22) Kweon, M.; Slade, L.; Levine, H.; Gannon, D. Cookie- versus cracker-baking − what's the difference? Flour functionality requirements explored by SRC and alveography. *Crit. Rev. Food Sci. Nutr.* **2014**, *54*, 115−138.
(23) Laguerre, M.; Chen, B.; Lecomte, J.; Villeneuve, P.; McClements, D. J.; Decker, E. A. Antioxidant properties of chlorogenic acid and its alkyl esters in stripped corn oil in combination with phospholipids and/or water. *J. Agric. Food Chem.* **2011**, *59*, 10361−10366.

DOI: 10.1021/acs.jafc.5b01085
J. Agric. Food Chem. 2015, 63, 5821−5827

involved in amino acid decarboxylation could be the results of a horizontal gene transfer (possibly from Gram-negative bacteria) and could be located in genomic islands, as already demonstrated for tyrosine decarboxylase operon.[18,19]

The presence of relevant amounts of BAs in food is associated with a massive growth of decarboxylating bacteria. Then, in unfermented foods, BA concentration has been considered as a spoilage index.[10] By contrast, in fermented foods the presence of complex microbial communities necessary for their production is often associated with high BA (among which is PUT) accumulation. According to a report of the EFSA,[10] PUT was found at median values of 26.9 mg/kg in fermented sausages and 82 mg/kg in fish sauce, whereas in dairy products this value was <50 mg/kg; higher PUT contents were found in fermented vegetables.

LAB are common components of the microbial population responsible for the production of several fermented foods. Their use in competitive strategies has been deeply studied in recent decades,[20−22] and recently the effect of the relationships between bioprotective LAB and decarboxylative bacteria has been described.[23−25] They can produce a wide range of metabolites, such as organic acids, diacetyl, acetoin, hydrogen peroxide, antifungal peptides, and bacteriocins, which are often able to inhibit or kill other microorganisms without safety implications.[26,27] During growth, LAB produce these antimicrobial substances, which are released and accumulated in the medium. Thus, the separation of cells from the cultural broth produces cell free supernatants (CFSs), which may exert interesting antimicrobial activity. The effects of CFSs from specific LAB on TYR and other BA production by common foodborne pathogens (FBPs) have been studied.[28] From this perspective, this work has the aim to investigate the impact of CFSs from some LAB strains on PUT and other monoamine and polyamine formation by FBPs in a specific decarboxylase medium. In particular, the effects of CFSs on the decarboxylase activities of *Salmonella* Paratyphi A, *Listeria monocytogenes*, *Staphylococcus aureus*, and *Escherichia coli* were assessed in ornithine decarboxylase broth (ODB).

MATERIALS AND METHODS

Bacterial Strains and Culture Conditions. LAB strains, which are *Lactococcus lactis* subsp. *lactis* IL 1403 (*Lc. lactis* subsp. *lactis*), *Leuconostoc mesenteroides* subsp. *cremoris* DSMZ 20346 (*Leuc. mesenteroides* subs. *cremoris*), *Pediococcus acidilactici* ATCC 25741 (*Pc. acidilactici*), and *Streptococcus thermophilus* NCFB 2392 (*Str. thermophilus*) were obtained from Sutcu Imam University (Kahramanmaraş, Turkey) in BGML stock culture.

The four selected foodborne pathogens were *Staphylococcus aureus* ATCC 29213 (*Staph. aureus*), *Escherichia coli* ATCC 25922 (*E. coli*), *Listeria monocytogenes* ATCC 7677 (*L. monocytogenes*), which were bought from American Type Culture Collection (Rockville, MD, USA), and *Salmonella* Paratyphi A NCTC 13 (*S.* Paratyphi A), which was purchased from National Collections of Industrial Food and Marine Bacteria (Aberdeen, UK).

Preparation of Cell-free Supernatants from Lactic Acid Bacteria. The CFSs were prepared using the medium in which LAB strains grew. In particular, LAB were pregrown in 10 mL of De Man, Rogosa, and Sharpe (MRS; Merck) medium (1%, v/v) with overnight incubation at 37 °C, and then 7.5 mL of the bacterial culture was added aseptically to 750 mL of MRS medium in a sterile 1000 mL bottle. Bacteria in the bottle were incubated at 37 °C for 16 h without shaking. A cell-free supernatant was taken by centrifuging at 9000 rpm for 20 min under refrigeration (at 4 °C) from bacterial suspension. The cell-free supernatant was sterilized using a Sartorius membrane filter (0.22 μm).

Determination of Antimicrobial Assay of LAB Strains. The antimicrobial activity of CFSs from the LAB against *E. coli*, *Staph. aureus*, *L. monocytogenes*, and *S.* Paratyphi A was achieved by using the well diffusion assay. More information about determination of antimicrobial activity has been reported by Toy et al.[28]

Foodborne Pathogen Growth in Ornithine Decarboxylase Medium. The production of PUT by all foodborne pathogen strains used in this work was monitored using ornithine decarboxylase broth (ODB) as proposed by Klausen and Huss.[29] ODB contains 2 g/L peptone, 1 g/L Lab-Lemco powder (Oxoid CM0017, Hampshire, UK), 5 g/L NaCl (Merck 1.06404.1000, Darmstadt, Germany), 8.02 g/L L-ornithine HCl (Sigma H8125), and 5 mg/L pyridoxal HCl (Sigma P9130, Steinheim, Germany). The ODB also contains glutamic acid, arginine, lysine, tyrosine, and tryptophan that come from peptone and beef extract, which are calculated as 304, 170, 132, 14, and 16 mg/L, respectively.

The broth pH was adjusted at 7.0 according to their optimum growth pH with 1 M NaOH or 6% trichloroacetic acid (Riedel-de Haen 27242, Seelze, Germany). The ODB was pipetted in 10, 7.5, and 5 mL bottles and then autoclaved at 121 °C for 15 min prior to use. Two different concentrations, which are 50% (5 mL of CFS + 5 mL of ODB) and 25% (2.5 mL of CFS + 7.5 mL of ODB) of CFS, were prepared. The control was prepared as only ODB without CFS.

Foodborne pathogen strains were grown in nutrient broth (Merck 1.05443.0500, Darmstadt, Germany). Each precultured foodborne pathogen strain was inoculated 1% (v/v) in ODB for each CFS concentration and control. All of them were incubated at their optimum growth temperature for 72 h. After that, 5 mL of the bacterial cultures was removed to separate bottles, and then 2 mL trichloroacetic acid was added. They were centrifuged at 3000*g* for 10 min and then filtered through a filter paper (Millipore). Finally, 4 mL of filtrate was taken for derivatization stage to analyze BAs using HPLC.

Derivatization of Bacterial Supernatant. For derivatization of standard and bacterial supernatant, a stock solution (2%) of benzoyl chloride dissolved in acetonitrile was used. For derivatization of standard amine solutions, 100 μL was taken (4 mL of bacterial supernatant) from each free base standard solution (10 mg/mL). One milliliter of 2 M NaOH was added, followed by 1 mL of 2% benzoyl chloride and the solution mixed on a vortex mixer for 1 min. The reaction mixture was left at room temperature for 5 min and then centrifuged (3000*g*) for 10 min. After that, the benzoylation was stopped by adding 2 mL of saturated NaCI mixture, and the mixture was extracted twice with 2 mL of diethyl ether. The upper organic layer was moved into a clean tube after mixing. Afterward, the organic layer was evaporated to dryness in a stream of nitrogen. Finally, the residue was dissolved in 1 mL of acetonitrile, and 10 μL aliquots were injected into the HPLC for BA determination.

Analytical Method. Biogenic amine analysis was achieved according to the method of Ozogul et al.[30] and measured in milligram amines per liter of broth. The confirmation of BA production was accomplished using a rapid HPLC method with a reversed phase column by using a gradient elution program. Ammonia and trimethylamine separations were done using the same injection of the BA determination.

A Shimadzu Prominence HPLC apparatus (Shimadzu, Kyoto, Japan) equipped with an SPD-M20A diode array detector and two binary gradient pumps (Shimadzu LC-10AT), an autosampler (SIL 20AC), a column oven (CTO-20AC), and a communication bus module (CBM-20A) with valve unit FCV-11AL was used. The column was ODS Hypersil (5 μm, 250 × 4.6 mm) for the BA analyses, and it was purchased from Phenomenex (Macclesfield, Cheshire, UK).

Chromatographic separation was done by continuous gradient elution with acetonitrile and HPLC grade water. The gradient started at 60% HPLC grade water and was then decreased to 40% in 20 min. The total separation time was <20 min, and the gradient was run for 25 min to ensure full separation. The injection volume was 10 μL and detection was monitored at 254 nm.

Statistical Analysis. The data gathered from CFS of LAB strains were processed using one-way analysis of variance (ANOVA), SPSS 15.0 for Windows (SPSS Inc., Chicago, IL, USA). The level of

DOI: 10.1021/acs.jafc.5b02410
J. Agric. Food Chem. 2015, 63, 5828−5835

Table 1. Polyamines Produced (mg/L) by Foodborne Pathogens in ODB[a]

biogenic amine[b]	*S.* Paratyphi A NCTC 13	*E. coli* ATCC 25922	*L. monocytogenes* ATCC 7677	*Staph. aureus* ATCC 29213
PUT	4991.3b (±49.9)	2630.9d (±109.4)	5902.0a (±77.5)	3514.7c (±155.2)
CAD	25.1b (±2.6)	32.7a (±3.0)	36.8a (±1.5)	30.2ab (±2.3)
SPD	372.2a (±19.5)	228.1b (±18.7)	399.3a (±13.6)	247.2b (±29.0)
SPN	7.5b (±0.7)	1.1c (±0.1)	23.5a (±0.8)	9.0b (±1.0)
AGM	26.5b (±0.8)	28.5b (±4.1)	31.4b (±0.8)	48.2a (±4.7)

[a]The data are reported as mean values ($n = 4$); standard deviation is given in parentheses. Values in the same row followed by different letters (a–d) are significantly different ($p < 0.05$). [b]PUT, putrescine; CAD, cadaverine; SPD, spermidine; SPN, spermine; AGM, agmatine.

significance was set at $p < 0.05$. Means were compared by Duncan t tests.

RESULTS AND DISCUSSION

pH Values of CFSs and Antimicrobial Activity of LAB Strains. The pH values of CFSs of *Str. thermophilus*, *Lc. lactis* subsp. *lactis*, *Leuc. mesenteroides* subsp. *cremoris*, and *Pc. acidilactici* were 4.06, 4.15, 4.06, and 4.35, respectively, in accordance with the data previously reported by Toy et al.[28] The initial pH of the ODB medium was 7. The pH values of the media obtained by adding, respectively, 25 and 50% of CFS to ODB were 4.86 and 5.66 for *Str. thermophilus*, 4.91 and 5.75 for *Lc. lactis* subsp. *lactis*, 4.93 and 5.68 for *Leuc. mesenteroides* subsp. *cremoris*, and 5.15 and 5.97 for *Pc. acidilactici*.

All of the CFSs resulting from the tested LAB strains' growth showed antimicrobial effect against *E. coli*, *Staph. aureus*, *L. monocytogenes*, and *S.* Paratyphi A according to the well diffusion assay employed. In fact, all of the inhibition zones were >8 mm of diameter, with the highest effect by CFS of *Str. thermophilus* against *Staph. aureus* (data not shown).

Putrescine and Other Polyamines Produced by Foodborne Pathogens. Putrescine-forming FBPs produced not only PUT but also other polyamines, that is, CAD, SPD, SPN, and AGM, besides other BAs. Although lysine and other amino acids were not added directly into ODB, the medium contained peptone and beef extract. For this reason, the observed quantity of other BAs derived from the transformation of amino acids was made available from these protein sources.

Polyamines produced by *S.* Paratyphi A, *E. coli*, *L. monocytogenes*, and *Staph. aureus* in ODB are presented in Table 1. Significant differences ($p < 0.05$) among the species for each amine were observed. With regard to PUT, *L. monocytogenes* and *S.* Paratyphi A were responsible for the highest accumulation, producing 5902 and 4991 mg/L, respectively. The PUT amount produced by *S.* Paratyphi is slightly higher than the theoretical maximum allowed by the ornithine added to the medium (5330 mg/L). The excess of production can be partially attributed to the biodegradative pathway, due to the presence of other sources of precursors (ornithine but also arginine) in the other medium constituents (peptone and Lab-Lemco powder). In any case, also the contribution of the biosynthetic pathway to PUT accumulation cannot be excluded, even if this contribution cannot be quantified under the adopted conditions. Also, the other two species were able to accumulate high levels of PUT, because a high source of free ornithine is available in the decarboxylase broth. Furthermore, SPD was accumulated in high level by all of the species studied (ranging from 228.1 to 399.3 mg/L). PUT can be converted into SPD through the action of several enzymes, the most important of which are methionine adenosyltrasferase, *S*-adenosyl methionine decarboxylase, and spermidine synthase,[11] and then it is not surprising that SPD is produced proportionally to the amounts of PUT. *L. monocytogenes* ATCC 7677 was the highest producer of CAD, SPD, and SPN, whereas *Staph. aureus* accumulated the higher quantity of AGM. These amines have a key role in the response of *E. coli* to oxidative and acidic stresses.[31,32] Similar mechanisms were observed in *Salmonella enterica* and *Vibrio vulnificus*.[33,34] Furthermore, many recent works demonstrated that polyamine biosynthesis and transport mechanisms are involved in classical virulence factors responsible for bacterial pathogenesis. These aspects have been elucidated in *Shigella*[35] and *Helicobacter pylori*.[36]

Effects of CFSs on Putrescine Production by Foodborne Pathogens. The effects of CFSs of LAB strains on PUT accumulation by foodborne pathogens were studied by adding 25 or 50% of supernatants to ODB. The LAB strains employed in this study were previously tested for their decarboxylating potential in MRS broth, and only traces of BAs were found (data not reported).

PUT accumulations in CFS-added samples are reported in Figure 1 for the four foodborne pathogens. In the evaluation of

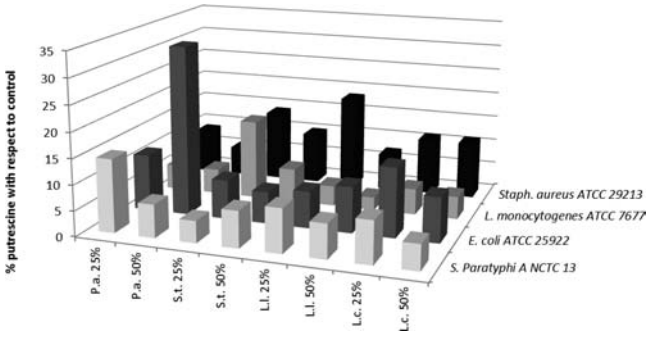

Figure 1. Percentage of putrescine produced by FBPs with respect to control effected by the addition of 25 or 50% of CFSs from LAB.

these data it has to be considered that the dilution rate between CFS and ODB necessarily modified the amount of ornithine available for the decarboxylation, which decreased to 4.0 mg/L in the samples with a 50:50 ratio (ODB/CFS) and to 6 mg/L in the samples with a 75:25 ratio. For this reason, the data are expressed as percentage of PUT accumulated with respect to the control samples (foodborne pathogens in ODB without the addition of CFSs). All of the CFSs reduced the accumulation of PUT by ≥65%. In general, all of the 50% CFSs samples resulted in a lower PUT concentration if compared to the correspondent 25% CFSs samples, with the exception of *E. coli* in the presence of *Pc. acidilactici* and *Lc. lactis* subsp. *lactis* CFSs and *S.* Paratyphi A in the presence of *Str. thermophilus* CFSs. *Salmonella* Paratyphi A and *L. monocytogenes* showed the most relevant inhibition of PUT accumulation. In the samples

DOI: 10.1021/acs.jafc.5b02410
J. Agric. Food Chem. 2015, 63, 5828–5835

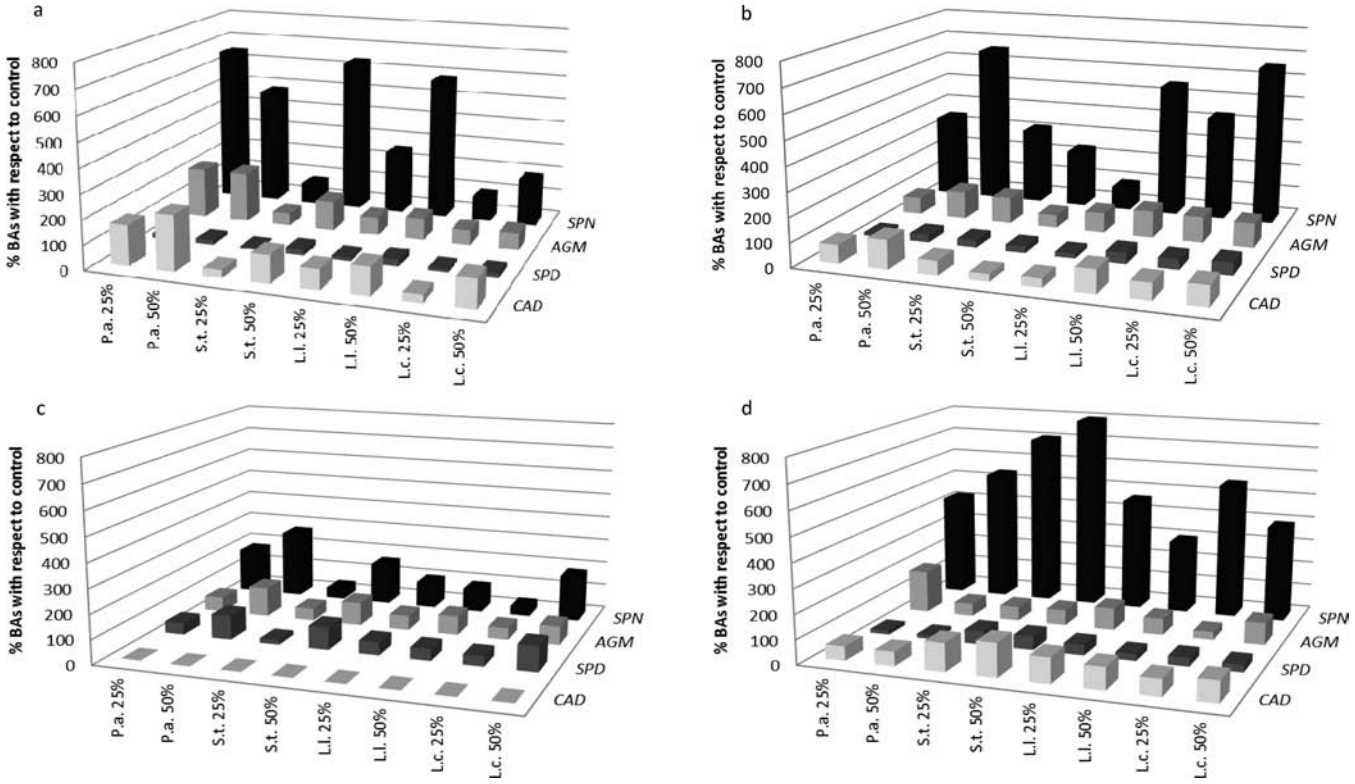

Figure 2. Percentage of cadaverine (CAD), spermine (SPN), spermidine (SPD), and agmatine (AGM) produced by FBPs with respect to control effected by the addition of 25 or 50% of CFSs from LAB: (a) *S.* Paratyphi A NCTC 13; (b) *E. coli* ATCC 25922; (c) *L. monocytogenes* ATCC 7677; (d) *Staph. aureus* ATCC 29213.

inoculated with this strain, PUT amount was between 5 and 10% of the amount found in the control (ODB). On the contrary, the decarboxylating activities of *Staph. aureus* and *E. coli* were less inhibited by CFSs. All of the strains tested in CFS had a decrease in PUT accumulation which was higher than that expected considering only the dilution effect of ODB. On the other hand, also the CFSs contained peptides and amino acids that could act as precursors for the decarboxylating activity. The reduction in the yield of ornithine decarboxylation was the result of the inhibiting effect of the CFS. Undoubtedly, the presence of lactic acid played a major role in this inhibition, even if the pH of the media added with CFSs was not prohibitive for the growth of the species tested in these trials.

Ozogul[23] observed that in histidine decarboxylase broth (in the absence of ornithine added) the growth in coculture of the same foodborne pathogen strains with *Lc. lactis* subsp. *lactis* and *Str. thermophilus* determined an increase of PUT, justifying the protective role exerted by this BA, which confers to cells a competitive advantage.[6] By contrast, adjunct of CFSs determined an opposite trend in ODB in which, however, the concentration of precursor was very high, independent of the dilution effect of the addition of CFSs. The same trend was observed for the same strains in tyramine decarboxylase broth.[22] These data reflected an inhibition or a modification of the foodborne pathogen metabolism due to the presence of antibacterial compounds produced by LAB during their growth.[26]

Effects of CFSs on Other Polyamine Production by Foodborne Pathogens. The protective role of polyamines was well evidenced by the fact that the sum of CAD, SPN, SPD, and AGM increased in the samples with added CFSs. In fact, this trend is often opposite to PUT accumulation. This discrepancy was probably related to the amount of precursor for these BAs. In effect, the presence of extremely high ornithine concentration can mask some metabolic response of the cells. The variation in polyamine accumulation with respect to the control samples is reported in Figure 2. Some differences can be found in the behavior of these BAs in relation to the foodborne pathogens. SPD was produced in lower amount with respect to control in many samples, especially by Gram-negative foodborne pathogens, whereas SPN increased drastically in the major part of the samples with respect to the control. This increase was particularly evident in *Staph. aureus* and less marked in *L. monocytogenes*. This latter species was characterized by the lower increase of polyamines. PUT is the precursor for the synthesis of SPD and SPN, which were obtained by successive addition of aminopropyl group to this BA,[11] and this may explain the relevant increase of SPD in all samples. SPN and SPD can have a strong protective effect, especially for nucleic acids, and their production is regulated by the cells under stress conditions.[11,37]

The production of CAD, which derives from the decarboxylation of lysine, is scarcely affected by the presence of CFSs, with the exception of the samples inoculated with *L. monocytogenes* in which CAD accumulation was drastically reduced, whereas in *S.* Parathyphi A in the presence of *Pc. acidilactici* a higher increment of CAD was observed.

Finally, AGM, which derives from decarboxylation of arginine, increased in all of the samples. This BA can be also a precursor for the production of PUT, following the agmatine deiminase pathway in the Gram-positive bacteria[38] or the agmatinase pathway in Gram-negative bacteria.[6] This pathway strengthened the hypothesis that the extremely high production

DOI: 10.1021/acs.jafc.5b02410
J. Agric. Food Chem. 2015, 63, 5828−5835

Table 2. Effect of CFS from LAB on Ammonia and Other BA Production (mg/L) by Gram-Negative Bacteria in ODB[a]

	medium		biogenic amines[b]							
			AMN	HIS	DOP	PHEN	TRPT	SER	TYR	TMA
S. Paratyphi A NCTC 13	control (ODB)		728.8bc (±29.7)	289.1a (±27.6)	158.9b (±10.5)	154.8a (±7.9)	1.4d (±0.1)	25.0e (±1.1)	7.2f (±0.4)	0.2c (±0.1)
	Pc. acidilactici ATCC 25741	25%	787.3b (±23.2)	27.4d (±4.6)	120.9c (±14.9)	107.5b (±15.4)	11.5c (±0.6)	69.0c (±6.1)	54.3c (±8.4)	6.5a (±0.1)
		50%	778.7b (±28.8)	41.9c (±5.4)	141.4b (±10.0)	78.5c (±11.6)	10.0c (±0.6)	149.2a (±20.8)	81.1a (±12.4)	8.3a (±0.1)
	Str. ghermophilus NCFB 2392	25%	378.8e (±36.2)	25.4d (±0.8)	16.9g (±1.3)	32.6f (±6.1)	0.8d (±0.0)	21.1e (±1.5)	18.9e (±2.4)	0.4c (±0.1)
		50%	570.1d (±29.3)	124.6b (±14.2)	72.2d (±6.9)	63.4cd (±6.6)	11.1c (±0.7)	95.9b (±6.6)	68.4b (±9.0)	4.5a (±0.4)
	Lc. lactis subsp. *lactis* IL 1403	25%	451.8de (±12.1)	19.6e (±2.9)	36.5f (±5.4)	42.4e (±4.8)	28.7b (±3.1)	53.8c (±1.2)	31.7d (±5.7)	0.6 (±0.1)
		50%	651.3c (±38.5)	11.9f (±0.8)	75.5d (±0.5)	62.6cd (±5.3)	35.8a (±7.8)	61.1c (±4.7)	55.4c (±3.5)	3.8b (±0.2)
	Leuc. mesenteroides subsp. *cremoris* DSMZ 20346	25%	276.5f (±18.2)	4.2f (±0.1)	53.8e (±6.7)	29.6f (±1.4)	0.2e (±0.2)	35.1d (±1.6)	21.3e (±7.2)	2.3b (±0.1)
		50%	1462.1a (±66.9)	29.7d (±3.0)	343.7a (±38.6)	50.5d (±3.1)	3.1d (±0.2)	49.3d (±8.3)	55.7c (±9.5)	1.1c (±0.1)
E. coli ATCC 25922	control (ODB)		268.9e (±16.1)	87.2a (±3.9)	90.4c (±3.4)	114.0a (±16.5)	0.5f (±0.0)	11.5e (±2.8)	3.8e (±0.4)	0.1d (±0.1)
	Pc. acidilactici ATCC 25741	25%	726.8b (±32.9)	9.6d (±2.4)	82.4c (±11.5)	53.2d (±7.4)	26.7b (±7.5)	67.4c (±9.1)	42.3c (±7.1)	2.2b (±0.3)
		50%	817.0b (±42.4)	15.4c (±1.1)	152.1a (±10.9)	84.4b (±6.8)	14.1c (±1.1)	78.3b (±3.3)	81.0a (±10.5)	2.6b (±0.0)
	Str. thermophilus NCFB 2392	25%	545.8c (±18.5)	27.7b (±4.9)	113.8b (±8.1)	39.8e (±3.1)	4.4e (±0.5)	70.5bc (±7.2)	66.5b (±8.9)	5.1a (±0.1)
		50%	364.6f (±11.0)	15.8c (±0.3)	47.0d (±7.3)	37.6e (±3.9)	4.4e (±0.7)	104.2a (±9.6)	44.3c (±1.9)	1.7c (±0.3)
	Lc. lactis subsp. *lactis* IL 1403	25%	413.2d (±38.2)	5.7d (±0.7)	46.0d (±4.2)	39.8e (±1.7)	29.4b (±1.2)	45.3d (±1.8)	34.4d (±2.5)	1.5c (±0.6)
		50%	657.0c (±47.5)	12.6c (±1.5)	111.7b (±2.2)	71.4b (±7.1)	26.8b (±2.9)	80.5b (±7.8)	73.6a (±4.6)	5.4a (±0.3)
	Leuc. mesenteroides subsp. *cremoris* DSMZ 20346	25%	499.4d (±8.1)	24.3b (±4.5)	144.1a (±3.7)	62.9c (±6.0)	8.7d (±0.0)	56.4c (±7.0)	48.7c (±3.4)	3.5a (±0.4)
		50%	1153.6a (±115.0)	15.8c (±2.0)	86.7c (±3.6)	56.8d (±3.6)	58.5a (±6.2)	73.2b (±4.8)	57.3b (±3.0)	3.9a (±1.5)

[a]The data are reported as mean values ($n = 4$); standard deviation is given in parentheses. Values in the same row followed by different letters (a–f) are significantly different ($p < 0.05$). [b]AMN, ammonia; HIS, histamine; DOP, dopamine; PHEN, 2-phenylethylamine; TRPT, tryptamine; SER, serotonin; TYR, tyramine; TMA, trimethylamine; control, ODB. Concentration: 50% (5 mL of CFS + 5 mL of medium) and 25% (2.5 mL of CFS + 7.5 mL of medium).

DOI: 10.1021/acs.jafc.5b02410
J. Agric. Food Chem. 2015, 63, 5828−5835

Table 3. Effect of CFS from LAB on Ammonia and Other BA Production (mg/L) by Gram-Positive Bacteria in ODB[a]

	medium		biogenic amines[b]							
			AMN	HIS	DOP	PHEN	TRPT	SER	TYR	TMA
	control (ODB)		629.5c (±38.0)	111.5a (±17.7)	122.0f (±24.1)	194.0a (±7.9)	1.7d (±0.3)	17.9f (±0.6)	3.5f (±0.3)	0.4e (±0.2)
Staph. aureus ATCC 29213	*Pc. acidilactici* ATCC 25741	25%	739.9b (±68.4)	8.7e (±0.3)	188.2c (±20.1)	65.1c (±7.9)	10.2b (±1.2)	74.0d (±1.3)	68.5d (±5.3)	2.0e (±0.1)
		50%	666.4b (±0.4)	18.4d (±2.2)	136.3d (±2.5)	67.4c (±9.1)	8.1c (±1.6)	97.2b (±11.0)	76.2c (±8.0)	6.7b (±0.7)
	Str. thermophilus NCFB 2392	25%	707.3b (±10.6)	46.3b (±5.7)	140.0d (±9.2)	95.2b (±7.8)	8.5c (±1.4)	119.8b (±9.2)	100.5b (±7.8)	5.2c (±0.6)
		50%	836.7a (±61.8)	17.9d (±3.4)	63.8e (±1.0)	84.7b (±3.2)	10.4b (±2.2)	164.1a (±65.1)	135.1a (±6.5)	8.8a (±0.3)
	Lc. lactis subsp. *lactis* IL 1403	25%	573.2c (±29.4)	35.6c (±3.6)	153.7c (±9.0)	69.6c (±6.6)	57.9a (±4.7)	66.6d (±4.6)	65.0d (±6.2)	2.5d (±0.1)
		50%	598.7c (±34.3)	13.0d (±1.7)	160.7c (±7.2)	50.4d (±6.0)	4.4c (±0.5)	86.8c (±8.1)	75.2c (±7.8)	5.2b (±0.1)
	Leuc. mesenteroides subsp. *cremoris* DSMZ 20346	25%	856.6a (±70.6)	6.1e (±0.9)	330.0a (±44.1)	56.8d (±3.8)	5.9c (±0.3)	41.9e (±4.2)	59.4e (±7.6)	0.5e (±0.5)
		50%	661.9b (±71.7)	36.9c (±5.7)	284.9b (±23.7)	64.4c (±4.4)	12.5b (±2.8)	83.5c (±7.6)	72.0c (±0.3)	7.3a (±0.3)
	control (ODB)		873.2b (±9.9)	673.9a (±31.2)	116.2b (±15.8)	217.6a (±9.0)	8.6b (±0.5)	26.8c (±0.1)	7.5d (±0.2)	3.1b (±0.2)
L. monocytogenes ATCC 7677	*Pc. acidilactici* ATCC 25741	25%	418.9d (±59.2)	13.3d (±3.2)	275.2a (±28.6)	58.3c (±1.2)	119.0a (±59.2)	69.6a (±11.7)	41.7b (±6.6)	1.8c (±0.2)
		50%	963.3a (±36.3)	30.8c (±7.1)	170.5b (±12.8)	104.7b (±9.8)	13.5b (±2.1)	94.4a (±4.2)	79.6a (±11.5)	4.3a (±0.4)
	Str. thermophilus NCFB 2392	25%	563.4c (±40.1)	120.2b (±9.9)	110.4b (±2.2)	43.3d (±3.8)	2.5d (±1.3)	27.3c (±4.8)	27.1c (±8.7)	2.1c (±0.6)
		50%	830.7b (±56.2)	37.8c (±3.0)	138.4b (±19.2)	69.7c (±7.3)	6.5c (±1.8)	80.8a (±5.0)	93.9a (±4.8)	6.6a (±0.3)
	Lc. lactis subsp. *Lactis* IL 1403	25%	490.6d (±20.5)	15.1d (±0.2)	53.4d (±6.3)	50.2c (±5.5)	4.4c (±0.2)	40.8b (±5.9)	28.3c (±8.6)	1.9c (±0.1)
		50%	598.1c (±55.1)	11.4d (±1.8)	85.9c (±10.2)	39.1d (±5.5)	3.5c (±0.4)	47.7b (±1.5)	28.6c (±5.0)	3.7b (±0.2)
	Leuc. mesenteroides subsp. *cremoris* DSMZ 20346	25%	510.4cd (±21.2)	2.7e (±0.1)	30.9d (±5.6)	38.4d (±5.9)	2.2d (±0.7)	26.5c (±3.5)	24.7c (±2.9)	2.8b (±1.9)
		50%	755.7b (±34.9)	7.4d (±0.7)	56.4d (±5.1)	68.2b (±5.7)	6.3c (±0.6)	53.9b (±5.0)	36.7b (±3.5)	4.5a (±0.5)

[a]The data are reported as mean values ($n = 4$); standard deviation is given in parentheses. Values in the same row followed by different letters (a–f) are significantly different ($p < 0.05$). [b]AMN, ammonia; HIS, histamine; DOP, dopamine; PHEN, 2-phenylethylamine; TRPT, tryptamine; SER, serotonin; TYR, tyramine; TMA, trimethylamine; control, ODB. Concentration: 50% (5 mL of CFS + 5 mL of medium) and 25% (2.5 mL of CFS + 7.5 mL of medium).

DOI: 10.1021/acs.jafc.5b02410
J. Agric. Food Chem. 2015, 63, 5828−5835

of PUT observed in some species can be based on sources different from the ornithine added to ODB.

The results regarding these other BAs are reported in Tables 2 and 3 for Gram-negative and Gram-positive foodborne pathogens, respectively. Some common trends can be found in these data. HIS was characterized by a marked concentration decrease in all samples. This trend was particularly evident in the samples of *L. monocytogenes*. This strain produced 673.9 mg/L of HIS in the control and amounts variable between 2.7 and 120.2 mg/L in the presence of LAB CFSs. Similar behavior was observed also for 2-phenylethylamine, deriving from decarboxylation of phenylalanine, even if the decrease was less pronounced. By contrast, tyramine, which was accumulated in very low concentrations in the controls (between 3.5 and 7.5 mg/L), showed in all the CFS adjunct broths a marked increase. These behaviors can be probably attributed to the different availabilities of precursors in the CFSs.

The results of this study showed that all of the CFSs employed reduced the accumulation of PUT by ≥65%. This could be due to the production of antimicrobial substances or the presence of the weak organic acids, contained in CFSs, that, decreasing pH quickly, inhibited microbial growth. On the other hand, the other polyamines increased in the samples with added CFSs, due to their cell protective role. For this reason, the use of CFSs in the food sector can have a double role. In fact, it can reduce the accumulation of some BAs, but it seems to increase the presence of others. To prevent the growth of pathogenic bacteria and its unfavorable compounds' formation in fermented food, bacteriocinogenic LAB strains may be used as starter cultures, cocultures, or bioprotective cultures to improve food quality and safety. Further studies aimed to a deep understanding of the metabolic pathways that bring about BA production are needed.

AUTHOR INFORMATION

Corresponding Author

*(F.O.) Mail: Department of Seafood Processing Technology, Faculty of Fisheries, University of Cukurova, 01330 Balcalı, Adana, Turkey. Phone: (90) 322 3386084, ext. 2961. Fax: (90) 322 3386439. E-mail: fozogul@cu.edu.tr.

Funding

We thank the Scientific Research Projects Unit in Cukurova University for their financial support (Research Project SUF2010YL7).

Notes

The authors declare no competing financial interest.

REFERENCES

(1) Bardócz, S. Polyamines in food and their consequences for food quality and human health. *Trends Food Sci. Technol.* **1995**, *6*, 341−346.

(2) Emborg, J.; Dalgaard, P. Formation of histamine and biogenic amines in cold-smoked tuna: an investigation of psychrotolerant bacteria from samples implicated in cases of histamine fish poisoning. *J. Food Prot.* **2006**, *69*, 897−906.

(3) Mohan, C. O.; Ravishankar, C. N.; Gopal, T. K. S.; Kumar, K. A.; Lalitha, K. V. Biogenic amines formation in seer fish (*Scomberomorus commerson*) steaks packed with O_2 scavenger during chilled storage. *Food Res. Int.* **2009**, *42*, 411−416.

(4) Ladero, V.; Calles-Enríquez, M.; Fernandéz, M.; Alvarez, M. A. Toxicological effects of dietary biogenic amines. *Curr. Nutr. Food Sci.* **2010**, *6*, 145−156.

(5) Wunderlichová, L.; Bûnková, L.; Koutný, M.; Jančová, P.; Buňka, F. Formation, degradation, and detoxification of putrescine by foodborne bacteria: a review. *Compr. Rev. Food Sci. Food Saf.* **2014**, *13*, 1012−1030.

(6) Hou, M. H.; Lin, S. B.; Yuann, J. M.; Lin, W. C.; Wang, A. H.; Kan, L. L. Effects of polyamines on the thermal stability and formation kinetics of DNA duplexes with abnormal structure. *Nucleic Acids Res.* **2001**, *29*, 5121−5128.

(7) Kaur-Sawhney, R.; Tiburcio, A. F.; Altabella, T.; Galston, A. W. Polyamines in plants: an overview. *J. Cell. Mol. Biol.* **2003**, *2*, 1−12.

(8) Largue, E.; Sabater-Molina, M.; Zamora, S. Biological significance of dietary polyamines. *Nutrition* **2007**, *23*, 87−95.

(9) Konings, W. N.; Lolkema, J. S.; Bolhuis, H.; van Veen, H. W.; Poolman, B.; Driessen, A. J. M. The role of transport processes in survival of lactic acid bacteria. *Antonie van Leeuwenhoek* **1997**, *71*, 117−128.

(10) EFSA. Scientific Opinion on risk based control of biogenic amine formation in fermented foods. *EFSA J.* **2011**, *9*, 2393−2486.

(11) Shah, P.; Swiatlo, E. A multifaceted role for polyamines in bacterial pathogens. *Mol. Microbiol.* **2008**, *68*, 4−16.

(12) Lucas, P. M.; Blancato, V. S.; Claisse, O.; Magni, C.; Lolkema, J. S.; Lonvaud-Funel, A. Agmatine deiminase pathway genes in *Lactobacillus brevis* are linked to the tyrosine decarboxylation operon in a putative acid resistance locus. *Microbiology* **2007**, *153*, 2221−2230.

(13) Coton, M.; Romano, A.; Spano, G.; Romano, A.; Spano, G.; Ziegler, K.; Vetrana, C.; Desmarais, C.; Lonvaud-Funel, A.; Lucas, P.; Coton, E. Occurrence of biogenic amine-forming lactic acid bacteria in wine and cider. *Food Microbiol.* **2010**, *27*, 1078−1085.

(14) Ladero, V.; Coton, M.; Ferńandez, M.; Buron, N.; Marťın, M. C.; Guichard, H.; Coton, E.; Alvarez, M. A. Biogenic amines content in Spanish and French natural ciders: application of qPCR for quantitative detection of biogenic amine-producers. *Food Microbiol.* **2011**, *28*, 554−561.

(15) Ladero, V.; Fernández, M.; Calles-Enríquez, M.; Sánchez-Llana, E.; Cañedo, E.; Martín, M. C.; Alvarez, M. A. Is biogenic amines production a strain-dependent trait in enterococci? *Food Microbiol.* **2012**, *30*, 132−138.

(16) Mah, J. H.; Hwang, H. J. Inhibition of biogenic amine formation in a salted and fermented anchovy by *Staphylococcus xylosus* as a protective culture. *Food Control* **2009**, *20*, 796−801.

(17) Chang, M.; Chang, H. C. Development of a screening method for biogenic amine producing *Bacillus* spp. *Int. J. Food Microbiol.* **2012**, *153*, 269−274.

(18) Coton, E.; Coton, M. Evidence of horizontal transfer as origin of strain to strain variation of the tyramine production trait in *Lactobacillus brevis*. *Food Microbiol.* **2009**, *26*, 52−57.

(19) Rossi, F.; Rizzotti, L.; Felis, G. E.; Torriani, S. Horizontal gene transfer among microorganisms in food: current knowledge and future perspectives. *Food Microbiol.* **2014**, *42*, 232−243.

(20) Gaggia, F.; Di Gioia, D.; Baffoni, L.; Biavati, B. The role of protective and probiotic cultures in food and feed and their impact in food safety. *Trends Food Sci. Technol.* **2011**, *22*, 58−66.

(21) Rodgers, S. Novel applications of live bacteria in food services: probiotics and protective cultures. *Trends Food Sci. Technol.* **2008**, *19*, 188−197.

(22) Beshkova, D.; Frengova, G. Bacteriocins from lactic acid bacteria: microorganisms of potential biotechnological importance for the dairy industry. . *Eng. Life Sci.* **2012**, *12*, 419−432.

(23) Ozogul, F. Effects of specific lactic acid bacteria species on biogenic amine production by foodborne pathogen. *Int. J. Food Sci. Technol.* **2011**, *46*, 478−484.

(24) Kuley, E.; Balıkcı, E.; Ozogul, I.; Gökdogan, S.; Ozogul, F. Stimulation of cadaverine production by foodborne pathogens in the presence of *Lactobacillus, Lactococcus*, and *Streptococcus* spp. *J. Food Sci.* **2012**, *77*, 650−658.

(25) Tabanelli, G.; Montanari, C.; Bargossi, E.; Lanciotti, R.; Gatto, V.; Felis, G.; Torriani, S.; Gardini, F. Control of tyramine and histamine accumulation by lactic acid bacteria using bacteriocin forming lactococci. *Int. J. Food Microbiol.* **2014**, *190*, 14−23.

DOI: 10.1021/acs.jafc.5b02410
J. Agric. Food Chem. 2015, 63, 5828−5835

(26) Ghanbari, M.; Jami, M.; Domig, K. J.; Kneifel, W. Seafood biopreservation by lactic acid bacteria − a review. *LWT−Food Sci.Technol.* **2013**, *54*, 315−324.
(27) Privat, K.; Thonart, P. Action des cultures protectrices: cas des germes lactiques sur la flore alimentaire indésirable. *Biotechnol. Agron. Soc. Environ.* **2011**, *15*, 339−348.
(28) Toy, N.; Ozogul, F.; Ozogul, Y. The influence of the cell free solution of lactic acid bacteria on tyramine production by food borne-pathogens in tyrosine decarboxylase broth. *Food Chem.* **2015**, *173*, 45−53.
(29) Klausen, N. K.; Huss, H. H. A rapid method for detection of histamine-producing bacteria. *Int. J. Food Microbiol.* **1987**, *5*, 137−146.
(30) Ozogul, F. Production of biogenic amines by *Morganella morganii*, *Klebsiella pneumoniae* and *Hafnia alvei* using a rapid HPLC method. *Eur. Food Res. Technol.* **2004**, *219*, 465−469.
(31) Chattopadhyay, M. K.; Tabor, C. W.; Tabor, H. Polyamines protect *Escherichia coli* cells from the toxic effect of oxygen. *Proc. Natl. Acad. Sci. U. S. A.* **2003**, *100*, 2261−2265.
(32) Jung, I. L.; Kim, I. G. Polyamines and glutamate decarboxylase-based acid resistance in *Escherichia coli*. *J. Biol. Chem.* **2003**, *278*, 22846−22852.
(33) Lee, Y. H.; Kim, B. H.; Kim, J. H.; Yoon, W. S.; Bang, S. H.; Park, Y. K. CadC has a global translational effect during acid adaptation in *Salmonella enterica* serovar *typhimurium*. *J. Bacteriol.* **2007**, *189*, 2417−2425.
(34) Kim, J. S.; Choi, S. H.; Lee, J. K. Lysine decarboxylase expression by *Vibrio vulnificus* is induced by SoxR in response to superoxide stress. *J. Bacteriol.* **2006**, *188*, 8586−8592.
(35) Durand, J. M.; Bjork, G. R. Putrescine or a combination of methionine and arginine restores virulence gene expression in a tRNA modification-deficient mutant of *Shigella flexneri*: a possible role in adaptation of virulence. *Mol. Microbiol.* **2003**, *47*, 519−527.
(36) Patchett, S. E.; Katelaris, P. H.; Zhang, Z. W.; Alstead, E. M.; Domizio, P.; Farthing, M. J. Ornithine decarboxylase activity is a marker of premalignancy in longstanding *Helicobacter pylori* infection. *Gut* **1996**, *39*, 807−810.
(37) Iarashi, K.; Kashiwagi, K. Modulation of cellular function by polyamines. *Int. J. Biochem. Cell Biol.* **2010**, *42*, 39−51.
(38) Romano, A.; Trip, H.; Lonvaud-Funel, A.; Lolkema, J. S.; Lucasa, P. M. Evidence of two functionally distinct ornithine decarboxylation systems in lactic acid bacteria. *Appl. Environ. Microbiol.* **2012**, *78*, 1953−1961.

DOI: 10.1021/acs.jafc.5b02410
J. Agric. Food Chem. 2015, 63, 5828−5835

different in samples, depending on the relative source of nitrogen.

Perini et al.[3] report the use of stable isotope ratio analysis to verify the authenticity of *Passito* wine. The effect of the grape's withering process on the variability of the $(D/H)_I$, $(D/H)_{II}$, and $\delta^{13}C$ of wine ethanol and the $\delta^{18}O$ of wine water were monitored. The production of PDO Erbaluce di Caluso Passito at five different vineyards in the Piedmont (Italy) was considered in two successive years. The results show that the isotopic parameters $(D/H)_I$, $(D/H)_{II}$, and $\delta^{13}C$ of ethanol did not change during the withering period, whereas the $\delta^{18}O$ of water and ethanol tended to decrease.

However, to better define univocal parameters, isotope ratios, expressed as $\delta^{13}C$, are preferably determined by the use of gas chromatography−combustion isotope ratio mass spectrometry (GC-C-IRMS) to fix a variable number of $\delta^{13}C$ values relative to pure compounds in the food investigated. The approach allows the preseparation of the components of interest in a capillary column, with the aim of directly determining the $\delta^{13}C$ value, through a combustion chamber followed by the isotope ratio MS instrument section. Different analytical approaches to GC-C-IRMS analyses applied to several food types such as coffee samples of different geographic origins and fatty acids (methyl esters) of different natural sources will be proposed, as well as specific examples of the characterization of various natural compounds.

NEW METHODS FOR QUALITY AND SAFETY CONTROL

Food quality and safety have been highly topical for the past 10 years in the public debate, in food policy, in industry, and, last but not least, in research. To ensure quality and food safety for consumers, it is essential develop analytical methods that are fast, sensitive, solventless, inexpensive, and suitable for automation and more transferable at industrial scale, ensuring control over the whole food chain.

One of the main problems in ensuring food safety is the presence of contaminants, and several papers in this issue have developed new methods for the determination of food toxins.

OTA is the only mycotoxin with legal limits in the European Union (EU) for wine; in contrast, there is no EU legislation imposed for aflatoxins and ochratoxin B (OTB). A study was focused on the development, by using immunoaffinity column cleanup and HPLC-FLD method in 57 red wines produced in Sicily, of a reproducible and sensitive analytical method for six mycotoxins: OTA, OTB, aflatoxin B_1 (AFB_1), aflatoxin B_2 (AFB_2), aflatoxin G_1 (AFG_1), and aflatoxin G_2 (AFG_2).

This study is the first report of OTA, OTB, and the main aflatoxins content in red Sicilian wines. The analytical method reported represents a real advantage in the field of mycotoxin surveillance in foods and shows that there is a real risk of contamination in wine.

The use of noninvasive tools for food processing and quality control is highly recommendable. In this respect, the detection of food flavors via gas sensing is surely a valuable option; in fact, flavors depend on the volatile molecules present in food and on their release, which is strongly influenced by the composition of the matrix. In one of the presented works was developed a gas sensor array based on quartz crystal microbalances (QCMs) modified with gold nanoparticles bearing peptide moieties. Results demonstrated the ability of the QCM gas sensor array under development to be used in the discrimination of food samples with different aroma patterns.

A simple and fast HPAEC-PAD analytical method with good sensitivity has been developed for the determination and quantification of carbohydrates in honey. The technique allows the simultaneous determination of minor and major saccharides without pretreatment of sample that, always, causes the loss of minor sugars. The analytical method was applied to honeys of different botanical origins, and the performance of this method was validated according to range, linearity, calibration curves, limit of detection, and limit of quantification.

In comparison with HPLC-RI, which is used as an official method, HPAEC-PAD was more sensitive and faster, with high specificity and improved peak resolution.

In one study was reported an optimized analytical method for the evaluation of fatty acid composition in lentils by using GC-FID. The results showed that there are five main fatty acids in lentils (palmitic, stearic, oleic, linoleic, and linolenic acids) and that unsaturated fatty acids are prevalent with respect to saturated ones. Indeed, in all types of lentil samples analyzed, the predominant fatty acid was linoleic acid, whereas the least concentrated one was stearic acid. Finally, it is very interesting that in lentils the ratio between omega-6 and omega-3 fatty acids coincides with that in the Recommended Dietary Allowances (RDA).

BOTANICAL AND NUTRACEUTICAL PRODUCTS

Nutraceuticals are foods or food ingredients that have defined physiological effects. They do not easily fall into the legal categories of food or drug and often inhabit a gray area between the two. These products in general terms cover health promotion and "optimal nutrition"; the concept of enhanced performance, both physically and mentally; and reduction of disease risk factors.

Botanical extracts represent a large segment of nutraceuticals and present additional problems relating to the complex nature and composition of these products. The term "botanicals", in this context, can represent the whole plant but also parts of plants, such as algae, fungi, and lichens. This word includes also specific preparations from these materials involving extraction, distillation, fractionation, purification, concentration, and fermentation processes. All of these botanicals need to be first recognized by the botanical name of the plant according to the binomial system (genus, species, variety, and author) and the part used (e.g., leaf, root, and fruit).[4]

The wide diffusion of these products requires new analytical methods to control their quality, guarantee their safety, and contribute to the scientific studies aimed to evaluate their beneficial effects.

In the X Italian Congress of Food Chemistry a whole day was dedicated to this hot topic, and different results were presented aimed in particular to control the quality of the vegetal matrix.

A chromatographic method for the qualitative and quantitative characterization of peel of different species of citrus was developed to obtain a total evaluation of the phytocomplex and to verify the eventual content of protoalkaloids such as synephrine. Twenty-four constituents comprising flavones, flavanones, polymethoxyflavonoids, and protoalkaloids were fully identified. Fourteen major constituents were quantified using a validated HPLC method with UV−vis. Synephrine was present in all samples except grapefruit.

Another work reported a study on Limone dell'Etna, a brand recently launched by citrus growers for lemon fruits produced in that area with the aim of enhancing and promoting Limone

DOI: 10.1021/acs.jafc.5b00324
J. Agric. Food Chem. 2015, 63, 5837−5840

dell'Etna production and contributing to an increase in the value of a product that, due to its peculiar qualities, could be awarded with a European certified label. Qualitative parameters (total soluble solids, titratable acidity, pH) and health-promoting components such as ascorbic acid, flavanones, and hydroxycinnamic acids of the two different varieties have been determined at fruit maturity.

Also, the stigmas from different samples of *Crocus sativus* cultivated in Italy (Tuscany and Umbria) have been analyzed to characterize this product from a quality point of view. The identification and quantification of crocins, safranal, picrocrocin, and flavonols were mainly carried out by applying an integrated approach by HPLC-DAD and NMR to control the hydroalcoholic and aqueous extracts, respectively.

The term "nutraceuticals" can be applied also to new formulations proposed for celiac patients to improve the quality of their diet. In the presented study, the chemical characterization and the quality evaluation of two different gluten-free breads with added chestnut flour were performed. In particular, protein and fat contents, fatty acid and volatile profiles, antioxidant capacity, and glycemic index were measured for each sample, and the results obtained for gluten-free breads were compared with those obtained for breads with added chestnut flour. The results showed that the addition of chestnut flour leads to a product with a higher nutritional profile.

NEW METHODS TO DETECT BIOACTIVE METABOLITES IN FOODS

A more accurate determination of the bioactive compounds in foods is a hot topic of recent years. At the same time, the development of innovative analytical methods more suitable to this aim is one of the targets of the *Journal of Agricultural and Food Chemistry*.

The presence of significant amounts of bioactive molecules may provide health benefits and play an important role in the prevention and risk reduction of some chronic diseases. Among these, the stilbenes, a class of compounds present in small fruits such as grapes and berries, act as natural protective agents to defend the plant against viral and microbial attack, excessive ultraviolet exposure, and disease. A work of this Congress applied HRGC equipped with FID and MS detectors, operating in selected ion monitoring (SIM) mode, to quantify *trans*-resveratrol and *trans*-pterostilbene in commercial blueberry samples, considering both the free and conjugated forms. Another work reports the characterization of the anthocyanin fraction of nine sweet cherry cultivars, grown in an experimental field of Vignola (Emilia Romagna). For this purpose was developed an extraction and purification method by SPE, and then the recovered anthocyanin fraction was characterized by HPLC-MS and MS-MS. This study aims to give some parameters suitable to evaluate cherry fruit quality, focusing on healthy compounds, especially considering the achievement of the Protected Geographical Indication (PGI) obtained in 2012 for this fruit. An optimization of the extraction procedure for the simultaneous recovery of anthocyanins, flavonols, flavan-3-ols, and stilbenes by HPLC-DAD-MS for the characterization of cv. Apulia Rose seedless table grape was also reported. The grape skins (cv. Apulia Rose) were extracted by means of three technologies (namely, solid to liquid, ultrasonic-assisted, and microwave-assisted extractions) under various different experimental conditions (namely, solvent type, solvent-to-solid ratio, and time contact) to determine the effect of these conditions on the yield of phenolic compounds. On the basis of quantitative HPLC-MS/MS analyses, ultrasonic-assisted extraction in methanol appeared to be the most efficient condition to extract the aforementioned compounds simultaneously. In addition, the solvent-to-solid ratio was found to have a critical role in extraction efficiency.

The coffee plant not only is a source to produce the well-known drink but also has a large floral display with strong scent and produces more fruits and seeds when pollinated by bees. In view of these aspects it is not surprising to encounter coffee honey as a side-product of coffee production, albeit rare and almost unexploited to date. By an integrated analytical approach the authors gave an overview of the composition of this product, evidencing the main differences with respect to citrus honeys. Even if further studies need to be done, the authors suggest caffeine and theobromine as reliable markers to trace coffee honey authenticity.[5]

Di Lorenzo et al.[6] reported the use of HPLC-PDA-ESI-MS^n and NMR methodologies to evaluate the chemical composition of five Sicilian unifloral honeys produced in purity by the local black honeybees. In detail, the analyzed honeys were lemon and orange honeys (*Citrus limon* and *Citrus aurantium*), sulla honey (*Hedysarum coronarium*), dill honey (*Anethum graveolens*), and loquat honey (*Eriobotrya japonica*).

This analysis allowed the description of the phytochemical composition of each type of honey and the identification of many compounds that were found in these types of honey for the first time.

EFFECTS OF STORAGE AND TECHNOLOGICAL PROCESSES ON FOODS

During food storage the primary goal is to prevent the proliferation of bacteria, fungi, molds, and other microorganisms that, inside the food, can produce undesirable or toxic substances and to retard the oxidation of the edible oils and fat. Indubitably, the availability of specific strategies designed to inhibit the aging or degradation that may occur during storage is of great relevance in food chemistry.

A study focused on the investigation of the effects of different drying technologies on the volatile fraction of three Italian rice cultivars coupling headspace solid phase microextraction (HS-SPME) to gas chromatography−mass spectrometry (GC-MS) was also reported. Paddy rice from selected cultivars was treated both with traditional hot air technology and with static microwave drying. Analytical results on differently processed rice, after home-cooking, showed changes in the volatile fraction profile, in particular between aroma compounds. The results give information on the actual distribution of aroma precursor as a function of the progressive drying process and can be correlated to the sensory quality of the final product.

Due to the presence of an amino group on the side chain, modifications on lysine residues, N^{ϵ}-(2-furoylmethyl)-L-lysine (furosine), N^{ϵ}-(carboxymethyl)-L-lysine (CML), N^{ϵ}-(carboxyethyl)-L-lysine (CEL), are the most widely used marker to monitor the thermal damage on proteic constituents. The authors propose a method suitable to achieve not only a simultaneous detection of the main markers but also characterization by high sensitivity, good reproducibility, and repeatability in several food matrices through stable isotope dilution assay and ESI-MS. The possibility of selectively recovering the external parts of barley by a process of progressive pearling has been investigated for production of functional breads. The authors used three different series of substituted flours, adding increasing percentages (from 5 to 25%) of external parts to

DOI: 10.1021/acs.jafc.5b00324
J. Agric. Food Chem. 2015, 63, 5837−5840

prepare the breads. As expected, the use of enriched flours improved the functional properties of the breads, in accord with the original properties of the barley fractions.[7]

CONCLUSIONS

This special issue of *Journal of Agricultural and Food Chemistry* contains a selection of papers that were presented at the X Italian Congress of Food Chemistry (CHIMALI 2014) in Florence, Italy, July 6−10, 2014. There are many papers derived from collaborations between different universities and also some papers obtained from cooperation with important Italian companies.

We thank all contributors for making available their experience in food research and devoting their time to making this special issue a volume containing information of great interest to researchers working in food chemistry and food analysis. We also thank all of the companies that, by their sponsorship, have contributed to the good performance of this national event.

We are also grateful to the Editorial Board of *Journal of Agricultural and Food Chemistry* for giving us the opportunity to publish this special issue. We give special thanks to the previous Editor in Chief, James Seiber, who accepted our proposal to dedicate an issue to the X Italian Congress of Food Chemistry. Finally, our thanks to the new Editor in Chief, Thomas Hofmann, and his editorial assistant, Ivonne Hofmann-Sellier, who helped us to carefully supervise the final version of this special issue. We believe this issue will be useful to improve the cross-fertilization of ideas in the fascinating area of food and nutraceutical products.

Nadia Mulinacci*
Marzia Innocenti

Department, Pharmaceutical and Nutraceutical Division, NEUROFARBA, University of Florence, Via Ugo Schiff 6, Sesto Fiorentino, Italy

AUTHOR INFORMATION

Corresponding Author

*(N.M.) Phone: +39 055 4573773. Fax: +39 055 4573737. E-mail: nadia.mulinacci@unifi.it.

Notes

The authors declare no competing financial interest.

REFERENCES

(1) Rodríguez-Ramírez, R.; González-Córdova, A. F.; Vallejo-Cordoba, B. Review: Authentication and traceability of foods from animal origin by polymerase chain reaction-based capillary electrophoresis. *Anal. Chim. Acta* **2011**, *685*, 120−126.

(2) Paolini, M.; Ziller, L.; Husted, S.; Camin, F. Discrimination between organic and conventional flour using compound-specific amino acid δ^{15}N analysis. *J. Agric. Food Chem.* **2015**, DOI: 10.1021/acs.jafc.5b00662.

(3) Perini, M.; Torchio, F.; Rolle, L.; Marianella, R. M.; Di Martino, V.; Simoni, M.; Gerbi, V.; Camin, F. H. C and O stable isotope ratios of "Passito" wine. *J. Agric. Food Chem.* **2015**, DOI: 10.1021/acs.jafc.5b02127.

(4) Gulati, O. P.; Berry Ottaway, P. Legislation relating to nutraceuticals in the European Union with a particular focus on botanical-sourced products. *Toxicology* **2006**, *221*, 75−87.

(5) Navarini, L.; Colomban, S.; Schievano, E.; Illy Belci, A.; Turello, L.; Mammi, S. Preliminary characterization of monofloral *Coffea* spp. honey: correlation between potential biomarkers and pollen content. *J. Agric. Food Chem.* **2015**, DOI: 10.1021/jf506359u.

(6) Di Lorenzo, A.; P.Sobolev, A.; Curti, V.; Tenore, G. C.; Mannina, L.; Daglia, M. Chemical composition of different botanical origin honeys produced by Sicilian black honeybees (*Apis mellifera* ssp. *sicula*). *J. Agric. Food Chem.* **2015**, DOI: 10.1021/j506192s.

(7) Blandino, M.; Locatelli, M.; Sovrani, V.; Coïsson, J. D.; Rolle, L.; Travaglia, F.; Giacosa, S.; Bordiga, M.; Scarpino, V.; Reyneri, A.; Arlorio, M. Progressive pearling of barley kernel: chemical characterization of pearling fractions and effect of their inclusion on the nutritional and technological properties of wheat bread. *J. Agric. Food Chem.* **2015**, DOI: 10.1021/jf506193p.

DOI: 10.1021/acs.jafc.5b00324
J. Agric. Food Chem. 2015, 63, 5837−5840

history of organic plants. This has partly been addressed by compound-specific isotope analysis of N and O of plant-derived nitrate, which has proven promising for organic authentication of vegetables.[1,13] However, due to the inherently low nitrate contents of most generative plant tissue, it remains unclear if stable isotope analysis of nitrate from cereal grains is feasible. Consequently, this calls for the development of novel analytical methods for authenticity testing of organic crops.

The stable isotope ratio of carbon $^{13}C/^{12}C$ (expressed as $\delta^{13}C$) has also been investigated as well for organic authentication. In C3 plants, $\delta^{13}C$ is affected by water availability and drought stress, but also shows significant interactions with nutrient availability and fertilization,[14,15] which frequently can be systematically different between organic and conventional systems. Additionally, $\delta^{13}C$ values can be related to a different contribution and isotopic ratio of CO_2 from soil respiration or from other sources (e.g., a CO_2-enriched atmosphere in the greenhouse) to plant photosynthesis.[16−18] The soil management practices used in organic systems and the use of green manure may lead to higher microbial activity in organic soils compared to conventionally grown.

Traditionally, stable isotope analysis has relied on measurements of bulk plant tissue, but emerging methods aimed at individual chemical compounds provide a means of obtaining a more in-depth understanding.[19] GC-C-IRMS has been utilized for examining the effects of land use and fertilizer practices on $\delta^{15}N$ value of individual amino acids in soil.[20] Previous studies[21] also showed that the $\delta^{15}N$ signatures of individual amino acids (e.g., histidine and phenylalanine) can be used to discriminate between different plant species in relation to the acquisition of available N sources. Amino acids are indeed the dominant low molecular weight nitrogen-bearing biomolecules in plants, and the pattern of isotopic fractionation during synthesis of these compounds records a range of information about the growth environment, such as the form of plant-available nitrogen in the soil.

New and more sensitive markers are needed to verify the authenticity of organically grown plants, and this study is thus timely and of practical relevance. We investigated the feasibility of using compound-specific nitrogen and carbon isotope analysis of plant-derived amino acids for differentiation between organically and conventionally grown wheat. The study was conducted on common wheat from Danish field trials and on durum wheat from Italian on-farm studies.

MATERIALS AND METHODS

Reagents and Reference Materials. L-Amino acid standards at ≥98% purity (alanine, aspartic acid, glutamic acid, glycine, isoleucine, norleucine, leucine, phenylalanine, proline, and valine) and analytical grade cation-exchange resin (Amberlite IR120 hydrogen form) were purchased from Sigma-Aldrich. All other solvents (dichloromethane, isopropanol, acetone, and ethyl acetate) and reagents (triethylamine and acetic anhydride) used were of analytical grade and purchased from Sigma-Aldrich and VWR (Milan, Italy).

Plant Materials and Sampling. Eighteen samples of winter wheat (*Triticum aestivum* L. cv. Tommi) were grown at three different Danish geographical locations: Flakkebjerg (FL), Foulum (FO), and Jyndevad (JY). The plants were grown in three systems (one conventional and two organic) under controlled conditions in a long-term field trial and were sampled in 2007 and 2008. The conventional system (CS) relied on the use of pesticides and synthetic fertilizers, whereas the organic systems (OSA and OSB) were managed in full compliance with the guidelines for organic farming (European Community Council Regulation EEC 2091/91 and EC 834/2007). The two organic systems OSA and OSB differed with regard to nutrient input. In the OSA system pig manure was imported from conventional farms, whereas the OSB system relied on nutrient input from green manures originating from cover crops being mixtures of grasses and N_2-fixing legumes. Fertilizer application rates as well as the percentage content of C and N in wheat samples are shown in Table 1. A map of the locations, soil characteristics, further details regarding field trials, climatic conditions, sampling of wheat grains and sample preparation are described elsewhere.[22]

Table 1. Danish Wheat: Sample Location, Agricultural System, Production Year, Fertilizer Application Rate, and Content of C and N in Wheat Samples in the Three Cropping Systems in Two Years

location	system[a]	year	fertilizer (nitrogen source) (kg/ha)	C (%)	N (%)
Flakkebjerg	Org (OSA)	2007	115	41.8	1.5
Flakkebjerg	Org (OSA)	2008	100	41.6	1.4
Foulum	Org (OSA)	2007	105	42.2	1.5
Foulum	Org (OSA)	2008	110	41.4	1.5
Jyndevad	Org (OSA)	2007	105	42.0	1.5
Jyndevad	Org (OSA)	2008	65	40.9	1.3
Flakkebjerg	Org (OSB)	2007	0	42.3	1.5
Flakkebjerg	Org (OSB)	2008	5	41.8	1.5
Foulum	Org (OSB)	2007	0	42.2	1.6
Foulum	Org (OSB)	2008	0	41.4	1.4
Jyndevad	Org (OSB)	2007	0	42.3	1.7
Jyndevad	Org (OSB)	2008	0	41.2	1.5
Flakkebjerg	Conv (CS)	2007	165	42.5	2.3
Flakkebjerg	Conv (CS)	2008	170	41.7	2.1
Foulum	Conv (CS)	2007	165	42.3	2.0
Foulum	Conv (CS)	2008	165	41.8	2.0
Jyndevad	Conv (CS)	2007	160	42.1	1.9
Jyndevad	Conv (CS)	2008	155	41.2	1.7

[a]CS, conventional; OSA, organic with animal manure; OSB, organic with green manures.

In addition to the 18 samples from Denmark, 17 samples of durum wheat (*Triticum turgidum* ssp. durum cv. Khorasan, Senatore Cappelli, Simeto, or Levante) were collected from commercial farms in 2012 in the main wheat-producing regions of Italy (Basilicata, $n = 7$; Molise, $n = 7$; and Emilia-Romagna, $n = 3$). Wheat was grown in each location in either a conventional system (CS, with mineral fertilizer) or an organic system (with organic fertilizer, OSA; or after 5 years of legumes, OSB; or without any fertilizer). The organic systems were managed in full compliance with the guidelines for organic farming (European Community Council Regulation EC 834/2007) for at least 8 years prior to the sample production. The systems were all based on stockless crop production but were managed differently depending on soil characteristics, climate, and farm structure. In the conventional system, pesticides and inorganic fertilizers were used according to usual farming practice. Nutrient supply in the organic system was based on the crop rotation built fertility and in some cases addition of commercial pelleted organic fertilizers. No irrigation was used for any of the organic and conventional fields. Information about location, cropping system, variety, and fertilizers used as well as the percentage content of C and N in wheat samples is reported in Table 2. All durum wheat samples were harvested at maturity and consequently on different days in the different regions (from mid-June until mid-July).

EA-IRMS Analysis. The $\delta^{15}N$ and $\delta^{13}C$ values of pure non-derivatized single amino acids and of bulk samples were measured using an elemental analyzer (Flash EA 1112, Thermo Scientific, Bremen, Germany), equipped with an autosampler (Finnigan AS 200, Thermo Scientific) and interfaced through a ConFlo IV dilutor device (Thermo Finnigan, Bremen, Germany) with a DELTA V isotope ratio mass spectrometer (Thermo Scientific). The isotopic values were calculated against L-glutamic acid USGS 40 (IAEA-International Atomic Energy Agency, Vienna, Austria), fuel oil NBS-22 (IAEA), and sugar IAEA-CH-6

DOI: 10.1021/acs.jafc.5b00662
J. Agric. Food Chem. 2015, 63, 5841−5850

Table 2. Italian Durum Wheat: Sampling Location, Agricultural System, Variety, Fertilizer Application Rate and Type, and Content of C and N in Durum Wheat Samples in the Italian Cropping Systems

location	system[a]	variety	fertilizer (nitrogen source)	C (%)	N (%)
Basilicata	Org (OSA)	Khorasan	32 kg N/ha (organic fertilizer)	42.3	1.8
Basilicata	Org (OSA)	Khorasan	32 kg N/ha (organic fertilizer)	42.8	1.9
Basilicata	Org (OSA)	Senatore Cappelli	32 kg N/ha (organic fertilizer)	43.2	2.3
Basilicata	Org (OSA)	Senatore Cappelli	32 kg N/ha (organic fertilizer)	43.1	2.3
Molise	Org (OSA)	Simeto	36 kg N/ha (organic fertilizer)	43.3	1.8
Molise	Org (OSA)	Simeto	36 kg N/ha (organic fertilizer)	43.0	2.1
Emilia-Romagna	Org (OSB)	Levante	5 years of Lucerne (*Medicago sativa*) cultivation	42.6	2.3
Emilia-Romagna	Org (OSB)	Levante	5 years of Lucerne (*Medicago sativa*) cultivation	43.2	2.4
Emilia-Romagna	Org (OSB)	Levante	5 years of Lucerne (*Medicago sativa*) cultivation	43.2	2.4
Molise	Org	Senatore Cappelli	nothing	42.8	1.8
Molise	Org	Senatore Cappelli	nothing	42.6	1.7
Molise	Conv (CS)	Simeto (R)	75 kg N/ha (mineral fertilizer)	42.3	2.6
Molise	Conv (CS)	Simeto (R)	75 kg N/ha (mineral fertilizer)	43.2	2.5
Molise	Conv (CS)	Simeto (A)	120 kg N/ha (mineral fertilizer)	42.9	2.2
Basilicata	Conv (CS)	Khorasan	100 kg N/ha (mineral nitrate)	43.1	2.5
Basilicata	Conv (CS)	Khorasan	100 kg N/ha (mineral nitrate)	43.1	2.4
Basilicata	Conv (CS)	Senatore Cappelli	100 kg N/ha (mineral nitrate)	43.8	2.9

[a]Conv, conventional; Org, organic.

for $^{13}C/^{12}C$ and against L-glutamic acid USGS 40 and potassium nitrate IAEA-NO3 for $^{15}N/^{14}N$.

The content of N and C was measured using IRMS (ANCA-SL elemental analyzer coupled to a 20-20 Tracermass mass spectrometer, Sercon Ltd., Crewe, UK). Quality assurance was performed by duplicate measurements of all samples as well as analysis of Certified Reference Materials (NIST 1515, NIST 8436, and 141d acetanilide $CH_3CONHC_6H_5$, National Institute of Standards and Technology) as previously described.[22]

Hydrolysis of Protein and Purification. Wheat samples were defatted three times with petroleum ether/ethyl ether (2:1 v/v, 30 mL) homogenizing with an Ultraturrax device (model X-620, Staufen, Germany; 11500 rpm for 3 min) and using a centrifuge (ALC PK 131R, Thermo Electron Corp., Germany; 4100 rpm for 6 min) to separate the ether from the residue. The defatted powdered samples were left open to air-dry and then stored at room temperature until analysis.

Acid hydrolysis was conducted to obtain individual amino acids from protein: 250 mg of lipid-extracted sample was digested with 2 mL of 6 M HCl at 110 °C for 24 h in a PTFE-capped Pyrex vial. After cooling, the hydrolyzed solution was filtered on glass wool, and the solution was blown to dryness under N_2 and redissolved in 2 mL of 0.1 M HCl. A known quantity of norleucine (8 mg mL^{-1} in 0.1 M HCl) was added as internal standard, and the solution was stored at −20 °C.

Amino acids were purified through ion-exchange chromatography on an Amberlite IR120 cation-exchange resin, previously saturated with H^+ on all exchange sites. This was accomplished by soaking the resin overnight in 3 M NaOH, followed by washing in distilled water and soaking overnight in 6 M HCl, after washing with distilled water. The H^+ saturated resin was pipetted into a glass pipet column fitted with a quartz wool plug, and a fraction of the hydrolyzed sample (500 μL) was added to the column. Salts were removed with distilled water and the amino acids eluted with NH_4OH (10 wt %) and then dried under N_2 before derivatization. Under those conditions, the resin does not cause any isotopic fractionation.[23,24]

Derivatization. Amino acids were analyzed after *N*-acetylisopropyl derivatization based on the method reported elsewhere.[25] Samples were first esterified in 1 mL of acidified isopropanol (1:4 acetyl chloride/isopropanol) at 100 °C for 1 h. Esterifying reagents were evaporated under a gentle stream of nitrogen at 40 °C, and dried esters were rinsed with two sequential 250 μL aliquots of dichloromethane to remove reagents in excess. Amino acid esters were acylated with 1 mL of acetic anhydride/triethylamine/acetone solution (1:2:5 v/v) at 60 °C for 10 min. The reagents were evaporated under a N_2 stream at room temperature, and dried derivatives were dissolved in 1 mL of saturated NaCl−water solution and 1 mL of ethyl acetate and mixed vigorously. The organic phase containing the amino acids was collected and dried under nitrogen at room temperature. Residual water was removed with two sequential 250 μL aliquots of dichloromethane. Finally, samples were dissolved in 200 μL of ethyl acetate and stored at −20 °C until analysis.

GC-C-IRMS Analysis. The isotopic values of 10 amino acids, alanine (Ala), aspartate (Asx), glutamate (Glx), glycine (Gly), isoleucine (Ile), leucine (Leu), phenylalanine (Phe), proline (Pro), threonine (Thr), and valine (Val), were determined by GC-C-IRMS (Figure 1).

Due to the acid hydrolysis, asparagine (Asn) and glutamine (Gln), present in wheat, are converted into aspartic acid (Asp) and glutamic acid (Glu), respectively. Therefore, the $\delta^{15}N$ and $\delta^{13}C$ values determined of Asx and Glx represent the nitrogen and carbon isotopic value of both aspartate + asparagine and glutamate + glutamine, respectively.[24]

Individual amino acid isotopic analysis was carried out using a Trace GC Ultra (GC IsoLink + ConFlo IV, Thermo Scientific) interfaced with an IRMS (DELTA V, Thermo Scientific) through an open split interface and with a single-quadrupole GC-MS (ISQ Thermo Scientific) to identify the compounds. For $\delta^{15}N$ analysis 0.8−1.0 μL of each sample was injected in splitless mode by an autosampler (Triplus, Thermo Scientific). A HP-INNOWAX capillary column (60 m × 0.32 mm i.d. × 0.25 μm film thickness; Agilent) with He as carrier gas (at a flow of 1.4 mL/min) was used. The injector temperature was set at 250 °C, and the oven temperature of the GC started at 40 °C, at which it was held for 2 min before heating at 40 °C/min to 140 °C, at 2.5 °C/min to 180 °C, at 6 °C/min to 220 °C, and finally at 40 °C/min to 250 °C and held for 15 min. For $\delta^{13}C$ analysis 1.0 μL of each sample was injected in split mode and a stronger polar column was used to obtain higher and sharper peaks (ZB-FFAP capillary column, 30 m × 0.25 mm i.d. × 0.25 μm film thickness; Phenomenex). The oven temperature of the GC started at 40 °C, at which it was held for 1 min before heating at 15 °C/min to 120 °C, at 3 °C/min to 190 °C, and finally at 5 °C/min to 250 °C and held for 7 min.

The eluted compound was combusted into N_2, CO_2, and H_2O in a combustion furnace reactor operated at 1030 °C and composed of a nonporous alumina tube (320 mm length) containing three wires

DOI: 10.1021/acs.jafc.5b00662
J. Agric. Food Chem. 2015, 63, 5841−5850

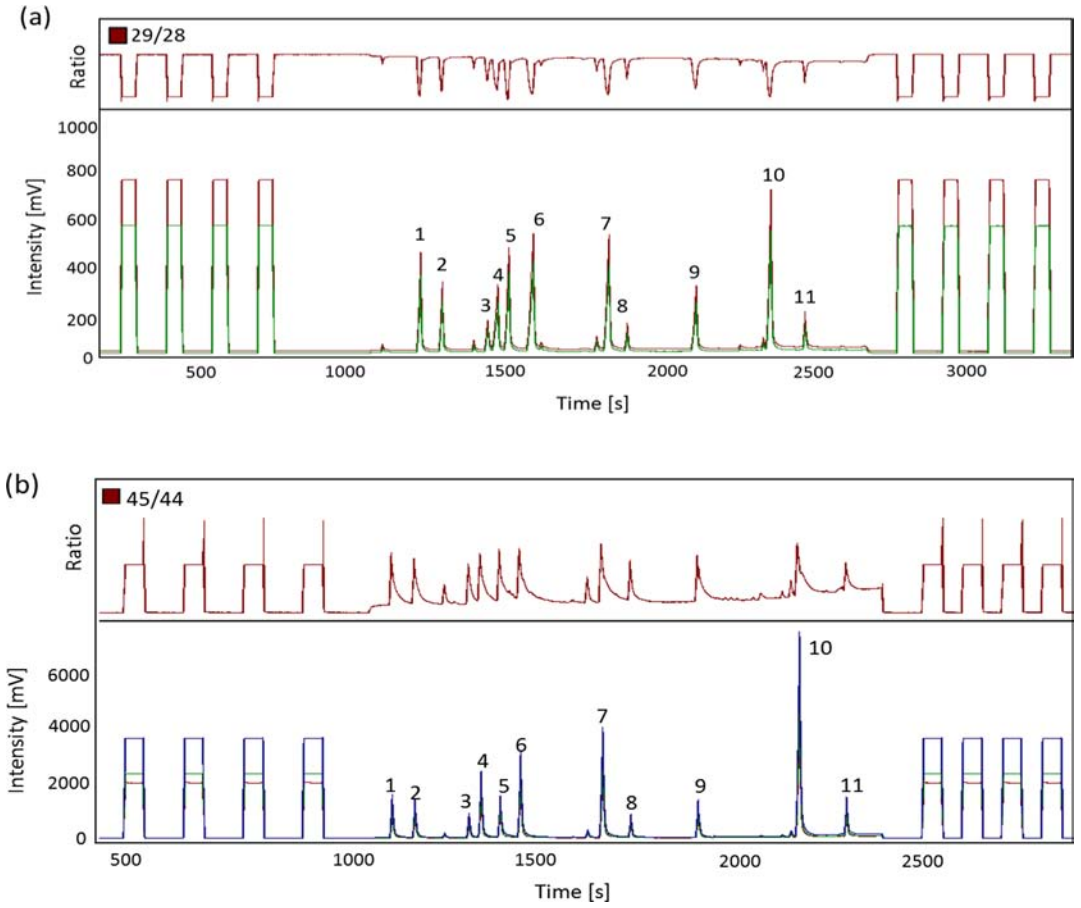

Figure 1. GC-C-IRMS chromatogram of *N*-acetyl-isopropyl derivatives of amino acids in a wheat sample (nitrogen isotopic ratio (a) and carbon isotopic ratio (b)). Peaks: 1, Ala; 2, Val; 3, Ile; 4, Leu; 5, Gly; 6, Nleu (internal standard); 7, Pro; 8, Thr; 9, Asx; 10, Glx; 11, Phe. The four first and last peaks of each panel are reference gas signals.

(Ni/Cu/Pt, 0.125 mm diameter, 240 mm identical length) braided and centered end-to-end within the tube. Water vapor was removed by a water-removing trap, consisting of a Nafion membrane. During $\delta^{15}N$ analysis a liquid nitrogen trap was added after the combustion oxidation reactor to remove CO_2 from the oxidized and reduced analyte.

To monitor instrumental performance a mixture of L-amino acid standards was derivatized and the $\delta^{15}N$ and $\delta^{13}C$ values were measured by GC-C-IRMS before each analytical run. Moreover, the isotopic value of the internal standard norleucine added to each sample was checked. Norleucine was chosen as internal standard because it is not naturally present in wheat. The $\delta^{15}N$ and $\delta^{13}C$ values of pure norleucine (+14.0 and −27.6‰, respectively) and of the pure L-amino acids (see below) were determined by EA-IRMS. The analytical run was accepted when the differences between GC-C-IRMS and EA-IRMS values were, at most, ± 1.0 and ±1.5‰, respectively, for $\delta^{15}N$ and $\delta^{13}C$.

Data Analysis and Corrections. All of the $\delta^{15}N$ and $\delta^{13}C$ values are reported relative to reference N_2 and CO_2 of known nitrogen and carbon isotopic composition, respectively, introduced directly into the ion source at the beginning and end of each run (Figure 1). All samples were measured in triplicate, and the isotope ratios were expressed in δ‰ versus atmospheric nitrogen for $\delta^{15}N$ and V-PDB (Vienna − Pee Dee Belemnite) for $\delta^{13}C$ according to eq 1

$$\delta = \left[\frac{(R_s - R_{std})}{R_{std}}\right] \quad (1)$$

where R_s is the isotope ratio measured for the sample and R_{std} is the isotope ratio of the internationally accepted standard.

Measured $\delta^{13}C$ values for derivatized amino acids are the product of both the carbon native to the molecule and the contribution from the reagents used for derivatization. The $\delta^{13}C$ values of the mixture of standard amino acids measured by EA-IRMS and their respective *N*-acetylisopropyl esters obtained with GC-C-IRMS are presented in the Supporting Information (SI 1). Therefore, an empirical correction[26] was applied to determine the effective carbon isotope value. Correction factors were calculated by determining the $\delta^{13}C$ values of the underivatized amino acid standards (EA-IRMS) and the derivatized amino acid standards (GC-C-IRMS):

$$n_{cd}\delta^{13}C_{cd} = n_c\delta^{13}C_c + n_d\delta^{13}C_d \quad (2)$$

n is the number of moles of carbon, and the subscripts c, d, and cd represent the compounds of interest, the derivative group, and the derivatized compound, respectively.

When calculating the uncertainty of $\delta^{13}C$ measurement (see below), we considered measurement errors as well as the total analytical error, which arises from the different derivatization steps:

$$\sigma_c^2 = \sigma_s^2\left(\frac{n_s}{n_c}\right)^2 + \sigma_{sd}^2\left(\frac{n_s + n_d}{n_c}\right)^2 + \sigma_{cd}^2\left(\frac{n_c + n_d}{n_c}\right)^2 \quad (3)$$

n is the number of moles of carbon, and the subscripts c, cd, d, s, and sd, represent the underivatized compound, the derivatized compound, the derivatizing reagent, the underivatized standard, and the derivatized standard, respectively.

Accuracy and Precision of GC-C-IRMS. To test the accuracy of the determination of amino acid isotopic values, we compared the $\delta^{15}N$ and $\delta^{13}C$ values of the mixture of standard amino acids measured by GC-C-IRMS with the isotopic values of pure nonderivatized single amino acids obtained with EA-IRMS. The $\delta^{15}N$ and $\delta^{13}C$ values determined by EA-IRMS were the mean of two measurements, whereas the $\delta^{15}N$ and $\delta^{13}C$ values determined by GC-C-IRMS were the average of three runs. Both

DOI: 10.1021/acs.jafc.5b00662
J. Agric. Food Chem. 2015, 63, 5841−5850

$\delta^{15}N$ and $\delta^{13}C$ values obtained from EA-IRMS were linearly correlated with those from GC-C-IRMS after derivatization, as shown in the Supporting Information (SI 2 and SI 3), and the difference between the values measured by EA-IRMS and by GC-C-IRMS after empirical correction was not higher than ±0.5 and ±1.6‰ for $\delta^{15}N$ and $\delta^{13}C$, respectively (SI 1).

To evaluate the precision, 10 replicates of the reference amino acid mixture were derivatized, and each of them was analyzed by GC-C-IRMS in triplicate. The precision (1σ) of GC-C-IRMS determinations was on average ±0.4‰ for $\delta^{15}N$ and ±0.8‰ for $\delta^{13}C$.

To evaluate the uncertainty of measurements for all of the processes, a wheat sample was hydrolyzed and derivatized 10 times, and each of the samples was analyzed by GC-C-IRMS. The standard deviation obtained (1σ) was on average ±0.3‰ for $\delta^{15}N$ and ±1.0‰ for $\delta^{13}C$ (Supporting Information (SI 4).

Statistical Analysis. The data were statistically evaluated using Statistica v 9 (StatSoft Italia srl, Padua, Italy).

RESULTS AND DISCUSSION

Wheat Amino Acid $\delta^{15}N$ and $\delta^{13}C$ Values. The $\delta^{15}N$ and $\delta^{13}C$ values of the amino acids Ala, Val, Ile, Leu, Gly, Pro, Thr, Asx, Glx, and Phe from the 18 Danish and from the 17 Italian wheat grain samples are shown in the Supporting Information (SI 5 and SI 6), whereas the mean and standard deviation (SD) values across agricultural systems are reported in Tables 3 and 4.

From the $\delta^{15}N$ values it is evident that the ^{15}N content between different amino acids can vary significantly due to isotopic fractionation occurring during N metabolism within the plant. Ammonium (NH_4^+) from soil is assimilated directly into plant amino acid metabolism via the enzyme glutamine synthetase, whereas nitrate (NO_3^-) undergoes sequential reduction to nitrite and then subsequently to ammonia via the nitrate and nitrite reductase enzymes.[27] The first amino acid produced by ammonia assimilation is glutamine, which therefore plays a central role in the amino acid metabolism. Glutamate and then other amino acids are produced by the transfer of the amide of glutamine to keto acids and by transamination.[28] It follows that in our case the $\delta^{15}N$ of glutamic acid derived from acid hydrolysates of glutamic acid and glutamine (Glx) represents the main source of imported nitrogen being a product of the net flux of N entering and leaving the Gln and Glu pools.

Figure 2a shows mean values of differences between the $\delta^{15}N$ values of Ala, Val, Ileu, Leu, Gly, Pro, Thr, Asx, and Phe and that of Glx across all 35 wheat samples. This allows comparison of the $\delta^{15}N$ value of single amino acids normalizing the possible variation caused by the external nitrogen source (e.g., fertilizer practices, soil composition, location). The $\delta^{15}N$ relative trend among amino acids is in agreement with the results reported in other studies.[29] As compared to the $\delta^{15}N$ value of Glx (Figure 2a), the $\delta^{15}N$ values of Phe (+4.4 ± 1.4‰) and Pro (+1.0 ± 0.8‰) are higher. The relative ^{15}N enrichment of Phe and Pro compared to the other amino acids in cereal grains is in agreement with the scientific literature on the subject, concluding that there is an isotopic fractionation associated with this enzymatic reaction.[29] Phenylalanine ammonia-lyase catalyzes the deamination of Phe, and the kinetic isotope effect associated with this reaction leaves the residual Phe enriched in ^{15}N, whereas the ^{15}N enrichment of Pro is caused by a kinetic isotope effect associated with the enzymes (proline dehydrogenase and Δ^1-pyrrolidine-5-carboxylate dehydrogenase) involved in its catabolism.[29,30]

The $\delta^{15}N$ values of Ala (−3.1 ± 1.5‰), Val (−1.4 ± 1.4‰), Ileu (−4.1 ± 1.8‰), Leu (−5.7 ± 1.3‰), Gly (−5.0 ± 1.8‰), Thr (−9.8 ± 2.5‰), and Asx (−2.9 ± 1.6‰) are lower than the

Table 3. Amino Acid $\delta^{15}N$ and $\delta^{13}C$ Values of Danish Wheat Samples[a]

		wheat amino acid $\delta^{15}N$ and $\delta^{13}C$ values (‰)																			
		Ala		Val		Ile		Leu		Gly		Pro		Thr		Asx		Glx		Phe	
system		N	C	N	C	N	C	N	C	N	C	N	C	N	C	N	C	N	C	N	C
CS	mean	1.1b	−24.9b	2.7b	−30.8	0.1b	−26.9	−1.2b	−34.0	−1.2b	−14.7	5.9b	−28.1	−6.4b	−14.6	0.8b	−25.2	5.3b	−26.1b	8.6b	−26.5
	SD	1.0	0.7	0.9	0.7	0.9	0.9	1.2	0.8	1.9	1.4	0.7	0.8	1.8	0.5	1.1	1.0	1.1	0.3	0.7	1.4
OSB	mean	1.7b	−23.7a	3.3b	−30.3	0.3b	−26.1	−1.0b	−33.7	−1.5b	−13.4	6.1b	−26.8	−5.4b	−12.5	1.1b	−24.1	5.3b	−24.6a	9.4b	−26.4
	SD	1.3	0.5	1.6	0.9	1.7	0.7	1.7	0.5	2.5	1.0	2.1	0.7	1.3	1.1	1.8	0.9	2.3	0.6	1.7	1.6
OSA	mean	6.2a	−24.1b	8.4a	−30.2	5.1a	−26.1	3.6a	−33.8	3.2a	−13.4	10.4a	−27.3	−0.2a	−12.8	6.0a	−24.4	9.3a	−24.0a	14.5a	−27.2
	SD	1.7	1.0	1.3	1.4	1.4	1.6	1.5	0.7	1.3	1.6	0.8	1.4	2.7	3.1	1.0	2.0	0.9	1.0	0.8	1.7

[a]Values are the means of three analytical replicates. CS, conventional; OSB, organic with green manures; OSA, organic with animal manure; SD, standard deviation. Significantly different mean values (HSD Tukey's, $p < 0.05$) of wheat samples from the three systems across locations are indicated with letters "a" and "b".

DOI: 10.1021/acs.jafc.5b00662
J. Agric. Food Chem. 2015, 63, 5841−5850

Table 4. Amino Acid $\delta^{15}N$ and $\delta^{13}C$ Values of Italian Wheat Durum Samples[a]

		wheat amino acid $\delta^{15}N$ and $\delta^{13}C$ values (‰)																			
		Ala		Val		Ile		Leu		Gly		Pro		Thr		Asx		Glx		Phe	
system		N	C	N	C	N	C	N	C	N	C	N	C	N	C	N	C	N	C	N	C
CS	mean	1.2	−22.5a	3.1	−30.9	0.4	−27.0	−1.4	−34.9a	0.8	−15.8ab	5.2	−26.2a	−4.5	−13.1ab	2.4	−24.3	4.1	−27.0b	8.4	−26.2a
	SD	1.9	1.9	2.8	1.5	2.6	1.3	2.2	1.0	2.2	2.1	2.2	1.5	1.8	1.9	2.3	3.0	2.3	0.9	2.2	1.2
OSB	mean	1.2	−27.0b	3.6	−32.7	1.4	−28.7	−1.7	−37.1b	1.1	−21.1b	5.2	−29.4b	−3.4	−17.0b	2.7	−25.8	3.9	−22.8a	9.8	−33.4b
	SD	3.9	0.1	2.9	0.3	4.2	0.2	2.7	1.1	2.1	2.5	3.1	0.8	5.3	2.5	3.4	0.8	2.2	0.6	2.8	3.5
OSA	mean	4.1	−22.8a	4.9	−31.5	2.9	−26.6	1.0	−34.5a	2.0	−15.0a	7.6	−25.3a	−3.2	−11.5a	4.4	−24.5	6.2	−23.8a	10.5	−27.1ab
	SD	2.9	1.9	3.3	1.2	3.4	1.7	3.4	0.6	3.6	3.5	3.0	1.0	4.0	2.0	3.3	1.5	2.6	1.4	2.7	2.9
nothing	mean	3.0	−23.9ab	4.6	−31.9	1.9	−28.5	1.6	−35.5ab	3.4	−17.3ab	7.2	−26.9ab	−4.7	−13.1ab	3.2	−25.6	6.6	−24.4a	10.5	−32.5ab
	SD	2.5	0.1	2.6	0.4	3.9	0.2	0.9	1.0	4.1	1.1	2.5	0.2	4.2	0.6	3.7	2.5	3.0	0.8	1.3	7.9

[a]Values are the means of three analytical replicates. CS, conventional; OSB, organic with green manure; OSA, organic with animal manure; nothing, organic without fertilizer treatment; SD, standard deviation. Significantly different mean values (HSD Tukey's, $p < 0.05$) between groups are indicated with letters "a" and "b".

$\delta^{15}N_{Glx}$ value. These amino acids are principally produced during transamination of precursors, amino acids (e.g., glutamic acid), and keto acids. Previous studies[31] have reported that enzymatic reactions of transamination involved in plant metabolism induced a kinetic isotope effect leading to the lower $\delta^{15}N$ values in NH_2 of product amino acid and that the extent of isotopic fractionation may vary depending on the reaction rates.

The mean $\delta^{13}C$ value of plant material is fixed by that of the primary carbon source (CO_2) and by the kinetic isotope effect of the CO_2-binding reaction (RuBP-carboxylase and PEP-carboxylase, respectively). The pattern of aliphatic amino acids and aromatic amino acids derived from glucose and shikimic acid, respectively, reflects the resulting ^{13}C distribution of these precursors, and it is supplemented by the introduction of additional C atoms depleted by the kinetic isotope effect on the PEP−carboxylase reaction.[32] Figure 2b shows mean values of differences between the $\delta^{13}C$ values of Ala, Val, Ileu, Leu, Gly, Pro, Thr, Asx, and Phe and that of Glx across all 35 wheat samples from all three agricultural systems and locations. $\delta^{13}C$ values of Gly (+9.6 ± 3.3‰) and Thr (+11.6 ± 2.7‰) were higher than the $\delta^{13}C_{Glx}$ value, whereas the $\delta^{13}C$ values of Val (−6.1 ± 2.2‰), Ileu (−2.0 ± 2.1‰), Leu (−9.6 ± 2.1‰), Pro (−2.1 ± 2.2‰), and Phe (−2.7 ± 4.0‰) were lower. The measured $\delta^{13}C$ values of Ala and Asx were very similar to that of Glx (within ±2.5 and ±2.4‰, respectively) in all of the wheat samples.

$\delta^{15}N$ and $\delta^{13}C$ Amino Acid Values for Organic Authentication. In Tables 3 and 4 the mean and standard deviation of the data grouped according to agricultural system across locations in Denmark and Italy, respectively, as well as the results of the honestly significantly difference (HSD) for unequal N Tukey's test are reported.

Grouping the Danish samples according to the agricultural systems, Tukey's test results (Table 3) showed that conventionally grown wheat had significantly lower $\delta^{15}N$ values than the organic wheat OSA, whereas it was not distinguishable from the organic wheat fertilized with green manure (OSB). This corresponds with results from bulk tissue analysis in previous studies.[1] This finding clearly highlights the limitation of $\delta^{15}N$ as a marker of organic production when plant fertilization is based on N_2-fixing green manures. On the other hand, the $\delta^{13}C$ value of Glx was significantly ($p < 0.05$) lower in the conventional wheat compared to both organic systems (OSA and OSB). $\delta^{15}N$ values of plant amino acids are clearly affected by the nitrogen source, which in this case results in similar $\delta^{15}N$ values for CS and OSB samples. In contrast, $\delta^{13}C$ is more linked to the different characteristics of the field under conventional and organic regimens in terms of water availability, drought stress, and nutrient availability, which influence the photosynthetic activity and stomatal conductance of leaves.[14−18] Here we found lower $\delta^{13}C$ values in the conventional wheat, which is expected to be due to a higher stomatal conductance in these plants due to the higher nitrogen content (as reported in Tables 1 and 2). Indeed, previous studies[33] showed that the maximum CO_2 assimilation rates and maximum stomatal conductance, when measured under higher N availability conditions, as typically observed in conventional crops, did lead to a higher discrimination of RuBisCo against $^{13}CO_2$. In contrast, N deficiency, as in the case of organic crops, can induce stomatal closure, which is caused by a lower ratio of the N-regulated plant hormones cytokinin and abscisic acid. This leads to a reduced discrimination against $^{13}CO_2$ and thereby higher $\delta^{13}C$ values. Lower $\delta^{13}C$ values were also observed in proteins extracted from conventional apples,[34]

DOI: 10.1021/acs.jafc.5b00662
J. Agric. Food Chem. 2015, 63, 5841−5850

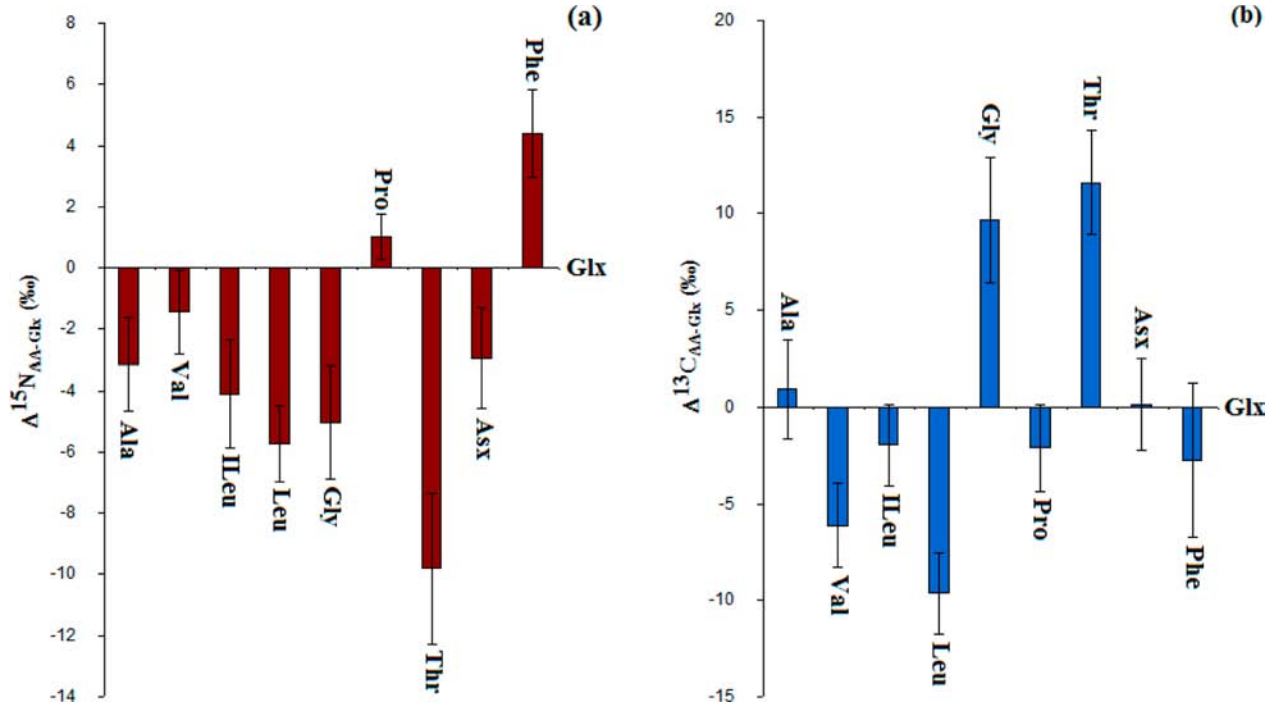

Figure 2. Differences between the δ^{15}N (a) and δ^{13}C (b) values of Ala, Val, Ileu, Leu, Gly, Pro, Thr, Asx, and Phe and the δ^{15}N and δ^{13}C of Glx for all of the Danish and Italian wheat samples. Bars represent mean values ± SD (n = 35).

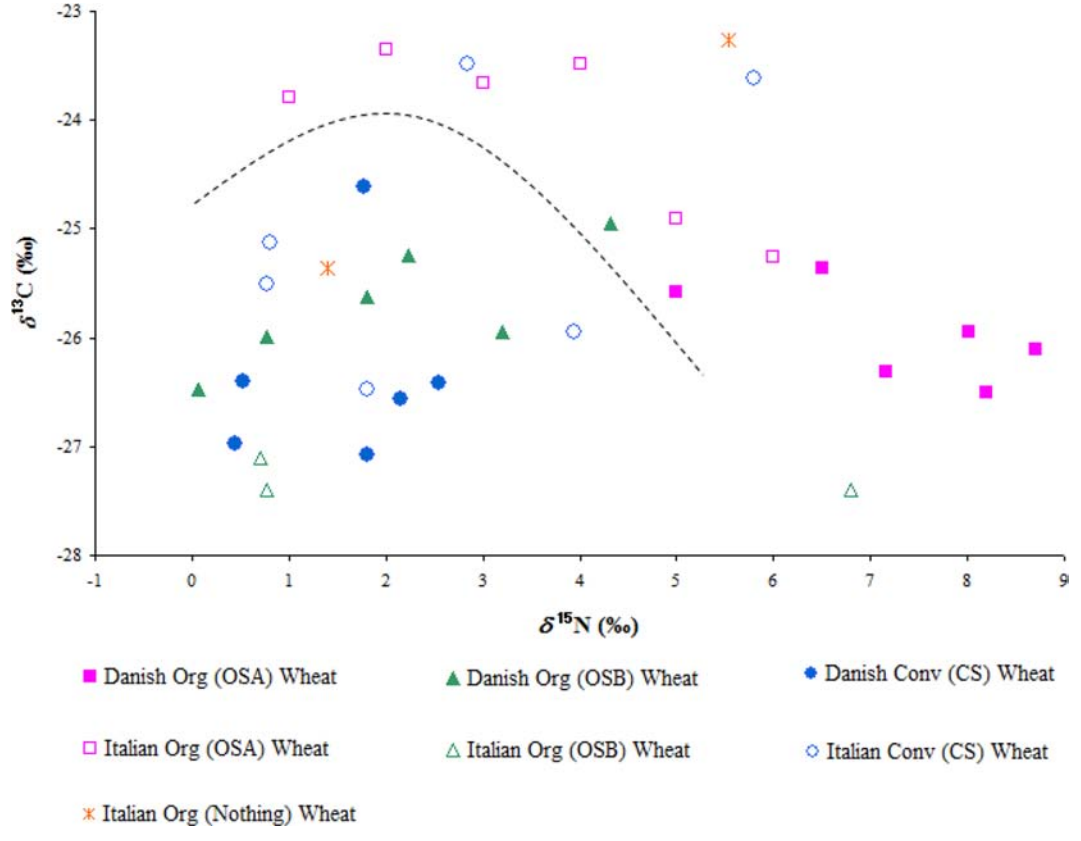

Figure 3. δ^{15}N plotted against δ^{13}C in bulk tissue samples of Danish and Italian wheat samples. Circles are CS (conventional), squares are OSA (organic with animal manure), triangles are OSB (organic with green manure), and stars are nothing (organic without fertilizer treatment). Solid and open symbols indicate Danish and Italian samples, respectively. Please note that the dashed line is only for illustrative purposes and does not represent statistical analysis.

but not in conventional onions and cabbages[15] or in soil of conventional grassland.[35]

Applying Tukey's test on δ^{15}N amino acid values of the Italian durum wheat samples grouped according to the agricultural

DOI: 10.1021/acs.jafc.5b00662
J. Agric. Food Chem. 2015, 63, 5841−5850

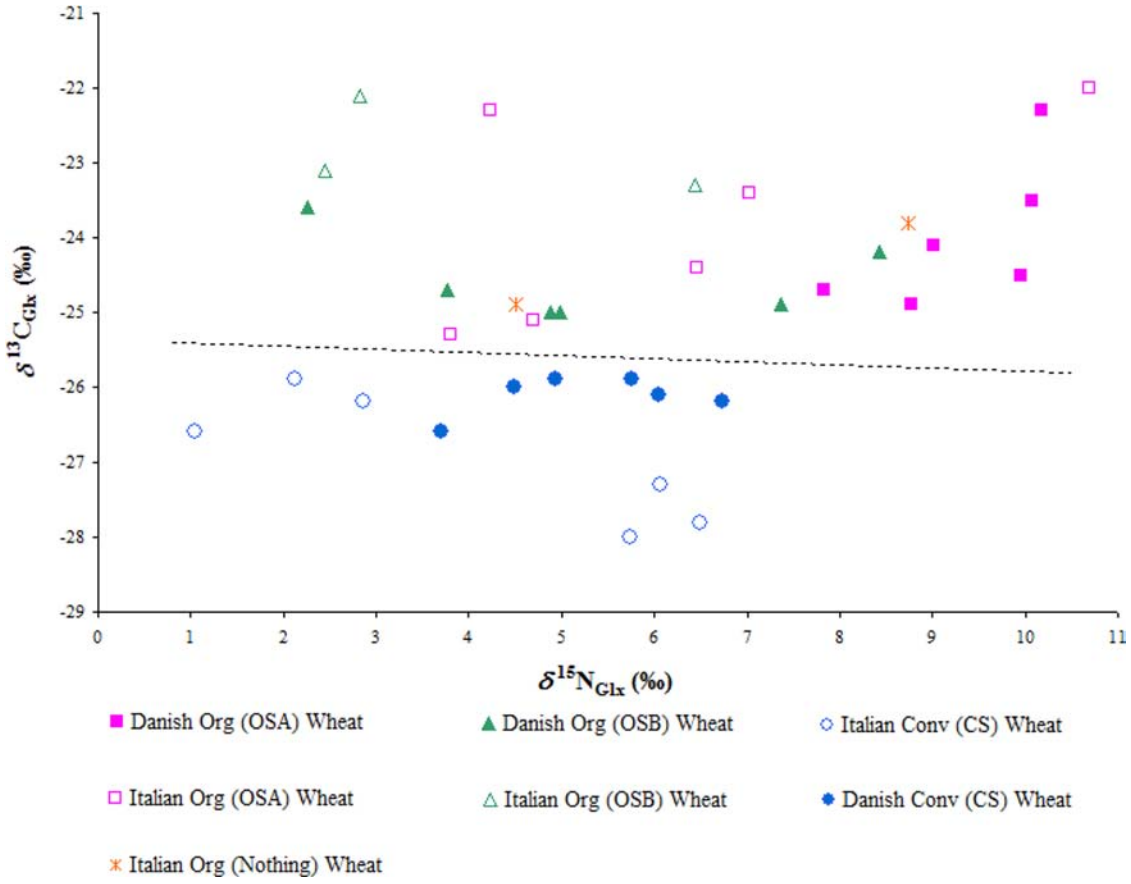

Figure 4. δ^{15}N in Glx plotted against δ^{13}C in Glx of Danish and Italian wheat samples. Circles are CS (conventional), squares are OSA (organic with organic fertilizer), triangles are OSB (organic with green manure), and stars are nothing (organic without fertilizer treatment). Solid and open symbols indicate Danish and Italian samples, respectively. Please note that the dashed line is only for illustrative purposes and does not represent statistical analysis.

regimen, no significant differences between the four groups were observed (Table 4). Conventionally cultivated durum wheat was not distinguishable from either the organic wheat OSA (fertilized with organic fertilizer) or OSB (fertilized with green manure) or organic wheat grown without fertilization. The main reason for this finding is that we considered samples produced in different Italian regions (Emilia Romagna, Basilicata, Molise) potentially characterized by different δ^{15}N values of the soil.

As observed for Danish wheat and also for Italian durum, the δ^{13}C values of some amino acids were significantly different between agricultural regimens. In particular the δ^{13}C of Glx was significantly lower ($p < 0.05$) in the conventional samples compared to organic systems (OSA, OSB, nothing) as for Danish samples.

On the basis of Tukey's test results we decided to consider all Danish and Italian samples together focusing on δ^{15}N and δ^{13}C values of Glx for discriminating between the agricultural systems. Moreover, we considered δ^{15}N and δ^{13}C values of bulk tissue wheat grain samples, taking the data from the literature for Denmark[1] and measuring the samples from Italy to conduct a direct comparison with the compound-specific data. Figure 3 shows the distribution of δ^{15}N and δ^{13}C values of Danish and Italian bulk tissue samples, whereas Figure 4 shows the same distribution for δ^{15}N and δ^{13}C values of Glx. The bulk tissue analysis allowed separation of wheat samples grown with the use of animal manure (OSA) from samples grown using synthetic fertilizers (CS), but it was impossible to distinguish the agricultural system based on legumes as green manures (OSB) from the conventional one, as discussed above.

However, the δ^{15}N and δ^{13}C values of Glx (Figure 4) improved the discrimination between the conventional and organic agricultural systems. In particular, the δ^{13}C value of Glx was able to distinguish organic samples from those grown in the conventional agricultural system—even when including the variations caused by wheat species, variety, harvest period, geographical location, etc.

Previous studies[36] have shown that multivariate statistical analysis can be a tool to improve the discrimination between different foods (e.g., organic and conventional). Linear discriminant analysis (LDA) is probably the most frequently used supervised pattern recognition method, which is based on maximization of the ratio of between-class variance and minimization of the ratio of within-class variance. LDA was performed using the data set composed by all wheat samples (35 organic and conventional samples) and 20 variables (δ^{15}N and δ^{13}C amino acid values) to establish if it is possible to enhance the separation between agricultural regimens. After application of LDA, three discriminant functions were calculated, and Figure 5 shows the score plot of the wheat samples using as axes the first two functions that explain 91.2% of total variance.

The three categories of wheat (OSA, OSB, and CS) were well separated across the principal component Rad 1. The latter correlates negatively with δ^{15}N Pro (−2.849) and δ^{13}C Val (−2.158) and positively with δ^{15}N Phe (3.436) and δ^{15}N Glx (2.622). Rad 2 improves the separation between OSA and the

DOI: 10.1021/acs.jafc.5b00662
J. Agric. Food Chem. 2015, 63, 5841−5850

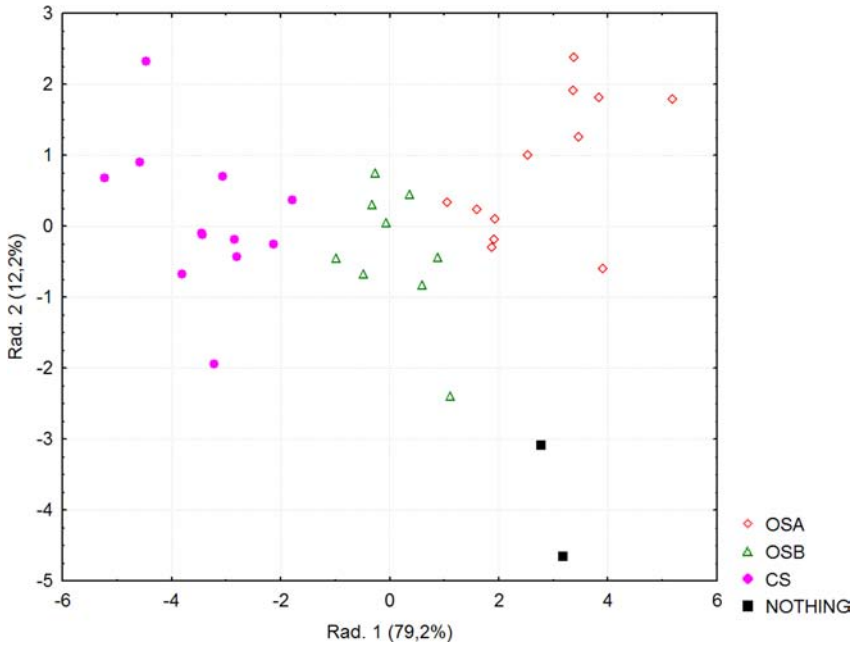

Figure 5. LDA scores plot of nitrogen and carbon isotope analysis of amino acids for organic and conventional wheat samples.

"nothing" group and correlates negatively with δ^{15}N Leu (−1.339), δ^{15}N ILeu (−1.036), and δ^{15}N Glx (−1.018), whereas it correlates positively with δ^{15}N Ala (1.314). δ^{13}C Glx did not correlate significantly with Rad 1 and Rad 2 because it is capable of separating organic from conventional samples but not the three types of organic agricultural systems.

We can conclude that compound-specific δ^{15}N and δ^{13}C analysis of plant-derived amino acids represents a promising tool for verification of the fertilization history of crops. δ^{13}C of glutamic acid and glutamine, in particular, but also the combination of δ^{15}N and δ^{13}C of the 10 amino acids Ala, Val, Ile, Leu, Gly, Pro, Thr, Asx, Glx, and Phe did improve the separation between organic and conventional wheat, even when organic wheat production was based on fertilization and crop rotation using N_2-fixing plants. It is recommended that the novel method is tested on a larger set of samples and across different plant species and locations to further evaluate the applicability of compound-specific stable isotope analysis of amino acids for organic authentication.

■ ASSOCIATED CONTENT

Supporting Information

Supplemental tables and figure. The Supporting Information is available free of charge on the ACS Publications website at DOI: 10.1021/acs.jafc.5b00662.

■ AUTHOR INFORMATION

Corresponding Author

*(M.P.) Fax: +39 0461 6152288. Phone: +39 0461 615525. E-mail: mauro.paolini@fmach.it.

Funding

We acknowledge the financial support provided by the CORE Organic II Funding Bodies, being partners of the FP7 ERA-NET Project, CORE Organic II (Coordination of European Transnational Research in Organic Food and Farming systems, Project No. 249667) via the AuthenticFood Project. The Danish Council for Independent Research − Technology and Production Sciences also provided financial support via the COM-ISO project (DFF-1337-00055). Financial support was also obtained from the Ministry of Food, Agriculture and Fisheries, Denmark, via the OrgTrace Research Project (3304-FOJO-05-45-01), which was coordinated by the International Centre for Research in Organic Food Systems (ICROFS).

Notes

The authors declare no competing financial interest.

■ ACKNOWLEDGMENTS

We acknowledge the persons involved in sample production, sampling, and data collection: J. E. Olesen and colleagues from the CROPSYS project; Cristina Micheloni, Fabia Montalbano, Paolo Di Luzio, Riccardo Bocci, and Vincenzo Ritunnano, Az. Agr. Bioland, Gravina di Puglia (BA), Az. Agr. Mazzarella Giuseppe, Gravina di Puglia (BA), Az. Agr. Tuotolo Federico, Termoli (CB), Az. Agr. Ruggiero Ilaria Beatrice, matrice (CB), and Az. Agr. Contarini Alessandro, Codigoro (FE).

■ REFERENCES

(1) Laursen, K. H.; Mihailova, A.; Kelly, S. D.; Epov, V. N.; Bérail, S.; Schjoerring, J. K.; Donard, O. F. X.; Larsen, E. H.; Pedentchouk, N.; Marca-Bell, A. D.; Halekoh, U.; Olesen, J. E.; Husted, S. Is it really organic? − Multi-isotopic analysis as a tool to discriminate between organic and conventional plants. *Food Chem.* **2013**, *141*, 2812−2820.

(2) Laursen, K. H.; Schjoerring, J. K.; Kelly, S. D.; Husted, S. Authentication of organically grown plants − advantages and limitations of atomic spectroscopy for multi-element and stable isotope analysis. *TrAC, Trends Anal. Chem.* **2014**, *59*, 73−82.

(3) Capuano, E.; Boerrigter-Eenling, R.; van der Veer, G.; van Ruth, M. S. Analytical authentication of organic products: an overview of markers. *J. Sci. Food Agric.* **2013**, *93*, 12−28.

(4) Bateman, A. S.; Kelly, S. D.; Woolfe, M. Nitrogen isotope composition of organically and conventionally grown crops. *J. Agric. Food Chem.* **2007**, *55*, 2664−2670.

(5) Choi, W. J.; Ro, H. M.; Lee, S. M. Natural ^{15}N abundances of inorganic nitrogen in soil treated with fertilizer and compost under changing soil moisture regimes. *Soil Biol. Biochem.* **2003**, *35*, 1289−1298.

(6) Wassenaar, L. I. Evaluation of the origin and fate of nitrate in the Abbotsford aquifer using the isotopes of ^{15}N and ^{18}O in NO_3^-. *Appl. Geochem.* **1995**, *10*, 391−404.

DOI: 10.1021/acs.jafc.5b00662
J. Agric. Food Chem. 2015, 63, 5841−5850

(7) Kerley, S. J.; Jarvis, S. C. Preliminary studies of the impact of excreted N on cycling and uptake of N in pasture systems using natural abundance stable isotope discrimination. *Plant Soil* **1996**, *178*, 287−294.
(8) Camin, F.; Perini, M.; L. Bontempo, L.; Fabroni, S.; Faedi, W.; Magnani, S.; Baruzzi, G.; Bonoli, M.; Tabilio, M. R.; Musmeci, S.; Rossmann, A.; Kelly, S. D.; Rapisarda, P. Potential isotopic and chemical markers for characterising organic fruits. *Food Chem.* **2011**, *125*, 1072−1082.
(9) Flores, P.; Lopez, A.; Fenoll, J.; Hellína, P.; Kelly, S. Classification of organic and conventional sweet peppers and lettuce using a combination of isotopic and bio-markers with multivariate analysis. *J. Food Compos. Anal.* **2013**, *31*, 217−223.
(10) Hohmann, M.; Christoph, N.; Wachter, H.; Holzgrabe, U. ^{1}H NMR profiling as an approach to differentiate conventionally and organically grown tomatoes. *J. Agric. Food Chem.* **2014**, *62*, 8530−8540.
(11) Zotarelli, L.; Zatorre, N. P.; Boddey, R. M.; Urquiaga, S.; Jantalia, C. P.; Julio C. Franchini, J. C.; Alves, B. J. R. Influence of no-tillage and frequency of a green manure legume in crop rotations for balancing N outputs and preserving soil organic C stocks. *Field Crop Res.* **2012**, *132*, 185−195.
(12) van Klinken, G. J.; Richards, M. P.; Hedges, R. E. M. In *Biogeochemical Approaches to Paleodietary Analysis*, 1st ed.; Ambrose, S. H., Katzenburg, M., Eds.; Springer: New York, 2000; pp 39−63.
(13) Mihailova, A.; Pedentchouk, N.; Kelly, S. D. Stable isotope analysis of plant-derived nitrate − novel method for discrimination between organically and conventionally grown vegetables. *Food Chem.* **2014**, *154*, 238−245.
(14) Adams, M. A.; Grierson, P. F. Stable isotopes at natural abundance in terrestrial plant ecology and ecophysiology: An update. *Plant Biol.* **2001**, *3*, 299−310.
(15) Hoegberg, P.; Johannisson, C.; Hallgren, J. E. Studies of ^{13}C in the foliage reveal interactions between nutrients and water in forest fertilization experiments. *Plant Soil* **1993**, *152*, 207−214.
(16) Georgi, M.; Voerkelius, S.; Rossmann, A.; Grassmann, J.; Schnitzler, W. H. Multielement isotope ratios of vegetables from integrated and organic production. *Plant Soil* **2005**, *275*, 93−100.
(17) Šantrůčková, H.; Bird, M. I.; Lloyd, J. Microbial processes and carbon-isotope fractionation in tropical and temperate grassland soils. *Funct. Ecol.* **2000**, *14*, 108−114.
(18) Schmidt, H. L.; Rossmann, A.; Voerkelius, S.; Schnitzler, W. M.; Georgi, M.; Grassmann, J.; Zimmermann, G.; Winkler, R. Isotope characteristics of vegetables and wheat from conventional and organic production. *Isot. Environ. Health Stud.* **2005**, *41*, 223−228.
(19) van Leeuwen, K. A.; Prenzler, P. D.; Ryan, D.; Camin, F. Gas chromatography-combustion-isotope ratio mass spectrometry for traceability and authenticity in foods and beverages. *Compr. Rev. Food Sci. Food Saf.* **2014**, *13*, 814−837.
(20) Bol, R.; Ostle, N. J.; Balesdent, J.; Petzke, K. J.; Cockburn, J. Influence of long-term fertilizer and manure on the distribution and ^{15}N natural abundance values of amino acids in the Versailles '42 parcelles': preliminary results. *Abstr. Pap. Am. Chem. Soc.* **2001**, *No. 221*, 534.
(21) Bol, R.; Ostle, N. J.; Petzke, K. J. Compound specific plant amino acid δ^{15}N values differ with functional plant strategies in temperate grassland. *J. Plant Nutr. Soil Sci.* **2002**, *165*, 661−667.
(22) Laursen, K. H.; Schjoerring, J. K.; Olesen, J. E.; Askegaard, M.; Halekoh, U.; Husted, S. Multielemental fingerprinting as a tool for authentication of organic wheat, barley, faba bean, and potato. *J. Agric. Food Chem.* **2011**, *59*, 4385−4396.
(23) Takano, Y.; Kashiyama, Y.; Ogawa, N. O.; Chikaraishi, Y.; Ohkouchi, N. Isolation and desalting with cation-exchange chromatography for compound-specific nitrogen isotope analysis of amino acids: application to biogeochemical samples. *Rapid Commun. Mass Spectrom.* **2010**, *24*, 2317−2323.
(24) Styring, A. K.; Kuhl, A.; Knowles, T. D. J.; Fraser, R. A.; Bogaard, A.; Evershed, R. P. Practical consideration in the determination of compound-specific amino acid δ^{15}N values in animal and plant tissues by gas chromatography-combustion-isotope ratio mass spectrometry, following derivatisation to their *N*-acetylisopropyl esters. *Rapid Commun. Mass Spectrom.* **2012**, *26*, 2328−2334.
(25) Corr, L. T.; Berstan, R.; Evershed, R. P. Optimisation of derivatization procedures for the determination of δ^{13}C values of amino acids by gas chromatography/combustion/isotope ratio mass spectrometry. *Rapid Commun. Mass Spectrom.* **2007**, *21*, 3759−3771.
(26) Docherty, G.; Jones, V.; Evershed, R. P. Practical and theoretical considerations in the gas chromatography/combustion/isotope ratio mass spectrometry δ^{13}C analysis of small polyfunctional compounds. *Rapid Commun. Mass Spectrom.* **2001**, *15*, 730−738.
(27) Lea, P. J.; Ireland, R. J. In *Plant Amino Acids. Biochemistry and Biotechnology*; Singh, B. K., Ed.; Dekker: New York, 1999; pp 1−47.
(28) Wada, E.; Yoneyama, T.; Minagawa, M.; Ando, T.; Fry, B. D. In *Stable Isotopes in the Biosphere*, 1st ed.; Kyoto University Press: Kyoto, Japan, 1995; pp 92−102.
(29) Styring, A. K.; Fraser, R. A.; Bogaard, A.; Evershed, R. P. Cereal grain, rachis and pulse seed amino acid δ^{15}N values as indicators of plant nitrogen metabolism. *Phytochemistry* **2013**, *97*, 20−29.
(30) Hermes, J. D.; Weiss, P. M.; Cleland, W. W. Use of ^{15}N and deuterium isotope effects to determine the chemical mechanism of phenylalanine ammonia lyase. *Biochemistry* **1985**, *24*, 2959−2967.
(31) Macko, S. A.; Estep, M. L. F.; Engel, M. H.; Hare, P. E. Kinetic fractionation of stable nitrogen isotopes during amino acid transamination. *Geochim. Cosmochim. Acta* **1986**, *50*, 2143−2146.
(32) Wada, E.; Yoneyama, T.; Minagawa, M.; Ando, T.; Fry, B. D. In *Stable Isotopes in the Biosphere*, 1st ed.; Kyoto University Press: Kyoto, Japan, 1995; pp 17−35.
(33) Waraich, E. A.; Ahmad, R.; Saifullah; Ahmad, A. Water stress and nitrogen management effects on gas exchange, water relations, and water use efficiency in wheat. *J. Plant Nutr.* **2011**, *34*, 1867−1882.
(34) Bat, K. B.; Vidrih, R.; Nečemer, M.; Vodopivec, B. M.; Mulič, I.; Kump, P.; Ogrinc, N. Characterization of Slovenian apples with respect to their botanical and geographical origin and agricultural production practice. *Food Technol. Biotechnol.* **2012**, *50*, 107−116.
(35) Klaus, V. H.; Holzel, N.; Prati, D.; Schmitt, B.; Schoning, I.; Schrumpf, M.; Fischer, M.; Kleinebecker, T. Organic vs. conventional grassland management: do N-15 and C-13 isotopic signatures of hay and soil samples differ? *PLoS One* **2013**, *8*, No. 78134.
(36) Camin, F.; Larcher, R.; Nicolini, G.; Bontempo, L.; Bertoldi, D.; Perini, M.; Schlicht, C.; Schellenberg, A.; Thomas, F.; Heinrich, K.; Voerkelius, S.; Horacek, M.; Ueckermann, H.; Froeschl, H.; Wimmer, B.; Heiss, G.; Baxter, M.; Rossmann, A.; Hoogewerff, J. Isotopic and elemental data for tracing the origin of European olive oils. *J. Agric. Food Chem.* **2010**, *58*, 570−577.

DOI: 10.1021/acs.jafc.5b00662
J. Agric. Food Chem. 2015, 63, 5841−5850

Table 1. Withering Procedures for *Passito* Wine Samples

DOC denomination	geographical origin	type of withering	grape variety	year
		In a Fruit-Drying Room (*Fruttaio*)		
Erbaluce di Caluso Passito	north, Piedmont	on trellises, controlled temperature	Erbaluce	2011, 2012
Oltrepò Pavese Moscato Passito	north, Lombardy	on trellises, controlled temperature	Moscato	2012
Loazzolo Passito	north, Piedmont	on trellises, natural	Moscato	2011, 2012, 2013
Ramandolo Passito[a]	north, Friuli Venezia Giulia	on trellises, forced ventilation	Verduzzo	2013
Colli Orientali del Friuli	north, Friuli Venezia Giulia	in boxes, controlled temperature	Verduzzo	2011
Picolit	north, Friuli Venezia Giulia	in boxes, controlled temperature	Picolit	2011, 2012
Strevi Passito	north, Piedmont	in boxes, controlled temperature	Moscato	2013
Recioto di Gambellara	north, Veneto	hung, controlled temperature	Garganega	2011, 2012
Montefalco Sagrantino Passito	central, Umbria	on trellises, forced ventilation	Sagrantino	2011, 2012, 2013
Verdicchio dei Castelli di Jesi Passito	central, Marche	on trellises, controlled temperature	Verdicchio	2012, 2013
Vin Santo del Chianti	central, Tuscany	on trellises, controlled temperature	Trebbiano	2011, 2012, 2013
Vin Santo del Chianti Classico	central, Tuscany	in boxes, controlled temperature	Trebbiano	2012, 2013
		En Plein Air		
Albana di Romagna Passito	north, Emilia Romagna	over-ripening on the plants	Albana	2012
Ramandolo Passito[a]	north, Friuli Venezia Giulia	over-ripening on the plants	Verduzzo	2011
Ramandolo Passito[a]	north, Friuli Venezia Giulia	on trellises, covered	Verduzzo	2012
Moscato di Noto passito	south, Sicily	over-ripening on the plants	Moscato	2012, 2013
Passito di Manduria	south, Apulia	over-ripening on the plants	Primitivo	2012, 2013
Moscato di Trani	south, Apulia	over-ripening on the plants	Moscato	2012, 2013
Alghero passito	south, Sardinia	on trellises, covered	Nasco	2011, 2012, 2013

[a]For the *Ramandolo Passito* different withering procedures were adopted in the three years.

with hanging of the grapes) were considered in two successive years. Moreover, numerous samples of different traditional Italian *passito* wines from grapes taken at different stages of withering and withered in different conditions were taken into account, focusing on the $\delta^{18}O$ of water.

The final aim was to define the isotopic characteristics of Italian *passito* wines and to check whether isotopic methods can be used for authenticity verification for this type of wine.

The novelty of this study lies in the fact that for the first time, the effect of grape withering processes (up to 5 months) on the variability of the $(D/H)_I$, $(D/H)_{II}$, $\delta^{13}C$, and $\delta^{18}O$ of wine ethanol and the $\delta^{18}O$ of wine and must water was monitored during the production of *passito* wines considering different types of withering and different years. The monitoring carried out becomes very important, because variations in the isotopic values with withering can lead to wrong interpretation of the data and therefore to false conclusions about the authenticity of the samples.

MATERIALS AND METHODS

Grape Samples. The study focused on *Erbaluce di Caluso Passito* DOC, a wine produced with Erbaluce white grapes grown in the province of Turin (Piedmont, northwestern Italy) during 2011 and 2012.[21] The grape samples were withered in five different cellars with fruit-drying rooms (*fruttaio*) located in Caluso (N 45.301045, E 7.894921), identified as ER-A, ER-B, and ER-C, in San Giorgio Canavese (N 45.333054, E 7.798944), ER-D, and in Piverone, ER-E (N 45.445302, E 8.006088), and the producers guaranteed respect of the procedural guidelines (G.U no. 248). ER-A withered the grapes by hanging them, ER-B put the product on wicker trellises, ER-C and ER-D withered the grapes in small boxes (holding about 5 kg), and ER-E used big boxes (holding about 20 kg), both in single layers. Two tons of Erbaluce grapes were withered for all cellars and years. During withering, relative humidity and temperature were monitored in each cellar using a Hobo data logger (Onset, Bourne, MA, USA). In 2011, the withering process was faster due to specific climatic conditions. In particular, the relative humidity percentage (RH%) in the first period of withering was low (60−65%) and the sugar increment achieved was about 10 °Brix. In 2012, the RH% in the first period of dehydration was 70−82%, with a low sugar concentration (+3 °Brix) in some cellars (EC-A, EC-D, EC-D). In this case, a longer processing time was necessary to obtain the minimum sugar content for the production of *Erbaluce di Caluso Passito* wine in accordance with its production discipline. In 2012 one sample of fresh grapes from ER-C was also withered in controlled climatic conditions (25 °C; 55 RH%) in a controlled chamber (ER-F).

Moreover, 78 grape samples used to produce 17 different traditional Italian *passito* wines (Table 1) were sampled in 2011, 2012, and 2013 by inspectors of the Italian Ministry of Agriculture. For each product, the grapes were collected immediately after harvesting and at the end of withering. In some cases an intermediate sample was also collected. We can identify two large groups (samples withered in the *fruttaio* and *en plein air*) and, within these, particular types of withering (e.g., on trellises, in boxes, or hung).

Vinification. For the study focused on *Erbaluce di Caluso*, a sample of about 10 kg of fresh and dried berries was used for must and wine production and analysis, with an interval of 4−5 weeks during the withering processes.

For the other traditional *passito* wines (Table 1), about 10 kg of fresh and dried berries was used for the must.

All samples of fresh and dried grapes were manually crushed and pressed, and the must was clarified with static decantation for 24 h, without adjuvants. In the must sample fermentation was arrested with sodium metabisulfite (800 mg/L).

For wine production each sample of must was inoculated with *Saccharomyces cerevisiae* (Uvaferm BC strain, Lallemand, Verona, Italy) rehydrated in each must and 1 g/L of yeast nutrient (Fermaind, Lallemand). Alcoholic fermentation took place at 25 °C in glass bottles with a bubbler valve in the cap.

Analysis. The D/H and $^{13}C/^{12}C$ isotope ratios of the alcohol obtained by distillation using Cadiot columns were determined following the official methods established by the International Organization of Vine and Wine (OIV), MA-AS-311-05 MA-AS-312-06, using site-specific natural isotope fractionation-nuclear magnetic resonance (SNIF-NMR) (FT-NMR AVANCE III 400, Bruker BioSpin GmbH, Karlsruhe, Germany) and isotope ratio mass spectrometry (IRMS) (SIRA II-VG ISOGAS, FISIONS, Rodano, Milano, Italy) interfaced with an elemental analyzer (Flash 1112, Carlo Erba, Milano, Italy). The D/H values were measured site-specifically in the methyl and methylene positions of ethanol [$(D/H)_I$ and $(D/H)_{II}$].

DOI: 10.1021/acs.jafc.5b02127
J. Agric. Food Chem. 2015, 63, 5851−5857

Table 2. Variation in Isotopic Values and Quality Parameters of Must and Wine with the Withering Period from the Harvest Date

chain	date of sampling	$\delta^{18}O_{VSMOW}$ (‰), must water	°Brix	pH	acidity (g/L) tartaric acid	$\delta^{18}O_{VSMOW}$ (‰), wine water	$\delta^{18}O_{VSMOW}$ (‰), ethanol	$(D/H)_I$ ppm ethanol	$(D/H)_{II}$ ppm ethanol	R ethanol	$\delta^{13}C_{VPDB}$ (‰), ethanol	pH	acidity (g/L) tartaric acid	glucose (g/L)	fructose (g/L)	glycerol (g/L)	ethanol (% vol)
ER-A 1	Sept 26, 2011	5.0	22.2	3.12	8.70	4.6	30.2	103.2	128.9	2.5	−26.6	3.29	8.1	nr[a]	nr	nd[b]	12.65
ER-A 2	Nov 7, 2011	3.2	28.8	3.49	6.70	3.0	28.3	103.3	132.5	2.6	−27.2	3.55	6.90	8	17	nd	14.1
ER-A 3	Dec 23, 2011	1.8	34.6	3.66	6.20	2.1	27.8	104.0	135.2	2.6	−27.7	3.75	6.35	23	78	nd	13.6
ER-B 1	Sept 26, 2011	6.0	30.4	3.38	8.30	5.5	31.1	103.3	134.2	2.6	−26.5	3.5	7.4	4	52	nd	14.05
ER-B 2	Nov 7, 2011	4.6	41.5	3.52	7.90	4.9	25.8	103.6	129.6	2.5	−27.5	3.58	6.80	124	159	nd	7.1
ER-B 3	Dec 23, 2011	−0.1	48.2	3.73	6.00	−0.2	24.3	103.1	124.5	2.4	−27.5	3.8	7.05	97	248	nd	7.3
ER-C 1	Sept 26, 2011	5.4	35.6	3.58	7.90	5.7	30.8	102.9	134.3	2.6	−27.0	3.63	6.8	33	81	nd	13.45
ER-C 2	Nov 7, 2011	0.7	45.8	3.62	5.70	1.0	25.2	101.9	129.6	2.5	−27.6	3.72	6.05	167	195	nd	6.5
ER-C 3	Dec 23, 2011	−0.3	47.4	3.87	6.70	0.1	22.9	102.4	131.9	2.6	−27.5	3.85	7.20	121	238	nd	5.9
ER-E 1	Sept 26, 2011	4.6	27.7	3.08	8.15	4.5	29.5	102.1	131.0	2.6	−28.0	3.22	7.75	2	15	nd	14.8
ER-E 2	Nov 7, 2011	3.2	38.8	3.33	6.70	3.3	28.5	102.5	131.7	2.6	−28.5	3.42	7.10	81	125	nd	10.2
ER-E 3	Dec 23, 2011	2.0	44.4	3.54	5.70	2.5	25.8	102.8	130.0	2.5	−28.4	3.59	6.80	93	201	nd	8.1
ER-A 1	Sept 25, 2012	4.3	25.2	3.17	8.40	4.0	29.5	101.7	131.1	2.6	−27.2	3.31	7.73	nr	nr	12.9	14.7
ER-A 2	Oct 17, 2012	2.7	27.1	3.25	7.09	2.5	27.1	101.8	130.8	2.6	−26.8	3.26	7.50	1	1	13.1	15.8
ER-A 3	Nov 21, 2012	1.7	30.2	3.26	7.80	1.7	27.1	101.8	129.1	2.5	−26.7	3.40	8.55	21	54	15.5	14.2
ER-A 4	Dec 18, 2012	0.4	33.8	3.29	8.48	1.0	24.8	100.4	125.9	2.5	−26.9	3.47	9.00	63	103	17.5	12.2
ER-A 5	Feb 15, 2013	1.1	40.5	3.58	6.45	1.6	25.6	102.8	129.4	2.5	−26.6	3.80	9.15	101	161	17.7	11.2
ER-B 1	Sept 25, 2012	5.3	27.3	3.34	7.46	5.3	30.6	102.0	133.5	2.6	−27.1	3.62	7.13	nr	nr	12.1	16.5
ER-B 2	Oct 17, 2012	2.1	32.2	3.49	6.75	1.8	28.4	100.2	130.2	2.6	−27.4	3.66	7.91	18	59	14.8	15.2
ER-B 3	Nov 21, 2012	−0.2	34.3	3.45	7.50	0.0	26.4	101.9	128.9	2.5	−26.5	3.65	8.85	55	92	17.2	13.4
ER-B 4	Dec 18, 2012	−1.3	40.0	3.65	7.01	−0.6	21.2	101.4	126.5	2.5	−26.5	3.90	8.78	118	156	19.3	10.4
ER-C 1	Sept 25, 2012	5.0	30.7	3.31	6.68	4.9	30.8	101.7	131.9	2.6	−26.1	3.50	6.90	7	36	13.6	15.9
ER-C 2	Oct 17, 2012	3.1	36.0	3.57	5.44	2.8	28.2	101.5	131.0	2.6	−26.7	3.67	7.05	54	108	16.4	13.3
ER-C 3	Nov 21, 2012	0.3	39.3	3.27	7.91	0.5	25.5	101.1	129.7	2.6	−27.3	3.44	9.23	113	149	18.3	10.9
ER-C 4	Dec 18, 2012	−0.7	43.4	3.41	6.45	−0.1	21.1	100.8	124.0	2.5	−27.2	3.59	8.18	169	191	18.6	7.2
ER-D 1	Sept 25, 2012	5.3	27.7	3.35	8.03	4.7	30.7	102.0	133.1	2.6	−26.8	3.59	7.65	nr	4	13.3	16.0
ER-D 2	Oct 17, 2012	4.1	30.0	3.34	7.24	3.7	29.9	102.0	131.5	2.6	−26.6	3.42	8.10	1	8	12.8	16.3
ER-D 3	Nov 21, 2012	2.5	35.5	3.28	8.63	3.0	28.1	102.2	130.1	2.5	−27.0	3.49	10.50	67	104	17.9	12.5
ER-D 4	Dec 18, 2012	2.4	36.5	3.46	8.03	2.8	26.4	102.8	129.1	2.5	−27.0	3.68	8.63	68	120	18.4	12.5
ER-D 5	Feb 15, 2013	3.3	46.6	3.51	8.63	3.0	26.5	103.0	133.1	2.6	−27.3	3.75	11.18	250	220	17.4	5.8
ER-E 1	Sept 25, 2012	4.6	25.1	3.26	7.13	4.0	29.0	101.3	130.0	2.6	−27.7	3.38	6.90	nr	nr	11.7	14.7
ER-E 2	Oct 17, 2012	3.6	28.1	3.33	6.30	3.2	28.0	101.4	131.2	2.6	−27.3	3.30	6.75	8	33	14.3	15.9
ER-E 3	Nov 21, 2012	1.8	31.8	3.44	6.00	1.4	26.4	101.1	128.3	2.5	−27.6	3.58	7.43	34	76	14.6	13.4
ER-E 4	Dec 18, 2012	0.3	34.9	3.43	5.93	0.6	24.2	101.5	127.8	2.5	−27.7	3.61	7.09	63	115	16.1	12.3
ER-E 5	Feb 15, 2013	0.0	39.9	3.6	5.81	0.3	23.5	101.7	129.0	2.5	−27.9	3.83	8.48	98	160	17.9	11.5
ER-C	Sept 25, 2012	5.0	30.7	3.31	6.68	4.9	30.8	101.70	131.90	2.60	−26.10	3.50	6.90	7	36	13.6	15.9
ER-F	Oct 17, 2012	9.7	48.8	3.57	6.00	9.6	33.8	102.20	122.70	2.40	−26.10	3.92	7.01	283	170	14.1	6.7

[a]nr, not detectable. [b]nd, not determined.

DOI: 10.1021/acs.jafc.5b02127
J. Agric. Food Chem. 2015, 63, 5851−5857

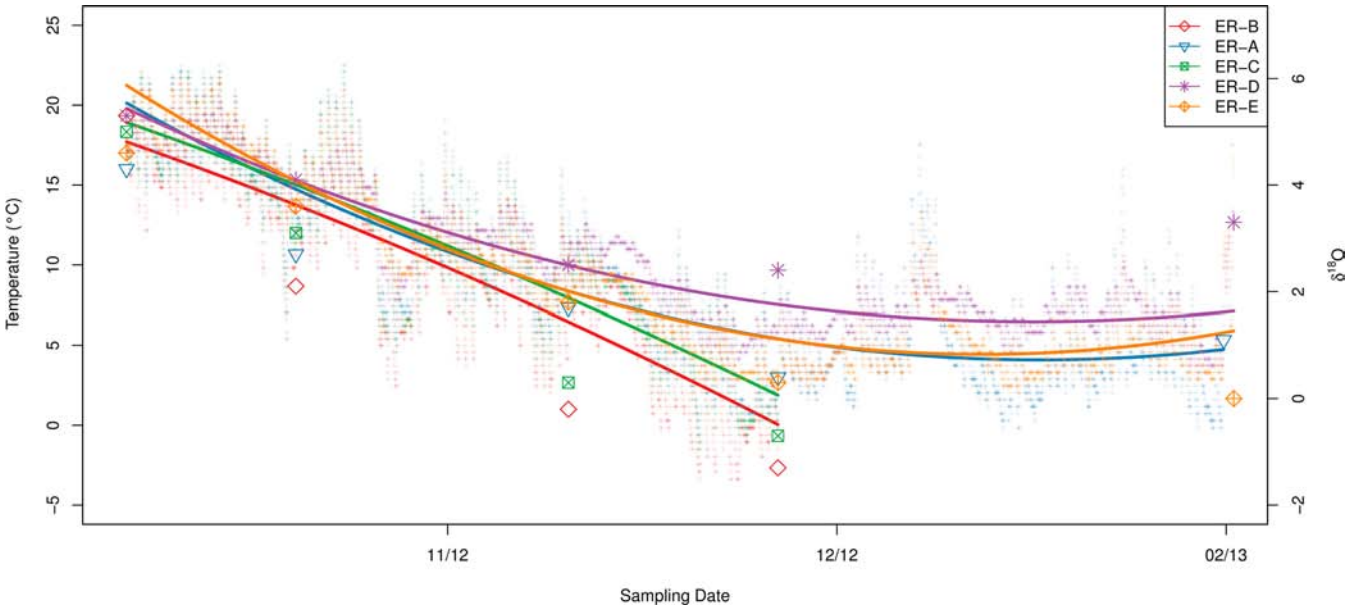

Figure 1. Variation in $\delta^{18}O$ with temperature in the *fruttaio*.

$^{18}O/^{16}O$ ratio analysis of wine and must water was performed using a SIRA II (VG Fisons, Middlewich, UK) connected to a water/CO_2 equilibration system Isoprep 1 (VG Fisons). The procedure is described in the OIV-MA-AS2-12 method (2009).

A DeltaPlus-XP isotope ratio mass spectrometer (IRMS) coupled to a thermal conversion/elemental analyzer (TC/EA) (both Thermo Scientific, Bremen, Germany) was used for $^{18}O/^{16}O$ analysis of ethanol samples following the procedure reported by Perini and Camin.[16]

The $^{13}C/^{12}C$ and $^{18}O/^{16}O$ values are denoted in delta in relation to the international V-PDB (Vienna-Pee Dee Belemnite) and V-SMOW (Vienna-Standard Mean Ocean Water) standards according to the general equation

$$\delta i\ \mathrm{E} = \frac{(i\ \mathrm{RSA} - i\ \mathrm{RREF})}{i\ \mathrm{RREF}}$$

where i is the mass number of the heavier isotope of element E (for example, ^{13}C); RSA is the respective isotope number ratio of a sample (such as for C, number of ^{13}C atoms/number of ^{12}C atoms or as $^{13}C/^{12}C$ approximation);[22,23] and RREF is the respective isotope number ratio of internationally recognized reference materials (see above).

The delta values are multiplied by 1000 and are expressed in units "per mil" (‰).

The working reference materials are specified in the OIV methods. A sample of wine was used to validate the whole analysis (distillation + measurement). With one sample of must we also allowed for fermentation. The final value was reported in a control chart, and if it was within the tolerance range, the whole session was validated.

The analytical uncertainties (estimated by combining within-laboratory reproducibility standard deviation with estimates of method and laboratory bias using proficiency test data)[24] of the measurements were 0.3‰, 0.6‰, 0.8 ppm, and 1.2 ppm for $\delta^{13}C$, $\delta^{18}O$, $(D/H)_I$, and $(D/H)_{II}$ in ethanol, respectively. For the $\delta^{18}O$ of water, the value was 0.3‰.

The alcohol content and residual sugar content were analyzed following the OIV-MA-AS312-01A and OIV MA-AS311-02 official methods.

Total soluble solid concentration (°Brix, as SSC) was measured with an Atago 0−32 °Brix temperature compensating refractometer (Atago Corp., Tokyo, Japan), and pH was determined with potentiometry, using a Crison electrode (Carpi, Italy). Titratable acidity (TA), expressed as grams of tartaric acid per liter, and ethanol expressed in % (v/v) were estimated using the OIV method. Glucose, fructose, and glycerol were quantified (as g/L) using a high-performance liquid chromatography system.[4]

Statistical Analysis. All statistical analysis was performed in R [R]. Linear modeling was applied to identify significant relationships between the $\delta^{18}O$ and temperature/humidity profiles recorded during withering. To account for differences in the initial conditions in the five different fruit-drying rooms, the initial conditions were subtracted from the $\delta^{18}O$, temperature, and humidity profiles before modeling. Modeling was then performed on the variation in temperature, humidity, and $\delta^{18}O$ shift. Stepwise model selection was performed using the MASS R package, freely available at the CRAN Web site (http://cran.r-project.org/),[25] and the best model was identified with the Akaike information criterion (AIC).

RESULTS AND DISCUSSION

Effect of Withering in Fruit Rooms (*Erbaluce di Caluso Passito*). In Table 2 the $\delta^{18}O$ values of must and wine water and the $(D/H)_I$, $(D/H)_{II}$, R, $\delta^{13}C$, and $\delta^{18}O$ values of wine ethanol are shown, together with some quality data for must and wine. Samples are grouped by cellar and year.

As expected, the sugar content in the grape increased with the degree of withering. The acidity of Erbaluce in the grape was normally very high. During the withering process the decrease in titratable acidity could be attributed to the concentration of cations, in particular K^+, caused by higher weight loss with salification of part of the tartaric acid, and to malic and citric acid depletion.[7] The must for *passito* production has a high sugar content and complete fermentation with *S. cerevisiae* is not possible. The alcohol content and yield generally depend on the initial sugar content in must, which influences yeast metabolism such as the production of glycerol.[26]

Of the isotopic parameters, $\delta^{18}O$ was most influenced by the degree of withering. In each of the five cellars, $\delta^{18}O$ decreased significantly from the starting value (from grapes immediately after harvesting) to the final value (grapes with a higher sugar content), with differences from −2 to −6‰ in must and wine water and from −2 to −10‰ in wine ethanol. As expected, the $\delta^{18}O$ of must was not different from that of wine.

The O stable isotope composition of grape juice is initially controlled by that of the source water and, as the grape berries

DOI: 10.1021/acs.jafc.5b02127
J. Agric. Food Chem. 2015, 63, 5851−5857

mature and approach harvest, by environmental conditions such as temperature and relative humidity, which control the degree of evapotranspiration, tending to enrich the grape water in ^{18}O.[20,27,28] Moreover, the $\delta^{18}O$ of grape water is affected by precipitation during the final development of the grape, with a relatively rapid response, due to stable isotope exchange with water vapor.[17]

Hermann et al. assumed that isotope fractionation takes place at leaf level and that isotopically modified water is transported into the grapes, where its isotopic signature should be preserved.[28] Other authors state that this fractionation takes place particularly in the leaves and also in the berry.[17,29] In a more recent paper,[30] isotope fractionation was also observed in a grape juice exposed to the atmosphere for several days, but protected from rain and snow.

In our study it is evident that grape water is also subject to isotopic fractionation after harvesting in grapes separated from the vines, when dehydration occurs. The decrease in $\delta^{18}O$ was coherent with the decrease in temperature recorded automatically every hour in the different fruit-drying rooms (Figure 1), but not with the variation in relative humidity (Supporting Information Figure S1).

To statistically evaluate the significance of relationships between $\delta^{18}O$ and temperature and humidity, a statistical modeling approach was applied. The rationale behind this is that the actual value for $\delta^{18}O$ shift is determined by the preceding average environmental conditions. By taking into account relative data (see Materials and Methods) the five different fruit-drying rooms can be considered as independent replicates of the same phenomenon.

The modeling was performed by considering the average temperature and humidity values in the period before each $\delta^{18}O$ analysis. To better characterize the process, three scenarios were examined, calculating the average temperature and humidity 1, 2, and 3 weeks before each $\delta^{18}O$ analysis. Each scenario was then modeled separately. In all cases a general linear model of the form $\delta^{18}O = A \times \text{temperature} + B \times \text{humidity} + C \times (\text{temperature} \times \text{humidity}) + D + \varepsilon$ was considered. This form is able to capture the separate effect of changes in temperature and humidity, the implicit contribution of time, and also the possible presence of an interaction effect between the two predictors. This separate modeling approach was preferred to a more complex linear model taking into account all of the possible factors and their interactions for two reasons: (a) the very small number of experimental points (only five time-resolved measurements of the isotopic ratios); (b) high correlations between the averages of temperature and humidity at the 1, 2, and 3 week intervals. In all three cases, the best model was found by stepwise model selection. For all three scenarios, stepwise selection indicated that the interaction term is not necessary to model the $\delta^{18}O$ shift during withering. In all cases, the optimal model had the form $\delta^{18}O = A \times \text{temperature} + B \times \text{humidity} + C + \varepsilon$, the level of significance for the two predictors in the three models being summarized in Table 3.

The results confirmed that temperature is the most significant parameter able to predict $\delta^{18}O$ variations in *passito* wine. By comparison of the adjusted R^2 for the three models (0.71 for week 1, 0.62 for week 2, and 0.57 for week 3, see Table 3), it is also possible to identify the model that shows the best fit with the experimental data. Considering that the 1 week model shows the highest adjusted R^2, it is possible to conclude that the average temperature and humidity in that period were better able to predict the isotopic shifts observed.

Table 3. Levels of Significance for the Modeling of $\delta^{18}O$ on the Basis of Temperature and Humidity

	estimate	std error	P value	signif level[a]
Week 1 (Adjusted R^2 = 0.71)				
C	−1.4	0.4	0.005	**
A (temperature)	0.27	0.04	8×10^{-6}	***
B (humidity)	−0.05	0.01	0.007	**
Week 2 (Adjusted R^2 = 0.62)				
C	−1.7	0.4	0.001	**
A (temperature)	0.3	0.06	1×10^{-4}	***
B (humidity)	−0.05	0.02	0.06	*
Week 3 (Adjusted R^2 = 0.57)				
C	−1.7	0.4	0.001	**
A (temperature)	0.27	0.05	2×10^{-4}	***
B (humidity)	−0.04	0.02	0.1	ns

[a]***, <0.0001; **, <0.001; *, < 0.1; ns, not significant.

It is interesting to note that by withering one of the grape samples (ER-F, 2012) in a temperature-controlled room with specific and constant temperature (25 °C) and humidity (55.5%), the grapes were dehydrated to about 49 °Brix in a short time (22 days) and the $\delta^{18}O$ value of wine increased from 4.9 to 9.6‰ (Table 2).

One reason for this is that in this case kinetic isotope fractionation takes place, as described by Ingraham et al. for wines obtained from grapes subjected to extreme evapotranspiration processes due to high daily temperatures and low humidity.[17] To simplify, kinetic or equilibrium isotope fractionation can occur in nature. Kinetic fractionation is a process that separates stable isotopes from one another by their mass during unidirectional processes. One naturally occurring example of kinetic fractionation is the evaporation of seawater to form clouds or the process of evapotranspiration observed in plants. Isotopically lighter water molecules (i.e., those with ^{16}O) evaporate more easily than the isotopically heavier ones, with ^{18}O. During this process the vapor becomes enriched with ^{16}O, whereas water becomes enriched in ^{18}O. Equilibrium isotope fractionation is the partial separation of isotopes between two or more compounds or phases in the thermodynamic equilibrium. Most equilibrium fractionation results from the reduction in vibrational energy (especially zero-point energy) when a heavier isotope is substituted for a lighter one.[31] An example of equilibrium isotope fractionation is the concentration of heavy isotopes of oxygen in liquid water compared with water vapor at low temperature (see Raleigh fractionation).[32]

It is possible to surmise that in the case of withering in the *fruttaio*, in the particular environmental conditions in the drying room, with low temperature and high humidity causing slow withering (up to 4 months and over), there is competition between at least two different processes: diffusive transport of water from the grape, but also isotopic exchange between the grape water and air humidity in the boundary layer at the interface between the skin and atmosphere, until an isotopic equilibrium is reached. The final result in this type of samples is a decrease in the $\delta^{18}O$ of grape water.

The $\delta^{18}O$ of ethanol obtained after distillation of *passito* samples showed good correlation with the $\delta^{18}O$ of *passito* wine water (R^2 = 0.78), as already observed.[16]

In contrast with $\delta^{18}O$, the $(DH)_I$ values of wine ethanol did not change during the experiment in either of the years considered ($P < 0.05$), also in the temperature-controlled room,

DOI: 10.1021/acs.jafc.5b02127
J. Agric. Food Chem. 2015, 63, 5851−5857

whereas the $(DH)_{II}$ and $\delta^{13}C$ values did change, but without any clear trend (Table 2). At all events, in most cases, both $(DH)_{II}$ and $\delta^{13}C$ tended to decrease with withering time (up to 1‰ for $\delta^{13}C$). This may be due to the fact that *passito* wines have a high sugar content, which can obstruct fermentation, in a similar way to sweet wines subject to the stopping of fermentation, with a subsequent decrease in $(DH)_{II}$ and $\delta^{13}C$.[33]

SURVEY OF ITALIAN *PASSITO* WINES

In this section we consider the $\delta^{18}O$ of must water for 78 samples of 17 different traditional Italian *passito* wines (Table 1), including *Erbaluce di Caluso*. For each sample we measured only the $\delta^{18}O$ of must water (Supporting Information Table S1), as this is the official parameter most influenced by withering, as described above.

The samples from northern Italian regions Piedmont, Lombardy, Emilia Romagna, Veneto, and Friuli Venezia Giulia (Figure 2a), subjected to postharvest drying of grapes in

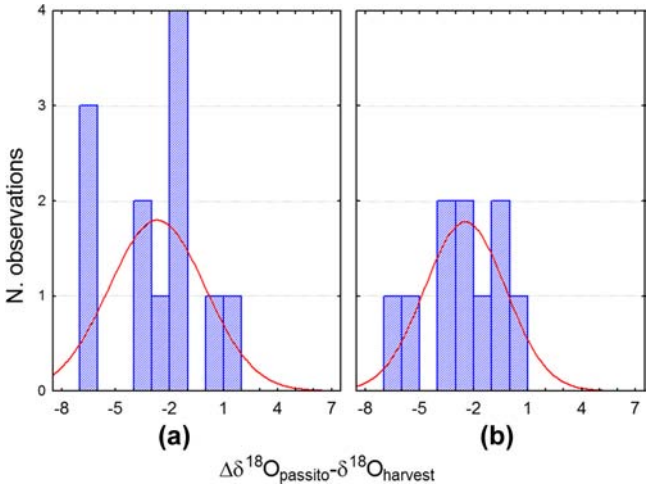

Figure 2. Difference between $\delta^{18}O$ of must water at the end of withering ($\delta^{18}O_{passito}$) and at harvest ($\delta^{18}O_{harvest}$). Withering was performed in northern (a) and central (b) Italy using *fruttaio*.

dedicated fruit rooms (*fruttaio*), showed a change in the $\delta^{18}O$ of water by −6.5‰, as observed above. In two cases (Figure 2a), Ramandolo 2013 (withering on trellises with forced ventilation) and Picolit 2011 (in boxes with controlled temperature) the $\delta^{18}O$ value increased by around 1‰, probably because withering took place in a shorter time (<1 month), which caused kinetic isotopic fractionation.

For the *passito* samples of regions in central Italy (Figure 2b), Tuscany, Marche, and Umbria, which also adopted withering in the *fruttaio*, $\delta^{18}O$ decreased up to −6‰.

For *passito* produced *en plein air* in the northern regions (Friuli Venezia Giulia and Emilia Romagna) (Figure 3a), climatic conditions caused equilibrium isotope fractionation, as in the *fruttaio*. Indeed a decrease in $\delta^{18}O$ was observed. In the southern regions of Apulia, Sicily, and Sardinia, in most cases $\delta^{18}O$ increased with withering (Figure 3b). Indeed, normally in these regions the grapes overripen on the plants in autumn, and due to the relatively higher temperature in these areas, kinetic evapotranspiration takes place. In two cases (*Passito di Manduria* and *Moscato di Trani*, both 2012) $\delta^{18}O$ decreased up to −4.6‰, probably because of precipitation, which could exchange with grape water.

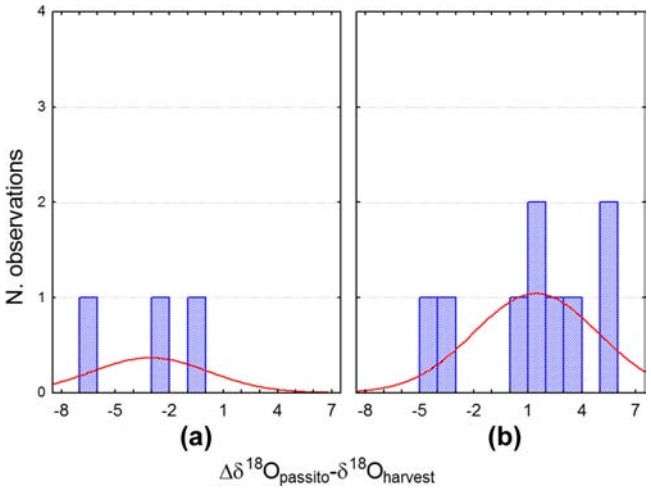

Figure 3. Difference between $\delta^{18}O$ of must water at the end of withering ($\delta^{18}O_{passito}$) and at harvest ($\delta^{18}O_{harvest}$). Withering was performed in northern (a) and southern Italy (b) *en plein air*.

The significant variation in the $\delta^{18}O$ of must and wine water and wine ethanol observed during withering have never previously been reported in the literature. This variation can lead to problems when interpreting data for detecting authenticity, if referring to an official wine databank based only on fresh grape wines. Indeed, decreases or increases of up to 6‰ can make the $\delta^{18}O$ values fall outside the limits defined by the European wine databank for an authentic wine for the declared origin,[34] with consequent false declaration of watering down or mislabeling. Furthermore, the ethanol $\delta^{18}O$ values of final samples were sometimes (ER-B, ER-C, and ER-E) outside the range proposed for authentic wine samples (from +24 to +36‰).[16] Particular attention must be therefore paid when the $\delta^{18}O$ data of *passito* wines is evaluated for fraud detection.

ASSOCIATED CONTENT

Supporting Information

Figure S1 and Table S1. The Supporting Information is available free of charge on the ACS Publications website at DOI: 10.1021/acs.jafc.5b02127.

AUTHOR INFORMATION

Corresponding Author

*(M.P.) Phone: +39-0461-615261. Fax: +39-0461-615288. E-mail: matteo.perini@fmach.it.

Notes

The authors declare no competing financial interest.

REFERENCES

(1) Disposizioni di attuazione della normativa comunitaria concernente l'organizzazione comune di mercato (OCM) del vino. Law of 20 February 2006, no. 82; G.U. n. 60 13/03/2006, Supp. N. 59; http://www.camera.it/parlam/leggi/06082l.htm.

(2) Domizio, P.; Lencioni, L. Vin Santo. *Adv. Food Nutr. Res.* **2011**, *63*, 41−100.

(3) Paronetto, L.; Dallaglio, F. Amarone: a modern wine coming from an ancient production technology. *Adv. Food Nutr. Res.* **2011**, *63*, 285−306.

(4) Giordano, M.; Rolle, L.; Zeppa, G.; Gerbi, V. Chemical and volatile composition of three Italian sweet white passito wines. *J. Int. Sci. Vigne Vin* **2009**, *43* (3), 159−170.

DOI: 10.1021/acs.jafc.5b02127
J. Agric. Food Chem. 2015, 63, 5851−5857

(5) Ribèreau-Gayon, P.; Maurjean, A.; Dubourdieu, D. The chemistry of wine. Stabilization and treatments. In *Handbook of Enology*, 2nd ed.; Wiley: Chichester, UK, 2006; Vol. 2, p 231.
(6) Chkaiban, L.; Botondi, R.; Bellincontro, A.; De Santis, D.; Kefalas, P.; Mencarelli, F. Influence of postharvest water stress on LOX, ADH and aroma biochemistry of Gewürztraminer grape dehydrated under controlled and uncontrolled thermohygrometric conditions. *Aust. J. Grape Wine Res.* **2007**, *13*, 142−149.
(7) Rolle, L.; Giordano, M.; Giacosa, S.; Vincenzi, S.; Río Segade, S.; Torchio, F.; Perrone, B.; Gerbi, V. CIEL*a*b* parameters of white dehydrated grapes as quality markers according to chemical composition, volatile profile and mechanical properties. *Anal. Chim. Acta* **2012**, *732*, 105−113.
(8) Vincenzi, S.; Tolin, S.; Cocolin, L.; Rantsiou, K.; Curioni, A.; Rolle, L. Proteins and enzymatic activities in Erbaluce grape berries with different response to the withering process. *Anal. Chim. Acta* **2012**, *732*, 130−136.
(9) Giacosa, S.; Torchio, F.; Río Segade, S.; Gaiotti, F.; Tomasi, D.; Lovat, L.; Vincenzi, S.; Rolle, L. Physico-mechanical evaluation of the aptitude of berries of red winegrape varieties to resist the compression in carbonic maceration vinification. *Int. J. Food Sci. Technol.* **2013**, *48*, 817−825.
(10) Dimensions, features and further information on counterfeiting − final report 2012; Ministry of Economic Development, Rome, Italy, July 2012; http://www.uibm.gov.it/attachments/Counterfeiting_Scope,%20characteristics%20and%20analyses.pdf.
(11) Martin, G. J. The chemistry of chaptalization. *Endeavour* **1990**, *14*, 137−143.
(12) Zhang, B. L.; Fourel, F.; Naulet, N.; Martin, G. J. Influence de l'expérimentation et du traitement de l'échantillon sur la précision et la justesse des mesures des rapports isotopiques (D/H) et (18O/16O). *OIV* **1992**, *918*, 1954/220792.
(13) Dordevic, N.; Camin, F.; Marianella, R. M.; Postma, G. J.; Buydens, L. M. C.; Wehrens, R. Detecting the addition of sugar and water to wine. *Aust. J. Grape Wine Res.* **2013**, *19*, 324−330.
(14) EEC Regulation No. 2347/91 on the collection of samples of wine products for the purposes of cooperation between Member States and for analysis by nuclear magnetic resonance, including analysis for the purposes of the Community databank.
(15) EEC Regulation No. 2348/91 establishing a databank for the results of analyses of wine products by nuclear magnetic resonance of deuterium.
(16) Perini, M.; Camin, F. δ^{18}O of ethanol in wine and spirits for authentication purposes. *J. Food Sci.* **2013**, *78* (6), 839−844.
(17) Ingraham, N.; Caldwell, E. Influence of weather on the stable isotopic ratios of wines: tools for weather/climate reconstruction. *J. Geophys. Res.* **1999**, *104*, 2185−2194.
(18) Rossmann, A.; Reniero, F.; Moussa, I.; Schmidt, H. L.; Versini, G.; Merle, M. H. Stable oxygen isotope content of water of EU databank wines from Italy, France and Germany. *Z. Lebensm. Unters. Forsch.* **1999**, *208*, 400−407.
(19) Martin, G. J.; Martin, M. L. Climatic significance of isotope ratios. *Phytochem. Rev.* **2003**, *2* (1−2), 179−190.
(20) Camin, F.; Dordevic, N.; Wehrens, R.; Neteler, M.; Delucchi, L.; Postma, G.; Buydens, L. Climatic and geographical dependence of the H, C and O stable isotope ratios of Italian wine. *Anal. Chim. Acta* **2015**, *853*, 384−390.
(21) Riconoscimento della denominazione di origine controllata e garantita dei vini "Erbaluce di Caluso" o "Caluso" e approvazione del relativo disciplinare di produzione. G.U no. 248 of 22.10 , 2010.
(22) Coplen, T. B. Guidelines and recommended terms for expression of stable-isotope-ratio and gas-ratio measurement results. *Rapid Commun. Mass Spectrom.* **2011**, *25*, 2538−2560.
(23) Brand, W. A.; Coplen, T. B. Stable isotope deltas: tiny, yet robust signatures in nature. *Isot. Environ. Health Stud.* **2012**, *48* (3), 393−409.
(24) Magnusson, B.; Näykk, T.; Hovind, H.; Krysell, M. *Handbook for Calculation of Measurement Uncertainty in Environmental Laboratories*, NT TR 537 - edition 3.1; Nordic Innovation: Stenbergsgata 25 NO-0170, Oslo, Norway, 2012; 46 pp .
(25) Venables, W. N.; Ripley, B. D. *Modern Applied Statistics with S*, 4th ed.; Springer: New York, 2002; ISBN 0-387-95457-0.
(26) Urso, R.; Rantsiou, K.; Dolci, P.; Rolle, L.; Comi, G.; Cocolin, L. Yeast biodiversity and dynamics during sweet wine production as determined by molecular methods. *FEMS Yeast Res.* **2008**, *8*, 1053−1062.
(27) Bricout, J. Recherches sur le fractionnement des isotopes stables de l'hydrogene et l'oxygene dans quelques vegetaux. *Rev. Cytol Biol. Veget-Bot* **1978**, *1*, 133−209.
(28) Hermann, A.; Voerkelius, S. Meteorological impact on oxygen isotope ratios of German wines. *Am. J. Enol. Vitic.* **2008**, *59* (2), 194−199.
(29) Gómez-Alonso, S.; García-Romero, E. Effect of irrigation and variety on oxygen (δ^{18}O) and carbon (δ^{13}C) stable isotope composition of grapes cultivated in a warm climate. *Aust. J. Grape Wine Res.* **2010**, *16* (2), 283−289.
(30) Hermann, A. Icewine authentication by stable oxygen isotope (δ^{18}O) measurements. *Am. J. Enol. Vitic.* **2014**, DOI: 6549910.5344/ajev.2014.13143.
(31) Faure, G.; Mensing, T. M. Principles of stable isotope distribution. In *Isotopes: Principles and Applications*, 3rd ed.; Wiley: New York, 2005; 928 pp.
(32) Emerson, S.; Hedges, J. Stable and radioactive isotopes. In *Chemical Oceanography and the Marine Carbon Cycle*; Cambridge University: Cambridge, UK, 2008; Vol. 5, pp 134−170.
(33) Perini, M.; Guzzon, R.; Simoni, M.; Malacarne, M.; Larcher, R.; Camin, F. The effect of stopping alcoholic fermentation on the variability of H, C and O stable isotope ratios of ethanol. *Food Control* **2014**, *40*, 368−373.
(34) Commission Regulation (EC) No. 555/2008 of 27 June 2008 laying down detailed rules for implementing Council Regulation (EC) No. 479/2008 on the common organisation of the market in wine as regards support programmes, trade with third countries, production potential and on controls in the wine sector. (30.06.2008). *Off. J. Eur. Union* **2008**, *L 170*.

DOI: 10.1021/acs.jafc.5b02127
J. Agric. Food Chem. 2015, 63, 5851−5857

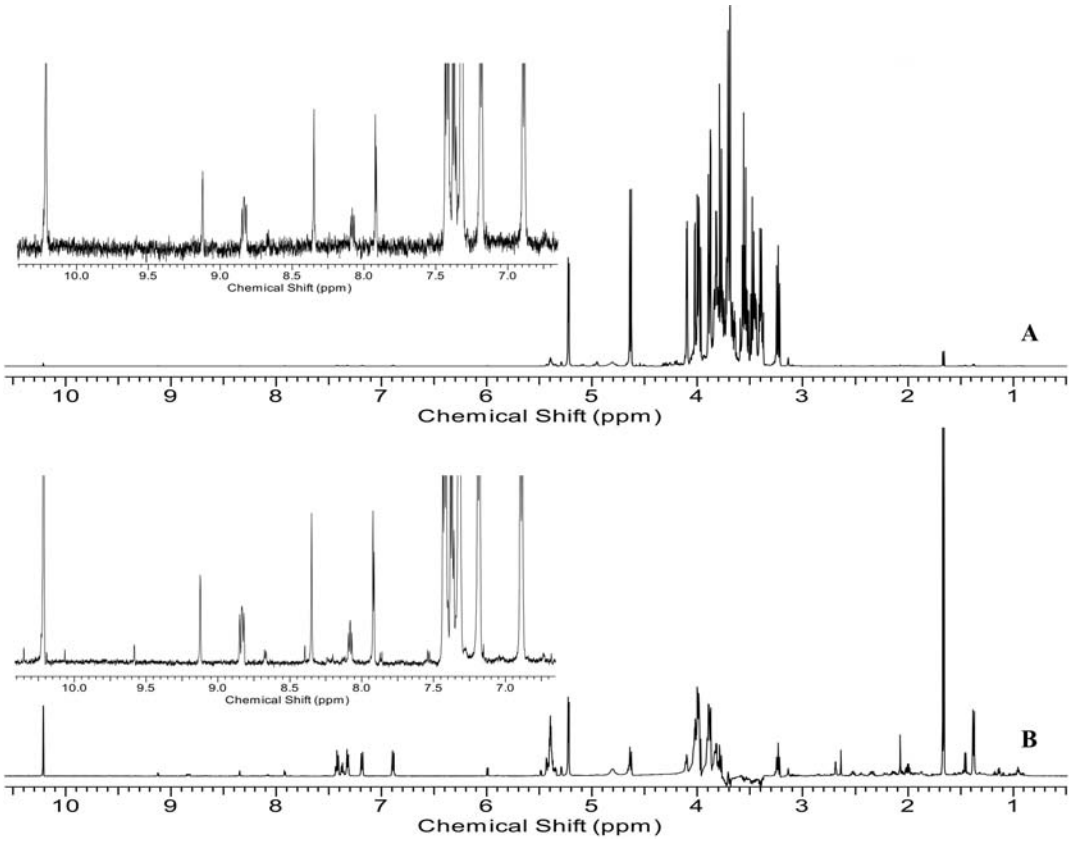

Figure 1. ^{1}H NMR spectra of coffee honey dissolved in D_2O and expansion of the aromatic region: (A) spectrum acquired with a one pulse sequence with presaturation of the water signal; (B) spectrum acquired with the modified DPFGSE sequence (see text).

99.9% *d*, Sigma-Aldrich, Milan, Italy), isobutyraldehyde (≥99%, Sigma-Aldrich, Milan, Italy), *N*,*N*-dimethylformamide (DMF, ≥99.99% (GC), Fluka-Sigma-Aldrich, Milan, Italy), calcium formate (standard for quantitative NMR, TraceCERT, Fluka-Sigma-Aldrich, Milan, Italy) were acquired as noted. Five millimeter precision glass NMR tubes 535-pp-7 and coaxial insert wgs-5bl were obtained from Wilmad (purchased through Sigma-Aldrich, Milan, Italy).

Honey Samples. Three different *Coffea* spp. honey samples were analyzed, two from Colombia and one from Honduras. The honey from Honduras (Capucas Miel) was purchased in a local market; the sample named Colombia 1 was produced by Apicalarama (Calarama Group) in the municipality of Chaparral, Department of Tolima, and the sample named Colombia 2 was produced on the farm Edén in the municipality of Apia, Department of Risaralda, both under the supervision of Jhon Ever Cardona (La Promotora de Bienes y Servicios Apicolas Proapis s.a.s.). These two honeys were obtained using an African species (*Apis mellifera scutellata*) known to be very aggressive; the bees that were used were duly selected and bred by J. E. Cardona for their limited aggressiveness.

Sample Preparation. About 180 mg of honey was dissolved in 550 μL of D_2O, precisely weighed. The volume obtained was measured, and 450 μL of the solution was transferred to 5 mm precision glass NMR tubes (Wilmad 535-pp).

NMR Spectroscopy. NMR experiments were recorded at 298 K using a Bruker Avance DMX600 spectrometer (Bruker Biospin GmbH Rheinstetten, Karlsruhe, Germany) operating at 599.90 MHz for ^{1}H and equipped with a 5 mm TXI xyz-triple gradient probe. The spectra were acquired using a double pulsed field gradient spin echo (DPFGSE) sequence,[11] modified by the addition of an inversion hard pulse after the first gradient in the G-S-G cluster, to obtain a G-π-S-G (G is a pulsed field gradient and S is a soft π pulse).[12] As a soft pulse, we used an inversion Reburp sequence of 1.2 kHz sweep width and 3867 ms duration centered at 4.00 ppm. All gradient pulses were followed by a 100 μs recovery delay. The relaxation delay was 65 s, and 72−256 scans were collected, resulting in acquisition times between 1 h and 30 min and 4 h and 55 min.

ACD software (ACD Laboratories 12.0, Toronto, ON, Canada) was used to process the spectra. An exponential window function with line broadenings of 0.3−0.5 Hz was applied before Fourier transformation. Phase and baseline corrections were performed manually, and the signal of the α H1 proton of glucose at 5.22 ppm was used as chemical shift reference.

Quantitative Analysis. To quantify absolute concentrations, a coaxial tube filled with an isobutyraldehyde solution in DMSO-d_6 was inserted in the NMR tube. This standard was chosen because its aldehydic proton resonates in our region of interest, not overlapping with any other signal. The solution was prepared by accurately weighing isobutyraldehyde and the DMSO-d_6 solvent, for a final concentration of the standard of 0.023 M. The accuracy of our quantitative analysis was demonstrated by the quantification of the formate signal in the spectrum of one of the aqueous honey samples using the standard addition method (weighed quantities of a standard solution of calcium formate in D_2O were added directly into the NMR tube and its concentration in the original sample extrapolated).

To calculate the concentration of the analytes, a scale factor of 0.108 was considered, corresponding to the ratio between the volume of the coaxial insert (V_c) and the volume occupied by the sample in the outer part of the NMR tube (V_s) calculated as reported by Rastrelli et al.[11] The absolute concentration of analytes (C_a) was determined by comparing the integral value of the area of the corresponding proton signal (I_a) and that of the aldehydic proton of isobutyraldehyde at 10.21 ppm (I_s), using the relationship C_a (mol/L) = $(I_a/I_s)(V_c/V_s)C_s$, where C_s is the concentration of the external standard.

The following formula gives the concentration of the analytes (in mg/kg): C_a (mg/kg) = C_a (mol/L) × MW_a × V_a (mL)/m_{honey}(kg), where MW_a is the molecular weight of the considered analyte, V_a is the volume of the honey solution in D_2O, and m_{honey} is the weight of the honey sample.

DOI: 10.1021/jf506359u
J. Agric. Food Chem. 2015, 63, 5858−5863

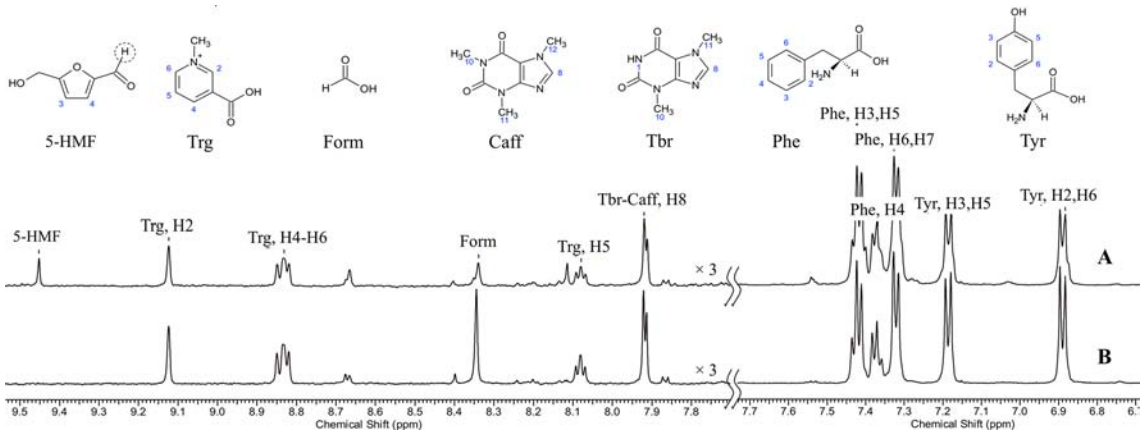

Figure 2. Aromatic region of Colombia 1 (A) and Colombia 2 (B) honey samples dissolved in D_2O. The chemical structures of the identified compounds and the corresponding assignments of the peaks are reported. 5-HMF, 5-hydroxymethylfurfural; Trg, trigonelline; Form, formic acid; Tbr, theobromine; Caff, caffeine; Phe, phenylalanine; Tyr, tyrosine.

The longitudinal relaxation time T_1 of all signals of interest, in the matrices and in the standard solutions, was determined using the inversion−recovery sequence. To produce quantitative data, the relaxation delay was at least 5 times the longest measured T_1, corresponding to the aldehydic signal of isobutyraldehyde in DMSO-d_6, determining a relaxation delay of 65 s.

Every sample was analyzed in duplicate, the spectra were processed four times, and data are reported as the mean ± standard deviation expressed as milligrams per kilogram of honey.

Pollen Analysis. Qualitative and quantitative melissopalynological analyses were carried out according to the UNI 11299:2008 method[13] by a specialized Italian laboratory.

RESULTS AND DISCUSSION

Optimization of the ^{1}H NMR Parameters. The metabolites that we wanted to quantify are present in up to hundreds of parts per million in coffee honey. ^{1}H NMR spectra of honey samples dissolved in water are dominated by the intense signals of sugar protons, which limit the value of the receiver gain (RG) that can be used and consequently the digitalization of very small signals. To overcome this problem, we utilized a DPFGSE sequence, modified with the insertion of a hard π pulse in the cluster [G-S-G] to obtain a G-π-S-G block.[12] As a result, the resonances in the sugar proton region are further defocused by the second gradient pulse, which allowed us to increase the RG by a factor of 128. The outcome of this approach is shown in Figure 1, where a normal spectrum obtained only with water presaturation is compared with a spectrum obtained with the modified DPFGSE sequence in the same amount of time. The improvement in S/N ratio is almost 4-fold.

To verify that the intensity of the signals of interest is not affected by the soft pulse, a 9 h long experiment was performed on one of the samples using the water presaturation sequence. The integral ratio of the signals of interest was the same as in the spectrum obtained with the modified sequence (not shown).

Spectral Analysis. Figure 2 displays the aromatic region of the ^{1}H NMR spectra (6.8−10 ppm) of Colombia 1 and Colombia 2 samples. A similar spectrum was obtained with the Honduras sample. The chemical formulas of the seven identified compounds and relative assignments are also shown.

For quantitative determination purposes, the integrals of the following signals were chosen: the sum of the three signals of phenylalanine divided by 5 (7.32, 7.36, and 7.42 ppm), the sum of the two signals of tyrosine divided by 4 (6.88 and 7.18 ppm), the singlet at 8.35 ppm for formic acid; the peak of the aldehydic proton at 9.45 ppm for 5-HMF; and the signal at 9.12 ppm for trigonelline. The signals of caffeine (7.91 ppm) and theobromine (7.92 ppm) are partially overlapped, and the integral values were extracted by deconvolution of the peaks. Table 1 shows the results of this quantification.

Table 1. Quantities of the Identified Metabolites in *Coffea* Honey Dissolved in D_2O

	concentration ± SD (mg/kg)		
	Honduras	Colombia 1	Colombia 2
caffeine	15.0 ± 0.6	52.0 ± 1.6	97.8 ± 1.4
theobromine	24.9 ± 0.9	99.9 ± 1.3	159.2 ± 6.2
trigonelline	23.0 ± 0.4	55.4 ± 2.2	85.7 ± 2.7
phenylalanine	220.1 ± 11.5	819.7 ± 12.4	795.4 ± 17.2
tyrosine	161.8 ± 4.0	499.5 ± 8.3	701.7 ± 18.9
formic acid	40.2 ± 0.8	11.3 ± 0.1	45.2 ± 0.6
5-HMF	23.7 ± 0.5	26.2 ± 2.9	not detected
Tbr/Caff molar ratio	1.79	2.01	1.75

The signals from phenylalanine and tyrosine are the strongest in this region of the spectrum. Amino acids are present in all types of honey and can have both plant and animal origins, the major source being pollen.[14,15] Several studies have demonstrated that amino acid composition is not sufficient to distinguish the botanical origin of honey samples, because rather high variability among honeys from the same botanical source and between honeys from different floral origin was found.[15,16] The content of phenylalanine and tyrosine we found is in the range reported in the literature.[4,15]

Formic acid is a natural component of honey and, together with the other organic acids present, contributes to honey's antibacterial and antioxidant activities. It presents high variability depending on the floral and geographical origins of the honey, and the values found in *Coffea* honey, reported in Table 1, are in the lower range reported in previous studies.[17]

5-HMF is present in only two samples, and in each case its concentration is well below the maximum values defined by the European Directive[18,19] (80 mg/kg for honeys of declared origin from regions with tropical climate).

DOI: 10.1021/jf506359u
J. Agric. Food Chem. 2015, 63, 5858−5863

Table 2. Honey Pollen Content

honey sample	*Coffea* pollen (%)	other pollens (%)
Colombia 1	64	Anacardiaceae (16); Myrtaceae (11); unknown (4), Verbenaceae (3); Labiatae (1); Compositae H (1); *Cordia* (1); *Stachys*; and Bombacaceae (present)
Colombia 2	95	Melastomataceae (3); Myrtaceae (1); Mimosaceae, *Senecio*, Compositae H, *Croton*, and Lauraceae (present)
Honduras	36	Compositae H (33); Melastomataceae (9); unknown (8); *Borreria* (3); Myrtaceae (2); Umbelliferae (1); Compositae T (1); *Liquidambar* (1); *Vernonia* (1); Anacardiaceae, *Citrus limon*, *Cordia*, and Sapindaceae (present)

The three purine and pyridine alkaloids, caffeine, theobromine, and trigonelline, are present in all of the analyzed samples and, until now, these had never been reported to be simultaneously present in any type of honey. Our data suggest that these compounds might be considered as chemical markers of *Coffea* as botanical origin. Caffeine is also present in other monofloral honeys, in particular, in *Citrus* spp. honeys but in much smaller amounts compared to the results of the current study on *Coffea* honey.[2,20] High amounts of caffeine (we found up to 98 ppm) are somewhat surprising because of the well-known toxic[21] and repellent effect of caffeine at high concentrations on honeybees.[22] It was recently reported that honeybees are deterred from drinking sucrose solutions containing caffeine at concentrations >100 ppm, although they preferred slightly caffeinated sucrose solutions over the control without caffeine.[23] Caffeine concentration in nectar does not exceed 58 ppm, even though levels of caffeine in vegetative and seed tissues of *Coffea* up to 24×10^3 ppm have been reported.[24] At the nectar level, caffeine does not exceed the bees' bitter taste threshold, implying that pollinators select pharmacologically active nectar (it enhances memories of reward) but not repellent. In fact, honeybees rewarded with caffeine were 3 times as likely to remember a learned floral scent as were honeybees rewarded with sucrose alone.[25]

For the first time, trigonelline was identified and quantified in *Coffea* honey samples; this compound had previously been identified in orange honey produced in Corsica.[3] Paraxanthine and theophylline were not found in our NMR spectra, probably because their concentrations were too low.

Theobromine has previously been reported in traces amounts in citrus honey.[2] The amounts of theobromine we determined were higher than those of caffeine. In fact, the amount of theobromine found in monofloral coffee honey seems too high considering its levels in coffee flowers. It has been reported that *C. arabica* flower parts (petals, stamens, and gynoecium) contain caffeine as the main purine alkaloid.[26] The gynoecium also contains theobromine (10−20% of caffeine) and no theophylline, whereas the other organs contain remarkably high values of theophylline (4−12% of caffeine) and <1% theobromine.[26] Moreover, although the absolute amounts of caffeine and theobromine vary in the three honey samples, their molar ratio remains fairly constant. These results suggest a possible role played by honeybee metabolism more than plant metabolism. The first step in metabolic degradation of caffeine in mammals is its demethylation, mainly to paraxantine (>80%),[27] whereas in plants, theophilline is the most important first metabolite.[28] We were not able to confirm this finding with the existing literature, but our data can be explained if theobromine is the main metabolic derivative in honeybees.

Blossom honey essentially consists of nectar concentrated by the activities of specialized bees in the hive. In the case of *Citrus* spp., during honey production, one should expect a much higher caffeine concentration in citrus honey than found in nectar; however, it has been calculated that about 95% of the nectar caffeine is removed or degraded by a still unknown mechanism.[2] In the present study, we found much higher amounts of caffeine in the honey, although the caffeine content in *Coffea* nectar is not much higher than in *Citrus* nectar. A possible explanation is that the strain of African bees used to produce *Coffea* honey and the *Apis mellifera* commonly used to produce *Citrus* honey metabolize caffeine in different ways. The remarkably high content of theobromine found in coffee honey could also be related to differing bee metabolisms. In our previous work, we compared honey produced by *A. mellifera* and by stingless bees; we detected differences clearly attributable to the different metabolism of the two species.[29]

Pollen Analysis. The percentage of *Coffea* pollen found in the three samples is reported in Table 2. For the two samples from Colombia, *Coffea* pollen >50%[30] makes the products "monofloral", whereas the Honduras sample can be classified as "multifloral".

We found an excellent correlation between the specific markers, caffeine, theobromine, and trigonelline, and the relative amount of specific *Coffea* pollen measured in the same sample. In Figure 3, the linear equations and the R^2 values

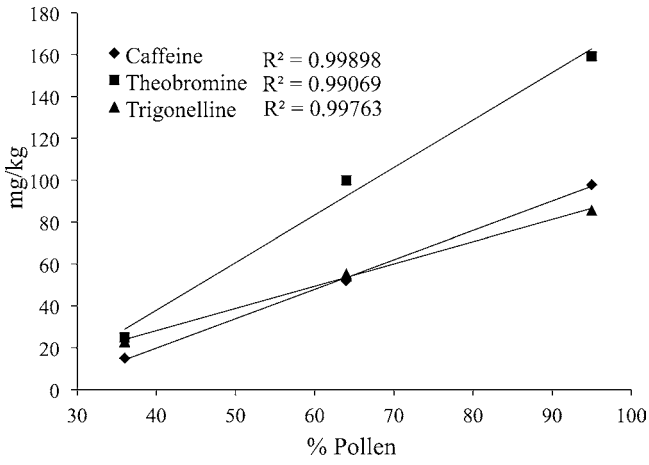

Figure 3. Linear correlation between marker content and the percentage of specific *Coffea* pollen measured in the three analyzed samples.

are reported. No correlation was found for phenylalanine (R^2 = 0.69), tyrosine (R^2 = 0.95), and formic acid (R^2 = 0.84). This is in line with our proposal that the former derivatives are specific for coffee honey, and the latter ones are not.

This result is important because it offers a way to validate our proposed method through comparison with an existing, accepted one. Indeed, melissopalynological analysis is universally recognized as the official technique to classify monofloral honey, although numerous drawbacks are associated with it. Among these are the time required and the need for experienced analysts. Many attempts have been put forth to

DOI: 10.1021/jf506359u
J. Agric. Food Chem. 2015, 63, 5858−5863

develop more objective methods, based on physical−chemical parameters, to certify the botanical origin of honey,[31−36] and NMR is emerging as a powerful technique in this regard.[37,38] The linear relationship between these two independent parameters might offer, for the first time in honey analysis, a sound and objective alternative to pollen determination.

The obvious limitation of the current study is that only three samples were analyzed. The reason for the small number of samples is also fairly understandable: coffee honey is not at all a common product; on the contrary, it is quite rare. The two monofloral samples we studied derive from a pilot project funded by the Ernesto Illy Foundation to promote beekeeping as an additional support to coffee cultivation activities in Colombia; the third sample was commercially available and was bought as "coffee honey", but the amount of *Coffea* pollen present was not sufficient to make it a monofloral product. Despite this limitation, the findings of the present study led to interesting hypotheses. To confirm these relevant hypotheses, our next study will be conducted with a higher number of samples, different origins, and different bee species.

This preliminary work also has a methodological value because it emphasizes the power of NMR in the characterization of complex mixtures, in the determination of botanical origin of honey, and in the simultaneous quantification of several compounds without the need for separation or derivatization. Moreover, the modified DPFGSE pulse sequence we used successfully suppressed the intense sugar signals, allowing the quantification of minor components in honey.

AUTHOR INFORMATION

Corresponding Author

*(E.S.) E-mail: elisabetta.schievano@unipd.it. Phone: +39 049 827 5742. Fax: +39 049 827 5829.

Notes

The authors declare no competing financial interest.

ACKNOWLEDGMENTS

We gratefully acknowledge the contribution of Jhon Ever Cardona (La Promotora de Bienes y Servicios Apicolas Proapis s.a.s.) in the technical supervision of the production of the honey samples from Colombia. We warmly thank Luca Turello and Stefano Scanferla (illycaffè spa) for their valuable technical support.

ABBREVIATIONS USED

DMF, *N*,*N*-dimethylformamide; DMSO, dimethyl sulfoxide; 5-HMF, 5-hydroxymethylfurfural; Trg, trigonelline; Form, formic acid; Tbr, theobromine; Caff, caffeine; Phe, phenylalanine; Tyr, tyrosine

REFERENCES

(1) Navarini, L.; Colomban, S.; Schievano, E.; Illy Belci, A.; Turello, L.; Mammi, S. Preliminary characterization of unifloral *Coffea* spp. honey. *Abstract book FoodMR2014*, Cesena, May 20−23, 2014; University of Bologna: Bologna, Italy, p 78.

(2) Kretschmar, J. A.; Baumann, T. W. Caffeine in citrus flowers. *Phytochemistry* **1999**, *52*, 19−23.

(3) Donarski, J. A.; Jones, S. A.; Charlton, A. J. Application of cryoprobe ^{1}H nuclear magnetic resonance spectroscopy and multivariate analysis for the verification of Corsican honey. *J. Agric. Food Chem.* **2008**, *56*, 5451−5456.

(4) Jerkovic, I.; Tuberoso, C. I. G.; Kus, P. M.; Marijanovic, Z.; Kranjac, M. Screening of *Coffea* spp. honey by different methodologies: theobromine and caffeine as chemical markers. *RSC Adv.* **2014**, *4*, 60557−60562.

(5) Bharti, S. K.; Roy, R. Quantitative ^{1}H NMR spectroscopy. *Trends Anal. Chem.* **2012**, *35*, 5−26.

(6) Pauli, G. F.; Jaki, B. U.; Lankin, D. C. Quantitative ^{1}H NMR: development and potential of a method for natural products analysis. *J. Nat. Prod.* **2005**, *68*, 133−149.

(7) Schievano, E.; Guardini, K.; Mammi, S. Fast determination of histamine in cheese by nuclear magnetic resonance (NMR). *J. Agric. Food Chem.* **2009**, *57*, 2647−2652.

(8) Schievano, E.; Finotello, C.; De Angelis, E.; Mammi, S.; Navarini, L. Rapid authentication of coffee blends and quantification of 16-*O*-methylcafestol in roasted coffee beans by nuclear magnetic resonance. *J. Agric. Food Chem.* **2014**, *62*, 12309−12314.

(9) Del Campo, G.; Berregi, I.; Caracena, R.; Zuriarrain, J. Quantitative determination of caffeine, formic acid, trigonelline and 5-(hydroxymethyl)furfural in soluble coffees by ^{1}H NMR spectrometry. *Talanta* **2010**, *81*, 367−371.

(10) Machado, A. R. T.; Lage, G. A.; Medeiros F. da S.: Filho, J. D. de S.; Pimenta, L. P. S. Quantitative analysis of trigonelline in some *Annona* species by proton NMR spectroscopy. *Nat. Prod. Bioprospect* **2013**, *3*, 158−160 (short communication).

(11) Rastrelli, F.; Schievano, E.; Bagno, A.; Mammi, S. NMR quantification of trace components in complex matrices by band-selective excitation with adiabatic pulses. *Magn. Reson. Chem.* **2009**, *47*, 868−872.

(12) Schievano, E.; Peggion, E.; Mammi, S. ^{1}H nuclear magnetic resonance spectra of chloroform extracts of honey for chemometric determination of its botanical origin. *J. Agric. Food Chem.* **2010**, *58*, 57−65.

(13) Ente Italiano di normazione (UNI). Honey − Microscopic or melissopalynological analysis. Norm 11299, 2008.

(14) Hendriksma, H. P.; Oxman, K. L.; Shafir, S. Amino acid and carbohydrate tradeoffs by honey bee nectar foragers and their implications for plant−pollinator interactions. *J. Insect Physiol.* **2014**, *69*, 56−59.

(15) Hermosin, I.; Chicon, R. M.; Cabezudo, M. D. Free amino acid composition and botanical origin of honey. *Food Chem.* **2003**, *83*, 263−268.

(16) Carratù, B.; Ciarocchi, M.; Mosca, M.; Sanzini, E. Free amino acids, oxalate and sulphate for honey characterization. *J. ApiProd. ApiMed. Sci.* **2011**, *3*, 81−88.

(17) Mato, I.; Huidobro, J. F.; Simal-Lozano, J.; Sancho, M. T. Rapid determination of nonaromatic organic acids in honey by capillary zone electrophoresis with direct ultraviolet detection. *J. Agric. Food Chem.* **2006**, *54*, 1541−1550.

(18) EU Directive 2001/110/CE of 02/12/2001 (L 10/47).

(19) Fallico, B.; Zappalà, M.; Arena, E.; Verzera, A. Effects of conditioning on HMF content in unifloral honeys. *Food Chem.* **2004**, *85*, 305−313.

(20) Swaileh, K. M.; Abdulkhaliq, A. Analysis of aflatoxins, caffeine, nicotine and heavy metals in Palestinian multifloral honey from different geographic regions. *J. Sci. Food Agric.* **2013**, *93*, 2116−2120.

(21) Detzel, A.; Wink, M. Attraction, deterrence or intoxication of bees (*Apis mellifera*) by plant allelochemicals. *Chemoecology* **1993**, *4*, 8−18.

(22) Mustard, J. A.; Dews, L.; Brugato, A.; Dey, K.; Wright, G. A. Consumption of an acute dose of caffeine reduces acquisition but not memory in the honey bee. *Behav. Brain Res.* **2012**, *232*, 217−224.

(23) Singaravelan, N.; Nee'man, G.; Inbar, M.; Izhaki, I. Feeding responses of free-flying honeybees to secondary compounds mimicking floral nectars. *J. Chem. Ecol.* **2005**, *31*, 2791−2804.

(24) Ashihara, H.; Crozier, A. Caffeine: a well known but little mentioned compound in plant science. *Trends Plant Sci.* **2001**, *6*, 407−413.

(25) Wright, G. A.; Baker, D. D.; Palmer, M. J.; Stabler, D.; Mustard, J. A.; Power, E. F.; Borland, A. M.; Stevenson, P. C. Caffeine in floral

DOI: 10.1021/jf506359u
J. Agric. Food Chem. 2015, 63, 5858−5863

nectar enhances a pollinator's memory of reward. *Science* **2013**, *339*, 1202−1204.
(26) Baumann, T. W. Some thoughts on the physiology of caffeine in coffee − and a glimpse of metabolite profiling. *Braz. J. Plant Physiol.* **2006**, *18*, 243−251.
(27) Perera, V.; Gross, A. S.; McLachlan, A. J. Measurement of CYP1A2 activity: a focus on caffeine as a probe. *Curr. Drug Metab.* **2012**, *13*, 667−678.
(28) Mazzafera, P. Catabolism of caffeine in plants and microorganisms. *Front. Biosci.* **2004**, *9*, 1348−1359.
(29) Schievano, E.; Mammi, S.; Menegazzo, I. Nuclear magnetic resonance as a method for prediction of geographical and entomological origin of pot honey. In *Pot-Honey: A Legacy of Stingless Bees*; Vit, P., Pedro, S. R. M., Roubik, D., Eds.; Springer: New York, 2013; pp 429−446.
(30) Beck, G.; Camps, G. Neue Spezifikationen fur Trachthonige. *Dtsch. Lebensm.-Rundsch.* **2009**, *105*, 105−110.
(31) Cuevas-Glory, L. F.; Pino, J. A.; Santiago, L. S.; Sauri-Duch, E. A review of volatile analytical methods for determining the botanical origin of honey. *Food Chem.* **2007**, *103*, 1032−1043.
(32) Jain, S. A.; Jesus, F. T.; Marchioro, G. M.; Araùjo, E. D. Extraction of DNA from honey and its amplification by PCR for botanical identification. *Food Sci. Technol.* **2013**, *33*, 753−756.
(33) Corvucci, F.; Nobili, L.; Melucci, D.; Grillenzoni, F. The discrimination of honey origin using melissopalynology and Raman spectroscopy techniques coupled with multivariate analysis. *Food Chem.* **2015**, *169*, 297−304.
(34) Anjos, O.; Iglesias, C.; Peres, F.; Martinez, J.; Garcia, A.; Taboada, J. Neural networks applied to discriminate botanical origin of honeys. *Food Chem.* **2015**, *175*, 128−136.
(35) Wang, J.; Kliks, M. M.; Qu, W.; Jun, S.; Shi, G.; Li, Q. X. Rapid determination of the geographical origin of honey based on protein fingerprinting and barcoding using MALDI TOF MS. *J. Agric. Food Chem.* **2009**, *57*, 10081−10088.
(36) Etzold, E.; Lichtenberg-Kraag, B. Determination of the botanical origin of honey an approach for routine analysis. *Eur. Food Res. Technol.* **2008**, *227*, 579−586.
(37) Schievano, E.; Morelato, E.; Facchin, C.; Mammi, S. Characterization of markers of botanical origin and other compounds extracted from unifloral honeys. *J. Agric. Food Chem.* **2013**, *61*, 1747−1755.
(38) Schievano, E.; Stocchero, M.; Morelato, E.; Facchin, C.; Mammi, S. An NMR-based metabolomic approach to identify the botanical origin of honey. *Metabolomics* **2012**, *8*, 679−690.

DOI: 10.1021/jf506359u
J. Agric. Food Chem. 2015, 63, 5858−5863

honey (*Eriobotrya japonica* (Thunb.) Lindl.), and almond honey (*Prunus dulcis* Mill. ex Rchb.).[10] The results showed that the tested honey samples presented higher phenolic content and antioxidant capacity than those produced by other honeybee subspecies from Sicily, other different Italian regions, and abroad.[10−14] Moreover, all tested honeys showed good antimicrobial activity against a broad spectrum of microorganisms.

Honey chemical characterization is generally studied with high-performance liquid chromatography coupled with diode array detection or electrospray ionization tandem mass spectrometry (HPLC-PDA or HPLC-ESI-MS/MS). These techniques are useful to reveal the presence of botanical biomarkers, α-dicarbonyl and phenolic compounds,[3,15] and contaminants.[16] Nevertheless, matrix interference, especially in the analysis of carbohydrates and peptides, and low sensitivity require the application of solid phase extraction (SPE) sample treatment before the analysis of the sugar- and peptide-derived fractions. Therefore, in most investigations carbohydrates are not determined or are evaluated as total sugar content according to spectrophotometric methods with a lack of specific knowledge on these components.[17−19] Given this scarce information about the chemical composition of *A. mellifera* ssp. *sicula* honeys, especially regarding carbohydrates and polyphenols, the present investigation represents an extension of our previous research[10] and is aimed to (1) investigate the chemical composition of two further honeys, sulla honey (*Hedysarum coronarium* L.) and dill honey (*Anethum graveolens* L.), with a multimethodological approach that consists of HPLC-PDA-ESI-MS^n and NMR spectroscopy; and (2) to extend the study of lemon, orange, and medlar honeys with NMR spectroscopy, to deepen the knowledge about their sugar and amino acid compositions. The combination of these techniques combines the advantages of liquid chromatography coupled with MS to those of NMR spectroscopy, which is a technique that has been recently employed in the field of food analysis, because it can lead both to "high-throughput" and simultaneous structural information on a wide range of metabolites and to the identification of specific metabolites or their classes. This approach allowed us to describe the phytochemical composition of each type of honey and identify many compounds that were found in these types of honeys for the first time. In addition, we could compare the metabolic profiles obtained by our analysis with those already reported in the literature and provide a first phytochemical composition for that kind of honey for which no chemical data are available in the literature.

MATERIALS AND METHODS

Chemicals and Materials. Millipore grade water was obtained with a Milli-Q water purification system (Millipore Corp., Billerica, MA, USA); formic acid, (−)-catechin, and luteolin were purchased from Sigma-Aldrich (Milan, Italy); LC-MS grade methanol was obtained from VWR International PBI srl (Milan, Italy). D_2O 99.9%D was purchased from EURISO-TOP (Saint-Aubin, France).

Honey Samples. *A. mellifera* ssp. *sicula* honey samples of different botanical origin, that is, sulla (*H. coronarium*), dill (*A. graveolens*), lemon (*C. limon*), orange (*C. arantium*), and medlar honeys (*E. japonica*), were obtained from an Italian independent apiarist (Carlo Amodeo, Termini Imerese, Palermo, Italy). Honey samples were harvested in 2014 by individual apiarists in the area of Termini Imerese (37°98′ N, 13°70′ E, Palermo, Italy). Samples were classified following the melissopalynological analysis[10] according to which the floral source was confirmed if the pollen content in the honeys was not lower than 10% (this percentage ranged between 27 and 61%). During the experiments, three samples for each botanical source were kept at 5 °C in the dark in airtight containers for <5 months until the analysis.

Sample Preparation for RP-HPLC-PDA-ESI-MS^n Analysis. One gram of each honey sample was added to 2 mL of Millipore grade water acidified with 0.1% formic acid. Each sample was purified with SPE, using an RP Sep-Pak Vac 6 cm^3 (1g) tC18 cartridge (Waters, Milford, MA, USA). After wetting the cartridge with methanol (10 mL) and conditioning it with 0.1% formic acid (10 mL), the polyphenol-enriched fraction (SPE_2 fraction) was eluted with 2 mL of a solution composed of methanol and 0.1% formic acid, 90:10% v/v, at a flow rate of 0.4 mL/min. The SPE_2 fraction was concentrated under a nitrogen stream until the volume of 130 μL, corresponding to a concentration of 7.69 mg/mL. After filtration with 0.45 and 0.20 μm nonsterile syringe filters, the concentrated SPE_2 fraction was submitted to RP-HPLC-PDA-ESI-MS^n analysis.

RP-HPLC-PDA-ESI-MS^n Analysis. All experiments were performed using a Thermo Finnigan Surveyor Plus HPLC, equipped with a quaternary pump, a Surveyor UV−vis diode array detector, and a LCQ Advantage Max ion trap mass spectrometer (Thermo Fisher Scientific, Waltham, MA, USA), connected through an ESI source.

The separation was carried out on a Gemini C18 110 Å (150 × 2 mm, 5 μm), equipped with an Ultra Cartridge C18 Peptide Security Guard Column, both from Phenomenex (Torrance, CA, USA). The mobile phase consisted of water acidified with 0.1% of formic acid (A) and methanol (B) and was eluted with the following gradient: from 2 to 5% B in 10 min, from 5 to 40% B in 50 min, from 40 to 60% B in 10 min, from 60 to 100% B in 10 min, followed by a 10 min isocratic run of 100% B. Total run time was 115 min, including column reconditioning. The flow rate was maintained at 0.3 mL/min, the autosampler and column temperatures were maintained at 4 and 25 °C, respectively. Chromatograms were monitored at 210, 254, and 280 nm; spectral data were collected within the range of 200−800 nm for all peaks. The ion trap was operated in data-dependent, full scan (m/z 100−1000), zoom scan, and MS^n mode. To obtain MS^2 data, a 35% collision energy and an isolation width of 2 m/z were applied. ESI source parameters had previously been optimized by flow injection analysis using (−)-catechin (10 ppm, in 0.1% formic acid and methanol, 50:50, v/v) and luteolin (5 ppm, in 0.1% formic acid and methanol, 50:50, v/v), for negative and positive ionization, respectively, to a ionization voltage of 3.5 kV, a capillary temperature of 200 °C, a sheath gas flow of 45 arbitrary units, and an auxiliary gas flow of 20 arbitrary units.

Sample Preparation for NMR Analysis. The samples were prepared dissolving 20 mg of honey in 700 μL of D_2O containing 3-(trimethylsilyl)propionic-2,2,3,3-d_4 acid sodium salt (TSP, 2 mM) as internal standard. Once a homogeneous solution was achieved using a vortex rotor, 700 μL of honey solution was transferred into a standard 5 mm NMR tube and subjected to NMR analysis.

NMR Analysis. The NMR spectra were recorded at 27 °C on a Bruker AVANCE 600 NMR spectrometer operating at the proton frequency of 600.13 MHz and equipped with a Bruker multinuclear z-gradient inverse probehead capable of producing gradients with a strength of 55 G cm^{-1} in the z-direction. ^{1}H spectra were referenced to methyl group signals of TSP (δ = 0.00 ppm) in D_2O. ^{1}H spectra were acquired by adding 64 transients with a recycle delay of 3 s. The residual HDO signal was suppressed using presaturation with a single soft pulse on the HDO resonance frequency applied during the relaxation delay followed by a strong observation pulse.

2D NMR experiments, namely, ^{1}H−^{1}H TOCSY, ^{1}H−^{13}C HSQC, and ^{1}H−^{13}C HMBC, were performed using the same experimental conditions previously reported.[20] The mixing time for the ^{1}H−^{1}H TOCSY was 80 ms, and the spin lock field was 6250 Hz. The HSQC experiments were performed using a coupling constant $^1J_{C-H}$ of 150 Hz, and the ^{1}H−^{13}C HMBC experiments were performed using a delay for the evolution of long-range couplings of 80 ms.

DOI: 10.1021/jf506192s
J. Agric. Food Chem. 2015, 63, 5864−5874

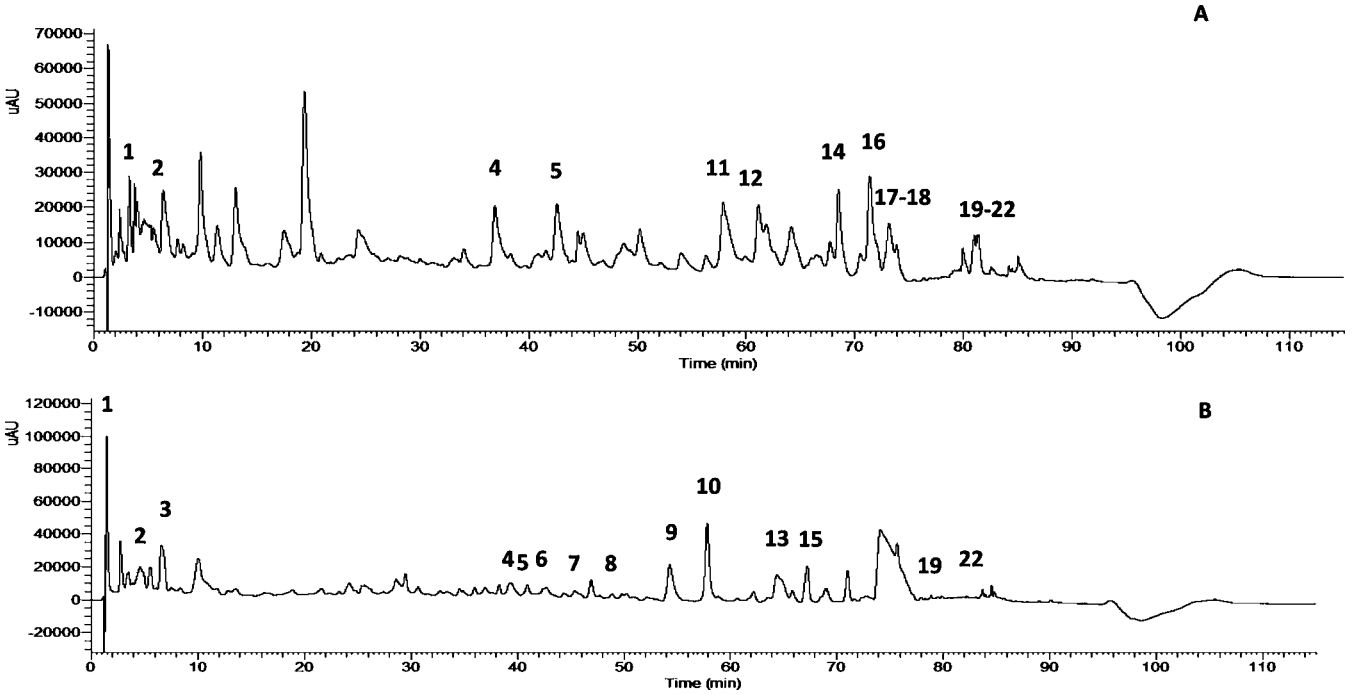

Figure 1. Chromatographic profile of SPE_2 fraction of sulla (A) and dill (B) honeys.

Table 1. Chromatographic Behavior and MS and MS^n Data of the Compounds Identified in Sulla and Dill Honeys

peak	RT (min)	λ_{max} (nm)	m/z	HPLC-ESI-MS^n m/z (% of base peak)	compound
1	2.29	260	195	177 (100), 49 (50)	4-methoxyphenyllactic acid[a,b]
2	6.86	260	191	111 (100), 129 (20)	citric acid[a,b]
3	6.96	257	166[c]	120 (100)	phenylalanine[b]
4	39.80	260	165	147 (100)	phenyllactic acid[a,b]
5	42.60	230	223[c]	205 (100), 121 (15)	dehydrovomifoliol[a,b]
6	42.80	230	223[c]	205 (100), 135 (22)	3-hydroxy-1-(2-methoxyphenyl)penta-1,4-dione[b]
7	44.80	260	137	93 (100)	*p*-hydroxybenzoic acid[b]
8	49.81	270	377[c]	243 (100), 172 (2)	riboflavin[b]
9	52.80	240	190[c]	162 (30), 173 (40)	kynurenic acid[b]
10	57.98	260	213[c]	181 (100), 154 (20), 121 (2)	methyl siringate[b]
11	58.39	257, 346	771	609 (100), 463 (10), 301 (5)	quercetin hexosyl rutinoside[a]
12	60.36	260, 350	755	300 (100), 301 (30), 609 (20)	quercetin rhamnosyl-hexosyl-rhamnoside[a]
13	65.70	250	243[c]	172 (65), 200 (60), 216 (70), 198 (5)	lumichrome[b]
14	65.96	255, 351	609	301 (100)	quercetin rutinoside[a]
15	67.22	250	265[c]	247 (100), 229 (20)	abscisic acid[b]
16	70.15	280	285	267 (100), 139	pinobanksin methyl ether[a]
17	71.09	270	593	285 (100)	kaempferol rutinoside[a]
18	71.51	287	271	253 (100), 225 (25)	pinobanksin[a]
19	79.65	290	255	213 (35), 151	pinocembrin[a,b]
20	79.93	255, 287	247	179 (100), 135 (20)	caffeic acid isoprenyl ester[a]
21	80.28	290, 326	313	253 (100), 271 (20)	pinobanksin acetate[a]
22	83.38	240	343[c]	240 (100)	pinobanksin butyrate[a,b]

[a]Compound identified in sulla honey. [b]Cmpound identified in dill honey. [c]Compound revealed by positive ionization mode.

RESULTS AND DISCUSSION

RP-HPLC-PDA-ESI-MS^n Analysis. RP-HPLC-PDA-ESI-MS^n analysis of sulla and dill honeys allowed the identification of 22 compounds, some of which were present in both honey samples. The chromatograms obtained from sulla and dill honey analyses are reported in Figure 1. The identification of these compounds was performed on the basis of their chromatographic behaviors; UV−vis, MS, and MS/MS spectra; and comparisons with literature data. The results obtained are summarized in Tables 1 and 2. For each compound, the retention time, the wavelength of maximum absorbance, m/z values of molecular ion, and its fragment ions are reported.

Nine flavonoids, among which were four flavonols (quercetin hexosyl rutinoside, quercetin rhamnosyl-hexosyl-rhamnoside, quercetin rutinoside, and kaempferol rutinoside), four flavanonols (dihydroflavonols, i.e. pinobanksin methyl ether, pinobanksin, pinobanksin acetate, and pinobanksin butyrate), and one flavanone (pinocembrin), were identified. Moreover, the analysis showed the presence of four organic acids (citric

DOI: 10.1021/jf506192s
J. Agric. Food Chem. 2015, 63, 5864−5874

Table 2. Presence of Nutrients and Bioactive Compounds in Sulla and Dill Honeys

compound	sulla honey[a]	dill honey[a]
flavonols		
quercetin hexosyl-rutinoside	+	−
quercetin rhamnosyl-hexosyl-rhamonoside	+	−
quercetin rutinoside	+	−
kaempferol rutinoside	+	−
flavanonols		
pinobanksin	+	−
pinobanksin methyl ethere	+	−
pinobanksin acetate	+	−
pinobanksin butyrate	+	+
flavanones		
pinocembrin	+	+
organic acids		
citric acid	+	+
lactic acid	+	+
succinic acid	+	+
acetic acid	+	+
4-methoxyphenyllactic acid	+	+
phenyllactic acid	+	+
kynurenic acid	−	+
phenolic acids and derivatives		
p-hydroxybenzoic acid	−	+
methyl siringate	−	+
caffeic acid isoprenyl ester	−	+
amino acids		
phenylalanine	−	+
proline	+	+
alanine	+	+
vitamins and metabolites		
riboflavin	−	+
lumichrome	−	+
norisoprenoid		
abscisic acid	−	+
other compounds		
dehydrovomifoliol	+	+
3-hydroxy-1-(2-methoxyphenyl)penta-1,4-dione	−	+

[a]+, found; −, not found.

acid, kynurenic acid, phenyllactic acid, and 4-methoxyphenyllactic acid), three phenolic acids and derivatives (*p*-hydroxybenzoic acid, caffeic acid isoprenyl ester, and methyl syringate), one vitamin and its main metabolite (riboflavin and lumichrome), one norisoprenoid (abscisic acid), one amino acid (phenylalanine), dehydrovomifoliol ((±)-1′-hydroxy-4′-keto-α-ionone), and 3-hydroxy-1-(2-methoxyphenyl)penta-1,4-dione.

As far as flavonoids are concerned, RP-HPLC-PDA-ESI-MS^n analysis of sulla honey showed the presence of flavonols, flavanonols, and a flavanone. In contrast, in dill honey just a flavanonol and a flavanone were detected. Peaks 11, 12, and 14 were identified as quercetin derivatives, because all of their MS^2 spectra showed the presence of quercetin aglycone at m/z 301. Peak 11 was assigned to quercetin hexosyl-rutinoside (MW 772) because the parent ion at m/z 771 produced fragment ions at m/z 609, due to the loss of a hexosyl moiety $[M - 162]^-$, and at m/z 463, corresponding to a hexosylated quercetin, due to the loss of the rutinoside group. Peak 12 was identified as quercetin-rhamnosyl-hexosyl-rhamnoside (MW 756) because its MS^2 spectrum showed the presence of a significant fragment ion at m/z 609, due to the loss of 146 Da that corresponded to a rhamnosyl unit. Moreover, the produced fragment ion corresponded to quercetin linked to a rhamnosyl moiety and a hexosyl one, $[301 + 146 + 162]^-$. Peak 14 was assigned to quercetin rutinoside (MW 610) on the basis of a comparison with literature data.[21] In fact, the pseudomolecular ion at m/z 609 produced a fragment ion at m/z 301, corresponding to the aglycone, due to the loss of the rutinoside moiety, $[M - 308]^-$. Peak 17 was assigned to kaempferol rutinoside (MW 594) because it produced a parent ion at m/z 593 and a fragment ion at m/z 285, corresponding to kaempferol aglycone and obtained by the loss of the rutinoside group.[21]

Of the flavanonols, peak 18 was identified as pinobanksin (MW 272) because the parent ion at m/z 271 produced the typical MS^2 spectrum already known in the literature,[22] characterized by the presence of fragment ions at m/z 253, due to the loss of H_2O, at m/z 243, corresponding to $[M - H - CO]^-$, at m/z 165, corresponding to $[M - H - H_2O - 2CO_2]^-$, at m/z 151 corresponding to the ion $[^{1,3}A]^-$, which derives from the cleavage of the C ring of the aglycone that undergoes retro-Diels–Alder scission. Peaks 16, 21, and 22 were assigned to pinobanksin derivatives. In more detail, peak 16 was identified as pinobanksin methyl ether (MW 286) because its MS/MS spectrum showed the presence of ions at m/z 252, due to the loss of the methyl group and a water molecule, at m/z 271, corresponding to the aglycone obtained by the loss of the methyl group, and at m/z 239 and 224 as previously reported.[23] Peak 21 was identified as pinobanksin acetate (MW 314). The assignment was possible by comparing the MS^2 spectrum with data already available in the literature.[23] The parent ion at m/z 313 produced fragment ions at m/z 271, corresponding to pinobanksin aglycone, obtained by the loss of the acetate (− 42 Da), and at m/z 253, due to the loss of a water molecule from the aglycone. Pinobanksin methyl ether and pinobanksin acetate were detected only in sulla honey, whereas pinobanksin butyrate, identified as peak 22, was found in both honey samples. The assignment was possible due to the fact that pinobanksin butyrate (MW 342) parent ion at m/z 343 produced a MS/MS spectrum as already reported by Chua et al.[24]

The flavanone, peak 19, was detected in both sulla and dill honeys and was identified as pinocembrin because the molecular ion at m/z 255 produced fragment ions at m/z 213, due to the loss of $[M - C_2H_2O^-]^-$, and at m/z 151, corresponding to the ion $[^{1,3}A]^-$, which derives from C ring cleavage by RDA scission, as reported by Ristivojević et al.[23]

The chemical structures of flavonoids detected in sulla and dill honeys are reported in Figure 2.

The presence of flavonoids in sulla honey is in agreement with earlier studies carried out on an Italian sulla honey sample in which quercetin and kaempferol aglycones were identified.[11] For the other flavonoids, this is the first report on the isolation and identification of flavanonols and a flavanone in sulla honey, to date. With regard to the absence of flavonols in dill honey, Ortan et al.[25] showed the presence of quercetin in *A. graveolens* flowers, leaves, and fruits, but no literature data have been reported on the potential content of these compounds in nectar and honey. Also in this case, this is the first report on the isolation and identification of pinobanksin butyrate and pinocembrin in dill honey.

DOI: 10.1021/jf506192s
J. Agric. Food Chem. 2015, 63, 5864−5874

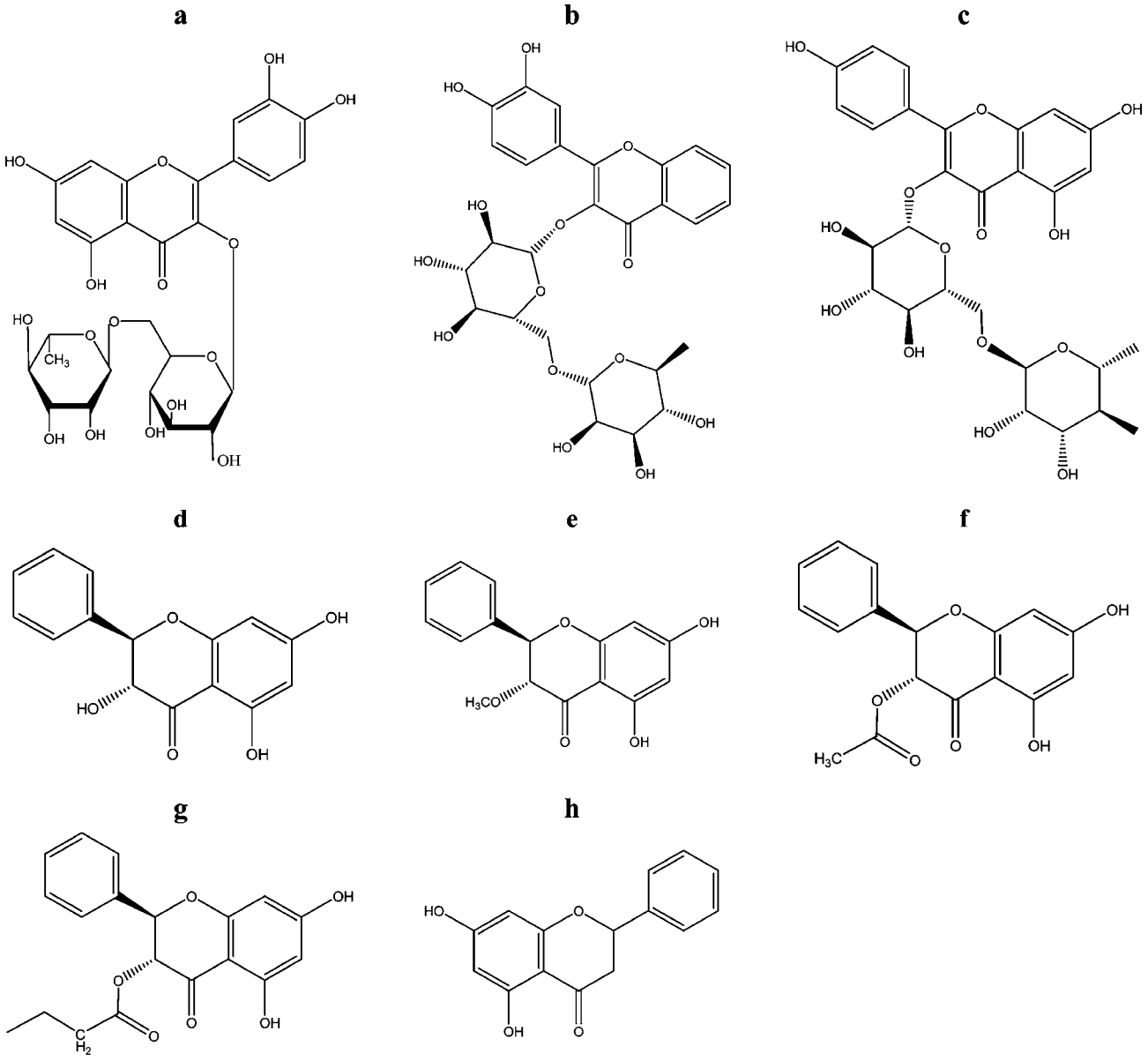

Figure 2. Chemical structures of flavonoids detected in sulla and dill honeys.

With regard to organic acids, the analysis showed the presence of four compounds belonging to this chemical class. In more detail, peak 2, detected in both sulla and dill honeys, was identified as citric acid (MW 192) because the parent ion $[M - H]^-$ at m/z 191 produced a fragment ion at m/z 129, corresponding to $[M - H - H_2O - CO_2]^-$, and another ion at m/z 111, due to the consequent loss of H_2O. Peaks 1 and 5 were identified as 4-methoxyphenyllactic acid (MW 196) and phenyllactic acid (MW 164), respectively. They were found in both sulla and dill honeys. In more detail, peak 1 was assigned to 4-methoxyphenyllactic acid because in the negative ionization mode the pseudomolecular ion at m/z 195 produced a MS/MS spectrum as previously reported in the literature by Oelschlaegel et al.[7] Peak 5 was identified as phenyllactic acid (MW 166) because its parent ion $[M - H]^-$ at m/z 165 produced fragment ions at m/z 147 and 119, corresponding to the neutral loss of H_2O and HCO_2H, respectively.[7] Peak 9, detected only in dill honey, was assigned to kynurenic acid (MW 189). Its parent ion $[M + H]^+$ at m/z 190 produced fragment ions at m/z 173 and 162, due to the loss of OH and a carbonyl group, respectively.

Phenyllactic acid is a common compound found in honeys. Its concentration ranges from several hundreds of millgrams per kilogram to <1 mg/kg and is strongly correlated to the typical honey sensorial properties.[5] Kynurenic acid derives from the tryptophan metabolic pathway and is the precursor of kynurenine and xanthurenic acid. Its presence in honey could be of interest due its biological and biochemical properties. Soto et al. showed the presence of kynurenic acid and derivatives in different botanical origin honeys. The highest kynurenic acid amounts were found in chestnut, blackberry, and multifloral honeys, with concentrations ranging from 103 to 141 to 3 mg/kg. Other kinds of honeys, such as oak, heather, orange, eucalyptus, thyme, sunflower, and acacia, were shown to contain lesser amounts (concentration <1 mg/kg) of this quinolone alkaloid. Nevertheless, no data are available on the presence of kynurenic acid in dill honey to date.[26]

DOI: 10.1021/jf506192s
J. Agric. Food Chem. 2015, 63, 5864−5874

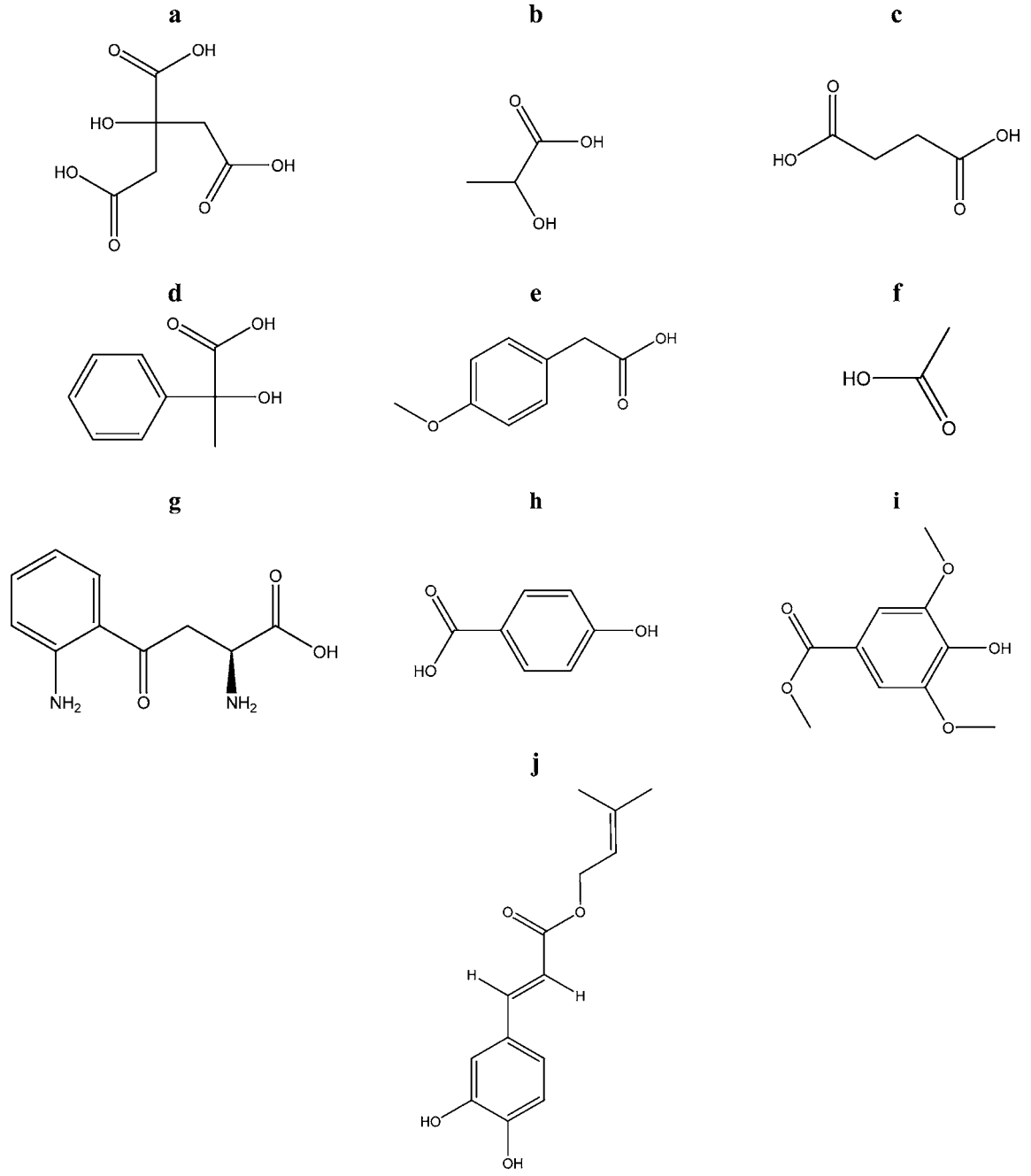

Figure 3. Chemical structures of organic acids, phenolic acids, and their derivatives detected in sulla and dill honeys.

As far as phenolic acids and derivatives are concerned, three substances were determined. Peak 7, detected only in dill honey, was identified as *p*-hydroxybenzoic acid (MW 138) because it presented a pseudomolecular ion $[M - H]^-$ at m/z 137, which produced a fragment ion at m/z 93, obtained by the loss of the carboxylic moiety. Peak 10, present only in dill honey, was assigned to methyl syringate (MW 212) because its parent ion $[M + H]^+$ at m/z 213 produced fragment ions at m/z 181, due to the loss of a carboxymethyl group, at m/z 154, corresponding to $[M - OCH_3CO]^+$, and at m/z 121, corresponding to $[M - (OCH_3)_2CO]^+$. Peak 20, identified only in sulla honey, was assigned to caffeic acid isoprenyl ester (MW 248). Its MS spectrum showed the presence of a parent ion $[M - H]^-$ at m/z 247, whereas its MS/MS spectrum presented ions at m/z 179, due to the loss of the isoprenyl group, and at m/z 135, obtained by the consequent loss of the carboxylic moiety.[27]

The chemical structures of organic acids, phenolic acids, and their derivatives detected in sulla and dill honeys are reported in Figure 3. Methyl syringate is a common phenolic derivative that was already detected in many honeys of different botanical origins such as robinia, rape, chestnut, clover, linden blossom, daendelion, sunflower, thyme, and manuka honeys.[28] The presence of this compound in sulla honey is in agreement with Jerković et al., who determined this compound by GC-MS analysis.[28] With regard to the other phenolic and hydroxycin-

DOI: 10.1021/jf506192s
J. Agric. Food Chem. 2015, 63, 5864−5874

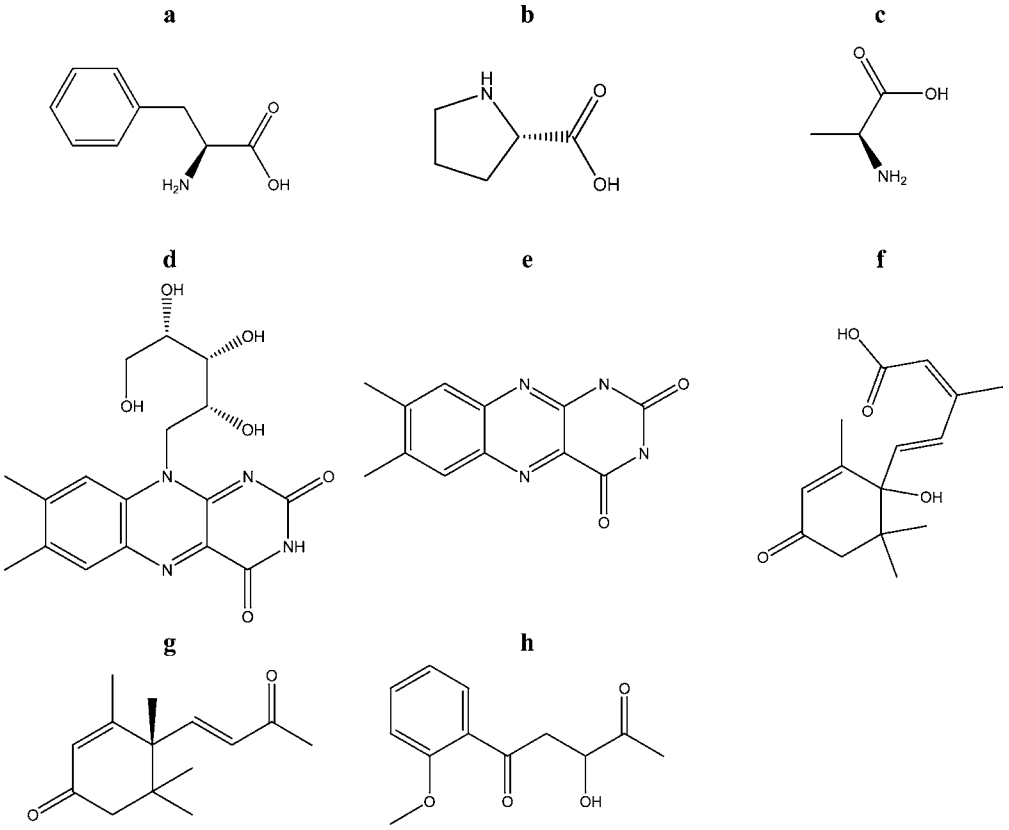

Figure 4. Chemical structures of other metabolites detected in sulla and dill honeys.

namic acids found in sulla and dill honeys, these compounds are typical secondary metabolites of plants,[29] widely distributed in many parts of the plants including flowers and nectars, and are identified in many different floral origin honeys.[10,15,30]

With regard to the other identified compounds, peak 3, found only in dill honey, was assigned to phenylalanine (MW 165) because its pseudomolecular ion at *m*/*z* 166 produced a fragment ion at *m*/*z* 120, due to the neutral loss of 46 Da, corresponding to HCOOH.

It is known that amino acids in honey are attributable to both animal and plant origin. The most abundant honey amino acid is proline, followed by phenylalanine, alanine, and glutamic acid. Phenylalanine content seems to be correlated to geographical origin, even if its presence is not always confirmed in honey, as reported by Kelly et al.[31]

In dill honey LC-MS/MS analysis showed also the presence of a riboflavin and lumichrome (7,8-dimethylalloxazin). The positive ionization mode allowed the identification of riboflavin (MW 376) as peak 8 because its MS/MS spectrum presented an intense fragment ion at *m*/*z* 243, corresponding to lumichrome, obtained from the partial loss of the ribitol moiety. Moreover, peak 13 was assigned to lumichrome (MW 242), because its MS^2 spectrum showed the presence of the same fragment ions as previously reported by Tuberoso et al.[5]

Lumichrome is a degradation product of riboflavin formed via a photochemical-induced cleavage of the ribityl group under neutral and acidic conditions. The presence of lumichrome was reported for the first time in 2011 by Tuberoso et al.[5] in thistle (*Galactites tomentosa* Moench) honey samples collected in different areas of Sardinia (Italy). More recently, the same authors reported that lumichrome occurs also in Dalmatian sage (*Salvia officinalis* L.) honey samples.[32] Our results show the occurrence of lumichrome in dill honey for the first time.

The present analysis allowed us to identify abscisic acid (MW 264), a norisoprenoid compound, derived from carotenoid degradation.[30] Abscisic acid was identified in dill honey as peak 15 because it showed fragment ions, derived from a parent ion $[M - H]^-$, at *m*/*z* 263, at *m*/*z* 219, due to the loss of the carboxylic group, and at *m*/*z* 201, corresponding to $[M - CO_3H]^-$.[33]

Abscisic acid acts as a plant hormone, inhibiting growth and helping plants to control stressful conditions. The presence of this compound in dill honey is not surprising as it is widely distributed in many honey varieties. With regard to sulla honey, the absence of abscisic acid confirms the results obtained by Jerković et al., who did not find this compound but revealed the presence of vomifoliol, a degradation product of abscisic acid.[28] On the other hand, we determined dehydrovomifoliol in both sulla and dill honeys.[7] In fact, LC-MS/MS analysis showed the presence of dehydrovomifoliol (detected in both sulla and dill honeys) and 3-hydroxy-1-(2-methoxyphenyl)penta-1,4-dione (found only in dill honey), which were previously identified in manuka honey (*Leptospermum scoparium* R.Forst. & G.Forst.) and were considered specific markers of this kind of honey.[7] The assignment was possible due to the presence in the literature of MS/MS spectra of these compounds that allowed a comparison.[7] Both compounds were identified in positive ionization mode, giving fragment ions at *m*/*z* 205 and 121 for dehydrovomifoliol (MW 222, peak 5) and at *m*/*z* 205 and 135 for 3-hydroxy-1-(2-methoxyphenyl)penta-1,4-dione (MW 222, peak 6), respectively.

The chemical structures of the other metabolites detected in sulla and dill honeys are reported in Figure 4.

DOI: 10.1021/jf506192s
J. Agric. Food Chem. 2015, 63, 5864−5874

NMR Analysis. In accordance with literature data,[34] the ^{1}H NMR spectrum of honey in an aqueous solution is dominated by the intense signals of glucose and fructose anomeric forms (Figure 5 is an example) where total ^{1}H NMR spectra of dill and sulla honeys are compared.

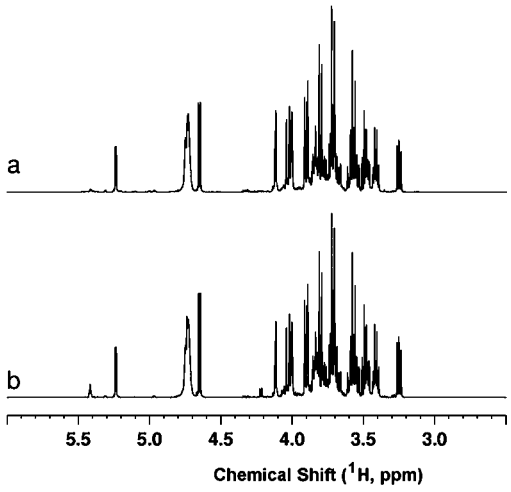

Figure 5. ^{1}H NMR spectra of dill (a) and sulla (b) honeys solutions in D_2O.

Apart from the signals of the principal components of the saccharide fraction, glucose and fructose, the signals of minor components are also observed in ^{1}H spectra. In Figure 6 the spectral region of anomeric protons (5.5−4.4 ppm) is reported not only for dill and sulla honeys but also for lemon, orange, and medlar ones. The complete assignment of these signals to individual compounds requires the application of $^{1}H-^{13}C$ HSQC-NMR with enhanced resolution in the ^{13}C dimension,[35] to overcome the overlapping of their ^{1}H and ^{13}C resonances,[34] the use of literature databases, and, in some cases, addition of standard compounds. The partial assignment obtained using 2D NMR experiments and literature data[34−36] was focused on ^{1}H signals not overlapped with other resonances. In this case the direct quantification by integration of corresponding ^{1}H signals was possible. Raffinose, kojiobiose, turanose, and nigerose were identified by virtue of their characteristic anomeric signals (Figure 6). The multiplet signal at 5.42 ppm showed a marked variation in the intensity among the five honeys. The structure of this multiplet (two doublets at 5.419 and 5.412 ppm partially overlapped) together with the corresponding ^{13}C correlations (a double spot in $^{1}H-^{13}C$ HSQC spectrum at 92.7 and 100.3 ppm) proves that it belongs to at least two different components. A detailed analysis of the literature data[34−36] revealed that at least seven di- and oligosaccharides have the anomeric CH group giving the signal with very similar ^{1}H (i.e., 5.42 ppm) and ^{13}C chemical shifts and usually present in honey: erlose, kestose, raffinose, sucrose, maltose, maltotriose, and maltotetraose. As verified by the direct addition of raffinose in our solution, the anomeric proton from the α-D-glucopyranose ring of raffinose gave a doublet signal at 5.435 ppm, and so raffinose can be excluded. The analysis of other ^{1}H and ^{13}C resonances including those outside the anomeric region indicated that kestose did not contribute to the signals at 5.419 and 5.412 ppm. Among the remaining sugars, sucrose and erlose were responsible for the doublet at

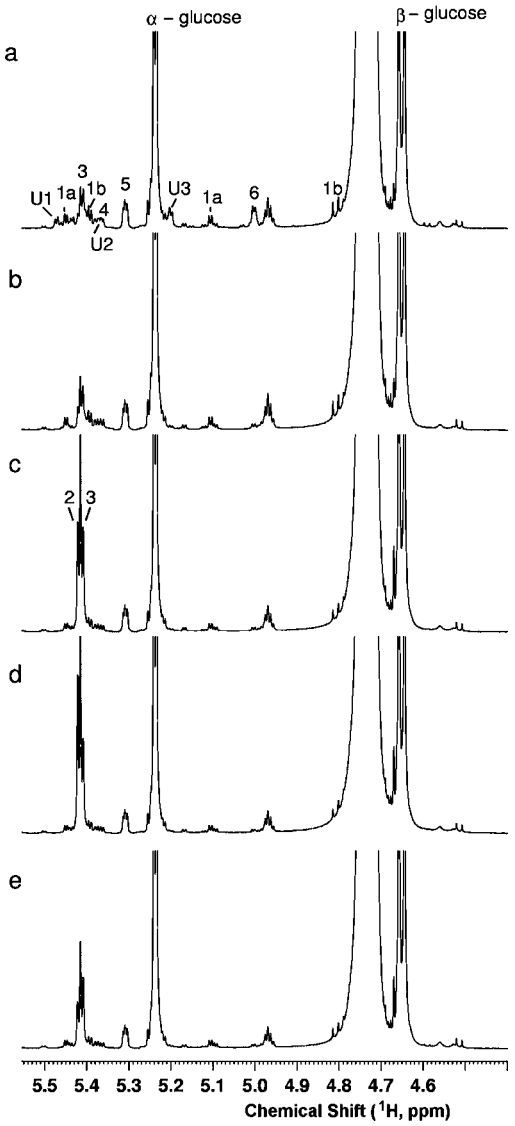

Figure 6. 5.5−4.4 ppm ^{1}H NMR spectral region of dill (a), medlar (b), sulla (c), orange (d), and lemon (e) honey solutions in D_2O. Assignments: 1a and 1b, kojibiose; 2, sucrose; 3, maltooligosaccharides; 4, nigerose; 5, turanose; 6, raffinose; U1, U2, U3, unassigned signals.

5.419 ppm, whereas erlose and maltose (according to $^{1}H-^{13}C$ HSQC experiment) contributed to the doublet at 5.412 ppm.

The quantification of raffinose, kojibiose, turanose, and nigerose in the five honeys has been performed by the integration of selected signals and normalization of integrals with respect to an internal standard (TSP) (Table 3). In the case of kojibiose and turanose, one of the anomeric forms (*O*-α-D-glucopyranosyl-(1→2)-β-D-glucopyranose and 3-*O*-α-D-glucopyranosyl-α-D-fructofuranose, respectively) was not quantified due to the absence of specific resonances not overlapped with the signals of the other sugars. As a consequence, the absolute content of kojibiose and turanose in honeys was underestimated. Nevertheless, taking into account that all of the anomeric forms were in equilibrium under the experimental conditions, the contents of kojibiose and turanose reported in Table 3 can be considered as relative values that can be compared between different samples.

DOI: 10.1021/jf506192s
J. Agric. Food Chem. 2015, 63, 5864−5874

Table 3. Sugar Concentrations in Sulla, Dill, Lemon, Orange, and Medlar Honeys According to NMR Analysis

	concentration (mg/g)				
sugar	sulla	dill	lemon	orange	medlar
raffinose	2.8 ± 0.1	25.7 ± 0.8	2.6 ± 0.1	2.2 ± 0.1	4.1 ± 0.1
kojibiose[a]	4.2 ± 0.1	6.7 ± 0.1	3.9 ± 0.1	3.9 ± 0.1	6.6 ± 0.1
turanose[b]	20.6 ± 0.4	22.6 ± 0.5	17.9 ± 0.2	18.0 ± 0.3	22.9 ± 0.4
nigerose	7.4 ± 0.1	nd	6.7 ± 0.2	6.8 ± 0.1	10.2 ± 0.3

[a]Only *O*-*α*-D-glucopyranosyl-(1→2)-*α*-D-glucolpyranose anomer. [b]Only 3-*O*-*α*-D-glucopyranosyl-*β*-D-fructofuranose and 3-*O*-*α*-D-glucopyranosyl-*β*-D-fructopyranose.

The values reported in Table 3 evidence the marked differences in the content of minor components of the saccharide fraction in the honeys of different botanical origins. Raffinose content showed a noticeable variation, whereas the contents of turanose were quite similar in all five honeys as well as to some extent the contents of kojibiose. The content of raffinose was particularly high in dill honey with respect to other honeys. The content of nigerose in dill honey was not determined due to overlapping of its signals with those of an unassigned compound (U2). It is noteworthy that dill honey contains still unidentified saccharides (denoted U1, U2, and U3 in Figure 6a) absent in the other four honeys, as suggested by ^{1}H NMR signals.

Especially in dill honey, the occurrence of carbohydrates such as kojibiose, turanose, and nigerose (Figure 7), which were shown to possess prebiotic effects in experimental animal studies, suggests that these honeys may exert prebiotic effects. These compounds have been found to show a large number of physiologic effects, such as increasing bifidobacteria numbers in the colon. This effect has been connected to other positive effects for human health such as the production of compounds able to inhibit potential pathogen growth, reduce blood ammonia levels, and produce vitamins and digestive enzymes. Moreover, the carbohydrates reported above showed also the capacity to increase calcium absorption and fecal weight and to decrease gastrointestinal transit time and blood lipid levels.[37,38]

Finally, in the region between 3 and 0.5 ppm (Figure 8a,b) characteristic signals of organic acids and amino acids are present. The signals of proline and lactic, acetic, and succinic acids were identified in this region in all honeys, but the intensity of proline and lactic and succinic acids resonances was much higher in dill compared to sulla honey. Another amino acid, phenylalanine, was identified only in dill (Figure 6c) and lemon honeys, whereas its content was too low to be detected in sulla (Figure 6d), medlar, and orange honeys. According to the literature, proline is the most abundant amino acid in honey followed by phenylalanine.[39] Moreover, alanine traces were observed only in the dill honey spectrum (Figure 8).

In conclusion, this investigation represents the first study of the chemical composition of sulla and dill honeys obtained in purity by Sicilian black honeybees performed with a combined method that includes HPLC-PAD-ESI-MS^n and NMR spectroscopy analyses. LC-MS/MS analysis allowed the identification of 22 compounds. In sulla honey, 14 compounds were identified, among which were 3 organic acids, 1 derivative of a phenolic acid, 4 flavonols, 1 flavanon, 4 flavanonols, and dehydrovomifoliol. In dill honey, 14 compounds were detected, among which were 4 organic acids, 2 phenolic acids and derivatives, 1 flavanonol, 1 flavanon, 1 B2 vitamin and its metabolite, 1 amino acid, 1 norisoprenoid compound, dehydrovomifoliol, and 3-hydroxy-1-(2-methoxyphenyl)penta-1,4-dione. Some compounds were previously detected in other

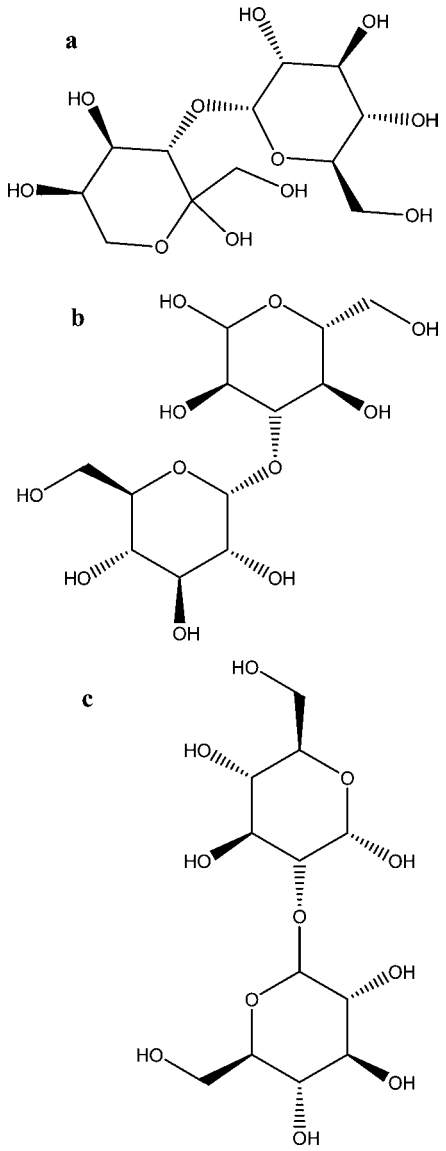

Figure 7. Chemical structures of (a) turanose (3-*O*-*α*-D-glucopyranosyl-*β*-D-fructopyranose), (b) nigerose (3-*O*-*α*-D-glucopyranosyl-D-glucose), and (c) kojibiose (2-*O*-*α*-D-glucopyranosyl-D-glucopyranose).

A. mellifera ssp. *sicula* honey samples of different botanical origins,[10] but for many other substances, this research represents the first report on their identification in these particular kinds of honey. NMR spectroscopy allowed the identification and quantification of several carbohydrates such as raffinose, kojibiose, turanose, and nigerose, the beneficial effects of which on nonpathogenic gut microorganism growth

DOI: 10.1021/jf506192s
J. Agric. Food Chem. 2015, 63, 5864−5874

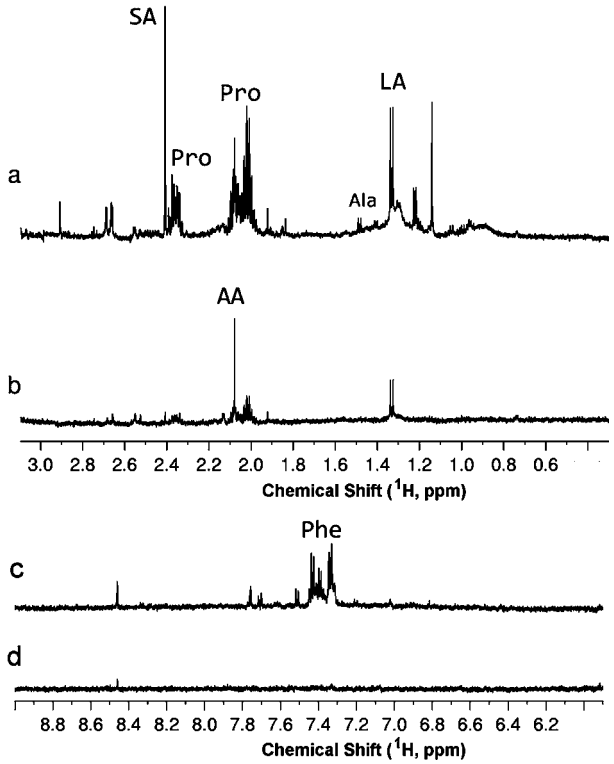

Figure 8. Two selected regions of ^{1}H NMR spectra of dill (a, c) and sulla (b, d) honey solutions in D_2O. Assignments: AA, acetic acid; Ala, alanine; LA, lactic acid; Phe, phenylalanine; Pro, proline; SA, succinic acid.

are well documented. Especially, the finding of the high content of turanose in all tested honeys and raffinose in dill honey justifies the prebiotic effect ascribed to honey.

The combination of these two methodologies allowed us to describe the phytochemical composition of each type of honey and identify many compounds that were found in these types of honey for the first time. In addition, we could compare the metabolic profiles obtained by our analysis with those already reported in the literature and provide the first phytochemical composition for that kind of honey for which no chemical data are available in the literature. On the basis of the obtained results, this combined approach can be applied conveniently for future honey analyses.

AUTHOR INFORMATION

Corresponding Author

*(M.D.) Phone: (39) 0382 987388. Fax: (39) 0382 422975. E-mail: maria.daglia@unipv.it.

Notes

The authors declare no competing financial interest.

REFERENCES

(1) Bogdanov, S.; Jurendic, T.; Sieber, R.; Gallmann, P. Honey for nutrition and health: a review. *J. Am. Coll. Nutr.* **2008**, *27*, 677−689.

(2) Khalil, M.-I.; Alam, N.; Moniruzzaman, M.; Sulaiman, S.-A.; Gan, S.-H. Phenolic acid composition and antioxidant properties of Malaysian honeys. *J. Food Sci.* **2011**, *76*, C921−928.

(3) Truchado, P.; Tourn, E.; Gallez, L. M.; Moreno, D. A.; Ferrerei, F.; Tomas-Barberan, F. A. Identification of botanical biomarkers in Argentinean Diplotaxis honeys: flavonoids and glucosinolates. *J. Agric. Food Chem.* **2010**, *58*, 12678−12685.

(4) White, J. W. Detection of honey adulteration by carbohydrate analysis. *J. Assoc. Off. Anal. Chem.* **1980**, *63*, 11−18.

(5) Tuberoso, C.; Bifulco, E.; Caboni, P.; Sarais, G.; Cottoglia, F. Lumichrome and phenyllactic acid as chemical markers of thistle (*Galactites tomentosa* Moench) honey. *J. Agric. Food Chem.* **2011**, *59*, 364−369.

(6) Tuberoso, C. I.; Bifulco, E.; Jerković, I.; Caboni, P.; Cabras, P.; Floris, I. Methyl syringate: a chemical marker of asphodel (*Asphodelus microcarpus* Salzm. et Viv.) monofloral honey. *J. Agric. Food Chem.* **2009**, *57*, 3895−3900.

(7) Oelschlaegel, S.; Gruner, M.; Wang, P.-N.; Boettcher, A.; Koelling-Speer, I.; Speer, K. Classification and characterization of manuka honeys based on phenolic compounds and methylglyoxal. *J. Agric. Food Chem.* **2012**, *60*, 7229−7237.

(8) Franck, P.; Garney, L.; Celebrano, G.; Solignac, M.; Cornuet, J.-M. Hybrid origins of honeybees from Italy (*Apis mellifera ligustica*) and Sicily (*Apis mellifera* ssp. *sicula*). *Mol. Ecol.* **2000**, *9*, 907−921.

(9) http://www.slowfood.com (accessed Feb 26, 2015).

(10) Tenore, G. C.; Ritieni, A.; Campiglia, P.; Novellino, E. Nutraceutical potential of monofloral honeys produced by the Sicilian black honeybees (*Apis mellifera* ssp. *sicula*). *Food Chem. Toxicol.* **2012**, *50*, 1955−1961.

(11) Pichichero, E.; Lorena, C.; Canini, A. Characterisation of the phenolic and flavonoid fractions and antioxidant power of Italian honeys of different botanical origin. *J. Sci. Food Agric.* **2009**, *89*, 609−616.

(12) Truchado, P.; López-Gálvez, F.; Gil, M. I.; Tomás-Barberán, F. A.; Allende, A. Quorum sensing inhibitory and antimicrobial activities of honeys and the relationship with individual phenolics. *Food Chem.* **2009**, *115*, 1337−1344.

(13) Escriche, I.; Kadar, M.; Juan-Borrás, M.; Domenech, E. Using flavonoids, phenolic compounds and headspace volatile profile for botanical authentication of lemon and orange honeys. *Food Res. Int.* **2011**, *44*, 1504−1513.

(14) Isla, M. I.; Craig, A.; Ordoñez, R.; Zampini, C.; Sayago, J.; Bedascarrasbure, E.; Alvarez, A.; Salomón, V.; Maldonado, L. Physico chemical and bioactive properties of honeys from northwestern Argentina. *LWT−Food Sci. Technol.* **2011**, *44*, 1922−1930.

(15) Marshall, S. M.; Schneider, K. R.; Cisneros, K. V.; Gu, L. Determination of antioxidant capacities, α-dicarbonyls, and phenolic phytochemicals in Florida varietal honeys using HPLC-DAD-ESI-MS(n). *J. Agric. Food Chem.* **2014**, *62*, 8623−8631.

(16) Wiest, L.; Buleté, A.; Giroud, B.; Fratta, C.; Amic, S.; Lambert, O.; Pouliguen, H.; Arnaudguilhem, C. Multi-residue analysis of 80 environmental contaminants in honeys, honeybees and pollens by one extraction procedure followed by liquid and gas chromatography coupled with mass spectrometric detection. *J. Chromatogr., A* **2011**, *1218*, 5743−5756.

(17) Dubois, M.; Gilles, K. A.; Hamilton, J. K.; Rebers, P. A.; Smith, F. Colorimetric method for determination of sugars and related substances. *Anal. Chem.* **1956**, *28*, 350−356.

(18) Miller, G. L. Use of dinitrosalicylic acid reagent for determination of reducing sugar. *Anal. Chem.* **1959**, *31*, 426−428.

(19) Khalil, M. I.; Moniruzzaman, M.; Boukraâ, L.; Benhanifia, M.; Islam, M. A.; Islam, M. N.; et al. Physicochemical and antioxidant properties of Algerian honey. *Molecules* **2012**, *17*, 11199−11215.

(20) Mannina, L.; Cristinzio, M.; Sobolev, A. P.; Ragni, P.; Segre, A. High-field nuclear magnetic resonance (NMR) study of truffles (*Tuber aestivum vittadini*). *J. Agric. Food Chem.* **2004**, *52*, 7988−7996.

(21) Kečkeš, S.; Gašić, U.; Ćirković Veličković, T.; Milojković-Opsenica, D.; Natić, M.; Tešić, Z. The determination of phenolic profiles of serbian unifloral honeys using ultra-high-performance liquid chromatography/high resolution accurate mass spectrometry. *Food Chem.* **2013**, *138*, 32−40.

(22) Pellati, F.; Orlandini, G.; Pinetti, D.; Benvenuti, S. HPLC-DAD and HPLC-ESI-MS/MS methods for metabolite profiling of propolis extracts. *J. Pharm. Biomed. Anal.* **2011**, *55*, 938−948.

(23) Ristivojević, P.; Trifković, J.; Gašić, U.; Andrić, F.; Nedić, N.; Tešić, Z.; Milojković-Opsenica, D. Ultrahigh-performance liquid

DOI: 10.1021/jf506192s
J. Agric. Food Chem. 2015, 63, 5864−5874

chromatography and mass spectrometry (UHPLC-LTQ/Orbitrap/MS/MS) study of phenolic profile of Serbian poplar type propolis. *Phytochem. Anal.* **2014**, DOI: 10.1002/pca.2544.
(24) Chua, L. S.; Rahaman, N. L.; Adnan, N. A.; Eddie Tan, T. T. Antioxidant activity of three honey samples in relation with their biochemical components. *J. Anal. Methods Chem.* **2013**, *2013*, article ID 313798, 8 pp.
(25) Ortan, A.; Popescu, M.-L.; Dinu-Pirvu, C.; Gaita, A.-L.; Campeanu, G. Contributions to the pharmacognostical study on *Anethum graveolens*, dill (*Apiaceae*). *Rom. Biotechnol. Lett.* **2009**, *14*, 4342−4348.
(26) Soto, M. A.; Ares, A. M.; Bernal, J.; Noza, M. J.; Bernal, J. L. Simultaneous determination of tryptophan, kynurenine, kynurenic and xanthurenic acids in honey by liquid chromatography with diode array, fluorescence and tandem mass spectrometry detection. *J. Chromatogr., A* **2011**, *1218*, 7592−7600.
(27) Medana, C.; Carbone, F.; Aigotti, R.; Appendino, G.; Baiocchi, C. Selective analysis of phenolic compounds in propolis by HPLC-MS/MS. *Phytochem. Anal.* **2008**, *19*, 32−39.
(28) Jerković, I.; Tuberoso, C. I. G.; Gugić, M.; Bubalo, D. Composition of sulla (*Hedysarum coronarium* L.) honey solvent extractives determined by GC/MS: norisoprenoids and other volatile organic compounds. *Molecules* **2010**, *15*, 6375−6385.
(29) Daglia, M.; Di Lorenzo, A.; Nabavi, S. F.; Talas, Z. S.; Nabavi, S. M. Polyphenols: well beyond the antioxidant capacity: gallic acid and related compounds as neuroprotective agents: you are what you eat! *Curr. Pharm. Biotechnol.* **2014**, *15*, 362−372.
(30) Sergiel, I.; Pohl, P.; Biesaga, M. Characterization of honeys according to their content of phenolic compounds using high performance liquid chromatography/tandem mass spectrometry. *Food Chem.* **2014**, *145*, 404−408.
(31) Kelly, M. T.; Blaise, A.; Larroque, M. Rapid automated high performance liquid chromatography method for simultaneous determination of amino acids and biogenic amines in wine, fruit and honey. *J. Chromatogr., A* **2010**, *1217*, 7385−7392.
(32) Tuberoso, C. I.; Jerković, I.; Bifulco, E.; Marijanovic, Z.; Congiu, F.; Bubalo, D. Riboflavin and lumichrome in Dalmatian sage honey and other unifloral honeys determined by LC-DAD technique. *Food Chem.* **2012**, *135*, 1985−1990.
(33) Xiong, L.; Zhu, J. K. Regulation of abscisic acid biosynthesis. *Plant Physiol.* **2003**, *133*, 29−36.
(34) Consonni, R.; Cagliani, L. R.; Cogliati, C. NMR characterization of saccharides in Italian honeys of different floral sources. *J. Agric. Food Chem.* **2012**, *60*, 4526−4534.
(35) Petersen, B. O.; Hindsgaul, O.; Meier, S. Profiling of carbohydrate mixtures at unprecedented resolution using high-precision ^{1}H-^{13}C chemical shift measurements and a reference library. *Analyst* **2014**, *139*, 401−406.
(36) Roslund, M. U.; Tähtinen, P.; Niemitzc, M.; Sjöholm, R. Complete assignments of the ^{1}H and ^{13}C chemical shifts and $J_{H,H}$ coupling constants in NMR spectra of D-glucopyranose and all D-glucopyranosyl-D-glucopyranosides. *Carbohydr. Res.* **2008**, *343*, 101−112.
(37) Sanz, M. L.; Polemis, N.; Morales, V.; Corzo, N.; Drakoularakou, A.; Gibson, G. R.; Rastall, R. A. In vitro investigation into the potential prebiotic activity of honey oligosaccharides. *J. Agric. Food Chem.* **2005**, *53*, 2914−2921.
(38) Al-Waili, N. S.; Salom, K.; Butler, G.; Al Ghamdi, A. A. Honey and microbial infections: a review supporting the use of honey for microbial control. *J. Med. Food* **2011**, *10*, 1079−1096.
(39) Belitz, H. D., Grosch, W., Schieberle, P., Eds. *Food Chemistry*, 4th ed.; Springer-Verlag: Berlin, Germany, 2009; pp 883−890.

DOI: 10.1021/jf506192s
J. Agric. Food Chem. 2015, 63, 5864−5874

source of phytochemicals.[13] The main challenge of adding these byproducts to bakery products is to find new processing strategies to incorporate more of the bioactive compounds in flour while still removing those parts of grain that confer inferior technological quality or affect safety.[3] In general, DF additions to baking lead to important reductions in the loaf volume, and a different texture of the breads is obtained; thus, the optimal proportion of DF addition to each different food should also be determined on the basis of sensory attributes.

The cereal grain fractionation technology, which could also be applied easily with a selective dry pearling process, is receiving a great deal of attention because of its capacity to efficiently separate negative and positive aspects, to produce new ingredients and flour mixes with technologically optimized functional and nutritional attributes.[14,15] The sequential pearling of wheat kernel and the incorporation of selected pearled fractions into the bread formula were studied in previous works.[16,17]

The effects of the inclusion of barley whole grain or bran fractions were previously reported by several authors, who focused separately on the nutritional benefits[18−22] or the technological consequences.[23−26] However, the addition of intermediate pearled barley fractions to breadmaking has not yet been considered.

The aims of this study were (i) to analyze the bioactive compound contents and detrimental factors in barley kernels, through a sequential pearling process, in order to use them as functional food ingredients; and (ii) to comprehensively evaluate the nutritional enhancement and the technological impact of the incorporation, at different replacement levels, of an intermediate pearled barley fraction into bread formulations.

MATERIALS AND METHODS

Field Barley Production. Two commercial winter barley varieties were cultivated side by side in the same field, in a medium-texture fertile soil in Carignano, northwestern Italy (44°53′8.69″ N, 7°41′16.75″ E, 232 m asl), during the 2011−2012 growing season, according to the normal crop management program applied in the growing area.

The compared barley varieties were Trasimeno (Geo Seed, Grinzano di Cervere, CN, Italy), a two-row cultivar, and Ketos (Limagrain Italia Spa, Busseto, PR, Italy), a six-row cultivar. Both cultivars have hulled grains.

Planting was conducted in 12 cm wide rows at a seeding rate of 450 seeds m^{-2} on October 24, 2011. The previous crop was maize for grain, and the seed bed was set after plowing (30 cm) and harrowing. A total of 130 kg N ha^{-1} was applied as a granular ammonium nitrate fertilizer, split equally between the tillering and stem elongation stages. Harvest was conducted with a combine-harvester on June 23, 2012. Kernel samples of each cultivar were stored at 4 °C until the beginning of the pearling tests.

Sequential Grain Pearling. Nine fractions of kernels from each cultivar were obtained through incremental pearling, following the approach proposed by Beta et al.[27] The pearling consisted of consecutive passages of barley whole grain and pearled grain in an abrasive-type grain testing mill (TM-05C model, Satake, Tokyo, Japan) at a constant speed of 1100 rpm and a frequency of 55 Hz. The pearling process was monitored by time control. After each assay, the laboratory pearler was cleaned thoroughly by means of dust aspiration and compressed air, to minimize equipment contamination. Initially, a 500 g portion of each unprocessed barley was subsampled from a 5 kg sample, and the remaining 4.5 kg was pearled. Starting with unprocessed grain, kernels were initially pearled to remove 5% of the original grain weight, and this resulted in a first fraction (0−5% w/w). The remaining kernels were then pearled to remove a second fraction of 5% (5−10% w/w). The pearling process was continued until another six fractions (designated 10−15, 15−20, 20−25, 25−30, 30−35, and 35−40%, respectively) plus a residual 60% of the kernel (40−100%) had been collected.

The whole grain samples and the residual 60% of the unprocessed kernels were milled using a laboratory centrifugal mill (ZM-100; Retsch, Haan, Germany) with a 1 mm opening. Then, both the milled and pearled samples (500 g) were ground to pass through a 0.5 mm sieve and stored at −25 °C until the chemical analyses.

Substitution of Flour with Barley Pearled Fraction in the Breadmaking Procedure. A functional ingredient was obtained from the barley pearling, following the approach proposed in a previous study focused on wheat.[17] The two-row Trasimeno barley, which showed the lower deoxynivalenol (DON) content and the higher β-glucan content, was chosen to prepare an intermediate pearled fraction, to obtain a functional ingredient that would preserve a high functional role, but without those parts of grain that could confer inferior technological quality or affect safety. Considering that the fiber, proteins, minerals, and antioxidant compounds are concentrated in the most external layers, but β-glucans are present in a greater concentration in the inner part of the barley kernel, the best compromise to preserve all of these functional compounds appeared to be the 15−25% (w/w) fraction. In fact, the total and insoluble DF in the selected pearled fraction was still high, and although the more external coarse fiber, located in the hull, and the more external endosperm layers were removed, a good β-glucan content was still provided.

Starting from unprocessed grain, the barley kernels were initially pearled to remove 15% of the original grain weight, according to the previously reported procedure, and this most external fraction was discarded. The remaining kernels were then pearled to remove a second 10% fraction of the original grain weight (15−25%), and this fraction was used to replace refined commercial breadmaking flour at different percentages.

Five mixtures of refined commercial breadmaking flour, with increasing replacement rates (5, 10, 15, 20, and 25%) of the selected pearled barley fraction, were obtained and employed for breadmaking. Refined flour and the selected pearled barley fraction were accurately mixed using a rotary laboratory blender (Beccaria S.r.l., Cuneo, Italy). The Chopin alveograph parameters of the commercial refined flour were deformation energy (W) = 325 J 10^{-4} and curve configuration ratio (P/L) 0.52. The particle size of the selected pearling fraction was similar to that of the refined commercial flour: in both cases, >80% of the particles were <200 μm.

The breads were made according to AACCI Method 10-10.03 for 3 kg of flour.[28] The formula contained salt (2% of flour weight), brewer's yeast (3% of flour weight), and the optimal water absorption, which was previously determined through a Mixolab rheological analysis. The dough was then mixed in a spiral mixer (Esmach, Bonpard Group, Vicenza, Italy) and divided into three pieces of approximately 400 g/piece, to obtain three loaves, which were placed in baking tins (10.5 × 6 cm^2, 6.5 cm deep). The mixing times were different for the refined commercial and the selected pearled barley fraction mixtures, to obtain an equivalent dough development. After fermentation (at 30 °C and a relative humidity of 85% for 120 min), the loaves were baked at 215 °C for 45 min.

The three composite loaves for each replacement level were used as replicates for chemical and technological analyses.

Chemicals. The total DF and mixed-linkage β-glucan kits for enzymatic determinations were supplied by Megazyme (Megazyme International Ireland Ltd., Wicklow, Ireland). The solvents (HPLC grade) and formic acid (50%, LC-MS grade) were purchased from Sigma-Aldrich (Milan, Italy). The water was obtained from a Milli-Q instrument (Millipore Corp., Bedford, MA, USA). The antibody-based immunoaffinity columns were supplied by VICAM (Waters Corp., Watertown, MA, USA). The analytical standards (purity ≥ 95%) and all other chemicals (reagent grade level) were purchased from Sigma-Aldrich.

Chemical Analyses on Pearling Fractions and Breads. *Sample Preparation.* Bread samples were ground in a laboratory mill (ZM-100; Retsch, Haan, Germany), and in the case of DF, total

DOI: 10.1021/jf506193p
J. Agric. Food Chem. 2015, 63, 5875−5884

Table 1. Ash, Protein, DF, and β-Glucan Contents, TAA, and DON Contamination in Barley Kernels[a]

			DF (%)			TAA (mmol TE kg^{-1})			
barley cv.	ash (%)	proteins (%)	total	insoluble	β-glucans (%)	DPPH MeOH	DPPH H_2O	ABTS	DON (μg kg^{-1})
Ketos (six-row)	2.5 b	10.2 a	27 a	22 a	2.7 b	10.3 a	26.1 a	30.6 a	178 a
Trasimeno (two-row)	2.8 a	9.3 b	20 b	14 b	4.4 a	10.4 a	26.7 a	28.3 b	<LOQ b
P (*F*)	<0.001	0.003	<0.001	<0.001	<0.001	0.076	0.123	<0.001	<0.001
SEM[b]	0.1	0.7	1.2	1.7	0.3	1.5	1.9	2.6	1.1

[a]The results are expressed on a dw basis. [b]SEM, standard error of means.

phenolic content (TPC), and total antioxidant activity (TAA) determinations, they were further freeze-dried (Heto Drywinner 8, Copenhagen, Denmark) and ground in an oscillatory mill (Mixer Mill MM440, Retsch GmbH). The pearled barley fractions, the whole flours, and the freeze-dried ground breads were sieved (particles size < 250 μm) prior to the TAA analyses.

Proximate Composition. Moisture, total proteins, ashes, dietary fiber (both total and insoluble), and β-glucan contents were determined as previously described.[16,17] The conversion factors employed to calculate the total protein content were 5.83 and 5.70 for barley and for wheat flour and bread, respectively.

Total Phenolic Content. TPC was determined on composite breads and on the flours employed to prepare the loaves. Phenolic extracts were prepared as previously reported,[17] and then 30−100 μL (according to the expected concentration) was made to react with 100 μL of Folin−Ciocalteu reagent and 350 μL of sodium carbonate (5%), adding distilled water to obtain a total volume of 2900 μL. After 1 h of incubation, the absorbance was measured at 760 nm (Evolution 60S spectrophotometer, Thermo Scientific, Milan, Italy). The results were expressed as ferulic acid equivalents through a calibration curve ($y = 0.0105x - 0.0563$; $R^2 = 0.994$; linearity range = 10−80 μg).

Total Antioxidant Activity. TAA was determined by employing DPPH$^•$ and ABTS$^{•+}$ methods (direct measurement on solid samples), as previously described.[16,17,29] DPPH$^•$ antiradical activity was determined in both methanolic (DPPH MeOH) and hydroalcoholic (DPPH H_2O) solutions.

As far as the DPPH MeOH method is concerned, the samples were opportunely weighed (0.5−20 mg, to obtain final inhibition percentage values <70%), and then 700 μL of methanol and 700 μL of a 100 μM DPPH$^•$ methanolic solution were added. The reaction was carried out in the dark under stirring for 25 min, and then the samples were promptly centrifuged for 1 min at 14000 rpm (Microcentrifuge 5417 R, Eppendorf Italia, Milan, Italy) and the absorbance was measured at 515 nm after exactly 30 min of reaction (Evolution 60S spectrophotometer, Thermo Scientific, Milan, Italy). A control solution (without sample) was tested under the same conditions to calculate the DPPH$^•$ inhibition percentage.

The DPPH H_2O method was performed as described for DPPH in the methanolic solution, but with the addition of 1400 μL of water and 1400 μL of the DPPH$^•$ methanolic solution to the solid samples.

ABTS$^{•+}$ reagent was prepared as described by Re et al.[30] and further diluted in a mixture of ethanol/water (50:50, v/v) to obtain an absorbance of 0.700 ± 0.020 at 734 nm. Samples were tested in the ratio of 0.5−10 mg per 6 mL of ABTS$^{•+}$ solution (inhibition percentage values < 70%). The reaction solutions were stirred for 25 min and then centrifuged at 14000 rpm for 1 min (Microcentrifuge 5417 R, Eppendorf Italia). Absorbance of the samples and control solutions was performed after exactly 30 min, and then the inhibition percentage values were calculated.

For all of the methods, the final results were expressed as millimoles of trolox equivalents (TE) per kilogram of sample (dw) through a calibration curve (DPPH, $y = 11.267x - 4.3171$, $R^2 = 0.982$, linearity range = 1−15 μg; ABTS, $y = 2.666x - 1.9208$, $R^2 = 0.986$, linearity range = 5−35 μg).

Deoxynivalenol Contamination. The DON content was analyzed on barley fractions obtained from the sequential pearling using a high-performance liquid chromatography (HPLC-MS-MS) method (range = 80−4000 μg kg^{-1}), as previously described by Sovrani et al.[16] The percentage of recovery, obtained using Certified Reference Materials (CRM Trilogy Analytical Laboratory, 2.1 mg kg^{-1} ± 0.2 mg kg^{-1}), was 79% (relative standard deviation = 6%). The limit of detection (LOD) and the limit of quantification (LOQ) were 5 and 16 μg kg^{-1}, respectively.

Breadmaking Technological Quality Analyses. *Rheological Properties of the Flour.* The mixing and pasting behaviors of the control and different replaced flours were studied using a Mixolab analyzer (Chopin Technologies, Paris, France), according to ICC Standard Method 173.[31] This instrument allows specific information to be obtained about the behavior of dough constituents (starch, protein, water) by continuously measuring the torque (Nm) produced by the passage of the dough between two mixing blades, subject to the dual stress of mixing and temperature changes.

Bread Crust and Crumb Color. The chromatic characteristics of the bread crust and crumb were determined using a Minolta Chroma Meter reflectance spectrophotometer (model CR-400, Minolta Co., Osaka, Japan). Standard illuminant C was used as the reference. The analysis was performed in triplicate at three different points for each loaf, for both the bread crust and crumb. The color values of *L**, *a**, and *b** were determined directly by the instrument, according to Commission Internationale de L'Eclairage methods.[32]

Combined Acoustic−Mechanical Analysis of the Bread Crust. A penetration test was carried out to assess the mechanical and acoustic properties of the bread crust, using a TA-XT Plus Texture Analyzer (SMS-Stable Micro Systems, Surrey, UK), combined with an AED Acoustic Envelope Detector supplied by the same manufacturer. Force and acoustic emission acquisitions were made simultaneously using the Texture Exponent software (Stable Micro Systems), with a data rate of 500 points per second during a compression/penetration test.[33] Each loaf was penetrated by a P/6 6 mm steel cylindrical probe, a deformation of 20 mm was applied with a test speed of 1 mm s^{-1}, and an instrumental trigger of 0.05 N was used. The microphone was placed at a fixed distance of 10 mm from the sample for the acoustic measurements. To minimize the noise, the acoustic measurements were filtered through an integrated 1 kHz high-pass filter, and a 24 dB instrumental gain was applied.

The analysis was performed in triplicate at three different points for each loaf. The following mechanical and acoustic parameters were determined from the force−distance and acoustic spectra according to the method of Piazza et al.:[33] total energy (mJ), maximum acoustic emission (dB (SPL)), and number of acoustic emission peaks using 15 dB (SPL) as the peak threshold value.[17]

Bread Volume. Loaf volume was determined 1 h after baking, by means of the rapeseed displacement method AACCI Standard 10-05.01.[34]

Bread Crumb Texture Profile Analysis. Texture measurements were performed on two slices (20 mm thick), cut from the central part of the three replicated loaves for each mixture of refined flour and pearled fraction, 4 h after baking. The bread slices were compressed in the central area using an SMS P/35 flat probe (Stable Micro Systems) for a 50% deformation of the slice with a waiting time between two bites of 30 s, using 1 mm s^{-1} as the speed test.[17] An instrumental trigger of 0.05 N was applied. The typical texture profile analysis parameters were determined from the force−distance curves and calculated by the software: hardness (N), cohesiveness (adimensional), gumminess (N), springiness (mm), chewiness (mJ), and resilience (adimensional).[35]

Statistical Analysis. All of the analyses were performed at least in triplicate. The results of the bread samples were reported as the means

DOI: 10.1021/jf506193p
J. Agric. Food Chem. 2015, 63, 5875−5884

Table 2. Ash, Protein, DF, and β-Glucan Contents, TAA, and DON Contamination in Pearled Barley Fractions[a]

barley cv.	kernel pearling fraction	ash (%)	proteins (%)	DF (%)		β-glucans (%)	TAA (mmol TE kg^{-1})			DON (μg kg^{-1})
				total	insoluble		DPPH MeOH	DPPH H_2O	ABTS	
Ketos (six-row)	0−5%	8.5 a	6.1 g	79 a	79 a	0.2 f	21 de	34 e	33 f	1074 a
	5−10%	7.0 b	9.4 f	68 b	66 b	1.2 e	45 b	77 c	114 b	532 b
	10−15%	6.4 c	18.3 bc	46 c	41 c	2.2 d	55 a	142 a	154 a	268 c
	15−20%	6.1 c	19.3 a	37 d	31 d	2.6 d	47 b	128 a	143 a	148 d
	20−25%	5.4 d	18.9 ab	23 e	20 e	3.5 c	31 c	98 b	95 c	110 e
	25−30%	4.3 e	17.7 c	21 e	14 f	4.0 b	25 d	59 d	66 d	73 f
	30−35%	3.3 f	16.2 d	19 e	9 g	4.5 ab	19 e	48 de	54 de	59 f
	35−40%	2.6 g	15.3 e	10 f	1 h	4.7 a	17 e	41 e	41 ef	52 f
	residue 40−100%	0.9 h	9.1 f	11 f	3 h	4.9 a	3 f	8 f	9 g	<LOQ g
	P (*F*)	<0.001	<0.001	<0.001	<0.001	<0.001	<0.001	<0.001	<0.001	<0.001
	SEM[b]	0.7	0.9	6.5	3.4	0.9	5.6	18.0	19.5	20
Trasimeno (two-row)	0−5%	9.4 a	5.3 f	72 a	71 a	0.8 g	20 e	45 de	30 f	<LOQ
	5−10%	7.3 b	9.6 d	65 b	64 b	1.2 g	31 d	66 c	61 cd	<LOQ
	10−15%	6.8 c	16.7 a	49 c	43 c	2.2 f	66 a	132 a	139 a	<LOQ
	15−20%	5.7 d	17.2 a	36 d	31 d	3.1 e	49 b	126 a	129 a	<LOQ
	20−25%	4.6 e	15.7 b	27 e	21 e	3.9 d	36 c	86 b	110 b	<LOQ
	25−30%	3.7 f	14.5 c	26 e	16 ef	4.6 cd	21 e	53 cd	66 c	<LOQ
	30−35%	3.0 g	13.9 c	19 f	12 fg	5.1 bc	16 f	47 de	50 de	<LOQ
	35−40%	2.6 h	14.1 c	22 ef	9 g	5.5 ab	14 f	40 e	40 e	<LOQ
	residue 40−100%	1.1 i	7.3 e	9 g	2 h	6.0 a	3 g	7 f	14 g	<LOQ
	P (*F*)	<0.001	<0.001	<0.001	<0.001	<0.001	<0.001	<0.001	<0.001	
	SEM[b]	0.3	0.9	5.4	4.2	1.3	4.9	13.4	13.4	

[a]Results are expressed on a dw basis. Means followed by different letters are significantly different (the level of significance is shown in the table). [b]SEM, standard error of means.

of the three loaf replicates. The analysis of variance (ANOVA) was used to compare the samples. The residual normal distribution was verified using the Kolmogorov−Smirnov test, whereas variance homogeneity was verified using the Levene test. Multiple-comparison tests were performed according to the REGW-Q test on treatment means. The SPSS for Windows, version 20.0 statistical package (SPSS Inc., Chicago, IL, USA), was used for the statistical analysis.

RESULTS AND DISCUSSION

Bioactive Compounds in the Whole Barley Kernel. The ash, protein, total and insoluble DF, and β-glucan contents, the DON contamination, and the TAA determined for the whole grain kernels are reported in Table 1. Except for the TAA obtained with the DPPH methods, ANOVA showed significant differences between the barley varieties used in this study. Trasimeno (two-row cultivar) reported a higher content of ash (+0.3%) and above all of β-glucans (+1.6%) than Ketos (six-row). Conversely, cv. Ketos had higher total and insoluble DF (+7%) and TAA, obtained through the ABTS method (+8%). As expected, the protein content was higher in the six-row barley (+1%). The DON content was under the LOQ for cv. Trasimeno, whereas the average contamination of this mycotoxin in the cv. Ketos kernel was 178 μg kg^{-1}.

The greatest difference between the compared cultivars is related to the almost double β-glucan content recorded in the two-row cultivar compared to the six-row one, thus confirming previous information.[36,37]

Even though the relative content of some compounds is genetically regulated (as in the case of β-glucans), their final absolute concentration is closely dependent on pedoclimatic and agronomic factors. For this reason, and considering that the observed varietal differences referred to a single year and a single cultivation location, further investigations should be conducted to improve the characterization of these barley cultivars.

Bioactive Compounds of the Pearled Barley Fractions. A total of 10 samples were obtained from each barley variety: the whole unprocessed grain and the 0−5, 5−10, 10−15, 15−20, 20−25, 25−30, 30−35, 35−40, and 40−100% fractions, obtained through the pearling process. The two first pearling passages (0−5 and 5−10%) led to an almost complete visual dehulling of the barley kernel, according to previous works.[15] The bioactive compound content in the fractions obtained from the sequential barley pearling is reported in Table 2. In both varieties, ANOVA showed highly significant differences ($P < 0.001$) between the kernel pearling fractions for all of the considered parameters. The first pearling fraction (0−5%) resulted in the highest content of the total and insoluble DF. Sequential pearling has shown that both the total and insoluble fibers decreased progressively from the external to the internal layers, whereas the β-glucan content increased going toward the inner kernel layers in both varieties, in agreement with the results of several authors.[38−40] According to Liu et al.,[15] the inner part of the barley kernel, after removal of 60% of the grain weight, showed a 27% higher β-glucan content than the whole kernel. In the cultivars considered in our study, the β-glucan contents of the residual part of the kernels after pearling (40−100%) were 79 and 38% higher than that of whole kernel, for the six-row and two-row barleys, respectively.

Comparing the β-glucan contents of the milling fractions of whole grain or pearled barley, Sullivan et al.[39] found the highest concentration in the middling fractions, followed by flour and, finally, by bran. Moreover, the authors reported that barley pearling (10% w/w) clearly affected the soluble and insoluble fiber contents in the milling fractions: the total DF of the grain

DOI: 10.1021/jf506193p
J. Agric. Food Chem. 2015, 63, 5875−5884

Table 3. Ash, Protein, DF, and β-Glucan Contents, TPC, and TAA in Refined Wheat Flour and Enriched Fractions Obtained through Barley Pearling[a]

			DF (%)				TAA (mmol TE kg^{-1})		
product	ash (%)	proteins (%)	total	insoluble	β-glucans (%)	TPC (mg kg^{-1})	DPPH MeOH	DPPH H_2O	ABTS
white flour	0.5 b	12.2 b	2.2 b	0.5 b	0.2 b	649 b	0.4 b	0.8 b	11.5 b
pearled barley fraction	5.1 a	18.1 a	24.7 a	23.1 a	3.3 a	5239 a	25.7 a	55.8 a	114.5 a
P (*F*)	<0.001	<0.001	0.002	0.004	<0.001	<0.001	<0.001	<0.001	<0.001
SEM[b]	0.1	0.3	0.7	1.2	0.09	75	1.1	2.9	5.9

[a]Results are expressed on a dw basis. Means followed by different letters are significantly different (the level of significance is shown in the table). [b]SEM, standard error of means.

Table 4. Mixolab Rheological Parameters[a] of Mixtures of Refined Wheat Flour and an Enriched Fraction Obtained through Barley Kernel Pearling

replacement level	water absorption (%)	DDT (min)	stability (min)	amplitude (nm)	C2 (Nm)	C3 (Nm)	C4 (Nm)	C5 (Nm)
0	55.0 f	3.5 a	8.7 a	0.09 b	0.42 a	1.82 a	1.61 a	2.33 a
5	57.2 e	3.6 a	6.4 bc	0.09 b	0.34 b	1.74 b	1.51 b	2.22 a
10	57.9 d	3.6 a	5.2 d	0.09 ab	0.29 de	1.72 b	1.49 b	2.22 a
15	58.5 c	3.3 a	5.6 d	0.09 ab	0.29 e	1.65 c	1.42 b	2.18 a
20	59.5 b	3.1 a	5.9 cd	0.10 ab	0.30 cd	1.66 c	1.46 b	2.28 a
25	60.5 a	3.1 a	6.9 b	0.11 a	0.31 c	1.63 c	1.43 b	2.25 a
P (*F*)	<0.001	0.096	<0.001	0.029	<0.001	<0.001	0.001	0.103
SEM[b]	0.30	0.51	0.62	0.02	0.01	0.04	0.08	0.12

[a]Mixolab parameters: water absorption, amount of water required for dough development; DDT, dough development time; stability, time of dough stability at a constant temperature; amplitude, dough elasticity; C2, protein weakness; C3, starch gelatinization; C4, hot gel stability; C5, starch retrogradation in the cooling phase; C2, C3, C4, and C5, end points of the corresponding mixing phases. Means followed by different letters are significantly different (the level of significance is shown in table). [b]SEM, standard error of means.

was decreased considerably by the pearling process. Conversely, there was little difference in the β-glucan content. In the study carried out by Marconi et al.,[41] the abrasive pearling fractions of barley hulled by approximately 10, 25, and 40% showed DF removals of 35, 55, and 71%, respectively, and β-glucan content removals of 5, 19, and 37%, respectively.

A progressive decrease in the percentage of ash was observed, because the mineral components are mainly distributed in the outer layers of the kernel.[41] Because useful elements and heavy metals, such as cadmium and lead, are included in ash, it could be useful to preserve the good mineral form present in cereals and remove the more contaminated fractions. In a previous experiment on wheat sequential pearling, heavy metals were found only in the most external fractions.[16]

The protein content was the lowest in the initial surface removal layer, which corresponded to the coarse hull fraction, whereas the highest content was observed in the 15−25 and 10−20% fractions, for Ketos and Trasimeno cultivars, respectively.

The 10−15 and 15−20% pearling fractions were those with the highest TAA. The next external layers (0−5 and 5−10%), consisting mainly of hull, and the next internal layers (20−25 and 25−30%) showed 48 and 44% lower TAA, respectively.

DON Contamination of the Pearled Barley Fractions. DON contamination in the barley fractions is reported in Table 2. The content of this mycotoxin was under the LOQ in all of the compared pearling fractions of cv. Trasimeno, thus confirming the data from whole grain kernels, whereas, for cv. Ketos, the outermost kernel layers had the highest DON contamination, which was 6 and 3 times higher than that of the whole kernel for the 0−5 and 5−10% fractions, respectively. These findings confirm that large concentrations of DON accumulate in the hulls of barley and that the application of processing strategies able to carefully remove the hull can lead to a significant reduction in the DON levels.[42]

As previously reported for wheat,[16] DON showed a decrease, going from the external to the internal layers, that followed a biphasic type pattern: a remarkable reduction was observed in the first pearling steps, and this was followed by a slower decrease. No significant differences were observed for DON contamination for the 25−30, 30−35, and 35−40% fractions. House et al.[43] reported that a grain mass loss of 15% through barley pearling reduced DON contamination by 34%.

Characterization of the Wheat Flour and Pearled Barley Fraction. The two-row Trasimeno barley, which showed the lower DON content and the higher β-glucan content, was chosen to prepare an intermediate pearled fraction, so as to obtain a functional ingredient that would preserve a high functional role, but without those parts of the grain that could confer inferior technological quality or affect safety. Considering that the fiber, proteins, minerals, and antioxidant compounds are concentrated in the most external layers, but β-glucans are present in a greater concentration in the inner part of the barley kernel, the best compromise to preserve all of these functional compounds appeared to be the 15−25% (w/w) fraction. In fact, the total and insoluble DF in the selected pearled fraction was still high, and although the more external coarse fiber, located in the hull, and the more external endosperm layers were removed, a good β-glucan content was still provided.

The refined commercial wheat flour and the selected pearled barley fraction were characterized for their chemical composition (ash, protein, DF, β-glucan, TPC content) and TAA (Table 3). The pearled barley fraction had 10, 1.5, 11, 14, and 8 times higher contents of ash, protein, DF, β-glucans, and TPC, respectively, than the refined commercial flour. Taking into account the different methods, the TAA of the pearled barley

DOI: 10.1021/jf506193p
J. Agric. Food Chem. 2015, 63, 5875−5884

Table 5. Crust Color, Texture, and Acoustic Emission Tests of Composite Bread with Refined Flour and Enriched Fractions Obtained through Barley Kernel Pearling[a]

	crust color			crust crunchiness		
replacement level	L^* (C)	a^* (C)	b^* (C)	total break energy (mJ)	max acoustic emission (dB, SPL)	no. of acoustic emission peaks (threshold 15 dB (SPL))
0	64.2 a	11.6 a	35.3 a	134 a	64.7 a	55 a
5	59.6 b	10.7 a	30.4 bc	90 b	62.7 ab	50 a
10	56.6 c	10.8 a	29.4 c	89 b	60.0 ab	23 b
15	50.0 e	11.0 a	29.5 c	84 bc	56.5 b	25 b
20	52.7 d	12.0 a	31.8 b	83 bc	55.1 b	18 b
25	54.2 d	11.1 a	31.9 b	73 c	45.2 c	12 b
P (F)	<0.001	0.403	<0.001	<0.001	<0.001	<0.001
SEM[b]	2.1	1.6	1.7	11.1	6.9	16.0

[a]Means followed by different letters are significantly different (the level of significance is shown in table). [b]SEM, standard error of means.

fraction was from 10 to 73 times higher than in the refined wheat flour.

Rheological Parameters of the Replaced Flours. Five mixtures of refined breadmaking flour, with an increasing replacement of the selected pearled barley fraction (5, 10, 15, 20, and 25%), were obtained and characterized for their rheological properties (Table 4); the refined flour (no replacement) was analyzed as the control.

The progressive replacement of flour with the pearled barley fraction significantly increased the amount of water required for the flour hydration process, although no differences were observed for the dough development time (DDT) at any replacement level. Compared to the control without the addition of the pearled fraction, the replacement at a 5% level significantly reduced dough stability and the C2 point (protein strength) by 26 and 20%, respectively. A further reduction was observed at the 10% level, of 40 and 31% for both parameters, respectively. Conversely, these parameters both increased slightly at higher replacement levels. Comparing the addition of bran from different cereals at different replacement levels to white flour, Sudha et al.[23] reported that barley bran (DF = 45%) led to the highest increase in water absorption (from 64 to 76%) and the greatest reduction in dough stability (from 7.0 to 3.5 min), whereas the DDT increased more for wheat, rice, and oat bran. According to Rosell et al.,[24] these differences are mainly related to the competition for water of the added barley fibers with the flour proteins and starch and to the negative physical and mechanical effects of fiber on the formation of the gluten network. Moreover, the increase in water absorption of the dough is also related to the nonstarch polysaccharide contents and β-glucans in particular.[44]

The dough amplitude was affected significantly only at the 25% level, whereas the starch gelatinization (C3 point) and amylase activity (C4) were already affected at 5% of substitution. A further significant reduction in the C3 value was observed for a 15% level of replacement. Conversely, increasing the replacement level of refined flour with the pearled barley fraction did not affect the C5 point (starch retrogradation). Dough resistant to extension, elasticity, and starch pasting properties has been reported to be affected significantly by the 15% inclusion of barley middlings in the bread formulation.[18]

Overall, compared to literature data referring to the addition of whole grain barley flour or other byproducts of barley processing,[18,19,25] the substitution of wheat flour with the selected intermediate pearling fraction has led to less dough weakening and, thus, a more contained reduction of dough stability.

Bread Technology Properties. The previously described composite flours were employed to prepare 5-, 10-, 15-, 20-, and 25%-substituted breads; a control bread was also prepared using the refined flour (without replacement) for comparison purposes. Bread samples were first analyzed for their technology properties: crust color, bread crunchiness and volume, and TPA test.

Bread Crust Color and Crunchiness. ANOVA showed significant differences in the L^* and b^* values for the crusts of bread made with different replacement levels of the refined flour with the pearled barley fraction (Table 5). An increase in the pearled fraction substitution resulted in a moderate reduction in the L^* (lightness) and the blue−yellow components (b^*). No significant changes were found for the redness (a^*) values.

In a previous work, no significant differences in crust color were observed for up to 10% blending with whole grain barley flour.[20] Sumner et al.[38] reported that the removal of the outer kernel layers resulted in an increase in lightness (L^*) of pearled barley grain and a reduction in the red (a^*) and yellow (b^*) values and showed intermediate values of L^*, a^*, and b^* between the hull and the inner pearled fractions for an intermediate pearling fraction similar to that used in the present study (15−24% w/w). In the breads obtained at replacement levels of 5 and 10%, the lightness (L^*) of the crust was reduced by 7 and 11%, respectively, compared to the control test. In the previous study based on pearled wheat fractions,[17] the reduction in crust lightness was found at the same replacement levels of 6 and 12%.

The results of the mechanical and acoustic property tests of the composite bread crust are reported in Table 5. The total break energy, which is the energy necessary to break the crust and to continue the compression until 20 mm of penetration, was already significantly reduced at the 5% replacement level, and a descending trend was observed as the flour replacement level was increased. A decreasing trend was also evidenced for both of the acoustic parameters that were evaluated (maximum acoustic emission and number of acoustic emission peaks, using a threshold value of 15 dB (SPL)) while increasing the replacement percentage. The maximum acoustic emission detected during compression was lower at each substitution, with significant differences from the 15% replacement level with respect to the control. A steep decrease in the parameter pertaining to the number of acoustic emission peaks was found between the control and the 10% replacement level samples,

DOI: 10.1021/jf506193p
J. Agric. Food Chem. 2015, 63, 5875−5884

which pointed out the loss of crust crunchiness in the substituted samples. The mechanical and acoustic crust evaluations showed a possible variation in the microstructure of the breads: this was also shown in extruded breads and was related to the water activity content and production parameters.[45,46]

Bread Volume, Bread Crumb Texture Profile Analysis, and Color. The increasing percentage of refined flour replacement with the pearled barley fraction led to a significant decrease in the bread volume (Figure 1). This effect already

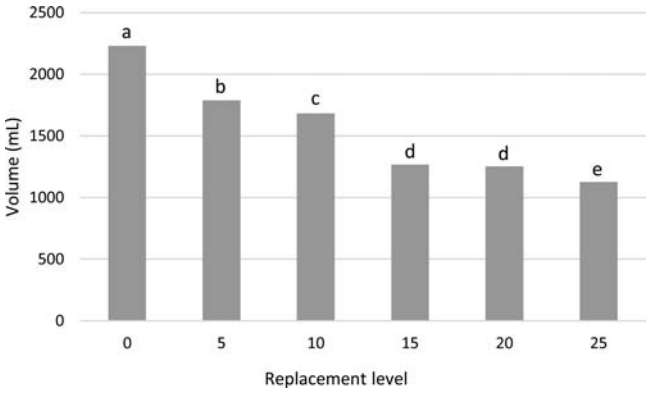

Figure 1. Volume of composite bread with refined flour and enriched fractions obtained through barley kernel pearling.

began at the 5% replacement of refined flour with the pearled fraction. At a 10% replacement level, the bread volume was reduced by 24%, compared to the control made with only refined wheat flour. The same reduction was reported by Gill et al.,[26,47] who included barley flour. At the same level of replacement, but using an intermediate pearled fraction obtained from wheat, the volume was reduced by 8% compared to the control.[17] A higher impact, on bread volume, of the inclusion of barley and other cereals, compared to wheat, was reported by Ragaee et al.:[21] the inclusion of 20% rye, barley, and oat whole grain flour led to reductions in loaf volume of 18, 27, and 28%, respectively. Conversely, the authors did not find any significant difference between a control bread and a 20% replacement of whole grain wheat flour. Gujral et al.[48] reported a reduction in loaf volume of 65% when 20% w/w of barley flour was incorporated in wheat bread.

The TPA parameters obtained during the analysis of the bread crumbs (Table 6) pointed out a variation in all of the parameters, excluding resilience, when the replacement level was increased. In particular, the force-related hardness parameter increased following the substitution increase, and the cohesiveness and springiness decreased slightly. In general, the variation in hardness predominated over cohesiveness and springiness in the variations of the derived parameters, such as gumminess and chewiness, thus evidencing a harder, gummier, and more difficult crumb to bite with the increased replacements. The differences are particularly clear for the 10% substitution.

The lower loaf volume and firmer crumb texture (hardness, gumminess, chewiness) with the inclusion of the pearled barley fraction may be attributed to gluten dilution caused by the addition of DF, which interfered with the optimal gluten matrix formation during fermentation and baking.[47] Moreover, no-starch polysaccharides could also have a profound impact on dough properties during breadmaking and could lead to a lower loaf volume and increasing bread firmness.[49] When added to wheat flour, β-glucans from barley could tightly bind to high amounts of water in the dough, suppress the availability of water to develop a gluten network, and cause rupture of the gas cells.[26,44]

Compared to the crust, for which an evolution in the lightness and some variations in the yellow color were perceived, the color of the bread crumbs was different. The evaluation of the bread crumb color showed an increase in both the a^* (red) and b^* (yellow) color components with an increase in the flour replacement, whereas the L^* (lightness) value showed a nonhomogeneous trend for the substitutions. A similar reduction in crumb brightness was observed for an increase in the whole flour barley substitution.[26]

Chemical Characterization of the Bread. The moisture, ash, DF, β-glucan, and TPC contents and the TAA of the bread increased linearly and significantly as the refined flour was replaced with the selected pearled barley fraction, whereas the protein content did not show a clear tendency (Table 7). In fact, although the pearled barley fraction presented much higher values than the refined commercial flour for the other parameters, the protein content was only 1.5 times higher. These results suggest that the contribution of the barley fraction alone is not sufficient to significantly improve the protein content of breads; for this reason, a linear increase, as in the case of the other parameters, was not observed.

Compared to the control (0% of replacement), the 5%-substituted bread showed a more than double content of insoluble DF, β-glucans, and TPC and, in the case of the DPPH

Table 6. Crumb Texture Profile Analysis of Composite Bread with Refined Flour and Enriched Fractions Obtained through Barley Kernel Pearling[a]

	bread crumbs						crumb color		
replacement level	hardness (N)	cohesiveness (−)	springiness (mm)	gumminess (N)	chewiness (mJ)	resilience (−)	L^* (C)	a^* (C)	b^* (C)
0	3.0 e	0.88 a	9.6 a	2.6 e	25.2 f	0.5 a	47.7 ab	0.6 e	12.8 c
5	4.6 de	0.85 ab	9.6 a	3.9 de	36.9 ef	0.5 a	43.0 cd	1.0 e	12.5 c
10	6.6 d	0.83 bc	9.3 ab	5.5 d	51.2 d	0.5 a	40.3 d	1.6 d	13.2 c
15	10.1 c	0.83 bc	9.2 ab	8.4 c	77.6 c	0.5 a	45.2 bc	2.8 c	17.4 b
20	16.3 b	0.81 cd	9.1 b	13.1 b	118.6 b	0.5 a	50.3 a	3.6 b	19.3 a
25	20.8 a	0.80 d	9.0 b	16.6 a	149.4 a	0.5 a	48.8 ab	4.1 a	20.2 a
P (F)	<0.001	<0.001	<0.001	<0.001	<0.001	0.253	<0.001	<0.001	<0.001
SEM[b]	2.8	0.03	0.4	2.0	17.3	0.04	3.32	0.5	1.6

[a]Volume and crumb texture profile analysis of composite bread with refined flour and enriched fractions obtained through barley kernel pearling. Means followed by different letters are significantly different (the level of significance is shown in table). [b]SEM, standard error of means.

DOI: 10.1021/jf506193p
J. Agric. Food Chem. 2015, 63, 5875−5884

Table 7. Moisture, Ash, Protein, DF, and β-Glucan Contents, TPC, and TAA of Composite Bread with Refined Flour and Enriched Fractions Obtained through Barley Kernel Pearling[a]

				DF (%)				TAA (mmol TE kg^{-1})		
replacement level	moisture (%)	ash (%)	proteins (%)	total	insoluble	β-glucans (%)	TPC (mg kg^{-1})	DPPH MeOH	DPPH H_2O	ABTS
0	25.8 e	2.7 e	12.6 c	2.9 d	1.1 e	0.15 f	501 e	0.17 e	1.47 e	9.4 e
5	26.7 d	2.9 d	12.9 b	3.8 d	2.3 d	0.33 e	1156 d	0.40 d	3.67 d	14.2 d
10	27.7 cd	3.2 c	13.2 a	5.9 c	4.2 c	0.52 d	1277 d	0.66 c	5.48 c	16.2 d
15	27.5 bc	3.5 b	12.5 c	7.2 b	4.7 bc	0.75 c	1939 c	0.57 c	6.02 c	14.6 c
20	28.4 bc	3.6 a	12.5 c	6.9 b	5.7 b	0.91 b	2211 b	1.07 b	9.84 b	19.8 b
25	30.0 a	3.6 a	12.7 c	11.6 a	7.6 a	1.07 a	2525 a	1.33 a	12.04 a	21.7 a
P (F)	<0.001	<0.001	<0.001	<0.001	<0.001	<0.001	<0.001	<0.001	<0.001	<0.001
SEM[b]	0.7	0.1	0.1	0.8	0.9	0.03	192	0.09	0.78	1.2

[a]Results are expressed on a dw basis. Means followed by different letters are significantly different (the level of significance is shown in the table). [b]SEM, standard error of means.

methods, also of TAA. Moreover, at this replacement level, a significant increase in the moisture (+0.9%) and ash (+0.14%) contents was observed compared to the refined control. A further significant increase in ashes, total and insoluble DF, β-glucans, and TAA was observed at a 10% replacement level, and a bread classified as a "source of fiber" (DF > 3%) and very close to being a "good source of fiber" (DF > 6%) was obtained.[50]

The supplementation of hulled barley whole grain flour led to a generally lower increase in DF compared to that reported in the present study: at a 15% level of substitution, Dhingra and Jood[20] reported increases of 10 and 7% in the total and insoluble fiber of bread, compared to a control, whereas no changes were observed for the ash content. Compared to whole grain barley flour, the intermediate pearled fraction also led to clearly higher increases in TPC and TAA. Compared to the control recipe, the bread enriched with 40% w/w of barley flour[26] presented TPC and TAA increases similar to those obtained in this study at a 5% replacement level. This is consistent with the fact that the external layers of barley kernels and, particularly, the selected pearled fraction employed for bread preparation have higher TAA than whole barley.

In conclusion, the results obtained in this work show that selected byproducts of barley pearling could be proposed as potential ingredients for the manufacture of functional foods rich in DF and antioxidant compounds. However, considering the technological impact on dough and bread properties, their amounts in the formulation of bakery products need to be considered carefully, taking into account the sensory acceptability of consumers and also the possible application strategies that could be introduced to mitigate these undesirable effects.

The inclusion of this pearled fraction could probably easily be applied to other bakery products that require lower leavening, such as biscuits, and this could result in the necessity of introducing fewer technological changes. However, to obtain enriched bread using these pearled barley fractions, it could be interesting to perform specific enzymatic or physical treatments or to modify the breadmaking process through the use of additives or sourdough fermentation.

AUTHOR INFORMATION

Corresponding Author

*(M.A.) Phone: +39-0321-375772. Fax: +39-0321-375751. E-mail: marco.arlorio@pharm.unipmn.it.

Funding

The research was conducted with the financial support of the European Union, Italian Economy and Finance Ministry, and the Regione Piemonte, as a part of the NUTRATEC project.

Notes

The authors declare no competing financial interest.

ACKNOWLEDGMENTS

We thank Claudio Bongiovanni, Fabiana Serafino, Silvia Tosco, and Andrea Maffia (Molini Bongiovanni, Cambiano, TO, Italy), Alessandra Gazzola and Federico Marinaccio (DISAFA), and Paola Lucchini, Silvia Lugli, and Chiara Prola (Dipartimento di Scienze del Farmaco) for their expert technical assistance.

ABBREVIATIONS USED

DDT, dough development time; DF, dietary fiber; DON, deoxynivalenol; dw, dry weight; TPC, total phenolic compounds; TAA, total antioxidant activity; TE, trolox equivalents; TPA, texture profile analysis

REFERENCES

(1) Siró, I.; Kápolna, E.; Kápolna, B.; Lugasi, A. Functional food. Product development, marketing and consumer acceptance − a review. *Appetite* **2008**, *51*, 456−467.

(2) Bartlomiej, S.; Rosicka-Kaczmarek, J.; Nebesny, E. Bioactive compounds in cereal grains − occurrence, structure, technological significance and nutritional benefits − a review. *Food Sci. Technol. Int.* **2012**, *18*, 559−568.

(3) Poutanen, K.; Sozer, N.; Della Valle, G. How can technology help to deliver more of grain in cereal foods for a healthy diet? *J. Cereal Sci.* **2014**, *59*, 327−336.

(4) Baik, B.; Ullrich, S. E. Barley for food: characteristics, improvement, and renewed interest. *J. Cereal Sci.* **2008**, *48*, 233−242.

(5) Brennan, C. S.; Cleary, L. J. The potential use of cereal (1→3, 1→4) β-D-glucans as functional food ingredients. Review. *J. Cereal Sci.* **2005**, *42*, 1−13.

(6) Vasanthan, T.; Temelli, F. Grain fractionation technologies for cereal β-glucan concentration. *Food Res. Int.* **2008**, *41*, 876−881.

(7) Food and Drug Administration. Food labelling: "Health claims: Soluble dietary fiber from certain food and coronary heart disease". In *Code of Federal Regulations* Title 21, Vol. 2, Part 101; Food and Drug Administration: Washington, DC, USA, 2006; available at http://www.accessdata.fda.gov/scripts/cdrh/cfdocs/cfcfr/CFRSearch.cfm?fr=101.81 (verified Nov 27, 2014).

(8) EFSA. Scientific Opinion on the substantiation of health claims related to beta-glucans from oats and barley and maintenance of normal blood LDL-cholesterol concentrations (ID 1236, 1299), increase in satiety leading to a reduction in energy intake (ID 851, 852), reduction of post-prandial glycaemic responses (ID 821, 824),

DOI: 10.1021/jf506193p
J. Agric. Food Chem. 2015, 63, 5875−5884

and "digestive function" (ID 850) pursuant to Article 13(1) of Regulation (EC) No. 1924/2006. *EFSA J.* **2011**, *9* (6), 2207, DOI: 10.2903/j.efsa.2011.2207.
(9) Lafiandra, D.; Riccardi, G.; Shewry, P. R. Improving cereal grain carbohydrates for diet and health. *J. Cereal Sci.* **2014**, *59*, 312−326.
(10) Hernanz, D.; Nuńez, V.; Sancho, A. I.; Faulds, C. B.; Williamson, G.; Bartolomé, B.; Gómez-Cordovés, C. Hydroxycinnamic acids and ferulic acid dehydrodimers in barley and processed barley. *J. Agric. Food Chem.* **2001**, *49*, 4884−4888.
(11) Liu, Q.; Yao, H. Antioxidant activities of barley seeds extracts. *Food Chem.* **2007**, *102*, 732−737.
(12) Jadhav, S. J.; Lutz, S. E.; Ghorpade, V. M.; Salunkhe, D. K. Barley: chemistry and value-added processing. *Crit. Rev. Food Sci. Nutr.* **1998**, *38*, 123−171.
(13) Holtekjølen, A. K.; Sahlstrøm, S.; Knutsen, S. H. Phenolic contents and antioxidant activities in covered whole-grain flours of Norwegian barley varieties and in fraction obtained after pearling. *Acta Agric. Scand., Sect. B* **2011**, *61*, 67−74.
(14) Hemery, Y.; Rouau, X.; Lullien-Pellrin, V.; Barron, C.; Abecassis, J. Dry process to develop wheat fractions and products with enhanced nutritional quality. *J. Cereal Sci.* **2007**, *46*, 327−347.
(15) Liu, K.; Barrows, F.; Obert, D. Dry fractionation methods to produce barley meals varying in protein, beta-glucan, and starch contents. *J. Food Sci.* **2009**, *74* (6), 487−499.
(16) Sovrani, V.; Blandino, M.; Scarpino, V.; Reyneri, A.; Coïsson, J. D.; Travaglia, F.; Locatelli, M.; Bordiga, M.; Montella, R.; Arlorio, M. Bioactive compound content, antioxidant activity, deoxynivalenol and heavy metal contamination of pearled wheat fractions. *Food Chem.* **2012**, *135*, 39−46.
(17) Blandino, M.; Sovrani, V.; Marinaccio, F.; Reyneri, A.; Rolle, L.; Giacosa, S.; Locatelli, M.; Bordiga, M.; Travaglia, F.; Coïsson, J. D.; Arlorio, M. Nutritional and technological quality of bread enriched with an intermediated pearled wheat fraction. *Food Chem.* **2013**, *141*, 2549−2557.
(18) Sullivan, P.; O'Flaherty, J.; Brunton, N.; Arendt, E.; Gallagher, E. The utilization of barley middlings to add value and health benefits to white breads. *J. Food Eng.* **2011**, *105*, 493−502.
(19) Cavallero, A.; Empilli, S.; Brighenti, F.; Stanca, A. M. High (1→3, 1→4)-β-glucan barley fractions in bread making and their effects on human glycemic response. *J. Cereal Sci.* **2002**, *36*, 59−66.
(20) Dhingra, S.; Jood, S. Organoleptic and nutritional evaluation of wheat breads supplemented with soybean and barley flour. *Food Chem.* **2001**, *77*, 479−488.
(21) Ragaee, S.; Guzar, I.; Dhull, N.; Seetharaman, K. Effect of fiber addition on antioxidant capacity and nutritional quality of wheat bread. *LWT − Food Sci. Technol.* **2011**, *44*, 2147−2153.
(22) Holtekjølen, A. K.; Bævre, A. B.; Rødbotten, M.; Berg, H.; Knutsen, S. H. Antioxidant properties and sensory profiles of bread containing barley flour. *Food Chem.* **2008**, *110*, 414−421.
(23) Sudha, M. L.; Vetrimani, R.; Leelavathi, K. Influence of fibre from different cereals on the rheological characteristics of wheat flour dough and on biscuit quality. *Food Chem.* **2007**, *100*, 1365−1370.
(24) Rosell, C. M.; Santos, E.; Collar, C. Physical characterization of fiber-enriched bread doughs by dual mixing and temperature constraint using the Mixolab®. *Eur. Food Res. Technol.* **2010**, *231*, 535−544.
(25) Rieder, A.; Holtekjølen, A. K.; Sahlstrøm, S.; Moldestad, A. Effect of barley and oat flour types and sourdoughs on dough rheology and bread quality of composite wheat bread. *J. Cereal Sci.* **2012**, *55*, 44−52.
(26) Gill, S.; Vasanthan, T.; Ooraikul, B.; Rossnagel, B. Wheat bread quality as influenced by the substitution of waxy and regular barley flour in their native and cooked forms. *J. Cereal Sci.* **2002**, *36*, 239−251.
(27) Beta, T.; Nam, S.; Dexter, J. E.; Sapirstein, H. D. Phenolic content and antioxidant activity of pearled wheat and roller-milled fractions. *Cereal Chem.* **2005**, *82*, 390−393.
(28) AACC International. AACCI method 10-10.03 (Optimized straight-dough bread-making method). In *Approved Methods of the AACC*,11th ed.; American Association of Cereal Chemistry: St. Paul, MN, USA, 2008.
(29) Locatelli, M.; Travaglia, F.; Coïsson, J. D.; Martelli, A.; Stévigny, C.; Arlorio, M. Total antioxidant activity of hazelnut skin (Nocciola Piemonte PGI): impact of different roasting conditions. *Food Chem.* **2010**, *119*, 1647−1655.
(30) Re, R.; Pellegrini, N.; Proteggente, A.; Pannala, A.; Yang, M.; Rice-Evans, R. Antioxidant activity applying an improved Abts+ radical cation decolorization assay. *Free Radical Biol. Med.* **1999**, *26*, 1231−1237.
(31) ICC. *Standard Methods of the International Association for Cereal Chemistry 110/1, 105/2, 106/2, 104/1, 173*; International Association for Cereal Science and Technology: Vienna, Austria, 2010.
(32) Commission Internationale de L'Eclairage. Colorimetry. *Publication CIE 15.2*; Vienna, Austria, 1986.
(33) Piazza, L.; Gigli, J.; Ballabio, D. On the application of chemometrics for the study of acoustic-mechanical properties of crispy bakery products. *Chemom. Intell. Lab. Syst.* **2007**, *86*, 52−59.
(34) AACC International. AACCI method 10-05.01 (Guidelines for measurement of volume by rapeseed displacement). In *Approved Methods of the AACC*, 11th ed.; American Association of Cereal Chemistry: St. Paul, MN, USA, 2008.
(35) Fik, M.; Surówka, K. Effect of prebaking and frozen storage on the sensory quality and instrumental texture of bread. *J. Sci. Food Agric.* **2002**, *82*, 1268−1275.
(36) Lehtonen, M.; Aikasalo, R. β-Glucan in two- and six-rowed barley. *Cereal Chem.* **1987**, *64*, 191−193.
(37) Andersson, A. A. M.; Lampi, A.-M.; Nyström, L.; Piironen, V.; Li, L.; Ward, J. L.; Gebruers, K.; Courtin, C. M.; Delcour, J. A.; Boros, D.; Fraś, A.; Dynkowska, W.; Rakszegi, M.; Bedõ, Z.; Shewry, P. R.; Åman, P. Phytochemical and dietary fiber components in barley varieties in the HEALTHGRAIN diversity screen. *J. Agric. Food Chem.* **2008**, *56*, 9767−9776.
(38) Sumner, A. K.; Gebre-Egziabher, A.; Tyler, R. T.; Rossnagel, B. G. Composition and properties of pearled and fines fractions from hulled and hull-less barley. *Cereal Chem.* **1985**, *62*, 112−116.
(39) Sullivan, P.; O'Flaherty, J.; Brunton, N.; Gee, V. L.; Arendt, E.; Gallagher, E. Chemical composition and microstructure of milled barley fractions. *Eur. Food Res. Technol.* **2010**, *230*, 579−595.
(40) Zheng, G. H.; Rossnagel, B. G.; Tyler, R. T.; Bhatty, R. S. Distribution of β-Glucan in the grain of hull-less barley. *Cereal Chem.* **2000**, *77*, 140−144.
(41) Marconi, E.; Graziano, M.; Cubadda, R. Composition and utilization of barley pearling by-products for making functional pastas rich in dietary fibre and β-glucans. *Cereal Chem.* **2000**, *77* (2), 133−139.
(42) Khatibi, P. A.; Berger, G.; Wilson, J.; Brooks, W. S.; McMaster, N.; Griffey, C. A.; Hicks, K. B.; Nghiem, N. P.; Schmale, D. G. A comparison of two milling strategies to reduce the mycotoxin deoxynivalenol in barley. *J. Agric. Food Chem.* **2014**, *62*, 4204−4213.
(43) House, J. D.; Nyachoti, C. M.; Abramson, D. Deoxynivalenol removal from barley intended as swine feed through the use of an abrasive pearling procedure. *J. Agric. Food Chem.* **2003**, *51*, 5172−5175.
(44) Holtekjølen, A. K.; Olsen, H. H. R.; Færgestad, E. M.; Uhlen, A. K.; Knutsen, S. H. Variations in water absorption capacity and baking performance of barley varieties with different polysaccharide content and composition. *LWT − Food Sci. Technol.* **2008**, *41*, 2085−2091.
(45) Marzec, A.; Lewicki, P. P.; Ranachowski, Z. Influence of water activity on acoustic emission of flat extruded bread. *J. Food Eng.* **2007**, *79*, 410−422.
(46) Gondek, E.; Jakubczyk, E.; Herremans, E.; Verlinden, B.; Hertog, M.; Vandendriessche, T.; Verboven, P.; Antoniuk, A.; Bongaers, E.; Estrade, P.; Nicolaï, B. M. Acoustic, mechanical and microstructural properties of extruded crisp bread. *J. Cereal Sci.* **2013**, *58*, 132−139.
(47) Gill, S.; Vasanthan, T.; Ooraikul, B.; Rossnagel, B. Wheat bread quality as influenced by the substitution of waxy and regular barley

DOI: 10.1021/jf506193p
J. Agric. Food Chem. 2015, 63, 5875−5884

flour in their native and extruded forms. *J. Cereal Sci.* **2002**, *36*, 219−237.
(48) Gujral, H. S.; Gaur, S.; Rosell, C. M. Effect of barley flour, wet gluten and ascorbic acid on bread crumb texture. *Food Sci. Technol. Int.* **2003**, *9*, 17−21.
(49) Courtin, C. M.; Delcour, J. A. Arabinoxylans and endoxylanases in wheat flour breadmaking. *J. Cereal Sci.* **2002**, *35*, 225−243.
(50) Codex Alimentarius. Codex guidelines for use of nutrition and health claims (CAC/GL 23-1997), 1997.

DOI: 10.1021/jf506193p
J. Agric. Food Chem. 2015, 63, 5875−5884

stitutions of $Pro_{182}Thr$ and $Tyr_{310}Cys$ in the *EPSPS* gene were recently reported in glyphosate-resistant sourgrass (*Digitaria insularis*).[31] The level of resistance due to these target site mutations is relatively low, ranging from 2- to 4-fold.[32]

Two other glyphosate resistance mechanisms have been reported more recently. Horseweed[33] and *Lolium* species[34] reduced the amount of glyphosate that reaches the target site by rapidly sequestering glyphosate into the vacuole. This mechanism has conferred 14-fold resistance to glyphosate.[34] A high level of resistance to glyphosate in Palmer amaranth (*Amaranthus palmeri*) and Italian ryegrass results from *EPSPS* gene amplification.[35,36] *EPSPS* gene amplification is heritable and correlates with glyphosate resistance in the F2 population.[35] How rare these resistance mechanisms are is not yet known. The case with Palmer amaranth indicates gene amplification could confer high levels of resistance.

Starting in the mid-2000s, some Italian ryegrass populations have been surviving the spring vegetation desiccation treatments in Arkansas (United States) about the same period it was reported in neighboring Mississippi.[16,37] The severity of escapes and reduction in weed control has been escalating. *Lolium* is the major weed problem in wheat in the southern United States. This is also a problem in corn and cotton as these crops are planted in the spring when Italian ryegrass is actively growing. Off-season application of glyphosate has historically been effective in reducing *Lolium* infestation. It also has already evolved resistance to acetyl-CoA carboxylase (ACCase) and acetolactate synthase (ALS) herbicides used in wheat.[38−43] The evolution of resistance to glyphosate has compromised preplant weed management options as well and has increased the risk of economic losses in crop production. The objectives of this study were to determine the level of resistance to glyphosate in the Arkansas *Lolium* populations and to investigate the mechanisms by which selected populations survive a previously lethal dose of glyphosate.

MATERIALS AND METHODS

Plant Materials. Mature panicles from suspected glyphosate-resistant Italian ryegrass were collected in Desha County, Arkansas, in 2009 and 2010. Des05, Des09, and D8 populations were collected from cotton fields; D4 and Des13 were from fallow fields; Des14 and Des15 populations were from soybean fields. Seeds were grown in a greenhouse maintained at 24/18 °C day/night temperatures with a 12 h photoperiod. Plants were watered daily and fertilized with Miracle-Gro, a water-soluble all-purpose plant food containing 15−30−15% NPK, every 2 weeks. Seedlings at three-leaf stage were sprayed with a discriminating dose of 870 g ae ha^{-1} glyphosate. The surviving plants were grown to maturity for seed increase, and seeds from all plants in the same population were bulked at harvest. Populations grown for seed increase were placed either in the greenhouse (8 m apart, with other species in between as physical barriers) or outdoors (25 m apart). Multiple plants from one population were grouped together to cross-pollinate. Seeds generated were used for the subsequent experiments. A susceptible population (98-3) that was not exposed to glyphosate selection was used as the susceptible standard (reference) in all experiments.

Experiment 1. Population Dose−Response Bioassay. Seeds were planted into flats (25 × 25 × 5 cm) filled with Sunshine Mix LC1 soil (Sun Gro Horticulture Canada Ltd., Vancouver, BC, Canada). Flats were equally divided in two greenhouses because of space limitations; one was maintained at 24/18 °C and the other at 30/25 °C day/night temperatures at 12 h photoperiod. Following emergence, plants were thinned to 15 seedlings per flat. Three- to four-leaf seedlings (98-3, Des05, Des14, D4, D8, and D13) were treated with eight doses of glyphosate from 0 to 13920 g ae ha^{-1}, which corresponds to 0−16 times the commercial dose of 870 g ae ha^{-1}. Treatments for 98-3 included a nontreated check and 11 doses of glyphosate from 13 to 3480 g ae ha^{-1} corresponding to $^1/_{64}$−4 times the commercial dose of glyphosate. MON 78623 (58% v/w potassium salt of *N*-(phosphonomethyl)glycine; Monsanto Co., St. Louis, MO, USA) was applied with 0.25% nonionic surfactant (NIS). Glyphosate treatments were applied using a laboratory sprayer equipped with a flat fan spray nozzle (TeeJet spray nozzles, Spraying Systems Co., Wheaton, IL, USA) delivering 187 L ha^{-1}. The experiment was conducted in a randomized complete block design with two replications. Each replication consisted of one tray (50 × 25 × 5 cm) accommodating two flats and placed in two greenhouses by replication.

The number of survivors was recorded at 28 days after treatment (28 DAT). Plants were cut at the soil surface and stored in a dryer for 3 days, and the dry weight was recorded. Data were expressed as percentage of biomass reduction relative to the nontreated control. Regression analysis was conducted using SAS JMP v. 10. The percent biomass reduction and percent mortality were fitted to a nonlinear, sigmoid, three-parameter logistic regression model defined by (eq 1)

$$Y = c/[1 + \exp(-a \times (X - b))] \quad (1)$$

where Y is the biomass reduction or mortality expressed as a percentage of the nontreated control, a is the growth rate, b is the inflection point, c is the asymptote, and X is the glyphosate dose. The dose needed to kill 50% (LD_{50}) of the population or cause 50% biomass reduction (GR_{50}) was calculated from the above equation.

Experiment 2. Single-Plant Dose−Response Bioassay. To determine the relationship of the *EPSPS* copy number in glyphosate-resistant plants and resistance level, dose−response assays were conducted using clones of 14 total individual plants from Des05, Des09, Des13, Des14, Des15, and D8 (Table 1). Enough clones were propagated for each plant to accommodate the dose range tested and calculate the resistance factor of each plant. Four plants from the susceptible standard 98-3 were used as reference. The dose−response assay was conducted in the greenhouse, maintained at 24/18 °C at 12 h photoperiod. To accomplish this, tillers (adventitious shoots at the base of grasses) of each plant were separated and planted in 15 cm pots to obtain 24 clones per plant that were sprayed with eight herbicide doses in three replicates. Resistant plants were treated with glyphosate at 0, 218, 435, 870, 1740, 3480, 6960, and 13920 g ae ha^{-1}, using a laboratory sprayer calibrated to deliver 187 L ha^{-1}. The susceptible plants were sprayed with seven doses of glyphosate at 0, 54, 109, 218, 435, 653, 870, and 1740 g ae/ha^{-1}. Glyphosate was

Table 1. Summary of *Lolium perenne* ssp. *multiflorum* Plants Used for Each Experiment

	plants used for each experiment			
	no. of plants cloned[a]	cloned plants from expt 2 plus others		
population	whole-plant dose−response bioassay (expt 2)	absorption and translocation (expt 3)	EPSPS gene sequencing (expt 4)[b]	EPSPS copy no. analysis (expt 5)
Des05	3	6	7 R, 5 S	10
Des09	1			1
Des13	2			2
Des14	4	6	13 R	10
Des15	3			3
D8	1			10
98-3	4	6	10 S	10
total	18			46

[a]Twenty-four clones of each plant were used to apply 8 doses (0, 218, 435, 870, 1740, 3480, 6960, and 13920 g ae ha^{-1}) for confirmed R plants and 7 doses (0, 54, 109, 218, 435, 653, 870, and 1740 g ae/ha^{-1}) for S plants. [b]R, resistant; S, susceptible.

DOI: 10.1021/acs.jafc.5b00018
J. Agric. Food Chem. 2015, 63, 5885−5893

applied with 0.25% NIS. The overall effects of glyphosate such as chlorosis, stunting, and desiccation were visually assessed at 28 DAT relative to the nontreated control, using a scale of 0−100 where 0 = no visible injury and 100 = complete death. Visible injury was regressed against glyphosate dose and modeled with a sigmoid, three-parameter, logistic function in SAS JMP ver.11 (eq 1). The amount of glyphosate needed to incur 50% injury (GR_{50}) was obtained from the regression equation.

Experiment 3. Absorption and Translocation of Glyphosate. Seeds from Des05, Des14, and 98-3 populations (Table 1) were planted in 2.5 cm pots in the greenhouse maintained at 24/18 °C day/night temperatures at 12 h photoperiod. Three weeks from emergence, when seedlings were 7.5−10 cm tall, formulated glyphosate (MON 78623) containing 0.25% NIS (Kinetic HV, Helena Chemical Co., Memphis, TN, USA) was sprayed at 870 g ae ha^{-1} in 187 L ha^{-1} spray volume and then spotted with 4 μL of herbicide solution containing 1.776 kBq ^{14}C-glyphosate. Plants were harvested at 24 and 48 h after treatment (HAT) and sectioned into four parts: treated leaf, above treated leaf, below treated leaf, and roots. To remove nonabsorbed glyphosate, the treated 5 cm portion of the treated leaf was rinsed for 15 s with 1 mL of a methanol/water (1:1 v/v) solution containing 0.25% v/v NIS. The rinsate was collected in a 20 mL scintillation vial, mixed with 10 mL of scintillation cocktail, and radioassayed by liquid scintillation spectroscopy (LSS) (Packard Tri-Carb 2100TR Liquid Scintillation Spectrometer, Packard Instrument Co., Downers Grove, IL, USA) to determine the amount of nonabsorbed ^{14}C. After rinsing dissection of the treated leaf, all plant parts were dried for 48 h at 50 °C. Individual plant parts were oxidized (Biological Oxidizer OX500, R. J. Harvey Instrument Corp., Tappan, NY, USA), and the released CO_2 was trapped in 15 mL of scintillation cocktail and radioassayed using LSS. Absorbed glyphosate was calculated by dividing the amount of ^{14}C recovered from the oxidized plant parts by the sum of the radioactivity contained in the leaf wash and that recovered from the oxidized plant parts. The distribution of ^{14}C-glyphosate in plant tissues was expressed as a percentage of absorbed radioactivity. The experiments were arranged in a completely randomized block design with four replicates. In the absorption experiment, a factorial scheme with two factors (population and harvest time) was tested by ANOVA. The translocation experiment, which had three factors (population, plant section, and harvest time), was also analyzed by ANOVA in SAS JMP Pro v.11.

Experiment 4. *EPSPS* Gene Sequencing. Two populations were randomly chosen for *EPSPS* gene sequencing (Table 1). Seeds from Des05 and Des14 populations were planted in 4.5 cm pots filled with Sunshine Mix LC potting soil. Tillers of 12 plants from Des05 and of 13 from Des14 were divided and transplanted into two pots. One set of clones was cut to 8 cm, allowed to regrow to 12 cm, and then sprayed with glyphosate at 870 g ae ha^{-1}. Clones that survived at 28 DAT were classified as resistant (R); otherwise, they were susceptible (S). Clones of all 13 plants from the Des14 population survived, whereas only 7 clones from the Des05 population remained alive at 28 DAT. The corresponding nontreated clones of verified R plants were used for sequencing of the *EPSPS* gene.

Young leaf tissues of 7 and 13 confirmed R plants from Des05 and Des14 populations, respectively, were harvested and stored at −80 °C for RNA extraction. In addition, leaf tissues of 5 and 10 S plants, respectively, from Des05 and 98-3 populations also were harvested. Leaf tissues were ground into fine powder in liquid nitrogen using a mortar and pestle. Total RNA was extracted using PureLink RNA Mini kit (Life Technologies, Carlsbad, CA, USA). First-strand complementary DNA (cDNA) was synthesized using Oligo$(dT)_{20}$ supplied in the Improm-II Reverse Transcription System first-strand cDNA synthesis kit (Promega, Madison, WI, USA). Forward primer LPM2F (5′-TSCAGCCCATCARGGAGATCT-3′) designed by Perez-Jones et al.[44] and reverse primer LPM2R1 (5′-CTAGTTCTT-CACGAAGGTGCTTA-3′) designed by Salas et al.[36] were used to amplify the *EPSPS* gene. The primer pair amplified a 915 bp fragment of the *EPSPS* region encompassing codon 106 where the known resistance-conferring point mutation occurs.

The polymerase chain reaction (PCR) was performed in a 25 μL reaction mixture consisting of 4 μL of cDNA, 0 0.4 μM of both forward and reverse primers, 12.5 μL of Taq2x master mix (New England Biolabs Inc., Ipswich, MA, USA), and nuclease-free water. The reaction mixture was loaded in a thermal cycler (PTC-200, MJ Research, Inc., Watertown, MA, USA) programmed for the following temperature profile: initial denaturation at 94 °C for 3 min, 35 cycles of 94 °C for 30 s; annealing at 57.5 °C for 30 s; elongation at 72 °C for 90 s, and final extension at 72 °C for 10 min. PCR products were cleaned using Wizard SV Gel and PCR Clean-Up System (Promega) before sequencing. The resulting DNA sequences were cleaned, aligned using the *EPSPS* sequence of Italian ryegrass as reference, and analyzed for polymorphisms using Sequencher v.5 and Bioedit v.7 software.

Experiment 5. *EPSPS* Copy Number Determination. Leaf tissues from 10 confirmed R plants of selected populations (Des05, Des14, and D8) and 10 plants of the S population 98-3 (Table 1) were harvested and stored at −80 °C. Plants used for whole-plant dose−response assays, glyphosate translocation studies, and gene sequence analysis were among those analyzed for gene copy number. Genomic DNA was extracted using the hexadecyltrimethylammonium bromide (CTAB) method[45] following the modification of Sales et al.[46] Approximately 100 mg of leaf tissue from each plant was ground to a fine powder in liquid nitrogen, transferred to a 1.5 mL centrifuge tube, and suspended in 500 mL of CTAB extraction buffer (100 mM Tris-HCl, pH 8.0, 20 mM ethylenediaminetetraacetic acid (EDTA), pH 8.0, 2 M NaCl, 2% CTAB, 2% polyvinylpyrrolidone-40, 1 mM phenanthroline, and 0.3% β-mercaptoethanol). The aqueous extracts were incubated in a water bath at 55 °C for 40 min, treated with RNase solution, and extracted with an equal volume of phenol/chloroform/isoamyl alcohol solution (25:24:1). Total nucleic acids were precipitated from the supernatant by the addition of an equal volume of isopropanol. The DNA pellet was washed with 500 μL of absolute ethanol, dried in a vacufuge for 5 min, and resuspended in 30 mL of Tris-EDTA buffer (10 mM Tris-HCl, pH 8.0, 1 mM EDTA). Genomic DNA was quantified using a NanoDrop spectrophotometer model ND-1000 (Thermo Scientific, Wilmington, DE, USA) and checked for quality by agarose gel electrophoresis.

Quantitative real-time PCR was used to measure the genomic copy number of *EPSPS* relative to cinnamoyl-CoA reductase (*CCR*) genomic copy number in Italian ryegrass. Primer sets and qPCR conditions were described previously.[36] Triplicate genomic DNA templates (10 ng) were amplified in a 25 μL reaction mixture using Bio-Rad iQ SYBR Green Supermix by the following thermoprofile on a Bio-Rad CFX96 Real-Time System PCR machine: 10 min at 94 °C, 40 cycles of 94 °C for 15 s, and 60 °C for 1 min then increasing the temperature by 0.5 °C every 5 s to generate the product melt-curve. Data were analyzed using CFX manager software (version 1.5). Primer efficiency and slope were 101.8% and −3.279 for *EPSPS* and were 98.64% and −3.355 for *CCR*, respectively. Negative controls did not have amplification products. Relative quantification of *EPSPS* was calculated as Δ^{Ct} = (Ct, *CCR* − Ct, *EPSPS*) according to the method described by Gaines et al.[35] Increase in *EPSPS* copy number was expressed as $2^{\Delta Ct}$. Each sample was run in three technical replicates to calculate the mean and standard error of the increase in *EPSPS* copy number. Results were expressed as fold increase in *EPSPS* copy number relative to *CCR*.

RESULTS AND DISCUSSION

Population Dose−Response Bioassay. Dose−response bioassay confirmed the resistance of Des05, Des13, Des14, D5, and D8 Italian ryegrass populations to glyphosate. The glyphosate dose that caused 50% growth reduction (GR_{50}) of the S population (98-3) was 101 g ae ha^{-1} glyphosate, whereas those of R populations ranged from 726 to 1264 g ae ha^{-1} glyphosate (Table 2 and Figure 1). Resistant populations Des05, Des14, Des13, D8, and D4 were, respectively, 7, 8, 9, 13, and 19 times less sensitive to glyphosate than the S

DOI: 10.1021/acs.jafc.5b00018
J. Agric. Food Chem. 2015, 63, 5885−5893

Table 2. GR_{50} and LD_{50} Values of Glyphosate-Resistant and -Susceptible *L. perenne* ssp. *multiflorum* Populations, Arkansas (United States)

population	GR_{50} (g ae ha^{-1})	R/S[a]	LD_{50} (g ae ha^{-1})	R/S[b]
Des05[c]	726 (629, 823)[d]	7	1702 (1419, 1986)[e]	9
Des14[c]	831 (771, 892)	8	1587 (1385, 1788)	9
D4[c]	1908 (1485, 2332)	19	2719 (2107, 3329)	15
D8[c]	1264 (1031, 1496)	13	2245 (1916, 2575)	12
D13[c]	917 (795, 1039)	9	1524 (1200, 1847)	8
98-3[d]	101 (91, 111)		184 (161, 207)	

[a]Resistance level (R/S) calculated using the GR_{50} of the resistant population relative to the susceptible standard. [b]Resistance level (R/S) calculated using the LD_{50} of the resistant population relative to the susceptible standard. [c]Glyphosate-resistant population. [d]Glyphosate-susceptible population. [e]Lower, 95%; upper, 95%.

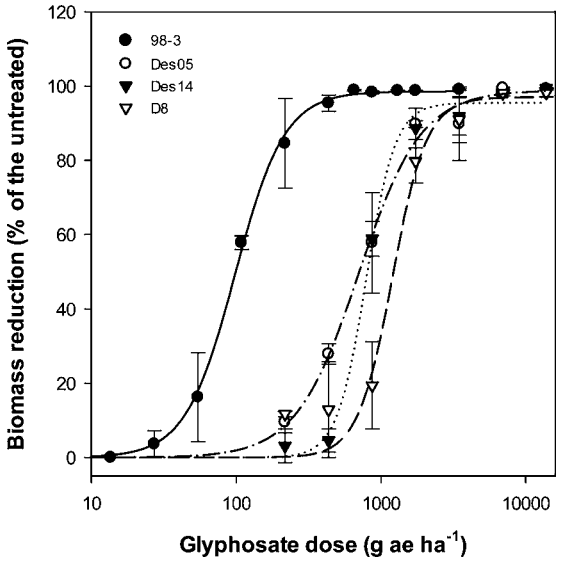

Figure 1. Shoot biomass reduction of selected *L. perenne* ssp. *multiflorum* populations, 28 days after treatment. Error bars are standard errors of the mean. Des05, Des14, and D8 had estimated 50% biomass reductions (GR_{50}) of 726, 831, and 1264 g ae ha^{-1} glyphosate, respectively. The susceptible 98-3 population had an estimated GR_{50} of 101 g ae ha^{-1} glyphosate.

population based on the R/S ratio calculated from GR_{50} values. The recommended field dose of glyphosate is 870 g ae ha^{-1}; thus, the R populations required 0.8−1.5 times the normal field dose of glyphosate to reduce aboveground biomass or ryegrass by 50%. The herbicide dose that caused 50% mortality (LD_{50}) of the 98-3 population was 184 g ae ha^{-1}, whereas those of the R populations ranged from 1524 to 2719 g ae ha^{-1} (Table 2 and Figure 2). On the basis of LD_{50} values, Des13, Des05, Des14, D8, and D4 populations had 8-, 9-, 9-, 12-, and 15-fold resistance relative to the 98-3 population (Table 2). These resistance levels are similar to the resistance levels calculated from the GR_{50} values. More than 1.8−3.1 times the commercial dose of glyphosate was needed to kill 50% of the resistant populations. Thus, growers would have to apply at least double these LD_{50} amounts to achieve 100% control in the corresponding fields; however, applying twice the normal dose is not recommended in commercial practice. The use of a higher dose also increases selection pressure and will accelerate the evolution of resistant populations.[47]

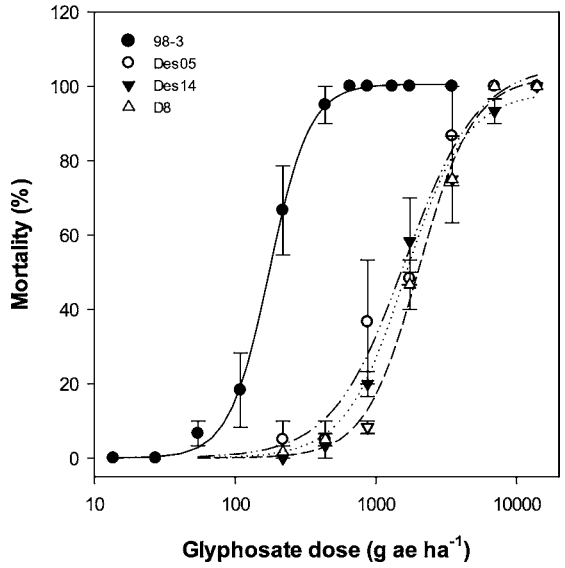

Figure 2. Mortality of selected glyphosate-resistant and -susceptible *L. perenne* ssp. *multiflorum* populations, 28 days after treatment. Error bars are standard errors of the mean. Des05, Des14, and D8 populations had estimated LD_{50} values of 1702, 1587, and 2245 g ae ha^{-1} glyphosate, respectively. The susceptible 98-3 population had an estimated LD_{50} of 184 g ae ha^{-1} glyphosate. LD_{50} is the amount of herbicide that kills 50% of the population.

The survival rate of populations is indicated by the LD_{50} values, which allows prediction of seed deposits into the soil seed bank or potential patch expansion of the resistant plants.[48] The GR_{50} values may differ slightly from the LD_{50} values, but together, these provide a better picture of population response to glyphosate. These inform us on the proportion of plants that are expected to survive a glyphosate application and how healthy these remaining plants are. The GR_{50} and LD_{50} values indicate that D4 and D8 populations are more resistant than Des05, Des14, and D13. The full dose of glyphosate at 870 g ae ha^{-1} is no longer sufficient to control these five R populations. The failure of glyphosate to control Italian ryegrass calls for alternative weed management approaches to mitigate the evolution of resistance.[37] The use of other herbicides, or the addition of other herbicides to glyphosate, is needed for complete weed control during field preparations prior to planting the crop. Resistance to glyphosate in these populations was lower than that of the first glyphosate-resistance population previously tested (Des03), which showed 23-fold resistance to glyphosate and required 3,880 g ae ha^{-1} glyphosate for 50% biomass reduction.[37] Nevertheless, the proportion of plants that escape glyphosate application in these populations already cause ecological concerns (of continuing resistance evolution) and economic detriment due to either yield loss from competition or additional costs for controlling escapes.

Uptake and Translocation of Glyphosate. Glyphosate is a potent herbicide because of its ability to translocate in the plant to the apical meristems, root, and underground reproductive organs of perennial plants via xylem and phloem.[49] It is possible that changes in the translocation pattern of glyphosate could endow resistance in plants. Glyphosate absorption was almost 60% in both S and R plants (Table 3). This result was similar to what was reported for glyphosate-R and -S Italian ryegrass from Mississippi[16] but differs from those in Chile,[50] where R and S plants absorbed >90% of ^{14}C-glyphosate at 48 HAT. On average 40 and 56% of

DOI: 10.1021/acs.jafc.5b00018
J. Agric. Food Chem. 2015, 63, 5885−5893

Table 3. ^{14}C Glyphosate Absorption and Distribution in Various Plant Tissues of Resistant and Susceptible *Lolium perenne* ssp. *multiflorum* Populations from Arkansas (United States)

	^{14}C-glyphosate absorption[a] (% of applied)		^{14}C-glyphosate distribution[a] (% of absorbed)							
			treated leaf		above treated leaf		below treated leaf		roots	
population	24 HAT[b]	48 HAT	24 HAT	48 HAT	24 HAT	48 HAT	24 HAT	48 HAT	24 HAT	48 HAT
Des05[c]	38	51	80	65	1	2	11	17	8	15
Des14[c]	44	59	79	68	1	1	12	19	8	12
98-3[d]	37	57	77	71	1	3	14	16	8	11

[a]Values are the average of four plants. [b]HAT, hours after treatment. [c]Resistant population. [d]Susceptible population.

applied glyphosate was absorbed by R and S plants at 24 and 48 HAT, respectively, and this response was not significantly different between R (Des05 and Des14) and S populations ($P > 0.05$).

Radioactivity recovered from the treated leaf represented glyphosate loaded into the leaf, but not translocated. The quantity of ^{14}C-glyphosate recovered from the treated leaf at 48 HAT was not different between R (65−68% of absorbed) and S (71% of absorbed) plants (Table 3). Translocation of ^{14}C-glyphosate into the roots and below the treated leaf was low, ranging from only 11 to 19%; the radioactivity accumulated above the treated leaf was nil (1−3% of absorbed). The proportion of ^{14}C-glyphosate recovered above the treated leaf, below the treated leaf, and in the roots increased between 24 and 48 HAT; however, no significant difference was detected between R and S populations in any plant sections at any harvest time. These results were similar to what was reported on *Lolium* populations from Australia[51] and California,[52] where the distribution patterns of ^{14}C-glyphosate did not differ between resistant and susceptible plants. On the contrary, glyphosate-resistant Italian ryegrass populations from Mississippi,[16] Oregon,[14] and Chile[50] showed reduced translocation of glyphosate. Among the Arkansas populations, however, resistance to glyphosate was not due to differences in uptake and translocation.

Partial *EPSPS* Gene Sequencing. A 915 bp PCR fragment of the *EPSPS* gene was amplified from cDNA of the R and S Italian ryegrass plants. This fragment encompassed amino acid positions 77−381 in the 444 amino acid long, mature EPSPS. The sequenced region included the domain where point mutations are known to confer resistance to glyphosate, for example, in corn at Pro_{106},[22−30] Gly_{101},[53] and Thr_{102}.[54] Mutations at Pro_{182} and Tyr_{310} were also observed in glyphosate-resistant sourgrass,[31] although the impact of these mutations on EPSPS enzyme activity has not been verified. Some nucleotide polymorphisms were detected in our recent research on Italian ryegrass; however, none was associated with resistance to glyphosate (data not shown). A mutation of Gly_{162}Ser was detected in one resistant Des14 plant, but this mutation was also found in a susceptible plant from Des05. Comparison of the *EPSPS* sequence between glyphosate-R and -S plants revealed both synonymous and nonsynonymous polymorphisms, but there were no amino acid changes in the catalytic sites that are known to confer resistance to glyphosate (data not shown). Therefore, mutations in the *EPSPS* gene known to endow resistance to glyphosate are not present in Des05 and Des14 Italian ryegrass populations or in the highly resistant population Des03.[37]

The absence of point mutations in the *EPSPS* gene that are exclusive to the R plants and the absence of other mutations previously associated with resistance to glyphosate indicate that target-site alteration is not the resistance mechanism in Des05 and Des14 populations. Considering that target-site mutation was also not found in the highly glyphosate-resistant population Des03,[36] it can be deduced that target-site mutation is not the mechanism of resistance among these tested glyphosate-resistant populations in Arkansas. It could also be that target-site mutation is a rare resistance mechanism among Arkansas Italian ryegrass populations for reasons not yet known. The rarity of target-site mutation as resistance mechanism to glyphosate is associated with the strong conservation of the catalytic site where glyphosate binds.[32] Glyphosate interacts with 17 invariant amino acids in the active site of the EPSPS protein[55] and mimics the transition state in the enol transfer reaction.[56] Because the active site of the EPSPS protein is highly conserved, any mutation at this site is deleterious and causes significant fitness penalty.[56] Single-site mutation at Thr_{97} to Ile or Pro_{101} to Ser[54] or Gly_{96} to Ala[53] in *Escherichia coli* impairs the binding of glyphosate but at the same time reduces affinity for the substrate phosphoenolpyruvate. Deleterious mutations of critical catalytic sites are not exclusive to EPSPS. Mutation in the *psbA* gene, which confers resistance to triazine herbicide, results in reduced agroecological fitness.[57] On the other hand, some mutations endowing target-site-based resistance to ACCase and ALS herbicides have little or no fitness costs.[12] Studies comparing glyphosate-resistant goosegrass with Pro_{106}Ser mutation versus susceptible population show some differences, but it is not yet evident whether there are any fitness costs associated with EPSPS-binding-site-based resistance.[58,59] Sammons et al.[32] reported that glyphosate has a very low risk for target-site resistance and this holds true to date. Thus, we are starting to find glyphosate-resistant populations that display resistance mechanisms other than target-site mutation.

***EPSPS* Genomic Copy Number Relative to *CCR*.** The degree of *EPSPS* gene amplification differed greatly among the resistant plants within each population, indicating high intrapopulation genetic variability. Genomic *EPSPS* copy number relative to *CCR* was 1 for S plants (n =10), whereas the relative *EPSPS* copy numbers for R plants (n = 30) were higher, ranging from 11 to 151 (Table 4 and Figure 3). The *EPSPS* copy number in Des05, Des14, and D8 resistant plants ranged from 11 to 121, from 24 to 97, and from 18 to 151, respectively. Italian ryegrass is an outcrossing species;[60] thus, a high degree of genetic diversity would be expected within a population. A broad range of *EPSPS* copy numbers also was detected in glyphosate-resistant Palmer amaranth, which is an obligate outcrossing species.[61] Individual plants that were subjected to both dose−response assay and *EPSPS* copy number analysis showed that the increase in copy number strongly correlated with the level of resistance to glyphosate (r = 0.80) (Figure 4). Plants with higher GR_{50} values had higher

DOI: 10.1021/acs.jafc.5b00018
J. Agric. Food Chem. 2015, 63, 5885−5893

Table 4. Summary Statistics of the Relative *EPSPS* Copy Number in Glyphosate-Resistant *L. perenne* ssp. *multiflorum* Populations, Arkansas (United States)

	EPSPS:CCR copy no.[a]					
population	mean	median	SD	CV	min	max
Des05	45	39	33	73	11	122
Des14	48	48	23	47	24	97
D8	80	84	47	59	18	151
98-3	1	1	0.2	20	0.8	1.4

[a]Values are averages of 10 plants.

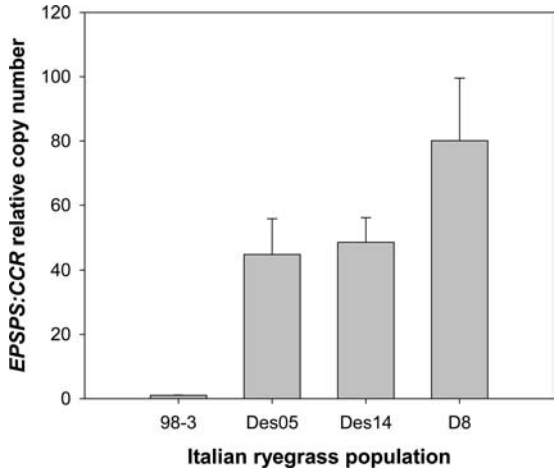

Figure 3. *EPSPS* relative genomic copy number in glyphosate-resistant and -susceptible *L. perenne* ssp. *multiflorum* plants. Relative copy number of *EPSPS* in resistant populations (D8, Des05, and Des14) ranged from 11 to 151 (n = 30), whereas the susceptible standard (98-3) contained a single copy (n = 10). Values are averages of 10 plants per population, with 3 technical replicates. Vertical bars represent the standard error of the mean.

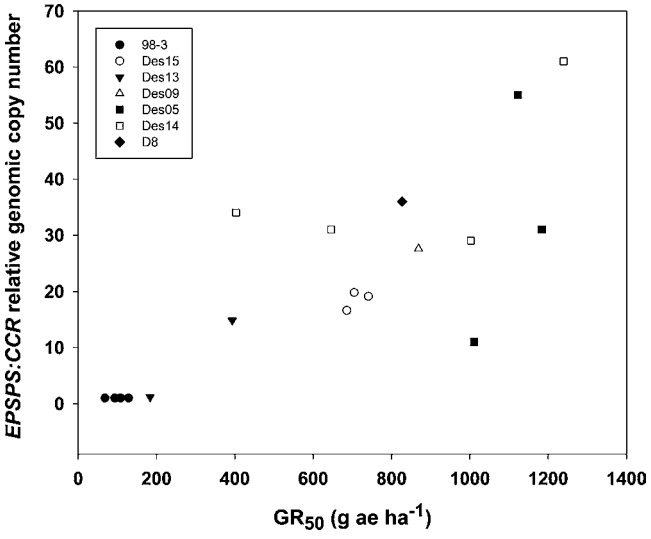

Figure 4. Relationship between the amount of glyphosate needed to incur 50% injury (GR_{50}) and the relative *EPSPS* genomic copy number (r = 0.80). Susceptible plants (98-3) had the lowest GR_{50} and *EPSPS* copy number.

EPSPS copy number (Figure 4). Other studies in Italian ryegrass[36] and Palmer amaranth[62,63] populations also reported positive correlation between *EPSPS* copy number and the level of resistance to glyphosate. The observation that plants with higher resistance levels to glyphosate had higher copies of *EPSPS* suggests that additional *EPSPS* gene copies have additive effects in conferring resistance to glyphosate.[61] Our data suggest that >10 *EPSPS* copies are necessary to survive the recommended field dose of glyphosate. Gaines et al.[61] reported that between 30 and 50 *EPSPS* genomic copies enabled *Amaranthus palmeri* to withstand the toxic effects of glyphosate. The EPSPS enzyme activity was not determined in this study; however, previous research[36,61] revealed that increased *EPSPS* copy number resulted in elevated EPSPS activity. Not all of the amplified genes may translate to increased level of protein (e.g., EPSPS) expression because transcriptional, post-transcriptional, and translational regulatory elements also play a crucial role in gene expression.[64] Salas et al.[36] observed that Italian ryegrass with similar *EPSPS* copy number did not show the same level of resistance. This could be a manifestation of some gene copies not resulting in a protein product or the involvement of other resistance mechanisms.

Amplification of the native, glyphosate-sensitive form of EPSPS enzymes had conferred resistance to glyphosate in chicory (*Cichorium intybus*), rock harlequin (*Capnoides sempervirens*), soybean (*Glycine max*), alfalfa (*Medicago sativa*), and tobacco (*Nicotiana tabacum*) in plant tissue culture with glyphosate selection.[65] Resistance to glyphosate in alfalfa, soybean, and tobacco from progressive selection in plant cell cultures is attributed to amplification of the *EPSPS* gene within the genome.[66] In addition, a glyphosate-tolerant wild carrot (*Daucus carota*) cell line generated by stepwise selection with glyphosate contained a 4−25-fold increase in *EPSPS*.[67] Similarly, a glyphosate-resistant petunia (*Petunia hybrida*) cell line contained a 20-fold increase in *EPSPS* gene copies.[68] Amplification of the *EPSPS* gene in Palmer amaranth from Georgia (United States) was recently reported by Gaines et al.[35] in which genomes of glyphosate-resistant plants contained from 5- to >160-fold more copies of the *EPSPS* gene, resulting in a 40-fold EPSPS overexpression. This Palmer amaranth population showed 6−8-fold resistance to glyphosate at the population level.[69] Although the EPSPS enzyme activity was not investigated in our study, various studies indicated that *EPSPS* gene amplification results in increased EPSPS enzyme activity in glyphosate-resistant plants.[65−67] Gene amplification can produce an abundant supply of EPSPS enzymes that are able to counteract the loss of metabolic function of enzyme molecules that are inhibited by glyphosate.[70] This affords the plant continued synthesis of aromatic acids for normal physiological function in the presence of glyphosate.

Given the lethal consequence of mutations in the binding site of the *EPSPS* gene, the selected glyphosate-resistant plants harbor other mechanisms of survival, such as *EPSPS* gene amplification. Gene duplication serves as a mechanism of adaptation to a changing environment such as environmental stresses.[71,72] Intense glyphosate usage as a selector will favor survival of plants with elevated copies of the glyphosate target gene *EPSPS*.[36] Amplification of *EPSPS* provides a certain level of glyphosate resistance in plants;[65] however, the stability of *EPSPS* gene amplification and the contribution of each additional copy are not clearly understood. *EPSPS* gene amplification in Palmer amaranth is heritable,[35] but the manner by which it is inherited is complex. Inheritance of *EPSPS* amplification in Palmer amaranth from North Carolina and Georgia was consistent with polygenic inheritance.[63,73] However, studies on plant cell culture revealed that gene

DOI: 10.1021/acs.jafc.5b00018
J. Agric. Food Chem. 2015, 63, 5885−5893

amplification varied considerably for different cell cultures.[65] Stable resistance was achieved with chicory,[74] tomato,[75] and tobacco,[76] but resistance to glyphosate was slowly reduced or lost entirely when glyphosate selection was removed in Madagascar periwinkle (*Catharanthus roseus*)[77] and wild carrot cell cultures.[78] In the absence of glyphosate selection pressure, resistance may be reduced, suggesting a fitness penalty for cells containing amplified genes.[65] However, the massive amplification of *EPSPS* gene in glyphosate-resistant Palmer amaranth did not cause any fitness cost.[79] Other than endowing resistance to glyphosate, no physiological advantage has been documented thus far as a consequence of *EPSPS* gene amplification.

In conclusion, the resistance to glyphosate in all Italian ryegrass populations analyzed is conferred by amplification of the *EPSPS* gene. This is the primary mechanism for resistance to glyphosate among Italian ryegrass populations in Arkansas. *EPSPS* copy number correlated positively with resistance level to glyphosate. The mechanism of *EPSPS* gene amplification and the nature of its heritability are not yet known. Information on the mechanism of amplification, stability, and genetic inheritance of copy number and fitness penalty that may be associated with *EPSPS* gene amplification is necessary to fully understand the novel mechanism of resistance to glyphosate due to *EPSPS* gene amplification in Italian ryegrass.

AUTHOR INFORMATION

Corresponding Author

*(N.R.B.) Phone: (479) 575-3984. Fax: (479) 575-3975. E-mail: nburgos@uark.edu.

Funding

This research was supported by the Arkansas Wheat Research and Promotion Board.

Notes

The authors declare no competing financial interest.

ACKNOWLEDGMENTS

We thank James Dickson for providing plant materials for the ryegrass germplasm collection. We also thank Seth Bernard Abugho, George Botha, Leopoldo Estorninos, Shilpa Singh, Vijay Singh, and Te Ming Tseng for their assistance in tissue collection and establishing greenhouse experiments.

ABBREVIATIONS USED

EPSPS, 5-enolpyruvylshikimate-3-phosphate synthase; ACCase, acetyl-CoA carboxylase; ALS, acetolactate synthase; NIS, nonionic surfactant; DAT, days after treatment; LSS, liquid scintillation spectroscopy; HAT, hours after treatment; R, glyphosate-resistant; S, glyphosate-susceptible; CCR, cinnamoyl-CoA reductase; CTAB, hexadecyltrimethylammonium bromide; PCR, polymerase chain reaction

REFERENCES

(1) Franz, J.; Mao, M.; Sikorski, J. *Glyphosate: A Unique Global Herbicide*; American Chemical Society: Washington, DC, USA, 1997; p 653.

(2) Duke, S. O.; Powles, S. B. Glyphosate: a once-in-a-century herbicide. *Pest Manage. Sci.* **2008**, *64*, 319−325.

(3) Powles, S. B.; Yu, W. Evolution in action: plants resistance to herbicides. *Annu. Rev. Plant Biol.* **2010**, *61*, 317−347.

(4) Steinrücken, H. C.; Amrhein, N. The herbicide glyphosate is a potent inhibitor of 5-enolpyruvyl-shikimic acid-3-phosphate synthase. *Biochem. Biophys. Res. Commun.* **1980**, *94*, 1207−1212.

(5) Dyer, W. E. Resistance to glyphosate. In *Herbicide Resistance in Plants: Biology and Biochemistry*; Powles, S. B., Holtum, J. A. M., Eds.; Lewis Publishers: Boca Raton, FL, USA, 1994; pp 229−237.

(6) Woodburn, A. Glyphosate: production, pricing and use worldwide. *Pest Manag. Sci.* **2000**, *56*, 309−312.

(7) Department of Agriculture, Economic Research Service (USDA ERS). Adoption of genetically engineered crops in the US [dataset]; available athttp://www.ers.usda.gov/Data/BiotechCrops/ (accessed Oct 12, 2011).

(8) Powles, S. B. Evolved glyphosate-resistant weeds around the world: lessons to be learnt. *Pest Manage. Sci.* **2008**, *64*, 360−365.

(9) Powles, S. B.; Lorraine-Colwill, D. F.; Dellow, J. J.; Preston, C. Evolved resistance to glyphosate in rigid ryegrass (*Lolium rigidum*) in Australia. *Weed Sci.* **1998**, *16*, 604−607.

(10) Heap, I. International Survey of Herbicide Resistant Weeds; available at http://www.weedscience.org (accessed Dec 26, 2014).

(11) Preston, C.; Wakelin, A. M.; Dolman, F. C.; Bostamam, Y.; Boutsalis, P. A decade of glyphosate-resistant *Lolium* around the world: mechanisms, genes, fitness, and agronomic management. *Weed Sci.* **2009**, *57*, 435−441.

(12) Powles, S. B.; Preston, C. Evolved glyphosate resistance in plants: Biochemical and genetic basis of resistance. *Weed Technol.* **2006**, *20*, 282−289.

(13) Lorraine-Colwill, D. F.; Powles, S. B.; Hawkes, T. R.; Hollinshead, P. H.l.; Warner, S. A. J.; Preston, C. Investigations into the mechanism of glyphosate resistance in *Lolium rigidum*. *Pestic. Biochem. Physiol.* **2003**, *74*, 62−72.

(14) Perez-Jones, A.; Park, K. W.; Polge, N.; Colquhoun, J.; Mallory-Smith, C. A. Investigating the mechanism of glyphosate resistance in *Lolium multiflorum*. *Planta* **2007**, *226*, 395−404.

(15) Yu, Q.; Cairns, A.; Powles, S. Glyphosate, paraquat and ACCase multiple herbicide resistance evolved in a *Lolium rigidum* biotype. *Planta* **2007**, *225*, 499−513.

(16) Nandula, V. K.; Reddy, K. N.; Poston, D. H.; Rimando, A. M.; Duke, S. O. Glyphosate tolerance mechanism in Italian ryegrass (*Lolium multiflorum*) from Mississippi. *Weed Sci.* **2008**, *56*, 344−349.

(17) Feng, P. C.; Tran, M.; Chiu, T.; Sammons, R. D.; Heck, G. R.; Jacob, C. A. Investigations into glyphosate-resistant *Conyza canadensis*: retention, uptake, translocation, and metabolism. *Weed Sci.* **2004**, *52*, 498−505.

(18) Koger, C. H.; Reddy, K. N. Role of absorption and translocation in the mechanism of glyphosate resistance in horseweed (*Conyza canadensis*). *Weed Sci.* **2005**, *53*, 84−89.

(19) Dinelli, G.; Marotti, I.; Bonetti, A.; Minelli, M.; Catizone, P.; Barnes, J. Physiological and molecular insight on the mechanisms of resistance to glyphosate in *Conyza canadensis* (L.) cronq. biotypes. *Pest Biochem. Physiol.* **2006**, *86*, 30−41.

(20) Riar, D. S.; Norsworthy, J. K.; Johnson, D. B.; Scott, R. C.; Bagavathiannan, M. Glyphosate resistance mechanism in a johnsongrass (*Sorghum halepense*) biotype from Arkansas. *Weed Sci.* **2011**, *59*, 299−304.

(21) Vila-Aiub, M. M.; Balbi, M. C.; Distéfano, A. J.; Fernández, L.; Hopp, E.; Yu, Q.; Powles, S. B. Glyphosate resistance in perennial *Sorghum halepense* (johnsongrass), endowed by reduced glyphosate translocation and leaf uptake. *Pest Manage. Sci.* **2011**, *68*, 430−436.

(22) Baerson, S. R.; Rodriguez, D. J.; Tran, M.; Feng, Y.; Biest, N. A.; Dill, G. M. Glyphosate-resistant goosegrass: Identification of a mutation in the target enzyme 5-enolpyruvylshikimate-3-phosphate synthase. *Plant Physiol.* **2002**, *129*, 1265−1275.

(23) Chong, J. L.; Wickneswari, R.; Ismail, B. S.; Salmijah, S. Nucleotide variability in the 5-enolpyruvylshikimate-3-phosphate synthase gene from *Eleusine indica* (L.) Gaertn. *Pak. J. Biol. Sci.* **2008**, *11*, 476−479.

(24) Ng, C. H.; Wickneswari, R.; Salmijah, S.; Teng, Y. T.; Ismail, B. S. Gene polymorphisms in glyphosate-resistant and -susceptible biotypes of *Eleusine indica* from Malaysia. *Weed Res.* **2003**, *43*, 108−115.

DOI: 10.1021/acs.jafc.5b00018
J. Agric. Food Chem. 2015, 63, 5885−5893

(25) Yuan, C.; Hsieh, Y.; Chiang, M. Glyphosate-resistant goosegrass in Taiwan: cloning of target enzyme (EPSPS) and molecular assay of field populations. *Plant Prot. Bull.* **2005**, *47*, 251−261.
(26) Kaundun, S. S.; Zelaya, I. A.; Dale, R. P.; Lycett, A. J.; Carter, P.; Sharples, K. R.; McIndoe, E. Importance of the P106S target-site mutation in conferring resistance to glyphosate in a goosegrass (*Eleusine indica*) population from the Philippines. *Weed Sci.* **2008**, *56*, 637−646.
(27) Jasieniuk, M.; Ahmad, R.; Sherwood, A.; Firestone, J.; Perez-Jones, A.; Lanini, W.; Mallory-Smith, C. A.; Stednick, Z. Glyphosate-resistant Italian ryegrass (*Lolium multiflorum*) in California: distribution, response to glyphosate and molecular evidence for an altered target enzyme. *Weed Sci.* **2008**, *56*, 496−502.
(28) Simarmata, M.; Penner, D. The basis for glyphosate resistance in rigid ryegrass (*Lolium rigidum*) from California. *Weed Sci.* **2008**, *56*, 181−188.
(29) Wakelin, A. M.; Preston, C. A target-site mutation is present in a glyphosate resistant *Lolium rigidum* population. *Weed Res.* **2006**, *46*, 432−440.
(30) Kaundun, S. S.; Dale, R. P.; Zelaya, I. A.; Dinelli, G.; Marotti, I.; McIndoe, E.; Cairns, A. A novel P106L mutation in EPSPS and an unknown mechanism(s) act additively to confer resistance to glyphosate in a South African *Lolium rigidum* population. *J. Agric. Food Chem.* **2011**, *59*, 3227−3233.
(31) De Carvalho, L. B.; Cruz-Hipolito, H. E.; Rojano-Delgado, A. M.; de Prado, R.; Gil-Humanes, J.; Barro, F.; de Castro, M. D. L. Pool of resistance mechanisms to glyphosate in *Digitaria insularis*. *J. Agric. Food Chem.* **2012**, *60*, 615−622.
(32) Sammons, R. D.; Heering, D. C.; Dinicola, N.; Glick, H.; Elmore, G. A. Sustainability and stewardship of glyphosate and glyphosate-resistant crops. *Weed Technol.* **2007**, *21*, 347−354.
(33) Ge, X.; d'Avignon, D. A.; Ackerman, J. J.; Sammons, R. D. Rapid vacuolar sequestration: the horseweed glyphosate resistance mechanism. *Pest Manage. Sci.* **2010**, *66*, 345−348.
(34) Ge, X.; d'Avignon, D. A.; Ackerman, J. J. H.; Collavo, A.; Sattin, M.; Ostrander, E. L.; Hall, E. L. L.; Sammons, R. D.; Preston, C. Vacuolar glyphosate-sequestration correlates with glyphosate resistance in ryegrass (*Lolium* spp.) from Australia, South America and Europe: a ^{31}P-NMR investigation. *J. Agric. Food Chem.* **2012**, *60*, 1243−1250.
(35) Gaines, T. A.; Zhang, W.; Wang, D.; Bukun, B.; Chrisholm, S. T.; Shaner, D. L.; Nissen, S. J.; Patzoldt, W. L.; Tranel, P. J.; Culpepper, A. S.; Grey, T. L.; Webster, T. M.; Vencill, W. K.; Sammons, R. D.; Jiang, J.; Preston, C.; Leach, J. E.; Westra, P. Gene amplification confers resistance in *Amaranthus palmeri*. *Proc. Natl. Acad. Sci. U.S.A.* **2010**, *107*, 1029−1034.
(36) Salas, R. A.; Dayan, F. E.; Pan, Z.; Watson, S. B.; Dickson, J. W.; Scott, R. C.; Burgos, N. R. *EPSPS* gene amplification in glyphosate-resistant Italian ryegrass (*Lolium perenne* ssp. *multiflorum*) from Arkansas. *Pest Manage. Sci.* **2012**, *68*, 1223−1230.
(37) Dickson, J. W.; Scott, R. C.; Burgos, N. R.; Salas, R. A.; Smith, K. L. Confirmation of glyphosate-resistant Italian ryegrass (*Lolium perenne* ssp. *multiflorum*) in Arkansas. *Weed Technol.* **2011**, *25*, 674−679.
(38) Kuk, Y. I.; Burgos, N. R.; Talbert, R. E. Cross- and multiple resistance of diclofop-resistant *Lolium* spp. *Weed Sci.* **2000**, *48*, 412−419.
(39) Kuk, Y. I.; Burgos, N. R. Cross-resistance profile of mesosulfuron-methyl resistant Italian ryegrass in the southern United States. *Pest Manage. Sci.* **2007**, *63*, 349−357.
(40) Kuk, Y. I.; Burgos, N. R.; Scott, R. C. Resistance profile of diclofop-resistant Italian ryegrass (*Lolium multiflorum*) to ACCase- and ALS-inhibiting herbicides in Arkansas, USA. *Weed Sci.* **2008**, *56*, 614−623.
(41) Chandi, A.; York, A. C.; Jordan, D. L.; Beam, J. B. Resistance to acetolactate synthase and acetyl Co-A carboxylase inhibitors in North Carolina Italian ryegrass (*Lolium perenne*). *Weed Technol.* **2011**, *25*, 659−666.
(42) Ellis, A. T.; Morgan, G. D.; Mueller, T. C. Mesosulfuron-resistant Italian ryegrass (*Lolium multiflorum*) biotype from Texas. *Weed Technol.* **2008**, *22*, 431−434.
(43) Ellis, A. T.; Steckel, L. E.; Main, C. L.; de Melo, M. S. C.; West, D. R.; Mueller, T. C. A survey for diclofop-methyl resistance in Italian ryegrass from Tennessee and how to manage resistance in wheat. *Weed Technol.* **2010**, *24*, 303−309.
(44) Perez-Jones, A.; Park, K. W.; Colquhoun, J.; Mallory-Smith, C.; Shaner, D. Identification of glyphosate-resistant Italian ryegrass (*Lolium multiflorum*) in Oregon. *Weed Sci.* **2005**, *53*, 775−779.
(45) Doyle, J. J.; Doyle, J. L. A rapid DNA isolation procedure for small quantities of fresh leaf tissue. *Phytochem. Bull.* **1987**, *19*, 11−15.
(46) Sales, M. A.; Shivrain, V. K.; Burgos, N. B.; Kuk, Y. I. Amino acid substitutions in the acetolactate synthase gene of red rice (*Oryza sativa*) confer resistance to imazethapyr. *Weed Sci.* **2008**, *56*, 485−489.
(47) Vargas, L.; Ulguim, A. R.; Agostinetto, D.; Magro, T. D.; Thuermer, L. Low level resistance of goosegrass (*Eleusine indica*) to glyphosate in Rio Grande do Sul-Brazil. *Planta Daninha* **2013**, *31*, 677−686.
(48) Burgos, N. R.; Tranel, P. J.; Streibig, J. C.; Davis, V. M.; Shaner, D.; Norsworthy, J. K.; Ritz, C. Review: Confirmation of resistance to herbicides and evaluation of resistance levels. *Weed Sci.* **2013**, *61*, 4−20.
(49) Shaner, D. L. Role of translocation as a mechanism of resistance to glyphosate. *Weed Sci.* **2009**, *57*, 118−123.
(50) Michitte, P.; De Prado, R.; Espinoza, N.; Ruiz-Santaella, J. P.; Gauvrit, C. Mechanisms of resistance to glyphosate in a ryegrass (*Lolium multiflorum*) biotype from Chile. *Weed Sci.* **2007**, *55*, 435−440.
(51) Feng, P. C. C.; Pratley, J. E.; Bohn, J. Resistance to glyphosate in *Lolium rigidum*. II. Uptake, translocation, and metabolism. *Weed Sci.* **1999**, *47*, 412−415.
(52) Simarmata, M.; Kaufmann, J. E.; Penner, D. Potential basis of glyphosate resistance in California rigid ryegrass (*Lolium rigidum*). *Weed Sci.* **2003**, *51*, 678−682.
(53) Eschenburg, S.; Healy, M. L.; Priestman, M. A.; Lushington, G. H.; Schonburnn, E. How the mutation glycine96 to alanine confers glyphosate insensitivity to 5-enolpyruvyl shikimate-3-phosphate synthase from *Escherichia coli*. *Planta* **2006**, *216*, 129−135.
(54) Funke, T.; Yang, Y.; Han, H.; Healy-Fried, M.; Olesen, S. Structural basis of glyphosate resistance resulting from the double mutation Thr97 → Ile and Pro101 → Ser in 5-enolpyruvylshikimate-3-phosphate synthase from *Escherichia coli*. *J. Biol. Chem.* **2009**, *284*, 9854−9860.
(55) Schonbrunn, E.; Eschenburg, S.; Shuttleworth, W. A.; Schloss, J. V.; Amrhein, N.; Evans, J. N. S.; Kabsch, W. Interaction of the herbicide glyphosate with its target enzyme EPSP synthase in atomic detail. *Proc. Natl. Acad. Sci. U.S.A.* **2001**, *98*, 1376−1380.
(56) Mizyed, S.; Wright, J. E. I.; Byczynski, B.; Berti, P. Identification of the catalytic residues of AroA (enolpyruvylshikimate 3-phosphate synthase) using partitioning analysis. *Biochemistry* **2003**, *42*, 6986−6995.
(57) Holt, J. S.; Thill, D. C. Growth and productivity of resistant plants. In *Herbicide Resistance in Plants: Biology and Biochemistry*; Powles, S. B.; Holtum, J. A. M., Eds.; Lewis: Boca Raton, FL, USA, 1994; pp 299−316.
(58) Ismail, B. S.; Chuah, T. S.; Salmijah, S.; Teng, Y. T.; Schumacher, R. W. Germination and seedling emergence of glyphosate-resistant and susceptible biotypes of goosegrass [*Eleusine indica* (L) Gaertn.]. *Weed Biol. Manage.* **2002**, *2*, 177−185.
(59) Lee, L. J. Glyphosate resistant goosegrass (*Eleusine indica*) in Malaysia and some of its morphological differences. *Proceedings of the 17th Asian-Pacific Weed Science Society Conference*, Bangkok, Thailand, 1999; pp 90−95.
(60) Terrell, E. E. *A Taxonomic Revision of the Genus Lolium*; Technical Bulletin 1392; U.S. Department of Agriculture, U.S. Government Printing Office: Washington, DC, USA, 1968; p 2.
(61) Gaines, T. A.; Shaner, D. L.; Ward, S. M.; Leach, J. E.; Preston, C.; Westra, P. Mechanism of resistance of evolved glyphosate-resistant

DOI: 10.1021/acs.jafc.5b00018
J. Agric. Food Chem. 2015, 63, 5885−5893

Palmer amaranth (*Amaranthus palmeri*). *J. Agric. Food Chem.* **2011**, *59*, 5886−5889.
(62) Ribeiro, D. N.; Pan, Z.; Duke, S. O.; Nandula, V. K.; Baldwin, B. S.; Shaw, D. R.; Dayan, F. E. Involvement of facultative apomixis in inheritance of EPSPS gene amplification in glyphosate-resistant *Amaranthus palmeri*. *Planta* **2014**, *239*, 199−212.
(63) Chandi, A.; Milla-Lewis, S. R.; Giacomini, D.; Westra, P.; Preston, C.; Jordan, D. L. Inheritance of evolved glyphosate resistance in a North Carolina Palmer amaranth (*Amaranthus palmeri*) biotype. *Int. J. Agron.* **2012**, DOI: 10.1155/2012/176108.
(64) Vogel, C.; Marcotte, E. M. Insights into the regulation of protein abundance from proteomic and transcriptomic analyses. *Nat. Rev. Genet.* **2012**, *13*, 227−232.
(65) Pline-Srnic, W. Physiological mechanisms of glyphosate resistance. *Weed Technol.* **2006**, *20*, 290−300.
(66) Widholm, J. M.; Chinnala, A. R.; Ryu, J.; Song, H.; Eggetta, T.; Brothertona, J. E. Glyphosate selection of gene amplification in suspension cultures of 3 plant species. *Physiol. Plant.* **2001**, *112*, 540−545.
(67) Suh, H.; Hepburn, A. G.; Kriz, A. L.; Widholm, J. M. Structure of the amplified 5-enolpyruvylshikimate-3-phosphate synthase gene in glyphosate resistant carrot cells. *Plant Mol. Biol.* **1993**, *22*, 195−205.
(68) Steinrucken, H. C.; Schulz, A.; Amrhein, N.; Porter, C. A.; Fraley, R. T. Overproduction of 5-enolpyruvyl-shikimate 3-phosphate synthase in a glyphosate-tolerant *Petunia hybrida* cell line. *Arch. Biochem. Biophys.* **1986**, *244*, 169−178.
(69) Culpepper, A. S.; Grey, T. L.; Vencill, W. K.; Kichler, J. M.; Webster, T. M.; Brown, S. M.; York, A. C.; Davis, J. W.; Hanna, W. W. Glyphosate-resistant Palmer amaranth (*Amaranthus palmeri*) confirmed in Georgia. *Weed Sci.* **2006**, *54*, 620−626.
(70) Powles, S. B. Gene amplification delivers glyphosate-resistant weed evolution. *Proc. Natl. Acad. Sci. U.S.A.* **2010**, *107*, 955−956.
(71) Zou, C.; Lehti-Shiu, M. D.; Thomashow, M.; Shiu, S.-H. Evolution of stress-regulated gene expression in duplicate genes of *Arabidopsis thaliana*. *PLoS Genet.* **2009**, *5*, No. e1000581.
(72) Kondrashov, F. A. Gene duplication as a mechanism of genomic adaptation to a changing environment. *Proc. R. Soc. B* **2012**, *279*, 5048−5057.
(73) Giacomini, D. A.; Westra, P.; Ward, S. M.; Sammons, R. D. The inheritance of amplified EPSPS gene copies in Palmer amaranth (*Amaranthus palmeri*). *Weed Sci. Soc. Am. Proc.* **2013**, *53*, 311.
(74) Sellin, C.; Forlani, G.; Dubois, J.; Nielsen, E.; Vasseur, J. Glyphosate tolerance in *Cichorium intybus* var magdebourg. *Plant Sci.* **1992**, *85*, 223−231.
(75) Smith, C. M.; Pratt, D.; Thompson, G. A. Increased 5-enolpyruvylshikimic acid 3-phosphate synthase activity in a glyphosate-tolerant variant strain of tomato cells. *Plant Cell Rep.* **1986**, *5*, 298−301.
(76) Goldsbrough, P. B.; Hatch, E. M.; Huang, B.; Kosinski, W. G.; Dyer, W. E.; Herrmann, K. M.; Weller, S. C. Gene amplification in glyphosate tolerant tobacco cellS. *Plant Sci.* **1990**, *72*, 53−62.
(77) Cresswell, R. C.; Fowler, M. W.; Scragg, A. H. Glyphosate-tolerance in *Catharanthus roseus*. *Plant Sci.* **1988**, *54*, 55−63.
(78) Murata, M.; Ryu, J. H.; Caretto, S.; Rao, D.; Song, H. S.; Widholm, J. M. Stability and culture medium limitations of gene amplification in glyphosate resistant carrot cell lines. *J. Plant Physiol.* **1998**, *152*, 112−117.
(79) Vila-Aiub, M. M.; Goh, S. S.; Gaines, T. A.; Han, H.; Busi, R.; Yu, Q.; Powles, S. B. No fitness cost of glyphosate resistance endowed by massive EPSPS gene amplification in *Amaranthus palmeri*. *Planta* **2014**, *239*, 793−801.

DOI: 10.1021/acs.jafc.5b00018
J. Agric. Food Chem. 2015, 63, 5885−5893

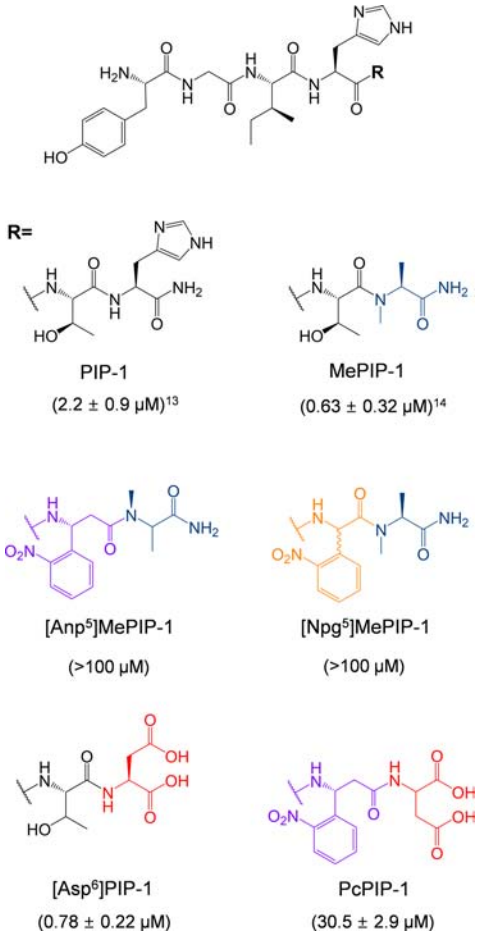

Figure 1. Structure of PIP-1 and its analogs. Anp, (*R*)-3-amino-3-(2-nitrophenyl)propionic acid; Npg, (*RS*)-(2-nitro)phenylglycine. Values in parentheses indicate EC_{50} for H_2O_2 generation.

at G1 phase and was rapidly inactivated by UV irradiation. This inactivation reactivated the cell cycle in all cells in a homogeneous and synchronous manner, allowing analysis of the cell cycle progress in detail.

In the present study, we designed a photocleavable PIP-1 analog to investigate the mechanisms underlying the stimulation period-dependent induction of late immune responses such as phytoalexin biosynthesis. The introduction of a photocleavable amino acid into PIP-1 successfully provided an analog, the activity of which can be "switched off" by UV irradiation. Using this analog, we explored key components that are associated with the initiation of phytoalexin biosynthesis in response to continuous stimulation with PIP-1.

MATERIALS AND METHODS

Plant Cell Culture. Tobacco cells (*Nicotiana tabacum* cv. Xanthi) were maintained as suspension cultures in 25 mL of liquid Linsmaier and Skoog (LS) medium at pH 5.75 containing 1-naphthalenacetic acid (10 μM), 5-benzyladenine (1 μM), and 3% of sucrose in a 100 mL Erlenmeyer flask. The cells were grown at 25 °C under continuous illumination on a rotary shaker (100 rpm) and subcultured every 2 weeks. The experiments were conducted using 9- and 10-day old subcultured tobacco cells.

Chemicals. *N*-(9-Fluorenylmethoxycarbonyl) (Fmoc)-NH-SAL resin, Cl-Trt(2-Cl)-Resin, and general Fmoc-protected amino acids were purchased from Watanabe Chemical Industries (Hiroshima, Japan). Fmoc-(*R*)-3-amino-3-(2-nitrophenyl)propionic acid was purchased from PepTech Corporation (Bedford, MA) and Fmoc-(*RS*)-(2-nitro)phenylglycine was synthesized as described by Rodenko et al.[20] (Carboxymethylaminocarbonyl)-4,4′-bis(dimethylamino)-diphenylamine sodium salt (DA-64), cycloheximide (CHX), and 3-hydroxy-3-methylglutaryl-coenzyme A (HMG-CoA) were purchased from Wako Pure Chemical Industries (Osaka, Japan), Nacalai Tesque (Kyoto, Japan), and Santa Cruz Biotechnology (Dallas, TX), respectively.

Synthesis of Photocleavable Analogs. An Fmoc solid-phase peptide synthesis strategy was used to synthesize photocleavable analogs. Deprotection of the Fmoc protecting group was conducted using 20% piperidine in DMF 3 times for 3, 3, and 20 min. Coupling of Fmoc-protected amino acids (3 equiv) was performed in the presence of *O*-(benzotriazole-1-yl)-1,1,3,3-tetramethyluronium hexafluorophosphate (HBTU) (3 equiv), 1-hydroxybenzotriazole (HOBt) (3 equiv), and *N*,*N*-diisopropylethylamine (DIPEA) (6 equiv) in *N*,*N*-dimethylformamide (DMF). Completion of the reaction was checked by Kaiser test.[22] After completion of all coupling reactions, the resin was washed with DMF, diethyl ether, and methanol and subsequently vacuum-dried. Peptide cleavage and removal of side-chain protecting groups were conducted using cleavage cocktails [TFA/triisopropylsilane/1,3-dimethoxybenzene (92.5:2.5:5) for Fmoc-SAL-resin attached peptides and TFA/triisopropylsilane/H_2O (95:2.5:2.5) for Cl-Trt(2-Cl)-resin attached peptides] for 2 h at room temperature. The reaction mixture was filtered, and the filtrate was mixed with cold diethyl ether to precipitate the peptides. The peptides were then vacuum-dried. For analogs containing (2-nitro)phenylglycine, dichloromethane was used instead of DMF throughout the process. Peptide purification was conducted by RP-HPLC using a 250 mm × 10 mm i.d., 5 μm, protein and peptide C18 semipreparative column (Grace, Columbia, MD), and lyophilized. Purified peptides were identified by electrospray ionization liquid chromatography−mass spectrometry (ESI-LC/MS) on an LCMS-2010 instrument (Shimadzu, Kyoto, Japan).

Measurement of H_2O_2 Generation. H_2O_2 generation was measured as described previously.[23] Suspension-cultured tobacco cells (0.2 g) were resuspended in 1 mL of assay buffer (175 mM mannitol, 0.5 mM $CaCl_2$, 0.5 mM K_2SO_4, 2.0 mM MES, pH 5.75) and incubated for 1 h at 25 °C using a tube rotator. Peptide samples were added to tobacco cell suspensions, and the cells were reincubated for 15 min at 25 °C. The supernatants (60 μL) were added to a 96-well microplate containing an H_2O_2 indicator solution (140 μL, 100 mM DA-64, 1 U/mL horseradish peroxidase, 100 mM PIPES, pH 7.0). This microplate was incubated for 10 min at 37 °C. The absorbance at 727 nm was observed using a Benchmark microplate reader (Bio-Rad, Hercules, CA). The amount of H_2O_2 was calculated using a calibration curve based on pure H_2O_2. As an index of activity, the concentration required for half-maximal responses (EC_{50}) was calculated using PRISM (GraphPad Software, La Jolla, CA).

Peptide Photolysis. The photocleavable analogs were dissolved in distilled water at 100 μM of final concentration. The solution was irradiated with UV light (365 nm, 10 mW/cm^2) using a Blak-ray B-100A UV lamp (UVP, Upland, CA). The UV-irradiated solution was analyzed with LCMS-2020 and LCMS-IT-TOF (Shimadzu) equipped with a 150 mm × 2.1 mm i.d., 3.6 μm, Aeris PEPTIDE XB-C18 reverse phase column (Phenomenex, Torrance, CA).

Cell Death Assay. Cell death was measured as described previously with modifications.[24] Cells (0.2 g) were treated with peptide samples and incubated for 24 h at 25 °C using a tube rotator. After incubation, the cell suspension was reincubated in Evans blue solution (Wako Pure Chemical Industries) at a final concentration of 0.01% for 15 min and then washed with distilled water 3 times to remove any unabsorbed dye. The washed cells were transferred into a new microtube containing 50% methanol and 1% SDS to extract the dye in dead cells and incubated for 1 h at 60 °C. The solution was centrifuged for 15 min at 1900*g*. Absorbance of the supernatant at 595 nm was measured on a microplate reader (Bio-Rad).

Quantitation of Capsidiol. Capsidiol content was quantitated as described previously.[13] Tobacco cells (0.6 g) resuspended in 3 mL of LS medium were incubated for 1 h. The cells were then treated with peptide samples and incubated for 24 h at 25 °C on a rotary shaker under continuous illumination. After incubation, capsidiol was

DOI: 10.1021/acs.jafc.5b01910
J. Agric. Food Chem. 2015, 63, 5894−5901

extracted from the culture medium using 4 mL of ethyl acetate twice and vacuum-dried. The residue was then dissolved in 1 mL of ethyl acetate and subjected to QP-2010 GC/MS analysis (Shimadzu), equipped with a 30 m × 0.25 mm, 0.25 μm phase thickness, DB-5MS capillary column (J & W Scientific, Folsom, CA). Other GC/MS conditions were described previously.[14] The amount of capsidiol was quantitated from the peak areas obtained in the total ion chromatogram, using a calibration curve based on an authentic standard purified from *Capsicum annuum* fruit.[25]

In-Gel Kinase Assay. In-gel kinase assay was performed as described previously with modifications.[26] Tobacco cells (0.6 g) resuspended in 3 mL of LS medium were incubated for 1 h at 25 °C. The cells were then treated with peptide samples and reincubated for 3 h. After all medium was removed, tobacco cells were ground in liquid nitrogen using a mortar and pestle. Powdered tobacco cells were homogenized using 1.5 mL of extraction buffer [50 mM HEPES, pH 7.4, 5 mM EDTA, 5 mM EGTA, 5 mM DTT, 10 mM NaF, 10 mM Na_3VO_4, 50 mM β-glycerophosphate, 1 mM 4-(2-aminoethyl)-benzenesulfonyl fluoride, 2 μg/mL antipain, 2 μg/mL aprotinin, and 2 μg/mL leupeptin] and centrifuged at 16 000*g* for 30 min at 4 °C. Protein extracts (10 μg) were electrophoresed on 12% SDS-polyacrylamide gels embedded with 0.25 mg/mL myelin basic protein (MBP) (Sigma, St. Louis, MO) as a kinase substrate. After electrophoresis, the gel was washed with washing buffer (20% 2-propanol, 50 mM Tris, pH 8.0) three times for 20 min each at room temperature to remove SDS and incubated with buffer A (50 mM Tris, pH 8.0, 5 mM DTT) for 1 h. The proteins in the gel were denatured using denaturation buffer (50 mM Tris−HCl, pH 8.0, 6 M guanidine·HCl, 20 mM DTT, 2 mM EDTA) twice for 30 min each. The kinases were allowed to renature by incubations in buffer A containing 0.04% of Tween 20 overnight at 4 °C with 5 changes of buffer. After equilibration in assay buffer (50 mM HEPES, pH 8.0, 2.0 mM DTT, 0.1 mM EGTA, and 20 mM $MgCl_2$) for 30 min at room temperature, the gel was incubated in 20 mL of assay buffer containing 30 μM ATP and 1.85 MBq of [γ-^{32}P]-ATP (111 TBq/mmol) (PerkinElmer, Waltham, MA) for 1 h at room temperature. The reaction was stopped by transferring the gel into a solution containing 10% trichloroacetic acid (w/v) and 1% sodium phosphate (w/v). The gel was washed five times with the same solution for 20 min each to remove any unincorporated [γ-^{32}P]-ATP and dried on filter paper using a vacuum gel-dryer. The dried gel was then exposed to BAS-MS 2040 imaging plates (Fujifilm, Tokyo, Japan) and analyzed using BAS-2500 (Fujifilm). Prestained size markers (Nacalai Tesque) were used to estimate the size of the kinases.

Gene Expression. Tobacco cells (0.6 g) suspended in 3 mL of LS medium were treated with peptide samples and incubated for 4 h at 25 °C. Incubated cells were collected by filtration and ground in liquid nitrogen using a mortar and pestle. Total RNA was extracted from powdered tobacco cells using TRIzol reagent (Life Technologies, Carlsbad, CA) according to the manufacturer's instructions. The RNA was then incubated with 10 U of RQ1 RNase-Free DNase (Promega, Madison, WI) for 30 min at 37 °C to degrade the DNA. cDNA was synthesized from 1 μg of total RNA using a PrimeScript RT reagent kit (Takara Bio, Otsu, Japan) according to the manufacturer's instructions. Quantitative reverse transcription polymerase chain reaction (qRT-PCR) was performed by Thermal Cycler Dice (Takara Bio) with amplification buffer (25 μL of final volume) containing 2 μL of cDNA template, SYBR *Premix Ex Taq* II (Takara Bio), and 0.4 μM of the following forward and reverse primer; *HMGR2*: 5′-GAGGG-GAGAGGAAAGTCTGTAG-3′ and 5′-TCTCTATGTTCTGAGCT-GGGTC-3′. *Actin* (5′-CCATTGGCTCAGAGAGGTTC-3′ and 5′-GTTGGAAGGTGCTGAGAG-3′) was used as a reference gene.[27]

Enzyme Assay. 3-Hydroxy-3-methylglutaryl coenzyme A reductase (HMGR) activity was measured as described previously.[28] In brief, tobacco cells (0.6 g) treated with peptide samples for 4 h were used for crude enzyme extraction. Tobacco cells were ground in liquid nitrogen using a mortar and pestle and homogenized using extraction buffer (50 mM Tris-HCl, 10 mM β-mercaptoethanol, 1% (w/v) PVP, pH 7.5). The mixture was centrifuged at 16 000*g* at 4 °C for 30 min, and the supernatant was used for measurement of HMGR activity after determining protein concentrations using a Bio-Rad protein assay reagent. The crude extract was added to the assay buffer (50 mM Tris-HCl, 0.3 mM HMG-CoA, 0.2 mM NADPH, and 4 mM DTT, pH 7.0), and NADPH oxidation was measured by monitoring a decrease in absorbance at 340 nm. One unit of HMGR enzyme is equivalent to the oxidation of 1 mM NADPH per minute. Elicitor-inducible HMGR activity was estimated by subtracting the constitutive activity in the absence of the elicitor from the activity in the presence of the elicitor.

RESULTS AND DISCUSSION

Design of Photocleavable PIP-1 Analogs and Evaluation of Their Elicitor Activity. In a previous contribution, we reported that PIP-1 can be rapidly hydrolyzed from its C-terminal end in the presence of tobacco cells and that no elicitor activity was observed when the C-terminal two residues were deleted.[14] The degradation-resistant analog MePIP-1 was obtained by attaching an *N*-methyl group to the amide bond between Thr and Ala residues (Figure 1). This analog exhibited elicitor activity higher than that of PIP-1 in terms of phytoalexin production. To obtain photocleavable PIP-1 analogs whose activity can be switched off by UV irradiation, the analogs must be stable against enzymatic degradation unless UV-irradiated. In this regard, MePIP-1 was suitable as a starting compound for development of photocleavable PIP-1 analogs. Therefore, we first substituted the Thr residue of MePIP-1 with a photocleavable amino acid (Anp) (Figure 1, [Anp^5]MePIP-1) because cleavage of the amide bond between His and Anp by UV irradiation was expected to produce inactive peptides. However, this analog did not show any measurable activity, even before UV irradiation (Figure 1). This lack of activity could be associated with the β-amino acid structure of Anp, which adds an additional carbon atom to the main peptide chain, possibly causing unfavorable structural changes preventing the interaction between the peptide and the receptor. Subsequently, we attempted to substitute the Thr residue with a photocleavable α-amino acid (Npg) (Figure 1, [Npg^5]MePIP-1), although substitution also resulted in loss of biological activity (Figure 1). In this case, the steric interaction between the 2-nitrobenzyl group and the neighboring terminal *N*-methyl group might have influence on the activity by changing the overall molecular conformation into the inactive form. Therefore, we explored different strategies to obtain new degradation-resistant PIP-1 analogs that could be suitable for designing photocleavable analogs.

While studying the relationship between structure and enzymatic degradation of PIP-1, it became apparent that the basic character of the C-terminal His residue could be important for the recognition by proteases derived from tobacco cells (data not published). Accordingly, we substituted the C-terminal His residue with an acidic amino acid, Asp, and replaced the C-terminal amide group with a carboxy group, which is known to increase PIP-1 elicitor activity (Figure 1, [Asp^6]PIP-1).[13] As expected, [Asp^6]PIP-1 displayed higher degradation resistance compared with that of PIP-1 without affecting elicitor activity (Figure 1 and Figure S1 in the Supporting Information). On the basis of the structure of [Asp^6]PIP-1, we designed a photocleavable analog as shown above. After substitution of the Thr residue of [Asp^6]PIP-1 with Anp (Figure 1, PcPIP-1), the resulting compound retained the elicitor activity and was resistant to degradation (Figures 1 and 2). In the following sections, we examine whether photocontrol of the elicitor activity of this analog is possible.

DOI: 10.1021/acs.jafc.5b01910
J. Agric. Food Chem. 2015, 63, 5894−5901

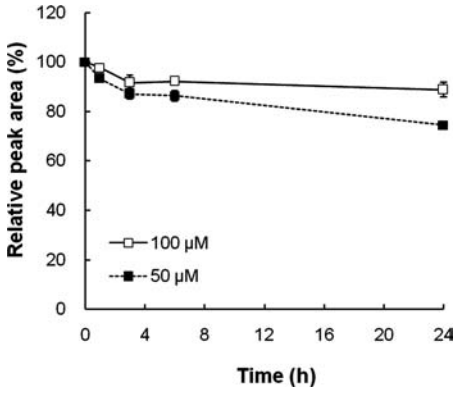

Figure 2. Degradation resistance of PcPIP-1 in the presence of tobacco cells. Relative amounts of PcPIP-1 in the cell culture medium after treatment are plotted (n = 2).

Photolysis of the Photocleavable PIP-1 Analog. We evaluated the reactivity of the photocleavable analog PcPIP-1 in aqueous solution under UV irradiation. ESI-LC/MS was used to monitor the degradation of PcPIP-1. When PcPIP-1 (m/z observed for $[M+2H]^{2+}$, 398.68; retention time, 15.1 min) was irradiated at 365 nm for 5 min, approximately 10% of the initial concentration was detected (Figure 3). Instead, several new peaks appeared in the chromatogram. The molecular masses of two peaks detected at 3.7 min (m/z 488.27 for $[M + H]^+$) and 6.3 min (m/z 489.26 for $[M + H]^+$) of retention time corresponded with those of YGIH-NH_2 and YGIH-OH, respectively, identified by comparing with synthesized standards. These peptides were considered to be produced by photolysis of the Anp residue, although the formation mechanism of the latter was not clear. The molecular mass of the other two peaks detected at 13.0 and 13.5 min of retention times was similar to that of the original peptide (m/z observed for $[M+2H]^{2+}$, 398.67; calculated, 398.66). These peaks were still detected after irradiation with UV light for an additional 10 min; however, only marginal levels of the original peptide were detected at that stage. MS/MS analysis showed that whereas fragment ions related to the amino acid sequence were regularly observed for the case of the original peptide, the two unknown peaks gave only two major fragment ions (Figure S2 in the Supporting Information). MS^3 analysis suggested that these fragment ions correspond to YGIH-NH_2 and 3-(2-nitrosophenyl)-3-oxopropanoyl aspartic acid, the expected photolyzed products of PcPIP-1. On the basis of these results, we assumed that these two unknown peaks observed after photolysis can be the structural isomers of an intermediate produced during photolysis of PcPIP-1. Previous studies have proposed that the photolysis of 2-nitrobenzyl compounds is a multistep process, and the decay of *aci*-nitro intermediates (Figure S3 in the Supporting Information) is considered to be rate-limiting.[29,30] By analogy, the photolysis of PcPIP-1 might involve the formation of relatively long-lived α-hydroxybenzyl intermediates;[31−33] therefore, it seems likely that the unknown peaks detected were associated with the 3-hydroxy-3-(2-nitrosophenyl) intermediate product, as shown in Figure S3 in the Supporting Information. The possible epimerization of this intermediate can account for the occurrence of two peaks with the same molecular mass.

Photocontrol of Activity of the Photocleavable PIP-1 Analog. To confirm that PcPIP-1 can be inactivated by UV irradiation, we first compared the defense-inducing activity of PcPIP-1 with and without UV irradiation. Regarding early-phase immune responses, treating cells with intact PcPIP-1 at 50 or 100 μM significantly increased the level of H_2O_2 generated (Figure 4A). Exposing PcPIP-1 to UV irradiation in the absence of tobacco cells reduced markedly its elicitor activity. When cells were treated with UV-irradiated PcPIP-1 at 50 and 100 μM, the level of H_2O_2 generated decreased by 6- and 2-fold, respectively. Exposing PcPIP-1 to UV irradiation also significantly affected the induction of the late-phase immune responses, such as HR-like cell death and phytoalexin production, compared with that by intact PcPIP-1. The levels of cell death induced by UV-irradiated PcPIP-1 were evidently lower than those induced by intact PcPIP-1 (Figure 4B). The production of capsidiol, the major phytoalexin in tobacco, also markedly differed between UV-irradiated and intact PcPIP-1; in this case, the activity was nearly entirely repressed by UV irradiation both at 50 and 100 μM (Figure 4C). These results indicated that UV-irradiated PcPIP-1, a mixture of the photolyzed products and intermediates, presents a level of elicitor activity sufficiently lower than that of intact PcPIP-1.

We then examined whether PcPIP-1 can be also inactivated by UV irradiation in the presence of tobacco cells. As shown in Figure 5A, when tobacco cells were UV-irradiated for 5, 10, or 15 min following treatment with PcPIP-1 at 100 μM for 1 h, a time-dependent decrease in capsidiol production was observed,

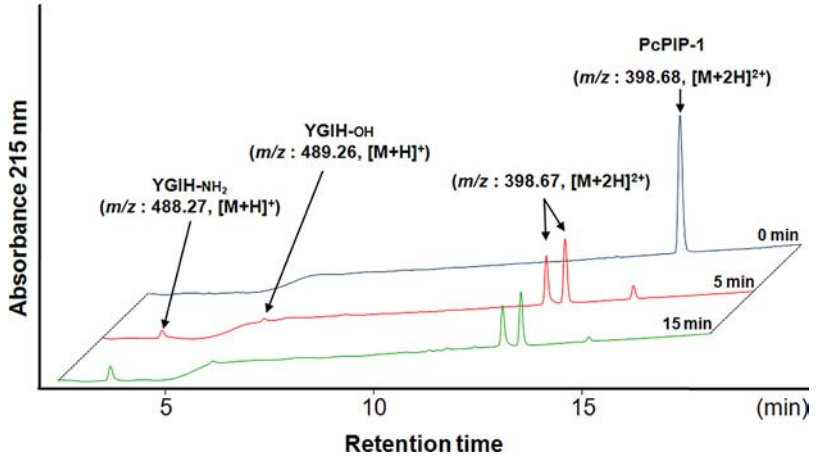

Figure 3. HPLC profile of photolyzed products of PcPIP-1 at 100 μM.

DOI: 10.1021/acs.jafc.5b01910
J. Agric. Food Chem. 2015, 63, 5894−5901

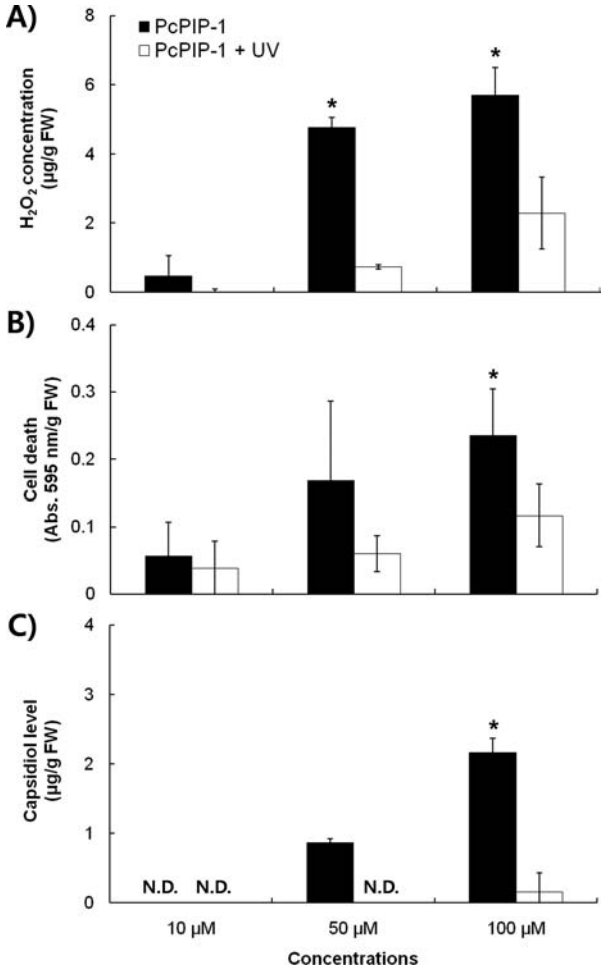

Figure 4. Comparisons of immune responses induced by PcPIP-1 between those with and without UV irradiation in the presence of tobacco cells. (A) H_2O_2 generation, (B) HR-like cell death, and (C) capsidiol production. Asterisks indicate significant difference at $P < 0.05$ according to the Student's paired *t*-test. Vertical bars indicate ±SD of three independent replicates. N.D.: not detected.

indicating that photolysis of PcPIP-1 occurred in the presence of tobacco cells similar to the process observed for aqueous solution in the absence of tobacco cells. These results were consistent with those from a previous study in which wash-out of PIP-1 from the cells 1 h after treatment resulted in no capsidiol production.[14] Therefore, our results confirmed that exposing PcPIP-1 to UV irradiation for 15 min was effective to inactivate it to entirely repress its action on tobacco cells. Capsidiol production after treatment with 100 μM of PIP-1 was not affected by 15 min of UV irradiation, indicating that UV irradiation per se had no negative effect on tobacco cells in relation to phytoalexin production.

Next, we investigated the stimulation period required to initiate capsidiol production in tobacco cells using PcPIP-1. Tobacco cells were treated with PcPIP-1 at 100 μM and irradiated with UV light for 15 min after 1, 3, 6, and 9 h. Capsidiol production was measured 24 h after treatment with PcPIP-1. Significant levels of capsidiol were detected when the cells were UV-irradiated 6 or 9 h after elicitation. By contrast, no capsidiol was detected when UV-irradiated 1 or 3 h after elicitation (Figure 5B). These results indicated that the continuous stimulation with PcPIP-1 for a time period between 3 and 6 h is required to induce phytoalexin production. These results were consistent with those from a previous study that used the cell-washing method to remove treated PIP-1 from the culture medium, where 3−6 h of continuous stimulation was required for capsidiol production.[14] However, the amount of capsidiol detected when PcPIP-1 was inactivated 6 or 9 h after elicitation by UV irradiation was much larger than that observed in the experiments using the cell-washing method. This is probably due to the difference in the degree of stresses placed on the tobacco cells. Cell-washing is more likely to damage cells than irradiation with UV light, possibly affecting negatively capsidiol biosynthesis. Moreover, the amount of the capsidiol accumulated in the extracellular fluid up to the time of cell-washing could have been lost, resulting in an underestimation of capsidiol production. Thus, our results showed that photocleavable PcPIP-1 presents several advantages as a tool to study phytoalexin induction mechanisms by elicitors because of its ability to stop the stimulation of the immune system rapidly but not aggressively, without damaging the cells or losing the phytoalexin accumulated in the medium.

Effect of PIP-1 Stimulation Period on Activation of Signaling Pathways and Biosynthesis Enzymes Important for Capsidiol Production. Following the recognition of pathogens or elicitors, MAP kinase cascades mediate the

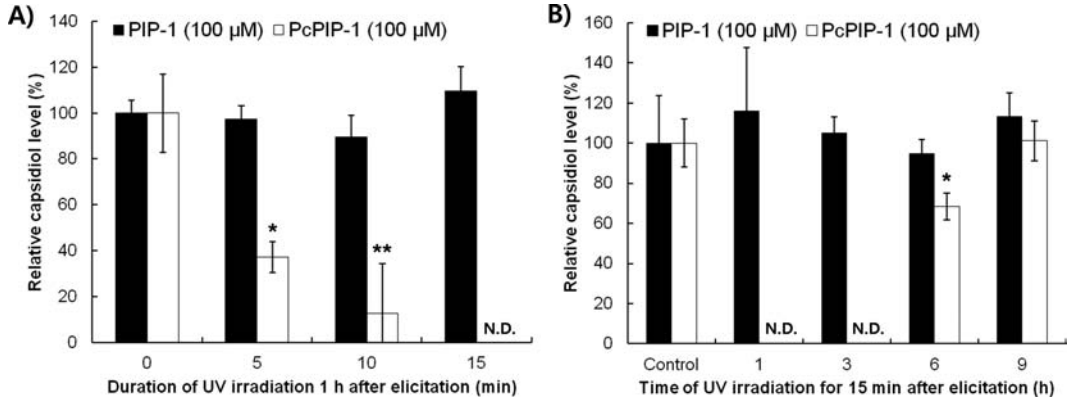

Figure 5. Comparisons of capsidiol production after treatment with PIP-1 and PcPIP-1 at 100 μM. (A) Effect of UV-irradiation period. UV irradiation for 0−15 min was applied 1 h after sample treatment, and 0 min was used as a control. (B) Effect of activation period. UV irradiation (15 min) was applied 1−9 h after sample treatment. Asterisks indicate significant difference compared with their control according to Tukey's multiple comparison test (*$P < 0.01$; **$P < 0.001$). Vertical bars indicate ±SD of three independent replicates. N.D.: not detected.

DOI: 10.1021/acs.jafc.5b01910
J. Agric. Food Chem. 2015, 63, 5894−5901

signaling pathway invoking late-phase immune responses.[9] In a previous study, we showed that PIP-1 induces activation of a 48 kDa kinase in tobacco cells,[14] which corresponds to a salicylic acid-induced protein kinase (SIPK).[26] From our previous study on the relationship between SIPK activation and capsidiol production, we concluded that a prolonged activation of SIPK induced by continuous elicitor stimulation is likely to be involved in the induction of capsidiol biosynthesis. However, which key components directly control capsidiol production in response to continuous stimulation with PIP-1 remains unknown.

3-Hydroxy-3-methylglutaryl CoA reductase (HMGR) acts as an upstream rate-limiting enzyme in the mevalonate pathway, and it plays an important role in the synthesis of isoprenoids essential for plant growth and development via constitutive activity that is likely to be regulated by *HMGR1*.[34] It was shown that the elicitor-inducible HMGR activity is considered to be responsible for capsidiol biosynthesis in tobacco cells,[35,36] which seems to be associated with *HMGR2*, an elicitor-inducible HMGR isogene in Solanaceae plants.[37,38] However, the mechanisms underlying the regulation of HMGR activity in response to elicitor treatment are poorly understood. In a previous study, we showed that short-term stimulation with PIP-1 induced the accumulation of *HMGR2* transcripts,[14] whereas no production of capsidiol was observed. In this regard, it is possible that HMGR activity is "switched on" only after continuous stimulation with PIP-1 via translational and/or post-translational regulatory mechanisms, leading to capsidiol production. Therefore, we investigated the relationship between the duration of stimulation with PIP-1 and the induction of HMGR activity along with the activation of SIPK using PcPIP-1.

We first examined the effect of the duration of stimulation with PIP-1 on SIPK activation. As shown in Figure 6A, SIPK activity increased significantly after 3 h of treatment with PcPIP-1. This enhancement of SIPK activity was much weaker when PcPIP-1 was inactivated by UV irradiation 1 h after elicitation. This result was consistent with our previous results obtained using the cell-washing method, where the enhanced SIPK activity decreased after washing out the elicitor.[14] However, the decrease in the SIPK activity was much sharper in the present study, compared to that observed using the cell-washing method. In the latter, high levels of the SIPK activity were still detected even after washing out the elicitor, probably due to physical stress or damage caused to the cells during washing operations. Our results here showed that the use of the photocleavable analog can effectively "switch off" elicitor-mediated MAP kinase activation including downstream responses, such as phosphorylation of its substrates. Thus, this method appears to be particularly advantageous for investigating key components important for capsidiol production in response to continuous stimulation with PIP-1 through MAP kinase signaling.

We then examined the effect of the duration of the stimulation with PIP-1 on the induction of *HMGR2* expression. Following treatment with either PIP-1 or PcPIP-1, *HMGR2* transcripts increased significantly regardless of UV irradiation (Figure 6B). This result clearly indicated that the short-term elicitor stimulation is enough for induction of the expression of *HMGR2*, as previously observed.[14] Treatment of protein synthesis inhibitor (CHX) did not suppress *HMGR2* expression induced by PcPIP-1, suggesting that de novo protein synthesis is not involved in this gene expression. Next, the effect of the

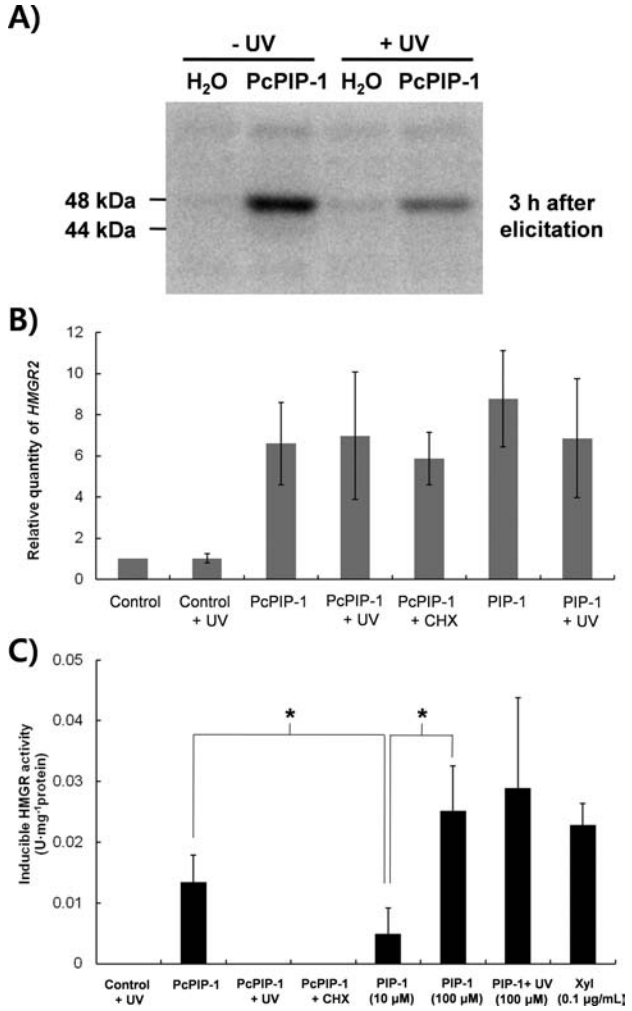

Figure 6. Effect of stimulation period on MAP kinase and HMGR activation. (A) Comparison of MAP kinase activity induced by PcPIP-1 (100 μM) between those with and without UV irradiation. UV irradiation (15 min) was applied 1 h after treatment with PcPIP-1. The activity of MAP kinase was measured 3 h after sample treatment by the in-gel kinase assay using MBP as a substrate. (B) Comparison of relative quantity of *HMGR2* transcripts. Suspension cultured tobacco cells were treated with 100 μM of PIP-1 or PcPIP-1. (C) Comparison of the elicitor-inducible HMGR activity. Suspension cultured tobacco cells were treated with xylanase (Xyl, 0.1 μg/mL), PIP-1 (10 and 100 μM), or PcPIP-1 (100 μM). Distilled water was used as a control. Increases in the activity from that of the control were shown as the inducible HMGR activity. +UV: UV irradiation for 15 min at 1 h after elicitation. +CHX: cycloheximide (10 μg/mL) treatment. The total RNA and crude enzyme were extracted 4 h after elicitation. Asterisks indicate significant difference at $P < 0.05$ according to the Student's paired *t*-test. Vertical bars indicate ±SD of three independent replicates.

duration of the stimulation with PIP-1 on the elicitor-inducible HMGR activity was examined. When a fungal elicitor xylanase, which is known to induce capsidiol production,[13,39,40] was treated, significant enhancement of the HMGR activity was observed (Figure 6C). Similar enhancement was observed after treatment with PIP-1 at 100 μM, which induces capsidiol production. This enhancement was not affected by UV irradiation, indicating that UV irradiation at this wavelength has no adverse effect on enhancement of the HMGR activity. Moreover, treatment with PIP-1 at 10 μM, which induces only

DOI: 10.1021/acs.jafc.5b01910
J. Agric. Food Chem. 2015, 63, 5894−5901

low levels of capsidiol production due to enzymatic degradation by tobacco cells, did not show significant enhancement of the HMGR activity. In the case of PcPIP-1, an increase in the HMGR activity was observed after treatment at 100 μM, where capsidiol production was induced. However, this enhancement was not induced when PcPIP-1 was inactivated by UV irradiation 1 h after treatment, where no capsidiol production was observed. Thus, production of capsidiol correlated well with enhancement of the HMGR activity. This suggests that the elicitor-inducible HMGR activity, which is switched on in response to continuous stimulation with PIP-1, is closely associated with the initiation of capsidiol biosynthesis, although the involvement of other factors cannot be ruled out. In addition, because CHX suppressed the enhancement of the HMGR activity, it is possible that de novo protein synthesis is involved in induction of the HMGR activity through translational or post-translational regulation mechanisms.

In a previous study, we showed that transient activation of SIPK induces only the accumulation of *HMGR2* transcripts and does not lead to capsidiol production, and that capsidiol production requires an increase in SIPK activity for at least 3 h.[14] In the present study, we showed that the increase in HMGR activity was also associated with the prolonged activation of SIPK activity. Therefore, it is possible that SIPK plays a dual role in immune response signaling pathways: induction of defense-related genes at an early phase and translational and/or post-translational activation of enzymes at a late phase. In fact, as shown in *Nicotiana benthamiana*, the expression of *HMGR2* is regulated by MAPK-mediated phosphorylation of WRKY8 transcription factors in response to pathogen inoculation.[41] Regarding translational or post-translational regulation of HMGR activity, recombinant HMGR1 from *Arabidopsis* has been shown to be inactivated in vitro by *Brassica oleracea* HMGR kinase A through phosphorylation of serine residues present in the catalytic domain.[42] In addition, HMGR activity has been demonstrated to be negatively regulated by protein phosphatase 2A that is considered to be a post-translational regulator of HMGR activity under stress conditions in *Arabidopsis*, and it was suggested that both active and inactive phosphorylation sites may exist in HMGR.[43] Thus, continuous stimulation with PIP-1 might influence phosphorylation of either these regulatory proteins or HMGR via kinase cascades including SIPK. Further investigations on variations in phosphorylation of regulatory proteins through continuous stimulation with PIP-1 would help understanding the regulatory mechanisms involved in phytoalexin biosynthesis in response to elicitors.

In summary, we designed photocleavable analogs to investigate which factors are involved in the initiation of phytoalexin production induced by PIP-1. An analog containing 3-amino-3-(2-nitrophenyl)propionic acid as the photocleavable residue exhibited a significant elicitor activity and was able to induce both early- and late-phase immune responses. This analog (PcPIP-1) was highly resistant to enzymatic degradation by tobacco cells, although it was easily inactivated through exposure to UV irradiation. Using this analog, we found that an increase in HMGR activity necessary for capsidiol production was significantly regulated by the stimulation period of PIP-1. To our knowledge, this study is the first report demonstrating that the continuous action of elicitor is required for activation of HMGR necessary for capsidiol production in tobacco cells.

■ ASSOCIATED CONTENT

Supporting Information

Degradation resistance of YGIHTD-OH in the presence of tobacco cells (Figure S1), MS/MS spectra of PcPIP-1 and its photolyzed products (Figure S2), and the structure of possible long-lived intermediate in the photolysis process of PcPIP-1 in aqueous solution (Figure S3). The Supporting Information is available free of charge on the ACS Publications website at DOI: 10.1021/acs.jafc.5b01910.

■ AUTHOR INFORMATION

Corresponding Author

*Tel/fax: +81-75-753-6123. E-mail: miyamasa@kais.kyoto-u.ac.jp.

Funding

This study was partly supported by MEXT KAKENHI (Grant 23580148), Japan.

Notes

The authors declare no competing financial interest.

■ ACKNOWLEDGMENTS

We are grateful to Professor Ritsuo Nishida and Dr. Hajime Ono (Kyoto University) for quantitative RT-PCR analysis.

■ REFERENCES

(1) Nürnberger, T.; Brunner, F.; Kemmerling, B.; Piater, L. Innate immunity in plants and animals: striking similarities and obvious differences. *Immunol. Rev.* **2004**, *198*, 249−266.

(2) Ausubel, F. M. Are innate immune signaling pathways in plants and animals conserved? *Nat. Immunol.* **2005**, *6*, 973−979.

(3) Hammond-Kosack, K. E.; Jones, J. D. G. Resistance gene-dependent plant defense responses. *Plant Cell* **1996**, *8*, 1773−1791.

(4) Glazebrook, J. Contrasting mechanisms of defense against biotrophic and necrotrophic pathogens. *Annu. Rev. Phytopathol.* **2005**, *43*, 205−227.

(5) Király, L.; Barna, B.; Király, Z. Plant resistance to pathogen infection: forms and mechanisms of innate and acquired resistance. *J. Phytopathol.* **2007**, *155*, 385−396.

(6) Bent, A. F.; Mackey, D. Elicitors, effectors, and R genes: the new paradigm and a lifetime supply of questions. *Annu. Rev. Phytopathol.* **2007**, *45*, 399−436.

(7) Albert, M. Peptides as triggers of plant defence. *J. Exp. Bot.* **2013**, *64*, 5269−5279.

(8) Zhao, J.; Davis, L. C.; Verpoorte, R. Elicitor signal transduction leading to production of plant secondary metabolites. *Biotechnol. Adv.* **2005**, *23*, 283−333.

(9) Meng, X.; Zhang, S. MAPK cascades in plant disease resistance signaling. *Annu. Rev. Phytopathol.* **2013**, *51*, 245−266.

(10) Boller, T.; Felix, G. A renaissance of elicitors: perception of microbe-associated molecular patterns and danger signals by pattern-recognition receptors. *Annu. Rev. Plant Biol.* **2009**, *60*, 379−406.

(11) Albert, M.; K. Jehle, A.; Lipschis, M.; Mueller, K.; Zeng, Y.; Felix, G. Regulation of cell behaviour by plant receptor kinases: pattern recognition receptors as prototypical models. *Eur. J. Cell Biol.* **2010**, *89*, 200−207.

(12) Gómez-Gómez, L.; Boller, T. Flagellin perception: a paradigm for innate immunity. *Trends Plant Sci.* **2002**, *7*, 251−256.

(13) Miyashita, M.; Oda, M.; Ono, Y.; Komoda, E.; Miyagawa, H. Discovery of a small peptide from combinatorial libraries that can activate the plant immune system by a jasmonic acid signaling pathway. *ChemBioChem* **2011**, *12*, 1323−1329.

(14) Kim, Y.; Komoda, E.; Miyashita, M.; Miyagawa, H. Continuous stimulation of the plant immune system by the peptide elicitor PIP-1 is required for phytoalexin biosynthesis in tobacco cells. *J. Agric. Food Chem.* **2014**, *62*, 5781−5788.

DOI: 10.1021/acs.jafc.5b01910
J. Agric. Food Chem. 2015, 63, 5894−5901

(15) Judkins, J. C.; Mahanti, P.; Hoffman, J. B.; Yim, I.; Antebi, A.; Schroeder, F. C. A photocleavable masked nuclear-receptor ligand enables temporal control of *C. elegans* development. *Angew. Chem., Int. Ed.* **2014**, *53*, 2110−2113.
(16) England, P. M.; Lester, H. A.; Davidson, N.; Dougherty, D. A. Site-specific, photochemical proteolysis applied to ion channels *in vivo*. *Proc. Natl. Acad. Sci. U. S. A.* **1997**, *94*, 11025−11030.
(17) Lawrence, D. S. The preparation and *in vivo* applications of caged peptides and proteins. *Curr. Opin. Chem. Biol.* **2005**, *9*, 570−575.
(18) Toebes, M.; Coccoris, M.; Bins, A.; Rodenko, B.; Gomez, R.; Nieuwkoop, N. J.; van de Kasteele, W.; Rimmelzwaan, G. F.; Haanen, J. B. A. G.; Ovaa, H.; Schumacher, T. N. M. Design and use of conditional MHC class I ligands. *Nat. Med.* **2006**, *12*, 246−251.
(19) Umezawa, N.; Noro, Y.; Ukai, K.; Kato, N.; Higuchi, T. Photocontrol of peptide function: backbone cyclization strategy with photocleavable amino acid. *ChemBioChem* **2011**, *12*, 1694−1698.
(20) Rodenko, B.; Toebes, M.; Hadrup, S. R.; van Esch, W. J.; Molenaar, A. M.; Schumacher, T. N.; Ovaa, H. Generation of peptide-MHC class I complexes through UV-mediated ligand exchange. *Nat. Protoc.* **2006**, *1*, 1120−1132.
(21) Parker, L. L.; Kurutz, J. W.; Kent, S. B.; Kron, S. J. Control of the yeast cell cycle with a photocleavable α-factor analogue. *Angew. Chem., Int. Ed.* **2006**, *45*, 6322−6325.
(22) Kaiser, E.; Colescott, R. L.; Bossinger, C. D.; Cook, P. I. Color test for detection of free terminal amino groups in the solid-phase synthesis of peptides. *Anal. Biochem.* **1970**, *34*, 595−598.
(23) Miyata, K.; Miyashita, M.; Nose, R.; Otake, Y.; Miyagawa, H. Development of a colorimetric assay for determining the amount of H_2O_2 generated in tobacco cells in response to elicitors and its application to study of the structure-activity relationship of flagellin-derived peptides. *Biosci., Biotechnol., Biochem.* **2006**, *70*, 2138−2144.
(24) Kadota, Y.; Watanabe, T.; Fujii, S.; Maeda, Y.; Ohno, R.; Higashi, K.; Sano, T.; Muto, S.; Hasezawa, S.; Kuchitsu, K. Cell cycle dependence of elicitor-induced signal transduction in tobacco BY-2 cells. *Plant Cell Physiol.* **2005**, *46*, 156−165.
(25) Whiteheah, I. M.; Threlfall, D. R.; Ewing, D. F. *Cis*-9,10-dihydrocapsenone: a possible catabolite of capsidiol from cell suspension cultures of *Capsicum annuum*. *Phytochemistry* **1987**, *26*, 1367−1369.
(26) Romeis, T.; Piedras, P.; Zhang, S.; Klessig, D. F.; Hirt, H.; Jones, J. D. G. Rapid Avr9- and Cf-9−dependent activation of MAP kinases in tobacco cell cultures and leaves: convergence of resistance gene, elicitor, wound, and salicylate responses. *Plant Cell* **1999**, *11*, 273−287.
(27) Wang, J.; Ming, F.; Pittman, J.; Han, Y.; Hu, J.; Guo, B.; Shen, D. Characterization of a rice (*Oryza sativa* L.) gene encoding a temperature-dependent chloroplast ω-3 fatty acid desaturase. *Biochem. Biophys. Res. Commun.* **2006**, *340*, 1209−1216.
(28) Mansouri, H.; Asrar, Z.; Szopa, J. Effects of ABA on primary terpenoids and Δ^9-tetrahydrocannabinol in Cannabis sativa L. at flowering stage. *Plant Growth Regul.* **2009**, *58*, 269−277.
(29) Yu, H.; Li, J.; Wu, D.; Qiu, Z.; Zhang, Y. Chemistry and biological applications of photo-labile organic molecules. *Chem. Soc. Rev.* **2010**, *39*, 464−473.
(30) McCray, J. A.; Trentham, D. R. Properties and uses of photoreactive caged compounds. *Annu. Rev. Biophys. Biophys. Chem.* **1989**, *18*, 239−270.
(31) Corrie, J. E. T.; Barth, A.; Munasinghe, V. R. N.; Trentham, D. R.; Hutter, M. C. Photolytic cleavage of 1-(2-nitrophenyl)ethyl ethers involves two parallel pathways and product release is rate-limited by decomposition of a common hemiacetal intermediate. *J. Am. Chem. Soc.* **2003**, *125*, 8546−8554.
(32) Peyser, J. R.; Flechtner, T. W. *N*-(α-hydroxy-2-nitrosobenzyl)-1-naphthamide: a photochemical intermediate. *J. Org. Chem.* **1987**, *52*, 4645−4646.
(33) Salerno, C. P.; Magde, D.; Patron, A. P. Enzymatic synthesis of caged NADP cofactors: aqueous NADP photorelease and optical properties. *J. Org. Chem.* **2000**, *65*, 3971−3981.
(34) Vranova, E.; Coman, D.; Gruissem, W. Network analysis of the MVA and MEP pathways for isoprenoid synthesis. *Annu. Rev. Plant Biol.* **2013**, *64*, 665−700.
(35) Chappell, J.; Nable, R. Induction of sesquiterpenoid biosynthesis in tobacco cell suspension cultures by fungal elicitor. *Plant Physiol.* **1987**, *85*, 469−473.
(36) Chappell, J.; VonLanken, C.; Vögeli, U. Elicitor-inducible 3-hydroxy-3-methylglutaryl coenzyme A reductase activity is required for sesquiterpene accumulation in tobacco cell suspension cultures. *Plant Physiol.* **1991**, *97*, 693−698.
(37) Choi, D.; Ward, B. L.; Bostock, R. M. Differential induction and suppression of potato 3-hydroxy-3-methylglutaryl coenzyme A reductase genes in response to *Phytophthora infestans* and to its elicitor arachidonic acid. *Plant Cell* **1992**, *4*, 1333−1344.
(38) Yoshioka, H.; Sugie, K.; Park, H. J.; Maeda, H.; Tsuda, N.; Kawakita, K.; Doke, N. Induction of plant gp91 *phox* homolog by fungal cell wall, arachidonic acid, and salicylic acid in potato. *Mol. Plant-Microbe Interact.* **2001**, *14*, 725−736.
(39) Lotan, T.; Fluhr, R. Xylanase, a novel elicitor of pathogenesis-related proteins in tobacco, uses a non-ethylene pathway for induction. *Plant Physiol.* **1990**, *93*, 811−817.
(40) Fluhr, R.; Sessa, G.; Sharon, A.; Ori, N.; Lotan, T., Pathogenesis-related proteins exhibit both pathogen-induced and developmental regulation. In *Adv. Mol. Genet. Plant-Microbe Interact. Vol. 1*; Hennecke, H., Verma, D., Eds.; Springer: Netherlands, 1991; Vol. *10*, pp 387−394.
(41) Ishihama, N.; Yamada, R.; Yoshioka, M.; Katou, S.; Yoshioka, H. Phosphorylation of the *Nicotiana benthamiana* WRKY8 transcription factor by MAPK functions in the defense response. *Plant Cell* **2011**, *23*, 1153−1170.
(42) Dale, S.; Arró, M.; Becerra, B.; Morrice, N. G.; Boronat, A.; Hardie, D. G.; Ferrer, A. Bacterial expression of the catalytic domain of 3−hydroxy-3−methylglutaryl-CoA reductase (isoform HMGR1) from *Arabidopsis thaliana*, and its inactivation by phosphorylation at ser577 by *Brassica oleracea* 3-hydroxy-3-methylglutaryl-CoA reductase kinase. *Eur. J. Biochem.* **1995**, *233*, 506−513.
(43) Leivar, P.; Antolín-Llovera, M.; Ferrero, S.; Closa, M.; Arró, M.; Ferrer, A.; Boronat, A.; Campos, N. Multilevel control of *Arabidopsis* 3-hydroxy-3-methylglutaryl coenzyme A reductase by protein phosphatase 2A. *Plant Cell* **2011**, *23*, 1494−1511.

DOI: 10.1021/acs.jafc.5b01910
J. Agric. Food Chem. 2015, 63, 5894−5901

Table 1. ^{13}C NMR Data (δ_C) of Compounds 1−6

position		1	2	position		3	4	5	6
	1	42.0	46.4		1	43.7	44.2	43.8	43.6
	2	36.3	35.7		2	36.9	37.2	36.8	36.6
	3	77.3	78.2		3	76.5	78.1	76.5	76.5
	4	51.1	50.9		4	51.6	51.9	51.6	51.7
	5	71.7	69.2		5	69.0	69.1	69.0	69.2
	6	62.1	47.7		6	53.9	54.4	53.9	54.9
	7	211.2	70.3		7	63.6	64.5	63.6	65.2
	8	72.1	23.0		8	123.1	123.0	123.0	123.3
	9	31.0	20.3		9	133.1	133.4	133.2	134.0
	10	78.2	19.3		10	147.2	146.9	147.2	147.0
	11	42.0	22.7		11	42.2	42.0	42.2	41.1
	12	42.2	41.9		12	40.5	40.7	40.5	40.8
	13	89.6	79.6		13	89.1	89.3	89.1	89.0
	14	84.1	210.0		14	82.0	82.2	82.0	81.1
	15	90.2	84.3		15	89.6	89.9	89.6	90.1
	16	13.9	15.4		16	14.1	14.2	14.0	14.1
	17	66.9	62.3		17	69.2	69.2	69.2	69.1
	18	33.5	15.4		18	112.8	113.1	112.8	112.2
	19	24.8	28.5		19	19.9	20.4	19.9	21.3
	20	21.8	22.1		20	24.6	24.7	24.6	24.5
3-OR	1	173.2	170.1	3-OR	1	173.4	125.7	174.1	173.3
	2	21.2	35.7		2	36.4	137.5	27.8	36.3
	3		17.7		3	18.1	123.4	8.9	17.9
	4		13.5		4	13.8	153.6		13.7
5-OR	1	173.5	129.1		5		150.9		
	2/6	27.5	129.5		6		164.5		
	3/5	9.1	128.1	5-OR	1	169.2	168.8	169.2	169.0
	4		133.0		2	20.8	20.6	20.8	20.7
	7		165.0	7-OR	1	170.4	130.4	170.4	126.6
7/10-OAc	1	169.1	171.8		2	21.0	129.3	21.0	137.1
	2	22.0	21.3		3		128.0		123.0
14/17-OR	1	126.2	125.5		4		132.6		153.0
	2	137.5	136.7		5		128.0		150.7
	3	123.1	123.3		6		129.3		164.5
	4	153.5	153.5		7		165.7		
	5	151.2	150.8	14-OR	1	125.8	126.8	125.7	170.2
	6	166.3	165.0		2	137.5	136.9	137.5	20.9
15-OAc	1	168.3			3	123.4	123.0	123.3	
	2	23.0			4	153.4	152.9	153.5	
					5	150.9	150.3	150.9	
					6	164.4	165.4	164.4	
				15-OAc	1	168.2	168.2	168.2	168.5
					2	22.3	22.6	22.3	22.6

TMS as an internal standard. ESIMS spectra were acquired on a Thermo Finnigan LCQ-Advantage mass spectrometer (Finnigan Co., Ltd., San Jose, CA, USA). HR-ESIMS were recorded by an IonSpec 7.0 T FTICR MS (IonSpec Co., Ltd., Lake Forest, CA, USA). HPLC purifications were finished on a CXTH system, equipped with a UV3000 detector at 210 nm (Beijing Chuangxintongheng Instruments Co., Ltd., Beijing, People's Republic of China). The HPLC column used was a 20 × 250 mm i.d., 5 μm, YMC-pack ODS-AM (YMC Co., Ltd., Kyoto, Japan). Silica gel (100−200 mesh) was used for column chromatography (Qingdao Haiyang Chemical Group Co., Ltd., Qingdao, People's Republic of China). Chemical reagents for isolation were of analytical grade and purchased from Tianjin Chemical Reagent Co. (Tianjin, People's Republic of China). Biological reagents were from Sigma Chemical Co.

Plant Material. The roots of *E. prolifera* were collected in July 2010 from Kunming, Yunnan province, People's Republic of China. The botanical identification was made by one of the authors (Y.G.), and a voucher specimen (No. 20100705) was deposited at the laboratory of the Research Department of Natural Medicine, College of Pharmacy, Nankai University, People's Republic of China.

Extraction and Isolation. The air-dried roots of *E. prolifera* (3.8 kg) were extracted with methanol three times (3 × 20 L) under reflux. The organic solvent was evaporated to afford a crude extract (900 g), which was suspended in H_2O (0.9 L) and then partitioned with ethyl acetate (3 × 0.9 L) to give the EtOAc-soluble portion (150 g). This portion was fractionated by silica gel column chromatography (silica gel, 1.0 kg; column, 9 × 70 cm), using a gradient solvent system of petroleum ether/acetone (100:0, 100:2, 100:4, 100:7, 100:11, 100:16, 100:23, 100:30, 100:40, and 0:100, 21 L for each gradient elution), to afford nine fractions (F_1−F_9) according to the TLC analyses. Fraction F_8 (eluted by petroleum ether/acetone, 100:30 and 100:40) was subjected to medium-pressure liquid chromatography (MPLC) over octadecylsilyl (ODS) eluting with a step gradient from 60 to 90% MeOH in H_2O to give four subfractions ($F_{8\text{-}1}$−$F_{8\text{-}4}$). Subfraction $F_{8\text{-}3}$ was further purified by preparative HPLC (YMC-pack ODS-AM, 250 × 20 mm i.d., 77% MeOH in H_2O) to afford compound **1** (t_R = 23

DOI: 10.1021/acs.jafc.5b02021
J. Agric. Food Chem. 2015, 63, 5902−5910

Table 2. ^{1}H NMR Data (δ_H) of Compounds 1−6[a]

position		1	2	position		3	4	5	6
	1α	2.94 dd (15.5, 10.3)	2.75 dd (14.7, 10.9)		1α	2.78 dd (15.8, 10.9)	2.86[b]	2.76 dd (15.8, 11.0)	2.83 dd (15.9, 10.8)
	β	2.46[b]	1.80 dd (14.7, 8.0)		β	2.69 dd (15.8, 9.1)	2.83[b]	2.65 dd (15.8, 9.0)	2.54 dd (15.9, 9.3)
	2	2.28 m	2.46 m		2	2.13 m	2.28 m	2.18 m	2.06 m
	3	5.53 t (3.8)	5.61 t (4.5)		3	5.31 t (3.2)	5.54 t (3.5)	5.31 t (3.5)	5.27 t (3.3)
	4	2.99 dd (11.1, 3.8)	3.01 dd (10.6, 4.5)		4	3.18 dd (11.1, 3.2)	3.42 dd (11.2, 3.5)	3.18 dd (11.1, 3.5)	3.10 dd (11.1, 3.3)
	5	5.90 d (11.1)	6.07 d (10.6)		5	5.95 d (11.1)	6.23 d (11.2)	5.96 d (11.1)	5.96 d (11.1)
	7		5.06 dd (5.8, 3.2)		7	4.86 d (6.1)	5.07 d (6.4)	4.85 d (6.1)	5.07 d (6.5)
	8	3.91 d (5.5)	1.61 m		8	6.10 dd (9.7, 6.1)	6.26 dd (9.8, 6.4)	6.10 dd (9.8, 6.1)	6.28 dd (9.7, 6.5)
			0.90 m		9	5.80 dd (9.7, 4.7)	5.85 dd (9.8, 5.4)	5.80 dd (9.8, 5.0)	5.94 dd (9.7, 5.5)
	9	2.52 m			11	3.29 m	3.34 m	3.24 m	3.15 m
	11	2.36 m	0.95 m		12	3.28 br s	3.50 d (3.8)	3.28 m	3.32 m
	12	4.53 d (12.2)	2.35 d (7.6)		14	5.25 br s	5.38 br s	5.24 s	5.03 br s
	14	5.35 br s			16	0.83 d (6.6)	0.89 d (6.7)	0.83 d (6.7)	0.81 d (6.7)
	16	0.88 d (6.6)	0.97 d (6.8)		17	4.06 d (8.7)	4.19 d (8.8)	4.06 d (8.8)	4.06 d (8.8)
	17	4.17 d (9.8)	5.33 d (12.1)			3.53 d (8.7)	3.65 d (8.8)	3.53 d (8.8)	3.60 d (8.8)
		3.66 d (9.8)	4.57 d (12.1)		18	4.99 s	4.93 s	4.99 s	4.76 s
	18	α 2.47[b]	1.03 s			4.86 s	4.83 s	4.85 s	4.64 s
		β 3.04 dd (12.2, 9.0)			19	1.88 s	1.88 s	1.88 s	1.87 s
	19	1.59 s	1.11 s		20	1.31 s	1.37 s	1.31 s	1.29 s
	20	1.22 s	1.61 s	3-OR	2	2.27 m	8.28 dt (7.9, 1.4)	2.31 q (7.5)	2.12 m
3-OR	2	2.01 s	2.12 m		3	1.62 m	7.43 dd (7.9,4.8)	1.12 t (7.5)	1.44 m
	3		1.43 m		4	0.94 t (7.4)	8.80 dd (4.8, 1.4)		0.78 t (7.4)
	4		0.77 d (7.4)		5		9.11 d (1.4)		
	5			5-OAc	2	1.99 s	1.96 s	1.99 s	1.94 s
5-OR	2/6	2.29 m	7.67 d (7.8)	7/10-OR	2	1.99 s	7.89 d (7.8)	1.99 s	8.25 d (7.9)
	3/5	1.12 t (7.6)	7.08 t (7.8)		3		7.31 t (7.8)		7.35 dd (7.9, 4.9)
	4		7.30 t (7.8)		4		7.46 t (7.8)		8.74 d (4.9)
7/10-OAc	2	1.90 s	1.88 s		5		7.31 t (7.8)		9.14 s
14/17-OR	2	8.36 d (7.9)	7.95 d (7.9)	7/10-OR	6		7.89 d (7.8)		
	3	7.40 dd (7.9, 4.9)	7.18 dd (7.6, 4.9)	14/17-OR	2	8.25 d (8.0)	8.06 dt (7.8, 1.4)	8.25 dt (7.9, 1.4)	2.06 s
	4	8.79 d (4.9)	8.68 d (4.9)		3	7.41 dd (8.0, 4.3)	7.18 dd (7.8, 4.8)	7.41 dd (7.9, 4.8)	
	5	9.22 br s	9.08 br s		4	8.79 d (4.3)	8.67 dd (4.8, 1.4)	8.78 dd (4.8, 1.4)	
15-OAc	2	2.24 s			5	9.06 s	9.07 d (1.4)	9.07 d (1.4)	
				15-OAc	2	2.08 s	2.33 s	2.08 s	2.21 s

[a]Assignments of ^{1}H NMR data are based on ^{1}H−^{1}H COSY, HMQC, and HMBC experiments. [b]Signals were in overlapped regions of the spectra, and the multiplicities could not be discerned.

min, 7.2 mg), and the purification of F_{8-4} by the same HPLC system (82% MeOH in H_2O) yielded compound **5** (t_R = 27 min, 11.5 mg). Fraction F_9 (eluted by petroleum ether/acetone, 100:40 and 0:100), using the above MPLC (60−90% MeOH in H_2O), provided four subfractions F_{9-1}−F_{9-4}. Compounds **2** (t_R = 32 min, 13.6 mg) and **8** (t_R = 21 min, 13.1 mg) were obtained from subfraction F_{9-2} by using the same HPLC system (73% MeOH in H_2O), and the following purification of subfraction F_{9-4} (77% MeOH in H_2O) afforded compound **4** (t_R = 24 min, 13.2 mg). Using the same MPLC system as for the above fractions, F_7 gave subfractions F_{7-1}−F_{7-4}. The following purification of subfraction F_{7-3} (73% MeOH in H_2O) produced compounds **3** (t_R = 35 min, 13.1 mg), **6** (t_R = 30 min, 13.8 mg), and **7** (t_R = 26 min, 15.0 mg).

*Prolifepene A, **1**:* white powder; $[\alpha]_D^{15}$ +27.5 (*c* 0.08, CH_2Cl_2); CD (CH_3CN) 216 (Δε +4.14), 237 (Δε −1.44) nm, 311 (Δε +9.42) nm; IR (KBr) ν_{max} 3422, 2934, 2875, 1734, 1637, 1395, 1249, 1226, 1082, and 1023 cm^{-1}; ^{13}C NMR (100 MHz, $CDCl_3$) and ^{1}H NMR (400 MHz, $CDCl_3$) data (Tables 1 and 2); ESIMS *m*/*z* 708 $[M + Na]^+$; HR-ESIMS *m*/*z* 708.2632 $[M + Na]^+$, calcd for $C_{35}H_{43}NNaO_{13}$, 708.2632.

*Prolifepene B, **2**:* white powder; $[\alpha]_D^{15}$ +16.9 (*c* 0.11, CH_2Cl_2); CD (CH_3CN) 200 (Δε +8.81), 215 (Δε +6.73), 234 (Δε −6.69), 300 (Δε +3.61) nm; IR (KBr) ν_{max} 3435, 2962, 2933, 1728, 1654, 1591, 1373, 1282, 1230, 1109, and 1025 cm^{-1}; ^{13}C NMR (100 MHz, $CDCl_3$) and ^{1}H NMR (400 MHz, $CDCl_3$) data (Tables 1 and 2); ESIMS *m*/*z* 728 $[M + Na]^+$; HR-ESIMS *m*/*z* 728.3041 $[M + Na]^+$, calcd for $C_{39}H_{47}NNaO_{11}$, 728.3047.

DOI: 10.1021/acs.jafc.5b02021
J. Agric. Food Chem. 2015, 63, 5902−5910

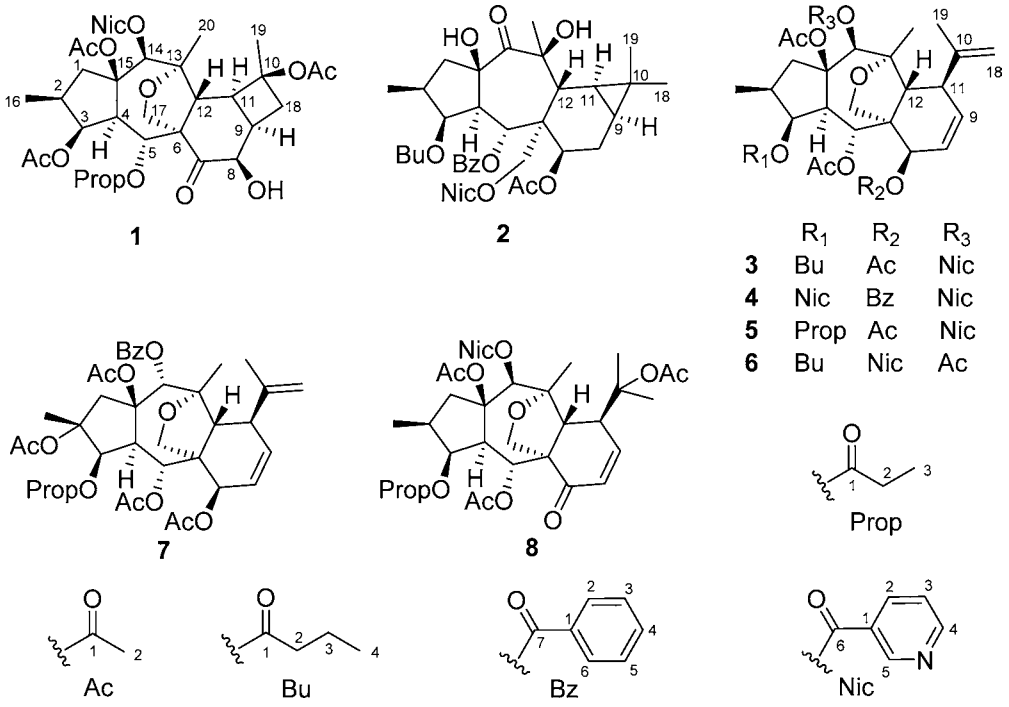

Figure 1. Structures of compounds **1**–**8** from *E. prolifera*.

*Prolifepene C, **3**:* white powder; $[\alpha]_D^{15}$ −43.8 (*c* 0.17, CH_2Cl_2); CD (CH_3CN) 202 ($\Delta\varepsilon$ +11.16), 216 ($\Delta\varepsilon$ −11.08), 244 ($\Delta\varepsilon$ +1.48) nm; IR (KBr) ν_{max} 2963, 2932, 2875, 1737, 1640, 1590, 1437, 1242, 1150, and 1024 cm^{-1}; ^{13}C NMR (100 MHz, $CDCl_3$) and ^1H NMR (400 MHz, $CDCl_3$) data (Tables 1 and 2); ESIMS *m*/*z* 668 $[M + H]^+$; HR-ESIMS *m*/*z* 668.3067 $[M + H]^+$, calcd for $C_{36}H_{46}NO_{11}$, 668.3071.

*Prolifepene D, **4**:* white powder; $[\alpha]_D^{15}$ −12.0 (*c* 0.10, CH_2Cl_2); IR (KBr) ν_{max} 2961, 2930, 1728, 1638, 1592, 1456, 1367, 1269, 1220, 1110, and 1026 cm^{-1}; ^{13}C NMR (100 MHz, $CDCl_3$) and ^1H NMR (400 MHz, $CDCl_3$) data (Tables 1 and 2); ESIMS *m*/*z* 787 $[M + Na]^+$; HR-ESIMS *m*/*z* 787.2841 $[M + Na]^+$, calcd for $C_{43}H_{44}N_2NaO_{11}$, 787.2843.

*Prolifepene E, **5**:* white powder; $[\alpha]_D^{15}$ −10.7 (*c* 0.60, CH_2Cl_2); IR (KBr) ν_{max} 2966, 2936, 1739, 1641, 1591, 1458, 1371, 1269, 1244, 1151, 1083, and 1025 cm^{-1}; ^{13}C NMR (100 MHz, $CDCl_3$) and ^1H NMR (400 MHz, $CDCl_3$) data (Tables 1 and 2); ESIMS *m*/*z* 676 $[M + Na]^+$; HR-ESIMS *m*/*z* 676.2734 $[M + Na]^+$, calcd for $C_{35}H_{43}NNaO_{11}$, 676.2734.

*Prolifepene F, **6**:* white powder; $[\alpha]_D^{15}$ −11.7 (*c* 0.12, CH_2Cl_2); IR (KBr) ν_{max} 2967, 2936, 1741, 1643, 1513, 1455, 1370, 1275, and 1224 cm^{-1}; ^{13}C NMR (100 MHz, $CDCl_3$) and ^1H NMR (400 MHz, $CDCl_3$) data (Tables 1 and 2); ESIMS *m*/*z* 668 $[M + H]^+$; HR-ESIMS *m*/*z* 668.3062 $[M + H]^+$, calcd for $C_{36}H_{46}NO_{11}$, 668.3071.

Computational Methods. The ECD calculations were performed according to the reported method.[29]

Antifungal Activity Assay. The antifungal activities of the isolated compounds were assayed against three pathogenic fungi (*Physalospora piricola*, *Alternaria solani*, and *Gibberella zeae*) using a mycelium growth inhibition method, the details of which have been previously reported.[30] The commercially available agricultural fungicides chlorothalonil and carbendazol were used as the corresponding positive controls. Compounds possessing good activities (inhibitory rate > 50% at 50 μg/mL) were further evaluated using the above-mentioned method with different concentrations.

RESULTS AND DISCUSSION

The ethyl acetate-soluble part of the methanol extract of the roots parts of *E. prolifera* was fractionated by silica gel column chromatography and MPLC and further purified by HPLC to afford six new (**1**–**6**) and two known (**7** and **8**) diterpenoids (Figure 1). The known compounds were identified by comparison of spectroscopic data with those reported in the literature as 2α,5α,7β,15β-tetra-*O*-acetyl-3β-*O*-propinoyl-14α-*O*-benzoyl-14-deoxomyrsinol, **7**,[31] and 3β-*O*-propionyl-5α,10,15β-tri-*O*-acetyl-14β-*O*-nicotinoyl-7-oxo-10,18-dihydromyrsinol, **8**.[14]

Compound **1** was obtained as a white powder. Its molecular formula was assigned as $C_{35}H_{43}NO_{13}$ on the basis of HR-ESIMS. The ^1H NMR spectrum of **1** exhibited four oxygenated methine protons [δ_H 5.53 (1H, t, *J* = 3.8 Hz, H-3), 5.90 (1H, d, *J* = 11.1 Hz, H-5), 3.91 (1H, d, *J* = 5.5 Hz, H-8), and 5.35 (1H, br s, H-14)], four aromatic protons [δ_H 8.36 (1H, d, *J* = 7.9 Hz), 7.40 (1H, dd, *J* = 7.9, 4.9 Hz), 8.79 (1H, d, *J* = 4.9 Hz), and 9.22 (1H, br s)], and a pair of oxygenated methylene protons [δ_H 4.17, and 3.66 (each 1H, d, *J* = 9.8 Hz, H_2-17)]. Additionally, seven methyl signals were also exhibited in the ^1H NMR spectrum. The ^{13}C NMR spectrum of **1** showed 35 carbon resonances (Table 1). From the ^1H and ^{13}C NMR spectra of **1**, three acetyl groups were apparent from the methyl singlets (δ_H 2.24, 2.01, and 1.90 s) and the corresponding carbons (Table 1). The above-mentioned four aromatic proton signals (Table 2), together with the typical carbon resonances, revealed the presence of one nicotinoyl group.[14] In addition to these substituent groups, a propionyl moiety (Tables 1 and 2) was deduced and defined from the methyl and methylene proton signals and the observation of the corresponding carbon signals (Tables 1 and 2).[13] Apart from the above 15 carbon signals for the substituent groups, there were additional 20 carbons displayed in the ^{13}C NMR spectrum, including 3 methyls, 3 methylenes, 9 methines, and 5 quaternary carbons based on the DEPT and HMQC spectra. These 20 typically skeletal carbons implied that compound **1** possessed a characteristic cyclomyrsinol-type diterpene skeleton according to the reported related diterpenes from the genus *Euphorbia*.[32−36] This skeleton of cyclomyrsinol-type diterpene was further confirmed by HMBC and ^1H–^1H COSY experiments,

DOI: 10.1021/acs.jafc.5b02021
J. Agric. Food Chem. 2015, 63, 5902−5910

in which the carbonyl signal at δ_C 211.2 was assigned to C-7, and the oxygenated carbon signals at δ_C 77.3, 71.7, 72.1, 78.2, 89.6, 84.1, 90.2, and 66.9 were attributed to C-3, C-5, C-8, C-10, C-13, C-14, C-15, and C-17, respectively. The positions of the acyloxy groups were deduced from the HMBC spectrum. The HMBC correlation of the carbonyl signal at δ_C 173.2 with the proton signal at δ_H 5.53 (H-3) demonstrated that one acetoxy group was attached at C-3. Similarly, the long-range couplings of the carbonyl carbon signals at δ_C 173.5 and 166.3 with the proton signals at δ_H 5.90 (H-5) and 5.35 (H-14) disclosed the presence of the propionyloxy group and the nicotinoyloxy group at C-5 and C-14, respectively. Because there were no long-range correlations of the skeletal protons with the carbonyl carbons of the two remaining acetoxy groups, it was therefore concluded that the two acetoxy groups were attached to quaternary carbons of the cyclomyrsinol skeleton. On the basis of the chemical shifts of skeletally oxygenated carbons and similar cyclomyrsinol diterpenes in the literature,[35,36] the residual acetoxy groups could only be located at C-10 and C-15, of which the C-10 acetoxy group was assigned by a NOESY experiment, indicating the NOESY correlations of H_3-19 (δ_H 1.59) to the methyl protons (δ_H 1.90) of the C-10 acetoxy group. Consequently, the other remaining acetoxy was assigned to C-15. By further analyzing the HMQC, HMBC, and $^1H-^1H$ COSY spectra (Figure 2), all of the proton and carbon signals were assigned unambiguously. Thus, the planar structure of **1** was established.

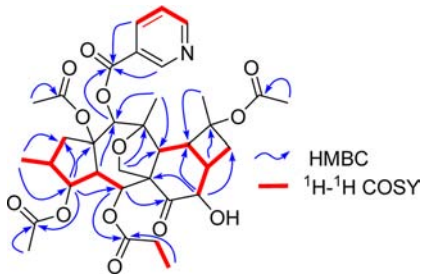

Figure 2. $^1H-^1H$ COSY and selected HMBC correlations of compound **1**.

The stereochemistry of **1** was elucidated as follows. The NOESY correlations of H-2/H-4, H-4/H-14, H-4/H_2-17, H-5/H-12, H-12/H_3-20, H-8/H-9, H_3-19/H-11, and H_3-19/H-9, but not of H-3/H-5, together with a Chem3D modeling revealed a conformation as shown in Figure 2. In this arrangement for compound **1**, the three rings, A, B, and C (5/7/6), were *trans*-fused with each other, H-12 proton and the C-15 acetoxy group were found to be in a β-position, and H-4 and C-17 were in an α-position. Another four-membered ring in the skeleton was *cis*-fused with ring C, and the H-9 and H-11 protons were assigned to be α-oriented correspondingly. In turn, the three methyl groups, Me-16, Me-19, and Me-20, were determined as β-, α-, and β-oriented, the acetoxy groups at C-3 and C-10 and the C-8 hydroxy group were all β-oriented, and the C-5 propionyloxy group was in an α-position according to this conformation of **1** and the above NOESY correlations. The relative configuration of **1** was therefore designated as shown in Figure 3.

The absolute configuration of **1** was established by the TDDFT ECD calculations[37−39] and substantiated by the octant rule. Starting from the conformation of **1** deduced from the NOESY correlations and Chem3D modeling, conformational

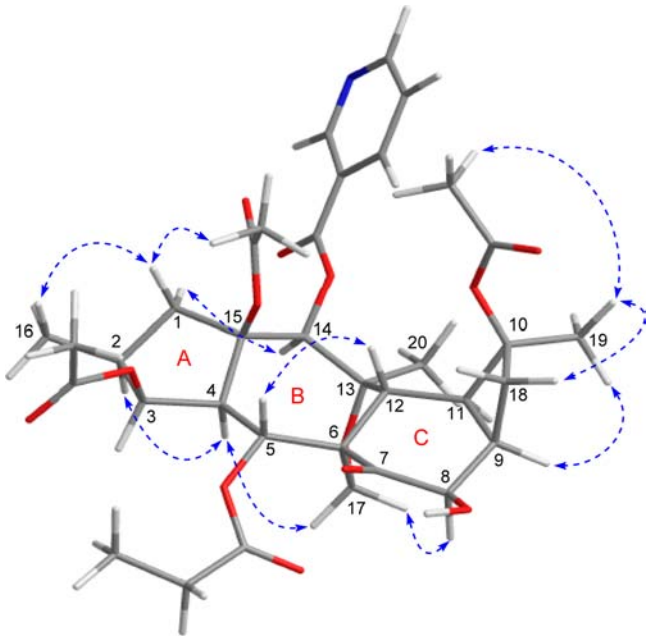

Figure 3. Conformation and key NOESY correlations of compound **1**.

searches with the MMFF94 force field by MOE software[40] and geometry optimizations by the Gaussian 09 package[41] were performed. Then, the ECD spectra were calculated at the CAM-B3LYP/SVP level with the CPCM model in acetonitrile. The obtained ECD spectrum of **1** (Figure 4) matched the experimental results closely, which suggested an absolute configuration of 2*S*,3*S*,4*R*,5*R*,6*S*,8*R*,9*R*,10*S*,11*S*,12*R*,13*R*,14*S*,-15*R* for compound **1**. The experimental ECD spectrum of **1** displayed a positive Cotton effect at 311 nm ($\Delta\varepsilon$ +9.42), corresponding to the n−π* transition of the cyclohexanone chromophore, which confirmed the absolute configuration of 2*S*,3*S*,4*R*,5*R*,6*S*,8*R*,9*R*,10*S*,11*S*,12*R*,13*R*,14*S*,15*R* unequivocally according to the octant rule.[42] On the basis of the above evidence, the structure of **1** was established as (2*S*,3*S*,4*R*,-5*R*,6*S*,8*R*,9*R*,10*S*,11*S*,12*R*,13*R*,14*S*,15*R*)-3β,10β,15-tri-*O*-acetyl-5α-*O*-propionyl-14β-*O*-nicotinoylcyclomyrsinol, which has been named prolifepene A.

Compound **2** had a molecular formula of $C_{39}H_{47}NO_{11}$ based on the HR-ESIMS. From the ^1H NMR spectrum of **2**, three oxygenated methine protons, a set of oxygenated methylene protons, nine aromatic protons, and six methyl signals were observed (Table 2). The ^{13}C NMR spectrum of **2** exhibited 39 carbon resonances. From the ^1H and ^{13}C NMR spectra, the methyl singlet (δ_H 1.88 s), together with the corresponding carbon signals (Table 1), implied the occurrence of one acetyl group, and the aromatic proton signals and the corresponding carbon resonaces (Table 1) revealed the presence of one nicotinoyl and one benzoyl group.[14,16] In addition, a butyryl group was also deduced and defined from the observation of the carbon signals (δ_C 170.1, 35.7, 17.7, and 13.5) and the corresponding proton signals (Table 2) based on those reported diterpenes with acyl groups in the literature.[13] Apart from the above 19 resonances for the substituent groups, the remaining 20 skeletal carbons in the ^{13}C NMR spectrum constituted a characteristic premyrsinol-type diterpene skeleton.[35,36]

To confirm the above deduction and position these substituent groups, the following HMQC, HMBC, and

DOI: 10.1021/acs.jafc.5b02021
J. Agric. Food Chem. 2015, 63, 5902−5910

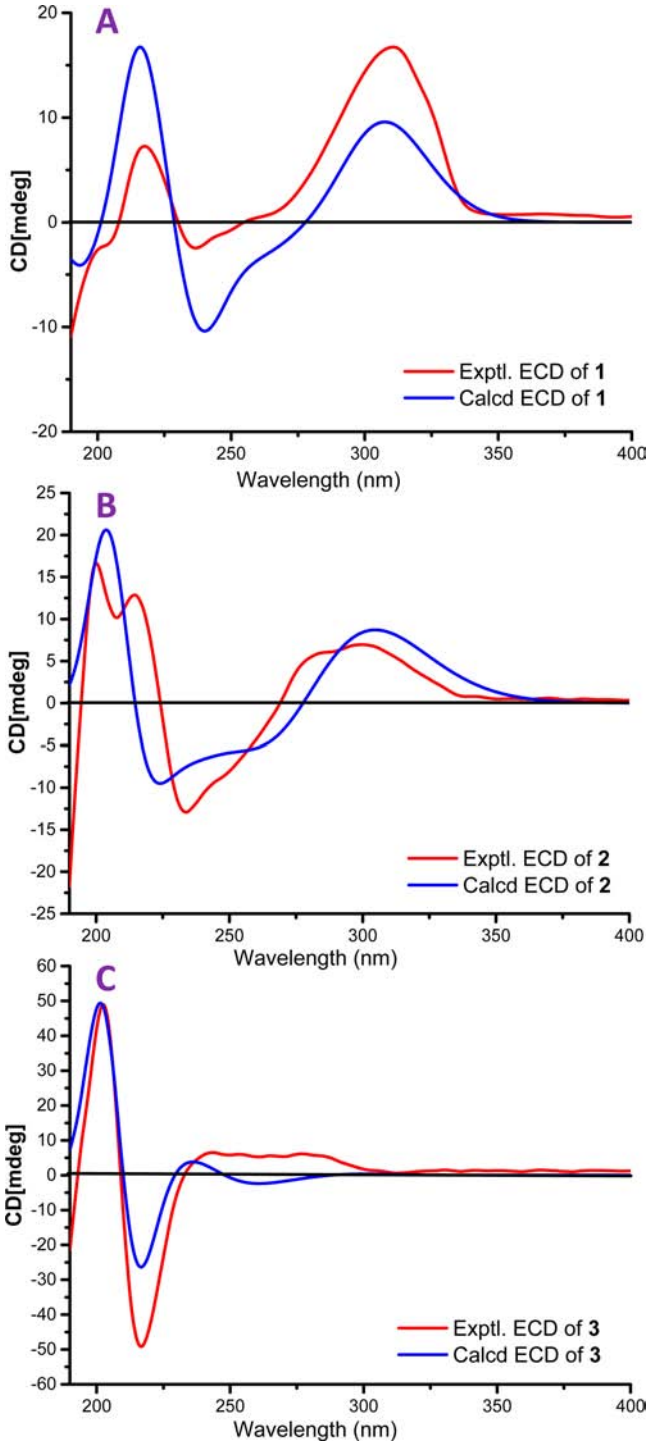

Figure 4. Calculated and experimental ECD spectra for compounds **1** (A), **2** (B), and **3** (C) in acetonitrile.

^{1}H−^{1}H COSY experiments were performed. By interpretation of the 2D NMR spectra, the presence of the above deduced acyl groups was substantiated and the characteristic premyrsinol-type diterpene skeleton was elucidated unequivocally, where the oxygenated carbons at δ_C 78.2, 69.2, 70.3, 79.6, 84.3, and 62.3 were attributed to C-3, C-5, C-7, C-13, C-15, and C-17, respectively. The locations of these acyloxy groups were determined by HMBC correlations. The long-range couplings of the protons H-3 (δ_H 5.61), H-5 (δ_H 6.07), H-7 (δ_H 5.06), and H_2-17 (δ_H 5.33 and 4.57) with the carbonyl carbons at δ_C 170.1, 165.0, 171.8, and 165.0 demonstrated that the butyryloxy group was located at C-3, the benzoyloxy group at C-5, the acetoxy group at C-7, and the nicotinoyloxy group at C-17, respectively. There were no additional acyloxy groups in compound **2**, indicating that the substituent groups at C-13 and C-15 could only be hydroxy groups, which was verified by the HR-ESIMS data. Further analyses of the HMQC, HMBC, and ^{1}H−^{1}H COSY data led to the assignments of all the proton and carbon signals. The planar structure with a premyrsinol-type diterpene skeleton for **2** was therefore elucidated. The relative configuration was elucidated on the basis of NOESY spectrum, which disclosed the correlations of H-2/H-4, H-3/H-4, H-4/H_3-20, H-5/H-12, H-7/H_2-17, H-9/H-11, H_2-17/H_3-20, and H-11/H_3-20. These NOESY correlations and the Chem3D modeling revealed that the three rings (5/7/6) forming the premyrsinol-type skeleton were *trans*-fused as those in **1**, the C-15 hydroxy group and H-12 proton were in a β-position, and C-17 and H-4 were in an α-position. Consequently, the C-3 butyryloxy, C-7 acetoxy, and C-13 hydroxy groups were assigned to be β-oriented, and the C-5 benzoyloxy group and H-9 and H-11 protons were determined as α-oriented according to the NOESY correlations. The relative configuration of compound **2** was therefore established. On the basis of the relative configuration of **2** deduced from the NOESY spectrum, the same procedures, conformational searches, geometry optimizations, and calculated ECD spectra as in the case of **1** were performed to determine the absolute configuration of **2**. As shown in Figure 5, the calculated ECD

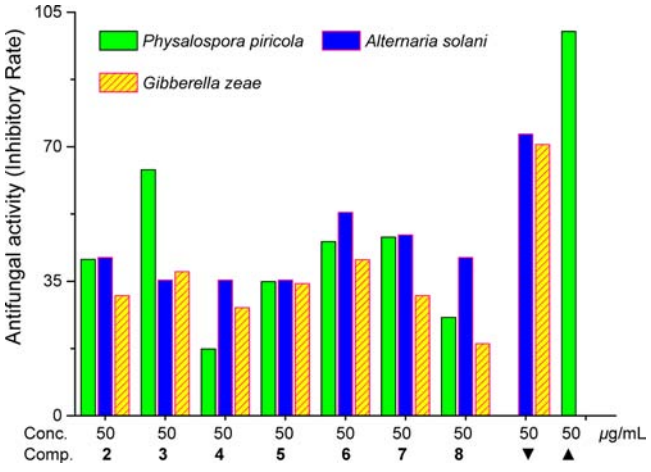

Figure 5. Antifungal effects of compounds **2**−**8** against three pathogenic fungi. Three common pathogenic fungi (*P. piricola*, *A. solani*, and *G. zeae*) were selected to evaluate the antifungal activities of compounds **2**−**8**. The biological data presented are the mean scores for each treatment across replicates. The symbols ▼ and ▲ indicate the positive controls chlorothalonil and carbendazol, respectively.

spectrum for (2*S*,3*S*,4*R*,5*R*,6*R*,7*R*,9*S*,11*S*,12*R*,13*S*,15*R*)-**2** was in good agreement with the experimental one. Therefore, the absolute configuration of **2** was assigned as 2*S*,3*S*,4*R*,5*R*,6*R*,7*R*,-9*S*,11*S*,12*R*,13*S*,15*R*. Thus, compound **2** was characterized as (2*S*,3*S*,4*R*,5*R*,6*R*,7*R*,9*S*,11*S*,12*R*,13*S*,15*R*)-3β-*O*-butyryl-5α-*O*-benzoyl-7β-*O*-acetyl-17-*O*-nicotinoylpremyrsinol and was given the trivial name prolifepene B.

Compound **3** was obtained as a white powder. Its HR-ESIMS corresponded to the molecular formula $C_{36}H_{45}NO_{11}$. From the ^{1}H and ^{13}C NMR spectra, three acetyl, one butyryl, and one nicotinoyl group were evident on the basis of those acyl groups

DOI: 10.1021/acs.jafc.5b02021
J. Agric. Food Chem. 2015, 63, 5902−5910

in compounds **1** and **2**. Apart from these carbon resonances for the acyl groups, there were 20 residual ones present in the ^{13}C NMR spectrum. The 20 skeletal carbons were sorted into 3 methyls, 3 methylenes, 10 methines, and 4 quaternary carbons with the aid of DEPT and HMQC spectra. According to these spectroscopic features, especially the terminal double bond (C-10 and C-18), and the diterpenoids isolated from the genus *Euphorbia*,[13,14] it could be deduced that compound **3** had a 14-deoxomyrsinol-type skeleton, which was confirmed by the following HMBC and $^{1}H-^{1}H$ COSY experiments. Correspondingly, the skeletal olefinic and oxygenated carbon signals at δ_C 123.1, 133.1, 147.2, 112.8, 76.5, 69.0, 63.6, 89.1, 82.0, 89.6, and 69.2 were assigned to C-8, C-9, C-10, C-18, C-3, C-5, C-7, C-13, C-14, C-15, and C-17, respectively. The locations of acyloxy groups were deduced from the HMBC spectrum, exhibiting the correlations of the protons H-3 (δ_H 5.31), H-5 (δ_H 5.95), H-7 (δ_H 4.86), and H-14 (δ_H 5.25) with the corresponding carbonyl carbons at δ_C 173.4, 169.2, 170.4, and 164.4. These HMBC correlations demonstrated the two acetoxy, one butyryloxy, and one nicotinoyl group to be attached at C-5, C-7, C-3, and C-14, respectively. The residual acetxoy group should be attached to quaternary carbons of the myrsinol skeleton due to the lack of long-range correlations of skeletal protons to the carbonyl carbon of the acyloxy moiety. On the basis of the chemical shifts of skeletally oxygenated carbons, this residual acetoxy group could only be located at C-15.[13,16] By further analyzing the 2D NMR spectra, the planar structure of **3** was elucidated.

The relative configuration of compound **3** was established by analyses of the NOESY spectrum, which showed the correlations of H-2/H-4, H-3/H-4, H-4/H-14, H-4/H_2-17, H-5/H-12, H-7/H-11, and H-12/H_3-20. According to these NOESY correlations, the relative configuration of **3** was as depicted in Figure 1, where the three rings (5/7/6) were similarly *trans*-fused with each other as those in compounds **1** and **2**; H-4 and H-11 protons and C-17 were found to be in an α-position, the C-3 butyryloxy, the C-7 and C-15 acetoxy, and the C-14 nicotinoyloxy group were all in a β-position, and the C-5 acetoxy was assigned as α-oriented. After definition of the relative configuration of **3**, the absolute configuration was assigned as 2*S*,3*S*,4*R*,5*R*,6*R*,7*R*,11*S*,12*R*,13*R*,14*S*,15*R*, by comparison of its experimental and calculated ECD spectra (Figure 4) using TDDFT method. On the basis of the above evidence, the structure of compound **3** (prolifepene C) was established as (2*S*,3*S*,4*R*,5*R*,6*R*,7*R*,11*S*,12*R*,13*R*,14*S*,15*R*)-3β-*O*-butyryl-5α,7β,15β-tri-*O*-acetyl-14β-*O*-nicotinoyl-14-deoxomyrsinol.

The ^{1}H and ^{13}C NMR spectra of compounds **4**–**6** were found to be similar to each other. Analyses of the ^{13}C and ^{1}H NMR spectra of the three compounds indicated that compounds **4**–**6** all possess the same 14-deoxomyrsinol-type diterpene scaffold as compound **3**.[35,36] The main differences between compounds **4**–**6** were found to be in the different substituent groups that occurred in each case. For compound **4**, five acyl groups (two acetyl, two nicotinoyl, and one benzoyl group) were deduced and determined according to its ^{13}C and ^{1}H NMR spectra. Using the same HMBC and NOESY experiments as for compounds **1**–**3**, the positions of these substituent groups and the relative configuration of compound **4** were determined, where one acetoxy group was located at C-5 with an α-orientation, the other acetoxy group was at C-15 with a β-orientation, the benzoyloxy group was at C-7 with a β-orientation, and the two nicotinoyloxy groups were at C-3 and C-14, both in a β-position. For compound **5**, besides the same three acetoxy groups and one nicotinoyloxy group as present in compound **3**, a propionyloxy moiety was deduced and defined on the basis of its ^{13}C and ^{1}H NMR data, which was located at C-3, replacing the butyryloxy group in compound **3**. Compound **6** was found to have the same acyl groups (three acetyl, one nicotinoyl, and one butyryl group) as compound **3**. From the evidence of the HMBC spectrum, the butyryloxy group was found to be located at C-3, the nicotinoyloxy group was at C-7, and the three acetoxy groups were at C-5, C-14, and C-15, respectively. The same relative configuration for all of compounds **3**–**6** was validated by the careful comparison of their NOESY spectra. On the basis of the above spectroscopic evidence, biosynthetic considerations, and absolute configuration of **3** elucidated by the TDDFT ECD method, the structures of compounds **4**–**6** were therefore elucidated as (2*S*,3*S*,4*R*,5*R*,6*R*,7*R*,11*S*,12*R*,13*R*,14*S*,15*R*)-3β,14β-di-*O*-nicotinoyl-5α,15β-di-*O*-acetyl-7β-*O*-benzoyl-14-deoxomyrsinol, (2*S*,3*S*,4*R*,5*R*,6*R*,7*R*,11*S*,12*R*,13*R*,14*S*,15*R*)-3β-*O*-propinoyl-5α,7β,15β-tri-*O*-acetyl-14β-*O*-nicotinoyl-14-deoxomyrsinol, and (2*S*,3*S*,4*R*,5*R*,6*R*,7*R*,11*S*,12*R*,13*R*,14*S*,15*R*)-3β-*O*-butyryl-5α,14α,15β-tri-*O*-acetyl-7β-*O*-nicotinoyl-14-deoxomyrsinol, which have been named prolifepenes D, E, and F, respectively.

E. prolifera is a poisonous plant, and its chemical constituents may be useful for the agricultural and medical industries.[27,28] To explore the potential biological effects of these diterpenes to serve agriculture, these isolated compounds from *E. prolifera* were preliminarily investigated for their antifungal activities against three pathogenic fungi (*G. zeae*, *P. piricola*, *A. solani*), which commonly infect crops, leading to severe crop yield reduction and dramatic economic losses in agriculture.[1] Carbendazol was used as a positive control and had an EC_{50} value of 0.43 μg/mL against *P. piricola*, and the other positive control, chlorothalonil, gave the corresponding EC_{50} values of 27.34 and 10.10 μg/mL against *A. solani* and *G. zeae*, respectively. At the concentration of 50 μg/mL, all of the evaluated compounds exhibited antifungal activities. Their preliminary antifungal activities are shown in Figure 5 (compound **1** was not assayed for antifungal effects because of inadequate amounts). For the pathogenic fungus *G. zeae*, all of the compounds showed weak or moderate antifungal effects at the concentration of 50 μg/mL. For the fungus *A. solani*, compound **6** showed a strong activity with an inhibitory rate of 53% and an EC_{50} value of 29.60 μg/mL. For the fungus *P. piricola*, compound **3** had a stronger activity than other compounds with an inhibitory rate of 64% and an EC_{50} value of 28.26 μg/mL.

In conclusion, six new and two known diterpenes were obtained from the roots of the plant *E. prolifera*. Their structures including the absolute configurations were elucidated by the NMR data analyses, the TDDFT ECD calculations, and the octant rule. The subsequent biological screenings indicated that these isolated compounds had antifungal activities against three phytopathogenic fungi. The results of our phytochemical investigation further revealed the chemical components of *E. prolifera* make it a poisonous and medicinal plant, and the biological screenings suggested that *E. prolifera* may be potentially useful to protect crops against phytopathogenic fungi; the bioactive compounds may probably be considered as candidate agents of antifungal agrochemicals for crop protection products.

DOI: 10.1021/acs.jafc.5b02021
J. Agric. Food Chem. 2015, 63, 5902–5910

■ ASSOCIATED CONTENT

Supporting Information

1D and 2D NMR and HR-ESIMS spectra of compounds **1**−**6**. The Supporting Information is available free of charge on the ACS Publications website at DOI: 10.1021/acs.jafc.5b02021.

■ AUTHOR INFORMATION

Corresponding Author

*(Y.G.) Phone/fax: +86-22-23502595. E-mail: victgyq@nankai.edu.cn.

Funding

This work was supported by the National Natural Science Foundation of China (Nos. 21372125 and 81102331).

Notes

The authors declare no competing financial interest.

■ REFERENCES

(1) Strange, R. N.; Scott, P. R. Plant disease: a threat to global food security. *Annu. Rev. Phytopathol.* **2005**, *43*, 83−116.

(2) Wang, L.; Li, C.; Zhang, Y.; Qiao, C.; Ye, Y. Synthesis and biological evaluation of benzofuroxan derivatives as fungicides against phytopathogenic fungi. *J. Agric. Food Chem.* **2013**, *61*, 8632−8640.

(3) Dodds, P. N.; Rathjen, J. P. Plant immunity: towards an integrated view of plant pathogen interactions. *Nat. Rev. Genet.* **2010**, *11*, 539−548.

(4) Dang, Q. L.; Kim, W. K.; Nguyen, C. M.; Choi, Y. H.; Choi, G. J.; Jang, K. S.; Park, M. S.; Lim, C. H.; Luu, N. H.; Kim, J. C. Nematicidal and antifungal activities of annonaceous acetogenins from *Annona squamosa* against various plant pathogens. *J. Agric. Food Chem.* **2011**, *59*, 11160−11167.

(5) Tareq, F. S.; Lee, M. A.; Lee, H. S.; Lee, Y. J.; Lee, J. S.; Hasan, C. M.; Islam, M. T.; Shin, H. J. Non-cytotoxic antifungal agents: isolation and structures of gageopeptides A−D from a *Bacillus* strain 109GGC020. *J. Agric. Food Chem.* **2014**, *62*, 5565−5572.

(6) Bai, Y. B.; Zhang, A. L.; Tang, J. J.; Gao, J. M. Synthesis and antifungal activity of 2-chloromethyl-1*H*- benzimidazole derivatives against phytopathogenic fungi in vitro. *J. Agric. Food Chem.* **2013**, *61*, 2789−2795.

(7) Cantrell, C. L.; Dayan, F. E.; Duke, S. O. Natural products as sources for new pesticides. *J. Nat. Prod.* **2012**, *75*, 1231−1242.

(8) Newman, D. J.; Cragg, G. M. Natural products as sources of new drugs over the 30 years from 1981 to 2010. *J. Nat. Prod.* **2012**, *75*, 311−335.

(9) Editorial Committee of Flora of China, Chinese Academy of Sciences. *Flora of China*; Science Press: Beijing, China, 1997; Vol. 44 (3), pp 118−121.

(10) Nanjing University of Chinese Medicine. *Dictionary of Chinese Herb Medicines*, 2nd ed.; Shanghai Scientific and Technologic Press: Shanghai, China, 2006; pp 131−132.

(11) Wu, D. G.; Sorg, B.; Hecker, E. Oligo- and macrocyclic diterpenes in Thymelaeaceae and Euphorbiaceae occurring and utilized in Yunnan (southwest China). 6. Tigliane type diterpene esters from latex of *Euphorbia prolifera*. *Phytother. Res.* **1994**, *8*, 95−99.

(12) Wu, D.; Sorg, B.; Hecker, E. New myrsinol-related polyfunctional pentacyclic diterpene esters from roots of *Euphorbia prolifera*. *J. Nat. Prod.* **1995**, *58*, 408−413.

(13) Xu, J.; Guo, Y.; Xie, C.; Li, Y.; Gao, J.; Zhang, T.; Hou, W.; Fang, L.; Gui, L. Bioactive myrsinol diterpenoids from the roots of *Euphorbia prolifera*. *J. Nat. Prod.* **2011**, *74*, 2224−2230.

(14) Xu, J.; Jin, D. Q.; Guo, Y.; Xie, C.; Ma, Y.; Yamakuni, T.; Ohizumi, Y. New myrsinol diterpenes from *Euphorbia prolifera* and their inhibitory activities on LPS-induced NO production. *Bioorg. Med. Chem. Lett.* **2012**, *22*, 3612−3618.

(15) Xu, J.; Jin, D. Q.; Song, H.; Guo, Y.; He, Y. Lathyrane diterpenes from *Euphorbia prolifera* and their inhibitory activities on LPS-induced NO production. *Fitoterapia* **2012**, *83*, 1205−1209.

(16) Li, J.; Xu, L.; Wang, F. P. New cytotoxic myrsinane-type diterpenes from *Euphorbia prolifera*. *Helv. Chim. Acta* **2010**, *93*, 746−752.

(17) Xu, J.; Yang, B.; Fang, L.; Wang, S.; Guo, Y.; Yamakuni, T.; Ohizumi, Y. Four new myrsinol diterpenes from *Euphorbia prolifera*. *J. Nat. Med.* **2013**, *67*, 333−338.

(18) Li, J.; Zhao, W.; Deng, L.; Li, X. R. Components of myrsinane-type diterpenes from *Euphorbia prolifera*. *Zhejiang Daxue Xuebao Yixue Ban* **2011**, *40*, 380−383.

(19) Xu, J.; Jin, D. Q.; Guo, P.; Xie, C.; Fang, L.; Guo, Y. Three new myrsinol diterpenes from *Euphorbia prolifera* and their neuroprotective activities. *Molecules* **2012**, *17*, 9520−9528.

(20) Zhang, W. J.; Chen, D. F.; Hou, A. J. New myrsinol diterpenes from *Euphorbia prolifera*. *Chin. J. Chem.* **2004**, *22*, 103−108.

(21) Jassbi, A. R. Chemistry and biological activity of secondary metabolites in *Euphorbia* from Iran. *Phytochemistry* **2006**, *67*, 1977−1984.

(22) Shi, Q. W.; Su, X. H.; Kiyota, H. Chemical and pharmacological research of the plants in genus *Euphorbia*. *Chem. Rev.* **2008**, *108*, 4295−4327.

(23) Vasas, A.; Hohmann, J. Euphorbia diterpenes: isolation, structure, biological activity, and synthesis (2008−2012). *Chem. Rev.* **2014**, *114*, 8579−8612.

(24) Wang, M.; Zhang, Q.; Wang, H.; Ren, Q.; Sun, Y.; Xie, C.; Xu, J.; Jin, D. Q.; Ohizumi, Y.; Guo, Y. Characterization and NO inhibitory activities of chemical constituents from an edible plant *Petasites tatewakianus*. *J. Agric. Food Chem.* **2014**, *62*, 9362−9367.

(25) Xu, J.; Zhang, Q.; Wang, M.; Ren, Q.; Sun, Y.; Jin, D. Q.; Xie, C.; Chen, H.; Ohizumi, Y.; Guo, Y. Bioactive clerodane diterpenoids from the twigs of *Casearia balansae*. *J. Nat. Prod.* **2014**, *77*, 2182−2189.

(26) Chen, H.; Xie, C.; Wang, H.; Jin, D. Q.; Li, S.; Wang, M.; Ren, Q.; Xu, J.; Ohizumi, Y.; Guo, Y. Sesquiterpenes inhibiting the microglial activation from *Laurus nobilis*. *J. Agric. Food Chem.* **2014**, *62*, 4784−4788.

(27) Li, Y. P.; Li, X. N.; Gao, L. H.; Li, H. Z.; Wu, G. X.; Li, R. T. Neopierisoids A and B, two new chlorinated 3,4-seco-grayanane diterpenoids with antifeedant activity from flowers of *Pieris japonica*. *J. Agric. Food Chem.* **2013**, *61*, 7219−7224.

(28) James, L. F.; Panter, K. E.; Gaffield, W.; Molyneux, R. J. Biomedical applications of poisonous plant research. *J. Agric. Food Chem.* **2004**, *52*, 3211−3230.

(29) Xu, J.; Ji, F.; Kang, J.; Wang, H.; Li, S.; Jin, D. Q.; Zhang, Q.; Sun, H.; Guo, Y. Absolute configurations and NO inhibitory activities of terpenoids from *Curcuma longa*. *J. Agric. Food Chem.* **2015**, DOI: 10.1021/acs.jafc.5b01584.

(30) Wang, M.; Zhang, Q.; Ren, Q.; Kong, X.; Wang, L.; Wang, H.; Xu, J.; Guo, Y. Isolation and characterization of sesquiterpenes from *Celastrus orbiculatus* and their antifungal activities against phytopathogenic fungi. *J. Agric. Food Chem.* **2014**, *62*, 10945−10953.

(31) Wang, L.; Yang, J.; Chi, Y. Q.; Ouyang, W. B.; Zang, Z.; Huang, S. X.; Cao, P.; Zhao, Y. A new myrsinol-type diterpene polyester from *Euphorbia dracunculoides* Lam. *Nat. Prod. Res.* **2015**, *29*, 1406−1413.

(32) Liu, Q.; Lu, D.; Jin, H.; Yan, Z.; Li, X.; Yang, X.; Guo, H.; Qin, B. Allelochemicals in the rhizosphere soil of *Euphorbia himalayensis*. *J. Agric. Food Chem.* **2014**, *62*, 8555−8561.

(33) Liu, Z. G.; Li, Z. L.; Bai, J.; Meng, D. L.; Li, N.; Pei, Y. H.; Zhao, F.; Hua, H. M. Anti-inflammatory diterpenoids from the roots of *Euphorbia ebracteolata*. *J. Nat. Prod.* **2014**, *77*, 792−799.

(34) Rédei, D.; Forgo, P.; Molnár, J.; Szabó, P.; Zorig, T.; Hohmann, J. Jatrophane diterpenoids with multidrug resistance-modulating activity from *Euphorbia mongolica* Prokh. *Tetrahedron* **2012**, *68*, 8403−8407.

(35) Vasas, A.; Sulyok, E.; Martins, A.; Rédei, D.; Forgo, P.; Kele, Z.; Zupkó, I.; Molnár, J.; Pinke, G.; Hohmann, J. Cyclomyrsinane and premyrsinane diterpenes from *Euphorbia falcata* modulate resistance of cancer cells to doxorubicin. *Tetrahedron* **2012**, *68*, 1280−1285.

(36) Sulyok, E.; Vasas, A.; Rédei, D.; Forgo, P.; Kele, Z.; Pinke, G.; Hohmann, J. New premyrsinane-type diterpene polyesters from *Euphorbia falcate*. *Tetrahedron* **2011**, *67*, 7289−7293.

(37) Zhang, Q.; Xiao, J.; Sun, Q. Q.; Qin, J. C.; Pescitelli, G.; Gao, J. M. Characterization of cytochalasins from the endophytic *Xylaria* sp. and their biological functions. *J. Agric. Food Chem.* **2014**, *62*, 10962−10969.
(38) Wang, D. M.; Zhang, C. C.; Zhang, Q.; Shafiq, N.; Pescitelli, G.; Li, D. W.; Gao, J. M. Wightianines A−E, dihydro-*β*-agarofuran sesquiterpenes from *Parnassia wightiana*, and their antifungal and insecticidal activities. *J. Agric. Food Chem.* **2014**, *62*, 6669−6676.
(39) Bruhn, T.; Schaumlöffel, A.; Hemberger, Y.; Bringmann, G. *SpecDis*, version 1.62; University of Wuerzburg: Germany, 2014.
(40) MOE 2013.08; Chemical Computing Group Inc., www.chemcomp.com.
(41) *Gaussian 09*, revision B, 01; Gaussian Inc.: Wallingford, CT, USA, 2010.
(42) Ye, X. L. *Stereochemistry*; Peking University Press: Beijing, China, 1999; pp 236−259.

DOI: 10.1021/acs.jafc.5b02021
J. Agric. Food Chem. 2015, 63, 5902−5910

N-Trimethylsilylimidazole (TMSI), *N*-methyl-*N*-trimethylsilylacetamide (MSA), *N*-trimethylsilyldiethylamine (TMSDEA), *N*-trimethylsilyldimethylamine (TMSDMA), *N*-methyl-*N*-trimethylsilyltrifluoroacetamide (MSTFA), *N*,*O*-bis(trimethylsilyl)-acetamide (BSA), and *N*,*O*-bis(trimethylsilyl)trifluoroacetamide (BSTFA) have also been used as silylation agents.[21] MSTFA was found to be superior in comparison to other reagents, giving better results for a broader range of analytes and producing fewer byproducts, especially when preceded with alkoxyamine treatment to prevent the formation of cyclic anomers.[22] This two-step procedure was further extended to other polar compounds present in multicomponent extracts, being now a gold standard in GC-MS-based metabolomics.[23]

However, as in vitro glycation mixtures often contain 50−200 mmol/L phosphate, that is, concentrations dramatically exceeding its dynamic range,[6,11,12] their analyses by GC-MS can be challenging. Additionally, peptides or proteins present in the mixture might also affect both method and instrument performance. Here we describe a new approach for the analysis of carbohydrates in heated model phosphate-buffered glycation systems containing D-glucose and peptide. The method relied on the removal of the phosphate component by SPE on polymer-based ion exchange cartridges followed by two-step derivatization with methoxyamine hydrochloride (MOA) and MSTFA and subsequent GC-MS analysis.

MATERIALS AND METHODS

Chemicals. Fmoc-rinkamide AM resin and Fmoc-L-Arg(Pbf)-OH (peptide synthesis grade) were bought from Iris Biotech GmbH (Marktredwitz, Germany). All other Fmoc-protected L-amino acids (peptide synthesis grade) were from ORPEGEN Pharma (Heidelberg, Germany). *N*,*N*′-Dimethylformamide (DMF, ≥99.8%), piperidine (≥99.5%), and dichloromethane (DCM, ≥99.9%) were purchased from Biosolve (Valkenswaard, The Netherlands). Trifluoroacetic acid (≥99.9%), α-D-glucose monohydrate (≥99.5%), D-(−)-fructose (≥99.5%), methanol (HPLC grade, ≥99.9%), 2-propanol (UV/IR grade, ≥99.9%), and D-(+)-sucrose (≥99.5%) were from Carl Roth GmbH & Co (Karlsruhe, Germany). L-(+)-Arabinose (≥99%), D-(+)-maltose monohydrate (≥98%), and D-(+)-mannose (≥98%) were from Merck KGaA (Darmstadt, Germany). MSTFA (≥95%) was bought from Macherey-Nagel (Düren, Germany). D-(+)-Galactose, D-(−)-ribose, D-(−)-mannitol, *myo*-inositol, diethyl ether (99%), and acetonitrile (≥99.9%, HPLC grade) were bought from VWR International GmbH (Dresden, Germany). 3-Deoxyglucosone (95%; 3-DG) was from Santa Cruz Biotechnology (Heidelberg, Germany). Ammonia solution (∼25% p.a.) was bought from KMF Laborchemie Handles GmbH (Lohmar, Germany). All other chemicals were purchased in required purities from Sigma-Aldrich Chemie GmbH (Taufkirchen, Germany). Water was purified in-house (resistance = 18 mΩ) on a PureLab Ultra Analytic System (ELGA Lab Water, Celle, Germany).

Peptide Synthesis. The sequence Ac-AFGSARASGA-NH_2 was synthesized on a Syro2000 multiple-peptide synthesizer (MultiSynTech GmbH, Witten, Germany) by 9-fluorenylmethoxycarbonyl/*tert*-butyl (Fmoc/^{t}Bu)-chemistry using 8 equiv (eq) of Fmoc-amino acid derivatives activated with 1,3-diisopropylcarbodiimide/hydroxybenzotriazol (DIC/HOBt) in DMF. N-Terminal acetylation was implemented in the automated synthesis by using 8 eq of acetic acid. After cleavage from the resin and removal of all protecting groups, the peptide was purified by RP-HPLC using 0.1% (v/v) aqueous trifluoroacetic acid (TFA) as ion pair reagent added to water (eluent A) and 60% (v/v) aqueous acetonitrile (eluent B) in 1% eluent B/min gradient (22−42% eluent B in 20 min). The purified peptide was reconstituted in 20% aqueous acetonitrile and split into aliquots of 50 nmol in 0.5 mL polypropylene tubes (Eppendorf AG, Hamburg, Germany). The solvent was removed under reduced pressure, and residues were stored at −20 °C.

In Vitro Glycation of the Model Peptide. The dried peptide aliquots were reconstituted in 100 μL of 100 mmol/L sodium phosphate buffer (pH 7.4) containing 18 μmol/L iron(II) sulfate in the presence or absence of 25 mmol/L D-glucose and incubated for 0, 30, 60, and 120 min at 95 °C under continuous shaking at 550 rpm. The incubated samples were cooled on ice, allowing the gas phase to condense completely and centrifuged (2 min at 2500*g*), and the reaction was quenched by the addition of 20 μL of a 6 mmol/L diethylenetriaminepentaacetic acid (DTPA) solution. Afterward, the samples were dried under vacuum and stored at −80 °C prior to GC-EI-MS analysis. The incubations performed in the absence of peptide served as controls.

Solid Phase Extraction. Ion exchange cartridges (mixed mode anion/cation exchanger CHROMABOND PSMix, 1 mL/100 mg, Macherey-Nagel), strong anion (CHROMABOND PSOH$^-$, 1 mL/100 mg, Macherey-Nagel), and weak anion exchanger (CHROMABOND HR-XAW, 45 μm, 1 mL/30 mg, Macherey-Nage) were conditioned with 3 mL of methanol and equilibrated with 3 mL of water. After the sample application, elution was performed in five steps: 1 mL of 5% (v/v) aqueous ammonia (E1), 1 mL of 5% (v/v) aqeuous acetic acid (E2), 1 mL of 50% (v/v) aqeuous methanol containing 10% (v/v) ammonia (E3), 1 mL of 50% aqeuous methanol containing 10% acetic acid (E4), and 1 mL of 20% methanol in acetone (E5). The individual fractions were dried under vacuum, and the carbohydrates and phosphate were analyzed by GC-MS after methoximation/trimethylsilylation.

For analysis of glycation mixtures, polymer-based mixed mode ion exchange SPE cartridges (CHROMABOND PSMix, 1 mL/100 mg, Macherey-Nagel) were conditioned and equilibrated with 3 mL (3 × 1 mL) of methanol and water, respectively. A 50 μL sample (n = 3) was diluted 20-fold with water and loaded, and carbohydrates were eluted with 10 mL of water. The eluates were lyophilized and reconstituted with 500 μL of 30% aqueous methanol. Eighty-five microliters of each diluted fraction was transferred to a 0.5 mL polypropylene tube, dried under vacuum, and stored at −20 °C prior to derivatization and GC-EI-MS analysis.

Method Standardization and Validation. Standardization and validation of the method was performed by a serial dilution (2−2.5-fold increment) of the authentic standard mixture (100 pmol/L−1 mmol/L each, 20 calibration levels, n = 3) in 30% aqueous methanol. The calibration mixtures were dried and derivatized directly or subjected to SPE (when spiked to the glycation matrix) before derivatization as described above. The experimentally determined limits of detection (LODs) were defined as 3.3 SD/m, where m is the slope of the calibration curve and SD is its standard deviation (calculated from the residual standard deviation of the relevant points in LDR).[24] The limits of quantitation (LOQs) were defined as the lower limit of the linear dynamic range, but not smaller that S/N = 10/1. The linear dynamic ranges (LDRs) were determined with 12 and 20 calibration levels (n = 3, increment 2.0−2.5) in the presence and absence of matrix, respectively. The accuracies were assessed using three calibration levels within the LDRs considering the SPE procedure. The uncertainty of the analysis was determined at the LOD for each analyte.

Derivatization Procedure and GC-MS. The samples were derivatized by employing a modification of the protocol described by Fiehn and co-workers.[22] In detail, 30 μL of freshly prepared 20 mg/mL MOA in pyridine solution was added to the dried sample and shaken at 600 rpm for 90 min at 30 °C. Then, 55 μL of MSTFA was added, and the sample was incubated for 30 min at 37 °C under continuous shaking at 600 rpm. The derivatized sample was transferred to a GC autosampler glass vial with micro inserts (NeoLab, Heidelberg, Germany) and subjected to GC-EI-MS analysis. One microliter of sample was injected by an A200S autosampler (CTC Analytics, Zwingen, Switzerland) into a Trace GC Ultra chromatograph equipped with a standard split/splitless injector (Thermo-Fisher Scientific, Bremen, Germany) as described in the Supporting Information (protocol S-1).

RESULTS

GC-EI-MS of Carbohydrate Derivatives. GC-MS analysis of the standard mixture containing 22 TMS-methoxime carbohydrate derivatives resulted in rich signal patterns in the corresponding total ion current (TIC) chromatograms (Figure 1). Individual analytes were typically represented by two well-resolved

DOI: 10.1021/jf505757m
J. Agric. Food Chem. 2015, 63, 5911−5919

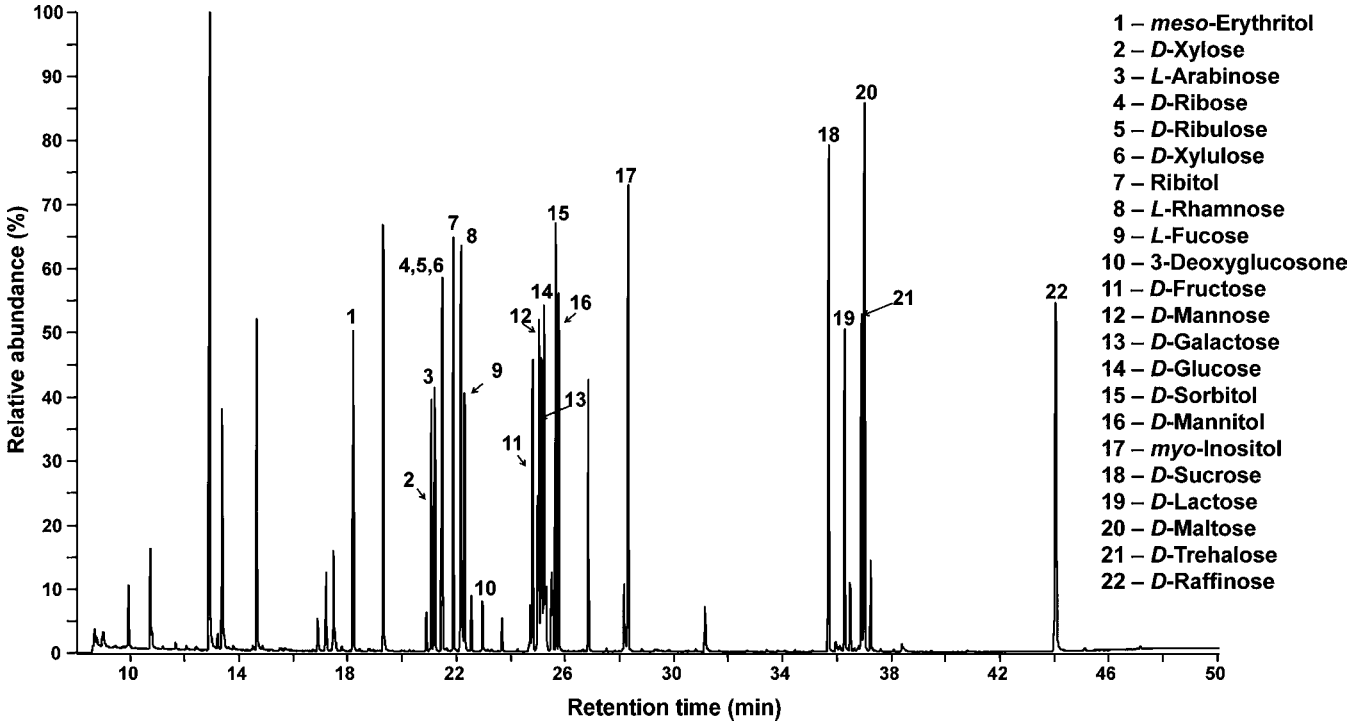

Figure 1. Total ion current chromatogram of TMS derivatives of carbohydrate methoximes identified in a 25 μmol/L carbohydrate standard mixture.

chromatographic peaks corresponding to *syn*- and *anti*-isomers of the TMS-methoximes. All carbohydrates were annotated by t_R and their characteristic MS fragmentation patterns. The numbers and intensities of the signals observed in the EI spectra (and, hence, obtained matches in spectra similarity search) were sufficient for unambiguous identification of analytes by spectra similarity (NIST database) or manual interpretation with a reversed match >900. Moreover, the annotation was confirmed by experiments performed with individual authentic standards. Extracted ion chromatograms (XICs) of the most intense and characteristic m/z values ($m/z \pm 0.5$) were integrated at specific retention times for relative and absolute quantitation.

When the temperature gradient from 40 to 350 °C was applied, baseline separation could be achieved for the majority of the sugars (Figure 1). However, some sugars, namely, D-ribose, D-ribulose, and D-xylulose (a diastereomer of D-ribulose), showed a strong coelution under these conditions (Figure S-1A). Moreover, the EI spectra of these analytes demonstrated a high similarity and absence of characteristic signals that made distinguishing these sugars impossible (Figure S-1B–D). Unfortunately, further optimization of the GC temperature gradient did not improve the separation of these three analytes. Therefore, in sugar mixtures, these unresolved signals were annotated as "ribose equivalents".

To assess the potential of our method for carbohydrate quantitation, we determined LODs and LOQs as well as LDRs for all analytes (Table S-1). For most of the analytes LODs were between 10 and 500 fmol (only L-fucose showed LOD of 1 pmol). The LOQs were in the range of 50–500 fmol, being higher only for L-rhamnose and L-fucose (1 and 2.5 pmol, respectively). The method showed a good linearity: the LDRs typically covered 3 orders of magnitude, whereas two analytes (D-sucrose and ribitol) produced linear GC-MS response over only 2 orders of magnitude. Only for two sugars, namely, L-rhamnose and L-fucose, the LDRs were $<10^2$.

Effects of Peptide and Phosphate on GC-MS Performance. Prior to application of our approach to the investigation of the protein/peptide Maillard reaction, it was necessary to characterize the effect of the glycation mixture components on the GC-MS responses of carbohydrates. For this, on the basis of the literature data,[6,11] we modeled a typical in vitro glycation reaction, based on 100 mmol/L phosphate buffer (pH 7.4), 18 μmol/L $FeSO_4$, and 0.5 mmol/L synthetic peptide Ac-AFGSARASGA-NH_2 simulating protein component. As this reaction was expected to be accompanied by the formation of multiple sugar intermediates, it contained three other carbohydrates besides glucose (D-mannose, D-fructose, and L-arabinose, each 20 μmol/L). Our results clearly demonstrated the absence of an essential effect of peptide Ac-AFGSARASGA-NH_2 on the recovery of carbohydrates (data not shown). However, in the presence of 100 mmol/L phosphate buffer, the GC-MS responses of all analytes were significantly decreased (Figure 2): up to a 57% reduction of signal intensities in comparison to the phosphate-free control was observed.

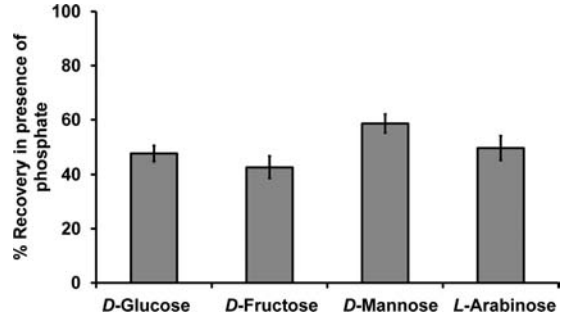

Figure 2. Effect of 100 mmol/L phosphate buffer (pH 7.4) on the intensity of characteristic chromatographic signals (peak areas) of the TMS-methoximes of D-glucose (m/z 319 ± 0.5), D-fructose (m/z 307 ± 0.5), D-mannose (m/z 319 ± 0.5), and L-arabinose (m/z 307 ± 0.5) obtained by GC-MS analysis of glycation mixtures. Recoveries were calculated in comparison to phosphate-free control.

DOI: 10.1021/jf505757m
J. Agric. Food Chem. 2015, 63, 5911–5919

Phosphate Removal by Ion Exchange SPE. To avoid this signal suppression, that is, to make our approach compatible with in vitro glycation systems, it was necessary to remove excess phosphate from the samples prior to derivatization and GC-MS analysis. For this, the same mixture of four carbohydrates, spiked to the above-mentioned phosphate-containing model glycation system, was depleted for phosphate anions by means of three polymeric ion exchange SPE materials (Figure 3). The analysis of the fractions revealed that total recoveries of all sugars from a strong cation/anion exchanger (PS-Mix) were higher than from the strong anion (PS-OH^-) and weak anion (HR-XAW) exchangers. Remarkably, the latter two phases demonstrated high variability of recovery for different sugars and generally lower recovery rates. The distribution of analyte between different SPE fractions was clearly favored for the flow-through fraction (72.3%), although 14% of recovered D-glucose was detected in the first elution fraction (5% aqueous ammonia, Figure 4A). In contrast, only a small portion of phosphate was recovered in the flow-through fraction, whereas most of this anion was eluted in the first three elution steps (5% aqueous ammonia, 5% aqeuous acetic acid, 50% aqeuous methanol containing 10% ammonia, Figure 4). Thereby, the weak anion exchanger had much lower phosphate removal efficiency than the other two tested phases. On the basis of these results, further method development was performed with the PS-Mix stationary phase.

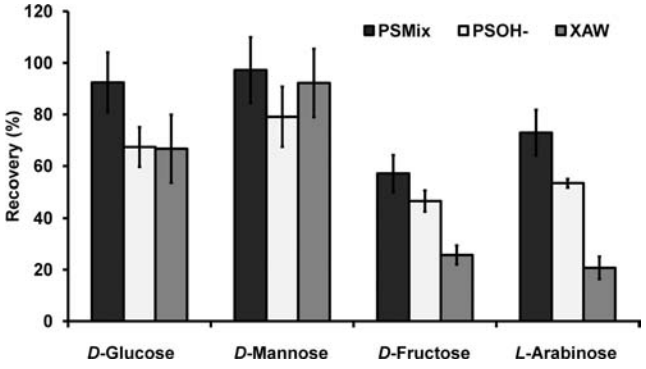

Figure 3. Total recoveries of D-glucose, D-mannose, D-fructose, and L-arabinose from mixed mode anion/cation exchange (PSMix), strong and weak anion exchange (PS-OH^- and HR-XAW, respectively) SPE cartridges (n = 5) after application of the 20 μmol/L carbohydrate mixture (D-glucose, D-fructose, D-mannose, and L-arabinose) in 100 mmol/L phosphate buffer (pH 7.4) containing 0.5 mmol/L synthetic peptide and 18 μmol/L $FeSO_4$. The eluates were dried and analyzed by GC-EI-MS after methoximation/trimethylsilylation.

In the next step, elution was optimized in terms of analyte recovery and degree of phosphate removal. As the abundance of phosphate was very high in the first three elution fractions and negligible in the flow-through fraction (Figure 4B), we replaced the elution steps with water (collected with the flow through) and 5% aqeuous formic acid. Indeed, when the mixture of four sugars (D-glucose, D-mannose, D-fructose, and L-arabinose, 20 μmol/L each) loaded on the PS-Mix cartridges was eluted with 0.9 mL of water, up to 85% of the total sugar recoveries were obtained (Figure S-2A). Moreover, even 0.9 mL of 5% aqueous formic acid resulted in enhanced elution of phosphate, whereas <0.5% of the total applied phosphate was recovered when elution was performed by the same volume of water (Figure S-2B). To increase the analyte recoveries, we applied higher elution volumes. Thereby, about a 30% increase in sugar recoveries was achieved when using 10 mL of water (Figure S-2A). Remarkably, it did not enhance the recovery of phosphate (Figure S-2B). Therefore, in further experiments elution was performed with 10 mL of water.

Finally, we verified the applicability of the established sample preparation scheme to the matrix used for in vitro glycation. For this, a solution of synthetic peptide Ac-AFGSARASGA-NH_2 (0.5 mmol/L) in 100 mmol/L phosphate buffer (pH 7.4) containing 18 μmol/L $FeSO_4$ was 20-fold diluted with water and spiked with the mixture of 22 carbohydrates (25 μmol/L). Fifty microliters of this mixture was subjected to the optimized SPE procedure, derivatized, and analyzed by GC-MS. In parallel, the same mixture was analyzed without SPE. Absolute quantitation of phosphate in the eluate fractions revealed >99% phosphate removal efficiency. Thereby, recoveries of the sugars were in the range of 60−95%, which was sufficient for quantitation.

Method Validation. The experimental procedure presented here was validated in terms of sensitivity, linearity, recovery, and precision. For the determination of method LODs, LOQs, and LDRs, serially diluted mixtures of 22 carbohydrates (n = 3) with analyte concentrations ranging from 1 nmol/L to 1 mmol/L were derivatized and analyzed by GC-MS after the SPE procedure. The method LODs (LOD_m) ranged from 10 to 210 fmol (Table 1). For most of the carbohydrates, the method LOQs (LOQ_m) were between 100 and 500 fmol, although for L-fucose it

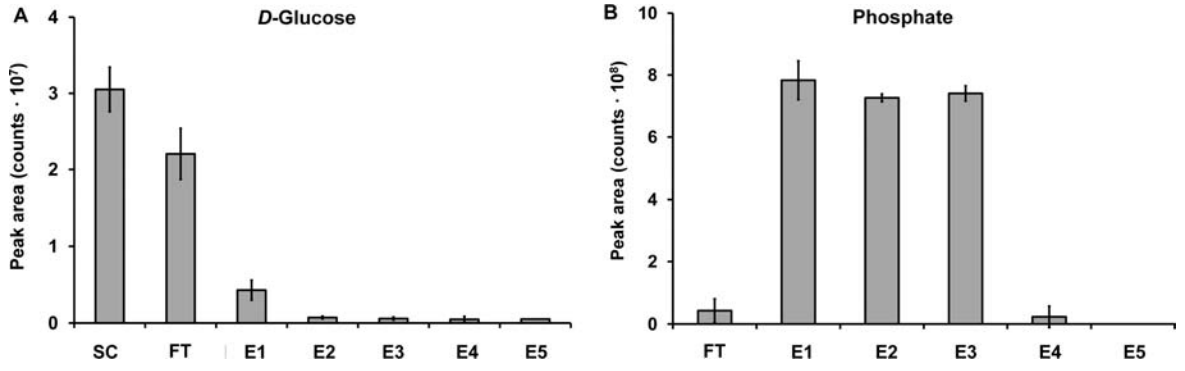

Figure 4. Intensities of D-glucose and phosphate signals (peak areas at m/z 319 ± 0.5 and 314 ± 0.5, respectively) in individual SPE (mixed mode anion/cation exchange, PSMix) fractions (n = 5): flow through (FT) and elution 1−5 (E1−E5). The carbohydrate mixture containing 20 μmol/L D-glucose, D-fructose, D-mannose, and L-arabinose was applied in 100 mmol/L phosphate buffer (pH 7.4) containing 0.5 mmol/L synthetic peptide and 18 μmol/L $FeSO_4$. The fractions were dried and analyzed by GC-EI-MS after methoximation/trimethylsilylation in parallel to sugars-only control (SC).

DOI: 10.1021/jf505757m
J. Agric. Food Chem. 2015, 63, 5911−5919

Table 1. Sensitivity and Linearity Parameters Obtained for the TMS-Methoximes of 22 Carbohydrate Standards Diluted in 100 mmol/L Phosphate Buffer (pH 7.4) Containing 18 μmol/L Fe_2SO_4 and 0.5 mmol/L Synthetic Peptide Ac-AFGSARASGA-NH_2 after Phosphate Removal prior to GC-MS Analysis[a]

compd	LOD_m[b] (fmol)	LOQ_m[b] (fmol)	LDR_m	slope	intercept	R^2	recovery[c] (%)	accuracy[d] (%)	uncertainty[e] (%)
1	140	250	2.0×10^2	0.31	-6×10^4	1.00	79.2	111	4.33
2	100	250	1.0×10^2	0.53	-4×10^4	0.99	89.6	103	12.8
3[f]	90	250	4.0×10^2	0.91	-2×10^6	1.00	74.4	98.6	8.93
4–6[g]	110	250	1.0×10^2	0.71	-5×10^4	1.00	83.7	106	6.04
7	60	500	2.0×10^2	0.52	-1×10^6	1.00	83.3	108	16.5
8	10	500	2.0×10^1	0.15	-3×10^4	1.00	86.6	102	10.3
9	70	2500	4.0×10^1	0.26	-1×10^5	1.00	80.6	97.7	3.61
10	80	250	1.0×10^2	0.29	-2×10^4	1.00	81.1	90.3	2.18
11	10	100	2.0×10^3	0.56	-1×10^5	0.99	69.0	96.6	6.74
12	26	100	1.0×10^2	0.79	-1×10^4	1.00	74.8	98.3	8.89
13	30	250	4.0×10^2	1.36	-4×10^6	0.99	79.9	102	4.39
14	70	70	1.4×10^2	0.92	-4×10^4	1.00	66.2	91.0	14.3
15	70	100	1.0×10^3	2.29	-4×10^6	1.00	88.2	94.0	17.9
16	60	100	1.0×10^2	0.94	-1×10^4	1.00	63.8	93.8	6.82
17	50	100	1.0×10^3	2.21	-2×10^6	1.00	92.1	91.2	0.82
18	210	210	4.8×10^1	2.31	-3×10^4	0.99	75.3	102	11.8
19	20	500	2.1×10^1	0.58	-2×10^4	1.00	78.1	103	2.61
20	40	250	4.0×10^2	2.51	-8×10^6	0.99	89.4	99.9	2.62
21	100	100	4.0×10^1	3.09	-9×10^4	0.99	76.3	96.2	11.3
22	120	250	4.0×10^2	4.11	-1×10^7	0.99	86.5	93.1	16.5

[a]All parameters were determined in independent dilution series ($n = 3$). [b]LODs and LOQs are given as fmol on column. [c]Sugar recoveries were calculated as the ratios of the calibration curve slopes obtained without and with SPE procedure. [d]Accuracy was determined using three calibration levels covering the lower, middle, and higher part of the LDRs. [e]Uncertainty was calculated at the LOD of each analyte. [f]Parameters determined for L-arabinose. [g]D-Ribose, D-ribulose, and D-xylulose were quantified as D-ribose equivalents.

was 2.5 pmol. Thus, for some analytes, the introduction of the SPE procedure resulted in an up to 5-fold decrease in their LODs and/or LOQs (Tables 1 and S-1). Moreover, for the majority of analytes an essential reduction of LDRs (defined for $R^2 \geq 0.99$) was observed; these values were typically 1 order of magnitude lower when the SPE procedure was applied (Tables 1 and S-1). The recoveries of the carbohydrates, calculated as the ratios of the calibration curve slopes obtained without and with the SPE procedure, were for most of the analytes >74%, although for three of them, namely, D-mannitol, D-glucose, and D-fructose, they were 63.8, 66.2, and 69.0%, respectively.

For the determination of intraday and interday precision, glycation mixtures ($n = 5$) were incubated for 60 min as described under Materials and Methods on three nonconsecutive days and analyzed by the workflow presented in Figure 5. The method demonstrated a high precision: for concentration determination neither intraday nor interday relative standard deviation (RSD%) exceeded 10%, whereas for retention times these values did not exceed 1% (Table S-2).

Quantitation of Sugar Intermediates in Model Glycation Mixtures. The established method was applied for the absolute quantitation of carbohydrate intermediates of the Maillard reaction. For this, D-glucose (25 mmol/L) was incubated in the absence and presence of synthetic peptide as described under Materials and Methods. GC-MS analysis of the glycation mixtures, performed after phosphate removal, revealed the formation of at least eight pentose and hexose monosaccharides present at least at one time point of incubation at concentrations exceeding LOQ_m, identified by characteristic retention times and similarity of EI mass spectra (Table 2). Peak areas were derived by integration of corresponding extracted ion chromatograms at retention times specific for each sugar. Quantitation relied on external calibration in authentic matrix. For this, the standard mixture was serially diluted with glycation medium and subjected to the ion exchange-based SPE procedure prior to GC-MS.

One of the detected sugars was D-glucose, whereas the rest were intermediates of Maillard reaction, demonstrating a characteristic kinetic behavior. The formation of two of them, D-mannose and D-fructose, increased over the incubation period. In the beginning of the reaction, the concentration of D-fructose increased more quickly in comparison to D-mannose. However, after 60 min of reaction, both hexoses showed a similar kinetic behavior (Table 3), achieving maximal concentrations after 120 min of incubation (up to 10.8% of initial D-glucose concentration). Similar kinetics was observed for D-ribose (and, probably, coeluting D-ribulose and D-xylulose), although it was below the LOQ up to 60 min of incubation both in the glycation mixtures and in controls. The maximal concentration of D-ribose in the reaction mixture (0.9% of initial D-glucose concentration) was observed in the absence of peptide after 2 h of incubation. Another pentose, arabinose, showed different kinetics: its maximal concentration (0.85 mmol/L, i.e., 3.4% of the initial D-glucose concentration) was achieved after 60 min of incubation and then decreased. As GC-MS analyses of the TMS-methoximes of D- and L-arabinose individually and in a mixture showed the same chromatographic behavior for both isomers (Figure S-3), most probably arabinose formed in the incubated samples was represented with the D-isomer. 3-Deoxyglucosone, *myo*-inositol, and D-xylose were also found both in the absence and in the presence of synthetic peptide. However, their concentrations at these reaction times were below corresponding LOQs; therefore, these sugars could not be absolutely quantified in this system.

DISCUSSION

Model reactions are known to be a convenient tool for the study of the Maillard reaction in protein systems. Typically, to

DOI: 10.1021/jf505757m
J. Agric. Food Chem. 2015, 63, 5911−5919

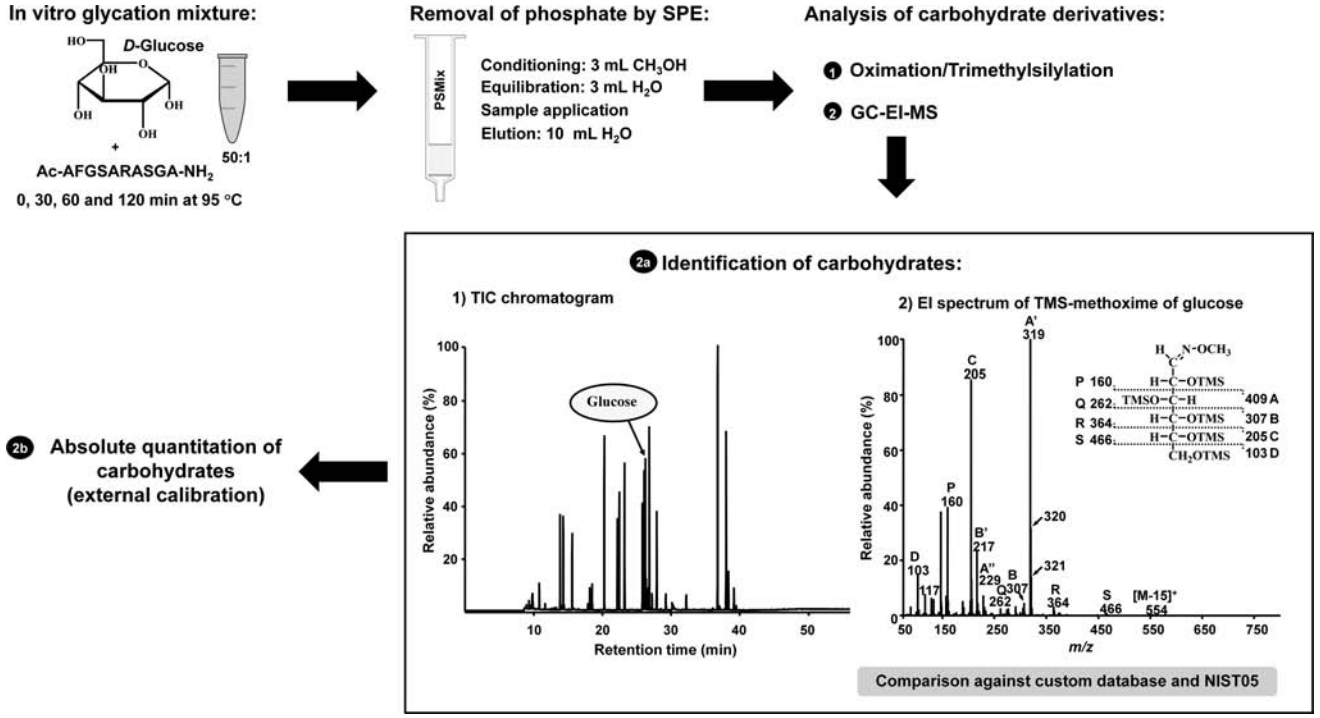

Figure 5. Experimental workflow for carbohydrate analysis.

Table 2. GC-MS Parameters of D-Glucose and the Main Products Formed during Its Thermal Degradation[a]

	t_R (min)		MS data
analyte	peak 1	peak 2	m/z (rel intensity, %)
D-glucose	25.2	25.4	160 (48), 205 (97), 217 (42), **319** (100)
D-mannose	24.9		160 (47), 205 (99), 217 (42), **319** (100)
D-fructose	24.7	24.9	103 (100), 205 (12), 217 (55), **307** (57)
3-DG	22.9	23.6	205 (10), 217 (7), **231** (100), 315 (4)
myo-inositol	28.2		191 (40), 217 (97), **305** (100), 318 (45)
arabinose	21.1		103 (100), 205 (13), 217 (50), **307** (47)
D-xylose	21.0		103 (100), 205 (14), 217 (49), **307** (44)
D-ribose[a]	21.4		103 (100), 205 (31), 217 (45), 263 (7), **307** (42)

[a] D-Ribose, D-ribulose, and D-xylulose were quantified as D-ribose equivalents. For all analytes, the boldfaced selective m/z and peak 1 were used for quantitation; 3-DG, 3-deoxyglucosone.

characterize the patterns of glycoxidative protein modifications, biologically relevant polypeptides, such as collagen,[25] bovine or human serum albumins (BSA and HSA, respectively),[26] were used. However, due to the large number of potential glycation sites, such mixtures are often too complex for efficient analysis of reaction pathways and mechanisms. Therefore, in the past decades, model peptide-based systems for the glycation of amino groups with selected glycation agents were established.[27] Recently we have described an advanced glycation model system based on arginine-containing peptides.[6] This approach provided adequate information about the peptide modifications and the kinetics of their formation. However, to reveal the underlying reaction mechanisms, this information needs to be complemented with knowledge about α-dicarbonyl and sugar profiles. As methods for comprehensive α-dicarbonyl analysis are well-established and reported elsewhere,[28] here we focused on carbohydrate profiling.

In the whole workflow of carbohydrate analysis, complete separation of all monosaccharides seems to be the most challenging task. Indeed, the differences in the structures of isomeric sugars are obviously too small to affect the chromatographic behavior of the analytes, and in this study, that was the case for D-ribose, D-ribulose, and D-xylulose (Figure S-1A). These three sugars could not be separated under any chromatographic conditions tested, without loss of selectivity in other sections of the chromatogram. Although Medeiros and Simoneit[29] recently separated ribose and xylulose TMS derivatives obtained without a methoximation step on a 5% phenyl-methylpolysiloxane column, their method suffered from coelution of fucose and xylose, galactose, and altrose, as well as arabitol and xylitol. Application of liquid chromatography (LC)-based techniques (LC-MS) resulted in compromised selectivity[30] and sensitivity,[31] although it can be successfully applied for the analysis of specific compound groups (e.g., dicarbonyls).[32] Remarkably, the LODs observed in this study for some monosaccharides (e.g., **1**, **3**, **7**, **11**, **12**, **13**, **15**, and **16**) and for all oligosaccharides (**18**–**22**) were lower than those observed with LC-MS,[33] GC-flame ionization detection (FID),[34] GC-MS,[23] and GC-MS/MS[35] methods. The values obtained here were also advantageous in comparison to those obtained with soft ionization techniques: ESI-MS,[36] MELDI-MS,[37] and MALDI-TOF-MS.[38] The lower method LODs and LOQs in comparison to the corresponding instrument values can be explained by different drying procedures: freeze-drying versus Speedvac. Additionally, reconstitution of dried SPE eluates in a low volume of derivatization mixture provided further increase of sensitivity due to the concentration effect (Tables 1 and S-1). Thus, in terms of both analyte coverage and selectivity, our method is, to the best of our knowledge, superior in comparison to those reported before. The sensitivity improvement can be also attributed to the double-focusing sector field mass analyzer used here, which is known for its high sensitivity.

Another challenge of multicomponent analysis is the interference between analytes and sample matrix (i.e., undefined compounds behind the scope of analysis) directly affecting

DOI: 10.1021/jf505757m
J. Agric. Food Chem. 2015, 63, 5911−5919

Table 3. Concentrations of D-Glucose and Main Sugar Glycation Intermediates at Each Incubation Time Point

	concentrations at each reaction time point[a] (mmol/L)							
	0 min		30 min		60 min		120 min	
analyte	control	Glc +Pept[a]	control	Glc+Pept[a]	control	Glc+Pept[a]	control	Glc+Pept[a]
D-glucose	25[b]	25[b]						
D-mannose	blq	blq	blq	blq	blq	0.17 ± 0.04 (0.7)[c]	0.50 ± 0.04 (2.0)[c]	0.30 ± 0.07 (1.2)[c]
D-fructose	blq	blq	0.64 ± 0.05 (2.5)[c]	1.04 ± 0.04 (4.2)[c]	1.10 ± 0.20 (4.4)[c]	1.22 ± 0.71 (4.9)[c]	2.70 ± 0.12 (10.8)[c]	2.38 ± 0.66 (9.5)[c]
3-DG[d]	blq	blq	blq	blq	blq	blq	blq	blq
myo-inositol	blq	blq	blq	blq	blq	blq	blq	blq
arabinose	blq	blq	0.47 ± 0.04 (1.9)[c]	0.42 ± 0.02 (1.7)[c]	0.85 ± 0.31 (3.4)[c]	0.46 ± 0.29 (1.8)[c]	0.76 ± 0.09 (3.1)[c]	0.84 ± 0.06 (3.4)[c]
D-xylose	blq	blq	blq	blq	blq	blq	blq	blq
D-ribose[e]	blq	blq	blq	blq	blq	blq	0.22 ± 0.03 (0.9)[c]	blq

[a]D-Glucose was heated in 100 mmol/L phosphate buffer (pH 7.4) containing 18 μmol/L $FeSO_4$ in the absence and presence of synthetic peptide Ac-AFGSARASGA-NH_2 at 95 °C during 2 h. The incubated samples were subjected to mixed mode anion/cation exchange (PSMix) SPE, derivatized with MOA/MSTFA, and analyzed by GC-EI-MS. [b]Initial D-glucose concentration. [c]Percentage of the initial glucose concentration. Data are expressed as mean ± SD; blq, below the limit of quantitation. [d]3-DG, 3-deoxyglucosone. [e]D-Ribose, D-ribulose, and D-xylulose were quantified as D-ribose equivalents.

analyte signal intensities. These events, generally denoted as matrix effects, result in signal enhancement or suppression and represent thereby an essential challenge in instrumental analyses.[39] Thus, this phenomenon was described for sugars: for example, glucose was reported to enhance the signals of lysine and fumaric and citric acids in plant samples.[19] Here, we observed that sugar-derived signals themselves could be suppressed in the presence of high (100 mmol/L) phosphate concentrations (Figure 2). Indeed, as this inorganic anion can be readily derivatized with MSTFA and converted into its volatile 3-TMS ether, it is involved in retention and separation, and, when present in concentrations exceeding column capacity, might interfere with analytes. Commonly, suppression effects within the GC-MS system can be explained by the formation of active sites in the analytical system.[40] Typically, the injector is the preferred part where these active sites can emerge. This might occur when a highly abundant analyte does not undergo quantitative derivatization and, due to compromised volatility, deposits in the liner. In such cases, subsequent injections with MSTFA as the solvent can furthermore provoke an in situ derivatization of these deposited remainders yielding irreproducible memory peaks in the corresponding chromatograms. Indeed, we observed such signals in MSTFA blank runs analyzed after the samples overloaded with phosphate (data not shown). This clearly indicated that formation of active sites could be responsible for the observed suppression effect (Figure 2).

Obviously, removal of phosphate from the samples before derivatization was the only way to escape this problem. Typically, SPE is the method of choice for this. As both analytes (i.e., sugars) and contaminating phosphate anions are polar substances, our strategy relied on the use of ion exchange cartridges. Surprisingly, a comparison of the three tested materials, that is, mixed mode anion/cation exchanger (PS-Mix), strong anion (PS-OH^-), and weak anion (HR-XAW) exchangers, applied to four carbohydrates dissolved in 100 mmol/L sodium phosphate buffer, revealed a consistently better recovery from the PS-Mix material in comparison to the other two phases (Figure 3). This improvement related to additional PS-H^+ functionality of the PS-Mix cartridges most probably can be attributed to the binding of iron and sodium cations, removing them from the mobile phase, where they otherwise could induce dipoles in the carbohydrate molecules that may lead to a more anionic character of the carbohydrates increasing the interaction with the $PSOH^-$ column material.

High analyte recoveries and method precision allowed the application of our approach to in vitro glycation reactions performed with arginine-containing peptide.[6] As early glycation was not described for arginine side chains yet, this peptide can be subjected exclusively to advanced glycation, that is, interaction with α-dicarbonyls, first of all glyoxal and methylglyoxal.[41] According to our results, the detected intermediates of dicarbonyl formation were mostly hexoses and pentoses (Table 2). In most cases, their origin can be explained by known pathways of the protein Maillard reaction or simple interconversion of monosaccharides (e.g., Lobry de Bruyn–Alberda van Ekenstein rearrangement driven by proton abstraction).[42] Thus, mannose and 3-deoxyglucosone can be generated from glucose via 1,2-endiol intermediate.[42] As the presence of the peptide did not influence fructose concentrations in the reaction mixture (Table 3), it can be concluded that this monosaccharide was generated solely from free glucose. Most probably, mannose was rather reactive toward the model peptide or its degradation was catalyzed by the peptide: its abundance was much lower when incubations were performed in the presence of peptide (Table 3). The formation of *myo*-inositol (even in trace amounts) apparently identified (Figure S-4) under the conditions of incubation seems to be confusing. In animals, this polyol is synthesized from glucose-6-phosphate in two enzymatic steps.[43] However, its nonenzymatic generation, to the best of our knowledge, was not described so far.

Generally, pentoses are well-known intermediates of protein Maillard reaction and typically generated in glucose-based glycation mixtures via retroaldolization.[44] All of them, especially aldoses, are potent glycation agents and readily react with free amino groups.[45] It can be assumed that, although ribose is much less abundant in the reaction mixtures (Table 3), it has an essentially higher reactivity in comparison to arabinose (represented here, most probably, with a D-isomer (Figure S-3)). Indeed, the concentration of ribose is significantly decreased in the presence of peptide, which might indicate its enhanced autoxidation. This enhancement, in turn, can be explained by the shift of chemical equilibrium due to the reaction of sugar autoxidation products with arginine residues. The same was observed for mannose, which is known to have a relatively low glycation potential.

In conclusion, our method allowed simultaneous quantitation of carbohydrates present in model glycation systems. Gas chromatographic analyses of sugars after two-step derivatization

DOI: 10.1021/jf505757m
J. Agric. Food Chem. 2015, 63, 5911−5919

with MOA and MSTFA showed very good performance and can be applied to the analysis of carbohydrate patterns in Maillard reaction mixtures. The method provided high sensitivity and precision for more than 10 relevant carbohydrates. After removal of >99% phosphate with mixed-mode ion exchange SPE, at least seven sugars (Maillard reaction intermediates) were identified by GC-MS and reproducibly quantified (RSD < 10%) using the peak areas of the corresponding extracted ion chromatograms. The method for the analysis of carbohydrates in model glycation mixtures established here can be used to get better insights into the mechanisms of protein Maillard reaction and pathways of AGE formation.

■ ASSOCIATED CONTENT

Supporting Information

Additional protocols, figures, tables, and references. The Supporting Information is available free of charge on the ACS Publications website at DOI: 10.1021/jf505757m.

■ AUTHOR INFORMATION

Corresponding Author

*(A.F.) Mail: Institut für Bioanalytische Chemie, Biotechnologisch-Biomedizinisches Zentrum, Deutscher Platz 5, 04103 Leipzig, Germany. Phone: +49 (0) 341 9731332. Fax: +49 (0) 341 9731339. E-mail: andrej.frolov@bbz.uni-leipzig.de.

Funding

We thank Prof. Dr. Ralf Hoffmann for financial support. We gratefully acknowledge financial support from the Deutsche Forschungsgemeinschaft (DFG, FR-3117/2-1 and HO-2222/7-1), the European Fund for Regional Structure Development (EFRE, European Union and Free State Saxony, and the Bundesministerium für Bildung and Forschung (BMBF) to R.H. and C.B.

Notes

The authors declare no competing financial interest.

■ ACKNOWLEDGMENTS

We thank Prof. Dr. Ralf Hoffmann for a critical reading of the manuscript and helpful discussions, as well as Antje Hutschenreuther for initial experiments and Divya Varadharajan for assistance in sample preparation.

■ ABBREVIATIONS USED

AGEs	advanced glycation end-products
GC-MS	gas chromatography−mass spectrometry
SPE	solid phase extraction
HPAEC	high-performance anion exchange chromatography
HILIC	hydrophilic interaction liquid chromatography
ELS	evaporative light scattering
PAD	pulsed amperometric detection
MS	mass spectrometry
EI	electron ionization
HMDS	hexamethyldisilazane
TMCS	trimethylchlorosilane
TMSI	*N*-trimethylsilylimidazole
MSA	*N*-methyl-*N*-trimethylsilylacetamide
TMSDEA	*N*-trimethylsilyldiethylamine
TMSDMA	*N*-trimethylsilyldimethylamine
MSTFA	*N*-methyl-*N*-trimethylsilyltrifluoroacetamide
BSA	*N*,*O*-bis(trimethylsilyl)acetamide
BSTFA	*N*,*O*-bis(trimethylsilyl) trifluoroacetamide
MOA	methoxyamine hydrochloride
DMF	dimethylformamide
DCM	dichloromethane
Fmoc/^{t}Bu	9-fluorenylmethoxycarbonyl/*tert*-butyl
TFA	trifluoroacetic acid
DIC/HOBt	3-diisopropylcarbodiimide/hydroxybenzotriazol
DTPA	diethylenetriaminepentaacetic acid
LODs	limits of detection
S/N	signal/noise
LOQs	limits of quantitation
TMS	trimethylsilyl
SD	standard deviation
RSD	relative standard deviation
TIC	total ion current
XICs	extracted ion chromatograms
LDR	linear dynamic ranges
BSA	bovine serum albumin
HSA	human serum albumin
LC	liquid chromatography
FID	flame ionization detection
FT	flow through
SC	sugars-only control

■ REFERENCES

(1) Ulrich, P.; Cerami, A. Protein glycation, diabetes, and aging. *Recent Prog. Horm. Res.* **2001**, *56*, 1−21.

(2) van Boekel, M. A. J. S. Formation of flavour compounds in the Maillard reaction. *Biotechnol. Adv.* **2006**, *24*, 230−233.

(3) Hodge, J. E. The Amadori rearrangement. *Adv. Carbohydr. Chem.* **1955**, *10*, 169−205.

(4) Heyns, K.; Noack, H. Die Umsetzung von D-Fructose mit L-Lysin und L-Arginin und deren Beziehung zu nichtenzymatischen Bräunungsreaktionen. *Chem. Ber.* **1962**, *95*, 720−727.

(5) Grillo, M. A.; Colombatto, S. Advanced glycation end-products (AGEs): involvement in aging and in neurodegenerative diseases. *Amino Acids* **2008**, *35*, 29−36.

(6) Frolov, A.; Schmidt, R.; Spiller, S.; Greifenhagen, U.; Hoffmann, R. Arginine-derived advanced glycation end products generated in peptide-glucose mixtures during boiling. *J. Agric. Food Chem.* **2014**, *62*, 3626−3635.

(7) Huttunen, H. J.; Fages, C.; Rauvala, H. Receptor for advanced glycation end products (RAGE)-mediated neurite outgrowth and activation of NF-κB require the cytoplasmic domain of the receptor but different downstream signaling pathways. *J. Biol. Chem.* **1999**, *274*, 19919−19924.

(8) Koschinsky, T.; He, C. J.; Mitsuhashi, T.; Bucala, R.; Liu, C.; Buenting, C.; Heitmann, K.; Vlassara, H. Orally absorbed reactive glycation products (glycotoxins): an environmental risk factor in diabetic nephropathy. *Proc. Natl. Acad. Sci. U. S. A.* **1997**, *94*, 6474−6479.

(9) Smuda, M.; Glomb, M. A. Fragmentation pathways during Maillard-induced carbohydrate degradation. *J. Agric. Food Chem.* **2013**, *61*, 10198−10208.

(10) Gobert, J.; Glomb, M. A. Degradation of glucose: reinvestigation of reactive α-dicarbonyl compounds. *J. Agric. Food Chem.* **2009**, *57*, 8591−8597.

(11) Thornalley, P. J.; Langborg, A.; Minhas, H. S. Formation of glyoxal, methylglyoxal and 3-deoxyglucosone in the glycation of proteins by glucose. *Biochem. J.* **1999**, *344* (Part 1), 109−116.

(12) Wells-Knecht, K. J.; Zyzak, D. V.; Litchfield, J. E.; Thorpe, S. R.; Baynes, J. W. Mechanism of autoxidative glycosylation: identification of glyoxal and arabinose as intermediates in the autoxidative modification of proteins by glucose. *Biochemistry* **1995**, *34*, 3702−3709.

(13) Usui, T.; Yoshino, M.; Watanabe, H.; Hayase, F. Determination of glyceraldehyde formed in glucose degradation and glycation. *Biosci., Biotechnol., Biochem.* **2007**, *71*, 2162−2168.

(14) Grandhee, S. K.; Monnier, V. M. Mechanism of formation of the Maillard protein cross-link pentosidine. Glucose, fructose, and ascorbate as pentosidine precursors. *J. Biol. Chem.* **1991**, *266*, 11649−11653.

DOI: 10.1021/jf505757m
J. Agric. Food Chem. 2015, 63, 5911−5919

(15) Cataldi, T. R. I.; Campa, C.; De Benedetto, G. E. Carbohydrate analysis by high-performance anion-exchange chromatography with pulsed amperometric detection: the potential is still growing. *Fresenius' J. Anal. Chem.* **2000**, *368*, 739−758.
(16) Buszewski, B.; Noga, S. Hydrophilic interaction liquid chromatography (HILIC) − a powerful separation technique. *Anal. Bioanal. Chem.* **2012**, *402*, 231−247.
(17) Anumula, K. R.; Dhume, S. T. High resolution and high sensitivity methods for oligosaccharide mapping and characterization by normal phase high performance liquid chromatography following derivatization with highly fluorescent anthranilic acid. *Glycobiology* **1998**, *8*, 685−694.
(18) Rakete, S.; Glomb, M. A. A novel approach for the quantitation of carbohydrates in mash, wort, and beer with RP-HPLC using 1-naphthylamine for precolumn derivatization. *J. Agric. Food Chem.* **2013**, *61*, 3828−3833.
(19) Koek, M. M.; Jellema, R. H.; van der Greef, J.; Tas, A. C.; Hankemeier, T. Quantitative metabolomics based on gas chromatography mass spectrometry: status and perspectives. *Metabolomics* **2011**, *7*, 307−328.
(20) Bentley, R.; Sweeley, C. C.; Makita, M.; Wells, W. W. Gas chromatography of sugars and other polyhydroxy compounds. *Biochem. Biophys. Res. Commun.* **1963**, *11*, 14−18.
(21) Ruiz-Matute, A. I.; Hernandez-Hernandez, O.; Rodriguez-Sanchez, S.; Sanz, M. L.; Martinez-Castro, I. Derivatization of carbohydrates for GC and GC-MS analyses. *J. Chromatogr. B: Anal. Technol. Biomed. Life Sci.* **2011**, *879*, 1226−1240.
(22) Fiehn, O.; Kopka, J.; Trethewey, R. N.; Willmitzer, L. Identification of uncommon plant metabolites based on calculation of elemental compositions using gas chromatography and quadrupole mass spectrometry. *Anal. Chem.* **2000**, *72*, 3573−3580.
(23) Koek, M. M.; Muilwijk, B.; van der Werf, M. J.; Hankemeier, T. Microbial metabolomics with gas chromatography/mass spectrometry. *Anal. Chem.* **2006**, *78*, 1272−1281.
(24) International Conference on the Harmonization of Technical Requirements for the Registration of Pharmaceuticals for Human Use; ICH harmonized tripartite guideline validation of analytical procedures: text and methodology Q2 (R1), 2005. Current Step 4 version, Parent Guideline dated 27 October 1994 (Complementary Guideline on Methodology dated 6 November 1996 incorporated in November 2005).
(25) Fu, M. X.; Wells-Knecht, K. J.; Blackledge, J. A.; Lyons, T. J.; Thorpe, S. R.; Baynes, J. W. Glycation, glycoxidation, and cross-linking of collagen by glucose. Kinetics, mechanisms, and inhibition of late stages of the Maillard reaction. *Diabetes* **1994**, *43*, 676−683.
(26) Frolov, A.; Hoffmann, R. Analysis of amadori peptides enriched by boronic acid affinity chromatography. *Ann. N. Y. Acad. Sci.* **2008**, *1126*, 253−256.
(27) Ehrlich, H.; Hanke, T.; Frolov, A.; Langrock, T.; Hoffmann, R.; Fischer, C.; Schwarzenbolz, U.; Henle, T.; Born, R.; Worch, H. Modification of collagen in vitro with respect to formation of N^{ε}-carboxymethyllysine. *Int. J. Biol. Macromol.* **2009**, *44*, 51−56.
(28) Gensberger, S.; Glomb, M. A.; Pischetsrieder, M. Analysis of sugar degradation products with α-dicarbonyl structure in carbonated soft drinks by UHPLC-DAD-MS/MS. *J. Agric. Food Chem.* **2013**, *61*, 10238−10245.
(29) Medeiros, P. M.; Simoneit, B. R. Analysis of sugars in environmental samples by gas chromatography-mass spectrometry. *J. Chromatogr., A* **2007**, *1141*, 271−278.
(30) Sevcik, R. S.; Mowery, R. A.; Becker, C.; Chambliss, C. K. Rapid analysis of carbohydrates in aqueous extracts and hydrolysates of biomass using a carbonate-modified anion-exchange column. *J. Chromatogr., A* **2011**, *1218*, 1236−1243.
(31) Fox, A. Chapter 23: A current perspective on analysis of sugar monomers using GC-MS and GC-MS/MS. In *Journal of Chromatography Library*; Ziad El, R., Ed.; Elsevier: Amsterdam, The Netherlands, 2002; Vol. 66, pp 829−843.
(32) Usui, T.; Yanagisawa, S.; Ohguchi, M.; Yoshino, M.; Kawabata, R.; Kishimoto, J.; Arai, Y.; Aida, K.; Watanabe, H.; Hayase, F. Identification and determination of alpha-dicarbonyl compounds formed in the degradation of sugars. *Biosci., Biotechnol., Biochem.* **2007**, *71*, 2465−2472.
(33) Henning, C.; Liehr, K.; Girndt, M.; Ulrich, C.; Glomb, M. A. Extending the spectrum of α-dicarbonyl compounds in vivo. *J. Biol. Chem.* **2014**, *289*, 28676−28688.
(34) Ciucanu, I.; Swallow, K. C.; Căpriţă, R. Micro-solid phase extraction with helical-solid-sorbent in the presence of organic solvent for gas chromatography−mass spectrometry analysis of per-O-methylated mono- and disaccharides. *Anal. Chim. Acta* **2004**, *519*, 93−101.
(35) Gómez-González, S.; Ruiz-Jiménez, J.; Priego-Capote, F.; Luque de Castro, M. a. D. Qualitative and quantitative sugar profiling in olive fruits, leaves, and stems by gas chromatography−tandem mass spectrometry (GC-MS/MS) after ultrasound-assisted leaching. *J. Agric. Food Chem.* **2010**, *58*, 12292−12299.
(36) Wunschel, D. S.; Fox, K. F.; Fox, A.; Nagpal, M. L.; Kim, K.; Stewart, G. C.; Shahgholi, M. Quantitative analysis of neutral and acidic sugars in whole bacterial cell hydrolysates using high-performance anion-exchange liquid chromatography−electrospray ionization tandem mass spectrometry. *J. Chromatogr., A* **1997**, *776*, 205−219.
(37) Qureshi, M. N.; Stecher, G.; Sultana, T.; Abel, G.; Popp, M.; Bonn, G. K. Determination of carbohydrates in medicinal plants − comparison between TLC, mf-MELDI-MS and GC-MS. *Phytochem. Anal.* **2011**, *22*, 296−302.
(38) Grant, G. A.; Frison, S. L.; Yeung, J.; Vasanthan, T.; Sporns, P. Comparison of MALDI-TOF mass spectrometric to enzyme colorimetric quantification of glucose from enzyme-hydrolyzed starch. *J. Agric. Food Chem.* **2003**, *51*, 6137−6144.
(39) Hutschenreuther, A.; Kiontke, A.; Birkenmeier, G.; Birkemeyer, C. Comparison of extraction conditions and normalization approaches for cellular metabolomics of adherent growing cells with GC-MS. *Anal. Methods* **2012**, *4*, 1953−1963.
(40) Poole, C. F. Matrix-induced response enhancement in pesticide residue analysis by gas chromatography. *J. Chromatogr., A* **2007**, *1158*, 241−250.
(41) Wolff, S. P.; Dean, R. T. Aldehydes and dicarbonyls in non-enzymic glycosylation of proteins. *Biochem. J.* **1988**, *249*, 618−619.
(42) Martins, S. I.; Marcelis, A. T.; van Boekel, M. A. Kinetic modelling of Amadori *N*-(1-deoxy-D-fructos-1-yl)-glycine degradation pathways. Part I − reaction mechanism. *Carbohydr. Res.* **2003**, *338*, 1651−1663.
(43) Holub, B. J. Metabolism and function of myo-inositol and inositol phospholipids. *Annu. Rev. Nutr.* **1986**, *6*, 563−597.
(44) Kerler, J.; Winkel, C.; Davidek, T.; Blank, I. Basic chemistry and process conditions for reaction flavours with particular focus on Maillard-type reactions. In *Food Flavour Technology*; Wiley-Blackwell: Chichester, UK, 2010; pp 51−88.
(45) Syrovy, I. Glycation of albumin: reaction with glucose, fructose, galactose, ribose or glyceraldehyde measured using four methods. *J. Biochem. Biophys. Methods* **1994**, *28*, 115−121.

DOI: 10.1021/jf505757m
J. Agric. Food Chem. 2015, 63, 5911−5919

providing a relatively high resolution for plant species discrimination.[17] However, the high level of sequence divergence is at the expense of sites conserved enough to standardize universal primers. In contrast, another widely utilized chloroplastic barcode, *rbcL* (large subunit of the ribulose-1,5-bisphosphate carboxylase/oxygenase gene), enables robust PCR amplification due to a high level of sequence conservation, but provides relatively poor resolution for discriminating plants at low taxonomic levels.[17,18] As a result, no single genomic region has yet been identified as the ultimate barcode, and it is often recommended that barcode regions be used in combination to meet specific research needs.[19,20]

In the present work, two noncoding regions from the chloroplast genome, the *trnL* (UAA) intron and the intergenic spacer between the *trnL* (UAA) 3′ exon and *trnF* (GAA) genes,[21] were used as DNA-barcodes for the discrimination of herbal species. Primers that anneal at conserved flanking coding regions and amplify variable noncoding sequences have long been available for these two barcode regions, and their universality has been shown with successful PCR amplifications from a wide range of taxonomic groups.[21,22,16] The rate of insertions/deletions (indels) in the two noncoding regions is at least as high as that of nucleotide substitutions.[22] The accumulation of indels is reflected by amplified fragment length polymorphisms that enable the discrimination of species based on size separation of the barcode amplicons. Such a discrimination capacity is remarkably useful in food authenticity analyses, because in the presence of multiple species in a food commodity, sequence analyses may fail to produce clean, reliable peaks from a mixture of divergent amplicons.[17] The length polymorphisms in the *trnL* (UAA) intron region of the chloroplast genome have been utilized for botanical origin authentication in food products in several studies. James and Schmidt[23] were successful in developing a simple, PCR-based assay that detects the presence of potential allergen food crops based on *trnL* (UAA) intron length polymorphisms. By taking advantage of the high fragment size resolution feature of capillary electrophoresis systems, Spaniolas et al.[24,25] displayed the potential of the *trnL* (UAA) intron length polymorphisms to identify the botanical origin of plant oils. When high-resolution melting (HRM) analysis was employed as the genotyping strategy, melting curves generated by the *trnL* (UAA) intron amplicons were sufficient to discriminate 11 nut species and detect hazelnut contamination in food products.[9] HRM analysis of the *trnL* (UAA) intron amplicons provided sufficient resolution to discriminate 13 legume species and allowed the detection of soybean (*Glycine max*)−lupine (*Lupinus* spp.) admixtures.[26] In addition, *trnL* (UAA) intron barcode-HRM analysis was successful in authenticating the Protected Designation of Origin (PDO) of legume species *Lathryus cleymenum*.[27] Utilization of a similar approach for species discrimination was also demonstrated in fruit juices.[28] With the present work, we propose a fast and reliable PCR-capillary electrophoresis (PCR-CE) barcode assay that involves the use of two plastid noncoding regions and test its efficiency to authenticate botanical origin on a set of 26 commercial herbal tea products that represent eight species that are common in herbal teas.

MATERIALS AND METHODS

Herbal Tea Samples and Reference Tissue. The herbal tea samples used in this work included 26 commercial herbal tea products in the form of tea bags. The sample set represented seven types of herbal teas commonly found in retail stores, including three single-ingredient products (sage tea, chamomile tea, and linden tea) and four blends of two herbal species (rose hip−hibiscus tea, peppermint−linden tea, peppermint−fennel tea, and anise−fennel tea). Each type of herbal tea was represented by four different commercial products from four different companies, except for peppermint−linden tea, which was represented by products from two companies. Herbal tea samples were purchased from retail stores. Because the aim of this study was to evaluate the performance of the plastid DNA-barcodes and not the herbal tea brands, company names are not provided. Samples of each herbal tea type were randomly assigned numbers (samples 1−4) regardless of the brand names.

Reference tissue samples of sage (*Salvia officinalis* L.), chamomile (*Matricaria chamomilla* L.), linden (*Tilia cordata* Mill.), rose hip (*Rosa canina* L.), hibiscus (*Hibiscus sabdariffa* L.), peppermint (*Mentha piperita* L.), fennel (*Foeniculum vulgare* Mill.), and anise (*Pimpinella anisum* L.) were obtained from Aegean University Botanical Garden and Herbarium Research and Application Center (Izmir, Turkey).

DNA Isolation. All DNA isolations were performed using a NucleoSpin Plant II Kit (Macherey Nagel, Duren, Germany) according to the manufacturer's instructions. For sample preparation, silica-dried tissue samples of reference herbal species were ground using a mortar and pestle, and 100 mg of ground tissue was used to isolate DNA. In-house admixtures of two, three, and four herbal species, prepared by mixing ground tissue from relevant reference samples, were also used for DNA extraction. Four different admixtures of pairs of herbal species (linden:peppermint; sage:anise; rose hip:chamomile; sage:linden) were prepared in two different admixing ratios of 95:5% and 99:1%. Admixtures of three (sage:anise:chamomile and linden:peppermint:chamomile) and four (chamomile:peppermint:anise:linden) herbal species were also prepared by mixing equal weights of ground reference tissue from all participant species. In the case of commercial products, the contents of multiple tea bags from each package were combined prior to sampling 100 mg of dried tissue. All DNA extractions (from reference tissue and commercial samples) were performed in two replicates. The concentration of DNA was measured using a Qubit 2.0 Fluorometer (Life Technologies, Thermo Fisher Scientific Inc., Waltham, MA, USA) with a dsDNA BR Assay Kit (Life Technologies). DNA integrity was checked on a 1.5% agarose gel.

PCR-CE Barcode Analysis. Primers that amplify the plastid *trnL* (UAA) intron (primers c and d) and the intergenic spacer between *trnL* (UAA) 3′ exon and *trnF* (GAA) gene (primers e and f) were introduced by Taberlet et al.[21] Primer sequences from the 5′ to 3′ direction are as follows: primer c, CGAAATCGGTAGACGCTACG; primer d, GGGGATAGAGGGACTTGAAC; primer e, GGTTCAAGTCCCTCTATCCC; and primer f, ATTTGAACTGGTGACACGAG. For simplicity, the two plastid barcodes are here named after the amplification primers as plastid-cd (Pl-cd) and plastid-ef (Pl-ef). Barcode regions were amplified in 20 μL reaction mixtures containing 1× Colorless GoTaq Flexi PCR buffer, 1.5 mM $MgCl_2$, 0.25 mM of each deoxyribonucleotide triphosphate (dNTP) (Promega Corp., Madison, WI, USA), 1 U of GoTaq G2 Flexi DNA Polymerase (Promega Corp.), 0.25 μM of each primer, and 5 ng of template DNA. Thermal cycling conditions consisted of one cycle of initial denaturation for 10 min at 94 °C, followed by 35 cycles of 94 °C for 30 s, 62 °C for 30 s, and 72 °C for 60 s, with a final extension step of 10 min at 72 °C. PCR mixtures with an alternative DNA polymerase [Q5 High-Fidelity DNA Polymerase (New England Biolabs Inc., Ipswich, MA, USA)] were prepared in a volume of 25 μL and contained 1× Q5 Reaction Buffer, 0.2 mM of each deoxyribonucleotide triphosphate (dNTP) (Promega Corp.), 0.5 U of Q5 High-Fidelity DNA Polymerase (New England Biolabs Inc.), 0.50 μM of each primer, and 5 ng of template DNA. Thermal cycling conditions consisted of one cycle of initial denaturation for 30 s at 98 °C, followed by 35 cycles of 98 °C for 10 s, 62 °C for 20 s, and 72 °C for 30 s, with a final extension step of 2 min at 72 °C. Barcode amplicons in the 96-well microtiter plates used for PCR amplification were directly loaded on a Qiaxcel Advanced capillary electrophoresis system (Qiagen, Valencia, CA, USA). No postamplification treatment was

DOI: 10.1021/acs.jafc.5b01255
J. Agric. Food Chem. 2015, 63, 5920−5929

Table 1. Barcode Amplicon Sizes of the Eight Herbal Species Used in This Study

herbal species	barcode Pl-cd [*trnL* (UAA) intron]	barcode Pl-ef (*trnL*−*trnF* intergenic spacer)	GenBank accession no.
Foeniculum vulgare	340 bp and 582 bp	434 bp	KT003613
Hibiscus sabdariffa	573 bp	260 bp and 469 bp	KT003612
Matricaria chamomilla	488 bp	442 bp	KT003608
Mentha piperita	580 bp	368 bp	KT003610
Pimpinella anisum	602 bp	432 bp	KT003611
Rosa canina	614 bp	472 bp	KT003614
Salvia officinalis	558 bp	370 bp	KT003607
Tilia cordata	628 bp	459 bp	KT003609

applied to the samples. The sample loading procedure did not involve a post-PCR labeling step, as the capillary cartridges provided with Qiaxcel DNA High Resolution Kits (Qiagen) are ready-to-use and filled with the staining dye−gel mixture. QX DNA Size Marker 50−800 bp, v2.0 (Qiagen) was used as the size standard, and QX Alignment Marker 15 bp/1000 bp (Qiagen) was used for aligning the size standard fragments. The high-resolution run method OM800 was applied with a sample injection time of 10 s. QIAxcel ScreenGel Software (Qiagen) was used for visualization of the barcode profiles. PCR-CE barcode assays were performed in three replicates for each DNA sample, and capillary electrophoresis runs were performed in two replicates.

Barcode DNA Sequencing. Primers that amplify the two barcodes, Pl-cd and Pl-ef, were used for dye-terminator sequencing. Sequencing targets were amplified in 20 μL reaction mixtures containing 1× Colorless GoTaq Flexi PCR buffer, 1.5 mM $MgCl_2$, 0.25 mM of each deoxyribonucleotide triphosphate (dNTP) (Promega Corp.), 1 U of GoTaq G2 Flexi DNA Polymerase (Promega Corp.), 0.25 μM of each primer, and 5 ng of template DNA. Thermal cycling conditions consisted of one cycle of initial denaturation for 10 min at 94 °C, followed by 35 cycles of 94 °C for 30 s, 62 °C for 30 s, and 72 °C for 45 s, with a final extension step of 10 min at 72 °C. For each reference/herbal tea sample, PCR reactions were performed in five replicates and combined during the purification step with the DNA Clean & Concentrator-5 Kit (Zymo Research, Irvine, CA, USA). Purified PCR products were used as template in dye-terminator sequencing reactions, prepared using GenomeLab DTCS Quick Start Kit (Beckman Coulter, Brea, CA, USA) according to the manufacturer's instructions. Sequencing reaction thermal cycling conditions were 30 cycles of 96 °C for 20 s, 50 °C for 20 s, and 60 °C for 4 min. The reaction mixture for each amplicon was then purified using ZR DNA Sequencing Clean-up Kit (Zymo Research), resuspended in 30 μL of sample loading solution (Beckman Coulter), and run on a Beckman CEQ8800 capillary electrophoresis device using the LFR-b method (injection voltage 2.0 kV for 10−15 s, separation temperature of 57 °C, separation voltage of 6.0 kV, separation time of 60 min). Sequence peaks were visualized with the "Sequencing" module of Beckman CEQ8800 software version 8.0 (Beckman Coulter). Alignment and assembly of sequences from forward and reverse directions and alignment of reference and sample sequences were performed using the "Investigator" module of the CEQ 8800 (Beckman Coulter) software. The MEGA V6.0 computer program[29] was used for cross-species sequence alignments with the ClustalW method. Homology search in GenBank Nucleotide Collection was carried out using "nucleotide blast" as the BLAST program with the "megablast" option optimized for identifying highly similar sequences. BankIt sequence submission tool (http://www.ncbi.nlm.nih.gov/WebSub/?form=history&tool=genbank) was used for sequence submission to the GenBank database.

RESULTS

Identification of Species Origin in Herbal Tea Products Using the PCR-CE Barcode Assays. The two plastid barcodes (barcode Pl-cd and barcode Pl-ef) were amplified using the DNA from the 8 reference samples and 26 commercial herbal tea products. Barcode amplicons were directly loaded on the capillary electrophoresis system without any post-PCR treatment. Because amplicons from the reference samples constituted the standards in the analysis, they were run simultaneously with the amplicons from the commercial tea samples. Sizes of the barcode amplicons are given in Table 1. A single fragment amplification pattern was observed for all of the species except for fennel and hibiscus, which yielded double bands for barcodes Pl-cd and Pl-ef, respectively. All eight herbal species displayed distinctive fragments with no two species yielding fragments of identical size for either of the two barcodes. The amplicon size of barcode Pl-cd ranged between 340 and 614 bp, whereas barcode Pl-ef amplicons ranged between 260 and 472 bp for the eight species. For barcode Pl-cd, the minimum fragment size difference (2 bp) was observed between fennel and peppermint, which produced fragments of 582 and 580 bp, respectively. However, fennel also displayed an additional 340 bp fragment in its barcode Pl-cd profile. For barcode Pl-ef, the minimum fragment size difference was 2 bp and was observed for fennel (434 bp) and anise (432 bp) and also sage (370 bp) and peppermint (368 bp) (Table 1). Similarly, rose hip and hibiscus produced barcode Pl-ef fragments of similar, but not identical, size (472 and 469 bp), with the latter yielding an additional band of 260 bp in its profile.

For the sage reference sample, the fragment sizes of the two barcodes were 558 and 370 bp for barcodes Pl-cd and Pl-ef, respectively (Table 1). Barcode sizes of all four commercial sage tea samples matched those of the standard reference (Figure 1), and no additional, unexpected fragments were observed for any of the samples in any of the replicate experiments. Therefore, we concluded that the botanical origins of the tested commercial sage tea products were true-to-label.

The chamomile reference sample gave Barcode Pl-cd and Pl-ef fragment sizes of 488 and 442 bp, respectively (Table 1). Barcode Pl-cd and Barcode Pl-ef profiles of three commercial chamomile tea samples (Figure 2, panels II−IV) perfectly matched with those of the reference sample, proving their identity as authentic chamomile tea. However, sample 4 (Figure 2, panel V) produced profiles that were inconsistent with the reference for both barcodes. In addition to the single 488 bp band expected for chamomile tea, sample 4 yielded an additional band of 564 bp length for barcode Pl-cd (Figure 2A, panel V). The barcode Pl-ef assay also produced an extra 359 bp band from sample 4, which was not expected for chamomile (Figure 2B, panel V). Similar results were obtained in all three replicate experiments with the two barcodes. Therefore, results of both barcode assays were in agreement and implied that sample 4 was either adulterated or contaminated with a plant species other than chamomile.

For the linden reference sample, the barcode Pl-cd and Pl-ef fragment lengths were 628 and 459 bp, respectively (Table 1).

DOI: 10.1021/acs.jafc.5b01255
J. Agric. Food Chem. 2015, 63, 5920−5929

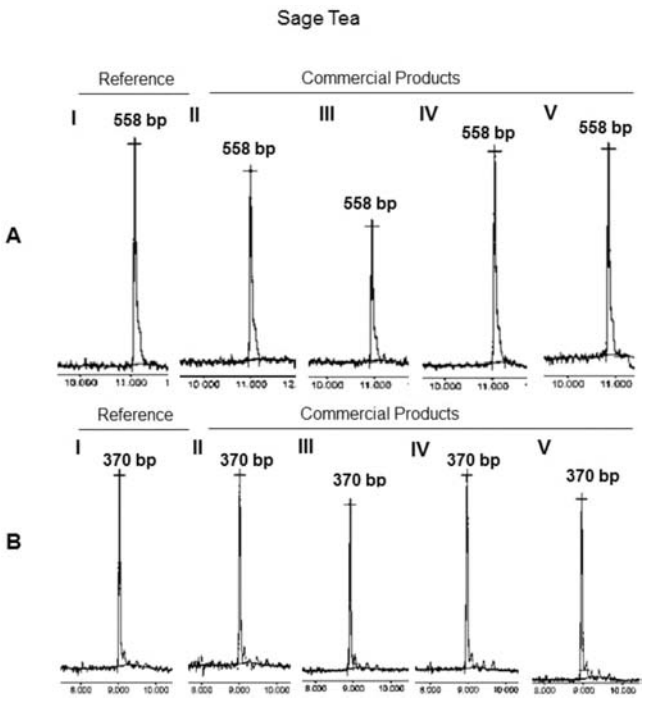

Figure 1. Capillary electropherograms displaying the results of the PCR-CE barcode assays applied on sage tea samples: (A) barcode Pl-cd assay; (B) barcode Pl-ef assay. Sample order is the same for rows A and B: I, sage reference sample; II, sage tea sample 1; III, sage tea sample 2; IV, sage tea sample 3; V, sage tea sample 4.

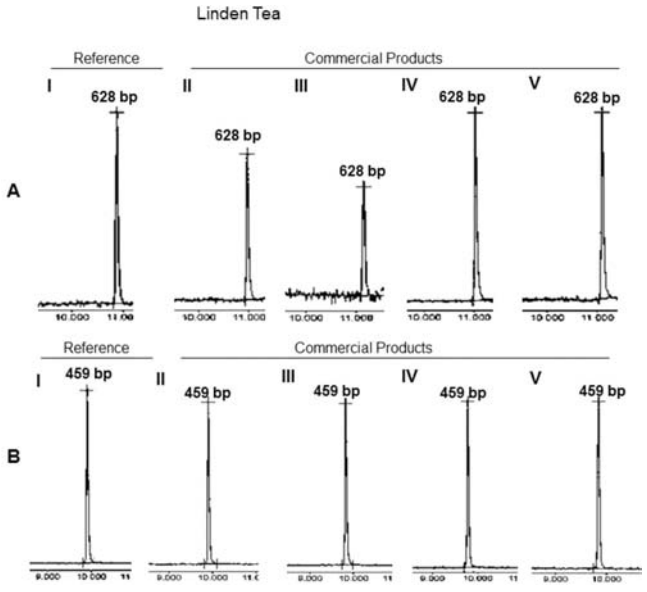

Figure 3. Capillary electropherograms displaying the results of the PCR-CE barcode assays applied on linden tea samples: (A) barcode Pl-cd assay; (B) barcode Pl-ef assay. Sample order is the same for rows A and B: I, linden reference sample; II, linden flower tea sample 1; III, linden flower tea sample 2; IV, linden flower tea sample 3; V, linden flower tea sample 4.

PCR-CE barcode analysis results of the reference and the four commercial linden flower tea samples were in concordance in all three replicate experiments, identifying the commercial samples as authentic linden tea (Figure 3). Peppermint−linden blends were also examined. According to the product labels, the ratio of peppermint in peppermint−linden blends was 20% for sample 1 and 30% in sample 2. The peppermint reference amplicons were 580 and 368 bp for barcodes Pl-cd and Pl-ef, respectively (Table 1). The two peppermint−linden commercial samples were successfully resolved by both barcodes with each barcode electropherogram displaying double bands of

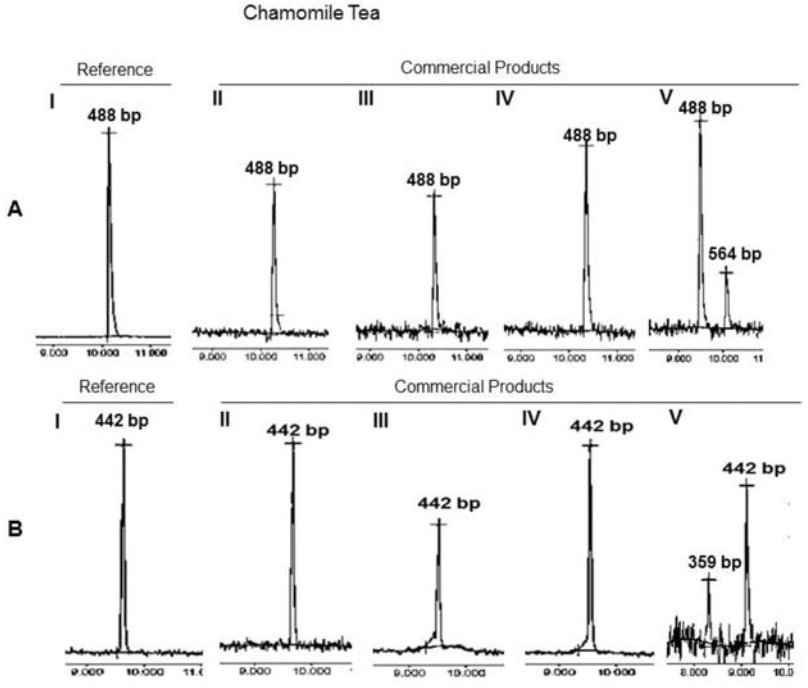

Figure 2. Capillary electropherograms displaying the results of the PCR-CE barcode assays applied on chamomile tea samples: (A) barcode Pl-cd assay; (B) barcode Pl-ef assay. Sample order is the same for rows A and B: I, chamomile reference sample; II, chamomile tea sample 1; III, chamomile tea sample 2; IV, chamomile tea sample 3; V, chamomile tea sample 4.

DOI: 10.1021/acs.jafc.5b01255
J. Agric. Food Chem. 2015, 63, 5920−5929

sizes identical to the references (Figure 4). In addition, no unexpected band other than the two species-specific fragments was observed in any of the replicate experiments with the two barcodes; therefore, the botanical origin of the two commercial products was identified as a blend of peppermint and linden as indicated on the labels.

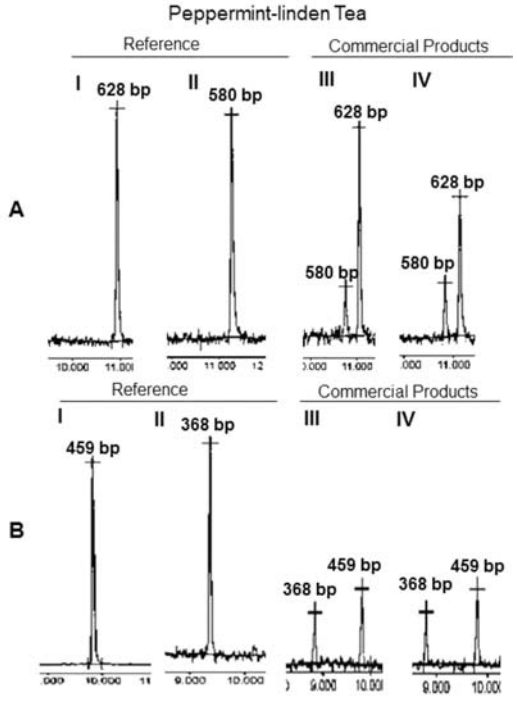

Figure 4. Capillary electropherograms displaying the results of the PCR-CE barcode assays applied on peppermint−linden tea samples: (A) barcode Pl-cd assay; (B) barcode Pl-ef assay. Sample order is the same for rows A and B: I, linden reference sample; II, peppermint reference sample; III, peppermint−linden tea sample 1; IV, peppermint−linden tea sample 2.

All four rose hip tea samples included in this work were blends of rose hip and hibiscus. The ratios of rose hip:hibiscus blends declared on the product labels were 70:30% for samples 1 and 3 and 60:40% for samples 2 and 4. Rose hip and hibiscus reference samples yielded barcode Pl-cd fragments of 614 and 573 bp, respectively (Table 1). Barcode Pl-cd analysis of the four commercial products was successful in clearly identifying both rose hip- and hibiscus-specific fragments (Figure 5A), and no additional band was observed to suspect the presence of undeclared plant material in the samples. The barcode Pl-ef profile of the hibiscus reference had two bands of 260 and 469 bp, whereas the rose hip reference produced a single 472 bp fragment (Table 1). When the commercial products were analyzed, the hibiscus-specific 260 bp fragment was readily identifiable in all four samples. However, the second, larger fragment could not be resolved by the capillary electrophoresis system in any of the replicate experiments because of the size similarity between the rose hip- and hibiscus-specific fragments (472 vs 469 bp) (Figure 5B, ,panels III−VI). As a result, whereas the presence of hibiscus in the samples was apparent by the presence of the 260 bp fragment, the mixture of the 472 and 469 bp fragments was identified as a single band within a size range of 470−472 bp. Nevertheless, barcode Pl-cd alone allowed distinguishing of species-specific amplification profiles when tested on rose hip−hibiscus blends.

Two types of fennel tea blends (anise−fennel tea and peppermint−fennel tea) were included in our analyses. Commercial samples of anise−fennel blends were labeled as either "fennel tea" or "anise−fennel tea" but always included anise in the list of ingredients. The ratio of anise in the blend was declared on the label of one product (sample 2) as 10%,

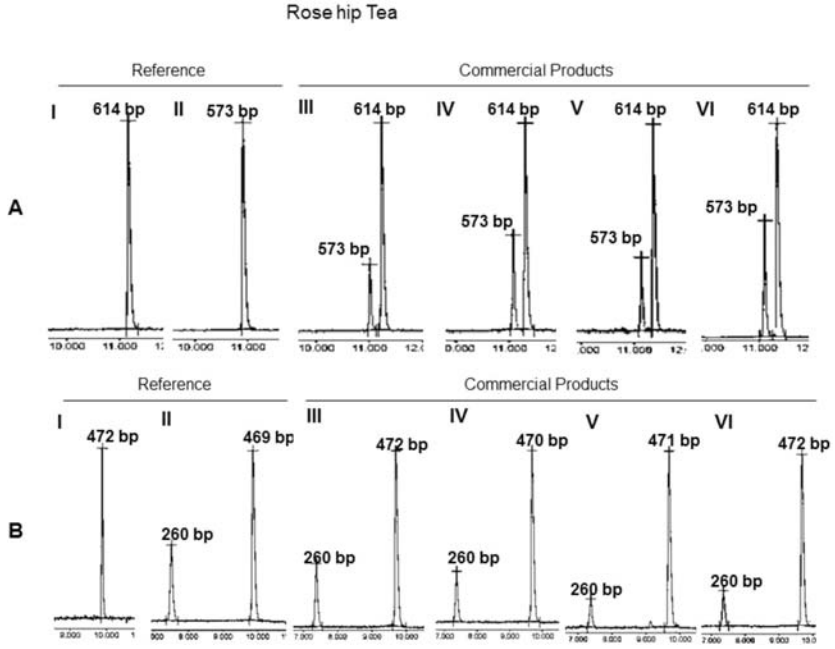

Figure 5. Capillary electropherograms displaying the results of the PCR-CE barcode assays applied on rose hip tea samples: (A) barcode Pl-cd assay; (B) barcode Pl-ef assay. Sample order is the same for rows A and B: I, rose hip reference sample; II, hibiscus reference sample; III, rose hip tea sample 1; IV, rose hip tea sample 2; V, rose hip tea sample 3; VI, rose hip tea sample 4.

DOI: 10.1021/acs.jafc.5b01255
J. Agric. Food Chem. 2015, 63, 5920−5929

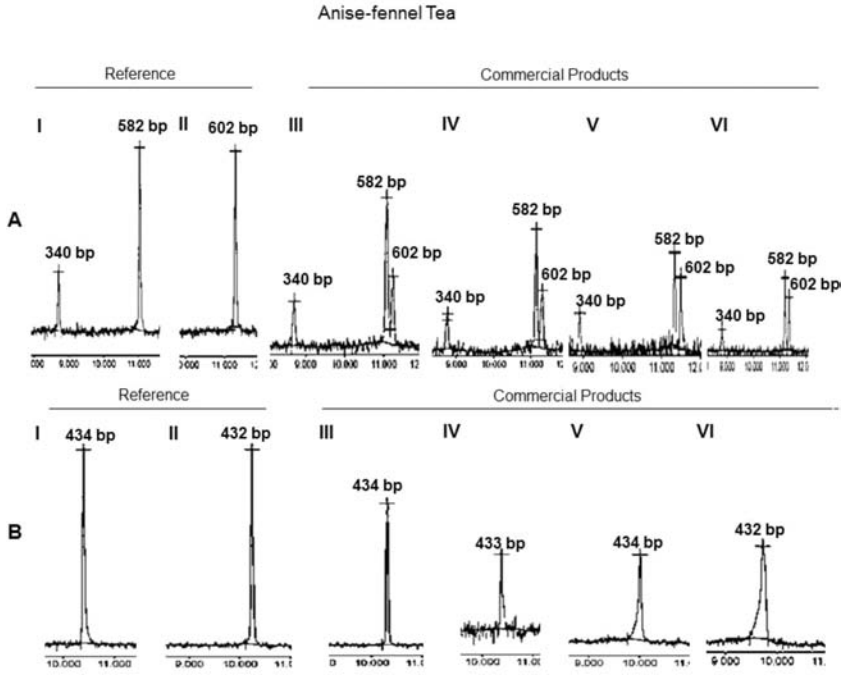

Figure 6. Capillary electropherograms displaying the results of the PCR-CE barcode assays applied on anise−fennel tea samples: (A) barcode Pl-cd assay; (B) barcode Pl-ef assay. Sample order is the same for rows A and B: I, fennel reference sample; II, anise reference sample; III, anise−fennel tea sample 1; IV, anise−fennel tea sample 2; V, anise−fennel tea sample 3; VI, anise−fennel tea sample 4.

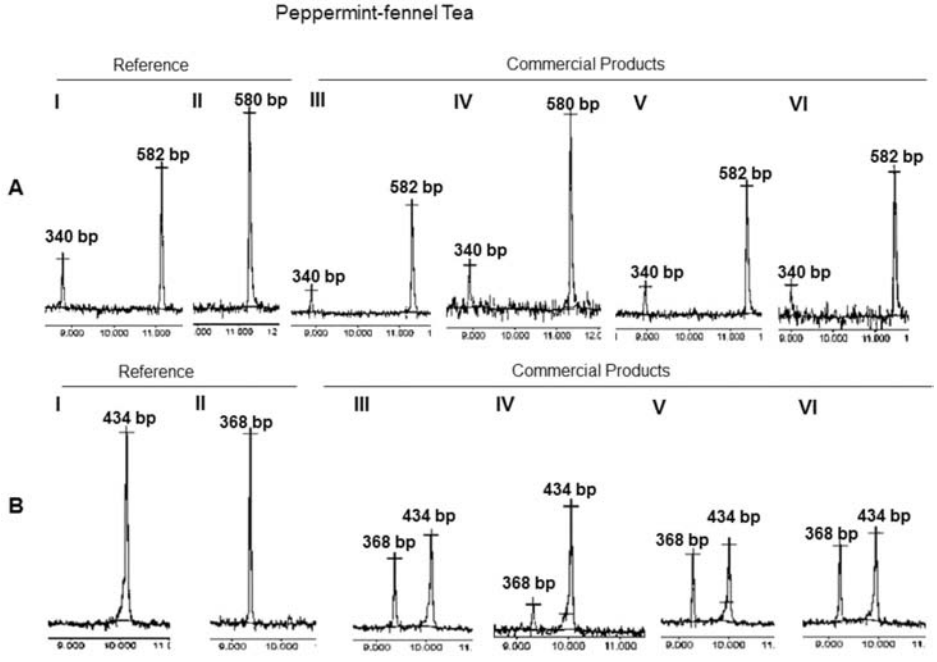

Figure 7. Capillary electropherograms displaying the results of the PCR-CE barcode assays applied on peppermint−fennel tea samples: (A) barcode Pl-cd assay; (B) barcode Pl-ef assay. Sample order is the same for rows A and B: I, fennel reference sample; II, peppermint reference sample; III, peppermint−fennel tea sample 1; IV, peppermint−fennel tea sample 2; V, peppermint−fennel tea sample 3; VI, peppermint−fennel tea sample 4.

but no ratio information was included in the ingredients list for the remaining three samples. The barcode Pl-cd amplification profile of fennel reference sample produced two bands of 340 and 582 bp, and the anise reference yielded a single 602 bp fragment (Table 1). All three fragments representing the two species were resolved by the capillary electrophoresis system, clearly displaying the presence of both species in the samples (Figure 6A). In addition, there were no unexpected amplicons in the profiles of the commercial samples to suspect contamination or adulteration. Fennel and anise references produced barcode Pl-ef amplicons of similar size (434 and 432 bp) (Table 1). Although we were able to reproducibly distinguish the two species from each other when amplicons from individual reference samples were run simultaneously, fennel- and anise-specific barcode Pl-ef fragments could not be resolved when amplified from the tea blends. Such samples had

DOI: 10.1021/acs.jafc.5b01255
J. Agric. Food Chem. 2015, 63, 5920−5929

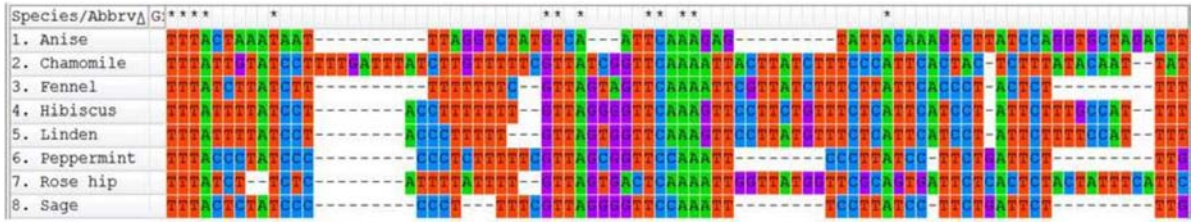

Figure 8. Portion of the alignment of plastid intergenic spacer (*trnL* (UAA) 3′ exon−*trnF* (GAA) gene) nucleotide sequences displaying indels and substitutions among eight herbal species.

single fragments of 432, 433, or 434 bp (Figure 6B, panels III−VI). Hence, barcode Pl-cd analysis was required to correctly identify the fennel−anise tea blends. For peppermint−fennel teas, blend ratio information was supplied on the labels of samples 1 and 2 as 90% fennel:10% peppermint. Barcode Pl-cd and Pl-ef amplicon sizes of the peppermint reference sample were 580 and 368 bp, respectively (Table 1). Because the 582 bp fragment from fennel and 580 bp fragment from peppermint could not be resolved, a two-fragment pattern with the 340 bp fennel-specific band and a larger band of either 580 (Figure 7A, panel IV) or 582 bp (Figure 7A, panels III, V, and VI) was observed for the peppermint−fennel tea samples as a result of barcode Pl-cd analysis. On the other hand, barcode Pl-ef was successful in clearly identifying the species-specific fragments of 434 bp (fennel) and 368 bp (peppermint) (Figure 7B). No unexpected barcode amplicon was observed in any of the replicate experiments to suspect the authenticity of the peppermint−fennel tea samples.

Sequencing Barcode Amplicons from Reference and Commercial Herbal Tea Samples. The two noncoding plastid barcodes used in this work represent single-copy sequences, as they are intended for use in plant phylogenetic inference.[21] Therefore, amplification profiles of both barcodes should have single fragments, and additional bands of lower intensity are regarded as nonspecific. Because the barcode Pl-ef amplification profile of hibiscus involved two fragments, only the larger fragment (469 bp), which was of comparable size with those from the remaining herbal species, was isolated from agarose gel for sequencing. Similarly, Spaniolas et al.[24] reported extra fragments in the *trnL* (UAA) intron amplification profiles of soybean (*Glycine max*) and corn (*Zea mays*), which they regarded as unspecific PCR byproducts. Alignment of barcode Pl-ef sequences from reference samples revealed several insertions/deletions of variable size among the sequences from the eight species, which resulted in the length polymorphisms among the barcode amplicons (Figure 8).

To verify the sequence identity between barcode amplicons from the reference samples and the commercial products, barcode fragments from the commercial tea samples were also sequenced. For the three single-ingredient herbal teas (sage, linden, and chamomile), barcode-Pl-ef sequences from the tea samples perfectly matched those from the references (data not shown). To identify the contaminant/adulterant species in chamomile tea sample 4, the extra fragments that appeared in the barcode Pl-cd (Figure 2A, panel V) and Pl-ef (Figure 2B, panel V) profiles of the sample were isolated from agarose gel and sequenced. Genbank database search identified the highest identity scores for homologous sequences from the *Rosmarinus officinalis* (rosemary) plastid genome for both barcodes. According to the BLAST homology search results, barcode Pl-cd sequence from the contaminant/adulterant species displayed an identity score of 96% with the rosemary sequence deposited under GenBank accession no. AY540465.1. Similarly, a 99% identity score was displayed for the barcode Pl-ef sequence and a rosemary plastid sequence entry (GenBank accession no. FJ490792.1). As a result, we predicted that rosemary was the source of the unexpected barcode fragments in the chamomile tea. Barcode Pl-ef PCR products from the commercial peppermint−fennel and peppermint−linden tea samples were separated by agarose gel electrophoresis to isolate species-specific fragments separately for sequencing. In concordance with the results of the PCR-CE barcode assays, sequences obtained from the commercial samples exactly matched the peppermint, fennel, and linden reference barcode sequences. Because barcode Pl-ef amplicons of rose hip and hibiscus (Figure 5B) and fennel and anise (Figure 6B) could not be resolved due to their size similarity, species-specific fragments of barcode Pl-cd were isolated and sequenced for the rose hip−hibiscus and anise−fennel commercial tea samples. Alignment of the sequence electropherograms showed that barcode sequences from the commercial tea samples were identical with the reference sequences for all four herbal species, thereby validating the results of the PCR-CE barcode analyses.

Determining the Threshold of Admixture Detection. To test the efficiency of the proposed methodology to identify blends of more than two herbal species and set a threshold of admixture detection, barcode Pl-cd assay was applied on in-house blends prepared using reference herbal samples (Figures 9 and 10). To improve the confidence in assessing the performance of the proposed methodology, experiments were carried out using two different types of DNA polymerases. The two admixtures prepared with tissue from three herbal species contained 33% of each species in the blends. The barcode Pl-cd assay was successful in identifying the botanical origin of the two blends as admixtures of sage, anise, and chamomile (Figure

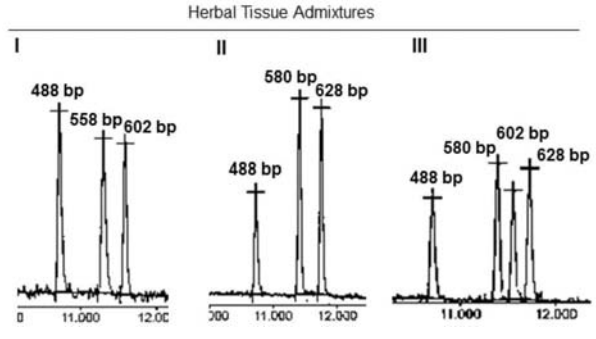

Figure 9. Capillary electropherograms displaying the results of the barcode Pl-cd assay applied on reference tissue admixtures of three and four herbal species. I, chamomile, sage, anise; II, chamomile, peppermint, linden; III, chamomile, peppermint, anise, linden.

DOI: 10.1021/acs.jafc.5b01255
J. Agric. Food Chem. 2015, 63, 5920−5929

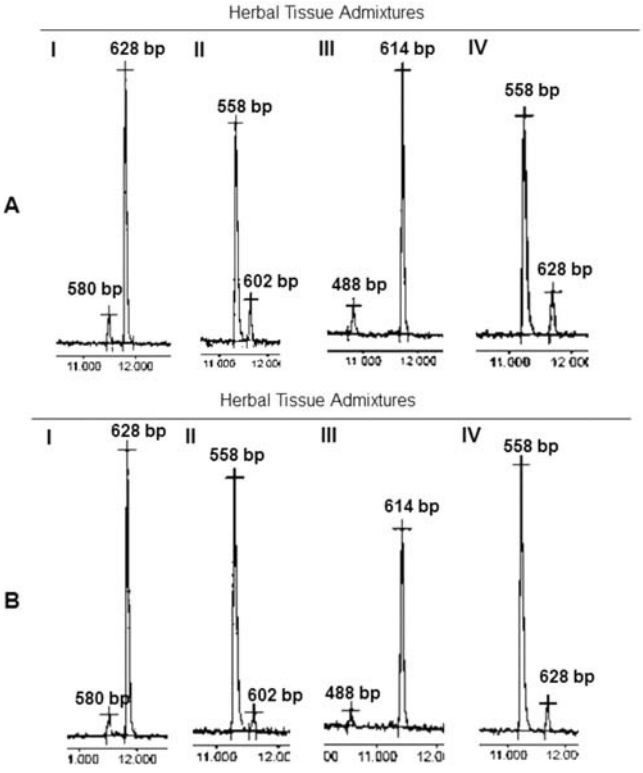

Figure 10. Capillary electropherograms displaying the results of the barcode Pl-cd assay applied on reference tissue admixtures of two herbal species: (A) 95:5% blends; (B) 99:1% blends. (A) I, 95% linden:5% peppermint; II, 95% sage:5% anise; III, 95% rose hip:5% chamomile; IV, 95% sage:5% linden. (B) I, 99% linden:1% peppermint; II, 99% sage:1% anise; III, 99% rose hip:1% chamomile; IV, 99% sage:1% linden.

9, panel I) and linden, peppermint, and chamomile (Figure 9, panel II). The admixture of four herbal species contained 25% of each species in the blend. When the barcode Pl-cd assay was applied on the admixture, barcode fragments of all four species (chamomile, peppermint, anise, and linden) were successfully resolved. Thus, the sample was correctly identified as a blend of four different species (Figure 9, panel III). Linden:peppermint, sage:anise, rose hip:chamomile, and sage:linden admixtures were prepared in two sets that contained the minor constituent at ratios of 5 and 1% in the blends. When the barcode Pl-cd assay was applied on these admixtures, barcode amplicons from the minor constituents (peppermint, anise, chamomile, and linden, respectively) were readily identifiable in all of the samples for both admixing ratios (Figure 10). Parallel experiments with both DNA polymerases (GoTaq G2 Flexi DNA Polymerase, Promega Corp.; and Q5 High-Fidelity DNA Polymerase, New England Biolabs Inc.) produced similar results with similar barcode amplicon peak heights obtained from the minor constituents (data not shown). As a result, the threshold of admixture detection of the proposed methodology was set as 1%.

DISCUSSION

It is almost impossible to identify substitution or contamination in herbal products because morphological features are lost during the processing of herbs into powders or fragmented products.[2] Identification often requires sophisticated analytical chemistry methods or diagnostic molecular approaches. In addition, substitution can easily be masked with food colorants and aromatics, resulting in products with indistinguishable color, taste, and smell. As a result, herbal products constitute an easy target for fraud or mislabeling, as evidenced by recent DNA-based studies that report a high frequency of substitution in herbal teas[1] and supplements.[2,14,15]

In this work, we tested the performance of plastid noncoding DNA length polymorphisms to authenticate the botanical origin of herbal teas. The plastid *trnL* (UAA) intron used in this work (barcode Pl-cd) was reported as a region of significant size variation, when sequences flanked by primers c and d[21] were compared for 706 plant species corresponding to 366 genera and 116 families.[16] Similarly, interspecific length polymorphisms that allowed species discrimination even within the same genus were shown for the plastid intergenic spacer [*trnL* (UAA) 3′ exon−*trnF* (GAA) gene],[21] which was used as the second barcode (barcode Pl-ef) in our study. By taking advantage of the length polymorphisms in the two noncoding barcode regions, we were able to verify the botanical origin and detect the presence of undeclared plant material in the tested herbal tea samples. For our sample set, the lowest ratio of an ingredient (10%) was declared for anise and peppermint in anise−fennel and peppermint−fennel blends. Our results showed that we could clearly detect the presence of a minor ingredient in a commercial sample with the PCR-CE assays (Figures 6A, panel IV, and 7B, panels III and IV). When the barcode Pl-cd assay was applied on herbal tissue admixtures of more than two species, all herbal constituents in the blends were correctly identified. Moreover, herbal ingredients present in minor quantities as low as 1% were readily detected in the tested blends. In addition, two different DNA polymerases were equally efficient in amplifying the barcode fragment from minor constituents to detectable quantities. As a result, the limit of the proposed methodology to identify herbal tissue admixtures was identified as 1%. We attribute this result to our barcode choice. Due to its high copy number in plant cells, the plastid genome is an ideal target for working with mixed samples of multiple species origin or highly processed samples with degraded DNA.[16]

Following a similar PCR-CE approach, Spaniolas et al.[24,25] used *trnL* (UAA) intron length polymorphisms for the authentication of the botanical origin of plant oils. While they were able to obtain barcode fragments of identical size as the references when they applied the PCR-CE assay on DNA from single plant species, amplicons with small size differences could not be resolved by the capillary electrophoresis system when PCR fragments from multiple species were analyzed. We also observed the problem of resolving small fragment size differences of 2−3 bp with barcode Pl-ef (Figure 5) and barcode Pl-cd (Figure 7A), when barcode amplicons from tea blends were analyzed. However, the use of a second barcode solved this problem in all three cases (Figures 5A, 6A, and 7B), resulting in the successful identification of herbal species in the tea blends. Thus, our results highlight the importance of using a combination of barcode regions to achieve sufficient species resolution. The use of barcode combinations is also valid when sample genotyping is based on sequencing. For example, Stoeckle et al.[1] investigated the authenticity of commercial herbal teas based on *rbcL* and *matK* sequences and reported that readable sequences could be obtained from 77 and 79% of the samples when *rbcL* and *matK* regions were sequenced, respectively. However, the success rate for sequencing either of the markers was much higher (90%). In our study, we

DOI: 10.1021/acs.jafc.5b01255
J. Agric. Food Chem. 2015, 63, 5920−5929

established reference barcode fragment length profiles and reference barcode sequences using reference tissue samples of the eight herbal species. We assessed the authenticity of the commercial samples by running reference and sample barcode amplicons simultaneously on the capillary electrophoresis. Thus, we were able to compare the electrophoretic mobility of the barcode amplicons from samples and references with high confidence. In addition, we verified our PCR-CE analysis results by comparing the reference and sample barcode sequences. Because we performed reference sequencing in our study, we did not face the problem of finding barcode sequences from the relevant species in public databases. When a reference sample set is not employed, the success of identifying the botanical origin of a sample depends on the availability of sequence for the species in the databases. For example, Stoeckle et al.[1] reported that barcode sequence records were missing in the GenBank database for about one-third of the herbal species listed on the labels of the tea samples they examined. In addition, it should be noted that, even when a sequence match is identified from a database, there is no certainty that the sequence entry is from a correctly identified plant.[2]

In this work, we used plastid DNA length polymorphisms for the authentication of botanical origin in herbal teas. While species identification based on barcode sequencing works well with single-ingredient samples, sequencing reactions may fail to produce clean, reliable sequences from samples of multiple species due to sequence divergence.[17] In that respect, barcode size variations improve the success rate in sequencing by enabling fragment isolation from a mixture of amplicons. By taking advantage of mitochondrial DNA length polymorphisms, Pun et al.[30] proposed a methodology that involved PCR fragment separation followed by sequencing for the identification of species from mixed samples of unknown identity. Barcode fragment size-based tests are especially suitable for food analyses, because species origin authentication of food products aims at identifying whether a sample is true-to-label or not. Therefore, it is feasible to set standards by analyzing sample barcode fragments with respect to barcode profiles of ingredients listed on the product label. Any deviation from the standards (i.e., reference profiles of the listed ingredients) can be further investigated by taking advantage of barcode length polymorphisms to separate and isolate the alien fragment for sequencing. By following such an approach, we were able to isolate and sequence contaminant/adulterant barcode amplicons from the suspected chamomile tea sample and search public databases for homologous sequence matches. On the basis of our results, we predicted that chamomile tea sample 4 contained rosemary and was mislabeled as a single-ingredient product.

It is important to note that the utility of the PCR-CE barcode assays proposed in this work is not limited to herbal teas but can be extended to authenticate all types of processed herbal products or raw material. When an appropriate genomic region with sufficient interspecific size variation is selected as the analyte, capillary electrophoresis analysis is a faster, more cost-efficient, less equipment and labor/expertise demanding, and relatively simple alternative to sequencing for herbal product authenticity analyses. PCR-CE assays can be standardized for individual products by employing references based on the ingredients list and applied as routine tests for the verification of botanical origin. PCR-CE assays can also be coupled with sequencing any time adulteration is suspected in a sample.

AUTHOR INFORMATION

Corresponding Author

*(S.D.) E-mail: samidoganlar@iyte.edu.tr. Phone: +90 232 750 7313.

Author Contributions

‖A.T.U. and A.O.U. contributed equally to this paper.

Notes

The authors declare no competing financial interest.

ACKNOWLEDGMENTS

We are grateful to Aegean University Botanical Garden and Herbarium Research and Application Center (Izmir, Turkey) for providing reference herbal material.

REFERENCES

(1) Stoeckle, M. Y.; Gamble, C. C.; Kirpekar, R.; Young, G.; Ahmed, S.; Little, D. P. Commercial teas highlight plant DNA barcode identification successes and obstacles. *Sci. Rep.* **2011**, *1*, 42.

(2) Newmaster, S. G.; Grguric, M.; Shanmughanandhan, D.; Ramalingam, S.; Ragupathy, S. DNA barcoding detects contamination and substitution in North American herbal products. *BMC Med.* **2013**, *11*, 222.

(3) Ekor, M. The growing use of herbal medicines: issues relating to adverse reactions and challenges in monitoring safety. *Front. Pharmacol.* **2014**, *4*, 177.

(4) Galimberti, A.; De Mattia, F.; Losa, A.; Bruni, I.; Federici, S.; Casiraghi, M.; Martellos, S.; Labra, M. DNA barcoding as a new tool for food traceability. *Food Res. Int.* **2013**, *50*, 55−63.

(5) Madesis, P.; Ganopoulos, I.; Sakaridis, I.; Argiriou, A.; Tsaftaris, A. Advances of DNA-based methods for tracing the botanical origin of food products. *Food Res. Int.* **2014**, *60*, 163−172.

(6) Lockley, A. K.; Bardsley, R. G. DNA-based methods for food authentication. *Trends Food Sci. Technol.* **2000**, *11*, 67−77.

(7) Pafundo, S.; Gulli, M.; Marmiroli, N. SYBR®GreenERreal-time PCR to detect almond in traces in processed food. *Food Chem.* **2009**, *116*, 811−815.

(8) Costa, J.; Mafra, I.; Oliveira, M. B. P. P. High resolution melting analysis as a new approach to detect almond DNA encoding for Pru du 5 allergen in foods. *Food Chem.* **2012**, *133*, 1062−1069.

(9) Madesis, P.; Ganopoulos, I.; Bosmali, I.; Tsaftaris, A. Barcode high resolution melting analysis for forensic uses in nuts: a case study on allergenic hazelnuts (*Corylus avellana*). *Food Res. Int.* **2013**, *50*, 351−360.

(10) Mayer, F.; Haase, I.; Graubner, A.; Heising, F.; Paschke-Kratzin, A.; Fischer, M. Use of polymorphisms in the γ-gliadin gene of spelt and wheat as a tool for authenticity control. *J. Agric. Food Chem.* **2012**, *60*, 1350−1357.

(11) Sonnante, G.; Montemurro, C.; Morgese, A.; Sabetta, W.; Blanco, A.; Pasqualone, A. DNA microsatellite region for a reliable quantification of soft wheat adulteration in durum wheat-based foodstuffs by real-time PCR. *J. Agric. Food Chem.* **2009**, *57*, 10199−10204.

(12) Marieschi, M.; Torelli, A.; Bruni, R. Quality control of saffron (*Crocus sativus* L.): development of SCAR markers for the detection of plant adulterants used as bulking agents. *J. Agric. Food Chem.* **2012**, *60*, 10998−11004.

(13) Olivieri, C.; Marota, I.; Rollo, F.; Luciani, S. Tracking plant, fungal and bacterial DNA in honey specimens. *J. Forensic Sci.* **2012**, *57*, 222−227.

(14) Baker, D. A.; Stevenson, D. W.; Little, D. P. DNA barcode identification of black cohosh herbal dietary supplements. *J. AOAC Int.* **2012**, *95*, 1023−1034.

(15) Wallace, L. J.; Boilard, S. M. A. L.; Eagle, S. H. C.; Spall, J. L.; Shokralla, S.; Hajibabaei, M. DNA barcodes for everyday life: routine authentication of natural health products. *Food Res. Int.* **2012**, *49*, 446−452.

DOI: 10.1021/acs.jafc.5b01255
J. Agric. Food Chem. 2015, 63, 5920−5929

(16) Taberlet, P.; Coissac, E.; Pompanon, F.; Gielly, L.; Miquel, C.; Valentini, A.; Vermat, T.; Corthier, G.; Brochmann, C.; Willerslev, E. Power and limitations of the chloroplastic trnL (UAA) intron for plant DNA barcoding. *Nucleic Acids Res.* **2007**, *35*, e14.
(17) Hollingsworth, P. M.; Graham, S. W.; Little, D. P. Choosing and using a plant DNA barcode. *PLoS One* **2011**, *6*, No. e19254.
(18) Dong, W.; Liu, J.; Yu, J.; Wang, L.; Zhou, S. Highly variable chloroplast markers for evaluating plant phylogeny at low taxonomic levels and for DNA barcoding. *PLoS One* **2012**, *7*, No. e35071.
(19) Chase, M. W.; Cowan, S.; Hollingsworth, P. M.; van den Berg, C.; Madrinan, S.; Petersen, G.; Seberg, O.; Jorgsensen, T.; Cameron, K. M.; Carine, M.; Niklas, P.; Hedderson, T. A. J.; Conrad, F.; Salazar, G. A.; Richardson, J. E.; Hollingsworth, M. L.; Barraclough, T. G.; Kelly, L.; Wilkinson, M. A proposal for a standardized protocol to barcode all land plants. *Taxon* **2007**, *56*, 295−299.
(20) CBOL Plant Working Group.. A DNA barcode for land plants. *Proc. Natl. Acad. Sci. U.S.A.* **2009**, *106*, 12794−12797.
(21) Taberlet, P.; Gielly, L.; Pautou, G.; Bouvet, J. Universal primers for amplification of three non-coding regions of chloroplast DNA. *Plant Mol. Biol.* **1991**, *17*, 1105−1109.
(22) Gielly, L.; Taberlet, P. The use of chloroplast DNA to resolve plant phylogenies: noncoding versus *rbcL* sequences. *Mol. Biol. Evol.* **1994**, *11*, 769−777.
(23) James, D.; Schmidt, A. M. Use of an intron region of a chloroplast tRNA gene (*trn*L) as a target for PCR identification of specific food crops including sources of potential allergens. *Food Res. Int.* **2004**, *37*, 395−402.
(24) Spaniolas, S.; Bazakos, C.; Awad, M.; Kalaitzis, P. Exploitation of the chloroplast *trn*L (UAA) intron polymorphisms for the authentication of plant oils by means of a Lab-on-a-Chip capillary electrophoresis system. *J. Agric. Food Chem.* **2008**, *56*, 6886−6891.
(25) Spaniolas, S.; Bazakos, C.; Spano, T.; Zoghby, C.; Kalaitzis, P. The potential of plastid *trn*L (UAA) intron polymorphisms for the identification of the botanical origin of plant oils. *Food Chem.* **2010**, *122*, 850−856.
(26) Madesis, P.; Ganopoulos, I.; Argiriou, A.; Tsaftaris, A. The application of Bar-HRM (barcode DNA-high resolution melting) analysis for authenticity testing and quantitative detection of bean crops (Leguminosae) without prior DNA purification. *Food Control* **2012**, *25*, 576−582.
(27) Ganopoulos, I.; Madesis, P.; Darzentas, N.; Argiriou, A.; Tsaftaris, A. Barcode high resolution melting (Bar-HRM) analysis for detection and quantification of PDO "Fava Santorinis" (*Lathyrus clymenum*) adulterants. *Food Chem.* **2013**, *133*, 505−512.
(28) Faria, M. A.; Magalhães, A.; Nunes, M. E.; Oliveira, M. B. P. P. High resolution melting of *trn*L amplicons in fruit juices. *Food Control* **2013**, *33*, 136−141.
(29) Tamura, K.; Stecher, G.; Peterson, D.; Filipski, A.; Kumar, S. MEGA6: Molecular Evolutionary Genetics Analysis version 6. 0. *Mol. Biol. Evol.* **2013**, *30*, 2725−2729.
(30) Pun, K. M.; Albrecht, C.; Castella, V.; Fumagalli, L. Species identification in mammals from mixed biological samples based on mitochondrial DNA control region length polymorphism. *Electrophoresis* **2009**, *30*, 1008−1014.

DOI: 10.1021/acs.jafc.5b01255
J. Agric. Food Chem. 2015, 63, 5920−5929

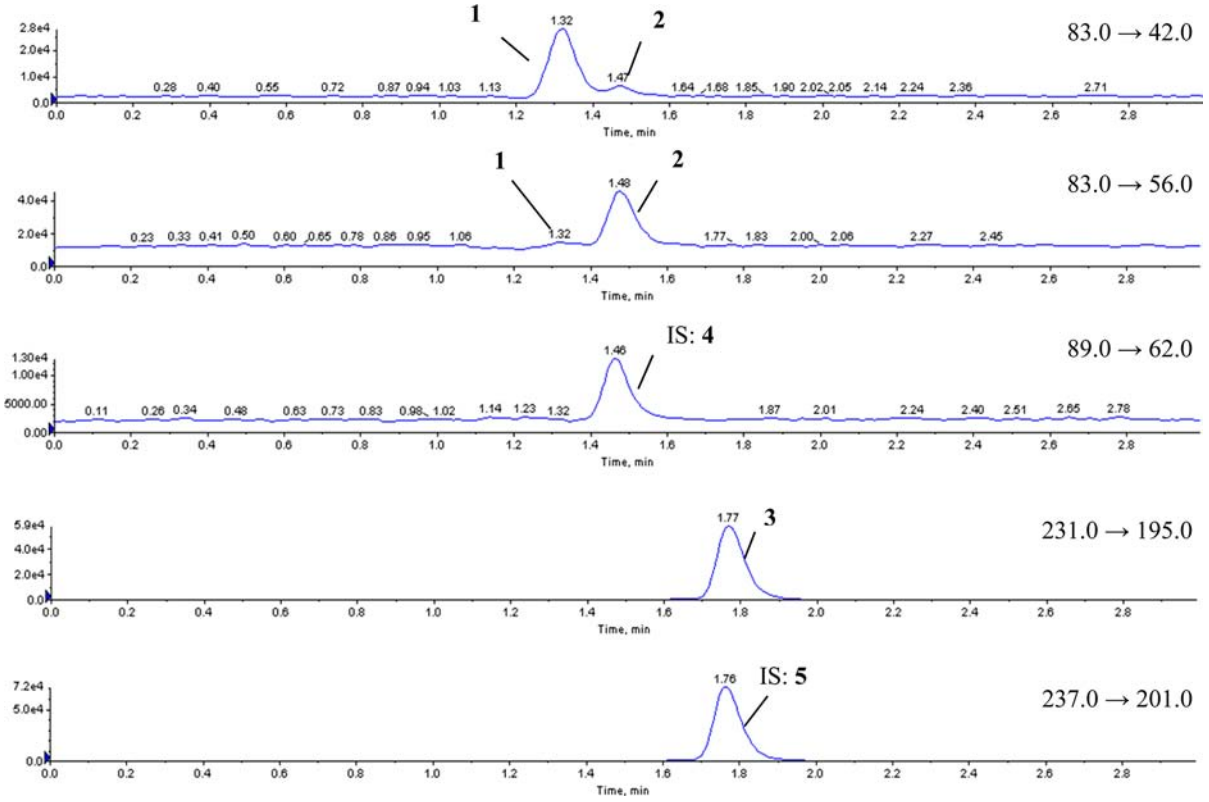

Figure 2. LC-MS/MS mass traces of the calibration standard solution at concentration levels of 0.51 ng/mL for 2-methylimidazole (**1**), 0.50 ng/mL for 4-methylimidazole (**2**), and 0.94 ng/mL for 2-acetyl-4-(1,2,3,4-tetrahydroxybutyl)imidazole (**3**).

ammonium chloride as a source of nitrogen, even though the high temperatures of 120−160 °C applied for the production of caramel food colorings would not be reached. This question was addressed in this study.

Analysis of the considered imidazoles is typically carried out by liquid chromatography−tandem mass spectrometry (LC-MS/MS) as their analysis by gas chromatography usually involves laborious derivatization reactions.[8,9] The available literature describes various methods for the determination of **1**−**3** in different matrices; however, only a few published methods exist for their simultaneous quantitation.[10,11] For example, Wang and Schnute described a UHPLC-MS/MS methodology using 4-methylimidazole-d_3 as an internal standard for their simultaneous determination in beverages using basic eluents under isocratic conditions on a C_{30} separation phase.[10] Schlee et al. published a method for the quantitation of **1**−**3** in caramel food colorings and cola beverages by LC-MS/MS with gradient elution under basic condition on a common C_{18} column without the use of an internal standard.[11]

Here we present an analytical method for the simultaneous and selective determination of the imidazoles **1**−**3** in licorice and other foodstuffs by high-performance liquid chromatography−tandem mass spectrometry applying stable-isotope dilution analysis (SIDA).[12,13] Chromatographic separation was achieved on a common C_{18} reversed-phase column within 3 min. Detection was carried out with the MS/MS system operating in multiple reaction monitoring (MRM) mode.

MATERIALS AND METHODS

Chemicals and Reagents. **1** and **2** were obtained from Sigma-Aldrich (Taufkirchen, Germany), **3** and [$^{13}C_6$]-2-acetyl-4-(1,2,3,4-tetrahydroxybutyl)imidazole (**5**, see Figure 1) were from ELFI Analytik GbR (Neufahrn, Germany), and 4-methylimidazole-d_6 (**4**, see Figure 1) was from Dr. Ehrenstorfer (Augsburg, Germany). HPLC grade methanol was purchased from Bernd Kraft (Duisburg, Germany), whereas formic acid, ammonia, potassium hexacyanoferrate(II) trihydrate, and zinc sulfate heptahydrate of analytical grade were from Merck (Darmstadt, Germany). Licorice samples (ammonium chloride content ≤2%) were purchased in local retail stores. Licorice products for the model assay were provided by the testing facility of a major German licorice manufacturer.

Stock Solutions. Stock solutions of **1**, **2**, and **4** were prepared by dissolving a suitable amount of the respective chemical in a mixture of methanol and purified water (MeOH/H_2O, 50:50 v/v) to obtain a concentration of 1 mg/mL. Stock solutions of **3** and **5** were prepared by dissolving a suitable amount of the respective substance in 0.1 M hydrochloric acid. Calibration levels of all analytes and internal standards were prepared by dilution of the respective stock solution with MeOH/H_2O (50:50 v/v) to obtain a respective concentration of 5 μg/mL. A calibration standard solution was prepared by mixing the standard solutions of **1**−**5** in MeOH/H_2O (50:50 v/v) and contained 5 ng/mL of **1**, **2**, and **4** as well as 10 ng/mL of **3** and **5**. This solution was further diluted with purified water (1:10). Internal standard solutions of **4** and **5** were prepared by appropriate dilution of the stock solutions with MeOH/H_2O (50:50 v/v) to a final concentration of 100 μg/mL.

Sample Preparation. All samples were finely ground and stored at room temperature prior to analysis. For equilibration, each sample (4 g) was placed in a 100 mL iodine determination flask, spiked with **4** (5 ng/mL, 200 μL) and **5** (10 ng/mL, 150 μL), and incubated at room temperature for 30 min. For extraction of the imidazoles methanol/water (50:50 v/v, 50 mL) was added, and the mixture was stirred for 30 min, followed by another volume of methanol/water (50:50 v/v, 50 mL) and subsequent sonication for 15 min at room temperature. Removal of proteins was achieved following the procedure of Carrez (150 g potassium hexacyanoferrate(II) trihydrate/L, 300 g zinc sulfate heptahydrate/L; 500 μL each). Finally, after filtration through a folded filter (Whatman, Germany), the obtained filtrates were diluted (for

DOI: 10.1021/acs.jafc.5b01493
J. Agric. Food Chem. 2015, 63, 5930−5934

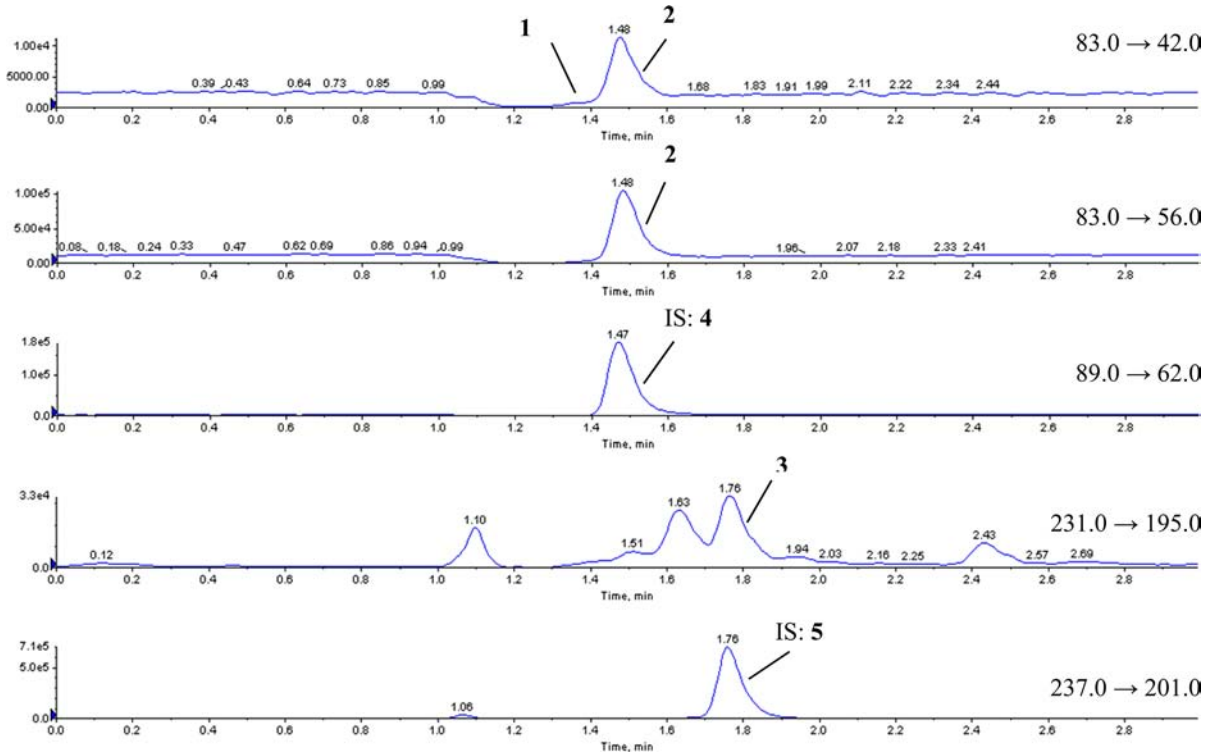

Figure 3. Example chromatogram of a licorice sample: 2-methylimidazole (**1**) ≤ LOD, 4-methylimidazole (**2**) = 1.09 mg/kg, and 2-acetyl-4-(1,2,3,4-tetrahydroxybutyl)imidazole (**3**) = 0.12 mg/kg.

analysis of **2** and **3**, with purified water 1:10; for analysis of **1**, with MeOH/H_2O 50:50 v/v 1:200) into HPLC vials.

LC-MS/MS Conditions. The LC-MS/MS system consisted of a 1260 Infinity HPLC from Agilent (Waldbronn, Germany) coupled to a TripleQuad 4500 tandem mass spectrometer from ABSCIEX (Darmstadt, Germany) through an electrospray ionization (ESI) interface in positive ionization mode (spray voltage, 3.0 kV; vaporizer temperature, 450 °C; curtain gas, 25 psi of N_2; collision energy, 25 V; Turbo V, ABSCIEX). Chromatographic separation was achieved on a Poroshell 120 EC-C_{18} (4.6 × 50 mm, 2.7 μm particle size, Agilent) under isocratic conditions (A/B, 50:50 v/v); A, 0.1% formic acid/methanol (99.5:0.5 v/v); B, 0.05% ammonia solution/methanol (90:10 v/v). The injection volume was 20 μL, and the flow rate was set to 0.45 mL/min. The following MRM transitions were used for analyte detection: **1**, m/z 83.0 → 42.0 (target), m/z 83.0 → 56.0 (qualifier); **2**, m/z 83.0 → 56.0 (target), m/z 83.0 → 42.0 (qualifier); **4**, m/z 89.0 → 62.0 (target), m/z 89.0 → 48.0 (qualifier); **3**, m/z 231.0 → 195.0 (target), m/z 231.0 → 153.0 (qualifier); **5**, m/z 237.0 → 201.0 (target), m/z 237.0 → 159.0 (qualifier).

Method Validation. Linearity was assessed by spiking a blank sample (licorice-free candy) at 10 different levels (0.005, 0.01, 0.025, 0.05, 0.10, 0.50, 1.00, 1.50, 2.50, and 5.00 mg/kg of **1**−**3**). LODs and LOQs of **1**−**3** were derived according to DIN 32645 by 10-fold analysis of a blank sample (direct method according to 5.3 of DIN 32645).[15] Total recovery was evaluated by spiking a blank sample to a final content of 1 mg/kg **1**−**3** followed by 6-fold analysis.[12,13] For the determination of intraday accuracy and interday precision, a licorice sample obtained from a local retail store was used.

RESULTS AND DISCUSSION

Method Development. One objective of this study was to develop and validate a method for the sensitive and simultaneous quantitation of the imidazoles **1**−**3**. Quantitative determination was carried out using commercially available **4** and **5** as internal standards (Figure 1). To achieve baseline separation of the **1** and **2** regioisomers, various parameters such as eluent composition, flow rate, temperature, and column material were evaluated. Separation of the analytes was tested on a C_{18} (Poroshell 120 EC-C18, Agilent) or a C_{30} (Acclaim C30, Thermo Scientific, Dreieich, Germany) reversed-phase column as well as on a porous graphitic carbon phase (Hypercarb, Thermo Scientific) while using a two-component eluent composed of A (0.05% aqueous ammonia solution, 100%, 0−2 min) and B (methanol, 100%, 2−3 min) at a flow of 0.45 mL/min. In addition, an isocratic eluent made from acidic and alkaline components (0.1% formic acid/methanol 99.5:0.5 v/v; 0.05% ammonia solution/methanol, 90:10 v/v) was evaluated, which, when used in combination with the Poroshell 120 EC-C18 column, provided an excellent baseline separation of **1**−**3** (Figure 2). Hence, the Poroshell 120 EC-C18 column and an eluent composed of acidic and basic components were used for further method development.

When complex licorice matrices were analyzed, ion suppression was observed for **1** when compared to the aqueous samples used for chromatography development. To remove the interfering matrix components a common Carrez clarification was introduced, and several dilution steps (1:10, 1:100, 1:200 v/v) of the sample solution injected into the LC-MS/MS system were evaluated to eliminate any remaining matrix effects. A recovery for **1** of 86% with acceptable sensitivity was finally achieved at a dilution of 1:200.

Although baseline-separated, the **1** and **2** regioisomers can also be distinguished from differences in their fragmentation behavior. Whereas **1** shows higher relative intensities at mass transition m/z 83 → 42, **2** shows higher intensity at mass transition m/z 83 → 56 (Figure 2). Figure 3 shows a typical chromatogram of a licorice sample recorded using the optimized LC-MS/MS conditions described above.

Method Validation. Following the guidelines laid out by Kromidas,[14] method validation included the following

DOI: 10.1021/acs.jafc.5b01493
J. Agric. Food Chem. 2015, 63, 5930−5934

Table 1. Method Validation Data

	2-methylimidazole	4-methylimidazole	2-acetyl-4-(1,2,3,4-tetrahydroxybutyl)imidazole
calibration range (mg/kg)	0.05−5.00 ($r^2 \geq 0.999$)	0.02−5.00 ($r^2 \geq 0.999$)	0.01−5.00 ($r^2 \geq 0.999$)
recovery (%)	86.1	99.4	99.5
limit of detection (LOD, mg/kg)	0.05	0.02	0.01
limit of quantitation (LOQ, mg/kg)	0.16	0.07	0.03
intraday accuracy (n = 12, %)		2.2	5.5
interday precision (n = 12, %)		9.3	10.2

parameters: intraday accuracy, interday precision, recovery, linearity, limit of detection (LOD), and limit of quantitation (LOQ). Validation data are summarized in Table 1.

Limits of detection and quantitation were estimated according to DIN 32645 and were 0.05 mg/kg for **1**, 0.02 mg/kg for **2**, and 0.01 mg/kg for **3** (LOD) as well as 0.03−0.16 mg/kg for all analytes (LOQ).[15] Linearity was evaluated by plotting the concentration of each analyte against the respective analyte/internal standard ratio (**2** was calibrated using **4** as the internal standard). Linearity in the range of LOD−5 mg/kg of licorice was shown for all 3 analytes by a coefficient of determination of ≥0.999. Intraday accuracies and interday precisions were calculated from 12 separate measurements and showed standard deviations ≤10.2% (Table 1). The developed methodology provided efficient recovery rates, which are in accordance with available literature data: **1**, 86%; **2**, 99%; **3**, 100%.[10,11]

Endogenous Formation. To check for endogenous formation of the imidazoles **1**−**3** in licorice in the presence of ammonium chloride, a model assay was conducted examining several coloring-free licorice products (n = 20; five levels of ammonium chloride in duplicate: 1, 2, 4, 6, and 8%). Depending on their manufacture, samples were further grouped into in-house types A, B, and C, where ammonium chloride had been added to the cooking mass either before (type A) or after (type B) the cooking process, whereas type C (here not under consideration) was simply dredged in solid ammonium chloride (see also Supporting Information, Figure S1). All model assays were conducted under typical industrial conditions at a testing facility of a major German licorice manufacturer, and samples were analyzed in our laboratory.

The results show a linear correlation (r^2 = 0.937) between the levels of endogenously formed **2** and the amount of added and concomitantly heated ammonium chloride when the ammonium chloride was added to the cooking mass before the cooking process (type A). The determined absolute levels of **2** (relative to the dry mass) were in the range from 0.02 (LOD) to 1.5 mg/kg. In type B licorice products, where ammonium chloride is added after the cooking process, most of the samples showed levels of **2** below the LOQ of 0.07 mg/kg. Only those products with 8% ammonium chloride showed levels at 0.09 mg/kg, just above the LOQ.

Endogenous formation of **3** in type A licorice products again depends on the amount of added and concomitantly heated ammonium chloride. A linear correlation between the endogenously generated amounts of **3** and the added ammonium chloride was derived with a coefficient of determination of r^2 = 0.909. The determined levels of **3** (relative to the dry mass) were in the range from 0.01 (LOD) to 0.17 mg/kg. In the case of type B licorice products all samples showed levels below an LOQ of 0.03 mg/kg.

Monitoring. Monitoring assays were subsequently carried out to examine the endogenous formation of **1**−**3** in 29 coloring-free licorice products. **1** was not observed in any of the samples, whereas levels of **2** and **3** were in the range of LOD−1.30 mg/kg (median, ≤LOQ) and LOD−0.10 mg/kg (median, ≤LOQ), respectively.

Maximum limits for **2** and **3** have not been defined for end products but are available for the caramel food colorings ammonia caramel E150c and sulfite ammonia caramel E150d (E150c, 200 mg/kg **2**, 10 mg/kg **3**; E150d, 250 mg/kg **2**).[5] Assuming that an amount of caramel food colorings of up to 2% is usually added to certain licorice products, the resultant carry-over produces a still acceptable content level for **2** of 4 mg/kg and a content level of 0.2 mg/kg for **3**. However, the determined levels of **2** and **3** formed in commercial licorice products by the addition of ammonium chloride were well below these theoretically derived maximum levels. The licorice products reviewed in this study can thus be judged safe with respect to a possible contamination by any of the imidazoles **1**−**3**.

■ ASSOCIATED CONTENT

Ⓢ Supporting Information

Schematic overview of the manufacture of type A, B, and C licorice products. The Supporting Information is available free of charge on the ACS Publications website at DOI: 10.1021/acs.jafc.5b01493.

■ AUTHOR INFORMATION

Corresponding Author

*(M.R.) Phone: +49-221-623061. Fax: +49-221-610477. E-mail: marion.raters@lci-koeln.de.

Notes

The authors declare no competing financial interest.

■ REFERENCES

(1) Moon, J. K.; Shibamoto, T. Formation of carcinogenic 4(5)-methylimidazole in Maillard reaction systems. *J. Agric. Food Chem.* **2011**, *59*, 615−618.

(2) IARC Working Group on the Evaluation of Carcinogenic Risks to Humans. IARC Monographs on the Evaluation of Carcinogenic Risks to Humans 101 (14), 2012; http://monographs.iarc.fr/ENG/Monographs/vol101/mono101-014.pdf (accessed Jan 20, 2015).

(3) IARC Working Group on the Evaluation of Carcinogenic Risks to Humans. IARC Monographs on the Evaluation of Carcinogenic Risks to Humans 101 (15), 2012; http://monographs.iarc.fr/ENG/Monographs/vol101/mono101-015.pdf (accessed Jan 20, 2015).

(4) Houben, G. F.; van Dokkum, W.; van Loveren, H.; Penninks, A. H.; Seinen, W.; Spanhaak, S.; Ockhuizen, T. Effects of Caramel Colour III on the number of blood lymphocytes: a human study on Caramel Colour III immunotoxicity and a comparison of the results with data from rat studies. *Food Chem. Toxicol.* **1992**, *30*, 427−430.

DOI: 10.1021/acs.jafc.5b01493
J. Agric. Food Chem. 2015, 63, 5930−5934

(5) Commission Regulation (EU) No. 231/2012 of 9 March 2012 laying down specifications for food additives listed in Annexes II and III to Regulation (EC) No. 1333/2008 of the European Parliament and of the Council Text with EEA relevance. *Off. J. Eur. Communities: Legis.* **2012**, *L83*, 1−295.
(6) Commission Directive 2008/128/EC laying down specific purity criteria concerning colours for use in foodstuffs. *Off. J. Eur. Communities: Legis.* **2008**, *L6*, 20−63.
(7) Commission Implementing Regulation (EU) No. 872/2012 of 1 October 2012 adopting the list of flavouring substances provided for by Regulation (EC) No. 2232/96 of the European Parliament and of the Council, introducing it in Annex I to Regulation (EC) No. 1334/2008 of the European Parliament and of the Council and repealing Commission Regulation (EC) No. 1565/2000 and Commission Decision 1999/217/EC. *Off. J. Eur. Communities: Legis.* **2012**, *L267*, 1−161.
(8) Fernandes, J. O.; Ferreira, M. A. Gas chromatographic-mass spectrometric determination of 4-(5) methylimidazole in ammonia caramel colour using ion-pair extraction and derivatization with isobutylchloroformate. *J. Chromatogr. A* **1997**, *786*, 299−308.
(9) Casal, S.; Fernandes, J. O.; Oliveira, M. B. P. P.; Ferreira, M. A. Gas chromatographic−mass spectrometric quantification of 4-(5-)methylimidazole in roasted coffee after ion-pair extraction. *J. Chromatogr. A* **2002**, *976*, 285−291.
(10) Wang, J.; Schnute, W. C. Simultaneous quantitation of 2-acetyl-4-tetrahydroxybutyl-imidazole, 2- and 4-methylimidazoles, and 5-hydroxymethylfurfural in beverages by ultrahigh-performance liquid chromatography−tandem mass spectrometry. *J. Agric. Food Chem.* **2012**, *60*, 917−921.
(11) Schlee, C.; Markova, M.; Schrank, J.; Laplagne, F.; Schneider, R.; Lachenmeier, D. W. Determination of 2-methylimidazole, 4-methylimidazole and 2-acetyl-4-(1,2,3,4-tetrahydroxy-butyl)imidazole in caramel colours and cola using LC/MS/MS. *J. Chromatogr. B: Anal. Technol. Biomed. Life Sci.* **2012**, *927*, 223−226.
(12) Dingel, A.; Goetze, S.; Raters, M.; Elsinghorst, P.; Matissek, R. Quantifizierung der Imidazole 4-MEI und THI in Zuckerkulör und anderen Lebensmitteln mittels SIVA-LC-MS/MS. *Lebensmittelchemie* **2013**, *67*, 166.
(13) Elsinghorst, P. W.; Raters, M.; Dingel, A.; Fischer, J.; Matissek, R. Synthesis and Application of ^{13}C-labeled 2-acetyl-4-((1*R*,2*S*,3*R*)-1,2,3,4-tetrahydroxybutyl)-imidazole (THI), an immunosuppressant observed in caramel food colorings. *J. Agric. Food Chem.* **2013**, *61*, 7494−7499.
(14) Kromidas, S. *Handbuch Validierung in der Analytik*; Wiley-VCH: Weinheim, Germany, 2000.
(15) DIN 32645:2008-11. *Chemical Analysis − Decision Limit, Detection Limit and Determination Limit under Repeatability Conditions − Terms, Methods, Evaluation*; Beuth Verlag GmbH: Berlin, Germany, 2008.

DOI: 10.1021/acs.jafc.5b01493
J. Agric. Food Chem. 2015, 63, 5930−5934

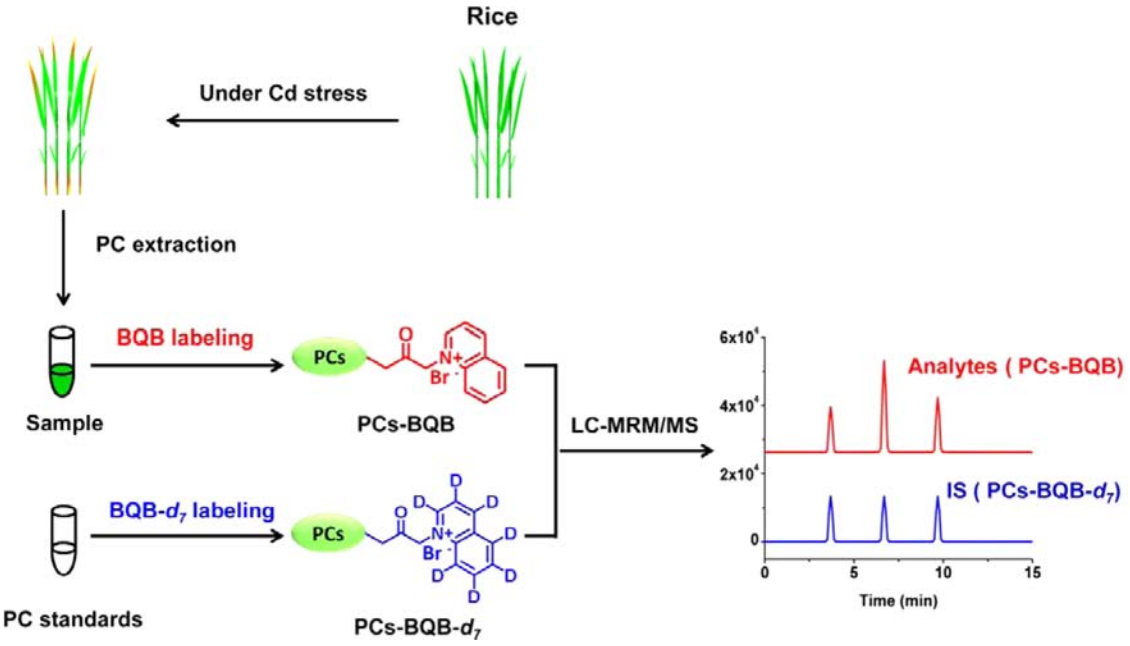

Figure 1. Schematic diagram of the principle of stable isotope labeling coupled with LC/MS analysis for PC determination.

analysis for the determination of phytohormones and carboxyl- and thiol-containing metabolites in plant and human urine samples.[20,24,25]

In this work, we developed a novel strategy by combing stable isotope labeling with LC/MS analysis to improve the identification and quantitation of PCs in rice samples. The schematic diagram of the principle of this method was shown in Figure 1. A pair of isotope-labeling reagents of ω-bromoacetonylquinolinium bromide (BQB) and BQB-d^7 were used to label the analytes in sample and PC standards, respectively, and then combined before LC/MS analysis. In this respect, the heavy labeled standards were used as the ISs for quantitation to minimize the matrix and ion suppression effect in MS analysis. In addition, the ionization efficiency of PCs was also greatly enhanced through the introduction of a permanently charged moiety of quaternary ammonium of BQB into the analytes. The established method was successfully applied to the sensitive quantitation of endogenous PCs in rice under Cd stress with different Cd concentrations and treatment time.

MATERIALS AND METHODS

Chemicals and Reagents. PCs (PC_2, PC_3, PC_4, PC_5, and PC_6) were purchased from Anaspec (Fremont, CA). Glycine and tris(2-carboxyethyl)phosphine hydrochloride salt (TCEP) were purchased from Sigma (St. Louis, MO). Formic acid and ethylenediaminetetraacetic acid (EDTA) were purchased from Sinopharm Chemical Reagent Co., Ltd. (Shanghai, China). Chromatographic-grade acetonitrile (ACN) was purchased from TEDIA Co., Inc. (Fairfield, OH). All other solvents and chemicals used were of analytical grade. The water used throughout the study was purified by a Milli-Q apparatus (Millipore, Bedford, MA). Stock standard solutions of PCs were prepared in 1.0 mM EDTA solution containing 0.05% formic acid at a concentration of 1.0 mM.

Rice Culture and Treatments. Rice seedings (*Oryza sativa* L. cv. Zhenghan No. 2) were germinated and grown by hydroponic culture in Hoagland's nutrient solution in a growth chamber with 70−80% relative humidity under a 16 h light (28 °C)/8 h dark (25 °C) photoperiod according to a previously described method, with some modifications.[26] Hoagland's nutrient solution contains 1.425 mM NH_4NO_3, 0.323 mM NaH_2PO_4, 0.513 mM K_2SO_4, 0.998 mM $CaCl_2$, 1.643 mM $MgSO_4$, 0.008 mM $MnCl_2$, 0.062 μM $(NH_4)_6Mo_7O_{24}$, 0.015 mM H_3BO_3, 0.122 μM $ZnSO_4$, 0.124 μM $CuSO_4$, 0.038 mM $FeCl_2$, and 0.062 mM citric acid. After 10 days of growing, the seedings with uniform size were subjected to Cd stress with different concentrations of $CdNO_3$ (0, 10, 100, 500, and 1000 μM). Rice seedings were harvested after Cd stress for 3 h, 3 days, and 7 days, then weighted, immediately frozen in liquid nitrogen, and stored at −80 °C.

Sample Preparation. Sample extraction was carried out according to a previously described method, with slight modifications.[7] Plant tissues (leafs and stems) were frozen in liquid nitrogen and ground into fine powder with a mortar and pestle. Then, 5 mg of plant powder was transferred into a 0.6 mL centrifuge tube and extracted with 50 μL of 0.1 M cold HCl (4 °C) containing 1 mM EDTA for 30 min. The exacted sample was centrifuged at 12 000 rpm for 30 min under 4 °C. Then, 30 μL of supernatant was added with 1 M NaOH (2 μL) to adjust the pH to 2 and then treated with 10 nmol of TCEP (10 mM, 1 μL) under 45 °C for 60 min.

Chemical Labeling. The chemical-labeling procedure was performed according to our previous work.[27] Briefly, 20 nmol of BQB (1 mM, 20 μL) was added to a 1.5 mL tube and dried under nitrogen gas. Subsequently, 90 μL of glycine−HCl buffer solution (5.0 mmol/L, pH 3.5) and 10 μL of treated plant extracts were added. The mixture was incubated at 60 °C for 60 min with shaking at 1500 rpm. The BQB-d_7-labeled PCs were added to serve as ISs for the quantitation. Then, 20 μL of samples were subjected to LC/MS analysis.

Liquid Chromatography−Electrospray Ionization−Tandem Mass Spectrometry (LC−ESI−MS/MS) Analysis. Analysis of samples was performed on the LC−ESI−MS/MS system consisting of an AB 3200 QTRAP mass spectrometer (Applied Biosystems, Foster City, CA) with an electrospray ionization source (Turbo Ionspray) and Shimadzu LC-20AD high-performance liquid chromatography (HPLC) (Tokyo, Japan) with two LC-20AD pumps, a SIL-20A auto sampler, a CTO-20AC thermostated column compartment, and a DGU-20A3 degasser. Data acquisition and processing were performed using AB SCIEX Analyst 1.5 software (Applied Biosystems, Foster City, CA). The HPLC separation was performed on a Shimadzu VP-ODS column (150 × 2.0 mm inner diameter, 5 μm, Tokyo, Japan) with a flow rate of 0.2 mL/min at 30 °C. Formic acid in water (0.1%, v/v, solvent A) and acetonitrile (solvent B) were employed as mobile phases. A gradient of 0−20 min from 5 to 40% B,

DOI: 10.1021/acs.jafc.5b01797
J. Agric. Food Chem. 2015, 63, 5935−5942

Figure 2. Chemical-labeling reaction for PCs using BQB.

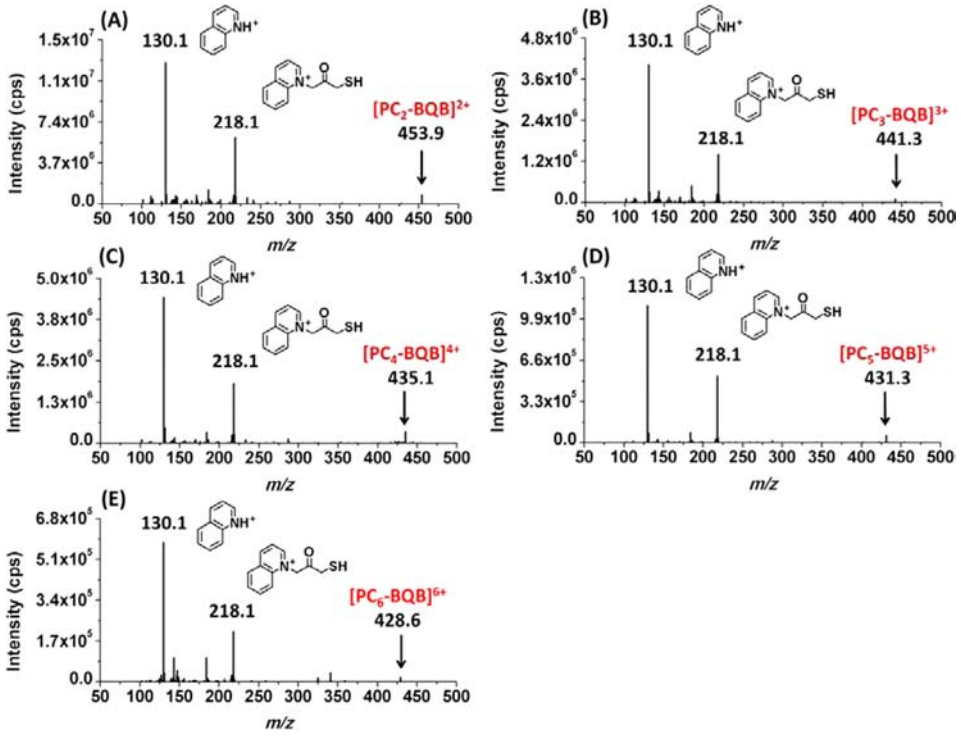

Figure 3. MS/MS spectra of the BQB-labeled PCs: (A) PC_2–BQB, (B) PC_3–BQB, (C) PC_4–BQB, (D) PC_5–BQB, and (E) PC_6–BQB.

20–25 min from 40 to 60% B, 25–26 min from 60 to 5% B, and 26–40 min at 5% B was used.

All BQB-labeled PCs were quantitated by multiple reaction monitoring (MRM) mode in positive mode. The optimal electrospray ionization (ESI) source conditions were as follows: turbo heater temperature (TEM), 550 °C; ion spray voltage, 4500 V; curtain gas, 30 psi; nebulizing gas (gas 1), 40 psi; and heated gas (gas 2), 60 psi.

Method Validation. To evaluate the linearity of the method, standards of PC–BQB at concentrations of 1, 2, 5, 10, 20, 50, 100, 200, and 500 nM fixed amounts of ISs ($PC_{2,3,4,6}$–BQB-d_7, 50 nM; PC_5–BQB-d_7, 10 nM) were used to construct calibration curves by plotting the peak area ratio (analyte/IS) against the PC–BQB concentrations with triplicate measurements. The residual plots were also considered, and the Durbin–Watson test was applied to prove linearity. The limits of detection (LODs) and limits of quantitation (LOQs) were determined at a concentration where the S/N ratios were 3 and 10, respectively.

The accuracy and precision of the developed method were assessed by the recoveries and the intra- and interday relative standard deviations (RSDs). Both recoveries and intra- and interday RSDs were calculated with PC standards spiked in rice tissue samples at three different concentrations. For each concentration, triplicate measurements were performed. The intraday variation was evaluated by repeating the process 3 times within 1 day, and the interday variation was investigated on 3 successive days.

RESULTS AND DISCUSSION

MS Behavior of BQB-Labeled PCs. The typical chemical labeling of PCs by BQB was shown in Figure 2. The results show that all of the thiol groups from the PCs could react with BQB, and the derivatives had several parent molecule ions with different charge states in the positive ESI–MS (see Figure S1 of the Supporting Information). This phenomenon might be attributed to the fact that the carboxy groups released the protons of derivatives during the ionization process and which then results in the derivatives containing one or several negative charges. It is benificial in identifying metabolites by multi-peaks in one analysis. Meanwhile, we found that the intensity of ions from derivatives with the most charge states were highest among the multiple parent molecule ions.

All of the parent molecule ions were subjected to ESI–MS/MS analysis to investigate the fragmentation behavior of BQB-labeled PCs. Figure 3 depicts the fragment ion spectra of BQB-labeled PC_2 ($[M]^{2+}$), PC_3 ($[M]^{3+}$), PC_4 ($[M]^{4+}$), PC_5 ($[M]^{5+}$), and PC_6 ($[M]^{6+}$). The results show that two common product ions at m/z 130.1 and 218.1 were observed for all of the derivatives. The product ion of m/z 130.1 was assigned to the fragment ion generated from the quinoline moiety of BQB, and

DOI: 10.1021/acs.jafc.5b01797
J. Agric. Food Chem. 2015, 63, 5935–5942

m/z 218.1 was assigned to the fragmentation of the C−S bond in derivatives. However, in comparison to the BQB-labeled PCs, the fragment ion spectra of unlabeled PCs were more complex (see Figure S2 of the Supporting Information).

Enhancement of Detection Sensitivity upon Chemical Labeling. The PCs can be ionized in ESI−MS with positive-ion mode. The MRM transitions of 540.1 → 336.0, 772.2 → 233.2, 1004.3 → 233.1, 1236.4 → 464.9, and 1468.4 → 772.0 for unlabeled PC_2, PC_3, PC_4, PC_5, and PC_6 were extracted, respectively, as a result of the highest signal intensity in the LC−MS analysis (Figure 4A). However, the ionization

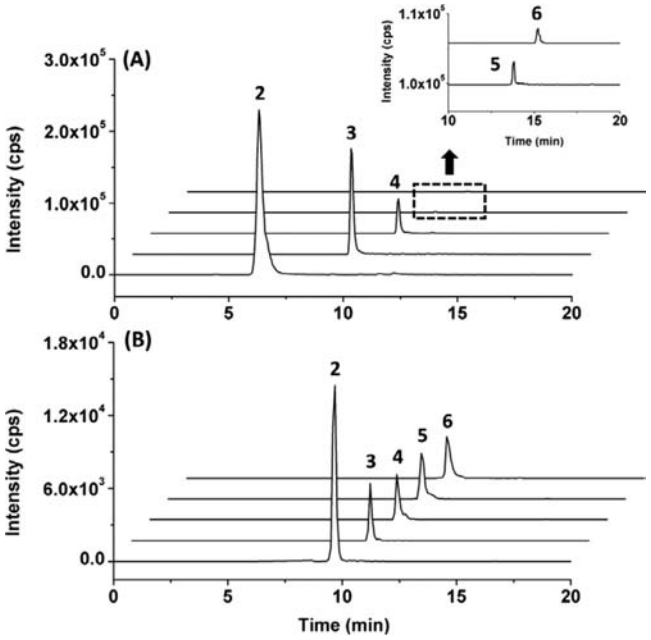

Figure 4. Extracted-ion chromatograms between unlabeled and BQB-labeled PC standards: (A) unlabeled PC_{2-5}, 10 μM; PC_6, 50 μM, 10 μL and (B) BQB-labeled PC_{2-5}, 0.1 μM; PC_6, 0.5 μM, 10 μL.

efficiency is normally poor, and the ionization efficiency dropped from PC_2 to PC_6. Previous studies demonstrated that introducion of an easily ionizable group into target componds by chemical labeling could obviously increase the detection sensitivities of analytes during ESI−MS analysis.[28−33] In this respect, chemical labeling of PCs by BQB that has a permanent charged moiety of quaternary ammonium may also largely enhance the ionization efficiencies of thiol compounds during ESI−MS analysis.

Here, we used the PC standards (PC_2, PC_3, PC_4, PC_5, and PC_6) to evaluate the enhancement of detection sensitivity upon chemical labeling by BQB under MRM mode. The detailed MRM conditions of BQB-labeled and unlabeled PCs were shown in Table 1 and Table S1 of the Supporting Information, respectively. Figure 4B shows the extracted ion chromatograms of BQB-labeled PC standards under MRM transitions. The transitions of $[M]^{n+}$ → 218.1 for BQB-labeled PCs were extracted because of the high signal intensity and low matrix interferences (Figure 4B). Although the PC concentrations labeled with BQB were 100-fold lower than unlabeled PCs, MS responses of BQB-labeled PCs were much more improved. We calculated the LODs of the unlabeled and BQB-labeled PCs under their own optimized MRM conditions, and the results show that the signal intensities of BQB-labeled PCs improved by 14.3−750.0-fold compared to the unlabeled PCs (Table 2). As shown in Figure 4B, the higher PC derivatives exhibited a strong peak tailing. The phenomenon may be due to the residue Si−OH of the silica-based stationary phase, which may strongly interact with the positively charged group(s) of derivatives. The higher PCs of derivatives have more numbers of the charged groups that lead to the strong peak tailing. We also found that the addition of formic acid at a higher concentration in the mobile phase could inhibit the tailing; however, it also caused the MS intensities to decrease. Taking the good peak shape and high intensities into consideration, we selected the formic acid concentration in the mobile phase as 0.1% (v/v).

Stability of BQB-Labeled PCs. The stability of the derivatives may greatly influence the reproducibility and sensitivity in determination of PCs. To examine the stability of the derivatives, the derivatives were left for 4 °C and determined every 24 h. The results indicated that the BQB derivatives of PCs could be stored at 4 °C for at least 1 week without a decrease of signal intensities (see Figure S3 of the Supporting Information). The RSDs were 2.2, 5.9, 3.3, 5.1, and 1.4 for the BQB-labeled PC_2, PC_3, PC_4, PC_5, and PC_6, respectively. It is worth noting that the PC−BQB derivatives should be placed in the vial of polyethylene to avoid the adsorption by the glass (Si−OH) vial.

Optimization of the TCEP and BQB. We investigated the effects of the contents of TCEP and BQB on the efficiencies of reduction of disulfide bonds and chemical labeling. Plant extract (without Cd stress) spiked with PCs (PC_{2-5}, 0.1 μM; PC_6, 0.5 μM) was used as the samples. To minimize the effect of instrumental variation, the same amounts of BQB-d_7-labeled PCs (PC_{2-5}, 0.1 μM; PC_6, 0.5 μM) were used as ISs and added to the samples prior to LC/MS analysis.

PCs are sensitive to oxidation during plant sample preparation and storage. The oxidation can occur in both inter- and intramolecular reactions via disulfide bond formation. El-Zohri et al. found intermolecular-oxidized PC_2 at m/z 1077 and PC_3 at m/z 1543,[16] and the intramolecular-oxidized PC_2 at m/z 770 were also observed in a previous study.[3] Thus, in the current study, the reducing agent was added to avoid the oxidation of PCs before chemical labeling. The reducing agent of TCEP ranging from 0 to 50 nmol was investigated, and the content of BQB was fixed at 30 nmol. As shown in Figure S4A of the Supporting Information, the peak intensity ratio (analyte/IS) of PC derivatives did not obvisouly change with the increase of TCEP from 0 to 10 nmol. We reason that the PC standards added in the plant extracts were all reduced PCs and were labeled with BQB immediately. However, the peak intensity ratio (analyte/IS) dropped with the increase of the TCEP amounts from 10 to 50 nmol, especially for PC_6, indicating that the efficiencies of chemical labeling may be suppressed by the excess content of TCEP. Consequently, 10 nmol of TCEP was used in the following experiments.

Because the plant sample mixture was much more complex than pure standards and BQB would be consumed by the target compounds as well as other thiol-containing interferents in the plant matrix, the amounts of labeling reagent were further optimized in the range of 1−30 nmol. As shown in Figure S4B of the Supporting Information, the peak intensity ratio (analyte/IS) of derivatives increased with the increase of the BQB content from 1 to 10 nmol and then reached a plateau when BQB contents exceeded 10 nmol. The highest chemical-labeling efficiencies of PC were achieved using 10 nmol of

DOI: 10.1021/acs.jafc.5b01797
J. Agric. Food Chem. 2015, 63, 5935−5942

Table 1. MRM Transitions and Optimal Parameters of Mass Spectrometry for BQB-Labeled PCs

PC−BQB	charge	precursor ion	product ion	DP (V)	EP (V)	CEP (V)	CE (V)	CXP (V)
PC_2−BQB	$[M]^{2+}$	453.9	130.1	50	7	15	40	3
			218.1			15	35	3
	$[M - H]^{+}$	906.7	777.4	90	10	37	40	7
			749.3			37	50	7
PC_3−BQB	$[M]^{3+}$	441.3	130.1	45	6	20	35	3
			218.1			20	37	3
	$[M - H]^{2+}$	661.3	130.1	55	7	25	55	3
			596.8			60	30	8
PC_4−BQB	$[M]^{4+}$	435.1	130.1	41	7	19	35	3
			218.1			17	35	3
	$[M - H]^{3+}$	579.6	130.1	41	8	26	50	3
			536.9			26	30	6
	$[M - 2H]^{2+}$	869.1	804.3	100	7	36	32	7
			740.0			36	38	8
PC_5−BQB	$[M]^{5+}$	431.3	130.1	45	6	20	35	3
			218.1			20	35	3
	$[M - H]^{4+}$	539.0	218.1	38	6	25	45	3
			499.9			25	35	7
	$[M - 2H]^{3+}$	718.4	130.1	50	7	31	65	4
			675.2			31	40	8
PC_6−BQB	$[M]^{6+}$	428.6	130.1	40	7	20	35	3
			218.1			20	35	3
	$[M - 2H]^{4+}$	643.0	130.1	37	7	20	50	3
			578.0			20	35	8
	$[M - 3H]^{3+}$	856.9	814.0	90	5	36	32	7
PC_2−BQB-d_7	$[M]^{2+}$	460.8	137.1	50	7	15	40	3
			225.1			15	35	3
PC_3−BQB-d_7	$[M]^{3+}$	448.4	137.1	45	6	20	35	3
			225.1			20	37	3
PC_4−BQB-d_7	$[M]^{4+}$	442.2	137.1	41	7	19	35	3
			225.1			17	35	3
PC_5−BQB-d_7	$[M]^{5+}$	438.4	137.1	45	6	20	35	3
			225.1			20	35	3
PC_6−BQB-d_7	$[M]^{6+}$	436.0	137.1	40	7	20	35	3
			225.1			20	35	3

Table 2. Comparison of LODs of Unlabeled and BQB-Labeled PC Standards under Their Own Optimized MS Conditions

	LODs (nmol)		
PC	unlabeled	BQB labeled	improved fold
PC_2	6.0×10^{-5}	2.4×10^{-6}	25.0
PC_3	1.0×10^{-4}	7.0×10^{-6}	14.3
PC_4	3.5×10^{-4}	6.2×10^{-6}	56.5
PC_5	2.2×10^{-3}	6.8×10^{-6}	323.5
PC_6	2.4×10^{-2}	3.2×10^{-5}	750.0

BQB. For more reliable quantitation of PCs in plant tissue, we used 20 nmol of BQB in the following experiments.

Method Validation. A series of experiments, including linearity, LODs and LOQs, recoveries, and precisions, were performed to validate the proposed method under optimized conditions. The results show that good linearity was obtained with a regression coefficient (R^2) higher than 0.9931 (see Table S2 of the Supporting Information). The residual plots show that a plot of the standardized residual versus the standardized predicted value revealed no particular pattern (i.e., data were randomly distributed around 0), no more than 5% of cases had

Table 3. Comparison of LODs with Previous Studies

		LODs (fmol)					
separation	detection	PC_2	PC_3	PC_4	PC_5	PC_6	reference
RP-HPLC	ESI−MS/MS	2.4	7.0	6.2	6.8	32.0	present method
HILIC	ESI−MS/MS	20.0	60.0	75.0	375.0	530.0	3
RP-HPLC	FLD	140.0	140.0	140.0			11
RP-HPLC	ED	78.0	6.0	86.0	59.0		15
CE	MS	3.0	39.0	42.0			18
RP-HPLC	ESI−MS/MS	30.6	100.8				19
RP-HPLC	ESI−MS/MS	8800.0	2400.0				17

DOI: 10.1021/acs.jafc.5b01797
J. Agric. Food Chem. 2015, 63, 5935−5942

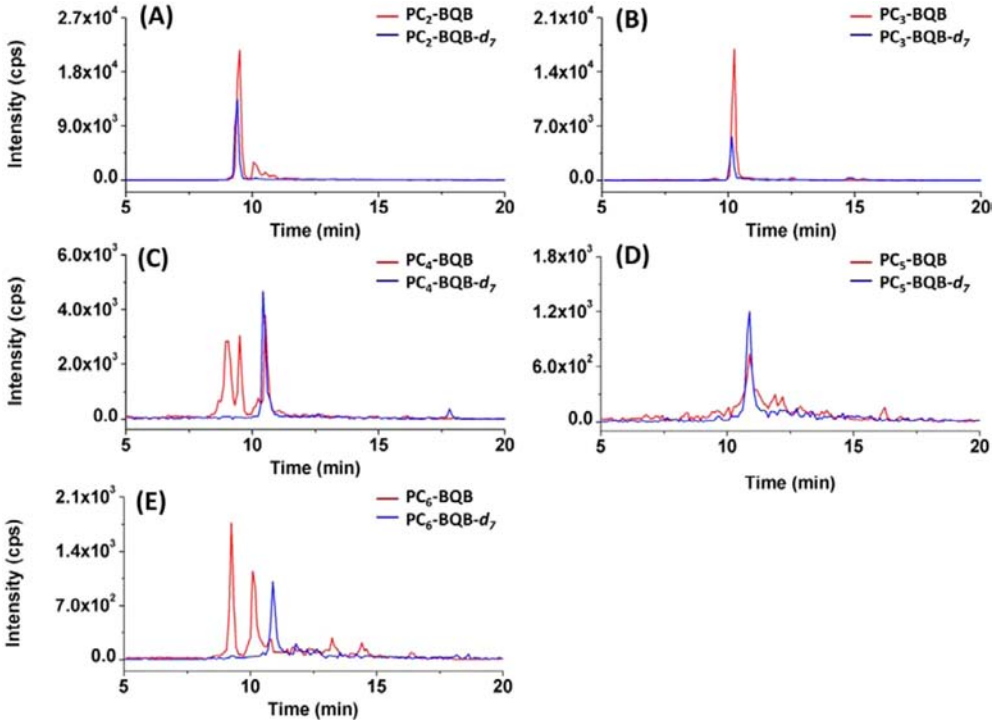

Figure 5. Typical extracted ion chromatogram of PCs from the plant treated with 100 μM Cd (3 days) and their corresponding ISs.

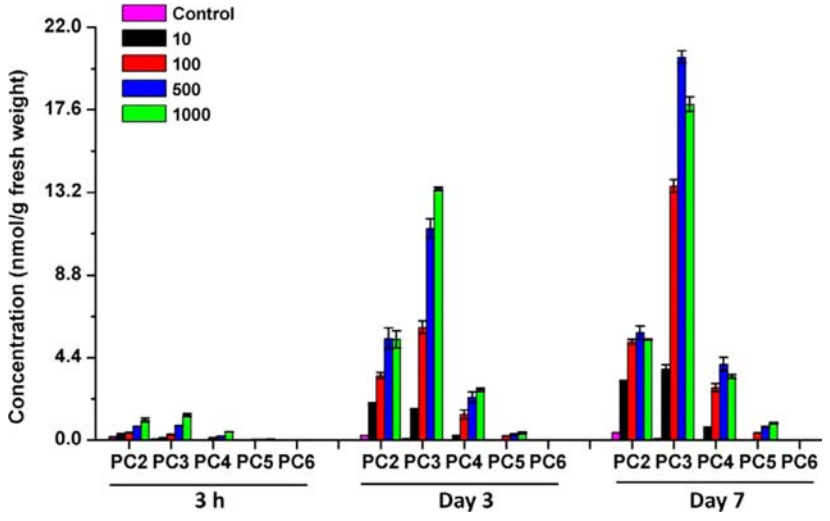

Figure 6. Content change of PCs in rice with Cd stress at different concentrations and time.

a standardized residual absolute value above 2, and the Durbin–Watson statistics were 2.1, 2.2, 1.2, 2.3, and 2.3 for PC_2, PC_3, PC_4, PC_5, and PC_6, respectively (between 1.5 and 2.5), indicating that the residuals were uncorrelated (see Figure S5 of the Supporting Information).[34] The LODs and LOQs for five PCs were in the range of 0.1–1.6 and 0.4–5.0 nM, respectively. Table 3 shows the comparison of the LODs obtained between our method and other methods reported in the literature.[3,11,15,17−19] Generally, the LODs obtained by the current method are much lower than those given in the literature, especially for the LODs of PC_4, PC_5, and PC_6, which were about 7–17 times lower than the lowest values reported in previous studies.[3,15,18]

The recoveries of five PCs were in the range of 71.6–93.1%, and the intra- and interday RSDs were less than 9.8 and 16.3%, respectively (see Table S3 of the Supporting Information), indicating that the accuracy and precision of the proposed method were satisfactory for the determination of PCs in plant samples.

Quantitation of Endogenous PCs in Plant Samples. In the present work, after 10 days of growing, rice samples were treated with Cd at different concentrations (0, 10, 100, 500, and 1000 μM) and collected after Cd stress for 3 h, 3 days, and 7 days. The real rice pictures under Cd stress with different concentrations and time were shown in Figure S6 of the Supporting Information. As seen, the rice under all of the Cd concentrations show the same appearance (green) at the Cd treatment time of 3 h and 3 days. However, at the treatment time of 7 days, the rice leaves turned yellow, starting from the 100 μM Cd concentration, and the inhibitory effects in plant

DOI: 10.1021/acs.jafc.5b01797
J. Agric. Food Chem. 2015, 63, 5935–5942

growth were also observed at the Cd concentrations of 500 and 1000 μM.

The concentrations of the PCs in those rice tissues were determined by the developed method. Figure 5 shows the typical extracted ion chromatogram of five PCs and their respective ISs from the plant treated with 100 μM Cd (3 days). As seen, the BQB-labeled PCs and the ISs (BQB-d_7-labeled PCs) were co-eluted on the chromatography, and the chromatographic isotope effect of BQB- and BQB-d_7-labeled standards was about 0.1 min.

The quantitation results (Figure 6 and Table S4 in Supporting Information) show that only PC_2 and PC_3 were observed in the control samples (0 μM Cd), indicating that PC_2 and PC_3 can be synthesized in plants even without heavy metal stress. For the rice under Cd stress, in comparison to the control samples, the contents of PC_2 and PC_3 under Cd stress at the concentrations of 10−1000 μM dramatically increased.

PC_4 and PC_5 were also detected in Cd-stressed rice. It is worth noting that PC_5 was first detected in the rice tissues in our study. PC_4 and PC_5 were induced by the Cd concentration greater than 10 μM, and PC_4 could also be found in rice under 10 μM Cd at the treatment time of 3 and 7 days. The results indicate that PC_4 was more easily synthesized than PC_5 in rice. The concentrations of PC_2, PC_3, and PC_4 in rice at 100 μM Cd stress (7 days) were consistent with previous work for the measurements of PCs in rice stems with 50 μM Cd stress for 7 days.[3] Generally, the contents of PCs in rice increased with the increase of the concentration and treatment time of Cd, indicating that the PCs have the role of detoxification for plants under Cd stress.[1]

Comparison of the Developed Method to Previous Methods. In comparison to previously published methods, our method has two major advantages. First, the detection sensitivity was significantly improved. As seen in Table 3, the LODs of PC_4, PC_5, and PC_6 obtained by the current method were 7, 8, and 17 times lower than the lowest values reported in the previous studies, respectively, and the LODs of PC_2 and PC_3 were also comparable to those lowest values. Because of the high detection sensitivity, PCs can be easily quantitated using only 5 mg of rice tissues and PC_5 was first detected in the rice tissues. Second, the accuracy for the identification and quantitation of PCs was also enhanced. The PC standards labeled with BQB-d_7 were used as the isotope ISs, which can calibrate the ion signal variation caused by matrix and ion suppression effects in MS analysis (Figure 5). Taken together, the method can significantly improve the detection sensitivity and accuracy for the identification and quantitation of PCs in plants.

In conclusion, we developed a stable isotope-labeling method combined with LC/MS analysis for the sensitive detection of PCs in rice. The plant samples and PC standards were labeled with BQB and BQB-d_7, respectively, then mixed, and analyzed by LC/MS. The BQB labeling improves the detection sensitivities of PCs by 14−750-fold because of the introduction of a permanent charged moiety of quaternary ammonium, and the BQB-d_7-labeled standards were used as the ISs for quantitation to minimize the severe matrix effect. Using the developed method, four endogenous PCs (PC_2, PC_3, PC_4, and PC_5) were successfully identified and quantitated in only 5 mg of rice samples under Cd stress, and PC_5 was first reported to exist in rice tissues by this method. The contents of PCs dramatically increased as the Cd concentrations and treatment time increased, suggesting that PCs have the role of detoxification in plants under Cd stress. This highly sensitive and reliable method can also be extended for the identification and quantitation of PCs in other samples.

■ ASSOCIATED CONTENT

Supporting Information

MRM transitions for PC data (Table S1), data for calibration, LOD, and LOQ (Table S2), data for recoveries and precisions (Table S3), PCs in rice (Table S4), MS spectra of BQB-labeled PCs (Figure S1), MS/MS spectra of the unlabeled PCs (Figure S2), stability of BQB (Figure S3), optimization of TCEP and BQB contents (Figure S4), residual plots (Figure S5), and pictures of rice under Cd stress (Figure S6). The Supporting Information is available free of charge on the ACS Publications website at DOI: 10.1021/acs.jafc.5b01797.

■ AUTHOR INFORMATION

Corresponding Author

*Telephone/Fax: +86-27-68755595. E-mail: yqfeng@whu.edu.cn.

Funding

The authors thank the financial support from the National Basic Research Program of China (973 Program) (2012CB720601 and 2013CB910702), the National Natural Science Foundation of China (21475098 and 91217309), and the Natural Scinence Foundation of Hubei Province, China (2014CFA002).

Notes

The authors declare no competing financial interest.

■ REFERENCES

(1) Gupta, D.; Vandenhove, H.; Inouhe, M. Role of phytochelatins in heavy metal stress and detoxification mechanisms in plants. In *Heavy Metal Stress in Plants*; Gupta, D. K., Corpas, F. J., Palma, J. M., Eds.; Springer: Berlin, Germany, 2013; pp 73−94.

(2) Rijstenbil, J. W.; Wijnholds, J. A. HPLC analysis of nonprotein thiols in planktonic diatoms: Pool size, redox state and response to copper and cadmium exposure. *Mar. Biol.* **1996**, *127*, 45−54.

(3) Cao, Z. Y.; Sun, L. H.; Mou, R. X.; Zhou, R.; Zhu, Z. W.; Chen, M. X. A novel method for the simultaneous analysis of seven biothiols in rice (*Oryza sativa* L.) using hydrophilic interaction chromatography coupled with electrospray tandem mass spectrometry. *J. Chromatogr. B: Anal. Technol. Biomed. Life Sci.* **2015**, *976*−*977*, 19−26.

(4) Dudka, S.; Miller, W. P. Accumulation of potentially toxic elements in plants and their transfer to human food chain. *J. Environ. Sci. Health, Part B* **1999**, *34*, 681−708.

(5) Hawrylak-Nowak, B.; Dresler, S.; Wójcik, M. Selenium affects physiological parameters and phytochelatins accumulation in cucumber (*Cucumis sativus* L.) plants grown under cadmium exposure. *Sci. Hortic.* **2014**, *172*, 10−18.

(6) Petraglia, A.; De Benedictis, M.; Degola, F.; Pastore, G.; Calcagno, M.; Ruotolo, R.; Mengoni, A.; Sanita di Toppi, L. The capability to synthesize phytochelatins and the presence of constitutive and functional phytochelatin synthases are ancestral (plesiomorphic) characters for basal land plants. *J. Exp. Bot.* **2014**, *65*, 1153−1163.

(7) Wawrzynski, A.; Kopera, E.; Wawrzynska, A.; Kaminska, J.; Bal, W.; Sirko, A. Effects of simultaneous expression of heterologous genes involved in phytochelatin biosynthesis on thiol content and cadmium accumulation in tobacco plants. *J. Exp. Bot.* **2006**, *57*, 2173−2182.

(8) Akhter, F.; McGarvey, B.; Macfie, S. M. Reduced translocation of cadmium from roots is associated with increased production of phytochelatins and their precursors. *J. Plant Physiol.* **2012**, *169*, 1821−1829.

DOI: 10.1021/acs.jafc.5b01797
J. Agric. Food Chem. 2015, 63, 5935−5942

(9) Figueira, E.; Freitas, R.; Guasch, H.; Almeida, S. F. Efficiency of cadmium chelation by phytochelatins in *Nitzschia palea* (Kützing) W. Smith. *Ecotoxicology* **2014**, *23*, 285−292.
(10) Aina, R.; Labra, M.; Fumagalli, P.; Vannini, C.; Marsoni, M.; Cucchi, U.; Bracale, M.; Sgorbati, S.; Citterio, S. Thiol-peptide level and proteomic changes in response to cadmium toxicity in *Oryza sativa* L. roots. *Environ. Exp. Bot.* **2007**, *59*, 381−392.
(11) Wu, Z.; Zhang, C.; Yan, J.; Ge, Y. Separation and quantification of cysteine, glutathione and phytochelatins in rice (*Oryza sativa* L.) upon cadmium exposure using reverse phase ultra performance liquid chromatography (RP-UPLC) with fluorescence detection. *Anal. Methods* **2013**, *5*, 6147.
(12) Dago, A.; Ariño, C.; Díaz-Cruz, J. M.; Esteban, M. Analysis of phytochelatins and Hg−phytochelatin complexes in *Hordeum vulgare* plants stressed with Hg and Cd: HPLC study with amperometric detection. *Int. J. Environ. Anal. Chem.* **2014**, *94*, 668−678.
(13) Dago, A.; Gonzalez, I.; Arino, C.; Martinez-Coronado, A.; Higueras, P.; Diaz-Cruz, J. M.; Esteban, M. Evaluation of mercury stress in plants from the Almaden mining district by analysis of phytochelatins and their Hg complexes. *Environ. Sci. Technol.* **2014**, *48*, 6256−6263.
(14) Dago, A.; Gonzalez, I.; Arino, C.; Diaz-Cruz, J. M.; Esteban, M. Chemometrics applied to the analysis of induced phytochelatins in *Hordeum vulgare* plants stressed with various toxic non-essential metals and metalloids. *Talanta* **2014**, *118*, 201−209.
(15) Diopan, V.; Shestivska, V.; Zitka, O.; Galiova, M.; Adam, V.; Kaiser, J.; Horna, A.; Novotny, K.; Liska, M.; Havel, L.; Zehnalek, J.; Kizek, R. Determination of plant thiols by liquid chromatography coupled with coulometric and amperometric detection in lettuce treated by lead(II) ions. *Electroanalysis* **2010**, *22*, 1248−1259.
(16) El-Zohri, M. H.; Cabala, R.; Frank, H. Quantification of phytochelatins in plants by reversed-phase HPLC−ESI−MS−MS. *Anal. Bioanal. Chem.* **2005**, *382*, 1871−1876.
(17) Simmons, D. B. D.; Hayward, A. R.; Hutchinson, T. C.; Emery, R. J. N. Identification and quantification of glutathione and phytochelatins from *Chlorella vulgaris* by RP-HPLC ESI−MS/MS and oxygen-free extraction. *Anal. Bioanal. Chem.* **2009**, *395*, 809−817.
(18) Kato, M.; Ishikawa, S.; Inagaki, K.; Chiba, K.; Hayashi, H.; Yanagisawa, S.; Yoneyama, T. Possible chemical forms of cadmium and varietal differences in cadmium concentrations in the phloem sap of rice plants (*Oryza sativa* L.). *Soil Sci. Plant Nutr.* **2010**, *56*, 839−847.
(19) Brautigam, A.; Wesenberg, D.; Preud'homme, H.; Schaumloffel, D. Rapid and simple UPLC−MS/MS method for precise phytochelatin quantification in alga extracts. *Anal. Bioanal. Chem.* **2010**, *398*, 877−883.
(20) Huang, Y. Q.; Wang, Q. Y.; Liu, J. Q.; Hao, Y. H.; Yuan, B. F.; Feng, Y. Q. Isotope labelling—Paired homologous double neutral loss scan-mass spectrometry for profiling of metabolites with a carboxyl group. *Analyst* **2014**, *139*, 3446−3454.
(21) Bruheim, P.; Kvitvang, H. F.; Villas-Boas, S. G. Stable isotope coded derivatizing reagents as internal standards in metabolite profiling. *J. Chromatogr A* **2013**, *1296*, 196−203.
(22) Ogawa, S.; Ooki, S.; Shinoda, K.; Higashi, T. Analysis of urinary vitamin D(3) metabolites by liquid chromatography/tandem mass spectrometry with ESI-enhancing and stable isotope-coded derivatization. *Anal. Bioanal. Chem.* **2014**, *406*, 6647−6654.
(23) Dai, W. D.; Huang, Q.; Yin, P. Y.; Li, J.; Zhou, J.; Kong, H. W.; Zhao, C. X.; Lu, X.; Xu, G. W. Comprehensive and highly sensitive urinary steroid hormone profiling method based on stable isotope-labeling liquid chromatography mass spectrometry. *Anal. Chem.* **2012**, *84*, 10245−10251.
(24) Huang, Y. Q.; Liu, J. Q.; Gong, H. Y.; Yang, J.; Li, Y. S.; Feng, Y. Q. Use of isotope mass probes for metabolic analysis of the jasmonate biosynthetic pathway. *Analyst* **2011**, *136*, 1515−1522.
(25) Liu, P.; Huang, Y. Q.; Cai, W. J.; Yuan, B. F.; Feng, Y. Q. Profiling of thiol-containing compounds by stable isotope labeling double precursor ion scan mass spectrometry. *Anal. Chem.* **2014**, *86*, 9765−9773.
(26) Oono, Y.; Yazawa, T.; Kawahara, Y.; Kanamori, H.; Kobayashi, F.; Sasaki, H.; Mori, S.; Wu, J.; Handa, H.; Itoh, T.; Matsumoto, T. Genome-wide transcriptome analysis reveals that cadmium stress signaling controls the expression of genes in drought stress signal pathways in rice. *PLoS One* **2014**, *9*, No. e96946.
(27) Huang, Y. Q.; Ruan, G. D.; Liu, J. Q.; Gao, Q.; Feng, Y. Q. Use of isotope differential derivatization for simultaneous determination of thiols and oxidized thiols by liquid chromatography tandem mass spectrometry. *Anal. Biochem.* **2011**, *416*, 159−166.
(28) Tang, Y.; Zheng, S. J.; Qi, C. B.; Feng, Y. Q.; Yuan, B. F. Sensitive and simultaneous determination of 5-methylcytosine and its oxidation products in genomic DNA by chemical derivatization coupled with liquid chromatography−tandem mass spectrometry analysis. *Anal. Chem.* **2015**, *87*, 3445−3452.
(29) Tang, Y.; Xiong, J.; Jiang, H. P.; Zheng, S. J.; Feng, Y. Q.; Yuan, B. F. Determination of oxidation products of 5-methylcytosine in plants by chemical derivatization coupled with liquid chromatography/tandem mass spectrometry analysis. *Anal. Chem.* **2014**, *86*, 7764−7772.
(30) Qi, B. L.; Liu, P.; Wang, Q. Y.; Cai, W. J.; Yuan, B. F.; Feng, Y. Q. Derivatization for liquid chromatography−mass spectrometry. *TrAC, Trends Anal. Chem.* **2014**, *59*, 121−132.
(31) Chen, M. L.; Fu, X. M.; Liu, J. Q.; Ye, T. T.; Hou, S. Y.; Huang, Y. Q.; Yuan, B. F.; Wu, Y.; Feng, Y. Q. Highly sensitive and quantitative profiling of acidic phytohormones using derivatization approach coupled with nano-LC−ESI−Q-TOF−MS analysis. *J. Chromatogr. B: Anal. Technol. Biomed. Life Sci.* **2012**, *905*, 67−74.
(32) Liu, J. F.; Yuan, B. F.; Feng, Y. Q. Determination of hexanal and heptanal in human urine using magnetic solid phase extraction coupled with *in-situ* derivatization by high performance liquid chromatography. *Talanta* **2015**, *136*, 54−59.
(33) Iwasaki, Y.; Nakano, Y.; Mochizuki, K.; Nomoto, M.; Takahashi, Y.; Ito, R.; Saito, K.; Nakazawa, H. A new strategy for ionization enhancement by derivatization for mass spectrometry. *J. Chromatogr. B: Anal. Technol. Biomed. Life Sci.* **2011**, *879*, 1159−1165.
(34) Long-Rossi, F.; Salsich, G. B. Pain and hip lateral rotator muscle strength contribute to functional status in females with patellofemoral pain. *Physiother. Res. Int.* **2010**, *15*, 57−64.

DOI: 10.1021/acs.jafc.5b01797
J. Agric. Food Chem. 2015, 63, 5935−5942

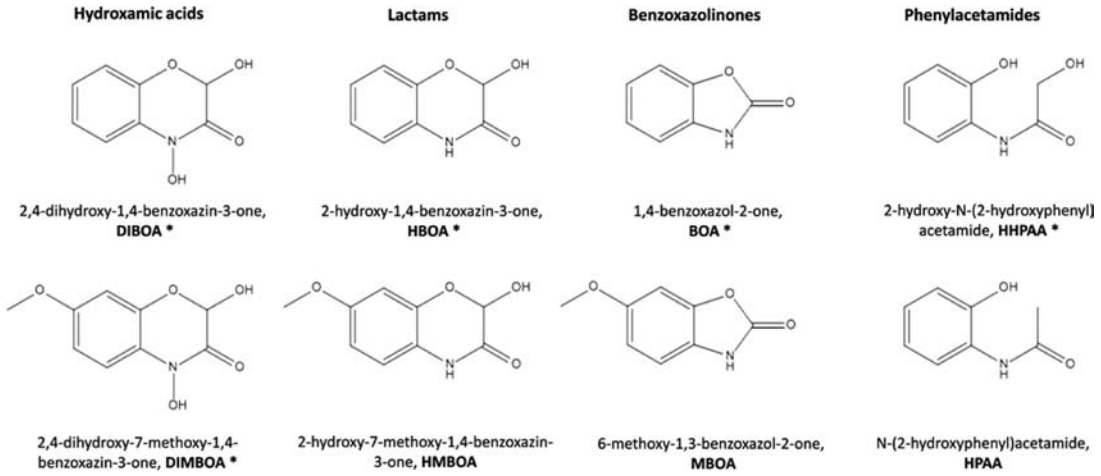

Figure 1. Molecular structures of the different benzoxazinoids exemplified with the most common compounds of each chemical class The asterisk (∗) indicates the compounds found in this study. In addition to aglycone forms, also the diglycoside and glucoside forms of DIBOA, DIMBOA, and HBOA were identified and analyzed in this study.

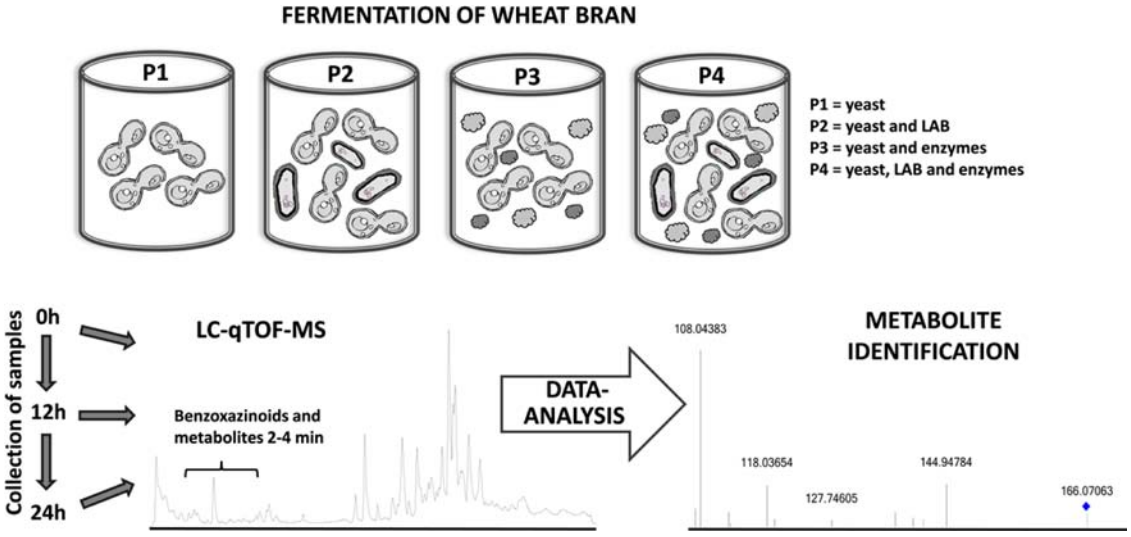

Figure 2. Schematic illustration of the study setup. Ground wheat bran was fermented in four different conditions (P1−P4). All conditions included equal amounts of yeast (*Kazachstania exigua*) at the start. In addition, conditions P2 and P4 included added lactic acid bacteria (*Lactobacillus brevis*), and conditions P3 and P4 had mixture of enzymes with cellulase, xylanase, β-glucanase, and α-amylase activity. Samples were collected at the start (0 h) and after 12 and 24 h of fermentation. LC-qTOF-MS analytics was used to study the effects of different fermentation conditions on the resulting benzoxazinoid metabolite profile.

Benzoxazinoids are highly bioactive compounds that have been suggested to even have pharmaceutical potential and may therefore have implications on health as part of the diet, as has been reviewed recently.[15] For example, benzoxazinoids have been reported to have antiallergenic and anti-inflammatory, as well as appetite suppressing effects in humans.[3,4,16−18] Additionally, benzoxazinoids may reduce cellular glucose uptake.[19] On the other hand, benzoxazinoids have also been found to be potent polyploidy-inducing agents in human-derived cell lines (HepG2 and HeLa), which has raised concern for their potential adverse health effects.[20,21] For phenylacetamides, no reports on bioactivity and potential effects on health are found. Whereas it is unclear whether benzoxazinoids, or potentially their metabolized forms, for example, phenylacetamides, have an impact on human metabolism, there is a need to understand the effect of different food-processing technologies on their content. It is known that soaking and boiling can considerably change the content of benzoxazinoids and their glycosides in grains or flakes and that they are released into water in notable amounts during such processing.[8] Sourdough fermentation combined with baking has been shown to effectively degrade DIBOA diglycoside and increase the amount of BOA and benzoxazinoid-related metabolite HPAA,[11,14] but whether the degradation was due to fermentation or baking is not known.

In the current study, we used a nontargeted liquid chromatography quadrupole time-of-flight mass spectrometry (LC-qTOF-MS) metabolite profiling approach with the aim of examining the effects of different fermentation conditions on the benzoxazinoid profile of wheat bran sourdoughs. The effect of different microbial contents (yeast, and yeast with lactic acid bacteria) as well as impact of cell wall degrading enzymes was evaluated.

MATERIALS AND METHODS

Materials. Commercial wheat bran (Fazer Mills, Lahti, Finland) was ground using a TurboRotor mill (Mahltechnik Görgens GmbH,

DOI: 10.1021/acs.jafc.5b00879
J. Agric. Food Chem. 2015, 63, 5943−5949

Table 1. Identified Benzoxazinoid Derivatives and Unknown Compounds with Molecular Formula, m/z of the Molecular Ion in ESI(−), Fragment Ions in ESI(−), Collision Energy (CE) Used for Fragmentation, Retention Time (rt), and References Used in Identification

putative ID	mol formula	m/z	MS/MS m/z	CE (eV)	rt	ref
DIMBOA diglycoside	$C_{21}H_{29}NO_{15}$	534.1457	192.0281, 164.0324, 149.0164	20	3.47	6
DIBOA diglycoside	$C_{20}H_{27}NO_{14}$	504.1362	162.0207, 180.0303, 134.0226, 108.0422	20	3.07	6
DIBOA glycoside	$C_{14}H_{17}NO_{9}$	342.0828	162.0179, 134.0213, 108.0419	20	3.42	6
HBOA diglycoside	$C_{20}H_{27}NO_{13}$	488.1407	164.0334	10	3.01	6
HBOA glycoside	$C_{14}H_{17}NO_{8}$	326.0883	164.0356	10	3.39	6
HHPAA	$C_{8}H_{9}NO_{3}$	166.0524	118.0453, 108.0422	20	2.89	11
BOA	$C_{7}H_{5}NO_{2}$	134.0254	78.047	20	3.52	6
unknown 1		150.0550	108.041, 107.035		3.03	
unknown 2		150.0552	108.042, 107.032		3.22	
unknown 3		188.0917	153.3879, 139.0272, 126.0841, 118.03662, 107.1137, 108.0512, 93.0216	20	3.67	
unknown 4		224.0553	178.0526, 162.0529, 144.0437, 134.0236, 118.0424, 108.05473, 78.0903	20	2.75	

Dormagen, Germany) to a median particle size of 160 μm. Enzymes used in fermentations 3 and 4 were Depol 740l (Biocatalyst Ltd., UK) and Grindamyl A1000 (Danisco, Denmark). Their enzyme activities are presented in Supporting Information Table 1. The yeast used in all fermentations was *Kazachstania exigua* (VTT C-81116), and the lactic acid bacteria (LAB) starter used in fermentations 2 and 4 was *Lactobacillus brevis* (VTT E-95612).

Bran Fermentations. Four different liquid fermentations (P1, yeast; P2, yeast + LAB; P3, yeast + enzymes; and P4, yeast + LAB + enzymes), containing bran and water (10:90 w/w) with an initial inoculum of ca. 10^6−10^7 cfu/mL for both starter cultures employed, were made as duplicates. The fermentations were performed in 1 L BIOSTAT QPlus bioreactors (Sartorius Stedim Biotech GmbH, Germany) in an anaerobic environment, which was created by a flow of nitrogen into the bottom of the fermentor. Preparation of the sourdoughs and process parameters can be found in the Supporting Information (Tables 2 and 3). Samples (285 g) were taken at 0, 12, and 24 h, freeze-dried (Lyovac GT 2, Steris GmbH, Germany; or Epsilon 2-25DS, Christ, Germany), and milled (Bamix, Switzerland and Retsch ZM 200, Retsch GmbH, Germany) to pass a 0.5 mm sieve. The process scheme for fermentations and sampling is illustrated in Figure 2.

Acidification. Acidity (pH and total titratable acids (TTA)) of the bioprocessed bran was determined from a suspension containing 5 g of bran sample and 50 mL of distilled water in an automatic titrator (Mettler Toledo titrator T50). After pH measurement, the suspension was titrated with 0.1 M NaOH to a final pH of 8.5. TTA value was expressed as the amount of NaOH used in milliliters per 10 g of sample.

Sample Preparation and LC-qTOF-MS Analyses. For LC-qTOF-MS analyses 100 mg of each freeze-dried and ground fermentation sample was weighed. The samples were extracted by vigorous shaking with 80% methanol for 30 min at room temperature using a Multi Reax shaker (Heidolph Instruments GmbH, Germany), centrifuged for 10 min at 6708*g* (7 °C), and filtered through a 0.2 μm PTFE membrane (PALL Corp., USA). Prior to analysis, samples were stored for 12 h at 6 °C. Metabolite profiling was carried out on an LC-qTOF-MS system consisting of a 1290 ultrahigh-performance liquid chromatograph (UHPLC) with a 6540 ultrahigh-definition (UHD) accurate-mass qTOF mass spectrometer (Agilent Technologies, USA). Separation of metabolites was performed using a 2.1 × 100 mm 1.8 μm particle size Agilent ZORBAX Eclipse XDB-C18 column (Agilent Technologies) thermostated at 50 °C. The mobile phase consisted of 0.1% of formic acid in water (phase A) and 0.1% of formic acid in methanol (phase B). The gradient program was as follows: 2−100% of B in 10 min, held at 100% of B for 4.5 min, 100−2% of B in 0.01 min, and held at 2% of B for 1.99 min. The mobile phase flow rate was 0.4 mL/min, and the sample injection volume was 1 μL. The instrument was equipped with an Agilent Jet Stream electrospray source and was operated in negative ionization mode with the following source parameters: drying gas flow rate, 11 L/min; gas temperature, 325 °C; pressure of nebulizer gas, 45 psi; Vcap, 3500 V; fragmentor, 100 V; skimmer, 45 V. The mass scan range was m/z 50−1600. For tandem mass spectrometry (MS/MS) analyses three different collision energies (10, 20, and 40 V) were used. The mass-axis was calibrated online during the analyses with two reference mass ions. Data acquisition was conducted with MassHunter Acquisition B.04.00 (Agilent Technologies).

Data Processing. Data were extracted using MassHunter Qualitative analysis B.05.00 (Agilent Technologies) using the "Find Compounds by Molecular Feature" function. Peaks were extracted by combining isotopes, sodium adducts, and dimers for specific "compounds". For compound alignment data were output into the Mass Profiler Professional software (version 2.2, Agilent Technologies, Santa Clara, CA, USA). Main emphasis on data analysis was laid on analyzing the benzoxazinoids, which typically elute at 2−4 min in our chromatographic conditions; therefore, the collection of signals for the data analysis was focused on this region. Compounds were identified on the basis of their accurate mass, molecular formula, and MS/MS fragmentation pattern. A heatmap chart was generated with Multi-experiment Viewer (MeV) software.[22,23]

RESULTS AND DISCUSSION

Identification of the Benzoxazinoid Compounds. Tentatively identified benzoxazinoids in wheat bran ferments included DIBOA diglycoside, DIBOA glycoside, HBOA diglycoside, HBOA glycoside, DIMBOA diglycoside, and BOA aglycone. All reported compounds were detected in negative electrospray ionization as molecular ions. The recorded MS/MS fragments of detected benzoxazinoid glycosides and metabolites are presented in Table 1, as well as references used for confirmation of identification. MS/MS fragmentation spectra for DIBOA and HBOA diglycoside and HHPAA with extracted ion chromatograms are presented in Figure 3. The fragmentation pattern of benzoxazinoid glycosides was analogical to that found earlier (Table 1; Figure 3).[6] Identification of the phenylacetamide HHPAA, a potential microbial conversion product of benzoxazinoids, was based on the fragmentation pattern showing major fragments at m/z 118.0453 and 108.0422 (Figure 3), which is in accordance with that reported earlier.[11] There were two signals (m/z 150.055 with retention time (rt) of 3.0 and 3.2 min) exhibiting the molecular mass and MS/MS fragmentation corresponding to phenylacetamide HPAA as reported earlier.[11] However, the structural difference between these two compounds could not be resolved, and therefore they are reported as unknowns (Table 1). Additionally, the data were searched for other earlier reported conversion products of benzoxazinoids,[24] but none were found. However, there were two metabolites formed

DOI: 10.1021/acs.jafc.5b00879
J. Agric. Food Chem. 2015, 63, 5943−5949

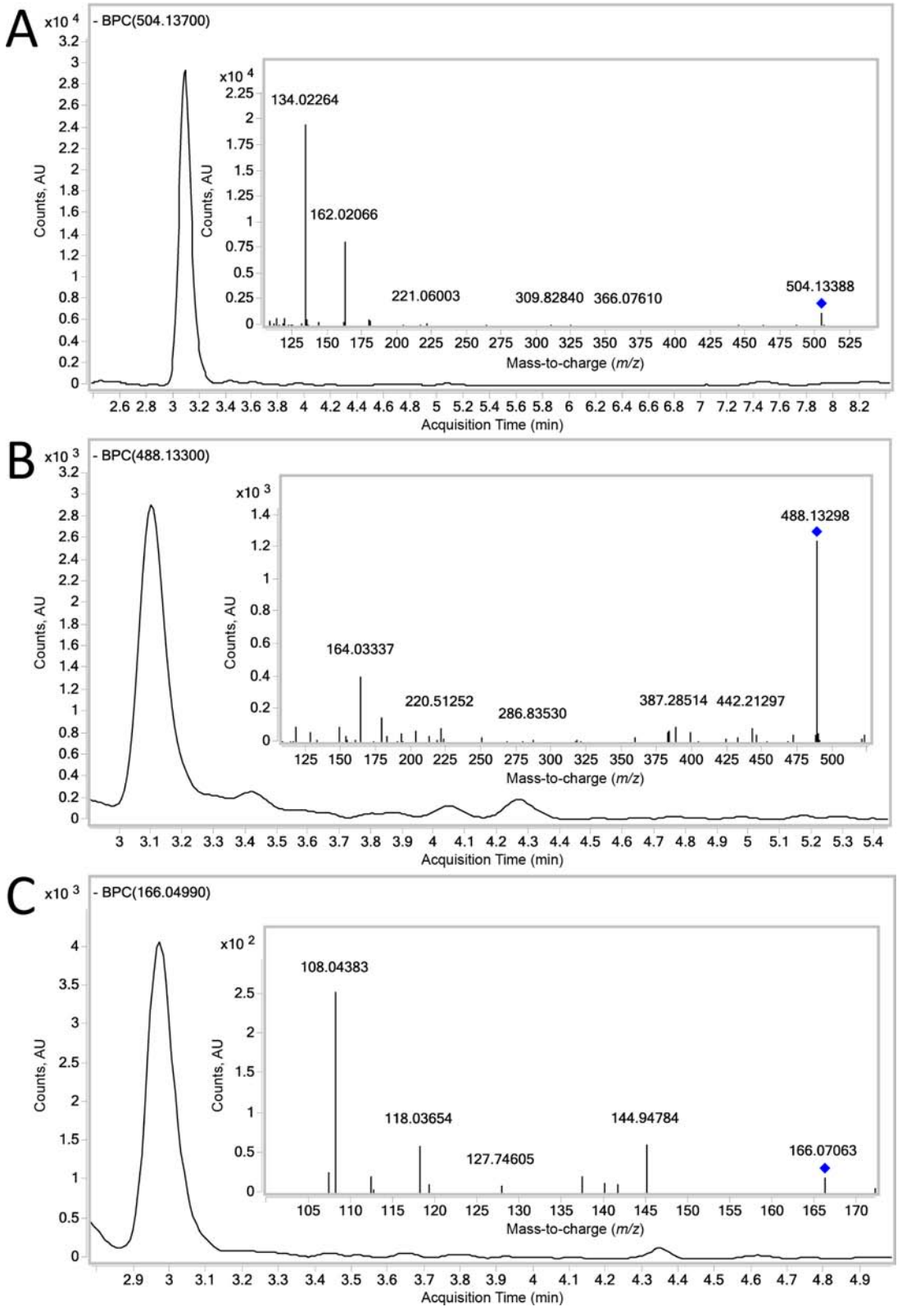

Figure 3. Extracted ion chromatograms in ESI(−) LC-qTOF-MS analysis for DIBOA diglycoside (A), HBOA diglycoside (B), and HHPAA (C) with MS/MS fragmentation spectra for each of the compounds.

during the fermentation (m/z 189.092 at 3.67 min and m/z 224.055 at 2.75 min), which had fragmentation pattern and retention time referring potentially to benzoxazinoid derived metabolites (Table 1). The ion with m/z 189.092 gave several fragment ions including m/z 118.037, 107.114, and 108.051, which were observed also for the benzoxazinoid compounds eluting in this same chromatographic region. Additionally, the unknown compound with m/z 224.055 resulted in MS/MS fragments of m/z 162.053, 134.024, 118.042, and 108.055, which are very close in mass to the ions observed for other

DOI: 10.1021/acs.jafc.5b00879
J. Agric. Food Chem. 2015, 63, 5943−5949

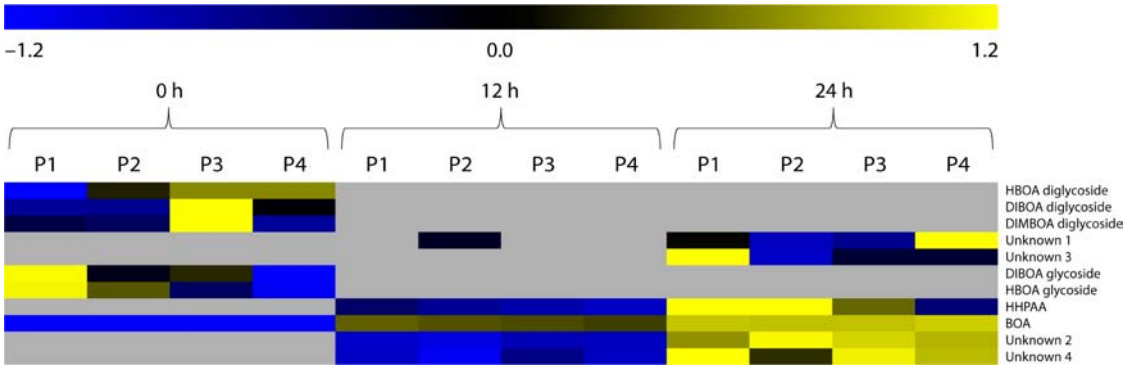

Figure 4. Heatmap representation of the tentatively identified benzoxazinoids and their conversion products in the different bioprocesses (P1−P4) during fermentation (0, 12, and 24 h). The signal abundances were row-wise normalized. The color coding indicates the abundance of each metabolite: yellow, high abundance; blue, low abundance; gray, no value.

benzoxazinoid compounds, including DIMBOA and HHPAA. We have recently observed this same unknown compound to be excreted in urine of mice after feeding with rye bran and, intriguingly, this compound was excreted in significantly higher levels when rye bran was fermented with yeast.[25]

Effects of Fermentation on the Benzoxazinoid Compounds. The relative intensities of the identified compounds had major differences during all four bioprocesses as visualized in a heatmap chart (Figure 4). Prior to fermentation (0 h), both the mono- and diglycoside derivatives of DIBOA, DIMBOA, and HBOA were found in all four fermentation conditions. Although our analytical method was not quantitative, it is worth mentioning that at the onset of fermentation we detected the largest peak areas for DIBOA and HBOA diglycosides (Figure 5), which have been shown to be

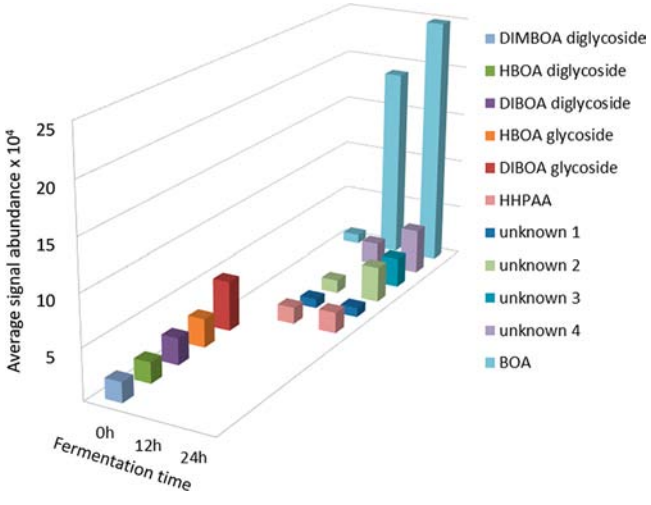

Figure 5. Average abundance of benzoxanoid derivatives and metabolites as relative peak areas plotted against fermentation time. The abundances from the different bioprocesses were combined.

the most abundant benzoxazinoids in wheat bran.[8] There were no benzoxazinoid aglycones or any of the potential degradation products detected prior to fermentation in any of the samples, except for a minor signal for BOA. Between 0 and 12 h of fermentation all di- and monoglycoside derivatives of benzoxazinoids were degraded in all of the tested fermentation conditions. In contrast, the breakdown products of DIBOA and HBOA, namely, BOA and HHPAA, as well as the several unknown compounds potentially derived from benzoxazinoids, were detected only from 12 h onward, showing highest accumulation at 24 h (Figures 4 and 5). One potential mediator for the compound conversion in the fermentation is the microbial metabolism in the bioprocess. Of the four fermentation methods used, P1 and P3 did not contain added lactic acid bacteria (LAB) but only the yeast, whereas in fermentations P2 and P4 a LAB starter was included. However, despite the differential bacterial regime, the fermentation method did not affect the degradation of glycosides and formation of other compounds including BOA and HHPAA (Figure 4). The pH decreased in all fermentations from 6.7 to an average of 4.8 during 24 h, and the use of LAB starter (P2 and P4) had only a slight additional 0.5 unit decrease in pH (Supporting Information (Table 4)). This slight difference in pH had no effect on the metabolic conversions. The lowered pH in fermentations without added LAB is most likely due to the growth of naturally occurring bacteria in the bran as has been demonstrated earlier.[26] Thus, the degradation of benzoxazinoid glycosides or formation of BOA and HHPAA was quite similar after two different types of fermentation irrespective of the microbial content. There were two unknown metabolites, which were produced mainly in either the fermentation containing yeast solely (P1; unknown 3, m/z 188.092) or after the fermentation with yeast, LAB, and enzymes (P4; unknown 1, m/z 150.055) referring to differential impact of the fermentation regime to the metabolic conversion (Figure 4). However, these two compounds remained unknown, similarly as two compounds that were produced in all of the fermentation conditions, which highlights the necessity of further structural analysis to understand the metabolic conversions of benzoxazinoid compounds during food processing.

In fermentations P3 and P4 enzyme preparations with cellulase, xylanase, β-glucanase, and α-amylase activities (Supporting Information (Table 1)) were used to modify the cereal cell wall structure and to release phytochemicals into the fermentation matrix.[27] With the application of enzymes in fermentation, the amount of phytochemicals in the dough can be modified; for example, the phenolic acids can be released from arabinoxylan.[27] This can further improve the bioaccessibility and bioavailability of these compounds.[28,29] Even when the sampling procedure was maintained as similar as possible for the four different fermentation conditions, the metabolic conversions seem to start rapidly after mixing the constituents of the fermentation mixture, as was suggested by the differences in the metabolite levels at the onset of the fermentation (0 h).

DOI: 10.1021/acs.jafc.5b00879
J. Agric. Food Chem. 2015, 63, 5943−5949

Interestingly, the fermentation together with yeast and the mixture of enzymes had the highest amount of the diglycoside conjugates of DIBOA, DIMBOA, and HBOA. This could be due to the enzymatic processing of the bran structure resulting in increased release of diglycoside conjugates to the fermentation media. In fermentation mixture P4 the mixture of enzymes was also added, but together with the LAB starter, which could boost the subsequent conversion of the digycosides and hence result in lower abundances of diglycosides when compared to the fermentation without the addition of LAB. However, the exact location of benzoxazinoids in the bran matrix is not yet studied, and thus the potential to increase their release by enzymatic treatment is only speculative. Detailed kinetic study would require quantitative targeted methods, which is currently not possible as not all of the detected compounds are available as commercial standards, and at the end of the fermentation process the levels of the main end products were relatively similar without striking differences between the different fermentation conditions.

In previous studies it has been demonstrated that boiling and soaking affect both the profile and the apparent concentration of benzoxazinoids in wheat.[8] Whereas it has been speculated that sourdough fermentation may be involved in altering the benzoxazinoid concentration in whole grain bread,[11] it was still unclear if this was due to the fermentation or the baking process. Our results clearly show that extensive structural conversions occur on benzoxazinoids during fermentation without baking, including degradation of benzoxazinoid glycosides and formation of HHPAA. The earlier finding of HHPAA glucuronide and sulfate as one of the most discriminatory signals for whole grain sourdough rye bread intake[11] suggests that HHPAA is bioavailable, as has also been shown in a postprandial study involving rye bran enriched diets.[14] Conversion of HHPAA was suggested to be postabsorptive metabolism,[11] although on the basis of our results this could equally be due to direct absorption of the metabolite present in sourdough bread. However, focused quantitative analyses are required to resolve the kinetics and dose−response relationship of this metabolite.

In our analysis, two signals potentially corresponding to HPAA were detected in the fermented products, but detailed identification could not be accomplished. HPAA has been previously detected in bread and was suggested to be a result from degradation of benzoxazinoid glycosides.[11] However, an alternative way of formation could be due to thermal processing during baking from HHPAA via dehydroxylation. Additionally, in our analysis, we observed unknown metabolites emerging in the sourdough process, which could potentially be of benzoxazinoid origin based on similarity in MS/MS fragments when compared with the identified metabolites. Therefore, it is possible that other, yet unknown, metabolized forms of benzoxazinoids are present in products involving sourdough fermentation and interestingly, as we recently observed, some of these seem to be also bioavailable and excreted in urine of mice after feeding with rye bran.[25]

In conclusion, we showed for the first time in a controlled fermentation that benzoxazinoid glycosides are degraded during fermentation and that HHPAA and BOA, conversion products of benzoxazinoids, alongside other potential metabolites of benzoxazinoid origin, are formed in sourdough. We also showed that the conversion was not remarkably affected by using lactic acid bacteria or enxymes in the fermentation in addition to yeast starter. This result emphasizes the potential of fermentation to modify the composition of phytochemicals embedded in the cereal matrix and the need to examine the effects of food processing on the phytochemical composition to be able to evaluate dietary effects at the molecular level.

■ ASSOCIATED CONTENT

Supporting Information

Tables 1−4. The Supporting Information is available free of charge on the ACS Publications website at DOI: 10.1021/acs.jafc.5b00879.

■ AUTHOR INFORMATION

Corresponding Author

*(O.S.) Department of Biology and Biological Engineering, Food Science, Chalmers University of Technology, Kemivägen 10, Gothenburg, Sweden. E-mail: otto.savolainen@chalmers.se. Phone: +46(0)317723813.

Funding

Funding from the Academy of Finland and Biocenter Finland is gratefully acknowledged.

Notes

The authors declare no competing financial interest.

■ ACKNOWLEDGMENTS

Ville Koistinen is acknowledged for assistance in the preparation of the figures and Miia Reponen for assistance in the LC-qTOF-MS analyses.

■ REFERENCES

(1) Sicker, D.; Frey, M.; Schulz, M.; Gierl, A. Role of natural benzoxazinones in the survival strategy of plants. *Int. Rev. Cytol.* **2000**, *198*, 319−346.

(2) Villagrasa, M.; Guillamon, M.; Labandeira, A.; Taberner, A.; Eljarrat, E.; Barcelo, D. Benzoxazinoid allelochemicals in wheat: distribution among foliage, roots, and seeds. *J. Agric. Food Chem.* **2006**, *54*, 1009−1015.

(3) Niemeyer, H. M. Hydroxamic acids derived from 2-hydroxy-2*H*-1,4-benzoxazin-3(4*H*)-one: key defense chemicals of cereals. *J. Agric. Food Chem.* **2009**, *57*, 1677−1696.

(4) Macias, F. A.; Marin, D.; Oliveros-Bastidas, A.; Molinillo, J. M. Rediscovering the bioactivity and ecological role of 1,4-benzoxazinones. *Nat. Prod. Rep.* **2009**, *26*, 478−489.

(5) Cambier, V.; Hance, T.; de Hoffmann, E. Non-injured maize contains several 1,4-benzoxazin-3-one related compounds but only as glucoconjugates. *Phytochem. Anal.* **1999**, *10*, 119−126.

(6) Hanhineva, K.; Rogachev, I.; Aura, A. M.; Aharoni, A.; Poutanen, K.; Mykkanen, H. Qualitative characterization of benzoxazinoid derivatives in whole grain rye and wheat by LC-MS metabolite profiling. *J. Agric. Food Chem.* **2011**, *59*, 921−927.

(7) Pedersen, H. A.; Laursen, B.; Mortensen, A.; Fomsgaard, I. S. Bread from common cereal cultivars contains an important array of neglected bioactive benzoxazinoids. *Food Chem.* **2011**, *127*, 1814−1820.

(8) Tanwir, F.; Fredholm, M.; Gregersen, P. L.; Fomsgaard, I. S. Comparison of the levels of bioactive benzoxazinoids in different wheat and rye fractions and the transformation of these compounds in homemade foods. *Food Chem.* **2013**, *141*, 444−450.

(9) Adhikari, K. B.; Laursen, B. B.; Lãrke, H. N.; Fomsgaard, I. S. Bioactive benzoxazinoids in rye bread are absorbed and metabolized in pigs. *J. Agric. Food Chem.* **2012**, *60*, 2497−2506.

(10) Adhikari, K. B.; Lãrke, H. N.; Mortensen, A. G.; Fomsgaard, I. S. Plasma and urine concentrations of bioactive dietary benzoxazinoids and their glucuronidated conjugates in rats fed a rye bread-based diet. *J. Agric. Food Chem.* **2012**, *60*, 11518−11524.

DOI: 10.1021/acs.jafc.5b00879
J. Agric. Food Chem. 2015, 63, 5943−5949

(11) Beckmann, M.; Lloyd, A. J.; Haldar, S.; Seal, C.; Brandt, K.; Draper, J. Hydroxylated phenylacetamides derived from bioactive benzoxazinoids are bioavailable in humans after habitual consumption of whole grain sourdough rye bread. *Mol. Nutr. Food Res.* **2013**, n/a.
(12) Zikmundova, M.; Drandarov, K.; Bigler, L.; Hesse, M.; Werner, C. Biotransformation of 2-benzoxazolinone and 2-hydroxy-1,4-benzoxazin-3-one by endophytic fungi isolated from *Aphelandra tetragona*. *Appl. Environ. Microbiol.* **2002**, *68*, 4863−4870.
(13) Zikmundova, M.; Drandarov, K.; Hesse, M.; Werner, C. Hydroxylated 2-amino-3*H*-phenoxazin-3-one derivatives as products of 2-hydroxy-1,4-benzoxazin-3-one (HBOA) biotransformation by *Chaetosphaeria* sp., an endophytic fungus from *Aphelandra tetragona*. *Z. Naturforsch., C: J. Biosci.* **2002**, *57*, 660−665.
(14) Hanhineva, K.; Keski-Rahkonen, P.; Lappi, J.; Katina, K.; Pekkinen, J.; Savolainen, O.; Timonen, O.; Paananen, J.; Mykkanen, H.; Poutanen, K. The postprandial plasma rye fingerprint includes benzoxazinoid-derived phenylacetamide sulfates. *J. Nutr.* **2014**, *144*, 1016−22.
(15) Adhikari, K. B.; Tanwir, F.; Gregersen, P. L.; Steffensen, S. K.; Jensen, B. M.; Poulsen, L. K.; Nielsen, C. H.; Høyer, S.; Borre, M.; Fomsgaard, I. S. Benzoxazinoids: cereal phytochemicals with putative therapeutic and health-protecting properties. *Mol. Nutr. Food Res.* **2015**, n/a−n/a.
(16) Rosenfeld, M. J.; Forsberg, S. R. Compounds for use in weight loss and appetite seppression in humans. U.S. Patent 7,507,731 B2, 2009.
(17) Poupaert, J.; Carato, P.; Colacino, E.; Yous, S. 2(3*H*)-benzoxazolone and bioisosters as "privileged scaffold" in the design of pharmacological probes. *Curr. Med. Chem.* **2005**, *12*, 877−885.
(18) Otsuka, H.; Hirai, Y.; Nagao, T.; Yamasaki, K. Anti-inflammatory activity of benzoxazinoids from roots of *Coix lachryma-jobi* var. ma-yuen. *J. Nat. Prod.* **1988**, *51*, 74−79.
(19) Bharathkumar, H.; Sundaram, M. S.; Jagadish, S.; Paricharak, S.; Hemshekhar, M.; Mason, D.; Kemparaju, K.; Girish, K. S.; Basappa; Bender, A.; Rangappa, K. S. Novel benzoxazine-based aglycones block glucose uptake in vivo by inhibiting glycosidases. *PLoS One* **2014**, *9*, No. e102759.
(20) Buchmann, C. A.; Nersesyan, A.; Kopp, B.; Schauberger, D.; Darroudi, F.; Grummt, T.; Krupitza, G.; Kundi, M.; Schulte-Hermann, R.; Knasmueller, S. Dihydroxy-7-methoxy-1,4-benzoxazin-3-one (DIMBOA) and 2,4-dihydroxy-1,4-benzoxazin-3-one (DIBOA), two naturally occurring benzoxazinones contained in sprouts of Gramineae are potent aneugens in human-derived liver cells (HepG2). *Cancer Lett.* **2007**, *246*, 290−299.
(21) Arroyo, E.; Chinchilla, N.; Molinillo, J. M. G.; Macias, F. A.; Astola, A.; Ortiz, M.; Valdivia, M. M. Aneugenic effects of benzoxazinones in cultured human cells. *Mutat. Res., Genet. Toxicol. Environ. Mutagen.* **2010**, *695*, 81−86.
(22) Saeed, A. I.; Bhagabati, N. K.; Braisted, J. C.; Liang, W.; Sharov, V.; Howe, E. A.; Li, J.; Thiagarajan, M.; White, J. A.; Quackenbush, J. TM4 microarray software suite. *Methods Enzymol.* **2006**, *411*, 134−193.
(23) Saeed, A. I.; Sharov, V.; White, J.; Li, J.; Liang, W.; Bhagabati, N.; Braisted, J.; Klapa, M.; Currier, T.; Thiagarajan, M.; Sturn, A.; Snuffin, M.; Rezantsev, A.; Popov, D.; Ryltsov, A.; Kostukovich, E.; Borisovsky, I.; Liu, Z.; Vinsavich, A.; Trush, V.; Quackenbush, J. TM4: a free, open-source system for microarray data management and analysis. *BioTechniques* **2003**, *34*, 374−378.
(24) Fomsgaard, I. S.; Mortensen, A. G.; Carlsen, S. C. Microbial transformation products of benzoxazolinone and benzoxazinone allelochemicals − a review. *Chemosphere* **2004**, *54*, 1025−1038.
(25) Pekkinen, J.; Rosa-Sibakov, N.; Micard, V.; Keski-Rahkonen, P.; Lehtonen, M.; Poutanen, K.; Mikkänen, H.; Hanhineva, K. Amino acid-derived betaines dominate as urinary markers for rye bran intake in mice fed high-fat diet − a non-targeted metabolomics study. *Mol. Nutr. Food Res.* **2015**, n/a−n/a.
(26) Savolainen, O. I.; Coda, R.; Suomi, K.; Katina, K.; Juvonen, R.; Hanhineva, K.; Poutanen, K. The role of oxygen in the liquid fermentation of wheat bran. *Food Chem.* **2014**, *153*, 424−431.
(27) Nordlund, E.; Katina, K.; Aura, A.-M.; Poutanen, K. Changes in bran structure by bioprocessing with enzymes and yeast modifies the in vitro digestibility and fermentability of bran protein and dietary fibre complex. *J. Cereal Sci.* **2013**, *58*, 200−208.
(28) Anson, N. M.; Selinheimo, E.; Havenaar, R.; Aura, A. M.; Mattila, I.; Lehtinen, P.; Bast, A.; Poutanen, K.; Haenen, G. R. Bioprocessing of wheat bran improves in vitro bioaccessibility and colonic metabolism of phenolic compounds. *J. Agric. Food Chem.* **2009**, *57*, 6148−6155.
(29) Mateo Anson, N.; Aura, A. M.; Selinheimo, E.; Mattila, I.; Poutanen, K.; van den Berg, R.; Havenaar, R.; Bast, A.; Haenen, G. R. Bioprocessing of wheat bran in whole wheat bread increases the bioavailability of phenolic acids in men and exerts antiinflammatory effects ex vivo. *J. Nutr.* **2011**, *141*, 137−143.

DOI: 10.1021/acs.jafc.5b00879
J. Agric. Food Chem. 2015, 63, 5943−5949

In vitro models using cultured human intestinal cells have been shown to be useful for a more focused investigation of the absorption of dietary compounds. One such model, Caco-2 cultured intestinal cells, has been successfully used to study the characteristics of transepithelial transport of a variety of nutrients and dietary components.[23] This system has been adapted for use in iron uptake research[24] and has been used extensively to study iron nutritional qualities of a range of foods and food products. An advantage of the Caco-2 system is that it confers the ability to study Fe uptake effects of individual food components apart from other dietary factors. Using this in vitro system, Hu et al.[25] reported that flavonoid polyphenols in colored bean seed coats strongly inhibited Fe bioavailability in bean digests. Thus, polyphenols have been implicated in reduced iron nutrition, specifically in beans, by studies using a range of experimental systems.

In Fe bioavailability studies, polyphenols have commonly been grouped as Fe uptake inhibitors, with the implication that all members of this class of phytochemicals act in a similar manner. The generalized nature of the presumed inhibitory effect is illustrated by the way that polyphenols are typically measured. Most studies use the Folin−Ciocalteu method,[26] and results are reported as gallic acid equivalents.[27] Little information has been established concerning the effects of specific individual polyphenols on Fe bioavailability. This work set out to identify polyphenolic compounds present in black and white bean and to examine the relative Fe-inhibition properties of specific polyphenols using a Caco-2 cell assay.

MATERIALS AND METHODS

Chemicals. LC-MS grade acetonitrile, LC-MS grade methanol, LC-MS grade formic acid, quercetin 3-glucoside, kaempferol 3-glucoside, 3,4-dihydroxybenzoic acid, catechin, myricetin, quercetin, kaempferol, dimethyl sulfoxide (DMSO), glucose, hydrocortisone, insulin, selenium, triiodothyronine, and epidermal growth factor were purchased from Sigma-Aldrich (St. Louis, MO, USA). Myricetin 3-glucoside was purchased from Extrasynthese (Genay, France). Sodium bicarbonate and PIPES were from Fisher Scientific (Waltham, MA, USA). Fe standard (1000 μg/mL in 2% HCl) was from High-Purity Standards (Charleston, SC, USA). Modified Eagle's medium (MEM), Dulbecco's modified Eagle's medium (DMEM), and 1% antibiotic−antimycotic solution were purchased from Gibco (Grand Island, NY, USA).

Bean Sample Preparation. Dried black and "Great Northern" white beans (Goya Foods, Inc., Secaucus, NJ, USA) were purchased at a local market. Isolated seed coats were prepared by wrapping whole black and white beans in deionized water-soaked paper towels until seed coats began to wrinkle and separate from cotyledons. Seed coats were then removed with forceps, dried, and ground to a coarse powder with a mortar and pestle. Whole beans were rinsed with deionized water, autoclaved for 30 min, lyophilized, and ground with a coffee grinder. To 1 g of ground bean material (cooked whole beans or isolated seed coats) was added 5 mL of methanol/water (50:50 v/v). The slurry was vortexed for 1 min, placed in a 24 °C sonication water bath for 15 min, vortexed again for 1 min, and centrifuged at 4000*g* for 15 min. The supernatant was filtered with a 0.45 μm Teflon syringe filter and stored for later use in a −20 °C freezer. For use in Caco-2 assays, whole bean methanol/water extracts were dried in a rotary evaporator, weighed, and redissolved in an appropriate volume of pH 2 medium (140 mM NaCl and 5 mM KCl, pH adjusted with HCl) to achieve the desired extract concentration.

Preparation of Fe and Polyphenol Solutions. Fe stock solutions were prepared from 1000 mg/mL Fe standard in pH 2 medium. For use in Caco-2 assays, polyphenols were dissolved to a concentration of 1.6 mM in DMSO and diluted with pH 2 medium to achieve 400 μM stock solutions containing 25% DMSO. Stock solutions were further diluted with pH 2 medium to appropriate concentrations for use in Caco-2 assays. Maximum DMSO concentration in the highest polyphenol concentration treatments (30 μM) was 3.1%. For use as LC-MS standards, polyphenols were dissolved to a concentration of 4 mM in DMSO and diluted to 1 mM with MeOH/H_2O (50:50 v/v). These stock solutions were further diluted with 50:50 MeOH/H_2O for use in standard curves.

Caco-2 Assays. Assays were performed with Caco-2 cells cultured on the bottom surface of wells in 24-well culture plates (Costar 24 Well Clear TC-Treated Multiple Well Plates). Cells were grown in DMEM supplemented with 3.7 g/L sodium bicarbonate, 25 mM HEPES (pH 7.2), and 10% fetal bovine serum. Cells were seeded at passages 29−38, at a density of 50000 cells/cm^2 on collagen-treated plates. Under these culture conditions, the cells were confluent by day 4 postseeding and formed highly reproducible, differentiated cell monolayers with consistent protein concentrations over the course of numerous experiments. Cells were used in experiments 13 days postseeding.

Solutions containing bean extract and/or polyphenol(s) were prepared in 150 μL of pH 2 medium. Fifty microliters of iron standard diluted in the same medium was added to extract or polyphenol solutions to achieve 4 or 10 μM Fe final concentration, and combined solutions (200 μL) were incubated at room temperature for 15 min before addition of 1 mL of MEM, supplemented with 3.5 g/L glucose, 2.2 g/L sodium bicarbonate, 10 mmol/L piperazine-*N*,*N*′-bis[2-ethanesulfonic acid] (PIPES) (pH 7.0), 1% antibiotic−antimycotic solution, hydrocortisone (4 mg/L), insulin (5 mg/L), selenium (5 μg/L), triiodothyronine (34 μg/L), and epidermal growth factor (20 μg/L). A half milliliter of this combined solution was applied directly onto Caco-2 cell monolayers in 24-well plates. After overnight incubation at 37 °C, cells were washed twice with a buffered saline solution (130 mM NaCl, 5 mM KCl, 5 mM PIPES, pH 6.7) and then lysed by the addition of 500 μL of 18 MΩ water. Lysed cells were measured for ferritin and protein concentrations as described previously[24,25] with modifications. Ferritin data in Figures 1−4 were acquired using an immunoradiometric assay (FER-IRON II), and data in Figure 5 used an enzyme immunoassay (SPECTRO FERRITIN, both from RAMCO Laboratories, Stafford, TX, USA). Ferritin formation was used as a measure of iron uptake and was expressed in nanograms of ferritin per milligram of cell protein. Cell protein was quantified using the Bio-Rad DC protein assay kit (Bio-Rad Laboratories). Means and standard errors of three replications were calculated for both protein and ferritin concentrations.

LC-MS Analysis. Extracts and standards were analyzed with a Waters Acquity UPLC. Five microliter samples were injected and passed through an Acquity UPLC BEH Shield RP18, 1.7 μm, 2.1 × 100 mm, column (Waters) at 0.5 mL/min. The column was temperature-controlled at 40 °C. The mobile phase consisted of water with 0.1% formic acid (solvent A) and acetonitrile with 0.1% formic acid (solvent B). Polyphenols were eluted using linear gradients of 86.7−84.4% A in 1.5 min, 84.4−81.5% A in 0.2 min, 81.5−77% A in 2.8 min, 77−55% A in 0.5 min, 55−46% A in 1 min, and 46−86.7% A in 0.2 min and a 0.8 min hold at 86.7% A for a total 7 min run time. From the column, flow was directed into a Waters Acquity photodiode array detector set at 300−400 nm and a sampling rate of 20/s. Flow was then directed into the source of a Xevo G2 QTOF mass spectrometer (Waters Corp.), and ESI mass spectrometry was performed in negative ionization mode with a scan speed of 5/s in the mass range from 50 to 1200 Da. Capillary and cone gas voltages were set at 2.3 kV and 30 V, respectively. Desolvation gas flow was 800 L/h, and desolvation gas temperature was 400 °C. Source temperature was 140 °C. Lock-mass correction was used, with leucine enkephalin as the lock-mass standard and a scan frequency of 25 s. Instrumentation and data acquisition were controlled by MassLynx software. Individual polyphenols in bean samples were tentatively determined by mass using MarkerLynx software, and their identities were confirmed by comparison of LC retention times with authentic standards. Polyphenol standard curves for flavonoids were derived from integrated areas under UV absorption peaks from 10 replications.

DOI: 10.1021/acs.jafc.5b00531
J. Agric. Food Chem. 2015, 63, 5950−5956

Standard curves for catechin and 3,4-dihydroxybenzoic acid were constructed from MS ion intensities using 10 replications.

Statistical Analysis. Data are presented as the mean ± standard error of the mean (SEM) in Caco-2 assays of nanograms of ferritin per milligram of protein (Figures 1–5) and as the mean ± standard deviation (SD) for polyphenol concentrations (Table 1).

Table 1. Concentrations of Polyphenols Present in Extracts from Black Bean Seed Coats[a]

polyphenol	rt (min)	*m/z*	mean ± SD (μM)	p/i
myricetin 3-*O*-glucoside	2.80	479.0820	100.6 ± 5.1	i
quercetin 3-*O*-glucoside	3.69	463.0870	33.2 ± 1.6	i
kaempferol 3-*O*-glucoside	4.54	447.0919	17.6 ± 0.9	p
3,4-dihydroxybenzoic acid	1.03	153.0179	14.3 ± 2.5[b]	p
catechin	1.35	289.0706	10.2 ± 0.9[b]	p
myricetin	5.39	317.0292	7.4 ± 0.4	i
quercetin	5.80	301.0344	1.8 ± 0.1	i
kaempferol	6.26	285.0399	1.5 ± 0.1	p

[a]rt, retention time; p/i, promoter or inhibitor of iron uptake in Caco-2 assays. [b]Quantified by MS ion intensity. Other concentrations were determined by integration of UV absorption peak areas.

RESULTS

Increasing concentrations of extracts from whole white or black beans applied to Caco-2 cells in the presence of 10 μM Fe induced an increase in ferritin formation, reaching a maximum at extract concentrations of 0.1–0.2 mg/mL (Figure 1). At higher extract concentrations, ferritin formation declined, with a greater decrease observed in black bean extracts. In the absence of added Fe, ferritin formation remained around baseline levels in both white bean and black bean.

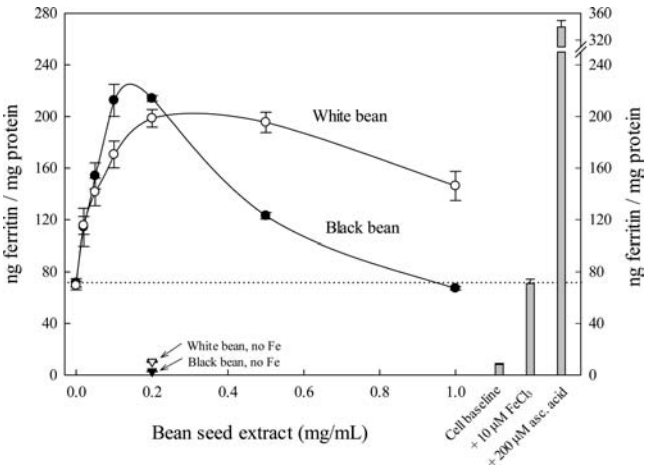

Figure 1. Ferritin formation in Caco-2 cells in response to various concentrations of extracts from whole white and black beans. Dotted line indicates ferritin response to 10 μM Fe alone. Error bars represent standard error of the mean and do not extend outside some data points.

When extracts from seed coats isolated from both black and white beans were applied to Caco-2 cells, the ferritin formation responses to the two types of bean were very different. The presence of white bean seed coats promoted ferritin formation at all extract concentrations, whereas seed coat extracts from black bean inhibited ferritin formation at all concentrations (Figure 2). In white bean seed coats, at extract concentrations of ≥0.2 mg/mL, ferritin production was double that of 10 μM Fe applied alone. Baseline levels of ferritin production were observed in the presence of both white and black bean seed coat extracts when Fe was withheld, demonstrating that enhanced ferritin production by white bean seed coats was not associated with higher endogenous Fe concentration in white bean seed coats. In striking contrast to the response to white bean seed coat extracts, black bean seed coat extracts strongly inhibited ferritin formation to nearly cell baseline levels at extract concentrations of ≥0.2 mg/mL (Figure 2).

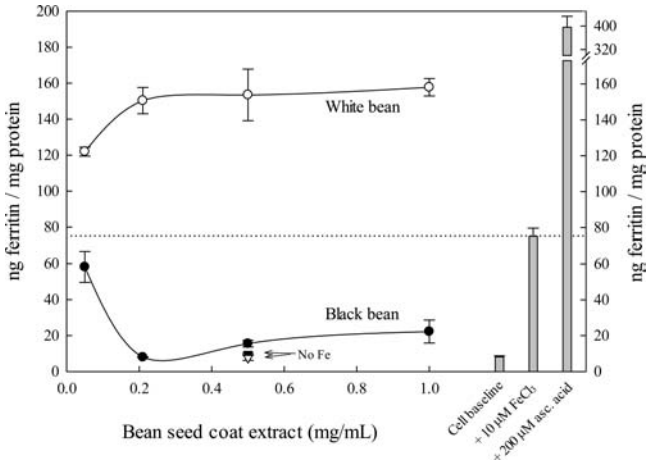

Figure 2. Ferritin formation in Caco-2 cells in response to various concentrations of extracts from white and black bean seed coats. Dotted line indicates ferritin response to 10 μM Fe alone. Error bars represent standard error of the mean and do not extend outside some data points.

Because it has been reported that polyphenols inhibit iron absorption in Caco-2 cells,[25,28] we investigated the effects of individual polyphenols on ferritin formation. Various concentrations of the flavonol myricetin, a polyphenol known to be present in black beans,[8] were added to whole black and white bean extracts (0.2 mg/mL) in a Caco-2 ferritin assay to test the response. Ferritin formation was inhibited in both black and white beans in the presence of myricetin at concentrations ≥10 μM Fe (Figure 3). In the absence of bean extract, 20 μM myricetin plus 10 μM inhibited ferritin formation down to cell baseline levels.

When supplied alone to Caco-2 cells, specific polyphenols had markedly varying effects on ferritin formation. At concentrations equimolar and greater than that of Fe, myricetin strongly inhibited ferritin formation (Figure 4). At higher myricetin concentrations, ferritin formation declined to cell baseline levels. The flavanol epicatechin induced a strong promotional effect on ferritin formation at all concentrations (Figure 4). The increase in ferritin production in the presence of epicatechin was Fe-dependent, as indicated by the low (cell baseline) level of ferritin formed when cells were supplied with 20 μM epicatechin in the absence of Fe (Figure 4).

To identify specific polyphenol composition, black and white bean seed coat extracts were analyzed by LC-MS. In black bean, the most abundant identifiable polyphenol was myricetin 3-*O*-glucoside, followed by lesser amounts of quercetin 3-*O*-glucoside and kaempferol 3-*O*-glucoside (Table 1). The benzoic acid, 3,4-dihydroxybenzoic acid, and the flavanol catechin were also present, followed by aglycones of the most abundant glycosylated flavonols (Table 1). White bean seed coat extracts contained no detectable amounts of these

DOI: 10.1021/acs.jafc.5b00531
J. Agric. Food Chem. 2015, 63, 5950–5956

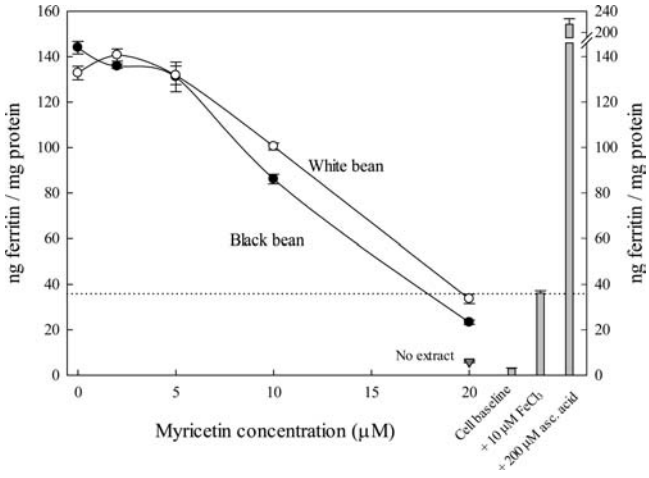

Figure 3. Ferritin formation in Caco-2 cells in response to various concentrations of myricetin plus 0.2 mg/mL extracts from whole white and black beans. Dotted line indicates ferritin response to 10 μM Fe alone. Error bars represent standard error of the mean and do not extend outside some data points.

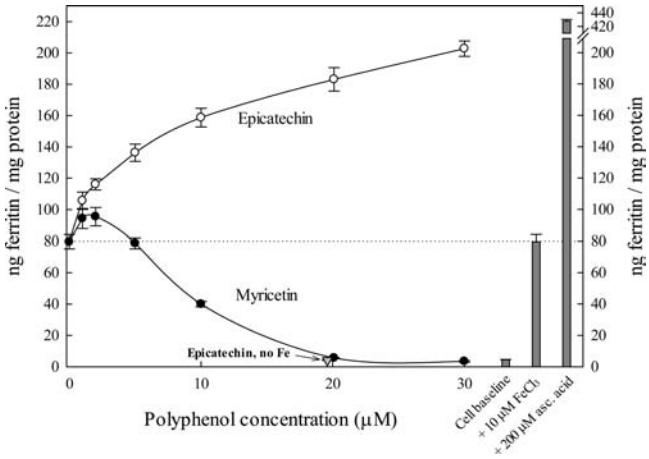

Figure 4. Ferritin formation in Caco-2 cells in response to various concentrations of epicatechin and myricetin, without bean extract. Dotted line indicates ferritin response to 10 μM Fe alone. Error bars represent standard error of the mean and do not extend outside some data points.

compounds. Anthocyanidins and anthocyanins, although present in black bean, were not considered in this study.

To examine the Fe bioavailability effects of the most abundant polyphenols present in black bean seed coats, each of the eight compounds listed in Table 1 was tested for its effect on ferritin formation with the Caco-2 assay. Kaempferol 3-*O*-glucoside, kaempferol, catechin, and 3,4-dihydroxybenzoic acid promoted ferritin production, whereas myricetin 3-*O*-glucoside, quercetin 3-*O*-glucoside, quercetin, and myricetin inhibited the formation of ferritin in a concentration-dependent manner (Figure 5). For all eight compounds, withholding Fe resulted in cell baseline levels of ferritin production. Relative Caco-2 ferritin responses varied somewhat among experiments as shown by slightly different values of Fe-alone and Fe plus ascorbic acid treatments. This is normal for Caco-2 bioassays, and it is important to note that in all cases, polyphenols showing either promotional or inhibitory effect on Fe bioavailability did so consistently. Experiments with individual polyphenols were repeated several times to confirm those observations.

DISCUSSION

In both in vitro and in vivo studies, whole colored beans and the seed coats from colored beans have consistently been shown to inhibit Fe bioavailability, and this inhibition has been demonstrated to be due to the presence of polyphenols in the seed coat.[2,15,22,29] As expected, in the present study, extracts of black bean whole seeds or seed coats inhibited ferritin production (i.e., cell Fe uptake) in Caco-2 cells to a much greater degree than similar extracts from white bean (Figures 1 and 2). The results clearly show that when the black bean seed coat is present, either as an extract from seed coats or whole seeds, the relative effect is one of inhibition of Fe uptake.

It should be noted that, although the primary focus of this study was the effects of polyphenols on Fe uptake, extracts from whole black and white beans and seed coats of white bean produced an enhancement of Fe uptake compared with supplying Caco-2 cells with Fe alone (Figures 1 and 2). The factor(s) present in cotyledons or seed coats responsible for increased ferritin formation cannot be determined from these results, but we can speculate that proteins and possibly phytate and/or other compounds present in extracts could help to solubilize Fe and make it available for absorption. This effect was concentration-dependent, with a maximum Fe uptake at about 0.2 mg/mL in both whole white and black bean extracts (Figure 1). This effect may be due, at least in part, to the presence of phytic acid in cotyledons. Under some conditions, low levels of phytic acid can actually promote Fe uptake in vitro,[30] whereas higher levels like those normally found in crops such as beans inhibit Fe uptake. As expected, the addition of ascorbic acid to Fe in controls (Figures 1−5) clearly demonstrated the power of this reducing agent to increase Fe uptake in Caco-2 assays.

It is also important to note that the low (near cell baseline) level of ferritin production in the absence of added Fe indicates that the compounds extracted from whole beans or seed coats (Figures 1 and 2) or individual polyphenols applied alone to Caco-2 cells (Figures 4 and 5) did not by themselves cause the ferritin formation response. Also, given that the extracts contained negligible amounts of Fe, it is very likely that the ferritin formation responses observed in these experiments were due to the interaction of extracted compounds with exogenously added Fe. Therefore, we can be confident that the in vitro conditions used in this work are suitable for characterizing both promotional and inhibitory effects of extractable compounds on Caco-2 cell Fe uptake.

There has been a consistent general assertion in the literature that all polyphenols inhibit Fe bioavailability.[31] This assumption is countered, however, by the results of the present study. Clearly, the addition of the flavonoid myricetin, a polyphenol known to be present in black beans,[8] to whole black and white bean extracts brought about a concentration-dependent decrease in Fe bioavailability (Figure 3). At myricetin concentrations >5 μM, the ferritin-promoting effects of whole bean extracts seen in Figure 1 were reversed by the addition of this individual polyphenol. Similarly, direct application of myricetin alone to Caco-2 cells brought about a strong decrease in Fe uptake at concentrations >5 μM (Figure 4).

On the other hand, the strong, concentration-dependent promotion of ferritin formation by epicatechin and catechin (Figures 4 and 5) and the moderate enhancement of Fe uptake

DOI: 10.1021/acs.jafc.5b00531
J. Agric. Food Chem. 2015, 63, 5950−5956

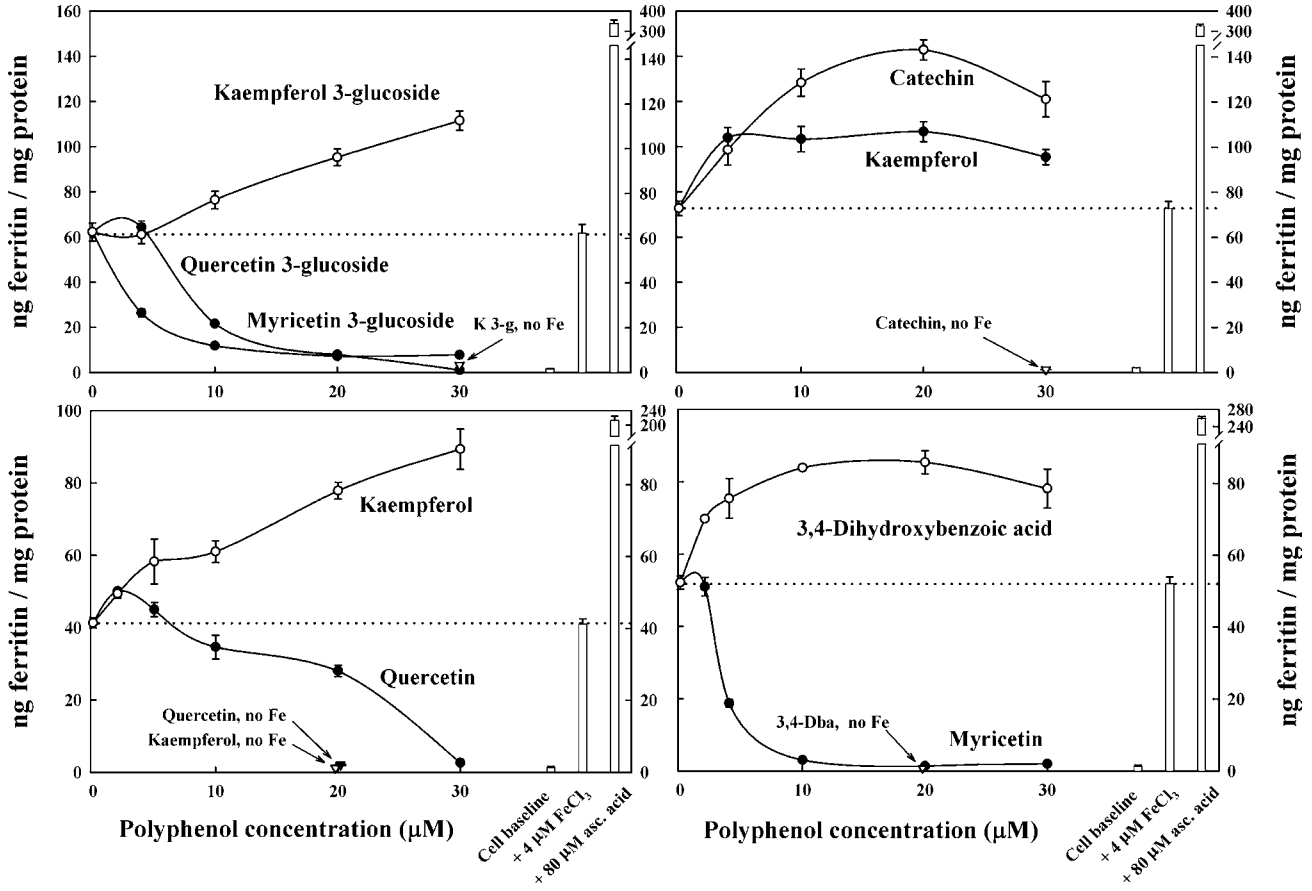

Figure 5. Ferritin formation in Caco-2 cells in response to various concentrations of eight polyphenols determined to be present in black bean seed coat extracts. Dotted line indicates ferritin response to 4 μM Fe alone. Error bars represent standard error of the mean and do not extend outside some data points.

by kaempferol, kaempferol 3-glucoside, and 3,4-dihydroxybenzoic acid (Figure 5), all applied directly to Caco-2 cells, are in contrast to the general assumption that polyphenols inhibit Fe uptake. As summarized in Table 1, of the eight most abundant non-anthocyanin polyphenols present in black bean seed coats, four were shown to be promoters of iron uptake in Caco-2 cells and four were shown to be inhibitors (Figure 5). This appears to be the first study to clearly show both inhibitory and promotional effects on Fe uptake by specific polyphenols. It is important to note that these cell culture experiments are relatively easy to carry out. Thus, we believe that this approach can be applied to characterize the effects of the multitude of other compounds present in staple food crops (and their interactions) that can influence Fe bioavailability.

The mechanism by which epicatechin and catechin promote Fe uptake is not known. One possible mechanism that may be involved with promotion is increased solubility of iron−epicatechin/catechin complexes coupled with favorable exchange kinetics at membrane-bound iron transport sites. This would tend to increase the amount of iron available for uptake by Caco-2 cells.

Another possible mechanism with some support in the literature is reduction of Fe^{3+} to Fe^{2+} by epicatechin. As shown in Figures 1−5, iron reduction by ascorbic acid had a strongly promoting effect on iron uptake in our Caco-2 system. If it occurs, iron reduction by epicatechin should also have a promoting effect. As reviewed by Perron et al.,[13] reduction of Fe^{3+} to Fe^{2+} by some polyphenols can occur, especially at low pH. Catechol[32] and epicatechin[33,34] have been demonstrated to reduce Fe^{3+} to Fe^{2+} at pH 2−3. In our experiments, polyphenols were incubated with Fe in pH 2 solution for 15 min and then added to pH 7-buffered MEM and quickly placed on Caco-2 cell monolayers. It is conceivable that this protocol was capable of generating sufficient Fe^{2+} to cause promotion of iron uptake before re-oxidation of Fe^{2+} to Fe^{3+} occurred. Re-oxidation of Fe^{2+} has been reported to occur with an increase in pH, but the kinetics with which this may occur is not well characterized.[32]

Iron reduction via the catecholate configuration on the B ring of epicatechin and catechin may be involved with increased Fe uptake.[13] Another promoter of iron uptake in our study, 3,4-dihydroxybenzoic acid, also contains a catecholate substructure. However, the promoters kaempferol and kaempferol 3-glucoside do not have either catecholate or gallate substructures, so their Fe-uptake promotional properties may proceed through another mechanism. On the other hand, the inhibitors quercetin, myricetin, and their glucosides do contain catecholate and gallate ligands, respectively. The inhibitory properties of those four polyphenols may occur simply by strongly binding iron and making it unavailable for uptake. Thus, a consistent polyphenol structure/iron bioavailability functional relationship influencing Fe bioavailability is not apparent in the major black bean polyphenols identified in this study.

We can speculate on the concentration-dependent inhibitory activity of myricetin on iron uptake (Figure 4) on the basis of

DOI: 10.1021/acs.jafc.5b00531
J. Agric. Food Chem. 2015, 63, 5950−5956

the well-documented ability of phenolic compounds to chelate iron.[35−37] Stability constant values for Fe^{3+}−myricetin complexes in the range of 10^5−10^9 have been reported,[9] and inhibition of iron uptake due to binding by polyphenols has been demonstrated in Caco-2 cells.[28,38] Thus, the iron uptake inhibition by myricetin shown in Figure 4 is consistent with previously published reports and suggests that it is due to iron−myricetin complexation and subsequent Fe uptake inhibition.

In black bean seed coats, the total concentration of the four iron uptake inhibitors was >3 times higher than the concentration of the four promoters (Table 1). Thus, it is not surprising that the net effect of black bean seed coat extracts containing all eight major polyphenols is a strong inhibition of iron uptake (Figure 2). However, implicit in this calculation is that the polyphenols studied here have a similar concentration effect on promotion or inhibition. In fact, examination of the curves in Figure 5 suggests that this assumption may not be true. For example, myricetin appears to be a more effective inhibitor than quercetin at a given concentration and catechin, a more effective promoter than kaempferol. It is not possible to deduce from the data in Figure 5 the net effect of combining promoters and inhibitors. Additional studies will be needed to establish the relative effectiveness of individual polyphenols and their interactions to promote or inhibit iron bioavailability.

It would appear that identification of polyphenols that can promote iron bioavailability raises the possibility of producing breeding lines with enhanced nutritional quality. The results reported here were obtained using an in vitro cell culture system, and it is not clear that the promotional effects observed using this system would extend to in vivo systems. Experiments with animal models or human feeding trials will be necessary to test the possibility. It is interesting that a human study of the effects of several polyphenols determined that, whereas gallic acid and tannic acid inhibited iron absorption, catechin produced no such inhibition.[39] This observation suggests that, even if polyphenol promotion of iron uptake in cell culture does not translate to promotion in vivo, breeding for reduced levels of inhibitory polyphenols as well as enhanced levels of promoting polyphenols may yield more nutritious staple foods.

AUTHOR INFORMATION

Corresponding Author

*(J.J.H.) Phone: (607) 254-4919. Fax: (607) 255-1132. E-mail: jjh16@cornell.edu.

Notes

The authors declare no competing financial interest.

ACKNOWLEDGMENTS

We thank Mary Bodis and Yongpei Chang for their invaluable assistance with Caco-2 experiments and for maintaining cell cultures. Expert technical advice concerning LC-MS was provided by Dr. Ted Thannhauser and Dr. Stuart Krasnoff.

REFERENCES

(1) WHO. Worldwide prevalence of anaemia 1993−2005. *WHO Global Database on Anaemia*; de Benoist, B., McLean, E., Egli, I., Cogswell, M., Eds.; World Health Organization: Geneva, Switzerland, 2008; pp 1−40.

(2) Ariza-Nieto, M.; Blair, M. W.; Welch, R. M.; Glahn, R. P. Screening of iron bioavailability patterns in eight bean (*Phaseolus vulgaris* L.) genotypes using the Caco-2 cell *in vitro* model. *J. Agric. Food Chem.* **2007**, *55*, 7950−7956.

(3) Torres, J.; Dominguez, S.; Cerda, M. F.; Obal, G.; Mederos, A.; Irvine, R. F.; Diaz, A.; Kremer, C. Solution behavior of *myo*-inositol hexakisphosphate in the presence of multivalent cations. Prediction of a neutral pentamagnesium species under cytosolic/nuclear conditions. *J. Inorg. Biochem.* **2005**, *99*, 828−840.

(4) Asenstorfer, R. E.; Wang, Y.; Mares, D. J. Chemical structure of flavonoid compounds in wheat (*Triticum aestivum* L.) flour that contribute to the yellow colour of Asian alkaline noodles. *J. Cereal Sci.* **2006**, *43*, 108−119.

(5) Dao, L.; Friedman, M. Chlorogenic acid content of fresh and processed potatoes determined by ultraviolet spectrophotometry. *J. Agric. Food Chem.* **1992**, *40*, 2152−2156.

(6) Franke, A. A.; Hankin, J. H.; Yu, M. C.; Maskarinec, G.; Low, S. H.; Custer, L. J. Isoflavone levels in soy foods consumed by multiethnic populations in Singapore and Hawaii. *J. Agric. Food Chem.* **1999**, *47*, 977−986.

(7) Beta, T.; Rooney, L. W.; Marovatsanga, L. T.; Taylor, J. R. N. Phenolic compounds and kernel characteristics of Zimbabwean sorghums. *J. Sci. Food Agric.* **1999**, *79*, 1003−1010.

(8) Lin, L.-Z.; Harnly, J. M.; Pastor-Corrales, M. S.; Luthria, D. L. The polyphenolic profiles of common bean (*Phaseolus vulgaris* L.). *Food Chem.* **2008**, *107*, 399−410.

(9) Sungur, S.; Uzar, A. Investigation of complexes tannic acid and myricetin with Fe(III). *Spectrochim. Acta, Part A* **2008**, *69*, 225−229.

(10) Mladenka, P.; Macakova, K.; Filipsky, T.; Zatloukalova, L.; Jahodar, L.; Bovicelli, P.; Silvestri, I. P.; Hrdina, R.; Saso, L. In vitro analysis of iron chelating activity of flavonoids. *J. Inorg. Biochem.* **2011**, *105*, 693−701.

(11) Hynes, M. J.; Coinceanainn, M. O. The kinetics and mechanisms of the reaction of iron(III) with gallic acid, gallic acid methyl ester and catechin. *J. Inorg. Biochem.* **2001**, *85*, 131−142.

(12) Ryan, P.; Hynes, M. J. The kinetics and mechanisms of complex formation and antioxidant behaviour of the polyphenols EGCg and ECG with iron(III). *J. Inorg. Biochem.* **2007**, *101*, 585−593.

(13) Perron, N. R.; Brumaghim, J. L. A review of the antioxidant mechanisms of polyphenol compounds related to iron binding. *Cell Biochem. Biophys.* **2009**, *53*, 75−100.

(14) Tako, E.; Glahn, R. P.; Laparra, J. M.; Welch, R. M.; Lei, X.; Kelly, J. D.; Rutzke, M. A.; Miller, D. D. Iron and zinc bioavailabilities to pigs from red and white beans (*Phaseolus vulgaris* L.) are similar. *J. Agric. Food Chem.* **2009**, *57*, 3134−3140.

(15) Tako, E.; Glahn, R. P. White beans provide more bioavailable iron than red beans: studies in poultry (*Gallus gallus*) and an *in vitro* digestion/Caco-2 model. *Int. J. Vitam. Nutr. Res.* **2010**, *80*, 416−429.

(16) Tako, E.; Blair, M. W.; Glahn, R. P. Biofortified red mottled beans (*Phaseolus vulgaris* L.) in a maize and bean diet provide more bioavailable iron than standard red mottled beans: studies in poultry (*Gallus gallus*) and an in vitro digestion/Caco-2 model. *Nutr. J.* **2011**, *10*, 113−122.

(17) Tako, E.; Beebe, S. E.; Reed, S.; Hart, J. J.; Glahn, R. P. Polyphenolic compounds appear to limit the nutritional benefit of biofortified higher iron black bean (*Phaseolus vulgaris* L.). *Nutr. J.* **2014**, *13*, 28.

(18) Grieger, J. A.; Haas, J. D.; Murray-Kolb, L. E.; Kris-Etherton, P.; Beard, J. L. Nutrient adequacy and food group consumption of Filipino novices and religious sisters over a nine month period. *Asia Pac. J. Clin. Nutr.* **2008**, *17*, 566−572.

(19) Tako, E.; Reed, S. M.; Budiman, J.; Hart, J. J.; Glahn, R. P. Higher iron pearl millet (*Pennisetum glaucum* L.) provides more absorbable iron that is limited by increased polyphenolic content. *Nutr. J.* **2015**, *14*, 11.

(20) Lynch, S. R.; Beard, J. L.; Dassenko, S. A.; Cook, J. D. Iron absorption from legumes in humans. *Am. J. Clin. Nutr.* **1984**, *40*, 42−47.

(21) Donangelo, C. M.; Woodhouse, L. R.; King, S. M.; Toffolo, G.; Shames, D. M.; Viteri, F. E.; Cheng, Z.; Welch, R. M.; King, J. C. Iron and zinc absorption from two bean (*Phaseolus vulgaris* L.) genotypes in young women. *J. Agric. Food Chem.* **2003**, *51*, 5137−5143.

DOI: 10.1021/acs.jafc.5b00531
J. Agric. Food Chem. 2015, 63, 5950−5956

(22) Petry, N.; Egli, I.; Zeder, C.; Walczyk, T.; Hurrell, R. Polyphenols and phytic acid contribute to the low iron bioavailability from common beans in young women. *J. Nutr.* **2010**, *140*, 1977−1982.
(23) Failla, M. L.; Chitchumronchokchai, C. *In vitro* models as tools for screening the relative bioavailabilities of provitamin A carotenoids in foods. *HarvestPlus Technical Monograph 3*; HarvestPlus: Washington, DC, USA, and Cali, Colombia, 2005; pp 1−33.
(24) Glahn, R. P.; Lee, O. A.; Yeung, A.; Goldman, M. I.; Miller, D. D. Caco-2 cell ferritin formation predicts nonradiolabeled food iron availability in an *in vitro* digestion Caco-2 cell culture model. *J. Nutr.* **1998**, *128*, 1555−1561.
(25) Hu, Y.; Cheng, Z.; Heller, L. I.; Krasnoff, S. B.; Glahn, R. P.; Welch, R. M. Kaempferol in red and pinto bean seed (*Phaseolus vulgaris* L.) coats inhibits iron bioavailability using an *in vitro* digestion/human Caco-2 cell model. *J. Agric. Food Chem.* **2006**, *54*, 9254−9261.
(26) Folin, O.; Ciocalteu, V. On tyrosine and tryptophane determinations in proteins. *J. Biol. Chem.* **1927**, *73*, 627−650.
(27) Singleton, V. L.; Orthofer, R.; Lamuela-Raventos, R. M. Analysis of total phenols and other oxidation substrates and antioxidants by means of Folin-Ciocalteu reagent. *Method Enzymol.* **1999**, *299*, 152−178.
(28) Ma, Q.; Kim, E.-Y.; Lindsay, E. A.; Han, O. Bioactive dietary polyphenols inhibit heme iron absorption in a dose-dependent manner in human intestinal Caco-2 cells. *J. Food Sci.* **2011**, *76*, H143−H150.
(29) Lung'aho, M. G.; Glahn, R. P. Use of white beans instead of red beans may improve iron bioavailability from a Tanzanian complementary food mixture. *Int. J. Vitam. Nutr. Res.* **2010**, *80*, 24−31.
(30) Engle-Stone, R.; Yeung, A.; Welch, R.; Glahn, R. Meat and ascorbic acid can promote Fe availability from Fe-phytate but not from Fe-tannic acid complexes. *J. Agric. Food Chem.* **2005**, *53*, 10276−10284.
(31) Mascitelli, L.; Goldstein, M. R. Inhibition of iron absorption by polyphenols as an anticancer mechanism. *QJM* **2011**, *104*, 459−461.
(32) Powell, H. K. J.; Taylor, M. C. Interactions of iron(II) and iron(III) with gallic acid and its homologues: a potentiometric and spectrophotometric study. *Aust. J. Chem.* **1982**, *35*, 739−756.
(33) Kennedy, J. A.; Powell, H. K. J. Polyphenol interactions with aluminum(III) and iron(III): their possible involvement in the podsolization process. *Aust. J. Chem.* **1985**, *38*, 879−888.
(34) Hider, R. C.; Liu, Z. D.; Khodr, H. H. Metal chelation of polyphenols. *Methods Enzymol.* **2001**, *335*, 190−203.
(35) Morel, I.; Lescoat, G.; Cillard, P.; Cillard, J. Role of flavonoids and iron chelation in antioxidant action. *Methods in Enzymol.* **1994**, *234*, 437−443.
(36) Fernandez, M. T.; Mira, M. L.; Florencio, M. H.; Jennings, K. R. Iron and copper chelation by flavonoids: an electrospray mass spectrometry study. *J. Inorg. Biochem.* **2002**, *92*, 105−111.
(37) Andjelkovic, M.; Van Camp, J.; De Meulenaer, B.; Depaemelaere, G.; Socaciu, C.; Verloo, M.; Verhe, R. Iron-chelation properties of phenolic acids bearing catechol and galloyl groups. *Food Chem.* **2006**, *98*, 23−31.
(38) Kim, E.-Y.; Ham, S.-K.; Shigenaga, M. K.; Han, O. Bioactive dietary polyphenolic compounds reduce nonheme iron transport across human intestinal cell monolayers. *J. Nutr.* **2008**, *138*, 1647−1651.
(39) Brune, M.; Rossander, L.; Hallberg, L. Iron absorption and phenolic compounds: importance of different phenolic structures. *Eur. J. Clin. Nutr.* **1989**, *43*, 547−557.

DOI: 10.1021/acs.jafc.5b00531
J. Agric. Food Chem. 2015, 63, 5950−5956

this food after oral administration to rats. We used an ether derivative compound with one OH (tyrosol ethyl ether, TEE), one with two OH (hydroxytyrosol ethyl ether, HTEE), and one with no OH in its structure (3,4-di-*o*-methylidene-hydroxytyrosol ethyl ether, MHTEE). Although MHTEE is a related phenolic compound not present in VOO, it was tested here as a "negative control" for antioxidant effects. Ethyl ether derivatives were used because of their greater lipid solubility and metabolic stability than natural compounds.[15,16] We chose the ethyl derivative with a short hydrocarbon chain for testing, because this made it more likely that the differences we observed between compounds were related to their basic chemical structure and the possible influence of the side chain. Moreover, by using different hydrocarbon chain lengths in the same experimental model, we aimed to show that the neuroprotective effect of the ethyl derivative was similar to that of the nonetherified compound.[17]

The sequence of our experiments was designed to answer the following questions: (1) Is the presence of OH important for the antioxidant effect of VOO polyphenols after oral administration? (2) Is there a relationship between the OH-antioxidant effect of VOO polyphenols and their neuroprotective effect after oral administration in rats? (3) Are the neuroprotective mechanisms of these compounds directly related to their antioxidant effects, and are the latter related to the OH groups, or are their neuroprotective effects explainable by other mechanisms?

MATERIALS AND METHODS

Chemicals. Lactate dehydrogenase reagent kits were obtained from Biosystem SA (Barcelona, Spain). HTEE (two OH in the chemical structure), TEE (one OH in the chemical structure), and MHTEE (no OH in the chemical structure) (Figure 1) were chemically synthesized

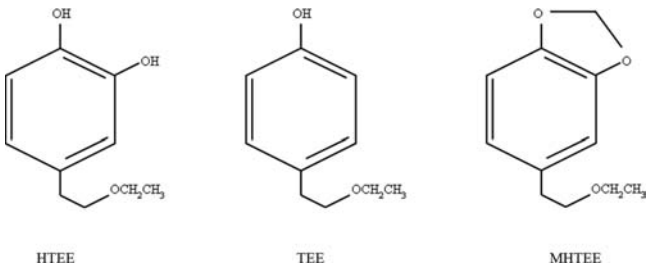

Figure 1. Chemical structures of hydroxytyrosol and hydroxytyrosyl alkyl ethers.

according to the methods of Madrona et al.[18] We chose the ethyl derivative to a long hydrocarbon chain in order not to interfere with the essential chemical structure in our explanation of how a known antioxidant affects these polyphenols. This approach allowed us to ascribe the differences between compounds to the basic chemical structure and the possible influence of the side chain. Moreover, research with different hydrocarbon chain lengths in the same experimental model showed that the ethyl derivative had a neuroprotective effect very similar to that of the nonetherified compound.[17]

Study Design. The animals (10 per group) were 2-month-old adult male Wistar rats (body weight 200−250 g). All rats were used in accordance with current Spanish legislation for animal care, use, and housing (EDL 2013/80847. BOE-A-2013-6271). The recommendations in the *Guide for the Care and Use of Laboratory Animals* (NIH publication 86-23, revised 1985) were followed, as well the Spanish Law on the Protection of Animals, where applicable. The study protocol was approved by the University of Malaga Ethics Committee for the Use of Animals.

Animals (10 rats per group) were distributed in seven groups: (1) control rats treated with saline, (2) rats treated with 10 mg/kg/day po (HTEE), (3) rats treated with 20 mg/kg/day po HTEE, (4) rats treated with 10 mg/kg/day po TEE, (5) rats treated with 20 mg/kg/day po TEE, (6) rats treated with 10 mg/kg/day po MHTEE, and (7) rats treated with 20 mg/kg/day po MHTEE. These doses were chosen according to results obtained in a previous study with HTEE, HTEE acetate, and HTEE ethyl ether in the same experimental model.[19,20] All compounds were given once per day for 7 days via an endogastric cannula at 10:00 a.m. The last dose was given 1 h before the animals were killed.

All rats were anesthetized with pentobarbital sodium (40 mg/kg ip) and were then decapitated with a guillotine.

In Vitro Model of Rat Brain Hypoxia−Reoxygenation. We used a previously described in vitro method of hypoxia−reoxygenation in brain slices.[21] The cortex and midbrain were cut coronally into 1 mm slices with a vibrating microtome (Capdem Instruments, San Francisco, CA, USA). The slices were placed in buffer (composition in mmol/L: 100 NaCl, 0.05 KCl, 24 $NaHCO_3$, 0.55 KH_2PO_4, 0.005 $CaCl_2$, 2 $MgSO_4$, 9.8 glucose, pH 7.4) and perfused with a mixture of 95% O_2 and 5% CO_2. After 30 min to reach equilibrium, the slices were placed in fresh buffer of the same composition except that the concentration of $CaCl_2$ was 3 mmol/L, that of $MgSO_4$ was 0.001 mmol/L, and no glucose was included. This solution was perfused with a mixture of 95% N_2 and 5% CO_2 for 20 min (hypoxia). Then the slices were placed in fresh buffer containing glucose, and the solution was perfused with a mixture of 95% O_2 and 5% CO_2 (reoxygenation).

Brain slices and/or incubation buffer were analyzed (1) after 30 min of incubation and before N_2 perfusion, (2) after 20 min of perfusion with N_2, and (3) after 180 min of reoxygenation. For all studies the tissues were quickly frozen in liquid nitrogen and stored at −80 °C until the day of the experiment, which was done not more than 7 days after the sample was frozen.

Analytical Techniques. All techniques were run in a single-blind manner; that is, the persons who did the assays were unaware of the origin and nature of the samples.

Lipid Peroxidation. To quantify lipid peroxidation, we measured thiobarbituric acid reactive substances (TBARS) in brain cell membrane-enriched fractions.[22] Absorbance was determined spectrophotometrically at 532 nm (FLUOstar-POLAEstar, BMG Labtechnologies. Offenburg, Germany). The results were expressed as nanomoles of TBARS per milligram of protein.

Glutathione Levels. Total glutathione was measured spectrofluorometrically.[23] Brain tissue was homogenized in 0.1 M sodium phosphate buffer (pH 8.0) with 25% phosphoric acid at a proportion of 1:20 and then centrifuged at 13000*g* for 15 min at 4 °C to obtain the supernatant. Cuvettes were prepared for spectrofluorometry with sodium phosphate buffer, the supernatant for each sample, and *o*-phthaldehyde. To determine the proportions of oxidized and reduced glutathione, we incubated the supernatant from each sample with 4-vinylpyridine and then proceeded as for as total glutathione.

Lactate Dehydrogenase Assay. Tissue damage was measured as lactate dehydrogenase (LDH) efflux. Enzyme activity was measured spectrophotometrically at 340 nm with a commercial kit (Cytotoxicity Detection Kit, Roche Applied Science, Barcelona, Spain) according to the manufacturer's instructions.

3-Nitrotyrosine. Brain tissue was homogenized (1:10 w/v) in a buffer containing 100 mM KH_2PO_4/K_2HPO_4 and 0.1% digitonin (pH 7.4). Then the homogenate was centrifuged at 5000*g* for 10 min at 4 °C. The amount of 3-nitrotyrosine in the supernatant was measured according to the manufacturer's instructions for the enzyme immunoassay kit.

Prostaglandin E_2. Brain tissues were snap-frozen in liquid nitrogen and stored until analysis. The samples were homogenized (1:10 w/v) in 15% methanol with 0.1 N phosphate-buffered saline (pH 7.5), then centrifuged at 37000*g* for 15 min at 4 °C. The supernatant was run through a C18 column (Bio-Rad Laboratories, Hercules, CA, USA) that had been activated with absolute methanol, followed by washing

DOI: 10.1021/acs.jafc.5b00627
J. Agric. Food Chem. 2015, 63, 5957−5963

Table 1. Oxidative Stress Variables in Oxygenated Brain Slices (N = 10 Rats per Group) after 7 Days of Treatment with 10 or 20 mg/kg/day po Hydroxytyrosol Ethyl Ether (HTEE), Tyrosol Ethyl Ether (TEE), or 3,4-Di-*o*-methylidene-hydroxytyrosol Ethyl Ether (MHTEE)[a]

compound (mg/kg/day po)	TBARS (nmol/mg protein)	GSH (μmol/g tissue)	% GSSG with respect to GSH+GSSG
control	2.3 ± 0.4	12.9 ± 4.6	16.1 ± 4.2
HTEE (10)	2.5 ± 0.4	11.9 ± 4.2	15.0 ± 7.7
HTEE (20)	2.2 ± 0.4	12.1 ± 3.5	15.3 ± 4.2
TEE (10)	2.5 ± 0.4	11.9 ± 2.3	16.2 ± 6.9
TEE (20)	2.5 ± 0.7	13.1 ± 2.3	15.1 ± 3.1
MHTEE (10)	2.5 ± 0.4	11.1 ± 3.1	17.3 ± 6.2
MHTEE (20)	2.5 ± 1.1	11.7 ± 4.6	17.2 ± 7.3

[a]TBARS, thiobarbituric acid reactive substances; GSH, reduced glutathione; GSSG, oxidized glutathione.

Table 2. Oxidative Stress Variables after the Reoxygenation Period after Hypoxia in Brain Slices (N = 10 Rats per Group) after 7 Days of Treatment with 10 or 20 mg/kg/day po Hydroxytyrosol Ethyl Ether (HTEE), Tyrosol Ethyl Ether (TEE), or 3,4-Di-*o*-methylidene-hydroxytyrosol Ethyl Ether (MHTEE)[a]

compound (mg/kg/day po)	TBARS (nmol/mg protein)	GSH (μmol/g tissue)	% GSSG with respect to GSH+GSSG
control	5.0 ± 1.5	6.5 ± 2.3	22.5 ± 5.4
HTEE (10)	3.2 ± 1.5[b]	6.6 ± 1.5	20.0 ± 9.7
HTEE (20)	2.6 ± 1.5[b]	6.6 ± 3.5	20.9 ± 13.1
TEE (10)	4.6 ± 1.5	5.9 ± 2.7	22.1 ± 6.6
TEE (20)	4.5 ± 1.5[b]	6.4 ± 2.7	21.3 ± 12.4
MHTEE (10)	4.6 ± 1.5	6.9 ± 3.1	24.2 ± 12.0
MHTEE (20)	4.8 ± 1.5	6.7 ± 3.5	21.2 ± 11.2

[a]TBARS, thiobarbituric acid reactive substances; GSH, reduced glutathione; GSSG, oxidized glutathione. [b]$p < 0.001$ with respect to control group.

with distilled water. After the sample had been assayed, the column was washed with 15% methanol in distilled water followed by petroleum ether. Prostaglandins were eluted with methyl formate. The samples were then dried at room temperature under a nitrogen current and reconstituted with phosphate-buffered saline. The concentration of prostaglandin E_2 was measured with a commercial enzyme immunoassay (GE Healthcare UK Limited, Little Chalfont, Buckinghamshire, UK).

Interleukin 1β (IL1β). The tissue was homogenized in a volume of 1 mL of a buffer (4 °C, pH 7.2) containing 50 mM Tris, 1 mM EDTA, 6 mM $MgCl_2$, 1 mM phenylmethanesufonyl fluoride, 5 μg/mL leupeptin, 1 mg/mL antipain, 1 mg/mL aprotinin, and 1 mg/mL soybean trypsin inhibitor. After mixing, the samples were transferred to silicone tubes, then sonicated (VC-50T Vibracell, Sonics Materials, Newtown, CT, USA) for 5−10 s, and centrifuged at 14000*g* for 10 min at 4 °C. Then the supernatant was collected and processed according to the instructions for commercial kits for IL1β determination.

Statistical Methods. The data in the text, tables, and figures are expressed as the mean ± standard deviation of 15 animals or measurements. All statistical analyses were done with the Statistical Package for Social Sciences v. 19.0 (SPSS Co., Chicago, IL, USA). One-way analysis of variance followed by Bonferroni transformation and unpaired Student's t tests were used. To establish a possible relationship between cell death (LDH efflux) and other biochemical variables, Pearson correlation coefficients were calculated. In all cases, statistical significance was assumed at a value of $p < 0.05$.

RESULTS AND DISCUSSION

There were no statistically significant differences between control samples and samples from rats treated with HTEE, TEE, or MHTEE in the mean value of TBARS or reduced (GSH) or oxidized (GSSG) glutathione in oxygenated brain slices (Table 1). After the oxygenation period in brain slices tested with the hypoxia−reoxygenation experimental model, TBARS production increased from 2.3 ± 0.6 nmol/mg protein before anoxia to 5.0 ± 1.6 nmol/mg protein after reoxygenation ($p < 0.0001$). After ex vivo treatment with HTEE, TBARS production was inhibited, whereas TEE showed significant inhibition only at 20 mg/kg/day and MHTEE did not produce significant changes (Table 2).

In the experiments with brain hypoxia−reoxygenation, GSH decreased from 12.9 ± 4.6 to 6.5 ± 2.2 μmol/g tissue ($p < 0.0001$), and the percentage of GSSG with respect to GSH +GSSG increased from 16.1 ± 4.1 to 22.5 ± 5.3% ($p < 0.01$). None of the compounds modified GSH concentration or the percentage of GSSG with respect to GSH+GSSG (Table 2).

The antioxidant effect of hydroxytyrosol (two OH groups) and some esterified and etherified derivatives has been reported (see reviews by Raederstorff and Granados-Principal)[5,24] in chemical matrices, in cell culture, and in whole animal organs including rat brain tissue.[7,19,25,26] This effect has also been demonstrated in ex vivo experiments.[17] Tyrosol (one OH group) has demonstrated a weak antioxidant effect[27] that was approximately 25% of the effect of hydroxytyrosol in cell cultures.[28] The results of the present study confirmed these differences, because the antioxidant effect of TEE was about 20−22% that of HTEE.

The present study demonstrates the relationship between the antiperoxidative effect of these compounds and the presence of OH groups in brain tissue after oral administration to rats. Our results are further supported by the absence of an antioxidant effect of MHTEE, which lacks OH groups. Therefore, two phenolic compounds in VOO exhibited very different antioxidant potencies: one (HTEE) had a clear antioxidant effect, whereas the other (TEE) had little effect on oxidative stress in brain tissue.

Therefore, the catechol group influences the antioxidant effect of VOO polyphenols in rat brain tissue after oral administration.

In our hypoxia−reoxygenation experiments, LDH efflux increased from 0.2 ± 0.04 to 2.9 ± 0.7 arbitrary units/mg tissue ($p < 0.0001$). All three compounds reduced LDH efflux after

DOI: 10.1021/acs.jafc.5b00627
J. Agric. Food Chem. 2015, 63, 5957−5963

oral treatment for 7 days in comparison to control group (Figure 2).

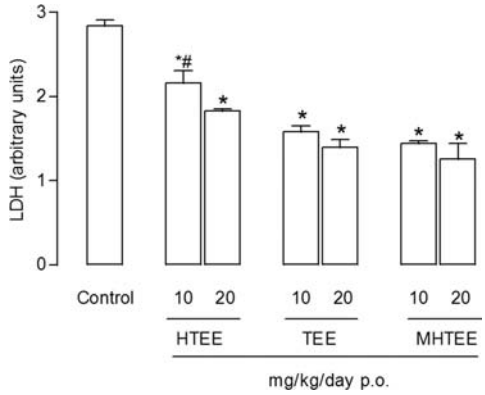

Figure 2. Lactate dehydrogenase efflux (LDH) measured after reoxygenation of brain slices in animals (N = 10 per group) treated for 7 days po with saline (control), hydroxytyrosol ethyl ether (HTEE) (two OH in the chemical structure), tyrosol ethyl ether (TEE) (one OH), or 3,4-di-*o*-methylidene-hydroxytyrosol ethyl ether (MHTEE) (no OH). (∗) $p < 0.001$ with respect to control group; (#) $p < 0.05$ with respect to HTEE 20 mg/kg/day and to TEE and MHTEE 10 and 20 mg/kg/day.

These results confirm the neuroprotective effect of hydroxytyrosol, HTEE acetate, and HTEE ethyl ether reported previously with the same experimental method as we used here.[7,17,19,20] Oxidative stress plays an important role in the process of neuronal death in brain ischemia,[29,30] and antioxidant compounds have thus been postulated to act as neuroprotective agents.[29] According to this hypothesis the polyphenolic compound with the greatest antioxidant potency (HTEE, with two OH) should have a greater neuroprotective effect than TEE (with one OH and a weak antioxidant effect). By this reasoning MHTEE, which lacks OH in its structure and has no antioxidant effect in brain tissue, would be expected to have little or no neuroprotective effect. In our experimental model, however, this prediction was not fully met, because TEE and MHTEE in fact showed greater neuroprotective potency than HTEE.

Tyrosol ethyl ether has shown neuroprotective effects in vitro[31] and in vivo.[10,32] In our experiments the antioxidant effect of TEE was proportionatey lower than its cytoprotective effect.

The antioxidant effect of these compounds influences only part of their neuroprotective action. This makes it necessary to consider other pathways of brain damage that might explain the overall neuroprotective effect of VOO polyphenols, particularly those involving TEE. In this study we explored two main neurotoxic pathways: nitrosative stress and some inflammatory mediators. The concentration of 3-nitrotyrosine, as an index of peroxynitrite formation in brain slices, increased from 1.2 ± 0.3 nmol/100 mg tissue before anoxia to 3.7 ± 0.8 nmol/100 mg tissue ($p < 0.001$) after reoxygenation. All three compounds inhibited 3-nitrotyrosine production at a dose of 20 mg/kg/day (Figure 3). There was no relationship between 3-nitrotyrosine inhibition and the number of OH groups in the chemical structure of the compounds we compared here.

The inhibition of nitrosative stress by olive oil polyphenols has been reported previously,[25,32] and hydroxytyrosol reduces the neuronal cytotoxicity induced by nitric oxide donors.[33]

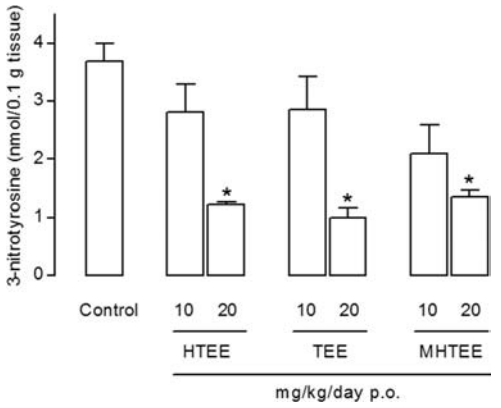

Figure 3. Peroxynitrite concentration (3-nitrotyrosine) measured after reoxygenation of brain slices in animals (N = 10 per group) treated for 7 days po with saline (control), hydroxytyrosol ethyl ether (HTEE) (two OH in the chemical structure), tyrosol ethyl ether (TEE) (one OH), or 3,4-di-*o*-methylidene -hydroxytyrosol ethyl ether (MHTEE) (no OH). (∗) $p < 0.0001$ with respect to control group and with respect to each 10 mg/kg/day group.

Moreover, hydroxytyrosol and tyrosol are known to act as nitrogen radical scavengers[34] and to prevent protein nitration induced by peroxynitrites.[35] This effect seems to be independent of their antioxidant effect, because their inhibitory profiles differ for oxidative and nitrosative stress in this experimental model with rat brain slices. Moreover, MHTEE (which had no antioxidant effect) had an inhibitory effect on 3-nitrotyrosine concentration after reoxygenation in brain slices.

With regard to inflammatory mediators, prostaglandin E_2 concentration in brain slices increased from 15.1 ± 6.2 pg/100 g tissue before anoxia to 57.0 ± 24.7 pg/100 mg tissue after reoxygenation ($p < 0.0001$). In this experimental model IL1β increased from 10.1 ± 4.1 pg/100 mg tissue before anoxia to 34.5 ± 12.7 pg/100 mg tissue after reoxygenation ($p < 0.0001$). All three polyphenol compounds inhibited prostaglandin E_2 production, whereas only HTEE inhibited IL1β production (Figure 4).

Hydroxytyrosol was previously found to inhibit type-2 cyclooxygenase (COX-2) in peripheral human blood cells.[25,36] Activation of the inducible isoform of COX in brain tissue and the prostaglandin synthesis resulting from this activation have been related to some aspects of ischemic damage,[37] and the inhibition of COX-2 correlated with a neuroprotective effect of some nonsteroidal anti-inflammatory drugs in the same experimental model as we used in this study.[21] This effect seems to be independent of the antioxidant effect because exposure to TEE (weak antioxidant effect) and MHTEE (no antioxidant effect) had an even greater effect than exposure to HTEE.

With regard to our results for IL1β inhibition, research with cultured human leukocytes showed that hydroxytyrosol inhibited the expression of stimulatory factors for cytokine synthesis (NF, STAT-1α, IRF-1) and, in general, the majority of inflammatory mediators.[32,38−40] Specifically, Rosignoli et al.[40] reported the importance for this effect of two OH groups at the ortho position, because other derivatives without these groups (dialdehyde elenolic acid) had no anti-inflammatory activity in activated human monocytes.

According to these results, TEE may exert its neuroprotective effect through mechanisms other than a (weak) antioxidant

DOI: 10.1021/acs.jafc.5b00627
J. Agric. Food Chem. 2015, 63, 5957−5963

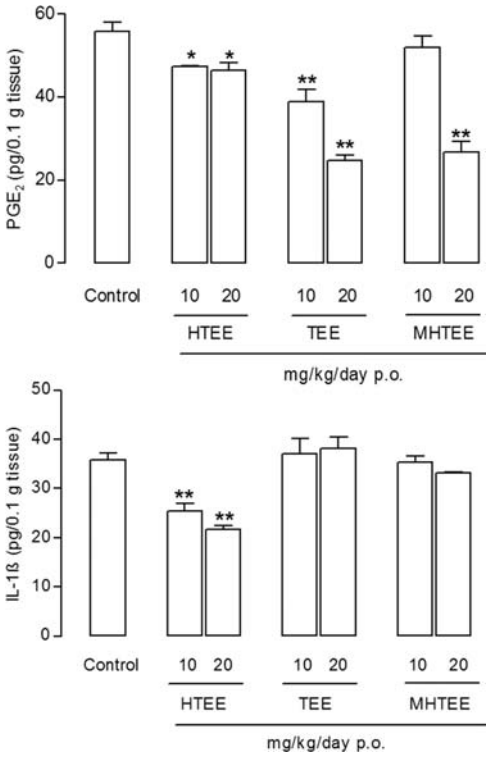

Figure 4. Prostaglandin E_2 (PGE_2) and interleukin 1β (IL1β) concentrations measured after reoxygenation of brain slices in animals (N = 10 per group) treated for 7 days po with saline (control), hydroxytyrosol ethyl ether (HTEE) (two OH in the chemical structure), tyrosol ethyl ether (TEE) (one OH), or 3,4-di-*o*-methylidene-hydroxytyrosol ethyl ether (MHTEE) (no OH). (*) $p < 0.01$; (**) $p < 0.001$ with respect to control group.

effect, for example, by inhibiting nitrosative stress or prostaglandin production.

To determine the possible contribution of each of these biochemical pathways to the neuroprotective effect of these compounds and to determine whether the presence of OH groups influenced this effect, we calculated Pearson correlation coefficients for the relationship between LDH efflux and variables identified in the hypoxia−reoxygenation model (Table 3). This analysis suggested that two types of mechanism may be responsible for the neuroprotective effect of VOO polyphenols: (1) an antioxidant effect, probably related to the presence of catechol groups (the neuroprotective effect of TEE and MHTEE was not significantly related to their effect on brain oxidative stress); (2) other effects (inhibition of nitrosative stress and inflammatory mediators) independent of their antioxidant effect and unrelated to the presence of catechol groups (TEE and MHTEE exerted these inhibitory effects).

Table 3. Pearson Correlation Coefficients between LDH Efflux and Oxidative and Nitrosative Stress and Inflammatory Mediators[a]

relationship between LDH and:	HTEE (two OH)	TEE (one OH)	MHTEE (no OH)
TBARS	0.72[b]	0.45	0.08
GSH	0.44	0.04	0.03
GSSSG	0.09	0.04	0.04
3-NT	0.78[b]	0.67[b]	0.66[b]
PGE_2	0.72[b]	0.79[b]	0.64[b]
IL1β	0.61[b]	0.41	0.41

[a]TBARS, thiobarbituric acid reactive substances; GSH, reduced glutathione; GSSG, oxidized glutathione; 3-NT, 3-nitrotyrosine; PGE_2, prostaglandin E_2; IL1β, interleukin 1β. [b]$p < 0.001$.

In conclusion, this study demonstrates that the presence of the catechol group in the chemical structure of VOO polyphenols is an important factor that contributes to their antioxidant effect in rat brain tissue, and that partly explains their neuroprotective effect. Inhibition of oxidative stress in the model of cerebral hypoxia−reoxygenation is not the only neuroprotective mechanism in which these compounds are involved. Other components of olive oil with a weak antioxidant effect, such as tyrosol, might also have a neuroprotective effect by modifying other biochemical pathways, for example, by inhibiting nitrosative stress or prostaglandin production. The neuroprotective effect of VOO in our experimental model may be the result of a combination of these mechanisms for HTEE and TEE, among other compounds. Further experiments designed to test combinations of these polyphenols will be needed to fully characterize the mechanisms behind their neuroprotective effect.

AUTHOR INFORMATION

Corresponding Author

*(J.A.G.-C.) Mail: Department of Pharmacology, School of Medicine, University of Malaga, Campus de Teatinos s/n, 29071 Malaga, Spain. Phone: +34 952 131567. Fax: +34 952 131568. E-mail: correa@uma.es.

Funding

This work was supported in part by Grant P09-AGR-5098 (Proyecto de Investigación de Excelencia, Consejería de Innovación, Ciencia y Empresa, Junta de Andalucía, Spain).

Notes

The authors declare no competing financial interest.

ACKNOWLEDGMENTS

We thank K. Shashok for improving the use of English in the manuscript.

REFERENCES

(1) Estruch, R.; Ros, E.; Salas-Salvadó, J.; Covas, M. I.; Corella, D.; Arós, F.; Gómez-Gracia, E.; Ruiz-Gutiérrez, V.; Fiol, M.; Lapetra, J.; Lamuela-Raventos, R. M.; Serra-Majem, L.; Pintó, X.; Basora, J.; Muñoz, M. A.; Sorlí, J. V.; Martínez, J. A.; Martínez-González, M. A. PREDIMED Study Investigators. Primary prevention of cardiovascular disease with Mediterranean diet. *N. Engl. J. Med.* **2013**, *368*, 1279−1290.

(2) Martínez-Lapiscina, E. H.; Clavero, P.; Toledo, E.; San Julián, B.; Sanchez-Tainta, A.; Corella, D.; Lamuela-Raventós, R. M.; Martínez, J. A.; Martínez-Gonzalez, M. A. Virgin olive oil supplementation and long-term cognition: the PREDIMED-NAVARRA randomized trial. *J. Nutr., Health Aging* **2013**, *17*, 544−552.

(3) Mitjavila, M. T.; Fandos, M.; Salas-Salvadó, J.; Covas, M. I.; Borrego, S.; Estruch, R.; Lamuela-Raventós, R.; Corella, D.; Martínez-Gonzalez, M. A.; Sánchez, J. M.; Bulló, M.; Fitó, M.; Tormos, C.; Cerdá, C.; Casillas, R.; Moreno, J. J.; Iradi, A.; Zaragoza, C.; Chaves, J.; Sáez, G. T. The Mediterranean diet improves the systemic lipid and DNA oxidative damage in metabolic syndrome individuals. A randomized, controlled, trial. *Clin. Nutr.* **2013**, *32*, 172−178.

(4) Konstantinidou, V.; Covas, M. I.; Muñoz-Aguayo, D.; Khymenets, O.; de la Torre, R.; Saez, G.; Tormos, C.; Toledo, E.; Marti, A.; Ruiz-Gutiérrez, V.; Ruiz Mendez, M. V.; Fito, M. In vivo nutrigenomic effects of virgin olive oil polyphenols within the frame of

DOI: 10.1021/acs.jafc.5b00627
J. Agric. Food Chem. 2015, 63, 5957−5963

the Mediterranean diet: a randomized controlled trial. *FASEB J.* **2010**, *24*, 2546−2557.
(5) Raederstorff, D. Antioxidant activity of olive polyphenols in humans: a review. *Int. J. Vitam. Nutr. Res.* **2009**, *79*, 152−165.
(6) Povie, G.; Villa, G.; Ford, L.; Pozzi, D.; Schiesser, C. H.; Renaud, P. Role of catechol in the radical reduction of B-alkylcatecholboranes in presence of methanol. *Chem. Commun.* **2012**, *46*, 803−805.
(7) Cabrerizo, S.; De La Cruz, J. P.; López-Villodres, J. A.; Muñoz-Marín, J.; Guerrero, A.; Reyes, J. J.; Labajos, M. T.; González-Correa, J. A. Role of the inhibition of oxidative stress and inflammatory mediators in the neuroprotective effects of hydroxytyrosol in rat brain slices subjected to hypoxia reoxygenation. *J. Nutr. Biochem.* **2013**, *24*, 2152−2157.
(8) Hu, T.; He, X.-W.; Jiang, J.-G.; Xu, X.-L. Hydroxytyrosol and its potential therapeutic effects. *J. Agric. Food Chem.* **2014**, *62*, 1449−1455.
(9) Romero, C.; Brenes, M. Analysis of total content of hydroxytyrosol and tyrosol in olive oils. *J. Agric. Food Chem.* **2012**, *60*, 9017−9022.
(10) Bu, Y.; Rho, S.; Kim, J.; Kim, M. Y.; Lee, D. H.; Kim, S. Y.; Choi, H.; Kim, H. Neuroprotective effect of tyrosol on transient focal cerebral ischemia in rats. *Neurosci. Lett.* **2007**, *414*, 218−221.
(11) González-Correa, J. A.; Muñoz-Marín, J.; Arrebola, M. M.; Guerrero, A.; Narbona, F.; López-Villodres, J. A.; De La Cruz, J. P. Dietary virgin olive oil reduces oxidative stress and cellular damage in rat brain slices subjected to hypoxia-reoxygenation. *Lipids* **2007**, *42*, 921−929.
(12) Azaizeh, H.; Halahlih, F.; Najami, N.; Brunner, D.; Faulstich, M.; Tafesh, A. Antioxidant activity of phenolic fractions in olive mill wastewater. *Food Chem.* **2012**, *134*, 2226−2234.
(13) Ruiz Gutierrez, V.; de la Puerta, R.; Catalá, A. The effect of tyrosol, hydroxytyrosol and oleuropein on the non-enzymatic lipid peroxidation of rat liver microsomes. *Mol. Cell. Biochem.* **2001**, *217*, 35−41.
(14) Bendini, A.; Cerretani, L.; Carrasco-Pancorbo, A.; Gómez-Caravaca, A. M.; Segura-Carretero, A.; Fernández-Gutiérrez, A.; Lercker, G. Phenolic molecules in virgin olive oils: a survey of their sensory properties, health effects, antioxidant activity and analytical methods. An overview of the last decade. *Molecules* **2007**, *12*, 1679−1719.
(15) Pereira-Caro, G.; Mateos, R.; Saha, S.; Madrona, A.; Espartero, J. L.; Bravo, L.; Kroon, P. A. Transepithelial transport and metabolism of new lipophilic ether derivatives of hydroxytyrosol by enterocyte-like Caco-2/TC7 cells. *J. Agric. Food Chem.* **2010**, *58*, 11501−11509.
(16) Bernini, R.; Crisante, F.; Barontini, M.; Tofani, D.; Balducci, V.; Gambacorta, A. Synthesis and structure/antioxidant activity relationship of novel catecholic antioxidant structural analogues to hydroxytyrosol and its lipophilic esters. *J. Agric. Food Chem.* **2012**, *60*, 7408−7416.
(17) Muñoz-Marín, J.; De La Cruz, J. P.; Guerrero, A.; López-Leiva, I.; López-Villodres, J. A.; Reyes, J. J.; Espartero, J. L.; Madrona, A.; Labajos, M. T.; González-Correa, J. A. Cytoprotective effect of hydroxytyrosyl alkyl ether derivatives after oral administration to rats in a model of glucose-oxygen deprivation in brain slices. *J. Agric. Food Chem.* **2012**, *60*, 7659−7564.
(18) Madrona, A.; Pereira-Caro, G.; Mateos, R.; Rodríguez, G.; Trujillo, M.; Fernández-Bolaños, J.; Espartero, J. L. Synthesis of hydroxytyrosyl alkyl ethers from olive oil waste waters. *Molecules* **2009**, *14*, 1762−1772.
(19) Guerrero, A.; De la Cruz, J. P.; Muñoz-Marín, J.; LópezVillodres, J. A.; Madrona, A.; Espartero, J. L.; Gonzalez Correa, J. A. Neuroprotective effect of alkyl hydroxytyrosol ethers in rat brain slices subjected to a hypoxia-reoxygenation model. *Food Chem.* **2012**, *134*, 2176−2183.
(20) González-Correa, J. A.; Navas, M. D.; Lopez-Villodres, J. A.; Trujillo, M.; Espartero, J. L.; De La Cruz, J. P. Neuroprotective effect of hydroxytyrosol and hydroxytyrosol acetate in rat brain slices subjected to hypoxia-reoxygenation. *Neurosci. Lett.* **2008**, *446*, 143−146.
(21) López-Villodres, J. A.; De La Cruz, J. P.; Muñoz-Marin, J.; Guerrero, A.; Reyes, J. J.; González-Correa, J. A. Cytoprotective effect of nonsteroidal antiinflammatory drugs in rat brain slices subjected to reoxygenation after oxygen-glucose deprivation. *Eur. J. Pharm. Sci.* **2012**, *45*, 624−631.
(22) De La Cruz, J. P.; Guerrero, A.; González-Correa, J. A.; Arrebola, M. M.; Sánchez de la Cuesta, F. Antioxidant effect of acetylsalicylic and salicylic acid in rat brain slices subjected to hypoxia. *J. Neurosci. Res.* **2004**, *75*, 280−290.
(23) Hissin, P. J.; Hilf, R. A fluorometric method for determination of oxidized and reduced glutathione in tissues. *Anal. Biochem.* **1976**, *74*, 214−226.
(24) Granados-Principal, S.; Quiles, J. L.; Ramirez-Tortosa, C. L.; Sanchez Rovira, P.; Ramirez-Tortosa, M. C. Hydroxytyrosol: from laboratory investigations to future clinical trials. *Nutr. Rev.* **2010**, *68*, 191−206.
(25) González-Correa, J. A.; López-Villodres, J. A.; Asensi, R.; Espartero, J. L.; Rodríguez-Gutiérez, G.; De La Cruz, J. P. Virgin olive oil polyphenol hydroxytyrosol acetate inhibits in vitro platelet aggregation in human whole blood: comparison with hydroxytyrosol and acetylsalicylic acid. *Br. J. Nutr.* **2009**, *101*, 1157−1164.
(26) Pereira-Caro, G.; Sarriá, B.; Madrona, A.; Espartero, J. L.; Goya, L.; Bravo, L.; Mateos, R. Alkyl hydroxytyrosyl ethers show protective effects against oxidative stress in HepG2 cells. *J. Agric. Food Chem.* **2011**, *59*, 5964−5976.
(27) Ruiz Gutierrez, V.; de la Puerta, R.; Catalá, A. The effect of tyrosol, hydroxytyrosol and oleuropein on the non-enzymatic lipid peroxidation of rat liver microsomes. *Mol. Cell. Biochem.* **2001**, *217*, 35−41.
(28) Deiana, M.; Corona, G.; Incani, A.; Loru, D.; Rosa, A.; Atzeri, A.; Paola-Melis, M.; Assunta-Dessì, M. Protective effect of simple phenols from extravirgin olive oil against lipid peroxidation in intestinal Caco-2 cells. *Food Chem. Toxicol.* **2010**, *48*, 3008−3016.
(29) Albarracin, S. L.; Stab, B.; Casas, Z.; Sutachan, J. J.; Samudio, I.; Gonzalez, J.; Gonzalo, L.; Capani, F.; Morales, L.; Barreto, G. E. Effects of natural antioxidants in neurodegenerative disease. *Nutr. Neurosci.* **2012**, *15*, 1−9.
(30) Chen, H.; Yoshioka, H.; Kim, G. S.; Jung, J. E.; Okami, N.; Sakata, H.; Maier, C. M.; Narasimhan, P.; Goeders, C. E.; Chan, P. H. Oxidative stress in ischemic brain damage: mechanisms of cell death and potential molecular targets for neuroprotection. *Antioxid. Redox Signaling* **2011**, *14*, 1505−1517.
(31) Shi, T. Y.; Feng, S. F.; Xing, J. H.; Wu, Y. M.; Li, X. Q.; Zhang, N.; Tian, Z.; Liu, S. B.; Zhao, M. G. Neuroprotective effects of Salidroside and its analogue tyrosol galactoside against focal cerebral ischemia in vivo and H_2O_2-induced neurotoxicity in vitro. *Neurotoxic. Res.* **2012**, *21*, 358−367.
(32) Zhang, X.; Cao, J.; Zhong, L. Hydroxytyrosol inhibits pro-inflammatory cytokines, iNOS, and COX-2 expression in human monocytic cells. *Naunyn-Schmiedeberg's Arch. Pharmacol.* **2009**, *379*, 581−586.
(33) Schaffer, S.; Müller, W. E.; Eckert, G. P. Cytoprotective effects of olive mill wastewater extract and its main constituent hydroxytyrosol in PC12 cells. *Pharmacol. Res.* **2010**, *62*, 322−327.
(34) Rietjens, S. J.; Bast, A.; de Vente, J.; Haenen, G. R. The olive oil antioxidant hydroxytyrosol efficiently protects against the oxidative stress-induced impairment of the NO• response of isolated rat aorta. *Am. J. Physiol. Heart Circ. Physiol.* **2007**, *292*, H1931−H1936.
(35) Deiana, M.; Aruoma, O. I.; Bianchi, M. L.; Spencer, J. P.; Kaur, H.; Halliwell, B.; Aeschbach, R.; Banni, S.; Dessi, M. A.; Corongiu, F. P. Inhibition of peroxynitrite dependent DNA base modification and tyrosine nitration by the extra virgin olive oil-derived antioxidant hydroxytyrosol. *Free Radical Biol. Med.* **1999**, *26*, 762−769.
(36) Reyes, J. J.; De La Cruz, J. P.; Muñoz-Marin, J.; Guerrero, A.; Lopez-Villodres, J. A.; Madrona, A.; Espartero, J. L.; González-Correa, J. A. Antiplatelet effect of new lipophilic hydroxytyrosol alkyl ether derivatives in human blood. *Eur. J. Nutr.* **2013**, *52*, 591−599.
(37) Candelario-Jalil, E.; Fiebich, B. L. Cyclooxygenase inhibition in ischemic brain injury. *Curr. Pharm. Design.* **2008**, *14*, 1401−1418.

DOI: 10.1021/acs.jafc.5b00627
J. Agric. Food Chem. 2015, 63, 5957−5963

(38) Maiuri, M. C.; De Stefano, D.; Di Meglio, P.; Irace, C.; Savarese, M.; Sacchi, R.; Cinelli, M. P.; Carnuccio, R. Hydroxytyrosol, a phenolic compound from virgin olive oil, prevents macrophage activation. *Naunyn-Schmiedeberg's Arch. Pharmacol.* **2005**, *371*, 457−465.
(39) Richard, N.; Arnold, S.; Hoeller, U.; Kilpert, C.; Wertz, K.; Schwager, J. Hydroxytyrosol is the major anti-inflammatory compound in aqueous olive extracts and impairs cytokine and chemokine production in macrophages. *Planta Med.* **2011**, *77*, 1890−1897.
(40) Rosignoli, P.; Fuccelli, R.; Fabiani, R.; Servili, M.; Morozzi, G. Effect of olive oil phenols on the production of inflammatory mediators in freshly isolated human monocytes. *J. Nutr. Biochem.* **2013**, *24*, 1513−1519.

DOI: 10.1021/acs.jafc.5b00627
J. Agric. Food Chem. 2015, 63, 5957−5963

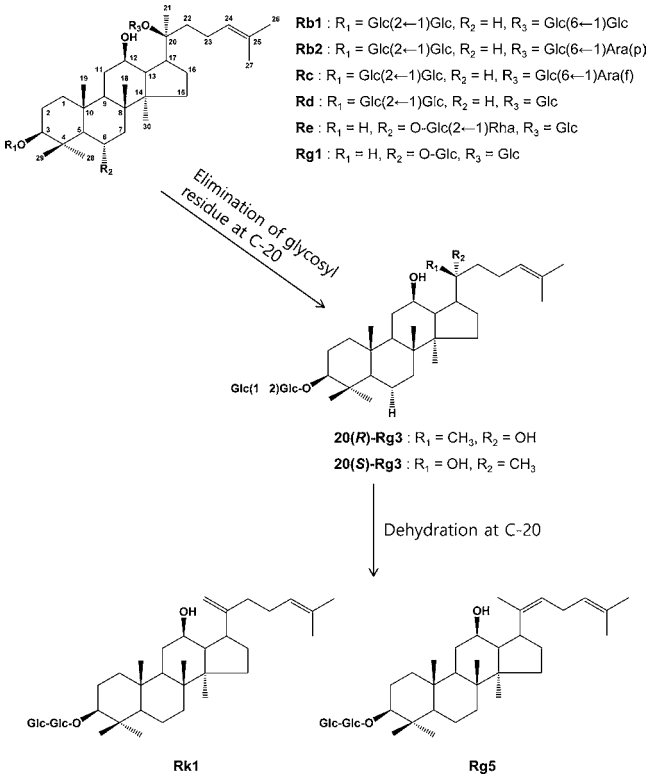

Figure 1. Structures of ginsenosides: −Glc, D-glucopyranosyl; −Rha, L-rhamnopyranosyl; −Ara(f), L-arabinofuranosyl; and −Ara(p): L-arabinopyranosyl.

MATERIALS AND METHODS

Chemicals and Reagents. Standard ginsenosides, including Rb1, Rb2, Rc, Rd, Re, Rg3, Rk1, and Rg5 (purity of 98−100%) were purchased from Ambo Institute (South Korea). Dulbecco's modified Eagle's medium (DMEM) and fetal bovine serum (FBS) were purchased from Invitrogen Co. (Grand Island, NY). Primary antibodies for c-Jun N-terminal kinase (JNK), phospho-JNK, p53, and cleaved caspase-3 as well as all secondary antibodies were obtained from Cell Signaling Technology, Inc. (Danvers, MA). The EZ-Cytox cell viability assay kit was purchased from ITSBIO (Seoul, South Korea). Acetonitrile and water used were of high-performance liquid chromatography (HPLC) grade, obtained from Fisher Scientific (Pittsburgh, PA), and glacial acetic acid was of analytical grade, purchased from Sigma-Aldrich (St. Louis, MO).

Preparation of Processed Ginseng Using Microwave Irradiation. White ginseng (WG) was processed using microwave irradiation as reported previously.[16] In brief, aliquots (200 mg) of the dry extract of WG were added to 1 mL of water in a 10 mL container of a microwave irradiator (model 908005) manufactured by CEM Company. WG was irradiated with microwaves in the sealed container at a temperature of 150 °C and power of 100 W (2455 MHz frequency) for 60 min. Microwave-irradiated dry extracts of ginseng (MG) were freeze-dried to obtain microwave-irradiated process products. Microwave irradiation was performed at a pressure of 20 atm. Vessel pressure was automatically controlled by the microwave irradiator.

Purification of Ginsenoside-Containing Fractions. MG extract (50 g) was subjected to open-column chromatography on a Diaion HP-20 (Mitsubishi Chemical Co., Ltd., Tokyo, Japan) and eluted stepwise with 5 L of distilled water and MeOH. The respective fractions were evaporated to yield the water eluate (MG−H_2O, 38 g) and the MeOH eluate (MG−MeOH, 10 g).

Analysis of Ginsenosides. Ginsenosides were identified and quantified using a previously reported method.[13] An analytical reversed-phase HPLC system comprised of a solvent degasser (Agilent, G1322A), binary pump (Agilent, G1312C), and model 380 evaporative light scattering detector (ELSD, Agilent) was used in the analysis. The standard solutions containing 1−100 μg of each ginsenoside were injected onto the HPLC column, with all calibration curves showing good linearity (R^2 > 0.995). The analysis was repeated 2 times for the assessment of repeatability.

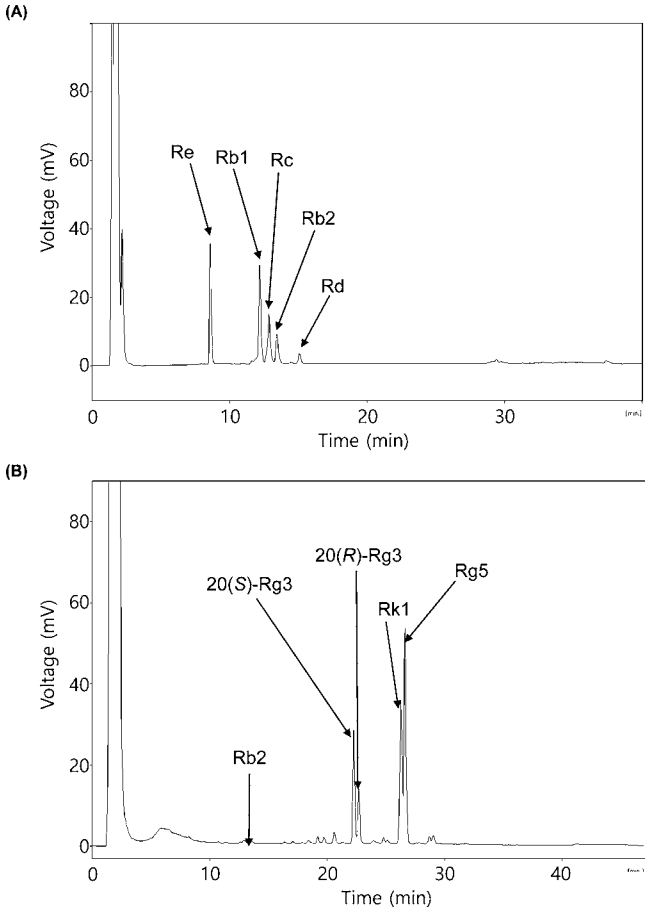

Figure 2. Structural changes in ginsenosides present in ginseng extract induced by microwave irradiation. (A) HPLC chromatogram presenting peaks corresponding to ginsenosides (Re, Rb1, Rc, Rb2, and Rd) present in raw ginseng. (B) HPLC chromatogram presenting peaks corresponding to ginsenosides [20(*S*)-Rg3, 20(*R*)-Rg3, Rk1, and Rg5] present in microwave-processed ginseng.

Protective Effect against Oxidative Damage in Kidney Cells. The protective effect against oxidative nephrotoxicity was evaluated in LLC-PK1 cells.[17] LLC-PK1 (pig kidney epithelium, CL-101) cells were cultured in DMEM supplemented with 10% FBS, 1% penicillin/streptomycin, and 4 mM L-glutamine at 37 °C with 5% CO_2 in air. Cells were seeded in 96-well culture plates at 1 × 10^4 cells/well and allowed to adhere for 24 h. Thereafter, test samples with or without cisplatin (25 μM) were added to the culture medium. Epigallocatechin gallate (EGCG) was used as a positive control. After 24 h of incubation, the cell viability was evaluated using the EZ-Cytox cell viability assay kit.

Protective Effect against Cisplatin-Induced Nephrotoxicity in Mice. All procedures involving the use of live animals as described in this study were approved in May 2013 by the Institutional Animal Care and Use Committee of the Korea Institute of Science and Technology and strictly followed the National Institutes of Health (NIH) guidelines for humane treatment of animals. Male C57/BL6 mice, 9−10 weeks of age, were obtained from Orient Bio Co., Ltd. (Seongnam, South Korea). They were kept on a 12 h light/dark cycle and given free access to water and a normal diet. The mice were subsequently divided into 6 groups that were similar in their initial body weights and assigned to the following treatment groups: group 1, vehicle-treated mice received water alone (no ginseng treatment; n = 4); group 2, cisplatin-treated mice received water alone (no ginseng treatment; n = 4); group 3, cisplatin-treated mice received WG extract (100 mg/kg) in aqueous

DOI: 10.1021/acs.jafc.5b00782
J. Agric. Food Chem. 2015, 63, 5964−5969

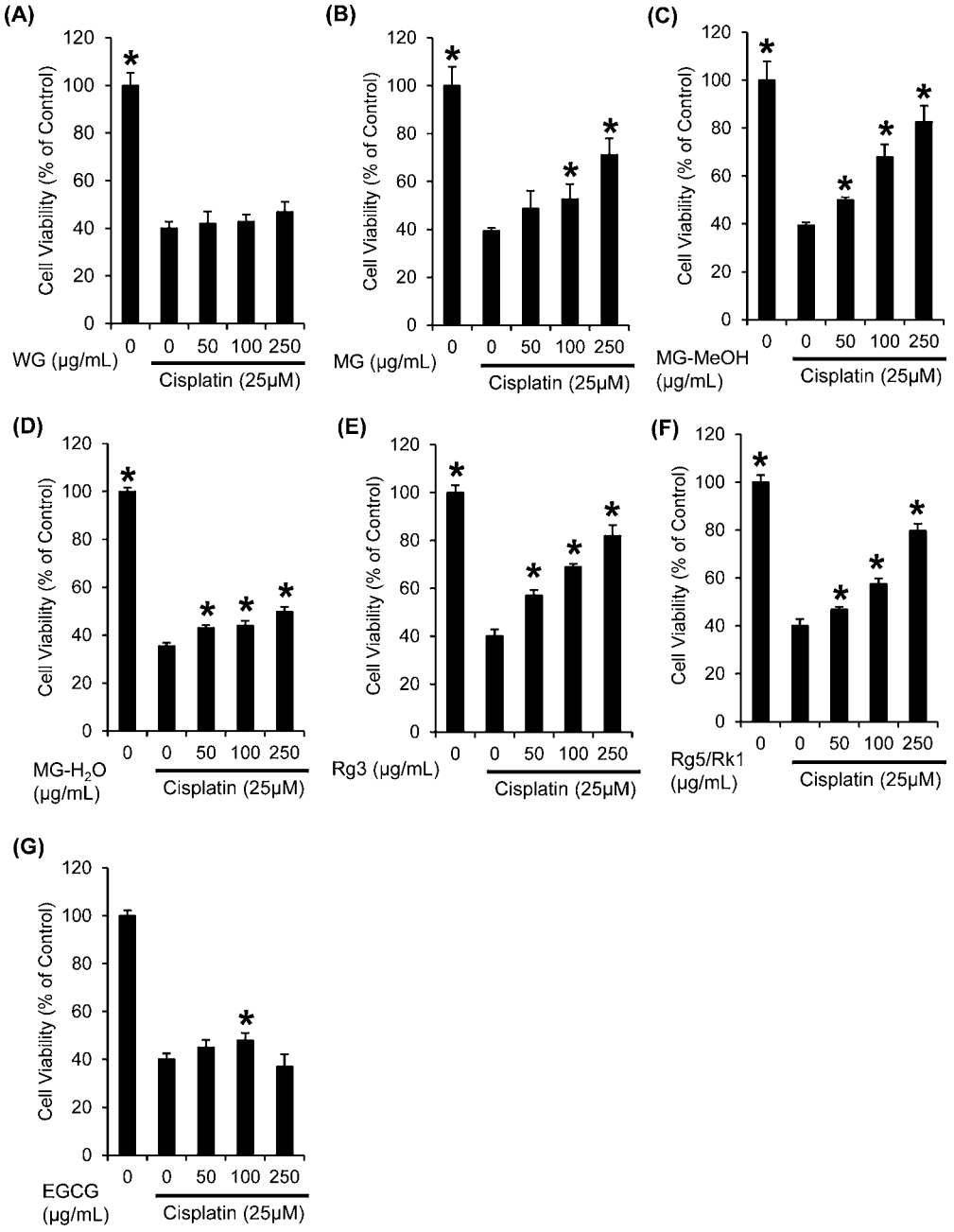

Figure 3. Comparison of the protective effects of WG, MG, MG−MeOH, MG−H_2O, Rg3, Rg5/Rk1, and EGCG against cisplatin-induced cytotoxicity in LLC-PK1 cells. (∗) $p < 0.05$ compared to the cisplatin-treated control value.

solution orally for 10 days (cisplatin + WG; $n = 4$); group 4, cisplatin-treated mice received MG extract (100 mg/kg) in aqueous solution orally for 10 days (cisplatin + MG; $n = 4$); group 5, cisplatin-treated mice received MG−MeOH (25 mg/kg) in aqueous solution orally for 10 days (cisplatin + MG−MeOH; $n = 4$); and group 6, cisplatin-treated mice received NAC (100 mg/kg) in aqueous solution orally for 10 days (cisplatin + NAC; $n = 4$). Samples were orally administered daily, while vehicle-treated rats were given water. After 10 days, mice in the five treatment groups (cisplatin, cisplatin + WG, cisplatin + MG, cisplatin + MG−MeOH, and cisplatin + NAC) were intraperitoneally administered a single dose of cisplatin (16 mg/kg of body weight) in 0.9% saline. Mice were sacrificed 3 days after cisplatin administration under light ether anesthesia. Blood samples were collected in tubes containing 0.18 M ethylenediaminetetraacetic acid (EDTA) from the abdominal aorta.

Analyses of Plasma Biomarkers. Blood samples were centrifuged at 3000*g* for 10 min at 4 °C. The plasma creatinine levels were measured by a rate-blanked kinetic Jaffe method.

Western Blotting Analysis. Whole-cell extracts were then prepared according to the instructions of the manufacturer using RIPA buffer (Cell Signaling Technology, Danvers, MA) supplemented with 1× protease inhibitor cocktail and 1 mM phenylmethylsulfonyl fluoride. Proteins were separated by electrophoresis, blotted onto polyvinylidene fluoride (PVDF) transfer membrane, and analyzed with epitope-specific primary and secondary antibodies.

Statistical Analysis. Statistical significance was determined through the one-way analysis of variance (ANOVA), followed by a multiple-comparison test with Bonferroni adjustment. p values lower than 0.05 were considered statistically significant (SPSS 11.5 software).

3. RESULTS AND DISCUSSION

The chromatograms for each of the prepared ginseng extracts are shown in panels A and B of Figure 2. The processing conditions for microwave treatment of ginseng extracts were optimized,[16]

DOI: 10.1021/acs.jafc.5b00782
J. Agric. Food Chem. 2015, 63, 5964−5969

and conditions resulting in the highest amounts of ginsenosides Rg3, Rg5, and Rk1 were selected. Ginsenosides were identified and quantified as reported previously.[13,16] As shown in panels A and B of Figure 2, each of the ginsenosides Re (114 μg), Rb1 (158 μg), Rc (94 μg), Rb2 (74 μg), and Rd (8 μg) content was decreased in WG, while the ginsenosides Rg3 (105 μg), Rk1 (151 μg), and Rg5 (275 μg) content increased in MG by microwave irradiation at 150 °C for 60 min. Ginsenosides 20(*S*)-Rg3 and 20(*R*)-Rg3 are produced by the elimination of the glycosyl residue at carbon-20 of protopanaxadiol-type saponins, such as ginsenosides Rb1, Rb2, Rc, and Rd during the steaming process.[11,18,19] Ginsenoside Rg3 is converted to Rg5 and Rk1 by further dehydration at the carbon-20 position by high pressure and temperature.[13,19]

Using LLC-PK1 renal epithelial cells as the *in vitro* model, we compared the protective activities of WG, MG, MG−MeOH, MG−H_2O, ginsenoside Rg3 epimers, and ginsenoside Rg5/Rk1 against cisplatin-induced oxidative renal damage. The ginsenoside stereoisomers were used as mixtures because of the difficulty in preparing a single ingredient with high purity. On the basis of previously collected data, 25 μM cisplatin, which results in approximately 60% cell death, was selected for further study. Loss of cell viability was noted after 24 h incubations of samples at a range of ginsenoside concentrations (0, 50, 100, and 250 μg/mL) with cisplatin (25 μM). The renoprotective effect of MG was observed to be stronger than that of WG (panels A and B of Figure 3). Additionally, we have assessed the renoprotective effects of the water and MeOH elution fractions of MG (MG−H_2O and MG−MeOH) to identify the main active components. On the basis of our observations, the MeOH fraction increased cell viability at a concentration of 50 μg/mL, while no amelioration in cell viability was observed following treatment with MG−H_2O (panels C and D of Figure 3). High concentrations of ginsenosides-20(*S*)-protopanaxadiol (ginsenosides Rb1, Rb2, Rc, Rd, Rg3, Rg5, and Rk1) and 20(*S*)-protopanaxatriol (ginsenosides Re and Rg1) are already known to be eluted in the MeOH fraction,[11] suggesting that the observed renoprotective activity of the MeOH elute is likely due to ginsenosides. Consequently, we investigated the renoprotective effects using ginsenosides Rg3 and Rg5/Rk1, the content of which was increased by microwave processing. Ginsenosides Rg3 and Rg5/Rk1 were found to significantly ameliorate cisplatin-induced reduction in cell viability in a dose-dependent manner (panels E and F of Figure 3). This protective effect was stronger than that of EGCG (Figure 3). We have also confirmed that MG and its active components did not affect the anticancer activity of cisplatin (see Figure S1 of the Supporting Information).

Figure 4 presents the protein expression levels of P-JNK, JNK, p53, and cleaved caspase-3 in the control and treated (WG, MG, and MG−MeOH) cells. The blocking of JNK−p53−caspase-3 signaling cascade plays a vital role in mediating the protective effect of renoprotectants against oxidative cytotoxicity in cultured LLC-PK1 cells.[20−22] Cisplatin-induced nephrotoxicity was previously correlated with the formation of oxidative stress, which can activate JNK.[23,24] Treatments with antioxidants and caspase inhibitors were shown to ameliorate cisplatin-related nephrotoxicity.[25] The important roles of JNK activation have emphasized the regulation of apoptosis pathways as well as inflammation.[26−28] In LLC-PK1 cells, p53 is activated by cisplatin, and p53 inhibition by pharmacological and molecular approaches reduces cisplatin-induced apoptosis.[29,30] Expression of JNK and p53 proteins in LLC-PK1 cells recovered markedly after treatments with MG and MG−MeOH but not with WG

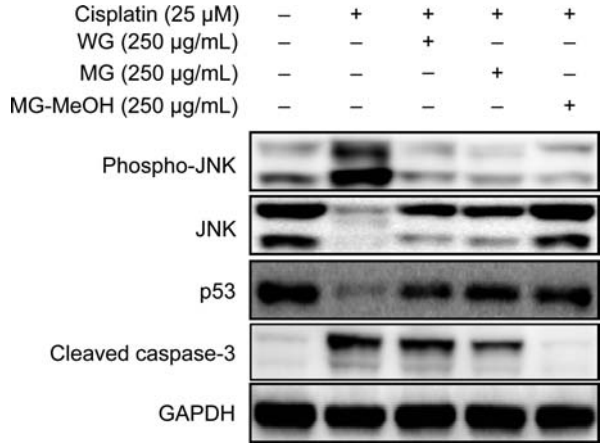

Figure 4. Comparison of the effects of WG, MG, and MG−MeOH on the expression of proteins P-JNK (46 and 54 kDa), JNK (46 and 54 kDa), p53 (53 kDa), and cleaved caspase-3 (17 and 19 kDa) in LLC-PK1 cells. Western blot assays were performed in triplicate for each protein and were repeated at least 3 times. The presence or absence of samples is indicated by a plus or minus sign, respectively.

(Figure 4). To further investigate the ability of MG and MG−MeOH to prevent apoptosis, the renal expression of cleaved caspase-3 was measured. In these experiments, MG significantly reduced the expression of cleaved caspase-3 (Figure 4). Figure 5 presents the expression of proteins P-JNK, JNK, p53,

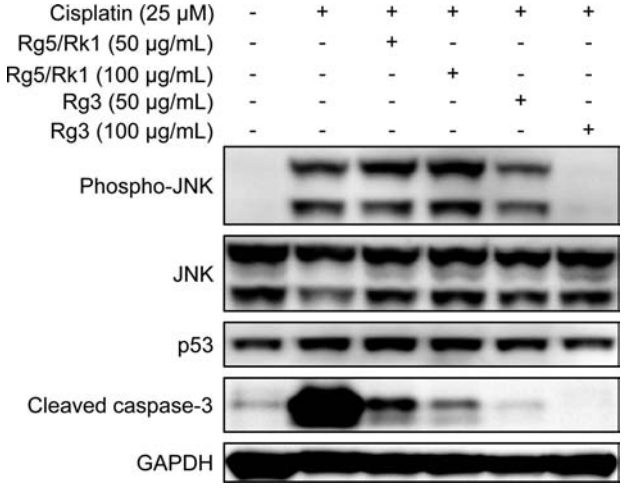

Figure 5. Comparison of the effect of ginsenosides Rg3 (50 and 100 μg/mL) and Rg5/Rk1 (50 and 100 μg/mL) on the expression of proteins P-JNK (46 and 54 kDa), JNK (46 and 54 kDa), p53 (53 kDa), and cleaved caspase-3 (17 and 19 kDa) in LLC-PK1 cells. Western blot assays were performed in triplicate for each protein and were repeated at least 3 times. The presence or absence of samples is indicated by a plus or minus sign, respectively.

and cleaved caspase-3 in control and experimental cells treated with ginsenoside Rg3 (at 50 and 100 μg/mL) or Rg5/Rk1 (50 and 100 μg/mL). Expression of JNK and p53 proteins in LLC-PK1 cells was markedly increased following treatment with Rg3 and Rg5/Rk1. Additionally, the elevated expression of cleaved caspase-3 following cisplatin treatment was significantly attenuated by ginsenosides Rg5/Rk1 and, more potently, by ginsenoside Rg3 co-treatments (Figure 5).

To determine whether MG and its ginsenoside fraction elicit renoprotective effects *in vivo*, we used cisplatin-induced renal

DOI: 10.1021/acs.jafc.5b00782
J. Agric. Food Chem. 2015, 63, 5964−5969

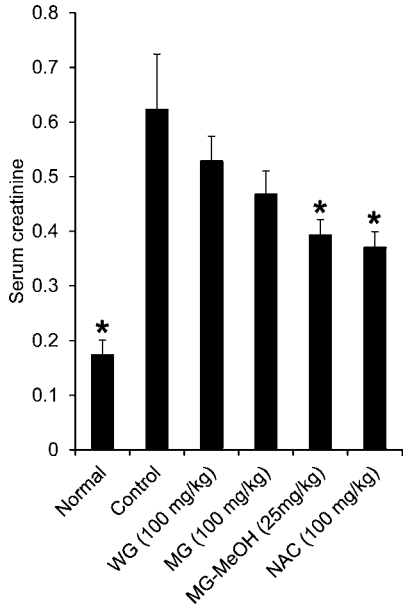

Figure 6. Protective effects of microwave-processed ginseng extract against cisplatin-induced renal damage in mice. (*) $p < 0.05$ compared to the cisplatin-treated control value.

oxidative-damaged mice as an *in vivo* model. Cisplatin-injected mice exhibited increased serum levels of creatinine compared to the vehicle-treated animals (Figure 6). Serum creatinine is a tried and true marker of kidney injury.[31,32] Elevated serum creatinine levels in cisplatin-treated mice were slightly attenuated by co-treatment with WG. In particular, increased serum creatinine levels were significantly reduced by administration of MG and, more potently, MG−MeOH, which contains ginsenosides Rg3, Rg5, and Rk1 (Figure 6). The renoprotective effect of MG−MeOH was as strong as that of NAC, which has been found to be effective in attenuating nephrotoxicity induced by cisplatin.[33] Therefore, co-treatment with MG and its active ginsenosides afforded significant protection against cisplatin-induced nephrotoxicity in mice.

In summary, we demonstrated that MG and its active ginsenosides Rg3, Rg5, and Rk1 showed a protective effect against cisplatin-induced nephrotoxicity in cultured kidney cells and mice. We found that ginsenosides Rg3, Rg5, and Rk1, generated during the heat treatment of ginseng, ameliorate renal damage by regulating inflammation and apoptosis. The experimental results provide convincing evidence for kidney protection effects of MG and its active ginsenosides, both *in vitro* and *in vivo*, supporting its therapeutic potential. Future studies will focus on the effect of MG and its active ginsenosides on unexplored areas, such as diabetic nephropathy.

■ ASSOCIATED CONTENT

Supporting Information

Effects of MG and its active components on the anti-proliferative effect of cisplatin in PC3 prostate cancer cells (Figure S1) (PDF). The Supporting Information is available free of charge on the ACS Publications website at DOI: 10.1021/acs.jafc.5b00782.

■ AUTHOR INFORMATION

Corresponding Authors

*Telephone: 82-31-750-5402. Fax: 82-31-750-5416. E-mail: kkang@gachon.ac.kr.

*Telephone: 82-33-650-3502. Fax: 82-33-650-3508. E-mail: ham0606@kist.re.kr.

Author Contributions

†Jun Yeon Park and Pilju Choi contributed equally to this work.

Funding

This work was supported by the Korea Institute of Science and Technology Institutional Program (2Z04390) and Industrial Infrastructure Program for Fundamental Technologies (N0000885), which is funded by the Ministry of Trade, Industry and Energy (MOTIE, South Korea).

Notes

The authors declare no competing financial interest.

■ REFERENCES

(1) Noori, S.; Mahboob, T. Antioxidant effect of carnosine pretreatment on cisplatin-induced renal oxidative stress in rats. *Indian J. Clin. Biochem.* **2010**, *25*, 86−91.

(2) Li, J.; Jiang, K.; Qiu, X.; Li, M.; Hao, Q.; Wei, L.; Zhang, W.; Chen, B.; Xin, X. Overexpression of CXCR4 is significantly associated with cisplatin-based chemotherapy resistance and can be a prognostic factor in epithelial ovarian cancer. *BMB Rep.* **2014**, *47*, 33−38.

(3) Rosenberg, B.; Vancamp, L.; Krigas, T. Inhibition of cell division in escherichia coli by electrolysis products from a platinum electrod. *Nature* **1965**, *205*, 698−699.

(4) Siddik, Z. H. Cisplatin: Mode of cytotoxic action and molecular basis of resistance. *Oncogene* **2003**, *22*, 7265−7279.

(5) Wang, D.; Lippard, S. J. Cellular processing of platinum anticancer drugs. *Nat. Rev. Drug Discovery* **2005**, *4*, 307−320.

(6) Forbes, J. M.; Coughlan, M. T.; Cooper, M. E. Oxidative stress as a major culprit in kidney disease in diabetes. *Diabetes* **2008**, *57*, 1446−1454.

(7) Heyman, S. N.; Rosen, S.; Rosenberger, C. A role for oxidative stress. *Contrib. Nephrol.* **2011**, *174*, 138−148.

(8) Baek, S. H.; Piao, X. L.; Lee, U. J.; Kim, H. Y.; Park, J. H. Reduction of cisplatin-induced nephrotoxicity by ginsenosides isolated from processed ginseng in cultured renal tubular cells. *Biol. Pharm. Bull.* **2006**, *29*, 2051−2055.

(9) Lee, J. H.; Lee, W.; Lee, S.; Jung, Y.; Park, S. H.; Choi, P.; Kim, S. N.; Ham, J.; Kang, K. S. Important role of Maillard reaction in the protective effect of heat-processed ginsenoside Re-serine mixture against cisplatin-induced nephrotoxicity in LLC-PK1 cells. *Bioorg. Med. Chem. Lett.* **2012**, *22*, 5475−5479.

(10) Huang, Y. C.; Chen, C. T.; Chen, S. C.; Lai, P. H.; Liang, H. C.; Chang, Y.; Yu, L. C.; Sung, H. W. A natural compound (ginsenoside Re) isolated from *Panax ginseng* as a novel angiogenic agent for tissue regeneration. *Pharm. Res.* **2005**, *22*, 636−646.

(11) Kang, K. S.; Ham, J.; Kim, Y. J.; Park, J. H.; Cho, E. J.; Yamabe, N. Heat-processed *Panax ginseng* and diabetic renal damage: Active components and action mechanism. *J. Ginseng Res.* **2013**, *37*, 379−388.

(12) Park, E. H.; Kim, Y. J.; Yamabe, N.; Park, S. H.; Kim, H. K.; Jang, H. J.; Kim, J. H.; Cheon, G. J.; Ham, J.; Kang, K. S. Stereospecific anticancer effects of ginsenoside Rg3 epimers isolated from heat-processed American ginseng on human gastric cancer cell. *J. Ginseng Res.* **2014**, *38*, 22−27.

(13) Kim, Y. J.; Yamabe, N.; Choi, P.; Lee, J. W.; Ham, J.; Kang, K. S. Efficient thermal deglycosylation of ginsenoside Rd and its contribution to the improved anticancer activity of ginseng. *J. Agric. Food Chem.* **2013**, *61*, 9185−9191.

(14) Zhu, J.; Kuznetsov, A. V.; Sandeep, K. P. Numerical simulation of forced convection in a duct subjected to microwave heating. *Heat Mass Transfer* **2007**, *43*, 255−264.

(15) Cuccurullo, G.; Giordano, L.; Viccione, G. An analytical approximation for continuous flow microwave heating of liquids. *Adv. Mech. Eng.* **2015**, *5*, 929236.

(16) Choi, P.; Park, J. Y.; Kim, T.; Park, S. H.; Kim, H.; Kang, K. S.; Ham, J. Improved anticancer effect of ginseng extract by microwave-assisted processing through the generation of ginsenosides Rg3, Rg5 and Rk1. *J. Funct. Foods* **2015**, *14*, 613−622.

DOI: 10.1021/acs.jafc.5b00782
J. Agric. Food Chem. 2015, 63, 5964−5969

(17) Yokozawa, T.; Cho, E. J.; Hara, Y.; Kitani, K. Antioxidative activity of green tea treated with radical initiator 2,2′-azobis(2-amidinopropane) dihydrochloride. *J. Agric. Food Chem.* **2000**, *48*, 5068−5073.
(18) Park, H. W.; In, G.; Han, S. T.; Lee, M. W.; Kim, S. Y.; Kim, K. T.; Cho, B. G.; Han, G. H.; Chang, I. M. Simultaneous determination of 30 ginsenosides in *Panax ginseng* preparations using ultra performance liquid chromatography. *J. Ginseng Res.* **2013**, *37*, 457−467.
(19) Kim, I. W.; Sun, W. S.; Yun, B. S.; Kim, N. R.; Min, D.; Kim, S. K. Characterizing a full spectrum of physico-chemical properties of (20*S*)- and (20*R*)-ginsenoside Rg3 to be proposed as standard reference materials. *J. Ginseng Res.* **2013**, *37*, 124−134.
(20) Kim, T.; Kim, Y. J.; Han, I. H.; Lee, D.; Ham, J.; Kang, K. S.; Lee, J. W. The synthesis of sulforaphane analogues and their protection effect against cisplatin induced cytotoxicity in kidney cells. *Bioorg. Med. Chem. Lett.* **2015**, *25*, 62−66.
(21) Lee, D.; Kim, K. H.; Moon, S. W.; Lee, H.; Kang, K. S.; Lee, J. W. Synthesis and biological evaluation of chalcone analogues as protective agents against cisplatin-induced cytotoxicity in kidney cells. *Bioorg. Med. Chem. Lett.* **2015**, *25*, 1929−1932.
(22) Tayem, Y.; Green, C. J.; Motterlini, R.; Foresti, R. Isothiocyanate−cysteine conjugates protect renal tissue against cisplatin-induced apoptosis via induction of heme oxygenase-1. *Pharmacol. Res.* **2014**, *81*, 1−9.
(23) Hannemann, J.; Baumann, K. Nephrotoxicity of cisplatin, carboplatin and transplatin. A comparative *in vitro* study. *Arch. Toxicol.* **1990**, *64*, 393−400.
(24) Xiao, T.; Choudhary, S.; Zhang, W.; Ansari, N. H.; Salahudeen, A. Possible involvement of oxidative stress in cisplatin-induced apoptosis in LLC-PK1 cells. *J. Toxicol. Environ. Health, Part A* **2003**, *66*, 469−479.
(25) Zhong, L. F.; Zhang, J. G.; Zhang, M.; Ma, S. L.; Xia, Y. X. Protection against cisplatin-induced lipid peroxidation and kidney damage by procaine in rats. *Arch. Toxicol.* **1990**, *64*, 599−600.
(26) Bokemeyer, D.; Sorokin, A.; Dunn, M. J. Multiple intracellular MAP quinase signaling cascades. *Kidney Int.* **1996**, *49*, 1187−1198.
(27) Xia, Z.; Dickens, M.; Raingeaud, J.; Davis, R. J.; Greenberg, M. E. Opposing effects of ERK and JNK−p38 MAP kinases on apoptosis. *Science* **1995**, *270*, 1326−1331.
(28) Hwang, Y. J.; Lee, E. J.; Kim, H. R.; Hwang, K. A. Molecular mechanisms of luteolin-7-*O*-glucoside-induced growth inhibition on human liver cancer cells: G2/M cell cycle arrest and caspase-independent apoptotic signaling pathways. *BMB Rep.* **2013**, *46*, 611−616.
(29) Jiang, M.; Yi, X.; Hsu, S.; Wang, C. Y.; Dong, Z. Role of p53 in cisplatin-induced tubular cell apoptosis: Dependence on p53 transcriptional activity. *Am. J. Physiol. Renal, Fluid Electrolyte Physiol.* **2004**, *287*, 1140−1147.
(30) Cummings, B. S.; Schnellmann, R. G. Cisplatin-induced renal cell apoptosis: Caspase 3-dependent and -independent pathways. *J. Pharmacol. Exp. Ther.* **2002**, *302*, 8−17.
(31) Pickering, J. W.; Endre, Z. H. The definition and detection of acute kidney injury. *J. Renal Inj. Prev.* **2013**, *3*, 21−25.
(32) Ko, J. Y.; Park, J. H. Mouse models of polycystic kidney disease induced by defects of ciliary proteins. *BMB Rep.* **2013**, *46*, 73−79.
(33) Luo, J.; Tsuji, T.; Yasuda, H.; Sun, Y.; Fujigaki, Y.; Hishida, A. The molecular mechanisms of the attenuation of cisplatin-induced acute renal failure by *N*-acetylcysteine in rats. *Nephrol., Dial., Transplant.* **2008**, *23*, 2198−2205.

DOI: 10.1021/acs.jafc.5b00782
J. Agric. Food Chem. 2015, 63, 5964−5969

suppression at higher DP. MS detection is more sensitive, but also more expensive, and typical MS approaches (e.g., electrospray ionization) do not have the molecular weight range to directly measure higher DP proanthocyanidins. Moreover, at higher DP, proanthocyanidins may form ions with multiple charges and/or undergo fragmentation. Due to the redox properties of polyphenols in cocoa, HPLC with electrochemical detection (ECD) could be employed for the identification and separation of a wide array of compounds in a single run. Our laboratory and others have successfully used this technique for the separation and detection of flavan-3-ol monomers.[18,19] The underlying unique redox chemistry of compounds makes ECD typically more selective and sensitive than UV and fluorescence detectors.[20] To our knowledge, proanthocyanidins of DP > 3 have not previously been analyzed by reversed-phase HPLC-ECD.

Polyphenols play an important role in the sensory characteristics of cocoa and chocolate products. With both bitter and astringent properties, these compounds in excess can negatively affect consumer acceptability.[21] Cocoa alkalization ("Dutching") is a process during which cocoa powder or nibs are exposed to a basic solution at increased temperatures. Resulting products are often darker in color, less astringent and bitter, and more dispersible compared to their unalkalized counterparts. Previous studies have reported that commercially available cocoa powders that had been subjected to "heavy alkalization" had up to 90% loss of total polyphenols (TP) and significantly reduced levels of proanthocyanidins.[22] Although suggestive, this study is limited by the fact that the authors did not alkalize the cocoa powder samples themselves, and no information regarding time, temperature, and concentration of alkali was provided. Instead, the degree of alkalization was based on the pH and color of the commercial product with lighter colored and lower pH products considered less alkalized. This approach discounts variability in the native pH of cocoa beans as well as differences in the levels of proanthocyanidins based on country of origin, harvest time, etc. In the absence of a direct examination of the effect of alkali treatment on proanthocyanidin content as a function of time, it is difficult to develop a predictive model to balance desirable sensory and ingredient functionality with retention of putative bioactive molecules.

Studies that have evaluated the direct effect of alkalization have focused on monomeric polyphenols or proanthocyanidin dimers, and few data are available regarding the effect of alkalization on proanthocyanidins of high DP. Due to the biological significance of high DP proanthocyanidins, such data are critical for understanding the potential bioactivity differences in various cocoa products.[14,23] In the present study we developed a new reversed phase HPLC-ECD method to separate and quantitate flavan-3-ol monomers and proanthocyanidins of DP 2−7. We demonstrate the usefulness of this new method by examining the effects of alkalization on individual flavan-3-ol monomers and proanthocyanidins of DP up to 7 and use the data to develop an initial predictive model of alkali-induced proanthocyanidin degradation.

MATERIALS AND METHODS

Materials. Commercial cocoa powder with a single batch code was sourced locally from a supermarket. Total polyphenols were estimated using the Folin−Ciocalteu reagent (Sigma-Aldrich, St. Louis, MO, USA). Cocoa proanthocyanidin standards were provided by the Hershey Co. (Hershey, PA, USA). All other chemicals were of the highest grade commercially available.

Alkalization of Cocoa Samples. Cocoa powder (15 g) was combined with 135 mL of ultrapure water and a stir bar in a 250 mL. The mixture was stirred at 400 rpm until the cocoa powder was dispersed. While stirring, samples were heated to 92 °C and a predetermined volume of 4.0 M sodium hydroxide solution was added to bring the starting pH of the solution to pH 8. Samples were removed at seven time points: heating onset, when the solution reached 92 °C (6 min after application of heat), and 0.5, 5, 15, 30, and 60 min after base addition. Upon removal, samples were poured into preweighed tubes and cooled in an ice−water bath prior to storage at −80 °C. Samples were freeze-dried to obtain a dry cocoa powder. Alkalization was repeated twice (overall $n = 7$ per treatment and time point).

Sample Preparation. After alkalization, the lipids were removed from cocoa samples by extraction three times with 10 volumes of hexane with continuous agitation for 10 min. After each extraction, the solvent was decanted. Lipid-free cocoa powder was air-dried for 24 h, and the defatted mass was recorded. A polyphenol-enriched fraction was prepared by sequentially extracting the defatted cocoa material with 30 mL of acetone/water (70:30, v/v) and 30 mL of methanol/water (50:50, v/v) with continuous agitation for 10 min. Following each extraction, the mixture was centrifuged at 1776*g* for 4 min. The supernatant from each extraction was then combined, the organic solvent was removed under vacuum, and the remaining water was frozen at −80 °C and lyophilized under 0.1 Pa vacuum. Extracts were stored at −80 °C until later use. Prior to analysis, cocoa extracts were redissolved in DMSO at 10 mg/mL.

HPLC Analysis. Cocoa flavan-3-ols and proanthocyanidins were analyzed using an HPLC system consisting of two LC-20AD pumps, an SIL-20AC refrigerated autosampler (Shimadzu Scientific, Kyoto, Japan), and an ESA 5500 coulochem electrode array system (CESA; Chelmsford, MA, USA). The potentials of the CEAS were set at −100, 100, 300, and 500 mV. A 150 mm × 4.6 mm, 5 μm, Supelcosil LC-18 column (Supelco, Bellefonte, PA, USA) was used for chromatographic separation. The mobile phases consisted of solvent A (30 mM sodium phosphate monobasic buffer, 1.75% acetonitrile, and 0.125% tetrahydrofuran, pH 3.35) and solvent B (15 mM sodium phosphate monophosphate buffer, 58.5% acetonitrile, and 12.5% tetrahydrofuran, pH 3.45). Mobile phase conditions started at 4% B with isocratic flow for 7 min. The concentration of B increased linearly to 17% at 25 min, to 33% B at 45 min, and to 98% B at 60 min. Mobile phase conditions were held at 98% B for 3 min prior to re-equilibration to 4% B. The flow rate was 1.0 mL/min, and the column temperature was maintained at 35 °C. For HPLC analysis, cocoa extracts (10 mg/mL in DMSO) were diluted 10-fold in 0.2% ascorbic acid in deionized water and filtered through a 0.45 μM PTFE filter (VWR International, Radnor, PA, USA). Injection volume was 30 μL. Samples were normalized to a standardized extract. Quantitation of **1** and **2** was based on a detector potential of 100 mV. Quantitation of **3**−**8** was based on a detector potential of 300 mV.

Kinetic Analysis. Kinetic analyses were carried out using GraphPad Prism (La Jolla, CA, USA). Data were fitted to a two-phase exponential decay model described by

$$Y = \text{span}\,\beta \times e^{-K\beta \times X} + \text{span}\,\alpha \times e^{-K\alpha \times X} + \text{plateau}$$

Y is concentration; span β and span α are constants that indicate the portions of the concentration−time curve in the slow and fast decay portions, respectively; K_β and K_α are the rate constants for the slow and fast portions, respectively, of the concentration−time curve; and plateau is the concentration at infinity. Initial and terminal half-lives ($t_{1/2\alpha}$ and $t_{1/2\beta}$) are equivalent to $0.6392/K$.

Color and pH Analysis. Sample pH was determined using a pH meter. Color was analyzed by L, a, b values using a CR400 Hunter colorimeter (Minolta, Osaka, Japan) calibrated to a white standard provided with the instrument. Samples were equilibrated to 25 °C, 10 mL of sample was placed in a clear plastic sample tray, and the L, a, b

DOI: 10.1021/acs.jafc.5b02661
J. Agric. Food Chem. 2015, 63, 5970−5975

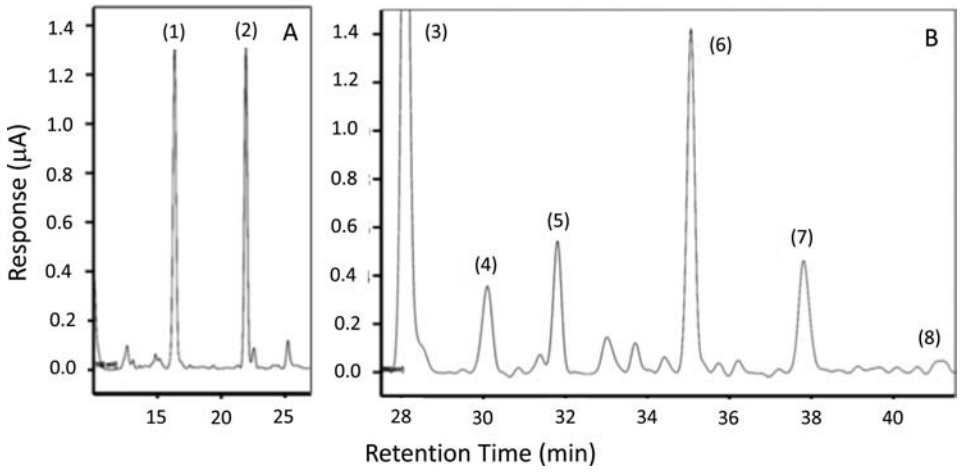

Figure 2. HPLC-ECD analysis of the flavan-3-ols and proanthocyanidins in a cocoa sample.

Table 1. Within- and Between-Day Variation of HPLC-ECD Method[a]

day		1	2	3	4	5	6	7	8
1	mean ± SD (mg/g)	0.9 ± 0.1	10.2 ± 0.8	11.8 ± 0.8	4.4 ± 0.5	3.6 ± 0.3	3.6 ± 0.1	1.0 ± 0.1	0.6 ± 0.0
	RSD (%)	8.1	8.1	7.0	6.7	8.3	1.6	6.9	8.6
2	mean ± SD (mg/g)	0.9 ± 0.1	10.6 ± 0.8	11.2 ± 0.3	4.4 ± 0.5	3.6 ± 0.3	3.6 ± 0.1	1.2 ± 0.0	0.6 ± 0.6
	RSD (%)	13.1	8.0	2.5	11.6	8.7	1.6	2.1	10.7
3	mean ± SD (mg/g)	1.0 ± 0.1	10.9 ± 0.7	12.6 ± 0.8	4.1 ± 0.1	4.1 ± 0.3	3.7 ± 0.2	1.2 ± 0.0	0.6 ± 0.0
	RSD (%)	12.3	6.4	6.4	2.4	7.0	5.1	3.2	5.0
between-day	mean ± SD (mg/g)	0.9 ± 0.1	10.5 ± 0.8	11.9 ± 0.9	4.3 ± 0.4	3.8 ± 0.4	3.7 ± 0.1	1.2 ± 0.1	0.6 ± 0.0
	RSD (%)	11.4	7.2	7.3	8.2	9.4	3.3	9.8	8.2

[a]Within-day and between-day relative standard deviation (%RSD) was determined using a standard cocoa powder with known amounts of proanthocyanidins.

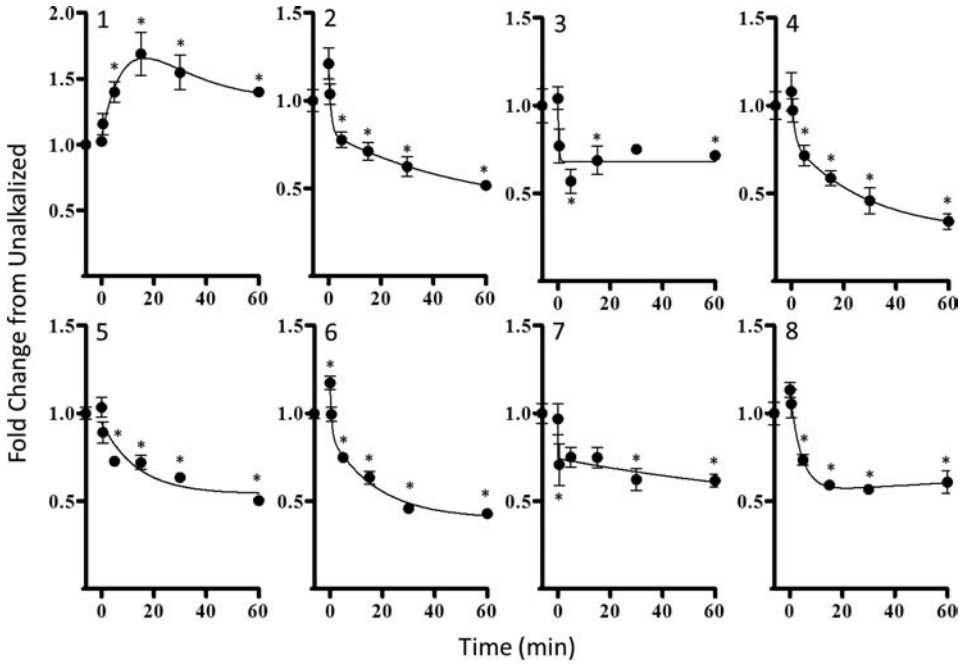

Figure 3. Effect of alkalization on the levels of individual flavan-3-ols and proanthocyanidins in cocoa powder. Data were fitted to a two-phase exponential decay model. Data represent the mean ± SEM. ∗ indicates $p < 0.05$ compared to unalkalized control.

values were measured. Color difference (ΔE) from unalkalized control was calculated as previously reported.[26]

$$\Delta E = \sqrt{(\Delta L^2 + \Delta a^2 + \Delta b^2)}$$

DOI: 10.1021/acs.jafc.5b02661
J. Agric. Food Chem. 2015, 63, 5970−5975

Total Phenolics Determination. Total phenolics were measured as previously described.[14] For total phenolic analysis, cocoa extract was dissolved in DMSO (final concentration = 10 mg/mL). The extract was then combined with 79 volumes of deionized water and 5 volumes of of Folin−Ciocalteu reagent and mixed for 5 min. The reaction was stopped by the addition of 15 volumes of 1.9 M sodium carbonate. After 30 min of incubation at 37 °C, the absorbance at λ 765 nm was measured and compared to a standard curve of gallic acid.

Statistical Analysis. All statistical analyses were carried out using GraphPad Prism (La Jolla, CA, USA). Mean ± standard error of the mean (SEM) was reported for HPLC-ECD data (flavan-3-ol monomers and proanthocyanidin content). Relative percent standard deviation (RSD) was calculated for within- and between-day variations from three replicate samples each run on three separate days. Mean ± SEM was reported for pH and color analysis. ΔE was calculated using unalkalized sample as the control. When applicable, comparison between treatments was calculated using one-way ANOVA with Tukey's HSD test. Significance was achieved at $p < 0.05$.

RESULTS AND DISCUSSION

In the present study, we developed a new reversed phase HPLC-ECD for the analysis of cocoa polyphenols and used that method to monitor alkali-induced changes in the content and composition of polyphenols in cocoa powder. To our knowledge, this is the first report of separation and quantitation of proanthocyanidins by HPLC-ECD.

The present chromatographic separation resulted in well-resolved peaks with high signal-to-noise ratio. Compounds **1** and **2** eluted at 16.4 and 22 min, respectively (Figure 2). Proanthocyanidin retention time was directly proportional to DP (Figure 2). The ECD response was greater for **1** and **2** compared to the proanthocyanidins. The ECD response was linear with respect to concentration of the individual flavan-3-ols and proanthocyanidins over a range of 1.5−15 μg (R^2 = 0.956−0.999). Within- and between-day variations of the new method are shown in Table 1. All compounds had between-day RSD values <10% except for **1** (11.4%).

In addition to the peaks that were identified with authenticated standards, several peaks that eluted after 41.2 min were well resolved. These peaks could represent higher DP proanthocyanidins, but a lack of high-quality, authenticated standards precluded their identification. Additional studies with such standards may increase the usefulness of the method.

All treatments resulted in a significant increase in the content of **1** compared to unalkalized cocoa ($p < 0.05$) (Figure 3). Concentrations of **1** increased by 69% during the first 15 min of alkalization and then began to slowly decline. Concentrations of **2** were significantly reduced after the first 5 min of alkalization, and treatment for 60 min resulted in a 47% reduction. These results are consistent with those previously reported.[24,25] Two potential mechanisms underlie these opposite trends. First, **2** may undergo epimerization to **1**.[24,25] Second, there is evidence that **2** may be preferentially added to proanthocyanidins during polymerization. Although **1** could act as a nucleophilic unit for attack, previous research has shown that 75−81% of terminal proanthocyanidin subunits are **2**.[26,27]

The concentration of **3**−**8** decreased as a function of alkalization time (Figure 3). The proanthocyanidins showed an initial rapid decay, likely due to condensation to form compounds with higher DP, followed by a slowing of the decay function. The levels of **4**, **5**, **6**, and **8** were significantly reduced after 5 min of alkalization. Interestingly, **3** deviated from the general trend of the other proanthocyanidins. Alkalization for 5 and 15 min significantly reduced **3** to its lowest value; however, upon further alkalization, the content **3** increased to levels comparable to that of the unroasted control. This increase could be a result of the formation of new dimers from flavan-3-ol subunits.

Degradation kinetics of proanthocyanidins were best modeled by a two-phase exponential decay model. Half-lives and R^2 values are shown (Table 2). A two-phase exponential decay model may best predict changes in cocoa proanthocyanidins during alkaline processing due to the continual degradation and formation of proanthocyanidins of various degrees of polymerization. It is interesting to note the model fits relatively well for proanthocyanidins composed of an odd number of flavan-3-ol subunits, whereas the changes in proanthocyanidins with an even number of subunits are not well explained by the model. Because of the poor fit of the model to **3** and **7**, the predicted half-lives are suspect. Similarly, because **1** initially increased, the model fit the data poorly and half-lives were not determined. More research is needed to better understand the mechanism behind proanthocyanidin condensation and the stability of individual proanthocyanidins under basic conditions to further refine this model.

Table 2. Half-Lives of Cocoa Flavan-3-ols and Proanthocyanidins[a]

	$t_{1/2\alpha}$ (min)	$t_{1/2\beta}$ (min)	R^2
1	n/a	n/a	0.458
2	0.62	37.73	0.749
3	0.25	5.62×10^{15}	0.379
4	0.82	20.09	0.705
5	9.43	9.43	0.640
6	0.44	12.49	0.917
7	7.60×10^{-33}	80.78	0.268
8	2.98	769.50	0.780

[a]Half-lives were derived by fitting concentration vs time data to a two-phase exponential decay model. R^2 represents the goodness of fit of the model to the data. n/a indicates that the concentration increased rather than decreased with time.

To provide context for the changes observed in individual compounds, we determined the effect of alkali treatment on cocoa powder color and total phenolic content. Alkalization increased cocoa pH compared to unalkalized cocoa powder (7.48−8.03 vs 5.57) (Table 3). As expected, alkaline treatment resulted in a time-dependent darkening (Figure 4). These pH changes and color changes are within the range of commercially available cocoa powders reported previously and correspond to "medium" to "heavily" alkalized cocoa powders as defined in that study.[22] To evaluate the differences between overall color of the samples, ΔE was calculated, using unalkalized averages for L, a, and b as the control. The human eye can perceive a difference in color if ΔE exceeds a value of 1.[28] All treatments resulted in a $\Delta E > 1$ and were significantly different from the unalkalized samples ($p < 0.05$), and all treatments with base addition were significantly different from samples that were preheated with no alkali. L, a, and b values all followed an inverse trend with increasing degree of alkalinization. Lower L values correspond with a darker appearance, whereas lower a and b values correspond with less red and less yellow, respectively (Table 3).[28] These results are important because one of the primary uses of alkalization today is to modify the color of cocoa, which was successfully achieved in this study.[22]

DOI: 10.1021/acs.jafc.5b02661
J. Agric. Food Chem. 2015, 63, 5970−5975

Table 3. Effect of Alkalization on pH and Color[a]

treatment	final pH	color			
		L	*a*	*b*	Δ*E*
unalkalized	5.57 ± 0.04	32.9 ± 0.6	9.3 ± 0.3	12.0 ± 0.5	0.00
preheat (92 °C, 6 min, no alkali)	5.57 ± 0.01	31.3 ± 0.1	8.6 ± 0.0	10.0 ± 0.2	2.62
time postalkali addition (min)					
0.5	8.03 ± 0.02*	28.6 ± 0.6	7.0 ± 0.4	8.2 ± 0.4	6.18
5	7.89 ± 0.06*	28.9 ± 0.2	7.5 ± 0.3	8.5 ± 0.3	5.59
15	7.70 ± 0.04*	29.3 ± 0.2	7.6 ± 0.2	8.6 ± 0.4	5.20
30	7.71 ± 0.01*	29.2 ± 0.5	7.6 ± 0.4	8.6 ± 1.0	5.28
60	7.48 ± 0.06*	28.7 ± 0.3	7.1 ± 0.1	7.9 ± 0.4	6.30

[a]All time points postalkali addition were significantly different from the unalkalized and preheated samples in terms of *L*, *a*, *b*, and Δ*E* values.

Figure 4. Representative images of the effect of alkalization on cocoa color.

Total phenolics were significantly reduced compared to the unalkalized control for all treatments ($p < 0.05$) (Figure 5). At 60 min, alkalization resulted in a 20.4% loss of phenolic compounds. Our results are consistent with trials in a previous study that reported a 26% loss in total polyphenols after alkalization at 1% NaOH for 20 min at 0.02 MPa.[29] The findings, although significant, are much less dramatic than those previously reported in the literature. Previous studies have reported a 60.5% decrease in total phenolics at similar final pH value.[22] The authors characterized this cocoa as a "medium alkalized" product. Another study reported a 60% loss in total flavonoids as quantified by LC-UV for cocoa with a pH ≤7.2.[10] These differences may be due to the fact that previous studies used commercially obtained products rather than samples alkalized in-house.

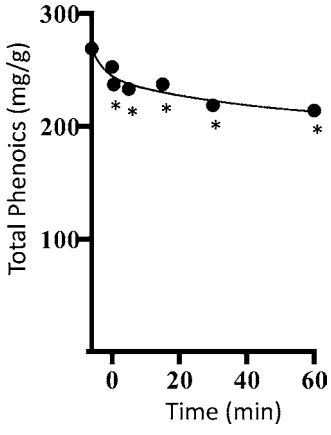

Figure 5. Effect of alkalization on the total polyphenol content in cocoa. Data represent the mean ± SEM. ∗ indicates $p < 0.05$ compared to unalkalized cocoa.

In the setting of a cocoa-processing facility, it is likely that large batches of alkalized cocoa are stored at room temperature for longer periods of time prior to use. In the present study, we extracted cocoa samples immediately after alkalization and stored the extracts at −80 °C to prevent further loss. These differences in postalkalization handling may account in part for the differences in total polyphenolics observed. In addition, because the panels of products used in previous studies are likely of different geographic origin and may have undergone different postharvest processing (i.e., fermentation and roasting), they likely have differences in polyphenol content and composition that are independent of alkalization.

Overall, the present study demonstrates the usefulness of HPLC-ECD for the analysis of flavan-3-ols as well as proanthocyanidins up to DP 7. Furthermore, although alkalization at pH 8 for 1 h, which resulted in a significant color change, reduced total phenolics by 20%, this reduction does not fully explain changes in individual polyphenols. We propose two-phase exponential decay as an initial model to predict alkali-induced polyphenol loss. Future mechanistic studies on proanthocyanidin polymerization could greatly improve the field and lead to improved prediction of proanthocyanidin composition based on processing conditions.

AUTHOR INFORMATION

Corresponding Author

*(J.D.L.) Phone: (814) 865-5223. Fax: (814) 863-6132. E-mail: jdl134@psu.edu.

Funding

This work was supported by a grant from the National Institutes of Health (AT004678) and by the Silvio and Edith Crespo Award in Chocolate Research to J.D.L.

Notes

The authors declare no competing financial interest.

DOI: 10.1021/acs.jafc.5b02661
J. Agric. Food Chem. 2015, 63, 5970−5975

■ ACKNOWLEDGMENTS

We thank Dr. Gregory Ziegler for the use of key pieces of laboratory equipment as well as helpful discussion. We also thank Dr. Ryan Elias for helpful discussion.

■ ABBREVIATIONS USED

CEAS, coulochem electrode array system; DP, degree of polymerization; ECD, electrochemical detection

■ REFERENCES

(1) Kim, H.; Keeney, P. G. (−)-Epicatechin content in fermented and unfermented cocoa beans. *J. Food Sci.* **1984**, *49*, 1090−1092.
(2) Wollgast, J.; Anklam, E. Review on polyphenols in *Theobroma cacao*: changes in composition during the manufacture of chocolate and methodology for identification and quantification. *Food Res. Int.* **2000**, *33*, 423−447.
(3) Becker, K.; Geisler, S.; Ueberall, F.; Fuchs, D.; Gostner, J. M. Immunomodulatory properties of cacao extracts potential consequences for medical applications. *Front. Pharmacol.* **2013**, *4*.10.3389/fphar.2013.00154
(4) Gu, Y.; Yu, S.; Lambert, J. D. Dietary cocoa ameliorates obesity-related inflammation in high fat-fed mice. *Eur. J. Nutr.* **2014**, *53*, 149−158.
(5) Steinberg, F. M.; Bearden, M. M.; Keen, C. L. Cocoa and chocolate flavonoids: implications for cardiovascular health. *J. Am. Diet. Assoc.* **2003**, *103*, 215−223.
(6) Vinson, J. A.; Proch, J.; Bose, P.; Muchler, S.; Taffera, P.; Shuta, D.; Samman, N.; Agbor, G. A. Chocolate is a powerful ex vivo and in vivo antioxidant, an antiatherosclerotic agent in an animal model, and a significant contributor to antioxidants in the European and American diets. *J. Agric. Food Chem.* **2006**, *54*, 8071−8076.
(7) Ohno, M.; Sakamoto, K. Q.; Ishizuka, M.; Fujita, S. Crude Cacao *Theobroma cacao* extract reduces mutagenicity induced by benzo[*a*]-pyrene through inhibition of CYP1A activity in vitro. *Phytother. Res.* **2009**, *23*, 1134−1139.
(8) Prior, R. L.; Gu, L. W. Occurrence and biological significance of proanthocyanidins in the American diet. *Phytochemistry* **2005**, *66*, 2264−2280.
(9) Weisburger, J. H. Chemopreventive effects of cocoa polyphenols on chronic diseases. *Exp. Biol. Med.* **2001**, *226*, 891−897.
(10) Andres-Lacueva, C.; Monagas, M.; Khan, N.; Izquierdo-Pulido, M.; Urpi-Sarda, M.; Permanyer, J.; Lamuela-Raventos, R. M. Flavanol and flavonol contents of cocoa powder products: Influence of the manufacturing process. *J. Agric. Food Chem.* **2008**, *56*, 3111−3117.
(11) Kothe, L.; Zimmermann, B. F.; Galensa, R. Temperature influences epimerization and composition of flavanol monomers, dimers and trimers during cocoa bean roasting. *Food Chem.* **2013**, *141*, 3656−3663.
(12) Langer, S.; Marshall, L. J.; Day, A. J.; Morgan, M. R. A. Flavanols and methylxanthines in commercially available dark chocolate: a study of the correlation with nonfat cocoa solids. *J. Agric. Food Chem.* **2011**, *59*, 8435−8441.
(13) Counet, C.; Collin, S. Effect of the number of flavanol units on the antioxidant activity of procyanidin fractions isolated from chocolate. *J. Agric. Food Chem.* **2003**, *51*, 6816−6822.
(14) Gu, Y.; Hurst, W. J.; Stuart, D. A.; Lambert, J. D. Inhibition of key digestive enzymes by cocoa extracts and procyanidins. *J. Agric. Food Chem.* **2011**, *59*, 5305−5311.
(15) Kelm, M. A.; Johnson, J. C.; Robbins, R. J.; Hammerstone, J. F.; Schmitz, H. H. High-performance liquid chromatography separation and purification of cacao (*Theobroma cacao* L.) procyanidins according to degree of polymerization using a diol stationary phase. *J. Agric. Food Chem.* **2006**, *54*, 1571−1576.
(16) Robbins, R. J.; Leonczak, J.; Li, J.; Johnson, J. C.; Collins, T.; Kwik-Uribe, C.; Schmitz, H. H. Determination of flavanol and procyanidin (by degree of polymerization 1−10) content of chocolate, cocoa liquors, powder(s), and cocoa flavanol extracts by normal phase high-performance liquid chromatography: collaborative study. *J. AOAC Int.* **2012**, *95*, 1153−1160.
(17) Hurst, W. J.; Stanley, B.; Glinski, J. A.; Davey, M.; Payne, M. J.; Stuart, D. A. Characterization of primary standards for use in the HPLC analysis of the procyanidin content of cocoa and chocolate containing products. *Molecules* **2009**, *14*, 4136−4146.
(18) Subagio, A.; Sari, P.; Morita, N. Simultaneous determination of (+)-catechin and (−)-epicatechin in cacao and its products by high-performance liquid chromatography with electrochemical detection. *Phytochem. Anal.* **2001**, *12*, 271−276.
(19) Murphy, K. J.; Chronopoulos, A. K.; Singh, I.; Francis, M. A.; Moriarty, H.; Pike, M. J.; Turner, A. H.; Mann, N. J.; Sinclair, A. J. Dietary flavanols and procyanidin oligomers from cocoa (*Theobroma cacao*) inhibit platelet function. *Am. J. Clin. Nutr.* **2003**, *77*, 1466−1473.
(20) Milbury, P. E. Analysis of complex mixtures of flavonoids and polyphenols by high-performance liquid chromatography electrochemical detection methods. *Methods Enzymol.* **2001**, *335*, 15−26.
(21) Harwood, M. L.; Ziegler, G. R.; Hayes, J. E. Tolerance for high flavanol cocoa powder in semisweet chocolate. *Nutrients* **2013**, *5*, 2258−2267.
(22) Miller, K. B.; Hurst, W. J.; Payne, M. J.; Stuart, D. A.; Apgar, J.; Sweigart, D. S.; Ou, B. Impact of alkalization on the antioxidant and flavanol content of commercial cocoa powders. *J. Agric. Food Chem.* **2008**, *56*, 8527−8533.
(23) Dorenkott, M. R.; Griffin, L. E.; Goodrich, K. M.; Thompson-Witrick, K. A.; Fundaro, G.; Ye, L.; Stevens, J. R.; Ali, M.; O'Keefe, S. F.; Hulver, M. W.; Neilson, A. P. Oligomeric cocoa procyanidins possess enhanced bioactivity compared to monomeric and polymeric cocoa procyanidins for preventing the development of obesity, insulin resistance, and impaired glucose tolerance during high-fat feeding. *J. Agric. Food Chem.* **2014**, *62*, 2216−27.
(24) Kofink, M.; Papagiannopoulos, M.; Galensa, R. (−)-Catechin in cocoa and chocolate: occurrence and analysis of an atypical flavan-3-ol enantiomer. *Molecules* **2007**, *12*, 1274−1288.
(25) Payne, M. J.; Hurst, W. J.; Miller, K. B.; Rank, C.; Stuart, D. A. Impact of fermentation, drying, roasting, and Dutch processing on epicatechin and catechin content of cacao beans and cocoa ingredients. *J. Agric. Food Chem.* **2010**, *58*, 10518−10527.
(26) Xie, D. Y.; Dixon, R. A. Proanthocyanidin biosynthesis − still more questions than answers? *Phytochemistry* **2005**, *66*, 2127−2144.
(27) Vidal, S.; Cartalade, D.; Souquet, J. M.; Fulcrand, H.; Cheynier, V. Changes in proanthocyanidin chain length in winelike model solutions. *J. Agric. Food Chem.* **2002**, *50*, 2261−2266.
(28) Rodriguez, P.; Perez, E.; Guzman, R. Effect of the types and concentrations of alkali on the color of cocoa liquor. *J. Sci. Food Agric.* **2009**, *89*, 1186−1194.
(29) Li, Y.; Zhu, S.; Feng, Y.; Xu, F. F.; Ma, J. G.; Zhong, F. Influence of alkalization treatment on the color quality and the total phenolic and anthocyanin contents in cocoa powder. *Food Sci. Biotechnol.* **2014**, *23*, 59−63.

DOI: 10.1021/acs.jafc.5b02661
J. Agric. Food Chem. 2015, 63, 5970−5975

Neu5Gc should not be used in human food because of potential immunological problems.[27]

Galacto-oligosaccharide mixtures (GOS) with degrees of polymerization (DP) from 2 to 9, which are synthesized from lactose by enzymatic transgalactosylation using specific microbial β-galactosidases, have shown to be functional food products with excellent prebiotic functions.[28] These ingredients are broadly applied in the infant food sector. Depending on the enzyme used, GOS contains an array of linear and branched $(Gal)_nGlc$ oligosaccharides with different substitution patterns. For one of these products, prepared with *Bacillus circulans* β-galactosidase, the ensemble up to DP5 comprises >40 components.[29−34]

In view of reported functions of both GOS and sialylated oligosaccharides, taking into account the low amounts of sialyl-oligosaccharides in cow's milk, it is hypothesized that partial sialylation of GOS (Sia-GOS) will generate mixtures of compounds that combine the different properties, meaning novel products with broad functionalities both for the food (Sia = Neu5Ac) and feed (Sia = Neu5Gc) industries. To this end we have chosen *Trypanosoma cruzi trans*-sialidase (TcTS), recombinantly produced in *E. coli* and capable of transferring sialic acid from various artificial and natural Sia(α2−3)Gal(β1−x)-glycans (sialogalactoglycans) to Gal(β1−x)-glycans (asialogalactoglycans), as the biocatalyst (for a review, see ref 35). For the aimed for food and feed products, bovine κ-casein-derived glycomacropeptide (GMP) (>99% Neu5Ac; <1% Neu5Gc) and bovine blood plasma glycoprotein mixture (BPG) (45% Neu5Ac; 55% Neu5Gc) were selected, respectively, as sialic acid donor substrates. Using the sialic acid acceptor substrates GOS and specific DP GOS, analytical information was collected about the formed Sia-GOS mixtures and patented.[36,37] A related study, but without analytical details, to such an approach has been patented earlier for the system GOS/GMP/*Trypanosoma congolense trans*-sialidase.[38] Parallel to our work some sialyltransfer studies have appeared on the sialylation of GOS with GMP using TcTS, *Trypanosoma rangeli trans*-sialidase, and *Pasteurella multocida trans*-sialidase.[39−41]

Recently, we have reported a basic study focused on the reaction kinetics, efficiency, and specificity of the (α2−3)-sialylation of terminal Gal residues of the GOS components 3′-galactosyl-lactose, 4′-galactosyl-lactose, and 6′-galactosyl-lactose, using TcTS combined with the donors 2-*O*-(4-methylumbelliferyl)-α-*N*-acetylneuraminic acid (4-MU-Neu5Ac) and GMP. Interestingly, also the internal Gal residue of 6′-galactosyl-lactose turned out to be sialylated.[42] In a further study, of importance for the exploration of potential food and feed applications, here, we present our detailed results, including matrix-assisted laser-desorption ionization time-of-flight mass spectrometry (MALDI-TOF-MS) and nuclear magnetic resonance (NMR) studies, on the sialylation of Vivinal GOS and GOS DP with the sialic acid donors GMP (Neu5Ac donor) and BPG (Neu5Ac/Neu5Gc donor) and the biocatalyst TcTS.

MATERIALS AND METHODS

Chemicals. Vivinal GOS was obtained from FrieslandCampina Domo (Borculo, The Netherlands). Bovine κ-casein-derived glycomacropeptide (GMP) was provided by FrieslandCampina Innovation Center (Wageningen, The Netherlands). Bovine blood plasma glycoprotein (BPG) preparations were supplied by Darling Ingredients Nederland BV (Son, The Netherlands). *N*-Acetylneuraminic acid (Neu5Ac), *N*-glycolylneuraminic acid (Neu5Gc), 2-*O*-(4-methylumbelliferyl)-α-*N*-acetylneuraminic acid (4MU-Neu5Ac), and *N*-acetylneuraminyl(α2−3)lactose (3′-SL) were obtained from Carbosynth Ltd. (Compton, UK). *N*-Glycolylneuraminyl(α2−3)lactose was a gift of Prof. Dr. T. Urashima (Obihiro, Japan). D_2O (99.9 atom % D) was acquired from Cambridge Isotope Laboratories Ltd. (Andover, MA, USA).

TcTS Production and Purification. Recombinant TcTS enzyme batches were produced in *E. coli* BL21(DE3) (Invitrogen, Carlsbad, CA, USA) using plasmid pTrcTS611/2[43] (a gift of Prof. Dr. A. C. C. Frasch, Buenos Aires, Argentina), as previously described.[42] The specific transglycosylation activity of TcTS was determined as 1.0 μmol/min/mg using 4MU-Neu5Ac and lactose as substrates and quantitative detection of *N*-acetylneuraminyl(α2−3)lactose using high-pH anion-exchange chromatography with pulsed-amperometric detection (HPAEC-PAD) analysis.

Isolation of Vivinal GOS DP Fractions by Size Exclusion Chromatography. Vivinal GOS was fractionated on a Bio-Gel P-2 Fine (45−90 μm) column (60 × 5 cm) using demineralized water as eluent at a flow rate of 1 mL/min and 40 °C. The separation was followed by an RI-101 Shodex refractive index detector (Showa Denko Europe GmbH, Munich, Germany). Carbohydrate-containing fractions (5 mL) were screened with MALDI-TOF-MS and pooled according to DP.

Analysis of Sialic Acid Content and Linkage Type of Bovine κ-Casein-Derived GMP and Bovine BPG. To determine the total sialic acid content of GMP and BPG, samples were incubated with 0.1 M HCl for 1 h at 80 °C, then neutralized with 1 M NaOH, and, after dilution with dimethyl sulfoxide, subjected to HPAEC-PAD analysis. For quantification of released Neu5Ac and Neu5Gc, use was made of calibration curves of known concentrations of both sialic acids. Following the same analysis protocol, the ratios of (α2−3)- and (α2−6)-linked sialic acid in GMP and BPG were determined by comparing the release of sialic acid by linkage-type nonspecific sialidase A (Prozyme, Hayward, CA, USA) and (α2−3)-specific sialidase S (Prozyme). Enzymatic incubations were carried out according to the manufacturer's protocols.

Enzyme Incubations. All TcTS incubations were performed in 50 mM sodium citrate buffer (pH 5.0) containing 30 mM NaCl at 25 °C. Reactions were stopped by placing on ice or at −20 °C until further processing. Samples for HPAEC-PAD analysis were diluted with 95% dimethyl sulfoxide.

TcTS incubations with 3.5 mg/mL Vivinal GOS (DP1−DP9; average DP of 3, corresponding to 2 mM) and 67.5 mg/mL GMP [corresponding to 5 mM (α2−3)-linked Neu5Ac] were carried out for 24 h. Sample aliquots were evaluated by HPAEC-PAD and MALDI-TOF-MS.

TcTS incubations with different GOS DPs (each at 3 mM) and 85 mg/mL GMP [corresponding to 6 mM (α2−3)-linked Neu5Ac] were carried out for various times, depending on the application. Sample aliquots were evaluated by HPAEC-PAD, and incubation mixtures were further subjected to weak anion-exchange chromatography (AEX) on Resource Q, followed by ^{1}H NMR analysis, MALDI-TOF-MS, or $NaBH_4$ reduction, as described below.

TcTS incubations with 65 mg/mL BPG (corresponding to 2 mM total sialic acid) and 4 mM lactose, GOS DP3, or GOS DP4 were carried out for various times, and samples were taken for evaluation by HPAEC-PAD. Obtained sialyl-lactose mixtures (24 h) were subjected to preparative HPAEC-PAD analysis to yield pure Neu5Ac(α2−3)lactose and Neu5Gc(α2−3)lactose. Obtained Sia-GOS products (48 h) were separated into mono-Sia-GOS and di-Sia-GOS fractions by AEX on Resource Q, and purified sialylated products were desalted prior to ^{1}H NMR analysis, as described below.

Isolation of Sialylated GOS Products by Weak AEX. To remove sialic acid donor glycoconjugates, incubation mixtures were filtered on Amicon Ultra 15 mL filters (10000 NMWL membrane) (Millipore) following the manufacturer's protocol. Then, samples were desalted on CarboGraph solid-phase extraction (SPE) columns (300 mg; Grace, Breda, The Netherlands). After washing with 0.1% trifluoroacetic acid, oligosaccharides were eluted with 25% aqueous acetonitrile, containing 0.1% trifluoroacetic acid as eluent, and

DOI: 10.1021/acs.jafc.5b01505
J. Agric. Food Chem. 2015, 63, 5976−5984

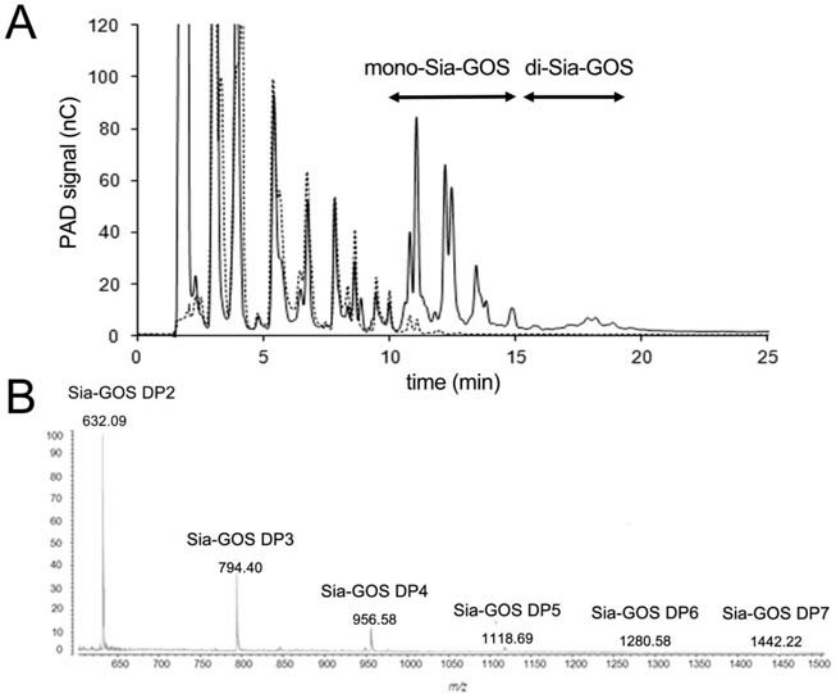

Figure 1. (A) HPAEC-PAD profile on CarboPac PA-1 of compounds in the Vivinal GOS/GMP/TcTS reaction mixture (incubation at 25 °C and pH 5.0) at t = 0 h (dotted line) and t = 24 h (solid line). The regions of formed mono-Sia-GOS and di-Sia-GOS are marked. (B) MALDI-TOF-MS spectrum (negative-ion mode) of the monocharged fraction of the Vivinal GOS/GMP/TcTS reaction mixture, showing $[M - H]^-$ quasi-molecular ions for mono-Sia-GOS DP2−DP7.

lyophilized. (Sialylated) oligosaccharide mixtures were fractionated on a 1 mL Resource Q anion-exchange column (GE Healthcare, Uppsala, Sweden) fitted in an Äkta Performance Fast Protein Liquid Chromatography system (GE Healthcare), equipped with a UV detector (214 and 280 nm) and a conductivity cell. The column was subsequently eluted with 3 mL of water, a linear gradient of 0−8% 0.5 M NaCl over 5 min, and a linear gradient of 8−50% 0.5 M NaCl in 6 min, at a flow rate of 1 mL/min. Neutral, monocharged, and dicharged oligosaccharide fractions were collected, desalted on CarboGraph columns (see above for conditions), and subjected to structural analysis.

Reduction of Disialylated GOS Fractions. Resource Q disialylated GOS fractions were treated with $NaBH_4$ (10 mg/mL) for 2 h at room temperature, followed by neutralization by dropwise addition of 4 M acetic acid (pH paper check). Formed boric acid was removed in vacuo by coevaporation with methanol. After lyophilization from water, the samples were subjected to MALDI-TOF-MS and HPAEC-PAD analyses.

High-pH Anion-Exchange Chromatography−Pulsed Amperometric Detection. Analytical analyses of oligosaccharides were carried out by HPAEC-PAD on a Dionex ICS-3000 system (Thermo Scientific, Amsterdam, The Netherlands), equipped with a CarboPac PA-1 column, as previously described.[42] Preparative isolation of Neu5Ac(α2−3)lactose and Neu5Gc(α2−3)lactose was performed on a Dionex ICS-5000 system, equipped with a CarboPac PA-1 guard column (50 × 4 mm) and a CarboPac PA-1 column (250 × 9 mm), using a gradient of 30−600 mM sodium acetate in 0.1 M NaOH (1 mL/min). Desalting was performed on CarboGraph columns (see above for conditions).

MALDI-TOF-MS. MALDI-TOF-MS experiments were performed on an Axima mass spectrometer (Shimadzu Kratos Inc., Manchester, UK), as previously described.[42]

NMR Spectroscopy. ^{1}H NMR spectra were recorded at a probe temperature of 298 K on a Varian Inova 600 spectrometer (NMR Center, University of Groningen) or on a Bruker DRX-500 spectrometer (Bijvoet Center, Department of NMR Spectroscopy, Utrecht University). Samples were exchanged twice with D_2O with intermediate lyophilization and then dissolved in 650 μL of D_2O. Proton chemical shifts are expressed in parts per million in reference to internal acetone (δ^1H 2.225). Suppression of the HOD signal was achieved by applying a WET1D pulse (600 MHz spectra) or a WEFT pulse (500 MHz spectra).

RESULTS AND DISCUSSION

TcTS Catalyzed Formation of Sia-GOS from GMP and Vivinal GOS. For the sialylation reaction of Vivinal GOS, the following characteristics of the donor GMP and the acceptor GOS have been recently documented. The used GMP preparation (MW 10 kDa) has a total sialic acid content of 3.6% (w/w), corresponding to 0.12 mmol/g dry matter; the ratio of Neu5Ac and Neu5Gc is 99:1.[42] The *O*-glycans of GMP contain both (α2−3)-linked and (α2−6)-linked Neu5Ac; the percentage of (α2−3)-linked Neu5Ac is 59% (w/w).[42] The used Vivinal GOS preparation contains free Glc (18.5%), free Gal (1.7%), DP2 products (42.5%), DP3 products (23.6%), DP4 products (10.2%), DP5 products (3.0%), and DP6−DP9 products (<0.5%). At present, the structures of >40 components have been elucidated (>98% of the oligosaccharides), being mainly linear and branched reducing (major) and linear nonreducing (minor) $(Gal)_nGlc$ oligosaccharides (Supporting Information Scheme S1). The common small basic structural fragments, which are nearly only elongated by Gal(β1−4) residues, are five disaccharides, namely, Gal(β1−2)Glc, Gal(β1−3)Glc, Gal(β1−4)Glc, Gal(β1−6)Glc, and Glc(α1−1β)Gal, and four branched trisaccharides, namely, Gal(β1−2)[Gal(β1−6)]Glc, Gal(β1−3)[Gal(β1−6)]Glc, Gal-(β1−4)[Gal(β1−6)]Glc, and Gal(β1−2)[Gal(β1−4)]Glc.[33,34]

A mixture of GOS (3 mM) and GMP (80 mg/mL; containing 6 mM (α2−3)-linked Neu5Ac) was incubated with TcTS (1 μg/mL) for 24 h at 25 °C and pH 5.0. The chosen time, temperature, and pH are based on the optimal

DOI: 10.1021/acs.jafc.5b01505
J. Agric. Food Chem. 2015, 63, 5976−5984

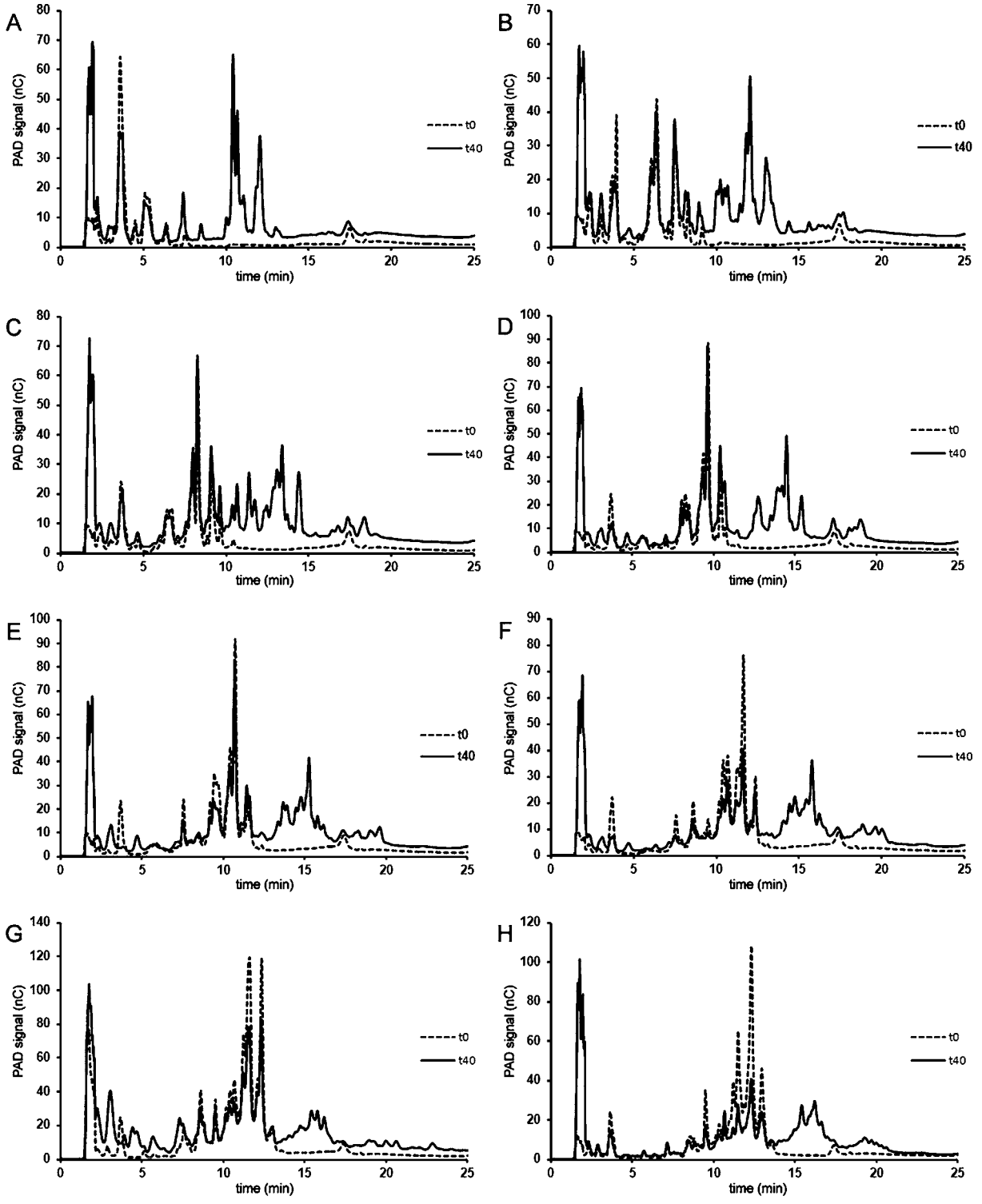

Figure 2. HPAEC-PAD profiles on CarboPac PA-1 of compounds in GOS DP2−DP9/GMP/TcTS reaction mixtures (incubation at 25 °C and pH 5.0) at t = 0 h (dotted line) and t = 40 h (solid line): (A) GOS DP2; (B) GOS DP3; (C) GOS DP4; (D) GOS DP5; (E) GOS DP6; (F) GOS DP7; (G) GOS DP8; (H) GOS DP9.

conditions established earlier for the transfer of Neu5Ac from 4MU-Neu5Ac to lactose, yielding Neu5Ac(α2−3)lactose.[42] Comparison of the HPAEC profile on CarboPac PA-1 (PAD detection) of the obtained reaction mixture after t = 24 h with that of GOS at t = 0 h showed a quite different peak pattern, reflecting a complex mixture of GOS and Sia-GOS components (Figure 1A). Clearly, the peaks in the higher retention time region reflect negatively charged Sia-GOS components. Closer inspection of the HPAEC profile of the reaction mixture revealed that two product pools were distinguishable on the basis of their retention times: a major pool of products with retention times between 10 and 15 min, expected to be mono-Sia-GOS components, and a minor pool of products with retention times between 16 and 20 min, expected to be

DOI: 10.1021/acs.jafc.5b01505
J. Agric. Food Chem. 2015, 63, 5976−5984

Table 1. MALDI-TOF-MS Analyses (Negative-Ion Mode) of Mono-Sia-GOS and Di-Sia-GOS Obtained from Incubations of GOS DP2−DP6 with GMP and TcTS[a]

	mono-Sia-GOS		di-Sia-GOS			
	$[M - H]^-$		$[M - H]^-$		$[M - 2H + Na]^-$	
DP GOS	expected	observed	expected	observed	expected	observed
DP2	632.20	632.33				
DP3	794.26	794.52	1085.35	1085.68	1107.33	1107.52
DP4	956.31	956.60	1247.40	1247.38	1269.39	1269.64
DP5	1118.36	1118.44	1409.46	1409.62	1431.44	1431.15
DP6	1280.42	1280.72	1571.51	1572.00	1593.49	1594.30

[a]The observed m/z values are averages of five and three independent measurements for the mono- and disialylated products, respectively.

Table 2. Percentages of Conversion of GOS into Sia-GOS and Mono-Sia-GOS/Di-Sia-GOS Ratios (Determined from Resource Q Chromatograms Using UV 214 nm Responses), Obtained from TcTS Incubations for 32 h at 25 °C with GMP and GOS DP2−DP9

DP GOS	conversion (%)[a] GOS → Sia-GOS	mono-Sia-GOS[b] (%)	di-Sia-GOS[b] (%)
DP2	56 ± 5	100	
DP3	36 ± 2	90 ± 3	10 ± 3
DP4	35 ± 4	87 ± 4	13 ± 4
DP5	37 ± 5	86 ± 2	14 ± 2
DP6	36 ± 5	89 ± 4	11 ± 4
DP7	19 ± 1	84 ± 1	16 ± 1
DP8	14 ± 2	81 ± 4	19 ± 4
DP9	20 ± 3	79 ± 2	21 ± 2

[a]Conversion percentages were determined in duplicate. [b]Mono- and di-Sia-GOS percentages were measured in triplicate (DP3−DP6) and duplicate (DP7−DP9).

disialylated-GOS (di-Sia-GOS) components. The latter structures can be formed from GOS components containing two terminal Gal units, which are both targets for sialylation by TcTS or from 6′-galactosyl-lactose (here terminal and internal Gal can be sialylated) present in GOS.[33,34,42] Note that mono-Sia-GOS components can originate from GOS structures with one and two terminal Gal units (and from 6′-galactosyl-lactose). After working up the reaction mixture, indeed AEX on Resource Q (UV detection at 214 nm) yielded a peak in the monocharged and in the dicharged region of sialylated oligosaccharides (data not shown). MALDI-TOF-MS analysis (negative-ion mode) of the monocharged fraction revealed a series of quasi-molecular $[M - H]^-$ ions for monosialylated GOS (mono-Sia-GOS) of GOS DP2−DP7 (m/z 632.09, 794.40, 956.58, 1118.69, 1280.58, 1442.22) (Figure 1B). The molar ratio of mono-Sia-GOS and di-Sia-GOS, based on the UV detection of C═O in Neu5Ac at 214 nm, taking into account the number of Neu5Ac units (one or two) in the detected molecules, was determined to be 97:3. The relatively low percentage of di-Sia-GOS is caused by the relatively high percentage of GOS DP2 (42.5%, w/v; i.e., lactose and other GOS DP2 components), which cannot form di-Sia-GOS structures.

TcTS Incubations of GMP with GOS DP2−DP9 Fractions. As is evident from the above experiment, incubation of GOS with GMP and TcTS leads to a highly complex mixture of GOS + Sia-GOS components with concomitant overlap in retention times on CarboPac PA-1 using HPAEC-PAD. Therefore, it was decided to separate GOS in its DP fractions and to incubate them separately with GMP and TcTS. To this end Vivinal GOS was fractionated on Bio-Gel P-2, yielding GOS fractions ranging from DP1 to DP9 (Supporting Information Figure S1). Each GOS DP fraction (3 mM), except DP1, was incubated with GMP [80 mg/mL; containing 6 mM (α2−3)-linked Neu5Ac] and TcTS (1 μg/mL) for 40 h at 25 °C and pH 5.0. HPAEC-PAD analysis on Carbo-Pac PA-1 (Figure 2) showed for all DP fractions the formation of product peaks with increased retention times, indicating that GOS DP2−DP9 were all suitable acceptor substrates for TcTS.

Separation of the reaction mixtures by AEX on Resource Q (UV detection at 214 nm) yielded two charged fractions for all DPs ≥3 (for DP4, see Figure S2). MALDI-TOF-MS analysis (negative-ion mode) of the charged fractions prepared from GOS DP2−DP6 confirmed in each case, except DP2 (only mono-Sia-GOS), the presence of both mono-Sia-GOS and di-Sia-GOS components (Table 1). When incubation experiments were followed over time, the total Sia-GOS and di-Sia-GOS formations were found to be maximal after 32 h of incubation at 25 °C (Table 2). The conversion of GOS to Sia-GOS was the highest for DP2 (about 56%), about 36% for medium-length GOS chains (DP3−DP6), and about 17% for long-chain GOS (DP7−DP9), respectively, indicating that TcTS has a preference for shorter GOS acceptors.

As the GOS preparation contains reducing linear (one terminal Gal unit) and branched (two terminal Gal units) oligosaccharides and nonreducing linear oligosaccharides (two terminal Gal units), di-Sia-GOS can originate from reducing branched as well as from nonreducing linear oligosaccharides. To make these two groups of di-Sia-GOS components visible, the di-Sia-GOS fractions obtained from GOS DP4 and DP5 were incubated with $NaBH_4$, whereby the reducing branched oligosaccharides were converted into their corresponding oligosaccharide-alditols. In HPAEC-PAD analyses on CarboPac PA-1, oligosaccharide-alditols have shorter retention times than their reducing oligosaccharide analogues,[44] but nonreducing oligosaccharides will retain their retention times. Inspection of the HPAEC-PAD profiles (Figure S3) before and after reduction, together with MALDI-TOF-MS analysis (data not

DOI: 10.1021/acs.jafc.5b01505
J. Agric. Food Chem. 2015, 63, 5976−5984

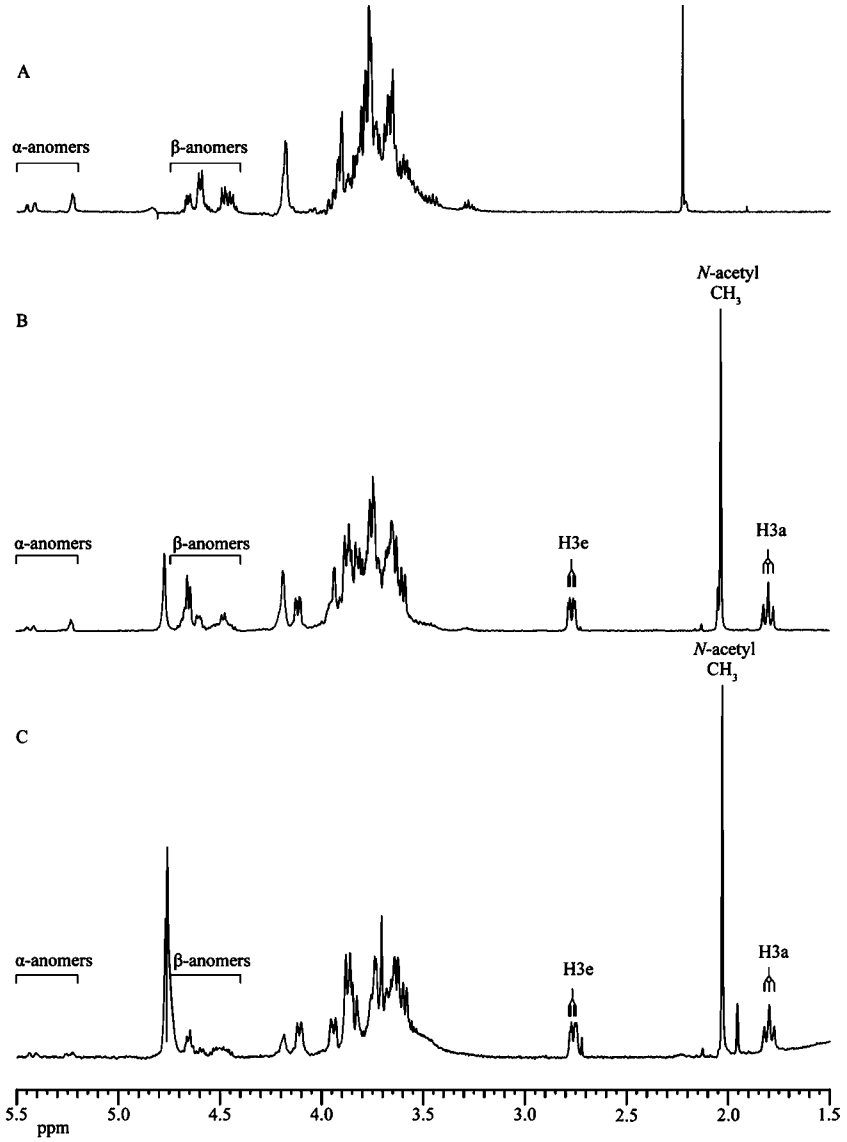

Figure 3. 500 MHz ^{1}H NMR spectra, recorded in D_2O at 298 K, of (A) GOS DP4, (B) DP4 mono-Sia-GOS, and (C) DP4 di-Sia-GOS. The sialylated GOS DP4 fractions were obtained from the incubation of GOS DP4 with GMP and TcTS.

shown), showed that the majority of the di-Sia peaks shifted to shorter retention times, in agreement with the finding that nonreducing oligosaccharides form only a very minor part of GOS.[34]

As a typical example of the NMR analysis of the different Sia-GOS DP fractions, a short discussion of the spectra of mono-Sia-GOS DP4 (MALDI-TOF-MS: $[M - H]^-$, 956.60) and di-Sia-GOS DP4 (MALDI-TOF-MS: $[M - H]^-$, 1247.38) is presented. The ^{1}H NMR spectrum of the DP4 GOS acceptor [a mixture of at least 15 DP4 structures in which the D-Glc*p* unit is mono or disubstituted by D-Gal*p* residues (monomeric, dimeric, or trimeric fragments); see Scheme S1[34]] is shown in Figure 3A. It shows α-anomeric peaks at δ 5.449 and 5.406, reflecting the GOS DP4 components with 2-, 2,4-, 2,6-, and 1,2-O-substituted α-D-Glc*p* residues; the α-anomeric signals in the range δ 5.25−5.22 reflect the GOS DP4 components with 1-, 3-, 4-, 6-, 3,6-, and 4,6-O-substituted α-D-Glc*p* residues, whereas the signals at δ 4.221 and 4.164 correspond with H-6a signals of 6-O-substituted D-Glc*p* residues (i.e., β- and α-anomeric forms of reducing D-Glc*p*, respectively) present in part of the GOS DP4 ensemble. The signals in the range of δ 4.75−4.40 stem from β-D-Glc*p* and β-D-Gal*p* H-1 atoms, and those in the range of δ 4.20−4.17 from β-D-Gal*p* H-4 atoms of GOS DP4 components containing 3- (very minor) and/or 4-O-substituted (major) β-D-Gal*p* residues.[33,34] Comparison of the ^{1}H NMR spectrum of mono-Sia-GOS DP4 (Figure 3B) with that of GOS DP4 (Figure 3A) shows, besides several signals shifting in the β-anomeric region, three clear additional signals that have similar peak areas. The new signals at δ 2.763 and 1.799 belong to the Neu5Ac H-3e and H-3a atoms of Neu5Ac(α2−3) residues [Neu5Ac(α2−3)Gal regions: H-3e, δ 2.75−2.76; H-3a, δ 1.79−1.80[45]] and the new signal at δ 4.112 is the Gal H-3 signal of 3-O-substituted β-D-Gal*p* units (a terminal Gal residue in GOS), in accordance with the Neu5Ac(α2−3)Gal sequence. Note that Neu5Ac(α2−6) H-3e and H-3a atoms of the Neu5Ac(α2−6)Gal sequence resonate in the regions δ 2.67 and 1.70−1.72, respectively.[45] The monosialylation follows from a comparison of the H-1 surface areas of the α-and β-anomeric Glc/Gal residues with those of the Neu5Ac H-3e signal, showing a 3.4:1 ratio for Glc/

DOI: 10.1021/acs.jafc.5b01505
J. Agric. Food Chem. 2015, 63, 5976−5984

Gal:Neu5Ac, fitting to a monosialylation of DP4 structures. Following a similar reasoning, the ^{1}H NMR spectrum of di-Sia-GOS (Figure 3C) can be interpreted [Neu5Ac(α2−3) H-3e, δ 2.760; H-3a, δ 1.794]. The disialylation is reflected by a 1.6:1 ratio for Glc/Gal:Neu5Ac, fitting to disialylated DP4 structures. Note that β-anomeric signals close to the HOD peak suffer from cosuppression, resulting in underestimation of the Glc/Gal amount in this approach.

Sialylation of Lactose with BPG as Sialic Acid Donor and TcTS as Catalyst. For the decoration of GOS with both Neu5Ac and Neu5Gc, a bovine BPG preparation was selected as sialic acid donor. Blood plasma glycoprotein preparations are a rich source of *N*- and *O*-glycans terminated by (α2→3)- and (α2→6)-linked sialic acids.[25,46,47] Total sialic acid analysis of BPG, after mild acid hydrolysis, by HPAEC-PAD yielded a content of 0.7% (w/w), corresponding to 23.4 μmol/g dry matter (w/w), of which 45% was Neu5Ac and 55% Neu5Gc. By comparing the amount of sialic acid released by the linkage-type nonspecific sialidase A and the (α2−3)-specific sialidase S, the percentages of (α2−3)-linked Neu5Ac and Neu5Gc in BPG were determined to be 60 and 40%, respectively.

To test the sialic acid transfer reaction with BPG as donor, first lactose was applied as acceptor. To this end BPG [65 mg/mL; corresponding with 0.54 and 0.44 mM (α2−3)-linked Neu5Ac and Neu5Gc, respectively] was incubated with TcTS (1 μg/mL) and lactose (4 mM) for 24 h at 25 °C and pH 5.0, and the products Neu5Ac(α2−3)lactose and Neu5Gc(α2−3)lactose were quantified by HPAEC-PAD on CarboPac PA-1 [Figure 4; the relative response factor of Neu5Gc(α2−3)lactose

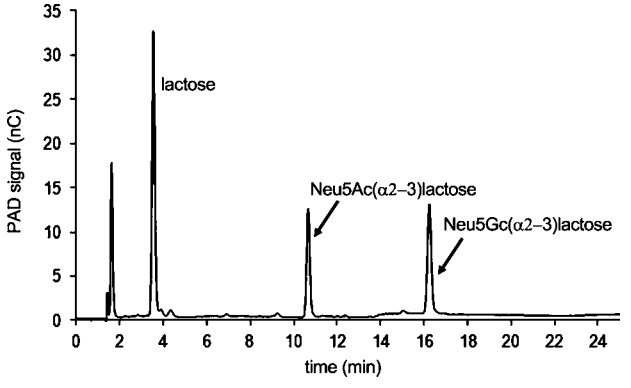

Figure 4. HPAEC-PAD profile on CarboPac PA-1 of the product mixture obtained from the incubation of lactose with BPG (24 h, 25 °C, pH 5.0), showing the formation of Neu5Ac(α2−3)lactose and Neu5Gc(α2−3)lactose.

is 1.2 times that of Neu5Ac(α2−3)lactose]. MALDI-TOF-MS analysis of the mixture revealed quasi-molecular ions $[M - H]^-$ at m/z 631.88 (Neu5Ac product) and m/z 647.87 (Neu5Gc product). Both products were isolated on CarboPac PA-1 and subjected to ^{1}H NMR analysis, showing the typical ^{1}H NMR parameters for (α2−3)-linked Neu5Ac (H-3e, δ 2.759; H-3a, δ 1.801; NAc, δ 2.030) and (α2−3)-linked Neu5Gc (H-3e, δ 2.777; H-3a, δ 1.820; NGc, δ 4.121).[45] Under the applied conditions, it was found that 33% of total Neu5Ac and 20% of total Neu5Gc could be transferred to lactose, which means that the percentage of transfer of (α2−3)-linked Neu5Ac and (α2−3)-linked Neu5Gc amounted to 55 and 50%, respectively.

Sia-GOS Obtained from TcTS Incubations with BPG and GOS DP3 and DP4. As incubations with GOS would lead to highly complex mixtures of Sia-GOS, built from components of different DP with only Neu5Ac, only Neu5Gc, and in the case of reducing branched oligosaccharides and nonreducing linear oligosaccharides also with both Neu5Ac and Neu5Gc, pilot experiments were carried out with GOS DP3 and DP4.

Both GOS DP fractions (4 mM) were incubated with BPG [65 mg/mL; corresponding with 0.54 and 0.44 mM (α2−3)-linked Neu5Ac and Neu5Gc, respectively] and TcTS (1 μg/mL) for 48 h at 25 °C and pH 5.0. When compared with the HPAEC profiles of the starting materials, HPAEC-PAD analysis showed in both cases above 10 min the formation of two nearly identical product pools, suggesting that both Neu5Ac(α2−3)GOS and Neu5Gc(α2−3)GOS were formed in similar ratios [Figure 5; compare with Figure 2B (DP3) and 2C (DP4) for

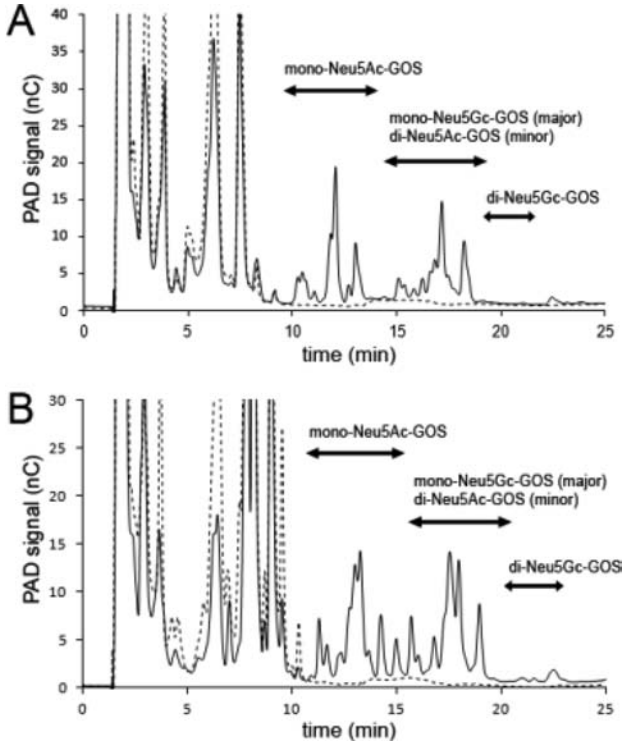

Figure 5. HPAEC-PAD profiles on CarboPac PA-1 of compounds in GOS DP3/BPG/TcTS and GOS DP4/BPG/TcTS reaction mixtures (incubation at 25 °C and pH 5.0 for 48 h): (A) GOS DP3; (B) GOS DP4.

only Neu5Ac(α2−3)GOS]. The sialylated GOS DP3 and DP4 reaction mixtures were separated by AEX on Resource Q, and the ratios of the mono-Sia-GOS and di-Sia-GOS fractions were determined to be 97:3 and 98:2, respectively (not optimized). The mono-Sia-GOS fractions were collected and subjected to ^{1}H NMR analysis (Figure S4). The NMR spectra showed overlap of the Neu5Ac and Neu5Gc signals; assignment of the chemical shifts led to the conclusion that both mono-Sia-GOS fractions contain (α2−3)-linked Neu5Ac (H-3e, δ 2.761; H-3a, δ 1.798) and (α2−3)-linked Neu5Gc (H-3e, δ 2.782; H-3a, δ 1.814) (^{1}H NMR data for Sia-GOS of DP3 are shown). Also, the presence of both *N*-acetyl and *N*-glycolyl signals at δ 2.031 and 4.122 was consistent with the presence of Neu5Ac and Neu5Gc in the products.

Conclusions. The presented data show that the *trans*-sialidase of *T. cruzi* is capable of transferring (α2−3)-linked sialic acid from the low-cost naturally available bovine donor

DOI: 10.1021/acs.jafc.5b01505
J. Agric. Food Chem. 2015, 63, 5976−5984

substrates GMP and BPG to GOS (total Vivinal GOS or derived specific GOS DPs), thus forming novel sialylated oligosaccharide mixtures (Sia-GOS) in excellent yields. Detailed analytical data for these complex mono-Sia-GOS and di-Sia-GOS mixtures were collected, substantiating the course of the decoration reactions. As the used donors contain the two basic members of the sialic acid family, Neu5Ac and Neu5Gc, nearly only (Neu5Ac in GMP) or in an attractive ratio, when focused on Neu5Gc (55% Neu5Gc) (BPG), they are highly suitable to be further explored for potential applications in both the food and feed industry, respectively. The protocols developed in this study are currently upgraded for the generation of larger batches of Sia-GOS products. When available, these products can be evaluated for food (GOS + Neu5Ac-GOS) and feed (GOS + Neu5Ac/Neu5Gc-GOS) applications in terms of combined prebiotic/antiadhesive properties. This holds for preparations obtained from both total GOS or from specific DP fractions of GOS. Moreover, separation of mono- and di-Sia-GOS fractions generates possibilities for testing them individually.

■ ASSOCIATED CONTENT

Ⓢ Supporting Information

Supplemental figures and scheme. The Supporting Information is available free of charge on the ACS Publications website at DOI: 10.1021/acs.jafc.5b01505.

■ AUTHOR INFORMATION

Corresponding Author

*(L.D.) Phone: 31-50-3632150. Fax: 31-50-3632154. E-mail: l.dijkhuizen@rug.nl.

Funding

This project was jointly financed by the European Union, European Regional Development Fund and the Ministry of Economic Affairs, Agriculture and Innovation, Peaks in the Delta, the Municipality of Groningen, and the Provinces of Groningen, Fryslân, and Drenthe, as well as the Dutch Carbohydrate Competence Center (CCC WP6).

Notes

The authors declare no competing financial interest.

■ ACKNOWLEDGMENTS

We thank A. C. C. Frasch (Universidad Nacional General San Martin, Buenos Aires, Argentina) for the gift of plasmid pTrcTS611/1.

■ ABBREVIATIONS USED

AEX, anion-exchange chromatography; BMOs, bovine milk oligosaccharides; BPG, bovine blood plasma glycoprotein mixture; DP, degree of polymerization; GMP, bovine κ-casein-derived glycomacropeptide; GOS, galacto-oligosaccharides; HMOs, human milk oligosaccharides; HPAEC-PAD, high-pH anion-exchange chromatography coupled with pulsed amperometric detection; MALDI-TOF-MS, matrix-assisted laser desorption ionization time-of-flight mass spectrometry; 4MU, 4-methylumbelliferyl; Neu5Ac, *N*-acetylneuraminic acid; Neu5Gc, *N*-glycolylneuraminic acid; NMR, nuclear magnetic resonance; SDS-PAGE, sodium dodecyl sulfate−polyacrylamide gel electrophoresis; Sia, sialic acid; SOSs, sialylated oligosaccharides; TcTS, *Trypanosoma cruzi trans*-sialidase; UV, ultraviolet

■ REFERENCES

(1) Boehm, G.; Stahl, B. Oligosaccharides from milk. *J. Nutr.* **2007**, *137*, 847S−849S.

(2) Hale, T. W.; Hartmann, P. E. *Textbook of Human Lactation*, 1st ed.; Hale Publishing: Amarillo, TX, USA, 2007.

(3) Gabrielli, O.; Zampini, L.; Galeazzi, T.; Padella, L.; Santoro, L.; Peila, C.; Giuliani, F.; Bertino, E.; Fabris, C.; Coppa, G. V. Preterm milk oligosaccharides during the first month of lactation. *Pediatrics* **2011**, *128*, e1520−e1531.

(4) Urashima, T.; Asakuma, S.; Messer, M. Milk oligosaccharides. In *Comprehensive Glycoscience: From Chemistry to Systems Biology*; Kamerling, J. P., Boons, G.-J., Lee, Y. C., Suzuki, A., Taniguchi, N., Voragen, A. G. J., Eds.; Elsevier Science: Amsterdam, The Netherlands, 2007; Vol. 4, pp 695−724.

(5) Wu, S.; Tao, N.; German, J. B.; Grimm, R.; Lebrilla, C. B. Development of an annotated library of neutral human milk oligosaccharides. *J. Proteome Res.* **2010**, *9*, 4138−4151.

(6) Wu, S.; Grimm, R.; German, J. B.; Lebrilla, C. B. Annotation and structural analysis of sialylated human milk oligosaccharides. *J. Proteome Res.* **2011**, *10*, 856−868.

(7) Hong, Q.; Ruhaak, L. R.; Totten, S. M.; Smilowitz, J. T.; German, J. B.; Lebrilla, C. B. Label-free absolute quantitation of oligosaccharides using multiple reaction monitoring. *Anal. Chem.* **2014**, *86*, 2640−2647.

(8) Bode, L. Human milk oligosaccharides: every baby needs a sugar mama. *Glycobiology* **2012**, *22*, 1147−1162.

(9) Hickey, R. M. The role of oligosaccharides from human milk and other sources in prevention of pathogen adhesion. *Int. Dairy J.* **2012**, *22*, 141−146.

(10) Yu, Z.-T.; Chen, C.; Newburg, D. S. Utilization of major fucosylated and sialylated human milk oligosaccharides by isolated human gut microbes. *Glycobiology* **2013**, *23*, 1281−1292.

(11) Shang, J.; Piskarev, V. E.; Xia, M.; Huang, P.; Jiang, X.; Likhosherstov, L. M.; Novikova, O. S.; Newburg, D. S.; Ratner, D. M. Identifying human milk glycans that inhibit norovirus binding using surface plasmon resonance. *Glycobiology* **2013**, *23*, 1491−1498.

(12) Ten Bruggencate, S. J. M.; Bovee-Oudenhoven, I. M. J.; Feitsma, A. L.; van Hoffen, E.; Schoterman, M. H. C. Functional role and mechanisms of sialyllactose and other sialylated milk oligosaccharides. *Nutr. Rev.* **2014**, *72*, 377−389.

(13) Gopal, P. K.; Gill, H. S. Oligosaccharides and glycoconjugates in bovine milk and colostrum. *Br. J. Nutr.* **2000**, *84* (Suppl. 1), S69−S74.

(14) Tao, N.; DePeters, E. J.; Freeman, S.; German, J. B.; Grimm, R.; Lebrilla, C. B. Bovine milk glycome. *J. Dairy Sci.* **2008**, *91*, 3768−3778.

(15) Tao, N.; DePeters, E. J.; German, J. B.; Grimm, R.; Lebrilla, C. B. Variations in bovine milk oligosaccharides during early and middle lactation stages analyzed by high-performance liquid chromatography-chip/mass spectrometry. *J. Dairy Sci.* **2009**, *92*, 2991−3001.

(16) Mariño, K.; Lane, J. A.; Abrahams, J. L.; Struwe, W. B.; Harvey, D. J.; Marotta, M.; Hickey, R. M.; Rudd, P. M. Method for milk oligosaccharide profiling by 2-aminobenzamide labeling and hydrophilic interaction chromatography. *Glycobiology* **2011**, *21*, 1317−1330.

(17) Aldredge, D. L.; Geronimo, M. R.; Hua, S.; Nwosu, C. C.; Lebrilla, C. B.; Barile, D. Annotation and structural elucidation of bovine milk oligosaccharides and determination of novel fucosylated structures. *Glycobiology* **2013**, *23*, 664−676.

(18) Mehra, R.; Barile, D.; Marotta, M.; Lebrilla, C. B.; Chu, C.; German, J. B. Novel high-molecular weight fucosylated milk oligosaccharides identified in dairy streams. *PLoS One* **2014**, *9*, e96040.

(19) Fong, B.; Ma, K.; McJarrow, P. Quantification of bovine milk oligosaccharides using liquid chromatography-selected reaction monitoring-mass spectrometry. *J. Agric. Food Chem.* **2011**, *59*, 9788−9795.

(20) Urashima, T.; Taufik, E.; Fukuda, K.; Asakuma, S. Recent advances in studies on milk oligosaccharides of cows and other domestic farm animals. *Biosci. Biotechnol. Biochem.* **2013**, *77*, 455−466.

(21) Liu, Z.; Moate, P.; Cocks, B.; Rochfort, S. Simple liquid chromatography-mass spectrometry method for quantification of major free oligosaccharides in bovine milk. *J. Agric. Food Chem.* **2014**, *62*, 11568−11574.

DOI: 10.1021/acs.jafc.5b01505
J. Agric. Food Chem. 2015, 63, 5976−5984

(22) Albrecht, S.; Lane, J. A.; Marino, K.; Al Busadah, K. A.; Carrington, S. D.; Hickey, R. M.; Rudd, P. M. A comparative study of free oligosaccharides in the milk of domestic animals. *Br. J. Nutr.* **2014**, *111*, 1313−1328.
(23) Smit, H.; Gaastra, W.; Kamerling, J. P.; Vliegenthart, J. F. G.; de Graaf, F. K. Isolation and structural characterization of the equine erythrocyte receptor for enterotoxigenic *Escherichia coli* K99 fimbrial adhesin. *Infect. Immun.* **1984**, *46*, 578−584.
(24) Kyogashima, M.; Ginsburg, V.; Krivan, H. C. *Escherichia coli* K99 binds to *N*-glycolylsialoparagloboside and *N*-glycolyl-GM3 found in piglet small intestine. *Arch. Biochem. Biophys.* **1989**, *270*, 391−397.
(25) Mouricout, M.; Petit, J. M.; Carias, J. R.; Julien, R. Glycoprotein glycans that inhibit adhesion of *Escherichia coli* mediated by K99 fimbriae: Treatment of experimental colibacillosis. *Infect. Immun.* **1990**, *58*, 98−106.
(26) Martín, M.-J.; Martín-Sosa, S.; Hueso, P. Binding of milk oligosaccharides by several enterotoxigenic *Escherichia coli* strains isolated from calves. *Glycoconjugate J.* **2002**, *19*, 5−11.
(27) Padler-Karavani, V.; Yu, H.; Cao, H.; Chokhawala, H.; Karp, F.; Varki, N.; Chen, X.; Varki, A. Diversity in specificity, abundance, and composition of anti-Neu5Gc antibodies in normal humans: potential implications for disease. *Glycobiology* **2008**, *18*, 818−830.
(28) Van Leusen, E.; Torringa, E.; Groenink, P.; Kortleve, P.; Geene, R.; Schoterman, M.; Klarenbeek, B. Industrial applications of galactooligosaccharides. In *Food Oligosaccharides: Production, Analysis and Bioactivity*; Moreno, F. J., Sanz, M. L., Eds.; Wiley Blackwell IFT Press: Oxford, UK, 2014; pp 470−522.
(29) Yanahira, S.; Kobayashi, T.; Suguri, T.; Nakakoshi, M.; Miura, S.; Ishikawa, H.; Nakajima, I. Formation of oligosaccharides from lactose by *Bacillus circulans* β-galactosidase. *Biosci. Biotechnol. Biochem.* **1995**, *59*, 1021−1026.
(30) Fransen, C. T. M.; Van Laere, K. M. J.; van Wijk, A. A. C.; Brüll, L. P.; Dignum, M.; Thomas-Oates, J. E.; Haverkamp, J.; Schols, H. A.; Voragen, A. G. J.; Kamerling, J. P.; Vliegenthart, J. F. G. α-D-Glc*p*-(1↔1)-β-D-Gal*p*-containing oligosaccharides, novel products from lactose by the action of β-galactosidase. *Carbohydr. Res.* **1998**, *314*, 101−114.
(31) Coulier, L.; Timmermans, J.; Bas, R.; van den Dool, R.; Haaksman, I.; Klarenbeek, B.; Slaghek, T.; van Dongen, W. In-depth characterization of prebiotic galacto-oligosaccharides by a combination of analytical techniques. *J. Agric. Food Chem.* **2009**, *57*, 8488−8495.
(32) Rodriguez-Colinas, B.; Poveda, A.; Jimenez-Barbero, J.; Ballesteros, A. O.; Plou, F. J. Galacto-oligosaccharide synthesis from lactose solution or skim milk using the β-galactosidase from *Bacillus circulans*. *J. Agric. Food Chem.* **2012**, *60*, 6391−6398.
(33) Van Leeuwen, S. S.; Kuipers, B. J. H.; Dijkhuizen, L.; Kamerling, J. P. Development of a ^{1}H NMR structural-reporter-group concept for the analysis of prebiotic galacto-oligosaccharides of the [β-D-Gal*p*-(1→*x*)$_n$-D-Glc*p* type. *Carbohydr. Res.* **2014**, *400*, 54−58.
(34) Van Leeuwen, S. S.; Kuipers, B. J. H.; Dijkhuizen, L.; Kamerling, J. P. ^{1}H NMR analysis of the lactose/β-galactosidase-derived galacto-oligosaccharide components of Vivinal® GOS up to DP5. *Carbohydr. Res.* **2014**, *400*, 59−73.
(35) Schauer, R.; Kamerling, J. P. The chemistry and biology of trypanosomal *trans*-sialidases: virulence factors in Chagas disease and sleeping sickness. *ChemBioChem* **2011**, *12*, 2246−2264.
(36) Sallomons, E.; Wilbrink, M. H.; Sanders, P.; Kamerling, J. P.; van Vuure, C. A.; Hage, J. A. Methods for providing sialylated oligosaccharides. Patent WO2013/085384 A1; priority date, Dec 7, 2011; international publication date, June 15, 2013.
(37) Wilbrink, M. H.; ten Kate, G. A.; Sanders, P.; Sallomons, E.; Klarenbeek, B.; Hage, H.; van Vuure, C. A.; Verdonk, J. M. A. J.; Dijkhuizen, L.; Kamerling, J. P. Enzymatic decoration of galacto-oligosaccharides with sialic acid. *Abstracts, 10th Carbohydrate Bioengineering Meeting*, Prague, Czech Republic, 2013; p 246.
(38) Schmitt, J.; Boehm, G.; Stahl, B.; Schauer, R.; Tiralongo, E.; Schrader, S. Trans-sialidases obtained from *Trypanosoma congolense*. U.S. Patent 7,655,784 B2; priority date, Jan 4, 2007; international publication date, Feb 2, 2010.
(39) Holck, J.; Larsen, D. M.; Michalak, M.; Li, H.; Kjærulff, L.; Kirpekar, F.; Gotfredsen, C. H.; Forssten, S.; Ouwehand, A. C.; Mikkelsen, J. D.; Meyer, A. S. Enzyme catalysed production of sialylated human milk oligosaccharides and galactooligosaccharides by *Trypanosoma cruzi* trans-sialidase. *New Biotechnol.* **2014**, *31*, 156−165.
(40) Jers, C.; Michalak, M.; Larsen, D. M.; Kepp, K. P.; Li, H.; Guo, Y.; Kirpekar, F.; Meyer, A. S.; Mikkelsen, J. D. Rational design of a new *Trypanosoma rangeli* trans-sialidase for efficient sialylation of glycans. *PLoS One* **2014**, *9*, e83902.
(41) Guo, Y.; Jers, C.; Meyer, A. S.; Arnous, A.; Li, H.; Kirpekar, F.; Mikkelsen, J. D. A *Pasteurella multocida* sialyltransferase displaying dual *trans*-sialidase activities for production of 3′-sialyl and 6′-sialyl glycans. *J. Biotechnol.* **2014**, *170*, 60−67.
(42) Wilbrink, M. H.; ten Kate, G. A.; van Leeuwen, S. S.; Sanders, P.; Sallomons, E.; Hage, J. A.; Dijkhuizen, L.; Kamerling, J. P. Galactosyl-lactose sialylation using *Trypanosoma cruzi trans*-sialidase as the biocatalyst and bovine κ-casein-derived glycomacropeptide as the donor substrate. *Appl. Environ. Microbiol.* **2014**, *80*, 5984−5991.
(43) Buschiazzo, A.; Campetella, O.; Frasch, A. C. C. *Trypanosoma rangeli* sialidase: cloning, expression and similarity to *T. cruzi* trans-sialidase. *Glycobiology* **1997**, *7*, 1167−1173.
(44) Corradini, C.; Cavazza, A.; Bignardi, C. High-performance anion-exchange chromatography coupled with pulsed electrochemical detection as a powerful tool to evaluate carbohydrates of food interest: Principles and applications. *Int. J. Carbohydr. Chem.* **2012**, ID 487564, *2012*, 1−13.10.1155/2012/487564
(45) Vliegenthart, J. F. G.; Kamerling, J. P. ^{1}H NMR structural-reporter-group concepts in carbohydrate analysis. In *Comprehensive Glycoscience: From Chemistry to Systems Biology*; Kamerling, J. P., Boons, G.-J., Lee, Y. C.; Suzuki, A., Taniguchi, N., Voragen, A. G. J., Eds.; Elsevier Science: Amsterdam, The Netherlands, 2007; Vol. 2, pp 133−191.
(46) Clemetson, K. J. Blood glycoproteins. In *Glycoproteins II/New Comprehensive Biochemistry*; Montreuil, J., Vliegenthart, J. F. G., Schachter, H., Eds.; Elsevier: Amsterdam, The Netherlands, 1997; Vol. 29b, pp 173−201.
(47) Montreuil, J.; Spik, G.; Mazurier, J. Transferrin superfamily. In *Glycoproteins II/New Comprehensive Biochemistry*; Montreuil, J., Vliegenthart, J. F. G., Schachter, H., Eds.; Elsevier: Amsterdam, The Netherlands, 1997; Vol. 29b, pp 203−242.

DOI: 10.1021/acs.jafc.5b01505
J. Agric. Food Chem. 2015, 63, 5976−5984

world-leading contributors to the development of methods for positional analysis of glycerolipids: "the assays of stereo- and regioisomers are more demanding than conventional lipid analyses...All of the methods are subject to improvement".[19]

Attempts to solve these problems include a comprehensive procedure employing an off-line two-dimensional HPLC-MS technique.[20−23] Its advantage is an ability to identify and quantitate a number of TG regioisomers (e.g., the data for 11 TG species were presented in one study).[20] However, with MS-based detection other issues arise: some TG species in the sample present linear calibration plots, whereas others possess nonlinear plots, complicating the data processing.[24] Here, it was concluded that linearity should not be assumed as nonlinear calibration plots may be obscured by scatter in the data or by plots where there is only slight curvature. Additional care and processing of the data are thus required to ensure the highest confidence in the results. Indeed, different MS detectors are known to give different ratios of isomeric TGs.[23] For example, when ionizing OOP, the OO/OP ratio of fragment ions varies from 51 with a Thermo Orbitrap to 64 with a Bruker Ion trap, whereas ionization of OPO with the same instruments provides OO/OP ratios of 16 and 21, respectively. Similarly, ionization of SOO provides OO/SO ratios ranging from 50 for a Bruker Ion trap to 70 for a Bruker QqTOF instrument, whereas OSO provides OO/SO ratios of 17 and 22, respectively, for the same instruments. Another recently reported study uses off-line two-dimensional chromatography by applying nonaqueous reversed phase (RP)-HPLC followed by Ag^+-HPLC of the selected fractions using evaporative light scattering detection (ELSD).[25] When two-dimensional chromatography is not used, separation of isomers and potential contaminants remains problematic, and the resulting chromatograms can be complex and unresolved;[22,23] among others, the separation of the OPO/POO pair has not been solved.

The goal of this work was to establish a convenient and reliable method by which to separate structurally similar TGs, with the targeted quantitation of OPO. A range of techniques was investigated with a view to comparing the advantages and limitations of each. This paper details efforts to provide a robust separation and analytical method that provides data with a high level of confidence and for which a range of potential contaminants were considered.

MATERIALS AND METHODS

Chemicals and Materials. Oleic, linoleic, elaidic, and stearic acids and glycerol were purchased from Sigma-Aldrich (USA). 1-Monopalmitoylglycerol, 1,3-dipalmitoylglycerol, 1,2-dipalmitoylglycerol, 1,3-dioleoyl 2-palmitoylglycerol (OPO), *rac* 1,2-dioleoyl-3-palmitoylglycerol (OOP), 1,2-dipalmitoyl-3-oleoylglycerol (PPO), 1,3-dipalmitoyl-2-oleoylglycerol (POP), tripalmitin (PPP), triheptadecanoin (HHH), triolein (OOO), trielaidin (EEE), trilaurin, trimyristin, tristearin, triarachidin, tribehenin, tripalmitolein, tripetroselinin, trielaidin, tri-11-eicosenoin, trierucin, trilinolein, and trilinolenin were purchased from Sigma-Aldrich (St. Louis, MO, USA). The triglyceride mix TG2-TG10 was from Supelco (Sigma-Aldrich, St. Louis, MO, USA). Commercial samples for analysis included sample 1, a dietary ingredient comprising dairy milk solids blended with OPO-containing oil; sample 2, OPO oil; sample 3, OPO oil (samples, 1, 2 and 3 were kind donations of industrial food grade products from a New Zealand company); and sample 4, infant formula.

POP and PPO were synthesized from 1,3-dipalmitoylglycerol and 1,2-dipalmitoylglycerol, respectively, and oleic acid, with dicyclohexylcarbodiimide (DCC) as the coupling agent.[26] A mixture of 1-palmitoyl-2,3-distearoyl-, 1-stearoyl-2-linoleoyl-3-palmitoyl-, 1-linoleoyl-2-stearoyl-3-palmitoyl-, and 1,2-dilinoleoyl-3-palmitoylglycerols was prepared from 1-monopalmitoylglycerol and a mixture of stearic and linoleic acids (1.00:1.03 mol/mol) using the same method. Similarly, a mixture of tristearin, triolein, 1-stearoyl-2,3-dioleoyl-, 1,3-dioleoyl-2-stearoyl-, 1,2-distearoyl-3-oleoyl-, and 1,3-distearoyl-2-oleoylglycerols was prepared from glycerol and a mixture of stearic and oleic acids (1.00:1.00 mol/mol). Synthetic samples were purified by column chromatography on Merck silica gel 70−230 mesh 100 Å grade 10184 (Sigma-Aldrich, St. Louis, MO, USA) with the consecutive use of hexane, hexane/dimethyl ether (99:1, by v/v), and hexane/diethyl ether (95:5, by v/v) solvent systems and controlled by TLC using Merck HPTLC silica gel 60 10 × 10 cm (Darmstadt, Germany) in hexane/diethyl ether/formic acid (80:20:2, v/v/v) with detection by iodine vapor. The composition of the samples was assessed by GC-FID. The regiospecific distribution of the saturated, monounsaturated, and diunsaturated fatty acids in triacylglycerols was assessed using NMR spectroscopy,[27] with the spectrum acquisition parameters modified as presented under NMR Spectroscopy below. DCC was from Acros Organics (Fisher Scientific, Pittsburgh, PA, USA). The same approach was used to synthesize a mixture of OOO, OOE, OEO, OEE, EOE, and EEE starting from oleic and elaidic acids (1.00:1.04 mol/mol) and glycerol. HPLC solvents (acetone, acetonitrile, *n*-hexane) were Merck LiChrosolv solvents for liquid chromatography (Sigma-Aldrich).

Extraction of TGs from Infant Formula. A 2 g sample of the infant formula powder (sample 4) was extracted using a modification of the method of Svennerholm and Fredman[28] to ensure that polar lipids (required for other assays, not related to this work) were also extracted. The original method was modified as follows: 2 g of powder was combined with 6 mL of water and mixed with 16 mL of methanol. This solution was then extracted sequentially with chloroform (8 mL) and 1:1 chloroform/methanol (16 mL) and twice with 2:1 chloroform/methanol (12 mL) with the use of ultrasonication (5 min/extraction). The centrifuged lipid extracts from each extraction were combined and transferred to a separating funnel and washed with water (23 mL) and then with 10% aqueous KCl (3 mL). The lower (organic, chloroform-rich) layer was dried and constituted the crude lipid extract. A portion (40 mg) of the crude lipid extract was dissolved in $CHCl_3$ (2 mL) and purified by passage through a Phenomenex Strata 500 mg silica SPE column (Torrance, CA, USA). Elution with chloroform (4 mL) produced a TG-rich fraction, which was dried under a stream of nitrogen gas and used directly for RP-HPLC.

GC-FID. Fatty acid methyl esters (FAMEs) were prepared from samples 1−3 by direct transmethylation without prior lipid extraction. Sample 4 was extracted as described above and converted into FAMEs.[29] GC analysis of the FAMEs was performed on a Trace GC Ultra gas chromatograph (Thermo Fisher Scientific, Waltham, MA, USA) equipped with a flame ionization detector (FID) and TraceGold TG-WaxMS capillary column of dimensions 30 m × 0.25 mm i.d., 0.25 μm (Thermo Fisher Scientific, Waltham, MA, USA). Helium (99.99%) was used as carrier gas (Air Products, Allentown, PA, USA), and a split ratio of 100:1 was maintained. Injector and detector temperatures were both set at 280 °C, and the oven was held at 190 °C for 50 min. Individual peaks of FAME were identified by comparison with standards of FAME and by equivalent chain length values.[30]

GC-FID analysis of acylglycerols was performed on the same gas chromatograph equipped with a CP-TAP CB UniMetal capillary column of dimensions 25 m × 0.25 mm i.d., 0.1 μm, supplied by Agilent (Santa Clara, CA, USA). Samples were injected in splitless mode. Helium (99.99%) was used as carrier gas (Air Products). Injector and detector temperatures were set to 350 and 370 °C, respectively. The oven temperature was raised from 60 to 200 °C at a rate of 120 °C/min, then increased to 320 °C at a rate of 20 °C/min, followed by a rise to 360 °C at a rate of 1 °C/min, and was maintained at that temperature for 6 min.

NMR Spectroscopy. In a typical experiment 20−45 mg of a sample was dissolved in 0.75 mL of $CDCl_3$. ^{13}C NMR spectra were recorded at 125.7 MHz with WALTZ16 proton composite pulse decoupling on a Bruker Avance III NMR spectrometer (Bruker, Billerica, MA, USA) equipped with an automatic tuning 5 mm multinuclear probe at 303 K. The pulse program ZGIG, which was

DOI: 10.1021/acs.jafc.5b01835
J. Agric. Food Chem. 2015, 63, 5985−5992

supplied with Bruker TopSpin2.6 spectrometer software, was used for suppression of nuclear Overhauser effects via inverse gate proton decoupling. Acquisition parameters were as follows: 90° ^{13}C observe pulse, 11.0 μs; spectral width, 2011 Hz (16 ppm) centered on the carbonyl region at 171 ppm; 32768 real and imaginary FID data points collected during the 8.146 s FID data acquisition time, followed by a 22 s recovery delay time to ensure a pulse repetition time of >5 times the longest expected longitudinal relaxation time T1. A total of 800 scans were collected, requiring almost 7 h per spectrum.

Because this part of the study involved quantitation, some comments on digital handling at the receiver stage are warranted. Although analog to digital converter oversampling and the standard Bruker "sharp" digital filter were used in conjunction with a 125 kHz analog filter, routine "on the fly" linear prediction (as implemented by the Bruker "baseopt" parameter) was not used to correct the initial FID data points to align them to the true time zero of the FID near the center of the excitation observe pulse. The FID was zero filled once to 32768 real data points, and a 0.06 Hz exponential weighting function was applied before Fourier transformation.

RP-HPLC. Semipreparative nonaqueous RP-HPLC was performed using a Gilson HPLC system (Middleton, MI, USA) comprising two Gilson 306 pumps and a Gilson 811C dynamic mixer. The mobile phase was 70:30 acetone/acetonitrile run under isocratic conditions at a flow rate of 4 mL/min for a duration of 72 min. The column, a Phenomenex Prodigy 5 μm 100A 250 × 10 mm ODS column, was operated at room temperature. Detection was at 210 nm using a Gilson UV−vis 156 detector. Because the methods employed isocratic elution, no further column conditioning was necessary between samples. Nevertheless, 80 mL of solvent was allowed to flow through the column between runs, at 4 mL/min. Samples of the oil were prepared by dissolving approximately 100 mg of the oil in 1 mL of the mobile phase. Three injections of 300 μL were made for each sample, and the collected fractions were pooled for subsequent analysis. For the infant formula, 30−40 mg of the extracted TG sample was dissolved in 300 μL of acetone and injected in one dose. Fractions were evaporated using a rotary evaporator and transferred to a vial using hexane. The hexane was evaporated under a stream of nitrogen, the sample weighed, and the solution made up with an accurately measured volume of hexane or isooctane.

Ag$^+$-HPLC. Analytical silver ion HPLC was performed on a Waters H-class Acquity UHPLC system (Milford, MA, USA) with UV at 205 nm (PDA) and ELSD detectors in series, using Agilent ChromSpher 5 Lipids columns (Santa Clara, CA, USA).[31,32] The Waters Acquity ELS detector settings were as follows: detector gain, 500; gas pressure (compressed air), 240 kPa; nebulizer set to cooling; and drift tube temperature, 60 °C. Three columns (250 × 4.6 mm) were connected in series and maintained at 25 °C. The mobile phase was 0.5% acetonitrile in *n*-hexane (sonicated to ensure complete mixing), and the flow rate was 1.0 mL/min. Samples were prepared at 10 mg/mL in hexane, and injection volumes of 2−5 μL were used for the high OPO samples and UV detection. Lower concentrations were employed when the ELSD was used for detection (approximately 2 mg/mL).

For high OPO samples, the method involving preparative nonaqueous RP-HPLC to generate an OPO-enriched fraction with analysis by Ag$^+$-HPLC with UV detection at 205 nm was the most effective. For the low OPO samples (<1% OPO), a weighed amount of the extracted TG fraction was used for the nonaqueous RP-HPLC, and an amount of 40 mg proved useful. There was no need to weigh the recovered fraction, which was dried of solvent and made up in 500 μL of *n*-hexane for Ag$^+$-HPLC using ELSD as the detector. A standard curve could be prepared using OPO at 0.2 mg/mL in *n*-hexane. Injections of between 1 and 10 μL were sufficient to prepare a standard curve, using the syringe on board the HPLC apparatus. Similar volumes were found appropriate for injection of samples in both the high OPO and low OPO procedures. For the work described here the UV-based standard curve for OPO was linear for the range from 3 to 16 μg injected. The ELSD standard curve conformed to a power curve in the range 0.2−1.2 μg of OPO injected.[33]

RESULTS AND DISCUSSION

^{13}C NMR Spectroscopy. The use of ^{13}C NMR spectroscopy of carboxyl carbons is accurate and convenient to determine the regiospecific distribution of saturated, *cis*-9 and *cis*-11 monounsaturated and polyunsaturated fatty acids in TGs.[27] Although this method was unable to provide data sufficient to detail the regiospecific distribution of individual fatty acids in complex mixtures, it was helpful to determine the ratio of saturated fatty acids in the α-positions (*sn*-1,3) of triacylglycerols to those in the β-position (*sn*-2). The optimal conditions for recording the spectra and securing details on the allocation of the signals to link those with the identity of the responsible compound were facilitated by the use of TG standards, both as discrete individual components and in mixtures of molecules. Dairy-derived samples (sample 1) afforded a distinctive set of signals for the carboxyl carbon atoms of the saturated fatty acids, in both the *sn*-1,3 and *sn*-2 positions. This was attributed to the presence of short-chain saturated fatty acids in the dairy TGs (Figure 1).

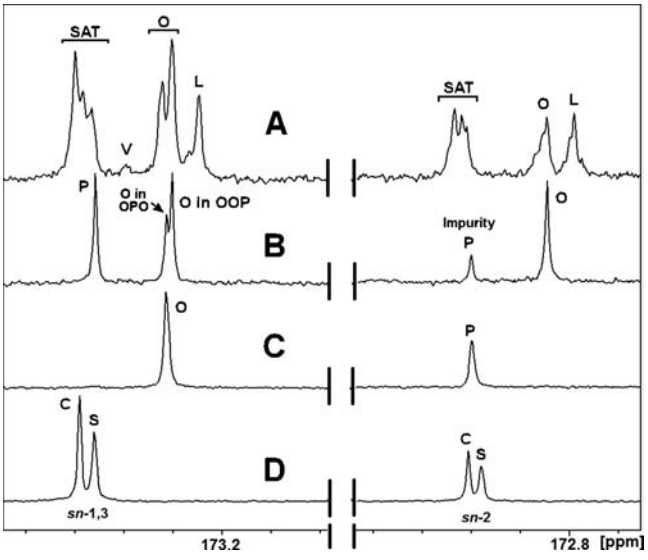

Figure 1. ^{13}C NMR spectra: (A) sample 1 (dietary ingredient); (B) OOP; (C) OPO standard; (D) mixture of tricaproin (CCC) with tristearin (SSS), with peak allocations. Note that the commercially obtained reference sample of OOP in fact contained 19.7% of an impurity, identified as OPO, with a saturated acid in the β-position.

If it is beneficial to have saturated fatty acids (any) in the middle of the TG molecule and unsaturated acids (any) at the side carbons of a glycerol moiety, then ^{13}C NMR spectroscopy is seemingly the best option to provide the relevant data for such indiscriminate requirements. For example, using the data from a previous study,[34] one may calculate that in human milk triacylglycerols, 47.1 mol % of colostrum-derived saturated fatty acids are located in the *sn*-2 position (72.0 ± 2.6% of total fatty acids in the *sn*-2 position are saturated), ignoring the identity of the fatty acids concerned. In transitional milk 45.9 mol % of the saturated fatty acids are located in the *sn*-2 position (77.1 ± 8.8% of *sn*-2 fatty acids are saturated), and in mature milk 45.5 mol % of the saturated fatty acids are located in the *sn*-2 position (79.1 ± 1.3% of *sn*-2 fatty acids are saturated). There is evidently very little variation in the level of saturated fatty acids in the *sn*-2 position between colostrum, transitional milk, and mature milk. Our data on saturated fatty acids in the *sn*-2

DOI: 10.1021/acs.jafc.5b01835
J. Agric. Food Chem. 2015, 63, 5985−5992

position of the samples investigated in the present study, given in mole percent of total saturated fatty acids present in the sample, are as follows: sample 1, 34.9 mol % (46.0% of *sn*-2 fatty acids are saturated); sample 2, 52.9 mol % (72.6% of *sn*-2 fatty acids are saturated); and sample 3, 52.4 mol % (80.3% of *sn*-2 fatty acids are saturated).

Given the data presented above, it would seem reasonable to use total "*sn*-2 saturates" as one of the parameters when infant formulas are compared to human milk. Although limited, the method is appealing and may provide sufficient information when dealing with infant constipation issues. Specifically, the work of Quinlan et al.,[7] published before OPO-enriched formulas started to gain popularity, leads to the identification of some interesting trends. Using data from that study it was possible to calculate that the amount of insoluble calcium salts of saturated fatty acids in the stools of formula-fed infants was substantially higher than that in breast milk-fed infants. Between formula-fed and breast milk-fed infants, the difference was approximately 36 times higher for lauric, 33 times for myristic, 24 times for palmitic, and 8 times for stearic acid, excreted in the form of calcium salts. These elevated levels of insoluble soaps, seemingly produced from triacylglycerols with saturated fatty acids in *sn*-1 and/or *sn*-3 positions, were linked to an increased incidence of hard stools and constipation in infants. An advantage of the use of the ^{13}C NMR spectroscopic method was that the results were produced as mole percent, making it easy to estimate the potential loss of calcium due to the formation of calcium soaps from non-*sn*-2-linked fatty acids in dietary TGs.

A downside of the method was in its low throughput, because the time required for recording a spectrum is 6−7 h using a sample size of 20−30 mg. It is possible that the use of larger samples with different NMR probes may reduce the time required for analysis while retaining the accuracy of the method. A recent publication shows that optimization of the parameters reduces the recording time even in the case of complex mixtures of triacylglycerols from fish oils.[35]

Other signals in ^{13}C NMR spectra, for example, those of α-CH_2 carbon atoms or of olefinic carbons, may also be helpful in providing information about the regiospecific distribution of fatty acids in triacylglycerols.[36] An alternative HSQC-TOCSY NMR method[37] was employed for the analysis of palmitoyl- and oleoyl-containing standards of triacylglycerols, but cannot resolve the present analytical problem.

GC-FID and GC-MS analysis. In contrast to ^{13}C NMR spectroscopy, GC-based analysis of TGs provides information on molecular species composition but no data on the regiospecific distribution of fatty acids. Due to the difficulties faced in volatilizing TGs, a high-temperature methylsilicone phase presented an obvious choice. This allows the separation of the compounds according to the number of carbon atoms in the molecule. An improved option would be medium-polarity phenyl-methylpolysiloxane phases that allow separation according to the number of the double bonds within a group of TGs with the same carbon number.[38]

The target compound, OPO, is a triacylglycerol with 52 carbon atoms in the fatty acid moieties containing two double bonds, TG52:2 in shorthand notation. The column employed in the present study allowed the baseline separation of TG52:0, TG52:1, TG52:3, and TG52:4 (see Figure 2). Despite this ability to separate isomers, OPO remained indistinguishable from its regioisomer, OOP, when this column was used (Figure 2). Incomplete separation of OPO/OOP from stearoyl-linoleyl-

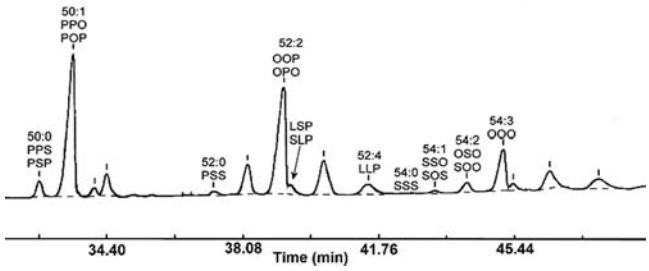

Figure 2. GC separation of sample 1 triacylglycerols in the area of interest according to the number of carbon atoms and unsaturation in the fatty acid residues. Only the peaks with retention times identical to those of the reference TG samples used are labeled.

palmitoyl (SLP) glycerols present in both human milk and some infant formulas[10] was also seen (marked with an arrow in Figure 2).

There are a number of questions yet to be addressed in the GC analysis of TGs, one being the applicability of different injectors to various types of oils.[39] An observation made in one study[39] is that, at least for some oils, a common split/splitless injector may produce results as good as more sophisticated programmed temperature injectors. The study also shows the importance of determining and using the response factors for individual TGs. For example, the difference in relative response between TG50:1 (POP) and TG54:2 (SOO) varied by almost 50%. In our experiments the difference in relative response between POP and OPO was approximately 15%. If average common values were used instead of specific values for response factors, the error can be significant, leading to unreliable data. Attempts in the present study to add a MS dimension by using a Shimadzu GCMS-QP2010-FID instrument were unsuccessful due to the upper temperature limit for the heated GC-MS interface being too low (350 °C) for a reliable transfer of the TGs of interest and were thus not pursued.

HPLC. Initial attempts to analyze TG mixtures by Ag^+-HPLC alone, even with two or three Ag^+ columns in line, yielded poor results. The sample being injected was thus simplified by adding a semipreparative RP-HPLC step and collecting the group of TGs that would contain the target OPO (Figure 3). Obviously, if other TGs are also of interest for regiospecific analysis, the relevant fractions may be collected during the same run. This "TG52:2" fraction (outlined area in

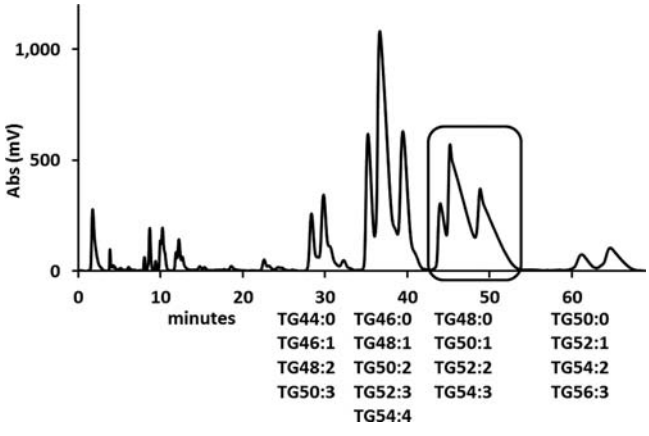

Figure 3. RP-HPLC trace of sample 3. Detection was by UV at 210 nm. The fraction collected for Ag^+-HPLC assay is identified.

DOI: 10.1021/acs.jafc.5b01835
J. Agric. Food Chem. 2015, 63, 5985−5992

Figure 3) produced by RP-HPLC could, apart from OPO, theoretically contain TGs 48:0, 50:1, 52:2, 53:4, 56:4, 58:5, 60:6, 62:7, 64:8, 66:9, etc., because these species demonstrate chromatographically similar behavior under the conditions employed. Of these, the following have been reported in analyses of human milk and infant formulas: 48:0 (PPP), 50:1 (PPO, POP, SMO and its isomers), TG52:2 (OOP, OPO, SLP), and 54:3 (OOO, SOL, SLnS).[10]

Ag^+-HPLC of an OPO/OOP mixture demonstrated that these isomers are clearly separable using this type of chromatography (Figure 4, trace A). Saturated, monounsaturated, and triunsaturated TGs are not expected to overlap with OPO and/or OOP in Ag^+-HPLC. It was still important to exclude the possibility of OPO/OOP overlapping with other diunsaturated TGs that might be present in the sample, namely, SLP and its regioisomers. Accordingly, a mixture of SLP isomers was prepared, and it was confirmed that those are clearly separated from OPO in Ag^+-HPLC under the conditions used (Figure 4, trace B). Under these conditions, OPO and OOP were also distinct from POP and PPO (Figure 4, trace C). Although the complete separation of LSP and OOP was not achieved (Figure 4, trace D), LSP is not reported among the TGs found in human milk and its substitutes[10] and is therefore unlikely to interfere if OOP content is to be determined. Confirmation of the peak identity was obtained by collection of the putative OPO peak and subsequent FAME analysis thereof by GC after hydrolysis and conversion of the free fatty acids into their methyl esters. Additionally, a sample spiked with authentic OPO showed coelution of the OPO peaks. Sample-derived OOP was also found to coelute with authentic OOP. Adlof[40] reported that silver ion HPLC also allows the separation of saturated TGs possessing shorter homologues due to their higher retention times. In the present experiments with three Ag^+-HPLC columns connected in series, good separation of monounsaturated homologues (SSO and PPO) was achieved, whereas diunsaturated TGs (SOO, OOP, OSO, and OPO) demonstrated good but incomplete separation (Figure 5).

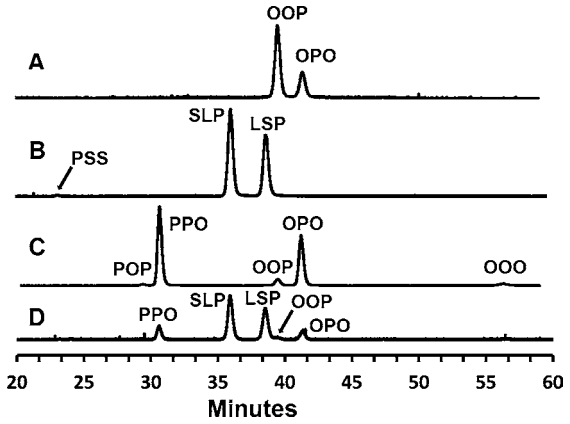

Figure 4. Ag^+-HPLC separation of OPO from the other TGs that may be present in the RP-HPLC "TG52:2" fraction: (A) OOP/OPO mixture; (B) SLP/LSP mixture; (C) sample 2 "TG52:2" fraction; (D) sample 2 "TG52:2" fraction + SLP/LSP mixture.

Although it was tempting to try to improve the separation by increasing the number of columns (e.g., four in line) in the hope that the RP-HPLC fractionation step might be omitted, a significant increase in the time required for analysis would be incurred. Additionally, the danger that polyunsaturated TGs with higher retention times will accumulate in the columns and interfere with subsequent assays made the RP-HPLC/Ag^+-HPLC option more attractive. Moreover, due to the low loading capacity of analytical Ag^+-HPLC columns, the RP-HPLC step was beneficial, because it allowed an increase in the relative content of all "TG52:2" components, thus increasing the sensitivity and accuracy of the method. An extra advantage of employing the two-step HPLC is that there was no need to prepare high-purity triacylglycerols for injection, because contaminants that might be present in oils or lipid extracts (e.g., phospholipids, sterol esters, etc.) were either rejected at the RP-HPLC step or did not fit into the OPO window in Ag^+-HPLC. Also, potential overlap with OSO was avoided by the two-step method.

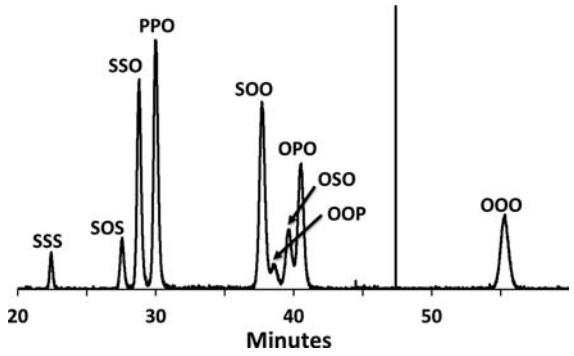

Figure 5. Separation of homologous unsaturated TGs by Ag^+-HPLC: SSO and PPO, SOO and OOP, and OSO and OPO. Detection was by ELSD.

Two more possibilities exist in which the OPO fraction may be contaminated with triacylglycerols of similar mobility during Ag^+ chromatography. The first was that dairy fats are known to contain *trans* fatty acids,[41] which demonstrate higher mobility than their *cis* isomers in Ag^+ chromatography.[42] It was consequently possible that triacylglycerols, which contain shorter chain fatty acids, and *trans* fatty acids may have retention times similar to that of OPO. Approximations have been made from analyses of trielaidin (EEE) versus OOO behavior, and the effect of chain-shortening on the behavior of saturated TGs has been investigated.[40] These observations suggest that, to compensate for an increase in mobility due to one *trans* double bond present, the triacylglycerol in question must have a lower number of carbon atoms. It would therefore be rejected at the RP-HPLC step in the present method and cause no problems during Ag^+ chromatography. In the second, it was possible that entities with the same or even higher number of carbon atoms and higher levels of unsaturation than OPO and containing a *trans* fatty acid (e.g., a TG54:3) may be a source of contamination in the "TG52:2" fraction from the RP-HPLC step. It was anticipated that the chromatographic behavior of one or more of EEE, EEO, EOE, EOO, OEO, and OOO may overlap with OPO. To address this possibility a mixture of TG54:3 containing oleic and elaidic acids was prepared and subjected to Ag^+-HPLC. Pleasingly, OPO was clearly separated from its nearest neighbor EEO (Figure 6).

A reversed-order approach (compared to ours) two-dimensional for analysis of TGs has been reported. Online Ag^+-HPLC and RP-HPLC with detection by UV, ELSD, and PI-APCI-MS was employed.[43] Both UV and ELSD methods of detection performed poorly (probably due to a low loading capacity of

DOI: 10.1021/acs.jafc.5b01835
J. Agric. Food Chem. 2015, 63, 5985−5992

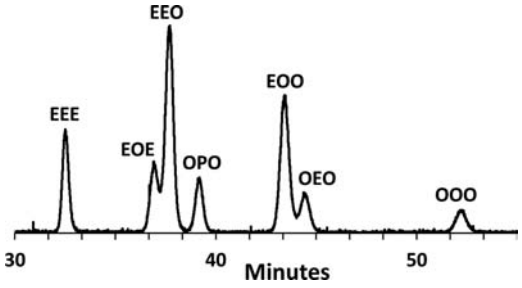

Figure 6. Ag^+-HPLC separation of OPO from isomeric TG54:3 with various numbers of *trans* double bonds.

the column used for the separation in the first dimension (a cation exchanger coated with silver nitrate).

As ELSD detectors are in common use in many analytical laboratories, the application of either UV or ELSD for the detection of a range of molecules is now routine. In this work a UV detector and ELSD in series were used for optimum reliability of the data. It was clear that UV detection was only useful for the high OPO samples. The limit of detection with UV at 205 nm was approximately 1.5 μg of OPO injected (at this level the ELSD peak was above scale). Using ELSD, the limit of detection was an order of magnitude lower at around 0.2 μg of OPO injected. Lipid samples with low levels of OPO such as the infant formula used in this work would be difficult to analyze using UV detection. Whereas ELSD was particularly useful for low OPO samples, the range of detection was narrower and the detector quickly moved off scale with samples containing higher levels of OPO; this would require sample dilution to obtain accurate data. For this reason, the use of an UV detector for those samples where the OPO level is high remained the method of choice. The UV standard curve for OPO was found to be linear for the range from 3 to 16 μg injected, whereas the ELSD standard curve conformed to a power curve in the range of 0.2−1.0 μg of OPO injected. The nondestructive nature of UV detection was also useful for collection of fractions from Ag^+-HPLC for any subsequent analysis (e.g., GC-FID of FAMEs). The combined results produced by different approaches to the analysis of OPO-containing mixtures are presented in Table 1.

Calibration and Statistical Data. For ELSD, good linearity (R^2 = 0.999 over nine discrete calibration curves set up over a period of 3 days using freshly prepared samples) was shown between 0.2 and 1.0 μg injected when using a log curve of the response. This also demonstrated the good repeatability of the method. For UV detection, good linearity (R^2 = 0.999) was obtained between 3 and 16 μg injected. The method was found to be reproducible when using three individual lipid samples (extracted from the infant formula as described above). For n = 13, the average content of OPO in the lipid was found to be 5.77 ± 0.24 mg/g of lipid, with RSD = 4.1%. The median was 5.72 mg/g and the range, 0.90 mg/g. For ELSD, the LOD was calculated as 0.1 μg injected weight of OPO, whereas the LOQ was calculated as 0.3 μg injected weight of OPO.[44]

In summary, the results demonstrate that ^{13}C NMR spectroscopy was useful to provide high-level "rough" data relating to the level of saturated fatty acids in the *sn*-2 position of TGs, but lacked the power (with the protocols employed) to provide structural information on those saturated fatty acids. The combination of RP-HPLC with UV detection at 210 nm, followed by Ag^+-HPLC of the selected OPO-containing fraction with either UV detection or ELSD, presented a reliable and robust method by which quantitative data for OPO content could be generated from complex matrices. Usefully, OPO was well separated from all other likely diunsaturated and/or *trans* triunsaturated TGs, thereby avoiding signals from non-OPO TGs that would give falsely elevated readings for OPO. The UV and ELSD detection methods provide complementary ranges for detection as indicated by their respective calibration curves. The method presented allowed good limits of detection and of quantitation. Because the combination of techniques draws together a set of procedures that are designed to specifically deal with complex matrices, the applicability of the method is likely to be wide-ranging and, thus, readily transferrable to other complex matrices and foodstuffs. It is expected, however, that some fine-tuning of one or both of the HPLC methods would be required, depending on the analytes of interest.

■ ASSOCIATED CONTENT

Supporting Information

Abbreviations used, response factors, calculations of saturated fatty acids in the *sn*-2 position, calibration data, linearity data, reproducibility results, determination of limit of detection. The Supporting Information is available free of charge on the ACS Publications website at DOI: 10.1021/acs.jafc.5b01835.

■ AUTHOR INFORMATION

Corresponding Authors

*(M.V.) Phone: +644 931 3394. Fax: +644 931 3055. E-mail: mikhail.vyssotski@callaghaninnovation.govt.nz.

*(D.B.G.W.) Phone: +644 463 0065. Fax: +644 931 3055. E-mail: bradley.williams@vuw.ac.nz.

Notes

The authors declare no competing financial interest.

Table 1. Analysis of OPO Oils, Dietary Ingredient, and Infant Formula by Different Techniques

method:	RP-HPLC/Ag^+-HPLC	RP-HPLC/GC[a]	RP-HPLC/GC[a,b]	GC[a,c]	GC[a,c]	^{13}C NMR		GC[d]
analyte:	OPO	OPO+OOP +SLP	OPO+OOP	TG52:2	TG52	saturated FA in *sn*-2, of total saturated acids	saturated FA in *sn*-2, of total FA in *sn*-2	P[e]
expressed as:	wt %	area %	area %	wt %	wt %	mol %	mol %	wt %
sample 1	9.2	11.9	9.9	8.3	14.8	34.9	46.0	18.4
sample 2	20.4	28.7	27.6	20.5	33.2	52.9	72.6	37.6
sample 3	20.8	24.3	23.8	20.6	29.2	52.4	80.3	46.7
sample 4	0.07	na[f]	na	0.08	2.8	33.9	81.6	31.9

[a]GC-FID of triacylglycerols. [b]SLP calculated using fatty acids data (GC). [c]Internal standards: HHH, POP. Relative response factor determined for OPO. [d]GC-FID of fatty acid methyl esters. [e]P = palmitic acid. [f]na, not assessed.

DOI: 10.1021/acs.jafc.5b01835
J. Agric. Food Chem. 2015, 63, 5985−5992

■ ACKNOWLEDGMENTS

We are grateful to Callaghan Innovation for funding and to colleagues from Callaghan Innovation as follows: David Kyle for identifying the OPO assay problem, Rosemary Webby for skilled extraction of the infant formula, Andrew MacKenzie for reviewing the manuscript, and Donal Krouse for assistance with the statistics calculations.

■ REFERENCES

(1) Jensen, R. G.; Ferris, A. M.; Lammi-Keefe, C. J.; Henderson, R. A. Lipids of bovine and human milks: a comparison. *J. Dairy Sci.* **1990**, *73*, 223−40.

(2) Straarup, E. M.; Lauritzen, L.; Faerk, J.; Høy, C.-E.; Michaelsen, K. F. The stereospecific triacylglycerol structures and fatty acid profiles of human milk and infant formulas. *J. Pediatr. Gastroenterol. Nutr.* **2006**, *42*, 293−299.

(3) Garcia, C.; Lutz, N. W.; Confort-Gouny, S.; Cozzone, P. J.; Armand, M.; Bernard, M. Phospholipid fingerprints of milk from different mammalians determined by ^{31}P NMR: towards specific interest in human health. *Food Chem.* **2012**, *135*, 1777−1783.

(4) Iwamori, M.; Takamizawa, K.; Momoeda, M.; Iwamori, Y.; Taketani, Y. Gangliosides in human, cow and goat milk, and their abilities as to neutralization of cholera toxin and botulinum type A neurotoxin. *Glycoconjugate J.* **2008**, *25*, 675−683.

(5) Bar-Yoseph, F.; Lifshitz, Y.; Cohen, T. Review of *sn*-2 palmitate oil implications for infant health. *Prostaglandins, Leukotrienes Essent. Fatty Acids* **2013**, *89*, 139−143.

(6) EFSA panel on dietetic products, scientific opinion on the substantiation of a health claim related to beta-palmitate and increased calcium absorption pursuant to Article 14 of Regulation (EC) No. 1924/2006. *EFSA J.* **2011**, *9*, 2289, and references cited therein.

(7) Quinlan, P. T.; Lockton, S.; Irwin, J.; Lucas, A. L. The relationship between stool hardness and stool composition in breast- and formula-fed infants. *J. Pediatr. Gastroenterol. Nutr.* **1995**, *20*, 81−90.

(8) Wennermark, M.; Raveh, P. InFat^{TM} premium fat for infant formula: fat closer to human milk. *Agro Food Ind. Hi-Tech* **2012**, *23*, 16−17.

(9) Sidnell, A.; Greenstreet, E. Infant nutrition − review of lipid innovation in infant formula. *Nutr. Bull.* **2011**, *36*, 373−380.

(10) Kurvinen, J.-P.; Sjövall, O.; Kallio, H. Molecular weight distribution and regioisomeric structure of triacylglycerols in some common human milk substitutes. *J. Am. Oil Chem. Soc.* **2002**, *79*, 13−22.

(11) Son, J.-M.; Lee, J.-H.; Hong, S.-T.; Lee, K.-S.; Park, H.-K.; Kwon, K.-I.; Lee, K.-T. Determination of positional fatty acid and triacylglycerol compositions of selected infant formulas. *Han'guk Sikp'um Yongyang Kwahak Hoechi* **2011**, *40*, 1256−1264.

(12) Christie, W. W.; Han, X. *Lipid Analysis − Isolation, Separation, Identification and Lipidomic Analysis*, 4th ed.; Oily Press: Bridgwater, UK, 2010; pp 261−267.

(13) Kalo, P. Regiospecific analysis of triacylglycerols. *Lipid Technol.* **2013**, *25*, 230−234.

(14) Takagi, T.; Ando, Y. Stereospecific analysis of triacyl-*sn*-glycerols by chiral high-performance liquid chromatography. *Lipids* **1991**, *26*, 542−547.

(15) Kuksis, A.; Marai, L.; Myher, J. J. Triglyceride structure of milk fats. *J. Am. Oil Chem. Soc.* **1973**, *50*, 193−201.

(16) Sahin, N.; Akoh, C. C.; Karaali, A. Lipase-catalyzed acidolysis of tripalmitin with hazelnut oil fatty acids and stearic acid to produce human milk fat substitutes. *J. Agric. Food Chem.* **2005**, *53*, 5779−5783.

(17) Ha, J. K.; Lindsay, R. C. Release of volatile branched-chain and other fatty-acids from ruminant milk fats by various lipases. *J. Dairy Sci.* **1993**, *76*, 677−690.

(18) Turon, F.; Bonnot, F.; Caro, Y.; Pina, M.; Graille, J. Acyl migration incidence on accuracy of a triacylglycerol regioanalysis − a theoretical evaluation. *Chem. Phys. Lipids* **2003**, *125*, 41−48.

(19) Kuksis, A.; Itabashi, Y. Regio- and stereospecific analysis of glycerolipids. *Methods* **2005**, *36*, 172−185.

(20) Dugo, P.; Favoino, O.; Tranchida, P. Q.; Dugo, G.; Mondello, L. Off-line coupling of non-aqueous reversed-phase and silver ion high-performance liquid chromatography-mass spectrometry for the characterization of rice oil triacylglycerol positional isomers. *J. Chromatogr. A* **2004**, *1041*, 135−142.

(21) Hu, J.; Wei, F.; Dong, X.-Y.; Lv, X.; Jiang, M.-L.; Li, G.-M.; Chen, H. Characterization and quantification of triacylglycerols in peanut oil by off-line comprehensive two-dimensional liquid chromatography coupled with atmospheric pressure chemical ionization mass spectrometry. *J. Sep. Sci.* **2013**, *36*, 288−300.

(22) Lísa, M.; Velínská, H.; Holčapek, M. Regioisomeric characterization of triacylglycerols using silver-ion HPLC/MS and randomization synthesis of standards. *Anal. Chem.* **2009**, *81*, 3903−3910.

(23) Holčapek, M.; Dvořáková, H.; Lísa, M.; Jimenéz Girón, A.; Sandra, P.; Cvačka, J. Regioisomeric analysis of triacylglycerols using silver-ion liquid chromatography−atmospheric pressure chemical ionization mass spectrometry: comparison of five different mass analyzers. *J. Chromatogr. A* **2010**, *1217*, 8186−8194.

(24) Ramaley, L.; Herrera, L. C.; Melanson, J. E. Applicability of non-linear versus linear fractional abundance calibration plots for the quantitative determination of triacylglycerol regioisomers by tandem mass spectrometry. *Rapid Commun. Mass Spectrom.* **2013**, *27*, 1251−1259.

(25) Kadivar, S.; De Clercq, N.; Nusantoro, B. P.; Le, T. T.; Dewettinck, K. Development of an offline bidimensional high-performance liquid chromatography method for analysis of stereo-specific triacylglycerols in cocoa butter equivalents. *J. Agric. Food Chem.* **2013**, *61*, 7896−7903.

(26) Barsukov, L. I.; Batrakov, S. G.; Bergelson, L. D.; Dyatlovitskaya, E. V.; Molotkovsky, J. G.; Prokazova, N. V. In *Lipid Biochemical Preparations*, Bergelson, L. D., Ed.; Elsevier/North-Holland Biomedical Press: Amsterdam, The Netherlands, 1980.

(27) Gouk, S. W.; Cheng, S. F.; Ong, A. S. H.; Chuah, C. H. Rapid and direct quantitative analysis of positional fatty acids in triacylglycerols using ^{13}C NMR. *Eur. J. Lipid Sci. Technol.* **2012**, *114*, 510−519.

(28) Svennerholm, L.; Fredman, P. A procedure for the quantitative isolation of brain gangliosides. *Biochim. Biophys. Acta, Lipids Lipid Metab.* **1980**, *617*, 97−109.

(29) Carreau, J. P.; Dubacq, J. P. Adaptation of a macro-scale method to the micro-scale for fatty acid methyl transesterification of biological lipid extracts. *J. Chromatogr.* **1978**, *151*, 384−390.

(30) Stránský, K.; Jursík, T.; Vítek, A.; Skořepa, J. An improved method of characterizing fatty acids by equivalent chain length values. *J. High Resolut. Chromatogr.* **1992**, *15*, 730−740.

(31) Adlof, R. O. Analysis of triacylglycerol positional isomers by silver ion high performance liquid chromatography. *J. High Resolut. Chromatogr.* **1995**, *18*, 105−107.

(32) Adlof, R. O.; List, G. R. Synthesis and analysis of symmetrical and nonsymmetrical disaturated/monounsaturated triacylglycerols. *J. Agric. Food Chem.* **2003**, *51*, 2096−2099.

(33) Mathews, B. T.; Higginson, P. D.; Lyons, R.; Mitchell, J. C.; Sach, N. W.; Snowden, M. J.; Taylor, M. R.; Wright, A. G. Improving quantitative measurements for the evaporative light scattering detector. *Chromatographia* **2004**, *60*, 625−633.

(34) Haddad, I.; Mozzon, M.; Frega, N. G. Trends in fatty acids positional distribution in human colostrum, transitional, and mature milk. *Eur. Food Res. Technol.* **2012**, *235*, 325−332.

(35) Gouk, S. W.; Cheng, S. F.; Malon, M.; Hock Ong, A. S.; Chuah, C. H. Critical considerations for fast and accurate regiospecific analysis of triacylglycerols using quantitative ^{13}C NMR. *Anal. Methods* **2013**, *5*, 2064−2073.

(36) Andreotti, G.; Lamanna, R.; Trivellone, E.; Motta, A. ^{13}C NMR spectra of TAG: an easy way to distinguish milks from different animal species. *J. Am. Oil Chem. Soc.* **2002**, *79*, 123−127.

(37) Simova, S.; Ivanova, G.; Spassov, S. L. Alternative NMR method for quantitative determination of acyl positional distribution in

DOI: 10.1021/acs.jafc.5b01835
J. Agric. Food Chem. 2015, 63, 5985−5992

triacylglycerols and related compounds. *Chem. Phys. Lipids* **2003**, *126*, 167−176.
(38) Geeraert, E.; Sandra, P. Capillary GC of triglycerides in fats and oils using a high temperature phenylmethylsilicone stationary phase, part 1. *J. High Resolut. Chromatogr.* **1985**, *8*, 415−422.
(39) Christie, W. W. High-temperature gas chromatography of triacylglycerols − a cautionary note? http://lipidlibrary.aocs.org/topics/gcoftg/index.htm (accessed June 3, 2015).
(40) Adlof, R. O. Normal-phase separation effects with lipids on a silver ion high-performance liquid chromatography column. *J. Chromatogr. A* **1997**, *764*, 337−340.
(41) Jensen, R. G. The composition of bovine milk lipids: January 1996 to December 2000. *J. Dairy Sci.* **2002**, *85*, 295−350.
(42) Christie, W. W. *Lipid Analysis*, 3rd ed.; Oily Press: Bridgwater, UK, 2003; pp 260−261.
(43) van der Klift, E. J. C.; Vivó-Truyols, G.; Claassen, F. W.; van Holthoon, F. L.; van Beek, T. A. Comprehensive two-dimensional liquid chromatography with ultraviolet, evaporative light scattering and mass spectrometric detection of triacylglycerols in corn oil. *J. Chromatogr. A* **2008**, *1178*, 43−55.
(44) Sardella, R.; Gioiello, A.; Ianni, F.; Venturoni, F.; Natalini, B. HPLC/ELSD analysis of amidated bile acids: an effective and rapid way to assist continuous flow chemistry processes. *Talanta* **2012**, *100*, 364−371.

DOI: 10.1021/acs.jafc.5b01835
J. Agric. Food Chem. 2015, 63, 5985−5992

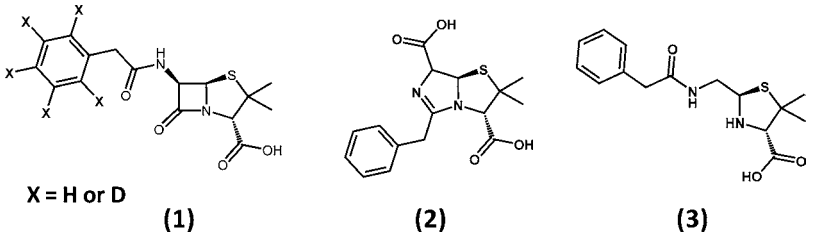

Figure 1. Schematic representation of the chemical structures of penicillin G or penicillin G-d_5 (**1**), penillic acid (**2**), and penilloic acid (**3**).

Table 1. Recovery of Penicillin G, Penillic Acid, and Penilloic Acid from Three Citrus Matrices Fortified in Triplicate[a]

	LC-MS absolute recovery (RSD, %)			LC-MS corrected recovery (RSD, %) using internal standards
analyte concn (ng/g)	penicillin G 335 → 114	penillic acid 335 → 128	penilloic acid 309 → 174	penicillin G 335 → 114
orange matrix				
0.1	63 (23)	70 (20)	73 (11)	100 (17)
0.25	89 (8)	63 (5)	73 (8)	118 (8)
1	69 (8)	66 (3)	69 (5)	99 (6)
10	60 (14)	67 (6)	62 (9)	101 (3)
grapefruit matrix				
0.1	43 (15)	50 (10)	60 (2)	80 (10)
0.25	51 (12)	61 (10)	57 (8)	88 (7)
1	59 (2)	63 (5)	57 (2)	93 (7)
10	50 (9)	64 (2)	51 (4)	97 (5)
lemon matrix				
0.1	33 (6)	56 (6)	57 (6)	77 (5)
0.25	40 (16)	73 (17)	61 (12)	87 (2)
1	41 (5)	65 (1)	57 (4)	97 (10)
10	38 (4)	67 (5)	55 (7)	99 (4)

[a]Only the most selective ion products are shown.

agents.[21,22] For example, in the presence of acids or bases, the highly strained β-lactam ring opens to give an array of products (metabolites) such as penicilloic acid, penicillinic acid, penicillamine, penilloaldehyde, aminopenicillanic acid, penaldic acid, penamaldic acid, isopenicillic acid, penillic acid, and penilloic acid. Of these, the most abundant are penillic acid, **2**, and penilloic acid, **3**.[22−29] The instability of penicillin G emphasizes the importance of designing an analytical method that identifies not only penicillin G but also potential metabolites.

To the best of our knowledge, no method has been reported for the analysis of penicillin G and its metabolites in citrus matrices. In this paper, we present a sensitive method to quantitate penicillin G and its metabolites (penillic and penilloic acids) with high selectivity in a variety of citrus matrices using ultra-high performance liquid chromatography coupled with triple-quadrupole tandem mass spectrometry (UHPLC-MS/MS). Throughout method development, we systematically investigated the extraction process and matrix effects to optimize quantitative accuracy and precision. Because of the potential use of penicillin G to treat citrus greening disease, it is necessary to develop a reliable method for the extraction and identification of penicillin G residues. This method is useful to quantitatively monitor the presence of penicillin G and its metabolites in citrus fruits post-treatment.

MATERIALS AND METHODS

Reagents. Penicillin G potassium salt (99.4%) and internal standard (penicillin G-d_5 potassium salt) (98.4%) were provided by o2si Smart Solutions (Charleston, SC, USA). Penilloic acid (96.3%) and penillic acid (99.3%) were purchased from LGC Standards (Wesel, Germany). HPLC grade hexane, acetonitrile (with and without 1% formic acid), methanol, and water (with and without 1% formic acid) were provided by Fisher Scientific (Pittsburgh, PA, USA). Anhydrous monosodium phosphate, disodium phopshate, and ammonium acetate were purchased from Sigma-Aldrich (St. Louis, MO, USA).

Buffer Solution Preparation. The phosphate buffer solution (PBS) (0.1 M, pH 7) was prepared by dissolving anhydrous NaH_2PO_4 (5.8 g, 0.0483 mol) and Na_2HPO_4 (8.15 g, 0.0574 mol) in 1 L of deionized (DI) water. Ammonium acetate ($NH_4C_2H_3O_2$) buffer (0.05 M, pH 6.7) was prepared by dissolving ammonium acetate (4.0 g, 0.0519 mol) in 1 L of DI water.

Preparation of Standard Stock Solutions. Individual stock solutions of penicillin G potassium salt, penilloic acid, penillic acid, and internal standard penicillin G-d_5 at 1000 μg/mL were made by dissolving the standard (after adjusting for salt content and purity) in a mixture of water and acetonitrile (1:1, v/v). These stock standard solutions were stored at −20 °C for an extended period of time (>5 months) with no issues.

Preparation of Mixed Intermediate Standard Solutions (Int-A) (1 μg/mL = 1 ng/μL). The above stock solutions, each at 1000 μg/mL, were used to prepare a mixed standard solution (Int-A) containing penicillin G, penillic acid, and penilloic acid, each at a concentration of 1 μg/mL. These were prepared by adding 100 μL of each standard stock solution into the same 100 mL volumetric flask. The flask was filled to the mark with phosphate buffer (0.1 M, pH 7). Preparation of intermediate solutions at concentrations of 2, 5, 20, 100, 200, and 300 ng/mL was carried out on each day of batch extraction/analysis by further diluting Int-A. The intermediate internal standard solution containing 1 μg/mL penicillin G-d_5 was prepared by adding 100 μL of the penicillin G-d_5 stock solution (1000 μg/mL) into a 100 mL volumetric flask, which was subsequently filled to the mark with phosphate buffer (0.1 M, pH 7). This was further diluted with

DOI: 10.1021/acs.jafc.5b02030
J. Agric. Food Chem. 2015, 63, 5993−6000

phosphate buffer to make an internal standard intermediate solution at a concentration of 40 ng/mL.

Calibration Curve Preparation. To prepare 800 μL of the individual calibration standards, 100 μL of the penicillin G-d_5 internal standard intermediate standard (40 ng/mL) was added to each of six different autosampler vials. Then to each vial was added 100 μL of each intermediate standard (2, 5, 20, 100, 200, 300 ng/mL). This was followed by the addition of 600 μL of ammonium acetate buffer. It should be noted that the calibration curve was prepared out of matrix for the quantitation of penicillin G because an internal standard was used to compensate for ion suppression and recovery losses during the extraction procedure. Because no isotopically labeled standards are available for penillic or penilloic acids, a calibration curve in matrix was used. The in-matrix curve was prepared by carrying six separate 2 g samples of matrix through the extraction process. The extracted matrix samples were evaporated in 50 mL centrifuge tubes and labeled 1−6. To each sample of dried matrix was added 100 μL of the correspondingly labeled mixed intermediate standard (2, 5, 20, 100, 200, 300 ng/mL) along with 700 μL of ammonium acetate buffer.

Sample Fortification. The fortified samples were made by spiking 2 g of the different citrus matrices (lemon, orange, and grapefruit) with 100 μL of four intermediate mixed standard solutions (2, 5, 20, and 200 ng/mL) and 100 μL of the internal standard intermediate solution (40 ng/mL). Overall, four spikes were made for each matrix to reach final concentrations of 0.1, 0.25, 1, and 10 ng/g of penicillin G, penillic acid, and penilloic acid in each spike. The concentration of the internal standard spiked into the matrix was constant in all samples (2 ng/g). Reagent (2 g of water) and matrix blanks were not fortified with internal standard and were used as negative controls.

Penicillin G Extraction from Citrus Matrices. Citrus fruit samples were purchased (from retail stores) and immediately stored at −80 °C. The entire frozen fruits were then homogenized to a powder-like consistency using a robot coupe with a 7 mm thick stainless steel blade (Robot Coupe, Ridgeland, MS, USA), and a 2 g portion was immediately weighed into a 50 mL polypropylene centrifuge tube. Then, 4 mL of PBS buffer (0.1 M, pH 7) was added, and the samples were fortified with 100 μL of internal standard. Each of four separate samples was then spiked with the intermediate standards, in triplicate, as shown in Table 1. The samples were shaken using a vortex mixer for 10 min at 1100 rpm. Four milliliters of hexane was added to the mixture followed by additional shaking in the vortex mixer (10 min at 1100 rpm). Then, the samples were centrifuged at 4000 rpm for 15 min to separate the aqueous and organic layers. The hexane layer was then discarded using a Pasteur pipette, and the aqueous layer was then transferred to an Amicon Ultra 50000 M_w membrane filtration device (Millipore, Darmstadt, Germany). Centrifugation at 4000 rpm for 15 min filtered solids and residual hexane from the aqueous layer. The filtrate was washed with 2 mL of phosphate buffer followed by further centrifugation (15 min, 4000 rpm) resulting in a filtered aqueous solution containing extracted penicillin G and its metabolites.

SPE Cleanup of Penicillin G. Oasis HLB, 6 cc, 200 mg SPE extraction cartridges (Waters, Milford, MA, USA) were prewashed sequentially with 3 mL of methanol, 3 mL of H_2O, and 3 mL of PBS buffer. The sample extract was loaded onto the SPE column, and the column was washed with 2 mL of phosphate buffer. Then, a slight vacuum was applied to dry the SPE columns. Penicillin G and metabolites were eluted from the SPE columns with 3 mL of acetonitrile into clean 50 mL polypropylene centrifuge tubes. The eluate was evaporated to dryness using a stream of N_2 at 40 °C for 1 h. Ammonium acetate buffer (800 μL) was then immediately added. The extract was mixed by vortexing for 20 s and followed by filtration through a 0.2 μm PVDF filter for LC-MS/MS analysis.

LC-MS/MS Method. The LC-MS/MS included an ACQUITY UPLC I-Class System (Waters) connected to an API 6500 Qtrap (AB Sciex, Toronto, ON, Canada) triple-quadrupole mass spectrometer. Analyses were carried out using electrospray ionization (ESI) in positive-ion mode using multiple reactions monitoring (MRM). Optimized mass spectrometer parameters for the detection of penicillin G and its metabolites were obtained through infusion studies. The parameters optimized were declustering potential (DP), entrance potential (EP), collision energy (CE), and collision cell exit potential (CXP). The MS/MS product ion spectra of the standards and experimental samples were obtained using a target-oriented screening approach in enhanced product ion (EPI) scan mode. The source parameters (ion source voltage (4500 V), curtain gas (30 psi), heater gas (45 psi), and ion source temperature (400 °C)) were identical in MRM and EPI scan modes. Separation of the test compounds was achieved using a 150 mm × 2.1 mm i.d., 1.7 μm, Acquity C18 column. The mobile phase composition was (A) water with 0.1% formic acid and (B) acetonitrile with 0.1% formic acid. The column temperature was maintained at 40 (±1) °C. The gradient began at 95:5 of A:B with a flow of 0.2 mL/min. The gradient was changed to 5:95 of A:B over a course of 10 min followed by a 5 min hold at 5:95 of A:B. Over 0.1 min, the gradient was changed to 95:5 of A:B with a concomitant change in flow rate to 0.4 mL/min. After 4 min, the flow was reduced to 0.2 mL/min over the course of 0.1 min. This was held for 0.8 min to complete the LC gradient (20 min total run time).

Method Validation. This analytical method was validated by independently analyzing three different matrices (lemon, orange, and grapefruit); each matrix was studied in triplicate. A multipoint, in-matrix calibration curve was used to calculate the concentration of penillic acid and penilloic acid in the spikes. The penicillin G is calculated from a multipoint, in-solvent calibration curve with an isotopically labeled internal standard (penicillin G-d_5). Calibrants were used at levels ranging from 0.25 ng/g (equivalent to 0.1 ng/g in sample) through 37.5 ng/g (equivalent to 15 ng/g in sample). A minimum of five data points for linear and quadratic regression lines were required, but any combination of standards may be used for quantitation. Curves were fit with $1/x$ weighting with an R^2 value >0.99. It is the policy of the laboratory to set limit of detection (LOD) and limit of quantitation (LOQ) values at levels greater than the minimum 3× and 10× general requirements, respectively, such that daily instrument variance, matrix effects, procedural errors, etc., do not result in failures to meet validated LODs and LOQs for studies taking place over extended periods of time. It is also the policy of the laboratory to verify LOD and LOQ reporting levels using spiked sample matrix. In short, the laboratory may set LOD and LOQ values to levels greater than the minimum detected signal at 3× or 10× on the instrument on the basis of the needs of the method and the desired ruggedness of the method. The LOD for this method was set to the lowest concentration validated in this study at 0.1 ng/g in matrix, whereas the LOQ was set at 0.25 ng/g. Both of these levels exceed the 3× and 10× requirements for the primary transition. Values below the LOD are reported as not detected (ND). Values between the LOD and LOQ are reported as below the quantitation limit (BQL). Values at and above the LOQ are reported as actual values.

RESULTS AND DISCUSSION

Citrus matrices contain a variety of compounds including sugars, citric acid, vitamin C, folic acid, potassium, phytochemicals (e.g., limonoids, flavanoids, etc.), and essential oils (e.g., limonene, octanal, copaene, dodecanal, etc.).[30−33] These various products are distinct in their structures and properties; this must be taken into consideration when attempts are made to extract specific molecules of interest such as penicillin G and its metabolites (penillic acid and penilloic acid) (Figure 1). These products are amphiphilic, containing a benzyl group at one end and one or two carboxylic acids at the other. The presence of carboxylic acid groups increases the polarity of these molecules, which makes them highly soluble in water and easily extracted using an aqueous medium. It is worth noting that penicillin G contains a fused β-lactam ring system, which is susceptible to ring-opening under acidic and alkaline conditions, as well as under enzymatic activity. It can easily be transformed or isomerized into many other compounds such as penillic, penilloic, and penaldic acids, penicillamine, and

DOI: 10.1021/acs.jafc.5b02030
J. Agric. Food Chem. 2015, 63, 5993−6000

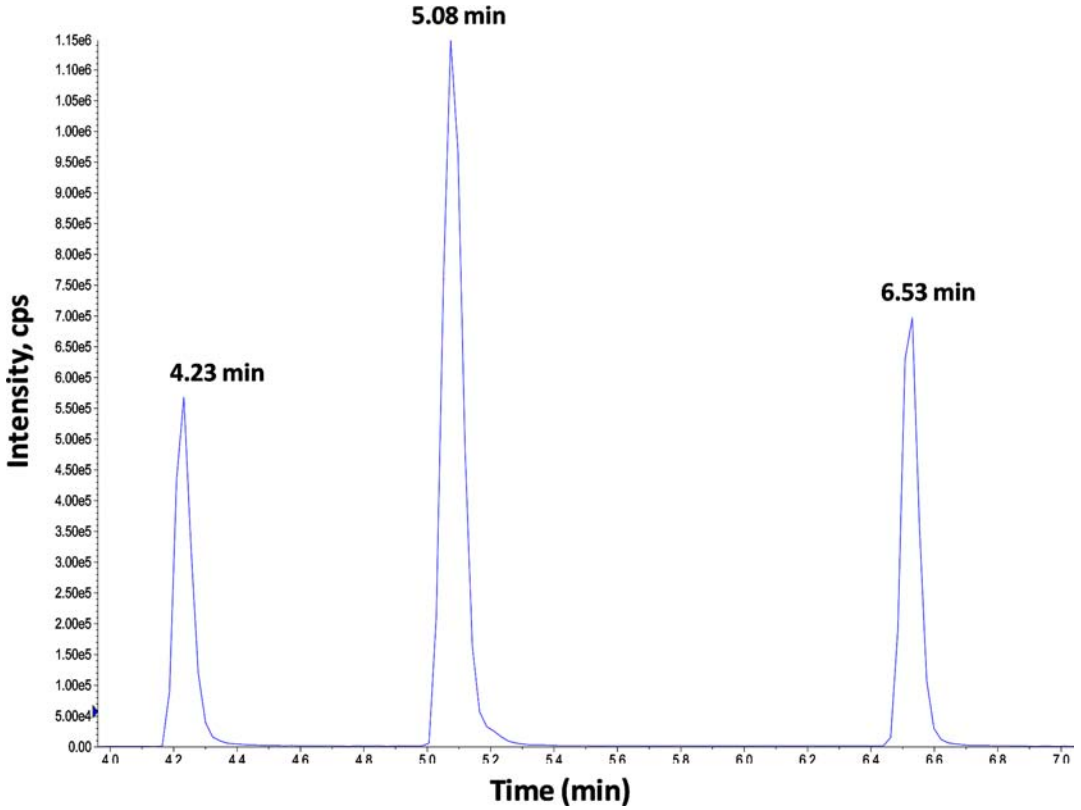

Figure 2. LC chromatogram of the three analytes showing their retention times with 6.53 min for penicillin G, 5.08 min for penilloic acid, and 4.23 min for penillic acid.

penilloaldehyde. Once infected citrus trees are treated with penicillin G, we believe various environmental conditions including heat, rain, sunlight, and contact with biological nucleophiles, acids, or bases might lead to the decomposition of penicillin G and formation of penicillin metabolites.[21] Therefore, it is important to identify these metabolites when fully assessing the treatment of citrus trees with penicillin G. This motivated us to incorporate penilloic acid and penillic acid metabolites (commercially available) into our extraction and analytical method because they may be present even after penicillin G has fully decomposed. This information guided us in the development of our method for the extraction of penicillin G and its metabolites from citrus matrices as observed by LC-MS/MS analysis.

Extraction Method Optimization. Samples were fortified with an internal standard solution containing only penicillin G-d_5 as well as an intermediate mixed standard solution containing penicillin G, penilloic acid, and penillic acid. After fortification, liquid/liquid extraction using a phosphate buffer (pH 7) and hexane solvent was carried out. The buffer helps to prevent degradation of penicillin G because it is more stable at pH 7, whereas the hexane removes nonpolar components from the sample. This increases the longevity of the C18 columns used on the liquid chromatograph instruments and decreases the probability of ion enhancement or suppression. Next, the aqueous phase was cleaned using a membrane filtration device to remove completely insoluble components. Finally, we used an amphiphilic OASIS HLB column to trap and purify the analytes from hydrophilic contaminants. The analytes were then eluted with acetonitrile, dried, reconstituted with an organic buffer (ammonium acetate), and injected in the LC-MS instrument. This method of extraction has been successfully used to extract penicillin G, penillic acid, and penilloic acid with absolute recoveries ranging from 35 to 70% depending on the matrix used, the compound of interest, and the fortification level. Recoveries as calculated for penicillin G using the internal standard had a range of 77−118% (Table 1).

LC-MS/MS Analysis. Solutions (1 ng/μL) of penicillin G, penicillin G-d_5, penillic acid, and penilloic acid were independently infused into the AB Sciex 6500 mass spectrometer to verify precursor/product ion masses. A Q1MS scan mode was used to identify the precursor ion of each compound. Once identified, the DP was optimized for each precursor ion. Then, product ion scan mode was used to find the product ions. A scan range from 100 to 340 Da was used to allow for observation of low mass product ions as well as the precursor ion. A collision energy ramp (5−80 eV) allowed for determination of the best confirming product ions for each precursor in terms of sensitivity and unique mass values. Using a MRM scan mode, in conjunction with automated compound optimization mode, the DP, CE, EP, and CXP were optimized for each product ion. The precursor to product ion transitions were found to be 335 → 176, 335 → 160, and 335 → 114 (amu) for penicillin G, 309 → 263, 309 → 174, and 309 → 128 (amu) for penilloic acid, 335 → 289, 335 → 243, 335 → 176, and 335 → 128 (amu) for penillic acid, and 335 → 181, 335 → 160, and 335 → 114 (amu) for penicillin G-d_5. Using the optimized parameters, subjection of the standards to LC-MS analysis allowed for observation of retention times and ion ratios between precursor and product ions. Penicillin G and its metabolites were separated on a reversed-phase LC column under the given gradient conditions within 20 min. Figure 2 shows the LC chromatogram of these three compounds. Typical retention times of 6.53, 5.08, and 4.23

DOI: 10.1021/acs.jafc.5b02030
J. Agric. Food Chem. 2015, 63, 5993−6000

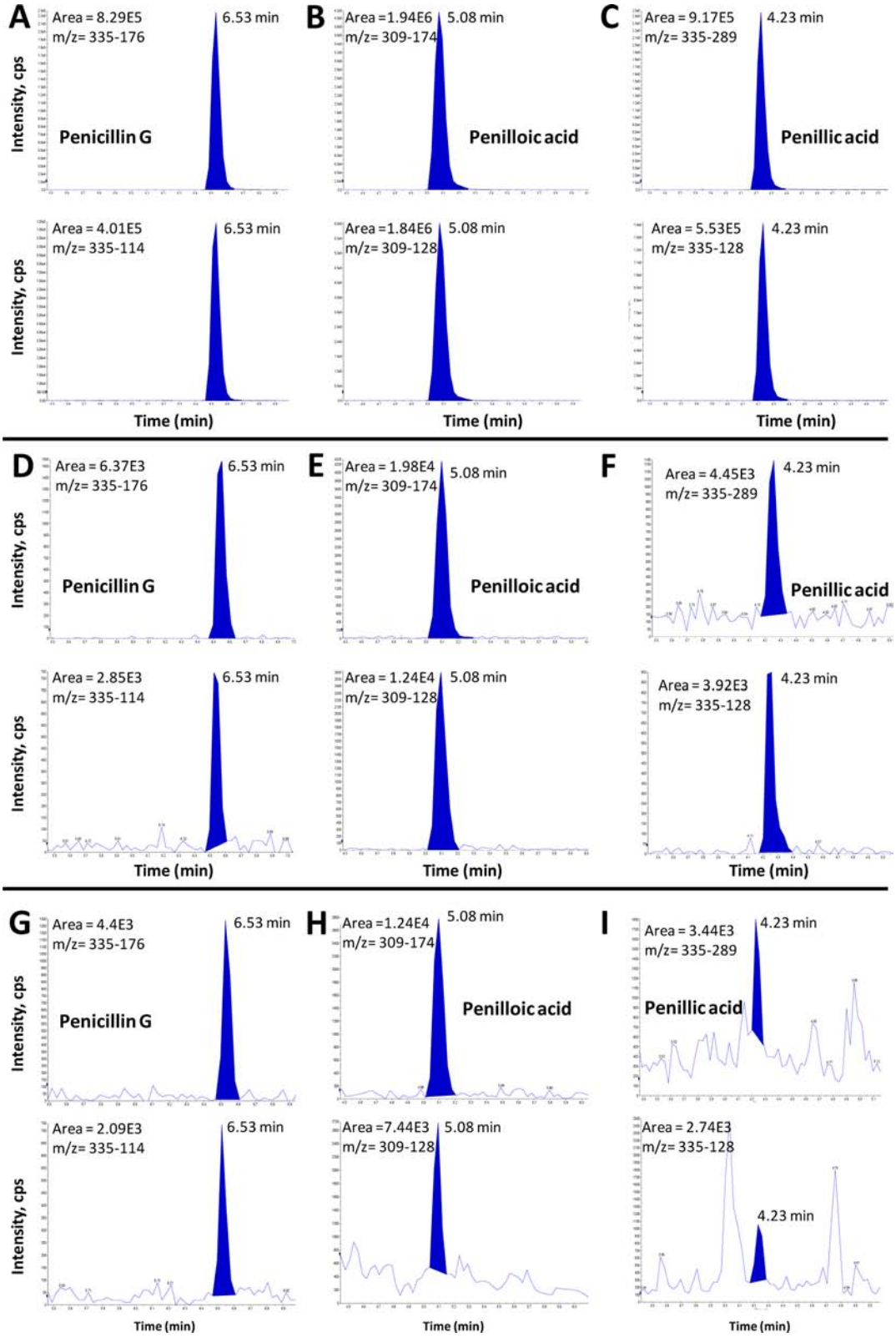

Figure 3. Extracted ion chromatograms collected at standard concentrations of 15 ng/mL in solvent (A–C), 0.1 ng/mL in solvent (D–F), and 0.1 ng/mL in grapefruit matrix (G–I) for penicillin G (*m/z* 176 and 114), penilloic acid (*m/z* 174 and 128), and penillic acid (*m/z* 289 and 128), respectively. These ion products were used for quantitation and precursor confirmation.

min were observed for penicillin G, penilloic acid, and penillic acid, respectively. These retention times reflect expectations based on the chemical structures (i.e., polarity) of these compounds. On one hand, the shortest retention (for penillic acid) can be explained by the high polarity of the two carboxylic acid groups along with the imidazoline heterocycle. Penicillin G, on the other hand, features only one carboxylic acid group along with a nonpolar benzyl group contributing to its longer

DOI: 10.1021/acs.jafc.5b02030
J. Agric. Food Chem. 2015, 63, 5993–6000

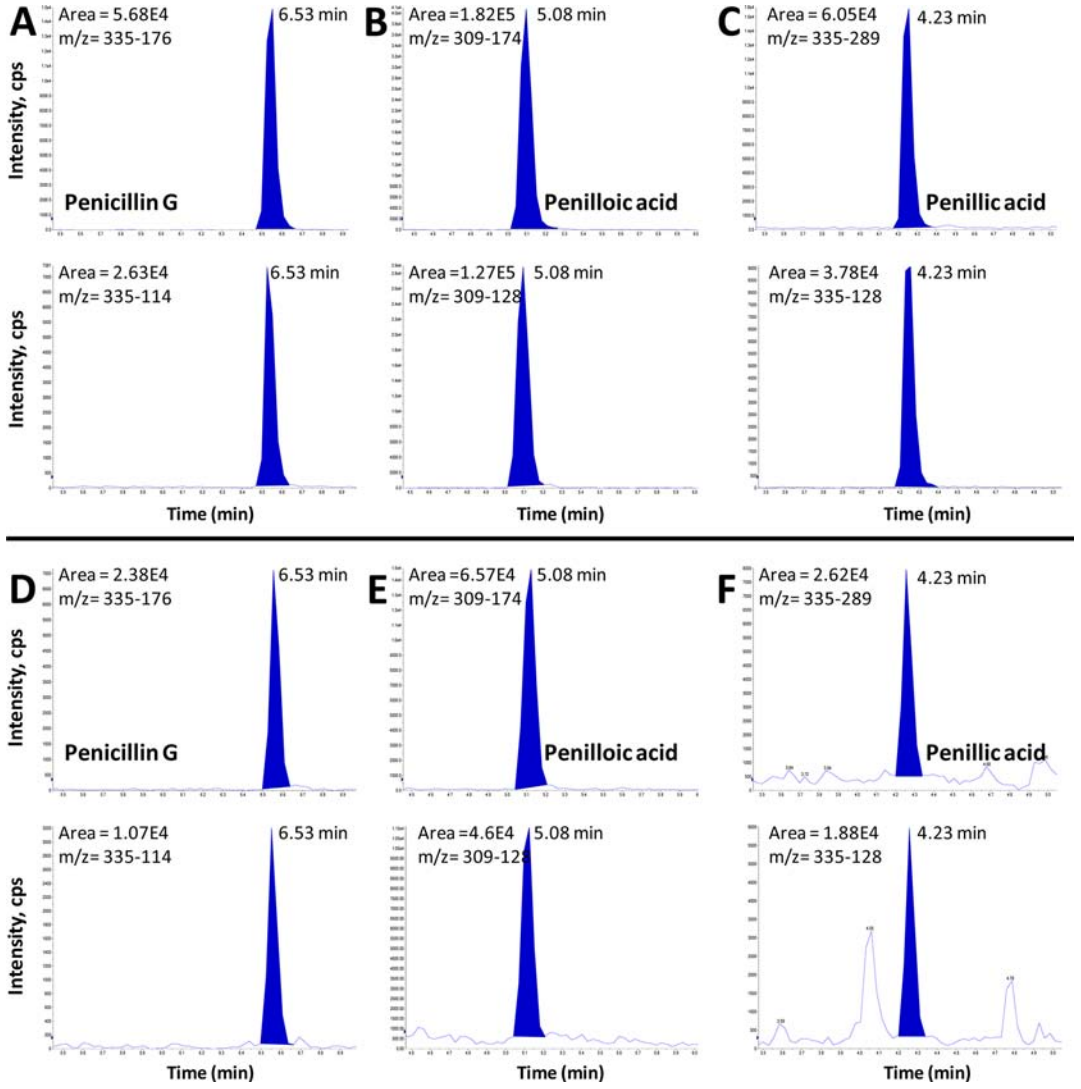

Figure 4. Chromatograms of two product ions of standards in solvent (A–C) and of fortified (spiked) samples in grapefruit matrix (D–F), each at a concentration of 1 ng/mL. The absolute difference in ion ratios between standards in solvent and fortified grapefruit matrix were found to be 1.3, 0.2, and 9% for penicillin G, penilloic acid, and penillic acid, respectively.

retention time of 6.53 min (Figure 1). Panels A–C of Figure 3 show representative LC-MS chromatograms of the most sensitive two product ion signals at a concentration of 15 ng/mL sample in solvent. To demonstrate the ability of this method to function at the LOD, the same chromatograms are shown in Figure 3D–F and in Figure 3G–I at a concentration of 0.1 ng/mL in solvent and grapefruit matrix, respectively. At the LOD level (100 ppt), matrix interference is clearly observed; however, detection of the product ions is still possible (Figure 3I). The product ion transitions used for quantitation purposes were selected on the basis of both the sensitivity and the presence of a clean background. The transitions used for quantitation are 335 → 114, 309 → 174, and 335 → 128 for penicillin G, penillic acid, and penilloic acid, respectively.

Fortifications and Recoveries Results. The method was tested in triplicate to determine its accuracy and precision, and the results are shown in Table 1. Penicillin G, penilloic acid, and penillic acid were each examined in three different citrus commodities (orange, grapefruit, and lemon) at four different concentrations (0.1, 0.25, 1, and 10 ng/g of matrix). The commodities were extracted within the same day to limit the extent of penicillin G degradation in the citrus matrices. The three analytes were then extracted and analyzed by UHPLC/ESI-MS/MS along with a set of samples prepared in solvent at identical concentrations. Preliminary experiments indicated that the instrumental response varies with the absence or presence of citrus matrix. Therefore, to compensate for the effects of the matrix suppression, matrix-matched calibration standard curves (in-matrix curves) were used to quantitate the analytes and obtain what we call absolute recovery. Because of the availability of the standard, penicillin G can be quantified using isotopically labeled penicillin G-d_5 internal standard, which accounts for recovery losses, ion suppression, and degradation of the analytes during the extraction process. Absolute recoveries of the three analytes used in this study from fortified citrus were calculated using a matrix-matched calibration standard curve, and the correlation of coefficient values (R^2) were consistently >0.99. To generate these curves, standards were dissolved in a solution (containing the matrix components) at concentrations varying from 0.1 to 15 ng/g. To quantitate the absolute recoveries of the analytes, chromato-

DOI: 10.1021/acs.jafc.5b02030
J. Agric. Food Chem. 2015, 63, 5993–6000

grams were used to plot the in-matrix calibration points, which were fitted using a $1/x$ weighted quadratic curve. On the other hand, the calibration curve obtained using the isotopically labeled internal standard, penicillin G-d_5, was fitted using $1/x$ linear regression.

The effect of matrix on the area counts for all of the analytes in the three matrices was also investigated. We determined the effect of ion suppression on the signal in all of the citrus matrices. The matrix ion suppression was found to be about 18, 39, and 19% in lemon, 25, 42, and 32% in orange, and 32, 42, and 28% in grapefruit for penicillin G, penilloic acid, and penillic acid, respectively. These data indicate that there is a slight difference in the ion suppression when the matrix is varied. Table 1 shows the absolute recoveries of penicillin G, penillic acid, and penilloic acid along with their relative standard deviations (RSD). Samples were analyzed in triplicate for each matrix as measured by the in-matrix curve. It also shows the recovery of penicillin G as calculated by the internal standard. The recoveries of penilloic acid and penillic acid at each of the four concentrations ranged from 50 to 73% with an average RSD value of <10%. However, the matrix seems to affect the recovery of penicillin G with an average of 70, 50, and 38% recovery in orange, grapefruit, and lemon, respectively. This is probably due to the instability of penicillin G at low pH during the extraction process. We anticipated having lower pH in the lemon matrix than in the grapefruit and orange matrices. To confirm this, we measured the pH of each matrix after stabilization with 4 mL of phosphate buffer and found the pH to be 4.0 for lemon, 5.5 for grapefruit, and 6.0 for orange. Furthermore, we studied the stability of penicillin G and penicillin G-d_5 in the final extract from lemon over the course of 1 week. The final extract, with a pH 7.0 after reconstitution with ammonium acetate buffer, was stored at 10 °C in the LC autosampler. Under these conditions, no significant changes were observed in the concentrations of penicillin G and penicillin G-d_5.

The recovery of penicillin G obtained when corrected with internal standard was nearly 100%. Low recoveries were observed in grapefruit and lemon (about 70−80%) at low levels of fortification (0.1 and 0.25 ppb). Differing matrices did not affect ion ratios, which closely corresponded to the ion ratios observed for in-solvent standards (Figure 4). Figure 4 shows an example of the chromatograms of two ion products of penicillin G, penillic acid, and penilloic acid dissolved in solvent and in fortified/extracted samples (spikes) at 1 ng/mL. These chromatograms demonstrate the consistency of ion ratios (RSD < 10%). The recoveries and RSDs indicate that our method provides good accuracy and precision for the determination of penicillin G and its metabolites in citrus.

In conclusion, an efficient method for the extraction, identification, and quantitation of penicillin G and its metabolites in a variety of citrus fruits (lemon, orange, and grapefruit) has been developed and optimized using UHPLC-MS/MS. Combining liquid/liquid extraction with solid phase extraction cartridges served as a simple and rapid technique for the extraction of penicillin G and the metabolites of interest (penilloic acid and penillic acid). Two product ion transitions per analyte, along with the ion ratios, were used for data acquisition and analyte confirmation, resulting in a highly selective method. Penicillin G and its metabolites can be detected with a limit of detection (LOD) of 0.1 ng/g when 2 g of citrus is extracted. This method is currently used by the Florida Department of Agriculture and Consumer Services to test actual citrus for the presence of penicillin G and its metabolites from trees that have been affected by the greening disease and treated with penicillin G.

AUTHOR INFORMATION

Corresponding Author

*(F.A.) Phone: (850) 617-7523. E-mail: fadi.aldeek@freshfromflorida.com.

Funding

We thank the Citrus Plant Greening Foundation for financial support.

Notes

The authors declare no competing financial interest.

ACKNOWLEDGMENTS

We thank Mariana Herceg, Rebecca Riddle, Qi Huanwu, and Amy Brown from the Department of Agriculture and Consumer Services (FDACS), Tallahassee, Florida, for their assistance with sample preparation and homogenization. We also thank Dr. Daniel Biggerstaff from o2si smart solutions for the preparation of the internal standard solution of penicillin G-d_5. We are grateful to Dr. Xiaoan Sun, FDACS-DPI Plant Pathologist, and Dr. Greg Hodges, FDACS-DPI Chief-Entomology, Nematology and Plant Pathology, for their contributions to the field studies, development of the treatment protocol, and various helpful discussions.

REFERENCES

(1) Folimonova, S. Y.; Achor, D. S. Early events of citrus greening (huanglongbing) disease development at the ultrastructural level. *Phytopathology* **2010**, *100*, 949−958.

(2) Gopal, K.; Sudarsan, S.; Gopi, V.; Naidu, L. N.; Ramaiah, M.; Sreenivasulu, Y.; Wesley, E. Detection of huanglongbing (citrus greening) disease by nucleic acid spot hybridization. *Z. Naturforsch., C: J. Biosci.* **2009**, *64*, 711−716.

(3) Hajeri, S.; Killiny, N.; El-Mohtar, C.; Dawson, W. O.; Gowda, S. Citrus tristeza virus-based RNAi in citrus plants induces gene silencing in *Diaphorina citri*, a phloem-sap sucking insect vector of citrus greening disease (huanglongbing). *J. Biotechnol.* **2014**, *176*, 42−49.

(4) Jagoueix, S.; Bove, J. M.; Garnier, M. PCR detection of the two 'Candidatus' Liberobacter species associated with greening disease of citrus. *Mol. Cell. Probes* **1996**, *10*, 43−50.

(5) Li, X. H.; Li, M. Z.; Won Suk, L.; Reza, E.; Ashish, R. M. Visible-NIR spectral feature of citrus greening disease. *Guang Pu Xue Yu Guang Pu Fen Xi* **2014**, *34*, 1553−1559.

(6) Nageswara-Rao, M.; Irey, M.; Garnsey, S. M.; Gowda, S. Candidate gene markers for Candidatus Liberibacter asiaticus for detecting citrus greening disease. *J. Biosci.* **2013**, *38*, 229−237.

(7) Plotto, A.; Baldwin, E.; McCollum, G.; Manthey, J.; Narciso, J.; Irey, M. Effect of Liberibacter infection (huanglongbing or "greening" disease) of citrus on orange juice flavor quality by sensory evaluation. *J. Food Sci.* **2010**, *75*, S220−S230.

(8) Teixeira Ddo, C.; Saillard, C.; Eveillard, S.; Danet, J. L.; da Costa, P. I.; Ayres, A. J.; Bove, J. Candidatus Liberibacter americanus, associated with citrus huanglongbing (greening disease) in Sao Paulo State, Brazil. *Int. J. Syst. Evol. Microbiol.* **2005**, *55*, 1857−1862.

(9) Lu, L.; Cheng, B.; Du, D.; Hu, X.; Peng, A.; Pu, Z.; Zhang, X.; Huang, Z.; Chen, G. Morphological, molecular and virulence characterization of three Lencanicillium species infecting Asian citrus psyllids in Huangyan citrus groves. *J. Invertebr. Pathol.* **2015**, *125*, 45−55.

(10) Tiwari, S.; Gondhalekar, A. D.; Mann, R. S.; Scharf, M. E.; Stelinski, L. L. Characterization of five CYP4 genes from Asian citrus psyllid and their expression levels in Candidatus Liberibacter asiaticus-infected and uninfected psyllids. *Insect Mol. Biol.* **2011**, *20*, 733−744.

DOI: 10.1021/acs.jafc.5b02030
J. Agric. Food Chem. 2015, 63, 5993−6000

(11) Zhang, M.; Powell, C. A.; Benyon, L. S.; Zhou, H.; Duan, Y. Deciphering the bacterial microbiome of citrus plants in response to 'Candidatus Liberibacter asiaticus'-infection and antibiotic treatments. *PLoS One* **2013**, *8*, No. e76331.
(12) Zhang, M.; Powell, C. A.; Guo, Y.; Benyon, L.; Duan, Y. Characterization of the microbial community structure in Candidatus Liberibacter asiaticus-infected citrus plants treated with antibiotics in the field. *BMC Microbiol.* **2013**, *13*, 112−121.
(13) Bove, J. M.; Bonnet, P.; Garnier, M.; Aubert, B. Penicillin and tetracycline treatments of greening disease-affected citrus plants in the glasshouse, and the bacterial nature of the prokaryote associated with greening. *Eighth IOCV Conference*; International Organization of Citrus Virologists: Riverside, CA, USA, 1980; pp 102−107
(14) Chung, K.; Zhisheng, W. A study on the use of antibiotics to control citrus huanglungbin. *Proceeding of the 6th International Asia Pacific Workshop on Integrated Health Management*; FAO: Rome, Italy, 1991; pp 40−48
(15) Blanchflower, W. J.; Hewitt, A. S.; Kennedy, D. G. Confirmatory assay for the simultaneous detection of five penicillins in muscle, kidney and milk using liquid chromatography-electrospray mass spectrometry. *Analyst* **1994**, *119*, 2595−2601.
(16) Daeseleire, E.; De Ruyck, H.; Van Renterghem, R. Confirmatory assay for the simultaneous detection of penicillins and cephalosporins in milk using liquid chromatography/tandem mass spectrometry. *Rapid Commun. Mass Spectrom.* **2000**, *14*, 1404−1409.
(17) Heller, D. N.; Ngoh, M. A. Electrospray ionization and tandem ion trap mass spectrometry for the confirmation of seven β-lactam antibiotics in bovine milk. *Rapid Commun. Mass Spectrom.* **1998**, *12*, 2031−2040.
(18) Holstege, D. M.; Puschner, B.; Whitehead, G.; Galey, F. D. Screening and mass spectral confirmation of β-lactam antibiotic residues in milk using LC-MS/MS. *J. Agric. Food Chem.* **2002**, *50*, 406−411.
(19) Wang, J. Confirmatory determination of six penicillins in honey by liquid chromatography/electrospray ionization-tandem mass spectrometry. *J. AOAC Int.* **2004**, *87*, 45−55.
(20) Ball, C. Agilent Technologies Inc., Wilmington, DE, USA, personal communication.
(21) Schwartz, M. A. Mechanism of degradation of penicillin G in acidic solution. *J. Pharm. Sci.* **1965**, *54*, 472−473.
(22) Schwartz, U.; Weidel, W. On the mechanism of action of penicillin. Ii. demonstration of a penicillin-induced hydrolytic degradation of murein and murein precursors in E. coli B. *Z. Naturforsch., B: J. Chem. Sci.* **1965**, *20*, 153−157.
(23) Li, D.; Yang, M.; Hu, J.; Zhang, Y.; Chang, H.; Jin, F. Determination of penicillin G and its degradation products in a penicillin production wastewater treatment plant and the receiving river. *Water Res.* **2008**, *42*, 307−317.
(24) Navarro, P. G.; Blazquez, I. H.; Osso, B. Q.; Martinez de las Parras, P. J.; Puentedura, M. I.; Garcia, A. A. Penicillin degradation catalysed by Zn(II) ions in methanol. *Int. J. Biol. Macromol.* **2003**, *33*, 159−166.
(25) Sumita, Y.; Fukasawa, M.; Mitsuhashi, S.; Inoue, M. Degradation of penicillin-binding protein 2′ in methicillin-resistant Staphylococcus aureus. *Chemotherapy* **1995**, *41*, 172−177.
(26) Tropilo, J.; Kiszczak, L.; Piusinski, W.; Len artowicz-Kubrat, Z. L.; Leszczynska, K. Subchronic toxicity of penicillin G and products of its thermal degradation after peroral administration. *Rocz. Panstw. Zakl. Hig.* **1988**, *39*, 389−395.
(27) Oeppinger, H.; Koernlein, M. On the nomenclature of penicillin and its decomposition products. *Arzneim.-Forsch.* **1960**, *10*, 95−98.
(28) Rodante, F.; Vecchio, S.; Tomassetti, M. Kinetic analysis of thermal decomposition for penicillin sodium salts: model-fitting and model-free methods. *J. Pharm. Biomed. Anal.* **2002**, *29*, 1031−1043.
(29) Toshkov, A.; Kuiumdzhiev, D.; Noeva, K. Penicillin and certain of its decomposition products as factors responsible for morphological changes in some bacteria. *Izv. Mikrobiol. Inst.* **1960**, *11*, 191−199.
(30) Kim, M. J.; Yang, K. W.; Kim, S. S.; Park, S. M.; Park, K. J.; Kim, K. S.; Choi, Y. H.; Cho, K. K.; Hyun, C. G. Chemical composition and anti-inflammation activity of essential oils from Citrus unshiu flower. *Nat. Prod. Commun.* **2014**, *9*, 727−730.
(31) Lopez-Munoz, G. A.; Antonio-Perez, A.; Diaz-Reyes. Quantification of total pigments in citrus essential oils by thermal wave resonant cavity photopyroelectric spectroscopy. *Food Chem.* **2015**, *174*, 104−109.
(32) Ruiz, B.; Flotats, X. Citrus essential oils and their influence on the anaerobic digestion process: an overview. *Waste Manage.* **2014**, *34*, 2063−2079.
(33) Wang, J.; Chen, H. P.; Liu, Y. P.; Wei, Z. Chemical variability of essential oils in peels collected in different time from Citrus reticulata 'Ponkan'. *J. Chinese Med. Mater.* **2013**, *36*, 1922−1925.

DOI: 10.1021/acs.jafc.5b02030
J. Agric. Food Chem. 2015, 63, 5993−6000

concert with the UGT enzymes to eliminate foreign compounds from the body.[20] Contribution of MRP2 to excretion of glucuronides has been well established.[21−24] However, the role of MRP4 in transporting glucuronides remains elusive despite the fact that estradiol 17-β-D-glucuronide is shown to be a substrate for transport by MRP4.[25]

In our previous study, it was shown that cellular glucuronidation was altered by inhibiting the exporter activity or decreasing exporter expression.[26,27] However, the mechanisms underlying the dependence of UGT metabolism on glucuronide efflux remain elusive. The objective of the present study was to explore the role of futile recycling (or deglucuronidation) in the disposition of two flavonoids (i.e., genistein and apigenin) using UGT1A1-overexpressing HeLa cells (or HeLa1A1 cells). Deglucuronidation refers to the β-glucuronidase (GUSB)-mediated hydrolysis reaction in which glucuronidated metabolites were converted back to the parent compounds. The pharmacokinetics of both aglycone and glucuronide in HeLa1A1 and MRP4 knocked-down cells were determined and compared after administration of the aglycone. A two-compartment pharmacokinetic model incorporating the deglucuronidation process was established and used to describe the data. Our result revealed that the effect of glucuronide efflux on total glucuronidation was through a futile recycling mechanism.

CHEMICALS AND METHODS

Chemicals. The pLVX-mCMV-ZsGreen-PGK-Puro vector was purchased from BioWit Technologies (Shenzhen, China). The anti-GUSB (human β-glucuronidase) and anti-GAPDH antibodies were purchased from Abcam (Cambridge, MA, USA). Uridine diphosphoglucuronic acid (UDPGA), alamethicin, and D-saccharic-1,4-lactone monohydrate were purchased from Sigma-Aldrich (St. Louis, MO, USA). Apigenin and genistein were purchased from Aladdin Reagents (Shanghai, China). Apigenin-7-*O*-glucuronide (or apigenin glucuronide (AG)) and genistein-7-*O*-glucuronide (or genistein glucuronide (GG)) were synthesized in our laboratory using rat liver microsomes as described.[28]

Cell Culture. HeLa1A1 cells and MRP4 knock-down HeLa1A1 cells (referred to as HeLa1A1-MRP4-shRNA cells) were seeded into six-well plates at a density of 4.0×10^5 cells/well and were grown using Dulbecco's modified Eagle's medium (DMEM) supplemented with 10% fetal bovine serum (FBS). On day 2 post seeding, the cells were used for the glucuronide excretion experiments. The procedures for establishment of HeLa1A1 and HeLa1A1-MRP4-shRNA cells have been detailed in our previous publications.[26,27] In HeLa1A1-MRP4-shRNA cells, the protein level of MRP4 was reduced to 35% as compared to HeLa1A1 cells.[27]

Development of GUSB Transfected HeLa Cells. HeLa cells were stably transfected with the cDNA of human GUSB using the lentiviral approach following our published procedures.[26] In brief, the full-length cDNA (1956 bp) of GUSB was PCR-amplified from the commercial pMD18-T plasmid (Sino Biologic Inc., Beijing, China). After purification, GUSB cDNA was ligated into the pLVX-mCMV-ZsGreen-PGK-Puro vector. The recombinant vector was then incorporated in the generation of lentiviral particles that were used to transduce the HeLa cells. Stably transfected cells were obtained by puromycin selection and named HeLa-GUSB cells.

Detection of GUSB mRNA by Reverse Transcription-Polymerase Chain Reaction (RT-PCR). Cells were collected, and total RNA isolation was performed using the TRIzol extraction method. The total RNA was converted to cDNA using the iScript cDNA synthesis kit according to the manufacturer's protocol (Bio-Rad, Hercules, CA, USA). The PCR conditions were as follows: 3 min of denaturation at 95 °C followed by 30 cycles of 20 s at 95 °C, 30 s at 55 °C, and 30 s at 72 °C and a final step of 72 °C for 5 min using Taq DNA polymerase (TransGen Biotech, Beijing, China). The forward primer was 5′-GTCGCGGGAGTGCAAGGAG-3′, and the reverse primer was 5′-TGTTGATGGCGATAGTGATT-3′. After RT-PCR, agarose gel electrophoresis was performed, and DNA bands were visualized under UV light.

Glucuronidation Assay. The aglycones (i.e., genistein and apigenin) were incubated with HeLa1A1 cell lysate to determine the rates of glucuronidation as described in our publications.[29−31] In brief, in addition to the aglycone (substrate), the incubation medium contained the lysate (26.5 μg/mL), $MgCl_2$ (0.88 mM), saccharolactone (4.4 mM), alamethicin (22 μg/mL), and UDPGA (3.5 mM) in 50 mM potassium phosphate (pH 7.4). The reaction was terminated by adding ice-cold acetonitrile (containing the internal standard biochanin A). The samples were vortexed and centrifuged at 18000*g* for 15 min. The supernatant was subjected to UPLC analysis. All experiments were performed in triplicate.

Modeling of Enzyme Kinetics. Kinetic parameters were derived by fitting the substrate inhibition equation (eq 1) to the data of reaction rates versus substrate concentrations.[32,33] Substrate inhibition refers to inhibition of enzyme activity at high substrate concentrations. Parameter estimation was performed using Graphpad Prism (San Diego, CA, USA).

$$V = \frac{V_{max} \times [S]}{K_m + [S]\left(1 + \frac{[S]}{K_{si}}\right)} \quad (1)$$

K_m is the Michaelis constant, V_{max} is the maximal velocity, and K_{si} is the substrate inhibition constant.

Glucuronide Excretion Experiments. The excretion experiment was performed essentially as described.[26,27] In brief, all culture wells were washed twice with 37 °C HBSS (pH 7.4). Then, the cells were incubated at 37 °C with HBSS (2 mL) containing the aglycone (i.e., genistein or apigenin). At each time point (i.e., 0.5, 1, 1.5, and 2 h), a 200 μL aliquot of extracellular medium was sampled and immediately replaced with the same volume of dosing solution. With the addition of 100 μL of acetonitrile (containing the internal standard biochanin A), the concentrations of glucuronides were measured by UPLC. After sampling at the last time point, the medium was rapidly removed by suction. The cells were processed, and intracellular aglycone and glucuronide were measured following our published procedures.[27]

A different set of experiments was performed to obtain the aglycone/glucuronide levels (both extracellular and intracellular) versus time profiles. The cells in culture wells were incubated with the aglycone at a dose of 2.5 nmol. At each time point (i.e., 10, 20, and 30 min and 1, 1.5, and 2 h), the incubation medium was sampled from the culture wells ($n = 3$). The residual medium was rapidly removed by suction. The cells were processed, and intracellular aglycone and glucuronide were measured following our published procedures.[27]

The excretion rate (ER) of intracellular glucuronide was calculated according to eq 2

$$ER = V\frac{dC}{dt} \quad (2)$$

where V is the volume of the incubation medium, C is the cumulative concentration of the glucuronide, and t is the incubation time.

The fraction of dose metabolized (f_{met}), an indicator of the extent of drug glucuronidation, was calculated exactly as described (eq 3).[27]

$$f_{met} = \frac{\text{excreted glucuronide} + \text{intracelluar glucuronide}}{\text{dosed aglycone}} \quad (3)$$

Pharmacokinetic Modeling and Data Fitting. A two-compartment model (Figure 1), consisting of the (incubation/extracellular) medium and the cell compartments, was used to describe the transport and glucuronidation in HeLa1A1 cells. The mass balance equations are shown (eqs 4−7). Transport of the aglycone (A) across the cell membrane occurred with the clearance CL_d, representing passive diffusion. Glucuronide (G) formation followed substrate inhibition kinetics described by V_{max}, K_m, and K_{si}. Excretion of glucuronide followed linear kinetics with the first-order rate constant K_{ef}. Similarly,

DOI: 10.1021/acs.jafc.5b00983
J. Agric. Food Chem. 2015, 63, 6001−6008

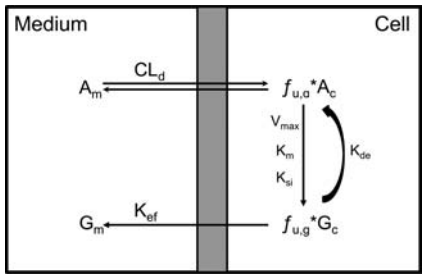

Figure 1. Schematic representation of a two-compartment model that describes the glucuronidation of flavonoids and excretion of their glucuronides in HeLa1A1 cells. Please refer to the text for the definition of each parameter.

conversion of glucuronide back to the aglycone (futile recycling or deglucuronidation) obeyed the linear kinetics (K_{de}). $f_{u,a}$ and $f_{u,g}$ denote the unbound fractions of aglycone and conjugate in the cell compartment, respectively. The model assumed (1) glucuronidation was the only metabolic pathway and (2) transport of aglycone across the membrane was a nonsaturable (linear) process.

Modeling and data fitting were performed using MATLAB (The Mathworks Inc., Natick, MA, USA). In data fitting, the protein binding of glucuronide was assumed to be unity ($f_{u,g} = 1$). Also the K_m and K_{si} were fixed as the corresponding values derived from the in vitro glucuronidation assays.

$$\frac{dA_m}{dt} = -\frac{CL_d}{V_m}A_m + \frac{CL_d}{V_c}f_{u,a}A_c \quad (4)$$

$$\frac{dA_c}{dt} = \frac{CL_d}{V_m}A_m - \frac{CL_d}{V_c}f_{u,a}A_c - \frac{f_{u,a}A_cV_{max}}{V_cK_m + f_{u,a}A_c + \frac{(f_{u,a}A_c)^2}{V_cK_{si}}} + K_{de}f_{u,g}G_c \quad (5)$$

$$\frac{dG_m}{dt} = K_{ef}f_{u,g}G_c \quad (6)$$

$$\frac{dG_c}{dt} = \frac{f_{u,a}A_cV_{max}}{V_cK_m + f_{u,a}A_c + \frac{(f_{u,a}A_c)^2}{V_cK_{si}}} - K_{ef}f_{u,g}G_c - K_{de}f_{u,g}G_c \quad (7)$$

Preparation of Cell Lysate. Cells collected in 50 mM potassium phosphate buffer (pH 7.4) were disrupted by sonication for 15 min in an ice-cold water bath. Cell lysate was obtained by centrifugation (4 °C) at 1000*g* for 5 min. Protein concentration was determined by Bio-Rad protein assay kit using bovine serum albumin as a standard.

Protein Binding Assay. Binding of the aglycones (genistein and apigenin) to cell lysate was measured using the rapid equilibrium dialysis system (RED) (Thermo Scientific, Rockford, IL, USA) as described.[34] In brief, the sample chamber was filled with 400 μL of the aglycone in HBSS (pH 7.4) containing the cell lysate (0.4 mg/mL). The buffer chamber was filled with 600 μL of blank buffer. The filled RED device was incubated at 100 rpm at 37 °C for 4 h (sufficient for reaching equilibrium) using an Eppendorf E24 incubator shaker (Hamburg, Germany). After incubation, a 50 μL aliquot from each chamber was mixed with 200 μL of acetonitrile, vortexed, and centrifuged for 15 min at 18000*g*, and the concentration of aglycone in the supernatant was determined by UPLC. The unbound fraction (fu) was calculated using the equation

$$fu = \frac{[S]_{buffer\ chamber}}{[S]_{sample\ chamber}}$$

where $[S]_{buffer\ chamber}$ and $[S]_{sample\ chamber}$ are the concentrations of aglycone in the respective chambers at the end of the incubation.

The fraction of unbound (fu) values versus genistein concentration was fitted to a Michaelis–Menten-like equation (eq 8) using the Graphpad Prism v5 software

$$fu = \frac{f_{u\text{-}max}[S]}{K_s + [S]} \quad (8)$$

where $f_{u\text{-}max}$ is the maximal fraction unbound and K_s is the concentration of genistein at half $f_{u\text{-}max}$.

Hydrolysis of Glucuronides by GUSB. The HeLa-GUSB or HeLa cell lysate was incubated with glucuronides (GG and AG) to determine the rates of glucuronide hydrolysis as described.[27] The assayed concentration ranges for GG and AG were 2.5–160 and 3.75–120 μM, respectively. The hydrolysis rate of GUBS was derived by subtracting the hydrolysis rate of HeLa cell lysate from that of HeLa-GUSB cell lysate.

Quantification of Aglycones and Glucuronides by UPLC Analysis. Concentrations of aglycones and their glucuronides were determined by using a Waters ACQUITY UPLC system equipped with a BEH column (2.1 × 50 mm, 1.7 μm; Waters). Elution was performed using a gradient of 2.5 mM ammonium acetate in water (mobile phase A) versus acetonitrile (mobile phase B) at a flow rate of 0.45 mL/min. The gradient program was 5% B at 0–0.5 min, 5–40% B at 0.5–1.2 min, 40% B at 1.2–1.5 min, 40–95% B at 1.5–2.8 min, 95% B at 2.8–3.3 min, and 95–5% B at 3.3–4 min. The detection wavelengths were 258 and 340 nm for genistein/GG and apigenin/AG, respectively.

Western Blotting. The cell lysate (40 μg of total protein) was analyzed by SDS-PAGE (8% acrylamide gels), and the proteins were transferred onto PVDF membranes (Millipore, Bedford, MA, USA). Blots were probed with the anti-GUSB antibody and the anti-GAPDH antibody (as internal loading control) followed by horseradish peroxidase-conjugated rabbit anti-goat IgG (Santa Cruz Biotechnology, Santa Cruz, CA, USA). Protein bands were detected by enhanced chemiluminescence (ECL).

Statistical Analysis. Data are expressed as the mean ± SD (standard deviation). Mean differences between treatment and control groups were analyzed by Student's *t* test. The level of significance was set at $p < 0.05$ (*) or $p < 0.01$ (**) or $p < 0.001$ (***).

RESULTS

Binding of Genistein and Apigenin to HeLa1A1 Cell Lysate. Protein binding of genistein to cell lysate was concentration dependent (Figure 2A). The unbound fraction (fu) showed a hyperbolic curve with respect to the genistein concentration (Figure 2A). The data were well characterized by a Michaelis–Menten-like equation (eq 8) with a $f_{u\text{-}max}$ value of 0.84 and a K_s value of 0.39 μM. By contrast, protein binding of apigenin to cell lysate was concentration independent, showing an average fu value of 0.37 (Figure 2B). The results suggested that there was a high possibility that genistein and apigenin bound to intracellular proteins once inside the cells.

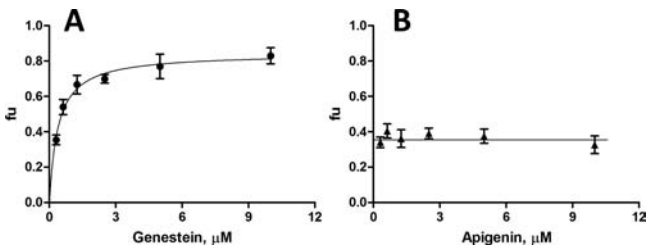

Figure 2. Protein binding of (A) genistein (0.31–10 μM) to HeLa1A1 cell lysate and (B) apigenin (0.31–10 μM) to HeLa1A1 cell lysate. Each data point is the average of three determinations with error bar representing the standard deviation.

DOI: 10.1021/acs.jafc.5b00983
J. Agric. Food Chem. 2015, 63, 6001–6008

Glucuronidation of Genistein and Apigenin by HeLa1A1 Cell Lysate. The HeLa1A1 cell lysate was able to generate glucuronides from the aglycones genistein and apigenin. Glucuronidation of the two compounds consistently obeyed substrate inhibition kinetics (V_{max} = 0.10 nmol/min/mg, K_m = 0.54 μM, and K_{si} = 2.0 μM for genistein; V_{max} = 0.19 nmol/min/mg, K_m = 0.56 μM, and K_{si} = 3.7 μM for apigenin) (Figure 3). Compared to genistein, glucuronidation of apigenin showed a higher intrinsic clearance value ($CL_{int} = V_{max}/K_m$). This suggested that apigenin was glucuronidated more efficiently by cell lysate.

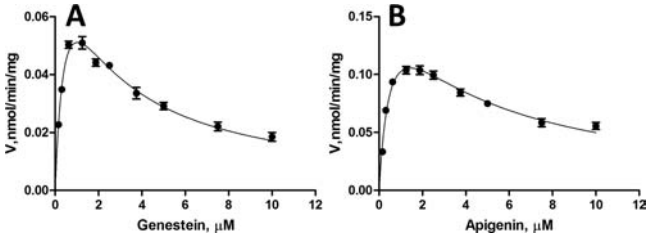

Figure 3. Kinetic profile of (A) glucuronidation derived from incubation of genistein with HeLa1A1 cell lysate and (B) glucuronidation derived from incubation of apigenin with HeLa1A1 cell lysate. Each data point is the average of three determinations with error bar representing the standard deviation.

Excretion of GG and AG in HeLa1A1 Cells. Genistein glucuronide (GG) was efficiently generated and excreted after incubation of the aglycone (loading doses of 1.25−20 nmol) with the cells. The excretion rates of GG ranged from 0.40 to 0.69 nmol/min/mg. Of note, the excretion rate of GG decreased ($p < 0.05$) significantly with an increase in the loading dose of genistein (Figure 4A). In response to dose escalation, the intracellular level of GG also decreased ($p < 0.05$), whereas the intracellular level of genistein increased ($p < 0.01$) (Figure 4B,C).

Likewise, apigenin glucuronide (AG) was efficiently generated and excreted after incubation of the aglycone (loading doses of 1.25−20 nmol) with the cells. The excretion rates ranged from 0.84 to 1.1 nmol/min/mg. Interestingly, the excretion rate of AG was highest at the intermediate dose of 5 nmol (Figure 5A). Dose escalation from 1.25 to 5 nmol caused a substantial increase in the intracellular level of AG ($p < 0.001$) (Figure 5B). However, further increase of the dose from 5 to 20 nmol did not alter the intracellular level of AG (Figure 5B). By contrast, the intracellular level of apigenin markedly rose as the loading dose increased ($p < 0.001$) (Figure 5C).

Expression of GUSB in HeLa, HeLa1A1, and HeLa1A1-MRP4-shRNA Cells. Expression of GUSB in HeLa and the modified cells was determined at both mRNA and protein levels (Figure 6). The mRNA of GUSB was found significantly in three cell lines (Figure 6A). Also, all three cell lines expressed the GUSB proteins at an identical level (Figure 6B). Clearly, transfection of HeLa cells did not alter protein expression of GUSB. The results suggested that GUBS within the cells may be involved in cellular glucuronidation.

Hydrolysis of Glucuronides (GG and AG) by GUSB. The hydrolysis kinetics of GG and AG by the GUSB enzyme were determined and compared. GUSB catalyzed the hydrolysis of two glucuronides at a wide range of concentrations (Figure 7). Determination of the kinetic parameters such K_m and V_{max} was unlikely because the reaction rates were linearly related to the tested substrate concentrations (Figure 7). However, we were able to estimate the intrinsic clearance (CL_{int}) by performing linear regression. The estimated CL_{int} values were 115 and 151 μL/h/mg for GG and AG, respectively (Figure 7). The CL_{int} value for AG was higher than that for GG ($p < 0.05$), suggesting that AG was more efficiently hydrolyzed by GUSB compared to GG.

Disposition of Genistein in HeLa1A1 versus HeLa1A1-MRP4-shRNA Cells. The concentration−time profiles were determined for extracellular genistein and GG and for intracellular genistein and GG in control versus MRP4 knocked-down (shRNA-MRP4) cells at a dose of 2.5 nmol of genistein (Figure 8). Knock-down of MRP4 led to a substantial decrease in excretion of GG (30.2%, $p < 0.01$) (Figure 8A) and in the f_{met} value (29.6%, $p < 0.01$) (Figure 8A,B). A reduction in cellular glucuronidation caused by MRP4 silencing was accompanied by elevations in both extracellular and intracellular levels of the aglycone (genistein) (Figure 8C,D). The two-compartment pharmacokinetic model featuring a futile recycling or deglucuronidation process (K_{de}) was well fitted to the data (Table 1 and Figure 8). The derived K_{ef} values were 20 and 9.1 1/h for control and shRNA-MRP4 cells, respectively (Table 1). A significant decrease (54.5%, $p < 0.01$) in the rate constant for glucuronide efflux was well consistent with decreased expression of MRP4 due to gene silencing.

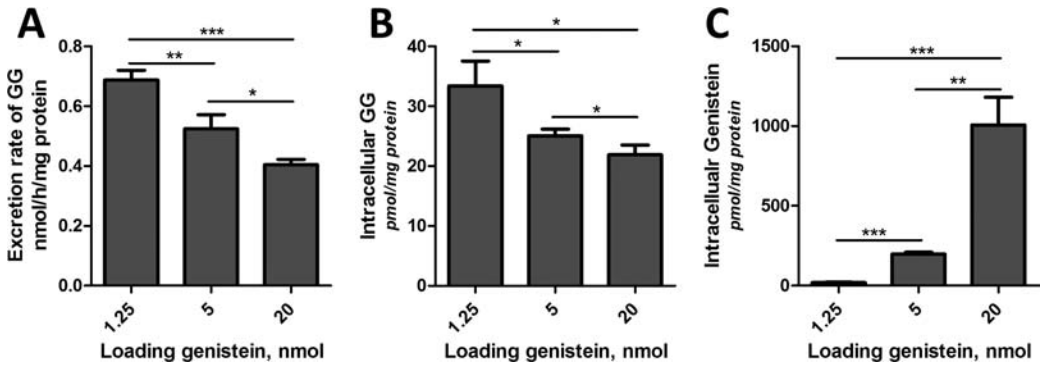

Figure 4. Disposition of genistein in HeLa1A1 cells at different doses: (A) excretion rates of genistein glucuronide (GG) at different loading doses; (B) intracellular amounts of GG at 2 h under different loading doses; (C) intracellular amounts of genistein at 2 h under different loading doses. Each data point is the average of three determinations with error bar representing the standard deviation (n = 3). (*) $p < 0.05$; (**) $p < 0.01$; (***) $p < 0.001$.

DOI: 10.1021/acs.jafc.5b00983
J. Agric. Food Chem. 2015, 63, 6001−6008

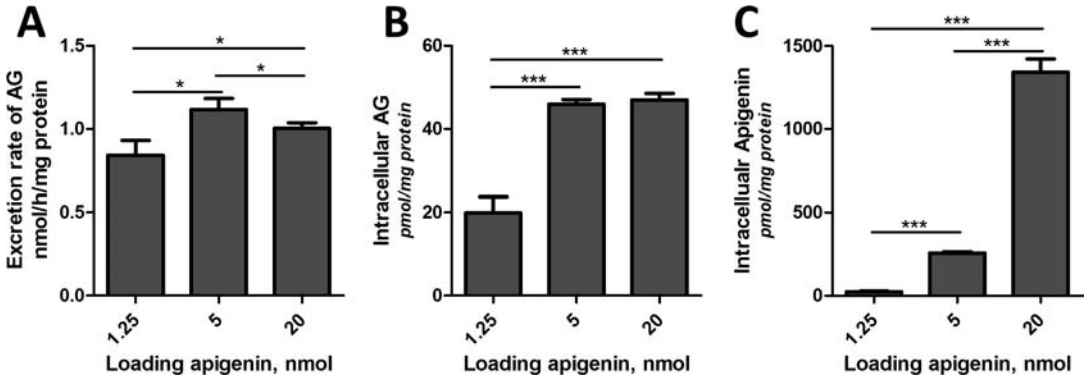

Figure 5. Disposition of apigenin in HeLa1A1 cells at different doses: (A) excretion rates of apigenin glucuronide (AG) at different loading doses; (B) intracellular amounts of AG at 2 h under different loading doses; (C) intracellular amounts of apigenin at 2 h under different loading doses. Each data point is the average of three determinations with error bar representing the standard deviation (n = 3). (*) $p < 0.05$; (***) $p < 0.001$.

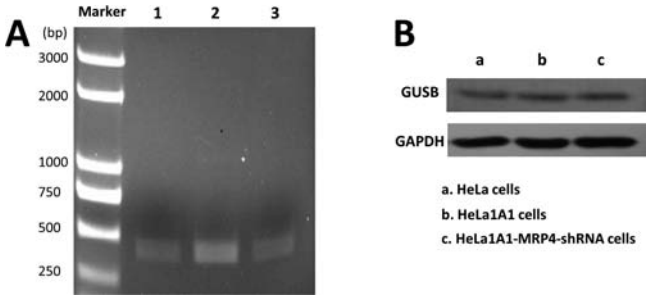

Figure 6. Expression of GUSB in wild-type HeLa, HeLa1A1, and HeLa1A1-MRP4-shRNA cells: (A) mRNA expression of GUSB in wild-type HeLa and modified cells (lanes: 1, detection of GUSB mRNA in wild-type HeLa cells; 2, detection of GUSB mRNA in HeLa1A1 cells; 3, detection of GUSB mRNA in HeLa1A1-MRP4-shRNA cells); (B) Western blots of the cell lines against GUSB.

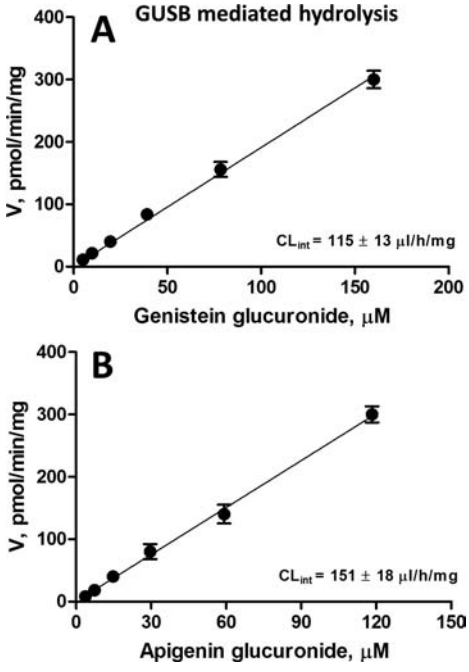

Figure 7. Hydrolysis of genistein glucuronide (A) and apigenin glucuronide (B) by GUSB enzyme. Each data point is the average of three determinations with error bar representing the standard deviation.

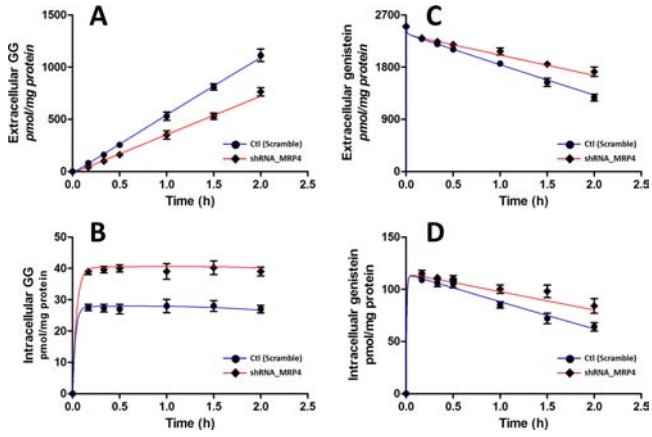

Figure 8. Pharmacokinetic profiles for genistein disposition in HeLa1A1 and shRNA-MRP4 transfected cells at the dose of 2.5 nmol: (A) extracellular GG−time profile; (B) intracellular GG−time profile; (C) extracellular genistein−time profile; (D) intracellular genistein−time profile. Solid lines are predicted data from the pharmacokinetic model depicted in Figure 1.

Disposition of Apigenin in HeLa1A1 versus HeLa1A1-MRP4-shRNA Cells. The concentration−time profiles were determined for extracellular apigenin and AG and for intracellular apigenin and AG in control versus shRNA-MRP4 cells at a dose of 2.5 nmol of apigenin (Figure 9). As observed for genistein, MRP4 silencing resulted in significant decreases in excretion of AG (30.5%, $p < 0.01$) (Figure 9A) and in the f_{met} value (27.7%, $p < 0.01$) (Figure 9A,B). Reduced glucuronidation in the shRNA-MRP4 cells was accompanied by elevations in both extracellular and intracellular levels of the aglycone (apigenin) (Figure 9C,D). Similarly, the data were well described by the two-compartment pharmacokinetic model incorporating the futile recycling process (Table 1 and Figure 9). The derived K_{ef} values were 23 and 12 1/h for control and shRNA-MRP4 cells, respectively (Table 1). A significant reduction (47.8%, $p < 0.01$) in the efflux rate constant was well consistent with a compromised efflux capacity due to decreased expression of MRP4.

DISCUSSION

In this study, the pharmacokinetics of both flavonoid (genistein or apigenin) and generated glucuronide in HeLa1A1 and MRP4 knocked-down cells were determined and compared after administration of the flavonoid. Consistent with our

DOI: 10.1021/acs.jafc.5b00983
J. Agric. Food Chem. 2015, 63, 6001−6008

Table 1. Fitted Parameters for Glucuronidation of Two Flavonoids and Efflux of Their Glucuronides in HeLa1A1 Cells

	genistein		apigenin	
parameter	control cells	MRP4 knockdown cells	control cells	MRP4 knockdown cells
K_m (μM)	0.54[a]	same as control	0.56[a]	same as control
K_{si} (μM)	2.0[a]	same as control	3.7[a]	same as control
V_{max} (pmol/min)	33 ± 2.5	same as control	58 ± 3.1	same as control
$f_{u,a}$	0.040 ± 0.0048	same as control	0.023 ± 0.0030	same as control
CL_d (mL/h)	13 ± 3.3	same as control	94 ± 7.4	same as control
K_{de} (1/h)	15 ± 2.8	same as control	25 ± 3.6	same as control
K_{ef} (1/h)	20 ± 2.9	9.1 ± 0.23	23 ± 1.3	12 ± 1.3

[a]Assigned values from in vitro metabolism kinetics.

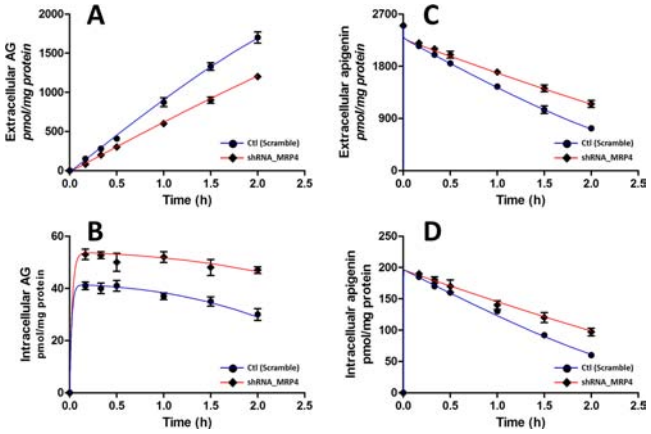

Figure 9. Pharmacokinetic profiles for apigenin disposition in HeLa1A1 and shRNA-MRP4 transfected cells at the dose of 2.5 nmol: (A) extracellular AG−time profile; (B) intracellular AG−time profile; (C) extracellular apigenin−time profile; (D) intracellular apigenin−time profile. Solid lines are predicted data from the pharmacokinetic model depicted in Figure 1.

previous study,[27] knock-down of MRP4 led to significant reductions in glucuronide excretion and total glucuronidation (representing one aspect of glucuronidation−efflux interplay). In addition, the pharmacokinetic data (in the control versus shRNA-MRP4 cells) were well described by a two-compartment model incorporating the futile recycling process (characterized by the rate constant K_{de}) (Figures 8 and 9). Furthermore, we showed that the GUSB enzyme was expressed in HeLa and the modified cells (Figure 6). Also, GUSB enzyme was capable of catalyzing efficient hydrolysis of the flavonoid glucuronides back to their parent compounds. Taken together, our results indicated that the futile recycling (enabled by GUSB-mediated deglucuronidation) was essential for the occurrence of glucuronidation−efflux interplay.

Glucuronidation of the two model flavonoids (i.e., genistein and apigenin) followed substrate inhibition kinetics (Figure 3). It should be noted that glucuronidation of many other flavonoids by UGT1A1 displays substrate inhibition.[32,35,36] The mechanisms for substrate inhibition in glucuronidation reactions remain elusive.[32] Nevertheless, the substrate inhibition may be attributable to an allosteric (inhibitory) binding site within the enzyme and/or formation of a ternary dead-end enzyme complex.[32] The substrate inhibition kinetics can be used to explain why the excretion rates of GG decreased as the loading dose of genistein increased (Figure 4A). The loading dose ranged from 1.25 to 20 nmol, corresponding to an incubation concentration range of 0.625−10 μM. Within the range of 0.625−10 μM, the rate of glucuronidation decreased with an increase in the substrate concentration (Figure 3A). Likewise, a decrease in the rate of AG excretion when loading apigenin was increased from 5 to 20 nmol (i.e., from 2.5 to 10 μM in terms of incubation concentration) can be well explained by the substrate inhibition kinetics wherein the glucuronidation rate at 10 μM was smaller than that at 2.5 μM (Figures 5A and 3B).

In vitro protein binding assays showed that genistein and apigenin bound significantly to cell lysate at a high protein concentration of 0.4 mg/mL, indicating that intracellular binding of the two compounds to proteins may be substantial (Figure 2). This was well consistent with the low values of derived fu values (0.040 and 0.023 for genistein and apigenin, respectively) from pharmacokinetic modeling (Table 1). On the other hand, the derived kinetic parameters for glucuronidation reactions were not corrected using protein binding (Figure 3). This was because binding of the aglycones (log P = 1.7−2.7) to cell lysate (at a low protein concentration of 26.5 μg/mL) in the glucuronidation assays was negligible (fu > 0.99) based on the Hallifax and Houston model. This model has been shown to accurately predict the fu values for the compounds with intermediate lipophilicity.[37]

Flavonoids are a large class of compounds with many types of health benefits such as anticancer and anti-inflammatory effects.[38−40] However, extensive glucuronidation is a significant barrier to the bioavailability of flavonoids, limiting their therapeutic uses. Therefore, a better understanding of the factors that govern glucuronidation of flavonoids would contribute to solving the problem of low bioavailability. The current study and our previous ones showed that reduced glucuronidation of flavonoids was attained by inhibiting exporter activity and decreasing exporter expression.[26,27] Hence, it represented a promising approach to modulate the bioavailability of flavonoids by manipulating the activities of efflux transporters such as MRP4.

Disposition of genistein and apigenin in HeLa1A1 cells (and MRP4 knocked-down cells) was adequately characterized by the two-compartment pharmacokinetic model (Figure 1). The pharmacokinetic model assumed that the aglycones passed the cell membranes freely by passive diffusion. This assumption was valid as passive diffusion was the predominant mechanism for transport of the two flavonoids.[41,42] The model also assumed that efflux of glucuronides followed a linear (nonsaturable) kinetics described by the first-order rate constant K_{ef}. The linear transport kinetics appeared to be valid because saturation of the efflux transporters was not observed for intracellular glucuronides of up to 60 pmol/mg protein (data not shown). In addition, protein binding of glucuronides was not considered (i.e., $f_{u,g}$ = 1) in data fitting; this was reasonable as binding of

DOI: 10.1021/acs.jafc.5b00983
J. Agric. Food Chem. 2015, 63, 6001−6008

polar glucuronides to cellular proteins was negligible or nonexistent.

Knock-down of the efflux transporter MRP4 leading to reduced glucuronidation of flavonoids represented one aspect of glucuronidation−efflux interplay, as also noted previously.[27] In the current study, we provided the first experimental evidence that the futile recycling (deglucuronidation) enabled by GUSB was necessary for this interplay of glucuronidation with glucuronide efflux to occur. Futile recycling appeared to bridge the two processes (i.e., glucuronide formation and excretion), making the interplay of glucuronidation−efflux feasible.[19] Impaired glucuronide efflux (due to decreased transporter expression) led to an elevation in the intracellular level of glucuronide (Figures 8 and 9). A rise in intracellular glucuronide was associated with an increase in the rate of futile recycling according to the first-order kinetics (the conversion rate = K_{de} × intracellular glucuronide) (Figure 1). As a consequence, total formation of glucuronide was altered (i.e., reduced) in the cells. On the contrary, in the absence of futile recycling, glucuronide formation was independent of its downstream process excretion; thus, impact of glucuronide excretion on its formation was impossible.[19]

Use of HeLa1A1 cells (and transporter knock-down cell lines) for glucuronide transport studies was more advantageous compared to the membrane vesicles or the monolayer cells (e.g., MDCK) overexpressing a single transporter. This was because the HeLa1A1 cells expressing an array of transporters were a closer mimic of the in vivo situations. In addition, synthesis of glucuronide (lacking in commercial availability) was avoided as glucuronide can be generated from dosed aglycone by the cells. Moreover, the HeLa1A1 cells were free of concerns raised in identification studies of glucuronide transporters using membrane vesicle or monolayer cells.[22] First, drug glucuronides poorly cross cellular membranes by passive diffusion. Therefore, use of polarized monolayers (expressing a transporter) with administration of glucuronide can be problematic. This was because the glucuronide will not enter the cells.[22] Second, studies with inside-out vesicles are time-consuming and challenging.[22]

In summary, glucuronidation of two flavonoids (i.e., genistein and apigenin) and excretion of their glucuronides were investigated using HeLa1A1 cells. Glucuronidation of these two flavonoids by cell lysate consistently followed substrate inhibition kinetics. GG or AG was efficiently generated and excreted after incubation of the aglycone with the cells. Knock-down of MRP4 resulted in a substantial reduction in the excretion of GG and AG. A significant reduction was also observed for cellular glucuronidation of genistein and apigenin. The alterations in glucuronide excretion and cellular glucuronidation were well characterized by a two-compartment pharmacokinetic model incorporating the process of futile recycling. This study provided the first experimental evidence that the effect of glucuronide efflux on total glucuronidation was through a futile recycling mechanism.

AUTHOR INFORMATION

Corresponding Author

*(B.W.) Phone: (+86) 020-8522-0482. Fax: (+86) 020-8522-0482. E-mail: bj.wu@hotmail.com.

Author Contributions

‖H.S. and X.Z. contribute equally to this work.

Funding

This work was supported by the Natural Science Foundation of Guangdong Province (Grant 2014A030306014).

Notes

The authors declare no competing financial interest.

ABBREVIATIONS USED

BCRP/Bcrp	breast cancer resistance protein
DMEM	Dulbecco's modified Eagle's medium
FBS	fetal bovine serum
$f_{u\text{-}max}$	maximal fraction unbound
GUSB	β-glucuronidase
K_m	Michaelis−Menten constant;
K_s	concentration of genistein at half $f_{u\text{-}max}$
K_{si}	substrate inhibition constant;
MRP	multidrug resistance-associated protein
MS	mass spectroscopy
P-gp	P-glycoprotein
QTOF	quadrupole time-of-flight
UDPGA	uridine diphosphoglucuronic acid
UGT	UDP-glucuronosyltransferase
UPLC	ultra performance liquid chromatography
V_{max}	maximal velocity

REFERENCES

(1) Kola, I.; Landis, J. Can the pharmaceutical industry reduce attrition rates? *Nat. Rev. Drug Discovery* **2004**, *8*, 711−716.

(2) Costa, A.; Sarmento, B.; Seabra, V. An evaluation of the latest in vitro tools for drug metabolism studies. *Expert Opin. Drug Metab. Toxicol.* **2014**, *1*, 103−119.

(3) Ingle, J. N.; Buzdar, A. U.; Schaid, D. J.; Goetz, M. P.; Batzler, A.; Robson, M. E.; Northfelt, D. W.; Olson, J. E.; Perez, E. A.; Desta, Z.; Weintraub, R. A.; Williard, C. V.; Flockhart, D. A.; Weinshilboum, R. M. Variation in anastrozole metabolism and pharmacodynamics in women with early breast cancer. *Cancer Res.* **2010**, *8*, 3278−3286.

(4) Reinhardt, D.; Berdel, D.; Heimann, G.; Kusenbach, G.; von Berg, A.; Johnson, E.; Steinijans, V. W.; Staudinger, H. Steady state pharmacokinetics, metabolism and pharmacodynamics of theophylline in children after unequal twice-daily dosing of a new sustained-release formulation. *Chronobiol. Int.* **1987**, *3*, 369−380.

(5) Ortiz de Montellano, P. R. *Cytochrome P450: Structure, Mechanism, and Biochemistry*; Kluwer Academic/ Plenum: New York, 2005.

(6) Jancova, P.; Anzenbacher, P.; Anzenbacherova, E. Phase II drug metabolizing enzymes. *Biomed. Pap.* **2010**, *2*, 103−116.

(7) Tang, L.; Zhou, J.; Yang, C. H.; Xia, B. J.; Hu, M.; Liu, Z. Q. Systematic studies of sulfation and glucuronidation of 12 flavonoids in the mouse liver S9 fraction reveal both unique and shared positional preferences. *J. Agric. Food Chem.* **2012**, *12*, 3223−3323.

(8) Wells, P. G.; Mackenzie, P. I.; Chowdhury, J. R.; Guillemette, C.; Gregory, P. A.; Ishii, Y.; Hansen, A. J.; Kessler, F. K.; Kim, P. M.; Chowdhury, N. R.; Ritter, J. K. Glucuronidation and the UDP-glucuronosyltransferases in health and disease. *Drug Metab. Dispos.* **2004**, *3*, 281−290.

(9) Evans, W. E.; Relling, M. V. Pharmacogenomics: translating functional genomics into rational therapeutics. *Science* **1999**, *5439*, 487−491.

(10) Rowland, A.; Miners, J. O.; Mackenzie, P. I. The UDP-glucuronosyltransferases: their role in drug metabolism and detoxification. *Int. J. Biochem. Cell Biol.* **2013**, *6*, 1121−1132.

(11) Tukey, R. H.; Strassburg, C. P. Human UDP-glucuronosyltransferases: metabolism, expression, and disease. *Annu. Rev. Pharmacol. Toxicol.* **2000**, *40*, 581−616.

(12) Nagar, S.; Blanchard, R. L. Pharmacogenetics of uridine diphosphoglucuronosyltransferase (UGT) 1A family members and its

DOI: 10.1021/acs.jafc.5b00983
J. Agric. Food Chem. 2015, 63, 6001−6008

role in patient response to irinotecan. *Drug Metab. Rev.* **2006**, *3*, 393−409.
(13) Higgins, C. F. ABC transporters: physiology, structure and mechanism − an overview. *Res. Microbiol.* **2001**, *3*−*4*, 205−210.
(14) Russel, F. G.; Koenderink, J. B.; Masereeuw, R. Multidrug resistance protein 4 (MRP4/ABCC4): a versatile efflux transporter for drugs and signalling molecules. *Trends Pharmacol. Sci.* **2008**, *4*, 200−207.
(15) DeGorter, M. K.; Xia, C. Q.; Yang, J. J.; Kim, R. B. Drug transporters in drug efficacy and toxicity. *Annu. Rev. Pharmacol. Toxicol.* **2012**, *52*, 249−273.
(16) Giacomini, K. M.; Huang, S. M.; Tweedie, D. J.; Benet, L. Z.; Brouwer, K. L.; Chu, X.; Dahlin, A.; Evers, R.; Fischer, V.; Hillgren, K. M.; Hoffmaster, K. A.; Ishikawa, T.; Keppler, D.; Kim, R. B.; Lee, C. A.; Niemi, M.; Polli, J. W.; Sugiyama, Y.; Swaan, P. W.; Ware, J. A.; Wright, S. H.; Yee, S. W.; Zamek-Gliszczynski, M. J.; Zhang, L. Membrane transporters in drug development. *Nat. Rev. Drug Discovery* **2010**, *3*, 215−236.
(17) Homolya, L.; Váradi, A.; Sarkadi, B. Multidrug resistance-associated proteins: export pumps for conjugates with glutathione, glucuronate or sulfate. *BioFactors* **2003**, *1*−*4*, 103−114.
(18) Siissalo, S.; Laine, L.; Tolonen, A.; Kaukonen, A. M.; Finel, M.; Hirvonen, J. Caco-2 cell monolayers as a tool to study simultaneous phase II metabolism and metabolite efflux of indomethacin, paracetamol and 1-naphthol. *Int. J. Pharm.* **2010**, *1*−*2*, 24−29.
(19) Wu, B. Pharmacokinetic interplay of phase II metabolism and transport: a theoretical study. *J. Pharm. Sci.* **2012**, *1*, 381−393.
(20) Jeong, E. J.; Liu, X.; Jia, X.; Chen, J.; Hu, M. Coupling of conjugating enzymes and efflux transporters: impact on bioavailability and drug interactions. *Curr. Drug Metab.* **2005**, *5*, 455−468.
(21) van de Wetering, K.; Zelcer, N.; Kuil, A.; Feddema, W.; Hillebrand, M.; Vlaming, M. L.; Schinkel, A. H.; Beijnen, J. H.; Borst, P. Multidrug resistance proteins 2 and 3 provide alternative routes for hepatic excretion of morphine-glucuronides. *Mol. Pharmacol.* **2007**, *2*, 387−394.
(22) Fahrmayr, C.; König, J.; Auge, D.; Mieth, M.; Fromm, M. F. Identification of drugs and drug metabolites as substrates of multidrug resistance protein 2 (MRP2) using triple-transfected MDCK-OATP1B1-UGT1A1-MRP2 cells. *Br. J. Pharmacol.* **2012**, *6*, 1836−1847.
(23) Zamek-Gliszczynski, M. J.; Hoffmaster, K. A.; Humphreys, J. E.; Tian, X.; Nezasa, K.; Brouwer, K. L. Differential involvement of Mrp2 (Abcc2) and Bcrp (Abcg2) in biliary excretion of 4-methylumbelliferyl glucuronide and sulfate in the rat. *J. Pharmacol. Exp. Ther.* **2006**, *1*, 459−467.
(24) Zamek-Gliszczynski, M. J.; Day, J. S.; Hillgren, K. M.; Phillips, D. L. Efflux transport is an important determinant of ethinylestradiol glucuronide and ethinylestradiol sulfate pharmacokinetics. *Drug Metab. Dispos.* **2011**, *10*, 1794−1800.
(25) Chen, Z. S.; Lee, K.; Kruh, G. D. Transport of cyclic nucleotides and estradiol 17-β-D-glucuronide by multidrug resistance protein 4. Resistance to 6-mercaptopurine and 6-thioguanine. *J. Biol. Chem.* **2001**, *36*, 33747−33754.
(26) Quan, E.; Wang, H.; Dong, D.; Zhang, X.; Wu, B. Characterization of chrysin glucuronidation in UGT1A1-overexpressing HeLa cells: elucidating the transporters responsible for efflux of glucuronide. *Drug Metab. Dispos.* **2015**, *4*, 433−443.
(27) Zhang, X.; Dong, D.; Wang, H.; Ma, Z.; Wang, Y.; Wu, B. Stable Knock-down of Efflux Transporters Leads to Reduced Glucuronidation in UGT1A1-Overexpressing HeLa Cells: The Evidence for Glucuronidation-Transport Interplay. *Mol. Pharmaceutics* **2015**, *4*, 1268−1278.
(28) Liu, H.; Wu, Z.; Ma, Z.; Wu, B. Glucuronidation of macelignan by human liver microsomes and expressed UGT enzymes: identification of UGT1A1 and 2B7 as the main contributing enzymes. *Biopharm. Drug Dispos.* **2014**, *9*, 513−524.
(29) Liu, H.; Sun, H.; Lu, D.; Zhang, Y.; Zhang, X.; Ma, Z.; Wu, B. Identification of glucuronidation and biliary excretion as the main mechanisms for gossypol clearance: in vivo and in vitro evidence. *Xenobiotica* **2014**, *8*, 696−707.
(30) Fu, J.; Liu, H.; Xing, H.; Sun, H.; Ma, Z.; Wu, B. Comparative analysis of glucuronidation of ethanol in treeshrews, rats and humans. *Xenobiotica* **2014**, *12*, 1067−1073.
(31) Sun, H.; Wang, H.; Liu, H.; Zhang, X.; Wu, B. Glucuronidation of capsaicin by liver microsomes and expressed UGT enzymes: reaction kinetics, contribution of individual enzymes and marked species differences. *Expert Opin. Drug Metab. Toxicol.* **2014**, *10*, 325−336.
(32) Wu, B. Substrate inhibition kinetics in drug metabolism reactions. *Drug Metab. Rev.* **2011**, *4*, 440−456.
(33) Hutzler, J. M.; Tracy, T. S. Atypical kinetic profiles in drug metabolism reactions. *Drug Metab. Dispos.* **2002**, *4*, 355−362.
(34) Sun, H.; Zhang, T.; Wu, Z.; Wu, B. Warfarin is an effective modifier of multiple UDP-glucuronosyltransferase enzymes: evaluation of its potential to alter the pharmacokinetics of zidovudine. *J. Pharm. Sci.* **2015**, *1*, 244−256.
(35) Tang, L.; Singh, R.; Liu, Z.; Hu, M. Structure and concentration changes affect characterization of UGT isoform-specific metabolism of isoflavones. *Mol. Pharmaceutics* **2009**, *5*, 1466−1482.
(36) Wu, B.; Xu, B.; Hu, M. Regioselective glucuronidation of flavonols by six human UGT1A isoforms. *Pharm. Res.* **2011**, *8*, 1905−1918.
(37) Gao, H.; Steyn, S. J.; Chang, G.; Lin, J. Assessment of in silico models for fraction of unbound drug in human liver microsomes. *Expert Opin. Drug Metab. Toxicol.* **2010**, *5*, 533−542.
(38) Benavente-García, O.; Castillo, J. Update on uses and properties of citrus flavonoids: new findings in anticancer, cardiovascular, and anti-inflammatory activity. *J. Agric. Food Chem.* **2008**, *56*, 6185−6205.
(39) Kamiyama, M.; Shibamoto, T. Flavonoids with potent antioxidant activity found in young green barley leaves. *J. Agric. Food Chem.* **2012**, *60*, 6260−6267.
(40) Friedman, M. Antibacterial, antiviral, and antifungal properties of wines and winery byproducts in relation to their flavonoid content. *J. Agric. Food Chem.* **2014**, *62*, 6025−6042.
(41) Hu, M.; Chen, J.; Lin, H. Metabolism of flavonoids via enteric recycling: mechanistic studies of disposition of apigenin in the Caco-2 cell culture model. *J. Pharmacol. Exp. Ther.* **2003**, *1*, 314−321.
(42) Liu, Y.; Hu, M. Absorption and metabolism of flavonoids in the caco-2 cell culture model and a perused rat intestinal model. *Drug Metab. Dispos.* **2002**, *4*, 370−377.

DOI: 10.1021/acs.jafc.5b00983
J. Agric. Food Chem. 2015, 63, 6001−6008

antagonistic mechanism, can satisfy long-term concerns over food safety and the environment in the mushroom industry.

The objectives of this study were to search for a new biological control agent against mushroom red bread mold disease from the *A. bisporus* mushroom cultivation substrate obtained from a commercial mushroom operation and to isolate and investigate the biological properties of the antimicrobial lipopeptide from the antagonistic *Bacillus* sp. strain.

MATERIALS AND METHODS

Fungi. The pathogenic fungus strain M21 (*N. sitophila*) was isolated from a contaminated *A. bisporus* compost-based cultivation substrate in a commercial *Agricus* mushroom factory in Shandong, China. Primers ITS1 (5′- TCCGTAGGTGAACCTGCGC-3′) and ITS4 (5′- TCCTCCGCTTATTGATATGC-3′) were used to amplify the internal transcribed space regions (ITS) of 18S rDNA sequences of M21.[15] PCR sequences were aligned and compared with those available in the GenBank database using the BLAST program.[16] Then the homology of the sequence was determined. A phylogenetic tree was constructed according to the neighbor-joining method using MEGA 4.0 based on the 18S rDNA sequence. Nucleotide sequence data for the pathogenic fungus have been submitted to GenBank database under accession number KM588213.

The fungi *Trichoderma harzianum* (ACCC30371), *Fusarium solani* (ACCC36223), *F. graminearum* (ACCC37686), *Botrytis cinerea* (ACCC36028), and *F. incarnatum* (CFCC 84580) were supplied by the Agricultural Culture Collection of China and the China Forestry Culture Collection Center.

Bacteria. A total of 600 colonies of bacteria were separated from *A. bisporus* mushroom composts by the serial dilution method.[17] Bacteria thus isolated were tested for their antifungal activity against the pathogenic fungus *N. sitophila* M21.

The bacterium B154, one of the antifungal strains, was characterized using the API 50 CHB system (BioMerieux, Marcy l'Etoile, France). Microscopic observation and biochemical features were tested as described previously.[18,19] To confirm biochemical identification, a partial sequence analysis of the 16S rDNA was performed. PCR amplification of the 16S rDNA gene of strain B154 with universal forward (5′-AGAGTTTGATCCTGGCTCAG-3′) and reverse (5′-GGCTACCTTGTTACGACTT-3′) primers was carried out.[20] The 16S sequence for B154 was deposited in GenBank (KM588212). A neighbor-joining tree was constructed based on the 16S rDNA sequences of bacterial strains. A *gyrA* fragment corresponding to *Bacillus subtilis gyrA* positions 42 to 1066 was PCR amplified by using primers *gyrA*-forward (5′-CAGTCAGGAAATGCGTACGTCCTT-3′) and *gyrA*-reverse (5′-CAAGGTAATGCTCCAGGCATTGCT-3′).[21] The *gyrA* sequence for B154 was deposited in GenBank (KR296983).

In Vitro Antagonism Experiments. The ability of the B154 strain to inhibit the growth of various fungal pathogens was tested in Petri dishes containing a potato dextrose agar (PDA) medium. The mycelial plugs of *N. sitophila*, *T. harzianum*, *F. incarnatum*, *F. solani*, *F. graminearum*, and *B. cinerea* were cultivated in the center of the plates at 28 °C, and the bacteria were inoculated on the edges. The slow growth fungi were inoculated on the plate 24−48 h prior to the bacteria. The inhibition of fungal growth was evaluated by the percentage of reduction of mycelium expansion compared to control plates without bacteria. The mycelial growth inhibition (MGI) percentage was calculated according to the equation MGI = $(A_0 - A_1)/A_0 \times 100$, where A_0 is the area of mycelium on control plates and A_1 is the area of mycelium on plates inoculated with B154.[22] The antagonism assay was conducted three times, and all treatments in each assay contained three replicates.

Selection of the Best Medium for Production of Antifungal Activity. To select the best culture medium for optimal production of antifungal activity, several broth media were tested: tryptic soya broth (TSB), Luria−Bertani broth (LB), nutrient broth (NB), and tryptic yeast (TY).[23] Incubation was performed at 30 °C with shaking at 150 rpm/min for 24 h. Cell growth was monitored by optical density measurement at 600 nm, and any secreted antifungal activity found in the culture supernatant was described by the diameter of the clear zone.

Fermentation and Kinetic Production of Antifungal Compounds. Bacterial fermentation was carried out in a gyratory shaker (150 rpm/min) at 30 °C. Antifungal activity was detected after incubating the producer strain in TSB medium for 56 h. We collected 10 mL of the culture at an interval of 4 h for the determination of cell growth, and the anti-*N. sitophila* activity in the supernatant was obtained by measuring the diameter of the clear zone. The pH of the medium was monitored regularly throughout the culture period.[24]

Antifungal Activity of the Compound. The activity of the antifungal compound produced by B154 was measured by the disc diffusion assay on all purification extracts and by using high-performance liquid chromatography (HPLC) fractions to determine where the antifungal compounds were eluted.[25] Arbitrary units (AU) of antifungal activity were calculated by the reciprocal of the highest dilution showing inhibition per milliliter of antifungal compound fraction. The antagonism assay was conducted three times, and all treatments in each assay contained three replicates.

Isolation and Purification of Antifungal Compound by Ion Exchange Chromatography. The antifungal compound was recovered by 20% ammonium sulfate precipitation of the B154 culture supernatant.[12] The precipitate was collected and dialyzed by distilled water in 3.5 kDa dialysis tubing. The resulting solution was concentrated by lyophilization, and the solid was dissolved in sterile milli-Q water to obtain the crude bioactive substance (1.0 mg/mL).

The crude extract (10 mL) was loaded onto a DEAE-Sephadex A50 (1.5 cm × 15 cm i.d.) column (GE Healthcare, Uppsala, Sweden) previously equilibrated with Tris-HCl buffer (25 mM, pH 8.0). A gradient of 0−1 M NaCl in buffer was run through the column at 0.5 mL/min.[26] The eluent was monitored at 280 nm using an HD5 spectrophotometer (Huxi Analysis, Shanghai, China), and fractions were collected every 5 min. All samples were assayed for antifungal activity, and the antifungal fractions were collected and concentrated by ultrafiltration with an Ultra-15 centrifugal filter concentrator (Millipore, Darmstadt, Germany).

Ultraviolet Spectrum. The ultraviolet absorption spectrum of the antibiotic collected from the ion exchange column was measured using a UV-1800 recording spectrophotometer (Shimadzu, Kyoto, Japan) from 200 to 600 nm.[27]

Detection of Antifungal Activity in Tricine-SDS-PAGE Gel. Tricine sodium dodecyl sulfate-polyacrylamide gel electrophoresis (Tricine-SDS-PAGE) was performed with active fractions from each purification step using a Mini Protean tetra cell vertical gel electrophoresis unit (Bio-Rad, Hercules, CA).[25] TSB medium, culture supernatant, dialyzed 20% ammonium sulfate fraction, and the antifungal fraction that had been purified by ion exchange chromatography were loaded onto the gel; ultra low molecular weight protein markers (Sigma-Aldrich, St Louis, MO) were used for size reference.

After electrophoresis, three duplicate gels were fixed in 500 mL of 50% (v/v) methanol/10% (v/v) acetic acid for 30 min and stained with 0.025% Coomassie brilliant blue G-250 (Bio-Rad, Hercules, CA) in 10% acetic acid/45% ethanol.

pH and Heat Stability. The concentrated antifungal fractions collected from ion exchange column were filter-sterilized using 0.22 μm filters (Millipore, Darmstadt, Germany) and lyophilized. Each aliquot was dissolved in 200 μL of buffer within the range of pH 2−12 adjusted with diluted HCl or NaOH. After incubation for 2 h at 25 °C and neutralization to pH 7, residual activity against *N. sitophila* was tested.

We evaluated thermal stability after incubation of antifungal fractions at different temperatures for 30 min or after autoclaving at 121 °C for 20 min. After the samples were cooled at room temperature, we quantitated residual inhibitory antifungal activity.

Effect of Proteolytic Enzymes. The effect of the proteolytic enzymes proteinase K, pepsin, trypsin, and papain on antifungal activity was investigated. Enzymes were dissolved in Tris-HCl buffer

DOI: 10.1021/acs.jafc.5b02218
J. Agric. Food Chem. 2015, 63, 6009−6018

(50 mM, pH 7.8) and were added to the antifungal fraction at a mass ratio of 1:10 and 1:5. After incubation at 37 °C for 2 h, solutions were incubated at 90 °C for 5 min and cooled at room temperature. The residual antifungal activity in the supernatant was tested. The untreated antifungal fraction and the enzymes alone in buffer were used as controls.

Conidial Germination Inhibition Assays. We examined the inhibitory effect of the purified antifungal fractions on conidial spore germination of *N. sitophila*.[28,29] The antifungal fractions were serially diluted with PDA to a final concentration of 30, 20, or 10 μg/mL. Sterile phosphate buffer (20 mM, pH 6.8) was used as a control. A 10 mL sample of the mixture was added into Petri dishes, and the *N. sitophila* spore suspension at a concentration of 10^5 cfu/mL was prepared and inoculated by spreading in the Petri dishes. After 6 h of incubation at 25 °C, the plates were observed by optical microscopy. When the length of the germ tube was longer than the radius of the spore, the spore was rated as germinated. At least 200 spores were counted on each plate. Each treatment was conducted in triplicate, and the experiments were repeated twice. The relative germination inhibition (RI) of the treatment compared to the control was calculated by percentage, using the following formula:

$$RI = (N_0 - N) \times 100/N_0$$

where RI is the relative inhibition, N_0 the number of germinated spores on the control plates, and N the number of germinated spores on the treatment plates.

Slices of pathogenic fungal spores were dyed by lactophenol cotton blue and observed using a B203 LED microscope (Optec instrument, Chongqing, China).

SEM Analyses. The effect of antifungal extracts from B154 on *N. sitophila* hyphae and spores was examined by scanning electron microscopy (SEM).[10] The antifungal fractions were diluted with potato dextrose broth (PDB) to a final concentration of 30 μg/mL. Spore suspension (10^5 cfu/mL) and the hyphae were added to the PDB medium. After incubation at 28 °C for 24 h in a shaker at 50 rpm/min, the spore and hyphae were harvested for SEM. Samples were sputter-coated with gold palladium in an IB-3 nanotech sputter-coating apparatus (EIKO, Osaka, Japan) and then examined using an S-3400N SEM (Hitachi, Tokyo, Japan).

Antifungal Activity of Bacteria B154 on *A. bisporus* Mushrooms. We studied the in vivo effect of the antifungal bacterium B154 against the pathogen fungus *N. sitophila* in the mushroom beds and recorded the associated yields of *A. bisporus*. The experimental cultivation trials of *A. bisporus* were conducted at the JiuFa Mushroom Test Demonstration Factory in cooperation with China Agricultural University. Suspensions of the fungus *N. sitophila* (10^3 cfu/mL) were mixed with the spawned compost (1 L suspension/m^2 of compost) on mushroom beds. One liter each of B154 fermentation broth (fermented for 24, 48, or 72 h) was mixed thoroughly with compost to inhibit the fungal pathogen. For comparison, there were two controls. In one control, only the pathogen fungus was mixed with compost (negative control); in the other (positive control), neither the pathogen nor the antagonistic bacteria B154 was used. Closed mushrooms were harvested, counted, and weighed daily. At the end of the third flush, yields were determined and expressed as kilograms per square meter. Each treatment was replicated three times, and these experiments were repeated twice.

Purification of Antifungal Active Compounds. The antifungal compounds collected through the DEAE-Sephadex A50 column from *B. subtilis* B154 were purified by a 1200 series HPLC system (Agilent Technologies, Wilmington, DE) using a ODS-A reverse phase (RP) C18 column, 4.6 mm × 250 mm i.d., 120 A (YMC, Allentown, PA) with a linear gradient elution of deionized water and acetonitrile.[30] Mobile phase: 0.05% trifluoroacetic acid water solution (A), acetonitrile (B). Flow rate: 0.8 mL/min. Gradient program: 30% B in 0−5 min; 30−45% B in 5−10 min; 45−80% B in 10−60 min; 80−100% B in 60−80 min; 100% B in 80−90 min. This step was repeated several times, and peaks with the same retention time were collected for determination of activity. The final active collection was dried, weighed, and used for studies of chemical characterization.

Analysis of Antifungal Conpound by MALDI-TOF MS Analysis. The HPLC-purified compound was analyzed on a 4800 Plus matrix-associated laser desorption ionization time-of-flight mass spectrometry (MALDI-TOF-MS) system (Applied Biosystems, Foster, CA).[31,32] For MALDI-TOF-MS analysis, HPLC fractions extracted from *B. subtilis* B154 were mixed with α-cyano-4-hydroxycinnamic acid (α-CHCA) saturated in 50% (v/v) acetonitrile containing 0.1% trifluoroacetic acid in equal amounts, applied to the MALDI sample plate, and left to air-dry.

ESI-MS/MS Analysis. Electrospray ionization tandem mass spectrometry (ESI-MS/MS) analysis of antifungal compound was performed on a SYNAPT G2-Si quadrupole time-of-flight (Q-TOF) mass spectrometry system (Waters MS Technologies, Manchester, UK).[31,33] MS survey scans in a mass range of m/z 100−2000 and of 30 s duration were run. The electrospray source was operated at a spray cone voltage of 80 V, a capillary voltage of 3 kV, and a source temperature of 100 °C. For the ESI experiment, the nanoflow gas pressure was set at the 0.5 bar, and the purge gas flow was set at 10 mL/min. Helium was used as the collision gas.

Statistical Analysis. All data were presented as the mean ± standard deviation (SD). One-way analysis of variance (ANOVA) and Duncan's multiple range tests were used to determine significant differences ($p < 0.05$) between the means using the statistical software SPSS 18.0 (IBM Corp., Armonk, NY).

RESULTS AND DISCUSSION

Identification of Pathogenic Fungus M21 and Antifungal Bacterium B154. The BLAST results based on the ITS sequence showed M21 had the highest similarity (100%) with *Neurospora sitophila* (GU192459.1) The phylogenetic tree constructed based on the ITS sequence indicated M21 closely clustered with *N. sitophila* as well. Mycelium of M21 was white and villiform (Figure 1A). After growing on PDA medium for 3

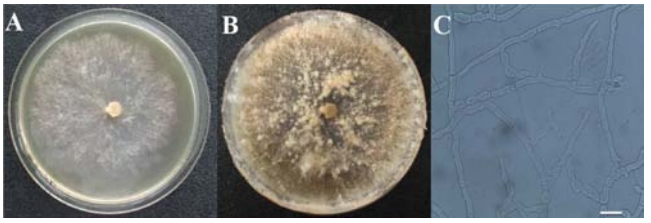

Figure 1. Colonial morphology (A), spore (B), and hyphal characteristics (C) of *N. sitophila* M21. Mycelia of *N. sitophila* M21 were amplified 40 times. Scale bar is 20 μm.

d, several orange spores formed (Figure 1B). M21 mycelium amplified 40 times showed that the diameter of its hypha was about 10−12 μm, and many hypha branches formed (Figure 1C). The combination of colony traits, mycelium morphological traits, and molecular characteristics allowed us to identify pathogenic fungus M21 as *N. sitophila*. The red bread mold (*N. sitophila*) is one of the major diseases threatening mushroom production.[3,34] *N. sitophila* became epidemic rapidly, when the room temperature and humidity were relatively high, leading to inhibition of primordial formation and reduction in yield.

Strain B154 isolated from the *A. bisporus* mushroom compost had the highest activity against the strain M21 (Figure 2A). Therefore, strain B154 was used in the subsequent investigation. The colonies of bacterial strain B154 were white, and its morphology was irregular (Figure 2B). A preliminary identification of this strain through phenotypical and

DOI: 10.1021/acs.jafc.5b02218
J. Agric. Food Chem. 2015, 63, 6009−6018

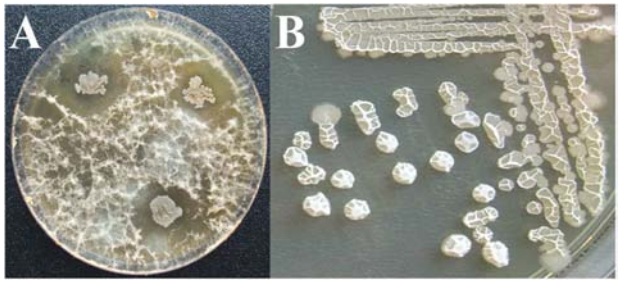

Figure 2. Growth inhibition of *N. sitophila* by the bacterial strain B154 (A) and the morphology of the colonies of B154 (B).

biochemical characteristics showed that this isolate belonged to the genus *Bacillus*. It is a Gram-positive bacillus, motile spore-forming organism and is catalase- and oxidase-positive. The tests of hydrogen sulfide, indole production, and Voges–Proskauer were positive. The use of an API 50 CHB kit with the APILAB Plus software indicated 99.6% identity with *B. subtilis*.

The BLAST results indicated that strain B154 had 100% similarity with *Bacillus subtilis* (NCDO1769) according to the sequence of the 16S rDNA gene. Phylogenetic trees constructed based on the 16S rDNA gene also indicated that B154 closely clustered with *B. subtilis*.

Because strain B154 identified as *B. subtilis* group on the basis of 16S rDNA sequence analysis is not satisfactory, we applied another method to obtain more reliable species identification. We performed *gyrA* sequencing preliminarily identified as *B. subtilis* on the basis of 16S rDNA sequencing. Cluster analysis of the *gyrA* sequence of B154 with those from the study of Chun and Bae[35] showed that strain B154 was identified as *B. subtilis* subsp. *subtilis*.

Antifungal Activity Spectrum. When tested in vitro against two fungal species of mushroom pathogens (*N. sitophila* and *T. harzianum*) and four phytopathogens (*F. incarnatum*, *F. solani*, *F. graminearum*, and *B. cinerea*), *B. subtilis* strain B154 could inhibit the mycelia growth of all of the fungi (Table 1).

Table 1. Antagonism Developed by *B. subtilis* Strain B154 on PDA Plates Against Various Fungal Pathogens

fungal pathogen	MGI (%)[a]
Neurospora sitophila	7.5 ± 0.4
Trichoderma harzianum	26.7 ± 0.6
Fusarium incarnatum	4.3 ± 0.2
Fusarium solani	7.1 ± 0.5
Fusarium graminearum	7.6 ± 0.3
Botrytis cinerea	38.3 ± 0.4

[a]MGI: relative mycelia growth inhibition percentage per bacterial colony. Data are expressed as the mean ± SD, $n = 9$.

The MGI of B154 on *N. sitophila* was 7.5%, and the MGI on *T. harzianum* was 26.7%. *B. subtilis* had inhibitory ability against various plant fungal pathogens, such as *Fusarium oxysporum*, *Exserohilum turcicum*,[12] and *Alternaria alternate*.[30] Our study indicated that strain B154 isolated from *A. bisporus* mushroom compost provided a broad spectrum of antifungal activities against both plant and mushroom pathogenic fungi; thus, it would be a potential effective alternative to chemical fungicides, especially in the mushroom industry.

Kinetic Production of the Antifungal Activity in the Optimized Medium. The antagonism potential of B154 could play a major role in biocontrol because of the production of antifungal compounds. Variation in the composition of the culture medium was shown previously to affect the production of antimicrobial activity.[23,36] The production of antifungal activity by strain B154 was tested in various media (Figure 3A).

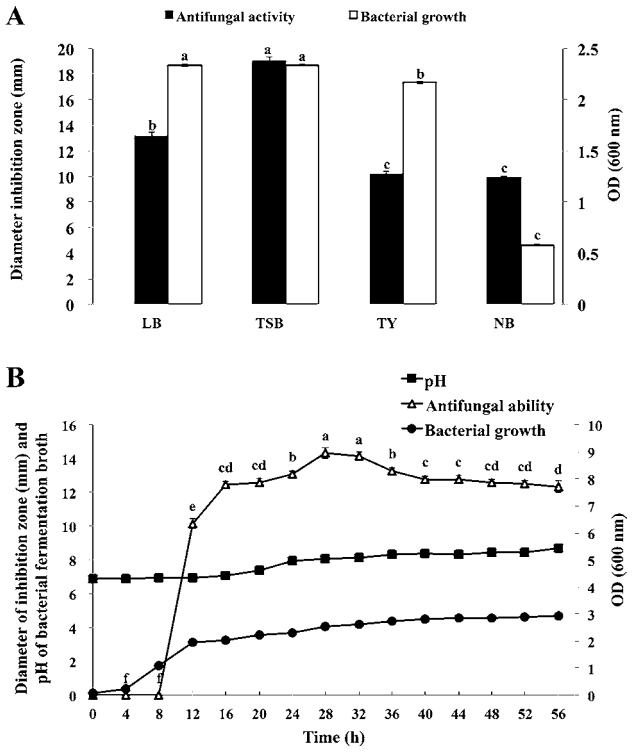

Figure 3. Effect of various growth media (A) and the kinetic study (B) of biomass and antifungal activity produced by *Bacillus* strain B154. Bacterial growth was evaluated by optical density measurement at 600 nm. Antifungal activity against *N. sitophila* was expressed as the diameter of the inhibition zone (in millimeters). Columns in the graph marked by different lower case letters for each mean are significantly different at $p < 0.05$ using Duncan's multiple-range tests. Data are expressed as mean ± SD of triplicate assays.

The TSB medium allowed maximum biomass accumulation and the highest antifungal activity against *N. sitophila*. The activity obtained by culturing in LB medium dropped significantly compared to TSB medium ($p < 0.05$), while the biomass in these two kinds of media was the same.

Synthesis of antimicrobial compounds by *Bacillus* species generally starts at the end of the exponential phase and reaches its maximum level during the stationary phase.[37,38] During the growth period of B154 in TSB medium, antifungal activity against *N. sitophila* (diameter of inhibition zone was 10.17 mm) was detected during the exponential growth phase (12 h after inoculation), and maximum antifungal activity (inhibition zone was 14.33 mm) was attained during the stationary phase (28 h after inoculation) (Figure 3B). This meant that the bacterium could produce high levels of the bioactive substance within a short period. Medium pH was monitored throughout the experiment and increased from 7 to 8.7 at 56 h.

Ultraviolet Spectrum and Tricine-SDS-PAGE Gel Detection of Antifungal Compound Purified by Ion Exchange Chromatography. Ion exchange chromatography of B154 culture extract on a DEAE-Sephadex A50 column contained one unadsorbed fraction and one adsorbed fraction

DOI: 10.1021/acs.jafc.5b02218
J. Agric. Food Chem. 2015, 63, 6009–6018

(**1** and **2**). Of these fractions, only fraction **2** showed strong antifungal activity (Figure 4A). The antibiotic was eluted from the DEAE-Sephadex matrix in 0.55−0.6 M NaCl.

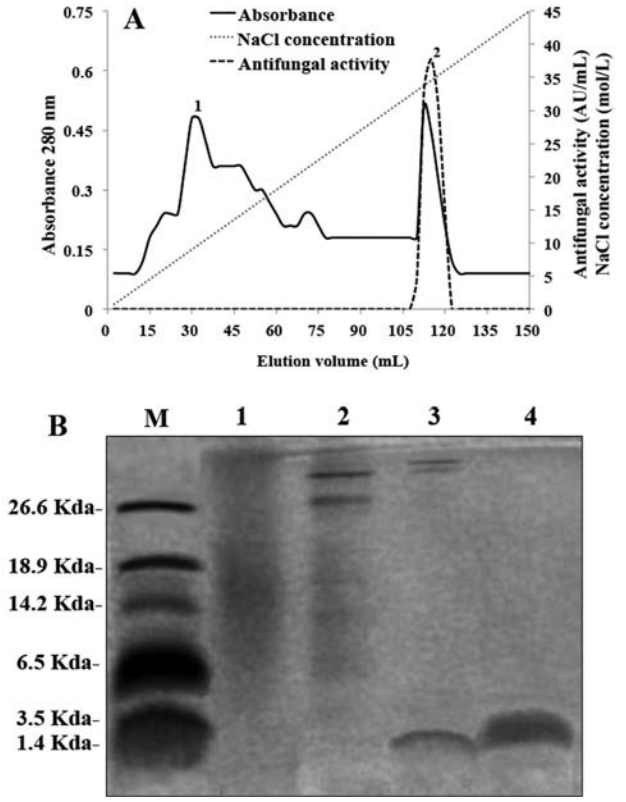

Figure 4. Ion exchange chromatography on a DEAE-Sephadex A50 column (A) and tricine-SDS-PAGE (B) of peptide antibiotic purification fraction. Slanting line across the chromatography indicates linear NaCl concentration gradient (0−0.75 M) employed to elute the adsorbed fractions **1** and **2**. Data are expressed as the mean, $n = 9$. Tricine-SDS-PAGE: (lane M) polypeptide SDS-PAGE standards; (lane 1) TSB medium; (lane 2) culture supernatant; (lane 3) dialyzed 20% ammonium sulfate precipitate; (lane 4) antifungal peptide purified by ion exchange chromatography.

Purification of the biologically active component from the culture medium is summarized in Table 2. The initial 20% ammonium sulfate precipitation yielded 47.2% of the original activity, and 25.5% of the initial activity was recovered by ion exchange chromatography.

Table 2. Yields of Chromatographic Fractions with Antifungal Activity Obtained at Different Stages of Purification from Culture Supernatant of *B. subtilis* B154

	volume (mL)	total protein (mg)	total activity[a] (AU)	activity recovery[b] (%)
culture supernatant	200.0	3712.6 ± 19.7	7522 ± 23.1	−
$(NH_4)_2SO_4$ precipitate	25.0	55.6 ± 2.9	3552.1 ± 53.2	47.2
ion exchange peak	12.5	12.7 ± 0.1	1917.7 ± 38.6	25.5

[a]Activity is expressed as activity units (AU) against *N. sitophila*. [b]Activity recovery indicates the percentage of initial activity. Data are expressed as the mean ± SD, $n = 9$.

The absorbance spectrum for the antibiotic measured in milli-Q water showed absorbance maxima at 236 and 275 nm, and there was no appreciable absorbance above 300 nm. *B. subtilis* is the producer of cyclic lipopeptides, for example, molecules of seven amino acids with a β-fatty acid.[26,39] The ultraviolet spectrum of the antibiotic suggested that our strain might be a producer of cyclic lipopeptides with antifungal activity. The absorbance maximum between 220 and 240 nm was due to the presence of tyrosine.[27]

The active fraction that was purified by ion exchange column, the TSB medium, the culture supernatant, and 20% ammonium sulfate precipitate were loaded onto a tricine gel containing 16.5% separating gel. The active bands were visualized with Coomassie brilliant blue G-250 solution (Figure 4B). Compared to the polypeptide marker, the molecular mass of purified peptide (lane 4) was estimated to be approximately 1.4 kDa. Tricine-SDS-PAGE confirmed the purity of the antibiotic preparation. The culture supernatant (lane 2) produced many bands of stained contaminated material. Evidently, almost all of this contaminated material was removed by the purification protocol (lane 4). Although ion exchange extraction actually decreased antibiotic activity relative to the previous step (ammonium sulfate precipitate) (Table 2), the ion exchange protocol was very effective at eliminating colored material contaminating the sample, and it separated the antibiotic peak from other peaks seen in the chromatogram.

pH, Heat Stability, and Effect of Proteolytic Enzymes on Antifungal Peptide. The antifungal activity of the purified peptide from the ion exchange column was conserved until 90 °C. In addition, it was stable within a wide range of pH (4−10). The antifungal activity was severely reduced at pH 2−3 and at a pH higher than 10 ($p < 0.5$). This heat-stable property was also observed in other antimicrobial metabolites produced by *Bacillus* species.[40,41] Temperature and pH stability of the antifungal peptide can provide greater application for the food and agrochemical industries.

The treatment of the antifungal peptide with different proteases, such as proteinase K, pepsin, papain, and trypsin, in enzyme/peptide mass ratios of 1:10 and 1:5 (w/w) for 2 h at 37 °C, did not affect its antifungal activity. The resistance of the antifungal peptide to the proteases might be attributed to the cyclic structure of the peptide, which inhibits the enzymatic action of proteases on peptides.[25]

Effect of *B. subtilis* B154 Antifungal Compound upon *N. sitophila* Conidia and Hyphae. We evaluated the ability of the B154 antibiotic compound purified by ion exchange column on arresting the germination of *N. sitophila* conidia by an in vitro bioassay (Figure 5). The RI rate for conidial germination increased with an increase in the antibiotic peptide concentration (Figure 5A). At 10 μg/mL, *B. subtilis* B154 antibiotic peptide reduced the number of germinated spores by 7.7%, at 20 μg/mL by 28.4%, and at 30 μg/mL by 83.4%. The subsequent development of branched mycelia in untreated (Figure 5B,a) or antifungal peptide treated (Figure 5B,b−d) discs observed by light microscopy showed that the development of *N. sitophila* conidia was arrested at the stage of the germ tube. Conidial germination represents the first step in triggering an asexual life cycle of aerial pathogenic fungi and the spread of the disease.[29] Therefore, the use of micro-organisms that produce antifungal compounds that inhibit conidial germination is a potential means of biocontrol for fungal disease.[42]

DOI: 10.1021/acs.jafc.5b02218
J. Agric. Food Chem. 2015, 63, 6009−6018

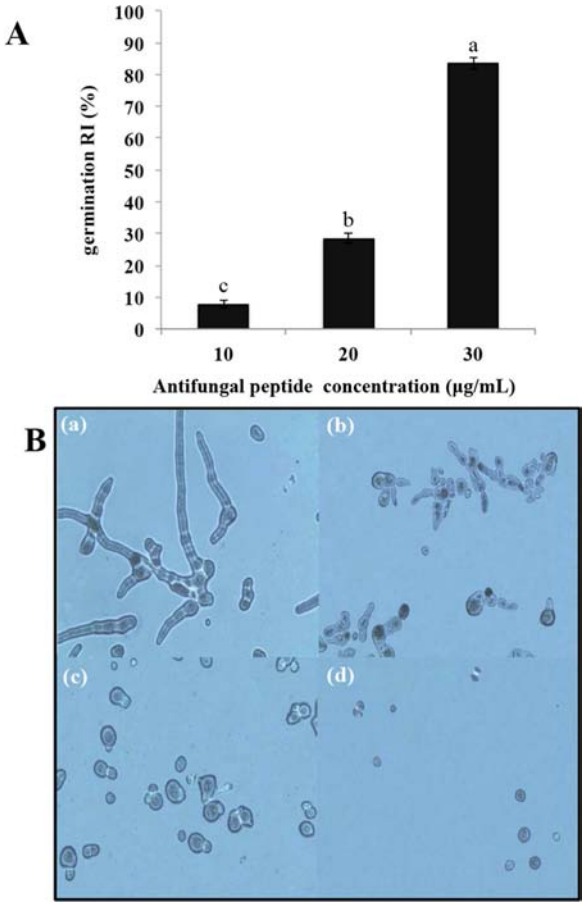

Figure 5. Influence of *B. subtilis* B154 antibiotic peptide on *N. sitophila* conidial germination. Columns in the graph marked by different lower case letters for each mean are significantly different at $p < 0.05$ using Duncan's multiple-range tests. Data are expressed as mean ± SD (n = 6). (B, a) Germination of control conidial spores; (B, b) spores in the presence of 10 μg/mL antifungal peptide; (B, c) spores treated with 20 μg/mL antifungal peptide; (B, d) the same effect produced by 30 μg/mL antifungal peptide extract from strain B154.

The surface appearance of hyphae and spores observed by SEM showed that the control hyphae and conidia of *N. sitophila* grew normally and were smooth with no breakage (Figure 6A,C), while the structures of hyphae and spores treated with B154 antifungal peptide were damaged and irregular (Figure 6B,D). When treated with antifungal peptide, the hyphae were deformed, distorted, wilted on the surface, and cavitated, and the conidia displayed a collapsed morphology characterized by distortion, shrinking, and loss of turgor. These findings support the hypothesis that the secretion of antifungal compounds, such as lipopeptides, is the primary mechanism contributing to the deleterious effect of the *B. subtilis* strain against conidial germination and hyphae growth of fungi.[43]

Antifungal Activity of Bacteria B154 on *A. bisporus* Mushrooms. B154, which was effective against the particular pathogen *N. sitophila* M21 in vitro, was selected to test for *A. bisporus* mushroom yield. B154 notably enhanced the yield of *A. bisporus* ($p < 0.05$) compared to a negative control (Figure 7). Among the three fermentation times (24, 48, and 72 h) during which the bacteria inoculum was tested in the *N. sitophila*-contaminated mushroom beds, 72 h was shown to be best in terms of mushroom yield.

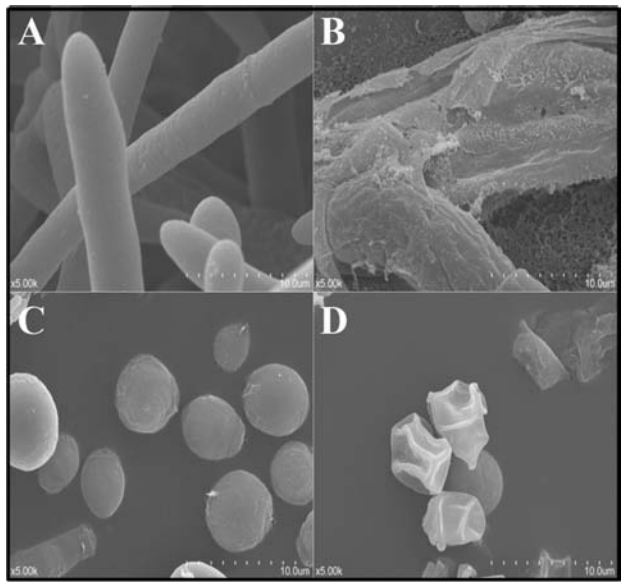

Figure 6. SEM of *N. sitophila* spores and hyphae after the antifungal peptide treatment: A, the control hyphae; B, hyphae treated with antifungal peptide; C, control spores; D, spores treated with antifungal peptide. Bars represent 10 μm.

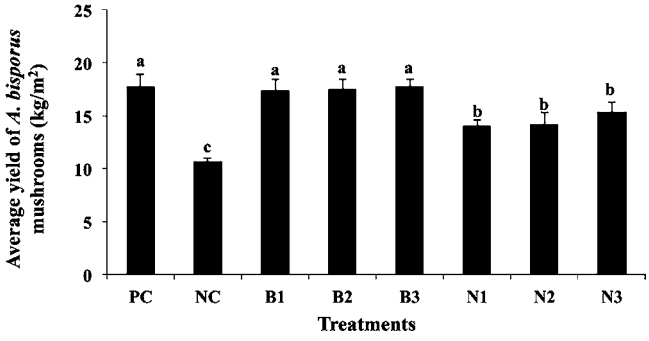

Figure 7. Results of *B. subtilis* B154 inhibition of *N. sitophila* in the compost of *A. bisporus* mushrooms. PC, positive control; NC, negative control; B1, inoculated with bacteria inoculum at 24 h; B2, bacteria inoculum at 48 h; B3, bacteria inoculum at 72 h; N1, inoculated with both fungal and bacteria inoculum at 24 h; N2, fungal and bacteria inoculum at 48 h; N3, fungal and bacteria inoculum at 72 h. Columns marked by different lower case letters for each mean are significantly different at $p < 0.05$ using Duncan's multiple-range tests. Data are expressed as mean ± SD (n = 6).

Few reports on controlling the phyto-pathogens using antibiotics produced by *B. subtilis* in vivo appear in the literature. The lipopeptide bacillomycin D derived from *B. subtilis* could inhibit the growth of *Aspergillus flavus* on corn.[10] However, antibiotics have not yet been commercialized extensively because of low production yields and high purification costs.[44] We inoculated the fermentation broth of *B. subtilis* B154 directly in the *A. bisporus* mushroom cultivation substrate to investigate the biocontrol ability of B154 on fungal pathogen *N. sitophila* in vivo. Our results indicated that *B. subtilis* B154 isolated from the *A. bisporus* mushroom compost might be a potential safety control agent against red bread mold, as it could colonize and proliferate in the mushroom cultivation substrates to compete with the fungal pathogens.

Isolation and Mass Spectrometry Analysis of the Active Compound. Using reverse phase HPLC, six pure

DOI: 10.1021/acs.jafc.5b02218
J. Agric. Food Chem. 2015, 63, 6009−6018

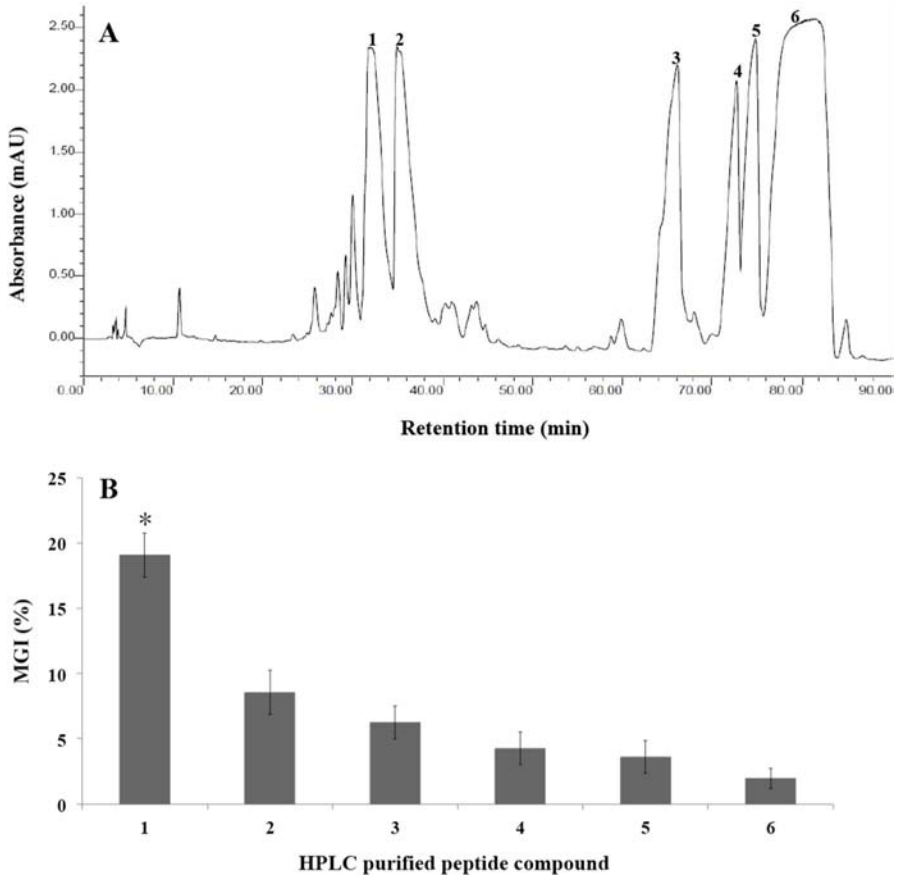

Figure 8. Reverse phase HPLC chromatogram (A) and anti-*N. sitophila* activity (B) of antifungal compounds. Six antifungal compounds were labeled compounds **1**−**6**. The column marked by a star for the mean is significantly different at $p < 0.05$ using Duncan's multiple-range tests. Data are expressed as mean ± SD ($n = 3$).

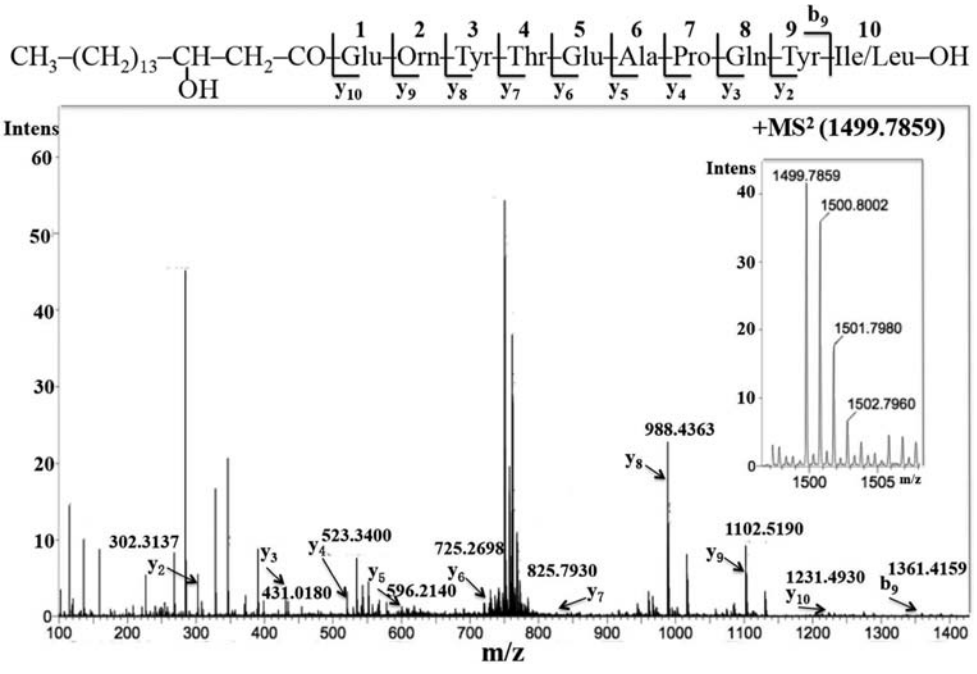

Figure 9. ESI-MS/MS spectra of the purified antifungal compound **1** against *N. sitophila* from *B. subtilis* B154.

antifungal compounds (labeled compounds **1**−**6**) were obtained (Figure 8A). Compound **1** had the highest antifungal activity against the mushroom pathogen *N. sitophila* (Figure 8B).

DOI: 10.1021/acs.jafc.5b02218
J. Agric. Food Chem. 2015, 63, 6009−6018

Compound **1** was further purified with RP-HPLC and then analyzed by MALDI-TOF-MS and ESI-MS/MS. The molecular weight of the purified chemical having antifungal activity was elucidated by MALDI-TOF-MS spectrometry. Data from the positive ion mass spectrum analysis showed that $[M + H]^+$ ion peak was 1499.7633; therefore, the molecular weight of compound **1** was 1498.7633 Da. Many strains of *Bacillus* species were reported to secrete antimicrobial lipopeptides, such as surfactin (m/z 994−1065), iturins (m/z 1028−1073), and fengycin (m/z 1421−1566), which can play important roles in the control of plant diseases.[10,45,46] The fengycin family could be readily distinguished by its distinctly higher masses in the m/z range of 1421−1566.[31,45,47,48] Compound **1** yielded a mass at 1499.7633; therefore, this compound was probably fengycin.

Fengycins are cyclic depsipeptides formed by lactonization involving the side chain −OH of Tyr_3 and C-terminal −COOH of Ile_{10}. The fengycins also possess a three-residue tail segment, and the N-terminal of the decapeptide segment is acylated with a β-hydroxy fatty acid.[49] The peptide sequences of fengycin variants from various *Bacilli* strains have been determined by MALDI-MS and LC-ESI-MS. Two classes of fengycins, A and B, have been reported thus far. Fengycin A has ^{D}Ala at position 6, while fengycin B has ^{D}Val in that position. Within each class, further heterogeneity was observed corresponding to the presence of a β−OH fatty acid, with the chain length varying from C_{14}−C_{19}.[47,48] Under collision-induced dissociation conditions, intense product ions corresponding to cleavage of Glu_1-Orn_2 (m/z 1066 or 1094) and Orn_2-Tyr_3 (m/z 952 or 980) are readily observed and have been used as diagnostics for identifying fengycin variants with the amino acids replacement within the macrocyclic moiety.[47,48] ESI-MS/MS spectrometry analysis of $[M + H]^+$ (m/z 1499.7633) was conducted further to confirm the structure of compound **1**. The ESI-MS/MS spectrum of the compound **1** ion (m/z 1499.7859) yielded two key product ions (y_9 m/z 1102.5.5, and y_8 m/z 988.4), which were not indicative of either of these two classes, demonstrating that compound **1** was a potential new fengycin type lipopeptide (Figure 9).

In the present study, specific residues have been inferred at the individual residue positions based on the mass shifts observed upon fragmentation. For example, a shift of 71 Da has been assigned to an Ala while a shift of 129 Da is assigned to a Glu residue. However, assignments based exclusively on the basis of mass spectrometry may not readily distinguish between isomeric residues like Ile (113 Da) and Leu (113 Da).[31] Based on the product ions (y_2−y_{10}, b_9) of the ESI-MS/MS spectrum of compound **1** (Figure 9), the composition of the amino acid residue was (Glu_1-Orn_2-Tyr_3-Thr_4-Glu_5-Ala_6-Pro_7-Gln_8-Tyr_9-Ile/Leu_{10}), a C_{17} β-hydroxy fatty acid chain connected with the N-terminal of Glu_1.

Fengycins exhibit antifungal activity against some filamentous fungi in vitro;[12] however, to date, no investigator has reported the antifungal application of fengycins in the control of mushroom mold. This work opens the possibility for biocontrol of red bread mold disease in commercial mushroom crops.

In conclusion, the new fengycin type lipopeptide is a potent antifungal component isolated from the *B. subtilis* B154, providing a valuable tool for resistance against pathogenic fungi in mushroom compost. In addition, the management of the microbial community in substrate during *A. bisporus* cultivation, such as inoculation of *Bacillus* spp., can be a way to optimize the growth of *A. bisporus* by increasing the competitive ability against the red bread mold *N. sitophila*. The bacterium B154 can act as a potential alternative to fungistats that inhibit fast-growing fungal antagonists. These findings are of great importance because peptide produced by bacteria or antagonistic microbe would be a way to help *Agaricus* compete with other fungal antagonists and thus to improve edible mushroom production and food safety.

■ ASSOCIATED CONTENT

Ⓢ Supporting Information

Phylogenetic position of *N. sitophila* M21 (Figure S1); neighbor-joining tree of the bacterial strains (A), and *gyrA* gene sequences (B) obtained in this study and others downloaded from GenBank at NCBI (Figure S2); effect of heat, pH, and hydrolytic enzyme treatment on the antifungal activity from B154 strain (Table S1). The Supporting Information is available free of charge on the ACS Publications website at DOI: 10.1021/acs.jafc.5b02218.

■ AUTHOR INFORMATION

Corresponding Author

*Tel.: +86-10-62737620. Fax: +86-10-62736474. E-mail: shen5000@cau.edu.cn.

Funding

The authors express gratitude to China Scholarship Council for providing the State Scholarship Fund to pursue research study at Harvard Medical School in the United States. This work was supported by the Special Fund for Agro-scientific Research in the Public Interest (200803033).

Notes

The authors declare no competing financial interest.

■ ABBREVIATIONS USED

PDA, potato dextrose agar; MGI, mycelial growth inhibition; TSB, tryptic soya broth; LB, Luria−Bertani broth; NB, nutrient broth; TY, tryptic yeast; RP-HPLC, reverse phase high-performance liquid chromatography; AU, arbitrary units; tricine-SDS-PAGE, tricine sodium dodecyl sulfate-polyacrylamide gel electrophoresis; RI, relative germination inhibition; PDB, potato dextrose broth; SEM, scanning electron microscopy; MALDI-TOF-MS, matrix-associated laser desorption ionization time-of-flight mass spectrometry; ESI-MS/MS, electrospray ionization tandem mass spectrometry; α-CHCA, α-cyano-4-hydroxycinnamic acid

■ REFERENCES

(1) Foulongne-Oriol, M.; Spataro, C.; Cathalot, V.; Monllor, S.; Savoie, J. M. An expanded genetic linkage map of an intervarietal *Agaricus bisporus* var. *bisporus* x *A. bisporus* var. burnettii hybrid based on AFLP, SSR and CAPS markers sheds light on the recombination behaviour of the species. *Fungal Genet. Biol.* **2010**, *47*, 226−236.

(2) Adams, L. S.; Chen, S.; Phung, S.; Wu, X.; Ki, L. White button mushroom (*Agaricus bisporus*) exhibits antiproliferative and proapoptotic properties and inhibits prostate tumor growth in athymic mice. *Nutr. Cancer* **2008**, *60*, 744−756.

(3) Largeteau, M.; Savoie, J. M. Microbially induced diseases of *Agaricus bisporus*: biochemical mechanisms and impact on commercial mushroom production. *Appl. Microbiol. Biotechnol.* **2010**, *86*, 63−73.

(4) Velázquez-Cedeño, M.; Farnet, A. M.; Mata, G.; Savoie, J. M. Role of *Bacillus* spp. in antagonism between *Pleurotus ostreatus* and *Trichoderma harzianum* in heat-treated wheat-straw substrates. *Bioresour. Technol.* **2008**, *99*, 6966−6973.

DOI: 10.1021/acs.jafc.5b02218
J. Agric. Food Chem. 2015, 63, 6009−6018

(5) Boiko, O. A.; Mel'nichuk, M. D.; Ivanova, T. V. Spread, diagnosis, and prevention of diseases of the button mushroom. *Russ. Agricult. Sci.* **2009**, *35*, 94−95.
(6) Yildiz, A.; Karakaplan, M.; Aydin, F. Studies on *Pleurotus ostreatus* (Jacq. ex Fr.) Kum. var. *salignus* (Pers. ex Fr.) Konr. et Maubl.: cultivation, proximate composition, organic and mineral composition of carpophores. *Food Chem.* **1998**, *61*, 127−130.
(7) Bailey, A. M.; Collopy, P. D.; Thomas, D. J.; Sergeant, M. R.; Costa, A. M. S. B.; Barker, G. L. A.; Mills, P. R.; Challen, M. P.; Foster, G. D. Transcriptomic analysis of the interactions between *Agaricus bisporus* and *Lecanicillium fungicola*. *Fungal Genet. Biol.* **2013**, *55*, 67−76.
(8) Compant, S.; Clément, C.; Sessitsch, A. Plant growth-promoting bacteria in the rhizo- and endosphere of plants: Their role, colonization, mechanisms involved and prospects for utilization. *Soil Biol. Biochem.* **2010**, *42*, 669−678.
(9) Santoyo, G.; Orozco-Mosqueda, M. d. C.; Govindappa, M. Mechanisms of biocontrol and plant growth-promoting activity in soil bacterial species of *Bacillus* and *Pseudomonas*: a review. *Biocontrol Sci. Techn.* **2012**, *22*, 855−872.
(10) Gong, Q.; Zhang, C.; Lu, F.; Zhao, H.; Bie, X.; Lu, Z. Identification of bacillomycin D from *Bacillus subtilis* fmbJ and its inhibition effects against *Aspergillus flavus*. *Food Control* **2014**, *36*, 8−14.
(11) Schallmey, M.; Singh, A.; Ward, O. P. Developments in the use of *Bacillus* species for industrial production. *Can. J. Microbiol.* **2004**, *50*, 1−17.
(12) Hu, L. B.; Shi, Z. Q.; Zhang, T.; Yang, Z. M. Fengycin antibiotics isolated from B-FS01 culture inhibit the growth of *Fusarium moniliforme* Sheldon ATCC 38932. *FEMS Microbiol. Lett.* **2007**, *272*, 91−98.
(13) Stein, T. *Bacillus subtilis* antibiotics: structures, syntheses and specific functions. *Mol. Microbiol.* **2005**, *56*, 845−857.
(14) Fravel, D. R. Commercialization and implementation of biocontrol. *Annu. Rev. Phytopathol.* **2005**, *43*, 337−359.
(15) Dettman, J. R.; Harbinski, F. M.; Taylor, J. W. Ascospore morphology is a poor predictor of the phylogenetic relationships of *Neurospora* and *Gelasinospora*. *Fungal Genet. Biol.* **2001**, *34*, 49−61.
(16) NCBI, Basic Local Aligment Search Tool. http://www.ncbi.nlm.nih.gov/BLAST/ (accessed May 11, 2015).
(17) Xu, M.; Sheng, J.; Chen, L.; Men, Y.; Gan, L.; Guo, S.; Shen, L. Bacterial community compositions of tomato (*Lycopersicum esculentum* Mill.) seeds and plant growth promoting activity of ACC deaminase producing *Bacillus subtilis* (HYT-12−1) on tomato seedlings. *World J. Microbiol. Biotechnol.* **2014**, *30*, 835−845.
(18) Clauss, D.; Berkeley, R. C. W. *Bergey's Manual of Determinative Bacteriology*; Sneath, P. H. A., Ed.; Williams & Wilkins: Baltimore, 1986; Vol. 2, pp 1105−1141.
(19) Macfadden, J. F. *Biochemical Tests for Identification of Medical Bacteria*, 3rd ed.; Lippincott Williams & Wilkins: Philadelphia, 2000; p 912.
(20) Weisburg, W. G.; Barns, S. M.; Pelletier, D. A.; Lane, D. J. 16S ribosomal DNA amplification for phylogenetic study. *J. Bacteriol.* **1991**, *173*, 697−703.
(21) Rooney, A. P.; Price, N. P.; Ehrhardt, C.; Swezey, J. L.; Bannan, J. D. Phylogeny and molecular taxonomy of the *Bacillus subtilis* species complex and description of *Bacillus subtilis* subsp. *inaquosorum* subsp. nov. *Int. J. Syst. Evol. Microbiol.* **2009**, *59*, 2429−2436.
(22) Touré, Y.; Ongena, M.; Jacques, P.; Guiro, A.; Thonart, P. Role of lipopeptides produced by *Bacillus subtilis* GA1 in the reduction of grey mould disease caused by *Botrytis cinerea* on apple. *J. Appl. Microbiol.* **2004**, *96*, 1151−1160.
(23) Tabbene, O.; Ben Slimene, I.; Bouabdallah, F.; Mangoni, M. L.; Urdaci, M. C.; Limam, F. Production of anti-methicillin-resistant staphylococcus activity from *Bacillus subtilis* sp. Strain B38 newly isolated from soil. *Appl. Biochem. Biotechnol.* **2009**, *157*, 407−419.
(24) Song, B.; Rong, Y. J.; Zhao, M. X.; Chi, Z. M. Antifungal activity of the lipopeptides produced by *Bacillus* amyloliquefaciens anti-CA against *Candida albicans* isolated from clinic. *Appl. Microbiol. Biotechnol.* **2013**, *97*, 7141−7150.
(25) Lee, H.; Churey, J. J.; Worobo, R. W. Purification and structural characterization of bacillomycin F produced by a bacterial honey isolate active against *Byssochlamys fulva* H25. *J. Appl. Microbiol.* **2008**, *105*, 663−673.
(26) Maldonado, M.; Corona, J.; Gordillo, M.; Navarro, A. Isolation and partial characterization of antifungal metabolites produced by *Bacillus* sp. IBA 33. *Curr. Microbiol.* **2009**, *59*, 646−650.
(27) Bechard, J.; Eastwell, K. C.; Sholberg; Mazza, G.; Skura, B. Isolation and partial chemical characterization of an antimicrobial peptide produced by a strain of *Bacillus subtilis*. *J. Agric. Food Chem.* **1998**, *46*, 5355−5361.
(28) Angelini, P.; Pagiotti, R.; Granetti, B. Effect of antimicrobial activity of *Melaleuca alternifolia* essential oil on antagonistic potential of *Pleurotus* species against *Trichoderma harzianum* in dual culture. *World J. Microbiol. Biotechnol.* **2008**, *24*, 197−202.
(29) Romero, D.; De Vicente, A.; Olmos, J. L.; Dávila, J. C.; Pérez-García, A. Effect of lipopeptides of antagonistic strains of *Bacillus subtilis* on the morphology and ultrastructure of the cucurbit fungal pathogen *Podosphaera fusca*. *J. Appl. Microbiol.* **2007**, *103*, 969−976.
(30) Gong, M.; Wang, J. D.; Zhang, J.; Yang, H.; Lu, X. F.; Pei, Y.; Cheng, J. Q. Study of the antifungal ability of *Bacillus subtilis* strain PY-1 *in vitro* and identification of its antifungal substance (iturin A). *Acta Biochim. Biophys. Sin.* **2006**, *38*, 233−240.
(31) Pathak, K.; Keharia, H.; Gupta, K.; Thakur, S.; Balaram, P. Lipopeptides from the banyan endophyte, *Bacillus subtilis* K1: mass spectrometric characterization of a library of fengycins. *J. Am. Soc. Mass Spectrom.* **2012**, *23*, 1716−1728.
(32) Tanaka, K.; Ishihara, A.; Nakajima, H. Isolation of anteiso-C17, iso-C17, iso-C16, and iso-C15 Bacillomycin D from *Bacillus* amyloliquefaciens SD-32 and their antifungal activities against plant pathogens. *J. Agric. Food Chem.* **2014**, *62*, 1469−1476.
(33) Rivillas-Acevedo, L. A.; Soriano-García, M. Isolation and biochemical characterization of an antifungal peptide from *Amaranthus hypochondriacus* Seeds. *J. Agric. Food Chem.* **2007**, *55*, 10156−10161.
(34) Komoń-Zelazowska, M.; Bissett, J.; Zafari, D.; Hatvani, L.; Manczinger, L.; Woo, S.; Lorito, M.; Kredics, L.; Kubicek, C. P.; Druzhinina, I. S. Genetically closely related but phenotypically divergent *Trichoderma* species cause green mold disease in *oyster* mushroom farms worldwide. *Appl. Environ. Microb.* **2007**, *73*, 7415−7426.
(35) Chun, J.; Bae, K. Phylogenetic analysis of *Bacillus subtilis* and related taxa based on partial *gyrA* gene sequences. *Antonie van Leeuwenhoek* **2000**, *78*, 123−127.
(36) Motta, A. S.; Brandelli, A. Influence of growth conditions on bacteriocin production by *Brevibacterium linens*. *Appl. Microbiol. Biotechnol.* **2003**, *62*, 163−167.
(37) Bizani, D.; Brandelli, A. Characterization of a bacteriocin produced by a newly isolated *Bacillus* sp. Strain 8 A. *J. Appl. Microbiol.* **2002**, *93*, 512−519.
(38) von der Weid, I.; Alviano, D. S.; Santos, A. L. S.; Soares, R. M. A.; Alviano, C. S.; Seldin, L. Antimicrobial activity of *Paenibacillus peoriae* strain NRRL BD-62 against a broad spectrum of phytopathogenic bacteria and fungi. *J. Appl. Microbiol.* **2003**, *95*, 1143−1151.
(39) Yu, G. Y.; Sinclair, J. B.; Hartman, G. L.; Bertagnolli, B. L. Production of iturin A by *Bacillus amyloliquefaciens* suppressing *Rhizoctonia solani*. *Soil Biol. Biochem.* **2002**, *34*, 955−963.
(40) Aunpad, R.; Na-Bangchang, K. Pumilicin 4, A novel bacteriocin with anti-MRSA and anti-VRE activity produced by newly isolated bacteria *Bacillus pumilus* strain WAPB4. *Curr. Microbiol.* **2007**, *55*, 308−313.
(41) Korenblum, E.; von Der Weid, I.; Santos, A. L. S.; Rosado, A. S.; Sebastián, G. V.; Coutinho, C. M. L. M.; Magalhães, F. C. M.; de Paiva, M. M.; Seldin, L. Production of antimicrobial substances by *Bacillus subtilis* LFE-1, *B. Firmus* H2O-1 and *B. licheniformis* T6−5 isolated from an oil reservoir in Brazil. *J. Appl. Microbiol.* **2005**, *98*, 667−675.
(42) Bélanger, R. R., Dik, A. J., Menzies, J. G. Powdery mildews. Recent advances toward integrated control. In *Plant-Microbe*

DOI: 10.1021/acs.jafc.5b02218
J. Agric. Food Chem. 2015, 63, 6009−6018

Interactions and Biological Control; Boland, G. J., Kuykendall, L. D., Eds.; Dekker: New York, 1998; pp 89−109.
(43) Romero, D.; Pérez-García, A.; Rivera, M. E.; Cazorla, F. M.; de Vicente, A. isolation and evaluation of antagonistic bacteria towards the cucurbit powdery mildew fungus *Podosphaera fusca*. *Appl. Microbiol. Biotechnol.* **2004**, *64*, 263−269.
(44) de Faria, A. F.; Teodoro-Martinez, D. S.; de Oliveira Barbosa, G. N.; Gontijo Vaz, B.; Serrano Silva, Í.; Garcia, J. S.; Tótola, M. R.; Eberlin, M. N.; Grossman, M.; Alves, O. L.; Regina Durrant, L. Production and structural characterization of surfactin (C14/Leu7) produced by *Bacillus subtilis* isolate LSFM-05 grown on raw glycerol from the biodiesel industry. *Process Biochem.* **2011**, *46*, 1951−1957.
(45) Ongena, M.; Jacques, P. *Bacillus* lipopeptides: versatile weapons for plant disease biocontrol. *Trends Microbiol.* **2008**, *16*, 115−125.
(46) Zhang, T.; Shi, Z. Q.; Hu, L. B.; Cheng, L. G.; Wang, F. Antifungal compounds from *Bacillus subtilis* B-FS06 inhibiting the growth of *Aspergillus flavus*. *World J. Microbiol. Biotechnol.* **2008**, *24*, 783−788.
(47) Vater, J.; Kablitz, B.; Wilde, C.; Franke, P.; Mehta, N.; Cameotra, S. S. Matrix-assisted laser desorption ionization-time of flight mass spectrometry of lipopeptide biosurfactants in whole cells and culture filtrates of *Bacillus subtilis* C-1 isolated from petroleum sludge. *Appl. Environ. Microb.* **2002**, *68*, 6210−6219.
(48) Pecci, Y.; Rivardo, F.; Martinotti, M. G.; Allegrone, G. LC/ESI-MS/MS characterisation of lipopeptide biosurfactants produced by the *Bacillus licheniformis* V9T14 strain. *J. Mass Spectrom.* **2010**, *45*, 772−778.
(49) Vanittanakom, N.; Loeffler, W.; Koch, U.; Jung, G. Fengycin-A novel antifungal lipopeptide antibiotic produced by *Bacillus subtilis* F-29−3. *J. Antibiot.* **1986**, *39*, 888−901.

DOI: 10.1021/acs.jafc.5b02218
J. Agric. Food Chem. 2015, 63, 6009−6018

Table 1. Designed Primer Sets for RT-PCR[a]

gene	primer	5′−3′	size (bp)
PI3K	sense	ACAAAGCTCTACTCTAGGCGTG	242
	antisense	TTACCAGCATGGTCATGGGC	
Akt	sense	AGAGAGCCGAGTCCTACAGAATA	133
	antisense	CCGAGAGAGGTGGAAAAACA	
GSK-3β	sense	TCGTCCATCGATGTGTGGTC	202
	antisense	TTGTCCAGGGGTGAGCTTTG	
GS	sense	TTGCCAGAATGCACGCAGAA	125
	antisense	TGCCTGCATCATCTGTTGAC	
β-actin	sense	GATCGATGCCGGTGCTAAGA	367
	antisense	TCCTATGGGAGAACGGCAGA	

[a]Primer sets designed for RT-PCR to evaluate the expressions of PI3K, Akt, GSK-3β, and GS at gene level. The specific primers, which include both sense and antisense, were designed separately and followed the designing principles.

environment for 7 days. Then the animals were randomly divided into normal control group (NC) and diabetic control group (DC). The NC group, consisting of 20 rats, was fed a normal chow diet during the whole study, whereas the other group was fed a high-fat diet (HFD). After a month, the HFD rats were injected intraperitoneally with STZ solution at a dose of 30 mg/(kg·body weight (bw)). The STZ was dissolved in citrate buffer at pH 4.2−4.5. The rats in the NC group were injected with the citrate buffer vehicle. Seventy-two hours after injection, the rats in the DC group with blood glucose level ≥11.1 mmol/L were considered as T2DM rats and would be used in future experiments. These T2DM rats were fed the HFD throughout the whole study. Then the T2DM rats were randomly divided into three groups with 10 animals each. The first group (low-dosage group, LD) received D-pinitol at 30 mg/(kg·bw·day), the second group (high-dosage group, HD) received D-pinitol at 60 mg/(kg·bw·day), and the last one received distilled water only (diabetes control group, DC). Ten rats were chosen from the normal control group to receive D-pinitol at 60 mg/(kg·bw·day) as the normal high-dosage control group (NH).

Oral Glucose Tolerance Test (OGTT) and Insulin Tolerance Test (ITT). OGTT was performed in overnight-fasted rats from every group. Vehicle (distilled water) was orally administered to NC and DC groups. Doses of 30, 60, and 60 mg/kg D-pinitol were orally administered to LD, HD, and NH groups, respectively. Twenty minutes later, all of the rats were orally administered glucose at a dose of 2 g/kg. Blood was withdrawn from the tip of the tail at 0, 30, 60, and 120 min from all five groups to measure the blood glucose level.

ITT were performed in overnight-fasted rats from all groups 3 days after the OGTT. Twenty minutes after administration of the vehicle (distilled water) and D-pinitol, the rats were injected with insulin intraperitoneally at a dose of 0.15 U/kg. Similar to the procedure for OGTT, blood samples were withdrawn at 0, 30, 60, and 120 min after the injection of insulin, and the blood glucose level was measured.

Biochemical Analysis. The fasting blood glucose (FBG) level was determined by using the blood glucose meter and test strips each week. The fasting serum insulin (FINS) was determined by ELISA kit. The insulin sensitivity index (ISI) was calculated following the formula ISI = Ln (1/FINS × FBG). The homeostasis model assessment-β (HOMA-β) was calculated following the formula HOMA-β = (20 × FINS)/(FBG − 3.5). All of the parameters were performed according to the manufacturer's instructions. The blood samples and viscera organs were stored at −80 °C in the refrigerator for future research.

Real-Time Polymerase Chain Reaction (RT-PCR) Analysis. RT-PCR was operated to determine the expression levels of the genes. Total RNA was extracted from liver using Trizol reagent, and the concentration of the total RNA was determined by the ultraviolet spectrophotometer. It was converted to DNA by using a RT-PCR kit, and the reaction was performed according to the manufacturer's instructions. The specific primers, which include both sense and antisense, were used for the amplification of DNA (Table1).

Western Blot Analysis. The expression of protein including PI3Kp85 (85 kDa), PI3Kp110 (110 kDa), Akt (60 kDa), p-Akt (60 kDa), GSK-3β (46 kDa), and GS (81−85 kDa) was analyzed by Western blot. In brief, 100 mg of liver was homogenized in RIPA buffer for 10 min, followed by centrifugation at 10000 rpm for 5 min at 4 °C. The supernatant was transferred to a new clean centrifuge tube, and the Bradford colorimetric method was used to determine the concentration of the total protein. The tissue protein (50−70 μg) was subjected to 10% SDS-PAGE for 0.5 h at 80 V and for 2.5 h at 100 V, to separate the target protein from the others. Proteins were transferred to a nitrocellulose membrane for 3 h at 300 mA by wet transfer equipment. The membrane was incubated in blocking solution containing 5% nonfat dried milk for 2 h at room temperature. Subsequently, the membrane was exposed to the desired primary antibodies, PBS containing PI3Kp85 antibody (1:1000), PI3Kp110 antibody (1:1000), Akt antibody (1:1000), p-Akt (Ser473) antibody (1:2000), GSK-3β (1:1000), and GS (1:1000), incubated with the membrane at 4 °C overnight; β-actin (43 kDa) was used as control protein. After incubation with the secondary antibody for 2 h at room temperature, the membrane was exposed to chemiluminescent reagent (ECL) for about 5−10 min. The expressions of the proteins on the membranes with fluorescence were exposed to X-ray photographic films in a darkroom, and the band densities were quantified.

Immunohistochemistry. Liver tissues embedded in paraffin were performed on 5 μm paraffin sections for immunohistochemical staining. The paraffin sections were dewaxed and rehydrated before being dipped into 0.01 M citrate buffer (pH 6.0) with a boiling water reaction to retrieve antigen. The paraffin sections were incubated with 3% H_2O_2 to quench the activity of endogenous peroxidase. Then the sections were incubated in the solution containing 3% BSA to block nonspecific binding sites, whereas endogenous avidin-binding activity was inhibited by continuous treatment with avidin−biotin. The following steps of the immunodetection experiment were operated according to the manufacturer's instruction for the SABC (rabbit IgG)−POD Kit. For each antibody, a negative control was included in which the primary antibody was replaced with phosphate buffer saline (PBS).

Table 2. Effect of D-Pinitol on Body Weight of Experimental Rats[a]

	body weight (g)			
group	0 weeks	1 week	3 weeks	5 weeks
NC	425.50 ± 14.12	456.50 ± 24.01**	478.50 ± 21.60**	496.50 ± 27.18**
DC	420.00 ± 28.55	368.63 ± 31.92	375.00 ± 26.01	380.75 ± 30.73
LD	413.60 ± 15.63	380.80 ± 16.19	366.20 ± 12.48	385.00 ± 14.76
HD	433.20 ± 29.75	393.80 ± 30.72	408.80 ± 25.55*	424.20 ± 17.87*
NH	417.80 ± 32.51	435.20 ± 19.72	477.00 ± 30.94	492.00 ± 34.26

[a]The effect of D-pinitol on body weight is exhibited in this table. The rats in DC group were significantly lighter than the normal ones. After treatment with D-pinitol, body weight of the rats in HD group was significantly higher than the ones in DC group. We evaluated (*)$p < 0.05$ as significant and (**) $p < 0.01$ as very significant. Values are the means ± SD, and each group contained 10 rats.

DOI: 10.1021/acs.jafc.5b01238
J. Agric. Food Chem. 2015, 63, 6019−6026

Table 3. Effect of D-Pinitol on Fasting Blood Glucose of Experimental Rats[a]

	fasting blood glucose (mmol/L)				
group	0 weeks	1 week	3 weeks	5 weeks	reduction rate (%)
NC	5.0 ± 0.57**	4.6 ± 0.57**	5.0 ± 0.56**	4.8 ± 1.18**	
DC	18.6 ± 3.00	20.2 ± 2.95	23.1 ± 6.26	21.1 ± 4.31	
LD	18.7 ± 5.35	21.3 ± 6.03	19.9 ± 4.13	16.9 ± 3.02**	9.63
HD	19.0 ± 2.20	18.5 ± 2.58	18.6 ± 3.01*	16.6 ± 2.56**	12.63
NH	4.7 ± 0.30	4.3 ± 0.38	4.5 ± 0.72	4.2 ± 0.44	

[a]Data in this table show the effect of D-pinitol on FBG. The FBG levels of the rats in LD and HD groups had a tendency to reduce during the treatment. Both LD and HD groups had very significant differences compared with DC group in FBG after 5 weeks of treatment. We evaluated (*) $p < 0.05$ as significant and (**) $p < 0.01$ as very significant. Values are the means ± SD, and each group contained 10 rats.

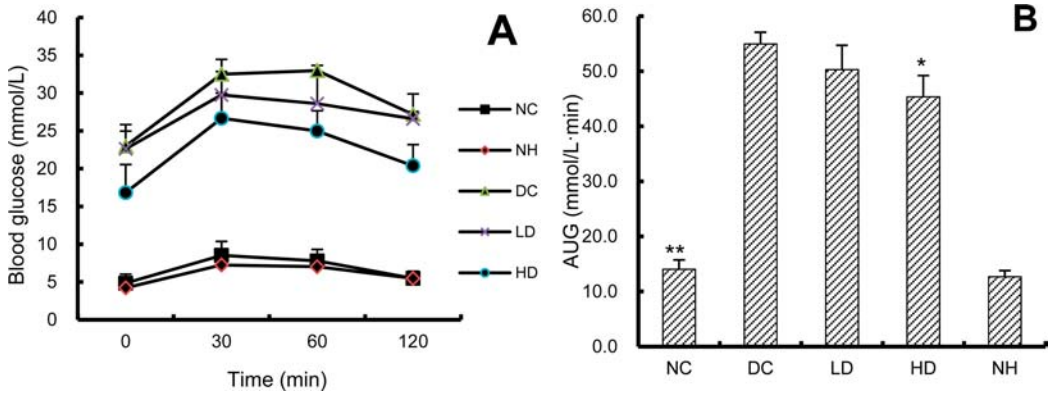

Figure 1. OGTT was performed after 4 weeks of treatment in all experimental rats. Animals in LD, HD, and NH groups received D-pinitol orally; rats in NC and DC groups received vehicle only. Twenty minutes after that, all groups received oral glucose at dosage of 2 g/kg. Blood samples were collected at 0, 30, 60, and 120 min after administration of glucose. Each point is the mean ± SD of 10 separate rats. The area under curve of panel A was calculated and exhibited in panel B). (*) $p < 0.05$ compared with the DC group was considered as significant difference. (**) $p < 0.01$ was very significantly different compared with the DC group.

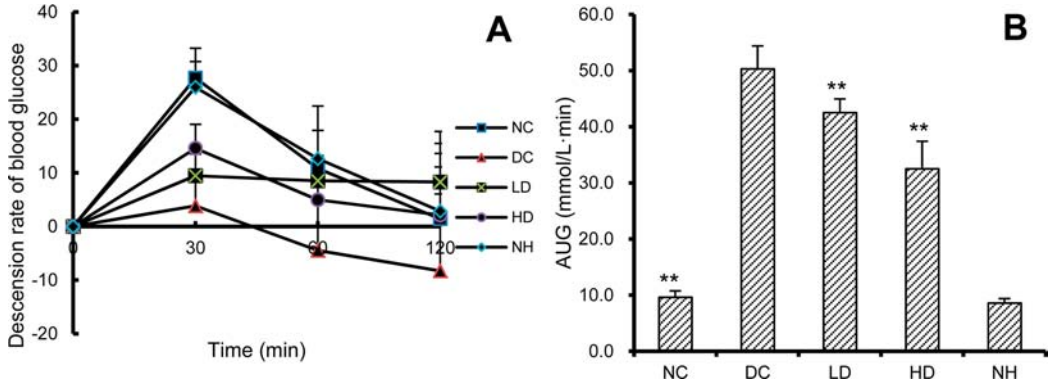

Figure 2. ITT was performed in all experimental rats 3 days after OGTT. Rats in the LD, HD, and NH groups received D-pinitol orally, whereas NC and DC groups received vehicle only. Rats were injected with insulin at 0.15 U/kg intraperitoneally, and blood samples were withdrawn at 0, 30, 60, and 120 min after injection. Each point is the mean ± SD of 10 separate rats. The area under curve of panel A was calculated and exhibited in panel B. (**) $p < 0.01$ was very significantly different compared with the DC group.

Statistical Analysis. All of the data were presented as means ± SD. The *t* test was used to exhibit the significance of differences between samples. These differences were considered significant when $p < 0.05$, whereas $p < 0.01$ was regarded as very significant (SPSS version 20.0, Statistical Package for the Social Sciences Software, SPSS Inc., Chicago, IL, USA).

RESULTS

D-Pinitol Increased Body Weight and Reduced Fasting Blood Glucose. Body weight and FBG of all the experimental rats were measured each week, and Table 2 reveals the body weight of all groups. There was a remarkable difference in body weight between normal rats and diabetic rats ($p < 0.01$). The body weight of the DC group was significantly lower than that of the NC group during the whole experiment ($p < 0.05$). Supplementation of D-pinitol to the diabetic rats showed a significant increase in body weight after 5 weeks of treatment compared to the DC group ($p < 0.05$).

Table 3 shows the level of FBG of all rats. The level of FBG of diabetic rats was significantly higher than that of the normal rats. D-Pinitol exhibited a positive effect on hypoglycemic activity in diabetic rats. The reduction rates of FBG in LD and HD groups were 9.63 and 12.63% separately. The LD group and HD group

DOI: 10.1021/acs.jafc.5b01238
J. Agric. Food Chem. 2015, 63, 6019−6026

Table 4. Effect of D-Pinitol on Insulin Sensitivity of Experimental Rats[a]

	insulin sensitivity		
group	FINS (mIU/L)	ISI	HOMA-β
NC	13.11 ± 1.55**	−4.06 ± 0.19**	260.88 ± 150.43**
DC	20.07 ± 3.17	−6.13 ± 0.15	20.77 ± 5.07
LD	18.29 ± 2.56	−5.89 ± 0.18	23.04 ± 6.91
HD	14.18 ± 2.14*	−5.40 ± 0.17*	24.55 ± 9.77
NH	13.86 ± 1.75	−4.10 ± 0.20	301.39 ± 128.29

[a]Data in this table suggested that rats in the DC group had a higher concentration of insulin in serum than that in normal groups. D-Pinitol helped to lower the contents of FINS and increased ISI of the rats in the LD and HD groups. (*) $p < 0.05$ was considered as significant and (**) $p < 0.01$ as very significant. Values are the means ± SD, and each group contained 10 rats.

both showed very significant decrease compared with the DC group ($p < 0.01$).

On the basis of the data, it can be concluded that D-pinitol is useful to increase the body weight and decrease FBG level in HFD/STZ-induced diabetic rats.

D-Pinitol Improved OGTT and ITT of Diabetic Rats. After 4 weeks of treatment with D-pinitol, overnight-fasted rats were subjected to an OGTT. Oral supplementation of glucose (2 g/kg) increased blood glucose level within 30 min, and it remained at a high level over the next 90 min in DC rats. The blood glucose level rose to the peak as well in NC rats, but dropped to the initial level after 120 min. Treatment with D-pinitol (60 mg/(kg·bw)) in diabetic rats inhibited the rise in blood glucose levels significantly after oral glucose administration (Figure 1A). The results of OGTT were expressed as overall area under curve of glucose (AUG) over 120 min, and the AUG of the HD group was markedly less than that of DC group (Figure 1B, $p < 0.05$).

Three days after OGTT, all rats were evaluated for ITT after an overnight fast. After intraperitoneally injected insulin at 0.5 U/kg, the blood glucose levels at 30, 60, and 120 min revealed that normal rats took more advantage of insulin than the diabetic rats (Figure 2A). Significant differences between the DC group ($p < 0.05$) and D-pinitol dosage groups suggested that D-pinitol increased the utilization of insulin and improved the insulin sensitivity of the diabetic rats as well (Figure 2B).

D-Pinitol Enhanced Insulin Sensitivity of T2DM Rats. The investigation studied whether D-pinitol could exert an insulin-sensitizing activity in T2DM rats. As Table 4 illustrates, treatment with D-pinitol increased ISI. Fasting blood insulin content stayed at a high level in DC and LD groups, whereas the HD group showed a significant decrease compared with the DC group ($p < 0.05$). When treated with D-pinitol, the diabetic rats showed a tendency of HOMA-β enhancement.

D-Pinitol Ameliorated Insulin Resistance through the PI3K/Akt Pathway. In this investigation we evaluated the effects of D-pinitol on PI3K, Akt, GSK-3β, and GS at the gene level with RT-PCR, inquiring into the molecular mechanism of D-pinitol in improving insulin resistance. The RT-PCR consequences in Figure 3 indicated that D-pinitol-treated groups increased the expression of PI3K, Akt, and GS at the gene level with the relativity of β-actin. The expression of GSK-3β was decreased in LD and HD groups, which were both very significantly different to the DC group ($p < 0.01$).

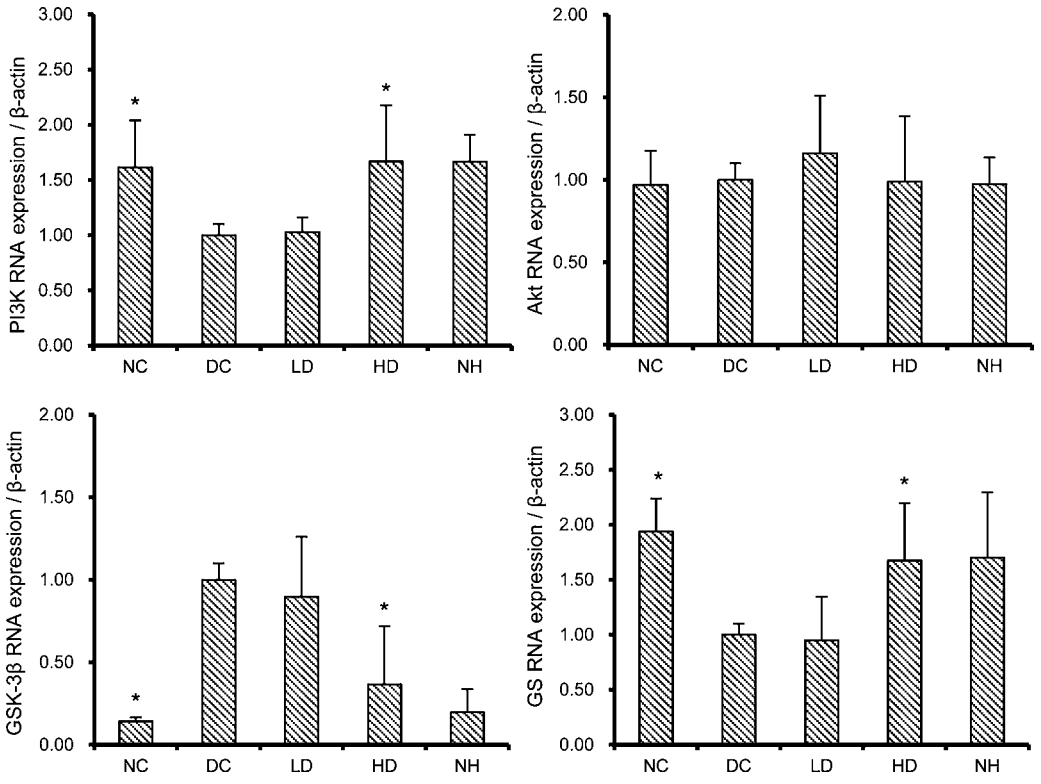

Figure 3. Total RNA was extracted from liver using Trizol reagent, and the concentration of the total RNA was determined by the ultraviolet spectrophotometer. RT-PCR was operated according to the manufacturer's instructions of the RT-PCR kits, and the results in this figure demonstrate the effect of D-pinitol on the genes in the PI3K/Akt pathway. (*) $p < 0.05$ compared with the DC group was considered as significantly different. Values are the means ± SD, and each group contained 10 samples.

DOI: 10.1021/acs.jafc.5b01238
J. Agric. Food Chem. 2015, 63, 6019−6026

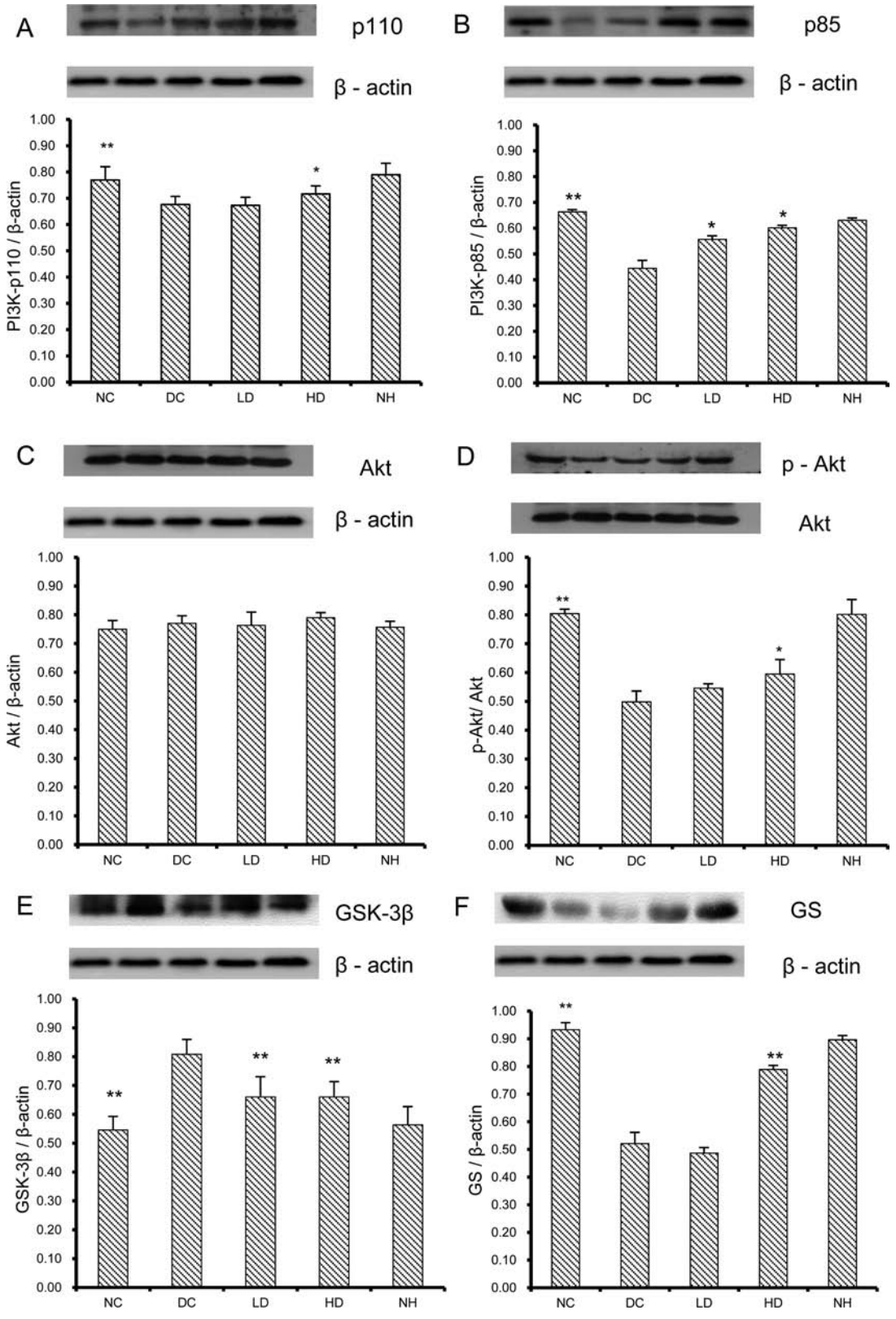

Figure 4. Western blot was used to express the effect of D-pinitol on the key proteins in PI3K/Akt pathway. The proteins of p85, p110, Akt, p-Akt, GSK-3β, and GS in liver tissue were extracted by RIPA and separated by 10% SDS-PAGE. Similar results were obtained in three independent experiments. Photos are representative images. Values are the means ± SD. (*) $p < 0.05$ compared with the DC group was considered as significantly different. (**) $p < 0.01$ was very significantly different compared with the DC group.

We also evaluated the expression of the main proteins in the PI3K/Akt pathway. PI3K is a kind of phosphatidylinositol kinase, which comprises a catalytic subunit (p110) and a regulatory subunit (p85). The p85 subunit is coupled with tyrosine-phosphorylated receptor tyrosine kinases, and the p110 subunit is required for G-protein-mediated activation of PI3K. D-Pinitol

DOI: 10.1021/acs.jafc.5b01238
J. Agric. Food Chem. 2015, 63, 6019−6026

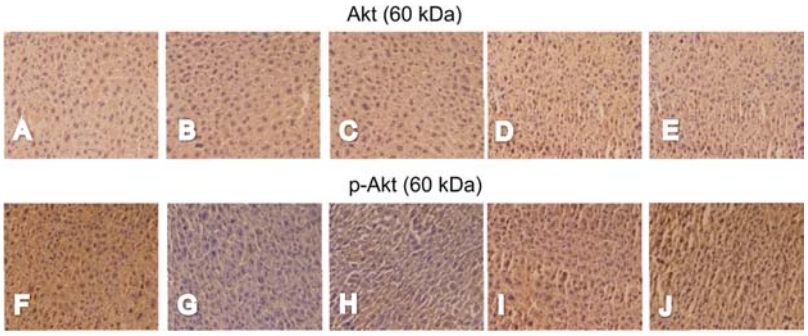

Figure 5. Immunohistochemical staining was performed on the 5 μm paraffin sections embedded with liver tissues. All staining steps were performed according to the manufacturer's instruction of SABC (rabbit IgG)−POD Kit. The staining outcomes were observed by microscope at 200 times magnification.

significantly increased the expression of p110 and p85 in diabetic rats (Figure 4A,B, $p < 0.05$). Akt and p-Akt were measured in this study to determine whether PI3K downstream signaling was affected by D-pinitol in diabetic rats. The results in Figure 4C,D suggested that D-pinitol treatment was associated with a significant increase in phosphorylation of Akt in liver tissue compared with the DC ($p < 0.05$). To gain some insight into the molecular mechanism for the effect of D-pinitol on glycogen synthesis, we assessed the levels of GSK-3β protein and GS protein (Figure 4E,F); the expression quantity of GSK-3β protein was decreased remarkably in D-pinitol-treated groups, and the expression of GS protein was increased.

The results showed that D-pinitol treatment significantly enhanced the expression of the main proteins in the PI3K/Akt pathway and then indicated that D-pinitol had a positive effect on liver insulin transduction.

Immunohistochemistry Test on Paraffin Sections. Immunohistochemistry staining of Akt and p-Akt suggested that liver tissues were completely stained in each group (Figure 5). There was no obvious difference in the staining of Akt in all groups. Increased immunostaining of p-Akt was observed in liver tissues of normal control rats, whereas the staining of p-Akt was markedly diminished in the DC group. Greater immunostaining for p-Akt in the HD group was presented in the tissues compared with diabetic control, whereas the LD group showed no obvious difference compared with the DC group.

DISCUSSION

T2DM is one of the most complicated worldwide epidemics in recent decades. T2DM, caused by insulin resistance, is associated with both hyperglycemic and hyperlipidemia. An imbalance of insulin sensitivity between the liver and peripheral tissue as well as endocrine pancreatic function damage may lead to T2DM.[14] Besides, T2DM is always the original reason causing many chronic diseases. Therefore, it is very important to find an appropriate way for better treatments and precaution strategies of T2DM. There are numerous investigations establishing animal models to mimicking T2DM. On the basis of the experimental characteristics, we chose SD rats as our experimental animals, which more easily obtain the pathological features resembling T2DM.[15] The rats were fed a HFD for 4 weeks and then injected with low-dose STZ, which would closely mimic the metabolic characteristic of human T2DM.[16,17] The liver plays a significant role in glycemic control between meals because it is the main organ that regulates glucose transformation.[18] In traditional medicines, along with the antidiabetic activity, negative consequences appeared and puzzled the patients. Some herbs and natural compounds were found to have hypoglycemic effect in recent studies.[19] D-Pinitol is a natural compound extracted from Pinaceae plants or Leguminosae and was reported as having a hypoglycemic effect.[20]

In summary, on the basis of our results, D-pinitol showed dose-dependent reduction of FBG and improvement of body weight, oral glucose tolerance, and insulin tolerance of T2DM rats. D-Pinitol lowered the concentration of FINS in diabetic rats, which meant it is helpful to enhance the insulin sensitivity of the body, and relieved the symptom of insulin resistance. D-Pinitol treatment also enhanced ISI, which meant D-pinitol increased the ability of the body to take advantage of insulin to accelerate glucose metabolism. We considered HOMA-β as the indicator to evaluate the function of pancreatic β-cells. However, D-pinitol showed a weak effect on pancreatic β-cells in this investigation. These results proved the positive effects of D-pinitol on relieving hyperglycemia and insulin resistance in T2DM rats. It also strengthened the ability of the body in glucose tolerance and the sensitivity to insulin. The PI3K/Akt pathway plays an important role in the metabolic effect of insulin,[21,22] and Akt/PKB is a critical node downstream of the PI3K/Akt pathway. Any fluctuation of Akt activation causes the pathophysiological properties of various complex diseases.[23,24] D-Pinitol, in this research, had favorable effects on mediating the activation of PI3K/Akt pathway signaling and alleviating insulin resistance of T2DM rats. The expressions of PI3Kp85 and PI3Kp110 subunits in D-pinitol-treated groups showed a dose-dependent increasing tendency. During the experiment, stimulation with high-density insulin can cause up-regulation of PI3Kp85 protein, which would give a negative feedback on insulin sensitivity in return and affect the activity of downstream molecules to inhibit the continuous conduction of signal.[25]

D-Pinitol also increased the amounts of phosphorylated Akt at Ser473 in a dose-dependent manner, and p-Akt inhibited the GSK-3β protein directly. GSK-3β activity can be acutely inactivated by insulin signaling through insulin receptor substrate-1 (IRS-1), PI3K, and the action of Akt to phosphorylate specific serine residues on the enzyme. An additional substrate of GSK-3β is IRS-1, and phosphorylation of IRS-1 on serine/threonine residues leads to impairment of insulin signaling.[26] Therefore, GSK-3β can negatively modulate the insulin action on GS protein and, potentially, on glucose transport activity.

Besides, according to the data, rats in the NH group exhibited no difference from the NC group, which explained that D-pinitol has no negative effect on normal rats.

DOI: 10.1021/acs.jafc.5b01238
J. Agric. Food Chem. 2015, 63, 6019−6026

In conclusion, D-pinitol relieves insulin resistance through the PI3K/Akt pathway, thereby reducing the concentration of blood glucose. We confirmed that this study investigated the probable mechanism of D-pinitol in relieving symptoms of T2DM, and D-pinitol can be developed into an effective drug for the treatment of T2DM when sufficient further research on D-pinitol can be performed.

AUTHOR INFORMATION

Corresponding Author

*(Z.Z.) Phone: (+86) 022 60912431. Fax: (+86) 022 60912431. E-mail: zhangzesheng@tust.edu.cn.

Funding

This research is supported by the National Science-Technology Pillar Program (2012BAD33B05) and the Program for Changjiang Scholars and Innovative Research Team in University of the Ministry of Education of the People's Republic of China (Grant IRT1166).

Notes

The authors declare no competing financial interest.

ABBREVIATIONES USED

HFD	high-fat diet
STZ	streptozocin
SD	Sprague−Dawley
T2DM	type 2 diabetes mellitus
FBG	fasting blood glucose
OGTT	oral glucose tolerance test
ITT	insulin tolerance test
FINS	fasting serum insulin
ISI	insulin sensitivity index
HOMA-β	homeostasis model assessment-β
PI3K	phosphatidylinositol-3-kinase
Akt	protein kinase B
p-Akt	phospho-Akt
GSK-3β	glycogen synthesis kinase-3β
GS	glycogen synthesis
IRS-1	insulin receptor substrate-1
NC	normal control group
DC	diabetic control group
LD	low-dosage group
HD	high-dosage group
NH	normal high-dosage group
RT-PCR	real-time polymerase chain reaction
ECL	chemiluminescent reagent
PBS	phosphate buffer saline
SPSS	statistical product and service solutions
AUG	area under curve of glucose

REFERENCES

(1) Zhang, B. B.; Moller, D. E. New approaches in the treatment of type 2 diabetes. *Curr. Opin. Chem. Biol.* **2000**, *4*, 461−467.

(2) Sharma, A. K.; Bharti, S.; Goyal, S.; Arora, S.; Nepal, S.; Kishore, K.; Joshi, S.; Kumari, S.; Arya, D. S. Upregulation of PPARγ by *Aegle marmelos* ameliorates insulin resistance and β-cell dysfunction in high fat diet fed-streptozotocin induced type 2 diabetic rats. *Phytother. Res.* **2011**, *25*, 1457−1465.

(3) Gandhi, G. R.; Stalin, A.; Balakrishna, K.; Ignacimuthu, S.; Paulraj, M. G.; Vishal, R. Insulin sensitization via partial agonism of PPARγ and glucose uptake through translocation and activation of GLUT4 in PI3K/p-Akt signaling pathway by embelin in type 2 diabetic rats. *Biochim. Biophys. Acta, Gen. Subj.* **2013**, *1830*, 2243−2255.

(4) Lo, H.-Y.; Ho, T.-Y.; Li, C.-C.; Chen, J.-C.; Liu, J.-J.; Hsiang, C.-Y. A novel insulin receptor-binding protein from *Momordica charantia* enhances glucose uptake and glucose clearance in vitro and in vivo through triggering insulin receptor signaling pathway. *J. Agric. Food Chem.* **2014**, *62*, 8952−8961.

(5) Anderson, A. B.; MacDonald, D. L.; Fischer, H. O. L. The structure of pinitol1. *J. Am. Chem. Soc.* **1952**, *74*, 1479−1480.

(6) Anderson, A. B. Pinitol from sugar pine stump wood. *Ind. Eng. Chem.* **1953**, *45*, 593−596.

(7) Kim, M. J.; Yoo, K. H.; Kim, J. H.; Seo, Y. T.; Ha, B. W.; Kho, J. H.; Shin, Y. G.; Chung, C. H. Effect of pinitol on glucose metabolism and adipocytokines in uncontrolled type 2 diabetes. *Diabetes Res. Clin. Pract.* **2007**, *77*, S247−S251.

(8) Hudlicky, T.; Price, J. D.; Rulin, F.; Tsunoda, T. Efficient and enantiodivergent synthesis of (+)- and (−)-pinitol. *J. Am. Chem. Soc.* **1990**, *112*, 9439−9440.

(9) Kang, M.-J.; Kim, J.-I.; Yoon, S.-Y.; Kim, J. C.; Cha, I.-J. Pinitol from soybeans reduces postprandial blood glucose in patients with type 2 diabetes mellitus. *J. Med. Food* **2006**, *9*, 182−186.

(10) Yamashita, Y.; Yamaoka, M.; Hasunuma, T.; Ashida, H.; Yoshida, K.-i. Detection of orally administered inositol stereoisomers in mouse blood plasma and their effects on translocation of glucose transporter 4 in skeletal muscle cells. *J. Agric. Food Chem.* **2013**, *61*, 4850−4854.

(11) Dang, N. T.; Mukai, R.; Yoshida, K.; Ashida, H. D-Pinitol and myo-inositol stimulate translocation of glucose transporter 4 in skeletal muscle of C57BL/6 mice. *Biosci., Biotechnol., Biochem.* **2010**, *74*, 1062−7.

(12) Avramoglu, R. K.; Basciano, H.; Adeli, K. Lipid and lipoprotein dysregulation in insulin resistant states. *Clin. Chim. Acta* **2006**, *368*, 1−19.

(13) Mehdi, M. Z.; Vardatsikos, G.; Pandey, S. K.; Srivastava, A. K. Involvement of Insulin-like growth factor type 1 receptor and protein kinase Cδ in bis(maltolato)oxovanadium(IV)-induced phosphorylation of protein kinase B in HepG2 cells. *Biochemistry* **2006**, *45*, 11605−11615.

(14) Buse, J. B. Type 2 diabetes mellitus in 2010: individualizing treatment targets in diabetes care. *Nat. Rev. Endocrinol.* **2011**, *7*, 67−68.

(15) Båvenholm, P. N.; Pigon, J.; Östenson, C.-G.; Efendic, S. Insulin sensitivity of suppression of endogenous glucose production is the single most important determinant of glucose tolerance. *Diabetes* **2001**, *50*, 1449−1454.

(16) Srinivasan, K.; Ramarao, P. Animal models in type 2 diabetes research: an overview. *Indian J. Med. Res.* **2007**, *125*, 451−72.

(17) Karasawa, H.; Nagata-Goto, S.; Takaishi, K.; Kumagae, Y. A novel model of type 2 diabetes mellitus based on obesity induced by high-fat diet in BDF1 mice. *Metab., Clin. Exp.* **2008**, *58*, 296−303.

(18) Srinivasan, K.; Viswanad, B.; Asrat, L.; Kaul, C. L.; Ramarao, P. Combination of high-fat diet-fed and low-dose streptozotocin-treated rat: a model for type 2 diabetes and pharmacological screening. *Pharmacol. Res.* **2005**, *52*, 313−320.

(19) Kuzuya, T.; Nakagawa, S.; Satoh, J.; Kanazawa, Y.; Iwamoto, Y.; Kobayashi, M.; Nanjo, K.; Sasaki, A.; Seino, Y.; Ito, C.; Shima, K.; Nonaka, K.; Kadowaki, T. Report of the Committee on the classification and diagnostic criteria of diabetes mellitus. *Diabetes Res. Clin. Pract.* **2002**, *55*, 65−85.

(20) Sivakumar, S.; Subramanian, S. P. Pancreatic tissue protective nature of D-pinitol studied in streptozotocin-mediated oxidative stress in experimental diabetic rats. *Eur. J. Pharmacol.* **2009**, *622*, 65−70.

(21) Jiang, S.; Ren, D.; Li, J.; Yuan, G.; Li, H.; Xu, G.; Han, X.; Du, P.; An, L. Effects of compound K on hyperglycemia and insulin resistance in rats with type 2 diabetes mellitus. *Fitoterapia* **2014**, *95*, 58−64.

(22) Vareda, P. M. P.; Saldanha, L. L.; Camaforte, N. A. d. P.; Violato, N. M.; Dokkedal, A. L.; Bosqueiro, J. R. *Myrcia bella* leaf extract presents hypoglycemic activity via PI3k/Akt insulin signaling pathway. *Evidence-Based Complement. Altern. Med.* **2014**, *2014*, No. 543606.

(23) Manning, B. D.; Cantley, L. C. AKT/PKB signaling: navigating downstream. *Cell* **2007**, *129*, 1261−1274.

(24) Liu, S.-H.; Chang, Y.-H.; Chiang, M.-T. Chitosan reduces gluconeogenesis and increases glucose uptake in skeletal muscle in

DOI: 10.1021/acs.jafc.5b01238
J. Agric. Food Chem. 2015, 63, 6019−6026

streptozotocin-induced diabetic rats. *J. Agric. Food Chem.* **2010**, *58*, 5795−5800.
(25) Nolan, C. J.; Damm, P.; Prentki, M. Type 2 diabetes across generations: from pathophysiology to prevention and management. *Lancet* **2011**, *378*, 169−181.
(26) Wang, L.-Y.; Wang, Y.; Xu, D.-S.; Ruan, K.-F.; Feng, Y.; Wang, S. MDG-1, a polysaccharide from *Ophiopogon japonicus*, exerts hypoglycemic effects through the PI3K/Akt pathway in a diabetic KKAy mouse model. *J. Ethnopharmacol.* **2012**, *143*, 347−354.

DOI: 10.1021/acs.jafc.5b01238
J. Agric. Food Chem. 2015, 63, 6019−6026

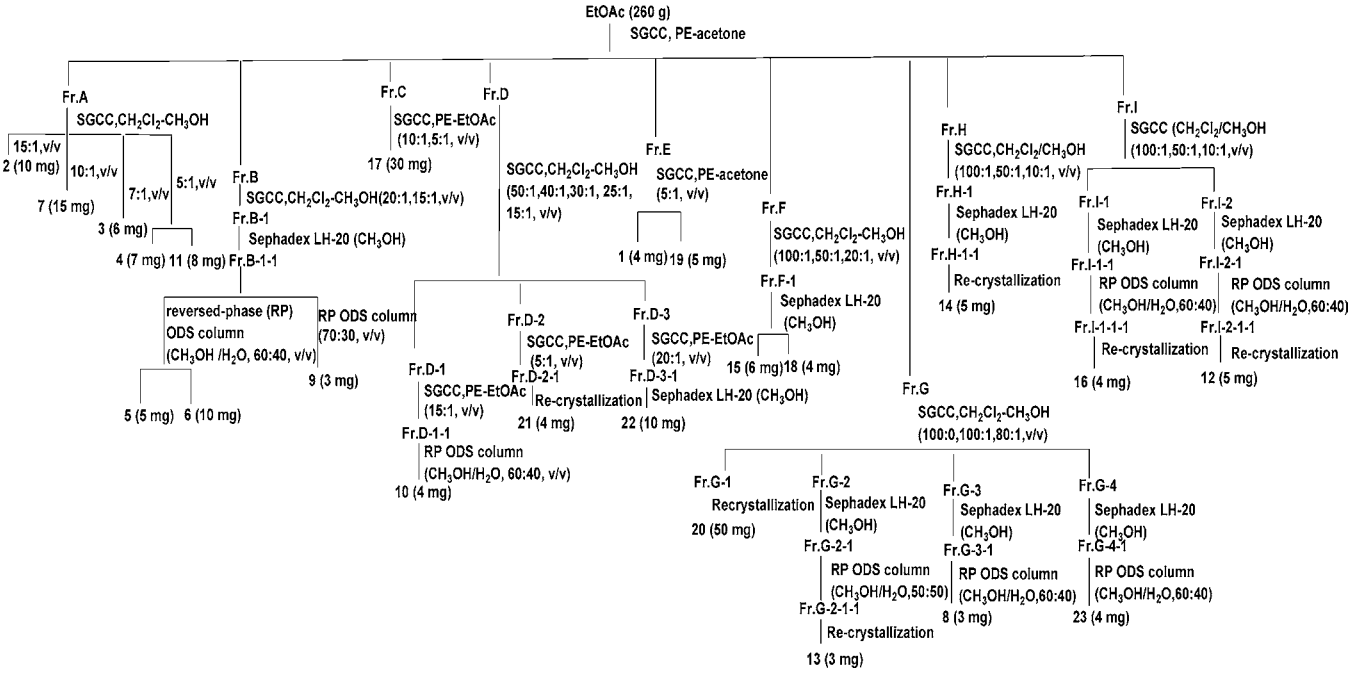

Figure 1. Schematic representation of the extraction and isolation procedure.

voucher specimen was deposited in Shenyang Pharmaceutical University.

General Experimental Procedures. Column chromatography (CC) was performed with silica gel (SiO_2 300−400 mesh, Qingdao Marine Chemical Group, Co. Qingdao, Shandong, China), reversed phase ODS (300−400 mesh, Agela Technologies Co. Tianjin, China), and Sephadex LH-20 (Pharmacia, Co. Tokyo, Japan). NMR spectra were recorded with a Bruker ARX-600 (^{1}H, 600 MHz; ^{13}C, 150 MHz) spectrometer in DMSO-d_6 or $CDCl_3$ with tetramethylsilane as internal standard. All other chemical agents, including CH_3OH, ethanol, petroleum ether, ethyl acetate, and *n*-butanol, were of analytical grade and were obtained from Tianjin DaMao Chemical Reagents Co. (Tianjin, China)

Extraction and Isolation. To obtain the active constituents, the stems of green asparagus (30 kg) were extracted with 75% EtOH (bp 78.1 °C) under reflux at 80 °C, on the basis of the results of several published references.[9,10] After evaporation of the alcohol, the residual aqueous solution was subsequently extracted with water, petroleum ether (PE, 388 g), ethyl acetate (EtOAc, 260 g), and *n*-butanol (*n*-BuOH, 200 g). The extraction and isolation scheme is shown in Figure 1.

Phytochemical study of green asparagus led to the isolation of 23 compounds, including 7 steroids (**1**−**7**), 2 esters (**8**, **11**), 3 arynes (**9**, **10**, **12**), 1 lignin (**13**), 3 flavonoids (**14**−**16**), 4 alkaloids (**17**−**20**), and 3 aliphatic series (**21**−**23**): 24(*R*)-24-ethyl-5α-cholestane-3β,5,6β-triol (**1**),[11] stigmasterol (**2**),[12] (22*E*,24*S*)-5α,8α-epidioxy-24-methylcholesta-6,22-dien-3β-ol (**3**),[13] 5α,8α-epidioxy-(20*S*,22*E*,24*R*)-ergosta-6,22-dien-3β-ol (**4**),[14] 24(*S*)-cycloart-25-ene-3β,24-diol (**5**),[15] α-spinasterol (**6**),[16] yamogenin (**7**),[17] 1,3-*O*-diferuloylglycerol (**8**),[18] methyl *p*-hydroxycinnamate (**11**),[19] 4-[5-(4-methoxyphenoxy)-3-penten-1-ynyl] phenol (**9**),[20] 4-[5-(4-hydroxyphenoxy)-3-penten-1-ynyl]phenol (**10**),[20] 4,4-dihydroxy-2-methyl-3-[(4-hydroxyphenyl)ethynyl]biphene (**12**),[21] syringaressinol (**13**),[22] quercetin (**14**),[23] kaempferol (**15**),[24] quercitrin (**16**),[25] aurantiamide acetate (**17**),[26] neoechinulin A (**18**),[27] 3-pyridinecarboxylic acid, 1,6-dihydro-6-oxo-methyl ester (**19**), 2-(2-hydroxytetracosanoylmino)-1,3,4-octadecanetriol (**20**),[28] hexadecanoic acid, 2,3-dihydroxypropyl ester (**21**),[29] 12,13,15-trihydroxy-9-octadecenoic acid (**22**),[30] and 2-octadecendioic acid (**23**).[31] The known compounds **1**−**23** (Figure 2) were identified by comparison of their NMR data with those reported in the literature. The purity of each compound ranged from 95 to 98%, as determined by HPLC analysis. Furthermore, compounds **1**, **3**, **5**, **11**, **12**, and **17**−**20** were extracted from the *Asparagus* genus for the first time.

Cell Culture. Murine hepatic stellate cells (t-HSC/Cl-6) were routinely maintained in Dulbecco's modified Eagle medium (DMEM) supplemented with 10% heat-inactivated fetal bovine serum and antibiotics (100 U/mL penicillin and streptomycin) in a humidified atmosphere containing 5% CO_2 at 37 °C.

Cell Viability Assay. t-HSC/Cl-6 cells were cultured in 96-well plates (1×10^4 cells/well) overnight and then treated with the individual compounds at various concentrations with or without TNF-α for another 48 h. Cell viability was then assessed by the MTT assay. After removal of all of the remaining liquid in the wells, 100 μL of fresh medium containing MTT reagent (5 μg/mL) was added to each well and incubated for 3 h at 37 °C. After that, the formazan crystals were dissolved with dimethyl sulfoxide, and the reduction of cell viability was determined by measuring the absorbance at 490 nm using a microplate reader. For this experiment, each of the 23 compounds was dissolved in dimethyl sulfoxide to give a 0.1 M stock solution.

RNA Extraction and Quantitative RT-PCR. Total RNA was extracted from the treated cells. The quality and quantity of RNA were determined. Quantitative real-time PCR was carried out using the ABI Prism 7900-HT sequence detection system (96 wells) as described.[32] The following primers were designed for mouse cytokine analysis: tumor necrosis factor-α (TNF-α), forward 5′-CCCTCACACTCAGATCATCTTCT-3′ and reverse 5′-GCTACGACGTGGGCTACAG-3′; IL-6, forward 5′-TAGTCCTTCCTACCCCAATTTCC-3′ and reverse 5′-TTGGTCCTTAGCCACTCCTTC-3′; TGF-β1, forward 5′-ACCTGCAAGACCATCGACAT-3′ and reverse 5′-GGTTTTCTCATAGATGGCGT-3′; activin C, forward 5′-CCGTGAGATTGGCTGGAAT-3′ and reverse 5′-GCGTTGGCTTTGAGCAGAT-3′. β-Actin was used as internal control.

Western Blotting Analyses. In addition to RNA, total protein was also extracted from the treated cells. In brief, the cells were lysed in RIPA buffer (Cell Signaling Technology, USA) for 15 min on water ice. After brief sonication, the cell lysate was centrifuged at 14000*g* for 15 min at 4 °C. The supernatant was resolved by SDS-PAGE using 12% gel. The proteins in the gel were then transferred to a nitrocellulose membrane. The following primary antibodies were used for immunoblotting: anti-TGF-β1 (1:1000), anti-p-Smad2 (1:1000), anti-activin C (1:1000), anti-p-ERK (1:1000), anti-p-JNK (1:1000), anti-c-Jun (1:1000), anti-c-Fos (1:1000), and anti-β-actin

DOI: 10.1021/acs.jafc.5b01490
J. Agric. Food Chem. 2015, 63, 6027−6034

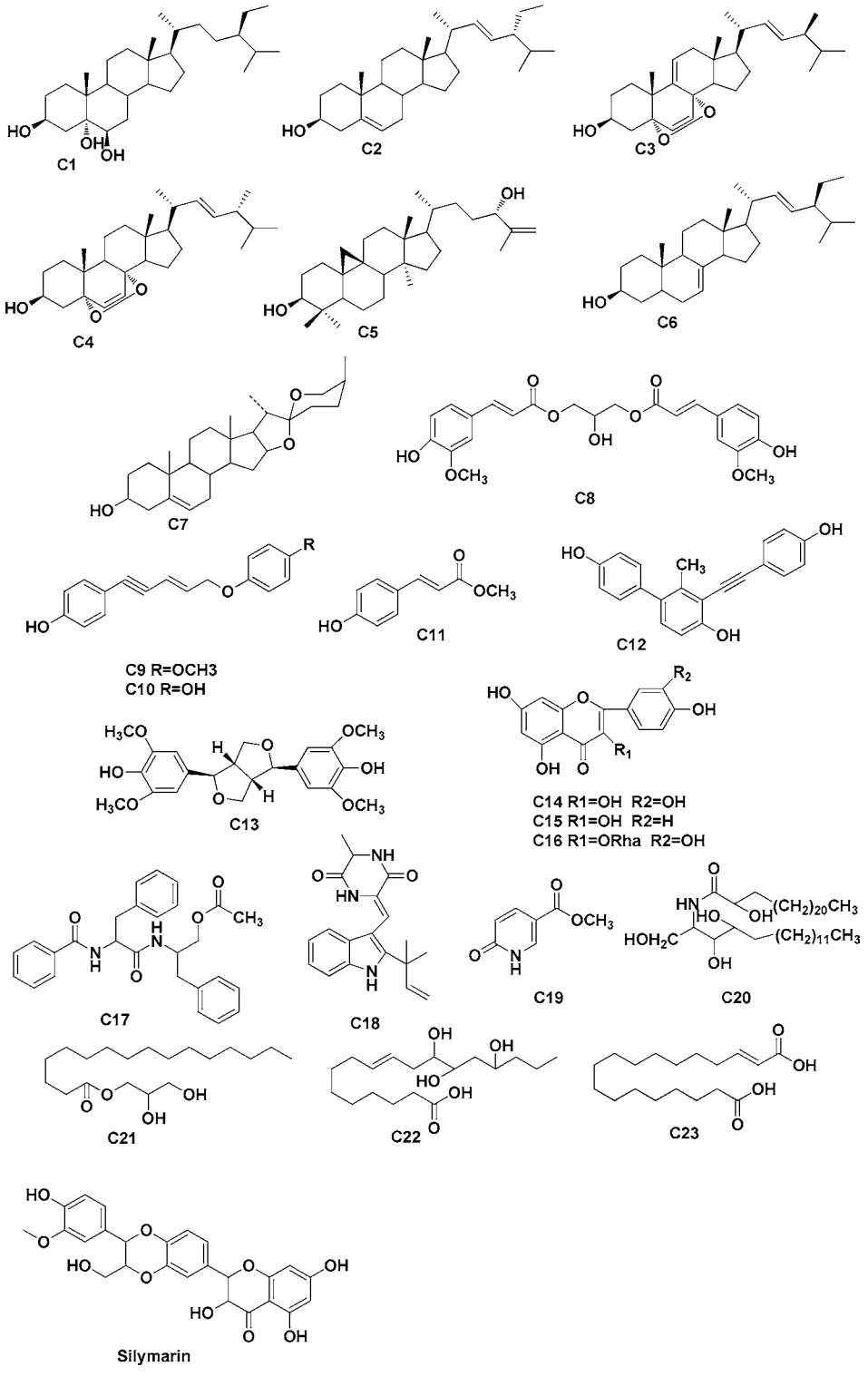

Figure 2. Chemical structures of isolated compounds **1**−**23** and silymarin.

(1:3000). Signals were detected by an enhanced chemiluminescence technique (Amersham Life Science, USA).

Quantification of the Active Compounds from Green Asparagus. For HPLC analysis, the top four active compounds (**3**, **4**, **10**, **12**) were analyzed using a HPLC system (LC3000, Beijing ChuangXinTongHeng Science & Technology Co., Ltd., Beijing, China) equipped with a UV lamp (Beijing ChuangXinTongHeng Science & Technology Co., Ltd.) and a C_{18} reversed-phase analytical column (Agilent HC-C18, 4.6 × 250 mm, 5 μm; Agilent Technologies Inc., Santa Clara, CA, USA). The HPLC mobile phase was composed of methanol (solvent A) and water (solvent B). The linear gradient elution system was as follows: 0−20 min, 53−65% (v/v) A; 20−30 min, 65−80% (v/v) A; 30−45 min, 80−90% (v/v) A; 45−60 min, 90−100% (v/v) A, and 60−90 min, 100% (v/v) A, at a flow rate of 1 mL/min. The quantification of the top four active compounds by UV was performed at 210 nm. The column temperature was maintained at 30 °C, and the injection volume was 20 μL. In addition, to quantitate the top four active compounds, namely, (22*E*,24*S*)-5α,8α-epidioxy-24-methylcholesta-6,22-dien-3β-ol, 5α,8α-epidioxy-(20*S*,22*E*,24*R*)-ergosta-6,22-dien-3β-ol, 4-[5-(4-hydroxyphenoxy)-3-penten-1-ynyl]phenol,

DOI: 10.1021/acs.jafc.5b01490
J. Agric. Food Chem. 2015, 63, 6027−6034

and 4,4-dihydroxy-2-methyl-3-[(4-hydroxyphenyl)ethynyl]biphene, were measured at concentrations of 0.025, 0.05, 0.1, 0.2, and 0.5 g/L to prepare a calibration curve for each compound. The percentage of the top four active compounds was calculated using eq 1:

$$\%\ \text{of compd} = A(\text{peak area of compd}) / A(\text{total peak areas of compd}) \times 100 \quad (1)$$

Statistical Analysis. All of the results were expressed as means ± SDs of three determinations at each concentration for each sample. Analysis of variance (ANOVA) was performed, and the mean separation was done by LSD ($p \leq 0.05$) using the SPSS 16.0 program for Windows (SPSS Inc., Chicago, IL, USA).

The HPLC chromatograms were recorded and analyzed using a CXTH-3000 Data Station (CXTH Co., Ltd., Beijing, China), and the results were calculated using Windows Excel 2010.

RESULTS

Phytochemical Characterization. Phytochemical investigation of the stem of green asparagus resulted in the isolation of 23 compounds, including 7 steroids, 2 esters, 3 arynes, 1 lignan, 3 flavonoids, 4 alkaloids, and 3 aliphatic series. Among these, compounds **1**, **3**, **5**, **11**, **12**, and **17**−**20** were obtained from this genus for the first time. The structures of compounds **1**−**23** were determined using a combination of NMR spectra and then identified by comparison of the spectral data with those reported in the literature (Table 1).

Among the tested compounds, compounds **3**, **4**, **7**, **8**, **10**−**12**, **16**, and **20** showed potent antihepatic fibrosis activity, and the relative order of potency was **10** > **12** > **3** > **8** > **4** > **20** > **16** > **7** > **11** as depicted in Table 2. We concluded that the high activity of compounds **10** and **12** could be due to their acetylenic bonds, whereas a significant difference was observed between the activity of compounds **9** and **10**, both of which had the same skeleton, except for the 16-hydroxyl (**10**) or methoxyl (**9**), suggesting that the hydroxyls may be more important for the antihepatic fibrosis activity. In addition, comparison of compounds **1**−**7** showed that the antihepatic fibrosis capacities of steroidal compounds may be influenced by the ring containing oxygen.

Quantification of the Top Four Active Compounds. The contents of **3**, **4**, **10**, and **12** in *A. officinalis* L. were determined by HPLC-UV analysis and are shown in Table 3.

Preliminary Screening of Inhibitory Activity against Self-Activated t-HSC/Cl-6 Cells. All of the extracts and compounds isolated were assayed for their inhibitory activities against self-activated t-HSC/Cl-6 cells, and the results are shown in Table 2. The PE- and EtOAc-extracted fractions greatly inhibited the activation of t-HSC/Cl-6 cells, with IC_{50} values of 87.77 and 45.52 μg/mL, respectively. At the same time, compounds **3**, **4**, **7**, **8**, **10**−**12**, **16**, and **20** isolated from the EtOAc-extracted fraction were more potent than the positive control drug silymarin (IC_{50} = 352.11 μM) or Fufang BiejiaRuangan Pian (IC_{50} = 212.34 μg/mL) at inhibiting the activation of t-HSC/Cl-6 cells, with IC_{50} values of 76.70, 111.08, 172.70, 95.22, 36.65, 196.30, 56.04, 166.34, and 125.11 μM, respectively. The inhibitory activity of these compounds against the activation of t-HSC/Cl-6 cells suggested that they might contribute to the inhibitory activity of the EtOAc-extracted fraction against hepatic fibrosis. Furthermore, the strong inhibitory activity of compounds **10** and **12** toward the activated t-HSC/Cl-6 cells could possibly be related to their different phytochemical properties.

Table 1. Compounds Isolated from the Stems of Green Asparagus

kind	compd	name	ref
steroids	**1**	24(*R*)-24-ethyl-5α-cholestane-3β,5,6β-triol	11
	2	stigmasterol	12
	3	(22*E*,24*S*)-5α,8α-epidioxy-24-methylcholesta-6,22-dien-3β-ol	13
	4	5α,8α-epidioxy-(20*S*,22*E*,24*R*)-ergosta-6,22-dien-3β-ol	14
	5	24(*S*)-cycloart-25-ene-3β,24-diol	15
	6	α-spinasterol	16
	7	yamogenin	17
esters	**8**	1,3-*O*-diferuloylglycerol	18
	11	methyl *p*-hydroxycinnamate	19
arynes	**9**	4-[5-(4-methoxyphenoxy)-3-penten-1-ynyl] phenol	20
	10	4-[5-(4-hydroxyphenoxy)-3-penten-1-ynyl] phenol	20
	12	4,4-dihydroxy-2-methyl-3-[(4-hydroxyphenyl) ethynyl]biphene	21
lignan	**13**	syringaressinol	22
flavonoids	**14**	quercetin	23
	15	kaempferol	24
	16	quercitrin	25
alkaloids	**17**	aurantiamide acetate	26
	18	neoechinulin A	27
	19	3-pyridinecarboxylic acid, 1,6-dihydro-6-oxo-methyl ester	
	20	2-(2-hydroxytetracosanoylmino)-1,3,4-octadecanetriol	28
aliphatic series	**21**	hexadecanoic acid, 2,3-dihydroxypropyl ester	29
	22	12,13,15-trihydroxy-9-octadecenoic acid	30
	23	2-octadecenedioic acid	31

Growth Inhibitory Effects of Compounds 3, 4, 10, and 12 toward TNF-α-Activated t-HSC/Cl-6 Cells. HSC activation, which includes initiation and perpetuation, is an early event in liver fibrogenesis. The activation of HSCs converts normal, quiescent vitamin A-rich cells into myofibroblast-like cells characterized by proliferation, chemotaxis, fibrogenesis, contractility, matrix degradation, retinoid loss, and the release of white blood cell chemoattractant/cytokine.[33−37] On the basis of the preliminary growth inhibitory screening data and considering the yield of phytochemical isolation, compounds **3**, **4**, **10**, and **12** were subjected to further investigation (Figure 3); **8** was not evaluated due to its low yield, although it also has better inhibitory activity on self-activated t-HSC/Cl-6 cells. t-HSC/Cl-6 cells were treated with these compounds (one at a time) plus TNF-α for 48 h, and the growth of the t-HSC/Cl-6 cells was determined. According to the data shown in Figure 3, compounds **3**, **4**, and **10**, but not **12**, could significantly decrease the growth of activated t-HSC/Cl-6 in a dose-dependent manner, and the extents of growth inhibition exerted by these compounds were even greater than that exerted by the positive control silymarin.

DOI: 10.1021/acs.jafc.5b01490
J. Agric. Food Chem. 2015, 63, 6027−6034

Table 2. Inhibitory Activities of Crude Extract and Isolated Compounds from Green Asparagus

extract/compd	IC_{50} (μM),[a] hepatic fibrosis	extract/compd	IC_{50} (μM/μg/mL),[a] hepatic fibrosis
1	>200	**16**	166.34 ± 1.13[b]
2	>200	**17**	>200
3	76.70 ± 1.68[b]	**18**	>200
4	111.08 ± 3.90[b]	**19**	>200
5	>200	**20**	125.11 ± 1.55[b]
6	>200	**21**	>200
7	172.70 ± 1.33[b]	**22**	>200
8	95.22 ± 1.61[c]	**23**	>200
9	>200	PE extract[c]	87.77 ± 0.62[d]
10	36.65 ± 1.49[b]	EtOAc extract[c]	45.52 ± 0.71[d]
11	196.30 ± 15.94[b]	*n*-BuOH extract[c]	160.56 ± 8.96[d]
12	56.04 ± 1.49[b]	water extract[c]	>200
13	>200	**positive control**	
14	>200	silymarin	352.11 ± 0.19
15	>200	Fufang Biejia Ruangan Pian[c]	261.29 ± 2.46

[a]IC_{50} values, expressed as means ± SDs, were calculated from the least-squares regression equations in the plot of the logarithm of three graded concentrations vs % inhibition using SPSS 16.0 program for Windows (SPSS Inc., Chicago, IL, USA). [b]Significant differences with respect to positive control (silymarin) at the $p < 0.01$ level. [c]The concentration unit of these extracts is μg/mL. [d]Significant differences with respect to positive control (Fufang Biejia Ruangan Pian) at the $p < 0.01$ level.

Table 3. Retention Times and Contents of 3, 4, 10, and 12 As Resolved by HPLC Analysis

compd	regression eq	R^2	retention time (min)	%
3	$y = 36.95x - 0.062$	0.999	57.048	0.012
4	$y = 14.94x + 0.132$	0.999	62.043	0.016
10	$y = 436.4x - 1.865$	0.999	33.848	0.069
12	$y = 161.2x - 0.112$	0.999	14.385	0.016

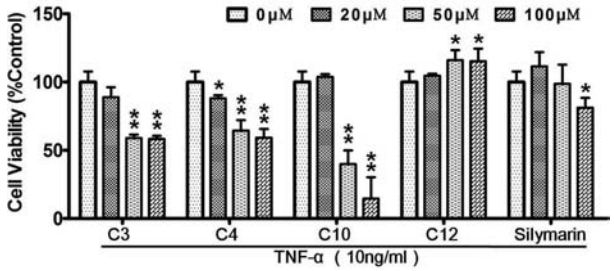

Figure 3. Effects of compounds **3**, **4**, **10**, and **12** on the viability of murine hepatic stellate cells (t-HSC/Cl-6). t-HSC/Cl-6 cells were seeded in 96-well plates (1×10^4 cells/well) for 24 h and then treated with TNF-α (10 ng/mL) and the four compounds at various concentrations for 48 h. Silymarin with TNF-α (10 ng/mL) was used as positive control. Viable cell numbers were estimated via MTT assay. Data represent the means ± SDs of three independent experiments, each performed in triplicate. (*) $p \leq 0.05$; (**) $p \leq 0.01$.

Compounds 3, 4, 10, and 12 Decrease Cytokine Released by TNF-α-Activated t-HSC/Cl-6 Cells. Besides HSC activation, ECM deposition and other events like oxidative stress, inflammation, and immune responses are also involved in the fibrogenic response. The levels of transforming growth factor beta 1 (TGF-β1) and activin C (Figure 4), both of which are HSC activation-associated factors, were increased in TNF-α activated t-HSC/Cl-6 cells. In addition, the levels of TNF-α and IL-6 were also increased in these cells. However, treatment of these cells with compounds **3**, **4**, **10**, and **12** decreased the transcript levels of both TGF-β1 and activin C, as well as inhibiting the release of TNF-α, while having no effect on the level of IL-6.

Compounds 3, 4, 10, and 12 Change the Expression Levels of HSC Activation-Associated Genes. TGF-β1 produced by HSCs acts as a potent fibrogenic signal as it increases the production of collagen I and other matrix constituents such as fibronectin and proteoglycans.[35,38] These effects are induced by the interaction between TGF-β1 and the membrane receptor complex formed by TβRI and TβRII, leading to the phosphorylation of intracellular mediators, namely, Smad proteins (Figure 5). The antifibrotic mechanism is mainly the result of the down-regulation of the TGF-β1/Smad signaling pathway. To further investigate the antifibrotic mechanism of the tested compounds, changes in the expression levels of genes associated with TGF-β1/Smad signaling pathway and its downstream target genes were determined. Upon stimulation with TNF-α, the expression levels of TGF-β1, activin C, and p-Smad2 were increased. At the same time, increased levels of phosphorylated extracellular signal-regulated kinsase (ERK) and c-Jun N-terminal kinases (JNKs) were also detected. Down-regulation of the expression of TGF-β1 and activin C and modulation of its intracellular mediators Smad2 by **3**, **4**, **10**, and **12** were observed in the present study. The above-mentioned compounds attenuated TNF-α-induced ERK and JNK phosphorylations and also the expression level of c-Fos and c-Jun, the downstream targets of JNK.

DISCUSSION

In present study, 23 compounds (purity > 95%, % is referred to HPLC analysis) were isolated from green asparagus, and 9 of them were obtained from this genus for the first time. The structures of compounds **1**−**23** were determined using a combination of ^{1}H and ^{13}C NMR spectra and then identified by comparison of the spectral data with those reported previously in the literature.

During chronic liver injury, HSCs are activated, and their subsequent proliferation can cause ECM deposition, leading to scar formation and fibrosis. During the early stages of liver disease and hepatic fibrosis, the infiltrated immune cells produce and release high levels of TNF-α and IL-1β. Therefore, TNF-α has been implicated as a key effector molecule in the activation of HSCs through regulating the levels of cytokines, chemokines, and other adhesion molecules. Medicinal plants are often safe, cost-effective, and versatile and are therefore popular potential antifibrotic agents. There are two ways by which medicinal plants and their bioactive compounds and extracts could reduce liver fibrosis: inhibition of HSC activation and reduction of ECM deposition. In the present study, we investigated the effect of the crude extract of green asparagus as well as of the pure compounds isolated from the extract on TNF-α-activated quiescent HSCs.

Perpetuation of HSC activation results in the maintenance of the activated phenotype and therefore the generation of fibrosis.[39] Scars are formed through changes in HSC behavior, such as proliferation, fibrogenesis, contractility, chemotaxis, retinoid loss, white blood cell chemoattractant/cytokine release,

DOI: 10.1021/acs.jafc.5b01490
J. Agric. Food Chem. 2015, 63, 6027−6034

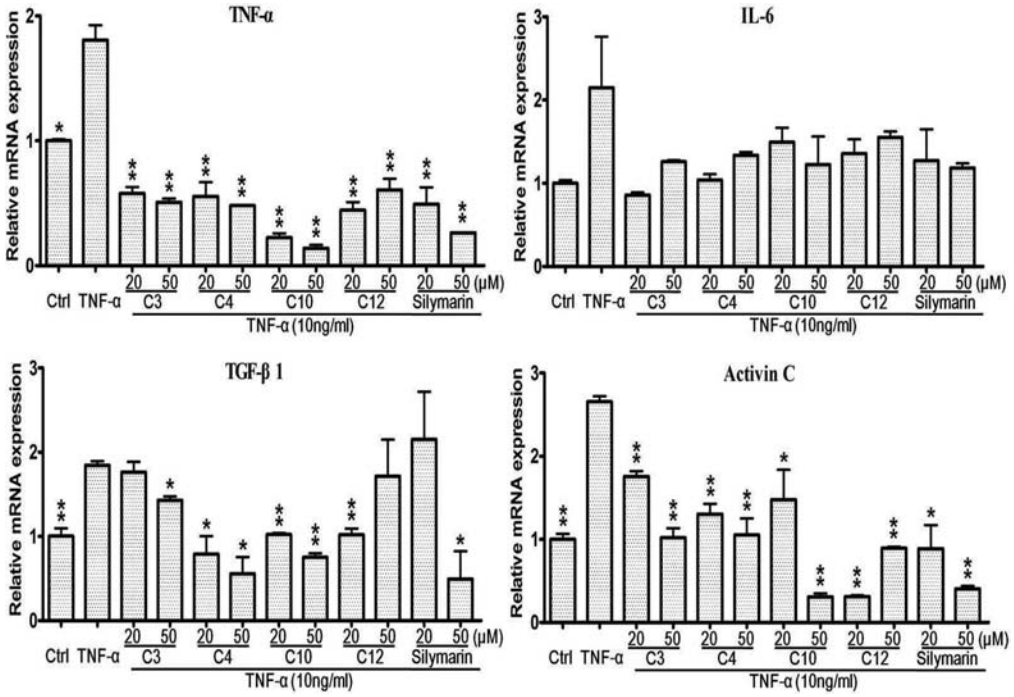

Figure 4. Changes in the expression levels of marker genes involved in inflammation (TNF-α, IL-6) and fibrosis (TGF-β1, activin C) in t-HSC/Cl-6 cells induced by the four compounds (**3**, **4**, **10**, and **12**). RNA was extracted from t-HSC/Cl-6 cells with or without TNF-α (10 ng/mL) and the four compounds or silymarin (positive control) at different concentrations for 48 h and subjected to real-time PCR analysis. Asterisks indicate significant differences in mRNA levels of TNF-α, IL-6, TGF-β1, or activin C with respect to TNF-α treatment only at the (*) $p \leq 0.05$ and (**) $p \leq 0.01$ levels, respectively.

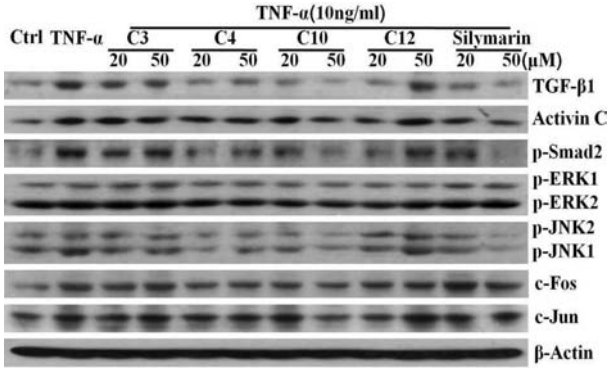

Figure 5. Inhibition of TGF-β/Smad-signaling-associated proteins mediated by the four compounds (**3**, **4**, **10**, and **12**) in t-HSC/Cl-6 cells. The levels of TGF-β/Smad signaling-associated proteins in t-HSC/Cl-6 cells activated with TNF-α (10 ng/mL) with or without the compounds for 48 h were determined and compared. β-Actin was used as a loading control. All experiments were performed three times. Representative data are shown.

and matrix degradation.[35] Cell proliferation further promotes liver fibrosis by increasing the number of collagen-producing cells. However, the growth of TNF-α-activated t-HSC/Cl-6 cells was significantly inhibited by compounds **3**, **4**, and **10**, and in dose-dependent manner, which suggested that bioactive compounds from green asparagus could improve liver fibrosis via inhibition of the proliferation of activated HSCs.

Inflammation and immune responses are involved in the initiation and perpetuation of fibrosis.[33,34,36,37] These pathways are potential targets for therapy aiming to reduce hepatic fibrosis. High levels of TNF-α released by immune cells are usually detected during the early stages of liver disease and hepatic fibrosis. The compounds from green asparagus could reduce TNF-α level in a time- and dose-dependent manner. This suggested that the inhibition of HSC activation by the compounds purified from green asparagus were probably due to their anti-inflammation capacity, stemming from the suppression of TNF-α expression.

Activation of TGF-β1/Smad signaling is one of the most important pro-fibrogenic pathways.[40] The disruption of this pathway is a common mode of action exerted by antifibrotic plants. Our findings were consistent with findings reported by other investigators. The compounds from green asparagus could decrease the level TGF-β1 and the phosphorylation of Smad2. Meanwhile, the phosphorylated forms of ERK and JNK, as well as the expression levels of c-Fos and c-Jun, the downstream targets of JNK, were also decreased. Impressively, activin C, a closely related member of the TGF-β superfamily of growth and differentiation factors, has been shown to inhibit regenerative DNA synthesis in hepatic cells and liver regeneration and to induce apoptosis.[41−45] In direct contrast, Wada et al. reported that overexpression or recombinant activin C stimulates DNA synthesis and growth of AML12 and AML12tAR cells and accelerates liver regeneration.[46,47] The present data showed that in TNF-α-activated t-HSC/Cl-6 cells, the level of activin C was increased, and after treatment with the compounds, it was reduced, but only at certain concentrations of the compounds.

In summary, our results demonstrated that compounds from green asparagus could inhibit HSC activation by inhibiting the proliferation of activated HSCs and attenuating TNF-α level. Moreover, TGF-β1/Smad signaling and MAPKs (ERK and JNK) signaling pathways were also involved in the antifibrosis mechanism of the tested compounds. Therefore, the current tested compounds from green asparagus may prove to be good

DOI: 10.1021/acs.jafc.5b01490
J. Agric. Food Chem. 2015, 63, 6027−6034

potential agents for the therapy of hepatic fibrosis. However, it should be noted that liver fibrosis treatment should take into account the versatility of its pathogenesis and should act upon all pathways involved, beginning with HSC activation and ECM deposition.

As a widely consumed vegetable worldwide, the current findings will no doubt have a positive effect on the search for protection against hepatic fibrosis, However, considering the contents analysis results in the current study, it may be difficult to acquire the necessary amount of the active compounds to protect against hepatic fibrosis unless a sufficient intake of asparagus can be ensured. It may therefore be necessary to produce green asparagus extracts or compounds and use them as a food supplement. Further study of the bioactive components from green asparagus on suppressing the development of hepatic fibrosis in vivo and at the clinical level will be necessary.

AUTHOR INFORMATION

Corresponding Authors

*(Y.Z.) Mail: Department of Traditional Chinese Medicine, Shenyang Pharmaceutical University, 103 Wenhua Road, Shenyang 110016, China. Phone: +86-24-23986521. E-mail: zyq4885@126.com.

*(X.B.) Mail: College of Life Science, Liaoning University, 66 Chongshan Road, Shenyang 110036, China. Phone: +86-24-62202232. Fax: +86-24-62202232. E-mail: xiulibi@gmail.com, xiulibi@lnu.edu.cn.

Author Contributions

‖C.Z. and C.J. contributed equally.

Funding

The work was financially supported by a program of Liaoning Excellent Talents in University to X.B. (LETU LR 2014001); the National Science Foundation of China to X.B. (Grants 81272333 and 81472821); and the Construction of R&D institute of state original new drug at Benxi of Liaoning Province to Y.Z. (2009ZX09301-012-105B).

Notes

The authors declare no competing financial interest.

ACKNOWLEDGMENTS

We express our gratitude to Senior Engineer Wen Li and Yi Sha from Shenyang Pharmaceutical University for the measurements of NMR spectra. We thank Dr. Alan K. Chang (Liaoning University) for revising the language of the manuscript.

REFERENCES

(1) Li, C.; Mao, R.; Li, Z.; Wang, Y.; Liu, X. Composition analysis and nutritional evaluation of the asparagus. *Mod. Food Sci. Technol.* **2011**, *27*, 1260−1263.

(2) Hafizur, R. M.; Kabir, N.; Chishti, S. Asparagus officinalis extract controls blood glucose by improving insulin secretion and β-cell function in streptozotocin-induced type 2 diabetic rats. *Br. J. Nutr.* **2012**, *108*, 1586−1595.

(3) Kim, B. Y.; Cui, Z. G.; Lee, S. R.; Kim, S. J.; Kang, H. K.; Lee, Y. K.; Park, D. B. Effects of *Asparagus officinalis* extracts on liver cell toxicity and ethanol metabolism. *J. Food Sci.* **2009**, *74*, H204−H208.

(4) Mormone, E.; George, J.; Nieto, N. Molecular pathogenesis of hepatic fibrosis and current therapeutic approaches. *Chem.-Biol. Interact.* **2011**, *193*, 225−231.

(5) Sanchez-Valle, V.; Chavez-Tapia, N. C.; Uribe, M.; Mendez-Sanchez, N. Role of oxidative stress and molecular changes in liver fibrosis: a review. *Curr. Med. Chem.* **2012**, *19*, 4850−4860.

(6) Reeves, H. L.; Friedman, S. L. Activation of hepatic stellate cells − a key issue in liver fibrosis. *Front. Biosci., Landmark Ed.* **2002**, *7*, d808−d826.

(7) Bataller, R.; Brenner, D. A. Liver fibrosis. *J. Clin. Invest.* **2005**, *115*, 209−218.

(8) Lim, Y. S.; Kim, W. R. The global impact of hepatic fibrosis and end-stage liver disease. *Clin. Liver Dis.* **2008**, *12*, 733−746 vii. .

(9) Sun, Z.; Huang, X.; Kong, L. A new steroidal saponin from the dried stems of *Asparagus officinalis* L. *Fitoterapia* **2010**, *81*, 210−213.

(10) Terada, K.; Honda, C.; Suwa, K.; Takeyama, S.; Oku, H.; Kamisako, W. Acetylenic compounds isolated from cultured cells of *Asparagus officinalis*. *Chem. Pharm. Bull.* **1995**, *43*, 564−566.

(11) Notaro, G.; Piccialli, V.; Sica, D. 3β,5α,6β-6P-Trihydroxylated sterols with a saturated nucleus from two populations of the marine sponge clzona copiosa. *J. Nat. Prod.* **1991**, *54*, 1570−1575.

(12) Ge, F.; Wang, Y.; Wang, J.; Yu, H.; Li, Z. Research on main bioactive components in red fermented rice. *J. Kunming Univ. Sci. Technol.* **2012**, *37*, 61−64.

(13) Ioannou, E.; Abdel-Razik, A. F.; Zervou, M.; Christofidis, D.; Alexi, X.; Vagias, C.; Alexis, M. N.; Roussis, V. 5α,8α-Epidioxysterols from the gorgonian *Eunicella cavolini* and the ascidian *Tridemnum inarmatum*: isolation and evaluation of their antiproliferative activity. *Steroids* **2009**, *74*, 73−80.

(14) Xu, Y.; Zhang, H. W.; Yu, C. Y.; Lu, Y.; Chang, Y.; Zou, Z. M. Norcyperone, a novel skeleton norsesquiterpene from *Cyperus rotundus* L. *Molecules* **2008**, *13*, 2474−2481.

(15) Pei, Y.; Wu, Q.; Shi, Y. Triterpenoids and other constituents from *Euphorbia humifusa*. *J. Chin. Chem. Soc.* **2007**, *54*, 1565−1572.

(16) Wang, B.; Li, J.; Zhao, Y.; Hu, C. Study of triterpenes from *Buddleia officinalis*. *J. Beijing Med. Univ.* **1996**, *28*, 472−477.

(17) Yang, Q.; Yang, C. Steroidal constituents of *Aspidistra elatior* from Yongshan, Yunnan. *Acta. Bot. Yunnanica* **2000**, *22*, 109−115.

(18) Luo, J.; Li, L.; Kong, L. Preparative separation of phenylpropenoid glycerides from the bulbs of *Lilium lancifolium* by high-speed counter-current chromatography and evaluation of their antioxidant activities. *Food Chem.* **2012**, *131*, 1056−1062.

(19) Pitchai, P.; Vlagi, R.; Mohan, P. S.; Gengan, R. M. A novel alkaloid,four alkaloid precursors and a coumarin form *Feronia Iimonia*. *Indian J. Chem., Sect. B: Org. Chem. Incl. Med. Chem.* **2012**, *51B*, 1771−1775.

(20) Terada, K.; Honda, C.; Suwa, K.; Takeyama, S.; Oku, H.; Kamisako, W. Acetylenic compounds isolated from cultured cells of *Asparagus officinalis*. *Chem. Pharm. Bull.* **1995**, *43*, 564−566.

(21) Xu, K. P.; Zou, H.; Li, F. S.; Xiang, H. L.; Zou, Z. X.; Long, H. P.; Li, J.; Luo, Y. J.; Li, Y. J.; Tan, G. S. Two new selaginellin derivatives from *Selaginella tamariscina* (Beauv.) Spring. *J. Asian Nat. Prod. Res.* **2011**, *13*, 356−360.

(22) Cheng, Y.; Zhou, J.; Ding, Z. Phenolic Constituents from *Manglietia crassipes*. *Acta Bot. Yunnanica* **2000**, *22*, 365−367.

(23) Ding, Y.; Guo, Y.; Ren, Y.; Dou, D.; Li, Q. Isolation of flavonoids from male flowers of *Eucommia ulmoides* and their anti-oxidantive activities. *Chin. Tradit. Herb. Drugs* **2014**, *45*, 323−327.

(24) Ni, F.; Chen, Z.; Xu, Q.; Yang, S.; Chen, D. Chemical constituents from *Rhodiola sachalinensis*. *Chin. Tradit. Herb. Drugs* **2013**, *44*, 798−802.

(25) Wang, P.; Luo, J.; Yang, M.; Kong, L. Chemical constituents of *Lobelia chinensis*. *Chin. Tradit. Herb. Drugs* **2013**, *44*, 794−797.

(26) Xu, J.; Zeng, S.; Qu, H. Chemical constituents from *Violayedoensis*. *Chin. Tradit. Herb. Drugs* **2010**, *41*, 1423−1425.

(27) Li, Y.; Li, X.; Kim, M. K.; Jung, S.; Choi, H. D.; Rho, J. R.; Son, B. W. Golmaenone, a new diketopiperazine alkaloid from the marine-derived fungus *Aspergillus* sp. *Chem. Pharm. Bull.* **2004**, *52*, 375−376.

(28) Qin, L.; Li, B.; Guan, J.; Zhang, G. Chemical study on *Aspergillus* sp. *Chin. J. Appl. Environ. Biol.* **2007**, *13*, 66−68.

(29) Li, F.; Deng, S.; Rao, Z.; Wu, H.; Xu, J.; Liu, X.; Zhong, H.; Zhao, D. A study on the chemical constituents of the South China sea hard coral *Montipora ramosa* bernard. *Chin. J. Mar. Drugs* **1997**, *61*, 4−6.

DOI: 10.1021/acs.jafc.5b01490
J. Agric. Food Chem. 2015, 63, 6027−6034

(30) Zhang, W.; Xiao, K.; Yang, G.; Chen, H. New compounds named sanleng acid from *Sparganiun stoloniferum*. *Chin. Tradit. Herb. Drugs* **1995**, *26*, 125−126.
(31) Sharma, A.; Chattopadhyay, S.; Mamdapur, V. R. PPL catalyzed monoesterification of α,ω-dicarboxylic acids. *Biotechnol. Lett.* **1995**, *17*, 939−942.
(32) Bi, X.; Xia, X.; Mou, T.; Jiang, B.; Fan, D.; Wang, P.; Liu, Y.; Hou, Y.; Zhao, Y. Anti-tumor activity of three ginsenoside derivatives in lung cancer is associated with Wnt/β-catenin signaling inhibition. *Eur. J. Pharmacol.* **2014**, *742*, 145−152.
(33) Friedman, S. L. Mechanisms of hepatic fibrogenesis. *Gastroenterology* **2008**, *134*, 1655−1669.
(34) Rockey, D. C. Translating an understanding of the pathogenesis of hepatic fibrosis to novel therapies. *Clin. Gastroenterol. Hepatol.* **2013**, *11*, 224−231 e1−5. .
(35) Friedman, S. L. Hepatic stellate cells: protean, multifunctional, and enigmatic cells of the liver. *Physiol. Rev.* **2008**, *88*, 125−172.
(36) Lee, U. E.; Friedman, S. L. Mechanisms of hepatic fibrogenesis. *Best. Pract. Res. Clin. Gastroenterol.* **2011**, *25*, 195−206.
(37) Jiao, J.; Friedman, S. L.; Aloman, C. Hepatic fibrosis. *Curr. Opin. Gastroenterol.* **2009**, *25*, 223−229.
(38) George, J.; Roulot, D.; Koteliansky, V. E.; Bissell, D. M. In vivo inhibition of rat stellate cell activation by soluble transforming growth factor β type II receptor: a potential new therapy for hepatic fibrosis. *Proc. Natl. Acad. Sci. U. S. A.* **1999**, *96*, 12719−12724.
(39) Safadi, R.; Friedman, S. L. Hepatic fibrosis − role of hepatic stellate cell activation. *MedGenMed* **2002**, *4*, 27.
(40) Mauviel, A. Transforming growth factor-β: a key mediator of fibrosis. *Methods Mol. Med.* **2005**, *117*, 69−80.
(41) Gold, E. J.; Zhang, X.; Wheatley, A. M.; Mellor, S. L.; Cranfield, M.; Risbridger, G. P.; Groome, N. P.; Fleming, J. S. βA- and βC-activin, follistatin, activin receptor mRNA and βC-activin peptide expression during rat liver regeneration. *J. Mol. Endocrinol.* **2005**, *34*, 505−515.
(42) Takamura, K.; Tsuchida, K.; Miyake, H.; Tashiro, S.; Sugino, H. Activin and activin receptor expression changes in liver regeneration in rat. *J. Surg. Res.* **2005**, *126*, 3−11.
(43) Chabicovsky, M.; Herkner, K.; Rossmanith, W. Overexpression of activin β(C) or activin β(E) in the mouse liver inhibits regenerative deoxyribonucleic acid synthesis of hepatic cells. *Endocrinology* **2003**, *144*, 3497−3504.
(44) Lau, A. L.; Kumar, T. R.; Nishimori, K.; Bonadio, J.; Matzuk, M. M. Activin βC and βE genes are not essential for mouse liver growth, differentiation, and regeneration. *Mol. Cell. Biol.* **2000**, *20*, 6127−6137.
(45) Vejda, S.; Erlach, N.; Peter, B.; Drucker, C.; Rossmanith, W.; Pohl, J.; Schulte-Hermann, R.; Grusch, M. Expression of activins C and E induces apoptosis in human and rat hepatoma cells. *Carcinogenesis* **2003**, *24*, 1801−1809.
(46) Wada, W.; Maeshima, A.; Zhang, Y. Q.; Hasegawa, Y.; Kuwano, H.; Kojima, I. Assessment of the function of the βC-subunit of activin in cultured hepatocytes. *Am. J. Physiol.−Endocrinol. Metab.* **2004**, *287*, E247−E254.
(47) Wada, W.; Medina, J. J.; Kuwano, H.; Kojima, I. Comparison of the function of the β(C) and β(E) subunits of activin in AML12 hepatocytes. *Endocr. J.* **2005**, *52*, 169−175.

DOI: 10.1021/acs.jafc.5b01490
J. Agric. Food Chem. 2015, 63, 6027−6034

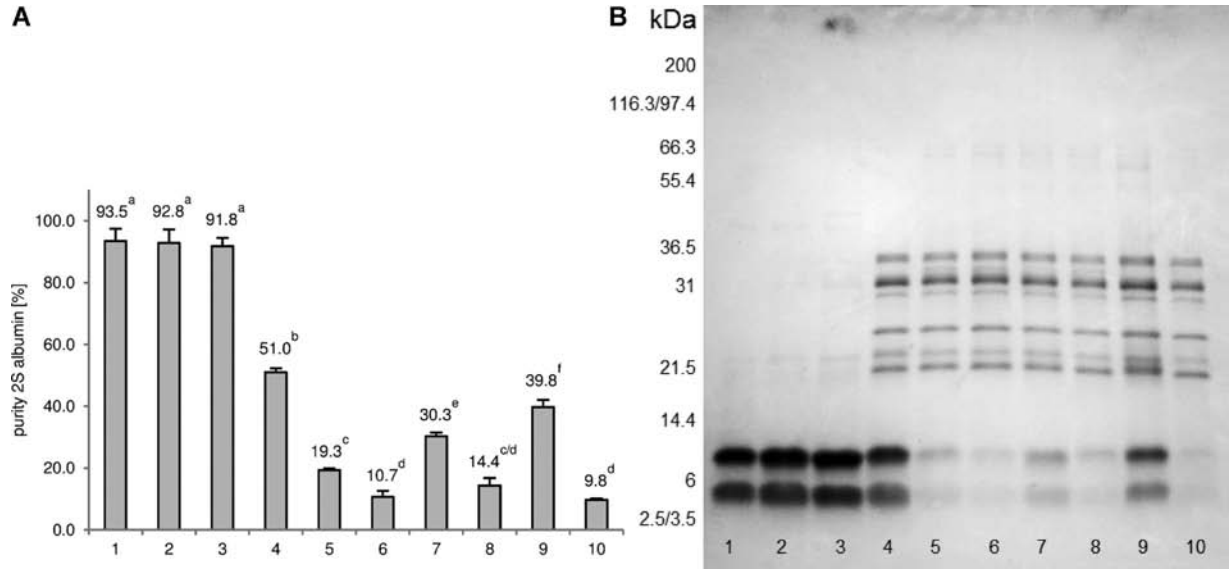

Figure 1. Effect of buffer system on 2S extraction. (A) Purity of 2S albumin extracts from mustard given as percentage of the total extracted protein in different buffer systems. Superscript letters indicate significance groups ($p \leq 0.05$): 1, glycine (100 mM, pH 2.5); 2, acetate (100 mM, pH 3.6); 3, citrate (100 mM, pH 4.0); 4, citrate (100 mM, pH 5.0); 5, MES (100 mM, pH 6.0); 6, MOPS (100 mM, pH 7.0); 7, Tris (100 mM, pH 8.0); 8, glycine (100 mM, pH 9.0); 9, bicarbonate (100 mM, pH 11.0); 10, Millipore H_2O. (B) Representative SDS-PAGE gel. Numbering is according to (A).

Preparation of Defatted Seed and Nut Flour. All seeds and nuts containing more than ∼40% fat (sunflower seeds, hazel nuts, pistachio seeds, Brazil nut seeds, sesame seeds, pecan seeds, cashew seeds, walnuts, and peanut seeds) were defatted twice prior to analysis. Seeds and nuts were crushed for 2−3 s in a knife mill (Grindomix GM 100, Retsch, Haan, Germany), resulting in a coarse flour. The first defatting step was performed by adding *n*-pentane (1 g/10 mL) and continuous stirring for 2 h at room temperature. The slurry was sieved and air-dried overnight. All seeds and nuts containing <40% fat (mustard seeds, buckwheat seeds, chickpea seeds, soybean seeds) as well as the pre-defatted material were separately milled to a fine powder using a nitrogen-cooled rotor-mill (Pulverisette, 1 mm mesh width, Fritsch, Idar Oberstein, Germany). Subsequently, the powder was defatted using *n*-pentane as described above. The defatted flour was stored at −20 ± 2 °C.

Extraction of Proteins. Proteins were extracted from the defatted flour by vigorous shaking (Mini shaker, VWR, 550 rpm) for 2 h in a 10-fold excess of different buffers (150 mg flour/1.5 mL buffer) at different temperatures. The slurry was centrifuged for 30 min at 9000*g* (Universal 16, Hettich, Spenge, Germany), and the supernatant was used for subsequent SDS-PAGE analysis immediately to avoid protein precipitation.

Optimization of Extraction. Four different parameters were systematically optimized to obtain optimal conditions for extraction: the buffer system (a), the extraction temperature (b), the molarity of the extraction buffer (c), and the pH of the extraction buffer (d). All experiments were carried out in biological triplicates using mustard seeds, and results were transferred to the other seeds and nuts. The pH was adjusted with an accuracy of ±0.03.

Experiment a included the following buffer systems: glycine−HCl buffer (100 mM, pH 2.5), sodium acetate−acetic acid buffer (100 mM, pH 3.6), sodium citrate−HCl buffer (100 mM, pH 4.0), sodium citrate−HCl buffer (100 mM, pH 5.0), MES−HCl buffer (100 mM, pH 6.0), MOPS−HCl buffer (100 mM, pH 7.0), Tris−HCl buffer (100 mM, pH 8.0), glycine−HCl buffer (100 mM, pH 9.0), sodium bicarbonate−HCl buffer (100 mM, pH 11.0). In this first experiment the molarity of all buffer solutions was 100 mM, and the pH was in the optimal buffering range of the respective buffer system. As 2S albumins are traditionally extracted using water, extraction with Millipore H_2O was in addition included in this study.

Experiment b was performed at extraction temperatures of 4, 23, and 60 °C, respectively. Molarity and pH values were not modified compared to experiment a.

Experiment c was performed using buffer molarities of 20, 50, 100, 200, 500, and 1000 mM, respectively. The pH value was not modified.

Experiment d was performed to assess extraction performance over the complete pH range of the respective buffer systems. For that purpose the lower limit of the pH range was increased in steps of ∼0.5 pH unit until the upper limit was reached.

Sodium Dodecyl Sulfate−Polyacrylamide Gel Electrophoresis (SDS-PAGE). Protein samples were separated by Tris−glycine SDS-PAGE using precast gels (Any kD Mini-PROTEAN TGX Gels, 15 well, 15 μL) and a Mini-PROTEAN Tetra cell (Bio-Rad). Protein solutions (10 μL) were diluted with Millipore H_2O to a volume of 150 μL and mixed with 50 μL pf 4× reducing sample loading buffer (2-ME in Bio-Rad 4× Laemmli Sample Buffer according to the manual). After the samples had been heated at 95 °C for 5 min, a volume of 10 μL per lane was loaded. Gels were run for 30 min at 200 V and stained for 2 h with Coomassie blue staining solution (500 mg of Coomassie brilliant blue R-250, 400 mL of methanol, 100 μL of acetic acid, filled to 1 L). After destaining, the gels were documented with a Chemidoc XRS system (Bio-Rad) and analyzed with the software ImageJ 1.48v (National Institutes of Health, Bethesda, MD, USA).

Buffer Exchange. Buffer exchange was performed using PD-10 desalting columns containing 8.3 mL of Sephadex G-25 medium (GE Healthcare, Uppsala, Sweden) according to the gravity protocol of the manufacturer. The column was equilibrated with 30 mL of phosphate buffered saline (1× PBS, 12 mM phosphate), and the flow-through was discarded. A sample volume of 0.5 mL was applied to the column, and 2.0 mL of equilibration buffer was added after the sample had entered the packed bed. Again, the flow-through was discarded. The elution was carried out with 5 mL of phosphate buffered saline (1× PBS, 12 mM phosphate), and the eluate was manually fractionated into ∼0.5 mL fractions. A qualitative protein test of all fractions was performed with protein assay reagent (Protein Assay, Bio-Rad) according to the method of Bradford using 20 μL of sample, 40 μL of Bradford reagent, and 140 μL of H_2O.[12] All fractions containing protein (indicated by blue color) were combined and used for further analyses.

Circular Dichroism (CD) Spectroscopy. CD studies were carried out by recording data in the far-UV region (250−200 nm) on a Jasco

DOI: 10.1021/acs.jafc.5b01634
J. Agric. Food Chem. 2015, 63, 6035−6040

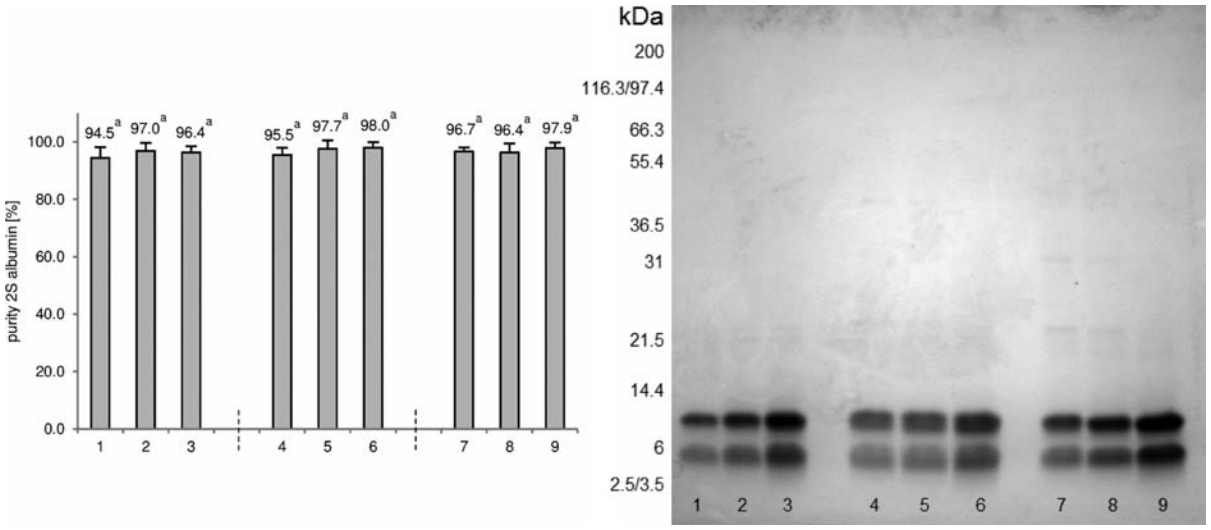

Figure 2. Effect of temperature on 2S extraction. Purity of extracted 2S albumins from mustard at different extraction temperatures. Superscript letters indicate significance groups ($p \leq 0.05$): 1, glycine (100 mM, pH 2.5, 4 °C); 2, glycine (100 mM, pH 2.5, 23 °C); 3, glycine (100 mM, pH 2.5, 60 °C); 4, acetate (100 mM, pH 3.6, 4 °C); 5, acetate (100 mM, pH 3.6, 23 °C); 6, acetate (100 mM, pH 3.6, 60 °C); 7, citrate (100 mM, pH 4.0, 4 °C); 8, citrate (100 mM, pH 4.0, 23 °C); 9, citrate (100 mM, pH 4.0, 60 °C).

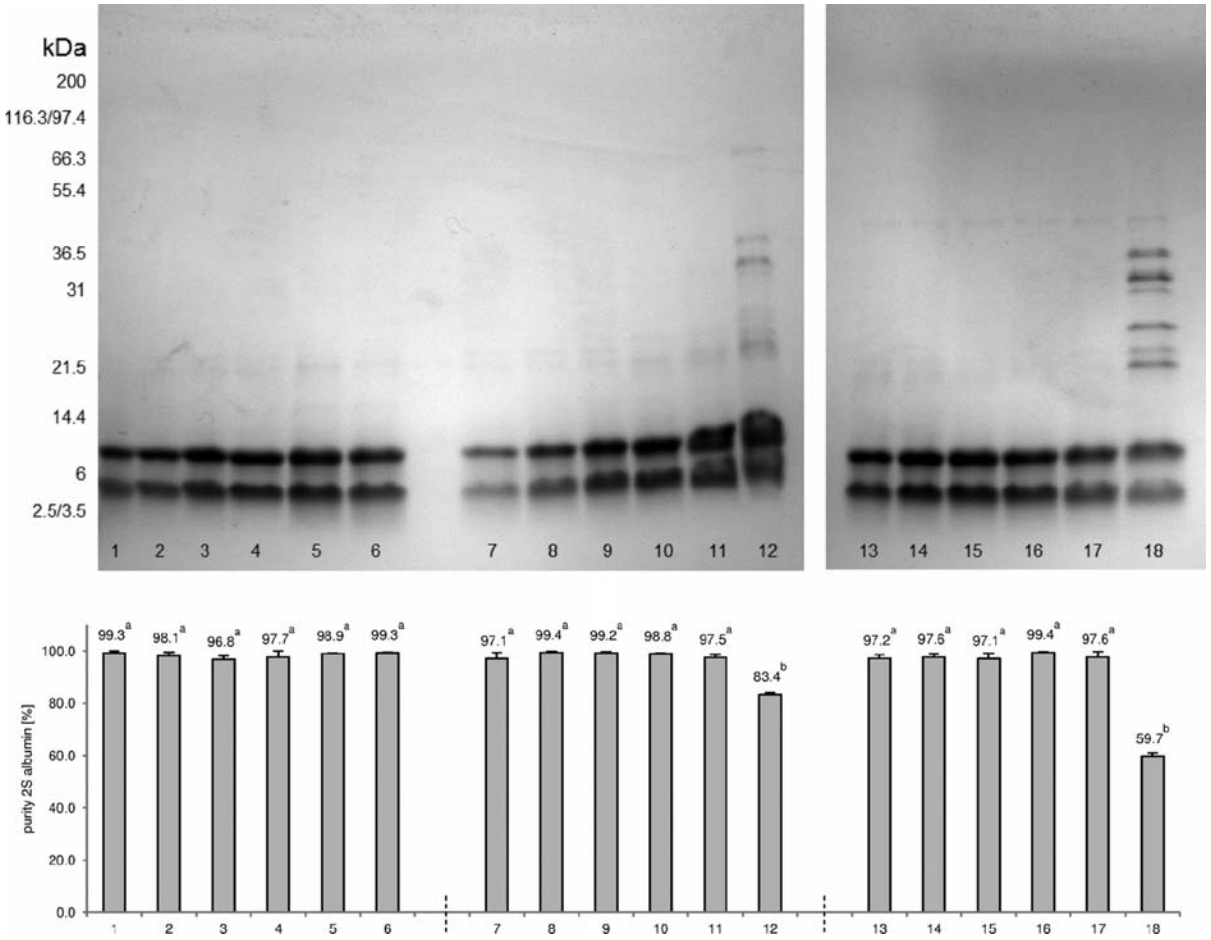

Figure 3. Effect of buffer molarity on 2S albumin extraction; purity of mustard 2S albumin extract with buffers of different molarity. Superscript letters indicate significance groups ($p \leq 0.05$): 1, glycine (20 mM, pH 2.5, 60 °C); 2, glycine (50 mM, pH 2.5, 60 °C); 3, glycine (100 mM, pH 2.5, 60 °C); 4, glycine (200 mM, pH 2.5, 60 °C); 5, glycine (500 mM, pH 2.5, 60 °C); 6, glycine (1000 mM, pH 2.5, 60 °C); 7, acetate (20 mM, pH 3.6, 60 °C); 8, acetate (50 mM, pH 3.6, 60 °C); 9, acetate (100 mM, pH 3.6, 60 °C); 10, acetate (200 mM, pH 3.6, 60 °C); 11, acetate (500 mM, pH 3.6, 60 °C); 12, acetate (1000 mM, pH 3.6, 60 °C); 13, citrate (20 mM, pH 4.0, 60 °C); 14, citrate (50 mM, pH 4.0, 60 °C); 15, citrate (100 mM, pH 4.0, 60 °C); 16, citrate (200 mM, pH 4.0, 60 °C); 17, citrate (500 mM, pH 4.0, 60 °C); 18, citrate (1000 mM, pH 4.0, 60 °C).

DOI: 10.1021/acs.jafc.5b01634
J. Agric. Food Chem. 2015, 63, 6035−6040

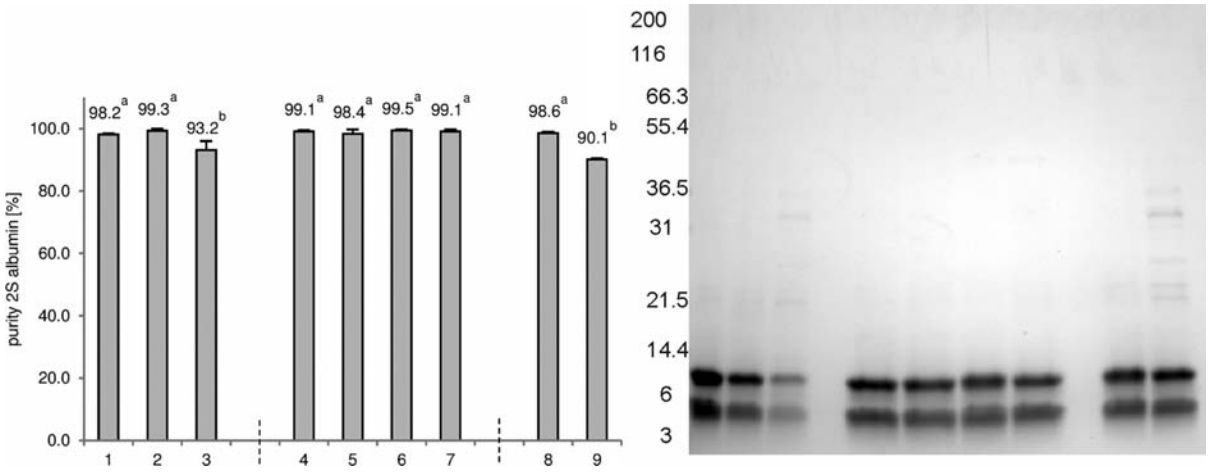

Figure 4. Effect of pH on mustard 2S albumin extraction; purity of 2S albumin extract at various pH values. Superscript letters indicate significance groups ($p \leq 0.05$): 1, glycine (100 mM, pH 2.5, 60 °C); 2, glycine (100 mM, pH 3.0, 60 °C); 3, glycine (100 mM, pH 3.5, 60 °C); 4, citrate (100 mM, pH 2.5, 60 °C); 5, citrate (100 mM, pH 3.0, 60 °C); 6, citrate (100 mM, pH 3.5, 60 °C); 7, citrate (100 mM, pH 4.0, 60 °C); 8, acetate (100 mM, pH 3.6, 60 °C); 9, acetate (100 mM, pH 4.0, 60 °C).

J810 spectropolarimeter in a 1 mm pathlength quartz cuvette (4 mL) at room temperature. The protein concentration was determined by Nanodrop 1000 (Thermo Scientific, Dreieich, Germany) and adjusted to 100 μg/mL. Spectra were recorded with a scanning speed of 100 nm/min and accumulated over four measurements. All samples were analyzed in 1× PBS (12 mM phosphate) after buffer exchange.

SDS-PAGE Gel Analysis. To exclude gel-to-gel differences due to staining/destaining interferences and limited linearity of Coomassie brilliant blue dye, we performed relative quantitation of single gel lanes. The protein purity given in the results are described by relative signal intensities of 2S albumin signals compared to other proteins in the same lane of the respective gel and represent the 2S albumin content as a percentage of the total protein extracted in a single sample. Using the software ImageJ 1.48v (National Institutes of Health, USA), the background of the gel was subtracted and every lane was plotted individually. The relative protein content was calculated as the sum of 2S albumin signals (large and small subunit) divided by the summarized peak areas of the sample (defined as 100%). The analysis is exemplified in the Supporting Information (Figure S1).

Statistical Analysis. All experiments were carried out as biological triplicates, and SPSS Statistics version 22 (IBM, Ehningen, Germany) was used to compare means. A one-way analysis of variances (ANOVA) was performed to evaluate the relationship between extraction conditions (independent variable) and the change in the 2S albumin percentage (dependent variable). A Tukey HSD post hoc test with a 95% confidence interval was used to evaluate pairwise differences among means.

RESULTS AND DISCUSSION

Effect of Buffer System. Ten different buffer systems were used to survey selective extraction of 2S albumins from mustard seeds (results are summarized in Figure 1 and Table S1). With regard to the 2S albumin yield, we observed considerable differences. The use of very acidic buffer systems (glycine (100 mM, pH 2.5), acetate (100 mM, pH 3.6), and citrate (100 mM, pH 4.0)) results in efficient and selective 2S albumin extraction with purities >90% and no significant differences between these three buffer systems. All remaining buffers gave only poor 2S albumin purities between 9.8 and 51.0% and a strongly reduced yield as demonstrated by SDS-PAGE (Figure 1B). Notably, the lowest purity and yield were observed for water (Figure 1, sample 10). This is of particular interest, as current methods in place for 2S albumin isolation mainly use water for the extraction. Garino et al. purified hazelnut 2S albumins by extraction with water at 4 °C and subsequent purification with SEC and RP-HPLC.[10] On the basis of our initial results, not only 2S albumin purity but also total protein yield can be improved by systematic optimization of extraction conditions. Furthermore, additional chromatographic purification is not necessary for most downstream applications.

Effect of Extraction Temperature. For further optimization, we chose the three most promising buffer systems (glycine (100 mM, pH 2.5), acetate (100 mM, pH 3.6), and citrate (100 mM, pH 4.0)) and assessed effects of different extraction temperatures (4, 23, and 60 °C, respectively). The molarity of all buffers was 100 mM, and the pH was set to 2.5 for glycine buffer, 3.6 for acetate buffer, and 4.0 for citrate buffer. An overview of the results is given in Table S1 and Figure 2. The statistical classification into significance groups demonstrates that 2S albumin purities were not affected by the extraction temperature in the above-mentioned three buffer systems. Increasing temperatures resulted, however, in higher total protein yield for all three buffers, leading to enhanced extraction efficiency at 60 °C compared to extraction at 23 and 4 °C (Figure 2, not statistically evaluated). Therefore, extraction at 60 °C was chosen for further experiments.

Effect of Molarity. Molarities between 20 and 1000 mM were tested for the three most promising buffer systems, glycine, acetate, and citrate, and the extraction was carried out at 60 °C. It has to be noted that 2S albumins are highly thermostable, and we did not observe relevant structural modifications (see also CD Spectroscopy; Supporting Information). The pH was set to 2.5 for glycine buffer, 3.6 for acetate buffer, and 4.0 for citrate buffer, respectively, and the effects of molarity on extraction are shown in Table S1 and Figure 3.

For the glycine buffer system, no significant difference in 2S albumin purity is observed when buffer molarities are modified from 20 to 1000 mM. For the acetate and citrate buffer no significant difference in purity is observed between 20 and 500 mM. For both buffers, purity is significantly reduced when using a buffer molarity of 1000 mM (Figure 3). Obviously a high buffer molarity, on the one hand, favors the extraction of high total protein amounts but, on the other hand, results in reduced selectivity and thus decreasing 2S purity. As high amounts of buffer salts are not beneficial for many analytical

DOI: 10.1021/acs.jafc.5b01634
J. Agric. Food Chem. 2015, 63, 6035−6040

routines, an intermediate buffer molarity of 100 mM was chosen for further experiments.

Effect of pH. As the pH of the buffer system was the most critical parameter in the initial experiment, we further assessed the influence of different pH values for the three most promising acidic buffers (glycine, acetate, and citrate) at molar buffer concentrations of 100 mM and 60 °C. Extraction of 2S albumins was analyzed for the three buffers over the respective buffering pH range in steps of ~0.5 pH unit. Results are summarized in Table S1 and Figure 4.

For the glycine buffer, an increase in pH to 3.5 resulted in reduced purity compared to extraction at pH 2.5 or 3.0. The citrate buffer showed equal purity of extracted 2S albumins over the complete pH range between 2.5 and 4.0. In contrast, an increase of pH of the acetate buffer from 3.6 to 4.0 led to a significant decrease in purity.

Optimized Buffer Conditions. We demonstrate that not a single optimal buffer system exists, but the extraction must comply with certain conditions: In our approach the most important parameter is the acidic pH of the buffer system and consequently glycine, acetate, or citrate buffers that have optimal buffering capacity between pH 2.5 and 4.0 resulted in the highest 2S albumin purity and high protein yield. The extraction temperature had no significant influence on purity, but elevated temperatures resulted in increased 2S albumin yield. This is especially interesting as 2S albumins are highly thermostable.[9] Optimal results with respect to buffer molarity are obtained in a broad range between 20 and 500 mM. Notably, the purity of 2S extracts is reduced when buffer molarity is further increased.

Performance Control and Transferability. As the optimized acidic buffer conditions are not common for protein extraction, we analyzed the secondary structure of the acidic protein extract and compared it to a 2S albumin fraction extracted in 100 mM Tris-HCl, pH 8.0, and purified by SEC. Extractions with three different acidic buffer systems (100 mM glycine, pH 2.5, 60 °C; 100 mM acetate, pH 3.6, 60 °C; and 100 mM citrate, pH 4.0, 60 °C) were compared with the SEC-purified 2S albumins using CD spectroscopy. To eliminate the influence of different buffers on CD spectra, a buffer exchange step to 12 mM phosphate buffer was included for all samples prior to CD spectroscopy. For all samples, we obtained CD spectra typical for 2S albumins (which mainly consist of α-helical structures), and no significant differences between the acidic extracts and the SEC-purified 2S albumins extracted with Tris buffer were observed (Figure 5), demonstrating that acidic extraction conditions do not interfere with 2S albumin structure.

As it is intended to provide a method generally applicable for the extraction of 2S albumins, we assessed the transferability from mustard to further seeds and nuts (see Materials and Methods). For 9 of 13 matrices included in this study, we observed excellent purity of 2S albumin extract and very good yield as exemplified in Figure 6. The crude protein was extracted with 100 mM Tris-HCl, pH 8.0, 23 °C (with an addition of 2 M NaCl for extraction of walnut according to the method of Sathe et al.[13]) and was compared to the extraction with 100 mM glycine, pH 2.5, 60 °C. Notably, selective 2S albumin extraction was not obtained for food matrices from legumes (peanut, chickpea, and soybean), and sunflower showed significantly reduced selectivity (Figure 6). As we did not observe phylogenetic clustering of extractable and "non-extractable" 2S albumin sequences (data not shown), we assume that differences in food matrices underlie reduced selectivity of the extraction for peanut, chickpea, soybean, and sunflower 2S albumins.

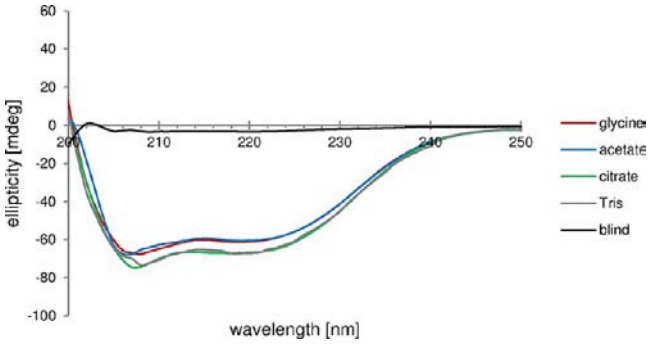

Figure 5. Circular dichroism spectroscopy of acidic buffers (glycine, acetate, and citrate) at 60 °C and 2S albumin preparation purified with GPC after Tris extraction at 20 °C. No significant differences in spectra are observed, and all obtained spectra are typical for 2S albumins, which are rich in α-helical secondary structure.

In our study we present a simple, rapid, and selective method for the isolation of 2S albumins from different seeds and nuts. We achieved 2S albumin purities up to 99% and excellent yield for our model protein Sin a 1 from mustard seeds and demonstrate excellent transferability to other allergenic seeds and nuts. In comparison to conventional chromatography-based purification methods (IEX, SEC, RP-HPLC), the newly developed method requires only minimal laboratory equipment and allows in principle unlimited protein yield with higher protein concentration compared to currently used chromatographic methods.

The purification of 2S albumins is relevant for different fields of interest in allergen research. With the selective extraction presented in this study, the production of allergen extracts from different natural sources that contain a single allergen with its natural variants and isoforms is feasible. Due to the pronounced stability of 2S albumins, neither acidic pH nor elevated extraction temperature influences the structure as demonstrated by CD spectroscopy.

Consequently, component-resolved diagnostic (CRD) of natural allergens might become possible. Today, allergen preparations for CRD are derived from recombinant expression as crude allergen extracts from natural sources are too complex and might not be reproducible.[14] Using selective extraction of 2S albumins results in the high yield of an isolated allergen with its isoforms and variants that might be employed (after a further purification step if necessary) for CRD. Although crude natural extracts are too complex for allergen diagnosis, isolated recombinant single isoforms of allergens do not reflect the natural complexity of allergens such as 2S albumins. Selective extraction might be an alternative for 2S albumins. It has to be noted that we did not investigate the immunological properties of the 2S extracts obtained in this study, which would be an essential prerequisite when aiming to use such extracts for CRD. Trace amounts of residual further allergens such as 11S legumins or 7S vicilins might influence the immunological properties, and this interference has to be ruled out. However, the high yield of 2S allows for efficient further downstream purification if necessary.

DOI: 10.1021/acs.jafc.5b01634
J. Agric. Food Chem. 2015, 63, 6035−6040

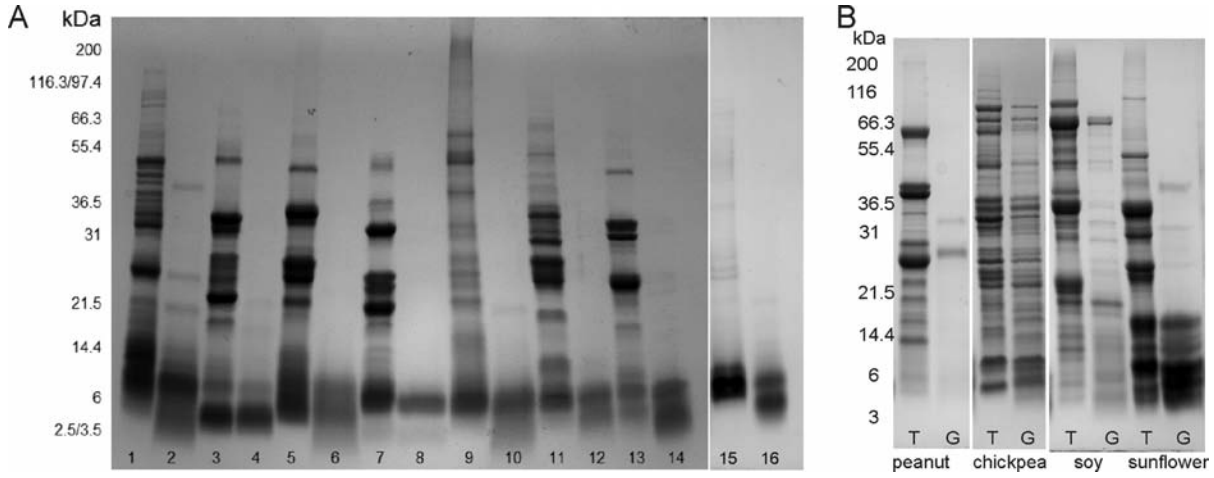

Figure 6. Transfer of optimized 2S extraction conditions to further seed and nut matrices. Total protein extract is performed with T = Tris-HCl (100 mM, pH 8.0, 23 °C), and 2S-selective extraction is done with G = glycine (100 mM, pH 2.5, 60 °C), respectively. (A) Allergenic foods from which 2S albumins are efficiently and selectively extracted: 1, buckwheat-T; 2, buckwheat-G; 3, cashew-T; 4, cashew-G; 5, hazelnut-T; 6, hazelnut-G; 7, Brazil nut-T; 8, Brazil nut-G; 9, pecan nut-T; 10, pecan nut-G; 11, pistachio-T; 12, pistachio-G; 13, sesame-T; 14, sesame-G; 15, walnut-T; 16, walnut-G. (B) Foods from which 2S albumins are not sufficiently extracted. Note that the SDS-PAGE conditions are not optimized to separate 2S albumin subunits.

■ ASSOCIATED CONTENT

Supporting Information

Figure S1 and Table S1. The Supporting Information is available free of charge on the ACS Publications website at DOI: 10.1021/acs.jafc.5b01634.

■ AUTHOR INFORMATION

Corresponding Author

*(J.B.) Phone: +49 251 8333392. Fax: +49 251 833396. E-mail: jbrockm@uni-muenster.de.

Funding

M.H. was supported by a grant from the Heinrich-Stockmeyer-Stiftung, Bad Rothenfelde.

Notes

The authors declare no competing financial interest.

■ ACKNOWLEDGMENTS

We thank Katrin Bassen for the excellent preparation of food photographs used in the table of contents (TOC).

■ REFERENCES

(1) Breiteneder, H.; Radauer, C. A classification of plant food allergens. *J. Allergy Clin. Immunol.* **2004**, *113*, 821−830.

(2) Hara-Hishimura, I.; Takeuchi, Y.; Inoue, K.; Nishimura, M. Vesicle transport and processing of the precursor to 2S albumin in pumpkin. *Plant J.* **1993**, *4*, 793−800.

(3) Moreno, F. J.; Clemente, A. 2S albumin storage proteins: what makes them food allergens? *Open Biochem. J.* **2008**, *2*, 16−28.

(4) Jyothi, T. C.; Sinha, S.; Singh, S. A.; Surolia, A.; Appu Rao, A. G. Napin from *Brassica juncea*: thermodynamic and structural analysis of stability. *Biochim. Biophys. Acta, Proteins Proteomics* **2007**, *1774*, 907−919.

(5) Hummel, M.; Wigger, T.; Brockmeyer, J. Characterization of mustard 2S albumin allergens by bottom-up, middle-down, and top-down proteomics: a consensus set of isoforms of Sin a 1. *J. Prot. Res.* **2015**, *14*, 1547−1556.

(6) Downs, M.; Semic-Jusufagic, A.; Simpson, A.; Bartra, J.; Fernandez-Rivas, M.; Rigby, N. M.; Taylor, S.; Baumert, J. L.; Mills, E. N. C. Characterization of low molecular weight allergens from English walnut (*Juglans regia*). *J. Agric. Food Chem.* **2014**, *62*, 11767−11775.

(7) Menendez-Arias, L.; Moneo, I.; Dominguez, J.; Rodriguez, R. Primary structure of the major allergen of yellow mustard (*Sinapis alba* L.) seed, Sin a 1. *Eur. J. Biochem.* **1988**, *177*, 159−166.

(8) Liu, C.; Wang, H.; Cui, Z.; He, X.; Wang, X.; Zeng, X.; Ma, H. Optimization of extraction and isolation for 11S and 7S globulins of soybean seed storage protein. *Food Chem.* **2007**, *102*, 1310−1316.

(9) Moreno, F. J.; Maldonado, B. M.; Wellner, N.; Mills, C. Thermostability and in vitro digestibility of a purified major allergen 2S albumin (Ses i 1) from white sesame seeds (*Sesamum indicum* L.). *Biochim. Biophys. Acta, Proteins Proteomics* **2005**, *1752*, 142−153.

(10) Garino, C.; Zuidmeer, L.; Marsh, J.; Lovegrove, A.; Morati, M.; Versteeg, S.; Schilte, P.; Shewry, P.; Arlorio, M.; van Ree, R. Isolation, cloning, and characterization of the 2S albumin: a new allergen from hazelnut. *Mol. Nutr. Food Res.* **2010**, *54*, 1257−1265.

(11) Galbas, M.; Porzucek, F.; Woźniak, A.; Słomski, R.; Selwet, M. Isolation of low-molecular albumins of 2S fraction from soybean (*Glycine max* (L.). *Acta Biochim. Polym.* **2013**, *60*, 107−110.

(12) Bradford, M. M. A rapid and sensitive method for the quantitation of microgram quantities of protein utilizing the principle of protein-dye binding. *Anal. Biochem.* **1976**, *72*, 248−254.

(13) Sathe, S. K.; Venkatachalam, M.; Sharma, G. M.; Kshirsagar, H. H.; Teuber, S. S.; Roux, K. H. Solubilization and electrophoretic characterization of select edible nut seed proteins. *J. Agric. Food Chem.* **2009**, *57*, 7846−7856.

(14) Valenta, R.; Lidholm, J.; Niederberger, V.; Hayek, B.; Kraft, D.; Grönlund, H. The recombinant allergen-based concept of component-resolved diagnostics and immunotherapy (CRD and CRIT). *Clin. Exp. Allergy* **1999**, *29*, 896−904.

DOI: 10.1021/acs.jafc.5b01634
J. Agric. Food Chem. 2015, 63, 6035−6040

of Trp-His in the gut using the intestinal epithelial cell line HT-29.

MATERIALS AND METHODS

Materials. Trp-His was purchased from GL Biochem (Shanghai, China). His-Trp was purchased from Kokusan Chemical (Osaka, Japan). Nifedipine (a dihydropyridine (DHP) L-type Ca^{2+} channel blocker) and verapamil (a phenylalkylamine (PAA) L-type Ca^{2+} channel blocker) were obtained from Sigma-Aldrich (St. Louis, MO, USA). (*S*)-(−)-Bay K 8644, a specific L-type Ca^{2+} channel agonist, was purchased from Santa Crutz Biotechnology (Dallas, TX, USA).

Induction of Colitis in Vivo and Treatment with Trp-His. All animal experiments were approved by the University of Guelph Animal Care Committee and carried out in accordance with the Canadian Council of Animal Care Guide to the Care and Use of Experimental Animals (eAUP no. 1536). The experiments for induction of DSS-induced colitis in mice were performed as previously described.[7] Briefly, female BALB/c mice (6−8 weeks, 18−20 g; Charles River Laboratories, Montreal, QC, Canada) were group housed with a 12 h light/dark cycle and allowed unrestricted access to standard food and water. Trp-His (100 or 250 mg/kg body weight (BW)/day) or vehicle (sterilized water) was given to mice via oral administration for 14 days. On the seventh day, 5% (w/v) DSS (MW 36−50 kDa; MP Biomedicals, Solon, OH, USA) was added to drinking water to induce acute colitis and continued for the following 7 days. The negative control mice received water only, and the positive group received water with DSS for 7 days. BWs were measured on a daily basis, and the daily weight changes were expressed as mean percentage change relative to the initial weight. Mice were humanely euthanized on day 14. Colons were collected and sectioned longitudinally, and tissue samples were flash frozen and stored at −80 °C for further analysis.

Clinical Evaluation of Colitis. Mice were inspected daily for stool consistency, presence of blood in stool, or general appearance. The clinical scoring was calculated as described by Maxwell et al.[23] and defined as follows: stool score, 0 = normal, 1 = moist/sticky stool, 2 = soft stool, 3 = diarrhea; stool blood score, 0 = no blood, 1 = evidence of blood in stool or around anus, 2 = severe bleeding; mouse appearance, 0 = normal, 1 = ruffled fur or altered gait, 2 = lethargic or moribund.

Measurement of Cytokine Concentrations in Colon. Measurement of tumor necrosis factor (TNF)-α and interleukin (IL)-6 in mouse colon tissues was carried out as previously described.[7] Briefly, tissue samples were homogenized in ice-cold PBS containing proteinase inhibitors (1 mM phenylmethanesulfonyl fluoride (PMSF), 0.1 mM ethylenediaminetetraacetic acid (EDTA), 10 μg/mL aprotinin, 10 μg/mL leupeptin, and 10 μg/mL pepstatin A; Sigma-Aldrich) using a Polytron homogenizer (PT 1200, Kinematica AG, Luzern, Switzerland) for 3 min and centrifuged at 10000*g* for 10 min. Protein concentration of the homogenate supernatant was measured by DC protein assay (Bio-Rad Laboratories, Hercules, CA, USA), according to the manufacturer's instructions. The supernatants and cytokine standards were added to an anti-mouse TNF-α antibody (1:500; BD Bioscience, Mississauga, ON, Canada) or IL-6 antibody (1:250; BD Bioscience)-coated plate and incubated for 2 h at 37 °C. Next, a biotinylated anti-mouse TNF-α antibody (1:500; BD Bioscience) or IL-6 antibody (1:500; BD Bioscience) was incubated for 1 h at 37 °C. Avidin−horseradish peroxidase (Av-HRP, 1:2000; BD Bioscience) was added for 0.5 h at 37 °C. Then, 100 μL of 3,3′,5,5′-tetramethylbenzidine (TMB) and 25 μL of 0.25 M H_2SO_4 were added to each well. The absorbance was measured at 450 nm by a plate reader (iMark model 550, Bio-Rad).

RNA Isolation, cDNA Synthesis, and RT-PCR. The colons were homogenized in Trizol reagent (Life Technologies, Carlsbad, CA, USA), and total RNA was extracted from the aqueous phase by using an Aurum Total RNA Mini Kit (Bio-Rad) according to the manufacturer's instructions. The quantity and quality of the total RNA were verified by Nano Drop ND-1000 (Thermo Scientific, Waltham, MA, USA). RNA (1 μg) was reverse transcribed using a qScript cDNA Synthesis Kit (Quanta BioSciences, Gaithersburg, MD, USA), and real-time quantitative PCR was carried out using PerfeCTa SYBR Green Supermix (Quanta Biosciences) on a MyiQ single-color real-time PCR detection system (Bio-Rad) as previously described.[9] The primer sequences used were follows: β-actin, forward, 5′-GAAATCGTGCGTGACATCAAAG-3′, reverse, 5′-TGTAGTTCATGGATGCCACAG-3′; TNF-α, forward, 5′-CCCCAAAGGGATGAGAAGTT-3′, reverse, 5′-CACTTGGTGGTTTGCTACGA-3′; IL-6, forward, 5′-CCGGAGAGGAGACTTCACAG-3′, reverse, 5′-CAGAATTGCCATTGCACAAC-3′; IL-1β, forward, 5′-GGATGAGGACATGAGCACCT-3′, reverse, 5′-AGCTCATATGGGTCCGACAG-3′; interferon (IFN)-γ, forward, 5′-GCTCTTCCTCATGGCTGTTT-3′, reverse, 5′-GTCACCATCCTTTTGCCAGT-3′; monocyte chemoattractant protein (MCP)-1, forward, 5′-CCCAATGAGTAGGCTGGAGA-3′, reverse, 5′-TCTGGACCCATTCCTTCTTG-3′, IL-10, forward, 5′-GCCTTATCGGAAATGATCCA-3′, reverse, 5′-AGGGGAGAAATCGATGACAG-3′. These primers were obtained from the University of Guelph Laboratory Services Molecular Biology Section (Guelph, ON, Canada). Results are presented as fold expression change relative to negative control. Relative gene expression was calculated according to the $2^{-\Delta\Delta Ct}$ method[24] using mouse β-actin as reference gene.

Cell Culture ant Treatment. Human intestinal epithelial cell line HT-29 (HTB-38; American Type Culture Collection, Manassas, VA, USA), was grown in McCoy's 5A medium (Sigma-Aldrich) supplemented with 100 units/mL penicillin−streptomycin and 10% fetal bovine serum (FBS; Life Technologies). HT-29 cells (2.0×10^5 cells/well) were grown in 12- or 24-well tissue culture plates (Corning, Corning, NY, USA) until confluent monolayers were obtained. The confluent monolayers were rinsed with Hank's balanced salt solution (HBSS) and incubated for 2 h with peptides (Trp-His or His-Trp), L-type Ca^{2+} channel blocker, or agonist at the indicated concentrations in McCoy's 5A medium containing 5% FBS. The negative and positive control cells were treated with medium alone for 2 h. After peptide treatment, TNF-α (2 ng/mL; Life Technologies) was added and cells were incubated for 2 h. For the competitive assay, an L-type Ca^{2+} channel agonist, Bay K 8644, was added to the cells 1 h after the addition of peptide/blocker and incubated along with the peptide/blocker for 1 h before the addition of TNF-α. The culture supernatants were collected, and IL-8 concentrations were measured by ELISA as described previously[25] with minor modification. Briefly, the supernatants and IL-8 standards were added to an anti-human IL-8 antibody (1:1000; BD Bioscience)-coated plate and incubated for 2 h at 37 °C. Next, a biotinylated anti-human IL-8 antibody (1:2000; BD Bioscience) was incubated for 1 h at 37 °C. Av-HRP (1:2000) was added for 0.5 h at 37 °C, and then 50 μL of TMB and 25 μL of 0.25 M H_2SO_4 were added to each well. The absorbance was measured at 450 nm as mentioned above.

Cell Viability. Cell viability during peptide/TNF-α treatment was measured using the WST-1 Cell Proliferation Reagent (Roche Applied Science, Indianapolis, IN, USA) according to the manufacturer's instructions, and viability was calculated as a percent relative to untreated cells.

Western Blot Analysis. Cell monolayers were rinsed with HBSS and incubated for 2 h with peptide or medium, followed by TNF-α (2 ng/mL) for 1 or 2 h. Cells were then washed twice with ice-cold PBS and lysed in 100 μL of ice-cold radio-immunoprecipitation assay (RIPA) buffer containing Halt Protease and Phosphatase Inhibitor Cocktail and 0.5 M EDTA (Thermo Scientific). The supernatants were collected following centrifugation at 10000*g* for 25 min. The protein concentration was measured by a DC protein assay. An aliquot of sample was mixed with NuPAGE LDS Sample Buffer (4×) (Life Technologies) and incubated for 5 min at 95 °C. The samples (containing 30 μg of total protein) were separated on a 10% sodium dodecyl sulfate−polyacrylamide gel electrophoresis (SDS-PAGE) gel and transferred to a polyvinylidene difluoride (PVDF) membrane (Pall Corp., Port Washington, NY, USA). The membrane was probed with primary antibody (1:1000) overnight at 4 °C. The antibodies used were rabbit monoclonal antiphospho-c-jun N-terminal kinase (JNK) (Thr^{183}/Tyr^{185}), JNK, phospho-IκBα (Ser^{32}) (Cell Signaling Tech-

DOI: 10.1021/acs.jafc.5b01682
J. Agric. Food Chem. 2015, 63, 6041−6050

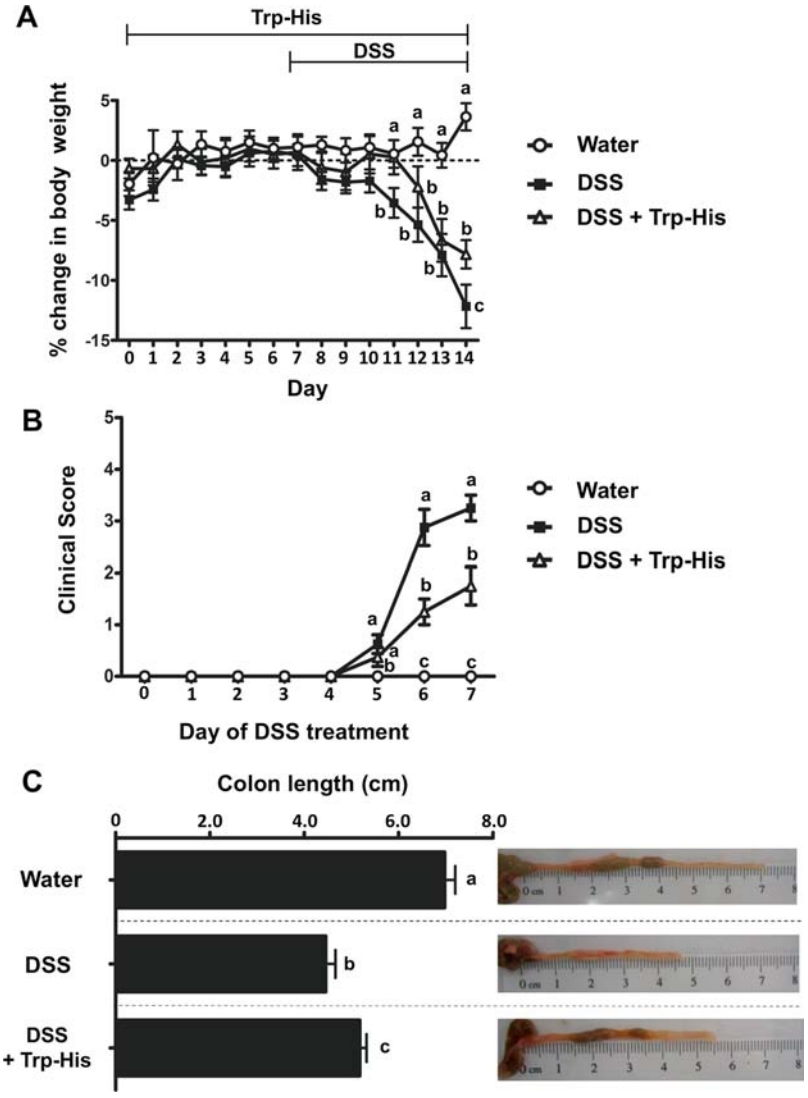

Figure 1. Effect of Trp-His on DSS-induced colitis signs and weight loss. Mice were given 100 mg/kg BW Trp-His for 14 days. On the seventh day, colitis was induced with 5% (w/v) DSS added to drinking water. (A) Mice were weighed daily, and changes in body weight are reported as percent change relative to the initial weight. (B) Mice were scored daily for clinical signs of DSS-induced colitis. (C) After 14 days, colons were removed and measured from the end of the cecum to the anus. Data represent means ± SEM (n = 8/group). Unless indicated, no significant difference was observed between groups. Values without a common letter are significantly different at $P < 0.05$.

nology, Danvers, MA, USA); and mouse monoclonal antiphospho-p38 (Tyr^{182}), p38, extracellular signal-related kinase 1/2 (ERK), IκBα, and rabbit monoclonal anti-phospho-ERK (Thr^{177}) (Santa Crutz Biotechnology). The membrane was washed and incubated with HRP-conjugated anti-mouse or anti-rabbit IgG (1:2000; GE Healthcare, Mississauga, ON, Canada) for 1 h at room temperature. Proteins were detected with ECL Plus Western Blotting Detection Reagent using a Typhoon FLA 9500 scanner (GE Healthcare). Densitometry was performed using NIH ImageJ software (Image Processing and Analysis in Java, National Institutes of Health, http://rsbweb.nih.gov/ij/).

Statistical Analysis. The results are expressed as the mean ± SEM. Statistical analyses were performed using GraphPad Prism version 5.0 (GraphPad, San Diego, CA, USA). Statistical differences between curves were analyzed using two-way analysis of variance (ANOVA) followed by Tukey's multiple-comparison test. Statistical differences between individual groups were determined using one-way ANOVA followed by Tukey's multiple-comparison test. $P < 0.05$ was considered statistically significant.

RESULTS

Preventative Effects of Trp-His on DSS-Induced Colitis in Mice. Administration of DSS in mice causes symptoms of colitis similar to those seen in human ulcerative colitis, including weight loss, diarrhea, bloody stool, and colon shortening.[26] On the fourth day of DSS treatment (day 11 of the study) (Figure 1A), the positive control mice (DSS) began to lose weight when compared with the negative control mice (water). Mice receiving Trp-His for 14 days (DSS + Trp-His) attenuated significantly ($P < 0.05$) DSS-induced weight loss on the seventh day of DSS treatment (day 14) (Figure 1A). An increase in clinical scores was also observed in DSS-treated groups beginning on the fifth day of DSS treatment, and the administration of Trp-His significantly ($P < 0.01$) reduced the severity of DSS-induced clinical signs on the sixth and seventh days (Figure 1B). No clinical signs were observed in mice before the start of DSS treatment (data not shown). As shown in Figure 1C, shortening of colon length, which is a typical sign of DSS-induced colitis, was significantly ($P < 0.05$) attenuated

DOI: 10.1021/acs.jafc.5b01682
J. Agric. Food Chem. 2015, 63, 6041−6050

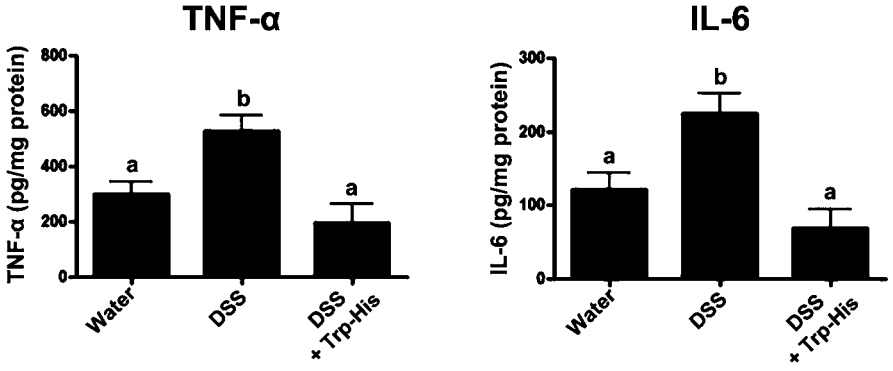

Figure 2. Effect of Trp-His on pro-inflammatory cytokine production in the colon of DSS-treated mice. TNF-α and IL-6 in the colonic tissue were measured by ELISA. Data represent means ± SEM (n = 8/group). Values without a common letter are significantly different at $P < 0.05$.

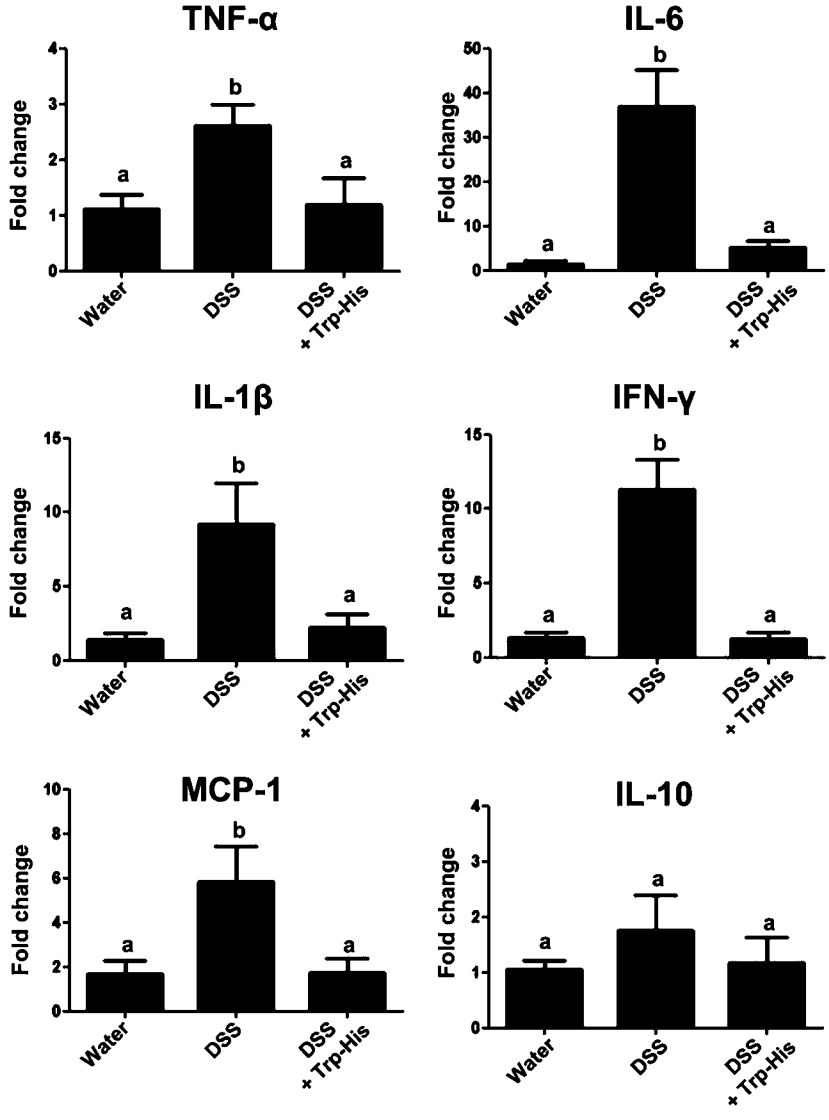

Figure 3. Effect of Trp-His on cytokine gene expression in the colon of DSS-treated mice. Relative mRNA expressions of the pro-inflammatory cytokines TNF-α, IL-6, IL-1β, IFN-γ, and MCP-1 and the anti-inflammatory cytokine IL-10 were measured by real-time PCR. Results are expressed as fold change to negative control (water) mice. Mouse β-actin was used for the internal control. Data represent means ± SEM (n = 8/group). Values without a common letter are significantly different at $P < 0.05$.

in DSS + Trp-His group, compared with the DSS group (water, 7.0 ± 0.2 cm; DSS, 4.5 ± 0.2 cm; WH, 5.2 ± 0.1 cm). Mice receiving the high dose (250 mg/kg BW) for 14 days also prevented these characteristic symptoms of colitis in a separate experiment and the potential of anti-colitis by high dose was similar to those observed by low dose (see Supporting Information Figure 1). We further evaluated the effect of Trp-His (100 mg/kg BW) administration on the DSS-induced

DOI: 10.1021/acs.jafc.5b01682
J. Agric. Food Chem. 2015, 63, 6041−6050

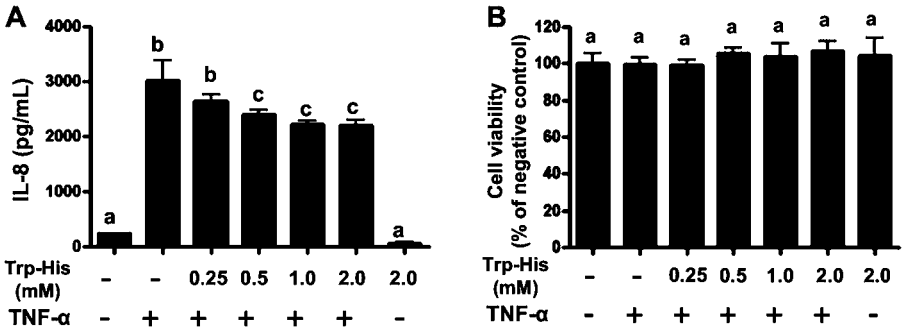

Figure 4. Effect of peptides on IL-8 secretion in HT-29 cells. (A) HT-29 cells were pretreated with medium or Trp-His at indicated concentrations for 2 h followed by TNF-α (2 ng/mL) for 2 h. IL-8 concentrations in the supernatants were measured by ELISA. Results are expressed as cytokine picograms per milliliter. (B) The viability of cells treated with Trp-His and/or TNF-α was analyzed by WST-1. Data represent means ± SEM of at least three independent tests. Values without a common letter are significantly different at $P < 0.05$.

expression of inflammatory mediators in the colonic tissues. As shown in Figure 2, treatment with Trp-His markedly ($P < 0.01$) attenuated the production of TNF-α and IL-6 when compared with the DSS mice (TNF-α, water, 229.2 ± 40.1 pg/mg protein, DSS, 527.6 ± 52.2 pg/mg protein, DSS + Trp-His, 198.5 ± 60.5 pg/mg protein; IL-6, water, 121.1 ± 22.8 pg/mg protein, DSS, 225.0 ± 32.3 pg/mg protein, DSS + Trp-His, 69.5 ± 27.4 pg/mg protein). In addition, Trp-His significantly inhibited the mRNA expression of pro-inflammatory cytokines and chemokines, including TNF-α ($P < 0.05$), IL-6 ($P < 0.01$), IL-1β ($P < 0.01$), IFN-γ ($P < 0.01$), and MCP-1 ($P < 0.01$) when compared with the DSS mice (Figure 3). There was no significant difference in the expression of anti-inflammatory cytokine IL-10. These findings suggested that Trp-His can exert potent anti-inflammatory effects in the colon of DSS-treated mice.

Effect of Trp-His on IL-8 Production in TNF-α-Stimulated HT-29 Cells. We explored the underlying mechanisms of anti-inflammatory effect of Trp-His using an intestinal epithelial cell line HT-29. TNF-α (2 ng/mL) was used to induce cellular inflammatory responses in HT-29 cells, and IL-8, a predominant pro-inflammatory chemokine produced in TNF-α-stimulated HT-29 cells,[27] was measured as an indicator of intestinal inflammation. As shown in Figure 4A, Trp-His significantly ($P < 0.05$) inhibited TNF-α-induced IL-8 secretion in HT-29 cells. Trp-His alone had no effect on IL-8 secretion. It was confirmed that Trp-His had no toxic effect at all concentrations used here (Figure 4B). The lowest concentration that significantly suppressed IL-8 production, 0.5 mM, was selected for further in vitro study.

Blocking Effect of L-Type Ca^{2+} Channels by Trp-His on TNF-α-Induced IL-8 Secretion. To clarify the structural requirement of Trp-His to exert an anti-inflammatory effect in HT-29 cells, the reverse sequence peptide of Trp-His, that is, His-Trp was used. Interestingly, His-Trp also significantly ($P < 0.01$) inhibited TNF-α-induced IL-8 secretion, and its inhibitory potential was to a similar degree as Trp-His (Figure 5A). As noted in our previous study, Trp-His can prevent an intracellular Ca^{2+}-mediated signaling via the blockade of L-type Ca^{2+} channels, and this blocking effect is similar to that of the reverse sequence peptide His-Trp.[18] This evidence allowed us to consider the involvement of L-type Ca^{2+} channels blocking in the regulation of IL-8 secretion induced by TNF-α. As specific inhibitors/activators of L-type Ca^{2+} channels, nifedipine, which binds to an extracellular side of the Ca^{2+} channel protein, verapamil (inhibitor), which binds to an intracellular side of the Ca^{2+} channel protein, and Bay K 8644 (activator) were selected. As shown in Figure 5B, both inhibitors

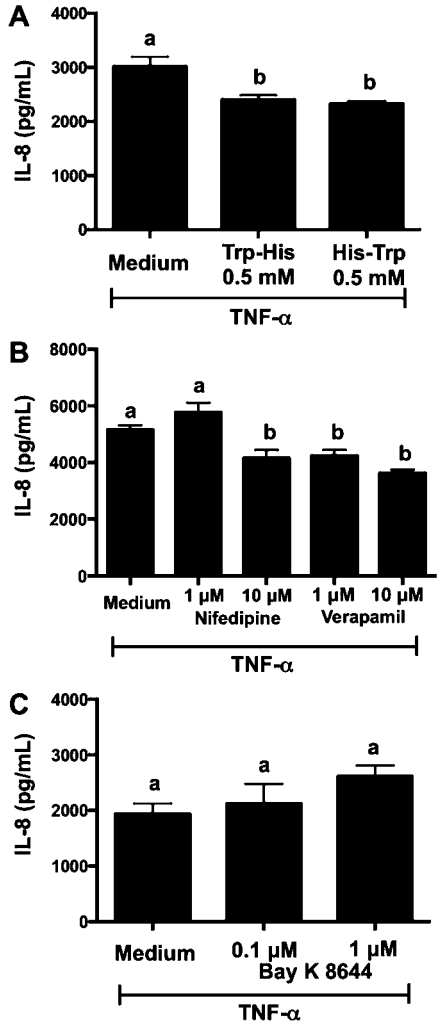

Figure 5. Effect of L-type Ca^{2+} channel blockers/agonist on IL-8 secretion in HT-29 cells. HT-29 cells were pretreated for 2 h with medium ((A) Trp-His or His-Trp, (B) nifedipine or verapamil, (C) Bay K 8644) at indicated concentrations followed by TNF-α (2 ng/mL) for 2 h. IL-8 concentrations in the supernatants were measured by ELISA. Results are expressed as cytokine picograms per milliliter. Data represent means ± SEM of at least three independent tests. Values without a common letter are significantly different at $P < 0.05$.

DOI: 10.1021/acs.jafc.5b01682
J. Agric. Food Chem. 2015, 63, 6041−6050

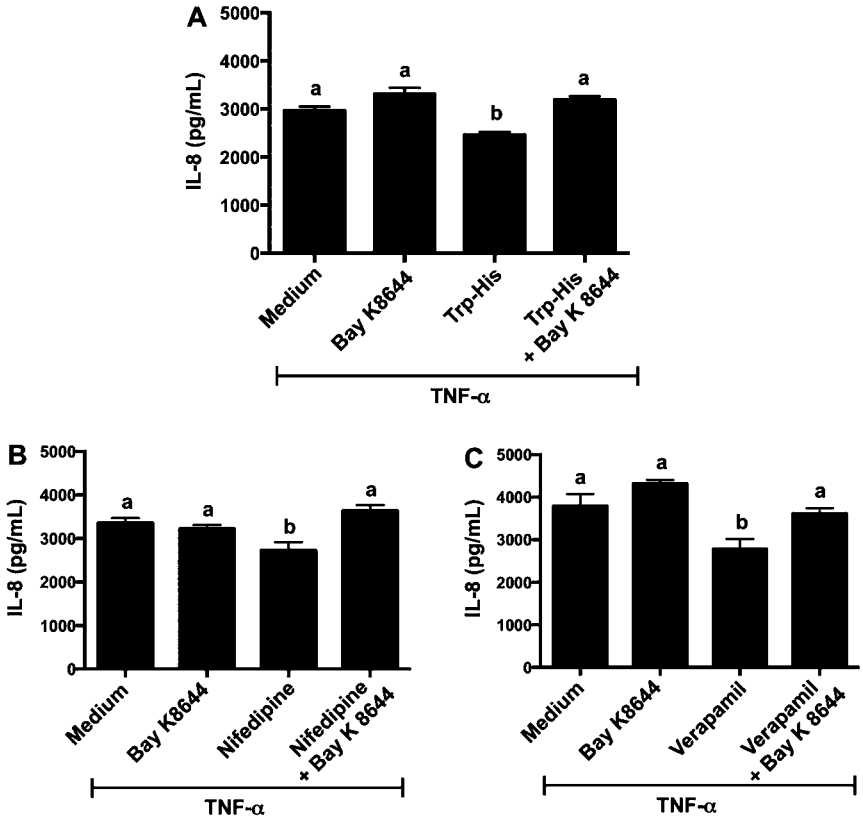

Figure 6. Effect of the combination of Trp-His or Ca^{2+} channel blockers with Bay K 8644. HT-29 cells were pretreated with medium, Bay K 8644 (0.1 μM), (A) Trp-His (0.5 mM), (B) nifedipine (10 μM), or (C) verapamil (1 μM). Bay K 8644 was added to the cells 1 h after the addition of Trp-His/blocker and incubated along with the peptide/blocker for 1 h before the addition of TNF-α (2 ng/mL). IL-8 concentrations in the supernatants were measured by ELISA. Results are expressed as cytokine picograms per milliliter. Data represent means ± SEM of at least three independent tests. Values without a common letter are significantly different at $P < 0.05$.

significantly ($P < 0.05$) reduced TNF-α-induced IL-8 production. In contrast, Bay K 8644 did not seem to affect the IL-8 secretion (Figure 5C), suggesting that the blockade of L-type Ca^{2+} channels may contribute to the decrease in IL-8 secretion observed here. To investigate whether the blockade of L-type Ca^{2+} channels by Ca^{2+} channel-blocking peptide Trp-His was similarly involved in the reduction of IL-8 production, cells were pretreated with Bay K 8644 (0.1 μM) in the presence of Trp-His (0.5 mM), followed by TNF-α treatment. The inhibitory effect of Trp-His on IL-8 secretion was completely abolished in the presence of Bay K 8644 (Figure 6A). Likewise, the inhibitory potential of nifedipine (10 μM) or verapamil (1 μM) was also abolished by Bay K 8644 (Figure 6B,C). These results indicate that the blocking effect of Trp-His on L-type Ca^{2+} channels is involved in the inhibition of IL-8 secretion in TNF-α-stimulated HT-29 cells. To further elucidate the anti-inflammatory effects of Trp-His on the TNF-α-mediated signals that control cytokine/chemokine production, we examined the effect of Trp-His on TNF-α-induced activation of mitogen-activated protein kinases (MAPKs) and nuclear factor (NF)-κB pathways. HT-29 cells were first treated with Trp-His, followed by stimulation with TNF-α for 1 or 2 h. Western blot analysis of total cell lysates using anti-phospho-MAPKs antibodies revealed that Trp-His significantly ($P < 0.05$) decreased TNF-α-induced phosphorylation of p38 and ERK after TNF-α stimulation for 2 h and that of JNK after 1 h stimulation when compared with TNF-α-treated cells (Figure 7A-C). Since phosphorylation of IκBα leads to the activation of NF-κB in TNF-α-stimulated HT-29 cells,[28] the involvement of Trp-His in the phosphorylation of IκBα was also investigated. As shown in Figure 7D, the phosphorylation level of IκBα was significantly ($P < 0.05$) increased after TNF-α stimulation for 1 h, and this was significantly ($P < 0.05$) reduced by treatment with Trp-His. These findings demonstrate that Trp-His can regulate TNF-α-mediated MAPKs/NF-κB signaling pathways in HT-29 cells.

DISCUSSION

The present study demonstrated that oral administration of Trp-His (100 mg/kg BW/day) significantly reduced the typical DSS-induced colitis symptoms and exerted anti-inflammatory effects in the mouse model of colitis. In vitro, the blocking effect of Trp-His on L-type Ca^{2+} channels contributed to the attenuation of TNF-α-induced IL-8 secretion in intestinal epithelial cell line HT-29. We further elucidated that Trp-His inhibited the activation of p38, ERK, JNK, and IκBα, which control pro-inflammatory mediator production.

Although the etiology of IBD is still unclear, overproduction of pro-inflammatory cytokines and chemokines has been shown to play an important role in the progression of colitis. TNF-α, IL-6, and IL-1β have been reported as key cytokines to amplify mucosal immune responses in IBD patients.[29] Current evidence suggests that IFN-γ and TNF-α are involved in the dysfunction of intestinal epithelial barrier, leading to the excessive entry of antigens, which initiates the inflammatory responses.[30] Chemokines such as MCP-1 promote the infiltration/migration of immune cells to areas of inflammation.[31] Our previous studies have demonstrated that dietary di/tripeptides could attenuate

DOI: 10.1021/acs.jafc.5b01682
J. Agric. Food Chem. 2015, 63, 6041−6050

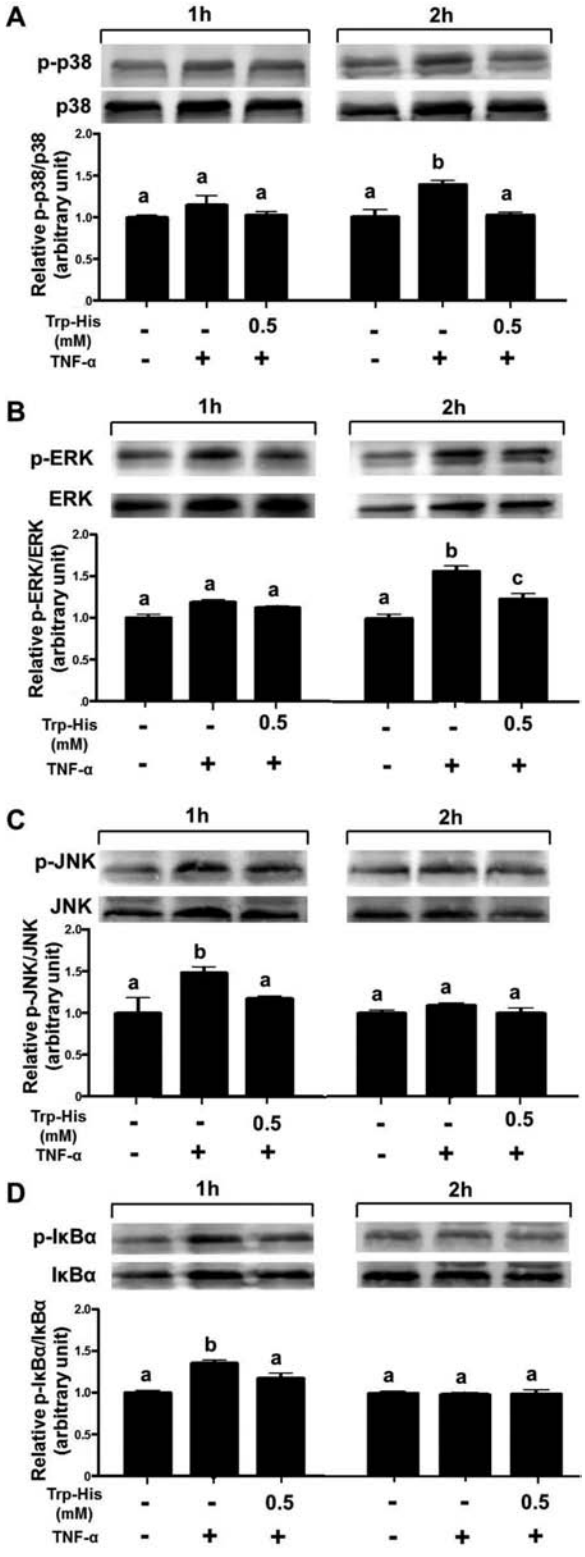

Figure 7. Effect of Trp-His on the phosphorylation of MAPKs and IκBα. HT-29 cells were pretreated with Trp-His followed by TNF-α (2 ng/mL) for 1 or 2 h. The expression of phosphorylated or total MAPKs in HT-29 cells was determined by Western blotting. The respective means of (A) p-p38/p38, (B) p-ERK/ERK, (C) p-JNK/JNK, and (D) p-IκBα/IκBα are reported as a ratio relative to the negative control. Data represent means ± SEM of at least three independent tests. Values without a common letter are significantly different at $P < 0.05$.

the development of colitis via down-regulating the expression of pro-inflammatory mediators in animal models of colitis.[8,9,12] Here, we observed that Trp-His reduced DSS-induced colitis signs, including BW loss, colon shortening, and diarrhea, and attenuated the local expression of TNF-α, IL-6, IL-1β, IFN-γ, and MCP-1 in the colon of DSS-treated mice. These results are consistent with a previous study which demonstrated that tripeptide Val-Pro-Tyr[9] at a similar dose could lessen the severity of colitis in DSS-treated mice. This would suggest that Trp-His may exert its anti-inflammatory effects by regulating the local expression of cytokines/chemokines, thereby contributing to the prevention of DSS-induced colitis development.

To elucidate the underlying mechanisms of anti-colitis by Trp-His, we further examined the anti-inflammatory effect of Trp-His in vitro. The HT-29 human colon carcinoma cell line has been shown to be a useful model for studying the physiology and immune function of intestinal epithelial cells, and the pattern of secretion of cytokines such as IL-8 by TNF-α stimulation was found to be similar in HT-29 cells and freshly isolated human colon epithelial cells.[32,33] Cho et al.[34] reported that the phytochemical arvelexin (4-methoxyindole-3-acetonitrile) inhibited TNF-α-mediated IL-8 production via NF-κB inactivation in HT-29 cells, and its anti-inflammatory potential was correlated with anti-colitis activity in DSS-treated mice. Here, we observed that Trp-His reduced TNF-α-induced IL-8 secretion by HT-29 cells. Interestingly, His-Trp, a Ca^{2+} channel-blocking peptide,[18] and L-type Ca^{2+} channel blockers (nifedipine and verapamil) also exert the inhibitory potential of TNF-α-induced IL-8 production. The expression of L-type Ca^{2+} channels, not other N- or P-type, has been confirmed in the same cell line, HT-29.[35] Furthermore, the elevation of $[Ca^{2+}]_i$ promotes the intracellular inflammatory signaling, leading to the production of IL-8 in an intestinal epithelial cell.[36] These reports imply that L-type Ca^{2+} channels may be a potential target for controlling inflammatory responses in HT-29 cells. The specific L-type Ca^{2+} channel agonist Bay K 8644 was employed here to confirm whether the anti-inflammatory effects of Trp-His were mediated via blockade of L-type Ca^{2+} channels. As expected, the combination treatment of Trp-His with Bay K 8644 completely abolished the inhibitory effect of Trp-His on TNF-α-induced IL-8 production. Similarly, the inhibitory effect of nifedipine (DHP type blocker) or verapamil (PAA type blocker) on IL-8 production was also abolished by Bay K 8644. These results are consistent with the paper by Zahradnikova et al.[37] which showed that the presence of Bay K 8644 reduced the inhibitory potency of the Ca^{2+} channel by a DHP-type blocker (in a competitive manner) or a PAA-type blocker (in a negative allosteric interaction). This would suggest that the blockade of L-type Ca^{2+} channels by Trp-His may contribute to the regulation of the TNF-α-induced inflammatory responses in HT-29 cells.

The activation of p38, ERK, JNK, and NF-κB was involved in the TNF-α-induced IL-8 secretion in HT-29 cells.[38] Western blot analysis in our present study demonstrated that the phosphorylation of MAPKs and IκBα was reduced by Trp-His in TNF-α-stimulated HT-29 cells. These results are consistent with studies which demonstrated that anti-inflammatory polyphenols can exert their effect by attenuating MAPKs activation after 1 h of stimulation with TNF-α in a human intestinal epithelial cell line,[39] and the NF-κB activation in TNF-α-stimulated HT-29 cells was shown to be induced without the degradation of IκBα.[40] These data suggest that Trp-His could exert anti-inflammatory effects via the inhibition

DOI: 10.1021/acs.jafc.5b01682
J. Agric. Food Chem. 2015, 63, 6041−6050

of MAPKs and NF-κB activation in TNF-α-mediated signaling pathways. The binding of TNF-α to TNF receptors initiates the forming of a signaling complex with TNF receptor-associated factors (TRAFs), thereby the complex activating MAPK kinase kinases (MAPKKKs), resulting in the subsequent activation of Ca^{2+}-dependent MAPKs and NF-κB.[41] In addition, activation of Ca^{2+}/CaM-dependent protein kinase II (CaMK II) also contributes to NF-κB activation in TNF-α-mediated inflammatory responses.[42] The activated CaMK II is involved in the facilitation of Ca^{2+} entry by phosphorylating the intracellular site of L-type Ca^{2+} channel.[43] In our previous study, Trp-His suppressed the phosphorylation of L-type Ca^{2+} channel via the inhibition of CaMK II activation in VSMCs.[19] Moreover, we recently demonstrated that the CaMK II inhibition by Trp-His would be caused by the inhibition of Ca^{2+}−CaM formation with the binding free energy of −49.1 kJ/mol in in silico analysis.[44] We successfully determined that Trp-His was absorbed as the peptide form into Sprague−Dawley rat blood, showing a maximal level at 1 h after single oral administration at 10 mg/kg BW (maximal concentration, 28.7 ± 8.9 pmol/mL plasma), and the peptide was preferably transported across the intestinal membrane by a proton-coupled peptide transporter 1 (PepT1).[15] Thus, these findings allow us to consider that the underlying mechanisms of the anti-inflammatory effect by Trp-His may be involved in the regulation of the CaMK II-related signaling through the blockade of L-type Ca^{2+} channels and/or the inhibition of Ca^{2+}−CaM formation on the intestine (Figure 8). Further studies are needed for clarifying whether Trp-His and other Ca^{2+} channel-blocking peptides can regulate Ca^{2+}−CaM/CaMK II-mediated inflammatory signaling so as to attenuate inflammatory responses.

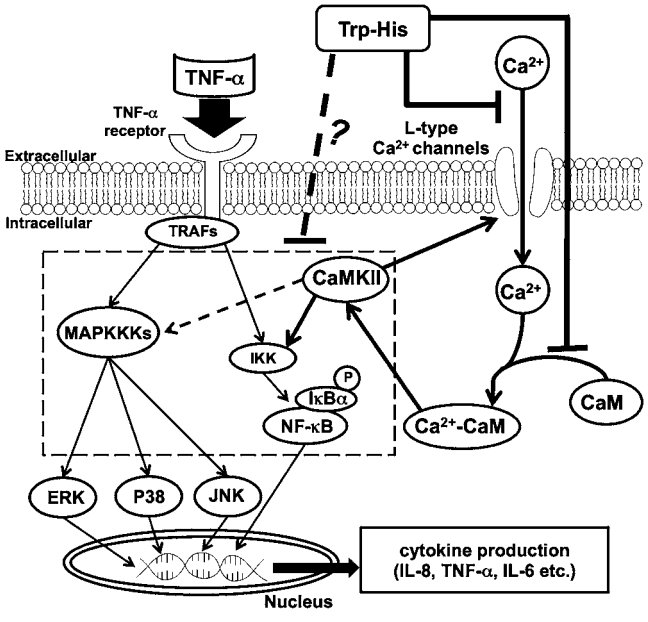

Figure 8. Possible role of Trp-His on the regulation of TNF-α-induced inflammatory signaling pathways in the intestine. The present study provides the first evidence that Trp-His reduces the TNF-α-induced IL-8 secretion through the blockade of L-type Ca^{2+} channels and inhibits the activation of MAPKs/NF-κB in HT-29 cells. Trp-His would attenuate the phosphorylation of L-type Ca^{2+} channels via the inhibition of CaMK II[19] and inhibit the formation of Ca^{2+}−CaM complex that is required for CaMK II activation.[44] Considering that the activated CaMK II is involved in the regulation of the subsequent TNF-α-mediated inflammatory signaling pathways, these data suggest that Trp-His may play a potential role in the inhibition of Ca^{2+}−CaM/CaMK II pathways.

In conclusion, the present study demonstrated that the anti-atherosclerotic peptide Trp-His prevented the development of DSS-induced colitis in mice in part by down-regulating the expression of pro-inflammatory cytokines. Trp-His significantly reduced TNF-α-induced IL-8 secretion through the blockade of L-type Ca^{2+} channels in HT-29 intestinal epithelial cells, which suggests that the blockade of L-type Ca^{2+} channels may play a beneficial role in attenuating the intestinal inflammatory responses. The anti-inflammatory activity of Trp-His was also associated with the inhibition of Ca^{2+} signaling pathway-mediated activation of MAPKs (p38, JNK, and ERK) and IκBα. Therefore, L-type Ca^{2+} channel blocking peptides such as Trp-His would be a potential preventative peptide for the amelioration of intestinal inflammation.

■ ASSOCIATED CONTENT

Ⓢ Supporting Information

Supplemental Figure 1. The Supporting Information is available free of charge on the ACS Publications website at DOI: 10.1021/acs.jafc.5b01682.

■ AUTHOR INFORMATION

Corresponding Author

*(Y.M.) Phone: (519) 824-4120. Fax: (519) 824-6631. E-mail: ymine@uoguelph.ca.

Funding

This study was supported in part by the Advanced Foods and Materials Network (AFMNet), part of the Networks of Centre of Excellence (NCE), Canada, to Y.M., a grant-in-aid from the Ministry of Education, Science, Sports and Culture of Japan (No. 22248014) to T.M., and the JSPS Research Fellowship for Young Scientists to Y.K.

Notes

The authors declare no competing financial interest.

■ ACKNOWLEDGMENTS

We thank Annette Morrison, Maka Natsvlishvili, and Jackie Rombeek for their assistance with the animal studies.

■ ABBREVIATIONS USED

Av-HRP, avidin-horseradish peroxidase; BW, body weight; $[Ca^{2+}]_i$, intracellular Ca^{2+} concentration; CaM, calmodulin; CaMK II, Ca^{2+}/CaM-dependent protein kinase II; CD, Crohn's disease; DHP, dihydropyridine; DSS, dextran sulfate sodium; EDTA, ethylenediaminetetraacetic acid; ERK, extracellular signal-regulated kinase 1/2; FBS, fetal bovine serum; HBSS, Hank's balanced salt solution; IBD, inflammatory bowel disease; IFN, interferon; IL, interleukin; JNK, c-jun N-terminal kinase; MAPKs, mitogen-activated protein kinases; MCP, monocyte chemoattractant protein; PAA, phenylalkylamine; PMSF, phenylmethanesulfonyl fluoride; PVDF, polyvinylidene difluoride; SDS-PAGE, sodium dodecyl sulfate−polyacrylamide gel electrophoresis; TMB, 3,3′,5,5′-tetramethylbenzidine; TNF, tumor necrosis factor; TRAFs, TNF receptor-associated factors; UC, ulcerative colitis; VSMCs, vascular smooth muscle cells

■ REFERENCES

(1) Macdermott, R. Alterations of the mucosal immune system in inflammatory bowel disease. *J. Gastroenterol.* **1996**, *31*, 907−916.

DOI: 10.1021/acs.jafc.5b01682
J. Agric. Food Chem. 2015, 63, 6041−6050

(2) Calder, P. C.; Albers, R.; Antoine, J. M.; Blum, S.; Bourdet-Sicard, R.; Ferns, G. A.; Folkerts, G.; Friedmann, P. S.; Frost, G. S.; Guarner, F.; Lovik, M.; Macfarlane, S.; Meyer, P. D.; M'Rabet, L.; Serafini, M.; Eden, W. V.; Loo, J. V.; Dias, W. V.; Virdy, S.; Winklhofer-Roob, B. M.; Zhao, J. Inflammatory disease processes and interactions with nutrition. *Br. J. Nutr.* **2009**, *101*, S1−S45.
(3) Gentschew, L.; Ferguson, L. R. Role of nutrition and microbiota in susceptibility to inflammatory bowel diseases. *Mol. Nutr. Food Res.* **2012**, *56*, 524−535.
(4) Pithadia, A. B.; Jain, S. Treatment of inflammatory bowel disease (IBD). *Pharmacol. Rep.* **2011**, *63*, 629−642.
(5) Stallmach, A.; Hagel, S.; Bruns, T. Adverse effects of biologics used for treating IBD. *Best Pract. Res. Clin. Gastroenterol.* **2010**, *24*, 167−182.
(6) Lee, M.; Kovacs-Nolan, J.; Yang, C.; Archbold, T.; Fan, M. Z.; Mine, Y. Hen egg lysozyme attenuates inflammation and modulates local gene expression in a porcine model of dextran sodium sulfate (DSS)-induced colitis. *J. Agric. Food Chem.* **2009**, *57*, 2233−2240.
(7) Kobayashi, Y.; Rupa, P.; Kovacs-Nolan, J.; Turner, P. V.; Matsui, T.; Mine, Y. Oral administration of hen egg white ovotransferrin attenuates the development of colitis induced by dextran sodium sulfate in mice. *J. Agric. Food Chem.* **2015**, *63*, 1532−1539.
(8) Young, D.; Ibuki, M.; Nakamori, T.; Fan, M.; Mine, Y. Soy-derived di- and tripeptides alleviate colon and ileum inflammation in pigs with dextran sodium sulfate-induced colitis. *J. Nutr.* **2012**, *142*, 363−368.
(9) Kovacs-Nolan, J.; Zhang, H.; Ibuki, M.; Nakamori, T.; Yoshiura, K.; Turner, P. V.; Matsui, T.; Mine, Y. The PepT1-transportable soy tripeptide VPY reduces intestinal inflammation. *Biochim. Biophys. Acta, Gen. Subj.* **2012**, *1820*, 1753−1763.
(10) Wada, S.; Sato, K.; Ohta, R.; Wada, E.; Bou, Y.; Fujiwara, M.; Kiyono, T.; Park, E. Y.; Aoi, W.; Takagi, T.; Nito, Y.; Yoshikawa, T. Ingestion of low dose pyroglutamyl leucine improves dextran sulfate sodium-induced colitis and intestinal microbiota in mice. *J. Agric. Food Chem.* **2013**, *61*, 8807−8813.
(11) Shi, Y.; Rupa, P.; Jiang, B.; Mine, Y. Hydrolysate from eggshell membrane ameliorates intestinal inflammation in mice. *Int. J. Mol. Sci.* **2014**, *15*, 22728−22742.
(12) Zhang, H.; Kovacs-Nolan, J.; Kodera, T.; Eto, Y.; Mine, Y. γ-Glutamyl cysteine and γ-glutamyl valine inhibit TNF-α signaling in intestinal epithelial cells and reduce inflammation in a mouse model of colitis via allosteric activation of the calcium-sensing receptor. *Biochim. Biophys. Acta, Mol. Basis Dis.* **2015**, *1852*, 792−804.
(13) Kim, C. J.; Kovacs-Nolan, J.; Yang, C.; Archbold, T.; Fan, M. Z.; Mine, Y. L-Cysteine supplementation attenuates local inflammation and restores gut homeostasis in a porcine model of colitis. *Biochim. Biophys. Acta, Gen. Subj.* **2009**, *1790*, 1161−1169.
(14) Kim, C. J.; Kovacs-Nolan, J.; Yang, C.; Archbold, T.; Fan, M. Z.; Mine, Y. L-Tryptophan exhibits therapeutic function in a porcine model of dextran sodium sulfate (DSS)-induced colitis. *J. Nutr. Biochem.* **2010**, *21*, 468−475.
(15) Tanaka, M.; Hong, S. M.; Akiyama, S.; Hu, Q. Q.; Matsui, T. Visualized absorption of anti-atherosclerotic dipeptide, Trp-His, in Sprague-Dawley rats by LC-MS and MALDI-MS imaging analyses. *Mol. Nutr. Food Res.* **2015**, n/a.
(16) Matsui, T.; Sato, M.; Tanaka, M.; Yamada, Y.; Watanabe, S.; Fujimoto, Y.; Imaizumi, K.; Matsumoto, K. Vasodilating dipeptide Trp-His can prevent atherosclerosis in Apo E-deficient mice. *Br. J. Nutr.* **2010**, *103*, 309−313.
(17) Hansson, G. K. Inflammation, atherosclerosis, and coronary artery disease. *N. Engl. J. Med.* **2005**, *352*, 1685−1695.
(18) Wang, Z.; Watanabe, S.; Kobayashi, Y.; Tanaka, M.; Matsui, T. Trp-His, a vasorelaxant di-peptide, can inhibit extracellular Ca^{2+} entry to rat vascular smooth muscle cells through blockade of dihydropyridine-like L-type Ca^{2+} channels. *Peptides* **2010**, *31*, 2060−2066.
(19) Kobayashi, Y.; Fukuda, T.; Tanaka, M.; Matsui, T. The anti-atherosclerotic di-peptide, Trp-His, inhibits the phosphorylation of voltage-dependent L-type Ca^{2+} channels in rat vascular smooth muscle cells. *FEBS Open Bio* **2012**, *2*, 83−88.
(20) Bang, L.; Chapman, T.; Goa, K. Lercanidipine: a review of its efficacy in the management of hypertension. *Drugs* **2003**, *63*, 2449−2472.
(21) Wang, X. T.; Nagaba, Y.; Cross, H. S.; Wrba, F.; Zhang, L.; Guggino, S. E. The mRNA of L-type calcium channel elevated in colon cancer: protein distribution in normal and cancerous colon. *Am. J. Pathol.* **2000**, *157*, 1549−1562.
(22) Sabatino, A. D.; Rovedatti, L.; Kaur, R.; Spencer, J. P.; Brown, J. T.; Morisset, V. D.; Biancheri, P.; Leakey, N. A.; Wilde, J. I.; Scott, L.; Corazza, G. R.; Lee, K.; Sengupta, N.; Knowles, C. H.; Gunthorpe, M.; Mclean, P. G.; MacDonald, T. T.; Kruidenier, L. Targeting gut T cell Ca^{2+} release-activated Ca^{2+} channels inhibits T cell cytokine production and T-box transcription factor T-bet in inflammatory bowel disease. *J. Immunol.* **2009**, *183*, 3454−3462.
(23) Maxwell, J. R.; Brown, W. A.; Smith, C. L.; Byrne, F. R.; Viney, J. L. Methods of inducing inflammatory bowel disease in mice. *Curr. Protoc. Pharmacol.* **2009**, *47*, 5.58.1−5.58.37.
(24) Livak, K. J.; Schmittgen, T. D. Analysis of relative gene expression data using real-time quantitative PCR and the $2^{-\Delta\Delta Ct}$ method. *Methods* **2001**, *25*, 402−408.
(25) Katayama, S.; Xu, X.; Fan, M. Z.; Mine, Y. Antioxidative stress activity of oiligophosphopeptides derived from hen egg yolk phosvitin in Caco-2 cells. *J. Agric. Food Chem.* **2006**, *54*, 773−778.
(26) Okayasu, I.; Hatakeyama, S.; Yamada, M.; Ohkusa, T.; Inagaki, Y.; Nakaya, R. A novel method in the induction of reliable experimental acute and chronic ulcerative colitis in mice. *Gastroenterology* **1990**, *98*, 694−702.
(27) Eckmann, L.; Jung, H. C.; Schurer-Maly, C.; Panja, A.; Morzycka-wroblewska, E.; Kagnoff, M. Differential cytokine expression by human intestinal epithelial cell lines: regulated expression of interleukin 8. *Gastroenterology* **1993**, *105*, 1689−1697.
(28) Russo, M. P.; Bennett, B. L.; Manning, A. M.; Brenner, D. A.; Jobin, C. Differential requirement for NF-κB-inducing kinase in the induction of NF-κB by IL-1β, TNF-α, and Fas. *Am. J. Physiol.−Cell Physiol.* **2002**, *283*, C347−C357.
(29) Reimund, J. M.; Wittersheim, C.; Dumont, S.; Muller, C. D.; Baumann, R.; Poindron, P.; Duclos, B. mucosal inflammatory cytokine production by intestinal biopsies in patients with ulcerative colitis and Crohn's disease. *J. Clin. Immunol.* **1996**, *16*, 144−150.
(30) Wang, F.; Schwarz, B. T.; Graham, W. V.; Wang, Y.; Su, L.; Clayburgh, D. R.; Abraham, C.; Turner, J. R. IFN-γ-induced TNFR2 expression is required for TNF-dependent intestinal epithelial barrier dysfunction. *Gastroenterology* **2006**, *131*, 1153−1163.
(31) Khan, W. I.; Motomura, Y.; Wang, H.; El-Sharkawy, R. T.; Verdu, E. F.; Verma-Gandhu, M.; Rollins, B. J.; Collins, S. M. Critical role of MCP-1 in the pathogenesis of experimental colitis in the context of immune and enterochromaffin Cells. *Am. J. Physiol. Gastrointest. Liver Physiol.* **2006**, *291*, G803−G811.
(32) Rousset, M. The human colon carcinoma cell lines HT-29 and Caco-2: two in vitro models for the study of intestinal differentiation. *Biochimie* **1986**, *68*, 1035−1040.
(33) Jung, H. C.; Eckmann, L.; Yang, S. K.; Panja, A.; Fierer, J.; Morzycka-Wroblewska, E.; Kagnoff, M. F. A distinct array of proinflammatory cytokines is expressed in human colon epithelial cells in response to bacterial invasion. *J. Clin. Invest.* **1995**, *95*, 55−65.
(34) Cho, E. J.; Shin, J. S.; Chung, K. S.; Lee, Y. S.; Cho, Y. W.; Baek, N. I.; Chung, H. G.; Lee, K. T. Arvelexin inhibits colonic inflammation by suppression of NF-κB activation in dextran sulfate sodium-induced mice and TNF-α-induced colonic epithelial cells. *J. Agric. Food Chem.* **2012**, *60*, 7398−7407.
(35) Zawadzki, A.; Liu, Q.; Wang, Y.; Melander, A.; Jeppsson, B.; Thorlacius, H. Verapamil inhibits L-type calcium channel mediated apoptosis in human colon cancer cells. *Dis. Colon Rectum* **2008**, *51*, 1696−1702.
(36) Yu, Y.; De Waele, C.; Chadee, K. Calcium-dependent interleukin-8 gene expression in T84 human colonic epithelial cells. *Inflammation Res.* **2001**, *50*, 220−226.
(37) Zahradnikova, A.; Minarovic, I.; Zahradnik, I. Competitive and cooperative effects of Bay K 8644 on the L-type calcium channel

DOI: 10.1021/acs.jafc.5b01682
J. Agric. Food Chem. 2015, 63, 6041−6050

current inhibition by calcium channel antagonists. *J. Pharmacol. Exp. Ther.* **2007**, *322*, 638−645.
(38) Jijon, H. B.; Panenka, W. J.; Madsen, K. L.; Parsons, H. G. MAP kinases contribute to IL-8 secretion by intestinal epithelial cells via a posttranscriptional mechanism. *Am. J. Physiol. Cell Physiol.* **2002**, *283*, C31−C41.
(39) Rodríguez-Ramiro, I.; Ramos, S.; López-Oliva, E.; Agis-Torres, A.; Bravo, L.; Goya, L.; Martín, M. A. Cocoa polyphenols prevent inflammation in the colon of azoxymethane-treated rats and in TNF-α-stimulated Caco-2 cells. *Br. J. Nutr.* **2013**, *110*, 206−215.
(40) Jobin, C.; Haskill, S.; Mayer, L.; Panja, A.; Sartor, R. Evidence for altered regulation of IκBα degradation in human colonic epithelial cells. *J. Immunol.* **1997**, *158*, 226−234.
(41) Sethu, S.; Melendez, A. J. New developments on the TNFα-mediated signalling pathways. *Biosci. Rep.* **2011**, *31*, 63−76.
(42) Théâtre, E.; Bours, V.; Oury, C. A P2X ion channel-triggered NF-κB pathway enhances TNF-α-induced IL-8 expression in airway epithelial cells. *Am. J. Respir. Cell Mol. Biol.* **2009**, *41*, 705−713.
(43) Lee, T. S.; Karl, R.; Moosmang, S.; Lenhardt, P.; Klugbauer, N.; Hofmann, F.; Kleppisch, T.; Welling, A. Calmodulin kinase II is involved in voltage-dependent facilitation of the L-type $Ca_v1.2$ calcium channel: identification of the phosphorylation sites. *J. Biol. Chem.* **2006**, *281*, 25560−25567.
(44) Kumrungsee, T.; Saiki, T.; Akiyama, S.; Nakashima, K.; Tanaka, M.; Kobayashi, Y.; Matsui, T. Inhibition of calcium-calmodulin complex formation by vasorelaxant basic dipeptides demonstrated by in vitro and in silico analyses. *Biochim. Biophys. Acta, Gen. Subj.* **2014**, *1840*, 3073−3078.

DOI: 10.1021/acs.jafc.5b01682
J. Agric. Food Chem. 2015, 63, 6041−6050

assess host responses to the implantation of biomaterials and the exposure of ionizing radiation.[17,18] It has been used to evaluate the anti-inflammatory potentials of vanillin and ginger extract on experimental colitis.[16] It also has been utilized to monitor the anti-inflammatory effects of medicinal herbs on LPS-induced acute systemic inflammation and carbon tetrachloride-induced chronic hepatitis.[19,20] Immunohistochemical (IHC) staining was further performed to elucidate the anti-inflammatory mechanisms of ginger and zingerone. Our findings suggested that ginger and zingerone were likely to be broad-spectrum anti-inflammatory agents in most organs that suppressed the activation of NF-κB, the production of interleukin-1β (IL-1β), and the infiltration of inflammatory cells.

MATERIALS AND METHODS

Chemicals. LPS (from *Escherichia coli* 055:B5), zingerone, and 3-(4,5-dimethylthiazol-2-yl)-2,5-diphenyl tetrazolium bromide (MTT) were purchased from Sigma (St. Louis, MO). MG-132, a NF-κB inhibitor, was purchased from Santa Cruz (Dallas, TX). D-Luciferin was purchased from Xenogen (Hopkinton, MA). Mouse monoclonal antibody against p65 was purchased from Chemicon (Temecula, CA). Rabbit polyclonal antibodies against IL-1β and CD11b were purchased from Santa Cruz (Dallas, TX) and Abcam (Cambridge, UK), respectively.

Preparation of Ginger Extract. Dried ginger was purchased from Xin Lung Chinese Herbal Medicine Pharmacy (Taichung, Taiwan). The voucher specimen has been deposited in Graduate Institute of Chinese Medicine, China Medical University. Ginger was ground to a fine powder and extracted by mixing 20 g of powder with 100 mL of ethanol at room temperature with shaking. Three days later, the supernatant was collected and stored at −30 °C for further analysis.

Cell Culture. Recombinant HepG2/NF-κB cells, which carried NF-κB-driven luciferase genes, were constructed previously.[19] HepG2/NF-κB cells were maintained in Dulbecco's modified Eagle's medium (Life Technologies, Gaithersburg, MD) supplemented with 10% fetal bovine serum (Hyclone, Logan, Utah) and incubated at 37 °C with 5% CO_2.

Luciferase Assay and Cell Viability Assay. HepG2/NF-κB cells (2×10^7 cells) were seeded in a 96-well plate and incubated at 37 °C overnight. LPS (100 ng/mL), MG-132 (5 μM), or various amounts of ginger and zingerone were then added to cells and incubated at 37 °C for 24 h. Cell viability was analyzed by MTT colorimetric assay as described previously.[19] Luciferase assay was performed as described previously.[19] Relative NF-κB activity was calculated by dividing the relative luciferase units (RLUs) of compound-treated cells by the RLUs of solvent-treated cells.

Animal Experiments. Transgenic mice carrying the luciferase genes driven by NF-κB-responsive elements were constructed as described previously.[17] Mouse experiments were conducted under ethics approval from China Medical University Animal Care and Use Committee (Permit No. 97-28-N).

Six-week-old female transgenic mice were randomly divided into four groups of five mice: (1) mock, no treatment; (2) LPS, (3) LPS/ginger, and (4) LPS/zingerone. Mice were challenged intraperitoneally with 1 mg/kg LPS and then orally with 100 mg/kg ginger extract or zingerone 10 min later. Four hours later, mice were imaged for the luciferase activity and subsequently sacrificed for *ex vivo* imaging and IHC staining.

***In Vivo* and *ex Vivo* Bioluminescence Imaging.** Bioluminescence imaging was performed as described previously.[17] Briefly, for *in vivo* imaging, mice were injected intraperitoneally with 150 mg/kg D-luciferin, placed in the IVIS Imaging System 200 Series chamber (Xenogen, Hopkinton, MA) 5 min later, and imaged for 1 min. Photons emitted from bodies were quantified using Living Image software (Xenogen, Hopkinton, MA).The intensity of the signal from bodies was quantified as the sum of all photon counts per second and presented as photon/s. For *ex vivo* imaging, mice were injected with D-luciferin and sacrificed 5 min later. The organs were removed immediately, placed in the IVIS chamber, and imaged for 1 min. The intensity of signal was quantified as the sum of all detected photon counts per second with the region of interest and presented as photon/(s·cm^2·steradian (sr)).

Cytokine Enzyme-Linked Immunosorbent Assay (ELISA). The amounts of proinflammatory cytokines, including IL-1β and tumor necrosis factor-α (TNF-α), in sera were quantified using Quantikine Mouse ELISA kits (R&D Systems, Minneapolis, MN). Briefly, mouse sera were added to wells coated with anti-IL-1β or anti-TNF-α antibodies and incubated at room temperature for 2 h. Biotinylated anti-mouse IL-1β or TNF-α antibodies, and avidin-horseradish peroxidase were added sequentially to wells. After a final wash, chromogenic substrate (tetramethylbenzidine) was added, and the reaction was stopped with 2 N H_2SO_4. The absorbance at 450 nm was measured using an ELISA reader (Multiskan GO, Thermo Scientific, Waltham, MA).

IHC Staining. Parafilm-embedded small intestines were cut into 5-μm-thick sections, deparaffinized in xylene, and rehydrated in graded ethanol. Sections were incubated with anti-p65, anti-IL-1β, or anti-CD11b antibodies overnight at 4 °C and then incubated with a biotinylated secondary antibody (Zymed Laboratories, Carlsbad, CA) for 20 min at room temperature. Finally, the sections were incubated with avidin−biotin complex reagent and stained with 3,3′-diaminobenzidine according to manufacturer's protocol (Histostain-Plus, Zymed Laboratories, Carlsbad, CA).

Statistics Analysis. Data were presented as mean ± standard error. Student's *t*-test was used for the comparison between two experiments. A value of $p < 0.05$ was considered statistically significant.

RESULTS

Ginger and Zingerone Suppressed LPS-Induced NF-κB Activities in Cells. Zingerone is a phenolic alkanone of ginger extract (Figure 1), and the content of zingerone was approximately 0.01 mg/mL in ethanolic extract of ginger by high-performance liquid chromatography analysis (see Supplementary Figure 1 of the Supporting Information). We first analyzed the effects of ginger and zingerone on LPS-induced NF-κB activation in cells. HepG2/NF-κB cells were treated with LPS, followed by MG-132 or various amounts of ginger and zingerone. As shown in Figure 2, LPS increased the NF-κB activity by 4-fold, compared with mock-treated cells. MG-132, a well-known NF-κB inhibitor, significantly suppressed LPS-

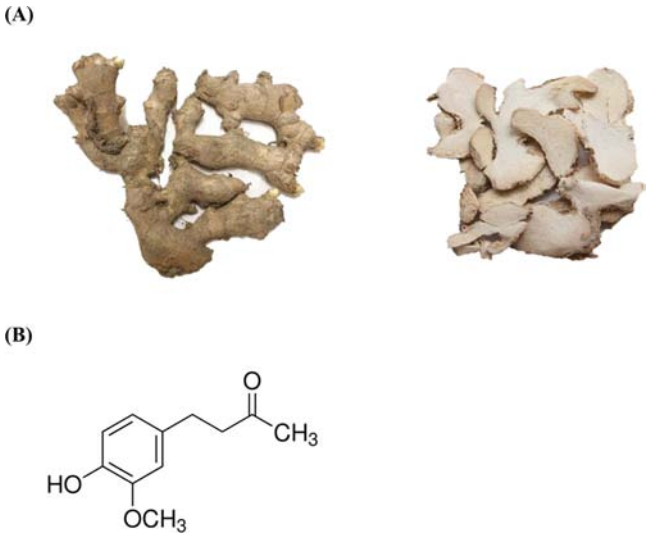

Figure 1. Ginger and zingerone. (A) Morphology of whole parts and cross sections of dried ginger. (B) Chemical structure of zingerone.

DOI: 10.1021/acs.jafc.5b01801
J. Agric. Food Chem. 2015, 63, 6051−6058

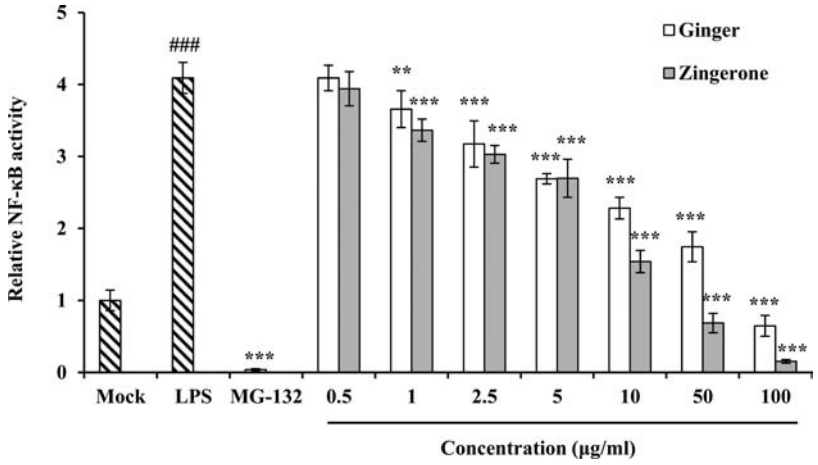

Figure 2. Effects of ginger and zingerone on LPS-induced NF-κB activities in cells. HepG2/NF-κB cells were treated with 100 ng/mL LPS and various amounts of ginger extract and zingerone. MG-132 (5 μM) was used as a positive control. NF-κB activity was measured 24 h later by luciferase assay. Results are expressed as relative NF-κB activity, which is presented as the comparison with RLU relative to solvent-treated cells. Values are mean ± standard error (n = 6). $^{###}p < 0.001$, compared with mock. $^{**}p < 0.01$, $^{***}p < 0.001$, compared with LPS.

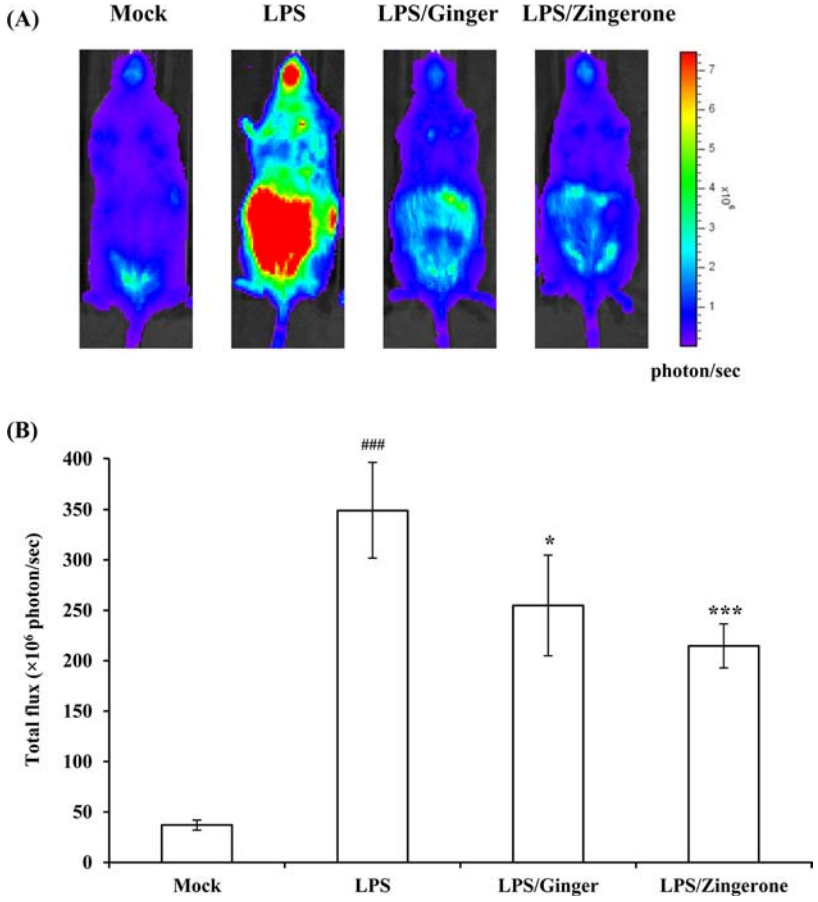

Figure 3. NF-κB-driven luminescence in living mice. (A) *In vivo* image. Transgenic mice were administered 1 mg/kg LPS and then treated with 100 mg/kg ginger or zingerone. Four hours later, mice were injected intraperitoneally with D-luciferin and imaged for 1 min. The color overlay on the image represents the photons per second emitted from mice, as indicated by the color scale. Photos are representative images (n = 5/group). (B) Quantification of photon emission from the whole body. Values are mean ± standard error. $^{###}p < 0.001$, compared with mock. $^{*}p < 0.05$, $^{***}p < 0.001$, compared with LPS.

induced NF-κB activities. Ginger and zingerone decreased NF-κB activities induced by LPS, and the decrease displayed a dose-dependency. The maximal inhibition (84.5% ± 3.5% and 96.2% ± 0.6%) was observed at 100 μg/mL ginger and zingerone, respectively. Moreover, zingerone was more effective than ginger in the inhibition of LPS-induced NF-κB activity. No visible cytotoxic effects were observed, judged by MTT assay (data not shown). These findings suggested that ginger and zingerone significantly suppressed NF-κB activities induced by LPS in cells.

DOI: 10.1021/acs.jafc.5b01801
J. Agric. Food Chem. 2015, 63, 6051−6058

Ginger and Zingerone Suppressed LPS-Induced Inflammation in Mice. The *in vivo* anti-inflammatory effects of ginger and zingerone were then analyzed by NF-κB bioluminescent imaging. Ginger extract or zingerone was orally given to transgenic mice, which had been challenged with 1 mg/kg LPS. The NF-κB-dependent bioluminescence was monitored 4 h later. As shown in Figure 3, LPS induced an approximately 4-fold increase in NF-κB-driven luminescent intensity, compared with mock-treated animals. The induced luminescence was observed over the whole body, and the strongest luminescence appeared in the abdominal region. Ginger and zingerone significantly decreased the LPS-induced luminescent intensity by 26.9% ± 14.3% and 38.5% ± 6.2%, respectively. These findings suggested that ginger and zingerone suppressed LPS-induced NF-κB-dependent luminescence in mice.

NF-κB plays a crucial role in the regulation of immunity. We wondered whether the intensity of NF-κB-driven luminescence was correlated with inflammation. The amount of proinflammatory cytokines, including IL-1β and TNF-α, in sera were therefore quantified by ELISA. As shown in Figure 4, LPS

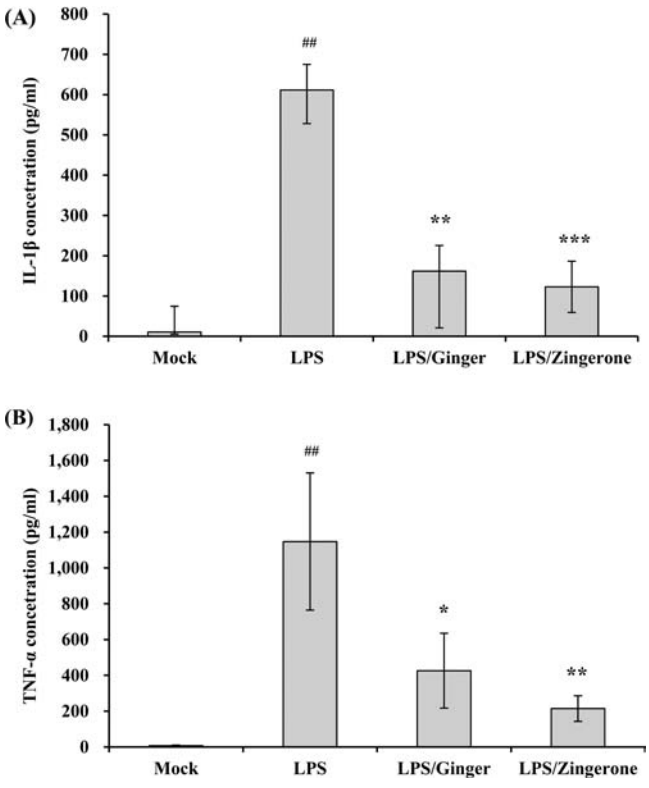

Figure 4. Effects of ginger and zingerone on LPS-induced IL-1β and TNF-α production in sera. Transgenic mice were challenged with 1 mg/kg LPS and then given with 100 mg/kg ginger or zingerone. Four hours later, mice were sacrificed, and the amount of IL-1β (A) and TNF-α (B) in sera was quantified by ELISA. Values are mean ± standard error (n = 5/group). ##p < 0.01, compared with mock. *p < 0.05, **p < 0.01, ***p < 0.001, compared with LPS.

significantly increased the amount of IL-1β and TNF-α in sera by 55.6 ± 7.6 and 172 ± 57.5 fold, respectively. However, ginger and zingerone significantly decreased LPS-induced IL-1β and TNF-α production in sera. Ginger reduced the production of IL-1β and TNF-α by 73.5% ± 23% and 63.9% ± 18.2%, respectively, while zingerone decreased IL-1β and TNF-α production by 79.9% ± 10.4% and 81.3% ± 6.2%, respectively. These data suggested that ginger and zingerone suppressed LPS-induced systemic inflammation in mice. Moreover, the correlation between NF-κB-dependent luminescent intensity and cytokine production indicated the representative of NF-κB-driven luminescence on the degree of inflammation.

Ginger and Zingerone Suppressed LPS-Induced Inflammation in Most Organs. Previous studies have shown that ginger or zingerone displayed anti-inflammatory efficacies in individual organs, such as liver, lung, brain, and colon. We would like to know whether ginger and zingerone exhibited broad-spectrum anti-inflammatory actions in most organs. Transgenic mice were therefore challenged with LPS and orally administered ginger extract and zingerone, and NF-κB-driven luminescence in organs was monitored 4 h later. As shown in Figure 5, luminescent intensities of organs were increased by LPS, suggesting that intraperitoneal injection of LPS induced inflammation in most organs. The maximal induction of luminescence by LPS was observed in kidney (15.9 ± 8 fold), followed by intestine (15.2 ± 6 fold), brain (10.4 ± 1.4 fold), heart (5.7 ± 1.5 fold), liver (4.7 ± 1.9 fold), spleen (4.7 ± 1.2 fold), lung (3.7 ± 1.4 fold), and stomach (2.7 ± 0.7 fold). Administration of ginger and zingerone significantly decreased LPS-induced NF-κB-driven luminescence in most organs. The maximal inhibition of LPS-induced luminescence by ginger and zingerone was observed in intestine, followed by kidney, liver, heart, and brain. Zingerone significantly decreased LPS-induced luminescence in lung, while ginger slightly decreased luminescent signals in lung. Moreover, both ginger and zingerone slightly decreased LPS-induced luminescent intensities in spleen.

We further analyzed the anti-inflammatory effects of ginger and zingerone in different segments of small intestine. We divided the small intestine into 35 segments, and the length ratio of duodenum, jejunum, and ileum was 1:3:2. The intensity of signal from each segment was quantified as photon/s. The suppression of LPS-induced luminescent signal by ginger or zingerone was further represented as the inhibitory percentage. As shown in Figure 6, LPS increased NF-κB-driven luminescence in whole small intestine, and strong luminescence was observed from segment 17 to 30, which corresponded to the region between midjejunum and midileum. Both ginger and zingerone suppressed LPS-induced bioluminescent intensity in whole small intestine, and the inhibition from segment 14 to 35 was >50% by ginger and zingerone. Overall, these data suggested that ginger and zingerone displayed broad-spectrum anti-inflammatory activities in most organs. Additionally, *ex vivo* imaging first showed that LPS induced a more severe inflammation in the region spanning from midjejunum to midileum. Moreover, LPS-induced luminescent signal in the junction of jejunum and ileum was suppressed efficiently by ginger and zingerone.

Ginger and Zingerone Inhibited LPS-Induced NF-κB Activation, IL-1β Production, and Inflammatory Cell Infiltration in Small Intestine. IHC staining was further performed to analyze the anti-inflammatory effects and mechanisms of ginger and zingerone in small intestine. As shown in Figure 7, the number of IL-1β-positive cells was increased by LPS, compared with mock. However, the expression of IL-1β-positive area was decreased by ginger and zingerone. In addition, LPS increased the number of CD11b-positive cells, including monocytes and granulocytes, while ginger and zingerone inhibited the expression of CD11b-

DOI: 10.1021/acs.jafc.5b01801
J. Agric. Food Chem. 2015, 63, 6051−6058

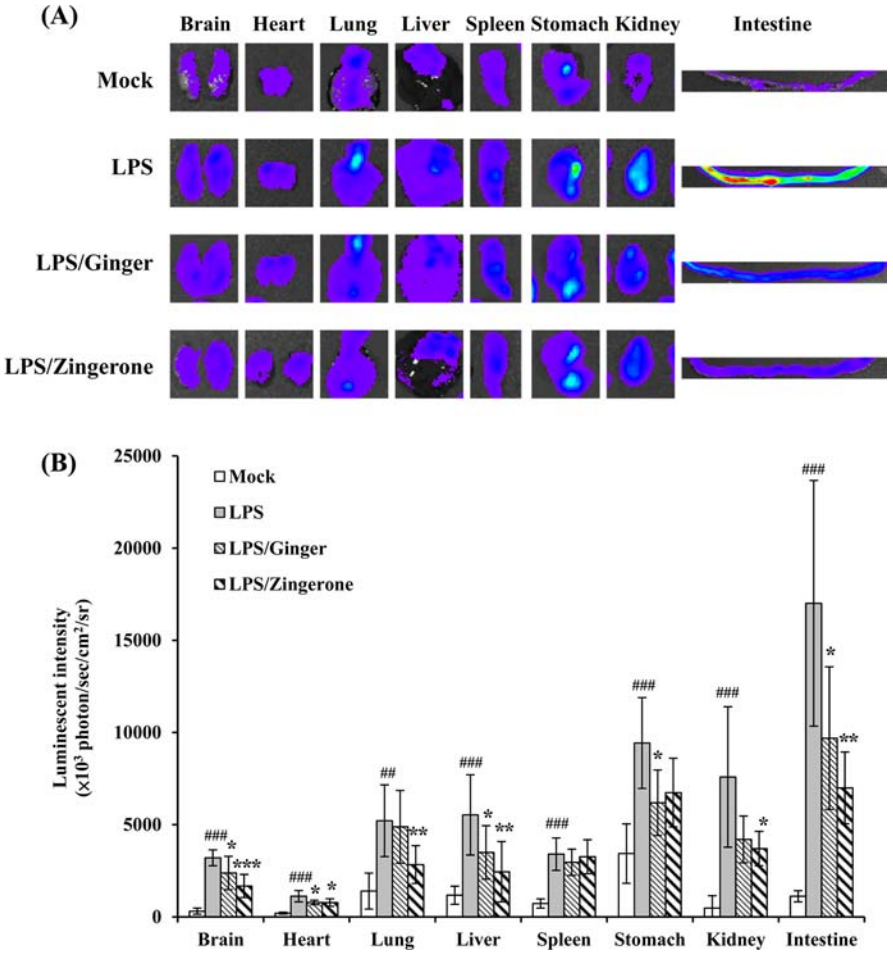

Figure 5. NF-κB-dependent luminescence in individual organs. (A) *Ex vivo* imaging. Transgenic mice were administered 1 mg/kg LPS and then treated with 100 mg/kg ginger or zingerone. Four hours later, mice were injected intraperitoneally with D-luciferin. Five minutes later, mice were sacrificed, and organs were excised rapidly and subjected to imaging (n = 5/group). (B) Quantification of photon emissions from organs. Values are mean ± standard error. ##p < 0.01, ###p < 0.001, compared with mock. *p < 0.05, **p < 0.01, ***p < 0.001, compared with LPS.

positive area. These data suggested that ginger and zingerone suppressed the production of IL-1β and the infiltration of inflammatory cells, resulting in the amelioration of LPS-inflammation in small intestine.

Because NF-κB plays a critical role in inflammation, we analyzed the level of NF-κB activity by IHC staining. The monoclonal antibody used here was against p65 nuclear localization sequence, which was blocked by inhibitory IκB when NF-κB was inactivated. LPS increased the number of p65-positive cells, while ginger and zingerone decreased the p65-positive area. These findings suggested the inhibition of LPS-induced inflammation byginger and zingerone might be through NF-κB signaling pathway.

DISCUSSION

In this study, we comprehensively evaluated the anti-inflammatory effects of ginger and zingerone by NF-κB bioluminescent imaging. Because of the light absorption by pigmented molecules and the low spatial resolution of bioluminescent imaging, we performed *ex vivo* imaging to monitor the effects of ginger and zingerone on individual organs.[21] Previous studies have shown that ginger extract and zingerone display anti-inflammatory activities in specific organs. For example, ginger extracts ameliorate LPS-induced hepatic injury and experimental colitis in mice.[16,22] Administration of ginger extracts significantly represses paw and joint swelling in rats with severe chronic adjuvant arthritis.[23] Ginger also exhibits a protective role on the diabetic brain by modulating the astroglial response to the injury in rats.[24] Moreover, zingerone attenuates LPS-induced lung injury in mice.[15] By NF-κB bioluminescent imaging, we found that administration of ginger and zingerone inhibited LPS-induced NF-κB-driven luminescence in brain, lung, liver, and colon. However, we newly identified that ginger and zingerone reduced LPS-induced luminescent intensities in heart, stomach, kidney, and small intestine. In addition, the maximal inhibition of LPS-induced luminescent signal by ginger and zingerone was observed in intestines, followed by kidney. The *in vivo* metabolism or pharmacokinetics of ginger and zingerone has been reported. After oral administration of 2 g of ginger extract in human, the glucuronide and sulfate metabolites of ginger components, such as gingerols and shogaol, are detected in plasma and gastrointestinal tract.[25] Oral dosage (100 mg/kg) of zingerone in rats results in the urinary excretion of glucuronide and sulfate conjugates of zingerone.[26] The distribution of ginger extract and zingerone in gastrointestinal tract and kidney might explain their anti-inflammatory effects in small intestine and kidney. Because of the correlation between NF-κB-driven luminescent signals and inflammation, we speculated that ginger and zingerone exhibited broad-spectrum anti-inflammatory activities

DOI: 10.1021/acs.jafc.5b01801
J. Agric. Food Chem. 2015, 63, 6051−6058

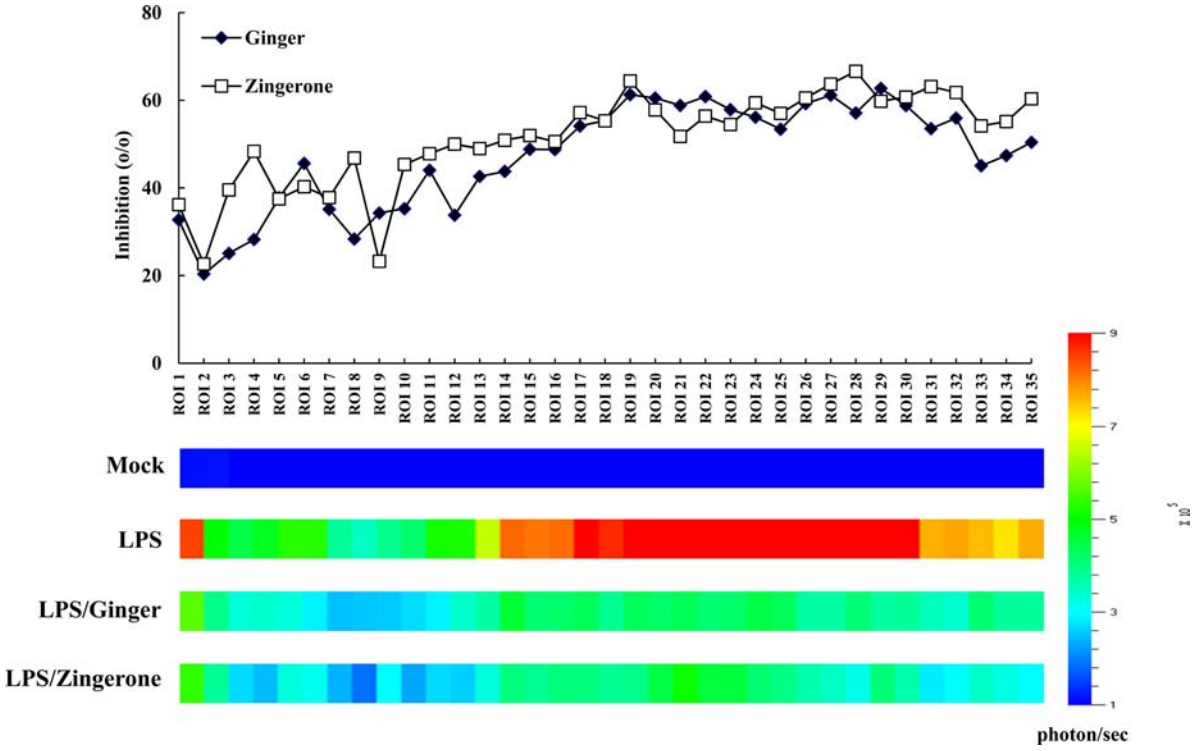

Figure 6. Anti-inflammatory effects of ginger and zingerone in various segments of small intestine. Transgenic mice were challenged with 1 mg/kg LPS and then given 100 mg/kg ginger or zingerone. Four hours later, mice were injected intraperitoneally with D-luciferin. Five minutes later, mice were sacrificed, and organs were excised rapidly and subjected to image. Small intestine was divided equally into 35 segments, and the photon emission from each segment was quantitated. Results are expressed as inhibition (%). Heatmap of small intestine is shown on the bottom. The color overlay on the heatmap represents the photons per second emitted from each segment of small intestine, as indicated by the color scale.

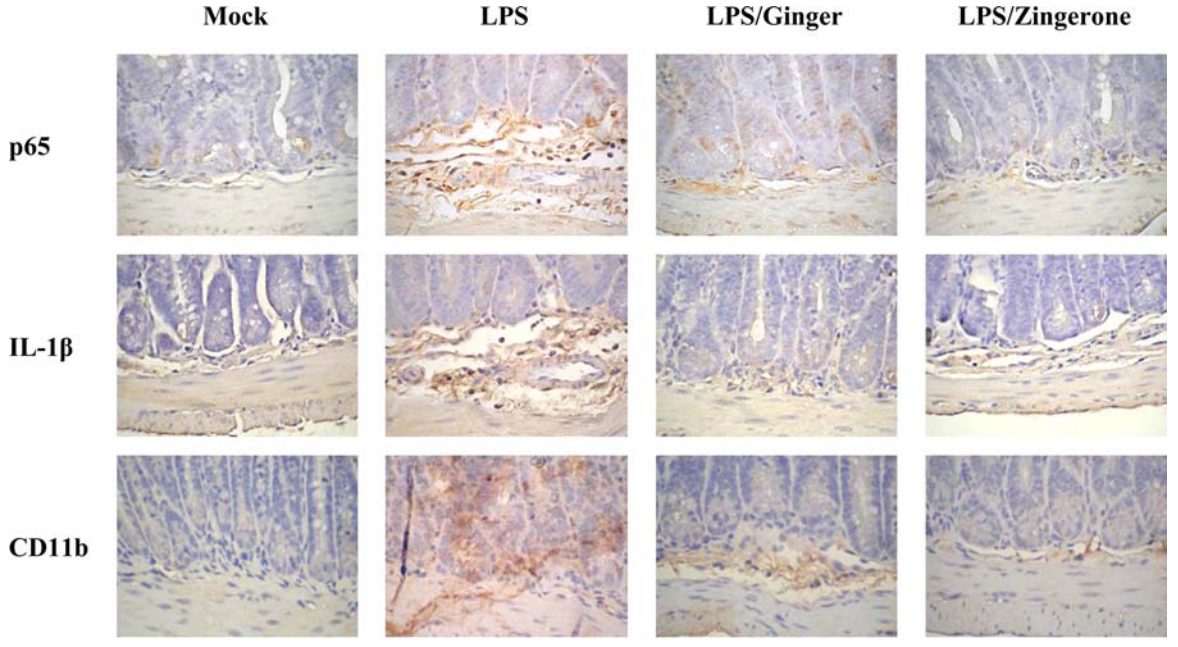

Figure 7. IHC staining analysis of p65, IL-1β, and CD11b in jejunum. Transgenic mice were challenged with 1 mg/kg LPS and then given 100 mg/kg ginger or zingerone. Four hours later, mice were sacrificed. Section of midjejunum was stained with antibodies against p65, IL-1β, and CD11b (400× magnification). Photos are representative images (n = 5/group).

that suppressed the LPS-induced inflammation in various organs.

Anti-inflammatory mechanisms of ginger and its constituents have been analyzed in *in vitro* and *in vivo* studies. For instance, ginger extract ameliorates LPS-induced hepatic injury via inhibiting the production of proinflammatory cytokines and attenuating the mitogen-activated protein kinases and NF-κB signaling pathways.[22] It also inhibits the activities of cyclooxygenase-2 (COX-2) and inducible nitric oxide synthase (iNOS) and thus inhibits the synthesis of prostaglandins and

DOI: 10.1021/acs.jafc.5b01801
J. Agric. Food Chem. 2015, 63, 6051−6058

NO, mediators of inflammation.[27] Ginger derivatives, such as 6-shogaol, reduce osteoarthritis symptoms by inhibiting toll-like receptor 4 (TLR-4)-mediated innate immunity and cathepsin-k activity.[28] 6-Shogaol also displays a neuroprotective effect via inhibiting iNOS, COX-2, proinflammatory cytokines, and NF-κB activities in LPS-treated microglial cells.[14] In addition, 1-dehydro-10-gingerdione inhibits TLR-4-mediated signaling cascades and cytokine expression via blockade of LPS binding to myeloid differentiation protein 2, a coreceptor of TLR-4 in macrophages.[29] In this study, we found that ginger and zingerone inhibited LPS-induced NF-κB activities in various organs in mice. Ginger and zingerone also suppressed the nuclear translocation of NF-κB subunit p65, the production of IL-1β, and the infiltration of granulocytes in small intestine. Overall, this study suggested that ginger and zingerone shared a common anti-inflammatory mechanism by inhibiting NF-κB activities and proinflammatory cytokine production in LPS-induced systemic inflammation. Moreover, ginger exhibits a nonsteroidal anti-inflammatory activity via inhibiting the activities of COX-2 and iNOS in other studies, probably explaining why ginger displayed a broad-spectrum anti-inflammatory activity in various organs in this study.

Detailed anti-inflammatory effects of ginger and zingerone in small intestine were evaluated here. It is interesting to find that LPS increased NF-κB-driven luminescence in the entire small intestine, especially from the middle portion of jejunum to the end of ileum. It is known that LPS activates macrophages, neutrophils, and dendritic cells via binding to TLR-4 and activating downstream NF-κB activity. The activated immune cells then initiate the inflammatory response and present antigens to lymphocytes in lymph nodes.[30] In comparison with duodenum, jejunum and ileum have abundant Peyer's patches, organized lymphoid nodules, in mice. Thus, we speculated that LPS induced maximal NF-κB-driven luminescence in jejunum and ileum might result from the abundance of Peyer's patches. We also found that ginger and zingerone suppressed LPS-induced NF-κB-dependent bioluminescent signals in the entire small intestine, especially in the region between midjejunum and midileum. Zingerone possesses the vanillyl moiety, which is considered important for the activation of vanilloid receptor 1 (VR1) expressed in nociceptive sensory neurons.[31] A recent study shows that activated VR1 protects against LPS-mediated renal injury possibly via reducing renal inflammation responses.[32] In addition, sensory VR1 has been found to modulate cytokine response to LPS and thereby induce the subsequent anti-inflammatory effect in the gut mucosa.[33] VR1 nerve fibers are observed within enteric ganglia of jejunum and ileum,[34] probably explaining why zingerone displayed more activities in jejunum and ileum than in duodenum.

In conclusion, we comprehensively evaluated the anti-inflammatory effects of ginger and zingerone on LPS-induced systemic inflammation via NF-κB bioluminescent imaging. Our data showed for the first time that ginger and zingerone suppressed NF-κB-driven luminescence in most organs. In addition, our findings suggested that ginger and zingerone are likely to be broad-spectrum anti-inflammatory agents that suppress the activation of NF-κB, the production of IL-1β, and the infiltration of inflammatory cells in most organs.

■ ASSOCIATED CONTENT

Ⓢ Supporting Information

HPLC profile of ginger extract (Supplementary Figure S1). The Supporting Information is available free of charge on the ACS Publications website at DOI: 10.1021/acs.jafc.5b01801.

■ AUTHOR INFORMATION

Corresponding Author

*Telephone: +886 4 22053366, ext. 3302. Fax: +886 4 22032295. E-mail: cyhsiang@mail.cmu.edu.tw.

Author Contributions

#C.-Y.H. and H.-M.C. equally contributed to this work.

Funding

This work was supported by grants from Ministry of Science and Technology (NSC101-2320-B-039-034-MY3, NSC102-2632-B-039-001-MY3, and MOST 104-2815-C-039-012-B), China Medical University (CMU102-NSC-04 and CMU103-SR-44), and CMU under the Aim for Top University Plan of the Ministry of Education, Taiwan.

Notes

The authors declare no competing financial interest.

■ ABBREVIATIONS USED

COX-2, cyclooxygenase-2; ELISA, enzyme-linked immunosorbent assay; IHC, immunohistochemical; iNOS, inducible nitric oxide synthase; IL-1β, interleukin-1β; LPS, lipopolysaccharide; MTT, 3-(4,5-dimethylthiazol-2-yl)-2,5-diphenyl tetrazolium bromide; NO, nitric oxide; NF-κB, nuclear factor-κB; RLU, relative luciferase unit; sr, steradian; TLR-4, toll-like receptor 4; TNF-α, tumor necrosis factor-α; VR1, vanilloid receptor 1

■ REFERENCES

(1) Ryan, J. L.; Heckler, C. E.; Roscoe, J. A.; Dakhil, S. R.; Kirshner, J.; Flynn, P. J.; Hickok, J. T.; Morrow, G. R. Ginger (*Zingiber officinale*) reduces acute chemotherapy-induced nausea: A URCC CCOP study of 576 patients. *Supportive Care Cancer* **2012**, *20*, 1479−1489.

(2) Dabaghzadeh, F.; Khalili, H.; Dashti-Khavidaki, S.; Abbasian, L.; Moeinifard, A. Ginger for prevention of antiretroviral-induced nausea and vomiting: a randomized clinical trial. *Expert Opin. Drug Saf.* **2014**, *13*, 859−866.

(3) Chopra, A.; Saluja, M.; Tillu, G.; Sarmukkaddam, S.; Venugopalan, A.; Narsimulu, G.; Handa, R.; Sumantran, V.; Raut, A.; Bichile, L.; Joshi, K.; Patwardhan, B. Ayurvedic medicine offers a good alternative to glucosamine and celecoxib in the treatment of symptomatic knee osteoarthritis: A randomized, double-blind, controlled equivalence drug trial. *Rheumatology* **2013**, *52*, 1408−1417.

(4) Bartels, E. M.; Folmer, V. N.; Bliddal, H.; Altman, R. D.; Juhl, C.; Tarp, S.; Zhang, W.; Christensen, R. Efficacy and safety of ginger in osteoarthritis patients: A meta-analysis of randomized placebo-controlled trials. *Osteoarthritis Cartilage* **2015**, *23*, 13−21.

(5) Black, C. D.; Herring, M. P.; Hurley, D. J.; O'Connor, P. J. Ginger (*Zingiber officinale*) reduces muscle pain caused by eccentric exercise. *J. Pain* **2010**, *11*, 894−903.

(6) Rahnama, P.; Montazeri, A.; Huseini, H. F.; Kianbakht, S.; Naseri, M. Effect of *Zingiber officinale* R. rhizomes (ginger) on pain relief in primary dysmenorrhea: A placebo randomized trial. *BMC Complementary Altern. Med.*. **2012**, *12*, No. 92.

(7) Mozaffari-Khosravi, H.; Talaei, B.; Jalali, B. A.; Najarzadeh, A.; Mozayan, M. R. The effect of ginger powder supplementation on insulin resistance and glycemic indices in patients with type 2 diabetes: A randomized, double-blind, placebo-controlled trial. *Complementary Ther. Med.* **2014**, *22*, 9−16.

DOI: 10.1021/acs.jafc.5b01801
J. Agric. Food Chem. 2015, 63, 6051−6058

(8) Jung, H. W.; Yoon, C. H.; Park, K. M.; Han, H. S.; Park, Y. K. Hexane fraction of Zingiberis Rhizoma Crudus extract inhibits the production of nitric oxide and proinflammatory cytokines in LPS-stimulated BV2 microglial cells via the NF-kappaB pathway. *Food Chem. Toxicol.* **2009**, *47*, 1190−1197.
(9) Podlogar, J. A.; Verspohl, E. J. Antiinflammatory effects of ginger and some of its components in human bronchial epithelial (BEAS-2B) cells. *Phytother. Res.* **2012**, *26*, 333−336.
(10) Li, F.; Nitteranon, V.; Tang, X.; Liang, J.; Zhang, G.; Parkin, K. L.; Hu, Q. *In vitro* antioxidant and anti-inflammatory activities of 1-dehydro-[6]-gingerdione, 6-shogaol, 6-dehydroshogaol and hexahydrocurcumin. *Food Chem.* **2012**, *135*, 332−327.
(11) Huang, S. H.; Lee, C. H.; Wang, H. M.; Chang, Y. W.; Lin, C. Y.; Chen, C. Y.; Chen, Y. H. 6-Dehydrogingerdione restrains lipopolysaccharide-induced inflammatory responses in RAW 264.7 macrophages. *J. Agric. Food Chem.* **2014**, *62*, 9171−9179.
(12) Rahmani, A. H.; Shabrmi, F. M.; Aly, S. M. Active ingredients of ginger as potential candidates in the prevention and treatment of diseases via modulation of biological activities. *Int. J. Physiol. Pathophysiol. Pharmacol.* **2014**, *6*, 125−136.
(13) Ha, S. K.; Moon, E.; Ju, M. S.; Kim, D. H.; Ryu, J. H.; Oh, M. S.; Kim, S. Y. 6-Shogaol, a ginger product, modulates neuroinflammation: A new approach to neuroprotection. *Neuropharmacology* **2012**, *63*, 211−223.
(14) Moon, M.; Kim, H. G.; Choi, J. G.; Oh, H.; Lee, P. K.; Ha, S. K.; Kim, S. Y.; Park, Y.; Huh, Y.; Oh, M. S. 6-Shogaol, an active constituent of ginger, attenuates neuroinflammation and cognitive deficits in animal models of dementia. *Biochem. Biophys. Res. Commun.* **2014**, *449*, 8−13.
(15) Xie, X.; Sun, S.; Zhong, W.; Soromou, L. W.; Zhou, X.; Wei, M.; Ren, Y.; Ding, Y. Zingerone attenuates lipopolysaccharide-induced acute lung injury in mice. *Int. Immunopharmacol.* **2014**, *19*, 103−109.
(16) Hsiang, C. Y.; Lo, H. Y.; Huang, H. C.; Li, C. C.; Wu, S. L.; Ho, T. Y. Ginger extract and zingerone ameliorated trinitrobenzene sulphonic acid-induced colitis in mice via modulation of nuclear factor-κB activity and interleukin-1β signalling pathway. *Food Chem.* **2013**, *136*, 170−177.
(17) Ho, T. Y.; Chen, Y. S.; Hsiang, C. Y. Noninvasive nuclear factor-κB bioluminescence imaging for the assessment of host-biomaterial interaction in transgenic mice. *Biomaterials* **2007**, *28*, 4370−4377.
(18) Chang, C. T.; Lin, H.; Ho, T. Y.; Li, C. C.; Lo, H. Y.; Wu, S. L.; Huang, Y. F.; Liang, J. A.; Hsiang, C. Y. Comprehensive assessment of host responses to ionizing radiation by nuclear factor-κB bioluminescence imaging-guided transcriptomic analysis. *PLoS One* **2011**, *6*, No. e23682.
(19) Li, C. C.; Hsiang, C. Y.; Lo, H. Y.; Pai, F. T.; Wu, S. L.; Ho, T. Y. Genipin inhibits lipopolysaccharide-induced acute systemic inflammation in mice as evidenced by nuclear factor-κB bioluminescent imaging-guided transcriptomic analysis. *Food Chem. Toxicol.* **2012**, *50*, 2978−2986.
(20) Li, C. C.; Hsiang, C. Y.; Wu, S. L.; Ho, T. Y. Identification of novel mechanisms of silymarin on the carbon tetrachloride-induced liver fibrosis in mice by nuclear factor-κB bioluminescent imaging-guided transcriptomic analysis. *Food Chem. Toxicol.* **2012**, *50*, 1568−1575.
(21) Badr, C. E. Bioluminescence imaging: Basics and practical limitations. *Methods Mol. Biol.* **2014**, *1098*, 1−18.
(22) Choi, Y. Y.; Kim, M. H.; Hong, J.; Kim, S. H.; Yang, W. M. Dried ginger (*Zingiber officinalis*) inhibits inflammation in a lipopolysaccharide-induced mouse model. *Evidence-Based Complementary Altern. Med.* **2013**, *2013*, No. 914563.
(23) Sharma, J. N.; Srivastava, K. C.; Gan, E. K. Suppressive effects of eugenol and ginger oil on arthritic rats. *Pharmacology* **1994**, *49*, 314−318.
(24) El-Akabawy, G.; El-Kholy, W. Neuroprotective effect of ginger in the brain of streptozotocin-induced diabetic rats. *Ann. Anat.* **2014**, *196*, 119−128.
(25) Yu, Y.; Zick, S.; Li, X.; Zou, P.; Wright, B.; Sun, D. Examination of the pharmacokinetics of active ingredients of ginger in humans. *AAPS J.* **2011**, *13*, 417−426.
(26) Monge, P.; Scheline, R.; Solheim, E. The metabolism of zingerone, a pungent principle of ginger. *Xenobiotica* **1976**, *6*, 411−423.
(27) Yu, Y. S.; Hsu, C. L.; Yen, G. C. Anti-inflammatory effects of the roots of *Alpinia pricei* Hayata and its phenolic compounds. *J. Agric. Food Chem.* **2009**, *57*, 7673−7680.
(28) Villalvilla, A.; da Silva, J. A.; Largo, R.; Gualillo, O.; Vieira, P. C.; Herrero-Beaumont, G.; Gómez, R. 6-Shogaol inhibits chondrocytes' innate immune responses and cathepsin-K activity. *Mol. Nutr. Food Res.* **2014**, *58*, 256−266.
(29) Park, S. H.; Kyeong, M. S.; Hwang, Y.; Ryu, S. Y.; Han, S. B.; Kim, Y. Inhibition of LPS binding to MD-2 co-receptor for suppressing TLR4-mediated expression of inflammatory cytokine by 1-dehydro-10-gingerdione from dietary ginger. *Biochem. Biophys. Res. Commun.* **2012**, *419*, 735−740.
(30) Morris, M. C.; Gilliam, E. A.; Li, L. Innate immune programing by endotoxin and its pathological consequences. *Front. Immunol.* **2015**, *5*, 680.
(31) Dedov, V. N.; Tran, V. H.; Duke, C. C.; Connor, M.; Christie, M. J.; Mandadi, S.; Roufogalis, B. D. Gingerols: A novel class of vanilloid receptor (VR1) agonists. *Br. J. Pharmacol.* **2002**, *137*, 793−798.
(32) Wang, Y.; Wang, D. H. Deletion of the transient receptor potential vanilloid type 1 channel exacerbates renal inflammation induced by lipopolysaccharide in mice. *FASEB J.* **2013**, *27*, 721.10.
(33) Assas, B. M.; Miyan, J. A.; Pennock, J. L. Cross-talk between neural and immune receptors provides a potential mechanism of homeostatic regulation in the gut mucosa. *Mucosal Immunol.* **2014**, *7*, 1283−1289.
(34) Vinuesa, A. G.; Sancho, R.; García-Limones, C.; Behrens, A.; ten Dijke, P.; Calzado, M. A.; Muñoz, E. Vanilloid receptor-1 regulates neurogenic inflammation in colon and protects mice from colon cancer. *Cancer Res.* **2012**, *72*, 1705−1716.

DOI: 10.1021/acs.jafc.5b01801
J. Agric. Food Chem. 2015, 63, 6051−6058

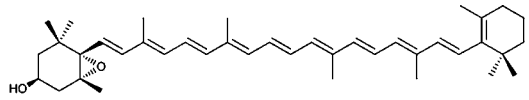
(3*S*,5*R*,6*S*)-β-Cryptoxanthin-5,6-epoxide **1**

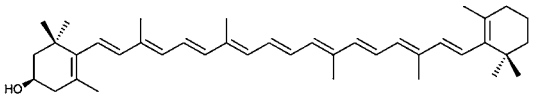
β-Cryptoxanthin **2**

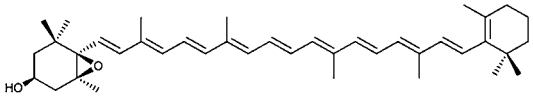
(3*S*,5*S*,6*R*)-β-Cryptoxanthin-5,6-epoxide **3**

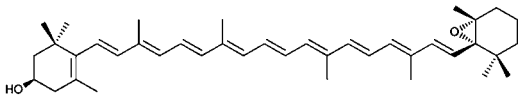
(3*R*,5′*R*,6′*S*)-β-Cryptoxanthin-5′,6′-epoxide **4**

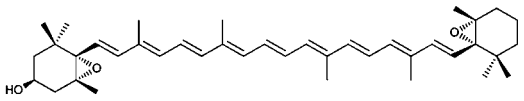
(3*S*,5*R*,6*S*,5′*R*,6′*S*)-β-Cryptoxanthin-5,6,5′,6′-diepoxide **5**

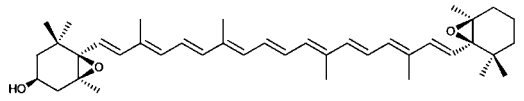
(3*S*,5*S*,6*R*,5′*S*,6′*R*)-β-Cryptoxanthin-5,6,5′,6′-diepoxide **6**

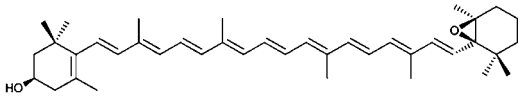
(3*R*,5′*S*,6′*R*)-β-Cryptoxanthin-5′,6′-epoxide **7**

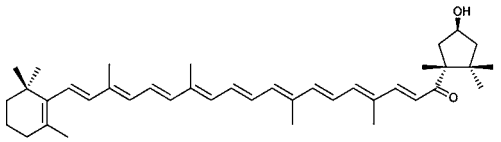
Cryptocapsin **8**

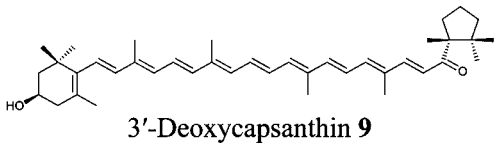
3′-Deoxycapsanthin **9**

Figure 1. Structures of carotenoids from red mamey and related compounds.

DRX Avance II (500/125 MHz for $^{1}H/^{13}C$) spectrometer (Bruker Corp., Billerica, MA, USA). Chemical shifts are referenced to internal TMS (^{1}H) or to the residual solvent signals (^{13}C).

MS Analysis. Samples were dissolved in MeOH and infused directly using a Fusion 100 T syringe pump (Thermo Fisher, Waltham, MA, USA) to a Q-Exactive quadrupole-orbitrap hybrid mass spectrometer (Thermo Fisher) with HESI source operated in positive ion mode. Data acquisition and analysis were performed by using Xcalibur (version 2.2 SP1.48). The source was operated with a spray voltage of 3500 V. Both sheath and auxiliary gases were nitrogen delivered at 10 and 2 L/min, respectively. The capillary temperature was set to 200 °C, whereas the ESI source heater was set to 40 °C. The RF level of the S-lenses was set to 70. For full MS experiments aimed at exact mass identification, we used the isolation window of m/z 50−750. By MS/MS experiments performed with the aim of structural elucidation of the β-cryptoxanthin-epoxides, we used the precursor ion isolation window of m/z 567.4−569.4. High-energy collision cell was used for fragmentation at four different collision energy levels, 10, 15, 20, and 25%. In the lists of MS results the first value is always the m/z of the corresponding compound; all other ions are products of fragmentation.

The exact mass measurements (HRESITOFMS) were performed using a Waters Q-TOF Premier mass spectrometer (Waters Corp., Milford, MA, USA). The sample was dissolved in MeOH and measured in positive electrospray ionization mode.

HPLC-DAD Analysis. A Dionex P680 gradient pump with a Dionex PDA-100 detector and Chromeleon 6.70 software was used. The analytical HPLC separation was carried out on an end-capped C30 column with 250 mm × 4.6 mm i.d., 5 μm, YMC C30 (YMC Co. Ltd.). Eluents were (A) MeOH/methyl *tert*-butyl ether (MTBE)/H_2O (81:15:4) and (B) MeOH/MTBE/H_2O (6:90:4). The chromatography was performed in linear gradient from 100% A eluent to 50% B mixture in 45 min, with a 1 mL/min flow.

The chiral HPLC-DAD separation was carried out on a 250 × 4.6 mm i.d., 3 μm, Chiralcel OD column (Daicel, Chemical Industries, Ltd.). Eluents were (A) MeOH/EtOH (1:1) and (B) MeCN/EtOH (1:1). The chromatography was performed in linear gradient from 100% A eluent to 100% B mixture in 30 min, with a 1 mL/min flow. HPLC-DAD analysis was performed with a Dionex HPLC system (Thermo Fisher Scientific).

Semipreparative HPLC. A model 1050 Hewlett-Packard chromatograph (Hewlett-Packard Development Co., Palo Alto, CA, USA) equipped with a diode array detector and HP ChemStation software was used. The separation was carried out on an end-capped C30 column with a 250 mm × 4.6 mm i.d., 5 μm, YMC C30 with an isocratic system of MeOH/MTBE/H_2O (7:16:4), with 2.5 mL/min flow, monitored at 450 nm.

HPLC-ECD analysis. Chiral HPLC separations were performed with a Jasco HPLC system using Chiralpak IA column with 250 mm × 4.6 mm i.d., 5 μm (Daicel, Chemical Industries, Ltd.) and *n*-hexane/propan-2-ol (9:1) eluent at a flow rate of 1.0 mL/min for **4** and **7** (Figure 1). HPLC-UV and OR chromatograms of the stereoisomeric mixtures were recorded with Jasco MD-910 multiwavelength and OR-2090Plus chiral detector, respectively. The online ECD and UV spectra were measured simultaneously by stopping the flow at the UV absorption maximum of each peak. The values of the ECD ellipticity (ϕ) were not corrected for the concentration. Three consecutive scans were recorded and averaged for an HPLC-ECD spectrum with standard sensitivity, 2 nm bandwidth and 1 s response. The background HPLC-ECD spectrum of the eluent was recorded in the same way.

Plant Material. Matured fruits were purchased at the Metropolitan public market in Panama City, Panama.

Extraction and Isolation. The pulp of red mamey (500 g) was homogenized in a porcelain mortar with 50 g of $NaHCO_3$ and extracted with acetone until no more color was observed. The extract was diluted with a mixture of Et_2O/*n*/hexane (1:1), washed with H_2O to remove acetone, dried (Na_2SO_4), and evaporated. The residue was dissolved in Et_2O and saponified with methanolic KOH. After saponification, the ethereal solution was washed to remove alkali and evaporated. The residue was subjected to open column chromatography (Al_2O_3 Brockman grade III) using an increasing percentage of ether in *n*-hexane.

The mixture of β-cryptoxanthin 5,6- and 5′,6′-epoxide was contained in the fraction that eluted with 15−25% diethyl ether. The specific epoxides were isolated by semiprepative HPLC, with several consecutive injections.

Cryptocapsin, **8**, was isolated from the fraction that eluted with 50% ether. This fraction was submitted to open column chromatography on

DOI: 10.1021/acs.jafc.5b01936
J. Agric. Food Chem. 2015, 63, 6059−6065

$CaCO_3$ (Merck) with toluene/hexane (30:70). Five colored zones could be separated: zone 1, 10 mm brick red band (mixture of cryptocapsin 5,8-epoxides[29] and 3′-deoxycapsorubin;[30] zone 2, 10 mm pink band, cryptocapsin 5,6-epoxide;[29] zone 3, 20 mm red band of cryptocapsin, **8**; zone 4, 10 mm pink band, 3′-deoxycapsanthin 5,6-epoxide;[29] zone 5, 3 mm yellow band of cryptoxanthin 5,6,5′,6′-diepoxide.[29] After processing (cutting the column into pieces and extracting), zones 2−5 were crystallized from benzene by the addition of hexane, yielding 4 mg of cryptocapsin 5,6-epoxide, 8 mg of cryptocapsin, **8**, 0.5 mg of 3′-deoxycapsanthin 5,6-epoxide, and 0.5 mg of cryptoxanthin 5,6,5′,6′-diepoxide.[29]

3′-Deoxycapsanthin, **9**, was isolated in pure form by additional column chromatography of a fraction eluted with 30% ether. This fraction was submitted to open column chromatography on $CaCO_3$ with toluene/hexane (20:80). After development, three zones were visible: zone 1, 6 mm pale yellow band, unidentified mixture; zone 2, 50 mm yellow band, mixture of β-cryptoxanthin 5,8- and 5′,8′-epoxides; zone 3, 20 mm pink band, 3′-deoxy-capsanthin, **9**. After processing, zone 3 was crystallized from benzene by the addition of hexane, yielding 2 mg of 3′-deoxy-capsanthin, **9**.

Preparation of Semisynthetic β-Cryptoxanthin-5′,6′-epoxides. To a solution of β-cryptoxanthin acetate (108 mg) in Et_2O (360 mL) at room temperature was added 9.2 mL of 0.339 M concentration monoperoxyphthalic acid (Et_2O solution). The mixture was kept under N_2, in the dark. After 12 h, the mixture was washed with 5% aqueous $NaHCO_3$ solution, the organic phase was dried (Na_2SO_4), and a 30% KOH/MeOH solution (∼100 mL) was added. After 16 h, the solution was washed with H_2O until neutral and dried (Na_2SO_4), and the solvent was evaporated.

Column Chromatography of β-Cryptoxanthin-epoxide Mixture. The residue was dissolved in hexane and submitted to open column chromatography on $CaCO_3$ (Biogal, Debrecen, Hungary) with eluent toluene/hexane (20:80). Picture after development: 5 mm bright yellow (zone 1, not identified); 10 mm intermediate zone; 60 mm bright yellow (zone 2, mixture of β-cryptoxanthin-diepoxides and -5,6-epoxides); 10 mm pale ochre (zone 3, β-cryptoxanthin 5′,6′-epoxides). After processing, zone 3 was crystallized from benzene by the addition of hexane yielding 6 mg of mixture of β-cryptoxanthin-5′,6′-epoxides, **4** and **7**.

(3*S*,5*R*,6*S*)-β-Cryptoxanthin-5,6-epoxide [(3*S*,5*R*,6*S*)-3-Hydroxy-5,6-dihydro-5,6-epoxy-β,β-caroten-3-ol, 1]: orange crystals, UV−vis (benzene) λ_{max} 434 (sh), 457, 487 nm, λ_{max} after acid treatment, 418, 438, 465 nm; UV−vis (hexane) λ_{max} (log ε) 475sh (3.93), 447 (4.00), 423sh (3.84), 398sh (3.58), 377sh (3.30), 330 (3.03), 267 (3.33); ^{1}H NMR (400 MHz, $CDCl_3$) δ 0.98 (3H, s, H-16), 1.03 (6H, s, H-16′, H-17′), 1.15 (3H, s, H-17), 1.19 (3H, s, H-18), 1.26 (2H, overlapping, H_{ax}-2, OH), 1.46 (2H, m, H-2′), 1.63 (4H, overlapping, H_{eq}-2, H_{ax}-4, H-3′), 1.72 (3H, s, H-18′), 1.93 (3H, s, H-19), 1.96 (3H, s, H-19′), 1.97 (6H, s, H-20, H-20′), 2.02 (2H, t, J = 6.8 Hz, H-4′), 2.39 (1H, m, H_{eq}-4), 3.90 (1H, s, H-3), 5.88 (1H, d, J = 15.4 Hz, H-7), 6.16 (1H, m, H-7′), ∼6.25 (8H, overlapped, H-8, H-10, H-12, H-14, H-8′, H-10′, H-12′, H-14′), ∼6.63 (4H, overlapped, H-11, H-15, H-11′, H-15′); ECD [hexane, λ (nm) (Δε), $c = 1.98 \times 10^{-4}$ M] 472sh (1.27), 444 (1.38), 418sh (1.06), 333 (1.82), 270 (−5.41), 238 (1.78), 215 (−4.53), 199 (0.48), negative below 197 nm; MS m/z 568.43 $[M]^+$, 553.40 $[M - 16 + H]^+$, 488.36 $[M - C_6H_8]^+$, 476.36 $[M - C_7H_8]^+$, 461.34 $[M - C_7H_8O]^+$, 415.30 $[M - 153]^+$; t_R = 17.5 min on a C30 column.

(3*R*,5′*R*,6′*S*)-β-Cryptoxanthin-5′,6′-epoxide [(3*R*,5′*R*,6′*S*)-3-Gydroxy-5′,6′-dihydro-5′,6′-epoxy-β,β-caroten-3-ol, 4]: orange crystals, UV−vis (benzene) λ_{max} 434 (sh), 457, 487 nm, λ_{max} after acid treatment, 416, 438, 465 nm; UV−vis (hexane) λ_{max} (log ε) 475sh (3.97), 445 (4.02), 422sh (3.83), 396sh (3.52), 373sh (3.14), 332 (2.77), 267 (3.26), 199 (3.09); ^{1}H NMR (400 MHz, $CDCl_3$) δ 0.94 (3H, s, H-16′), 1.07 (7H, s, H-2′, H-16, H-17), 1.10 (3H, s, H-17′), 1.15 (3H, s, H-18′), 1.26 (1H, s, OH), 1.43 (2H, m, H-3′), 1.48 (2H, m, H_{ax}-2, H-2′), 1.74 (3H, s, H-18), 1.76 (1H, m, H-4′), 1.79 (1H, m, H_{eq}-2), 1.90 (1H, m, H-4′), 1.93 (3H, s, H-19′), 1.96 (6H, s, H-20, H-20′), 1.97 (3H, s, H-19), 2.04 (1H, m, H_{ax}-4), 2.38 (1H, m, H_{eq}-4), 4.00 (1H, s, H-3), 5.88 (1H, d, J = 15.6 Hz, H-7′), 6.11 (1H, m, H-7), 6.15 (1H, m, H-8), 6.16 (1H, d, J = 11.0 Hz, H-10), 6.19 (1H, d, J = 11.0 Hz, H-10′), 6.26 (2H, overlapped, H-14, H-14′), 6.29 (1H, d, J = 15.6 Hz, H-8′), 6.36 (1H, d, J = 15.0 Hz, H-12), 6.37 (1H, d, J = 15.0 Hz, H-12′), 6.62 (4H, overlapped, H-11, H-15, H-11′, H-15′); ECD [hexane, λ (nm) (Δε), $c = 1.32 \times 10^{-4}$ M] 474sh (2.10), 448 (2.49), 412sh (1.68), 333 (3.81), 273 (−13.46), 238 (7.71), 216 (−8.51), 200 (1.33), negative below 198 nm; MS m/z 568.43 $[M]^+$, 553.40 $[M - 16 + H]^+$, 488.36 $[M - C_6H_8]^+$, 476.36 $[M - C_7H_8]^+$, 461.34 $[M - C_7H_8O]^+$, 415.30 $[M - 153]^+$; t_R = 14.5 min on a C30 column.

Mixture of (3*R*,5′*R*,6′*S*)-β-Cryptoxanthin-5′,6′-epoxide, 4, and (3*R*,5′*S*,6′*R*)-β-Cryptoxanthin-5′,6′-epoxide, 7: orange crystals, UV−vis (benzene) λ_{max} 434 (sh), 457, 487 nm, λ_{max} after acid treatment, 416, 438, 465 nm; ^{1}H NMR (400 MHz, $CDCl_3$) δ 0.94 (3H, s, H-16′), 1.07 (1H, m, H-2′), 1.07 (6H, s, H-16, H-17), 1.10 (3H, s, H-17′), 1.15 (3H, s, H-18′), 1.44 (2H, m, H-3′), 1.48 (2H, m, H_{ax}-2, H-2′), 1.74 (3H, s, H-18), 1.75 (1H, m, H-4′), 1.77 (1H, m, H_{eq}-2), 1.91 (1H, m, H-4′), 1.93 (3H, s, H-19′), 1.96 (6H, s, H-20, H-20′), 1.97 (3H, s, H-19), 2.04 (1H, m, H_{ax}-4), 2.41 (1H, m, H_{eq}-4), 4.00 (1H, s, H-3), 5.87 (1H, d, J = 15.6 Hz, H-7′), 6.11 (1H, d, J = 15.4 Hz, H-7), 6.15 (1H, d, J = 15.4 Hz, H-8), 6.16 (1H, d, J = 11.3 Hz, H-10), 6.19 (1H, d, J = 11.7 Hz, H-10′), 6.26 (2H, m, H-14, H-14′), 6.29 (1H, d, J = 15.6 Hz, H-8′), 6.36 (1H, d, J = 14.8 Hz, H-12), 6.37 (1H, d, J = 15.1 Hz, H-12′), 6.61 (1H, dd, J = 11.7, 15.1 Hz, H-11′), 6.63 (2H, m, H-15, H-15′), 6.64 (1H, dd, J = 11.3, 14.8 Hz, H-11); ^{13}C NMR ($CDCl_3$) δ 12.74 (CH_3, C-19), 12.79 (CH_3, C-20′), 12.81 (CH_3, C-20), 13.01 (CH_3, C-19′), 17.12 (C-3′), 21.16 (CH_3, C-18′), 21.60 (CH_3, C-18), 25.92 (CH_3, C-17′), 26.01 (CH_3, C-16′), 28.76 (CH_3, C-16), 30.13 (C-4′), 30.29 (CH_3, C-17), 33.85 (C-1′), 35.78 (C-2′), 37.13 (C-1), 42.60 (C-4), 48.50 (C-2), 65.10 (C-3), 65.50 (C-5′), 71.38 (C-6′), 124.16 (C-7′), 124.78 (C-11′), 124.96 (C-11), 125.59 (C-7), 126.16 (C-5), 130.05 (C-15), 130.19 (C-15′), 131.32 (C-10), 131.94 (C-10′), 132.59 (C-14), 132.76 (C-14′), 134.48 (C-9′), 135.69 (C-9), 136.38 (C-13), 136.54 (C-13′), 137.27 (C-8′), 137.59 (C-12), 137.79 (C-6), 137.98 (C-12′), 138.50 (C-8); MS m/z 568.43 $[M]^+$, 553.40 $[M - 16 + H]^+$, 488.36 $[M - C_6H_8]^+$, 476.36 $[M - C_7H_8]^+$, 461.34 $[M - C_7H_8O]^+$, 415.30 $[M - 153]^+$. **4** t_R = 6.55 min and **7** t_R = 7.02 min on a Chiralcel OD column. **4** t_R = 4.11 min and **7** t_R = 3.87 min on a Chiralpak IA column (hexane/propan-2-ol 9:1). **4** HPLC-ECD [hexane/propan-2-ol 9:1, λ (nm) (φ)] 332 (4.95), 273 (−19.70), 238 (11.00), 215 (−13.80). **7** HPLC-ECD [hexane/propan-2-ol 9:1, λ (nm) (φ)] 332 (−4.66), 292sh (−1.14), 266 (7.61), 245sh (2.91), 233 (−2.79), 216 (6.95).

3′-Deoxycapsanthin [(3*R*,5′*R*)-3-Hydroxy-β,κ-caroten-6′-one, 9]. red crystals, UV−vis (benzene) λ_{max} 484 nm λ_{max} after reduction 434, 457, 487 nm; ^{1}H NMR (500 MHz, $CDCl_3$) δ 0.86 (3H, s, H-16′), 1.08 (6H, s, H-16, H-17), 1.12 (3H, s, H-17′), 1.18 (3H, s, H-18′), 1.48 (1H, m H_{ax}-4′), 1.50 (1H, m, H_{ax}-2), 1.54 (1H, m, H_{eq}-2), 1.68 (1H, m, H_{eq}-2′), 1.72 (1H, m H-3′), 1.74 (3H, s, H-18), 1.78 (1H, m H_{eq}-2), 1.97 (3H, s, H-19), 1.98 (6H, s, H-20, H-19′), 1.99 (3H, s, H-20′), 2.06 (1H, m, H_{ax}-4), 2.40 (1H, m, H_{eq}-4), 2.54 (1H, m, H_{eq}-4′), 4.02 (1H, m, H-3), 6.13 (1H, d, H-7), 6.14 (1H, d, H-8), 6.17 (1H, d, H-10, $J_{10/11}$ = 11.7 Hz), 6.27 (1H, d, H-14, $J_{14/15}$ = 11.4 Hz), 6.34 (1H, d, H-14′, $J_{14'/15'}$ = 10.8 Hz), 6.37 (d, 1H, H-12, $J_{11/12}$ = 14.7 Hz), 6.48 (1H, d, H-7′), 6.52 (1H, d, H-12′, $J_{11'/12'}$ = 15.4 Hz), 6.56 (1H, d, H-10′, $J_{10'/11'}$ = 11.3 Hz), 6.61 (1H, m, H-11′), 6.65 (1H, m, H-15′), 6.68 (1H, dd, H-11), 6.69 (1H, m, H-15), 7.34 (1H, d, H-8′, $J_{7'/8'}$ = 15 Hz); ^{13}C NMR ($CDCl_3$) δ 12.7 (CH_3, C-20), 12.8 (CH_3, C-19, C-20′), 12.9 (CH_3, C-19′), 19.5 (C-18′), 19.7 (C-3′), 21.4 (C-18), 24.3 (C-17′), 25.4 (C-16′), 28.5 (C-17), 30.0 (C-16), 34.2 (C-4′), 40.3 (C-2′), 42.3 (C-4), 48.3 (C-2), 65.0 (C-3), 121.1 (CH, C-7′), 123.8 (C-11′), 125.1 (C-11), 125.5 (C-8), 129.6 (C-15′), 131.0 (C-10), 131.2 (C-15), 132.1 (C-14), 134.8 (C-14′), 137.1 (C-12), 138.2 (C-7), 140.2 (C-10′), 141.7 (C-12′), 146.2 (C-8′); ECD [hexane, λ (nm) (φ)] 347 (3.65), 337sh (2.31), 294 (−15.05), 285sh (−14.00), 253 (9.74), 243sh (7.53), 225 (−8.77), 205 (0.78), negative below 203 nm; MS m/z 568.43 $[M]^+$; HRESITOFMS m/z 568.4262 (calcd for $C_{40}H_{56}O_2$, 568.4280).

Cryptocapsin (3′*R*,5′*R*)-3′-hydroxy-β,κ-caroten-6′-one, 8): red crystals; UV/vis (benzene) λ_{max} 484 nm, λ_{max} after reduction 434, 457, 487 nm; ^{1}H NMR (400 MHz, $CDCl_3$) δ 0.84 (3H, s, H-17′),

DOI: 10.1021/acs.jafc.5b01936
J. Agric. Food Chem. 2015, 63, 6059−6065

1.03 (6H, s, H-16, H-17), 1.21 (3H, s, H-16′), 1.37 (3H, s, H-18′), 1.47 (2H, m, H-2), 1.49 (1H, m, H_{ax}-4′), 1.62 (2H, m, H-3), 1.69 (1H, m, H_{ax}-2′), 1.72 (3H, s, H-18), 1.96 (3H, s, H-20), 1.98 (6H, s, H-19′, H-20′), 1.99 (3H, s, H-19), 2.00 (1H, m, H_{eq}-2′), 2.02 (2H, m, H-4), 2.96 (1H, d, J = 14.4 Hz, H_{eq}-4′), 4.51 (1H, m, H-3′), 6.12−6.73 (15H, br overlapping, H-7, H-8, H-10, H-11, H-12, H-14, H-15, H-7′, H-10′, H-11′, H-12′, H-14′, H-15′), 7.33 (1H, d, J = 15.0 Hz, H-8′); MS m/z 568.43 $[M]^+$.

RESULTS AND DISCUSSION

The extraction of red mamey was performed as described previously.[28] Column chromatography of the extract on aluminum oxide and calcium carbonate resulted in 1 mg of β-cryptoxanthin-5,6-epoxide, **1**, 1.5 mg of β-cryptoxanthin-5′,6′-epoxide, **4**, 2 mg of 3′-deoxycapsanthin, **9**, and 8 mg of cryptocapsin, **8**.

Structure Elucidation of Natural β-Cryptoxanthin 5,6- and 5′,6′-Epoxides. The β-cryptoxanthin monoepoxides, **1** and **4** exhibited UV−vis maxima at (434), 457, and 487 nm in benzene, which was in accordance with the 5,6- or 5′,6′-epoxy group. Upon acidification with dilute HCl solution, a 20 nm hypsochromic shift of the above transition was observed, which was characteristic of the conversion to the corresponding furanoid oxide.

Mass spectrometry helped to identify the location of the epoxide groups unequivocally. The compound eluted at the retention time of 14.5 min had the molecular ion at (m/z) 568.43. Fragmentation of this mass even with relatively low fragmentation energies produced a large number of ions. The fragmentation profile was very similar to that reported earlier for β-cryptoxanthin.[31] Characteristic ions were observed at values of m/z 553.40 ($[M - 16 + H]^+$ or protonated β-cryptoxanthin), 488.36 ($[M - C_6H_8]^+$), 476.36 ($[M - C_7H_8]^+$), 461.34 ($[M - C_7H_8O]^+$), and 415.30 ($[M - 153]^+$), loss of the hydroxylated ring with cleavage at the 7,8 carbon−carbon bond from the protonated molecule, and several fragment ions corresponding to cleavages of the polyene chain.

The other compound eluting at the retention time of 17.5 min had the molecular ion at (m/z) 568.43, as well. The fragmentation of this compound seemed to be almost identical to the fragmentation of the other compound with the retention time of 14.5 min. It contained the same high abundant ions, but the most intensive differed. To clarify the position of the epoxidation we calculated the theoretical masses of two ions (169.12340 and 171.13769), which contain the six-membered ring, four methyl groups, the epoxide, and the hydroxyl groups as they all together could occur in the tandem spectra only if the position of the epoxidation is 5,6. All of the tandem spectra were analyzed using mass isolation ranges of 169.11−169.13 and 171.13−171.15, and these two ions (Figure 2) were observed only in the spectra of the compound with the retention time of 17.5 min. Their intensities applying 25% HCD cell energy were 3 and 6% of the intensity of the precursor ion (568.43) or 0.01 and 0.02% of the total ion chromatogram.

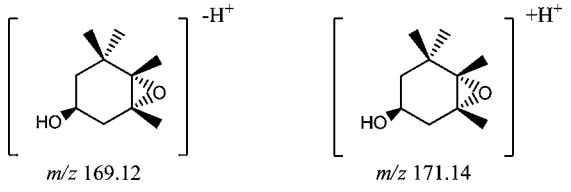

Figure 2. Two ions, m/z 169.12 and 171.14, used for the differentiation of 5,6- and 5′,6′-epoxides.

In the ^{1}H NMR spectrum of compound **1**, methyl group signals were observed at 1.03 ppm (six protons) and 1.72 ppm (three protons) due to the C-16′, C-17′, and C-18′ methyl groups of the unsubstituted β-ring and at 0.98 and 1.15 ppm (C-16, C-17) and 1.19 ppm (C-18) of the 3-hydroxy-5,6-epoxy-5,6-dihydro-β-ring.[32]

The structural elucidation of compounds **1** and **4** was supported by the ^{1}H and ^{13}C NMR measurements, which were in good agreement with the literature data.[18,32]

In the 3-hydroxy β-end group, the δ(H) of CH_2(4) differed significantly for the *cis*- and *trans*-epoxide (relative to OH) and, therefore, proved the (3*S*,5*R*,6*S*)-configuration of **1**. Because the (5′*S*,6′*R*)- or (5′*R*,6′*S*)-configuration of the epoxy β-end groups cannot be distinguished in the ^{1}H NMR spectra, the elucidation of the configuration at the nonhydroxylated end group was achieved by electronic circular dichroism (ECD) measurements.

Carotenoid-5,6-epoxides exhibit strongly conservative ECD spectra comparable to those of other carotenoids with a substituted β-end group. The influence of additional substituents such as a OH group at C(3) or C(3′) is rather small,[33] and thus ECD spectra of the epoxides are governed by the absolute configuration of the epoxy group. The ECD spectra of **1** showed positive Cotton effects (CEs) at 472, 444, 418, 333, 238, and 199 nm and negative ones at 270 and 215 nm. The ECD spectrum of **1** (Figure 3) was compared with those of the related (5*R*,6*S*)- and (5*S*,6*R*)-5,6-epoxy-β-carotene,[34,35] which allowed the assignment of the absolute configuration of **1** as (3*S*,5*R*,6*S*).

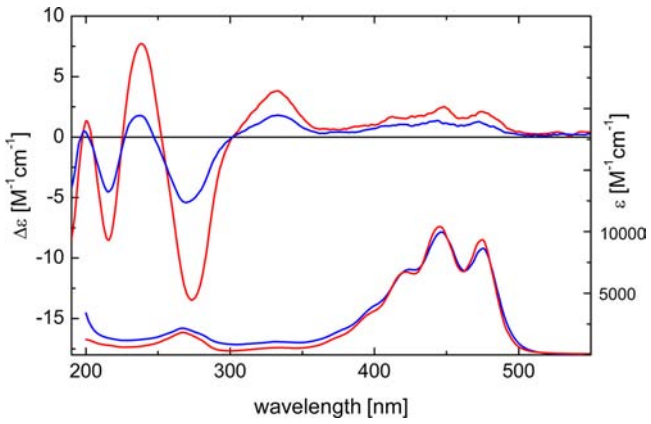

Figure 3. ECD and UV−vis spectra of (3*S*,5*R*,6*S*)-β-cryptoxanthin-5,6-epoxide, **1** (blue curves), and (3*R*,5′*R*,6′*S*)-β-cryptoxanthin-5′,6′-epoxide, **4** (red curves), in acetonitrile.

Although the β-cryptoxanthin-5′,6′-epoxide, **4**, contained the epoxide moiety in the other end group, its ECD spectrum showed the same CEs for the corresponding transitions as the β-cyryptoxanthin 5,6-epoxide, **1**, which determined the absolute configuration as (3*R*,5′*R*,6′*S*). In this way, the compound eluted at 14.5 min was identified as (3*R*,5′*R*,6′*S*)-β-cryptoxanthin 5′,6′-epoxide, **3**, whereas the compound eluted at 17.4 min was (3*S*,5*R*,6*S*)-β-cryptoxanthin 5,6-epoxide, **1**.

Investigation of Semisynthetic β-Cryptoxanthin-5′,6′-epoxides. Earlier, from a mixture of synthetic epoxidation products of β-cryptoxanthin, we could isolate and crystallize a

DOI: 10.1021/acs.jafc.5b01936
J. Agric. Food Chem. 2015, 63, 6059−6065

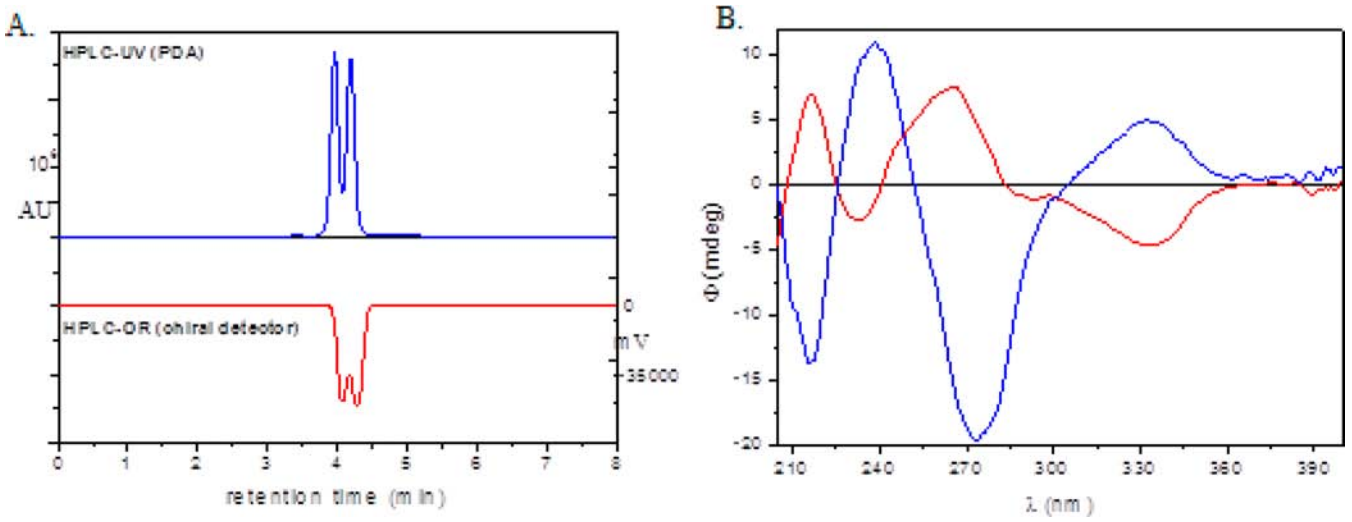

Figure 4. (A) HPLC-UV and HPLC-OR chromatograms of a mixture of (3*R*,5′*R*,6′*S*)- and (3*R*,5′*S*,6′*R*)-cryptoxanthin-5′,6′-epoxide diastereomers, **4** and **7**, on a Chiralpak IA column (hexane/isopropanol 9:1). (B) HPLC-ECD spectra of cryptoxanthin-5′,6′-epoxide diastereomers (3*R*,5′*R*,6′*S*)-, **4** (blue curve), and (3*R*,5′*S*,6′*R*)-, **7** (red curve), in hexane/isopropanol 9:1.

5′,6′-epoxide derivative, which had been reported as the (3*R*,5′*R*,6′*S*)-epoxide, **4**.[18]

To have a further identification aid of the *β*-cryptoxanthin 5′,6′-epoxide, the compound was prepared again semisynthetically from *β*-cryptoxanthin by oxidation with monoperoxy phthalic acid. This furnished the necessary amount for the NMR investigations. After isolation of the mixture of the *syn*- and *anti*-mono-5′,6′-epoxides, which are nondistinguishable by nuclear magnetic resonance, the assignment of the ^{1}H and ^{13}C signals furnished by 2D techniques ($^{1}H-^{13}C$ HSQC, $^{1}H-^{13}C$ HMBC measurements, $^{1}H-^{1}H$ COSY) was possible. The end-group carrying the epoxide moiety has shown the known ambivalent behavior considering the assignment of the proton signals, whereas the signal of the 3-OH-*β* end-group was assigned unequivocally. However, the resulting chemical shifts were in good accordance with the published data.[18] The identification of *β*-cryptoxanthin 5′,6′-epoxide of natural origin was confirmed by semisynthetic counterpart in the further analytical investigations.

HPLC reinvestigation of this semisynthetic compound with a chiral stationary phase showed that this sample contains two components with identical UV−vis spectra and sign of optical rotation. The epoxidation of *β*-cryptoxanthin could produce two diastereomeric 5′,6′-epoxy derivatives, which could not be separated by column chromatography using calcium carbonate or HPLC using C18 or C30 columns. However, separation of (5′*R*,6′*S*)- and (5′*S*,6′*R*)-cryptoxanthin-5′,6′-epoxide diastereomers, **4** and **7**, respectively, was achieved on Chiralcel OD and Chiralpak IA HPLC columns, which showed approximately equal amounts of the two diastereomers (Figure 4). Comparison of the retention times of the semisynthetic compounds with that of natural *β*-cryptoxanthin-5′,6′-epoxide, **4**, on Chiralcel OD column showed that the first-eluting diastereomer was the natural one. On the Chiralpak IA column, this elution order was apparently reversed. The HPLC-ECD spectra of the diastereomeric (3*R*,5′*R*,6′*S*)-, **4**, and (3*R*,5′*S*,6′*R*)-, **7**, showed opposite CEs for the corresponding ECD transitions, but they were not mirror image curves (Figure 4B). On the basis of the ECD spectra of natural (3*R*,5′*R*,6′*S*)-, **4**, the (3*R*,5′*R*,6′*S*) absolute configuration was assigned to the second-eluting diastereomer.

Structure Elucidation of Cryptocapsin 8 and 3′-Deoxycapsanthin 9. The isolation of cryptocapsin was described earlier from red mamey.[29] All of the spectroscopic data of the isolated compound were identical with the data reported in the literature.[31,32]

The UV−vis spectrum of 3′-deoxycapsanthin, **9** (λ_{max} 484 nm in benzene, 498 and 469 nm in hexane) was in agreement with the chromophore conjugated with a carbonyl group. Reduction of **9** with $NaBH_4$ gave an approximately 1:1 mixture of the corresponding diastereomeric alcohols. The UV−vis spectrum of this mixture showed the expected fine structure and a hypsochromic shift (λ_{max} 434, 457, 487 nm in benzene). The molecular formula of **9** was determined to be $C_{40}H_{56}O_2$ by HPLC-MS. The ^{13}C and ^{1}H NMR assignments for **9** were made on the basis of 1D (^{1}H) and 2D (COSY, HSQC) experiments and by comparison with capsanthin and sapotexanthin. In compound **9**, methyl group signals could be attributed to an unsubstituted *κ*-ring. The ^{13}C and ^{1}H NMR data of **9** were similar to those of sapotexanthin, except for the *β*-end group signals (*δ* H-3, *δ* C-3).[28] The ^{1}H signal at *δ* 4.02 and the ^{13}C signal at *δ* 65.0 indicated that the hydroxy group is attached to the cyclohexane and not the *κ*-ring.[32,36] The connection of H-2, H-3, and H-4 protons from the *β*-end group and the connection of H-2′, H-3′, and H-4′ protons from the *κ*-end group were confirmed on the basis of COSY measurements. All other ^{1}H and ^{13}C data and *all-E* polyene chain were in good accordance with literature data.[32,36]

The ECD spectrum of **9** showed positive CEs at 347, 253, and 205 nm and negative ones at 294 and 225 nm with pronounced shoulders (Figure 5). These ECD transitions are governed by the C-5′ chirality center, which is adjacent to the carbonyl group conjugating with the decaene moiety. On the basis of the ECD spectrum, the absolute configuration of **9** could be determined as (3*R*,5′*R*).[36]

If *β*-cryptoxanthin-5,6,5′,6′-diepoxide is present in high amounts in a plant, it usually triggers the production of cryptocapsin-5,6-epoxide and 3′-deoxycapsanthin-5,6-epoxide. The 3-hydroxy *κ*-end group forms from a 3-hydroxy-5,6-epoxy-*β* end group by pinacol rearrangement, which is a common process in carotenoid biosynthesis. In this way the cryptocapsin, **8**, could be formed from *β*-cryptoxanthin 5,6-epoxide, **1**, in red

DOI: 10.1021/acs.jafc.5b01936
J. Agric. Food Chem. 2015, 63, 6059−6065

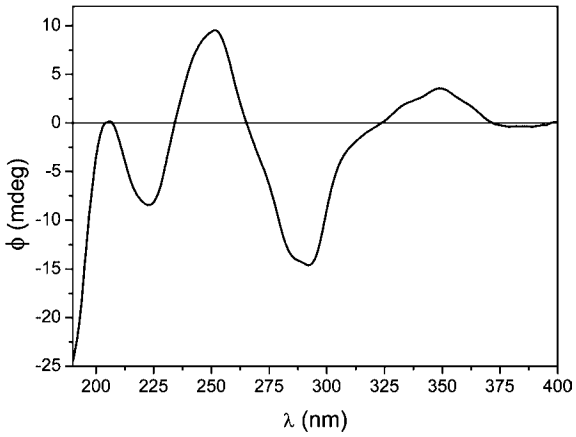

Figure 5. ECD spectrum of **9** in hexane.

mamey. Similarly, the nonhydroxylated 5,6-epoxy-β-ring could result in the nonhydroxylated κ-ring, for example, 3′-deoxycapsanthin **9** forms from β-cryptoxanthin 5′,6′-epoxide **4** (Figure 6).

Our results confirm recently published observations: In red mamey, both the enzyme responsible for the epoxidation of the nonhydroxylated rings and the enzyme that catalyzes the rearrangement of the epoxides should be highly active to produce the detected carotenoids in such a high concentration.[21,28,29] It has been also confirmed that natural 5,6-epoxy carotenoids bear the 5*R*,6*S* configuration independent of the presence or absence of the hydroxyl group on the six-membered ring. During the synthesis of semisynthetic epoxides the compound with 5*S*,6*R* configuration is obtained, as well. Our study has also shown that the two epoxide isomers can be separated only on a chiral column if the ring is not hydroxylated. In the light of these new findings old data about similar compounds should be rechecked.

AUTHOR INFORMATION

Corresponding Author

*(J.D.) Phone: +36-72-503-650, ext. 28833. Fax: +36-72-503-650, ext. 28826. E-mail: jozsef.deli@aok.pte.hu.

Funding

Financial support was achieved by OTKA Grants K 83898, 105871, 105459, and 115931 (Hungarian National Research Foundation).

Notes

The authors declare no competing financial interest.

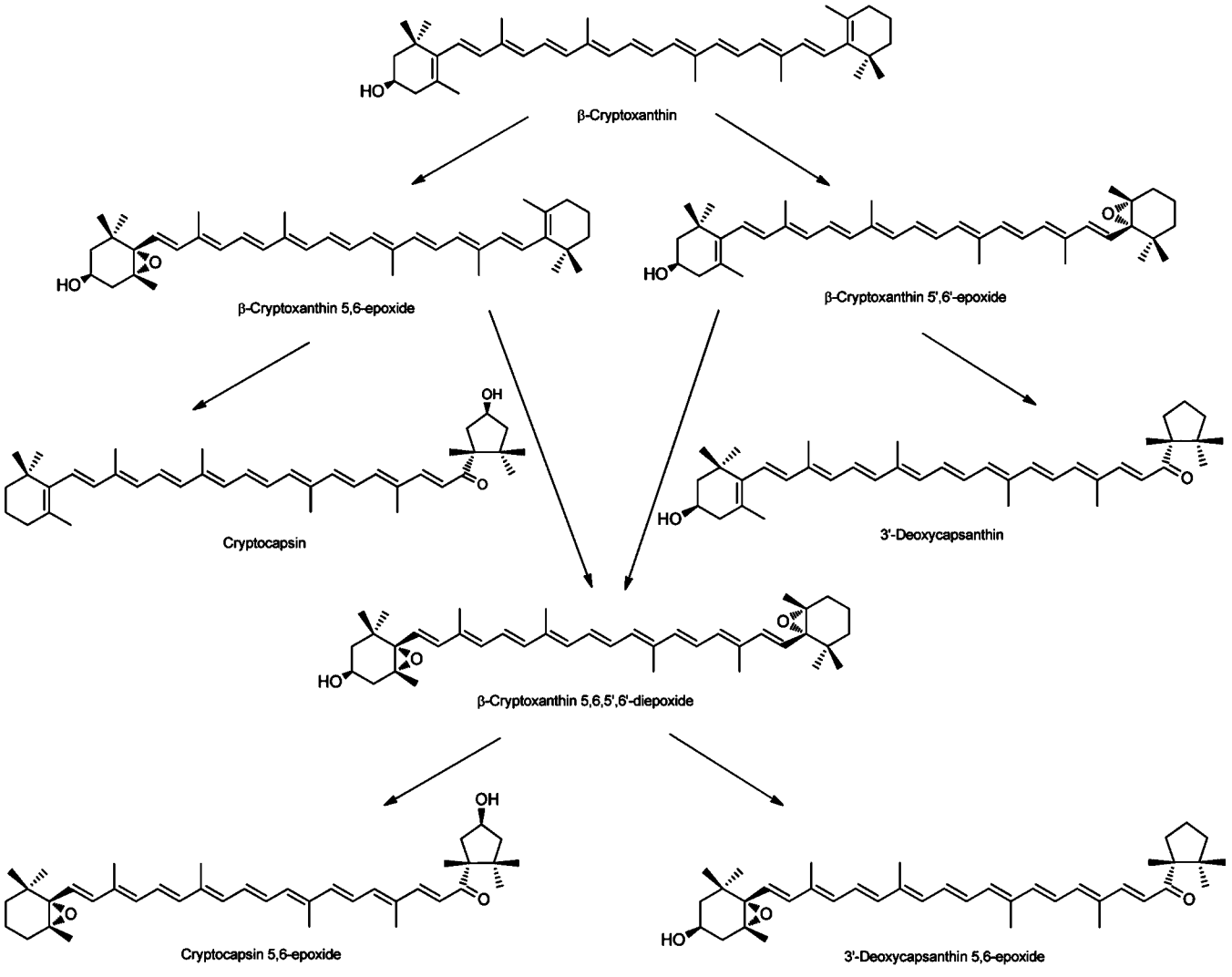

Figure 6. Proposed biosynthetic pathway.

DOI: 10.1021/acs.jafc.5b01936
J. Agric. Food Chem. 2015, 63, 6059−6065

■ ACKNOWLEDGMENTS

We thank Dr. L. Drahos for performing the HR-ESI-TOF-MS measurement. We also thank J. Rigó, R. Lukács, and Zs. Götz for their assistance. The present scientific contribution is dedicated to the 650th anniversary of the foundation of the University of Pécs, Hungary.

■ REFERENCES

(1) Curl, A. L.; Bailey, G. F. The carotenoids of ruby red grapefruit. *J. Food Sci.* **1957**, *22*, 63−68.
(2) Curl, A. L.; Bailey, G. F. The carotenoids of navel oranges. *J. Food Sci.* **1961**, *26*, 442−447.
(3) Curl, A. L. The carotenoids of cling peaches. *J. Food Sci.* **1959**, *24*, 413−421.
(4) Curl, A. L. The carotenoids of Japanese persimmons. *J. Food Sci.* **1960**, *25*, 670−674.
(5) Curl, A. L. The carotenoids of red bell peppers. *J. Agric. Food Chem.* **1962**, *10*, 504−509.
(6) Curl, A. L. The carotenoids of Italiana prunes. *J. Food Sci.* **1963**, *28*, 623−626.
(7) Purcell, A. E. Carotenoids of goldrush sweetpotato flakes. *Food Technol.* **1962**, *16*, 99−102.
(8) Subbarayan, C.; Cama, H. R. Carotenoids in *Carica papaya* (papaya fruit). *Indian J. Chem.* **1964**, *2*, 451−454.
(9) Yamamoto, H. Y. Comparison of the carotenoids in yellow- and red-fleshed *Carica papaya*. *Nature* **1964**, *20*, 1049−1050.
(10) Yokoyama, H.; Vandercook, C. E. Citrus carotenoids I. Comparison of carotenoids in mature-green and yellow lemons. *J. Food Sci.* **1967**, *32*, 42−48. Yokoyama, H.; White, M. J. Carotenoids in the flavedo of Marsh seedless grapefruit. *J. Agric. Food Chem.* **1967**, *15*, 693−696.
(11) Schaller, D. R.; Von Elbe, J. H. The carotenoids in Montmorency cherries. *J. Food Sci.* **1971**, *36*, 712−713.
(12) Gross, J.; Gabai, M.; Lifshitz, A. Carotenoids in juice of Shamouti orange. *J. Food Sci.* **1971**, *36*, 466−473.
(13) Gross, J.; Gabai, M.; Lifshitz, A. A comparative study of the carotenoid pigments in juice of Shamouti, Valencia and Washington oranges, three varieties of *Citrus sinensis*. *Phytochemistry* **1972**, *11*, 303−308.
(14) Rahman, F. M. M.; Buckle, K. A. Pigment changes in capsicum cultivars during maturation and ripening. *Int. J. Food Sci. Technol.* **1980**, *15*, 241−249.
(15) Noga, G.; Lenz, F. Separation of citrus carotenoids by reversed-phase high-performance liquid chromatography. *Chromatographia* **1983**, *17*, 139−142.
(16) Matus, Z.; Deli, J.; Szabolcs, J. Carotenoid composition of yellow pepper during ripening: isolation of β-cryptoxanthin 5,6-epoxide. *J. Agric. Food Chem.* **1991**, *39*, 1907−1914.
(17) Godoy, H. T.; Rodriguez-Amaya, D. B.; Connor, A. E.; Britton, G. Confirmation of the structure of papaya β-cryptoxanthin monoepoxide. *Food Chem.* **1990**, *36*, 281−286.
(18) Molnár, P.; Deli, J.; Matus, Z.; Tóth, G.; Steck, A.; Pfander, H. Partial synthesis and characterization of the mono- and diepoxides of β-cryptoxanthin. *Helv. Chim. Acta* **1997**, *80*, 221−229.
(19) Thompson, A. J.; Jackson, A. C.; Parker, R. A.; Morpeth, D. R.; Burbidge, A.; Taylor, I. B. Abscisic acid biosynthesis in tomato: regulation of zeaxanthin epoxidase and 9-*cis*-epoxy-carotenoid dioxygenase mRNAs by light/dark cycles, water stress and abscisic acid. *Plant Mol. Biol.* **2000**, *42*, 833−845.
(20) Kalala, M.; Cowan, A. K.; Molnár, P.; Tóth, G. (9*Z*)-Epoxy-carotenoid cleavage enzyme activity from the *Citrus* cell-free system for ABA biosynthesis. *S. Afr. J. Bot.* **2001**, *67*, 376−377.
(21) Bouvier, F.; Hugueney, P.; d'Harlingue, A.; Kuntz, M.; Camara, B. Xanthophyll biosynthesis in chromoplast: isolation and molecular cloning of an enzyme catalyzing the conversion of 5,6-epoxycarotenoid into ketocarotenoid. *Plant J.* **1994**, *6*, 45−54.
(22) Deli, J.; Matus, Z.; Tóth, G. Carotenoid composition in the fruits of *Capsicum annuum* cv. Szentesi Kosszarvú during ripening. *J. Agric. Food Chem.* **1996**, *44*, 711−716.
(23) Deli, J.; Tóth, G. Carotenoid composition of the fruits of *Capsicum annuum* cv. Bovet 4 during ripening. *Z. Lebensm. Unters.Forschung A* **1997**, *205*, 388−391.
(24) Deli, J.; Molnár, P.; Matus, Z.; Tóth, G. Carotenoid composition in the fruits of red paprika (*Capsicum annuum* var. *lycopersiciforme rubrum*) during ripening; biosynthesis of carotenoids in red paprika. *J. Agric. Food Chem.* **2001**, *49*, 1517−1523.
(25) Deli, J.; Matus, Z.; Tóth, G. Carotenoid composition in the fruits of *Asparagus officinalis*. *J. Agric. Food Chem.* **2000**, *48*, 2793−2796.
(26) Deli, J.; Molnár, P.; Ősz, E.; Tóth, G. Analysis of the carotenoids of the fruits of *Asparagus falcatus*; Isolation of 5,6-diepikarpoxanthin. *Chromatographia* **2000**, *51*, S183−187.
(27) Deli, J.; Molnár, P.; Matus, Z.; Tóth, G.; Steck, A.; Pfander, H. Isolation and characterization of 3,5,6-trihydroxy-carotenoids from petals of *Lilium tigrinum*. *Chromatographia* **1998**, *48*, 27−31.
(28) Murillo, E.; McLean, R.; Britton, G.; Agócs, A.; Nagy, V.; Deli, J. Sapotexanthin, an A-provitamin carotenoid isolated from mamey (*Pouteria sapota*). *J. Nat. Prod.* **2011**, *74*, 283−285.
(29) Gulyás-Fekete, G.; Murillo, E.; Kurtán, T.; Papp, T.; Illyés, T. Z.; Drahos, L.; Visy, J.; Agócs, A.; Turcsi, E.; Deli, J. Cryptocapsinepoxide-type carotenoids from red mamey *Pouteria sapota*. *J. Nat. Prod.* **2013**, *76* (4), 607−614.
(30) Murillo, E.; Mosquera, Y.; Kurtán, T.; Gulyás-Fekete, G.; Nagy, V.; Deli, J. Isolation and characterization of two novel capsorubin like carotenoids from the red mamey (*Pouteria sapota*). *Helv. Chim. Acta* **2012**, *95* (6), 983−988.
(31) van Breemen, R. B.; Dong, L.; Pajkovic, N. D. Atmospheric pressure chemical ionization tandem mass spectrometry of carotenoids. *Int. J. Mass Spectrom.* **2012**, *312*, 163−172.
(32) Englert, G. NMR spectroscopy. In *Carotenoids*; Britton, G., Liaaen-Jensen, S., Pfander, H., Eds.; Birkhauser: Basel, Switzerland, 1995; Vol. 1B, p 147.
(33) Buchecker, R.; Noack, K. CD spectroscopy. In *Carotenoids*; Britton, G., Liaaen-Jensen, S., Pfander, H., Eds.; Birkhauser: Basel, Switzerland, 1995; Vol. 1B, p 81.
(34) Acemoglu, M.; Eugster, C. H. (5*R*,6*S*,5′*R*,6′*S*)-5,6,5′,6′-Diepoxy-β,β-carotene − synthesis, spectroscopical and chiroptical properties, and HPLC-behaviour. *Helv. Chim. Acta* **1984**, *67*, 184−190.
(35) Eschenmoser, W.; Eugster, C. H. Synthesis and chirality of (5*S*,6*R*)-5,6-epoxy-5,6-dihydro-β,β-carotene and (5*R*,6*R*)-5,6-dihydro-β,β-carotene-5,6-diol, a compound with unepected solubility characteristics. *Helv. Chim. Acta* **1978**, *61*, 822−831.
(36) Maoka, T.; Akimoto, N.; Fujiwara, Y.; Hashimoto, K. Structure of new carotenoids with the 6-oxo-κ end group from the fruits of paprika *Capsicum annuum*. *J. Nat. Prod.* **2004**, *67*, 115−117.

DOI: 10.1021/acs.jafc.5b01936
J. Agric. Food Chem. 2015, 63, 6059−6065

Table 1. Moisture and Oil Contents of Pomaces of Five Italian Cultivars Processed at Different Temperatures and Times of Malaxation[a]

	malaxation temperature = 25 °C						malaxation temperature = 30 °C					
	control		FTC[b]		FTC		control		FTC		FTC	
	30 min		15 min		20 min		30 min		15 min		20 min	
cv. Ottobratica												
moisture content (%)	62.4	(0.3)a	62.9	(0.4)a	62.3	(0.5)a	63.3	(0.1)a	63.5	(0.8)a	63.2	(1.3)a
oil content (% dw)	13	(0.3)ab	13.2	(0.3)a	13.1	(0.5)ab	12.1	(0.3)b	12.5	(0.4)ab	12.2	(0.5)ab
cv. Cellina di Nardò												
moisture content (%)	62.3	(1.2)a	62.1	(0.4)a	61.9	(1.1)a	63.1	(0.5)a	63.3	(0.8)a	62.5	(0.3)a
oil content (% dw)	15	(0.4)a	15	(0.8)a	14.9	(0.8)a	14.1	(0.1)a	14.2	(0.2)a	14	(0.4)a
cv. Peranzana												
moisture content (%)	62.7	(0.2)ab	62.7	(0.8)ab	62.1	(0.4)a	62.5	(0.4)ab	63.4	(0.2)b	63	(0.5)ab
oil content (% dw)	12.5	(0.3)a	12.3	(0.4)a	11.9	(0.3)ab	11	(0.5)bc	10.3	(0.5)c	10.6	(0.4)c
cv. Coratina												
moisture content (%)	63.7	(0.4)a	64.7	(0.6)a	64.8	(0.9)a	64.4	(0.2)a	65.7	(1.7)a	64.3	(0.4)a
oil content (% dw)	11	(0.3)a	11	(0.2)a	10.4	(0.3)ab	10.5	(0.1)ab	10.6	(0.4)ab	10	(0.1)b
cv. Moraiolo												
moisture content (%)	63	(0.5)a	62.8	(0.9)ab	64.4	(0.5)ac	63.5	(0.4)abc	62.3	(0.7)b	64.8	(0.3)c
oil content (% dw)	15	(0.5)a	15.5	(0.6)a	15.5	(0.5)a	15.5	(0.7)a	15.2	(0.8)a	14.8	(0.7)a

[a]The data are the mean values of two independent experiments, and the standard deviation is reported in parentheses. Values in each row having different letters (a−c) are significantly different from one another ($p < 0.05$). [b]FTC, flash thermal conditioning.

have on the choice of the main parameters of the malaxation process, when coupled with a flash thermal treatment of the olive paste using a tubular heat exchanger with the common purpose of producing high-quality VOOs. The objectives of this study were to investigate the influence that the new technology could have on the quantitative and qualitative release of phenolic and volatile compounds into VOOs extracted from five Italian olive cultivars simultaneously to an interesting impact on the reduction of the time required for a traditional virgin olive oil mechanical extraction process.

MATERIALS AND METHODS

Chemicals. (3,4-Dihydroxyphenyl)ethanol (3,4-DHPEA) was obtained from Cayman Chemicals Ltd. (Ann Arbor, MI, USA), whereas (*p*-hydroxyphenyl)ethanol (*p*-HPEA) was obtained from Janssen Chemical Co. (Beerse, Belgium). The dialdehydic forms of elenolic acid linked to 3,4-DHPEA and *p*-HPEA (3,4-DHPEA-EDA and *p*-HPEA-EDA, respectively), the isomer of oleuropein aglycon (3,4-DHPEA-EA), (+)-1-acetoxypinoresinol, and (+)-pinoresinol were extracted from the VOO according to the method developed by Montedoro et al.[25] In short, the phenols were extracted from the oil (1 kg) using methanol/water 80:20 v/v (2 L). The mixture made of olive oil (1 kg) and methanol/water (500 mL) was homogenized for 3 min at 25 °C. Then, it was centrifuged at 3000 rpm for 20 min. After the recovery of the supernatant, that procedure was repeated three more times. After solvent evaporation and partial purification of the crude extract obtained from the olive fruit and VOO, phenolic separation was performed by semipreparative high-performance liquid chromatography (HPLC) analysis using a 9.4 mm i.d. × 500 mm Whatman Partisil 10 ODS-2 semipreparative column; the mobile phase was 0.2% acetic acid in water (pH 3.1) (A)/methanol (B) at a flow rate of 6.5 mL/min, whereas detection of the phenols was performed using a diode array detector (DAD).[25] The purity of all the substances obtained from direct extraction was tested by HPLC, and their chemical structures were verified by nuclear magnetic resonance (NMR), using the same operative conditions reported in previous papers.[25,26] Pure analytical standards of volatile compounds were purchased from Fluka and Aldrich (Milan, Italy).

Mechanical VOO Extraction Process. In this research, the VOOs were extracted from olives of the Ottobratica, Cellina di Nardò, Peranzana, Coratina, and Moraiolo cultivars. The Coratina olives, on the one hand, and the Peranzana olives, on the other, were harvested in the Apulia region, in the province of Bari, and in the province of Foggia, respectively, whereas the Cellina di Nardò originated from the Salento area of the Apulia region. The growing area of Ottobratica olive trees was the province of Reggio Calabria (Calabria), whereas Moraiolo trees are typical of the region of Umbria. All cultivars were harvested during the period between the end of October and the last week of November 2013, and the ripening stage of these olives, evaluated on the basis of the pigmentation index according to the method of Pannelli et al.,[24] was 0.95. The olives were processed within 48 h after harvesting. About 150 kg of each olive cultivar was processed using an industrial plant TEM 200 system (Toscana Enologica Mori, Tavarnelle Val di Pesa, Florence, Italy) consisting of a hammer mill, a malaxer with a gas controller system and a working capacity of 200 kg of olives, and a two-phase decanter; a UVPX 305 AGT 14 centrifuge (Alfa Laval S.p.A., Tavarnelle Val di Pesa, Florence, Italy) was used to separate the olive oil.

The control trial malaxation was carried out for 30 min at 25 or 30 °C.

The other tests were conducted using an EVO-Line heat exchanger (Alfa Laval S.p.A.) placed after the same hammer crusher used in the control trial. This was able to determine a flash thermal conditioning (FTC) of olive paste, and heated hot water to 35 and 40 °C to bring the pastes to 25 or 30 °C, respectively. The instantaneous heating of the paste was performed with a counter current, hot water flow, automatically regulated by specifically regulated valves, controlled by a programmable logic controller (PLC). Heated paste was sent to a covered malaxer, and the oil was extracted using the same industrial plant used for the control, following the flowchart illustrated by Esposto et al.[22]

The trials were performed to test two flash conditioning temperatures (25 and 30 °C) for 15 and 20 min of malaxation and, in addition, each experimental condition was repeated twice. Those times were calculated from the moment the inoperative malaxer was completely full.

VOO samples were stored in the dark at 13 °C until analysis. Samples of pomaces were stored at −25 °C until analysis. Two analytical replicates were performed in all of the samples.

VOO Analyses. *Legal Quality Parameters.* Free acidity, peroxide value, and UV absorption characteristics at 232 and 270 nm of oils obtained were measured in accordance with the European Union Official Methods.[27]

Oil Content. Foss-Let 15310 (A/S N. Foss Electric Denmark) was used for the quantitative evaluation of pomace oil content. Dry pomaces (22.5 g) were homogenized (Homogenizer, A/S N. Foss Electric

DOI: 10.1021/acs.jafc.5b01666
J. Agric. Food Chem. 2015, 63, 6066−6074

Table 2. Phenolic Composition (mg/kg) of VOO Control and FTC Obtained at Different Temperatures and Times of Malaxation[a]

	malaxation temperature = 25 °C						malaxation temperature = 30 °C					
	control		FTC[b]		FTC		control		FTC		FTC	
	30 min		15 min		20 min		30 min		15 min		20 min	
cv. Ottobratica												
3,4-DHPEA	6.5	(0.1)a	5.9	(0.2)b	5.6	(0.1)b	5.7	(0.2)b	7.0	(0.1)c	7.1	(0.2)c
p-HPEA	4.6	(0.04)a	3.7	(0.1)b	4.3	(0.1)c	3.2	(0.1)d	4.2	(0.1)c	3.8	(0.1)b
3,4-DHPEA-EDA	73.6	(3.5)a	99.2	(3.7)b	100.2	(4.9)b	90.2	(3.8)b	126.7	(4.0)c	134.3	(6.2)c
p-HPEA-EDA	17.3	(0.1)a	15.7	(0.9)a	23.7	(1.3)b	20.8	(2.3)b	28.2	(0.2)c	27.1	(0.9)c
(+)-1-acetoxypinoresinol	5.7	(0.7)a	5.8	(0.8)a	7.2	(1.1)ab	5.2	(0.8)a	6.5	(0.9)ab	8.5	(1.2)b
(+)-pinoresinol	35.1	(1.3)ab	36.3	(1.2)a	35.5	(1.6)ab	31.5	(1.9)b	37.7	(1.4)a	38.4	(1.5)a
3,4-DHPEA-EA	101.1	(6.1)a	112.4	(4.5)ab	122.3	(5.9)bc	119.7	(1.9)bc	123.7	(2.7)bc	127.4	(1.0)c
total phenol	244.0	(7.0)a	278.9	(5.9)b	298.9	(7.8)c	276.2	(4.8)b	333.9	(4.8)d	346.7	(6.4)d
cv. Cellina di Nardò												
3,4-DHPEA	5.6	(0.2)a	2.8	(0.1)bc	2.6	(0.1)b	4.7	(0.1)ac	3.2	(0.1)bc	1.6	(1.8)b
p-HPEA	4.5	(0.02)a	3.0	(0.2)b	3.4	(0.3)b	3.1	(0.6)b	3.5	(0.4)b	2.9	(0.1)b
3,4-DHPEA-EDA	196.9	(2.5)a	217.5	(4.0)bc	221.7	(6.0)bd	210.5	(7.1)acde	222.9	(10.5)be	230.0	(7.6)b
p-HPEA-EDA	80.7	(2.1)a	79.8	(0.1)a	88.7	(0.5)b	86.3	(1.0)ab	91.0	(4.4)bc	95.8	(3.6)c
(+)-1-acetoxypinoresinol	8.8	(0.3)a	8.7	(0.4)a	8.1	(0.4)a	8.3	(0.5)a	8.3	(0.3)a	8.4	(0.4)a
(+)-pinoresinol	11.3	(0.6)a	11.0	(0.5)a	10.6	(0.6)a	10.8	(0.6)a	9.6	(0.9)a	10.0	(0.8)a
3,4-DHPEA-EA	153.0	(2.8)a	159.2	(0.1)a	173.9	(0.2)b	170.5	(5.2)b	182.6	(2.3)c	194.4	(2.2)d
total phenol	460.8	(4.3)a	482.1	(4.1)ab	509.0	(6.1)cd	494.2	(8.8)bc	521.2	(11.6)d	543.0	(8.9)e
cv. Peranzana												
3,4-DHPEA	2.1	(0.2)a	2.5	(0.2)ab	1.5	(0.2)c	2.5	(0.2)a	2.3	(0.1)a	3.8	(0.1)d
p-HPEA	2.5	(0.2)a	4.0	(0.1)b	3.3	(0.1)c	3.3	(0.1)cd	3.1	(0.2)d	4.1	(0.1)b
3,4-DHPEA-EDA	109.4	(2.5)a	113.2	(3.3)a	120.5	(6.2)a	179.5	(6.2)b	190.2	(2.0)b	214.2	(6.4)c
p-HPEA-EDA	34.8	(3.6)a	34.6	(1.3)a	40.1	(2.3)a	49.1	(2.3)b	50.3	(1.4)b	52.0	(0.7)b
(+)-1-acetoxypinoresinol	3.3	(0.5)a	4.6	(0.6)a	3.5	(0.5)a	3.5	(0.4)a	3.9	(0.5)a	4.0	(0.6)a
(+)-pinoresinol	13.1	(0.4)a	14.5	(0.8)b	13.2	(0.4)ab	13.2	(0.5)ab	13.0	(0.3)a	12.7	(0.6)a
3,4-DHPEA-EA	113.0	(5.6)a	120.3	(1.8)ab	128.9	(3.5)bc	134.9	(3.5)cd	142.6	(6.6)d	162.9	(5.4)e
total phenol	278.3	(7.1)a	293.7	(4.0)ab	311.0	(7.5)b	386.0	(7.5)c	405.5	(7.1)d	453.7	(8.4)e
cv. Coratina												
3,4-DHPEA	4.6	(0.04)a	3.5	(0.1)b	2.3	(0.1)c	3.5	(0.1)b	2.9	(0.1)d	2.8	(0.1)d
p-HPEA	3.6	(0.1)a	2.8	(0.1)b	2.8	(0.1)b	3.3	(0.1)a	2.6	(0.1)b	2.8	(0.2)b
3,4-DHPEA-EDA	258.3	(4.3)a	294.3	(8.2)b	329.3	(12.5)c	305.1	(16.6)b	336.5	(5.8)c	370.1	(0.6)d
p-HPEA-EDA	35.9	(1.6)a	37.5	(1.9)a	40.1	(1.1)ab	42.5	(0.2)b	51.0	(2.2)c	59.3	(2.8)c
(+)-1-acetoxypinoresinol	16.5	(0.6)a	15.8	(0.7)a	15.7	(0.7)a	14.8	(0.6)a	15.1	(0.7)a	16.6	(0.8)a
(+)-pinoresinol	9.9	(0.5)a	9.1	(0.6)ab	9.7	(0.4)a	8.9	(0.5)ab	8.0	(0.5)b	9.1	(0.6)ab
3,4-DHPEA-EA	234.1	(3.1)a	246.2	(3.8)a	278.2	(6.9)b	334.1	(9.3)c	351.6	(14.2)c	517.5	(6.6)d
total phenol	562.9	(5.6)a	609.2	(9.3)b	678.0	(14.4)c	712.4	(19.1)c	767.7	(15.6)d	978.4	(7.2)e
cv. Moraiolo												
3,4-DHPEA	2.9	(0.1)a	3.0	(0.2)a	2.3	(0.002)b	3.4	(0.1)c	3.8	(0.2)d	3.2	(0.1)ac
p-HPEA	2.0	(0.2)a	2.6	(0.04)b	2.5	(0.1)bc	1.5	(0.2)a	2.7	(0.1)bc	3.1	(0.3)c
3,4-DHPEA-EDA	214.1	(13.0)a	228.5	(7.8)a	236.2	(7.2)a	283.2	(5.4)b	287.2	(8.2)b	321.4	(21.0)d
p-HPEA-EDA	32.7	(1.6)a	37.4	(4.4)ab	38.3	(1.9)ab	38.2	(2.4)ab	40.4	(1.0)b	41.5	(2.0)b
(+)-1-acetoxypinoresinol	17.4	(0.7)a	17.3	(0.8)a	16.9	(0.9)a	16.7	(0.8)a	15.9	(0.8)a	15.4	(0.9)a
(+)-pinoresinol	20.7	(1.1)ab	20.5	(1.2)ab	19.7	(1.3)ab	21.6	(1.1)ab	18.3	(1.4)a	22.5	(1.1)b
3,4-DHPEA-EA	206.6	(7.7)a	212.5	(3.0)a	255.2	(9.8)bc	230.3	(3.6)ab	268.2	(13.1)c	298.1	(17.1)d
total phenol	496.4	(15.2)a	521.8	(9.5)a	571.2	(12.3)b	595.0	(6.9)bc	636.5	(15.5)c	705.3	(27.2)d

[a]The data are the mean values of two independent experiments analyzed in duplicate, and the standard deviation is reported in parentheses. Values in each row having different letters (a–d) are significantly different from one another ($p < 0.05$). [b]FTC, flash thermal conditioning.

Denmark) with 120 mL of tetrachloroethylene with the addition of a small amount of anhydrous sodium sulfate for 2 min and estimated.

Phenolic Compounds. The analysis of VOO was conducted with direct injection dissolving 1 g of oil in 5 mL of acetone, and then the solution was filtered through a polyvinylidene fluoride (PVDF) syringe filter (0.2 μm). As described by Selvaggini et al.,[28] HPLC analysis was performed using an Agilent Technologies system, model 1100, consisting of a vacuum degasser, a quaternary pump, an autosampler, a thermostated column compartment, a DAD, and a fluorescence detector (FLD), controlled by ChemStation (Agilent Technologies, Palo Alto, CA. USA), and used to process the chromatographic data. A Spherisorb ODS-1 250 mm × 4.6 mm with a particle size of 5 μm (Waters, Milford, MA, USA) column was used to evaluate the phenolic compounds. The mobile phase consisted of 0.2% acetic acid (pH 3.1) in water (solvent A)/ methanol (solvent B) at a flow rate of 1 mL/min, and the gradient changed as follows: 95% A for 2 min, 75% A in 8 min, 60% A in 10 min, 50% A in 16 min, 0% A in 14 min, and maintained for 10 min. Following the re-equilibration of the initial condition, equilibration was reached in 13 min; the total running time was 73 min. All phenolic compounds, except lignans, which were detected by FLD

DOI: 10.1021/acs.jafc.5b01666
J. Agric. Food Chem. 2015, 63, 6066–6074

Table 3. Volatile Composition (μg/kg) of VOO Control and FTC Obtained for cv. Ottobratica at Different Temperatures and Times of Malaxation[a]

	malaxation temperature = 25 °C						malaxation temperature = 30 °C					
	control		FTC[b]		FTC		control		FTC		FTC	
	30 min		15 min		20 min		30 min		15 min		20 min	
Aldehydes												
(*E*)-2-pentenal	83	(5)a	86	(6)a	89	(14)a	140	(4)b	119	(6)b	141	(20)b
hexanal	614	(11)a	797	(43)b	734	(76)ab	476	(11)c	851	(64)b	578	(44)ac
(*E*)-2-hexenal	102951	(2008)a	96193	(2703)a	95748	(11717)a	100563	(2504)a	105525	(2964)a	101875	(5567)a
(*E*,*E*)-2,4-hexadienal	1196	(127)a	1070	(55)a	1189	(42)a	965	(264)a	1026	(331)a	1260	(25)a
Alcohols												
1-penten-3-ol	191	(11)a	190	(6)a	194	(23)a	290	(9)b	280	(26)b	303	(57)b
(*E*)-2-penten-1-ol	30	(4)ab	24	(5)a	23	(8)a	42	(4)b	35	(1)a	43	(5)b
1-hexanol	2847	(50)a	2625	(273)a	2922	(310)a	2021	(73)b	2393	(300)ab	2430	(150)ab
(*Z*)-3-hexen-1-ol	1930	(267)a	1774	(335)ab	1585	(154)ab	1225	(142)b	1691	(249)ab	1659	(87)ab
(*E*)-2-hexen-1-ol	3301	(58)a	4339	(191)b	4089	(15)b	2382	(99)c	2933	(374)a	2812	(204)ac
Esters												
hexyl acetate	240	(43)a	94	(12)b	81	(9)b	112	(13)b	101	(19)b	74	(10)b
(*Z*)-3-hexenyl acetate	369	(30)a	156	(11)bc	122	(4)b	207	(11)cd	227	(26)d	157	(20)bc

[a]The data are the mean values of two independent experiments analyzed in duplicate, and the standard deviation is reported in parentheses. Values in each row having different letters (a−c) are significantly different from one another ($p < 0.05$). [b]FTC, flash thermal conditioning.

Table 4. Volatile Composition (μg/kg) of VOO Control and FTC Obtained for cv. Cellina di Nardò at Different Temperatures and Times of Malaxation[a]

	malaxation temperature = 25 °C						malaxation temperature = 30 °C					
	control		FTC[b]		FTC		control		FTC		FTC	
	30 min		15 min		20 min		30 min		15 min		20 min	
Aldehydes												
(*E*)-2-pentenal	44	(2)a	44	(7)a	43	(4)a	42	(3)a	44	(1)a	42	(3)a
hexanal	573	(13)ab	529	(19)a	474	(6)c	610	(20)b	603	(33)b	609	(14)b
(*E*)-2-hexenal	34780	(4709)a	35188	(2561)a	31328	(628)a	34085	(610)a	33158	(658)a	31288	(783)a
(*E*,*E*)-2,4-hexadienal	653	(26)a	673	(5)a	574	(10)ab	639	(28)a	465	(117)b	601	(7)ab
Alcohols												
1-penten-3-ol	103	(4)a	106	(8)a	103	(12)a	89	(5)a	108	(6)a	96	(4)a
(*E*)-2-penten-1-ol	14	(2)a	16	(3)a	16	(3)a	13	(2)a	16	(3)a	15	(2)a
1-hexanol	924	(27)a	782	(88)b	808	(41)ab	774	(45)b	814	(11)ab	734	(48)b
(*Z*)-3-hexen-1-ol	550	(22)a	498	(78)a	473	(49)a	442	(43)a	453	(6)a	450	(4)a
(*E*)-2-hexen-1-ol	845	(50)a	696	(72)ab	675	(24)ab	655	(26)ab	740	(154)ab	580	(49)b
Esters												
hexyl acetate	711	(56)a	639	(6)a	632	(71)a	679	(68)a	601	(12)a	700	(20)a
(*Z*)-3-hexenyl acetate	628	(53)a	556	(16)ab	494	(96)ab	489	(45)ab	426	(25)b	482	(50)ab

[a]The data are the mean values of two independent experiments analyzed in duplicate, and the standard deviation is reported in parentheses. Values in each row having different letters (a−c) are significantly different from one another ($p < 0.05$). [b]FTC, flash thermal conditioning.

operated at an excitation wavelength of 280 nm and emission at 339 nm,[29] were detected by DAD at 278 nm.

Volatile Compounds. Evaluation and quantification of volatile compounds in VOOs were performed by headspace solid-phase microextraction, followed by gas chromatography−mass spectrometry (HS-SPME/GC-MS), according to the method of Servili et al.[30] Six grams of oil with the addition of 50 μL of a standard methanolic solution, consisting of butanal, isobutyl acetate, and 1-nonanol, were mixed with vortex for 1 min, and then 3 g was placed into a 10 mL vial. To sample the headspace volatile compounds, solid-phase microextraction (SPME) was applied as follows: all of the vials were held at 35 °C, and then the SPME fiber (a 50/30 μm 1 cm long DVB/Carboxen/PDMS, Stableflex; Supelco, Inc., Bellefonte, PA, USA) was exposed to the vapor phase for 30 min to sample the volatile compounds. The fiber was then inserted into the gas chromatograph (GC) injector, set in splitless mode, using a splitless inlet liner of 0.75 mm i.d. for thermal desorption, where it was left for 10 min. All of the SPME operations were automated through the Varian CP 8410 autoinjector (Varian, Walnut Creek, CA, USA).

GC-MS Analysis. A Varian 4000 GC-MS equipped with a 1079 split/splitless injector (Varian) was used. A fused-silica capillary column was employed (DB-Wax-ETR, 50 m, 0.32 mm i.d., 1 μm film thickness; J&W Scientific, Folsom, CA, USA). The column was operated with helium at a constant flow rate of 1.7 mL/min, maintained with an electronic flow controller (EFC). The GC oven heating program began at 35 °C. This temperature was maintained for 8 min and then increased to 45 °C at a rate of 1.5 °C/min. This was then increased to 150 °C at a rate of 3 °C/min, to 180 °C at a rate of 4 °C/min, and finally to 210 °C at a rate of 3.6 °C/min. This temperature was held for 14.5 min. The total analysis time was 80 min. The injector temperature was maintained at 250 °C, the temperature for the transfer line was fixed at 170 °C, and the mass spectrometer was operated in the electron ionization (EI) mode at an ionization energy of 70 eV, with scanning in the mass range of m/z 25−350 at a scan rate of 0.79 s/scan and a manifold temperature of 150 °C. The GC-MS was operated with Varian MS Workstation Software, version 6.6. The volatile compounds were identified by comparing their mass spectra and retention times

DOI: 10.1021/acs.jafc.5b01666
J. Agric. Food Chem. 2015, 63, 6066−6074

Table 5. Volatile Composition (μg/kg) of VOO Control and FTC Obtained for cv. Peranzana at Different Temperatures and Times of Malaxation[a]

	malaxation temperature = 25 °C						malaxation temperature = 30 °C					
	control		FTC[b]		FTC		control		FTC		FTC	
	30 min		15 min		20 min		30 min		15 min		20 min	
Aldehydes												
(*E*)-2-pentenal	122	(1)a	138	(1)b	111	(1)c	148	(1)d	129	(3)e	136	(0)b
hexanal	613	(5)a	707	(3)b	611	(1)a	530	(2)c	526	(6)c	585	(20)d
(*E*)-2-hexenal	52400	(1980)ab	60320	(721)c	50945	(714)a	50865	(1478)a	54740	(891)b	49390	(566)a
(*E*,*E*)-2,4-hexadienal	1174	(41)ab	1575	(18)c	1408	(7)cd	1340	(51)ad	1013	(139)b	1214	(18)a
Alcohols												
1-penten-3-ol	403	(1)a	469	(8)b	304	(4)c	437	(3)d	335	(3)e	320	(1)f
(*E*)-2-penten-1-ol	40	(1)a	44	(1)b	27	(1)c	45	(1)b	33	(1)d	34	(1)d
1-hexanol	1428	(16)a	1714	(18)b	994	(22)c	1442	(57)a	1246	(16)d	1059	(6)c
(*Z*)-3-hexen-1-ol	1074	(3)a	1433	(21)b	893	(11)c	1387	(49)b	1016	(6)a	722	(7)d
(*E*)-2-hexen-1-ol	532	(26)a	505	(3)a	501	(19)a	612	(11)b	775	(19)c	953	(23)d
Esters												
hexyl acetate	634	(40)a	922	(37)b	900	(4)b	653	(45)a	772	(31)c	1060	(49)d
(*Z*)-3-hexenyl acetate	690	(6)a	786	(16)b	705	(10)a	656	(2)a	912	(38)c	1066	(42)d

[a]The data are the mean values of two independent experiments analyzed in duplicate, and the standard deviation is reported in parentheses. Values in each row having different letters (a−d) are significantly different from one another ($p < 0.05$). [b]FTC, flash thermal conditioning.

Table 6. Volatile Composition (μg/kg) of VOO Control and FTC Obtained for cv. Coratina at Different Temperatures and Times of Malaxation[a]

	malaxation temperature = 25 °C						malaxation temperature = 30 °C					
	control		FTC[b]		FTC		control		FTC		FTC	
	30 min		15 min		20 min		30 min		15 min		20 min	
Aldehydes												
(*E*)-2-pentenal	63	(3)a	51	(5)bc	66	(6)a	42	(3)b	43	(2)b	59	(3)ac
hexanal	1319	(94)ab	2004	(67)c	1523	(45)ad	1642	(37)d	1455	(188)a	1056	(139)b
(*E*)-2-hexenal	118175	(6325)a	119790	(1053)a	120475	(2728)a	114850	(4813)a	111975	(11246)a	104800	(5294)a
(*E*,*E*)-2,4-hexadienal	1442	(40)a	1536	(86)a	1591	(22)a	1580	(82)a	1549	(92)a	1658	(290)a
Alcohols												
1-penten-3-ol	230	(9)a	281	(38)a	376	(3)b	231	(14)a	227	(60)a	310	(38)ab
(*E*)-2-penten-1-ol	27	(4)abc	27	(4)abc	38	(3)a	21	(4)b	23	(5)bc	36	(4)a
1-hexanol	2065	(106)a	1400	(67)bc	1248	(179)b	1663	(139)c	1329	(114)bc	1074	(150)b
(*Z*)-3-hexen-1-ol	593	(35)a	452	(31)bc	459	(5)bc	454	(49)bc	490	(10)b	396	(44)c
(*E*)-2-hexen-1-ol	3551	(223)a	2112	(152)bc	1738	(198)b	2437	(345)c	1776	(106)b	1572	(169)b
Esters												
hexyl acetate	nd[c]		nd		nd		nd		nd		nd	
(*Z*)-3-hexenyl acetate	46	(7)a	19	(2)bc	14	(4)bc	24	(4)b	14	(4)bc	10	(2)c

[a]The data are the mean values of two independent experiments analyzed in duplicate, and the standard deviation is reported in parentheses. Values in each row having different letters (a−d) are significantly different from one another ($p < 0.05$). [b]FTC, flash thermal conditioning. [c]nd, not detected.

with those of authentic reference compounds. Integration of all the chromatographic peaks was performed by choosing the three masses with the highest intensities from among those specific for each compound, to selectively discriminate them from their nearest neighbors. The results of the peak areas were calculated on the basis of the relative calibration curve for each compound and expressed in g/kg of oil.[30]

Statistical Analysis. *Analysis of Variance (ANOVA).* The statistically significant differences of data were evaluated by one-way ANOVA. The SigmaPlot 12.3 was used (Systat Software Inc., San Jose, CA, USA).

Principal Component Analysis (PCA). The PCA model was built with 30 objects (6 oils for each cultivar analyzed) and 28 variables (legal quality parameters, acidity, peroxide value, K_{232}, K_{270}, ΔK; phenolic compounds, 3,4-DHPEA, *p*-HPEA, 3,4-DHPEA-EDA, *p*-HPEA-EDA, (+)-1-acetoxypinoresinol, (+)-pinoresinol, 3,4-DHPEA-EA, total phenol; volatile compounds, (*E*)-2-pentenal, hexanal, (*E*) 2-hexenal, (*E*,*E*)-2,4-hexadienal, sum of aldehydes, 1-penten-3-ol, (*E*)-2-penten-1-ol, 1-hexanol, (*Z*)-3-hexen-1-ol, (*E*)-2-hexen-1-ol, sum of alcohols, hexyl acetate, (*Z*)-3-hexenyl acetate, sum of esters, 1-penten-3-one) to analyze the influence of processing parameters on the analytical data of VOO. The SIMCA 13.0 chemometric package was used (Umetrics AB, Umeå, Sweden). The raw data of each variable were centered, with the subtraction of the mean, and autoscaled to unit variance, dividing these results by the standard deviation. The number of significant components was found by applying cross-validation.

RESULTS AND DISCUSSION

The impact of the flash thermal conditioning of the olive pastes was tested on five Italian olive cultivars (Ottobratica, Cellina di Nardò, Peranzana, Coratina, and Moraiolo) characterized by various origin areas.

Instead of heating it with the traditional malaxation processes, the first step was to analyze the effects of the FTC of the olive

DOI: 10.1021/acs.jafc.5b01666
J. Agric. Food Chem. 2015, 63, 6066−6074

Table 7. Volatile Composition (μg/kg) of VOO Control and FTC Obtained for cv. Moraiolo at Different Temperatures and Times of Malaxation[a]

	malaxation temperature = 25 °C						malaxation temperature = 30 °C					
	control		FTC[b]		FTC		control		FTC		FTC	
	30 min		15 min		20 min		30 min		15 min		20 min	
Aldehydes												
(*E*)-2-pentenal	74	(1)ab	67	(3)a	78	(8)b	72	(2)ab	65	(3)a	65	(2)a
hexanal	520	(30)a	484	(28)ab	435	(46)bc	484	(14)ab	405	(25)cd	415	(14)bd
(*E*)-2-hexenal	88395	(3143)ab	85435	(4183)ab	89843	(3366)a	83470	(3824)ab	78953	(4202)bc	71997	(644)c
(*E*,*E*)-2,4-hexadienal	1530	(155)a	1372	(71)ab	1385	(146)ab	1415	(182)a	1250	(68)ab	1038	(114)b
Alcohols												
1-penten-3-ol	276	(3)a	266	(8)ab	316	(7)ab	262	(17)a	241	(8)ab	250	(10)b
(*E*)-2-penten-1-ol	30	(2)a	30	(1)a	37	(3)b	30	(1)a	29	(1)a	30	(3)a
1-hexanol	1543	(190)a	1,189	(59)b	1120	(105)bc	1631	(89)a	890	(14)c	975	(92)bc
(*Z*)-3-hexen-1-ol	619	(17)ab	607	(32)abc	624	(9)ab	496	(30)cd	541	(71)ad	680	(57)b
(*E*)-2-hexen-1-ol	1933	(29)a	1738	(43)ab	1698	(462)bc	1758	(38)abc	1099	(60)d	1060	(100)d
Esters												
hexyl acetate	45	(4)a	15	(2)b	23	(3)cd	29	(2)c	16	(1)d	18	(2)d
(*Z*)-3-hexenyl acetate	145	(4)ab	102	(7)ac	153	(19)b	83	(5)c	118	(8)abc	153	(34)b

[a]The data are the mean values of two independent experiments analyzed in duplicate, and the standard deviation is reported in parentheses. Values in each row having different letters (a−d) are significantly different from one another ($p < 0.05$). [b]FTC, flash thermal conditioning.

paste on the parameters associated with the yield extraction. The FTC treatment, coupled with 15 and 20 min of malaxation time, longer than the time investigated by Esposto et al.,[22] corresponding to 10 min, determined a similar oil yield during the mechanical extraction process of the virgin olive oil, in comparison to the control trial. The differences between the control and the FTC trials, expressed as residual pomace oil, are not significant for any of the cultivars analyzed (Table 1).

Marketable parameters, free acidity, and peroxide values were unaffected by the FTC treatment of the paste for both the temperatures and malaxation times analyzed, showing that the thermal modification applied to the mechanical extraction process does not modify the normal chemical and biochemical processes of fat degradation, with a specific reference to residual lipase activities (data not shown).

The evaluation of K_{232}, K_{270}, and ΔK did not show significant modification due to the use of FTC in the olive paste in all of the cultivars studied (data not shown). Therefore, as already reported in a previous paper,[22] there are no negative effects on the legal quality parameters of virgin olive oil FTC at the two different temperatures and malaxation times compared to the respective control.

The data analysis of the phenolic composition of VOOs (Table 2) showed a strong variation depending on the cultivar processed. In all of the cultivars studied, the phenolic concentration of the oils, obtained with the FTC treatment, was always higher than those extracted by the traditional process. The increase of phenolic compounds was influenced by the processing parameters such as the temperature and time of malaxation applied after FTC. Indeed, an increase in the mixing time, post rapid thermal conditioning, corresponds to an increase of phenols released in the VOOs. The mixing time used, lower than in the control trials, already determined an improvement in the phenolic concentration after 15 min of malaxation, even though the main differences were observed in the oils extracted 20 min after FTC of the olive pastes at both temperatures tested.

In a previous study,[22] 10 min of malaxation applied after the FTC treatment of the olive pastes in cv. Peranzana was unable to enhance the phenolic concentration of VOOs compared with the traditional extraction process, highlighting the correct time of malaxation paste after an FTC treatment is at least 15 min. As a result, 15 min can be considered the minimum time required to improve cell wall degradation by the endogenous depolymerizing enzymes, which promote the release of phenols in the VOOs and in the vegetation waters.[31,32]

The most important differences in terms of phenolic compounds are mainly related to the oleuropein derivatives such as 3,4-DHPEA-EDA and 3,4-DHPEA-EA and, to a lesser extent, to the ligstroside derivatives that include *p*-HPEA and *p*-HPEA-EDA; these increases appear to be affected not only by the thermal treatment but also by the genetic origins of the Italian cultivars analyzed, confirming that the distribution of the values obtained under different extraction process conditions is strictly cultivar-dependent.[10] The results from the combinations of 30 °C and 20 min of malaxing time applied after FTC treatment, which enabled the highest concentrations of phenolic compounds to be extracted, indeed showed a great variation between the cultivars, with increases in the total phenols of 9.9, 17.5, 18.5, 25.5, and 37.3% for cultivars Cellina di Nardò, Peranzana, Moraiolo, Ottobratica, and Coratina, respectively. On the contrary, lignans such as (+)-1-acetoxypinoresinol and (+)-pinoresinol showed the lowest variability under the different operative conditions applied, validating a general stability of these compounds to almost all of the technological parameters involved in the mechanical extraction process of VOOs.[10,17,22]

The results relating to the volatile compounds (Tables 3−7) are interesting because they show a differentiated impact on the generation of aroma, of the operative conditions applied during the olive FTC, associated with the cultivar. As shown in Table 5, the use of flash heating produces an increase in esters, related to a "floral" sensory note in cv. Peranzana,[12] when the treatment was applied to the olive pastes at the times and temperatures tested; C_6 aldehydes, (*E*)-2-hexenal in particular, increase in the oils from cv. Peranzana malaxed for 15 min at 25 and 30 °C, whereas C_6 alcohols did not show a specific trend that can be associated with the paste treatment. Those results confirm, as reported in a previous paper,[22] the positive impact of FTC on the volatile composition of VOOs from cv. Peranzana but, at the same time, show that the FTC effect on the volatile compounds of VOO was strongly affected by the

DOI: 10.1021/acs.jafc.5b01666
J. Agric. Food Chem. 2015, 63, 6066−6074

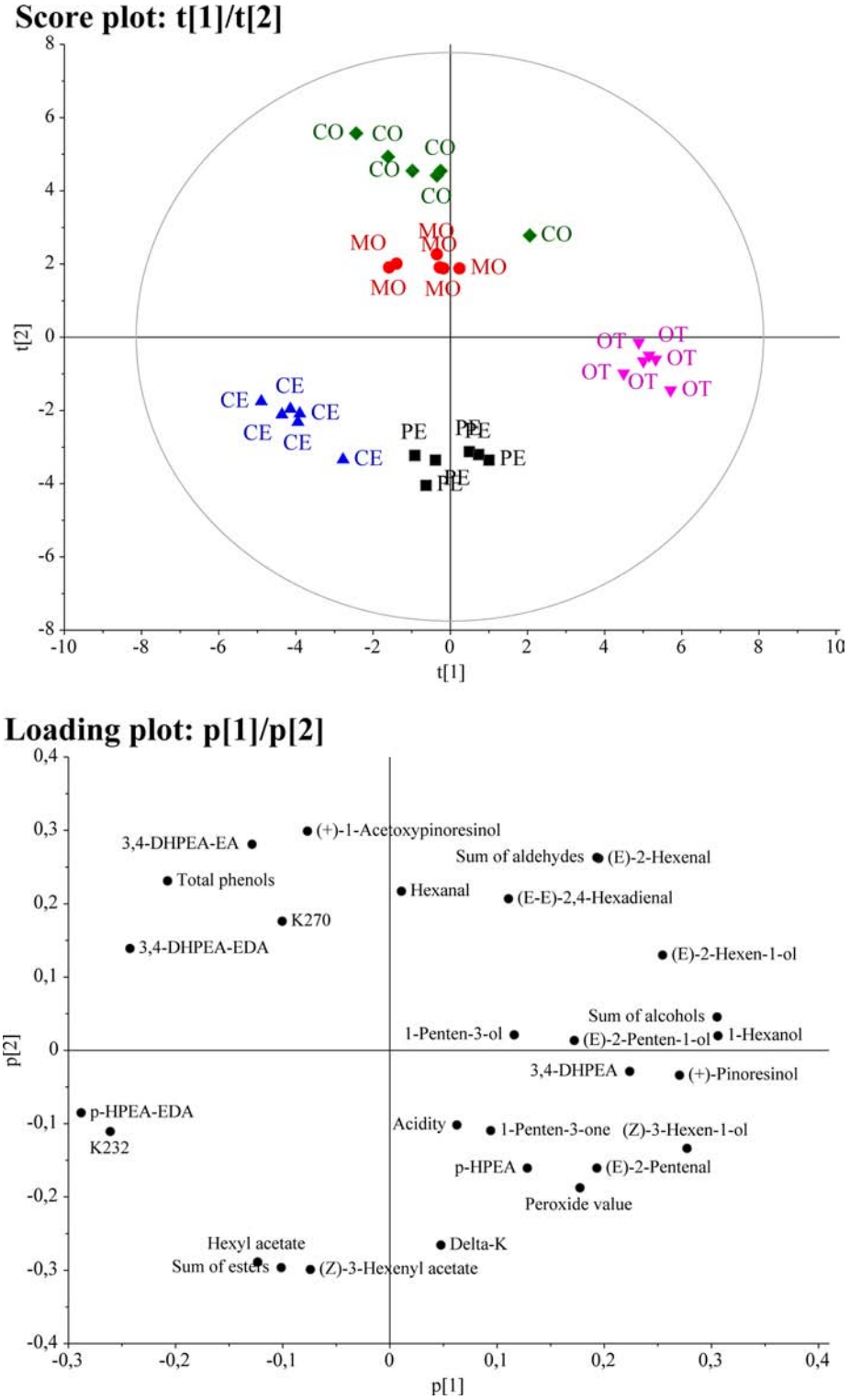

Figure 1. Score plot and loading plot of the first two principal components (explaining 34 and 31% of the total variance, respectively) of the PCA model built with VOOs obtained from five Italian olive cultivars under different malaxation conditions. CE, Cellina di Nardò; CO, Coratina; MO, Moraiolo; OT, Ottobratica; PE, Peranzana.

olive cultivar. VOOs from cultivars Coratina and Cellina di Nardò showed a restricted reduction in esters, whereas the C_6 unsaturated aldehydes did not show any significant modification (Tables 4 and 6). The C_6 alcohols, on the contrary, demonstrated a significant reduction in cv. Coratina, due to the FTC at both temperatures, whereas the VOO from cv. Cellina di Nardò showed no significant differences associated with the paste treatment. A reduction in esters, associated with the FTC, was also found in VOO from cv. Ottobratica and demonstrated at 25 °C that C_6 aldehydes were not affected by the application of flash heating treatment and that C_6 alcohols improved at 30 °C depending on the malaxation time, whereas no significant differences were found at 25 °C except for (*E*)-2-hexen-1-ol (Table 3). The oil obtained from cv. Moraiolo showed a

DOI: 10.1021/acs.jafc.5b01666
J. Agric. Food Chem. 2015, 63, 6066−6074

significant reduction in C_6 alcohols in all of the oils obtained by flash heating treatment of the olive pastes excluding (*Z*)-3-hexen-1-ol. A minor modification was observed, on the contrary, for the other volatile compounds (Table 7).

The reported results demonstrate that the impact of the flash heating treatment of the olive pastes on the phenolic composition of the VOO shows the same behavior characterized by a higher phenolic concentration in VOO obtained after FTC treatment in all of the cultivars. Those results can be explained by the improved activity of the thermal treatment on the endogenous enzymes, which catalyze the depolymerization of the cell walls and improve the release of phenols in the oil. The impact of FTC treatment on the lipoxygenase pathway appears to be cultivar-dependent. The genetic origin of the raw material affects not only the absolute activity of each enzyme involved in the lipoxygenase pathway but also their distribution in the constituent parts of the fruit.[12,33−35] Both of these aspects could explain the differences in the generation of aroma, observed using the same operative condition in various cultivars.

The PCA model reported in Figure 1, built with 30 objects and 28 variables, explains with five significant principal components 92% of the total variance (explaining each 34, 31, 17, 7, and 3%, respectively), summarizes the differences observed in previously reported results, and clearly highlights a discrimination of the VOO samples according to the cultivar origin. The first component put in evidence a discrimination of VOOs of cultivars Cellina di Nardò and Ottobratica, and the loading plot shows that this separation is mainly due to the secoiridoid derivatives, such as 3,4-DHPEA-EDA and *p*-HPEA-EDA, present in greater concentrations in the first cultivar, and saturated and unsaturated C_6 alcohols and (+)-pinoresinol, higher in cv. Ottobratica and, as indicated in Tables 3 and 4, the content of these compounds for this cultivar are about 4 times higher than for cv. Cellina di Nardò. VOOs from cultivars Coratina and Moraiolo, characterized by high concentrations of the phenolic compounds and a volatile profile with high contents of (+)-1-acetoxypinoresinol, 3,4-DHPEA-EA, (*E*)-2-hexenal, and hexanal by a side and a low concentration of esters by the other, are located in the upper side of the second component and discriminated by VOOs from cultivars Peranzana and Cellina di Nardò, which are positioned on the opposite side. The concentrations of the phenolic compound (+)-1-acetoxypinoresinol is about 5-fold, whereas 3,4-DHPEA-EA is more than twice in cv. Coratina with respect to cv. Peranzana; also, the values found for the aldehydes above-mentioned are 2-fold higher in the objects present in the upper side of the second principal component.

AUTHOR INFORMATION

Corresponding Author

*(G.V.) Phone: +39 075 5857903. Fax: +39 075 5857916. E-mail: gianluca.veneziani@unipg.it.

Funding

This study was kindly supported by Alfa Laval SpA (Tavarnelle Val di Pesa, Florence, Italy), Consorzio Olivicolo Italiano UNAPROL—Italy (Projects Reg. UE 1220/2011), and Progetto MIUR CLUSTER CL.A.N.—Agrifood AREA1—Nutrizione e salute Pros.IT (CTN01_00230_413096).

Notes

The authors declare no competing financial interest.

ABBREVIATIONS USED

VOO, virgin olive oil; FTC, flash thermal conditioning; PLC, programmable logic controller; 3,4-DHPEA, (3,4-dihydroxyphenyl)ethanol; *p*-HPEA, (*p*-hydroxyphenyl)ethanol; 3,4-DHPEA-EDA, dialdehydic form of decarboxymethyl elenolic acid linked to (3,4-dihydroxyphenyl) ethanol; *p*-HPEA-EDA, dialdehydic form of decarboxymethyl elenolic acid linked to (*p*-hydroxyphenyl)ethanol; 3,4-DHPEA-EA, isomer of the oleuropein aglycon; HPLC, high-performance liquid chromatography; DAD, diode array detector; NMR, nuclear magnetic resonance; PVDF, polyvinylidene fluoride; FLD, fluorescence detector; HS-SPME, headspace solid-phase microextraction; GC-MS, gas chromatography−mass spectrometry; ANOVA, analysis of variance; PCA, principal component analysis

REFERENCES

(1) Caruso, G.; Gucci, R.; Urbani, S.; Esposto, S.; Taticchi, A.; Di Maio, I.; Selvaggini, R.; Servili, M. Effect of different irrigation volumes during fruit development on quality of virgin olive oil of cv. Frantoio. *Agric. Water Manage.* **2014**, *134*, 94−103.

(2) Inglese, P.; Famiani, F.; Galvano, F.; Servili, M.; Esposto, S.; Urbani, S. Factors affecting extra-virgin olive oil composition. *Hortic. Rev.* **2011**, *38*, 83−147.

(3) Chiacchierini, E.; Mele, G.; Restuccia, D.; Vinci, G. Impact evaluation of innovative and sustainable extraction technologies on olive oil quality. *Trends Food Sci. Technol.* **2007**, *18*, 299−305.

(4) Oliveras-López, M. J.; Berná, G.; Jurado-Ruiz, E.; López-García de la Serrana, H.; Martín, F. Consumption of extra-virgin olive oil rich in phenolic compounds has beneficial antioxidant effects in healthy human adults. *J. Funct. Foods* **2014**, *10*, 475−484.

(5) Parkinson, L.; Keast, R. Oleocanthal, a phenolic derived from virgin olive oil: a review of the beneficial effects on inflammatory disease. *Int. J. Mol. Sci.* **2014**, *15*, 12323−12334.

(6) Gill, C. I. R.; Hashim, Y. Z. H.-Y.; Servili, M.; Rowland, I. Olive oil and its phenolic components and their effects on early- and late stage events in carcinogenesis. In *Olives and Olive Oil in Health and Disease Prevention*; Preedy, V. R., Watson, R. R., Eds.; Academic Press: Oxford, UK, 2010; pp 1005−1012.

(7) Reboredo-Rodríguez, P.; González-Barreiro, C.; Cancho-Grande, B.; Simal-Gándara, J. Improvements in the malaxation process to enhance the aroma quality of extra virgin olive oils. *Food Chem.* **2014**, *158*, 534−545.

(8) Stefanoudaki, E.; Koutsaftakis, A.; Harwood, J. L. Influence of malaxation conditions on characteristic qualities of olive oil. *Food Chem.* **2011**, *127*, 1481−1486.

(9) Gómez-Rico, A.; Inarejos-García, A. M.; Salvador, M. D.; Fregapane, G. Effect of malaxation conditions on phenol and volatile profiles in olive paste and the corresponding virgin olive oils (*Olea europaea* L. cv. Cornicabra). *J. Agric. Food Chem.* **2009**, *57*, 3587−3595.

(10) Selvaggini, R.; Esposto, S.; Taticchi, A.; Urbani, S.; Veneziani, G.; Di Maio, I.; Sordini, B.; Servili, M. Optimization of the temperature and oxygen concentration conditions in the malaxation during the oil mechanical extraction process of four Italian olive cultivars. *J. Agric. Food Chem.* **2014**, *62*, 3813−3822.

(11) Youssef, O.; Mokhtar, G.; Abdelly, C.; Mohamed, S. N.; Mokhtar, Z.; Flamini, G. Changes in volatile compounds and oil quality with malaxation time of Tunisian cultivars of *Olea europea*. *Int. J. Food Sci. Technol.* **2013**, *48*, 74−81.

(12) Angerosa, F.; Servili, M.; Selvaggini, R.; Taticchi, A.; Esposto, S.; Montedoro, G. Volatile compounds in virgin olive oil: occurrence and their relationship with the quality. *J. Chromatogr. A* **2004**, *1054*, 17−31.

(13) Pastore, G.; D'Aloise, A.; Lucchetti, S.; Maldini, M.; Moneta, E.; Peparaio, M.; Raffo, A.; Sinesio, F. Effect of oxygen reduction during malaxation on the quality of extra virgin olive oil (cv. Carboncella)

DOI: 10.1021/acs.jafc.5b01666
J. Agric. Food Chem. 2015, 63, 6066−6074

extracted through "two-phase" and "three-phase" centrifugal decanters. *LWT—Food Sci. Technol.* **2014**, *59*, 163−172.
(14) Jiménez, B.; Sánchez-Ortiz, A.; Rivas, A. Influence of the malaxation time and olive ripening stage on oil quality and phenolic compounds of virgin olive oils. *Int. J. Food Sci. Technol.* **2014**, *49*, 2521−2527.
(15) Catania, P.; Vallone, M.; Pipitone, F.; Inglese, P.; Aiello, G.; La Scalia, G. An oxygen monitoring and control system inside a malaxation machine to improve extra virgin olive oil quality. *Biosyst. Eng.* **2013**, *114*, 1−8.
(16) Taticchi, A.; Esposto, S.; Veneziani, G.; Urbani, S.; Selvaggini, R.; Servili, M. The influence of the malaxation temperature on the activity of polyphenoloxidase and peroxidase and on the phenolic composition of virgin olive oil. *Food Chem.* **2013**, *136*, 975−983.
(17) Servili, M.; Taticchi, A.; Esposto, S.; Urbani, S.; Selvaggini, R.; Montedoro, G. Influence of the decrease in oxygen during malaxation of olive paste on the composition of volatiles and phenolic compounds in virgin olive oil. *J. Agric. Food Chem.* **2008**, *56*, 10048−10055.
(18) Parenti, A.; Spugnoli, P.; Masella, P.; Calamai, L. The effect of malaxation temperature on the virgin olive oil phenolic profile under laboratory scale conditions. *Eur. J. Lipid Sci. Technol.* **2008**, *110*, 735−741.
(19) Puértolas, E.; Martínez de Marañón, I. Olive oil pilot-production assisted by pulsed electric field: impact on extraction yield, chemical parameters and sensory properties. *Food Chem.* **2015**, *167*, 497−502.
(20) Leone, A.; Tamborrino, A.; Romaniello, R.; Zagaria, R.; Sabella, E. Specification and implementation of a continuous microwave-assisted system for paste malaxation in an olive oil extraction plant. *Biosyst. Eng.* **2014**, *125*, 24−35.
(21) Toschi, T. G.; Berardinelli, A.; Cevoli, C.; Iaccheri, E.; Di Lecce, G.; Bendini, A.; Ragni, L. Effectiveness of the mechanical excitation applied to the olive paste: possible improving of the oil yield, in malaxation phase, by vibration systems. *J. Agric. Eng.* **2013**, *44* (225), 166−169.
(22) Esposto, S.; Veneziani, G.; Taticchi, A.; Selvaggini, R.; Urbani, S.; Di Maio, I.; Sordini, B.; Minnocci, A.; Sebastiani, L.; Servili, M. Flash thermal conditioning of olive pastes during the olive oil mechanical extraction process: impact on the structural modifications of pastes and oil quality. *J. Agric. Food Chem.* **2013**, *61*, 4953−4960.
(23) Gómez-Rico, A.; Fregapane, G.; Salvador, M. D. Effect of cultivar and ripening on minor components in Spanish olive fruits and their corresponding virgin olive oils. *Food Res. Int.* **2008**, *41*, 433−440.
(24) Pannelli, G.; Servili, M.; Selvaggini, R.; Baldioli, M.; Montedoro, G. F. Effect of agronomic and seasonal factors on olive (*Olea europaea* L.) production and on the qualitative characteristics of the oil. *Acta Hortic.* **1994**, *356*, 239−244.
(25) Montedoro, G. F.; Servili, M.; Baldioli, M.; Selvaggini, R.; Miniati, E.; Macchioni, A. Simple and hydrolyzable compounds in virgin olive oil. 3. Spectroscopic characterization of the secoiridoids derivatives. *J. Agric. Food Chem.* **1993**, *41*, 2228−2234.
(26) Servili, M.; Baldioli, M.; Selvaggini, R.; Macchioni, A.; Montedoro, G. F. Phenolic compounds of olive fruit: one- and two-dimensional nuclear magnetic resonance characterization of nüzhenide and its distribution in the constitutive parts of fruit. *J. Agric. Food Chem.* **1999**, *47*, 12−18.
(27) E.U. 2003 November 6, Regulation 1989/03 amending Regulation (EEC) No 2568/91 on the characteristics of olive oil and olive-pomace oil and on the relevant methods of analysis modifies the CEE n. 2568/91 on olive oils and pomace olive oils characteristics and relative analysis methods. *Off. J. Eur. Communities* **2003**, *295/57*, 13/11.
(28) Selvaggini, R.; Servili, M.; Urbani, S.; Esposto, S.; Taticchi, A.; Montedoro, G. F. Evaluation of phenolic compounds in virgin olive oil by direct injection in high-performance liquid chromatography with fluorometric detection. *J. Agric. Food Chem.* **2006**, *54*, 2832−2838.
(29) Servili, M.; Baldioli, M.; Selvaggini, R.; Miniati, E.; Macchioni, A.; Montedoro, G. F. High-performance liquid chromatography evaluation of phenols in olive fruit, virgin olive oil, vegetation waters and pomace and 1D- and 2D-nuclear magnetic resonance characterization. *J. Am. Oil Chem. Soc.* **1999**, *76*, 873−882.
(30) Servili, M.; Selvaggini, R.; Taticchi, A.; Montedoro, G. F. Headspace composition of virgin olive oil evaluated by solid phase microextraction: relationship with the oil sensory characteristics. In *Food Flavours and Chemistry: Advances of the New Millennium*; Spanier, A. M., Shahidi, F., Parliment, T. H., Mussinan, C., Ho, C. T., Tratratas Contis, E., Eds.; The Royal Society of Chemistry: London, UK, 2001; pp 236−247.
(31) Heredia, A.; Gullién, R.; Jiménez, A.; Bolaños, G. F. Olive fruit glycosidases. Factor affecting their extraction. *Z. Lebensm. Unters. Forsch.* **1992**, *194*, 561−565.
(32) Vierhuis, E.; Servili, M.; Baldioli, M.; Schols, H. A.; Voragen, A. G. J.; Montedoro, G. F. Effect of enzyme treatment during the mechanical extraction of olive oil on phenolic compounds and polysaccharides. *J. Agric. Food Chem.* **2001**, *49*, 1218−1223.
(33) Kalua, C. M.; Allen, M. S.; Bedgood, D. R., Jr.; Bishop, A. G.; Prenzler, P. D.; Robards, K. Olive oil volatile compounds, flavour development and quality: a critical review. *Food Chem.* **2007**, *100*, 273−286.
(34) Luaces, P.; Sanz, C.; Pérez, A. G. Thermal stability of lipoxygenase and hydroperoxide lyase from olive fruit and repercussion on olive oil aroma biosynthesis. *J. Agric. Food Chem.* **2007**, *55*, 6309−6313.
(35) Padilla, M. N.; Hernández, M. L.; Sanz, C.; Martínez-Rivas, J. M. Functional characterization of two 13-lipoxygenase genes from olive fruit in relation to the biosynthesis of volatile compounds of virgin olive. *J. Agric. Food Chem.* **2009**, *57*, 9097−9107.

DOI: 10.1021/acs.jafc.5b01666
J. Agric. Food Chem. 2015, 63, 6066−6074

via the Maillard reaction followed by a self-assembly method; that is, the Maillard dry-heat conjugates were heated in a water bath at the isoelectric point of β-conglycinin, where it showed the lowest polydispersity index value. The size distribution, turbidity, morphology, ζ-potential, and conformation of nanogels were investigated to characterize the nanogels. The mechanism of nanogel formation was systematically analyzed, and the stability of nanogels was also observed.

MATERIALS AND METHODS

Materials. Soy β-conglycinin was separated from defatted soybean flour (obtained from Shandong Gaotang Lanshan Group Corp., Shandong, China) on the basis of the method of Nagano et al.[19] The protein content of β-conglycinin was 84.03% (Kjeldahl, N × 5.71). Dextran (molecular weight 48−90 kDa) and 8-anilino-1-naphthalenesulfonic acid (ANS) were supplied by Sigma (St. Louis, MO, USA). All reagents were of analytical grade unless specified. All solutions were prepared by using deionized water.

Synthesis of Soy β-Conglycinin−Dextran Conjugates. Soy β-conglycinin and dextran powder mixtures with weight ratios of 1:1 were dissolved in distilled water and lyophilized. The lyophilized powder was dry-heated at 60 °C with a relative humidity of 79% in a desiccators containing saturated KBr in the bottom for 4 days. The resultant samples were dissolved in distilled water and centrifuged (10000*g*, 15 min, 25 °C). The supernatant was then freeze-dried, and the products were soy β-conglycinin−dextran conjugates.

Fabrication of Soy β-Conglycinin−Dextran Nanogels. The Maillard conjugates were dispersed in double-distilled water to reach a soy β-conglycinin concentration of 1 mg/mL. The pH of the completely solubilized conjugate solution was acidified to 4.8 by stepwise addition of 0.1 mol/L HCl. The solution was then placed in a water bath without stirring at a temperature of 95 °C for 50 min. The resultant soy β-conglycinin−dextran nanogels solution was either kept at 4 °C or freeze-dried.

To evaluate the effect of pH on the size distributions of nanogels, the conjugates were acidified to pH 3.8, 4.3, 4.8, 5.3, or 5.8 and subsequently incubated in water baths at 80 °C for 30 min. Other steps were as described above. To study the effect of protein concentration, conjugate solutions at concentrations ranging from 0.5 to 10 mg/mL were used and heated at 80 °C for 30 min. Other steps were as described above. To investigate the effect of the heating temperature, the conjugate solutions were heated at 75, 80, 85, 90, or 95 °C for 30 min. Other steps were as described above. To observe the effect of heating time on size distributions of nanogels, the Maillard products were heated in water baths at 95 °C for 5−60 min. Other steps were as described above.

Sodium Dodecyl Sulfate−Polyacrylamide Gel Electrophoresis (SDS-PAGE). SDS-PAGE was performed according to the methodology of Laemmli[20] with a 12% acrylamide separating gel and a 5% stacking gel. The samples were dissolved in 0.125 mol/L Tris-HCl buffer that contained 1% (w/v) sodium dodecyl sulfate, 2% (v/v) 2-mercaptoethanol, 5% (v/v) glycerol, and 0.025% (w/v) bromophenol blue. The sample solutions (5 mg/mL, 10 μL) were heated for 5 min in boiling water before electrophoresis. After electrophoresis, the gels were stained for protein for 2.5 h and for carbohydrate for 16 h with Coomassie brilliant blue R-250 and periodate−Schiff solution, respectively.[21] The gel stained for protein was then destained with 10% (v/v) methanol and 10% (v/v) acetic acid.

Degree of Glycation (DG). The DG of soy β-conglycinin−dextran conjugates was estimated using trinitrobenzenesulfonic acid (TNBS) reaction according to Adler-Nissen with some modifications.[22] A sample solution (1 mg/mL, 0.5 mL) was mixed with $NaHCO_3$ (4 wt %, 0.5 mL), sodium dodecyl sulfate (0.1 wt %, 0.5 mL), and TNBS (0.1 wt %, 0.5 mL). The solution was then incubated at 40 °C for 2 h, followed by the addition of 0.25 mL of 1 N HCl to quench the reaction. The absorbance of the solution was measured by using a UV2300 ultraviolet−visible spectrophotometer (Tianmei Ltd., Shanghai, China) at a wavelength of 340 nm. DG was determined as

$$DG = [(A_0 - A_1)/A_0] \times 100\%$$

where A_0 and A_1 were the absorbance of solutions before and after glycation, respectively.

Dynamic Light Scattering Measurements. The size distributions of the samples were conducted on a Zetasizer Nano-ZS instrument (Malvern Instruments, Worcestershire, UK) with a fixed scattering angle of 173° equipped with a 4 mW He−Ne laser (633 nm wavelength). The sample was placed in a 1 cm × 1 cm cuvette (PCS8501) and analyzed three times at 25 °C. The apparent average hydrodynamic diameter (D_h) and polydispersity index (PDI) were obtained.

ζ-Potential Measurements. The ζ-potentials of samples were also examined on the Zetasizer Nano-ZS instrument. ζ-Potentials were calculated by using Dispersion Technology software according to the Smoluchowski approximation in an automatic mode.[23] Each sample was analyzed in triplicate.

Turbidity Measurements. Native β-conglycinin, β-conglycinin/dextran mixtures, and β-conglycinin−dextran conjugate powders were dissolved in distilled water to achieve the final protein concentration of 1 mg/mL. The pH values of the solutions were acidified to 4.8 using 0.1 mol/L HCl. The solutions were then placed in a water bath at 95 °C for different times (0−60 min).The turbidity of each sample was assessed by measuring the transmittance of sample solution at a wavelength of 540 nm on a UV2300 ultraviolet−visible spectrophotometer (Tianmei Ltd.).[24]

Surface Hydrophobicity (H_0) Measurements. Surface hydrophobicity was obtained by using the ANS as fluorescence probe following the method described by Haskard and Li-Chan[25] with some modifications. Briefly, samples were dissolved in buffer solutions (0.01 mol/L, pH 7.0) to reach desired protein concentrations (0.02−0.2 mg/mL). Aliquots of ANS stock solution (8×10^{-3} mol/L, 20 μL) were mixed with each sample solution (4 mL). The mixtures were then shaken fully on a vortex mixer and stored in the dark for 3 min before measurements. Fluorescence intensity (FI) was analyzed on an F7000 fluorescence spectrophotometer (Hitachi Co., Tokyo, Japan) with wavelengths of 390 nm (excitation) and 470 nm (emission) at 25 °C. The FI value at each concentration minus the FI value of the blank (without added ANS) was calculated as the final FI value. The initial slope of the final FI value versus protein concentration (mg/mL) was obtained by a linear regression analysis and used as an index of H_0. Each sample was conducted three times.

Circular Dichroism (CD) Spectroscopy. CD spectra were recorded on an MOS-450 spectropolarimeter (BioLogic Science Instrument, Grenoble, France). The far-UV CD spectrum probed the secondary structures. Each sample was placed in a 2 mm quartz cuvette with the protein concentration of 0.1 mg/mL and scanned from 180 to 260 nm. The near-UV CD spectrum probed the tertiary structures. Each sample was placed in a 10 mm quartz cuvette with a protein concentration of 2 mg/mL and scanned over a wavelength range from 260 to 340 nm. For each measurement, the spectrum was an average of eight scans. All determinations were carried out in triplicate.

Atomic Force Microscopy (AFM). AFM images were captured in tapping mode on a Multimode 8 scanning probe microscope (Bruker Inc., Billerica, MA, USA) equipped with a silicon cantilever (FESPA, Bruker Corp, Santa Barbara, CA, USA) of 125 μm length. Aliquots (2 μL) of sample previously diluted to 5 μg/mL with deionized water were deposited on a freshly cleaved mica substrate and air-dried for overnight before imaging.

Scanning Electron Microscopy (SEM). SEM image was acquired on a Nova NanoSEM 430 (FEI NanoPorts, Eindhoven, The Netherlands) at 10 kV accelerating voltage. The preparation of specimen for SEM was the same as AFM. The specimen was coated with gold followed by imaging.

Transmission Electron Microscopy (TEM). TEM image was recorded on a JEM-2100F electron microscopy at an accelerating voltage of 80 kV. Aliquots (10 μL) of dispersions (diluted to 3 μg/μL with deionized water, previously) were dropped on the carbon membrane support copper grid. Excessive dispersions were removed by filter paper and dried for 5 min. Ten microliters of 1% (w/v)

DOI: 10.1021/acs.jafc.5b01778
J. Agric. Food Chem. 2015, 63, 6075−6083

phosphotungstic acid was placed on the copper grid and stained for 5 min before removing it with filter paper, and the grid was dried overnight at ambient temperature.

Data Analysis. All measurements were performed in triplicate if not specified. Significance of difference was analyzed using analysis of variance (ANOVA) and Tukey's test at 5% level of probability (SPSS 17.0 for Windows statistical software).

RESULTS AND DISCUSSION

Characteristics of Soy β-Conglycinin−Dextran Conjugates Formed by Maillard Dry-Heating Reaction. The process of Maillard conjugation involves three stages.[26] In the initial stage, an amino group was condensed with a carbonyl group to synthesize a Schiff base, which then cyclizes to an N-substituted glycosylamine. It subsequently goes through Amadori rearrangement to produce a more stable Amadori rearrangement product (ARP, 1-amino-1-deoxy-2-ketose).[27] The ARP undergoes a complex series of reactions to form multiple colored compounds in the following stages.[28] The reaction is often limited to the initial stage to prevent the occurrence of highly colored and poorly characterized products.

The formation of Maillard-type protein−polysaccharide complexes was confirmed by SDS-PAGE and TNBS test. Figure 1A exhibits the protein staining SDS-PAGE pattern; the

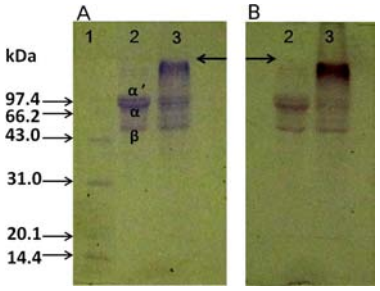

Figure 1. SDS-PAGE patterns for β-conglycinin/dextran samples: (A) protein stain; (B) carbohydrate stain. Lanes: 1, protein marker; 2, native β-conglycinin; 3, β-conglycinin−dextran conjugates. Arrows indicate the boundary between the stacking and separating gels.

characteristic bands of β-conglycinin (subunits of α′, α, and β) were detected in lane 2, which is consistent with Zhang.[29] However, when it comes to lane 3, a shift of bands toward the top of separating gels was visualized after the Maillard reaction, which is clear evidence that compounds with high molecular weight were developed. The migration of dextran can be elided because it carries no charge, the effect of noncovalent interactions on SDS-PAGE may be ignored because they were disrupted in the reducing condition, and an intense bank accumulated on the top of separating gels in carbohydrate staining pattern (Figure 1B, lane 3), all of which strongly verified the covalent attachment of dextran to β-conglycinin.

The degree of glycation was evaluated by quantifying the loss of available amino groups of β-conglycinin after Maillard reaction using the TNBS method. The DG of the Maillard dry-heating products prepared by us was around 16.7%.

Characteristics of Soy β-Conglycinin−Dextran Nanogels Fabricated by Self-Assembly Approach. DLS is a quantitative and effective tool to investigate the particle size and size distribution of nanogels.

As mentioned above, Schmitt and co-workers reported spherical microgels exhibiting colloidal stability were formed in a narrow pH range near the isoelectric point (p*I*) of β-lactoglobulin. The p*I* of β-conglycinin is 4.8.[30] Therefore, in this study, the effect of pH on the formation of nanogels was studied by heating (80 °C) the soy β-conglycinin−dextran conjugates (1 mg/mL) at the pH range of 3.3−5.8. As shown in Figure 2, when the pH was shifted toward the p*I*, the mean

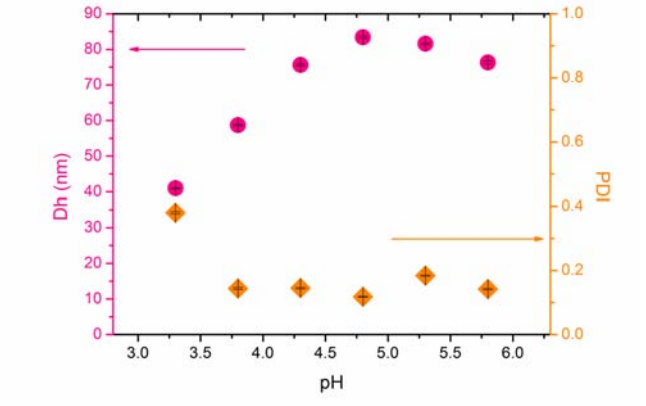

Figure 2. D_h and PDI of nanogels prepared by heating the β-conglycinin−dextran conjugates (1 mg/mL) in a water bath at 80 °C for 30 min at different pH values.

hydrodynamic diameter (D_h) increased, whereas the polydispersity index (PDI) decreased, implying that the nanoparticles were more uniform at p*I*. There was a dominant interaction, electrostatic repulsion, and hydrophobic attraction during the heat-induced gelating process. When the pH decreased from 4.3 to 3.3 or increased from 5.3 to 5.8, β-conglycinin carried more charges, resulting in stronger long-range electrostatic repulsion and weaker short-range hydrophobic aggregation. Therefore, the β-conglycinin molecules were separated from each other, which may weaken the gelation ability of protein and make it unfavorable to the formation of homogeneous nanogels. On the other hand, at the isoelectric point where β-conglycinin carried zero net charge and nanogels displayed the lowest PDI value, the electrostatic repulsion can be ignored and hydrophobic attraction was strong enough to construct well-defined nanonetwork hydrogels.

Figure 3 exhibits the influence of β-conglycinin concentration on the DLS result of nanogels, which were prepared by heating (80 °C) the conjugates (0.5−10 mg/mL) at pH 4.8. The increment of β-conglycinin gradually increased the D_h and PDI values of nanogels (from 79.26 to 123.65 nm and from 0.189 to 0.276, separately). A higher concentration of β-conglycinin brings molecules closer together. As a consequence, the mean particle size increased as the concentration increased. Furthermore, when the protein concentration was increased to ≥8 mg/mL, the turbidity of the solution markedly increased and the mobility of the solution sharply diminished. In the following study we adopted 1 mg/mL as the optimal protein concentration to form nanogels.

A heat treatment of proteins above their denaturation temperature is a prerequisite for unfolding the hydrophobic groups and forming gels.[31] Because the denaturation temperature of β-conglycinin is 60−75 °C,[32] a heating temperature range of 75−95 °C was used to study the formation of nanogels. As shown in Figure 4, the D_h and PDI of nanogels did not change significantly when the heating temperature

DOI: 10.1021/acs.jafc.5b01778
J. Agric. Food Chem. 2015, 63, 6075−6083

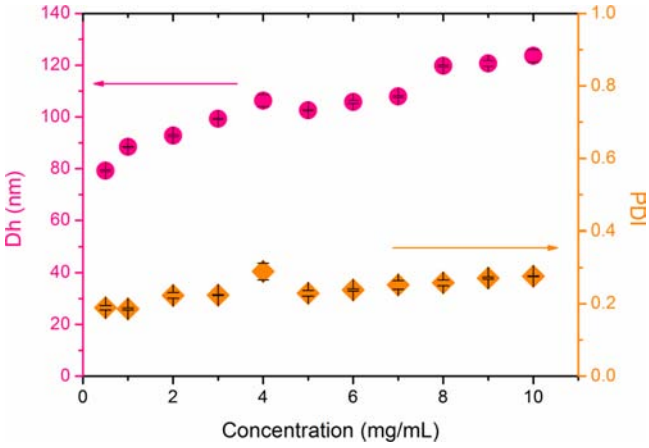

Figure 3. DLS results of nanogels prepared by heating the β-conglycinin–dextran conjugates with different concentrations at 80 °C for 30 min.

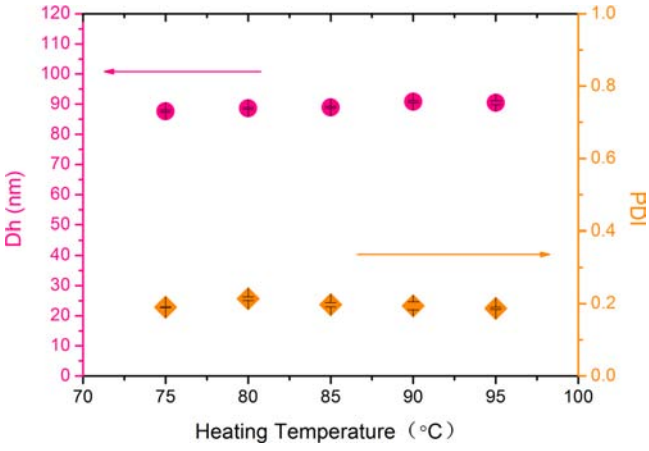

Figure 4. D_h and PDI of nanogels prepared by heating 1 mg/mL β-conglycinin–dextran conjugates at different temperatures for 30 min.

improved. Because the lowest PDI value appeared at 95 °C, we chose a heating temperature of 95 °C for nanogel synthesis.

The size distribution of nanogels (Figure 5) and the turbidity of native β-conglycinin and β-conglycinin/dextran mixture as well as nanogels (Figure 6) as a function of heating time were

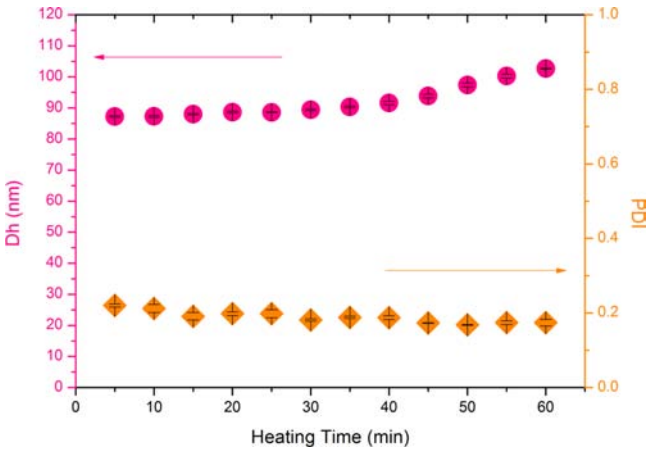

Figure 5. D_h and PDI of nanogels prepared by heating 1 mg/mL β-conglycinin–dextran conjugates at 95 °C for different times.

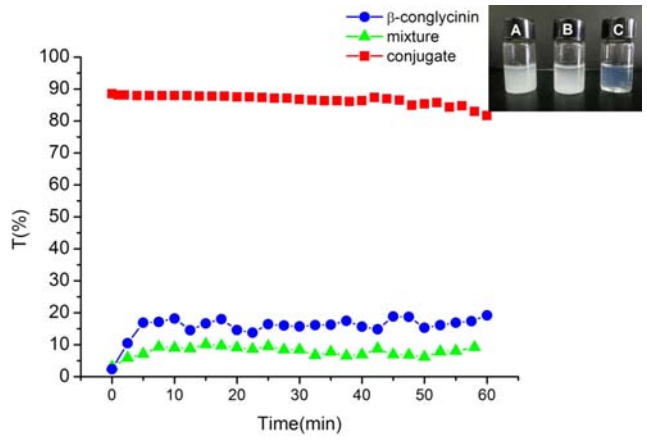

Figure 6. Turbidity of β-conglycinin, β-conglycinin/dextran mixture, and β-conglycinin–dextran conjugates incubated in a water bath at 95 °C for 0–60 min. (Inset) Photographs of β-conglycinin (A), β-conglycinin/dextran mixture (B), and β-conglycinin–dextran conjugates (C) heated in a water bath at 95 °C for 60 min.

investigated. As shown in Figure 5, when the heating time increased, the particle size did not grow markedly and PDI dropped slightly. It is notable that the PDI value fell below 0.2 after 15 min of heating, indicating that homogeneous dispersed nanogels were formed in a broad heating time range of 15–60 min. We used a 50 min heat treatment to the conjugates in the following study. As shown in Figure 6, depletion flocculation appeared after a heat treatment to β-conglycinin, and a similar phenomenon was found by Chen and co-workers.[33] Precipitation was also observed in the presence of free dextran, indicating that the individual dextran molecules cannot prevent the β-conglycinin molecules from aggregating. However, when the conjugates were heated, no coagula were found and the solution was translucent. Therefore, the dextran grafted to β-conglycinin not only can suppress the protein coagulation but also can improve the solubility of protein.

Taken together, heating 1 mg/mL soy β-conglycinin–dextran conjugates at pH 4.8 in a water bath at 95 °C for 50 min was chosen to prepare nanogels in the following study.

Morphology, Formation Mechanism, and Structure of Soy β-Conglycinin–Dextran Nanogels. *Morphology and Formation Mechanism.* Atomic force microscopy has been proved to be helpful for detecting 3D information on nanoscale particles.[34] Scanning electron microscopy is available to obtain 2D information by examining the surfaces of samples,[35] whereas transmission electron microscopy is valuable for investigating the structures of specimens,[36] both of which produce 2D images.

DLS and AFM were carried out to determine the dimensions and morphology of β-conglycinin–dextran conjugates and nanogels as well as to probe the effect of self-assembly on the aggregation of protein. DLS data show that after self-assembly, the D_h of particles increased from 73.21 to 83.33 nm, whereas the polydispersity index reduced from 0.184 to 0.096, which indicates that the particles in nanogel solution were more homogeneous. The AFM images exhibit that the conjugates (Figure 7A) were irregular aggregations and the nanogels (Figure 7B) were approximately spherical in shape. In comparison, there were far fewer aggregates and more uniform globules in the nanogels than conjugates. The DLS and AFM analyses imply that self-assembly of the amphiphilic conjugates

DOI: 10.1021/acs.jafc.5b01778
J. Agric. Food Chem. 2015, 63, 6075–6083

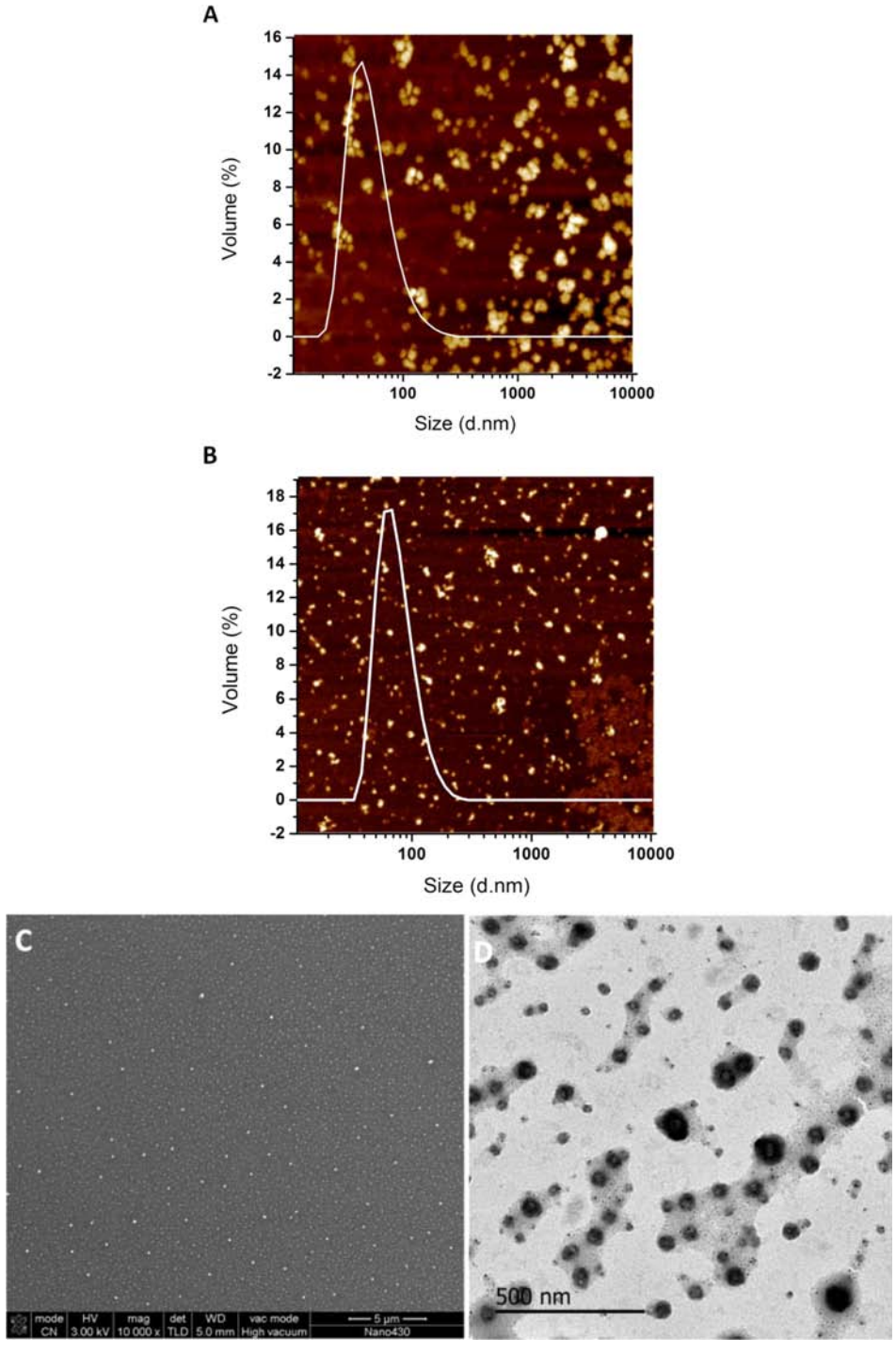

Figure 7. AFM images and size distribution of β-conglycinin−dextran conjugates (A) and nanogels (B); SEM image (C) and TEM image (D) of β-conglycinin−dextran nanogels.

can form spherical particles and deplete self-aggregates of β-conglycinin.

The SEM image presented in Figure 7C illustrates that the well-dispersed nanogels were of globular shape with narrow particle distribution. The TEM image (Figure 7D) verifies that the nanogels were characterized by spherical shapes with core−shell structure having a dark shell and a light core. The phenomenon found in the TEM image may be rationalized by the following mechanism: a heat treatment to conjugates could cause the β-conglycinin to unfold, promote macroscopic aggregates, and form macro gels, but the dextran covalently attached to the β-conglycinin through Maillard reaction restrained the β-conglycinin from aggregating due to the steric hindrance of dextran; it, therefore, served as the barrier for the inner β-conglycinin molecules, which cross-linked with each other by attractive forces (e.g., hydrophobic, disulfide bonds).[37] Hence, the flexible and hydrophilic dextran chains constituted the dark shell region, whereas the hydrophobic cross-linked β-conglycinins constituted the light core region (Figure 7D).

ζ-Potential. The ζ-potential of β-conglycinin, β-conglycinin/dextran mixture, and β-conglycinin−dextran nanogels was monitored at various pH values (Figure 8). The samples

DOI: 10.1021/acs.jafc.5b01778
J. Agric. Food Chem. 2015, 63, 6075−6083

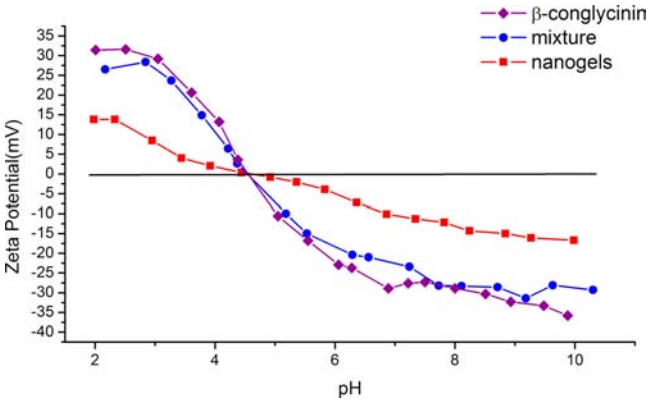

Figure 8. Zeta potential of native β-conglycinin, β-conglycinin/dextran mixture, and β-conglycinin−dextran nanogels at different pH values.

were positively or negatively charged at the pH above or below p*I*, and they carried zero net charge near the p*I*. It is worth noting that the ζ-potential of nanogels was pronouncedly lower in magnitude compared with native β-conglycinin as well as mixture, and the difference was even larger when the pH was farther from the p*I*. Harada and Kataoka synthesized core−shell-like polyion complex micelles developed from lysozyme and poly(ethylene glycol)−poly(aspartic acid) block copolymer (PEG−P (ASP)).[38] The ζ-potential of these associates was about zero because the PEG corona could sterically stabilize the micelles. Riley and co-workers reported that the ζ-potential of nanoparticles prepared from poly(lactic acid) (PLA)−PEG copolymers was negligible when compared with PLA nanoparticles, and they attributed this phenomenon to the PEG segment that shielded the carboxyl acid end groups of the PLA chains.[39] Likewise, the ζ-potential profile of nanogels in Figure 8 further confirmed the aforementioned finding that β-conglycinin cores were covered with nonionic dextran blocks. The coated dextran shielded the inner protein and, therefore, it weakened the electrostatic repulsion of protein in different cores. However, the nanogel solution still carried several net charges at the pH farther from the p*I*. This phenomenon may be attributed to the presence of native β-conglycinin in the solution, which neither conjugated with dextran nor fabricated nanogels.

Circular Dichroism Spectroscopy. CD spectroscopy has been proved as a reliable method to reveal the conformational structure of protein.[40] The far-UV spectrum (in the region of 190−250 nm) estimates the secondary conformation of protein, whereas the near-UV fingerprint (in the region of 260−340 nm) exhibits the tertiary structure of protein.

The far-UV curves of native β-conglycinin, β-conglycinin/dextran mixture, β-conglycinin−dextran conjugates, and nanogels were presented in Figure 9A. The spectrum of native β-conglycinin showed two negative dichroic peaks around 208 and 217 nm, a positive bank in the vicinity of 195 nm, and a zero-crossing near 200 nm, suggesting that the secondary composition of native β-conglycinin was mainly β-sheet.[41] There was no significant difference in secondary structure among the native protein, mixture, and conjugates. However, as to nanogels, the mean residue ellipticity at 208 and 217 nm largely decreased, which indicated that the secondary conformation of nanogels changed and the β-sheet content increased.

The near-UV spectra are shown in Figure 9B. The native β-conglycinin exhibited a positive peak at 270 nm, and the

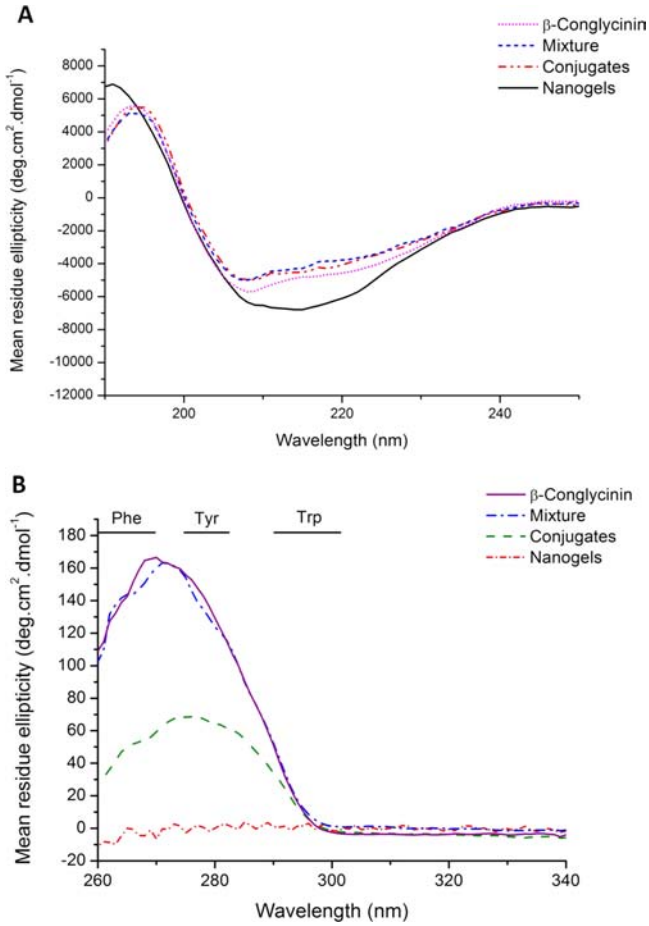

Figure 9. Far-UV CD spectra (A) and near-UV CD spectra (B) of native β-conglycinin, β-conglycinin/dextran mixture, and β-conglycinin−dextran conjugates and nanogels.

dichroic curve of mixture was similar to that of β-conglycinin. However, a decrease in the magnitude of the bank was observed after glycation, demonstrating that aromatic side chains were exposed to some extent during Maillard reaction.[42] It is worth noting that the positive peak of nanogels disappeared and the intensity of the spectrum was relatively low, clearly indicating that the tertiary structure of protein was totally destroyed after further heating of the Maillard dry-heat conjugates.

Surface Hydrophobicity. H_0 was determined by fluorescence probe methods using the ANS probe, which can access the hydrophobic groups on the surface of proteins and bind with the aromatic amino acid residues. H_0 has been used to reflect the 3D structure and conformational changes of protein.[25] Figure 10 exhibits the changes of H_0 at pH 7.0 with various specimens. The surface hydrophobicity of the mixture decreased slightly compared with the native β-conglycinin, suggesting that the free dextran had little effect on the H_0 of protein. Moreover, there was no substantial difference ($P < 0.05$) in H_0 between the conjugates and native β-conglycinin. This phenomenon might be attributed to the conjecture that H_0 is determined not only on the degree of partial denaturation of β-conglycinin during the Maillard dry-heat process, which is prone to increase it, but also on the degree of glycation, which is prone to decrease it. However, further heat treatment of conjugates caused a pronounced enhancement in H_0 of the nanogels. It is well-known that heat treatment will lead to the

DOI: 10.1021/acs.jafc.5b01778
J. Agric. Food Chem. 2015, 63, 6075−6083

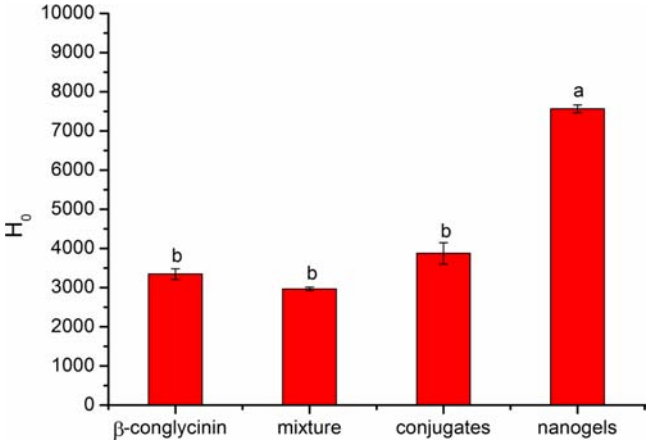

Figure 10. Surface hydrophobicity (H_0) of native β-conglycinin, β-conglycinin/dextran mixture, β-conglycinin–dextran conjugates, and nanogels. Different letters (a, b) above columns indicate significant differences ($P < 0.05$).

thermal denaturation of protein and subsequent exposure of nonpolar amino acids. Consequently, the surface hydrophobicity of β-conglycinin in nanogels was higher than that of the native protein and conjugates. The result indicates that the tertiary structure of nanogels was changed, which is consistent with the previous CD study.

Because the core of nanogels was composed of cross-linked β-conglycinins, the hydrophobic groups of which were exposed to the surface of protein, it is likely that several well-defined hydrophobic compartments were developed inside the core of nanogels, which might be available to deliver hydrophobic compounds due to the hydrophobic attraction between β-conglycinins and compounds.

Stability of Soy β-Conglycinin–Dextran Nanogels. The nanogels prepared at pH 4.8 were then incubated at various pH values. Figure 11A illustrates that the particle size and size distribution of nanogels did not change significantly from pH 2 to 12, suggesting that the nanogels were resistant to pH change. When the pH was farther from the p*I*, the β-conglycinins in the core were prone to separate from each other, but the cross-linking structure of β-conglycinins, which were formed in the heating process, made the nanogels remain stable in solution. On the other hand, when the pH was at/around the p*I*, the β-conglycinins in different cores tended to aggregate due to the lack of electrostatic repulsion; however, the glucan shells acted as shields to prevent the proteins from aggregating owing to the hydrophilicity and steric hindrance of dextrans. The results were in accordance with the aforementioned self-assembly mechanism of nanogels.

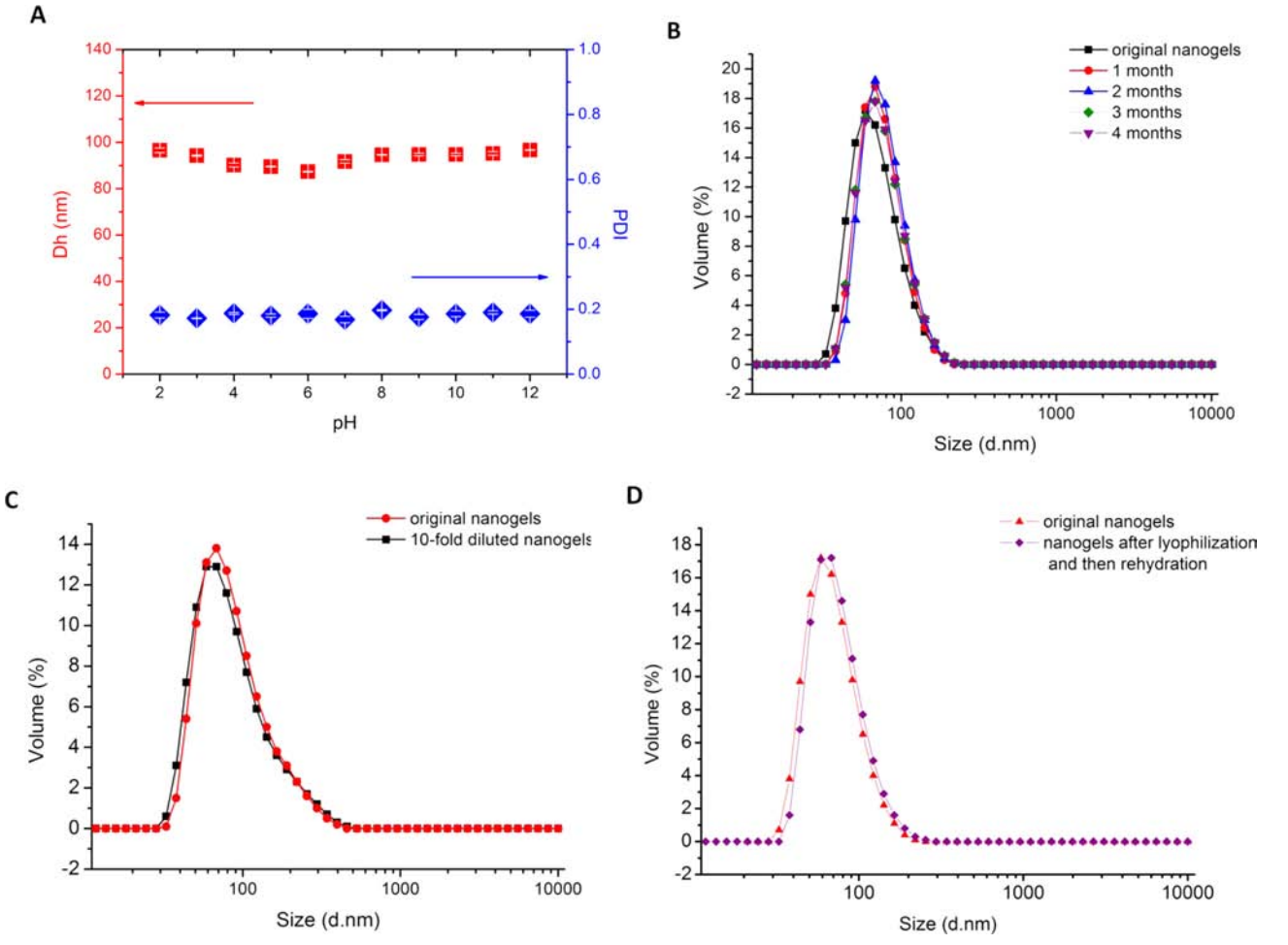

Figure 11. (A) D_h and PDI of nanogels under different pH conditions; (B) size distribution of freshly prepared nanogels and after storage for 1, 2, 3, or 4 months; (C) size distribution of nanogels as prepared and diluted to 0.1 mg/mL; (D) size distribution of nanogels as prepared and freeze-dried followed by rehydration.

DOI: 10.1021/acs.jafc.5b01778
J. Agric. Food Chem. 2015, 63, 6075–6083

No aggregates were found in the nanogel solution and, together with the particle size and polydispersity values (Figure 11B), were maintained after 4 months of storage at 4 °C without antiseptics, indicating that the nanogels were initially in thermodynamic equilibrium.[38] The narrow Gaussian fit of nanogels (Figure 11C), which were diluted to 0.1 mg/mL (10-fold), reconfirms that the cross-linking structures of nanogels are fairly stable. Furthermore, the lyophilized nanogels were water-dispersible, and there is no considerable change in the particle size of nanogels that were freeze-dried followed by rehydrating versus the original ones (Figure 11D). All of these outstanding properties are favorable to the practical application of nanogels in the food industry.

The synthesis of nanogels was illustrated in Figure 12. Amphiphilic soy β-conglycinin−dextran conjugates were formed by dextran covalently attaching to protein via the Maillard reaction. The amphiphilic graft copolymers subsequently self-assembled to fabricate core−shell nanogels. The grafted dextran afforded a shell to the inner cross-linked β-conglycinins and in turn improved the stability of nanogels. The formerly buried hydrophobic groups were exposed to the surface of β-conglycinin and constructed several hydrophobic compartments in the core, which may offer great potential to deliver hydrophobic compounds due to the hydrophobic interaction between the nanogels and the compounds.

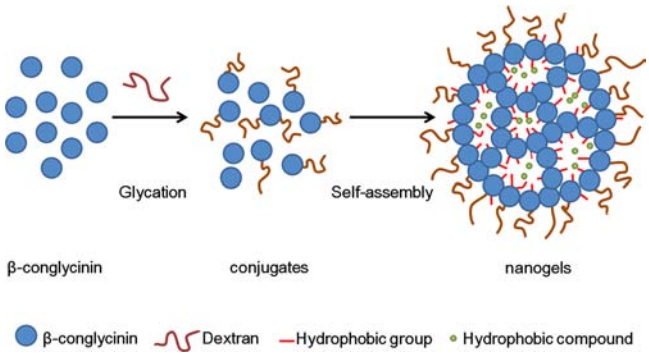

Figure 12. Illustration of the synthesis of β-conglycinin−dextran nanogels.

In conclusion, soy β-conglycinin−dextran nanogels were successfully produced via a self-assembly method at the isoelectric point of β-conglycinin. The nanogels were spherical with core−shell structures, as evidenced by AFM, SEM, and TEM as well as ζ-potential studies, and the hydrodynamic diameter was around 90 nm. Surface hydrophobicity and CD analyses clearly indicated that the structures of β-conglycinins were destroyed and the hydrophobic groups were exposed to the surface of protein to form hydrophobic compartments in the cores. The nanogels were fairly stable against long-term storage, pH change, lyophilization, or dilution. These valuable properties and the low toxicity of nanogels may provide a promising way to deliver hydrophobic compounds, and further research will emphasize the loading and unloading bioactive substance.

AUTHOR INFORMATION

Corresponding Author

*(J.-R.Q.) E-mail: jrqi@scut.edu.cn. Phone: +86 20 87114262. Fax: +86 20 87114263.

Funding

We appreciate the Chinese National Natural Science Fund (serial no. 31370036, 31301432), the Research Fund for Pearl River S&T Nova Program of Guangzhou (201506010063), and the project supported by Guangdong Natural Science Foundation (S2013010012097) for financial support.

Notes

The authors declare no competing financial interest.

REFERENCES

(1) Whitesides, G. M.; Boncheva, M. Beyond molecules: self-assembly of mesoscopic and macroscopic components. *Proc. Natl. Acad. Sci. U. S. A.* **2002**, *99*, 4769−4774.

(2) Whitesides, G. M.; Grzybowski, B. Self-assembly at all scales. *Science* **2002**, *295*, 2418−2421.

(3) Paulson, J. A.; Mesbah, A.; Zhu, X.; Molaro, M. C.; Braatz, R. D. Control of self-assembly in micro- and nano-scale systems. *J. Process Control* **2015**, *27*, 38−49.

(4) Schmitt, C.; Bovay, C.; Vuilliomenet, A. M.; Rouvet, M.; Bovetto, L.; Barbar, R.; Sanchez, C. Multiscale characterization of individualized beta-lactoglobulin microgels formed upon heat treatment under narrow pH range conditions. *Langmuir* **2009**, *25*, 7899−7909.

(5) Ho, K. M.; Li, W. Y.; Lee, C. H.; Yam, C. H.; Gilbert, R. G.; Li, P. Mechanistic study of the formation of amphiphilic core−shell particles by grafting methyl methacrylate from polyethylenimine through emulsion polymerization. *Polymer* **2010**, *51*, 3512−3519.

(6) Torchilin, V. P. Structure and design of polymeric surfactant-based drug delivery systems. *J. Controlled Release* **2001**, *73*, 137−172.

(7) Wang, D.; Wang, X. Amphiphilic azo polymers: molecular engineering, self-assembly and photoresponsive properties. *Prog. Polym. Sci.* **2013**, *38*, 271−301.

(8) Zhang, K.; Fang, H.; Shen, G.; Taylor, J. S.; Wooley, K. L. Well-defined cationic shell crosslinked nanoparticles for efficient delivery of DNA or peptide nucleic acids. *Proc. Am. Thorac. Soc.* **2009**, *6*, 450−457.

(9) Kato, A.; Minaki, K.; Kobayashi, K. Improvement of emulsifying properties of egg white proteins by the attachment of polysaccharide through Maillard reaction in a dry state. *J. Agric. Food Chem.* **1993**, *41*, 540−543.

(10) Sato, R.; Sawabe, T.; Saeki, H. Characterization of fish myofibrillar protein by conjugation with alginate oligosaccharide prepared using genetic recombinant alginate lyase. *J. Food Sci.* **2005**, *70*, 58−62.

(11) Dickinson, E. Interfacial structure and stability of food emulsions as affected by protein−polysaccharide interactions. *Soft Matter* **2008**, *4*, 932−942.

(12) Akhtar, M.; Dickinson, E. Whey protein−maltodextrin conjugates as emulsifying agents: an alternative to gum arabic. *Food Hydrocolloids* **2007**, *21*, 607−616.

(13) Wu, N. N.; Zhang, J. B.; Tan, B.; He, X. T.; Yang, J.; Guo, J.; Yang, X. Q. Characterization and interfacial behavior of nanoparticles prepared from amphiphilic hydrolysates of beta-conglycinin-dextran conjugates. *J. Agric. Food Chem.* **2014**, *62*, 12678−12685.

(14) Li, J.; Yu, S.; Yao, P.; Jiang, M. Lysozyme-dextran core-shell nanogels prepared via a green process. *Langmuir* **2008**, *24*, 3486−3492.

(15) Kang, I.; Yoon, J.; Lee, Y.; Choi, J.; Yang, J.; Chang, S. T.; Lee, J.; Lee, J.; Yoo, P. J.; Park, J. Stable vesicle assemblies on surfaces of hydrogel nanoparticles formed from a polysaccharide modified with lipid moieties. *Chem. Eng. J.* **2015**, *263*, 38−44.

(16) MacKinnon, N.; Guérin, G.; Liu, B.; Gradinaru, C. C.; Macdonald, P. M. Liposome-hydrogel bead complexes prepared via biotin− avidin conjugation. *Langmuir* **2009**, *25*, 9413−9423.

(17) Qi, J. R.; Yang, X. Q.; Liao, J. S. Improvement of functional properties of acid-precipitated soy protein by the attachment of dextran through Maillard reaction. *Int. J. Food Sci. Technol.* **2009**, *44*, 2296−2302.

DOI: 10.1021/acs.jafc.5b01778
J. Agric. Food Chem. 2015, 63, 6075−6083

(18) de Souza Ferreira, E.; Silva, M. A.; Demonte, A.; Neves, V. A. β-Conglycinin (7S) and glycinin (11S) exert a hypocholesterolemic effect comparable to that of fenofibrate in rats fed a high-cholesterol diet. *J. Funct. Foods* **2010**, *2*, 275−283.
(19) Nagano, T.; Hirotsuka, M.; Mori, H.; Kohyama, K.; Nishinari, K. Dynamic viscoelastic study on the gelation of 7S globulin from soybeans. *J. Agric. Food Chem.* **1992**, *40*, 941−944.
(20) Laemmli, U. K. Cleavage of structural proteins during the assembly of the head of bacteriophage T4. *Nature* **1970**, *227*, 680−685.
(21) Cerri, P. S.; Sasso-Cerri, E. Staining methods applied to glycol methacrylate embedded tissue sections. *Micron* **2003**, *34*, 365−372.
(22) Adler-Nissen, J. Determination of the degree of hydrolysis of food protein hydrolysates by trinitrobenzenesulfonic acid. *J. Agric. Food Chem.* **1979**, *27*, 1256−1262.
(23) Sarmiento, F.; Ruso, J. M.; Prieto, G.; Mosquera, V. ζ-Potential study on the interactions between lysozyme and sodium n-alkylsulfates. *Langmuir* **1998**, *14*, 5725−5729.
(24) Damodaran, S.; Kinsella, J. E. Effect of conglycinin on the thermal aggregation of glycinin. *J. Agric. Food Chem.* **1982**, *30*, 812−817.
(25) Haskard, C. A.; Li-Chan, E. C. Y. Hydrophobicity of bovine serum albumin and ovalbumin determined using uncharged (PRODAN) and anionic (ANS-) fluorescent probes. *J. Agric. Food Chem.* **1998**, *46*, 2671−2677.
(26) Hodge, J. E. Dehydrated foods, chemistry of browning reactions in model systems. *J. Agric. Food Chem.* **1953**, *1*, 928−943.
(27) Liu, J.; Ru, Q.; Ding, Y. Glycation a promising method for food protein modification: physicochemical properties and structure, a review. *Food Res. Int.* **2012**, *49*, 170−183.
(28) Spotti, M. J.; Martinez, M. J.; Pilosof, A. M.; Candioti, M.; Rubiolo, A. C.; Carrara, C. R. Influence of Maillard conjugation on structural characteristics and rheological properties of whey protein/dextran systems. *Food Hydrocolloids* **2014**, *39*, 223−230.
(29) Zhang, X.; Qi, J. R.; Li, K. K.; Yin, S. W.; Wang, J. M.; Zhu, J. H.; Yang, X. Q. Characterization of soy β-conglycinin-dextran conjugate prepared by Maillard reaction in crowded liquid system. *Food Res. Int.* **2012**, *49*, 648−654.
(30) Iwabuchi, S.; Yamauchi, F. Determination of glycinin and β-conglycinin in soybean proteins by immunological methods. *J. Agric. Food Chem.* **1987**, *35*, 200−205.
(31) Baier, S.; McClements, D. J. Impact of preferential interactions on thermal stability and gelation of bovine serum albumin in aqueous sucrose solutions. *J. Agric. Food Chem.* **2001**, *49*, 2600−2608.
(32) Renkema, J. M.; Gruppen, H.; Van Vliet, T. Influence of pH and ionic strength on heat-induced formation and rheological properties of soy protein gels in relation to denaturation and their protein compositions. *J. Agric. Food Chem.* **2002**, *50*, 6064−6071.
(33) Chen, N.; Lin, L.; Sun, W.; Zhao, M. Stable and pH-sensitive protein nanogels made by self-assembly of heat denatured soy protein. *J. Agric. Food Chem.* **2014**, *62*, 9553−9561.
(34) Yang, H.; Wang, Y.; Lai, S.; An, H.; Li, Y.; Chen, F. Application of atomic force microscopy as a nanotechnology tool in food science. *J. Food Sci.* **2007**, *72*, 65−75.
(35) Gwaze, P.; Annegarn, H. J.; Huth, J.; Helas, G. Comparison of particle sizes determined with impactor, AFM and SEM. *Atmos. Res.* **2007**, *86*, 93−104.
(36) Kaminskyj, S. G.; Dahms, T. E. High spatial resolution surface imaging and analysis of fungal cells using SEM and AFM. *Micron* **2008**, *39*, 349−361.
(37) Zhou, H.; Sun, X.; Zhang, L.; Zhang, P.; Li, J.; Liu, Y. N. Fabrication of biopolymeric complex coacervation core micelles for efficient tea polyphenol delivery via a green process. *Langmuir* **2012**, *28*, 14553−14561.
(38) Harada, A.; Kataoka, K. Novel polyion complex micelles entrapping enzyme molecules in the core: preparation of narrowly-distributed micelles from lysozyme and poly (ethylene glycol)-poly (aspartic acid) block copolymer in aqueous medium. *Macromolecules* **1998**, *31*, 288−294.
(39) Riley, T.; Govender, T.; Stolnik, S.; Xiong, C. D.; Garnett, M. C.; Illum, L.; Davis, S. S. Colloidal stability and drug incorporation aspects of micellar-like PLA-PEG nanoparticles. *Colloids Surf., B* **1999**, *16*, 147−159.
(40) Kelly, S. M.; Jess, T. J.; Price, N. C. How to study proteins by circular dichroism. *Biochim. Biophys. Acta, Proteins Proteomics* **2005**, *1751*, 119−139.
(41) Xu, C.-h.; Yu, S.-j.; Yang, X.-q.; Qi, J.-r.; Lin, H.; Zhao, Z.-g. Emulsifying properties and structural characteristics of β-conglycinin and dextran conjugates synthesised in a pressurised liquid system. *Int. J. Food Sci. Technol.* **2010**, *45*, 995−1001.
(42) Xu, C.-h.; Yang, X.-q.; Yu, S.-j.; Qi, J.-r.; Guo, R.; Sun, W.-W.; Yao, Y.-J.; Zhao, M.-M. The effect of glycosylation with dextran chains of differing lengths on the thermal aggregation of β-conglycinin and glycinin. *Food Res. Int.* **2010**, *43*, 2270−2276.

DOI: 10.1021/acs.jafc.5b01778
J. Agric. Food Chem. 2015, 63, 6075−6083

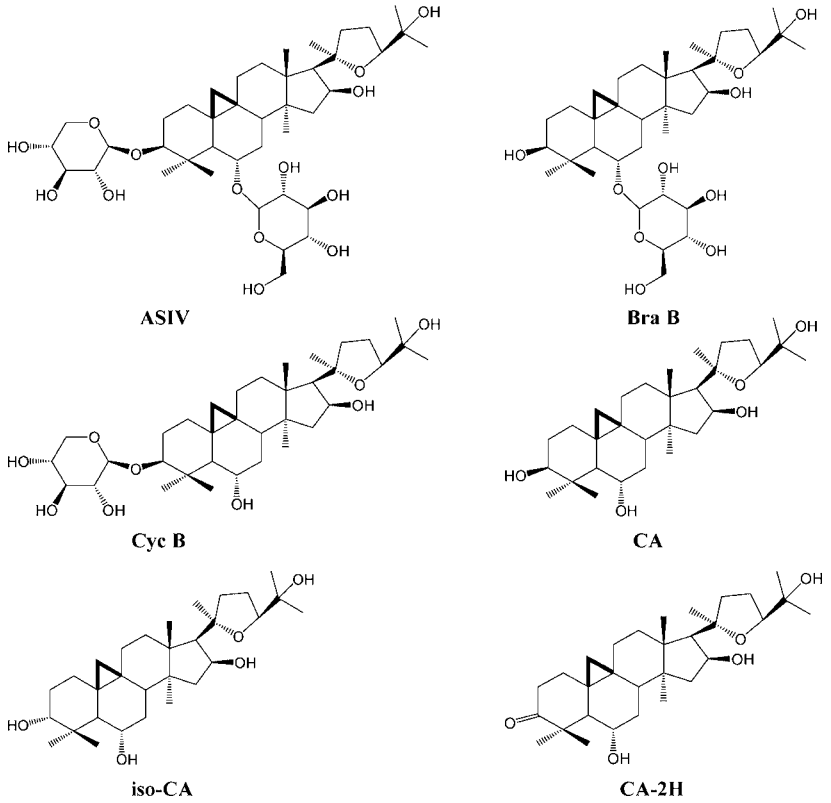

Figure 1. Chemical structures of ASIV and its metabolites. ASIV, astragaloside; Bra B, brachyoside B; Cyc B, cyclogaleginoside B; CA, cycloastragenol; iso-CA, iso-cycloastragenol; CA-2H, dehydrogenated metabolite of CA.

the disposition of ASIV is still missing. In addition, the activity of intestinal microbiota is predicted to change enterohepatic circulation of metabolites secreted from the liver and affect the *in vivo* distribution of xenobiotics. Elucidation of the effect of the intestinal microbiome on the disposition of ASIV will be a great help in understanding its bioactivities and bioavailability. Therefore, the present study aimed to investigate the enterohepatic circulation of ASIV and assess the impact of the activity of the intestinal microbiome on the disposition of ASIV.

MATERIALS AND METHODS

Chemicals. ASIV (purity > 98%) and CA (purity > 98%) were supplied by Shanghai Winherb Medical Technology Co. Ltd. (Shanghai, China). Ketoconazole (the internal standard, IS, purity > 99%) was obtained from the National Institute for the Control of Pharmaceutical and Biological Products (Beijing, China). Solutol HS 15 was provided by BASF Co. (Ludwigshafen, Germany). BBL brain−heart infusion (BHI) and rat liver S9 were purchased from Becton Dickinson Co. (Franklin Lakes, NJ, USA). Hemin bovine and vitamin K1 were supplied by Shanghai Yuanye Biotech Co. (Shanghai, Chaina). L-Cystine was provided by Biosharp Co. (Anhui, China). β-Nicotinamine adenine dinucleotide phosphate (reduced form, NADPH) was purchased from Xinjingke Biotechnology Co. (Beijing, China). HPLC grade acetonitrile was obtained from Fisher Chemicals (Fair Lawn, NJ, USA). Distilled water, prepared from demineralized water, was used throughout the study. All other chemicals and solvents were of analytical grade and used without further purification.

Animals. Male Sprague−Dawley (SD) rats (200 ± 10 g) were obtained from Laboratory Animal Center of Shenyang Pharmaceutical University (Shenyang, China). They were kept in a temperature- and humidity-controlled (temperature, 25 ± 2 °C; humidity, 52.6 ± 5.3%) environment with a reverse 12 h light/dark cycle. After a week of acclimation, the animals were fasted 12 h before experiments. During the period of experiment, animals had free access to food and autoclaved distilled water except those under anesthesia with urethane. All experimental procedures were performed in accordance with the guidelines of the Experimental Animal Care and Use Committee of Shenyang Pharmaceutical University (Shenyang, China). The experimental animal ethic review approval number was SYPU-IACUC-2014-0039.

Pharmacokinetic Study. *Oral Administration.* Six male rats were given a single intragastrical (ig) administration of 10 mg/kg ASIV dissolved in 0.5% sodium carboxymethyl cellulose (CMC-Na). The dosage was selected according to the published literature[12] as well as the clinical dosage of Radix Astragali (20−100 g/day) and the content of ASIV in Radix Astragali (≥0.04%). The rats were slightly anesthetized by diethyl ether before blood collection. Blood samples (200 μL) of rats obtained from the periorbital sinus vein were collected into heparinized tubes before administration (0 h) and at 0.5, 1.0, 2.0, 3.0, 4.0, 5.0, 6.0, 8.0, 10, and 12 h after administration. Plasma was separated by centrifugation at 4000*g* for 5 min and stored at −70 °C until analysis.

Intravenous Administration. Six male rats were treated with a dose of 1.5 mg/kg ASIV from the caudal vein on the basis of reported documents.[11,17,29] The injection solution is prepared in 10% (w/v) Solutol HS 15 in saline. After the rats were slightly anesthetized by diethyl ether, blood samples (200 μL) were collected from the periorbital sinus vein into heparinized tubes before administration (0 h) and at 0.083, 0.167, 0.33, 0.5, 1.0, 2.0, 4.0, 6.0, 8.0, 10, and 12 h after dosing. Plasma was separated by centrifugation at 4000*g* for 5 min and stored at −70 °C until analysis.

Enterohepatic Circulation Experiments in Bile Duct Cannulation Rat Model. *Oral Administration Experimental Design.* Twelve male rats were randomly divided into two groups. One group of rats (n = 6) received bile duct cannulation surgery before being given a dosage of 10 mg/kg ASIV from the duodenum. In brief, the animals were anesthetized by an intraperitoneal (ip) injection of urethane (1 g/kg). A 1 cm cut was made to expose the jugular vein for each rat. Then the vein was cut, and a cannula made of polyethylene-

DOI: 10.1021/acs.jafc.5b00168
J. Agric. Food Chem. 2015, 63, 6084−6093

20 tubing was inserted. After the cannula and the vein were tied with sterilized suture, a 4 cm cut was made to open the abdominal cavity of the rat. The bile duct was separated from the surrounding tissue, and a polyethylene-10 tubing was inserted into the duct. When bile flow out of the cannulation was seen without restriction, the cannula was secured with sutures. After that, ASIV solution (1 mg/mL in 0.5% CMC-Na) in a syringe was slowly injected into the duodenum through an intravenous infusion needle at about 6 cm below pylorus. The injection rate was controlled at 0.1 mL/min by a syringe pump. Another six control rats were treated with the same procedure except bile duct drainage.

With the tolerance of rats to surgery and the pharmacokinetic profiles of ASIV and its metabolites after an ig administration of ASIV taken into consideration, blood samples (200 μL) of bile duct-cannulated rats and control rats were collected from the jugular vein at only four time points: before administration (0 h) and at 2.0, 8.0, and 10 h after administration. Plasma was separated by centrifugation at 4000*g* for 5 min. Bile samples were collected into 1.5 mL centrifuge tubes in 30 min before administration and every 30 min after administration until 10 h. Plasma and bile samples were stored at −70 °C until analysis.

Intravenous Administration Experimental Design. Six male rats having bile duct and jugular vein cannulation surgery (by the same method as described above) were given an injection of ASIV at a dose of 1.5 mg/kg from the caudal vein. Another six rats having only jugular vein cannulation surgery were labeled as controls. The control rats also received an iv injection of 1.5 mg/kg ASIV from the caudal vein after surgery. Blood samples (200 μL) of rats in both groups were obtained from the jugular vein and collected into heparinized tubes before administration (0 h) and at 2.0, 8.0, and 10 h after administration. Plasma was separated by centrifugation at 4000*g* for 5 min. Bile samples were collected into 1.5 mL centrifuge tubes in 30 min before administration and every 30 min after administration until 10 h. Plasma and bile samples were stored at −70 °C until analysis.

Rat Intestinal S9 Fraction Preparation. Rat intestinal S9 fraction was prepared from male SD rats according to a published procedure with a slight modification.[30] In brief, rats were anesthetized with urethane (1 g/kg), and then rat whole intestines were cut out and flushed with ice-cold saline containing 1 mM dithiothreitol. After the intestines were pooled from six rats, they were washed twice with the ice-cold washing solution (consisting of 8 mM KH_2PO_4, 5.6 mM Na_2HPO_4, 1.5 mM KCl, 96 mM NaCl, 27 mM sodium citrate, and 0.04 mg/mL phenylmethanesulfonyl fluoride (PMSF)). After they had been dried with paper, the intestinal strips were cut open, and mucosal cells were scraped off in a 4 °C cold room. The mucosal cells were centrifuged at 900*g* for 5 min at 4 °C and washed twice in 50 mL of the homogenization buffer (consisting of 10 mM, pH 7.4, KH_2PO_4, 250 mM sucrose, 1 mM EDTA, and 0.04 mg/mL PMSF). The cells were resuspended in 15 mL of the homogenization buffer. After 15 min of centrifugation at 9000*g* and 4 °C, the supernatant was collected, aliquoted, and stored at −70 °C until use. Protein concentration was determined by using the Coomassie brilliant blue colorimetric method.

In Vitro Metabolism of ASIV and CA by Rat Liver and Intestinal S9 Fraction. ASIV (1 μM) or CA (1 μM) was mixed with liver or intestinal S9 fraction (the final protein concentrations were 1 mg/mL), potassium chloride (10 mM), magnesium chloride (10 mM), and 1.0 mM NADPH in 50 mM potassium phosphate buffer (pH 7.4). The total volume was 200 μL. The reaction was initiated by the addition of a solution of NADPH after 5 min of pre-incubation. After incubation at 37 °C for 0 and 1 h, the reaction was terminated by the addition 200 μL of cold methanol (0 °C). The mixture was centrifuged at 4000*g* for 5 min, and the supernatant was stored at −20 °C until analysis. Controls were prepared in the same manner, except for the presence of NADPH. Blank samples were assayed without substrate to exclude analytical interference by the matrix.

In Vitro Metabolism of ASIV and CA by Rat Intestinal Microbiota. Five healthy male rats were housed in individual steel metabolism cages. Fresh feces were collected and immediately stored at −70 °C until use. Pooled feces (2.5 g from five rats, 0.5 g/rat) were mixed with 20 mL of culture medium of BHI containing 37 μg/mL BHI, 5 μg/mL hemin bovine, 0.5 mg/mL L-cystine, and 0.02% vitamin K1.[31] The fecal suspension was centrifuged at 300*g* for 5 min. The resultant supernatant was transferred into another clean tube and centrifuged at 4000*g* for 10 min; then the residue was resuspended in 15 mL of culture medium of BHI to produce intestinal bacteria solution. ASIV (20 μM) or CA (1 μM) was mixed with 20 μL of intestinal bacteria solution and 180 μL of culture medium of BHI. The total volume was 200 μL. The mixture was incubated at 37 °C under anaerobic conditions for 0, 2, 4, 8, 12, 24, 36, and 48 h. The reaction was stopped by the addition of 200 μL of cold methanol (0 °C). The mixture was centrifuged at 4000*g* for 5 min, and the supernatant was stored at −20 °C until analysis. Control and blank samples were prepared in the same manner without bacteria solution and substrate, respectively.

Effect of Activity of Intestine Microbiota on the Disposition of ASIV. *Comparison of Metabolism of ASIV by Intestinal Microbiota from Rats Pretreated with and without Antibiotics.* Five male rats were given a mixture solution of streptomycin sulfate and bacitracin (1:1, w/w; 200 mg/kg) dissolved in sterilized water through gavage twice daily for 6 days to inhibit the activity of intestinal microbiome. Another five rats without the treatment of antibiotics were used as controls. Fresh fecal samples from five control rats and those from five antibiotic-pretreated rats were collected individually and pooled separately. Then intestinal bacteria solutions from the two different fecal samples were prepared and incubated with 20 μM ASIV by the corresponding methods as described above. After incubation at 37 °C for 0, 4, 8, 12, and 24 h, the reaction was stopped by the addition of 200 μL of cold methanol (0 °C). The mixture was centrifuged at 4000*g* for 5 min, and the supernatant was stored at −20 °C until analysis. Control and blank samples were prepared in the same manner without bacteria solution and substrate, respectively.

Antibiotics used to inhibit the activity of gut microbiota may interact with the analyte, which might interfere with the study result. Therefore, we determined the potential interference of antibiotics to the biotransformation ASIV in intestinal microbiota. ASIV (20 μM) in the presence of streptomycin sulfate and bacitracin (1:1, w/w; 0.08, 0.4, or 2 mg/mL) was mixed with 20 μL of intestinal bacteria solution and 180 μL of culture medium of BHI. After incubation at 37 °C for 0 and 4 h, the reaction was stopped by the addition of 200 μL of cold methanol (0 °C). The mixture was centrifuged at 4000*g* for 5 min, and the supernatant was stored at −20 °C until analysis. Control and blank samples were prepared in the same manner without bacteria solution and substrate, respectively.

Comparison of Pharmacokinetics of ASIV in Rats Pretreated with and without Antibiotics. Six male rats were treated with antibiotics according to the same method as mentioned above. After an overnight fast, antibiotic-pretreated rats received an ig dose of 10 mg/kg ASIV dissolved in 0.5% CMC-Na. The rats were under light diethyl ether anesthesia before blood collection. Blood samples (200 μL) were collected from the periorbital sinus vein into heparinized tubes before administration (0 h) and at 0.5, 1.0, 2.0, 3.0, 4.0, 5.0, 6.0, 8.0, 10, and 12 h after administration. Plasma was separated by centrifugation at 4000*g* for 5 min and stored at −70 °C until analysis. The rats given an ig dose of ASIV in pharmacokinetic study were used as controls.

Sample Preparation. For plasma and bile samples, a 10 μL aliquot of the IS solution (4.0 μM ketoconazole in methanol) and a 100 μL aliquot of methanol were added into a 50 μL aliquot of sample. The mixture was vortex-mixed for 1 min. After being centrifuged at 15000*g* for 5 min, a 5 μL aliquot of the supernatant of each sample was injected for LC-MS/MS analysis.

For the samples in in vitro metabolism studies, a 10 μL aliquot of the IS solution (4.0 μM ketoconazole in methanol) and a 50 μL aliquot of methanol were added into 100 μL of sample. Then the mixture was prepared according to the same method as that for plasma and bile samples.

LC-MS/MS Analysis. The chromatographic separation was performed on a Venusil ASB C18 column (150 × 4.6 mm, 5 μm, Agela, Tianjin, China). Methanol (A) and 5 mM ammonium acetic acid (B) were used as mobile phase for elution. The gradient was controlled as follows: 0−1.0 min, 60% A; 1.0−2.0 min, 60−90% A;

DOI: 10.1021/acs.jafc.5b00168
J. Agric. Food Chem. 2015, 63, 6084−6093

2.0−5.5 min, 90% A; 5.5−6.0 min, 90−60% A; 6.0−8.0 min, 60% A. The retention times of ASIV, Bra B, Cyc B, CA, iso-CA, CA-2H, and IS were around 4.5, 4.8, 4.7, 5.1, 6.0, 5.3, and 4.2 min, respectively.

An API 4000 triple-quadrupole tandem mass spectrometer (Applied Biosystem/MDS SCIEX, Foster City, CA, USA) with Turboionspray source (TIS) was operated in positive ion mode. Quantification was performed using the multiple reactions monitoring (MRM) method. The MRM transitions and compound-dependent parameters for ASIV and its metabolites are listed in Table 1. The main working parameters

Table 1. MRM Transitions and Compound-Dependent Parameters for ASIV and Its Metabolites

compound	MRM transition	DP	EP	CE	CXP
ASIV	m/z 785 → 143	44	10	16	10
CA and iso-CA	m/z 491 → 143	33	10	16	15
CA-2H[a]	m/z 489 → 143	33	10	16	15
Bra B[a]	m/z 653 → 143	44	10	16	10
Cyc B[a]	m/z 623 → 143	44	10	16	10
ketoconazole (IS)	m/z 531 → 489	120	10	55	15

[a]Without the standards of CA-2H, Bra B, and Cyc B, the compound-dependent parameters of CA were adopted for the determination of CA-2H and those of ASIV were used for the quantification of Bra B and Cyc B because of similarity in chemical structure.

were set as follows: ionspray voltage, 4.5 kV; ion source temperature, 350 °C; gas 1, 40 psi; gas 2, 45 psi; curtain gas, 15 psi. Analyte concentrations were determined using the software Analyst 1.5.

The assay of ASIV and CA was validated according to the guidance for bioanalytical method validation.[32] The calibration curves were constructed in concentration ranges of 2.55−510 nM for ASIV and 1.02−204 nM for CA with good linearity showing correlation coefficients (r) better than 0.993. Without the standard of iso-CA, the amount of iso-CA was calculated from the standard curves of CA. The same method was applied by Zhou et al. to investigate the pharmacokinetics of iso-CA in rats after an oral dose of 40 mg/kg ASIV.[13] The intra- and interday precisions were lower than 13.6% for ASIV and CA, and the accuracy was within ±12.1% deviation from the nominal values of the analytes. Due to the lack of standards of Bra B and Cyc B, their concentrations were expressed as peak area ratios of analyte/IS in the study.

Data Analysis. The pharmacokinetic parameters of ASIV, CA, and iso-CA were estimated by noncompartmental method using the DAS 3.2.0 pharmacokinetic program (Chinese Pharmacology Society) because the noncompartmental model is a robust population model and it provides additional information on the random variation component existing between animals. The maximum plasma concentrations (C_{max}) and the corresponding peak time (t_{max}) were observed from the individual drug plasma concentration−time profile. The terminal elimination rate constant (k_e) was estimated by log−linear regression of concentrations observed during the terminal phase of elimination. The elimination half-life ($t_{1/2}$) was calculated as 0.693/k_e. The area under the plasma concentration−time curve was calculated by the linear trapezoidal rule.

Data are reported as the mean ± SD. Independent Student t tests and one-way ANOVA with Tukey−Kramer multiple-comparison (post hoc) tests (Minitab, version 14) were used to evaluate statistical differences. Differences were considered statistically significant when p values were <0.05.

RESULTS AND DISCUSSION

Pharmacokinetic Study. *Oral Administration.* The mean plasma concentration−time curves of ASIV, CA, and iso-CA in rats after an ig dose of 10 mg/kg ASIV are shown in Figure 2A. The main pharmacokinetic parameters of ASIV, CA, and iso-CA are presented in Table 2. ASIV reached the maximum level (C_{max}) of 34.5 ± 20.6 nM at 2.0 h, whereas its metabolites, CA

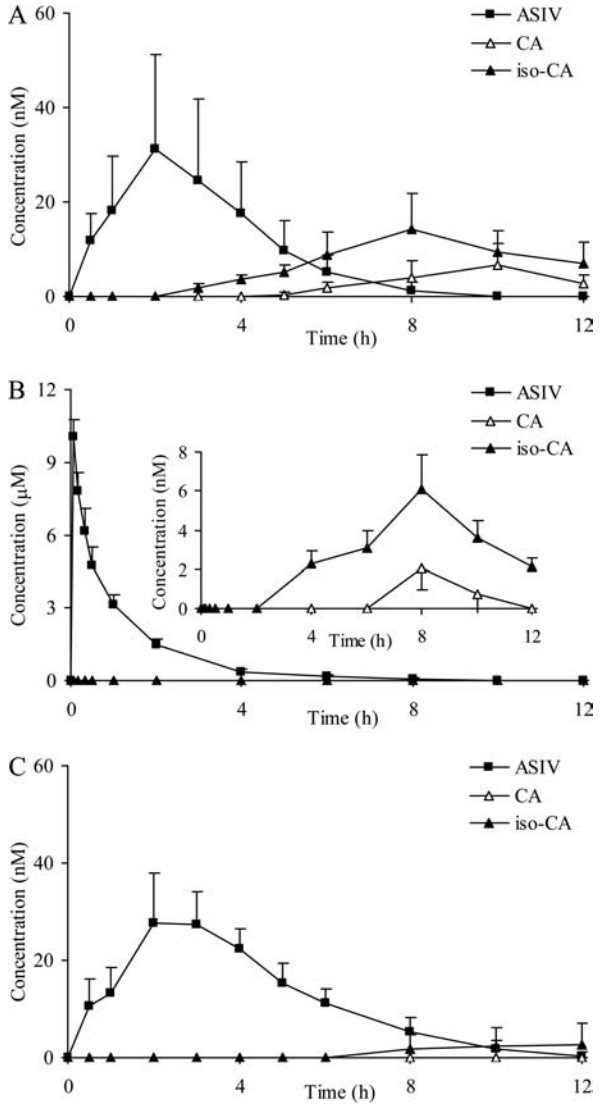

Figure 2. Mean plasma concentration−time curves of ASIV, CA,and iso-CA in control rats after an intragastrical (ig) administration of 10 mg/kg ASIV (A) or an intravenous (iv) administration of 1.5 mg/kg ASIV (B) and in antibiotic-pretreated rats after an ig administration of 10 mg/kg ASIV (C). Each point represents the mean ± SD (n = 6).

and iso-CA, achieved their maximum concentrations comparatively late at approximately 8 h. As reported by Zhou et al.,[13] ASIV predominated in the forms circulated in blood after ingestion. The contributions of ASIV, CA, and iso-CA to the total exposure (the sum of AUC values of ASIV, CA, and iso-CA) were 51.0, 12.5, and 36.5%, respectively (Table 2). No other metabolites of ASIV were observed in rat plasma.

Multiple peaks often appear in plasma concentration−time curves of xenobiotics with enterohepatic circulation. However, there was not a secondary peak in the concentration−time curve of ASIV. This phenomenon probably resulted from the slow and approximately uniform absorption of ASIV from the small intestine, because ASIV showed similar low absorption rates in rat duodenum, jejunum, and ileum.[32]

Intravenous Administration. Pharmacokinetics of ASIV and its metabolites in rats were studied after an iv injection of 1.5 mg/kg ASIV. The mean plasma concentration−time curves of ASIV, CA, and iso-CA are shown in Figure 2B. The corresponding pharmacokinetic parameters are summarized in

DOI: 10.1021/acs.jafc.5b00168
J. Agric. Food Chem. 2015, 63, 6084−6093

Table 2. Pharmacokinetic Parameters of ASIV, CA, and Iso-CA in Control Rats after an Intragastrical (ig) Administration of 10 mg/kg ASIV or an Intravenous (iv) Administration of 1.5 mg/kg ASIV and in Antibiotic-Pretreated Rats after an ig Administration of 10 mg/kg ASIV

			parameters			
rats	administration route	analyte	$t_{1/2}$ (h)	C_{max} (nM)	T_{max} (h)	AUC_{0-t} (nM·h)
control	ig (n = 6)	ASIV	1.71 ± 1.16	34.5 ± 20.6	2.00 ± 0.63	109 ± 55
		CA[a]		7.09 ± 4.76	9.67 ± 0.82	26.8 ± 17.9
		iso-CA	4.77 ± 3.26	14.3 ± 7.5	8.00 ± 0.00	77.9 ± 35.1
	iv (n = 6)	ASIV[b]	1.29 ± 0.41	10020 ± 727		10086 ± 1323
		CA[a]		2.46 ± 0.44	8.33 ± 0.82	5.56 ± 1.60
		iso-CA	3.05 ± 1.06	6.07 ± 1.76	8.00 ± 0.00	32.2 ± 5.3
antibiotic-pretreated	ig (n = 6)	ASIV	1.99 ± 0.33	32.4 ± 7.8	2.83 ± 0.98	135 ± 30
		CA[c]				
		iso-CA[a]		4.41 ± 4.01[d]	11.0 ± 1.2	16.4 ± 15.0[d]

[a]The valid time points were not enough for the calculation of $t_{1/2}$. [b]The C_{max} data were obtained from the plasma samples collected at 0.083 h after injection. [c]The concentration of CA in antibiotic-pretreated rats after an ig dose of ASIV was too low to be detected. [d]The data obtained in antibiotic-pretreated rats were significantly different from those obtained in control rats after ig administration of ASIV according to Student's t test ($p < 0.05$).

Table 2. When rats received an iv injection of ASIV, ASIV traveled in rat systemic circulation mainly as itself. Very tiny amounts of CA and iso-CA were detected in rat plasma from 4 h after administration. The contributions of ASIV, CA, and iso-CA to the total exposure were 99.7, 0.05, and 0.3%, respectively (Table 2). Compared with the corresponding data obtained after ig administration, the contribution of CA and iso-CA to the total exposure decreased >100 times after iv injection (0.05 vs 12.5% for CA and 0.3 vs 36.5% for iso-CA), suggesting that the intestinal tract might contribute more than the liver to the biotransformation of ASIV.

Enterohepatic Circulation Experiment in Bile-Duct Cannulation Rat Model. *Oral Administration Experiment.* To investigate the effect of enterohepatic circulation on the disposition of ASIV, we compared the plasma distribution of ASIV and its metabolites between rats with and without bile-duct cannulation (control) at 2, 8, and 10 h after administration of ASIV from the duodenum. Time points of 2, 8, and 10 h were the t_{max} values of ASIV, iso-CA, and CA, respectively, as shown in the pharmacokinetic study of ASIV after oral administration (Figure 2A and Table 2).

The plasma concentrations of ASIV, CA, and iso-CA in control rats at 2 h were 29.5 ± 10.1 nM, undetectable, and undetectable, respectively; at 8 h they were 2.68 ± 2.26 nM, undetectable, and 2.64 ± 0.89 nM, respectively; and at 10 h they were undetectable, 5.05 ± 2.53 nM, and 9.37 ± 4.23 nM, respectively. After rats received bile-duct drainage surgery, the plasma amount of ASIV at 2 h (8.51 ± 3.91 nM) was significantly lower than that in control rats at the same point (Figure 3). Moreover, the amounts of CA and iso-CA in bile-duct cannulated rats became immeasurable at 8 and 10 h (Figure 3). These data declared that enterohepatic circulation played an important role in the disposition of ASIV after oral administration.

Biliary excretion of ASIV and its metabolites was assayed to partly profile the enterohepatic circulation process of ASIV. Figure 4 shows the bile excretion of ASIV, Bra B, and Cyc B in rats after duodenal administration of ASIV. Due to the lack of standards of Bra B and Cyc B, their excretion concentrations were expressed as peak area ratio of analyte/IS (Figure 4B). The biliary excretion of ASIV reached a plateau at 3 h after dosing (Figure 4A). The accumulative bile excretion of ASIV in

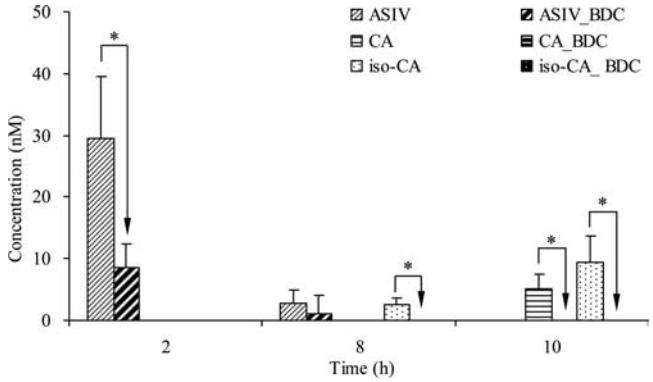

Figure 3. Comparison of plasma concentrations of ASIV, CA, and iso-CA between rats treated with and without bile-duct cannulation after administration of 10 mg/kg ASIV from the duodenum. The concentrations of ASIV, CA, and iso-CA in control rats are labeled "ASIV", "CA", and "iso-CA", respectively; those in cannulated rats are labeled "ASIV_BDC", "CA_BDC", and "iso-CA_BDC", respectively. Each point represents the mean ± SD (n = 6). The asterisk (*) indicates the differences of plasma concentration between control and cannulated rats are significant according to Student's t test ($p < 0.05$).

10 h, calculated as [(amount of ASIV in bile/dose) × 100], was 0.015%.

Although obvious amounts of ASIV, Bra B, and Cyc B were excreted from bile after rats received ASIV from the duodenum, the biliary excretion amounts of CA, iso-CA, and CA-2H were not detectable. Zhou et al. found that when 5 μM ASIV was incubated with rat intestinal bacteria, Bra B and Cyc B were formed after 0.5 and 8 h of incubation, respectively, whereas CA, iso-CA, and CA-2H were not found in the first 8 h.[13] This result suggested that the formation rates of Bra B and Cyc B from ASIV by intestinal microbiota were faster than those of CA, iso-CA, and CA-2H. The undetectable biliary excretion of CA, iso-CA, and CA-2H probably resulted from the slow hydrolysis of ASIV, Bra B, and Cyc B in the intestine and/or liver.

Intravenous Administration Experiment. In the present study, we also compared the plasma distribution of ASIV and its metabolites between bile-duct cannulated rats and control rats after iv injection. Neither CA nor iso-CA was found in

DOI: 10.1021/acs.jafc.5b00168
J. Agric. Food Chem. 2015, 63, 6084−6093

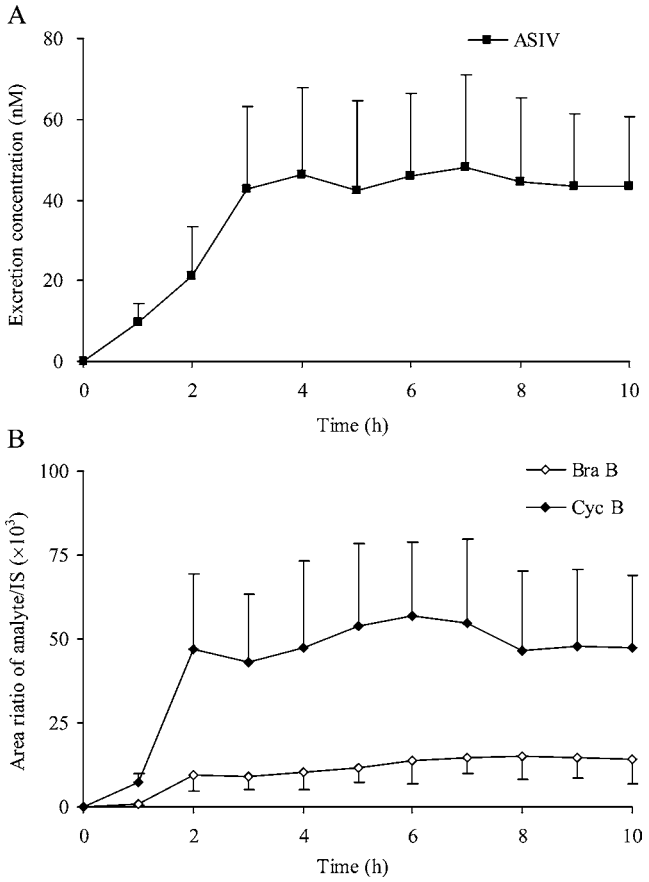

Figure 4. Bile excretion profiles of ASIV (A) and its metabolites (B) in rats following a dose of 10 mg/kg ASIV through the duodenum. In panel B, the excretion amounts of Bra B and Cyc B are expressed as peak area ratio of analyte/IS without the standards of Bra B and Cyc B. Each point represents the mean ± SD (n = 6).

control and bile-duct cannulated rats at 2, 8, and 10 h after iv injection. The plasma concentrations of ASIV in control rats at 2, 8, and 10 h were 1292 ± 198, 133 ± 26, and 36.5 ± 10.9 nM, respectively. The amount of ASIV in the bile-duct cannulation group of rats was kept at a level similar to that in the control group at the same time point, which was 1263 ± 230 nM at 2 h, 136 ± 19 nM at 8 h, and 37.2 ± 9.8 nM at 10 h.

Bile sample assay revealed that no metabolites (including Bra B, Cyc B, CA, iso-CA, and CA-2H) except ASIV were excreted from bile after iv injection of ASIV. The accumulative bile excretion of ASIV in 10 h after iv adminstration was 27.4%. Although more than one-fourth of the dosage was excreted from bile in 10 h, the plasma level of ASIV after iv injection was not affected by bile-duct drainage surgery. These data were further proof for the limited adsorption of ASIV in the intestine. In addition, the low cumulative bile excretion of ASIV after duodenal administration (0.015%) was also believed to come from the poor intestinal absorption of ASIV. Bra B and Cyc B, two deglycosylated metabolites of ASIV, were secreted from bile when rats received ASIV through the duodenum (Figure 3); however, they were not found in bile when rats were given ASIV intravenously. This result indicated that intestinal hydrolysis of ASIV was critical for the formation of Bra B and Cyc B.

After summarizing the results of enterohepatic circulation experiments, we proposed that ASIV was first slowly hydrolyzed to Bra B and Cyc B by gut microbiota; these compounds then distributed in the liver via portal vein and were quickly excreted with bile. CA was formed from the repeated hydrolysis of ASIV, Bra B, and Cyc B by gut microbiota via enterohepatic circulation, and iso-CA was generated from CA by gut microbiota and/or hepatic enzymes (Figure 5). To test and supplement our hypotheses, we investigated the metabolism of ASIV and CA by rat liver S9 fraction, intestinal S9 fraction, and intestinal microbiota.

In Vitro Metabolism of ASIV and CA by Rat Liver and Intestinal S9 Fraction. In vitro hepatic and intestinal enzyme metabolism of ASIV and CA was studied using rat liver and intestinal S9 fraction in the presence of NADPH. ASIV was comparatively stable to rat liver and intestinal S9 fraction. After ASIV (1 μM) was incubated with rat liver or intestinal S9 fraction at 37 °C for 1 h, none of the metabolites, such as Bra B, Cyc B, CA, iso-CA, and CA-2H, was observed in the incubation samples, which agreed with the reported data obtained from rat liver microsome.[13]

Iso-CA was one of the major components circulating in rat blood after oral administration of ASIV. It was generated from CA via CA-2H.[13] Therefore, we investigated the metabolism of CA in rat liver and intestinal S9 fraction to illuminate the role of liver and intestine in the formation of iso-CA. It was reported that CA was extensively metabolized by rat liver microsome and produced several monohydroxylated metabolites as well as a few hydroxylated and dehydrogenated metabolites.[24] In our study, CA underwent moderate metabolism in rat liver S9 fraction but was hardly biotransformed by intestinal S9 fraction. When CA was incubated with rat liver S9 fraction at 37 °C for 1 h, approximately 25% of CA was metabolized, of which 6% was converted to iso-CA. CA-2H as well as two hydroxylated metabolites of CA and two hydroxylated and dehydrogenated

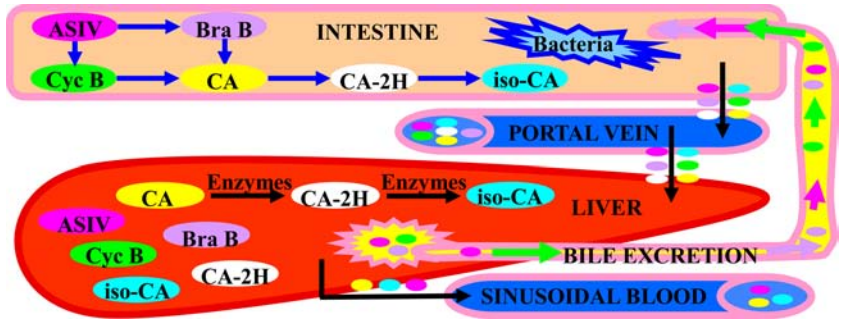

Figure 5. Schematic representation of disposition pathways of ASIV in enterohepatic circulation. Pink, purple, green, yellow, blue, and white particles stand for ASIV, Bra B, Cyc B, CA, iso-CA, and CA-2H, respectively.

DOI: 10.1021/acs.jafc.5b00168
J. Agric. Food Chem. 2015, 63, 6084−6093

metabolites of CA was also observed in rat liver S9 fraction (data not shown).

In Vitro Metabolism of ASIV and CA by Rat Intestinal Bacteria. The metabolic profile of ASIV against incubation time in rat intestinal bacteria is plotted in Figure 6. To

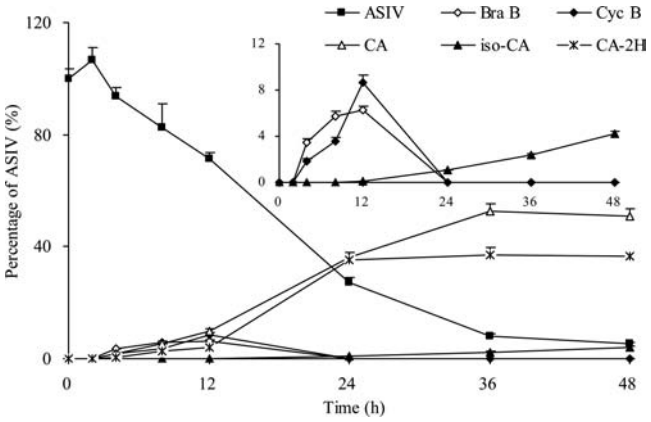

Figure 6. Remaining amount of ASIV and the formation amounts of Bra B, Cyc B, CA, iso-CA, and CA-2H after incubation of 20 μM ASIV with rat intestinal bacteria at 37 °C. The amounts of ASIV, Bra B, Cyc B, CA, iso-CA, and CA-2H were calculated as percentages of the initial amount of ASIV before incubation. Each point represents the mean ± SD (n = 3).

intuitively compare the metabolism rate of substrate and the generation rates of metabolites, the remaining amount of ASIV and the formation amounts of Bra B, Cyc B, CA, iso-CA, and CA-2H in incubation solution were expressed as percentages of the initial amount of ASIV before incubation. Despite the lack of standards of Bra B, Cyc B and CA-2H, we calculated their amounts by the following method based on the observation that there were no other metabolites of ASIV after incubation except Bra B, Cyc B, CA, iso-CA, and CA-2H, and hence the metabolized amount of ASIV equaled the total generation amount of the five metabolites. After 24 h of incubation, only ASIV, CA, iso-CA, and CA-2H were detected in incubation solution. The amounts of ASIV, CA, and iso-CA were determined from the calibration curves of ASIV and CA, respectively. The formation amount of CA-2H at this time point (24 h) was calculated by (100% − remaining amount of ASIV% − formation amount of CA% − formation amount of iso-CA%), which was 36.3%. Then the formation amounts of CA-2H at other time points were calculated by comparing their peak area ratio to the peak area ratio at 24 h. By a similar method, we figured out the generation amounts of Bra B and Cyc B at each time point. The generation curves of Bra B, Cyc B, and CA-2H plotted by this way were not very accurate because of measurement and calculation errors, but this method was convenient to illuminate the metabolic behavior of ASIV in gut bacteria.

ASIV was slowly metabolized by the intestinal microbiome. After 4 h of incubation, ASIV began to be converted to Bra B, Cyc B, CA, and CA-2H by intestinal bacteria. The formation rates of Bra B, Cyc B, CA, and CA-2H after 4 h of incubation were 3.47 ± 0.29, 1.87 ± 0.19, 1.69 ± 0.15, and 0.59 ± 0.06%, respectively, suggesting that ASIV was metabolized to Bra B by intestinal bacteria more quickly than to other metabolites. This result was coincident with the observation of Zhou et al.[13] The remaining amount of ASIV in incubation solution linearly declined along with time from 4 to 24 h. After 24 h of incubation, about 72% of ASIV was metabolized by gut bacteria, among which 36% was converted to CA, 35% to CA-2H, and 1% to iso-CA%. Given that iso-CA was generated from CA via CA-2H, formation time courses of the metabolites of ASIV indicated that the conversion from CA-2H to iso-CA seemed to be the rate-limiting step for the generation of iso-CA in the intestine.

When 1 μM CA reacted with intestinal bacteria, its metabolism rate was much slower than that of ASIV (Figure 7). No other metabolites except CA-2H and iso-CA were found

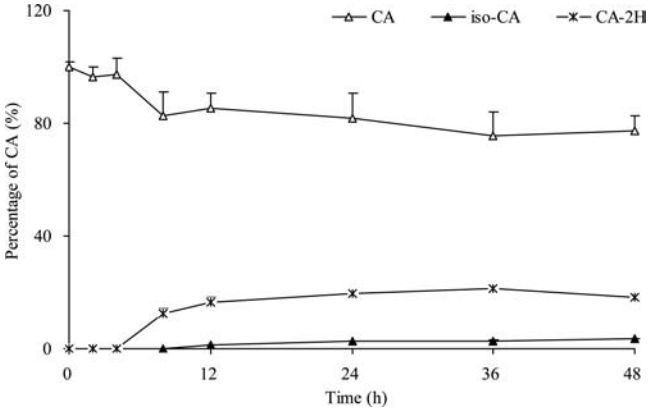

Figure 7. Remaining amount of CA and the formation amounts of iso-CA and CA-2H after incubation of 1 μM CA with rat intestinal bacteria at 37 °C. The amounts of CA, iso-CA, and CA-2H were calculated as percentages of the initial amount of CA before incubation. Each point represents the mean ± SD (n = 3).

in the intestinal bacteria incubation samples of CA. The total biotransformation amount of CA was <30% after 48 h of incubation, of which around 3.5% was converted to iso-CA (Figure 7). The amount of CA-2H generated was obtained by (100% − remaining amount of CA% − formation amount of iso-CA%). Although the production amount of CA-2H was >15% after 12 h of incubation, the formation amount of iso-CA was <1.5%, which further confirmed that the formation rate of iso-CA in the intestine depends on the conversion rate of CA-2H.

Taken together, in vitro metabolism of ASIV in S9 fraction and in gut microbiota showed that ASIV was not metabolized by the liver and intestinal S9 fraction but was slowly hydrolyzed by gut bacteria. This result demonstrated that deglycosylation of ASIV in the intestinal tract was a crucial step for the formation of CA. Although the intestine is likely to be the more important organ responsible for the disposition of ASIV, in vitro metabolism data of CA suggested that the liver might have a bigger role in the generation of iso-CA because the formation rate of iso-CA from CA was faster in the liver S9 fraction (6% in 1 h) than that in the intestinal microbiome (3.5% in 48 h).

Effect of Activity of Intestine Microbiota on the Disposition of ASIV. *Comparation of Metabolism of ASIV by Intestinal Microbiota from Rats Pretreated with and without Antibiotics.* Hydrolysis of ASIV by gut microbiota is a key factor in the disposition of ASIV after oral administration. To investigate the influence of the activity of the intestinal microbiota on the deglycosylation of ASIV, in vitro gut microbial conversion of ASIV was compared between the intestinal microbiota obtained from antibiotic-pretreated rats and that from control rats by the method as described under

DOI: 10.1021/acs.jafc.5b00168
J. Agric. Food Chem. 2015, 63, 6084−6093

Materials and Methods. Antibiotic-pretreated models represent one relatively simple strategy to study the role of intestinal bacteria in xenobiotic metabolism, although antibiotics cannot eliminate all microorganisms from the intestine. Streptomycin sulfate and bacitracin are the common antibiotics applied to attenuate the activity of intestinal bacteria.[33,34]

The metabolic behaviors of ASIV in control gut bacteria and antibiotic-pretreated intestinal bacteria are shown in Figure 8.

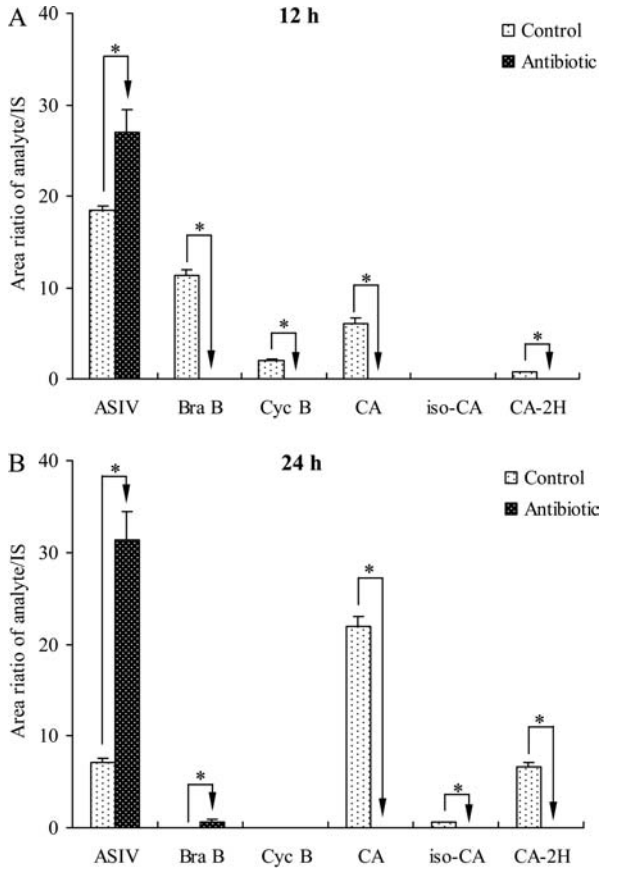

Figure 8. Remaining amount of ASIV and the formation amounts of Bra B, Cyc B, CA, iso-CA, and CA-2H after incubation of 20 μM ASIV with rat intestinal bacteria obtained from control rats (control) and from antibiotic-pretreated rats (antibiotic) at 37 °C for 12 h (A) and 24 h (B). The amounts of ASIV, Bra B, Cyc B, CA, iso-CA, and CA-2H were expressed as peak area ratio of analyte/IS. Each point represents the mean ± SD (n = 3). The asterisk (∗) indicates the differences are significant according to Student's t test ($p < 0.05$).

To intuitively contrast the difference in the metabolism of ASIV between control and antibiotic-pretreated gut microbiota, the amounts of ASIV, Bra B, Cyc B, CA, iso-CA, and CA-2H were expressed as peak area ratio of analyte/IS. When ASIV (20 μM) was incubated with control gut bacteria at 37 °C for 12 h, around 30% of ASIV was metabolized (Figure 6). Antibiotics obviously inhibited the metabolism of ASIV by intestinal microbiome. No metabolites of ASIV were observed in antibiotic-pretreated gut microbiota samples over the same time period (12 h, Figure 8A). After 24 h of incubation, >70% of ASIV was converted in control intestinal microbiota (Figure 6), whereas only a trace of Bra B was produced from ASIV by antibiotic-pretreated gut bacteria (Figure 8B).

To assess the potential interference of antibiotics to the hydrolysis of ASIV by intestinal microbiota, ASIV was simultaneously incubated with low, middle, and high concentrations of streptomycin sulfate and bacitracin (1:1, w/w) in control gut bacteria at 37 °C for 4 h. The generated amounts of Bra B, Cyc B, and CA were concentration-independently decreased by antibiotics (Figure 9). It seemed

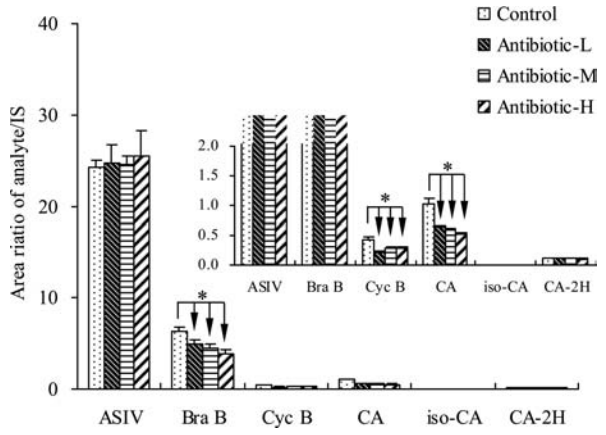

Figure 9. Remaining amount of ASIV and the formation amounts of Bra B, Cyc B, CA, iso-CA, and CA-2H after 20 μM ASIV was incubated with and without antibiotics in control rat intestinal bacteria at 37 °C for 4 h. The final concentrations of antibiotics (streptomycin sulfate/bacitracin = 1:1, w/w) in incubation solution were 0 (control), 0.08 (antibiotic-L), 0.4 (antibiotic-M), or 2 mg/mL (antibiotic-H), respectively. The amounts of ASIV, Bra B, Cyc B, CA, iso-CA, and CA-2H are expressed as peak area ratio of analyte/IS. Each point represents the mean ± SD (n = 3). The asterisk (∗) indicates the differences are significant according to one-way ANOVA test ($p < 0.05$).

that antibiotics interfered with the hydrolysis of ASIV. However, with further investigation, we believed that the decreased generation by antibiotics mainly resulted from the bacteriostasis action of antibiotics rather than its interference with the biotransformation of ASIV, because the microbial culture experiment showed that the colony amount of gut bacteria in the presence of antibiotics was obviously less than that in the absence of antibiotics after 4 h of incubation (data not shown). As shown in Figure 9, the formation rate of CA-2H was not affected by antibiotics. It is well-known that there are a lot of species of microorganisms existing in mammal intestines. The unchanged formation rate of CA-2H was probably caused by the fact that the microbiotas responsible for the biotransformation from CA to CA-2H were not suppressed by streptomycin sulfate and bacitracin.

Comparative Disposition of ASIV in Rats Pretreated with and without Antibiotics. An in vivo experiment is the ultimate model to study the effect of intestinal microbiota on xenobiotic disposition. In the present study, we compared the pharmacokinetics of ASIV and its metabolites in rats treated with and without antibiotics. After rats received antibiotics for 6 days, they were given 10 mg/kg ASIV through gavage. The mean plasma concentration−time curves of ASIV, CA, and iso-CA in antibiotic-pretreated rats are shown in Figure 2C. The C_{max}, t_{max}, $t_{1/2}$, and AUC_{0-t} values of ASIV in antibiotic-pretreated rats were 32.4 ± 7.8 nM, 2.83 ± 0.98 h, 1.99 ± 0.33 h, and 135 ± 30 nM·h, respectively (Table 2). The pharmacokinetic profile of ASIV in antibiotic-pretreated rats was similar to that in control rats (Figure 2A,C), which might be caused by passive diffusion of ASIV in intestinal

DOI: 10.1021/acs.jafc.5b00168
J. Agric. Food Chem. 2015, 63, 6084−6093

absorption.[16] Nevertheless, the plasma concentrations of CA in antibiotic-pretreated rats were immeasurable. Moreover, the C_{max} (4.41 ± 4.01 nM) and AUC_{0-t} (16.4 ± 15.0 nM·h) values of iso-CA in antibiotic-pretreated rats were significantly less than the corresponding data obtained from control rats (Table 2). The result indicated that the disposition of ASIV was obviously affected by the activity of intestinal bacteria after oral administration. Antibiotic treatments altered the intestinal microbiota composition of rodents.[35,36] Streptomycin and bacitracin inhibited the activity of Lactobacillaceae, which includes species capable of hydrolyzing saponins.[37,38] This might be one reason why the exposure of CA and iso-CA in antibiotic-pretreated rats was lower than in control rats. The alteration in rat microbial composition caused by streptomycin and bacitracin and the bacteria species involved in the hydrolysis of ASIV need to be further investigated.

Genetics, infant feeding patterns, antibiotic usage, sanitary living conditions, and long-term dietary habits are known to shape the composition of the gut microbiome.[39] Gut microbiota affects the metabolism of some natural compounds and synthetic drugs and resultantly affects their bioactivity or toxicity.[18,19,40−42] Our study shows that the metabolism of ASIV by intestinal microbiome was a crucial step in the disposition of ASIV, rather than that by hepatic and intestinal enzymes. Variations in intestinal microbiota induced by physiological or pathological conditions may change the disposition of ASIV and subsequently influence the potential health benefits of ASIV. Therefore, gut microbiota should be considered as a critical factor for understanding the bioactivities of ASIV.

AUTHOR INFORMATION

Corresponding Author

*(H.X.) Phone: +86 24 23986985. Fax: +86 24 23986250. E-mail: xhy1020@gmail.com, xhy411@163.com.

Notes

The authors declare no competing financial interest.

ACKNOWLEDGMENTS

We thank Dr. Jinghua Xu of Shenyang Pharmaceutical University for her invaluable work and advice in the treatment of animals.

REFERENCES

(1) Zu, Y. G.; Yan, M. M.; Fu, Y. J.; Liu, W.; Zhang, L.; Gu, C. B.; Efferth, T. Determination and quantification of astragalosides in Radix Astragali and its medicinal products using LC−MS. *J. Sep. Sci.* **2007**, *32* (4), 517−525.

(2) Chu, C.; Cai, H. X.; Ren, M. T.; Liu, E. H.; Li, B.; Qi, L. W.; Li, P. Characterization of novel astragaloside malonates from Radix Astragali by HPLC with ESI quadrupole TOF MS. *J. Sep. Sci.* **2010**, *33* (4−5), 570−581.

(3) Kwon, H. J.; Park, Y. D. Determination of astragalin and astragaloside content in Radix Astragali using high-performance liquid chromatography coupled with pulsed amperometric detection. *J. Chromatogr. A* **2012**, *1232* (2), 212−217.

(4) Chen, P.; Xie, Y. Q.; Shen, E.; Li, G.G.; Yu, Y.; Zhang, C. B.; Yang, Y. Z.; Zou, Y. Z.; Ge, J. B.; Chen, R. Z.; Chen, H. Z. Astragaloside IV attenuates myocardial fibrosis by inhibiting TGF-beta1 signaling in coxsackievirus B3-induced cardiomyopathy. *Eur. J. Pharmacol.* **2011**, *658* (2−3), 168−175.

(5) Zhang, D. W.; Bian, Z. P.; Xu, J. D.; Wu, H. F.; Gu, C. R.; Zhou, B.; Chen, X. J.; Yang, D. Astragaloside IV alleviates hypoxia/reoxygenation-induced neonatal rat cardiomyocyte injury via the protein kinase a pathway. *Pharmacology* **2012**, *90* (1−2), 95−101.

(6) Chan, W. S.; Durairajan, S. S. K.; Lu, J. H.; Wang, Y.; Xie, L. X.; Kum, W. F.; Koo, I.; Yung, K. K. L.; Li, M. Neuroprotective effects of Astragaloside IV in 6-hydroxydopamine-treated primary nigral cell culture. *Neurochem. Int.* **2009**, *55* (6), 414−422.

(7) Zhang, N.; Wang, X. H.; Mao, S. L.; Zhao, F. Astragaloside IV improves metabolic syndrome and endothelium dysfunction in fructose-fed rats. *Molecules* **2011**, *16* (5), 3896−3907.

(8) Yung, L. Y.; Lam, W. S.; Ho, M. K.; Hu, Y.; Ip, F. C.; Pang, H.; Chin, A. C.; Harley, C. B.; Ip, N. Y.; Wong, Y. H. Astragaloside IV and cycloastragenol stimulate the phosphorylation of extracellular signal-regulated protein kinase in multiple cell types. *Planta Med.* **2012**, *78* (2), 115−121.

(9) Commission of the Chinese Pharmacopoeia, Chinese Pharmacopoeia Part I, 2010, 283−284.

(10) Gu, Y.; Wang, G.; Pan, G.; Fawcett, J. P.; A, J.; Sun, J. Transport and bioavailability studies of astragaloside IV, an active ingredient in Radix Astragali. *Basic Clin. Pharmacol. Toxicol.* **2004**, *95* (6), 295−298.

(11) Du, Y.; Zhang, Q.; Chen, G. G.; Wei, P.; Tu, C. Y. Pharmacokinetics of Astragaloside IV in rats by liquid chromatography coupled with tandem mass spectrometry. *Eur. J. Drug Metab. Pharmacokinet.* **2005**, *30* (4), 269−273.

(12) Huang, C.; Wang, G.; Li, H.; Xie, H.; Sun, J.; Lv, H.; Lv, T. Sensitive and selective liquid chromatography-electrospray ionisation-mass spectrometry analysis of astragaloside-IV in rat plasma. *J. Pharm. Biomed. Anal.* **2006**, *40* (3), 788−793.

(13) Zhou, R. N.; Song, Y. L.; Ruan, J. Q.; Wang, Y. T.; Yan, R. Pharmacokinetic evidence on the contribution of intestinal bacterial conversion to beneficial effects of astragaloside IV, a marker compound of astragali radix, in traditional oral use of the herb. *Drug Metab. Pharmacokinet.* **2012**, *27* (6), 586−597.

(14) Zhang, Q.; Zhu, L. L.; Chen, G. G.; Du, Y. Pharmacokinetics of astragaloside IV in beagle dogs. *Eur. J. Drug Metab. Pharmacokinet.* **2007**, *32* (2), 75−79.

(15) Huang, C. R.; Wang, G. J.; Wu, X. L.; Li, H.; Xie, H. T.; Lv, H.; Sun, J. G. Absorption enhancement study of astragaloside IV based on its transport mechanism in Caco-2 cells. *Eur. J. Drug Metab. Pharmacokinet.* **2006**, *31* (1), 5−10.

(16) Huang, H. P.; Liu, C. X.; Li, Y. L.; Gao, G. L. Study on absorption kinetics of astragaloside IV in rats intestines. *Zhongguo Zhong Yao Za Zhi* **2008**, *33* (13), 1609−1611.

(17) Zhang, W. D.; Zhang, C.; Liu, R. H.; Li, H. L.; Zhang, J. T.; Mao, C.; Moran, S.; Chen, C. L. Preclinical pharmacokinetics and tissue distribution of a natural cardioprotective agentastragaloside IV in rats and dogs. *Life Sci.* **2006**, *79* (8), 808−815.

(18) Kang, M. J.; Kim, H. G.; Kim, J. S.; Oh, D. G.; Um, Y. J.; Seo, C. S.; Han, J. W.; Cho, H. J.; Kim, G. H.; Jeong, T. C.; Jeong, H. G. The effect of gut microbiota on drug metabolism. *Expert Opin. Drug Metab. Toxicol.* **2013**, *9* (10), 1295−1308.

(19) Jeong, H. G.; Kang, M. J.; Kim, H. G.; Oh, D. G.; Kim, J. S.; Lee, S. K.; Jeong, T. C. Role of intestinal microflora in xenobiotic-induced toxicity. *Mol. Nutr. Food Res.* **2013**, *57* (1), 84−99.

(20) Tomás-barberán, F. A.; Mine, Y. A key to understanding the effects of food bioactives in health, gut microbiota. *J. Agric. Food Chem.* **2013**, *61* (41), 9755−9757.

(21) Saad, R.; Rizkallah, M. R.; Aziz, R. K. Gut pharmacomicrobiomics: the tip of an iceberg of complex interactions between drugs and gut-associated microbes. *Gut Pathog.* **2012**, *4* (1), 16.

(22) Selma, M.; Espín, J. C.; Tomás-Barberán, F. A. Interaction between phenolics and gut microbiota: role in human health. *J. Agric. Food Chem.* **2009**, *57* (15), 6485−6501.

(23) Wang, S.; Zhai, C.; Liu, Q.; Wang, X.; Ren, Z.; Zhang, Y.; Zhang, Y.; Wu, Q.; Sun, S.; Li, S.; Qiao, Y. Cycloastragenol, a triterpene aglycone derived from Radix astragali, suppresses the accumulation of cytoplasmic lipid droplet in 3T3-L1 adipocytes. *Biochem. Biophys. Res. Commun.* **2014**, *450* (1), 306−311.

(24) Zhu, J.; Lee, S.; Ho, M. K.; Hu, Y.; Pang, H.; Ip, F. C.; Chin, A. C.; Harley, C. B.; Ip, N. Y.; Wong, Y. H. In vitro intestinal absorption

DOI: 10.1021/acs.jafc.5b00168
J. Agric. Food Chem. 2015, 63, 6084−6093

and first-pass intestinal and hepatic metabolism of cycloastragenol, a potent small molecule telomerase activator. *Drug Metab. Pharmacokinet.* **2010**, *25* (5), 477−486.
(25) Liu, H.; Yang, J.; Du, F.; Gao, X.; Ma, X.; Huang, Y.; Xu, F.; Niu, W.; Wang, F.; Mao, Y.; Sun, Y.; Lu, T.; Liu, C.; Zhang, B.; Li, C. Absorption and disposition of ginsenosides after oral administration of *Panax notoginseng* extract to rats. *Drug Metab. Dispos.* **2009**, *37* (12), 2290−2298.
(26) Gu, Y.; Wang, G. J.; Sun, J. G.; Jia, Y. W.; Wang, W.; Xu, M. J.; Lv, T.; Zheng, Y. T.; Sai, Y. Pharmacokinetic characterization of ginsenoside Rh2, an anticancer nutrient from ginseng, in rats and dogs. *Food Chem. Toxicol.* **2009**, *47* (9), 2257−2268.
(27) Feng, L.; Wang, L.; Hu, C.; Jiang, X. Pharmacokinetics, tissue distribution, metabolism, and excretion of ginsenoside rg1 in rats. *Arch. Pharmacal Res.* **2010**, *33* (12), 1975−1984.
(28) Yu, K.; Chen, F.; Li, C. Absorption, disposition, and pharmacokinetics of saponins from Chinese medicinal herbs: what do we know and what do we need to know more? *Curr. Drug Metab.* **2012**, *13* (5), 577−598.
(29) Xu, M.; Yin, J.; Xie, L.; Zhang, J.; Zou, C.; Zou, J.; Liu, F.; Ju, W.; Li, P. Pharmacokinetics and tolerance of total astragalosides after intravenous infusion of astragalosides injection in healthy Chinese volunteers. *Phytomedicine* **2013**, *20* (12), 1105−1111.
(30) Chen, J.; Lin, H.; Hu, M. Metabolism of flavonoids via enteric recycling: role of intestinal disposition. *J. Pharmacol. Exp. Ther.* **2003**, *304* (3), 1228−1235.
(31) Ruan, J.; Leong, W.; Wang, Y. Characterization of metabolism and in vitro permeability study of notoginsenoside R1 from Radix notoginseng. *J. Agric. Food Chem.* **2010**, *58* (9), 5770−5776.
(32) U.S. Food and Drug Administration. *Guidance for Industry: Bioanalytical Method Validation*; U.S. Food and Drug Administration, Center for Drug Evaluation and Research: Washington, DC, USA, 2001.
(33) Kinouchi, T.; Kataoka, K.; Miyanishi, K. Biological activities of the intestinal microflora in mice treated with antibiotics or untreated and the effects of the microflora on absorption and metabolic activation of orally administered glutathione conjugates of K-region epoxides of 1-nitropyrene. *Carcinogenesis* **1993**, *14* (5), 869−874.
(34) Xing, J.; Chen, X.; Sun, Y.; Luan, Y.; Zhong, D. Interaction of baicalin and baicalein with antibiotics in the gastrointestinal tract. *J. Pharm. Pharmacol.* **2005**, *57* (6), 743−750.
(35) Ferreira, R. B. R.; Gill, N.; Willing, B. P.; Antunes, L. C. M.; Russell, S. L.; Croxen, M. A.; Finlay, B. B. The intestinal microbiota plays a role in salmonella-induced colitis independent of pathogen colonization. *PLoS One* **2011**, *6* (5), No. e20338.
(36) Wlodarska, M.; Willing, B.; Keeney, K. M.; Menendez, A.; Bergstrom, K. S.; Gill, N.; Russell, S. L.; Vallance, B. A.; Finlay, B. B. Antibiotic treatment alters the colonic mucus layer and predisposes the host to exacerbated citrobacter rodentium-induced colitis. *Infect. Immun.* **2011**, *79* (4), 1536−1545.
(37) Chi, H.; Ji, G. E. Transformation of ginsenosides Rb1 and Re from Panax ginseng by food microorganisms. *Biotechnol. Lett.* **2005**, *27* (11), 765−771.
(38) Kim, S.; Min, J.; Quan, L.; Lee, S.; Yang, D.; Yang, D. Enzymatic transformation of ginsenoside rb1 by lactobacillus pentosus strain 6105 from kimchi. *J. Ginseng Res.* **2012**, *36* (3), 291−297.
(39) Voreades, N.; Kozil, A.; Weir, T. L. Diet and the development of the human intestinal microbiome. *Front. Microbiol.* **2014**, *5*, No. 494.
(40) Jin, M. J.; Kim, I. S.; Kim, D.; Yoo, H. H. Effects of intestinal microbiota on the bioavailability of geniposide in rats. *J. Agric. Food Chem.* **2014**, *62* (40), 9632−9636.
(41) Niu, T.; Smith, D. L.; Yang, Z.; Gao, S.; Yin, T. J.; Jiang, Z. H.; You, M.; Gibbs, R. A.; Petrosino, J. F.; Hu, M. Bioactivity and bioavailability of ginsenosides are dependent on the glycosidase activities of the A/J mouse intestinal microbiome defined by pyrosequencing. *Pharm. Res.* **2013**, *30* (3), 836−846.
(42) Zhang, Y.; Limaye, P. B.; Renaud, H. J.; Klaassen, C. D. Effect of various antibiotics on modulation of intestinal microbiota and bile acid profile in mice. *Toxicol. Appl. Pharmacol.* **2014**, *277* (2), 138−145.

DOI: 10.1021/acs.jafc.5b00168
J. Agric. Food Chem. 2015, 63, 6084−6093

diseases, and oxidative stress has been shown to activate extracellular signal-regulated kinases (ERK) 1/2 simultaneously.[25,26] Interestingly, previous results also show that antioxidants (e.g., *N*-acetyl-L-cysteine, NAC) added before other toxin treatment can rescue cells from cytotoxicity induced by the toxin through decreased oxidative damage.[27] In addition, the ERK signaling pathway is one of the major pathways of T lymphocyte proliferation and IL-2 production.[28−30] Until now, the interaction of AFB_1-induced immunotoxicity and the ERK1/2 pathway in T lymphocyte proliferation is relatively unexplored.

Because a lot of research shows AFB_1 exposure could exert oxidative stress in cell culture model,[31] we hypothesize that (i) AFB_1 could induce immunotoxicity in primary porcine splenocytes and (ii) AFB_1 induced decreases of porcine splenocyte proliferation and IL-2 production by oxidative stress mediated ERK1/2 MAPK signaling pathway. Thus, our objective was to evaluate the effect of different concentrations of AFB_1 on the anti-CD3-induced primary porcine splenocytes proliferation and IL-2 production, intracellular redox status, and expression of p-ERK1/2 MARK protein and to determine whether intracellular oxidative stress and the phosphorylation of the ERK1/2 MARK pathway are novel mechanisms involved in AFB_1-induced immunotoxic properties in primary porcine splenocytes.

MATERIALS AND METHODS

Animal and Cell Culture. The use of experimental animals and the following procedures were approved by the Nanjing Agricultural University Animal Care Committee. Fifty normal Meishan pigs (half males and half females), aged 30 days and weighing 8 ± 2 kg, were collected from the breeding center of Jiangsu Polytechnic College of Agriculture and Forestry and killed. The spleens were removed and placed in Hanks' solution and then disrupted mechanically under a clean bench, after which they were carefully layered on the surface of lymphocyte separation medium (Tianjin Hematology Institute, Chinese Academy of Medical Sciences, China). Isolated spleen lymphocytes were adjusted and supplemented with enriched RPMI-1640 medium (Invitrogen, USA), which was added with 10% fetal bovine serum (FBS), penicillin (20 mg/mL), and streptomycin (20 mg/mL) and cultivated at 37 °C in the incubator with 5% CO_2, and subsequently evaluated for the viability of isolated spleen lymphocyte by 0.4% trypan blue dye exclusion. We detected lymphocyte proliferation at 24, 36, 48, 60, and 72 h in the beginning stage of the experiment. However, we found that cell proliferation at 60 h had the best results by flow cytometry, so we detected cell proliferation only at 60 h in the following experiment. In previous literature, the antigen-specific response is more sensitive to AFB_1 exposure than the mitogen-specific response in pigs, so we selected only anti-CD3 stimulation rather than mitogen stimulation in the present experiment.

AFB_1 (Sigma, USA) was dissolved in DMSO (1 mg/mL), and final mycotoxin concentrations were diluted in the culture medium. Cells without any AFB_1 and with 0.4% final concentration of DMSO were used as the control group.

Spleen Lymphocyte Proliferation Assay. Spleen lymphocytes (1×10^6 cells/well) were treated with various concentrations of AFB_1 in the absence or presence of anti-pig-CD3 mAb (clone PPT3, Abcam, UK) and cultivated in 96-well plates for 60 h. In the splenocyte viability experiment, AFB_1 was exposed at 0, 0.5, 1, 2, 4, 8, 10, and 20 μg/mL concentrations. In cell proliferation analysis, AFB_1 was treated at 0, 1, 2, 4, and 8 μg/mL concentrations. Subsequently, 3-(4,5-dimethylthiazol-2-yl)-2,5-diphenyltetrazolium bromide (MTT) solution (Sigma, USA) was added at 5 mg/mL concentration, and the plate was oscillated for 10 min by enzyme-labeled instrument (Bio-Rad, USA). Finally, the optical density (OD) value was assessed as absorbance at 490 nm. All samples were assayed in quadruplicate.

To assess T-cell proliferation, 1×10^6 cells/well CFSE-stained splenocytes were cultivated in 24-well plates accompanied by RPMI-1640 medium to a final volume of 1 mL. After 60 h, splenocytes were centrifuged and wash with phosphate buffered saline (PBS) once, then stained with anti-CD3-PEcy5 (Abcam, UK) and prepared for flow cytometry analysis. Flow cytometry was used and enabled by FACSCalibur (BD Biosciences, USA). Color compensation was achieved using an appropriate single fluorochrome-labeled sample. Data were analyzed using FlowJo 7.6.5 (TreeStar).

Determination of IL-2 in Splenocytes. Splenocytes (1×10^6 cells/well) were seeded in 96-well plates and treated with various concentrations of AFB_1 (0, 1, 2, 4, and 8 μg/mL) in the absence (controls) or presence of anti-pig-CD3 mAb for 60 h. The cell supernatants were then collected and assayed for IL-2 by ELISA (R&D Systems, USA). All samples were assayed in triplicate.

Oxidative Stress Analysis. Primary porcine splenocytes at a density of 2×10^6/well in 6-well plates were treated with AFB_1 at 0, 1, 2, 4, and 8 μg/mL for 60 h in the presence of anti-pig-CD3 mAb.

Intracellular glutathione (GSH) in splenocyte cytosol was measured as previously described,[32] using commercially available kits (Jiancheng, China), which are based on the reaction of 5,5′-dithiobis(2-nitrobenzoic acid) and GSH to 5-thio-2-nitrobenzoic acid. Cell extracts were prepared, and GSH was measured spectrophotometrically (412 nm). Protein concentration was determined according to the BCA method using commercially available kits (Beyotime, Jiangsu, China). Data were expressed as micromoles of GSH per gram of protein. All samples were assayed in triplicate.

Assessment of T-SOD enzymatic activity was performed according to a previously described method,[33] using commercially available kits (Jiancheng, China). The absorbance was measured at 525 nm for 10 min. One unit of T-SOD was defined as the enzyme amount responsible for 50% of the inhibition of epinephrine oxidation. T-SOD enzymatic activity was expressed as units (U) per milligram of protein. All samples were assayed in triplicate.

Intracellular malondialdehyde (MDA) in splenocyte cytosol was measured as previously described,[34] using commercially available kits (Jiancheng, China). All samples were assayed in triplicate.

Western Blot Analysis. Spleen lymphocyte suspension was cultured in a 6-well plate at a density of 2×10^6/well for 60 h with a density of 2×10^6 cells/well. After separation by SDS-PAGE, protein molecules on the gel were transferred onto a PVDF membrane and then probed using a specific antibody to quantitatively detect ERK (1/1000) (Cell Signaling Technology, USA) and p-ERK (1/2000) protein (Cell Signaling Technology, USA). After the first antibody reaction overnight, the PVDF membrane was washed by TBST three times and incubated for 60 min with horseradish peroxidase (HRP)-labeled anti-rabbit secondary antibody (Cell Signaling Technology, USA), diluted 1/5000 (v/v) in 5% (w/v) BSA TBST. Finally, the result of Western blot was detected by electrochemiluminescence (ECL) using the Amersham Hyperfilm ECL reagent.

Short Interfering RNA (siRNA) Transfection. Double-stranded RNA sequences were designed according to the sequence of ERK-specific siRNAs using Invitrogen BlockiT RNAi designer and were synthesized by Invitrogen. The ERK-specific siRNAs sequence was sense 5′-CUCCAAAGCUCUGGAUUUAtt-3′ and antisense 5′-UAA-AUCCAGAGCUUUGGAGtt-3′. The control siRNA had the sequence 5′-UUCUCCGAACGUGUCACGUTT-3′. Duplexes were resuspended in DEPC-treated water to obtain 20 mM solutions before use. T cells in RPMI-1640 medium without FBS or antibiotics were seeded in 6-well plates, 24-well plates, and 96-well plates after spleen lymphocytes were separated, and siRNA was introduced using the X-tremeGene siRNA transfection reagent (Roche, USA) according to the manufacturer's protocol.

Statistical Analysis. All of the data were analyzed statistically using the SPSS 18.0 for Windows statistical software package (Statistical Product and Service Solutions, Inc., USA). All results are presented as the mean ± SEM. We also performed a one-way ANOVA on the statistical analysis. Tukey's b (K) post-test was used to compare means of each group, and a *P* value was considered significant at 0.05.

DOI: 10.1021/acs.jafc.5b00433
J. Agric. Food Chem. 2015, 63, 6094−6101

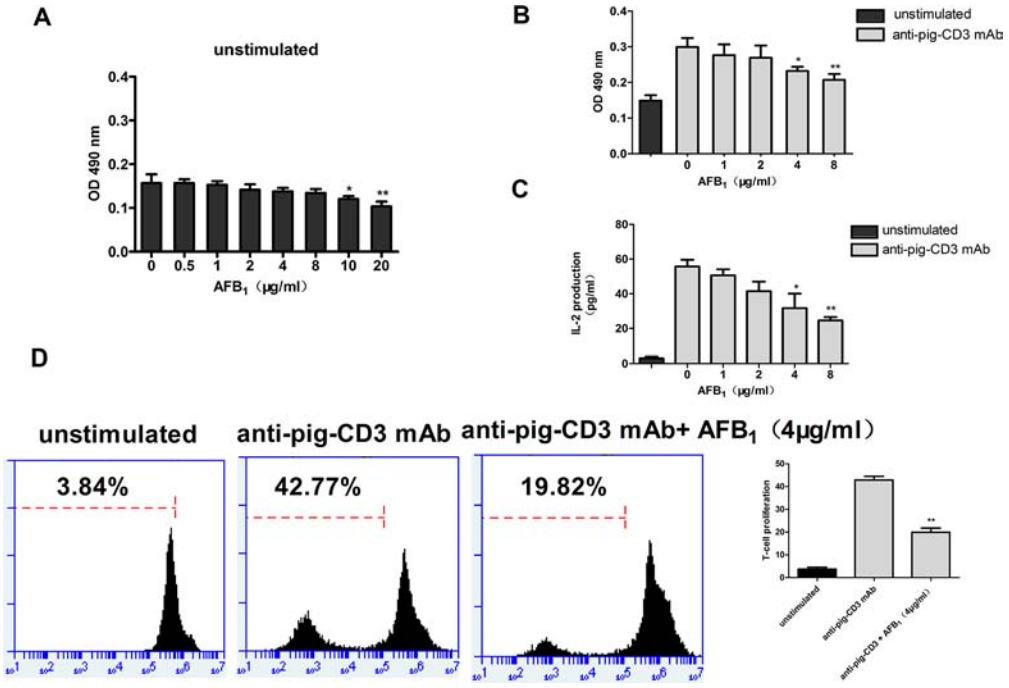

Figure 1. Effects of AFB_1 on the viability, cell proliferation, and IL-2 production in primary porcine splenocytes. Primary porcine splenocytes (1×10^6 cells/well) were treated with different concentrations of AFB_1 for 60 h without any stimulus (A) or stimulated by 2 μg/mL anti-pig-CD3 mAb (B) and were assayed by the MTT method. The values are presented as means ± SEM ($n = 4$). IL-2 production in splenocytes treated with different concentrations of AFB_1 and IL-2 concentrations was determined by ELISA (C). The values are presented as means ± SEM ($n = 3$). Significant differences with control were designated as $* P < 0.05$ and $** P < 0.01$. CD3+T-cell proliferation was monitored using CFSE labeling (D). Cells were stained with anti-CD3-PEcy5. CD3+T cells from the entire well were analyzed for proliferation by flow cytometry. The percentage of proliferating cells for each culture is indicated. A representative experiment from two separate experiments is shown.

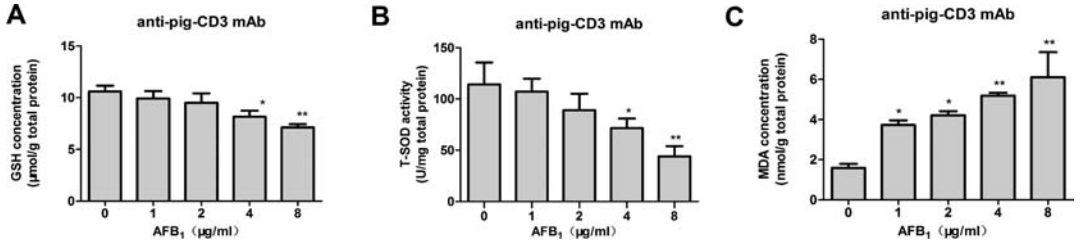

Figure 2. Effects of AFB_1 supplementation on oxidative stress capacity. Primary porcine splenocytes at a density of 2×10^6/well in 6-well plates were treated with AFB_1 at 1, 2, 4, and 8 μg/mL for 60 h in the presence of anti-CD3. Changed levels of GSH (A), T-SOD (B), and MDA (C) were assayed as described under Materials and Methods. The values are presented as means ± SEM ($n = 3$). Significant differences with control were designated as $*P < 0.05$ and $** P < 0.01$.

Supplementary Information. Primary porcine splenocytes were stimulated with 2 μg/mL anti-pig-CD3 mAb in the absence or presence of 5 mmol/L of NAC for 24 h, washed with PBS once, and then treated with AFB_1 (4 μg/mL) or not for another 36 h. Moreover, control and NAC treatment group were treated at the final concentration of 0.4% DMSO.

RESULTS

Effects of AFB_1 on Viability, Cell Proliferation, and IL-2 Production in Primary Porcine Splenocytes. To investigate the effect of AFB_1 treatment on the antigen-stimulated lymphocyte proliferation, we examined the effects of AFB_1 at various concentrations on splenocyte proliferation and IL-2 production. As shown in Figure 1, DMSO, the solvent of AFB_1, does not have a significant effect on splenocyte viability and proliferation of lymphocytes. However, the higher doses of AFB_1 (10 and 20 μg/mL) showed significant cytotoxic effect on the viability ($P < 0.05$) (Figure 1A). On the basis of this observation, the higher dose was excluded during our experiments. Over the range of concentrations of AFB_1 used, the proliferation of cells was significantly lowered by AFB_1 at 4 and 8 μg/mL in a dose-dependent manner ($P < 0.05$) (Figure 1B). A significant reduction in IL-2 production by anti-pig-CD3 stimulation was observed at concentrations of 4 and 8 μg/mL ($P < 0.05$). The inhibition indicates dose dependency (Figure 1C).

To confirm whether the proliferation evaluated by cell counting assay was due to T lymphocytes or total cells or any other cell type, CD3+T-cell proliferation was estimated by CFSE labeling of splenocytes and following anti-pig-CD3-PEcy5 staining. The T-cell proliferation measured by CFSE showed a pattern similar to that of MTT. Total CD3+T cells proliferated less in the toxin exposure group than in the control group with anti-pig-CD3 mAb regulated and treated (19.82 versus 42.77%, Figure 1D).

DOI: 10.1021/acs.jafc.5b00433
J. Agric. Food Chem. 2015, 63, 6094−6101

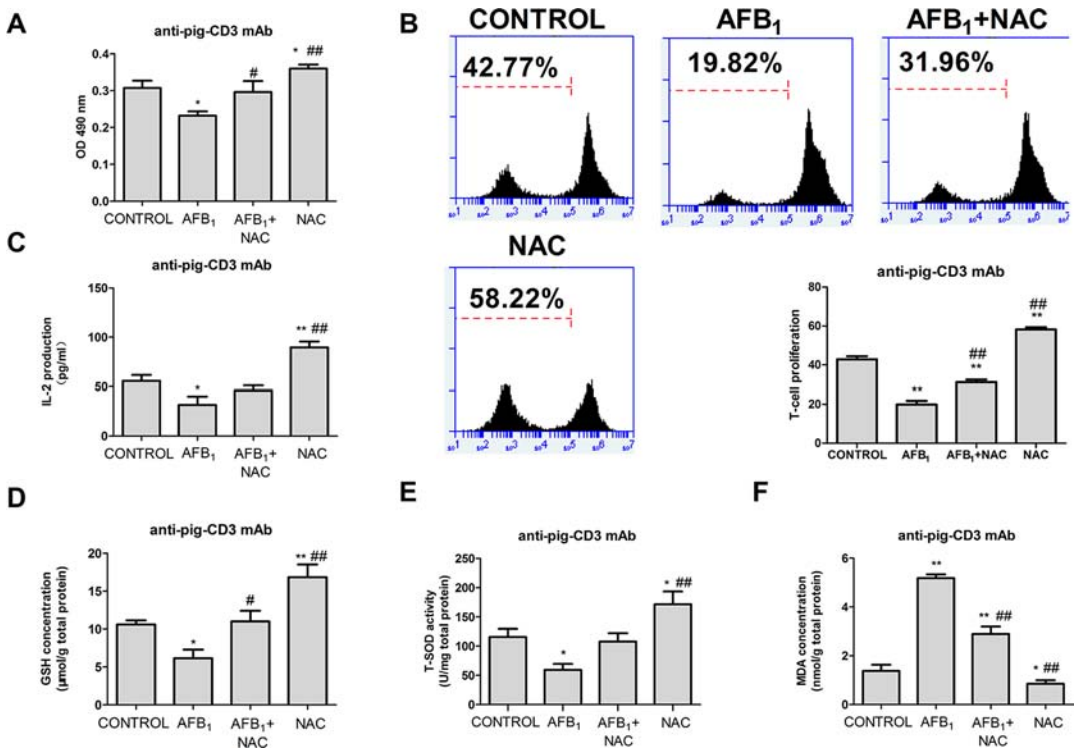

Figure 3. Effects of NAC on cell proliferation, IL-2, and redox activity induced by AFB_1 in primary porcine splenocytes. Primary porcine splenocytes were stimulated with anti-CD3 in the absence or presence of 5 mmol/L of NAC for 24 h and then inoculated with or without AFB_1 at 4 μg/mL for a further 36 h treatment. Cells were assayed for cell proliferation (A), IL-2 production (C), levels of GSH (D), T-SOD (E), and MDA (F). Data are presented as means ± SE of three independent experiments: ∗ $P < 0.05$ and ∗∗ $P < 0.01$ are statistically significant compared to control cells; # $P < 0.05$ and ## $P < 0.01$ are statistically significant compared to 4 μg/mL AFB_1-treated T cells. CD3+T-cell proliferation was monitored using CFSE labeling (B). Cells were stained with anti-CD3-PEcy5. CD3+T cells from the entire well were analyzed for proliferation by flow cytometry. The percentage of proliferating cells for each culture is indicated. A representative experiment from two separate experiments is shown.

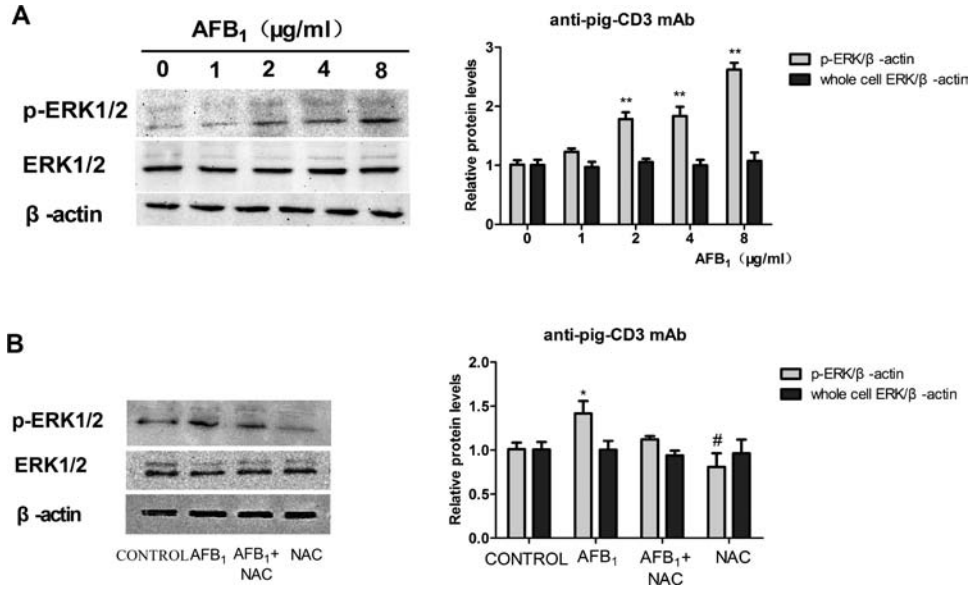

Figure 4. Western blot and densitometric analysis of ERK1/2 expression. Primary porcine splenocytes were treated with AFB_1 at 1, 2, 4, and 8 μg/mL for 60 h in the presence of anti-CD3 (A). Primary porcine splenocytes were stimulated with anti-CD3 in the absence or presence of 5 mmol/L of NAC for 24 h and then inoculated with or without AFB_1 at 4 μg/mL for a further 36 h treatment (B). Whole cell ERK expression/β-actin was used as a control. Densitometric analysis results are expressed as the ratio of phosphorylated ERK to β-actin and the whole cell ERK expression to β-actin. Graphical results are represented the mean ± SEM of three independent experiments: ∗ $P < 0.05$ and ∗∗ $P < 0.01$ are tatistically significant compared to control cells; # $P < 0.05$ and ## $P < 0.01$ are statistically significant compared to 4 μg/mL AFB_1-treated T cells.

Effects of AFB_1 Supplementation on Oxidative Stress Capacity. To investigate the effect of AFB_1 exposure on the parameters of oxidative stress, GSH, T-SOD, and MDA levels were measured in the splenocytes. Cells treated with AFB_1

DOI: 10.1021/acs.jafc.5b00433
J. Agric. Food Chem. 2015, 63, 6094−6101

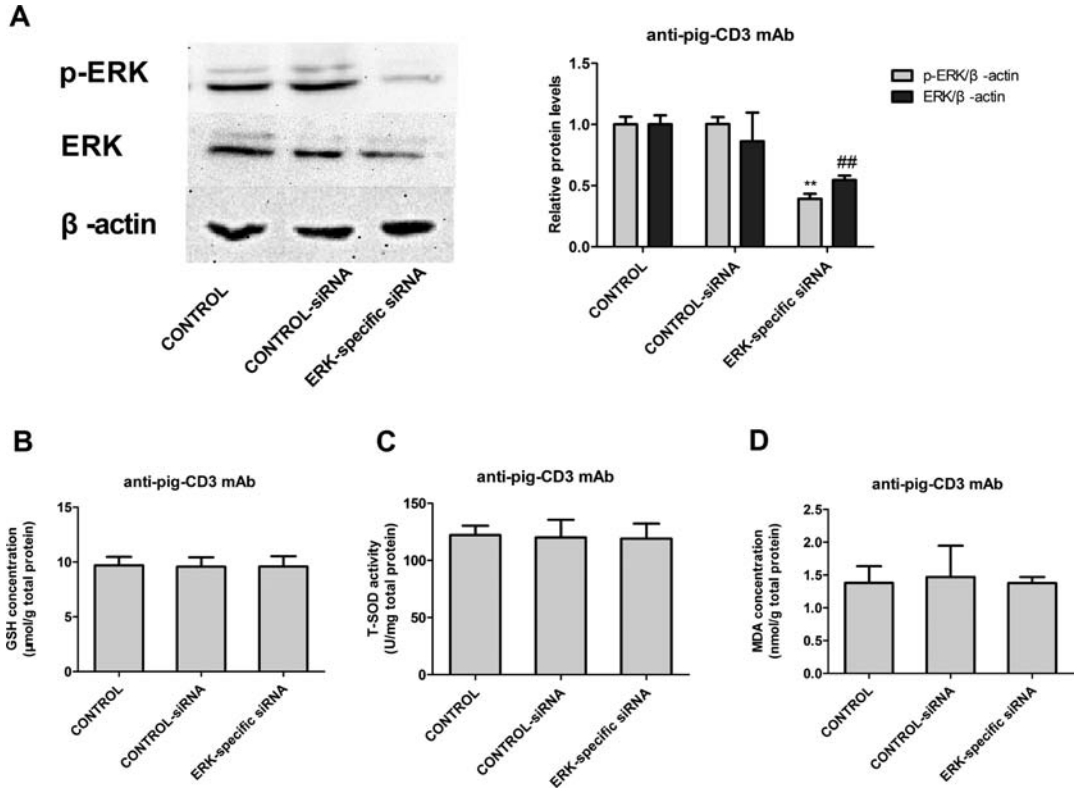

Figure 5. Effect of ERK-knockdown on ERK1/2 and p-ERK1/2 expression and oxidative stress in primary porcine splenocytes. Cell were transfected with either an ERK-specific siRNA or a control siRNA and cultured for 5 h before 4 μg/mL AFB_1 and 2 μg/mL anti-CD3 treatment. Cell samples were assayed for p-ERK and ERK protein levels (A) and GSH (B), T-SOD (C), and MDA (D) levels as described under Materials and Methods. Whole cell ERK expression/β-actin was used as a control. Densitometric analysis results are expressed as the ratio of phosphorylated ERK to β-actin and the whole cell ERK expression to β-actin. Graphical results are represented the mean ± SEM of three independent experiments: * and # indicate statistically significant difference from control (* and #, $P < 0.05$; ** and ##, $P < 0.01$).

showed a dose-dependent decrease in the intracellular concentrations of GSH. The minimal decreases of GSH levels appeared in activated splenocytes exposed to 8 μg/mL AFB_1 (Figure 2A) and GSH concentrations in the 4 μg/mL AFB_1 show a significant decrease compared with control splenocytes, whereas T-SOD presents the same trend (Figure 2B). To assess the MDA levels in primary porcine splenocytes, which is a marker of oxidative stress, we measured the results as shown in Figure 2C. In 0−8 μg/mL AFB_1-treated groups, MDA concentrations exhibit a dose-dependent increase. MDA concentrations in the 1 μg/mL AFB_1 show a significant enhancement compared with control splenocytes. The maximal increases of MDA level were observed in activated splenocytes incubated with 8 μg/mL AFB_1.

Effects of NAC on Cell Proliferation, IL-2, and Redox Activity Induced by AFB_1 in Primary Porcine Splenocytes. To determine whether a change of oxidative stress could affect T-cell proliferation, primary porcine splenocytes were stimulated with 2 μg/mL anti-pig-CD3 mAb in the absence or presence of 5 mmol/L of NAC for 24 h. As shown in Figure 3A, AFB_1 treatment exhibited significant toxicity, which was suppressed in NAC-treated cells ($P < 0.05$). The T-cell proliferation measured by CFSE showed a pattern similar to that of MTT (Figure 3B). Total CD3+T cells proliferated more in the NAC exposure group and the NAC and AFB_1 group than in the AFB_1 group with anti-pig-CD3 mAb treatment (58.22 and 31.96 versus 19.82%). We found that NAC alleviated AFB_1-induced cytotoxicity as demonstrated by increasing intracellular concentrations of GSH levels (Figure 3D) and decreasing MDA levels (Figure 3F), respectively, compared with the AFB_1 group ($P < 0.05$). However, NAC together with AFB_1 did not produce a significant increase in the IL-2 production and intracellular concentrations of T-SOD levels (Figure 3C,E).

Western Blot and Densitometric Analysis of p-ERK1/2 and ERK1/2 Expression. To determine if the AFB_1 treatment of primary porcine splenocytes affects expression of extracellular signal-regulated kinases, Western blot was used to measure protein levels of ERK1/2 protein in activated splenocytes. The significant change in p-ERK1/2 expression was associated with a dose-dependent increase in gray value. As shown in Figure 4A, in the cells exposed to various concentrations of AFB_1 (1−8 μg/mL), AFB_1 at a concentration of 2 μg/mL showed significantly higher ERK1/2 phosphorylation compared to the no-toxin group ($P < 0.01$). It has been assumed that the influence of AFB_1 on cell proliferation shows connections with p-ERK1/2 protein expression in T lymphocytes. As shown in Figure 4B, expression of p-ERK1/2 protein in activated splenocytes was decreased in NAC interaction with the AFB_1 group compared to the AFB_1 group.

Effect of ERK-Knockdown on ERK1/2 Expression and Oxidative Stress in Primary Porcine Splenocytes. The extent of ERK-knockdown was evaluated by determination of ERK1/2 protein levels after primary porcine splenocyte cells were transfected with either an ERK1/2-specific or a control siRNA. As shown in Figure 5, transfection of primary porcine splenocytes cells with ERK-specific siRNA led to a decrease in ERK1/2 protein levels compared with control cells, there being

DOI: 10.1021/acs.jafc.5b00433
J. Agric. Food Chem. 2015, 63, 6094−6101

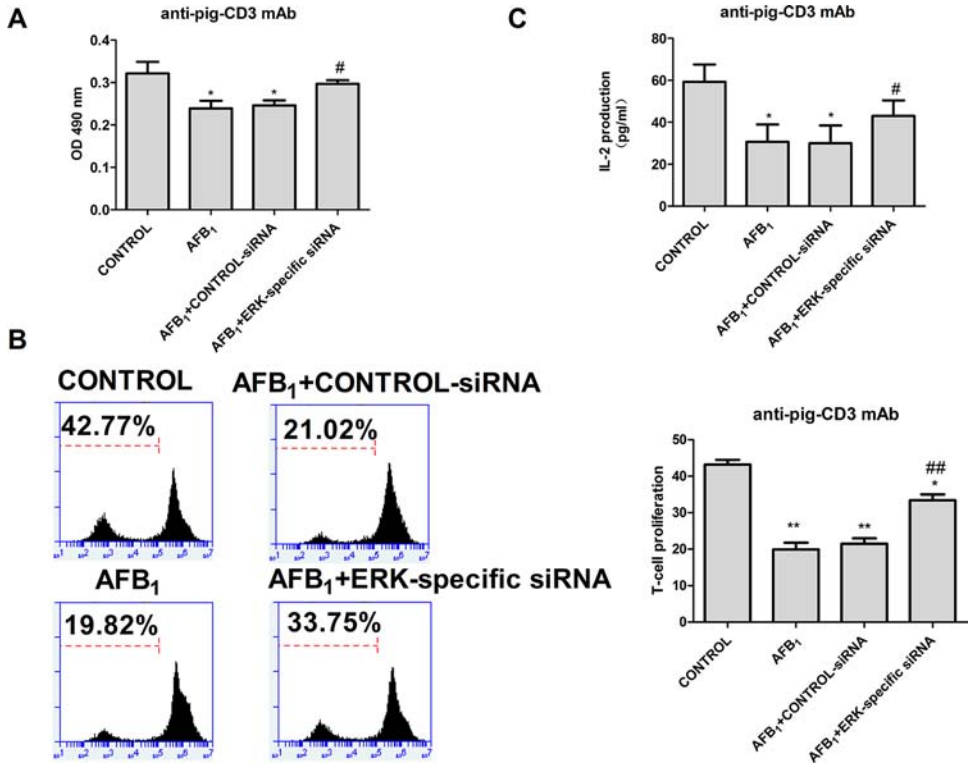

Figure 6. Alleviative effects of ERK1/2 knockdown on immunosuppression induced by AFB_1 in primary porcine splenocytes. Cells were transfected with either an ERK-specific siRNA or a control siRNA and cultured for 5 h before 4 μg/mL AFB_1 and 2 μg/mL anti-CD3 treatment. The transfected cells were assayed for proliferation by MTT (A) and IL-2 concentration by ELISA (C). Cells with only stimulus were used as control. Data are presented as means ± SE of three independent experiments: * $P < 0.05$, statistically significant compared to control cells; # $P < 0.05$, statistically significant compared to 4 μg/mL AFB_1-treated T cells. CD3+T-cell proliferation was monitored using CFSE labeling (B). Cells were stained with anti-CD3-PEcy5. CD3+T cells from the entire well were analyzed for proliferation by flow cytometry. The percentage of proliferating cells for each culture is indicated. A representative experiment from two separate experiments is shown.

a 65% decrease in p-ERK1/2 protein levels and a 55% decrease in whole cell ERK1/2, respectively (Figure 5A). Transfection of primary porcine splenocytes with siRNA targeted against ERK had no effects on the redox status as measured by intracellular GSH levels, T-SOD levels, and MDA levels (Figure 5B–D).

Alleviative Effects of ERK-Knockdown on Immunosuppression Induced by AFB_1 in Primary Porcine Splenocytes. To address whether ERK1/2 plays a key role in reducing the cytotoxicity of AFB_1 in primary porcine splenocytes, cells were cultured and then transfected with ERK-specific or control siRNA. After 5 h of transfection treatment, the medium was removed. Transfected cells were then cultured with AFB_1 at 4 μg/mL in the presence of anti-pig-CD3 mAb for a further 55 h. As shown in Figure 6, ERK-specific siRNA alleviated the immune toxicity of AFB_1, as demonstrated by increasing T-cell proliferation (Figure 6A) and IL-2 production (Figure 6C) ($P < 0.05$), but not in cells transfected with the siRNA control. The T-cell proliferation measured by CFSE showed a pattern similar to that of MTT (Figure 6B). Total CD3+T cells proliferated more in the ERK-specific siRNA group than in the AFB_1 exposure group and control siRNA group with anti-pig-CD3 mAb treatment (33.75 versus 19.82 and 21.02%).

DISCUSSION

Previous studies have indicated that an AFB_1-contaminated diet has been widely documented in many parts of the world and exposure to the toxin affects the immune response in pigs.[35,36] However, the detailed mechanisms of the immunotoxicity induced by AFB_1 have not been reported in pigs until now. The present work is the first to investigate the relationship of cell signaling pathway and the immunotoxicity induced by AFB_1. The present data showed that the effects of AFB_1-induced immunotoxicity were associated with oxidative damage and the ERK1/2 MAPK signaling pathway.

Costello et al. demonstrated an overall higher activation status achieved with CD3i/CD28i than with PHA.[37] Meissonnier et al.[8] supplied results that the antigen-specific response is more sensitive to AFB_1 than the mitogen-specific response in blood lymphocytes exposed to dietary AFB_1 from pigs. Therefore, we chose anti-CD3 stimulation rather than mitogen stimulation in the present experiment. Lymphocyte proliferation and IL-2 production were considered as measures to evaluate T-cell function in an in vitro experiment.[38] Our results showed that the vitality of AFB_1-induced unstimulated T cells was decreased dose dependently, but relatively insensitively, compared to the active T cells, which was consistent with a previous study that AFB_1 decreases lymphoid cell populations, especially activated lymphocytes.[8] In anti-CD3-induced T cells, 4–8 μg/mL AFB_1 exposures significantly inhibited T-cell proliferation and IL-2 production in the present work. Actually, concentrations of >8 μg/mL had been detected and had a continued declining trend (data not shown). To ensure the accuracy of the results, both MTT and flow cytometry were used as effective methods to measure the proliferation of T cells in the present experiment.

To our knowledge, reactive oxygen species (ROS) not only result from normal cellular metabolism but also are related to

DOI: 10.1021/acs.jafc.5b00433
J. Agric. Food Chem. 2015, 63, 6094–6101

the treatment of the drugs or environment pollutants.[39] Parveen et al. showed that 0.25 μg/mL AFB_1 caused a significant increase in oxidative stress in MDCK cells, which was demonstrated by a significant increase of MDA level and reduction of intracellular GSH level, as well as GPX1 activity and mRNA level.[40] Our results showed that AFB_1 treatment induced intracellular oxidative stress in the splenocyte, which is consistent with previous studies.[41]

The results from the NAC treatment experiments provided further evidence that AFB_1-induced T-cell inhibition is associated with cellular oxidative stress in splenocytes. NAC is a pharmacological antioxidant. Treatment of NAC in splenocytes reduced oxidative stress and resulted in an alleviation of T-cell proliferation. Xiao et al. confirmed that the significant toxicity induced by 4-ClBQ could be suppressed after NAC treatment in human keratinocytes.[27] Our study showed that NAC alleviated the immunotoxic effects of AFB_1, which indicated that the AFB_1-induced immunotoxic effects were due to an increase of redox status.

In previous research, ERK1 and ERK2 have been demonstrated as ultimately phosphorylated products from MAPK families, and the activated ERKs translocate to the nucleus and transcription factors, changing gene expression to promote growth, differentiation, or mitosis.[42] Also, the ERK signaling pathway is one of the major pathways of T-lymphocyte proliferation.[43] However, there is little research available on the relationship with the ERK pathway and immunosuppression of AFB_1. In our experiment, T cells were exposed to various concentrations of AFB_1 (1−8 μg/mL), and expression of ERK1/2 was increased at 2, 4, and 8 μg/mL in a dose-dependent manner. Our current results strongly indicated that AFB_1 exposure could activate the ERK1/2 signaling pathway in primary porcine splenocytes.

Above all, hypotheses were formulated that the change of phosphorylation of ERK1/2 seems likely correlated with ROS generation in certain aspects. In the previous study, Keshari et al. demonstrated ROS resulted in activation of ERK in PMNs, which is an important component of the innate immune system.[44] To examine oxidative stress as a function in the MAPK signaling pathway, NAC was added before AFB_1 exposure. The finding that NAC, a nonspecific antioxidant, down-regulated the phosphorylation of the ERK1/2-MAPK pathway in primary porcine splenocytes (Figure 4 B) further certified this hypothesis.

To further determine the specificity of the ERK1/2−MAPK pathway regulating AFB_1-induced oxidative stress and immune toxicity, experiments were repeated using ERK-specific siRNA, which can specifically block ERK1/2 expression (Figure 6). O'Connell et al. made a key contribution to the inhibition of the MAPK pathway resulting in attenuation of the CsA-induced mesangial cell alterations caused by oxidative stress.[45] Our results are consistent with the previous studies, which strongly indicate that ERK1/2-knockdown mitigates AFB_1-induced cellular immunity toxicity and the ERK pathway maybe is a key mechanism of T-cell suppression induced by AFB_1. It seems that AFB_1 exposure produced oxidative stress, and then oxidative stress activated the ERK signal pathway and resulted in the suppression of T-cell proliferation. The mechanisms by which oxidative stress and ERK1/2 phosphorylation correlated with interaction are relatively unexplored but undoubtedly important areas for future investigation.

AUTHOR INFORMATION

Corresponding Author

*(K.H.) Phone: +86-25-84395507. Fax: +86-25-84398669. E-mail: khhuang@njau.edu.cn.

Funding

This work was funded by the National Natural Science Foundation of China (31272627, 31472253), the Research Fund for Doctoral Program of Higher Education in China (20110097110014 and 20120097130002), and the Priority Academic Program Development of Jiangsu Higher Education Institutions (Jiangsu, China).

Notes

The authors declare no competing financial interest.

REFERENCES

(1) Wild, C. P. Aflatoxin exposure in developing countries: the critical interface of agriculture and health. *Food Nutr. Bull.* **2007**, *28*, S372−S380.

(2) Yunus, A. W.; Razzazi-Fazeli, E.; Bohm, J. Aflatoxin B(1) in affecting broiler's performance, immunity, and gastrointestinal tract: a review of history and contemporary issues. *Toxins* **2011**, *3*, 566−590.

(3) Wang, Y. K.; Yan, Y. X.; Li, S. Q.; Wang, H. A.; Ji, W. H.; Sun, J. H. Simultaneous quantitative determination of multiple mycotoxins in cereal and feedstuff samples by a suspension array immunoassay. *J. Agric. Food Chem.* **2013**, *61*, 10948−10953.

(4) Hamid, A. S.; Tesfamariam, I. G.; Zhang, Y.; Zhang, Z. G. Aflatoxin B1-induced hepatocellular carcinoma in developing countries: geographical distribution, mechanism of action and prevention. *Oncol. Lett.* **2013**, *5*, 1087−1092.

(5) Probst, C.; Njapau, H.; Cotty, P. J. Outbreak of an acute aflatoxicosis in Kenya in 2004: identification of the causal agent. *Appl. Environ. Microbiol.* **2007**, *73*, 2762−2764.

(6) Marin, S.; Ramos, A. J.; Cano-Sancho, G.; Sanchis, V. Mycotoxins: occurrence, toxicology, and exposure assessment. *Food Chem. Toxicol.* **2013**, *60*, 218−237.

(7) Thieu, N. Q.; Ogle, B.; Pettersson, H. Efficacy of bentonite clay in ameliorating aflatoxicosis in piglets fed aflatoxin contaminated diets. *Trop. Anim. Health Prod.* **2008**, *40*, 649−656.

(8) Meissonnier, G. M.; Pinton, P.; Laffitte, J.; Cossalter, A. M.; Gong, Y. Y.; Wild, C. P.; Bertin, G.; Galtier, P.; Oswald, I. P. Immunotoxicity of aflatoxin B1: impairment of the cell-mediated response to vaccine antigen and modulation of cytokine expression. *Toxicol. Appl. Pharmacol.* **2008**, *231*, 142−149.

(9) Mehrzad, J.; Devriendt, B.; Baert, K.; Cox, E. Aflatoxin B(1) interferes with the antigen-presenting capacity of porcine dendritic cells. *Toxicol. In Vitro* **2014**, *28*, 531−537.

(10) Marin, D. E.; Taranu, I.; Bunaciu, R. P.; Pascale, F.; Tudor, D. S.; Avram, N.; Sarca, M.; Cureu, I.; Criste, R. D.; Suta, V.; Oswald, I. P. Changes in performance, blood parameters, humoral and cellular immune responses in weanling piglets exposed to low doses of aflatoxin. *J. Anim. Sci.* **2002**, *80*, 1250−1257.

(11) Weaver, A. C.; See, M. T.; Hansen, J. A.; Kim, Y. B.; De Souza, A. L.; Middleton, T. F.; Kim, S. W. The use of feed additives to reduce the effects of aflatoxin and deoxynivalenol on pig growth, organ health and immune status during chronic exposure. *Toxins* **2013**, *5*, 1261−1281.

(12) Cai, F.; Gao, W.; Li, H.; Chen, J.; Li, Z. [Aflatoxin contamination of Chinese herbal medicine in China and its potential management strategies]. *Zhongguo Zhongyao Zazhi* **2010**, *35*, 2503−2507.

(13) Sun, G.; Wang, S.; Hu, X.; Su, J.; Zhang, Y.; Xie, Y.; Zhang, H.; Tang, L.; Wang, J. S. Co-contamination of aflatoxin B1 and fumonisin B1 in food and human dietary exposure in three areas of China. *Food Addit. Contam., Part A* **2011**, *28*, 461−470.

(14) Li, F. Q.; Li, Y. W.; Wang, Y. R.; Luo, X. Y. Natural occurrence of aflatoxins in Chinese peanut butter and sesame paste. *J. Agric. Food Chem.* **2009**, *57*, 3519−3524.

DOI: 10.1021/acs.jafc.5b00433
J. Agric. Food Chem. 2015, 63, 6094−6101

(15) Rothkotter, H. J.; Sowa, E.; Pabst, R. The pig as a model of developmental immunology. *Hum. Exp. Toxicol.* **2002**, *21*, 533−536.
(16) Fairbairn, L.; Kapetanovic, R.; Sester, D. P.; Hume, D. A. The mononuclear phagocyte system of the pig as a model for understanding human innate immunity and disease. *J. Leukocyte Biol.* **2011**, *89*, 855−871.
(17) Butler, J. E.; Lager, K. M.; Splichal, I.; Francis, D.; Kacskovics, I.; Sinkora, M.; Wertz, N.; Sun, J.; Zhao, Y.; Brown, W. R.; DeWald, R.; Dierks, S.; Muyidermans, S.; Lunney, J. K.; McCray, P. B.; Rogers, C. S.; Welsh, M. J.; Navarro, P.; Klobasa, F.; Habe, F.; Ramsoondar, J. The piglet as a model for B cell and immune system development. *Vet. Immunol. Immunopathol.* **2009**, *128*, 147−170.
(18) Almond, G. W. Research applications using pigs. *Vet. Clin. N. Am.−Food A* **1996**, *12*, 707−&.
(19) Delmulle, B. S.; De Saeger, S. M.; Sibanda, L.; Barna-Vetro, I.; Van Peteghem, C. H. Development of an immunoassay-based lateral flow dipstick for the rapid detection of aflatoxin B1 in pig feed. *J. Agric. Food Chem.* **2005**, *53*, 3364−3368.
(20) Murphy, K. M.; Ouyang, W.; Farrar, J. D.; Yang, J.; Ranganath, S.; Asnagli, H.; Afkarian, M.; Murphy, T. L. Signaling and transcription in T helper development. *Annu. Rev. Immunol.* **2000**, *18*, 451−494.
(21) Carter, L. L.; Zhang, X.; Dubey, C.; Rogers, P.; Tsui, L.; Swain, S. L. Regulation of T cell subsets from naive to memory. *J. Immunother.* **1998**, *21*, 181−187.
(22) Xie, A. N.; Zheng, X.; Khattar, M.; Schroder, P.; Stepkowski, S.; Xia, J. H.; Chen, W. H. TCR stimulation without co-stimulatory signals induces expression of "tolerogenic" genes in memory CD4 T cells but does not compromise cell proliferation. *Mol. Immunol.* **2015**, *63*, 406−411.
(23) Ren, F.; Chen, X.; Hesketh, J.; Gan, F.; Huang, K. Selenium promotes T-cell response to TCR-stimulation and ConA, but not PHA in primary porcine splenocytes. *PLoS One* **2012**, *7*, e35375.
(24) Boding, L.; Nielsen, M. W.; Bonefeld, C. M.; von Essen, M. R.; Nielsen, B. L.; Lauritsen, J. P.; Hansen, A. K.; Nielsen, M. M.; Kongsbak, M.; Rubin, M.; Vennegaard, M. T.; Odum, N.; Geisler, C. Polymorphisms of the T cell receptor CD3delta and CD3epsilon chains affect anti-CD3 antibody binding and T cell activation. *Mol. Immunol.* **2010**, *47*, 2450−2457.
(25) Srikumar, R.; Parthasarathy, N. J.; Manikandan, S.; Narayanan, G. S.; Sheeladevi, R. Effect of Triphala on oxidative stress and on cell-mediated immune response against noise stress in rats. *Mol. Cell. Biochem.* **2006**, *283*, 67−74.
(26) Satoh, T.; Nakatsuka, D.; Watanabe, Y.; Nagata, I.; Kikuchi, H.; Namura, S. Neuroprotection by MAPK/ERK kinase inhibition with U0126 against oxidative stress in a mouse neuronal cell line and rat primary cultured cortical neurons. *Neurosci. Lett.* **2000**, *288*, 163−166.
(27) Xiao, W.; Zhu, Y.; Sarsour, E. H.; Kalen, A. L.; Aykin-Burns, N.; Spitz, D. R.; Goswami, P. C. Selenoprotein P regulates 1-(4-chlorophenyl)-benzo-2,5-quinone-induced oxidative stress and toxicity in human keratinocytes. *Free Radical Biol. Med.* **2013**, *65*, 70−77.
(28) Kogkopoulou, O.; Tzakos, E.; Mavrothalassitis, G.; Baldari, C. T.; Paliogianni, F.; Young, H. A.; Thyphronitis, G. Conditional up-regulation of IL-2 production by p38 MAPK inactivation is mediated by increased Erk1/2 activity. *J. Leukocyte Biol.* **2006**, *79*, 1052−1060.
(29) Liang, Q.; Guo, L.; Gogate, S.; Karim, Z.; Hanifi, A.; Leung, D. Y.; Gorska, M. M.; Alam, R. IL-2 and IL-4 stimulate MEK1 expression and contribute to T cell resistance against suppression by TGF-β and IL-10 in asthma. *J. Immunol.* **2010**, *185*, 5704−5713.
(30) Hughes-Fulford, M.; Sugano, E.; Schopper, T.; Li, C. F.; Boonyaratanakornkit, J. B.; Cogoli, A. Early immune response and regulation of IL-2 receptor subunits. *Cell. Signalling* **2005**, *17*, 1111−1124.
(31) Ubagai, T.; Tansho, S.; Ito, T.; Ono, Y. Influences of aflatoxin B1 on reactive oxygen species generation and chemotaxis of human polymorphonuclear leukocytes. *Toxicol. In Vitro* **2008**, *22*, 1115−1120.
(32) Wu, X.; Wei, C.; Pan, C.; Duan, Y.; Huang, K. Regulation of expression and activity of selenoenzymes by different forms and concentrations of selenium in primary cultured chicken hepatocytes. *Br. J. Nutr.* **2010**, *104*, 1605−1612.
(33) Cardoso, H. D.; dos Santos Junior, E. F.; de Santana, D. F.; Goncalves-Pimentel, C.; Angelim, M. K.; Isaac, A. R.; Lagranha, C. J.; Guedes, R. C.; Beltrao, E. I.; Morya, E.; Rodrigues, M. C.; Andrade-da-Costa, B. L. Omega-3 deficiency and neurodegeneration in the substantia nigra: involvement of increased nitric oxide production and reduced BDNF expression. *Biochim. Biophys. Acta, Gen. Subj.* **2014**, *1840*, 1902−1912.
(34) Shen, H. M.; Ong, C. N.; Shi, C. Y. Involvement of reactive oxygen species in aflatoxin B1-induced cell injury in cultured rat hepatocytes. *Toxicology* **1995**, *99*, 115−123.
(35) del Rio Garcia, J. C.; Moreno Ramos, C.; Pinton, P.; Mendoza Elvira, S.; Oswald, I. P. [Evaluation of the cytotoxicity of aflatoxin and fumonisin in swine intestinal cells]. *Rev. Iberoam. Micol.* **2007**, *24*, 136−141.
(36) Viegas, S.; Veiga, L.; Figueredo, P.; Almeida, A.; Carolino, E.; Sabino, R.; Verissimo, C.; Viegas, C. Occupational exposure to aflatoxin B1 in swine production and possible contamination sources. *J. Toxicol. Environ. Health, Part A* **2013**, *76*, 944−951.
(37) Costello, E.; Munoz, M.; Buetti, E.; Meylan, P. R. A.; Diggelmann, H.; Thali, M. Gene transfer into stimulated and unstimulated T lymphocytes by HIV-1-derived lentiviral vectors. *Gene Ther.* **2000**, *7*, 596−604.
(38) Rosenthal, A. S. Determinant selection and macrophage function in genetic control of the immune response. *Immunol. Rev.* **1978**, *40*, 136−152.
(39) Ray, P. D.; Huang, B. W.; Tsuji, Y. Reactive oxygen species (ROS) homeostasis and redox regulation in cellular signaling. *Cell. Signalling* **2012**, *24*, 981−990.
(40) Parveen, F.; Nizamani, Z. A.; Gan, F.; Chen, X.; Shi, X.; Kumbhar, S.; Zeb, A.; Huang, K. Protective effect of selenomethionine on aflatoxin B1-induced oxidative stress in MDCK cells. *Biol. Trace Elem. Res.* **2014**, *157*, 266−274.
(41) Williams, M. S.; Henkart, P. A. Role of reactive oxygen intermediates in TCR-induced death of T cell blasts and hybridomas. *J. Immunol.* **1996**, *157*, 2395−2402.
(42) Zhang, W.; Liu, H. T. MAPK signal pathways in the regulation of cell proliferation in mammalian cells. *Cell Res.* **2002**, *12*, 9−18.
(43) Liu, Y.; Gao, X.; Deeb, D.; Arbab, A. S.; Dulchavsky, S. A.; Gautam, S. C. Anticancer agent xanthohumol inhibits IL-2 induced signaling pathways involved in T cell proliferation. *J. Exp. Ther. Oncol.* **2012**, *10*, 1−8.
(44) Keshari, R. S.; Verma, A.; Barthwal, M. K.; Dikshit, M. Reactive oxygen species-induced activation of ERK and p38 MAPK mediates PMA-induced NETs release from human neutrophils. *J. Cell. Biochem.* **2013**, *114*, 532−540.
(45) O'Connell, S.; Tuite, N.; Slattery, C.; Ryan, M. P.; McMorrow, T. Cyclosporine A-induced oxidative stress in human renal mesangial cells: a role for ERK 1/2 MAPK signaling. *Toxicol. Sci.* **2012**, *126*, 101−113.

DOI: 10.1021/acs.jafc.5b00433
J. Agric. Food Chem. 2015, 63, 6094−6101

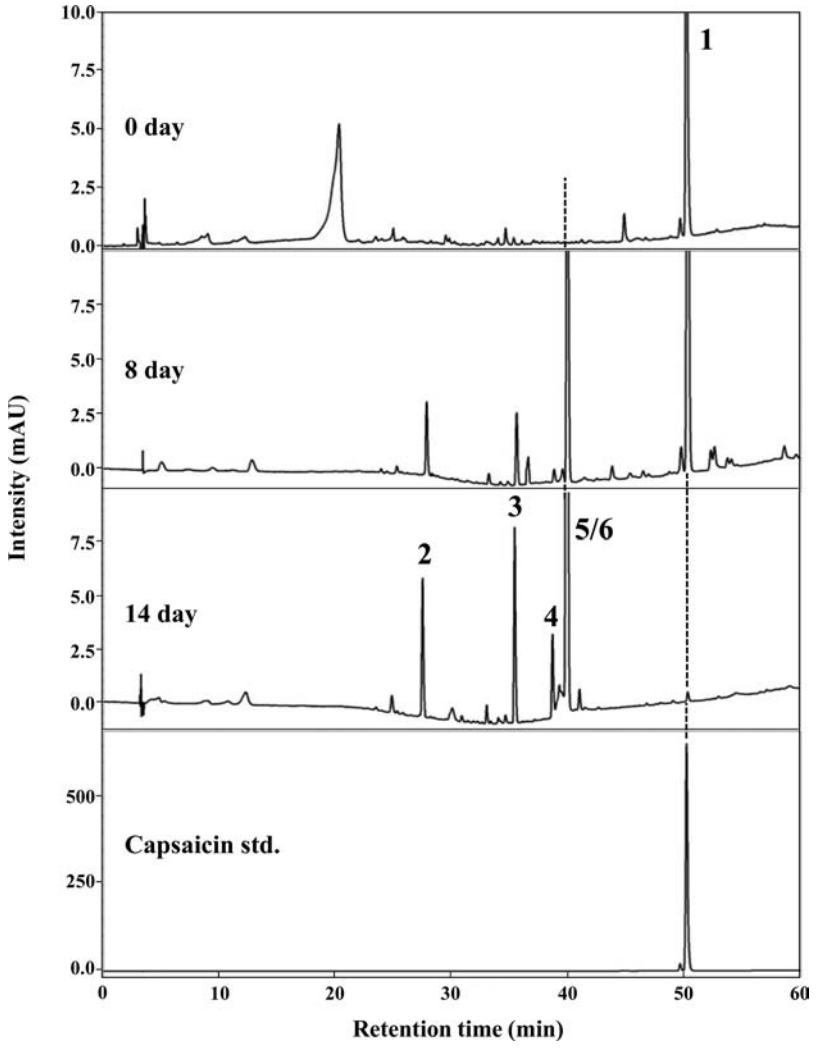

Figure 1. High-performance liquid chromatography chromatograms of capsaicin culture during incubation.

September 2014. The main ingredients were listed as red pepper powder, starch syrup, wheat flour, glutinous rice, *meju* made with soybean, and calcium. Capsaicin (purity, 50%) was obtained from Sigma-Aldrich Chemical Co. (St. Louis, MO, USA) and was purified as follows: Commercial capsaicin (purity, 50%) was dissolved in MeOH (0.3 mL). An aliquot of the capsaicin solution was subjected to preparative HPLC equipped with a Shim pack prep-ODS(H)KIT column (20 i.d. × 250 mm, 10 μm) (Shimadzu, Kyoto, Japan). Capsaicin was detected at 280 nm at a flow rate of 9.9 mL/min. Elution was achieved using a solvent mixture of MeOH/H_2O (7:3, v/v) as the mobile phase. Capsaicin (t_R 18.7 min, 240.6 mg, white powder) was collected, subjected to NMR and MS analyses, and used as a standard. The purity of capsaicin was >98.0%. *A. oryzae* KCCM 11372 was obtained from the Korean Culture Center for Microorganism (Seoul, Korea). Potato dextrose agar (PDA) and potato dextrose broth (PDB) were purchased from Difco Co. (Detroit, MI, USA). All solvents used for analyses were of HPLC grade. All other chemicals used were of reagent grade.

Incubation of Capsaicin with *A. oryzae*. Purified capsaicin (10 mg) was added to PDB (100 mL), inoculated with a 5% (v/w) spore suspension of *A. oryzae* and incubated for 14 days at 30 °C and 120 rpm in an incubator. The samples were collected at intervals of 0, 2, 4, 6, 8, 10, 12, and 14 days during the incubation and were stored immediately at −70 °C until analysis. *A. oryzae* was grown on PDA and maintained at 30 °C. The spores were inoculated to PDB and maintained in a shaker incubator at 30 °C and 120 rpm for 48 h. The cells were collected by centrifugation (890*g*, 15 min, at 4 °C), and starter culture was obtained.

HPLC Profile of Capsaicin Metabolites. The cultured capsaicin broth (1 mL) was centrifuged for 15 min, at 4 °C and 890*g*. The supernatant was extracted with EtOAc (6 mL, twice). The EtOAc fractions were combined and concentrated under vacuum. The EtOAc fraction was dissolved in 0.5 mL of 90% MeOH and subjected to reversed-phase-HPLC containing a photodiode array system operating at 200−800 nm. The capsaicin metabolites were separated on a Capcell Pak C18 column (UG-120, 4.6 mm i.d. × 250 mm, 5 μm) (Shisheido, Tokyo, Japan) at 40 °C using a gradient consisting of 100% H_2O (solvent A) to 100% MeOH (solvent B). The gradient was started with 50% B for 30 min, increased to 80% B at 50 min, and held at 100% B until 60 min. The flow rate was 1.0 mL/min.

Purification and Isolation of Capsaicin Metabolites. Purified capsaicin (200 mg) was added to PDB (2.0 L) and incubated for 14 days under the same conditions described above. Samples were collected at intervals of 0, 2, 4, 6, 8, 10, 12, and 14 days during the incubation. The cultured capsaicin broth was centrifuged for 15 min, at 4 °C and 890*g*. The supernatant was extracted with EtOAc (4 L, twice), and then the EtOAc fractions were combined and concentrated under vacuum. The EtOAc fraction was fractionated by octadecylsilane (ODS, 70−230 mesh) (YMC, Kyoto, Japan) column (3.0 cm × 80 cm i.d.) chromatography eluted with H_2O/MeOH (7:3−0:10, v/v, stepwise elution, each 300 mL). The fractions were subjected to TLC and grouped into 13 fractions (A−M). Each fraction was analyzed by HPLC under the conditions described above. The HPLC

DOI: 10.1021/acs.jafc.5b01730
J. Agric. Food Chem. 2015, 63, 6102−6108

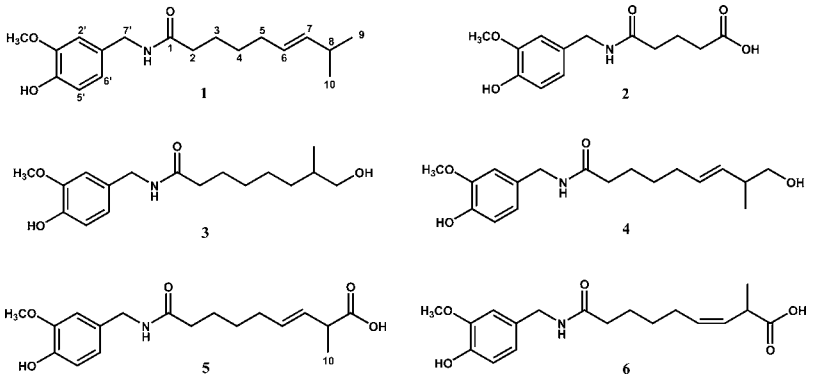

Figure 2. Structures of capsaicin and its metabolites isolated from capsaicin culture.

Table 1. ^{1}H Nuclear Magnetic Resonance Spectroscopic Data of the Capsaicin Metabolites

	δ_H (int, mult, J in Hz)				
position	2	3	4	5	6
1					
2	2.28 (2H, m)	2.22 (2H, t, 7.5)	2.23 (2H, m)	2.21 (2H, t, 7.5)	2.22 (2H, t, 7.5)
3	1.91 (2H, m)	1.63 (2H, m)	1.63 (2H, m)	1.63 (2H, m)	1.62 (2H, m)
4	2.32 (2H, m)	1.30 (2H, m)	1.38 (2H, m)	1.39 (2H, m)	1.40 (2H, m)
5		1.33 (2H, m)	2.02 (2H, m)	2.03 (2H, m)	2.04 (2H, m)
6a		1.39 (1H, m)	5.45 (1H, m)	5.53 (1H, dt, 15.5, 6.0)	5.54 (1H, dt, 12.5, 6.0)
6b		1.06 (1H, m)			
7		1.56 (1H, m)	5.33 (1H, m)	5.48 (1H, dt, 15.5, 7.5)	5.49 (1H, dt, 12.5, 7.0)
8		3.34 (2H, m)	3.40 (1H, m)	3.11 (1H, m)	3.02 (1H, m)
9		0.89 (3H, d, 7.0)	3.32 (2H, m)[a]		
10			0.89 (3H, d, 7.0)	1.20 (3H, d, 7.0)	1.19 (3H, d, 7.0)
2′	6.87 (1H, br s)	6.86 (1H, d, 1.0)	6.86 (1H, d, 1.5)	6.86 (1H, d, 1.5)	6.86 (1H, d, 1.5)
5′	6.73 (1H, d, 8.0)[a]	6.74 (1H, d, 8.0)	6.74 (1H, d, 8.0)	6.74 (1H, d, 8.0)	6.74 (1H, d, 8.0)
6′	6.73 (1H, br d, 8.0)[a]	6.71 (1H, br d, 8.0)	6.71 (1H, dd, 8.0, 1.5)	6.71 (1H, dd, 8.0, 1.5)	6.71 (1H, dd, 8.0, 1.5)
7′	4.26 (2H, s)	4.26 (2H, s)	4.26 (2H, s)	4.26 (2H, s)	4.52 (2H, s)
$-OCH_3$	3.84 (3H, s)	3.83 (3H, s)	3.83 (3H, s)	3.83 (3H, s)	3.82 (3H, s)

[a]The chemical shifts of H-5′ and H-6′ overlapped.

chromatograms showed high purity of fractions J (**3**, t_R 24.5 min, 4.5 mg), K (**4**, t_R 25.5 min, 93.6 mg), and L (a mixture of **5** and **6**, t_R 28.7 min, 12.8 mg). Fraction H (10.6 mg) was purified by HPLC equipped with a μBondapak C18 column (10 μm, 7.8 i.d. × 300 mm) (Waters, Milford, MA, USA) (flow rate, 5.0 mL/min; wavelength, 210 nm; elution, from 50 to 80% MeOH for 40 min) to give **2** (t_R 17.7 min, 1.0 mg). Thin-layer chromatography (TLC) was carried out by using silica gel TLC plates (0.25 mm thickness) (Merck, Rahway, NJ, USA) and developed using a mixture of EtOAc/HOAc/$CHCl_3$ (5:1:2, v/v/v). The spots were detected by UV light (254 nm) and 1% cerium(IV) sulfate ethanol solution spray.

Structural Analysis. NMR spectra were obtained with a ^{unit}INOVA 500 spectrometer (Varian, Walnut Creek, CA, USA). Methanol-d_4 (CD_3OD) (Acros Organics, Morris Plains, NJ, USA) containing tetramethylsilane was used as an analytical solvent. The mass spectra were acquired on a SYNAPT G2 hybrid (Waters, Cambridge, UK) and LCMS-8030 (Shimadzu, Kyoto, Japan) equipped with an electrospray ionization source (ESI-MS).

HPLC ESI MS/MS Analysis of the Capsaicin Metabolites Identified in Gochujang. Freeze-dried gochujang (1 g) was homogenized in MeOH (20 mL, twice). The mixture was filtered under vacuum through no. 2 filter paper (Whatman, Maidenstone, UK). The MeOH solutions were combined and concentrated under vacuum at 38 °C. The extracts were suspended in distilled water (10 mL) and partitioned with EtOAc (10 mL, three times). The EtOAc fraction was evaporated under vacuum at 38 °C and dissolved in MeOH/$CHCl_3$ (1:1, v/v, 4 mL), and then the fraction was analyzed using a high-performance liquid chromatography/electrospray ionization tandem mass spectrometer (HPLC-ESI/MS) (Shimadzu). Capsaicin and its metabolites (**1**−**6**) were separated under the chosen HPLC conditions [column, MG III (C18, 3 μm, 3.0 i.d. × 100 mm) (Shiseido); column temperature, 35 °C; flow rate, 0.3 mL/min (Shimadzu)]. The sample was eluted using a gradient system of H_2O (solvent A) to MeCN (solvent B) (both containing 0.3% formic acid), starting with 100% B, increasing to 20% A for 8 min, holding to 20% A for 16 min, increasing to 50% A for 30 min, increasing to 80% A for 35 min, increasing to 100% A for 40 min, and holding at 100% A for 45 min. The mass spectrometer was set up respectively for multiple reaction monitoring (MRM) with a dwell time of 0.1 s per transition to monitor the capsaicin metabolites: m/z 304.1 $[M - H]^-$ → 168.2 for **1**; m/z 268.3 $[M + H]^+$ → 137.1 for **2**, m/z 310.1$[M + H]^+$ → 174.3 for **3**, m/z 320.1$[M - H]^-$ → 184.1 for **4**, m/z 334.0 $[M - H]^-$→ 154.2 for **5** and **6**. The optimal MS conditions for **1**−**6** were employed: ESI source voltage, 3.5 kV; detector voltage, 45 V; heat block temperature, 400 °C; desolvation line temperature, 250 °C. Nebulizing gas and drying gas flows were 3.0 and 15.0 L/min, respectively. Argon was used as the collision gas at a pressure of 230 kPa. The optimized collision energies for **1**−**4** and **5** and/or **6** were 13.0, −16.0, −11.0, 13.0, and 19.0 V, respectively.

The contents of **1**−**6** in gochujang were quantitatively analyzed by HPLC ESI MS/MS analysis. Sample and standard solutions were prepared just before analysis. The calibration curves (n = 6) were constructed using **1**−**6** (0.1−50 ng) that were isolated from capsaicin broth incubated with *A. oryzae*. Accuracy and reproducibility were evaluated using the standard spike method. External standards of capsaicin and **1**−**6** were added to aliquots of gochujang at three

DOI: 10.1021/acs.jafc.5b01730
J. Agric. Food Chem. 2015, 63, 6102−6108

concentrations to determine their precision. The quantification and quantitation of capsaicin and its metabolites **1**−**6** in gochujang were performed in triplicate.

RESULTS AND DISCUSSION

Changes in Capsaicin and Its Metabolites in the Medium during *A. oryzae* Incubation. *A. oryzae* was incubated with capsaicin in PDB at 30 °C for 14 days. The supernatants (1 mL) obtained with the passage of time were extracted with EtOAc, and the H_2O and EtOAc fractions were analyzed by reversed-phase-HPLC. In the EtOAc fraction, the capsaicin peak decreased gradually depending on the incubation period (Figure 1). New metabolites were detected from 6 days of incubation, and then capsaicin was detected at detection limit concentration (100 pmol) at 14 days of incubation. No chemical transition was observed from H_2O fraction (data not shown), suggesting that capsaicin metabolites converted by *A. oryzae* were extracted in the EtOAc fraction. However, no chemical change of capsaicin was observed in PDB without *A. oryzae* at 30 °C for 14 days (data not shown).

Isolation and Identification of the Capsaicin Metabolites Converted by *A. oryzae*. Capsaicin was incubated with *A. oryzae* for 14 days, and the culture was solvent-fractionated to obtain the EtOAc fraction. Five converted metabolites **2**−**6** were purified and isolated from the EtOAc fraction of the capsaicin culture by ODS open-column chromatography and ODS-HPLC. The structures of the converted compounds were determined by NMR and ESI-MS analyses.

The molecular weight of metabolite **2** was determined to be 267, as established by a pseudomolecular ion peak at m/z 268.3 $[M + H]^+$ in the ESI-MS (positive) spectrum. The ^1H NMR spectrum of **2** was partially similar to that of **1**.[16] The ^1H NMR spectrum exhibited three trisubstituted benzene ring proton signals at δ 6.87 (1H, br s, H-2′), 6.73 (1H, d, J = 8.0 Hz, H-5′), and 6.73 (1H, d, J = 8.0 Hz, H-6′), one methoxyl proton signal at δ 3.84 (3H, s, $-OCH_3$), and one nitrogen-bearing methylene proton signal at δ 4.26 (2H, s, H-7′) (Table 1), indicating a vanillylamine moiety as a partial capsaicin structure. In addition, three sp^3 methylene carbon protons at δ 2.28 (2H, m, H-2), 1.91 (2H, m, H-3), and 2.32 (2H, m, H-4) were observed in the ^1H NMR spectrum. This result was also supported by the ^{13}C NMR spectrum, which contained 13 carbon signals including 7 sp^2 carbons with 5 quaternary carbons at δ 177.0−112.5 and 4 sp^3 carbons at δ 56.5−12.8 (Table 2). Considering the molecular weight of **2**, the chemical shifts in five sp^2 quaternary carbons indicated that one was a nitrogen-bearing carbonyl carbon at δ 175.3 (C-1) with evidence of a carbonyl carbon at δ 177.0 (C-4). Metabolite **2** was suggested to be *N*-vanillylcarbamoylbutanoic acid based on the ESI-MS and 1D NMR spectra. The complete NMR assignment and connectivity of **2** were further studied by $^1H-^1H$ correlation spectroscopy ($^1H-^1H$ COSY), heteronuclear single-quantum correlation (HSQC), and heteronuclear multiple-bond correlation (HMBC) experiments. Vanillyl and carbamoylbutanoic acid moieties were confirmed by the 2D NMR spectra. In particular, H-7′ was correlated with C-1 in the HMBC spectrum (Figure 3), indicating a vanillyl group was connected to the C-1 position of carbamoylbutanoic acid. Consequently, the structure of metabolite **2** was unambiguously determined to be *N*-vanillylcarbamoylbutanoic acid (Figure 2).

The molecular weight of metabolite **3** was 309 based on the pseudomolecular ion peaks detected at m/z 332.1 $[M + Na]^+$ and 310.1 $[M + H]^+$ in the ESI-MS (positive) spectrum, and the molecular formula ($C_{17}H_{27}NO_4$) was established by the HRESI-MS data (m/z 310.2021 $[M + H]^+$, calculated for $C_{17}H_{28}NO_4$, m/z 310.2018, +0.3 mDa). The ^1H NMR spectrum of **3** was related to that of **1**.[18] However, the ^1H NMR spectrum of **3** exhibited two upfield-shifted sp^3 methylene proton signals at δ 1.30 (2H, m, H-6) and 1.56 (1H, m, H-7) and one downfield-shifted sp^3 oxygenated methylene proton signal at δ 3.34 (2H, m, H-9′) (Table 1), compared to the proton signals of the olefinic double bond and the methyl group in capsaicin. The ^{13}C NMR spectrum revealed the presence of 17 carbon signals, including 7 sp^2 carbons with 4 quaternary carbons at δ 176.2−112.6 and 10 sp^3 carbons at δ 68.5−17.2 (Table 2). The side chain of **3** was suggested to be hydroxymethyloctanamide on the basis of the ESI-MS and 1D NMR spectra. The complete NMR assignment and connectivity of **3** were further determined by 2D NMR. The important correlations observed from the HMBC experiment are shown in Figure 3. In particular, correlations between H-9 and C-7 and C-8 were observed in the HMBC spectrum, indicating that the side chain of **3** was 8-hydroxy-7-methyloctanamide (Figure 3). Therefore, the structure of metabolite **3** was *N*-vanillyl-9-hydroxy-8-methyloctanamide (Figure 2), which is a new compound.

The molecular weight of metabolite **4** was 321 on the basis of the pseudomolecular ion peak detected at m/z 320.1 $[M - H]^-$ in the ESI-MS (negative) spectrum. The ^1H and ^{13}C NMR spectra of **4** were similar to those of **1**, except for an oxygenated methylene group. An oxygenated methylene proton and carbon signals were detected at δ 3.34 (2H, m, H-9) in the ^1H NMR spectrum (Table 1) and at δ 68.5 (C-9) in the ^{13}C NMR spectrum (Table 2), suggesting that **4** is a hydroxylated capsaicin (ω-hydroxycapsaicin). The ^1H and ^{13}C NMR spectra of **4** were consistent with those of ω-hydroxycapsaicin, which was isolated from *Capsicum annuum* (Banshou) previously.[19] Therefore, **4** was identified as ω-hydroxycapsaicin (Figure 2).

The molecular weight of fraction L was 335 on the basis of the pseudomolecular ion peak detected at m/z 334.2 $[M - H]^-$ in the ESI-MS (negative) spectrum, and the molecular formula ($C_{18}H_{25}NO_5$) was established by the HRESI-MS data (m/z

Table 2. ^{13}C NMR Nuclear Magnetic Resonance Spectroscopic Data of the Capsaicin Metabolites

	δ_C				
position	**2**	**3**	**4**	**5**	**6**
1	175.3	176.2	176.1	176.0	176.0
2	36.3	37.2	37.1	37.0	37.0
3	12.8	27.2	26.7	26.7	26.6
4	22.5	30.7	30.2	29.9	29.9
5	177.0	27.9	33.5	33.3	33.2
6		34.4	131.2	131.0	130.6
7		36.9	131.7	132.7	133.0
8		68.5	40.8	44.0	44.0
9		17.2	68.4	179.0	177.3
10			17.4	18.1	18.0
1′	142.1	131.7	134.5	131.6	131.6
2′	112.5	112.6	112.6	112.5	112.6
3′	149.2	149.1	149.1	149.1	149.1
4′	147.0	146.9	146.9	146.9	146.9
5′	116.2	116.2	116.2	116.2	116.2
6′	121.6	121.5	121.5	121.5	121.5
7′	44.1	44.1	44.1	44.1	44.2
$-OCH_3$	56.5	56.5	56.5	56.5	56.5

DOI: 10.1021/acs.jafc.5b01730
J. Agric. Food Chem. 2015, 63, 6102−6108

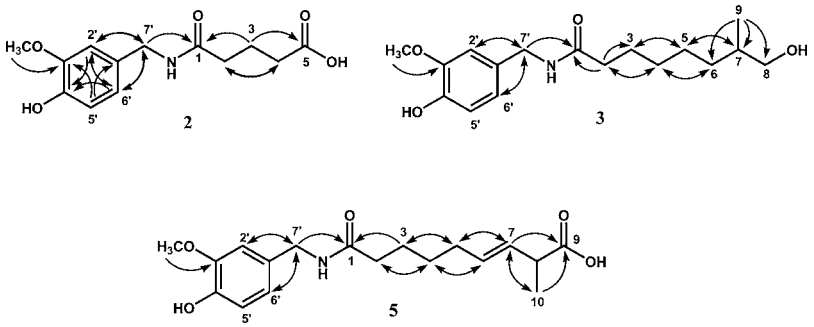

Figure 3. Heteronuclear multiple-bond correlation (HMBC) correlations (arrows) for **2**, **3**, and **5**.

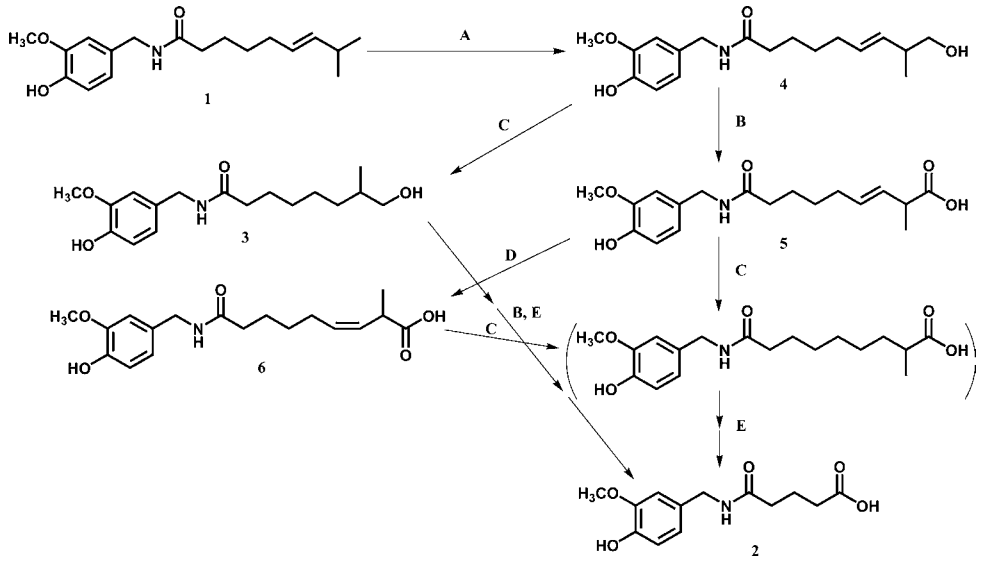

Figure 4. Proposed bioconversion mechanisms of the metabolite conversion from capsaicin by *A. oryzae*: (A) ω-hydroxylation; (B) alcohol oxidation; (C) hydrogenation; (D) isomerization; (E) α- and β-oxidations.

334.1655 $[M - H]^-$, calculated for $C_{18}H_{24}NO_5$, m/z 334.1654, +0.1 mDa). The ^1H and ^{13}C NMR spectra of fraction L showed evidence of a mixture of two compounds. These data suggest that the skeletal structure was similar, but the olefinic double bond differed. The ^1H NMR spectrum of fraction L had unequal methine proton signal intensity at a ratio of 2.5:1 (the main metabolite, **5**; the minor metabolite, **6**). The ^1H and ^{13}C NMR spectra of **5** were related to those of **1** and **4**, except for a carbonyl group. A carbonyl carbon signal at δ 179.0 (C-9) was observed in the ^{13}C NMR spectrum (Table 2), indicating that **5** contained a carboxylic group rather than a methyl alcohol group contained in **4**. The ESI-MS and 1D NMR results suggested that **5** was methyl-*N*-vanillylcarbamoyloctenoic acid. The complete NMR assignment and connectivity of **5** were further determined by 2D NMR. The olefinic double-bond position was side chain C-6 and C-7, based on the proton−proton correlations in the $^1H-^1H$ COSY experiment and the proton−carbon correlations in the HMBC experiment. In particular, correlations (Figure 3) of H-10 and H-7 to C-9 and of H-10 to C-7 were observed in the HMBC spectrum, indicating that the side chain of **5** was determined to be 8-methylcarbamoyl-6-octenoic acid (Figure 2). The olefinic double-bond signals of **5** overlapped with those of **6**. The olefinic double-bond signals of **5** were confirmed by the NOE experiment. The proton signals of the methyl group at δ 1.20 (H-10) and the olefinic double bond at δ 5.48−5.54 (H-6 and H-7) were enhanced when the proton signal of H-8 at δ 3.11was irradiated. The geometry of the olefinic double bond at C-6 and C-7 was the *trans* form, on the basis of their coupling constant value (15.5 Hz). Therefore, the structure of metabolite **5** was 8-methyl-*N*-vanillylcarbamoyl-6(*E*)-octenoic acid (Figure 2).

The ^1H and ^{13}C NMR spectra of metabolite **6** were closely related to those of metabolite **5**, except for different chemical shifts in the methine proton and olefinic double-bond carbon signals (Table 1). In particular, methine proton signals at δ 3.02 (H-8) were observed at 0.09 ppm upfield, the C-7 signal at δ 133.0 was shifted by 0.3 ppm, and the signals of C-6 at δ 130.6 and of C-9 at δ 177.3 were shifted by above 0.4 ppm compared to the ^1H and ^{13}C NMR spectra of **5**. The complete NMR assignment and connectivity of **6** were further confirmed by the $^1H-^1H$ COSY, HSQC, and HMBC experiments. The geometry of the olefinic double bond at C-6 and C-7 was the *cis* form, based on the NOE data and their coupling constant value (12.5 Hz). Consequently, the structure of metabolite **6** was 2-methyl-*N*-vanillylcarbamoyl-6(*Z*)-octenoic acid (Figure 2).

The structures of five metabolites converted from capsaicin by *A. oryzae* were determined by NMR and MS analyses. Metabolites **2**, **4**, and **5** have already been reported as capsaicin metabolites converted by *A. niger*.[15,16] However, the NMR study for the capsaicin metabolites **2** and **5** converted by *A. niger* was insufficient. Therefore, we performed complete assignments of them using NMR analysis to provide data as models for establishing the structures of the capsaicin

DOI: 10.1021/acs.jafc.5b01730
J. Agric. Food Chem. 2015, 63, 6102−6108

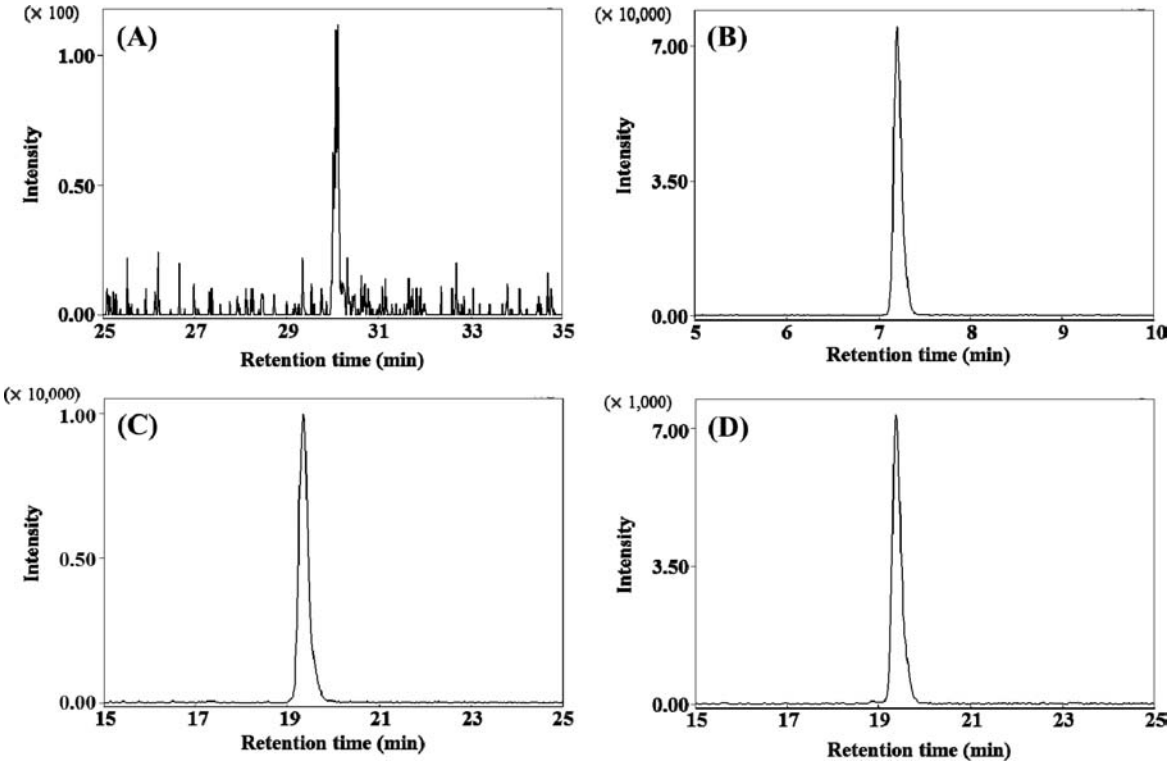

Figure 5. Multiple reaction monitoring chromatograms of (A) **1**, (B) **2**, (C) **4**, and (D) **5** and/or **6** in gochujang. Capsaicin and its metabolites were analyzed by LC-ESI-MS/MS. Capsaicin metabolites were detected by selective multiple reaction monitoring (MRM): m/z 304.1 $[M - H]^-$ → 168.2 for **1**; m/z 268.3 $[M + H]^+$ → 137.1 for **2**; m/z 320.1 $[M - H]^-$ → 184.1 for **4**; m/z 334.0 $[M - H]^-$→ 154.2 for **5** and **6**. Detailed procedures for LC-ESI-MS/MS analysis have been described under Materials and Methods.

metabolites in future research. Among the five metabolites, **3** and **6** are new capsaicin metabolites first reported in this study. *Streptomyces mobaraensis* and *Actinoplanes utahensis* hydrolyze capsaicin to vanillylamine and *trans*-8-methyl-6-nonenoic acid.[10−14] However, capsaicin hydrolysates (vanillylamine and *trans*-8-methyl-6-nonenoic acid) were not identified in this study. These observations indicate that capsaicin hydrolysis may not be a predominant pathway in *A. oryzae*. The conversion mechanisms by *A. oryzae* of capsaicin metabolites are proposed in Figure 4. Metabolite **4** was produced by the hydroxylation of capsaicin and was converted to **3** and **5** by β-oxidation and alcoholic oxidation, respectively. In addition, metabolite **6** was probably degraded from **5** by α- and β-oxidations via isomerization and/or hydrogenation, and **2** was likely produced from **3** by α- and β-oxidations.

Qualitative and Quantitative Analyses of the Capsaicin Metabolites in Gochujang. Capsaicin and its metabolites **1**−**6** in gochujang were quantitated by HPLC-ESI-MS using the isolated compounds as external standards. The EtOAc fraction obtained after solvent fractionation from gochujang MeOH extracts was analyzed by selective MRM detection and MS/MS. The capsaicin metabolites **1**, **2**, **4**, and **5** and/or **6** were detected at t_R 30.8, 7.2, 19.3, and 19.4 min on the MRM chromatogram of gochujang (Figure 5). The metabolites were identified using the retention times of authentic compounds **1**, **2**, **4**, and **5** and/or **6**. In this study, the identity of **5** and **6** on the EtOAc fraction MRM chromatogram could not be determined because **5** and **6** were a mixture when they were purified, suggesting that **5** and **6** are present in gochujang. However, metabolite **3** (t_R 16.0 min; limit of detection, 0.5 ng) was not detected on the MRM chromatogram of gochujang, suggesting no production of it or rapid conversion to other capsaicin metabolites, although this compound is produced during fermentation of gochujang. These results indicate that capsaicin metabolites **2**, **4**, and **5** and/or **6** are unambiguously present in gochujang.

Capsaicin and its metabolites **1**, **2**, **4**, and **5** and/or **6** were also analyzed quantitatively by selective MRM detection and MS/MS. The external calibration curve of each compound at a concentration range of 0.1−50 ng produced a good linear correlation ($R^2 > 0.99$). The dilution ratio of gochujang extract in MeOH/$CHCl_3$ was 1:800 (w/v). The repeatability of each metabolite ranged from 1.1 to 2.6%: **1**, 1.1%; **2**, 1.9%; **4**, 2.6%; and **5** and/or **6**, 2.4%. The recoveries of **1** (99.0 ± 1.1%), **2** (99.5 ± 1.9%), **4** (100.3 ± 2.6%), and **5** and/or **6** (101.0 ± 2.4%) ranged from 99.0 to 101.1%. Of the capsaicin metabolites, **5** and **6** (5607.8 ± 53.0 μg/100 g dry wt) were most abundantly found in gochujang, yet the abundance was lower than that of capsaicin (7671.4 ± 278.6 μg/100 g dry wt) (Table 3). Metabolites **2** (74.8 ± 1.4 μg/100 g dry wt) and **4**

Table 3. Contents of Capsaicin and Its Metabolites in Gochujang

metabolite	content[a] (μg/100 g dry wt)
1	7671.4 ± 278.6
2	74.8 ± 1.4
3	ND
4	38.1 ± 0.9
5 and/or **6**	5607.8 ± 53.0

[a]Data are expressed mean ± standard deviation of triplicate experiments.

DOI: 10.1021/acs.jafc.5b01730
J. Agric. Food Chem. 2015, 63, 6102−6108

(38.1 ± 0.9 μg/100 g dry wt) were present in small amounts in gochujang compared to **5** and/or **6**. In this study, most capsaicin was converted when *A. oryzae* was incubated with capsaicin in PDB at 30 °C for 14 days. However, capsaicin was found at greater content than capsaicin metabolites in gochujang product. It is considered because gochujang is a high viscous paste that is fermented from a primary mixture of red hot pepper powder, waxy rice flour, fermented soybean, and koji. Although capsaicin metabolite-related enzymes were secreted from *A. oryzae* during the fermentation of gochujang, the amounts and activities of the secreted enzymes may be relatively lower than those in PDB culture. Therefore, capsaicin may be converted slowly to capsaicin metabolites during the fermentation of gochujang. The varieties and contents of capsaicin metabolites in gochujang may be dependent upon the fermentation microorganisms and the extent of fermentation.

The contents of capsaicinoids in hot pepper were 46−77% for capsaicin, 21−40% for dihydrocapsaicin, 2−12% for nordihydrocapsaicin, and >2% for other capsaicin derivatives.[1,18] According to the results of a capsaicinoid sensory evaluation, the pungent intensity decreases in the order **1** (100) = dihydrocapsaicin (100) > nordihydrocapsaicin (57) > homodihydrocapsaicin (50) > homocapsaicin (43).[20] In addition, *N*-nonanoylvanillylamide, which contains a nine-carbon side chain, has the most pungent taste.[21] However, the pungency of capsaicin derivatives, which have more variable carbon side chains than that of *N*-nonanoylvanyllylamide, is lower.[22,23] Thus, the pungency of capsaicin derivatives may depend on the amide acylation and carbon side chain length. In addition, ω-hydroxycapsaicin has slightly weaker pungency than **1**.[19] All capsaicin metabolites identified in this study contain the carboxylic acid or hydroxyl groups, and **2** and **3** had fewer carbons in their side chain than **1**. Therefore, capsaicin metabolites are likely to be less pungent than capsaicin, although pungency was not evaluated in this study.

The five capsaicin metabolites converted by *A. oryzae* were elucidated by NMR and MS analyses. Also, the capsaicin metabolites in gochujang were all found except for **3**. Therefore, the capsaicin metabolites are likely produced from **1** during gochujang fermentation, and the product becomes less pungent than red hot pepper. These results will provide useful information to improve the quality and biological activity of gochujang to control pungency during fermentation. New alternatives for capsaicin products in food and pharmaceutical applications can be suggested for future study.

AUTHOR INFORMATION

Corresponding Author

*(J.-H.M.) Phone: +82-62-530-2141. Fax: +82-62-530-2149. E-mail: nutrmoon@jnu.ac.kr.

Funding

This research was supported by a grant from the Korea Food Research Institute (Project E0141501-02).

Notes

The authors declare no competing financial interest.

REFERENCES

(1) Contreras-Padilla, M.; Yahia, E. M. Changes in capsaicinoids during development, maturation, and senescence of chile peppers and relation with peroxidase activity. *J. Agric. Food Chem.* **1998**, *46*, 2075−2079.

(2) Dairam, A.; Fogel, R.; Daya, S.; Limson, J. L. Antioxidant and iron-binding properties of curcumin, capsaicin, and *S*-allylcysteine reduce oxidative stress in rat brain homogenate. *J. Agric. Food Chem.* **2008**, *56*, 3350−3356.

(3) Kawada, T.; Hagihara, K.; Iwai, K. Effects of capsaicin on lipid metabolism in rats fed a high fat diet. *J. Nutr.* **1986**, *116*, 1272−1278.

(4) Bode, A. M.; Dong, Z. The two faces of capsaicin. *Cancer Res.* **2011**, *71*, 2809−2814.

(5) Kwon, D. Y.; Kim, Y. S.; Ryu, S. Y.; Cha, M. R.; Yon, G. H.; Yang, H. J.; Kim, M. J.; Park, S. Capsiate improves glucose metabolism by improving insulin sensitivity better than capsaicin in diabetic rats. *J. Nutr. Biochem.* **2013**, *24*, 1078−1085.

(6) Park, J. M.; Lee, S. S.; Oh, H. I. Changes in chemical characteristics of traditional *Kochujang meju* during fermentation. *Korean J. Food Nutr.* **1995**, *8*, 184−191.

(7) Lee, K. H.; Lee, M. S.; Park, S. O. Studies on the microflora and enzymes influencing on Korean native *kochujang* (red pepper soybean paste) aging. *J. Korean Agric. Chem. Soc.* **1976**, *19*, 82−92.

(8) Kim, Y. S.; Oh, B. H.; Shin, D. H. Quality characteristics of Kochujang prepared with different *meju* fermented with *Aspergillus* sp. and *Bacillus subtilis*. *Food Sci. Biotechnol.* **2008**, *17*, 527−533.

(9) Cho, J. Y.; Lee, H. J.; Shin, H. C.; Lee, J. M.; Park, K. H.; Moon, J. H. Behavior of flavonoid glycosides contained in Korean red pepper paste (*gochujang*) during fermentation: participation of a β-glucosidase inhibitor. *Food Sci. Biotechnol.* **2013**, *22*, 1245−1252.

(10) Kim, H. E.; Han, S. Y.; Kim, Y. S. Quality characteristics of *gochujang meju* prepared different fermentation tools and inoculation time of *Aspergillus oryzae*. *Food Sci. Biotechnol.* **2010**, *19*, 1579−1585.

(11) Cho, S.; Moon, H. I.; Hong, G. E.; Lee, C. H.; Kim, J. M.; Kim, S. K. Biodegradation of capsaicin by *Bacillus licheniformis* SK1230. *Han'guk Eungyong Sangmyong Hwahakhoeji* **2014**, *57*, 335−339.

(12) Duarte, D. R.; Castillo, E.; Bárzana, E.; López-Munguía, A. Capsaicin hydrolysis by *Candida antarctica* lipase. *Biotechnol. Lett.* **2000**, *22*, 1811−1814.

(13) Koreishi, M.; Zhang, D.; Imanaka, H.; Imamura, K.; Adachi, S.; Matsuno, R.; Nakanishi, K. A novel acylase from *Streptomyces mobaraensis* that efficiently catalyzes hydrolysis/synthesis of capsaicins as well as *N*-acyl-L-amino acids and *N*-acyl-peptides. *J. Agric. Food Chem.* **2006**, *54*, 72−78.

(14) Romano, D.; Gandolfi, R.; Guglielmetti, S.; Molinari, F. Enzymatic hydrolysis of capsaicins for the production of vanillylamine using ECB deacylase from *Actinoplanes utahensis*. *Food Chem.* **2011**, *124*, 1096−1098.

(15) Lee, S. S.; You, I. S. Biodegradation mechanisms of capsaicin and its analogs (I): microbial ω-hydroxylation on capsaicin mixture. *Korean Biochem. J.* **1977**, *10*, 135−146.

(16) Lee, I. S.; Lee, S. S. Microbial transformation mechanism of capsaicinoids general biodegradation pattern of capsaicinoids by fungi. *Yakhak Hoeji* **1987**, *31*, 280−285.

(17) Onozaki, H.; Sasaoka, K.; Ezaki, H. Hydrolytic degradation of capsaicin by *Aspergillus niger* and *Aspergillus oryzae*. *J. Ferment Technol.* **1976**, *54*, 29−301.

(18) Lin, L. Z.; West, D. P.; Cordell, G. A. NMR assignments of *cis*- and *trans*- capsaicin. *Nat. Prod. Lett.* **1993**, *3*, 5−8.

(19) Ochi, T.; Takaishi, Y.; Kogure, K.; Yamauti, I. Antioxidant activity of a new capsaicin derivative from *Capsicum annuum*. *J. Nat. Prod.* **2003**, *66*, 1094−1096.

(20) Todd, P. H.; Bensinger, M. G.; Biftu, T. Determination of pungency due to capsicum by gas-liquid chromatography. *J. Food Sci.* **1977**, *42*, 660−665.

(21) Lee, S. J.; Han, M. S.; Chang, Y. I. Method for producing koji of hot pepper paste (gochujang) with reduced hotness, koji produced by the method, and hot pepper paste prepared from the koji. U.S. Patent 7,514,109, April 7, 2009.

(22) Castillo, E.; Torres-Gavilán, A.; Severiano, P.; Arturo, N.; López-Munguía, A. Lipase-catalyzed synthesis of pungent capsaicin analogues. *Food Chem.* **2007**, *100*, 1202−1208.

(23) Wang, J.; Peng, Z.; Zhou, S.; Zhang, J.; Zhang, S.; Zhou, X.; Zhang, X.; Peng, B. A study of pungency of capsaicinoid as affected by their molecular structure alteration. *Pharmacol. Pharm.* **2011**, *2*, 109−115.

DOI: 10.1021/acs.jafc.5b01730
J. Agric. Food Chem. 2015, 63, 6102−6108

and 5 days. Samples for Nano-PALDI MSI were cut from the fruit using a blade, and the frozen samples were set axially in a cryostat (CM-3050S; Leica, USA) at −25 °C. Samples were cut into serial sections (50 μm) and thaw-mounted on indium tin oxide glass slides for MSI.

MSI of Procymidone in Cucumbers. Standard procymidone dissolved in 70% methanol (Dr Ehrenstorfer, Germany) was used for the standards. Standard procymidone was desalted before MS measurement to detect a definite protonated ion. Standard procymidone (10 ppm) was dropped on an iron oxide nanoparticle-coated target MS plate. After drying the solution, ice water was dropped on the target position and immediately removed. High solubility sali-ions were almost purged from the procymidone sample. MSI was achieved by a Fourier-transform ion cyclotron resonance (FT-ICR) MS (SolariX, Bruker, Germany). An iron oxide nanoparticle (1 mg/mL) suspension was dispersed in methanolic solution and was sprayed on glass slides with an airbrush on some sections (nozzle caliber, 0.2 mm). The section surface was irradiated with 1000 laser shots in the positive ion detection mode of the mass spectrometer. To detect the laser spot area, the sections were scanned and a spot-to-spot center distance of 100 μm in each direction at the center and the pericarp of the cucumber was measured. For the pericarp, flesh, and seed regions, the related intensities were processed by discarding background peaks. The remaining intensities formed the set of variables that were used for imaging and semiquantitative analysis.

RESULTS AND DISCUSSION

Detection of Procymidone by GC-MS and Nano-PALDI-FT-ICR MS. GC-MS was used for the quantitative analysis of the pericarp, flesh, and whole fruit. The total ion chromatogram showed that the signal at 21.5 min corresponded to procymidone, which was consistent with the database value. We monitored the procymidone ion at m/z 283 and prepared a calibration curve over the range of 0.01−10 ppm. Selected ion monitoring of m/z 283 showed m/z 255, 212, 96, 67, and 53 as fragment ions.[9] The whole sample showed the same amount of procymidone residue regardless of the time stored, indicating that the amount of procymidone residue did not decrease during storage. In the pericarp region, the amount of procymidone decreased over time. There was a substantial decrease in the amount of procymidone residue between days 0 and 1 and subsequent days, whereas it did not change between days 1, 3, and 5. In contrast, the flesh showed a substantial increase in the amount of procymidone (Figure 1).

We investigated whether the increase in the concentration of the procymidone residue was caused by changes in the weight of the cucumber through the evaporation of water. The weight of the cucumbers did not change over time. Thus, the GC-MS results quantitatively showed the amount of procymidone in cucumbers.

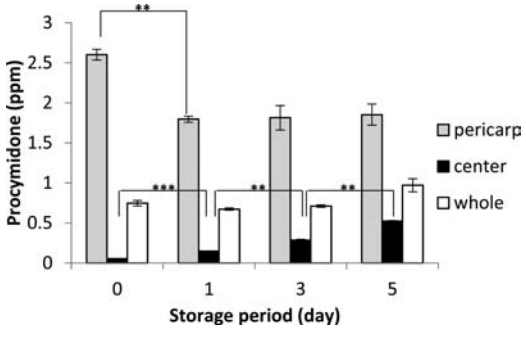

Figure 1. GC results for the concentration of procymidone in the pericarp, flesh, and whole cucumber. The values are expressed as the standard error of mean. (**) $p < 0.01$, and (***) $p < 0.001$ by Student's t test.

FT-ICR MS offers high resolution ($R = 10^5-10^6$) and accuracy ($\Delta m = 10^{-4}-10^{-3}$ u).[10−12] Thus, we could classify the molecular species from the exact mass (M_e) without tandem mass spectrometry. To confirm the ionization of procymidone by Nano-PALDI, a procymidone standard was ionized using an iron oxide nanoparticle ionization-assisting reagent. Procymidone ions at m/z 284.025, 306.007, and 321.981 corresponded to the protonated ion and the sodium and potassium adducts, respectively (Figure 2). The same signals were detected from the section of cucumber sample containing the procymidone standard, indicating that iron oxide-based Nano-PALDI ionized the procymidone in the cucumber sections (Figure 3).

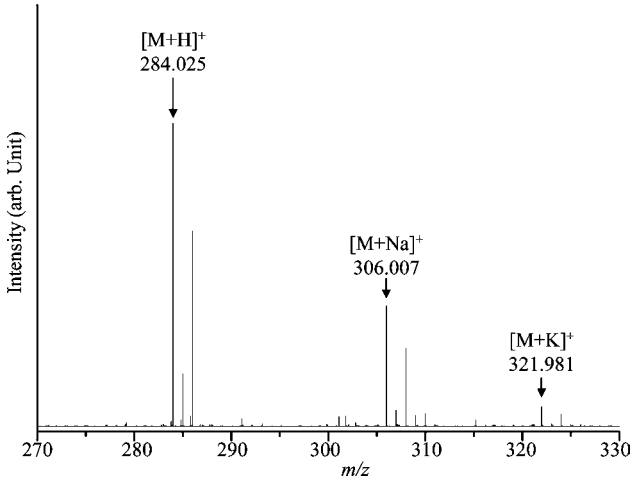

Figure 2. Nano-PALDI MS spectra of procymidone standard. m/z 284.025, 306.007, and 321.981 correspond to the protonated ion and sodium and potassium adducts of procymidone, respectively.

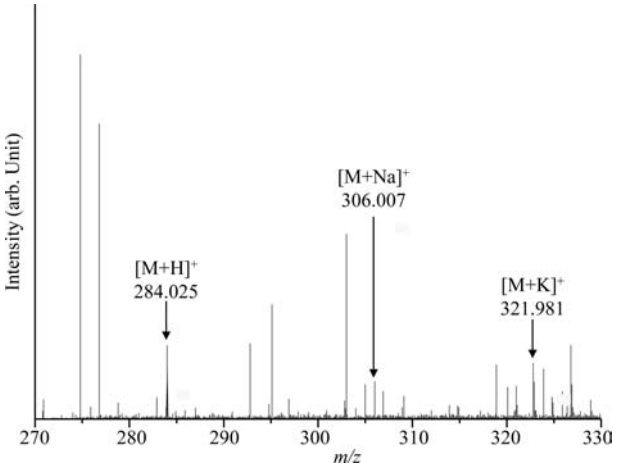

Figure 3. Mass spectrum of cucumber section containing procymidone.

Comparison of Storage Period. We imaged the localization of procymidone in cucumbers by MSI at a resolution of 100 μm to show whether procymidone was localized in any of the regions. The protonated ion signal was chosen as the procymidone target in the cucumber section because the images of the sodium and potassium adducts reflected the

DOI: 10.1021/acs.jafc.5b00957
J. Agric. Food Chem. 2015, 63, 6109−6112

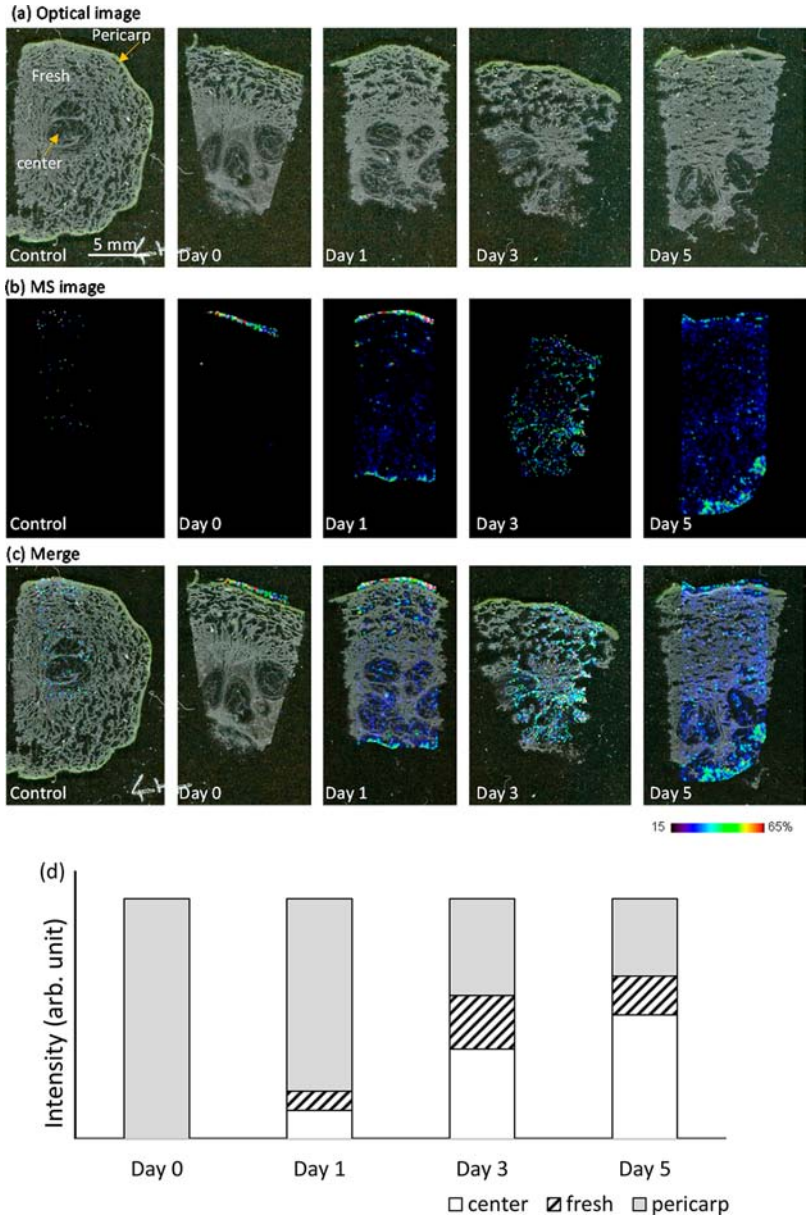

Figure 4. Procymidone distribution in cucumber control samples and samples sprayed with procymidone 0, 1, 3, and 5 days after harvest: optical image of cucumber sections (a); MSI of procymidone (b); merged optical and ion image (c); stacked bar chart of procymidone in the samples, reconstructed from the MSI data by binarization (d).

localization of the salt rather than that of the procymidone. A number of high-intensity signals were detected in the mass spectrum obtained from the samples containing procymidone. Thus, we could analyze the localization of procymidone from cucumber sample by MSI.

The optical image of the cucumber sections was used to determine the pericarp, flesh, and center regions of the tissue (Figure 4a). The control sample did not show the presence of procymidone. The cucumber samples that were sprayed with procymidone after harvest on day 0 showed procymidone in only the pericarp region and procymidone had not reached the inner region.

The image of the cucumber sample 1 day after harvest showed procymidone in the pericarp region in a ladder pattern. Procymidone migrated toward the inner region. Three days after harvest, procymidone was mainly present from the premedial flesh to the center region. Five days after harvest, procymidone was found in the center region. These images were not obtained on the same day; thus, we constructed the ion images by normalizing the signal intensity of m/z 284.025 (Figure 4b,c).

Semiquantitative regional analysis was performed by matching the MS intensities with the pericarp, flesh, and seed regions. The values were converted to the intensity per unit area. The total intensity ratios for samples 0, 1, 3, and 5 days after harvest were 3:2:1:1, 0:1:2:3, and 0:1:3:5 in the pericarp, flesh, and seed regions, respectively.

In the pericarp, the intensity for the day 0 sample was 3-fold higher than that for the day 3 and 5 samples. The intensity of the samples decreased over time. However, for the flesh the intensity increased in the day 1−3 samples and decreased in the day 5 sample. In contrast, the intensity of the center region gradually increased with time, indicating that procymidone reached the inner region and ended up in the center region

DOI: 10.1021/acs.jafc.5b00957
J. Agric. Food Chem. 2015, 63, 6109−6112

(Figure 4d). Penetration of procymidone occurred from day 1, and it was present in all sections of the cucumber by day 3 and became concentrated in the center, although some procymidone remained in the pericarp. These data show only relative comparison, although it was in good agreement with quantitative GC-MS data (Figure 1).We performed MSI of the localization of procymidone in cross sections of cucumbers. Nano-PALDI enabled imaging of the low molecular weight pesticide. MSI showed that procymidone migrated toward the center of the cucumber over 5 days. Visualization of pesticide gives us the time-dependent permeation aspect. MSI is a powerful tool for fundamental science, agricultural chemistry, food hygiene, and pesticide science.

Shu Taira[†]
Motomi Tokai[‡]
Daisaku Kaneko[§]
Hajime Katano[†]
Yasuko Kawamura-Konishi*[,‡]

[†]Department of Bioscience, Fukui Prefectural University, Eiheiji, Fukui 910-1195, Japan

[‡]Department of Food Science, Ishikawa Prefectural University, 1-308 Suematsu, Nonoichi-shi, Ishikawa-ken 921-8836, Japan

[§]Kyushu Institute of Technology, 1-1 Sensui, Tobata, Kitakyushu, Fukuoka 804-0015, Japan

AUTHOR INFORMATION

Corresponding Author

*(Y.K.-K.) E-mail: konishi@ishikawa-pu.ac.jp. Phone: +81-76-227-7454.

Funding

This research was supported by a Lotte grant and a SUNBOR grant to S.T.

Notes

The authors declare no competing financial interest.

ACKNOWLEDGMENTS

We are grateful to Dr. Nobuyuki Fukuoka for his kind help in this work.

REFERENCES

(1) Shiba, K.; Kaneko, H.; Yoshino, H.; Kakuta, N.; Iba, K.; Nakatsuka, I.; Yoshitake, A.; Yamada, H.; Miyamoto, J. Comparative metabolism of procymidone in rats and mice. *J. Pestic. Sci.* **1991**, *16*, 27−33.

(2) Mikami, N.; Satogami, H.; Miyamoto, J. Metabolism of procymidone in rats. *J. Pestic. Sci.* **1979**, *4*, 165−174.

(3) Simal Gandara, J.; Paseiro Losada, P.; Gonzalez Rodriguez, V.; Romero Rodriguez, A. Comparison of GC-MS and HPLC-UV for determination of procymidone in wine. *J. Agric. Food Chem.* **1993**, *41*, 674−677.

(4) Stoeckli, M.; Chaurand, P.; Hallahan, D. E.; Caprioli, R. M. Imaging mass spectrometry: a new technology for the analysis of protein expression in mammalian tissues. *Nat. Med.* **2001**, *7*, 493−496.

(5) Taira, S.; Shimma, S.; Osaka, I.; Kaneko, D.; Ichiyanagi, Y.; Ikeda, R.; Konishi-Kawamura, Y.; Zhu, S.; Tsuneyama, K.; Komatsu, K. Mass spectrometry imaging of the capsaicin localization in the *Capsicum* fruits. *Int. J. Biotechnol. Wellness Ind.* **2012**, *1*, 61−65.

(6) Zaima, N.; Goto-Inoue, N.; Hayasaka, T.; Setou, M. Application of imaging mass spectrometry for the analysis of *Oryza sativa* rice. *Rapid Commun. Mass Spectrom.* **2010**, *24*, 2723−2729.

(7) Taira, S.; Hashimoto, M.; Saito, K.; Shido, O. Visualization of decreased docosahexaenoic acid in the hippocampus of rats fed an n-3 fatty acid-deficient diet by imaging mass spectrometry. *J. Biophys. Chem.* **2012**, *3*, 221−226.

(8) Taira, S.; Sugiura, Y.; Moritake, S.; Shimma, S.; Ichiyanagi, Y.; Setou, M. Nanoparticle-assisted laser desorption/ionization based mass imaging with cellular resolution. *Anal. Chem.* **2008**, *80*, 4761−4766.

(9) Castillo-Sánchez, J.; Aguilera-del Real, A.; Rodriguez-Sánchez, M.; Valverde-García, A. Residue levels, decline curves, and plantation distribution of procymidone in green beans grown in greenhouse. *J. Agric. Food Chem.* **2000**, *48*, 2991−2994.

(10) Budzikiewicz, H.; Gross, J. H. Mass spectrometry. A textbook. *Anal. Bioanal. Chem.* **2005**, *381*, 1319−1320.

(11) Walk, T. B.; Trautwein, A. W.; Richter, H.; Jung, G. ESI fourier transform ion cyclotron resonance mass spectrometry (ESI-FT-ICR-MS): a rapid high-resolution analytical method for combinatorial compound libraries. *Angew. Chem., Int. Ed.* **1999**, *38*, 1763−1765.

(12) Asamoto, B. In *FT-ICR/MS*; 1991; p. Medium: X; Size: 306 pp.

DOI: 10.1021/acs.jafc.5b00957
J. Agric. Food Chem. 2015, 63, 6109−6112

dissolution in NaOH/urea aqueous solution. The effects of acid pretreatment time on DP, carbohydrate composition, kappa numbers, crystallinity indices, morphology, and dissolved proportions of lignocellulose were studied.

MATERIALS AND METHODS

Materials. Softwood unbleached kraft pulp (UKP) with a kappa number of about 28, another softwood unbleached kraft pulp (UKP′) with a higher lignin content, and a softwood thermomechanical pulp (TMP) were used as the wood pulp samples, which were kindly provided by Oji Paper Co., Ltd., Japan. $NaClO_2$ was purchased from Sigma-Aldrich Co. Other reagents and solvents were of laboratory grade and were used as received from Wako Pure Chemicals, Tokyo, Japan.

Chlorite Delignification. The UKP or TMP with a weight of 5 g was delignified by a mixture of 1 g of $NaClO_2$, 0.3 mL of acetic acid, and 160 g of water four times. The mixture was kept at room temperature. It took 40 min each time. The mixture was occasionally shaken by hand. Softwood bleached kraft pulp (BKP) with low lignin content and bleached TMP (BTMP) were finally obtained after filtration.

Dilute Acid Hydrolysis. Three grams of dried original pulp (UKP, UKP′, and TMP) or bleached pulp (BKP and BTMP) was dispersed in 100 g of 3% H_2SO_4 aqueous solution. The mixture was heated by water bath at 80 °C for different times (0.5, 1, 2, 3, or 4 h). After the acid hydrolysis, the pulps were separated by filtration and kept without drying. The pulp samples were coded as UKP-hydrolysis time (UKP-0.5, UKP-1, UKP-2, UKP-3, or UKP-4), UKP′-hydrolysis time (UKP′-4 or UKP′-8), TMP-hydrolysis time (TMP-4 or TMP-8), BKP-hydrolysis time (BKP-0.5, BKP-1, BKP-2, BKP-3, or BKP-4), and BTMP-hydrolysis time (BTMP-4), respectively. The pulps without acid treatment were coded UKP-0, BKP-0, UKP′-0, TMP-0, and BTMP-0, respectively.

Dissolution. The original pulp or acid-treated pulp was dispersed in a 7 wt % NaOH/12 wt % urea/81 wt % H_2O solution with pulp content of 1 wt %, and then the pulp dispersion was frozen and thawed. The resulting mixture was centrifuged at 10000 rpm for 10 min at 5 °C and then filtered.[16] The remaining undissolved fractions were washed by 7 wt % NaOH/12 wt % urea/81 wt % H_2O three times and further washed by water until they were neutral. Then they were dried in a vacuum oven with P_2O_5 at 40 °C for 48 h and weighed. The dissolved proportion of the pulp was calculated according to the equation

$$\text{dissolved proportion} = \frac{m_0 - m_1}{m_0} \times 100\% \quad (1)$$

where m_0 is the dry mass of the pulp before dissolution and m_1 is the dry mass of the residual undissolved pulp. The dissolved proportion measurements were repeated more than three times, and their average was obtained.

Film Preparation. UKP′-4 was dissolved in NaOH/urea solvent to obtain a lignocellulose solution with 4 wt % lignocellulose content. After centrifugation, the solution was cast on a glass plate and soaked in 5 wt % aqueous H_2SO_4 for 5 min, following the previously reported method.[19] The regenerated lignocellulose gel was washed thoroughly with water and air-dried at 23 °C and 50% relative humidity for more than 1 day to obtain the lignocellulose film.

Lignin Content Determination. The Klason method and kappa number method were used to determine the lignin content of the samples.[36]

Sugar Analysis. The carbohydrate compositions of the samples were determined by the alditol−acetate method.[37] Sulfuric acid (72 wt %, 1 mL) was added to 100 mg samples, kept at room temperature for 4 h, and then diluted with water to adjust the concentration of sulfuric acid at 4 wt %. Hydrolysis of the samples in 4 wt % sulfuric acid was performed in an autoclave at 120 °C for 1 h. After cooling to room temperature, the hydrolyzed solution was filtered by glass filter, and the filtrate was adjusted to 100 mL with water. As the internal standard, 1.00 mL of *myo*-inositol aqueous solution (1.00 mg/mL) was added into 5.00 mL of the cooled solution obtained above. The solution was neutralized by aqueous barium hydroxide solution to pH 5.5. After removal of the precipitate, about 20 mg of $NaBH_4$ was added to the filtrate, and the reaction mixture was kept at room temperature for 24 h. Excess $NaBH_4$ was degraded by acetic acid. After the mixture was evaporated to dryness, a small amount of methanol was added and dried. This was repeated several times, and then the mixture was heated in an oven at 105 °C for 15 min to ensure complete removal of the water. The dry residue was acetylated by 1 mL of acetic anhydride below 120 °C for 3 h and then analyzed by gas chromatography GC-14b with FID (Shimadzu Co., Kyoto, Japan) using a column TC-17 (fused-silica capillary column, 30 m, 0.25 mm i.d, GL Science Inc., Tokyo, Japan) with a temperature program of 20 min at 220 °C, injection temperature of 220 °C, and detector temperature of 230 °C.

X-ray Diffraction (XRD). The samples were dried in a vacuum oven with P_2O_5 at 40 °C for 48 h. XRD patterns of the samples were acquired in reflection mode using a RINT 2000 diffractometer (Rigaku, Tokyo, Japan) with monochromator-filtered Cu Kα radiation (λ = 0.15418 nm) at 40 kV and 40 mA. Scans were obtained from 4 to 40° 2θ at a speed of 1° per minute. The crystallinity index (CI) was calculated from the height ratio between the intensity of the crystalline region and total region according to Segal's method.[38,39]

Scanning Electron Microscopy (SEM). The surfaces of the wood pulps were coated with osmium using a Meiwafosis Neo osmium coater at 10 mA for 10 s and observed with a Hitachi S4800 field-emission SEM at 2 kV.

Optical Microscopy. The pulps were dispersed in the 7 wt % NaOH/12 wt % urea/81 wt % H_2O solutions with pulp content of 1 wt %, and then the pulp dispersions were frozen and thawed. The images of the final dispersions (or solutions) were observed by using an optical microscope (BX-50 with a digital camera DP-20, Olympus, Japan).

Viscosity-Average Degree of Polymerization (DP_v) measurement. The samples (0.04 g) were dissolved in 0.5 M copper ethylenediamine (20 mL) for 30 min. The intrinsic viscosity of the solution was obtained by using a Cannon−Fenske capillary viscometer, and the value was converted to DP_v values using the Mark−Houwink−Sakurada equation, $[\eta] = 0.57 \times DP_v$.[40]

Tensile Test. The tensile test of the lignocellulose film was performed using a Shimadzu EZ-TEST instrument equipped with a 500 N load cell. Rectangular strips 2 × 30 mm in size were cut from the lignocellulose film and tested with a span length of 10 mm at a rate of 1.0 mm min^{-1}. The film was conditioned at 23 °C and 50% relative humidity for 2 days before the test.

RESULTS AND DISCUSSION

Effect of Acid Treatment on Characteristics of Pulps. Figure 1 shows the yields of the wood pulps after acid

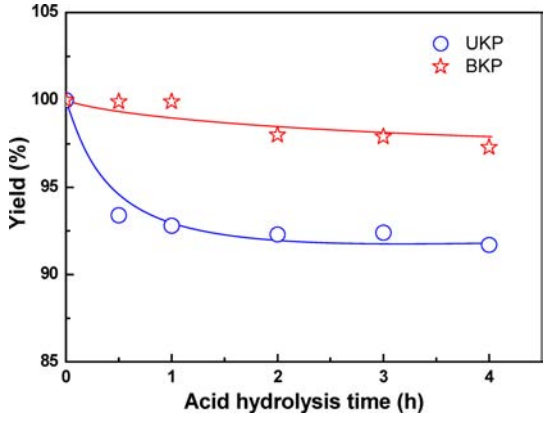

Figure 1. Effects of acid hydrolysis time on the yields of the wood pulps. Yield is based on the weight of the samples before acid hydrolysis.

DOI: 10.1021/acs.jafc.5b01714
J. Agric. Food Chem. 2015, 63, 6113−6119

hydrolysis based on the weight of the wood pulps before acid hydrolysis. The yields decreased only a little after acid hydrolysis. Even after 4 h of acid hydrolysis, the yield of softwood BKP was still high (97.3%) and slightly higher than 91.7% of softwood UKP. This was probably because BKP contains less acid soluble components, such as lignin and hemicellulose, after delignification compared with UKP. Especially, the yields of the wood pulps with different acid-treated times (0.5−4 h) were almost the same. As will be seen later, the amounts of the main components (cellulose, hemicellulose, and lignin) of the wood pulps barely changed under the mild dilute acid hydrolysis condition, which is the reason for the high yields of UKP and BKP after acid hydrolysis.

The kappa numbers of the wood pulps are shown in Figure 2. After acid hydrolysis, the kappa numbers of UKP and BKP slightly decreased and kept a similar level with different acid-treated times (0.5−4 h). Table 1 shows the carbohydrate compositions of the wood pulps before and after dilute sulfuric acid treatment. The results indicated that the hemicellulose contents of the pulps barely changed under the different acid treatment times (0.5−4 h). The results of carbohydrate compositions together with the kappa numbers (Figure 2) and yields of the pulps (Figure 1) confirmed that the amounts of the main components (cellulose, hemicellulose, and lignin) of UKP and BKP were almost unchanged for the different acid hydrolysis times, and in this case their influence on the dissolution of wood pulp in NaOH/urea system could be excluded.

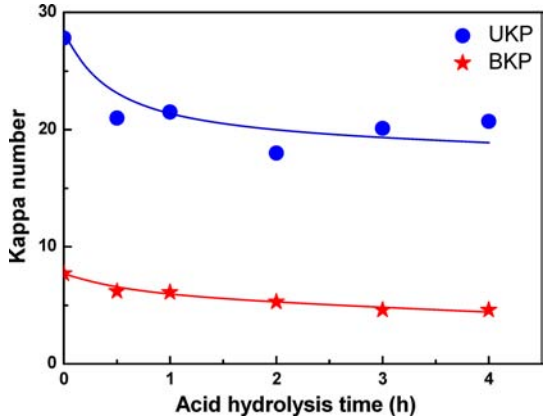

Figure 2. Effects of acid hydrolysis time on the kappa numbers of the wood pulps.

Table 1. Carbohydrate Compositions of the Wood Pulps before and after Pretreatment by Sulfuric Acid Hydrolysis

sample	glucose (%)	xylose (%)	mannose (%)	galactose (%)
UKP-0	71.1	6.5	5.0	0.8
UKP-0.5	78.3	6.5	6.8	0.8
UKP-1	83.1	7.3	5.4	0.2
UKP-2	84.7	7.2	5.7	0.6
UKP-3	81.1	7.2	3.8	0.5
UKP-4	84.1	6.9	5.4	0.4
BKP-0	82.1	7.4	5.6	0.8
BKP-0.5	83.3	7.4	5.6	0.5
BKP-1	84.8	7.5	5.5	0.5
BKP-2	85.4	7.2	6.0	0.6
BKP-3	85.9	6.8	5.5	0.5
BKP-4	86.9	7.2	5.5	0.5

Figure 3 shows the XRD patterns of the wood pulps before and after acid hydrolysis, and the effects of acid hydrolysis time on the crystallinity indices (CI) of the wood pulps are shown in Figure S1. Compared with the original wood pulp, the crystallinity indices of the acid hydrolysis pulps increased. The crystallinity indices of UKP increased from 66 to 77% and that of BKP increased from 73 to 79%, with the increase in acid hydrolysis time from 0 to 4 h. Moreover, the increase in the crystallinity index of UKP after 1 h of acid hydrolysis was more than that of BKP; this was probably due to there being more amorphous components present in UKP-0 than in BKP-0, such as lignin, hemicellulose, and amorphous cellulose.

SEM images of the wood pulps before and after acid hydrolysis are shown in Figure 4. UKP-0 and BKP-0 show relatively smooth and flat surfaces, and many random microfibril bundles were present on the surface of UKP-0, probably owing to the S1 layer of the wood fiber. However, after acid hydrolysis, these random microfibril bundles disappeared and some oriented fiber bundles appeared, forming a rough surface. This change in morphology of wood fiber was probably due to the S1 layer of the wood fiber having been removed by acid hydrolysis and the secondary wall of the wood fiber appearing.[34] Moreover, compared with UKP, the change in morphology of BKP after acid hydrolysis was more obvious. The surface of BKP became very rough, and some microfibril bundles were stripped from the surface of the wood fiber after acid hydrolysis. This may have been because lignin exerted a preventative influence on the acid hydrolysis of wood fiber, and the lower lignin content of BKP compared with UKP led to a greater change in morphology after the acid hydrolysis.

Dissolution of Acid-Treated Unbleached Kraft Pulp and Bleached Kraft Pulp. Figure 5 shows the photos of different UKP/NaOH/urea solutions and BKP/NaOH/urea solutions after freezing and thawing. The UKP-0/NaOH/urea solution and BKP-0/NaOH/urea solution were not transparent. However, after 2 h of acid pretreatment, UKP and BKP gave transparent NaOH/urea solution, suggesting that most of the UKP-2 and BKP-2 was dissolved in the NaOH/urea solution.

The effect of acid pretreatments on the dissolution of wood pulps was also studied by optical microscopy. The relevant optical microscope images of different UKP/NaOH/urea solutions after freezing and thawing are shown in Figure 6. In the case of the UKP-0/NaOH/urea dispersion, most of the wood fibers kept their original morphology, although some of the wood fibers were swollen. However, even after 0.5 h of acid hydrolysis, the morphology of UKP-0.5 changed obviously. Most pulps were dissolved or became highly swollen fibers, fragments, balloons, or flat rings in the insoluble fractions. Moreover, with increasing acid hydrolysis time, the insoluble fractions were reduced. UKP-3/NaOH/urea shows a clear solution image, indicating that after 3 h of acid hydrolysis, the wood pulp almost completely dissolved in the NaOH/urea aqueous solution.

Figure 7 shows the dissolved proportions and DP_v of wood pulps pretreated by dilute sulfuric acid. After 4 h of acid hydrolysis, DP_v of UKP and BKP decreased from 1150 to 550 and from 1300 to 520, respectively, whereas the dissolved proportions of UKP and BKP increased from 20.7 to 94.7% and

DOI: 10.1021/acs.jafc.5b01714
J. Agric. Food Chem. 2015, 63, 6113−6119

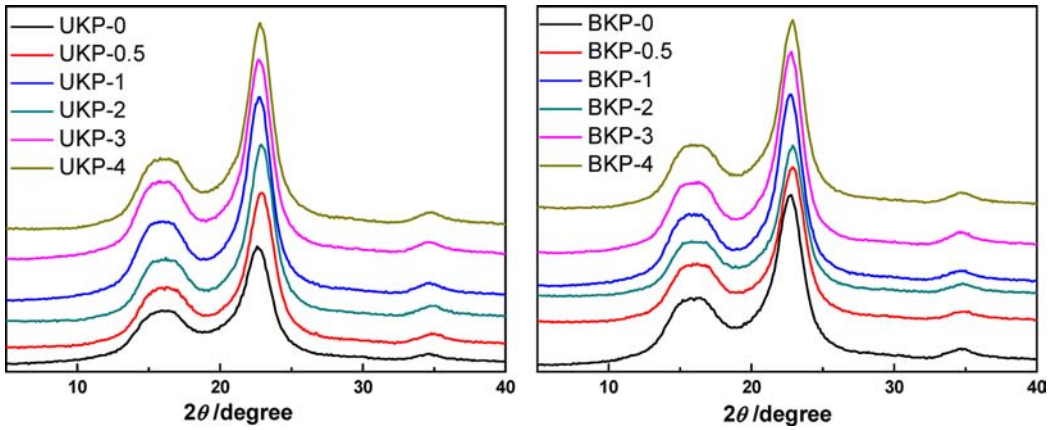

Figure 3. XRD patterns of the wood pulps before and after acid hydrolysis.

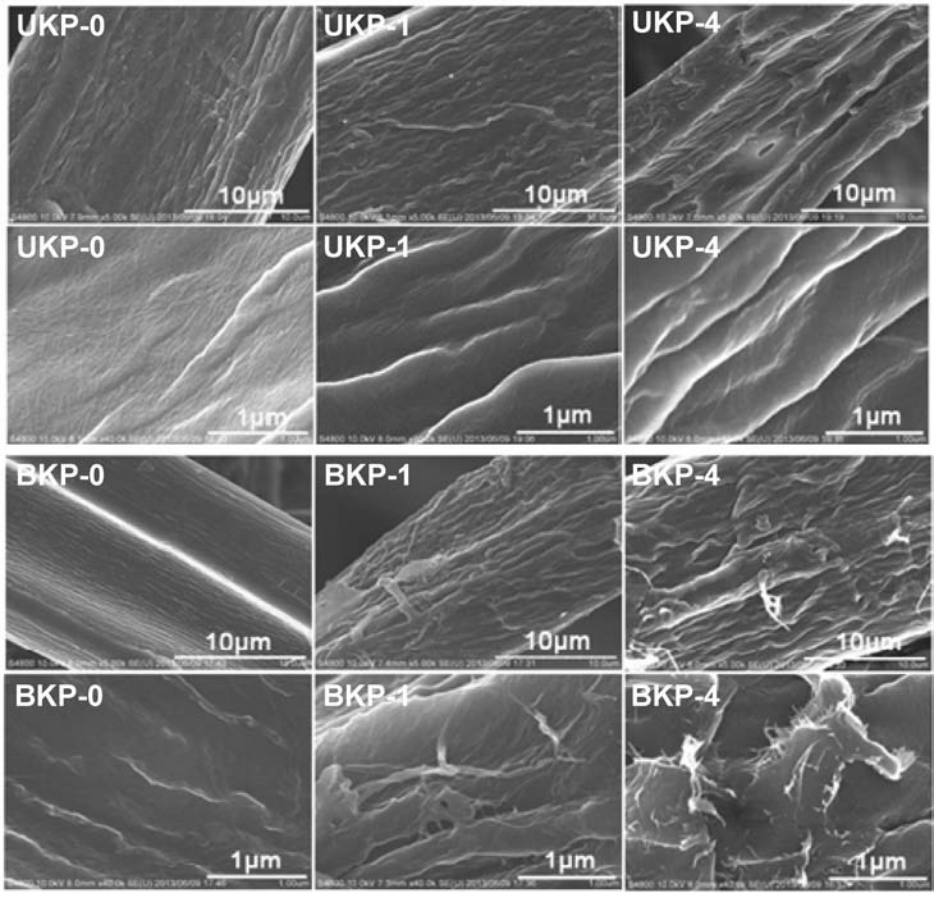

Figure 4. SEM images of the wood pulps before and after acid hydrolysis.

from 20.5 to 96.3%, respectively. It was indicated that the wood pulps with lower DP had higher dissolved proportions in the NaOH/urea solvent system, which was similar to the dissolution of cotton linters cellulose in this solvent system.[24] In fact, even though the acid hydrolysis time was only 2 h, the dissolved proportions of UKP-2 and BKP-2 had already increased to about 90%, which was much better than those of the untreated UKP-0 and BKP-0. Moreover, the dilute acid-treated wood pulps still kept a relatively high DP_v of about 600. Furthermore, this figure also shows that under the same acid hydrolysis conditions, the dissolved proportions of UKP and BKP were similar. This indicated that the main factor influencing the dissolved proportion of the wood pulp in this case is the molecular weight of the wood pulp, and the effect of lignin content could be neglected. However, it does not mean that the presence of lignin does not affect the dissolution of the pulps into this solvent. After acid hydrolysis, the lignin molecule must be cut into smaller fragments even though they are not removed from the pulp.[41] This fragmentation of lignin must affect the interaction between lignin and polysaccharide. The results of dissolved proportions of the wood pulps were in good agreement with the results of their appearances (Figure 5) and optical microscope images (Figure 6).

DOI: 10.1021/acs.jafc.5b01714
J. Agric. Food Chem. 2015, 63, 6113−6119

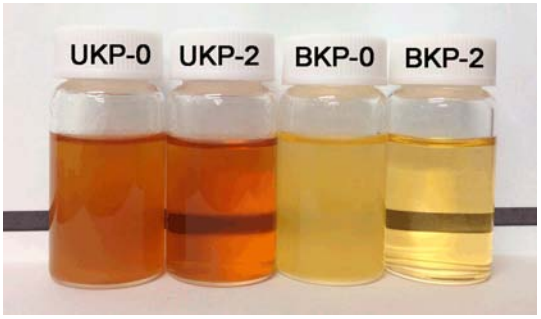

Figure 5. Photographs of different UKP/NaOH/urea solutions and BKP/NaOH/urea solutions after freeze and thaw.

To further confirm that wood pulp with low molecular weight was easily dissolved in NaOH/urea solvent, regenerated wood pulps were prepared by regeneration of once-dissolved pulp with ethanol. DP_v values of the original wood pulp samples and the regenerated wood pulp samples are shown in Figure 8. BKP-3 with a low DP_v of 530 almost completely dissolved in NaOH/urea solvent (Figure 7). After dissolution and regeneration, DP_v of the regenerated BKP-3 was about 400, not much lower than that of the original BKP-3. This result indicated that the dissolution of wood pulp in NaOH/urea solvent followed by regeneration resulted in only a slight degradation of cellulose. Furthermore, UKP-1 and BKP-1 could not completely dissolve in the NaOH/urea solvent. The DP_v of the regenerated UKP-1 was about 410, which was much lower than that of the original UKP-1 (700). The DP_v of the regenerated BKP-1 was about 390, also much lower than that of the original BKP-1 (730). This indicates again that the low molecular weight fraction of pulp was easy to dissolve in the NaOH/urea solvent, which is consistent with the results of the dissolved proportions shown in Figure 7.

Dissolution of Wood Pulps with High Lignin Contents. To study whether the acid-treated pulp with high lignin content (>3%) could dissolve in NaOH/urea solvent or not, the different acid hydrolysis pulps with relatively high lignin contents were dissolved, and their relevant dissolved proportions are shown in Table 2. UKP′ had a lignin content of 6.1%. After acid hydrolysis for 4 h, it could dissolve well in NaOH/urea solvent, and its dissolved proportion increased from 20 to 93%. The dissolved proportion of the original TMP was very low (about 10%), probably due to its high lignin content (about 29%). After acid hydrolysis for 4 h, the dissolved proportion of TMP increased to 33%, although the dissolved proportion was still very low. Even after acid hydrolysis for 8 h, TMP still could not completely dissolve and the dissolved proportion was <40%. After delignification of TMP by $NaClO_2$, the obtained BTMP had a lignin content of about 13.5%. After 4 h of acid hydrolysis of BTMP, the dissolved proportion of the obtained BTMP-4 increased from 45 to 96%, which indicated that, even though the lignin content of BTMP-4 was still as high as 14.2%, it could dissolve well in NaOH/urea solvent.

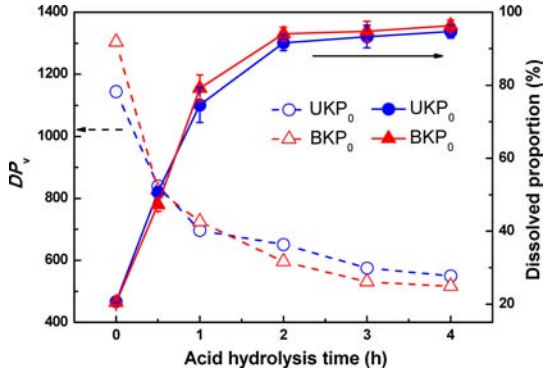

Figure 7. Effects of acid hydrolysis time on the dissolved proportions and viscosity-average degrees of polymerization (DP_v) of the wood pulps.

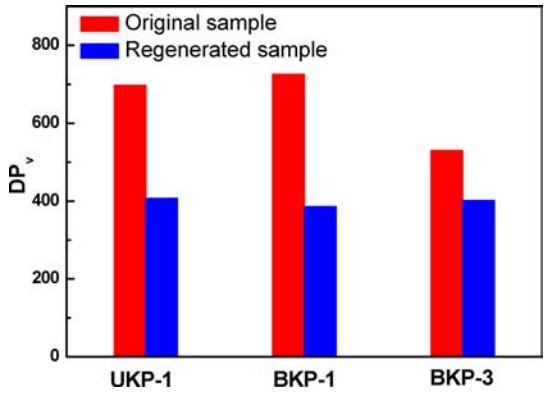

Figure 8. Viscosity-average degrees of polymerization (DP_v) of the wood pulps (UKP-1, BKP-1, and BKP-3) and their relevant regenerated samples prepared by dissolution in NaOH/urea solution followed by regeneration with ethanol.

Table 2. Dissolved Proportions of Different Pulp Species before and after Acid Treatment

sample	Klason lignin content (%)	dissolved proportion (%)
UKP′-0	6.1	19.7 ± 0.7
UKP′-4	6.9	93.4 ± 2.1
TMP-0	28.7	10.5 ± 0.2
TMP-4	32.3	33.3 ± 0.1
TMP-8	33.3	37.6 ± 0.8
BTMP-0	13.5	42.8 ± 2.8
BTMP-4	14.2	95.6 ± 3.6

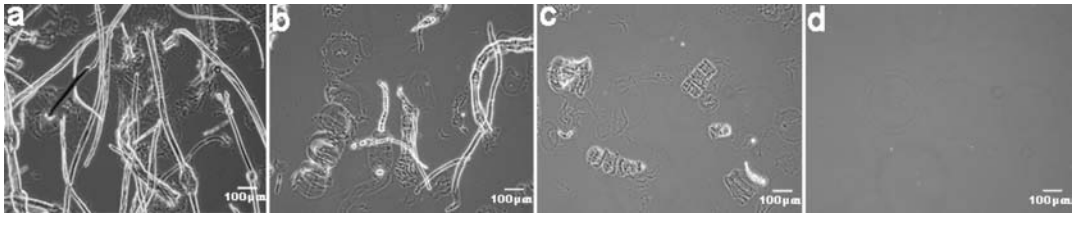

Figure 6. Optical microscopy images of different UKP/NaOH/urea solutions after freeze and thaw: (a) UKP-0; (b) UKP-0.5; (c) UKP-1; (d) UKP-3.

DOI: 10.1021/acs.jafc.5b01714
J. Agric. Food Chem. 2015, 63, 6113−6119

The dissolution of wood pulps in NaOH/urea solvent can be visualized as a map plotted along the DP_v and lignin contents of the wood pulps (Figure 9). This map shows how both the DP_v and lignin contents influenced the dissolved proportions of wood pulps. When DP_v was as high as 1300, the wood pulp, even though it had a low lignin content of 1.2%, could not dissolve well. On the other hand, when the lignin content was too high (e.g., 33.3%), the wood pulp, even though it had a relatively low DP_v of about 400, still could not dissolve well. However, when both the DP_v and lignin content were not so high, as shown in the green region of Figure 9, the wood pulps could almost completely dissolve in NaOH/urea solvent with dissolved proportions >90%. For instance, the UKP′-4 pulp with DP_v of about 500 and lignin content of 6.9% could dissolve in NaOH/urea solvent and achieve a maximum pulp concentration of 4 wt % in the obtained lignocellulose solution. Moreover, lignocellulose materials could be prepared from these wood pulp/NaOH/urea solutions. Figure 10 shows appearances of the UKP′-4 pulp, the relevant lignocellulose film, and the stress−strain curve of the lignocellulose film. The film with yellow color exhibited good transparency and bendability. It possessed a tensile strength of 82 MPa, Young's modulus of 3.7 GPa, and elongation at break of 10.3%. These lignocellulose films are promising as new biobased materials and the applications of lignocellulose would be widely expanded. This may promote the creation of new material and chemical streams from nonfood agriculture to high-tech industry. Meanwhile, the enhanced utilization of these wood resources, together with adequate artificial management of forests and tree plantations, would help to create a sustainable and low-carbon society.

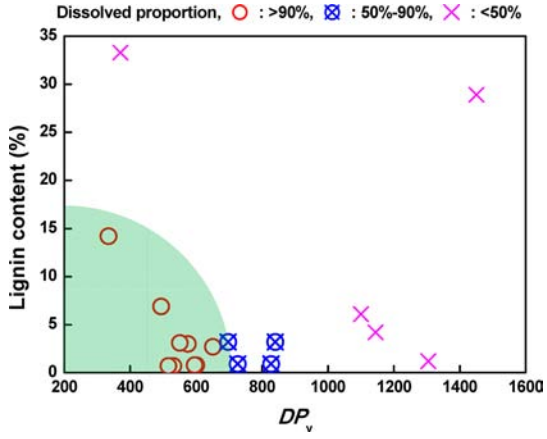

Figure 9. Dissolved proportion map of wood pulps in NaOH/urea solvent in terms of their DP_v and lignin contents.

■ ASSOCIATED CONTENT

Supporting Information

Effects of acid hydrolysis time on the crystallinity indices (CI) of the wood pulps. The Supporting Information is available free of charge on the ACS Publications website at DOI: 10.1021/acs.jafc.5b01714.

■ AUTHOR INFORMATION

Corresponding Authors

*(Z.S.) E-mail: zqshi2010@gmail.com.
*(Q.Y.) E-mail: yql0377@gmail.com.

Funding

We acknowledge support by the China Scholarship Council (CSC) for Z.S.

Notes

The authors declare no competing financial interest.

■ ACKNOWLEDGMENTS

We acknowledge Prof. Akira Isogai of The University of Tokyo for supply of the viscometer and optical microscopy for this work and support by the China Scholarship Council (CSC) for ZS.

■ REFERENCES

(1) Mohanty, A. K.; Misra, M.; Drzal, L. T. Sustainable bio-composites from renewable resources: Opportunities and challenges in the green materials world. *J. Polym. Environ.* **2002**, *10*, 19−26.
(2) Dhepe, P. L.; Fukuoka, A. Cracking of cellulose over supported metal catalysts. *Catal. Surv. Asia* **2007**, *11*, 186−191.
(3) Biermann, C. J. *Handbook of Pulping and Papermaking*; Academic Press: San Diego, CA, USA, 1996.
(4) Klemm, D.; Kramer, F.; Moritz, S.; Lindström, T.; Ankerfors, M.; Gray, D.; Dorris, A. Nanocelluloses: A new family of nature-based materials. *Angew. Chem., Int. Ed.* **2011**, *50*, 5438−5466.
(5) Eichhorn, S. J.; Dufresne, A.; Aranguren, M.; Marcovich, N. E.; Capadona, J. R.; Rowan, S. J.; Weder, C.; Thielemans, W.; Roman, M.; Renneckar, S.; Gindl, W.; Veigel, S.; Keckes, J.; Yano, H.; Abe, K.; Nogi, M.; Nakagaito, A. N.; Mangalam, A.; Simonsen, J.; Benight, A. S.; Bismarck, A.; Berglund, L. A.; Peijs, T. Review: Current international research into cellulose nanofibres and nanocomposites. *J. Mater. Sci.* **2010**, *45*, 1−33.
(6) Isogai, A.; Saito, T.; Fukuzumi, H. TEMPO-oxidized cellulose nanofibers. *Nanoscale* **2011**, *3*, 71−85.

Figure 10. Appearances of the UKP′-4 pulp (left) and the relevant lignocellulose film (middle) and the stress−strain curve of the lignocellulose film (right) prepared by dissolution of UKP′-4 in NaOH/urea solvent followed by regeneration in 5% H_2SO_4.

DOI: 10.1021/acs.jafc.5b01714
J. Agric. Food Chem. 2015, 63, 6113−6119

(7) Rubin, E. M. Genomics of cellulosic biofuels. *Nature* **2008**, *454*, 841−845.
(8) Hari Krishna, S.; Chowdary, G. V. Optimization of simultaneous saccharification and fermentation for the production of ethanol from lignocellulosic biomass. *J. Agric. Food Chem.* **2000**, *48*, 1971−1976.
(9) Binder, J. B.; Raines, R. T. Simple chemical transformation of lignocellulosic biomass into furans for fuels and chemicals. *J. Am. Chem. Soc.* **2009**, *131*, 1979−1985.
(10) Sun, N.; Li, W.; Stoner, B.; Jiang, X.; Lu, X.; Rogers, R. D. Composite fibers spun directly from solutions of raw lignocellulosic biomass dissolved in ionic liquids. *Green Chem.* **2011**, *13*, 1158−1161.
(11) Li, J.; Lu, Y.; Yang, D.; Sun, Q.; Liu, Y.; Zhao, H. Lignocellulose aerogel from wood-ionic liquid solution (1-allyl-3-methylimidazolium chloride) under freezing and thawing conditions. *Biomacromolecules* **2011**, *12*, 1860−1867.
(12) Wang, Z. G.; Yokoyama, T.; Chang, H. M.; Matsumoto, Y. Dissolution of beech and spruce milled woods in LiCl/DMSO. *J. Agric. Food Chem.* **2009**, *57*, 6167−6170.
(13) Lu, F. C.; Ralph, J. Non-degradative dissolution and acetylation of ball-milled plant cell walls: high-resolution solution-state NMR. *Plant J.* **2003**, *35*, 535−544.
(14) Le Moigne, N.; Navard, P. Dissolution mechanisms of wood cellulose fibres in NaOH−water. *Cellulose* **2010**, *17*, 31−45.
(15) Isogai, A.; Atalla, R. H. Dissolution of cellulose in aqueous NaOH solutions. *Cellulose* **1998**, *5*, 309−319.
(16) Cai, J.; Zhang, L. N. Rapid dissolution of cellulose in LiOH/urea and NaOH/urea aqueous solutions. *Macromol. Biosci.* **2005**, *5*, 539−548.
(17) Cai, J.; Zhang, L. N.; Liu, S. L.; Liu, Y. T.; Xu, X. J.; Chen, X. M.; Chu, B.; Guo, X. L.; Xu, J.; Cheng, H.; Han, C. C.; Kuga, S. Dynamic self-assembly induced rapid dissolution of cellulose at low temperatures. *Macromolecules* **2008**, *41*, 9345−9351.
(18) Li, R.; Wang, S.; Lu, A.; Zhang, L. N. Dissolution of cellulose from different sources in an NaOH/urea aqueous system at low temperature. *Cellulose* **2015**, *22*, 339−349.
(19) Yang, Q. L.; Fukuzumi, H.; Saito, T.; Isogai, A.; Zhang, L. N. Transparent cellulose films with high gas barrier properties fabricated from aqueous alkali/urea solutions. *Biomacromolecules* **2011**, *12*, 2766−2771.
(20) Shi, Z. Q.; Gao, H. C.; Feng, J.; Ding, B. B.; Cao, X. D.; Kuga, S.; Wang, W. J.; Zhang, L. N.; Cai, J. In-situ synthesis of robust conductive cellulose/polypyrrole composite aerogels and their potential application in nerve regeneration. *Angew. Chem., Int. Ed.* **2014**, *53*, 5380−5384.
(21) Fang, Y.; Duan, B.; Lu, A.; Liu, M. L.; Liu, H. L.; Xu, X. J.; Zhang, L. N. Intermolecular interaction and the extended wormlike chain conformation of chitin in NaOH/urea aqueous solution. *Biomacromolecules* **2015**, *16*, 1410−1417.
(22) Duan, B.; Zheng, X.; Xia, Z. X.; Fan, X. L.; Guo, L.; Liu, J. F.; Wang, Y. F.; Ye, Q. F.; Zhang, L. N. Highly biocompatible nanofibrous microspheres self-assembled from chitin in NaOH/urea aqueous solution as cell carriers. *Angew. Chem., Int. Ed.* **2015**, *54*, 5152−5156.
(23) Shi, Z. Q.; Yang, Q. L.; Cai, J.; Kuga, S.; Matsumoto, Y. Effects of lignin and hemicellulose contents on dissolution of wood pulp in aqueous NaOH/urea solution. *Cellulose* **2014**, *21*, 1205−1215.
(24) Qi, H. S.; Chang, C. Y.; Zhang, L. N. Effects of temperature and molecular weight on dissolution of cellulose in NaOH/urea aqueous solution. *Cellulose* **2008**, *15*, 779−787.
(25) Battista, O. A. Hydrolysis and crystallization of cellulose. *Ind. Eng. Chem.* **1950**, *42*, 502−507.
(26) Nickerson, R. F.; Habrle, J. A. Cellulose intercrystalline structure. *Ind. Eng. Chem.* **1947**, *39*, 1507−1512.
(27) Battista, O. A. Hydrolysis and crystallization of cellulose. *Ind. Eng. Chem.* **1950**, *42*, 502−507.
(28) Millet, M. A.; Moore, W. E.; Saeman, J. F. Preparation and properties of hydrocellulose. *Ind. Eng. Chem.* **1954**, *46*, 1493−1497.
(29) Håkansson, H.; Ahlgren, P.; Germgård, U. The degree of disorder in hardwood kraft pulps studied by means of LODP. *Cellulose* **2005**, *12*, 327−335.
(30) Saha, B. C.; Iten, L. B.; Cotta, M. A.; Wu, Y. V. Dilute acid pretreatment, enzymatic saccharification and fermentation of wheat straw to ethanol. *Process Biochem.* **2005**, *40*, 3693−3700.
(31) Rinaldi, R.; Schüth, F. Acid hydrolysis of cellulose as the entry point into biorefinery schemes. *ChemSusChem* **2009**, *2*, 1096−1107.
(32) Kumar, P.; Barrett, D. M.; Delwiche, M. J.; Stroeve, P. Methods for pretreatment of lignocellulosic biomass for efficient hydrolysis and biofuel production. *Ind. Eng. Chem. Res.* **2009**, *48*, 3713−3729.
(33) Adel, A. M.; El-Wahab, Z. H. A.; Ibrahim, A. A.; Al-Shemy, M. T. Characterization of microcrystalline cellulose prepared from lignocellulosic materials. Part I. Acid catalyzed hydrolysis. *Bioresour. Technol.* **2010**, *101*, 4446−4455.
(34) Trygg, J.; Fardim, P. Enhancement of cellulose dissolution in water-based solvent via ethanol−hydrochloric acid pretreatment. *Cellulose* **2011**, *18*, 987−994.
(35) Gong, X.; Wang, Y.; Tian, Z.; Zheng, X.; Chen, L. Controlled production of spruce cellulose gels using an environmentally "green" system. *Cellulose* **2014**, *21*, 1667−1678.
(36) Lin, S. Y.; Dence, C. W. *Methods in Lignin Chemistry*; Springer: Berlin, Germany, 1992.
(37) Borchardt, L. G.; Piper, C. V. A gas chromatographic method for carbohydrates as alditol-acetates. *Tappi* **1970**, *53*, 257−260.
(38) Segal, L.; Creely, J. J.; Martin, A. E., Jr; Conrad, C. M. An empirical method for estimating the degree of crystallinity of native cellulose using the X-ray diffractometer. *Text. Res. J.* **1959**, *29*, 786−794.
(39) Alexander, L. E. *X-ray Diffraction Methods in Polymer Science*; Wiley-Interscience: New York, 1969.
(40) Shinoda, R.; Saito, T.; Okita, Y.; Isogai, A. Relationship between length and degree of polymerization of TEMPO-oxidized cellulose nanofibrils. *Biomacromolecules* **2012**, *13*, 842−849.
(41) Adler, E. Lignin chemistry-past, present and future. *Wood Sci. Technol.* **1977**, *11*, 169−218.

DOI: 10.1021/acs.jafc.5b01714
J. Agric. Food Chem. 2015, 63, 6113−6119

compounds (VOCs) contributing to the reduction of the ozone layer and overall leading to poor air quality. These facts led to new agricultural practices such as anaerobic soil disinfestation and biofumigation. Both techniques involve incorporating in the soil large quantities of fresh organic material. To qualify as a good cover crop for the management of plant-parasitic nematodes, the crop should be a poor host for the nematodes and lower the population after incorporation into the soil.[19] *E. sativa* cv. Nemat was found to be a poor host for *M. incognita*, *Meloidogyne javanica*, and *Meloidogyne hapla* when tested as a cover crop in a greenhouse treatment.[20]

Much of the scientific research on rucola extracts deals with their biological activities, but to the best of our knowledge, there are no reports on the nematicidal activity of *E. sativa* and its volatile phytochemicals on *M. incognita*. In the present study we investigated (1) the chemical characterization of the volatilome of *E. sativa* by means of solid phase microextraction (SPME) followed by GC-MS analysis, (2) the synthesis of the most abundant compound present in volatilome and the nematocidal activity (EC_{50}) of the secondary metabolites of rucola, (3) the disruption of the parasites' biological cycle in host roots treated with fresh rucola powder, and (4) the efficacy of field-grown rucola, incorporated in situ, on root-knot nematodes.

MATERIALS AND METHODS

Chemicals. Carbon disulfide, erucin, iberin, and sulforaphane were obtained from Santa Cruz Biotechnology (Dallas, TX, USA); butyl isothiocyanate, isobutyl isothiocyanate, 2-ethylfuran, (*E*)-2-hexenal, pentyl isothiocyanate, hexyl isothiocyanate, (*E*)-3-hexen-1-ol, (*Z*)-3-hexen-1-ol, 2-furoic acid, ethyl 2-furoate, 2-furanacetic acid, tetrahydrothiophene, 3-pentanone, dimethyl sulfoxide, and *β*-cyclocitral were obtained from Sigma-Aldrich (Milano, Italy). Methanol was of high-performance liquid chromatography grade.

General Procedure for the Synthesis of (*E*)- and (*Z*)-3-Hexenyl Acetate. (*Z*)-3-Hexenyl acetate and (*E*)-3-hexenyl acetate were prepared as reported in the literature, with slight modifications.[21] (*Z*)- or (*E*)-3-hexen-1-ol (0.3 g, 2.99 mmol) and 4-(*N*,*N*-dimethylamino)pyridine (DMAP) (0.44 g, 3.59 mmol) were dissolved in 7.5 mL of diethyl ether. Acetic anhydride (0.37 g, 3.59 mmol) was then added dropwise with stirring, rapidly producing a white precipitate. The reaction mixture was warmed to 40 °C and stirred for 4 h. The crude mixture was then diluted with diethyl ether and washed with water (10 mL), 10% HCl (3 × 8 mL) and saturated $NaHCO_3$ (3 × 10 mL). The combined organic phase was dried over Na_2SO_4 and then concentrated under vacuum to provide the desired acetate as a pale yellow oil.^{1}H spectra, recorded on a UnitInova 500 MHz spectrometer (Varian, Walnut Creek, CA, USA), are consistent with those reported in the literature.[21]

Plant Material. Commercial *E. sativa* was obtained from a local market in Cagliari (Sardinia, Italy) on March 2014. Samples were used fresh and a voucher specimen was deposited at the Department of Life and Environmental Sciences, University of Cagliari, Cagliari, Italy, for species identification.

GC-MS Analysis. SPME analysis was performed following the method proposed by Jirovetz et al.[22] with minor modifications. Prior to analysis, the aerial parts of a sample of *E. sativa* were first ground to a paste in a mortar; 3 g of this paste was then placed into a 20 mL SPME vial, 75.5 × 22.5 mm, which was tightly closed with a septum and allowed to equilibrate for 5 min at 60 °C, and then the fiber was exposed to the headspace.

The extraction was carried out on a 1 cm DVB/CAR/PDMS 50/30 Stableflex (Supelco, Milano, Italy) SPME fiber. The fiber was preconditioned at 270 °C for 1 h in a Gerstel MPS bake-out station, according to the manufacturer's instructions. Prior to and after each analysis, the fiber underwent a further bake-out step for 5 min at 250 °C. The extraction time was fixed to 30 min, based on a previous optimization. After the extraction, the fiber was desorbed for 2 min into a Gerstel CIS6 PTV injector operating at 250 °C in a splitless mode.

Compound separation and identification was first performed on an Agilent 7890 GC equipped with a Gerstel MPS autosampler, coupled with an Agilent 7000C MSD detector. The chromatographic separation was performed on a VF-Wax 60 m × 0.25 mm i.d., 0.5 μm (J&W Scientific, Folsom, CA, USA), with the following temperature program: 40 °C for 4 min, then increased to 150 °C at a rate of 5.0 °C/min, held for 3 min, then increased to 240 °C at a rate of 10 °C/min, and held for 12 min. Helium was used as the carrier gas at a constant flow of 1 mL/min. The MS detector was set as follows: EI ion source operating at 70 eV, full scan acquisition range between *m*/*z* 40 and 650, scan rate of 7.1 cycles/s. Source and quadrupole temperatures were respectively 230 and 150 °C; He and N_2 were used respectively as quenching and collision gas at flows of 2.5 and 1 mL/min, respectively. Further injections were performed, as a confirmation, on a 3800 gas chromatograph directly coupled with a 2000 ion trap mass detector (Varian, Milano, Italy). The separation was achieved on an HP-5MS column of 30 m, 0.25 mm i.d., 0.25 μm (J&W Scientific), with the following temperature program: 50 °C for 5 min, then increased to 250 at a rate of 3.0 °C/min, held for 10 min, and then increased to 300 °C at a rate of 10.0 °C/min. The MS detector was programmed as follows: EI ion source operating at 70 eV, acquisition range between *m*/*z* 40 and 650, scan rate of 1 scan/s. The trap, manifold, and transfer line temperature were set to 200, 80, and 200 °C, respectively. Compounds were identified using their MS data (Mass Spectral Library NIST08 MS), the linear retention indices, and comparison with authentic standard (when available). The data were processed using a MassHunter Workstation B.06.00 SP1.

Nematode Paralysis Bioassays. A population of *M. incognita* of Italian origin was reared on tomato (*Solanum lycopersicum* Mill.) cv. Roma VF for 2 months in a glasshouse at 25 ± 5 °C. Batches of 30 egg masses (averaging 4500 eggs/batch) were collected from infected tomato roots and placed on 2 cm sieves (215 μm diameter), positioned on a 3.5 cm Petri dish. Distilled water was used as a natural hatching agent.[23]The eggs were then incubated in a growth chamber at 25 ± 2 °C, in the dark. First-emerging second-stage juveniles (J2) were discarded, and only second-stage juveniles collected after 2 days were used for the experiments. Compounds identified in rucola, including carbon disulfide and erucin, were tested on nematodes in a dose range of 1−1000 mg/L using fosthiazate as a chemical control. As part of this study, we also tested a series of structurally related isothiocyanates such as methyl isothiocyanate, butyl isothiocyanate, isobutyl isothiocyanate, pentyl isothiocyanate, hexyl isothiocyanate, benzyl isothiocyanate, phenyl isothiocyanate, and allyl isothiocyanate. Stock solutions of pure compounds were prepared in methanol to overcome insolubility, using aqueous Tween 20 (0.3% v/v) for further dilutions. The final concentration of methanol in each well never exceeded 1% (v/v) because preliminary experiments showed that this concentration was not toxic to the nematodes.[23] Distilled water as well as a mixture of methanol and aqueous Tween 20 at 0.3% (v/v) served as controls. In all cases, working solutions were prepared containing twice the test concentration and mixed in 96-well cell culture plates at a ratio of 1:1 (v/v) with a suspension of 25 nematodes added to each well. Multiwell plates were covered to avoid evaporation and maintained in the dark at 20 °C. Juveniles were observed with the aid of an inverted microscope (Zeiss, Gottingen, Germany) at 20× after 1 and 3 days for pure compounds and extracts of *E. sativa*, respectively. The nematodes were at this point moved to plain water after washing through a 20 μm sieve to remove the excess test compounds. Numbers of motile and paralyzed nematodes were assessed by pricking the juvenile body with a needle, and they were counted. Paralysis experiments were performed three times, and every treatment was replicated six times.

Experiment with Containerized Plants. For this experiment we used a clay loam soil, free of root-knot nematodes, with 1.3% organic matter and a pH of 7.8 that was collected from a noncultivated field at the Aristotle University of Thessaloniki Farm (Greece). The soil was sieved through a 3 mm sieve and partially air-dried overnight. The soil was mixed with sand at a ratio of 2:1 to obtain the mixture used for the

DOI: 10.1021/acs.jafc.5b02425
J. Agric. Food Chem. 2015, 63, 6120−6125

Table 1. Percentage Composition (n = 6) of Rucola Volatile Phytochemicals Determined by SPME/GC-MS Analysis, Listed in Order of Elution

		DB-WAX		HP-5MS			
peak	volatile compound[a]	t_r[b] (min)	LRI[c]	t_r[b] (min)	LRI[c]	ID[d]	area %[e]
1	carbon disulfide	6.12	744	1.72	613	MS, RI	3.6 ± 0.9
2	2-ethylfuran	11.50	933	2.61	702	MS, RI, STD	0.8 ± 0.2
3	tetrahydrothiophene	16.70	1127			MS, STD	2.4 ± 0.1
4	2-pentenal	17.48	1151	3.35	747	MS, RI	0.2 ± 0.1
5	1-penten-3-ol	18.26	1175	2.42	683	MS, RI	0.8 ± 0.1
6	3-ethylthiophene	18.77	1190			MS, RI	0.3 ± 0.1
7	D-limonene	19.37	1209	13.50	1027	MS, RI, STD	1.6 ± 0.7
8	(*E*)-2-hexenal	20.36	1241	5.85	849	MS, RI, STD	2.2 ± 0.7
9	methyl isothiocyanate	21.06	1265	3.18	736	MS, RI, STD	0.5 ± 0.1
10	hexyl acetate	21.63	1283			MS, RI	1.2 ± 0.2
11	methyl thiocyanate	22.23	1302	2.75	711	MS, RI, STD	1.2 ± 0.1
12	(*E*)-3-hexenyl acetate	22.72	1319			MS, RI, STD	1.7 ± 0.4
13	(*Z*)-2-penten-1-ol	22.87	1324	3.63	765	MS, RI	0.2 ± 0.1
14	(*Z*)-3-hexenyl acetate	23.08	1331	12.58	1008	MS, RI, STD	22.7 ± 1.6
15	(*E*)-2-hexenyl acetate	23.50	1346	13.09	1019	MS, RI	1.0 ± 0.1
16	1-hexanol	23.97	1362			MS, RI	0.7 ± 0.2
17	(*E*)-3-hexen-1-ol	24.36	1376		853	MS, RI, STD	0.7 ± 0.2
18	(*Z*)-3-hexen-1-ol	25.01	1398	6.18	858	MS, RI, STD	15.9 ± 2.3
19	nonanal	25.40	1412	17.33	1105	MS, RI	6.2 ± 0.3
20	unknown	26.85	1463				0.9 ± 0.1
21	(*Z*)-3-hexen-1-yl butyrate	27.15	1473	21.34	1180	MS, RI	4.8 ± 0.8
22	1-butene 4-isothiocyanate coeluting with (*Z*)-3-hexenyl isopentanoate	27.50	1485	11.39, 23.51	983, 1234	MS, RI	6.1 ± 2.3
23	(*Z*)-3-hexenyl pentanoate	27.95	1501	23.67	1238	MS, RI	1.4 ± 0.5
24	1-pentyl isothiocyanate	28.44	1517	16.99	1098	MS, RI, STD	1.0 ± 0.1
25	4-methylpentyl isothiocyanate	30.12	1572	20.16	1163	MS, RI	4.5 ± 0.4
26	hexyl isothiocyanate	31.54	1624	21.89	1199	MS, RI, STD	2.3 ± 0.1
27	β-cyclocitral	32.53	1665	22.80	1219	MS, RI, STD	1.2 ± 0.1
28	(*Z*)-3-hexenyl hexanoate	32.68	1672			MS, RI	0.7 ± 0.1
29	(*Z*)-3-hexenyl lactate	34.13	1740	30.34	1388	MS, RI	1.2 ± 0.8
30	4-ethylbenzaldehyde	34.47	1757			MS, RI	0.4 ± 0.2
31	unknown	36.6	1881				0.3 ± 0.3
32	β-ionone	38.15	1989	34.37	1485	MS, RI	1.7 ± 0.1
33	1-isothiocyanate-3-(methylthio)propane	39.01	2051	26.94	1310	MS, RI	1.0 ± 0.1
34	erucin	41.23	2208	32.17	1432	MS, RI, STD	8.6 ± 1.3

[a]Compounds in order of linear retention index on DB-WAX column. [b]Retention time on DB-WAX column in GC-MS or HP5-MS column. [c]Linear retention index (LRI) from a linear equation between each pair of straight-chain alkanes (C7−C23). [d]Identification method: LRI agrees with LRIs in the literature; MS, compared with NIST 08 Mass Spectral Database; STD, compared with authentic strandard solutions. [e]Peak area of each compound/sum of total peak area.

bioassays. It was separated into seven plastic bags, which received appropriate amounts of fresh rucola paste to achieve concentrations from 4 to 100 mg/g, whereas a treatment with plain water was used as control. Each soil sample was then inoculated with 2500 nematodes of *M. incognita* and was used for transplanting 7-week-old, at the six-leaf stage, tomato plants, cv. Belladonna, into plastic pots containing 200 g of soil, which were maintained at 27 °C and 60% relative humidity for a 16 h photoperiod; each pot received 20 mL of water every 3 days. Forty days later, root samples were stained with acid fuchsin,[24] and the following variables were assessed: fresh root and shoot weight and total number of females and galls of nematodes per gram of root at 10×, under uniform illumination by transparent light within tissue sample. The experiment was conducted twice, and the treatments were always arranged in a completely randomized design with five replicates.

Field Experiment. To verify the efficacy under field conditions *E. sativa* was planted in the field and, after having reached full growth, it was incorporated in soil that subsequently was planted with tomatoes. Specifically, the experiment consisted of two treatments, namely (1) rucola seeds planted in full field surface at a concentration of 5 g/m^2 and (2) an untreated control. Each treatment consisted of four replicates, and each plot area was 10 m^2. One month later when rucola had reached full growth, it was mechanically incorporated in the soil. A week later 7-week-old, at the six-leaf stage, tomato plants, cv. Belladonna, were transplanted. No other treatments were performed for nematode control during the culture period, and the efficacy was assessed 73 days post transplanting by uprooting the plants and categorizing with root index for RKN infection. Successively, the weight of roots and aerial parts was recorded.

Statistical Analysis. For containerized bioassays, data were expressed as a percentage decrease in the number of females and galls per gram of root corrected for the control, according to Abbott's formula:

$$\text{corrected \%} = 100 \times \left(1 - \frac{\text{no. of females in treated plot}}{\text{no. of females in control pot}}\right)$$

It was fitted in the log−logistic model[25] to estimate the concentration causing a 50% decrease in females per gram of root (EC_{50} value). In this regression equation, the rucola paste concentration (mg/g) was the independent variable (x) and the number of females and galls of nematodes (percentage decrease over water control) was the dependent variable (y). Additionally, Tuckey's test was used to

DOI: 10.1021/acs.jafc.5b02425
J. Agric. Food Chem. 2015, 63, 6120−6125

separate treatment differences and root or shoot fresh weight, $P \leq 0.05$. Because ANOVA indicated no significant treatment by time interaction (between runs of experiments), means were averaged over experiments.

Because paralysis in solvent (methanol, Tween-20) did not significantly differ from that observed in distilled water, the percentages of paralyzed nematodes were corrected by eliminating the natural paralysis in the water control (0−5% of total number of nematodes) according to the Schneider−Orelli formula[26]

$$\text{corrected \%} = [(\%\ \text{mortality in treatment} - \%\ \text{mortality in control}) / (100 - \%\ \text{mortality in control})] \times 100$$

and they were analyzed (ANOVA) combined over time. Because ANOVA indicated no significant treatment by time interaction, means were averaged over experiments. Corrected percentages of paralyzed nematodes treated with tested compounds were subjected to nonlinear regression analysis using the log−logistic equation proposed by Seefeldt et al.:[25]

$$Y = C + (D - C)/\{1 + \exp[b(\log(x) - \log(EC_{50}))]\}$$

C = lower limit, D = upper limit, b = slope at EC_{50}, and EC_{50} = test substances' concentration required for 50% death/paralysis of nematodes after elimination of the control (natural death/paralysis). In the regression equation, the test substances' concentration was the independent variable (x) and the paralyzed nematodes (percentage increase over water control) was the dependent variable (y). The mean value of the six replicates per test substance concentration and immersion period was used to calculate the EC_{50} value. Mean data values were reported with the respective standard deviations.

RESULTS AND DISCUSSION

SPME is a useful analytical technique for the semiquantitation of volatile compounds in different matrices, whereas GC-MS is used for compound identification. With these techniques, we identified 32 compounds in *E. sativa* paste; (*Z*)-3-hexenyl acetate was the most abundant, followed by (*Z*)-3-hexen-1-ol, with relative percentages of 22.7 ± 1.6 and 15.9 ± 2.3, respectively (Table 1). Stereoisomers of (*E*)- and (*Z*)-3-hexen-1-ol are produced by plants when mechanical damage occurs and may have indirect plant defense signaling properties.[27] The level of the isothiocyanate erucin in the *E. sativa* volatilome was 8.6 ± 1.3%, although Jirovetz et al.[22] reported levels of approximately 14.2%.

According to Cataldi et al.,[28] the most abundant glucosinolates isolated from rucola leaves are glucoerucin, 4-methylpentyl glucosinolate, 1-hexyl glucosinolate, glucoraphanin, 4-mercaptobutyl glucosinolate, progoitrin, sinigrin, and glucobrassicin.[28] In fact, three of the isothiocyanates deriving from the three first mentioned glucosinolates reported above were identified in *E. sativa* after GC-MS analysis (Table 1).

When we tested the nematicidal activity of rucola volatile compounds, we found that erucin, pentyl isothiocyanate, hexyl isothiocyanate, 2-(*E*)-hexenal, 2-ethylfuran, and methyl thiocyanate were the most active, with EC_{50} values of 3.2 ± 1.7, 11.1 ± 5.0, 11.3 ± 2.6, 15.0 ± 3.3, 16 ± 5.0, and 18.1 ± 0.6 mg/L after 24 h of incubation with nematodes, whereas the EC_{50} for (*Z*)-3-hexen-1-ol was 323 ± 91 mg/L (Table 2). Figure 1 reports the chemical structures of the most active compounds tested. On the other hand, furan derivatives such as 2-furoic acid, ethyl 2-furoate, and 2-furanacetic acid were not active at 100 mg/L (Table 2). Furthermore, β-cyclocitral found in trace amounts in leaves of *E. sativa*[29] was not active at 100 mg/L. Interestingly, acetates of (*E*)- and (*Z*)-3-hexen-1-ol were not

Table 2. EC_{50} Values (n = 4) of Tested Compounds against *M. incognita* Calculated after 1 Day of Nematode Immersion in Test Solutions

compound	$EC_{50/1day}$ (mg/L ± SD)
(**1**) erucin	3.2 ± 1.7
(**2**) methyl isothiocyanate	7.9 ± 3.1
(**3**) pentyl isothiocyanate	11.1 ± 5.0
(**4**) hexyl isothiocyanate	11.3 ± 2.6
(**5**) (*E*)-2-hexenal	15.0 ± 3.3
(**6**) 2-ethylfuran	16 ± 5.0
(**7**) methyl thiocyanate	18.1 ± 0.6
(**8**) (*Z*)-3-hexen-1-ol	323 ± 91
(**9**) 3-pentanone	>100
(**10**) tetrahydrothiophene	>100
(**11**) (*Z*)-3-hexenyl acetate	>400
(**12**) (*E*)-3-hexenyl acetate	>400
(**13**) carbon disulfide	>500
(**14**) (*E*)-3-hexen-1-ol	>700
(**15**) benzyl isothiocyanate[a]	1.9 ± 0.3
(**16**) allyl isothiocyanate[a]	6.6 ± 2.5
(**17**) butyl isothiocyanate[a]	12 ± 8.0
(**18**) sulforaphane	152 ± 35
(**19**) iberin	180 ± 21
(**20**) 2-furoic acid	>100
(**21**) ethyl 2-furoate	>100
(**22**) 2-furanacetic acid	>100
(**23**) β-cyclocitral	>100
(**24**) isobutyl isothiocyanate	>200
(**25**) phenyl isothiocyanate[a]	>1000
(**26**) fosthiazate[a]	0.4 ± 0.3

[a]Data published by Aissani et al.[8]

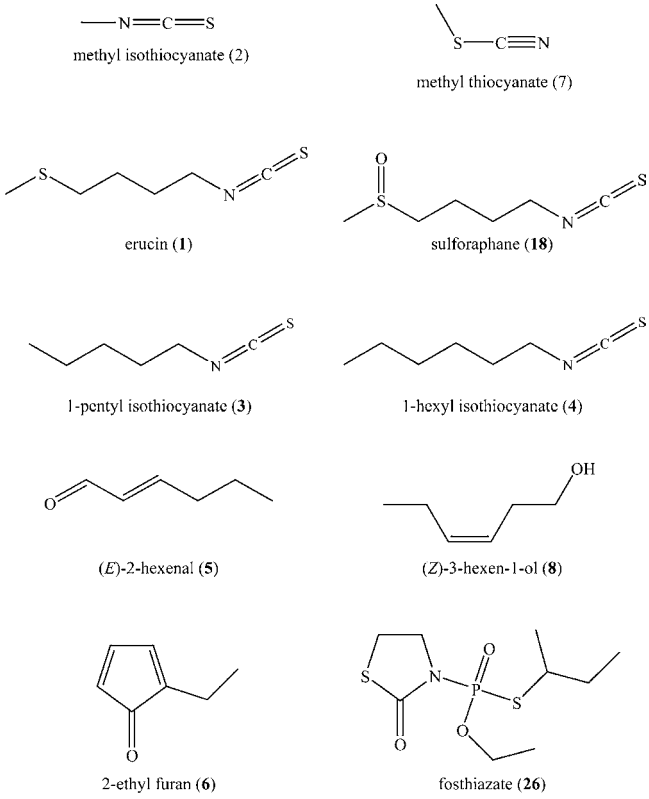

Figure 1. Chemical structures of most active nematicidal compounds.

DOI: 10.1021/acs.jafc.5b02425
J. Agric. Food Chem. 2015, 63, 6120−6125

active at concentrations >400 mg/L. Among isothiocyanate derivatives, not found in the *E. sativa* volatilome, the most effective in paralyzing *M. incognita* was benzyl isothiocyanate, followed by allyl isothiocyanate and butyl isothiocyanate, exhibiting $EC_{50/1day}$ values of 1.9 ± 0.3, 6.6 ± 2.5, and 12 ± 8 mg/L, respectively. It is noteworthy that isobutyl isothiocyanate and phenyl isothiocyanate were not active at concentrations >200 and >1000 mg/L, respectively. Sulforaphane was 50 times less active if compared with its reduced isothiocyanate analogue erucin (EC_{50} = 152 ± 35 mg/L), whereas iberin showed an EC_{50} of 180 ± 21 mg/L. Finally, carbon disulfide and (*E*)-3-hexen-1-ol were not found active at concentrations >500 and >700 mg/L, respectively. Interestingly, in our in vitro conditions, butyl isothiocyanate showed a fumigant activity at 160 mg/L (data not shown). Slight structural differences among isothiocyanates conferred significantly different nematicidal effects. This suggests that the biological activity is not only a concentration-dependent function but also related to the alkyl chain characteristics. Notably, Caboni et al.[7] observed that nematodes treated with different isothiocyanates were paralyzed in a straight shape with evident internal vacuolization (Figure 2). The same evidence

Figure 2. *M. incognita* J2 before (A) and after (B) a 24 h immersion in erucin at 10 mg/L. After treatment, nematodes were paralyzed in a straight shape, and internal vacuoles were evident.

was observed when nematodes were treated with some V-ATPase inhibitors such as α,β,γ,δ-unsaturated aldehydes and pyocyanin.[30,31] Conversely, nematodes treated with the organophosphorous fosthiazate were paralyzed in a coiling shape.[7] When the methanolic extract of fresh rucola paste was tested against *M. incognita*, a clear dose−response relationship was established and significant paralysis/death of nematodes was evident after 3 days of exposure with a calculated EC_{50} value of 93 ± 59 mg/L (data not shown). According to the results of our experiment with containerized tomato plants infested with *M. incognita*, when *E. sativa* paste was incorporated to the growing medium, it decreased root infestation and increased plant growth in a dose-response manner. The EC_{50} values based on the numbers of females and galls were calculated at 20.02 ± 1.65 (95% CI, 16.64−23.41) and 20.75 ± 1.65 (95% CI, 16.99−24.53) mg/g, respectively. The treatment of tomato plants with rucola paste induced fresh shoot weight increase (Table 3), whereas no root weight increase was observed.

Most interestingly, rucola used as a soil amendant fully controlled RKN under our field conditions. Specifically, on the basis of the galling index, all roots were severely knotted in control plants and the root system was absent (root index 10) due to secondary infections by soil pathogens, whereas in rucola-treated plants no knots were evident (root index 1).

Table 3. Weight Increase of Aerial Parts after Treatment with Rucola Paste in Nematode-Infested Tomato Plants

E. sativa paste (mg/g)	aerial part weight[a] (g)
0	4.45 ± 0.24c
4	4.99 ± 0.15cb
8	5.61 ± 0.05cbd
16	6.23 ± 0.36cbd
32	7.35 ± 0.26d
64	7.14 ± 0.16d
128	6.95 ± 0.15bd

[a]Data are presented as means of five replicates with standard deviations. Means followed by the same letter are not significantly different according to Tukey's test ($P \leq 0.05$).

In the literature reporting on the use of soil amendants in RKN management, the family Brassicaceae is probably the most cited due to the isothiocyanate levels observed in its members.[32] This is the first study on the nematicidal properties of the volatilome of *E. sativa* on *M. incognita*, which shows the possibility of its potential use as an intercrop plant. Intercropping, being a cost-effective, environmentally friendly pest management method, can be easily used in developing countries.

In our previous works, we largely stressed the importance of compound volatility in the nematicidal character of various botanical extracts.[5] This feature is essential for delivering the active substance to the inner parts of the soil infested by nematodes. Herein we report the high activity in containerized and field experiments of rocket and attribute it to its isothiocyanates contents. Nevertheless, under field conditions the efficacy of the isothiocyanates decreases due to their short half-life, making mandatory the repetition of applications,[8] a fact that should not be underestimated. The fate in soil of pure isothiocyanates is to be studied with regard to their half-life as ingredients in complex botanical soil amendments. This together with the cost effectiveness of respective treatments could establish a nematode control method suitable for integrated crop management.

AUTHOR INFORMATION

Corresponding Author

*(P.C.) Phone: +39 070 675 8617. Fax: +39 070 675 8612. E-mail: caboni@unica.it.

Notes

The authors declare no competing financial interest.

ACKNOWLEDGMENTS

We are grateful to Margherita Addis (AGRIS Sardegna, Italy) for helpful suggestions. We are particularly indebted to Prof. Renato Iori and Dr. Gina De Nicola (CRA-Bologna, Italy).

ABBREVIATIONS USED

SPME solid phase microextraction; GC-MS gas chromatography−mass spectrometry; ITC isothiocyanates; RKN root-knot nematodes

REFERENCES

(1) Reynolds, A. M.; Dutta, T. K.; Curtis, R. S. C.; Power, S. J.; Gaur, H. S.; Kerry, B. R. Chemotaxis can take plant-parasitic nematodes to the source of a chemo-attractant via the shortest possible routes. *J. R. Soc., Interface* **2011**, *8*, 568−577.

DOI: 10.1021/acs.jafc.5b02425
J. Agric. Food Chem. 2015, 63, 6120−6125

(2) Isman, M. B. Botanical insecticides, deterrents, and repellents in modern agriculture and an increasingly regulated world. *Annu. Rev. Entomol.* **2006**, *51*, 45−66.
(3) Tian, B.; Yang, J.; Zhang, K. Q. Bacteria used in the biological control of plant parasitic nematodes: Populations, mechanisms of action, and future prospects. *FEMS Microbiol. Ecol.* **2007**, *61*, 197−213.
(4) Whittaker, R. H.; Feeny, P. P. Allelochemics: chemical interactions between species. *Science* **1971**, *171*, 757−770.
(5) Ntalli, N. G.; Caboni, P. Botanical nematicides: a review. *J. Agric. Food Chem.* **2012**, *60*, 9929−9940.
(6) Caboni, P.; Saba, M.; Tocco, G.; Casu, L.; Murgia, A.; Maxia, A.; Menkissoglu-Spiroudi, U.; Ntalli, N. Nematicidal activity of mint aqueous extracts against the root-knot nematode *Meloidogyne incognita*. *J. Agric. Food Chem.* **2013**, *61*, 9784−9788.
(7) Caboni, P.; Sarais, G.; Aissani, N.; Tocco, G.; Sasanelli, N.; Liori, B.; Carta, A.; Angioni, A. Nematicidal activity of 2-thiophenecarboxaldehyde and methylisothiocyanate from caper (*Capparis spinosa*) against *Melodogyne incognita*. *J. Agric. Food Chem.* **2012**, *60*, 7345−7351.
(8) Aissani, N.; Tedeschi, P.; Maietti, A.; Brandolini, V.; Vincenzo, L. G.; Caboni, P. Nematicidal activity of allylisothiocyanate from horseradish (*Armoracia rusticana*) roots against *Meloidogyne incognita*. *J. Agric. Food Chem.* **2013**, *61*, 4723−4727.
(9) Bennett, R. N.; Rosa, E. A.; Mellon, F. A.; Kroon, P. A. Ontogenic profiling of glucosinolates, flavonoids, and other secondary metabolites in *Eruca sativa* (salad rocket), *Diplotaxis erucoides* (wall rocket), *Diplotaxis tenuifolia* (wild rocket), and *Bunias orientalis* (Turkish rocket). *J. Agric. Food Chem.* **2006**, *54*, 4005−4015.
(10) Steinmetz, K. A.; Potter, J. D. Vegetables, fruit, and cancer. II. Mechanisms. *Cancer Causes Control* **1991**, *2*, 427−442.
(11) Fenwick, G. R.; Heaney, R. K.; Mullin, W. J. Glucosinolates and their breakdown products in food and food plants. *CRC Crit. Rev. Food Sci. Nutr.* **1983**, *18*, 123−201.
(12) Wu, H.; Masler, E. P.; Rogers, S. T.; Chen, C.; Chitwood, D. J. Benzylisothiocyanate affects development, hatching and reproduction of the soybean cyst nematode *Heterodera glycines*. *Nematology* **2014**, *4*, 495−504.
(13) Brown, P. D.; Morra, M. J. Control of soil-borne plant pests using glucosinolate-containing plants. *Adv. Agron.* **1997**, *61*, 167−231.
(14) Nair, K. S. S.; McEwen, F. L. Host selection by the adult cabbage maggot, *Hylemya brassicae* (Diptera: Anthomyiidae): effect of glucosinolates and common nutrients on oviposition. *Can. Entomol.* **1976**, *108*, 1021−1030.
(15) Feeny, P.; Paauwe, K. L.; Demong, N. J. Flea beetles and mustard oils: host plant specificity of *Phyllotreta cruciferae* and *Phyllotreta striolata* adults (Coleoptera: Chrysomelidae). *Ann. Entomol. Soc. Am.* **1970**, *63*, 832−841.
(16) Vincent, C.; Steward, R. K. Effect of allyl isothiocyanate on field behavior of crucifer-feeding flea beetles (Coleoptera: Chrysomelidae) (*Phyllotreta cruciferae*, *Psylliodes punctulata*, *Phyllotreta bipustulata*, *Phyllotreta striolata*, rutabagas). *J. Chem. Ecol.* **1984**, *10*, 33−39.
(17) Hovanitz, W.; Chang, V. C. S.; Honch, G. The effectiveness of different isothiocyanates on attracting larvae of *Pieris rapae*. *J. Res. Lepidoptera* **1963**, *1*, 249−259.
(18) Huang, X.; Renwick, J. A. A. Relative activities of glucosinolates as oviposition stimulants for *Pieris rapae* and *P. napi oleracae*. *J. Chem. Ecol.* **1994**, *20*, 1025−1037.
(19) Viaene, N. M.; Abawi, G. S. Management of *Meloidogyne hapla* on lettuce in organic soil. *Plant Dis.* **1998**, *82*, 945−952.
(20) Edwards, S.; Ploeg, A. Evaluation of 31 potential biofumigant brassicaceous plants as hosts for three meloiodogyne species. *J. Nematol.* **2014**, *46*, 287−295.
(21) Ward, D.; Villanueva, L. A.; Allred, G. D.; Payne, S. C.; Semones, M. A.; Liebeskind, L. S. Synthesis, characterization, and configurational lability of (η^3-allyl)dicarbonyl[hydrotris(1-pyrazolyl)-borato]molybdenum complexes bearing substituents at the termini: thermodynamic preference for the anti stereoisomer. *Organometallics* **1995**, *14*, 4132−4156.
(22) Jirovetz, L.; Smith, D.; Buchbauer, G. Aroma compound analysis of *Eruca sativa* (Brassicaceae) SPME headspace leaf samples using GC, GC-MS, and olfactometry. *J. Agric. Food Chem.* **2002**, *50*, 4643−4646.
(23) Caboni, P.; Ntalli, G. N.; Aissani, N.; Cavoski, I.; Angioni, A. Nematicidal activity of (*E*,*E*)-2,4-decadienal and (*E*)-2-decenal from *Ailanthus altissima* against *Meloidogyne javanica*. *J. Agric. Food Chem.* **2012**, *60*, 1146−1151.
(24) Byrd, K. R. B.; Kirkpatrick, T. An improved technique for clearing and staining plant tissues for detection of nematodes. *J. Nematol.* **1983**, *15*, 142−143.
(25) Seefeldt, S. S.; Jensen, J. E.; Fuerst, E. P. Log-logistic analysis of herbicide rate response relationships. *Weed Technol.* **1995**, *9*, 218−227.
(26) Puntener, W. *Manual for Field Trials in Plant Protection*, 2nd ed.; Ciba Geigy: Basel, Switzerland, 1981; p 205.
(27) Ruther, J.; Kleier, S. Plant-plant signalling: ethylene synergizers volatile emission in *Zea mays* induced by exposure to (*Z*)-3-hexen-1-ol. *J. Chem. Ecol.* **2005**, *31*, 2217−2222.
(28) Cataldi, T. R. I.; Rubino, A.; Lelario, F.; Bufo, S. A. Naturally occurring glucosinolates in plant extracts of rocket salad (*Eruca sativa* L.) identified by liquid chromatography coupled with negative ion electrospray ionization and quadrupole ion-trap mass spectrometry. *Rapid Commun. Mass Spectrom.* **2007**, *21*, 2374−2388.
(29) Blaževic, I.; Mastelic, J. Free and bound volatiles of rocket (*Eruca sativa* Mill.). *Flavour Fragrance J.* **2008**, *23*, 278−285.
(30) Caboni, P.; Aissani, N.; Cabras, T.; Falqui, A.; Marotta, R.; Liori, B.; Ntalli, N.; Sarais, G.; Sasanelli, N.; Tocco, G. Potent nematicidal activity of phthalaldehyde, salicylaldehyde, and cinnamic aldehyde against *Meloidogyne incognita*. *J. Agric. Food Chem.* **2013**, *61*, 4723−4727.
(31) Caboni, P.; Tronci, L.; Liori, B.; Tocco, G.; Sasanelli, N.; Diana, A.; Tulipaline, A. Structure-activity aspects as a nematicide and V-ATPase inhibitor. *Pestic. Biochem. Physiol.* **2014**, *112*, 33−39.
(32) Matthiessen, J. N.; Kirkegaard, J. A. Biofumigation and enhanced biodegradation: opportunity and challenge in soil borne pest and disease management. *Crit. Rev. Plant Sci.* **2006**, *25*, 235−265.

DOI: 10.1021/acs.jafc.5b02425
J. Agric. Food Chem. 2015, 63, 6120−6125

Recently, several artificial diets and in vitro rearing techniques have been developed for *A. mellifera* larvae.[18,22−25] On the basis of these new diets and rearing methods, we here describe a dietary exposure assay for assessing the direct toxicity of insecticidal compounds to *A. mellifera* larvae. We then used the dietary exposure assay to evaluate the potential toxicity of Cry1C and Cry2A to *A. mellifera* larvae. These Cry proteins have been expressed in rice and other plants for the control of lepidopteran rice pests, such as *Chilo suppressalis* (Walker) (Lepidoptera: Crambidae) and *Scirpophaga incertulas* (Walker) (Lepidoptera: Pyralidae).[26,27] In addition, biochemical and histopathological experiments were conducted to further evaluate the potential toxicity of the two Cry proteins on this species.

MATERIALS AND METHODS

Insects. Worker larvae of *A. mellifera* were obtained from three colonies at the Institute of Plant Protection, CAAS. The queens were individually confined in cages (45 × 55 × 65 cm) with an empty comb, where they were permitted to lay eggs for 24 h. On the second day after the eggs hatched, the combs were transferred to the laboratory, and the 1.5−2.0 day old larvae were used for experiments.

Larvae of a *Bt*-susceptible strain of *C. suppressalis* were obtained from a colony that had been maintained on an artificial diet for over 50 generations in our laboratory. The *C. suppressalis* larvae were used to test the bioactivity of the Cry proteins (as described later).

Chemical Compounds. Commercial royal jelly and yeast extract were purchased from China-Bee Science & Technology Development Co., Ltd. (Beijing, People's Republic of China) and Oxoid Ltd. (Hampshire, England), respectively. D-(+)-glucose, D-(+)-fructose, bovine serum albumin (BSA), and soybean trypsin inhibitor (SBTI) were purchased from Sigma-Aldrich (St. Louis, MO, USA). Cry1C and Cry2A proteins were purchased from Envirotest-China (agent for Envirologix Inc., Portland, MA, USA; www.envirotestchina.com). The *Bt* proteins were produced and purified at the Department of Biochemistry, Case Western Reserve University (Cleveland, OH, USA; contact person Dr. Marianne Pusztai-Carey). The protoxins from *Bt* had been expressed as single-gene products in *Escherichia coli*. The *E. coli* expressed protoxin inclusion bodies were dissolved and trypsinized and then isolated and purified by ion exchange HPLC; the pure fractions were finally desalted and lyophilized. Purity was about 94−96%. The bioactivity of the Cry proteins was verified in a sensitive-insect bioassay using neonate larvae of *C. suppressalis* that were reared for 7 days with artificial diet containing a range of Cry protein concentrations (see Bioactivity of Cry Protein in Diets). The EC_{50} (toxin concentration resulting in 50% weight reduction in comparison to the control) values of our protein batches were estimated to be 18.1 and 1310 ng/mL for Cry1C and Cry2A, respectively.[50]

Artificial Diet and Rearing Technique for *A. mellifera* Larvae. Diet making and rearing techniques have been described in more detail elsewhere.[25] The artificial diet for *A. mellifera* larvae contained 50% royal jelly, 4% glucose, 8% fructose, 37% double-distilled water, and 1% yeast extract. The sugars and the yeast extract were dissolved in distilled water, and freshly thawed royal jelly was added to the mixture and mixed thoroughly by hand. The prepared diets were added to 5 mL centrifuge tubes and stored at −20 °C until they were used. Before they were provided to *A. mellifera* larvae, the diets were thawed and brought to 34 °C in a water bath.

A plastic grafting tool for bee larva was used to gently and individually transfer *A. mellifera* larvae (1.5−2.0 days old) to cells (diameter 1.6 cm) of 24-well cell culture plates (Corning Inc., Corning, NY, USA). After they were transferred, the larvae were examined with a stereo microscope to confirm that they were alive. An Eppendorf pipet was used to carefully add artificial diet to each cell such that the bee larvae floated on the food. The plates were covered with lids and placed in a desiccator containing 10% sulfuric acid (resulting in 90% RH) and incubated in a climatic chamber at 34 ± 1 °C in darkness. New diet was added daily after unconsumed diet in each cell was gently removed with a vacuum pump. Each larva was provided with 100 μL of diet per day for the first 2 days and then with 200 μL per day until defecation. Defecation was determined to have occurred when yellow, stringy material or uric acid crystals were observed. Once defecation occurred (i.e., once the larvae were mature), each larva was removed from the cell, gently blotted on tissue papers to remove the food on the body surface, weighed, and then transferred to a new 24-cell plate, the cells of which were lined with tissue paper on the bottoms and walls. The plates were then placed in a desiccator containing a saturated NaCl−water solution (resulting in 70% RH) in a climatic chamber at 34 ± 1 °C in darkness until adult emergence. Larvae were observed every 12 h (9:00 am and 9:00 pm) for development and mortality.

Response of *A. mellifera* Larvae to SBTI in the Dietary Assay. Previous studies have confirmed that SBTI is toxic to *A. mellifera*.[7,9,23,28] Therefore, SBTI was used as a positive control to verify that the artificial diet and our dietary exposure assay could be used to detect toxicity.

A stock solution of SBTI was diluted with distilled water and mixed into the *A. mellifera* larval artificial diet to give concentrations of 0, 0.1, 1, and 10 mg/g FW of diet. The experimental system and the provision of diets were the same as those described in the previous section. There were 3 replicates per treatment, and each replicate contained 24 larvae. The larvae were examined for development and mortality every 12 h. When the larvae matured (as indicated by the occurrence of defecation), they were weighed.

Toxicity of *Bt* Proteins to *A. mellifera* Larvae. *Effects on Life Table Parameters.* Larvae were fed one of five diets, which were prepared by treating the artificial diet with (1) Cry1C (50 μg/g FW of diet), (2) Cry2A (400 μg/g FW of diet), (3) BSA (400 μg/g FW of diet; negative control), (4) SBTI (1 mg/g FW diet; positive control), or (5) no added protein (blank control). The experimental conditions and the feeding system were the same as those described earlier. Diets were prepared 3 days before initiation of this experiment and were stored at −20 °C until used. BSA was used here as a nontoxic protein control, because a previous study showed that feeding of BSA does not affect the survival and development of honey bees and a parasitoid Hymenoptera.[23,29] There were 5 replicates pre treatment, and each replicate contained 15 larvae. Insect development and mortality were recorded twice per day (9:00 am and 9:00 pm), and the mature larvae were weighed.

Uptake of Cry Protein by A. mellifera Larvae. *A. mellifera* larvae were fed artificial diet containing no toxin (the control), Cry1C at 50 μg/g FW of diet, or Cry2A at 400 μg/g FW of diet as described in the previous section. After 2 and 4 days of feeding, six larvae were collected per treatment. Additional larvae were allowed to pupate before six pupae were collected per treatment. The larvae and pupae were stored at −20 °C until Cry concentrations were measured.

The concentrations of Cry proteins in individual larvae and pupae were measured by double-antibody sandwich enzyme-link immunosorbent assay (DAS-ELISA) using Cry1C and Cry2A detection kits from EnviroLogix (Portland, MA, USA). The insects were washed in phosphate buffered saline Tween-20 (PBST) (provided with the kit) to remove Cry proteins from body surfaces before analysis. Cry protein was extracted and ELISA measurements were performed following the manufacturer's instructions. Optical density (OD) values were read with a microplate spectrophotometer (PowerWave XS2, BioTek, Winooski, VT, USA). The concentrations of Cry proteins were calculated by calibrating the OD values to a range of concentrations of Cry protein standards provided with the kit.

Bioactivity of Cry Protein in Diets. The bioactivity of Cry proteins in *A. mellifera* larval diets was assessed in three subsamples that were collected from the pure diet (untreated with Cry protein) or diets containing Cry1C (at 50 μg/g FW of diet) or Cry2A (at 400 μg/g FW of diet) that had been exposed to bee larvae for 1 day. The bioactivity of Cry proteins was determined with a sensitive-insect bioassay that used *C. suppressalis* larvae. For Cry protein extraction, a 50 mg sample of each of the three diets was homogenized with 2 mL of PBST buffer (provided with the ELISA kit as described above). After the preparations were centrifuged at 15.8*g*, the supernatants were

DOI: 10.1021/acs.jafc.5b01662
J. Agric. Food Chem. 2015, 63, 6126−6132

appropriately diluted and thoroughly incorporated into the artificial diet for *C. suppressalis* larvae.[30] The artificial diets were cut into slices and placed in Petri dishes (6 cm diameter, 1 cm height) with neonate larvae of *C. suppressalis* (one slice and one larva per dish). The Petri dishes were then sealed with Parafilm. Each treatment was represented by 30 replicate dishes. After 7 days, the *C. suppressalis* larvae were weighed.

Enzyme Activity Analysis. *A. mellifera* worker larvae (1.5−2.0 days old) were fed pure diets or diets containing BSA (at 400 μg/g FW of diet), Cry1C (at 50 μg/g FW of diet), Cry2A (at 400 μg/g FW of diet), or SBTI (at 1 mg/g FW of diet) as described earlier. After 4 days of feeding exposure, seven larvae were collected per treatment and stored at −20 °C before the activity levels of four gut enzymes (the total protease, tryptase, aminopeptidase, and α-naphthyl acetate esterase (α-NAE)) were measured using ELISA kits from Beijing Luyuan Bode Biotechnology Co., Ltd. (Beijing, People's Republic of China). Samples were homogenized at 4 °C in 300 μL of 0.15 mol/L NaCl.[31] The homogenates were then centrifuged at 3000*g* for 10 min at 4 °C, and the resulting supernatants were used for analysis of the enzymatic activities following the manufacturer's instructions. The optical density (OD) values were read with a microplate spectrophotometer (PowerWave XS2, BioTek, Winooski, VT, USA). The activity levels of test enzymes were calculated by calibrating the OD values to a range of concentrations of standards provided with the kits.

Histopathology. *A. mellifera* larvae (1.5−2.0 days old) were fed artificial diet containing no added protein, BSA at 400 μg/g FW of diet, Cry1C at 50 μg/g FW of diet, Cry2A at 400 μg/g FW of diet, or SBTI at 1 mg/g FW of diet. After 4 days of feeding exposure, five larvae were collected per treatment. The midguts of the larvae were fixed in a 10% (v/v) paraformaldehyde solution for at least 24 h at 4 °C. Tissues were sectioned at 4 μm thickness with a microtome (Leica, R2235, Wetzlar, Germany). The sections were stained with hematoxylin-eosin stain, and images were captured with a digital camera (Olympus, DP73, Japan) mounted on a microscope (Olympus, BX63, Japan).

Data Analysis. In the bioassays with SBTI or Cry proteins, statistical comparisons were made between each treatment and the control (pure artificial diet) by Dunnett's tests after one-way ANOVAs showed a significant effect for any life table parameter. Student's *t* tests were used to compare the weights of *C. suppressalis* larvae that were fed artificial diets containing the extract from untreated diet vs extracts from diets containing Cry proteins. One-way ANOVAs were used to compare enzyme activities among treatments, and Dunnett's tests were used to separate the means between each toxin treatment and the control.

All statistical analyses were conducted using the software package SPSS (version 13 for Windows, 2004).

RESULTS

Response of *A. mellifera* Larvae to SBTI. In the diet-only control treatment, >95% of the worker larvae developed to pupae (Figure 1A), and >90% developed to adults (Figure 1B). With an increasing concentration of SBTI in the diet, the survival rates of *A. mellifera* were steadily reduced (Figure 1), and no larvae survived to the pupal stage at the highest SBTI concentration of 10 mg/g fresh weight (FW) of diet (data not shown). Pupal and adult development and larval weight were not significantly affected by SBTI at 0.1 mg/g FW diet (Dunnett's test; $P > 0.05$) (Figure 1A−D), but SBTI at 1.0 mg/g FW diet significantly decreased the pupation rate (Dunnett's test; $P = 0.006$) (Figure 1A), eclosion rate ($P = 0.012$) (Figure 1B), and mature larvae fresh weight ($P = 0.003$) (Figure 1D) and significantly prolonged larval development time (days to defecation) (Dunnett's test; $P = 0.023$) (Figure 1C).

Toxicity of *Bt* Proteins to *A. mellifera* Larvae. *Effects on Life Table Parameters.* *A. mellifera* pupation rate, eclosion rate, larval development time (days to defecation), days to the adult stage, mature larval weight, and adult weight did not significantly differ among the untreated control diet and diets containing BSA, Cry1C, or Cry2A proteins (Dunnett's test: BSA, $P = 0.999$, 0.837, 0.711, 1.000, 0.999, and 0.998, respectively; Cry1C, $P = 0.999$, 1.000, 0.351, 0.421, 0.998, and 0.983, respectively; Cry2A, $P = 0.999$, 0.999, 0.405, 0.699, and 0.788, respectively) (Table 1). *A. mellifera* pupation rate and eclosion rate were decreased by feeding the diet containing SBTI in comparison to those fed control diet (by 13.3 and 17.3%, respectively), although the differences were not significant (Dunnett's test; $P = 0.058$ and 0.054 for pupation rate and eclosion rate, respectively). The developmental time of *A. mellifera* larvae (days to defecation and to adult) were also not significantly affected by the diet containing SBTI (Dunnett's test: $P = 0.12$ for larval development time, $P = 0.68$ for days to adult) (Table 1). In contrast, the mean weights of mature larvae and of newly emerged adults were significantly reduced by SBTI (Dunnett's test, $P < 0.001$) (Table 1).

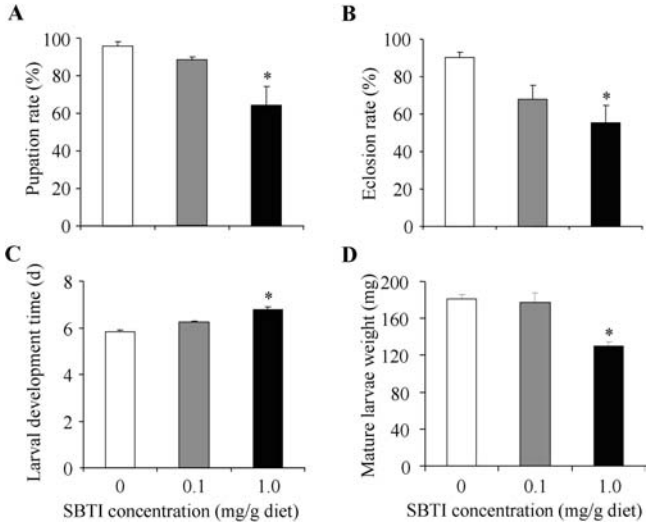

Figure 1. Life-table parameters of *Apis mellifera* larvae fed an artificial diet containing different concentrations of SBTI. An asterisk denotes a significant difference between the treatment and the control ($P < 0.05$). No larva reached the pupal stage at the highest SBTI concentration of 10 mg/g diet (data not shown). Values are means + SE, $n = 3$.

Uptake of Bt Proteins by A. mellifera Worker Larvae. ELISA measurements revealed that all *A. mellifera* larvae contained considerable amounts of Cry1C or Cry2A, but no Cry protein was detected in pupae when they were fed diets containing the corresponding *Bt* proteins. After 2 and 4 days of feeding, the mean ± SE concentrations of Cry1C in *A. mellifera* larvae were 0.61 ± 0.04 and 0.82 ± 0.14 μg/g of FW insect, respectively. For Cry2A, the concentrations detected after 2 and 4 days of feeding were 29.11 ± 2.01 and 18.70 ± 1.02 μg/g FW insects, respectively. No Cry protein was detected in larvae or pupae fed with control diet.

Bioactivity of Bt Proteins. After *C. suppressalis* larvae were fed for 7 days in the sensitive-insect bioassay, the mean ± SE weights per larva were 1.71 ± 0.12, 0.92 ± 0.11, and 0.19 ± 0.11 mg when the artificial diet contained extract from the control bee diet, extract from the bee diet containing Cry1C protein, and extract from the bee diet containing Cry2A, respectively (Figure 2). According to the Student's *t* test, the difference relative to the diet containing control extract was

DOI: 10.1021/acs.jafc.5b01662
J. Agric. Food Chem. 2015, 63, 6126−6132

Table 1. Life Table Parameters of *Apis mellifera* Worker Larvae Fed Pure Artificial Diet (Untreated Control) or Artificial Diet Containing the Protein BSA (400 μg/g Diet; Negative Control), Cry2A (400 μg/g Diet), Cry1C (50 μg/g Diet), or SBTI (1 mg/g Diet; Positive Control)[a]

parameter	untreated control	BSA	Cry2A	Cry1C	SBTI
pupation rate (%)	90.67 ± 2.67	92.00 ± 3.27	92.00 ± 3.89	89.33 ± 1.63	77.33 ± 5.09
eclosion rate (%)	85.33 ± 3.89	90.67 ± 3.40	86.67 ± 4.71	85.33 ± 3.27	68.00 ± 7.12
larval development time (days)	5.79 ± 0.15	5.98 ± 0.20	6.06 ± 0.07	6.08 ± 0.05	6.20 ± 0.12
time to adult (days)	18.68 ± 0.21	18.66 ± 0.28	18.59 ± 0.05	18.46 ± 0.10	18.96 ± 0.20
mature larval weight (mg)	199.02 ± 3.35	200.34 ± 4.98	190.70 ± 5.39	197.15 ± 3.65	151.43 ± 9.31*
emergence weight of adults (mg)	137.06 ± 4.73	138.56 ± 5.11	131.17 ± 4.96	134.39 ± 2.84	101.80 ± 5.41*

[a]Each protein treatment was compared to the control. Dunnett's test was used for all comparisons. An asterisk denotes a significant difference between a treatment and the untreated control ($P < 0.001$). Values are means ± SE, $n = 5$.

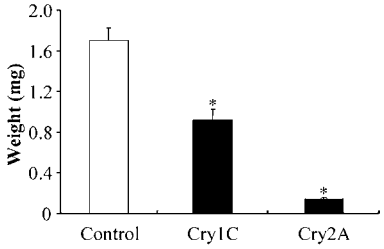

Figure 2. Weight of *Chilo suppressalis* larvae fed for 2 days on an artificial diet that contained an extract from pure bee artificial diet (control) or extracts from bee diets containing Cry1C or Cry2A. An asterisk denotes a significant difference between the treatment and the control ($P < 0.05$). Values are means + SE, $n = 30$.

significant for the diet containing Cry1C extract ($t = 4.91$, $df = 57$, $P < 0.001$) and for the diet containing Cry2A extract ($t = 11.91$, $df = 54$, $P < 0.001$) (Figure 2).

Enzyme Activity in A. mellifera Worker Larvae. The activities of the total protease, tryptase, aminopeptidase, and α-naphthyl acetate esterase (α-NAE) were similar when *A. mellifera* larvae were fed the untreated control diet or diets containing BSA, Cry1C, or Cry2A protein (Dunnett's test; $P > 0.1$) (Table 2). When *A. mellifera* larvae were fed a diet containing SBTI, the activity levels of all test enzymes were significantly increased relative to the control (Dunnett's test; all $P < 0.001$).

Histopathology of A. mellifera Larvae after Ingestion of Cry Proteins. Midgut sections from *A. mellifera* larvae that had ingested BSA, Cry1C, Cry2A, or SBTI, as well as midguts from control larvae that had not been exposed to the toxins, were examined microscopically for histopathological effects. Midguts of *A. mellifera* larvae had a monolayer epithelial cell structure (Figure 3). For larvae fed pure diet or diet containing BSA or

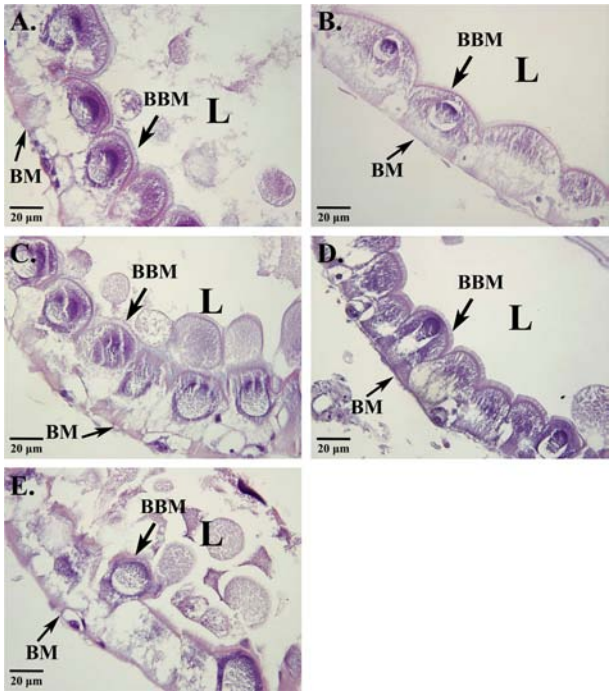

Figure 3. Light micrographs of midgut sections of *Apis mellifera* larvae fed for 4 days on artificial diets containing no toxin (A), BSA at 400 μg/g diet (B), Cry1C at 50 μg/g diet (C), Cry2A at 400 μg/g diet (D), or SBTI at 1 mg/g diet (E). Note that the brush border membranes (BBM) of the epithelial cells (ECs) are clear and that the ECs are homogeneous and intact in the midguts of larvae that consumed a diet without toxin or a diet with BSA, Cry1C, or Cry2A. For larvae that consumed a diet with SBTI, however, the BBMs are lysed and the ECs showed signs of degeneration. BM = base membrane, L = lumen.

Table 2. Enzyme Activity Levels in *Apis mellifera* Worker Larvae Fed Pure Artificial Diet (Untreated Control) or Artificial Diet Containing the Protein BSA (400 μg/g Diet; Negative Control), Cry2A (400 μg/g Diet), Cry1C (50 μg/g Diet), or SBTI (1 mg/g Diet; Positive Control)[a]

	enzyme activity level			
treatment	total protease (U/L ± SE)	tryptase (U/mL ± SE)	aminopeptidase (U/L ± SE)	α-NAE (IU/mL ± SE)
untreated control	131.79 ± 2.67	104.59 ± 5.47	5.73 ± 0.21	31.57 ± 0.76
BSA	151.48 ± 10.93	113.68 ± 3.47	6.18 ± 0.23	33.03 ± 0.61
Cry2A	154.55 ± 6.49	115.85 ± 5.05	5.98 ± 0.14	33.04 ± 1.33
Cry1C	140.28 ± 17.03	102.10 ± 3.46	5.92 ± 0.20	31.15 ± 0.98
SBTI	229.76 ± 5.04*	137.93 ± 5.02*	7.11 ± 0.24*	40.77 ± 1.36*

[a]Each protein treatment was compared to the control, and an asterisk denotes a significant difference between a treatment and the untreated control ($P < 0.05$). The Dunnett's test was used for all comparisons. Values are means ± SE, $n = 8–10$.

DOI: 10.1021/acs.jafc.5b01662
J. Agric. Food Chem. 2015, 63, 6126−6132

Cry proteins, the epithelial cells (ECs) were intact and aligned, and their brush border membranes (BBMs) were clearly visible (Figure 3A–D). There was no apparent difference between midgut sections from control larvae and from larvae fed Cry1C or Cry2A protein. For the larvae fed on a diet containing SBTI, however, the ECs showed signs of degeneration and had separated from the basal membrane (BM) and the BBM of ECs lysed (Figure 3E).

DISCUSSION

Evaluating the potential adverse effects of IRGE plants on valued nontarget organisms typically starts with laboratory experiments that measure the potential toxicity of the insecticidal proteins produced by IRGE plants.[4,32−34] These experiments are referred to as tier 1 studies and are conducted under controlled, worst-case exposure conditions. In the tier 1 assays, purified insecticidal proteins are normally delivered directly to test species by incorporating them into artificial diets at high concentrations. These concentrations are much higher than those encountered in the field and thus yield conservative results: i.e., they tend to overestimate adverse effects.[33−35] Tier 1 assays require a suitable method for delivering insecticidal compounds to the test organism and arriving at conclusive results.[33,34,36]

Artificial diets and in vitro rearing techniques for *A. mellifera* larvae have been developed, and these are useful for conducting dietary exposure assays that assess the potential toxicity of insecticidal compounds.[18−20,22−25,37−39] The artificial diet and the procedure for feeding *A. mellifera* larvae used in the present study were the same as those described by Huang.[25] The >90% survival rate with this diet satisfies the basic criterion of >80% survival for diets used for tier 1 assays.[32−34] In addition to the untreated pure diet control, diet containing the nontoxic protein BSA was included as a negative control treatment in our experiments for further evaluation of how the test system and test conditions, including the diet used in the study, affect the mortality and development of *A. mellifera* larvae. This negative control treatment could ensure nutritional equivalence between dietary treatments, and it assisted in determining whether observed effects are related to the test compounds.[33] Likewise, the survival rate of *A. mellifera* larvae in this negative control treatment was >90%, suggesting that there was no apparent background effect with the diet used in the current dietary testing system.

Positive control treatments are particularly useful in dietary exposure assays with the purposes of indicating whether the test compound is actually ingested and confirming the sensitivity of the testing system. In addition, positive controls may function as useful references to permit comparison to other test results.[33,34] Compounds used as a positive control should be readily accepted and toxic to the test organism and have properties similar to those of the test compounds in terms of their route of toxicity.[33,34] SBTI was used to determine the ability of our dietary exposure assay because it is known to be readily accepted and toxic to bees[23] and is an orally active compound, as are the tested Cry proteins. Dose-dependent responses to dietary SBTI were observed for all of the measured life table parameters for worker larvae. This demonstrated that the test system used in the current study was capable of efficiently detecting dietary effects of insecticidal compounds. In addition, these results indicated that artificial diet containing SBTI at 1 mg/g FW of diet is a useful positive control.

After validating the dietary exposure assay described in the present study, we evaluated the potential toxicities of purified Cry1C at 50 μg/g diet and Cry2A at 400 μg/g diet to *A. mellifera* worker larvae. These can be regarded as worst-case exposure scenarios, because these concentrations in the diet are >10 times higher than the Cry protein concentrations in pollen of the current *Bt* rice lines (mean concentrations of Cry1C and Cry2A are 2.6 μg/g dry weight of T1C-19B pollen and 33.5 μg/g dry weight in T2A-1 pollen, respectively[40,41]). Pollen is the only route by which honeybee larvae would be exposed to Cry proteins, because rice does not produce nectar. Considering that *A. mellifera* larvae ingest only small amounts of plant pollen,[8] the concentrations of Cry proteins used in this study are much higher than the Cry protein levels likely encountered by *A. mellifera* under natural conditions. Our results indicate that *A. mellifera* larvae were not negatively affected when fed a diet containing Cry1C or Cry2A proteins. Feeding on diets containing SBTI at 1 mg/g FW, in contrast, significantly reduced the survival and weight of *A. mellifera* larvae. The results also demonstrated that *A. mellifera* larvae did ingest the insecticidal compounds that were incorporated in the diet of our assay and that our experimental system was capable of detecting the adverse dietary effects caused by toxic compounds.

To further determine the quantity of Cry proteins ingested by *A. mellifera* worker larvae, the contents of Cry proteins were measured by ELISA in larvae fed for 2 or 4 days on diets that contained Cry protein. High concentrations of both Cry proteins were detected in *A. mellifera* larvae, confirming that the larvae did ingest the Cry proteins. Interestingly, no Cry protein was detected in pupae that had developed from larvae that had fed on both Cry protein treatments. The likely reason for the absence of Cry protein in the pupae is the fact that the bee larvae empty their gut before pupation. The absence of Cry proteins in pupae developing from larvae that had consumed Cry protein containing diet was also documented for the ladybird beetles *Stethorus punctillum* and *Propylea japonica* (Coleoptera: Coccinellidae),[42,43] suggesting that those insects also empty their guts before pupation. This is not the case for lacewings (Neuroptera: Chrysopidae), however, because insecticidal proteins such as *Galanthus nivalis* agglutinin and Cry proteins could still be detected in lacewing pupae or adults that developed from larvae that ingested these compounds.[30,44,45]

To have confidence in the findings that Cry1C and Cry2A do not affect larval *A. mellifera*, the bioactivity of the test compounds during the feeding assay needs to be confirmed.[33,34] A bioassay with the *Bt* protein sensitive species *C. suppressalis* was conducted to test the bioactivity of the Cry1C and Cry2A proteins in the artificial bee diet. The 7 day larval weight was selected as the measurement end point because it has been proven to be a credible and sensitive parameter for assessing the possible impact of *Bt* toxins on this sensitive test insect.[30,42,46] The results demonstrated that *A. mellifera* larvae had ingested large amounts of bioactive Cry1C or Cry2A protein. We therefore conclude that *A. mellifera* larvae are not sensitive to Cry1C or Cry2A at concentrations that are much higher than those potentially encountered under natural conditions.

The activities of four gut enzymes (the total protease, tryptase, aminopeptidase, and α-naphthyl acetate esterase) have been widely used to indicate the potential toxicity of insecticidal compounds.[21,28] Our results showed that consumption of

DOI: 10.1021/acs.jafc.5b01662
J. Agric. Food Chem. 2015, 63, 6126−6132

Cry1C or Cry2A did not affect the activity of these enzymes in *A. mellifera* larvae, while the activity levels of all analyzed enzymes were significantly increased in *A. mellifera* larvae fed on a diet containing SBTI in comparison to those fed control diet. A similar pattern of change in the activity of these enzymes has been observed for *Folsomia candida* (Collembola: Isotomidae) fed purified Cry1C and Cry2A.[47] These results further demonstrate that Cry1C and Cry2A do not affect *A. mellifera* larvae. In addition, microscopy revealed that the midgut brush border membranes of *A. mellifera* larvae were not damaged after ingestion of Cry1C or Cry2A protein. Because the BBM is the locus of Cry protein activity in sensitive organisms,[28,31] this provided additional evidence that neither Cry protein is toxic to *A. mellifera* larvae.

In summary, we used toxicological, biochemical, and histopathological techniques to assess the toxicity of Cry1C and Cry2A proteins to *A. mellifera* worker larvae. These techniques have been widely used in previous studies to evaluate the potential toxicity of insecticidal compounds on arthropods.[21,28,48] With the integrated application of these techniques, a convincing conclusion can be drawn that Cry1C and Cry2A have no acute toxicity to *A. mellifera* larvae at concentrations that are more than 10 times higher than those detected in pollen from *Bt*-transgenic plants. The results are consistent with previous studies in which the purified *Bt* proteins Cry1Ac, Cry1Ab, Cry1A.105, Cry2A, and Cry3Bb1 were found to be nontoxic to *A. mellifera* larvae or adults.[14,17,20,49] Thus, we conclude that the planting of GE crops including *Bt* rice expressing such *Bt* proteins poses a negligible risk to *A. mellifera*.

AUTHOR INFORMATION

Corresponding Authors

*Y.-H.L.: tel, +86-10-62815947; fax, +86-10-62896114; e-mail, yunhe.li@hotmail.com.

*Y.-F.P.: e-mail, yfpeng@vip.qq.com.

Funding

The study was supported by the National GMO New Variety Breeding Program of PRC (2014ZX08011-02B) and (2014ZX08011-001).

Notes

The authors declare no competing financial interest.

REFERENCES

(1) James, C. Global status of commercialized biotech/GM crops: 2014. ISAAA Brief No. 49 (International Service for the Acquisition of Agri-Biotech Applications, Ithcaca, NY, USA). 2014.

(2) Sanvido, O.; Romeis, J.; Gathmann, A.; Gielkens, M.; Raybould, A.; Bigler, F. Evaluating environmental risks of genetically modified crops-ecological harm criteria for regulatory decision-making. *Environ. Sci. Policy* **2012**, *15*, 82−91.

(3) Li, Y.; Peng, Y.; Hallerman, E.; Wu, K. Biosafety management and commercial use of genetically modified crops in China. *Plant Cell Rep.* **2014**, *33*, 565−573.

(4) Romeis, J.; Bartsch, D.; Bigler, F.; Candolfi, M. P.; Gielkens, M. M. C.; Hartley, S. E.; Hellmich, R. L.; Huesing, J. E.; Jepson, P. C.; Layton, R.; Quemada, H.; Raybould, A.; Rose, R. I.; Schiemann, J.; Sears, M. K.; Shelton, A. M.; Sweet, J.; Vaituzis, Z.; Wolt, J. D. Assessment of risk of insect-resistant transgenic crops to nontarget arthropods. *Nat. Biotechnol.* **2008**, *26*, 203−208.

(5) Morse, R. A.; Calderone, N. W. The value of honey bees as pollinators of US crops in 2000. *Bee Culture.* **2000**, *128*, 1−15.

(6) Klein, A. M.; Vaissiere, B. E.; Cane, J. H.; Steffan-Dewenter, I.; Cunningham, S. A.; Kremen, C.; Tscharntke, T. Importance of pollinators in changing landscapes for world crops. *Proc. R. Soc. London, Ser. B* **2007**, *274*, 303−313.

(7) Malone, L. A.; Pham-Deleguep, M. H. Effects of transgene products on honey bees (*Apis mellifera*) and bumblebees (*Bombus* sp.). *Apidologie* **2001**, *32*, 287−304.

(8) Babendreier, D.; Kalberer, N.; Romeis, J.; Fluri, P.; Bigler, F. Pollen consumption in honey bee larvae: a step forward in the risk assessment of transgenic plants. *Apidologie* **2004**, *35*, 293−300.

(9) Babendreier, D.; Kalberer, N. M.; Romeis, J.; Fluri, P.; Mulligan, E.; Bigler, F. Influence of *Bt*-transgenic pollen, *Bt*-toxin and protease inhibitor (SBTI) ingestion on development of the hypopharyngeal glands in honeybees. *Apidologie* **2005**, *36*, 585.

(10) Baker, H.; Baker, I. The occurrence and significance of amino acids in floral nectar. *Plant Syst. Evol.* **1986**, *151*, 175−186.

(11) Crailsheim, K. The protein balance of the honey bee worker. *Apidologie* **1990**, *21*, 417−429.

(12) Kaftanoglu, O.; Linksvayer, T. A.; Page, R. E., Jr Rearing honey bees, *Apis mellifera*, *in vitro* 1: Effects of sugar concentrations on survival and development. *J. Insect Sci.* **2011**, *11* (96), 1−10.

(13) Romeis, J.; Raybould, A.; Bigler, F.; Candolfi, M. P.; Hellmich, R. L.; Huesing, J. E.; Shelton, A. M. Deriving criteria to select arthropod species for laboratory tests to assess the ecological risks from cultivating arthropod-resistant genetically engineered crops. *Chemosphere* **2013**, *90*, 901−909.

(14) Malone, L. A.; Burgess, E. P. J.; Gatehouse, H. S.; Voisey, C. R.; Tregidga, E. L.; Philip, B. A. Effects of ingestion of a *Bacillus thuringiensis* toxin and a trypsin inhibitor on honey bee flight activity and longevity. *Apidologie* **2001**, *32*, 57−68.

(15) Hanley, A. V.; Huang, Z. Y.; Pett, W. L. Effects of dietary transgenic *Bt* corn pollen on larvae of *Apis mellifera* and *Galleria mellonella*. *J. Apic. Res.* **2003**, *42*, 77−81.

(16) Rose, R.; Dively, G. P.; Pettis, J. Effects of *Bt* corn pollen on honey bees: emphasis on protocol development. *Apidologie* **2007**, *38*, 368−377.

(17) Duan, J. J.; Marvier, M.; Huesing, J.; Dively, G.; Huang, Z. Y. A meta-analysis of effects of *Bt* crops on honey bees (Hymenoptera: Apidae). *PLoS One* **2008**, *3* (1), e1415.

(18) Hendriksma, H. P.; Härtel, S.; Steffan-Dewenter, I. Honey bee risk assessment: new approaches for *in vitro* larvae rearing and data analyses. *Methods Ecol. Evol.* **2011**, *2*, 509−517.

(19) Hendriksma, H. P. Testing pollen of single and stacked insect-resistant *Bt*-maize on *in vitro* reared honey bee larvae. *PLoS One* **2011**, *6* (12), e28174.

(20) Hendriksma, H. P.; Härtel, S.; Babendreier, D.; von der Ohe, W.; Steffan-Dewenter, I. Effects of multiple *Bt* proteins and GNA lectin on *in vitro*-reared honey bee larvae. *Apidologie* **2012**, *43*, 549−560.

(21) Han, P.; Niu, C. Y.; Biondi, A.; Desneux, N. Does transgenic Cry1Ac + CpTI cotton pollen affect hypopharyngeal gland development and midgut proteolytic enzyme activity in the honey bee *Apis mellifera* L. (Hymenoptera, Apidae)? *Ecotoxicology* **2012**, *21*, 2214−2221.

(22) Malone, L. A.; Tregidga, E. L.; Todd, J. H.; Burgess, E. P.; Philip, B. A.; Markwick, N. P.; Poulton, J.; Christeller, J. T.; Lester, M. T.; Gatehouse, H. S. Effects of ingestion of a biotin-binding protein on adult and larval honey bees. *Apidologie* **2002**, *33*, 447−458.

(23) Brødsgaard, H. F.; Brødsgaard, C. J.; Hansen, H.; Lövei, G. L. Environmental risk assessment of transgene products using honey bee (*Apis mellifera*) larvae. *Apidologie* **2003**, *34*, 139−145.

(24) Silva, I. C.; Message, D.; Cruz, C. D.; Campos, L. A.; Sousa-Majer, M. J. Rearing Africanized honey bee (*Apis mellifera* L.) brood under laboratory conditions. *GMR, Genet. Mol. Res.* **2009**, *8*, 623−9.

(25) Huang, Z. Y. *A standardized procedure for in vitro rearing of honey bee larvae*. California Department of Agriculture. 2009; http://www.cdpr.ca.gov/docs/registration/reevaluation/larval_protocol.pdf (accessed 10 March 2015).

(26) Chen, H.; Tang, W.; Xu, C.; Li, X.; Lin, Y.; Zhang, Q. Transgenic indica rice plants harboring a synthetic *cry2A** gene of

DOI: 10.1021/acs.jafc.5b01662
J. Agric. Food Chem. 2015, 63, 6126−6132

Bacillus thuringiensis exhibit enhanced resistance against lepidopteran rice pests. *Theor. Appl. Genet.* **2005**, *111*, 1330−7.
(27) Tang, W.; Chen, H.; Xu, C. G.; Li, X. H.; Lin, Y. J.; Zhang, Q. F. Development of insect-resistant transgenic indica rice with a synthetic *cry1C* gene. *Mol. Breed.* **2006**, *18*, 1−10.
(28) Burgess, E. P.; Malone, L. A.; Christeller, J. T. Effects of two proteinase inhibitors on the digestive enzymes and survival of honey bees (*Apis mellifera*). *J. Insect Physiol.* **1996**, *42*, 823−828.
(29) Bell, H. A.; Kirkbride-Smith, A. E.; Marris, G. C.; Edwards, J. P.; Gatehouse, A. M. R. Oral toxicity and impact on fecundity of three insecticidal proteins on the gregarious ectoparasitoid *Eulophus pennicornis* (Hymenoptera: Eulophidae). *Agric. For. Entomo.* **2004**, *6*, 215−222.
(30) Li, Y.; Hu, L.; Romeis, J.; Wang, Y.; Han, L.; Chen, X.; Peng, Y. Use of an artificial diet system to study the toxicity of gut-active insecticidal compounds on larvae of the green lacewing *Chrysoperla sinica*. *Biol. Control* **2014**, *69*, 45−51.
(31) Schnepf, E.; Crickmore, N.; Van Rie, J.; Lereclus, D.; Baum, J.; Feitelson, J.; Zeigler, D. R.; Dean, D. H. *Bacillus thuringiensis* and its pesticidal crystal proteins. *Microbiol. Mol. Biol. Rev.* **1998**, *62*, 775−806.
(32) Rose, R. *White paper on tier-based testing for the effects of proteinaceous insecticidal plant-incorporated protectants on non-target invertebrates for regulatory risk assessment*. USDA-APHIS and US Environmental Protection Agency: Washington, DC, USA., 2007.
(33) Romeis, J.; Hellmich, R. L.; Candolfi, M. P.; Carstens, K.; De Schrijver, A.; Gatehouse, A. M.; Herman, R. A.; Huesing, J. E.; McLean, M. A.; Raybould, A. Recommendations for the design of laboratory studies on non-target arthropods for risk assessment of genetically engineered plants. *Transgenic Res.* **2011**, *20*, 1−22.
(34) Li, Y. H.; Romeis, J.; Wu, K. M.; Peng, Y. F. Tier-1 assays for assessing the toxicity of insecticidal proteins produced by genetically engineered plants to non-target arthropods. *Insect Sci.* **2014**, *21*, 125−134.
(35) Duan, J. J.; Lundgren, J. G.; Naranjo, S.; Marvier, M. Extrapolating non-target risk of *Bt* crops from laboratory to field. *Biol. Lett.* **2010**, *6*, 74−77.
(36) Romeis, J.; McLean, M. A.; Shelton, A. M. When bad science makes good headlines: *Bt* maize and regulatory bans. *Nat. Biotechnol.* **2013**, *31*, 386−387.
(37) Lima, M. A. P.; Pires, C. S. S.; Guedes, R. N. C.; Nakasu, E. Y. T.; Lara, M. S.; Fontes, E. M. G.; Sujii, E. R.; Dias, S. C.; Campos, L. A. O. Does Cry1Ac *Bt*-toxin impair development of worker larvae of Africanized honey bee? *J. Appl. Entomol.* **2011**, *135*, 415−422.
(38) Aupinel, P.; Fortini, D.; Michaud, B.; Medrzycki, P.; Padovani, E.; Przygoda, D.; Maus, C.; Charriere, J. D.; Kilchenmann, V.; Riessberger-Galle, U. Honey bee brood ring-test: method for testing pesticide toxicity on honeybee brood in laboratory conditions. *Julius-Kühn-Archiv.* **2010**, *423*, 96−102.
(39) Lehrman, A. Does pea lectin expressed transgenically in oilseed rape (*Brassica napus*) influence honey bee (*Apis mellifera*) larvae? *Environ. Biosaf. Res.* **2007**, *6*, 271−278.
(40) Wang, Y.; Li, Y.; Romeis, J.; Chen, X.; Zhang, J.; Chen, H.; Peng, Y. Consumption of *Bt* rice pollen expressing Cry2Aa does not cause adverse effects on adult *Chrysoperla sinica* Tjeder (Neuroptera: Chrysopidae). *Biol. Control* **2012**, *61*, 246−251.
(41) Li, Y.; Chen, X. P.; Hu, L.; Romeis, J.; Peng, Y. F. *Bt* rice producing Cry1C protein does not have direct detrimental effects on the green lacewing *Chrysoperla sinica* (Tjeder). *Environ. Toxicol. Chem.* **2014**, *33* (6), 1391−1397.
(42) Zhang, X.; Li, Y.; Romeis, J.; Yin, X.; Wu, K.; Peng, Y. Use of a pollen-based diet to expose the ladybird beetle *Propylea japonica* to insecticidal proteins. *PLoS One* **2014**, *9* (1), e85395.
(43) Li, Y. H.; Romeis, J. *Bt* maize expressing Cry3Bb1 does not harm the spider mite, *Tetranychus urticae*, or its ladybird beetle predator. *Biol. Control* **2010**, *53*, 337−344.
(44) Li, Y. H.; Romeis, J. Impact of snowdrop lectin (*Galanthus nivalis* agglutinin; GNA) on adults of the green lacewing, *Chrysoperla carnea*. *J. Insect Physiol.* **2009**, *55*, 136−143.
(45) Hogervorst, P. A. M.; Ferry, N.; Gatehouse, A. M. R.; Wäckers, F. L.; Romeis, J. Direct effects of snowdrop lectin (GNA) on larvae of three aphid predators and fate of GNA after ingestion. *J. Insect Physiol.* **2006**, *52*, 614−624.
(46) Huang, F.; Leonard, B. R.; Gable, R. H. Comparative susceptibility of European corn borer, Southwestern corn borer, and sugarcane borer (Lepidoptera: Crambidae) to Cry1Ab protein in a commercial *Bacillus thuringiensis* corn hybrid. *J. Econ. Entomol.* **2006**, *99*, 194−202.
(47) Yang, Y.; Chen, X.; Cheng, L.; Cao, F.; Romeis, J.; Li, Y.; Peng, Y. Toxicological and biochemical analyses demonstrate no toxic effect of Cry1C and Cry2A to *Folsomia candida*. *Sci. Rep.* **2015**, in press.
(48) Rodrigo-Simón, A.; de Maagd, R. A.; Avilla, C.; Bakker, P. L.; Molthoff, J.; González-Zamora, J. E.; Ferré, J. Lack of detrimental effects of *Bacillus thuringiensis* Cry toxins on the insect predator *Chrysoperla carnea*: a toxicological, histopathological, and biochemical analysis. *Appl. Environ. Microbiol.* **2006**, *72*, 1595−1603.
(49) Sims, S. R. Host activity spectrum of the CryIIA *Bacillus thuringiensis* subsp. *kurstaki* protein: effects on lepidoptera, diptera, and non-target arthropods. *Southwestern Entomol.* **1997**, *22*, 395−404.
(50) Li, Y.-H. Unpublished results.

DOI: 10.1021/acs.jafc.5b01662
J. Agric. Food Chem. 2015, 63, 6126−6132

Table 1. Accession Numbers, Country of Origin, Days from Sowing to 50% Flowering and Maturity, Plant Height, Seed Coat Color, and Seed β-ODAP Concentration [% of seed dry weight (DW)] of Seven Grass Pea (*Lathyrus sativus* L.) Genotypes Measured in Plants Grown in the Field in 2012

accession no.	origin	days to 50% flowering	days to maturity	plant height (mm)	seed coat color	seed β-ODAP concentration (% DW)
IF 225	Slovakia	65.0	105.0	416	cream	2.53
IF 2156	Bangladesh	59.0	93.0	320	light brown	1.81
Dingxi	China	64.5	107.8	423	cream	1.72
IF 1942	Bangladesh	58.0	90.5	374	light brown	1.66
IF 1347	Syria	61.0	95.0	352	light brown	1.58
IF 1312	Syria	63.0	99.0	339	dark brown	1.51
IF 1310	Syria	63.0	100.0	355	dark brown	1.22

ODAP, β-isoxazolinon-alanine, and found that there was no difference in the incorporation of the precursor in seeds of high- and low-β-ODAP genotypes, suggesting that the differences in β-ODAP among genotypes was likely the result of differences in the biosynthesis and amount of the precursor of β-ODAP near maturity. It is therefore not clear whether the accumulation or catabolism of β-ODAP at vegetative and reproductive stages is associated with the final concentration of β-ODAP in seeds at maturity.

As the basis for genotypic variation in the amount and concentration of β-ODAP in seeds and the effect of water stress on this genotypic variation is not known, an experiment on the accumulation and catabolism of β-ODAP in vegetative and reproductive tissues of seven grass pea genotypes varying in seed β-ODAP concentration was conducted at three levels of water availability. We hypothesized that variation in amount and concentration of β-ODAP in seeds is determined by the accumulation and/or catabolism of β-ODAP in vegetative and reproductive tissues at the early reproductive phase and that the variation in the amount and concentration of β-ODAP in seeds with varying water availability is determined as a result of the processes of accumulation and catabolism in these tissues. The purpose of the present study was to (1) track the variation in β-ODAP concentration and amount in leaves and pods of seven grass pea genotypes at flowering, podding, and maturity; (2) examine whether water stress affected the distribution of β-ODAP at these stages; and (3) determine the relationship between amount and concentration of β-ODAP in seeds in the vegetative and early reproductive stages at three levels of water availability.

MATERIALS AND METHODS

Plant Materials and Growth Conditions. Seven genotypes of grass pea (six genotypes from the International Centre for Agricultural Research in Dry Areas and one local cultivar, Dingxi, from China) were planted on April 4, 2013 at the Yuzhong Experiment Station of Lanzhou University, Yuzhong, Gansu province, China (35°51′ N, 104°07′S; altitude, 1620 m). The genotypes had similar phenologies, differing by 6 days in time to flowering; plant height varied from 320 to 420 mm; seed coat color varied from cream to dark brown; and seed β-ODAP concentration varied more than 200% when the genotypes were planted in the field at the Yuzhong Experiment Station of Lanzhou University in 2012 (Table 1). The experimental site has a typical semiarid climate with an accumulated rainfall of 202.5 mm, a mean temperature of 14.5 °C, and a mean relative humidity of 58% during the growing season (March−July). Ten uniform seeds of the seven genotypes were each sown in 45 plastic pots (0.26 m diameter, 0.30 m high) containing 8.0 kg of a dry silty-loam loess soil (haplic greyxems[34]) and vermiculite mixture (soil:vermiculite = 2:1, v/v) with a field capacity (FC, the percentage of water in the soil when the soil is fully saturated, then allowed to drain for 48 h) of 30.8%; the pots were placed in a rainout shelter that was open when rain was not forecast. Ten DAS, the plants were thinned to five seedlings per pot. Nitrogen (0.68 g of NH_4NO_3) and phosphorus (1.58 g of KH_2PO_4) were supplied as a solution to each pot before sowing. Three water treatments were imposed: (1) Well-watered (WW): pots were watered daily in the late afternoon to 80% FC throughout the growing period. (2) Moderate water-stressed (WS): pots were kept at 80% FC until 35 DAS when soil water content (SWC) was allowed to fall to 50% FC and maintained at 50% FC to maturity by daily watering in the late afternoon until maturity. (3) Severe WS: pots were kept at 80% FC until 35 DAS when the SWC was allowed to fall to 35% FC and maintained at 35% FC by daily watering in the late afternoon to maturity.

Days to 50% flowering and maturity were recorded and dry matter of different organs measured at flowering (54 DAS), early podding (75 DAS), and maturity (103 DAS). At flowering and podding, plants were cut off at soil level and separated into stems and leaves at flowering and leaves, stems, and pods at early podding. They were then dried in a forced-draft oven at 80 °C for 24 h, and dry weights (DW) were recorded. Fresh leaf (0.5 g) and pod (0.5 g) material at flowering and podding stages were sampled for measurement of β-ODAP concentration. At maturity, plants were cut off at soil level and separated into stems, leaves, pod walls and grain and then dried in a forced-draft oven at 80 °C for 24 h; DW was then recorded. Total grain number was counted and individual grain DW (seed size) was calculated as grain DW/total grain number. A subsample (about 1.0 g) of air-dried seeds was collected at maturity to measure β-ODAP concentration. β-ODAP amount for each plant organ was calculated as product of the β-ODAP concentration and the DW of each organ.

There were 21 different treatment combinations (7 genotypes, each with 3 water treatments), with 15 pots per treatment, giving a total of 315 pots. At both flowering (54 DAS) and early podding (75 DAS), 3 of the 15 pots per treatment were harvested for DW measurements and 3 for β-ODAP concentration, while at maturity the three remaining pots were harvested. The experiment was arranged as a complete randomized block design with three replicate blocks.

β-ODAP Concentration. β-ODAP concentration was analyzed using the methods of Wang et al.[35] and Yan et al.[36] Dry seeds (0.5 g) were ground to powder using a mini ball mill (FZ102, Zhongxing Ltd. Beijing, China) or fresh leaves (0.5 g) or fresh pods (0.5 g) were homogenized with 4.5 mL of ethanol/water (7:3, v/v) and extracted for 24 h at room temperature. The mixture was centrifuged for 0.25 h at 150 000*g* with 0.5 mL of supernatant dried under vacuum. A 100 μL of 0.5 M $NaHCO_3$ solution was used to dissolve the residue, and then 100 μL of the reagent (100 mg of 1-fluoro-2,4-dinitrobenzene in 10 mL of acetonitrile) was added to the mixture for derivatization which was completed in 0.75 h at 60 °C. After the mixture was cooled to room temperature, 0.8 mL of 0.01 M KH_2PO_4 solution was added to the above reaction mixture; then the mixture was vortexed for 10 s and filtered through a 0.45 μm membrane filter. A 20 μL sample of the product was taken for high-performance liquic chromatography (HPLC) analysis using a HPLC system (Agilent 1200, Waldbronn, Germany) to detect β-ODAP concentration. The chromatographic conditions were set as follows: Phenomenex C 18 column of 3.9 × 150 mm; mobile phase, acetonitritle/0.1 M KH_2PO_4, 17/83 (v/v); column temperature, 40 °C; flow rate, 1/60 mL/s; detection wave, 360 nm. The mobile solutions were filtered through a 0.45 μm membrane filter and degassed before use in the HPLC system. ODAP (containing 80% β-ODAP, and 20% α-

DOI: 10.1021/acs.jafc.5b01729
J. Agric. Food Chem. 2015, 63, 6133−6141

Table 2. Days to 50% Flowering [Days after Sowing (DAS)], Days to Maturity (DAS), Leaf Dry Weight (DW, g/plant), Pod DW (g/plant), Aboveground DW (g/plant), Grain DW (g/plant), Grain Number (/plant), and Individual Grain Dry Weight (DW, g/seed) in Seven Grass Pea (*Lathyrus sativus* L.) Genotypes Subjected to Three Water Regimes [80% field capacity (FC), 50% FC, and 35% FC][a]

				leaf DW		pod DW	above ground DW	grain DW	grain number	individual grain DW
water	genotype	days to 50% flowering	days to maturity	flowering	podding	podding	maturity	maturity	maturity	maturity
80% FC	IF 225	50	99	1.6	2.2	1.6	7.9	3.1	18.1	0.182
	IF 2156	43	91	1.0	0.8	2.2	4.1	2.2	17.7	0.126
	Dingxi	55	103	1.4	2.3	1.9	9.9	4.5	22.6	0.179
	IF 1942	44	91	1.0	1.0	2.2	5.0	2.7	20.9	0.104
	IF 1347	47	94	1.1	1.3	2.1	5.9	2.9	27.5	0.102
	IF 1312	44	91	1.3	1.5	2.3	6.9	3.2	26.9	0.100
	IF 1310	48	94	1.1	1.3	2.1	5.4	2.7	24.3	0.105
	mean	47	95	1.2	1.5	2.1	6.4	3.0	22.6	0.128
50% FC	IF 225	48	91	1.1	1.0	1.7	4.5	2.0	13.3	0.106
	IF 2156	42	87	0.8	0.6	1.2	2.8	1.5	14.8	0.073
	Dingxi	52	93	1.0	1.3	2.1	5.6	2.7	12.7	0.141
	IF 1942	43	88	0.8	0.5	2.0	3.3	1.9	16.8	0.082
	IF 1347	46	91	0.8	0.9	1.7	4.1	2.3	22.5	0.054
	IF 1312	43	87	1.0	0.5	1.7	3.5	1.8	13.1	0.087
	IF 1310	47	90	0.7	0.7	2.2	3.3	1.9	19.5	0.055
	mean	46	90	0.9	0.8	1.8	3.9	2.0	16.1	0.085
35% FC	IF 225	46	89	0.9	0.5	1.1	2.7	1.2	7.7	0.119
	IF 2156	42	84	0.5	0.3	1.2	1.8	1.0	10.1	0.077
	Dingxi	52	91	0.7	0.8	0.6	2.3	0.9	4.8	0.235
	IF 1942	43	84	0.6	0.4	1.2	1.9	1.0	10.6	0.076
	IF 1347	46	89	0.5	0.4	1.1	2.0	1.1	13.7	0.051
	IF 1312	43	84	0.8	0.5	1.6	2.4	1.3	12.2	0.058
	IF 1310	47	84	0.7	0.5	1.5	2.7	1.5	14.8	0.047
	mean	46	86	0.7	0.5	1.2	2.3	1.1	10.6	0.095
	$LSD_{0.05(W)}$	**1.0	***0.9	***0.04	***0.1	***0.2	***0.09	***0.2	***1.6	***0.013
	$LSD_{0.05(G)}$	***1.6	***1.5	***0.07	***0.2	**0.3	***0.14	***0.3	***2.4	***0.019
	$LSD_{0.05(W\times G)}$	n.s.	***2.5	*0.12	***0.3	**0.5	***0.80	***0.5	*4.2	***0.034

[a]Least significant differences (LSD) for each column are given: $LSD_{0.05(W)}$ for water treatments, $LSD_{0.05(G)}$ for genotypes, $LSD_{0.05(W\times G)}$ for water treatment by genotype interactions (n.s., no significant difference; *, $P < 0.05$; **, $P < 0.01$; ***, $P < 0.001$).

ODAP, provided by Prof. Zhixiao Li, School of Chemistry and Chemical Engineering, Lanzhou University, Lanzhou, Gansu Province, China) was used as a standard for quantitative analysis.

Statistical Analyses. Data were analyzed by two-way ANOVA (water treatments and genotypes) using Genstat 12.1 (VSN International Ltd., Hemel Hempstead, UK). Where significant effects were found, least significant difference (LSD) values at $P = 0.05$ are presented. Linear regressions between the amount or concentration of β-ODAP in the seeds and the amount of β-ODAP in the leaves and pods during growth were analyzed by Origin 8.0 (Microcal Software Inc. Northampton, Massachusetts, United States). Ordinary least-squares (OLS) regression analysis was used to test linear Y − linear X relationships, and OLS slope heterogeneity among water treatments was tested using the Standardized Major Axis Tests and Routines (SMATR) (version 2.0, NSW, Australia).[37]

RESULTS

Phenology. In the WW treatment, the seven genotypes reached 50% flowering in 43−55 DAS (mean, 47 DAS) with IF 2156, IF 1942, and IF 1312 flowering first and the local cultivar, Dingxi, flowering last (Table 2). Water stress reduced the time to 50% flowering by 1−2 days at both 50% FC and 35% FC (Table 2). In the WW treatment, maturity varied from 91 DAS in the early flowering genotypes to 103 DAS in Dingxi (mean, 95 DAS); at 50% FC, the time to maturity decreased by 5 days, and at 35% FC it decreased by a further 4 days (Table 2).

Plant Dry Weight, Grain Yield, and Yield Components. In the WW treatment (80% FC), the local cultivar, Dingxi, had the most aboveground DW and grain DW at maturity with 9.9 and 4.5 g/plant, respectively, of the seven grass pea genotypes, followed by IF 1312 and IF 225 (aboveground DW 6.9−7.9 g/plant and grain DW 3.1−3.2 g/plant); then IF 1942, IF 1310, and IF 1347 (aboveground DW 5.0−5.9 g/plant and grain DW 2.7−2.9 g/plant); with the least aboveground DW and grain DW at maturity observed in IF 2156 (4.1 and 2.2 g/plant, respectively) (Table 2). In the WW treatment, the seven genotypes ranked differently for pod DW (including seed) at early podding (75 DAS), leaf DW at flowering (54 DAS), and early podding (75 DAS) when compared to the seed DW at maturity (Table 2). Reducing available water to 50% FC significantly decreased aboveground DW and seed DW at maturity by 40% and 33%, respectively, on average across genotypes, and reducing of available water to 35% FC reduced aboveground DW and seed DW by a further 41% and 45%, respectively (62−65% less than in the WW treatment) (Table 2). There was a highly significant interaction between genotypes and water treatments, with aboveground DW and seed DW of the local cultivar, Dingxi,

DOI: 10.1021/acs.jafc.5b01729
J. Agric. Food Chem. 2015, 63, 6133−6141

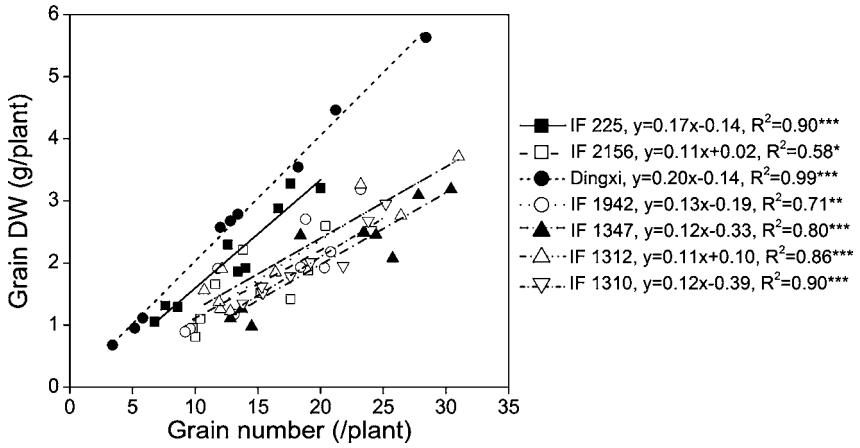

Figure 1. Relationship between grain dry weight (DW) and grain number in seven grass pea (*Lathyrus sativus* L.) genotypes. The lines are the fitted ordinary least-squares (linear) regressions (regression data shown).

decreasing by 40−43% at 50% FC and by 77−80% at 35% FC, compared to 30−39% and 44−50% at 50% FC and 35% FC, respectively, in genotype IF 1310 (Table 2). Leaf and pod DW at podding decreased with decreasing water availability in a similar manner and percentage to seed DW (Table 2). The reduction in leaf and pod DW in the local cultivar, Dingxi, was greater than that in IF 1310 as water availability decreased from 80% FC to 35% FC (Table 2). The large reduction in seed DW with water stress in Dingxi (Table 2) was associated with a large decrease (44% at 50% FC and 79% at 35% FC) in seed number (Table 2). This contrasts with the smaller decrease in seed numbers in IF 1310 (20% at 50% FC and 39% at 35% FC) with water stress (Table 2). The reduction in seed DW with water stress was associated with a decrease in grain number in all genotypes (Table 2, Figure 1). Seed size (individual grain DW) decreased in all genotypes when the water treatment decreased from 80% FC to 50% FC, but it increased in some genotypes when the water stress treatment decreased to 35% FC (Table 2), such that the reduction in seed DW with WS was not associated with individual grain DW (data not shown).

***β*-ODAP Concentration in Leaves, Pods, and Seeds.** *β*-ODAP concentration in leaves at flowering varied significantly among genotypes, from 0.79% in IF 1310 to 1.58% in IF 1347 in the WW treatment (Table 3). In all genotypes the concentration of *β*-ODAP in the leaves decreased between flowering and podding, which varied with genotype (Table 3). Water stress increased *β*-ODAP concentration in the leaves at both flowering and early podding, but the only significant interaction was at flowering when the severe stress treatment (35% FC) induced a significant increase in *β*-ODAP concentration in IF 225, IF 2156, and IF 1347 (Table 3).

At maturity when plants senesce, *β*-ODAP can be detected only in seeds and not in the leaves, stems, roots, or pod walls.[27,32] Therefore, we measured *β*-ODAP concentration in whole pods (including developing seeds) at early podding but only in seeds at maturity. In the WW treatment, IF 1312 had the highest pod *β*-ODAP concentration at 2.51%, while IF 1310 had the lowest at 0.65% at podding; there was a significant reduction (more than 1% decrease on average across genotypes) in *β*-ODAP concentration in seeds at maturity compared with pods at early podding (Table 3). The concentration of *β*-ODAP in seeds varied from 0.85% in IF 1312 to 0.22% in IF 1310 in the WW treatment (Table 3). In all genotypes except IF 1312, water stress (50% FC) significantly increased *β*-ODAP concentration in pods

Table 3. Leaf *β*-ODAP Concentration [% Dry Weight (DW)] at Flowering [54 Days after Sowing (DAS)] and Early Podding (75 DAS), Pod *β*-ODAP Concentration (% DW) at Early Podding (75 DAS), and Seed *β*-ODAP Concentration (% DW) at Maturity (103 DAS) in Seven Grass Pea (*Lathyrus sativus* L.) Genotypes Given Three Water Regimes [80% Field Capacity (FC), 50% FC, and 35% FC][a]

β-ODAP concentration		leaves		pods	seeds
water	genotype	flowering	podding	podding	maturity
80% FC	IF 225	1.33	0.58	1.64	0.59
	IF 2156	1.50	0.45	1.67	0.77
	Dingxi	1.17	0.79	1.85	0.57
	IF 1942	1.28	1.09	1.80	0.58
	IF 1347	1.58	1.38	1.59	0.68
	IF 1312	1.32	0.73	2.51	0.85
	IF 1310	0.79	0.76	0.65	0.22
	mean	1.28	0.83	1.67	0.61
50% FC	IF 225	1.96	0.68	2.11	0.80
	IF 2156	1.61	1.01	4.23	0.78
	Dingxi	1.13	0.89	2.44	0.76
	IF 1942	2.20	1.08	2.13	0.75
	IF 1347	1.84	1.65	2.27	0.75
	IF 1312	1.30	1.12	1.96	0.67
	IF 1310	1.24	0.97	0.96	0.29
	mean	1.61	1.06	2.30	0.69
35% FC	IF 225	2.10	0.97	4.03	0.81
	IF 2156	2.48	0.97	3.54	0.88
	Dingxi	1.21	1.01	7.22	0.90
	IF 1942	1.84	1.04	3.76	0.75
	IF 1347	3.16	2.22	4.02	0.86
	IF 1312	1.67	0.89	2.72	1.02
	IF 1310	1.20	1.79	1.20	0.52
	mean	1.95	1.27	3.78	0.82
	$LSD_{0.05(W)}$	***0.22	**0.23	***0.40	***0.09
	$LSD_{0.05(G)}$	***0.34	***0.35	***0.61	***0.15
	$LSD_{0.05(W\times G)}$	**0.59	n.s.	***1.05	n.s.

[a]Least significant differences (LSD) for each column are given: $LSD_{0.05(W)}$ for water treatments, $LSD_{0.05(G)}$ for genotypes, $LSD_{0.05(W\times G)}$ for water treatment by genotype interactions (n.s., no significant difference; *, $P < 0.05$; **, $P < 0.01$; ***, $P < 0.001$).

DOI: 10.1021/acs.jafc.5b01729
J. Agric. Food Chem. 2015, 63, 6133−6141

at early podding and increased it further at 35% FC (Table 3). Similarly, water stress increased the concentration of β-ODAP in seeds at maturity, but the low seed β-ODAP genotype, IF 1310, was consistently low in all three water treatments (Table 3). It is notable that the ranking for seed β-ODAP concentration in the seven genotypes in the moderate WS (50% FC) treatment (Table 3) was the same as that observed in the field in 2012 (Table 1).

Contrary to previous observations,[38−40] there was no association between seed size (individual grain weight, Table 2) or seed color (Table 1) with the β-ODAP concentration in the seed (Table 3) in the limited number of genotypes used in this study.

β-ODAP Amount in Leaves, Pods, and Seeds. As the amount of β-ODAP in the tissues is a product of β-ODAP concentration and tissue DW, it is a measure of the net accumulation, synthesis minus catabolism, and redistribution of β-ODAP by the plant. In the WW treatment, IF 225 had the greatest, while IF 1310 had the least, amount of β-ODAP in the leaves at flowering (Table 4). Over all the genotypes, water shortage significantly reduced the amount of β-ODAP in the leaves at flowering from 15.6 mg/plant at 80% FC to 14.1 mg/plant at 50% FC to 12.4 mg/plant at 35% FC, and there was a significant genotype by water interaction in the leaves of IF 1942 that had more β-ODAP at 50% FC than at 80% FC (Table 4). Nevertheless, IF 225 had the most and IF 1310 had the least β-ODAP in the leaves at flowering in all three levels of water supply (Table 4). Generally, the amount of β-ODAP decreased in the leaves between flowering and early podding, more so at 35% FC than 50% FC and less so at 80% FC (Table 4).

In the WW treatment, IF 1312 had the most and IF 1310 had the least β-ODAP in pods at early podding and in seeds at maturity (Table 4). The amount of β-ODAP in pods at early podding generally increased from 80% FC to 50% FC to 35% FC, except in IF 2156, Dingxi, IF 1312, and IF 1310 (Table 4), but the amount of β-ODAP in seeds at maturity decreased with increasing water stress such that the amount of β-ODAP in mature seeds was about 54% of that in pods at podding at 80% FC, 36% at 50% FC, and 23% at 35% FC (Table 4). IF 1310 had the least β-ODAP in seeds at maturity in all soil water treatments (Table 4).

Changes in β-ODAP Amount in Leaves and Pods between Different Stages of Growth. In the WW treatment (80% FC), there was a significant reduction in β-ODAP in the leaves between flowering and early podding in IF 225, IF 2156, IF 1942, and IF 1312 (Table 5). The average reduction across the seven genotypes was greater for all genotypes at 50% (5.9 mg/plant) and 35% FC (6.5 mg/plant) than at 80% FC (3.6 mg/plant) (Table 5). In contrast, the amount of β-ODAP in the pods at early podding increased relative to the amount in the leaves at flowering in all seven genotypes and all three water treatments (Table 5). The increase in β-ODAP in pods was greater with decreased water availability; the mean increase for all grass pea genotypes was 19.2 mg/plant at 80% FC, 24.9 mg/plant at 50% FC, and 28.0 mg/plant at 35% FC (Table 5). The amount of β-ODAP in pods decreased from early podding to maturity (at maturity, the seed β-ODAP amount is the same as pod β-ODAP amount as there is no β-ODAP in the pod wall) in all seven genotypes in all water treatments (Table 5). The reduction in β-ODAP in pods increased as the water deficit became more severe; the mean reduction for the seven genotypes was 16.1 mg/plant at 80% FC, 24.9 mg/plant at 50% FC, and 31.2 mg/plant at 35% FC (Table 5). Water shortage did not significantly affect the sum of β-ODAP in leaves and pods at the early podding stage, but there was significant variation among genotypes from 68.2 mg/plant in IF 1312 to 23.7 mg/plant in IF 1310 in the WW treatment (Table 5). IF 1310 consistently had the least β-ODAP in leaves and pods at 23.7 to 27.7 mg/plant, while the genotype with the greatest amount varied from IF 1312 at 80% FC to Dingxi at 50% FC to Dingxi and IF 1347 at 35% FC (Table 5).

Table 4. Leaf β-ODAP Amount (mg/plant) at Flowering [54 Days after Sowing (DAS)] and Early Podding (75 DAS), Pod β-ODAP Amount (mg/plant) at Early Podding (75 DAS), and Seed β-ODAP Amount (mg/plant) at Maturity (103 DAS) in Seven Grass Pea (*Lathyrus sativus* L.) Genotypes Given Three Water Regimes [80% Field Capacity (FC), 50% FC, and 35% FC][a]

β-ODAP amount		leaves		pods	seeds
water	genotype	flowering	podding	podding	maturity
80% FC	IF 225	20.6	12.8	27.0	18.5
	IF 2156	15.5	3.7	36.6	17.3
	Dingxi	15.9	18.2	35.9	26.1
	IF 1942	13.4	10.5	39.6	15.7
	IF 1347	17.6	18.3	33.0	19.9
	IF 1312	17.3	10.6	57.6	27.5
	IF 1310	8.9	10.0	13.7	6.0
	mean	15.6	12.0	34.8	18.7
50% FC	IF 225	21.6	7.0	36.4	16.2
	IF 2156	12.8	6.4	49.5	12.0
	Dingxi	11.5	11.5	51.4	20.5
	IF 1942	17.6	5.2	42.6	14.5
	IF 1347	14.1	14.2	37.8	17.6
	IF 1312	12.4	6.1	34.0	11.8
	IF 1310	8.6	6.7	21.0	5.5
	mean	14.1	8.2	39.0	14.0
35% FC	IF 225	18.0	5.3	45.9	9.9
	IF 2156	12.7	3.3	41.7	8.4
	Dingxi	8.4	8.0	44.8	8.3
	IF 1942	11.0	4.0	44.9	7.6
	IF 1347	15.6	8.1	44.8	9.5
	IF 1312	13.1	4.3	42.8	13.1
	IF 1310	8.1	8.7	17.9	7.7
	mean	12.4	6.0	40.4	9.2
	$LSD_{0.05(W)}$	***1.3	***1.8	**3.1	***1.6
	$LSD_{0.05(G)}$	***2.0	***2.7	***4.7	***2.5
	$LSD_{0.05(W\times G)}$	**3.5	n.s.	***8.2	***4.3

[a]Least significant differences (LSD) for each column are given: $LSD_{0.05(W)}$ for water treatments; $LSD_{0.05(G)}$ for genotypes; $LSD_{0.05(W\times G)}$ for water treatment by genotype interactions (n.s., no significant difference; *, $P < 0.05$; **, $P < 0.01$; ***, $P < 0.001$)

Relationship between the Amount or Concentration of β-ODAP in Seeds at Maturity and the Amount of β-ODAP in Tissues during Growth. There was no significant ($P > 0.05$) association between the amount of β-ODAP in leaves at either flowering or podding and the amount or concentration of β-ODAP in seeds at maturity (data not shown). However, there was a significant ($P < 0.05$) positive correlation between the sum of leaf and pod β-ODAP amount at early podding and seed β-ODAP concentration at maturity in all three water treatments (Figure 2a). There was no significant difference in the slope among the three water treatments, but the concentration of β-ODAP in seeds at 35% FC was higher than that of the other two water treatments (Figure 2a). There was also a positive

DOI: 10.1021/acs.jafc.5b01729
J. Agric. Food Chem. 2015, 63, 6133−6141

Table 5. Changes in Leaf β-ODAP Amount (mg/plant) and Pod β-ODAP Amount (mg/plant) between Flowering (F), Podding (P), and Maturity (M), and the Sum of Leaf and Pod β-ODAP Amounts (mg/plant) at P (75 DAS) in Seven Grass Pea (*Lathyrus sativus* L.) Genotypes Given Three Water Regimes [80% Field Capacity (FC), 50% FC, and 35% FC][a]

water	genotype	change in leaf β-ODAP amount between F and P	Change in β-ODAP amount between leaves at F and pods at P	change in pod β-ODAP amount between P and M	sum of leaf and pod β-ODAP amounts at P
80% FC	IF 225	−7.8	+6.4	−8.5	39.8
	IF 2156	−11.8	+21.1	−19.3	40.3
	Dingxi	+2.3	+20.0	−9.8	54.1
	IF 1942	−2.9	+26.2	−23.9	50.1
	IF 1347	+0.7	+15.4	−13.1	51.3
	IF 1312	−6.7	+40.3	−30.1	68.2
	IF 1310	+1.1	+4.8	−7.7	23.7
	mean	−3.6	+19.2	−16.1	46.8
50% FC	IF 225	−14.6	+14.8	−20.2	43.4
	IF 2156	−6.4	+36.7	−37.5	55.9
	Dingxi	−0.0	+39.9	−30.9	62.9
	IF 1942	−12.4	+25.0	−28.1	47.8
	IF 1347	+0.1	+23.7	−20.2	52.0
	IF 1312	−6.3	+21.6	−22.2	40.1
	IF 1310	−1.9	+12.4	−15.5	27.7
	mean	−5.9	+24.9	−24.9	47.1
35% FC	IF 225	−12.7	+27.9	−36.0	51.2
	IF 2156	−9.4	+29.0	−33.3	45.0
	Dingxi	−0.4	+36.4	−36.5	52.8
	IF 1942	−7.0	+33.9	−37.3	48.9
	IF 1347	−7.5	+29.2	−35.3	52.9
	IF 1312	−8.8	+29.7	−29.7	47.1
	IF 1310	+0.6	+9.8	−10.2	26.6
	mean	−6.5	+28.0	−31.2	46.4
	$LSD_{0.05(W)}$	***1.2	***1.9	***1.7	n.s.
	$LSD_{0.05(G)}$	***1.9	***2.9	***2.6	***3.5
	$LSD_{0.05(W\times G)}$	***3.3	***5.1	***4.4	***6.1

[a]Least significant differences (LSD) for each column are given: $LSD_{0.05(W)}$ for water treatments; $LSD_{0.05(G)}$ for genotypes; $LSD_{0.05(W\times G)}$ for water treatment by genotype interactions (n.s., no significant difference; *, $P < 0.05$; **, $P < 0.01$; ***, $P < 0.001$).

relationship between the amount of β-ODAP in seeds at maturity and the sum of leaf and pod β-ODAP amounts at 80% FC and 50% FC, but not at 35% FC, with no increase in the amount of β-ODAP in seeds relative to the amount of β-ODAP in leaves and pods at podding in severely stressed plants (Figure 2b). There was also a significant ($P < 0.05$) positive association between the change in β-ODAP amount between leaves at flowering and pods at early podding, and seed β-ODAP concentration at maturity in all three water treatments (Figure 3a), and with the amount of β-ODAP in seeds at maturity in the WW and moderate WS (50% FC) treatments (Figure 3b). There was no significant ($P > 0.05$) relationship between the change in leaf β-ODAP between flowering and podding, nor in the change in β-ODAP amount in the pods between podding and maturity and the seed β-ODAP concentration and amount at maturity (Table 6).

DISCUSSION

Grass pea differs genotypically in the concentration of β-ODAP in seeds at maturity. In this study we confirmed this and showed that the concentration of β-ODAP in seeds increased with water shortage but that a low β-ODAP genotype maintained the lowest β-ODAP concentration at all levels of water availability. We have shown that the variation in seed β-ODAP concentration at maturity is associated with the net (synthesis minus catabolism) amount of β-ODAP in pods and leaves at early podding in all three water treatments. This was associated with a marked increase in the amount of β-ODAP in pods at early podding compared with leaves at flowering, but not with the marked reduction in the amount of β-ODAP in seeds at maturity compared with pods at early podding, suggesting that the concentration of β-ODAP in seeds is likely the result of synthesis of β-ODAP or its precursor, β-isoxazolinon-alanine, in the early reproductive phase and the possible transfer of β-ODAP from leaves to pods and seeds. Genotypes ranked on the basis of their seed β-ODAP concentration in the field in 2012 had the same ranking as the ranking at the moderate stress (50% FC) treatment in the rainout shelter. However, the concentration of β-ODAP in seeds showed a genotype by environment interaction in that the rankings differed in the WW (80% FC) and severe WS (35% FC) treatments.

Effect of Water Stress on Biomass Accumulation, Grain Yield, and Yield Components. Reducing water supply to 50% FC and 35% FC had a marked effect on the growth of grass pea plants, reducing leaf DW at flowering and early podding as well as aboveground DW and seed DW at maturity by 40% and 33%, respectively, at 50% FC, and by 65% and 62%, respectively, at 35% FC. The reduction in grain DW by water stress in the seven genotypes was largely due to a reduction in grain number, with grain size largely unaffected; grain size even increased in the large-seeded genotype Dingxi which had a large reduction in grain number under severe water shortage. This result is consistent with other results with grass pea; water stress reduced

DOI: 10.1021/acs.jafc.5b01729
J. Agric. Food Chem. 2015, 63, 6133−6141

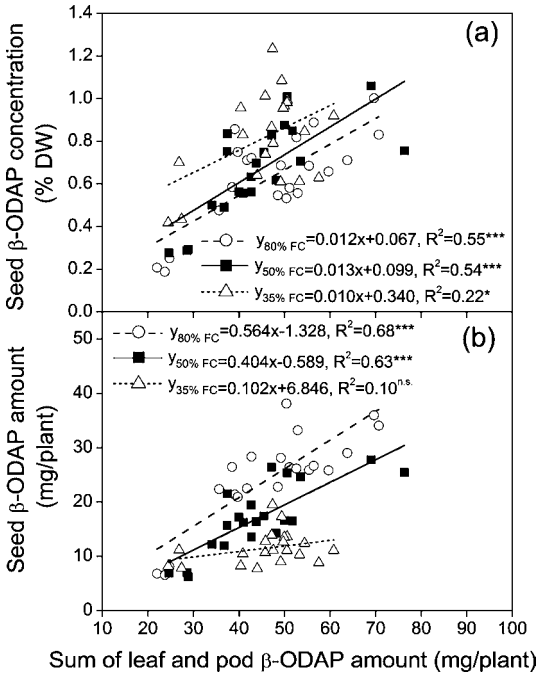

Figure 2. Relationship between (a) seed β-ODAP concentration and (b) seed β-ODAP amount at maturity and sum of leaf and pod β-ODAP amounts at podding in seven grass pea genotypes maintained at three water regimes: well-watered (80% field capacity, FC), moderate water stress (50% FC), and severe water stress (35% FC). The line is the fitted ordinary least-squares (linear) regression (regression data shown).

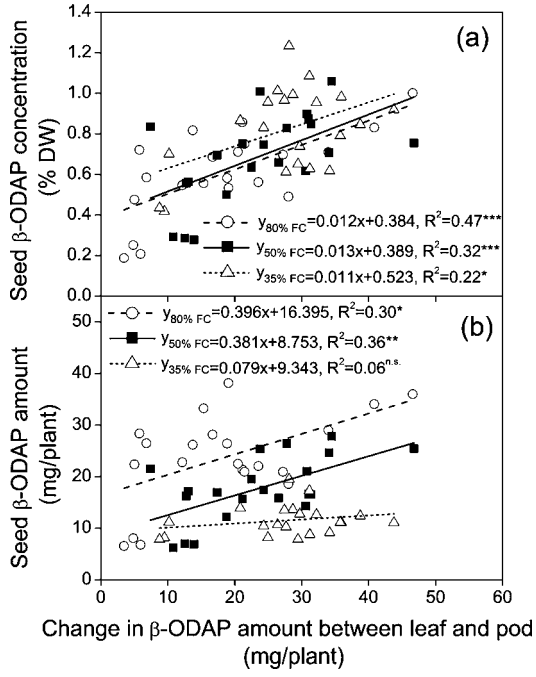

Figure 3. Relationship between (a) seed β-ODAP concentration and (b) seed β-ODAP amount at maturity and the change in β-ODAP amount between leaves at flowering and pods at early podding in seven grass pea cultivars maintained at three water regimes: well-watered (80% field capacity, FC), moderate water stress (50% FC), and severe water stress (35% FC). The line is the fitted ordinary least-squares (linear) regression (regression data shown).

the number of filled pods, grain number, grain DW, pod length, and pod wall DW, but not individual grain DW in the large-seeded (0.18 g/seed) *Lathyrus sativus* L. genotype Dingxi.[41] On the other hand, *Lathyrus sativus* L. cv. Ceora which has small seeds at 0.12 g/seed, produced smaller seeds (0.09 g/seed) and fewer seeds (from 269.5 to 124.0 per plant) when subjected to terminal water stress.[31] These results are consistent with those of Cocks et al.[28] who showed that a large-seeded (0.19 g/seed) grass pea accession, SEL 526, maintained its seed size, while a small-seeded (0.12 g/seed) accession had smaller seeds (0.09 g/seed) with increasing severe water stress.

Effect of Water Stress on β-ODAP Concentration and Amount. In this study, water stress increased β-ODAP concentration in leaves, pods, and seeds in all seven genotypes, more so with lower water supply. This result is consistent with previous results showing that water shortage increased β-ODAP concentration in different tissues of grass pea[28,29,42] but does not agree with observations by Gusmao et al.[30] and Kong et al.[31] that terminal drought induced no change in β-ODAP concentration of seeds. However, while the concentration of β-ODAP increased in this study, the amount of β-ODAP in the leaves at flowering and podding, and in the seeds at maturity, significantly decreased when the water supply decreased from 80% FC to 35% FC because of the reduction in DW in leaves, pods, and seeds with water shortage.

Accumulation and Catabolism of β-ODAP during the Vegetative and Reproductive Period. Jiao et al.[27] showed that the concentration of β-ODAP in leaves gradually declined with age. In the present study, leaf β-ODAP concentration also decreased from flowering to early podding. As there was little change in leaf DW over this period, this represents a loss in β-ODAP by either catabolism or translocation to the developing pods. The concentration of β-ODAP in seeds at maturity was lower than that in pods (containing seeds) at podding in all seven grass pea genotypes. This loss in β-ODAP concentration was associated with a large loss in the amount of β-ODAP in seeds at maturity relative to that in pods at podding, particularly in the severe WS treatment (35% FC). This suggests that there was considerable catabolism of β-ODAP in the senescing and maturing grass pea plants.

The reduction in the amount of β-ODAP in leaves from flowering to early podding was not associated ($P > 0.05$) with the concentration of β-ODAP in seeds at maturity, but there was a significant positive relationship between the increased amount of β-ODAP in leaves at flowering and pods at early podding, suggesting that variation in seed β-ODAP concentration may be related to differences in synthesis of new β-ODAP in pods at early podding rather than any transfer from leaves to pods, particularly as the amount of β-ODAP in pods at the podding stage was far higher than the amount of β-ODAP in leaves at flowering or podding.

The amount and concentration of β-ODAP in seeds at maturity was positively associated with the sum of leaf and pod β-ODAP amounts at podding, further suggesting that the amount of leaf and pod β-ODAP at this early reproductive stage jointly affected the final β-ODAP concentration in seeds. This was true in the genotype, IF 1310, which had the lowest amount and concentration of β-ODAP in seeds amount at maturity and the lowest amount of β-ODAP in leaves and pods at podding of seven grass pea genotypes. This is consistent with the observations by Kuo et al.[33] that genotypes differing in seed β-ODAP concentration differ in the biosynthesis of its precursor, not in the conversion of the precursor to β-ODAP; we suggest that the synthesis and accumulation of β-ODAP and its precursor in the vegetative and early reproductive stages determines the

DOI: 10.1021/acs.jafc.5b01729
J. Agric. Food Chem. 2015, 63, 6133−6141

Table 6. Relationships between the Change in β-ODAP Amounts in Leaves between Flowering (F) and Early Podding (P), and the Change in β-ODAP Amounts between Pods at P and Maturity (M), and Seed β-ODAP Concentration and Amount at Maturity Across Seven Grass Pea (*Lathyrus sativus* L.) Genotypes Maintained at Three Water Regimes [80% field capacity (FC), 50% FC, and 35% FC][a]

X	Y	water treatment	slope	intercept	R^2
change in leaf β-ODAP amounts	seed β-ODAP concentration	80% FC	0.017	0.543	0.21[n.s.]
		50% FC	0.001	0.681	0.00[n.s.]
		35% FC	0.012	0.743	0.08[n.s.]
between F and P	seed β-ODAP amount	80% FC	0.154	23.19	0.01[n.s.]
		50% FC	−0.130	18.42	0.02[n.s.]
		35% FC	0.204	10.20	0.11[n.s.]
change in pod β-ODAP amounts	seed β-ODAP concentration	80% FC	0.010	0.501	0.19[n.s.]
		50% FC	0.010	0.490	0.09[n.s.]
		35% FC	0.006	0.642	0.08[n.s.]
between P and M	seed β-ODAP amount	80% FC	0.030	23.46	0.00[n.s.]
		50% FC	0.158	14.56	0.03[n.s.]
		35% FC	0.014	11.12	0.00[n.s.]

[a]n.s., not significant ($P > 0.05$).

concentration in seeds at maturity. The strong association between the sum of β-ODAP in leaves and pods at early podding and final concentration in seeds at maturity could also be used to predict final β-ODAP concentration in the seed by measuring the β-ODAP level in the vegetative tissues at the early reproductive stage. Water stress did not significantly affect the relationship between seed β-ODAP concentration and the sum of leaf and pod β-ODAP at podding. However, severe water stress significantly reduced the slope between the amount of β-ODAP in seeds and the sum of leaf and pod β-ODAP amounts compared to the WW treatment, indicating that the severe WS treatment reduced the transfer of β-ODAP from leaves and pods at the early reproductive stage to seeds at maturity.

In summary, the variation among genotypes in seed β-ODAP concentration is a result of variation in the net accumulation (synthesis and catabolism) of β-ODAP during both the vegetative and reproductive phases. Water shortage affects this accumulation of β-ODAP in leaves and pods at podding differently among genotypes and hence induces differences in β-ODAP concentration in seeds at maturity. While the genotype by water supply interaction has been observed previously, the present study provides evidence that the differences among genotypes starts in the vegetative stage and is not simply determined by differences in synthesis in the late reproductive phase.

AUTHOR INFORMATION

Corresponding Authors

*UWA Institute of Agriculture and Centre for Plant Genetics and Breeding, The University of Western Australia, M080, Perth, WA 6009, Australia. Tel: +61 418 286 487. E-mail: neil.turner@uwa.edu.au.

*State Key Laboratory of Grassland Agroecosystems, Institute of Arid Agroecology, School of Life Sciences, Lanzhou University, Lanzhou 730000, Gansu Province, China. Tel: +86-931-8914500. Fax: +86-931-8914500. E-mail: xiongyc@lzu.edu.cn.

Funding

The research was funded by the Chinese Scholarships Council, Doctoral Fund of Ministry of Education of China (20110211110022), International Cooperation Program of Ministry of Science and Technology of China (2015DFG31840), State Technology Support Program (2015BAD22B04), Overseas Masters Program of Ministry of Education (Ms2011LZDX059), and the Fundamental Research Funds for the Central Universities of China (lzujbky-2015-br02).

Notes

The authors declare no competing financial interest.

ABBREVIATIONS USED

β-ODAP, β-N-oxalyl-L-α, β-diaminopropionic acid; DAS, days after sowing; DW, dry weight; FC, field capacity; LSD, least significant difference; OLS, ordinary least-squares; SWC, soil water content; WS, water-stressed; WW, well-watered

REFERENCES

(1) Jackson, M. T.; Yunus, A. G. Variation in the grass pea (*Lathyrus sativus* L.) and wild species. *Euphytica* **1984**, *33*, 549−559.

(2) Siddique, K. H. M.; Loss, S. P.; Herwig, S. P.; Wilson, J. M. Growth, yield and neurotoxin (ODAP) concentration of three *Lathyrus* species in Mediterranean-type environments of Western Australia. *Aust. J. Exp. Agric.* **1996**, *36*, 209−218.

(3) Al-Doss, A. A.; Assaeed, A. M.; Soliman, A. S. Growth characters and yield of some selected lines of grass pea (*Lathyrus sativus*). *J. King Saud Univ., Agric. Sci.* **1998**, *10*, 67−72.

(4) Campbell, C. G.; Mehra, R. B.; Agrawal, S. K.; Chen, Y. Z.; Abd El-Moneim, A. M.; Khawaja, H. I. T.; Yadov, C. R.; Tay, J. U.; Araya, W. Current status and future strategy in breeding grasspea (*Lathyrus sativus*). *Euphytica* **1993**, *73*, 167−175.

(5) Hanbury, C. D.; White, C. L.; Mullan, B. P.; Siddique, K. H. M. A review of the potential of *Lathyrus sativus* L. and *L. cicera* L. grain for use as animal feed. Anim. *Anim. Feed Sci. Technol.* **2000**, *87*, 1−27.

(6) Low, R. K. C.; Rotter, R. G.; Marquardt, R. R.; Campbell, G. C. Use of *Lathyrus sativus* L. (var. Seminis albi) as a foodstuff for poultry. *Br. Poult. Sci.* **1990**, *31*, 615−625.

(7) Tamburino, R.; Guida, V.; Pacifico, S.; Rocco, M.; Zarelli, A.; Parente, A.; Maro, A. D. Nutritional values and radical scavenging capacities of grass pea (*Lathyrus sativus* L.) seeds in Valle Agricola district, Italy. *Aust. J. Crop Sci.* **2012**, *6*, 149−156.

(8) Kumar, S.; Bejiga, G.; Ahmed, S.; Nakkoul, H.; Sarker, A. Genetic improvement of grass pea for low neurotoxin (β-ODAP) content. *Food Chem. Toxicol.* **2011**, *49*, 589−600.

DOI: 10.1021/acs.jafc.5b01729
J. Agric. Food Chem. 2015, 63, 6133−6141

(9) Hillocks, R. J.; Maruthi, M. N. Grass pea (*Lathyrus sativus*): Is there a case for further crop improvement? *Euphytica* **2012**, *186*, 647−654.
(10) Rao, S. L. N.; Adiga, P. R.; Sarma, P. S. The isolation and characterization of β-N-oxalyl-L-α, β-diaminopropionic acid: A neurotoxin from the seeds of *Lathyrus sativus*. *Biochemistry* **1964**, *3*, 432−436.
(11) Spencer, P. S.; Ludolph, A.; Dwivedi, M. P.; Roy, D.; Hugon, J.; Schaumburg, H. H. Lathyrism: evidence for role of the neuroexcitatory amino acid BOAA. *Lancet* **1986**, *328*, 1066−1067.
(12) Haimanot, R. T.; Kidane, Y.; Wuhib, E.; Kalissa, A.; Alemu, T.; Zein, Z. A.; Spencer, P. S. Lathyrism in rural northwestern Ethiopia: a highly prevalent neurotoxic disorder. *Int. J. Epidemiol.* **1990**, *19*, 664−672.
(13) Yan, Z. Y.; Spencer, P. S.; Li, Z. X.; Liang, Y. M.; Wang, Y. F.; Wang, C. Y.; Li, F. M. *Lathyrus sativus* (grass pea) and its neurotoxin ODAP. *Phytochemistry* **2006**, *67*, 107−121.
(14) Lambein, F.; Kuo, Y. H. Lathyrism. *Grain Legumes* **2009**, *54*, 8−9.
(15) Koh, H. L.; Lau, A. J.; Chan, E. C. Y. Hydrophilic interaction liquid chromatography with tandem mass spectrometry for the determination of underivatized dencichine (β-N-oxalyl-l-α, β-diamino propionic acid) in *Panax* medicinal plant species. *Rapid Commun. Mass Spectrom.* **2005**, *19*, 1237−1244.
(16) Dahiya, B. S.; Jeswani, L. M. Estimation of genetic variances by full-sib and half-sib analysis in grass-pea. *Indian J. Agr. Sci.* **1974**, *44*, 829−832.
(17) Dahiya, B. S.; Jeswani, L. M. Genotype X environment interactions for neurotoxic principle (BOAA) in grass pea. *Indian J. Agr. Sci.* **1975**, *45*, 437−439.
(18) Ramanujam, K. L.; Sethi, K. L.; Rao, S. L. N. Stability of neurotoxin content in khesari. *Indian J. Genet. Plant Breed.* **1980**, *40*, 300−304.
(19) Bell, E. A. Nonprotein amino acids of plants: significance in medicine, nutrition, and agriculture. *J. Agric. Food Chem.* **2003**, *51*, 2854−2865.
(20) Campbell, C. G. *Grass pea, Lathyrus sativus L. Promoting the conservation and use of underutilized and neglected crops. 18. Institute of Plant Genetic and Crop Plant Research*; Gatersleben/International Plant Genetic Resources Institute: Rome, Italy. 1997.
(21) Abd El-Moneim, A. M.; Van Dorrestein, B.; Baum, M.; Mulugeta, W. Improving the nutritional quality and yield potential of grasspea (*Lathyrus sativus* L.). *Food Nutr. Bull. Suppl.* **2000**, *21*, 493−496.
(22) Grela, E. R.; Rybiński, W.; Klebaniuk, R.; Matras, J. Morphological characteristics of some accessions of grass pea (*Lathyrus sativus* L.) grown in Europe and nutritional traits of their seeds. *Genet. Resour. Crop Evol.* **2010**, *57*, 693−701.
(23) Grela, E. R.; Rybiński, W.; Matras, J.; Sobolewska, S. Variability of phenotypic and morphological characteristics of some *Lathyrus sativus* L. and *Lathyrus cicera* L. accessions and nutritional traits of their seeds. *Genet. Resour. Crop Evol.* **2012**, *59*, 1687−1703.
(24) Tavoletti, S.; Iommarini, L.; Mogliani, L. Agronomic, qualitative (β-ODAP) and molecular variability in grasspea populations of the Marche region (central Italy). *Food Chem. Toxicol.* **2011**, *49*, 601−606.
(25) Hussain, M.; Chowdhury, B.; Haque, R.; Lambein, F. Effect of water stress, salinity, interaction of cations, stage of maturity of seeds and storage devices on the ODAP content of *Lathyrus sativus*. In *Lathyrus and Lathyrism, a Decade of Progress*; Haimanot, R. T., Lambein, F., Eds.; University of Ghent: Ghent, Belgium, 1997; pp 107−110.
(26) Haque, R. M.; Kuo, Y. H.; Lambein, F.; Hussain, M. Effect of environmental factors on the biosynthesis of the neuro-excitatory amino acid beta-ODAP (beta-N-oxalyl-L-alpha, beta-diaminopropionic acid) in callus tissue of *Lathyrus sativus*. *Food Chem. Toxicol.* **2011**, *49*, 583−588.
(27) Jiao, C. J.; Xu, Q. L.; Wang, C. Y.; Li, F. M.; Li, Z. X.; Wang, Y. F. Accumulation pattern of toxin β-ODAP during lifespan and effect of nutrient elements on β-ODAP content in *Lathyrus sativus* seedlings. *J. Agric. Sci.* **2006**, *144*, 369−375.
(28) Cocks, P.; Siddique, K. H. M.; Hanbury, C. *Lathyrus - A new grain legume*; No. 99/150; Rural Industries Research and Development Corporation: Kingston, Australia, 2000.
(29) Yang, H. M.; Zhang, X. Y.; Wang, G. X. Relationships between stomatal character, photosynthetic character and seed chemical composition in grass pea at different water availabilities. *J. Agric. Sci.* **2004**, *142*, 675−681.
(30) Gusmao, M.; Siddique, K. H. M.; Flower, K.; Nesbitt, H.; Veneklaas, E. J. Water deficit during the reproductive period of grass pea (*Lathyrus sativus* L.) reduced grain yield but maintained seed size. *J. Agron. Crop Sci.* **2012**, *198*, 430−441.
(31) Kong, H.; Palta, J. A.; Siddique, K. H. M.; Stefanova, K.; Xiong, Y. C.; Turner, N. C. Photosynthesis is reduced, and seeds fail to set and fill at similar soil water contents in grass pea (*Lathyrus sativus* L.) subjected to terminal drought. *J. Agron. Crop Sci.* **2014**, n/a.
(32) Addis, G.; Narayan, R. K. J. Developmental variation of the neurotoxin, β-N-oxalyl-l-α, β-diamino propionic acid (ODAP), in *Lathyrus sativus*. *Ann. Bot.* **1994**, *74*, 209−215.
(33) Kuo, Y. H.; Khan, J. K.; Lambein, F. Biosynthesis of the neurotoxin β-ODAP in developing pods of *Lathyrus sativus*. *Phytochemistry* **1994**, *35*, 911−913.
(34) FAO-UNESCO. Soil map of the world: Revised legend. *World Soil Resources Report*; No. 60; FAO: Rome, 1988.
(35) Wang, F.; Chen, X.; Chen, Q.; Qin, X. C.; Li, Z. X. Determination of neurotoxin 3-N-oxalyl-2, 3-diaminopropionic acid and non-protein amino acids in *Lathyrus sativus* by precolumn derivatization with 1-fluoro-2, 4-dinitrobenzene. *J. Chromatogr. A* **2000**, *883*, 113−118.
(36) Yan, Z. Y.; Jiao, C. J.; Wang, Y. P.; Li, F. M.; Liang, Y. M.; Li, Z. X. A method for the simultaneous determination of β-ODAP, α-ODAP, homoarginine and polyamines in *Lathyrus sativus* by liquid chromatography using a new extraction procedure. *Anal. Chim. Acta* **2005**, *534*, 199−205.
(37) Falster, D. S.; Warton, D. I.; Wright, I. J. SMATR: Standardised major axis tests and routines, version 2.0, 2006. http://www.bio.mq.edu.au/ecology/SMATR.
(38) Dahiya, B. S. Seed morphology as an indicator of low neurotoxin in *Lathyrus sativus* L. *Qual. Plant. - Plant Foods Hum. Nutr.* **1976**, *25*, 391−394.
(39) Roy, D. N.; Rao, K. V. Physicochemical values in different varieties of *Lathyrus sativus* and their interrelationships. *J. Agric. Food Chem.* **1978**, *26*, 687−689.
(40) Gresta, F.; Rocco, C.; Lombardo, G. M.; Avola, G.; Ruberto, G. Agronomic characterization and α- and β-ODAP determination through the adoption of new analytical strategies (HPLC-ELSD and NMR) of ten Sicilian accessions of grass pea. *J. Agric. Food Chem.* **2014**, *62*, 2436−2442.
(41) Xiong, J.-L.; Kong, H.-Y.; Akram, N. A.; Bai, X.; Ashraf, M.; Tan, R.-Y.; Siddique, K. H. M.; Xiong, Y.-C.; Turner, N. C. 24-epibrassinolide increases growth, grain yield and β-ODAP production in seeds of well-watered and moderately water-stressed grass pea. *Plant Growth Regul.* **2015**, (accepted 27 May 2015), DOI: 10.1007/s10725-015-0087-1.
(42) Xing, G. S.; Cui, K. R.; Li, J.; Wang, Y. F.; Li, Z. X. Water stress and accumulation of β-N-Oxalyl-L-α, β-diaminopropionic acid in grass pea (*Lathyrus sativus*). *J. Agric. Food Chem.* **2001**, *49*, 216−220.

DOI: 10.1021/acs.jafc.5b01729
J. Agric. Food Chem. 2015, 63, 6133−6141

Table 1. General Information about the Phytase Products Used in the in Vitro Digestion Model

	name in this work						
	EC1	EC2	EC3	BSP	CB	PL	AN
trademark	Quantum	Quantum Blue	PhyzymeXP	AxtraPHY	Ronozyme Hiphos	Ronozyme NP	Natuphos
supplier	AB Vista	AB Vista	Danisco	Danisco	Novozymes/ DSM	Novozymes/ DSM	BASF
donor organism	*Escherichia coli*	*Escherichia coli*	*Escherichia coli*	*Buttiauxella* sp.	*Citrobacter braakii*	*Peniophora lycii*	*Aspergillus niger*
production organism	*Trichoderma reesei*	*Trichoderma reesei*	*Schizosaccharomyces pombe*	*Trichoderma reesei*	*Aspergillus oryzae*	*Aspergilus oryzae*	*Aspergillus niger*
formulation	liquid	liquid	liquid	liquid	liquid	liquid	solid

a final concentration of 10 U mL^{-1}. Phytic acid dodecasodium salt, pancreatin from porcine pancreas (4 × USP), and pepsin from porcine gastric mucosa (>250 U mg^{-1}) were obtained from Sigma (Steinheim, Germany). Ultrasep ES 100 RP18 was purchased from Bischoff (Leonberg, Germany) and AG1 X-4, 100−200 mesh, resin from Bio-Rad (München, Germany). All reagents were of analytical grade.

Standard Phytase Activity Assay. The phytase activity assay was performed according to the method of Greiner et al.[9] Briefly, 10 μL of an appropriately diluted phytase preparation was incubated with 350 μL of phytate solution (2.5 mM of sodium phytate in 100 mM sodium acetate−acetic acid buffer, pH 5.5) at 37 °C. After an incubation time of 30 min, the liberated inorganic phosphate was measured by using a modification of the ammonium molybdate method.[10] One unit of phytase activity was defined as 1 μmol of P released in 1 min at test conditions. Blanks were performed by adding stop solution prior to enzyme addition.

Biochemical Characterization of the Phytases. To study the pH dependency of the phytase activity, the following buffers were used: pH 2.0−3.5, glycine−HCl; pH 4.0−5.5, sodium acetate−acetic acid; pH 6.0−7.0, sodium acetate−HCl; and pH 8.0−9.0, Tris−HCl.

To determine kinetic constants, the incubation mixture consisted of 350 μL of incubation buffer (100 mM glycine−HCl, pH 3.0, or 100 mM sodium acetate−acetic acid, pH 5.0) containing sodium phytate in a serial dilution of a concentrated stock solution (20 mM). Kinetic constants (K_M, k_{cat}) were calculated from Michaelis−Menten plots of the data. For the calculation of k_{cat}, the molecular masses of the nonglycosylated phytases were used: 42 kDa for the phytase from *Escherichia coli*,[9] 45 kDa for the phytases from *Peniophora lycii*[11] and *Buttiauxella*,[12] 47 kDa for the *Citrobacter braakii* phytase,[13] and 49 kDa for the *Aspergillus niger* phytase.[14]

Phytase inactivation by pepsin was determined by incubating 20 mU of the different phytase preparations in 100 mM glycine−HCl, pH 3.0, containing 3000 U of pepsin for 45 min at 37 °C. As a control the pH stability of the different phytases was determined under the same conditions. After incubation, residual phytase activity was determined using the standard phytase assay.

To study the dependency of phytase activity by ionic strength, 50 mM sodium acetate−acetic acid buffer (pH 4−5.5) was used and ionic strength was increased by adding NaCl to 600 mM.

Simulation of Poultry Digestive Tract. A simple in vitro degradation model was used to simulate the digestive tract of poultry, respectively, the crop, stomach (proventriculus and gizzard), and small intestine.[15] Because poultry diets are usually corn−soybean-based, ground wheat was used as a model feed in this study. The intrinsic wheat phytase was inactivated by microwave treatment of the ground wheat. One gram of ground wheat was incubated with 3 or 6 mL of 50 mM sodium acetate−acetic acid buffer, pH 5.0, buffer containing different amounts of phytase activity (0, 250, 500, 750, and 1000 U kg^{-1}) at 40 °C for 30 min. Subsequent stomach simulations were performed by adding 280 μL of 1 M HCl and 520 μL of 50 mM sodium acetate−acetic acid buffer, pH 3, containing 21 mg mL^{-1} pepsin to the crop digesta. The entire mixture was incubated at 40 °C for 45 min under continuous shaking at 100 rpm on a rotary shaker to guarantee a homogeneous distribution of all ingredients. Simulations of the small intestine were performed by adding 650 μL of 1 M $NaHCO_3$ and 650 μL of 14.8 mg mL^{-1} aqueous pancreatin solution to the stomach digesta. The entire mixture was incubated at 40 °C for 60 min. Inorganic P release and *myo*-inositol phosphate (IP_6−IP_3) quantification were used to follow phytate dephosphorylation throughout the simulated digestion. The samples obtained from the simulated digestion studies were freeze-dried overnight, and 1 g of the freeze-dried samples was extracted with 20 mL of 2.4% HCl for 3 h at room temperature. The resulting suspensions were centrifuged (30 min, 10000 rpm). The supernatants were collected and used for inorganic phosphate determination[10] and *myo*-inositol phosphate quantification.[16]

Quantification of the Liberated Inorganic Phosphate. The liberated phosphate was quantified by using a modification of the ammonium molybdate method.[10] One and a half milliliters of a freshly prepared solution of acetone/2.5 M sulfuric acid/10 mM ammonium molybdate (2:1:1 v/v) and thereafter 100 μL of 1.0 M citric acid were added to 400 μL of the suitably diluted supernatants or to the mixtures of the phytase activity assays. Any cloudiness was removed by centrifugation prior to the measurement of absorbance at 355 nm. To quantify the released phosphate, a calibration curve was produced over the range of 5−600 nmol of phosphate.

Quantification of *myo*-Inositol Phosphates. Two milliliter aliquots of the supernatants were diluted with water to give a final volume of 60 mL. The entire solution was applied to a column (0.7 × 15 cm) containing 0.5 g of AG 1-X4 200−400-mesh resin. The column was washed with 25 mL of water and 25 mL of 25 mM HCl. Then *myo*-inositol phosphates were eluted with 25 mL of 2 M HCl. The eluates obtained were concentrated in a vacuum evaporator and dissolved in 1 mL of water. Then 20 μL of the samples was chromatographed on Ultrasep ES 100 RP18 (2 × 250 mm). The column was run at 45 °C and 0.2 mL min^{-1} of an eluant consisting of formic acid/methanol/water/tetrabutylammonium hydroxide (44:56:5:1.5 v/v), pH 4.25, as described by Sandberg and Ahderinne.[17] A mixture of the individual *myo*-inositol phosphate esters (IP_3−IP_6) was used as a standard.

RESULTS AND DISCUSSION

Biochemical Properties of the Phytases Used in the in Vitro Degradation Model. Some enzymatic properties of seven commercially available phytase products were determined under identical assay conditions. All phytases have been produced in genetically modified microorganisms. Therefore, it is assumed that the major constituent of the phytase products analyzed is the respective phytase, and the enzymatic properties determined reflect those of the enzyme in question. Phytases from five different donor organisms have been used in this study (Table 1). Two are of fungal (*A. niger*, *P. lycii*) and three of bacterial origin (*E. coli*, *C. braakii*, *Buttiauxella* sp.). On the basis of the carbon in the *myo*-inositol ring of phytate at which hydrolysis is initiated, the commercial phytase products consist either of a 3-phytase (*A. niger*) or a 6-phytase (*E. coli*, *P. lycii*, *C. braakii*, *Buttiauxella* sp.). Furthermore, variants of the above-mentioned phytases with significant improvements over the

DOI: 10.1021/acs.jafc.5b01996
J. Agric. Food Chem. 2015, 63, 6142−6149

Table 2. Enzymatic Properties of the Phytase Products Used in the in Vitro Digestion Model

	EC1	EC2	EC3	BSP	CB	PL	AN
pH range (80% of the optimal activity)	4.0−5.0	3.5−5.0	3.0−5.0	3.0	3.0−4.5	4.5−5.5	4.5−5.5
phytase activity at pH 3.0[a] (%)	92.5	101.3	82.8	235.1	145.7	12.5	64.2
phytase activity at pH 7.0[a] (%)	0.8	2.2	1.7	0.5	0.6	7.8	7.0
K_M (μM) for phytate at pH 5.0 and 37 °C	228	142	285	272	364	75	35
k_{cat} (s^{-1}) for phytate at pH 5.0 and 37 °C	1545	1821	1327	1054	1478	1532	318
K_M (μM) at pH 3.0 and 37 °C	257	178	302	311	427	98	142
k_{cat} (s^{-1}) at pH 3.0 and 37 °C	1012	1274	984	768	1061	824	170
residual activity (%) (pH 3.0, 37 °C, 45 min)							
without pepsin	95	98	92	87	93	58	81
with 3000 U pepsin	93	98	92	85	92	34	47
optimal ionic strength (mM NaCl)	50−100	50−200	100−200	50−200	50−200	50−200	50−600

[a]Phytase activity at pH 5.5 was taken as 100%.

parent enzymes through selective molecular modifications have found their way to the marketplace.[2] In addition, the expression system used for phytase production has an effect on the enzymatic character of the phytase. Last but not least, postfermentation activities such as product formulation and optimization can influence the properties of the final phytase preparation.[2] Therefore, phytases of the same origin might exhibit differences in their enzymatic properties as also shown for the *E. coli* phytases in this study (Table 2; Figure 1).

With respect to phytate dephosphorylation in the gastrointestinal tract of poultry, the low pH (pH 4−5) in the forestomach (crop) as well as in the proventriculus and gizzard (pH 2−5) has to be considered.[2,15] The small intestine of poultry, however, presents a neutral pH environment (pH 6.5−7.5).[15] Thus, pH optima and pH activity profile of supplementary phytases generally determine their ability to develop catalytic activity in the aforementioned gastrointestinal compartments.[18] All phytase preparations studied showed an acid pH optimum for phytate dephosphorylation and were shown to be virtually inactive above pH 7.0 (Figure 1A,B; Table 2). Thus, the phytase preparations included in the study are expected to act most efficiently under the conditions present in the forestomach, proventriculus, and gizzard of poultry. Under intestinal pH conditions the phytases exhibit almost no phytate-degrading capability. However, considerable differences in their pH activity profiles have been observed. Even if the site of phytase action in the gastrointestinal tract of poultry has received little attention so far, the crop was reported to be very likely the primary site of phytate dephosphorylation by supplementary phytase.[19] With regard to the bioefficacy of supplementary phytase, it has also to be considered that phytases are in general supplemented according to their activity determined at standard conditions (pH 5.5, 37 °C, 5 mmol/L sodium phytate).[20] Therefore, their phytate-degrading activity will differ at other pH conditions. In Table 2, the relative phytate-degrading activities of the phytase preparations included in the studies at pH 3.0 (represents the pH conditions in the proventriculus and gizzard of the birds) and pH 7.0 (represents the pH conditions in the small intestine of the birds) are displayed. Compared to their phytate-degrading activities at pH 5.5, some of the phytase preparation studied exhibited a similar (EC1, EC2, EC3), a significantly higher (BSP, CB), or a significantly lower (PL, AN) phytate-degrading capability at pH 3.0. The lowest relative activity was determined for PL (12.5%) and the highest for BSP (235.1%). At pH 7.0 all phytase preparations included in the study showed a very low phytate-degrading capability compared to that at pH 5.5. The phytate-degrading activity at pH 7.0 of all enzymes has been found to be below 8% compared to the activity at pH 5.5.

Furthermore, it must be considered that bioefficacy is not only determined by the pH activity profile of the phytase but, among others, by its kinetic constants for phytate hydrolysis, its stability under the pH conditions of the crop or stomach, and its susceptibility to pepsin degradation and the electrostatic environment in the crop or stomach.[18] Even if so far not proven by animal studies, a high affinity for phytate and *myo*-inositol pentakisphosphate, high turnover numbers with both compounds, and narrow substrate specificity are concluded to be desirable properties for phytases used as feed additives.[18] In Table 2, the kinetic constants (K_M, k_{cat}) of the phytase preparations included in the studies for phytate dephosphorylation at pH 5.0 (represents the pH conditions in the crop of the birds) and pH 3.0 (represents the pH conditions in the proventriculus and gizzard of the birds) are given. For all phytase products the turnover numbers (k_{cat}) were lower and the Michaelis−Menten constants (K_M) higher at pH 3.0 than at pH 5.0. Thus, all phytases acted more rapidly on and exhibited a higher affinity toward phytate at pH 5.0 compared to pH 3.0. Relatively low K_M values have been found for AN and PL at pH 5.0 and for PL at pH 3.0. However, AN also exhibited relatively low turnover number at both pH values. A higher affinity toward sodium phytate of *A. niger*[14] and *P. lycii*[11,14] phytases compared to the phytases from *E. coli*,[9] *C. braakii*,[13] and *Buttiauxella*[12] has already been reported.

With the exception of PL all phytase products included in the study showed a remarkable stability at pH values representing the conditions of the proventriculus and gizzard of the birds (Table 2). PL exhibited 58% residual phytase activity after exposure at pH 3.0 and 37 °C for 45 min, whereas with all other phytase products residual activities >80% have been observed. These data are in good agreement with already published data on the pH stability of the phytases studied.[9,12,13,21] The effectiveness and limitations of feed supplementation with phytases may also depend on their susceptibility to proteolytic cleavage. By incubating the phytase products with pepsin at pH 3.0, differences in their ability to withstand degradation by this digestive protease were observed (Table 2). The bacterial phytases seem to be pepsin tolerant (residual activity >85%), whereas the fungal phytases retained only 34% (PL) and 47% (AN) of their initial activity after pepsin digestion. These data are in good agreement with already published data on the susceptibility of phytases to proteolytic cleavage by pepsin.[13,22−25]

DOI: 10.1021/acs.jafc.5b01996
J. Agric. Food Chem. 2015, 63, 6142−6149

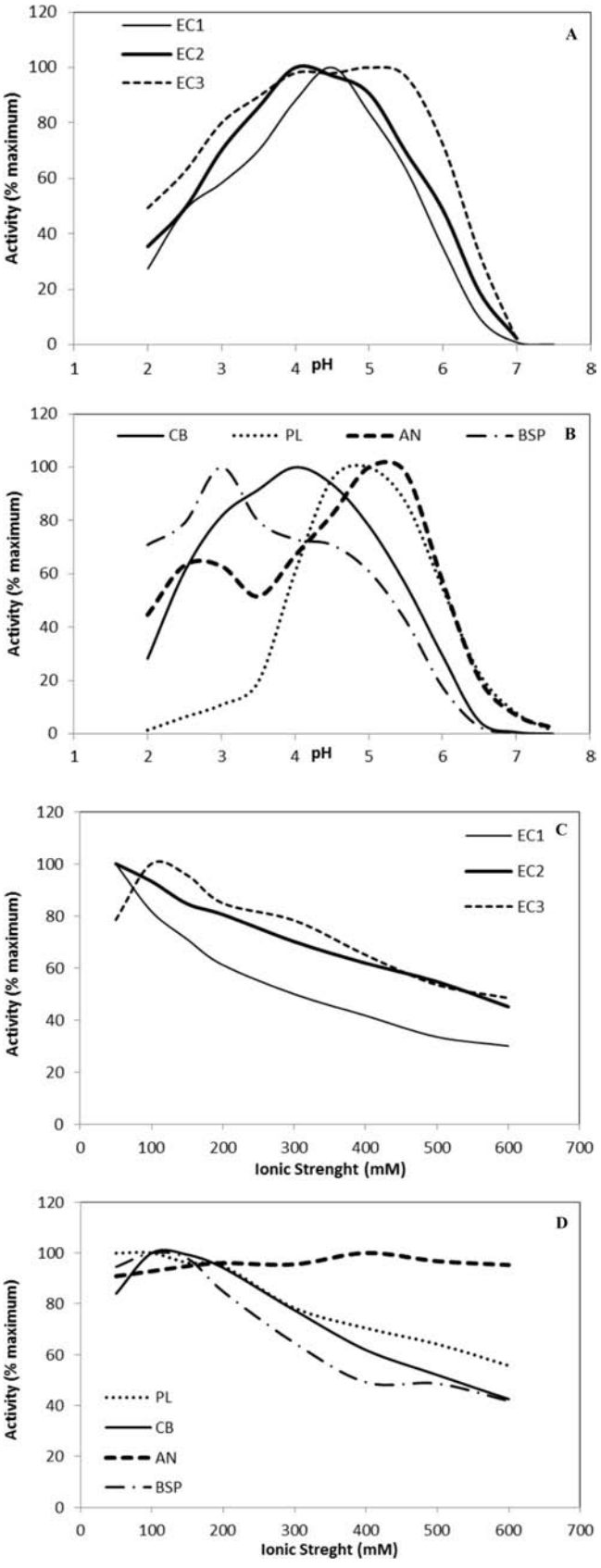

Figure 1. Effect of pH (A, B) and ionic strength (C, D) on phytase activity of the phytase products used in the in vitro degradation model.

In addition, it was already shown that the electrostatic environment could have an effect on phytase activity. The pH profiles of the phytases from *A. niger* and *E. coli*, for example, have been modified by both the buffer and the introduction of salt (NaCl, $CaCl_2$).[26] Addition of NaCl up to 600 mM to increase the ionic strength of the phytase environment resulted in a strong inhibition of all phytase products with the exception of AN (Figure 1C,D).

No clear conclusion about the bioefficacy of the phytase products could be drawn from the enzymatic properties determined. Some enzymatic properties would point to a certain phytase product as better suited for application as an animal feed supplement; some other enzymatic properties would give preference to a different phytase product (Table 2). Furthermore, there is no evidence that a single property is more important with respect to bioefficacy. A better performance in vivo is a conjunction of all enzymatic properties as well as the interaction with phosphatase activity occurring in the gastrointestinal tract.[18] Thus, enzymatic properties could only be guidelines on potential functionality of phytases in animal feeds and digestive systems.

Phytase Performance in an in Vitro Simulation of Poultry Digestive Tract. The effect of seven commercial phytase products on phytate dephosphorylation was studied in an in vitro simulation of the digestive tract of poultry based on that of Zyla and co-workers.[15] The simulation included some key conditions of the crop, stomach (proventriculus and gizzard), and small intestine of the birds. In general, supplementation of animal feed with 250−1000 U kg^{-1} is recommended by the phytase suppliers.[27−29] Therefore, 250, 500, 750, and 1000 U kg^{-1} were used in this simulation study. Whole wheat flour (ground wheat grains) was used as a feed matrix. The intrinsic wheat phytase activity was reduced to 27.6 ± 2.1 U kg^{-1} dry matter by microwave treatment. Thus, the residual activity of the intrinsic wheat phytase corresponds to 11% of the phytase activity added to the simulation at the lowest dose. A complete inactivation of the intrinsic wheat phytase could not be achieved by microwave treatment, and structural changes of the wheat by microwave treatment could not be avoided. To simulate the crop two different volumes of buffer were used. The lower volume (3 mL per gram of wheat flour) represented much better the conditions in the digestive track of the birds with respect to viscosity. However, it was extremely difficult to homogeneously distribute the phytase added throughout the entire crop content by mixing, because the mixture had a pasty consistency. To overcome this problem, 6 mL of buffer per gram of microwave-treated wheat flour was used in a second setup. Phytate dephosphorylation was followed by quantification of phytate (IP_6) and partly phosphorylated *myo*-inositol phosphates (IP_5−IP_3) as well as the inorganic phosphate (P_i) released. The variation of the analytical methods applied was determined using 10 replicates of the artificial crop, stomach, and intestine digesta without phytase addition. The standard deviation of P_i, IP_6, and IP_{total} (IP_6 + IP_5 + IP_4 + IP_3) represented 5−15% of the average (coefficient of variation; CV), whereas the standard deviation of the partly phosphorylated *myo*-inositol phosphates represented 30−100% of average. The high CVs for IP_3, IP_4, and IP_5 can be explained by the fact that these are transient forms in the phytate degradation pathway and occur in a significantly lower concentration compared to IP_6 and P_i. Conclusions drawn from the simulated digestion studies were therefore based only on IP_6, IP_{total}, and P_i.

The following trends in the simulated gastrointestinal degradation studies have been observed: IP_6 as well as IP_{total}

DOI: 10.1021/acs.jafc.5b01996
J. Agric. Food Chem. 2015, 63, 6142−6149

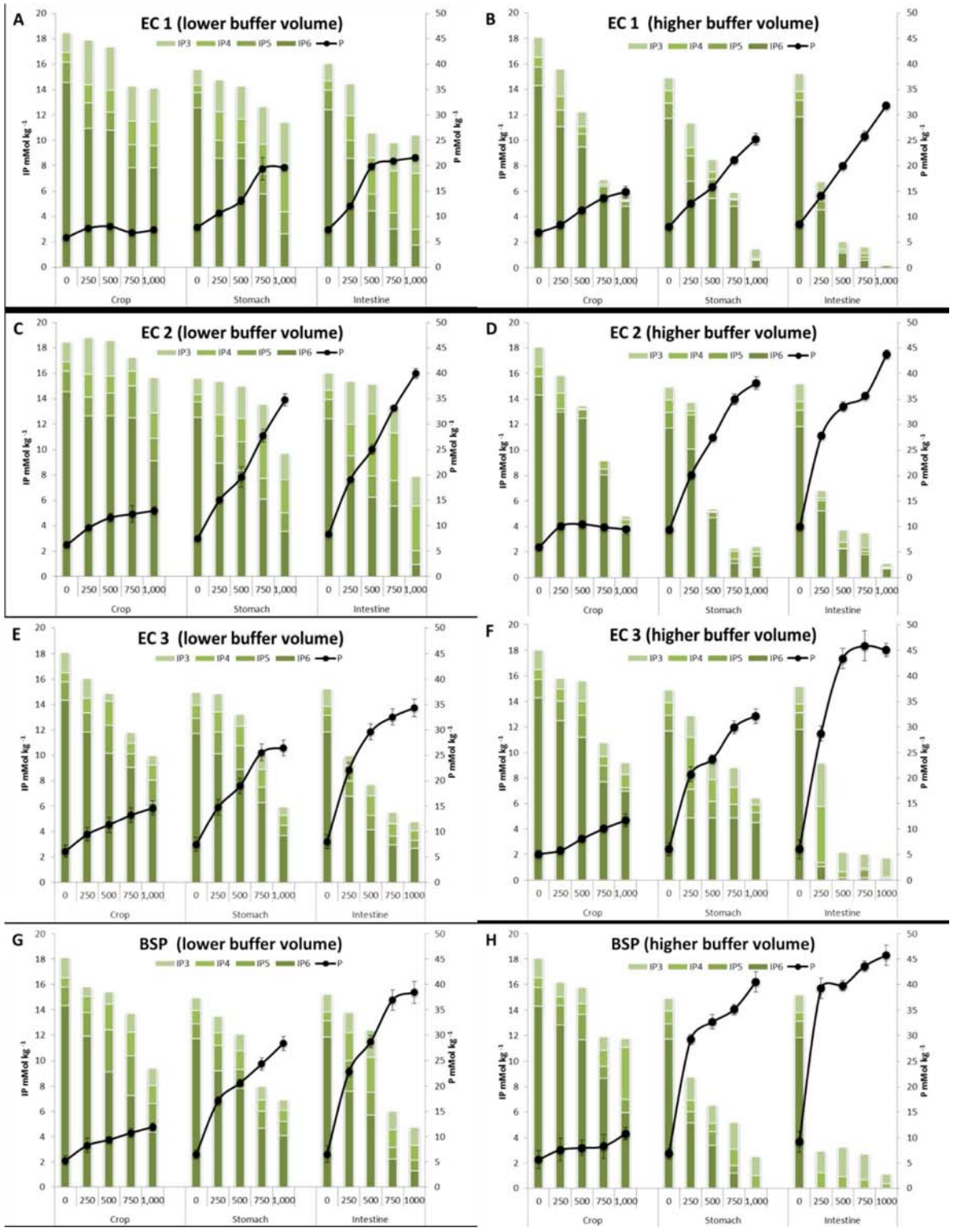

Figure 2. continued

DOI: 10.1021/acs.jafc.5b01996
J. Agric. Food Chem. 2015, 63, 6142−6149

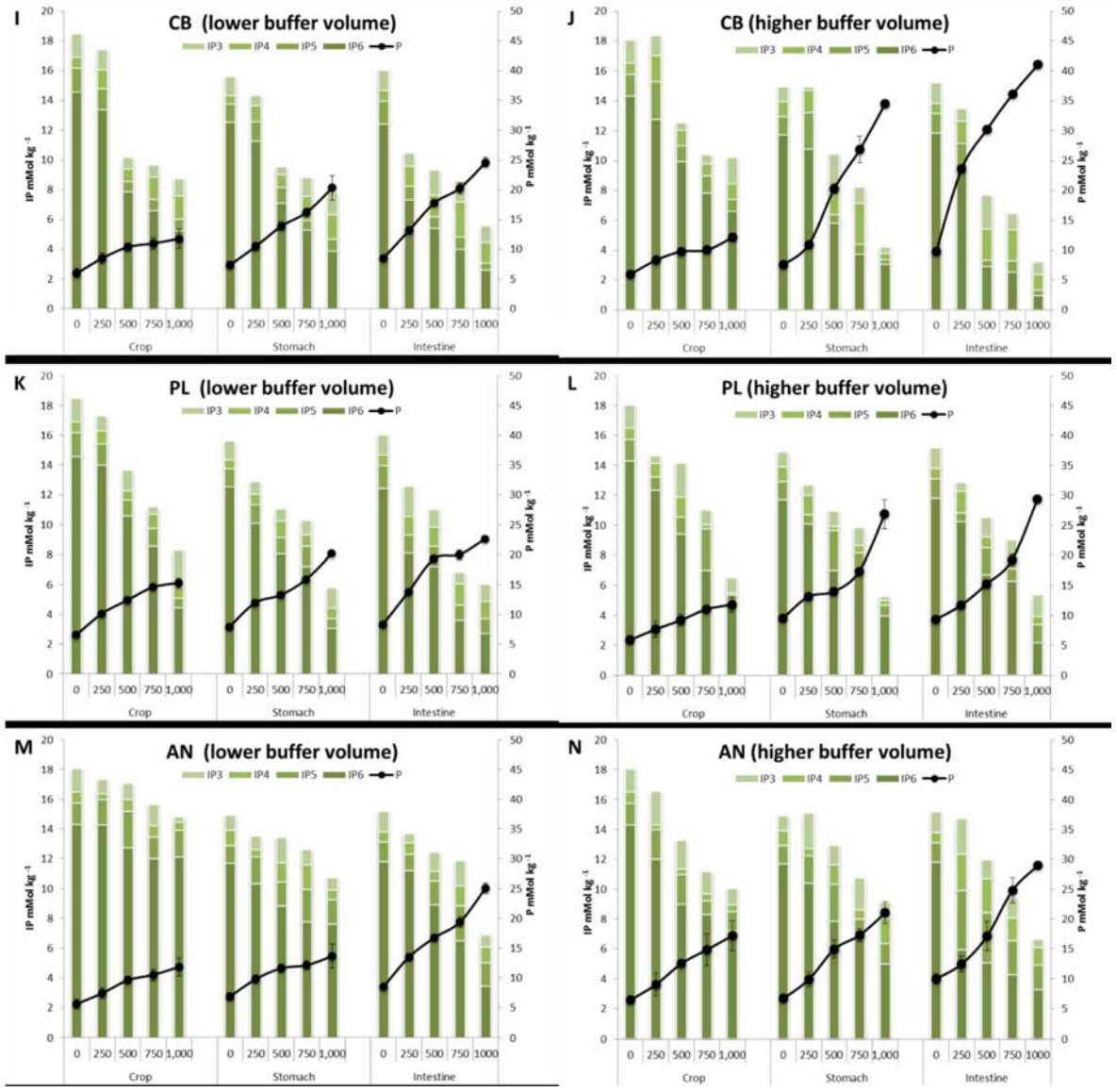

Figure 2. Enzymatic phytate dephosphorylation during in vitro simulation of poultry digestive tract quantified by reversed-phase high-performance liquid chromatography of *myo*-inositol phosphates (columns: IP_6 to IP_3) and P_i (dots and black lines). In the individual graphs the data obtained for the phytase products EC1, EC2, EC3, BSP, CB, PL, and AN are shown. A, C, E, G, I, K, and M represent the lower buffer volume, whereas B, D, F, H, J, L, and N the higher buffer volume. For every enzyme and buffer system samples were analyzed after simulation of the crop, crop and stomach, as well as crop, stomach, and small intestine at increasing phytase doses (0−1000 U kg^{-1}).

decreased, whereas P_i increased with increasing phytase supplementation (Figure 2). This result was expected, because phytases were added to release the organically bound phosphate in the phytate molecule. Histidine acid phytases (HAP) as used in this study are capable of releasing up to five phosphate moieties from the phytate molecule.[18] However, P_i release determined experimentally and P_i release calculated from the HPLC data of *myo*-inositol phosphate turnover did not match. The calculated values were always higher. The impossibility to quantify IP_2 and IP_1 with the HPLC method applied might explain this observation at least in part, because the difference in IP_{total} during in vitro digestion compared to IP_{total} in the diets was taken as IP_1 for P_i release calculations. The experimentally determined P_i release in the in vitro degradation system was comparable to values already available in the literature. In poultry, P availability was reported to increase up to 1 g P kg^{-1} of feed when feeds are supplemented with 766 U kg^{-1} of HAP phytase.[30,31] P_i release in the in vitro degradation system at 750 U kg^{-1} phytase was determined to be 0.83 ± 0.24 g P kg^{-1} (lower buffer volume) and 0.93 ± 0.31 g P kg^{-1} (higher buffer volume), respectively. Selle et al.[31] reported that 42% of the organically bound phosphate from phytate was released under the conditions mentioned above, whereas the corresponding values in the in vitro degradation system were 72.7 ± 6.8% (lower buffer volume) and 85.6 ± 9.7% (higher buffer volume), respectively. However, this study was performed with microwave-treated ground wheat, whereas Selle et al.[31] used a complete feed. A higher buffer volume and, respectively, a lower viscosity in the in vitro digestion studies resulted in general in improved IP_6 dephosphorylation and in lower IP_{total} and higher P_i amounts (Figure 2). The extent of the improvement in the release of the organically bound phosphate dephosphorylation was dependent on the phytase used. EC1 and EC2 were most sensitive to modification of the

DOI: 10.1021/acs.jafc.5b01996
J. Agric. Food Chem. 2015, 63, 6142−6149

Table 3. Phytase Activity Needed To Achieve a 50% Reduction in IP_6 and an Increase in P_i of 50% of the Maximum Reachable Value[a]

	EC1	EC2	EC3	BSP	CB	PL	AN
lower buffer volume							
50% IP_6	326 (0.95)	319 (0.86)	395 (0.92)	323 (0.92)	445 (0.87)	418 (0.80)	586 (0.89)
50% P_i	2194 (0.84)	955 (0.94)	1159 (0.93)	952 (0.94)	2200 (0.97)	2606 (0.89)	2398 (0.93)
higher buffer volume							
50% IP_6	148 (0.94)	211 (0.82)	140 (0.76)	129 (0.88)	269 (0.96)	480 (0.75)	503 (0.90)
50% P_i	1459 (0.97)	780 (0.86)	636 (0.86)	654 (0.77)	841 (0.94)	1719 (0.82)	1773 (0.93)

[a]Values (U kg^{-1}) obtained by nonlinear fit of the observed data; coefficient of determination in parentheses.

buffer volume, whereas BSP, CB, and EC3 were moderately sensitive and PL as well as AN showed similar behaviors at both buffer volumes. Apparently, bacterial phytases were more affected by the modification in buffer volume during in vitro digestion, which may suggest that viscosity is of more concern regarding bioefficacy of bacterial compared to fungal phytases. In contrast to the enzymatic dephosphorylation of phytate in a buffered system, no real accumulation of partially phosphorylated *myo*-inositol phosphates such as IP_4 or IP_3 has been observed in the in vitro digestion system (Figure 2). A reduced mobility of the phytase and the *myo*-inositol phosphate molecules due to the higher viscosity in the in vitro digestion compared to the buffered system seems to result in the preference of the phytase to act upon the just released *myo*-inositol phosphate instead of binding a different phytate molecule into its active site. As expected from their pH profiles (Table 2; Figure 1), the major site of action of the different phytase products used was determined to be the stomach, but a significant *myo*-inositol phosphate dephosphorylation was also observed in the crop (Figure 2). About 80−90% of the enzymatic *myo*-inositol phosphates dephosphorylation occurred in the stomach and crop.

All phytase products included in the study were capable of releasing the organically bound phosphate from *myo*-inositol phosphate moiety. Their relative performances, however, were remarkably different (Figure 2). When the enzymatic properties of the different phytases (Table 2) as well as incubation time in the different parts of the intestinal tract and the phytate concentration in the microwave-treated ground wheat are taken into consideration, all phytases should be able to dephosphorylate all phytate accessible in the wheat to *myo*-inositol monophosphate, the final phytate dephosphorylation product of histidine acid phytases, even at the lowest dose (250 U kg^{-1}) used. Because IP_6, IP_5, IP_4, and IP_3 were still present in the intestinal samples of the in vitro degradation system, further parameters need to affect phytase performance. An attempt was made to explain enzyme performance in the in vitro degradation system by considering incubation time and substrate concentrations in the different parts of the digestive tract as well as pH dependence of enzymatic activity individually and in combination. Neither correlation tables nor component analysis or regression plots were able to explain the differences in phytase performance (data not shown). Therefore, further parameters such as lower catalytic activity toward precipitated forms of phytate, product inhibition (P_i) of enzymatic activity, reduction in enzymatic activity due to adsorption processes, and limited access of the phytase to phytate because of mobility and physical constraints may affect phytase performance.

Due to the vast number of parameters affecting phytase performance in the in vitro degradation system used as well as in animal studies, an in vitro system will hardly be able to fully mimic the in vivo situation. Besides determination of the enzymatic properties of a phytase, however, in vitro simulation is considered as a good complementary tool to preselect promising phytase candidates as a feed supplement. To compare the different enzyme products used in the study, the phytase activity needed to achieve a 50% reduction in IP_6 and a 50% release of the P_i bound to the *myo*-inositol ring was estimated using nonlinear fit of a negative exponential model of the observed data (Table 3). According to the model, between 319 and 581 U phytase per kilogram of microwave-treated ground wheat was needed to achieve a 50% reduction in IP_6, whereas between 952 and 2606 U phytase per kilogram of ground wheat was required to release 50% of the P_i bound to the *myo*-inositol ring when the lower buffer volume was used. With the higher buffer volume, the corresponding values were estimated to be 129−503 and 636−1791 U per kilogram of microwave-treated ground wheat, respectively. Thus, significantly lower phytase activity values were calculated to achieve a 50% reduction in IP_6 compared to a 50% release of the organically bound P_i. This result was expected because in the former case more or less 50% of the IP_6 present in the microwave-treated ground wheat was converted to IP_5, and in the latter case all IP_6 was enzymatically dephosphorylated to IP_3. In addition, it must be considered that partially phosphorylated *myo*-inositol phosphates are dephosphorylated with a different velocity compared to IP_6 and that the rate of phosphate release decreases progressively as the enzymatic reaction proceeds.

The differences in the behavior of the different commercially available phytase products in the in vitro degradation model system do not precisely reflect their performance in the animal. Therefore, the model cannot be used to rank phytases with respect to their bioefficacy, but it is considered as a simple and useful tool to evaluate the suitability of a phytase to be used as a feed supplement. Although relevant factors such as dietary P levels, intestinal phytase, and P absorption are not implemented in the system, this approach might help to reduce the number of feeding trials when searching for a better suited phytase for animal feed application in the initial screening phase. Based on of the phytase activity needed to achieve either a 50% reduction in IP_6 or a 50% release of the organically bound P_i, studies are currently carried out to establish a threshold value for the need to conduct animal feeding trials with the phytase in question. Furthermore, these studies should answer the question of whether the in vitro model will prove satisfactory when only the higher buffer volume is used and only P_i is quantified. In that case, the model system is more easily handled; the in vitro studies are less time-consuming and need less analytical effort. Further research work is in progress to study the value of in

DOI: 10.1021/acs.jafc.5b01996
J. Agric. Food Chem. 2015, 63, 6142−6149

vitro models with more realistic feed formulations for poultry and swine.

AUTHOR INFORMATION

Corresponding Author

*(R.G.) Mail: Department of Food Technology and Bioprocess Engineering, Max Rubner-Institut, Federal Research Institute of Nutrition and Food, Haid-and-Neu-Straße 9, 76131 Karlsruhe, Germany. Phone: ++49 (0)721 6625 300. Fax: ++49 (0)721 6625 303. E-mail: ralf.greiner@mri.bund.de.

Funding

This work was supported by a Georg Forster Research Postdoctoral Fellowship (Humboldt Foundation).

Notes

The authors declare no competing financial interest.

ACKNOWLEDGMENTS

We thank AB Vista, Danisco, Novozymes/DSM, and BASF for kindly providing us with the phytase preparations used in the study.

REFERENCES

(1) Dorozhkin, S. V.; Epple, M. Biological and medical significance of calcium phosphates. *Angew. Chem., Int. Ed.* **2002**, *41*, 3130−3146.

(2) Menezes-Blackburn, D.; Greiner, R. Enzymes used in animal feed: leading technologies and forthcoming developments. In *Functional Polymers in Food Science*; Cirillo, G., Spizzirri, G., Lemma, F., Eds.; Wiley: Calabria, Italy, 2014; pp 47−73.

(3) Abelson, P. A potential phosphate crisis. *Science* **1999**, *283*, 2015.

(4) Ashley, K.; Cordell, D.; Mavinic, D. A brief history of phosphorus: from the philosopher's stone to nutrient recovery and reuse. *Chemosphere* **2011**, *84*, 737−746.

(5) Shastak, Y.; Rodehutscord, M. Determination and estimation of phosphorus availability in growing poultry and their historical development. *World's Poult. Sci. J.* **2013**, *69*, 569−586.

(6) Zeller, E.; Schollenberger, M.; Witzig, M.; Shastak, Y.; Kühn, I.; Hoelzle, L. E.; Rodehutscord, M. Interactions between supplemented mineral phosphorus and phytase on phytate hydrolysis and inositol phosphates in the small intestine of broilers. *Poult. Sci.* **2015**, DOI: 10.3382/ps/pev087.

(7) Mullaney, E.; Daly, C.; Ullah, A. Advances in phytase research. *Adv. Appl. Microbiol.* **2000**, *47*, 158−200.

(8) Lei, X.; Porres, J.; Mullaney, E.; Brinch-Pedersen, H. Phytase: source, structure and application. In *Industrial Enzymes: Structure, Function and Applications*; Polaina, J., MacCabe, A. P., Eds.; Springer: Dordrecht, The Netherlands, 2007; pp 505−529.

(9) Greiner, R.; Konietzny, U.; Jany, K. Purification and characterization of two phytases from Escherichia coli. *Arch. Biochem. Biophys.* **1993**, *303*, 107−113.

(10) Heinonen, J. K.; Lahti, R. J. A new and convenient colorimetric determination of inorganic orthophosphate and its application to the assay of inorganic pyrophosphatase. *Anal. Biochem.* **1981**, *113*, 313−317.

(11) Lassen, S. F.; Breinholt, J.; Østergaard, P. R.; Brugger, R.; Bischoff, A.; Wyss, M.; Fuglsang, C. C. Expression, gene cloning, and characterization of five novel phytases from four Basidiomycete fungi: *Peniophora lycii*, *Agrocybe pediades*, a *Ceriporia* sp., and *Trametes pubescens*. *Appl. Environ. Micobiol.* **2001**, *67*, 4701−4707.

(12) Shi, P.; Huang, H.; Wang, Y.; Luo, H.; Wu, B.; Meng, K.; Yang, P.; Yao, B. A novel phytase gene appA from *Buttiauxella* sp. GC21 isolated from grass carp intestine. *Aquaculture* **2008**, *275*, 70−75.

(13) Kim, H.-W.; Kim, Y.-O.; Lee, J.-H.; Kim, K.-K.; Kim, Y.-J. Isolation and characterization of a phytase with improved properties from *Citrobacter braakii*. *Biotechnol. Lett.* **2003**, *25*, 1231−1234.

(14) Ullah, A. H. J.; Sethumadhavan, K. *PhyA* gene product of *Aspergillus ficuum* and *Peniophora lycii* produces dissimilar phytases. *Biochem. Biophys. Res. Commun.* **2003**, *301*, 463−468.

(15) Zyła, K.; Gogol, D.; Koreleski, J.; Świątkiewicz, S.; Ledoux, D. R. Simultaneous application of phytase and xylanase to broiler feeds based on wheat: *in vitro* measurements of phosphorus and pentose released from wheats and wheat-based feeds. *J. Sci. Food Agric.* **1999**, *79*, 1832−1840.

(16) AOAC. Phytate in foods, anion-exchange method, No. 986.11. *Official Methods of Analysis*, 15th ed.; AOAC: Arlington, VA, USA, 1990; pp 800−801.

(17) Sandberg, A. S.; Ahderinne, R. HPLC method for determination of inositol tri-, tetra-, penta-, and hexaphosphates in foods and intestinal contents. *J. Food Sci.* **1986**, *51*, 547−550.

(18) Greiner, R.; Konietzny, U. Phytases: biochemistry, enzymology and characteristics relevant to animal feed use. In *Enzymes in Farm Animal Nutrition*; Bedford, M., Partridge, G., Eds.; CABI Publishing: Wallingford, UK, 2010; pp 96−128.

(19) Selle, P.; Ravindran, V. Microbial phytase in poultry nutrition. *Anim. Feed Sci. Technol.* **2007**, *135*, 1−41.

(20) Engelen, A. J.; van der Heeft, F. C.; Randsdorp, P. H. G.; Smit, E. L. C. Simple and rapid determination of phytase activity. *J. AOAC Int.* **1994**, *77*, 760−764.

(21) Greiner, R.; Gomes da Silva, L.; Couri, S. Purification and characterisation of an extracellular phytase from *Aspergillus niger* 11T53A9. *Braz. J. Microbiol.* **2009**, *40*, 795−807.

(22) Elkhalil, E. A. I.; Männer, K.; Borriss, R.; Simon, O. *In vitro* and *in vivo* characteristics of bacterial phytases and their efficacy in broiler chickens. *Br. Poult. Sci.* **2007**, *48*, 64−70.

(23) Igbasan, F. A.; Männer, K.; Miksch, G.; Borriss, R.; Farouk, A.; Simon, O. Comparative studies on the *in vitro* properties of phytases from various microbial origins. *Arch. Tierernaehr.* **2000**, *53*, 353−373.

(24) Rodriguez, E.; Porres, J. M.; Han, Y.; Lei, X. G. Different sensitivity of recombinant *Aspergillus niger* phytase (*r-phyA*) and *Escherichia coli* pH 2.5 acid phosphatase (*r-AppA*) to trypsin and pepsin *in vitro*. *Arch. Biochem. Biophys.* **1999**, *365*, 262−267.

(25) Simon, O.; Igbasan, F. *In vitro* properties of phytases from various microbial origins. *Int. J. Food Sci. Technol.* **2002**, *37*, 813−822.

(26) Ullah, A. H. J.; Sethumadhavan, K.; Mullaney, E. J. Salt effect on the pH profile and kinetic parameters of microbial phytases. *J. Agric. Food Chem.* **2008**, *56*, 3398−3402.

(27) Commission Regulation (EC) No. 785/2007 of 4 July 2007 concerning the authorisation of 6-phytase EC 3.1.3.26 (Phyzyme XP 5000G Phyzyme XP 5000L) as a feed additive. *Off. J. Eur. Union* **2007**, *L 175/5−L 175/7*.

(28) Commission Regulation (EC) No. 1141/2007 of 1 October 2007 concerning the authorisation of 3-phytase (Rovabio Phy AP and Rovabio Phy LC) as a feed additive. *Off. J. Eur. Union* **2007**, *L 256/17−256/19*.

(29) Commission Regulation (EU) No. 891/2010 of 8 October 2010 concerning the authorisation of a new use of 6-phytase as a feed additive for turkeys. *Off. J. Eur. Union* **2010**, *L 266/4−266/5*.

(30) Selle, P.; Ravindran, V.; Cowieson, A. Phytate and phytase. In *Enzymes in Farm Animal Nutrition*; Bedford, M., Partridge, G., Eds.; CABI Publishing: Wallingford, UK, 2010; pp 160−205.

(31) Simons, P.; Versteegh, H.; Jongbloed, A. W.; Kemme, P.; Slump, P.; Bos, K.; Wolters, M.; Beudeker, R.; Verschoor, G. Improvement of phosphorus availability by microbial phytase in broilers and pigs. *Br. J. Nutr.* **1990**, *64*, 525−540.

NOTE ADDED AFTER ASAP PUBLICATION

This paper was published ASAP on July 2, 2015, with an error to Table 1. The corrected version reposted with the issue on July 15, 2015.

DOI: 10.1021/acs.jafc.5b01996
J. Agric. Food Chem. 2015, 63, 6142−6149

The solubility of chlorpyrifos in water is very low, and the analysis has to be carried out in toxic solvents such as DMF. The reduction potential of chlorpyrifos on mercury-based electrodes is almost close to the hydrogen evolution potential, which complicates the estimation of sensing currents (peak currents). In this work we tried to overcome these disadvantages by developing a newer modified electrode for the sensing of chlorpyrifos.

Due to the high affinity of nano-TiO_2 on phosphate groups, it was used as a sensor probe along with nafion for the electrochemical sensing of the organophosphate pesticide fenitrothion.[19] Cellulose acetate (CA) is a porous material that is used to immobilize the enzymes, bacteria, and metal nanoparticles. The advantages of CA membrane are good stability in alcohol-based electrolyte, biocompatibility, easy film-forming properties, and low cost.[20,21] Titanium dioxide immobilized on a cellulose acetate membrane, a hybrid material, shows a very attractive electrocatalytic property and stability in sensor applications.[22,23] Nano-TiO_2/cellulose acetate is a complex material with no chemical interaction between TiO_2 particles and cellulose acetate, which are only physically mixed. However, very few studies were available in the literature using this composite modified electrode in sensor applications. Studies on the analysis of pesticides on this composite modified electrode were not reported in the literature.

In this paper, we report the preparation, characterization, and application of a nano-TiO_2/cellulose acetate modified glassy carbon electrode (n-TiO_2/CA/GCE) for the electrochemical sensing of chlorpyrifos. SEM was used for surface characterization. Cyclic voltammetry, differential pulse voltammetry, and amperometry were used as sensing techniques.

EXPERIMENTAL PROCEDURES

Apparatus. Cyclic votammetry (CV), differential pulse votammetry (DPV), and amperometry were performed with the computer-controlled Autolab PGSTAT 30 (Eco Chemie, Utrecht, The Netherlands) electrochemical system. DPV was recorded with the following optimized instrumental settings: modulation amplitude, 40 mV; modulation step, 4 mV; and set scan rate, 8 mV s^{-1}. For electrochemical experiments, a 10 mL glass cell with a TiO_2/cellulose acetate coated glassy carbon electrode (GCE Alfa Aesar, 3 mm diameter) as the working electrode, platinum foil as the counter electrode, and saturated calomel electrode (SCE) as the reference electrode was used. SEM analysis was done with a Hitachi model S-3000H with 20 kV acceleration voltage. HPLC analysis was carried out with an LC-10AT pump and an SPD-10A detector (Shimadzu, Kyoto, Japan) at 254 nm with a Shimpack CLC ODS-18 column. Prior to electrochemical measurements, the solution was deareated by purging with pure nitrogen for 15 min. All electrochemical experiments were carried out at 30 ± 1 °C.

Reagents and Chemicals. Chlorpyrifos was purchased from AccuStandard, New Haven, CT, USA. A stock solution of chlorpyrifos (2424 μM) was prepared in methanol. Tetra-*n*-butyl ammonium bromide was purchased from Alfa Aesar, and its 0.05 M solution was prepared in 60:40 methanol/water (v/v). It was used as the solvent−supporting electrolyte system. The nano-TiO_2 powder was prepared as follows, and the details are available in the literature.[24] Titanium(IV) butoxide (10 g) was dissolved in cyclohexanol solvent. To this solution a premixed solution containing water, cyclohexanol, and hexadecyltrimethylammonium bromide was added at room temperature. After 12 h, triethylamine was added to precipitate TiO_2 powder. The TiO_2 powder was separated, washed with acetone, and dried in air at 353 K for 2 h. The dried powder was calcined at 773 K to give nano-TiO_2 powder. Other reagents used were of analytical reagent grade.

Preparation of n-TiO_2 /CA/GCE. The GC electrode was hand polished with fine emery papers (1/0, 2/0, 3/0, 4/0), rinsed thoroughly with Millipore water, cleaned successively in 10% NaOH solution, 1:1 HNO_3/water (v/v), and MeOH, each for 2 min, and dried in air.[25] Before modification of the GC electrode, the reproducibility of the bare GC electrode was checked with the recording of cyclic voltammetric responses of a potassium ferrocyanide/ferricyanide redox system in 0.1 M KCl as reported in the literature.[26]

Cellulose acetate solution was prepared by following the procedure available in the literature.[27,28] Cellulose acetate (0.2 g) was dissolved in solvents containing 12.7 mL of acetone and 10.6 mL of cyclohexanone and stirred for 3 h to get a homogeneous solution.

The modifier solution n-TiO_2/CA was prepared by mixing 4 mg of nano-TiO_2 powder into 4 mL of the above prepared cellulose acetate solution and stirred for 1 h. This solution was used for modification of the GC electrode. The GC electrode was coated with 8 μL of n-TiO_2/CA solution by the drop−dry method. This 8 μL modifier solution contains 4.36 μL of acetone, 3.64 μL of cyclohexanone, 8 ng of TiO_2 powder, and 0.05264 ng of cellulose acetate. The coated GC electrode was dried in air for 3 h. A very thin film was seen on the GC surface. This modified n-TiO_2/CA/GCE was used for electrochemical measurements.

RESULTS AND DISCUSSION

Surface Morphology of n-TiO_2/CA/GCE. An SEM image of the composite modified GCE is shown in Figure 1. From the figure, it can be seen that the composite film uniformly covered the surface of the GCE with pores and shrinking of the film. The nano-titania particles are spread on the surface.

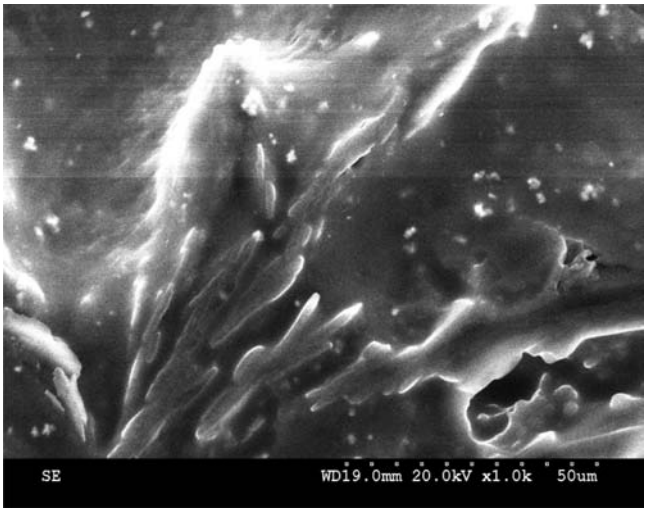

Figure 1. SEM image of n-TiO_2/CA/GCE.

Optimization of Modified Electrode Preparation. The volume of nano-TiO_2/cellulose acetate solution used for modification of the GCE surface was optimized by recording cyclic voltammetry of 50 μM chlorpyrifos in 0.05 M on n-TiO_2/CA/GCE in TBAB 60:40 methanol/water (Figure 2). The peak current increases with the increase in the volume of nano-TiO_2/cellulose acetate solution up to 8 μL. A further increase in the volume of nano-TiO_2/cellulose composite solution on GCE results in a decrease in the peak current value. This may be due to the formation of thicker films, which may render the mass transport difficult, so the optimum volume of 8 μL was used to modify the electrode surface.

Cyclic Voltammetric Analysis. Figure 3 shows the cyclic voltammetric response of 50 μM chlorpyrifos at n-TiO_2/CA/

DOI: 10.1021/acs.jafc.5b02057
J. Agric. Food Chem. 2015, 63, 6150−6156

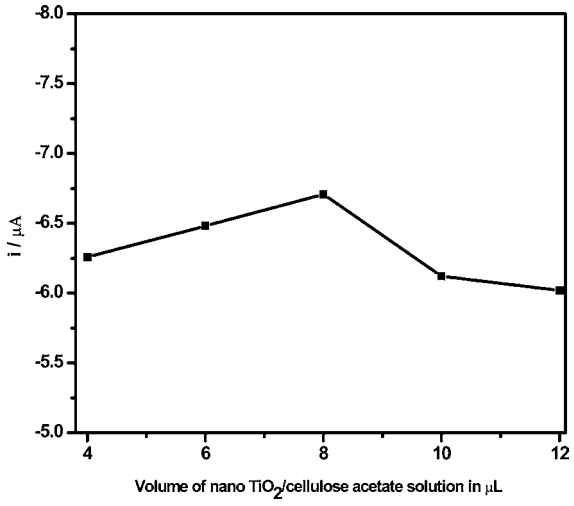

Figure 2. Effect of volume of nano-TiO_2/cellulose acetate composite solution on the peak current of 50 μM chlorpyrifos in 60:40 (v/v) methanol/water containing 0.05 M TBAB at 100 mV s^{-1}.

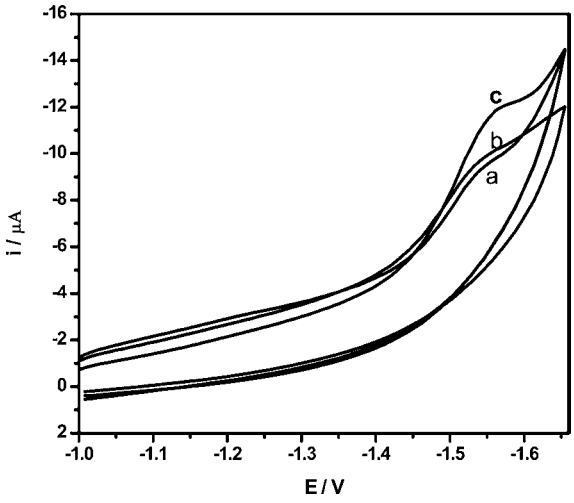

Figure 3. Cyclic voltammograms of 50 μM chlorpyrifos at (a) bare GCE, (b) cellulose acetate modified GCE, and (c) n-TiO_2/CA/GCE in 0.05 M TBAB 60:40 (v/v) methanol/water containing 0.05 M TBAB at 100 mV s^{-1}.

GCE. The reduction peak is observed at around −1.55 V. This peak is due to the electroreduction of −C═N of the pyridine ring of the chlorpyrifos via a $2e^-$ transfer step as reported earlier.[11−13]

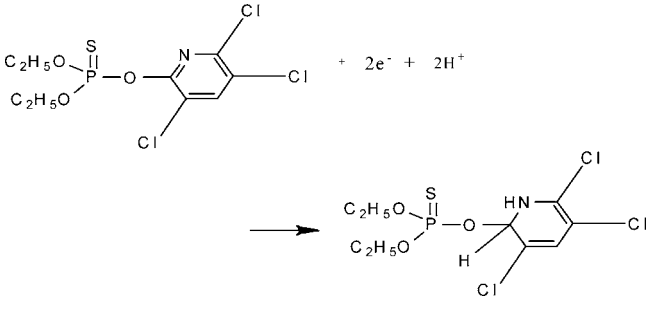

No peaks are observed on the reverse scan, which means that the reduction process is irreversible. The peak current increases with the increase in the scan rates and the concentrations. A linear relationship between the peak currents and the square root of the scan rates reveals that the reduction process is diffusion controlled. The reduction of C═N of the pyridine ring is difficult and occurs very close to the hydrogen evolution region and sometimes completely overlaps with the background reduction, that is, hydrogen evolution. However, the attachment of three chlorine atoms in the pyridine ring delocalizes the electrons at the −C═N− bond and, consequently, enhances the reduction of the −C═N− bond of the pyridine ring at lesser negative potentials.[11] However, studies on the direct reduction of chlorpyrifos are limited. The reduction of chlorpyrifos was carried out on the bare glassy carbon electrode (Figure 3a), cellulose acetate modified GCE (Figure 3b), and n-TiO_2/CA/GCE (Figure 3c). The n-TiO_2/CA/GCE gives a high sensing current when compared to the CA/GCE and bare GCE. The presence of TiO_2 nanoparticles in the cellulose acetate matrix leads to the shift of hydrogen evolution nearly by 200 mV more cathodic region, which improves the measurement of true sensing current of chlorpyrifos. The peak observed on bare GCE is close to the hydrogen evolution potential. Cellulose acetate is a negatively charged membrane, which is a good matrix for the incorporation of TiO_2 nanoparticles due to the physical interaction of TiO_2 nanoparticles with cellulose acetate,[29] which was confirmed by FT-IR analysis. Figure 4

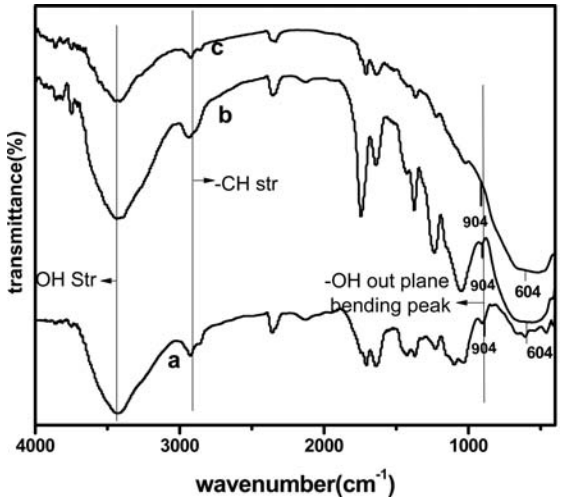

Figure 4. FTIR spectra of (a) cellulose acetate, (b) nano-TiO_2, and (c) nano-TiO_2/cellulose acetate composite.

shows the FTIR spectra of the CA, nano-TiO_2, and n-TiO_2/CA composites. The peaks are identified as follows: The broad peak at 3430 cm^{-1} is due to the −OH stretching frequencies. The broad peak around 2900 cm^{-1} is due to the −C−H stretching frequencies. The absorption peak around 1700 cm^{-1} is due to the C═O stretching frequencies.[30,31] The −C−H bending vibration peak around 904 cm^{-1} and the −OH out-of-plane bending peak around 600 cm^{-1} are of low intensity in the composite film (Figure 4c). The IR absorption peaks above 2000 cm^{-1} are intense and are composition dependent. All three IR spectra show similar characteristics, which demonstrates that the interaction between titania particles and cellulose acetate film matrix is through physical adsorption and not chemical bonding.

The presence of TiO_2 in the cellulose acetate increases the sensing current of chlorpyrifos, which is due to the electrocatalytic activity of TiO_2 nanoparticles. The pores in the film may also contribute to the increase in the peak currents. Figure

DOI: 10.1021/acs.jafc.5b02057
J. Agric. Food Chem. 2015, 63, 6150−6156

5 shows the effect of various concentrations of chlorpyrifos on the peak current of chlorpyrifos. The peak current increases

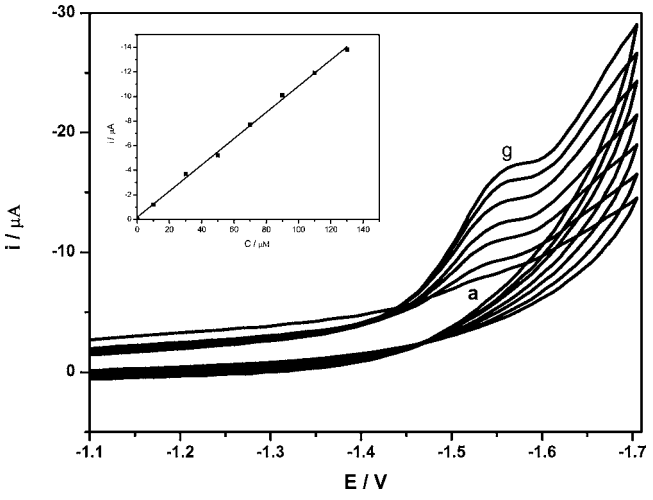

Figure 5. Influence of various concentrations of chlorpyrifos on the peak current, (a) 10, (b) 30, (c) 50, (d) 70, (e) 90, (f) 110, (g) 130 μM, at nano-TiO_2/cellulose acetate modified GCE in 60:40 (v/v) methanol/water containing 0.05 M TBAB at 100 mV s^{-1}. (Inset) Calibration graph.

with the increase in the concentrations of chlorpyrifos ranging from 10 to 130 μM (inset graph in Figure 5). The limit of detection (LOD) and limit of quantitation (LOQ) were calculated from the calibration graph constructed with concentration of chlorpyrifos on the *x*-axis and reduction current on the *y*-axis using the relationships LOD = $3s/m$ and LOQ = $10s/m$, where *s* is the standard deviation of the intercept and *m* is the slope of the calibration curve.[32] The LOD is 4.4 μM, and the LOQ is 14.7 μM.

Differential Pulse Voltammetric Analysis. Typical DPV curves at various concentrations of chlorpyrifos are shown in Figure 6. The peak current obtained after subtracting the background current increases with the increase in the

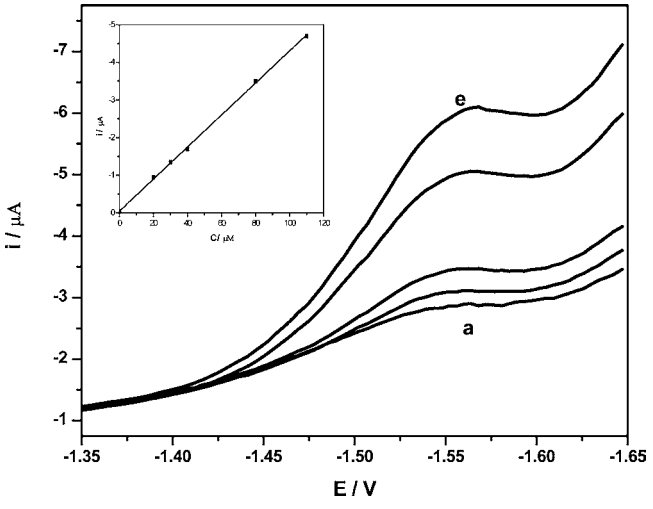

Figure 6. Differential pulse voltammetric response of various concentrations of chlorpyrifos, (a) 20, (b) 30, (c) 40, (d) 50, (e) 80, and (f) 110 μM, at nano-TiO_2/cellulose acetate modified GCE in 60:40 (v/v) methanol/water containing 0.05 M TBAB. (Inset) Calibration graph.

concentration of chlorpyrifos. The peak current varies linearly with an increase in the concentration of chlorpyrifos from 20 to 110 μM (inset in Figure 6). The LOD and the LOQ values are 3.5 and 11.7 μM, respectively. The analytical parameters obtained on various electrodes reported in the literature are presented in Table 1. Although the reduction potential of chlorpyrifos on nano-TiO_2/cellulose acetate modified GCE is higher than the values reported on mercury-based electrodes, from an environmental point of view, mercury is not a suitable material for sensing. The reduction potentials are comparable with the PEDOT modified and carbon paste modified electrodes. The nano-TiO_2/cellulose acetate modified GCE presented in this work is stable, reproducible, and biocompatible and, moreover, the preparation of the modified electrode is simple.

Amperometric Analysis. Figure 7 shows the amperometric response of chlorpyrifos at nano-TiO_2/cellulose acetate modified GCE. It was recorded at a constant potential of −1.5 V. The reduction current increases for each addition of chlorpyrifos, and the steady state current was measured. The peak current varies linearly with the increase in concentration of chlorpyrifos from 20 to 340 μM (inset in Figure 7). The LOD and the LOQ values are 11.8 and 39.2 μM, respectively.

Reproducibility and Stability of n-TiO_2/CA/GCE. The electrochemical responses are affected by the surface chemistry of carbon−oxygen functionalities present on the GC electrode and cleanliness, that is, the absence of adsorbed impurities.[33−36] In the present work GC was hand polished with finer emery papers to remove the oxide layers and adsorbed impurities on the electrode surface. Then the GC electrode was throughouly washed with Millipore water to remove the loosely adsorbed particles on the GC surface. The GC electrode was further chemically cleaned with NaOH, HNO_3, and MeOH. The electron transfer rates of redox reactions and reproducibility on the GC electrode are controlled by the distribution of surface oxides. The distribution of surface oxides was modified by exposing the GC electrode to NaOH and HNO_3. The surface of GC contains C—OH and C═O functional groups. The relative density of these species varies with the chemical treatments with NaOH and HNO_3. Treatment with NaOH increases the surface coverage of C—OH and with HNO_3 increases the surface coverage of C═O. Methanol is a less aggressive cleaning agent, which desorbs the solution impurities.[37,38] Bare GC electrodes pretreated by the above methods gave reproducible voltammetric responses for the ferrocyanide/ferricyanide redox system in 0.1 M KCl. Hence, the above pretreatment procedures were adopted in the present work.

First, the reproducibility of the bare GC electrode pretreated with emery papers and chemical agents such as NaOH, HNO_3, and MeOH was established by recording the cyclic voltammetric responses of ferricyanide/ferrocyanide in 0.1 M KCl.[26] The pretreatment procedures used in this work were sufficient to give reproducible CV responses. The pretreated GC electrode was used for modification with n-TiO_2/CA composite film. The modified GC electrode was potentiostatically cycled from the rest potential to the hydrogen evolution potential at slow sweep rates, for example, 10 mV s^{-1} in supporting electrolyte solution. After a few cycles, the background current was stable and reproducible. Then cyclic voltammograms were recorded for the reduction of chlorpyrifos on n-TiO_2/CA/GCE.

DOI: 10.1021/acs.jafc.5b02057
J. Agric. Food Chem. 2015, 63, 6150−6156

Table 1. Comparison of Analytical Parameters on Various Modified Electrodes

method	electrode[a]	linear range	LOD	LOQ	ref
DPASV	HMDE (−1.2 V)	9.9×10^{-8}–5.96×10^{-7} M	9.9×10^{-8} M		11
DPV	HMDE (−1.2 V)	$(5.7–28.5) \times 10^{-8}$ M	4.0×10^{-10} M	1.2×10^{-9} M	13
cyclic voltammetry	PEDOT/GCE (−1.6 V)	10×10^{-10}–7×10^{-7} M	8×10^{-10} M		15
DPP	DME (−1.2 V)	9.7×10^{-7}–6.9×10^{-6} M	8.7×10^{-7} M		12
DPAdSV	CMCPE (−1.2 V)	2.8×10^{-10}–5.7×10^{-6} M	2.2×10^{-10} M		14
cyclic voltammetry	TiO_2/CA/GCE (−1.5 V)	$(10.0–30) \times 10^{-6}$ M	4.4×10^{-6} M	14.7×10^{-6} M	present work
DPV	TiO_2/CA/GCE (−1.5 V)	$(20.0–110) \times 10^{-6}$ M	3.5×10^{-6} M	11.7×10^{-6} M	present work
amperometry	TiO_2/CA/GCE	$(20.0–340) \times 10^{-6}$ M	11.8×10^{-6} M	39.2×10^{-6} M	present work

[a]The value given in parentheses is the reduction potential.

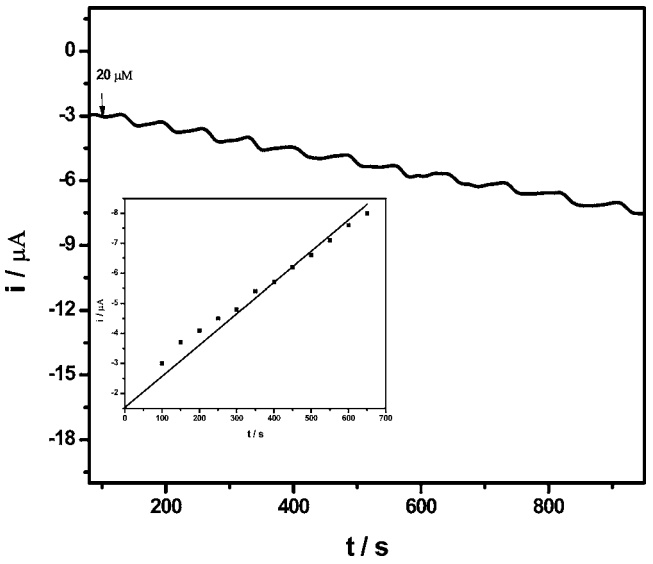

Figure 7. Amperometric response of chlorpyrifos for the constant addition of 20 μM at nano-TiO_2/cellulose acetate modified GCE in 60:40 (v/v) methanol/water containing 0.05 M TBAB. (Inset) Calibration graph.

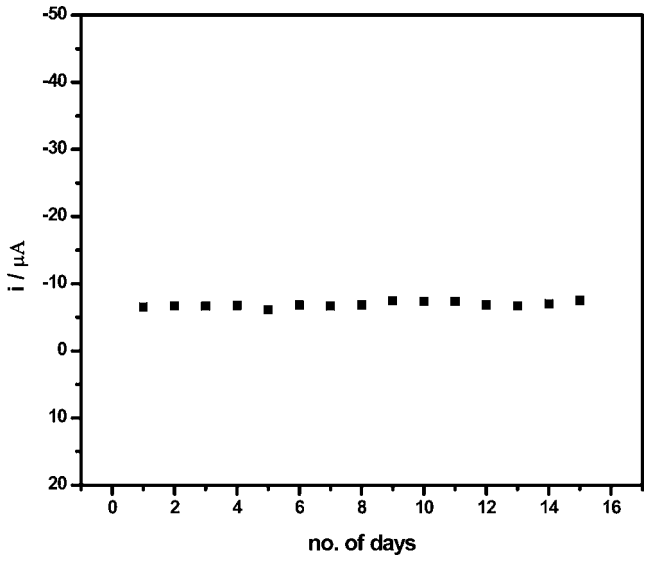

Figure 8. Stability of the n-TiO_2/CA/GCE electrode over time for the addition of 50 μM chlorpyrifos in 60:40 (v/v) methanol/water containing 0.05 M TBAB at 100 mV s^{-1}.

Reproducibility of the electrochemical response of this electrode was checked by carrying out a series of seven repetitive experiments for the fixed concentration of 50 μM chlorpyrifos. The peak currents are reproducible with the relative standard deviation of 2.54%. The reproducible response of the modified electrode with respect to time was checked (Figure 8). After the modification, the same electrode was used for the sensing of chlorpyrifos for 15 days successively. The peak currents are reproducible with the relative standard deviation of 5.3%. The stability of the electrode was also checked. After 40 cycles of cyclic voltammetric scans, the peak current variation from the initial current was 2.8% only. This shows that the nano-TiO_2/cellulose acetate film is highly stable and reproducible.

Interference Study. The interference study of several inorganic species and pesticides on the reduction signal of 50 μM chlorpyrifos was carried out using cyclic voltammetry. The concentration of the pesticides and the interfering ions were taken in 1:1 ratio. The inorganic ions such as Ca^{2+}, Mg^{2+}, Na^+, NH_4^+, and K^+ do not interfere with the chlorpyrifos reduction signal. Possible interferences with the other nitroaromatic pesticides such as methyl parathion and fenitrothion were also checked. These pesticides are reduced at around −700 mV on n-TiO_2/CA/GCE, whereas chlorpyrifos is reduced at around −1.55 V. The wide variation in the reduction potential makes it possible to determine chlorpyrifos even in the presence of these nitropesticides. The possible interference of chlorocompounds such as chlorophenol, chloroaniline, and chlorobenzene was also analyzed. The reduction of these chlorocompounds is not observed on this electrode under the present experimental conditions, and these chlorocompounds do not show any interference in the sensing signal of chlorpyrifos (Figure 9).

Real Sample Analysis. *Chlorpyrifos-Spiked Water Analysis.* The analytical utility of the above methods was checked with the water sample, which was collected at the Central Electrochemical Research Institute (CECRI) premises. It was tested for the presence of chlorpyrifos. Chlorpyrifos was absent in the water sample. Therefore, a 100 μM concentration of chlorpyrifos was spiked into the water sample and was thoroughly shaken for 1 h. Then it was extracted by using dichloromethane. A small amount of anhydrous sodium sulfate was added to the extracted sample to remove traces of water. The solvent was slowly evaporated to get the residue. The chlorpyrifos residue was dissolved in solvent supporting electrolyte and was used as analyte for electrochemical experiments. The recovery rates obtained in electrochemical techniques are summarized in Table 2. The results are compared with the HPLC method.

Commercial Sample Analysis. The commercial chlorpyrifos sample was analyzed using nano-TiO_2/cellulose acetate modified GCE as a sensor probe. One hundred milliliters of commercial chlorpyrifos was purchased from the local market, which contains approximately 20% (v/v) chlorpyrifos. The

DOI: 10.1021/acs.jafc.5b02057
J. Agric. Food Chem. 2015, 63, 6150−6156

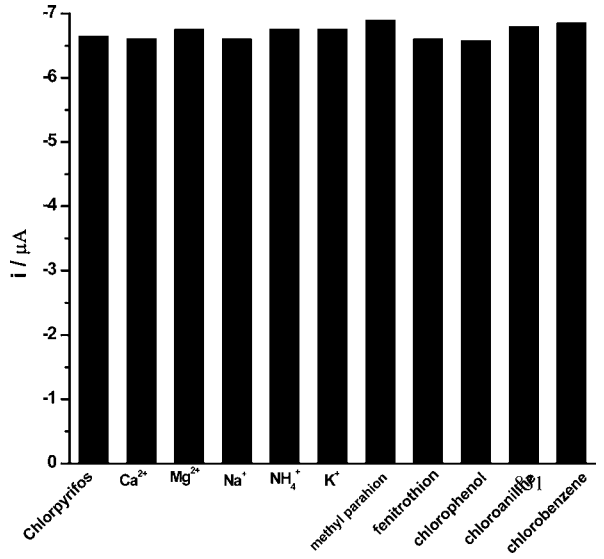

Figure 9. Interference study of various inorganic metal ions and pesticides on the reduction signal of 50 μM chlorpyrifos at n-TiO_2/CA/GCE in 60:40 (v/v) methanol/water containing 0.05 M TBAB at 100 mV s^{-1}.

Table 2. Recovery Study of Chlorpyrifos in Spiked Water Samples

method	amount added (μM)	amount recovered[a] (μM) ± SD	recovery rate (%)
cyclic voltammetry	100	91.84 ± 0.18	91.84
differential pulse voltammetry	100	96.28 ± 0.11	96.28
amperometry	100	96.46 ± 0.01	96.46
HPLC	100	98.80 ± 0.08	98.80

[a]Number of samples analyzed was 6.

actual concentration of the commercial samples was determined using an HPLC technique and was taken as reference value. It was diluted to 100 μM. Then it was used as an analyte in cyclic voltammetry, differential pulse voltammetry, and amperometry to verify the concentrations specified by the manufacturer. The concentration obtained in electroanalytical techniques is given in Table 3. The results obtained with electroanalytical techniques are comparable with the results obtained in the HPLC method.

Table 3. Commercial Sample Analysis

method	concn (%)[a,b] (v/v)
cyclic voltammetry	17.5 ± 0.50
differential pulse voltammetry	18.00 ± 0.09
amperometry	16.5 ± 0.08
HPLC	18.61 ± 0.10

[a]Concentration specified by the manufacturer is approximately 20% (v/v). [b]Number of samples assayed was 6.

Soil Analysis. Ten milliliters of chlorpyrifos was taken from the 100 mL commercial chlorpyrifos pack, which contains 20% (v/v) chlorpyrifos, and it was diluted to 1000 mL. Then this pesticide was sprayed on a pomegranate tree using an air sprayer. After 1 week, 112.6 g of soil under the pomegranate plant was collected and thoroughly ground. Then it was extracted as per the procedure explained above. The extracted sample was analyzed by electroanalytical techniques and HPLC measurements. The numer obtained in HPLC measurements is taken as reference value. The results obtained in electrochemical techniques are well comparable with the HPLC techniques (Table 4), so the electrochemical sensor using this nano-TiO_2-cellulose acetate modified electrode is promising for the analysis of environmental samples.

Table 4. Soil Sample Analysis

electroanalytical technique	concn (μM)[a,b]
cyclic voltammetry	91.62 ± 0.31
differential pulse voltammetry	91.64 ± 0.23
amperometry	102 ± 0.12
HPLC	99.6 ± 0.08

[a]Number of samples analyzed was 6. [b]Total weight of the soil was 112.6 g.

In this study a stable, reproducible, and biocompatible nano-TiO_2/cellulose acetate modified electrode was developed and used for the analysis of chlorpyrifos. The presence of TiO_2 nanoparticles increases the sensing current of chlorpyrifos, which enhances the sensitivity of the sensor. Moreover, the presence of TiO_2 nanoparticles in the cellulose acetate matrix shifts the hydrogen evolution markedly, which improves the measurement of true sensing current of chlorpyrifos. The modified electrode is highly stable with respect to time so that the electrode once modified can be used many times for the sensing of chlorpyrifos. The electrode modification procedure outlined in this work is also simple. The nano-TiO_2/cellulose acetate film on the glassy carbon electrode surface is highly stable in alcoholic medium, which makes this physically mixed composite material suitable for the determination of chlorpyrifos in alcoholic medium. This modified electrode replaces the mercury sensing electrode in the determination of chlorpyrifos. The materials used in the preparation of the modified electrode are cheap. The modified electrode can easily be renewed for subsequent analysis. The analytical utility of the proposed method was checked in the spiked water sample and the commercial sample.

AUTHOR INFORMATION

Corresponding Author

*(M.C.) Phone: +91 4565 241552. Fax: +91 4565 227779, 227713. E-mail: yemchand@yahoo.com.

Funding

We thank the Department of Science and Technology, New Delhi, India, for financial support. A.K. thanks the Council of Scientific and Industrial Research (CSIR), New Delhi, India, for awarding a Senior Research Fellowship (SRF).

Notes

The authors declare no competing financial interest.

REFERENCES

(1) Venkata Mohan, S.; Sirisha Ra, N. C.; Sarma, P. N.; Reddy, S. J. Degradation of chlorpyrifos contaminated soil by bioslurry reactor operated in sequencing batch mode: bioprocess monitoring. *J. Hazard. Mater.* **2004**, *116*, 39−48.

(2) De Silva, P. M. C. S; Samayawardhena, L. A. Effects of chlorpyrifos on reproductive performances of guppy (*Poecilia reticulata*). *Chemosphere* **2005**, *58*, 1293−1299.

DOI: 10.1021/acs.jafc.5b02057
J. Agric. Food Chem. 2015, 63, 6150−6156

(3) Environment Canada. Canadian water quality guidelines, prepared by the Canadian Council of Resource and Environment Ministers, 1987.
(4) Cometa, M. F.; Buratti, F. M.; Fortuna, S.; Lorenzini, P.; Volpe, M. T.; Parisi, L. E; Testai, E.; Meneguz, A. Cholinesterase inhibition and alterations of hepatic metabolism by oral acute and repeated chlorpyrifos administration to mice. *Toxicology* **2007**, *234*, 90−102.
(5) Ray, D. E. Chronic effects of low level exposure to anticholinesterases — a mechanistic review. *Toxicol. Lett.* **2008**, *103*, 527−533.
(6) Richardson, R. J.; Moore, T. B.; Kayyali, U. S.; Randall, J. C. Chlorpyrifos: Assessment of potential for delayed neurotoxicity by repeated dosing in adult hens with monitoring of brain acetylcholinesterase, brain and lymphocyte neurotoxic esterase, and plasma butyrylcholinesterase activities. *Fundam. Appl. Toxicol.* **1993**, *21*, 89−96.
(7) Inman, R. D.; Kiigemagi, U.; Deinzer, M. L. Determination of chlorpyrifos and 3,5,6 trichloro-2-pyridinol residues in peppermint hay and peppermint oil. *J. Agric. Food Chem.* **1981**, *29*, 321−323.
(8) Oliva, J.; Navarro, J. S.; Barba, A.; Navarro, G. Determination of chlorpyrifos,penconazole,fenarimol, vinclozolin and metalaxyl in grapes, must and wine by on-line microextraction and gas chromatography. *J. Chromatogr. A* **1999**, *833*, 43−51.
(9) Brzak, K. A.; Harms, D. W.; Bartels, M. J.; Nolan, R. J. Determination of chlorpyrifos, chlorpyrifos oxon, and 3,5,6-trichloro-2-pyridinol in rat and human blood. *J. Anal. Toxicol.* **1998**, *22*, 203−210.
(10) Mauldin, R. E.; Primus, T. M.; Buettgenbach, T. A.; Johnston, J. J. A simple HPLC method for the determination of chlorpyrifos in black oil sunflower seeds. *J. Liq. Chromatogr. Relat. Technol.* **2006**, *29*, 339−348.
(11) El-Shahawi, M. S.; Kamal, M. M. Determination of the pesticide chlorpyrifos by cathodic adsorptive stripping voltammetry. *Fresenius' J. Anal. Chem.* **1998**, *362*, 344−347.
(12) Al-Meqbali, A. S. R.; El-Shahawi, M. S.; Kamal, M. M. Differential pulse polarographic analysis of chlorpyrifos insecticide. *Electroanalysis* **1998**, *1*, 784−786.
(13) Pelit, F. O.; Ertas, H.; Ertas, F. N. Development of an adsorptive catalytic stripping voltammetric method for the determination of an endocrine disruptor pesticide chlorpyrifos and its application to the wine samples. *J. Appl. Electrochem.* **2011**, *41*, 1279−1285.
(14) Sirisha, K.; Mallipattu, S.; Reddy, S. R. J. Differential pulse adsorptive stripping voltammetric determination of chlorpyrifos at a sepiolite modified carbon paste electrode. *Anal. Lett.* **2007**, *40*, 1939−1950.
(15) Manisankar, P.; Viswanathan, S.; Pushpalatha, A. M.; Rani, C. Electrochemical studies and square wave stripping voltammetry of five common pesticides on poly 3,4-ethylenedioxythiophene modified wall-jet electrode. *Anal. Chim. Acta* **2005**, *528*, 157−163.
(16) Li, H.; Li, L.; Xu, Q.; Hu, X. Poly(3-hexylthiophene)/TiO_2 nanoparticle-functionalized electrodes for visible light and low potential photoelectrochemical sensing of organophosphorus pesticide chlorpyrifos. *Anal. Chem.* **2011**, *83*, 9681−9686.
(17) Xie, C.; Li, H.; Li, S.; Wu, J.; Zhang, Z. Surface molecular self-assembly for organophosphate pesticide imprinting in electropolymerized poly(*p*-aminothiophenol) membranes on a gold nanoparticle modified glassy carbon electrode. *Anal. Chem.* **2010**, *82*, 241−249.
(18) Samet, Y.; Agengui, L.; Abdelhedi, R. Anodic oxidation of chlorpyrifos in aqueous solution at lead dioxide electrodes. *J. Electroanal. Chem.* **2010**, *650*, 152−158.
(19) Kumaravel, A.; Chandrasekaran, M. A biocompatible nano TiO_2/nafion composite modified glassy carbon electrode for the detection of fenitrothion. *J. Electroanal. Chem.* **2010**, *650*, 163−170.
(20) Kumaravel, A.; Vincent, S.; Chandrasekaran, M. Development of an electroanalytical sensor for γ-hexachlorocyclohexane based on a cellulose acetate modified glassy carbon electrode. *Anal. Methods* **2013**, *5*, 931−938.
(21) Wu, S.; Liu, J.; Bai, X.; Tan, W. Stability improvement of prussian blue by a protective cellulose acetate membrane for hydrogen peroxide sensing in neutral media. *Electroanalysis* **2010**, *22*, 1906−1910.
(22) Hoffmann, A. A.; Dias, S. L. P.; Benvenutti, E. V.; Lima, E. C.; Paavan, F. A.; Rodrigues, J. R.; Scotti, R.; Ribeiro, E. S.; Gushikem, Y. Cationic dyes immobilized on cellulose acetate surface modified with titanium dioxide:Factorial design and an application as sensor for NADH. *J. Braz. Chem. Soc.* **2007**, *18*, 1462−1472.
(23) Hoffmann, A. A.; Dias, S. L. P.; Rodrigues, J. R.; Paavan, F. A.; Benvenutti, E. V.; Lima, E. C. Methylene blue immobilized on cellulose acetate with titanium dioxide: an application as sensor for ascorbic acid. *J. Braz. Chem. Soc.* **2008**, *19*, 943−949.
(24) Kamalan Kirubakaran, A. M.; Selvaraj, M.; Maruthan, K.; Jeyakumar, D. Synthesis and characterization of nanosized titanium dioxide and silicon dioxide for corrosion resistance applications. *J. Coat. Technol. Res.* **2012**, *9*, 163−170.
(25) Xu, C.; Wu, K.; Hu, S.; Cui, D. Electrochemical detection of parathion at a glassy carbon electrode modified with hexadecane. *Anal. Bioanal. Chem.* **2002**, *373*, 284−288.
(26) Noel, M.; Anantharaman, P. N. Voltammetric studies on a glassy carbon electrode. Part II. Factors influencing the simple electron transfer reactions-the $K_3[Fe(CN)_6]$-$K_4[Fe(CN)_6]$ system. *Analyst* **1985**, *110*, 1095−1103.
(27) Wang, J.; Golden, T.; Li, R. Cobalt/phthalocyanine/cellulose acetate chemically modified electrodes for electrochemical detection in flow streams.Multifunctional operation based upon the coupling of electrocalalysis and permeability. *Anal. Chem.* **1988**, *60*, 1642−1645.
(28) Wu, S.; Liu, J.; Bai, X. W. Stability improvement of Prussian Blue by a protective cellulose acetate membrane for Hydrogen peroxide sensing in neutral media. *Electroanalysis* **2010**, *22*, 1906−1910.
(29) Jin, X.; Xu, J.; Wang, X.; Xie, Z.; Liu, Z.; Liang, B.; Chen, D.; Shen, G. Flexible TiO_2/cellulose acetate hybrid film as a recyclable photocatalyst. *RSC Adv.* **2014**, *4*, 12640−12648.
(30) Ilharco, L. M.; Brito de Barros, R. Aggregation of pseudoisocyanine iodide in celluloseacetate films: Structural characterization by FTIR. *Langmuir* **2000**, *16*, 9331−9337.
(31) Ugur, S. S.; Sariisik, M.; Aktas, A. H. Nano-TiO_2 based multilayer film deposition on cotton fabrics for UV-protection. *Fibers Polym.* **2011**, *12*, 190−196.
(32) Skoog, D.; Holler, K.; Nieman, T. *Principles of Instrumental Analysis*, 5th ed.; Harrcourt Brace College Publishers: Orlando, FL, USA, 1998; pp *13*, 14.
(33) Ray, K. G., III; McCreery, R. L. Characterisation of the surface carbonyl and hydroxyl coverage on glassy carbon electrodes using Raman Spectroscopy. *J. Electroanal. Chem.* **1999**, *469*, 150−158.
(34) McCreery, R. L. *Electrochemical Properties of Carbon Surfaces, Interfacial Chemistry*; Wiechowski, A., Ed.; Dekker: New York, 1999; Chapter 35, pp 631−643.
(35) Chen, P.; McCreery, R. L. Control of electron transfer kinetics at glassy carbon electrodes by specific surface modifications. *Anal. Chem.* **1996**, *68*, 3958−3965.
(36) Ping, W. X.; Lan, Z.; Wen-Rong, L.; Ping, D. J.; Qing, C. H.; Nan, C. G. Study on the interfacial behavior of Melatonin with an activated electrode. *Electroanalysis* **2012**, *14*, 1654−1660.
(37) Braga, O.; Comprestrini, C. I.; Vieira, I. C.; Spinelli, A. Sulfadiazine determination in pharmaceuticals by electrochemical reduction on a glassy carbon electrode. *J. Braz. Chem. Soc.* **2010**, *21*, 813−820.
(38) Jain, R.; Sharma, S. Glassy carbon electrode modification with multiwalled carbon nanotubes sensor for the quantification of antihistamin drug phenaramine in solubilised systems. *J. Pharm. Anal.* **2012**, *1*, 56−61.

DOI: 10.1021/acs.jafc.5b02057
J. Agric. Food Chem. 2015, 63, 6150−6156

Recently, matrix-assisted laser desorption/ionization time-of-flight mass spectrometry (MALDI-TOF-MS)-based approaches have been developed for biological fluid profiling, showing their potential in the quali-quantitative analysis of milk proteins and peptides.[8] MALDI-TOF-MS has the advantage of requiring small amounts of even heterogeneous samples, permitting their analysis in a very short time. In particular, detection of α-lactalbumin, β-lactoglobulin, and $\gamma 2/\gamma 3$-casein isoforms during protein profiling (PR-P) of whey and skimmed milk samples has been used to reveal definite species-associated milk frauds.[9−13] Linear regression analysis of the resulting mass spectra quantified nondeclared milk material even in low amounts.[13] Recently, MALDI-TOF-MS PR-P of skimmed samples combined with multivariate calculation techniques allowed an accurate estimate of the levels of adulteration in bovine−goat−sheep milk mixtures.[14] No similar applications were developed to assess fraudulent addition of powdered material to fresh milk. Direct serum or skimmed milk PR-P applications did not find a counterpart at the peptide level. In fact, peptide profiling (PE-P) approaches were developed only when contemplating additional experimental steps consisting of the enzymatic digestion (with trypsin or plasmin) of the whole milk samples or of selected proteins preventively resolved by electrophoresis.[4,5,15−20] This experimental setup severely affected the time necessary for entire analysis and highly complicated the nature of the resulting MALDI-TOF spectra, generally determining the need for additional chromatographic steps for an accurate quantification of the adulteration percentages.

In this study, an integrated platform for the combined peptidomic and proteomic profiling of milk samples has been developed to rapidly reveal illegal adulterations due to the addition of either nondeclared bovine material to water buffalo, goat, and ovine milks or of powdered bovine material to the fresh counterpart. To this purpose, specific peptide and protein markers of fresh bovine milk (BM), water buffalo milk (WM), ovine milk (OM), and goat milk (GM) were identified after direct analysis of skimmed samples. Markers of TT were characterized in fresh bovine milk (BM), pasteurized milk (PM), ultra-high-temperature (UHT) milk (UM), and powdered milk (IM) samples. Principal components (PCs) scores of ad hoc prepared species- or TT-associated adulterated milk samples were subjected to partial least-squares (PLS) regression, allowing an accurate estimate of the fraud extents in test samples at either protein and peptide level.

EXPERIMENTAL PROCEDURES

Sample Preparation. Fresh raw BM, WM, OM, and GM samples were collected from local farms after morning milking, stored at 4 °C, and assayed within 5 h. Bovine PM, UM, and IM samples from different (20 in number) commercial brands were purchased from supermarkets and used before their expiration date (Supporting Information Table S2). In all cases, 25 different samples were analyzed for each type of milk.

For adulteration studies, binary mixtures of BM in WM, OM, and GM counterparts or IM in BM were prepared at 1, 2, 5, 10, 15, 20, 30, 40, and 50% v/v values. Three independent samples were prepared for each specific binary mixture.

All milk samples or their binary mixtures were defatted by centrifugation at 3000 rpm, for 30 min, at 4 °C. A part of the corresponding skimmed material (20 μL) was directly analyzed by MALDI-TOF-MS for the generation of the corresponding protein profiles. The remaining material (200 μL) was diluted 1:1 v/v with water, transferred onto Amicon Ultra devices (3 kDa cutoff) (Millipore), and filtered by centrifugation at 10000 rpm, at 4 °C. Two technical replicates were prepared for each filtrate. Peptides from filtrates were directly analyzed by MALDI-TOF-MS or extracted with C_{18}ZipTip devices (Millipore) and then subjected to MS analysis.

MALDI-TOF-MS Profiling Measurements. Before MALDI-TOF-MS PR-P, skimmed milk samples were diluted 1:100 with water. Each sample (0.5 μL) was mixed with 0.5 μL of a solution of sinapinic acid (10 mg/mL) (Bruker Daltonics, Bremen, Germany) in 0.1% v/v trifluoroacetic acid (TFA) and 30% v/v acetonitrile (ACN), placed onto a Ground Steel Target (Bruker Daltonics), and dried at room temperature. Before MALDI-TOF-MS PE-P, peptide samples (0.5 μL) were mixed with 0.5 μL of a solution of α-cyano-4-hydroxycinnamic acid (25 mg/mL) (Bruker Daltonics) in 0.1% v/v TFA and 30% v/v ACN, placed onto the instrument target reported above, and dried at room temperature.

Protein and peptide samples were analyzed by MALDI-TOF-MS using an UltraflexExtreme mass spectrometer (Bruker Daltonics) equipped with the FlexControl software package (version 3.4, Bruker Daltonics).[21] In all cases, spectral acquisition methods were developed to maximize the number of signals present in the mass spectra and the corresponding signal-to-noise ratios. In the case of PR-P measurements, spectra were recorded in the positive linear mode (LM) (laser frequency, 1000 Hz; ion source 1 voltage, 25.19 kV; ion source 2 voltage, 23.59 kV; lens voltage, 7.50 kV; sample rate, 0.31; mass range, 5000−20000 Da). Five independent spectra (1000 shots at random positions on the same target place, for spectrum) were automatically collected, calibrated externally by using the Protein Calibration Standard 1 (Bruker Daltonics), and subsequently analyzed. In the case of PE-P measurements, spectra were recorded both in the positive LM (laser frequency, 1000 Hz; ion source 1 voltage, 25.19 kV; ion source 2 voltage, 23.94 kV; lens voltage, 6.50 kV; sample rate, 0.16; mass range, 500−5000 Da) and in the positive reflector mode (RM) (laser frequency, 1000 Hz; ion source 1 voltage, 25.19 kV; ion source 2 voltage, 22.50 kV; lens voltage, 8.50 kV; reflector, 26.83 kV; reflector 2, 13.75 kV; sample rate, 0.63; mass range, 500−5000 Da). Ten independent spectra (500 shots at random positions on the same target place, for spectrum) for each peptide mixture were automatically collected, externally calibrated by using Peptide Calibration Standard 2 (Bruker Daltonics), and subsequently analyzed.

Bioinformatics and Statistics. FlexAnalysis (version 3.4) and ClinProt Tools (version 2.2) software packages (Bruker Daltonics) were used for the analysis of all MALDI-TOF-MS data, which included spectral mass adjustment (compression by a factor of 10 in the total mass range), optional smoothing (using the Savitsky−Golay algorithm with a frame size of 25 Da), spectral baseline subtraction, normalization, internal peak alignment, and peak picking. Pretreated data were then subjected to visualization and statistical analysis. Peptides or proteins showing a statistically significant difference in signal intensity or mass value were determined by means of Wilcoxon (PWKW), Anderson−Darling (PAD,) and t (PTTA) tests. A class prediction model was set up by Genetic Alghorithms (GA). Discriminant peaks were considered those presenting at least a p value <0.000001 among the PWKW, PAD, and PTTA ones. Finally, a principal components analysis (PCA) of the spectra was performed, which was carried out by an external MATLAB software tool integrated into ClinPro Tools software.

With regard to adulterated milk, corresponding PCs scores were subjected to PLS regression by XLSTAT software (Microsoft). Adulteration prediction at two points (5 and 15% v/v) was obtained by the forecast function of Excel software (Microsoft), using PLS results as matrix reference data.

RESULTS AND DISCUSSION

To define an optimal method for the suitable discrimination of milk samples by MALDI-TOF-MS profiling, dedicated procedures were set up for the combined analysis of the corresponding protein and peptide components. Due to the composition complexity of each milk type, various experimental protocols were developed for this purpose, which were

DOI: 10.1021/acs.jafc.5b02384
J. Agric. Food Chem. 2015, 63, 6157−6171

compared a posteriori for their discrimination performances. PR-P assays were performed directly on diluted skimmed milk samples.[9−14] On the other hand, PE-P measurements were realized on diluted low molecular mass skimmed milk filtrates that were then straightly analyzed by MALDI-TOF-MS or extracted with concentration devices before MS analysis. Attempts to assay peptides directly in diluted skimmed milk samples were unsuccessful in terms of recognition performances (data not shown). Different instrument acquisition ranges were assessed for protein and peptide analysis; in the latter case, the effect of a spectral acquisition in LM and RM was also evaluated (see below). Optimized procedures were used for milk speciation, for the characterization of commercial bovine milk samples subjected to various TTs, and finally for the detection of adulterated test samples as result of the addition of nondeclared material.

On the whole, a data set of 3500 MALDI-TOF mass spectra was recorded for the speciation of raw milk from four animal species. In particular, 500 mass spectra were acquired for the corresponding PR-P (5 spectral replicas for 25 milk samples from totally different individuals of each animal species); a representative example is reported in Figure 1. A thousand mass spectra were acquired for the corresponding PE-P of milk filtrates (10 spectral replicas for 25 milk samples from totally different individuals of each animal species) either in LM and in RM; representative examples are reported in Supporting Information Figures S1 and S2. Five hundred mass spectra were acquired for the corresponding PE-P of milk filtrates subjected to C_{18}ZipTip enrichment (5 spectral replicas for 25 milk samples from totally different individuals of each animal species) either in LM or in RM; representative examples are reported in Supporting Information Figure S3 and in Figure 2.

A data set analogous to that reported above was recorded in the case of BM and commercial thermally treated PM, UM, and IM samples. A representative example of the corresponding PR-P spectra is reported in Figure 3. Similarly, exemplificative PE-P spectra of milk filtrates acquired either in LM or in RM are shown in Supporting Information Figures S4 and S5, respectively. Peptide MALDI-TOF spectra of milk filtrates subjected to C_{18}ZipTip enrichment recorded either in LM or in RM are presented in Supporting Information Figure S6 and in Figure 4, respectively.

Finally, a data set of 3780 MALDI-TOF mass spectra was recorded for the detection of adulterated milk samples as a result of the addition of nondeclared material. Experiments were performed to identify adulteration either from raw BM added to WM, OM, or GM, and from IM added to BM. In particular, 540 mass spectra were acquired for the corresponding PR-P (5 spectral replicas of the 9 percentage values assayed for each kind of adulteration; experiments were performed on triplicate samples) (data not shown); 1080 mass spectra were acquired for the corresponding PE-P of milk filtrates (10 spectral replicas of the 9 percentage values assayed for each kind of adulteration; experiments were performed on triplicate samples) either in LM or in RM (data not shown); 540 mass spectra were acquired for the corresponding PE-P of milk filtrates subjected to C_{18}ZipTip enrichment (5 spectral replicas of the 9 percentage values assayed for each kind of adulteration; experiments were performed on triplicate samples) either in LM or in RM (data not shown).

In each case, statistical analysis of mass spectra of pure milk samples allowed the identification of discriminant signals on the basis of intensity and/or mass values. Class prediction model

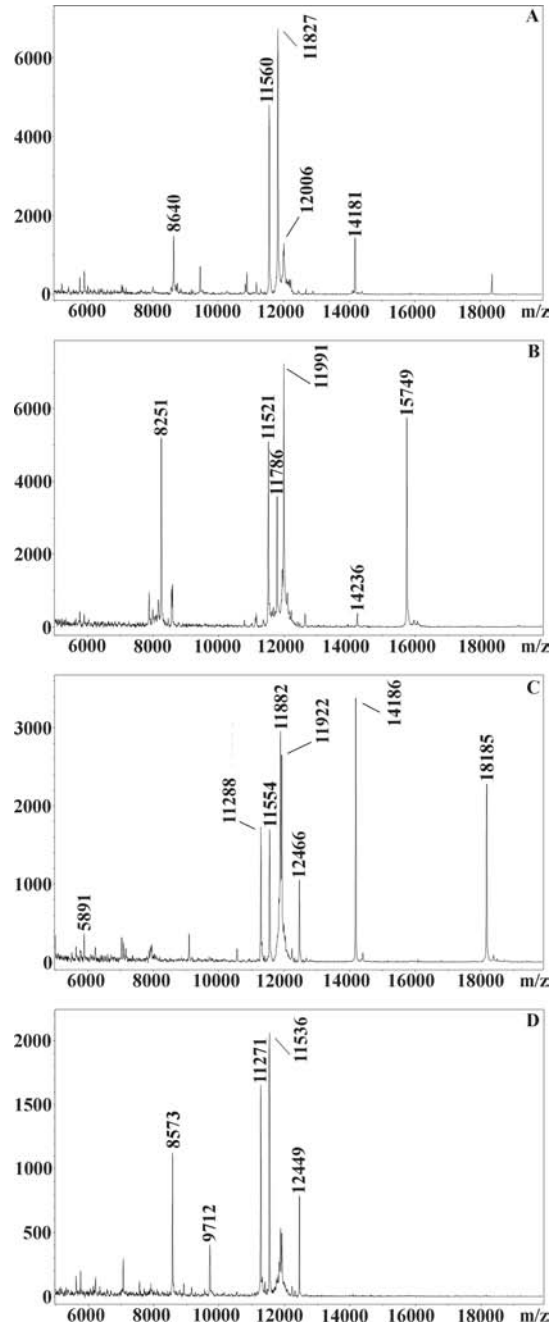

Figure 1. MALDI-TOF-MS PR-P in LM of diluted milk samples. Spectra refer to BM (A), WM (B), GM (C), and OM (D). MH^+ signals corresponding to identified marker molecules are highlighted by reporting the associated mass values.

was set up by GA; marker proteins or peptides were identified by means of their PWKW, PAD, and PTTA p values. Corresponding data for milk speciation are shown in Supporting Information Table S3 (PR-P, 23 markers), Supporting Information Table S4 (PE-P in LM, 65 markers), Supporting Information Table S5 (PE-P in RM, 106 markers), Supporting Information Table S6 (PE-P in LM after C_{18}ZipTip enrichment, 63 markers), and Supporting Information Table S7 (PE-P in RM after C_{18}ZipTip enrichment, 95 markers), together with additional statistical parameters. Corresponding data for the characterization of thermally treated commercial bovine milks are shown in Supporting Information Table S8

DOI: 10.1021/acs.jafc.5b02384
J. Agric. Food Chem. 2015, 63, 6157−6171

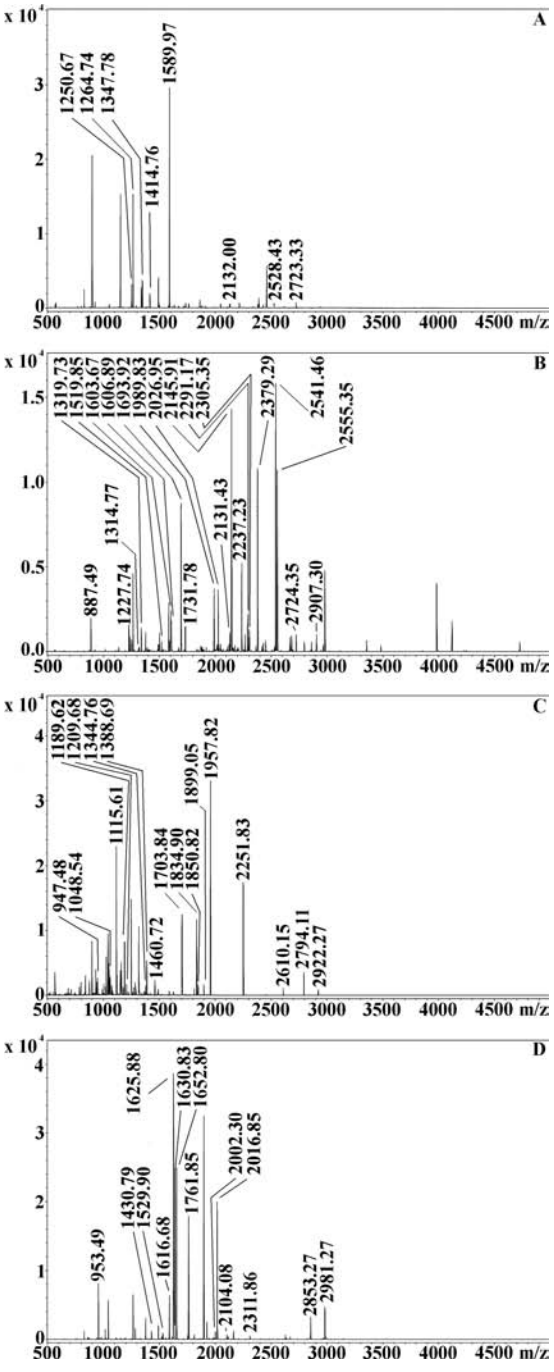

Figure 2. MALDI-TOF-MS PE-P in RM of diluted milk filtrates subjected to C_{18}ZipTip enrichment resulting from BM (A), WM (B), GM (C), and OM (D). MH^+ signals corresponding to identified marker molecules are highlighted by reporting the associated mass values.

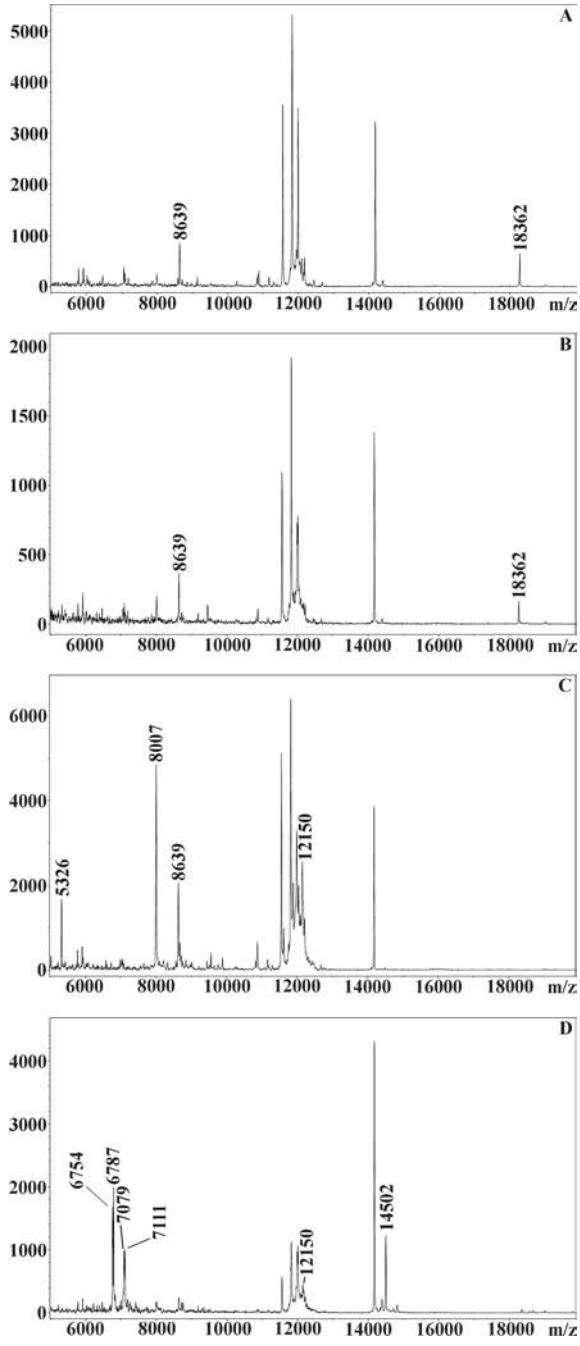

Figure 3. MALDI-TOF-MS PR-P in LM of diluted thermally treated commercial milk samples. Spectra refer to fresh BM (A), PM (B), UM (C), and IM (D). MH^+ signals corresponding to identified marker molecules are highlighted by reporting the associated mass values.

(PR-P, 10 markers), Supporting Information Table S9 (PE-P in LM, 27 markers), Supporting Information Table S10 (PE-P in RM, 47 markers), Supporting Information Table S11 (PE-P in LM after C_{18}ZipTip enrichment, 46 markers), and Supporting Information Table S12 (PE-P in RM after C_{18}ZipTip enrichment, 53 markers), together with additional statistical parameters. As expected, a number of common peptide markers occurred between analyses performed in LM and RM. In particular, 43, 39, 18, and 23 common peptide markers were observed during PE-P on milk filtrates for speciation, on C_{18}ZipTip-enriched milk samples for speciation, on milk filtrates for TT characterization, and on C_{18}ZipTip-enriched milk samples for TT characterization, respectively. Importantly, data from PWKW, PAD, and PTTA analyses defined the recognition capability of each specific assay; corresponding results are reported in Tables 1 and 2. They demonstrate that milk speciation (100% recognition capability) was guaranteed in the case of MALDI-TOF-MS profiling measurements performed either on proteins from milk filtrates, on peptides from milk filtrates analyzed in RM, or on peptides from C_{18}ZipTip-enriched milk filtrates analyzed in both LM and RM, notwithstanding the heterogeneous polypeptide composition of

DOI: 10.1021/acs.jafc.5b02384
J. Agric. Food Chem. 2015, 63, 6157−6171

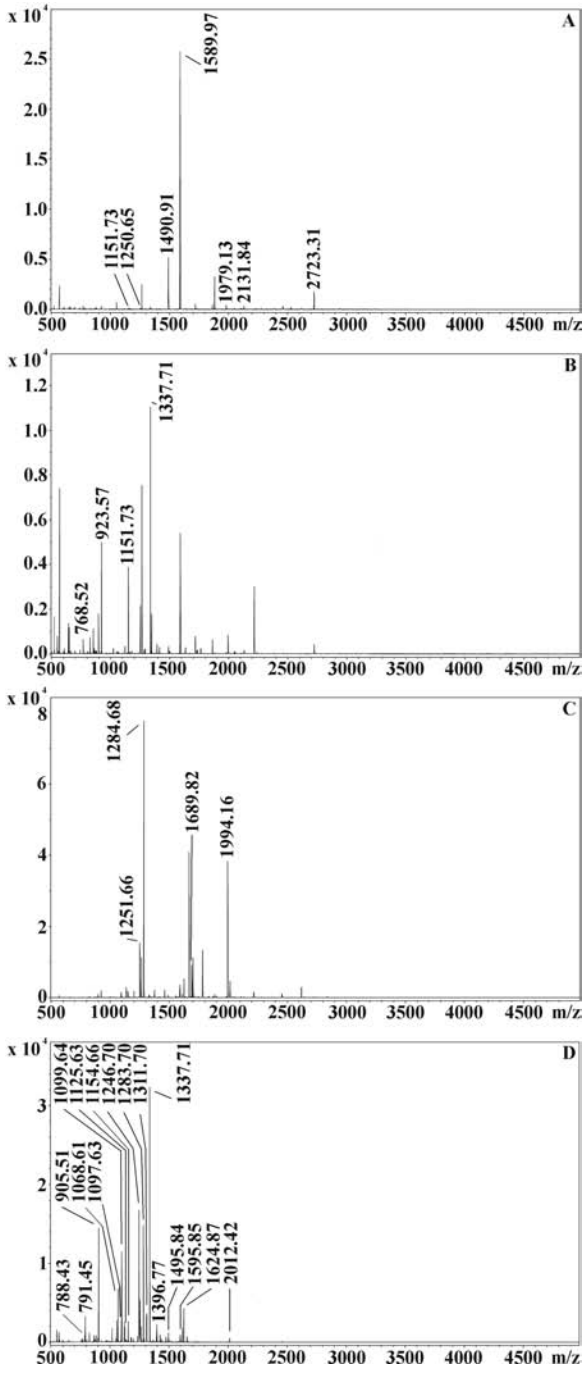

Figure 4. MALDI-TOF-MS PE-P in RM of milk filtrates subjected to C_{18}ZipTip enrichment from thermally treated commercial milk samples. Spectra refer to fresh BM (A), PM (B), UM (C), and IM (D). MH^+ signals corresponding to identified marker molecules are highlighted by reporting the associated mass values.

this biological fluid[16,18,22] (Table 1). Conversely, the characterization of the TT of commercial bovine milks was ensured only in the case of peptides from C_{18}ZipTip-enriched milk filtrates analyzed in RM (Table 2). The latter result is probably dependent on the higher complexity of the protein and peptide mixtures present in commercial milk samples;[5,15,17,19,20,23−26] it also emphasizes that the method used for spectral acquisition can highly affect the recognition capability of the whole platform. On this basis, particular care is necessary for the initial setup of the PR-P and PE-P experimental conditions to

Table 1. ClinProt Model Generation Report for the Speciation of Milk Samples from Different Animal Species (Cow, Buffalo, Goat, and Sheep)

molecular targets/acquisition method	cross validation (%)	recognition capability (%)
proteins from diluted samples/LM	95.11	100.00
peptides from C_{18}ZipTip-enriched diluted milk filtrates/RM	89.43	100.00
peptides from diluted milk filtrates/RM	90.10	100.00
peptides from C_{18}ZipTip-enriched diluted milk filtrates/LM	89.11	100.00
peptides from diluted milk filtrates/LM	77.47	97.39

Table 2. ClinProt Model Generation Report for the Recognition of Thermally Treated Commercial Milk Samples (Raw, Pasteurized, Ultrahigh-Temperature, and Powdered)

molecular targets/acquisition method	cross validation (%)	recognition capability (%)
proteins from diluted samples/LM	87.82	97.19
peptides from C_{18}ZipTip-enriched diluted milk filtrates/RM	89.69	100.00
peptides from diluted milk filtrates/RM	90.07	96.46
peptides from C_{18}ZipTip-enriched diluted milk filtrates/LM	86.94	98.04
peptides from diluted milk filtrates/LM	82.44	98.00

guarantee the maximum number of signals present in the mass spectra and of the corresponding signal-to-noise ratios. These instrumental settings have to be maintained during the whole analysis of the different milk samples with the aim of not compromising the recognition capability of the whole platform.

As expected, PCA of the data reported in Supporting Information Tables S3−S12 was in line with the recognition capability values reported in Tables 1 and 2. For example, panels A and B of Figure 5 show the PCA 3D scatter plots of results from BM, WM, GM, and OM proteins analyzed in LM and from BM, WM, GM, and OM C_{18}ZipTip-enriched peptides in RM, respectively, which were used for milk speciation. A good separation of the colored spots was evident in both cases. Similarly, panels A and B of Figure 6 show the PCA 3D scatter plots of results from BM, PM, UM, and IM proteins analyzed in LM and from BM, PM, UM and IM C_{18}ZipTip-enriched peptides in RM, respectively, which were used for the recognition of the material thermal treatment. Although more appreciable in a three-dimensional representation, well-resolved colored spots were evident also in these cases. Best dot separation occurred in the case of peptides. Less-resolved PCA 3D scatter plots were obtained in the case of the remaining methods used for milk speciation (Supporting Information Figure S7) and for the recognition of milk TT (Supporting Information Figure S8).

On the basis of the data reported in Tables 1 and 2, Figures 5 and 6, and Supporting Information Figure S7 and S8 and the capability of this MS platform to perform independent analyses on different molecules (proteins and peptides), we conclude that complementary information associated with the highest recognition capability values for milk speciation and for thermal treatment characterization are obtained when diluted skimmed milk samples and C_{18}ZipTip-enriched diluted skimmed milk filtrates are analyzed for the respective protein and peptide content in LM and RM, respectively.

DOI: 10.1021/acs.jafc.5b02384
J. Agric. Food Chem. 2015, 63, 6157−6171

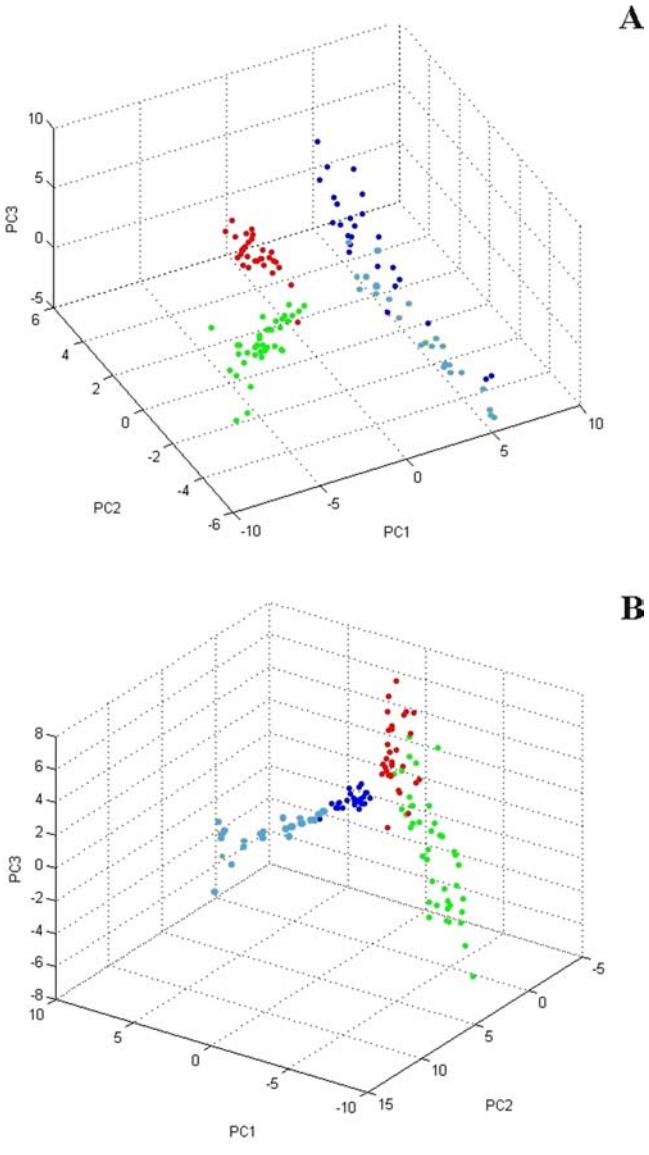

Figure 5. PCA scatter plot of protein (A) and peptide (B) MALDI-TOF-MS data in milk samples having different animal origins. Data referring to BM, WM, GM, and OM are highlighted in red, green, blue, and light blue, respectively. MALDI-TOF-MS PR-P experiments were performed in LM on diluted milk samples. MALDI-TOF-MS PE-P experiments were performed in RM on diluted milk filtrates subjected to C_{18}ZipTip enrichment.

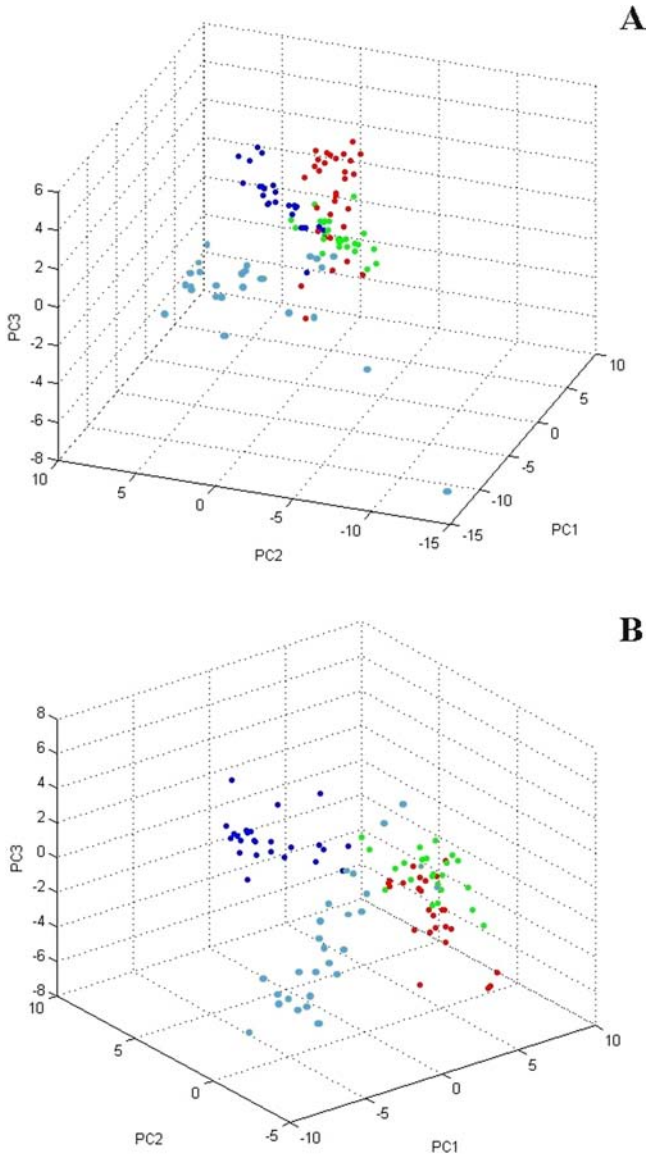

Figure 6. PCA scatter plot of protein (A) and peptide (B) MALDI-TOF-MS data in milk samples subjected to different thermal treatments. Data referring to fresh BM, PM, UM, and IM are highlighted in red, green, blue, and light blue, respectively. MALDI-TOF-MS PR-P experiments were performed in LM on diluted milk samples. MALDI-TOF-MS PE-P experiments were performed in RM on diluted milk filtrates subjected to C_{18}ZipTip enrichment.

Marker Assignment. Marker protein signals recognized for milk speciation (Supporting Information Table S3 and Figure 1) and for TT recognition (Supporting Information Table S8 and Figure 3) were associated with specific components on the basis of literature data[9−14,17] and mass calculations. As expected, most of the signals were assigned to α-lactalbumin and β-lactoglobulin, as well as to γ2/γ3-caseins and proteoso peptones resulting from the activity of milk plasmin on β-casein.[17,27−29] In particular, γ2-caseins and γ3-caseins were identified as marker signals in BM, WM, GM, and OM; α-lactalbumins were assigned markers in BM, WM, and GM; β-CN fragments (98−207) were discriminant signals in GM and OM; β-lactoglobulin, proteoso peptones p.p.8.I., and β-casein fragments (1−68) and (69−209) were discriminant molecules in GM, BM, and WM, respectively (Table 3). The latter complementary peptides originated after specific proteolysis at K_{68}; this lysine is exclusively present within the water buffalo β-casein sequence.[4,17]

When compared to data reported above, PR-P of thermally treated milk samples identified a reduced number of protein markers, that is, proteoso peptones p.p.8.I. (BM, PM, and UM), β-lactoglobulin (BM and PM), α-lactalbumin adduct with lactose (Δm = +324) (IF), γ2-casein (UM), and its adduct with lactose (IM) (Table 4). Various nonassigned marker species were specific for UM and IM; the corresponding hypothetical lactose adducts were present only in IM.

Finally, marker peptide signals from C_{18}ZipTip-enriched diluted skimmed milk filtrates recognized for speciation (Supporting Information Table S7 and Figure 2) and for TT recognition (Supporting Information Table S12 and Figure 4) were associated with specific components based on MALDI-

DOI: 10.1021/acs.jafc.5b02384
J. Agric. Food Chem. 2015, 63, 6157−6171

Table 3. Marker Species Recognized during MALDI-TOF-MS Protein Profiling for Milk Speciation[a]

DAve	description	exptl MH^+	theor MH^+ (UniProt Code)
	Bovine Milk		
36.26	α-lactalbumin	14181	14179 (P00711)
29.46	γ2-casein/β-casein f(106−209)	11827	11825 (P02666)
17.55	γ3-casein/β-casein f(108−209)	11560	11560 (P02666)
15.97	unknown	12006	
10.29	proteoso peptone p.p.8.I/β-casein f(29−105)	8640	8638 (P02666)
33.66	β-casein f(69−209)	15749	15750 (Q9TSI0)
30.90	unknown	11991	
30.39	γ3-casein/β-casein f(108−209)	11521	11520 (Q9TSI0)
27.62	β-casein f(1−68)P_5	8251	8252 (Q9TSI0)
20.56	γ2-casein/β-casein f(106−209)	11786	11785 (Q9TSI0)
16.63	α-lactalbumin variant B	14236	14236
36.26	α-lactalbumin variant A	14186	14187 (P00712)
29.02	unknown	11882	
21.33	γ3-casein/β-casein f(108−207)	11288	11287 (Q95L76)
16.48	unknown	11922	
15.17	unknown	5891	
14.06	γ2-casein/β-casein f(106−207)	11554	11553 (Q95L76)
9.48	β-casein f(98−207)	12466	12466 (Q95L76)
8.66	β-lactoglobulin	18185	18187 (P02756)
	Ovine Milk		
36.25	γ2-casein/β-casein f(106−207)	11536	11535 (P11839)
31.26	γ3-casein/β-casein f(108−207)	11271	11270 (P11839)
22.59	unknown	8573	
14.40	β-casein f(98−207)	12449	12448 (P11839)
9.48	unknown	9712	

[a]MS experiments were performed in linear mode as reported under Experimental Procedures. Difference value between the maximal and the minimal average peak/area intensity of all classes (DAve) (see ClinProt Tools software for details), protein/polypeptide name, and experimental/theoretical MH^+ (average) value are reported. Theoretical MH^+ values were calculated according to the amino acid sequence entries present in the UniProt Knowledge Database and the corresponding post-translational modifications. P, phosphate; f, fragment. α-Lactalbumin variant B mass value was calculated according to dedicated studies.[35].

Table 4. Marker Species Recognized during MALDI-TOF-MS Protein Profiling of Thermally Treated Commercial Milk Samples[a]

DAve	description	exptl MH^+	theor MH^+ (UniProt Code)
	Raw Milk		
10.88	proteoso peptone p.p.8.I/β-casein f(29−105)	8639	8638 (P02666)
4.46	β-lactoglobulin variant A	18362	18364 (P02754)
	Pasteurized Milk		
10.88	proteoso peptone p.p.8.I/β-casein f(29−105)	8639	8638 (P02666)
4.46	β-lactoglobulin variant A	18362	18364 (P02754)
	UHT Milk		
38.27	unknown	8007	
24.64	unknown	5326	
10.88	proteoso peptone p.p.8.I/β-casein f(29−105)	8639	8638 (P02666)
6.19	γ2-casein + lactose/β-casein f(106−209) + lactose	12150	12149 (P02666)
	Powdered Milk		
40.19	unknown	6787	
24.82	unknown	6754	
22.77	unknown at m/z 6787 + lactose	7111	
16.40	unknown at m/z 6754 + lactose	7079	
7.51	α-lactalbumin + lactose	14502	14503 (P00711)
6.19	γ2-casein/β-casein f(106−209) + lactose	12150	12149 (P02666)

[a]MS experiments were performed in linear mode as reported under Experimental Procedures. Difference value between the maximal and the minimal average peak/area intensity of all classes (DAve) (see ClinProt Tools software for details), protein/polypeptide name, and experimental/theoretical MH^+ (average) values are reported. Theoretical MH^+ values were calculated according to the bovine amino acid sequence entries present in the UniProt Knowledge Database and the corresponding post-translational modifications. The Amadori adduct is indicated with + lactose; f, fragment.

DOI: 10.1021/acs.jafc.5b02384
J. Agric. Food Chem. 2015, 63, 6157−6171

Table 5. Marker Species Recognized during MALDI-TOF-MS Peptide Profiling for Milk Speciation[a]

DAve	accession code	description	exptl MH^+	theor MH^+	modification(s)	error (Da)	sequence	score	LIFT	CID
				Bovine Milk						
709.31	P02666	β-casein	1589.97	1589.93		−0.04	EPVLGPVRGPFPIIV	54	yes	
476.00	P02666	β-casein	1264.74	1264.70		−0.04	EPVLGPVRGPFP	55		yes
57.52		unknown	2132.00				nd		yes	
56.66	P02662	α_{S1}-casein	1250.67	1250.60		−0.07	QKEDVPSERY	37		yes
56.16		unknown	1347.78				nd		yes	
44.51	P80195	glycosylation-dependent cell adhesion molecule 1	2723.33	2723.36		0.03	ILNKPEDETHLEAQPTDASAQFIR	126	yes	
30.65	P02666	β-casein	1414.76	1414.71		−0.05	VPYPQRDMPIQA	47		yes
11.41		unknown	2528.43				nd		yes	
				Buffalo Milk						
827.39		unknown	2541.46				nd		yes	
564.57		unknown	2145.91				nd		yes	
313.56	S94080212	glycosylation-dependent cell adhesion molecule 1	1693.92	1693.89		−0.03	SSRQPQNQNPKLPLS	75	yes	
168.81		unknown	2555.35				nd		yes	
119.65	P11840	κ-casein	2026.95	2026.89	Q→pyroE (N-term); Q→E (at Q_3, Q_5 or Q_7)	−0.06	QEQNQEQPIRCEKEER	49	yes	
97.33		unknown	2379.29				nd		yes	
95.92	S94080212	glycosylation-dependent cell adhesion molecule 1	2724.35	2724.30		−0.05	ILNEPEDETHLEAQPTDASAQFIR	135	yes	
56.19		unknown	1731.78				nd		yes	
55.09		unknown	2237.23				nd		yes	
52.43		unknown	2291.17				nd		yes	
50.79	Q3HW31	β-casein	887.49	887.46		−0.03	YPFPGPIP	21	yes	yes
50.35	E1BMU2	cytoglobin isoform X1	1989.83	1989.96	M_6Ox	0.13	KVPGEMEIERRERSEE	21	yes	
43.21	S94080212	glycosylation-dependent cell adhesion molecule 1	1606.89	1606.86		−0.03	SRQPQNQNPKLPLS	23	yes	
25.18	S94080212	glycosylation-dependent cell adhesion molecule 1	1519.85	1519.83		−0.02	RQPQNQNPKLPLS	33	yes	
24.69		unknown	2131.43				nd		yes	
23.15		unknown	1603.67				nd		yes	
19.93	Q3HW31	β-casein	1314.77	1314.74		−0.03	SLVYPFPGPIPK	67		yes
18.00	S94080212	glycosylation-dependent cell adhesion molecule 1	1319.73	1319.71		−0.02	RQPQNQNPKLP	24	yes	
17.13	Q9TSI0	β-casein	1227.74	1227.71		−0.03	LVYPFPGPIPK	41		yes
10.62		unknown	2907.30				nd		yes	
8.79		unknown	2305.35				nd		yes	
				Goat Milk						
993.43	P02670	κ-casein	1957.82	1957.79	Q_1→pyroE	−0.03	QEQNQEQPICCEKDER	3.75		yes
858.47	W5PJE0	serum amyloid A protein	1899.05	1898.94		−0.11	SGKDPNHFRPAGLPDKY	39	yes	
576.54	A5JST2	serum amyloid A protein	1834.90	1834.85	Q_1→pyroE	−0.05	QGWGTFLREAGQGAKDM	110	yes	
336.00	P33048	β-casein	1115.61	1115.56		−0.05	REQEELNVV	32	yes	
221.76	A5JST2	serum amyloid A protein	1703.84	1703.81	Q_1→pyroE	−0.03	QGWGTFLREAGQGAKD	92	yes	

J. Agric. Food Chem. 2015, 63, 6157−6171
DOI: 10.1021/acs.jafc.5b02384

Table 5. continued

DAve	accession code	description	exptl MH^+	theor MH^+	modification(s)	error (Da)	sequence	score	LIFT	CID
				Goat Milk						
171.67	P02670	κ-casein	2922.27	2922.30	Q_1→pyroE	0.03	QEQNQEQPICCEKDERFFDDKIAK	4.15		yes
131.71	P02670	κ-casein	2794.11	2794.20	Q_1→pyroE	0.09	QEQNQEQPICCEKDERFFDDKIA	4.33		yes
126.32	P02670	κ-casein	2251.83	2251.93	Q_1→pyroE	0.10	QEQNQEQPICCEKDERFF	3.64		yes
23.52	P02670	κ-casein	2610.15				nd		yes	
22.48	A5JST2	serum amyloid A protein	1388.69	1388.66		−0.03	AYRDMKEANYK	48		yes
17.91		unknown	947.48				nd		yes	
16.79		unknown	1048.54				nd		yes	
15.96	A3EY52	butyrophilin subfamily 1 member A1	1460.72	1461.62		0.90	MGEDSASGDIETLH	77		yes
15.35	A3F9D6	lactoperoxidase	1344.76	1344.73		−0.03	GQVWEESLKRL	60		yes
15.04	P33049	α_{S2}-casein	1209.68	1209.66		−0.02	TNAIPYVRYL			yes
11.37	A5JST2	serum amyloid A protein	1850.82	1850.84	Q_1→pyroE; M_{17}Ox	0.02	QGWGTFLREAGQGAKDM	102	yes	
11.10		unknown	1189.62				nd		yes	
				Ovine Milk						
810.55	P02669	κ-casein	2016.85	2016.84	Q_1→pyroE	−0.01	QEQNQEQRICCEKDER			yes
563.21	W5PJR5	serum amyloid A protein	1761.85	1761.85	Q_1→pyroE	0.00	QGLGTFLREAGQGAKDM	102	yes	
455.43	B0LRN2	serum amyloid A protein	1625.88	1625.81	D→N (D_1 or D_{12})	−0.07	DPNHFRPAGLPDKY	60	yes	
302.85	P42819	serum amyloid A	1652.80	1652.81		0.01	DPNHFRPPGLPDKY	57	yes	
174.48	P11839	β-casein	1630.83	1630.79		−0.04	REQEELNVVGETVE	39		yes
118.53		unknown	2311.86				nd		yes	
98.44		unknown	2853.27				nd		yes	
89.56	W5Q6Z7	cohesin subunit SA-3	2981.27	2981.24	Q_1→pyroE	−0.03	QQELEELLQSSFLDEDEVYSLAATLK	27	yes	
71.12	B0LRN2	serum amyloid A protein	953.49	953.45		−0.04	DPNHFRPA	40	yes	
46.23	P04653	α_{S1}-casein	1529.90	1529.82		−0.08	SPEVLNENLLRFV	65	yes	
35.47		unknown	2104.08				nd		yes	
35.33		unknown	2002.30				nd		yes	
25.50		unknown	1616.68				nd		yes	
23.68	P04653	α_{S1}-casein	1430.79	1430.76		−0.03	SPEVLNENLLRF	46	yes	

[a]MS experiments were performed in reflectron mode as reported under Experimental Procedures. Most intense MH^+ signals reported in Supporting Information Table S7 were subjected to fragmentation analysis for structural assignment (see Supporting Information for experimental details). Difference value between the maximal and the minimal average peak/area intensity of all classes (DAve) (see ClinProt Tools software for details), UniProt/NCBI sequence code (the latter highlighted in *italics*), protein name, experimental/theoretical MH^+ (monoisotopic) value, modifications(s), mass error (in Da), peptide sequence, MASCOT/SEQUEST score (the latter highlighted in *italics*), and the mass spectrometry method used for peptide assignment (LIFT or CID) are reported. Theoretical MH^+ values were calculated according to the indicated UniProt/NCBI sequence entries. nd, not determined.

J. Agric. Food Chem. 2015, 63, 6157−6171
DOI: 10.1021/acs.jafc.5b02384

Table 6. Marker Species Recognized during MALDI-TOF-MS Peptide Profiling of Thermally Treated Commercial Milk Samples[a]

DAve	accession code	description	exptl MH^+	theor MH^+	modification(s)	error (Da)	sequence	score	LIFT	CID
				Raw Milk						
144.16	P02666	β-casein	1589.97	1589.94		−0.03	EPVLGPVRGPFPIIV	54	yes	
32.55		unknown	1490.91				nd		yes	
18.21		unknown	1979.13				nd		yes	
15.94	P02666	β-casein	1151.73	1151.69		−0.04	GPVRGPFPIIV	26		yes
14.19		unknown	2131.84				nd		yes	
11.05	P80195	glycosylation-dependent cell adhesion molecule 1	2723.31	2723.36		0.05	ILNKPEDETHLEAQPTDASAQFIR	126	yes	
10.03	P02662	α_{S1}-casein	1250.65	1250.60		−0.05	QKEDVPSERY	37		yes
				Pasteurized Milk						
129.77	P02662	α_{S1}-casein	1337.71	1337.68		−0.03	HIQKEDVPSER	23	yes	yes
26.06	P02663	α_{S2}-casein	923.57	923.53		−0.04	IPYVRYL	46	yes	yes
18.96	P81265	polymeric immunoglobulin receptor	768.52	769.42		0.90	AAPAGAAIQ_	29		yes
15.94	P02666	β-casein	1151.73	1151.69		−0.04	GPVRGPFPIIV	28		yes
				UHT Milk						
262.34	P02666	β-casein	1284.68	1284.64		−0.04	RELEELNVPGE	59		yes
120.64	P02666	β-casein	1994.16	1994.15		−0.01	LYQEPVLGPVRGPFPIIV	45	yes	yes
76.91	P02663	α_{S2}-casein	1251.66	1251.75		0.09	TKVIPYVRYL	29		yes
41.20	P02662	α_{S1}-casein	1689.83	1689.82		−0.01	PIGSENSEKTTMPLW	112	yes	
				Powdered Milk						
129.77	P02662	α_{S1}-casein	1337.71	1337.68		−0.03	HIQKEDVPSER	53		yes
97.04	P02662	α_{S1}-casein	905.51	905.48		−0.03	NENLLRF	39		yes
73.78	P02666	β-casein	1283.70	1283.65	E→Q (E_2, E_4, E_5, or E_{11})	−0.05	RELEELNVPGE	58	yes	yes
72.10		unknown	791.45				nd		yes	
63.23	P02666	β-casein	1624.87	1624.85	E→Q (E_2, E_4, E_5, E_{11}, or E_{14})	−0.02	RELEELNVPGEIVE	51		yes
54.19	P02754	β-lactoglobulin	1246.70	1245.58		−1.12	TPEVDDEALEK	77		yes
53.94	P02666	β-casein	1396.77	1396.74	E→Q (E_2, E_4, E_5, or E_{11})	−0.03	RELEELNVPGEI	30		yes
33.77	P02666	β-casein	1068.61	1068.56		−0.05	YPVEPFTES	26		yes
28.44	P02666	β-casein	1311.70	1311.71		0.01	YQEPVLGPVRGP	58		yes
25.01	P02663	α_{S2}-casein	1595.85	1594.71	S_7phospho	−1.14	KTVDMESTEVFTK	98		yes
21.07	P02666	β-casein	1495.84	1495.80	E→Q (E_2, E_4, E_5, or E_{11})	−0.04	RELEELNVPGEIV	34		yes
20.13	P02662	α_{S1}-casein	1099.64	1099.61		−0.03	EVLNENLLR	46		yes
17.41	P02666	β-casein	788.43	788.41		−0.02	RELEEL	27		yes
16.39	P02666	β-casein	1097.63	1097.59	E→Q (E_2, E_4 or E_5)	−0.04	RELEELNVP	43		yes
12.48	P02666	β-casein	1154.66	1154.61		−0.05	LTLTDVENLH	67		yes
8.86	P02666	β-casein	1125.63	1125.61	Q_7→E	−0.02	VVPPFLQPEV	43		yes
5.69	P02662	α_{S1}-casein	2012.42	2014.00		1.57	IPNPIGSENSEKTTMPLW	46		yes

[a]MS experiments were performed in reflectron mode as reported under Experimental Procedures. Most intense MH^+ signals reported in Supporting Information Table S12 were subjected to fragmentation analysis for structural assignment (see Supporting Information for experimental details). Difference value between the maximal and the minimal average peak/area intensity of all classes (DAve) (see ClinProt Tools software for details), UniProt/NCBI sequence code (the latter highlighted in *italics*), protein name, experimental/theoretical MH^+ (monoisotopic) value, modifications(s), mass error (in Da), peptide sequence, MASCOT/SEQUEST score (the latter highlighted in *italics*), and the mass spectrometry method used for peptide assignment (LIFT or CID) are reported. Theoretical MH^+ values were calculated according to the indicated UniProt/NCBI sequence entries. nd, not determined.

TOF/TOF and nanoLC-ESI-LIT-MS/MS analyses (see Supporting Information for experimental details). Fragmentation data were obtained from peptide mixtures loaded on the MALDI plates also used for PE-P experiments and directly analyzed by nanoLC-ESI-LIT-MS/MS analysis; in the latter case, specific data searching for peptides having a mass value coincident with that of the marker species was realized. This combined approach identified 38 marker peptides for milk speciation as deriving from β-casein (BM, WM, GM, and OM), α_{S1}-casein (BM and OM), α_{S2}-casein (GM), glycosylation-dependent cell adhesion molecule 1 (BM and WM), κ-casein (WM, GM, and OM), cytoglobin isoform X1 (WM), serum amyloid A protein (GM and OM), butyrophilin subfamily 1 member A1 (GM), lactoperoxidase (GM), and cohesin subunit SA-3 (OM), some of which bear specific modifications (Table 5). Similarly, 28 marker peptides for TT recognition were

DOI: 10.1021/acs.jafc.5b02384
J. Agric. Food Chem. 2015, 63, 6157−6171

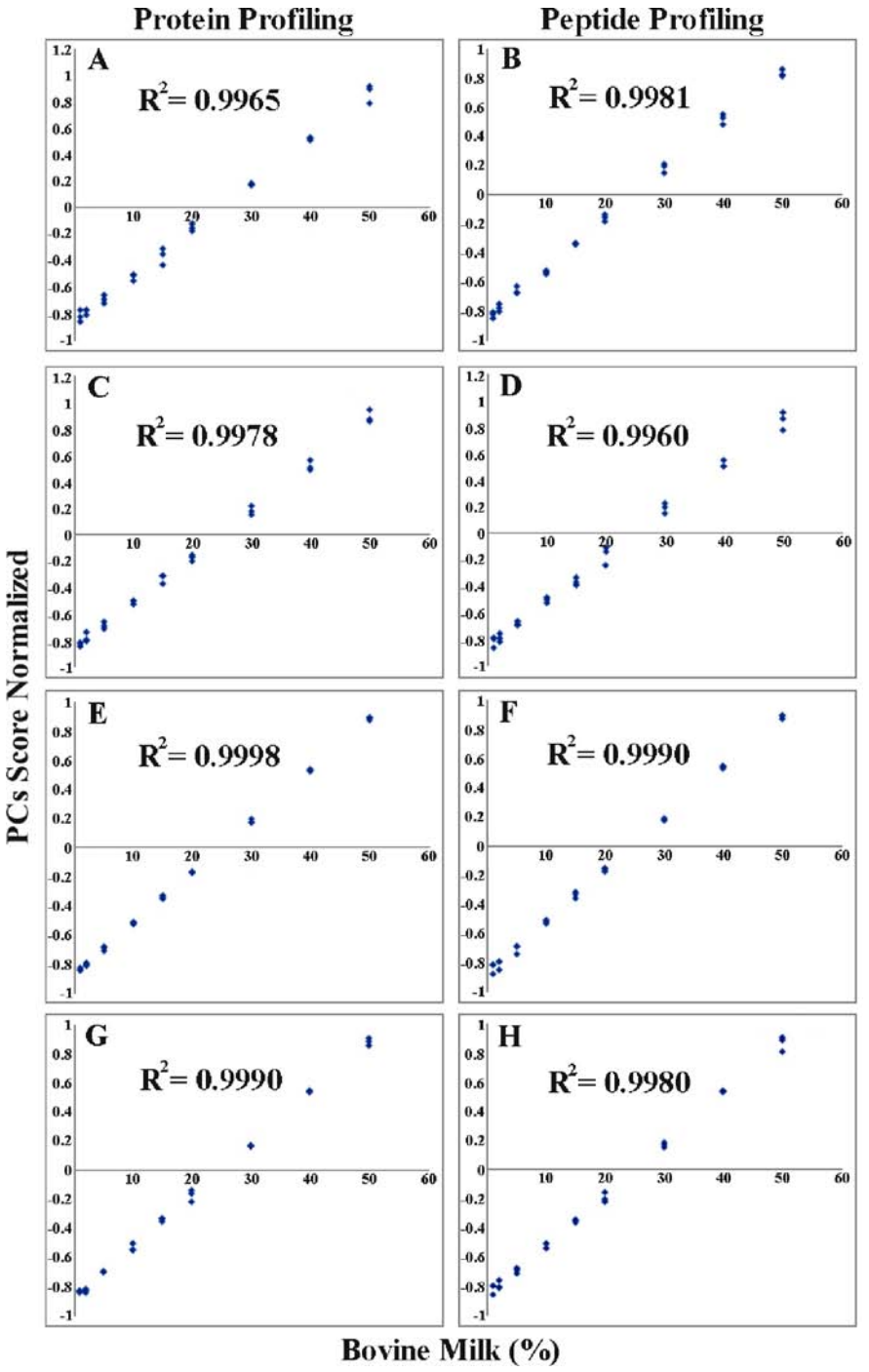

Figure 7. PLS plot of MALDI-TOF-MS data deriving from protein (A, C, E, and G) and peptide (B, D, F, and H) profiling experiments on adulterated milk samples resulting from the addition of BM to WM (A, B), GM (C, D), and OM (E, F) or of fresh BM to IM (G, H). MALDI-TOF-MS PR-P experiments were performed in LM on diluted milk samples. MALDI-TOF-MS PE-P experiments were performed in RM on diluted milk filtrates subjected to C_{18}ZipTip enrichment. The different dots show the concentration of BM in the mixture in relation to the normalized PC scores.

identified as deriving from β-casein (BM, PM, UM, and IM), α_{S1}-casein (BM, PM, UM, and IM), α_{S2}-casein (PM, UM, and IM), glycosylation-dependent cell adhesion molecule 1 (BM), and polymeric immunoglobulin receptor (PM) (Table 6). In the case of either milk speciation or thermal treatment recognition, the slight difference in the nature of the marker molecules identified with PR-P and PE-P experiments should be associated with the molecular mass value of intact proteins, which may exceed the instrument mass range we used, and the resistance of specific proteins to proteases that may hamper the production of the corresponding peptides.

Adulteration. Platform capability to recognize milk adulteration due to the addition of either nondeclared BM to WM, GM, and OM or IM to fresh BM was verified with PR-P and PE-P by analyzing nine impure milk samples, which were prepared in triplicate following the addition of different BM volumes into WM, GM, and OM to generate 1, 2, 5, 10, 15, 20, 30, 40, and 50% v/v binary mixtures. Similarly, adulterated samples having identical mixed concentrations were prepared

DOI: 10.1021/acs.jafc.5b02384
J. Agric. Food Chem. 2015, 63, 6157−6171

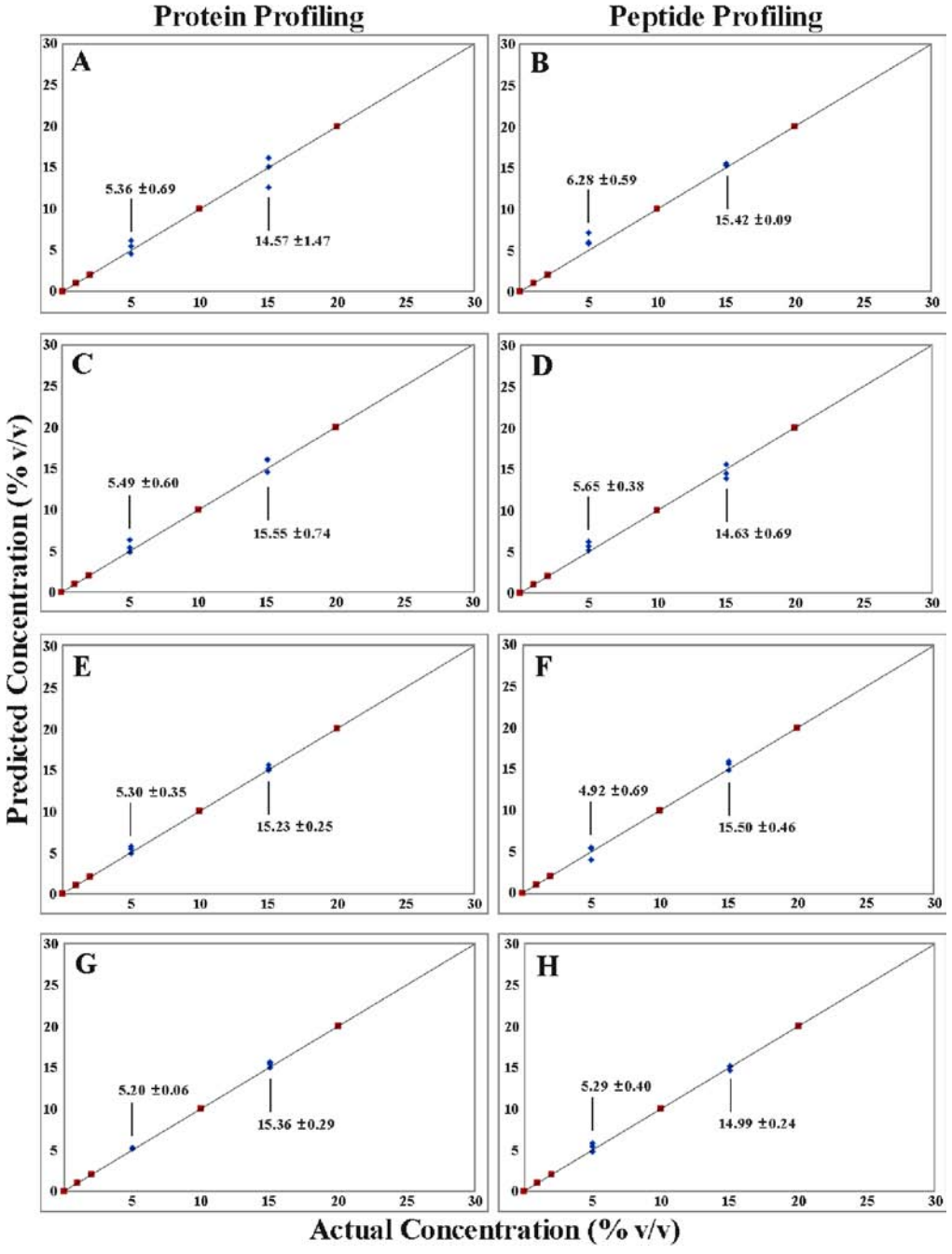

Figure 8. Plots showing the predicted levels of milk adulteration after MALDI-TOF-MS protein (A, C, E, and G) and peptide (B, D, F, and H) profiling experiments. The different panels represent data for adulterated samples resulting from the addition of BM to WM (A, B), GM (C, D), and OM (E, F). Data for adulterated samples resulting from the addition of fresh BM to IM are also shown (G, H). MALDI-TOF-MS PR-P experiments were performed in LM on diluted milk samples. MALDI-TOF-MS PE-P experiments were performed in RM on diluted milk filtrates subjected to C_{18}ZipTip enrichment. Blue squares represent the training data set, whereas the red rhombuses indicate the test set. The predicted levels of milk adulteration are reported ± SD.

when IM was added to BM. After spectral processing according to the procedures already set up for pure materials, MALDI-TOF-MS data of these binary mixtures were subjected to PCA. Resulting PCA data also included variance, PC score, and coefficient values. These data were then used for PLS regression calculations. Figure 7 shows the PLS regression plot of each binary mixture, as deriving from PR-P and PE-P analyses. An optimal linearity of the data was observed in each case. Normalized values for two adulterated test samples analyzed in triplicate were then used to get a prediction of the corresponding percentages of adulteration. Plots of the predicted adulteration levels, as estimated from the above-mentioned PLS model on the basis of the corresponding PR-P and PE-P data, are reported in Figure 8. Data from PR-P and PE-P analyses matched each other and were in good agreement with real adulteration percentages (5 and 15%) within experimental error. These results demonstrated the good capability of this platform to predict illegal adulteration levels of unknown milk samples when they are processed together with proper adulteration standards. They also demonstrated the

DOI: 10.1021/acs.jafc.5b02384
J. Agric. Food Chem. 2015, 63, 6157−6171

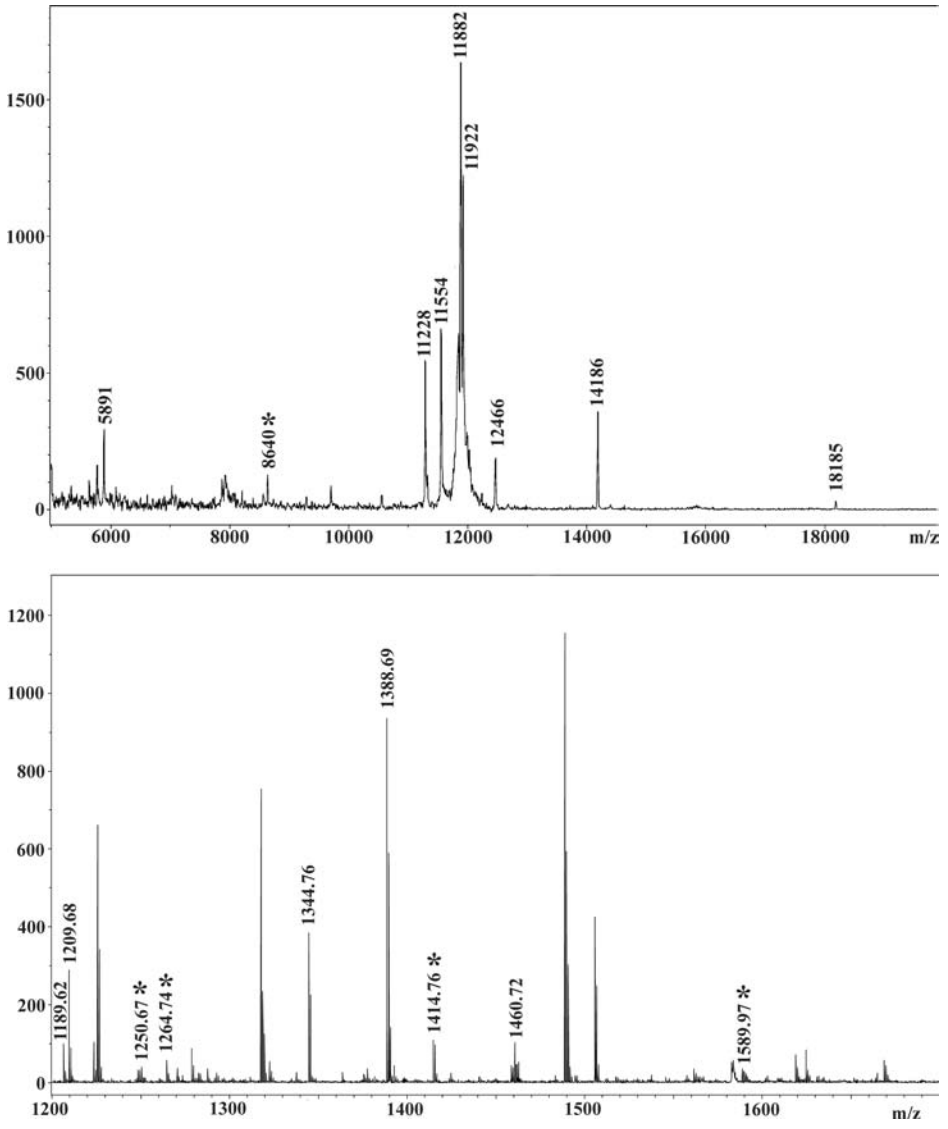

Figure 9. Cropped regions of the MALDI-TOF-MS PR-P and PE-P spectra of a GM sample containing 5% v/v BM. MALDI-TOF-MS PR-P was performed in LM on diluted milk samples. MALDI-TOF-MS PE-P was performed in RM on diluted milk filtrates subjected to C_{18}ZipTip enrichment. MH^+ signals corresponding to GM and BM marker molecules are highlighted by reporting the associated mass values; those associated with BM adulteration are marked with an asterisk.

importance of having an analytical system that provides simultaneously two independent adulteration measurements realized on diluted skimmed milk samples and C_{18}ZipTip-enriched diluted skimmed milk filtrates, which are analyzed for the respective protein and peptide contents, respectively. As an example, Figure 9 shows the simultaneous detection of bovine protein and peptide markers in the PR-P and PE-P spectra of an adulterated GM sample containing 5% v/v BM.

Conclusions. The development of a versatile and fast method for the detection of fraudulent adulterations in milk is a very important issue, due to the economic impact that these frauds have in dairy productions.[6] As mentioned before, a number of analytical methods have been developed for this purpose, which have the disadvantage of being sometimes time-consuming, suitable only for a specific milk assay (speciation or TT analysis), useful for a unique animal species to animal species milk discrimination, and/or eventually not adaptable for global screening of milk samples (Supporting Information Table S1). To overcome these limits and take advantage of previous applications of the ClinProt technology for biomarker recognition and disease prediction in humans,[30,31] a MALDI-TOF-MS platform for combined PR-P and PE-P of milk samples has been here developed, which recognizes markers either for speciation in BM, WM, GM, and OM or for thermal treatment in BM, PM, UM, and IM, quickly assigning the nature of a pure unknown material. This platform was developed by taking advantage of other applicable studies in the biomedical research field.[32−34] Platform capability to recognize milk adulteration due to the addition of small volumes either of nondeclared BM to WM, GM, and OM or of IM to fresh BM was verified by analyzing different ad hoc prepared binary mixtures and specific test samples. In the latter case, concentration values were predicted according to independent PR-P and PE-P analyses and verified a posteriori to be coincident with real data.

With respect to previous papers describing the use of PR-P analysis on diluted skimmed samples for milk speciation,[9−14] this study extends this method to the analysis of TT and

DOI: 10.1021/acs.jafc.5b02384
J. Agric. Food Chem. 2015, 63, 6157−6171

introduces an independent, complementary measurement based on an ad hoc developed PE-P approach that has been set up to integrate protein data with additional information on other molecules, that is, peptides, validating final results. When coupled to a robust statistical evaluation of the resulting data, this platform ultimately permits the typing of milk and the correlation of MALDI spectra with quantitative adulteration values. By introducing PE-P analysis in the sample-processing pipeline, this integrated profiling approach also permits the detection of adulterations due to the addition of powdered material into fresh milk, broadening the applicative scenario of the MALDI profiling techniques in dairy science. The high-throughput character of the MALDI ionization technique and its versatility in answering a number of issues related to the certification of raw materials used in dairy industry suggest the massive use of this platform in milk analysis with the aim to preserve product tradition and value.

■ ASSOCIATED CONTENT

Supporting Information

Additional tables and figures as cited in the text. The Supporting Information is available free of charge on the ACS Publications website at DOI: 10.1021/acs.jafc.5b02384.

■ AUTHOR INFORMATION

Corresponding Author

*(A.S.) Proteomics & Mass Spectrometry Laboratory, ISPAAM, National Research Council, via Argine 1085, Naples I-80147, Italy. E-mail: andrea.scaloni@ispaam.cnr.it. Phone: +39 (081) 5966006. Fax: +39 (081) 5965291.

Author Contributions

‖M.S. and S.A. gave an equal contribution to this work.

Funding

This work was supported by funds from the Italian Ministry of Economy and Finance to CNR for the project "Innovazione e sviluppo del Mezzogiorno − Conoscenze Integrate per Sostenibilità ed Innovazione del *Made in Italy* Agroalimentare" − Legge n.191/2009 and from Regione Campania for the Project "QUARC − Qualità delle produzioni tipiche campane ed il suo territorio: approcci innovativi ed integrati per rafforzare la competitività del sistema Agroalimentare" (A.G.C.6 − settore 1), bando CAMPUS.

Notes

The authors declare no competing financial interest.

■ REFERENCES

(1) Bertoni, G.; Calamari, L.; Maianti, M. G. Producing specific milks for speciality cheeses. *Proc. Nutr. Soc.* **2001**, *60*, 231−246.

(2) Johnson, M. E.; Lucey, J. A. Major technological advances and trends in cheese. *J. Dairy Sci.* **2006**, *89*, 1174−1178.

(3) Gerosa, S.; Skoet, J. *Milk Availability: Trends in Production and Demand and Medium-Term Outlook*; FAO of the United Nations ESA Working Paper 12-01; FAO: Rome, Italy, 2012.

(4) Di Luccia, A.; Picariello, G.; Trani, A.; Alviti, G.; Loizzo, P.; Faccia, M.; Addeo, F. Occurrence of beta-casein fragments in cold-stored and curdled river buffalo (*Bubalus bubalis* L.) milk. *J. Dairy Sci.* **2009**, *92*, 1319−1329.

(5) Calvano, C. D.; Monopoli, A.; Loizzo, P.; Faccia, M.; Zambonin, C. Proteomic approach based on MALDI-TOF MS to detect powdered milk in fresh cow's milk. *J. Agric. Food Chem.* **2013**, *61*, 1609−1617.

(6) Commission Regulation (EU) No. 273/2008, Methods for the analysis and the evaluation of the quality milk and dairy products. *Off. J. Eur. Communities* **2008**, *L88*, 1−115.

(7) Addeo, F.; Garro, G.; Intorcia, N.; Pellegrino, L.; Resmini, P.; Chianese, L. Gel electrophoresis and immunoblotting for the detection of casein proteolysis in cheese. *J. Dairy Res.* **1995**, *62*, 297−309.

(8) Villar-Garea, A.; Griese, M.; Imhof, A. Biomarker discovery from body fluids using mass spectrometry. *J. Chromatogr. B: Anal. Technol. Biomed. Life Sci.* **2007**, *849*, 105−114.

(9) Angeletti, R.; Gioacchini, A. M.; Seraglia, R.; Piro, R.; Traldi, P. The potential of matrix-assisted laser desorption/ionization mass spectrometry in the quality control of water buffalo mozzarella cheese. *J. Mass Spectrom.* **1998**, *33*, 525−531.

(10) Fanton, C.; Delogu, G.; Maccioni, E.; Podda, G.; Seraglia, R.; Traldi, P. Matrix-assisted laser desorption/ionization mass spectrometry in the dairy industry 2. The protein fingerprint of ewe cheese and its application to detection of adulteration by bovine milk. *Rapid Commun. Mass Spectrom.* **1998**, *12*, 1569−1573.

(11) Cozzolino, R.; Passalacqua, S.; Salemi, S.; Malvagna, P.; Spina, E.; Garozzo, D. Identification of adulteration in milk by matrix-assisted laser desorption/ionization time-of-flight mass spectrometry. *J. Mass Spectrom.* **2001**, *36*, 1031−1037.

(12) Cozzolino, R.; Passalacqua, S.; Salemi, S.; Garozzo, D. Identification of adulteration in water buffalo mozzarella and in ewe cheese by using whey proteins as biomarkers and matrix-assisted laser desorption/ionization mass spectrometry. *J. Mass Spectrom.* **2002**, *37*, 985−991.

(13) Cunsolo, V.; Muccilli, V.; Saletti, R.; Foti, S. MALDI-TOF mass spectrometry for the monitoring of she-donkey's milk contamination or adulteration. *J. Mass Spectrom.* **2013**, *48*, 148−153.

(14) Nicolaou, N.; Xu, Y.; Goodacre, R. MALDI-MS and multivariate analysis for the detection and quantification of different milk species. *Anal. Bioanal. Chem.* **2011**, *399*, 3491−3502.

(15) Calvano, C. D.; de Ceglie, C.; Monopoli, A.; Zambonin, C. G. Detection of sheep and goat milk adulterations by direct MALDI-TOF MS analysis of milk tryptic digests. *J. Mass Spectrom.* **2012**, *47*, 1141−1149.

(16) Baum, F.; Fedorova, M.; Ebner, J.; Hoffmann, R.; Pischetsrieder, M. A sensitive and effective proteomic approach to identify she-donkey's and goat's milk adulterations by MALDI-TOF MS fingerprinting. *J. Proteome Res.* **2013**, *12*, 5447−5462.

(17) Somma, A.; Ferranti, P.; Addeo, F.; Mauriello, R.; Chianese, L. Peptidomic approach based on combined capillary isoelectric focusing and mass spectrometry for the characterization of the plasmin primary products from bovine and water buffalo beta-casein. *J. Chromatogr. A* **2008**, *1192*, 294−300.

(18) Cuollo, M.; Caira, S.; Fierro, O.; Pinto, G.; Picariello, G.; Addeo, F. Toward milk speciation through the monitoring of casein proteotypic peptides. *Rapid Commun. Mass Spectrom.* **2010**, *24*, 1687−1696.

(19) De Simone, C.; Picariello, G.; Mamone, G.; Stiuso, P.; Dicitore, A.; Vanacore, D.; Chianese, L.; Addeo, F.; Ferranti, P. Characterisation and cytomodulatory properties of peptides from Mozzarella di Bufala Campana cheese whey. *J. Pept. Sci.* **2009**, *15*, 251−258.

(20) Holland, J. W.; Gupta, R.; Deeth, H. C.; Alewood, P. F. Proteomic analysis of temperature-dependent changes in stored UHT milk. *J. Agric. Food Chem.* **2011**, *59*, 1837−1846.

(21) Mastrogiacomo, R.; D'Ambrosio, C.; Niccolini, A.; Serra, A.; Gazzano, A.; Scaloni, A.; Pelosi, P. An odorant-binding protein is abundantly expressed in the nose and in the seminal fluid of the rabbit. *PLoS One* **2014**, *9*, e111932.

(22) Dallas, D. C.; Guerrero, A.; Parker, E. A.; Garay, L. A.; Bhandari, A.; Lebrilla, C. B.; Barile, D.; German, J. B. Peptidomic profile of milk of Holstein cows at peak lactation. *J. Agric. Food Chem.* **2014**, *62*, 58−65.

(23) Arena, S.; Renzone, G.; Novi, G.; Paffetti, A.; Bernardini, G.; Santucci, A.; Scaloni, A. Modern proteomic methodologies for the characterization of lactosylation protein targets in milk. *Proteomics* **2010**, *10*, 3414−3434.

(24) Arena, S.; Renzone, G.; Novi, G.; Scaloni, A. Redox proteomics of fat globules unveils broad protein lactosylation and compositional

DOI: 10.1021/acs.jafc.5b02384
J. Agric. Food Chem. 2015, 63, 6157−6171

changes in milk samples subjected to various technological procedures. *J. Proteomics* **2011**, *74*, 2453−2475.
(25) Renzone, G.; Arena, S.; Scaloni, A. Proteomic characterization of intermediate and advanced glycation end-products in commercial milk samples. *J. Proteomics* **2015**, *117*, 12−23.
(26) Meltretter, J.; Wust, J.; Pischetsrieder, M. Modified peptides as indicators for thermal and nonthermal reactions in processed milk. *J. Agric. Food Chem.* **2014**, *62*, 10903−10915.
(27) Eigel, W. N. Identification of proteose-peptone component 5 as a plasmin-derived fragment of bovine beta-casein. *Int. J. Biochem.* **1981**, *13*, 1081−1086.
(28) Andrews, A. T. Proteinases in normal bovine milk and their action on caseins. *J. Dairy Res.* **1983**, *50*, 45−55.
(29) Eigel, W. N.; Hofmann, C. J.; Chibber, B. A. K.; Tomik, J. M.; Keenen, T. W.; Mertz, E. T. Plasmin-mediated proteolysis of casein in bovine milk. *Proc. Natl. Acad. Sci. U. S. A.* **1979**, *76*, 2244−2248.
(30) Solassol, J.; Jacot, W.; Lhermitte, L.; Boulle, N.; Maudelonde, T.; Mangé, A. Clinical proteomics and mass spectrometry profiling for cancer detection. *Expert Rev. Proteomics* **2006**, *3*, 311−320.
(31) Magni, F.; Van Der Burgt, Y. E.; Chinello, C.; Mainini, V.; Gianazza, E.; Squeo, V.; Deelder, A. M.; Kienle, M. G. Biomarkers discovery by peptide and protein profiling in biological fluids based on functionalized magnetic beads purification and mass spectrometry. *Blood Transfus.* **2010**, *8* (Suppl. 3), s92−s97.
(32) Terracciano, R.; Preianò, M.; Palladino, G. P.; Carpagnano, G. E.; Barbaro, M. P.; Pelaia, G.; Savino, R.; Maselli, R. Peptidome profiling of induced sputum by mesoporous silica beads and MALDI-TOF MS for non-invasive biomarker discovery of chronic inflammatory lung diseases. *Proteomics* **2011**, *11*, 3402−3414.
(33) Preianò, M.; Pasqua, L.; Gallelli, L.; Galasso, O.; Gasparini, G.; Savino, R.; Terracciano, R. Simultaneous extraction and rapid visualization of peptidomic and lipidomic body fluids fingerprints using mesoporous aluminosilicate and MALDI-TOF MS. *Proteomics* **2012**, *12*, 3286−3294.
(34) Preianò, M.; Falcone, D.; Maggisano, G.; Montalcini, T.; Navarra, M.; Paduano, S.; Savino, R.; Terracciano, R. Assessment of pre-analytical and analytical variables affecting peptidome profiling of gingival crevicular fluid by MALDI-TOF mass spectrometry. *Clin. Chim. Acta* **2014**, *437*, 120−128.
(35) Chianese, L.; Caira, S.; Lilla, S.; Pizzolongo, F.; Ferranti, P.; Pugliano, G.; Addeo, F. Primary structure of water buffalo alpha-lactalbumin variants A and B. *J. Dairy Res.* **2004**, *71*, 14−19.

DOI: 10.1021/acs.jafc.5b02384
J. Agric. Food Chem. 2015, 63, 6157−6171

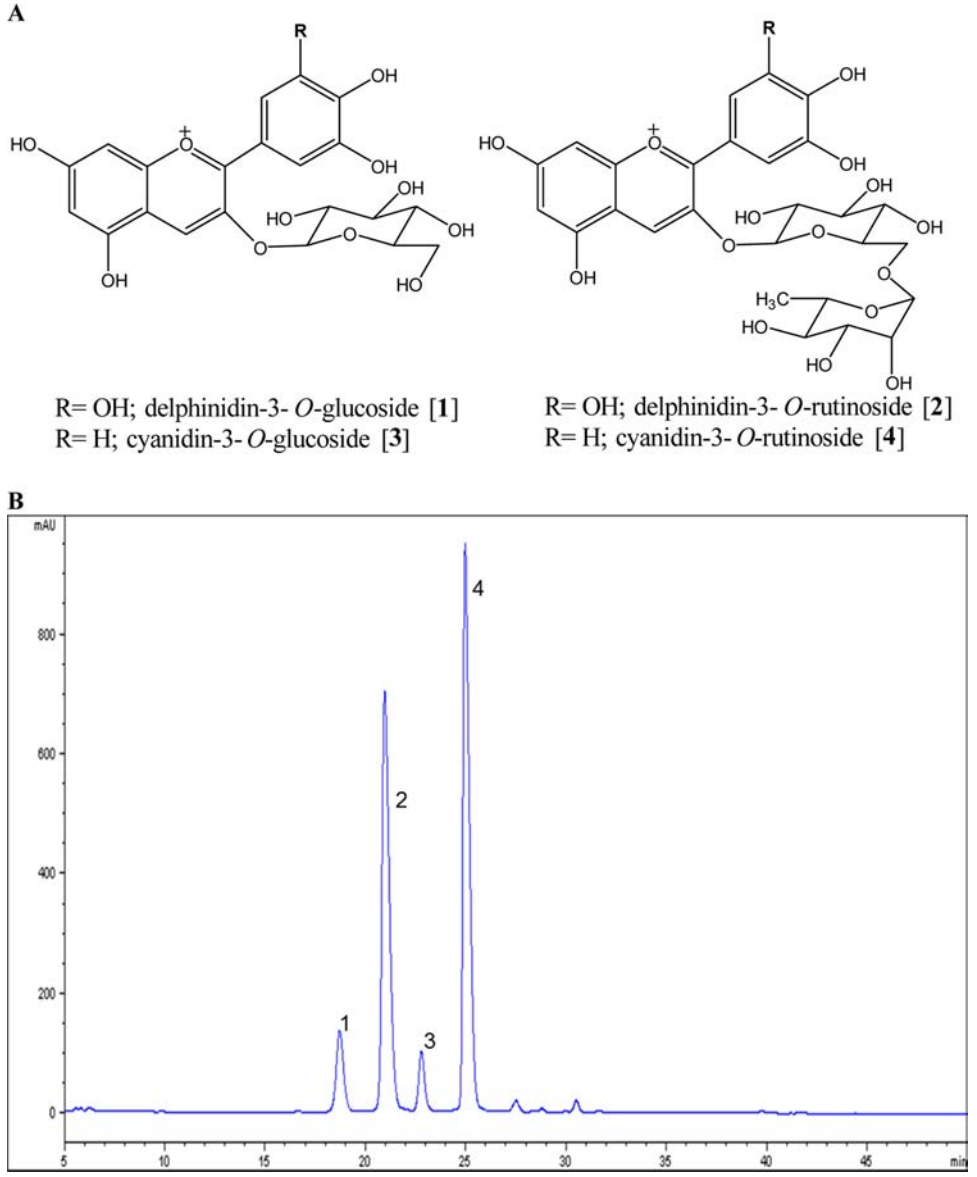

Figure 1. Chemical structures of black currant anthocyanins (A) and their respective HPLC-DAD chromatogram peaks. Peak numbers correspond to Table 1 and 2 labels.

equally distributed between cyanidin and delphinidin aglycones[24] and, therefore, provides an attractive model to investigate these differences. Moreover, anthocyanins represent the most abundant phenolic compounds in black currants, with other minor phenolics contributing to <5% of black currant powdered extract.[25] Protocatechuic and gallic acids are major breakdown metabolites of cyanidin- and delphinidin-type anthocyanins, respectively.[26]

The present study was designed to examine the preventive effect of anthocyanin-rich black currant extract on the development of obesity and hyperglycemia induced by feeding a high-fat diet in C57BL/6 mouse polygenic obesity model with intact and antibiotic-disrupted gut microbiome. Major anthocyanins and their phenolic acid metabolites were identified in feces and gastrointestinal tissue samples from these animals.

MATERIALS AND METHODS

Chemicals. The anthocyanins cyanidin- and delphinidin- 3-*O*-β-glucosides (HPLC grade standards) were purchased from Polyphenols Laboratories AS (Sandnes, Norway). All other chemical reagents and solvents were purchased from Sigma (St. Louis, MO, USA). A commercial black currant powdered extract (Active Cassis Extract 30) was kindly provided by Eddie Shiojima (Just the Berries, Palmerston North, New Zealand). Total anthocyanin content of the black currant powdered extract was 32.4%, and its anthocyanin composition was 41.4% delphinidin-3-*O*-rutinoside, 11.2% delphinidin-3-*O*-glucoside, 42.4% cyanidin-3-*O*-rutinoside, and 5.0% cyanidin-3-*O*-glucoside according to the manufacturer's certificate of analysis (Figure 1).

Animals and Diets. All animal experiments were performed according to procedures approved by the NC Research Campus Institutional Animal Care and Use Committee in the David H. Murdock Research Institute, an AAALAC accredited animal care facility.

Male, 6-week-old, C57BL/6J mice were purchased from Jackson Laboratory (Bar Harbor, ME, USA) and housed four animals per cage under controlled temperature (24 ± 2 °C) and light (12 h light−dark cycle, lights on at 7:00 a.m.). Immediately upon arrival, animals were

DOI: 10.1021/acs.jafc.5b00963
J. Agric. Food Chem. 2015, 63, 6172−6180

allowed to adapt to the new conditions for 7 days, and handling the animals was performed daily during this time to reduce the stress of physical manipulation. Mice were then randomized into ad libitum access to Research Diets (New Brunwick, NJ, USA) low 10 kcal% fat diet D12450J (LFD, 3.85 kcal/g, n = 24) or high 60 kcal% fat diet D12492 (HFD, 5.24 kcal/g, n = 24) and tap water for 6 weeks (weeks 1−6).

Lean and obese mice were further randomized to control low-fat diet (LFD, n = 8), control high-fat diet (HFD, n = 8), and the respective low-fat (LFD+C, n = 16) and high-fat (HFD+C, n = 16) black currant-supplemented treatment groups (1% black currant powdered extract, weight on g/kcal basis, incorporated in LFD or HFD diet by Research Diets). Because typical 24 h food intake for a C57BL/6 mouse is 2.5−3.0 g or 10−12 kcal/g body weight,[27] the animals were expected to consume an average of 25 mg/day of black currant powdered extract or 8 mg/day of black currant anthocyanins. Mice were kept on the respective diets for an additional 8 weeks (weeks 7−14). Animal weight and food intake (accounting for spillage) were recorded weekly for the duration of the study. All animal diets were kept at −80 °C for long-term storage and stability, and freshly thawed food was dispensed to animals every 3−4 days to limit phytochemical degradation in food matrix.

Antibiotic Knockdown of Endogenous Gut Microbiome. An antibiotic cocktail (0.5 g/L vancomycin, 1 g/L neomycin sulfate, 1 g/L metronidazole, 1 g/L ampicillin) previously shown to be sufficient to deplete all detectable commensal bacteria[28] was administered in drinking water ad libitum to half of the animals on LFD+C and HFD +C supplemented with black currant powdered extract (n = 8, LFD +CA and HFD+CA groups, respectively) for the entire duration of the black currant feeding study (weeks 7−14).

Oral Glucose and Insulin Tolerance Tests. For the oral glucose tolerance test, mice were fasted overnight (16 h) and received an oral gavage of D-glucose (1.5 g/kg body weight, Sigma). For the insulin tolerance test, mice were fasted for 4 h and received an intraperitoneal injection of insulin (0.75 U/kg body weight, Santa Cruz Biotechnology). Blood glucose concentrations were measured at 0, 15, 30, 60, and 120 min after glucose or insulin challenge in blood samples obtained from tail-tip bleedings, using a glucometer (Lifescan, Johnson and Johnson).

Sample Collection. Fecal samples from mice were collected, weighed, and pooled by cage midway (week 10) and at the end of the black currant feeding study (week 14) and stored at −80 °C. At the end of the experiment, blood was collected by heart puncture after CO_2 inhalation. Gastrointestinal tissues (stomach, duodenum, jejunum, ileum, cecum, and colon) and luminal digesta were collected and stored at −80 °C to determine the temporal sequence and signaling events that are responsible for changes in physiology and metabolism.

Anthocyanin and Metabolite Extraction. Anthocyanins were extracted from feces, gastrointestinal digesta, and gastrointestinal wall tissue using 60% aqueous methanol (1% trifluoroacetic acid acid) following a previously reported method for the rapid analysis of various anthocyanins in rats.[29]

HPLC and LC-MS Analysis. The phytochemical composition of ACE30 black currant powdered extract was analyzed in triplicate by LC-MS in positive mode (Agilent G1312B-1200 series Infinity Quaternary HPLC system coupled with Agilent 6530A accurate-mass quadrupole time-of-flight MS with Agilent Jet Stream source). Dry samples were reconstituted with 500 μL of 80% methanol, and 5 μL was injected onto an Agilent ZORBAX Eclipse Plus C18 column (3 × 100 mm, 1.8 μm). A gradient from 30% acetonitrile in 0.1% formic acid to 90% acetonitrile in 0.1% formic acid was used for HPLC separation. Mass data were acquired with the following parameters: drying gas temperature, 300 °C; drying gas flow, 7 L/min; nebulizer pressure, 40 psi; sheath gas temperature, 350 °C; sheath gas flow, 10 L/min; capillary voltage, 3500 V; nozzle voltage, 500 V; fragmentor voltage, 150 V; skimmer voltage, 65 V; octopole RF peak voltage, 750 V. Standard curves for compounds of interest were obtained in a linear dynamic range of 10−50000 pg and used for quantitative analysis. Peak area was determined by Agilent MassHunter Qualitative Analysis (version B.05.00) software.

Individual anthocyanins and phenolic acids were quantified by HPLC as described in our previous publication.[30] Briefly, filtered samples were injected (10 μL) into a 1200 HPLC system (Agilent Technologies) equipped with a UV−vis diode array detector (DAD), controlled-temperature autosampler (4 °C), and column compartment (30 °C) using a reversed-phase Supelcosil LC-18 column, 25 mm × 4.6 mm × 5 μm (Supelco, Bellefonte, PA, USA). Standard curves were calculated using peak areas at UV of 520 or 325 nm for anthocyanins (as cyanidin 3-O-glucoside or delphinidin 3-O-glucoside equivalents) or phenolic acids, respectively, and the known injected concentrations for the standards.

Statistics. Data were analyzed by one-way ANOVA followed by Dunnett's multiple-range tests using Prism 6.0 (GraphPad Software, San Diego, CA, USA). Body weight gain and glucose tolerance were analyzed by two-factor repeated-measures ANOVA, with time and treatment as independent variables. All data are presented as means ± SEM. Significant differences were accepted when the P value was <0.05.

RESULTS

Characterization of Black Currant Powdered Extract and Diets. The LC/JS-ESI/Q-TOF/MS was used for initial untargeted characterization and quantification of the major phytochemicals in ACE30 black currant powdered extract prior to food incorporation studies. Five major phytochemicals were identified in the extract (Table 1). Citric acid was a major weak organic acid present in the powdered extract in the amount of 279 mg/g. Total anthocyanin content of the extract was 323 mg/g, together with citric acid this accounted for 60% of components present in the ACE30 extract. Four anthocyanins were routinely quantified in the powdered extracts and tissue samples by subsequent HPLC-DAD analysis (Figure 1). ACE30 extract contained two cyanidin-based anthocyanins and two delphinidin-based anthocyanins in approximately equal amounts (153 vs 170 mg/g). On the other hand, 3-O-rutinosides were 5 times more abundant in the powdered extract as compared to their 3-O-glucoside counterparts (271 vs 52 mg/g). Anthocyanins represented the most abundant phenolic compounds in black currants, with other minor phenolics contributing to <5% of black currant powdered extract as shown by us previously.[25]

Table 1. Characterization and Quantification of Major Components in ACE30 Black Currant Powdered Extract Using LC-MS

peak	phytochemical composition	other name	m/z $[M]^+$	concentration (mg/g extract)
	citric acid		192	279
1	delphinidin-3-O-glucoside	mirtillin	465	36
2	delphinidin-3-O-rutinoside	tulipanin	611	134
3	cyanidin-3-O-glucoside	chrysanthemin	449	16
4	cyanidin-3-O-rutinoside	antirrhinin	595	137

Incorporation of ACE30 extract in animal food at the 1% level was performed at the same grams per kilocalorie basis (Table 2). Anthocyanin levels in the diet remained stable for at least 4 days at room temperature and for the duration of the study when diets were stored at −80 °C (data not shown).

DOI: 10.1021/acs.jafc.5b00963
J. Agric. Food Chem. 2015, 63, 6172−6180

Table 2. Anthocyanin Composition of ACE30-Incorporated Diets

peak	anthocyanin	concentration[a] (μg/g diet) LFD	HFD
1	delphinidin-3-*O*-glucoside	334 ± 26.4	423 ± 98.0
2	delphinidin-3-*O*-rutinoside	930 ± 65.0	1195 ± 264
3	cyanidin-3-*O*-glucoside	173 ± 14.5	219 ± 46.2
4	cyanidin-3-*O*-rutinoside	1015 ± 68.7	1321 ± 286
	total quantified cyanidins	1189 ± 83.2	1540 ± 332
	total quantified delphinidins	1264 ± 91.4	1618 ± 361
	total quantified 3-*O*-rutinosides	1946 ± 133	2516 ± 549
	total quantified 3-*O*-glucosides	507 ± 41.0	643 ± 143
	total quantified anthocyanins	2451 ± 175	3158 ± 690

[a]LFD, low-fat diet; HFD, high-fat diet.

Changes of Body Weight, Food Intake, and Food Efficiency. Six-week-old mice were fed LFD or HFD for 6 weeks to initiate development of obesity in the HFD animals (Figure 2). Next, the treatment groups were presented with anthocyanin-enriched diets and control (tap water) or antibiotic-supplemented tap water for an additional 8 weeks. There were no abnormal clinical signs throughout the entire study. After 14 weeks, mice fed HFD developed 48% larger body weights as compared to their LFD controls (30.8 vs 45.6 g, Figure 2A). Incorporation of 1% black currant powdered extract into the respective diets for 8 weeks resulted in 8−10% smaller body weights in animals receiving anthocyanin treatment, irrespective of fat content of the diet (LDF+C and HFD+C groups). However, body weight loss was absent in anthocyanin-treated animals with disrupted gut microbiome due to the addition of antibiotic cocktail to their drinking water (LFD+CA and HFD+CA groups, Figure 2B).

Food intake was not significantly different among all treatment groups and varied in the range of 2.4−3.0 g/mouse/day (Figure 2C). The caloric intake was significantly higher in HFD animals; however, neither supplementation with the black currant extract nor antibiotic cocktail affected food intake of the treatment animals respective to their controls (Figure 2D). Therefore, the data suggest that anthocyanin supplementation decreased mouse body weight without affecting the food or caloric intake.

Feed efficiency (%), calculated as (body weight gain/food intake) × 100 ratio, was higher in HFD groups (Figure 3). Supplementation with black currant powdered extract decreased feed efficiency in LFD+C and HFD+C mice. Upon disruption of gut microbiome with antibiotic cocktail in the drinking water, a trend to increase feed efficiency was observed in HFD+CA but not LFD+CA mice.

Anthocyanins in Fecal Samples. We observed the intense red/purple coloration of the small intestine, cecal, and fecal content samples only from anthocyanin-fed mice. HFD diet alone was responsible for a 20% increase in fecal pellet weight as compared to LFD controls. Neither anthocyanin treatment nor antibiotic cocktail supplementation changed the number or size of fecal pellet output in treated animals as compared to the respective LFD or HFD controls (Figure 4). Relative anthocyanins and their phenolic acid metabolite concentrations found in fecal samples after 4 and 8 weeks of treatment are summarized in Table 3.

No significant differences in metabolism or fecal output of anthocyanins or their respective phenolic acids were observed

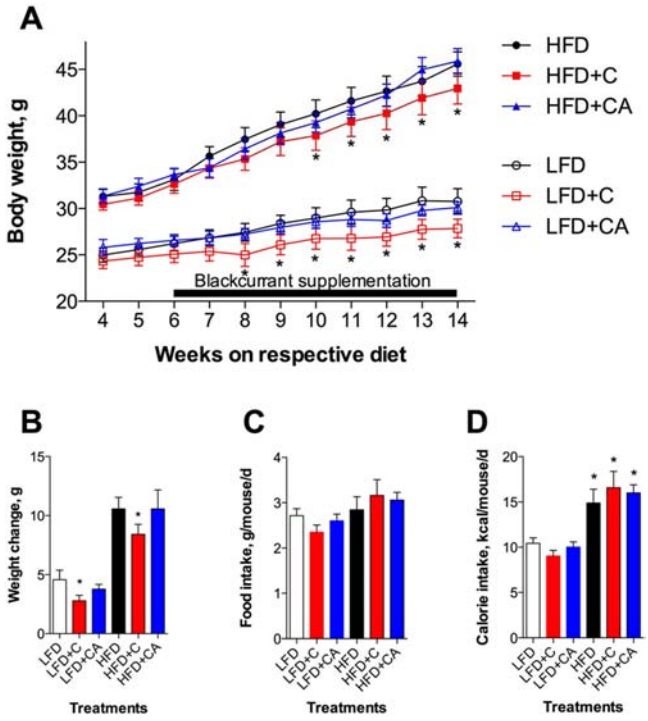

Figure 2. Effects of black currant and gut microbiome on body weight (A), body weight gain (B), food intake (C), and calorie intake (D) in the C57BL/6J mice. Six-week-old male mice were fed a low- or high-fat diet for 6 weeks. Lean and obese mice were further randomized to control low-fat diet (LFD), control high-fat diet (HFD), and the respective low-fat (LFD+C) and high-fat (HFD+C) black currant-supplemented treatment groups (1% black currant powdered extract incorporated in LFD or HFD) and kept on the same diet for an additional 8 weeks. An antibiotic cocktail was administered in drinking water ad libitum to half of the animals on black currant-supplemented treatment groups (LFD+CA and HFD+CA groups, respectively) for the entire duration of the black currant feeding study (weeks 7−14). Animal weight and food intake were recorded weekly for the duration of the study. Results are expressed as means ± SEM, $n = 8$. Body weight gain was analyzed by two-factor repeated-measures ANOVA, with time and treatment as independent variables. (∗) $P < 0.05$ versus respective LFD or HFD control. One-way ANOVA, Dunnett's post hoc test. Body weight gain was analyzed by two-factor, repeated-measures ANOVA, with time and treatment as independent variables.

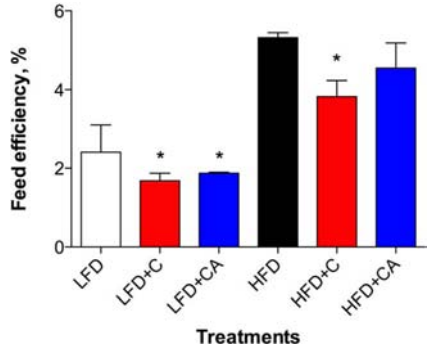

Figure 3. Effects of black currant and gut microbiome on feed efficiency in the C57BL/6J mice fed low- and high-fat diets. Animals received low-fat diet (LFD) or high-fat diet (HFD) or black currant-supplemented treatment groups (1% black currant extract) LFD+C or HFD+C for 8 weeks. Feed efficiency was calculated as (body weight gain/food intake) × 100 ratio. (∗) $P < 0.05$ versus respective LFD or HFD control. One-way ANOVA, Dunnett's post hoc test.

DOI: 10.1021/acs.jafc.5b00963
J. Agric. Food Chem. 2015, 63, 6172−6180

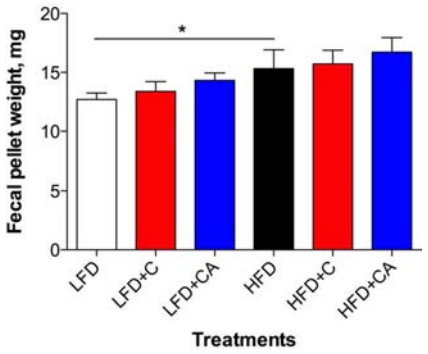

Figure 4. Effects of black currant and gut microbiome on fecal excretion in the C57BL/6J mice fed low- and high-fat diets. Animals received low-fat diet (LFD) or high-fat diet (HFD) or black currant-supplemented treatment groups (1% black currant extract incorporated in LFD or HFD; LFD+C or HFD+C) for 8 weeks. Results are expressed as means ± SEM. (*) $P < 0.05$ versus respective LFD or HFD control. One-way ANOVA, Dunnett's post hoc test.

between LFD+C and HFD+C treatments. Administration of antibiotic cocktail to LFD+CA and HFD+CA groups resulted in marked 16−25-fold increases in anthocyanin content of feces. The effect was more pronounced in lean animals, suggesting that the gut microbiome was more active at biotransformation of anthocyanins than in their obese counterparts. The 3-*O*-rutinosides seemed to be the most susceptible to microbial biotransformation (24−55-fold increases in lean and 16−28-fold increase in obese animals receiving antibiotic cocktail in drinking water for week 10 of the study). Among all molecules tested, cyanidin-type anthocyanins showed the most dramatic increase in fecal content upon disruption of gut microbiome (28−55-fold for week 10; 32−51-fold for week 14 of treatment).

We also observed a parallel decrease in phenolic acid metabolites in feces of antibiotic-treated animals. Both gallic acid (delphinidin-derived metabolite) and protocatechuic acid (cyanidin-derived metabolite) fecal contents decreased 2−4-fold depending on the time of analysis (Table 3).

Anthocyanins in Gastrointestinal Wall Tissues. Jejunum, cecum, and colon gastrointestinal wall tissues collected from each diet group were analyzed to compare anthocyanin and phenolic acid profiles. Anthocyanin ratio profiles from jejunum tissues were very similar to those in the original extract (Table 4). Administration of antibiotic cocktail to LFD+CA and HFD+CA groups resulted in marked 2−5-fold increases in anthocyanin content of jejunum tissues. The effect was more pronounced in lean animals (4−5-fold) versus obese mice (1.5−2-fold), suggesting that, once again, the intact gut microbiome was more active at biotransformation of anthocyanins. Even though cyanidin- and delphinidin-type anthocyanins were present in black currant powdered extract and diet in almost equal concentrations (Tables 1 and 2), a strong preference for selective absorption of gallic acid (delphinidin-derived metabolite) was evident as compared to protocatechuic acid (cyanidin-derived metabolite) levels in the jejunum walls (Table 4). An approximately 3-fold enrichment in gallic acid over protocatechuic acid was observed in the jejunum of lean LFD+C and LFD+CA mice, and this ratio dropped to <2-fold in obese HFD+C and HFD+CA animals. Because similar ratios were observed in both intact and antibiotic-treated animals, this effect was likely independent of gut microbiome.

Smaller amounts of anthocyanins were also observed in cecum (Table 5) and colon (Table 6) walls. A small parallel increase in anthocyanin and phenolic acid metabolite content was observed in the colon as animals LFD+CA and HFD+CA were treated with antibiotic cocktail; however, generally lower amounts of tissue metabolites suggested that these tissues were less likely to absorb the bioactive anthocyanins from diet. Phenolic acid content was increased in cecum tissue compared to jejunum tissue (with the exception of HFD+CA animals)

Table 3. Individual Anthocyanins and Phenolic Acids Recovered from the Feces (Week 10)

	concentration[a] (μg/g feces)			
	LFD+C	LFD+CA	HFD+C	HFD+CA
Week 10				
total anthocyanins	**244 ± 5.82**	**6307 ± 891**	**293 ± 68.9**	**4834 ± 826**
delphinidin-3-*O*-glucoside	39.5 ± 8.69	134 ± 38.6	33.5 ± 7.39	94.2 ± 111
delphinidin-3-*O*-rutinoside	121.4 ± 3.06	2941 ± 1084	160 ± 36.7	2635 ± 850
cyanidin-3-*O*-glucoside	25.7 ± 5.96	60.0 ± 11.8	20.2 ± 4.15	46.0 ± 5.05
cyanidin-3-*O*-rutinoside	57.9 ± 5.77	3172 ± 757	79.9 ± 20.5	2230 ± 813
total phenolic acids	**81.5 ± 55.7**	**32.6 ± 5.91**	**93.3 ± 64.8**	**30.0 ± 0.06**
gallic acid	47.2 ± 33.6	16.3 ± 3.74	59.0 ± 42.0	16.2 ± 0.41
protocatechuic acid	34.4 ± 22.1	16.3 ± 2.17	34.3 ± 22.8	13.7 ± 0.35
Week 14				
total anthocyanins	**251 ± 0.49**	**4203 ± 820**	**347 ± 69.0**	**9906 ± 235**
delphinidin-3-*O*-glucoside	39.0 ± 7.35	45.7 ± 7.92	37.9 ± 7.20	150.0 ± 41.9
delphinidin-3-*O*-rutinoside	126 ± 6.72	2169 ± 216	193 ± 41.7	4939 ± 209
cyanidin-3-*O*-glucoside	26.0 ± 7.15	12.8 ± 0.83	23.2 ± 3.11	98.0 ± 90.2
cyanidin-3-*O*-rutinoside	60.5 ± 7.16	1976 ± 617	92.3 ± 16.3	4719 ± 158
total phenolic acids	**58.8 ± 18.0**	**47.9 ± 20.9**	**77.0 ± 0.90**	**48.6 ± 5.18**
gallic acid	31.6 ± 10.9	19.2 ± 9.2	42.6 ± 3.38	35.6 ± 4.57
protocatechuic acid	27.2 ± 7.05	28.7 ± 11.7	34.4 ± 2.48	12.8 ± 0.62

[a]LFD+C, low-fat diet supplemented with black currant extract; LFD+CA, low-fat diet supplemented with black currant extract and antibiotic cocktail; HFD+C, high-fat diet supplemented with black currant extract; HFD+CA, high -fat diet supplemented with black currant extract and antibiotic cocktail.

DOI: 10.1021/acs.jafc.5b00963
J. Agric. Food Chem. 2015, 63, 6172−6180

Table 4. Individual Anthocyanins and Phenolic Acids Recovered from the Jejunum (Week 14)

	concentration[a] (μg/g tissue)			
	LFD+C	LFD+CA	HFD+C	HFD+CA
total anthocyanins	**35.2 ± 14.1**	**154 ± 12.3**	**111 ± 74.0**	**195 ± 33.3**
delphinidin-3-*O*-glucoside	6.90 ± 0.86	28.7 ± 13.1	23.8 ± 15.4	27.0 ± 12.7
delphinidin-3-*O*-rutinoside	11.4 ± 5.48	54.8 ± 0.83	37.9 ± 27.7	68.6 ± 46.0
cyanidin-3-*O*-glucoside	6.26 ± 1.54	22.0 ± 7.67	18.6 ± 10.8	25.3 ± 11.9
cyanidin-3-*O*-rutinoside	10.6 ± 6.24	48.2 ± 7.58	30.9 ± 20.2	74.2 ± 46.8
total phenolic acids	**29.0 ± 8.08**	**14.0 ± 5.49**	**21.4 ± 11.0**	**38.1 ± 35.4**
gallic acid	22.2 ± 7.34	10.3 ± 2.81	12.4 ± 9.31	26.3 ± 28.2
protocatechuic acid	6.81 ± 0.74	3.70 ± 2.68	9.32 ± 1.67	11.8 ± 7.17

[a]LFD+C, low-fat diet supplemented with black currant extract; LFD+CA, low-fat diet supplemented with black currant extract and antibiotic cocktail; HFD+C, high-fat diet supplemented with black currant extract; HFD+CA, high-fat diet supplemented with black currant extract and antibiotic cocktail.

Table 5. Individual Anthocyanins and Phenolic Acids Recovered from the Cecum (Week 14)

	concentration[a] (μg/g tissue)			
	LFD+C	LFD+CA	HFD+C	HFD+CA
total anthocyanins	**16.5 ± 8.17**	**52.7 ± 23.9**	**23.7 ± 0.58**	**18.4 ± 17.6**
delphinidin-3-*O*-glucoside	2.16 ± 3.05	7.00 ± 4.06	n/a	3.48 ± 4.91
delphinidin-3-*O*-rutinoside	2.60 ± 3.72	19.8 ± 12.9	6.40 ± 0.76	n/a
cyanidin-3-*O*-glucoside	2.79 ± 3.95	5.38 ± 1.36	5.61 ± 0.05	14.9 ± 12.7
cyanidin-3-*O*-rutinoside	8.97 ± 2.55	20.5 ± 5.50	11.7 ± 0.23	n/a
total phenolic acids	**57.6 ± 5.86**	**53.3 ± 1.10**	**24.3 ± 17.1**	**30.0 ± 0.06**
gallic acid	50.0 ± 4.11	33.1 ± 3.53	14.5 ± 16.4	18.9 ± 12.6
protocatechuic acid	7.60 ± 1.75	20.2 ± 2.43	9.86 ± 0.62	11.0 ± 3.41

[a]n/a, not available; LFD+C, low-fat diet supplemented with black currant extract; LFD+CA, low-fat diet supplemented with black currant extract and antibiotic cocktail; HFD+C, high-fat diet supplemented with black currant extract; HFD+CA, high-fat diet supplemented with black currant extract and antibiotic cocktail.

Table 6. Individual Anthocyanins and Phenolic Acids Recovered from the Colon (Week 14)

	concentration[a] (μg/g tissue)			
	LFD+C	LFD+CA	HFD+C	HFD+CA
total anthocyanins	**15.5 ± 12.8**	**53.9 ± 4.82**	**41.5 ± 9.24**	**61.0 ± 29.2**
delphinidin-3-*O*-glucoside	3.10 ± 4.38	5.51 ± 0.82	2.44 ± 3.44	2.13 ± 3.01
delphinidin-3-*O*-rutinoside	3.56 ± 5.63	25.0 ± 4.31	20.8 ± 8.44	27.4 ± 10.1
cyanidin-3-*O*-glucoside	2.57 ± 3.63	n/d	n/d	2.13 ± 3.01
cyanidin-3-*O*-rutinoside	6.23 ± 0.28	23.4 ± 0.31	18.3 ± 4.25	28.8 ± 12.3
total phenolic acids	**n/d**	**n/d**	**n/d**	**n/d**
gallic acid	n/d	n/d	n/d	n/d
protocatechuic acid	n/d	n/d	n/d	n/d

[a]n/d, not detected LFD+C, low-fat diet supplemented with black currant extract; LFD+CA, low-fat diet supplemented with black currant extract and antibiotic cocktail; HFD+C, high-fat diet supplemented with black currant extract; HFD+CA, high-fat diet supplemented with black currant extract and antibiotic cocktail.

and diminished below detection levels in the colon tissue. These data may reflect increased biotransformation of anthocyanins in the cecum and further degradation of phenolic acid metabolites into simple phenols in the colon.[23]

Effect on Glucose Metabolism and Insulin Sensitivity. Baseline blood glucose levels were measured at week 14 of the study after an overnight fast (Figure 5, time point 0 min). Black currant supplementation or gut microbiome disruption had no effect on blood glucose in animals on LFD (Figure 5A). Baseline blood glucose levels did not differ for HFD and HFD +C groups as well (Figure 5B). However, HFD+CA mice without functional gut microbiome showed a 45% increase in baseline blood glucose (284 mg/dL) versus HFD controls or HFD+C animals with black currant supplementation (193 mg/dL). The HFD group blood glucose levels were significantly higher at 30, 60, and 120 min after oral gavage as compared with the LFD mice, whereas the anthocyanin treatment (HFD +C) significantly reversed peak blood glucose concentration at 60 min (Figure 5B). Despite black currant supplementation, mice with disrupted gut microbiome (HFD+CA) showed high peak blood glucose values similar to those of untreated HFD controls (Figure 5B).

Insulin sensitivity was enhanced in LFD animals receiving black currant supplementation, even when their gut microbiome was suppressed by antibiotic cocktail (Figure 5C). HFD mice developed insulin resistance as expected, whereas black currant-supplemented HFD+C mice showed improved insulin sensitivity at 30, 60, and 120 min after insulin injection (Figure 5D). Suppression of gut microbiome had a dramatic negative effect on insulin sensitivity in HFD+CA animals: despite black

DOI: 10.1021/acs.jafc.5b00963
J. Agric. Food Chem. 2015, 63, 6172−6180

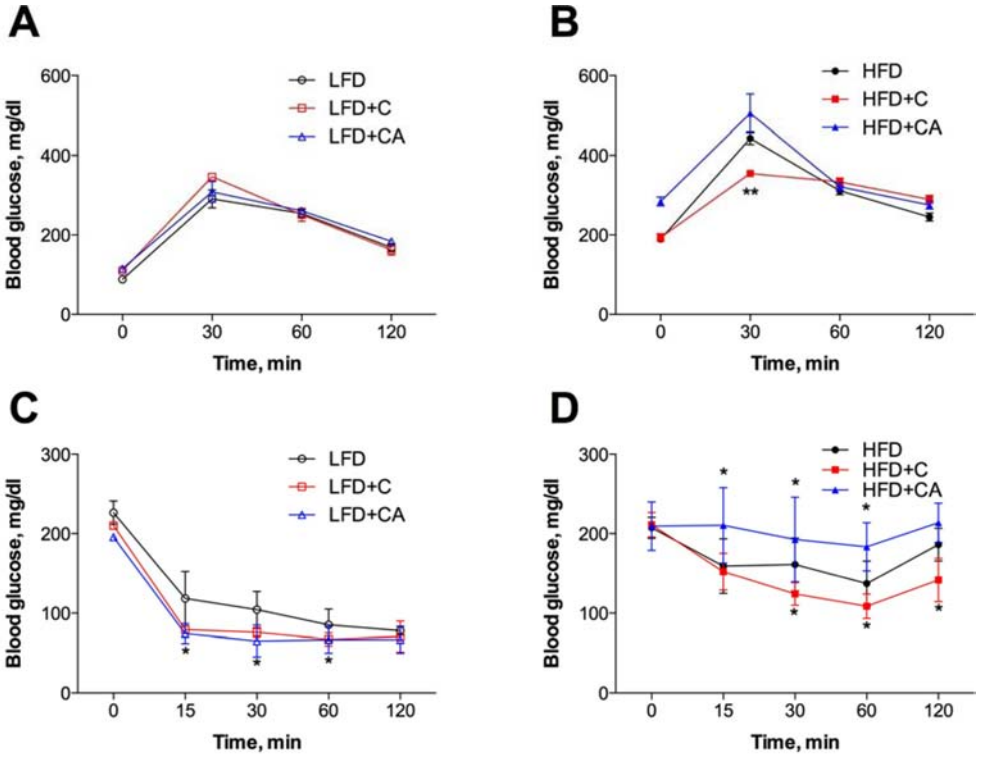

Figure 5. Chronic insulin-sensitizing effect of black currant supplementation on oral glucose tolerance test on low-fat diets (A) and high-fat diets (B) and insulin tolerance test on low-fat diets (C) and high-fat diets (D) in the C57BL/6J mice. Eight-week-old male mice were fed a low- or high-fat diet for 6 weeks. Lean and obese mice were further randomized to control low-fat diet (LFD), control high-fat diet (HFD), and the respective low-fat (LFD+C) and high-fat (HFD+C) black currant-supplemented treatment groups (1% black currant extract incorporated in LFD or HFD diet) and kept on the same diet for an additional 8 weeks. An antibiotic cocktail was administered in drinking water ad libitum to half of the animals on black currant-supplemented treatment groups (LFD+CA and HFD+CA groups, respectively) for the entire duration of the black currant feeding study (weeks 7−14). For oral glucose tolerance test, mice were fasted overnight (16 h) and received oral gavage of D-glucose (1.5 g/kg body weight). For insulin tolerance test, mice were fasted for 4 h and received intraperitoneal injection of insulin (0.75 U/kg body weight). Blood glucose concentrations were measured at 0, 15, 30, 60, and 120 min after glucose or insulin challenge in blood samples obtained from tail-tip bleedings, using a glucometer. Values are means ± SEM. (*) $P < 0.05$ and (**) $P < 0.01$ when compared with LFD or HFD control by one-way ANOVA followed by Dunnett's post hoc test.

currant supplementation, the insulin tolerance curve remained virtually flat for the duration of the testing, showing significant degree of insulin resistance at all time points tested (15−120 min).

DISCUSSION

Bioactive anthocyanins are of substantial health-promoting interest as their daily intake is 180−200 mg in the United States and may be significantly higher in other countries where more fruits and vegetables are consumed on a regular basis.[31] A single serving of anthocyanin-rich berries may contribute in excess of 100−200 mg of anthocyanins to a regular diet,[32] which is 5−10-fold higher than the daily intake of other flavonoids, such as quercetin or apigenin.[33] Anthocyanins are structurally diverse compounds that are present in plants in different concentrations and have various degrees of hydroxylation, methylation, glycosylation, and acylation.[3] This inherent diversity may be responsible for the lack of equivocal results from animal and human studies, because predominantly delphinidin- and malvidin-containing fruits are more likely to improve metabolic and cardiovascular disease risk biomarkers (i.e blueberry,[16] black currant and bilberry,[17,18] or grapes[19]), whereas cyanidin-based supplementation strategies offer less protection (i.e., elderberry,[20] blood orange,[21] or purple carrot[22]). In this study, we focused on the effects of black currant powdered extract on glucose metabolism and insulin sensitivity in diet-induced obese mice with intact and antibiotic-disrupted gut microbiome. The predominant flavonoids in the extract (Tables 1 and 2) were four anthocyanins that are equally distributed between cyanidin and delphinidin aglycones (Figure 1), in agreement with previously published data.[24] Anthocyanins represented the most abundant phenolic compounds in black currants, with other minor phenolics contributing to <5% of black currant powdered extract as shown by our previous work.[25]

Reduced body weight associated with 1% black currant powdered extract supplementation was observed together with no change in food intake (Figure 2). In this study mice consumed on average between 2.5 and 3.0 g food/animal/day, which is equal to ingestion of 8−10 mg/animal/day (300−400 mg/kg/day) of black currant anthocyanins. The human equivalent dose for this study was estimated at 25 mg/kg/day or 1.5 g/day of total anthocyanins for an average adult.[34] This dose was 8 times larger than an average anthocyanin intake in a regular U.S. diet[31] and could be achieved by incorporating 3−4 cups of fresh black currants (250−750 mg anthocyanins/100 g fruit)[35,36] or wild blueberries (350−550 mg anthocyanins/100 g fruit)[37] in the diet. Citric acid present in the black currant powdered extract was not likely to contribute to beneficial effects of black currant anthocyanin supplementation on obesity and metabolic disease, as obese patients show significantly

DOI: 10.1021/acs.jafc.5b00963
J. Agric. Food Chem. 2015, 63, 6172−6180

higher values in the level of citric acid as a result of natural changes in intermediate metabolism components associated with obesity.[38]

The majority of studies focusing on anthocyanin absorption have shown that the bioavailability of anthocyanins is low. The maximum black currant anthocyanin concentration in plasma reached 0.4 μM (t_{max} = 15 min) and returned to baseline after 7 h.[24] Gastrointestinal tissues, however, receive longer exposure time to anthocyanins that could increase their absorption in the tissue walls. Indeed, in this study we observed concentrations up to 35 and 111 μg/g anthocyanins in the jejunum tissue of LFD and HFD mice, respectively, and these levels increased to 154 and 195 μg/g tissue in antibiotic-treated animals (Table 4).

Anthocyanin concentrations were much lower in cecum and colon tissues, suggesting that black currant anthocyanins are maximally absorbed in the jejunum—a conclusion that is consistent with previous observations.[24] On the other hand, gallic and protocatechuic acid levels were highest in cecum and largely undetectable in colon tissues (Table 5). Even though cyanidin- and delphinidin-type anthocyanins were present in black currant extract and diet in almost equal concentrations, a strong preference for selective absorption of gallic acid was evident as compared to protocatechuic acid in the jejunum (Table 4). Because similar ratios were observed in both intact and antibiotic-treated animals, this effect was likely independent of gut microbiome.

We observed that the gut microbiome was crucial for the protective effect of black currant anthocyanins against obesity and associated insulin resistance (Figure 5). Indeed, germ-free HFD mice gained more weight than controls.[39] At the same time, addition of antibiotic cocktail to drinking water decreased anthocyanin biotransformation in the gut, which resulted in higher anthocyanin concentrations in the gastrointestinal tissues (Tables 4−6) and feces (Table 3). Cyanidin-based anthocyanins showed the most dramatic increase in fecal content upon disruption of gut microbiome, suggesting their high susceptibility to microbial degradation in the gut. At the same time, an approximately 3-fold enrichment in gallic acid (major delphinidin-derived metabolite) over protocatechuic acid (major cyanidin-derived metabolite) was observed in the jejunum of both intact and antibiotic-treated animals. These observations may explain why plants or foods rich in cyanidin-type anthocyanins are less effective in preventing metabolic and inflammatory disorders in animal and human studies. Higher gastrointestinal tissue levels of anthocyanins in antibiotic-treated animals, however, did not correlate with metabolic health outcomes, possibly indicating that not intact anthocyanins but their gut microbiome metabolites are partially responsible for these effects.

In conclusion, consumption of black currant powdered extract decreases weight gain of the LFD and HFD fed C57Bl/6J mice with healthy gut microbiome. Feces of gut microbiome-deficient mice showed an increase in anthocyanins and a decrease in their phenolic acid metabolites, whereas a corresponding increase was observed in the jejunum tissue. Cyanidin-type anthocyanins were much more sensitive to gut microbiome metabolism than delphinidins. Thus, gut microbiome was crucial for the protective effect of black currant anthocyanins against obesity and associated insulin resistance.

AUTHOR INFORMATION

Corresponding Author

*(S.K.) Phone: (704) 250-5459. Fax: (704) 250-5425. E-mail: komarnytsky@ncsu.edu.

Present Address

§(T.D.) Program of Thai Traditional Medicine, Faculty of Science and Technology, Rajamangala University of Technology Srivijaya, 109 Thung Song, Nakhon Si Thammarat, Thailand 80110.

Funding

This work was supported in part by NCSU Research and Innovation seed grant 2012-2246 (M.A.L., S.K.), NCSU faculty start-up funds (S.K.), and the Cell Culture and Phenotyping Core of the Plants for Human Health Institute, North Carolina State University.

Notes

The authors declare no competing financial interest.

REFERENCES

(1) White, M. F. Insulin signaling in health and disease. *Science* **2003**, *302*, 1710−1711.

(2) Manco, M.; Putignani, L.; Bottazzo, G. F. Gut microbiota, lipopolysaccharides, and innate immunity in the pathogenesis of obesity and cardiovascular risk. *Endocr. Rev.* **2010**, *31*, 817−844.

(3) Tsuda, T. Dietary anthocyanin-rich plants: biochemical basis and recent progress in health benefits studies. *Mol. Nutr. Food Res.* **2012**, *56*, 159−170.

(4) Tsuda, T.; Horio, F.; Uchida, K.; Aoki, H.; Osawa, T. Dietary cyanidin 3-*O*-β-D-glucoside-rich purple corn color prevents obesity and ameliorates hyperglycemia in mice. *J. Nutr.* **2003**, *133*, 2125−2130.

(5) Kwon, S. H.; Ahn, I. S.; Kim, S. O.; Kong, C. S.; Chung, H. Y.; Do, M. S.; Park, K. Y. Anti-obesity and hypolipidemic effects of black soybean anthocyanins. *J. Med. Food* **2007**, *10*, 552−556.

(6) Prior, R. L.; Wu, X.; Gu, L.; Hager, T. J.; Hager, A.; Howard, L. R. Whole berries versus berry anthocyanins: interactions with dietary fat levels in the C57BL/6J mouse model of obesity. *J. Agric. Food Chem.* **2008**, *56*, 647−653.

(7) Qin, B.; Anderson, R. A. An extract of chokeberry attenuates weight gain and modulates insulin, adipogenic and inflammatory signalling pathways in epididymal adipose tissue of rats fed a fructose-rich diet. *Br. J. Nutr.* **2012**, *108*, 581−587.

(8) Hwang, Y. P.; Choi, J. H.; Han, E. H.; Kim, H. G.; Wee, J. H.; Jung, K. O.; Jung, K. H.; Kwon, K. I.; Jeong, T. C.; Chung, Y. C.; Jeong, H. G. Purple sweet potato anthocyanins attenuate hepatic lipid accumulation through activating adenosine monophosphate-activated protein kinase in human HepG2 cells and obese mice. *Nutr. Res.* **2011**, *31*, 896−906.

(9) Wu, T.; Qi, X.; Liu, Y.; Guo, J.; Zhu, R.; Chen, W.; Zheng, X.; Yu, T. Dietary supplementation with purified mulberry (*Morus australis* Poir) anthocyanins suppresses body weight gain in high-fat diet fed C57BL/6 mice. *Food Chem.* **2013**, *141*, 482−487.

(10) Wu, T.; Tang, Q.; Yu, Z.; Gao, Z.; Hu, H.; Chen, W.; Zheng, X.; Yu, T. Inhibitory effects of sweet cherry anthocyanins on the obesity development in C57BL/6 mice. *Int. J. Food Sci. Nutr.* **2014**, *65*, 351−359.

(11) Hogan, S.; Canning, C.; Sun, S.; Sun, X.; Zhou, K. Effects of grape pomace antioxidant extract on oxidative stress and inflammation in diet induced obese mice. *J. Agric. Food Chem.* **2010**, *58*, 11250−11256.

(12) Benn, T.; Kim, B.; Park, Y. K.; Wegner, C. J.; Harness, E.; Nam, T. G.; Kim, D. O.; Lee, J. S.; Lee, J. Y. Polyphenol-rich black currant extract prevents inflammation in diet-induced obese mice. *J. Nutr. Biochem.* **2014**, *25*, 1019−1025.

(13) Marques, A. Y.; Dragano, N. R.; Lenquiste, S. A.; Batista, A. G.; Palazzo, C. C.; Marostica, M. R., Jr. Freeze-dried jaboticaba peel

DOI: 10.1021/acs.jafc.5b00963
J. Agric. Food Chem. 2015, 63, 6172−6180

powder rich in anthocyanins did not reduce weight gain and lipid content in mice and rats. *Arch. Latinoam. Nutr.* **2012**, *62*, 37−43.
(14) Prior, R. L.; Wilkes, S.; Rogers, T.; Khanal, R. C.; Wu, X.; Hager, T. J.; Hager, A.; Howard, L. Dietary black raspberry anthocyanins do not alter development of obesity in mice fed an obesogenic high-fat diet. *J. Agric. Food Chem.* **2010**, *58*, 3977−3983.
(15) van Dam, R. M.; Naidoo, N.; Landberg, R. Dietary flavonoids and the development of type 2 diabetes and cardiovascular diseases: review of recent findings. *Curr. Opin. Lipidol.* **2013**, *24*, 25−33.
(16) Stull, A. J.; Cash, K. C.; Johnson, W. D.; Champagne, C. M.; Cefalu, W. T. Bioactives in blueberries improve insulin sensitivity in obese, insulin-resistant men and women. *J. Nutr.* **2010**, *140*, 1764−1768.
(17) Karlsen, A.; Retterstol, L.; Laake, P.; Paur, I.; Bohn, S. K.; Sandvik, L.; Blomhoff, R. Anthocyanins inhibit nuclear factor-κB activation in monocytes and reduce plasma concentrations of pro-inflammatory mediators in healthy adults. *J. Nutr.* **2007**, *137*, 1951−1954.
(18) Zhu, Y.; Xia, M.; Yang, Y.; Liu, F.; Li, Z.; Hao, Y.; Mi, M.; Jin, T.; Ling, W. Purified anthocyanin supplementation improves endothelial function via NO-cGMP activation in hypercholesterolemic individuals. *Clin. Chem.* **2011**, *57*, 1524−1533.
(19) Hansen, A. S.; Marckmann, P.; Dragsted, L. O.; Finne Nielsen, I. L.; Nielsen, S. E.; Gronbaek, M. Effect of red wine and red grape extract on blood lipids, haemostatic factors, and other risk factors for cardiovascular disease. *Eur. J. Clin. Nutr.* **2005**, *59*, 449−455.
(20) Curtis, P. J.; Kroon, P. A.; Hollands, W. J.; Walls, R.; Jenkins, G.; Kay, C. D.; Cassidy, A. Cardiovascular disease risk biomarkers and liver and kidney function are not altered in postmenopausal women after ingesting an elderberry extract rich in anthocyanins for 12 weeks. *J. Nutr.* **2009**, *139*, 2266−2271.
(21) Giordano, L.; Coletta, W.; Tamburrelli, C.; D'Imperio, M.; Crescente, M.; Silvestri, C.; Rapisarda, P.; Reforgiato Recupero, G.; De Curtis, A.; Iacoviello, L.; de Gaetano, G.; Rotilio, D.; Cerletti, C.; Donati, M. B. Four-week ingestion of blood orange juice results in measurable anthocyanin urinary levels but does not affect cellular markers related to cardiovascular risk: a randomized cross-over study in healthy volunteers. *Eur. J. Nutr.* **2012**, *51*, 541−548.
(22) Wright, O. R.; Netzel, G. A.; Sakzewski, A. R. A randomized, double-blind, placebo-controlled trial of the effect of dried purple carrot on body mass, lipids, blood pressure, body composition, and inflammatory markers in overweight and obese adults: the QUENCH trial. *Can. J. Physiol. Pharmacol.* **2013**, *91*, 480−488.
(23) Faria, A.; Fernandes, I.; Norberto, S.; Mateus, N.; Calhau, C. Interplay between anthocyanins and gut microbiota. *J. Agric. Food Chem.* **2014**, *62*, 6898−6902.
(24) Walton, M. C.; Hendriks, W. H.; Broomfield, A. M.; McGhie, T. K. Viscous food matrix influences absorption and excretion but not metabolism of black currant anthocyanins in rats. *J. Food Sci.* **2009**, *74*, H22−H29.
(25) Mbeunkui, F.; Grace, M. H.; Yousef, G. G.; Lila, M. A. Isolation and characterization of flavonols from black currant by high-performance counter-current chromatography and electrospray ionization tandem mass spectrometry. *J. Sep. Sci.* **2012**, *35*, 1682−1689.
(26) Keppler, K.; Humpf, H. U. Metabolism of anthocyanins and their phenolic degradation products by the intestinal microflora. *Bioorg. Med. Chem.* **2005**, *13*, 5195−5205.
(27) Ellacott, K. L.; Morton, G. J.; Woods, S. C.; Tso, P.; Schwartz, M. W. Assessment of feeding behavior in laboratory mice. *Cell Metab.* **2010**, *12*, 10−17.
(28) Wang, Z.; Klipfell, E.; Bennett, B. J.; Koeth, R.; Levison, B. S.; Dugar, B.; Feldstein, A. E.; Britt, E. B.; Fu, X.; Chung, Y. M.; Wu, Y.; Schauer, P.; Smith, J. D.; Allayee, H.; Tang, W. H.; DiDonato, J. A.; Lusis, A. J.; Hazen, S. L. Gut flora metabolism of phosphatidylcholine promotes cardiovascular disease. *Nature* **2011**, *472*, 57−63.
(29) He, J.; Magnuson, B. A.; Giusti, M. M. Analysis of anthocyanins in rat intestinal contents − impact of anthocyanin chemical structure on fecal excretion. *J. Agric. Food Chem.* **2005**, *53*, 2859−2966.
(30) Yousef, G. G.; Brown, A. F.; Funakoshi, Y.; Mbeunkui, F.; Grace, M. H.; Ballington, J. R.; Loraine, A.; Lila, M. A. Efficient quantification of the health-relevant anthocyanin and phenolic acid profiles in commercial cultivars and breeding selections of blueberries (*Vaccinium* spp.). *J. Agric. Food Chem.* **2013**, *61*, 4806−4815.
(31) Kuhnau, J. The flavonoids. A class of semi-essential food components: their role in human nutrition. *World Rev. Nutr. Diet.* **1976**, *24*, 117−191.
(32) McGhie, T. K.; Ainge, G. D.; Barnett, L. E.; Cooney, J. M.; Jensen, D. J. Anthocyanin glycosides from berry fruit are absorbed and excreted unmetabolized by both humans and rats. *J. Agric. Food Chem.* **2003**, *51*, 4539−4548.
(33) Hertog, M. G.; Hollman, P. C.; Katan, M. B.; Kromhout, D. Intake of potentially anticarcinogenic flavonoids and their determinants in adults in The Netherlands. *Nutr. Cancer* **1993**, *20*, 21−29.
(34) Reagan-Shaw, S.; Nihal, M.; Ahmad, N. Dose translation from animal to human studies revisited. *FASEB J.* **2008**, *22*, 659−661.
(35) Slimestad, R.; Solheim, H. Anthocyanins from black currants (*Ribes nigrum* L.). *J. Agric. Food Chem.* **2002**, *50*, 3228−3231.
(36) Hellstrom, J.; Hietaranta, T.; Karhu, S.; Mattila, P.; Tiirikka, T.; Vetelainen, M. High variability in anthocyanin contents between different blackcurrant varieties. *NJF Report* **2010**, *6*, 116−118.
(37) Hosseinian, F. S.; Beta, T. Saskatoon and wild blueberries have higher anthocyanin contents than other Manitoba berries. *J. Agric. Food Chem.* **2007**, *55*, 10832−10838.
(38) Stuchlikova, E.; Hruskova, J.; Tenorova, M.; Novotna, B.; Komarkova, A.; Riedl, O. Some changes in intermediary metabolism of obese patients. *Clin. Chim. Acta* **1961**, *6*, 571−577.
(39) Fleissner, C. K.; Huebel, N.; Abd El-Bary, M. M.; Loh, G.; Klaus, S.; Blaut, M. Absence of intestinal microbiota does not protect mice from diet-induced obesity. *Br. J. Nutr.* **2010**, *104*, 919−929.

DOI: 10.1021/acs.jafc.5b00963
J. Agric. Food Chem. 2015, 63, 6172−6180

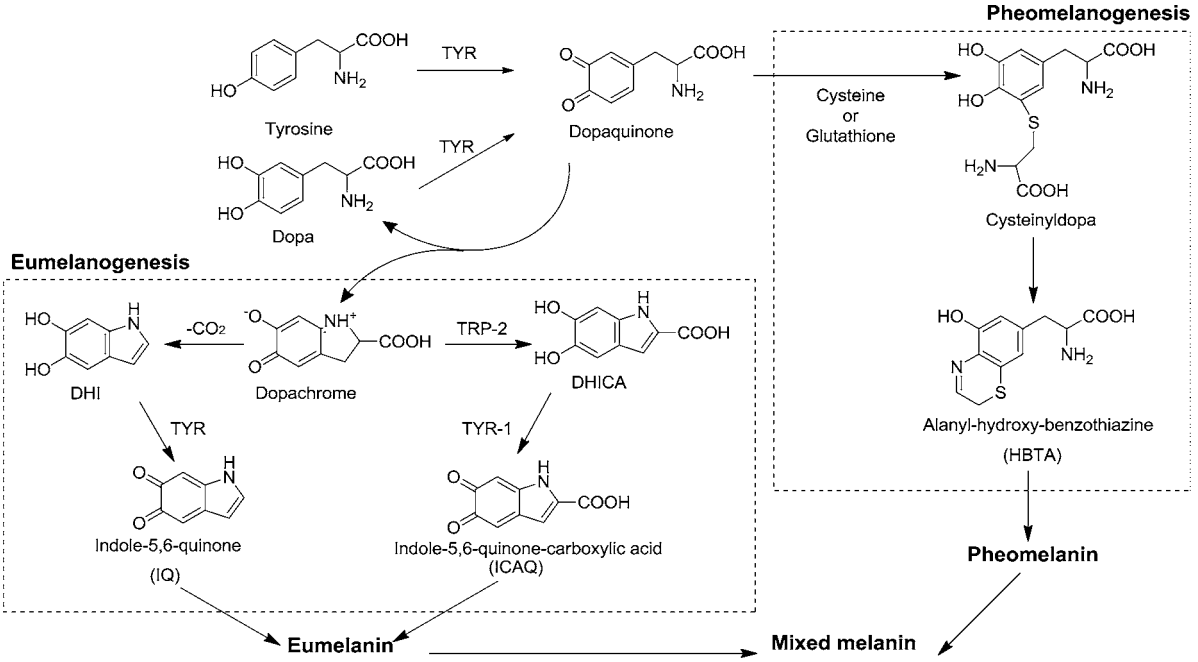

Figure 1. Biosynthetic pathway of melanin involving mushroom tyrosinase. Melanin biosynthesis includes eumelanogenesis and pheomelanogenesis that generate eumelanin and pheomelanin, respectively.

tion of tyrosine to DOPA and the oxidation of DOPA to dopaquinone during melanin formation from tyrosine.[9] In plants, tyrosinase is responsible for browning, which occurs after the long-term storage of fruits and vegetables.[10] In animals, tyrosinase is responsible for skin and hair pigmentation and skin anomalies, namely, hypo- (vitiligo) or hyper- (freckles or flecks) pigmentation.[11,12] Moreover, tyrosinase may play a role in neurodegenerative diseases (e.g., Parkinson's disease) and cancer.[13,14] Therefore, tyrosinase is a crucial topic in the fields of medicine, agriculture, and cosmetics, and considerable attention has been paid to developing and screening for tyrosinase inhibitors.[15]

Some tyrosinase inhibitors, such as hydroquinone,[16,17] arbutin,[18] kojic acid,[19,20] azelaic acid,[21,22] and electron-rich phenols,[23] have been used in cosmetics. However, only a few such inhibitors are sufficiently potent for practical use and are in compliance with safety regulations. Therefore, continual efforts have been exerted to obtain tyrosinase inhibitors synthetically (in laboratories)[24−26] and naturally (through plant extractions).[27−29] Recently, we used phage-displayed tetrapeptide inhibitors[30] and a T1 compound from *Gastrodia elata*,[31] and other researchers have employed peptide-derived compounds for tyrosinase inhibition.[4,32,33] Certain short-sequence oligopeptides, **P3** and **P4**, inhibit mushroom tyrosinase with no cytotoxicity to human melanocyte.[32] The tyrosinase inhibitory potency of kojic acid−tripeptide is superior to that of kojic acid.[34] In addition, a mimosine tetrapeptide, mimosine−FFY, exhibits a marked tyrosinase inhibitory ability when the half-maximal inhibitory concentration (IC_{50}) is 18.3 μM.[33] Peptides are reported to bind with exact specificity to their in vivo targets, resulting in an exceptionally high potency of action and relatively few off-target side effects.[35] Thus, tyrosinase inhibitors have great potential for use as skin-whitening components in medicine and cosmetics.

In a previous study, we established a reasonable and reliable pharmacophore model for screening potent natural products for mushroom tyrosinase inhibition. We identified a potent natural product, A5,[36] that exhibits an apparent tyrosinase inhibitory ability. Moreover, the structure of A5 resembled that of the dipeptide **WY**. Therefore, in this study, we synthesized 20 × 20 dipeptides to comprehensively investigate their tyrosinase inhibitory ability. We found that cysteine-containing dipeptides exhibit an outstanding inhibitory potency against tyrosinase among all others. The tyrosine moiety of tyrosine-containing dipeptides competes with the substrate binding site of tyrosinase to reduce tyrosinase activity. Dipeptides (**CA**, **YC**, **PD**, and **DY**) exhibiting divergent inhibition against tyrosinase were subjected to a cell viability assay and melanin content assessment to study their effects on cytotoxicity and depigmentation. In addition, to identify dipeptides with the strongest tyrosinase inhibitory potency, the IC_{50} values of cysteine-containing dipeptides, which are superior to those of other dipeptides, were calculated. This study reveals the functional roles of the cysteine residue positional preference and the selectivity of specific amino acids of dipeptides for inhibiting tyrosinase. The results can be applied in developing inhibitors for interrupting melanin biosynthesis.

MATERIALS AND METHODS

Materials. Molecular docking studies were conducted using Genetic Optimization for Ligand Docking (GOLD; GlaxoSmithKline PLC, Astex Technology Ltd., Cambridge Crystallographic Data Centre). All calculations were performed at the National Center for High-Performance Computing in Taiwan. Mushroom tyrosinase, L-tyrosine, and a potassium phosphate buffer (PBS, NaH_2PO_4−Na_2HPO_4, 67 mM, pH 6.8) were purchased from Sigma-Aldrich (St. Louis, MO, USA). All 400 peptides (purity = 0.95%) used in this study were custom-synthesized by Kelowna International Scientific, Inc. (New Taipei City, Taiwan).

Methods. *Examination of the Inhibitory Potency of Dipeptides against Tyrosinase.* A tyrosinase inhibition assay was performed, according to a previously reported method,[36] on the synthesized 20 × 20 dipeptides to investigate their effects on tyrosinase activity.[37] In brief, 25 μL of a 5 mM dipeptide solution, 125 μL of a 5 mM L-tyrosine, and 80 μL of a 67 mM PBS were mixed and added to each well of a 96-well enzyme-linked immunosorbent assay plate, which was incubated at 25 °C for 5 min. Subsequently, 20 μL of a 1250 U/mL mushroom tyrosinase

DOI: 10.1021/acs.jafc.5b01026
J. Agric. Food Chem. 2015, 63, 6181−6188

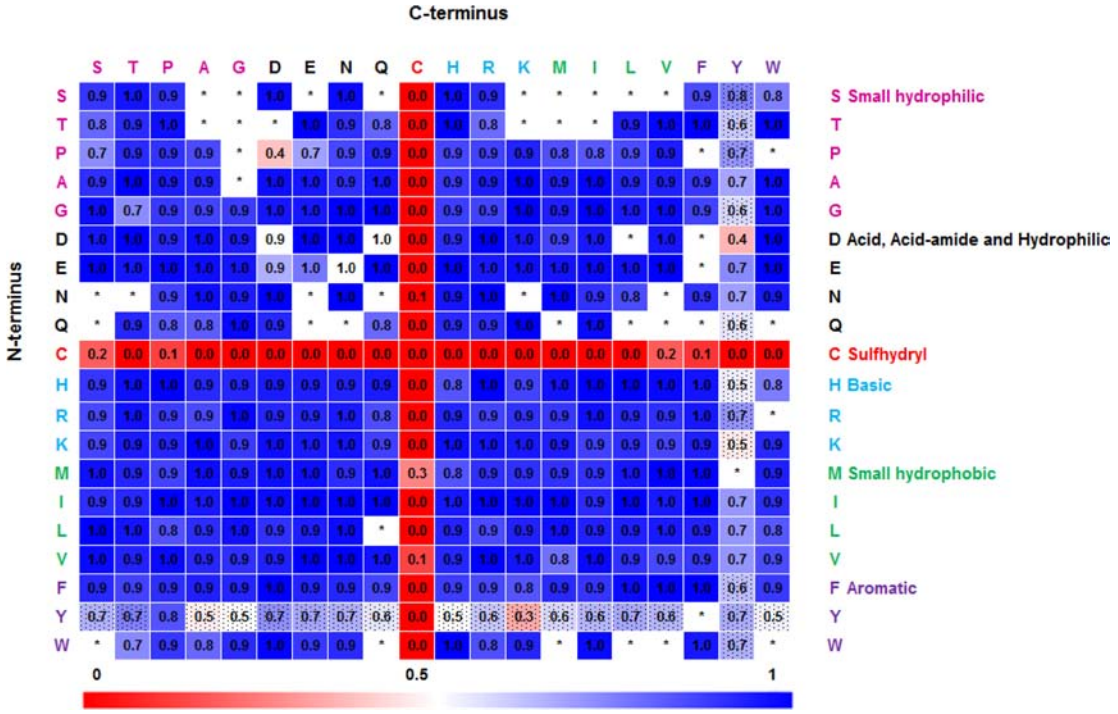

Figure 2. 20 × 20 dipeptide-based tyrosinase inhibition matrix. The comprehensive pre-estimation of the inhibitory ability of 20 × 20 dipeptides against mushroom tyrosinase is summarized in the matrix. The *Y*-axis represents the amino acids that constitute the N terminus of the dipeptides, and the *X*-axis represents the 20 amino acids that constitute the C terminus of the dipeptides. According to the chemical properties of the side chains, 20 amino acids are divided into eight categories: (1) G; (2) nonpolar aliphatic amino acids, A, V, L, I, and P; (3) nonpolar aromatic amino acids, F, W, and Y; (4) polar hydroxyl amino acids, S and T; (5) sulfur amino acids, C and M; (6) amidic amino acids, N and Q; (7) polar negative amino acids, D and E; and (8) polar positive amino acids, R, H, and K. The numbers in each small square with different colors are inhibition indices, which represent the distinct levels of tyrosinase activities. The scale of inhibition indices is from 0 (complete abolished tyrosinase activity; red) to 1 (full tyrosinase activity; blue). An asterisk denotes that the dipeptides are not completely dissolved in ddH_2O. The dipeptides that change the color of the reaction solution and therefore might interfere with the results are marked with a dotted pattern.

solution was added to each well; thus, the final volume in each well was 250 μL. The plate was incubated again at 25 °C for 5 min. In addition, the same concentrations of kojic acid and β-arbutin under the same conditions as those in the wells were used as controls. The amount of dopachrome produced was determined against a blank (solution without tyrosinase) and recorded using a spectrophotometer (Varian Cary 50 Bio UV−visible spectrophotometer) at 475 nm every 10 s for 10 min. The amount of dopachrome produced in the reaction solution was determined using a previously described method.[37] The tyrosinase activity was calculated using the equation

$$\text{tyrosinase activity } \% = \left(\frac{S - B}{C}\right) \times 100$$

where S is the OD_{475} absorbance of the test samples, B is the OD_{475} absorbance of the blank, and C is the OD_{475} absorbance of controls. The IC_{50} of cysteine-containing dipeptides was determined by performing dose-dependent inhibition experiments in triplicate.

Cell Viability and Melanin Quantification Assay. Normal human epidermal melanocytes were purchased from Cascade Biologics (Portland, OR, USA) and cultured in Medium 254 supplemented with human melanocyte growth supplement (Cascade Biologics). During the experiment, confluent cells were trypsinized and suspended in melanocyte growth medium M2 containing 2×10^5 cells/mL. The cells were then placed in 96-well plates (2×10^4 cells/well) for the cell viability assay and in 24-well plates (1×10^5 cells/well) for the melanin content assay. After 24 h, the cells were treated with arbutin (50 μM, 2.5 mM), kojic acid (50 μM, 500 μM), and 1, 10, and 100 μM **CA**, **YC**, **PD**, and **DY**. The cells were then incubated at 37 °C for 72 h. Cell viability was determined using the MTT assay.[38,39] For measuring the melanin content, the melanocyte pellets were dissolved in 1 N hot NaOH (70 °C) for 1 h and centrifuged for 10 min at 10000*g*. The optical density (OD_{405}) of supernatant in each cell of the plate was measured using a microplate reader (Molecular Devices Spectra Max M2).

Molecular Modeling. Models of the dipeptides in complex with tyrosinase were built using molecular docking analysis. GOLD (version 5.2) featuring the Goldscore scoring function was used to predict the positions of dipeptides at the active sites. All cofactors and water molecules were removed before docking. Three-dimensional (3D) structures of the desired dipeptides were generated and optimized through energy minimization by using Discovery Studio version 4.0 (Accelrys Software, Inc., San Diego, CA, USA) and further docked into the active sites of mushroom tyrosinase (PDB ID 2Y9X) by turning on the flexible docking option. Initially, 100 genetic algorithm cycles of computation were performed with ligand torsion angles varying between −180° and 180°. The search efficiency was set at 200% to explore the docking conformational space. All other parameters were applied as the default settings. Finally, from the 100 docking conformations of each dipeptide, the conformation with the highest GOLD fitness score was examined to investigate its binding with the mushroom tyrosinase active site by using Goldscore. The molecular models of the dipeptide−tyrosinase complexes were presented using PyMOL software (http://www.pymol.org).

RESULTS

Comprehensive Investigation of Inhibitory Abilities of 20 × 20 Dipeptides against Tyrosinase. In our previous study, we found a natural product, A5,[36] that exhibits an apparent tyrosinase inhibitory ability. Moreover, the structure of A5 resembles that of dipeptide **WY**. To investigate the inhibitory potency of dipeptides against mushroom tyrosinase, 400 dipeptides were constructed and subjected to the tyrosinase inhibition assay. Their inhibitory abilities were pre-estimated and

DOI: 10.1021/acs.jafc.5b01026
J. Agric. Food Chem. 2015, 63, 6181−6188

summarized in a 20 × 20 dipeptide matrix (Figure 2). The result showed that 5 mM cysteine-containing dipeptides completely ceased the activity of tyrosinase (normalized percentage inhibition index is 0.0−0.3; Figure 2). In addition, 5 mM **PD**, **DY**, and **YK** reduced the activity of tyrosinase by 60−70%. However, dipeptides with a tyrosine residue located at the C or N terminus exerted moderate effects on tyrosinase inhibitory formation efficiency; their normalized inhibition index was approximately 0.5−0.7. The remaining dipeptides showed little or no inhibition against tyrosinase, and some did not even completely dissolve in double-distilled (dd) H_2O (46 peptides labeled with asterisks). Twenty-seven dipeptides (the color of the reaction solution changed; therefore, these might have interfered with the result) are denoted with a dotted pattern (Figure 2).

Cell Viability and Melanin Quantification Assay. According to the 20 × 20 dipeptide matrix for the inhibition of tyrosinase (Figure 2), we randomly selected four dipeptides, two cysteine-containing dipeptides (**CA** and **YC**) and two non-cysteine-containing dipeptides (**PD** and **DY**), to estimate their effects on cell viability and melanogenesis. The cell viability of human normal melanocytes treated with 1.0, 10, and 100 μM dipeptides (**CA**, **YC**, **PD**, and **DY**) is shown in Figure 3; no

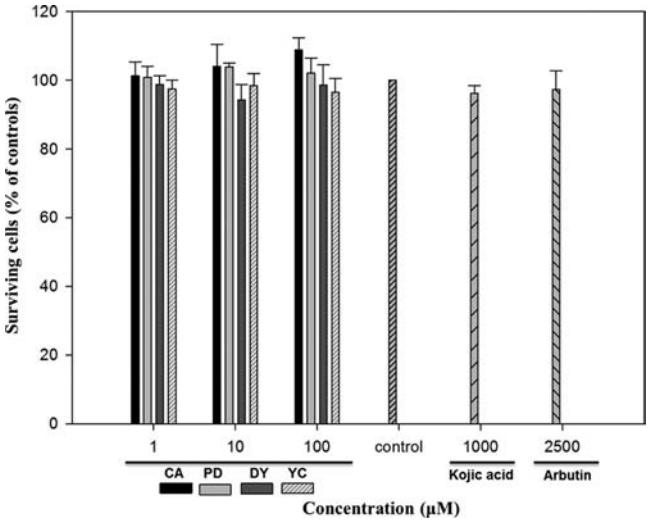

Figure 3. Effects of arbutin, kojic acid, and dipeptides **CA**, **YC**, **PD**, and **DY** on cell viability.

significant cell death was observed under these conditions compared with the controls. The depigmenting effects of these dipeptides were estimated under the same conditions as those of the cell viability assay (Table 1). The results revealed that **CA** and **PD** attenuated 5.6 and 16.5% melanin content, respectively, at 100 μM; notably, **PD** could attenuate 20−30% melanin content at 400 μM. However, **YC** and **DY** showed little or no antimelanogenesis effects.

Table 1. Effects of Dipeptides CA, YC, PD, and DY on Melanogenesis in Normal Human Epidermal Melanocytes

	melanin content (%)			
peptide ID	1 μM	10 μM	100 μM	400 μM
CA	94.5 ± 1.8	93.4 ± 2.9	94.4 ± 1.8	
YC	85.9 ± 3.3	90.2 ± 5.7	109.7 ± 1.8	
PD	88.6 ± 1.1	87.0 ± 2.1	83.5 ± 1.2	71.5 ± 1.5
DY	91.1 ± 3.4	92.8 ± 2.4	102.9 ± 1.3	
kojic acid, 50 μM		97.7 ± 1.8		
kojic acid, 500 μM		91.6 ± 1.0		
β-arbutin, 50 μM		102.1 ± 4.6		
β-arbutin, 2.5 mM		90.6 ± 1.8		

Determination of Inhibitory Potency (IC_{50}) against Tyrosinase. The pre-estimation of the effects of dipeptides on tyrosinase inhibition demonstrated that cysteine-containing dipeptides markedly reduced the activity of tyrosinase. We further determined the IC_{50} to precisely investigate and compare the functional variations. The IC_{50} values of N-terminal cysteine-containing dipeptides are shown in Table 2. According to the table, most of the values ranged from 2.0 to 22.6 μM, showing the effective inhibitory potency, except for **CP** (IC_{50} = 55.8 μM). In addition, **CS**, **CY**, **CF**, **CC**, **CI**, **CM**, and **CQ** considerably inhibited tyrosinase; the IC_{50} was <5 μM. In particular, **CE** exhibited the strongest potency in inhibiting tyrosinase (IC_{50} = 2.0 μM). The inhibition scales of most C-terminal cysteine-containing dipeptides ranged from 4.5 to 140 μM, less potent than the inhibition scales of N-terminal cysteine-containing dipeptides (Table 2). The dipeptides that showed comparable inhibitory potency with those of the C-terminal cysteine-containing dipeptides were **IC**, **NC**, **QC**, **FC**, and **VC** (IC_{50} < 10 μM).

Molecular Modeling. Cysteine-containing dipeptides (**CE**, **CS**, **CY**, **CA**, and **CW**) significantly decreased the activities of tyrosinase (by >6-fold) compared with **EC**, **SC**, **YC**, **AC**, and **WC**. To elucidate the functional deviations of these cysteine-containing dipeptides, we further analyzed the structural interactions of these dipeptides with mushroom tyrosinase by using molecular modeling. Dipeptides **CE**, **CS**, **CY**, **CA**, and **CW** and their reverse forms (**EC**, **SC**, **YC**, **AC**, and **WC**) were docked into the active sites of mushroom tyrosinase (PDB ID 2Y9X), and their detailed molecular interactions were analyzed (Supporting Information Table S1). The result showed that the cysteine residues of all dipeptides most likely contacted closely with the binuclear copper ions at the active sites of tyrosinase, regardless of their location (N or C terminus; Supporting Information Figure S1). In addition, **CE**, with the most profound tyrosinase inhibitory ability, showed extensive strong molecular interactions with tyrosinase (Supporting Information Figure S2 and Table S1). The electrostatic and cation−π interactions supported by residues His244, Asn260, Glu256, and Phe264 were commonly observed within the docked **CE**, **CD**, **CS**, **CY**, **CA**, and **CW**. In addition, hydrogen bonds and hydrophobic interactions were observed among **CE**, **CS**, **CY**, and **CW** active-site residues Arg268, Gly281, Ser282, and Val283 (Supporting Information Table S1). Molecular modeling of **CD** was performed to clarify its functional divergence with **CE**. The result showed that only four of six molecular interactions were observed between tyrosinase and **CD**. The molecular interactions of **EC**, **SC**, **YC**, **AC**, and **WC** with tyrosinase are summarized in Table S1. All N-terminal cysteine-containing dipeptides exhibited electrostatic attractions with Glu256, hydrogen-bond interactions with Asn260, and hydrophobic interactions with Val283. In addition, the molecular models of tyrosine-containing dipeptides, **YK** and **DY**, in complex with mushroom tyrosinase were observed (Figure 4). The tyrosine moiety of **YK** and **DY** went deep into the substrate binding pocket, and π−π interactions were observed between the phenol ring of tyrosine and the imidazole ring of His263. The lysine moiety of **YK** interacted with Phe264 and Arg268 through cation−π interactions and electrostatic interactions, respectively (Figure 4D). The dipeptide **DY** interacted with H85, Ser282, and

DOI: 10.1021/acs.jafc.5b01026
J. Agric. Food Chem. 2015, 63, 6181−6188

Table 2. Comparison of Tyrosinase Inhibitory Ability (IC_{50}) among N-Terminal Cysteine-Containing Dipeptides (Cx) and C-Terminal Cysteine-Containing Dipeptides (xC) in ddH_2O for 10 and 30 min[a]

dipeptide	IC_{50}	SEM	xC/Cx	dipeptide	IC_{50}	SEM	xC/Cx
CE	2.0	0.3	70.7	CG	5.9	2.5	4.1
EC*	140.1	16.7		GC	24.6	8.5	
CS	4.5	2.8	6.3	CR	8.0	3.0	4.0
SC	28.3	5.4		RC	32.3	12.9	
CY	3.1	0.7	42.4	CW	5.4	1.5	8.8
YC*	131.6	26.4		WC	47.3	2.5	
CF	2.7	0.2	3.0	CL	8.0	2.4	1.8
FC	7.9	1.3		LC	14.5	2.1	
CC	3.2	0.4	1.0	CA	9.6	5.7	6.5
CC	3.2	0.4		AC	62.2	17.1	
CI	4.0	0.9	1.1	CT	8.2	2.1	5.3
IC	4.5	0.5		TC*	44.0	15.3	
CM	4.9	0.8	2.2	CH	10.7	2.1	1.9
MC	10.7	1.6		HC*	20.0	6.9	
CQ	3.5	1.0	1.7	CN	22.6	8.8	0.2
QC	5.9	0.3		NC	5.3	0.8	
CK	5.9	0.5	6.8	CD	14.1	4.6	4.0
KC	39.9	2.4		DC*	56.1	8.9	
CV	8.2	2.1	1.0	CP*	55.8	4.6	0.4
VC	8.3	1.5		PC	20.3	1.0	

[a]SEM denotes the standard error of mean. An asterisk represents the dipeptides that did not completely dissolve in ddH_2O.

Val283 through electrostatic attractions, hydrogen bonding, and hydrophobic interactions, respectively (Figure 4C).

DISCUSSION

According to our previous finding that a natural compound, A5,[36] which possesses potent tyrosinase inhibitory ability, resembles the structure of dipeptide **WY**, dipeptides have great potential for tyrosinase inhibitor development. In this study, we comprehensively estimated 20 × 20 dipeptides for mushroom tyrosinase inhibition, and the results revealed that cysteine-containing dipeptides significantly inhibit tyrosinase. The IC_{50} of cysteine-containing dipeptides was determined for investigating the positional preference of the cysteine residue and the selectivity of functional amino acids against tyrosinase. The results revealed that N-terminal cysteine-containing dipeptides outperformed the C-terminal cysteine-containing dipeptides in inhibiting tyrosinase, and **CE** exhibited the strongest inhibitory potency (IC_{50} = 2.0 μM) (Table 2). In addition, most of the cysteine-containing dipeptides exhibited modest divergence in their inhibitory abilities when the cysteine residue was reversed at the terminus. By contrast, the inhibitory abilities of **CE**, **CS**, **CY**, **CA**, and **CW** decreased >6-fold when the cysteine residues shifted from the N terminus to the C terminus. Furthermore, an extensively attenuated inhibition of tyrosinase was observed; the inhibitory potencies of **CY**−**YC** and **CE**−**EC** were reduced 42.4- and 70.7-fold, respectively. These results indicate that the glutamic acid residue (**E**) is more functional at the C terminus than at the N terminus of dipeptides for inhibition, and the hydroxyl groups of serine and tyrosine residues at the C terminus, not the N terminus, considerably contribute to the inhibitory ability. Moreover, the bulk indole ring of the tryptophan residue located at the C terminus of dipeptides is more bioactive in inhibiting tyrosinase than that located at the N terminus. This study not only demonstrates the importance of the positional preference of the cysteine residue but also reveals the selectivity of the functional amino acids of cysteine-containing dipeptides for inhibiting tyrosinase.

The functional variations resulting from the positional preference of the cysteine residue and the selectivity of specific amino acids among N- and C-terminal cysteine-containing dipeptides were further analyzed using molecular modeling. According to the models, the cysteine residue most likely coordinates with the binuclear copper ions through the sulfur atom of the cysteine residue, regardless of its location (N or C terminus; Figure S1). In addition, one anion−π interaction, one hydrogen bond, and two electrostatic forces were frequently observed in all N-terminal cysteine-containing dipeptides for tyrosinase interactions (Table S1). However, only one hydrogen bond, one hydrophobic bond, and one electrostatic interaction were frequently observed in all C-terminal cysteine-containing dipeptides for tyrosinase interaction. Thus, these variations may mainly cause a functional divergence between N- and C-terminal cysteine-containing dipeptides in the inhibition of tyrosinase. The different inhibitory efficacies of the N-terminal cysteine-containing dipeptides against tyrosinase can be explained by their corresponding interactions with tyrosinase. For example, **CE** and **CY** display a maximum of six molecular interactions with tyrosinase; therefore, they show the strongest inhibitory ability (Figure S1 and Table S1), and **CA**, featuring the fewest molecular interactions with tyrosinase, exhibits the weakest inhibitory potency (Table S1). Similar explanations can be applied to interpret the diverse inhibitory efficiency of C-terminal cysteine-containing dipeptides, except for **EC** and **YC**; their inferior inhibitory ability compared with that of **SC** and **AC** may result from incomplete dissolution in ddH_2O. Moreover, the glutamic acid residue of **CE**, with a longer carboxyl side chain than that of aspartic acid, results in four extra molecular interactions with the active-site residues of tyrosinase (Figure S1A and Table S1), causing a stronger inhibitory ability than that of **CD**. Furthermore, the tryptophan residue of **CW** additionally contacts tyrosinase (one electrostatic interaction with His224, one hydrogen bond with the main chain of Gly281, and an extra hydrophobic interaction with Phe264), rendering it more efficient than **WC** in the inhibition of tyrosinase.

DOI: 10.1021/acs.jafc.5b01026
J. Agric. Food Chem. 2015, 63, 6181−6188

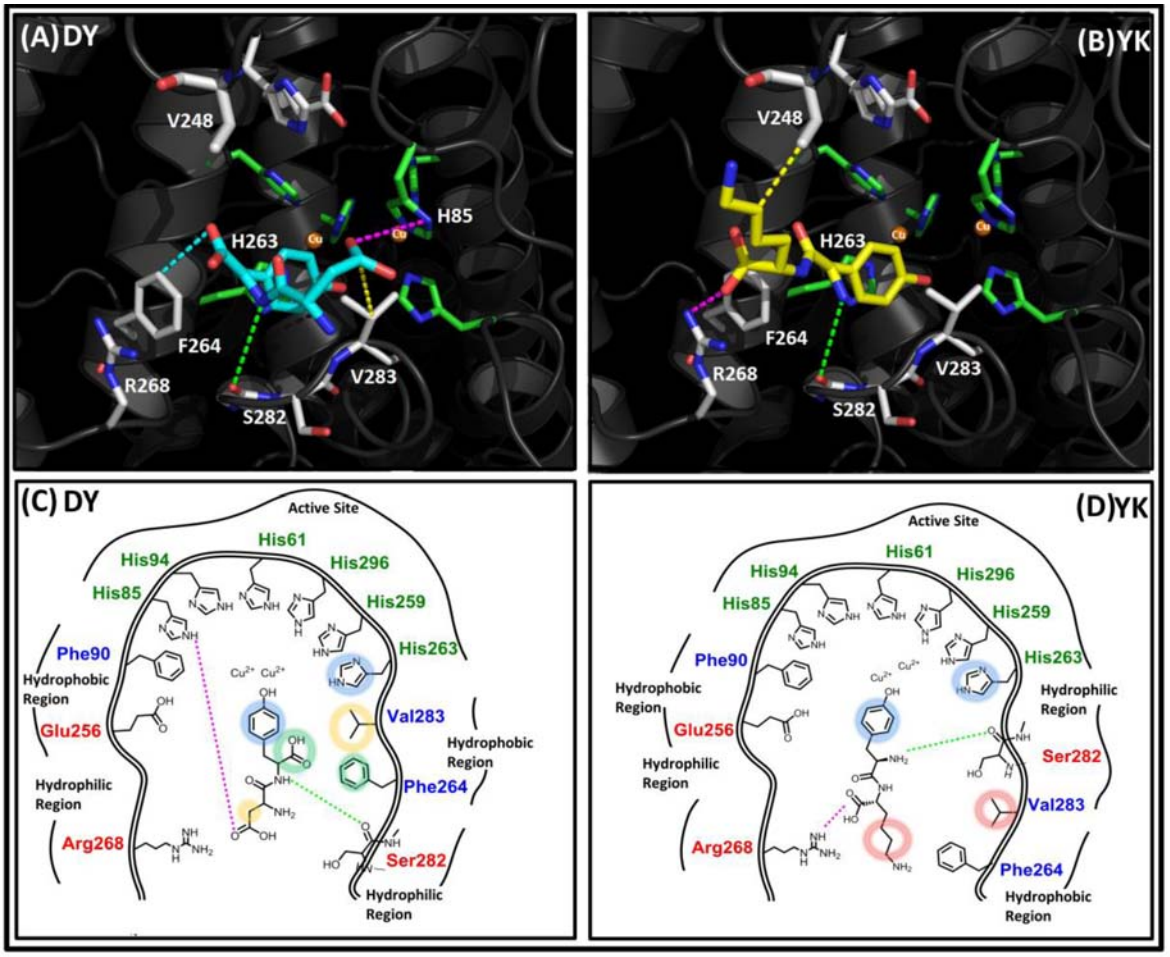

Figure 4. Molecular models of dipeptides **DY** and **YK** in complex with mushroom tyrosinase. (A) Docking model of the dipeptide **DY** (cyan) at the active sites of mushroom tyrosinase. (B) Docking model of the dipeptide **YK** (yellow) in complex with mushroom tyrosinase. The residues interacting with dipeptides **DY** and **YK** are denoted by white and green (six histidine residues), respectively. Green, magenta, and cyan dashed lines represent the H-bonding, electrostatic, and anion−π interactions, respectively, and yellow lines represent the hydrophobic interactions. (C) 2D schematic of the interactions between the dipeptide **DY** and active-site residues of mushroom tyrosinase. (D) 2D schematic of the interactions between the dipeptide **YK** and active-site residues of mushroom tyrosinase. In 2D schemes, green and magenta dashed lines denote H-bonding and electrostatic interactions, respectively; circles in distinct colors represent the relative hydrophobic and/or π−π interactions among the dipeptide and active-site residues of mushroom tyrosinase, respectively.

In this study, the inhibitory abilities of dipeptides were investigated in the presence of tyrosine as the tyrosinase substrate, and dipeptide activity was evaluated for dopachrome formation. Therefore, the inhibition of tyrosinase activity could be accomplished by one of the following: (a) reducing agents, leading to the reduction of dopaquinone; (b) *o*-dopaquinone scavengers, such as thiol-containing compounds; (c) alternative enzyme substrates−phenolic compounds; (d) nonspecific enzyme inactivators, such as acids or bases; or (e) specific tyrosinase inactivator−mechanism-based inhibitors, also called suicide substrates.[7] Cysteine-containing dipeptides are similar to *o*-dopaquinone scavengers, which react with dopaquinone, causing the formation of thiol−dopa conjugates. In vivo, cysteine and GSH are natural thiol compounds that form pheomelanin instead of eumelanin.[40] Similarly, cysteine-containing dipeptides have the potential to form dopaquinone conjugates, thus attenuating dopachrome formation, abolishing eumelanin synthesis, and increasing the pheomelanin amount (Figure 1). The structural components of **CE**, the most potent dipeptide in the inhibition of dopachrome formation, exhibit similarities with those of GSH (Figure 1). Thus, we proposed that cysteine-containing dipeptides can either interact with the active sites of tyrosinase or act as the *o*-dopaquinone scavenger to inhibit dopachrome formation. However, this was disproved by our HPLC and mass spectrometry analysis results (Figure S3, Table S2, and Figure S4). To clarify and identify the possible inhibition mechanism of cysteine-containing dipeptides against tyrosinase, we performed HPLC to purify the products of both N-terminal and C-terminal cysteine-containing dipeptides that reacted with tyrosinase. In addition, mass spectrometry was employed to determine the precise molecular weight of the purified samples. The results showed that none of the peaks corresponding to cysteinyldopa-peptides—the products resulting from the reactions of cysteine-containing dipeptides interacting with dopaquinone—was observed in the HPLC profile, and no molecular weight equilibrant to cysteinyldopa-peptide was identified using mass spectrometry (Figure S4). These results reveal that cysteine-containing dipeptides most likely bind and inhibit tyrosinase directly, instead of interacting with dopaquinone to form cysteinyldopa-peptide.

However, the tyrosine-containing dipeptides possibly belong to the alternative enzyme substrate, where the tyrosine entity can

DOI: 10.1021/acs.jafc.5b01026
J. Agric. Food Chem. 2015, 63, 6181−6188

compete with the tyrosine substrate at the active site of tyrosinase. To elucidate the inhibition mechanism of tyrosine-containing dipeptides against tyrosinase, **CY**, **DY**, **YC**, and **YK** were directly reacted with tyrosinase in the absence of a substrate (tyrosine); the absorbance at 400 and 475 nm of the products was then evaluated. The result showed that the products obtained from the reactions of **CY** and **YC** interacting with tyrosinase exhibited no absorption at 400 and 475 nm (Figure S5A), respectively, indicating that none of the products belongs to a dopachrome-containing and/or dopaquinone-containing peptide. This proved that cysteine-containing dipeptides are inhibitors that use the cysteine moiety mainly to interact with the active site of tyrosinase instead of using the tyrosine. The products from **DY** and **YK** showed weak absorption at 400 nm but not at 475 nm (Figure S5B), indicating that the tyrosine-containing dipeptides are substrate-like inhibitors subject to further catalysis by tyrosinase to form dopaquinone-containing dipeptide. These results clarify that the tyrosine-containing dipeptides act as substrate binding at the active site of tyrosinase, thus exhibiting varying inhibitory efficacies against tyrosinase. When these tyrosine-containing dipeptides exhibit a favorable affinity with tyrosinase, dopachrome formation is attenuated. In addition, approximately 27 tyrosine-containing dipeptides that changed the color of the tyrosinase reaction solutions were observed. Therefore, free tyrosine can react with tyrosinase and form dopachrome. However, tyrosine in a dipeptide can be oxidized by tyrosinase, thus inhibiting dopachrome formation.

Conventional pharmaceutical skin-whitening drugs, such as hydroquinone,[16,17] arbutin,[18] and kojic acid,[19,20] are insufficient because they are reported to be severely carcinogenic and damage the structural architecture of several tissues.[41−43] Moreover, an intriguing recent story was published on a skin-whitening rhododendrol, which has been withdrawn from the cosmetic market because of its toxicity.[44] Recently, several studies have discovered novel proteins and peptides from natural resources, such as the housefly,[45] silk,[46] honey,[47] wheat,[48] and milk,[49] for tyrosinase inhibition. In particular, cyclic peptides,[50] short-sequence oligopeptides,[32] kojic acid tripeptide,[34] mimosine tetrapeptides,[33] and octameric peptides[15] have been thoroughly investigated to determine their tyrosinase inhibitory ability. The current study is the first on the systematical annotation of critical amino acids that constitute potent dipeptides for tyrosinase inhibition in dopachrome formation. The cytotoxicity and depigmenting effects of cysteine-containing **YC** and **CA**, as well as the less potent noncysteine-containing **PD** and **DY**, were examined using cell viability and melanin quantification assays. No significant cytotoxicity was observed in these dipeptide-treated melanocytes, and **CA** and **PD** attenuated 5.6 and 16.5% melanin content, respectively, at 100 μM. In addition, the cells treated with dipeptide **PD** (400 μM) could reduce 20−30% of melanin content. This indicates that the inhibitory effects of **CA** and **PD** on melanin production are not attributable to their cytotoxicity, and **CA** and **PD** can be safely used in skin-whitening products without influencing melanocyte growth.

In conclusion, this study provides insight into the functional role of the cysteine residue positional preference and the selectivity of specific amino acids of cysteine-containing dipeptides for the inhibition of tyrosinase. Therefore, the findings can be applied in developing new inhibitors against tyrosinase.

■ ASSOCIATED CONTENT

Ⓢ Supporting Information

Five figures (S1, S2, S3, S4, and S5) and two tables (S1 and S2). The Supporting Information is available free of charge on the ACS Publications website at DOI: 10.1021/acs.jafc.5b01026.

■ AUTHOR INFORMATION

Corresponding Author

*(N.-W.H.) Phone: +886-4-7232105, ext. 3421; Fax: +886-4-7211156. E-mail: nady@cc.ncue.edu.tw.

Author Contributions

‖T.-S.T., K.-C.T., and W.-C.C. contributed equally to this work.

Funding

This study was supported by the National Research Institute of Chinese Medicine, Ministry of Health and Welfare (MM10211-0153 and MM10401-0394) and the Ministry of Science and Technology (MOST 103-2320-B-077-001-MY3 to K.-C.T.), Taipei, Taiwan.

Notes

The authors declare no competing financial interest.

■ ACKNOWLEDGMENTS

We thank Chia-Ying Wu, Jin-Yu Shiu, and Chia-Chia Chang (Institute of Biotechnology, National Changhua University of Education, Changhua, Taiwan) for their input and assistance. In addition, we are grateful to the National Center for High-Performance Computing for use of computers and facilities. The computational work of GOLD and Discovery Studio was conducted at the National Center for High-Performance Computing, Taiwan.

■ REFERENCES

(1) Lee, H. E.; Kim, E. H.; Choi, H. R.; Sohn, U. D.; Yun, H. Y.; Baek, K. J.; Kwon, N. S.; Park, K. C.; Kim, D. S. Dipeptides Inhibit Melanin Synthesis in Mel-Ab Cells through Down-Regulation of Tyrosinase. *Korean J. Physiol. Pharmacol.* **2012**, *16*, 287−291.

(2) Brenner, M.; Hearing, V. J. The protective role of melanin against UV damage in human skin. *Photochem. Photobiol.* **2008**, *84*, 539−549.

(3) Schallreuter, K.; Slominski, A.; Pawelek, J. M.; Jimbow, K.; Gilchrest, B. A. What controls melanogenesis? *Exp. Dermatol.* **1998**, *7*, 143−150.

(4) Wang, H. M.; Chen, C. Y.; Wen, Z. H. Identifying melanogenesis inhibitors from Cinnamomum subavenium with in vitro and in vivo screening systems by targeting the human tyrosinase. *Exp. Dermatol.* **2011**, *20*, 242−248.

(5) Lo, C. Y.; Liu, P. L.; Lin, L. C.; Chen, Y. T.; Hseu, Y. C.; Wen, Z. H.; Wang, H. M. Antimelanoma and antityrosinase from Alpinia galangal constituents. *Sci. World J.* **2013**, *2013*, No. 186505.

(6) Iozumi, K.; Hoganson, G. E.; Pennella, R.; Everett, M. A.; Fuller, B. B. Role of tyrosinase as the determinant of pigmentation in cultured human melanocytes. *J. Invest. Dermatol.* **1993**, *100*, 806−811.

(7) Chang, T. S. An updated review of tyrosinase inhibitors. *Int. J. Mol. Sci.* **2009**, *10*, 2440−2475.

(8) Seo, S. Y.; Sharma, V. K.; Sharma, N. Mushroom tyrosinase: recent prospects. *J. Agric. Food Chem.* **2003**, *51*, 2837−2853.

(9) Passi, S.; Nazzaro-Porro, M. Molecular basis of substrate and inhibitory specificity of tyrosinase: phenolic compounds. *Br. J. Dermatol.* **1981**, *104*, 659−665.

(10) Marusek, C. M.; Trobaugh, N. M.; Flurkey, W. H.; Inlow, J. K. Comparative analysis of polyphenol oxidase from plant and fungal species. *J. Inorg. Biochem.* **2006**, *100*, 108−123.

(11) Katsambas, A. D.; Stratigos, A. J. Depigmenting and bleaching agents: coping with hyperpigmentation. *Clin Dermatol* **2001**, *19*, 483−488.

DOI: 10.1021/acs.jafc.5b01026
J. Agric. Food Chem. 2015, 63, 6181−6188

(12) Solano, F.; Briganti, S.; Picardo, M.; Ghanem, G. Hypopigmenting agents: an updated review on biological, chemical and clinical aspects. *Pigm. Cell Res.* **2006**, *19*, 550−571.
(13) Asanuma, M.; Miyazaki, I.; Ogawa, N. Dopamine- or L-DOPA-induced neurotoxicity: the role of dopamine quinone formation and tyrosinase in a model of Parkinson's disease. *Neurotoxic. Res.* **2003**, *5*, 165−176.
(14) Pan, T.; Li, X.; Jankovic, J. The association between Parkinson's disease and melanoma. *Int. J. Cancer* **2011**, *128*, 2251−2260.
(15) Schurink, M.; van Berkel, W. J.; Wichers, H. J.; Boeriu, C. G. Novel peptides with tyrosinase inhibitory activity. *Peptides* **2007**, *28*, 485−495.
(16) Arndt, K. A.; Fitzpatrick, T. B. Topical use of hydroquinine as a depigmenting agent. *J. Am. Med. Assoc.* **1965**, *194*, 117−119.
(17) Fitzpatrick, T. B.; Arndt, K. A.; el-Mofty, A. M.; Pathak, M. A. Hydroquinone and psoralens in the therapy of hypermelanosis and vitiligo. *Arch. Dermatol.* **1966**, *93*, 589−600.
(18) Germanas, J. P.; Wang, S.; Miner, A.; Hao, W.; Ready, J. M. Discovery of small-molecule inhibitors of tyrosinase. *Bioorg. Med. Chem. Lett.* **2007**, *17*, 6871−6875.
(19) Ahn, S. M.; Rho, H. S.; Baek, H. S.; Joo, Y. H.; Hong, Y. D.; Shin, S. S.; Park, Y. H.; Park, S. N. Inhibitory activity of novel kojic acid derivative containing trolox moiety on melanogenesis. *Bioorg. Med. Chem. Lett.* **2011**, *21*, 7466−7469.
(20) Elsner, P., Maibach, H. I., Eds. *Cosmeceuticals: Drugs vs. Cosmetics*; CRC Press: Boca Raton, FL, USA, 2000.
(21) Breathnach, A. C.; Nazzaro-Porro, M.; Passi, S.; Zina, G. Azelaic acid therapy in disorders of pigmentation. *Clin. Dermatol* **1989**, *7*, 106−119.
(22) Rigoni, C.; Toffolo, P.; Serri, R.; Caputo, R. [Use of a cream based on 20% azelaic acid in the treatment of melasma]. *G. Ital. Dermatol. Venereol.* **1989**, *124*, I−VI.
(23) Jimbow, K. *N*-Acetyl-4-*S*-cysteaminylphenol as a new type of depigmenting agent for the melanoderma of patients with melasma. *Arch. Dermatol.* **1991**, *127*, 1528−1534.
(24) Hamidian, H.; Tagizadeh, R.; Fozooni, S.; Abbasalipour, V.; Taheri, A.; Namjou, M. Synthesis of novel azo compounds containing 5(4*H*)-oxazolone ring as potent tyrosinase inhibitors. *Bioorg. Med. Chem.* **2013**, *21*, 2088−2092.
(25) Hamidian, H. Synthesis of novel compounds as new potent tyrosinase inhibitors. *BioMed Res. Int.* **2013**, *2013*, No. 207181.
(26) Zhu, T. H.; Cao, S. W.; Yu, Y. Y. Synthesis, characterization and biological evaluation of paeonol thiosemicarbazone analogues as mushroom tyrosinase inhibitors. *Int. J. Biol. Macromol.* **2013**, *62*, 589−595.
(27) Liang, C.; Lim, J. H.; Kim, S. H.; Kim, D. S. Dioscin: a synergistic tyrosinase inhibitor from the roots of Smilax china. *Food Chem.* **2012**, *134*, 1146−1148.
(28) Zheng, Z. P.; Tan, H. Y.; Wang, M. Tyrosinase inhibition constituents from the roots of *Morus australis*. *Fitoterapia* **2012**, *83*, 1008−1013.
(29) Sarkhail, P.; Sarkheil, P.; Khalighi-Sigaroodi, F.; Shafiee, A.; Ostad, N. Tyrosinase inhibitor and radical scavenger fractions and isolated compounds from aerial parts of *Peucedanum knappii* Bornm. *Nat. Prod. Res.* **2013**, *27*, 896−899.
(30) Lee, Y. C.; Hsiao, N. W.; Tseng, T. S.; Chen, W. C.; Lin, H. H.; Leu, S. J.; Yang, E. W.; Tsai, K. C. Phage display-mediated discovery of novel tyrosinase-targeting tetrapeptide inhibitors reveals the significance of N-terminal preference of cysteine residues and their functional sulfur atom. *Mol. Pharmacol.* **2015**, *87*, 218−230.
(31) Chen, W. C.; Tseng, T. S.; Hsiao, N. W.; Lin, Y. L.; Wen, Z. H.; Tsai, C. C.; Lee, Y. C.; Lin, H. H.; Tsai, K. C. Discovery of highly potent tyrosinase inhibitor, T1, with significant anti-melanogenesis ability by zebrafish in vivo assay and computational molecular modeling. *Sci. Rep.* **2015**, *5*, No. 7995.
(32) Abu Ubeid, A.; Zhao, L.; Wang, Y.; Hantash, B. M. Short-sequence oligopeptides with inhibitory activity against mushroom and human tyrosinase. *J. Invest. Dermatol.* **2009**, *129*, 2242−2249.
(33) Upadhyay, A.; Chompoo, J.; Taira, N.; Fukuta, M.; Gima, S.; Tawata, S. Solid-phase synthesis of mimosine tetrapeptides and their inhibitory activities on neuraminidase and tyrosinase. *J. Agric. Food Chem.* **2011**, *59*, 12858−12863.
(34) Noh, J. M.; Kwak, S. Y.; Kim, D. H.; Lee, Y. S. Kojic acid-tripeptide amide as a new tyrosinase inhibitor. *Biopolymers* **2007**, *88*, 300−307.
(35) Craik, D. J.; Fairlie, D. P.; Liras, S.; Price, D. The future of peptide-based drugs. *Chem. Biol. Drug Des.* **2013**, *81*, 136−147.
(36) Hsiao, N. W.; Tseng, T. S.; Lee, Y. C.; Chen, W. C.; Lin, H. H.; Chen, Y. R.; Wang, Y. T.; Hsu, H. J.; Tsai, K. C. Serendipitous discovery of short peptides from natural products as tyrosinase inhibitors. *J. Chem. Inf. Model.* **2014**, *54*, 3099−3111.
(37) Takahashi, M.; Takara, K.; Toyozato, T.; Wada, K. A novel bioactive chalcone of Morus australis inhibits tyrosinase activity and melanin biosynthesis in B16 melanoma cells. *J. Oleo Sci.* **2012**, *61*, 585−592.
(38) Kumar, K. J.; Yang, J. C.; Chu, F. H.; Chang, S. T.; Wang, S. Y. Lucidone, a novel melanin inhibitor from the fruit of *Lindera erythrocarpa* Makino. *Phytother. Res.* **2010**, *24*, 1158−1165.
(39) Wang, K. H.; Lin, R. D.; Hsu, F. L.; Huang, Y. H.; Chang, H. C.; Huang, C. Y.; Lee, M. H. Cosmetic applications of selected traditional Chinese herbal medicines. *J. Ethnopharmacol.* **2006**, *106*, 353−359.
(40) del Marmol, V.; Ito, S.; Bouchard, B.; Libert, A.; Wakamatsu, K.; Ghanem, G.; Solano, F. Cysteine deprivation promotes eumelanogenesis in human melanoma cells. *J. Invest. Dermatol.* **1996**, *107*, 698−702.
(41) McGregor, D. Hydroquinone: an evaluation of the human risks from its carcinogenic and mutagenic properties. *Crit. Rev. Toxicol.* **2007**, *37*, 887−914.
(42) Philips, N.; Burchill, D.; O'Donoghue, D.; Keller, T.; Gonzalez, S. Identification of benzene metabolites in dermal fibroblasts as non-phenolic: regulation of cell viability, apoptosis, lipid peroxidation and expression of matrix metalloproteinase 1 and elastin by benzene metabolites. *Skin Pharmacol. Physiol.* **2004**, *17*, 147−152.
(43) Charlin, R.; Barcaui, C. B.; Kac, B. K.; Soares, D. B.; Rabello-Fonseca, R.; Azulay-Abulafia, L. Hydroquinone-induced exogenous ochronosis: a report of four cases and usefulness of dermoscopy. *Int. J. Dermatol.* **2008**, *47*, 19−23.
(44) Ito, S.; Ojika, M.; Yamashita, T.; Wakamatsu, K. Tyrosinase-catalyzed oxidation of rhododendrol produces 2-methylchromane-6,7-dione, the putative ultimate toxic metabolite: implications for melanocyte toxicity. *Pigm. Cell Melanoma Res.* **2014**, *27*, 744−753.
(45) Daquinag, A. C.; Sato, T.; Koda, H.; Takao, T.; Fukuda, M.; Shimonishi, Y.; Tsukamoto, T. A novel endogenous inhibitor of phenoloxidase from Musca domestica has a cystine motif commonly found in snail and spider toxins. *Biochemistry* **1999**, *38*, 2179−2188.
(46) Kato, N.; Sato, S.; Yamanaka, A.; Yamada, H.; Fuwa, N.; Nomura, M. Silk protein, sericin, inhibits lipid peroxidation and tyrosinase activity. *Biosci., Biotechnol., Biochem.* **1998**, *62*, 145−147.
(47) Ates, S.; P, S.; Cokmus, C. Partial characterization of a peptide from honey that inhibits mushroom polyphenol oxidase. *J. Food Biochem.* **2001**, *25*, 127−137.
(48) Okot-Kotber, M.; L, A.; Yong, K. J.; Bagorogoza, K. Activity and inhibition of polyphenol oxidase in extracts of bran and other milling fractions from a variety of wheat cultivars. *Cereal Chem.* **2001**, *78*, 514−520.
(49) Chen, M. J.; L, J.; Sheu, J. F.; Lin, C. W.; Chuang, C. L. Study on skin care properties of milk kefir whey. *Asian-Australas. J. Anim. Sci.* **2006**, *19*, 905−908.
(50) Morita, H.; Kayashita, T.; Kobata, H.; Gonda, A.; Takeya, K.; Itokawa, H. Pseudostellarins D−F, new tyrosinase inhibitory cyclic peptides from *Pseudostellaria heterophylla*. *Tetrahedron* **1994**, *50*, 9975−9982.

DOI: 10.1021/acs.jafc.5b01026
J. Agric. Food Chem. 2015, 63, 6181−6188

Table 1. Major Fatty Acids Identified in Germ

ion m/z	RT	adduct	error (ppm)	RDB	MS^2 data	formula	tentative identification	abbreviation
279.2320	4.57	$[M + H]^+$	0.513	3.5	MS2 [279.2]: **261.2 (100)**,[a] 243.2 (58), 223.1 (27), 209.2 (30), 195.1 (21), 137.2 (31), 123.2(42), 109.2(35), 95.2 (38); MS3 [279.2→261.2]: **243.3 (100)**, 173.2 (13), 135.2 (13); MS4 [279.2→261.2→243.3]: 215.2 (12), 201.2 (44), 187.3 (61), 173.2 (100), 161.2 (28), 159.2 (45), 147.3 (22), 145.2 (50), 133.2 (20), 131.3 (26)	$C_{18}H_{30}O_2$	α-linolenic acid	C18:3
277.2172	4.63	$[M - H]^-$	−0.373	4.5	MS2 [277.2]: **259.4 (41)**, 257.3 (7), 233.3 (100), 205.3 (4), 179.3 (5)			
281.2473	5.93	$[M + H]^+$	−0.735	2.5	MS2 [281.2]: **263.2 (100)**, 245.2 (19); MS3 [281.2→263.2]: **245.2 (100)**; MS4 [281.2→263.2→245.2]: 217.1 (26), 203.2 (43), 189.2 (93), 175.2 (96), 163.3 (39), 161.2 (100), 149.2 (37), 147.1 (71), 135.1 (29), 133.2 (55), 121.2 (28), 119.1 (26), 109.2 (13), 107.2 (11), 105.2(16), 95.2 (17), 81.2 (13)	$C_{18}H_{32}O_2$	linoleic acid	C18:2
279.2329	5.95	$[M - H]^-$	−0.192	3.5	MS2 [279.2]: **261.3 (100)**, 259.3 (5), 243.3 (5); MS3 [279.2→261.2]: 243.3 (100), 233.5 (16), 219.1 (22), 205.4 (16), 109.2 (25), 107.3 (17)			
257.2475	6.87	$[M + H]^+$	−0.026	0.5	MS2 [257.2]: **239.3 (100)**, 225.2 (24), 187.2 (22), 183.2 (17), 173.1 (20), 169.2 (17), 103.2 (20), 89.0 (28)	$C_{16}H_{32}O_2$	palmitic acid	C16:0
255.2330	6.91	$[M - H]^-$	0.182	1.5	MS2 [255.2]: **237.3 (100)**, 236.7 (11), 211.2 (21), 193.3 (12)			
283.2630	7.43	$[M + H]^+$	−0.554	1.5	MS2 [283.3]: **265.3 (100)**, 247.3 (27); MS3 [283.3→265.3]: **247.3 (100)**; MS4 [283.3→265.3→247.3]: 205.2 (26), 191.2 (65), 177.3 (97), 165.2 (19), 163.2 (100), 151.2 (17), 149.1 (98), 137.1 (19), 135.1 (73), 123.2 (19), 121.2 (48), 109.2 (30), 107.2 (19), 95.2 (34), 93.2 (17), 81.2 (24)	$C_{18}H_{34}O_2$	oleic acid	C18:1
281.2484	7.48	$[M - H]^-$	−0.724	2.5	MS2 [281.2]: **263.3 (100)**			
285.2786	9.76	$[M + H]^+$	−0.725	0.5	MS2 [285.2]: 271.0 (23), **267.3 (35)**, 257.2 (20), 253.1 (100)	$C_{18}H_{36}O_2$	stearic acid	C18:0
283.2639	9.82	$[M - H]^-$	−1.248	1.5	MS2 [283.3]: **265.3 (100)**, 251.2 (11), 239.5 (20), 221.3 (26)			
311.2945	10.36	$[M + H]^+$	0.138	1.5	MS2 [311.3]: **293.2 (100)**, 275.3 (24); MS3 [311.3→293.2]: **275.4 (100)**; MS4 [311.3→293.2→275.4]: 219.3 (60), 205.2 (70), 191.3 (80), 177.2 (72), 163.2 (70), 149.2 (100), 135.2 (66), 121.2 (59), 109.2 (24), 107.2 (29), 93.2 (22)	$C_{20}H_{38}O_2$	gadoleic acid	C20:1
309.2796	10.45	$[M - H]^-$	−0.982	2.5	MS2 [309.3]: **291.4 (100)**, 265.4 (54), 209.2 (67)			

[a]Characteristic ions for identification are in bold. Same as other tables.

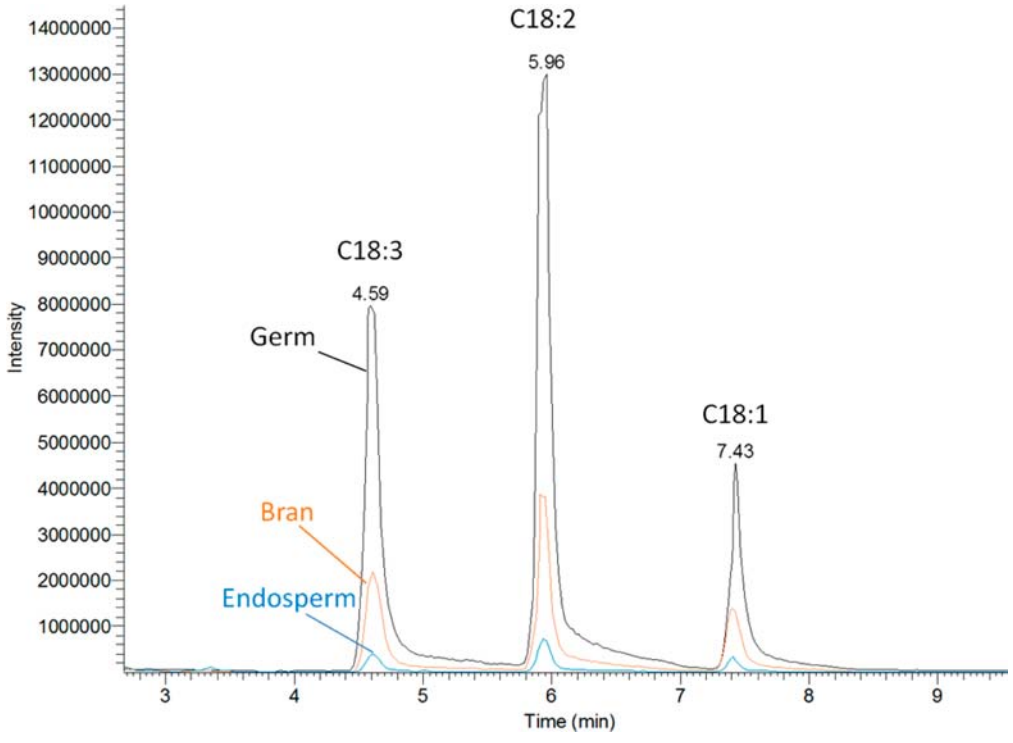

Figure 1. Extracted ion chromatograms of fatty acid ions at m/z 277.21−277.23, 279.23−279.24, and 281.24−281.25 in ESI negative mode.

DOI: 10.1021/acs.jafc.5b01599
J. Agric. Food Chem. 2015, 63, 6189−6211

Table 2. Oxylipins Putatively Identified in Germ

ion m/z	RT	adduct	error (ppm)	formula	RDB	MS^2 data	tentative identification	abbreviation
329.2334	1.05	$[M-H]^-$	0.160	$C_{18}H_{34}O_5$	2.5	MS2 [329.2]: 314.1 (10), 311.3 (100), 293.4 (48), 291.2 (7), 275.3 (31), 229.3 (35), 211.2 (34), 201.2 (61), 199.3 (29), 197.2 (8), 183.3 (7), 181.2 (17), 171.3 (73), 169.2 (12)	9,12,13-trihydroxy-10-octadecenoic acid	9,12,13-THODE
309.2071	1.16	$[M-H]^-$	−0.106	$C_{18}H_{30}O_4$	4.5	MS2 [309.2]: 291.3 (100), 273.3 (4), 265.3 (5), 251.4 (4), 221.3 (8), 209.3 (9), 195.3 (20), 185.2 (7), 171.2 (8)	9-hydroperoxy-10,12,15-octadecatrienoic acid	
311.2228	1.32	$[M-H]^-$	0.055	$C_{18}H_{32}O_4$	3.5	MS2 [311.2]: 293.4 (97), 275.4 (8), 267.3 (20), 249.2 (9), 241.4 (6), 223.3 (11), 211.3 (11), 184.1 (24), 183.2 (100), 171.2 (6)	9-hydroxy-13-oxo-10-octadecenoic acid; 13-hydroxy-9-oxo-10-octadecenoic acid	13-oxo-9-HODE; 9-oxo-13-HODE
313.2384	1.41	$[M-H]^-$	−0.105	$C_{18}H_{34}O_4$	2.5	MS2 [313.2]: 295.3 (100), 277.4 (19), 213.2 (4), 201.2 (7), 195.3 (13), 183.3 (60), 129.3 (4); MS3 [313.2→295.3]: 277.3 (100), 251.4 (24), 211.3 (10), 195.3 (56), 181.3 (12), 179.3 (44), 171.2 (12), 113.2 (7)	12,13-dihydroxy-9-octadecenoic acid	12,13-DiHOME(9)
293.2122	1.65	$[M-H]^-$	−0.062	$C_{18}H_{30}O_3$	4.5	MS2 [293.2]: 275.4 (100), 265.4 (6), 249.3 (7), 235.3 (20), 224.2 (6), 205.4 (9), **195.2 (18)**, 179.2 (7); MS3 [293.2→275.4]: 257.3 (10), 231.3 (100), 177.3 (9)	(9Z,11*E*)-13-keto-9,11-octadecadienoic acid	13-KODE
295.2276	1.68	$[M-H]^-$	−0.908	$C_{18}H_{32}O_3$	3.5	MS2 [295.2]: 277.4 (100), 267.5 (3), 259.3 (2), 251.3 (47), 223.3 (5), 213.2 (5), 197.1 (9), 195.3 (13), 179.2 (18), 171.2 (16), 169.2 (9), 167.3 (2), 153.2 (11), 151.2 (20), 141.3 (29)	13-hydroxy-9,11-octadecadienoic acid	13-HODE
295.2276	1.96	$[M-H]^-$	−0.908	$C_{18}H_{32}O_3$	3.5	MS2 [295.2]: 277.3 (100), 251.4 (7), 195.2 (23), 179.2 (14), **171.2 (34)**	9-hydroxy-10,12-octadecadienoic acid	9-HODE
293.2122	2.06	$[M-H]^-$	−0.062	$C_{18}H_{30}O_4$	4.5	MS2 [293.2]: 275.2 (67), 249.3 (47), 235.3 (17), 209.3 (7), **197.3 (36)**, **185.3 (100)**, 179.2 (9), 167.2 (10), 149.2 (7), 141.3 (10), 125.3 (8), 113.2 (26)	(10*E*,12*Z*)-9-keto-10,12-octadecadienoic acid	9-KODE
297.2434	2.19	$[M-H]^-$	−0.398	$C_{18}H_{34}O_3$	2.5	MS2 [297.2]: **279.3 (100)**, 253.5 (9), **251.4 (17)**, 235.3 (10), 198.2 (5), 197.2 (14), 184.2(9), 183.2 (24), 171.3 (45), 157.3 (12), 155.2 (6)	9,10-epoxyoctadecanoic acid	9,10-EODA
297.2434	5.11	$[M-H]^-$	−0.398	$C_{18}H_{34}O_3$	2.5	MS2 [297.2]: **297.5 (24)**, 281.1 (6), 279.2 (100), 253.4 (85), 251.3 (49), 240.1 (7), 235.2 (15), 183.1 (92)	9,10-epoxyoctadecanoic acid	9,10-EODA

enabled the analysis of a wide range of compounds from fatty acids to intact high molecular weight lipids such as sterol esters and TGs. UHPLC-HRAM-MS^n has been used to analyze polyphenols, glucosinolates, flavonoids, etc., in this laboratory.[13−17] The fuzzy chromatography mass spectrometric (FCMS) fingerprinting combined PCA was used to visualize the chemical difference between WF and RF. In comparison with full LC separation, FCMS aims to obtain an adequate separation one class of compounds from another as fast as possible on a relatively short (≤50 mm) column. Although optimal separation cannot be achieved on each individual compound, FCMS can avoid ion suppression effects to some extent and speed up high-throughput analysis.

EXPERIMENTAL PROCEDURES

Chemicals. HPLC grade methanol, formic acid, and *n*-butanol were purchased from VWR International, Inc. (Clarksburg, MD, USA). HPLC water was prepared from distilled water using a Milli-Q system (Millipore Laboratories, Bedford, MA, USA).

Materials and Sample Preparation. The bran, germ, and endosperm of the same brand were purchased from local grocery stores. Bran and germ flakes were ground into fine powder and then passed through a 60 mesh sieve. One hundred milligrams of each sample was extracted with 4.0 mL of water-saturated *n*-butanol[5,6,11,18] using a sonicator (Advanced Sonic Processing Systems, Oxford, CT, USA) at 16 kHz with 300 W power for 40 min. The slurry mixture was centrifuged at 13000*g* for 15 min in a Contifuge 28RS centrifuge (Heraeus, South Plainfield, NJ, USA) at 4 °C. The supernatant was filtered through a 17 mm (0.20 μm) PVDF syringe filter (VWR Scientific, Seattle, WA, USA) and stored at −80 °C until analysis. For FCMS analysis, whole wheat flour and all purpose unbleached flour from three different brands were used as WF and RF, respectively. Each of the six samples was extracted in triplicate. The injection volume for all samples was 2 μL.

UHPLC-HRAM-MS^n Conditions. The UHPLC-HRAM-MS^n system consisted of an LTQ Orbitrap XL MS with an Accela 1250 binary pump, a PAL HTC Accela TMO autosampler, an Accela PDA detector (Thermo Fisher Scientific, San Jose, CA, USA), and a G1316A column compartment (Agilent, Santa Clara, CA, USA). APCI and ESI detection were investigated in both the positive and negative ion modes. The ESI conditions were set as follows: sheath gas at 80 (arbitrary units), auxiliary and sweep gas at 10 (arbitrary units), spray voltage at −4.0 kV for negative mode and at 4.5 kV for positive mode; capillary temperature at 300 °C; capillary voltage at −50 V for negative mode and at 50 V for positive mode; and tube lens offset at −120 V for negative mode and at 120 V for positive mode. APCI source was operated at 450 °C, the heated capillary temperature was 275 °C, the corona discharge current was set to 5.0 μA, and sheath gas (N_2) and auxiliary gas (N_2) were at 60 and 5 arbitrary units, respectively. The scan event cycle used a FT full scan mass spectrum at a resolving power of 30000 and three data-dependent MS^2, MS^3, MS^4 events acquired by LTQ triggered by the most intensive ion from each previous scan event. The automated gain control (AGC) target value was set to 200,000 for FT full scan and to 10,000 for IT MS^n scan, respectively. MS^n activation parameters used an isolation width of 1 amu, maximum ion injection time of 200 ms, normalization collision energy at 35%, and activation time of 30 ms.

DOI: 10.1021/acs.jafc.5b01599
J. Agric. Food Chem. 2015, 63, 6189−6211

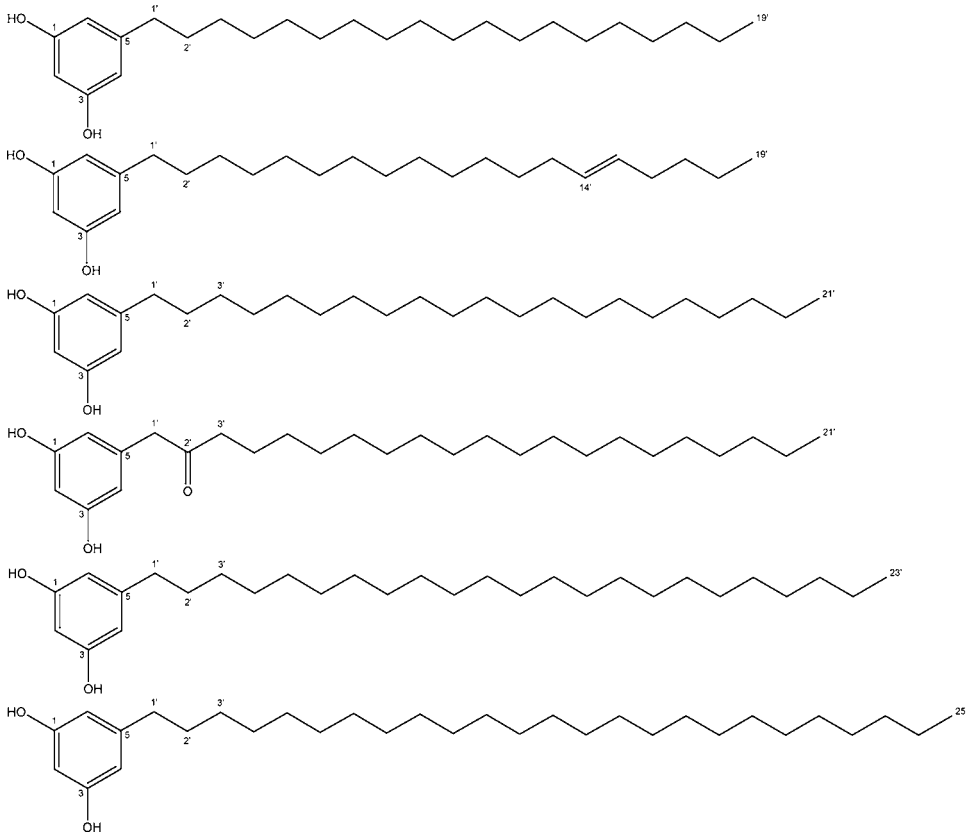

Figure 2. Structures of 5-*n*-alk(en)ylresorcinols present in wheat.

Table 3. Alk(en)ylresorcinols Identified from Bran

ion *m/z*	RT	error (ppm)	formula	RDB	MS^2 data	abbreviation
345.2788	5.83	−0.020	$C_{23}H_{36}O_2$	5.5	MS2 [345.3]: 327.6 (21), 275.5 (12), 261.5 (17), 177.0 (21), 163.1 (63), **123.1 (100)**	AR-C17:2
371.2946	6.81	0.385	$C_{25}H_{38}O_2$	6.5	MS2 [371.3]: **355.2 (36)**, 301.3 (32), 275.2 (38), 259.1 (72), 240.9 (36), **177.2 (53)**, **163.2 (100)**, 147.1 (37), 137.2 (46), 129.1 (60), **123.1 (99)**	AR-C19:3
347.2945	7.32	0.124	$C_{23}H_{38}O_2$	4.5	MS2 [347.3]: **123.1 (100)**; MS3 [347.3→123.1]: 95.0 (100), 65.1 (11)	AR-C17:1
391.3207	7.69	0.072	$C_{25}H_{42}O_3$	4.5	MS2 [391.3]: 373.4 (62), 348.2 (10), 233.2 (12), **149.1 (100)**, 139.1 (21), **123.0 (10)**	AR-C19:oxo
373.3101	8.14	−0.019	$C_{25}H_{40}O_2$	5.5	MS2 [373.3]: **357.1 (52)**, 341.2 (28), 289.2 (16), 275.3 (21), 261.3 (27), **163.2 (56)**, 149.3 (18), 137.2 (19), **123.2 (100)**	AR-C19:2
349.3104	9.56	0.839	$C_{23}H_{40}O_2$	3.5	MS2 [349.3]: 334.4 (2), 123.2 (4), **111.0 (100)**; MS3 [349.3→111.0]: 93.2 (100)	AR-C17:0
375.3259	10.09	0.381	$C_{25}H_{42}O_2$	4.5	MS2 [375.3]: **123.1 (100)**; MS3 [375.3→123.1]: 95.1 (100), 77.0 (5), 67.1 (17)	AR-C19:1
419.3519	10.66	−0.072	$C_{27}H_{46}O_3$	4.5	MS2 [419.4]: **401.4 (100)**, 177.1 (14), **163.1 (35)**, **149.2 (35)**, **123.1 (29)**; MS3 [419.4→401.4]: 319.4 (14), 177.1 (20), 163.2 (76), 149.1 (100), 123.2 (58)	AR-C21:oxo
375.3259	10.25	0.381	$C_{25}H_{42}O_2$	4.5	MS2 [375.3]: **123.1 (100)**; MS3 [375.3→123.1]: 95.1 (100), 67.2 (23)	AR-C19:1
377.3416	12.78	0.511	$C_{25}H_{44}O_2$	3.5	MS2 [377.3]: 127.0 (2), **123.1 (2)**, **111.2 (100)**; MS3 [377.3→111.2]: 93.2 (100)	AR-C19:0
403.3572	13.24	0.354	$C_{27}H_{46}O_2$	4.5	MS2 [403.4]: **123.1 (100)**; MS3 [403.4→123.1]: 95.2 (100), 57.1 (14)	AR-C21:1
447.3835	13.86	0.228	$C_{29}H_{50}O_3$	4.5	MS2 [447.4]: **429.4 (100)**, 177.3 (12), **163.1 (39)**, 149.1 (30); MS3 [447.4→429.4]: 347.3 (10), 333.4 (9), 177.2 (14), 163.2 (85), **149.1 (100)**, **123.1 (34)**	AR-C23:oxo
429.3729	14.31	0.193	$C_{29}H_{48}O_2$	5.5	MS2 [429.4]: 411.5 (24), **401.5 (24)**, 341.2 (18), 219.2 (13), 205.3 (26), **191.3 (14)**, **177.3 (20)**, 175.1 (6), **165.2 (100)**, **163.2 (17)**, **149.2 (6)**; MS3 [429.4→165.1]: **137.2 (100)**, 119.3 (11), 109.3 (20), 67.2 (4)	AR-C23:2

DOI: 10.1021/acs.jafc.5b01599
J. Agric. Food Chem. 2015, 63, 6189−6211

Table 3. continued

ion m/z	RT	error (ppm)	formula	RDB	MS^2 data	abbreviation
405.3730	15.86	0.293	$C_{27}H_{48}O_2$	3.5	MS2 [405.4]: 387.4 (40), 251.2 (28), 169.1 (27), 140.8 (79), 127.2 (75), 124.8 (67), **123.3 (100)**	AR-C21:0
431.3884	16.42	0.099	$C_{29}H_{50}O_2$	4.5	MS2 [431.4]: 413.6 (8), 361.5 (8), 347.3 (9), 333.4 (17), 319.1 (12), 305.3 (8), 291.4 (5), 277.2 (7), 137.2 (5), **123.1 (100)**	AR-C23:1
433.4042	18.91	0.193	$C_{29}H_{52}O_2$	3.5	MS2 [433.4]: 433.8 (78), 415.7 (72), 405.5 (70), 279.4 (50), 265.1 (41), 251.4 (49), 237.5 (41), 197.2 (61), 182.7 (41), 169.0 (52), 167.4 (56), 155.2 (100), 138.1 (41), **123.2 (59)**	AR-C23:0
461.4355	21.92	0.192	$C_{31}H_{56}O_2$	3.5	MS2 [461.4]: **111.2 (100)**	AR-C25:0

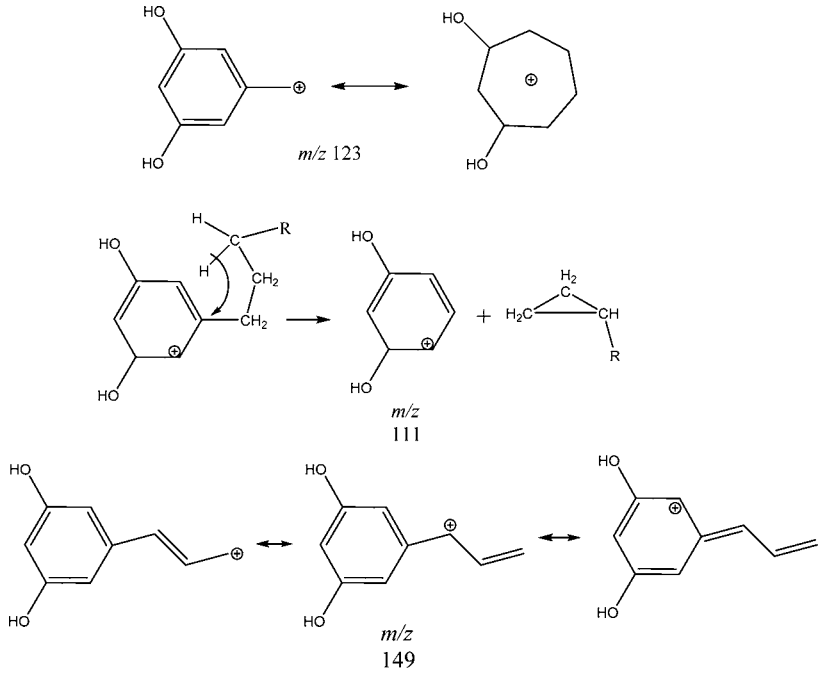

Figure 3. Proposed characteristic ions from CID spectra of ARs in positive mode.

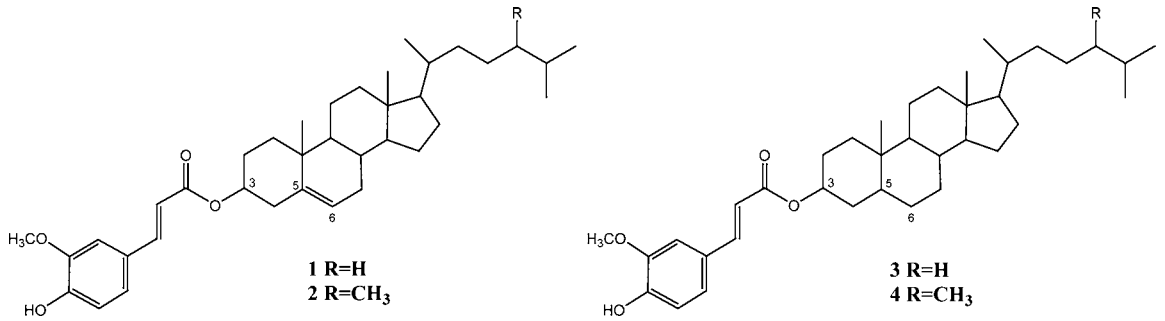

Figure 4. Structures of γ-oryzanol identified in wheat bran: **1**, campesteryl ferulate; **2**, sitosteryl ferulate; **3**, campestanyl ferulate; **4**, sitostanyl ferulate.

The LC separation was carried out on a Poroshell 120EC-C_{18} column (2.1 × 150 mm, 2.7 μm) (Agilent, Santa Clara, CA, USA) with a flow rate of 0.4 mL/min. The mobile phase consisted of a combination of A (0.1% formic acid in water) and B (0.1% formic acid in methanol). A gradient elution program was employed as follows: 85% B at 0−3.0 min, 90% B at 5.0−7.0 min, 95−100% B over 15.0−20.0 min, and held at 100% B until 100.0 min. The column temperature was set at 40 °C.

A Poroshell 120EC-C_{18} column (3.0 × 50 mm, 2.7 μm) was used for FCMS fingerprinting with the same flow rate and temperature. The flowing elution gradient was 85% B at 0−1.0 min, 100% B at 1.1−3.7 min, and 85% B at 3.8−5.0 min.

Data Processing for PCA. Each FCMS fingerprint consisted of a one-dimensional matrix (ion counts versus mass for m/z 100−1300 in nominal resolution), obtained by averaging spectra acquired from 0.1 to 5.0 min. The nominal masses of each FCMS spectrum were exported to Excel (Microsoft, Inc., Bellingham, WA, USA) from Xcalibur for data preprocessing. The preprocessing in Excel involved combining MS fingerprints of all the samples into one matrix, sorting the data by sample names, and aligning the masses (each spectrum had a different number of masses because the m/z below the detection threshold would not be exported into the mass list from the spectrum). A zero was inserted for each missing m/z, using an Excel macro written in-house.

DOI: 10.1021/acs.jafc.5b01599
J. Agric. Food Chem. 2015, 63, 6189−6211

Table 4. γ-Oryzanols Identified from Bran

ion m/z	RT	adduct	error (ppm)	formula	RDB	MS^2 data	tentative identification
573.3943	21.73	$[M-H]^-$	−1.105	$C_{38}H_{54}O_4$	12.5	MS2 [573.4]: **558.4 (100)**	24-methylenecholesterol ferulate
573.3943	21.96	$[M-H]^-$	−1.105	$C_{38}H_{54}O_4$	12.5	MS2 [573.4]: **558.5 (100)**, **193.2 (4)**	24-methylenecholesterol ferulate
601.4261	23.33	$[M-H]^-$	−0.222	$C_{40}H_{58}O_4$	12.5	MS2 [601.4]: **586.6 (100)**, **193.1 (1)**	cycloartenyl ferulate
575.4105	24.30	$[M-H]^-$	−0.145	$C_{38}H_{56}O_4$	11.5	MS2 [575.4]: **560.5 (100)**, **193.2 (3)**; MS3 [575.4→560.5]: **545.5 (100)**; MS4 [575.4→560.5→545.5]: 501.5 (7), **179.1 (100)**	campesteryl ferulate
601.4261	24.30	$[M-H]^-$	−0.222	$C_{40}H_{58}O_4$	12.5	MS2 [601.4]: **586.6 (100)**, **193.1 (1)**	cycloartenyl ferulate
603.4417	25.17	$[M-H]^-$	−0.304	$C_{40}H_{60}O_4$	11.5	MS2 [603.4]: **588.5 (100)**, **193.2 (2)**	cycloartanyl ferulate
589.4261	25.39	$[M-H]^-$	−0.227	$C_{39}H_{58}O_4$	11.5	MS2 [589.4]: **574.5 (100)**, **193.1 (3)**; MS3 [589.4→574.5]: **559.5 (100)**; MS4 [589.4→574.5→559.5]: **179.0 (100)**	sitosteryl ferulate
577.4261	25.41	$[M-H]^-$	−0.231	$C_{38}H_{58}O_4$	10.5	MS2 [577.4]: **562.5 (100)**, **193.1 (3)**; MS3[577.4→562.5]: 547.5 (5), 534.5 (21), 518.6 (95), 518.0 (16), 178.2 (12), **177.1 (100)**	campestanyl ferulate
591.4413	26.58	$[M-H]^-$	−0.987	$C_{39}H_{60}O_4$	10.5	MS2 [591.4]: **576.5 (100)**; MS3 [591.4→576.5]: 561.7 (4), 548.5 (18), **532.6 (100)**, 532.0 (15), 178.2 (9), **177.1 (93)**	sitostanyl ferulate

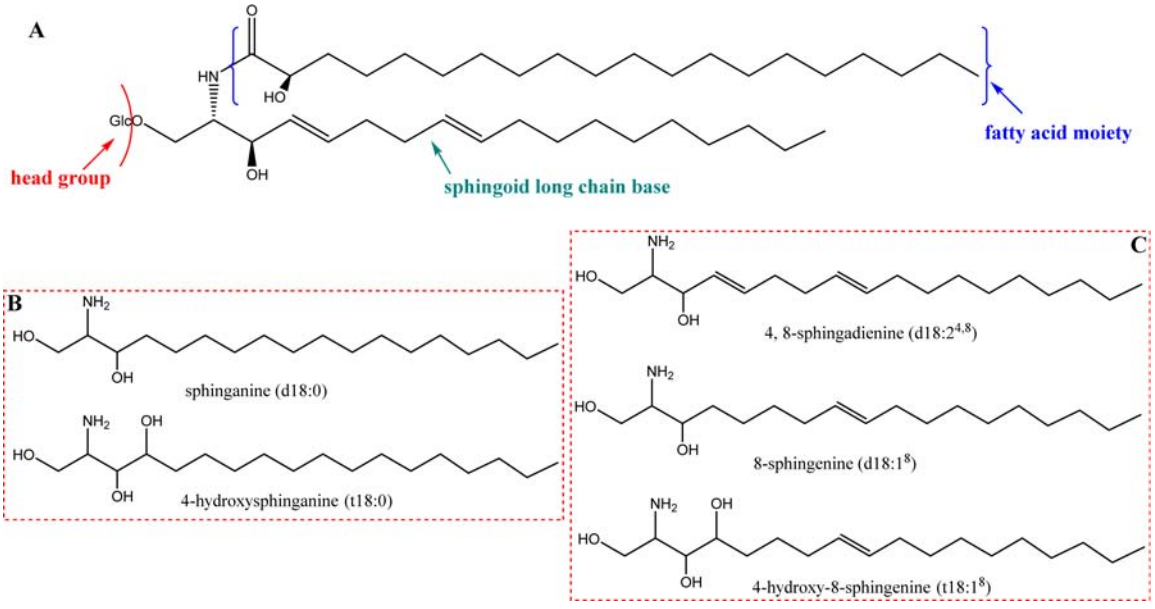

Figure 5. Structures of wheat sphingolipids.

One data matrix for each acquisition mode was obtained: APCI +, APCI−, ESI+, and ESI−. The data matrices were then imported to software SIMCA-P (version 13.0 Umetrics, Umea, Sweden) for PCA.

RESULTS AND DISCUSSION

ESI- and APCI-HRAM-MS^n detection in both positive and negative ionization modes were used to obtain complementary information on the structural features and the conjugated forms of lipids. The total ion chromatograms (TICs) of germ acquired in APCI(±) and ESI(±) are shown in the Supporting Information (Figure S1). From first glance, most of the peaks appearing in the negative spectra were eluted before 40 min; those were identified as free FA, oxylipins, γ-oryzanol, phospholipids, sphingolipids, galactolipids, etc., whereas for positive spectra, DGs were identified from peaks eluting around 20−30 min, ARs were found mainly prior to DGs, and the majority of the peaks eluted after 40 min were identified as TGs. Identification of the lipid compounds was based on chromatographic behavior, accurate mass measurements, consecutive MS^2−MS^4 analyses, ring-plus-double-bond equivalent (RDB), and comparison with data in the literature. A total of 155 lipid compounds were tentatively identified from germ, bran, and endosperm. The MS^n data listed in the tables were from the milling fraction with the most reliable spectra in terms of peak intensity.

Identification of Free Fatty Acids. The FAs of wheat and wheat products have been studied by many investigators in the form of methyl derivatives by gas chromatography (GC).[9] When liquid chromatography is used, the FAs can be analyzed directly without being converted to their methyl esters. The characteristic fragmentation of free FA in APCI negative and positive

DOI: 10.1021/acs.jafc.5b01599
J. Agric. Food Chem. 2015, 63, 6189−6211

Table 5. Characteristic Anion of 2-Hydroxy Fatty Acids in Sphingolipids

Length (n=)	anion of 2-OH fatty acids 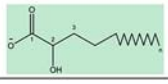	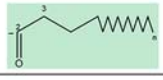	Structure
16	271	225	16:0(2OH)
18	299	253	18:0(2OH)
20	327	281	20:0(2OH)
22	355	309	22:0(2OH)
23	365	ND[1]	23:2(2OH)
23	367	ND	23:1(2OH)
23	369	323	23:0(2OH)
24	381	335	24:1(2OH)
24	383	337	24:0(2OH)
25	397	351	25:0(2OH)
26	409	363	26:1(2OH)
26	411	365	26:0(2OH)

[1]Not observed in this work.

modes is demonstrated in Figure S2. The putative identification of wheat free FAs and APCI(±) data are listed in Table 1. The distributions of the three most abundant free FAs across endosperm, bran, and germ are compared in Figure 1 with the germ fraction giving the highest peaks.

Identification of Oxylipins. Oxylipins are a diverse family of secondary metabolites that are produced by oxidative metabolism of polyunsaturated fatty acids (PUFA), such as linolenic acid and linoleic acid.[19−22] In plants, oxylipins serve as signal molecules in developmental processes (e.g., pollen formation) and in defense mechanisms (e.g., pathogenesis, wounding, and herbivores).[23] Milling, baking, and storage are known to trigger autoxidation, leading to the formation of additional oxylipins. A whole-grain wheat feeding study on pigs[24] also found that oxylipins in the plasma of pigs correlated with WF and RF bread consumed, with higher oxylipin concentrations found after consumption of WF. It is not clear whether oxylipins may have health detrimental effects or may just be considered as markers for the shelf life of flour. The oxylipins in wheat are tentatively identified in Table 2 using APCI negative MS, MS^2, and MS^3 spectra and literature research.[19−22,25−28] The characteristic MS^2 and MS^3 spectra in APCI negative mode are shown in Figure S3.

Identification of Alk(en)ylresorcinols. Alkylresorcinols and alkenylresorcinols are amphiphilic derivatives of 1,3-dihydroxybenzene with an odd-numbered alkyl or alkenyl chain at position 5 of the benzene ring (Figure 2). ARs have been extensively evaluated as biomarkers for the intake of whole-grain and bran products of wheat and rye.[29,30] Among commonly consumed foods, ARs have been reported to be found mainly in the bran fraction of cereal grains,[31,32] where homologues with alkyl chains in the range of C15−C25 dominate, although derivatives with unsaturated and oxygenated side chains also exist. The MS/MS spectra of three ARs,

Table 6. Ceramides and Cerebrosides Identified from Wheat

ion m/z	RT	adduct	error (ppm)	formula	RDB	MS^2 data	tentative identification
712.5369	15.40	$[M-H]^-$	−0.008	$C_{40}H_{75}O_9N$	4.5	MS2 [712.5]: **550.5 (45)**, **532.5 (100)**, **271.3 (10)**; MS3 [712.5→532.5]: 514.5 (26), **340.4 (51)**, **324.4 (90)**, **306.4 (100)**, 278.2 (59), **225.4 (53)**	GlcCer(d18:$2^{4,8}$/16:0(2OH))
714.5525	16.37	$[M-H]^-$	−0.078	$C_{40}H_{77}O_9N$	3.5	MS2 [714.5]: **552.6 (56)**, **534.6 (100)**, **271.3 (6)**; MS3 [714.5→534.6]: 516.6 (13), 296.4 (15), 280.3 (63), 253.3 (26), **225.3 (100)**	GlcCer(d18:1^8/16:0(2OH))
716.5682	18.07	$[M-H]^-$	−0.009	$C_{40}H_{79}O_9N$	2.5	MS2 [716.6]: **554.8 (58)**, **536.5 (100)**, **271.3 (10)**	GlcCer(d18:0/16:0(2OH))
740.5680	18.10	$[M-H]^-$	−0.278	$C_{42}H_{79}O_9N$	4.5	MS2 [740.6]: **578.6 (46)**, **560.6 (100)**, **299.4 (14)**; MS2 [740.6]: 684.0 (9), 678.9 (10), 672.0 (5), 578.5 (35), 560.5 (100), **299.4 (5)**, 279.0 (14)	GlcCer(d18:$2^{4,8}$/18:0(2OH))
742.5839	19.17	$[M-H]^-$	0.059	$C_{42}H_{81}O_9N$	3.5	MS2 [742.6]: 712.1 (5), 710.8 (5), 699.8 (9), 625.9 (7), **580.7 (33)**, **562.7 (100)**, 503.8 (20), **299.5 (6)**	GlcCer(d18:1^8/18:0(2OH))
768.5994	20.98	$[M-H]^-$	−0.138	$C_{44}H_{83}O_9N$	4.5	MS2 [768.6]: **606.6 (48)**, **588.6 (100)**, 570.6 (3), **327.4 (7)**, **281.3 (2)**	GlcCer(d18:$2^{4,8}$/20:0(2OH))
770.6151	22.01	$[M-H]^-$	−0.073	$C_{44}H_{85}O_9N$	3.5	MS2 [770.6]: **608.6 (54)**, **590.7 (100)**, 489.4 (5), 415.3 (4), **327.4 (9)**, 279.3 (54); MS3 [770.6→590.7]: 572.5 (6), 562.7 (10), 352.4 (17), 309.4 (13), **281.4 (100)**	GlcCer(d18:1^8/20:0(2OH))
840.6570	22.76	$[M-H]^-$	−0.025	$C_{48}H_{91}O_{10}N$	4.5	MS2 [840.7]: **678.8 (25)**, **660.5 (8)**, 436.5 (100), **381.4 (17)**, **335.5 (10)**	GlcCer(t18:1^8/24:1(2OH))
822.6460	23.90	$[M-H]^-$	−0.555	$C_{48}H_{89}O_9N$	5.5	MS2 [822.7]: 754.1 (10), **660.7 (54)**, **642.6 (100)**, **381.4 (9)**, **335.4 (3)**	GlcCer(d18:$2^{4,8}$/24:1(2OH))

DOI: 10.1021/acs.jafc.5b01599
J. Agric. Food Chem. 2015, 63, 6189−6211

Table 6. continued

ion m/z	RT	adduct	error (ppm)	formula	RDB	MS^2 data	tentative identification
842.6721	24.95	$[M - H]^-$	−0.678	$C_{48}H_{93}O_{10}N$	3.5	MS2 [842.7]: 773.7 (8), **680.7 (19)**, **662.6 (12)**, **438.5 (100)**, **383.6 (16)**, **337.4 (13)**	GlcCer(t18:1[8]/24:0(2OH))
654.6041	25.19	$[M - H]^-$	−0.149	$C_{40}H_{81}O_5N$	1.5	MS2 [654.6]: **410.4 (24)**, 398.4 (23), **355.5 (100)**, **309.5 (31)**	Cer(t18:0/22:0(2OH))
680.6194	25.52	$[M - H]^-$	−0.658	$C_{42}H_{83}O_5N$	2.5	MS2 [680.6]: 662.6 (11), 612.3 (6), **436.5 (24)**, **424.5 (30)**, **381.4 (100)**, **335.5 (23)**, 267.5 (6)	Cer(t18:0/24:1(2OH))
824.6620	26.20	$[M - H]^-$	−0.129	$C_{48}H_{91}O_9N$	4.5	MS2 [824.7]: 794.3 (57), **662.7 (37)**, **644.6 (100)**, **383.5 (17)**, **337.6 (4)**	GlcCer(d18:2[4,8]/24:0(2OH))
668.6197	26.61	$[M - H]^-$	−0.221	$C_{41}H_{83}O_5N$	1.5	MS2 [668.6]: 650.7 (8), 424.5 (26), 412.5 (11), **369.4 (100)**, **323.4 (25)**, 267.3 (8), 255.3 (6)	Cer(t18:0/23:0(2OH))
680.6198	26.72	$[M - H]^-$	−0.070	$C_{42}H_{83}O_5N$	2.5	MS2 [680.6]: 662.6 (10), 612.0 (7), **438.4 (18)**, **426.5 (12)**, **383.4 (100)**, **337.5 (14)**	Cer(t18:1[8]/24:0(2OH))
826.6777	27.20	$[M - H]^-$	−0.068	$C_{48}H_{93}O_9N$	3.5	MS2 [826.7]: 780.6 (50), 758.9 (56), **664.6 (50)**, **646.6 (100)**, **383.3 (12)**	GlcCer(d18:1[8]/24:0(2OH))
682.6353	28.05	$[M - H]^-$	−0.290	$C_{42}H_{85}O_5N$	1.5	MS2 [682.6]: **438.5 (19)**, 426.5 (18), **383.4 (100)**, **337.5 (20)**; MS3 [682.6→383.4]: **337.4 (100)**	Cer(t18:0/24:0(2OH))
696.6511	29.59	$[M - H]^-$	−0.069	$C_{43}H_{87}O_5N$	1.5	MS2 [696.7]: **452.5 (22)**, 440.6 (21), **397.6 (100)**, **351.5 (21)**	Cer(t18:0/25:0(2OH))
710.6663	31.23	$[M - H]^-$	−0.701	$C_{44}H_{89}O_5N$	1.5	MS2 [710.7]: 466.5 (18), 454.5 (20), **411.4 (100)**, **365.5 (25)**	Cer(t18:0/26:0(2OH))

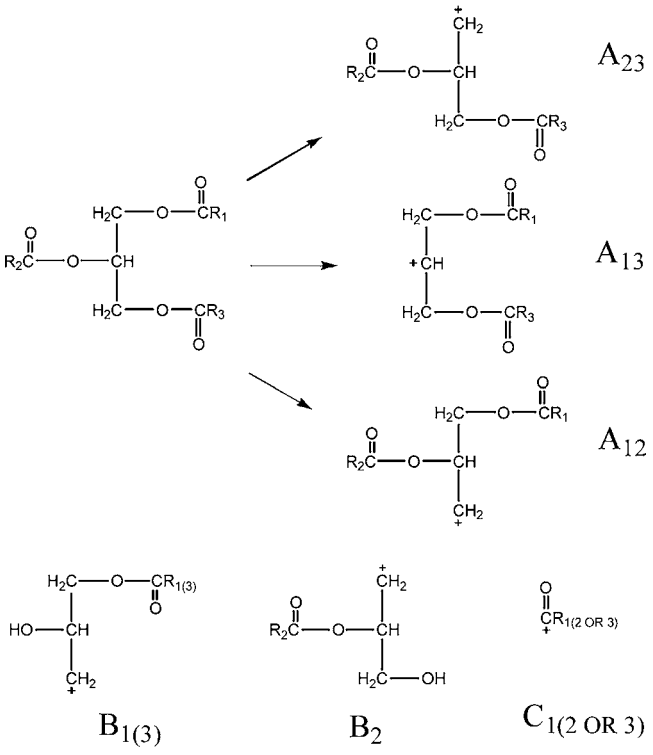

Figure 6. Structures and notation of the fragment ions of TGs/DGs and other acylglycerols used in this work.

representing unsaturated, oxygenated, and saturated species, are shown in Figure S4. Seventeen ARs were tentatively identified from the bran sample in Table 3 using APCI positive MS, MS^2, and MS^3 spectra and literature research (Figure 3).[32,33]

Table 7. Abbreviations of Acyls and Characteristic Fragment Ions of TGs/DGs

name	symbol	CN:DB[a]	ion B	ion B − H_2O	ion C	ion C − H_2O
myristic	M	C14:0	285	267	211	193
palmitoleic	Po	C16:1	311	293	237	219
palmitic	P	C16:0	313	295	239	221
linolenic	Ln	C18:3	335	317	261	243
linoleic	L	C18:2	337	319	263	245
oleic	O	C18:1	339	321	265	247
stearic	S	C18:0	341	323	267	249
gadoleic	G	C20:1	367	349	293	275
arachidic	A	C20:0	369	351	295	277
erucic	E	C22:1	395	377	321	303

[a]CN, carbon number; DB, double bond.

Identification of γ-Oryzanols. γ-Oryzanol is a mixture of ferulic acid esters of sterols and triterpene alcohols (Figure 4), which is generally found in rice, particularly in the bran fraction.[34−36] It has also been identified in wheat,[37,38] but in low concentrations, 6.3 mg/100 g, as compared with those in brown rice, 60.2−65.6 mg/100 g.[35]

The molecular mass of γ-oryzanol could be resolved by APCI in negative mode on the basis of the formation of the deprotonated anion $[M - H]^-$. The positive mode spectra generated the cation of the intact triterpene alcohol or sterol moieties ($[M + H - 194]^+$ from neutral loss of ferulic acid[36,38] as major peak and protonated ion $[M + H]^+$ in low abundance. CID spectra of deprotonated molecular ions showed abundant ions of $[M - H - CH_3]^{\bullet-}$ resulting from the loss of a methyl group in the ferulic acid moiety. Another anion, $[M - H - 2CH_3]^{\bullet-}$, could be yielded for sterol ferulates with a double bond between

DOI: 10.1021/acs.jafc.5b01599
J. Agric. Food Chem. 2015, 63, 6189−6211

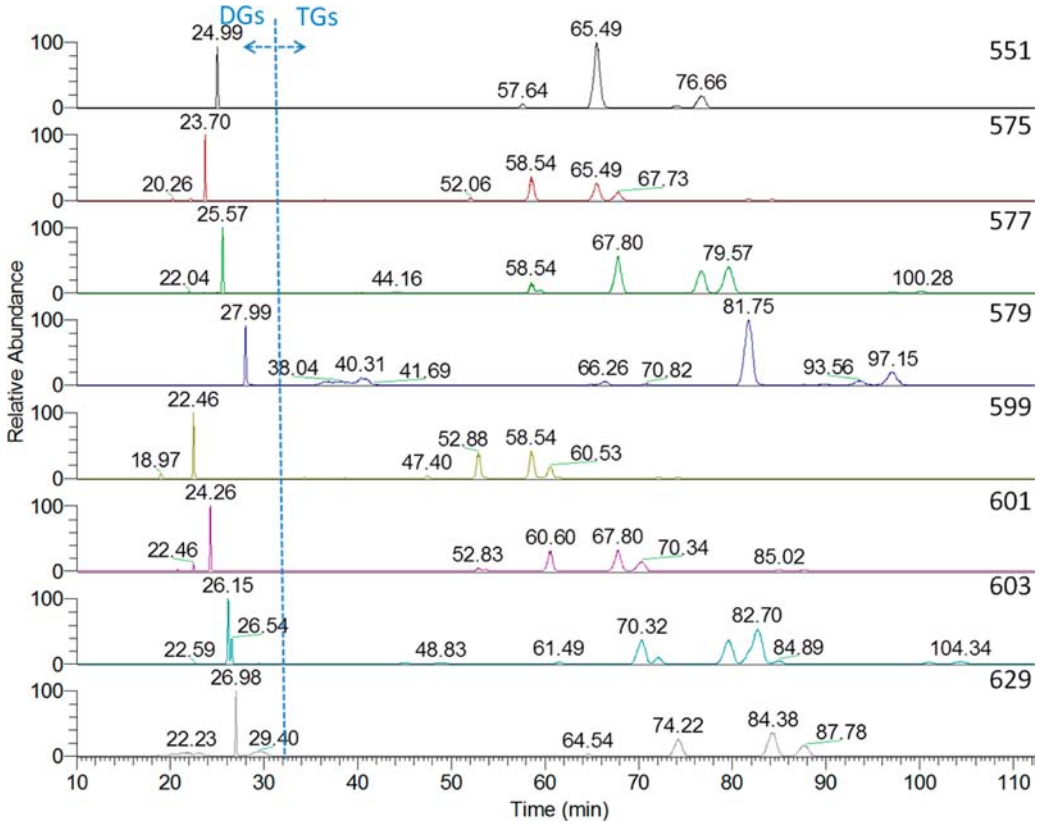

Figure 7. Extracted ion chromatograms of A ions of DGs/TGs at mass range 551.50−551.52, 575.50−575.51, 577.51−577.53, 579.53−579.54, 599.50−599.51, 601.51−601.23, 603.53−603.54, or 629.54−629.56 in APCI positive mode.

Table 8. Diglycerides (DGs) and Triglycerides (TGs) Tentatively Identified from Germ

ion m/z	RT	adduct[a]	error (ppm)[b]	formula[a]	RDB	MS^2 data	abbreviation
613.4823	19.18	$[M + H]^+$	−0.573	$C_{39}H_{64}O_5$	7.5	MS2 [613.5]: 595.5 (100), 594.9 (10), 539.5 (23), 521.4 (29), 503.4 (17); MS3 [613.5→595.5]: 577.6 (53), 559.5 (31), 539.6 (100), 521.4 (63), 503.6 (45), 425.4 (26), 411.5 (21), 397.3 (29), 351.4 (25)	LnLn
595.4720	19.18	$[M + H - H_2O]^+$	−0.146	$C_{39}H_{63}O_4^+$	8.5	MS2 [595.5]: 539.6 (100), 521.6 (47), **317.3 (70)**, **261.3 (18)**, 211.3 (22)	
615.4982	20.85	$[M + H]^+$	−0.165	$C_{39}H_{66}O_5$	6.5	MS2 [615.5]: **597.6 (100)**, 517.5 (8), 503.5 (6), 491.6 (5), **337.4 (6)**, **317.4 (4)**; MS3 [615.5→597.6]: 579.6 (47), 561.5 (20), 541.5 (81), 523.4 (100), 505.6 (35), **317.4 (27)**; MS4 [615.5→597.6→523.4]: 505.4 (100)	LLn
597.4880	20.85	$[M + H - H_2O]^+$	0.440	$C_{39}H_{65}O_4^+$	7.5	MS2 [597.5]: 541.4 (100), 523.4 (63), 505.5 (25), **337.4 (18)**, **319.3 (19)**, **317.3 (34)**, **263.2 (19)**, **261.3 (22)**, **245.3 (11)**, **243.2 (16)**	
591.4980	22.10	$[M + H]^+$	−0.510	$C_{37}H_{66}O_5$	4.5	MS2 [591.5]: 573.4 (100), **335.4 (36)**, **317.4 (19)**, **313.3 (48)**, **261.3 (24)**, **243.3 (6)**; MS3 [591.5→573.4]: 517.5 (18), 499.5 (19), **317.3 (100)**, **313.3 (21)**, **261.3 (39)**, **243.3 (9)**	PLn
573.4882	22.10	$[M + H - H_2O]^+$	0.807	$C_{37}H_{65}O_4^+$	5.5	MS2 [573.5]: 499.5 (16), **317.4 (100)**, **313.3 (54)**, **261.3 (56)**, **243.2 (33)**, **239.2 (15)**	
617.5133	22.46	$[M + H]^+$	−1.055	$C_{39}H_{68}O_5$	5.5	MS2 [617.5]: 599.5 (100); MS3 [617.5→599.5]: 581.6 (16), 543.5 (100), 525.7 (55), 507.7 (14), **337.4 (23)**, **319.2 (31)**, **263.3 (33)**, **245.3 (14)**	LL
599.5032	22.46	$[M + H - H_2O]^+$	−0.312	$C_{39}H_{67}O_4^+$	6.5	MS2 [599.5]: 581.6 (16), 543.5 (100), 525.7 (55), 507.7 (14), **337.4 (23)**, **319.2 (31)**, **263.3 (33)**, **245.3 (14)**	
593.5135	23.72	$[M + H]^+$	−0.452	$C_{37}H_{68}O_5$	3.5	MS2 [593.5]: 575.7 (79), 574.9 (26), 501.4 (5), 353.4 (4), **337.4 (89)**, **319.3 (5)**, **313.3 (100)**, 279.3 (5), **263.3 (17)**, 257.2 (7), **245.3 (14)**, **239.2 (6)**	PL
575.5039	23.72	$[M + H - H_2O]^+$	0.891	$C_{37}H_{67}O_4^+$	4.5	MS2 [575.5]: 501.5 (11), **319.4 (60)**, **313.3 (100)**, **263.3 (51)**, **245.4 (31)**, **239.1 (13)**, **221.3 (5)**, 175.3 (11)	

DOI: 10.1021/acs.jafc.5b01599
J. Agric. Food Chem. 2015, 63, 6189−6211

Table 8. continued

ion m/z	RT	adduct[a]	error (ppm)[b]	formula[a]	RDB	MS^2 data	abbreviation
619.5292	24.26	$[M + H]^+$	−0.648	$C_{39}H_{70}O_5$	4.5	MS2 [619.5]: 601.5 (100), 545.5 (22), 527.5 (37), **339.4 (4)**, **337.3 (5)**; MS3 [619.5→601.5]: 583.6 (19), 545.4 (47), 527.5 (100), **317.4 (4)**; MS4 [619.5→601.5→527.5]: 509.7 (100), 499.7 (12), 491.6 (5), 457.6 (11), 445.4 (10), 443.6 (11), 429.5 (20), 317.6 (6), **245.3 (5)**	OL
601.5195	24.26	$[M + H - H_2O]^+$	0.770	$C_{39}H_{69}O_4^+$	5.5	MS2 [601.5]: 583.6 (14), 545.4 (100), 527.5 (71), 509.5 (31), **339.5 (28)**, **319.4 (29)**, **265.3 (26)**, **263.4 (25)**, **247.3 (13)**, **245.4 (19)**	
551.5039	24.99	$[M + H - H_2O]^+$	0.930	$C_{35}H_{67}O_4^+$	2.5	MS2 [551.5]: **313.2 (4)**, 297.3 (3), **295.4 (5)**, 257.4 (3), **239.1 (100)**, **221.1 (12)**	PP
595.5290	25.57	$[M + H]^+$	−1.010	$C_{37}H_{70}O_5$	2.5	MS2 [595.5]: **577.6 (100)**, **339.4 (100)**, **313.4 (100)**, 283.3 (12), **265.4 (25)**, 257.4 (17), **247.3 (11)**, **239.2 (14)**	PO
577.5191	25.57	$[M + H - H_2O]^+$	0.109	$C_{37}H_{69}O_4^+$	3.5	MS2 [577.5]: 503.5 (8), **321.4 (8)**, **313.3 (28)**, 303.4 (4), **265.4 (100)**, **247.4 (39)**, **239.2 (27)**, **221.2 (4)**	
621.5449	26.15	$[M + H]^+$	−0.566	$C_{39}H_{72}O_5$	3.5	MS2 [621.5]: 603.7 (100), 547.5 (12), 529.5 (39), 511.6 (8), **339.3 (74)**, **321.2 (4)**, **265.4 (22)**, **247.3 (10)**	OO
603.5350	26.15	$[M + H - H_2O]^+$	0.518	$C_{39}H_{71}O_4^+$	4.5	MS2 [603.5]: 529.6 (19), 511.6 (6), **339.3 (24)**, **321.4 (12)**, **265.3 (100)**, **247.3 (31)**; **MS3 [603.5→265.3]: 247.4 (100)**	
621.5449	26.54	$[M + H]^+$	−0.566	$C_{39}H_{72}O_5$	3.5	NA	SL
603.5350	26.54	$[M + H - H_2O]^+$	0.518	$C_{39}H_{71}O_4^+$	4.5	MS2 [603.5]: **341.4 (100)**, **319.3 (57)**, **263.4 (50)**, **245.3 (28)**	
647.5604	26.98	$[M + H]^+$	−0.775	$C_{41}H_{74}O_5$	4.5	MS2 [647.6]: 629.6 (100), 573.5 (29), 555.6 (34), 537.6 (6), **367.4 (6)**, **337.3 (6)**	GL
629.5508	26.98	$[M + H - H_2O]^+$	0.735	$C_{41}H_{73}O_4^+$	5.5	MS2 [629.5]: 611.6 (30), 573.6 (100), 555.5 (66), 537.6 (18), 461.4 (9), **367.5 (9)**, **349.4 (17)**, **293.3 (12)**, **263.3 (15)**, **245.2 (5)**	
579.5348	27.99	$[M + H - H_2O]^+$	0.195	$C_{37}H_{71}O_4^+$	2.5	MS2 [579.5]: **323.4 (22)**, **267.3 (37)**, **249.3 (16)**, **239.0 (100)**	PS
623.5605	28.53	$[M + H]^+$	−0.644	$C_{39}H_{74}O_5$	2.5	MS2 [623.6]: 605.4 (100), **367.3 (27)**, **341.4 (38)**, **339.2 (29)**, **313.0 (11)**	mix of PG and SO
605.5504	28.53	$[M + H - H_2O]^+$	0.104	$C_{39}H_{73}O_4^+$	3.5	MS2 [605.5]: 531.5 (14), **349.4 (16)**, **341.4 (40)**, **321.4 (9)**, **313.3 (12)**, **293.4 (100)**, **275.4 (31)**, **267.1 (18)**, **265.3 (99)**, **249.3 (9)**, **247.3 (27)**, **239.0 (14)**, 179.3 (8)	
649.5762	29.07	$[M + H]^+$	−0.542	$C_{41}H_{76}O_5$	3.5	MS2 [649.6]: 631.8 (100), 631.1 (25), 575.6 (25), 557.5 (59), 367.4 (54), 339.5 (58), 293.4 (18), 265.5 (13)	GO
631.5660	29.07	$[M + H - H_2O]^+$	0.020	$C_{41}H_{75}O_4^+$	4.5	MS2 [631.6]: 613.6 (8), 575.6 (8), 574.5 (25), 557.6 (43), 556.5 (16), 539.6 (15), **367.4 (22)**, **349.4 (19)**, **339.4 (13)**, **323.3 (8)**, **321.1 (13)**, **293.3 (100)**, **275.3 (28)**, **265.4 (77)**, **247.3 (29)**	
649.5762	29.64	$[M + H]^+$	−0.542	$C_{41}H_{76}O_5$	3.5	NA	AL
631.5660	29.64	$[M + H - H_2O]^+$	0.020	$C_{41}H_{75}O_4^+$	4.5	MS2 [631.6]: 574.5 (63), 557.3 (28), 556.4 (34), **369.5 (100)**, 367.4 (17), **319.4 (64)**, 293.3 (40), 265.3 (21), **263.3 (48)**, **245.4 (25)**, 203.3 (14)	
675.5920	30.05	$[M + H]^+$	−0.299	$C_{43}H_{78}O_5$	4.5	MS2 [675.6]: 657.7 (100), 601.7 (32), 583.6 (38)	EL
657.5816	30.05	$[M + H - H_2O]^+$	−0.057	$C_{43}H_{77}O_4^+$	5.5	MS2 [657.6]: 639.7 (22), 601.6 (100), 583.7 (60), 565.6 (29), **395.4 (15)**, **377.5 (14)**, **321.4 (29)**, **319.2 (18)**, **303.4 (14)**, **263.3 (21)**, **245.4 (15)**	
873.6973	39.38	$[M + H]^+$	0.723	$C_{57}H_{92}O_6$	11.5	MS2 [873.7]: 855.7 (36), 803.7 (15), **595.5 (100)**, 593.5 (60), 335.5 (4); MS3 [873.7→595.5]: 577.8 (50), 539.5 (59), 521.5 (52), **317.2 (100)**, **243.2 (43)**	LnLnLn
890.7234	39.38	$[M + NH_4]^+$		$C_{57}H_{92}O_6$		MS2 [890.7]: 873.8 (100), **595.5 (55)**	
875.7130	42.98	$[M + H]^+$	0.780	$C_{57}H_{94}O_6$	10.5	MS2 [875.7]: 857.6 (49), **597.5 (66)**, **595.6 (100)**, 337.4 (7); MS3 [875.7→597.5]: 579.6 (30), 541.5 (100), 523.5 (72), **337.4 (29)**, **335.2 (24)**, **319.4 (40)**, **317.2 (98)**, **263.3 (35)**, **261.1 (47)**, **243.3 (23)**	LnLnL

DOI: 10.1021/acs.jafc.5b01599
J. Agric. Food Chem. 2015, 63, 6189−6211

Table 8. continued

ion m/z	RT	adduct[a]	error (ppm)[b]	formula[a]	RDB	MS^2 data	abbreviation
892.7388	42.98	$[M + NH_4]^+$		$C_{57}H_{94}O_6$		MS2 [892.7]: 875.6 (100), **597.5 (46)**, **595.5 (34)**	
851.7131	46.74	$[M + H]^+$	0.919	$C_{55}H_{94}O_6$	8.5	MS2 [851.7]: 833.6 (19), **595.5 (100)**, 539.5 (12), 521.6 (17)	LnLnP
868.7384	46.74	$[M + NH_4]^+$		$C_{55}H_{94}O_6$		MS2 [868.7]: 851.6 (100), **595.5 (60)**, **573.5 (47)**; MS3 [868.7→573.5]: 499.6 (17), **317.3 (100)**, **313.4 (32)**, **261.3 (52)**, **243.2 (15)**	
877.7284	47.47	$[M + H]^+$	0.493	$C_{57}H_{96}O_6$	9.5	MS2 [877.7]: 859.8 (46), 599.5 (31), **597.6 (100)**; MS3 [877.7→597.5]: 579.7 (26), 541.6 (100), 523.5 (77), 505.6 (28), **337.4 (27)**, **335.3 (18)**, **319.3 (33)**, **317.4 (91)**, **263.3 (32)**, **261.3 (40)**, **245.3 (15)**, **243.3 (21)**	LLnL
894.7516	47.47	$[M + NH_4]^+$		$C_{57}H_{96}O_6$		MS2 [894.8]: 877.6 (100), **599.5 (23)**, **597.6 (42)**	
827.7122	49.04	$[M + H]^+$	−0.141	$C_{53}H_{94}O_6$	6.5	MS2 [827.7]: **599.5 (100)**; MS3 [827.7→599.5]: 543.4 (100), 525.5 (52), 507.6 (20), **337.3 (17)**, **319.4 (24)**, **263.4 (16)**; MS3 [827.7→547.5]: **319.5 (98)**, **285.3 (43)**, **263.4 (100)**, **245.3 (32)**, **211.1 (54)**	MLL
844.7385	49.04	$[M + NH_4]^+$		$C_{53}H_{94}O_6$		MS2 [844.7]: 827.7 (100), **599.6 (36)**, **547.6 (23)**	
853.7281	52.06	$[M + H]^+$	0.156	$C_{55}H_{96}O_6$	7.5	MS2 [853.7]: 835.6 (20), **597.5 (100)**; MS3 [853.7→597.5]: 579.5 (16), 541.4 (100), 523.5 (58), 505.6 (19), **337.4 (9)**, **319.4 (9)**, **317.3 (25)**, **261.3 (11)**, **243.2 (8)**	PLnL
870.7534	52.06	$[M + NH_4]^+$		$C_{55}H_{96}O_6$		MS2 [870.8]: 853.8 (100), **597.5 (61)**, **575.6 (28)**, **573.4 (22)**	
879.7435	52.88	$[M + H]^+$	−0.133	$C_{57}H_{98}O_6$	8.5	MS2[879.8]: 861.7 (44), **599.6 (100)**; MS3 [879.7→599.5]: 581.6 (14), 543.4 (100), 525.6 (57), 507.6 (23), **337.2 (41)**, **319.3 (52)**, **263.3 (59)**, **245.3 (29)**	LLL
896.7672	52.88	$[M + NH_4]^+$		$C_{57}H_{98}O_6$		MS2 [896.8]: 879.6 (100), **599.5 (60)**; MS3 [896.8→879.6]: 861.7 (39), **599.6 (100)**, 597.5 (40), 525.5 (13)	
879.7435	53.60	$[M + H]^+$	−0.133	$C_{57}H_{98}O_6$	8.5	MS2 [879.8]: 861.7 (33), **599.6 (28)**, **597.6 (100)**, 541.5 (11), 523.5 (13), 339.4 (4)	LLnO
896.7679	53.60	$[M + NH_4]^+$		$C_{57}H_{98}O_6$		MS2 [896.8]: 879.6 (100), **601.5 (22)**, **599.6 (29)**, **597.6 (40)**; MS3 [896.8→879.7]: 861.8 (36), **599.5 (31)**, **597.6 (100)**	
855.7438	57.15	$[M + H]^+$	0.214	$C_{55}H_{98}O_6$	6.5	MS2 [855.7]: 837.8 (100), 757.7 (15), **601.5 (92)**, **573.5 (69)**, 545.4 (8), 527.6 (16), 517.3 (10), **339.3 (8)**	PoLO
872.7682	57.15	$[M + NH_4]^+$		$C_{55}H_{98}O_6$		MS2 [872.8]: 855.7 (72), 837.8 (16), **601.5 (100)**, **575.6 (54)**, **573.5 (95)**	
829.7290	57.64	$[M + H]^+$	1.245	$C_{53}H_{96}O_6$	5.5	MS2 [829.7]: 811.6 (67), **573.4 (100)**, **551.5 (40)**, 499.5 (7), 317.3 (38), 313.4 (6), 261.3 (25); MS3 [829.7→[573.5]: **317.4 (100)**, 313.3 (35), **261.3 (45)**, 243.3 (21)	PLnP
846.7551	57.64	$[M + NH_4]^+$		$C_{53}H_{96}O_6$		MS2 [846.8]: 829.7 (30), 811.7 (21), **573.5 (100)**, **551.5 (40)**, 317.3 (10), 261.2 (6)	
855.7438	58.54	$[M + H]^+$	0.214	$C_{55}H_{98}O_6$	6.5	MS2 [855.8]: 837.7 (22), **599.6 (100)**; MS3 [855.8→599.5]: 581.6 (16), 543.5 (100), 525.5 (51), 507.6 (21), **337.4 (11)**, **319.4 (12)**, **263.3 (13)**, **245.3 (8)**; MS3 [855.8→575.5]: **319.4 (67)**, **313.3 (91)**, **263.3 (100)**, **245.3 (52)**, **239.1 (28)**	PLL
872.7682	58.54	$[M + NH_4]^+$		$C_{55}H_{98}O_6$		MS2 [872.8]: 855.6 (100), **599.5 (52)**, **575.5 (47)**; MS3 [872.8→855.6]: 837.8 (19), 757.5 (6), **599.5 (100)**, 543.6 (8), 525.5 (13)	
881.7601	60.54	$[M + H]^+$	0.944	$C_{57}H_{100}O_6$	7.5	MS2 [881.8]: 863.7 (30), **601.6 (10)**, **599.5 (100)**; MS3 [881.8→601.5]: 545.6 (70), 544.5 (100), 527.7 (67), 526.6 (53), **339.4 (39)**, **337.4 (32)**, **319.3 (69)**, **265.4 (63)**, **263.3 (63)**, **247.4 (17)**, **245.3 (40)**	LLO
898.7858	60.54	$[M + NH_4]^+$		$C_{57}H_{100}O_6$		MS2 [898.8]: 881.7 (100), **601.5 (55)**, **599.6 (47)**	
881.7601	61.49	$[M + H]^+$	0.944	$C_{57}H_{100}O_6$	7.5	MS2 [881.8]: **603.5 (41)**, **599.5 (100)**; MS3 [881.8→599.5]: 543.5 (100), 525.5 (62), 507.6 (18), **339.4 (28)**, **317.3 (67)**, **265.3 (20)**, **261.3 (34)**, **243.4 (14)**; MS3 [881.8→603.5]: **339.4 (25)**, **321.3 (11)**, **265.2 (100)**, **247.2 (23)**	OLnO
898.7858	61.49	$[M + NH_4]^+$		$C_{57}H_{100}O_6$		NA	

DOI: 10.1021/acs.jafc.5b01599
J. Agric. Food Chem. 2015, 63, 6189−6211

Table 8. continued

ion m/z	RT	adduct[a]	error (ppm)[b]	formula[a]	RDB	MS^2 data	abbreviation
855.7438	61.53	$[M + H]^+$	0.214	$C_{55}H_{98}O_6$	6.5	MS2 [855.8]: 837.7 (22), **599.6 (100)**, 575.6 (2), **313.4 (4)**; MS3 [855.8→599.6]: 581.5 (86), 563.6 (46), 543.5 (100), 525.5 (73), 507.7 (33), **339.4 (28)**, **317.1 (15)**, **261.2 (9)**, **243.2 (6)**	PLnO
872.7682	61.53	$[M + NH_4]^+$		$C_{55}H_{98}O_6$		MS2 [872.8]: 855.6 (100), 837.7 (25), **599.5 (69)**, **577.6 (43)**, **573.5 (40)**	
881.7601	62.92	$[M + H]^+$	0.944	$C_{57}H_{100}O_6$	7.5	MS2 [881.8]: 863.9 (23), **597.6 (100)**; MS3 [881.8→597.6]: 579.5 (68), 561.5 (46), 541.5 (96), 523.5 (100), 521.5 (24), 505.5 (52), 317.3 (25)	LLnS
898.7858	62.92	$[M+NH_4]^+$		$C_{57}H_{100}O_6$		MS2 [898.8]: 881.7 (100), **603.5 (37)**, **601.6 (32)**, **597.5 (50)**, 337.6 (7)	
907.7752	64.66	$[M + H]^+$	0.311	$C_{59}H_{102}O_6$	8.5	MS2 [907.8]: 889.7 (41), 627.6 (30), **597.5 (100)**; MS3 [907.8→627.5]: 571.4 (34), **317.4 (100)**, **293.3 (40)**, **261.1 (33)**	LLnG
924.8021	64.66	$[M + NH_4]^+$		$C_{59}H_{102}O_6$		MS2 [924.8]: 907.7 (100), **629.7 (15)**, **627.6 (25)**, **597.5 (52)**	
831.7441	65.49	$[M + H]^+$	0.581	$C_{53}H_{98}O_6$	4.5	MS2 [831.7]: 813.6 (14), **575.4 (100)**, **551.5 (51)**; MS3 [831.7→575.5]: 501.6 (15), **319.3 (82)**, **313.3 (100)**, **263.4 (73)**, **245.3 (40)**, **239.2 (14)**; MS3 [831.7→551.5]: **239.3 (100)**, **221.3 (16)**	PLP
848.7703	65.49	$[M + NH_4]^+$		$C_{53}H_{98}O_6$		MS2 [848.8]: 831.8 (2), **575.5 (100)**, **551.4 (41)**	
857.7603	67.80	$[M + H]^+$	1.204	$C_{55}H_{100}O_6$	5.5	MS2 [857.8]: 839.7 (25), **601.6 (100)**, 577.6 (4), 575.6 (4); MS3 [857.8→575.5]: 501.6 (26), **319.3 (68)**, **313.4 (100)**, **263.3 (100)**, **245.3 (66)**, **239.1 (24)**; MS3 [857.8→601.5]: 545.4 (100), 527.5 (73), 509.6 (26), **339.4 (18)**, **319.4 (14)**, **265.3 (15)**, **263.4 (17)**; MS3 [857.8→577.5]: **313.3 (59)**, **265.3 (100)**, **247.4 (41)**, **239.2 (43)**	PLO
874.7852	67.80	$[M+NH_4]^+$		$C_{55}H_{100}O_6$		MS2 [874.8]: 857.6 (39), **601.5 (100)**, **577.5 (56)**, **575.5 (58)**	
883.7760	70.32	$[M + H]^+$	1.225	$C_{57}H_{102}O_6$	6.5	MS2 [883.8]: 865.7 (46), **601.6 (100)**; MS3 [883.8→601.6]: 583.5 (21), 545.5 (100), 527.5 (75), 509.5 (29), **319.4 (6)**, **265.4 (4)**, **263.3 (4)**, **245.2 (6)**	OLO
900.8003	70.32	$[M + NH_4]^+$		$C_{57}H_{102}O_6$		MS2 [900.8]: 883.8 (39), **603.5 (40)**, **601.6 (100)**; MS3 [900.8→601.6]: 545.6 (100), 527.3 (67), **339.5 (68)**, **319.3 (69)**, **265.3 (36)**, **263.3 (49)**, **245.3 (35)**	
883.7762	72.08	$[M + H]^+$	1.225	$C_{57}H_{102}O_6$	6.5	MS2 [883.8]: 865.7 (24), **599.5 (100)**; MS3 [883.8→603.5]: 529.6 (22), 511.4 (23), **341.5 (100)**, **319.4 (80)**, **263.3 (91)**, **245.3(46)**; MS3 [883.8→599.5]: 581.6 (12), 543.5 (100), 525.5 (43), 507.5 (16), **337.3 (14)**, **319.4 (15)**, **263.3 (15)**, **245.2 (10)**	LLS
900.8003	72.08	$[M + NH_4]^+$		$C_{57}H_{102}O_6$		MS2 [900.8]: 883.6 (100), **603.6 (57)**, **599.4 (61)**	
551.5034	74.07	ion A		$C_{51}H_{98}O_6$		MS2 [551.5]: **313.3 (6)**, **295.1 (5)**, **239.2 (100)**, **221.2 (24)**	PPP
824.7717	74.07	$[M + NH_4]^+$		$C_{51}H_{98}O_6$		MS2 [824.8]: **551.5 (100)**; MS3 [824.8→551.5]: 295.3 (33), 239.3 (100), 221.3 (16)	
909.7910	74.22	$[M + H]^+$	0.476	$C_{59}H_{104}O_6$	7.5	MS2 [909.8]: 891.7 (43), **629.7 (12)**, **599.5 (100)**; MS3 [909.8→629.5]: 573.7 (100), 555.7 (72), **367.4 (44)**, **349.3 (17)**, **319.4 (65)**, **293.4 (78)**, **275.5 (44)**, **263.2 (64)**, **245.4 (26)**; MS3 [909.8→599.5]: 543.5 (100), 525.5 (52), 507.6 (20), **337.4 (15)**, **319.4 (18)**, **263.4 (23)**, **245.3 (13)**	LLG
926.8160	74.22	$[M + NH_4]^+$		$C_{59}H_{104}O_6$		MS2 [926.8]: 909.7 (100), **629.6 (58)**, **599.6 (42)**	
833.7601	76.66	$[M + H]^+$	0.999	$C_{53}H_{100}O_6$	3.5	MS2 [833.8]: **577.7 (100)**, **551.5 (75)**; MS3 [833.8→551.5]: **239.2 (100)**, **221.3 (13)**; MS3 [833.8→577.5]: **321.3 (14)**, **313.4 (32)**, **265.3 (100)**, **247.3 (28)**, **239.1 (24)**	POP
850.7860	76.66	$[M + NH_4]^+$		$C_{53}H_{100}O_6$		MS2 [850.8]: **577.6 (100)**, **551.5 (26)**	
859.7755	79.64	$[M + H]^+$	0.678	$C_{55}H_{102}O_6$	4.5	MS2 [859.8]: 841.7 (18), **603.5 (100)**, **577.5 (79)**; MS3 [859.8→577.5]: 321.3 (12), **313.3 (32)**, **265.4 (100)**, **247.4 (31)**, **239.2 (28)**; MS3 [859.8→603.5]: 529.5 (36), **339.3 (47)**, **321.4 (15)**, **265.3 (100)**, **247.4 (31)**	POO
876.8011	79.64	$[M + NH_4]^+$		$C_{55}H_{102}O_6$		MS2 [876.8]: **603.6 (56)**, **577.5 (100)**	
859.7755	81.75	$[M + H]^+$	0.678	$C_{55}H_{102}O_6$	4.5	MS2 [859.8]: 841.6 (35), **603.6 (75)**, **579.5 (100)**, **575.5 (72)**	PLS

DOI: 10.1021/acs.jafc.5b01599
J. Agric. Food Chem. 2015, 63, 6189−6211

Table 8. continued

ion m/z	RT	adduct[a]	error (ppm)[b]	formula[a]	RDB	MS^2 data	abbreviation
876.8011	81.75	$[M + NH_4]^+$		$C_{55}H_{102}O_6$		MS2 [876.8]: 859.5 (11), **603.6 (83)**, **579.6 (70)**, **575.5 (100)**	
885.7906	82.70	$[M + H]^+$	0.037	$C_{57}H_{104}O_6$	5.5	MS2 [885.8]: 867.9 (15), **603.5 (100)**, 529.6 (11); MS3 [885.8→603.5]: 529.6 (28), **339.3 (50)**, **321.2 (13)**, **265.3 (100)**, **247.3 (35)**	OOO
902.8176	82.70	$[M + NH_4]^+$		$C_{57}H_{104}O_6$		MS2 [902.8]: 885.6 (20), **603.4 (100)**	
885.7906	84.31	$[M + H]^+$	0.037	$C_{57}H_{104}O_6$	5.5	MS2 [885.8]: 867.9 (18), **629.5 (100)**; MS3 [885.8→629.5]: 611.6 (18), 573.6 (100), 555.5 (69), 537.6 (18), **367.5 (12)**, **319.3 (12)**, **293.3 (13)**, **263.3 (14)**, **245.3 (7)**; MS3 [885.8→605.5]: 349.4 (25), 341.4 (29), **313.4 (26)**, **293.4 (100)**, **275.3 (33)**, 239.2 (27); MS3 [885.8→575.5]: 501.5 (23), **319.3 (74)**, **313.3 (57)**, **263.3 (100)**, **245.3 (64)**, **239.1 (25)**	PLG
902.8176	84.31	$[M + NH_4]^+$		$C_{57}H_{104}O_6$		MS2 [902.8]: 885.6 (53), **629.5 (100)**, **605.5 (49)**, **575.5 (53)**	
911.8065	87.78	$[M + H]^+$	0.310	$C_{59}H_{106}O_6$	6.5	MS2 [911.8]: 893.7 (87), **629.5 (100)**, **601.5 (59)**; MS3 [911.8→629.5]: 611.6 (17), 573.6 (100), 555.5 (73), **367.4 (20)**, **293.4 (20)**, **263.3 (20)**	OLG
928.8334	87.78	$[M + NH_4]^+$		$C_{59}H_{106}O_6$		MS2 [928.8]: 911.4 (63), **631.7 (78)**, **629.5 (100)**, **601.6 (81)**; MS3 [928.8→631.6]: 573.8 (14), 557.6 (51), **367.4 (31)**, **349.4 (21)**, **339.4 (16)**, **293.4 (100)**, **275.4 (31)**, **265.4 (65)**, **247.3 (13)**	
911.8065	91.05	$[M + H]^+$	0.310	$C_{59}H_{106}O_6$	6.5	MS2 [911.8]: 893.7 (21), **599.5 (100)**; MS3 [911.8→599.5]: 543.6 (100), 525.6 (39), 507.6 (21), **319.3 (12)**, **263.3 (15)**; MS3 [911.8→631.6]: **369.2 (46)**, **319.2 (100)**, **263.4 (23)**, **245.4 (31)**	LLA
928.8334	91.05	$[M+NH_4]^+$		$C_{59}H_{106}O_6$		MS2 [928.8]: 911.8 (100), **631.6 (69)**, **599.4 (55)**	
937.8220	93.40	$[M + H]^+$	0.141	$C_{61}H_{108}O_6$	7.5	MS2 [937.8]: 919.9 (43), 657.7 (13), **599.6 (100)**, 543.6 (15), 525.6 (13)	LLE
954.8480	93.40	$[M + NH_4]^+$		$C_{61}H_{108}O_6$		MS2 [954.8]: 937.8 (100), **657.6 (50)**, **599.6 (46)**; MS3 [954.8→599.5]: 581.6 (15), 543.6 (100), 525.5 (49), 507.5 (21), **337.4 (23)**, **319.3 (15)**, **263.3 (15)**, **245.3 (11)**; MS3 [954.8→657.6]: 601.6 (58), **395.5 (41)**, **377.6 (18)**, **321.4 (100)**, **319.6 (25)**, **263.2 (34)**, **245.3 (14)**	
861.7905	96.91	$[M + H]^+$	−0.078	$C_{55}H_{104}O_6$	3.5	MS2 [861.8]: **605.4 (100)**, **579.6 (83)**, **577.7 (71)**; MS3 [861.8→605.5]: 531.2 (14), **341.4 (17)**, **321.4 (13)**, **265.2 (100)**, **247.2 (21)**; MS3 [861.8→577.5]: **313.3 (26)**, **265.3 (100)**, **247.4 (21)**, **239.2 (27)**	POS
878.8170	96.91	$[M + NH_4]^+$		$C_{55}H_{104}O_6$		MS2 [878.8]: 861.7 (13), **605.5 (100)**, **579.6 (54)**, **577.6 (89)**	
887.8062	100.28	$[M + H]^+$	−0.020	$C_{57}H_{106}O_6$	4.5	MS2 [887.8]: 869.7 (26), **631.6 (100)**, **605.6 (52)**, **577.5 (42)**; MS3 [887.8→577.5]: **321.3 (18)**, **313.2 (17)**, **265.3 (100)**, **247.2 (29)**, **239.1 (36)**; MS3 [887.8→631.6]: 557.5 (66), **367.4 (23)**, **349.2 (25)**, **339.6 (34)**, **321.2 (22)**, **293.4 (100)**, **275.4 (25)**, **265.4 (73)**, **247.4 (19)**	POG
904.8326	100.28	$[M + NH_4]^+$		$C_{57}H_{106}O_6$		MS2 [904.8]: 887.8 (8), **631.6 (100)**, **605.6 (86)**, **577.5 (74)**	
913.8221	104.34	$[M + H]^+$	0.254	$C_{59}H_{108}O_6$	5.5	MS2 [913.8]: 895.7 (23), **631.6 (100)**, **603.5 (44)**; MS3 [913.8→603.5]: 339.4 (71), 265.3 (100), 247.4 (27); MS3 [913.8→631.6]: 557.6 (58), **367.4 (30)**, **349.3 (32)**, **339.4 (32)**, **293.3 (100)**, **275.2 (44)**, **265.2 (85)**, **247.3 (38)**	OOG
930.8481	104.34	$[M + NH_4]^+$		$C_{59}H_{108}O_6$		MS2 [930.8]: 913.8 (43), **631.5 (100)**, **603.5 (85)**	
913.8221	107.23	$[M + H]^+$	0.254	$C_{59}H_{108}O_6$	5.5	MS2 [913.8]: 895.7 (17), **657.6 (100)**, 601.6 (21), 583.5 (14); MS2 [913.8→657.6]: 639.5 (31), 601.6 (100), 583.7 (73), 565.5 (21), **321.5 (16)**, **263.4 (17)**	PLE
930.8481	107.23	$[M + NH_4]^+$		$C_{59}H_{108}O_6$		MS2 [930.8]: 913.9 (39), **657.5 (100)**, **633.6 (31)**, **575.7 (15)**; MS3 [930.8→657.6]: 639.6 (18), 601.6 (100), 583.7 (69), **321.4 (20)**, **303.3 (17)**, **263.4 (14)**, **245.3** (7); MS3 [930.8→633.6]: 614.1 (14), 559.7 (24), 559.1 (15), 451.9 (22), **377.5 (31)**, **321.5 (100)**, **303.5 (33)**, **239.1 (13)**; MS3 [930.8→575.5]: **319.3 (99)**, **313.3 (73)**, **263.3 (100)**, **245.4 (50)**, **239.1 (21)**	

[a]For $[M + H - H_2O]^+$, formula of cation is listed; for other ions, formula of neutral molecules is listed. [b]Error of adduct ions or fragment ions was not reported.

DOI: 10.1021/acs.jafc.5b01599
J. Agric. Food Chem. 2015, 63, 6189−6211

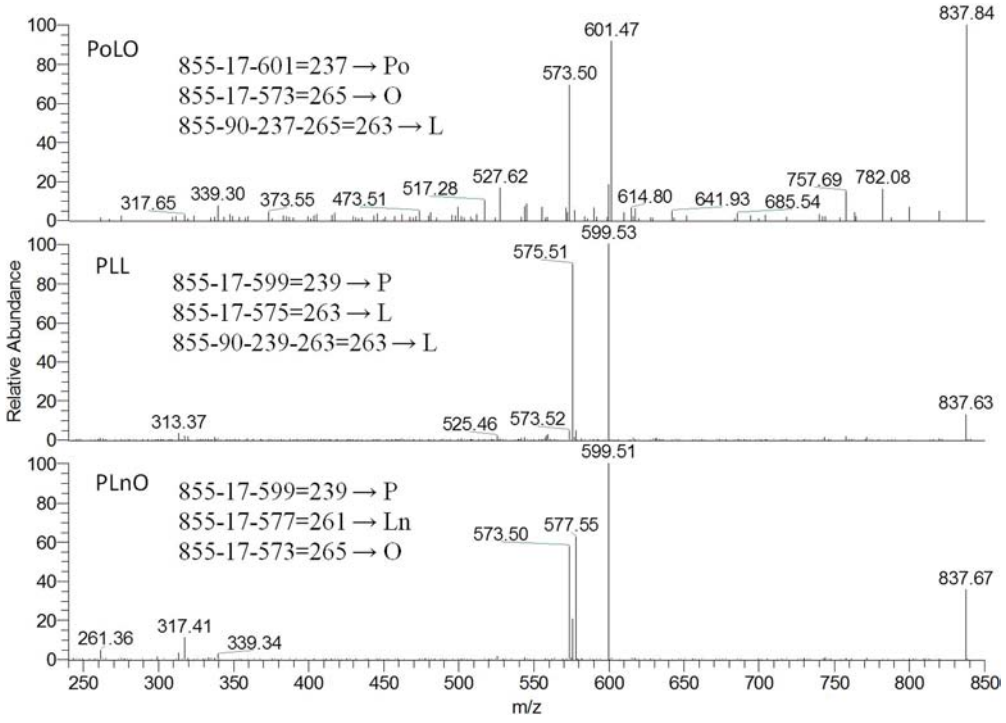

Figure 8. APCI+ MS^2 spectra of $[M + H]^+$ ions from TG isomers at m/z 855.7.

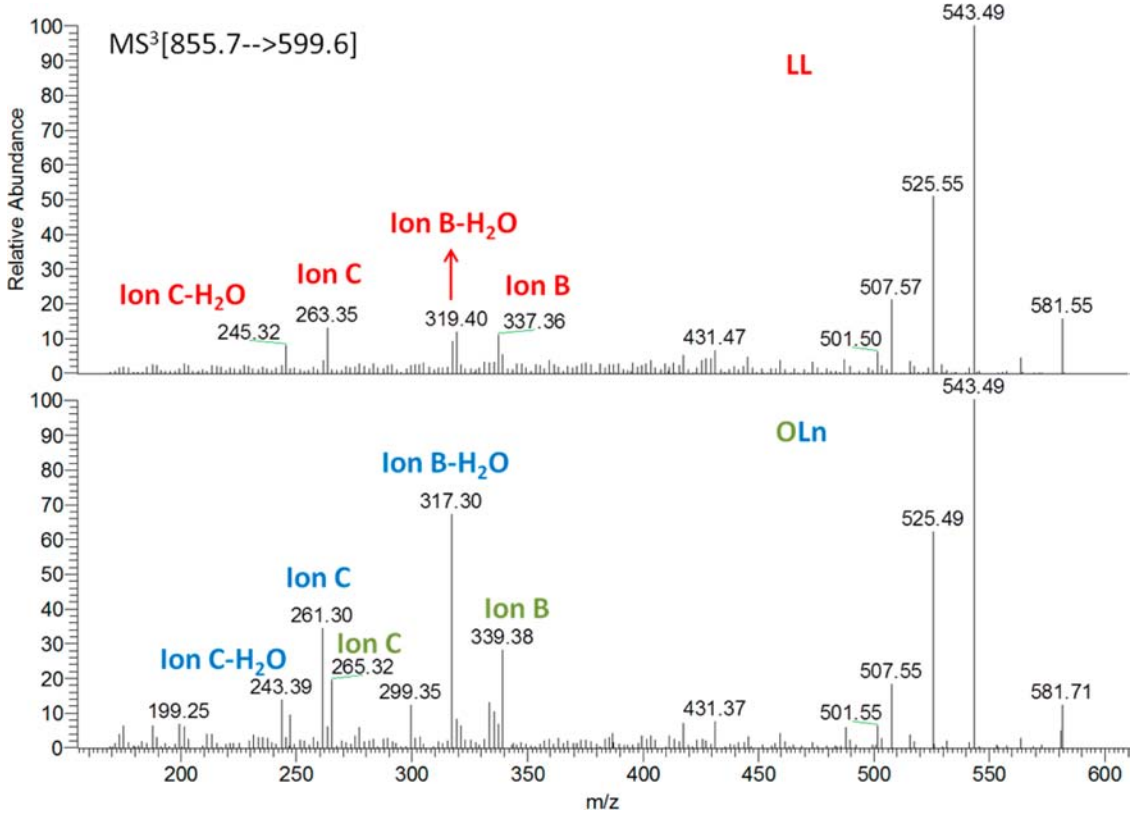

Figure 9. APCI+ MS^3 spectra of A ions from TG isomers [855.7→599.6].

C-5 and C-6. Characteristic ions also include deprotonated ferulic acid at m/z 193 as well as a fragment at m/z 177 derived from deprotonated ferulic acid.[36] The APCI(±) MS^n spectra of campestanyl ferulate re shown in Figure S5. The major γ-oryzanol components were deduced by combining APCI positive and negative data, listed in Table 4.

Identification of Sphingolipids. Sphingolipids constitute a class of distinct compounds that are both endogenous to mammalian cells and available exogenously through dietary consumption. These unique lipids are composed of a sphingoid long-chain base, a fatty acid tethered to the amino group of the sphingosine, and a variable polar headgroup (Figure 5A).

DOI: 10.1021/acs.jafc.5b01599
J. Agric. Food Chem. 2015, 63, 6189−6211

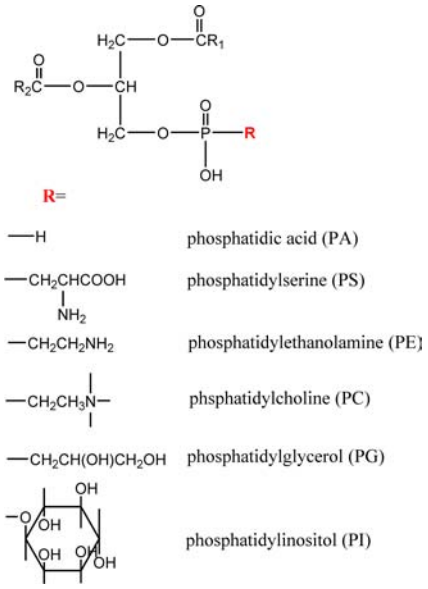

Figure 10. Structures and abbreviations of common wheat phospholipids.

The sphingosine base and the fatty acid constitute ceramide. There is considerable structural variation among the sphingolipids of different organisms with respect to the types of polar head groups and ceramide backbones. The principal molecular species of sphingolipids reported in wheat include the dihydroxy long-chain base sphinganine (d18:0) and the trihydroxy long-chain base 4-hydroxysphinganine (t18:0) for ceramide (Figure 5B) AND 4,8-sphingadienine (d18:2[4,8]), 8-sphingenine (d18:1[8]), and 4-hydroxy-8-sphingenine (t18:1[8]) for glucosylceramide (Figure 5C). The major fatty acids in wheat sphingolipids are 2-hydroxy fatty acids, and the major sugar in wheat monoglycosyl ceramide (cerebroside) is glucose.[39]

In APCI/ESI negative mode, ceramide and cerebroside compounds mainly yielded $[M - H]^-$ and $[M + FA - H]^-$ ions, due to the formation of adducts with formic acid in the mobile phase. The acid adducts were useful diagnostic ions as sphingolipid selective markers. All cerebrosides gave product ions $[M - H - 162]^-$ and $[M - H - 180]^-$ in their MS^2 spectra (Table 6; Figure S6). Anions of 2-hydroxy fatty acids, which can be used to determine the length of the fatty acyl chain moiety, are listed in Table 5.[40,41] Twelve cerebrosides and seven ceramides were tentatively identified (Table 6). Their distributions in three milling fractions were about the same on the basis of the peak areas in their extracted ion chromatography.

Identification of Triglycerides and Diglycerides. According to the literature,[18] TGs in whole wheat contain mainly linoleic acid (59%), palmitic acid (16.7%), and oleic acid (16.5%) with lower concentrations of some other fatty acids, such as linolenic acid (4.3%), arachidic acid (1.9%), palmitoleic acid (0.7%), and stearic acid (0.3%).

The APCI full scan spectra of TGs showed primarily two types of structurally important ions, "molecular ions" ($[M + H]^+$ and $[M + NH_4]^+$) and "diglycerides" $[M - RCOO]^+$ ions, the fragment ions formed by the loss of one fatty acid molecule from the $[M + H]^+$ ion of TGs (Figure 6, A ions). In the ESI full scan spectra, adduct ions $[M + NH_4]^+$ and $[M + Na]^+$ were observed instead of protonated molecules $[M + H]^+$, and no obvious fragment ions were produced. Therefore, the molecular masses of the individual TGs can be readily determined from the peaks of $[M + H]^+$ and $[M + NH_4]^+$ in APCI spectra, or $[M + NH_4]^+$ and $[M + Na]^+$ in ESI spectra, respectively. DGs formed A ions by losing a molecule of water from their $[M + H]^+$ ion. Another abundant fragment ion in the MS/MS spectra of TGs is formed by subsequent losses of a fatty acid molecule and an acyl RCO (B ions). Furthermore, dehydrated ion B, acyl ions (C ions), and dehydrated C ions were observed as well. The structure of the fragment ions observed in both the APCI and ESI MS/MS spectra are shown in Figure 6. The masses of acyls and characteristic fragment ions of TGs/DGs are listed in Table 7.

Molecular weight can also be determined from ions A or C using the following equations:

$$[M + H]^+ = C_1 + C_2 + C_3 + 90$$

$$A_{12} = C_1 + C_2 + 73$$

$$C_1 = [M + H]^+ - A_{23} - 17$$

$$C_2 = [M + H]^+ - A_{13} - 17$$

$$C_3 = [M + H]^+ - A_{12} - 17$$

The above equations are very helpful in elucidating composition of saturated TGs, which showed no or extremely low intensity of $[M + H]^+$ ions in APCI spectra.

Extracted ion chromatograms of A ions could be reconstructed to deconvolute the overlapping peaks, facilitating the identification of TGs/DGs with the same A ion (Figure 7). Every TG molecule contains three distinct attachment sites for fatty acids.

Table 9. Characteristic Ions of Phospholipids

	ESI				
	positive		negative		
compound	molecular ions	fragment ions	molecular ions	fragment ions	*sn*-2/*sn*-1[a]
PE	$[M + H]^+$	$[M + H - 141]^+$	$[M - H]^-$	R_1COO^-, R_2COO^-	>1
PC	$[M + H]^+$	*m/z* 184	$[M + FA - H]^-$	$[M - 15]^-$	>1
PG			$[M - H]^-$	R_1COO^-, R_2COO^-	>1
PS			$[M - H]^-$	$[M - H - 87]^-$, $[M - H - 87 - R_2COOH]^-$, $[M - H - 87 - R_1COOH]^-$, R_1COO^-, R_2COO^-	<1
PA	$[M + NH_4]^+$	$[M + H - 98]^+$	$[M - H]^-$	R_1COO^-, R_2COO^-, $[M - H - R_2COOH]^-$, $[M - H - R_1COOH]^-$, $[M - R_2CO]^-$	<1
PI			$[M - H]^-$	*m/z* 241, R_1COO^-, R_2COO^-, $[M - H - R_2COOH]^-$, $[M - H - R_1COOH]^-$, $[M - R_2CO]^-$	<1

[a]Ion intensity ratio of *sn*-2/*sn*-1 acyl substituent.

DOI: 10.1021/acs.jafc.5b01599
J. Agric. Food Chem. 2015, 63, 6189−6211

Table 10. Phospholipids Tentatively Identified from Endosperm

ion m/z	RT	adduct	error (ppm)	formula	RDB	MS^2 data	abbreviation
518.3241	2.58	$[M + H]^+$	−0.03	$C_{26}H_{48}O_7NP$	3.5	MS2 [518.3]: 500.3 (100), **184.2 (29)**	LPC(18:3)
562.3145		$[M + FA - H]^-$		$C_{26}H_{48}O_7NP$		MS2 [562.3]: 502.4 (100)	
520.3398	3.31	$[M + H]^+$	0.066	$C_{26}H_{50}O_7NP$	2.5	MS2 [520.3]: 502.4 (100), **184.1 (30)**	LPC(18:2)
564.3290		$[M+FA-H]^-$		$C_{26}H_{50}O_7NP$		MS2 [564.3]: **504.3 (100)**; MS3 [564.3→504.3]: 279.3 (100), 242.2 (2), 224.2 (2); MS4 [564.3→504.3→279.3]: 261.3 (100), 259.5 (8), 243.2 (2), 205.5 (2)	
496.3401	4.02	$[M + H]^+$	0.673	$C_{24}H_{50}O_7NP$	0.5	MS2 [496.3]: 478.4 (100), **184.1 (36)**; MS3 [496.3→478.4]: 419.2 (100), 283.4 (7), 163.2(6)	LPC(16:0)
540.3306		$[M+FA-H]^-$		$C_{24}H_{50}O_7NP$		MS2 [540.3]: 480.3 (100); MS3 [540.3→480.3]: 255.3 (100), 242.2 (2), 224.3 (3)	
522.3555	4.60	$[M + H]^+$	0.161	$C_{26}H_{52}O_7NP$	1.5	MS2 [522.4]: 504.3 (100), **184.2 (31)**; MS3 [522.4→504.3]: 445.3 (100), 309.5 (5), 265.3 (5), 163.1 (4)	LPC(18:1)
566.3462		$[M + FA - H]^-$		$C_{26}H_{52}O_7NP$		MS2 [566.3]: 506.3 (100); MS3 [566.3→506.4]: 281.3 (100), 242.2 (2), 224.1 (2)	
524.3708	6.42	$[M + H]^+$	−0.507	$C_{26}H_{54}O_7NP$	0.5	MS2 [524.4]: 506.5 (100), **184.2 (33)**; MS3 [524.4→506.5]: 447.4 (100), 311.4 (11)	LPC(18:0)
568.3618		$[M + FA - H]^-$		$C_{26}H_{54}O_7NP$		MS2 [568.4]: 508.4 (100); MS3 [568.4→508.4]: 283.4 (100)	
824.5448	17.31	$[M + FA - H]^-$	0.112	$C_{44}H_{78}O_8NP$		MS2 [824.5]: **764.5 (100)**; MS3 [824.5→764.5]: 504.4 (11), 502.4 (14), 279.3 (100), 277.3 (63)	PC(18:3/18:2)
800.5444	18.61	$[M + FA - H]^-$	−0.307	$C_{42}H_{78}O_8NP$		MS2 [800.5]: **740.5 (100)**, **277.5 (2)**	PC(16:0/18:3)
826.5603	18.85	$[M + FA - H]^-$	−0.069	$C_{44}H_{80}O_8NP$		MS2 [826.6]: **766.5 (100)**; MS3 [826.6→766.5]: 504.4 (13), **279.4 (100)**; MS4 [826.6→766.5→279.4]: 261.4 (100), 259.6 (2)	PC(18:2/18:2)
802.5604	20.17	$[M + FA - H]^-$	0.053	$C_{42}H_{80}O_8NP$		MS2 [802.6]: **742.5 (100)**; MS3 [802.6→742.5]: 504.4 (2), 480.3 (13), 462.4 (2), **279.3 (100)**, **255.3 (29)**; MS4 [802.6→742.5→279.3]: 261.3 (100), 259.4 (8), 243.0 (3)	PC(16:0/18:2)
804.5763	22.10	$[M + FA - H]^-$	0.364	$C_{42}H_{82}O_8NP$		MS2 [804.6]: 744.5 (100); MS3 [804.6→744.5]: 480.5 (13), 462.4 (1), **281.3 (100)**, **255.4 (27)**; MS4 [804.6→744.5→281.4]: 281.6 (70), 263.4 (100), 97.1 (23)	PC(16:0/18:1)
828.5759	20.74	$[M + FA - H]^-$	−0.130	$C_{44}H_{82}O_8NP$		MS2 [828.6]: 768.6 (100); MS3 [828.6→768.6]: 506.4 (11), 504.4 (11), 281.3 (100), 279.3 (79)	PC(18:2/18:1)
830.5916	22.66	$[M + FA - H]^-$	−0.069	$C_{44}H_{84}O_8NP$		MS2 [830.6]: 770.6 (100); MS3 [830.6→770.6]: 506.4 (12), **281.4 (100)**	PC(18:1/18:1)
478.2928	3.33	$[M + H]^+$	−0.033	$C_{23}H_{44}O_7NP$	2.5	MS2 [478.3]: 460.3 (16), 337.4 (19), 326.6 (7), 324.3 (8), 306.5 (100)	LPE(18:2)
476.2782		$[M - H]^-$	−0.131	$C_{23}H_{44}O_7NP$	3.5	MS2 [476.3]: 402.3 (2), 279.3 (100), 196.2 (2), 153.2 (2); MS3 [476.3→279.3]: 261.3 (100), 259.4 (5), 243.3 (4)	
454.2930	4.04	$[M + H]^+$	0.406	$C_{21}H_{44}O_7NP$	0.5	NA	LPE(16:0)
452.2783		$[M - H]^-$	0.083	$C_{21}H_{44}O_7NP$	1.5	MS2 [452.3]: 378.4 (7), **255.3 (100)**, 153.1 (11); MS3 [452.3→255.3]: 237.2 (100)	
738.5062	17.39	$[M + H]^+$	−0.855	$C_{41}H_{72}O_8NP$	6.5	MS2 [738.5]: **597.5 (100)**; MS3 [738.5→597.5]: 541.2 (17), **319.4 (73)**, **317.4 (100)**, **263.3 (71)**, **261.2 (48)**, **245.2 (16)**, 187.3 (16), 175.2 (29)	PE(18:3/18:2)
736.4922		$[M - H]^-$	−0.106	$C_{41}H_{72}O_8NP$	7.5	MS2 [736.5]: 474.5 (4), 458.4 (9), 456.4 (18), **279.3 (100)**, **277.4 (47)**	
714.5074	19.11	$[M + H]^+$	0.569	$C_{39}H_{72}O_8NP$	4.5	MS2 [714.5]: **573.5 (100)**; MS3 [714.5→573.5]: 317.4 (100), **261.4 (87)**, **239.0 (84)**	PE(16:0/18:3)

DOI: 10.1021/acs.jafc.5b01599
J. Agric. Food Chem. 2015, 63, 6189−6211

Table 10. continued

ion m/z	RT	adduct	error (ppm)	formula	RDB	MS^2 data	abbreviation
712.4916		$[M - H]^-$	−0.678	$C_{39}H_{72}O_8NP$	5.5	MS2 [712.5]: 694.2 (9), 452.4 (15), 474.3 (4), **277.4 (100)**, **255.3 (49)**	
740.5236	19.36	$[M + H]^+$	1.511	$C_{41}H_{74}O_8NP$	5.5	MS2 **599.5 (100)**; MS3 [740.5→599.5]: 582.0 (14), 525.6 (40), 507.7 (31), 319.3 (100), **263.4 (88)**,**245.3 (28)**	PE(18:2/18:2)
738.5078		$[M - H]^-$	−0.173	$C_{41}H_{74}O_8NP$	6.5	MS2 [738.5]: 458.4 (15), **279.2 (100)**	
716.5233	20.65	$[M + H]^+$	1.143	$C_{39}H_{74}O_8NP$	3.5	MS2 [716.5]: **575.5 (100)**; MS3 [716.5→575.5]: 501.3 (24), 319.4 (38), **263.3 (100)**, **245.2 (29)**, **239.2 (36)**	PE(16:0/18:2)
714.5077		$[M - H]^-$	−0.319	$C_{39}H_{74}O_8NP$	4.5	MS2 [714.5]: 452.3 (19), **279.3 (100)**, **255.4 (48)**	
742.5394	23.45	$[M + H]^+$	1.709	$C_{41}H_{76}O_8NP$	4.5	NA	PE(18:1/18:2)
740.5236		$[M - H]^-$	0.022	$C_{41}H_{76}O_8NP$	5.5	MS2 [740.5]: 478.4 (5), 460.4 (17), 458.4 (10), **281.3 (77)**, **279.3 (100)**	
483.2729	4.23	$[M - H]^-$	0.119	$C_{22}H_{45}O_9P$	1.5	MS2 [483.3]: 415.3 (7), 255.3 (100), 153.1 (6); MS3 [483.3→255.3]: 237.2 (100)	LPG(16:0)
745.5025	23.91	$[M - H]^-$	−0.011	$C_{40}H_{75}O_{10}P$	4.5	MS2 [745.5]: 489.3 (14), **279.3 (100)**, **255.3 (65)**	PG(16:0/18:2)
769.5021	24.28	$[M - H]^-$	−0.53	$C_{42}H_{75}O_{10}P$	6.5	MS2 [769.5]: 507.4 (9), 489.4 (11), 415.2 (15), **279.2 (100)**	PG(18:2/18:2)
771.5181	25.25	$[M - H]^-$	−0.075	$C_{42}H_{77}O_{10}P$	5.5	MS2 [771.5]: 740.6 (11), **281.3 (100)**, **279.3 (79)**	PG(18:2/18:1)
831.5027	23.44	$[M - H]^-$	−0.243	$C_{43}H_{77}O_{13}P$	6.5	MS2 [831.5]: 784.6 (12), 771.7 (20), 770.5 (81), 575.3 (25), 571.5 (23), 553.4 (100), 413.3 (12), 391.2 (61), 297.1 (19), 277.4 (24), 255.3 (58), **241.1 (19)**	PI(16:0/18:3)
857.5176	23.93	$[M - H]^-$	−1.110	$C_{45}H_{79}O_{13}P$	7.5	MS2 [857.5]: 595.4 (19), 577.3 (100), 415.3 (53), 297.3 (13), 279.3 (82), **241.1 (8)**	PI(18:2/18:2)
833.5181	26.00	$[M - H]^-$	−0.542	$C_{43}H_{79}O_{13}P$	5.5	MS2 [833.5]: 671.5 (1), 577.3 (24), 571.4 (23), **553.4 (100)**, 415.2 (9), 391.3 (61), 297.2 (18), 279.3 (33), 255.3 (61), **241.1 (22)**	PI(16:0/18:2)
859.5339	27.39	$[M - H]^-$	−0.351	$C_{45}H_{81}O_{13}P$	6.5	MS2 [859.5]: 597.5 (19), 595.3 (16), 579.4 (100), 577.3 (78), 417.2 (59), 415.3 (41), 297.1 (19), 281.3 (72), 279.4 (65), **241.1 (10)**	PI(18:1/18:2)
835.5341	30.26	$[M - H]^-$	−0.122	$C_{43}H_{81}O_{13}P$	4.5	MS2 [835.5]: 766.6 (2), 673.6 (1), 597.5 (3), 579.4 (19), 571.5 (22), 553.3 (100), 417.3 (10), 391.3 (54), 315.3 (3), 297.1 (20), 281.3 (29), 255.3 (55), **241.0 (19)**	PI(16:0/18:1)
714.5071		$[M + NH_4]^+$		$C_{39}H_{69}O_8P$		MS2 [714.5]: 697.3 (100), 646.6 (7), **599.5 (60)**, 263.1 (1)	PA(18:2/18:2)
695.4653	23.04	$[M - H]^-$	−0.616	$C_{39}H_{69}O_8P$	6.5	MS2 [695.5]: 433.3 (30), 415.2 (83), **279.4 (100)**; MS3 [695.5→279.4]: 261.4 (100)	
690.5070		$[M + NH_4]^+$		$C_{37}H_{69}O_8P$		MS2 [690.5]: 679.2 (13), 673.1 (40), 672.2 (7), 644.5 (9), 622.7 (6), **575.6 (100)**	PA(16:0/18:2)
671.4656	24.79	$[M - H]^-$	−0.192	$C_{37}H_{69}O_8P$	4.5	MS2 [671.5]: 433.4 (4), 415.3 (28), 409.3 (52), 391.3 (96), **279.3 (45)**, **255.3 (100)**	
716.5233		$[M + NH_4]^+$		$C_{39}H_{71}O_8P$		MS2 [716.5]: 699.3 (59), 670.0 (19), 665.6 (18), **601.6 (100)**	PA(18:1/18:2)
697.4808	25.84	$[M - H]^-$	−0.377	$C_{39}H_{71}O_8P$	5.5	MS2 [697.5]: 435.5 (26), 433.4 (36), 417.4 (63), 415.3 (89), **281.3 (91)**, **279.3 (100)**	
673.4813	28.56	$[M - H]^-$	−0.117	$C_{37}H_{71}O_8P$	3.5	MS2 [673.5]: 604.7 (12), 417.2 (22), 409.3 (35), 391.3 (100), **281.5 (37)**, **255.2 (89)**	PA(16:0/18:1)
784.5132	21.23	$[M - H]^-$	−0.264	$C_{42}H_{76}O_{10}NP$	6.5	MS2 [784.5]: 737.9 (6), 715.9 (6), **697.6 (100)**, 417.3 (14), 415.2 (10), 281.4 (7), 279.5 (2)	PS(18:1/18:2)

These are numbered *sn*-1, *sn*-2, and *sn*-3, where *sn* stands for stereospecific numbering. Three identical acyls on the glycerol backbone ($R_1R_1R_1$) provide only a single A ion, whereas the $R_1R_1R_2$ or $R_1R_2R_1$ TGs produce two different types of A ions with a statistical abundance ratio of 2:1, and the $R_1R_2R_3$ TGs produce three different types of A ions with the statistical

DOI: 10.1021/acs.jafc.5b01599
J. Agric. Food Chem. 2015, 63, 6189−6211

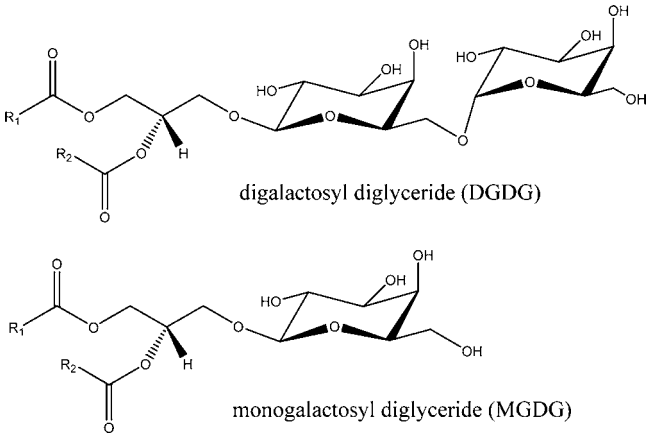

Figure 11. Major galactolipids in wheat.

abundance ratio of 1:1:1. In fact, the loss of RCOOH from the equivalent side position *sn*-1 and *sn*-3 is preferred compared to cleavage from the middle position *sn*-2.[42] The acyls in the *sn*-2 position are determined on the basis of relatively lower abundances of the A_{13} ions with respect to the A_{12} and A_{23} ions. The positions *sn*-1 and *sn*-3 are considered identical: the acyl with a lower mass is consistently attributed to the *sn*-1 position. The standard notation of TGs employs the initial of fatty acid names (Table 7), arranged in the order of their position on the glycerol skeleton (Table 8).

The fatty acids in the *sn*-2 position are much more unsaturated than those in positions *sn*-1 and *sn*-3 for both TGs and DGs. The positional distribution of fatty acids in DG isomers suggested that they originated from 1,2-diacyl-*sn*-glycerol,[10] so the DGs listed in Table 8 were arranged in the order of 1,2-diglycerides for simplicity.

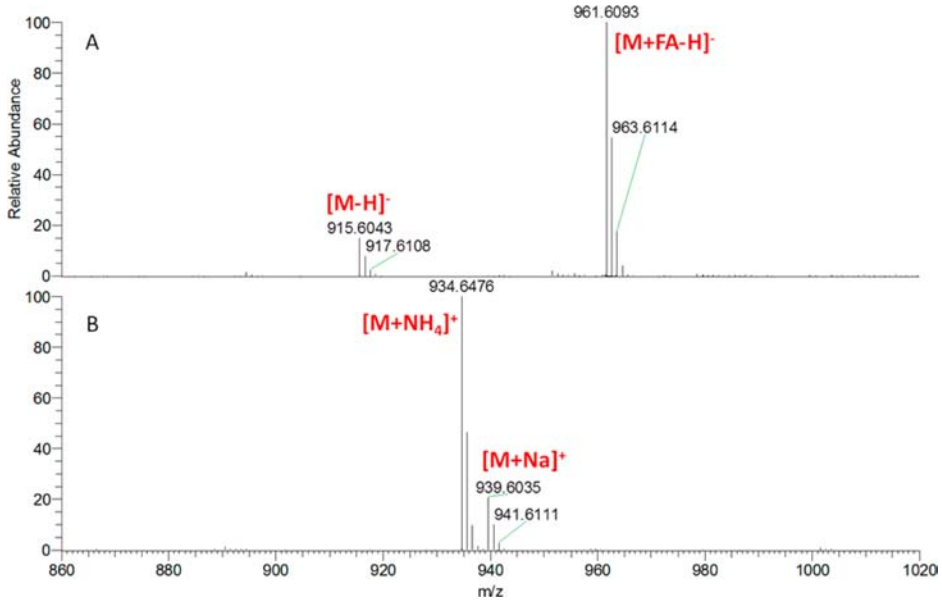

Figure 12. ESI mass spectra of DGDG (16:0/18:2): (A) negative mode; (B) positive mode.

Table 11. Galactolipids Tentatively Identified from Endosperm

ion *m/z*	RT	adduct	error (ppm)	formula	RDB	MS^2 data	tentative identification
677.3752	2.78	$[M-H]^-$	−0.265	$C_{33}H_{58}O_{14}$	5.5	MS2 [677.4]: 415.3 (34), **397.2 (100)**; MS3 [677.4→397.2]: 305.2 (79), 287.3 (43), 253.2 (35), 235.1 (100)	DGMG(18:2)
696.4174	2.89	$[M+NH_4]^+$				MS2 [696.4]: 678.6 (27), 661.3 (16), 516.6 (35), 499.1 (18), **355.2 (100)**, 337.3 (26), **263.3 (20)**, **245.3 (20)**	
937.5891	16.16	$[M-H]^-$	−0.315	$C_{51}H_{86}O_{15}$	9.5	MS2 [937.6]: 890.4 (47), 868.7 (29), **659.2 (98)**, **657.1 (100)**, 565.5 (15), 397.2 (21), 379.2 (64), **279.3 (39)**, **277.4 (18)**	DGDG(18:2/18:3)
956.6325	16.65	$[M+NH_4]^+$				MS2 [956.6]: 938.5 (16), 924.8 (16), **615.6 (100)**, 519.7 (8), 337.6 (2)	
939.6047	17.66	$[M-H]^-$	−0.367	$C_{51}H_{88}O_{15}$	8.5	MS2 [939.6]: 677.3 (22), **659.2 (100)**, 397.3 (37), 379.2 (44), 279.4 (32)	DGDG(18:2/18:2)
958.6489	18.21	$[M+NH_4]^+$				MS2 [958.7]: 940.4 (28), 786.6 (57), **617.6 (100)**, **599.5 (52)**	
913.5895	17.34	$[M-H]^-$	0.115	$C_{49}H_{86}O_{15}$	7.5	MS2 [913.6]: 897.6 (27), 887.6 (29), 880.8 (18), 869.8 (18), **657.3 (77)**, 653.0 (23), **635.1 (100)**, 397.1 (41), 379.1 (94), **277.3 (18)**	DGDG(16:0/18:3)
932.6318	17.87	$[M+NH_4]^+$				NA	
915.6043	18.93	$[M-H]^-$	−0.049	$C_{49}H_{88}O_{15}$	6.5	MS2 [915.6]: 677.1 (27), **659.2 (100)**, 653.3 (40), **635.3 (76)**, 397.2 (50), 379.1 (74), **279.2 (54)**, **255.3 (13)**	DGDG(16:0/18:2)

DOI: 10.1021/acs.jafc.5b01599
J. Agric. Food Chem. 2015, 63, 6189−6211

Table 11. continued

ion m/z	RT	adduct	error (ppm)	formula	RDB	MS^2 data	tentative identification
934.6478	19.43	$[M + NH_4]^+$				MS2 [934.7]: 916.3 (24), 879.4 (20), 866.7 (100), 804.7 (53), 745.5 (15), 693.1 (12), **593.5 (25)**, **575.6 (29)**, 337.2 (9)	
941.6205	19.44	$[M - H]^-$	−0.207	$C_{51}H_{90}O_{15}$	7.5	MS2 [941.6]: **661.3 (79)**, **659.2 (100)**, 415.2 (21), 397.2 (52), 379.2 (96), **281.2 (39)**, **279.3 (54)**	DGDG(18:2/18:1)
960.6642	19.95	$[M + NH_4]^+$				MS2 [960.7]: **619.4 (100)**, 601.5 (73), 337.7 (57)	
943.6360	21.24	$[M - H]^-$	−0.154	$C_{51}H_{92}O_{15}$	6.5	MS2 [943.6]: 927.5 (72), 896.6 (62), 875.8 (44), 874.8 (79), **661.3 (100)**, 397.2 (50), 379.1 (27), **281.6 (22)**	DGDG(18:1/18:1)
962.6794	21.68	$[M + NH_4]^+$				NA	
943.6360	21.59	$[M - H]^-$	−0.154	$C_{51}H_{92}O_{15}$	6.5	MS2 [943.6]: 928.1 (57), 925.0 (27), 915.7 (49), 913.8 (22), 911.2 (100), **663.6 (25)**, **659.4 (92)**, 397.3 (53), 379.1 (56), **283.5 (12)**	DGDG(18:2/18:0)
962.6794	22.04	$[M + NH_4]^+$				NA	
775.5366	17.93	$[M - H]^-$	0.037	$C_{45}H_{76}O_{10}$	8.5	MS2 [775.5]: 757.0 (25), 751.8 (46), 743.8 (27), 730.8 (28), 729.2 (39), 706.8 (54), **279.3 (100)**, **277.2 (58)**	MGDG(18:2/18:3)
794.5792	18.45	$[M + NH_4]^+$				MS2 [794.6]: 762.6 (9), 759.2 (10), **615.6 (100)**, 597.6 (12), 505.4 (3), 337.4 (8)	
777.5521	19.57	$[M - H]^-$	−0.157	$C_{45}H_{78}O_{10}$	7.5	MS2 [777.5]: 758.9 (2), 717.4 (4), 716.4 (17), 708.8 (3), 515.2 (4), **279.3 (100)**	MGDG(18:2/18:2)
796.5955	20.07	$[M + NH_4]^+$				MS2 [796.6]: 789.1 (20), 745.6 (13), 737.9 (12), 711.6 (12), **617.6 (100)**, 599.6 (33), 337.5 (5)	
779.5677	21.37	$[M - H]^-$	−0.220	$C_{45}H_{80}O_{10}$	6.5	MS2 [779.6]: 749.3 (16), 733.0 (20), 719.6 (66), 718.6 (76), 710.8 (17), **281.3 (100)**, **279.4 (66)**	MGDG(18:2/18:1)
798.6105	21.84	$[M + NH_4]^+$				MS2 [798.6]: 780.7 (20), 716.0 (12), **619.5 (100)**, 601.5 (96), 578.5 (17), 339.4 (18), 337.4 (12)	

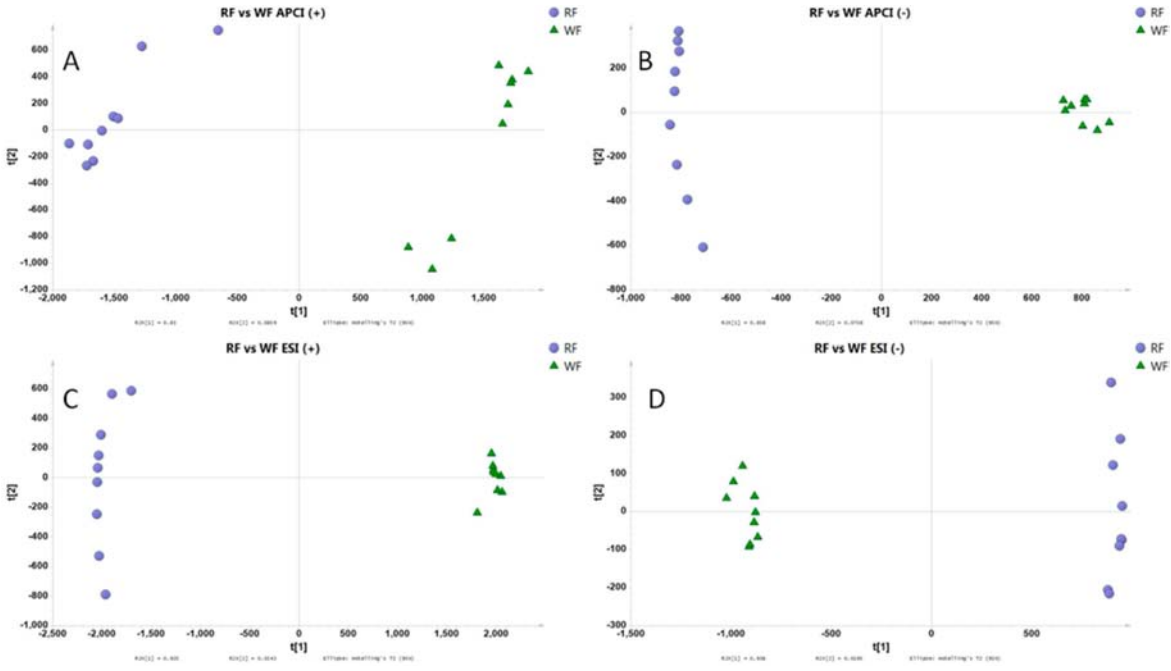

Figure 13. PCA score plot from flour sample RF and WF running on four data sets: (A) APCI+; (B) APCI−; (C) ESI+; (D) ESI−.

Isomers are common in TGs; A ions may or may not share the same value. Figure 8 shows the three MS^2 spectra of $[M + H]^+$ ion at m/z 855.7. The different A ion patterns indicate that there are three different TGs. Even though ions at m/z 599 were observed in the spectra of both PLL and PLnO, the MS^3 spectra of [855.7→599] could differentiate them from each other

DOI: 10.1021/acs.jafc.5b01599
J. Agric. Food Chem. 2015, 63, 6189−6211

unambiguously. As labeled in Figure 9, the compositions of ions at m/z 599 were LL for PLL and OLn for PLnO.

Identification of Glycerophospholipids. Phospholipids are the main constituents of biological membranes and have important structural and functional properties. They are made up of several distinct molecular classes with different polar head groups (Figure 10). Each phospholipid class consists of a mixture of many molecular species containing different combinations of fatty acids in the *sn*-1 and *sn*-2 positions on the glycerol backbone. The phospholipids are a minor proportion of wheat lipids except in the starchy endosperm, where they account for about 50% of the total lipids.[11]

A challenge in identifying phospholipids is that species from different structural classes may have the same masses. For example, exact masses of molecular cations of phosphatidylcholine (PC) and phosphatidylethanolamine (PE) may overlap because their heteroatom compositions are the same ($N_1O_8P_1$). Consequently, characteristic fragmentation behaviors of each class played an important role in the identification process. Positive ion ESI MS/MS provides information on the nature of the headgroup,

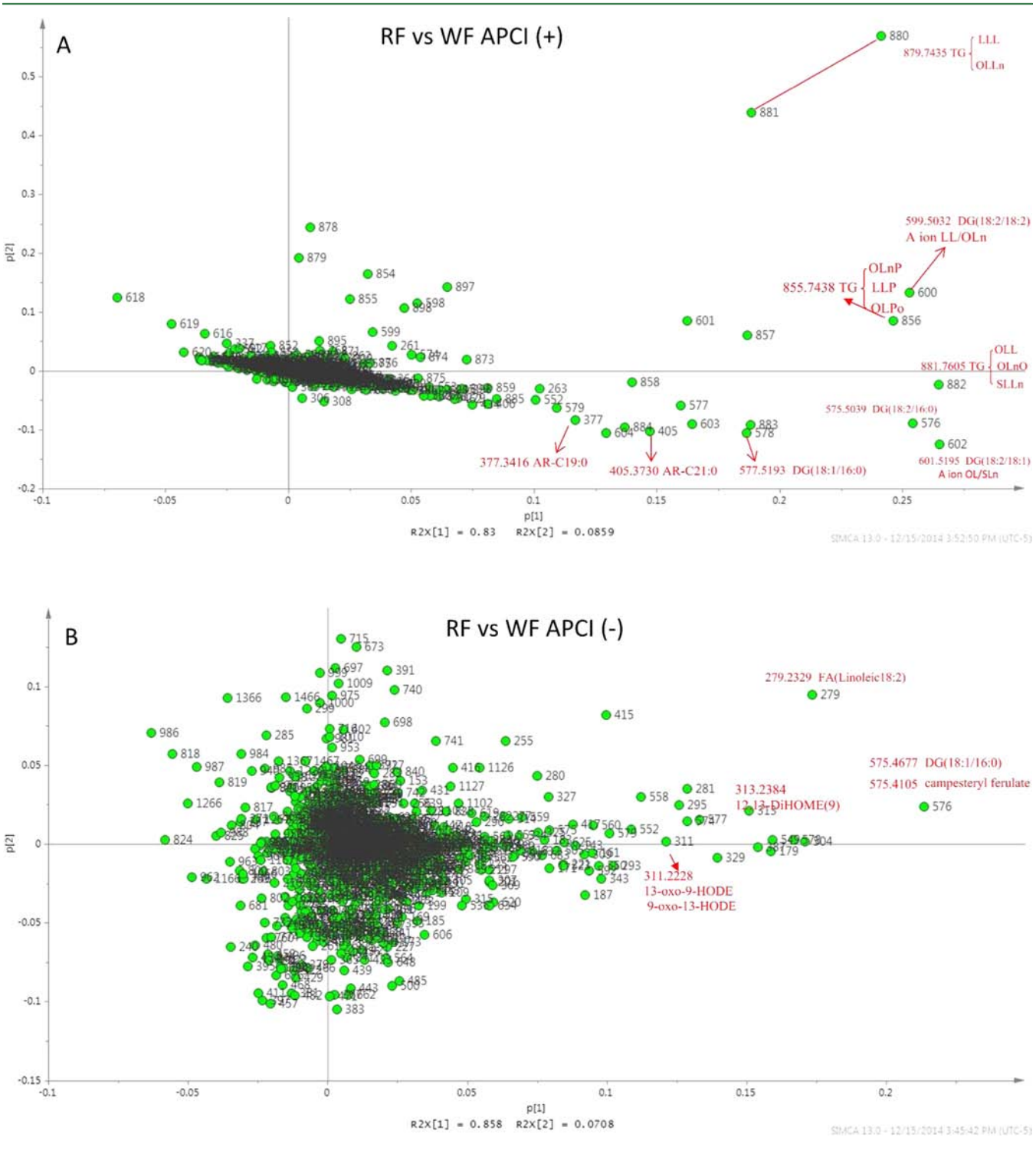

Figure 14. continued

DOI: 10.1021/acs.jafc.5b01599
J. Agric. Food Chem. 2015, 63, 6189−6211

Figure 14. PCA loading plot from flour sample RF and WF running on four data sets: (A) APCI+; (B) APCI−; (C) ESI+; (D) ESI−.

with the formation of an ion corresponding to the headgroup itself, or the loss of the headgroup from the molecular ion $[M + H]^+$ or NH_4^+ or Na^+ adducts. Acyl constituents were identified during negative ion MS/MS from the formation of their $RCOO^-$ or $[M - H - RCOOH]^-$ ions. Negative ESI MS spectra provided information on the regiochemistry of the phospholipids. The regiospecificity of the two acyl linkages could be clearly assigned on the basis of the intensity ratio of *sn*-2/*sn*-1 fragment ions. The ions used to characterize phospholipids in this study are summarized in Table 9. Characteristic MS^n spectra of PC, PE, PG, PI, PA, and PS identified in this work are shown in Figure S7. Tentative identification of the phospholipids with ESI negative data is listed in Table 10. The identification relied on the comparison of MS fragmentation behaviors between our data and the previously reported data.[43−46]

Identification of Galactolipids. Polar lipids, especially galactolipids, make important contributions to dough properties, baking performance, and resistance to bread staleness.[47,48] Plant seeds have a relatively low concentration of galactolipids compared to phospholipids and neutral lipids. The galactolipids

DOI: 10.1021/acs.jafc.5b01599
J. Agric. Food Chem. 2015, 63, 6189−6211

accounted for only about 3% of the total lipids of the seeds examined.[49]

Each of the two major galactolipid classes in wheat, DGDG and MGDG, is composed of various molecular species differing in chain length and the degree of saturation of their fatty acyl groups (Figure 11). The 2-position fatty acids of wheat galactolipids are highly unsaturated, containing 83% linoleic acid and 7% linolenic acid.[7]

Galactolipids were identified by comparing their positive and negative ESI spectra. As shown in Figure 12, the $[M - H]^-$/$[M + FA - H]^-$ and $[M + NH_4]^+$/$[M + Na]^+$ pairs were observed in ESI negative and positive mode, respectively. The MS^2 spectra of ions $[M - H]^-$ and $[M + NH_4]^+$ from DGDG (18:2/18:3) are shown in Figure S8. The principal product ions of $[M - H]^-$ were observed due to the cleavage of the fatty acid, giving $[M - H - R_1COOH]^-$ and $[M - H - R_2COOH]^-$. The less prominent ions were $[M - H - R_1COO - R_2COOH]^-$ at m/z 379 and fatty carboxylate anions R_1COO^- and R_2COO^-. These ions provide information on the composition of the two acyl groups. The $[M + NH_4]^+$ ion loses two galactosyl moieties to yield ions $[M + H - 162 - 162]^+$. One digalactosyl monoglyceride (DGMG), seven DGDG, and three MGDG compounds were identified mainly from endosperm (Table 11).

Lipids Discriminate Whole-Grain and Refined Wheat Flour. WF and RF data acquired by FCMS were used for PCA. Four different ionization modes (APCI+, APCI−, ESI+, and ESI−) were tested. The score plots of all four ionization methods are shown in Figure 13. All four PCA plots displayed excellent separation between RF and WF samples. The first two principal components cumulatively represented 91.6, 92.8, 94.9, and 95.6% of variance, respectively.

The corresponding loadings plots are presented in Figure 14. The loading plots reflect how much each of the variables contributed to the classification. However, different compound classes have different ionization efficiencies in different ionization modes, which lead to their different degrees of importance for discrimination in each mode. TGs/DGs respond to both APCI and ESI source, but form ions $[M + H]^+$/$[M + NH_4]^+$ and $[M + NH_4]^+$/$[M + Na]^+$, respectively, as mentioned above. Galactolipids show weak signals in APCI positive mode but very good signals in ESI positive mode. AR cannot be detected in ESI positive mode, but gives good signal in APCI positive mode.

TGs, DGs, and ARs contributed significantly to the separation in APCI+ mode (Figure 14A). Free FA, oxylipins, γ-oryzanol, or/and DGs contributed most to the separation in APCI− mode (Figure 14B). In ESI+ mode, galactolipids were mainly responsible for the discrimination of RF from WF, and TGs also appeared as characteristic ions of WF, whereas AR had poor ionization efficiency (Figure 14C). Phospholipids and galactolipids were the major contributors in ESI− mode (Figure 14D). The results of this study highlight the potential discriminatory compound categories between WF and RF. Sphingolipids did not show important roles in WF/RF discrimination.

■ ASSOCIATED CONTENT

Supporting Information

TICs of germ and characteristic MS^n spectra of each compound category. The Supporting Information is available free of charge on the ACS Publications website at DOI: 10.1021/acs.jafc.5b01599.

■ AUTHOR INFORMATION

Corresponding Author

*(P.C.) Mail: Food Composition and Methods Development Laboratory, Beltsville Human Nutrition Research Center, Agricultural Research Service, USDA, Building 161, BARC-East, 10300 Baltimore Avenue, Beltsville, MD 20705, USA. E-mail: pei.chen@ars.usda.gov. Phone: (301) 504-8144. Fax: (301) 504-8314.

Funding

This research is supported by the Agricultural Research Service of the U.S. Department of Agriculture and an Interagency Agreement with the Office of Dietary Supplements of the National Institutes of Health (Grant Y01 OD001298-01).

Notes

The authors declare no competing financial interest.

■ ABBREVIATIONS USED

WF, whole wheat flour; RF, refined wheat flour; FA, fatty acid; TG, triacylglycerol; DG, diacylglycerol; ARs, alk(en)-ylresorcinols; PUFA, polyunsaturated fatty acids; PC, phosphatidylcholine; LPC, lysophosphatidylcholine; PE, phosphatidylethanolamine; LPE, lysophosphatidylethanolamine; PG, phosphatidylglycerol; PA, phosphatidic acid; PS, phosphatidylserine; MGDG, monogalactosyl diglyceride; DGDG, digalactosyl diglyceride; DGMG, digalactosyl monoglyceride; PCA, principal component analysis; CID, collision-induced dissociation; TIC, total ion chromatogram

■ REFERENCES

(1) Aune, D.; Chan, D. S. M.; Lau, R.; Vieira, R.; Greenwood, D. C.; Kampman, E.; Norat, T., Dietary fibre, whole grains, and risk of colorectal cancer: systematic review and dose-response meta-analysis of prospective studies. *Br. Med. J.* **2011**, *343*, d661710.1136/bmj.d6617

(2) Kristensen, M.; Toubro, S.; Jensen, M. G.; Ross, A. B.; Riboldi, G.; Petronio, M.; Bugel, S.; Tetens, I.; Astrup, A. Whole Grain Compared with Refined Wheat Decreases the Percentage of Body Fat Following a 12-Week, Energy-Restricted Dietary Intervention in Postmenopausal Women. *J. Nutr.* **2012**, *142*, 710−716.

(3) Mellen, P. B.; Walsh, T. F.; Herrington, D. M. Whole grain intake and cardiovascular disease: A meta-analysis. *Nutr., Metab. Cardiovasc. Dis.* **2008**, *18*, 283−290.

(4) Lutsey, P. L.; Jacobs, D. R.; Kori, S.; Mayer-Davis, E.; Shea, S.; Steffen, L. M.; Szklo, M.; Tracy, R. Whole grain intake and its cross-sectional association with obesity, insulin resistance, inflammation, diabetes and subclinical CVD: The MESA Study. *Br. J. Nutr.* **2007**, *98*, 397−405.

(5) Fisher, N.; Broughton, M.; Peel, D.; Bennett, R. The lipids of wheat. II.—lipids of flours from single wheat varieties of widely varying baking quality. *J. Sci. Food Agric.* **1964**, *15*, 325−341.

(6) MacMurray, T.; Morrison, W. Composition of wheat-flour lipids. *J. Sci. Food Agric.* **1970**, *21*, 520−528.

(7) Morrison, W. Wheat lipid composition. *Cereal Chem.* **1978**, *55*, 548−558.

(8) Khan, K.; Shewry, P. R. *Wheat: Chemistry and Technology*; American Association of Cereal Chemists, Inc. (AACC): St. Paul, MN, USA, 2009.

(9) Burkwall, M.; Glass, R. The fatty acids of wheat and its milled products. *Cereal Chem.* **1965**, *42*, 236.

(10) Arunga, R.; Morrison, W. The structural analysis of wheat flour glycerolipids. *Lipids* **1971**, *6*, 768−776.

(11) Colborne, A. J.; Laidman, D. L. The extraction and analysis of wheat phospholipids. *Phytochemistry* **1975**, *14*, 2639−2645.

(12) Prinsen, P.; Gutiérrez, A.; Faulds, C. B.; del Río, J. C. Comprehensive Study of Valuable Lipophilic Phytochemicals in Wheat Bran. *J. Agric. Food Chem.* **2014**, *62*, 1664−1673.

DOI: 10.1021/acs.jafc.5b01599
J. Agric. Food Chem. 2015, 63, 6189−6211

(13) Sun, J. H.; Lin, L. Z.; Chen, P. Study of the mass spectrometric behaviors of anthocyanins in negative ionization mode and its applications for characterization of anthocyanins and non-anthocyanin polyphenols. *Rapid Commun. Mass Spectrom.* **2012**, *26*, 1123−1133.
(14) Sun, J.; Xiao, Z.; Lin, L. Z.; Lester, G. E.; Wang, Q.; Harnly, J. M.; Chen, P. Profiling polyphenols in five Brassica species microgreens by UHPLC-PDA-ESI/HRMS(n). *J. Agric. Food Chem.* **2013**, *61*, 10960−70.
(15) Lin, L.-Z.; Sun, J.; Chen, P.; Monagas, M. J.; Harnly, J. M. UHPLC-PDA-ESI/HRMS n Profiling Method To Identify and Quantify Oligomeric Proanthocyanidins in Plant Products. *J. Agric. Food Chem.* **2014**, *62*, 9387−9400.
(16) Lin, L.-Z.; Sun, J.; Chen, P.; Zhang, R.-W.; Fan, X.-E.; Li, L.-W.; Harnly, J. M. Profiling of Glucosinolates and Flavonoids in *Rorippa indica* (Linn.) Hiern.(Cruciferae) by UHPLC-PDA-ESI/HRMSn. *J. Agric. Food Chem.* **2014**, *62*, 6118−6129.
(17) Sun, J.; Liu, X.; Yang, T.; Slovin, J.; Chen, P. Profiling polyphenols of two diploid strawberry (*Fragaria vesca*) inbred lines using UHPLC-HRMS(n). *Food Chem.* **2014**, *146*, 289−98.
(18) Nelson, J.; Glass, R.; Geddes, W. The triglycerides and fatty acids of wheat. *Cereal Chem.* **1963**, *40*, 343−351.
(19) Levandi, T.; Puessa, T.; Vaher, M.; Toomik, P.; Kaljurand, M. Oxidation products of free polyunsaturated fatty acids in wheat varieties. *Eur. J. Lipid Sci. Technol.* **2009**, *111*, 715−722.
(20) Oliw, E. H.; Garscha, U.; Nilsson, T.; Cristea, M. Payne rearrangement during analysis of epoxyalcohols of linoleic and α-linolenic acids by normal phase liquid chromatography with tandem mass spectrometry. *Anal. Biochem.* **2006**, *354*, 111−126.
(21) Dufour, C.; Loonis, M. Regio-and stereoselective oxidation of linoleic acid bound to serum albumin: identification by ESI−mass spectrometry and NMR of the oxidation products. *Chem. Phys. Lipids* **2005**, *138*, 60−68.
(22) Orellana-Coca, C.; Adlercreutz, D.; Andersson, M. M.; Mattiasson, B.; Hatti-Kaul, R. Analysis of fatty acid epoxidation by high performance liquid chromatography coupled with evaporative light scattering detection and mass spectrometry. *Chem. Phys. Lipids* **2005**, *135*, 189−199.
(23) Farmer, E. E.; Alméras, E.; Krishnamurthy, V. Jasmonates and related oxylipins in plant responses to pathogenesis and herbivory. *Curr. Opin. Plant Biol.* **2003**, *6*, 372−378.
(24) Nørskov, N. P.; Hedemann, M. S.; Theil, P. K.; Knudsen, K. E. B. Oxylipins discriminate between whole grain wheat and wheat aleurone intake: a metabolomics study on pig plasma. *Metabolomics* **2013**, *9*, 464−479.
(25) Yuan, Z. X.; Rapoport, S. I.; Soldin, S. J.; Remaley, A. T.; Taha, A. Y.; Kellom, M.; Gu, J.; Sampson, M.; Ramsden, C. E. Identification and profiling of targeted oxidized linoleic acid metabolites in rat plasma by quadrupole time-of-flight mass spectrometry. *Biomed. Chromatogr.* **2013**, *27*, 422−432.
(26) Knoche, H. A study on the biosynthesis of *cis*-9,10-epoxyoctadecanoic acid. *Lipids* **1968**, *3*, 163−169.
(27) Vollenweider, S.; Weber, H.; Stolz, S.; Chételat, A.; Farmer, E. E. Fatty acid ketodienes and fatty acid ketotrienes: Michael addition acceptors that accumulate in wounded and diseased *Arabidopsis* leaves. *Plant J.* **2000**, *24*, 467−476.
(28) Wheelan, P.; Zirrolli, J. A.; Murphy, R. C. Low-energy fast atom bombardment tandem mass spectrometry of monohydroxy substituted unsaturated fatty acids. *Biol. Mass Spectrom.* **1993**, *22*, 465−473.
(29) Landberg, R.; Marklund, M.; Kamal-Eldin, A.; Åman, P. An update on alkylresorcinols−Occurrence, bioavailability, bioactivity and utility as biomarkers. *J. Funct. Foods* **2014**, *7*, 77−89.
(30) Bondia-Pons, I.; Barri, T.; Hanhineva, K.; Juntunen, K.; Dragsted, L. O.; Mykkänen, H.; Poutanen, K. UPLC-QTOF/MS metabolic profiling unveils urinary changes in humans after a whole grain rye versus refined wheat bread intervention. *Mol. Nutr. Food Res.* **2013**, *57*, 412−422.
(31) Landberg, R.; Kamal-Eldin, A.; Salmenkallio-Marttila, M.; Rouau, X.; Aman, P. Localization of alkylresorcinols in wheat, rye and barley kernels. *J. Cereal Sci.* **2008**, *48*, 401−406.
(32) Zhu, Y.; Conklin, D. R.; Chen, H.; Wang, L.; Sang, S. 5-Alk(en)ylresorcinols as the major active components in wheat bran inhibit human colon cancer cell growth. *Bioorg. Med. Chem.* **2011**, *19*, 3973−3982.
(33) Knödler, M.; Kaiser, A.; Carle, R.; Schieber, A. Profiling of alk(en)ylresorcinols in cereals by HPLC-DAD-APcI-MSn. *Anal. Bioanal. Chem.* **2008**, *391*, 221−228.
(34) Lerma-Garcia, M.; Herrero-Martinez, J.; Simó-Alfonso, E.; Mendonça, C. R.; Ramis-Ramos, G. Composition, industrial processing and applications of rice bran γ-oryzanol. *Food Chem.* **2009**, *115*, 389−404.
(35) Cho, J.-Y.; Lee, H. J.; Kim, G. A.; Kim, G. D.; Lee, Y. S.; Shin, S. C.; Park, K.-H.; Moon, J.-H. Quantitative analyses of individual γ-oryzanol (steryl ferulates) in conventional and organic brown rice (*Oryza sativa* L.). *J. Cereal Sci.* **2012**, *55*, 337−343.
(36) Fang, N.; Yu, S.; Badger, T. M. Characterization of triterpene alcohol and sterol ferulates in rice bran using LC-MS/MS. *J. Agric. Food Chem.* **2003**, *51*, 3260−3267.
(37) Nystrom, L.; Makinen, M.; Lampi, A. M.; Piironen, V. Antioxidant activity of steryl ferulate extracts from rye and wheat bran. *J. Agric. Food Chem.* **2005**, *53*, 2503−2510.
(38) Hakala, P.; Lampi, A. M.; Ollilainen, V.; Werner, U.; Murkovic, M.; Wahala, K.; Karkola, S.; Piironen, V. Steryl phenolic acid esters in cereals and their milling fractions. *J. Agric. Food Chem.* **2002**, *50*, 5300−5307.
(39) Fujino, Y.; Ohnishi, M. Sphingolipids in wheat grain. *J. Cereal Sci.* **1983**, *1*, 159−168.
(40) Zhu, Y.; Soroka, D. N.; Sang, S. Structure elucidation and chemical profile of sphingolipids in wheat bran and their cytotoxic effects against human colon cancer cells. *J. Agric. Food Chem.* **2013**, *61*, 866−874.
(41) Bandu, M. L.; Grubbs, T.; Kater, M.; Desaire, H. Collision induced dissociation of alpha hydroxy acids: Evidence of an ion-neutral complex intermediate. *Int. J. Mass Spectrom.* **2006**, *251*, 40−46.
(42) Jakab, A.; Héberger, K.; Forgács, E. Comparative analysis of different plant oils by high-performance liquid chromatography−atmospheric pressure chemical ionization mass spectrometry. *J. Chromatogr. A* **2002**, *976*, 255−263.
(43) Murphy, R. C.; Harrison, K. A. Fast atom bombardment mass spectrometry of phospholipids. *Mass Spectrom. Rev.* **1994**, *13*, 57−75.
(44) Taguchi, R.; Houjou, T.; Nakanishi, H.; Yamazaki, T.; Ishida, M.; Imagawa, M.; Shimizu, T. Focused lipidomics by tandem mass spectrometry. *J. Chromatogr. B: Anal. Technol. Biomed. Life Sci.* **2005**, *823*, 26−36.
(45) Fang, J.; Barcelona, M. J. Structural determination and quantitative analysis of bacterial phospholipids using liquid chromatography/electrospray ionization/mass spectrometry. *J. Microbiol. Methods* **1998**, *33*, 23−35.
(46) Pulfer, M.; Murphy, R. C. Electrospray mass spectrometry of phospholipids. *Mass Spectrom. Rev.* **2003**, *22*, 332−364.
(47) Gerits, L. R.; Pareyt, B.; Delcour, J. A. A lipase based approach for studying the role of wheat lipids in bread making. *Food Chem.* **2014**, *156*, 190−196.
(48) Pareyt, B.; Finnie, S. M.; Putseys, J. A.; Delcour, J. A. Lipids in bread making: Sources, interactions, and impact on bread quality. *J. Cereal Sci.* **2011**, *54*, 266−279.
(49) Gil, J. H.; Hong, J.; Choe, J. C.; Kim, Y. H. Analysis of fatty acyl groups of diacyl galactolipid molecular species by HPLC/ESI-MS with in-source fragmentation. *Bull. Korean Chem. Soc.* **2003**, *24*, 1163−1168.

DOI: 10.1021/acs.jafc.5b01599
J. Agric. Food Chem. 2015, 63, 6189−6211

Table 1. Nucleotide Sequences of the Primers Used for Real-Time Quantitative PCR

gene	accession no.	direction	primer sequence	product length, bp
PPARγ	DQ013884	forward	5′-TTCCAGGGGTGTCAGTTTCG-3′	99
		reverse	5′-TTGGTCATTCAGGTCAAGGTTTA-3′	
aP2	NM_001002817	forward	5′-TAGTAGATGATAAGTTGGTGGTGGAATG-3′	67
		reverse	5′-CTCTCATAAATTCTGGTAGCCGTGA-3′	
FAS	EF589048	forward	5′-TTGTCCTGGGAAGAGTGTAAGC-3′	94
		reverse	5′-CCTGAGGTCCCGAGATGGT-3′	
HSL	AY686758	forward	5′-ACCCTCGGCTGTCAACTTCTT-3′	90
		reverse	5′-ACTTTCTCCTCCTTGGTGCTAATCT-3′	
18S rRNA	AY265350	forward	5′-CCCACGGAATCGAGAAAGAG-3′	122
		reverse	5′-TTGACGGAAGGGCACCA-3′	

Reagents. DNJ was purchased from Sigma (D9305; Sigma, St. Louis, MO, USA), and DNJ stock solutions were made in deionized distilled water and later diluted in media or phosphate-buffered saline (PBS) prior to use in culture. Rosiglitazone (RGZ), a PPARγ agonist, was purchased from Cayman Chemical (CAS Registry No. 122320-73-4; Ann Arbor, MI, USA). Fetal bovine serum (FBS) was from Hyclone (Logan, UT, USA), BODIPY from Life Technologies (Carlsbad, CA, USA), and 4′,6-diamidino-2-phenylindole (DAPI) from Roche (Basel, Switzerland).

Frozen Section and HE Staining. Baimei is an important Chinese indigenous breed, an obese type with 32% fat in the carcass, whereas Large White pig is widely distributed in most of the world and is a lean type with 15% fat in the carcass. Four fat-type breed Bamei pigs and four lean-type breed Large White pigs at day 180 of age were provided by the experimental farm of Northwest A&F University. All pigs were killed at a slaughterhouse under the guidelines of Northwest A&F University Animal Care Committee. Half an hour post-mortem, 4−6 g samples were taken from LM muscle between the sixth and seventh rib. LM were dissected and rinsed with PBS. Samples were frozen in liquid nitrogen. For frozen section, the samples were fixed with 4% paraformaldehyde and kept at room temperature. Fixed tissues were dehydrated in 30% sucrose (v/v) and sectioned (10 μm) through a sliding microtome (Leica, Solms, Germany). Sections were stained with HE using standard pathologic procedures.[27] The slides were then dehydrated with 95 and 100% ethanol successively followed by xylene (2 × 5 min) and mounted with coverslips. The sections were observed and pictures taken through a microscope (Olympus, New York, NY, USA) at 100× magnification.

Isolation and Culture of Porcine Intramuscular Adipocytes. About 20−30 min post-mortem, 4−6 g of LM per piglet was collected from four piglets (2 of them at 1 day and the others at 2 days of age) and finely minced in 50 mL beakers containing 5 mL of Dulbecco's modified Eagle's medium (DMEM)/Nutrient Mixture F-12 (DMEM/F12; Gibco) with 0.2 mL of kanamycin solution (30 mg/mL) per gram of tissue, respectively. Intramuscular adipocytes were isolated using a type II collagenase (Gibco) method according to previous publications.[28,29] The cells were cultured using a previously published method.[30,31] Briefly, the finely minced tissues were digested at 37 °C for 120 min in a shaking water bath. Digesta were passed through sterile 178 and 74 μm steel mesh filters to isolate digested cells. Cells were rinsed with serum-free DMEM/F12 medium and centrifugation twice at 1500*g* for 10 min. Cells were resuspended in growth medium (GM), plated at 6×10^5 per 60 mm culture dish, and cultured in a 5% CO_2 incubator at 37 °C. Because adipocytes attach much earlier than myoblasts, the culture cells were rinsed three times with PBS to remove myoblasts, insoluble myofibrillar proteins, and other debris at 1 h after plating. Cells were cultured in GM until reaching 70−80% confluence, digested with 0.05% trypsin, collected by centrifugation 1000*g* for 5 min, resuspended in GM, and plated at a density of 2×10^4 cells/cm^2 in 6-well plates. Two days after 100% confluence, the cells were treated with DMEM/F12 supplemented with 10% FBS and the hormone cocktail IBMX−DEX−insulin (MDI; 0.5 mM IBMX, 1 nM DEX, and 5 ng/mL insulin) for 2 days. The medium was changed to differentiation medium (DM), including DMEM/F12 supplemented with 10% FBS and 5 ng/mL insulin, for another 2 days.

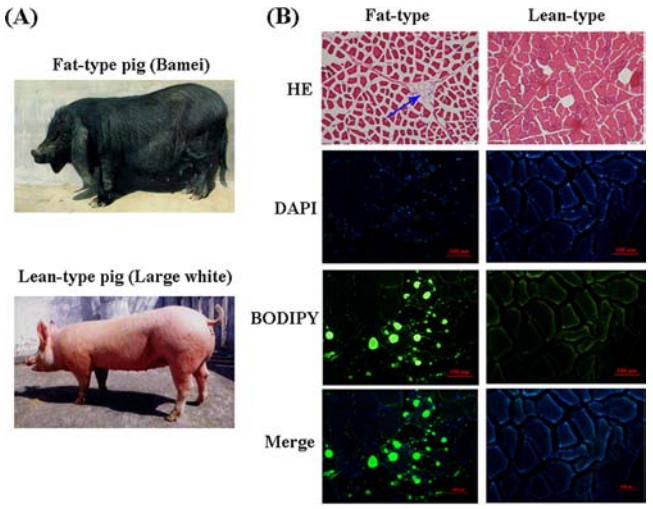

Figure 1. Morphologic observation of LM between obese and lean pigs at 180 days of age: (A) fat-type pig (Bamei) and lean-type pig (Large white); (B) intramuscular adipocyte in LM of fat-type and lean-type pigs. HE, hematoxylin and eosin staining, blue arrow indicates IMF adipocytes; BODIPY staining, lipids indicate green and blue nuclei stained with DAPI. Scale bar = 100 μm.

Table 2. Carcass Weight, Fat Percent and IMF Content of Bamei and Large White Pigs at 180 Days of Age

pig breed	carcass weight, kg	fat, %	IMF content, %
Bamei	37.48 ± 1.09**	31.03 ± 0.41**	4.42 ± 0.45**
Large White	68.74 ± 1.36	17.61 ± 0.27	2.37 ± 0.29

**indicates $P < 0.01$.

Cell Viability Analysis. Porcine intramuscular adipocyte viability was determined using the 3-(4,5-dimethylthiazol-2-yl)-2,5-diphenyltetrazolium bromide (MTT) assay. Cells were seeded in 24-well culture plates at a density of 2×10^4 cells/well, incubated for 48 h, treated with DNJ at various concentrations (2.0, 3.0, 4.0, 5.0, and 6.0 μM) or RSG (0.1, 0.2, 0.3, 0.4, and 0.5 mM) for 48 h to evaluate any dose-dependent effects of DNJ or RSG on cell growth and viability, cultured with 0.5 mg/mL MTT at 37 °C in a humidified atmosphere of 5% CO_2 for another 4 h, and solubilized with isopropanol. The viable cell number was directly proportional to the production of formazan measured spectrophotometrically at 563 nm.

DOI: 10.1021/acs.jafc.5b01680
J. Agric. Food Chem. 2015, 63, 6212−6220

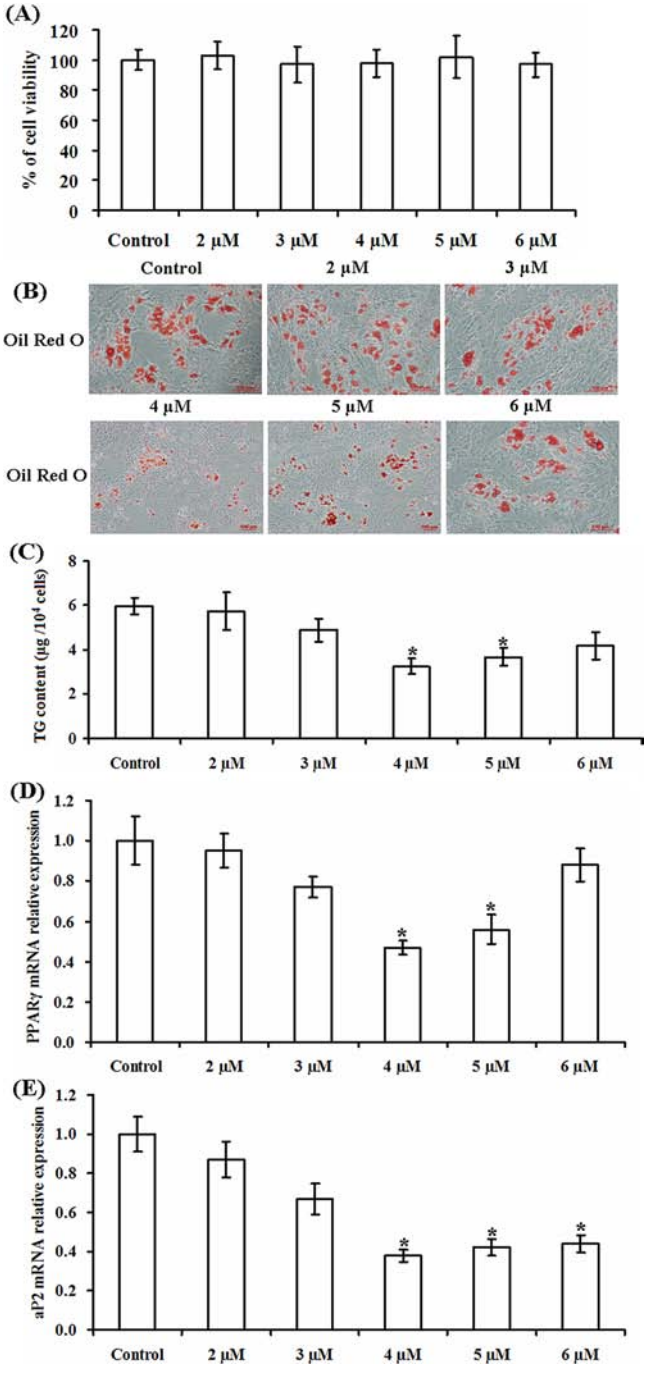

Figure 2. Effects of various concentrations of DNJ on porcine intramuscular preadipocyte differentiation. (A) Effect of DNJ on viability of porcine intramuscular preadipocyte as assessed by the MTT assay. Cells were treated with different concentrations (2.0−6.0 μM) of DNJ for 48 h and then assayed using MTT. (B) Intracellular lipids stained with Oil Red O. Intramuscular preadipocytes were treated with DMSO as control and the indicated concentrations of DNJ at day 8. (C) TG content (μg/10^4 cells) determined at day 8 after treatment. (D, E) mRNA levels of PPARγ and aP2 at day 8 after treatment. Gene mRNA expression was determined by qPCR, normalized to 18S rRNA and expressed relative to expression in the control. Each column represents the mean of four independent experiments ± SEM: (*) $p < 0.05$.

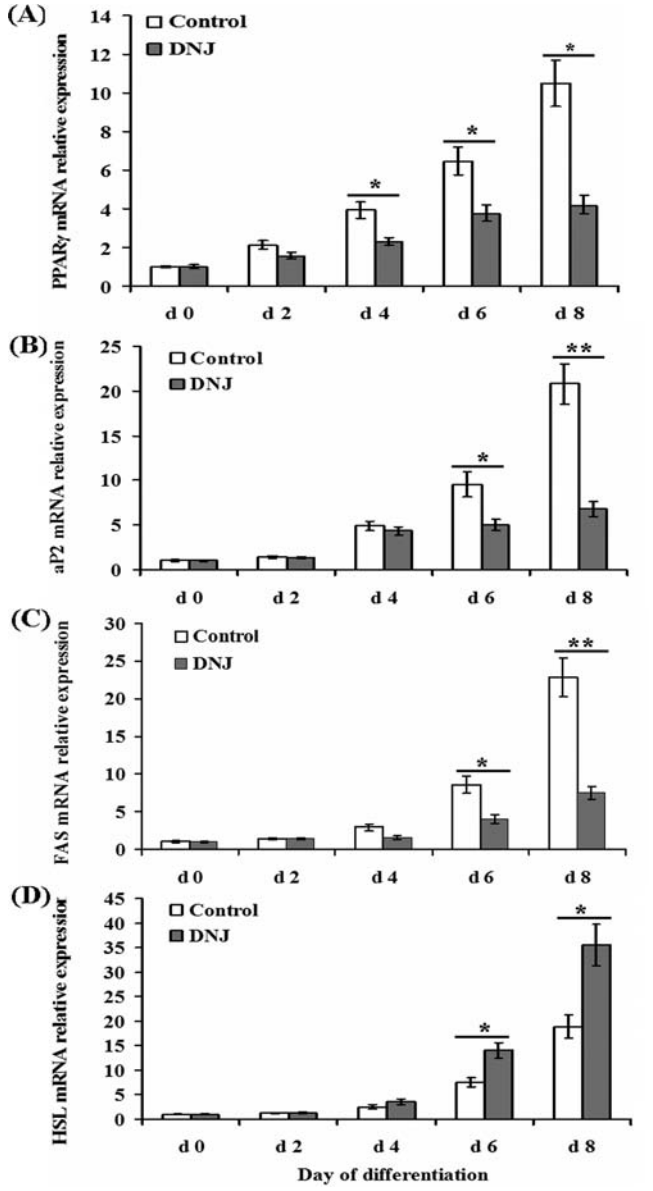

Figure 3. DNJ regulates mRNA expression of key adipogenic and lipolytic genes during lipogenesis of intramuscular preadipocytes: real-time qPCR analysis of (A) PPARγ, (B) AP$_2$, (C) FAS, and (D) HSL mRNA levels, respectively. Porcine intramuscular preadipocytes treated with 4 μM DNJ were induced differentiation and collected at days 0, 2, 4, 6, and 8. Gene mRNA expression was determined by qPCR, normalized to 18S rRNA, and expressed relative to expression in the control at day 0. Data indicate the mean ± SEM: (*) $p < 0.05$ and (**) $p < 0.01$.

Treatment with DNJ and RSG. For the DNJ experiment, porcine intramuscular adipocytes incubated in induced media of differentiation were treated with 0, 2, 3, 4, 5, or 6 μM DNJ for 8 days. For both DNJ and RSG experiment, at day 8 after treatment with 4 μM DNJ, intramuscular adipocytes were incubated with 0.4 mM RSG for 2 days. At the indicated time points, cells were stained by Oil Red O or BODIPY, a triacylglycerol content assay was performed, and total RNA and protein were extracted for analysis of gene expression.

Oil Red O Staining. Oil Red O staining was conducted according to a previously published method.[32]

BODIPY Staining. BODIPY staining was performed according to a previously published method.[32] The sections or cells were observed under fluorescence microscope (Nikon, Tokyo, Japan).

Triacylglycerol (TG) Content Assay. TG content analysis was conducted according to a previously published method.[32]

Real-Time Quantitative PCR. Total RNA was extracted from cells according to the manufacturer's instruction of TRIZOL reagent (Takara, Japan). The RNA concentration was determined, and reverse transcription was performed using the First-Strand cDNA Synthesis Kit

DOI: 10.1021/acs.jafc.5b01680
J. Agric. Food Chem. 2015, 63, 6212−6220

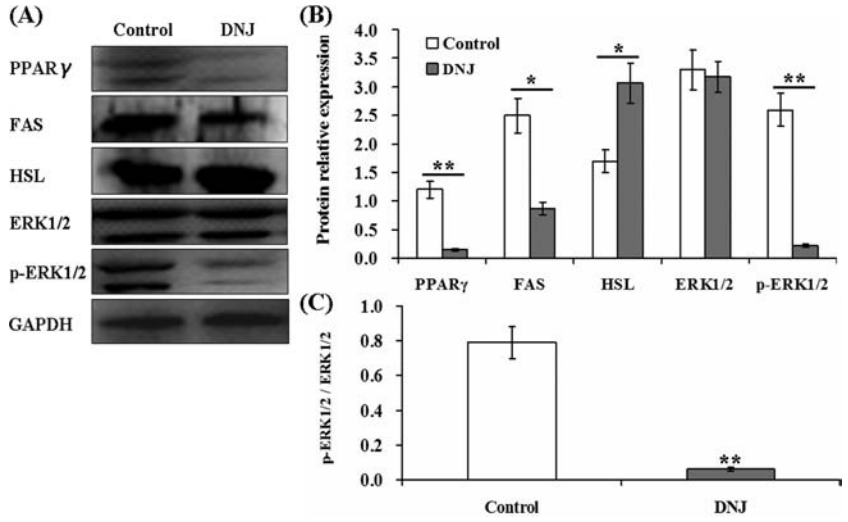

Figure 4. DNJ represses adipogenesis by inhibiting phosphorylation of ERK1/2: (A, B, C) ERK signaling in intramuscular adipocytes under DNJ stimulation condition. On reaching 70−80% confluence, the intramuscular preadipocytes were treated with DMSO as control and 4 μM DNJ for 2 days; the protein levels of adipogenic and lipolytic markers, phosphorylated ERK1/2 (p-ERK1/2), and ERK1/2 proteins were detected by Western blotting at day 8 of differentiation induction. GAPDH was applied as internal reference. Each column represents the mean of four batches ± SEM: (∗) $p < 0.05$ and (∗∗) $p < 0.01$.

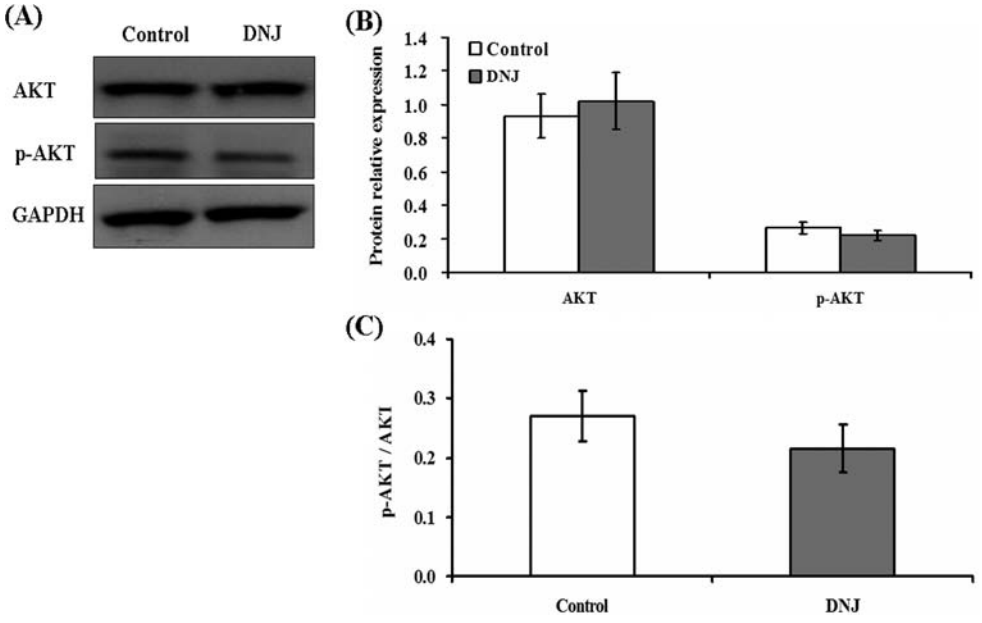

Figure 5. DNJ did not change the levels of AKT and p-AKT: (A, B, C) AKT signaling in intramuscular adipocytes under DNJ stimulation condition. On reaching 70−80% confluence, the intramuscular preadipocytes were treated with DMSO as control and 4 μM DNJ for 2 days; p-AKT and AKT proteins were detected by Western blotting at day 8 of differentiation induction. GAPDH was applied as internal reference. Each column represents the mean of four batches ± SEM.

(Takara, Japan) for qRT-PCR (Bio-Rad iQ5 multicolor Real-Time PCR Detection system) analysis of the functional genes. Real-time PCR was performed by using a Prime Script RT Reagent Kit (Perfect Real Time, Takara, Japan) according to the manufacturer's instructions. Primers are listed in Table 1. In this study, 18S rRNA (18S) was used as the reference gene. The 2-ΔΔCT method is used to analyze the relative changes in the expression of each gene mRNA.

Western Blot Analysis. Cells were lysed in lysis buffer (Beyotime, China), supplemented with 1 mM PMSF. Protein concentration was determined with a BCA protein assay kit (Tiangen, China). The proteins of each sample were separated by 12% SDS-PAGE and electrotransferred to PVDF membrane (Millipore, Bedford, MA, USA) for immunoblot analysis. The following primary antibodies were used: PPARγ (abcam, ab1948, 1:400), FAS (Santa Cruz, sc-20140, 1:300), HSL (cell signaling, 4107, 1:1000), ERK1/2 (cell signaling, 9102, 1:1000), p-ERK1/2 (cell signaling, 9101, 1:1000), AKT (Santa Cruz, sc-8312, 1:500), p-AKT (Santa Cruz, sc-7985-R, 1:500), and anti-GAPDH (Santa Cruz, sc-166574, 1:500), which was used as internal reference. After incubation with the appropriate HRP−conjugate secondary antibody, proteins were detected using a ChemiDoc XRS imaging system and analysis software Quantity One (Bio-Rad).

Statistical Analysis. All experimental data are obtained from four independent experiments. Values are expressed as means ± standard error of the mean (SEM). Statistics are calculated with SPSS statistics v19.0 software. Student's *t* test is used for individual comparisons. Multiple comparisons are assessed by one-way ANOVA followed by Dunnett's tests. Differences between groups are considered statistically significant if $P < 0.05$.

RESULTS

Intramuscular Adipocyte in Fat-Type and Lean-Type Pig Longissimus Dorsi Muscles. Bamei pig is a fat-type breed, and Large White pig is a lean-type breed (Figure 1A). Fat percent

DOI: 10.1021/acs.jafc.5b01680
J. Agric. Food Chem. 2015, 63, 6212−6220

and IMF content of Bamei pigs were significantly greater than that of Large White pigs at 180 days of age (Table 2). Using HE and BODIPY staining, the intramuscular adipocytes and IMF in LM of Bamei pigs were much greater than that of Large White pigs at 180 days of age (Figure 1B).

Effect of Various DNJ Concentrations on Adipogenesis of Porcine Intramuscular Adipocytes. As shown in Figure 2A, DNJ (2, 3, 4, 5, and 6 mM) was not toxic, so these five concentrations were used to test the effect of DNJ on adipogenesis of porcine intramuscular adipocytes. To evaluate the effect of DNJ on lipogensis of porcine intramuscular adipocytes, the cells were treated with different concentrations of DNJ including 0, 2, 3, 4, 5, and 6 μM for 8 days. The results indicated that lipid accumulation was significantly weakened in the treatment with 4 and 5 μM DNJ by Oil Red O staining (Figure 2B) and TG content assay ($p < 0.05$; Figure 2C). Moreover, the mRNA levels of key lipogenic gene PPARγ (4 and 5 μM DNJ; $p < 0.05$; Figure 2D) and aP2 (4, 5, and 6 μM DNJ; $p < 0.05$; Figure 2E) were markedly down-regulated at day 8 after treatment. On the basis of the above results, the following experiments were performed with 4 μM DNJ.

DNJ Inhibited Lipid Accumulation during Intramuscular Adipocyte Differentiation. To further examine the effects of 4 μM DNJ on key lipogenic and lipolytic genes during adipocyte differentiation, the time course of mRNA expressions of aP_2, PPARγ, FAS, and HSL were analyzed by real-time qRT-PCR at days 0, 2, 4, 6, and 8. The results indicated that mRNA levels of PPARγ were decreased at days 4, 6, and 8 compared with controls ($p < 0.05$; Figure 3A), mRNA levels of aP_2 were significantly reduced at days 6 ($p < 0.05$; Figure 3B) and 8 ($p < 0.01$; Figure 3B), and mRNA levels of FAS were down-regulated at days 6 ($p < 0.05$; Figure 3C) and 8 ($p < 0.01$; Figure 3C), whereas the mRNA levels of HSL were up-regulated at days 6 and 8 ($p < 0.05$; Figure 3D).

ERK Signaling Was Repressed in Intramuscular Adipocytes under DNJ Stimulation. To study the effect of DNJ on proteins that play a key role or involve signal transduction during differentiation, the total proteins were extracted from intramuscular adipocytes treated with 4 μM DNJ at day 8 after induction of differentiation for Western blot analysis. The results showed that protein levels of vital adipogenic genes, including PPARγ ($p < 0.01$) and FAS ($p < 0.05$), were significantly reduced (Figure 4), whereas the protein level of HSL ($p < 0.05$), which is a key lipolytic marker, markedly increased in the treatment (Figure 4). Interestingly, compared with the control, levels of ERK1/2 had no striking difference, but levels of phosphorylated ERK1/2 (p-ERK1/2) were markedly inhibited in the DNJ treatment ($p < 0.05$; Figure 4). In addition, levels of AKT and phosphorylated AKT (p-Akt) showed no difference (Figure 5). Therefore, the ERK signaling pathway was implicated in adipogenesis of intramuscular adipocytes under DNJ stimulation condition.

RGZ Improves Adipogenesis of Porcine Intramuscular Adipocytes. As shown in Figure 6A, RGZ (0.1, 0.2, 0.3, 0.4, and 0.5 mM) was not toxic, so these five concentrations were used to test the effect of RGZ on adipogenesis of porcine intramuscular adipocytes. TG contents in intramuscular adipocytes treated with RGZ (0.3, 0.4, and 0.5 mM) were significantly greater than the control ($p < 0.01$; Figure 6B). Moreover, compared with the control, the levels of PPARγ mRNA in cells treated with RGZ (0.3, 0.4, and 0.5 mM) were markedly up-regulated ($p < 0.01$; Figure 6C).

Inhibitory Adipogenesis of DNJ Is Attenuated by RGZ via Up-regulation of PPARγ Expression. To further investigate whether the ERK/PPARγ signaling pathway is involved in regulating adipogenesis of DNJ, the intramuscular adipocytes treated with 4 μM DNJ (for 8 days) were stimulated with 0.4 mM RGZ for 2 days (Figure 7A), then the treated cells were stained with BODIPY and Oil Red O to indicate lipogenesis; protein samples were subjected to a protein array to study the relevant kinases. The results showed that the inhibitory lipogenesis of DNJ was significantly attenuated by RGZ ($p < 0.05$; Figure 7B,C) and recovered the protein levels of PPARγ and FAS ($p < 0.05$; Figure 7D,E). Interestingly, the levels of ERK1/2 and its phosphorylation were not changed (Figure 7E,F) in intramuscular adipocytes treated with 4 μM DNJ plus 0.4 mM RSG. On the basis of the above results, the inhibitory adipogenesis of DNJ was attenuated by RSG via up-regulation of PPARγ. These findings indicate that DNJ inhibits adipogenesis through the ERK/PPARγ signaling pathway.

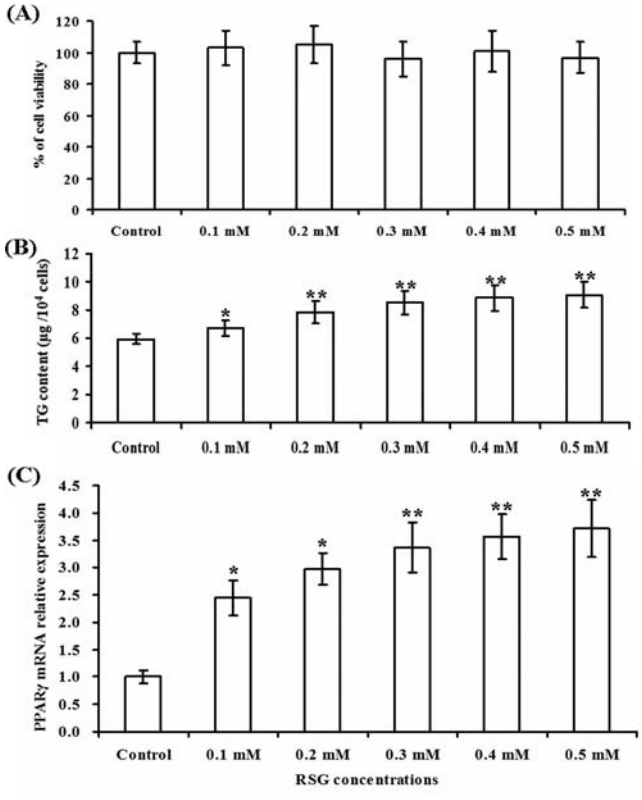

Figure 6. RSG improved adipogenesis in intramuscular adipocytes: (A) effect of rosiglitazone (RSG) on viability of porcine intramuscular preadipocyte as assessed by the MTT assay (cells were treated with different concentrations (0.1−0.5 mM) of RSG for 48 h and then assayed using MTT); (B) TG content (μg/10^4 cells) analyzed at day 8 after treatment; (C) real-time qPCR analysis of PPARγ mRNA levels. 18S rRNA was applied as internal reference. PPARγ mRNA expression was determined by qPCR, normalized to 18S rRNA, and expressed relative to expression in the control. Data indicate the mean ± SEM: (*) $p < 0.05$ and (**) $p < 0.01$.

DISCUSSION

China is the world's largest producer and consumer of pork. However, pork quality becomes bad because of the unfit IMF content. Our previous study showed that IMF content in LM of Bamei pig was much greater than that of Large White pig at 180 days of age.[33] In this study, intramuscular adipocyte and IMF content in fat-type and lean-type porcine LMs were directly

DOI: 10.1021/acs.jafc.5b01680
J. Agric. Food Chem. 2015, 63, 6212−6220

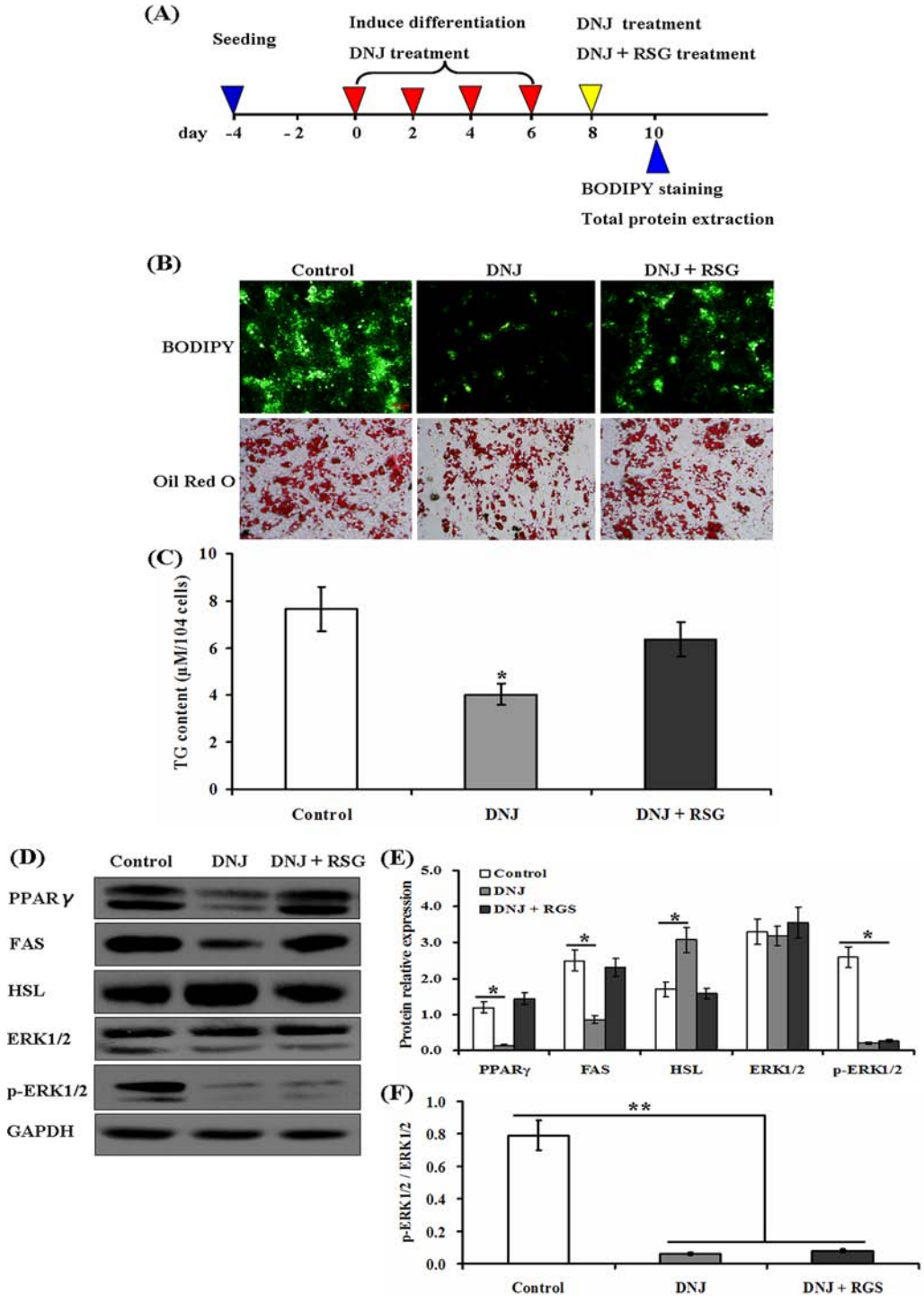

Figure 7. Inhibitory adipogenesis of DNJ was attenuated by RSG via up-regulation of PPARγ expression in intramuscular adipocytes: (A) experimental procedure for DNJ plus RSG treatment of porcine intramuscular adipocytes; (B) BODIPY and Oil Red O staining of intramuscular adipocytes under 4 μM DNJ condition at day 2 after treatment with 0.4 mM RSG; (C) TG content (μg/10^4 cells) analysis; (D, E, F) ERK signaling in intramuscular adipocytes under DNJ plus RSG stimulation condition. Each column represents the mean of four batches ± SEM: (∗) $p < 0.05$ and (∗∗) $p < 0.01$.

shown using HE and BODIPY staining. We think that the suitable IMF content and distribution in Bamei pork are involved in good meat quality.

Improvement of domestic animal meat quality is implicated in the regulatory mechanism of IMF deposition, which is modulated by adipogenensis of intramuscular adipocytes. Our previous studies found that some functional genes and natural extractions, including FoxO1 (Forkhead box O 1),[30,33] Sirt1 (Sirtuim 1),[32] Akt2 (protein kinase B 2),[32] C/EBPβ (CCAAT enhancer-binding protein B),[34] PU.1 (spleen focus forming virus proviral integration oncogene spi1),[35] resveratrol,[36] and camptothecin[31] regulated lipogenesis of porcine subcutaneous adipocytes through differentiation or apopotosis. It was reported that intake of DNJ suppressed lipid accumulation in rat liver and diet-induced obesity through increases in adiponectin in mice.[11,37] At present, the regulatory adipogenesis by DNJ in

DOI: 10.1021/acs.jafc.5b01680
J. Agric. Food Chem. 2015, 63, 6212−6220

porcine intramuscular adipocytes is still unknown. In this study, to explore the effect of DNJ on lipogenesis of intramuscular adipocytes, intramuscular adipocytes were isolated and cultured using the differential speed adherence method.[28] In accordance with Lee's results,[12] we found that DNJ did not affect intramuscular adipocyte viability. Likewise, RGZ, an agonist of PPARγ, was not toxic. DNJ at 4 μM decreased lipid acceleration and TG content, whereas 0.4 mM RGZ showed the opposite effects. Moreover, mRNA levels of key adipogenic genes including PPARγ and aP_2 were down-regulated in intramuscular adipocytes treated with 4 μM DNJ. On the basis of above findings, DNJ and RGZ may regulate IMF deposition by modulated lipogenesis of porcine intramuscular adipocytes.

Interestingly, in middle and later intramuscular adipocyte differentiation, mRNA and protein levels of PPARγ, aP_2, and FAS were markedly decreased, but the mRNA and protein levels of HSL were increased in the DNJ treatment. These results suggested that DNJ inhibited lipogenesis not only by down-regulation of lipogenic genes but also by up-regulation of lipolytic genes.

To investigate whether DNJ influences the activation of ERK1/2 during intramuscular adipocyte differentiation, we detected the levels of total and phosphorylated ERK1/2 in adipocytes treated with 4 μM DNJ at day 8. ERK1 and ERK 2 are members of the mitogen-activated protein kinase (MAPK) family, which play a pivotal role in intracellular signaling pathways of cellular proliferation and differentiation.[38] The blurry functions of ERK1/2 in adipogenesis were reported. Some researchers proved that phosphorylated ERK1/2 inhibited 3T3-L1 adipocyte differentiation by decreasing the activation of PPARγ.[39] In contrast, others reported that ERK1/2 activation has a positive association with adipogenesis in human mesenchymal stem cells and 3T3-L1 adipocytes.[38,40] We think that the opposite effects of ERK1/2 on lipogenesis may be related to different periods during differentiation. Consistent with the latter, our findings indicated that decreasing levels of phosphorylated ERK1/2 (p- ERK1/2) inhibited adipogenesis during the later period of intramuscular adipocyte differentiation at day 8 after treatment with DNJ. Meanwhile, expression levels of PPARγ and aP_2 have an apparently declining trend at days 6 and 8. Interestingly, the levels AKT and p-AKT were not changed under the DNJ treatment, indicating that Akt signaling was not involved in the lipogenesis of DNJ. Therefore, we think that DNJ may inhibit adipogenesis through the ERK/PPARγ signaling pathway intramuscular adipocytes.

To further explore whether ERK/PPARγ signaling is implicated in the regulatory lipogenesis of DNJ, the experiment of treatment with both DNJ and RSG was performed. Although levels of phosphorylated ERK1/2 and PPARγ in the treatment with DNJ were down-regulated, the level of PPARγ was recovered in treatment with DNJ plus RSG. DNJ inhibits lipogenesis of porcine intramuscular adipocyte via directly repressing the level of phosphorylated ERK1/2, then indirectly down-regulating the level of PPARγ through ERK signaling. Therefore, we conclude that DNJ inhibits IMF deposition by the ERK/PPARγ signaling pathway.

DNJ has been reported to be the main component of mulberry leaves, fruits, and silkworms.[41,42] Unlike chemical synthesis drugs, DNJ has no undesirable or significant side effects in vivo or in vitro.[3] Therefore, pork palatability and marbling may be changed by feeding a feedstuff containing a suitable concentration of DNJ, which will be further explored in the future.

A 2.5−3% IMF level is best for pork, but it is much closer to 4−7% in many Chinese indigenous pig breeds, such as the Neijiang pig and Hanjiang Black pig,[43] so DNJ may decrease pork IMF content. In introduced pig breeds, including Large White and Landrace,[43] their IMF contents are often below 2.5%, so it should be increased in these breeds.

In summary, DNJ suppresses lipid accumulation during differentiation of porcine intramuscular adipocytes by the ERK/PPARγ signaling pathway. We need to point out that the effects have been shown here for adipocytes of 1- or 2-day-old piglets and our method of possibly decreasing IMF deposition is only likely to be of practical usefulness for some breeds of pig that are particularly prone to fat deposition. These findings not only help us understand the mechanism whereby DNJ affects adipogenesis but may also provide a novel method to control intramuscular adipogenesis via DNJ for improving pork quality.

AUTHOR INFORMATION

Corresponding Author

*(W.-J.P.) Mail: No. 22 Xinong Road, Yangling, Shaanxi Province 712100, China. Phone: 86-29-87091017. Fax: 86-29-87092430. E-mail: pwj1226@nwsuaf.edu.cn.

Author Contributions

∥Guo-qiang Wang and Li Zhu contributed equally to this work.

Funding

This work was supported by the National Key Basic Research Programs of China (2015CB943102 and 2012CB124705), the National Natural Science Foundation of China (U1201213), the National Swine Industry Technology System Foundation (CARS-36), and the Natural Science Foundation of Shaanxi Province (2015JM3096).

Notes

The authors declare no competing financial interest.

ABBREVIATIONS USED

AKT, protein kinase B; aP_2, adipocyte fatty acid-binding protein 4; DAPI, 4′,6-diamidino-2-phenylindole; DMEM, Dulbecco's modified Eagle's medium; DNJ, 1-deoxynojirimycin; Erk, extracellular regulated protein kinase; FAS, fatty acid synthetase; FBS, fetal bovine serum; HE, hematoxylin and eosin; HSL, hormone-sensitive lipase; HUVECs, human umbilical vein endothelial cells; IMF, intramuscular fat; IBMX, isobutylmethylxanthine; LM, longissimus dorsi muscle; MTT, 3-(4,5-dimethylthiazol-2-yl)-2,5-diphenyltetrazolium bromide; PBS, phosphate buffer solution; PPARγ, peroxisome proliferator-activated receptor-γ; RSG, rosiglitazone

REFERENCES

(1) Kumar, S.; Narwal, S.; Kumar, V.; Prakash, O. α-Glucosidase inhibitors from plants: a natural approach to treat diabetes. *Pharmacogn. Rev.* **2011**, *5*, 19.

(2) Nakagawa, K.; Kubota, H.; Kimura, T.; Yamashita, S.; Tsuzuki, T.; Oikawa, S.; Miyazawa, T. Occurrence of orally administered mulberry 1-deoxynojirimycin in rat plasma. *J. Agric. Food Chem.* **2007**, *55*, 8928−8933.

(3) Kwon, H. J.; Chung, J. Y.; Kim, J. Y.; Kwon, O. Comparison of 1-deoxynojirimycin and aqueous mulberry leaf extract with emphasis on postprandial hypoglycemic effects: in vivo and in vitro studies. *J. Agric. Food Chem.* **2011**, *59*, 3014−3019.

(4) Kong, W.; Oh, S.; Ahn, Y.; Kim, K.; Kim, J.; Seo, S. Antiobesity effects and improvement of insulin sensitivity by 1-deoxynojirimycin in animal models. *J. Agric. Food Chem.* **2008**, *56*, 2613−2619.

DOI: 10.1021/acs.jafc.5b01680
J. Agric. Food Chem. 2015, 63, 6212−6220

(5) Oku, T.; Yamada, M.; Nakamura, M.; Sadamori, N.; Nakamura, S. Inhibitory effects of extractives from leaves of *Morus alba* on human and rat small intestinal disaccharidase activity. *Br. J. Nutr.* **2006**, *95*, 933−938.
(6) Onose, S.; Ikeda, R.; Nakagawa, K.; Kimura, T.; Yamagishi, K.; Higuchi, O.; Miyazawa, T. Production of the α-glycosidase inhibitor 1-deoxynojirimycin from *Bacillus* species. *Food Chem.* **2013**, *138*, 516−523.
(7) Li, Y.; Ji, D.; Zhong, S.; Lin, T.; Lv, Z.; Hu, G.; Wang, X. 1-Deoxynojirimycin inhibits glucose absorption and accelerates glucose metabolism in streptozotocin-induced diabetic mice. *Sci. Rep.* **2013**, *3*, 1377.
(8) Vichasilp, C.; Nakagawa, K.; Sookwong, P.; Higuchi, O.; Kimura, F.; Miyazawa, T. A novel gelatin crosslinking method retards release of mulberry 1-deoxynojirimycin providing a prolonged hypoglycaemic effect. *Food Chem.* **2012**, *134*, 1823−1830.
(9) Asai, A.; Nakagawa, K.; Higuchi, O.; Kimura, T.; Kojima, Y.; Kariya, J.; Miyazawa, T.; Oikawa, S. Effect of mulberry leaf extract with enriched 1-deoxynojirimycin content on postprandial glycemic control in subjects with impaired glucose metabolism. *J. Diabetes Invest.* **2011**, *2*, 318−323.
(10) Kimura, T.; Nakagawa, K.; Kubota, H.; Kojima, Y.; Goto, Y.; Yamagishi, K.; Oita, S.; Oikawa, S.; Miyazawa, T. Food-grade mulberry powder enriched with 1-deoxynojirimycin suppresses the elevation of postprandial blood glucose in humans. *J. Agric. Food Chem.* **2007**, *55*, 5869−5874.
(11) Tsuduki, T.; Nakamura, Y.; Honma, T.; Nakagawa, K.; Kimura, T.; Ikeda, I.; Miyazawa, T. Intake of 1-deoxynojirimycin suppresses lipid accumulation through activation of the β-oxidation system in rat liver. *J. Agric. Food Chem.* **2009**, *57*, 11024−11029.
(12) Lee, S. M.; Shin, M. J.; Hwang, K. Y.; Kwon, O.; Chung, J. H. 1-Deoxynojirimycin isolated from a Bacillus subtilis stimulates adiponectin and GLUT4 expressions in 3T3-L1 adipocytes. *J. Microbiol. Biotechnol.* **2013**, *23*, 637−643.
(13) Shuang, E.; Kijima, R.; Honma, T.; Yamamoto, K.; Hatakeyama, Y.; Kitano, Y.; Kimura, T.; Nakagawa, K.; Miyazawa, T.; Tsuduki, T. 1-Deoxynojirimycin attenuates high glucose-accelerated senescence in human umbilical vein endothelial cells. *Exp. Gerontol.* **2014**, *55*, 63−69.
(14) Do, H. J.; Lee, S.; Kim, Y. S.; Shin, M. Effect of 1-deoxynojirimycin on cholesterol efflux through ABCA1-LXRα pathway in 3T3-L1 adipocytes. *J. Funct. Foods* **2014**, *7*, 692−699.
(15) Wang, R.; Yang, C.; Hu, M. 1-Deoxynojirimycin inhibits metastasis of B16F10 melanoma cells by attenuating the activity and expression of matrix metalloproteinases-2 and-9 and altering cell surface glycosylation. *J. Agric. Food Chem.* **2010**, *58*, 8988−8993.
(16) Zhao, Y.; Liu, W.; Zhou, Y.; Zhang, X.; Murphy, P. V. *N*-(8-(3-Ethynylphenoxy)octyl-1-deoxynojirimycin suppresses growth and migration of human lung cancer cells. *Bioorg. Med. Chem. Lett.* **2010**, *20*, 7540−7543.
(17) Papandréou, M.; Barbouche, R.; Guieu, R.; Kieny, M. P.; Fenouillet, E. The α-glucosidase inhibitor 1-deoxynojirimycin blocks human immunodeficiency virus envelope glycoprotein-mediated membrane fusion at the CXCR4 binding step. *Mol. Pharmacol.* **2002**, *61*, 186−193.
(18) Wang, S.; Zhou, G.; Shu, G.; Wang, L.; Zhu, X.; Gao, P.; Xi, Q.; Zhang, Y.; Yuan, L.; Jiang, Q. Glucose utilization, lipid metabolism and BMP-Smad signaling pathway of porcine intramuscular preadipocytes compared with subcutaneous preadipocytes. *Cell. Physiol. Biochem.* **2013**, *31*, 981−996.
(19) Wood, J. D.; Enser, M.; Fisher, A. V.; Nute, G. R.; Richardson, R. I.; Sheard, P. R. Manipulating meat quality and composition. *Proc. Nutr. Soc.* **1999**, *58*, 363−370.
(20) Fernandez, X.; Monin, G.; Talmant, A.; Mourot, J.; Lebret, B. Influence of intramuscular fat content on the quality of pig meat-1. Composition of the lipid fraction and sensory characteristics of m. longissimus lumborum. *Meat Sci.* **1999**, *53*, 59−65.
(21) Hardin, B. J.; Campbell, K. S.; Smith, J. D.; Arbogast, S.; Smith, J.; Moylan, J. S.; Reid, M. B. TNF-α acts via TNFR1 and muscle-derived oxidants to depress myofibrillar force in murine skeletal muscle. *J. Appl. Physiol.* **2008**, *104*, 694−699.
(22) Ryan, A. S.; Buscemi, A.; Forrester, L.; Hafer-Macko, C. E.; Ivey, F. M. Atrophy and intramuscular fat in specific muscles of the thigh: associated weakness and hyperinsulinemia in stroke survivors. *Neurorehabil. Neural Repair* **2011**, *25*, 865−872.
(23) Noble, J. J.; Charles-Edwards, G. D.; Keevil, S. F.; Lewis, A. P.; Gough, M.; Shortland, A. P. Intramuscular fat in ambulant young adults with bilateral spastic cerebral palsy. *BMC Musculoskeletal Disord.* **2014**, *15*, 236.
(24) Casellas, J.; Vidal, O.; Pena, R. N.; Gallardo, D.; Manunza, A.; Quintanilla, R.; Amills, M. Genetics of serum and muscle lipids in pigs. *Anim. Genet.* **2013**, *44*, 609−619.
(25) Bendixen, E.; Danielsen, M.; Larsen, K.; Bendixen, C. Advances in porcine genomics and proteomics − a toolbox for developing the pig as a model organism for molecular biomedical research. *Briefings Funct. Genomics* **2010**, *9*, 208−219.
(26) Lunney, J. K. Advances in swine biomedical model genomics. *Int. J. Biol. Sci.* **2007**, *3*, 179−184.
(27) Hochstim, C. J.; Choi, J. Y.; Lowe, D.; Masood, R.; Rice, D. H. Biofilm detection with hematoxylin-eosin staining. *Arch. Otolaryngol., Head Neck Surg.* **2010**, *136*, 453−456.
(28) Hausman, G. J.; Poulos, S. P. A method to establish co-cultures of myotubes and preadipocytes from collagenase digested neonatal pig semitendinosus muscles. *J. Anim. Sci.* **2005**, *83*, 1010−1016.
(29) Jiang, S.; Wei, H.; Song, T.; Yang, Y.; Peng, J.; Jiang, S. Transcriptome comparison between porcine subcutaneous and intramuscular stromal vascular cells during adipogenic differentiation. *PLoS One* **2013**, *8*, e77094.
(30) Pang, W. J.; Yu, T. Y.; Bai, L.; Yang, Y. J.; Yang, G. S. Tissue expression of porcine FoxO1 and its negative regulation during primary preadipocyte differentiation. *Mol. Biol. Rep.* **2009**, *36*, 165−176.
(31) Pang, W. J.; Xiong, Y.; Wang, Y.; Tong, Q.; Yang, G. S. Sirt1 attenuates camptothecin-induced apoptosis through caspase-3 pathway in porcine preadipocytes. *Exp. Cell Res.* **2013**, *319*, 670−683.
(32) Pang, W. J.; Wang, Y.; Wei, N.; Xu, R. X.; Xiong, Y.; Wang, P.; Shen, Q. W.; Yang, G. S. Sirt1 inhibits Akt2-mediated porcine adipogenesis potentially by direct protein-protein interaction. *PLoS One* **2013**, *8*, e71576.
(33) Pang, W. J.; Wei, N.; Wang, Y.; Xiong, Y.; Chen, F. F.; Wu, W. J.; Zhao, C. Z.; Sun, S. D.; Yang, G. S. Obese and lean porcine difference of FoxO1 and its regulation through C/EBPβ and PI3K/GSK3β signaling pathway. *J. Anim. Sci.* **2014**, *92*, 1968−1979.
(34) Xiong, Y.; Pang, W. J.; Wei, N.; Wang, Y.; Ren, W. K.; Yang, G. S. Knockdown of both FoxO1 and C/EBPβ promotes adipogenesis in porcine preadipocytes through feedback regulation. *Cell Biol. Int.* **2013**, *37*, 905−916.
(35) Wei, N.; Wang, Y.; Xu, R. X.; Wang, G. Q.; Xiong, Y.; Yu, T. Y.; Yang, G. S.; Pang, W. J. PU.1 antisense lncRNA against its mRNA translation promotes adipogenesis in porcine preadipocytes. *Anim. Genet.* **2015**, *46*, 133−140.
(36) Pang, W. J.; Xiong, Y.; Zhang, Z.; Wei, N.; Chen, N.; Yang, G. S. Lentivirus-mediated Sirt1 shRNA and resveratrol independently induce porcine preadipocyte apoptosis by canonical apoptotic pathway. *Mol. Biol. Rep.* **2013**, *40*, 129−139.
(37) Tsuduki, T.; Kikuchi, I.; Kimura, T.; Nakagawa, K.; Miyazawa, T. Intake of mulberry 1-deoxynojirimycin prevents diet-induced obesity through increases in adiponectin in mice. *Food Chem.* **2013**, *139*, 16−23.
(38) Xu, B.; Ju, Y.; Song, G. Role of p38, ERK1/2, focal adhesion kinase, RhoA/ROCK and cytoskeleton in the adipogenesis of human mesenchymal stem cells. *J. Biosci. Bioeng.* **2014**, *117*, 624−631.
(39) Ling, H. Y.; Wen, G. B.; Feng, S. D.; Tuo, Q. H.; Ou, H. S.; Yao, C. H.; Zhu, B. Y.; Gao, Z. P.; Zhang, L.; Liao, D. F. MicroRNA-375 promotes 3T3-L1 adipocyte differentiation through modulation of extracellular signal regulated kinase signalling. *Clin. Exp. Pharmacol. Physiol.* **2011**, *38*, 239−246.
(40) Sale, E. M.; Atkinson, P. G.; Sale, G. J. Requirement of MAP kinase for differentiation of fibroblasts to adipocytes, for insulin

DOI: 10.1021/acs.jafc.5b01680
J. Agric. Food Chem. 2015, 63, 6212−6220

activation of p90 S6 kinase and for insulin or serum stimulation of DNA synthesis. *EMBO J.* **1995**, *14*, 674.

(41) Asano, N.; Yamashita, T.; Yasuda, K.; Ikeda, K.; Kizu, H.; Kameda, Y.; Kato, A.; Nash, R. J.; Lee, H. S.; Ryu, K. S. Polyhydroxylated alkaloids isolated from mulberry trees (*Morus alba L.*) and silkworms (*Bombyx mori L.*). *J. Agric. Food Chem.* **2001**, *49*, 4208−4213.

(42) Isabelle, M.; Lee, B. L.; Ong, C. N.; Liu, X.; Huang, D. Peroxyl radical scavenging capacity, polyphenolics, and lipophilic antioxidant profiles of mulberry fruits cultivated in southern China. *J. Agric. Food Chem.* **2008**, *56*, 9410−9416.

(43) Pang, W. J.; Bai, L.; Yang, G. S. Relationship among H-FABP gene polymorphism, intramuscular fat content, and adipocyte lipid droplet content in main pig breeds with different genotypes in western China. *Yichuan Xuebao* **2006**, *33*, 515−524.

DOI: 10.1021/acs.jafc.5b01680
J. Agric. Food Chem. 2015, 63, 6212−6220

the studies have focused on ACN-rich foods[14,16] or beverages,[17] which contain multiple compounds and different concentrations or subclasses of ACNs. Furthermore, the rates of absorption and elimination as well as the relative bioavailability of ACNs present in different foods in vivo are different.[18] Therefore, it is important to examine the direct effects of pure ACNs on liver injury to elucidate their mechanisms of action in vitro and in vivo.[19,20] However, to the best of our knowledge, the direct role of the purified monomer form of ACNs in liver injury remains unclear, and their effects on liver fibrosis in vivo has not been systematically studied.

In the present study, we aimed to explore whether cyanidin-3-*O*-*β*-glucoside (Cy-3-G), the most abundant monomer form of ACNs in plants,[21] could protect against liver damage caused by carbon tetrachloride (CCl_4), as well as suppress the paths of the activation of HSCs.

MATERIALS AND METHODS

Cy-3-G Extraction and Analyses. Black rice (*Oryza sativa* L. *indica*) was obtained from Guangdong province, China. ACNs were extracted from black rice following our previous methods.[10] Then, high purity Cy-3-G was isolated from ACNs by the method of medium-pressure liquid chromatography (MPLC). After analysis by HPLC-PAD, the purity of Cy-3-G was >96.5%. The detailed methods are shown in the Supporting Information.

Reagents and Antibodies. Antibody for *α*-smooth muscle actin (*α*-SMA) was purchased from Sigma-Aldrich (St. Louis, MO, USA) and for glyceraldehyde phosphate dehydrogenase (GAPDH) was obtained from Santa Cruz Biotechnology (Santa Cruz, CA, USA). Anti-desmin and anti-F4/80 antibodies were purchased from Abcam (Cambridge, UK); anti-CD45 antibody and Alex-488 conjugated goat anti-rabbit IgG secondary antibody were purchased from Goodbio Technology (Wuhan, China). All other secondary antibodies were obtained from Santa Cruz Biotechnology (Santa Cruz, CA, USA). Reagents for immunohistochemistry, such as hydrogen peroxide and diaminobenzidine (DAB), were obtained from Zhongshan Jinqiao Biotechnology (Beijing, China). 4′,6-Diamidino-2-phenylindole (DAPI) was purchased from Beyotime (Nantong, China). Fluorescent probe dihydroethidium (DHE) was from Calbiochem (San Diego, CA, USA). All other chemicals used in this study were of analytical grade from Sigma-Aldrich or Invitrogen unless otherwise noted.

Animals and Diets. This study was carried out in agreement with the recommendations of the Guide for the Care and Use of Laboratory Animals. All animal procedures were approved by the Animal Care and Protection Committee of Sun Yat-Sen University. SPF, male, C57BL/6 mice (8 weeks old) were purchased from the SYSU animal center (Guangzhou, China). The animals were maintained at 25 °C with a 12 h light/dark cycle and ad libitum access to water and chow. Mice were randomly divided into three groups (each with eight mice), including a control group, a CCl_4-treated group, and a Cy-3-G plus CCl_4 group. CCl_4-treated mice were given an intraperitoneal (ip) injection of 10% CCl_4 in olive oil (0.5 *μ*L pure CCl_4/g BW) twice weekly for 8 weeks, whereas the control group received vehicle only. At the same time, Cy-3-G (800 mg/kg diet) was added to standard diet, which was supplied for the Cy-3-G plus CCl_4 group; the other groups of mice lived on standard diet. All of the animals were sacrificed 72 h after the last dose of CCl_4 or vehicle. After narcotizing the mice by pentobarbital sodium, blood was collected by extirpating eyeballs for serum biochemistry analysis. Livers were excised, partly fixed for histological analysis, and the rest was frozen in liquid nitrogen and then stored at −80 °C until analyzed.

Determination of Serum Transaminase Levels and Cytokines. Serums were separated from blood by centrifuging under 4 °C, at 3000 *g* for 15 min, then alanine and aspartate aminotransferases (ALT and AST) were measured by an assay kit from Jiancheng Biotech (Nanjing, China) according to the manual. Serum cytokines (TNF-*α*, TGF-*β*, and IL-17) were analyzed by ELISA technique using commercial kits from eBioscience (San Diego, CA, USA).

Histological Study and Immunohistochemistry. Liver samples were separated and fixed in 10% neutral buffered formalin and then embedded in paraffin, sectioned to a thickness of 5 *μ*m. Then the slides were performed with hematoxylin and eosin (H&E) staining for general observation or with Sirius Red for collagen fiber detection.

Under a light microscope (Leica, Solms, German), inflammatory cell infiltration in hepatic lobules and necrosis were observed. Then, the inflammation activity were evaluated and divided into four parts: portal area inflammation (P), lobular inflammation (L), patch necrosis (PN), and bridging necrosis (including lobular necrosis, BN). Every item was recorded as 1, 2, 3, or 4 on the basis of degrees of pathological changes. The score counting formula was P + L + 2 × (PN + BN).[22] The percentage of fibrosis regions in the liver was measured on five high-power (200×) fields per slide and then calculated by Image-pro Plus 6.0. The observer was blinded to the group distribution when the analyses were made.

Immunostaining was performed on paraffin section. For the test of the activation of hepatic stellate cells, desmin was visualized with Alex-488 conjugated goat anti-rabbit IgG secondary antibody, and DAPI was used for nuclear staining. After the slides had been incubated with anti-F4/80 or anti-CD45 at 4 °C overnight, they were treated with labeled polymer horseradish peroxidase (HRP) secondary antibody for 1.5 h, followed by DAB staining. Positive cells were counted on five high-power (200×) fields per slide.

Measurements of MDA, SOD, and GSH. Liver tissue homogenates were prepared to measure hepatic malondialdehyde (MDA) following the commercial kit's instructions (Jiancheng Biotech, Nanjing, China). Superoxide dismutase (SOD) and glutathione (GSH) were measured by the commercial kits from Beyotime (Shanghai, China).

Measurements of ROS and Apoptosis. The frozen liver samples were cut into 10 *μ*m sections and fixed in paraformaldehyde. After being washed in phosphate buffer saline (PBS) three times, the slides were incubated with DHE (5 mmol/L) in a dark condition for 30 min at 37 °C for redundant reactive oxygen species (ROS) detection. DHE can be oxidized by superoxide and changed to ethidium bromide, which then binds to the DNA of the nucleus, and red fluorescence was detected through the fluorescence microscope (Leica, Solms, Germany) under the 580 nm exciting light.[23] Apoptosis of cells in the liver was detected by terminal-deoxynucleoitidyl transferase mediated nick end labeling (TUNEL) staining (Beyotime) according to the manual; the fluorescence was detected at 510 nm through a fluorescence microscope (Leica). Thereafter, the intensity of the fluorescence was analyzed by Image-pro Plus 6.0.

Protein Extraction and Western Blotting. Proteins were extracted from liver tissue, using RIPA lysis buffer (Beyotime) and 1% PMSF and 1% protease inhibitor cocktail (Sigma-Aldrich). The lysates were centrifuged at 12000 *g* for 15 min, and the supernatants were used for immunoblotting; meanwhile, the total protein concentration of the tissue homogenates was determined by BCA protein assay kit (Thermo, Rockford, IL, USA). Protein extractions were separated by using SDS-PAGE on 10% polyacrylamide gels and transferred to 0.45 *μ*m polyvinylidene fluoride (PVDF) membranes (Millipore, Billerica, MA, USA). After blocking for 2 h with 5% skimmed milk in TBS-T buffer (10 mM Tris, 150 mM NaCl, and 0.1% Tween-20), the membrane was incubated with primary antibodies against *α*-SMA or GAPDH at 4 °C for overnight. The membrane was incubated with HRP-conjugated secondary antibodies and using ECL Reagent Kit (Thermo) to make the film exposed. The band densities were quantified using an image analyzer, Quantity One System (Bio-Rad, Richmond, CA, USA). All protein quantifications were adjusted for the corresponding GAPDH level.

RNA Extraction and Quantitative Real-Time PCR. Total RNA was extracted from liver tissue with Trizol (Invitrogen, Carlsbad, CA, USA), according to the manufacturer's instructions. Then total RNA was reverse-transcribed to complementary DNA (cDNA) using the Reverse Transcription System by the cDNA Synthesis kit (Takara, Dalian, China). Quantitative real-time PCR was performed with SYBR Green Supermix kit (Takara) according to the manufacturer's instructions and played on a Vii7 system (ABI, Carlsbad, CA, USA).

DOI: 10.1021/acs.jafc.5b02181
J. Agric. Food Chem. 2015, 63, 6221−6230

Relative gene expression was calculated using the $2^{-\Delta\Delta Ct}$ method. Primers used in the test are shown in the Supporting Information.

Statistical Analysis. SPSS 16.0 (SPSS Inc., Chicago, IL, USA) was used for statistical analysis, and all results are presented as the mean ± SEM. Data were analyzed using Student's *t* test (for two groups), one-way ANOVA, and Dunnett's test (for three groups). Mann−Whitney's rank sum test was used to calculate the statistical significance of the pathological scores of inflammation. $P < 0.05$ was considered statistically significant. Graph bars were obtained using Graph Pad Prism 5.0 software (San Diego, CA, USA).

RESULTS

General Parameters and Histopathological Analysis. During the experiment period, mice with CCl_4 treatment showed a trend of reducing body weight and increasing relative liver weight compared to the control mice without statistical significance as shown in Table 1.

Table 1. Data from General Parameters Evaluated in Different Groups[a]

	control	CCl_4	CCl_4 + Cy-3-G
initial body wt (g)	26.05 ± 0.62	26.11 ± 0.79	26.39 ± 0 0.52
final body wt (g)	28.52 ± 0.73	28.00 ± 0.78	27.43 ± 0.44
food consumption (g/mouse/day)	2.74 ± 0.08	2.83 ± 0.12	2.67 ± 0.13
relative liver wt (%)	3.96 ± 0.13	4.24 ± 0.12	4.10 ± 0.29

[a]Body and relative liver weights were examined in the mice model. Results are expressed as mean ± SEM (n = 8 mice/each). Comparisons between all groups were evaluated using one-way analysis of variance (ANOVA).

To estimate the protective function of Cy-3-G on liver injury, H&E staining and Sirius staining were carried out on liver tissue slides (Figure 1). CCl_4-treated groups developed liver damage with the performance of hepatocellular lesions, inflammation, and liver fibrosis. Whereas Cy-3-G ameliorated the degree of patch necrosis, bridging necrosis and less inflammatory cells (mainly neutrophils) infiltrated into the portal area; fibrillar collagen sediment was rarely found in the portal/periportal area. The inflammatory scores were calculated (Figure 1C; Table 2), and Sirius Red staining for the fibrosis was evaluated (Figure 1D); Cy-3-G ameliorated both scores ($P < 0.05$). Therefore, according to histopathological analysis, Cy-3-G showed a protective effect on liver injury and fibrosis.

Cy-3-G Depressed the Activation of HSCs. HSCs are cores in the progression of liver injury. Their activation, accompanied by cytokine release and production of matrix molecules, proteases, and their inhibitors, finally leads to liver fibrosis. We investigated the suppressing effect of Cy-3-G on the activation of HSCs induced by CCl_4. As shown in Figure 2A, immunoblotting (left panel) and qRT-PCR (right panel) analysis revealed that α-SMA was less expressed in the Cy-3-G group compared to the CCl_4 group. In addition, desmin as another marker of the activated HSCs (Figure 2B,C) was less detected by immunostaining in the Cy-3-G-treated group compared with the CCl_4 group. Moreover, matrix metalloproteinase (MMP), such as MMP-2 and MMP-9, mRNA levels sharply increased in the CCl_4 group, whereas they were significantly decreased by the intervention of Cy-3-G (Figure 2D,E).

Cy-3-G Attenuated Oxidative Stress and Increased Antioxidant. Hepatic levels of ROS increased significantly (Figure 3A), and MDA, the terminal product of lipid peroxidation, elevated sharply after the treatment of CCl_4 (Figure 3B). However, Cy-3-G treatment significantly inhibited the oxidative stress levels of ROS and MDA ($P < 0.05$).

Glutathione (GSH) is an antioxidant, which can prevent damage from reactive oxygen species. After the treatment of CCl_4, the level of GSH significantly decreased (Figure 3C). With the supplementation of Cy-3-G, the level of GSH tends to recover, but without significant difference compared to the CCl_4 group ($P = 0.3102$). Antioxidant enzymes can protect cellular compounds against damage induced by free radicals. In the present study, total SOD was detected by the WST-1 assay. CCl_4 treatment caused a severe decrease of SOD level ($P < 0.05$), whereas addition of Cy-3-G to the diet ameliorated changes of the hepatic SOD activity significantly (Figure 3D).

Cy-3-G Ameliorated Apoptosis of Hepatic Cells. ALT and AST have been recognized as biomarkers of liver injury.[24] The activities of serum ALT and AST were respectively increased 92 and 83% in CCl_4-treated mice compared to the control group (Figure 4A,B). However, the treatment of Cy-3-G showed an inhibition of this elevation; it significantly ameliorated the level of ALT ($P < 0.05$) and decreased the level of AST ($P = 0.159$).

Apoptotic cells in the liver were detected by TUNEL staining (Figure 4C). Dying cells, with DNA damage, can be combined to the fluorescent dye (cyanine 3) by the catalysis of terminal deoxynucleotidyl transferase. Thereafter, cyanine 3 release red fluorescence under excitation of 510 nm light. After treatment with CCl_4, the apoptotic cells in the liver increased significantly. Although the number of apoptotic cells in the Cy-3-G group showed no significant differences compared to the CCl_4 group, it showed a trend of decrease ($P = 0.088$).

Cy-3-G Suppressed Leukocyte Recruitment but Had No Significant Effect on the Activation of Kupffer Cells. Administration of CCl_4 caused hepatocyte injury and followed with more infiltrating inflammatory cells. To investigate periportal inflammation in the liver, we performed immunostaining with anti-CD45 (Figure 5A), which was a biomarker of leukocytes.[25] In the CCl_4 group, positive cells increased nearly 30-fold (Figure 5B), compared to control animals. Adding Cy-3-G to the diet significantly alleviated the number of $CD45^+$ cells compared to the CCl_4 group.

Kupffer cells are resident macrophages in liver, which were activated by damage amplification and recruited from the bloodstream.[26] Upon activation, Kupffer cells release pro-inflammatory cytokines involving TNF-α and fibrogenic factors such as TGF-β1 and PDGF, which will stimulate HSCs to be activated.[27] F4/80 is a specific marker of activated Kupffer cells; after the treatment with CCl_4, F4/80 positive cells increased almost 13-fold compared with the control group (Figure 5C,D). Interestingly, Cy-3-G treatment had no significant effect compared with the CCl_4 group.

Cy-3-G Attenuated the Level of Pro-inflammation Cytokines and Increased the Level of Anti-inflammation Cytokine. Pro-inflammation cytokines are released from both injured hepatocytes and nonparenchymal cells, which play important roles in driving fibrogenesis. In our present study, TNF-α, IL-1α, and IL-17 were detected. After the treatment with CCl_4, TNF-α levels in the serum and tissue (Figure 6A,B) were increased nearly 1-fold compared to the control group, whereas they significantly decreased after treatment with Cy-3-G. However, detected by the qRT-PCR method, IL-1α had no significant changes in the CCl_4 or CCl_4 plus Cy-3-G (Figure 6C) groups. Previous studies have shown that monocyte

DOI: 10.1021/acs.jafc.5b02181
J. Agric. Food Chem. 2015, 63, 6221−6230

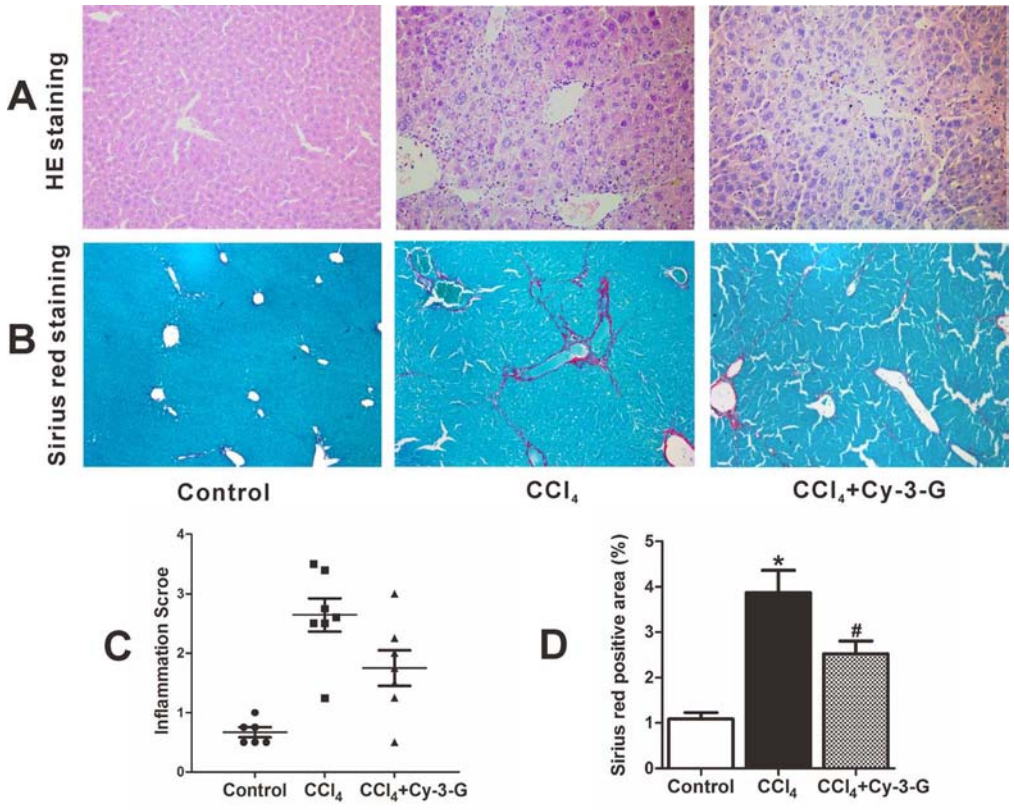

Figure 1. H&E staining and Sirius staining on liver tissue: (A) hematoxylin and eosin stain (the inflammation score was evaluated and calculated (C)); (B) Sirius Red staining (quantitative analysis of Sirius Red staining was carried out by using Image Pro-Plus (D)). All slides are based on the examination of five different fields, 200× magnifications. Results are expressed as the mean ± SEM; (*) $P < 0.05$, significantly different compared to the control group; (#) $P < 0.05$, significantly different compared to the CCl_4 group. $n = 6$ (control group) or 7 (other groups).

Table 2. Pathological Inflammatory Scores in Liver Tissues[a]

group	P + L + 2 × (PN + BN)	S0	S1	S2	S3	S4	*P*
control	0.667 ± 0.083	5	1	0	0	0	
CCl4	2.643 ± 0.280	0	1	4	2	0	0.001*
CCl_4+Cy-3-G	1.750 ± 0.299	1	3	3	0	0	0.017#

[a]The score of inflammation was given by P + L + 2 × (PN + BN) (P, portal area inflammation; L, lobular inflammation; PN, patch necrosis; BN, bridging necrosis). *n* (control): $n(CCl_4)$:$n(CCl_4$+Cy-3-G) = 6:7:7. Mann−Whitney's rank sum test was used to calculate the statistical significance: (*) $P < 0.05$ compared to the control group; (#) $P < 0.05$ compared to the CCl_4 group.

production of TNF-α was a critical downstream response to the IL-17 produced by Th17 cells.[28] The level of IL-17 was detected in both serum and liver tissue by ELISA; IL-17 elevated 1-fold in serum and 0.5-fold in liver tissue after the treatment with CCl_4, which were significantly decreased by Cy-3-G supplementation (Figure 6D,E). IL-10 is a kind of anti-inflammatory cytokine. In our present study, Cy-3-G treatment enhanced the relative mRNA expression of IL-10, which is suggestive of promotion of anti-inflammation cytokine (Figure 6F).

Cy-3-G Treatment Decreased Liver Growth Factors and MCP-1. HSCs are an important source of growth factors in the liver, but also respond to these factors. TGF-β1 and PDGF are two potent growth factors that stimulate activation and proliferation of HSCs.[29] The elevated levels of TGF-β1 and PDGF mRNA expression in the liver induced by CCl_4 were suppressed significantly by treatment with Cy-3-G (Figure 7A,C). Interestingly, Cy-3-G had no significant effect on the level of TGF-β1 in serum (Figure 7B). Monocyte chemotactic protein (MCP-1) is a kind of typical chemokine expressed in various cells in the liver, which in general promotes the migration of fibrogenic cells to the site of liver injury.[30] The relative mRNA expression of MCP-1 dropped nearly 1-fold after Cy-3-G intervention compared to the CCl_4 group (Figure 7D).

DISCUSSION

In our present study, we demonstrated that in CCl_4-treated mice, Cy-3-G extracted from black rice attenuated liver injury and fibrosis. Furthermore, we found that addition of Cy-3-G suppressed the activation of hepatic stellate cells, which may result from the amelioration of liver oxidative stress, hepatocyte apoptosis, and inflammation induced by CCl_4. To our knowledge, this is the first study showing the positive effects of Cy-3-G on CCl_4 injury mouse model and uncovers the possible paths of restraining activation of HSCs.

ACN extractions from plant foods were proved to have a series of benefits on various chronic diseases, but it is difficult to explain the biological mechanism of ACNs, because the food extractions usually contain an enormous variety of bioactive compounds. Through 2009, more than 600 kinds of ACNs had been extracted and identified from plants, such as Cy-3-G, Dp-3-G, and Pg-3-G.[31] Therefore, it is useful and valuable to study one composition of anthocyanin to elucidate the biological effects and the mechanism of actions. Cyanidin exists in about 50% of all ACNs in fruits and vegetables. Moreover, Cy-3-G is the most common anthocyanin with a glycoside.[32] In the

DOI: 10.1021/acs.jafc.5b02181
J. Agric. Food Chem. 2015, 63, 6221−6230

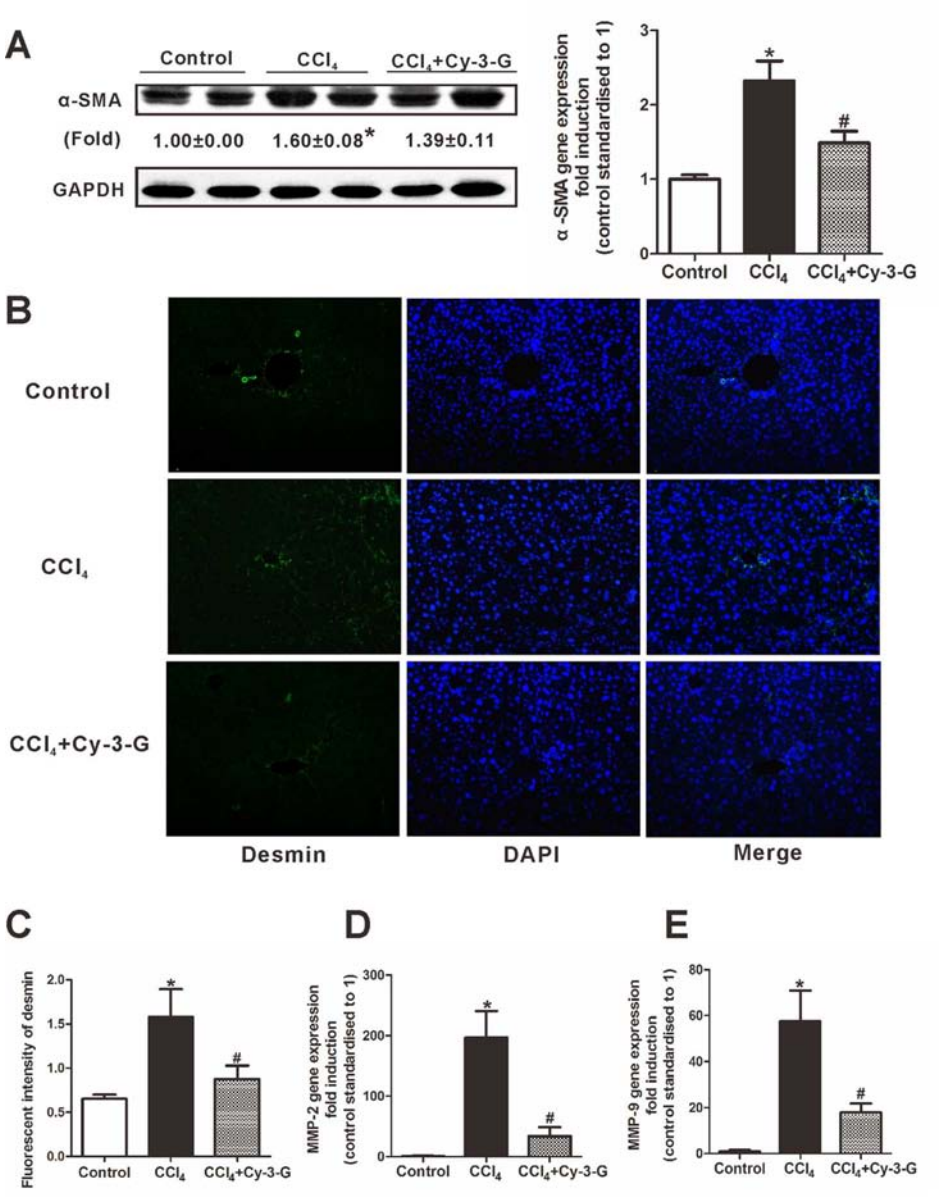

Figure 2. Cy-3-G attenuates the activation of HSCs in liver: (A) α-SMA protein (left panel) and mRNA (right panel) levels were evaluated; (B) desmin was detected by immunofluorescence and then qualified by the fluorescent intensity in every field (C); relative expressions of hepatic MMP-2 and MMP-9 mRNA levels were measured by RT-PCR (D, E). Values are expressed as the mean ± SEM, $n = 5$; (*) $P < 0.05$ compared to the control group; (#) $P < 0.05$ compared to the CCl_4 group.

present study, high-purity Cy-3-G as a monomer of anthocyanin was extracted from black rice and purified by MPLC, which has many merits including lower cost, higher speed, and greater loading of samples compared with the other purification methods.[33] Cy-3-G is nontoxic, and a moderate dose was adopted (800 mg/kg diet) for the present study according to previous researches in vivo.[34−36]

It has been reported that CCl_4 increases free radicals, which further causes lipid peroxidation of cellular and organelle membranes; thus, it is considered as one of the most widely used toxic agents to induce liver injury in animals.[37] We used a very low dose of CCl_4 (0.5 μL/g BW) injection for 8 weeks, which caused a moderate degree of liver injury according to histological analysis (Figure 1). Under this situation, we could investigate the preventive effects of Cy-3-G on liver fibrosis. The present study showed that supplementation of Cy-3-G has great effects on suppressing the liver fibrosis induced by CCl_4.

Hepatic fibrogenesis is a complex pathogenesis responding to various toxic stimuli. HSC activation is considered to play a key role in fibrotic progression. Activated HSCs were marked with higher expression of α-SMA, more desmin, and generation of collagen type I. In the present study, these elevated markers resulting from CCl_4 injection were significantly decreased with the treatment of Cy-3-G. Furthermore, MMP-2 and MMP-9 mRNA levels were significantly suppressed by Cy-3-G. It is universally recognized that MMPs are a family of zinc metallo-endopeptidases, which may contribute to the regression of liver fibrosis through cleavage of the fibrillar extracellular matrix. On the other hand, MMPs are promptly expressed by activated HSCs in response to diverse hepatic injury and are considered to promote disease progression.[38] Thus, MMPs play a dual role

DOI: 10.1021/acs.jafc.5b02181
J. Agric. Food Chem. 2015, 63, 6221−6230

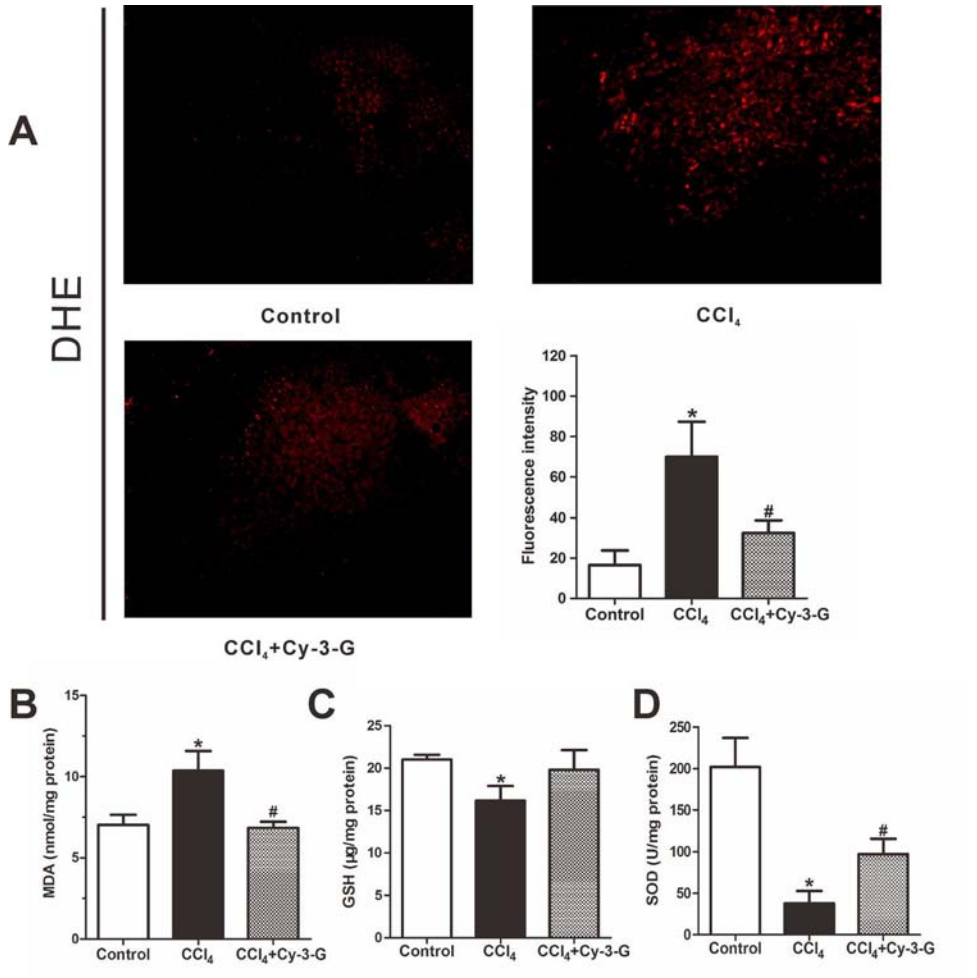

Figure 3. Cy-3-G attenuated oxidative stress and increased antioxidant defense system in CCl_4 administered mice: (A) liver ROS level detected by dihydroethidium (DHE) staining (representative photomicrographs (100×) are shown and mean of red fluorescence density of per field quantified by ImageJ (right panel)); (B) MDA, lipid peroxidation assessed in liver homogenate; (C) hepatic GSH and (D) SOD measured by commercial assay kit (n = 6−7, mean ± SEM; (∗) $P < 0.05$ versus control; (#) $P < 0.05$ versus CCl_4).

in liver fibrosis, depending on the timing of their production. The early temporary high expression of MMPs may destroy the surrounding tissue in order to deposit newly synthesized ECM.[39] In our present study, Sirius Red staining of liver collagens showed the liver fibrosis occurring at an early stage of the animal model, and MMP-2 and MMP-9 expression significantly increased in the CCl_4 group. Because of the early stage of liver fibrosis, MMPs are considered as markers of the activation of HSCs. Cy-3-G could decrease MMP-2 and MMP-9 expression, suggesting that Cy-3-G may suppress the activation of HSCs.

As is well-known, CCl_4 in vivo is metabolized by the cytochrome P450 system to highly reactive free radicals and reactive oxygen species, such as trichloromethyl (CCl_3) and trichloromethyl peroxyl (CCl_3O_2), which initiate lipid peroxidation and generate MDA.[16] Subsequently, elevated ROS attack hepatocytes, which leads to apoptosis.[40] By the treatment with Cy-3-G, ROS level and oxidative products such as MDA were significantly decreased and antioxidative SOD level increased to catalyze the dismutation of superoxide to hydrogen peroxide and oxygen. Nonetheless, GSH as a nonenzymatic defense substance slightly changed in the CCl_4 and Cy-3-G group, which may account for the balance between GSH and glutathione disulfide (GSSG) being restored efficiently at this early phase of liver injury, and the enzyme glutathione reductase was still available to bring GSSG back to GSH.[40] Thus, Cy-3-G showed no significant effect on GSH. ALT and AST were both considered sensitive indicators of hepatocyte integrity. It was revealed that either acute or chronic injury to the liver would eventually result in an increase of aminotransferases.[41] Furthermore, apoptosis is responsible for the physiological removal of unwanted cells, involving damaged cells.[42] We found that the treatment with Cy-3-G significantly diminished the liver apoptosis accompanied by the decreasing AST and ALT levels in circulation. These results indicated that Cy-3-G protective effects on hepatocytes may be related to the reduction of oxidative stress in the liver, similar to a previous report that ACNs or Cy-3-G could protect high glucose or methionine and choline deficiency caused by mouse hepatocyte apoptosis by modulating mitochondrial dysfunction and the PI3K/Akt pathway.[34,43]

The generation of oxidative stress together with the injured hepatocytes could increase tissue inflammation and drive disease progression more intensely.[44] This is reflected in our finding that CCl_4 up-regulated inflammation degree in the liver, whereas Cy-3-G treatment could attenuate liver inflammation significantly. To evaluate liver inflammation, a liver biopsy assessment system was employed to evaluate the inflammation

DOI: 10.1021/acs.jafc.5b02181
J. Agric. Food Chem. 2015, 63, 6221−6230

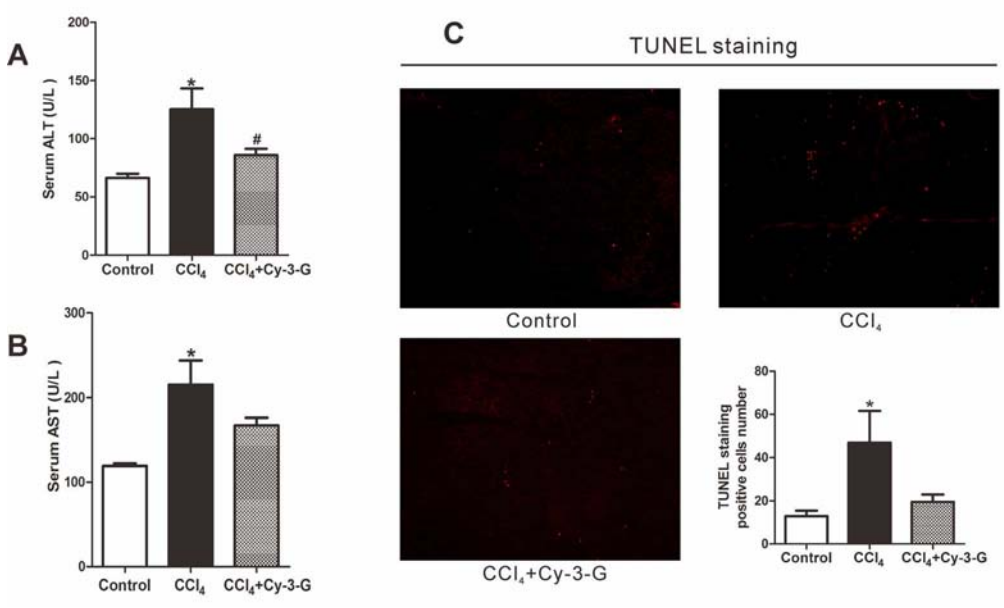

Figure 4. Cy-3-G alleviated apoptosis of hepatic cells. ALT (A) and AST (B) levels in the circulation were evaluated. Cell apoptosis in the liver tissue was detected by TUNEL assay (100×), and positive cells were counted in every field (C). Results are expressed as the mean ± SEM; (∗) $P < 0.05$ significantly different compared to the control group; (#) $P < 0.05$ versus the CCl_4 group.

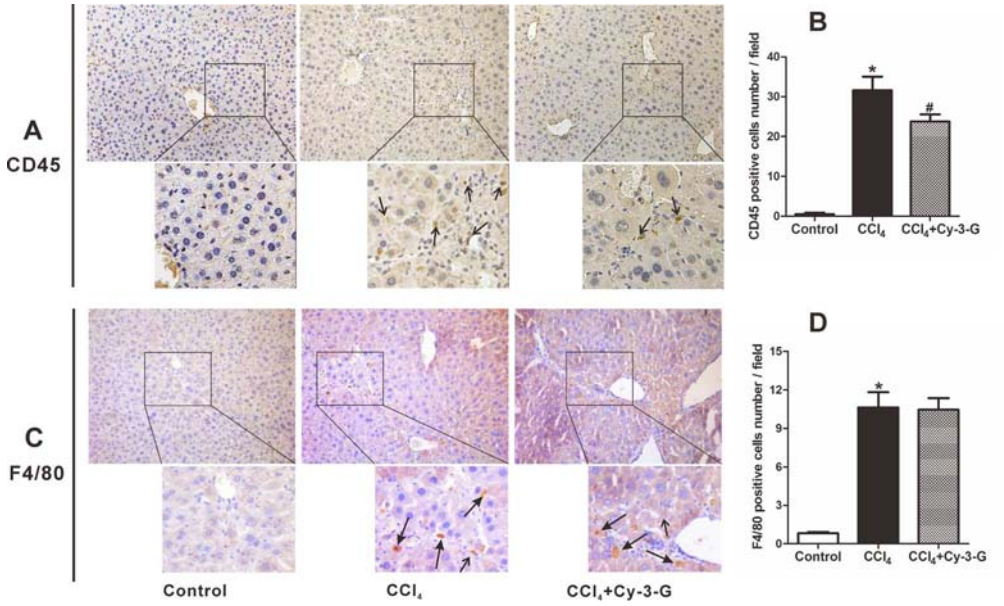

Figure 5. Effects of Cy-3-G on the inflammatory cells recruitment in CCl_4-treated mice. Immunostaining was performed on liver tissue sections. (A) Anti-CD45 was used to detect the infiltration of leukocytes in liver, and (B) F4/80 antibody was used to identify the activated Kupffer cells (magnification 200×). Five typical fields per slide were randomly examined, and then the numbers of positive cells in every field were counted and analyzed (C, D). Values are expressed as the mean ± SEM, $n = 5$; (∗) $P < 0.05$ compared to the control group; (#) $P < 0.05$ compared to the CCl_4 group.

score in our experiments.[22] As our present study showed, Cy-3-G could decrease neutrophils and attained a lower liver inflammation score (Figure 1; Table 2). Furthermore, it reduced liver CD45 positive cells, which were leukocytes, infiltrated to the periportal zone as inflammation cells (Figure 5). We also studied Kupffer cells, resident liver macrophages, which were also activated during liver injury. Activated Kupffer cells are enabled to launch biochemical attack and initiate interactions with HSCs by releasing a variety of biologically active mediators.[26] Interestingly, in our study, the results revealed that Cy-3-G had no significant suppressing effect on the activation of Kupffer cells in CCl_4-treated mice, which seems to be incompatible to previous protective effects on ROS or hepatocyte apoptosis. This phenomenon may be due to the early stage of liver injury and the weak effect of Cy-3-G on Kupffer cells.

With the progression of liver injury, pro-inflammatory cytokines, growth factors, and chemokines are released, which subsequently stimulate the activation of HSCs and migration. Not only are TNF-α, TGF-β, PDGF, and other cytokines produced by Kupffers but also infiltrating neutrophils, macrophages, or HSCs.[45] We identified that Cy-3-G could restrain

DOI: 10.1021/acs.jafc.5b02181
J. Agric. Food Chem. 2015, 63, 6221−6230

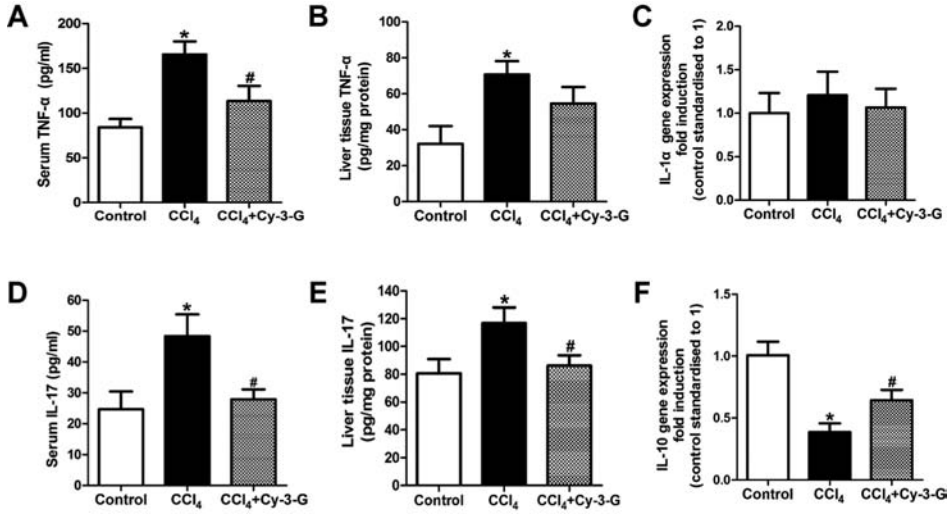

Figure 6. Cy-3-G ameliorated inflammatory cytokines induced by CCl_4 treatment in mice (A) TNF-α and (C) IL-17 in serum and liver tissues measured by ELISA assay. IL-1α (B) and (D) IL-10 mRNA in liver tissue were analyzed by qRT-PCR. Values are expressed as the mean ± SEM, n = 5; (∗) $P < 0.05$ compared to the control group; (#) $P < 0.05$ compared to the CCl_4 group.

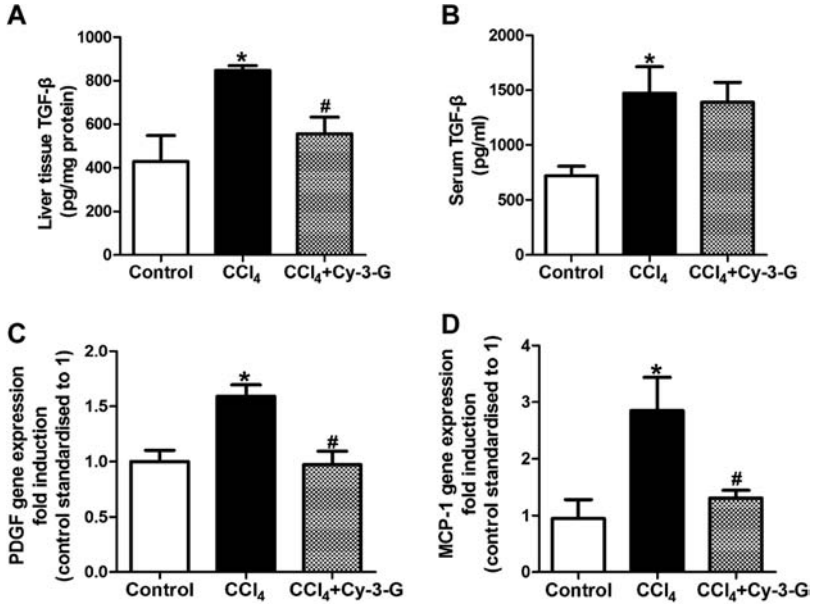

Figure 7. Cy-3-G decreased growth factors and MCP-1 in CCl_4-treated mice. TGF-β in liver tissue (A) and serum (B) were measured by ELISA assay. PDGF (C) and MCP-1(D) mRNA levels in liver tissue were analyzed by qRT-PCR. Values are expressed as mean ± SEM, n = 5; (∗) $P < 0.05$ compared to the control group; (#) $P < 0.05$ compared to the CCl_4 group.

the level of TNF-α, TGF-β, PDGF, and MCP-1 and increase the level of IL-10; the anti-inflammation effects are similar to the previous study about Cy-3-G on obesity, which might result from decreasing NF-κB activity.[46] Furthermore, we detected IL-17, which was significantly down-regulated by Cy-3-G in both liver and circulation. IL-17 is mainly secreted from Th17 cells that can promote tissue inflammation by induction of other pro-inflammatory mediators and recruitment of leukocytes to the site of inflammation.[47] In our present study, a Cy-3-G anti-inflammatory effect was evidenced by restraining inflammation cell recruitment and inflammatory cytokines in liver injury.

The paracrine and autocrine sources of cytokines will finally cause the activation of HSCs. It is assumed that Cy-3-G restrains HSC activation through two possible paths; the first was to suppress the path of generating inflammatory cytokines; the second might be to directly suppress the activation of HSCs (Scheme 1). Cy-3-G can be partly absorbed into circulation[48] and may have an opportunity to react with HSCs. Moreover, Cy-3-G was investigated to prevent HSC proliferation and collagen synthesis in vitro.[20]

In conclusion, Cy-3-G was able to attenuate liver injury and prevent fibrosis in CCl_4-treated mice. Moreover, Cy-3-G could reduce liver oxidative stress, alleviate apoptosis of hepatic cells, suppress liver inflammation, and finally restrain the activation of HSCs. Our study implied that regular intake of Cy-3-G in the daily diet could prevent the progression of hepatic fibrosis and be a potent element to treat liver injury. However, further studies are needed to fully understand the cellular and molecular mechanisms of Cy-3-G on HSCs.

DOI: 10.1021/acs.jafc.5b02181
J. Agric. Food Chem. 2015, 63, 6221−6230

Scheme 1. Cy-3-G Could Restrain HSC Activation Possibly by Two Paths: The First Was To Suppress the Path of Generating Inflammatory Cytokines; The Second Might Directly Suppress the Activation of HSCs

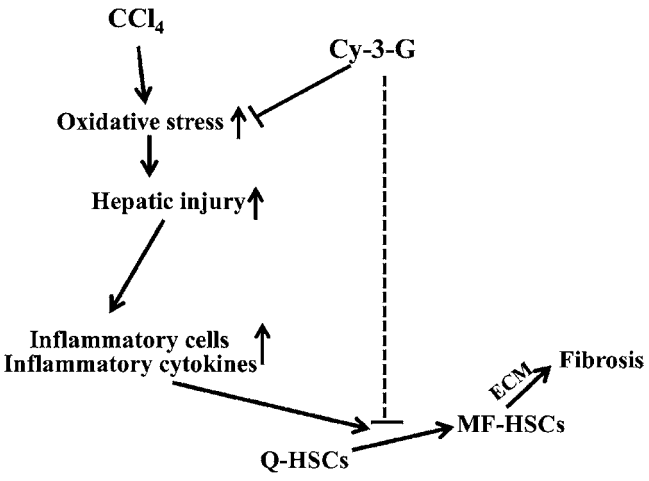

■ ASSOCIATED CONTENT

Supporting Information

Methods of Cy-3-G extraction and analysis from black rice (Supporting Information and Methods, Figure S1 and S2) and primer sequences for quantitative real-time PCR (Table S1). The Supporting Information is available free of charge on the ACS Publications website at DOI: 10.1021/acs.jafc.5b02181.

■ AUTHOR INFORMATION

Corresponding Authors

*(Y.Y.) Phone: 86-20-87330687. Fax: 86-20-87330446. E-mail: yangyan3@mail.sysu.edu.cn.

*(W.L.) Phone: 86-20-87331597. Fax: 86-20-87330446. E-mail: lingwh@mail.sysu.edu.cn.

Author Contributions

Xinwei Jiang and Wenhua Ling were in charge of the experimental design, implementing, and preparing for the manuscript. Tianran Shen and Xilan Tang participated in mouse feeding and treatment and helped with data analysis. Yan Yang and Honghui Guo helped with biochemical analysis and modification of the manuscript.

Funding

This study was supported by grants from the National Key Basic Research Program of China (973 Program, No. 2012CB517506) and National Natural Science Foundation of China (No. 81130052, 81372994).

Notes

The authors declare no competing financial interest.

■ ACKNOWLEDGMENTS

Lili Yang, Huilian Zhu, and Min Xia are acknowledged for supporting the research work with suggestions.

■ ABBREVIATIONS USED

Cy-3-G, cyanidin-3-*O*-*β*-glucoside; CCl_4, carbon tetrachloride; ACNs, anthocyanins; HSC, hepatic stellate cells; ECM, extracellular matrix; ROS, reactive oxygen species; ALT, alanine aminotransferase; AST, aspartate aminotransferase; *α*-SMA, *α*-smooth muscle actin; TNF-*α*, tissue necrosis factor-*α*; MCP-1, monocyte chemotactic protein-1; IL-1*α*, interleukin-1*α*; IL-17, interleukin-17; TGF-*β*, tissue growth factor-*β*; PDGF, platelet-derived growth factor; MMP-2, matrix metalloproteinases-2; MMP-9, matrix metalloproteinases-9; NAFLD, nonalcoholic fatty liver disease; NAS, NAFLD activity score

■ REFERENCES

(1) Friedman, S. L. Liver fibrosis − from bench to bedside. *J. Hepatol.* **2003**, *38*, 38−53.

(2) Wynn, T. A.; Ramalingam, T. R. Mechanisms of fibrosis: therapeutic translation for fibrotic disease. *Nat. Med.* **2012**, *18*, 1028−1040.

(3) Tacke, F.; Weiskirchen, R. Update on hepatic stellate cells: pathogenic role in liver fibrosis and novel isolation techniques. *Expert Rev. Gastroenterol. Hepatol.* **2012**, *6*, 67−80.

(4) Bataller, R.; Brenner, D. A. Liver fibrosis. *J. Clin. Invest.* **2005**, *115*, 209−218.

(5) Wobser, H.; Dorn, C.; Weiss, T. S.; Amann, T.; Bollheimer, C.; Büttner, R.; Schölmerich, J.; Hellerbrand, C. Lipid accumulation in hepatocytes induces fibrogenic activation of hepatic stellate cells. *Cell Res.* **2009**, *19*, 996−1005.

(6) Loria, P.; Marchesini, G.; Nascimbeni, F.; Ballestri, S.; Maurantonio, M.; Carubbi, F.; Ratziu, V.; Lonardo, A. Cardiovascular risk, lipidemic phenotype and steatosis. A comparative analysis of cirrhotic and non-cirrhotic liver disease due to varying etiology. *Atherosclerosis* **2014**, *232*, 99−109.

(7) Fardet, A.; Chardigny, J. M. Plant-based foods as a source of lipotropes for human nutrition: a survey of in vivo studies. *Crit. Rev. Food Sci. Nutr.* **2013**, *53*, 535−590.

(8) He, J.; Giusti, M. M. Anthocyanins: natural colorants with health-promoting properties. *Annu. Rev. Food Sci. Technol.* **2010**, *1*, 163−187.

(9) Hou, Z. H.; Qin, P. Y.; Ren, G. X. Effect of anthocyanin-rich extract from black rice (*Oryza sativa* L. japonica) on chronically alcohol-induced liver damage in rats. *J. Agric. Food Chem.* **2010**, *58*, 3191−3196.

(10) Xia, X.; Ling, W.; Ma, J.; Xia, M.; Hou, M.; Wang, Q.; Zhu, H.; Tang, Z. An anthocyanin-rich extract from black rice enhances atherosclerotic plaque stabilization in apolipoprotein E-deficient mice. *J. Nutr.* **2006**, *136*, 2220−2225.

(11) Hogan, S.; Canning, C.; Sun, S.; Sun, X. X.; Zhou, K. Q. Effects of grape pomace antioxidant extract on oxidative stress and inflammation in diet induced obese mice. *J. Agric. Food Chem.* **2010**, *58*, 11250−11256.

(12) Kurimoto, Y.; Shibayama, Y.; Inoue, S.; Soga, M.; Takikawa, M.; Ito, C.; Nanba, F.; Yoshida, T.; Yamashita, Y.; Ashida, H.; Tsuda, T. Black soybean seed coat extract ameliorates hyperglycemia and insulin sensitivity via the activation of AMP-activated protein kinase in diabetic mice. *J. Agric. Food Chem.* **2013**, *61*, 5558−5564.

(13) Morrison, M. C.; Liang, W.; Mulder, P.; Verschuren, L.; Pieterman, E.; Toet, K.; Heeringa, P.; Wielinga, P. Y.; Kooistra, T.; Kleemann, R. Mirtoselect, an anthocyanin-rich bilberry extract, attenuates non-alcoholic steatohepatitis and associated fibrosis in ApoE(*)3Leiden mice. *J. Hepatol.* **2015**, *62*, 1180−1186.

(14) Choi, J. H.; Hwang, Y. P.; Choi, C. Y.; Chung, Y. C.; Jeong, H. G. Anti-fibrotic effects of the anthocyanins isolated from the purple-fleshed sweet potato on hepatic fibrosis induced by dimethylnitrosamine administration in rats. *Food Chem. Toxicol.* **2010**, *48*, 3137−3143.

(15) Domitrović, R.; Jakovac, H. Antifibrotic activity of anthocyanidin delphinidin in carbon tetrachloride-induced hepatotoxicity in mice. *Toxicology* **2010**, *272*, 1−10.

(16) Ki, S. H.; Yang, J. H.; Ku, S. K.; Kim, S. C.; Kim, Y. W.; Cho, I. J. Red ginseng extract protects against carbon tetrachloride-induced liver fibrosis. *J. Ginseng Res.* **2013**, *37*, 45−53.

(17) Krajka-Kuzniak, V.; Szaefer, H.; Ignatowicz, E.; Adamska, T.; Oszmianski, J.; Baer-Dubowska, W. Effect of chokeberry (*Aronia melanocarpa*) juice on the metabolic activation and detoxication of carcinogenic *N*-nitrosodiethylamine in rat liver. *J. Agric. Food Chem.* **2009**, *57*, 5071−5077.

DOI: 10.1021/acs.jafc.5b02181
J. Agric. Food Chem. 2015, 63, 6221−6230

(18) Fang, J. Bioavailability of anthocyanins. *Drug Metab. Rev.* **2014**, *46*, 508−520.
(19) Choi, J. H.; Hwang, Y. P.; Park, B. H.; Choi, C. Y.; Chung, Y. C.; Jeong, H. G. Anthocyanins isolated from the purple-fleshed sweet potato attenuate the proliferation of hepatic stellate cells by blocking the PDGF receptor. *Environ. Toxicol. Pharmacol.* **2011**, *31*, 212−219.
(20) Bendia, E.; Benedetti, A.; Baroni, G. S.; Candelaresi, C.; Macarri, G.; Trozzi, L.; Di Sario, A. Effect of cyanidin 3-*O*-*β*-glucopyranoside on hepatic stellate cell proliferation and collagen synthesis induced by oxidative stress. *Dig. Liver Dis.* **2005**, *37*, 342−348.
(21) Guo, H.; Liu, G.; Zhong, R.; Wang, Y.; Wang, D.; Xia, M. Cyanidin-3-*O*-*β*-glucoside regulates fatty acid metabolism via an AMP-activated protein kinase-dependent signaling pathway in human HepG2 cells. *Lipids Health Dis.* **2012**, *11*, 10.
(22) Wei, J. IκB kinase-*β* inhibitor attenuates hepatic fibrosis in mice. *World J. Gastroenterol.* **2011**, *17*, 5203.
(23) Iwai, M.; Liu, H. W.; Chen, R.; Ide, A.; Okamoto, S.; Hata, R.; Sakanaka, M.; Shiuchi, T.; Horiuchi, M. Possible inhibition of focal cerebral ischemia by angiotensin II type 2 receptor stimulation. *Circulation* **2004**, *110*, 843−848.
(24) Ozer, J.; Ratner, M.; Shaw, M.; Bailey, W.; Schomaker, S. The current state of serum biomarkers of hepatotoxicity. *Toxicology* **2008**, *245*, 194−205.
(25) Thompson, M. D.; Awuah, P.; Singh, S.; Monga, S. P. Disparate cellular basis of improved liver repair in *β*-catenin-overexpressing mice after long-term exposure to 3,5-diethoxycarbonyl-1,4-dihydrocollidine. *Am. J. Pathol.* **2010**, *177*, 1812−1822.
(26) Baffy, G. Kupffer cells in non-alcoholic fatty liver disease: the emerging view. *J. Hepatol.* **2009**, *51*, 212−223.
(27) Rombouts, K.; Marra, F. Molecular mechanisms of hepatic fibrosis in non-alcoholic steatohepatitis. *Dig. Dis.* **2010**, *28*, 229−235.
(28) Rajesh, D.; Zhou, Y.; Jankowska-Gan, E.; Roenneburg, D. A.; Dart, M. L.; Torrealba, J.; Burlingham, W. J. Th1 and Th17 immunocompetence in humanized NOD/SCID/IL2rγnull mice. *Hum. Immunol.* **2010**, *71*, 551−559.
(29) Kisseleva, T.; Brenner, D. A. Role of hepatic stellate cells in fibrogenesis and the reversal of fibrosis. *J. Gastroenterol. Hepatol.* **2007**, *22* (Suppl.1), S73−S78.
(30) Marra, F.; DeFranco, R.; Grappone, C.; Milani, S.; Pastacaldi, S.; Pinzani, M.; Romanelli, R. G.; Laffi, G.; Gentilini, P. Increased expression of monocyte chemotactic protein-1 during active hepatic fibrogenesis: correlation with monocyte infiltration. *Am. J. Pathol.* **1998**, *152*, 423−430.
(31) Castañeda-Ovando, A.; Pacheco-Hernández, M. d. L.; Páez-Hernández, M. E.; Rodríguez, J. A.; Galán-Vidal, C. A. Chemical studies of anthocyanins: a review. *Food Chem.* **2009**, *113*, 859−871.
(32) Kong, J. Analysis and biological activities of anthocyanins. *Phytochemistry* **2003**, *64*, 923−933.
(33) Vivar-Quintana, A. M.; S.-B, C.; Rivas-Gonzalo, J. C. Anthocyanin derived pigments and colour of red wines. *Anal. Chim. Acta* **2002**, *458*, 147−155.
(34) Tang, X.; Shen, T.; Jiang, X.; Xia, M.; Sun, X.; Guo, H.; Ling, W. Purified anthocyanins from bilberry and black currant attenuate hepatic mitochondrial dysfunction and steatohepatitis in mice with methionine and choline deficiency. *J. Agric. Food Chem.* **2015**, *63*, 552−561.
(35) Wang, D.; Xia, M.; Gao, S.; Li, D.; Zhang, Y.; Jin, T.; Ling, W. Cyanidin-3-*O*-*β*-glucoside upregulates hepatic cholesterol 7*α*-hydroxylase expression and reduces hypercholesterolemia in mice. *Mol. Nutr. Food Res.* **2012**, *56*, 610−621.
(36) Guo, H.; Xia, M.; Zou, T.; Ling, W.; Zhong, R.; Zhang, W. Cyanidin 3-glucoside attenuates obesity-associated insulin resistance and hepatic steatosis in high-fat diet-fed and db/db mice via the transcription factor FoxO1. *J. Nutr. Biochem.* **2012**, *23*, 349−360.
(37) Starkel, P.; Leclercq, I. A. Animal models for the study of hepatic fibrosis. *Best Pract. Res. Clin. Gastroenterol.* **2011**, *25*, 319−333.
(38) Veidal, S. S.; Karsdal, M. A.; Vassiliadis, E.; Nawrocki, A.; Larsen, M. R.; Nguyen, Q. H. T.; Hägglund, P.; Luo, Y.; Zheng, Q.; Vainer, B.; Leeming, D. J. MMP mediated degradation of type VI collagen is highly associated with liver fibrosis − identification and validation of a novel biochemical marker assay. *PLoS One* **2011**, *6*, e24753.
(39) Hemmann, S.; Graf, J.; Roderfeld, M.; Roeb, E. Expression of MMPs and TIM Ps in liver fibrosis−a systematic review with special emphasis on anti-fibrotic strategies. *J. Hepatol.* **2007**, *46*, 955−975.
(40) Koek, G. H.; Liedorp, P. R.; Bast, A. The role of oxidative stress in non-alcoholic steatohepatitis. *Clin. Chim. Acta* **2011**, *412*, 1297−1305.
(41) Giannini, E. G.; Testa, R.; Savarino, V. Liver enzyme alteration: a guide for clinicians. *CMAJ* **2005**, *172*, 367−379.
(42) Guicciardi, M. E.; Malhi, H.; Mott, J. L.; Gores, G. J. Apoptosis and necrosis in the liver. *Compr. Physiol.* **2013**, *3*, 977−1010.
(43) Jiang, X.; Tang, X.; Zhang, P.; Liu, G.; Guo, H. Cyanidin-3-6O-*β*-glucoside protects primary mouse hepatocytes against high glucose-induced apoptosis by modulating mitochondrial dysfunction and the PI3K/Akt pathway. *Biochem. Pharmacol.* **2014**, *90*, 135−144.
(44) Donepudi, A. C.; Aleksunes, L. M.; Driscoll, M. V.; Seeram, N. P.; Slitt, A. L. The traditional ayurvedic medicine, *Eugenia jambolana* (jamun fruit), decreases liver inflammation, injury and fibrosis during cholestasis. *Liver Int.* **2012**, *32*, 560−573.
(45) Miura, K.; Yang, L.; van Rooijen, N.; Brenner, D. A.; Ohnishi, H.; Seki, E. Toll-like receptor 2 and palmitic acid cooperatively contribute to the development of nonalcoholic steatohepatitis through inflammasome activation in mice. *Hepatology* **2013**, *57*, 577−589.
(46) Seymour, E. M.; Lewis, S. K.; Urcuyo-Llanes, D. E.; Tanone, II; Kirakosyan, A.; Kaufman, P. B.; Bolling, S. F. Regular tart cherry intake alters abdominal adiposity, adipose gene transcription, and inflammation in obesity-prone rats fed a high fat diet. *J. Med. Food* **2009**, *12*, 935−942.
(47) Hammerich, L.; Heymann, F.; Tacke, F. Role of IL-17 and Th17 cells in liver diseases. *Clin. Dev. Immunol.* **2011**, *2011*, 345803.
(48) McGhie, T. K.; Walton, M. C. The bioavailability and absorption of anthocyanins: towards a better understanding. *Mol. Nutr. Food Res.* **2007**, *51*, 702−713.

DOI: 10.1021/acs.jafc.5b02181
J. Agric. Food Chem. 2015, 63, 6221−6230

sequencing (NGS), is a powerful and cost-efficient tool for discovering gene expression, novel genes, and differentially expressed genes. Due to its higher accuracy and dynamic range, RNA-seq is replacing other methods for quantifying gene expression, including microarray and serial analysis of gene expression (SAGE). RNA-seq is very sensitive and allows more precise quantification of differential gene expression, as well as the detection of low-abundance transcripts. Furthermore, RNA-seq is useful in nonmodel plants that lack a reference genome because the focus of sequencing is the coding regions. Therefore, the transcriptomes of various nonmodel agricultural crops have been assessed using RNA-seq, including olive,[24] chestnut,[25] and tea.[26] For model agriculture crops such as *Zea mays* and soybean, RNA-seq provides breeders with new tools and methodologies to discover genome-wide expression, to isolate novel transcripts, and to explore alternative RNA splicing events, which allow great steps forward in plant breeding.[27−29]

To investigate the transcriptional profiling in *A. membranaceus* hairy roots in response to MeJA, we used the next-generation Illumina/Solexa HiSeq2000 platform for RNA analysis (RNA-seq). The assembled and annotated transcriptome sequences provide a valuable resource for the molecular characterization of secondary metabolite biosynthesis in *A. membranaceus*. In addition, we identified most genes related to AST, calycosin, and CG biosynthesis in *A. membranaceus*. Transcriptional regulation of AST, calycosin, and CG biosynthetic genes and changes in AST, calycosin, and CG accumulation were investigated in the hairy roots of *A. membranaceus* treated with MeJA. These data may establish new approaches to maximize AST, calycosin, and CG production and biomass productivity in the hairy roots of *A. membranaceus*.

MATERIALS AND METHODS

Establishment of Hairy Root Transformation and MeJA Treatment. Excised cotyledons and leaves of *A. membranaceus* from 20-day-old seedlings were used as the explant materials for cocultivation with wild-type *Agrobacterium rhizogenes* strain R1000. The excised explants were dipped into a liquid *A. rhizogenes* culture in inoculation medium for 10 min, blotted dry on sterile filter paper, and incubated in the dark at 25 °C on agar-solidified half-strength (1/2) MS medium. After 2 days of cocultivation, the explant tissues were thoroughly washed with sterilized distilled water and transferred to a hormone-free 1/2 MS medium containing cefotaxime (500 mg/L). The hairy roots were induced from the wound sites after 20 days of inoculation. Genomic DNA was isolated from several different fast-growing hairy root lines using the method described by Edwards et al.[30] Polymerase chain reaction (PCR) analysis was then performed using primers that detect *rol* A, B, C, and D genes to confirm the integration of *A. rhizogenes* open reading frames into the recipient plant genome (data not shown).

For the next steps, approximately 200 mg of fresh hairy roots was transferred to 30 mL of 1/2 MS liquid medium in 100 mL flasks. Hairy root cultures were maintained at 25 °C on a gyratory shaker (100 rpm) in a growth chamber under standard cool white fluorescent tubes with a flux rate of 35 μmol s^{-1} m^{-2} and a 16-h photoperiod. For MeJA treatments, hairy root samples were treated with MeJA (Sigma) after 3 weeks of culture in 30 mL of 1/2 MS liquid medium. Hairy root samples were harvested 24 h after MeJA treatment. In another study (unpublished data), we found that the production of AST, calycosin, and CG in hairy roots treated with 100 μM MeJA was higher than that in the hairy roots treated with other concentrations of MeJA. Therefore, the hairy roots treated with 100 μM MeJA was chosen for the further transcriptome analysis. Untreated hairy roots were used as the control. The entire experiment was repeated three times, and three independent hairy root replicates were pooled for further analyses. All samples were frozen in liquid nitrogen immediately after harvesting and then stored at −80 °C or freeze-dried for total RNA isolation or HPLC analysis.

RNA Isolation and Illumina Sequencing. The samples were ground into powder using liquid nitrogen, and total RNA was isolated using a Plant Total RNA Mini Kit (Geneaid, Taiwan) according to the manufacturer's instructions. The quality and concentration of total extracted RNA was determined by 1% agarose gel electrophoresis and spectrophotometer analysis in a NanoVue Plus spectrophotometer (GE Healthcare Bio-Science Crop, USA). mRNA was purified from total RNA using Sera-Mag Magnetic Oligo(dT) beads (Illumina, San Diego, CA, USA). cDNA synthesis, library construction, and DNA sequencing were performed using Illumina/Solexa HiSeq2000 platform by SEEDERS Company (Daejeon, Korea). The resulting high-quality reads were then deposited in the Short Read Archive at the National Center for Biotechnology Information (NCBI) with the accession number SRR923811.

De Novo Assembly and Functional Annotation. Reads obtained using an Illumina sequencer were filtered and *de novo* assembled using Velvet and Oases at high *k*-mers of 57, 59.[31] *A. membranaceus* transcripts were searched against the plant genome information in Phytozome (http://www.phytozome.net/) with a wide range of *E*-value cutoff, from 1×10^{-100} to 1×10^{-6}. The numbers of annotated genes stabilize around cutoff values of 1×10^{-6} to 1×10^{-10} (data not shown). Therefore, we chose a default cutoff of 1×10^{-10} for best blast hit number. To assign function to each gene, gene ontology (GO) analysis and clusters of orthologous groups (COG) analyses were performed. To gain an overview of gene pathway networks, genes were mapped according to the Kyoto Encyclopedia of Genes and Genomes (KEGG). Genes encoding transcription factors were identified using the Plant Transcription Factor Database (http://planttfdb.cbi.edu.cn/).

Differentially Expressed Gene Analysis. Differential expression analysis was performed based on the negative-binomial distribution, as described by Anders and Huber.[32] Raw counts data for the control and MeJA-treated hairy roots were compared to determine the $\log_2$-fold change in abundance of each transcript. Differentially expressed genes were those having $\log_2$-fold change of ≤ -1 or ≥ 1 and a false discovery rate of ≤ 0.01.

Identification of Genes Related to AST, Calycosin, and CG Biosynthetic Pathways. Genes involved in the AST, calycosin, and CG biosynthetic pathways were searched for using functional annotation data based on the candidate gene names. In addition, the AST, calycosin, and CG biosynthetic genes of *Arabidopsis* obtained from The *Arabidopsis* Information Resource (TAIR) were used as queries to search for homologous sequences in *A. membranaceus* transcriptome database. Following this, each search sequence was confirmed by using the BLAST program in the National Center for Biotechnology Information GenBank database.

Quantitative Real-Time PCR. On the basis of the sequences of *A. membranaceus* 1-deoxy-D-xylulose 5-phosphate synthase (AmDXS), (*E*)-4-hydroxy-3-methylbut-2-enyl diphosphate synthase (AmHDS), acetoacetyl-coenzyme A thiolase (AmAACT), isopentenyl diphosphate isomerase (AmIDI), squalene synthase (AmSS), phenylalanine ammonia lyase (AmPAL1), cinnamic acid 4-hydroxylase (Am4CL), chalcone synthase (AmCHS1), chalcone isomerase (AmCHI), and isoflavone *O*-methyltransferase (AmIOMT), we designed real-time PCR primers using the Primer3 Web site (http://bioinfo.ut.ee/primer3-0.4.0/primer3/; Table S10, Supporting Information). Real-time PCR products were tested for specificity of fragment sizes, melting curves, and sequences by PCR, real-time PCR, and cloning into a T-Blunt vector for sequencing, respectively. The expression levels of these genes were normalized and then analyzed by relative quantification using the *A. membranaceus* adenine phosphoribosyl transferase housekeeping gene (NCBI Genbank accession number KF355974) as a reference. qRT-PCR was performed by previous paper.[33] Three replications for each sample were used in the real-time analyses.

DOI: 10.1021/acs.jafc.5b01822
J. Agric. Food Chem. 2015, 63, 6231−6240

Table 1. Summary of Sequences from *A. membranaceus* Transcriptome after Illumina Sequencing

	control hairy roots_1	control hairy roots_2	MeJA-treated hairy roots_1	MeJA-treated hairy roots_2	total
Raw Data					
number of reads	24 006 768	24 006 768	25 122 120	25 122 120	98 257 776
mean length (bp)	101	101	101	101	101
total base pairs	2 424 683 568	2 424 683 568	2 537 334 120	2 537 334 120	9 924 035 376
Trimmed Data					
number of reads	24 006 768	24 006 768	25 122 120	25 122 120	98 257 776
mean length (bp)	82.00	77.09	82.49	78.23	79.95
total base pairs	1 968 502 825	1 850 604 616	2 072 343 049	1 965 385 644	7 856 836 134
Paired-End Data					
number of reads	18 905 452	18 905 452	19 973 663	19 973 663	77 758 230
mean length (bp)	91.74	89.46	92.02	90.02	90.81
total base pairs	1 734 455 319	1 691 227 010	1 837 991 656	1 798 088 737	7 061 762 722

HPLC Analysis. The materials were freeze-dried and ground into a fine powder. AST I, AST II, AST III, AST IV, calycosin, and CG were analyzed by HPLC.[34,35] The concentration of each compound was determined using a standard curve. All samples were analyzed in triplicate.

Statistical Analysis. The data for gene expression and AST, calycosin, and CG content were analyzed using Statistical Analysis System software (SAS version 9.2). Treatment means were compared using Duncan's multiple range test.

RESULTS AND DISCUSSION

Illumina Sequencing and *De Novo* Sequence Assembly. cDNA libraries were constructed from *A. membranaceus* hairy roots treated with 100 μM MeJA for 24 h and from untreated hairy roots and sequenced. In total, 98 257 776 reads of 101 bp from 9 924 035 376 bp were obtained from the Illumina/Solexa HiSeq2000 platform (Table 1). Of these, 77 758 230 paired-end clean reads, with a mean length of 90.81 bp, were obtained from 98 257 776 trimmed reads. The clean reads were assembled into 48 636 transcripts (average length of 1398 bp), which were then clustered into 23 658 loci using Velvet and Oases at high *k*-mers of 57, 59 (Table 2).[31] Because our main goal was to study the nonredundant set of mRNA sequences for *A. membranaceus*, the longest or highest coverage transcript for each locus was chosen to produce 23 658 nonredundant cDNAs (genes), with an average length of 1161 bp, containing 10 311 full-length coding sequences. Distribution of the number of transcripts and genes organized by transcript length and gene length, respectively, are shown in Figure 1.

Table 2. Summary of Sequence Assembly from the *A. membranaceus* Transcriptome

	transcript	locus
number of sequences	48 636	23 658
minimum length (bp)	200	200
maximum length (bp)	14 974	11 135
mean length (bp)	1 398	1 161
annotated sequences	40 904	19 940
full-length coding sequences	21 899	10 311

Functional Annotation. A total of 40 904 transcripts clustering into 19 940 genes were annotated by searching against the plant genome information using Phytozome (http://www.phytozome.net/) with an *E*-value cutoff of 1×10^{-10} (Table S1, Supporting Information). Subsequently, GO and COG analyses were performed to classify the function of predicted *A. membranaceus* genes. GO analysis categorized 19 940 genes as biological process, cellular component, or molecular function (Figure 2). Each gene may have more than one GO term and be assigned to different GO categories. The dominant groups within the biological process, cellular component, and molecular function categories were cellular process (8402 members), cell part (13 182 members), and nucleotide binding (3748 members), respectively. A total of 17 189 genes were aligned to 25 categories of the COG database (Figure 3). The R category "general function prediction only" was the largest group (3505 members), followed by the T category "signal transduction mechanisms" (1996 members) and the S category "function unknown", which has no concrete assignment (1537 members). In addition, 4969 genes were mapped to 116 KEGG pathways (Table S2, Supporting Information). The biosynthesis of plant hormones, phenylpropanoids, terpenoids, and steroids were the three largest groups with 282, 210, and 184 identified genes, respectively. The analyses provided excellent material for the molecular characterization of genes related to secondary metabolite biosynthetic pathways in *A. membranaceus*.

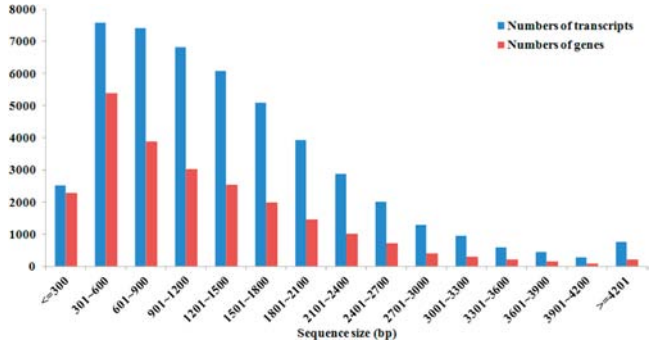

Figure 1. Distribution of transcript and gene numbers based on transcript and gene length, respectively.

Differentially Expressed Gene Analysis in *A. membranaceus* Hairy Roots in Response to MeJA. The differentially expressed gene (DEG) analysis between MeJA-treated and control hairy roots was performed using the DESeq method.[32] Genes were determined to be differentially expressed if they had a $\log_2$-fold change of ≤ -1 or ≥ 1 and a false discovery rate of ≤ 0.01. A total of 3374 genes were found to be differentially expressed in MeJA-treated hairy roots compared with control hairy roots. Of these, 2127 genes were up-regulated and 1247 genes were down-regulated by MeJA. BLASTx searches of 3374 DEGs against the plant genome

DOI: 10.1021/acs.jafc.5b01822
J. Agric. Food Chem. 2015, 63, 6231−6240

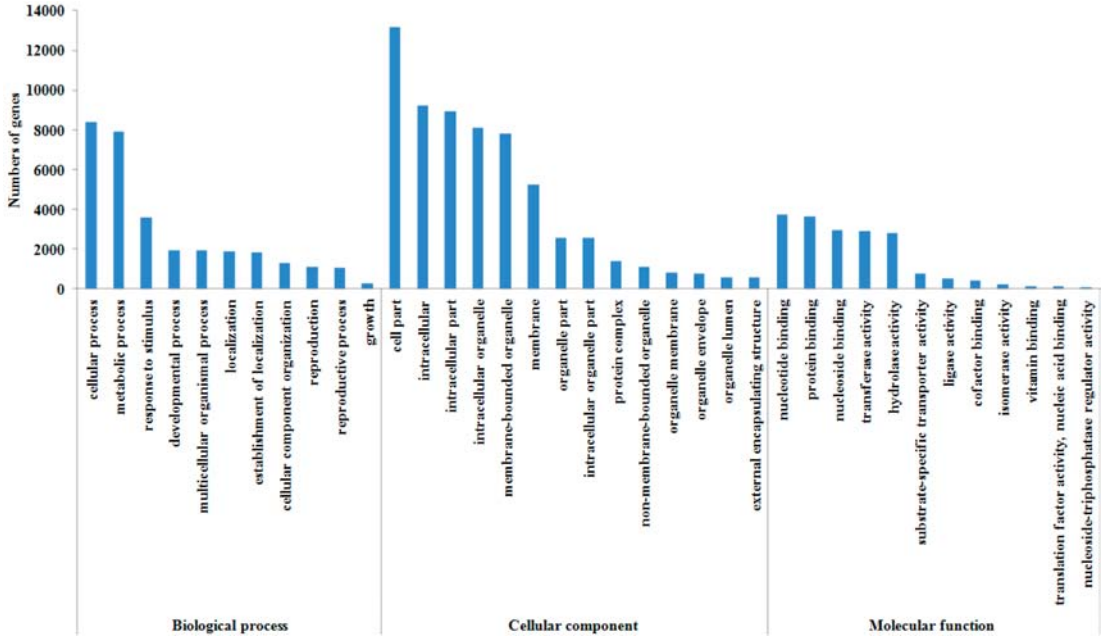

Figure 2. GO analysis of genes based on biological process, cellular component, and molecular function categories.

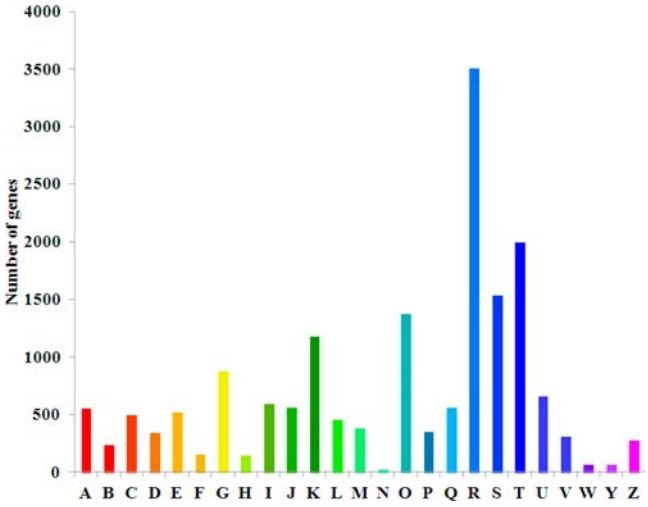

Figure 3. COG functional classification of genes. (A) RNA processing and modification; (B) chromatin structure and dynamics; (C) energy production and conversion; (D) cell cycle control, cell division, and chromosome partitioning; (E) amino acid transport and metabolism; (F) nucleotide transport and metabolism; (G) carbohydrate transport and metabolism; (H) coenzyme transport and metabolism; (I) lipid transport and metabolism; (J) translation, ribosomal structure, and biogenesis; (K) transcription; (L) replication, recombination, and repair; (M) cell wall/membrane/envelope biogenesis; (N) cell motility; (O) posttranslational modification, protein turnover, and chaperones; (P) inorganic ion transport and metabolism; (Q) secondary metabolite biosynthesis, transport, and catabolism; (R) general function prediction only; (S) function unknown; (T) signal transduction mechanisms; (U) intracellular trafficking, secretion, and vesicular transport; (V) defense mechanisms; (W) extracellular structures; (Y) nuclear structure; (Z) cytoskeleton.

information using Phytozome (http://www.phytozome.net/) with an E-value cutoff of 1×10^{-10} revealed that 2920 DEGs, including 1852 up-regulated genes and 1068 down-regulated genes, were annotated (Tables S3 and S4, Supporting Information, respectively). Furthermore, the KEGG analysis revealed that 667 up-regulated genes and 238 down-regulated genes could be mapped to 88 and 76 KEGG pathways, respectively (Tables S5 and S6, Supporting Information, respectively). Of these, MeJA up-regulated a large numbers of genes belonging to the biosynthesis of plant hormone group (71 genes), the biosynthesis of terpenoids and steroids group (44 genes), and the biosynthesis of phenylpropanoids group (34 genes) in *A. membranaceus* hairy roots. The application of MeJA stimulates the transcription of biosynthetic genes and accumulation of secondary metabolites in plants.[36−38] The annotated differentially expressed genes are an important and valuable resource for the identification of novel MeJA-responding genes and for the investigation of specific MeJA-regulated pathways in *A. membranaceus*.

Transcriptional Regulation of Transcription Factors in *A. membranaceus* Hairy Roots in Response to MeJA. Transcription factors are important elements in regulating plant responses to a range of abiotic and biotic stresses by controlling the expression patterns of genes involved in signaling pathways.[39,40] In the *A. membranaceus* transcriptome, 3784 genes encoding transcription factors were annotated (Table S7, Supporting Information). bHLH, NAC, WRKY, MYB-related, and bZIP are the five largest families of transcription factors and have 339, 292, 287, 281, and 227 members, respectively (Figure 4). Of the 3784 identified transcription factors, 395 were up-regulated and 250 were down-regulated by MeJA in *A. membranaceus* hairy roots (Tables S8 and S9, Supporting Information, respectively). A high number of transcription factors regulated by MeJA suggested that transcription factors play various roles in molecular mechanisms in response to MeJA as well as in the defense mechanisms of *A. membranaceus* hairy roots. Moreover, information about transcription factors will be helpful in investigating their roles in secondary metabolite biosynthesis in response to stresses.

MeJA Increases Transcription Levels of Genes Related to the AST Biosynthetic Pathway in *A. membranaceus* Hairy Roots. Triterpene ASTs are built from isopentenyl diphosphate, which is supplied from the cytosol mevalonic acid

DOI: 10.1021/acs.jafc.5b01822
J. Agric. Food Chem. 2015, 63, 6231−6240

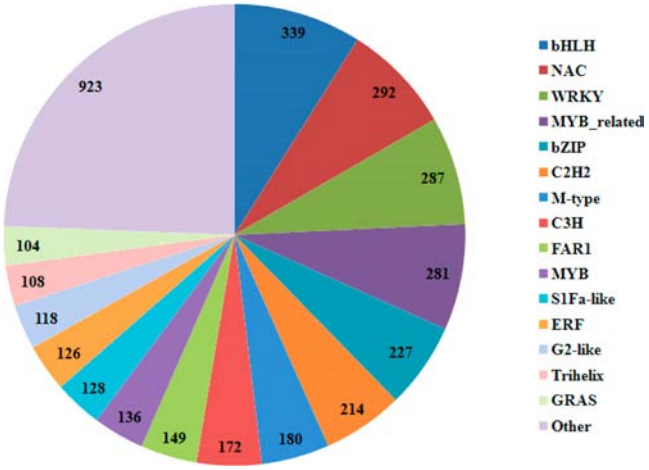

Figure 4. Numbers of genes encoding transcription factors.

(MVA) pathway and the plastid methylerythritol phosphate (MEP) pathway (Figure 5). On the basis of the functional annotation of the *A. membranaceus* transcriptome library, 17 novel genes were identified that encode enzymes related to the AST biosynthetic pathway (Table 3). In the MEP pathway, full-length coding sequences of AmDXS, 2-*C*-methyl-D-erythritol 4-phosphate cytidylyltransferase (AmMCT), 4-(cytidine 5′-phospho)-2-*C*-methyl-D-erithritol kinase (AmCMK), AmHDS, and (*E*)-4-hydroxy-3-methylbut-2-enyl diphosphate reductase (AmHDR) and partial-length coding sequences of 1-deoxy-D-xylulose 5-phosphate reductoisomerase (AmDXR) were found. Entire genes that are involved in the MVA pathway were isolated, including AmAACT, 3-hydroxy-3-methylglutaryl coenzyme A synthase (AmHMGS), 3-hydroxy-3-methylglutaryl-coenzyme A reductase (AmHMGR1, AmHMGR2, AmHMGR3), mevalonate kinase (AmMVK), phosphomevalonate kinase (AmPMK1, AmPMK2), mevalonate diphosphate decarboxylase (AmMVD), and AmIDI. In addition, full-length coding sequence of farnesyl diphosphate synthase (AmFDS), an enzyme that functions in the initial step of triterpene formation in the MVA pathway and MEP pathway, was also found in the *A. membranaceus* transcriptome library. These 17 novel AST biosynthetic genes of *A. membranaceus* share high similarity and identity with other orthologous genes (data not shown) and have been submitted to Genbank at the NCBI.

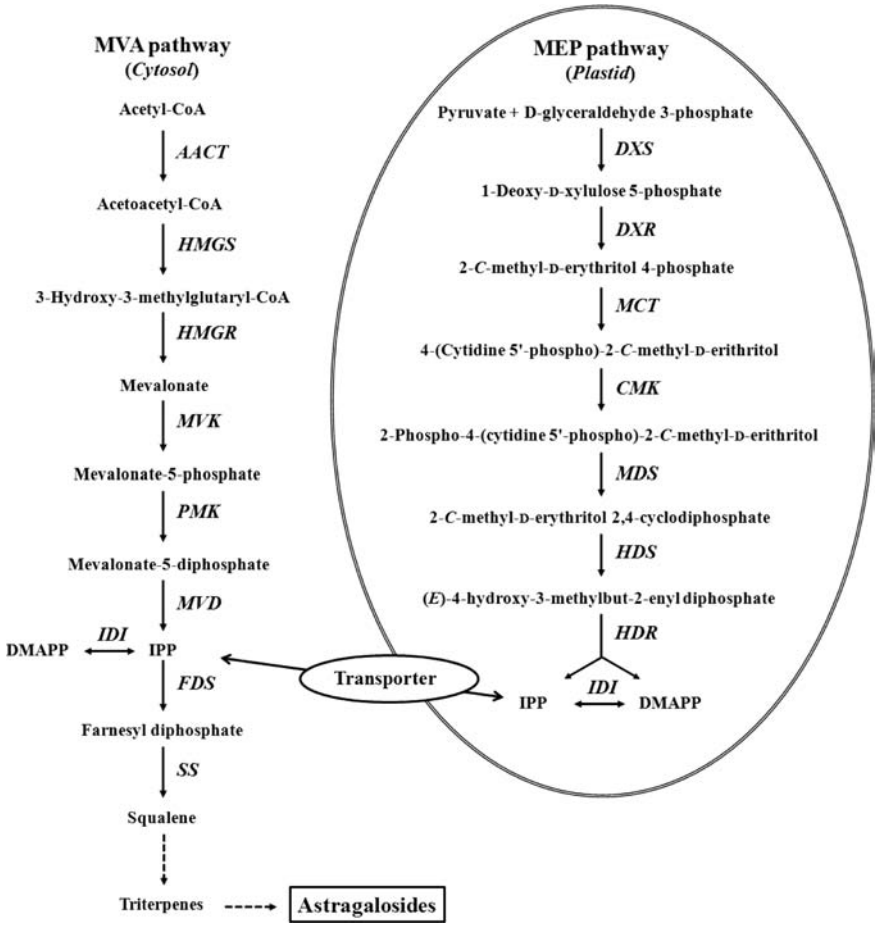

Figure 5. Proposed AST biosynthetic pathway in plants. AACT, acetoacetyl-CoA thiolase; CMK, 4-(cytidine 5′-diphospho)-2-*C*-methyl-D-erythritol kinase; DXR, 1-deoxy-D-xylulose 5-phosphate reductoisomerase; DXS, 1-deoxy-D-xylulose 5-phosphate synthase; FDS, farnesyl diphosphate synthase; HDR, (*E*)-4-hydroxy-3-methylbut-2-enyl diphosphate reductase; HDS, (*E*)-4-hydroxy-3-methylbut-2-enyl diphosphate synthase; HMGR, 3-hydroxy-3-methylglutaryl-CoA reductase; HMGS, 3-hydroxy-3-methylglutaryl-CoA synthase; IDI, isopentenyl diphosphate isomerase; MCT, 2-*C*-methyl-D-erythritol 4-phosphate cytidylyltransferase; MDS, 2-*C*-methyl-D-erythritol 2,4-cyclodiphosphate synthase; MVD, mevalonate diphosphate decarboxylase; MVK, mevalonate kinase; PMK, phosphomevalonate kinase; SS, squalene synthase ; DMAPP, dimethylallyl diphosphate; IPP, isopentenyl diphosphate.

DOI: 10.1021/acs.jafc.5b01822
J. Agric. Food Chem. 2015, 63, 6231−6240

Table 3. Candidate Genes for AST Biosynthesis in the *A. membranaceus* Transcriptome

gene name	gene ID	accession number (NCBI)	control hairy roots (RPKM)	MeJA-treated hairy roots (RPKM)	fold change
1-deoxy-D-xylulose 5-phosphate synthase (AmDXS)[a,b]	Locus_19738	KF355950	62	1 724	27.81
1-deoxy-D-xylulose 5-phosphate reductoisomerase (AmDXR)[a]	Locus_12894	KF355951	776	836	1.08
2-C-methyl-D-erythritol 4-phosphate cytidylyltransferase (AmMCT)[a,b]	Locus_9577	KF355952	97	100	1.03
4-(cytidine 5′-phospho)-2-C-methyl-D-erithritol kinase (AmCMK)[a,b]	Locus_28629	KF355953	69	136	1.97
(*E*)-4-hydroxy-3-methylbut-2-enyl diphosphate synthase (AmHDS)[a,b]	Locus_3604	KF355954	829	2 365	2.85
(*E*)-4-hydroxy-3-methylbut-2-enyl diphosphate reductase (AmHDR)[a,b]	Locus_21871	KF355955	1 179	2 588	2.20
acetoacetyl-coenzyme A thiolase (AmAACT)[a,b]	Locus_600	KF355956	5 817	18 711	3.22
3-hydroxy-3-methylglutaryl coenzyme A synthase (AmHMGS)[a,b]	Locus_212	KF355957	1 251	3 780	3.02
3-hydroxy-3-methylglutaryl-coenzyme A reductase (AmHMGR1)[a,b]	Locus_920	KF355958	2 401	9 314	3.88
AmHMGR2[a,b]	Locus_4326	KF355959	500	1 611	3.22
AmHMGR3[a,b]	Locus_19060	KF355960	331	1 929	5.83
mevalonate kinase (AmMVK)[a,b]	Locus_32998	KF355961	472	2 903	6.15
phosphomevalonate kinase (AmPMK1)[a,b]	Locus_2082	KF355962	494	1 072	2.17
AmPMK2[a,b]	Locus_8364	KF355963	47	4 686	99.70
mevalonate diphosphate decarboxylase (AmMVD)[a,b]	Locus_1511	KF355964	349	3 936	11.28
isopentenyl diphosphate isomerase (AmIDI)[a]	Locus_732	KF355965	2 571	25 244	9.82
farnesyl diphosphate synthase (AmFDS)[a,b]	Locus_1394	KF355966	1 921	15 097	7.86
squalene synthase (AmSS)	Locus_17877	HQ829974	1 225	18 025	14.71

[a]The genes identified in this study. [b]The full-length coding sequence genes.

RPKM values showed that most genes related to the AST biosynthetic pathway were up-regulated by the application of MeJA in *A. membranaceus* hairy roots. *AmPMK2*, *AmDXS*, and *AmSS* exhibited the highest increases in expression in MeJA-treated hairy roots, with fold changes of 99.7, 27.81, and 14.71, respectively (Table 3). Expression levels of five selected genes were validated by qRT-PCR (Figure 6A). Although the fold-changes of these genes were different than those detected by RNA-seq, their expression profiles were consistent with the RNA-seq. The same hairy root materials as those used for RNA-seq and qRT-PCR were used for HPLC analysis of AST I, AST II, AST III, and AST IV (Figure 6B). The accumulation of AST I, AST II, AST III, and AST IV was significantly increased by 2.98-, 2.85-, 2.30-, and 1.57-fold, respectively, in MeJA-treated hairy roots compared with control hairy roots. These results suggest that the accumulation of ASTs was tightly regulated by the expression levels of genes involved in the MVA and MEP pathways in *A. membranaceus* hairy roots in response to MeJA. Furthermore, large amounts of AST I, AST II, AST III, and AST IV were found in both control (2386.06, 774.85, 401.52, and 124.24 μg/g, respectively) and MeJA-treated (7104.02, 2205.2, 924.98, and 194.77 μg/g, respectively) hairy roots. These amounts were much higher than those of the natural roots of *A. membranaceus*.[10] Hairy roots of *A. membranaceus* may, therefore, be a good material for the production of ASTs.

MeJA Increases Transcription Levels of Genes Related to Calycosin and CG Biosynthetic Pathways in *A. membranaceus* Hairy Roots. AmPAL1, AmC4H1, AmCHS1, chalcone reductase (AmCHR), AmCHI, isoflavone synthase (AmIFS), and isoflavone 3′-hydroxylase (AmI3′H), which are involved in calycosin and CG biosynthetic pathways (Figure 7),[9] were also found in the *A. membranaceus* transcriptome library. In addition, seven new full-length coding

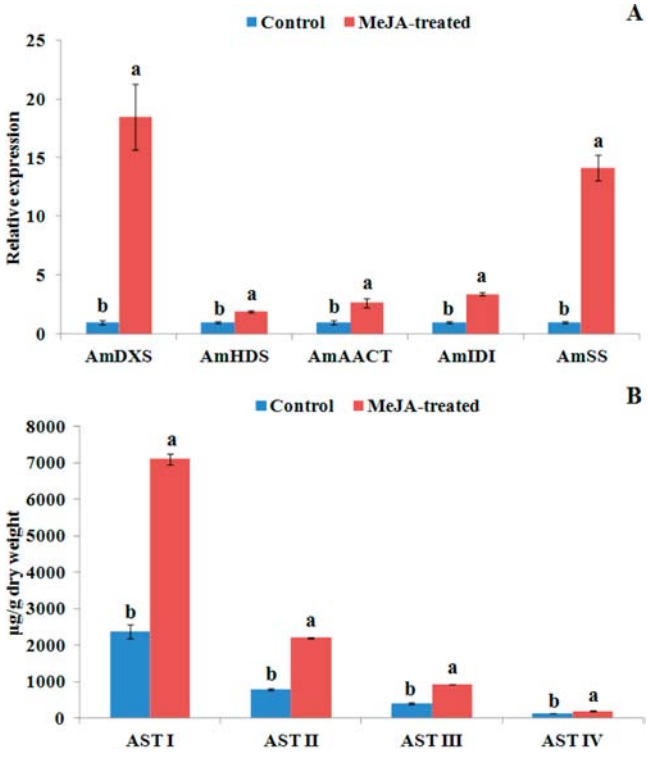

Figure 6. Expression levels of five selected AST biosynthetic genes determined by qRT-PCR (A) and AST content (B) in 100 μM MeJA-treated and untreated hairy roots. The height of each bar and the error bars show the mean and standard error, respectively, from three independent measurements. The letters a and b indicate significant differences at the 5% level by Duncan's multiple range test.

DOI: 10.1021/acs.jafc.5b01822
J. Agric. Food Chem. 2015, 63, 6231−6240

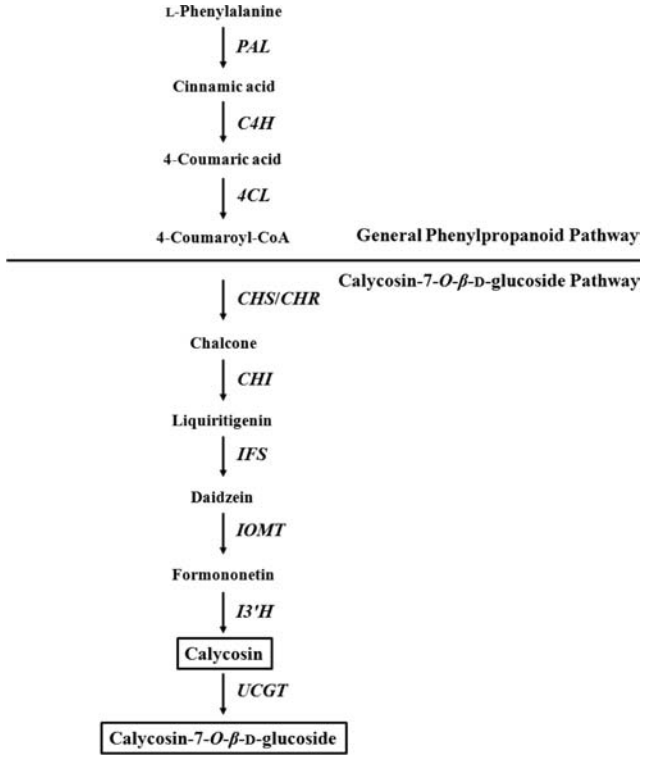

Figure 7. Proposed calycosin and CG biosynthetic pathways in plants. PAL, phenylalanine ammonia lyase; C4H, cinnamate-4-hydroxylase; 4CL, 4-coumaroyl CoA ligase; CHS, chalcone synthase; CHR, chalcone reductase; CHI, chalcone isomerase; IFS, isoflavone synthase; IOMT, isoflavone *O*-methyltransferase; I3′H, isoflavone 3′-hydroxylase; UCGT, UDP-glucose:calycosin-7-*O*-glucosyltransferase.

sequences (AmPAL2, AmPAL3, AmC4H2, Am4CL, AmCHS2, AmIOMT, and UDP-glucose:calycosin 7-*O*-glucosyltransferase (AmUCGT)) were identified (Table 4). BLAST searches of the NCBI Genbank database showed that they exhibited high homology to other orthologous genes (date not shown). The seven new calycosin and CG biosynthetic genes of *A. membranaceus* have been deposited into the NCBI Genbank (accession numbers shown in Table 4).

According to fold change values of RNA-seq, with the exception of *AmIOMT*, all calycosin and CG biosynthetic genes were up-regulated by MeJA in *A. membranaceus* hairy roots (Table 4). Expression levels of *AmUCGT*, *AmCHS1*, and *AmPAL3*, with fold changes of 7.07, 3.79, and 2.89, respectively, increased the most in MeJA-treated hairy roots compared with control hairy roots. qRT-PCR of five selected genes was performed to confirm the gene expression profiles analyzed by RNA-seq (Figure 8A). The higher expression levels of *AmPAL1*, *Am4CL*, *AmCHS1*, and *AmCHI* and the lower expression level of *AmIOMT* detected in MeJA-treated hairy roots by qRT-PCR supported the reliability of RNA-seq analyses. The higher expression levels of calycosin and CG biosynthetic genes were correlated with their higher accumulation in MeJA-treated hairy roots compared with control hairy roots (Figure 8B). Specifically, MeJA-treated hairy roots contained 23.61 μg/g of CG, whereas untreated hairy roots contained 17.75 μg/g. Untreated hairy roots did not accumulate calycosin, but hairy roots treated with MeJA contained 0.54 μg/g of calycosin. These data may not only broaden our understanding of the molecular mechanisms involved in the calycosin and CG biosynthetic pathways in *A. membranaceus* but also aid in their metabolic engineering in plants.

A. membranaceus, one of the most important Chinese traditional herbs, has a wide range of natural products.[6,7] MeJA application increased the expression levels of most genes related to AST, calycosin, and CG biosynthesis and their accumulation. Therefore, MeJA-treated hairy roots of *A. membranaceus* may be an excellent material for the production of ASTs, calycosin, and CG because of their biochemical stability and rapid growth rate.[41,42] On the other hand, although AST, calycosin, and CG were identified a long time ago, the complete biosynthetic pathway and biosynthetic genes of AST, calycosin, and CG are still largely unknown. Recently, based on the hypotheses that genes involved in secondary metabolite biosynthesis are often coordinately regulated at the transcriptional level, coexpression analysis has been widely used to identify new candidate genes in plants. There are numerous examples of successful gene discovery studies using this strategy such as the isolation of two glycosyltransferases involved in anthocyanin modification in *Arabidopsis thaliana*,[43] and the last

Table 4. Candidate Genes for Calycosin and CG Biosynthesis in the *A. membranaceus* Transcriptome

gene name	gene ID	accession number (NCBI)	control hairy roots (RPKM)	MeJA-treated hairy roots (RPKM)	fold change
phenylalanine ammonia-lyase (AmPAL1)	Locus_27697	EF567076	5 268	7 547	1.43
AmPAL2[a,b]	Locus_440	KF355967	2 016	2 301	1.14
AmPAL3[a,b]	Locus_28451	KF355968	715	2 069	2.89
cinnamate 4-hydroxylase (AmC4H1)	Locus_4902	HQ339960	3 548	7 540	2.13
AmC4H2[a,b]	Locus_15996	KF355969	27 465	62 687	2.28
4-coumaroyl:CoA-ligase (Am4CL)[a,b]	Locus_858	KF355970	3 526	5 750	1.63
chalcone synthase (AmCHS1)	Locus_1134	JQ048940	1 559	5 908	3.79
AmCHS2[a,b]	Locus_5993	KF355971	1 097	2 717	2.48
chalcone reductase (AmCHR)	Locus_9056	HM357239	17 888	22 132	1.24
chalcone isomerase (AmCHI)	Locus_17766	DQ205407	2 610	6 663	2.55
isoflavone synthase (AmIFS)	Locus_138	JF912329	26 250	39 575	1.51
isoflavone *O*-methyltransferase (AmIOMT)[a,b]	Locus_2606	KF355972	1 788	1 728	0.97
isoflavone-3′-hydroxylase (AmI3′H)	Locus_39	JQ609280	15 660	16 214	1.04
UDP-glucose:calycosin 7-*O*-glucosyltransferase (AmUCGT)[a,b]	Locus_30758	KF355973	365	2 582	7.07

[a]The genes identified in this study. [b]The full-length coding sequence genes.

DOI: 10.1021/acs.jafc.5b01822
J. Agric. Food Chem. 2015, 63, 6231−6240

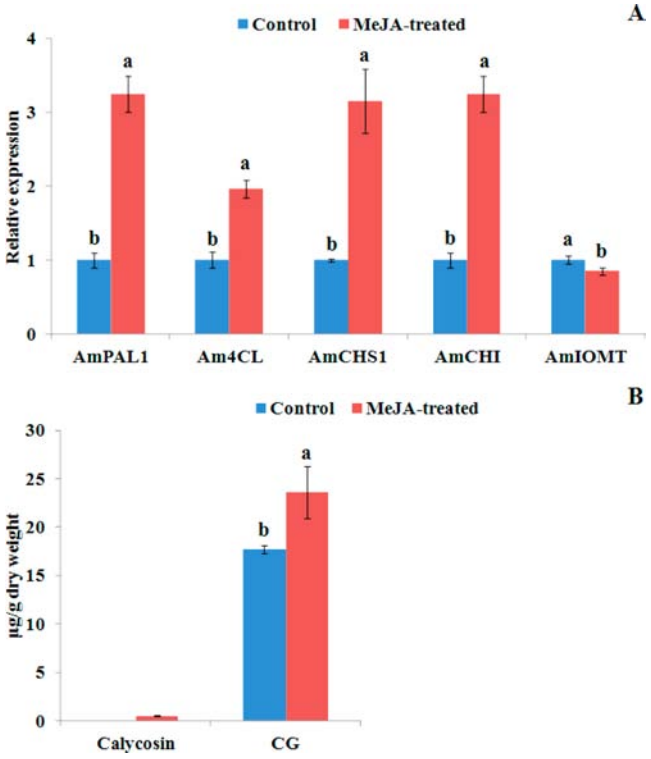

Figure 8. Expression levels of five selected calycosin and CG biosynthetic genes determined by qRT-PCR (A) and calycosin and CG content (B) in 100 μM MeJA-treated and untreated hairy roots. The height of each bar and the error bars show the mean and standard error, respectively, from three independent measurements. The letters a and b indicate significant differences at the 5% level by Duncan's multiple range test.

four missing steps of the seco-iridoid biosynthesis pathway in *Catharanthus roseus*.[44] The RNA-sequencing transcriptional profiling of *A. membranaceus* hairy roots in response to MeJA in this study will provide useful information to identify novel genes putatively involved in the downstream steps of the AST, calycosin, and CG biosynthetic pathways using coexpression analysis strategy.

Functional food, which contains numerous compounds beneficial to health, recently has attracted much interest. Therefore, much research has focused on developing efficient strategies to optimize the production of beneficial compounds for health in plants without gene modification or breeding. Among them, application of elicitors has been reported to efficiently affect the natural product accumulation in plants.[21−23] Here, we reported that application of MeJA significantly increased the accumulation of AST, calycosin, and CG in the hairy roots of *A. membranaceus*. This finding may provide a new method to develop functional food products having high concentrations of AST, calycosin, and CG in the future.

In conclusion, we identified 23 658 genes by high-throughput sequencing technology. There were 19 940 annotated genes, 4969 genes mapped to 116 KEGG pathways, and 3784 genes encoding transcription factors. RNA-seq analysis revealed that 2127 genes were up-regulated and 1247 genes were down-regulated by 100 μM MeJA in *A. membranaceus* hairy roots. In addition, we isolated 24 novel genes involved in the biosynthesis of ASTs, calycosin, and CG, chemical markers of the quality of *A. membranaceus*. The assembled and annotated transcriptome sequences provide a valuable resource for molecular characterization of ASTs, calycosin, and CG as well as other secondary metabolite biosynthetic pathways in *A. membranaceus*. The up-regulated biosynthesis of ASTs, calycosin, and CG in MeJA-treated hairy roots may lead to new approaches to maximize their production and biomass productivity in the hairy roots of *A. membranaceus*.

■ ASSOCIATED CONTENT

Supporting Information

Table S1, the annotation of transcripts; Table S2, the KEGG pathway analysis of genes; Table S3, the annotation of genes up-regulated by MeJA; Table S4, the annotation of genes down-regulated by MeJA; Table S5, KEGG pathway analysis of genes up-regulated by MeJA; Table S6, the KEGG pathway analysis of genes down-regulated by MeJA; Table S7, the annotation of genes encoding transcription factors; Table S8, the annotation of transcription factor genes up-regulated by MeJ; Table S9, the annotation of transcription factor genes down-regulated by MeJA; Table S10, primers used for qRT-PCR. The Supporting Information is available free of charge on the ACS Publications website at DOI: 10.1021/acs.jafc.5b01822.

■ AUTHOR INFORMATION

Corresponding Authors

*J. Lee. Phone: + 82-51-200-7592. Fax: +82-51-200-7505. E-mail: jhnlee@dau.ac.kr.

*S. U. Park. Phone: +82-42-821-5730. Fax: +82-42-822-2631. E-mail: supark@cnu.ac.kr.

Author Contributions

⊥P.A. Tuan and E. Chung contributed equally to this work.

Funding

This work was supported by the National Research Foundation of Korea (NRF) grant funded by the Korea government (MSIP) (No. 2015R1A2A2A01004054).

Notes

The authors declare no competing financial interest.

■ ABBREVIATIONS USED

AACT, acetoacetyl-CoA thiolase; CMK, 4-(cytidine 5′-diphospho)-2-*C*-methyl-D-erythritol kinase; DXR, 1-deoxy-D-xylulose 5-phosphate reductoisomerase; DXS, 1-deoxy-D-xylulose 5-phosphate synthase; FDS, farnesyl diphosphate synthase; HDR, (*E*)-4-hydroxy-3-methylbut-2-enyl diphosphate reductase; HDS, (*E*)-4-hydroxy-3-methylbut-2-enyl diphosphate synthase; HMGR, 3-hydroxy-3-methylglutaryl-CoA reductase; HMGS, 3-hydroxy-3-methylglutaryl-CoA synthase; IDI, isopentenyl diphosphate isomerase; MCT, 2-*C*-methyl-D-erythritol 4-phosphate cytidylyltransferase; MDS, 2-*C*-methyl-D-erythritol 2,4-cyclodiphosphate synthase; MVD, mevalonate diphosphate decarboxylase; MVK, mevalonate kinase; PMK, phosphomevalonate kinase; SS, squalene synthase; DMAPP, dimethylallyl diphosphate; IPP, isopentenyl diphosphate; PAL, phenylalanine ammonia lyase; C4H, cinnamate-4-hydroxylase; 4CL, 4-coumaroyl CoA ligase; CHS, chalcone synthase; CHR, chalcone reductase; CHI, chalcone isomerase; IFS, isoflavone synthase; IOMT, isoflavone *O*-methyltransferase; I3′H, isoflavone 3′-hydroxylase; UCGT, UDP-glucose:calycosin-7-*O*-glucosyltransferase

DOI: 10.1021/acs.jafc.5b01822
J. Agric. Food Chem. 2015, 63, 6231−6240

REFERENCES

(1) Rios, J. L.; Waterman, P. G. A review of the pharmacology and toxicology of *Astragalus*. *Phytother. Res.* **1997**, *11*, 411−418.

(2) Zhang, W. J.; Hufnag, P.; Binder, B. R.; Wojta, J. Anti-inflammatory activity of astragaloside IV is mediated by inhibition of NF-kappaB activation and adhesion molecule expression. *J. Thromb. Haemost.* **2003**, *90*, 904−914.

(3) Tang, L.; Liu, Y.; Wang, Y.; Long, C. Phytochemical analysis of an antiviral fraction of *Radix astragali* using HPLC-DAD-ESIMS/MS. *J. Nat. Med.* **2010**, *64*, 182−186.

(4) Zhang, Y. D.; Wang, Y. L.; Shen, J. P. Effects of *Astragalous* saponins on antiinflammation and antihypertension. *Acta Pharmacol. Sin.* **1984**, *19*, 333−337.

(5) Bedir, E.; Pugh, N.; Calis, I.; Pasco, D. S.; Khan, I. A. Immunostimulatory effects of cycloartane-type triterpene glycosides from *Astragalus* species. *Biol. Pharm. Bull.* **2000**, *23*, 834−837.

(6) Wu, F.; Chen, X. A review of pharmacological study on *Astragalus membranaceus* (Fisch.) Bge. *Zhong Yao Cai* **2004**, *27*, 232−234.

(7) Song, Z. H.; Ji, Z. N.; Lo, C. K.; Dong, T. T.; Zhao, K. J.; Li, O. T.; Haines, C. J.; Kung, S. D.; Tsim, K. W. Chemical and biological assessment of a traditional Chinese herbal decoction prepared from *Radix Astragali* and *Radix Angelicae Sinensis*: Orthogonal array design to optimize the extraction of chemical constituents. *Planta Med.* **2004**, *70*, 1222−1227.

(8) Xu, R. Y.; Nan, P.; Yang, Y.; Pan, H.; Zhou, T.; Chen, J. Ultraviolet irradiation induces accumulation of isoflavonoids and transcription of genes of enzymes involved in the calycosin-7-O-β-d-glucoside pathway in *Astragalus membranaceus* Bge. var. *mongholicus* (Bge.) Hsiao. *Physiol. Plant.* **2011**, *142*, 265−273.

(9) Pan, H.; Wang, Y.; Zhang, Y.; Zhou, T.; Fang, C.; Nan, P.; Wang, X.; Li, X.; Wei, Y.; J, C. Phenylalanine ammonia lyase functions as a switch directly controlling the accumulation of calycosin and calycosin-7-O-b-D-glucoside in *Astragalus membranaceus* var. *mongholicus* plants. *J. Exp. Bot.* **2008**, *59*, 3027−3037.

(10) Kwon, H. J.; Hwang, J.; Lee, S. K.; Park, Y. D. Astragaloside content in the periderm, cortex, and xylem of *Astragalus membranaceus* root. *J. Nat. Med.* **2013**, *67*, 850−855.

(11) Lai, P. K.; Chan, J. Y.; Cheng, L.; Lau, C. P.; Han, S. Q.; Leung, P. C.; Fung, K. P.; Lau, C. B. Isolation of anti-inflammatory fractions and compounds from the root of *Astragalus membranaceus*. *Phytother. Res.* **2012**, *27*, 581−587.

(12) Han, L.; Chen, K. J. Progress of experimental pharmacologic study on the effect of *Astragalus* on the cardiac vascular system. *Chin. J. Integr. Med.* **2000**, *20*, 234−237.

(13) Huang, C. L.; Lu, Y. P. Effect of *Astragalus* injection on insulin resistance in auxiliary treating patients with diabetes mellitus type 2. *Chin. J. Integr. Med.* **2003**, *23*, 779−780.

(14) Liu, Z. Q.; Li, Q. Z.; Qin, G. J. Effect of *Astragalus* injection on platelet function and plasma endothelin in patients with early stage diabetic nephropathy. *Chin. J. Integr. Med.* **2001**, *21*, 274−276.

(15) Fan, Y.; Wu, D. Z.; Gong, Y. Q.; Zhou, R. Y.; Hu, Z. B. Effects of calycosin on the impairment of barrier function induced by hypoxia in human umbilical vein endothelial cells. *Eur. J. Pharmacol.* **2003**, *481*, 33−40.

(16) Tang, D.; He, B.; Zheng, Z. G.; Wang, R. S.; Gu, F.; Duan, T. T.; Cheng, H. Q.; Zhu, Q. Inhibitory effects of two major isoflavonoids in *Radix Astragali* on high glucose-induced mesangial cells proliferation and AGEs-induced endothelial cells apoptosis. *Planta Med.* **2011**, *77*, 729−732.

(17) Chen, L.; Li, Z.; Tang, Y.; Cui, X.; Luo, R.; Guo, S.; Zheng, Y.; Huang, C. Isolation, identification and antiviral activities of metabolites of calycosin-7-O-β-D-glucopyranoside. *J. Pharm. Biomed. Anal.* **2011**, *56*, 382−389.

(18) Hirotani, M.; Zhou, Y.; Rut aTsutomu Furuya, H. Cycloartane triterpene glycosides from the hairy root cultures of *Astragalus membranaceus*. *Phytochemistry* **1994**, *37*, 1403−1407.

(19) Du, M.; Wu, X. J.; Ding, J.; Hu, Z. B.; White, K. N.; Branford-White, C. J. Astragaloside IV and polysaccharide production by hairy roots of *Astragalus membranaceus* in bioreactors. *Biotechnol. Lett.* **2003**, *25*, 1853−1856.

(20) Ionkova, I.; Momekov, G.; Proksch, P. Effects of cycloartane saponins from hairy roots of *Astragalus membranaceus* Bge., on human tumor cell targets. *Fitoterapia* **2010**, *81*, 447−451.

(21) Rischer, H.; Orešič, M.; Seppänen-Laakso, T.; Katajamaa, M.; Lammertyn, F.; Diaz, W. A.; Montagu, M. V.; Inzé, D.; Oksman-Caldentey, K. M.; Goossens, A. Gene-tometabolite networks for terpenoid indole alkaloid biosynthesis in *Catharanthus roseus* cells. *Proc. Natl. Acad. Sci. U.S.A.* **2006**, *103*, 5614−5619.

(22) Xu, H.; Park, N. I.; Li, X.; Kim, Y. K.; Lee, S. Y.; Park, S. U. Molecular cloning and characterization of phenylalanine ammonia-lyase, cinnamate 4-hydroxylase and genes involved in flavone biosynthesis in *Scutellaria baicalensis*. *Bioresour. Technol.* **2010**, *101*, 9715−9722.

(23) Liang, Y. S.; Kim, H. K.; Lefeber, A. W.; Erkelens, C.; Choi, Y. H.; Verpoorte, R. Identification of phenylpropanoids in methyl jasmonate treated *Brassica rapa* leaves using two-dimensional nuclear magnetic resonance spectroscopy. *J. Chromatogr. A* **2006**, *1112*, 148−155.

(24) Alagna, F.; D'Agostino, N.; Torchia, L.; Servili, M.; Rao, R.; Pietrella, M.; Giuliano, G.; Chiusano, M. L.; Baldoni, L.; Perrotta, G. Comparative 454 pyrosequencing of transcripts from two olive genotypes during fruit development. *BMC Genomics* **2009**, *10*, No. 399.

(25) Barakat, A.; DiLoreto, D. S.; Zhang, Y.; Smith, C.; Baier, K.; Powell, W. A.; Wheeler, N.; Sederoff, R.; Carlson, J. E. Comparison of the transcriptomes of American chestnut (*Castanea dentata*) and Chinese chestnut (*Castanea mollissima*) in response to the chestnut blight infection. *BMC Plant Biol.* **2009**, *9*, No. 51.

(26) Shi, C. Y.; Yang, H.; Wei, C. L.; Yu, O.; Zhang, Z. Z.; Jiang, C. J.; Sun, J.; Li, Y. Y.; Chen, Q.; Xia, T.; Wan, X. C. Deep sequencing of the *Camellia sinensis* transcriptome revealed candidate genes for major metabolic pathways of tea-specific compounds. *BMC Genomics* **2011**, *12*, No. 131.

(27) Pérez-de-Castro, A. M.; Vilanova, S.; Cañizares, J.; Pascual, L.; Blanca, J. M.; Díez, M. J.; Prohens, J.; Picó, B. Application of genomic tools in plant breeding. *Curr. Genomics* **2012**, *13*, 179−195.

(28) Li, P.; Ponnala, L.; Gandotra, N.; Wang, L.; Si, Y.; Tausta, S. L.; Kebrom, T. H.; Provart, N.; Patel, R.; Myers, C. R.; Reidel, E. J.; Turgeon, R.; Liu, P.; Sun, Q.; Nelson, T.; Brutnell, T. P. The developmental dynamics of the maize leaf transcriptome. *Nat. Genet.* **2010**, *42*, 1060−1067.

(29) Severin, A. J.; Woody, J. L.; Bolon, Y. T.; Joseph, B.; Diers, B. W.; Farmer, A. D.; Muehlbauer, G. J.; Nelson, R. T.; Grant, D.; Specht, J. E.; Graham, M. A.; Cannon, S. B.; May, G. D.; Vance, C. P.; Shoemaker, R. C. RNA-Seq Atlas of Glycine max: A guide to the soybean transcriptome. *BMC Plant Biol.* **2010**, *10*, No. 160.

(30) Edwards, K.; Johnstone, C.; Thompson, C. A simple and rapid method for the preparation of plant genomic DNA for PCR analysis. *Nucleic Acids Res.* **1991**, *19*, 1349.

(31) Schulz, M. H.; Zerbino, D. R.; Vingron, M.; Birney, E. Oases: Robust de novo RNAseq assembly across the dynamic range of expression levels. *Bioinformatics* **2012**, *28*, 1086−1092.

(32) Anders, S.; Huber, W. Differential expression analysis for sequence count data. *Genome Biol.* **2010**, *11*, No. R106.

(33) Tuan, P. A.; Thwe, A. A.; Kim, Y. B.; Kim, J. K.; Kim, S. J.; Lee, S.; Chung, S. O.; Park, S. U. Effects of white, blue, and red light-emitting diodes on carotenoid biosynthetic gene expression levels and carotenoid accumulation in sprouts of tartary buckwheat (Fagopyrum tataricum Gaertn.). *J. Agric. Food Chem.* **2013**, *61*, 12356−12361.

(34) Thwe, A. A.; Mai, N. T. T.; Li, X.; Kim, Y.; Kim, Y. B.; Uddin, M. R.; Kim, Y. S.; Bae, H.; Kim, H. H.; Lee, M. Y.; Park, S. U. Production of astragaloside and flavones from adventitious root cultures of *Astragalus membranaceus* var *mongholicus*. *Plant Omics J.* **2012**, *5* (5), 466−470.

(35) Pan, H.; Fang, C.; Zhou, T.; Wang, Q.; Chen, J. Accumulation of calycosin and its 7-O-beta-D-glucoside and related gene expression in seedlings of *Astragalus membranaceus* Bge. var. *mongholicus* (Bge.)

DOI: 10.1021/acs.jafc.5b01822
J. Agric. Food Chem. 2015, 63, 6231−6240

Hsiao induced by low temperature stress. *Plant Cell Rep.* **2007**, *26*, 1111−1120.
(36) Palazon, J.; Cusido Rosa, M.; Bonfill, M.; Mallol, A.; Moyano, E.; Morales, C.; Pinol, M. T. Elicitation of different Panax ginseng transformed root phenotypes for an improved ginsenoside production. *Plant Physiol. Biochem.* **2003**, *41*, 1019−1025.
(37) Komaraiah, P.; Reddy, G. V.; Reddy, P. S.; Raghavendra, A. S.; Ramakrishna, S. V.; Reddanna, P. Enhanced production of antimicrobial sesquiterpenes and lipoxygenase metabolites in elicitor-treated hairy root cultures of *Solanum tuberosum*. *Biotechnol. Lett.* **2003**, *25*, 593−597.
(38) Hayashi, H.; Huang, P.; Inoue, K. Up-regulation of soyasaponin biosynthesis by methyl jasmonate in cultured cells of *Glycyrrhiza glabra*. *Plant Cell Physiol.* **2003**, *44*, 404−411.
(39) Singh, K.; Foley, R. C.; Oñate-Sánchez, L. Transcription factors in plant defense and stress responses. *Curr. Opin. Plant Biol.* **2002**, *5*, 430−436.
(40) Glazebrook, J. Genes controlling expression of defense responses in *Arabidopsis* - 2001 status. *Curr. Opin. Plant Biol.* **2001**, *4*, 301−308.
(41) Georgiev, M. I.; Pavlov, A. I.; Bley, T. Hairy root type plant in vitro systems as sources of bioactive substances. *Appl. Microbiol. Biotechnol.* **2007**, *74*, 1175−1185.
(42) Srivastava, S.; Srivastava, A. K. Hairy root culture for mass-production of high value secondary metabolites. *Crit. Rev. Biotechnol.* **2007**, *27*, 29−43.
(43) Yonekura-Sakakibara, K.; Fukushima, A.; Nakabayashi, R.; Hanada, K.; Matsuda, F.; Sugawara, S.; Inoue, E.; Kuromori, T.; Ito, T.; Shinozaki, K.; Wangwattana, B.; Yamazaki, M.; K, S. Two glycosyltransferases involved in anthocyanin modification delineated by transcriptome independent component analysis in *Arabidopsis thaliana*. *Plant J.* **2012**, *69*, 154−167.
(44) Miettinen, K.; Dong, L.; Navrot, N.; Schneider, T.; Burlat, V.; Pollier, J.; Woittiez, L.; van der Krol, S.; Lugan, R.; Ilc, T.; Verpoorte, R.; Oksman-Caldentey, K. M.; Martinoia, E.; Bouwmeester, H.; Goossens, A.; Memelink, J.; Werck-Reichhart, D. The seco-iridoid pathway from Catharanthus roseus. *Nat. Commun.* **2014**, *5*, No. 3606.

DOI: 10.1021/acs.jafc.5b01822
J. Agric. Food Chem. 2015, 63, 6231−6240

Table 1. Apparent Amylose Content, Crystallinity of Native Rice Starches, and Weight-Based Amounts of Debranched Rice Starches[a]

code	cultivar	AAC (%)	crystallinity (%)	FrI (%)	FrII (%)	FrIIa (%)	FrIIb (%)
BP011	Youzaonuo	0.8^{h}	45.5^{a}	0.5^{f}	99.5^{a}	70.7^{a}	28.8^{a}
BP597	Lishuinuo	0.1^{h}	36.8^{ef}	0.2^{f}	99.8^{a}	69.2^{a}	30.6^{a}
BP601	Xiangnuo	0.1^{h}	42.9^{b}	1.5^{f}	98.5^{a}	69.9^{a}	28.6^{a}
BP005	Zhefu 504	14.6^{g}	41.0^{c}	16.8^{e}	83.2^{b}	58.0^{bc}	25.2^{b}
BP025	Ce 482	18.3^{e}	36.0^{ef}	18.2^{cd}	81.8^{b}	59.2^{b}	22.6^{c}
BP033	93−11	17.3^{f}	34.2^{gh}	19.7^{c}	80.3^{b}	58.1^{bc}	22.2^{c}
BP050	Xiushui 11	17.8^{ef}	34.7^{fg}	17.9^{d}	82.1^{b}	61.1^{b}	21.0^{c}
BP605	Zhonghua 11	17.4^{f}	37.3^{de}	16.7^{e}	83.3^{b}	59.7^{b}	23.6^{b}
BP015	Lemont	21.6^{d}	38.0^{de}	22.6^{b}	77.4^{c}	56.6^{c}	20.8^{c}
BP047	IR64	21.0^{d}	38.3^{de}	20.9^{c}	79.1^{b}	52.6^{e}	26.5^{a}
BP003	Jiayu 293	24.9^{c}	42.0^{bc}	25.6^{a}	74.4^{d}	56.6^{c}	17.8^{d}
BP028	Zhenshan B	27.7^{b}	37.9^{de}	20.9^{c}	79.1^{b}	56.4^{c}	22.7^{c}
BP578	Zaiyeqing 8	28.7^{a}	39.2^{cd}	23.4^{b}	76.6^{c}	54.8^{d}	21.8^{c}
BP628	LongB	28.1^{ab}	32.3^{h}	24.6^{ab}	75.4^{c}	53.7^{d}	21.7^{c}

[a]AAC and crystallinity data were taken from our previous report.[15] Values in the same column with different superscripts are significantly different ($p < 0.05$).

On the basis of the above investigations, the digestive properties of starch were influenced by both amylose content and amylopectin fine structure. However, the concerted interplay or contributions of amylose and amylopectin fine structures are not completely understood.

Genetic investigations into the mechanisms underlying the formation of SDS and RS content in rice starches are scarce. Some starch mutants such as *amylose extender*, in which the starch branching enzyme IIb (BEIIb) gene is defective, displayed high RS.[10] For a *japonica* high RS mutant "Jiangtangdao 1" with an RS value of 11.67%, BEIIb was found to be the causal gene for the elevated RS content.[11] For another high amylose mutant in *japonica* background (Goami 2), BEIIb was not the causal gene,[12] whereas the genetic controls for some other high RS mutants in *indica* background are still unknown.[13] Low glycemic index (GI) food is able to assist in the management or prevention of type II diabetes, a major chronic disease in developing countries where rice is the staple food. In a study of 235 varieties, the *Waxy* gene was the major gene associated with GI.[14] However, genetic control of the naturally occurring variations in SDS and RS contents in rice starch has not been reported.

To deepen the understanding of the "genetics−structure−functionality" relationships of rice starch, an investigation of diverse rice starch samples with different amylose contents and similar amylopectin fine structures or similar amylose contents (for example, waxy rice) and different amylopectin fine structure combinations is required. Previously, we examined 14 rice cultivars varying in the combination of AAC and gelatinization temperatures for their physicochemical and functional properties.[15] In this study, the same series of rice starch samples were analyzed for starch structure and digestibility. The objectives were (i) to determine the contribution of amylose content and amylopectin fine structure to the in vitro digestion properties of the selected rice starches and (ii) to delve into the genetic contribution of the starch synthesis related genes (SSRGs) to the starch structure and functional properties.

MATERIALS AND METHODS

Materials. Fourteen rice cultivars were selected in the current study and included three waxy (Youzaonuo, Lishuinuo, and Xiangnuo) and eleven normal (Zhefu 504, Ce 482, 93−11, Xiushui 11, Zhonghua 11, Lemont, IR64, Jiayu 293, Zhenshan B, Zaiyeqing 8, and LongB) types as described in a previous report (Table 1).[15] Sample preparation and starch isolation procedures have been previously described.

In Vitro Starch Digestibility. Samples of the starch fraction (550 mg, dry weight basis) were weighed in a screw-capped tube and heated in 10 mL of distilled water for 20 min with frequent mixing. Following this, 15 glass beads (0.5 mm diameter), guar gum (50 mg), and 10 mL of sodium acetate buffer (0.25 M, pH 5.2) were added to each tube. The tubes were then incubated with pancreatic α-amylase (50 units) and amyloglucosidase (35 units) at 37 °C in a shaking water bath. After 20 and 120 min of incubation, the hydrolysates (0.5 mL) were transferred to 20 mL of 80% ethanol to stop the reaction. The amount of released glucose was determined using a glucose oxidase assay kit (Megazyme, Bray, Co. Wicklow, Ireland). The percentages of glucose after 20 (SD_{20}) and 120 (SD_{120}) min incubations were calculated using a glucose standard curve to determine the percent starch digested. The contents of rapidly digestible starch (RDS), slowly digestible starch (SDS), and resistant starch (RS) in rice starch samples were determined according to a previous report.[1]

Gel-Permeation Chromatography (GPC). Rice starch (~3.5 mg) was dissolved in 100 μL of dimethyl sulfoxide (DMSO) with constant stirring overnight. Hot Milli-Q water (800 μL) and 100 μL of 0.1 M NaAc buffer (pH 4.5) were added to the starch−DMSO solution. Isoamylase (1 μL, from *Pseudomonas* sp., 1000 U/mL, EC 3.2.1.68, Megazyme, Bray, Co. Wicklow, Ireland) and 1 μL of pullulanase (from *Klebsiella planticola*, 700 U/mL, EC 3.2.1.41, Megazyme, Bray, Co. Wicklow, Ireland) were added to start the reaction, which was conducted overnight with slow and constant stirring at room temperature. A NaOH solution (100 μL 5 M) was added to the debranched starch sample, and the mixture was centrifuged and then analyzed by gel-permeation chromatography (GPC) on a column (1 × 90 cm) of Sepharose CL 6B (Pharmacia, Uppsala, Sweden) with 0.5 M NaOH as an eluent at a rate of 0.5 mL/min. The column was calibrated by using dextrans with known molecular weights. The carbohydrate content of the collected fractions (0.5 mL) was determined with phenol−sulfuric acid reagent.[16]

Amylopectin Fractionation and Chain-Length Distribution Determination. Amylopectin fractionation followed previous methods based on butanol−alcohol precipitation.[17,18] Purified amylopectin (9 mg) was dissolved in 450 μL of 100% DMSO with constant stirring overnight. The solution was then diluted with 2250 μL of Milli-Q water, and 300 μL of 0.1 M sodium acetate buffer (pH 4.5), 1 μL of isoamylase (from *Pseudomonas* sp., 1000 U/mL, EC 3.2.1.68, Megazyme, Bray, Co. Wicklow, Ireland), and 1 μL of pullulanase (from *Klebsiella planticola*, 700 U/mL, EC 3.2.1.41, Megazyme, Bray,

DOI: 10.1021/acs.jafc.5b02143
J. Agric. Food Chem. 2015, 63, 6241−6248

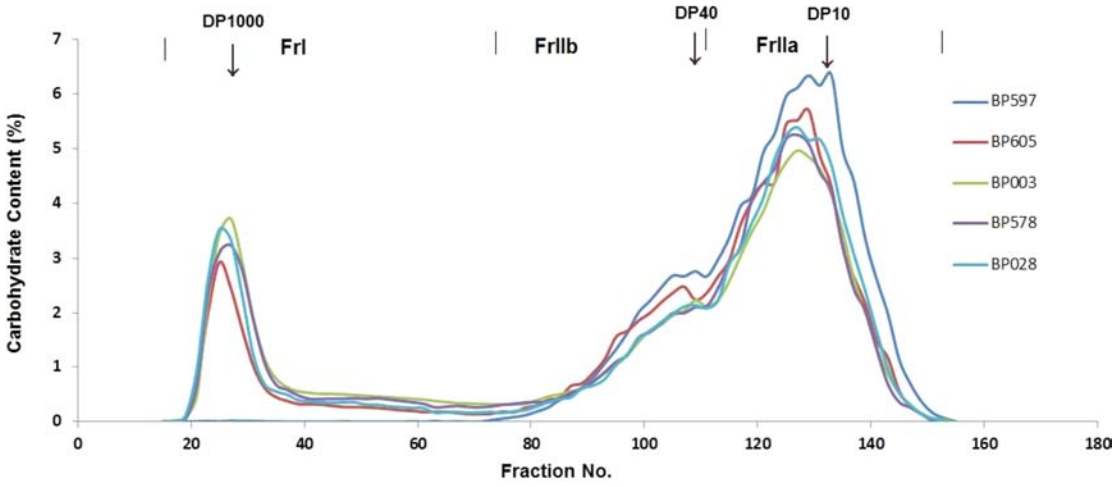

Figure 1. Molecular weight distributions on Sepharose CL 6B of debranched total starches from selected rice cultivars.

Table 2. Weight-Based Chain-Length Distribution and Average Chain Length of Debranched Amylopectins from Different Rice Starches[a]

	weight-based chain-length distribution (%)				
code	fa (DP 6−12)	fb_1 (DP 13−24)	fb_2 (DP 25−36)	fb_3 (DP > 36)	CL_{ap} (DP)
BP011	18.07^{e}	52.94^{bc}	14.05^{a}	14.93^{cd}	17.61^{a}
BP597	22.26^{b}	47.11^{e}	13.45^{ab}	17.18^{b}	17.01^{bc}
BP601	19.58^{c}	51.38^{c}	13.12^{bc}	15.92^{bc}	17.38^{ab}
BP005	18.18^{e}	51.59^{bc}	13.00^{bc}	17.23^{b}	17.76^{a}
BP025	22.48^{b}	49.84^{cd}	13.82^{a}	13.86^{e}	16.63^{cd}
BP033	24.71^{a}	48.51^{d}	13.26^{bc}	13.52^{e}	16.34^{d}
BP050	23.03^{ab}	48.73^{d}	13.39^{bc}	14.86^{cd}	16.60^{cd}
BP605	22.28^{b}	49.34^{d}	13.59^{ab}	14.79^{cd}	16.73^{cd}
BP015	20.06^{cd}	53.52^{b}	13.21^{bc}	13.21^{e}	17.06^{bc}
BP047	21.55^{b}	45.01^{f}	12.72^{c}	20.72^{a}	17.54^{a}
BP003	20.46^{cd}	55.67^{a}	13.07^{bc}	10.80^{f}	16.71^{cd}
BP028	18.98^{de}	52.37^{bc}	13.46^{ab}	15.20^{bcd}	17.44^{ab}
BP578	19.44^{de}	52.04^{bc}	13.11^{bc}	15.40^{bcd}	17.31^{ab}
BP628	20.11^{cd}	51.17^{c}	13.00^{bc}	15.72^{bcd}	17.21^{ab}

[a]Values in the same column with different superscripts are significantly different ($p < 0.05$).

Co. Wicklow, Ireland) were added. The debranching reaction was conducted at room temperature with constant stirring overnight and was terminated by heating. The sample was centrifuged and filtered (pore size 0.45 μm) before injection into the HPLC system.

The chain length distributions of debranched samples were analyzed with a method modified from a previous report using a high-performance anion-exchange chromatography (HPAEC) system (Dionex ICS-5000+, Sunnyvale, CA) coupled with a BioLC gradient pump and a pulsed amperometric detector (PAD).[18] The PAD signal was recorded by Chromeleon software (Version 6.8) and corrected to carbohydrate content.[19] Prior to loading of the sample, the column (250 mm × 4 mm, Carbo-Pac PA-100 with a guard column) was eluted at a rate of 1 mL/min with 150 mM NaOH for 20 min and then with a mixture of 150 mM NaOH (eluent A, 93%) and 150 mM NaOH containing 1 M NaOAc (eluent B, 7%) for 20 min. The elution gradient with a rate of 1 mL/min was as follows: from 0 to 1.3 min, 93% eluent A; from 1.3 to 10 min, eluent A changed from 93 to 82% linearly; from 10 to 19 min, from 82 to 78%; from 19 to 111 min, from 78 to 50%; from 111 to 113 min, from 50 to 93% (after which it returned to the starting mixture). The sample was injected during the initial 1.2−1.3 min.

Physicochemical Properties. The parameters of the physicochemical properties used in the current study were described in our previous report.[15]

Association Test. Since all of the 14 accessions were selected from our association panel,[20−22] the genotypes of all the SSRGs (Supplementary Table 1 in the Supporting Information) as well as other markers (i.e., microsatellites) were used in this study, to test the association among SSRGs, starch structure, and functionality (digestive properties). Due to the small amount of samples, the analysis of variance (ANOVA) and the kinship coefficient (K) models were performed with TASSEL Version 2.1 software. The P value determining whether a marker is associated with a trait was set at $P < 0.05$.

Statistical Analysis. All analyses were determined in triplicate. Statistical analysis was conducted using SigmaPlot 9.01 integrated with SigmaStat 3.11 (Systat Software, CA). The results were subjected to one-way analysis of variance (ANOVA) and Tukey's test to determine significant differences.

RESULTS AND DISCUSSION

Molecular Structure Characterization of Rice Starch. The debranched total starch samples were analyzed by gel-permeation chromatography (GPC) with Sepharose CL 6B to determine the molecular size distribution profiles. The typical profiles from selected starch samples are shown in Figure 1. Two major peaks were identified: the fraction from the first peak area (FrI) is amylose, while the fraction of the second

DOI: 10.1021/acs.jafc.5b02143
J. Agric. Food Chem. 2015, 63, 6241−6248

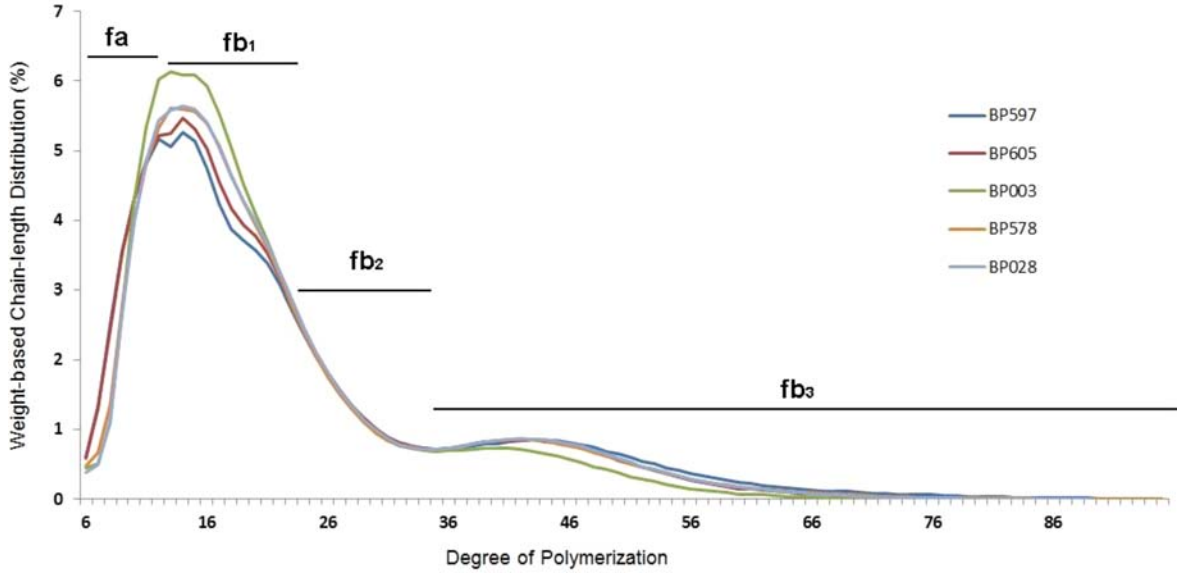

Figure 2. Chain-length profiles obtained by HPAEC of amylopectins from selected rice cultivars.

peak area (FrII) is amylopectin. FrII could be further divided into FrIIb and FrIIa, which are long- and short-unit chains of amylopectin, respectively (Figure 1). As expected, the percentage of FrI from waxy rice starch was low (0.2−1.5%), while nonwaxy rice starch had 16.7−25.6% FrI. The content of FrI followed the general trend of AAC as determined by the iodine reagent method (Table 1). Since the amylose contents obtained from Sepharose CL 2B (before debranching) and 6B (debranched) differ,[23] caution should be taken when comparing the AAC values obtained from the different methods.

Purified amylopectin debranched by enzymes was employed to determine the chain-length profile. The parameters of chain-length distribution and average chain length of amylopectin are summarized in Table 2, and a comparison of amylopectin chain-length distribution profiles from selected rice starch samples is presented in Figure 2. The weight-based chain-length distribution of debranched amylopectin was grouped into four fractions, fa (DP 6−12), fb_1 (DP 13−24), fb_2 (DP 25−36), and fb_3 (DP > 36), according to the division suggested by a previous report.[24] The percentages of fa, fb_1, fb_2, and fb_3 were 18.07%−24.71%, 45.01%−55.67%, 12.72%−14.05%, and 10.80%−20.72%, respectively. The average chain length in rice amylopectin was DP 16.34−17.76, which was in agreement with a previous report on waxy rice;[25] however, these values were lower than those in a recent report describing the average chain lengths of six waxy rice starches, which ranged from DP 21.9 to 24.3.[9] In another study, the average chain length of four waxy rice starches was from DP 20.0 to 20.7.[26] The results showed that amylopectin chain-length profiles from 3 waxy and 11 normal types were similar, which indicated that the amylopectin fine structure was independent of the amylose content. This result challenged a conclusion made in a previous report that amylose content was significantly correlated with amylopectin average chain length and the ratio of long chains to short chains.[27]

Amylopectin chains in high-amylose and intermediate-amylose rice were shown to be longer than those in waxy and low-amylose rice when four rice cultivars were compared;[7] however, when more cultivars were included as in this study, the trend was not clear (Table 2). Generally, waxy and low-amylose (BP005) rice starches had a higher degree of crystallinity than normal types. However, waxy type BP597 had a much lower degree of crystallinity. Notably, fb_1 (DP 13−24) chains in BP597 were lower and fb_3 (DP > 36) were higher than those in the other two waxy types (Table 2), indicating that fb_1 chains contributed to the formation of crystallinity while fb_3 hindered this formation. Normal type BP003 had a higher degree of crystallinity than other normal types, and the highest proportion of fb_1 chains and lowest proportion of fb_3 chains was observed in BP003 (Table 2), which further supported the roles of fb_1 and fb_3 chains in starch crystallinity. It has also been suggested that fb_1 chains form double helices that span the entire length of crystalline regions.[28]

In Vitro Digestibility of Rice Starch. The in vitro methodology for determining nutritional starch fractions was developed by Englyst and co-workers[1] and describes the likely rate and extent of glucose release from foods in the small intestine; it has been verified to match the mean proportion of starch recovered in ileostomy studies.[29,30] These nutritional fractions determine the bioavailability and likely physiological fate of the carbohydrate when it is consumed.[31]

The nutritional fractions of rice starch, including rapidly digestible starch (RDS), slowly digestible starch (SDS), and resistant starch (RS), are presented in Table 3. The RDS content of rice starch ranged from 78.5 to 87.5%. The lowest and highest RDS contents were observed in BP028 and BP011, respectively. Waxy rice starch types had relatively higher RDS content than normal types. SDS content from rice starch samples ranged from 1.2 to 6.0%, with the lowest content observed in BP011 and the highest in BP005. RS content varied from 10.1% (BP005) to 18.0% (BP578) (Table 3). It has been proposed that combining the fractions of SDS and RS was useful for comparison of starch types,[32] and normal rice starch showed relatively higher fractions of SDS and RS than waxy types; this phenomenon was also observed in the current study. Rice starch digestion properties were previously shown to be affected by amylopectin fine structure,[5] starch fine molecular structure, and crystalline structure.[9] RS has been correlated positively with amylose content in rice starch, while SDS decreased as amylose content increased.[7] RDS content of rice

DOI: 10.1021/acs.jafc.5b02143
J. Agric. Food Chem. 2015, 63, 6241−6248

Table 3. Digestion Properties of Starches from Selected 14 Rice Cultivars[a]

code	SD_{20} (%)	SD_{120} (%)	RDS (%)	SDS (%)	RS (%)
BP011	87.5 ± 1.4	88.7 ± 1.2	87.5^{a}	1.2^{c}	11.3^{e}
BP597	80.0 ± 0.9	83.8 ± 1.4	80.0^{ef}	3.8^{b}	16.2^{bc}
BP601	85.8 ± 0.6	89.4 ± 1.4	85.8^{ab}	3.7^{b}	10.6^{e}
BP005	84.0 ± 1.0	90.0 ± 0.9	84.0^{bc}	6.0^{a}	10.1^{e}
BP025	80.6 ± 0.9	83.5 ± 1.0	80.6^{e}	2.9^{bc}	16.5^{abc}
BP033	81.5 ± 1.6	84.8 ± 1.0	81.5^{d}	3.4^{b}	15.2^{c}
BP050	83.1 ± 1.0	86.0 ± 1.4	83.1^{c}	3.0^{bc}	14.0^{d}
BP605	85.5 ± 0.8	89.4 ± 0.8	85.5^{b}	3.9^{b}	10.6^{e}
BP015	82.8 ± 1.2	86.1 ± 1.1	82.8^{cd}	3.3^{b}	13.9^{d}
BP047	81.2 ± 1.0	84.6 ± 1.4	81.2^{de}	3.4^{b}	15.4^{c}
BP003	79.5 ± 0.8	82.8 ± 0.5	79.5^{e}	3.4^{b}	17.2^{ab}
BP028	78.5 ± 1.1	82.5 ± 0.6	78.5^{f}	4.1^{ab}	17.5^{ab}
BP578	80.6 ± 1.0	82.0 ± 0.6	80.6^{e}	1.4^{c}	18.0^{a}
BP628	80.4 ± 1.1	83.3 ± 0.6	80.4^{ef}	2.9^{bc}	16.7^{abc}

[a]Values in the same column with different superscripts are significantly different ($p < 0.05$).

starches decreased with increasing amylose content,[6] and waxy starches showed greater enzyme digestion than normal types.[33] Higher RDS content in waxy rice starch was attributed to the lower proportion of long chains in amylopectin (DP ≥ 37), the molecular weight in the molecular structure, the onset temperature of gelatinization and crystallinity, and the higher proportion of short A (DP 6−12) chains.[9]

Relating Starch Structure to Functional and Digestion Properties. Starch physicochemical and functional parameters including AAC, starch crystallinity, pasting, and thermal properties were adapted from our previous report.[15] The fraction of short chains (DP 6−12), fa, was negatively correlated with the degree of crystallinity ($r = -0.67$, $p < 0.01$) (Table 4). AAC was previously shown to be negatively correlated with the degree of crystallinity ($r = -0.62$, $p < 0.001$).[15] However, a higher proportion of short chains (DP 10−13) resulted in a higher degree of crystallinity and the degree of starch crystallinity decreased with increasing amylose content in a previous report.[34] Waxy types BP011 and BP601 and normal types BP028 and BP578 exhibited similar amylopectin chain-length profiles regardless of amylose content (Table 2). The waxy types had a higher degree of crystallinity than the normal. Waxy type BP597 had lower proportion of fb_1 chains and a relatively higher proportion of fb_3 chains than the other two waxy types; these differences in amylopectin structure contributed to a lower degree of crystallinity in BP597. On the basis of the above, the starch crystallinity was not affected by amylose content or amylopectin fine structure alone but by the interplay of amylose and amylopectin fine structure.

FrI consisted of debranched amylose and represented the amylose content; thus, it is not surprising that AAC showed a significant positive correlation with FrI ($r = 0.97$, $p < 0.001$) (Table 4). Breakdown viscosity (BD) was positively correlated with the amout of short chains (fa) but negatively correlated with the amount of fb_1 chains. A previous study also indicated that rice starches with higher proportions of fb_1 chains seemingly had lower BD values, whereas those with higher proportions of fa chains had higher BD values.[35] These observations were generally consistent with our current results. No significant correlation between BD and FrI was observed; however, FrI was positively correlated with CPV ($r = 0.78$, $p < 0.001$) and SB ($r = 0.82$, $p < 0.001$) (Table 4). When the starch paste was cooled, aggregation of leached amylose resulted in a strong gel due to the formation of hydrogen bonds from free amylose, which explained the current observed results, and similar observations were reported previously in rice starches with different amylose contents.[6] Gelatinization parameters, including T_o, T_p, and ΔH, had negative correlations with the proportion of short fa (DP 6−12) chains; fa chains were also negatively correlated with RVA pasting temperature ($r = -0.84$, $p < 0.001$) (Table 4). The average chain length of amylopectin (CL_{ap}) was found to be positively correlated with the degree of crystallinity, pasting, and gelatinization temperatures.

Pearson correlation coefficients between rice starch digestion properties and starch structural/functional parameters are presented in Table 5. RDS was negatively correlated with FrI ($r = -0.56$, $p < 0.05$) and AAC ($r = -0.62$, $p < 0.05$), respectively. RDS was positively correlated with amylose content in four lentil starch samples with a narrow range of amylose content from 30.6 to 33.9%.[36] Almost no correlation was found between RDS and amylose content when four rice cultivars with an amylose content of 1.7−55% were investigated.[7] However, RDS was negatively correlated with the AAC when four commercial rice varieties with amylose contents of 4.2−27.2% were studied.[6] The contradictory relationships between AAC and RDS content are because the effects of amylopectin fine structure were not considered.

RDS was positively correlated with the proportion of short chains, FrIIa ($r = 0.56$, $p < 0.05$) (Table 5). The lower proportion of longer branch chains (DP ≥ 37) and higher proportion of short A chains were observed to contribute to higher RDS content.[9] Previously, RDS was shown to be positively correlated with the proportion of DP 6−12 saccharides and negatively correlated with the proportion of DP 13−24 saccharides.[6] However, no significant correlation between amylopectin chain-length distributions and RDS was

Table 4. Correlations between Starch Structural Parameters and Functional Properties[a]

	AAC	crystallinity	BD	CPV	SB	P_{temp}	T_o	T_p	ΔH
fa	0.02	−0.67*	0.58*	−0.20	−0.41	−0.84***	−0.77**	−0.77**	−0.56*
fb_1	0.20	0.48	−0.54*	0.35	0.55*	0.63*	0.45	0.38	0.04
fb_2	−0.40	0.16	0.43	−0.54*	−0.50	−0.21	0.02	−0.03	0.11
fb_3	−0.21	0.03	0.09	−0.16	−0.23	−0.01	0.12	0.21	0.43
CL_{ap}	−0.15	0.55*	−0.43	0.07	0.20	0.69**	0.72**	0.77**	0.73**
FrI	0.97***	−0.46	−0.19	0.78***	0.82***	−0.02	−0.23	−0.30	−0.42
FrIIa	−0.94***	0.51	0.15	−0.76**	−0.59*	0.05	0.22	0.27	0.32
FrIIb	−0.85***	0.31	0.21	−0.69**	−0.63*	0.03	0.20	0.30	0.52

[a]Correlations are significant at (*) $P < 0.05$, (**) $P < 0.01$, and (***) $P < 0.001$, respectively.

DOI: 10.1021/acs.jafc.5b02143
J. Agric. Food Chem. 2015, 63, 6241−6248

Table 5. Correlations between Rice Starch Digestion Properties and Structural/Functional Parameters[a]

	RDS	SDS	RS
FrI	−0.56*	0.06	0.51
FrIIa	0.56*	−0.12	−0.49
FrIIb	0.46	0.04	−0.46
fa	−0.23	0.01	0.21
fb_1	0.05	−0.13	0.01
fb_2	0.34	−0.36	−0.17
fb_3	0.08	0.21	−0.17
CL_{ap}	0.23	0.10	−0.26
crystallinity	0.51	−0.09	−0.44
AAC	−0.62*	−0.03	0.60*
SP	0.78**	−0.13	−0.67*
PV	−0.46	0.40	0.26
BD	−0.04	0.09	−0.01
CPV	−0.66**	0.13	0.58*
SB	−0.38	−0.08	0.40
T_o	0.28	−0.11	−0.22
T_p	0.36	−0.06	−0.31
ΔH	0.19	−0.08	−0.15
HD	−0.75**	−0.17	0.76**
ADH	0.63*	0.19	−0.66*

[a]Correlations are significant at (*) $P < 0.05$ and (**) $P < 0.01$, respectively.

identified (Table 5). RVA setback was positively correlated with RDS when rice starch cultivars with similar amylose content were investigated.[5] This correlation was not observed in the current study, indicating that RVA breakdown as a screening tool for selection of rice cultivars with low RDS should be used with caution. In a previous report, SDS decreased as amylose content increased and the correlation between SDS and amylose content was high.[7] The content of combined SDS and RS in three waxy rice starches varied from 12.5% to 20.0%, indicating that amylopectin fine structure influenced the SDS/RS content. Normal starch types showed a significantly higher content of combined SDS and RS content than waxy starch types BP011 and BP601 (Table 3), suggesting that amylose increased the content of combined SDS and RS in rice starches. Hence, the concerted influence of amylose content and amylopectin fine structure contributed to the SDS/RS contents in rice starch.

Relating SSRG Markers to Starch Structure and Functional Properties. Previous studies have shown that *Wx* and *SSIIa* genes are responsible for the genetic control of AAC and gelatinization temperature, respectively.[37−40] In this study, these two genes were also shown to be associated with AAC and gelatinization (thermal) properties (data not shown). We found that *SSIIa* was responsible for the degree of crystallinity, the average chain length of amylopectin (CL_{ap}), and the amount of fa chains in amylopectin (Table 6). This is simply because SSIIa elongates the short A and B_1 chains with a degree of polymerization (DP) <10 to form long B_1 chains of amylopectin,[41] and the amount of fa chains (DP 6−12) and crystallinity were negatively correlated with gelatinization temperature (Table 4). The amount of fb_1 was found to be controlled by *SSIIIa* (Table 6). The *SSIIIa* mutant showed a decrease in DP 6−9 and DP 16−19 chains and an increase in DP 10−15 and DP 20−25 chains.[42] The pattern of the changes in chain length distributions could be explained as the amount of fb_1 chains (DP12−24) controlled by SSIIIa, which

Table 6. Putative SSRG Markers in Relation to Starch Crystallinity, Structure and Functionality Revealed by ANOVA and Kinship (K) Models

			ANOVA model		K model	
trait	locus	Chr	P	R^2	P	R^2
crystallinity	*SSIIa*	6	0.0014	0.5867	0.0014	0.5853
CL_{ap}	*SSIVb*	5	0.0482	0.3099	0.0483	0.3092
	SSIIa	6	0.0051	0.493	0.0051	0.4921
Fa	*SSIIa*	6	0.0013	0.5911	0.0013	0.5893
Fb_1	*SSIIIa*	8	0.0263	0.3484	0.0263	0.3477
Fb_2	*AGPL1*	5	0.0217	0.3667		
	Wx	6			0.0508	0.2816
FrI	*AGPL1*	5	0.0048	0.4977	0.0048	0.4944
	Wx	6	0.0093	0.4434	0.0060	0.2747
FrII	*AGPL1*	5	0.0048	0.4977	0.0048	0.4944
	Wx	6	0.0093	0.4434	0.0060	0.2747
FrIIa	*AGPL1*	5	0.0064	0.4755	0.0038	0.193
	Wx	6	0.0055	0.4879	0.0054	0.4839
FrIIb	*AGPL1*	5	0.0230	0.3613	0.0231	0.3604
	Wx	6			0.0325	0.211
RDS	*ISA2*	5	0.0374	0.3374	0.0372	0.2917
	Wx	6	0.0300	0.3353	0.0301	0.3294
RS	*Wx*	6	0.0179	0.385	0.0179	0.3821

specifically elongates B_2−B_4 long chains of amylopectin.[42] The amount of fb_2 chains was controlled by the ADP-Glucose pyrophosphorylase L1 (*AGPL1*) gene, a gene in the first step of starch biosynthesis. However, in the Kinship (K) model, *Wx* gene was also detected for the amount of fb_2 with a little higher P value ($P = 0.0508$) (Table 6). A previous report showed that superlong chains of amylopectin was controlled by *Wx* gene;[43] it is not known whether GBSS1 encoded by *Wx* works on the chains of DP 24−36 (fb_2) to form superlong chains in amylopectin.

Wx gene was also associated with the amount of fraction from the first peak area (FrI), which is amylose, and the FrIIa, which are short unit chains of amylopectin. This is supported by the correlation results among AAC, FrI, and FrIIa. Both the amount of FrIIa and FrIIb were also related to the *AGPL1* gene on chromosome 5, which was not reported before.

For the RDS, two SSRGs, *Wx* and the starch debranching enzyme gene *isoamylase II* (*ISA2*), were detected. Amylose content was negatively correlated with RDS; thus, it is possible that RDS was detected to be controlled by *Wx*. The *ISA2* gene is responsible for amylopectin biosynthesis,[44] which indicated that the amylopectin structure may play a role in the formation of RDS. However, the function of ISA2 in amylopectin biosynthesis is not well understood and only its expression pattern during grain filling was available.[44] Although *BEIIb* mutants generally had higher RS contents than their counterpart parents, the naturally occurring variation in RS among diverse rice germplasm was controlled by *Wx* gene (Table 6) but not by *BEIIb*. This could be explained by the relationships between AAC and RS (Table 5) and was also supported by a previous study on the genetic control of GI.[14]

CONCLUSION

This is the first study delving into the "genetics−structure−function" relationships of rice starches. The functional properties of rice starches, i.e. digestion properties, were influenced by amylose and amylopectin fine structure to different extents. Rice starch crystallinity was negatively

DOI: 10.1021/acs.jafc.5b02143
J. Agric. Food Chem. 2015, 63, 6241−6248

correlated with the proportion of fa chains in amylopectin. AAC was negatively correlated with RDS content but positively correlated with RS content in rice starch. *SSIIa* gene controls the degree of crystallinity and the amount of fa chains of amylopectin. *SSIIIa* gene controls the amount of fb1 chains. *Wx* gene controls the amount of FrI, FrIIa, RDS, and RS. *ISA2* gene also controls the RDS, which may suggest that RDS was also affected by the amylopectin structure, although no correlation between them was found. However, it should be noted that this is an initial test of these relationships, and further studies involving large sets of rice accessions will provide more in-depth insight. An understanding of the relationships among genetics, starch structure, and functionalities will assist plant breeders and food processors in the design of new rice varieties oriented to functional foods.

■ ASSOCIATED CONTENT

Ⓢ Supporting Information

Supplementary Table 1, giving the genotypes of starch synthesis related gene markers in 14 rice accessions. The Supporting Information is available free of charge on the ACS Publications website at DOI: 10.1021/acs.jafc.5b02143.

■ AUTHOR INFORMATION

Corresponding Authors

*Z.S.: tel, +86-21-34206613; fax, +86-21-34206613; e-mail, springsui@gmail.com.

*J.B.: tel, +86-571-86971932; fax, +86-571-86971421; e-mail, jsbao@zju.edu.cn.

Notes

The authors declare no competing financial interest.

■ ACKNOWLEDGMENTS

This work was financially supported by the National Natural Science Foundation of China (31101225, 31301419) and the Department of Science and Technology, Zhejiang Province (2015C32055), Fundamental Research Funds for the Central Universities at ZJU (2012QNA6013), and a Hong Kong GRF award (17106314, to H.C.).

■ ABBREVIATIONS

AAC, apparent amylose content; CL_{ap}, average chain length of amylopectin; BD, breakdown viscosity; CPV, cool paste viscosity; DP, degree of polymerization; GPC, gel permeation chromatography; HPAEC, high-performance anion-exchange chromatography; HPSEC, high-performance size exclusion chromatography; P_{temp}, pasting temperature; PV, peak viscosity; RDS, rapidly digestible starch; RS, resistant starch; SB, setback viscosity; SDS, slowly digestible starch; T_o, onset temperature of gelatinization; T_p, peak temperature of gelatinization; ΔH, enthalpy of gelatinization; SP, swelling power; HD, hardness; ADH, adhesiveness

■ REFERENCES

(1) Englyst, H. N.; Kingman, S. M.; Cummings, J. H. Classification and measurement of nutritionally important starch fractions. *Eur. J. Clin. Nutr.* **1992**, *46*, S33−S50.

(2) Soral-Smietana, M.; Wronkowska, M.; Amarowicz, R. Health-promoting function of wheat or potato resistant starch preparations obtained by physico-biochemical process. In *Starch: Advances in Structure and Function*; Barsby, T. L., Donald, A. M., Frazier, P. J., Eds.; The Royal Society of Chemistry: Cambridge, U.K., 2001; pp 116−128.

(3) Lehmann, U.; Robin, F. Slowly digestible starch - its structure and health implications: a review. *Trends Food Sci. Technol.* **2007**, *18*, 346−355.

(4) Nugent, A. P. Health properties of resistant starch. *Nutr. Bull.* **2005**, *30*, 27−54.

(5) Benmoussa, M.; Moldenhauer, K. A. K.; Hamaker, B. R. Rice amylopectin fine structure variability affects starch digestion properties. *J. Agric. Food Chem.* **2007**, *55*, 1475−1479.

(6) Chung, H. J.; Liu, Q.; Lee, L.; Wei, D. Z. Relationship between the structure, physicochemical properties and *in vitro* digestibility of rice starches with different amylose contents. *Food Hydrocolloids* **2011**, *25*, 968−975.

(7) Zhu, L. J.; Liu, Q. Q.; Wilson, J. D.; Gu, M. H.; Shi, Y. C. Digestibility and physicochemical properties of rice (*Oryza sativa* L.) flours and starches differing in amylose content. *Carbohydr. Polym.* **2011**, *86*, 1751−1759.

(8) Syahariza, Z. A.; Sar, S.; Hasjim, J.; Tizzotti, M. J.; Gilbert, R. G. The importance of amylose and amylopectin fine structures for starch digestibility in cooked rice grains. *Food Chem.* **2013**, *136*, 742−749.

(9) You, S. Y.; Lim, S. T.; Lee, J. H.; Chung, H. J. Impact of molecular and crystalline structures on *in vitro* digestibility of waxy rice starches. *Carbohydr. Polym.* **2014**, *112*, 729−735.

(10) Dhital, S.; Butardo, V. M.; Jobling, S. A.; Gidley, M. J. Rice starch granule amylolysis - Differentiating effects of particle size, morphology, thermal properties and crystalline polymorph. *Carbohydr. Polym.* **2015**, *115*, 305−316.

(11) Yang, R.; Sun, C.; Bai, J.; Luo, Z.; Shi, B.; Zhang, J.; Yan, W.; Piao, Z. A putative gene *sbe3-rs* for resistant starch mutated from SBE3 for starch branching enzyme in rice (*Oryza sativa* L.). *PLoS One* **2012**, *7*, e43026.

(12) Butardo, V. M.; Daygon, V. D.; Colgrave, M. L.; Campbell, P. M.; Resurreccion, A.; Cuevas, R. P.; Jobling, S. A.; Tetlow, I.; Rahman, S.; Morell, M.; Fitzgerald, M. Biomolecular analyses of starch and starch granule proteins in the high-amylose rice mutant goami 2. *J. Agric. Food Chem.* **2012**, *60*, 11576−11585.

(13) Shu, X.; Jia, L.; Ye, H.; Li, C.; Wu, D. Slow digestion properties of rice different in resistant starch. *J. Agric. Food Chem.* **2009**, *57*, 7552−7559.

(14) Fitzgerald, M. A.; Rahman, S.; Resurreccion, A. P.; Concepcion, J.; Daygon, V. D.; Dipti, S. S.; Kabir, K. A.; Klingner, B.; Morell, M. K.; Bird, A. R. Identification of a major genetic determinant of glycaemic index in rice. *Rice* **2011**, *4*, 66−74.

(15) Kong, X. L.; Zhu, P.; Sui, Z. Q.; Bao, J. S. Physicochemical properties of starches from diverse rice cultivars varying in apparent amylose content and gelatinization temperature combinations. *Food Chem.* **2015**, *172*, 433−440.

(16) Dubois, M.; Gilles, K. A.; Hamilton, J. K.; Rebers, P. A.; Smith, F. Colorimetric method for determination of sugars and related substances. *Anal. Chem.* **1956**, *28*, 350−356.

(17) Klucinec, J. D.; Thompson, D. B. Fractionation of high-amylose maize starches by differential alcohol precipitation and chromatography of the fractions. *Cereal Chem.* **1998**, *75*, 887−896.

(18) Kong, X. L.; Bertoft, E.; Bao, J. S.; Corke, H. Molecular structure of amylopectin from amaranth starch and its effect on physicochemical properties. *Int. J. Biol. Macromol.* **2008**, *43*, 377−382.

(19) Koch, K.; Andersson, R.; Åman, P. Quantitative analysis of amylopectin unit chains by means of high-performance anion-exchange chromatography with pulsed amperometric detection. *J. Chromatogr. A* **1998**, *800*, 199−206.

(20) Jin, L.; Lu, Y.; Xiao, P.; Sun, M.; Corke, H.; Bao, J. Genetic diversity and population structure of a diverse set of rice germplasm for association mapping. *Theor. Appl. Genet.* **2010**, *121*, 475−487.

(21) Xu, F. F.; Zhang, G.; Tong, C.; Sun, X.; Corke, H.; Sun, M.; Bao, J. S. Association mapping of starch physicochemical properties with starch biosynthesizing genes in waxy rice (*Oryza sativa* L.). *J. Agric. Food Chem.* **2013**, *61*, 10110−10117.

(22) Yang, F.; Chen, Y. L.; Tong, C.; Huang, Y.; Xu, F. F.; Li, K. H.; Corke, H.; Sun, M.; Bao, J. S. Association mapping of starch

DOI: 10.1021/acs.jafc.5b02143
J. Agric. Food Chem. 2015, 63, 6241−6248

physicochemical properties with starch synthesis-related gene markers in nonwaxy rice (*Oryza sativa* L.). *Mol. Breed.* **2014**, *34*, 1747−1763.
(23) Zhu, F.; Bertoft, E.; Källman, A.; Myers, A. M.; Seetharaman, K. Molecular structure of starches from maize mutants deficient in starch synthase III. *J. Agric. Food Chem.* **2013**, *61*, 9899−9907.
(24) Hanashiro, I.; Abe, J.; Hizukuri, S. A periodic distribution of the chain length of amylopectin as revealed by high-performance anion-exchange chromatography. *Carbohydr. Res.* **1996**, *283*, 151−159.
(25) Bertoft, E.; Zhu, Q.; Andtfolk, H.; Jungner, M. Structural heterogeneity in waxy-rice starch. *Carbohydr. Polym.* **1999**, *38*, 349−359.
(26) Wang, Y. J.; Wang, L. Structures of four waxy rice starches in relation to thermal, pasting, and textural properties. *Cereal Chem.* **2002**, *79*, 252−256.
(27) Cheetham, N. W. H.; Tao, L. P. The effects of amylose content on amylose molecular size, and on the average chain length of amylopectin in maize starches. *Carbohydr. Polym.* **1997**, *33*, 251−261.
(28) Du, S. K.; Jiang, H. X.; Ai, Y. F.; Jane, J. L. Physicochemical properties and digestibility of common bean (*Phaseolus vulgaris* L.) starches. *Carbohydr. Polym.* **2014**, *108*, 200−205.
(29) Silvester, K. R.; Englyst, H. N.; Cummings, J. H. Ileal recovery of starch from whole diets containing resistant starch measured *in vitro* and fermentation of ileal effluent. *Am. J. Clin. Nutr.* **1995**, *62*, 403−411.
(30) Englyst, H. N.; Hudson, G. J. The classification and measurement of dietary carbohydrates. *Food Chem.* **1996**, *57*, 15−21.
(31) Englyst, K. N.; Englyst, H. N. Detecting nutritional starch fractions. In *Starch in food: Structure, function and applications*; Eliasson, A. C., Ed.; Woodhead Publishing: Amsterdam, 2004; pp 541−559.
(32) Zhang, P. Y.; Hamaker, B. R. Banana starch structure and digestibility. *Carbohydr. Polym.* **2012**, *87*, 1552−1558.
(33) Srichuwong, S.; Jane, J. Physicochemical properties of starch affected by molecular composition and structure: a review. *Food Sci. Biotechnol.* **2007**, *16*, 663−674.
(34) Cheetham, N. W. H.; Tao, L. P. Variation in crystalline type with amylose content in maize starch granules: an X-ray powder diffraction study. *Carbohydr. Polym.* **1998**, *36*, 277−284.
(35) Kowittaya, C.; Lumdubwong, N. Molecular weight, chain profile of rice amylopectin and starch pasting properties. *Carbohydr. Polym.* **2014**, *108*, 216−223.
(36) Kaur, M.; Sandhu, K. S.; Lim, S. T. Microstructure, physicochemical properties and *in vitro* digestibility of starches from different Indian lentil (*Lens culinaris*) cultivars. *Carbohydr. Polym.* **2010**, *79*, 349−355.
(37) Bao, J. S. Toward understanding the genetic and molecular bases of the eating and cooking qualities of rice. *Cereal Foods World* **2012**, *57*, 148−156.
(38) Tian, Z.; Qian, Q.; Liu, Q.; Yan, M.; Liu, X.; Yan, C.; Liu, G.; Gao, Z.; Tang, S.; Zeng, D.; Wang, Y.; Yu, J.; Gu, M.; Li, J. Allelic diversities in rice starch biosynthesis lead to a diverse array of rice eating and cooking qualities. *Proc. Natl. Acad. Sci. U. S. A.* **2009**, *106*, 21760−21765.
(39) Umemoto, T.; Yano, M.; Satoh, H.; Shomura, A.; Nakamura, Y. Mapping of a gene responsible for the difference in amylopectin structure between japonica-type and indica-type rice varieties. *Theor. Appl. Genet.* **2002**, *104*, 1−8.
(40) Zhao, W. G.; Chung, J. W.; Kwon, S. W.; Lee, J. H.; Ma, K. H.; Park, Y. J. Association analysis of physicochemical traits on eating quality in rice (*Oryza sativa* L.). *Euphytica* **2013**, *191*, 9−21.
(41) Nakamura, Y.; Francisco, P. B.; Hosaka, Y.; Sato, A.; Sawada, T.; Kubo, A.; Fujita, N. Essential amino acids of starch synthase IIa differentiate amylopectin structure and starch quality between japonica and indica rice varieties. *Plant Mol. Biol.* **2005**, *58*, 213−227.
(42) Fujita, N.; Yoshida, M.; Kondo, T.; Saito, K.; Utsumi, Y.; Tokunaga, T.; Nishi, A.; Satoh, H.; Park, J. H.; Jane, J. L.; Miyao, A.; Hirochika, H.; Nakamura, Y. Characterization of SSIIIa-deficient mutants of rice: The function of SSIIIa and pleiotropic effects by SSIIIa deficiency in the rice endosperm. *Plant Physiol.* **2007**, *144*, 2009−2023.
(43) Hanashiro, I.; Itoh, K.; Kuratomi, Y.; Yamazaki, M.; Igarashi, T.; Matsugasako, J. I.; Takeda, Y. Granule-bound starch synthase I is responsible for biosynthesis of extra-long unit chains of amylopectin in rice. *Plant Cell Physiol.* **2008**, *49*, 925−933.
(44) Ohdan, T.; Francisco, P. B., Jr.; Sawada, T.; Hirose, T.; Terao, T.; Satoh, H.; Nakamura, Y. Expression profiling of genes involved in starch synthesis in sink and source organs of rice. *J. Exp. Bot.* **2005**, *56*, 3229−3244.

DOI: 10.1021/acs.jafc.5b02143
J. Agric. Food Chem. 2015, 63, 6241−6248

In food applications GlcN has been used to generate antimicrobial, antioxidant,[14] and taste-enhancing compounds;[15] to enrich beverages[16] or milk;[17] and to modify proteins to enhance their functionality in food systems. For instance, Hrynets et al.[18] took advantage of GlcN reactivity to create novel glycoproteins at moderate temperatures resulting in an enhanced solubility and emulsification capacity.

At the same time, studies have reported a link between GlcN supplementation and diabetes complications,[19,20] presumably due to GlcN-induced β-cell apoptosis and dysfunction.[21] Furthermore, Candiano et al.[22] indicated that GlcN possesses reactivity at physiological temperatures producing fluorescent pyrazine compounds derived from the cyclocondensation between two GlcN molecules, which were later reported to cause DNA strand breakage.[23]

Some of GlcN's effects, for instance, taste-enhancing and antimicrobial properties as well as protein modifications, are likely related to its high reactivity; however, to date no plausible explanations for this phenomenon have been provided. It is also surprising that only a few studies have focused on GlcN degradation at moderate temperatures (i.e., 37 °C)[24,25] and, to the best of our knowledge, no research has evaluated the formation of α-dicarbonyls (α-DCs) from this popular dietary supplement. It was expected that GlcN, a Heyns/Amadori-like compound, would rapidly form reactive intermediates such as α-DCs and several advanced and stable condensation products as compared to GlcNAc. Hence, the main objective of this study was to investigate the chemistry of GlcN degradation in vitro (nonenzymatic degradation) and to compare it to GlcNAc and a reaction mixture containing Glc + NH_3 (Glc-NH_3). To meet this objective, GlcNAc, Glc-NH_3, and GlcN were incubated at 37 °C, and α-DCs were analyzed over time using liquid chromatography and Orbitrap mass spectrometry. Condensation products were also evaluated over time using both spectroscopic and mass spectrometric techniques.

MATERIALS AND METHODS

Chemicals. *N*-Acetyl-D-glucosamine (≥99% purity), D-glucose (≥99.5% purity), D-glucosamine hydrochloride (≥99% purity), potassium phosphate monobasic and dibasic, sodium azide, HPLC grade solvents (acetonitrile, methanol, formic acid), glucosone (2-keto-D-glucose; ≥98.0% purity; M_w 178.14 Da), glyoxal (ethanedial; 40% in H_2O; M_w 58.04 Da), methylglyoxal (2-oxopropanal; 40% in H_2O; M_w 72.06 Da), diacetyl (butane-2,3-dione; ≥95.0% purity; M_w 86.09 Da), and 1,2-diaminobenzene were purchased from Sigma-Aldrich (St. Louis, MO, USA). 3-Deoxyglucosone (3-deoxy-D-*erythro*-hexosulose; ≥95% purity; M_w 162.14 Da) was obtained from Cayman Chemical (Ann Arbor, MI, USA). Ammonium hydroxide was purchased from Fisher Scientific. SPE tC-18 Sep-Pak Vac 6 cc columns were obtained from Waters (Milford, MA, USA). Filtration membranes (0.22 μm) were from Millipore (Billerica, MA, USA). Standard ion calibration solution (Pierce LTQ) for electrospray ionization in positive mode was purchased from Thermo Scientific (Rockford, IL, USA). All buffers and reaction mixtures were prepared with Milli-Q purified distilled water (Millipore, Bedford, MA, USA).

Experimental Design. In this study the nonenzymatic degradation of GlcN, GlcNAc, and Glc-NH_3 was evaluated over time at 0, 0.5, 1, 2, 3, 6, and 12 days in phosphate buffer at 37 °C using UV−vis and fluorescence spectroscopic analyses as well as mass spectrometric techniques. In the first part of the study, UV−vis and fluorescence profiles were assessed over time to understand the major changes occurring during the degradation reaction of the monosaccharides. In this regard, a total of 42 tubes (2 tubes × monosaccharide × incubation time) were randomly placed within the incubator, and the reaction was monitored over time. Three independent trials were conducted, resulting in six replicates per treatment.

Following this exploratory test, a dedicated study on α-DCs identification and production was conducted over time using the same design as reported before. Liquid chromatographic separations and mass spectrometry techniques were used to identify and quantify the major degradation products. Finally, the last part of this study focused on the production of fluorescent and stable condensation products obtained by the reaction between the main α-DCs produced during GlcN degradation and GlcN. In this regard, selected α-DCs (glucosone (G), 3-deoxyglucosone (3-DG), glyoxal (GO), and methylglyoxal (MGO)) were incubated with GlcN at equimolar concentrations for 0, 4, 8, 12, 24, and 48 h at 37 °C, and their UV−vis and fluorescence profiles were recorded. Three tubes per selected α-DC were incubated over time, resulting in six replicates.

Incubation of GlcNAc, Glc-NH_3, and GlcN Aliquots. Solutions (15 mg/mL) of GlcNAc, Glc-NH_3 (equimolar mixture), and GlcN were prepared in 50 mM phosphate buffer. The pH of the final solutions, 7.4, was adjusted (Denver Instrument UltraBasic pH Meter) if necessary. NaN_3 was added to a final concentration of 0.02% to prevent microbial growth. The reaction mixtures were transferred into plastic screw-cap tubes, randomly arranged within an incubator (New Brunswick Scientific, Edison, NJ, USA), and incubated at 37 °C. Samples aliquots were collected at 0.5, 1, 2, 3, 6, and 12 days. The controls were reaction solutions at 0 h. The pH value of the solution over time was checked, but not adjusted during the reaction to enable a natural time course generation of reaction's reactive intermediates. Decrease in pH within 0.3−0.45/0.5 unit was found for GlcN (6−12 reaction days, respectively) and within 0.1 unit for Glc-NH_3 solutions (12 reaction days).

Preparation of α-Dicarbonyls and Glucosamine Reaction Mixtures. Equimolar (2.5 mM) concentrations of GlcN and commercially available standards of G, 3-DG, GO, and MGO were solubilized in 50 mM phosphate buffer (pH 7.4), containing 0.02% NaN_3. Controls included fresh and incubated solutions of GlcN and each α-DC separately. All reaction mixtures were incubated at 37 °C for 4, 8, 12, 24, and 48 h.

Spectrophotometric Measurements. UV−vis absorbance and fluorescence spectra of 15 mg/mL solutions of GlcNAc, Glc-NH_3, and GlcN were recorded using the Spectramax M5 multimode microplate reader (Molecular Devices, Sunnyvale, CA, USA). For both analyses readings were taken with 1 cm quartz cuvettes and samples diluted (1:20, v/v) with 50 mM phosphate buffer (pH 7.4). The absorbance was recorded in the range of 200−500 nm. For fluorescence, the excitation wavelength was set at 347, and an emission was recorded from 364 to 600 nm. A blank (buffer) was subtracted from all spectra automatically. Absorbance (200−600 nm) and fluorescence (λ_{exc} = 347, λ_{em} = 364−600) of α-DC standards separately or in the mixture with GlcN were measured in the same way at the concentration of 2.5 mM. For all GlcN−α-DC mixtures, controls of incubated GlcN and respective incubated α-DCs for each time period were subtracted.

Free α-Dicarbonyl Compounds: Extraction, Identification, and Quantitation. *Solid Phase Extraction (SPE) and Derivatization Procedure.* The extraction procedure was based on a method reported by Papetti et al.[26] with slight modification. Briefly, collected over time aliquots of GlcNAc, Glc-NH_3, and GlcN were spiked with 0.006 g of 1,2-diaminobenzene (*o*-phenylenediamine (OPD)), the pH was adjusted to 3.00 ± 0.02 with 4 M HCl, and the mixture was derivatized at 37 °C for 1 h. The derivatized solution was passed through a preconditioned SPE cartridge (tC-18 Sep-Pak, Waters, Milford, MA, USA). The cartridge was washed with 2 mL of water, and quinoxalines were eluted with 4 mL of a MeOH/H_2O mixture (90:10, v/v) at a flow rate close to 2 mL/min. The first 1 mL was discarded, whereas the next 2 mL was used for analysis. The controls were treated exactly as collected sugar aliquots except no derivatizing agent was added. To ensure complete derivatization, a preliminary test was performed, where derivatization times of 0.5, 1, 2, 4, and 8 h were tested. The maximum peak area was reached after a derivatization for 1 h without further increase during longer derivatization times.

UHPLC-UV Analysis of Quinoxalines Derivatives Formed from α-Dicarbonyl Compounds and o-Phenylenediamine. α-DC analysis was conducted using an ultrahigh-performance liquid chromatography

DOI: 10.1021/acs.jafc.5b02664
J. Agric. Food Chem. 2015, 63, 6249−6261

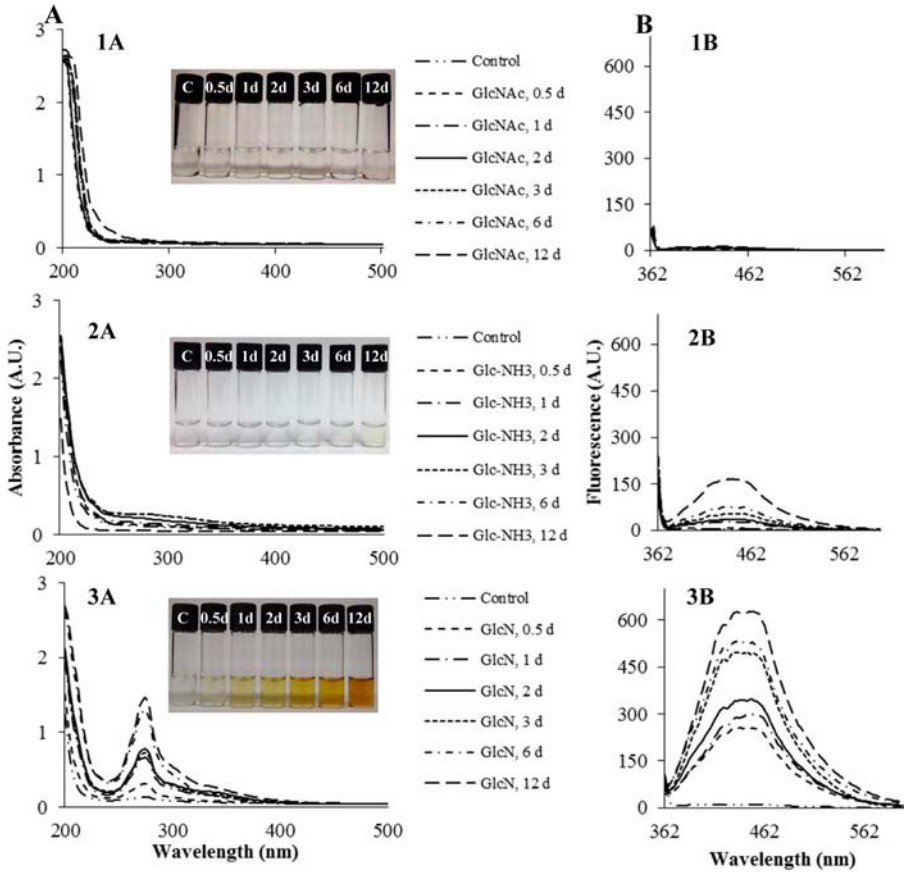

Figure 1. UV−vis absorbance (A) and fluorescence spectra (B) profiles of GlcNAc (1A, 1B), Glc-NH_3 (2A, 2B), and GlcN (3A, 3B) as a function of heating time from 0 to 12 days. The values are expressed in arbitrary units (A.U.). Inset images (left) show photographs of the corresponding incubated sugar solutions. The images were taken for nondiluted experimental solution incubated at 15 mg/mL.

apparatus (Shimadzu, Columbia, MD, USA) consisting of two pumps LC-30AD, an SPD-M20A photodiode array detector (PDA), a DGU-20A5 degasser, an SIL-30AC autosampler (operated at 4 °C), and a CTO-20 AC column oven. The UHPLC system was controlled by a personal computer equipped with LabSolutions software operating in Windows XP. The separation was achieved following the method described by Papetti et al.[26] using an Ascentis Express ES-C18 column (150 × 4.6 mm, 2.7 μm particles; Sigma-Aldrich, St. Louis, MO, USA) with a UHPLC precolumn filter (UltraShield Analytical Scientific Instruments, Richmond, CA, USA) operating at 25.0 ± 0.5 °C and a flow rate of 0.3 mL/min. The binary mobile phase consisted of (A) 0.1% formic acid in water and (B) methanol. The 120 min gradient is described as follows: 0−5 min, 90−85% A; 5−13 min, 85−80% A; 13−40 min, 80% A; 40−65 min, 80−70% A; 65−90 min, 70−50% A; 90−100 min, 50−0% A; 100−105 min, 0% A; and 105−110 min, 0−90% A; the column was then re-equilibrated with the initial mobile phase for 10 min. The injection volume was 5 μL. The PDA detector was set at 314 and 335 nm to record the peaks, and UV spectra were recorded from 215 to 420 nm. Before injection, sample solutions were filtered with a PVDF syringe filter (13 mm, 0.22 μm; Millipore Millex, Billerica, MA, USA).

Identification and Quantitation of Quinoxaline Derivatives. The identification of major α-DCs was based on comparison of their retention times of the reference compounds (quinoxalines derivatives of G, 3-DG, GO, MGO, and DA) and spectral characteristics. For unequivocal identification of the major α-DCs, 10 UHPLC peaks were manually collected and subjected to mass spectrometry analyses. The accurate mass and MS/MS fragmentation patterns were compared to authentic standards and to the reference data. Mass spectrometry analyses were performed in duplicates.

For quantitation external calibration was used. Each quinoxaline derivative was diluted to the final concentrations ranging from 60 to 2000 μM (G), from 30 to 2000 μM (3-DG), from 4.5 to 50 μM (GO), from 1.0 to 10 μM (MGO), and from 1.25 to 7.5 μM (DA). Calibration curves were prepared for each trial, and each concentration was analyzed in triplicate. The peak area was plotted against concentration, and the regression equations were calculated. The correlation coefficients for all calibration curves were $R^2 \geq 0.999$. The average (from three trials) limit of detection (LOD) was calculated as 2.15 ± 0.07 μM (G), 0.27 ± 0.00 μM (3-DG), 0.13 ± 0.00 μM (GO), 0.09 ± 0.00 μM (MGO), and 0.18 ± 0.00 μM (DA). The average limit of quantification (LOQ) was determined as 6.52 ± 0.21 μM (G), 0.81 ± 0.01 μM (3-DG), 0.39 ± 0.01 μM (GO), 0.27 ± 0.01 μM (MGO), and 0.55 ± 0.02 μM (DA) by assuming a signal-to-noise ratio (S/N) of 3:1 for LOD and 10:1 for LOQ. The following ranges of sample concentrations were extrapolated from the calibration curves: 169−861 μM (G), 67−1289 μM (3-DG), 7.9−32 μM (GO), 2.5−6.8 μM (MGO) and 1.9−3.7 μM (DA). These values were then expressed as milligrams per kilogram GlcN.

Direct Infusion Orbitrap Mass Spectrometry Analyses (DIMS). Collected α-DC fractions from UHPLC and GlcN aliquots (diluted in 50:50 (methanol/water, v/v)) were subjected to DIMS. All Orbitrap measurements were carried out by using the Ion Max electron spray ionization (ESI) source (Thermo Fisher Scientific) mounted on an LTQ Orbitrap XL (Thermo Scientific, San Jose, CA, USA). The Orbitrap mass analyzer was calibrated with standard ion calibration solutions (Pierce LTQ, Thermo Scientific). The following parameters were applied: sheath gas flow, 15 arbitrary units; auxiliary gas flow, 5 arbitrary units; and capillary temperature, 275 °C. Samples (3 μL) were injected manually by performing direct infusion using a 100 μL syringe (Hamilton, Reno, NV, USA) and the on-board syringe pump. DIMS analyses were performed at a mass resolution of 60000 at m/z 400, and spectra were acquired over the range of m/z 50−2000. The automatic gain control (AGC) target was set to 1e6 and the

DOI: 10.1021/acs.jafc.5b02664
J. Agric. Food Chem. 2015, 63, 6249−6261

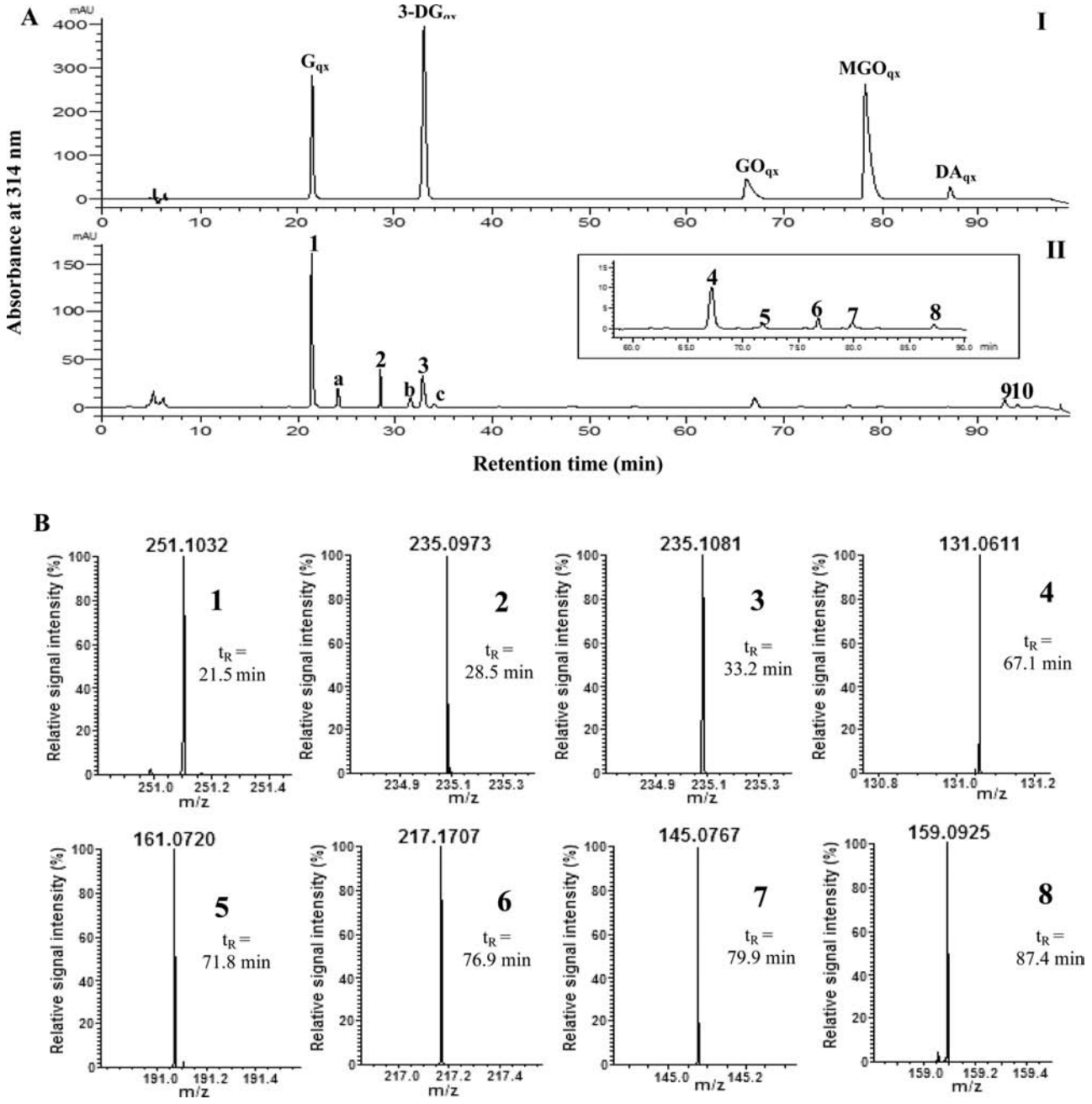

Figure 2. UHPLC and MS analyses of quinoxaline derivatives of α-dicarbonyl compounds produced from GlcN incubation over time. (A) (I) Chromatogram of a reference quinoxaline mixture of glucosone (G), 3-deoxyglucosone (3-DG), glyoxal (GO), methylglyoxal (MGO), and diacetyl (DA). (II) Representative chromatogram of GlcN incubated for 1 day, derivatized with OPD, and acquired by UHPLC with UV detection at 314 nm. Numbers indicate the peaks of the quinoxalines of (1) G, (2) unidentified α-DC, (3) 3-DG, (4) GO, (5) HPA, (6) 3,4-DGE, (7) MGO, (8) DA, (9) 4-GlcN-3-DG, and (10) 4-G-3-DG, and a, b, and c peaks correspond to non-OPD-derived GlcN condensation products. (Inset) Zoomed-in view of the peaks eluted at 60−90 min. (B) Precursor ions and retention times of the peaks corresponding to the same 10 numbers as indicated above for panel AII.

maximum injection time to 250 ms. For MS/MS experiments, ions of interest were isolated with an isolation width of 1−2 Da, and collision-induced dissociation was conducted at various voltages, which were optimized for each sample. An activation time of 30 ms was used with a tube lens voltage of 110 V and a capillary temperature of 275 °C. Data acquisition and processing were performed using Xcalibur software (Thermo Scientific).

Statistical Analysis. Spectroscopic profiles obtained from UV−vis and fluorescence analyses from the three different independent trials were averaged and reported as graphs. α-DC production over time was subjected to an analysis of variance (ANOVA) using the PROC MIXED procedure of SAS (v. 9.3, SAS Institute Inc., Cary, NC, USA). The model tested incubation time as a fixed variable and used the trial replication as a random variable. Tukey's honestly significant difference ($p < 0.05$) multiple-range test was conducted to determine differences between means.

RESULTS AND DISCUSSION

UV−Vis and Fluorescence Profiles of Nonenzymatic Modification of GlcNAc, Glc-NH_3, and GlcN over Time. UV−vis and fluorescent profiles can be a useful and simple tool to understand the major changes occurring during a reaction.

DOI: 10.1021/acs.jafc.5b02664
J. Agric. Food Chem. 2015, 63, 6249−6261

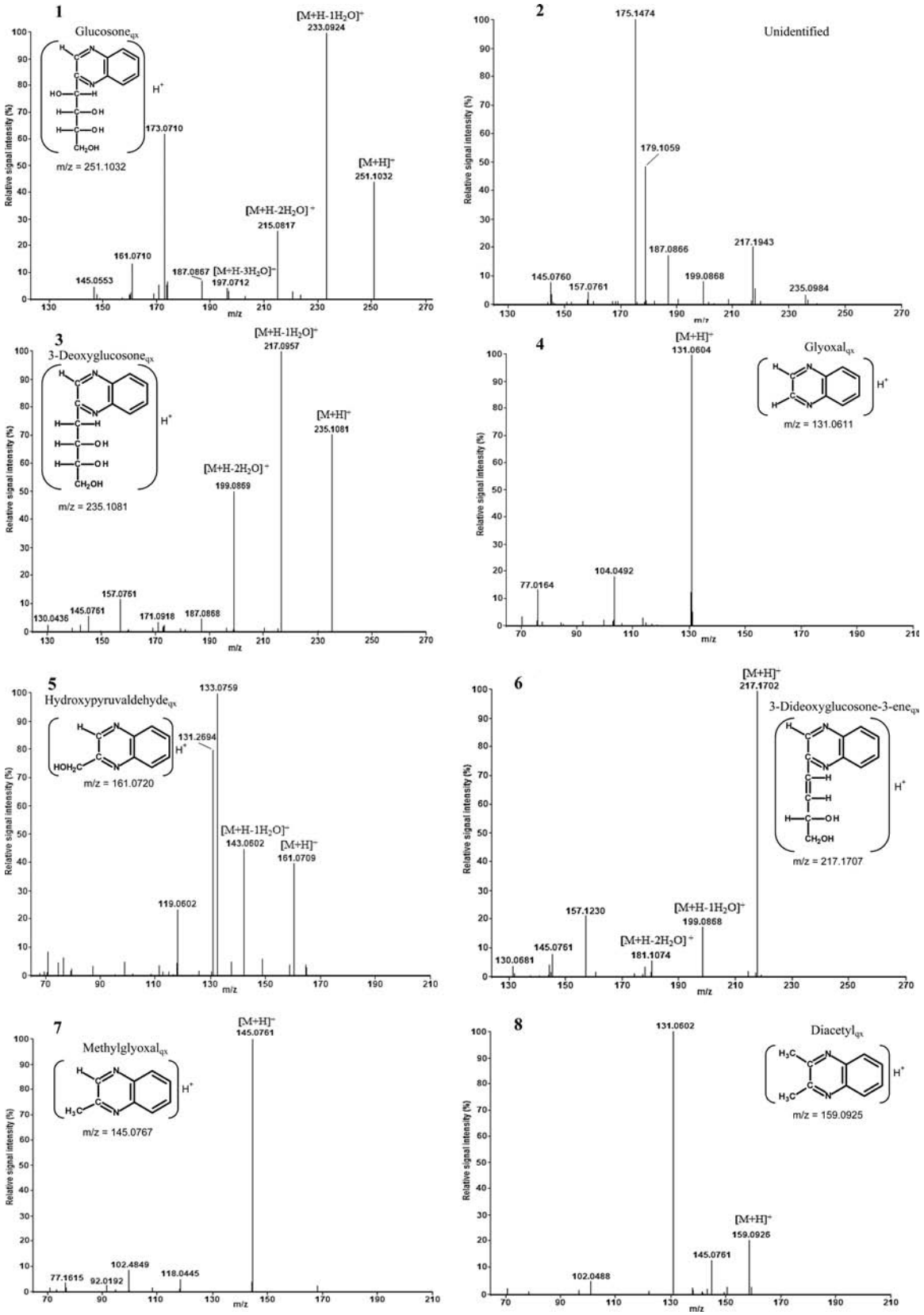

Figure 3. MS/MS spectra and structures of quinoxaline α-dicarbonyl compounds produced during GlcN degradation: (1) glucosone$_{qx}$; (2) unidentified α-DC$_{qx}$; (3) 3-deoxyglucosone$_{qx}$; (4) glyoxal$_{qx}$; (5) hydroxypyruvaldehyde$_{qx}$; (6) 3,4-dideoxyglucosone-3-ene$_{qx}$; (7) methylglyoxal$_{qx}$; (8) diacetyl$_{qx}$. The respective quinoxaline precursor ions are shown in Figure 2B.

Solutions of GlcNAc, GlcN, and Glc-NH$_3$ were incubated at 37 °C in phosphate buffer from 0 to 12 days, and their UV−vis absorbance and fluorescence profiles (Figure 1) were recorded to monitor their stability over time. No major changes in the

DOI: 10.1021/acs.jafc.5b02664
J. Agric. Food Chem. 2015, 63, 6249−6261

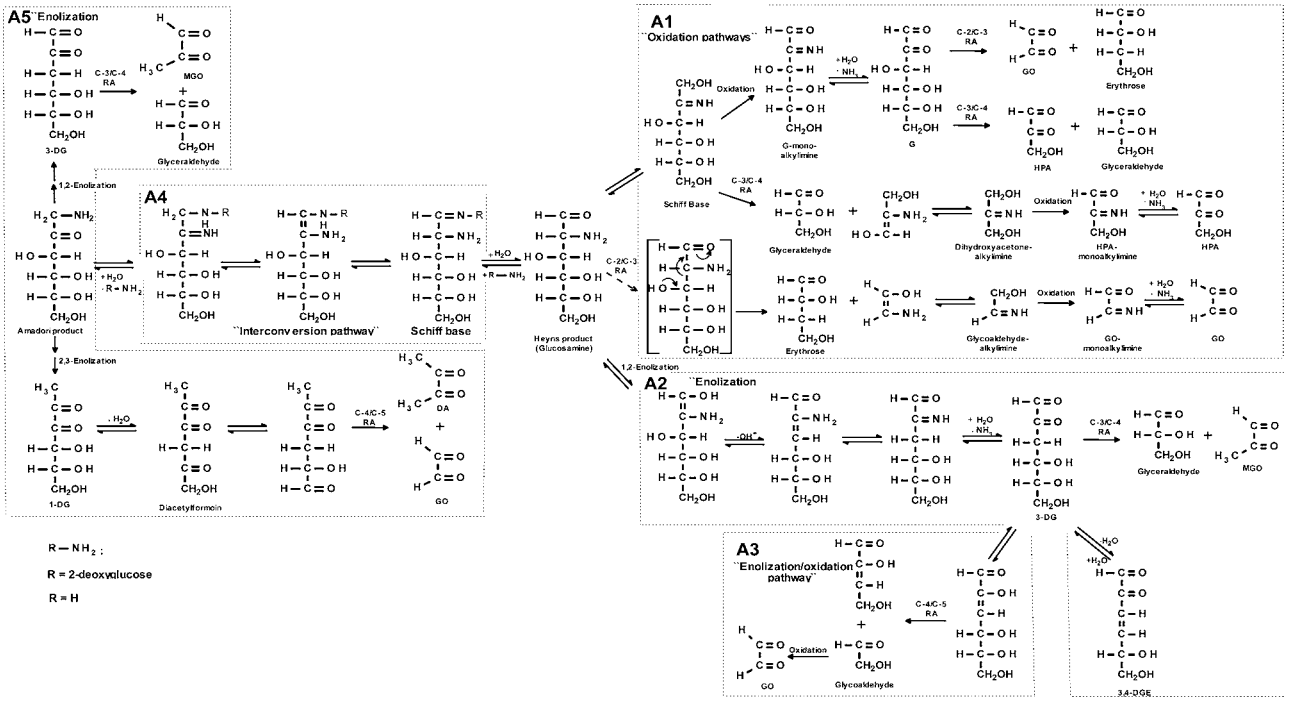

Figure 4. Proposed pathways of generation of α-dicarbonyl compounds from GlcN. G, glucosone; 3-DG, 3-deoxyglucosone; 1-DG, 1-deoxyglucosone; 3,4-DGE, 3,4-dideoxyglucosone-3-ene; GO, glyoxal; MGO, methylglyoxal; HPA, hydroxypyruvaldehyde; RA, retroaldolization.

absorbance over time were obtained for GlcNAc, except a slight increase at λ = 220−235 nm at 12 days. A minor absorbance increase was observed in the Glc-NH_3 mixture. On the contrary, steady increases of maxima of 274 and 320−360 nm were obtained for GlcN, suggesting a formation of products that absorb in the UV region. The increase in absorbance at 320 nm was lower than at 274 nm; however, the formation of a light yellow color was apparent after 0.5 day of incubation. The increase in UV absorbance at 274 and 320 nm was also reported by Zhang et al.,[27] who incubated 0.02 M GlcN at 37 °C for 50 h in phosphate buffer (pH 7.4). Candiano et al.[22] and Horowitz[25] indicated that the increase in UV absorption at around 274 nm is due to the formation of pyrazine compounds, which derive from the cyclocondensation between GlcN molecules, which have been confirmed by MS analysis (see Condensation Products from Nonenzymatic Modification of GlcN). At the same time the increase at 320 nm was attributed to the formation of soluble premelanoidins,[28] which was also confirmed by the production of a light yellow-brown color over incubation time (Figure 1(3A, inset)). In addition, this hyperchromicity at 320−340 nm was apparent at longer incubation times. No color production was observed for GlcNAc (Figure 1(1A inset)); the Glc-NH_3 mixture changed from slightly yellow to yellow over 6−12 days (Figure 1(2A inset)), whereas the time course of color development by GlcN was changed from yellowish to brown. The fluorescence profile showed a progressive increase in the emission (λ_{exc} 347 nm/λ_{em} 364−600 nm) intensity over time for GlcN. A broad peak was observed with a maximum intensity ranging from 420 to 450 nm. Glc-NH_3 also showed an increased fluorescence, however, with significantly lower intensity and reaction velocity; at 12 days fluorescence emission was around 3 times lower as compared to GlcN. On the other hand, the GlcNAc fluorescence profile did not change significantly over time. The wavelengths observed were typically used to assess the progress of the Maillard reaction and, more specifically, the development of advanced glycation products (AGEs).[29] Zhang et al.[24] reported the increase in fluorescence intensity (λ_{exc} 340 nm/λ_{em} 420 nm) during GlcN incubation at 37 °C and suggested an increase due to GlcN cyclocondensation and rearrangements. Candiano et al.[22] came to the same conclusion and further proved that the increase in fluorescence emission at 430 nm (λ_{exc} = 362 nm) in a lysine−GlcN reaction mixture was due to GlcN cyclocondensation. The same authors indicated that GlcN cyclocondensation products possessed optical and fluorescent properties of browning compounds, which in turn could explain an increase in color intensity over time (Figure 1(3A inset)). These preliminary results suggest that with prolonged heating time GlcN cyclocondensation and a variety of rearrangements occur and, thus, the formation of higher molecular weight colored compounds.

Identification and Quantitation of the Major α-Dicarbonyls Produced from GlcN Degradation by UHPLC and Mass Spectrometry Analyses. In the previous section, UV and fluorescence analyses were discussed to evaluate the formation of the final stable products of GlcN degradation (i.e., GlcN−GlcN autocondensation products). However, because GlcN is a Heyns-like compound, we hypothesized the production of α-DCs, which in turn have the potential to generate a variety of condensation products. α-DC are highly reactive compounds; thus, they were derivatized (condensation with OPD) to form stable quinoxalines, followed by UHPLC and MS analyses. Separation of quinoxalines achieved with chromatography[26] allowed for the identification of analytes. There were no α-DCs identified in GlcNAc samples up to 12 days of incubation, whereas lower production was observed in Glc-NH_3 samples at 12 days of reaction as compared to GlcN (see Figure S1 in the Supporting Information). Because the production of α-DCs at 37 °C from Glc-NH_3 was lower as compared to GlcN, the main focus

DOI: 10.1021/acs.jafc.5b02664
J. Agric. Food Chem. 2015, 63, 6249−6261

Table 1. Concentrations of Five Different α-Dicarbonyl Compounds Found in GlcN Incubated over Time[a]

	free α-dicarbonyl compounds (mg/kg of GlcN)							
α-dicarbonyl	0 days	0.5 day	1 day	2 days	3 days	6 days	12 days	p value[b]
glucosone	709 ± 68e	2634 ± 87f	3245 ± 90a	2710 ± 134b	2443 ± 85bc	2132 ± 89c	1131 ± 68d	**
3-deoxyglucosone	272 ± 19f	451 ± 32e	571 ± 27de	583 ± 33d	707 ± 63c	1905 ± 42b	4535 ± 82a	**
glyoxal	11.2 ± 1.2e	26.6 ± 2.1bc	34.9 ± 3.4a	28.4 ± 2.1b	24.9 ± 1.6c	17.7 ± 0.9d	12.6 ± 1.1e	**
methylglyoxal	nd[c]	4.5 ± 1.3e	5.5 ± 1.1de	6.4 ± 1.0cd	7.3 ± 0.8c	8.7 ± 0.9b	10.4 ± 2.3a	**
diacetyl	nd	nd	6.1 ± 1.1b	6.9 ± 0.9a	3.7 ± 1.0c	nd	nd	**

[a]All values are expressed as milligrams of α-dicarbonyl compound per kilogram of GlcN. The mean ± standard deviation of three independent experiments ($n = 6$) is shown. Values in the same row with different letters differ significantly ($p < 0.05$). [b]** indicates $p < 0.0001$. [c]nd, not detectable.

was to identify and quantify α-DCs derived from GlcN over time. Figure 2A illustrates the representative UHPLC chromatogram of standard α-DC compounds and α-DCs produced from GlcN incubated for 1 day. For confirmation of the peaks for which commercial standards were available and the identification of unknowns, the major peaks were collected and further subjected to MS analyses. Eight peaks in the UV chromatograms (Figure 2A(II)) were identified by their pseudomolecular peaks ($[M + H]^+$, as detected by MS (Figure 2B). Individual peaks 1−8 were identified as being (1) glucosone, m/z 251.1032; (2) unidentified α-dicarbonyl, m/z 235.0973; (3) 3-deoxyglucosone, m/z 235.1081; (4) glyoxal, m/z 131.0611; (5) 3-hydroxy-2-oxopropanal (hydroxypyruvaldehyde, HPA); m/z 161.0720; (6) 3,4-dideoxyglucosone-3-ene, m/z 217.1707; (7) methylglyoxal, m/z 145.0767; and (8) diacetyl, m/z 159.0925. On the basis of molecular weight and reference data,[26] peaks 9 and 10 were tentatively assigned to the quinoxaline derivatives of 2-amino-2-deoxy-4-glycosyl-5,6-dihydroxy-2-oxohexanal (4-GlcN-3-DG) and 4-glycosyl-5,6-dihydroxy-2-oxohexanal (4-Glc-3-DG), respectively (see precursor ions in Figure S2 in the Supporting Information). The peaks denoted a, b, and c showed m/z in the range of 317−355 (see Figure S3 in the Supporting Information). The nature of these peaks is not clear; however, it is suspected that they derived from a variety of condensation products of GlcN itself or GlcN with α-DCs (i.e., fructosazines). Hence, they are likely non-OPD condensed products, which are highly hydrophilic fructosazines missing the benzene portion of OPD and, despite their high molecular weight, elute at early retention times in the hydrophilic part of the gradient. The product ions and structures of quinoxaline derivatives of the seven identified peaks are shown in Figure 3. For G_{qx} the molecular ion and subsequent losses of three water molecules were observed. Mittelmaier et al.[30] found very similar fragmentation pattern with the loss of three water molecules, except the fragment ion at m/z 173.0 was dominant. Product ion spectra of $3\text{-}DG_{qx}$ and its dehydration product, $3,4\text{-}DGE_{qx}$, showed similar fragment ions, apart from the latter missing fragments at m/z 235.1081 and 171.0918. The MS/MS of the unidentified α-dicarbonyl (peak 2) showed two similar fragment ions (m/z 145.0760/1 and 157.0761) with $3\text{-}DG_{qx}$ and could be an indication of the presence of 1-deoxyglucosone (1-DG), 3-deoxygalactosone, or 4-deoxyglucosone. However, the presence of DA would support the presence of 1-DG, being a precursor of DA[41] (Figure 4A). There was a minimal tendency of fragmentation for GO_{qx} and MGO_{qx}, with three and five fragments, respectively, along with the highest intensity for precursor ions and fragment at m/z 77.0164 (77.1615 in MGO) typical for quinoxaline skeleton fragmentation.[31] For DAqx four major MS/MS fragment ions were found. Under the described MS/MS conditions m/z 161.0709, 143.0602, 133.0759, 131.2694, and 119.0602 were identified as the main fragments of the parent molecule ion (m/z 161.0720) of HPA_{qx}. The fragment ions from eight identified α-DCs were in accordance with previously reported quinoxalines in various foods, such as high-fructose corn syrup;[32] coffee, barley, and soy sauce;[26] and honey.[33] The MS/MS fragmentation and proposed structures of 4-GlcN-3-DG and 4-G-3-DG are reported in the Figure S3 in the Supporting Information. After identification of the α-DC presence, five of them were quantified, and the concentrations expressed in milligrams per kilogram of GlcN are given in Table 1. It was found that G, 3-DG, and GO were already present in control samples, suggesting the partial degradation of GlcN while stored in powder. Even though a freshly ordered GlcN was used in the analyses, rapid development of α-DCs could be a possible explanation for their presence in the nonheated sample. The elevated temperatures (90 °C for hydrolysis, 45 °C for evaporation, etc.) used during GlcN's extraction could induce its degradation and thus dicarbonyl compounds' development. At the beginning of the incubation G was the most abundant α-DC compound followed by 3-DG. However, after 1 day of incubation, the concentration of G decreased significantly ($p < 0.05$) from 3245 to 1131 mg/kg GlcN, along with a significant increase in the amount 3-DG. At 0.5 and 1 day of incubation, G concentration was around 6 times higher than that of 3-DG. After heating for 12 days, the concentration of 3-DG was 4 times higher than that of G. G is a product of oxidative degradation of Amadori or Heyns compounds (see proposed pathway in Figure 4) or autoxidation of sugar (i.e., glucose), whereas 3-DG is formed nonoxidatively through the enolization pathway.[34] These results suggest the prevalence of an oxidative pathway during the first days of incubation, whereas over time the enolization process dominates. In addition, a slight pH drop at 6 and 12 days could aid the 1,2-enolization to produce 3-DG.[35] The concentrations of the other α-DCs, GO, MGO, and DA, were significantly lower in comparison to G and 3-DG. The opposite relationship was observed between GO and MGO formation over time. Whereas the concentration of GO significantly ($p < 0.05$) decreased from 34.9 mg/kg at 1 day to 12.6 mg/kg GlcN after 12 days, the amount of MGO significantly ($p < 0.05$) increased from 4.5 to 10.4 mg/kg GlcN. DA reached the highest concentration at 2 days of incubation (6.9 mg/kg GlcN), dropped almost twice by 3 days, and was not detected with prolonged incubation. Obtained results confirm our hypothesis that GlcN is an unstable amino sugar that degrades more rapidly in phosphate buffer at 37 °C, whereas GlcNAc is stable in the condition used in this study.

Proposed Pathways of α-Dicarbonyl Formation from the Degradation of GlcN. Figure 4 reports the possible pathways

DOI: 10.1021/acs.jafc.5b02664
J. Agric. Food Chem. 2015, 63, 6249−6261

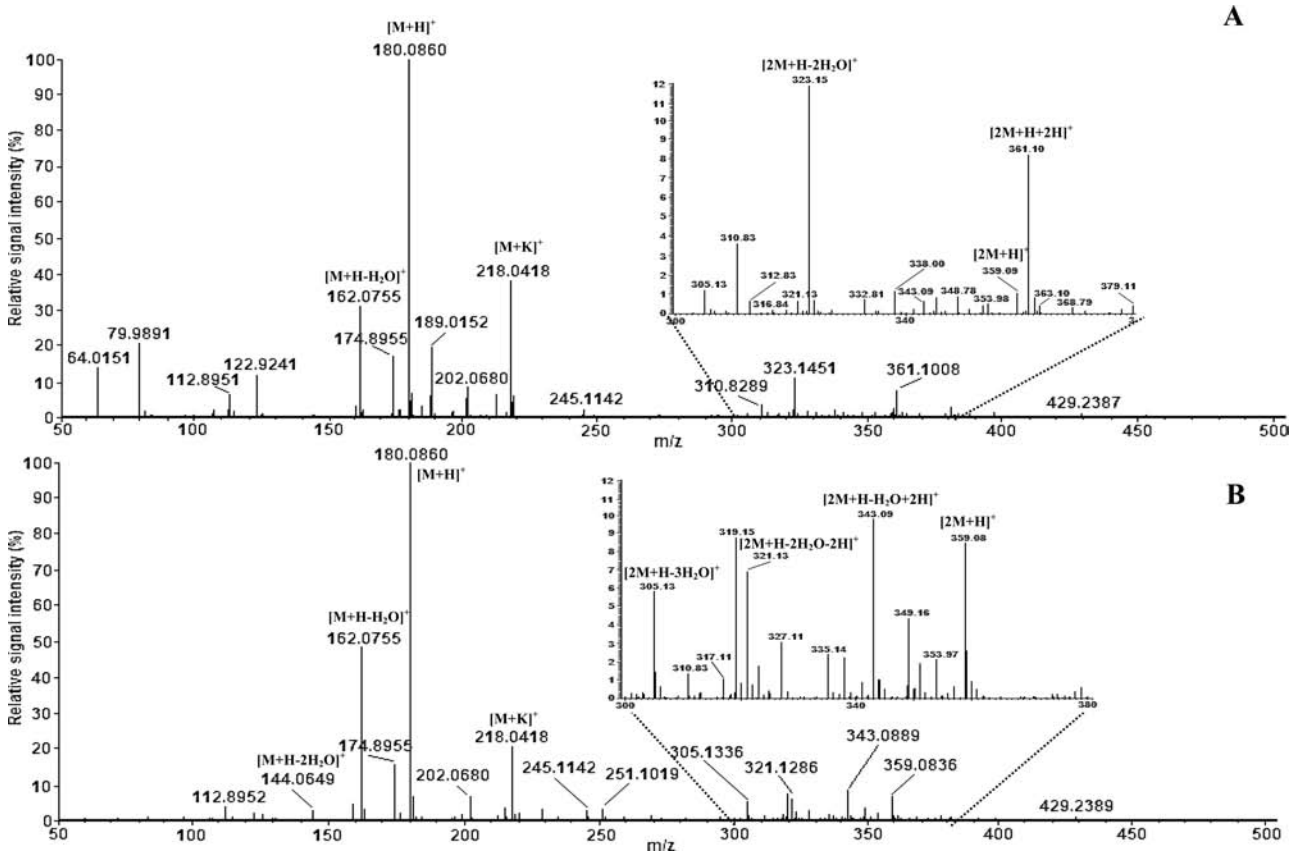

Figure 5. Mass spectrum of GlcN incubated at 0.5 (A) and 3 (B) days and directly infused into the LTQ Orbitrap−MS instrument. (Inset) Enlargement of the respective spectra in the range of m/z 300−380.

involved in the production of α-DCs identified in the present study. This scheme can be divided into "oxidation" (A1), "enolization" (A2, A5), "enolization/oxidation" (A3), and "interconversion" pathways. Glucosone, for instance, is most likely produced from an oxidative pathway (A1) with a mechanism similar to the one proposed by Hofmann et al.[36] and later verified by Gobert and Glomb.[37] Specifically, the imine or eminol form of GlcN would be directly oxidized to form monoalkylimines, which upon deamination will produce glucosone (Figure 4A1). Subsequently, through a retro-aldol cleavage between C-3 and C-4, G is proposed to form HPA, whereas the C-2/C-3 bond retroaldolization produces glyoxal.[36,38]

3-DG is proposed to be formed through the classical 1,2-enolization typical for the Heyns compound;[39] it has been reported that this compound can go only through the 1,2-enolization, as opposed to the Amadori compound, which can also undergo 2,3-enolization, where 2,3-enediol is deaminated to yield 1-DG.[40] However, Yaylayan and Huyghues-Despointes[39] reported that Heyns products can isomerize to Amadori compounds through an interconversion reaction, similar to Lobry de Bruyn-Alberda van Ekenstein transformation of fructose into glucose. In Figure 5A4 is a proposed reaction scheme in which GlcN interconverts into Amadori compounds via two possible condensation reactions: the first between two GlcN molecules and the second between GlcN and NH_3 formed during deamination of GlcN (see Figure S4 in the Supporting Information). The proposed interconversion pathway would also explain the presence of DA through 1-DG degradation[41] (Figure 4A5). However, other new chemical pathways might be involved in DA production. An increase in 3-DG was accompanied by increasing concentrations of MGO over time (Table 1). Several studies[42,43] suggested 3-DG as the precursor for MGO formation, which is based on the nonoxidative fragmentation of the retroaldolization pathway. In the model experiment of Thornalley et al.[44] 0.09 μM MGO was formed from 50 μM 3-DG, which accounts for 0.18%. In the current study, at 0.5 day, MGO accounted for 1% of 3-DG, whereas with incubation up to 12 days the percentage decreased to 0.23. GO is also proposed to be formed through oxidative (Figure 4A1) and enolization/oxidation pathways (Figure 4A3). Indeed, several pathways are proposed in the case of GO formation. The first, postulated by Hoffman et al.,[36] involves GO production from G as reported in Figure 4A1. The other potential mechanism is via enolization/oxidation pathways, by which GO might be produced from 3-DG (Figure 4A3) via vinylogous retroaldolization forming glycoaldehyde, which subsequently oxidizes to form GO.[45] The mechanism reported in Figure 4A1 is unique, where GO is proposed to originate from direct C-2/C-3 retroaldolization cleavage of GlcN in its aldosamine form, forming erythrose and a two-carbon enaminol compound that will subsequently undergo oxidation and deamination, forming GO. This would be an oxidative pathway similar to the one proposed by Hayashi and Namiki,[46] with the only difference that in this specific case the retro-aldol type cleavage would directly occur on the aldosamine form of GlcN and not on its Schiff base (imine) form. In the Namiki type of rearrangements, GO is produced before and independently of the G precursor. Hofmann and Heuberger[47] reported GO production in a glucose/L-alanine

DOI: 10.1021/acs.jafc.5b02664
J. Agric. Food Chem. 2015, 63, 6249−6261

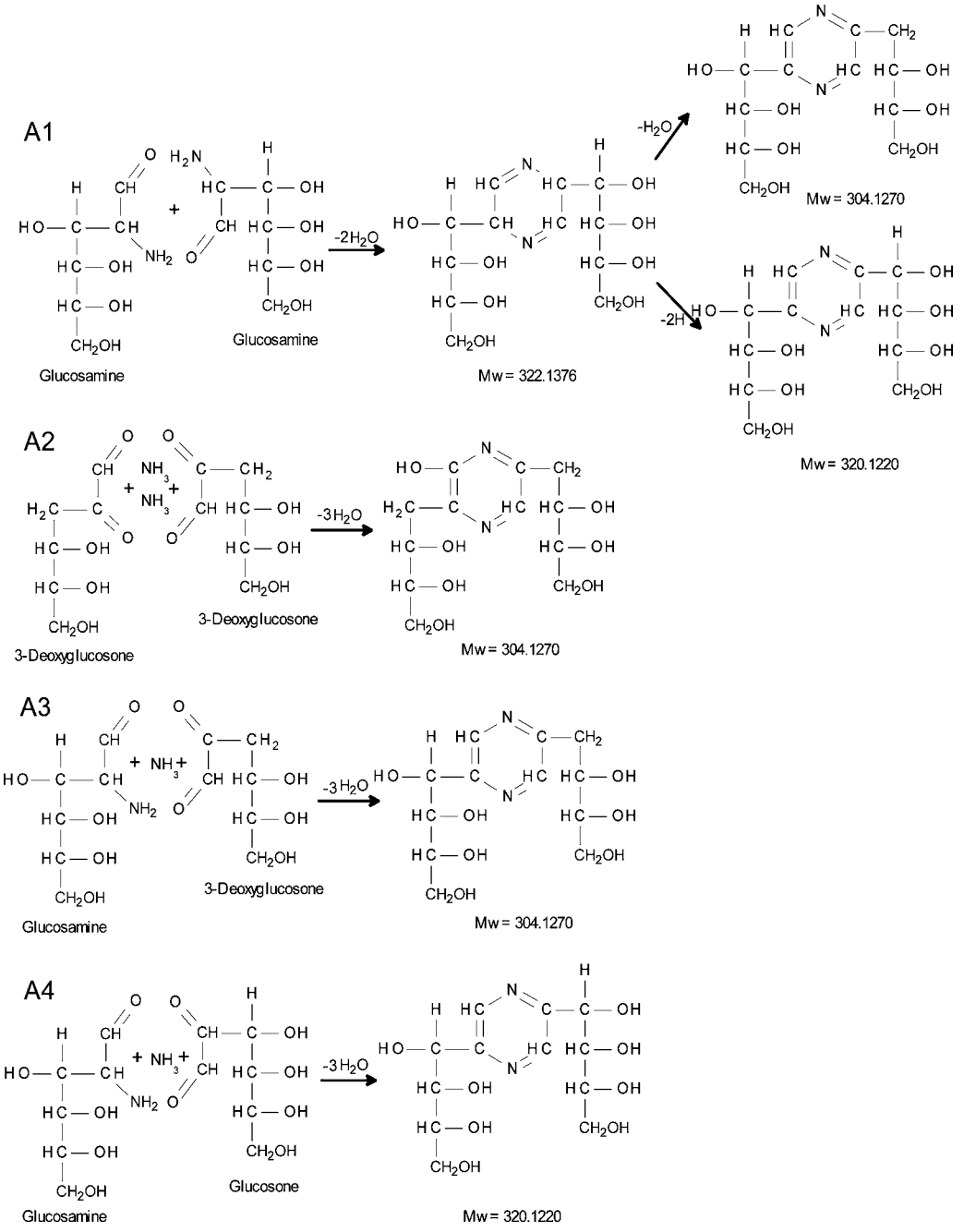

Figure 6. Proposed structures and theoretical monoisotopic molecular weights (M_w) of cyclocondensation products of GlcN only or GlcN and α-dicarbonyl compounds. Structures are shown as neutral molecules.

mixture (pH 7.0, phosphate buffer, 95 °C) at the early stages of the Maillard reaction, prior to deoxyosone formation. A steady decrease in the amount of G was associated with a decrease in GO concentrations (Table 1); therefore, it is plausible to propose both pathways described above as major routes for GO formation in the current study. HPA can also be produced in a similar manner as previously described for GO, with the only difference being that retroaldol degradation is proposed to occur at C-3/C-4 of the Schiff base form of GlcN (Figure 4A1).

Condensation Products from Nonenzymatic Modification of GlcN. As presented in Figure 1, incubation of GlcN results in an increased absorbance and fluorescence, suggesting products are generated over time. To further investigate, aliquots of GlcN incubated for 0.5 (Figure 5A) and 3 days (Figure 5B) were directly injected into a MS to obtain a compound profile. As shown in Figure 5A,B, several molecular ion species were observed. GlcN showed peaks at m/z 180.0860 corresponding to its protonated molecular ion $[M + H]^+$ and at m/z 162.0755 and 144.0649 corresponding to mono- and didehydrated GlcN, respectively. The m/z 218.0418 is likely due to GlcN's potassium adduct $[M + K]^+$, whereas m/z 359.0836 corresponds to $[2M + H]^+$, possibly due to *N*-glycoside formation between two GlcN molecules. m/z 361.1008 can also be due to an *N*-glycoside formation, but from a reduced GlcN molecule (i.e., 2-amino-2-deoxy-D-glucitol) and GlcN. Remarkably, several other species with pseudomolecular weights higher than m/z 300 were present. These species are the result of two types of reactions: cyclocondensation (Figure 6), which results

DOI: 10.1021/acs.jafc.5b02664
J. Agric. Food Chem. 2015, 63, 6249−6261

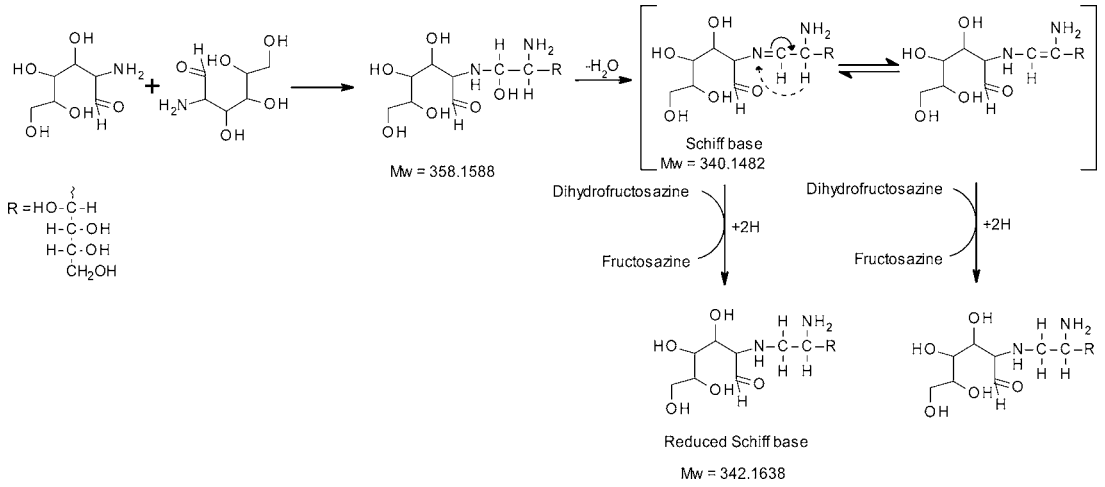

Figure 7. Proposed structures and theoretical monoisotopic molecular weights (M_w) of products deriving from GlcN acyclic condensation. Structures are shown as neutral molecules.

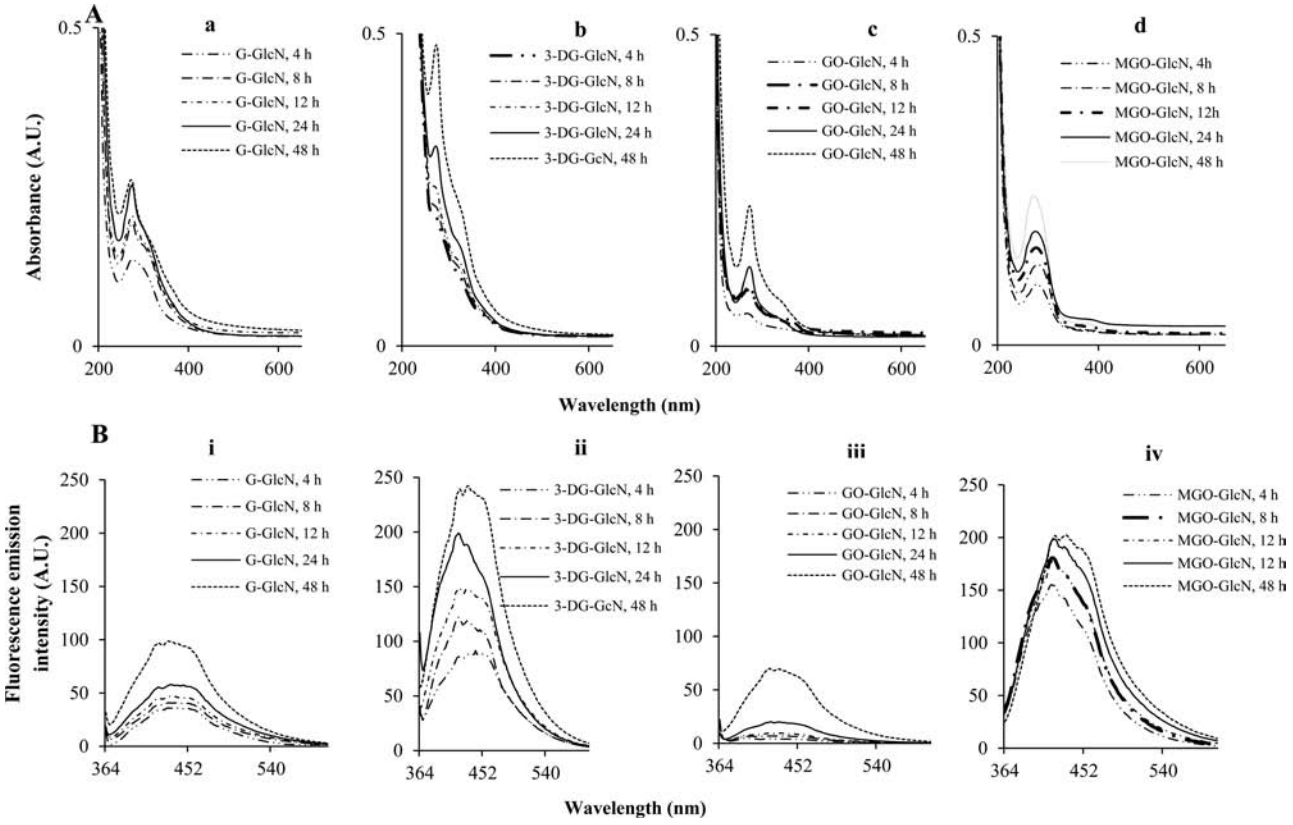

Figure 8. Absorbance (A) and fluorescence emission (B) spectra of control and incubated equimolar mixtures of GlcN and α-dicarbonyl compounds. (A) GlcN incubated with (a) G, (b) 3-DG, (c) GO, and (d) MGO. (B) GlcN incubated with (i) G, (ii) 3-DG, (iii) GO, and (iv) MGO.

in pyrazine ring formation, and acyclic condensation (Figure 7), during which no pyrazine rings are formed. One of the products of GlcN cyclocondensation, namely, dihydrofructosazine [2,5-bis(*arabino*-tetrahydroxybutyl)dihydropyrazine)], was identified at m/z 323.1451 (Figure 5A). This compound was originally identified and isolated by Candiano et al.[22] during the incubation of lysine in the presence of GlcN at 37 °C. The products at m/z 321.1286 and 305.1336 believed to be the products of dihydrofructosazine rearrangement produced fructosazine and deoxyfructosazine, respectively.[23] Similar products of GlcN incubation at m/z 321 and 323 were reported previously by Kashige et al.[23] while studying the possible involvement of GlcN-derived dihydrofructosazine in breaking DNA. It is also apparent that many other cyclocondensation products may be produced as a consequence of the reaction between GlcN and α-DCs via the mechanism proposed by Klinger.[48] The proposed reaction mechanisms between the most abundant α-DCs found in this study and GlcN are reported in Figure 6. The term "symmetric cyclocondensation" indicates a reaction scheme that involves two identical GlcN (Figure 6A1) or α-DC molecules (Figure 6A2), and "asymmetric cyclocondensation" refers to a reaction

DOI: 10.1021/acs.jafc.5b02664
J. Agric. Food Chem. 2015, 63, 6249−6261

that occurs between a specific α-dicarbonyl and GlcN (Figure 6A3,A4). Theoretically, the formation of all masses reported in Figure 6 is possible. The mass spectra of underivatized GlcN (Figure 5) at 0.5 and 3 days show the presence of the peaks which correspond to both "symmetric" (Figure 6A1,A2) and "asymmetric" (Figure 6A3,A4) cyclocondensation products, and in some cases the molecular weights of these products coincide (i.e., protonated m/z 305.1348, 321.1298, 323.1454). These data are also corroborated by Figure 8, which represents the UV−vis (Figure 8A) and fluorescence emission (Figure 8B) profiles of an equimolar mixture of G, 3-DG, GO, and MGO with GlcN over a period of incubation from 0 to 48 h. In all cases absorbance and fluorescence emission intensities increased over time owing to the formation of cyclocondensation reaction products. Hence, GlcN possesses a trapping effect to the nascent α-DCs produced from its degradation. Fluorophore formation was also reported[24] to represent the formation of heterocyclic compounds (i.e., pyrazines). Among four α-DCs tested, 3-DG appears to be the most reactive toward GlcN, judging from an extensive accumulation of fluorescence (240 units). 3-Deoxyosones predominantly form pyrazines and imidazoles with ammonia, which in turn are responsible for the sugar coloring.[40] Therefore, the accumulation of 3-DG (Table 1) and its reaction products with GlcN (Figure 8) over time could be partially responsible for GlcN browning with extended incubation periods (Figure 1(3A inset)).

An example of acyclic condensation is the peak at m/z of 343.0889 identified at 3 days of incubation. It is proposed that this molecular ion corresponds to a reduced Schiff base from a condensation between two molecules of GlcN. The possible mechanisms of formation are illustrated in Figure 7, where the reduction of the GlcN−GlcN Schiff base would be promoted from the dehydrogenation of the dihydrofructosazines to fructosazines. Supporting this phenomenon is the observed decrease in intensity of m/z 323.1451 during incubation from 0.5 to 3 days with a concomitant increase intensity of m/z at 321.1286 (Figure 5). Shimamura et al.[49] also reported the reducing capacity of dihydrofructosazine.

In summary, this research demonstrated that GlcN, and not GlcNAc, is the unstable compound, producing 1−6 mg of α-dicarbonyl compounds per gram of GlcN depending on incubation time. The cause of this reactivity lays in the nature of GlcN, which is a Heyns (aldosamine) compound with the potential to generate many reactive α-dicarbonyls, precursors of fluorescent heterocyclic compounds such as pyrazines. By contrast, acetylation of GlcN decreases its reactivity by blocking the nucleophilicity of the free $-NH_2$ group. Considering the ubiquities of GlcNAc in animal tissues, enzymatic acetylation appears to play a crucial role in minimizing the less stable GlcN, which has the potential to form endogenous reactive α-DCs. Also, research interests in GlcN application in food products are dramatically increasing. For instance, Jia et al.[50] proposed the bioconversion of GlcN to deoxyfructosazine and fructosazine to produce flavor compounds for the food industry. Uzzan et al.[17] enriched milk with GlcN with the hope of producing a functional food product; however, the experiment was compromised due to aggregation of milk protein upon pasteurization. This may indicate the cross-linking effects of α-DCs generated from GlcN degradation (unpublished results from our research group also support GlcN-induced myoglobin aggregation at moderate temperatures). In North America, GlcN has the legislative status of "natural health product" (or dietary supplement) and not of a food ingredient; for instance, a specific dose of 1.5 g daily is recommended to treat osteoarthritis. The U.S. Department of Agriculture does not recognize GlcN as "generally recognized as safe" due to lack of clinical studies that its consumption is safe in young children, pregnant women, and diabetics.[16] Hence, more studies are necessary for the use of GlcN as a food ingredient for both technological and safety reasons.

■ ASSOCIATED CONTENT

Ⓢ Supporting Information

Supplemental UHPLC-UV chromatograms of quinoxaline derivatives of α-dicarbonyl compounds produced from GlcNAc and Glc-NH_3 incubated for 12 days; precursor ions and MS/MS spectra of peaks 9 and 10 (from Figure 2II); production of ammonia during incubation of GlcN solutions from 0 to 12 days. The Supporting Information is available free of charge on the ACS Publications website at DOI: 10.1021/acs.jafc.5b02664.

■ AUTHOR INFORMATION

Corresponding Author

*(M.B.) Phone: (780) 248-1598. E-mail: mirko.betti@ualberta.ca.

Funding

This research was funded by grant from Alberta Innovates-Bio Solutions (Al Bio), ALMA, and Natural Sciences and Engineering Research Council (NSERC) of Canada to M.B.

Notes

The authors declare no competing financial interest.

■ ACKNOWLEDGMENTS

We thank Jack Moore at the Institute of Biomolecular Design (University of Alberta, Edmonton) for technical assistance in mass spectrometry experiments.

■ ABBREVIATIONS USED

α-DC, alpha-dicarbonyl compounds; AGEs, advanced glycation end-products; ANOVA, analysis of variance; COS, chitosan oligosaccharide; DA, diacetyl; 3-DG, 3-deoxyglucosone; 3,4-DGE, 3,4-dideoxyglucoson-3-ene; ESI, electrospray ionization; G, glucosone; GAGs, glycosaminoglycans; GFAT, glutamine:-fructose-6-phosphate-aminotransferase; Glc, glucose; GlcN, glucosamine; GlcN-6-P, glucosamine-6-phosphate; GlcNAc, *N*-acetyl-glucosamine; GO, glyoxal; HA, hyaluronic acid; HBP, hexosamine biosynthesis pathway; HPA, hydroxypyruraldehyde; LOD, limit of detection; LOQ, limit of quantification; MGO, methylglyoxal; MS, mass spectrometry; MS/MS, tandem mass spectrometry; nd, not detectable; OPD, *o*-phenylenediamine; PDA, photodiode array detector; RA, retroaldolization; SPE, solid phase extraction; UHPLC, ultra-high-performance liquid chromatography

■ REFERENCES

(1) Anderson, J. W.; Nicolosi, R. J.; Borzecella, J. F. Glucosamine effects in humans: a review of effects on glucose metabolism, side effects, safety considerations and efficacy. *Food Chem. Toxicol.* **2005**, *43*, 187−201.

(2) Block, J. A.; Oegema, T. R.; Sandy, J. D.; Plaas, A. The effects of oral glucosamine on joint health: is a change in research approach needed? *Osteoarthr. Cartil.* **2010**, *18*, 5−11.

(3) Uitterlinden, E. J.; Koevoet, J. L.; Verkoelen, C. F.; Bierma-Zeinstra, S. M.; Jahr, H.; Weinans, H.; Verhaar, J. A.; van Osch, G. J.

DOI: 10.1021/acs.jafc.5b02664
J. Agric. Food Chem. 2015, 63, 6249−6261

Glucosamine increases hyaluronic acid production in human osteoarthritic synovium explants. *BMC Musculoskeletal Disord.* **2008**, *9*, 120−127.
(4) Qu, C.-J.; Karjalainen, H. M.; Helminen, H. J.; Lammi, M. J. The lack of effect of glucosamine sulphate on aggrecan mRNA expression and (35)S-sulphate incorporation in bovine primary chondrocytes. *Biochim. Biophys. Acta, Mol. Basis Dis.* **2006**, *4*, 453−459.
(5) Einbu, A.; Varum, K. M. Characterization of chitin and its hydrolysis to GlcNAc and GlcN. *Biomacromolecules* **2008**, *9*, 1870−1875.
(6) Sibi, G.; Dhananjaya, K.; Ravikumar, K. R.; Mallesha, H.; Venkatesha, R. T. Preparation of glucosamine hydrochloride from crustacean shell waste and it's quantitation by RP-HPLC. *Am.−Eur. J. Sci. Res.* **2013**, *8*, 63−67.
(7) Schleicher, E. D.; Weigert, C. Role of the hexosamine biosynthetic pathway in diabetic nephropathy. *Kidney Int.* **2000**, *77*, S13−8.
(8) Salazar, J.; Bello, L.; Chavez, M.; Anez, R.; Rojas, J.; Bermudez, V. Glucosamine for osteoarthritis: biological effects, clinical efficacy, and safety on glucose metabolism. *Arthritis* **2014**, *2014*, 432463.
(9) Heyns, K.; Koch, W. Z. Über die bildung eines aminozuckers ausd-fruktose und ammoniak. *Z. Naturforsch., B: J. Chem. Sci.* **1952**, *7B*, 486−488.
(10) Mottram, D. S.; Elmore, J. S. Control of the Maillard reaction during the cooking of food. In *Controlling Maillard Pathways To Generate Flavors*, 3rd ed.; Mottram, D. S., Taylor, A. J., Eds.; ACS Symposium Series 1042; American Chemical Society: Washington, DC, USA, 2010; pp 143−155.
(11) Song, K.-H.; Kang, J.-H.; Woo, J.-K.; Nam, J.-S.; Min, H.-Y.; Lee, H. Y.; Kim, S.-Y.; Oh, S.-H. The novel IGF-IR/Akt−dependent anticancer activities of glucosamine. *BMC Cancer* **2014**, *14*, 31.
(12) Chesnokov, V.; Gong, B.; Sun, C.; Itakura, K. Anti-cancer activity of glucosamine through inhibition of N-linked glycosylation. *Cancer Cell Int.* **2014**, *14*, 45−55.
(13) Kantor, E. D.; Lampe, J. W.; Peters, U.; Shen, D. D.; Vaughan, T. L.; White, E. Use of glucosamine and chondroitin supplements and risk of colorectal cancer. *Cancer Cause Control.* **2013**, *24*, 1137−1146.
(14) Wu, S.; Hu, J.; Wei, L.; Du, Y.; Shi, X.; Zhang, L. Antioxidant and antimicrobial activity of Maillard reaction products from xylan with chitosan/chitooligomer/glucosamine hydrochloride/taurine model systems. *Food Chem.* **2014**, *148*, 196−203.
(15) Katsumata, T.; Nakakuki, H.; Tokunaga, C.; Fujii, N.; Egi, M.; Phan, T. H.; Mummalaneni, S.; DeSimone, J. A.; Lyall, V. Effect of Maillard reacted peptides on human salt taste and the amiloride-insensitive salt taste receptor (TRPV1t). *Chem. Senses* **2008**, *33*, 665−680.
(16) Kralovec, A.; Barrow, C. J. Glucosamine production and health benefits. In *Marine Nutraceuticals and Functional Food*, 1st ed.; Barrow, C., Shahidi, F., Eds.; CRC Press: Boca Raton, FL, USA, 2008; pp 198−227.
(17) Uzzan, M.; Nechrebeki, J.; Labuza, T. P. Thermal and storage stability of nutraceuticals in a milk beverage dietary supplement. *J. Food Sci.* **2007**, *72*, E109−114.
(18) Hrynets, Y.; Ndagijimana, M.; Betti, M. Non-enzymatic glycation of natural actomyosin (NAM) with glucosamine in a liquid system at moderate temperatures. *Food Chem.* **2013**, *139*, 1062−1072.
(19) Nakamura, M.; Barber, A. J.; Antonetti, D. A.; LaNoue, K. F.; Robinson, K. A.; Buse, M. G.; Gardner, T. W. Excessive hexosamines block the neuroprotective effect of insulin and induce apoptosis in retinal neurons. *J. Biol. Chem.* **2001**, *276*, 43748−43755.
(20) Hawkins, M.; Barzilai, N.; Chen, W.; Angelov, I.; Hu, M.; Cohen, P.; Rossetti, L. Increased hexosamine availability similarly impairs the action of insulin and IGF-1 on glucose disposal. *Diabetes* **1996**, *45*, 1734−1743.
(21) Zhang, X.; Tong, N.; Li, Y. Concurrently using rosiglitazone prevents glucosamine-induced islet and beta Cell apoptosis and dysfunction. *Cell Biochem. Funct.* **2010**, *28*, 509−514.
(22) Candiano, G.; Ghiggeri, G. M.; Gusmano, R.; Zetta, L.; Benfenati, E.; Icardi, G. Reaction of 2-amino-2-deoxyglucose and lysine: isolation and characterization of 2,5-bis(tetrahydroxybutyl)-pyrazine. *Carbohydr. Res.* **1988**, *184*, 67−75.
(23) Kashige, N.; Yamaguchi, T.; Mishiro, N.; Hanazono, H.; Miake, F.; Watanabe, K. Possible involvement of dihydrofructosazine in the DNA breaking activity of D-glucosamine. *Biol. Pharm. Bull.* **1995**, *18*, 653−658.
(24) Zhang, X.; Ma, Y.; Liu, H.; De Sa, P. F.; Brown, P. R.; Dain, J. A. Capillary electrophoresis separation of autocondensation glycation products of glucosamine. *J. Capill. Electrophor. Microchip. Technol.* **2003**, *1−2*, 33−37.
(25) Horowitz, M. I. Nonenzymatic modifications of amino sugars in vitro. *Arch. Biochem. Biophys.* **1991**, *288*, 317−323.
(26) Papetti, A.; Mascherpa, D.; Gazzani, G. Free α-dicarbonyl compounds in coffee, barley coffee and soy after in vitro digestion. *Food Chem.* **2014**, *164*, 259−265.
(27) Zhang, X.; Ma, Y.; Liu, H.; De Sa, P. F.; Brown, P. R.; Dain, J. A. Monitoring the formation of Maillard reaction products of glucosamine with fibrinogen and human serum albumin using capillary electrophoresis. *Anal. Biochem.* **2004**, *325*, 255−259.
(28) Fogliano, V.; Monti, S. M.; Musella, T.; Randazzo, G.; Ritieni, A. Formation of coloured Maillard reaction products in a gluten-glucose model system. *Food Chem.* **1999**, *66*, 293−299.
(29) Ferrer, E.; Alegria, A.; Farre, R.; Clemente, G.; Calvo, C. Fluorescence, browning index, and color in infant formulas during storage. *J. Agric. Food Chem.* **2005**, *53*, 4911−4917.
(30) Mittelmaier, S.; Fünfrocken, M.; Fenn, D.; Berlich, R.; Pischetsrieder, M. Quantification of the six major α-dicarbonyl contaminants in peritoneal dialysis fluids by UHPLC/DAD/MSMS. *Anal. Bioanal. Chem.* **2011**, *401*, 1183−1193.
(31) Pfeifer, Y. V.; Kroh, L. W. Investigation of reactive alpha-dicarbonyl compounds generated from the Maillard reactions of L-methionine with reducing sugars via their stable quinoxaline derivatives. *J. Agric. Food Chem.* **2010**, *58*, 8293−8299.
(32) Gensberger, S.; Mittelmaier, S.; Glomb, M. A.; Pischetsrieder, M. Identification and quantification of six major α-dicarbonyl process contaminants in high-fructose corn syrup. *Anal. Bioanal. Chem.* **2012**, *403*, 2923−2931.
(33) Mavric, E.; Wittmann, S.; Barth, G.; Henle, T. Identification and quantification of methylglyoxal as the dominant antibacterial constituent of Manuka (*Leptospermum scoparium*) honeys from New Zealand. *Mol. Nutr. Food Res.* **2008**, *52*, 483−489.
(34) Kerler, J.; Winkel, C.; Davidek, T.; Blank, I. Basic chemistry and process conditions for reaction flavours with particular focus on Maillard-type reactions. In *Food Flavour Technology*, 2nd ed.; Taylor, A. J., Linforth, R. S. T., Eds.; Blackwell Publishing: Chichester, UK, 2010; Vol. 2, pp 51−81.
(35) Sena, C. M.; Metafome, P.; Crisostomo, J.; Rodrigues, L.; Fernandes, R.; Pereira, P.; Seica, R. M. Methylglyoxal promotes oxidative stress and endothelial dysfunction. *Pharmacol. Res.* **2012**, *65*, 497−506.
(36) Hofmann, T.; Bors, W.; Stettmaier, K. Studies on radical intermediates in the early stage of the nonenzymic browning reaction of carbohydrates and amino acids. *J. Agric. Food Chem.* **1999**, *47*, 379−390.
(37) Gobert, J.; Glomb, M. A. Degradation of glucose: reinvestigation of reactive α-dicarbonyl compounds. *J. Agric. Food Chem.* **2009**, *57*, 8591−8597.
(38) Degen, J.; Hellwig, M.; Henle, T. 1, 2-dicarbonyl compounds in commonly consumed foods. *J. Agric. Food Chem.* **2012**, *60*, 7071−7079.
(39) Yaylayan, V. A.; Huyghues-Despointes, A. Chemistry of Amadori rearrangement products: analysis, synthesis, kinetics, reactions and spectroscopic properties. *Crit. Rev. Food Sci. Nutr.* **1994**, *34*, 321−369.
(40) Belitz, H.-D.; Grosch, W.; Schieberle, P. Carbohydrates. In *Food Chemistry*, 4th ed.; Belitz, H.-D., Grosch, W., Schieberle, P., Eds.; Springer-Verlag: Berlin, Germany, 2009; pp 248−337.
(41) Shibamoto, T. Diacetyl: occurrence, analysis, and toxicity. *J. Agric. Food Chem.* **2014**, *62*, 4048−4053.

DOI: 10.1021/acs.jafc.5b02664
J. Agric. Food Chem. 2015, 63, 6249−6261

(42) Weenen, H. Reactive intermediates and carbohydrate fragmentation in Maillard chemistry. *Food Chem.* **1998**, *62*, 393−401.
(43) Yaylayan, V. A.; Keyhani, A. Origin of carbohydrate degradation products in L-alanine/D-[13C]glucose model systems. *J. Agric. Food Chem.* **2000**, *48*, 2415−2419.
(44) Thornalley, P. J.; Langborg, A.; Minhas, H. S. Formation of glyoxal, methylglyoxal and 3-deoxyglucosone in the glycation of proteins by glucose. *Biochem. J.* **1999**, *344*, 109−116.
(45) Nursten, H. The chemistry of nonenzymic browning In *The Maillard Reaction: Chemistry, Biochemistry and Implications*, 1st ed.; Nursten, H., Ed.; Royal Society of Chemistry: Cambridge, UK, 2005; pp 5−30.
(46) Hayashi, T.; Namiki, M. Role of sugar fragmentation in the Maillard reaction. *Dev. Food Sci.* **1986**, *13*, 29−38.
(47) Hofmann, T.; Heuberger, S. The contribution of coloured Maillard reaction products to the total colour of browned glucose/l-alanine solutions and studies on their formation. *Z. Lebensm Unters. Forsch. A* **1999**, *208*, 17−26.
(48) Klinger, K. M.; Liebner, F.; Fritz, I.; Potthast, A.; Rosenau, T. Formation and ecotoxicity of N heterocyclic compounds on ammoxidation of mono- and polysaccharides. *J. Agric. Food Chem.* **2013**, *61*, 9004−9014.
(49) Shimamura, T.; Takamori, A.; Ukeda, H.; Sawamura, M. Reduction mechanism of tetrazolium salt XTT by a glucosamine derivative. *Biosci., Biotechnol., Biochem.* **2003**, *67*, 295−299.
(50) Jia, L.; Wang, Y.; Qiao, Y.; Qia, Y.; Hou, X. Efficient one-pot synthesis of deoxyfructosazine and fructosazine from D-glucosamine hydrochloride using a basic ionic liquid as a dual solvent-catalyst. *RSC Adv.* **2014**, *4*, 44253−44260.

DOI: 10.1021/acs.jafc.5b02664
J. Agric. Food Chem. 2015, 63, 6249−6261

novel industrial enzymes, such as cellulases, hemicellulases, polygalacturonases, and mannanases.[15,16] In this study, we used a fast and effective approach, combining degenerate PCR and thermal asymmetric interlaced PCR (TAIL-PCR), to identify a novel exochitinase gene from pig fecal environment DNA. Our aim was to characterize a novel exochitinase having application potentials in the food and feed industries.

MATERIALS AND METHODS

Sample Collection and DNA Extraction. Pig fecal sample used in this study was collected from Hebei province, China, and stored at −20 °C before use. Pig feces samples (0.5 g) were suspended in 40 mL of prewash buffer (100 mM Tris-HCl, pH 8.0), shaken at room temperature, and centrifuged for 10 min at 14000*g*. The pellet was then dissolved in 9.5 mL of lysis buffer (100 mM Tris-HCl, 100 mM EDTA, 1.5 M NaCl, lysozyme 10 mg/mL) followed by incubation at 37 °C for 2 h.[17] Then 500 μL of 10% sodium dodecyl sulfate and 1 mg of proteinase K were added, and incubation was continued at 70 °C for 30 min. After centrifugation at 14000*g* for 10 min, 9 mL of the supernatant was transferred to a fresh 40 mL tube. Then 9 mL of phenol/chloroform/isoamyl alcohol (25:24:1) mixture was added, mixed gently, and separated by centrifugation at 14000*g* (4 °C) for 10 min. The aqueous phase was transferred to a new 40 mL tube and the preview step repeated. The aqueous phase was transferred to fresh tubes, 0.8 volume of precooled isopropanol was added, and centrifugation was performed at 14000*g* for 10 min. Pellets were washed with ice-cold 75% (v/v) ethanol and dissolved in 1 mL of TE buffer (10 mM Tris-HCl; pH 8.0, 1 mM EDTA). Then the DNA were purified using a Gel Extraction Kit (Biomed Inc., China) according to the manufacturer's protocol and verified by electrophoresis on 1% agarose gels. The presence and size of purified DNA were determined by agarose gel electrophoresis with ethidium bromide staining.

Cloning and Sequence Analysis of the Chitinase Gene (*Echi47*). The conserved regions of glycosyl hydrolase (GH) family 18 chitinases were determined by aligning their amino acid sequences obtained from the NCBI database using CLUSTAL_X (version 1.8). The degenerate primer specific for GH 18 chitinases weas designed using the CODEHOP strategy.[18] Based on the sequence alignment analysis, two highly conserved regions, DG(I/V)D(I/L/F)DWEYP and YDING(F/I/M)W for GH 18 chitinases were identified, and the CODEHOP primer (CHIF, 5′-GGNRTNGAYHTNGAYTGGGAR-TAYCC-3′; CHIR: 5′-CCAATGNCCRTTDATRTCRTA-3′) was designed. The reaction mixture (50 μL) contained 2.5 U of LA *Taq* polymerase (Takara, Japan), 250 μM of each dNTP, 1.5 mM Mg^{2+} in the buffer supplied by the manufacturer (Takara, Japan), 0.5 μM of each primer, and ∼50 ng of template DNA. PCR was performed as follows: 95 °C for 5 min, followed by 8 cycles of 94 °C for 30 s, 48−52 °C (increasing by 0.5 °C after each cycle) for 30 s, and 72 °C for 30 s, then 25 cycles of 95 °C for 30 s, 56 °C for 30 s, and 72 °C for 30 s, and then a final extension at 72 °C for 5 min. PCR products of the appropriate size (280 bp) were recovered from 1.5% agarose gel using the Gel Extraction Kit (Biomed Inc., China), ligated into the vector pGEM-T-Easy (Promega, Madison, WI, USA), and transformed into *E. coli* DH5α following the manufacturer's protocols. Colonies were selected randomly, and then inserts of the correct size were sequenced. The positive transformants were randomly picked and sequenced by Sangon Inc. (Shanghai, China). Sequence similarity analysis and alignment were carried out using BLASTX (http://www.ncbi.nlm.nih.gov/BLAST/). The 5′ and 3′ flanking regions of the chitinase gene fragment were obtained using thermal asymmetric interlaced PCR.[19] The TAIL-PCR runs include primary, secondary, and tertiary amplifications[19] with arbitrary primers (LAD1, 5′-ACGATGGAC-TCCAGAVNVNNNGGAA-3′; LAD2, 5′-ACGATGGACTCCAGA-BNBNNNGGTT-3′; LAD3, 5′-ACGATGGACTCCAGAVVNVNN-NCCAA-3′; LAD4, 5′-ACGATGGACTCCAGABDNBNNNCGGT-3′; AC, 5′-ACGATGGACTCCAGA-3′) and specific primers (FSP1, 5′-TATCCTGCCAGTCCCGAGCAA-3′; FSP2, 5′-TCAATGAAG-CCGAGGATACCA-3′; FSP3, 5′-ATGAAGGATGTTTCCGAG-TTTGC-3′; RSP1, 5′-GCAAACTCGGAAACATCCTTCA-3′; RSP2, 5′-GCTCCTTCTTGCCACCTTTCT-3′; RSP3, 5′-GCTTGTTGC-TCGGGACTGG-3′). The tertiary PCR products of the expected sizes were purified and cloned into pMD18-T vectors (Takara, Japan) for sequencing.

Sequencing and Phylogenetic Analysis. Sequence analysis and multiple alignments were performed by Vector NTI 10.0 (Invitrogen) and BLAST programs (http://blast.ncbi.nlm.nih.gov/Blast.cgi), respectively. N-terminal signal peptide analysis was done using Signal IP version 4.0 (http://www.cbs.dtu.dk/services/SignalP/). Phylogenetic trees were constructed with MEGA version 4.0[20] using the neighbor-joining method. Confidence for tree topology was estimated on the basis of 1000 bootstrap replicates.

Heterogenous Expression and Purification. The gene (*Echi47*) sequence encoding a chitinase was amplified from the environmental genomic DNA. *Nco*I and *Xho*I sites (underlined) were added to the forward and reverse primers (EchiNcoI, 5′-CATGCCATGGGCA-AAGTCATCGTTGGATACTTC-3′; EchiXhoI, 5′-CCGCTCGAG-TGATCTTATTTTGTAGACCTCATT-3′), respectively. The PCR products were gel-purified, digested, and cloned into pET-28a (+) vector, and the recombinant plasmids were transformed into *E. coli* BL21 (DE3) competent cells. The positive transformants were cultured in 20 mL of LB medium containing 50 μg/mL kanamycin at 37 °C to an OD_{600} of 0.5−0.7. The recombinant enzyme was induced by 0.5 mM isopropyl-β-D-1-thiogalactopyranoside (IPTG), and the culture was further grown at 20 °C for 24 h. The recombinant protein was concentrated and purified by Ni-IDA agarose as described before.[21] Briefly, the bound recombinant chitinase (Echi47) was eluted with buffer (50 mM Tris-HCl pH 8.0, 500 mM NaCl, 150 mM imidazole). Fractions with high chitinase activity were pooled and dialyzed against 50 mM citrate buffer (pH 5.0). The purified chitinase was monitored by sodium dodecyl sulfate−polyacrylamide gel electrophoresis (SDS-PAGE). For detection of chitinase on gel, purified enzyme was added to SDS-PAGE sample buffer and heated at 100 °C for 5 min. The sample was separated with an 10% polyacrylamide gel containing 0.1% glycol chitin, and the gel was immersed in refolding buffer (50 mM Tris-HCl pH 7.5, 1% Triton X-100) at 37 °C overnight. The gel was washed with distilled water and then stained with 0.01% (w/v) CalcoXuor white M2R in 10 mM Tris-HCl (pH 7.5). After 5 min, the brightener solution was removed and the gel was washed with distilled water. The gel was placed on a UV transilluminator to visualize the lytic zone.[22]

The native molecular mass was estimated by Sephacryl S-100 HR column (1 cm × 40 cm) in 20 mM Tris-HCl buffer (pH 7.4) containing 100 mM NaCl at a flow rate of 0.3 mL/min. The molecular mass standards used were phosphorylase *b* (97.2 kDa), bovine serum albumin (66.0 kDa), albumin from egg chicken white (45.0 kDa), α-chymotrypsinogen A (type II from bovine pancreas, 25.7 kDa), and lysozyme (14.4 kDa).

Enzymatic Assay and Protein Determination. The chitinase activity was assayed using the dinitrosalicylic acid (DNS) method,[23] by measuring the reducing sugar. The standard reaction mixture consisting of 0.1 mL of enzyme, 0.1 mL of 1% (w/v) colloidal chitin, and 0.2 mL of 50 mM citrate buffer, pH 5.0, was incubated at 40 °C for 30 min. After incubation, the reaction was terminated by the addition of 0.4 mL of DNS reagent and boiled for 10 min. Then, the samples were rapidly cooled to room temperature and centrifuged at 14000*g* for 3 min. The absorbance of the supernatant was measured at 540 nm. One unit of chitinase activity (U) was defined as the amount of enzyme that releases 1 μmol of *N*-acetylglucosamine per minute under standard assay conditions. The protein concentration was determined according to the method of Lowry et al.[24] using bovine serum albumin (BSA) as the standard. The specific activity was expressed as units (U) per milligram of protein.

Enzyme Characterization. The optimal pH of the recombinant chitinase was determined using 50 mM various buffers within pH 3.0−10.0: citrate (pH 3.0−6.0), acetate (pH 4.0−6.0), phosphate (pH 5.0−7.0), 2-(morpholino)ethanesulfonic acid (MES, pH 6.5−7.5), Tris-HCl (pH 7.0−9.0), and *N*-cyclohexyl-2-aminoethanesulfonic acid (CHES, pH 8.0−10.0). For pH stability determination, residual activity was measured using the standard assay after the enzyme was

DOI: 10.1021/acs.jafc.5b01457
J. Agric. Food Chem. 2015, 63, 6262−6270

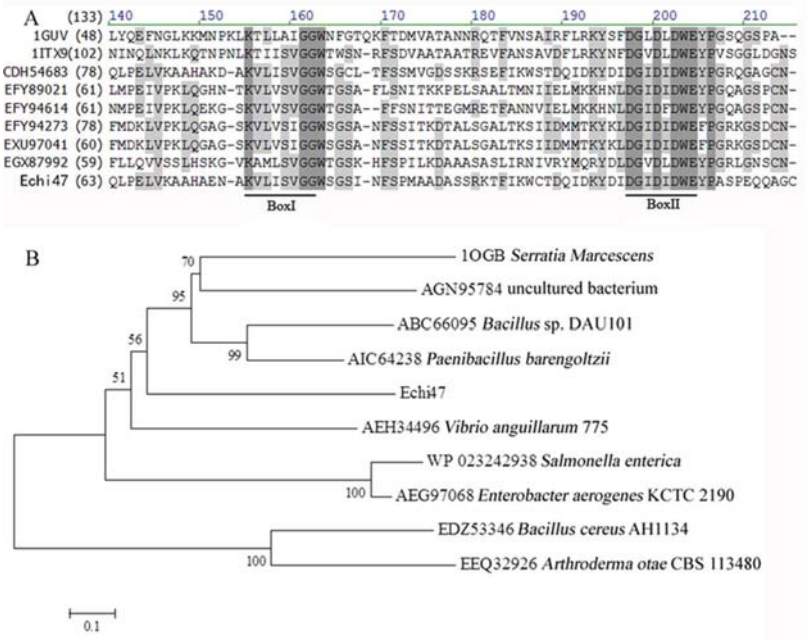

Figure 1. (A) Multiple-sequence alignment of the glycosyl hydrolase (GH) family 18 chitinase sequences. Protein motifs identified within the novel exochitinase Echi47 protein sequence include a chitin-binding motif (BoxI, SxGG) and a catalytic motif (BoxII, DxxDxDxE) with the active site (Glu, 112), indicating that it belongs to GH family 18. Accession numbers in GenBank are 1GUV (*Homo sapiens*), 1ITX (*Bacillus circulans*), CDH54683 (*Lichtheimia corymbifera* JMRC:FSU:9682), EFY89021 (*Metarhizium acridum* CQMa 102), EFY94614 (*Metarhizium robertsii* ARSEF 23), EFY94273 (*Metarhizium robertsii* ARSEF 23), EXU97041 (*Metarhizium robertsii*), and EGX87992 (*Cordyceps militaris* CM01). (B) Phylogenetic tree of the GH family 18 exochitinase based on protein sequence alignment of the catalytic domains. The tree was constructed by the neighbor-joining method using MEGA 4.0. The sequences were selected from GenBank.

incubated at 40 °C for 30 min in the different buffers. Optimal temperature of the purified chitinase was determined by the standard assay at the temperatures ranging from 20 to 70 °C; thermostability was measured after preincubation of enzyme at temperatures from 25 to 70 °C for 30 min.

The enzyme samples were preincubated with various metal ions and chemical reagents (Cu^{2+}, Ca^{2+}, Ni^{2+}, Mg^{2+}, Hg^{2+}, Zn^{2+}, Mn^{2+}, Co^{2+}, Na^{+}, Ba^{2+}, Ag^{+}, Fe^{3+}, Cr^{3+}, Fe^{2+}, K^{+}, EDTA, β-mercaptoethanol, and SDS) in 50 mM citrate buffer, pH 5.0, at 37 °C for 30 min. The residual activities were then measured by the standard assay. The relative activities were determined by comparison with control without metal ions or chemical reagents (100%).

Substrate Specificity and Kinetic Parameters. To evaluate the substrate specificity of the purified chitinase, Echi47 was incubated with 1% (w/v) of different substrates such as colloidal chitin, glycol chitin, glycol chitosan, powder chitin, powder shrimp shell, glucan, carboxymethyl cellulose, Avicel, or 10 mM *p*NP-GlcNAc.

Kinetic data were determined at 40 °C for 5 min using colloidal chitin as the substrate in 50 mM citrate buffer (pH 5.0) with concentrations ranging from 2 to 10 mg/mL. The Michaels−Mention constant (K_m) and maximum velocity (V_{max}) were determined from a Lineweaver−Burk plot.

Hydrolysis Properties of Echi47. The reaction mixture, containing 1% colloidal chitin and 0.5 U of purified chitinase (Echi47), was incubated at 40 °C for 2 h. Hydrolysis products were analyzed by thin-layer chromatography (TLC).[25] High-performance liquid chromatography (HPLC) was carried out in a Shodex sugar KS-802 column (Waters, Milford, MA, USA), which was eluted with acetonitrile/H_2O (100%) at a flow rate of 1 mL/min. The mixture of *N*-acetyl-COSs [(GlcNAc, $(GlcNAc)_2$, and $(GlcNAc)_3$)] was purchased from Megazyme International (Bray, Ireland) and used as the standards. *N*-Acetyl-COSs were eluted and monitored by recording absorption at 210 nm. $(GlcNAc)_2$, $(GlcNAc)_3$, and $(GlcNAc)_4$ were hydrolyzed by Echi47, respectively. The reaction mixture, containing a 0.5 mg solution of the corresponding substrate and 15 mU of purified enzyme in 100 μL of 50 mM citrate buffer (pH 5.0), was incubated at 40 °C for 40 min. Samples were withdrawn at various time points and were then boiled for 5 min to terminate the chitinase.

Protease Treatments. To determine resistance to proteases, the purified Echi47 (4 mU) was incubated with pepsin (pH 2.0; Sigma), trypsin (pH 7.0; Sigma), proteinase K (pH 7.5; Sigma), and flavor protease (pH 7.0; Novozymes) at a ratio of 1:10 (Echi47/protease, w/w) at 37 °C for 1 h. The residual activities were determined using the standard assay. The control was performed under the same conditions without Echi47.

Enzyme Stability and Activity under Simulated Gastric and Intestinal Conditions. The stabilities of Echi47 in simulated gastric fluid (SGF) and simulated intestinal fluid (SIF) were examined using a previously reported method with some modifications.[26] Purified Echi47 (0.2 U) was incubated in SGF or SIF at 37 °C for 20 min. Residual chitinase activity was determined using a standard assay. As a control, purified Echi47 was incubated in SGF and SIF without pepsin/trypsin under the same conditions. The results from three individual experiments were averaged.

The stomach and intestinal digestion phase was simulated according to the model described by Minekus et al.[27] with some modifications. Reaction systems (40 mL of each) containing 2.0 mg/mL NaCl, 200 mM glycine-HCl, 3.2 mg/mL pepsin, and 80 mg colloidal chitin were initially adjusted to pH 2.0 on ice, and then 500 μg of purified Echi47 with the specific activity of 6.84 U/mg was added. The mixture was incubated at 37 °C for 20 min, followed by further incubations for 20 min at pH 3.0, 4.0, 5.0, and 6.0, respectively. The pH changes were done while the reaction mixture was temporarily placed on ice. Finally, 10 mg/mL trypsin was added, the pH was adjusted to 6.8, and the mixture was incubated at 37 °C for 20 min. All procedures were conducted in a rotary incubator with shaking at 100 rpm. Samples (400 μL) were collected at the end of each phase and analyzed according to the DNS method.[23]

DOI: 10.1021/acs.jafc.5b01457
J. Agric. Food Chem. 2015, 63, 6262−6270

RESULTS

Amplification of the Chitinase Gene and Sequence Analysis. The PCR products (~280 bp for GH 18 chitinases) were amplified directly from environmental DNA by touchdown PCR. To obtain the full-length chitinase gene, the 5′ and 3′ fragments flanking the core regions were amplified by TAIL-PCR with three nested insertion-specific primers.[19] The full-length *Echi47* cDNA consisted of 1161 nucleotides (GenBank accession no. KP182406) and encoded an ORF of 386 amino acid residues with a predicted isoelectric point of 5.28. The diagnostic domains SxGG (chitin-binding motif) and DxxDxDxE (catalytic motif), a signature of GH18 chitinases,[28] are conserved in Echi47 (Figure 1A). The consensus sequence locates as DIDWE at positions from 110 to 115 in Echi47, where Glu112 in Echi47 is a putative catalytic residue in the active site.[4] According to the homology search of the deduced amino acid sequences by BLAST, Echi47 showed the identity of 35−77% to other chitinases. The amino acid sequence of Echi47 showed the highest identity of 77% to that of GH family 18 protein (accession no. CDH54683) from *Lichtheimia corymbifera* JMRC:FSU:9682. Echi47 shared 36% identity with the characterized chitinase (accession no. AFD19009) from *Coprinellus congregatus*.[29] Therefore, Echi47 may be a novel GH family 18 chitinase.

Enzyme Expression and Purification. The chitinase gene (*Echi47*) was successfully expressed in *E. coli* as soluble intracellular proteins with His-tags. The recombinant chitinase (Echi47) was purified from the crude cell extract by a single-step purification procedure using a Ni-IDA agarose resin column. It was purified 8.65-fold with a recovery yield of 56.7%. The purified enzyme migrated as a single band on SDS-PAGE with an apparent molecular mass of 47.6 kDa (Figure 2). The

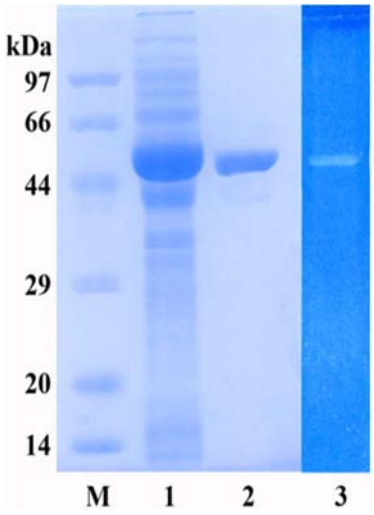

Figure 2. SDS-PAGE and zymogram of purified recombinant exochitinase (Echi47). Lanes: M, protein molecular weight marker; 1, crude extract; 2, purified Echi47; 3, zymogram of the purified chitinase.

lytic zone in the in-gel assay confirmed the chitinase activity of Echi47 (Figure 2). The native molecular mass of the enzyme was estimated to be 47 kDa by gel filtration chromatography on a Sephacryl S-100 HR column, indicating that it is a monomer.

Enzyme Characterization. The purified Echi47 had a maximum activity at pH 5.0 (Figure 3A). The enzyme was stable within pH 4.0−9.0 (Figure 3B). The optimal temperature of Echi47 was 40 °C (Figure 3C). The enzyme retained >50% of the maximum activity when assayed at 30−50 °C (Figure 3C). The enzyme was stable up to 45 °C (Figure 3D). Purified Echi47 was assayed using different substrates. Echi47 showed high activity toward colloidal chitin (6.84 U/mg), followed by glycol chitin (3.38 U/mg), but no activity toward glycol chitosan, powdered chitin, powdered shrimp shell, glucan, carboxymethyl cellulose, Avicel, and *p*NP-GlcNAc. The K_m, V_{max}, K_{cat}, and K_{cat}/K_m values using colloidal chitin as the substrate were 2.2 mg/mL, 12 U/mg, 0.0095 s^{-1}, and 0.0043 mg^{-1} s^{-1} mL, respectively.

The influence of metal ions on chitinase activity of Echi47 was tested by incubating 1 mM of various metal ions with the enzyme samples (Table 1). Among the metal ions and chemicals used, *β*-mercaptoethanol (129.3%), Ni^{2+} (118.4%), Na^{+} (112.8%), and Cr^{3+} (113.1%) increased the enzyme activity, whereas Hg^{2+} (20.5%), Ag^{+} (23.2%), Co^{2+} (64.9%), and EDTA (70.7%) decreased the activity of the enzyme. Ca^{2+}, Cu^{2+}, Mg^{2+}, Fe^{3+}, Zn^{2+}, Mn^{2+}, Ba^{2+}, Fe^{2+}, K^{+}, and SDS had negligible effect on enzyme activity (Table 1). The crustacean shell consists mainly of protein (30−40%), mineral salts (30−50%), and chitin (13−42%).[30] Cu^{2+}, Ca^{2+}, Mn^{2+}, Fe^{2+}, Zn^{2+}, and Ba^{2+} have been found in shrimp shells.[30]

Hydrolysis Properties of Echi47. Hydrolysis properties of Echi47 were analyzed by TLC and HPLC. When colloidal chitin was used as substrate, $(GlcNAc)_2$ was mostly produced in the initial stage. Small amounts of GlcNAc (2.9−8.3%) and $(GlcNAc)_3$ (11.8−2.4%) were detected (Table 2 and Figure 4); finally, at 24 h, the reaction mixture contained $(GlcNAc)_2$ (91.2%) and GlcNAc (8.8%). The amount of $(GlcNAc)_2$ was >10-fold higher than that of GlcNAc. The proportion of $(GlcNAc)_2$ slowly increased with prolonged incubation times (Table 2 and Figure 4A). The proportion of GlcNAc increased along with the reduction of $(GlcNAc)_3$ (Table 2). Moreover, $(GlcNAc)_4$ was hydrolyzed by Echi47 to yield exclusively $(GlcNAc)_2$ (Figure 4C). When $(GlcNAc)_3$ was used as a substrate, the products were $(GlcNAc)_2$ and GlcNAc. Echi47 hardly hydrolyzed $(GlcNAc)_2$.

Protease Resistance and Activity under Simulated Gastric and Intestinal Conditions. Echi47 exhibited excellent resistance to tested proteases, namely, trypsin (94.8%), proteinase K (98.3%), and flavor protease (98.3%), except pepsin (67.8%) (Figure 5). Moreover, Echi47 retained >80% activity at pH 3.0−6.8 at the whole stomach stage with or without the presence of pepsin after incubation in SGF and SIF at 37 °C for 20 min (Figure 6A). Under simulated alimentary tract conditions, Echi47 was very active and efficient in the degradation of substrate, releasing 21.1 mg of *N*-acetyl-COSs from 80 mg of colloidal chitin (Figure 6B).

DISCUSSION

Chitinase plays an important role in the decomposition of chitin and potential utilization of chitin as a renewable resource. Microorganisms are a major source of chitinases. However, only a tiny fraction of natural microorganisms can be cultured by conventional microbiological techniques.[13] A metagenome-based technique has recently been recognized as an attractive approach to mining novel genetic resources in the natural environment.[31] Many novel microbial enzymes have been successfully cloned from various environments, such as xylanase from compost-soil,[32] carboxylesterases from seawater,[33] and chitinase from suppressive soil.[14] Animal fecal microorganisms represent rich resources of novel glycoside hydrolases.[34]

DOI: 10.1021/acs.jafc.5b01457
J. Agric. Food Chem. 2015, 63, 6262−6270

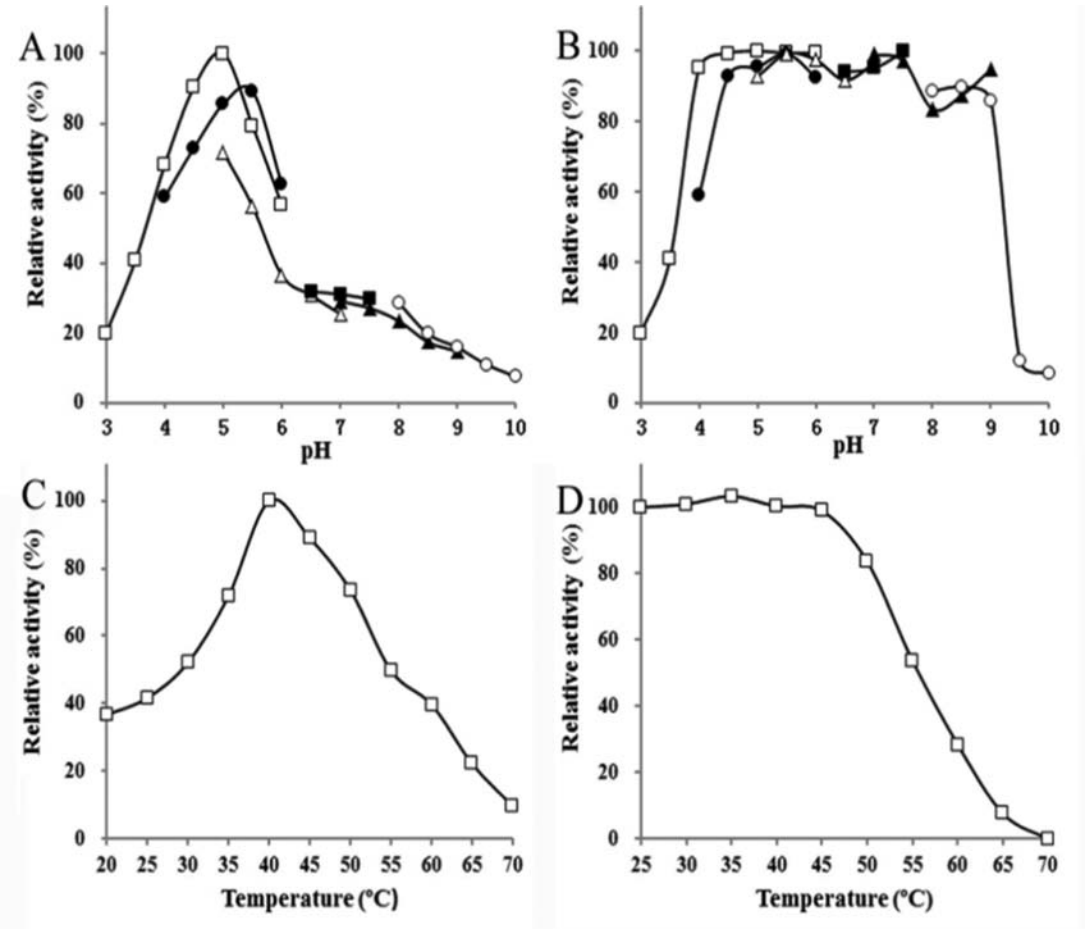

Figure 3. Characterization of purified Echi47: (A) effect of pH on Echi47; (B) pH stability of Echi47 [influence of pH and pH stability of Echi47 activity was determined at 40 °C using different buffers: citrate (□), acetate (●), phosphate (△), MES (■), Tris-HCl (▲), and CHES (○)]; (C) effect of temperature on Echi47 activity; (D) thermostability of Echi47 (temperature profiles were measured at different temperatures in 50 mM citrate buffer (pH 5.0)). Each value represents the mean ± SD (n = 3).

Table 1. Effects of Metal Ions and Chemical Reagents on the Activity of Echi47

chemical	specific activity[a] (U/mg)	relative activity (%)
none	6.84	100.0
Cu^{2+}	5.5 ± 0.2	80.1 ± 2.9
Ca^{2+}	6.4 ± 0.1	93.5 ± 1.5
Ni^{2+}	8.1 ± 0.12	118.4 ± 1.7
Mg^{2+}	5.8 ± 0.08	84.1 ± 1.2
Zn^{2+}	6.5 ± 0.37	94.3 ± 5.4
Hg^{2+}	1.4 ± 0.18	20.5 ± 2.6
Mn^{2+}	6.1 ± 0.29	89.9 ± 4.2
Co^{2+}	4.4 ± 0.23	64.9 ± 3.3
Na^{+}	7.7 ± 0.32	112.8 ± 4.7
Ba^{2+}	7.1 ± 0.57	103.1 ± 8.4
Ag^{+}	1.6 ± 0.25	23.2 ± 3.6
Fe^{3+}	5.7 ± 0.18	83.1 ± 2.6
Cr^{3+}	7.7 ± 0.12	113.1 ± 1.8
Fe^{2+}	6.8 ± 0.27	99 ± 4.0
K^{+}	7.0 ± 0.23	102.9 ± 3.4
EDTA	4.8 ± 0.15	70.7 ± 2.2
β-mercaptoethanol	8.8 ± 0.01	129.3 ± 0.2
SDS	6.1 ± 0.5	89.7 ± 7.3

[a]Activity was determined at 40 °C in 50 mM citrate (pH 5.0) for 30 min.

Table 2. HPLC Analysis of Colloidal Chitin Hydrolyzed by Echi47

	proportion of hydrolysate (%)		
reaction time (min)	GlcNAc	$(GlcNAc)_2$	$(GlcNAc)_3$
5	2.9 ± 0.13	85.4 ± 1.23	11.8 ± 0.15
15	3.9 ± 0.25	86.4 ± 1.1	9.8 ± 0.27
30	5.2 ± 0.03	87.5 ± 1.53	7.3 ± 0.03
60	5.9 ± 0.2	88.5 ± 2.27	5.6 ± 0.14
120	6.6 ± 0.27	88.5 ± 2.73	4.9 ± 0.22
240	8.3 ± 0.26	89.4 ± 3.23	2.4 ± 0.09

Therefore, a novel chitinase gene (*Echi47*) was directly cloned from pig fecal environment DNA, which is the first chitinase isolated from environmental DNA using a genomic walking PCR technique.

Microbial chitinases vary widely in their molecular masses, ranging from as low as 20 kDa to about 200 kDa.[3] Moreover, GH family 18 exochitinases have a size range of 40−60 kDa without carbohydrate-binding modules.[4] Thus, the molecular mass of Echi47 is similar to that of other exochitinases. The specific activity (6.84 U/mg) of the purified Echi47 toward colloidal chitin is higher than that of the chitinase from *Bacillus* sp. DAU101 (0.73 U/mg)[35] and *Vibrio parahemolyticus* (1.5 U/mg),[36] but lower than that of a chitinase from *Paenicibacillus barengoltzii* (19.9 U/mg).[5]

DOI: 10.1021/acs.jafc.5b01457
J. Agric. Food Chem. 2015, 63, 6262−6270

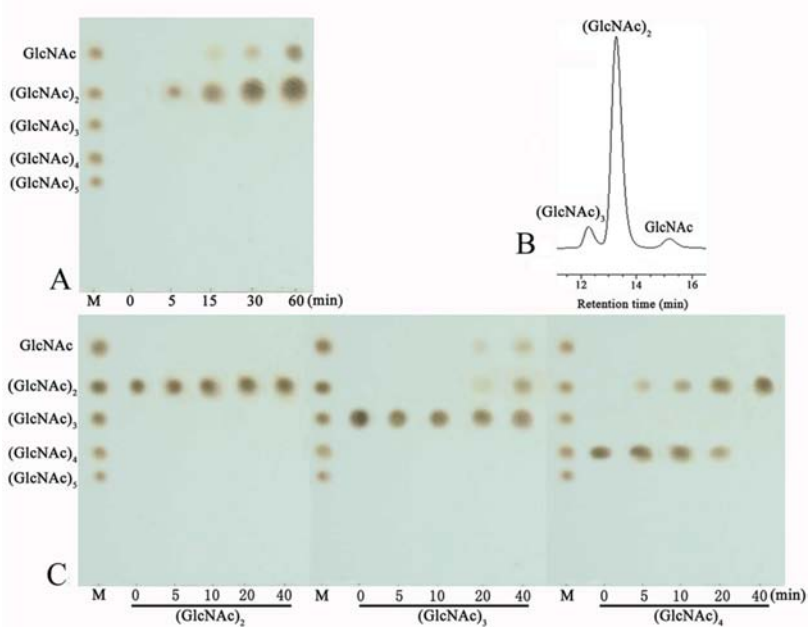

Figure 4. Hydrolysis properties of Echi47: (A) thin layer chromatography (TLC) analysis of colloidal chitin hydrolyzed by purified Echi47; (B) hydrolysis products from colloidal chitin by Echi47 at the stage of reaction (30 min); (C) TLC of various *N*-acetyl-COSs hydrolyzed by Echi47. The reaction mixture (100 μL) containing 0.5 mg of *N*-acetyl-COSs [$(GlcNAc)_2$, $(GlcNAc)_3$ or $(GlcNAc)_4$] in 50 mM citrate buffer (pH 5.0) was incubated with the enzyme (Echi47, 15 mU) at 40 °C. The reaction products were analyzed at the indicated times. Lanes: M, standard *N*-acetyl-COSs from GlcNAc to $(GlcNAc)_5$.

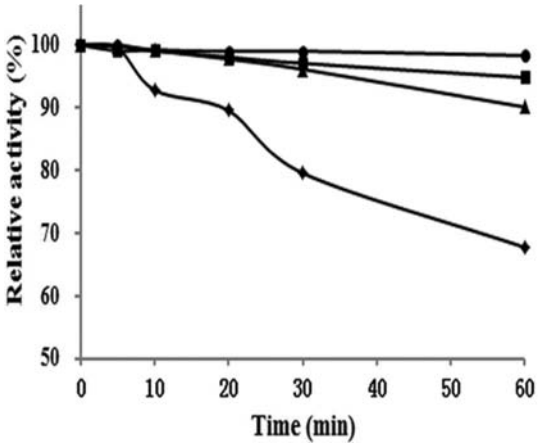

Figure 5. Effect of proteases on activity of purified Echi47. The influence of proteases on the activity of Echi47 was determined at 37 °C using different proteases: pepsin (◆), trypsin (■), proteinase K (▲), and flavor protease (●). Each value represents the mean ± SD (n = 3).

Microbial chitinases are found to be active over a wide range of temperatures (from 30 to 80 °C) and pH (from 3.0 to 10.0), depending on the source of microorganisms.[1,3] The optimal pH 5.0 of Echi47 is lower than that of an exochitinase from *Bacillus* sp. DAU101 (pH 7.5),[35] but higher than that of an exochitinase from *Microbispora* sp. V2 (pH 3.0).[37] Echi47 was most active at 40 °C (Figure 3A), which is intermediate compared with most other exochitinases, which have optimal temperatures in the range of 30−50 °C.[1,5] Interestingly, Echi47 exhibited similar optimal pH and temperature to the intestinal conditions, which make the enzyme valuable in several applications requiring acidic pH and low temperature. Additionally, the pH range for Echi47 activity (≥50% of the maximum activity between pH 4.0 and 9.0) is similar to the physicochemical conditions found for

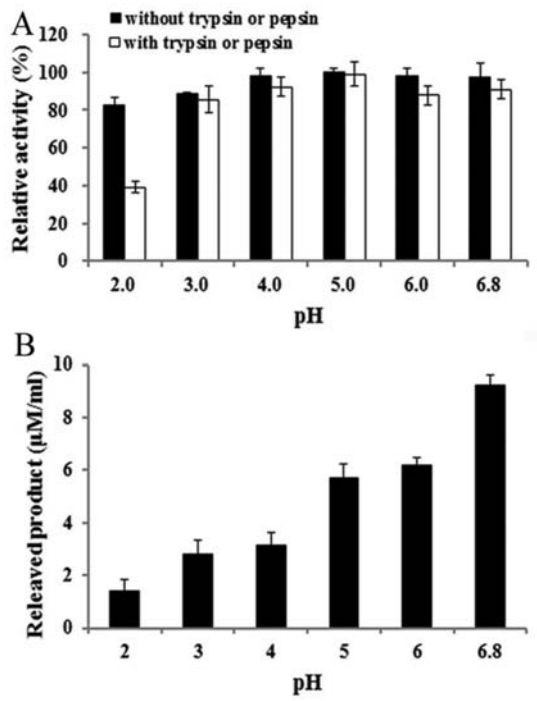

Figure 6. Stability and hydrolytic efficacy of Echi47 in simulated gastric fluid (SGF): (A) stability of the purified Echi47 in SGF (Echi47 stability was determined after incubation in SGF at pH 2.0−6.8 and 37 °C for 20 min; relative activity is expressed as a percentage of the initial activity of Echi47); (B) hydrolysis efficacy of Echi47 in SGF at different pH values. The degradation of colloidal chitin was measured after digestion at pH 2.0−6.8 or in a pH gradient according to gastric passage. Hydrolysis efficacy is calculated as the quantity of released reducing sugar. Each value in both panels represents the mean ± SD (n = 3).

DOI: 10.1021/acs.jafc.5b01457
J. Agric. Food Chem. 2015, 63, 6262−6270

the environments of warm-water fish,[10] which may be meaningful for use as aquaculture feed supplement.

Chitinases[1] are commonly inhibited by Hg^{2+}, Ag^{+}, Cu^{2+}, Zn^{2+}, Fe^{2+}, and Co^{2+}. Hg^{2+}, Ag^{+}, and Co^{2+} inhibited chitinase activity of Echi47. Hg^{2+} and Ag^{+} also inhibited activity of the chitinase from *Streptomyces violaceusniger*.[38] The activity of Echi47 was significantly stimulated by Ni^{2+}, Na^{+}, Cr^{3+}, and β-mercaptoethanol. The activity of Echi47 was stimulated by some of the tested metal ions and was inhibited by the metal ion chelating compound EDTA, suggesting that metals may be important in enzyme stability and/or activity. Additionally, the activity of Echi47 was enhanced by β-mercaptoethanol indicates the presence of sulfhydryl groups on the active site of the enzyme, which was confirmed by the inhibition by Hg^{2+}. Hg^{2+} may react with −SH groups in cysteine residues in the protein chain and disrupt the tertiary structure. Inhibition by Hg^{2+} and β-mercaptoethanol enhancement are similar to the case for the chitinases from *Streptomyces* species.[38]

To ensure efficient degradation of crystalline and inaccessible polymeric chitin substrates, chitinases often have one or more carbohydrate-binding modules (CBMs). CBMs' contribution to the efficiency of substrate conversion is not completely clear. The presence of CBMs increases substrate affinity as well as efficiency of chitin hydrolysis, especially in the hydrolysis of crystalline chitin forms.[38,39] The catalytic efficiency of chitinase-D (a single-domain chitinase from *Serratia proteamaculans*)[40] is increased, for degradation of insoluble chitin substrates, by fusing the heterologous CBMs such as PKD and CBP21. On the contrary, no such typical chitin-binding domain is present in single-domain Echi47, but it has a high affinity for chitin (K_m = 2.2 mg/mL), which is due to the conserved chitin-binding motif. The lack of CBMs in some chitinases suggests that a single catalytic domain is sufficient for catalytic activity of chintinase and further suggests that CBMs may facilitate hydrolysis of insoluble substrates but are not required for chitinase activity. Single-domain chitinases[41] such as Bce Chi36 and Echi47 may have good activity toward partially hydrolyzed or soluble chitin substrates.

Endochitinases randomly cleave β-1,4-glycosidic bonds of chitin, whereas exochitinases cleave the chain to form diacetylchitobiose.[35] $(GlcNAc)_2$ was mostly produced at the early stage of colloidal chitin hydrolyzed by Echi47, indicating that Echi47 is an exotype chitinase. This is similar to that of *Serratia marcescens* ChiB, which is identified as an exochitinase because it generates exclusively $(GlcNAc)_2$ from $(GlcNAc)_4$ and colloidal chitin at initial stage.[42] Exochitinases usually have a deep and tunnel-shaped substrate-binding site, but the endochitinases have a shallow and open substrate-binding site, which is relatively long and accommodates at least five sugar units.[4,43] The exomechanism can occur when the substrate is not released after successful cleavage but slides through the active site for the next cleavage event to occur.[43] In such a mechanism, chitin chains were degraded from one end with release of successive $(GlcNAc)_2$.[43] There is a growing appreciation of the potential of bioactive *N*-acetylchitooligosaccharides (especially *N*-acetylchitobiose). For instance, high antioxidant activities of GlcNAc and $(GlcNAc)_2$ produced by exochitinase from *Bacillus cereus* EW5 have been reported.[44] There are some reports on the bioproduction of $(GlcNAc)_2$.[2] For the production of specific *N*-acetyl-COSs, suitable enzymes and controlled reactions are the primary requisites.[45] $(GlcNAc)_2$ can be obtained as a major hydrolytic product from enzymes by controlling the ratio of *N*-acetyl-β-1,4-D-glucosaminidase to *N*,*N*′-diacetylchitobiohydrolase activities in the crude enzyme of *Aeromonas* sp. GJ-18.[2] $(GlcNAc)_2$ has also been produced from colloidal chitin by the chitinase from *Bacillus licheniformis* strain JS isolated from a mushroom bed.[45] Therefore, Echi47 may be useful for the production of $(GlcNAc)_2$.

The excellent resistance of enzymes to proteases is useful in the feed industries. The activity of the enzymes is inhibited somewhat by proteases and the pH (~7) in the intestine.[46] However, there are very few studies on the protease-resistant chitinases. Echi47 displayed excellent protease resistance as compared to other chitinases. The chitinase from *Aeromonas veronii* B565 has been found to be resistant to pepsin (55.8%), trypsin (81.6%), and proteinase K (59.9%).[10] Additionally, whether or not an enzyme can be used as feed additive depends on its activity and stability under alimentary tract conditions. To date, many other enzymes have high activity under simulated gastric conditions, such as β-galactosidase from *Bispora* sp. MEY-1 and exopolygalacturonase from *Klebsiella* sp. Y1.[26,46] Echi47 was stable and exhibited high hydrolytic ratio at low pH in the presence of pepsin. This is the first report on chitinase activity and stability under alimentary tract conditions. Supplementation of the diet with chitinase complexes containing endochitinases and exochitinases may be effective hydrolysis of chitin. Thus, these properties make Echi47 a potential feed additive.

AUTHOR INFORMATION

Corresponding Author

*(Z.J.) Phone: +86 10 62737689. Fax: +86 10 82388508. E-mail: zhqjiang@cau.edu.cn.

Funding

This work was financially supported by the National Science Fund for Distinguished Young Scholars (No. 31325021), the National High Technology Research and Development Program of China (No. 2012AA021505), and the National Natural Science Foundation of China (No. 31172239).

Notes

The authors declare no competing financial interest.

ABBREVIATIONS USED

BSA, bovine serum albumin; EDTA, ethylenediaminetetracetic acid; DNS, dinitrosalicylic acid; CHES, 2-(cyclohexylamino)-ethanesulfonic acid; MOPS, 3-(*N*-morpholino)propanesulfonic acid; MES, 2-(*N*-morpholino)ethanesulfonic acid; IPTG, isopropyl-β-D-1-thiogalactopyranoside; *N*-acetyl COSs, *N*-acetylchitooligosaccharides; Echi47, a glycosyl hydrolase (GH) family 18 exochitinase from the pig fecal environment; SDS-PAGE, sodium dodecyl sulfate−polyacrylamide gel electrophoresis; TLC, thin-layer chromatography

REFERENCES

(1) Karthik, N.; Akanksha, K.; Pandey, A. Production, purification and properties of fungal chitinases − a review. *Indian J. Exp. Biol.* **2014**, *52*, 1025−1035.

(2) Jung, W. J.; Park, R. D. Bioproduction of chitooligosaccharides: present and perspectives. *Mar. Drugs* **2014**, *12*, 5328−5356.

(3) Bhattacharya, D.; Nagpure, A.; Gupta, R. K. Bacterial chitinases: properties and potential. *Crit. Rev. Biotechnol.* **2007**, *27*, 21−28.

(4) Hartl, L.; Zach, S.; Seidl-Seiboth, V. Fungal chitinases: diversity, mechanistic properties and biotechnological potential. *Appl. Microbiol. Biotechnol.* **2012**, *93*, 533−543.

DOI: 10.1021/acs.jafc.5b01457
J. Agric. Food Chem. 2015, 63, 6262−6270

(5) Fu, X.; Yan, Q.; Yang, S.; Yang, X.; Guo, Y.; Jiang, Z. An acidic, thermostable exochitinase with β-*N*-acetylglucosaminidase activity from *Paenibacillus barengoltzii* converting chitin to *N*-acetyl glucosamine. *Biotechnol. Biofuels* **2014**, *7*, 174.
(6) Islam, R.; Datta, B. Diversity of chitinases and their industrial potential. *Int. J. Appl. Res.* **2015**, *1*, 55−60.
(7) Hamid, R.; Khan, M. A.; Ahmad, M.; Ahmad, M. M.; Abdin, M. Z.; Musarrat, J.; Javed, S. Chitinases: An update. *J. Pharm. Bioallied Sci.* **2013**, *5*, 21−29.
(8) Patil, R. S.; Ghormade, V. V.; Deshpande, M. V. Chitinolytic enzymes: an exploration. *Enzyme Microb. Technol.* **2000**, *26*, 473−483.
(9) Gutowska, M. A.; Drazen, J. C.; Robison, B. H. Digestive chitinolytic activity in marine fishes of Monterey Bay, California. *Comp. Biochem. Physiol., Part A: Mol. Integr. Physiol.* **2004**, *139*, 351−358.
(10) Zhang, Y.; Zhou, Z.; Liu, Y.; Cao, Y.; He, S.; Huo, F.; Qin, C.; Yao, B.; Ringø, E. High-yield production of a Chitinase from *Aeromonas veronii* B565 as a potential feed supplement for warm-water aquaculture. *Appl. Microbiol. Biotechnol.* **2014**, *98*, 1651−1662.
(11) Hobel, C. F.; Marteinsson, V. T.; Hreggvidsson, G. O.; Kristjansson, J. K. Investigation of the microbial ecology of intertidal hot springs by using diversity analysis of 16S rRNA and chitinase genes. *Appl. Environ. Microbl.* **2005**, *71*, 2771−2776.
(12) Terahara, T.; Ikeda, S.; Noritake, C.; Minamisawa, K.; Ando, K.; Tsuneda, S.; Harayama, S. Molecular diversity of bacterial chitinases in arable soils and the effects of environmental factors on the chitinolytic bacterial community. *Soil Biol. Biochem.* **2009**, *41*, 473−480.
(13) Amann, R. I.; Ludwig, W.; Schleifer, K. H. Phylogenetic identification and in situ detection of individual microbial cells without cultivation. *Microbiol. Rev.* **1995**, *59*, 143−169.
(14) Hjort, K.; Presti, I.; Elväng, A.; Marinelli, F.; Sjöling, S. Bacterial chitinase with phytopathogen control capacity from suppressive soil revealed by functional metagenomics. *Appl. Microbiol. Biotechnol.* **2014**, *98*, 2819−2828.
(15) Wang, W.; Archbold, T.; Kimber, M. S.; Li, J.; Lam, J. S.; Fan, M. Z. The porcine gut microbial metagenomic library for mining novel cellulases established from growing pigs fed cellulose-supplemented high-fat diets. *J. Anim. Sci.* **2012**, *90*, 400−402.
(16) Sae-Lee, R.; Boonmee, A. Newly derived GH43 gene from compost metagenome showing dual xylanase and cellulase activities. *Folia Microbiol.* **2014**, *59*, 409−417.
(17) Brady, S. F. Construction of soil environmental DNA cosmid libraries and screening for clones that produce biologically active small molecules. *Nat. Protoc.* **2007**, *2*, 1297−1305.
(18) Rose, T. M.; Henikoff, J. G.; Henikoff, S. CODEHOP (consensus-generate hybrid oligonucleotide primer) PCR primer design. *Nucleic Acids Res.* **2003**, *31*, 3763−3766.
(19) Huang, H. Q.; Wang, G. Z.; Zhao, Y. Y.; Shi, P. J.; Luo, H. Y.; Yao, B. Direct and efficient cloning of full-length genes from environmental DNA by RT-qPCR and modified TAIL-PCR. *Appl. Microbiol. Biotechnol.* **2010**, *87*, 1141−1149.
(20) Tamura, K.; Dudley, J.; Nei, M.; Kumar, S. MEGA4: molecular evolutionary genetics analysis (MEGA) software version 4.0. *Mol. Biol. Evol.* **2007**, *24*, 1596−1599.
(21) Katrolia, P.; Jia, H. Y.; Yan, Q. J.; Song, S.; Jiang, Z. Q.; Xu, H. B. Characterization of a protease-resistant α-galactosidase from the thermophilic fungus *Rhizomucor miehei* and its application in removal of raffinose family oligosaccharides. *Bioresour. Technol.* **2012**, *110*, 578−586.
(22) Trudel, J.; Asselin, A. Detection of chitinase activity after polyacrylamide gel electrophoresis. *Anal. Biochem.* **1989**, *178*, 362−366.
(23) Miller, G. L. Use of dinitrosalicylic acid reagent for determination of reducing sugar. *Anal. Chem.* **1959**, *31*, 426−428.
(24) Lowry, O. H.; Rosebrough, N. J.; Farr, A. L.; Randall, R. J. Protein measurement with the Folin phenol reagent. *J. Biol. Chem.* **1951**, *193*, 265−275.
(25) Rauvolfová, J.; Kuzma, M.; Weignerová, L.; Fialová, P.; Prikrylová, V.; Pisvejcová, A.; Macková, M.; Kren, V. β-*N*-acetylhexosaminidase-catalysed synthesis of nonreducing oligosaccharides. *J. Mol. Catal. B: Enzym.* **2004**, *29*, 233−239.
(26) Yuan, P.; Meng, K.; Wang, Y.; Luo, H.; Shi, P.; Huang, H.; Bai, Y.; Yang, P.; Yao, B. A protease-resistant exo-polygalacturonase from *Klebsiella* sp. Y1 with good activity and stability over a wide pH range in the digestive tract. *Bioresour. Technol.* **2012**, *123*, 171−176.
(27) Minekus, M.; Marteau, P.; Havenaar, R.; Huisintveld, J. H. J. A multicompartmental dynamic computer-controlled model simulating the stomach and small-intestine. *Altern. Lab. Anim.* **1995**, *23*, 197−209.
(28) Matsumoto, T.; Nonaka, T.; Hashimoto, M.; Watanabe, T.; Mitsui, Y. Three-dimensional structure of the catalytic domain of chitinase A1 from *Bacillus circulans* WL-12 at a very high resolution. *Proc. Jpn. Acad., Ser. B* **1999**, *75*, 269−274.
(29) Kang, Y.; Kim, H.; Choi, H. T. Biochemical characterization of chitinase 2 expressed during the autolytic phase of the Inky Cap *Coprinellus congregatus*. *J. Microbiol.* **2013**, *51*, 189−193.
(30) Synowiecki, J.; Al-Khateeb, N. A. Production, properties, and some new applications of chitin and its derivatives. *Crit. Rev. Food Sci. Nutr.* **2010**, *43*, 145−171.
(31) Uchiyama, T.; Abe, T.; Ikemura, T.; Watanabe, K. Substrate-induced gene-expression screening of environmental metagenome libraries for isolation of catabolic genes. *Nat. Biotechnol.* **2005**, *23*, 88−93.
(32) Verma, D.; Kawarabayasi, Y.; Miyazaki, K.; Satyanarayana, T. Cloning, expression and characteristics of a novel alkalistable and thermostable xylanase encoding gene (*Mxyl*) retrieved from compost-soil metagenome. *PLoS One* **2013**, *8*, No. e52459.
(33) Tchigvintsev, A.; Tran, H.; Popovic, A.; Kovacic, F.; Brown, G.; Flick, R.; Hajighasemi, M.; Egorova, O.; Somody, J. C.; Tchigvintsev, D.; Khusnutdinova, A.; Chernikova, T. N.; Golyshina, O. V.; Yakimov, M. M.; Savchenko, A.; Golyshin, P. N.; Jaeger, K. E.; Yakunin, A. F. The environment shapes microbial enzymes: five cold-active and salt-resistant carboxylesterases from marine metagenomes. *Appl. Microbiol. Biotechnol.* **2015**, *99*, 2165−2178.
(34) Lee, S.; Cantarel, B.; Henrissat, B.; Gevers, D.; Birren, B. W.; Huttenhower, C.; Ko, G. Gene-targeted metagenomic analysis of glucan-branching enzyme gene profiles among human and animal fecal microbiota. *ISME J.* **2014**, *8*, 493−503.
(35) Lee, Y. S.; Park, I. H.; Yoo, J. S.; Chung, S. Y.; Lee, Y. C.; Cho, Y. S.; Ahn, S. C.; Kim, C. M.; Choi, Y. L. Cloning, purification, and characterization of chitinase from *Bacillus* sp. DAU101. *Bioresour. Technol.* **2007**, *98*, 2734−2741.
(36) Kadokura, K.; Rokutani, A.; Yamamoto, M.; Ikegami, T.; Sugita, H.; Itoi, S.; Hakamata, W.; Oku, T.; Nishio, T. Purification and characterization of *Vibrio parahaemolyticus* extracellular chitinase and chitin oligosaccharide deacetylase involved in the production of heterodisaccharide from chitin. *Appl. Microbiol. Biotechnol.* **2007**, *75*, 357−365.
(37) Nawani, N. N.; Kapadnis, B. P.; Das, A. D.; Rao, A. S.; Mahajan, S. K. Purification and characterization of a thermophilic and acidophilic chitinase from *Microbispora* sp. V2. *J. Appl. Microbiol.* **2002**, *93*, 965−975.
(38) Hashimoto, M.; Ikegami, T.; Seino, S.; Ohuchi, N.; Fukada, H.; Sugiyama, J.; Shirakawa, M.; Watanabe, T. Expression and characterization of the chitin-binding domain of chitinase A1 from *Bacillus circulans* WL-12. *J. Bacteriol.* **2000**, *182*, 3045−3054.
(39) Eijsink, V. G.; Vaaje-Kolstad, G.; Varum, K. M.; Horn, S. J. Towards new enzymes for biofuels: lessons from chitinase research. *Trends Biotechnol.* **2008**, *26*, 228−235.
(40) Madhuprakash, J.; El Gueddari, N. E.; Moerschbacher, B. M.; Podile, A. R. Catalytic efficiency of chitinase-D on insoluble chitinous substrates was improved by fusing auxiliary domains. *PLoS One* **2015**, *10*, No. e0116823.
(41) Wang, S. Y.; Wu, S. J.; Thottappilly, G.; Locy, R. D.; Singh, N. K. Molecular cloning and structural analysis of the gene encoding *Bacillus cereus* exochitinase Chi36. *J. Biosci. Bioeng.* **2001**, *92*, 59−66.
(42) Brurberg, M. B.; Nes, I. F.; Eijsink, V. G. H. Comparative studies of chitinases A and B from *Serratia marcescens*. *Microbiology* **1996**, *142*, 1581−1589.

DOI: 10.1021/acs.jafc.5b01457
J. Agric. Food Chem. 2015, 63, 6262−6270

(43) Horn, S. J.; Sørbotten, A.; Synstad, B.; Sikorski, P.; Sørlie, M.; Vårum, K. M.; Eijsink, V. G. Endo/exo mechanism and processivity of family 18 chitinases produced by *Serratia marcescens*. *FEBS J.* **2006**, *273*, 491−503.
(44) Azam, M. S.; Kim, E. J.; Yang, H. S.; Kim, J. K. High antioxidant and DNA protection activities of *N*-acetylglucosamine (GlcNAc) and chitobiose produced by exolytic chitinase from *Bacillus cereus* EW5. *SpringerPlus* **2014**, *3*, 354.
(45) Waghmare, S. R.; Ghosh, J. S. Chitobiose production by using a novel thermostable chitinase from *Bacillus licheniformis* strain JS isolated from a mushroom bed. *Carbohydr. Res.* **2010**, *345*, 2630−2635.
(46) Wang, H.; Luo, H.; Bai, Y.; Wang, Y.; Yang, P.; Shi, P.; Zhang, W.; Fan, Y.; Yao, B. An acidophilic *β*-galactosidase from *Bispora* sp. MEY-1 with high lactose hydrolytic activity under simulated gastric conditions. *J. Agric. Food Chem.* **2009**, *57*, 5535−5541.

DOI: 10.1021/acs.jafc.5b01457
J. Agric. Food Chem. 2015, 63, 6262−6270

(MLC1) with a molecular mass of ∼18 kDa and the regulatory light chain (MLC2) with a molecular mass of ∼20 kDa.[20,22] It has been demonstrated that MLC2 is phosphorylated by its kinase, which is regulated the expression of IgE, and is reported to be increased in the smooth muscle of the allergen-sensitized human airway.[23] MLC has been reported to have IgE-binding activity in *L. vannamei*, *C. crangon*, and *P. monodon*, and the immunological effects of recombinant MLC have been analyzed in these organisms. However, it is unclear whether MLC is the major allergen in *P. clarkii*, nor has native MLC been characterized or the isoform identified.

The objectives of this study were to identify and purify MLC from *P. clarkii* and to analyze its physicochemical and immunological characteristics during changes in its secondary structure. We were able to clone the cDNA encoding the MLC proteins and to identify the allergenic MLC isoform. A homology model of the MLC structure was developed and used to predict its epitopes. These data will extend our understanding of MLC and provide valuable references for further research into the molecular nature of hypersensitivity to crayfish.

MATERIALS AND METHODS

Crayfish. Crayfish (*P. clarkii*) were purchased from a local market in Xiamen, China. Crayfish were peeled, and the muscle samples were collected and immediately used in the experiments or frozen at −70 °C for later analysis.

Chemicals. Diethylaminoethyl−Sephacel (DEAE−Sephacel) and Sephacryl S-200 HR were from Amersham Biosciences (Uppsala, Sweden). The protein standards for sodium dodecyl sulfate−polyacrylamide gel electrophoresis (SDS−PAGE) were from Fermentas (Vilnius, Lithuania), and the prestained protein standards for Western blot analysis were from New England BioLabs (Beverly, Massachusetts, USA). Horseradish peroxidase (HRP)-conjugated goat anti-human IgE antibody was from Kirkegaard and Perry Laboratories (Gaithersburg, Maryland, USA), and the enhanced chemiluminescence (ECL) substrate for Western blot analysis was from Pierce (Rockford, Illinois, USA). 3,3′,5,5′-Tetramethylbenzidine (TMB) was from Tiangen (Beijing, China). Ponceau S concentrate and porcine pancreatic enzymes were purchased from Sigma-Aldrich (St. Louis, Missouri, USA). Porcine pepsin was prepared in our laboratory. All reagents were of analytical grade.

Human Sera. Sera were collected from seven crustacean-allergic patients (nos. 749, 514, 974, 067, 785, 980, and 791), who were referred by the Medical Center of Jimei University in Xiamen, China. Serum samples from nonallergic (NA) individuals (nos. 780 and 981) were used as the negative controls. All patients and NA individuals voluntarily provided their sera (nos. U245749, U394514, T800974, U246067, U390785, U405980, U393791, U397780, and V490981). Written informed consent was obtained from each patient. The IgE level in each serum was measured with an ImmunoCAP assay (Phadia AB, Uppsala, Sweden), and the results are shown in Table 1. An ImmunoCAP score >0.35 kUA/L was considered positive. All sera were stored at −30 °C until analysis.

Purification of the Target Protein. The preliminary treatment was carried out as described previously,[24] with slight modifications. All procedures were performed at 0−4 °C unless otherwise stated. The crayfish muscle tissue was minced and homogenized with 10 vol (v/w) of ice-cold 50 mM NaCl buffer containing 2 mM $NaHCO_3$ and 10 mM EDTA. The homogenate was then centrifuged at 8000*g* for 10 min at 4 °C. The precipitate was resuspended in the same solution and then homogenized and centrifuged again four more times. The last precipitate, which contained the myofibrillar proteins, was washed three times with cold absolute acetone and dried completely. The dried powder was extracted overnight with 10 vol (v/w) of 20 mM Tris-HCl (pH 7.5) containing 1 M NaCl and 1 mM EDTA. The mixture was then centrifuged at 12 000*g* for 20 min at 4 °C. The supernatant was subjected to isoelectric precipitation at pH 4.0 with 1 N HCl. After centrifugation at 12 000*g* for 20 min at 4 °C, the precipitate was dissolved with 20 mM Tris-HCl (pH 7.5) and brought to pH 7.6 with 1 N NaOH and then subjected to ammonium sulfate fractionation with 41−60% saturated ammonium sulfate. Following centrifugation at 12 000*g* for 20 min at 4 °C, the precipitate was dissolved in 20 mM Tris-HCl (pH 7.5) containing 1 mM EDTA and then dialyzed in the same solution overnight. After centrifugation at 12 000*g* for 20 min at 4 °C, the supernatant was applied to a DEAE−Sephacel column (2.5 × 10 cm) and eluted with a linear gradient of 0−0.5 M NaCl at a flow rate of 0.6 mL/min. The fractions containing the target protein were concentrated by the ultrafiltration of a 3 kDa filtering membrane and then applied to a Sephacryl S-200 HR gel column (1.5 × 100 cm) equilibrated with 20 mM Tris-HCl (pH 7.5) containing 0.2 M NaCl. The column was eluted at a flow rate of 0.5 mL/min, and the fractions containing the target protein were collected and detected on a 12% SDS−PAGE gel stained with Coomassie Brilliant Blue R-250 (CBB). The protein concentrations in the eluted solutions were estimated by measuring the absorbance at 280 nm.

Table 1. Clinical and Laboratory Characterizations of Seven Crustacean-Allergic Patients and Two Nonallergic Individuals[a]

serum no.	age	sex	symptoms	sIgE shrimp (f24) by ImmunoCAP (kUA/L)
749	23	F	U, P	11.1
514	19	M	E, N	1.28
974	18	M	N, P	45.1
067	22	F	A, D, R	9.68
785	19	F	GIT, Dr	61.7
980	19	F	U, D, P	1.93
791	24	M	A, D	2.35
780	19	F	ND	0.15
981	23	M	ND	0.06

[a]F, female; M, male; U, urticaria; P, pruritus; E, emesis; N, nausea; A, asthma; D, dyspnea; R, rhinitis; GIT, gastrointestinal problems; Dr, diarrhea; ND, not determined/unknown.

Peptide Analysis by Matrix-Assisted Laser Desorption/Ionization Time-of-Flight Mass Spectrometry (MALDI-TOF-MS). After the 18 kDa target protein had migrated on the 12% SDS−PAGE gel and was stained with CBB, the band was cut from the gel and sent to Shanghai Applied Protein Technology Company Limited (Shanghai, China) to digest with trypsin for analysis with a 4800 Plus MALDI-TOF/TOF analyzer from Applied Biosystems (Foster City, California, USA), based on the method of Yan et al.[25] The MS conditions were as follows: laser source, ND; wavelength, 355 nm; accelerating voltage, 2 kV; and substrate, α-cyano-4-hydroxycinnamic acid. The positive ion mode was used, and the data were obtained automatically. The resulting peptide spectra were compared with those in the National Center for Biotechnology Information (NCBI) database.

Carbohydrate Content and Carbohydrate−Peptide Linkage Characterization. The total carbohydrate content of the 18 kDa target protein was determined with the phenol−sulfuric acid method,[26] with some modifications. In brief, 0.3 mL of 6% phenol in water was added to the sample solution (0.5 mL) in a test tube, and 1.5 mL of concentrated sulfuric acid was added slowly down the side of the tube. The tube was then vortexed, covered, and incubated for 20 min at 100 °C. After all the tubes were cooled to room temperature, the absorbance of each was read at 490 nm. All the experiments were performed in duplicate. The β-elimination was used to determine the carbohydrate−peptide linkages in the target protein, according to a previously described method.[6] The target protein sample (0.3 mg/mL, 90 μL) was mixed with 10 μL of 0.5 M NaOH and incubated at 37 °C for 16 h, after which the absorbance at 220−300 nm was measured. The target protein sample was replaced with the same volume of distilled water, as the blank, and NaOH was replaced with the same volume of distilled water, as the negative control. All experiments were performed in duplicate.

DOI: 10.1021/acs.jafc.5b01318
J. Agric. Food Chem. 2015, 63, 6271−6282

Thermal Stability and pH Stability. To determine the thermal stability of the 18 kDa target protein, it was incubated in buffer (10 mM Tris-HCl, pH 7.5) at different temperatures (30, 40, 50, 60, 70, 80, 90, and 100 °C) for 30 min. The protein was incubated at 0 °C as the control. To test its pH stability, the target protein was incubated for 1 h at room temperature in buffer at different pH (1.0, 2.0, 3.0, 4.0, 5.0, 7.0, 9.0, and 11.0). The protein was incubated at pH 7.5 as the control. Then all the samples were analyzed with 15% SDS−PAGE and dot blot.

Stability during Simulated Digestion. The stability of the target protein in vitro in simulated gastric fluid (SGF, pepsin) and simulated intestinal fluid (SIF, pancreatin) was assessed with the method of Chen et al.,[14] with some modifications. The total volume of the reaction solution was 1 mL. For gastric digestion, the ratio of pepsin to the target protein was 1:500 (w/w). An aliquot of 100 μL of the reaction solution was removed after different time intervals (0, 1, 2, 5, 10, 15, 30, or 60 min), and the reaction was immediately terminated by the addition of 30 μL of 200 mM Na_2CO_3. For intestinal digestion, the ratio of pancreatin to the target protein was 1:500 (w/w). The reactions were performed for 0, 1, 15, 30, 60, 120, 180, or 240 min, after which they were immediately terminated by heating at 95 °C for 5 min. A target protein sample, dissolved in SGF/SIF with no corresponding enzyme, was used as the undigested control. The final concentration of each sample was adjusted to 0.25 mg/mL. The samples were analyzed with 15% SDS−PAGE and a competitive inhibition enzyme-linked immunosorbent assay (ELISA).

Western Blot and Dot Blot Analysis. Western blot analysis was performed as described by Chen et al.,[14] with some modifications. Briefly, protein samples separated with SDS−PAGE were electrophoretically transferred to a nitrocellulose membrane, and then the transfer efficiency was determined by Ponceau S staining of the membrane. The membrane was washed with TBST (20 mM Tris-HCl, pH 8.0, containing 0.15 M NaCl and 0.05% Tween-20) and blocked with 5% skim milk in TBST. They were then incubated for 6 h at room temperature with human serum (diluted 1:4) as the primary antibody and washed with TBST. The membrane was then incubated for 1.5 h with HRP-labeled goat anti-human IgE antibody (diluted 1:20000) as the secondary antibody. After being extensively washed with TBST, the proteins were visualized with ECL. In the dot blot analysis, the samples were blotted onto the nitrocellulose membrane, blocked, and incubated with sera from patients (diluted 1:4) and HRP-labeled goat anti-human IgE antibody (diluted 1:20000) as described above. The signal was detected with ECL.

Indirect and Competitive Inhibition ELISA (ciELISA). Each well of a polystyrene 96-well ELISA plate (Nunc Maxisorb, Denmark) was coated with the 18 kDa target protein (0.2 μg) and incubated at 4 °C overnight or at 37 °C for 2 h. The coated plates were washed with TBST and blocked with 200 μL/well 5% skim milk at 37 °C for 2 h. After being washed and blocked, the coated plates were incubated at 37 °C for 2.5 h with 50 μL of patient serum (diluted 1:5 with 1% skim milk in TBST) as the primary antibody and then at 37 °C for 1.5 h with HRP-conjugated goat anti-human IgE (diluted 1:2000) as the secondary antibody. TMB (100 μL) was then added to each well and incubated at 37 °C for 20 min. After the reaction was terminated by the addition of 50 μL of 2 M sulfuric acid, the absorbance was measured at 450 nm with an automated ELISA plate reader (Benchmark 96; Bio-Rad Laboratories, Hercules, California, USA). The specific IgE-binding activity of the purified protein-derived digestion fragments was confirmed with a ciELISA, based on the method of Li et al.[27] In contrast to indirect ELISA, after the plates were blocked with 5% skim milk, 50 μL of human sera (diluted 1:2 with 1% skim milk in TBST) was mixed with the same volume of inhibitor sample (the purified protein-derived digestion fragments), in the concentration range of 0.025−50 μg/mL in another plate. After incubation at 37 °C for 1.5 h, 50 μL of the mixture (serum plus inhibitor) was transferred to the ELISA plate precoated with the purified protein as the allergen and incubated for 1.5 h at 37 °C. As above, after incubation with the secondary antibody and reaction with TMB, the absorbance at 450 nm was measured. The inhibition rate was calculated to evaluate the percentage of inhibition by each inhibitor sample using the following formula:

$$\text{inhibition rate } (\%) = ([X - Y]/[X - Z]) \times 100$$

where X is the absorbance of the patient's serum not incubated with the inhibitor, and Y and Z are the absorbance of an allergic patient's serum and control NA serum reacted with the inhibitor, respectively. All the samples were tested in duplicate and the mean values calculated.

Circular Dichroism (CD) Spectroscopy. Far-UV CD spectra were measured with a Chirascan circular dichroism spectrometer (Applied Photophysics Ltd., Surrey, UK). The measurements of purified protein in buffer (10 mM Tris-HCl, pH 7.5) were made at 25 °C using a rectangular quartz cuvette (Starna, Essex, UK) with a path length of 0.1 cm at a protein concentration of 0.12 mg/mL. The purified protein was treated at different temperatures (0 and 100 °C) for 30 min or at room temperature in different pH buffers (pH 1.0, 7.5, and 11.0) for 1 h. The samples were scanned three times at 1 nm/s at a bandwidth of 1 nm. The response time was 2 s, and the wavelength range was 190−260 nm. The data were averaged, and the spectrum of the sample-free control was subtracted. The secondary structures of the proteins were determined with the CDNN program (version 2.0) based on the variables of the amino acid sequence and the molecular weight of the target protein.[28]

Cloning and Sequencing the MLC Genes. Total RNA was prepared from crayfish (*P. clarkii*) muscle based on the TRIzol method.[29] The first-strand cDNA was synthesized with the TIANScript RT kit (Tiangen, Beijing, China), according to the manufacturer's instructions, and oligo$(dT)_{18}$ primers were designed according to the manufacturer's instructions. Based on the MALDI-TOF-MS results and the alignment of the MLC cDNA sequences of *C. crangon* and *P. monodon*, degenerate oligonucleotide primers were designed as the sense primers for PCR. Using these primers and the synthesized cDNA, a 300 bp fragment of the *MLC* gene was amplified by PCR in the GeneAmp 9700 thermal cycler (Applied Biosystems, Foster City, California, USA). The PCR thermal cycling program was 5 min at 94 °C, followed by 30 cycles of 45 s at 94 °C, 30 s at 57 °C, and 45 s at 72 °C, and a final extension at 72 °C for 7 min. The PCR product was purified by agarose gel electrophoresis and cloned into the pGEM-T Easy vector (Promega), and the DNA sequence was analyzed. 5′-RACE primers and 3′-RACE primers were designed based on the sequence information from the RT−PCR product. RACE and RACE−PCR were performed with the SMART RACE amplification kit (Clontech, Palo Alto, California, USA). The PCR amplification product was purified, cloned, and sequenced. The full-length gene sequences of the *MLC*s (*MLC1*, 1096 bp; *MLC2*, 1362 bp) were obtained by overlapping the RT−PCR fragment, the 3′-RACE fragment, and the 5′-RACE fragment. DNA nucleotide sequencing was performed with the ABI PRISM 3730 DNA analyzer (Applied Biosystems, Foster City, California, USA), and the sequences were compared with the nucleotide sequences in the GenBank database. The sequences were submitted to GenBank under accession numbers JX173714 (gil401606250) for *P. clarkii MLC1* cDNA and JX013934 (gil392499120) for *P. clarkii MLC2* cDNA.

Structural Modeling and Epitope Prediction. The three-dimensional structure of the target protein was simulated at the Web site http://swissmodel.expasy.org/ based on the homology modeling by the amino acid sequence of the target protein to search the suitable template. The continuous linear epitopes were predicted by the DNASTAR Protean software using the method of Kyte−Doolittle for hydrophilicity plot prediction, the method of Karplus−Schulz for flexible regions prediction, the method of Jameson−Wolf for antigenic index prediction, and the method of Emini for surface probability plot prediction. The peptide fragments were selected to satisfy the conditions: (i) highly hydrophilic; (ii) appropriate antigenic index; and (iii) situated in a flexible and surface-exposed region. Discontinuous conformational epitopes were predicted at the DiscoTope 2.0 server (http://www.cbs.dtu.dk/services/DiscoTope/) by the calculation of surface accessibility, a novel epitope propensity, and the propensity of residues in spatial proximity. The three-dimensional structure and epitopes were represented on the molecular surface of the protein with PyMOL.

DOI: 10.1021/acs.jafc.5b01318
J. Agric. Food Chem. 2015, 63, 6271−6282

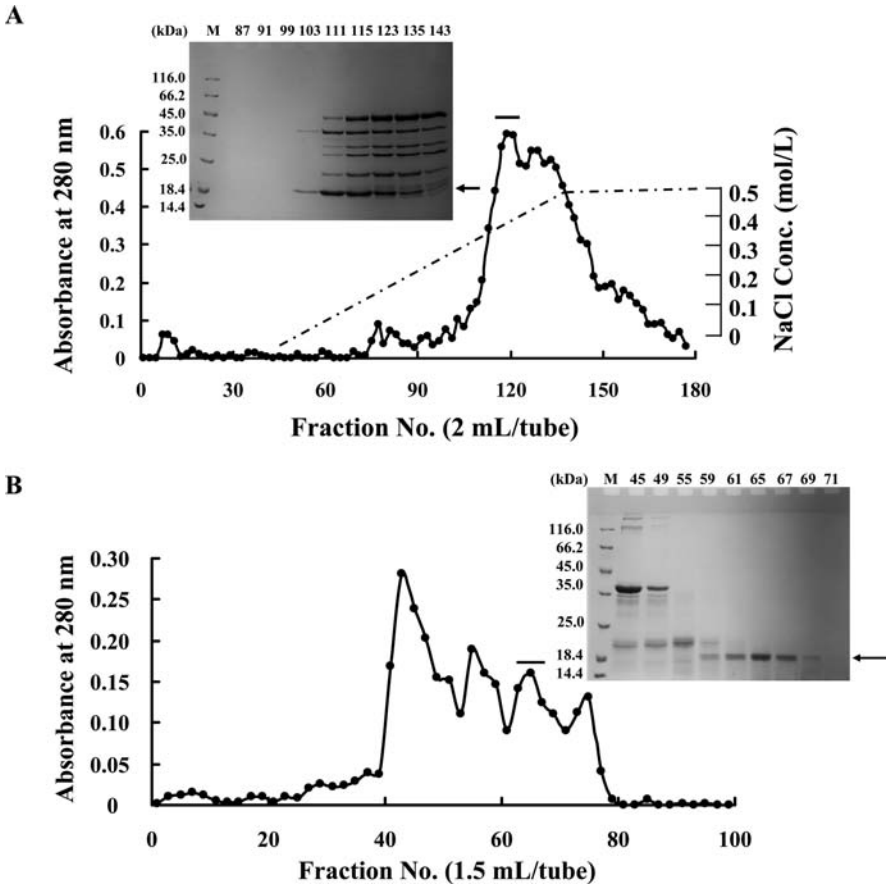

Figure 1. Chromatographic purification of the 18 kDa protein in crayfish. (A) DEAE−Sephacel chromatography. (B) Sephacryl S-200 HR gel chromatography. The numbers above the lanes correspond to the fraction numbers. Target protein fractions under the bar were pooled.

RESULTS

Purification of the 18 kDa Protein. The 18 kDa protein was purified from crayfish muscle with ammonium sulfate precipitation and sequential column chromatography on DEAE−Sephacel and Sephacryl S-200 HR. The fractions from the DEAE−Sephacel column were eluted with a linear gradient of 0−0.5 M NaCl (Figure 1A). The fractions that contained relatively high concentrations of the 18 kDa target protein were then pooled, concentrated, and separated on a Sephacryl S-200 HR gel-filtration column, which removed the contaminating proteins. After Sephacryl S-200 HR chromatography, the highly purified protein migrated on SDS−PAGE as a single band with a molecular weight of about 18 kDa (Figure 1B). Approximately 5.6 mg of the purified protein was obtained from 140 g of crayfish muscle.

Identification by MALDI-TOF-MS. The purified 18 kDa protein band was excised from the SDS−PAGE gel, destained, and digested in-gel with trypsin. The resulting peptides were analyzed with MALDI-TOF-MS. Peptide mass fingerprinting of the purified protein showed multiple peaks ranging from 800 to 4000 Da. The peaks with signal-to-noise ratios >50 were analyzed with MS/MS, as shown in Figure 2A. The effective peaks were compared with the NCBInr database using the Mascot 2.2 search engine. One peptide fragment containing 13 amino acid residues was 100% identical to MLC of *Drosophila yakuba* (gil 195503715) and 92.3% identical to that of *C. crangon* (gil 238477331) and *Marsupenaeus japonicas* (gil290908988) (Figure 2B). These results confirmed the purified 18 kDa protein as MLC.

Glycoprotein Characterization. The results of the phenol−sulfuric acid analysis indicated that the total carbohydrates in MLC accounted for about 4.3 ± 0.05% (w/w) of the whole protein. The β-elimination was used to determine the presence of O-linked glycans in the MLC structure. As shown in Figure 3A, when MLC was treated with alkali, the UV absorbance at 240 nm increased significantly compared with the absorbance before alkali treatment. This result indicates that one or more *O*-glycans may be present in the structure of MLC.

Thermal and pH Stability. Thermal and pH stabilities are accepted characteristics of most allergens. The thermal stability of purified MLC was analyzed with SDS−PAGE and dot blot. As illustrated in Figure 3B, MLC was stable after exposure to different temperatures, even up to 100 °C. MLC IgE-binding activity at different temperatures was determined with dot blot using the patients' sera. The IgE-binding activity of crayfish MLC was detected in this assay and did not increase or decrease obviously in the temperature range of 30−100 °C (Figure 3C).

The pH stability of purified crayfish MLC was also examined with SDS−PAGE and dot blot. As illustrated in Figure 3D, MLC remained stable when exposed to acidic (pH 1.0−5.0) and alkaline (pH 9.0, 11.0) conditions. Dot blot was also used to analyze the IgE-binding activity of MLC. Compared with the control, no obvious change was detected in the IgE-binding activity of MLC after exposure to different pH values (Figure 3E).

Stability during Digestion. It was determined whether MLC was stable under in vitro conditions simulating human gastrointestinal digestion. The stability of purified MLC in

DOI: 10.1021/acs.jafc.5b01318
J. Agric. Food Chem. 2015, 63, 6271−6282

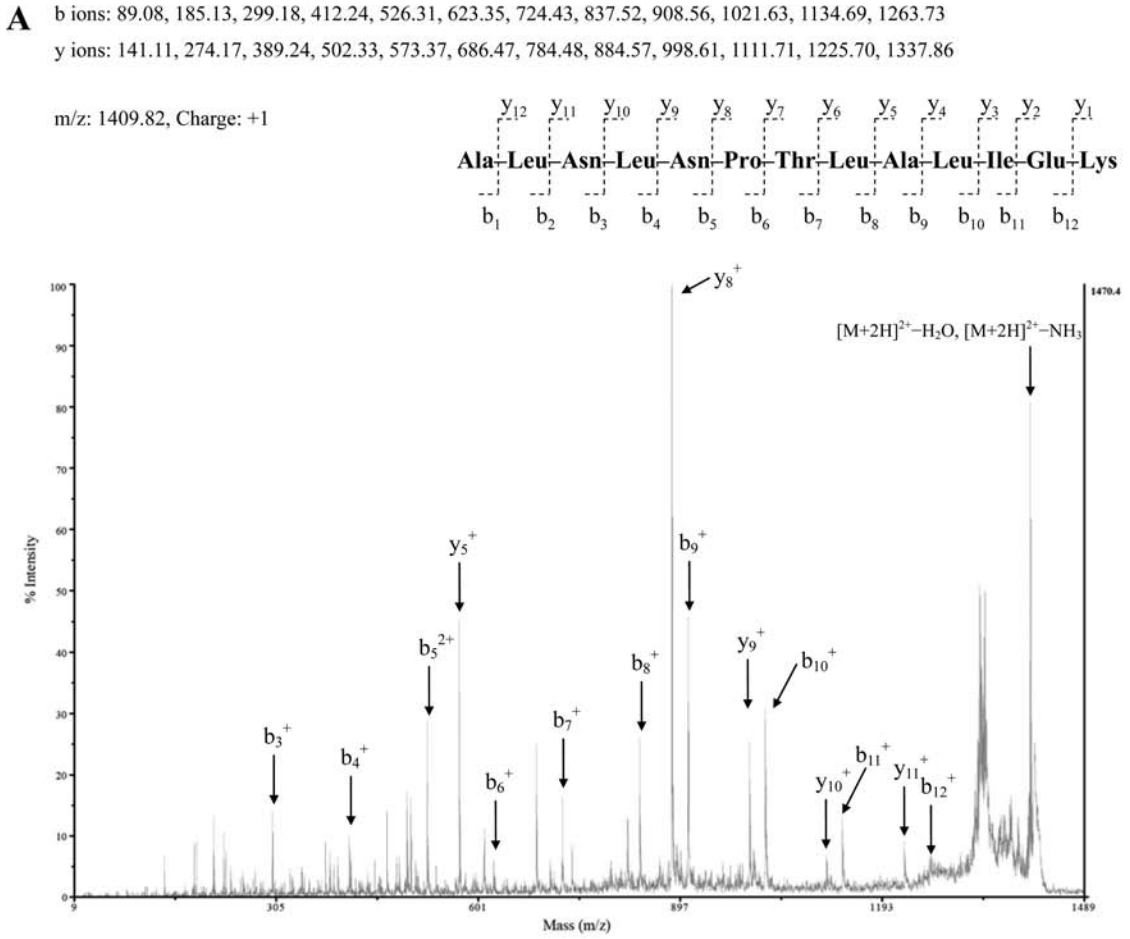

Figure 2. Mass spectrometric analysis of the 18 kDa protein in crayfish. (A) Map of MS/MS. (B) Protein sequence alignments of MLCs from *Procambarus clarkii*, *Drosophila yakuba*, *Crangon crangon*, and *Marsupenaeus japonicus*.

pepsin digestion was analyzed with SDS–PAGE. The original band (18 kDa) was gradually digested over time. Proteolytic fragments smaller than 14.4 kDa appeared after prolonged peptic digestion. The original band was digested into fragments smaller than can be resolved by SDS–PAGE by pepsin within 1 h (Figure 3F). In contrast, a single proteolytic fragment smaller than 14 kDa was observed after the pancreatin digestion of MLC. The ~14.4 kDa fragment appeared after 15 min and remained undigested up to 240 min (Figure 3G). Competitive inhibition ELISA was used to analyze the IgE-binding activity of the MLC-derived digestion fragments. As shown in Figure 3H, the IgE-binding activity of the digested fragments was reduced by pancreatin digestion but not significantly with pepsin digestion. When the concentration of the inhibitor was 2.5 μg/mL, the inhibition rate of the pepsin digestion fragments was 80%, whereas that of the undigested MLC was 85%, and the inhibition rate of the pancreatin digestion fragments was only 57%. The pepsin digestion fragments at a concentration of 0.095 μg/mL were capable of binding 50% of the IgE epitopes bound by undigested MLC at 0.075 μg/mL, whereas the pancreatic digestion fragments had a 50% inhibition rate at concentrations up to 0.224 μg/mL. This indicates that pepsin digestion had little effect on the IgE-binding activity of MLC. However, the IgE-binding activity of MLC that had been digested by pancreatin over a period of 4 h was reduced compared with that of the undigested MLC sample.

Secondary Structure of Purified MLC. Far-UV CD spectra were examined to confirm the predicted structure of purified MLC and to evaluate the effects of different physicochemical conditions on the protein's secondary structure. As shown in Figure 4, the control curves (0 °C and pH 7.5) displayed two minima, around 222 and 208 nm, and one maximum around 190

DOI: 10.1021/acs.jafc.5b01318
J. Agric. Food Chem. 2015, 63, 6271–6282

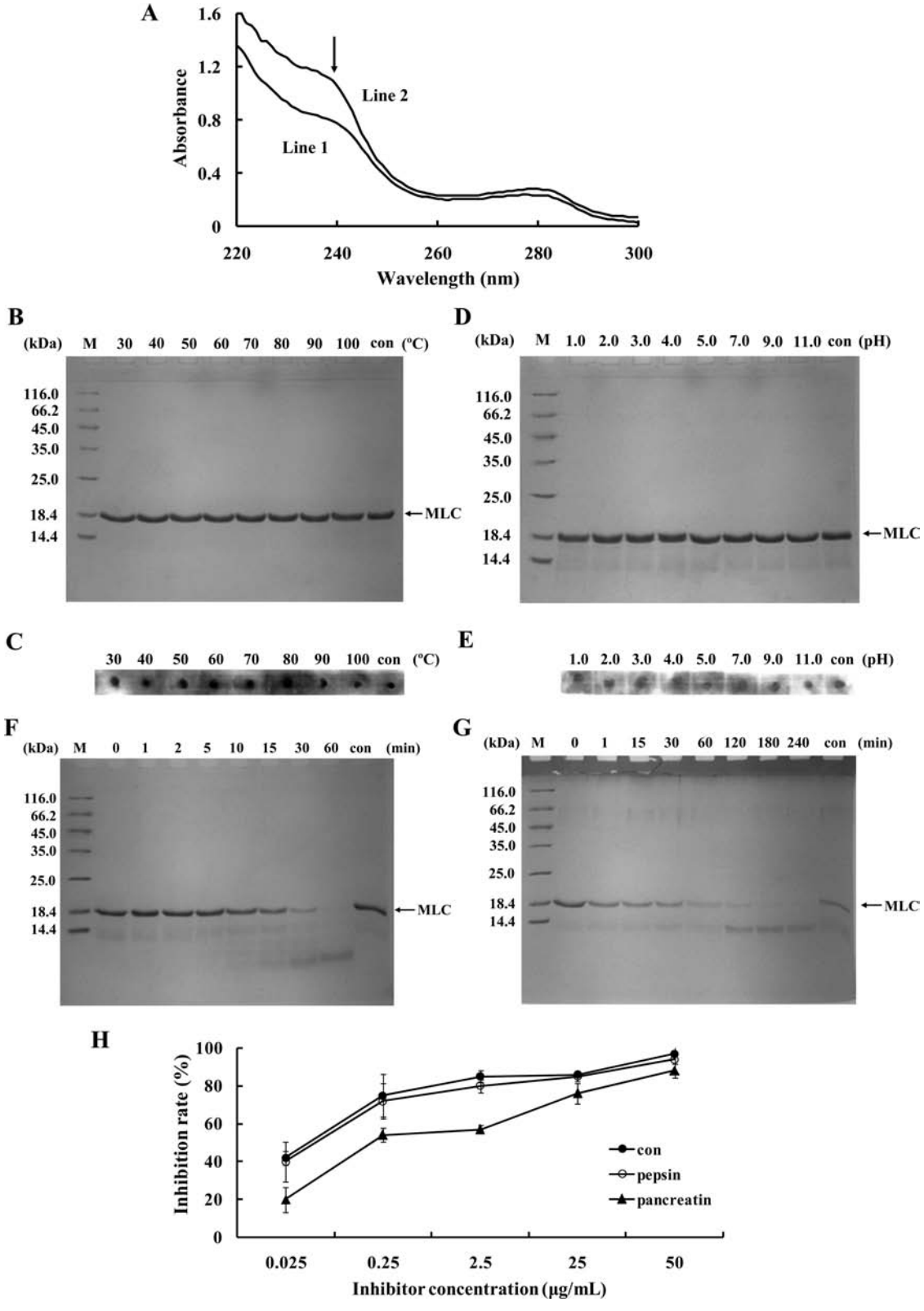

Figure 3. Physicochemical characterization of purified crayfish MLC. (A) UV spectral analysis of the purified MLC. Line 1: untreated MLC. Line 2: MLC treated with low-concentration alkali. The change at 240 nm is marked by an arrow. (B) SDS−PAGE analysis of the thermal stability of MLC. con: MLC was incubated at 0 °C. (C) Dot blot of thermally treated MLC. con: MLC was incubated at 0 °C. (D) SDS−PAGE analysis of the pH stability of MLC. con: MLC was incubated at pH 7.5. (E) Dot blot of MLC treated with different pH values. con: MLC was incubated at pH 7.5. (F) SDS−PAGE analysis of MLC stability to pepsin digestion. con: MLC was untreated with pepsin. (G) SDS−PAGE analysis of MLC stability to pancreatin digestion. con: MLC was untreated with pancreatin. M, protein marker; con, control. (H) ciELISA of the digested fragments of MLC. MLC digested by pepsin (○, 1 h); pancreatin (▲, 4 h); and undigested (●).

DOI: 10.1021/acs.jafc.5b01318
J. Agric. Food Chem. 2015, 63, 6271−6282

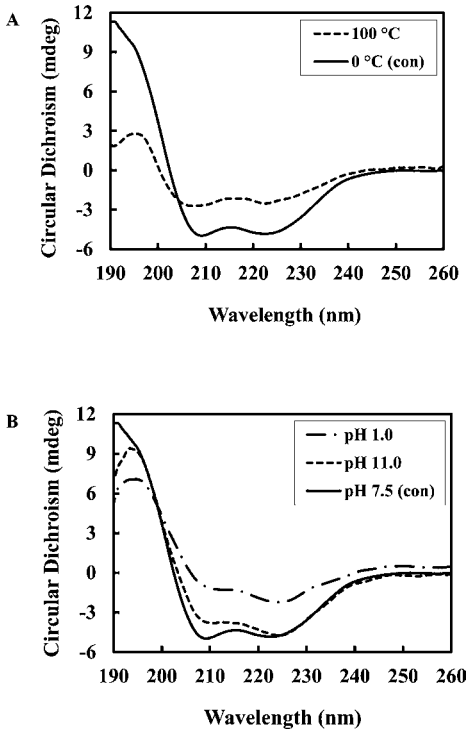

Figure 4. Effects of different experimental conditions on the stability of purified crayfish MLC1. (A) CD spectral analysis of MLC1 subjected to high temperature (100 °C, - - -) or 0 °C (—) as the control. (B) CD spectral analysis of MLC1 subjected to strong acid (pH 1.0, -·-·-); strong alkali (pH 11.0, - - -), or pH 7.5 (—) as the control.

nm, which are typical of α-helical secondary structures, although there was no fully canonical shapes that reflect the presence of other secondary structures, such as the extended strands, the β-turns, and/or the random coils. At 0 °C, the secondary structure was 33.5% α-helices, 16.2% extended strands, and 34.2% random coils. However, high-temperature treatments had a noticeable effect on the secondary structure, significantly increasing the extended strands (23.5%), which are characterized by a maximum at around 195 nm, and partially increasing the β-turns and/or the random coils (Figure 4A). Extended strands (25.6%) and random coils (39.3%) were also markedly increased after strong acid treatment, whereas strong alkali did not significantly increase the extended strands (19.2%) (Figure 4B). Among the different treatments tested, the secondary structure of purified crayfish MLC was most effectively altered by high temperature and strong acid.

Determination of the Predominant Epitope Type of Purified MLC. The IgE-binding activity of the purified crayfish MLC in folded form (with indirect ELISA and dot blot analysis, Figure 5A,B) was compared with MLC in its denatured, linear form (Western blot analysis, Figure 5C), with seven individual serum samples (nos. 749, 514, 974, 067, 785, 980, and 791) from crustacean-allergic patients and two sera from NA individuals that were pooled (nos. 780 and 981). With indirect ELISA (Figure 5A), the IgE from each of the seven sera bound to the native folded MLC, at least 2-fold higher than that of the negative control sera. In the dot blot analysis, all seven sera reacted with the native folded MLC, but no IgE-binding activity was detected in the negative control sera (Figure 5B). However, as shown in Figure 5C, only three sera (nos. 067, 785, and 791) reacted weakly to the denatured, linear MLC in the Western blot analysis. This indicates that the native folded MLC has higher IgE-binding activity than the denatured linear MLC.

Cloning and Sequencing MLC1. To identify the isoform of the purified MLC and to predict of the MLC structures, the *MLC1* gene was cloned. As shown in Figure 6A, the full-length gene sequence of crayfish *MLC1* is 1096 bp, including the ATG start codon at nucleotides (nt) 63−65, the TAA stop codon at nt 523−525, and the poly-A tail. The open reading frame of crayfish *MLC1* is 462 bp, and the predicted protein consisted of 153 amino acid residues, with a predicted molecular weight of 17.59 kDa by DNASTAR EditSeq software, which is equivalent to the ∼18 kDa molecular weight estimated with SDS−PAGE (Figure 1B). The protein has a predicted isoelectric point of 4.58 by DNASTAR EditSeq software. There are two potential N-glycosylation sites in the amino acid sequence of crayfish MLC1 (marked with a box in Figure 6A), which were identified by the conserved motif Asn−X−Ser/Thr/Cys. A protein sequence alignment showed that the MLC proteins from different crustacean species share high homology (Figure 6B). The amino acid sequence of crayfish MLC1 was 92.81% identical to the amino acid sequence of *C. crangon* MLC (gil238477331) and *M. japonicus* MLC (gil290908988), 84.97% to *Palaemon varians* MLC (gil238683675), 64.05% to *Periplaneta americana* MLC (gil 359326577), and 53.80% to *Artemia franciscana* MLC (gil 152013723).

Cloning and Sequencing MLC2. The *MLC2* gene was also cloned to distinguish between the isoforms of MLC. The full-length gene sequence of crayfish *MLC2* is 1362 bp, including the ATG start codon at nt 63−65, the TAA stop codon at nt 589−591, and the poly-A tail (Figure 6C). The open reading frame of crayfish *MLC2* is 528 bp, and the predicted protein consists of 175 amino acid residues, with a predicted molecular weight of 19.07 kDa and a predicted isoelectric point of 4.21 by DNASTAR EditSeq software. There is only one potential N-glycosylation site in the amino acid sequence of crayfish MLC2 (marked with a box in Figure 6C). A protein sequence alignment showed that the sequence homology of MLC1 and MLC2 is only 14.2%, whereas the MLC2 proteins of different crustacean species share relatively high homology (Figure 6D). The amino acid sequence of crayfish MLC2 is 62.92% identical to the amino acid sequence of *P. monodon* MLC2 (gil357640499) and *L. vannamei* MLC (gil 184198734).

Structural Modeling and Epitope Prediction in Crayfish MLC. The three-dimensional structure of crayfish MLC1 was determined based on its amino acid sequence by a homology model (template: 4QBD, 56.95% identity, Figure 7A). Crayfish MLC1 is mainly composed of α-helices (54.25%) and random coils (22.22%), with a few β-turns or extended strands analyzed by SOPMA secondary structure prediction. This is roughly consistent with the results of the CD spectral analysis. The conformational epitopes were identified with the DiscoTope 2.0 server, and the most likely regions included 10 discontinuous amino acid residues (25, 57−60, 96−99, and 136). The 10 predicted discontinuous epitope residues were molecularly mapped onto the three-dimensional structure of crayfish MLC1 and formed four conformational epitopes (labeled with slate in Figure 7B). The linear (continuous) epitopes of crayfish MLC1 were predicted with the DNASTAR Protean software based on its secondary structure. Three continuous regions (amino acid residues 53−58, 76−83, and 95−99) of linear epitopes occurred in the most hydrophilic, flexible, and surface-exposed regions and were shown in blue on the model of crayfish MLC1 (Figure 7C). Crayfish MLC2 is also mainly composed of

DOI: 10.1021/acs.jafc.5b01318
J. Agric. Food Chem. 2015, 63, 6271−6282

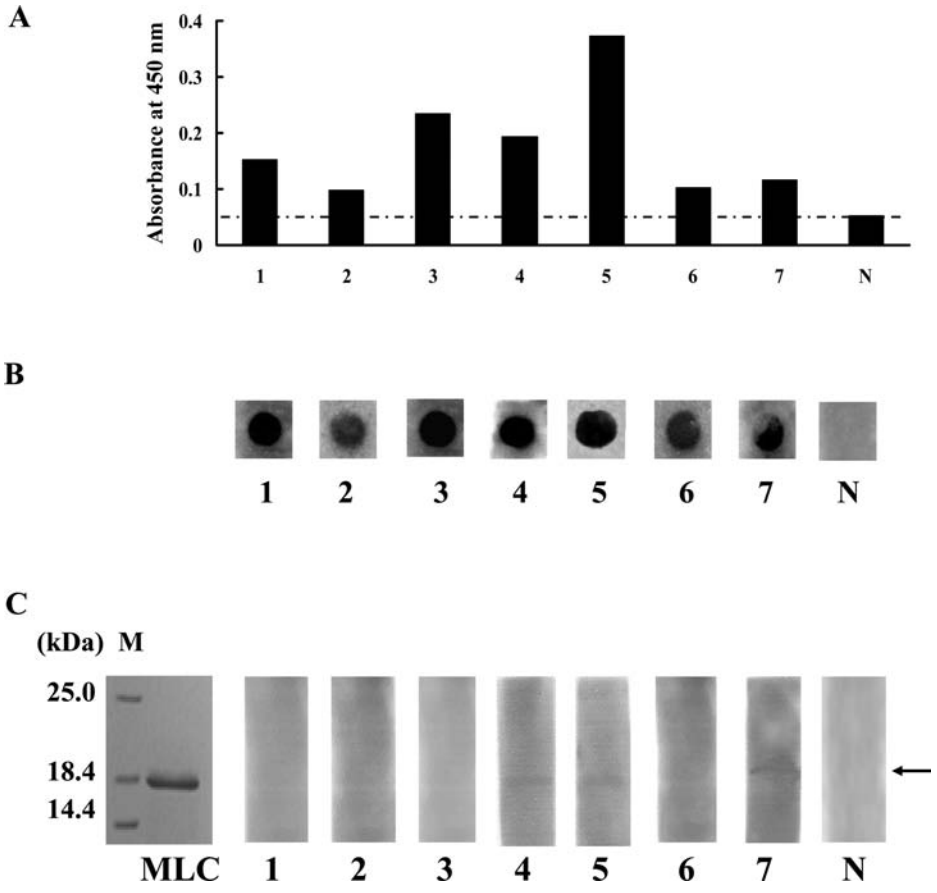

Figure 5. Comparison of IgE reactivity to native and denatured MLC from crayfish. 1−7: sera of seven crustacean-allergic patients (corresponding to serum nos. 749, 514, 974, 067, 785, 980, and 791); N: pooled sera from nonallergic individuals (nos. 780 and 981) as the negative control. (A) ELISA. (B) Dot blot. (C) Western blot. M, protein marker; MLC, SDS−PAGE analysis of the purified MLC.

α-helices (49.14%) and random coils (32.57%), with a few β-turns or extended strands. The most likely regions of conformational epitopes were 47 discontinuous residues (amino acid residues 31−32, 34−36, 38−39, 41−47, 49−71, 73−79, and 81−83), which composed a major conformational epitope. Three continuous regions (amino acid residues 5−11, 92−99, and 169−172) of linear epitopes were predicted (data not shown).

DISCUSSION

The growing international trade in crayfish has increased its popularity and the frequency of its consumption, which has been accompanied by an increase in the incidence of allergic diseases.[1,2] MLC was identified as a novel allergen in the white leg Pacific shrimp (*L. vannamei*),[18] the North Sea Shrimp (*C. crangon*),[10] and the black tiger prawn (*P. monodon*).[19] A previous study of crayfish TM demonstrated that an undefined myofibrillar protein, with a molecular mass about 18 kDa, had IgE-binding activity in the sera from crustacean-allergic patients.[9] It was inferred to be a new allergen in *P. clarkii*, although it is unclear whether this *P. clarkii* protein was MLC and, if so, which isoform it might be. This study was undertaken to determine whether this 18 kDa protein was MLC.

Few studies have purified native MLC for further analysis. In this study, the 18 kDa protein was purified by a combination of isoelectric precipitation, ammonium sulfate precipitation, ion exchange, and size exclusion chromatography and identified as MLC with MALDI-TOF-MS. The MLC content in muscle tissue is very low compared with the content of crayfish AK.[14] Only 11 sera from 137 sera collected from crayfish-allergic patients (which also had IgE-binding activity to other crustaceans) reacted with *P. clarkii* MLC in a serological assay. This indicates that MLC is a minor allergen in *P. clarkii* and may cross-react with the myofibrillar proteins of other crustaceans.

The molecular mass of crayfish MLC is 18 kDa, which is similar to that of *C. crangon* MLC, smaller than that of *L. vannamei* MLC (20 kDa), and larger than that of *P. monodon* MLC (16 kDa). It is interesting that the cloned sequence of the purified MLC was highly homologous to *C. crangon* MLC (Figure 6B), whereas *L. vannamei* MLC (gil184198734) was only 13.11% identical and *P. monodon* MLC (gil357640499) only 13.97% identical to the purified MLC, whereas the *L. vannamei* and *P. monodon* MLCs were 62.92% identical to MLC2 from *P. clarkii* (gil392499121). This indicates that the purified MLCs from *P. clarkii* and MLC from *C. crangon* are MLC1, and that the MLCs from *L. vannamei* and *P. monodon* are MLC2. Because MLC1 is the essential light chain and MLC2 is the regulatory light chain, further studies should be performed to determine whether MLC2 in *P. clarkii* is also allergenic and to compare the allergenic properties of MLC1 and MLC2.

Most food allergens share similar physicochemical characteristics in that they are glycoproteins, relatively stable to heat and acid−alkali, and may remain allergenic after digestion.[14] In this study, the total carbohydrate content of MLC1 was about 4.3 ± 0.05% (w/w) of the whole protein. Two identical potential N-glycosylated sites (Asn−Gly−Thr) were identified by analyzing

DOI: 10.1021/acs.jafc.5b01318
J. Agric. Food Chem. 2015, 63, 6271−6282

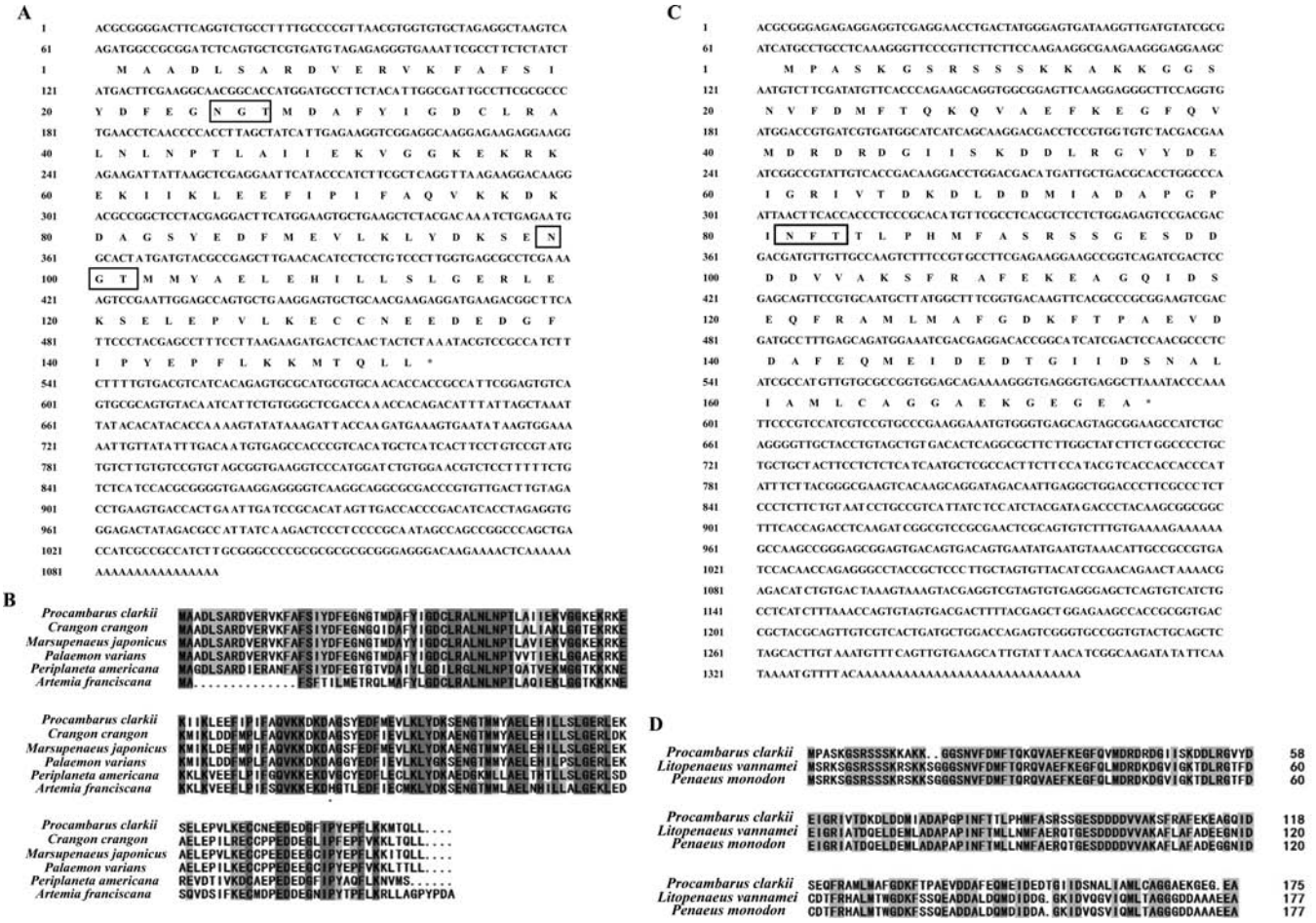

Figure 6. Cloning *MLC* genes and sequence alignment of crayfish MLC proteins. (A) Nucleotide and deduced amino acid sequences of crayfish MLC1 (the N-glycosylation site is marked with a box). (B) Sequence alignment of crayfish MLC1 and the MLC proteins of other crustaceans. (C) Nucleotide and deduced amino acid sequences of crayfish MLC2 (the N-glycosylation site is marked with a box). (D) Sequence alignment of crayfish MLC2 and the MLC proteins of other crustaceans.

the primary structure and mass spectra of the protein. The carbohydrates in crayfish SCP are reported to constitute about 4.9% of the protein, with one N-glycosylation site. MLC and SCP have reportedly similar characteristics, and data in this report support this conclusion.[6,18] An O-linked glycan in the MLC1 structure was detected with β-elimination. The O-glycan, which occurs in clusters along short regions of the peptide chain that contain repeating units of Ser and Thr, is unstable under alkaline conditions at low temperature. After NaOH treatment, Ser and Thr are transformed into α-amino acids. Both of these unsaturated amino acids display characteristic UV absorption at 240 nm.[6] According to the typical characterization of glycoproteins, MLC1 is a glycoprotein. N- and O-linked allergenic glycoproteins, which have common core structures, are associated with the induction of an IgE response in allergic patients.[30] The N-glycosylated sites of MLC1 were partially at the predicted epitope regions (amino acid residues 25 and 99). Therefore, the relationship between the allergenicity and glycosylation of crayfish MLC1 warrants further research.

In this study, MLC1 was stable at 30−100 °C and under strongly acidic and alkaline conditions and retained its IgE-binding activity at different temperatures and pH value. In contrast, a study by Kamath et al.[19] demonstrated that IgE binding to MLC of *P. monodon* was only detected in heated prawn extract and not in raw prawn extract. It was inferred that the thermal stability of MLC1 differs from that of MLC2. The thermal stability and pH stability of crayfish MLC1 were similar to those of TM, another myofibrillar protein and the major allergen of shellfish, which is stable under acidic and alkaline conditions and retains its IgE-binding activity after high-temperature and high-pressure processing.[31] However, the IgE-binding activities of crayfish myosinogens AK and SCP are reduced at high temperatures or under different acidic or alkaline conditions.[6,14] It has been reported that, under different physiological and experimental conditions, some allergens may undergo conformational changes that cause the exposure of different combinations of epitopes recognized by the IgE antibodies of allergic subjects.[18] In this study, the changes in the secondary structure of crayfish MLC1 under severe conditions, including high temperature (100 °C), strong acid (pH 1.0), and strong alkali (pH 11.0), were assessed to observe the changes in its secondary structure. High temperature and strong acid treatments had significant effects on the secondary structure of MLC1, but its IgE-binding activity remained intact despite the changes in its structure. A future study should focus on effective processing methods to mask or disrupt the IgE epitopes. Food allergens generally remain intact during gastrointestinal digestion. Crayfish MLC1 appeared to be more resistant to gastric digestion than to intestinal digestion and retained its immunological activity (detected with ciELISA).

DOI: 10.1021/acs.jafc.5b01318
J. Agric. Food Chem. 2015, 63, 6271−6282

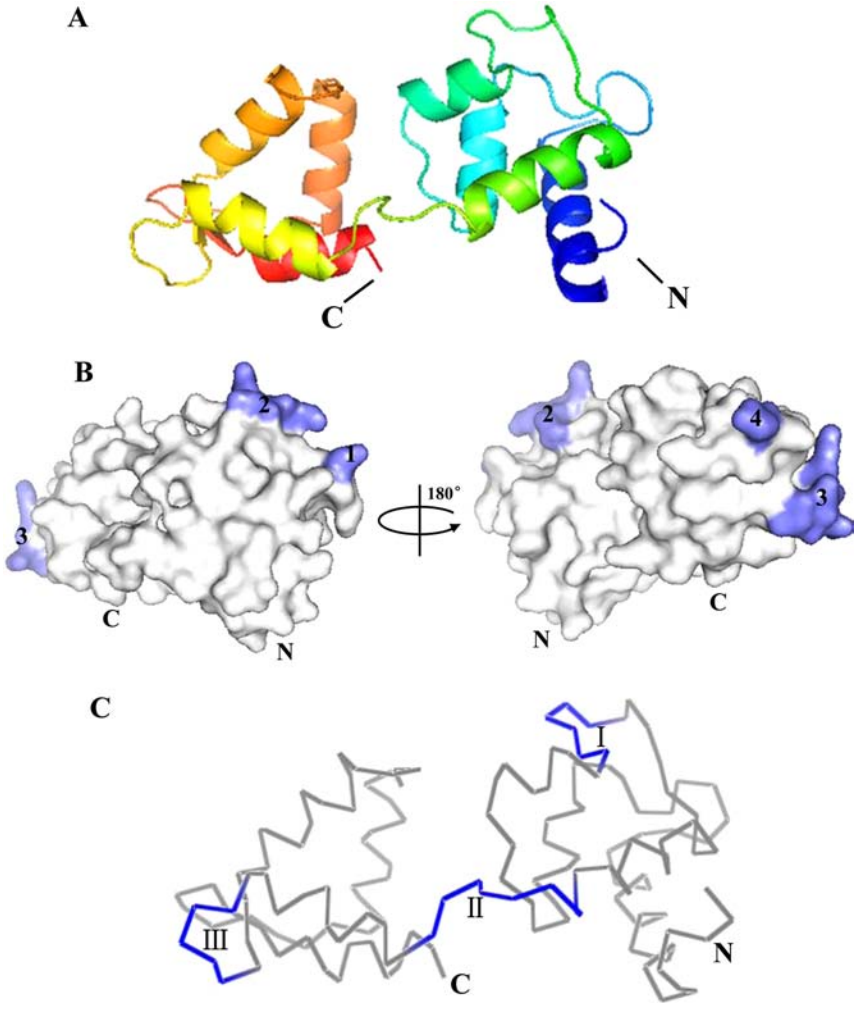

Figure 7. Structural modeling and epitope prediction of crayfish MLC1. (A) Three-dimensional structure of crayfish MLC1. N and C indicate the N- and C-termini, respectively. (B) Molecular mapping of the conformational epitopes of crayfish MLC1 onto its three-dimensional structure. The areas occupied by the conformational epitopes are shown in slate. Epitopes 1−4 are Asn^{25}, Lys^{57}−Glu^{60}, Lys^{96}−Asn^{99}, and Glu^{136}, respectively. (C) Molecular mapping of the linear epitopes of crayfish MLC1 onto its three-dimensional structure. The areas occupied by the linear epitopes are shown in blue. Epitopes I−III, Gly^{53}−Arg^{58}, Lys^{76}−Ser^{83}, and Asp^{95}−Asn^{99}, respectively.

Interestingly, MLC1 was degraded after gastrointestinal digestion, but the degraded fragments had IgE-binding activity almost equivalent to that of the undigested MLC1 sample. In a previous study, crayfish AK and SCP were also degraded to varying degrees by gastrointestinal digestion but remained immunologically active.[6,14] Certain IgE-binding sites on crayfish MLC1 are thought to be left intact by digestive enzymes, and the major IgE-binding sites of allergens in crayfish are stable after digestion. It was reported that Ca^{2+} binding was essential for the formation of the conformation structure of calcium-binding proteins like parvalbumin, and the depletion of Ca^{2+} resulted in the reduction of IgE-binding activity.[32,33] MLC belongs to the EF-hand superfamily, and the influences of Ca^{2+} on the structure of MLC and its allergenicity need further research.

The epitopes can be classified as continuous or discontinuous. Continuous epitopes can be identified in denatured proteins and peptide fragments, whereas discontinuous epitopes depend on the higher-order structures of the native protein.[34] The study of epitopes is critical to understanding the nature of allergens and the improvement of diagnosis, detection, and therapies. To determine the predominant IgE epitope type in crayfish MLC1, indirect ELISA and dot blot analysis were performed on folded MLC1 and Western blot analysis was performed on the unfolded MLC1 with sera from allergic individuals. In both the indirect ELISA and the dot blot analysis, the native MLC1 was immobilized on the plate or a nitrocellulose membrane, respectively. In both of these assays, the folded MLC1 was found to maintain IgE binding under high heat and different pH conditions for all allergic sera tested. In the Western blot, where MLC1 was in denatured or linear form, only the serum IgE from three allergic individuals displayed weakly positive binding. These results imply that the conformational epitopes of MLC1 are predominantly recognized by IgE, rather than the linear epitopes. Considering that the IgE binding by unfolded MLC1 is significantly reduced compared to the folded MLC1, it is possible that the digested fragments retain some structural features that are able to compete with intact MLC1 for IgE binding.

The conformational and linear epitopes of the crayfish MLCs were also predicted in silico. MLC1 was predicted to contain four conformation epitopes and three linear epitopes, and the regions formed by amino acids 57−60 and 96−99 contained both conformational and linear epitopes. MLC2 also showed a major predicted conformational epitope and three linear epitopes. MLC2 clearly was predicted to have more epitopes than MLC1,

DOI: 10.1021/acs.jafc.5b01318
J. Agric. Food Chem. 2015, 63, 6271−6282

but it was not recognized by the IgE in sera from crustacean-allergic patients in a previous study. However, in future studies, it will be important to investigate IgE binding to MLC2 with the same patient sera used in this study for MLC1. Fundamental studies of allergens focus on IgE-binding epitopes, which are used as biomarkers to predict the clinical reactivity of subjects who are sensitized to a specific food, and provide alternative immunotherapeutic strategies.[35] If some parallels can be found between predicted and the experimental IgE-binding patterns, perhaps efforts to reduce the allergenicity of food and diagnostic tools may be improved via epitope prediction tools. Also, recombinant MLC1 and MLC 2 can be used to aid in clinical diagnoses and in further research to provide basic information for the hypersensitization to crayfish and the evaluation of food allergies.

■ ASSOCIATED CONTENT

Supporting Information

Additional experimental details. The Supporting Information is available free of charge on the ACS Publications website at DOI: 10.1021/acs.jafc.5b01318.

■ AUTHOR INFORMATION

Corresponding Author

*Phone: +86-592-6183383. Fax: +86-592-6180470. E-mail: gmliu@jmu.edu.cn.

Funding

This work was supported by the Grant from the National Natural Scientific Foundation of China (31171660, U1405214) and the Foundation for Innovative Research Team of Jimei University (2010A005).

Notes

The authors declare no competing financial interest.

■ REFERENCES

(1) Lee, A. J.; Gerez, I.; Shek, L. P.-C.; Lee, B. W. Shellfish allergy—an Asia-Pacific perspective. *Asian Pac. J. Allergy Immunol.* **2012**, *30*, 3−10.

(2) Pedrosa, M.; Boyano-Martínez, T.; García-Ara, C.; Quirce, S. Shellfish Allergy: a Comprehensive Review. *Clin. Rev. Allergy Immunol.* **2014**, DOI: 10.1007/s12016-014-8429-8.

(3) Mona, M. H.; Geasa, N.; Sharshar, K.; Morsy, E. Chemical composition of freshwater crayfish (*Procambarus clarkii*) and its nutritive value. *Egyptian J. Aquatic Biol. Fisheries* **2000**, *4*, 19−34.

(4) Fahmy, S. R.; Hamdi, S. A.; Abdel-Salam, H. A. Curative effect of dietary freshwater and marine crustacean extracts on carbon tetrachloride-induced nephrotoxicity. *Aust. J. Basic Applied Sci.* **2009**, *3*, 2118−2129.

(5) *China Fisheries Yearbook*; China Agricultural Press: Beijing, China, 2014 (in Chinese).

(6) Chen, H. L.; Cao, M. J.; Cai, Q. F.; Su, W. J.; Mao, H. Y.; Liu, G. M. Purification and characterisation of sarcoplasmic calcium-binding protein, a novel allergen of red swamp crayfish (*Procambarus clarkii*). *Food Chem.* **2013**, *139*, 213−223.

(7) Leung, P. S.; Chen, Y. C.; Mykles, D. L.; Chow, W. K.; Li, C. P.; Chu, K. H. Molecular identification of the lobster muscle protein tropomyosin as a seafood allergen. *Mol. Mar. Biol. Biotechnol.* **1998**, *7*, 12−20.

(8) Reese, G.; Ayuso, R.; Lehrer, S. B. Tropomyosin: an invertebrate pan-allergen. *Int. Arch. Allergy Immunol.* **1999**, *119*, 247−258.

(9) Lin, J. W.; You, H. Y.; Shen, H. W.; Cao, M. J.; Cai, Q. F.; Liu, G. M. Purification and Allergenic Analysis of Procambarus clarkii Tropomyosin. *J. Jimei Uni. (Natural Sci.)* **2012**, *17*, 167−174.

(10) Bauermeister, K.; Wangorsch, A.; Garoffo, L. P.; Reuter, A.; Conti, A.; Taylor, S. L.; Lidholm, J.; DeWitt, Å. M.; Enrique, E.; Vieths, S. Generation of a comprehensive panel of crustacean allergens from the North Sea Shrimp Crangon crangon. *Mol. Immunol.* **2011**, *48*, 1983−1992.

(11) Abdel Rahman, A. M.; Kamath, S. D.; Gagné, S. b.; Lopata, A. L.; Helleur, R. Comprehensive proteomics approach in characterizing and quantifying allergenic proteins from northern shrimp: toward better occupational asthma prevention. *J. Proteome Res.* **2013**, *12*, 647−656.

(12) Rosmilah, M.; Shahnaz, M.; Zailatul, H.; Noormalin, A.; Normilah, I. Identification of tropomyosin and arginine kinase as major allergens of *Portunus pelagicus* (blue swimming crab). *Trop. Biomed.* **2012**, *29*, 467−478.

(13) Shen, H. W.; Cao, M. J.; Cai, Q. F.; Ruan, M. M.; Mao, H. Y.; Su, W. J.; Liu, G. M. Purification, cloning, and immunological characterization of arginine kinase, a novel allergen of *Octopus fangsiao*. *J. Agric. Food Chem.* **2012**, *60*, 2190−2199.

(14) Chen, H. L.; Mao, H. Y.; Cao, M. J.; Cai, Q. F.; Su, W. J.; Zhang, Y. X.; Liu, G. M. Purification, physicochemical and immunological characterization of arginine kinase, an allergen of crayfish (*Procambarus clarkii*). *Food Chem. Toxicol.* **2013**, *62*, 475−484.

(15) Shiomi, K.; Sato, Y.; Hamamoto, S.; Mita, H.; Shimakura, K. Sarcoplasmic calcium-binding protein: identification as a new allergen of the black tiger shrimp Penaeus monodon. *Int. Arch. Allergy Immunol.* **2008**, *146*, 91−98.

(16) Ayuso, R.; Grishina, G.; Ibáñez, M. D.; Blanco, C.; Carrillo, T.; Bencharitiwong, R.; Sánchez, S.; Nowak-Wegrzyn, A.; Sampson, H. A. Sarcoplasmic calcium-binding protein is an EF-hand-type protein identified as a new shrimp allergen. *J. Allergy Clin. Immunol.* **2009**, *124*, 114−120.

(17) Piboonpocanun, S.; Jirapongsananuruk, O.; Tipayanon, T.; Boonchoo, S.; Goodman, R. E. Identification of hemocyanin as a novel non-cross-reactive allergen from the giant freshwater shrimp *Macrobrachium rosenbergii*. *Mol. Nutr. Food Res.* **2011**, *55*, 1492−1498.

(18) Ayuso, R.; Grishina, G.; Bardina, L.; Carrillo, T.; Blanco, C.; Ibáñez, M. D.; Sampson, H. A.; Beyer, K. Myosin light chain is a novel shrimp allergen, Lit v 3. *J. Allergy Clin. Immunol.* **2008**, *122*, 795−802.

(19) Kamath, S. D.; Rahman, A. M. A.; Voskamp, A.; Komoda, T.; Rolland, J. M.; O'Hehir, R. E.; Lopata, A. L. Effect of heat processing on antibody reactivity to allergen variants and fragments of black tiger prawn: a comprehensive allergenomic approach. *Mol. Nutr. Food Res.* **2014**, *58*, 1144−1155.

(20) Funkenstein, B.; Skopal, T.; Rapoport, B.; Rebhan, Y.; Du, S.; Radaelli, G. Characterization and functional analysis of the 5′ flanking region of myosin light chain-2 gene expressed in white muscle of the gilthead sea bream (Sparus aurata). *Comp. Biochem. Physiol., Part D: Genomics Proteomics* **2007**, *2*, 187−199.

(21) Han, F.; Wang, Z. Y.; Wang, X. Q. Characterization of myosin light chain in shrimp hemocytic phagocytosis. *Fish Shellfish Immunol.* **2010**, *29*, 875−883.

(22) Liu, J.; Han, L. N.; Zhang, Q.; Wang, Q. L.; Chang, Q.; Zhuang, H.; Liu, J.; Li, M.; Yu, D.; Kang, Z. S. Cloning and molecular characterization of a myosin light chain gene from Puccinia striiformis f. sp. tritici. *World J. Microbiol. Biotechnol.* **2014**, *30*, 631−637.

(23) Balhara, J.; Redhu, N. S.; Shan, L.; Gounni, A. S. IgE Regulates the Expression of smMLCK in Human Airway Smooth Muscle Cells. *PLoS One* **2014**, *9*, e93946.

(24) Huang, M. C.; Ochiai, Y. Fish fast skeletal muscle tropomyosins show species-specific thermal stability. *Comp. Biochem. Physiol., Part B: Biochem. Mol. Biol.* **2005**, *141*, 461−471.

(25) Yan, L. J.; Zhan, C. L.; Cai, Q. F.; Weng, L.; Du, C. H.; Liu, G. M.; Su, W. J.; Cao, M. J. Purification, characterization, cDNA cloning and in vitro expression of a serine proteinase from the intestinal tract of sea cucumber (*Stichopus japonicus*) with collagen degradation activity. *J. Agric. Food Chem.* **2014**, *62*, 4769−4777.

(26) Dubois, M.; Gilles, K. A.; Hamilton, J. K.; Rebers, P.; Smith, F. Colorimetric method for determination of sugars and related substances. *Anal. Chem.* **1956**, *28*, 350−356.

(27) Li, Z.; You, J.; Luo, Y. K.; Wu, J. P. Purification and characterization of parvalbumin isotypes from grass carp (*Ctenopharyngodon idella*). *J. Agric. Food Chem.* **2014**, *62*, 6212−6218.

DOI: 10.1021/acs.jafc.5b01318
J. Agric. Food Chem. 2015, 63, 6271−6282

(28) Böhm, G.; Muhr, R.; Jaenicke, R. Quantitative analysis of protein far UV circular dichroism spectra by neural networks. *Protein Eng., Des. Sel.* **1992**, *5*, 191−195.
(29) Guo, C.; Cao, M. J.; Liu, G. M.; Lin, X. S.; Hara, K.; Su, W. J. Purification, characterization, and cDNA cloning of a myofibril-bound serine proteinase from the skeletal muscle of crucian carp (*Carassius auratus*). *J. Agric. Food Chem.* **2007**, *55*, 1510−1516.
(30) Fötisch, K.; Vieths, S. N-and O-linked oligosaccharides of allergenic glycoproteins. *Glycoconjugate J.* **2001**, *18*, 373−390.
(31) Yu, H. L.; Cao, M. J.; Cai, Q. F.; Weng, W. Y.; Su, W. J.; Liu, G. M. Effects of different processing methods on digestibility of *Scylla paramamosain* allergen (tropomyosin). *Food Chem. Toxicol.* **2011**, *49*, 791−798.
(32) Moraes, A.; Ackerbauer, D.; Kostadinova, M.; Bublin, M.; Oliveira, G. A.; Ferreira, F.; Almeida, F.; Breiteneder, H.; Valente1, A. P. Solution and high-pressure NMR studies of the structure, dynamics, and stability of the cross-reactive allergenic cod parvalbumin Gad m 1. *Proteins: Struct., Funct., Genet.* **2014**, *82*, 3032−3042.
(33) Swoboda, I.; Bugajska-Schretter, A.; Linhart, B.; Verdino, P.; Keller, W.; Schulmeister, U.; Sperr, W. R.; Valent, P.; Peltre, G.; Quirce, S.; Douladiris, N.; Papadopoulos, N. G.; Valenta, R.; Spitzauer, S. A recombinant hypoallergenic parvalbumin mutant for immunotherapy of IgE-mediated fish allergy. *J. Immunol.* **2007**, *178*, 6290−6296.
(34) Barlow, D.; Edwards, M.; Thornton, J. Continuous and discontinuous protein antigenic determinants. *Nature* **1986**, *322*, 747−748.
(35) Mao, H. Y.; Cao, M. J.; Maleki, S. J.; Cai, Q. F.; Su, W. J.; Yang, Y.; Liu, G. M. Structural characterization and IgE epitope analysis of arginine kinase from *Scylla paramamosain*. *Mol. Immunol.* **2013**, *56*, 463−470.

DOI: 10.1021/acs.jafc.5b01318
J. Agric. Food Chem. 2015, 63, 6271−6282

human hydrolyzed plasma was <67 nM for enterolignans and <1 nM for plant lignans. The concentration of lignans in hydrolyzed pig plasma was <2 nM for enterolactone and close to zero for plant lignans and enterodiol.

Test Urine. The concentrations of lignans in unhydrolyzed and hydrolyzed human urine were <3.4 and 100 nM for enterolignans and <0.05 and 17 nM for plant lignans, respectively. Unhydrolyzed urine from pigs contained only traces of lignans. The concentration of lignans in hydrolyzed pig urine was <6.7 nM for enterolactone and <0.2 nM for enterodiol and plant lignans.

Sample Hydrolysis. Plasma samples of 0.5 mL were treated with 1 mL of freshly dissolved β-glucuronidase (≥300000 units/g solid)/sulfatase (≥10000 units/g solid) (2 mg/mL in 50 mM sodium acetate buffer, pH 5) and incubated in a shaker at 37 °C in 19 h according to the method of Smeds et al.[9] Urine samples of 0.25 mL used for the quantitation of plant lignans and 2.5 μL for the quantitation of enterolignans were also treated with 1 mL of β-glucuronidase (2 mg/mL in 50 mM sodium acetate buffer, pH 5) and incubated in a shaker at 37 °C in 19 h. The optimal hydrolysis time for urine samples was determined by incubating samples for longer and shorter periods of time, where 19 h was the time at which lignans reached their maximal concentration. After incubation, 1 mL of 0.2% of formic acid was added, and the samples were centrifuged for 15 min at 4 °C at 60*g* and then ready for solid phase extraction (SPE).

SPE Cleanup of Plasma and Urine. Samples were cleaned up using SPE C18-E columns or SPE C18-E 96-well plates from Phenomenex (Torrance, CA, USA). The SPE method included conditioning, washing, and elution of lignans. The C18-E column or 96-well plate was conditioned with acetonitrile and then with water. Afterward, the samples were loaded and allowed to elute slowly through the C18 material. The column or plate was then washed with 0.5 mL of 5% methanol for plasma or with 20% methanol for urine. Lignans from plasma and urine were eluted with 150 and 300 μL of 100% acetonitrile, respectively. The eluted samples were then diluted to 25% acetonitrile with 450 and 900 μL of water containing glycocholic acid (glycine-1^{13}C) as IS. A final concentration of IS was 20 ng/mL. IS was used for autosampler correction and matrix effects validation. Samples were spun at 10 °C for 5 min prior to LC-MS/MS measurements.

LC-MS/MS Equipment and Method. The LC-MS/MS measurements were performed on a microLC 200 series from Eksigent/AB Sciex (Redwood City, CA, USA) and QTrap 5500 mass spectrometer from AB Sciex (Framingham, MA, USA). The mass spectrometer was equipped with an ESI source. The microLC was equipped with an Ascentis C18 column, 100 mm × 1.0 mm with 3.0 μm partical size from Sigma-Aldrich. The LC conditions were as follows: Eluent A consisted of water with 0.1% formic acid and eluent B was acetonitrile with 0.1% formic acid. The column was equilibrated for 3 min. The gradient started at 75% eluent A and 25% eluent B, was held constant for 1 min, then increased to 85% eluent B during 3.3 min and kept constant for 0.5 min. The total run time was 7.8 min. The autosampler racks were kept at 10 °C, and the column oven was set to 23 °C. Negative mode was used for ionization. The flow injection analysis (FIA) was performed to optimize the turbo V source of the instrument, where curtain gas was set to 20 psig, nebulizer gas (gas1) to 50 psig, heater gas (gas2) to 60 psig, and temperature to 300 °C and ionization spray was operated at −4500 eV. Deprotonated molecules were detected in MRM mode. The compound-dependent parameters were optimized for each lignan by syringe infusion of pure standard and are shown in Table 1. Data analysis was performed in Analyst software 1.6 from AB Sciex.

Calibration Curves. Calibration curves had 7−12 points depending on the analyte. The mixture of pure solvents was prepared in 25% acetonitrile in the range of 0.0244−100 ng/mL. IS was added to the calibration curves at a final concentration of 20 ng/mL. The analyte/internal standard concentration ratio was plotted against the analyte/internal standard peak area ratio as a linear regression curve with $1/x$ weighting.

Accuracy, Precision, and Recovery. The accuracy, precision, and recovery of the lignans were tested at three concentrations, low, medium, and high, using five measurements per concentration. Plasma samples were tested at 0.0977, 1.56, and 50 ng/mL, respectively. Urine samples were tested at 0.39, 1.56, and 50 ng/mL, respectively. For determination of the accuracy and precision at low and medium concentrations, the unhydrolyzed plasma and urine were spiked with standards after SPE extraction, whereas at high concentration hydrolyzed plasma and urine were used. Recoveries of the lignans were determined by spiking plasma and urine with standards prior to enzymatic hydrolysis and SPE using unhydrolyzed plasma and urine for low and medium concentrations and hydrolyzed plasma and urine for high concentration. Blank hydrolyzed or unhydrolyzed plasma and urine were used to subtract the background during the calculations. Quality control (QC) samples were used to validate the interbatch variation. Ten QC samples were used for each run.

Table 1. Compound-Dependent LC-MS/MS Parameters: Declustering Potential (DP), Entrance Potential (EP), Collision Energy (CE), and Cell Exit Potential (CEP)

	Q1 mass (m/z)	Q3 mass (m/z)	DP (V)	EP (V)	CE (eV)	CEP (V)
enterolactone	297.1	189.1	−140	−10	−26	−21
enterodiol	301.1	253.1	−140	−10	−32	−19
matairesinol	357.2	82.9	−145	−10	−26	−7
hydroxymatairesinol	373.1	217.1	−115	−10	−32	−13
secoisolariciresinol	361.2	165.0	−150	−10	−34	−11
lariciresinol	359.1	329.0	−40	−10	−16	−21
isolariciresinol	359.2	344.0	−165	−10	−26	−31
pinoresinol	357.2	151.0	−155	−10	−24	−11
syringaresinol	417.1	181.0	−170	−10	−26	−13
medioresinol	387.2	151.0	−15	−10	−26	−25

Statistics. The accuracy describes the percentage deviation of the mean from the true value. Accuracy was calculated as relative error (ER) of replicated measurements, with acceptance criteria that it should not deviate by >±20% at low concentration or by >±15% at medium and high concentrations. The precision describes the closeness of individual measurements of an analyte applied to the multiple samples. Precision was calculated as relative standard deviation (RSD), where it should not exceed by >20% at low concentration or by >15% at medium and high concentrations. The recovery of the analyte represents the amount of the analyte recovered after the sample preparation procedure. Recovery was calculated as a percentage of the analyte recovered after the SPE procedure. The interbatch precision was validated using QC samples, which can provide the bases of accepting or rejecting the run. The acceptance criterion was that at least 67% of QC samples were within an RSD of 15%. Matrix effects were investigated by calculating the matrix factor (MF) for lignan and IS as the ratio between the peak area in the presence of matrix and in the absence of matrix. If the ratio was close to 100%, no ion suppression had occurred. The IS-normalized MF was calculated by dividing the MF of the analyte with the MF of the IS. The RSD of the IS-normalized MF should not exceed >15%.

Method Validation. The method was validated according to the guidelines of the U.S. Food and Drug Administration (FDA)[12] and European Medicines Agency of Science Medicines Health.[13]

RESULTS

SPE Cleanup. The sample cleanup procedure presented in this paper was developed and optimized for both low and high numbers of plasma and urine samples. Therefore, both single SPE C18 columns and SPE C18 plates can be used. The sample cleanup was kept as simple as possible to minimize transfer losses and labor time involved. A simplified sample cleanup procedure is far more amenable for a high throughput of samples.

Chromatographic Analysis. Chromatographic parameters were optimized to achieve high resolution and efficiency at

DOI: 10.1021/acs.jafc.5b01275
J. Agric. Food Chem. 2015, 63, 6283−6292

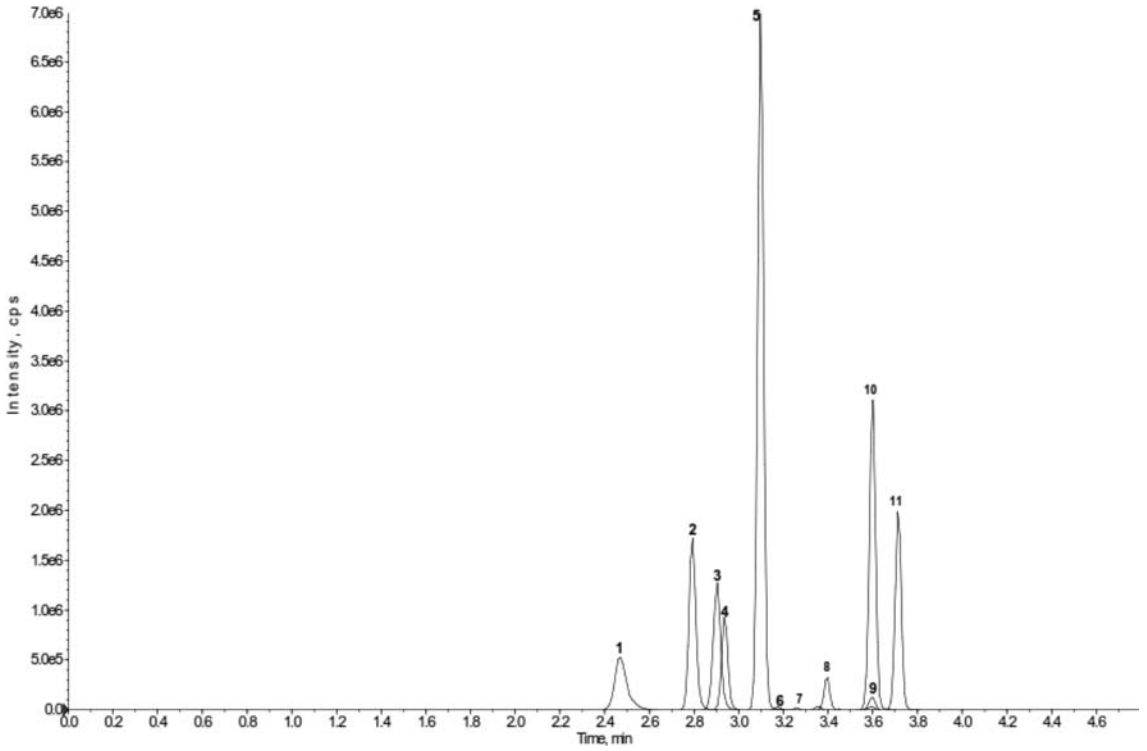

Figure 1. Typical MRM chromatogram of lignan standards at 50 ng/mL. Peaks: 1, isolariciresinol, RT 2.47 min; 2, secoisolariciresinol, RT 2.79 min; 3, hydroxymatairesinol, RT 2.90 min; 4, lariciresinol, RT 2.94 min; 5, enterodiol, RT 3.10 min; 6, syringaresinol, RT 3.17 min; 7, medioresinol, RT 3.26 min; 8, internal standard, RT 3.40 min; 9, pinoresinol, RT 3.60 min; 10, matairesinol, RT 3.60 min; 11, enterolactone, RT 3.71 min.

minimum run time. Good chromatographic separation was achieved at a short run time of 4.8 min, which is desirable when the number of samples is high. Only 2 of 10 lignans had similar retention times (RT) (Figure 1). Isolariciresinol had the lowest affinity to the C18 column, as indicated by the broader peak shape compared to the other lignans. Isolariciresinol was also the first lignan, eluting at 2.47 min, followed by secoisolariciresinol with RT of 2.79 min (Figure 1). Variation in the RT was negligible, with interbatch variation of <6 s. However, column-to-column variation of 10 s was observed. The chromatographic method was optimized using the standards prepared for the standard curve. These series of standards were also used to ensure the reproducibility of the chromatographic method and MS performance and were run each intra- and interbatch. No carry-over effect was observed when running blank samples containing only solvent and zero samples containing the solvent and the internal standard (data not shown). Zero samples also ensured the reproducibility of the IS.

Method Validation. *Quantitative Validation.* Calibration curves of pure standards were used to quantitate unknown concentrations of lignans in plasma and urine. The calibration curves generally consisted of 11 or 12 points; however, in the case of pinoresinol, syringaresinol, and medioresinol, they consisted of 7−10 points. The lower limit of quantitation (LLOQ) was accepted as the lowest standard on the calibration curve if the analyte response was at least 5 times the response of the blank sample. The highest standard defined the upper limit of quantitation (ULOQ). All calibration curves showed good linearity throughout the used range of concentration with LLOQ accuracy varying from 85 to 97% and precision below 20% and ULOQ accuracy from 90 to 105% and precision below 15%. The LLOQ and ULOQ and the corresponding regression coefficients for each lignan are listed in Table 2.

Table 2. Lower Limit of Quantitation (LLOQ) and Upper Limit of Quantitation (ULOQ) and Their Corresponding Regression Coefficients (r)

	LLOQ, nM (ng/mL)	ULOQ, nM (ng/mL)	r
enterolactone	0.16 (0.048)	167.6 (50)	0.9993
enterodiol	0.081 (0.024)	165.4 (50)	0.9997
matairesinol	0.068 (0.024)	139.5 (50)	0.9997
hydroxymatairesinol	0.13 (0.048)	133.6 (50)	0.9992
secoisolariciresinol	0.067 (0.024)	138.0 (50)	0.9997
lariciresinol	0.14 (0.048)	277.5 (100)	0.9996
isolariciresinol	0.068 (0.024)	277.5 (100)	0.9998
pinoresinol	0.27 (0.0975)	279.9 (100)	0.9994
syringaresinol	1.9 (0.78)	239.0 (100)	0.9977
medioresinol	4.0 (1.56)	257.5 (100)	0.998

Matrix Effect Validation. Ion suppression of ESI in MS instruments is a well-known problem. Several methods can be used for the validation of ion suppression due to matrix effects. Because both hydrolyzed and unhydrolyzed plasma and urine contained lignans in different concentrations, which would complicate the standard curve calculations, it was decided to use standards of three concentrations spiked into the pure solvent and SPE extracted plasma and urine. This experiment established that any matrix effect on the analyte response was corrected by a corresponding decrease in the IS response and thus permitted the use of calibration curves in pure solvent. Even though the IS corrected for possible matrix effects, the matrix factor (MF) was calculated for each lignan and IS (data not shown). Furthermore, the average MF was calculated for IS of human and pig plasma and urine and used as a measure indicating the influence of the matrix on the ionization of

DOI: 10.1021/acs.jafc.5b01275
J. Agric. Food Chem. 2015, 63, 6283−6292

lignans. The MFs for human and pig plasma were 99 and 98%, respectively, showing that no ion suppression had occurred. The MF of hydrolyzed versus unhydrolyzed plasma was also compared, but no differences were observed. In the case of enterolignans in urine the MF was close to 100%, whereas it was more variable when plant lignans were measured. Because 10 times more sample volume was used for measuring the plant lignans, variation in MF between the human and pig urine and unhydrolyzed versus hydrolyzed urine was observed. The MFs of the human hydrolyzed and unhydrolyzed urine were 90 and 69%, respectively. The MFs of the pig hydrolyzed and unhydrolyzed urine were 82 and 72%, respectively. The RSD of the IS normalized MF was then calculated for each of the three concentrations of human and pig urine and found to be not greater than 15%.

Accuracy, Precision, and Recovery. The accuracy, precision, and recovery were the main parameters used for the validation of the method. They were tested by the addition of the standards at three concentrations, low, medium, and high (Tables 3 and 4). The low concentration of plasma was chosen as 3 times the LLOQ of the standard curve, and in the case of urine 5 times the LLOQ was chosen, due to higher concentrations of lignans in the test urine. Because the ULOQ was set to 100 ng/mL, the high concentration was selected as the second highest concentration on the standard curve. In the case of precision and accuracy the standards were added to plasma and urine after the SPE procedure to be able to test the matrix effects and overall instrument performance. With regard to recovery of the lignans, the standards were added before the enzymatic hydrolysis and SPE procedure to test the affinity of the lignans to the SPE sorbent. In general, the results in Tables 3 and 4 show good or acceptable accuracy, precision, and recovery for all of the lignans tested in this study.

In the case of plasma (Table 3), the accuracy varied from −2.4% for hydroxymatairesinol to 12.7 and 8.9% for enterolactone and enterodiol, respectively, for human plasma at low concentration. This was opposite for pig plasma, where enterodiol and enterolactone showed the best accuracies of 1.6 and 4.7%, respectively, whereas secoisolariciresinol and hydroxymatairesinol had accuracies of 20 and 16.9%, respectively. At medium and high concentrations the method showed good or acceptable accuracy and precision, which was lower than the acceptance criteria of ±15%. Also, high or acceptable recoveries were observed for all of the lignans for human and pig plasma at all three concentrations.

In the case of urine (Table 4), the precision and accuracy of plant lignans, when corrected by the IS, were acceptable even though some ion suppression due to matrix effect had occurred. The concentration of enterolactone in human urine was too high to be able to calculate accuracy, precision, and recovery at low concentration. In general, the recoveries for enterolactone and enterodiol were high at all three concentrations, whereas in the case of plant lignans recoveries at high concentration were slightly lower compared to low and medium concentrations.

Selectivity and Sensitivity. Panels A and B of Figure 2 show the selectivity of the method in both human test plasma and urine spiked with low concentration of standards for all lignans except pinoresinol, syringaresinol, and medioresinol, where spiked concentrations were medium and high, respectively. A high selectivity of the method was demonstrated for plasma samples, where low background with no interfering peaks was observed (Figure 2A). Only a few additional peaks were visible for isolariciresinol, hydroxymatairesinol, lariciresinol, and

Table 3. Accuracy, Precision, and Recovery of Human and Pig Plasma Lignans at Low (L) = 0.0977 ng/mL, Medium (M) = 1.56 ng/mL, and High (H) = 50 ng/mL Concentrations, n = 5

	human plasma									pig plasma								
	accuracy (RE %)			precision (±RSD %)			recovery (%)			accuracy (RE %)			precision (±RSD %)			recovery (%)		
	L	M	H	L	M	H	L	M	H	L	M	H	L	M	H	L	M	H
enterolactone	12.7	5.9	1.4	20.0	7.6	2.6	99.4 ± 13.2	101.9 ± 8.9	95.4 ± 4.4	4.7	1.5	5.4	10.7	4.6	2.2	102.7 ± 12.3	104.2 ± 12.9	95.7 ± 3.8
enterodiol	8.9	4.9	1.5	16.5	4.2	2.2	104.4 ± 4.5	93.0 ± 2.4	96.2 ± 2.2	1.6	6.9	−1.5	4.7	7.3	2.7	80.0 ± 8.9	80.0 ± 9.3	103.5 ± 6.7
matairesinol	−4.0	2.9	0.1	6.4	2.8	1.4	93.7 ± 10.2	96.5 ± 2.5	82.8 ± 2.6	14.7	8.7	5.7	5.2	7.3	2.7	89.7 ± 12.5	89.1 ± 11.5	92.5 ± 4.8
hydroxymatairesinol	−2.4	0.6	−2.2	6.6	4.7	1.7	63.9 ± 5.5	76.3 ± 5.2	94.6 ± 4.4	−16.9	−12.4	−3.6	17.4	7.1	3.0	65.2 ± 14.1	66.5 ± 7.0	79.6 ± 5.1
secoisolariciresinol	−4.4	−2.1	−2.0	13.6	3.0	1.5	96.7 ± 16.7	86.3 ± 5.2	94.0 ± 3.7	20.0	13.5	1.7	5.4	3.8	2.0	98.7 ± 9.0	80.2 ± 3.8	83.2 ± 5.7
lariciresinol	8.3	0.5	4.0	16.3	3.3	2.5	102.6 ± 9.9	83.6 ± 5.2	91.2 ± 2.2	−17.2	−10.0	−1.5	15.2	6.3	1.4	83.8 ± 9.6	95.7 ± 3.8	87.6 ± 5.9
isolariciresinol	−8.7	0.2	−0.1	19.3	1.2	2.1	107.7 ± 3.4	88.8 ± 1.8	76.7 ± 3.5	13.5	3.3	1.1	9.5	10.1	3.9	88.3 ± 8.2	81.1 ± 3.8	87.6 ± 5.8
pinoresinol	8.1	0.6	−4.0	10.3	4.2	2.1	76.5 ± 4.5	93.4 ± 10.1	83.9 ± 4.9	13.2	−4.8	3.6	9.6	0.9	2.5	96.8 ± 5.5	85.5 ± 7.6	92.9 ± 4.1
syringaresinol	nq[a]	3.7	−4.7	nq	10.8	1.7	nq	107.6 ± 11.0	84.4 ± 4.3	nq	0.9	3.8	nq	10.5	5.5	nq	99.1 ± 3.2	79.4 ± 4.6
medioresinol	nq	nq	−1.6	nq	nq	4.3	nq	nq	97.3 ± 5.9	nq	nq	−2.5	nq	nq	4.4	nq	nq	81.8 ± 1.7

[a]Not quantitated.

DOI: 10.1021/acs.jafc.5b01275
J. Agric. Food Chem. 2015, 63, 6283−6292

Table 4. Accuracy, Precision, and Recovery of Human and Pig Urine Lignans at Low (L) = 0.0977 ng/mL, Medium (M) = 1.56 ng/mL, and High (H) = 50 ng/mL Concentrations, $n = 5$

	human urine									pig urine								
	accuracy (RE %)			precision (±RSD %)			recovery (%)			accuracy (RE %)			precision (±RSD %)			recovery (%)		
	L	M	H	L	M	H	L	M	H	L	M	H	L	M	H	L	M	H
enterolactone	nq	14.3	11.5	nq	3.3	0.4	nq	100.3 ± 15.3	94.0 ± 5.0	20.0	15.0	11.5	3.6	3.3	0.4	92.9 ± 2.6	102.9 ± 20.7	94.3 ± 5.8
enterodiol	14.1	5.6	- 3.9	4.5	2.8	0.9	101.3 ± 6.0	103.3 ± 3.2	96.7 ± 3.0	10.3	5.6	−3.9	4.4	2.9	0.9	88.6 ± 3.3	100.6 ± 19.8	84.6 ± 5.5
matairesinol	−5.2	−11.8	−10.1	5.7	3.9	1.2	97.3 ± 10.7	108.9 ± 3.7	79.8 ± 2.3	7.4	−11.9	−6.6	11.4	1.3	3.4	91.5 ± 12.5	86.2 ± 5.6	82.1 ± 1.7
hydroxymatairesinol	−9.6	−12.9	−9.4	9.0	9.3	2.8	95.8 ± 6.8	63.3 ± 9.0	48.8 ± 2.3	−9.5	−12.9	−10.7	6.9	4.9	4.0	94.7 ± 14.1	118.5 ± 24.8	49.4 ± 4.1
secoisolariciresinol	−3.5	−5.9	−8.0	5.8	3.4	0.3	87.0 ± 12.1	102.2 ± 8.4	68.0 ± 4.0	2.6	4.1	4.6	4.5	3.3	3.3	93.5 ± 6.0	97.7 ± 10.0	68.4 ± 3.7
lariciresinol	11.0	5.6	−8.5	8.3	10.0	2.7	101.1 ± 9.9	103.6 ± 5.5	83.4 ± 3.9	14.7	−10.8	−6.4	12.0	3.7	4.6	85.8 ± 9.8	86.9 ± 11.9	73.1 ± 3.4
isolariciresinol	3.5	−4.5	−4.3	6.0	7.6	1.4	81.7 ± 11.2	92.7 ± 9.3	91.6 ± 5.6	14.1	−3.5	−5.1	3.0	9.3	7.4	91.2 ± 5.1	85.7 ± 12.1	89.6 ± 5.7
pinoresinol	−1.7	0.5	−6.0	3.1	9.3	3.3	60.9 ± 11.8	78.4 ± 5.8	72.1 ± 5.6	7.6	2.7	−4.3	10.0	12.0	1.3	78.9 ± 15.5	106.3 ± 10.2	96.7 ± 6.6
syringaresinol	nq[a]	10.4	−6.2	nq	13.5	3.4	nq	104.4 ± 7.7	78.8 ± 5.5	nq	6.5	7.6	nq	8.1	10.4	nq	86.5 ± 12.6	86.0 ± 7.8
medioresinol	nq	nq	−5.1	nq	nq	10.4	nq	nq	82.9 ± 4.2	nq	nq	5.8	nq	nq	8.4	nq	nq	93.3 ± 6.6

[a]Not quantitated.

syringaresinol. Similar high selectivity was observed for pig plasma (data not shown). In the case of urine higher background and more additional peaks were visible on the chromatograms compared to plasma (Figure 2B). However, no peaks interfered with the signal of the analytes. Moreover, a very low noise level at around 100−700 cps in intensity for plasma and around 200−1500 cps in intensity in the case of urine (Figure 3) increased the sensitivity of the method, allowing quantitation at low concentrations, as described in the quantitative validation section. No difference in noise level or number of additional/interfering peaks was observed for unhydrolyzed versus hydrolyzed plasma (data not shown).

Standard Stability. Repeated analyses of the standard curve over a 3 month period showed that the standards were stable for at least 1 month. Short-term stability of IS in water was also tested by comparison of the IS areas from 4 to 24 h. The result indicated that IS was stable for at least 1 day.

Real Sample Analyses. The applicability of the developed LC-MS/MS method was verified by measuring plant lignans and enterolignans in human and pig plasma and urine from two ongoing studies. Human plasma and urine were obtained from a Nordic lifestyle intervention study involving 24 men with early-stage prostate cancer, where 16 male participants were prescribed a high-lignan diet (HLD, based on whole grain rye) and 8 were used as control and were provided a low-lignan diet (LLD, based on refined wheat) during 6 months. Participants in the HLD group were prescribed 1200 g of whole grain rye per week. The detailed explanation of the intervention is described elsewhere.[14,15] The pig plasma and urine were collected from 10 pigs kept on HLD (based on whole grain rye) and 10 pigs kept on LLD (based on refined wheat) for 3 weeks and 1 week of wash-out LLD in the beginning of the study. Details of this study will be presented elsewhere. The samples from these two studies were run in batches together with 10 QC samples for each batch. Interbatch precision of pig plasma and urine was measured using QC samples of low and high concentrations, whereas in the case of human plasma and urine only one concentration was used (Table 5). The acceptance criterion of RSD of 15% was fulfilled in all cases except one; hydroxymatairesinol, at low concentration, had an RSD of 24.2%. However, this is in agreement with the low recovery and high deviation for this lignan in pig plasma at low concentration previously described under Method Validation. The results of human and pig studies are presented in Table 6. Furthermore, Figures 4 and 5 demonstrate MRM chromatograms of lignans in one of the plasma and urine samples from humans and pigs.

DISCUSSION

SPE Cleanup. One of the advantages of our developed cleanup procedure is the possibility to prepare both urine and plasma samples on the same SPE plate because the procedures are similar. Another simplification of the developed cleanup procedure is that no evaporation or resuspension of the extracted sample is necessary prior to LC-MS/MS, compared to the previously reported SPE methods.[7−9,16,17] After extraction of the analytes from the SPE plate or column, the samples can be diluted and analyzed directly on the LC-MS/MS instrument. Evaporation of the sample is usually time-consuming, and resuspension can contribute to the losses of the analytes.

Chromatographic Analysis. The separation of lignans was achieved with a run time of only 4.8 min, the lowest run time reported so far.[7−9,18] For comparison, Smeds et al.[8,9] reported

DOI: 10.1021/acs.jafc.5b01275
J. Agric. Food Chem. 2015, 63, 6283−6292

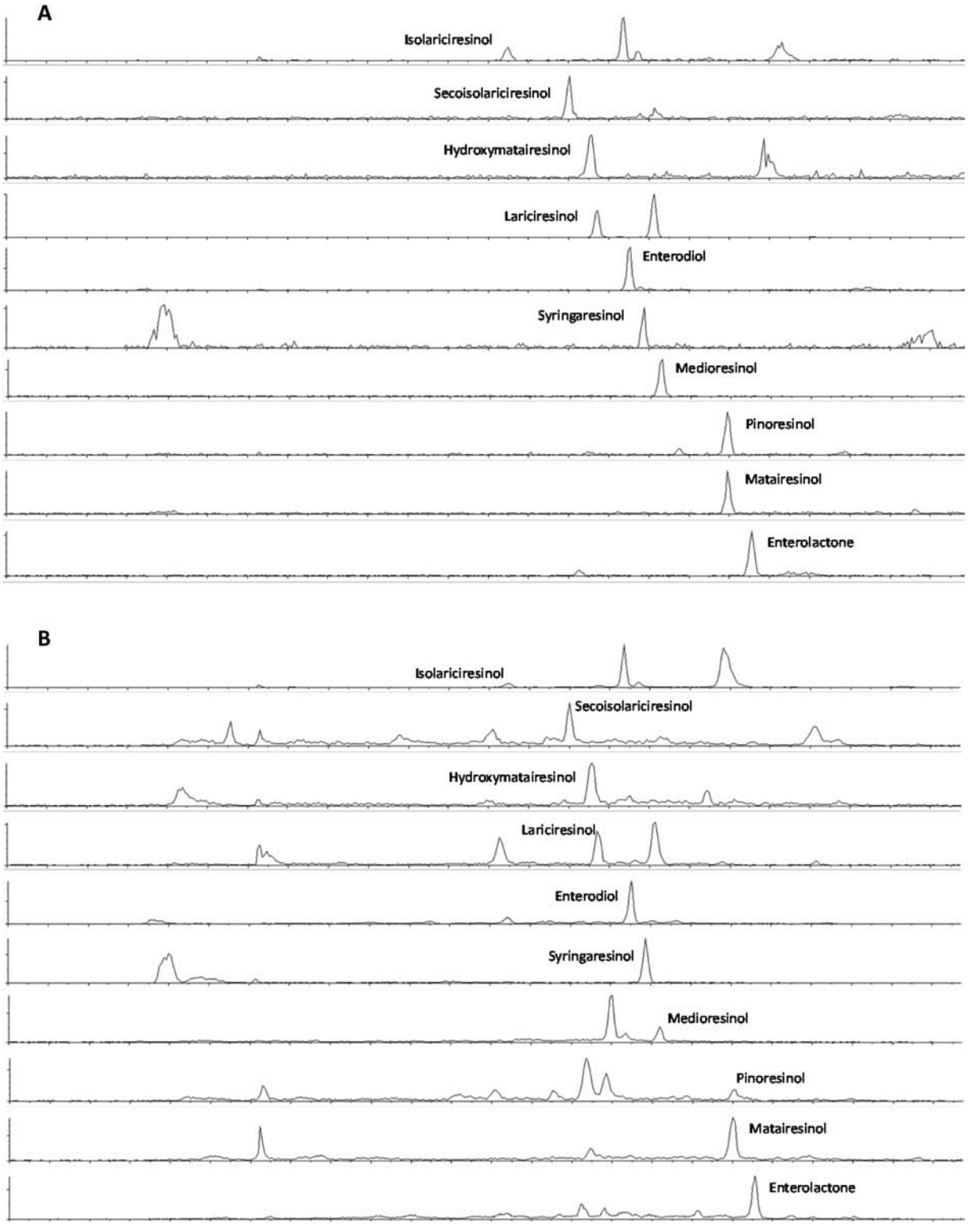

Figure 2. MRM chromatogram of lignans in test plasma spiked with 0.0977 ng/mL of standards for all lignans except pinoresinol, syringaresinol, and medioresinol, where spiked concentrations were 1.56 and 50 ng/mL respectively (A). Extracted ion MRM chromatogram of lignans in test urine spiked with 0.39 ng/mL of standards for all lignans except pinoresinol, syringaresinol, and medioresinol, where spiked concentrations were 1.56 and 50 ng/mL, respectively (B).

run times of 17 and 18 min to separate similar numbers of lignans. However, shorter run times were reported for separation of phytoestrogens in human serum[10] and urine,[11] where only enterolignans were included. The low run time is favorable when large numbers of samples are analyzed, which can effectively minimize the analytical time and therefore decrease the cost of analyses.

Method Validation. *Quantitative Validation.* The sensitivity of the method was demonstrated by low LLOQ and low noise level of the blank test plasma and urine. The sensitivity

DOI: 10.1021/acs.jafc.5b01275
J. Agric. Food Chem. 2015, 63, 6283−6292

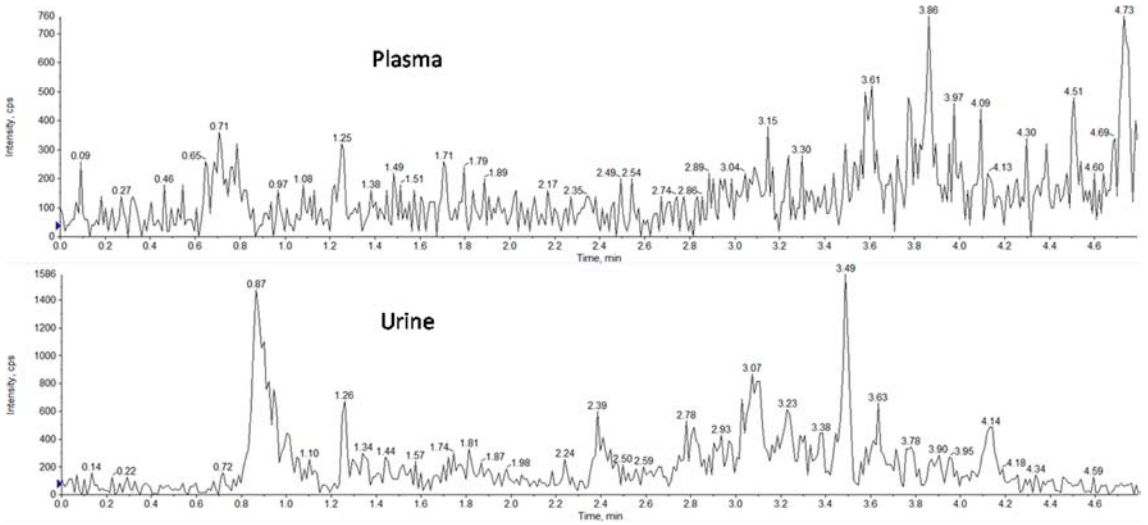

Figure 3. Typical MRM chromatogram of noise level in plasma and urine.

Table 5. Interbatch Precision of Human and Pig Plasma and Urine, Represented as ±RSD, n = 10 (Quality Control Samples (QC) at Low (L) and High (H) Concentration of Lignans)

	human plasma	human urine	pig plasma		pig urine	
	H	H	L	H	L	H
enterolactone	4.9	5.6	8.1	6.4	4.2	2.9
enterodiol	5.9	7.1	nq	6.5	6.4	3.4
matairesinol	10.8	5.3	nq	10.8	2.5	10.4
hydroxymatairesinol	nq[a]	8.8	24.2	8.2	4.0	6.6
secoisolariciresinol	6.2	12.0	8.0	4.9	8.6	5.7
lariciresinol	6.4	7.4	13.0	9.6	4.7	8.6
isolariciresinol	12.6	8.0	14.2	6.8	6.3	3.2
pinoresinol	14.0	5.2	nq	nq	5.5	6.0
syringaresinol	nq	12.2	nq	nq	9.7	4.8
medioresinol	nq	nq	nq	nq	nq	nq

[a]Not quantitated.

was 10−100 times higher depending on the lignan analyzed compared to the previously reported LC-MS/MS method of Smeds et al.[9] This was achieved without the need for concentrating the sample during the SPE procedure; on the contrary, the samples were diluted four times. This improved sensitivity is probably due to the use of the most recent LC-MS/MS system in our laboratory compared to the methods reported nearly 10 years ago. However, newer LC-MS/MS methods recently reported for the determination of phytoestrogens in human serum and urine did not show similar sensitivity either.[10,11] Prasain et al.[10] measured enterolignans in serum at LLOQ of 1 ng/mL, which is >10 times higher than LLOQ of our method. Moreover, to our knowledge no LC-MS/MS method has been published before on the quantitation of pinoresinol, syringaresinol, and medioresinol in plasma and urine. However, the LLOQ for syringaresinol and medioresinol was much higher compared to that of other plant lignans, and therefore syringaresinol was only possible to measure in urine, whereas medioresinol could not be measured in plasma or in urine.

Matrix Effects and Selectivity. Matrix-based and solvent-based calibration curves can be constructed to analyze the matrix effects on the instrument response[7,19] or to analyze the standards at three concentrations both dissolved in solvent and spiked into SPE extracted plasma and urine.[9,20] On the basis of the results of the spiking experiment, no matrix effects were detected for hydrolyzed or unhydrolyzed human and pig plasma, which is in agreement with previous analyses of human plasma reported by Smeds et al.[8,9] The selectivity was not

Table 6. Real Sample Analyses of Human Plasma Presented As Averaged (nM ± SD) and Urine As Averaged (μM/mM* or nM/mM of Creatinine ± SD), Low-Lignan Diet (LLD) following a High-Lignan Diet (HLD)[a]

	human plasma		human urine		pig plasma		pig urine	
	LLD	HLD	LLD	HLD	LLD	HLD	LLD	HLD
enterolactone	41.9 ± 35.7	59.6 ± 60.5	0.8* ± 0.7	1.4* ± 2.2	5.1 ± 1.8	150.5 ± 28.4	0.09* ± 0.03	4.8* ± 1.1
enterodiol	5.5 ± 10.8	10.0 ± 21.1	0.1* ± 0.1	0.2* ± 0.3	0.1 ± 0.07	3.1 ± 1.1	3.7 ± 1.7	55.9 ± 26.4
matairesinol	0.9 ± 0.6	0.6 ± 0.3	13.2 ± 6.0	15.3 ± 3.3	nq[b]	0.6 ± 0.3	0.9 ± 0.3	15.4 ± 9.7
hydroxymatairesinol	0.1 ± 0.1	0.2 ± 0.2	0.6 ± 0.4	1.1 ± 0.9	0.8 ± 0.3	0.9 ± 0.3	5.5 ± 2.6	3.4 ± 2.2
secoisolariciresinol	5.5 ± 5.8	3.1 ± 3.8	3.2 ± 2.5	4.3 ± 9.5	0.4 ± 0.1	1.1 ± 0.5	1.2 ± 0.5	10.5 ± 5.0
lariciresinol	0.9 ± 0.6	0.7 ± 0.4	18.3 ± 9.8	16.1 ± 7.3	0.5 ± 0.1	2.4 ± 0.5	2.0 ± 0.5.0	25.2 ± 11.6
isolariciresinol	3.5 ± 3.5	2.5 ± 3.5	73.9 ± 54.6	64.9 ± 43.2	0.3 ± 0.1	0.6 ± 0.3	0.9 ± 0.5	2.0 ± 0.4
pinoresinol	2.2 ± 2.5	2.0 ± 3.0	60.0 ± 32.8	75.8 ± 28.6	nq	nq	1.3 ± 1.1	16.5 ± 9.3
syringaresinol	nq	nq	5.3 ± 1.4	8.6 ± 4.4	nq	nq	1.6 ± 0.3	31.4 ± 14.2
medioresinol	nq	nq	nq	nq	nq	nq	nq	nq

[a]The numbers of samples for human plasma and urine of LLD were n = 8 and HLD n = 16 and for pig plasma and urine of both LLD and HLD were n = 10. [b]Not quantitated.

DOI: 10.1021/acs.jafc.5b01275
J. Agric. Food Chem. 2015, 63, 6283−6292

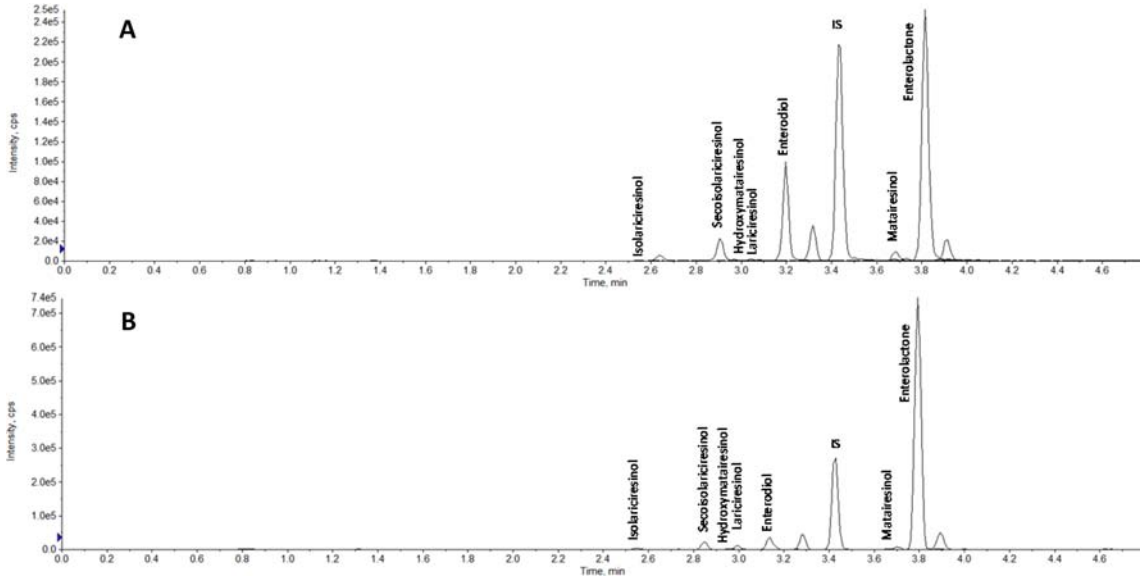

Figure 4. MRM chromatogram of lignans in one human plasma sample (A) and one pig plasma sample (B) from real sample analyses.

affected by hydrolysis of the plasma, where no additional or interfering peaks were observed. Prasain et al.[10] had detected minor to moderate matrix effects when analyzing phytoestrogens in serum. In our study, we measured minor to moderate matrix effects when analyzing plant lignans in urine. Moreover, a difference in matrix effects between hydrolyzed and unhydrolyzed urine was also measured. Our result showed that less ion suppression occurred after hydrolysis of the urine sample. However, no difference in the noise level or selectivity was observed for hydrolyzed/unhydrolyzed urine. To minimize the matrix effects in urine when plant lignans are measured, it is possible to use less sample volume.

Accuracy, Precision, and Recovery. In general, the accuracy and precision of this method for plasma and urine at low, medium, and high concentrations were good or acceptable. As expected, at the low concentration the accuracy and precision had higher deviation compared to the medium and high concentrations. Valentin-Blasini et al.[7] have also reported that the accuracy of their method increased with increasing analyte concentration.

In the case of plasma, at high concentration the accuracy was very good with an ER of only 0.1−4.7% in human plasma and 1.1−5.7% in pig plasma. Similarly, precision was also high at high concentration. At low concentration higher variation was observed among the lignans; also, the differences between human and pig plasma were greater. For example, in the case of enterodiol and enterolactone, the difference between the accuracy of these lignans in human versus pig plasma can probably be explained by the fact that no enterodiol and enterolactone were detected in unhydrolyzed test pig plasma, whereas traces of this compound were detected in human unhydrolyzed test plasma. The opposite situation was observed for hydroxymatairesinol, where low concentration of this compound was detected in both hydrolyzed and unhydrolyzed test pig plasma and no hydroxymatairesinol was detected in human test plasma.

Recoveries of enterolactone and enterodiol were high, not lower than 90% for human plasma and 80% for pig plasma. These data are comparable to previously reported recoveries for enterolignans by others using GC-MS, LC-MS, and LC with coulometric electrode array detector.[7−9,18,19,21] Lower recoveries of 68−91% for enterolignans in human plasma were reported by Nurmi et al.[22] using LC with coulometric electrode array detector and in serum by Prasain et al.[10] Recoveries for plant lignans in plasma were more varied, with the lowest recovery for hydroxymatairesinol, 63.9−94.6% for human plasma and 65.2−79.6% for pig plasma. Similarly low recoveries of 65−69% for hydroxymatairesinol were reported by Smeds et al.[8] Penalvo et al.[18] reported recoveries varying from 77 to 86% for plant lignans in human plasma. Our recoveries for other plant lignans except hydroxymatairesinol in human plasma varied from 76.5 to 107.7%, which is comparable to recoveries reported by Penalvo et al.[18]

In the case of urine, the recoveries for enterolactone and enterodiol were high at all three concentrations and therefore in accordance with recoveries reported elsewhere.[7,16,20] Plant lignans have shown high recoveries at low and medium concentrations, whereas recoveries were slightly lower at high concentration, except pinoresinol. Because our test urine when hydrolyzed contained higher concentrations of lignans compared to unhydrolyzed urine, this could have influenced the result.

Test Plasma and Urine. The increased concentration of lignans after hydrolysis of the plasma and urine was expected because lignans and especially enterolactone and enterodiol have been detected almost exclusively as conjugates of glucuronic acid and sulfate in human serum and urine.[23,24] The results of this study show that pig plasma and urine, similarly to human plasma and urine, contain lignans mainly in conjugated form.

Real Sample Analyses. As consumption of diet containing a high level of lignans is associated with a higher concentration of lignans in the blood and urine compared to a diet containing a low level of lignans, we have tested this newly developed method on real samples from two studies, with humans and with pigs. The analyses of human plasma and urine showed large interindividual variation in the concentration of lignans, which was expected because absorption and bioconversion of lignans depend greatly on the microbiota of the individual. Large interindividual variation in humans was also observed in other studies.[9,25,26] Therefore, the difference between participants consuming HLD and LLD was not so pronounced compared to the pig study, where dietary intake is under more strict control.

DOI: 10.1021/acs.jafc.5b01275
J. Agric. Food Chem. 2015, 63, 6283−6292

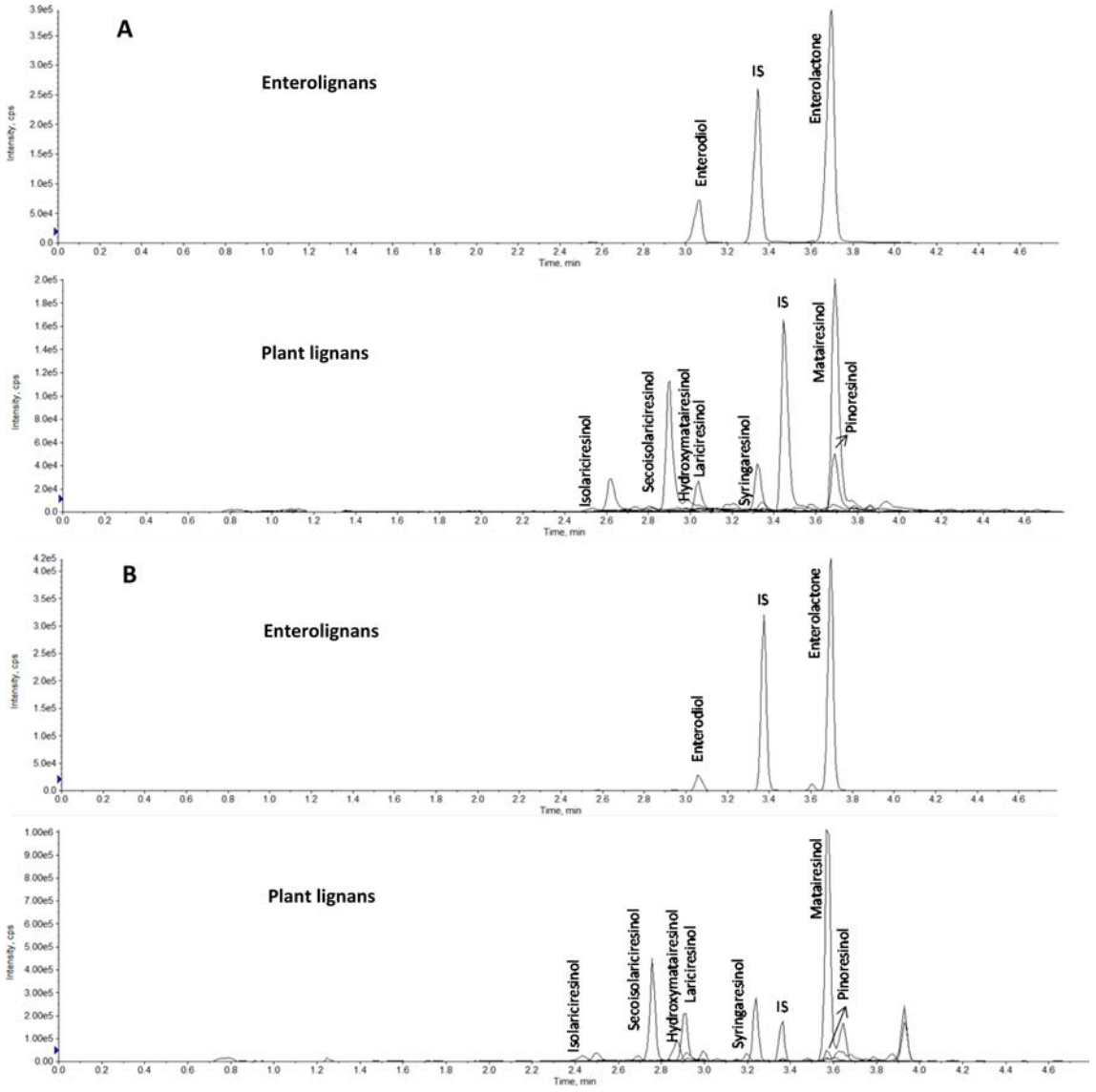

Figure 5. Extracted ion MRM chromatogram of lignans in one human urine sample (A) and one pig urine sample (B) from real sample analyses.

The difference between HLD and LLD in the pig study was large, which was as expected. The two types of diets, used in this pig study, have previously been used in model experiments with pigs, where large differences in lignan concentration between HLD and LLD in the plasma and urine were observed.[27,28] Moreover, interindividual variation among the pigs is much lower compared to humans, because the pigs genetically are more homogeneous and compliant to the experimental diets. It can be noted that the ratio between enterodiol and enterolactone in human plasma and urine was 3−5 times higher compared to pig plasma and urine. This indicates that pigs have a higher capacity to convert enterodiol to enterolactone compared to humans, probably due to a different microbiota. Moreover, the ratio between plant lignans and enterolignans in human plasma and urine after consumption of HLD was also 3−5 times higher compared to pig plasma and urine after consumption of the HLD. In contrast, when the two species consumed a LLD, the ratios between plant lignans and enterolignans in both human and pig plasma and urine were similar. This again can indicate differences in the absorption and bioconversion of lignans between humans and pigs and that the pig's conversion of plant lignans to enterolignans is more efficient. In general, the concentration of enterolignans in plasma and urine from both humans and pigs was higher compared to plant lignans, which is in accordance with our current knowledge that the majority of plant lignans are converted to enterolignans prior to uptake from the gut.[1]

The current paper presents a fast and easy (around 200 samples per day) LC-MS/MS method to quantitate two enterolignans, enterolactone and enterodiol, and eight plant lignans, matairesinol, hydroxymatairesinol, secoisolariciresinol, lariciresinol, isolariciresinol, syringaresinol, medioresinol, and pinoresinol, in biofluids from humans and pigs. The merit of our approach was to simplify the SPE cleanup and to shorten the analytical time used per sample without compromising the analytical performances of our method in terms of accuracy, precision, reproducibility, and sensitivity. Although we were successful in simplifying the SPE cleanup, some matrix effects were observed when plant lignans in urine samples were measured. This problem can be minimized by using a lower sample volume, because the concentration of plant lignans in urine is quite high. Furthermore, the method was successfully applied to quantitate lignans after the

DOI: 10.1021/acs.jafc.5b01275
J. Agric. Food Chem. 2015, 63, 6283−6292

consumption of HLD and LLD in plasma and urine. The lignans could be quantitated at pico- to nanomolar concentrations with good accuracy and precision. Moreover, the method is applicable for large numbers of samples and allows simultaneous analyses of plasma and urine from humans and pigs with a wide range of lignan concentrations.

AUTHOR INFORMATION

Corresponding Author

*(N.P.N.) Phone: +45 8715 7724. Fax: +45 8715 4249. E-mail: Natalja.Norskov@anis.au.dk.

Funding

We thank the Danish Council for Strategic Research for financing the project "The effects of enterolignans in chronic diseases − ELIN" (11964).

Notes

The authors declare no competing financial interest.

REFERENCES

(1) Axelson, M.; Sjovall, J.; Gustafsson, B. E.; Setchell, K. D. R. Origin of lignans in mammals and identification of a precursor from plants. *Nature* **1982**, *298*, 659−660.

(2) Setchell, K. D. R.; Lawson, A. M.; Mitchell, F. L.; Adlercreutz, H.; Kirk, D. N.; Axelson, M. Lignans in man and in animal species. *Nature* **1980**, *287*, 740−742.

(3) Setchell, K. D. R.; Lawson, A. M.; Borriello, S. P.; Harkness, R.; Gordon, H.; Morgan, D. M. L.; Kirk, D. N.; Adlercreutz, H.; Anderson, L. C.; Axelson, M. Lignan formation in man − microbial involvement and possible roles in relation to cancer. *Lancet* **1981**, *318*, 4−7.

(4) Saarinen, N. M.; Smeds, A.; Makela, S. I.; Ammala, J.; Hakala, K.; Pihlava, J. M.; Ryhanen, E. L.; Sjoholm, R.; Santti, R. Structural determinants of plant lignans for the formation of enterolactone in vivo. *J. Chromatogr. B: Anal. Technol. Biomed. Life Sci.* **2002**, *777*, 311−319.

(5) Adlercreutz, H. Lignans and human health. *Crit. Rev. Clin. Lab. Sci.* **2007**, *44*, 483−525.

(6) Peterson, J.; Dwyer, J.; Adlercreutz, H.; Scalbert, A.; Jacques, P.; McCullough, M. L. Dietary lignans: physiology and potential for cardiovascular disease risk reduction. *Nutr. Rev.* **2010**, *68*, 571−603.

(7) Valentin-Blasini, L.; Blount, B. C.; Rogers, H. S.; Needham, L. L. HPLC-MS/MS method for the measurement of seven phytoestrogens in human serum and urine. *J. Exposure Anal. Environ. Epidemiol.* **2000**, *10*, 799−807.

(8) Smeds, A.; Hakala, K. Liquid chromatographic-tandem mass spectrometric method for the plant lignan 7-hydroxymatairesinol and its potential metabolites in human plasma. *J. Chromatogr. B: Anal. Technol. Biomed. Life Sci.* **2003**, *793*, 297−308.

(9) Smeds, A. I.; Hakala, K.; Hurmerinta, T. T.; Kortela, L.; Saarinen, N. M.; Makela, S. I. Determination of plant and enterolignans in human serum by high-performance liquid chromatography with tandem mass spectrometric detection. *J. Pharm. Biomed. Anal.* **2006**, *41*, 898−905.

(10) Prasain, J. K.; Arabshahi, A.; Moore, D. R.; Greendale, G. A.; Wyss, J. M.; Barnes, S. Simultaneous determination of 11 phytoestrogens in human serum using a 2 min liquid chromatography/tandem mass spectrometry method. *J. Chromatogr. B: Anal. Technol. Biomed. Life Sci.* **2010**, *878*, 994−1002.

(11) Parker, D. L.; Rybak, M. E.; Pfeiffer, C. M. Phytoestrogen biomonitoring: an extractionless lc-ms/ms method for measuring urinary isoflavones and lignans by use of atmospheric pressure photoionization (appi). *Anal. Bioanal. Chem.* **2012**, *402*, 1123−1136.

(12) Guidance for Industry: Bioanalytical Method Validation; U.S. Department of Health and Human Services, Food and Drug Administration, Center for Drug Evaluation and Research (CDER), Center of Veterinary Medicine (CVM), May 2001; available at http://www.Fda.Gov/drugs/guidancecomplianceregulatoryinformation/guidances/default.Htm.

(13) Guideline on Bioanalytical Method Validation. Eurpean Medicines Agency of Science Medicine Health. Committee for Medicinal Products for Human Use (CHMP), February 2012; available at http://www.Ema.Europa.Eu/docs/en_gb/document_library/scientific_guideline/2011/08/wc500109686.Pdf.

(14) Landberg, R.; Andersson, S. O.; Zhang, J. X.; Johansson, J. E.; Stenman, U. H.; Adlercreutz, H.; Kamal-Eldin, A.; Aman, P.; Hallmans, G. Rye whole grain and bran intake compared with refined wheat decreases urinary c-peptide, plasma insulin, and prostate specific antigen in men with prostate cancer. *J. Nutr.* **2010**, *140*, 2180−2186.

(15) Moazzami, A. A.; Zhang, J. X.; Kamal-Eldin, A.; Aman, P.; Hallmans, G.; Johansson, J. E.; Andersson, S. O. Nuclear magnetic resonance-based metabolomics enable detection of the effects of a whole grain rye and rye bran diet on the metabolic profile of plasma in prostate cancer patients. *J. Nutr.* **2011**, *141*, 2126−2132.

(16) Grace, P. B.; Taylor, J. I.; Botting, N. P.; Fryatt, T.; Oldfield, M. F.; Bingham, S. A. Quantification of isoflavones and lignans in urine using gas chromatography/mass spectrometry. *Anal. Biochem.* **2003**, *315*, 114−121.

(17) Jacobs, E.; Kulling, S. E.; Metzler, M. Novel metabolites of the mammalian lignans enterolactone and enterodiol in human urine. *J. Steroid Biochem. Mol. Biol.* **1999**, *68*, 211−218.

(18) Penalvo, J. L.; Nurmi, T.; Haajanen, K.; Al-Maharik, N.; Botting, N.; Adlercreutz, H. Determination of lignans in human plasma by liquid chromatography with coulometric electrode array detection. *Anal. Biochem.* **2004**, *332*, 384−393.

(19) Kuijsten, A.; Buijsman, M.; Arts, L. C. W.; Mulder, P. P. J.; Hollman, P. C. H. A validated method for the quantification of enterodiol and enterolactone in plasma using isotope dilution liquid chromatography with tandem mass spectrometry. *J. Chromatogr. B: Anal. Technol. Biomed. Life Sci.* **2005**, *822*, 178−184.

(20) Nurmi, T.; Voutilainen, S.; Nyyssonen, K.; Adlercreutz, H.; Salonen, J. T. Liquid chromatography method for plant and mammalian lignans in human urine. *J. Chromatogr. B: Anal. Technol. Biomed. Life Sci.* **2003**, *798*, 101−110.

(21) Edel, A. L.; Aliani, M.; Pierce, G. N. Supported liquid extraction in the quantitation of plasma enterolignans using isotope dilution GC/MS with application to flaxseed consumption in healthy adults. *J. Chromatogr. B: Anal. Technol. Biomed. Life Sci.* **2013**, *912*, 24−32.

(22) Nurmi, T.; Adlercreutz, H. Sensitive high-performance liquid chromatographic method for profiling phytoestrogens using coulometric electrode array detection: application to plasma analysis. *Anal. Biochem.* **1999**, *274*, 110−117.

(23) Adlercreutz, H.; Vanderwildt, J.; Kinzel, J.; Attalla, H.; Wahala, K.; Makela, T.; Hase, T.; Fotsis, T. Lignan and isoflavonoid conjugates in human urine. *J. Steroid Biochem. Mol. Biol.* **1995**, *52*, 97−103.

(24) Adlercreutz, H.; Fotsis, T.; Lampe, J.; Wahala, K.; Makela, T.; Brunow, G.; Hase, T. Quantitative-determination of lignans and isoflavonoids in plasma of omnivorous and vegetarian women by isotope-dilution gas-chromatography mass-spectrometry. *Scand. J. Clin. Lab. Invest.* **1993**, *53*, 5−18.

(25) Zeleniuch-Jacquotte, A.; Adlercreutz, H.; Akhmedkhanov, A.; Toniolo, P. Reliability of serum measurements of lignans and isoflavonoid phytoestrogens over a two-year period. *Cancer Epidemiol. Biomarkers Prev.* **1998**, *7*, 885−889.

(26) Morton, M. S.; Chan, P. S. F.; Cheng, C.; Blacklock, N.; MatosFerreira, A.; AbranchesMonteiro, L.; Correia, R.; Lloyd, S.; Griffiths, K. Lignans and isoflavonoids in plasma and prostatic fluid in men: samples from Portugal, Hong Kong, And the United Kingdom. *Prostate* **1997**, *32*, 122−128.

(27) Laerke, H. N.; Mortensen, M. A.; Hedemann, M. S.; Knudsen, K. E.; Bach; Penalvo, J. L.; Adlercreutz, H. Quantitative aspects of the metabolism of lignans in pigs fed fibre-enriched rye and wheat bread. *Br. J. Nutr.* **2009**, *102*, 985−994.

(28) Knudsen, K. E. B.; Serena, A.; Kjaer, A. K. B.; Tetens, I.; Heinonen, S. M.; Nurmi, T.; Adlercreutz, H. Rye bread in the diet of pigs enhances the formation of enterolactone and increases its levels in plasma, urine and feces. *J. Nutr.* **2003**, *133*, 1368−1375.

DOI: 10.1021/acs.jafc.5b01275
J. Agric. Food Chem. 2015, 63, 6283−6292

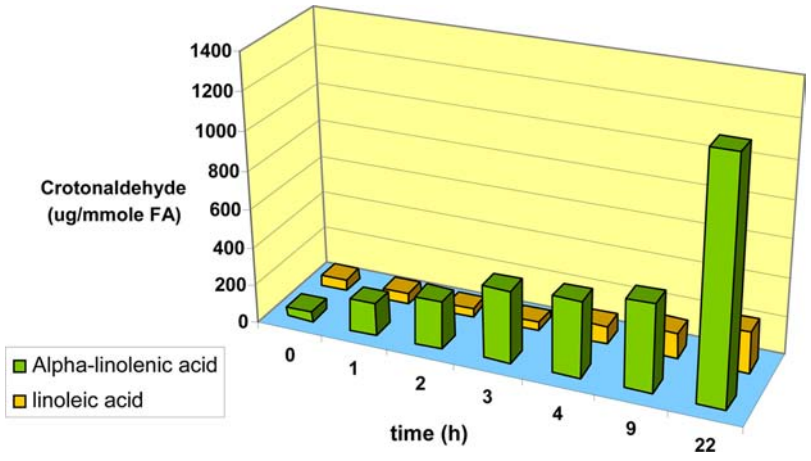

Figure 1. Formation of crotonaldehyde over time.

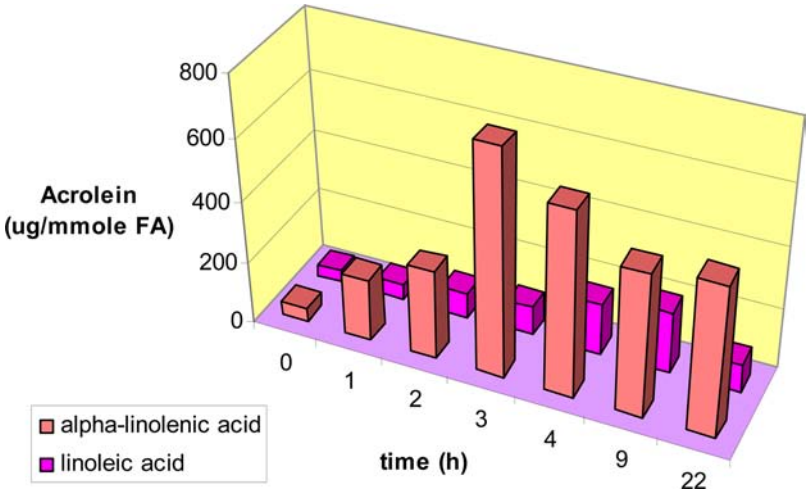

Figure 2. Formation of acrolein over time.

Chromatography was performed using an Agilent 1200 LC system. LC separations were performed using a Zorbax 300SB-C18 column (4.6 × 150 mm; 5 μm; Agilent Technologies) with a flow rate of 1 mL/min. Solvent A was 0.1% formic acid in water, and solvent B was 0.1% formic acid in acetonitrile. A linear gradient was performed as follows: 35% B at 0 min, 85% B at 25 min, 85% B at 30 min, 35% B at 31 min, and 35% B at 35 min.

Semipreparative HPLC. Purification of carbonyl–DNPH was conducted on an Agilent 1260 preparative system. A Zorbax 300SB-C18 column (9.4 × 250 mm; 5 μm; Agilent Technologies) was used with a flow rate of 12 mL/min. Solvent A was 0.1% formic acid in water, and solvent B was 0.1% formic acid in acetonitrile. A linear gradient was performed as follows: 35% B at 0 min, 85% B at 30 min, 85% B at 35 min, 35% B at 40 min, and 35% B at 45 min.

NMR. 1D NMR spectra were acquired on a Varian 300 MHz spectrometer (Palo Alto, CA, USA). Pyridine-d_5 was used as solvent, and VNMR 6.1c and Mestre-C were used for data processing.

Statistical Analysis. Data were expressed as means ± standard deviation (SD) and represent three independent analyses. Statistical significance was examined using Student's t test comparison between the means. A p value of >0.05 was considered statistically significant.

RESULTS AND DISCUSSION

α-Linolenic acid and linoleic acid were used as study material representing omega-3 and omega-6 fatty acids, respectively. They separately underwent autoxidation. Carbonyl compounds generated were derivatized by DNPH. LC-ESI-TOF was used to get the exact mass of each carbonyl derivative, and structure identification was conducted through product ion mode of LC-ESI-MS/MS. Detailed fragmentation paths followed the fragmentation scheme set up by Kölliker and Oehme.[11] For example, a molecular weight of 58.0418 represents acetone derivative and propanal derivative; differentiation of those compounds depended on the fragmentation patterns provided by product ion mode of triple quadrupole. On the basis of the characteristics of DNPH derivatives of carbonyl, ketone showed a much higher m/z 179 ion, and aldehyde showed abundant m/z 163. Therefore, through the ion patterns, compounds particularly with same molecular weight could be identified. All carbonyls were divided into three groups according to their molecular weight. The first group contained small monocarbonyls having a molecular weight of <120. In this group, α-linolenic acid and linoleic acid could generate nearly the same types of carbonyl compounds such as acetaldehyde, acrolein, crotonaldehyde, and pentanal. However, hexanal was detected in linoleic acid oxidation, and heptanal was generated from α-linolenic acid oxidation. Acrolein and crotonaldehyde were reported as highly reactive carbonyls, which can cross-link to DNA and protein and induce certain degenerative diseases.[12,13] Even though acrolein and crotonaldehyde could be detected in both omega-6 and omega-3 fatty acids, the amount generated from them was still a question. Therefore, oxidation of α-

DOI: 10.1021/acs.jafc.5b02376
J. Agric. Food Chem. 2015, 63, 6293–6296

linolenic acid and linoleic acid was conducted separately in a time course manner followed by derivatization by DNPH. MRM was used to quantify acrolein and crotonaldehyde derivatives. Figures 1 and 2 show that α-linolenic acid could generate more crotonaldehyde and acrolein than could linoleic acid. Pan and Chung reported that acrolein and crotonladehyde adducts were primarily derived from omega-3 polyunsaturated fatty acids when deoxyguanosine 5′-monophosphate was separately incubated with different polyunsaturated fatty acids including docosahexaenoic acid, α-linolenic acid, and eicosapentaenoic acid as well as omega-6 fatty acids linoleic acid and arachidonic acid.[14] Their results were perfectly consistent with ours. In accordance with the mechanism of acrolein formation from arachidonic acid,[13] an acrolein formation pathway from α-linolenic acid was proposed in Figure 3. Acrolein can be

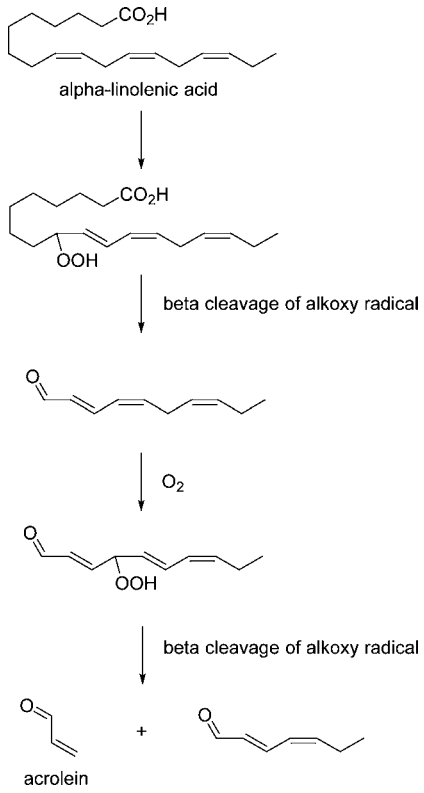

Figure 3. Proposed mechanism pathway of acrolein formation.

released from β-cleavage of lipid hydroperoxide of the corresponding alkoxy radical, which gives an aldehyde and an alkyl fragment (Figure 3). This mechanism pathway explained why hexanal was seen in the oxidation of linoleic acid, whereas heptanal was detected from the oxidation of α-linolenic acid. This mechanism pathway also indicated that both omega-3 fatty acids and omega-6 fatty acids went through the same β-cleavage of lipid hydroperoxide. Study of acrolein−DNA adducts also indicated that formation of adducts was independent from fatty acid type, but its yield related to the number of double bonds in the fatty acids.[14] This result indirectly supported the mechanism pathway of acrolein formation.

The second group contained the medium monoaldehyde having molecular weight >120 but <200. DNPH-derivatized reaction mixture was separated by semipreparative HPLC to get different fractions according to their UV absorbance. 9-Oxononanoic acid fraction accounting for the major peak was collected and identified through ^{1}H NMR. HNE and EDE were identified on the basis of standard comparison. 9-Oxononanoic acid could be found from both linoleic acid and α-linolenic acid and accounted for the biggest peak during separation. HNE and EDE could be identified only from linoleic acid oxidation. The formation pathways of 9-oxononanoic acid, as well as HNE and EDE generated from linoleic acid, are shown in Figure 4. The

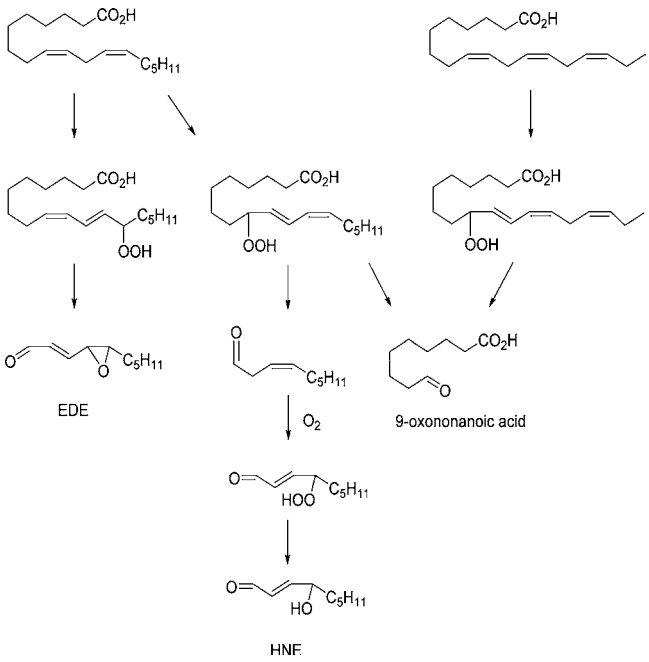

Figure 4. Formation pathways of carbonyl compounds from α-linolenic acid and linoleic acid.

peroxide group attaches to the ninth position of either α-linolenic acid or linoleic acid to form hydroperoxide products. Concurrently, 4-hydroperoxy-2-nonenal was generated only from linoleic acid, which is the precursor for HNE. One more double bond and the position of double bonds cause α-linolenic acid to go through a different oxidation pathway. As compared with dicarbonyl generation in the third group, glyoxal and methylglyoxal could be found in both fatty acids, but malondialdehyde could be detected only from α-linolenic acid under our condition. Three isomers of four-carbon dicarbonyl were shown in the oxidation of α-linolenic acid, whereas only one isomer was found from linoleic acid oxidation. A five-carbon dicarbonyl can be detected from α-linolenic acid, but it was undetectable from linoleic acid. Those results suggested α-linolenic acid might generate more dicarbonyls than would linoleic acid, which explained a limited number of medium-size monoaldehydes generating from α-linolenic acid. Because of the limitation of derivatization agent DNPH, we could not identify those four-carbon and five-carbon dicarbonyls. A new derivatization agent will be studied in the future. The oxidation mechanism of short-chain omega-3 fatty acids (α-linolenic acid) is the same as that of long-chain omega-3 fatty acids (EPA and DHA) because they all are oxidized into hydroperoxides and degraded into acrolein via β-scission. However, more study of long-chain omega-3 fatty acids is still needed to understand the mechanism and potential safety issues.

α-Linolenic acid (an omega-3 fatty acid) can generate more acrolein and crotonaldehyde, which are toxic compounds, in vitro than can linoleic acid, an omega-6 fatty acid. Under certain

DOI: 10.1021/acs.jafc.5b02376
J. Agric. Food Chem. 2015, 63, 6293−6296

circumstances, omega-3 fatty acids are also easily degraded to dicarbonyl compounds, which can bind with proteins.[10] However, omega-3 fatty acids have been considered as health improvement components for a long time. Many products with fortified omega-3 fatty acids are widely accepted by consumers. On the basis of our results, the safety of omega-3 fatty acids should be re-evaluated in vivo. Storage conditions for preventing the oxidation of omega-3 fatty acids should also be addressed.

Yu Wang*
Ping Cui
Food Science and Human Nutrition, Citrus Research and Education Center, University of Florida, Lake Alfred, Florida 33850, United States

AUTHOR INFORMATION

Corresponding Author
*(Y.W.) Phone: (863) 956-8673. Fax: (863) 956-5896. E-mail: yu.wang@ufl.edu.

Notes
The authors declare no competing financial interest.

ABBREVIATIONS USED

ROS, reactive oxygen species; RNS, reactive nitrogen species; RCS, reactive carbonyl species; DNPH, 2,4-dinitrophenylhydrazine; 13-HPODE, 13-hydroperoxy-octadecadienoic acid; EDE, 4,5-epoxy-2(*E*)-decenal; ONE, 4-oxo-2(*E*)-nonenal; HNE, 4-hydroxy-2(*E*)-nonenal; DODE, 9,12-dioxo-10(*E*)-dodecenoic acid; AGEs, advanced glycation end products

REFERENCES

(1) Lee, S. H.; Williams, M. V.; DuBois, R. N.; Blair, I. A. Cyclooxygenase-2-mediated DNA damage. *J. Biol. Chem.* **2005**, *280*, 28337−28346.
(2) Williams, V. M.; Lee, S. H.; Pollack, M.; Blair, I. A. Endogenous lipid hydroperoxide-mediated DNA-adduct formation in Min mice. *J. Biol. Chem.* **2006**, *281*, 10127−10133.
(3) Jian, W.; Arora, J. S.; Oe, T.; Shuvaev, V. V.; Blair, I. A. Induction of endothelial cell apoptosis by lipid hydroperoxide-derived bifunctional electrophiles. *Free Radical Biol. Med.* **2005**, *39*, 1162−1176.
(4) Jian, W.; Lee, H. S.; Mesaros, C.; Oe, T.; Elipe, M. V. S.; Blair, I. A. A novel 4-oxo-2(*E*)-nonenal-derived endogenous thiadiazabicyclo glutathione adduct formed during cellular oxidative stress. *Chem. Res. Toxicol.* **2007**, *20*, 1008−1018.
(5) Doorn, J. A.; Petersen, D. R. Covalent modification of amino acid nucleophiles by the lipid peroxidation products 4-hydroxy-2-nonenal and 4-oxo-2-nonenal. *Chem. Res. Toxicol.* **2002**, *15*, 1445−1450.
(6) Liu, Z.; Minkler, P. E.; Sayre, L. M. Mass spectroscopic characterization of protein modification by 4-hydroxy-2-(*E*)-nonenal and 4-oxo-2-(*E*)-nonenal. *Chem. Res. Toxicol.* **2003**, *16*, 901−911.
(7) Sayre, L. M.; Lin, D.; Yuan, Q.; Zhu, X.; Tang, X. Protein adducts generated from products of lipid oxidation: focus on HNE and ONE. *Drug Metab. Rev.* **2006**, *38*, 651−675.
(8) Schaur, R. J. Basic aspects of the biochemical reactivity of 4-hydroxynonenal. *Mol. Aspects Med.* **2003**, *24*, 149−159.
(9) Williams, M. V.; Wishnok, J. S.; Tannenbaum, S. R. Covalent adducts arising from the decomposition products of lipid hydorperoxides in the presence of cytochrome *c*. *Chem. Res. Toxicol.* **2007**, *20*, 767−775.
(10) Dmitriev, L. F.; Titov, V. N. Lipid peroxidation in relation to ageing and the role of endogenous aldehydes in diabetes and other age-related diseases. *Ageing Res. Rev.* **2010**, *9*, 200−210.
(11) Kölliker, S.; Oehme, M.; Dye, C. Structure elucidation of 2,4-dinitrophenylhydrazine derivatives of carbonyl compounds in ambient air by HPLC/MS and multiple MS/MS using atmospheric chemical ionization in the negative ion mode. *Anal. Chem.* **1998**, *70*, 1979−1985.
(12) Minko, I. G.; Kozekov, I. D.; Harris, T. M.; Rizzo, C. J.; Lloyd, R. S.; Stone, M. P. Chemistry and biology of DNA containing 1,N(2)-deoxyguanosine adducts of the α,β-unsaturated aldehydes acrolein, crotonaldehyde, and 4-hydroxynonenal. *Chem. Res. Toxicol.* **2009**, *22*, 759−778.
(13) Esterbauer, H.; Schaur, R. J.; Zollner, H. Chemistry and biochemistry of 4-hydroxynonenal, malonaldehyde and related aldehydes. *Free Radical Biol. Med.* **1991**, *11*, 81−128.
(14) Pan, J.; Chung, F.-L. Formation of cyclic deoxyguanosine adducts from ω-3 and ω-6 polyunsaturated fatty acids under oxidative conditions. *Chem. Res. Toxicol.* **2002**, *15*, 367−372.

DOI: 10.1021/acs.jafc.5b02376
J. Agric. Food Chem. 2015, 63, 6293−6296

solvent, which makes its more attractive for routine or aquatic environment analysis.[16] CO_2 has many advantages including its nontoxicity, nonflammability, and easy purification. In addition, a combination of SFC and mass spectrometry could improve the sensitivity using postcolumn polar solvent compensation technology. Furthermore, SFC-MS/MS may be easier to achieve than LC-MS due to the high proportion of volatile CO_2, which enhances the evaporation step during the ionization process.[17] This green technique is becoming more popular. In addition, QuEChERS (quick, easy, cheap, effective, rugged, and safe) sample preparation approaches have been proposed for the analysis of aquatic environmental samples. The procedure for dispersive solid-phase extraction in the QuEChERS method is easy to perform. In comparison to the traditional SPE approach, dispersive-SPE saves time, labor, and solvent by using a much smaller quantity of sorbent.[18] Therefore, we established a method with low cost, faster separation, and better resolution for tebuconazole using SFC-MS/MS.

To the best of our knowledge, this paper provides the first enantioselective analysis of tebuconazole in water and zebrafish samples using SFC-MS/MS. The results from this study will provide a new reference for the development of green chromatographic separation of chiral compound, as well as offer an important foundation for future aquatic safety and accurate risk assessment.

MATERIALS AND METHODS

Chemicals and Reagents. Racemic tebuconazole (98.7% purity) was obtained from the China Standard Material Center (Beijing, China). High-purity CO_2 (≥99.999%) and N_2 (≥99.999%) were acquired from Haike Yuanchang Gas (Beijing, China). HPLC grade acetonitrile and methanol were purchased from Fisher Scientific (Shanghai, China). Ultrapure water was obtained from a Milli-Q system (Bedford, MA, USA). Analytical grade NaCl, $MgSO_4$, and acetonitrile were purchased from Beihua Fine-Chemicals Co. (Beijing, China). The sorbents including primary−secondary amine (PSA) (40 μm), C18 (40 μm), and Florisil (120−400 mesh size) were obtained from Agela Technologies Inc. (Newark, DE, USA). The mobile phase solvents were distilled and filtered through a 0.22 μm pore size filter membrane (Tengda, Tianjin, China) prior to the determination.

The standard stock solutions (100 mg/L) of racemic tebuconazole were prepared in pure acetonitrile. The standard working solutions of *rac*-tebuconazole at 0.01, 0.05, 0.1, 0.5, 1.0, and 5.0 mg/L were prepared in pure acetonitrile from the stock solution by serial dilution. The concentrations of each enantiomer were 0.005, 0.025, 0.05, 0.25, 0.5, and 2.5 mg/L. All of the solutions were protected from light using aluminum foil and stored in a refrigerator at 4 °C prior to analysis. The working standard solutions exhibited no degradation for 3 months.

Supercritical Fluid Chromatography−Tandem Triple-Quadrupole Mass Spectrometry (SFC-MS/MS). An ACQUITY UPC^2 system (Waters, Milford, MA, USA), which was equipped with a binary solvent manager, column manager, convergence manager, sample manager-FL, and Waters 515 compensation pump, was used for the separation of the analytes. The column used for the separation of the stereoisomers of tebuconazole was a 150 mm × 4.6 mm i.d., 3 μm particle size, Chiralpak IA-3 (Daicel, Japan). This column was coated with amylose tris-3,5-dimethylphenylcarbamate. Three additional chiral columns including a Chiralpak IA [amylose tris (3,5-dimethylphenycarbamate), 5 μm], Chiralpak IB-3 [cellulose tris(3,5-dimethylphenylcarbamate), 3 μm], and Chiralpak IC-3 [cellulose tris(3,5-dichlophenylcarbamate), 3 μm] were employed. The separation was carried out using an isocratic elution with solvent A (CO_2) and solvent B (methanol) ratio of 87:13 (v/v) at a flow rate of 2.0 mL/min for 5 min. The ABPR 2200 psi was selected. The flow rate of the 515 compensation pump was 0.15 mL/min, which used 0.1% FA-MeOH (v/v) as a postcolumn additive. The temperature of the column and sample manager were maintained at 30 and 25 °C, respectively. In each run, 1 μL of the sample was injected.

The parameters including the capacity factor (k), separation factor (α), and resolution (Rs) were calculated from the formulas $k = (t - t_0)/t_0$, $\alpha = k_2/k_1$, and $Rs = 2(t_2 - t_1)/(W_1 + W_2)$, where t_0 is the void time at the given conditions (t_0 = 0.85 min, determined using 1,3,5-tri*tert*-butylbenzene), t is the retention time, k is the retention factor, and W is the baseline peak width.

A triple-quadrupole Xevo-TQD mass spectrometer (Waters Inc., Milford, MA, USA) equipped with an electrospray ionization source (ESI) was used to quantify the tebuconazole stereoisomers. The analyses were performed in ESI$^+$ with a 3.5 kV capillary voltage, 150 °C source temperature, and 500 °C desolvation temperature. A 50 L/h cone gas flow and a 900 L/h desolvation gas flow were employed. The nebulizer gas was 99.95% N_2, and the collision gas was 99.99% Ar at a pressure of 2×10^{-3} mbar in the T-Wave cell. MassLynx NT v. 4.1 software (Waters) was used to collect and analyze the obtained data.

Multiple reaction monitoring (MRM) mode was used for MS detection. The monitoring conditions were optimized for tebuconazole. A dwell time of 130 ms per ion pair was used to maintain the high sensitivity of the analysis, and a number of data points across the chromatographic peak were required. The typical conditions were as follows: the cone voltage of tebuconazole was 39 V; m/z 308.1 was selected as the precursor ion for tebuconazole, m/z 70.02 was selected for the product quantitative ion, and m/z 125.03 was selected for the qualitative ion when the collision energy was set to 23 and 37 V (see Table S1 of the Supporting Information). Under the conditions, the retention times of (+)-*S*-tebuconazole and (−)-*R*-tebuconazole were approximately 3.26 and 3.60 min, respectively (Figure 1). These settings were utilized for all subsequent studies.

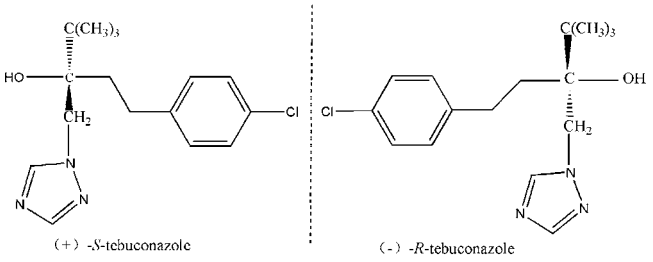

Figure 1. Chemical structures of tebuconazole stereoisomers.

The micropreparation of the stereoisomers was achieved using an Agilent 1100 series HPLC system (Agilent Technology, Waldbronn, Germany) coupled with an online OR-2090 detector (Jasco, Japan). The separation employed *n*-hexane/isopropanol (90:10, v/v) as the mobile phase at 30 °C on a CHIRALPAK AS-H column. It was a 250 mm × 4.6 mm i.d., 5 μm column (Daicel, Japan), which was coated with tris(*S*)-1-phenylethylcarbamate.

Sample Preparation. The water and zebrafish samples (total length of 2.0 ± 1.0 cm, weight of 0.1 ± 0.05 g) were not contaminated by the target analyte. All of the zebrafish were healthy. Each zebrafish was homogenized. Approximately 2.0 g of the blank zebrafish samples (2.0 mL water) was weighed into a 10 mL PTFE centrifuge tube. Suitable concentrations of tebuconazole standard solutions were added to the tube and vortexed for 30 s, followed by equilibration for 2 h at room temperature to allow the pesticide to distribute evenly. Two milliliters of acetonitrile was added, and the tube was vortexed for 3 min. Then, 1 g of NaCl was added to the mixtures. The tube was vortexed again for 1 min followed by centrifugation for 5 min at a relative centrifugal force (RCF) of 2599*g*. Next, 1.0 mL of the upper layer was transferred into a single-use 2 mL centrifuge tube containing 150 mg of Florisil and 150 mg of anhydrous $MgSO_4$ (for the water samples, 1.0 mL of the upper layer was filtered directly using a 0.22-μm nylon syringe filter for SFC-MS/MS injection). The tubes were vortexed for 30 s and centrifuged for 5 min at RCF 2400*g*. Finally, the resulting supernatant (acetonitrile) was filtered using a 0.22-μm nylon syringe filter for SFC-MS/MS injection.

DOI: 10.1021/acs.jafc.5b02450
J. Agric. Food Chem. 2015, 63, 6297−6303

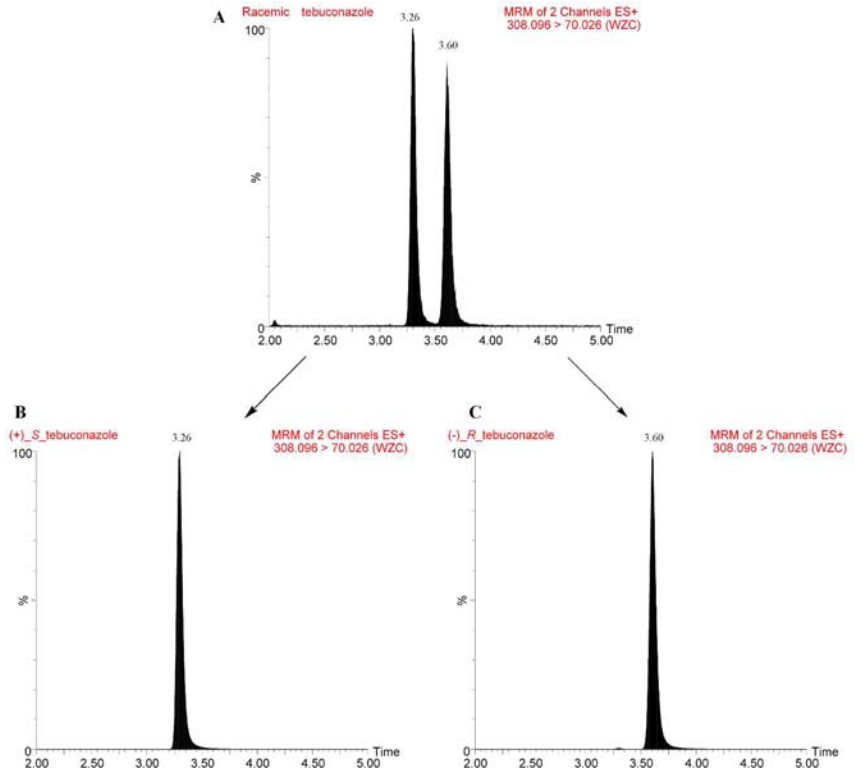

Figure 2. SFC-MS/MS chromatograms for the separation of tebuconazole enantiomers on a Chiralpak IA-3 chiral column: A, chromatogram of racemic tebuconazole; B, SFC-MS/MS chromatogram of (+)-*S*-tebuconazole; C, SFC-MS/MS chromatogram of (−)-*R*-tebuconazole.

For the SPE, the extraction volume was 6 mL, and the cleanup procedure involved transferring 3 mL of the upper layer into rotary evaporation bottles to evaporate to dryness followed by redissolving in a 1 mL mixture (acetone/*n*-hexane = 1:9, v/v). Then 1 mL of solution was passed slowly through a Florisil SPE cartridge at a flow rate of approximately 1 mL/min. The cartridges were preconditioned using 5 mL of acetone/*n*-hexane = 1:9 (v/v) followed by 5 mL of *n*-hexane. Next, a 10 mL mixed solution (acetone/*n*-hexane = 1:9, v/v) was added to elute the target analytes. Then, the organic solvent was evaporated to dryness using a rotary evaporator (30 °C, 0.09 MPa). The resulting residue was redissolved in 1 mL of ACN and filtered using a 0.22-μm nylon syringe filter for chromatographic injection.

For determination of the authentic samples, the water and zebrafish samples were obtained from a bioaccumulation test (Beijing, China); collected 24 h after an exposure period, the spiked solutions were prepared by adding *rac*-tebuconazole dissolved in acetone to deionized water for a final concentration of 1.0 mg/L.

Method Validation. The following parameters were used to evaluate the performance of the developed method: specificity, linearity, limit of detection (LOD), limit of quantitation (LOQ), matrix effect, accuracy, precision, and stability.

Blank samples (water and zebrafish) were analyzed by monitoring the characteristics of selected ion chromatograms. The linearity of the method was determined by analyzing the standard solutions and three matrices in triplicate at five concentrations ranging from 5 to 500 μg/kg for each enantiomer.

The matrix-dependent LOD and LOQ were determined using the blank and calibration standards consisting of water and zebrafish matrices. The LOD for the enantiomers of the chiral pesticide was regarded as the concentration with a signal-to-noise (S/N) ratio of 3, and the LOQ was defined as the concentrations that produced a signal-to-noise ratio of 10. These values were estimated from the chromatogram corresponding to the lowest point used in the matrix-matched calibration. The matrix effect can be computed as follows:

$$\text{matrix effect (ME, \%)} = [(\text{slope of calibration curves in matrix} - \text{slope of calibration curves in solvent})/\text{slope of calibration curves in solvent}] \times 100\%$$

The recovery assays were carried out to investigate the accuracy and precision of the method. Five replicates of the spiked samples at different levels (i.e., 10, 100, and 1000 μg/kg) for water and zebrafish were prepared on three different days. The precision under these conditions for repeatability, which is expressed as the relative standard deviation (RSD), was determined by the intra- and interday assays.

The stability was determined in acetonitrile and in the matrix. The stability of the stock solution was tested monthly by injection of a newly prepared working solution. The stability of the spiked samples (100 mg/kg) with tebuconazole was evaluated monthly, and all of the samples used in the stability test were stored at −20 °C. The results were analyzed using Student's *t* test ($P < 0.05$).

RESULTS AND DISCUSSION

Optimization of Enantioseparation Conditions. *Selection of the Chiral Column.* Four chiral columns (i.e., Chiralpak IA-3, Chiralpak IA, Chiralpak IB-3, and Chiralpak IC-3) were tested for their ability to separate the tebuconazole enantiomers under the same chromatographic conditions. The stationary phase of the four columns was polysaccharide chiral stationary phase. These chiral stationary phases exhibited good feasibility due to their individual chiral carbohydrate monomers and long-range helical secondary structure, which affect the separations. Among the four tested columns, the best chromatographic separation of the two tebuconazole enantiomers was achieved with Chiralpak IA-3 and IA columns (Figure 2). Chiralpak IB-3 and IC-3 columns exhibited insufficient discrimination ability for the tebuconazole stereoisomers. Due to the particle size of the columns and the retention time, Chiralpak IA-3 was chosen. However, Chiralpak IB-3 and IC-3 columns were filled with

DOI: 10.1021/acs.jafc.5b02450
J. Agric. Food Chem. 2015, 63, 6297−6303

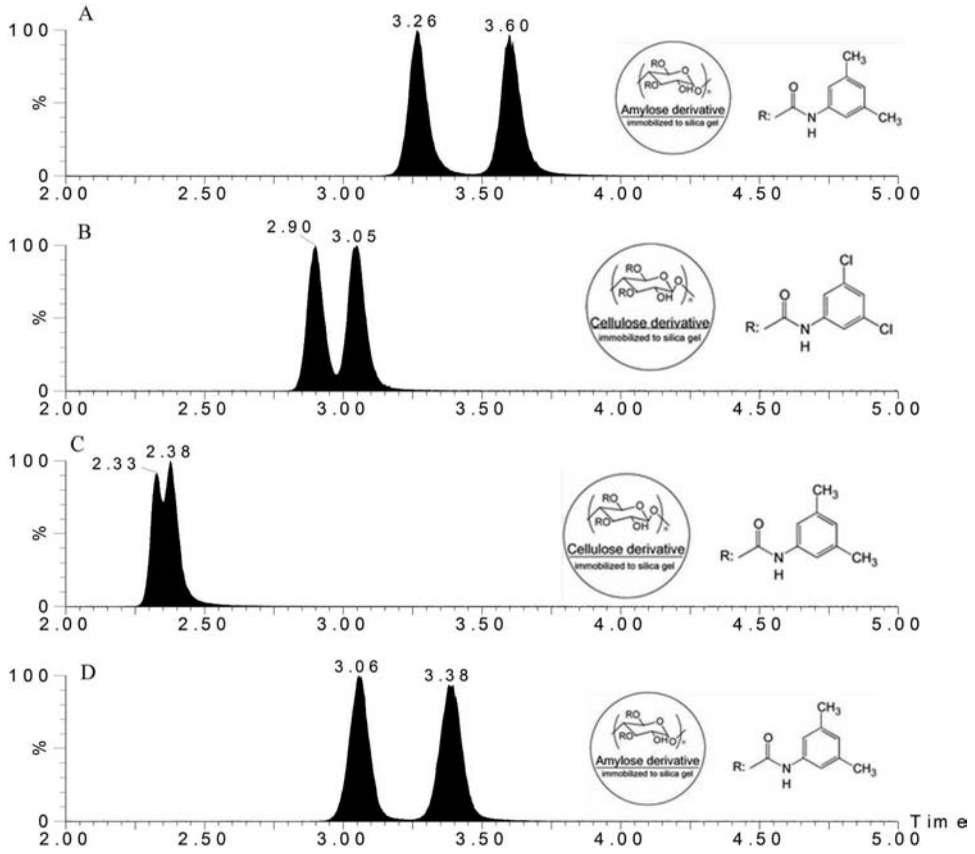

Figure 3. Typical SFC-MS/MS (MRM) chromatograms of tebuconazole on four columns: A, Chiralpak IA-3; B, Chiralpak IC-3; C, Chiralpak IB-3; D, Chiralpak IA.

derivatives of cellulose chiral stationary phase. In addition, Chiralpak IA-3 and IA columns were filled with derivatives of an amylose chiral stationary phase. The polar carbamate groups of CDMPC were thought to be the main chiral recognition regions because those can physically interact with the analytes via hydrogen bonds with the NH groups and dipole−dipole interactions with the C═O groups.[19] The derivatives of amylose exhibited higher recognition abilities for tebuconazole. Flutriafol has a structure similar to that of tebuconazole, which has also been well separated on a Chiralpak IA-3 column using SFC-MS/MS.[20]

In comparison to the 5-μm particles in the Chiralpak IA chiral column, Chiralpak IA-3 has 3-μm particles, and this column exhibited a highly effective chiral separation capacity for tebuconazole. On the basis of the solvent consumption, peak shape, and retention time, the Chiralpak IA-3 column was the optimal choice. The benefits of using columns with smaller particle sizes for chiral analysis have been previously discussed.[21]

Composition of the Mobile Phase. Different compositions of the mobile phase were investigated to achieve good separation of the tebuconazole enantiomers on the Chiralpak IA-3 column. Comparative analysis assays were conducted using methanol, ethanol, 2-propanol, 1-butanol, and acetonitrile. The results indicated that tebuconazole enantiomers were well separated when methanol was used as the modifier. In contrast, lower Rs values were obtained when ethanol and 1-butanol were employed. However, the two enantiomers cannot be separated using acetonitrile or 2-propanol as the modifier.

Different ratios of the modifier (methanol) were also tested (Figure 3A). The retention time of the enantiomers was shorter as the proportion of methanol increased. This result may be due to the strong elution ability of methanol. Finally, CO_2/methanol (83:17, v/v) was chosen as the mobile phase due to the relatively better resolution (2.75) and shorter retention times (3.26, 3.60 min).

Effect of the Auto Back Pressure Regulator (ABPR) Pressure. The ABPR settings can affect the retention time by changing the density of the mobile phase prior to the release of pressure.[20] The retention time decreased as the ABPR pressure increased from 1600 to 4000 psi (Figure 3B). However, the instrument system pressure would be beyond this range at higher ABPR pressures. In addition, higher ABPR pressure is disadvantageous for the lifetime of the chiral columns. Therefore, an ABPR pressure of 2200 psi was the optimal choice.

Effect of Column Temperature. Temperature plays an important role in chiral separation.[22] The column temperature affects the selectivity and retention in SFC-MS/MS. In this study, the column temperature was evaluated from 25 to 40 °C during the chiral separation. The results for the retention time and separation factor indicated that the temperature exhibited only a slight influence on the chiral separation. The two enantiomers were both well separated at all of the tested temperatures. The column temperature was ultimately set to 30 °C. The results were similar to those reported by Li et al.[6]

Flow Rate of the Mobile Phase. Different flow rates of the mobile phase were investigated on the basis of a mobile phase consisting of CO_2/methanol (83:17, v/v). As shown in Figure

DOI: 10.1021/acs.jafc.5b02450
J. Agric. Food Chem. 2015, 63, 6297−6303

3C, the retention time was shorter as the flow rate of the mobile phase increased. Methanol has a strong elution ability. The volume of methanol increased with the high flow rates. Therefore, the elution ability increased due to the high velocity. A rate of 2 mL/min was selected for better resolution (2.75) and a relatively suitable retention time (3.26, 3.60 min).

Flow Rate of the Compensation Pump Solvent. The compensation pump was used to provide the compensation solution, which could improve the ionization efficiency of ESI-MS/MS. A mixture of 0.1% formic acid/methanol is often selected as a compensation solvent. In this study, different flow rates of the compensation pump solvent in a range of 0.15−0.45 mL/min were examined. The results indicated that the flow rate of the compensation pump solvent had no effect on the retention time and resolution. However, this flow rate influenced the peak area (Figure 3D). For comprehensive consideration, the optimal choice was 0.15 mL/min, which provided high peak areas for the tebuconazole enantiomers.

Elution Order of Tebuconazole Enantiomers. The relationships between the absolute configurations and optical rotations (ORs) of the tebuconazole enantiomers were determined in a previous study.[23] Each single isomer and racemic tebuconazole were individually subjected to SFC-MS/MS determination under the same chromatographic conditions mentioned above. In this study, the enantiomer that eluted first was (+)-*S*-tebuconazole, followed by (−)-*R*-tebuconazole. The results were similar to the separation using LC-MS/MS reported by Li et al.[7]

Optimization of Extraction and Cleanup Procedure. The extraction and cleanup procedures are important for residue analysis. The water samples were relatively clean with few impurities. Therefore, the water samples were directly extracted with acetonitrile without purification. For the zebrafish samples, different extraction solvents (acetonitrile and acetonitrile (saturated with *n*-hexane)) were investigated first (Figure 4). The results indicated that acetonitrile extraction performed the best. A comparison between dispersive and solid-phase extraction for the cleanup step was carried out for the zebrafish samples. The dispersive cleanup procedure in the QuEChERS method was simple. Florisil, which is a normal-phase sorbent, can effectively remove lipid interferences. The results indicated that the recovery was high with 150 mg of Florisil. Dispersive solid-phase extraction (D-SPE) exhibited more interaction between the sample and the sorbent, which contributed to better recoveries, improved the cleanup by removing the interferences, and generated less waste due to the smaller volume of organic solvent employed in the sample preparation.[24]

The results indicated that the recoveries were <80% with SPE. Therefore, the QuEChERS method was the optimal choice, and this approach saved time, money, and solvent compared to traditional SPE.

Method Validation. *Specificity, Linearity, and Matrix Effect.* The blank samples (water and zebrafish) were analyzed to evaluate the specificity of the previously mentioned method, and no interference was detected at the retention time of each enantiomer. Linear regression analysis was performed in a concentration range of 5.0−500 μg/kg for each enantiomer. Table S2 in the Supporting Information provides the standard solution and matrix-matched calibration curves (acetonitrile, water, and zebrafish) for each enantiomer, including the slopes and coefficients of determination (R^2). The results indicated that a mean R^2 > 0.9933 was obtained for each enantiomer.

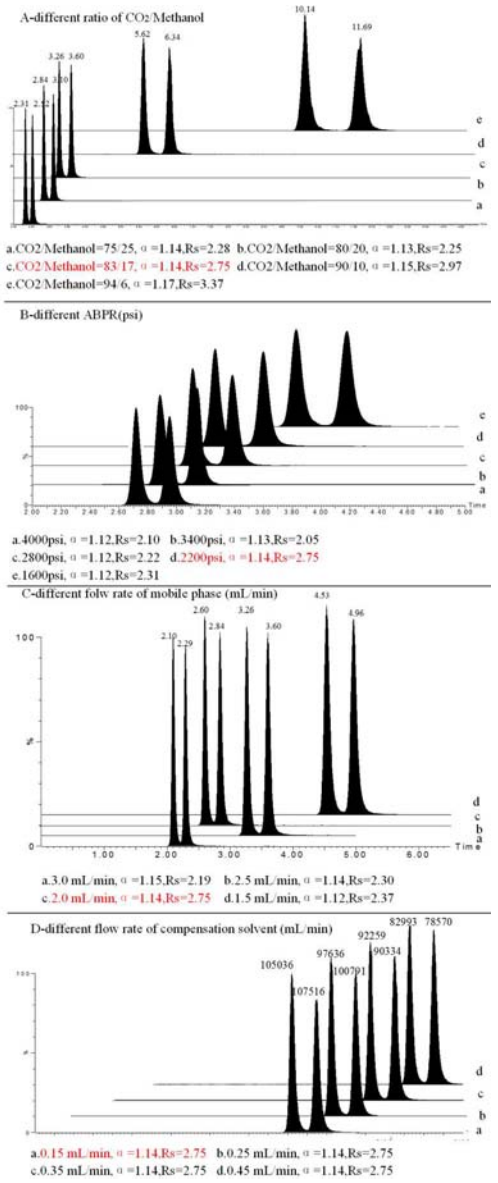

Figure 4. Comparison of effects of different parameters (A, ratio of CO_2/methanol; B, ABPR; C, flow rate of mobile phase; D, flow rate of compensation solvent) on the enantioseparation of tebuconazole enantiomers.

The matrix effects result from coeluting matrix components that affect the ionization of the target analyte, resulting either in ion suppression or in ion enhancement in some cases.[25] Matrix effects can be highly variable and difficult to control or predict. In this study, the matrix effects were investigated by comparing the standards in the solvent with the matrix-matched standards. As shown in Table S2 in the Supporting Information, signal suppression was observed for tebuconazole in the matrices, based on the slope ratios of the matrix/acetonitrile in the range of 0.007−0.010, and the slope values were 99.0 and 99.3%. In general, the suppression or enhancement effect originates from the inadequate removal of endogenous compounds, such as phospholipids, fatty acids, saccharides, phenols, and pigments.[26] Therefore, external matrix-matched standards were selected to obtain more accurate quantification results.

LODs and LOQs. In this study, the LODs for each enantiomer were estimated to be 0.3−0.4 μg/kg and obtained

DOI: 10.1021/acs.jafc.5b02450
J. Agric. Food Chem. 2015, 63, 6297−6303

from all five replicated extractions and analyses of spiked samples at the lowest spiked levels (10 μg/kg). The LOQs in the two sample matrices were 1.0−1.32 μg/kg for the compound based on five replicates at 10 μg/kg.

Accuracy and Precision. The recoveries and RSDs of each enantiomer were measured by spiking the blank samples with three different concentrations (i.e., 10, 100, and 1000 μg/kg) and then analyzing them in quintuplicate (see Table S3 of the Supporting Information). All of the recoveries were determined from analyses of the target compounds in the water and zebrafish samples. The precision of the method was determined using repeatability and reproducibility studies. The intraday precision (expressed as the RSD_r) was measured by comparing the standard deviation of the recovery percentages of the spiked samples run on the same day. The interday precision (expressed as the RSD_R) was determined by analyzing spiked samples from three different days. As shown in Table S3 in the Supporting Information, satisfactory mean recovery values (79.8−108.4%) and precisions were obtained. All of the experimental RSD values were <7.1% at the three fortified concentration levels. In general, the intraday (n = 5) and interday RSDs (n = 15) for the proposed method ranged from 0.7 to 7.1% and from 2.1 to 6.0%, respectively. Figure 4 shows typical chromatograms of the water and zebrafish blanks and spiked samples. On the basis of the results from the recovery studies, satisfactory precisions and accuracies were achieved for the analysis of tebuconazole enantiomers in water and zebrafish samples (Figure 5). In addition, the stabilities of tebuconazole

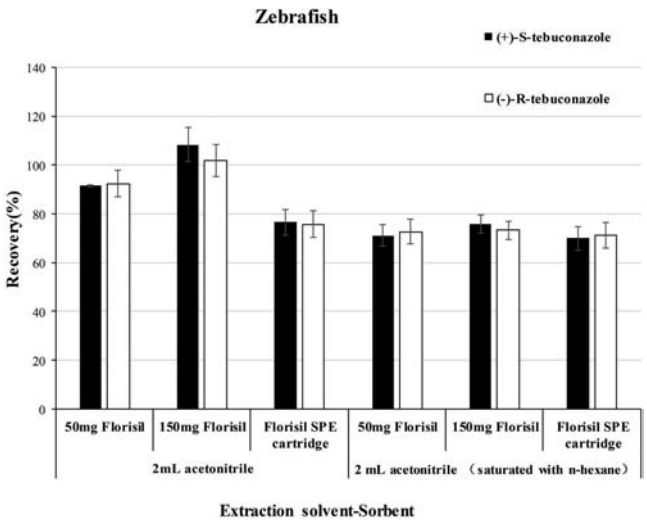

Figure 5. Effect of different kinds of sorbents and extraction solvents for tebuconazole enantiomers in zebrafish at 100 μg/kg level (n = 5).

were evaluated, and no significant difference (P > 0.05) was observed from the solvent and matrix storage treatments, as previously described.

Application to Authentic Samples. The effectiveness of this method for measuring trace levels of *rac*-tebuconazole was evaluated in water and zebrafish samples. (+)-*S*-Tebuconazole and (−)-*R*-tebuconazole in the water and zebrafish samples were detected after 24 h at concentrations of 0.33 ± 0.05 and 0.35 ± 0.04 mg/kg and 3.67 ± 0.46 and 3.06 ± 0.42 mg/kg, respectively.

In the current study, a simple and reliable method using SFC-ESI-MS/MS has been successfully established and validated for the stereoselective determination of tebuconazole in water and zebrafish. On the basis of a modified QuEChERS method, the target compounds were extracted and purified by acetonitrile and Florisil, respectively. This approach is simple and rapid with good mean recoveries and excellent linearities compared to the traditional SPE method. Satisfactory results were obtained for real samples. The current study developed an analytical method to detect tebuconazole enantiomers in water and zebrafish samples using SFC-MS/MS and also to provide technical support for future studies investigating the bioaccumulation, metabolism, and fate of tebuconazole enantiomers in aquatic environments to minimize the risk posed by tebuconazole to humans, animals, and the ecosystem.

■ ASSOCIATED CONTENT

Ⓢ Supporting Information

Experimental parameters and SFC-MS/MS conditions for analysis of tebuconazole (Table S1); comparison of matrix-matched calibration and solvent calibration with all of the range at 5− 500 μg/kg for each enantiomer (Table S2); and accuracy and precision of the proposed method in the two studied matrices at three spike levels (Table S3). The Supporting Information is available free of charge on the ACS Publications website at DOI: 10.1021/acs.jafc.5b02450.

■ AUTHOR INFORMATION

Corresponding Author

*(Y.Z.) Phone: +86-01-62815908. Fax: +86-01-62815908. E-mail: zhengyongquan@ippcaas.cn.

Funding

This work was financially supported by the National Natural Science Foundation of China (31272071).

Notes

The authors declare no competing financial interest.

■ ABBREVIATIONS USED

SSE, signal suppression/enhancement; RT, retention time; ABPR, auto back pressure regulator; UPC^2, ultraperformance convergence chromatography; SFC, supercritical fluid chromatography; MRM, multiple reaction monitoring; MS, mass spectrometry; ESI, electrospray ionization; CSP, chiral stationary phase

■ REFERENCES

(1) Yu, L.; Chen, M.; Liu, Y.; Gui, W.; Zhu, G. Thyroid endocrine disruption in zebrafish larvae following exposure to hexaconazole and tebuconazole. *Aquat. Toxicol.* **2013**, *138*, 35−42.

(2) Montuelle, B.; Dorigo, U.; Bérard, A.; Volat, B.; Bouchez, A.; Tlili, A.; Gouy, V.; Pesce, S. The periphyton as a multimetric bioindicator for assessing the impact of land use on rivers: an overview of the Ardières-Morcille experimental watershed (France). *Hydrobiologia* **2010**, *657*, 123−141.

(3) Zubrod, J. P.; Bundschuh, M.; Schulz, R. Effects of subchronic fungicide exposure on the energy processing of *Gammarus fossarum* (Crustacea; Amphipoda). *Ecotoxicol. Environ. Saf.* **2010**, *73*, 1674−1680.

(4) Toni, C.; Loro, V. L.; Santi, A.; de Menezes, C. C.; Cattaneo, R.; Clasen, B. E.; Zanella, R. Exposure to tebuconazol in rice field and laboratory conditions induces oxidative stress in carp (*Cyprinus carpio*). *Comp. Biochem. Physiol., Part C: Toxicol. Pharmacol.* **2011**, *153*, 128−132.

(5) Sancho, E.; Villarroel, M.; Fernandez, C.; Andreu; Ferrando, M. Short-term exposure to sublethal tebuconazole induces physiological impairment in male zebrafish (*Danio rerio*). *Ecotoxicol. Environ. Saf.* **2010**, *73*, 370−376.

DOI: 10.1021/acs.jafc.5b02450
J. Agric. Food Chem. 2015, 63, 6297−6303

(6) Li, Y.; Dong, F.; Liu, X.; Xu, J.; Li, J.; Kong, Z.; Chen, X.; Zheng, Y. Enantioselective determination of triazole fungicide tebuconazole in vegetables, fruits, soil and water by chiral liquid chromatography/tandem mass spectrometry. *J. Sep. Sci.* **2012**, *35*, 206−215.
(7) Li, Y.; Dong, F.; Liu, X.; Xu, J.; Han, Y.; Zheng, Y. Enantioselectivity in tebuconazole and myclobutanil non-target toxicity and degradation in soils. *Chemosphere* **2015**, *122*, 145−153.
(8) Sanz-Landaluze, J.; Pena-Abaurrea, M.; Munoz-Olivas, R.; Camara, C.; Ramos, L. Zebrafish (*Danio rerio*) Eleutheroembryo-based procedure for assessing bioaccumulation. *Environ. Sci. Technol.* **2015**, *49*, 1860−1869.
(9) Zhou, Y.; Li, L.; Lin, K.; Zhu, X.; Liu, W. Enantiomer separation of triazole fungicides by high-performance liquid chromatography. *Chirality* **2009**, *21*, 421−427.
(10) Wang, P.; Jiang, S.; Liu, D.; Wang, P.; Zhou, Z. Direct enantiomeric resolutions of chiral triazole pesticides by high-performance liquid chromatography. *J. Biochem. Biophys. Methods* **2005**, *62*, 219−230.
(11) Wu, Y.; Lee, H.; Li, S. High-performance chiral separation of fourteen triazole fungicides by sulfated *β*-cyclodextrin-mediated capillary electrophoresis. *J. Chromatogr., A* **2001**, *912*, 171−179.
(12) Wang, X.; Wang, X.; Zhang, H.; Wu, C.; Wang, X.; Xu, H.; Wang, X.; Li, Z. Enantioselective degradation of tebuconazole in cabbage, cucumber, and soils. *Chirality* **2012**, *24*, 104−111.
(13) Toribio, L.; del Nozal, M. J.; Bernal, J. L.; Jiménez, J. J.; Alonso, C. Chiral separation of some triazole pesticides by supercritical fluid chromatography. *J. Chromatogr., A* **2004**, *1046*, 249−253.
(14) Souza Caldas, S.; Marian Bolzan, C.; Jaime de Menezes, E.; Laura Venquiaruti Escarrone, A.; de Martinez Gaspar Martins, C.; Bianchini, A.; Gilberto Primel, E. A vortex-assisted MSPD method for the extraction of pesticide residues from fish liver and crab hepatopancreas with determination by GC-MS. *Talanta* **2013**, *112*, 63−68.
(15) Andreu-Sanchez, O.; Paraiba, L. C.; Jonsson, C. M.; Carrasco, J. M. Acute toxicity and bioconcentration of fungicide tebuconazole in zebrafish (*Danio rerio*). *Environ. Toxicol.* **2012**, *27*, 109−116.
(16) Zhou, Q.; Gao, B.; Zhang, X.; Xu, Y.; Shi, H.; Yu, L. L. Chemical profiling of triacylglycerols and diacylglycerols in cow milk fat by ultra-performance convergence chromatography combined with a quadrupole time-of-flight mass spectrometry. *Food Chem.* **2014**, *143*, 199−204.
(17) Novakova, L.; Grand-Guillaume Perrenoud, A.; Nicoli, R.; Saugy, M.; Veuthey, J. L.; Guillarme, D. Ultra high performance supercritical fluid chromatography coupled with tandem mass spectrometry for screening of doping agents. I: Investigation of mobile phase and MS conditions. *Anal. Chim. Acta* **2015**, *853*, 637−646.
(18) Anastassiades, M.; Lehotay, S. J.; Stajnbaher, D.; Schenck, F. J. Fast and easy multiresidue method employing acetonitrile extraction/partitioning and "dispersive solid-phase extraction" for the determination of pesticide residues in produce. *J. AOAC Int.* **2003**, *86*, 412−431.
(19) Qiu, J.; Dai, S.; Zheng, C.; Yang, S.; Chai, T.; Bie, M. Enantiomeric separation of triazole fungicides with 3-mum and 5-muml particle chiral columns by reverse-phase high-performance liquid chromatography. *Chirality* **2011**, *23*, 479−486.
(20) Tao, Y.; Dong, F.; Xu, J.; Liu, X.; Cheng, Y.; Liu, N.; Chen, Z.; Zheng, Y. Green and sensitive supercritical fluid chromatographic-tandem mass spectrometric method for the separation and determination of flutriafol enantiomers in vegetables, fruits, and soil. *J. Agric. Food Chem.* **2014**, *62*, 11457−1164.
(21) Biba, M.; Regalado, E. L.; Wu, N.; Welch, C. J. Effect of particle size on the speed and resolution of chiral separations using supercritical fluid chromatography. *J. Chromatogr., A* **2014**, *1363*, 250−256.
(22) Toribio, L.; Bernal, J.; Martin, M.; Bernal, J.; Del Nozal, M. Effects of organic modifier and temperature on the enantiomeric separation of several azole drugs using supercritical fluid chromatography and the Chiralpak AD column. *Biomed. Chromatogr.* **2014**, *28*, 152−158.
(23) Shapovalova, E.; Shpigun, O.; Nesterova, L.; Belov, M. Determination of the optical purity of fungicides of the triazole series. *J. Anal. Chem.* **2004**, *59*, 255−259.
(24) Wilkowska, A.; Biziuk, M. Determination of pesticide residues in food matrices using the QuEChERS methodology. *Food Chem.* **2011**, *125*, 803−812.
(25) Chambers, E.; Wagrowski-Diehl, D.; Lu, Z.; Mazzeo, J. Systematic and comprehensive strategy for reducing matrix effects in LC/MS/MS analyses. *J. Chromatogr. B: Anal. Technol. Biomed. Life Sci.* **2007**, *852*, 22−34.
(26) Li, M.; Liu, X.; Dong, F.; Xu, J.; Kong, Z.; Li, Y.; Zheng, Y. Simultaneous determination of cyflumetofen and its main metabolite residues in samples of plant and animal origin using multi-walled carbon nanotubes in dispersive solid-phase extraction and ultrahigh performance liquid chromatography-tandem mass spectrometry. *J. Chromatogr., A* **2013**, *1300*, 95−103.

DOI: 10.1021/acs.jafc.5b02450
J. Agric. Food Chem. 2015, 63, 6297−6303

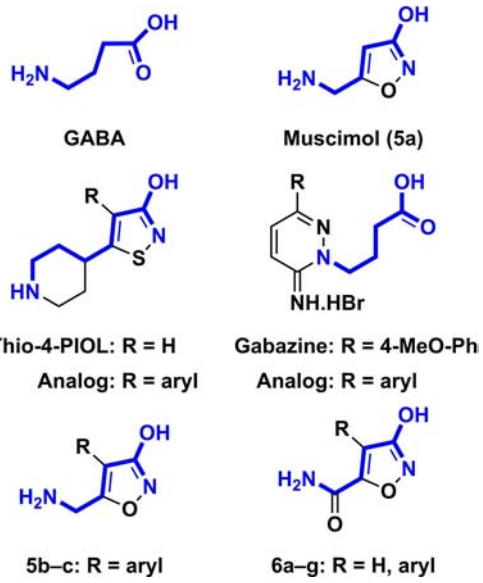

Figure 1. Chemical structures of GABA, muscimol, thio-4-PIOL, gabazine, and the synthesized analogues. Bold blue lines represent the GABA structural scaffold.

(Tokyo, Japan), unless otherwise noted. All air- and moisture-sensitive reactions were performed under an argon atmosphere using oven-dried glassware. Reactions were monitored by thin layer chromatography (TLC silica gel 60 F254 plates, Merck KGaA, Darmstadt, Germany) using UV light or a $KMnO_4$ spray reagent. Column chromatography was performed using silica gel (Wakogel C-200, 75–150 μm, Wako). Melting points were determined using a YANACO MP-500D micro melting point apparatus and are uncorrected. ^{1}H (400 MHz) and ^{13}C (100 MHz) NMR spectra were recorded on a JEOL JNM A-400 spectrometer. Chemical shifts are reported in parts per million (ppm) on the δ scale, and coupling constants (J) are in hertz (Hz). Spin multiplicities are abbreviated as follows: s (singlet), bs (broad singlet), d (doublet), t (triplet), and m (multiplet). Mass spectra (MS) were measured using the positive electrospray ionization mode (ESI) on a Waters XEVO mass spectrometer, and high-resolution mass spectra (HRMS) were obtained using ESI on a Waters SYNAPT G2 spectrometer.

*Synthesis of Methyl 3-Hydroxy-5-isoxazolecarboxylate (**2**).*[17] Dimethyl acetylenedicarboxylate (1.4 g, 10.0 mmol) was added to a solution of 1,8-diazabicyclo[5.4.0]undec-7-ene (1.8 g, 12.0 mmol) and *N*-hydroxyurea (760 mg, 10.0 mmol) in methanol (15 mL) at 0 °C under argon. The solution was stirred at 0 °C for 30 min and then at room temperature for 12 h. After the solvent was evaporated, the residue was dissolved in water (25 mL) and acidified to pH 1 with concentrated HCl. The product was extracted with Et_2O (3 × 30 mL), and the combined organic phases were washed with brine, dried over Na_2SO_4, and evaporated under reduced pressure. The obtained solid was recrystallized from chloroform to give **2** as a light yellow solid (840 mg, 59% yield): ^{1}H NMR (400 MHz, DMSO-d_6) δ 11.97 (1H, s, OH), 6.76 (1H, s, Ar–H), 3.87 (3H, s, $COOCH_3$).

*Synthesis of 3-Benzyloxy-5-methoxycarbonylisoxazole (**3**).*[18] A mixture of **2** (2.1 g, 15 mmol) and K_2CO_3 (3.1 g, 22.5 mmol) in acetone (30 mL) was heated at 70 °C for 1 h. Benzyl bromide (3.8 g, 22.5 mmol) was added dropwise, and the mixture was stirred at 50 °C for 12 h. The mixture was filtered, and the filtrate was concentrated under reduced pressure. Water (30 mL) was added to the filtrate, and the product was extracted with Et_2O (3 × 30 mL). The combined organic phases were washed with brine, dried over Na_2SO_4, and evaporated under reduced pressure. Column chromatography (hexane/EtOAc 15:1) gave **3** as a colorless oil (3.1 g, 87% yield): ^{1}H NMR (400 MHz, $CDCl_3$) δ 7.54–7.28 (5H, m, Ar–H), 6.57 (1H, s, Ar–H), 5.32 (2H, s, OCH_2), 3.95 (3H, s, $COOCH_3$); MS m/z 255.9 $[M + Na]^+$.

*Synthesis of 3-Benzyloxy-5-carbamoylisoxazole (**4**).* A mixture of **3** (466 mg, 2.0 mmol) and aqueous ammonia (5 mL, 28%) was stirred at room temperature for 12 h. The mixture was concentrated to dryness under reduced pressure. Water (15 mL) was added to the residue, and the mixture was extracted with EtOAc (3 × 15 mL). The combined organic phases were washed with brine, dried over Na_2SO_4, and evaporated under reduced pressure to afford **4** as a white solid (395 mg, 91% yield): mp 162–164 °C; ^{1}H NMR (400 MHz, $CDCl_3$): δ 7.48–7.32 (5H, m, Ar–H), 6.59 (1H, s, Ar–H), 6.43 (1H, bs, $CONH_2$), 5.87 (1H, bs, $CONH_2$), 5.31 (2H, s, OCH_2); MS m/z 241.1 $[M + Na]^+$.

*Synthesis of Muscimol Hydrobromide (**5a**).*[19] Borane in THF (1 M, 5 mL, 5.0 mmol) was slowly added to a solution of **4** (480 mg, 2.2 mmol) in dry THF (15 mL) at 0 °C. The solution was stirred at room temperature for 16 h. After acidification (pH 1) with 4 M HCl, the solution was stirred for 1 h and concentrated under reduced pressure. The residue was suspended in water, and the solution was made basic (pH 10) with 4 M NaOH. The product was extracted with EtOAc (3 × 30 mL); the combined organic phases were washed with brine, dried over Na_2SO_4, and evaporated under reduced pressure to afford a light yellow oil. The oil was dissolved in a solution of HBr in AcOH (10 mL, 30%), and the mixture was stirred at room temperature for 24 h. The reaction mixture was concentrated with a subsequent azeotropic treatment of MeOH/toluene (1:1) three times, and the residue was recrystallized (MeOH/Et_2O) to give **5a** as a light brown solid (179 mg, 42% yield): ^{1}H NMR (400 MHz, DMSO-d_6) δ 11.25 (1H, bs, OH), 8.45 (3H, bs, NH_2·HBr), 6.18 (1H, s, Ar–H), 4.14 (2H, s, CH_2); ^{13}C NMR (100 MHz, DMSO-d_6) δ 170.14, 165.22, 96.04, 34.29; HRMS m/z calcd for $C_4H_7N_2O_2$ $[M - Br]^+$ 115.0508, found 115.0502.

*Synthesis of 5-Carbamoyl-3-isoxazolol (**6a**).* Compound **4** (349 mg, 1.6 mmol) was suspended in a solution of HBr in AcOH (10 mL, 30%), and the mixture was stirred at room temperature for 24 h. The reaction mixture was concentrated with a subsequent azeotropic treatment of MeOH/toluene (1:1) three times, and the residue was recrystallized (MeOH/EtOAc) to give **6a** as a white solid (152 mg, 74% yield): mp 236–239 °C (dec); ^{1}H NMR (400 MHz, DMSO-d_6) δ 11.61 (1H, bs, OH), 8.15 (1H, bs, $CONH_2$), 7.81 (1H, bs, $CONH_2$), 6.54 (1H, s, Ar–H); ^{13}C NMR (100 MHz, DMSO-d_6) δ 170.40, 163.58, 157.39, 97.69; HRMS m/z calcd for $C_4H_5N_2O_3$ $[M + H]^+$ 129.0295, found 129.0290.

*Synthesis of 3-Benzyloxy-5-carbamoyl-4-iodoisoxazole (**7**).* A mixture of **4** (1.1 g, 5 mmol), $Pd(OAc)_2$ (112 mg, 0.5 mmol), CsOAc (2.3 g, 12 mmol), $NaHCO_3$ (420 mg, 5 mmol), I_2 (3.8 g, 15 mmol), 4 Å molecular sieves (150 mg), and *N*-methylformamide (30 mL) was stirred at 75 °C for 16 h. After cooling, the reaction mixture was added to $Na_2S_2O_4$ (solid) until the color stopped changing, and then it was filtered through Celite, which was thoroughly washed with EtOAc. The combined organic phases were washed with water twice and then with brine, dried over Na_2SO_4, and evaporated under reduced pressure. Column chromatography (hexane/EtOAc 10:1) gave **7** as a light yellow solid (980 mg, 57% yield): mp 179–182 °C; ^{1}H NMR (400 MHz, $CDCl_3$) δ 7.50–7.35 (5H, m, Ar–H), 6.43 (1H, bs, $CONH_2$), 5.94 (1H, bs, $CONH_2$), 5.37 (2H, s, OCH_2); MS m/z 366.9 $[M + Na]^+$.

*General Procedure for the Synthesis of 4-Aryl-3-benzyloxy-5-carbamoylisoxazole (**8b–8g**).* A mixture of **7** (1 mmol), an arylboronic acid (1.5 mmol), $Pd(PPh_3)_2Cl_2$ (0.08 mmol), DMF (5 mL), and aqueous K_2CO_3 (0.5 mL, 3 M, 1.5 mmol) was stirred at 80 °C for 24 h. After cooling, the reaction mixture was filtered through Celite and diluted using Et_2O. The organic phase was washed with water and brine, dried over Na_2SO_4, and evaporated under reduced pressure. Column chromatography (hexane/EtOAc) gave **8b–8g**.

*3-Benzyloxy-4-(3-biphenylyl)-5-carbamoylisoxazole (**8b**):* white solid; yield 82%; mp 145–147 °C; ^{1}H NMR (400 MHz, $CDCl_3$) δ 7.93 (1H, s, Ar–H), 7.70–7.26 (13H, m, Ar–H), 6.40 (1H, bs, $CONH_2$), 5.78 (1H, bs, $CONH_2$), 5.42 (2H, s, OCH_2); ^{13}C NMR (100 MHz, $CDCl_3$) δ 169.88, 157.95, 156.60, 141.09, 140.78, 135.39, 129.03, 128.83, 128.74, 128.60, 128.56, 128.09, 127.58, 127.37, 127.20, 126.59, 114.21, 72.27; MS m/z 371.0 $[M + H]^+$, 393.0 $[M + Na]^+$.

DOI: 10.1021/acs.jafc.5b01843
J. Agric. Food Chem. 2015, 63, 6304–6312

*3-Benzyloxy-5-carbamoyl-4-(2-naphthyl)isoxazole (**8c**):* white solid; yield 69%; mp 138−140 °C; ^{1}H NMR (400 MHz, $CDCl_3$) δ 8.14 (1H, s, Ar−H), 7.88−7.73 (4H, m, Ar−H), 7.72−7.26 (7H, m, Ar−H), 6.39 (1H, bs, $CONH_2$), 5.84 (1H, bs, $CONH_2$), 5.43 (2H, s, OCH_2); ^{13}C NMR (100 MHz, $CDCl_3$) δ 169.90, 157.95, 156.60, 135.33, 133.21, 132.90, 129.75, 129.58, 128.49, 128.37, 127.90, 127.74, 127.63, 127.26, 126.74, 126.23, 123.56, 114.31, 72.17; MS *m*/*z* 367.0 $[M + Na]^+$.

*3-Benzyloxy-4-(4-biphenylyl)-5-carbamoylisoxazole (**8d**):* white solid; yield 90%; mp 164−167 °C; ^{1}H NMR (400 MHz, $CDCl_3$) δ 7.80−7.28 (14H, m, Ar−H), 6.39 (1H, bs, $CONH_2$), 5.75 (1H, bs, $CONH_2$), 5.42 (2H, s, OCH_2); ^{13}C NMR (100 MHz, $CDCl_3$) δ 169.98, 158.03, 156.59, 141.72, 140.66, 135.48, 132.23, 132.13, 130.49, 128.84, 128.67, 128.60, 128.47, 128.08, 127.59, 127.19, 126.95, 125.21, 114.11, 72.34; MS *m*/*z* 371.0 $[M + H]^+$.

*3-Benzyloxy-5-carbamoyl-4-(1-naphthyl)isoxazole (**8e**):* white solid; yield 77%; mp 154−156 °C; ^{1}H NMR (400 MHz, $CDCl_3$) δ 7.95−7.25 (12H, m, Ar−H), 6.05 (1H, bs, $CONH_2$), 5.72 (1H, bs, $CONH_2$), 5.34 (2H, s, OCH_2); ^{13}C NMR (100 MHz, $CDCl_3$) δ 170.35, 158.09, 157.37, 135.23, 133.66, 131.57, 129.83, 128.97, 128.52, 128.41, 128.05, 126.56, 126.25, 125.26, 125.19, 123.84, 112.32, 72.02; MS *m*/*z* 367.1 $[M + Na]^+$.

*3-Benzyloxy-5-carbamoyl-4-(6-methoxy-2-naphthyl)isoxazole (**8f**):* light yellow solid; yield 67%; mp 124−126 °C; ^{1}H NMR (400 MHz, $CDCl_3$) δ 8.07 (1H, s, Ar−H), 7.78−7.65 (3H, m, Ar−H), 7.46−7.30 (5H, m, Ar−H), 7.18−7.10 (2H, m, Ar−H), 6.40 (1H, bs, $CONH_2$), 6.06 (1H, bs, $CONH_2$), 5.42 (2H, s, OCH_2), 3.91 (3H, s, OCH_3); ^{13}C NMR (100 MHz, $CDCl_3$) δ 169.92, 158.40, 158.21, 156.39, 135.41, 134.54, 129.90, 129.50, 128.55, 128.45, 127.86, 127.79, 126.57, 121.23, 119.11, 114.35, 105.61, 72.12, 55.32; MS *m*/*z* 397.1 $[M + Na]^+$.

*3-Benzyloxy-5-carbamoyl-4-(6-hydroxy-2-naphthyl)isoxazole (**8g**):* light yellow solid; yield 43%; mp 177−179 °C; ^{1}H NMR (400 MHz, DMSO-d_6) δ 9.73 (1H, s, Ar−OH), 8.11 (1H, bs, $CONH_2$), 7.97 (1H, s, Ar−H), 7.85 (1H, bs, $CONH_2$), 7.75−7.05 (10H, m, Ar−H), 5.41 (2H, s, OCH_2); ^{13}C NMR (100 MHz, DMSO-d_6) δ 169.11, 158.67, 158.25, 155.96, 135.67, 134.12, 129.56, 128.60, 128.37, 128.24, 127.93, 127.31, 127.06, 125.49, 120.77, 118.98, 111.59, 108.54, 71.63; MS *m*/*z* 383.1 $[M + Na]^+$.

*Synthesis of 5-Aminomethyl-4-(3-biphenylyl)-3-isoxazolol Hydrobromide (**5b**).* Compound **5b** was prepared from **8b** (185 mg, 0.5 mmol) according to the procedure described for **5a**. Recrystallization (MeOH/Et_2O) gave **5b** as a white solid (69 mg, 40%): mp 220−222 °C; ^{1}H NMR (400 MHz, CD_3OD) δ 7.75−7.30 (9H, m, Ar−H), 4.36 (2H, s, CH_2); ^{13}C NMR (100 MHz, CD_3OD) δ 163.30, 160.88, 143.29, 141.79, 130.50, 129.95, 129.33, 128.72, 128.66, 128.38, 128.07, 128.02, 111.90, 35.40; HRMS *m*/*z* calcd for $C_{16}H_{15}N_2O_2$ $[M - Br]^+$ 267.1134, found 267.1143.

*Synthesis of 5-Aminomethyl-4-(2-naphthyl)-3-isoxazolol Hydrobromide (**5c**).* Compound **5c** was prepared from **8c** (196 mg, 0.57 mmol) according to the procedure described for **5a**. Recrystallization (MeOH/Et_2O) gave **5c** as a brown solid (85 mg, 47%): mp 226−228 °C; ^{1}H NMR (400 MHz, CD_3OD) δ 8.01−7.86 (4H, m, Ar−H), 7.65−7.50 (3H, m, Ar−H), 4.41 (2H, s, CH_2); ^{13}C NMR (100 MHz, CD_3OD) δ 170.22, 160.92, 134.85, 134.37, 129.63, 129.09, 128.77, 127.69, 127.20, 126.21, 112.05, 35.56; HRMS *m*/*z* calcd for $C_{14}H_{13}N_2O_2$ $[M - Br]^+$ 241.0977, found 241.0989.

*Synthesis of 4-(3-Biphenylyl)-5-carbamoyl-3-isoxazolol (**6b**).* Compound **6b** was prepared from **8b** (333 mg, 0.9 mmol) according to the procedure described for **6a**. Recrystallization (MeOH/EtOAc) gave **6b** as a white solid (210 mg, 83%): mp 193−195 °C; ^{1}H NMR (400 MHz, DMSO-d_6) δ 12.03 (1H, bs, OH), 8.09 (1H, bs, $CONH_2$), 7.90 (1H, s, Ar−H), 7.82 (1H, bs, $CONH_2$), 7.71−7.27 (8H, m, Ar−H); ^{13}C NMR (100 MHz, DMSO-d_6) δ 168.62, 158.59, 158.30, 140.04, 139.77, 128.87, 128.42, 128.35, 128.05, 127.43, 126.62, 126.19, 111.31; HRMS *m*/*z* calcd for $C_{16}H_{13}N_2O_3$ $[M + H]^+$ 281.0921, found 281.0914.

*Synthesis of 5-Carbamoyl-4-(2-naphthyl)-3-isoxazolol (**6c**).* Compound **6c** was prepared from **8c** (189 mg, 0.55 mmol) according to the procedure described for **6a**. Recrystallization (MeOH/EtOAc) gave **6c** as a light yellow solid (95 mg, 68%): mp 221−223 °C; ^{1}H NMR (400 MHz, DMSO-d_6) δ 12.02 (1H, bs, OH), 8.10 (1H, s, Ar−H), 8.06 (1H, bs, $CONH_2$), 7.95−7.88 (3H, m, Ar−H), 7.79 (1H, bs, $CONH_2$), 7.66 (1H, d, *J* = 8.3 Hz, Ar−H), 7.58−7.47 (2H, m, Ar−H); ^{13}C NMR (100 MHz, DMSO-d_6) δ 168.58, 158.39, 158.28, 132.33, 132.19, 128.35, 127.80, 127.25, 126.92, 126.23, 126.02, 124.96, 111.33; HRMS *m*/*z* calcd for $C_{14}H_{11}N_2O_3$ $[M + H]^+$ 255.0770, found 255.0785.

*Synthesis of 4-(4-Biphenylyl)-5-carbamoyl-3-isoxazolol (**6d**).* Compound **6d** was prepared from **8d** (222 mg, 0.6 mmol) according to the procedure described for **6a**. Recrystallization (MeOH/EtOAc) gave **6d** as a white solid (112 mg, 67%): mp 278−280 °C (dec); ^{1}H NMR (400 MHz, DMSO-d_6) δ 12.03 (1H, bs, OH), 8.09 (1H, bs, $CONH_2$), 7.82 (1H, bs, $CONH_2$), 7.80−7.50 (6H, m, Ar−H), 7.48−7.34 (3H, m, Ar−H); ^{13}C NMR (100 MHz, DMSO-d_6) δ 168.61, 158.56, 158.20, 139.65, 139.58, 129.96, 128.86, 127.48, 126.61, 126.54, 126.04, 110.98; HRMS *m*/*z* calcd for $C_{16}H_{12}N_2O_3Na$ $[M + Na]^+$ 303.0740, found 303.0738.

*Synthesis of 5-Carbamoyl-4-(1-naphthyl)-3-isoxazolol (**6e**).* Compound **6e** was prepared from **8e** (330 mg, 0.96 mmol) according to the procedure described for **6a**. Recrystallization (MeOH/EtOAc) gave **6e** as a white solid (128 mg, 52%): mp 189−191 °C; ^{1}H NMR (400 MHz, DMSO-d_6) δ 11.77 (1H, bs, OH), 7.96 (2H, d, *J* = 7.8 Hz, Ar−H), 7.92 (1H, bs, $CONH_2$), 7.68 (1H, bs, $CONH_2$), 7.59−7.41 (5H, m, Ar−H); ^{13}C NMR (100 MHz, DMSO-d_6) δ 169.34, 159.28, 157.69, 133.03, 131.46, 128.66, 128.44, 128.07, 126.08, 125.76, 125.39, 125.15, 110.58; HRMS *m*/*z* calcd for $C_{14}H_{11}N_2O_3$ $[M + H]^+$ 255.0770, found 255.0785.

*Synthesis of 5-Carbamoyl-4-(6-methoxy-2-naphthyl)-3-isoxazolol (**6f**).* Compound **6f** was prepared from **8f** (243 mg, 0.65 mmol) according to the procedure described for **6a**. Recrystallization (MeOH/EtOAc) gave **6f** as a white solid (115 mg, 62%): mp 242−244 °C (dec); ^{1}H NMR (400 MHz, DMSO-d_6) δ 11.99 (1H, bs, OH), 8.03 (2H, bs, $CONH_2$), 7.85−7.70 (4H, m, Ar−H), 7.63 (1H, dd, *J* = 8.8, 2.0 Hz, Ar−H), 7.32 (1H, d, *J* = 2.4 Hz, Ar−H), 7.17 (1H, dd, *J* = 8.8, 2.4 Hz, Ar−H), 3.89 (3H, s, OCH_3); ^{13}C NMR (100 MHz, DMSO-d_6) δ 168.72, 158.58, 158.05, 157.71, 133.70, 129.52, 128.31, 127.89, 127.83, 125.99, 122.60, 118.64, 111.58, 105.90, 55.21; HRMS *m*/*z* calcd for $C_{15}H_{12}N_2O_4Na$ $[M + Na]^+$ 307.0695, found 307.0691.

*Synthesis of 5-Carbamoyl-4-(6-hydroxy-2-naphthyl)-3-isoxazolol (**6g**).* Compound **6g** was prepared from **8g** (90 mg, 0.25 mmol) according to the procedure described for **6a**. Recrystallization (MeOH/EtOAc) gave **6g** as a white solid (52 mg, 77%): mp 210−213 °C; ^{1}H NMR (400 MHz, DMSO-d_6) δ 11.94 (1H, bs, OH), 9.70 (1H, bs, OH), 8.05−7.50 (6H, m, Ar−H and $CONH_2$), 7.36−7.05 (2H, m, Ar−H); ^{13}C NMR (100 MHz, DMSO-d_6) δ 168.73, 158.61, 157.91, 155.78, 129.56, 128.37, 128.12, 127.56, 127.11, 125.29, 121.64, 118.81, 111.69, 108.51; HRMS *m*/*z* calcd for $C_{14}H_{11}N_2O_4$ $[M + H]^+$ 271.0719, found 271.0714.

Preparation of cRNAs of Housefly RDL and Their Expression in *Xenopus* Oocytes. The cRNAs of four housefly RDL variants (DDBJ accession no. AB177547, complete cds of RDL_{bd}; AB824728, partial cds of exon 3a version; AB824729, partial cds of exon 6c version) were prepared as previously described.[20] In brief, the cDNA templates of four *Rdl* variants (ac, bc, ad, and bd) including the upstream RNA polymerase promoter site were obtained by PCR amplification from pBluescript KS(−)-$MdRdl_{ac}$, -$MdRdl_{bc}$, -$MdRdl_{ad}$, and -$MdRdl_{bd}$ using KOD -Plus- ver. 2 (Toyobo, Tokyo, Japan), a forward primer, 5′-TGTAAAACGACGGCCAGT-3′, and a reverse primer, 5′-CAGGAAACAGCTATGACC-3′. The PCR products were purified using the illustra GFX PCR DNA and Gel Band Purification Kit (GE Healthcare UK, Ltd., Little Chalfont, UK), and the integrity of amplified cDNAs was confirmed by sequence analysis. The capped cRNAs were synthesized using T7 polymerase (mMessage mMachine T7 Ultra Kit; Ambion, Austin, TX, USA). The cRNAs were precipitated with LiCl, dissolved in sterile RNase-free water, and stored at −20 °C until use.

Mature female African clawed frogs (*Xenopus laevis*) were anesthetized with 0.1% (w/v) ethyl *m*-aminobenzoate methanesulfonate in water. The ovarian lobes were dissected out and then treated

DOI: 10.1021/acs.jafc.5b01843
J. Agric. Food Chem. 2015, 63, 6304−6312

Scheme 1. Synthesis of Muscimol and Target Compounds[a]

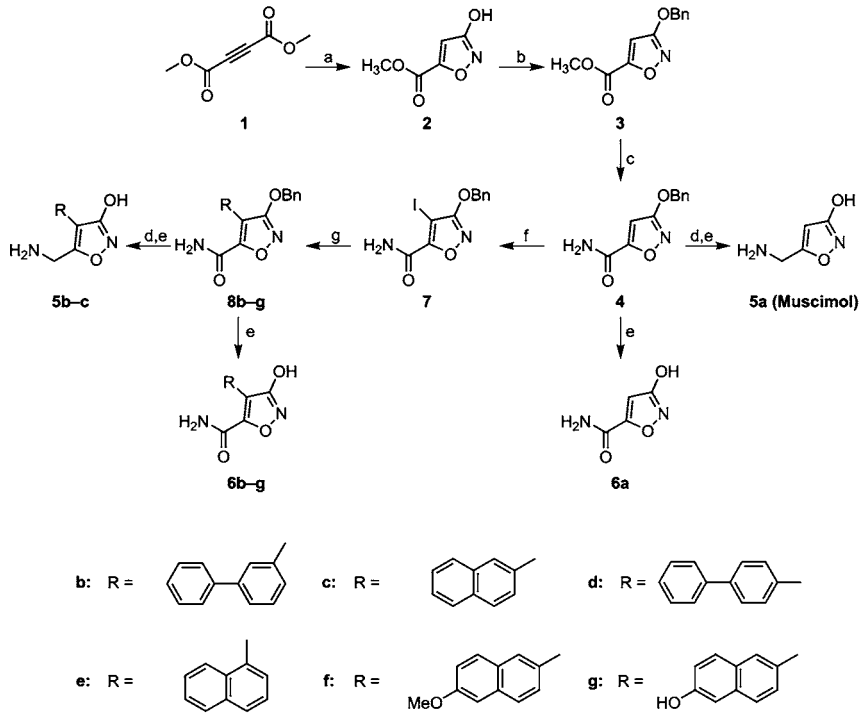

[a]Reagents and conditions: (a) *N*-hydroxyurea, 1,5-diazabicyclo[5.4.0]undec-5-ene, MeOH, 0 °C; (b) benzyl bromide, K_2CO_3, acetone, 70 °C; (c) aqueous NH_3, room temperature; (d) BH_3, THF, room temperature; (e) 30% HBr in AcOH, room temperature; (f) I_2, $Pd(OAc)_2$, CsOAc, $NaHCO_3$, DMF, 75 °C; (g) $RB(OH)_2$, $PdCl_2(PPh_3)_2$, K_2CO_3, DMF, 80 °C.

with collagenase (2 mg/mL, Sigma-Aldrich) in a Ca^{2+}-free standard oocyte solution (Ca^{2+}-free SOS) (100 mM NaCl, 2 mM KCl, 1 mM $MgCl_2$, 5 mM HEPES, pH 7.6) at room temperature for 90−120 min. The oocytes were then gently washed with sterile SOS (100 mM NaCl, 2 mM KCl, 1.8 mM $CaCl_2$, 1 mM $MgCl_2$, 5 mM HEPES, pH 7.6) containing gentamycin (50 μg/mL, Life Technologies, Thermo Fisher Scientific Inc., Waltham, MA, USA), penicillin (100 U/mL, Life Technologies), streptomycin (100 μg/mL, Life Technologies), and sodium pyruvate (2.5 mM, Sigma-Aldrich). Each oocyte was injected cytoplasmically with 5 ng of cRNA dissolved in RNase-free water (9.2 nL), and then the oocytes were incubated in sterile SOS for 48 h at 16 °C.

Two-Electrode Voltage Clamp (TEVC) Recordings. Electrophysiological experiments were performed as previously described.[14] Briefly, GABA-induced currents were recorded at a holding potential of −80 mV using an Oocyte Clamp OC-725C amplifier (Warner Instruments, Hamden, CT, USA) and Data-Trax2 software (World Precision Instruments Inc., Sarasota, FL, USA). The glass capillary electrodes were fabricated using a micropipette puller (P-97, Sutter Instrument, Novato, CA, USA) and filled with 2 M KCl (resistance ranging from 0.5 to 2.0 MΩ). Oocytes were placed in a recording bath that was continuously perfused with SOS at 18−22 °C.

For agonist assays, GABA dissolved in SOS was applied to oocytes for 3 s, at intervals of 30−60 s, to ensure a full recovery from desensitization. Concentration−response curves were generated by sequential applications of increasing concentrations of GABA. Muscimol hydrobromide was dissolved in SOS and tested using the same procedure as GABA. For antagonist assays, 3-isoxazolols were dissolved in DMSO and then diluted with SOS to the desired concentrations [DMSO, ≤0.1% (v/v)]. The test compound solution was added to the perfusate after two successive control applications of GABA and was then applied consecutively for the remainder of the experiments. Antagonist solutions were perfused alone for 30 s before their coapplication with GABA. GABA, at a concentration corresponding to the EC_{50} for each variant, was then coapplied with an antagonist for 3 s, and the coapplication was repeated at 30−60 s intervals to obtain the highest constant inhibition. All experiments were performed using at least four different oocytes obtained from at least two different frogs.

EC_{50} and IC_{50} values were obtained from concentration−response data by nonlinear regression analysis using OriginPro 8J (OriginLab, Northampton, MA, USA). Statistical significance was assessed using one-way analysis of variance (ANOVA) followed by Duncan's multiple-range test.

Insecticidal Assays. The WHO/SRS strain of houseflies (*M. domestica*) was used to examine the insecticidal activity of **6b**. Compound **6b** dissolved in DMSO (0.1 μL) at various concentrations was injected into the dorsal side of the thorax of adult female houseflies (3−5 days after eclosion). This volume of DMSO solution alone did not affect the viability of houseflies. A total of 12−15 houseflies was used at each concentration. The injected houseflies were maintained with sugar and water at 25 °C. The number of dead or paralyzed flies was counted after 24 h. The experiments were replicated five times. The LD_{50} value was calculated from the mean values of mortality at three dosages using the Probit method.

Molecular Modeling and Ligand Docking Studies. A recently published X-ray crystal structure of the homopentameric human β3 GABAR (PDB ID 4COF)[21] was used as a template to construct a housefly RDL_{ac} GABAR homology model. A sequence alignment of the RDL_{ac} and β subunits was carried out using ClustalW software, and this was used to build all five subunits simultaneously using MOE 2011.10 software (Chemical Computing Group, Montreal, Canada). The obtained pentamer model was optimized geometrically using the AMBER99 force field. GABA and muscimol were created in the zwitterionic forms, and compound **6b** was created in a deprotonated hydroxyl form using MOE Builder. Potential docking sites were searched using SiteFinder of MOE. The created ligands were docked into the potential binding site of the generated model using the ASEDock program (2011.01.27, Chemical Computing Group) with default parameters. The energies of the receptor and ligands were minimized using the MMFF94x force field. The stable conformations of ligands were obtained by a conformational search. The binding

DOI: 10.1021/acs.jafc.5b01843
J. Agric. Food Chem. 2015, 63, 6304−6312

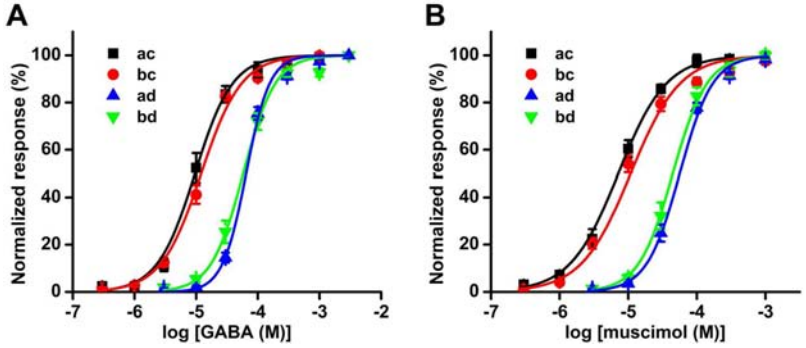

Figure 2. Agonist responses of the four splice variants of housefly RDL GABARs expressed in *Xenopus* oocytes: (A) GABA concentration−response curves of the four variants; (B) muscimol concentration−response curves of the four variants. Responses were normalized relative to the maximum currents induced by 1 mM GABA in the ac and bc variants and by 3 mM GABA in the ad and bd variants. No significant differences were observed in the maximum currents induced by muscimol and GABA in each variant, indicating that muscimol is a full agonist. Data represent means ± SEM (n = 6−9).

mode with the highest score was chosen for the final representation. Structural images were visualized using PyMOL ver. 1.3 (Schrödinger, Tokyo, Japan).

RESULTS AND DISCUSSION

Chemistry. A new, convenient strategy to synthesize 4-aryl-substituted muscimols and 4-aryl-5-carbamoyl-3-isoxazolols starting from dimethyl acetylenedicarboxylate (**1**) was established and is outlined in Scheme 1. 3-Isoxazolol **2** was synthesized from **1** according to a reported method,[17] and the hydroxyl group was protected to give 3-benzyloxyisoxazole **3**.[18] Ammonolysis of ester **3** to amide **4** was followed by reduction with borane and deprotection with hydrobromic acid to afford muscimol hydrobromide (**5a**). Treatment of **4** with 30% hydrobromic acid in acetic acid afforded 5-carbamoyl-3-isoxazolol (**6a**). To introduce aromatic groups into the 4-position of the isoxazole ring, **4** was first iodinated at this position using iodine and $Pd(OAc)_2$ as a catalyst to give **7**.[22] The Suzuki−Miyaura cross-coupling reaction of **7** with the appropriate arylboronic acids in the presence of a palladium catalyst afforded analogues **8b**−**8g** in 43−90% yields, the hydroxyl groups of which were deprotected with hydrobromic acid to give **6b**−**6g**. Compounds **5b**−**5c** were obtained by reduction and subsequent deprotection of **8b** and **8c**, as described for **5a**.

Differential Sensitivity of Housefly GABAR Variants to GABA and Muscimol. Similar to the case of *D. melanogaster*,[5] four splice variants (ac, ad, bc, and bd) of RDL are endogenously generated by alternatively splicing exons 3 (a and b) and 6 (c and d) of *Rdl* in houseflies. The two amino acid residues that differ between the sequences encoded by exons 3a and 3b are located upstream of the agonist-interacting region of the RDL subunit, and the 10 residues that differ between the sequences encoded by exons 6c and 6d are located in a region including loops F and C (Figure S1), which are predicted to be generally involved in the interaction with agonists in Cys-loop receptors.[23] In the present study, the four variants of housefly RDL were expressed in *Xenopus* oocytes, and their responses to the agonists GABA and muscimol were first investigated using a TEVC method.

Application of GABA to the oocytes expressing housefly RDL GABARs induced concentration-dependent inward currents in all four variants when the voltage was clamped at −80 mV. The GABA concentration−response curves show that the order of variants giving higher sensitivity to GABA is $RDL_{ac} \approx RDL_{bc} > RDL_{ad} \approx RDL_{bd}$ (Figure 2A); the EC_{50} values are given in Table 1. The finding that the alternative splicing of exon 3 did not affect the sensitivity to GABA suggests that the two variable residues in exon 3 may not be involved in the interaction with GABA. RDL_{ac} GABARs showed ∼6-fold higher sensitivity to GABA than RDL_{ad} GABARs, and RDL_{bc} GABARs had ∼5-fold higher sensitivity than RDL_{bd} GABARs. This finding indicates that the alternative splicing of exon 6 significantly influences GABA potency in the RDL variants of housefly GABARs. Similarly, muscimol (**5a**) was a more potent full agonist in the ac and bc variants than in the ad and bd variants (Figure 2; Table 1). These different potencies of GABA and muscimol in the four variants are similar to those in *Drosophila* RDL variants.[6−8] The changes of agonist potencies may be due to the residue difference in loop(s) F and/or C in the orthosteric binding site.

Table 1. Potencies of GABA and Muscimol in the Four Splice Variants of Housefly RDL GABARs[a]

	GABA		muscimol	
variant	EC_{50} (μM)	n_H	EC_{50} (μM)	n_H
RDL_{ac}	10.6 ± 1.6a	1.74 ± 0.23	7.1 ± 0.7a	1.25 ± 0.16
RDL_{bc}	12.2 ± 0.7a	1.62 ± 0.24	10.2 ± 1.0a	1.18 ± 0.10
RDL_{ad}	64.1 ± 3.8b	2.29 ± 0.10	54.1 ± 2.2b	1.98 ± 0.26
RDL_{bd}	59.0 ± 5.7b	1.77 ± 0.21	45.8 ± 4.7b	1.76 ± 0.16

[a]Data are means ± SEM (n = 6−9). n_H is the Hill coefficient. Different letters within a column indicate statistically significant difference at $p < 0.01$.

Antagonism of Housefly GABAR Variants by Synthesized Analogues. We examined the activity of synthesized compounds against RDL GABARs from three insect species. The compounds were first tested against common cutworm (*Spodoptera litura* Fabricius) and small brown planthopper (*Laodelphax striatellus* Fallén) RDL_{bd} GABARs expressed in *Drosophila* S2 cells using the fluorescent imaging plate reader (FLIPR) membrane potential (FMP) assays, as previously reported.[14] Unexpectedly, synthesized analogues other than muscimol failed to show significant activity at 100 μM in both insect receptors (data not shown). In contrast to these results, significant results were obtained against housefly RDL GABARs, prompting further investigation described below. These contrasting results suggest that structural or functional

DOI: 10.1021/acs.jafc.5b01843
J. Agric. Food Chem. 2015, 63, 6304−6312

differences in the orthosteric binding sites of RDL GABARs might exist between insect species.

As agonist potencies vary by the variant, synthesized analogues were assessed for their functional characteristics in the four RDL variants of housefly GABARs expressed in *Xenopus* oocytes using a TEVC method. Analogues were first tested at 100 μM in the absence and in the presence of the EC_{50} of GABA to determine if they are agonists or antagonists. Unlike muscimol, all synthesized analogues showed no agonism but exhibited antagonism at 100 μM in the four RDL variants.

In a previous study, we found that the 4-(3-biphenylyl)-thio-4-PIOL and 4-(2-naphthyl)-thio-4-PIOL analogues showed competitive antagonism in housefly RDL_{ac} GABARs and common cutworm RDL_{bd} GABARs, indicating that the 3-biphenyl and 2-naphthyl groups are beneficial for competitive antagonists of insect GABARs.[14] Thus, these groups were introduced into the 4-position of muscimol (**5a**) to afford **5b** and **5c**. Both compounds showed antagonism at 100 μM in all four RDL variants of housefly GABARs, albeit with <40% inhibition of GABA-induced currents (Figure 3A). Although

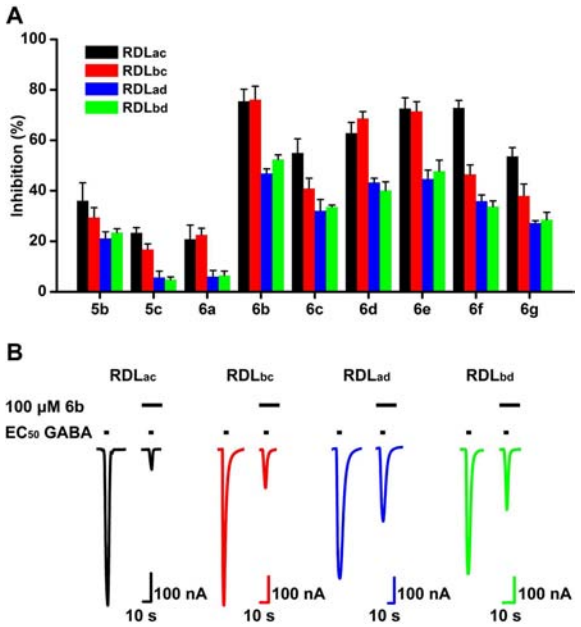

Figure 3. Inhibition of GABA-induced currents by the 3-isoxazolol analogues in the four splice variants of housefly RDL GABARs expressed in *Xenopus* oocytes: (A) inhibition of GABA-induced currents by synthesized analogues at 100 μM in the four variants (data represent means ± SEM (n = 4–6)); (B) examples of GABA-induced currents inhibited by 100 μM **6b** in the four variants. The EC_{50} of GABA for each variant (Table 1) was used to induce control currents in each oocyte.

the potencies of these analogues were low, these results indicate that the 3-isoxazolol scaffold may be useful for developing antagonists of housefly GABARs and that the bicyclic aromatic system at the 4-position of the isoxazole ring may be beneficial for antagonistic activity as it was in thio-4-PIOL analogues.

Replacement of the aminomethyl group of muscimol (**5a**) with a carbamoyl group to give **6a** changed the function of muscimol from an agonist to an antagonist in the four variants, with ~20% inhibition of GABA-induced currents at 100 μM in RDL_{ac} and RDL_{bc} GABARs and ~6% inhibition in RDL_{ad} and RDL_{bd} GABARs. These findings indicate that the protonated amino group is needed for agonist activity and that the carbamoyl group at the 5-position favors antagonism rather than agonism. The introduction of a 3-biphenylyl group at the 4-poisiton of **6a** to give **6b** markedly increased the antagonistic activity against the four variants, leading to 75.5, 76.1, 46.9, and 52.4% inhibition of GABA-induced currents in RDL_{ac}, RDL_{bc}, RDL_{ad}, and RDL_{bd} GABARs, respectively (Figure 3A). Figure 3B shows that GABA-induced currents were inhibited by the 3-biphenylyl analogue (**6b**) at 100 μM in the four RDL variants. Compound **6c**, with a 2-naphthyl substitution at the 4-position of the isoxazole ring, also exhibited higher inhibition than **6a** in all four variants, but relatively lower inhibition compared with **6b**. Additionally, two different aromatic groups, 4-biphenylyl and 1-naphthyl, were introduced into the 4-position to yield **6d** and **6e**, respectively. The inhibition of GABA-induced currents by **6d** and **6e** in the four variants was comparable to the inhibition by **6b**. These findings indicate that analogues with bicyclic aromatic groups at the 4-position of the isoxazole ring are well tolerated at the binding site and that they are effective in inhibiting GABA-induced current in housefly GABARs. To investigate whether the electron-donating groups on the aromatic group at the 4-position increase activity, a methoxyl and a hydroxyl group were introduced to the 6-position of the 2-naphthyl group of **6c** to afford **6f** and **6g**, respectively. Compounds **6f** and **6g** were comparable in activity to **6c** in the four variants, although inhibition by **6f** in the ac variant was higher than that of **6c** (Figure 3A). Overall, the synthesized analogues **5b**, **5c**, and **6b**–**6g** were more potent against RDL_{ac} and RDL_{bc} GABARs than against RDL_{ad} and RDL_{bd} GABARs (Figure 3A), with from ~1.5- to ~4-fold higher inhibition in the former than in the latter. The different sensitivities of the four variants to the synthesized analogues are similar to those of the agonists GABA and muscimol, implying that the synthesized analogues bind to the same site as agonists.

Compounds **6b**–**6g**, which exerted relatively greater inhibitory effects, were further evaluated in RDL_{ac} GABARs with the generation of antagonist concentration–response curves in the presence of 10 μM (EC_{50}) GABA (Figure 4A). The 3-biphenylyl analogue (**6b**), with an IC_{50} value of 30.0 μM, is among the analogues that displayed the greatest antagonism in the ac variant (Table 2). The replacement of the 3-biphenylyl group with a 2-naphthyl and a 4-biphenylyl group to yield **6c** and **6d** resulted in 2.3- and 1.8-fold increases in the IC_{50} value, respectively. The 1-naphthyl analogue (**6e**) had a potency similar to that of **6b** in the ac variant. Thus, the 3-biphenyl group is advantageous compared with the 4-biphenyl group; the 1-naphthyl group is preferable to the 2-naphthyl group. The introduction of a methoxy group into the naphthyl group of **6c** to yield **6f** led to a 1.9-fold increased potency in the ac variant, whereas the potency of **6g**, in which a hydroxyl group was introduced, was similar to that of **6c** in the ac variant.

Compound **6b** was further examined for its potencies in other RDL variants of housefly GABARs. Figure 4B shows concentration–response curves for **6b** in the presence of the EC_{50} of GABA in the four variants. No significant differences were observed in the IC_{50} values of **6b** between the ac and bc variants or between the ad and bd variants, whereas the IC_{50} values of **6b** in the ad and bd variants were ~3-fold greater compared with those in the ac and bc variants (Table 2). These findings were analogous to those in the EC_{50} values of GABA and muscimol in the four variants, indicating that **6b** most likely acts on the same site as agonists. The different amino acid residues in the region encoded by exon 6 in different variants

DOI: 10.1021/acs.jafc.5b01843
J. Agric. Food Chem. 2015, 63, 6304–6312

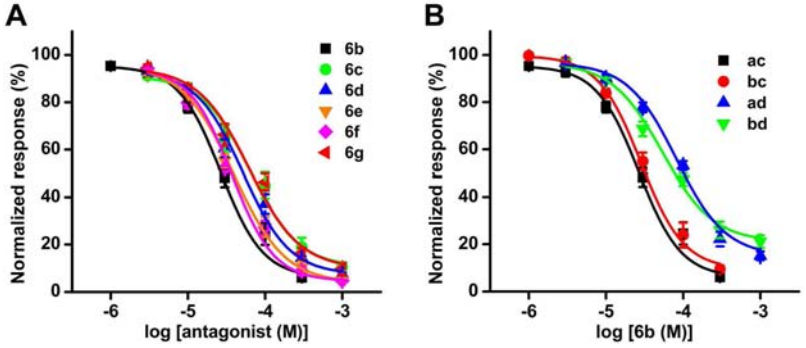

Figure 4. Effects of the 3-isoxazolol analogues on GABA-induced currents in housefly RDL GABARs expressed in *Xenopus* oocytes: (A) concentration−response inhibition curves of 4-aryl-5-carbamoyl-3-isoxazolols (**6b**−**6g**) in the housefly RDL_{ac} variant; (B) concentration−response inhibition curves of **6b** in four GABAR variants. Responses were normalized relative to currents induced by the EC_{50} of GABA for each variant. Data represent means ± SEM (n = 4−6).

Table 2. Inhibition of GABA (EC_{50})-Induced Currents by 4-Aryl-5-carbamoyl-3-isoxazolols (6b−6g) in the Four Variants of Housefly RDL GABARs[a]

	IC_{50} (μM)			
compd	RDL_{ac}	RDL_{bc}	RDL_{ad}	RDL_{bd}
6b	30.0 ± 2.6a	34.3 ± 2.4a	107.2 ± 8.1b	96.0 ± 4.9b
6c	67.7 ± 3.0c	>100	>100	>100
6d	53.3 ± 3.4d	ND	>100	>100
6e	38.5 ± 4.9a	ND	≈ 100	>100
6f	36.0 ± 3.5a	ND	>100	>100
6g	64.9 ± 2.7cd	>100	>100	>100

[a]Data are means ± SEM (n = 4). Different letters within a row and a column indicate statistically significant difference at $p < 0.01$ and $p < 0.05$, respectively. ND, not determined.

may cause the difference in the sensitivity to competitive antagonists and agonists.

Mode of Antagonism. To determine whether synthesized 3-isoxazolols act as competitive antagonists, the GABA concentration−response relationships in the presence and absence of **6b** were examined in the ac variant. The GABA concentration−response curves made a parallel rightward shift with increasing **6b** concentration, indicating a competitive mechanism (Figure 5). The EC_{50} values of GABA in the presence of 30 and 100 μM **6b** were 27.2 and 55.6 μM, respectively. The potency of GABA was decreased 2.6- and 5.2-fold in the presence of 30 and 100 μM **6b**, respectively, whereas

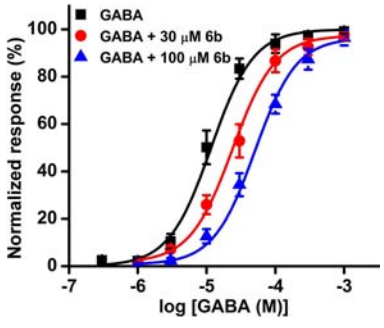

Figure 5. GABA concentration−response curves of housefly RDL_{ac} GABARs in the presence and absence of 30 and 100 μM **6b**. Responses were normalized relative to the maximum current induced by 1 mM GABA in each oocyte. Data represent means ± SEM (n = 4−6).

the efficacy of GABA remained unchanged. These results indicate that **6b** competes with GABA for the orthosteric site to stabilize the closed conformation of chloride channels.

Insecticidal Activity. Competitive antagonists stabilize the closed conformation of GABAR channels and should thus exert insecticidal effects when they act at insect GABARs. There is no information about the insecticidal action of competitive antagonists. We therefore investigated whether **6b**, which showed the highest antagonism, has intrinsic insecticidal activity by injection into adult female houseflies. As a result, **6b** proved to be insecticidal, with an LD_{50} value of 5.6 (4.9−6.3) nmol/fly (95% confidence interval in parentheses). The finding that **6b** shows insecticidal activity by definition is somewhat encouraging, although the activity was not prominent and was observed by injection but not topical application.

Molecular Interaction between Ligands and Housefly RDL GABAR. To understand the molecular mechanisms of the interaction between 3-isoxazolols and insect GABARs, GABA, muscimol, and the 3-biphenylyl analogue (**6b**) were docked into the orthosteric binding site of a housefly RDL_{ac} GABAR homology model constructed on the basis of the X-ray crystal structure of the human homopentameric β3 GABAR. The β3 subunit shares 38.7% amino acid identity with the RDL_{ac} subunit. The most likely binding poses were selected on the basis of the score and are shown in Figure 6. The orthosteric site of Cys-loop receptors, which is located in the extracellular interface of two adjacent subunits (Figure S2), is formed by loops A−C from the principal subunit and loops D−F from the complementary subunit.[24] Similarly, the orthosteric binding pocket of the constructed model is basically formed by Phe144, Val146, Glu202, Ser203, Phe204, Gly205, Ile245, Leu247, and Arg254 from the principal subunit and by Tyr88, Leu90, Tyr107, Arg109, and Met224 from the complementary subunit. The distance between two key residues, Glu202 and Arg109, is approximately 9.0 Å.

The docking simulation showed that the protonated amino groups of GABA and muscimol are located close to Glu202 of loop B and that they form an electrostatic interaction and hydrogen bonds with this residue (Figure 6A,B). Arg109 of loop D electrostatically interacts with the deprotonated carboxyl group of GABA and the deprotonated hydroxyl group (or the isoxazole ring) of muscimol. In addition, Arg109 serves as a hydrogen bond donor for the carboxylate of GABA and the hydroxyl oxygen or the nitrogen atom of muscimol. These important interactions were observed in the docking

DOI: 10.1021/acs.jafc.5b01843
J. Agric. Food Chem. 2015, 63, 6304−6312

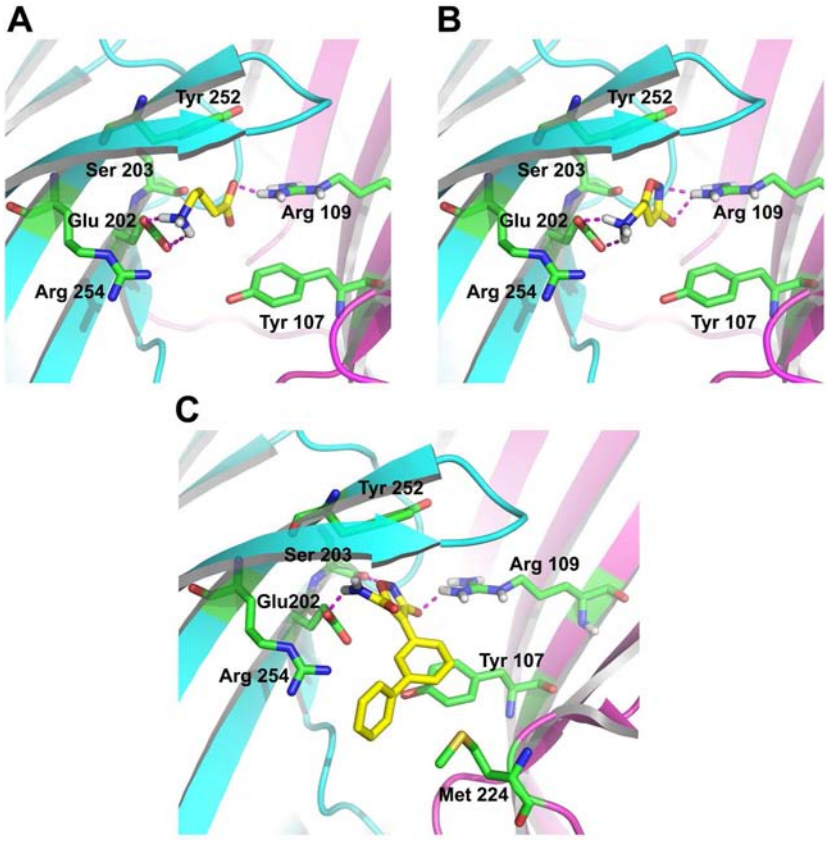

Figure 6. Simulation of the docking of GABA, muscimol, and **6b** into the orthosteric binding site of a housefly RDL_{ac} GABAR homology model: (A) docking of GABA into the orthosteric site; (B) docking of muscimol; (C) docking of **6b**. The crystal structure of the homopentameric human β3 GABAR (PDB 4COF) was used as a template to construct the model.

simulation results using another housefly RDL GABAR homology model in our previous studies and are apparently conserved in *Drosophila* RDL GABARs.[14,15,25−27] Tyr252 of loop C, which surrounds the protonated amino group of GABA and muscimol, may produce a cation−π interaction, as proposed for *Drosophila* RDL GABARs.[25−27] Similar orientations and interactions of GABA and muscimol in the binding site indicate that these two agonists interact with housefly RDL GABARs in an identical mode.

Docking of the 4-(3-biphenylyl) analogue (**6b**) to the homology model of the housefly RDL_{ac} GABAR predicts that the 5-carbamoyl-3-isoxazolol scaffold of **6b** lies between Glu202 (loop B) and Arg109 (loop D) in the same orientation as muscimol. Similar to the cases of GABA and muscimol, the side chain of Arg109 electrostatically interacts with the deprotonated hydroxyl group of **6b** and forms a hydrogen bond with the same group; the side chain of Glu202 functions as a hydrogen acceptor for the carbamoyl group of **6b**. Furthermore, the two amino acid residues, Arg254 of loop C and Tyr107 of loop D, surround the 3-biphenylyl group of **6b**. The present docking studies of **6b** predict that the 3-biphenylyl group points out of the binding site and may form a cation−π interaction with Arg254 and a $\pi-\pi$ interaction with Tyr107. The orientation of the 3-biphenylyl group is in contrast with that of the 4-substitution of thio-4-PIOL analogues in our previous study.[14] This difference may be due to the different templates used in the homology modeling. It has yet to be elucidated which orientation is feasible.

In conclusion, we synthesized a novel class of housefly competitive GABAR antagonists (**6b**−**6g**) by replacing the aminomethyl group of muscimol with a carbamoyl group and simultaneously introducing bicyclic aromatic groups at the 4-position. All of the analogues exhibited antagonism of the four splice variants of housefly GABARs, the most potent compound being 4-(3-biphenylyl)-5-carbamoyl-3-isoxazolol (**6b**). The potencies of **6b** in RDL_{ac} and RDL_{bc} GABARs were ∼3-fold greater than those in RDL_{ad} and RDL_{bd} GABARs, and this potency difference in these variants is similar to the potency difference of agonists. The identification of a novel series of competitive GABAR antagonists serves to widen the current scope for insecticidal chemicals competitively acting at the orthosteric sites beyond those of gabazine and thio-4-PIOL derivatives.

■ ASSOCIATED CONTENT

Supporting Information

Alignments of amino acid sequences encoded by exons 3a, 3b, 6c, and 6d of housefly *Rdl* (Figure S1); view of the orthosteric binding pocket in a housefly RDL_{ac} GABAR homology model (Figure S2). The Supporting Information is available free of charge on the ACS Publications website at DOI: 10.1021/acs.jafc.5b01843.

■ AUTHOR INFORMATION

Corresponding Author

*(Y.O.) E-mail: ozoe-y@life.shimane-u.ac.jp. Phone: +81-852-32-6573. Fax: +81-852-32-6573.

DOI: 10.1021/acs.jafc.5b01843
J. Agric. Food Chem. 2015, 63, 6304−6312

Funding

This work was supported in part by JSPS KAKENHI Grant 26292031.

Notes

The authors declare no competing financial interest.

■ ACKNOWLEDGMENTS

We thank Dr. I. Ikeda and K. Nomura (Faculty of Life and Environmental Science, Shimane University) for their useful advice and technical assistance.

■ ABBREVIATIONS USED

DMSO, dimethyl sulfoxide; EC_{50}, half-maximal effective concentration; GABA, γ-aminobutyric acid; GABAR, GABA receptor; IC_{50}, half-maximal inhibitory concentration; LD_{50}, median lethal dose; PCR, polymerase chain reaction; RDL, an insect GABAR subunit; *Rdl*, RDL-encoding gene; SOS, standard oocyte solution; TEVC, two-electrode voltage clamp; thio-4-PIOL, 5-(4-piperidyl)-3-isothiazolol

■ REFERENCES

(1) Purves, D.; Augustine, G. J.; Fitzpatrick, D.; Hall, W. C.; LaMantia, A.-S.; White, L. E. In *Neuroscience*, 5th ed.; Sinauer Associates: Sunderland, MA, USA, 2012; pp 25−140.

(2) Ozoe, Y. γ-Aminobutyrate- and glutamate-gated chloride channels as targets of insecticides. In *Advances in Insect Physiology*; Ephraim, C., Ed.; Academic Press: Burlington, MA, USA, 2013; Vol. 44, pp 211−286.

(3) Ozoe, Y.; Takeda, M.; Matsuda, K. γ-Aminobutyric acid receptors: a rationale for developing selective insect pest control chemicals. In *Biorational Control of Arthropod Pests*; Ishaaya, I., Horowitz, A. R., Eds.; Springer: Heidelberg, Germany, 2009; pp 131−162.

(4) Buckingham, S. D.; Sattelle, D. B. GABA receptors of insects. In *Insect Pharmacology: Channels, Receptors, Toxins and Enzymes*; Gilbert, L. I., Gill, S. S., Eds.; Academic Press: London, UK, 2010; pp 29−64.

(5) ffrench-Constant, R. H.; Rocheleau, T. A. *Drosophila* γ-aminobutyric acid receptor gene *Rdl* shows extensive alterntive splicing. *J. Neurochem.* **1993**, *60*, 2323−2326.

(6) Hosie, A. M.; Sattelle, D. B. Agonist pharmacology of two *Drosophila* GABA receptor splice variants. *Br. J. Pharmacol.* **1996**, *119*, 1577−1585.

(7) Hosie, A. M.; Buckingham, S. D.; Presnail, J. K.; Sattelle, D. B. Alternative splicing of a *Drosophila* GABA receptor subunit gene identifies determinants of agonist potency. *Neuroscience* **2001**, *102*, 709−714.

(8) Jones, A. K.; Buckingham, S. D.; Papadaki, M.; Yokota, M.; Sattelle, B. M.; Matsuda, K.; Sattelle, D. B. Splice-variant- and stage-specific RNA editing of the *Drosophila* GABA receptor modulates agonist potency. *J. Neurosci.* **2009**, *29*, 4287−4292.

(9) Ozoe, Y.; Asahi, M.; Ozoe, F.; Nakahira, K.; Mita, T. The antiparasitic isoxazoline A1443 is a potent blocker of insect ligand-gated chloride channels. *Biochem. Biophys. Res. Commun.* **2010**, *391*, 744−749.

(10) Lahm, G. P.; Cordova, D.; Barry, J. D.; Pahutski, T. F.; Smith, B. K.; Long, J. K.; Benner, E. A.; Holyoke, C. W.; Joraski, K.; Xu, M.; Schroeder, M. E.; Wagerle, T.; Mahaffey, M. J.; Smith, R. M.; Tong, M.-H. 4-Azolylphenyl isoxazoline insecticides acting at the GABA gated chloride channel. *Bioorg. Med. Chem. Lett.* **2013**, *23*, 3001−3006.

(11) Nakao, T.; Banba, S.; Nomura, M.; Hirase, K. Meta-diamide insecticides acting on distinct sites of RDL GABA receptor from those for conventional noncompetitive antagonists. *Insect Biochem. Mol. Biol.* **2013**, *43*, 366−375.

(12) Ozoe, Y.; Kita, T.; Ozoe, F.; Nakao, T.; Sato, K.; Hirase, K. Insecticidal 3-benzamido-*N*-phenylbenzamides specifically bind with high affinity to a novel allosteric site in housefly GABA receptors. *Pestic. Biochem. Physiol.* **2013**, *107*, 285−292.

(13) Casida, J. E. Golden age of RyR and GABA-R diamide and isoxazoline insecticides: common genesis, serendipity, surprises, selectivity, and safety. *Chem. Res. Toxicol.* **2015**, *28*, 560−566.

(14) Liu, G.; Furuta, K.; Nakajima, H.; Ozoe, F.; Ozoe, Y. Competitive antagonism of insect GABA receptors by 4-substituted 5-(4-piperidyl)-3-isothiazolols. *Bioorg. Med. Chem.* **2014**, *22*, 4637−4645.

(15) Rahman, M. M.; Liu, G.; Furuta, K.; Ozoe, F.; Ozoe, Y. Synthesis of 1,3-di- and 1,3,4-trisubstituted 1,6-dihydro-6-iminopyridazines as competitive antagonists of insect GABA receptors. *J. Pestic. Sci.* **2014**, *39*, 133−143.

(16) Rahman, M. M.; Akiyoshi, Y.; Furutani, S.; Matsuda, K.; Furuta, K.; Ikeda, I.; Ozoe, Y. Competitive antagonism of insect GABA receptors by iminopyridazine derivatives of GABA. *Bioorg. Med. Chem.* **2012**, *20*, 5957−5964.

(17) Frey, M.; Jäger, V. Synthesis of *N*-substituted muscimol derivatives including *N*-glycylmuscimol. *Synthesis* **1985**, *12*, 1100−1104.

(18) Riess, R.; Schön, M.; Laschat, S.; Jäger, V. Evaluation of protecting groups for 3-hydroxyisoxazoles − short access to 3-alkoxyisoxazole-5-carbaldehydes and 3-hydroxyisoxazole-5-carbaldehyde, the putative toxic metabolite of muscimol. *Eur. J. Org. Chem.* **1998**, *3*, 473−479.

(19) Krogsgaard-Larsen, P.; Christensen, S. B. Structural analogues of GABA. A new convenient synthesis of muscimol. *Acta Chem. Scand.* **1976**, *30*, 281−282.

(20) Eguchi, Y.; Ihara, M.; Ochi, E.; Shibata, Y.; Matsuda, K.; Fushiki, S.; Sugama, H.; Hamasaki, Y.; Niwa, H.; Wada, M.; Ozoe, F.; Ozoe, Y. Functional characterization of *Musca* glutamate- and GABA-gated chloride channels expressed independently and coexpressed in *Xenopus* oocytes. *Insect Mol. Biol.* **2006**, *15*, 773−783.

(21) Miller, P. S.; Aricescu, A. R. Crystal structure of a human $GABA_A$ receptor. *Nature* **2014**, *512*, 270−275.

(22) Wang, X. C.; Hu, Y.; Bonacorsi, S.; Hong, Y.; Burrell, R.; Yu, J. Q. Pd(II)-catalyzed C−H iodination using molecular I_2 as the sole oxidant. *J. Am. Chem. Soc.* **2013**, *135*, 10326−10329.

(23) Buckingham, S. D.; Biggin, P. C.; Sattelle, B. M.; Brown, L. A.; Sattelle, D. B. Insect GABA receptors: splicing, editing, and targeting by antiparasitics and insecticides. *Mol. Pharmacol.* **2005**, *68*, 942−951.

(24) Miller, P. S.; Smart, T. G. Binding, activation and modulation of Cys-loop receptors. *Trends Pharmacol. Sci.* **2010**, *31*, 161−174.

(25) Ashby, J. A.; McGonigle, I. V.; Price, K. L.; Cohen, N.; Comitani, F.; Dougherty, D. A.; Molteni, C.; Lummis, S. C. R. GABA binding to an insect GABA receptor: a molecular dynamics and mutagenesis study. *Biophys. J.* **2012**, *103*, 2071−2081.

(26) Comitani, F.; Cohen, N.; Ashby, J.; Botten, D.; Lummis, S. C. R.; Molteni, C. Insights into the binding of GABA to the insect RDL receptor from atomistic simulations: a comparison of models. *J. Comput.-Aided Mol. Des.* **2014**, *28*, 35−48.

(27) McGonigle, I.; Lummis, S. C. R. Molecular characterization of agonists that bind to an insect GABA receptor. *Biochemistry* **2010**, *49*, 2897−2902.

DOI: 10.1021/acs.jafc.5b01843
J. Agric. Food Chem. 2015, 63, 6304−6312

Table 1. Characteristics of the Studied 2-Ketones and Eight Flavor Molecules[a]

compound	M (g/mol)	ρ(g/mL)	c_w (g/L)	P^0 (Pa)	supplier	c (mg/m^3)
validation: 2-ketones						
2-butanone	72.11	0.806	76	1.3×10^4	Acros	8.06
2-pentanone	86.13	0.808	21	5.3×10^3	Sigma-Aldrich	8.08
2-hexanone	100.16	0.811	7.8	1.8×10^3	Sigma-Aldrich	8.11
2-heptanone	114.19	0.819	2.2	655	Alfa Aesar	8.19
2-octanone	128.21	0.820	0.88	249	Fluka	8.20
2-nonanone	142.24	0.823	0.17	86	SAFC	8.23
citrus molecules						
ethyl acetate	88.12	0.901	30	1.3×10^4	Firmenich	9.01
trans-2-hexenal	98.16	0.847	5.3	629	Firmenich	8.47
ethyl butanoate	116.16	0.880	2.8	1.9×10^3	Firmenich	8.80
octanal	128.24	0.823	0.39	199	Firmenich	8.23
1-octanol	130.26	0.826	0.81	13	Firmenich	8.26
citral	152.26	0.891	0.085	12	Firmenich	8.91
citronellal	154.28	0.855	0.039	34	Firmenich	8.55
citronellol	156.30	0.858	0.11	2.3	Firmenich	8.58

[a]The density, ρ, solubility, c_w, and vapor pressure, P^0, are given at 25 °C. P^0 and c_w values of the citrus flavor molecules are results from, respectively, the MPBWIN and the WSKOW models of EPI Suite at 25 °C.[21]

Henry's constants for more complex flavor molecules and their temperature dependence.

We have developed a methodology to rapidly measure air−water Henry's constants as a function of temperature. It is suitable for a wide range of H values and is based on equilibrium static headspace analysis (ESHA). A solution of volatiles is equilibrated with air in a closed vessel, and then a sample of the air is led through a deactivated fused silica capillary and heated to 130 °C (to avoid condensation issues) into the ionization source (atmospheric pressure chemical ionization) of a quadrupole mass spectrometer (APCI-MS),[15] which is referred to as an MS-Nose. It has a detection threshold of >∼0.01 mg/m^3 of volatiles in the headspace.[15] Note that a proton transfer reaction mass spectrometer (PTR-MS) could also be used.[16] The mass spectrometer is calibrated with a liquid reference. As discussed previously,[17] liquid calibration can be a source of uncertainty, but correct practice gives data comparable to those obtained from the internally calibrated phase ratio variation (PRV) method.[17,18] With the PRV method, the depletion from the liquid to the gas phase is explicitly used for different liquid−gas ratios, to calculate the partition coefficient. However, as elegant as this internal calibration is, the latter is suited for only a limited number of compounds and temperatures, as significant partitioning into the air, that is, H > ∼0.1, is required for accurate results.

To demonstrate consistency with existing methods, we measure Henry's constants for a series of 2-ketones, for which reliable values are known.[3,19,20] We then apply the method to a set of volatiles regularly used to create citrus flavors (herein referred to as citrus flavor molecules).

MATERIALS AND METHODS

Chemicals. The 2-ketones and flavor molecules used in this study are 2-butanone (CAS Registry No. 78-93-3 Acros), 2-pentanone (CAS Registry No. 107-87-9, Sigma-Aldrich), 2-hexanone (CAS Registry No. 591-78-6, Sigma-Aldrich), 2-heptanone (CAS Registry No. 110-43-0, Alfa Aesar), 2-octanone (CAS Registry No. 111-13-7, Fluka), 2-nonanone (CAS Registry No. 821-55-6, SAFC), and cyclopentane (CAS Registry No. 287-92-3, Sigma-Aldrich). Ethyl acetate (CAS Registry No. 141-78-6), *trans*-2-hexenal (CAS Registry No. 6278-26-3), ethyl butanoate (CAS Registry No. 105-54-4), octanal (CAS Registry No. 124-13-0), 1-octanol (CAS Registry No. 111-87-5), citral (CAS Registry No. 5392-40-5), citronellal (CAS Registry No. 2385-77-5), and citronellol (CAS Registry No. 106-22-9) were all obtained internally at Firmenich S.A. All of the molecules and their charachteristics are listed in Table 1. Values for the solubility, c_w, vapor pressure, P^0, and Henry's constant, H, were estimated using, respectively, the MPBWIN (v1.42), WSKOW (v1.41), and HENRYWIN (v3.10) model of the Estimation Program Interface (EPI) Suite.[21]

The molecules were first dissolved in dimethyl sulfoxide (DMSO; CAS Registry No. 67-68-5, Sigma-Aldrich) and then transferred to water. This two-step procedure accelerates dissolution and improves reliability. To determine if the presence of DMSO in any way perturbed the baseline of the molecules being quantified, a DMSO blank was injected into the MS prior to a standard injection. It was observed that DMSO blank did not affect the MS signal. The final concentrations in the aqueous phase, c, are listed in Table 1. They were always <0.1 ppm to ensure that the volatile could be considered being at infinite dilution.

Instrumentation. The MS-NOSE (Micromass ZMD, Manchester, UK; APCI-MS (quadrupole) was operated under the following conditions: corona voltage, 3.8 kV; cone voltage, 14 V; source temperature, 105 °C; heated sample transfer line (deactivated fused silica SGE Analytical) temperature, 130 °C; heated interface gas temperature, 105 °C; and sampling flow rate, 25 mL/min. The signal used for calibration was produced by direct injection of a continuous flow (1 μL/min) of the volatile dissolved in cyclopentane into a controlled air flow (10 L/min). A correction was made for the signal of pure cyclopentane by subtracting the signal produced by the pure cyclopentane from the standard signal.

Headspace Measurements. Figure 1 shows the setup. An aqueous solution (100 mL) of the flavor molecule was transferred to a 250 mL Pyrex bottle containing a Teflon-coated magnetic stirrer. Room temperature measurements were made in a temperature-controlled laboratory (T = 21.0 ± 0.1 °C). For measurements at 35 and 50 °C, the bottles were heated by a heat jacket (Hillesheim, Waghäusel Germany). The bottle was closed with a Teflon cap equipped with a small electric fan (2.5 × 2.5 × 0.5 cm, Conrad.CH Part MFB25B-05) hanging in the headspace. The fan and the magnetic stirrer (300 rpm) ensured good mixing of both phases. Stable signals were obtained after about 15 min of continuous mixing. Therefore, the closed system was allowed to equilibrate for 20 min, and then the volatiles in the headspace were sampled via the heated transfer line (130 °C to avoid condensation issues) of the MS-NOSE for 1 min at a flow rate of 25 mL/min. The signals were corrected by subtracting the signal from the headspace of distilled water, to allow for the effects of humidity and background signal from the laboratory air. For each

DOI: 10.1021/acs.jafc.5b01517
J. Agric. Food Chem. 2015, 63, 6313−6318

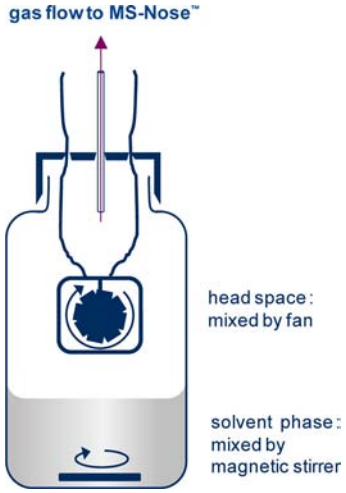

Figure 1. Schematic setup of the static headspace measurement.

stock solution of flavor in DMSO and at each temperature, the results of triplicate measurements were averaged.

RESULTS

Validation with 2-Ketones. To validate the use of the MS-NOSE to determine Henry's constants of mixtures of volatiles,

Table 2. Henry's Constants for a Series of 2-Ketones at 21 °C Measured as One Mixture[a]

	$H = c_{hs}/c$ at 294 K		H at 298 K, EPI Suite	
compound	literature	this work	bond	group
2-butanone	0.0018	0.0018 ± 0.0001	0.0027	0.0023
2-pentanone	0.0026	0.0027 ± 0.0001	0.0036	0.0032
2-hexanone	0.0030	0.0030 ± 0.0001	0.0047	0.0046
2-heptanone	0.0040	0.0040 ± 0.0001	0.0063	0.0065
2-octanone	0.0052	0.0058 ± 0.0001	0.0084	0.0091
2-nonanone	0.0065	0.0062 ± 0.0001	0.011	0.013

[a]The literature values are interpolated from Figure 8 in Brachet and Chaintreau,[3] and H was calculated from the HENRYWIN model of EPI Suite using the bond and the group estimation method at 25 °C.

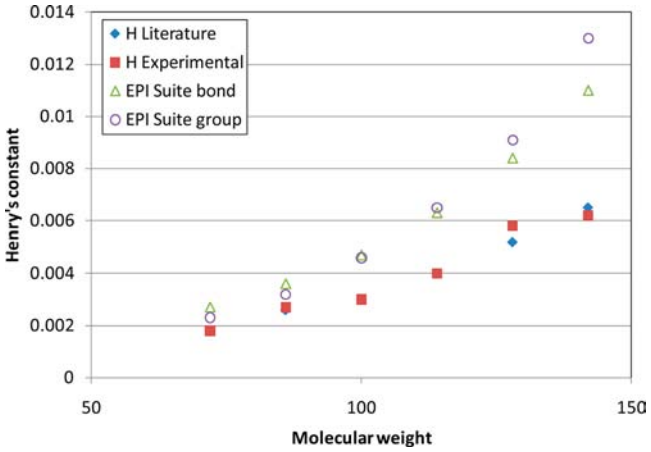

Figure 2. Henry's constants at 21 °C for a series of 2-ketones as a function of molecular weight measured with the MS-NOSE, reported in the literature,[3] and computed at 25 °C with the HENRYWIN model of EPI Suite using the bond and group estimation methods.[21]

Table 3. Henry's Constants for a Set of Citrus Flavor Molecules at 294 K Measured Individually, Including Values Reported in the Literature,[11,17,19] from the HENRYWINTM Model of EPI Suite Using the Bond and Group Estimation Methods for T = 298 K[21]

	literature		$H \times 10^3$, EPI Suite		this work
compound	$H \times 10^3$	T (K)	bond	group	$H \times 10^3$
citral			15	1.8	0.99 ± 0.07
citronellol			2.3	0.87	0.69 ± 0.03
1-octanol	1.0	298[14]	1.3	1.6	1.19 ± 0.21
trans-2-hexenal	3.0	298[14]	4.0	1.9	1.66 ± 0.17
ethyl acetate	7.0	298[14]	9.5	6.5	5.8 ± 0.1
ethyl butanoate	15	293[12]	17	13	10.3 ± 0.5
	15	293[14]			
octanal	21	298[14]	15	20	13.8 ± 0.4
citronellal			28	11	11.9 ± 0.7

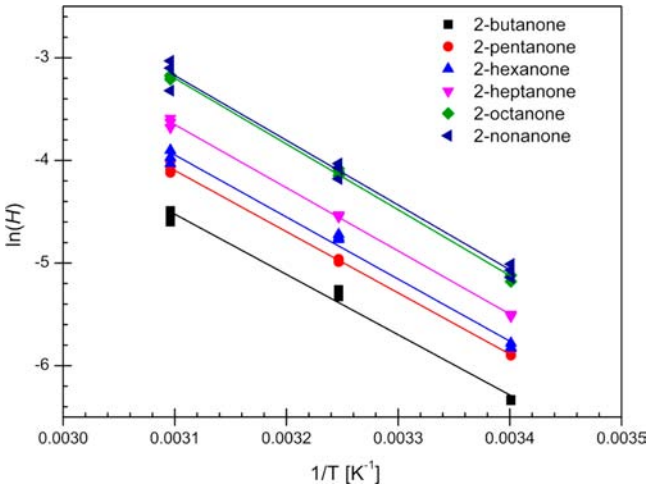

Figure 3. Measured Henry's constants at different temperatures for a series of 2-ketones, including the data from Table 2.

a series of 2-ketones was measured at room temperature using the above method and the values compared to those obtained in the literature.[3] The measured signal of the MS-NOSE, I_s, was translated into the concentration of volatile in the headspace expressed in milligrams per cubic meter, c_{hs}, using the calibration constant, I_{ref}, measured as described above. Notably for volatiles that strongly partition into the headspace, the concentration in the aqueous phase, c, will be significantly lowered by the partitioning. This effect can be taken into account by a straightforward correction to calculate the Henry's constant:

$$H = \frac{c_{hs}}{c - c_{hs}\frac{V_{hs}}{V_{aq}}} \quad (4)$$

c is the added concentration of volatile in the aqueous phase, V_{hs} the volume of the headspace, and V_{aq} the volume of the aqueous phase. For our setup V_{hs}/V_{aq} was 2.2.

Table 2 lists Henry's constants of the 2-ketones, measured as one component at room temperature, including the standard deviation over three repeated measurements. For comparison, interpolated data from Brachet and Chaintreau at 21 °C are included[3] as well as calculated values at 25 °C using EPI Suite.[21] The same data are plotted in Figure 2 as a function of

DOI: 10.1021/acs.jafc.5b01517
J. Agric. Food Chem. 2015, 63, 6313−6318

Table 4. Enthalpies and Entropies of Solution Measured in This Work by Regression Analysis of Figure 3 Compared to Literature Values

	ΔH_{sol} (kJ/mol)		ΔS_{sol} (J/mol K)		
compound	this work	literature[a]	this work	literature[a]	ref
2-butanone	−48 ± 2	−43	−114 ± 5	−92	3, 20,
		−41		−143	22[b]
2-pentanone	−49 ± 1	−48	−120 ± 2	−115	3, 20,
		−46		−161	22[b]
2-hexanone	−50 ± 2	−52	−123 ± 6	−129	3, 20,
		−49		−174	22[b]
2-heptanone	−51 ± 1	−55	−128 ± 1	−141	3, 20,
		−52		−187	22[b]
2-octanone	−53 ± 1	−58	−138 ± 2	−155	3, 20,
		−55		−202	22[b]
2-nonanone	−52 ± 1	−61	−136 ± 2	−166	3, 20,
		−63		−236	22[b]
ethyl acetate	−42 ± 2	−41	−100 ± 5	na[c]	13, 19
		−41			
octanal	−58 ± 6	−48.8	−161 ± 18	na	13
1-octanol	−58 ± 1	−61	−143 ± 5	na	13, 19
		−74			

[a] ΔH_{sol} and ΔS_{sol} obtained from the data in Figure 8 of Brachet and Chaintreau.[3] [b] ΔH_s (g → aq) and ΔS_s (g → aq) as reported in Table 14 of Abraham.[22] [c] na, data not available.

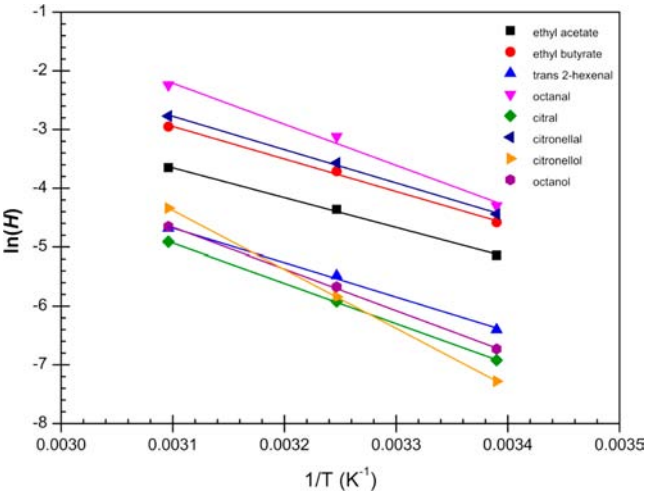

Figure 4. Measured Henry's constants at different temperatures for a set of citrus flavor molecules.

Table 5. Experimental Enthalpies and Entropies of Solution of a Set of Citrus Flavor Molecules Determined from Figure 4

compound	ΔH_{sol} (kJ/mol)	ΔS_{sol} (J/mol K)
ethyl acetate	−42 ± 2	−100 ± 5
trans-2-hexenal	−48 ± 3	111 ± 8
ethyl butyrate	−46 ± 2	118 ± 8
octanal	−58 ± 6	−161 ± 18
1-octanol	−58 ± 1	−143 ± 5
citral	−57 ± 1	−135 ± 2
citronellal	−47 ± 2	123 ± 6
citronellol	−83 ± 1	−221 ± 1

the molecular weight of the 2-ketones, which shows that in all cases the general trends are similar; however, the calculated values are offset compared to the measured values. In summary, our methodology yields Henry's constants with a standard

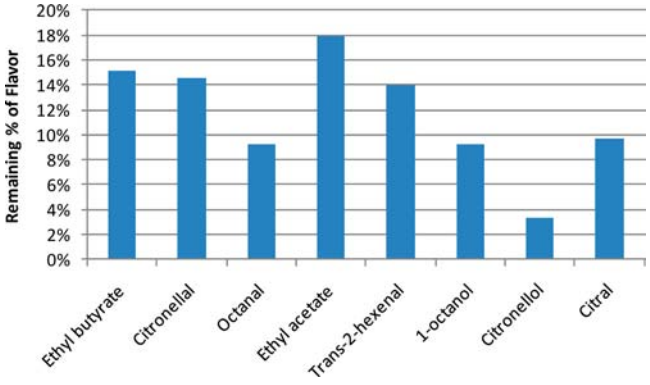

Figure 5. Relative flavor profile at temperature of consumption (50 °C), as compared to preparation at 90 °C. Concentration of headspace at 90 °C is set at 100%.

deviation of ∼10% based on replicates and absolute values that are in good agreement with values reported in the literature.[3] It also shows the need for experimental values as modeled values (EPI Suite) tend to overestimate the Henry's constants for the ketones at higher molecular weights, by up to 100% as shown in Figure 2.

Citrus Flavor Molecules. A set of eight molecules typical of a citrus flavor were selected, including the well-studied molecules ethyl acetate, ethyl butanoate, octanal, and 1-octanol and the less studied *trans*-2-hexenal, citral, citronellal, and citronellol. The molecules are chosen to cover a wide range of solubilities and vapor pressures. The flavor molecules were measured individually. The results are listed in Table 3, including Henry's constants from the literature and estimates calculated using the HENRYWIN model of EPI Suite using the bond and group estimation methods.[21]

In line with our findings for the 2-ketones, we observed a standard deviation in the measured Henry's constants of about 10% within triplicate measurements of the same stock solution of a specific flavor molecule. Our results are in agreement with

DOI: 10.1021/acs.jafc.5b01517
J. Agric. Food Chem. 2015, 63, 6313−6318

reported experimental values for the esters,[3] (Table 2) and octanal and 1-octanol.[19] For these molecules, values from EPI Suite tend to overestimate the experimental values with deviations up to 70%. For the other four molecules, each containing one or more unsaturated bond(s), EPI Suite values overestimate the experimental ones by up to 80% using the group method and by up to an order of magnitude using the bond method. This shows that modeling can give good estimations for Henry's constants (100% deviation for group contribution estimation methods is not uncommon), if an adequate model is used. Nevertheless, for practical purposes there is a strong need to have more reliable values.

Temperature Dependence. To allow the use of measured Henry's constants for the modeling of food processing and consumption, we extended the method to higher temperatures (35 and 50 °C). The experimental setup could easily be heated first in a water bath and then transferred to a heat jacket, without affecting the stirring of the aqueous phase and the headspace. We first tested the method on 2-ketones, for which the results are shown in Figure 3. Because Henry's constants characterize an equilibrium partitioning between two phases, their temperature dependence can be described by van't Hoff's equation:

$$\ln(H) = -\frac{\Delta S_{sol}}{R} + \frac{\Delta H_{sol}}{RT} \quad (5)$$

Here ΔS_{sol} and ΔH_{sol} are respectively the entropy and the enthalpy of solution. The extracted values are listed in Table 4 and compared to literature values deduced from Henry's constants,[3] and measured directly with microcalorimetry.[20,22] For the citrus flavor molecules, ΔH_{sol} values were available for ethyl acetate, octanal, and 1-octanol. The reproducibility of ΔH_{sol} over independent repeated measurements is estimated to be around 10% ΔH_{sol}, whereas ΔS_{sol} shows a larger variability of ≥30% ΔS_{sol}. With this in mind, our results are in excellent agreement with values reported in the literature.

We applied the validated methodology to the citrus flavor molecules. It is clear from the results in Figure 4 that not all molecules have the same temperature dependence, hence the need to determine experimentally the correct values. Table 5 shows the experimental entropies and enthalpies of solution. Within this set of flavor molecules, we found slight differences in ΔH_{sol}, which are directly related to the partitioning of the flavor molecules at higher temperatures. To put these results into context, we take the set of molecules as a hypothetical citrus flavor for fruit tea prepared by a flavorist at room temperature. If one would prepare tea with this flavor, the resulting profile that one would smell while brewing the tea would be very different as the relative presence of the flavor molecules into the humid headspace can vary up to 3 orders of magnitude. This highlights the difficulties in creating flavors for hot and cold beverages and food products, as well as the large differences in the effect of heat treatment on the different volatiles. The bar chart in Figure 5 demonstrates the well-known experience that the taste of fruit tea can be quite disappointing after the attractive smell: the tea cools quickly in the mouth to about 50 °C, reducing the relative amount of volatiles in the headspace by up to an order of magnitude, as well as distorting the flavor profile. This calculation clearly demonstrates that the knowledge of temperature-dependent Henry's constants is crucial for the creation of flavors for hot and cold products. As shown, modeling (using, e.g., EPI Suite) is not accurate enough to give good predictions of the Henry's constants, so the technology described here will be very useful to obtain reproducible and reliable Henry's constants.

AUTHOR INFORMATION

Corresponding Author

*(S.A.) E-mail: Shane.Avison@Firmenich.com. Phone: +41 22 780 21 86. Fax: +41 22 780 27 35.

Present Address

#(K.v.G.) Firmenich S.A., Route de La Plaine 125, CH-1283 La Plaine, Switzerland.

Funding

The BNF Programme Berne is warmly acknowledged for support of K.v.G. and M.P. This research is part of a project funded by the CTI, Switzerland, Grant 14936.1.

Notes

The authors declare no competing financial interest.

ABBREVIATIONS USED

APCI-MS, atmospheric pressure chemical ionization mass spectrometry; PTR-MS, proton transfer reaction mass spectrometry; ESHA, equilibrium static headspace analysis

REFERENCES

(1) Overbosch, P.; Afterof, W. G. M.; Haring, P. G. M. Flavor release in the mouth. *Food Rev. Int.* **1991**, *7* (2), 137−184.

(2) Martuscelli, M.; Savary, G.; Pittia, P.; Cayot, N. Vapour partition of aroma compounds in strawberry flavoured custard cream and effect of fat content. *Food Chem.* **2008**, *108* (4), 1200−1207.

(3) Brachet, A.; Chaintreau, A. Determination of air-to-water partition coefficients using automated multiple headspace extractions. *Anal. Chem.* **2005**, *77* (10), 3045−3052.

(4) Nielsen, F.; Olsen, E.; Fredenslund, A. Henry's law constants and infinite dilution activity coefficients for volatile organic compounds in water by a validated batch air stripping method. *Environ. Sci. Technol.* **1994**, *28* (12), 2133−2138.

(5) Straver, E. J. M.; De Loos, T. W. Determination of Henry's law constants and activity coefficients at infinite dilution of flavor compounds in water at 298 K with a gas-chromatographic method. *J. Chem. Eng. Data* **2005**, *50* (4), 1171−1176.

(6) Wieland, F.; Gloess, A. N.; Yeretzian, C. *Measuring Partition Coefficients of VOCs and their Temperature Dependence by Dynamic Stripping and Proton-Transfer Reaction Time-of-Flight Mass Spectrometry (PTR-ToF-MS)*, 5th International PTR-MS Conference, Austria, 2011.

(7) Pollien, P.; Jordan, A.; Lindinger, W.; Yeretzian, C. Liquid-Air Partitioning of Volatile Compounds in Coffee: Dynamic Measurements using Proton-Transfer-Reaction Mass Spectrometry. *Int. J. Mass Spectrom.* **2003**, *228*, 69−80.

(8) Pollien, P.; Lindinger, C.; Glöss, A. N.; Yeretzian, C. *Measuring Partition Coefficients of VOCs Using a Dynamic, PTR-MS-Coupled Method*, 4th International PTR-MS Conference, Austria, 2009; pp 221−226.

(9) Pollien, P.; Yeretzian, C. *Liquid-Air Partition Coefficients of Coffee Flavour Compounds: A Novel Approach Using Proton-Transfer-Reaction Mass-Spectrometry*, 19éme Colloque Scientifique International, Italy, 2002.

(10) Karl, T.; Yeretzian, C.; Jordan, A.; Lindinger, W. Dynamic measurements ofpartition coefficients using proton-transfer-reaction mass spectrometry (PTR-MS). *Int. J. Mass Spectrom.* **2003**, *223-224*, 383−395.

(11) Copolovici, L.; Niinemets, U. Salting-in and salting-out effects of ionic and neutral osmotica on limonene and linalool Henry's law constants and octanol/water partition coefficients. *Chemosphere* **2007**, *69* (4), 621−629.

(12) Hwang, I. C.; Kwak, H. Y.; Park, S. J. Determination and prediction of K_{ow} and dimensionless Henry's constant (H) for 6 ether

DOI: 10.1021/acs.jafc.5b01517
J. Agric. Food Chem. 2015, 63, 6313−6318

compounds at several temperatures. *J. Ind. Eng. Chem.* **2010**, *16* (4), 629−633.
(13) Kühne, R.; Ebert, R. U.; Schüürmann, G. Prediction of the temperature dependency of Henry's law constant from chemical structure. *Environ. Sci. Technol.* **2005**, *39* (17), 6705−6711.
(14) Hilal, S. H.; Ayyampalayam, S. N.; Carreira, L. A. Air−liquid partition coefficient for a diverse set of organic compounds: Henry's law constant in water and hexadecane. *Environ. Sci. Technol.* **2008**, *42* (24), 9231−9236.
(15) Taylor, A. J.; Linforth, R. S. T. Direct mass spectrometry of complex volatile and non-volatile flavour mixtures. *Int. J. Mass Spectrom.* **2003**, *223−224*, 179−191.
(16) Avison, S. J. Real-Time Flavor Analysis: Optimization of a Proton-Transfer-Mass Spectrometer and Comparison with an Atmospheric Pressure Chemical Ionization Mass Spectrometer with an MS-Nose Interface. *J. Agric. Food Chem.* **2013**, *61* (9), 2070−2076.
(17) Tromelin, A.; Ayed, C.; Lubbers, S.; Pagès-Hélary, S.; Andriot, I.; Guichard, E. Proposed alternative phase ratio variation method for the calculation of liquid-vapour partition coefficients of volatiles. *J. Chromatogr. A* **2012**, *1263*, 158−168.
(18) Ettre, L. S.; Welter, C.; Kolb, B. Determination of gas-liquid partition coefficients by automatic equilibrium headspace-gas chromatography utilizing the phase ratio variation method. *Chromatographia* **1993**, *35* (1−2), 73−84.
(19) Abraham, M. H.; Whiting, G. S.; Fuchs, R.; Chambers, E. J. Thermodynamics of solute transfer from water to hexadecane. *J. Chem. Soc., Perkin Trans. 2* **1990**, *2*, 291−300.
(20) Gatta, G. D.; Stradella, L.; Venturello, P. Enthalpies of solvation in cyclohexane and in water for homologous aliphatic ketones and esters. *J. Solution Chem.* **1981**, *10* (3), 209−220.
(21) *Estimation Programs Interface Suite for Microsoft® Windows, v 4.11*; U.S. Environmental Protection Agency: Washington, DC, USA, 2012.
(22) Abraham, M. H. Thermodynamics of solution of homologous series of solutes in water. *J. Chem. Soc., Faraday Trans. 1* **1984**, *80* (1), 153−181.

DOI: 10.1021/acs.jafc.5b01517
J. Agric. Food Chem. 2015, 63, 6313−6318

Table 1. Calculated $TEAC_{calcd}$ and Experimental $TEAC_{exptl}$ Values Obtained for the Studied Samples by EPR Spectroscopy[a]

no.	sample	V (mL)	%I	I_{100}	$TEAC_{calcd}$ (μmol TE/100 mL)	$TEAC_{exptl}$ (μmol TE/100 mL)	relative error (%)
S1	lemon balm 1	0.002	8.22	638596.26	646.6	688	6.4
S2	lemon balm 1′	0.014	97.1	680166.58	688.7	688	0.1
S3	lemon balm 2	0.002	14.1	697610.64	706.3	738	4.5
S4	lemon balm 2′	0.012	86.1	683262.10	691.8	738	6.7
S5	heartsease 1	0.120	85.0	64917.08	65.7	66	0.4
S6	heartsease 1′	0.140	95.1	64932.30	65.7	66	0.4
S7	heartsease 2	0.080	69.6	69461.10	70.3	64	8.9
S8	heartsease 2′	0.120	82.7	61563.65	62.3	63	2.7
S9	menthe 1	0.015	25.8	177667.15	179.9	177	1.6
S10	menthe 1′	0.0525	94.0	178924.16	181.1	177	2.3
S11	menthe 2	0.0225	47.6	182095.76	184.4	172	6.7
S12	menthe 2′	0.045	80.2	170238.13	172.4	172	0.2
S13	horsetail 1	0.025	50.0	170440.20	172.6	156	9.6
S14	horsetail 1′	0.040	73.3	169399.4	171.5	156	9.0
S15	horsetail 2	0.015	33.9	212671.4	215.3	186	13.6
S16	horsetail 2′	0.040	72.3	165871.96	167.9	186	10.7
S17	nettle 1	0.040	44.7	77608.82	78.6	75	4.5
S18	nettle 1′	0.060	59.9	73743.99	74.6	75	0.5
S19	nettle 2	0.030	40.3	103106.19	104.4	89	14.7
S20	nettle 2′	0.100	97.2	95252.86	96.4	89	7.7
S21	chamomile 1	0.040	46.6	82944.04	84.0	86	2.4
S22	chamomile 1′	0.070	71.9	87678.43	88.8	86	3.1
S23	chamomile 2	0.060	63.8	83641.46	84.7	91	7.5
S24	chamomile 2′	0.080	76.4	84040.21	85.1	91	6.9
S25	eyebright 1	0.008	76.0	855266.69	866.0	1007	16.3
S26	eyebright 1′	0.01	89.4	844233.56	854.8	1007	17.8
S27	eyebright 2	0.008	74.0	830029.33	840.4	917	9.1
S28	eyebright 2′	0.012	96.8	783472.58	793.3	917	15.6
S29	hypericum 1	0.006	59.7	844269.16	854.8	823	3.7
S30	hypericum 1′	0.009	78.8	802565.39	812.6	823	1.3
S31	hypericum 2	0.003	27.4	755117.08	764.6	746	2.4
S32	hypericum 2′	0.007	59.9	743393.45	752.7	746	0.9
S33	fennel 1	0.350	87.9	19028.01	19.3	23	19.5
S34	fennel 1′	0.400	96.3	19102.52	19.3	23	19.0
S35	fennel 2	0.350	90.2	20443.73	20.7	21	1.5
S36	fennel 2′	0.400	94.6	18756.50	19.0	21	10.7
S37	ground coffee a1	0.007	71.2	892645.69	903.8	963	6.5
S38	ground coffee a1′	0.008	81.0	919585.92	931.1	963	3.4
S39	ground coffee a2	0.003	35.9	891823.22	903.0	919	1.8
S40	ground coffee a2′	0.004	44.4	877871.08	888.9	919	3.4
S41	ground coffee b1	0.004	48.0	938364.31	950.1	1058	11.3
S42	ground coffee b1′	0.007	69.8	873475.20	884.4	1058	19.6
S43	ground coffee b2′	0.005	52.9	869463.2	880.4	915	3.9
S44	ground coffee b2′	0.008	73.9	827889.0	838.3	915	9.1
S45	ground coffee c1	0.007	83.9	1077659.5	1091.2	1239	13.5
S46	ground coffee c1′	0.008	93.5	1088833.2	1102.5	1239	12.4
S47	ground coffee c2	0.006	76.7	1107222.8	1121.1	1240	10.6
S48	ground coffee c2′	0.007	85.9	1106820.7	1120.7	1240	10.6
S49	instant coffee a1	0.005	47.9	782747.1	792.6	830	4.7
S50	instant coffee a1′	0.007	65.2	811268.02	821.4	830	1.0
S51	instant coffee a2	0.006	65.1	923779.7	935.4	948	1.3
S52	instant coffee a2′	0.008	79.0	893824.31	905.0	948	4.8
S53	instant coffee b1	0.004	70.1	1375626.50	1392.9	1239	11.0
S54	instant coffee b1′	0.007	96.6	1274621.34	1290.6	1239	4.0
S55	instant coffee b2	0.004	70.5	1385570.666	1402.9	1283	8.5
S56	instant coffee b2′	0.007	96.6	1274621.342	1290.6	1283	0.6
S57	instant decaffeinated coffee a1	0.0015	69.1	2317997.892	2347.1	2147	8.5
S58	instant decaffeinated coffee a1′	0.0025	78.0	2134273.302	2161.1	2147	0.6
S59	instant decaffeinated coffee a2	0.0025	77.2	2108618.061	2135.1	2073	2.9
S60	instant decaffeinated coffee a2′	0.0035	83.8	1871337.538	1984.9	2073	9.4

DOI: 10.1021/acs.jafc.5b01478
J. Agric. Food Chem. 2015, 63, 6319−6324

Table 1. continued

no.	sample	V (mL)	%I	I_{100}	$TEAC_{calcd}$ (μmol TE/100 mL)	$TEAC_{exptl}$ (μmol TE/100 mL)	relative error (%)
S61	instant decaffeinated coffee b1	0.001	18.1	1246402.553	1262	1496	18.5
S62	instant decaffeinated coffee b1′	0.0025	53.2	1377434.707	1394.7	1496	7.3
S63	instant decaffeinated coffee b2	0.001	31.5	1400887.636	1418.5	1492	5.2
S64	instant decaffeinated coffee b2′	0.004	69.9	1371595.897	1388.8	1492	7.4
S65	espresso coffee a1	0.007	44.3	562630.0452	569.7	649	14
S66	espresso coffee a1′	0.013	87.1	642252.5487	650.3	649	0.2
S67	espresso coffee a2	0.011	78.1	661043.0	669.3	690	3.1
S68	espresso coffee a2′	0.012	87.1	692086.3584	700.8	690	1.5
S69	espresso coffee b1	0.014	64.4	422755.2747	428	458.1	7.0
S70	espresso coffee b1′	0.018	80.9	432031.9939	437.4	458.1	4.7
S71	espresso coffee b2	0.014	76.9	517972.1808	524.5	461.4	12
S72	espresso coffee b2′	0.019	89.8	464136.8967	469.9	461.4	1.8
S73	black currant nectar 1	0.014	66.8	440522.7068	446	436.4	2.2
S74	black currant nectar 1′	0.02	85.6	417322.0496	422.5	436.4	3.3
S75	black currant nectar 2	0.008	57.6	635511.3281	643.5	686.6	6.7
S76	black currant nectar 2′	0.01	78.0	720621.496	729.6	686.6	5.9
S77	orange juice 1	0.01	81.2	754783.6141	764.2	765.4	0.2
S78	orange juice 1′	0.0105	82.6	736282.0769	745.5	765.4	2.7
S79	orange juice 2	0.006	52.8	749176.354	758.6	727.5	4.1
S80	orange juice 2′	0.0105	86.7	779067.9429	788.8	727.5	7.8

[a]Abbreviations: %I, inhibition (%) of the EPR signal of the DPPH free radical; I_{100}, value calculated from the equation describing the relationship between %I and V corresponding to a 100 mL sample; $TEAC_{calcd}$, Trolox equivalent antioxidant capacity calculated by model; $TEAC_{exptl}$, Trolox equivalent antioxidant capacity determined by EPR spectroscopy; a,b,c, various manufacturers.

Such studies are very time-consuming and costly. To reduce the cost and time of measurement, attempts have been made to determine the antioxidant capacity on the basis of empirical or semiempirical mathematical models.[27] This new method allows researchers to reduce the time and costs associated with determining the TEAC value more than five times. In accordance with the above, the goal of this study was to develop and assess an empirical model allowing for an estimation of total antioxidant capacity, along with conversion into Trolox equivalents, among others, depending on the standard curve utilized, and using EPR spectroscopy and DPPH as the free radical standard for a variety of food products.

MATERIALS AND METHODS

Chemicals and Samples. DPPH (Sigma-Aldrich, Poznań, Poland) was used as the source of free radicals. To quantify the antioxidant capacity of the tinctures, Trolox (Acros Organics, Geel, Belgium) was used. All other chemicals and solvents were of analytical grade and used without further purification.

The model was constructed on the basis of the antioxidant capacity, determined by EPR spectroscopy, for a wide range of food products available on the market and in pharmacies with varied antioxidant capacity (substances with both strong and weak antioxidant properties): tea, wine, juice, and herbs.

The study was performed on 20 samples of white wines and 40 red wine samples measured immediately after opening. The following were tested: sweet wines (10 samples), semisweet wines (10 samples), semidry wines (10 samples), and dry wines (30 samples), with differing antioxidant properties. The second group of products represented 24 sample juices. The juices differed in the type of fruit that was used for their production, color, percent fruit content, and turbidity. The following beverages were included in the study: 12 juices (orange, apple, grapefruit, citron, raspberry), 10 drinks (red grape, orange, apple, grapefruit, black currant), and 8 nectars (cherry, plum, apple, black currant). All commercial juices, drinks, and nectars were used immediately after opening. Fresh juice obtained by squeezing also was measured immediately after preparation.

Thirty-six samples of tea produced by various manufacturers were also used: black tea (12 samples), green tea (12 samples), and Earl Gray tea (12 samples). An infusion was prepared from each tea by pouring 200 mL of boiling water over one tea bag.

Moreover, 24 samples of herbs (thyme, lemon balm, sage, heartsease, menthe, chamomile) were used. One hundred milliliters of boiling water was poured over teabags filled with herbs, and the tea was infused for a length of time suggested by the manufacturer.

Tests of the model were performed on samples of herbs, coffees, and juices available on the market and in pharmacies. Thirty-six samples of herbs (lemon balm (S1−S4), heartsease (S5−S8), menthe (S9−S12), horsetail (S13−S16), nettle (S17−S20), chamomile (S21−S24), eyebright (S25−S28), hypericum (S29−S32), fennel (S33−S36)) were used. One hundred milliliters of boiling water was poured over tea bags filled with herbs, and the tea was infused for a length of time suggested by the manufacturer. Thirty-two samples of coffee, ground coffee (S37−S48), instant coffee (S49−S56), instant decaffeinated coffee (S57−S64), and espresso coffee (S65−S72), were also used. The coffee differed in species and manufacturer. An infusion was prepared from each coffee by pouring 150 mL of boiling water over 2 g of coffee. The last group of products used for testing included 12 samples of juices produced by various manufacturers (black currant juices (S73−S76) and orange juices (S77−S80)) (Table 1).

Determination of Antioxidant Capacity. Trolox equivalent antioxidant capacity ($TEAC_{exptl}$) was determined using the method described previously.[4,7,20] The regression equation for the linear relationship between the percent inhibition of EPR signal intensity and the mole number of Trolox was assessed as $\%I = 987.60V + 16.36$, where %I is the inhibition (%) and V is the volume of the sample (mL). This equation was used to calculate the antioxidant capacity of the studied samples in micromoles of TE per 100 mL of the studied sample. The percent inhibition of the EPR spectrum was calculated according to the following equation: $\%\ \text{inhibition} = [(I_0 I)/I_0] \times 100\%$, where I_0 is the area of the EPR spectrum of DPPH (control sample) and I is the area of the EPR spectrum of DPPH with sample.

A typical reaction mixture contained 1 mL of 200 μmol/L DPPH solution in ethanol together with 0.002−0.4 mL of sample, depending on the manifested antioxidant properties. For all samples, the regression equation of the linear relationship between the percent

DOI: 10.1021/acs.jafc.5b01478
J. Agric. Food Chem. 2015, 63, 6319−6324

inhibition (%I) of the EPR signal intensity and the volume of sample (V) was determined. On the basis of this equation the %I corresponding to 100 mL of the studied sample was calculated (I_{100}). Then, from the standard curve obtained for Trolox, the antioxidant capacity given in micromoles of TE per 100 mL of sample was defined. To indicate antioxidant capacity measured using the DPPH by EPR spectroscopy $TEAC_{exptl}$ is used.

EPR spectra were obtained with a Bruker EMX EPR spectrometer (Bruker-Biospin, Karlsruhe, Germany) operating at the X-band frequency at room temperature. The typical instrument parameters were as follows: central field, 3480 G; modulation amplitude, 2.0 G; time constant, 40.96; gain, 1×10^4 G; microwave power, 20.12 mW.

Mathematical Model. The mathematical model was based on three variables: $x = V$, $y = \%I$, and $z = I_{100}$, where V is the volume of antioxidant added to the DPPH free-radical solution (mL), %I is the inhibition (%) of the EPR signal of the DPPH free radical, and I_{100} is the value calculated from the equation describing the relationship between %I and V corresponding to a 100 mL sample. The approximation procedure starts from the variable separation $z(x,y) = f(x)g(y)$. Taking into account the qualitative behavior of the data, that is, a strong decay with respect to x, the volume of antioxidant added to the DPPH, and a boundedness with respect to y, the inhibition, the function $f(x)$ is represented as a Laurent series, which includes terms with negative degrees only

$$f(x) = \sum_{n=0}^{\infty} f_n x^{-n}$$

and $g(y)$ as the Taylor series

$$g(y) = \sum_{m=0}^{\infty} g_m y^m$$

around the origin of coordinates $(x,y) = (0,0)$ that results in the following formal double series:

$$z(x, y) = \sum_{n=0}^{\infty} \sum_{m=0}^{\infty} g_m f_n x^{-n} y^m \quad (1)$$

As the next step, the polynomial cutoff $\max(n) = N$ is reproduced. The properties of the obtained Laurent polynomial guarantee that the product eq 1 with finitely many negative terms exists.

The last step consists of the choice of the maximal polynomial index for x terms in such a way that $\max(m_n) = N - n$. Thus, the final expression takes the form

$$z(x, y) = \sum_{n=0}^{N} \sum_{m=0}^{N-n} f_n g_m x^{-n} y^m$$

For $N = 3$

$$z(x, y) = a_0 + a_1 y + a_2 y^2 + a_3 y^3 + \frac{a_4 + a_5 y + a_6 y^2}{x} + \frac{a_7 + a_8 y}{x^2} + \frac{a_9}{x^3} \quad (2)$$

where $a_0 = f_0 g_0$, $a_1 = f_0 g_1$, $a_2 = f_0 g_2$, $a_3 = f_0 g_3$, $a_4 = f_1 g_0$, $a_5 = f_1 g_1$, $a_6 = f_1 g_2$, $a_7 = f_2 g_0$, $a_8 = f_2 g_1$, and $a_9 = f_3 g_0$.

Fitting Model to Experimental Data. The model eq 2 was fitted to 1000 data points of EPR spectroscopy measurements.

For each sample, $TEAC_{exptl}$ was determined in three trials, according to the standard method of determining antioxidant capacity, described above, using EPR spectroscopy and DPPH as the free radical. Adjustable parameters a_i were estimated by a nonlinear regression procedure using the Levenberg–Marquardt algorithm in double precision. The set of a_i coefficients and the adjusted coefficient of determination for the nonlinear regression, adj-R^2, are listed in Table 2. One can see that the data satisfy the assumed function with high accuracy.

Table 2. Coefficients of Equation 2 together with the Adjusted Coefficient of Determination for the Nonlinear Regression, Adj-R^2

a_0	−50924 ± 1005
a_1	−1493 ± 110
a_2	47.23 ± 7.63
a_3	−0.277 ± 0.012
a_4	2842 ± 440
a_5	32.887 ± 8.399
a_6	0.446 ± 0.058
a_7	−4.782 ± 0.39
a_8	−0.0438 ± 0.0095
a_9	0.00329 ± 0.00047
adj-R^2	0.91

Testing of the Mathematical Model. The model was tested on 20 sample food products, that is, for 80 EPR spectroscopy measurements.

For each sample, $TEAC_{exptl}$ was determined twice, according to the standard method of determining antioxidant capacity, described above, using EPR spectroscopy and DPPH as the free radical. Next, for two randomly selected volumes of antioxidant sample added to 1 mL of DPPH solution, the EPR measurements were repeated (80 measurements) and %I of the DPPH free radical of EPR signal was determined. On the basis of the value of the V of antioxidant added to the free radical solution, as well as %I of the DPPH free radical EPR signal, the I_{100} value was determined using the model eq 2. On the basis of the I_{100} value the antioxidant capacity $TEAC_{calcd}$ was calculated according to the equation $\%I = 987.60V + 16.36$. Subsequently, the average $TEAC_{exptl}$ values were determined from the two series on the basis of seven measurements in each series, the average calculated $TEAC_{calcd}$ values were determined from the model on the basis of two measurements for each series for each studied sample, and these values were compared to each other.

Statistical Analysis. The presented data are the mean values, whereas errors were calculated as standard deviation (SD). Determination coefficients (R^2), obtained $TEAC_{exptl}$, and expected $TEAC_{calcd}$ were calculated by the Pearson test with a level of significance of $p = 0.05$.

RESULTS AND DISCUSSION

A plot of the proposed model and the observed data points is useful to determine how well the model fits the data. Model eq 2 and the observations are plotted in Figure 1. It is evident from the figure that a definite trend exists in the data and that the model eq 2 proficiently performed the task of capturing that trend. Note that the model was fitted to a larger data set than that shown.

One way of evaluating how well the model fits and predicts the data is to compute not only the deviations between the model and the actual data, analysis of the randomness of the residual plots, and normality of the errors but also deviations between the model and the new data. The proposed mathematical equation allows for a determination of the antioxidant capacity of food products based on a single EPR spectroscopy measurement. The value of the experimental TEAC antioxidant capacity for the products, selected for testing of the model, was situated in the wide range between 21 μmol TE/100 mL of the sample and 2347 μmol TE/100 mL (Table 1). The values of TEAC for the studied food samples are consistent with the TEAC values that have been determined through the use of other research methods described in the literature.[1,28,29]

DOI: 10.1021/acs.jafc.5b01478
J. Agric. Food Chem. 2015, 63, 6319−6324

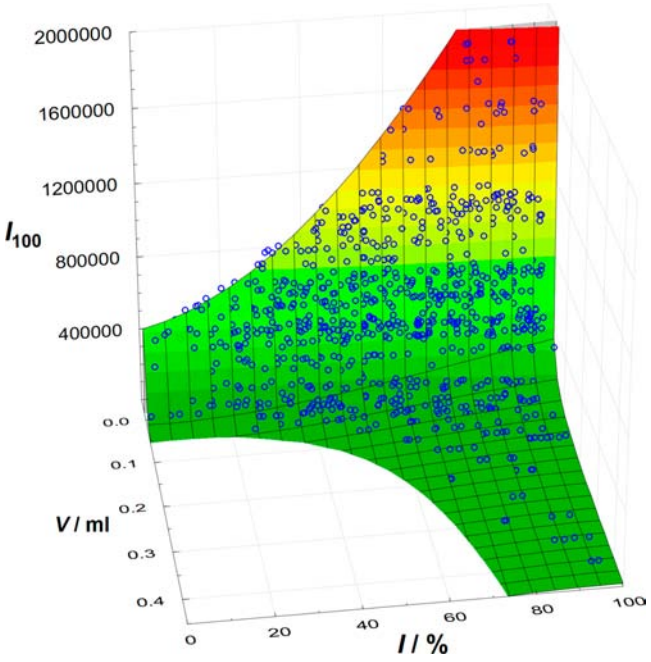

Figure 1. I_{100} as a function of the inhibition of the EPR signal, I, and the volume of antioxidant added to the DPPH solution, V. Points are experimental data on V–I surface calculated using eq 2.

The determination coefficient between TEAC $_{calcd}$ and TEAC $_{exptl}$ was found to be $R^2 = 0.98$ (Figure 2).

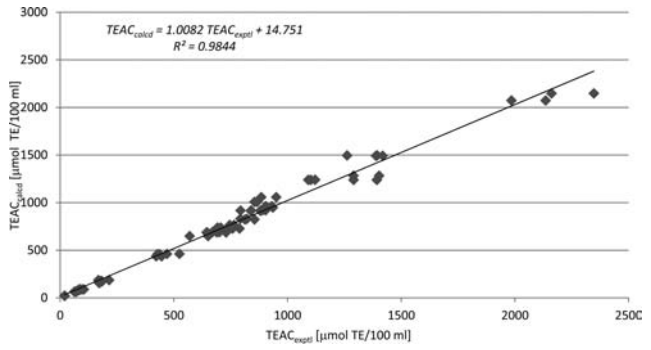

Figure 2. Regression between calculated ($TEAC_{calcd}$) and experimental ($TEAC_{exptl}$) antioxidant capacity.

On the basis of the mathematical model and test conducted, it was concluded that the average relative percentage error of $TEAC_{calcd}$ versus $TEAC_{exptl}$ was 6.6% (95% confidence intervals, CI, 5.5–7.7). It should be noted that for 40 of 80 measurements the value of the error is below 5%, and for 62 of the 80 measurements it was below 10%. The proposed model works for both strong and weak antioxidants. For strong antioxidants (TEAC > 200) the average relative percentage error was found to be 6.5% (95% CI, 5.1–7.8), whereas for weak antioxidants (TEAC < 200) it was 6.8% (95% CI, 4.5–9.0). Such an agreement between $TEAC_{exptl}$ and $TEAC_{calcd}$, as well as an agreement with values found in the literature, indicates the possibility of using this method, which connects mathematical modeling with EPR spectroscopy, for evaluating antioxidant capacities.

For each product the average $TEAC_{exptl}$ and $TEAC_{calcd}$ values from the two series in Figure 3 are presented.

The average relative error for the determined average TEAC calculated values amounted to only 5.25%, which indicates a high utility of the proposed model. To obtain the average antioxidant capacity value via the standard method for determining antioxidant capacity using EPR spectroscopy and DPPH free radicals, it is necessary to perform 22 separate EPR measurements. With the proposed model it is sufficient to perform between two and four EPR experimental and calculated TEAC values to obtain comparable accuracy. Moreover, thanks to the utilization in the model of the I_{100} value, the model offers the possibility of determining the antioxidant capacity in various standards. It is sufficient to develop a standard curve for a standard other than Trolox, to obtain, from one series of measurements, the antioxidant capacities expressed in different standard equivalents.

AUTHOR INFORMATION

Corresponding Author

*(J.P.) Phone: +48 323591446. E-mail: justyna.polak@us.edu.pl.

Notes

The authors declare no competing financial interest.

ACKNOWLEDGMENTS

M.C. appreciates the inspiring discussion with Prof. Eugene B. Postnikov from the Department of Theoretical Physics, Kursk State University, Russia.

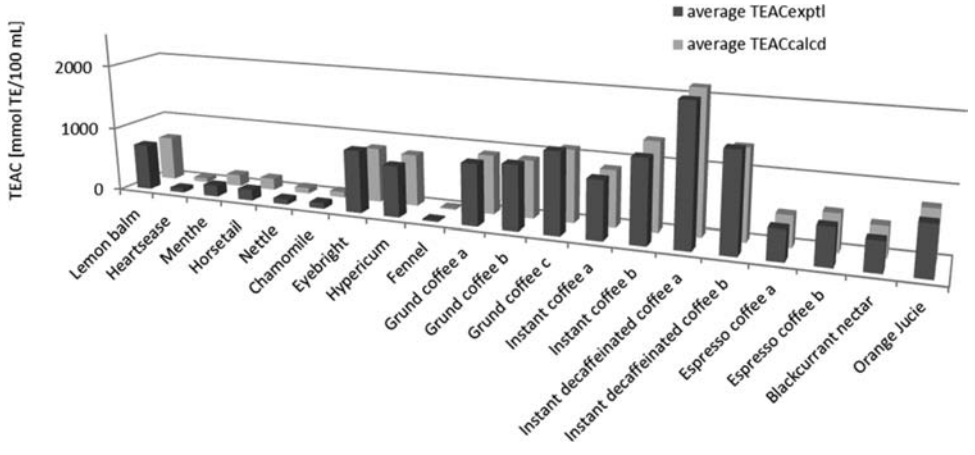

Figure 3. Average values of experimental and calculated TEAC of investigated samples (a, b, and c are various manufacturers).

DOI: 10.1021/acs.jafc.5b01478
J. Agric. Food Chem. 2015, 63, 6319–6324

REFERENCES

(1) Fasseas, M.; Mountzouris, K. Antioxidant activity in meat treated with oregano and sage essential oils. *Food Chem.* **2008**, *106*, 1188−1194.

(2) Gheldof, N.; Wang, X. H.; Engeseth, N. J. Identification and quantification of antioxidant components of honeys from various floral sources. *J. Agric. Food Chem.* **2002**, *50*, 5870−5877.

(3) Riberio-Tafulo, P. A.; Queniros, R. B.; Deleru-Matos, C. M.; Ferreina Moneti-Sales, M. Control and comparsion of the antioxidant capacity of beers. *Food Res. Int.* **2010**, *43*, 1702−1709.

(4) Bartoszek, M.; Polak, J. An electron paramagnetic resonance study of antioxidant properties of alcoholic beverages. *Food Chem.* **2012**, *132*, 2089−2093.

(5) Stasko, A.; Brezova, V.; Mazur, M.; Certik, M.; Kalinak, M.; Gescheidt, G. A comperatice study on the antioxidant properties of slovakian and austrian wines. *Lebensm.-Wiss. Technol.* **2008**, *41*, 2126−2135.

(6) Escarpa, A.; Gonzalez, M. C. Approach to the content of total extractable phenolic compounds from diffrent food samples by comparsion of chromatogaphic and spectrophotometric methods. *Anal. Chim. Acta* **2001**, *427*, 119−127.

(7) Polak, J.; Bartoszek, M.; Stanimirova, I. A study of the antioxidant properties of beers using electron. *Food Chem.* **2013**, *141*, 3042−3049.

(8) Tabart, J.; Kevers, C.; Pincemail, J.; Defraigne, J. O.; Dommesa, J. Comparative antioxidant capacities of phenolic compounds measured by various tests. *Food Chem.* **2009**, *113*, 1226−1233.

(9) Karadag, A.; Ozcelik, B.; Saner, S. Received: Review of methods to determine antioxidant capacities. *Food Anal. Methods.* **2009**, *2*, 41−60.

(10) Molyneux, P. The use of the stable free radical diphenylpicryl-hydrazyl (DPPH) for estimating antioxidant activity. *Songklanakarin J. Sci. Tehchnol.* **2004**, *26*, 211−219.

(11) Campos, A.; Escobar, J.; Lissi, E. A. The total reactive antioxidant potential (TRAP) and total antioxidant reactive (TAR) of *Ilex paraguayensis* extracts and red wine. *J. Braz. Chem. Soc.* **1996**, *7*, 43−49.

(12) Ou, B.; Huang, D.; Hampsch-Woodill, M.; Flanagan, J.; Deemer, E. Analysis of antioxidant activities of common vegetables employing oxygen radical absorbance capacity 83 (ORAC) and ferric reducing antioxidant power (FRAP) assays: a comparative study. *J. Agric. Food Chem.* **2002**, *50*, 3122−3128.

(13) Ninfali, P.; Bacchioccaa, M.; Biagiottia, E.; Servilib, M.; Montedorob, G. Validation of the oxygen radical absorbance capacity (ORAC) parameter as a new index of quality and stability of virgin olive oil. *J. Am. Oil Chem. Soc.* **2002**, *10*, 977−982.

(14) Arts, M. J. T. J.; Dallinga, S.; Voss, H. P.; Haenen, G.; Bast, A. A new approach to asess the total antioxidant capacity using the TEAC. *Food Chem.* **2004**, *88*, 567−570.

(15) Miller, N. J.; Rice-Evans, C. A. Factors influencing the antioxidant activity determined by the $ABTS^{+\bullet}$ radical cation assay. *Free Radical Res.* **1997**, *26*, 195−199.

(16) Gheldof, N.; Wang, X. H.; Engeseth, N. J. Identification and quantification of antioxidant components of honeys from various floral sources. *J. Agric. Food Chem.* **2002**, *50*, 5870−587.

(17) Polovka, M.; Brezova, V.; Stasko, A. Antioxidant properties of tea investigated by EPR spectroscopy. *Biophys. Chem.* **2003**, *106*, 39−56.

(18) Tzika, E. D.; Papadimitriou, V.; Sotiroudis, T. G.; Xenakis, A. Antioxidant properties of fruits and vegetables shots and juices: an electron paramagnetic resonance study. *Food Biophys.* **2008**, *3*, 48−53.

(19) Zalibera, M.; Stasko, A.; Slebodova, A.; Jancovicova, V.; Cermakova, T.; Brezova, V. Antioxidant and radical-scavenging activities of Slovak honeys − an electron paramagnetic resonance study. *Food Chem.* **2008**, *110*, 512−521.

(20) Polak, J.; Bartoszek, M. The study of antioxidant capacity of varieties of nalewka, a traditional Polish fruit liqueur, using EPR, NMR and UV−vis spectroscopy. *J. Food Compos. Anal.* **2015**, *40*, 114−119.

(21) Morsy, M. A.; Khaled, M. M. Novel EPR characterization of the antioxidant activity of tea leaves. *Spectrochim. Acta, Part A* **2002**, *58*, 1271−1277.

(22) Unno, T.; Yayabe, F.; Hayakawa, T.; Tsuge, H. Electron spin resonance spectroscopic evaluation of scavenging activity of tea catechins on superoxide radicals generated by a phenazine methosulfate and NADH system. *Food Chem.* **2002**, *76*, 259−265.

(23) Brezova, V.; Slebodova, A.; Stasko, A. Coffee as a source of antioxidants: an EPR study. *Food Chem.* **2009**, *114*, 859−868.

(24) Stasko, A.; Liptakowa, M.; Malik, F.; Misik, V. Free radical scavening activities of white and red wines: an EPR trapping study. *Appl. Magn. Reson.* **2002**, *22*, 101−113.

(25) Stasko, A.; Polovka, M.; Brezova, V.; Biskupic, S.; Malik, F. Tokay wines as scavengers of free radicals (an EPR study). *Food Chem.* **2006**, *96*, 185−196.

(26) Brezova, V.; Polovka, M.; Stasko, A. The influence of additives on beer stability investigated by EPR spectroscopy. *Spectrochim. Acta, Part A* **2002**, *58*, 1279−1291.

(27) Jäntschi, L.; Sestras, R.; Bolboacs, S. Modeling the antioxidant capacity of red wine from different production years and sources under censoring. *Comput. Math. Method. M.* **2013**, *2013*, 1−7, doi.org/10.1155/2013/267360,.

(28) Santini, A.; Ferracane, R.; Mikusová, P.; Eged, S.; Srobárová, A.; Meca, G.; Mañes, J.; Ritieni, A. Influence of different coffee drink preparations on ochratoxin A content and evaluation of the antioxidant activity and caffeine variations. *Food Control* **2011**, *22*, 1240−1245.

(29) Miller, N. J.; Rice-Evans, C. A. The relative contributions of ascorbic acid and phenolic antioxidants to the total antioxidant activity of orange and apple fruit juices and blackcurrant drink. *Food Chem.* **1997**, *6o* (3), 331−337.

DOI: 10.1021/acs.jafc.5b01478
J. Agric. Food Chem. 2015, 63, 6319−6324

MATERIALS AND METHODS

Materials. Chlorothalonil, phthalide, quintozene, pentachlorophenol, 2,4-dichlorophenoxyacetic acid (2,4-D), and 2,4,5-trichlorophenoxyacetic acid (2,4,5-T) were purchased from Wako Pure Chemical Industries (Osaka, Japan). The pesticides used for residue analysis were of analytical grade. *N*-Hydroxysuccinimide (NHS) and 1-ethyl-3-(3-dimethylaminopropyl)carbodiimide hydrochloride (EDC) were purchased from Wako Pure Chemical Industries and Dojindo Laboratories (Kumamoto, Japan), respectively. Bovine serum albumin (BSA, Pro. No. A7888) was purchased from Sigma-Aldrich (St. Louis, MO, USA). Sodium dodecyl sulfate (SDS) and guanidine hydrochloride (GdnHCl) were purchased from Nacalai Tesque (Kyoto, Japan). Horseradish peroxidase-labeled anti-mouse IgG (H+L) antibody from rabbit (Invitrogen) and 96-well microtiter plates (Nunc MaxiSorp) were purchased from Thermo Fisher Scientific (New York, NY, USA). All other chemicals and reagents were of analytical grade and purchased from Wako Pure Chemical Industries or Nacalai Tesque. Anti-chlorothalonil mouse monoclonal antibody (MoAb TPN9A; IgG_1) and the conjugate of *N*-(pentachlorophenoxyacetyl)glycine and BSA (TPN−BSA) were prepared as described previously.[12]

SPR-sensor. SPR-sensors consisted of commercially available instruments of microflow type (Biacore T200; GE Healthcare Europe, Munich, Germany) and a sensor chip, which was coated with carboxymethyldextran (CM5; GE Healthcare Europe). They were functionalized via the following steps based on the instruction manual.

1. Immobilization of TPN−BSA. TPN−BSA was covalently bound to the chip surface by the active ester method. The sensor chip was put to the instrument and was initially rinsed with 10 mmol/L PBS (10 mmol/L phosphate buffer adjusted to pH 7.0, 150 mmol/L NaCl) modified with 0.005% Tween 20 at 5 μL/min for 600 s. A mixture of 80 μL of EDC (400 mmol/L) and 80 μL of NHS (100 mmol/L) in distilled water was made to flow to the channel for 350 s to esterify the carboxyl group of the sensor chip with NHS. The TPN−BSA solution (17 or 44 μg/mL) was dissolved in acetic acid buffer (10 mmol/L; adjusted to pH 5.0) and flowed for 45, 60, 90, or 120 s to bind the activated carboxyl groups to the amino-group residues of TPN−BSA. Ethanolamine (1 mol/L; adjusted to pH 8.5) was made to flow for 350 s to block the residual carboxyl groups. After a rinse with running buffer (50 mmol/L phosphate buffer adjusted to pH 7.0, 75 mmol/L NaCl, 5.0% methanol, and 0.1% BSA), the sensor chip was used for chlorothalonil determination.

2. Premixture of MoAb TPN9A and Chlorothalonil. On the other hand, chlorothalonil was dissolved in methanol and serially diluted to concentrations from 7.8 to 1000 ng/mL in tubes. The diluents were further diluted 10-fold with distilled water, resulting in concentrations from 0.78 to 100 ng/mL in 10% methanol. MoAb TPN9A was also diluted to concentrations from 1.56 to 60 μg/mL with 100 mmol/L PBS (100 mmol/L phosphate buffer adjusted to pH 7.0, 150 mmol/L NaCl) modified with 0.2% BSA, as described previously.[12] The prepared chlorothalonil solution (75 μL) was mixed with the MoAb TPN9A solution (75 μL) in tubes. In this phase, the complex between the MoAb TPN9A and chlorothalonil was formed.

3. Reaction of MoAb TPN9A Not Bound to Chlorothalonil with the Immobilized TPN−BSA. The tubes were put to the instrument. Each mixture was made to flow to the sensor at 20 μL/min for 180 s to react the free MoAb TPN9A, which was not bound to chlorothalonil, with TPN−BSA on the chip. Immediately after the reaction, the flowing solution was replaced with running buffer at 20 μL/min for 180 s.

4. Dissociation of the Bound MoAb TPN9A from the Immobilized TPN−BSA. The sensor chip must be regenerated by removal of the bound antibody from the immobilized TPN−BSA. As the condition, two kinds of solutions were used for the dissociation of the bound MoAb TPN9A after examinations had been carried out to optimize the conditions as described in the results. The dissociation solution A was GdnHCl (3.0 mol/L) in acetic acid (1.0 mol/L; pH 1.9), and the dissociation solution B was 0.2% SDS. The sensor chip was initially washed with solution A at 20 μL/min for 60 s. After 60 s of rinsing with distilled water at 20 μL/min, it was washed again with solution B at 20 μL/min for 120 s. The sensor chip on which the MoAb TPN9A had been dissociated was used again by repeating each of the above steps between (2) premixture of MoAb TPN9A and chlorothalonil and (4) dissociation of the bound MoAb TPN9A from the immobilized TPN-BSA.

5. Data Processing. Raw data were output as a resonance unit (RU), where 1000 RU was defined as 0.1 degree of the refractive index shift by the SPR phenomenon. The actual response curve was drawn; the *x*-axis represented chlorothalonil concentration, and the *y*-axis represented the ΔRUs between the starting point of the reaction and a time point of 180 s.

Indirect Competitive (ic)-ELISA. ic-ELISA was developed as described previously.[12] TPN−BSA (1 μg/mL) was dissolved in 10 mmol/L PBS and added to each well of a 96-well microtiter plate at 100 μL/well. The plate was incubated overnight at 4 °C. Blocking buffer (10 mmol/L PBS modified with 0.4% BSA) was added at 300 μL/well after the wells were washed once with washing buffer (10 mmol/L PBS modified with 0.02% Tween 20). The plate was incubated at 25 °C for 1 h, and the solution was removed from the wells. Chlorothalonil standards were prepared at concentrations from 0.05 to 200 ng/mL in 10% methanol, and the solutions were added at 50 μL/well. The MoAb TPN9A was dissolved in 100 mmol/L PBS with 0.2% BSA and was prepared to a concentration (100 ng/mL) showing an absorbance between 1.0 and 2.0 at 450 nm in this ic-ELISA. MoAb TPN9A was added at 50 μL/well to each well immediately after the standard was added. The plate was incubated at 25 °C for 1 h. After three washings with the washing buffer, horseradish peroxidase-labeled anti-mouse IgG (H+L) antibody, which was diluted 2000-fold in 10 mmol/L PBS with 0.2% BSA, was added at 100 μL/well. The plate was incubated at 25 °C for 1 h. After three washings with the washing buffer, the color development solution (100 μg/mL 3,3′,5,5′-tetramethylbenzidine, 0.006% H_2O_2, 100 mmol/L acetic acid; adjusted to pH 5.5) was added at 100 μL/well. After 10 min at 25 °C, 0.5 mol/L sulfuric acid was added at 100 μL/well to stop the color development reaction. The absorbance was measured at 450 nm by the microplate reader, xMark (Bio-Rad Laboratories, Hercules, CA, USA).

Treatment of Vegetable Samples. Lettuce, cabbage, and long green onion (200 g of each), purchased from a market in Kyoto city, were used for recovery examinations. Cucumber and eggplant (1.0 kg of each), harvested from the experimental farm at the National Institute for Agro-Environmental Sciences, were used for correlation examinations between the SPR-sensor and HPLC. Phosphoric acid solution (phosphoric acid/water = 1:9 v/v) was added at a ratio of 1:2 (w/w) to the vegetable samples and homogenized by a blender. Chlorothalonil was added to the homogenized samples. The final concentrations ranged from 1.0 to 10 mg/kg for the recovery examinations and from 0.2 to 5.5 mg/kg for the correlation examinations.

For the SPR-sensor, pretreatment of the homogenized samples was carried out according to the same procedure as that of direct competitive (dc)-ELISA, as described previously.[12] Methanol (25 mL) was added to the samples (7.5 g) in a 50 mL tube hermetically sealed with a screw cap. The tube was vigorously shaken for 30 min to extract chlorothalonil. The mixture was centrifuged at 3000 rpm at room temperature for 10 min. The supernatant was diluted 8.5-fold with distilled water to become 10% methanol equivalent. The diluted sample was applied to the SPR-sensor without other pretreatments.

For HPLC, acetone was added at 100 mL/sample to the homogenized samples (20 g) and extracted for 3 min, using a homogenizer (Polytron PT2100; Kinematica, Lucerne, Switzerland). The mixture was filtered through a funnel with diatomite by suction. The residue was then re-treated with 50 mL of acetone. Both filtered extracts were mixed and concentrated to 30 mL by evaporation at a temperature lower than 40 °C, in a flask. The sample was transferred to a separating funnel with 100 mL of 10% sodium chloride solution. The above flask was washed with 100 mL of hexane, and the washed solution was also transferred to the funnel. After vigorous shaking for 5 min, a hexane layer was recovered. The liquid−liquid partition was repeated twice. The recovered hexane layer was mixed with

DOI: 10.1021/acs.jafc.5b01980
J. Agric. Food Chem. 2015, 63, 6325−6330

appropriate quantities of anhydrous sodium sulfate. After the filtration, the solution was transferred to a flask and evaporated to dryness at a temperature lower than 40 °C. The dried residue was dissolved with 5 mL of hexane. The dissolved solution was applied to a column in which Florisil (5 g) and anhydrous sodium sulfate (5 g) were filled up with hexane. After the column was washed with hexane (100 mL), chlorothalonil was eluted with a mixture of ethyl acetate and hexane (1:9, v/v; 150 mL). The eluate was dried by evaporation and redissolved with hexane (2.0 mL). A portion of the solution (0.5 mL) was dried by evaporation and redissolved with methanol (1.0 mL). The methanol solution was applied to HPLC.

HPLC Analysis. The HPLC system consisted of an Agilent 1100 series equipped with a quaternary pump, an autosampler, a column oven, and a diode array detector. The wavelength for chlorothalonil detection was 246 nm. The column was a SunFire C18 reversed-phase column (5 μm, 4.6 i.d. × 250 mm; Waters, Milford, MA, USA) with a guard column (5 μm, 4.6 i.d. × 20 mm). The mobile phase was methanol/water (70:30, v/v). The flow rate was 1.0 mL/min, the column oven temperature was 40 °C, and the injection volume was 20 μL.

RESULTS AND DISCUSSION

Development of the SPR-sensor. An SPR-sensor was developed for chlorothalonil determination, using MoAb TPN9A and antigen TPN−BSA. The TPN part of the TPN−BSA has a chlorothalonil-like structure as shown in Figure 1 and reacts with MoAb TPN9A as described

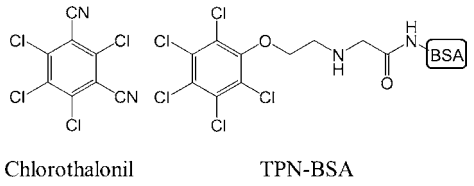

Figure 1. Structures of chlorothalonil and TPN−BSA.

previously.[12] Because the structure is much more chemically stable than that of the binding site in the MoAb TPN9A, TPN−BSA was chosen for immobilization on the sensor chip surface, as it was expected to tolerate the dissociation condition of the TPN−BSA and TPN9A complex.

The TPN−BSA was immobilized at several concentrations and reaction times to determine the optimum conditions: 17 μg/mL and 90 s, 44 μg/mL and 45 s, 44 μg/mL and 60 s, and 44 μg/mL and 120 s. The RU values changed depending on the concentration and the reaction time as shown in Figure 2. Sufficient signal was acquired at a condition of 44 μg/mL and 120 s. These conditions were the minimum concentration of TPN−BSA and time required to obtain a sufficient signal.

The sensor chip should be repeatedly regenerated by dissociation of MoAb TPN9A from the TPN−BSA immobilized on the chip surface. The recommended condition in the instruction manual was SDS (up to 0.5%) or GdnHCl (up to 5.0 mol/L). Only 10% of MoAb TPN9A was dissociated from TPN−BSA by 0.2% SDS, as shown in Figure 3, whereas 84% of MoAb TPN9A was dissociated by 3.0 mol/L GdnHCl, but the dissociation was still incomplete. The k_d value, which was determined after the condition was optimized, was 3×10^{-5} mol/L/s. The result means that the complex is difficult to dissociate at these conditions. Such a phenomenon has already been reported by Svitel et al. for the complex of 2,4-D−BSA and anti-2,4-D antibody.[19] Anti-2,4-D antibody was successfully dissociated from the sensor chip surface by using a non-covalently bound 2,4-D−concanavalin A conjugate instead of a

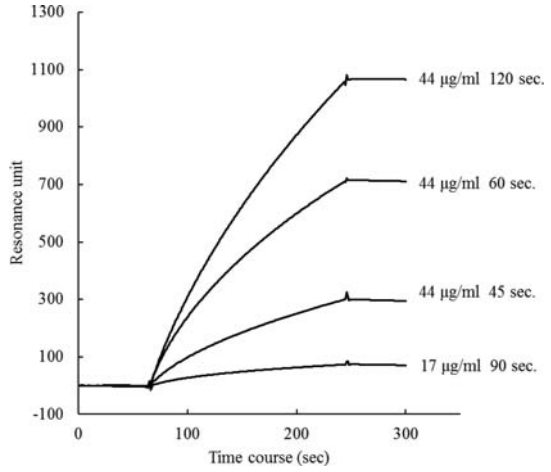

Figure 2. Typical time course of the MoAb TPN9A (7.5 μg/mL) reaction with the immobilized TPN−BSA in the SPR-sensor. The numerals on the right show TPN−BSA concentrations and reaction times for the immobilization.

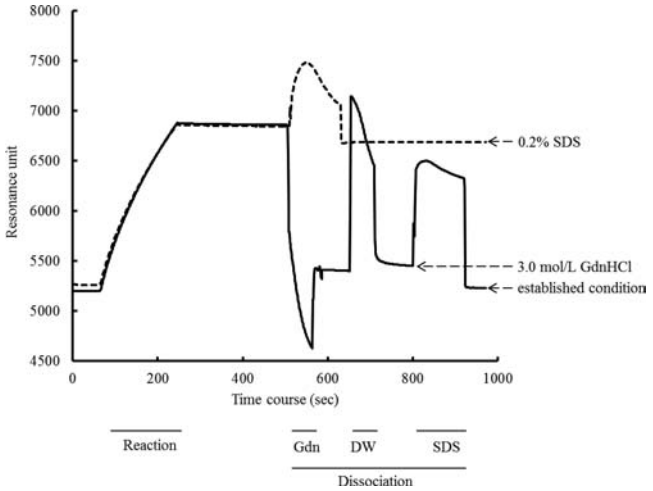

Figure 3. Dissociation of the MoAb TPN9A bound to the immobilized TPN−BSA on the sensor chip. Solid line shows the time course of the signal for the established condition. Dashed line shows the time course of the signal for the dissociation by 0.2% SDS.

2,4-D-BSA conjugate, with which sugar chains were covalently immobilized on the sensor chip surface. This idea was useful for the regeneration of the sensor chip, but re-immobilization of 2,4-D−concanavalin A was necessary for each test. Improvement of the dissociation condition was therefore examined using a combination of GdnHCl and SDS. The dissociation condition was consequently established such that GdnHCl (3.0 mol/L) in acetic acid (1.0 mol/L) was initially made to flow for 60 s, followed by flowing distilled water for 60 s to remove the GdnHCl residue and, finally, 0.2% SDS was made to flow for 120 s. The baseline returned completely to the initial level at this condition, as shown in Figure 3. The established condition made it possible for the sensor chip to be used continuously for 200 cycles, after which the microchannel was physically destroyed by delamination of the thin gold film. This suggests that salting-out by GdnHCl is an effective way to dissociate the complex, and the residual part was dissociated with the surfactant potency of SDS. The MoAb TPN9A and the TPN−BSA complex may have heterogeneous binding forces.

DOI: 10.1021/acs.jafc.5b01980
J. Agric. Food Chem. 2015, 63, 6325−6330

Reactivity in the SPR-sensor. Various concentrations of the MoAb TPN9A solution (1.88−60 μg/mL) were initially applied to the sensor chip, on which TPN−BSA (44 μg/mL) was immobilized, to determine the application dose of MoAb. The minimum required concentration of MoAb TPN9A was 7.5 μg/mL to achieve a ΔRU value of >400 at a time point of 180 s after injection. In turn, this concentration was set as the application dose.

Chlorothalonil solutions were mixed with equal volumes of the MoAb TPN9A solution and then applied to the SPR-sensor. The ΔRU value decreased with an increase in the chlorothalonil concentration (0.78−100 ng/mL), as shown in Figure 4. The K_a value was calculated as 1×10^{10} $(mol/L)^{-1}$

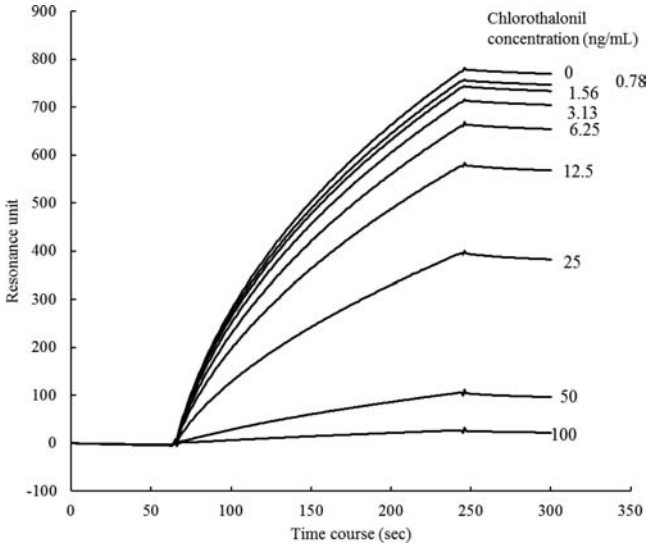

Figure 4. Typical time course of the MoAb TPN9A reaction not bound to chlorothalonil with the immobilized TPN−BSA in the SPR-sensor.

from the results of the SPR-sensor. The inhibition curve 180 s after sample injection for the SPR-sensor was compared with that for ic-ELISA, as shown in Figure 5. The values of 20, 50, and 80% inhibition concentration (IC_{20}, IC_{50}, and IC_{80}) were 8.0, 25, and 44 ng/mL, respectively, for the SPR-sensor. The reactivity at IC_{50} was 10-fold lower than that acquired by ic-ELISA, with which the IC_{20}, IC_{50}, and IC_{80} values were 0.44, 2.5, and 12 ng/mL, respectively. The SPR-sensor required a 44-fold higher concentration of TPN−BSA for immobilization compared with ic-ELISA, which was 44 μg/mL in the SPR-sensor as shown in Figure 2 but 1 μg/mL in the ic-ELISA. The high concentration for the SPR-sensor was derived from the mechanism to monitor the direct signal of the antigen−antibody interaction, differing from signal amplification by horseradish peroxidase in the ic-ELISA. This would be the reason that the sensitivity between them was different as shown in Figure 5, although the same MoAb was used for their constitutions. On the other hand, the SPR-sensor required only 15 min to examine chlorothalonil and showed high reproducibility. The relative standard deviations (RSDs) of SPR were 0.76% (6.25 ng/mL), 2.0% (25 ng/mL), and 8.5% (44 ng/mL) for chlorothalonil, whereas the RSDs of ic-ELISA were 3.8% (0.44 ng/mL), 4.8% (3.1 ng/mL), and 8.6% (13 ng/mL). Thus, the SPR-sensor would be a useful immunoassay method for a simple, quick, and accurate determination, although it had lower sensitivity than ic-ELISA.

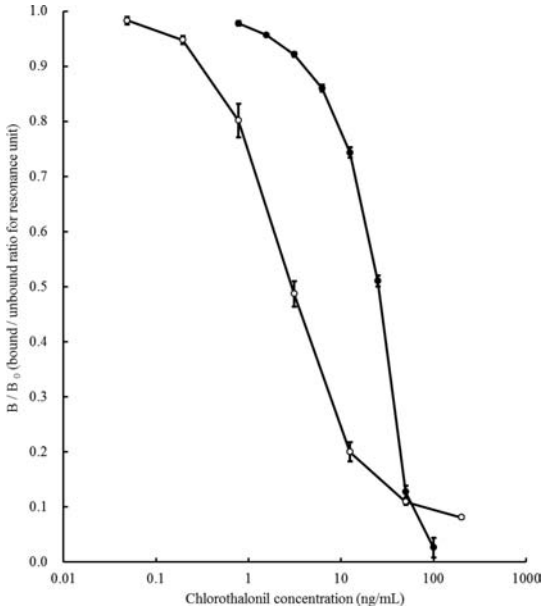

Figure 5. Inhibition curves by chlorothalonil in the ic-ELISA (○) and in the SPR-sensor (●). Each data point is the mean of three replicates from independent examinations. Error bars indicate standard deviations.

Cross-reactivity was examined by the SPR-sensor for structurally related pesticides. The results were slightly less specific compared to those acquired by ic-ELISA, as described in Table 1. Compared with the results of ic-ELISA, phthalide

Table 1. Cross-Reactivity of MoAb TPN9A with Chlorothalonil and the Other Structurally Related Pesticides

Pesticide	CR (%)[a] ELISA	CR (%)[a] SPR	Pesticide	CR (%) ELISA	CR (%) SPR
chlorothalonil			pentachlorophenol		
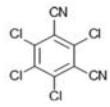	100	100	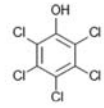	<0.7[b]	1.2
phthalide			2,4-D		
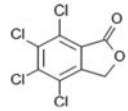	22	9.1	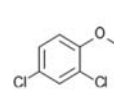	<0.7	<2.0
quintozene			2,4,5-T		
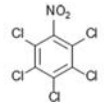	17	22.6	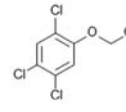	<0.7	6.5

[a]CR (%) shows cross-reactivity (%) compared to chlorothalonil. [b]<0.7 shows less than 0.7%.

examined by the SPR-sensor had a slightly lower cross-reactivity, but quintozene, pentachlorophenol, and 2,4,5-T had slightly higher cross-reactivities. The SPR-sensor monitors the early response of the antigen−antibody interactions, whereas ic-ELISA monitors the saturated interactions after 1 h. Because both assays showed only minor differences, it was confirmed that the specificity was a particular characteristic of the MoAb TPN9A.

DOI: 10.1021/acs.jafc.5b01980
J. Agric. Food Chem. 2015, 63, 6325−6330

The MRLs of chlorothalonil are set from 0.5 to 50 mg/kg in vegetables in Japan. On the other hand, the SPR-sensor showed a working range from 6.5 to 42 ng/mL. The MRL values were included in concentrations that were 70-fold higher than the working range, for which the dilution rate was usually used for the pretreatment of vegetables in dc-ELISAs.[12] The developed SPR-sensor showed adequate sensitivity to determine chlorothalonil residues in vegetables.

Recovery of Chlorothalonil Spiked into Vegetables. Recovery examination was carried out to confirm applicability of the SPR-sensor in determining chlorothalonil residues in vegetables. Lettuce in the Asteraceae family, cabbage in the Brassicaceae family, and Welsh onion in the Alliaceae family, which are typical leaf vegetables, were chosen as representative species. The vegetable samples before spiking with chlorothalonil had not contained any detectable chlorothalonil in the SPR-sensor (the data not shown). The recovery results within the day are shown in Table 2, and the results across several days

Table 2. Intraday Validation of Chlorothalonil Recovered from Vegetables by SPR-sensor[a]

	lettuce[b]		cabbage[b]		long green onion[b]	
spike (mg/kg)	recovery	RSD	recovery	RSD	recovery	RSD
1	96	3.3	103	9.9	NT	NT
2	90	7.1	90	3.5	118	2.7
4	NT[c]	NT	103	13.5	NT	NT
5	NT	NT	NT	NT	103	3.1
10	NT	NT	NT	NT	114	7.4

[a]Each data point is the mean of three replicates for independent examination. [b]The values show recovery (%) and RSD (%). [c]NT, not tested.

Table 3. Interday Validation of Chlorothalonil Recovered from Vegetables by SPR-sensor[a]

	lettuce[b]		cabbage[b]		long green onion[b]	
spike (mg/kg)	recovery	RSD	recovery	RSD	recovery	RSD
1	101	12.6	105	10.4	NT	NT
2	90	7.1	92	9.2	115	6.8
4	NT[c]	NT	107	7.9	NT	NT
5	NT	NT	NT	NT	112	7.5
10	NT	NT	NT	NT	111	8.7

[a]Each data point is the mean of three replicates for independent examination. [b]The values show recovery (%) and RSD (%). [c]NT, not tested.

are shown in Table 3. The SPR-sensor showed good recovery results for both examinations. The recovery ranged from 90 to 118% within the day and from 90 to 115% across several days. The RSD ranged from 2.7 to 13.5% within the day and from 6.8 to 12.6% across several days. These results showed that the developed SPR-sensor has adequate accuracy for the determination of chlorothalonil residues in the vegetables. It was suggested that the SPR-sensor would be applicable to a wide range of vegetables.

Examination of the Correlation between HPLC and SPR-sensor. The results of recovery were confirmed by HPLC analysis, using eggplants and cucumbers, which are typical fruit vegetables. As shown in Figure 6, although the analytical values generally have a bias toward the proposed method (slope = 1.2)

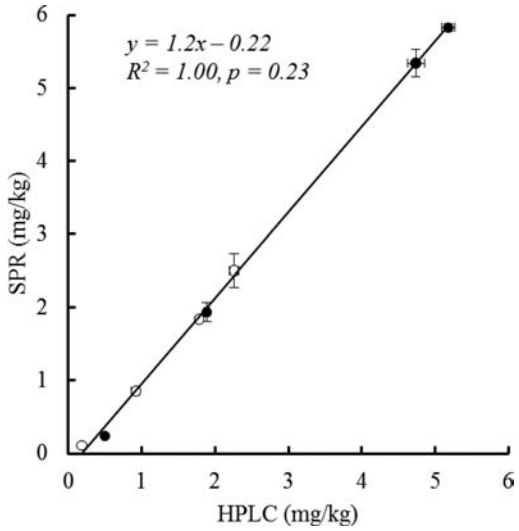

Figure 6. Correlation between the results of the SPR-sensor and the results of HPLC: (○) eggplant; (●) cucumber. Each data point is the mean of three replicates from independent examinations. Error bars indicate standard deviations.

and have y-intercept of −0.22, no significant difference was found in the values obtained from both methods (R^2 = 1.00 and p = 0.23). The results showed that the SPR-sensor developed could determine the chlorothalonil residues in vegetables with adequate quantitative performance in addition to HPLC analysis.

In conclusion, this study showed that the SPR-sensor developed was applicable for the rapid determination of chlorothalonil residues in vegetables around the MRL, although the sensitivity and cross-reactivity were less effective than with the ic-ELISA. The principle of SPR is quite simple, making the real-time determination of pesticides possible. It would be useful for rapid and accurate pesticide residue analysis in garden crops.

AUTHOR INFORMATION

Corresponding Author

*(S.M.) Phone: +81 75 366 5265. Fax: +81 75 925 5491. E-mail: miyake@astem.or.jp.

Present Addresses

[Π](F.O.) Ryukoku University, Otsu, Shiga 520-2194, Japan.
[∞](Y.M.-Y.) Kyoto College of Nutritional & Medical Science, Ukyo-ku, Kyoto 616-8326, Japan.

Funding

This study was supported by the Aichi Science and Technology Foundation and by the Kyoto Integrated Science & Technology Bio-Analysis Center (KIST-BIC).

Notes

The authors declare no competing financial interest.

ACKNOWLEDGMENTS

We express our appreciation to Dr. Jun Wada and Mr. Naohiro Tomari for their advice and to Ms. Shiho Yamaji and Ms. Asako Yamaguchi for their assistance.

DOI: 10.1021/acs.jafc.5b01980
J. Agric. Food Chem. 2015, 63, 6325−6330

■ ABBREVIATIONS USED

BSA, bovine serum albumin; dc, direct competitive; ELISA, enzyme-linked immunosorbent assay; HPLC, high-performance liquid chromatography; ic, indirect competitive; MRL, maximum residue limit; RSD, relative standard deviation; RU, resonance unit; SDS, sodium dodecyl sulfate; SPR, surface plasmon resonance

■ REFERENCES

(1) Chlorothalonil. In *The Pesticide Manual*, 16th ed.; MacBean, C., Ed.; British Crop Protection Council: Hampshire, UK, 2012; pp 194−196.

(2) Akiyama, Y.; Matsuoka, T.; Yoshioka, N.; Akamatsu, S.; Mitsuhashi, T. Pesticide residues in domestic agricultural products monitored in Hyogo Prefecture, Japan, FY 1995−2009. *J. Pestic. Sci.* **2011**, *36*, 66−72.

(3) Kurt-Karakus, P. B.; Teixeira, C.; Small, J.; Muir, D.; Bidleman, T. F. Current-use pesticides in inland lake waters, precipitation, and air from Ontario, Canada. *Environ. Toxicol. Chem.* **2011**, *30*, 1539−1548.

(4) Ripley, B. D.; Lissemore, L. I.; Leishman, P. D.; Denomme, M. A.; Ritter, L. Pesticide residues on fruits and vegetables from Ontario, Canada, 1991−1995. *J. AOAC Int.* **2000**, *83*, 196−213.

(5) el-Nabarawy, I. M.; Carey, W. F. Improved method for determination of chlorothalonil and related residues in cranberries. *J. Assoc. Off. Anal. Chem.* **1988**, *71*, 358−360.

(6) Hladik, M. L.; Kuivila, K. M. Analysis of chlorothalonil and three degradates in sediment and soil. *J. Agric. Food Chem.* **2008**, *56*, 2310−2314.

(7) Jongen, M. J.; Engel, R.; Leenheers, L. H. Determination of the pesticide chlorothalonil by HPLC and UV detection for occupational exposure assessment in greenhouse carnation culture. *J. Anal. Toxicol.* **1991**, *15*, 30−34.

(8) Yamamoto, A.; Miyamoto, I.; Kitagawa, M.; Moriwaki, H.; Miyakoda, H.; Kawasaki, H.; Arakawa, R. Analysis of chlorothalonil by liquid chromatography/mass spectrometry using negative-ion atmospheric pressure photoionization. *Anal. Sci.* **2009**, *25*, 693−697.

(9) Yeung, J. M.; Newsome, W. H. Determination of chlorothalonil in produce by enzyme immunoassay. *Bull. Environ. Contam. Toxicol.* **1995**, *54*, 444−450.

(10) Watanabe, E.; Miyake, S.; Ito, S.; Baba, K.; Eun, H.; Ishizaka, M.; Endo, S. Reliable enzyme immunoassay detection for chlorothalonil: fundamental evaluation for residue analysis and validation with gas chromatography. *J. Chromatogr. A* **2006**, *1129*, 273−282.

(11) Takahashi, Y.; Hayashi, A.; Sakurai, A.; Umezu, T.; Wada, Y. Immunological analysis of deposition of chlorothalonil applied by fogging techniques. *J. Pestic. Sci.* **1996**, *21*, 65−67.

(12) Okazaki, F.; Hirakawa, Y.; Yamaguchi-Murakami, Y.; Harada, A.; Watanabe, E.; Iwasa, S.; Narita, H.; Miyake, S. Development of direct competitive ELISA for residue analysis of fungicide chlorothalonil in vegetables. *Shokuhin Eiseigaku Zasshi* **2014**, *55*, 65−72.

(13) Tomassetti, M.; Martini, E.; Campanella, L. New immunosensors operating in organic phase (OPIEs) for analysis of triazinic pesticides in olive oil. *Electroanalysis* **2012**, *24*, 842−856.

(14) Garcia-Febrero, R.; Valera, E.; Muriano, A.; Pividori, M.; Sanchez-Baeza, F.; Marco, M. An electrochemical magneto immunosensor (EMIS) for the determination of paraquat residues in potato samples. *Anal. Bioanal. Chem.* **2013**, *405*, 7841−7849.

(15) Cesarino, I.; Moraes, F.; Lanza, M.; Machado, S. Electrochemical detection of carbamate pesticides in fruit and vegetables with a biosensor based on acetylcholinesterase immobilized on a composite of polyaniline−carbon nanotubes. *Food Chem.* **2012**, *135*, 873−879.

(16) Ribeiro, F.; Barroso, M.; Morais, S.; Viswanathan, S.; de Lima-Neto, P.; Correia, A.; Oliveira, M.; Delerue-Matos, C. Simple laccase-based biosensor for formetanate hydrochloride quantification in fruits. *Bioelectrochemistry* **2014**, *95*, 7−14.

(17) March, C.; Manclús, J.; Jiménez, Y.; Arnau, A.; Montoya, A. A piezoelectric immunosensor for the determination of pesticide residues and metabolites in fruit juices. *Talanta* **2009**, *78*, 827−833.

(18) Harris, R. D.; Luff, B. J.; Wilkinson, J. S.; Piehler, J.; Brecht, A.; Gauglitz, G.; Abuknesha, R. A. Integrated optical surface plasmon resonance immunoprobe for simazine detection. *Biosens. Bioelectron.* **1999**, *14*, 377−386.

(19) Svitel, J.; Dzgoev, A.; Ramanathan, K.; Danielsson, B. Surface plasmon resonance based pesticide assay on a renewable biosensing surface using the reversible concanavalin A monosaccharide interaction. *Biosens. Bioelectron.* **2000**, *15*, 411−415.

(20) Mauriz, E.; Calle, A.; Abad, A.; Montoya, A.; Hildebrandt, A.; Barcelo, D.; Lechuga, L. M. Determination of carbaryl in natural water samples by a surface plasmon resonance flow-through immunosensor. *Biosens. Bioelectron.* **2006**, *21*, 2129−2136.

(21) Kim, S. J.; Gobi, K. V.; Iwasaka, H.; Tanaka, H.; Miura, N. Novel miniature SPR immunosensor equipped with all-in-one multi-microchannel sensor chip for detecting low-molecular-weight analytes. *Biosens. Bioelectron.* **2007**, *23*, 701−707.

(22) Farré, M.; Martínez, E.; Ramón, J.; Navarro, A.; Radjenovic, J.; Mauriz, E.; Lechuga, L.; Marco, M. P.; Barceló, D. Part per trillion determination of atrazine in natural water samples by a surface plasmon resonance immunosensor. *Anal. Bioanal. Chem.* **2007**, *388*, 207−214.

(23) Mauriz, E.; Calle, A.; Manclus, J. J.; Montoya, A.; Lechuga, L. M. Multi-analyte SPR immunoassays for environmental biosensing of pesticides. *Anal. Bioanal. Chem.* **2007**, *387*, 1449−1458.

(24) Gouzy, M.-F.; Keß, M.; Krämer, P. M. A SPR-based immunosensor for the detection of isoproturon. *Biosens. Bioelectron.* **2009**, *24*, 1563−1568.

(25) Mauriz, E.; García-Fernández, C.; Mercader, J.; Abad-Fuentes, A.; Escuela, A.; Lechuga, L. Direct surface plasmon resonance immunosensing of pyraclostrobin residues in untreated fruit juices. *Anal. Bioanal. Chem.* **2012**, *404*, 2877−2886.

(26) Tomassetti, M.; Martini, E.; Campanella, L.; Favero, G.; Sanzó, G.; Mazzei, F. A new surface plasmon resonance immunosensor for triazine pesticide determination in bovine milk: a comparison with conventional amperometric and screen-printed immunodevices. *Sensors* **2015**, *15*, 10255−10270.

DOI: 10.1021/acs.jafc.5b01980
J. Agric. Food Chem. 2015, 63, 6325−6330

identification of which compounds were chelated to the elements.[18]

Some foods with high nutrient content have been used as supplements to meals to improve nutritional values. Nevertheless, antinutritional compounds (phytate, fibers, lignin, and others) can affect the expected result of these supplementations. For example, bread prepared with amaranth flour (which has a high content of iron) was evaluated using bioavailability studies to verify the contribution of this supplementation on its nutritional value. Furthermore, the bioavailable iron fraction was not increased due to the high phytate content in amaranth flour.[19]

The babassu mesocarp has been used as a food supplement, but its composition is not well-known nor is its effect on nutrient bioacessibility. This work aimed to study methods for assessing the interactions of Cu, Fe, and Zn with mesocarp and its effect on the bioaccessibility of these elements in dry whole milk and lignin, with and without babassu mesocarp as supplement, using simulated gastrointestinal digestion.

MATERIALS AND METHODS

Apparatus. An inductively coupled plasma optical emission spectrometer (ICP OES, iCAP 6300 Duo, Thermo Fisher Scientific, Cambridge, UK) equipped with axial and radial viewed plasma, a charge-injection device (CID) detector, an Echelle polychromator, and a radiofrequency source of 27.12 MHz was used for Cu, Fe, Zn, Ca, and Mg determination. The instrumental conditions for the analysis were 1250 W of power, 12 L min^{-1} of plasma gas, 0.5 L min^{-1} of auxiliary gas, and 0.2 L min^{-1} of nebulizer gas. A Babington nebulizer combined with a cyclonic spray chamber was used as sample introduction system. The selected wavelengths were 184.006 nm (Ca), 324.754 nm (Cu), 259.940 nm (Fe), 285.213 nm (Mg), and 202.548 nm (Zn).

A simultaneous atomic absorption spectrometer (SIMAA-6000, PerkinElmer, Norwalk, CT, USA) equipped with a longitudinal Zeeman-effect background corrector, Echelle optical arrangement, solid-state detector, and a standard transversely heated graphite atomizer (THGA) tube with a pyrolytically coated integrated platform was used when the analysis required greater sensitivity, for instance, in the determination of Cu and Fe. The spectrometer was operated using hollow cathode lamps, and the solutions were delivered into the graphite tube by means of an AS-72 autosampler. The instrumental conditions and heating program are shown in Table 1.

Table 1. Instrumental Conditions and Heating Program for the Simultaneous Determination of Cu and Fe by SIMAAS[a]

Instrumental Conditions				
element	wavelength (nm)	current (mA)		slit width (nm)
Cu	324.8	12		0.7
Fe	248.3	25		0.7
Heating Program				
step	temperature (°C)	ramp (s)	hold (s)	Ar flow (mL min^{-1})
drying I	110	1	30	250
drying II	130	15	30	250
pyrolysis	1200	10	20	250
atomization	2000	0	5	0
cleaning	2500	1	3	250

[a]Pyrolysis and atomization temperatures were selected on the basis of the most and least volatile analyte to be simultaneously determined. No chemical modifier was used. The injection temperature of the graphite tube was 30 °C, and the pipet speed of the injection was 100%.

Samples and standard reference materials (SRM) were digested using a high-pressure microwave oven (Speedwave 4, Berghof, Eningen, Germany) equipped with 12 TFM-PTFE vessels (model DAC-17) and infrared sensors for individual temperature and pressure measurements.

Mesocarp and milk drying procedures were carried out in a drying oven, model Q317M-32 (Quimis, São Paulo, SP, Brazil). A shaker table, model Q225 M (Quimis), was used for solution homogenization and stirring during the extraction procedures. For simulated gastrointestinal digestion, a water bath at 36 °C was used at 90 rpm for 120 min (model Q226M2, Quimis). A centrifuge, model Q222TM (Quimis), was used for phase separation. A pH meter, model PH-710 (Unity, Guarulhos, SP, Brazil), was used for pH adjustment of the samples.

Reagents and Samples. All solutions were prepared with high-purity deionized water (18.2 MΩ cm) obtained in a Milli-Q water purification system (Millipore, Belford, MA, USA).

Reference solutions were prepared from Titrisol standard analytical solutions containing 1000 mg L^{-1} iron ($FeCl_3$), copper ($CuCl_2$), zinc ($ZnCl_2$), calcium ($CaCl_2$), and magnesium ($MgCl_2$) (Merck, Darmstadt, Germany) after dilution in HNO_3 0.1% (v v^{-1}) (Merck).

Nitric acid 65% (w v^{-1}) (Merck) and hydrogen peroxide 30% (w v^{-1}) (Merck) were used for sample digestion in a microwave oven, and hydrochloric acid (Merck) and sodium hydroxide (Merck) solutions were used for pH adjustments.

Gastrointestinal fluids were prepared using NaCl (Merck), pepsin (CAS Registry No. 9001-75-6) (Sigma-Aldrich, Saint Louis, MO, USA), HCl (Merck), $NaHCO_3$ (Reagen, Rio de Janeiro, Brazil), K_2HPO_4 (Synth, Diadema, Brazil), NaOH (Merck), pancreatin (CAS Registry No. 8049-47-6) (Sigma-Aldrich), and bile salts (Sigma-Aldrich).

The dialysis procedure was performed using cellulose membranes (Sigma-Aldrich) in 32 mm tubes with 12.4 kDa porosity.

To check the accuracy of the analytical method used for the total determination of the elements, standard reference materials (SRM) of peach leaves (SRM 1547) and bovine liver (SRM 1577c) from the National Institute of Standards and Technology (NIST) were analyzed.

Babassu mesocarp flour samples, purchased in Maranhão state communities, dry milk (Ninho, Nestlé, São Paulo, Brazil), alkaline lignin powder (Sigma-Aldrich), and phytic acid solution 50% (w w^{-1}) (Sigma-Aldrich) were used in simulated gastrointestinal digestion assays.

Procedure. For the total determination of the elements, a mass of 200 mg of mesocarp, milk, or SRMs (SRM 1547 and SRM 1577c) were digested in a microwave oven with 2.0 mL of HNO_3 plus 1.0 mL of H_2O_2 plus 3.0 mL of H_2O, using a heating program in three steps (first step, temperature = 140 °C, ramp = 5 min, hold = 1 min; second step, temperature = 180 °C, ramp = 4 min, hold = 5 min; third step, temperature = 200 °C, ramp = 4 min, hold = 10 min). After digestion, the samples were diluted with deionized water until a final volume of 10 mL and analyzed by ICP OES for Fe, Zn, Ca, and Mg determination. The same solutions were used for Cu determination in a graphite furnace (SIMAA-6000). The calibrations for both techniques were prepared using reference solutions in equivalent acid concentration media of the digestion procedure (HNO_3 2% v v^{-1}). The determination of Ca and Mg was performed in the mesocarp and milk because these elements are considered macronutrients and, consequently, to determine if their presence during the process can influence the bioaccessibility of Cu, Fe, and Zn.

A mass around 2 g of babassu mesocarp was used to extract phytate and other complexing substances with 200 mL of water at pH 7 and 12, adjusted with NaOH. The mixtures were agitated on a shaker table for 30 min (400 rpm), and the mesocarp extract was separated using simple filtration. The residue from the extraction at pH 12 was washed again with NaOH (pH 12) and subsequently washed with three aliquots of water (200 mL) and later dried at 60 °C.

To confirm the extraction of phytate, a standard solution of phytic acid was extracted from mesocarp (obtained at pH 7 and 12) and was scanned in a range between 260 and 800 nm by UV molecular

DOI: 10.1021/acs.jafc.5b01947
J. Agric. Food Chem. 2015, 63, 6331−6337

Table 2. Experimental Conditions Used to Investigate the Bioaccessibility of Cu, Fe, and Zn[a]

assay	sample	addition	fraction analyzed	determination
Cu, Fe, and Zn bioaccessibility in mesocarp	200 mg of mesocarp		soluble fraction	Cu and Fe by SIMAAS, Zn by ICP OES
Cu, Fe, and Zn recovery after addition to the washed mesocarp (pH 12)	200 mg of mesocarp	0.018 mg of Cu^{II} 0.28 mg of Fe^{III} 0.14 mg of Zn^{II}	soluble fraction	Cu, Fe, and Zn by ICP OES
effect of Ca on Cu, Fe, and Zn bioaccessibility	200 mg of mesocarp	0.018 mg of Cu^{II} 0.28 mg of Fe^{III} 0.14 mg of Zn^{II} 0.88 mg of Ca^{II}	soluble fraction	Cu, Fe, and Zn by ICP OES
effect of Mg on Cu, Fe, and Zn bioaccessibility	200 mg of mesocarp	0.018 mg of Cu^{II} 0.28 mg of Fe^{III} 0.14 mg of Zn^{II} 0.067 mg of Mg^{II}	soluble fraction	Cu, Fe, and Zn by ICP OES
Cu, Fe, and Zn bioaccessibility in milk	100 mg of milk		soluble and dialyzable fraction	Cu by SIMAAS, Fe and Zn by ICP OES
Cu, Fe, and Zn bioaccessibility in presence of milk + mesocarp	100 mg of milk 100 mg of mesocarp		soluble and dialyzable fraction	Cu by SIMAAS, Fe and Zn by ICP OES
Cu, Fe, and Zn bioaccessibility in presence of milk + lignin	100 mg of milk 3.2 mg of lignin		soluble and dialyzable fraction	Cu by SIMAAS, Fe and Zn by ICP OES

[a]The gastrointestinal digestion used 3.0 mL of gastric fluid (pH ∼1.5) added to sample. The mixture was shaken (100 rpm) in a thermostatic bath at 36 °C for 2 h, and 0.4 mL of $NaHCO_3$ 3% (w v^{-1}) was added to adjust the pH to 6.8. An aliquot of 3.0 mL of intestinal fluid (pH ∼6.5) was added, and the extract solution was shaken and centrifuged to separate the supernatant.

Table 3. Concentration of Elements in Mesocarp, Milk, and SRMs as well as Addition and Recovery Test and Limits of Detection[a]

		Cu[b] ($\mu g\ g^{-1}$)	Fe[c] ($\mu g\ g^{-1}$)	Zn[c] ($\mu g\ g^{-1}$)	Ca[c] (mg g^{-1})	Mg[c] (mg g^{-1})
bovine liver (SRM 1577c)	certified	275.2 ± 4.6	197.94 ± 0.65	181.1 ± 1.0	0.131 ± 0.010	0.620 ± 0.042
	found	229 ± 4	177 ± 4	173 ± 4	0.130 ± 0.007	0.55 ± 0.01
	recovery	83	90	95	99	90
peach leaves (SRM 1547)	certified	3.7 ± 0.4	218 ± 14	17.9 ± 0.4	15.6 ± 0.2	4.32 ± 0.08
	found	3.5 ± 0.4	195 ± 23	16.73 ± 0.07	14.1 ± 0.09	3.89 ± 0.04
	recovery	95	89	93	90	90
milk	concentration	0.23 ± 0.03	236 ± 6	33 ± 0.7	9.1 ± 0.2	0.77 ± 0.01
	addition	2.5	250	25	5	0.5
	recovery	84	110	84	95	109
mesocarp	concentration	4.07 ± 0.07	16 ± 1	2.9 ± 0.3	0.40 ± 0.02	0.57 ± 0.01
	addition	5	10	1.0	0.25	0.5
	recovery (%)	99	116	85	95	104
limit of detection (LOD)		0.1	0.2	0.02	0.0006	0.0006

[a]The total determination of the elements used a mass of 200 mg of mesocarp, milk, or SRMs for digestion in a microwave oven. After digestion, the solution was diluted with deionized water to 10 mL and analyzed. [b]Analysis by SIMAAS. [c]Analysis by ICP OES (n = 3 samples).

absorption spectrophotometry. The pH of each solution was adjusted to 7 before the scan.

Aliquots of Cu, Fe, and Zn reference solutions were added to 2 mL of extracts, the pH was adjusted to 7, and the solution was diluted with water to 3 mL for a final concentration in the 10−300 mg L^{-1} range. Then, the solutions were homogenized on a shaker table for 30 min (400 rpm) and centrifuged at 1700 rpm, and the supernatants were analyzed by ICP OES. A similar procedure was used for the washed mesocarp, adding Cu, Fe, and Zn reference solutions to 50 mg of washed mesocarp and diluting until to 5 mL.

The concentrations of Cu, Fe, and Zn were also determined in the extracts and in a blank prepared for washed mesocarp additions. Thus, the recoveries of additions were calculated as follows: (obtained concentration − blank concentration)/added concentration) × 100%.

The in vitro gastrointestinal digestion procedure was employed to assess the bioaccessibility of the mineral nutrients (Cu, Fe, and Zn) using fluids prepared according to U.S. Pharmacopeia XXIV recommendations.[20] The gastric fluid was prepared by dissolving 0.2 g of NaCl and 0.32 g of pepsin in water. Afterward, 7.0 mL of HCl 10% (v v^{-1}) was added, and this solution was diluted to 100 mL with

DOI: 10.1021/acs.jafc.5b01947
J. Agric. Food Chem. 2015, 63, 6331−6337

deionized water. The intestinal fluid was prepared by dissolving 0.68 g of K_2HPO_4, 1.0 g of pancreatin, 1.25 g of bile salts, and 7.7 mL of NaOH (0.2 mol L^{-1}) and diluted in deionized water to 100 mL.

The general procedure followed to simulate gastrointestinal digestion used 3.0 mL of gastric fluid (pH ~1.5) added to 200 mg of mesocarp. The mixture was shaken continuously (100 rpm) in a thermostatic bath at 36 °C for 2 h. To proceed with the intestinal digestion step, it was necessary to add 0.4 mL of $NaHCO_3$ 3% (w v^{-1}) to adjust the pH to 6.8. Then, 3.0 mL of intestinal fluid (pH ~6.5) was added, and the extract solution was shaken again using the same conditions reported in the gastric step and centrifuged to separate the supernatant. A dialysis procedure was performed to simulate nutrient absorption by human organisms. The supernatants (2 mL) were added into bags formed from cellulose membranes, tied with polyethylene tapes, and immersed into tubes filled with 30 mL of water. After 12 h, the membrane was carefully opened, and the solution was collected from inside and analyzed. The dialyzed fraction was determined by subtracting the retained concentration in membrane from the soluble fraction.[21] The varied conditions established to investigate the Cu, Fe, and Zn bioaccessibility by in vitro gastrointestinal assays are shown in Table 2.

The calibrations for analyses of in vitro gastrointestinal digestions samples by ICP OES and SIMAAS were prepared using reference solutions in HNO_3 0.1% (v v^{-1}). For ICP OES analyzes, the matrix interference effect was evaluated by addition and recovery test. Furthermore, for Fe and Cu determination by SIMAAS, the matrix interference effect was evaluated by comparing calibration curves using reference solutions in sample, blank (gastrointestinal fluid), and HNO_3 0.1% (v v^{-1}).

RESULTS AND DISCUSSION

Total Determination of Elements. The concentrations of Cu, Fe, Zn, Ca, and Mg in mesocarp and milk samples were determined by ICP OES, after microwave oven acid digestion (Table 3). Furthermore, in Table 3 are also shown the method accuracy evaluation by SRMs analysis and addition/recovery test results. The results of SRMs analyses present recoveries ranging from 83 to 99%. Good recoveries (84−116%) were also obtained in addition/recovery tests (Table 3).

The concentrations of Fe and Ca in milk were similar to the information contained in the manufacturer's label (200 μg g^{-1} Fe and 9.4 mg g^{-1} Ca). There was no information about other elements on the milk label to be compared. However, except Cu and Fe, all results were in agreement with those described by the Brazilian Table of Food Composition (TACO) (1.1 μg g^{-1} Cu, 5.0 μg g^{-1} Fe, 27 μg g^{-1} Zn, 8.9 mg g^{-1} Ca, and 0.77 mg g^{-1} Mg).[22] The concentration of Fe was about 40 times greater than the TACO value, owing to the milk sample being enriched with iron pyrophosphate.

By comparison of the obtained concentrations for mesocarp with values previously determined by our group (2.1 μg g^{-1} Cu, 16 μg g^{-1} Fe, 2.4 μg g^{-1} Zn, 432 μg g^{-1} Ca, and 679 μg g^{-1} Mg),[23] differences could be observed for the Cu and Mg concentrations, but for the other elements, the results were similar. When the results were compared with the TACO table values (2.2 μg g^{-1} Cu, 183 μg g^{-1} Fe, 3 μg g^{-1} Zn, 610 μg g^{-1} Ca, and 390 μg g^{-1} Mg), only Zn presented similar values. These differences may be related to the factors that can modify its mineral composition, such as origin, soil, and climate.[23]

Reference daily intakes (RDIs) for essential human nutrition elements have been established by the U.S. Food and Drug Administration (FDA), for instance, Cu (2 mg), Fe (18 mg), Zn (15 mg), Ca (1000 mg), and Mg (400 mg).[24] Considering a portion of 26 g (two spoons) of mesocarp consumed, the contribution percentages to RDIs are 5, 2, 1, 1, and 4% for Cu, Fe, Zn, Ca, and Mg, respectively.

Evaluation of Cu, Fe, and Zn Interaction with the Extract of Babassu Mesocarp. The mesocarp extract obtained at pH 12 had a darker brown color than that obtained at pH 7. This difference must be related to the greater ability of the pH 12 solution to extract organic acids (mainly phytic acid) that are bound to the matrix.

Phytic acid could be the main complexing substance extracted from mesocarp, as this compound is found in high concentrations in vegetables because it has the function of storing phosphorus and energy. Phytic acid also has the ability to bind to metal ions, forming stable complexes.[6−8]

Spectrophotometric analysis of the extracts showed that the spectra of phytic acid and the extracts were similar, and both had a maximum absorbance at 272 nm, demonstrating the presence of this substance in the extract.

The addition of elements in both extracts (pH 7 and 12 solutions) was done with the final pH adjusted to 7, which is similar to the intestinal condition. After the addition of elements to the extracts, a brown precipitate was formed and extract solution discoloration was observed. In aqueous solutions at pH 7, Fe^{III} and Cu^{II} may hydrolyze and precipitate as hydroxides. However, even with the possibility of Fe^{III} and Cu^{II} hydrolysis, the precipitate formed in the extract from mesocarp was provided not only by hydrolysis of these ions but also by complexation with phytate. The discoloration of the extract solutions and the increasing volume of the precipitate indicated that the compound present in the solution had precipitated together with the elements.

The recoveries of elements added (determined in supernatant) to the babassu mesocarp extracts from pH 7 (Figure 1a) and pH 12 (Figure 1b) solutions, after centrifugation, are shown in Figure 1. If only hydrolysis was considered, high Cu and Fe recoveries were not expected, especially for lower addition concentrations. However, the results show that complexes formed between these elements and phytate until a certain concentration, minimizing the effect of hydrolysis, making them more soluble and increasing recovery. The recovery is higher for the extract at pH 12 (Figure 1b) because it contains a higher concentration of phytate. It is well-known that the higher the concentration of cations bound to phytate, the lower the complex solubility. For example, monoferric phytate is highly soluble, whereas tetraferric phytate is insoluble.[25]

This experiment demonstrates that the phytate extract of the babassu mesocarp can strongly interact with Cu^{II} and Fe^{III}, and less so with Zn^{II}, at pH 7.

Evaluation of Cu, Fe, and Zn Interaction with Washed Mesocarp. The recovery of Cu^{II}, Fe^{III}, and Zn^{II} added to the washed mesocarp is shown in Figure 1c. These additions were carried out to evaluate the behavior of these ions in the presence of solid mesocarp, after weakly bound complexing compounds had been removed during the washing. It can be seen that the recoveries of Cu and Fe in the supernatants were <20%. These low recoveries cannot prove their interaction with washed mesocarp because they can be attributed to the hydrolysis and precipitation of Cu^{II} and Fe^{III} at pH 7. On the other hand, at this pH the Zn^{II} does not hydrolyze. However, at lower added element concentrations, lower recoveries for Zn were observed, demonstrating a possible interaction with the complexing compounds that were not extracted from the mesocarp. The increase in recovery may be indicative of saturation of the binding sites in the mesocarp compounds. Therefore, a low concentration of Zn was able to interact with

DOI: 10.1021/acs.jafc.5b01947
J. Agric. Food Chem. 2015, 63, 6331−6337

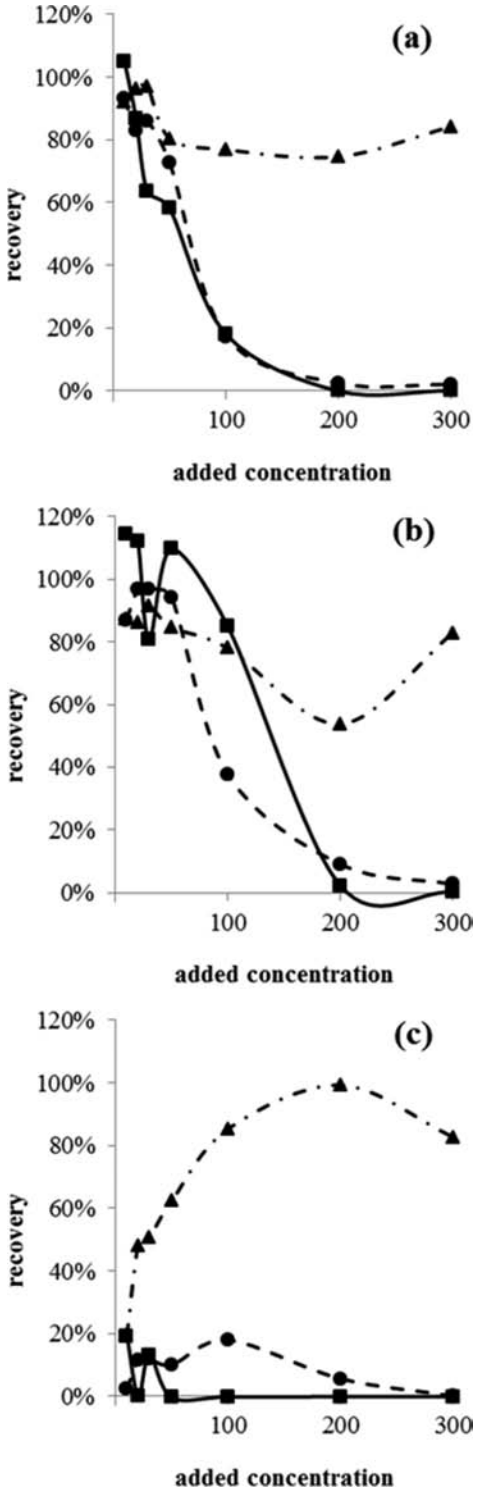

Figure 1. Recovery of Cu (●), Fe (■), and Zn (▲) added to the extract prepared (a) at pH 7 or (b) at pH 12 and (c) in the washed mesocarp.

mesocarp occupying all binding sites. Thus, when a higher concentration was added, the excess of Zn remained in solution.

In Vitro Gastrointestinal Digestion of Babassu Mesocarp. The addition and recovery test shows that ICP OES analyses did not present significant matrix interference effect. The obtained recoveries range from 87 to 107%. Matrix interference was also not observed for SIMAAS analyses. The ratio between the slopes obtained from HNO_3 0.1% (v v^{-1}) solutions and sample and blank media range from 1.0 to 1.2; thus, no significant difference was observed, allowing the calibration with reference solutions in HNO_3 0.1% (v v^{-1}).

The gastrointestinal digestion of babassu mesocarp showed that Fe and Zn present in this material are not extracted, but Cu presented a soluble fraction (96%). This indicates that, besides the presence of Fe and Zn in the babassu mesocarp, as shown in Table 3, these elements are not bioaccessible.

The supernatants of the gastrointestinal digestions with Cu^{II}, Fe^{III}, and Zn^{II} addition exhibited a dark color, possibly caused by the extraction of phytic acid and subsequent complexation with elements such as Fe, as observed in previous results.

Table 4 presents the recoveries of Cu, Fe, and Zn that were added to the babassu mesocarp during gastrointestinal digestion, without and with the addition of Ca^{II} and Mg^{II}. These elements were added in concentrations similar to those present in milk. Without Ca and Mg, 65% of the Cu, 48% of the Fe, and 75% of the Zn remained in the supernatant solution. It is likely that the other fractions of Cu, Fe, and Zn were bound to the compounds present in the mesocarp or precipitate. With the addition of 67 μg of Mg^{II} to the simulated gastrointestinal digestion, the recovery values were not significantly changed (65% for Cu, 49% for Fe, and 73% for Zn). However, with the addition of 880 μg of Ca^{II}, Fe^{III}, and Zn^{II}, recoveries undergo alteration, decreasing to 41% for Fe and 56% for Zn. In this case, the concentration of soluble Cu was also almost the same under all conditions.

Table 4. Addition and Recovery Tests for Fe, Cu, and Zn in Gastrointestinal Digestion of Babassu Mesocarp in the Presence of Ca and Mg[a]

	recovery mass (μg)		
element	without Ca and Mg	with Ca addition	with Mg addition
Fe	134 ± 3	115 ± 2	138 ± 7
Cu	11.7 ± 0.2	11.6 ± 0.3	11.5 ± 0.4
Zn	105 ± 5	78 ± 6	103 ± 3

[a]Addition of 18 μg of Cu, 280 μg of Fe, and 140 μg of Zn.

Upon the addition of Ca^{II}, the color of the solution was clearer than that without Ca^{II}. The dark color of the solution can be related to soluble phytate complexes. Therefore, discoloration caused by the addition of Ca^{II} indicates a decrease in phytate complex solubility. Calcium forms complexes with phytate, and these complexes (Ca−phytate) can bind Zn^{II} and Fe^{III}, forming complexes that are even more insoluble than just Fe−phytate and Zn−phytate complexes.[25]

In Vitro Gastrointestinal Digestion of Milk with Mesocarp and Lignin. In principle, the studies performed to evaluate the bioaccessibility of the elements with babassu mesocarp all utilized standard solutions, which was very important to a better understanding of the system.

To simulate a situation closer to reality, tests were conducted to assess the bioaccessibility of Cu, Fe, and Zn in the gastrointestinal digestion of whole dried milk and milk in the presence of mesocarp and lignin. The Cu, Fe, and Zn bioaccessibility values are shown in Figure 2. In each case, the first column in the graphs (white bar) refers to the total concentration of elements present in the weighed mass of milk and mesocarp. The second column (gray bar) represents the soluble fractions obtained during gastrointestinal digestions, after centrifugation and analysis of supernatant, and the last

DOI: 10.1021/acs.jafc.5b01947
J. Agric. Food Chem. 2015, 63, 6331−6337

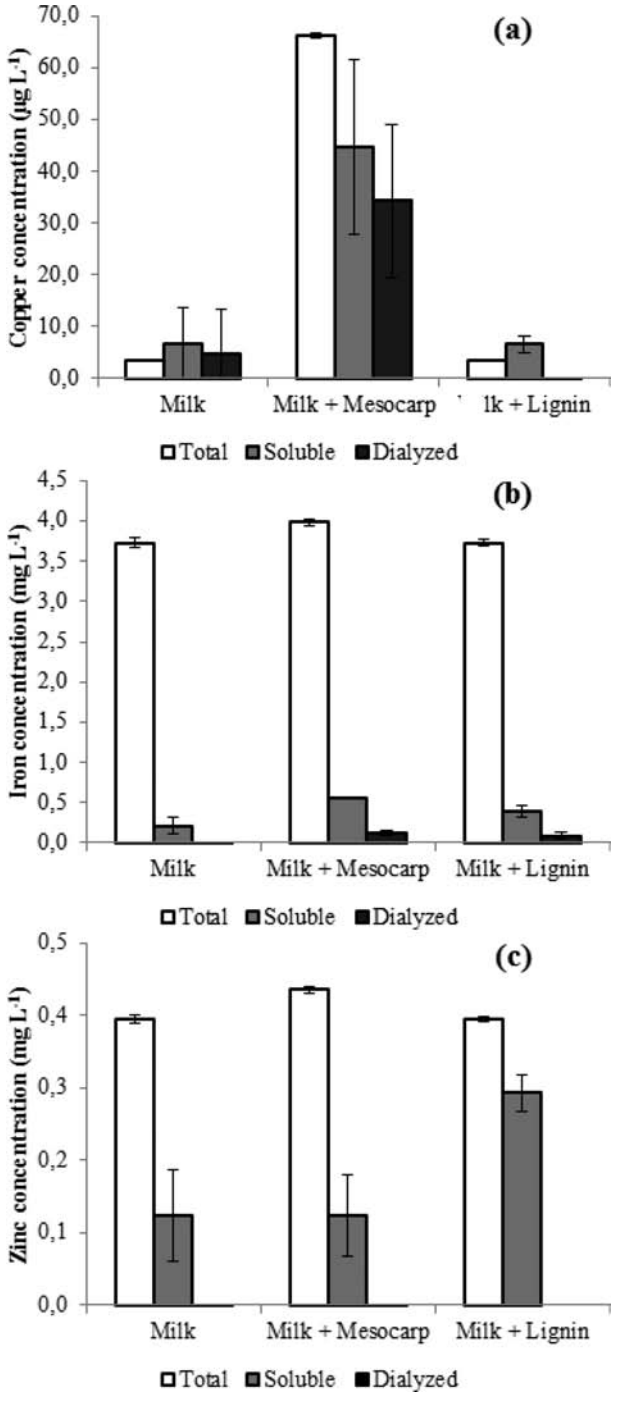

Figure 2. (a) Cu, (b) Fe, and (c) Zn bioaccessibility in milk and in a mixture of milk and mesocarp as well as in a mixture of milk and lignin.

column (black bar) represents the concentration of these elements dialyzed in the cellulose membrane (the fraction that migrated throughout the membrane).

The concentration of Cu in milk is low, but it is fully bioaccessible, as shown in Figure 2a. A comparison of the total and soluble Fe and Zn contents (Figure 2b,c) shows that they are not fully solubilized during the milk gastrointestinal digestion. Furthermore, after dialysis, these elements were completely retained inside the membrane, indicating they were associated with high molecular weight compounds, which probably could decrease their bioaccessibility. The results observed for Fe are very interesting, as the milk used in this research was enriched with ferric pyrophosphate by the manufacturer. This iron compound is widely used for fortify foods. Although it is known that it presents low bioavailabity when compared to other iron species, such as ferrous sulfate, studies demonstrate that it suffers less negative effect of antinutritional compounds.[26,27]

When the milk was mixed with mesocarp, the total concentration of Cu increased meaning fully, owing to the presence of mesocarp that has a concentration 20 times higher than in milk. Consequently, the soluble and dialyzed fractions observed in Figure 2a are from mesocarp. Thus, it was not possible to evaluate the effect on Cu bioaccessibility in milk. The addition of mesocarp to milk increased the concentration of soluble Fe (Figure 2b) and its dialyzed fraction compared to the digestion of milk alone. Fe hydrolyzes and precipitates at intestinal pH; however, nutrients present in food, such as amino acids and peptides, can bind to Fe, turning it soluble and, consequently, bioavailable.[28] Thus, substances present in milk, such as casein or other binding compounds, can form a soluble complex with Fe, thereby enhancing the Fe bioaccessibility in mesocarp. Another suggested explanation is that compounds present in the mesocarp (e.g., phytate) may also form soluble compounds of the elements, depending on their concentrations. The soluble and dialyzed fractions of Zn in the mixture of milk and mesocarp remained unchanged compared to the milk alone (Figure 2c); thus, the mesocarp does not influence Zn bioaccessibility in milk.

Although lignin increases the elements' soluble fractions, the dialyzed fractions were still very low. However, these elements, even when soluble, may not be bioaccessible for absorption by the body, because they are strongly associated with lignin, which is a compound of high molecular weight.

In conclusion, total elemental determination showed that mesocarp babassu contained Fe, Cu, and Zn; however, Fe and Zn are not available after in vitro gastrointestinal digestion. Therefore, the mesocarp cannot be considered as a source of these nutrients. Only Cu was extracted during the simulated digestion, having a soluble fraction of 96%. Furthermore, it was observed that the mesocarp could interact with these elements, and phytate was the main compound responsible for these interactions. It was also noted that Fe^{III} and Cu^{II} ions may hydrolyze and precipitate at intestinal pH, inhibiting their absorption by human organisms. The negative effects on Cu, Fe, and Zn bioaccessibility observed in the studies using reference solutions did not occur when digestion of the milk mixtures was performed. The presence of mesocarp did not reduce the available fractions of elements.

AUTHOR INFORMATION

Corresponding Author

*(P.V.O.) Phone: +55 11 3091 8516. Fax: +55 11 3091 2161. E-mail: pvolivei@iq.usp.br.

Funding

We are grateful to Conselho Nacional de Desenvolvimento Científico e Tecnológico (CNPq) and Fundação de Amparo à Pesquisa do Estado de São Paulo (FAPESP) for financial support. We thank the CNPq for the research opportunities and fellowships provided.

Notes

The authors declare no competing financial interest.

DOI: 10.1021/acs.jafc.5b01947
J. Agric. Food Chem. 2015, 63, 6331−6337

■ ACKNOWLEDGMENTS

We thank Nova Analítica Imp. Exp. Ltda. for providing the microwave oven and ICP OES.

■ REFERENCES

(1) Vinhal, J. O.; Lima, C. F.; Barbosa, L. C. A. Analytical pyrolyis of the kernel and oil of babassu palm (*Orbignya phalerata*). *J. Anal. Appl. Pyrolysis* **2014**, *107*, 73−81.

(2) Pessoa, R. S.; Franca, E. L.; Ribeiro, E. B.; Lanes, P. K. D.; Chaud, N. G. A.; Moraes, L. C. A.; Honorario-Franca, A. C. Microemulsion of babassu oil as a natural product to improve human immunes system function. *Drug Des., Dev. Ther.* **2015**, *9*, 21−31.

(3) Miotto, F. R. C.; Restle, J.; Neiva, J. N. M.; Maciel, R. P.; Fernandes, J. J. d. R. Intake and digestibility of sheep diets containing levels of babassu-mesocarp meal. *Rev. Cienc. Agron.* **2012**, *43*, 792−801.

(4) Souza, M. G.; Vieira, E. C.; Oliveira, P. V. Determination of As, Cd e Pb in babassu nut and mesocarp, sapucaia, xixa and brazilian nut by atomic absorption spectrometry. *Quim. Nova* **2009**, *32*, 1442−1446.

(5) Souza, L. F.; Macedo, G. D.; Missio, R. L.; Neiva, J. N. M.; Restle, J.; Melo, J. C.; de Sousa Júnior, A.; dos Santos, R. P.; Silva, A. G. M. E.; Borges, I. Bromatological composition and kinetics of rumen for feeds containing babassu residue. *Rev. Cienc. Agron.* **2014**, *45*, 177−185.

(6) Gupta, R. K.; Gangoliya, S. S.; Singh, N. K. Reduction of phytic acid and enhancement of bioavailable micronutrients in food grains. *J. Food Sci. Technol.* **2015**, *52*, 676−684.

(7) Dost, K.; Tokul, O. Determination of phytic acid in wheat and wheat products by reverse phase high performance liquid chromatography. *Anal. Chim. Acta* **2006**, *558*, 22−27.

(8) Kumar, V.; Sinha, A. K.; Makkar, H. P.; Becker, K. Dietary roles of phytate and phytase in human nutrition: a review. *Food Chem.* **2010**, *120*, 945−959.

(9) Amalraj, A.; Pius, A. Bioavailability of calcium and its absorption inhibitors in raw and cooked green leafy vegetables commonly consumed in India − an *in vitro* study. *Food Chem.* **2015**, *170*, 430−436.

(10) Torre, M.; Rodriguez, A. R.; Saura-Calixto, F. Interactions of Fe(II), Ca(II) and Fe(III) with high dietary fibre materials: a physicochemical approach. *Food Chem.* **1995**, *54*, 23−31.

(11) Tejado, A.; Pena, C.; Labidi, J.; Echeverria, J.; Mondragon, I. Physico-chemical characterization of lignins from different sources for use in phenol−formaldehyde resin synthesis. *Bioresour. Technol.* **2007**, *98*, 1655−1663.

(12) Fly, A.; Fahey, G.; Czarnecki-Maulden, G. Iron bioavailability from diets containing isolated or intact sources of lignin. *Biol. Trace Elem. Res.* **1998**, *62*, 83−100.

(13) Etcheverry, P.; Grusak, M. A.; Fleige, L. E. Application of *in vitro* bioacessibility and bioavailability methods for calcium, carotenoids, folate, iron, magnesium polyphenols, zinc, and vitamins B-6, B-14, D, and E. *Front. Physiol.* **2012**, *3*, 1−22.

(14) Hur, S. J.; Lim, B. O.; Decker, E. A.; McClements, D. J. *In vitro* human digestion models for food applications. *Food Chem.* **2011**, *125*, 1−12.

(15) Perales, S.; Barberá, R.; Lagarda, M. J.; Farré, R. Availability of iron from milk-based formulas and fruit juices containing milk and cereals estimated by *in vitro* methods (solubility, dialysability) and uptake and transport by Caco-2 cells. *Food Chem.* **2007**, *102*, 1296−1303.

(16) Thompson, B.; Sharp, P.; Elliott, R.; Al-Mutairi, S.; Fairweather-Tait, S. J. Development of a modified Caco-2 cell model system for studying iron availability in eggs. *J. Agric. Food Chem.* **2010**, *58*, 3833−3839.

(17) da Silva, E. D.; Heerdt, G.; Cidade, M.; Pereira, C. D.; Morgon, N. H.; Cadore, S. Use of *in vitro* digestion method and theoretical calculations to evaluate the bioaccessibility of Al, Cd, Fe and Zn in lettuce and cole by inductively coupled plasma mass spectrometry. *Microchem. J.* **2015**, *119*, 152−158.

(18) Lestienne, I.; Caporiccio, B.; Besançon, P.; Rochette, I.; Trèche, S. Relative contribution of phytates, fibers, and tannins to low iron and zinc in vitro solubility in pearl millet (*Pennisetum glaucum*) flour and grain fractions. *J. Agric. Food Chem.* **2005**, *53*, 8342−8348.

(19) Sanz-Penella, J. M.; Laparra, J. M.; Sanz, Y.; Haros, M. Bread supplemented with amaranth (*Amaranthus cruentus*): effect of phytates on *in vitro* iron absorption. *Plant Foods Hum. Nutr.* **2012**, *67*, 50−56.

(20) Test solutions. In *The United States Pharmacopeia and The National Formulary*, USP24-NF19; The United States Pharmacopeial Convention: Rockville, MD, USA, 2000; pp 2235−2236.

(21) Nascimento, A. N.; Naozuka, J.; Oliveira, P. V. *In vitro* evaluation of Cu and Fe bioavailability in cashew nuts by *off-line* coupled SEC−UV and SIMAAS. *Microchem. J.* **2010**, *96*, 58−63.

(22) NEPA/UNICAMP (Núcleo de Estudos e Pesquisas em Alimentação/Universidade Estadual de Campinas). Banco de dados. In *Tabela Brasileira de Composição dos Alimentos (TACO)*, 4th ed.; Fórmula: Campinas, Brazil, 2011; pp 64−88.

(23) Naozuka, J.; Carvalho Vieira, E.; Nascimento, A. N.; Oliveira, P. V. Elemental analysis of nuts and seeds by axially viewed ICP OES. *Food Chem.* **2011**, *124*, 1667−1672.

(24) Dolan, S. P.; Capar, S. G. Multi-element analysis of food by microwave digestion and inductively coupled plasma-atomic emission spectrometry. *J. Food Compos. Anal.* **2002**, *15*, 593−615.

(25) Rouchon, V.; Pellizzi, E.; Duranton, M.; Vanmeert, F.; Janssens, K. Combining XANES, ICP-AES, and SEM/EDS for the study of phytate chelating treatments used on iron gall ink damaged manuscripts. *J. Anal. At. Spectrom.* **2011**, *26*, 2434−2441.

(26) Walczyk, T.; Kastenmayer, P.; Bonsmann, S. S.; Zeder, C.; Grathwohl, D.; Hurrell, R. F. Ferrous ammonium phosphate ($FeNH_4PO_4$) as a new food fortificant: iron bioavailability compared to ferrous sulfate and ferric pyrophosphate from an instant milk drink. *Eur. J. Nutr.* **2013**, *52*, 1361−1368.

(27) Zhu, L.; Glahn, R. P.; Nelson, D.; Miller, D. D. Comparing soluble ferric pyrophosphate to common iron salts and chelates as sources of bioavailable iron in a Caco-2 cell culture model. *J. Agric. Food Chem.* **2009**, *57*, 5014−5019.

(28) Miller, D. D.; Schricker, B. R.; Rasmussen, R. R.; Van Campen, D. An *in vitro* method for estimation of iron availability from meals. *Am. J. Clin. Nutr.* **1981**, *34*, 2248−2256.

DOI: 10.1021/acs.jafc.5b01947
J. Agric. Food Chem. 2015, 63, 6331−6337

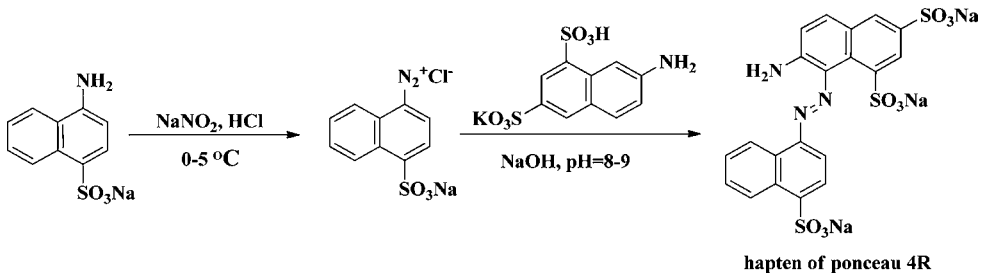

Figure 1. Synthesis of the hapten for ponceau 4R.

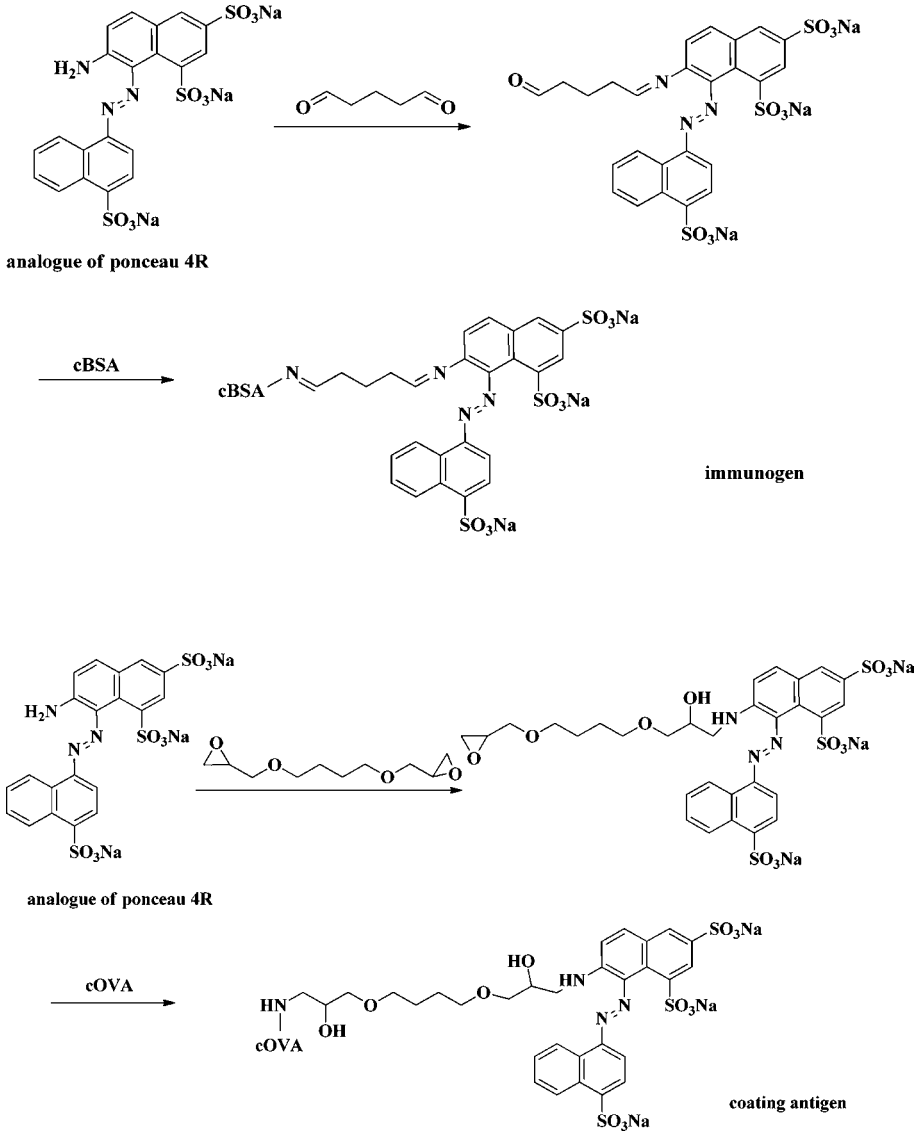

Figure 2. Synthesis of the immunogen and coating antigen for ponceau 4R.

Sciences (Military Medical Institute, Beijing, China). 3,3′,5,5′-Tetramethylbenzidine (TMB) was purchased from Shanghai Sangon Biological Engineering Technology (Sangon Biotech Co., Ltd., Shanghai, China). Dimethylformamide (DMF) and glutaraldehyde of chemical grade were supplied by Guangfu Fine Chemical Research Institute (Guangfu Chemical Co., Tianjin, China). Sodium 4-aminonaphthalene-1-sulfonate and sodium 7-aminonaphthalene-1,3-disulfonate were from TCI (Tokyo Kasei Kogyo Co., Ltd., Tokyo, Japan).

The buffers included (1) phosphate-buffered saline (PBS, pH 7.4), composed of 138 mM NaCl, 1.5 mM KH_2PO_4, 7 mM Na_2HPO_4, and 2.7 mM KCl; (2) washing buffer (PBST), a PBS solution containing 0.05% (v/v) of Tween 20; (3) coating buffer, 0.01 M carbonate buffer (15 mM Na_2CO_3 and 35 mM $NaHCO_3$, pH 9.6); (4) blocking buffer, PBS mixed with 1% of OVA and 0.05% (v/v) of Tween 20; (5) substrate buffer (TMB + H_2O_2), 400 mL of 0.6% TMB−DMSO mixed with 100 mL of 1% H_2O_2 in citrate−acetate buffer (pH 5.5); and (6) borate buffer (pH 8.5), 94.5 mM sodium tetraborate and 151.4 mM NaCl.

The instruments used in this study were listed as follows: (1) The model 680 microplate reader was from Bio-Rad Laboratories Headquarters (Bio-Rad, Hercules, CA, USA) for immunoassay signal

DOI: 10.1021/acs.jafc.5b02129
J. Agric. Food Chem. 2015, 63, 6338−6345

Table 1. Cross-Reactivity (CR) of ELISA for Ponceau 4R and Related Compounds

Compound	Structure	IC_{50} (ng/mL)	CR (%)
Ponceau 4R	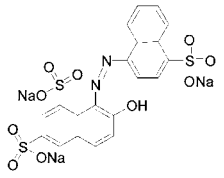	36.82	100
Sunset yellow FCF	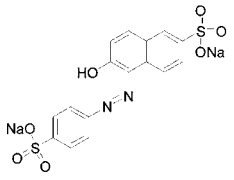	>50000	<0.07
Tartrazine	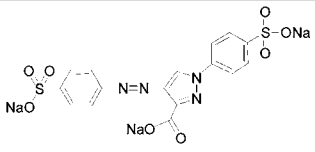	>50000	<0.07
Amaranth	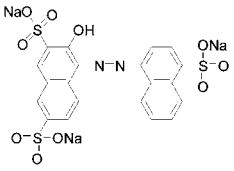	>10000	<0.3
Chromotrope FB	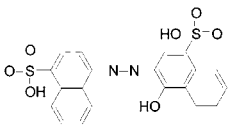	>50000	<0.07
Crocein orange G	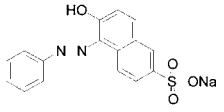	>50000	<0.07

collection. (2) A Shimadzu UV-1800 (Kyoto, Japan) was used to detect the UV−vis spectra of conjugates. (3) A Bruker Avance 400 NMR spectrometer (Bruker BioSpin, Zurich, Switzerland) was applied to record the ^1H (400 MHz).

Synthesis of Hapten for Ponceau 4R. To prepare immunogen, a hapten of ponceau 4R was synthesized by the following steps (Figure 1). First, 1.0 mmol of 4-aminonaphthalene-1-sulfonate and 1.1 mmol of $NaNO_2$ were sufficiently mixed and added into 4.0 mL of 12.0 M HCl. This mixture was allowed to react at 0−5 °C for 1 h. Second, the mixture was added into the DMF solution (250 μL) containing 1.0 mmol of sodium 7-aminonaphthalene-1,3-disulfonate. Subsequently, 10 M NaOH was used to adjust the pH of the solution to 8−9, and the mixture was kept at 4 °C for 5 h for reaction. Finally, the product was filtered and the precipitate was collected, which served as the hapten of ponceau 4R.

Preparation of Immunogen and Coating Antigen. BSA and OVA were used to prepare the immunogen and coating antigen of ponceau 4R, respectively. To improve the yield of the reaction, the carboxylic acid groups of the carrier protein were converted into primary amine groups with an excess of ethylenediamine as described previously.[33] The activated proteins were named cBSA and cOVA, respectively.

The immunogen and coating antigen of ponceau 4R were initially synthesized in this study, and the details of preparation were described as follows (Figure 2). Accurately weighed cBSA (97.2 mg, 1.43 μmol) and hapten of ponceau 4R (30.2 mg, 0.05 mmol) were dissolved into 6.0 and 3.0 mL of borate buffer, respectively. Then, these two solutions were fully mixed. Next, 98 μL of glutaraldehyde (25%, 0.25 mmol) was added dropwise to the mixture, and it was stirred for reaction at room temperature for 5 h. The product was dialyzed against PBS and distilled water for 3 days, respectively, and the dialysate was refreshed at intervals of 8 h. Finally, the purified resultant, which was the immunogen of ponceau 4R, was lyophilized and stored at −20 °C for further use.

The coating antigen of ponceau 4R was prepared by using BDE as the linker (Figure 2). BDE (13.3 μL; 0.07 mmol) was added into the solution of cOVA (31.5 mg, 0.7 μmol), which was dissolved in 4 mL of borate buffer and then reacted for 24 h. To this solution was dropwise

DOI: 10.1021/acs.jafc.5b02129
J. Agric. Food Chem. 2015, 63, 6338−6345

added hapten of ponceau 4R (14.8 mg, 0.0245 mmol) dissolved into 3 mL of borate buffer, and reaction was continued for another 24 h at room temperature. The coating antigen of ponceau 4R was obtained via the purification steps mentioned above.

Preparation of Polyclonal Antibody. Animal treatments were based on the guidelines of the Chinese Association for Laboratory Animal Sciences. Two male New Zealand white rabbits (2−2.5 kg) were used to produce anti-ponceau 4R polyclonal antibodies by multiple-site subcutaneous injections. The blank blood (1.0 mL) was collected beforehand. In the first immunization, 0.5 mL of normal saline containing 0.5 mg of immunogen and 0.5 mL of cFA was emulsified and subcutaneously injected at the rabbits' back. Then, three booster injections at intervals of 2 weeks followed by the first immunization, and the injected dosage decreased to 0.25 mg of immunogen plus 0.5 mL of iFA and 0.5 mL of normal saline. For the fifth immunization, 0.25 mg of immunogen in 1 mL of normal saline was administered. Seven days after the final injection, the rabbits were exsanguinated by heart puncture under general anesthetic, and the antiserum was collected by coagulation and centrifugation. It was stored at −20 °C until use.

Optimization of the Immunoassay. The concentrations of coating antigen and antibody were optimized first by the checkerboard procedure. The 96-well microplate was coated with the coating antigen at various concentrations (0.001, 0.01, 0.1, 0.5, 1.0, 5.0 μg/mL), and it was incubated at 37 °C for 2 h. After removal of the excess coating antigen by washing with PBST, the blocking buffer was added and the plate was incubated at 37 °C for 2 h subsequently. The antibodies with different dilutions were added (dilution ratio of 1:2500−1:320000, 100 μL per well) after washing with PBST. The plate was incubated at 37 °C for 2 h and washed. Then, goat anti-rabbit IgG-HRP (1:2000, 100 μL) was added into each well and incubated for 0.5 h at 37 °C. Finally, TMB substrate solution was added, which was incubated for 10 min, and the enzymatic reaction was stopped by the addition of 2 M HCl (100 μL per well). Subsequently, the absorbance at 450 nm was recorded. The concentration of antibody and coating antigen with the absorbance value correspondent with their dilution ratio was selected as the optimal condition for further study.

Indirect Competitive ELISA (icELISA). An icELISA procedure was developed under the optimal concentration of coating antigen and antibody, which was studied above. The icELISA was similar to the description above, except that 50 μL of competitor diluent (ponceau 4R) was added before the addition of antibodies. The competitive curve was generated by plotting absorbance at 450 nm versus the logarithm of ponceau 4R concentration. The IC_{50} values were determined to reflect the sensitivity of the assay, which represented the concentration that half of the binding of the antibody to the coating antigen was inhibited.

For the cross-reactivity study, other selected azo dyes were added instead of ponceau 4R at different concentrations from 0.0001 to 10000 ng/mL. Five structural analogues were selected for cross-reactivity study including sunset yellow FCF, tartrazine, amaranth, chromotrope FB, and crocein orange G. The cross-reactivity (CR%) values were calculated to evaluate the specificity of the antibody according to the following equation:

$$CR\% = IC_{50\ \text{ponceau 4R}}/IC_{50\ \text{other pigments}} \times 100\%$$

The accuracy and precision of the method were evaluated by detecting ponceau 4R solutions (1, 100, 10000 ng/mL) five times per day, which was performed for 3 days to calculate the intra- and interassay variations of the method.

Application of the icELISA in Food Samples. To investigate the matrix effects, three food samples including grape juice, a carbonated beverage, and RIO cocktail, in which the use of ponceau 4R as a color additive was permitted, were obtained from local supermarkets. Before detection with the proposed icELISA, the samples were treated simply as follows: carbonated beverage was boiled to remove CO_2 and then centrifuged at 10000*g* for 10 min, grape juice and RIO cocktail were centrifuged at 10000*g* for 10 min and then filtered by a 0.25 μm filter membrane. The matrices were then diluted into a series of concentrations before analysis.

IC_{50} values of ponceau 4R in each prepared sample were compared with that in PBS to obtain the optimum dilution. Recoveries and coefficients of variation (CVs) were determined by the performance of the icELISA in different matrices spiked with ponceau 4R at levels of 50, 100, and 200 ng/mL.

$$\text{recovery}\ (\%) = (\text{concentration measured}/\text{concentration spiked}) \times 100\%$$

Statistical Analysis. All of the experiments in the research were performed at least three times. The data are expressed as the mean ± standard deviation (SD).

RESULTS AND DISCUSSION

Synthesis of Hapten for Ponceau 4R. It is well-known that a small molecule has only immunoreactivity and does not have any immunogenicity. Therefore, ponceau 4R cannot elicit an immune response independently in the bodies of animals. It must be connected to a carrier protein to obtain the capacity of being immunogenic. The important condition of connection with carrier protein is the existence of active groups in the structures of hapten, such as hydroxyl, carboxyl, and amino groups, which could react with protein under relatively mild conditions. As shown in Table 1, there is a hydroxyl group at

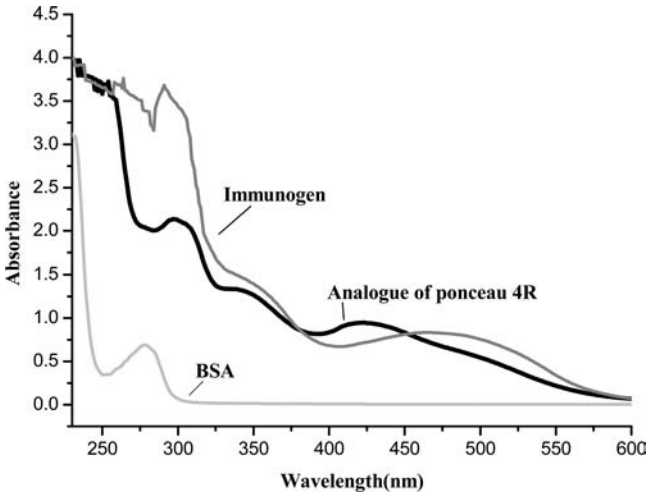

Figure 3. UV spectra of BSA (light gray), hapten (black), and immunogen (dark gray).

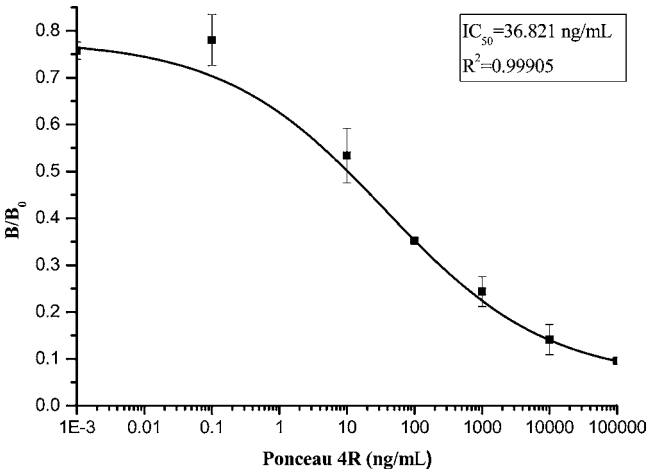

Figure 4. Inhibition curve of the icELISA for ponceau 4R.

DOI: 10.1021/acs.jafc.5b02129
J. Agric. Food Chem. 2015, 63, 6338−6345

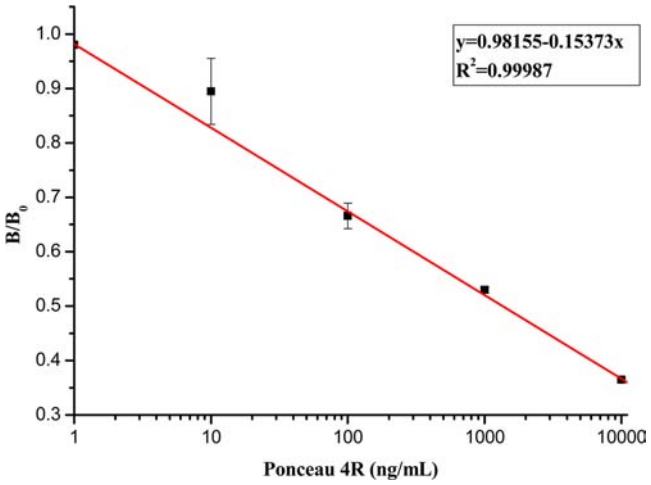

Figure 5. Standard curve of the developed icELISA for ponceau 4R.

Table 2. Coefficients of Variation for Detection of Ponceau 4R Standard Solutions in PBS by ELISA

ponceau 4R solution (ng/mL)	serial no.	detected (ng/mL) day 1	day 2	day 3
1	1	0.978	1.023	0.984
	2	0.998	1.012	0.965
	3	0.983	0.991	0.995
	4	0.983	0.997	0.963
	5	1.013	1.045	0.963
	average	0.989	1.014	0.974
	intra-assay CV (%)	1.7	2.1	1.5
	interassay CV (%)	17.7		
100	1	114.30	95.68	119.81
	2	105.66	107.43	119.82
	3	118.21	103.37	106.26
	4	103.32	104.17	109.03
	5	119.54	109.11	117.78
	average	112.20	103.90	114.50
	intra-assay CV (%)	6.5	5.0	5.6
	interassay CV (%)	13.8		
10000	1	11113.41	10837.27	10360.12
	2	11587.23	10306.18	9928.94
	3	10748.35	10695.87	10593.74
	4	11021.00	10476.19	10056.61
	5	10748.35	100471.44	10207.24
	average	11043.70	10471.40	10229.30
	intra-assay CV (%)	2.8	2.7	2.3
	interassay CV (%))	10.6		

position 7, which is adjacent to the azo bond. However, it was reported that azo−hydrazone tautomerism might happen in similar structures.[34] To improve the efficiency of the connecting reaction, a hapten of ponceau 4R was designed and synthesized as shown in Figure 1. A primary amine was introduced into the structure of ponceau 4R, which could react with aldehyde groups or carboxyl groups simply. The synthesized hapten was tested by ^{1}H NMR, and the results were as follows: ^{1}H NMR (400 MHz, DMSO) δ 8.273−8.282 (t, 2H), 8.121 (s, 1H), 8.092 (s, 1H), 8.032 (s, 1H), 8.012 (s, 1H), 7.639 (s, 1H), 7.494 (s, 1H), 7.367 (s, 1H), 7.240 (s, 1H). The NMR data demonstrated that the hapten was synthesized successfully.

Characterization of Immunogen and Coating Antigen. In this study, glutaraldehyde was used to link the hapten and protein (cBSA). The procedure of synthesis is shown in Figure 2. By this method, a linker with a five-carbon length was introduced, which might be beneficial for the specific recognition of the organism. UV−vis spectrophotometry was used to evaluate the effectiveness of the conjugation reaction, and the UV−vis spectra of cBSA, analogue of ponceau 4R, and the immunogen are shown in Figure 3. The characteristic absorption peak of the analogue of ponceau 4R locates at 300 and 420 nm, and that of cBSA appears at 278 nm. However, the maximal absorbance of immunogen is observed at 480 nm, and there is an obviously enhanced peak at 290 nm, which indicates that a red-shift happens. The results of the UV−vis spectra could preliminarily demonstrate that the synthesis of immunogen succeeds.

Characterization of Polyclonal Antibodies. The titer or the highest dilution of the antibody, which represents the lowest concentration needed to get a positive result by ELISA, was measured first. The anti-ponceau 4R polyclonal antibody was doubly diluted, and the titer of the produced antibody was found to be 1:20000. Second, the concentration of the coating antigen and the proper dilution of the antibody for ELISA were optimized. The optimal working concentration of the coating antigen is 2 μg/mL, and the selected dilution of the antibody was 1:4000. On the basis of the optimized conditions, an indirect competitive ELISA was developed by using ponceau 4R as the competitor.

The sensitivity of the assay was evaluated by IC_{50} value from the inhibition curve as shown in Figure 4. The IC_{50} of the proposed icELISA is 36.82 ng/mL, and the limit of detection (LOD, IC_{20}) is 0.80 ng/mL. Additionally, the standard curve of the method was obtained as shown in Figure 5. The standard curve exhibits a wide linear range of 1−10000 ng/mL and good linearity (R^2 = 0.99987, n = 5) with a standard curve equation of $y = 0.98155 - 0.15373x$, where x represents the logarithm of ponceau 4R concentration and y is the ratio of the absorbance value at 450 nm with competitor (B) to that value without competitor (B_0).

The specificity of the anti-ponceau 4R polyclonal antibody was studied by cross-reactivity. Five structural analogues of ponceau 4R were selected as listed in Table 1, and their IC_{50} values were detected by the proposed icELISA. The cross-reactivity of each analogue was calculated as shown in Table 1. It is indicated that the prepared antibody was highly specific with low cross-reactivity to each selected pigment (<0.3). It was remarkable that the structure of one analogue, amaranth, was very similar to that of ponceau 4R. However, the cross-reactivity was considerably low, which demonstrated that the substituent position of sulfonate significantly influences the specificity of the antibody. It also reflected that the synthesis of the immunogen using glutaraldehyde was advisible. The linker with a five-carbon length introduced into the immunogen seemed proper, which might contribute to adequate exposure of the hapten for specific recognition.

DOI: 10.1021/acs.jafc.5b02129
J. Agric. Food Chem. 2015, 63, 6338−6345

Table 3. Recovery and Coefficient of Variation (CV) for Ponceau 4R Detection in Food Samples by ELISA

		intra-assay			interassay	
sample	spiked (ng/mL)	detected (ng/mL)	recovery (%)	CV (%)	detected (ng/mL)	CV (%)
grape juice	50	50.71 ± 4.23	101.24	7.51	49.78 ± 4.04	8.11
	100	99.68 ± 1.54	99.68	1.54	100.93 ± 2.42	2.40
	200	202.92 ± 5.37	101.46	2.64	201.17 ± 4.23	2.10
carbonated beverage	50	47.48 ± 4.64	94.96	9.78	48.49 ± 4.27	8.80
	100	103.77 ± 6.28	103.77	6.05	99.84 ± 9.13	9.14
	200	195.36 ± 4.24	97.68	4.24	194.44 ± 20.58	10.58
RIO cocktail	50	49.01 ± 5.75	98.02	11.73	47.96 ± 4.95	10.33
	100	93.87 ± 7.61	93.87	8.11	95.02 ± 6.93	7.30
	200	197.82 ± 7.47	98.91	3.77	198.34 ± 10.07	5.08

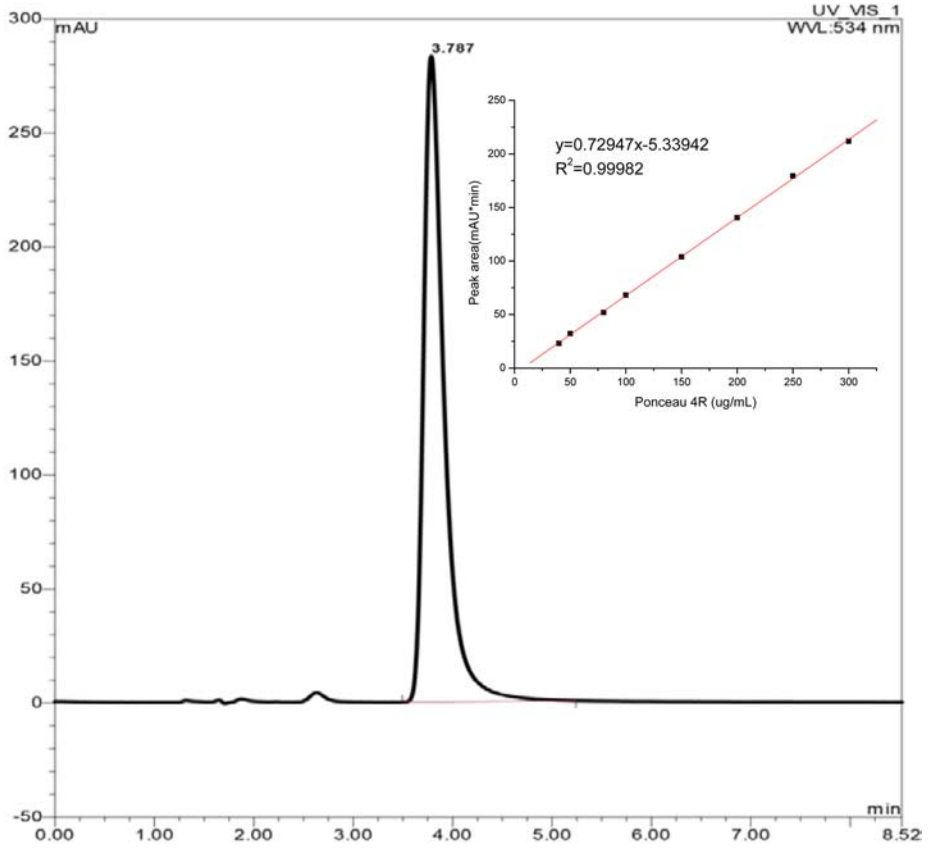

Figure 6. Confirmatory HPLC chromatogram of ponceau 4R and linear standard curve of the HPLC analysis.

Table 4. Determination of Ponceau 4R by icELISA and HPLC Methods

	ELISA			HPLC		
added (μg/mL)	measured (μg/mL)	recovery (%)	CV (%)	measured (μg/mL)	recovery (%)	CV (%)
100	110.27 ± 2.97	110.27	2.69	99.59 ± 0.54	99.59	0.54
200	197.64 ± 5.61	98.82	2.84	202.30 ± 5.31	101.15	2.62
250	247.85 ± 3.52	99.14	1.42	254.37 ± 2.28	101.75	0.90
LOD	0.80 ng/mL			0.74 μg/mL		
working range	1−10000 ng/mL			40−300 μg/mL		

To evaluate the accuracy and precision of the assay, three levels of ponceau 4R standard solutions in PBS (1, 100, and 10000 ng/mL) were prepared and detected by the developed icELISA for three consecutive days, which was repeated five times per day. The intra-assay variation and interassay variation were calculated, and the results are listed in Table 2. As shown, the intra-assay variations range from 1.7 to 6.5%, and the interassay variations were <17.7%. The results reflected that the proposed icELISA was accurate and precise for ponceau 4R determination in PBS.

DOI: 10.1021/acs.jafc.5b02129
J. Agric. Food Chem. 2015, 63, 6338−6345

Performance of the Developed icELISA in Foods. The matrix of real samples might interfer with the detection, and it is important to reduce matrix interferences. Three available food samples, which are allowed to add ponceau 4R as pigment, were collected, including grape juice, a carbonated beverage, and RIO cocktail. To minimize the matrix effects, these samples were treated simply and diluted, respectively. The recovery study was performed with the optimized dilution of each sample: grape juice, 1:20; carbonated beverage, 1:10; and RIO cocktail, 1:50. The recoveries of ponceau 4R in these three samples at three different fortified levels are listed in Table 3, and they range from 93.87 to 103.77%. The intra-assay variation is <11.73%, and the interassay variation is <10.58%. The results showed that the developed icELISA for ponceau 4R was stable and reproducible in the food sample detections. It also has the advantage of simplicity in sample preparation, which is a potential tool fitting for field tests of ponceau 4R.

Comparison with HPLC Method. To vertify the accuracy of the proposed icELISA for ponceau 4R, the method of HPLC was employed for comparison. The standard curve shown in Figure 6 exhibited excellent linearity from 40 to 300 μg/mL with the R^2 up to 0.99982. During the detection range of HPLC, 100, 200, and 250 μg/mL were chosen to determine the quantitative examination of ELISA and HPLC (Table 4), which showed that ELISA had results consistent with those of HPLC, and it was more sensitive, with a lower limit of detection, 0.80 ng/mL, and a wider working range, 1−10000 ng/mL, than HPLC as shown in Table 4. (F test showed the variances between ELISA and HPLC were not significantly different and $P > 0.05$.)

In conclusion, an icELISA was developed for the detection of ponceau 4R based on the polyclonal antibody produced in this study. The antibody was specific to ponceau 4R, which had low cross-reactivity with its analogues (<0.3). The good performance of the antibody was derived from the well-synthesized hapten and immunogen by a novel design. All of the data showed that the icELISA for ponceau 4R proposed in this study was sensitive, accurate, specific, stable, and reproducible with a LOD of 0.80 ng/mL. Additionally, this method exhibited the advantages of simplicity, convenience, rapidity, and inexpensiveness. It provides an alternative for the determination of ponceau 4R, which is especially suitable for its monitoring in food samples.

AUTHOR INFORMATION

Corresponding Authors

*(Y.Y.) Phone:+86-(22)-23499986. Fax:+86-(22)-23507760. E-mail: yinyongmei@nankai.edu.cn.

*(R.X.) E-mail: xirimo@nankai.edu.cn.

Author Contributions

#The first three authors contributed equally to this work.

Funding

This work was financially supported by the National Natural Science Foundation (No. 81173017, No. 31101277, No. 81402896), the International Science & Technology Cooperation Program of China (No. 2015DFR40460), the National High-Tech Research and Development Program of China (863 Program) (No. 2014AA022303), the Tianjin Science and Technology Program (No. 11ZCGHHZ01200, No. 12ZXCXSY08400, No. 12JCQNJC08900), and the Tianjin Research Program of Application Foundation and Advanced Technology (13JCZDJC29700).

Notes

The authors declare no competing financial interest.

REFERENCES

(1) Mikkelsen, H.; Larsen, J. C.; Tarding, F. Hypersensitivity reactions to food colours with special reference to the natural colour annatto extract (butter colour). *Arch. Toxicol. Suppl.* **1978**, *1*, 141−143.

(2) Ibero, M.; Eseverri, J. L.; Barrosso, C.; Botey, J. Dyes, preservatives and salicylates in the induction of food intolerance and/or hypersensitivity in children. *Allergol. Immunopathol (Madr).* **1982**, *10*, 263−268.

(3) Kolly, M.; Pecoud, A.; Frei, P. C. Additives contained in drug formulations most frequently prescribed in Switzerland. *Ann. Allergy* **1989**, *62*, 21−25.

(4) Sako, F.; Kobayashi, N.; Watabe, H.; Taniquchi, N. Cytotoxicity of food dyes on cultured fetal rat hepatocytes. *Toxicol. Appl. Pharmacol.* **1980**, *54*, 285−292.

(5) Ashida, H.; Hashimoto, T.; Tsuji, S.; Kanazawa, K.; Danno, G. Synergistic effects of food colors on the toxicity of 3-amino-1,4-dimethyl-5H-pyrido[4,3-b]indole (Trp-1) in primary cultured rat hepatocytes. *J. Nutr. Sci. Vitaminol.* **2000**, *46*, 130−136.

(6) Agarwal, K.; Mukherjee, A.; Sharma, A. In vivo cytogenetic studies on male mice exposed to Ponceau 4R and β-carotene. *Cytobios* **1992**, *74*, 23−28.

(7) Chung, K. T. Mutagenicity and carcinogenicity of aromatic amines metabolically produced from azo dyes. *J. Environ. Sci. Health C: Environ. Carcinog. Ecotoxicol. Rev.* **2000**, *18*, 51−74.

(8) Tsuda, S.; Murakami, M.; Matsusaka, N.; Kano, K.; Taniguchi, K.; Sasaki, Y. F. DNA damage induced by red food dyes orally administered to pregnant and male mice. *Toxicol. Sci.* **2001**, *61*, 92−99.

(9) Talaska, G.; Al-Zoughool, M. Aromatic amines and biomarkers of human exposure. *J. Environ. Sci. Health. C. Environ. Carcinog. Ecotoxicol. Rev.* **2003**, *21*, 133−164.

(10) Chen, Q. C.; Mou, S. F.; Hou, X. P.; Riviello, J. M.; Ni, Z. M. Determination of eight synthetic food colorants in drinks by high-performance ion chromatography. *J. Chromatogr. A* **1998**, *827*, 73−81.

(11) Dossi, N.; Toniolo, R.; Susmel, S.; Pizzariello, A.; Bontempelli, G. Simultaneous RP-LC determination of additives in soft drinks. *Chromatographia* **2006**, *63*, 557−562.

(12) Wu, H.; Guo, J. B.; Du, L. M.; Tian, H.; Hao, C. X.; Wang, Z. F.; Wang, J. Y. A rapid shaking-based ionic liquid dispersive liquid phase microextraction for the simultaneous determination of six synthetic food colourants in soft drinks, sugar-and gelatin-based confectionery by high-performance liquid chromatography. *Food Chem.* **2013**, *141*, 182−186.

(13) Feng, F.; Zhao, Y.; Yong, W.; Sun, L.; Jiang, G.; Chu, X. Highly sensitive and accurate screening of 40 dyes in soft drinks by liquid chromatography−electrospray tandem mass spectrometry. *J. Chromatogr. B: Anal. Technol. Biomed. Life Sci.* **2011**, *879*, 1813−1818.

(14) Minioti, K. S.; Sakellariou, C. F.; Thomaidis, N. S. Determination of 13 synthetic food colorants in water-soluble foods by reversed-phase high-performance liquid chromatography coupled with diode-array detector. *Anal. Chim. Acta* **2007**, *583*, 103−110.

(15) Zhang, J.; Gao, N.; Zhang, Y. Method development and validation for the determination of five synthetic food colorants in alcoholic beverages by reversed-phase high performance liquid chromatography coupled with diode-array detector. *Anal. Lett.* **2007**, *40*, 3080−3094.

(16) Yoshioka, N.; Ichihashi, K. Determination of 40 synthetic food colors in drinks and candies by high-performance liquid chromatography using a short column with photodiode array detection. *Talanta* **2008**, *74*, 1408−1413.

(17) Ma, M.; Luo, X.; Chen, B.; Su, S.; Yao, S. Simultaneous determination of water-soluble and fat-soluble synthetic colorants in foodstuff by high-performance liquid chromatography−diode array detection−electrospray mass spectrometry. *J. Chromatogr. A* **2006**, *1103*, 170−176.

(18) Berzas Nevado, J. J.; Guiberteau Cabanillas, C.; Contento Salcedo, A. M. Method development and validation for the

DOI: 10.1021/acs.jafc.5b02129
J. Agric. Food Chem. 2015, 63, 6338−6345

simultaneous determination of dyes in foodstuffs by capillary zone electrophoresis. *Anal. Chim. Acta* **1999**, *378*, 63−71.
(19) Frazier, R. A.; Inns, E. L.; Dossi, N.; Ames, J. M.; Nursten, H. E. Development of a capillary electrophoresis method for the simultaneous analysis of artificial sweeteners, preservatives and colours in soft drinks. *J. Chromatogr. A* **2000**, *876*, 213−220.
(20) Ryvolová, M.; Táborský, P.; Vrábel, P.; Krásenský, P.; Preisler, J. Sensitive determination of erythrosine and other red food colorants using capillary electrophoresis with laser-induced fluorescence detection. *J. Chromatogr. A* **2007**, *1141*, 206−211.
(21) Yang, X.; Qin, H.; Gao, M.; Zhang, H. Simultaneous detection of Ponceau 4R and tartrazine in food using adsorptive stripping voltammetry on an acetylene black nanoparticle-modified electrode. *J. Sci. Food Agric.* **2011**, *91*, 2821−2825.
(22) Xie, Y.; Li, Y.; Sun, Y.; Wang, H.; Qian, H.; Yao, W. Theoretical calculation (DFT), Raman and surface-enhanced Raman scattering (SERS) study of ponceau 4R. *Spectrochim. Acta, Part A* **2012**, *96*, 600−604.
(23) Aziz, F.; Sherwani, S. K.; Akhtar, S. S.; Kazmi, S. U. Development of an in-house enzyme-linked immunosorbent assay based on surface whole cell antigen for diagnosis of Helicobacter pylori infection in patients with gastroduodenal ulcer disease. *World J. Microbiol. Biotechnol.* **2014**, *30*, 305−315.
(24) Cui, Y.; Liu, K.; Xu, C.; Liu, F.; Li, Q. X.; Liu, S.; Wang, B. Development of a sensitive monoclonal antibody-based indirect competitive enzyme-linked immunosorbent assay for analysing chlorantraniliprole residues. *Food Chem.* **2014**, *143*, 293−299.
(25) Dzuman, Z.; Vaclavikova, M.; Polisenska, I.; Veprikova, Z.; Fenclova, M.; Zachariasova, M.; Hajslova, J. Enzyme-linked immunosorbent assay in analysis of deoxynivalenol: investigation of the impact of sample matrix on results accuracy. *Anal. Bioanal. Chem.* **2014**, *406*, 505−514.
(26) Miao, W. B.; Wei, B. W.; Yang, R. J.; Wu, C. H.; Lou, D.; Jiang, W.; Zhou, Z. J. Highly specific and sensitive detection of bisphenol A in water samples using an enzyme-linked immunosorbent assay employing a novel synthetic antigen. *New J. Chem.* **2014**, *38*, 669−675.
(27) Gazzaz, S. S.; Rasco, B. A.; Dong, F. M. Application of immunochemical assays to food analysis. *Crit. Rev. Food Sci. Nutr.* **1992**, *32*, 197−229.
(28) Wigfield, Y. Y.; Grant, R. Analysis for atrazine in fortified commeal and comsusing a commercialy available enzyme immuno-assay microtiter plate. *Bull. Environ. Contam. Toxicol.* **1993**, *51*, 171−177.
(29) Hoegger, D.; Morier, P.; Vollet, C.; Heini, D.; Reymond, F.; Rossier, J. S. Disposable microfluidic ELISA for the rapid determination of folic acid content in food products. *Anal. Bioanal. Chem.* **2007**, *387*, 267−275.
(30) Zhang, T.; Xue, H.; Zhang, B.; Zhang, Y.; Song, P.; Tian, X.; Xing, Y.; Wang, P.; Meng, M.; Xi, R. Determination of folic acid in milk, milk powder and energy drink by an indirect immunoassay. *J. Sci. Food Agric.* **2012**, *92*, 2297−2304.
(31) Zhao, C.; Liu, W.; Ling, H.; Lu, S.; Zhang, Y.; Liu, J.; Xi, R. Preparation of anti-gatifloxacin antibody and development of an indirect competitive enzyme-linked immunosorbent assay for the detection of gatifloxacin residue in milk. *J. Agric. Food Chem.* **2007**, *55*, 6879−6884.
(32) Lu, S. X.; Zhang, Y.; Liu, J.; Zhao, C.; Liu, W.; Xi, R. Preparation of antipefloxacin antibody and development of an indirect competitive enzyme-linked immunosorbent assay for detection of pefloxacin residue in chicken liver. *J. Agric. Food Chem.* **2006**, *54*, 6995−7000.
(33) Ren, L.; Meng, M.; Wang, P.; Xu, Z.; Eremin, S. A.; Zhao, J.; Yin, Y.; Xi, R. Determination of sodium benzoate in food product by fluorescence polarization immunoassay. *Talanta* **2014**, *121*, 136−143.
(34) Hihara, T.; Okada, Y.; Morita, Z. Azo-hydrazone tautomerism of phenylazonaphthol sulfonates and their analysis using the semi-empirical molecular orbital PM5 method. *Dyes Pigm.* **2003**, *59*, 25−41.

DOI: 10.1021/acs.jafc.5b02129
J. Agric. Food Chem. 2015, 63, 6338−6345

(analytical reagent grade), acetonitrile (HPLC grade), dichloromethane (laboratory reagent grade), hexane (GLC, pesticide residue grade), and methanol (HPLC grade) were obtained from Thermo-Fisher Scientific (Loughborough, UK); benzyl mercaptan (BM) was from Sigma-Aldrich (Poole, UK); phosphate buffered saline (PBS) was from Biomérieux (Marcy l'Etoile, France); Sephadex LH-20 was from GE Healthcare (Little Chalfont, UK); and ultrapure water (MQ H_2O) was from a Milli-Q Plus system (Millipore, Watford, UK).

Preparation of Plant Extracts and Tannin Fractions. Eighteen different plant materials were used: aerial plants of *Onobrychis viciifolia* (OV) were collected on June 7, 2012 (Barham, Kent, UK); *Trifolium repens* flowers were collected from at NIAB (Cambridge, UK; sample TRa) or purchased from Zioła z Kurpi (Jednorożec, Poland; sample TRb); *Lespedeza cuneata* (LC) pellets were from Sims Brothers Seed Co. (Union Springs, AL, USA); *Betulae folium* leaves (*Betula pendula* Roth and/or *Betula pubescens* Ehrh.; BP), *Tilia inflorescentia* flowers (T; a mixture of *Tilia cordata*, *Tilia platyphyllos*, and *Tilia vulgaris* L), *Salicis cortex* bark (SA) from various *Salix* spp. (including *Salix purpurea* L.; *Salix daphnoides* Vill.; *Salix fragilis* L.), and *Ribes nigrum* leaves (sample RNb) were from Flos (Mokrsko, Poland); *Corylus avellana* (CA) pericarp was from Société Inovfruit (Musidan, France); *Juglandis folium* leaves of *Juglans regia* L. (JR) were from Kawon (Gostyń, Poland); inner bark of *Pinus sylvestris* (PS) was from University of Turku (Turku, Finland); *Salix babylonica* catkins (SB) were collected on May 26, 2012 (Emmer Green, UK); *Salix caprea* (SCL and SCT) leaves and twigs were harvested on June 19, 2012 (Goring-on-Thames, UK); *Ribes nigrum* leaves (sample RNa) and *Ribes rubrum* leaves (RR) were collected on August 13, 2012, from Hildred PYO farm (Goring-on-Thames, UK); *Theobroma cacao* beans (TC) were from Peru (imported by "Detox your world" Inc., Norfolk, UK); and *Vitellaria paradoxa* (VP) meal (i.e., residue of VP nuts after fat extraction) was from AarhusKarlshamm Sweden AB, Sweden. Samples OV and TRa were lyophilized; samples PS, CA, SCL, SCT, RNa, and RR were dried at room temperature for <10 days and then stored at room temperature. The different botanical families[23] of each plant are indicated in Table 2.

Extracts were prepared according to the method of Stringano et al.[24] with a few modifications. Plant samples (50 g; <1 mm sieve) were extracted with 70% acetone/H_2O (500 mL, 7:3, v/v) and filtered under vacuum. Chlorophyll and lipids were removed with dichloromethane (125 mL) by liquid−liquid extraction. The remaining solvents were removed from the aqueous phase on a rotary evaporator at 35 °C. The aqueous extracts were centrifuged for 3 min at 4500 rpm (Jouan CR3i multifunction centrifuge) to remove the remaining chlorophyll, insoluble particles, and some precipitates. Extracts were freeze-dried and stored at −20 °C.

Extracts were purified on Sephadex LH-20 chromatographic columns to remove impurities (mainly sugars and small phenolics) with water. Elution with acetone/H_2O (3:7, v/v) yielded fraction 1 CTs (F1); a second elution with acetone/H_2O (1:1, v/v) yielded fraction 2 CTs (F2). In total 36 (18 F1 and 18 F2) fractions were tested using *H. contortus* and *T. colubriformis* infective third-stage larvae (L3).

Tannin Analysis by Thiolytic Degradation and HPLC. The purified CT fractions were subjected to thiolytic degradation as described by Gea et al.[25] with some changes for the analysis of CT contents (% CT) and features (size in terms of mean degree of polymerization, mDP; percentage of prodelphinidins and procyanidins within CTs, % PD and % PC; and percentage of *trans* vs *cis* flavanols, % *trans*, and % *cis*). Freeze-dried samples (4 mg) were weighed into 10 mL glass tubes, and methanol (1.5 mL) was added, followed by acidified methanol (0.5 mL of 3.3% HCl/in MeOH), benzyl mercaptan (50 μL), and a magnetic stirrer. The tube was capped and heated at 40 °C for 1 h in a water bath. Water (2.5 mL) was added to stop the reaction, and the internal standard (0.5 mL of taxifolin: 0.05 mg/mL) was added. Samples were analyzed within 48 h by RP-HPLC.[25]

Gastrointestinal Nematodes. The third-stage larvae (L3) were obtained from feces of donor goats, kept indoors and infected monospecifically, with AH susceptible strains of either *H. contortus* or *T. colubriformis*. The facilities hosting the animals and trial performance met French ethical and welfare rules (agreement C 31 555 27 of August 19, 2010).

Coproculture were maintained for 12 days at 23 °C to obtain the third-stage larvae. Larvae were then recovered from feces using the Baerman technique and stored at 4 °C in a horizontally vented cap flask at a concentration of 1000−1500 L3/mL. Prior to use, the larvae were checked to ensure that at least 90% of them were mobile and ensheathed.

Larval Exsheathment Inhibition Assay (LEIA). The larval exsheathment inhibition assay was performed as described by Bahuaud et al.[26] to compare the inhibitory effects of the various tannin fractions (F1 and F2) on the exsheathment process of *H. contortus* and *T. colubriformis*. For both nematode species a batch of 2-month-old larvae was used to perform the in vitro assays.

Briefly, 1000 ensheathed L3 larvae (*H. contortus* or *T. colubriformis*) were first incubated for 3 h at 20 °C with one of the fractions at serial dilutions from 600, 300, 150, 75, to 37.5 μg/mL in PBS (0.1 M phosphate, 0.05 M NaCl, pH 7.2). In addition to all of the tested fractions, negative controls (L3 in PBS) were run in parallel. After incubation, the larvae were washed and centrifuged, three times in PBS, and then submitted to the artificial exsheathment process by contact with a solution containing sodium hypochlorite (2% w/v) and sodium chloride (16.5% w/v), which had been diluted 1 to 350 in PBS. The exsheathment kinetics were measured under a microscope at ×200 magnification by identifying the proportion of exsheathed larvae. Regular examination was performed at 0, 20, 40, and 60 min after contact with the exsheathment solution. The exsheathment percentage was calculated according to the formula (number of exsheathed larvae) × 100/(number of exsheathed larvae + ensheathed larvae). For each fraction, four replicates were run per concentration and observation time to examine the exsheathment kinetics.

Statistical Analyses of the Results. The effective concentration that causes 50% exsheathment inhibition (EC_{50}) for each tannin fraction was calculated at 60 min (using the software Probit Polo Plus). First, a nonparametric rank correlation of Spearman was calculated using a 2 by 2 correlation to evaluate the relationship between the structural parameters characterizing the tannin fractions and also the relationship between the in vitro AH activity (EC_{50} of each fraction) and quantitative (% CT) and qualitative parameters (mDP, % PD and *trans*) of the respective F1, F2, and combined F1 and F2 (F1+F2) fractions. Significant values ($P < 0.05$) and (close to significance) values ($P < 0.10$) are reported.

Then multivariate analyses, principal component analyses (PCA), were performed separately for each nematode species on the basis of the combined data of F1+F2 to obtain an overall synthesis of the relationships between the effects on larval exsheathment and the main CT features. The five variables composing the column of the two PCA matrices included quantitative (% CT) and qualitative parameters (mDP, % PD and % *trans* values) plus the EC_{50} per species. The 36 rows of the matrix corresponded to the F1 and F2 data of the 18 plant samples. All statistical analyses were performed using Systat 9 software (SPSS Ltd.).

RESULTS

Tannin Analysis and Relationships between Structural Parameters. The parameters that characterized the 18 CT samples are provided in Table 1. The average % CT, mean degree of polymerization (mDP), and % prodelphinidins (PD) values were higher in the F2 compared with the F1 fraction, whereas the mean % *trans* values were lower for F2. The Spearman correlation coefficients were positive and significant between the F1 and F2 fractions for mDP ($r = 0.583$, $P < 0.05$, df = 16), % PD ($r = 0.975$, $P < 0.01$, df = 16), and % *trans* ($r = 0.728$, $P < 0.05$, df = 16), which is due to the fact that these 15 plant species produce different CT types. There was no correlation for the % CT in both fractions ($r = 0.082$, NS, df = 16).

When the Spearman correlation test was applied to the combined F1+F2 data ($n = 36$ samples), there were positive

DOI: 10.1021/acs.jafc.5b00831
J. Agric. Food Chem. 2015, 63, 6346−6354

Table 1. Chemical Characterization of Two Tannin Fractions from 18 Plant Resources (F1 and F2 Fractions; % PC = 100 − % PD; % *cis* = 100 − % *trans*)

scientific name	family[23]	common name/sample	% CT ± SD		mDP ± SD		% PD ± SD		% *trans* ± SD	
			F1	F2	F1	F2	F1	F2	F1	F2
Onobrychis viciifolia	Leguminosae	sainfoin/whole plant	37.2 ± 4.5	100 ± 4.1	2.8 ± 0.1	8.7 ± 0.0	72.0 ± 0.3	64.9 ± 0.1	33.3 ± 0.2	20.9 ± 0.3
Trifolium repens[a]	Leguminosae	white clover/flower	11.7 ± 0.4	100 ± 2.4	1.8 ± 0.0	8.6 ± 0.0	98.3 ± 0.3	98.7 ± 0.0	82.2 ± 0.1	41.1 ± 0.6
Trifolium repens[b]	Leguminosae	white clover/flower	13.4 ± 0.4	82.4 ± 2.0	3.1 ± 0.1	12.7 ± 0.0	98.1 ± 0.1	98.8 ± 0.0	74.2 ± 0.2	38.2 ± 0.0
Lespedeza cuneata	Leguminosae	sericea lespedeza/pellets	42.1 ± 0.2	82.6 ± 1.4	5.0 ± 0.0	11.3 ± 0.3	92.4 ± 0.1	92.3 ± 0.0	34.7 ± 0.0	24.8 ± 0.2
Betula spp.	Betulaceae	birch/leaf	12.9 ± 0.3	63.6 ± 2.5	2.2 ± 0.0	8.3 ± 0.1	44.7 ± 0.1	58.9 ± 0.1	59.3 ± 0.1	29.3 ± 0.1
Corylus avellana	Corylaceae	hazelnut/pericarp	49.2 ± 1.1	67.5 ± 0.6	4.6 ± 01	9.2 ± 0.1	18.3 ± 0.9	20.9 ± 0.8	59.0 ± 0.11	52.2 ± 0.35
Juglans regia L.	Juglandaceae	walnut/leaf	21.8 ± 1.4	69.0 ± 1.7	2.9 ± 0.0	12.3 ± 0.1	9.3 ± 0.4	30.9 ± 0.0	56.1 ± 0.0	23.7 ± 0.0
Pinus sylvestris L.	Pinaceae	pine/inner bark	54.0 ± 2.0	79.0 ± 2.4	2.3 ± 0.0	6.6 ± 0.2	15.1 ± 0.6	11.2 ± 1.7	51.9 ± 0.7	21.9 ± 1.8
Tilia L.	Tiliaceae	lime tree/flower	47.5 ± 2.8	91.7 ± 3.8	2.0 ± 0.0	7.9 ± 0.1	1.1 ± 0.0	0.9 ± 0.1	16.4 ± 0.0	4.4 ± 0.1
Salix spp	Salicaceae	white willlow/bark	23.1 ± 1.7	83.3 ± 0.6	2.0 ± 0.1	9.9 ± 0.0	0.0 ± 0.0	6.0 ± 0.0	63.0 ± 0.2	21.9 ± 0.0
Salix babylonica	Salicaceae	weeping willow/catkins	40.2 ± 2.8	97.4 ± 2.2	2.9 ± 0.0	8.0 ± 0.3	24.6 ± 0.1	33.0 ± 1.7	44.5 ± 0.2	42.3 ± 1.2
Salix caprea	Salicaceae	goat willow/leaf	51.5 ± 0.1	83.8 ± 1.8	2.1 ± 0.1	5.3 ± 0.1	5.8 ± 0.3	4.8 ± 0.6	93.2 ± 0.3	95.8 ± 0.2
Salix caprea	Salicaceae	goat willow/twigs	72.0 ± 1.1	93.2 ± 11	2.1 ± 0.0	5.3 ± 0.1	15.6 ± 0.9	21.3 ± 0.71	59.4 ± 0.1	37.2 ± 0.4
Ribes nigrum[a]	Grossilariaceae	black currant/leaf	59.8 ± 1.3	100.0 ± 1.7	2.5 ± 0.0	6.5 ± 0.1	93.7 ± 0.07	94.5 ± 0.11	87.2 ± 0.1	93.0 ± 0.1
Ribes nigrum[b]	Grossilariaceae	black currant/leaf	55.5 ± 3.2	77.1 ± 3.9	3.8 ± 0.0	11.8 ± 0.1	94.0 ± 0.0	95.3 ± 0.0	91.5 ± 0.1	81.2 ± 0.1
Ribes rubrum	Grossilariaceae	red currant/leaf	57.7 ± 9.1	68.2 ± 1.1	4.9 ± 0.0	10.0 ± 0.1	85.8 ± 0.4	90.4 ± 0.1	55.7 ± 1.1	35.6 ± 0.9
Theobroma cacao	Malvaceae	cocoa/seed	58.5 ± 2.9	75.5 ± 8.1	2.3 ± 0.0	5.4 ± 0.1	0.0 ± 0.2	0.0 ± 0.0	8.7 ± 0.2	3.7 ± 0.1
Vitellaria paradoxa	Sapotaceae	shea/meal	33.0 ± 0.6	44.9 ± 0.8	2.2 ± 0.1	4.1 ± 0.1	76.3 ± 0.1	72.5 ± 0.1	41.4 ± 0.3	40.2 ± 0.1
		mean value	40.2 ± 9.2	81.1 ± 7.4	2.8 ± 0.5	8.4 ± 1.3	44.6 ± 20.2	49.7 ± 19.4	56.2 ± 12.4	39.3 ± 13.3

[a]Sample a. [b]Sample b.

DOI: 10.1021/acs.jafc.5b00831
J. Agric. Food Chem. 2015, 63, 6346−6354

Table 2. EC_{50} Values by Parasite and by Fraction (F1 or F2) from Each Tannin-Containing Resource Tested

plant	abbreviation	family[26]	*H. contortus* EC_{50} (95% CI) (μg/mL)		*T. colubriformis* EC_{50} (95% CI) (μg/mL)	
			F1	F2	F1	F2
Onobrychis viciifolia	OVF1/OV2	Leguminosae	62.7 (49.9−76.5)	212 (182−250)	203 (131−322)	147 (99−230)
Trifolium repens (a)	TRaF1/TRaF2	Leguminosae	287 (249−328)	177 (131−239)	110 (82.1−145)	152 (109−210)
Trifolium repens (b)	TRbF1/TRbF2	Leguminosae	37.5 < (0.7−74.4)[a]	37.5 < (0.08−42.4)[a]	132 (92.3−186)	110 (63.2−166)
Lespedeza cuneata	LCF1/LCF2	Leguminosae	78.2 (28.1−157)	37.5 <(2.5−55.3)[a]	198 (108−366)	94.9 (50.5−140)
Corylus avellana	CAF1/C1F2	Corylaceae	166 (82.5−441)	143 (104−170)	351 (287−441)	329 (209−671)
Juglans regia L.	JRF1/JRF2	Juglandaceae	94.7 (65.5−115)	70.6 (46.9−106)	258 (130−386)	243 (169−384)
Betula spp.	BPF1/BPF2	Betulaceae	62.8 (58.6−82)	62.6 (19.0−90.3)	226 (163−335)	125 (86.7−169)
Pinus sylvestris L.	PSF1/PSF2	Pinaceae	236 (192−290)	144 (125−167)	184 (121−305)	135.9 (112−163)
Tilia L. spp.	TF1/TF2	Tiliaceae	113 (82−157)	88.7 (66.1−107)	459 (353−660)	297 (258−335)
Salix spp.	SAF1/SAF2	Salicaceae	188 (137−241)	138 (117−154)	300 (271−333)	191 (126−294)
Salix babylonica	SBF1/SBF2	Salicaceae	174 (120−206)	128 (69.8−166)	181 (152−214)	108 (83.8−132)
Salix caprea (twigs)	SCTF1/SCTF2	Salicaceae	195 (142−266)	132 (97.6−184)	385 (296−459)	125 (94.9−159)
Salix caprea (leaves)	SCLF1/SCLF2	Salicaceae	196 (86−217)	161 (133−191)	377 (316−435)	316 (243−420)
Ribes nigrum (sample a)	RNaF1/RNaF2	Grossulariaceae	145 (85−259)	157 (124−203)	145 (123−169)	89.5 (70.1−111)
Ribes nigrum (sample b)	RNbF2/RNbF2	Grossulariaceae	48.7 (78.1−158)	59.2 (18.5−111)	315 (212−592)	209 (140−344)
Ribes rubrum	RRF1/RRF2	Grossulariaceae		97.8 (85.4−305)	130 (84.5−199)	124 (99.5−152)
Theobroma cacao	TCF1/TCF2	Malvaceae	208 (168−246)	65.2 (34.1−95.7)	76.1 (24.3−130)	122 (94.8−200)
Vitellaria paradoxa	VP1/VP2	Sapotaceae	37.5 < (0.7−29.1)[a]	37.5 < (0.48−36.5)[a]	169 (115−288)	76.0 (65.7−86.7)
		mean values	136.9 ± 74.1	108.1 ± 53.2	233 ± 54.3	166 ± 39.9

[a]Calculation of the EC_{50} values relying on the Polo Plus software gave the following values for the effects against *H. contortus* for *T. repens* (b), fraction F1 = 33.2 μg/mL and fraction F2 = 14.5 μg/mL; for *L. cuneate*, fraction F2 = 29.4 μg/mL; and for *V. paradoxa*, fraction F1 = 13.6 μg/mL and fraction F2 = 16.5 μg/mL.

correlation coefficients between % CT and mDP values (r = 0.696; P < 0.01; df = 34). A nonsignificant negative correlation existed between % CT and % *trans* (r = −0.261; NS; df = 34) and between % PD and mDP values (r = 0.270; NS; df = 34). This absence of a link between % PD and mDP is important because column chromatography of CTs from the same plant material tends to lead to fractions, where % PD and mDP are positively correlated (unpublished observations). Therefore, these F1 and F2 fractions enable the investigation of relationships between CT structures and AH activities. Trends were observed for % PD and % *trans* (r = 0.300; P < 0.08; df = 34).

Anthelmintic Activity. The different fractions affected the larval exsheathment process in a dose-dependent way. The EC_{50} values for each of the F1 and F2 fractions per plant sample were used to characterize the AH activity and are shown for *H. contortus* and *T. colubriformis* in Table 2. For both parasites, EC_{50} values were generally lower with F2 than with F1 fractions. In addition, overall, EC_{50} values calculated for *H. contortus* were lower than those of *T. colubriformis*, suggesting that *H. contortus* was more susceptible to these fractions. Thus, the calculation of Spearman's correlation coefficients between EC_{50} values, obtained respectively for F1 and F2, showed significant and positive values for both species separately, that is, *H. contortus* (r = 0.642; P < 0.05; df = 15) and *T. colubriformis* (r = 0.688; P < 0.01; df = 16). However, there were no correlations between the EC_{50} values of the F1 fractions between *H. contortus* and *T. colubriformis* (r = −0.056; NS; df = 15) and also not for the F2 fractions (r = 0.397; NS; df = 16). Finally, there were also no correlations between the EC_{50} values of both parasite species with the F1+F2 combined data (r = 0.164; NS; df = 33).

Figure 1 shows the EC_{50} score values in rank order for *H. contortus* and *T. colubriformis*, respectively. The 25% of the most effective plants against both GIN species (i.e., lowest EC_{50} values) were *Vitellaria paradoxa*, *Trifolium repens*, *Lespedeza cuneata*, *Ribes nigrum*, *Theobroma cacao*, and *Betula* spp. In addition, *Onobrychis viciifolia* was active against *H. contortus*, and *Ribes rubrum* and *Salix babylonica* were active against *T. colubriformis*.

Table 3 presents the Spearman's correlation coefficients between the EC_{50} values and the various CT parameters for both nematode species in terms of the F1, F2, and the combined (F1+F2) data. For *H. contortus*, there were negative trends between EC_{50} and mDP and % PD of the F1 fraction and between EC_{50} and mDP of the F1+F2 data. The correlation between EC_{50} and % PD was negative and significant for the F1+F2 data. Somewhat surprisingly, a significant positive correlation was noted for EC_{50} values and % CT of the F2 fractions.

In contrast, for *T. colubriformis* there were no correlations with mDP or % CT. Instead, negative correlation coefficients between EC_{50} and % PD were close to significance for F1 (r = −0.453; P < 0.10; df = 16) and F2 (r = −0.439; P < 0.10; df = 16) and were significant for the combined (F1+F2) fractions (r = −0.403; P < 0.05; df = 34).

When PCA was applied separately to either *H. contortus* or *T. colubriformis*, the two main components of axis 1 were mDP and % CT. For axis 2, % PD appeared as the key component. The plane defined by the combination of axes 1 and 2 (Figure 2) represented 67% of the overall variability for *H. contortus* and close to 70% for *T. colubriformis*.

The main objective of the PCA was to analyze the overall combined relationships between the different variables and the effects on exsheathment as assessed by the EC_{50} values (Figure 2). Variables that are positively related are located on the same side of the plane. In contrast, variables that are negatively related are located in diagonally opposed quadrants. Analyses of these planes for both GIN species tend to confirm the 2 by 2 Spearman's correlation results. For *Haemonchus*, the EC_{50} values were in opposition to % PD and mDP values and, to a lesser

DOI: 10.1021/acs.jafc.5b00831
J. Agric. Food Chem. 2015, 63, 6346−6354

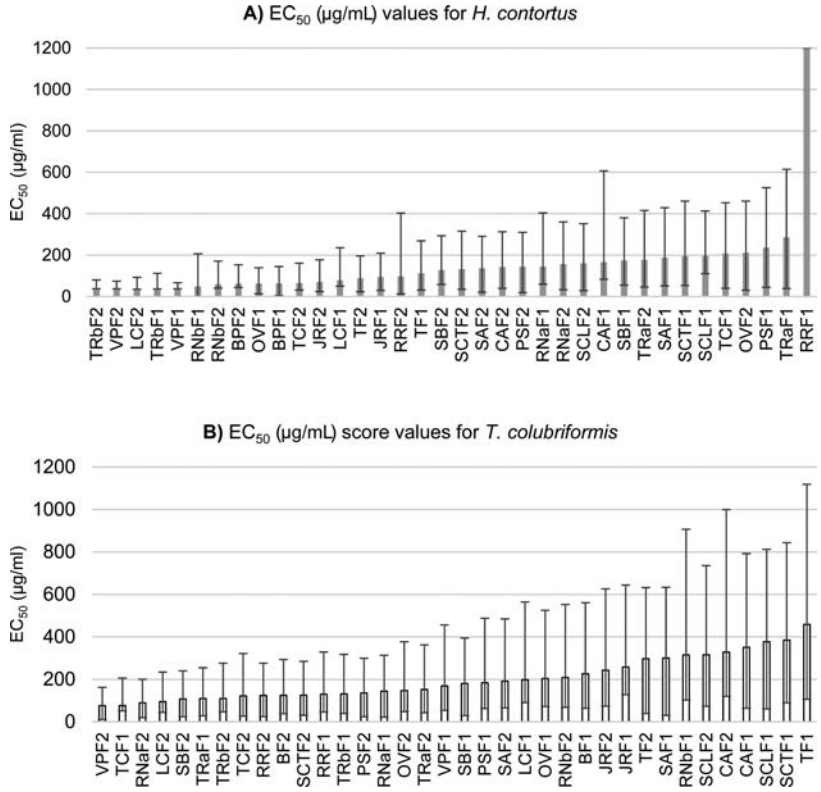

Figure 1. EC_{50} values (and 95% confidence interval) scores for (A) *Haemonchus contortus* and (B) *Trichostrongylus colubriformis* using F1 and F2 fractions from the 18 tannin-containing plant resources.

Table 3. Spearman's Correlation Coefficients for Anthelmintic Activity by Nematode Species According to Tannin Content and Structural Parameters in F1 and/or F2 Fractions

	Haemonchus contortus EC_{50} (μg/mL)						*Trichostrongylus colubriformis* EC_{50} (μg/mL)					
	F1 (df = 15)		F2 (df = 16)		F1+F2 (df = 33)		F1 (df = 16)		F21 (df = 16)		F1+F2 (df = 34)	
variable	*r* value	*P* value	*r* value	*P* value	*r* value	*P* value	*r* value	*P* value	*r* value	*P* value	*r* value	*P* value
% CT	0.30	0.44	0.61[a]	0.50	0.12	0.29	0.10	0.43	0.01	0.43	−0.22	0.28
mDP	−0.46[b]	0.44	−0.28	0.43	−0.33[b]	0.29	−0.17	0.43	0.19	0.43	−0.26	0.28
% PD	−0.44[b]	0.44	−0.22	0.43	−0.35[a]	0.34	−0.46[b]	0.43	−0.43[b]	0.43	−0.40[a]	0.34
% trans	0.08	0.44	0.12	0.43	0.18	0.29	0.12	0.43	−0.01	0.43	0.24	0.28

[a] $P < 0.05$. [b] $P < 0.10$.

extent, to the % CT. For *Trichostrongylus*, the EC_{50} values were mainly in opposition to % PD.

DISCUSSION

The study evaluated 36 CT fractions from 18 sources (15 plant species). These plants were chosen because they present a wide range of different CT features in terms of mDP, % PD, and % *trans* values. It was expected that this variation would allow exploring the relationships between CTs and their AH activities. These particular CT parameters have been described previously as being involved in their biological activities.[10,19,20,22,27−29] From these 15 plant species 18 tannin extracts were obtained that yielded two related CT fractions (i.e., F1 and F2 fractions). These 36 samples were used to test the effects of quantitative and qualitative differences between CTs. The range of CT concentrations tested with these fractions was chosen on the basis of previous in vitro data, which had been obtained with plant extracts of known CT concentrations.[16,26,27]

Three in vitro assays are available to explore the interactions between tannins and infective third-stage larvae of gastrointestinal nematodes;[30] these are the larval migration inhibition assay (LMIA), the larval feeding inhibition assay (LFIA), and the LEIA, which has been used in the current study. The LEIA has been widely used to screen the AH activity of either plant extracts,[26,30] tannin fractions,[8,10] or flavan-3-ol monomers.[21,22] The LEIA has proved to be simple and reproducible and, like the LFIA, it also has the advantage that it allows calculation of EC_{50} values, which is rarely the case for the LMIA. Moreover, LEIA has been related to similar in vivo processes.[31] The LEIA was performed with 2-month-old larvae for both nematode species to allow comparison of EC_{50} values obtained with the F1 and F2 fractions of each plant sample and between the two nematodes species.

Overall, CT contents (% CT) were higher in the F2 than in the F1 fractions, and the EC_{50} values for F2 calculated for both nematodes were, in most cases, lower than for F1 fractions. This suggests a role for the % CT in the antiparasitic effect. Similar results were obtained by Williams et al.[20] for the AH

DOI: 10.1021/acs.jafc.5b00831
J. Agric. Food Chem. 2015, 63, 6346−6354

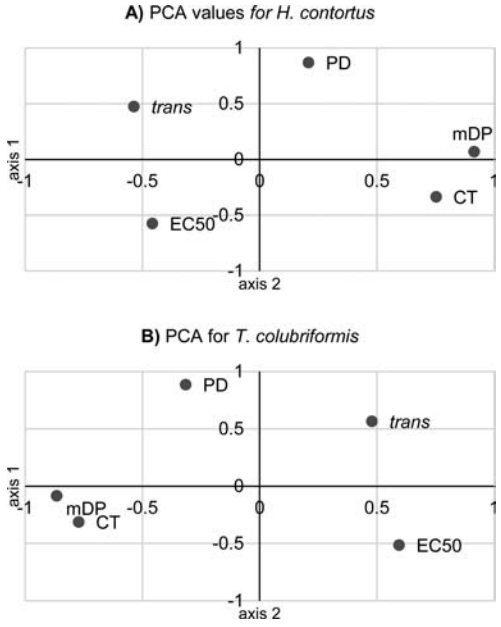

Figure 2. Multivariate principal component analyses (PCA) explained to condensed tannins for each parasite species: (A) *H. contortus*; (B) *T. colubriformis*. For both nematode species, the matrix was composed of 5 variables and 36 lines corresponding to 2 fractions (F1 and F2) of a range of 18 tannin-containing samples. Abbreviations: EC_{50} values based on LEIA (low values reflect high anthelmintic activities), CT (condensed tannins content, units g CT/100 g fraction); mDP (mean degree of polymerization of tannins); PD (% of prodelphinidins) *trans* (% of *trans* flavan-3-ols). The planes represent 67% of the variability for *H. contortus* and 70% for *T. colubriformis*, respectively.

effects against *Ascaris suum* with a subset of these F1 and F2 fractions. Many studies, based on different in vitro tests, have reported a dose-dependent AH effect when using tannin-containing plant extracts. For example, for some legume forages such dose-dependent effects have been described for (i) *O. viciifolia* (sainfoin) with the larval migration inhibition assay (LMIA),[7] LEIA,[31] egg hatch assay (EHA),[28] and larval development inhibition assay (LDIA);[28] and for (ii) *L. pedunculatus* and *L. corniculatus* extracts with the LMIA and LDIA,[27,28] the larval feeding inhibition assay (LFIA), and LEIA.[9] Although, surprisingly, there was a significant positive correlation between CT content and AH activity of the F2 fractions for *H. contortus*, there was no significant correlation when the F1+F2 data were combined. Similarly, Naumann et al.[19] also found no relationship between CT content and the AH activity against *H. contortus* L3 when comparing fractions from three legumes (*Lespedeza stuevei*, *L. cuneata*, and *Arachis glabrata*). Novobilský et al.[10] compared the effects of different CT fractions from *O. viciifolia* on cattle nematodes of either the abomasum (*Ostertagia ostertagi*) or the small intestine (*Cooperia oncophora*). These authors also did not obtain consistent correlations between the CT contents and the in vitro AH activity as measured by LFIA.

This discrepancy in relationship between dose and AH activity obtained with either CT-containing extracts or fractions could perhaps be related to other compounds that are also present in extracts.[7,21] Indeed, Molan et al.[22] also reported deleterious effects of flavan-3-ol monomers against *T. colubriformis* at different life cycle stages, that is, eggs (EHA) and larvae (LDIA, LMIA). The highest AH effect occurred with the epigallocatechin gallate (EGCG) monomer. This observation was confirmed by further studies with green tea fractions that were tested against *Teladorsagia circumcincta* and *T. colubriformis*, where higher EGCG content was linked with a higher AH effect.[8] Similarly, when monomeric subunits of CT were tested in the LEIA on *H. contortus* and *T. colubriformis*,[21] a higher AH activity was observed with (i) the monomeric subunits of PDs (i.e., gallocatechin, epigallocatechin) and (ii) the galloyl derivatives of both PDs and procyanidins.

Besides the possible contribution of CT concentration toward explaining antiparasitic activities, several authors have also suggested that CT structures (or quality) could explain some of the observations.[8−10,19,20,22] For instance, it has been proposed that the biological activity is affected by the hydroxylation at the B-ring in flavan-3-ol monomers and in polymers, where the presence of an additional hydroxyl group (OH) increases the interaction with proteins. This could explain the generally higher activity of PDs compared to PCs. In addition, activity is also increased when galloyl groups are present.[21,32−34]

Results of the 2 by 2 calculations of Spearman's correlation coefficients as well as multivariate analyses (PCA) tended to confirm that the in vitro AH activity in terms of EC_{50} was related to CT structural features for both *H. contortus* and *T. colubriformis*. In addition, our results suggest that different mechanisms appear to be involved for each nematode species. For *H. contortus*, AH activity appeared stronger for CTs with higher PD contents and larger sizes (mDP values), although, as described by Williams et al.,[20] there was no effect of mDP or % PD within F2 fractions on the EC_{50} values. For the F1 fractions, lower EC_{50} values were associated with higher % PD and larger tannins (higher mDP values). Novobilský et al.[10] suggested that mDP was a key factor in the LFIA against L3 of *O. ostertagi* and *C. oncophora* after testing *O. viciifolia* extracts and fractions.

However, Naumann et al.[19] found no clear evidence for CT size and inhibition of *H. contortus* motility. However, only a narrow range of CT sizes was investigated. Conversely to the present data, Manoralaki[35] found that lower mDP values were correlated with higher AH activity when extracts from 40 *O. viciifolia* accessions were tested by LEIA against *H. contortus*. Similarly, Barrau et al.[7] found that a fraction that contained CTs (<2000 Da) plus flavonol glycosides had higher AH effects against *H. contortus* larvae than a fraction that contained only CTs (>2000 Da). At this stage, it is important to note that the complexity of plant extract compositions and difficulties in purifying CTs are likely to account for some of these apparent contradictions. Acetone/water extracts from CT-containing plants consist of CTs plus low molecular weight phenolic compounds (flavones, flavonols, flavonol glycosides, etc.). In addition, CTs usually occur as complex mixtures that contain low to high molecular weight tannins, and the mDP value simply describes the average "tannin size" rather than the distribution profile of all CTs. In fact, we recently discovered that mixtures of CTs and flavonoids had higher AH activities than CTs on their own.[36] Kozan et al.[37] also reported that flavonol glycosides (luteolin-7-β-*O*-glucopyranoside and quercetin-3-*O*-β-glucopyranoside) from *Vicia pannonica* var. *purpuracens* might also participate in the modulation of bioactivity of the highly AH extract and fractions against trichostrongylid larvae. This emphasizes that the proximity of biochemical structure between flavonol glycosides and CT (which are flavan-3-ols' polymers) could suggest a similar or close mechanism of action for both types of compounds. Taken together, the presence of non-CT compounds (such as flavonoid monomers) could, therefore, explain the apparently contradictory observations by Manoralaki[35]

DOI: 10.1021/acs.jafc.5b00831
J. Agric. Food Chem. 2015, 63, 6346−6354

and Barrau et al.[7] The F1 fractions had only half the CT contents of F2 fractions (Table 1). However, the combination of F1+F2 data gave a close to significant correlation of EC_{50} and mDP values (Table 3).

In contrast, for *T. colubriformis*, % PD was consistently (F1, F2, and combined F1+F2) related to AH activity. This agrees with other reports on *T. colubriformis* larvae, which found higher AH in vitro effects of PD-rich compared with PC-rich tannins.[21,22]

Interestingly, there were different susceptibilities between the two parasite species, which suggested that *H. contortus* was more susceptible than *T. colubriformis*. This is indicated by the overall lower EC_{50} values for the abomasal species with both types of CT fractions. Molan et al.[8] also pointed out that the abomasal nematode *T. circumcincta* was more susceptible than *T. colubriformis* to the AH effects of flavan-3-ol monomers and oligomeric CTs in the LMIA. The same conclusion was drawn from in vitro studies that examined extracts from different woody plants (*Rubus fructicosus*, *Quercus robur*, and *Corylus avellana*) against *H. contortus*, *T. circumcincta*, and *T. colubriformis* based on LMIA and LEIA tests.[16] However, other authors found no such differences in the response to quebracho or *O. viciifolia* extracts[11,31] between abomasal or intestinal species. Moreno-Gonzalo et al.[38,39] even found a higher in vitro susceptibility of *T. colubriformis* compared to *H. contortus* and *T. circumcincta* when measuring the AH activity of extracts from different heather species (*Calluna vulgaris*, *Erica cinerea*, and *E. umbellata*). It remains to be seen whether differences in assay conditions could account for some of these contradictory results. Moreover, it will be worth exploring whether there exist species-specific differences in the quality of larval sheath proteins between the abomasal and intestinal species to better understand the mode of actions of polyphenols against the different GIN species.

Although it is difficult to extrapolate from in vitro to in vivo results, our current data provide a screening of CT-containing plants whose AH properties will need to be explored further in controlled in vivo studies to develop their potential for on-farm exploitation. It is also worth noting that the CT fractions from three legumes ranked among the most effective ones (i.e., having the lowest EC_{50} values): *L. cuneata* pellets, *O. viciifolia* plants, and *T. repens* flowers (Figure 1). The past decade has seen an accumulation of in vivo results that confirm the AH effects of *L. cuneata* and *O. viciifolia* against the main GIN species whether offered to small ruminants in the form of freshly grazed pasture[40,41] or as hay,[15,17,42] silages,[42] or pellets.[18]

As far as *T. repens* is concerned, no other data are available because the genus *Trifolium* is usually considered as a tannin-free legume,[43] and consequently the various *Trifolium* species have received little attention for their antiparasitic potential. However, Carlsen and Fomsgaard[44] provided an extensive review of the secondary metabolites in *T. repens* and pointed out the high CT content in flowers. The current study found that CTs from *T. repens* flowers had a strong AH effect and confirmed the dose-dependent inhibition effects of *T. repens* tannins observed for *C. oncophora* in the LFIA.[45]

The CT fractions of *V. paradoxa* were also ranked as highly effective against both nematode species and suggested that some agro-industrial byproducts could be of interest for their antiparasitic properties. It is worth noting that AH effects on *H. contortus* and *T. colubriformis* were recently also described not only for cocoa seed but also for husk extracts using the EHA.[46]

In conclusion, our results showed that structural features of condensed tannins are key factors that affect the anthelmintic effects against gastrointestinal nematodes of ruminants. In addition, there were differences in the susceptibilities of the abomasal as the intestinal nematode species. These differences have been described previously in the literature and could be related to the fact that the nematode sheath proteins differ in these parasite species. This could perhaps affect their interactions with the tannins. It is worth also emphasizing that the current results have been acquired on infective larvae and that other assays that target other parasitic stages might have different outcomes. Further studies will be needed to explore these interactions at the molecular level.

AUTHOR INFORMATION

Corresponding Author

*(H.H.) Phone: +(33) 05-61-19-38-75. Fax: +(33) 05-61-19-32-43. E-mail: h.hoste@envt.fr.

Funding

The financial support of the European Commission through the PITN-GA-2011-289377, "LegumePlus" project, is sincerely acknowledged.

Notes

The authors declare no competing financial interest.

ACKNOWLEDGMENTS

We thank Alison and Dave Prudence for the *S. caprea* leaves and twigs, Hildred's PYO Farm for the *R. nigrum* and *R. rubrum* leaves, and P. Davy for the *O. viciifolia* plants. The *V. paradoxa* meal sample was kindly provided by AarhusKarlshamm Sweden AB, Sweden. We also deeply appreciate all of LegumePlus' fellows for help in collecting plant samples.

ABBREVIATIONS USED

GINs, gastrointestinal nematodes; CT, condensed tannins; AH, anthelmintic; mDP, mean degree of polymerization; PD, prodelphinidins; PC, procyanidins; PBS, phosphate buffered saline; LEIA, larval exsheathment inhibition assay; L3, infective stage nematode larvae; EC_{50}, effective concentration for 50% inhibition of larvae's exsheathment; LDIA, larval development inhibition assay; LFIA, larval feeding inhibition assay; EHA, egg hatch assay; LMIA, larval migration inhibition assay

REFERENCES

(1) Jackson, F.; Varady, M.; Bartley, D. J. Managing anthelmintic resistance in goats − can we learn lessons from sheep? *Small Ruminant Res.* **2012**, *103* (1), 3−9.

(2) Hoste, H.; Torres-Acosta, J. F. J. Non chemical control of helminths in ruminants: adapting solutions for changing worms in a changing world. *Vet. Parasitol.* **2011**, *180*, 144−154.

(3) Andlauer, W.; Fürst, P. Nutraceuticals: a piece of history, present status and outlook. *Food Res. Int.* **2002**, *35*, 171−176.

(4) Athanasiadou, S.; Houdijk, J.; Kyriazakis, I. Exploiting synergisms and interactions in the nutritional approaches to parasite control in sheep production systems. *Small Ruminant Res.* **2008**, *76*, 2−11.

(5) Hoste, H.; Martinez-Ortiz-de-Montellano, C.; Manolaraki, F.; Brunet, S.; Ojeda-Robertos, N.; Fourquaux, I.; Torres-Acosta, J. F. J.; Sandoval-Castro, C. A. Direct and indirect effects of bioactive tannin-rich tropical and temperate legumes against nematode infection. *Vet. Parasitol.* **2012**, *186*, 18−27.

(6) Terrill, T. H.; Miller, J. E.; Burke, J. M.; Mosjidis, J. A.; Kaplan, R. M. Experiences with integrated concepts for the control of *Haemonchus contortus* in sheep and goats in the United States. *Vet. Parasitol.* **2012**, *186*, 28−37.

(7) Barrau, E.; Fabre, N.; Fouraste, I.; Hoste, H. Effect of bioactive compounds from Sainfoin (*Onobrychis viciifolia* Scop.) on the *in vitro*

DOI: 10.1021/acs.jafc.5b00831
J. Agric. Food Chem. 2015, 63, 6346−6354

larval migration of *Haemonchus contortus*: role of tannins and flavonol glycosides. *Parasitology* **2005**, *131*, 531−538.
(8) Molan, A. L.; Sivakumaran, S.; Spencer, P. A.; Meagher, L. P. Green tea flavan-3-ols and oligomeric proanthocyanidins inhibit the motility of infective larvae of *Teladorsagia circumcincta* and *Trichostrongylus colubriformis in vitro*. *Res. Vet. Sci.* **2004**, *77*, 239−243.
(9) Novobilský, A.; Mueller-Harvey, I.; Thamsborg, S. M. Condensed tannins act against cattle nematodes. *Vet. Parasitol.* **2011**, *182*, 213−220.
(10) Novobilský, A.; Stringano, E.; Hayot Carbonero, C.; Smith, L. M. J.; Enemark, H. L.; Mueller-Harvey, I.; Thamsborg, S. M. *In vitro* effect of extracts and purified tannins of sainfoin (*Onobrychis viciifolia*) against two cattle nematodes. *Vet. Parasitol.* **2013**, *196*, 532−537.
(11) Athanasiadou, S.; Kyriazakis, I.; Jackson, F.; Coop, R. L. Direct anthelmintic effects of condensed tannins towards different gastrointestinal nematodes of sheep: *in vitro* and *in vivo* studies. *Vet. Parasitol.* **2001**, *99*, 205−219.
(12) Hoste, H.; Jackson, F.; Athanasiadou, S.; Thamsborg, S. M.; Hoskin, S. The effects of tannin-rich plants on parasitic nematodes in ruminants. *Trends Parasitol.* **2006**, *22*, 253−261.
(13) Joshi, B. R.; Kommuru, D. S.; Terrill, T. H.; Mosjidis, J. A.; Burke, J. M.; Shakya, K. P.; Miller, J. E. Effect of feeding sericea lespedeza leaf meal in goats experimentally infected with *Haemonchus contortus*. *Vet. Parasitol.* **2011**, *178*, 192−197.
(14) Max, R. A. Effect of repeated wattle tannin drenches on worm burdens, faecal egg counts and egg hatchability during naturally acquired nematode infection in sheep and goats. *Vet. Parasitol.* **2010**, *169*, 138−143.
(15) Terrill, T. H.; Dykes, G. S.; Shaik, S. A.; Miller, J. E.; Kouakou, B.; Kannan, G.; Burke, J. M.; Mosjidis, J. A. Efficacy of sericea lespedeza hay as a natural dewormer in goats: dose titration study. *Vet. Parasitol.* **2009**, *163*, 52−56.
(16) Paolini, V.; Fouraste, I.; Hoste, H. *In vitro* effects of three woody plant and sainfoin on third-stage larvae and adult worms of three gastrointestinal nematodes. *Parasitology* **2004**, *129*, 69−77.
(17) Paolini, V.; De La Farge, F.; Prevot, F.; Dorchies, Ph.; Hoste, H. Effects of the repeated distribution of sainfoin hay on the resistant and the resilience of goats naturally infected with gastrointestinal nematodes. *Vet. Parasitol.* **2005**, *127*, 277−283.
(18) Kommuru, D. S.; Barker, T.; Desai, S.; Burke, J. M.; Ramsay, A.; Mueller-Harvey, I.; Miller, J. E.; Mosjidis, J. A.; Kamisetti, N.; Terrill, T. H. Use of pelleted sericea lespedeza (*Lespedeza cuneata*) for natural control of coccidian and gastrointestinal nematodes in weaned goats. *Vet. Parasitol.* **2014**, *204*, 191−198.
(19) Naumann, H. D.; Armstrong, S. A.; Lambert, B. D.; Muir, J. P.; Tedeshi, L. O.; Kothmann, M. M. Effect of molecular weight and concentration of legume condensed tannins on *in vitro* larval migration inhibition of *Haemonchus contortus*. *Vet. Parasitol.* **2014**, *199*, 93−98.
(20) Williams, A. R.; Fryganas, C.; Ramsay, A.; Mueller-Harvey, I.; Thamsborg, S. T. Direct anthelmintic effects of condensed tannins from diverse plant sources against *Ascaris suum*. *PLoS One* **2014**, *9* (5), No. e97053, DOI: 10.1371/journal.pone.0097053.
(21) Brunet, S.; Hoste, H. Monomers of condensed tannins affect the larval exsheathment of parasitic nematodes of ruminants. *J. Agric. Food Chem.* **2006**, *54*, 7481−7487.
(22) Molan, A. L.; Meagher, L. P.; Spencer, P. A.; Sivakumaran, S. Effect of flavan-3-ols *in vitro* hatching, larval development and viability of infective larvae of *Trichostrongylus colubriformis*. *Int. J. Parasitol.* **2003**, *33*, 1691−1698.
(23) Blamey, M.; Grey-Wilson, C. *La Flore d'Europe Occidentale*; Flammarion: Paris, France, 2003.
(24) Stringano, E.; Gea, A.; Salminen, J.-P.; Mueller-Harvey, I. Simple solution for a complex problem: proanthocyanidins, galloyl glucoses and ellagitannins fit on a single calibration curve in high-performance-gel permeation chromatography. *J. Chromatogr. A* **2011**, *1218*, 7804−7812.
(25) Gea, A.; Stringano, E.; Brown, R. H.; Mueller-Harvey, I. *In situ* analysis and structural elucidation of sainfoin (*Onobrychis viciifolia*) tannins for high-throughput germplasm screening. *J. Agric. Food Chem.* **2011**, *59*, 495−503.
(26) Bahuaud, D.; Martinez-Ortiz De Montellano, C.; Chauveau, S.; Prevot, F.; Torres-Acosta, F.; Fouraste, I.; Hoste, H. Effects of four tanniferous plant extracts on the *in vitro* exsheathment of third-stage larvae of parasitic nematodes. *Parasitology* **2006**, *132*, 545−554.
(27) Molan, A. L.; Alexander, R. A.; Brookes, I. M.; McNabb, W. C. Effect of an extract from sulla (*Hedysarum coronarium*) containing condensed tannins on the migration of three sheep gastrointestinal nematodes *in vitro*. *Proc. N. Z. Soc. Anim. Prod.* **2000**, *60*, 21−25.
(28) Molan, A. L.; Waghorn, G. C.; McNabb, W. C. The impact of condensed tannins on egg hatching and larval development of *Trichostrongylus colubriformis*. *Vet. Rec.* **2002**, *150*, 65−69.
(29) Mueller-Harvey, I. Unravelling the conundrum of tannins in animal nutrition and health. *J. Sci. Food Agric.* **2006**, *86*, 2010−2037.
(30) Jackson, F.; Hoste, H. *In vitro* methods for the primary screening of plant products for direct activity against ruminant gastrointestinal nematodes. In *In Vitro Screening of Plant Resources for Extra Nutritional Attributes in Ruminants: Nuclear and Related Methodologies*; Vercoe, P. E., Makkar, H. P. S., Schlink, A. C., Eds.; FAO/IAEA Springer: Berlin, Germany, 2010; pp 24−45.
(31) Brunet, S.; Aufrere, J.; El Babili, F.; Fouraste, I.; Hoste, H. The kinetics of exsheathment of infective nematode larvae is disturbed in the presence of a tannin-rich plant extract (sainfoin) both *in vitro* and *in vivo*. *Parasitology* **2007**, *134*, 1253−1262.
(32) Brunet, S.; Jackson, F.; Hoste, H. Effects of sainfoin (*Onobrychis viciifolia*) extract and monomer of condensed tannins on the association of abomasal nematode larvae with fundic explants. *Int. J. Parasitol.* **2008**, *38*, 783−790.
(33) Li, C.; Leverence, R.; Trombley, J. D.; Xu, S.; Yang, J.; Tian, Y.; Reed, J. D.; Hagerman, A. E. High molecular weight persimmon (*Diospyros kaki* L.) proanthocyanidin, a highly galloylated, A-linked tannin with an unusual flavonol terminal unit, myricetin. *J. Agric. Food Chem.* **2010**, *58*, 9033−9042.
(34) Okuda, T.; Ito, H. Tannins of constant structure in medicinal and food plants − hydrolysable tannins and polyphenols related to tannins. *Molecules* **2011**, *16*, 2191−2217.
(35) Manolaraki, F. *Propriétés anthelminthiques du sainfoin (Onobrychis viciifolia): analyse des facteurs de variations et du rôle des composés phénoliques impliqués*. Ph.D. Dissertation, INP, Université de Toulouse, Toulouse, France, 2011.
(36) Klongsiriwet, C.; Quijada, J.; Williams, A. R.; Hoste, H.; Williamson, E.; Mueller-Harvey, I. 2014. Synergistic effects between condensed tannins and luteolin on *in vitro* larval exsheathment inhibition of *Haemonchus contortus*. In *Proceedings of XXVIIth International Conference on Polyphenols (ICP2014)*, Nagoya, Japan, Sept 2−6, 2014; ISBN 978-4-9907847-0-6), pp 601−602.
(37) Kozan, E.; Anul, S. A.; Tatli, I. I. *In vitro* anthelmintic effect of *Vicia pannonica* var. *purpurascens* on trichostrongylosis in sheep. *Exp. Parasitol.* **2013**, *134*, 299−303.
(38) Moreno-Gonzalo, J.; Manolaraki, F.; Frutos, P.; Hervas, G.; Celaya, R.; Osoro, K.; Ortega-Mora, L. M.; Hoste, H.; Ferre, I. *In vitro* effect of heather (Ericaceae) extracts on different development stages of *Teladorsagia circumcincta* and *Haemonchus contortus*. *Vet. Parasitol.* **2013**, *197*, 235−243.
(39) Moreno-Gonzalo, J.; Manolaraki, F.; Frutos, P.; Hervas, G.; Celaya, R.; Osoro, K.; Ortega-Mora, L. M.; Hoste, H.; Ferre, I. *In vitro* effect of heather extracts on *Trichostrongylus colubriformis* eggs, larvae and adults. *Vet. Parasitol.* **2013**, *197*, 586−594.
(40) Athanasiadou, S.; Tzamaloukas, O.; Kyriazakis, I.; Jackson, F.; Coop, R. L. Testing for direct anthelmintic effects of bioactive forages against *Trichostrongylus colubriformis* in grazing sheep. *Vet. Parasitol.* **2005**, *28*, 233−243.
(41) Mechineni, A.; Kommuru, D. S.; Gujja, S.; Mosjidis, J. A.; Miller, J. E.; Burke, J. M.; Ramsay, A.; Mueller-Harvey, I.; Kannan, G.; Lee, J. H.; Kouakou, B.; Terrill, T. H. Effect of fall-grazed sericea lespedeza (*Lespedeza cuneata*) on gastrointestinal nematode infections of growing goats. *Vet. Parasitol.* **2014**, *29*, 221−228.

DOI: 10.1021/acs.jafc.5b00831
J. Agric. Food Chem. 2015, 63, 6346−6354

(42) Heckendorn, F.; Häring, D. A.; Maurer, V.; Zinsstag, J.; Langhans, W.; Hertzberg, H. Effect of sainfoin (*Onobrychis viciifolia*) silage and hay on established populations of *Haemonchus contortus* and *Cooperia curticei* in lambs. *Vet. Parasitol.* **2006**, *142*, 293−300.
(43) Barry, T. N. The role of condensed tannins in the nutritional value of *Lotus pedunculatus* for sheep. 3. Rates of body and wool growth. *Br. J. Nutr.* **1985**, *54*, 217−221.
(44) Carlsen, S.; Fomsgaard, I. S. Biologically active secondary metabolites in white clover (*Trifolium repens* L.) − a review focusing on contents in the plant, plant−pest interactions and transformation. *Chemoecology* **2008**, *18*, 129−170.
(45) Desrues, O.; Enemark, H. L.; Mueller-Harvey, I.; Fryganas, C.; Thamsborg, S. M. Preliminary analysis of the relationship between structure and anthelmintic activity of condensed tannins in cattle nematodes. In *Proceedings 7th Novel Approaches to the Control of Helminths of Livestock*; Toulouse, France, March 25−28; 2013; p 46.
(46) Vargas-Magaña, J. J.; Torres-Acosta, J. F. J.; Aguilar-Caballero, A. J.; Sandoval-Castro, C. A.; Hoste, H.; Chan-Pérez, J. I. Anthelmintic activity of acetone−water extracts against *Haemonchus contortus* eggs: Interactions between tannins and other plant secondary compounds. *Vet. Parasitol.* **2014**, *206*, 322−327.

DOI: 10.1021/acs.jafc.5b00831
J. Agric. Food Chem. 2015, 63, 6346−6354

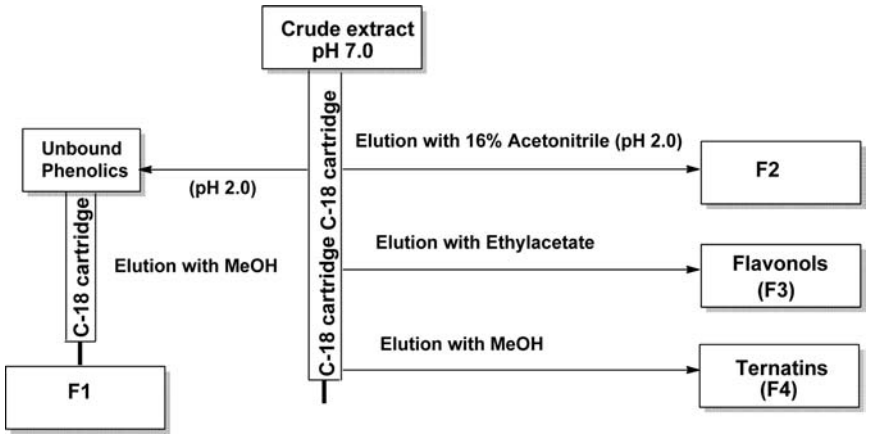

Figure 1. Fractionation scheme used for butterfly pea flower extracts to obtain fractions F1, F2, F3, and F4. Fractions F3 and F4 correspond to enriched fractions of quercetin glycosides and ternatin anthocyanins, respectively.

have been shown to have inhibitory effects on the COX-2 enzyme activity, important for generation of the PGE2 and PGD2, pro-inflammatory mediators.[15,16]

In the present study we hypothesize that the mixture of flavonols and anthocyanins present in the blue flower petals of *C. ternatea* would be responsible for the anti-inflammatory properties claimed by folklore use of butterfly pea extracts. To our knowledge this is the first report of the anti-inflammatory properties of polyphenols from *C. ternatea*. To accomplish our goal we identified the polyphenols by HPLC-DAD-ESI/MS^n, separated them in fractions, and characterized their anti-inflammatory properties, determining the molecular mechanism roles of flavonols and ternatin anthocyanin derivatives in reactive oxygen species (ROS) and nitric oxide (NO) suppression, NF-κB and iNOS modulation, and COX-2 inhibition.

MATERIALS AND METHODS

Materials. Butterfly pea flowers were collected in March 2012 from an uncultivated field near Bogor Agricultural University, Indonesia. The blue color petals of butterfly pea were blanched by steam at 100 °C for 6 min and cooled immediately by soaking in an ice bath, freeze-dried in a FreeZone 6L benchtop Freeze-Dry System model 77520 (Labconco, Kansas City, MO, USA), and shipped to Texas A&M University (College Station, TX, USA). The following chemicals were used in the experiments: 2′,7′-Dichlorofluorescin diacetate (DCFA), Griess reagent, sodium nitrite solution, Dulbecco's modified Eagle's medium (DMEM)/low glucose, phenol red-free DMEM/low glucose, penicillin/streptomyccn mixture, DMSO, and fetal bovine serum (FBS) were purchased from Sigma (St. Louis, MO, USA). Glucose was purchased from Acros Organics (Fair Lawn, NJ, USA), and sodium bicarbonate was purchased from Mallinckrodt Chemicals (Phillipsburg, NJ, USA). The CellTiter 96 AQ_{ueous} Non-Radioactive Cell Proliferation Assay Kit was purchased from Promega (Madison, WI, USA). Antibodies against iNOS, COX-2, and NPM/B23 and against p-NF-κB and actin were purchased from Cell Signaling Technology (Danvers, MA, USA) and Santa Cruz Biotechnology (Dallas, TX, USA), respectively. Macrophage RAW 264.7 (cell line TIB-71) was acquired from the American Type Culture Collection (ATCC) (Manassas, VA, USA). A COX Inhibitor Screening Assay Kit and DuP-697 were purchased from Cayman Chemicals (Ann Arbor, MI, USA).

FA, Folin−Ciocalteu reagent, sodium carbonate (Na_2CO_3), 6-hydroxy-2,5,7,8-tetramethyl-2-carboxylic acid (Trolox), 2,2′-azobis(2-amidinopropane) dihydrochloride (AAPH), fluorescein sodium salt, polyvinylpyrrolidine (PVPP), boric acid, β-mercaptoethanol, L-phenylalanine, *trans*-cinnamic acid, diphenyleneiodonium chloride (DPI), Na_2EDTA, ascorbic acid, diethyl dithiocarbamate, NADPH, Tris-HCl, sucrose, riboflavin, methionine, methanol (HPLC grade), and acetonitrile (HPLC grade) were purchased from Sigma Chemical Co. (St. Louis, MO, USA). Chlorogenic acid, nitrotetrazolium blue chloride (NBT), and Triton X-100 were purchased from Fisher Scientific (Houston, TX, USA).

Sample Preparation. A 0.1 g portion of lyophilized powder of butterfly pea was dissolved in a mixture of MeOH/acetone/H_2O (5:4:1) and stirred for 24 h at room temperature. The extract was blue in color, and the solution was centrifuged and concentrated at 4000 rpm (2147*g*) and 45 °C until all of the volatile solvents were evaporated in a Centrivap concentrator connected to a cold trap (Labconco, Kansas City, MO). MeOH/H_2O (8:2) was added to the concentrated mixture, and this solvent fraction was used to analyze the profiling of the compounds present in the butterfly pea extract by HPLC/MS.

TLC Analysis and Fractionation of Phenolic Compounds. The crude MeOH/acetone/H_2O extract was spotted in a TLC plate to determine the possible presence of terpenoids using the Liebermann Burchard test,[17] confirming no visible spots for terpenoids due likely to the fact that the solvent used did not remove terpenoids from the blue flower petal freeze-dried samples.

The crude extract was fractionated into phenolic acids (F1), anthocyanins (F2), flavonols (F3), and procyanidins/polymeric anthocyanins (F4) by solid-phase extraction using C18 cartridges as previously described[18] (Figure 1). Briefly, the aqueous extract was adjusted to pH 7.0 with 5 N NaOH. A total of 2 mL of extract was loaded in SEP Pack C18 cartridge (55−105 μm, Waters Corp., Milford, MA, USA) previously conditioned to pH 7.0 with 20 mL of 100% methanol and 50 mL of nanopure water (pH 7.0). The neutral phenolics were absorbed in the cartridge, whereas the phenolic acids were not. The cartridge was washed with 20 mL of water (pH 7.0). The water from the wash was combined with the phenolics that were not adsorbed in the cartridge and adjusted to pH 2.0. This mixture of compounds was loaded into a second cartridge previously conditioned at pH 2.0 with 20 mL of 100% methanol and 20 mL of nanopure water at pH 2.0. Phenolic acids bound to the matrix of the second cartridge (F1) were later eluted with 50 mL of 100% methanol. After the pH was adjusted to 2.0 in the first cartridge, elution of anthocyanins was accomplished by passing 20 mL of 16% acetonitrile at pH 2.0 (F2). The flavonols were eluted using 20 mL of 100% ethyl acetate (F3) and the anthocyanin polymers using 20 mL of 100% methanol (F4). Fractions eluted with low boiling point solvents (F1, F3, and F4) were completely evaporated at 45 °C using a Centrivap (Labconco, Kansas City, MO). Fraction F2 was evaporated using a rotavapor (Büchi, Flawil, Switzerland), at 50 °C and 200 mmHg of pressure. All fractions were kept under nitrogen gas at −20 °C for use in cell culture.

The butterfly pea crude extracts and fractions were analyzed by HPLC-MS. Identification of phenolic compounds was performed at 200−600 nm by a comparison of retention times and the MS/MS

DOI: 10.1021/acs.jafc.5b00928
J. Agric. Food Chem. 2015, 63, 6355−6365

Table 1. Identification of Anthocyanins and Flavonols from the Butterfly Pea Flower Crude Extract

peak	retention time	mass $[M + H]^+$	mass $[M - H]^-$	UV	MS^n	percentage area	identification
1	30.53	1296		237, 256, 314, 557	MS^2 **1296**: 1242, 810, 788, 658, 633, 611, 465, **303**	3.19	delphinidin derivative
2	35.75	1534		238, 290, 550	MS^2 **1534**: 1329, 1081, 779, 658, 611, 465, **303**	3.73	delphinidin derivative
3	38.41	1638		238, 290, 547	MS^2 **1638**: 1638, 1615, 1389, 1227, 1081, 1168, 964, 919, 860, 801, 633, 611, 517, 437, **303**, 180	4.60	ternatin B3
4	39.12	1167		221, 238, 290, 551	MS^2 **1167**: 1167, 919, 611, **303**, 180.8, 163.8, 149.07	2.83	ternatin D3
5	40.82		609	227, 238, 291, 382,	MS^2 **609**: **301**, 177	6.10	rutin
6	43.19	950		238, 265, 546	MS^2 **950**: 950, 658, 487, 465, **303**, 180.9, 163.12	11.50	delphinidin derivative
7	44.95		593	238, 253, 302, 312, 353	MS^2 **593**: 593, **301**	39.86	quercetin 3-*O*-dirhamnoside
8	46.32		753	223, 238, 290	MS^2 **753**: 447, **301**, 285, 180.9	7.10	manghaslin quercetin 3-[2G]-rhamnosylrutinoside
9	52.51	1638		223, 238, 292, 547	MS^2 **1638**: 1638, 1389, 1167, 919, 773, 703, 626, 535, **303**, 287, 180.8, 163.13	3.21	ternatin B2
10	53.51	1329		223, 238, 292, 549	MS^2 **1329**: 1329, 1081, 919, 471, 448, 314, **303**, 387, 180.8, 163.07, 149.09	3.91	ternatin B4
11	54.38	1491		223, 238, 292, 538	MS^2 **1491**: 1492, 1449, 1389, 1257, 1227, 919, 828, 763, 611, **303**, 264, 180.8, 163.12, 149.09	6.71	ternatin C2
12	60.20	1783		223, 238, 292, 550	MS^2 **1783**: 1783, 1535, 1255, 1167, 919, 898, **303**, 180.8	7.21	ternatin D1

fragments from the original crude extract, which was previously identified.

During the extraction process a yield of ∼72 mg of a MeOH/acetone/H_2O solvent crude extract powder was obtained per each 100 mg of freeze-dried petal powder. Additionally, during the fractionation process yields of ∼2.4, 1.2, 8.1, and 2.2 mg of fraction powders were obtained, respectively, for fractions F1, F2, F3, and F4 per each 20 mg of the MeOH/acetone/H_2O crude extract.

LC-MS Analysis and Conditions. Individual compounds were identified on the basis of retention time, UV spectra, and mass-to-charge ratio using LC-MS/MS. Chromatographic separations were performed on an LCQ Deca XP Max MS^n system (Thermo Finnigan, San Jose, CA, USA) equipped with an autosampler, a Surveyor 2000 quaternary pump, and a Surveyor UV 2000 PDA detector using a Hydro-RP_{18} phase (150 mm × 4.6 mm × 3 mm, Phenomenex, Torrance, CA, USA; particle size = 4 μm and pore size = 100 Å) and a guard column of the same chemistry. The elution gradients were performed with acetonitrile/methanol (1:1), formic acid (0.5:99.5, v/v) (phase A) and formic acid/water (0.5:99.5, v/v) (phase B). The applied elution conditions were as follows: 0−2 min, 2% A; 98% B; 3−5 min, 5% A, 95% B; 5−30 min, 20% A, 80% B; 30−72 min, 35% A, 65% B; 72−83 min, 100% A, 0% B; 83−85 min, isocratic, 100% A; 87−90 min, 2% A, 98% B to bring to the starting condition. The chromatograms were monitored at 365, 330 and 520 nm; complete spectral data were recorded in the range of 200−600 nm. Nitrogen was used as desolvation gas, at 275 °C and a flow rate of 60 L/h, and He gas was used as damping gas. Mass spectra were obtained on a MS Finnigan LCQ Deca XP Max, ion trap mass spectrometer coupled at the exit of the diode array detector and equipped with a *Z*-spray ESI source and run by Xcalibur version 1.3 software (Thermo Finnigan-Surveyor, San Jose, CA, USA). A potential of 30 V and a spray voltage of 1.5 kV were used on the capillary for negative ion mode. A potential of 6.8 V was used on the capillary for positive ion mode. The spray voltage was 4.57 kV, and the source block temperature was held at 285 °C. Results are reported in Table 1.

Analysis of Total Soluble Phenolics (PC) and Determination of Antioxidant Activity [Oxygen Radical Absorbance Capacity (ORAC) Value]. Total soluble phenolics were determined using the method described by Swain and Hillis.[19] Methanolic extracts (13 μL) were diluted with nanopure water (208 μL) in a 96-well microplate well, followed by the addition of 0.25 N Folin−Ciocalteu reagent (15 μL). The mixture was incubated for 3 min, and then 1 N Na_2CO_3 (26 μL) was added. The final mixture was incubated for 2 h at room temperature in the dark. Spectrophotometric readings at 725 nm were collected using a plate reader (Synergy HT, Bio-Tek Instruments, Inc., Winooski, VT, USA). Total phenolics were expressed as milligrams of chlorogenic acid equivalents per milligram of crude extract or fraction. The antioxidant activity was determined with the ORAC assay. The ORAC value was obtained using the procedure of Wu et al.[20] for hydrophilic ORAC with a slight modification as described by Villarreal-Lozoya et al.[21] Results are reported as micromoles Trolox equivalent per gram crude extract or fraction.

Cell Culture and Treatment of Butterfly Pea Extracts and Fractions (F3 and F4). RAW 264.7 macrophages were grown in the DMEM-low glucose (pH 7.2−7.4) including 4 g/L glucose, 3.7 g/L sodium bicarbonate, 10% FBS, and antibiotics (100 units/mL penicillin and 100 μg/mL streptomycin) in a humidified atmosphere with 5% CO_2 at 37 °C. Cells were used at a subculture of 5−9 in this study. It is important to record the approximate number of subcultures because in mammalian cell lines chromosomal aberrations have a tendency to increase with a high number of subculture. In this study we used a low number of subcultures associated with healthy cells.

For treatments of cells with butterfly pea extract and its fractions (F3 and F4), the cells were plated at 2×10^5 or 0.5×10^5 cells/well in 96-well black and clear-bottom plates (Costar, Cambridge, MA, USA) for MTS test and NO/ROS measurements and at 2×10^6 cells/well in 6-well plates (BD Biosciences, Franklin Lakes, NJ, USA) for Western blot analysis and then cultured overnight. The cells were treated with the growth medium containing 1 μg/mL lipopolysaccharide (LPS) for times indicated in this study either with or without a 1 or 5 h of pretreatment of butterfly pea extract and its fractions. The butterfly pea extract and its fractions were dissolved in the growth medium including 0.5% DMSO, which was used as a control in all experiments. Finally, cells and medium at the time points indicated in this study were used for various measurements.

Cell Viability Test. Macrophages were plated at $(0.5-2) \times 10^5$ cells/well in 96-well clear-bottom plates (Costar) and cultured overnight. The cells were treated with butterfly pea extract and its fractions for 24 h and were subjected to the cell viability test, which was evaluated in macrophages using the MTS assay kit (Promega, Madison, WI), according to the manufacturer's instructions. The quantity of formazan product was measured at 490 nm and is directly proportional to the mitochondrial dehydrogenase activity.

Detection of Extracellular Nitric Oxide and Intracellular Reactive Oxygen Species Production. Macrophages were plated at $(0.5-2) \times 10^5$ cells/well in 96-well black and clear bottom plates (Costar) and cultured overnight. The cells were stimulated by LPS for times indicated in this study either with or without a 1 and 5 h of

DOI: 10.1021/acs.jafc.5b00928
J. Agric. Food Chem. 2015, 63, 6355−6365

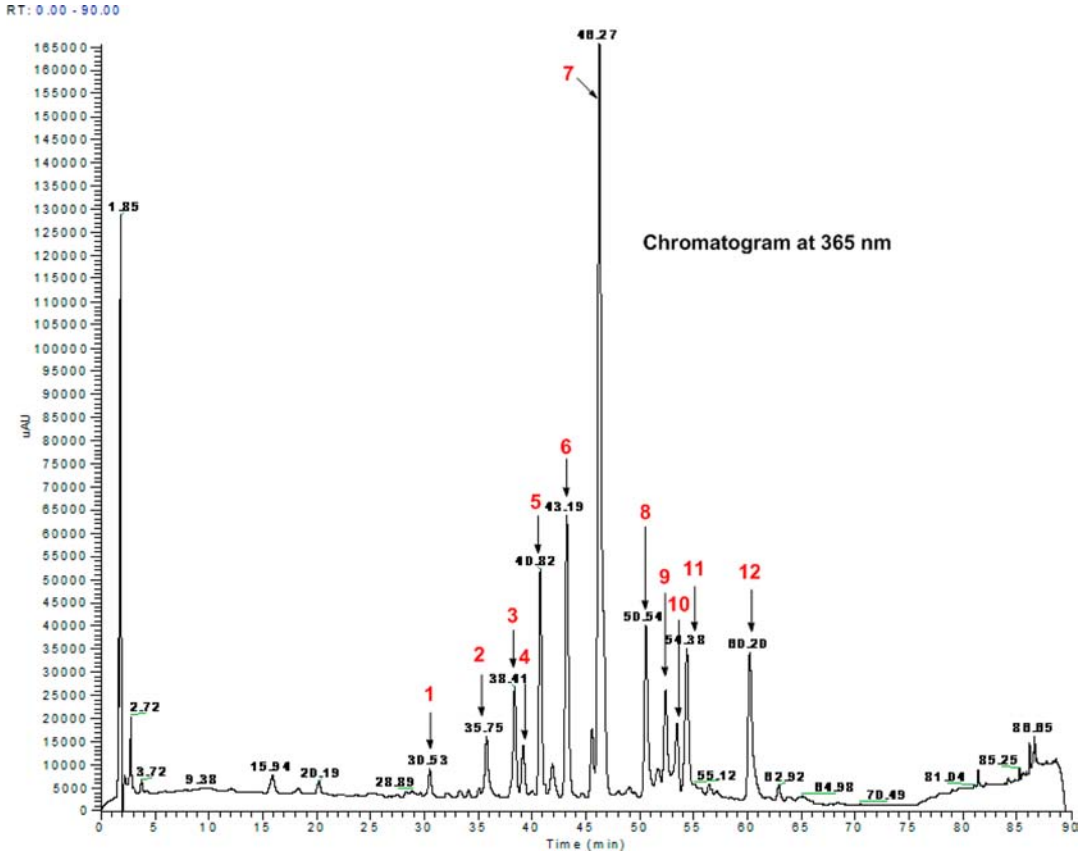

Figure 2. HPLC-MS chromatogram of the total butterfly pea flower extract at 365 nm. Identified quercetin glycoside and ternatin anthocyanin peaks are reported in Table 1. Peaks 1, 2, and 6 are delphinidin derivatives, peaks 3, 4, and 9−12 are ternatin anthocyanins, and peaks 5, 7, and 8 are quercetin glycosides.

pretreatment of butterfly pea extract and its fractions as described above. Finally, cells and medium were used for the ROS and NO detections, respectively.

The NO production was assessed by the accumulation of nitrite (NO_2^-) in the medium using a colorimetric reaction with the Griess reagent. However, because anthocyanins absorb in the 465−560 nm range similarly to the purple azo dye (λ_{max} = 540 nm), a reaction product of nitrite and Griess reagent, and thus interfere with detection of the purple azo dye, the measurement of nitrite (NO_2^-) in the medium including anthocyanins was carried out using an alternative method as described in Wang and Mazza.[22] Briefly, 50 μL of cell culture supernatants was obtained at 19 or 24 h after LPS treatment, and 100 mM sodium nitrite solution was diluted with nanopure water for the preparation of standards from 10 to 100 μM. To obtain absorbance of the anthocyanins interfering with detection of the purple azo dye, medium was mixed with a similar concentration of butterfly pea extract or fractions with ones used for cell treatments. Subsequently, the cell supernatants and standards were mixed with an equal (1:1) volume of Griess reagent, and finally absorbance was measured at 540 nm using a 96-well microplate reader (Synergy HT, Bio-Tek Instruments, Inc.). Eventually, the net absorbance of the product of Griess reaction was obtained by subtracting the absorbance of medium, including blue flower extract or fractions, from the total value.

The intracellular ROS production was measured by DCFA. Briefly, the cell culture medium was removed by aspiration at times indicated in this study after the LPS challenge, and subsequently cells were exposed to 10 μM DCFA in the phenol red/FBS-free DMEM for 30 min and then washed twice with the phenol red/FBS-free DMEM. Finally, fluorescence was read immediately at wavelengths of 485 nm for excitation and 528 nm for emission on a 96-well microplate reader (Synergy HT, Bio-Tek Instruments, Inc., Winooski, VT).

Preparation of Nuclear Extracts and Western Blot Analysis. The LPS stimulation was terminated by the addition of ice-cold PBS, and a modified procedure based on previous methods[23] was used for the preparation of nuclear extracts. Accordingly, 2×10^6 cells per well were washed twice with ice-cold PBS in 6-well plates and were resuspended in 200 μL of hypotonic lysis buffer (10 mM HEPES, pH 7.9; 10 mM KCl, and 1.5 mM $MgCl_2$) supplemented with a protease inhibitor cocktail. After 10 min at 4 °C, cells were lysed by the addition of 25 μL of 2.5% nonidet P-40 (final 0.3%) for 10 min at 4 °C. The tubes were gently vortexed for 15 s, and nuclei were collected by centrifugation at 8000*g* for 15 min in an Eppendorf 5417 R centrifuge (Ependdorf, Hamburg, Germany). The supernatants were stored at −80 °C (cytosolic extracts). The pellets were resuspended in 50 μL of extraction buffer (10 mM HEPES, pH 7.9; 100 mM NaCl, 1.5 mM $MgCl_2$, 0.1 mM EDTA, and 0.1 mM DTT) supplemented with protease inhibitor cocktail and mixed gently for 30 min at 4 °C. Finally, nuclear proteins were extracted by centrifugation at 13000*g* for 15 min, and aliquots of the supernatant were stored at −80 °C (nuclear extracts). The protein levels in the samples were then quantified using the colorimetric method with bicinchoninic acid solution. All steps of cell fractionation were carried out at 4 °C.

Nuclear and cytosolic proteins prepared as described above were loaded on a gel with a prestained, broad-range, molecular weight protein marker (Fermentas). Proteins were fractionated by electrophoresis using 10% polyacrylamide gels. The gels were transferred by wet blotting onto PVDF membranes (Millipore, Bedford, MA, USA). The membranes were blocked with 5% skim milk in Tris-buffered saline with 1% Tween-20 (TBS-T) for 1 h with gentle shaking. Membranes were then incubated overnight with a specific primary antibody against p-NF-κB p65 (1:1000), iNOS (1:1000), COX-2 (1:1000), NPM/B23 (1:1000), and actin (1:5000) at 4 °C. The membranes were washed four times with TBS-T and incubated for 1 h at room temperature with the secondary antibody conjugated with

DOI: 10.1021/acs.jafc.5b00928
J. Agric. Food Chem. 2015, 63, 6355−6365

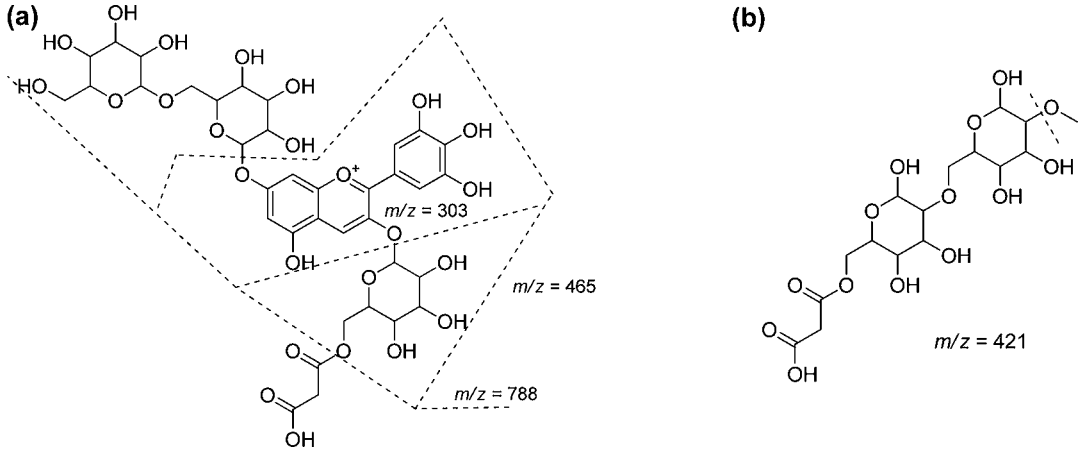

Figure 3. Ternatin anthocyanin from butterfly pea corresponding to peak 1. (a) Tentative description of the fragmentation pattern obtained by MS/MS fragmentation for peak 1 at RT 30.53 having a major MS^2 fragmentation peak at $[M + H]^+$ m/z 303 (delphinidin derivative). m/z 465 corresponds to the m/z 303 and sugar, and m/z 788 corresponds to the m/z 465 and dihexose. (b) Remaining part of the structure from the parent ion m/z 1296. The connectivity of this part is unknown, which could be confirmed by NMR.

horseradish peroxidase (HRP) at 1:5000 dilution. Specific bands were developed using a SuperSignal West Femto enhanced chemiluminescence (ECL) Western blotting detection kit (Pierce, Thermo Fisher Scientific, Inc., Rockford, IL, USA), and the signals were captured by Chemi Doc XRS (Bio-Rad Laboratories, Hercules, CA). Bands were quantified using densitometry with ImageJ software (NIH, Bethesda, MD, USA).

COX-2 Inhibitory Assay. The COX-2 inhibitory assay was carried out using a COX Inhibitor Screening Assay Kit following the manufacturer's instructions (Cayman Chemical, Ann Arbor, MI). Briefly, heme and COX-2 (human recombinant) enzyme were added to test tubes containing COX reaction buffer. The mixture was vortex and exposed either to blue flower extract or fractions or to DMSO (control) for 10 min at 37 °C. This was followed by the addition of arachidonic acid with further incubation for 2 min. Hydrochloric acid (1 M) was added to stop the COX reaction followed by the addition of stannous chloride ($SnCl_2$) solution. This assay measures $PGF_{2\alpha}$ derived from $SnCl_2$ reduction of PGH_2 produced in the COX-2 reaction, through an enzyme immunoassay kit.

Statistical Analysis. The data were analyzed using Student's t test or one-way analysis of variance (ANOVA) followed by the Tukey-HSD test, using the software JMP pro v10.0. Results are expressed as means ± standard errors (SE). Different letters show significant differences ($P < 0.05$).

RESULTS AND DISCUSSION

Characterization and Identification of Phenolic Compounds by LC-MS in Butterfly Pea Extracts and Fractions. Results by LC-MS analysis indicated that peaks 1−4, 6, and 9−12 belong to delphinidin/ternatin derivatives, which are responsible for the blue color in butterfly pea petals (Figure 2). Compound **1** at RT 30.53 with $[M + H]^+$ m/z 1296 yielded MS^2 fragments at m/z 1242, 810, 788, 658, 633, 611, 465, and 303. The fragmentation of m/z 788 can be explained tentatively from the parent ion due to the loss of a malonate group, whereas m/z 465 can be explained due to the loss of 323 Da from the precursor ion m/z 788, which could be due to the loss of a dihexose residue as explained in Figure 3. The remaining part of the structure (fragment m/z 421), obtained from the parent ion m/z 1296, is shown in Figure 3b. However, it was not possible to obtain the connectivity to Figure 3a. The base MS^2 peak at m/z 303 suggests the delphinidin core and hence the complete structure and its connectivity have to be established by NMR spectroscopy.

Compound **2** at RT 35.75 with $[M + H]^+$ m/z 1534 yielded MS^2 fragments at m/z 1329, 1081, 779, 658, 611, 465, and 303. The fragmentation of m/z 465 was similar to that of compound **1** with loss of a dihexose residue as explained in Figure 3, and the m/z 303 was due to a delphinidin core. This compound has not been reported before, and the complete structure could be elucidated by NMR spectroscopy.

Compound **3** at RT 38.41 with $[M + H]^+ m/z$ 1638 yielded MS^2 fragments at m/z 1638, 1615, 1389, 1227, 1081, 964, 860, 663, 611, 437, 303, and 180. This compound was identified as ternatin B3. Compound **4** at RT 39.12 with $[M + H]^+$ m/z 1167 gave MS^2 fragments 1167, 919, 611, 303, 180.8, 163.8, and 149.07; this compound was identified as ternatin D3. Compound **6** at RT 43.19 with $[M + H]^+$ m/z 950 gave MS^2 950, 658, 487, 465, 303, 180.9, and 163.12, and again this compound gave the familiar fragment of m/z 465 and 303, which defines the core structure of delphinidin hexose residue. However, the fragments and the structure were not reported and need to be confirmed by NMR. Compound **9** at RT 52.51 with $[M + H]^+$ m/z 1638 yielded MS^2 fragments at 1638, 1389, 1167, 919, 773, 703, 626, 535, 303, 287, 180.8, and 163.13, and this compound was identified as ternatin B2. Compound **10** at RT 53.51 gave $[M + H]^+$ m/z 1329 and yielded MS^2 fragmentation m/z 1329, 1081, 919, 471, 448, 314, 303, 387, 180.8, 163.07, and 149.09, and this compound was identified as ternatin B4. Compound **11** at RT 54.38 gave $[M + H]^+$ m/z 1491 and yielded MS^2 fragmentation m/z 1492, 1449, 1389, 1257, 1227, 919, 828, 763, 611, 303, 264, 180.8, 163.12, and 149.09, and this compound was identified as ternatin C2. Compound **12** at RT 60.20 gave $[M + H]^+$ m/z 1783 and yielded MS^2 fragments at 1783, 1535, 1255, 1167, 919, 898, 303, and 180, and this compound was identified as ternatin D1. Most of the ternatin derivatives were previously identified from *C. ternatea*, and their MS^2 and fragmentation patterns were in accordance with the literature[1,5]

Compounds **5**, **7**, and **8** gave a UV absorbance within the range of 290−360 nm and suggested that they belong to the flavonoid class (Figure 2). Compound **5** at RT 40.82 gave $[M - H]^-$ at m/z 753 and yielded fragments at 447, 301, 285, and 180.9. The fragment m/z 301 was due to the quercetin core, and the m/z 447 can be explained by the attachment of a rhamnosyl sugar on the quercetin moiety. Hence, this

DOI: 10.1021/acs.jafc.5b00928
J. Agric. Food Chem. 2015, 63, 6355−6365

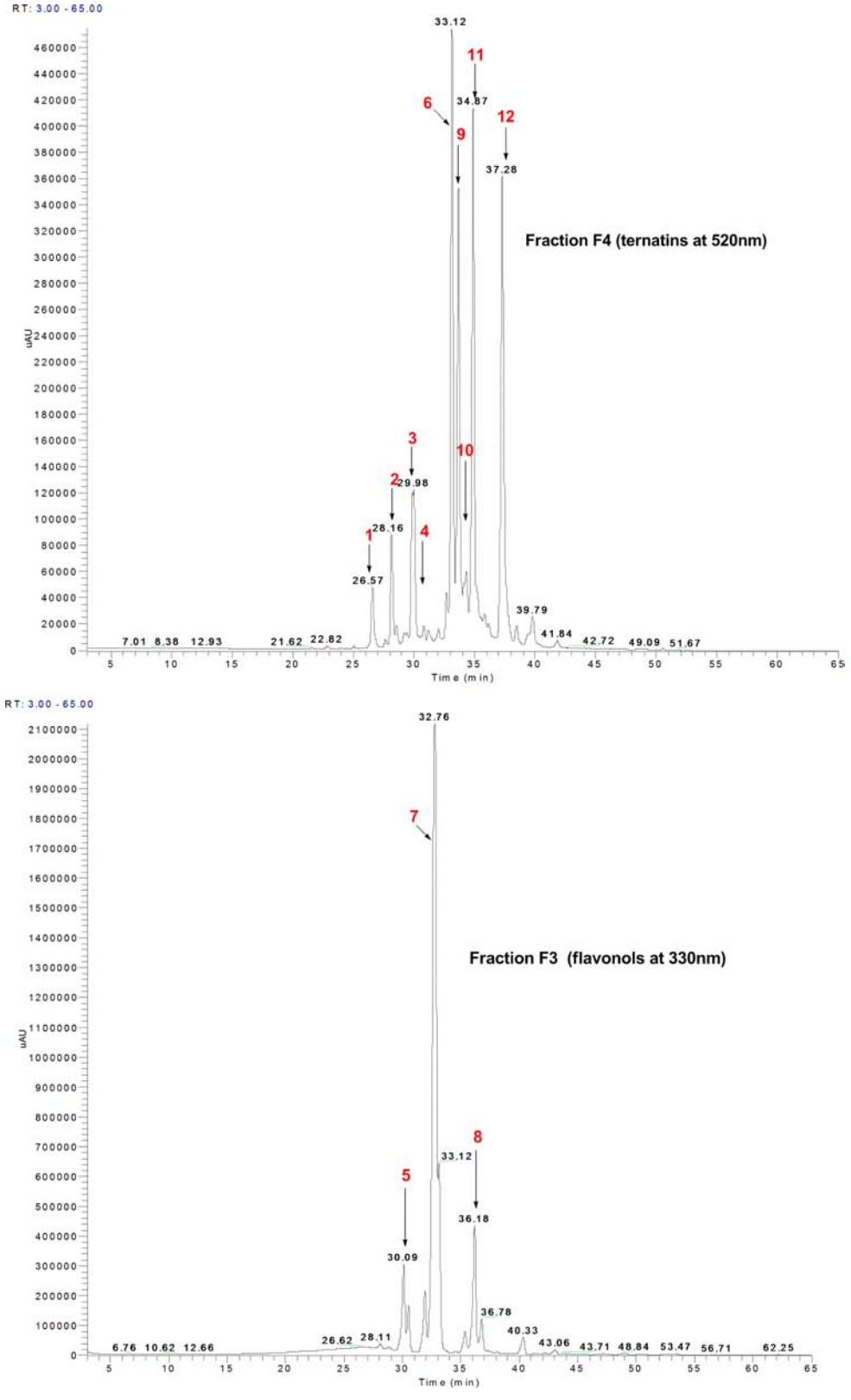

Figure 4. HPLC-MS profiling of the enriched flavonol (F3) and ternatin anthocyanin (F4) fractions from the flower petals of butterfly pea. Chromatograms of fractions F3 and F4 are reported at wavelengths of 330 and 520 nm, respectively. Identified peaks are reported in Table 1. Peaks 1, 2, 3, 4, 6, 9, 10, 11, and 12 from fraction F4 had corresponding areas of 3.5, 5.6, 4.3, 5, 20, 15.9, 4.3, 20.2, and 19.1%, respectively. On the other hand, peaks 5, 7, and 8 from fraction F3 had corresponding peak areas of 14.4, 76.7, and 8.8%, respectively.

compound was identified as manghaslin quercetin 3-[2G]-rhamnosylrutinoside. Compound **7** at RT 46.27 gave $[M - H]^-$ m/z 593 and a major MS^2 fragment 285, and the compound was identified as quercetin 3-*O*-dirhamnoside. Compound **8** at RT 50.54 gave $[M - H]^-$ at m/z 609 and yielded fragments at 301 and 177, and this compound was

DOI: 10.1021/acs.jafc.5b00928
J. Agric. Food Chem. 2015, 63, 6355−6365

Table 2. Yield, Phenolic Content, and Antioxidant ORAC Values for Butterfly Pea Extract and Fractions

extract	yield[a]	phenolic content[b]	antioxidant activity[c]
crude extract	20	0.0952	490.71
fraction F4	2.2	0.1041	260.63
fraction F3	8.1	0.0998	136.97

[a]Yield is expressed in mg of powder. [b]Phenolic content by the Folin–Ciocalteu assay is expressed in mg chlorogenic acid equivalents/mg of crude extract or fraction. [c]Antioxidant activity by the ORAC assay is expressed in μmol Trolox equivalent/g crude extract or fraction.

identified as rutin. Some of these flavonoids were already reported from the petals of butterfly pea.[1]

By solid-phase extraction using C_{18} cartridges, the crude extract was fractionated into phenolic acids (F1), anthocyanins (F2), flavonols (F3), and procyanidins/polymeric anthocyanins (F4) (Figure 1). Results indicated that the polyphenols identified above were present only in fractions F3 and F4, whereas no compounds were present in fractions F1 and F2. Thus, fraction F3, rich in flavonols, contained compounds **5**, **7**, and **8**, whereas fraction F4, rich in ternatin anthocyainins, contained compounds **1**–**4**, **6**, and **9**–**12** (Figure 4).

The fractionation processes showed that fraction F3 was ~3.6 times higher in powder yield compared to fraction F4, suggesting that flavonols constitute the main polyphenols present in butterfly pea extracts. This was also confirmed by actually determining the phenolic content of the fractions (Table 2). For example, fractions F4 and F3 had phenolic concentrations of 0.1041 and 0.099 mg phenolics/mg fraction extract, respectively. Because the powder yield of fractions F4 and F3 were 2.2 and 8.1 mg, respectively, per each 20 mg of crude extract, the amounts of phenolics present in those fraction F4 and F3 powders were 0.22902 and 0.8085 mg phenolics, respectively, confirming that quercetin glycosides are ~3.5 times higher than ternatin anthocyanins in the crude extract.

Furthermore, area chromatogram analysis of compounds indicated that flavonols present in fraction F3 had the following descending order for identified peak areas, 7 ≫ 5 > 8, corresponding to areas of 76.7, 14.4, and 8.8%, respectively (Figure 4). On the other hand, the area chromatogram analysis in fraction F4 indicated that ternatin anthocyanins had the following descending order for identified peak areas, 11 ~ 6 ~ 12 > 9 ≫ 2 ~ 4 ~ 3 ~ 10 > 1, corresponding to areas of 20.2, 20, 19.1, 15.9, 5.6, 5, 4.3, 4.3, and 3.5%, respectively (Figure 4). These results identify which individual compounds were more abundant in each fraction.

The antioxidant ORAC analysis of the dried flower and crude extract gave values of 1096 μmol Trolox equivalent/g dried flower and 490.7 μmol Trolox equivalent/g crude extract, respectively. On the other hand, ORAC analysis of fractions F3 and F4 gave values of 136.9 and 260.6 μmol Trolox equivalent/

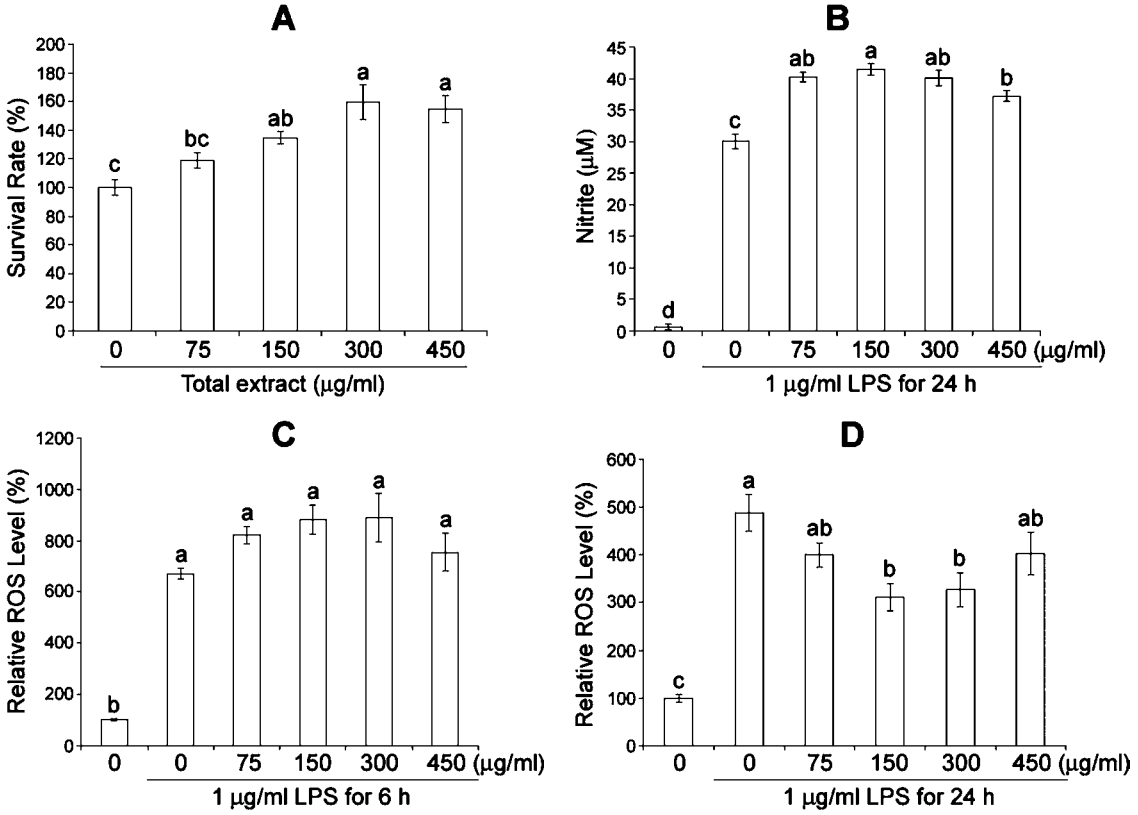

Figure 5. Effect of butterfly pea extract on cell viability and LPS-induced NO and ROS production. (A) Effect of butterfly pea extract on cell viability in macrophage cells. RAW 264.7 cells (2×10^5 cells/well in 96-well culture plates) were treated with 0–450 μg/mL blue flower extract for 24 h, and then the cell viability was measured by MTS assay. (B–D) Effect of blue flower extract on LPS-induced NO and ROS production. RAW 264.7 cells (2×10^5 cells/well in 96-well culture plates) were pretreated with 0–450 μg/mL blue flower extract for 1 h and then stimulated with LPS (1 μg/mL) for 6 or 24 h. Griess reagent was used to detect the generation of extracellular nitrite at 24 h after the LPS challenge (B), and DCFA was used to determine the generation of intracellular ROS at 6 h (C) and 24 h (D) after the LPS challenge. Data, obtained from at least four biological repeats, are shown as mean ± SE values. Different letters indicate significant differences by ANOVA/Tukey-HSD ($p < 0.05$).

DOI: 10.1021/acs.jafc.5b00928
J. Agric. Food Chem. 2015, 63, 6355–6365

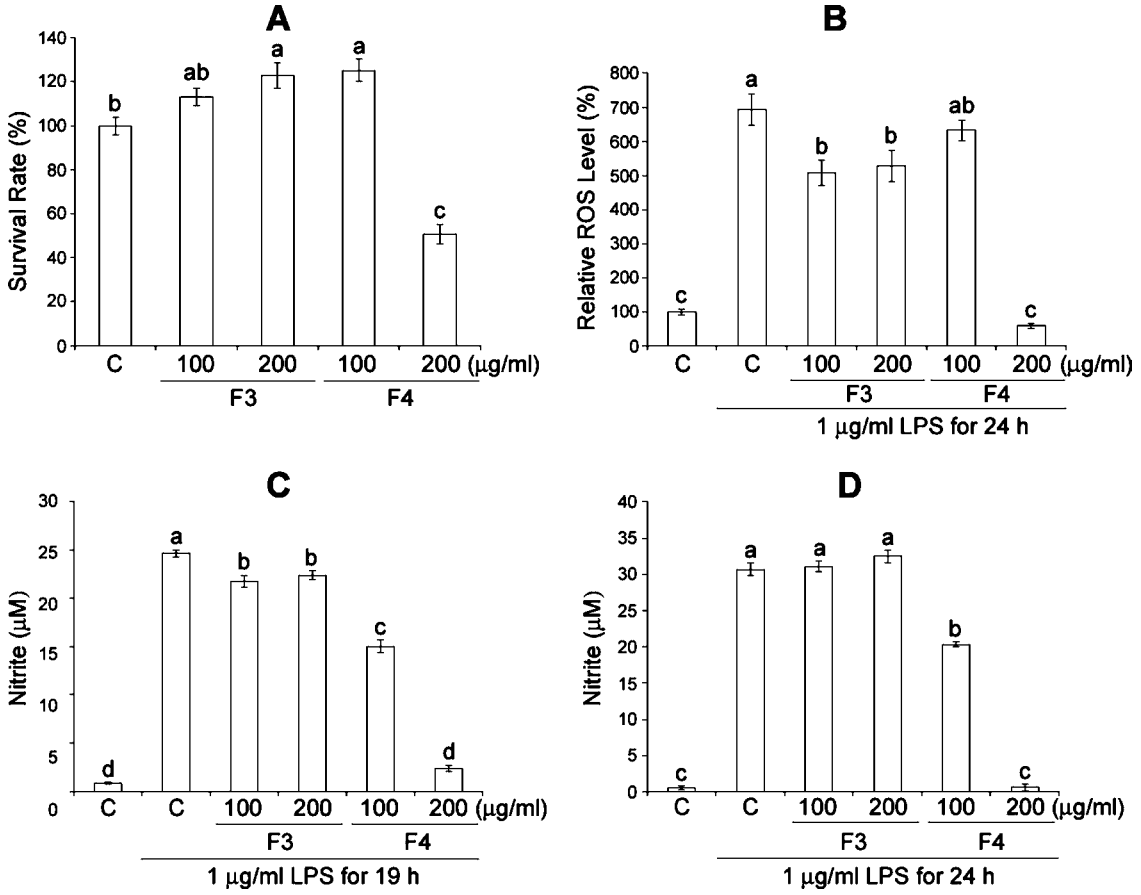

Figure 6. Effect of butterfly pea fractions (F3 and F4) on cell viability and LPS-induced ROS and NO production. (A) Effect of butterfly pea fractions (F3 and F4) on cell viability in macrophage cells. RAW 264.7 cells (0.5×10^5 cells/well in 96-well culture plates) were treated with 100 and 200 μg/mL blue flower fractions (F3 and F4) for 24 h, and then the cell viability was measured by MTS assay. (B–D) Effect of blue flower fractions (F3 and F4) on LPS-induced ROS and NO production. RAW 264.7 cells (0.5×10^5 cells/well in 96-well culture plates) were pretreated with 100 and 200 μg/mL butterfly pea fractions (F3 and F4) for 5 h and then stimulated with LPS (1 μg/mL) for 19 or 24 h. DCFA was used to determine the generation of intracellular ROS at 24 h after the LPS challenge (B), and Griess reagent was used to detect the generation of extracellular nitrite at 19 h (C) and 24 h (D) after the LPS challenge. "C", a control, indicates the pretreatment of 0.5% DMSO in DMEM with or without any LPS stimulation. Data, obtained from at least four biological repeats, are shown as mean ± SE values. Different letters indicate significant differences by ANOVA/Tukey-HSD ($p < 0.05$).

g fraction extract, respectively (Table 2). In general, both fractions showed scavenging properties of peroxyl radicals and potential antioxidant properties. The crude extracts and fractions F3 and F4 were used for the inflammation studies.

Effect of Blue Flower Butterfly Pea Extract and Fractions (F3 and F4) on LPS-Induced Inflammation. Here we assessed the effects of the total extract and its fractions (F3 and F4), prepared from butterfly pea, on inflammation in a LPS-stimulated RAW 264.7 macrophage cell line. Initially the effects of the total extract on inflammation were examined as follows: The MTS assay showed that a dose range of 75–450 μg/mL extract did not affect cell viability (Figure 5A), whereas the NO measurement suggested that the extract had no suppressive effect on LPS-induced NO production (Figure 5B). When LPS-induced ROS production was assessed using DCFA at 6 and 24 h after the LPS challenge, the extract dose range studied did not suppress ROS production at 6 h (Figure 5C); however, at 24 h after the LPS challenge, only doses of 150 and 300 μg/mL extract showed a significantly weak effect on the suppression of ROS production (Figure 5D).

Next, the fractions isolated from the blue flower extract (F3 and F4) were used to identify their possible protective roles against the LPS-induced inflammation process. The MTS assay confirmed that neither doses of 100 and 200 μg/mL of fraction F3 nor a dose 100 μg/mL of fraction F4 affected cell viability; however, a dose of 200 μg/mL of fraction F4 significantly affected it (Figure 6A), resulting in strong suppression effects of ROS and NO production (Figure 6B–D). Fraction F3 (100 and 200 μg/mL) showed a significantly weak effect on ROS suppression at 24 h after the LPS challenge, whereas a dose of 100 μg/mL fraction F4 had no effect (Figure 6B). Accordingly, the antioxidant properties of fractions F3 and F4 (observed with the ORAC assay) seem to be playing a role only in fraction F3, but not in fraction F4, within macrophage cells.

When LPS-induced NO production was assessed at 19 and 24 h after the LPS challenge, fraction F3 (100 and 200 μg/mL) exhibited a significantly slight effect on suppression of NO at 19 h; however, that effect disappeared at 24 h after the LPS challenge. On the other hand, a dose of 100 μg/mL of fraction F4 showed a significantly higher effect on the suppression of NO at 19 h compared to fraction F3, and this effect remained at 24 h after the LPS challenge (Figure 6C,D).

Furthermore, effects of fractions F3 and F4 on LPS-induced iNOS and COX-2 production and NF-κB activation were examined by Western blot analysis. At 19 h after the LPS challenge with 5 h pretreatments of 100 μg/mL of fractions F3

DOI: 10.1021/acs.jafc.5b00928
J. Agric. Food Chem. 2015, 63, 6355–6365

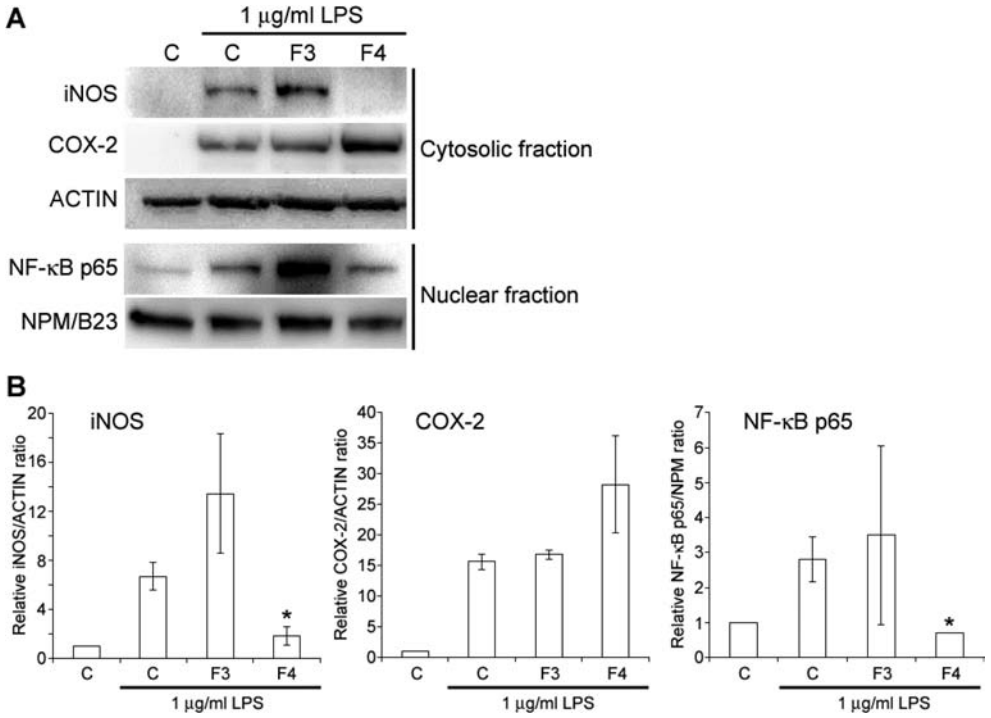

Figure 7. Effects of butterfly pea fractions (F3 and F4) on iNOS, COX-2, and NF-κB in macrophage cells. RAW 264.7 cells (2×10^6 cells/well in 6-well culture plates) were pretreated with 100 μg/mL butterfly pea fractions (F3 and F4) for 5 h and then stimulated with LPS (1 μg/mL) for 19 h. Subsequently, cytosolic and nuclear fractions were isolated as described under Materials and Methods and subjected to SDS-PAGE and Western blot analysis using specific antibodies against iNOS, COX-2, p-NF-κB, actin, and NPM/B23. The protein bands in panel A were detected by chemiluminescence. "C", a control, indicates the pretreatment of 0.5% DMSO in DMEM with or without any LPS stimulation, and actin and NPM/B23 were used to confirm the same amount of total cytosolic and nuclear proteins loaded, respectively. The histograms in panel B represent the relative protein levels measured by ImageJ software using protein bands obtained from panel A. Data, obtained from two biological repeats, are shown as the mean ± SE. Asterisks indicate significant differences by Student's t test ($p < 0.05$).

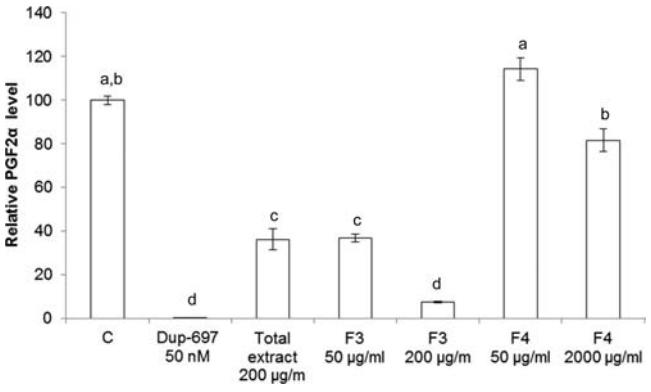

Figure 8. Effect of butterfly pea extract and fractions (F3 and F4) on COX-2 activity. DuP-607 was used as a positive control. The COX-2 inhibitory assay was evaluated using the COX Inhibitor Screening Assay Kit following the manufacturer's instructions (Cayman Chemical, Ann Arbor, MI, USA). Data obtained from three biological repeats are shown as mean ± SE values. Different letters indicate significant differences by ANOVA/Tukey-HSD ($p < 0.05$).

and F4, cell lysates were separated into cytosolic and nuclear fractions and then subjected to Western blot analyses to detect cytosolic iNOS and COX-2 and nuclear NF-κB. As shown in Figure 7, both fractions F3 and F4 had no significant effect on the suppression of LPS-induced COX-2 production. However, fraction F4 significantly suppressed the LPS-induced iNOS production and nuclear NF-κB translocation, whereas fraction F3 did not have that effect (Figure 7).

Inhibition of Cyclooxygenase-2 Activity of Butterfly Pea Extract and Fractions (F3 and F4). The effect of butterfly pea total extract and fractions (F3 and F4) on COX-2 activity is shown in Figure 8. The total blue flower extract and fraction F3 at two concentrations (50 and 200 μg/mL) showed a significant COX-2 inhibitory effect when compared to the control. Moreover, fraction F3 showed a dose-dependent COX-2 inhibitory effect, whereas fraction F4 did not show a significant effect. These results suggest that the flavonol compounds present in fraction F3 are responsible for the COX-2 inhibitory effect of the blue flower *C. ternatea* total extract.

Mechanistic Model of Anti-inflammatory Properties of Butterfly Pea Polyphenols. Macrophages produce various pro-inflammatory mediators when responding to pathogens such as TNFα, IL-1β, IL-6, IFNβ, COX-2, mPGES-1, and iNOS, but excessive production of the pro-inflammatory mediators leads to the development of diseases such as the metabolic syndrome.[24−26] Noticeably, production of the inflammatory mediators is mediated by TLR signaling pathways including the NF-κB, a redox-responsive transcription factor.[24,27,28] For example, binding of LPS, a pathogen-associated molecular pattern, to TLR4 receptor triggers generation of ROS from NADPH oxidase and mitochondria,[29−31] ROS-mediated redox changes activate the nuclear translocation of NF-κB via IκB and Ref-1,[23,28] and then the ROS-dependent NF-κB activation mediates the LPS-induced gene expressions such as *COX-2* and *IFN-β*.[24] Eventually, binding of the LPS-induced IFN-β to an IFN receptor triggers amplification of the iNOS expressions.[32−34] Therefore, this TLR pathway in

DOI: 10.1021/acs.jafc.5b00928
J. Agric. Food Chem. 2015, 63, 6355−6365

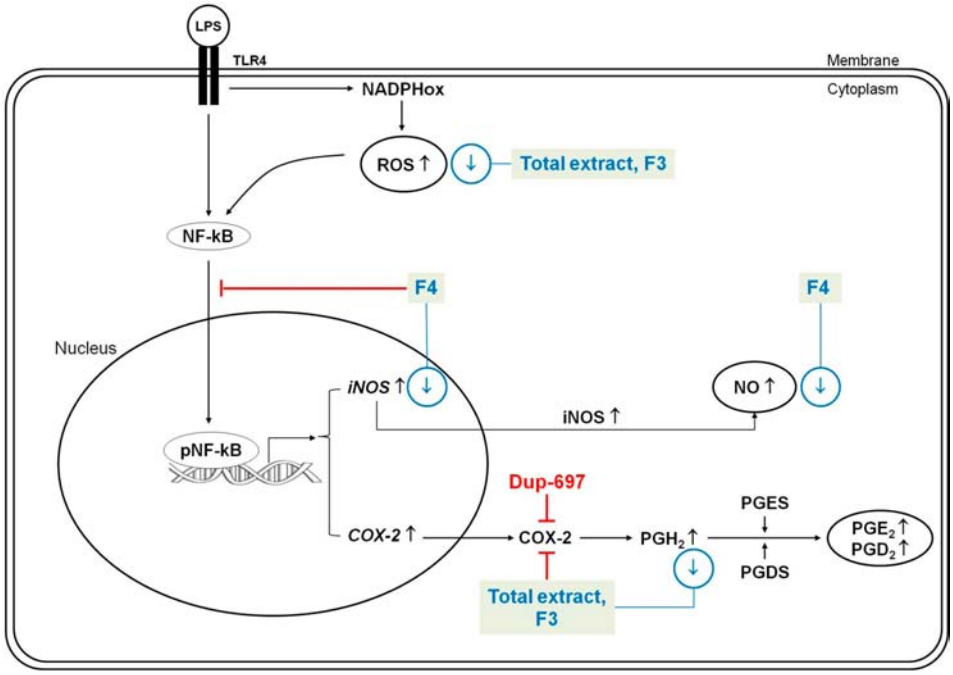

Figure 9. Anti-inflammatory roles of butterfly pea extract and its fractions (F3 and F4) in the TLR4 signaling pathway. Binding of LPS to TLR4 receptor triggers generation of ROS from NADPH oxidase and mitochondria. ROS-mediated redox activates the nuclear translocation of NF-κB via IκB and Ref-1. The NF-κB activation is ROS-dependent and mediates LPS-induced *COX-2* and *IFN-β* expressions. Binding of the LPS-induced IFN-β to an IFN receptor triggers amplification of the *iNOS* expressions. The blue flower extract and fraction F3 showed weak suppressive effects on LPS-induced ROS production. Fraction F3 had strong suppressive effects on PGH_2 production by inhibiting COX-2 enzyme activity. Fraction F4 suppressed *iNOS* expression and NF-κB activation, leading to a suppressive effect of LPS-induced NO production, but affected the COX-2 enzyme activity weakly, compared with fraction F3.

macrophage has guided the screening of many phytochemicals from various crops that have anti-inflammatory properties.

Here we assessed for the first time the effects of the blue flower *C. ternatea* extract and its fractions (F3 and F4) on anti-inflammation properties in a LPS-stimulated RAW 264.7 macrophage cell line. The extract and fraction F3 showed weak suppressive effects on LPS-induced ROS production (Figures 5D and 6B). This F3 fraction had strong suppressive effects on PGH2 production by inhibiting COX-2 enzyme activity (Figure 8) but affected weakly LPS-induced NO production (Figure 6C). On the other hand, fraction F4 suppressed iNOS expression and NF-κB activation (Figure 7), leading to the much stronger suppressive effect of LPS-induced NO production than that of fraction F3 (Figure 6C,D), but did not affect the COX-2 enzyme activity compared with the control and fraction F3 (Figure 8).

In summary, here we report for the first time the anti-inflammatory properties of polyphenols from butterfly pea extracts and identify two fractions, F3 and F4, suppressing the LPS-induced inflammation process through two distinct actions in the TLR pathway (Figure 9). In more detail, fraction F3, which includes quercetin glycosides, plays an important role as an inhibitor of COX-2 activity and as an antioxidant; however, its scavenging properties seem too weak to suppress ROS-mediated NF-κB activation (Figure 9). On the other hand, the ternatin anthocyanins present in fraction F4 suppress the nuclear NF-κB translocation and the protein expression of iNOS as well as NO production by inhibiting signaling factors, through a non-ROS suppression mechanism possibly downstream of ROS in macrophage cells (Figure 9). Accordingly, quercetin glycosides and ternatin anthocyanins from the blue flower petals of *C. ternatea* may be useful in the development of drugs or nutraceuticals protecting against chronic inflammatory diseases by suppressing the excessive production of pro-inflammatory mediators from macrophage cells. Additional, work is needed to confirm these results in in vivo studies as well as to evaluate different butterfly pea accessions that may contain different levels of anthocyanins and other flavonoids as reported in the works of Morris and Wang (2007) and Morris (2009).[35,36]

AUTHOR INFORMATION

Corresponding Author

*(L.C.-Z.) E-mail: lcisnero@tamu.edu. Phone: 979-8453244. Fax: 979-8450627.

Funding

We acknowledge funds from USAID Cooperative Agreement AID-497-A-11-00003 for research and educational activities at Bogor Agricultural University, Indonesia, and Texas A&M University, USA. W.Y.B. is supported by a grant from the National Institute of Biological Resources (NIBR), funded by the Ministry of Environment (MOE) of the Republic of Korea (ex; NIBR201512101).

Notes

The authors declare no competing financial interest.

ACKNOWLEDGMENTS

We thank Facundo Ibanez for technical support.

REFERENCES

(1) Kazuma, K.; Noda, N.; Suzuki, M. Flavonoid composition related to petal color in different lines of *Clitoria ternatea*. *Phytochemistry* **2003**, *64*, 1133−1139.

DOI: 10.1021/acs.jafc.5b00928
J. Agric. Food Chem. 2015, 63, 6355−6365

(2) Terahara, N.; Toki, K.; Saito, N.; Honda, T.; Matsui, T.; Osajima, Y. Eight new anthocyanins, Ternatins C1-C5 and D3 and Preternatins A3 and C4 from young *Clitoria ternatea* flowers. *J. Nat. Prod.* **1998**, *61*, 1361−1367.
(3) Jain, N. N.; Ohal, C.; Shroff, S.; Bhutada, R.; Somani, R.; Kasture, V.; Kasture, S. *Clitoria ternatea* and the CNS. *Pharmacol., Biochem. Behav.* **2003**, *75*, 529−536.
(4) Madhu, K. Phytochemical screening and antioxidant activity of in vitro grown plants *Clitoria ternatea* L. using DPPH assay. *Asian J. Pharm. Clin Res.* **2013**, *6*, 38−42.
(5) Terahara, N.; Oda, M.; Matsui, T.; Osajima, Y.; Saito, N.; Toki, K.; Honda, T. Five new anthocyanins, ternatins A3, B4, B3, B2, and D2, from *Clitoria ternatea* flowers. *J. Nat. Prod.* **1996**, *59*, 139−144.
(6) Izzi, V.; Masuelli, L.; Tresoldi, I.; Sacchetti, P.; Modesti, A.; Galvano, F.; Bei, R. The effects of dietary flavonoids on the regulation of redox inflammatory networks. *Front. Biosci., Landmark Ed.* **2012**, *17*, 2396−2418.
(7) Park, S.-J.; Shin, W.-H.; Seo, J.-W.; Kim, E.-J. Anthocyanins inhibit airway inflammation and hyperresponsiveness in a murine asthma model. *Food Chem. Toxicol.* **2007**, *45*, 1459−1467.
(8) Karlsen, A.; Retterstøl, L.; Laake, P.; Paur, I.; Kjølsrud-Bøhn, S.; Sandvik, L.; Blomhoff, R. Anthocyanins inhibit nuclear factor-κB activation in monocytes and reduce plasma concentrations of pro-inflammatory mediators in healthy adults. *J. Nutr.* **2007**, *137*, 1951−1954.
(9) Serafini, M.; Peluso, I.; Raguzzini, A. Flavonoids as anti-inflammatory agents. *Proc. Nutr. Soc.* **2010**, *69*, 273−278.
(10) Kowalski, J.; Samojedny, A.; Paul, M.; Pietsz, G. Apigenin inhibits release and gene expression of monocyte chemoattractant protein 1 (MCP-1) in J774.2 macrophages. *Wiad Lek.* **2005**, *59*, 634−638.
(11) García-Mediavilla, V.; Crespo, I.; Collado, P. S.; Esteller, A.; Sánchez-Campos, S.; Tuñón, M. J.; González-Gallego, J. The anti-inflammatory flavones quercetin and kaempferol cause inhibition of inducible nitric oxide synthase, cyclooxygenase-2 and reactive C-protein, and down-regulation of the nuclear factor kappaB pathway in Chang liver cells. *Eur. J. Pharmacol.* **2007**, *557*, 221−229.
(12) Ruiz, P. A.; Braune, A.; Hölzlwimmer, G.; Quintanilla-Fend, L.; Haller, D. Quercetin inhibits TNF-induced NF-κB transcription factor recruitment to proinflammatory gene promoters in murine intestinal epithelial cells. *J. Nutr.* **2007**, *137*, 1208−1215.
(13) Puangpraphant, S.; de Mejia, E. G. Saponins in yerba mate tea (*Ilex paraguariensis* A. St.-Hil) and quercetin synergistically inhibit iNOS and COX-2 in lipopolysaccharide-induced macrophages through NFκB pathways. *J. Agric. Food Chem.* **2009**, *57*, 8873−8883.
(14) Crespo, I.; García-Mediavilla, M. V.; Gutiérrez, B.; Sánchez-Campos, S.; Tuñón, M. J.; González-Gallego, J. A comparison of the effects of kaempferol and quercetin on cytokine-induced pro-inflammatory status of cultured human endothelial cells. *Br. J. Nutr.* **2008**, *100*, 968−976.
(15) Zhang, X. F.; Hung, T. M.; Phuong, P. T.; Ngoc, T. M.; Min, B.-S.; Song, K.-S.; Seong, Y. H.; Bae, K. Anti-inflammatory activity of flavonoids from *Populus davidiana*. *Arch. Pharmacal Res.* **2006**, *29*, 1102−1108.
(16) D'Mello, P.; Gadhwal, M. K.; Joshi, U.; Shetgiri, P. Modeling of COX-2 inhibitory activity of flavonoids. *Int. J. Pharm. Pharm. Sci.* **2011**, *3*, 33−40.
(17) Huang, T.; Chen, C.; Wefler, V.; Raftery, A. A stable reagent for the Liebermann-Burchard reaction. Application to rapid serum cholesterol determination. *Anal. Chem.* **1961**, *33*, 1405−1407.
(18) Noratto, G.; Porter, W.; Byrne, D.; Cisneros-Zevallos, L. Identifying peach and plum polyphenols with chemopreventive potential against estrogen-independent breast cancer cells. *J. Agric. Food Chem.* **2009**, *57*, 5219−5226.
(19) Swain, T.; Hillis, W. The phenolic constituents of *Prunus domestica*. I. The quantitative analysis of phenolic constituents. *J. Sci. Food Agric.* **1959**, *10*, 63−68.
(20) Wu, X.; Beecher, G. R.; Holden, J. M.; Haytowitz, D. B.; Gebhardt, S. E.; Prior, R. L. Lipophilic and hydrophilic antioxidant capacities of common foods in the United States. *J. Agric. Food Chem.* **2004**, *52*, 4026−4037.
(21) Villarreal-Lozoya, J. E.; Lombardini, L.; Cisneros-Zevallos, L. Phytochemical constituents and antioxidant capacity of different pecan [*Carya illinoinensis* (Wangenh.) K. Koch] cultivars. *Food Chem.* **2007**, *102*, 1241−1249.
(22) Wang, J.; Mazza, G. Quantification of nitrite in the presence of anthocyamns using Griess and GC/MS assays. *J. Food Biochem.* **2002**, *26*, 339−354.
(23) Song, J. D.; Lee, S. K.; Kim, K. M.; Kim, J. W.; Kim, J. M.; Yoo, Y. H.; Park, Y. C. Redox factor-1 mediates NF-κB nuclear translocation for LPS-induced iNOS expression in murine macrophage cell line RAW 264.7. *Immunology* **2008**, *124*, 58−67.
(24) Biswas, S. K.; Mantovani, A. Orchestration of metabolism by macrophages. *Cell Metab.* **2012**, *15*, 432−437.
(25) Arthur, J. S. C.; Ley, S. C. Mitogen-activated protein kinases in innate immunity. *Nat. Rev. Immunol.* **2013**, *13*, 679−692.
(26) Chawla, A.; Nguyen, K. D.; Goh, Y. S. Macrophage-mediated inflammation in metabolic disease. *Nat. Rev. Immunol.* **2011**, *11*, 738−749.
(27) Chandel, N. S.; Trzyna, W. C.; McClintock, D. S.; Schumacker, P. T. Role of oxidants in NF-κB activation and TNF-α gene transcription induced by hypoxia and endotoxin. *J. Immunol.* **2000**, *165*, 1013−1021.
(28) Kabe, Y.; Ando, K.; Hirao, S.; Yoshida, M.; Handa, H. Redox regulation of NF-κB activation: distinct redox regulation between the cytoplasm and the nucleus. *Antioxid. Redox Signaling* **2005**, *7*, 395−403.
(29) Hsing, C.-H.; Lin, M.-C.; Choi, P.-C.; Huang, W.-C.; Kai, J.-I.; Tsai, C.-C.; Cheng, Y.-L.; Hsieh, C.-Y.; Wang, C.-Y.; Chang, Y.-P. Anesthetic propofol reduces endotoxic inflammation by inhibiting reactive oxygen species-regulated Akt/IKKβ/NF-κB signaling. *PLoS One* **2011**, *6*, e17598.
(30) Bulua, A. C.; Simon, A.; Maddipati, R.; Pelletier, M.; Park, H.; Kim, K.-Y.; Sack, M. N.; Kastner, D. L.; Siegel, R. M. Mitochondrial reactive oxygen species promote production of proinflammatory cytokines and are elevated in TNFR1-associated periodic syndrome (TRAPS). *J. Exp. Med.* **2011**, *208*, 519−533.
(31) Hsu, H.-Y.; Wen, M.-H. Lipopolysaccharide-mediated reactive oxygen species and signal transduction in the regulation of interleukin-1 gene expression. *J. Biol. Chem.* **2002**, *277*, 22131−22139.
(32) Kovarik, P.; Stoiber, D.; Eyers, P. A.; Menghini, R.; Neininger, A.; Gaestel, M.; Cohen, P.; Decker, T. Stress-induced phosphorylation of STAT1 at Ser727 requires p38 mitogen-activated protein kinase whereas IFN-γ uses a different signaling pathway. *Proc. Natl. Acad. Sci. U. S. A.* **1999**, *96*, 13956−13961.
(33) Chan, E. D.; Riches, D. W. IFN-γ+ LPS induction of iNOS is modulated by ERK, JNK/SAPK, and p38 mapk in a mouse macrophage cell line. *Am. J. Physiol. Cell Physiol.* **2001**, *280*, C441−C450.
(34) Jacobs, A. T.; Ignarro, L. J. Lipopolysaccharide-induced expression of interferon-β mediates the timing of inducible nitric-oxide synthase induction in RAW 264.7 macrophages. *J. Biol. Chem.* **2001**, *276*, 47950−47957.
(35) Morris, J.; Wang, M. Anthocyanin and potential therapeutic traits in *Clitoria*, *Desmodium*, *Corchorus*, *Catharanthus* and *Hibiscus* species. In *Proceedings of the International Symposium on Medicinal and Nutraceutical Plants 756*; ISHS: Leuven, Belgium, 2007; pp 381−388
(36) Morris, J. Characterization of butterfly pea (*Clitoria ternatea* L.) accessions for morphology, phenology, reproduction and potential nutraceutical, pharmaceutical trait utilization. *Genet. Resour. Crop Evol.* **2009**, *56*, 421−427.

DOI: 10.1021/acs.jafc.5b00928
J. Agric. Food Chem. 2015, 63, 6355−6365

inhibitory sequences are thus largely unexplored. Although systematic analysis is advisable, the identification and isolation of novel inhibitory peptides in hydrolyzed protein mixtures are challenging tasks: indeed, they are usually based on sequential chromatographic separations of different fractions or components that have to be characterized and tested to identify putative sequences that must then be synthesized and tested for bioactivity. Thus, the development of novel methodologies for the discovery of new active sequences encrypted in food is strongly recommended. Within this framework, the computer-driven screening of peptide sequences may strongly support the discovery of new BPs.

Recently a number of in silico approaches have been successfully applied for the discovery of novel bioactive sequences, also toward ACE enzyme (e.g., ref 10). Basically, two main computer-aided frameworks have been applied so far. The former is based on the in silico simulation of enzymatic cleavage or digestion of protein sequences and the evaluation of the release of bioactive sequences (e.g., refs 10 and 11) by using inhibition assay or by checking the release of already known inhibitory peptides (e.g., ref 12). The second is based on the prediction of inhibitory activity of peptides through the use of computational strategies. Notably, most of them use statistical approach to infer activity solely on the basis of the physicochemical properties of peptides (e.g., ref 13). Nevertheless, when the activity requires a certain degree of a protein−ligand interaction, as in the case of peptide-mediated ACE inhibition, structure-based modeling is more advisable.[14] Therefore, with the aim to discover novel ACE inhibitory peptides from a previously reported peptidomic profile of digested samples of Parma dry-cured ham,[15] we report the benefits achieved by using a hybrid approach involving the integration of in vitro trials and in silico structure-based molecular modeling technique, the reliability of which in predicting the bioactivity of compounds, including peptides, has been previously assessed.[16−21] Parma dry-cured ham has been chosen as the case study because it is one of the most valuable brands in Italy with a significant commercialization in Europe, the United States, and Japan.[22,23] Even if it is among the most consumed traditional Italian cured-meat products,[24] there is a marked lack of data beyond the canonical nutritional values. Thus, the profiling of bioactive compounds, including BPs, is strongly advisable, also considering the efforts to better understand, and rationally improve, the content of health-protective compounds. In particular, dry-cured ham samples have been hydrolyzed by an in vitro simulated gastrointestinal digestion, and then the digested peptide mixtures have been fractionated by preparative LC and the ACE inhibitory activity of each fraction has been evaluated in vitro. In parallel, the priority ranking of peptides in terms of ACE-inhibitory activity has been done on the basis of computational predictions. Finally, in accordance with computational rank and relative occurrence within the most active fractions, some peptides have been synthesized and then assessed for their inhibitory activity by using an in vitro assay.

MATERIALS AND METHODS

In Silico Procedures. *Pharmachopore Models.* The anatomy of the ACE binding sites was investigated by using the Flapsite tool of FLAP software (Fingerprint for Ligand And Protein; http://www.moldiscovery.com),[25] and the GRID molecular interaction fields (MIFs) were used to investigate the corresponding pharmacophoric space.[26] The DRY probe was used to describe the potential hydrophobic interactions, whereas the sp2 carbonyl oxygen (O) and the neutral flat amino (N1) probes were used to describe the hydrogen bond acceptor and donor capacity of the target, respectively. All images were obtained using the software PyMol version 1.7 (http://www.pymol.org).

Molecular Modeling. The models for both C- and N-domains of ACE were derived from the Protein Data Bank (http://www.rcsb.org) structures having PDB codes 4APH and 4BZS, respectively.[27,28] Protein structures and ligands were processed by using the software Sybyl, version 8.1 (www.tripos.com). All atoms were checked for atom- and bond-type assignments. Amino- and carboxyl-terminal groups were set as protonated and deprotonated, respectively. Hydrogen atoms were computationally added to the protein and energy-minimized using the Powell algorithm with a coverage gradient of ≤0.5 kcal/(mol Å) and a maximum of 1500 cycles.

Docking Simulations and Rescoring Procedure. The coupling of GOLD, to perform docking simulations, and HINT software, as rescoring function, has been already proved to be effectively able to evaluate the bioactivity of small molecules,[16,20,21,29] including peptides.[30] The docking simulations of compounds were performed with the GOLD version 5.1 (CCDC; Cambridge, UK; http://www.ccd.cam.ac.uk). All crystallographic waters and ligands were removed, and 25 poses for each compound were generated. No constraints were set up, and the explorable space was defined in a radius of 10 Å from the centroid of the catalytic site. For each GOLD docking search, a maximum number of 100,000 operations were performed on a population of 100 individuals with a selection pressure of 1.1. Operator weights for crossover, mutation, and migration were set to 95, 95, and 10, respectively. The number of islands was set to 5 and the niche to 2. The hydrogen bond distance was set to 2.5 Å and the van der Waals linear cutoff to 4.0. Ligand flexibility options "flip pyramidal N", "flip amide bonds", and "flip ring corners" were allowed. Each best-scored pose according to GOLD scoring function was rescored by HINT. Owing to the huge dimension of the pocket, and to speed the spatial search, molecule positioning has been spatially restrained according to crystallographic pose of the inhibitory drug captopril,[31] whose pattern of interaction and volume occupancy are maintained also by all of the ligands cocrystallized so far.

The software HINT (Hydrophatic INTeraction)[32] was used as the rescoring function on the basis of previous studies attesting to the higher reliability of HINT scoring with respect to other scoring functions, as well as its successful use in the search for ligands for other targets and in the estimation of ligand-binding free energies. In more detail, the score provides the evaluation of thermodynamic benefits of protein−ligand interaction, and therefore low/negative scores indicate no appreciable protein−ligand interactions.[17,19−21,29,30,33−35] GOLD uses a Lamarckian genetic algorithm, and scores may slightly change from run to run. Therefore, to exclude a noncausative score assignment, we conducted simulations in quintuplicate, and the mean values are reported.

In Vitro Experimental Procedures. *Samples.* Parma dry-cured ham samples with 18 and 24 ripening months were provided by the Experimental Station for Food Preserving Industry (Parma, Italy). Samples of biceps femoris muscle were minced by a common mill (Moulinex, Milano, Italy) and stored at freezing temperature (−22 °C) until analysis.

Reagents and Solvents. Doubly distilled water was produced in our laboratory by a Millipore Alpha Q purification system (Waters, Billerica, MA, USA). Pepsin from porcine gastric mucosa, trypsin from porcine pancreas, α-chymotrypsin from bovine pancreas, α-amylase from barley malt (type VIIIa), uric acid, mucin from porcine stomach (type III), glucose, glucuronic acid, glucosamine hydrochloride, bovine serum albumin, pancreatin from porcine pancreas, lipase from porcine pancreas (type II), bovine and ovine bile, sodium dihydrogen phosphate, potassium chloride, sodium hydroxide, sodium phosphate dibasic dodecahydrate, monobasic potassium phosphate, acetonitrile, urea, methanol, trifluoroacetic, triisopropylsilane acid, DL-dithiothreitol, hippuryl-histidyl-leucine (HHL), angiotensin I converting enzyme (ACE; EC 3.4.15.1) from rabbit lung 0.1 U, and glycerol were all purchased from Sigma-Aldrich (St. Louis, MO, USA). Hydrochloric

DOI: 10.1021/acs.jafc.5b02303
J. Agric. Food Chem. 2015, 63, 6366−6375

acid (37% v/v), sodium hydroxide, sodium hydrogen carbonate, calcium chloride, ammonium chloride, potassium thiocyanate, and potassium hydroxide were purchased from Carlo Erba (Milan, Italy). Formic acid was purchased from Acros Organics (Geel, Belgium). Sodium chloride was purchased from AnalaR Normapur (Milan, Italy). Sodium sulfate was purchased from Riedel de Haen (Seelze, Germany). Magnesium chloride hexahydrate and boric acid were purchased from Fluka (Sigma-Aldrich, St. Louis, MO, USA).

Simulated Gastrointestinal Digestion. Simulated gastrointestinal digestion was recently applied to the study of the effect of dry-cured ham maturation time on the composition of the released peptide fraction:[15] the preparation of the relative artificial digestive juices (simulated salivary juice, simulated gastric juice, simulated duodenal juice, and bile) was performed according to the protocol of Versantvoort.[36]

Briefly, the digestion procedure was as follows: minced biceps femoris muscle (2 g) was dispersed in 3 mL of simulated salivary juice (pH 6.8 ± 0.2) and incubated at 37 °C under agitation with a vortex and a horizontal shaker (230 rpm) for 5 min. After this first step, 6 mL of the simulated gastric juice (pH 1.3 ± 0.2) was added, and the mixture was left to react for 2 h under the same conditions. The last step was the addition of bicarbonate (1 mL, 1 M), simulated duodenal juice (6 mL, pH 8.1 ± 0.2), and bile (3 mL, pH 8.2 ± 0.2), and the mixture was left to react at 37 °C for another 2 h under agitation on a horizontal shaker. The enzyme reaction was stopped by heating at 95 °C for 15 min and the mixture was centrifuged at 3200*g* for 20 min to separate the supernatant (chyme) and the pellet (residual matrix). The supernatant was subjected to a final cleanup step by a Sep-Pak C18 cartridge (Waters Co., Milford, MA, USA): after the cartridge was conditioned with CH_3OH (2 mL) and bidistilled water (3 mL), chyme was applied (2 mL), and after the first eluate had been discarded, peptides were eluted with 2 mL of a solution of H_2O/CH_3OH (50:50, v/v). The eluate (2 mL) was evaporated to dryness under nitrogen flow in an Eppendorf tube, and the residue was resuspended with 2 mL of aqueous formic acid (0.1%), centrifuged and, then, fractionated in semipreparative HPLC-UV (conditions reported below).

Semipreparative LC-UV Fractionation of Digested Samples. The digested mixture was fractionated by semipreparative HPLC-UV (λ = 214nm) by collecting one fraction per minute. The digested samples were separated by a RP column (JUPITER 5 μm, C18, 300 Å, 250 × 10 mm, Phenomenex, Bologna, Italy) using a semipreparative HPLC-UV (1525 binary HPLC pump, Waters, Billerica, MA, USA). The following gradient conditions were applied: eluent A, water with 0.1% formic acid and 0.2% acetonitrile; eluent B, acetonitrile with 0.1% formic acid; gradient, 0−12 min, 100% A; 12−77 min, linear from 100 to 50% A; 77−81 min, 50% A; 81−82 min, linear from 50 to 0% A; 82−90 min, 0% A; 90−91 min, linear from 0 to 100% A; 91−110 min, 100% A. Other parameters were as follows: flow rate, 5 mL/min; analysis time, 110 min; column temperature, room temperature; sample temperature, room temperature; injection volume, 2 mL; fractions collected every minute for a total of 51 fractions. The UV detector (2998 photodiode array, Waters) set at λ = 214 nm.

All collected fractions were evaporated to dryness at the rotavapor and dissolved in 2 mL of H_2O + 0.1% HCOOH for analyses.

UPLC-ESI-MS Analyses. UPLC/ESI-MS analyses were performed with a UPLC/ESI-MS system (UPLC Acquity Waters equipped with a single-quadrupole mass spectrometer, Waters Acquity Ultraperformance). Conditions were as follows: column, RP ACQUITY UPLC BEH 300, C18 (1.7 μm, 2.1 × 150 mm, Waters); gradient elution, eluent A, water with 0.1% formic acid and 0.2% acetonitrile, eluent B, acetonitrile with 0.1% formic acid; gradient, 0−7 min, 100% A; 7−50 min, linear from 100 to 50% A; 50−52.6 min, isocratic, 50% A; 52.6−53 min, linear from 50 to 0% A; 53−58.2 min, isocratic 0% A; 58.2−59 min, linear from 0 to 100% A; 59−72 min, isocratic 100% A. LC parameters: flow rate, 0.2 mL/min; analysis time, 72 min; column temperature, 35 °C; sample temperature, 18 °C; injection volume, 10 μL for fraction samples; 2 μL for the calibration curve of LGL peptide. MS parameters: full scan mode; acquisition time, 7−58.2 min; ionization type, ESI+ (positive ions); scan range, m/z 100−2000; capillary voltage, 3.2 kV; cone voltage, 30 V; source block temperature, 150 °C; desolvation temperature, 300 °C; cone gas flow, 100 L/h; desolvation gas flow, 650 L/h. Data were acquired and analyzed by MassLynx 4.0 software (Waters Co., Milford, MA, USA).

HPLC-ESI-MS/MS Analyses. HPLC/ESI-MS/MS analyses were performed using a HPLC (model Alliance 2695, Waters) equipped with a triple-quadrupole mass spectrometer (model Four Micro, Waters) and a RP column JUPITER 5 μm, C18, 300 Å, 250 × 2 mm i.d. (Phenomenex). Gradient elution was as follows: eluent A, water with 0.1% formic acid and 0.2% acetonitrile; eluent B, acetonitrile with 0.1% formic acid; gradient, 0−12 min, 100% A; 12−77 min, linear from 100 to 50% A; 77−81 min, 50% A; 81−82 min, linear from 50 to 0% A; 82−90 min, 0% A; 90−91 min, linear from 0 to 100% A; 91−110 min, 100% A. Samples (fractions) were first analyzed in full scan mode to identify the characteristic ions and the retention time of the unknown compounds and then in daughters scan modality, using a variable collision energy from 10 to 30 eV. HPLC/ESI-MS/MS parameters were as follows: flow rate, 0.2 mL/min; analysis time, 110 min; column temperature, 35 °C; sample temperature, 23 °C; injection volume, 10 μL for full scan mode and 30 μL for daughter scan mode; acquisition time, 90 min; ionization type, ESI+ (positive ions); scan range, m/z 100−2000; capillary voltage, 3.2 kV; cone voltage, 35 V; source block temperature, 100 °C; desolvation temperature, 200 °C; cone gas flow, 100 L/h; desolvation gas flow, 650 L/h. The peptide sequences were assigned on the basis of the obtained mass spectra and using the Bioinfomatics resource portal ExPasy with the tools FindPept (Swiss Institute of Bioinformatics, Switzerland) and with the web application "Proteomics Toolkit" (Institute for Systems Biology, Seattle, WA, USA).

Solid Phase Peptide Synthesis and Purification. Peptides were synthesized using solid phase peptide synthesis according to the Fmoc/*tert*-butyl strategy on Wang-resin (Wang, Calbiochem-Novabiochem, Läufelfingen, Switzerland) using a Syro I Fully Automated Peptide Synthesizer (Biotage, Uppsala, Sweden). Cleavage from the resin was performed using a trifluoroacetic acid (TFA)/triisopropylsilane (TIS)/H_2O/dithiothreitol (DTT) (94:1:2.5:2.5) solution, and peptides were purified by semipreparative RP-HPLC-UV (λ = 214 nm). The purity and molecular mass of peptides were determined by using a liquid chromatograph coupled to a mass spectrometer equipped with an electrospray ionization source (UPLC-ESI-MS).

Evaluation of ACE Inhibition. The percentage of ACE inhibitory activity for pure peptides and digested fractions was determined by using the methods of Cushman et al [37] and Nakamura et al,[38] with some modifications and according to the following equation: $I\% = [(ACE_{max} - B_{max}) - (ACE_{min} - B_{min})]/(ACE_{max} - B_{max}) \times 100$, where ACE_{max} is the maximum activity of ACE (in the absence of the peptides), ACE_{min} is the minimal activity of ACE (in the presence of the peptides), B_{max} is the control blank of ACE and B_{min} is the control blank of sample/digestion blank/pure peptide.

The following solutions were prepared: sodium borate buffer (0.1 M, NaBB) with NaCl (300 mM), pH 8.3; potassium phosphate buffer (0.01 M, KPB) with NaCl (500 mM), pH 7; 5 mM hippuryl-histidyl-leucine (HHL) in NaBB buffer; and ACE 0.1 U/mL in KPB + 5% glycerol (g/mL). The experiment is carried out at 37 °C in a thermostatic bath (WB-OD 24, Falc, Treviglio (BG), Italy) determining the following parameters: maximum activity of ACE (ACE_{max}) = 200 μL of HHL + 80 μL of NaBB + 20 μL of ACE; control blank of ACE (B_{max}) = 200 μL of HHL + 80 μL of NaBB + 20 μL of KPB; minimal activity of ACE (ACE_{min}) = 200 μL of HHL + 80 μL of sample (i.e., fraction or pure peptide) + 20 μL of ACE; control blank of sample (i.e., fraction or pure peptide) (B_{min}) = 200 μL of HHL + 80 μL of sample (i.e., fraction or pure peptide) + 20 μL of KPB. After 60 min of incubation, the reaction was quenched with 250 μL of HCl (1 N). The analysis was performed by HPLC-UV (Alliance 2695 separation, Waters, Billerica, MA, USA) with dual λ absorbance detector model 2487 (Waters), with the following conditions: column, RP JUPITER C18, 5 μm, 300 Å, 250 × 2 mm (Phenomenex); gradient elution, eluent A, water with 0.1% formic acid and 0.2% acetonitrile; eluent B, acetonitrile with 0.1% formic acid; gradient, 0−10 min, 100% A; 10−22.50 min, linear from

DOI: 10.1021/acs.jafc.5b02303
J. Agric. Food Chem. 2015, 63, 6366−6375

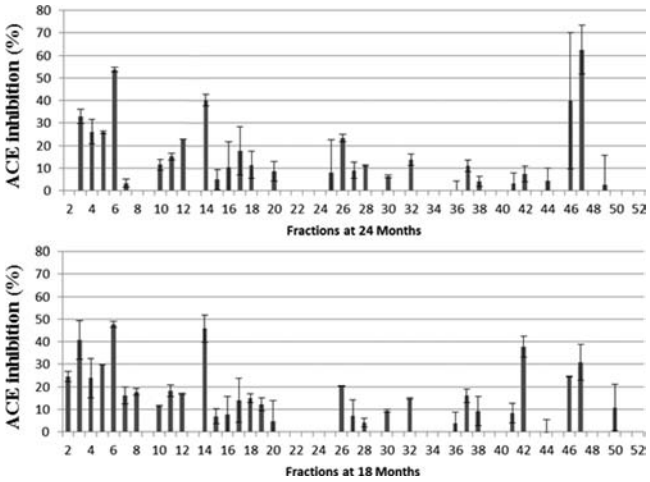

Figure 1. ACE-inhibitory activity of fractions collected after an in vitro gastrointestinal digestion of dry-cured hams at 18−24 months of aging time.

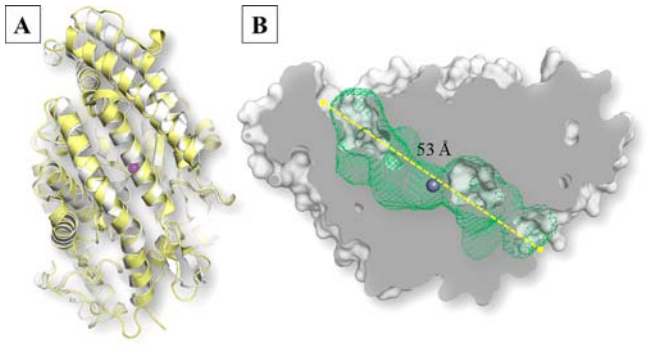

Figure 3. Three-dimensional representation of ACE structures: (A) structures overlapping C-terminal (white) and N-terminal (yellow) domains; (B) cut surface of N-terminal domain. The binding pocket is represented in mesh, and the dark sphere represents Zn ion.

100 to 50% A; 22.50−23.50 min, 50% A; 23.50−30 min, linear from 50 to 100% A; column temperature, 35 °C; sample temperature, room temperature; injection volume, 10 μL for sample fractions and 20 μL for pure peptides; acquisition time, 30 min; flow, 0.2 mL/min; UV detection, λ = 228. Data analysis was performed with Empower software (Waters Co., Milford, MA, USA).

The IC_{50} value is defined as the inhibitor concentration that is able to decrease ACE activity by 50%. To determine IC_{50}, different concentrations of peptides were prepared and their relative ACE inhibitory activity was evaluated. IC_{50} values were determined by plotting the percentage relative inhibition as a function of concentration of test compound.

Peptide Quantification. LGL was quantified by an external calibration curve. The calibration curve was set up by injecting 200 μL of LGL at different concentrations (from 1 to 125 μM) containing 4 μL of internal standard (1 mM Phe-Phe) in UPLC-ESI-MS with the analysis conditions reported above.

RESULTS AND DISCUSSION

ACE Inhibitory Activity of Digested Fractions. We have recently reported the characterization of the peptide mixture obtained by simulated gastrointestinal digestion of Parma dry-cured hams:[15] To characterize the ACE inhibitory activity of the obtained peptides, the digesta were fractionated by semi-preparative HPLC, and the different fractions were tested by in vitro assay, according to common procedures used to identify active sequences.[39] By performing a reverse phase HPLC separation with very tight fraction collection, we obtained 51 fractions: results of in vitro test are reported in Figure 1.

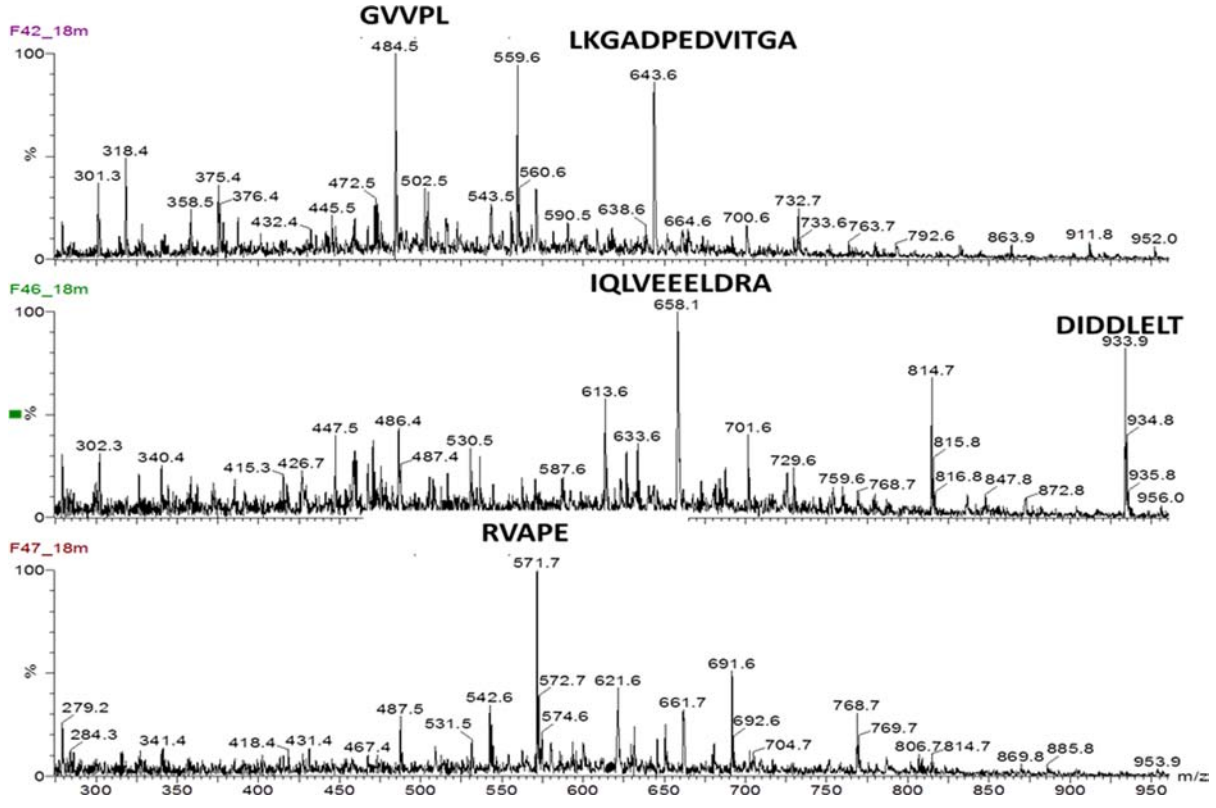

Figure 2. Mass spectra of fractions 42, 46, and 47 of samples at 18 months of aging time.

DOI: 10.1021/acs.jafc.5b02303
J. Agric. Food Chem. 2015, 63, 6366−6375

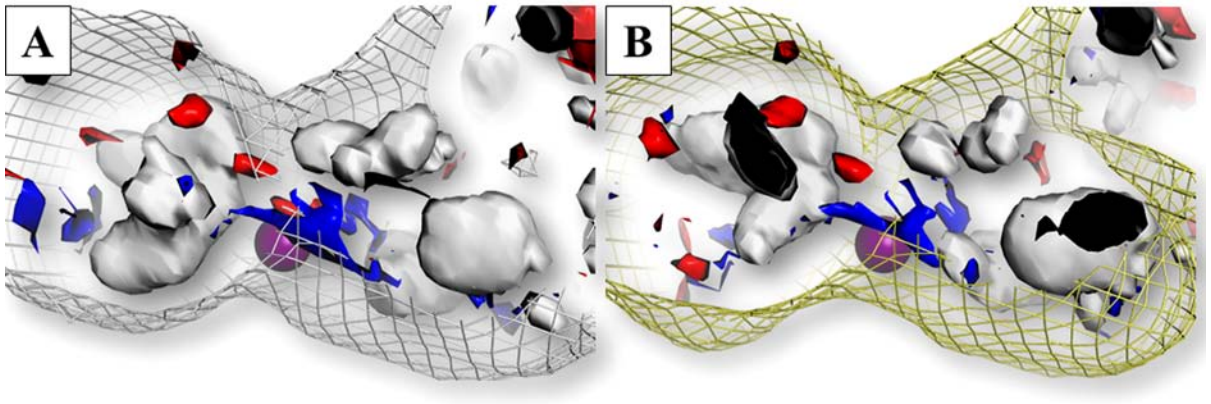

Figure 4. Anatomy of the binding sites: (A) C-terminal domain; (B) N-terminal domain. White, red, and blue contours identify regions sterically and energetically favorable for hydrophobic, H-bond acceptor, and H-bond donor groups, respectively (black regions are due to the back-lighted cut of some contours). The shape of the binding site is represented in mesh.

The inhibitory activity significantly differs among the different fractions, and differences were also observed as a function of aging time. In this respect, indeed, the most active fractions for digested ham sample at 24 months were found to be fractions 6, 14, 46, and 47, whereas for samples at 18 months also fraction 42 showed a relevant activity. To identify the peptides occurring in these fractions, MS and MS/MS analyses have been performed as previously reported.[15] The mass spectrum revealed a prevalence of dipeptides and free amino acids (mainly, tyrosine and phenylalanine) in the early eluted fractions (for both aging time). Conversely, longer peptides were found in fractions 42, 46, and 47: the identified sequences are RVAPE, IQLVEEELDRA, DIDDLELT, DIDSPPITAR, LKGADPEDVITGA, and GVVPL, as reported in Figure 2. Nevertheless, many other fractions have shown significant ACE inhibitory activity. It is worth noting that the activity of a specific fraction is determined by two possible contribution: (i) the activity of the occurring peptides or (ii) the total amount of peptides. Indeed, it is possible that a particular fraction shows high activity for the presence of a particularly active sequence in low amount or to the occurrence of a less active peptide in higher amount. Moreover, synergic effect may not be excluded. This mode of investigation is certainly time-consuming, and it is extremely difficult to quantify the peptides both with the total nitrogen evaluation method (Kjieldahl, owing to the low amount in collected fraction) and by chromatographic analysis (lack of authentic standards). Therefore, we have decided to use an innovative computer-aided framework for the research of novel active peptides by using the unbiased computational screening of sequences in comparison to the canonical piecemeal fractioning just applied.

In contrast with most other in silico approaches used for the analysis of ACE inhibition, we presented a structure-based procedure, based on the evaluation of protein−ligand interaction, which provides as output the qualitative evaluation of inhibitory activity together with the putative architecture of binding of each ACE−peptide complex. It should be kept in mind that insights concerning the spatial organization of enzyme−inhibitor complex are fundamental for the in-depth understanding of molecular mechanisms of action. Furthermore, they can serve for the rational design/optimization of strong inhibitors. As a general statement, it should be mentioned also that virtual screening can be a fast and cost-effective technique for analyzing huge amounts of sequences. Therefore, the systematic use for the analysis of peptidomes found in food digesta and/or hydrolyzed mixtures can be a promising straightforward first step toward the total profiling of the BP composition of food.

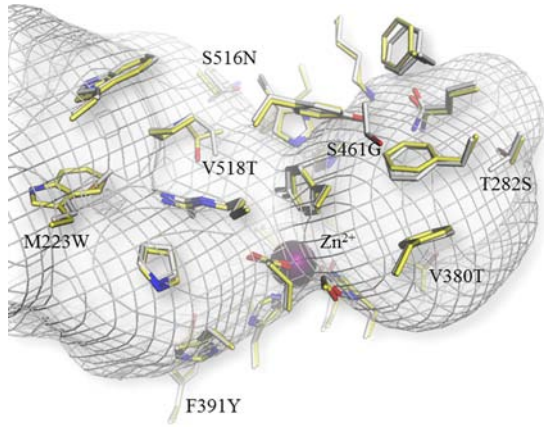

Figure 5. Comparison between catalytic sites of C-terminal and N-terminal domains. The shape of the pocket is represented in mesh, whereas lining amino acids are represented in sticks. The Zn ion is represented by a dark sphere. Residues of C-terminal and N-terminal domains are colored in white and yellow, respectively. Amino acid substitutions are highlighted by labels.

Computational Results. The underlying assumption at the basis of the use of docking-based strategy relies on the concept that the protein−ligand interaction is the sine qua non condition for the inhibitory activity. This means that the protein−ligand interaction is a necessary condition, even if occasionally not sufficient, for the enzymatic inhibition. Consequently, in the case of ACE, peptides able to stably interact with at least one of the two catalytic sites can reduce the conversion of substrates (e.g., angiotensin I in in vivo condition and HHL in in vitro assay), leading to true, substrate-like or pro-drug inhibition mechanisms. For this reason, the evaluation of the binding event at the catalytic site through docking simulations can be a straightforward technique to predict inhibitory potential of peptides. Specifically, to evaluate the enzyme−peptide complex formation, the coupling of docking simulations and rescoring procedures by using the HINT scoring function was chosen, the correlation with the free energy of binding being previously reported. [17]

Anatomy of the Pocket. The two catalytic domains originated from tandem gene duplication[40] and show the same 3D

DOI: 10.1021/acs.jafc.5b02303
J. Agric. Food Chem. 2015, 63, 6366−6375

Table 1. HINT Scores and Expected Activity of Peptides under Analysis

peptide sequence[a]	C-domain	N-domain	expected interaction
RVAPEEHPT	−5202	−3442	negative
VAPEEHPT	−3113	−5273	negative
LAPST	1046	416	positive
FQPS	−494	308	positive
APLNPK	−396	−4126	negative
PGIAD	195	728	positive
KLEGDLK	−211	−3021	negative
YPIEH methylated	−1238	−616	negative
TEAPLNPK	< −10000	−1859	negative
IVAPG	267	−228	positive
MDLER	1434	−2354	positive
ELV	503	581	positive
ALM*	1885	1200	positive
NSIM*	1001	848	positive
IIAPPER	−2734	−787	negative
DIR	−677	−1314	negative
IGGSI	846	283	positive
MDLE	729	365	positive
LQDLVDK	−1342	−2949	negative
LTEAPLNPK	−5231	< −10000	negative
PSIV	688	1558	positive
SFVTT*	1481	542	positive
DPV	1398	1463	positive
DLTDY	−5	−2265	negative
NWDDMEK	−2130	−410	negative
NVPI	400	−227	positive
KMEGDLNEM	−3471	−2962	negative
LTL	1030	1432	positive
LEGI	169	847	positive
SYELPDGQ	−2173	−2000	negative
PTVE	428	1242	positive
LGL*	2503	2285	positive
IKAKSALA	251	−852	positive
PEILPDGDHDLK	< −10000	< −10000	negative
SLSTEL	−1359	492	positive
LVL	1473	1641	positive
VEPEILPDGDHDLK	< −10000	< −10000	negative
TSLINTK	1094	−284	positive
VTV	1930	1180	positive
LKGADPEDVITGA	< −10000	−7295	negative
DIDSPPITAR	−3137	−3436	negative
GVVPL*	1075	−1129	positive
INAEL	−92	101	positive
PEILPDGDHDL	<−10000	−6684	negative
DQIISANPL	−3516	−2260	negative
LLASIDIDHT	< −10000	−3236	negative
TVKDLQHRL	−5802	< −10000	negative
IQLVEEELDRA	< −10000	< −10000	negative
DIDDLELT	−3807	−1487	negative
LFDKPVSPL	−7900	−1585	negative
RMKKNMEQTVK	< −10000	< −10000	negative
RVAPE	−735	−1897	negative
INTTLETKQ	−3525	−789	negative
NAYEESLDQLETLK	< −10000	< −10000	negative

[a]Peptides selected for experimental trials are denoted by an asterisk (*).

organization with 51% of sequence identity (according to global alignment by using the Needleman−Wunsch algorithm; http://www.ebi.ac.uk/Tools/psa/emboss_needle). Both domains hold a huge pocket with similar shape, which crosses the entire protein body (Figure 3). Analyses were focused on catalytic sites thus retracing the mode of action of inhibitory drugs (e.g., captopril and lisinopril).[41,42] The regions lining the catalytic site maintain the same organization in both domains, and both pockets share a prevalently hydrophobic environment (Figure 4), albeit they differ for seven amino acid substitutions (Figure 5).

Table 2. IC_{50} Values of Selected Peptides

sequence	IC_{50} (μM)
LGL	145
ALM	>1100
SFVTT	395
GVVPL	956
NSIM	>1100

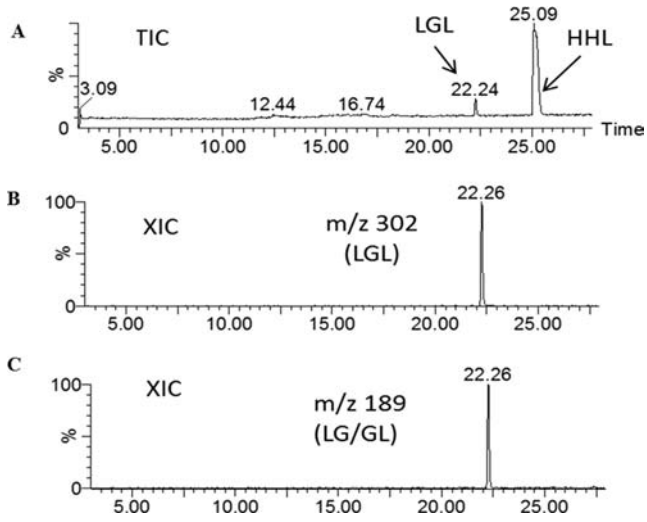

Figure 6. (A) TIC of LGL in the presence of ACE and HHL; (B) XIC of peptide LGL; (C) XIC of peptides LG/GL.

Data Collection. The peptide library was based on the peptidomic profile previously characterized after the in vitro physiological digestion of 18 and 24 months aged dry-cured ham.[15] However, in this study, solely those sequences that were unequivocally identified were considered, thus discarding those for which the Ile-Leu uncertainty subsisted (same M_w). Moreover, because most dipeptides were already known as active like I(L)F, GI(L), AI(L) (BIOPEP database, http://www.uwm.edu.pl/biochemia/index.php/pl/biopep), they were excluded throughout. Overall, a total of 54 sequences were analyzed (Table 1).

Predicted Activity. All of the computational results obtained for the analyzed sequences are reported in Table 1. A total of 25 peptides were predicted as active, and they ranged from three to five amino acids, with the exception of three peptides (i.e., IKAKSALA, SLSTEL, and TSLINTK).

Lead Peptide Identification and in Vitro Assessment of ACE Inhibition. Keeping in mind that the discovery of novel active sequences for future and more detailed analysis is one of the main goals of this work, we decided to synthesize and test for the in vitro ACE inhibition some of the strongest candidates identified by in silico analysis. Because we applied a previously assessed in silico procedure (as aforementioned), which has been followed by experimental confirmations of positive hits, no further validation of the model was needed. Thus, a total of five potentially active peptides were selected by

DOI: 10.1021/acs.jafc.5b02303
J. Agric. Food Chem. 2015, 63, 6366−6375

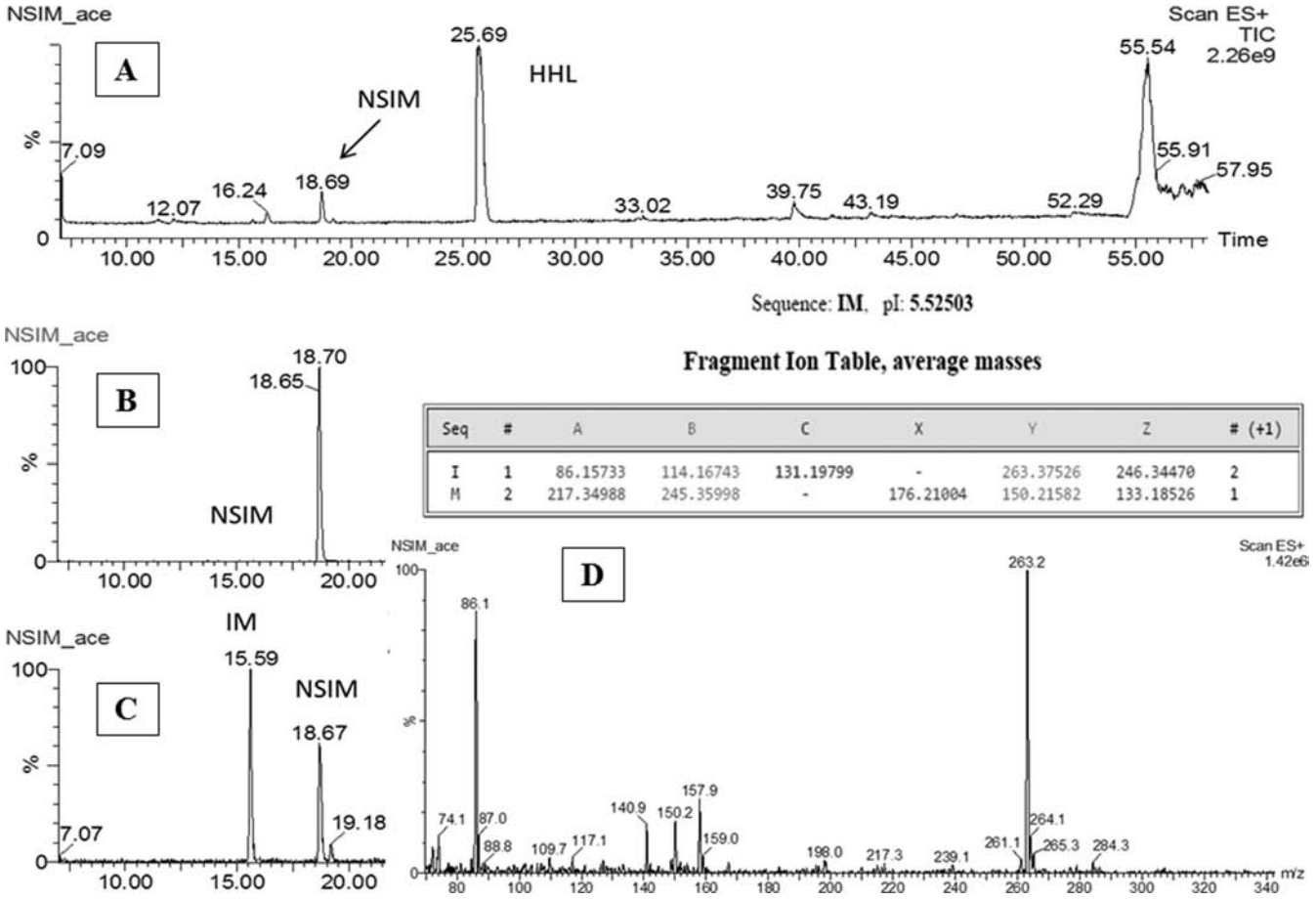

Figure 7. (A) TIC of mixture NSIM in the presence of ACE and HHL; (B) XIC of peptide NSIM; (C) XIC of peptide IM; (D) fragmentation in source of IM and theoretical fragmentation.

taking into account the in silico results and their occurrence in active fractions. The inclusion criteria were based (i) on the finding that short peptides may be easily absorbed through the intestinal epithelium,[5] thus having a greater physiological significance; (ii) on the relative abundance within the most active fraction of digested mixture, approximately evaluated on the basis of the most intense signals in the mass spectrum;[15] and (iii) on the computational results, with the aim to cover a reasonably high range of scores. Therefore, sequences ALM, NSIM, SFVTT, LGL, and GVVPL were synthesized by solid phase peptide synthesis, purified, and then assessed for ACE inhibitory activity. Specifically, LGL showed highest scores for both ACE domains; GVVPL, which was detected in relevant abundance in fraction 42, showed a putative interaction only with the C-domain; and ALM, NSIM, and SFVTT were arbitrarily selected among the remaining peptides with high scores. With respect to this, although a correlation between HINT scores and inhibitory activity cannot be sustained yet, because HINT scores have proved to be correlated with the free energy of binding (as aforementioned), it is reasonable to think that the selection of high-scoring peptides may increase the chances to discover truly active peptides. The inhibitory activity of peptides is expressed as half-maximal inhibitory concentration (IC_{50}), and results of ALM, NSIM, SFVT, LGL, and GVVPL are reported in Table 2. All of the tested peptides showed appreciable inhibitory activity, and the most active sequences were LGL, SFVTT, and GVVPL with IC_{50} values of 145, 395, and 956 μM, respectively. ALM, NSIM, SFVTT, and LGL occurred in fractions 32, 31, 33, and 37, respectively. Interestingly, NSIM and SFVTT were found in fractions with no appreciable activity, whereas ALM and LGL were found in fractions with a relatively low ACE-inhibitor activity (Figure 1). Conversely, GVVPL was present in one of the most active fractions (no. 42; Figure 1). Interestingly, to the best of our knowledge, these inhibitory sequences have never been identified previously.

Because the GL dipeptide is an already known ACE inhibitor[43] (not found in ham digesta), it was assessed whether LGL eventually acted as a pro-drug inhibitor (e.g., peptide converted to true inhibitor after hydrolysis by ACE [44]) upon enzymatic cleavage. Thus, the presence of the GL fragment in the inhibitory assay mixture was checked by UPLC-ESI-MS analysis. As reported in Figure 6, the GL fragment was not detected, and therefore a true inhibition mechanism can be proposed for LGL itself. The same was proposed also for ALM, SFVTT, and GVVPL because hydrolysis fragments were not observed (data not shown). Conversely, with regard to NSIM, a substrate mechanism can be proposed because the IM fragment was released in the assay medium (Figure 7). The pro-drug mechanism was excluded due to the low potency observed.

As far as the utility of this approach, we can easily affirm that, by the evaluation of the activity of single fractions, the GVVPL peptide would have been identified accordingly, due to the high abundance in one of the most active fractions. However, our results showed that the unbiased analysis of the entire peptidomic profile by using the in silico method allowed the

DOI: 10.1021/acs.jafc.5b02303
J. Agric. Food Chem. 2015, 63, 6366−6375

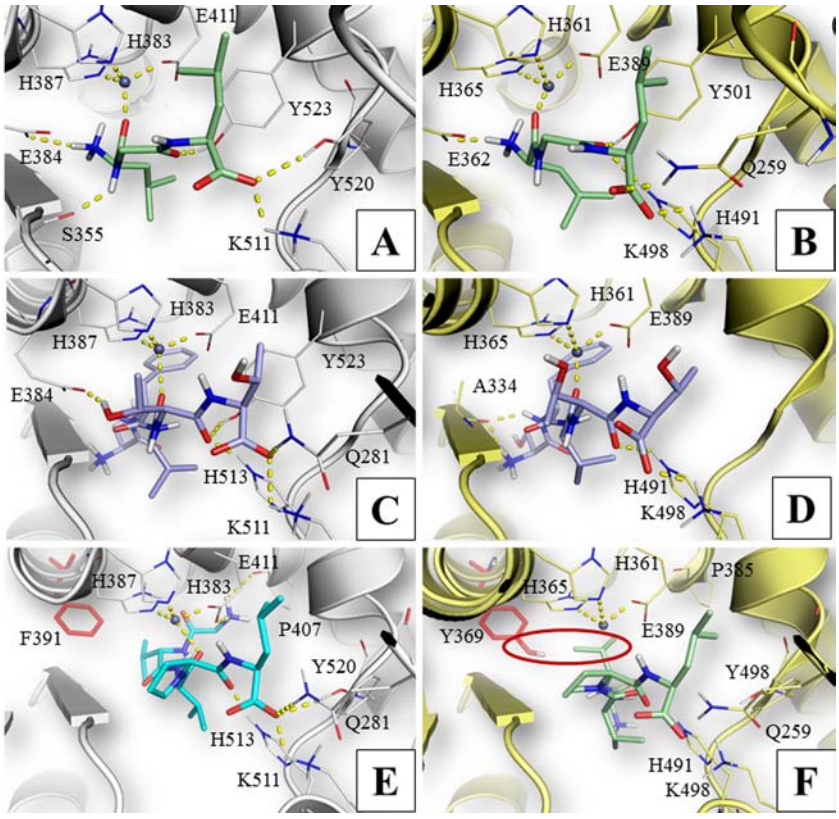

Figure 8. Binding architectures of the most active peptides: (A) LGL within the C-terminal domain; (B) LGL within the N-terminal domain; (C) SFVTT within the C-terminal domain; (D) SFVTT within the N-terminal domain; (E) GVVPL within the C-terminal domain; (F) GVVPL within the N-terminal domain. Amino acids involved in polar contacts and peptides are represented in thin and bold sticks, respectively. The Zn ion is represented in a dark sphere, whereas yellow dotted lines indicate polar contacts. The residues involved in the differential interaction of GVVPL are represented in red sticks, and the hydrophobic−polar mismatch is ringed in red. Because the interaction is predicted as missing, polar contacts between protein and GVVPL are not represented.

identification of other more active sequences (i.e., LGL and SFVTT), which would have been missed otherwise, being encrypted in low-activity fractions. Theoretically, at the present stage, the in silico method herein proposed is unable to distinguish ACE substrates from true inhibitors or pro-drug peptides because the interaction with the catalytic site is a common requirement. Nevertheless, with only the exception of NSIM, all peptides accounted for in vitro analysis proved to be true inhibitors.

Mode of Interaction of Active Peptides. Even if the two domains show some amino acid substitutions at the level of catalytic sites (Figure 5), they did not affect the capability of tested peptides to interact with both domains, with the exception of GVVPL, the binding of which with the N-terminal domain catalytic site was prevented mainly by the F391Y mutation. In particular, the hydroxyl group of Tyr369 within the N-terminal binding site interfered with the side chain of valine in position 2 (from N- to C-terminus), thus preventing the proper positioning of the GVVPL peptide. Therefore, it is proposed that the inhibitory activity of the GVVPL peptide is mediated preferably through the inhibition of the C-domain, whereas the other four peptides can have effects on both catalytic sites. The binding architectures of the three best peptides (LGL, SFVTT, and GVVPL) are reported in Figure 8.

Furthermore, it is worth mentioning that the simulation of the binding architecture can be a solid foothold for further enhancing active sequences. For example, with regard to GVVPL the lack of interaction with the N-terminal domain was predicted owing to charged interferences on valine in position 2. Therefore, it may be hypothesized that the proper substitution with a smaller side chain might increase the activity by gaining interaction with the N-terminal domain. Likewise, with the aim to pursue a domain-specific inhibitor, the loss of the interaction solely with one of the two catalytic sites could be searched. The F391Y mutation can be accounted, accordingly.

Quantification of LGL in Ham Samples. LGL is the most active peptide among those considered herein for in vitro assay. Actually, the gastrointestinal stability of inhibitory peptides and the resistance to cleavage by ACE are not always evaluated even if they are essential requirements for seeking in vivo effects. Keeping in mind that all peptides under analysis originated from gastrointestinal digestion of dry-cured ham samples, and considering that di- and tripeptides may be easily adsorbed by intestinal epithelium,[5] the true inhibitor LGL might be a sequence of great physiological relevance. Moreover, although effective absorption by intestinal epithelium should be considered, solely on the basis of the IC_{50} value, LGL might show a congruent range of activity with respect to the abundance per portion. Indeed, to determine the amount of this peptide in dry-cured ham digested samples, a calibration curve was set up plotting the ratio between the peak areas of LGL and FF (as internal standard) and the LGL concentration. In the digested mixtures of 24 and 18 months aged ham samples, the LGL peptide (M_w 301 g/mol) occurs respectively at concentrations of 62 ± 11 and 112 ± 36 μg/g. With regard to the bioaccessibility in respect to the in vitro gastrointestinal digestion

DOI: 10.1021/acs.jafc.5b02303
J. Agric. Food Chem. 2015, 63, 6366−6375

model, 829 μg of LGL is needed in to reach a concentration able to decrease ACE activity by 50% (which is contained in 13.4 and 7.4 g of 24 and 18 months aged ham, respectively). Furthermore, such a concentration is overcome by 7.5- and 13.5-fold when 24 and 18 months aged ham portions (100 g) are consumed. Therefore, one can hypothesize that physiologically relevant concentrations might be reached after dietary consumption of Parma ham, at least in the intestinal lumen. Accordingly, the high abundance in ham samples, together with the high activity observed in in vitro ACE inhibition, concur to elect LGL as a strong lead compound and also strongly support its inclusion in future and more detailed experimental investigations. Taken as a whole, our findings are an important step forward toward the in-depth and more informed characterization of such a relevant food product beyond its well-known nutritional properties.

AUTHOR INFORMATION

Corresponding Authors

*(P.C.) Phone: ++39-0521-905669. E-mail: pietro.cozzini@unipr.it.

*(G.G.) Phone: ++39-0521-906270. E-mail: gianni.galaverna@unipr.it.

Author Contributions

‖L.D. and S.P. contributed equally to the work.

Funding

This work was supported by the project "Hepiget-Advanced research in genomics and processing technologies for the Italian heavy pig production chain" financed by the AGER-Agroalimentare e Ricerca foundation (Italy).

Notes

The authors declare no competing financial interest.

ACKNOWLEDGMENTS

We acknowledge Prof. Glen E. Kellogg (Virginia Commonwealth University, Richmond, VA, USA; USA) for the HINT scoring function, Prof. Gabriele Cruciani (University of Perugia, Perugia, Italy) for kindly supplying the FLAP software, Dario Manfredi for programming support, and Dr. Roberta Virgili (Experimental Station for Food Preserving Industry, Parma, Italy) for the ham samples.

REFERENCES

(1) Puchalska, P.; Marina Alegre, M. L.; García López, M. C. Isolation and characterization of peptides with antihypertensive activity in foodstuffs. *Crit. Rev. Food Sci. Nutr.* **2015**, *55*, 521−551.

(2) Harnedy, P. A.; FitzGerald, R. J. Bioactive peptides from marine processing waste and shellfish: a review. *J. Funct. Foods* **2012**, *4*, 6−24.

(3) Hartmann, R.; Meisel, H. Food-derived peptides with biological activity: from research to food applications. *Curr. Opin. Biotechnol.* **2007**, *18*, 163−169.

(4) Kim, S.; Wijesekara, I. Development and biological activities of marine-derived bioactive peptides: a review. *J. Funct. Foods* **2010**, *2*, 1−9.

(5) De Leo, F.; Panarese, S.; Gallerani, R.; Ceci, L. R. Angiotensin converting enzyme (ACE) inhibitory peptides: production and implementation of functional food. *Curr. Pharm. Des.* **2009**, *15*, 3622−3643.

(6) Anthony, C. S.; Masuyer, G.; Sturrock, E. D.; Acharya, K. R. Structure based drug design of angiotensin-I converting enzyme inhibitors. *Curr. Med. Chem.* **2012**, *19*, 845−855.

(7) Iwaniak, A.; Minkiewicz, P.; Darewicz, M. Food-originating ACE inhibitors, including antihypertensive peptides, as preventive food components in blood pressure reduction. *Compr. Rev. Food Sci. Food Saf.* **2014**, *13*, 114−134.

(8) Yang, Y.; Marczak, E. D.; Yokoo, M.; Usui, H.; Yoshikawa, M. Isolation and antihypertensive effect of angiotensin I-converting enzyme (ACE) inhibitory peptides from spinach Rubisco. *J. Agric. Food Chem.* **2003**, *51*, 4897−4902.

(9) Nakashima, Y.; Arihara, K.; Sasaki, A.; Mio, H.; Ishikawa, S.; Itoh, M. Antihypertensive activities of peptides derived from porcine skeletal muscle myosin in spontaneously hypertensive rats. *J. Food Sci.* **2002**, *67*, 434−437.

(10) Lafarga, T.; O'Connor, P.; Hayes, M. Identification of novel dipeptidyl peptidase-IV and angiotensin-I-converting enzyme inhibitory peptides from meat proteins using in silico analysis. *Peptides* **2014**, *59*, 53−62.

(11) Asoodeh, A.; Haghighi, L.; Chamani, J.; Ansari-Ogholbeyk, M. A.; Mojallal-Tabatabaei, Z.; Lagzian, M. Potential angiotensin I converting enzyme inhibitory peptides from gluten hydrolysate: biochemical characterization and molecular docking study. *J. Cereal Sci.* **2014**, *60*, 92−98.

(12) Vermeirssen, V.; van der Bent, A.; Van Camp, J.; van Amerongen, A.; Verstraete, W. A quantitative in silico analysis calculates the angiotensin I converting enzyme (ACE) inhibitory activity in pea and whey protein digests. *Biochimie* **2004**, *86*, 231−239.

(13) Sagardia, I.; Roa-Ureta, R. H.; Bald, C. A new QSAR model, for angiotensin I-converting enzyme inhibitory oligopeptides. *Food Chem.* **2013**, *136*, 1370−1376.

(14) Gleeson, M. P.; Modi, S.; Bender, A.; Robinson, R. L.; Kirchmair, J.; Promkatkaew, M.; Hannongbua, S.; Glen, R. C. The challenges involved in modeling toxicity data in silico: a review. *Curr. Drug Metab.* **2012**, *18*, 1266−1291.

(15) Paolella, S.; Falavigna, C.; Faccini, A.; Virgili, R.; Sforza, S.; Dall'Asta, C.; Dossena, A.; Galaverna, G. Effect of dry-cured ham maturation time on simulated gastrointestinal digestion: characterization of the released peptide fraction. *Food Res. Int.* **2015**, *67*, 136−144.

(16) Amadasi, A.; Mozzarelli, A.; Meda, C.; Maggi, A.; Cozzini, P. Identification of xenoestrogens in food additives by an integrated in silico and in vitro approach. *Chem. Res. Toxicol.* **2009**, *22*, 52−63.

(17) Cozzini, P.; Fornabaio, M.; Marabotti, A.; Abraham, D. J.; Kellogg, G. E.; Mozzarelli, A. Simple, intuitive calculations of free energy of binding for protein-ligand complexes. 1. Models without explicit constrained water. *J. Med. Chem.* **2002**, *45*, 2469−2483.

(18) Delfosse, V.; Grimaldi, M.; Cavaillès, V.; Balaguer, P.; Bourguet, W. Structural and functional profiling of environmental ligands for estrogen receptors. *Environ. Health Perspect.* **2014**, *122*, 1306−1313.

(19) Dellafiora, L.; Dall'Asta, C.; Cruciani, G.; Galaverna, G.; Cozzini, P. Molecular Modelling approach to evaluate poisoning of topoisomerase I by alternariol derivatives. *Food Chem.* **2015**, DOI: 10.1016/j.foodchem.2015.02.083.

(20) Dellafiora, L.; Mena, P.; Cozzini, P.; Brighenti, F.; Del Rio, D. Modelling the possible bioactivity of ellagitannin-derived metabolites. In silico tools to evaluate their potential xenoestrogenic behavior. *Food Funct.* **2013**, *4*, 1442−1451.

(21) Dellafiora, L.; Mena, P.; Del Rio, D.; Cozzini, P. Modeling the effect of phase II conjugations on topoisomerase I poisoning: pilot study with luteolin and quercetin. *J. Agric. Food Chem.* **2014**, *62*, 5881−5886.

(22) Prosciutto di Parma, Consortium; http://www.prosciuttodiparma.com/en_UK/consortium/economic-figures.

(23) Cannata, S.; Ratti, S.; Meteau, K.; Mourot, J.; Baldini, P.; Corino, C. Evaluation of different types of dry-cured ham by Italian and French consumers. *Meat Sci.* **2010**, *84*, 601−606.

(24) Lucarini, M.; Saccani, G.; D'Evoli, L.; Tufi, S.; Aguzzi, A.; Gabrielli, P.; Marletta, L.; Lombardi-Boccia, G. Micronutrients in Italian ham: a survey of traditional products. *Food Chem.* **2013**, *140*, 837−842.

(25) Baroni, M.; Cruciani, G.; Sciabola, S.; Perruccio, F.; Mason, J. S. A common reference framework for analyzing/comparing proteins and

DOI: 10.1021/acs.jafc.5b02303
J. Agric. Food Chem. 2015, 63, 6366−6375

ligands. Fingerprints for Ligands and Proteins (FLAP): theory and application. *J. Chem. Inf. Model.* **2007**, *47*, 279−294.
(26) Carosati, E.; Sciabola, S.; Cruciani, G. Hydrogen bonding interactions of covalently bonded fluorine atoms: from crystallographic data to a new angular function in the GRID force field. *J. Med. Chem.* **2004**, *47*, 5114−5125.
(27) Kramer, G. J.; Mohd, A.; Schwager, S. L.; Masuyer, G.; Acharya, K. R.; Sturrock, E. D.; Bachmann, B. O. Interkingdom pharmacology of angiotensin-I converting enzyme inhibitor phosphonates produced by actinomycetes. *ACS Med. Chem. Lett.* **2014**, *5*, 346−351.
(28) Masuyer, G.; Schwager, S. L.; Sturrock, E. D.; Isaac, R. E.; Acharya, K. R. Molecular recognition and regulation of human angiotensin-I converting enzyme (ACE) activity by natural inhibitory peptides. *Sci. Rep.* **2012**, *2*, 717.
(29) Cozzini, P.; Dellafiora, L. In silico approach to evaluate molecular interaction between mycotoxins and the estrogen receptors ligand binding domain: a case study on zearalenone and its metabolites. *Toxicol. Lett.* **2012**, *214*, 81−85.
(30) Salsi, E.; Bayden, A. S.; Spyrakis, F.; Amadasi, A.; Campanini, B.; Bettati, S.; Dodatko, T.; Cozzini, P.; Kellogg, G. E.; Cook, P. F.; Roderick, S. L.; Mozzarelli, A. Design of *O*-acetylserine sulfhydrylase inhibitors by mimicking nature. *J. Med. Chem.* **2010**, *53*, 345−356.
(31) Akif, M.; Masuyer, G.; Schwager, S. L.; Bhuyan, B. J.; Mugesh, G.; Isaac, R. E.; Sturrock, E. D.; Acharya, K. R. Structural characterization of angiotensin I-converting enzyme in complex with a selenium analogue of captopril. *FEBS J.* **2011**, *278*, 3644−3650.
(32) Kellogg, E. G.; Abraham, D. J. Hydrophobicity: is LogP(o/w) more than the sum of its parts? *Eur. J. Med. Chem.* **2000**, *37*, 651−661.
(33) Fornabaio, M.; Cozzini, P.; Mozzarelli, A.; Abraham, D. J.; Kellogg, G. E. Simple, intuitive calculations of free energy of binding for protein-ligand complexes. 2. Computational titration and pH effects in molecular models of neuraminidase-inhibitor complexes. *J. Med. Chem.* **2003**, *46*, 4487−4500.
(34) Fornabaio, M.; Spirakis, F.; Mozzarelli, A.; Cozzini, P.; Abraham, D. J.; Kellogg, G. E. Simple, intuitive calculations of free energy of binding for protein-ligand complexes. 3. The free energy contribution of structural water molecules in HIV-1 protease complexes. *J. Med. Chem.* **2004**, *47*, 4507−4516.
(35) Marabotti, A.; Spyrakis, F.; Facchiano, A.; Cozzini, P.; Alberti, S.; Kellogg, G. E.; Mozzarelli, A. Energy-based prediction of amino acid-nucleotide base recognition. *J. Comput. Chem.* **2008**, *29*, 1955−1969.
(36) Versantvoort, C. H.; Oomen, A. G.; Van de Kamp, E.; Rompelberg, C. J.; Sips, A. J. Applicability of an in vitro digestion model in assessing the bioaccessibility of mycotoxins from food. *Food Chem. Toxicol.* **2005**, *43*, 31−40.
(37) Cushman, D. W.; Cheung, H. S. Spectrophotometric assay properties of the angiotensin-converting enzyme of rabbit lung. *Biochem. Pharmacol.* **1971**, *20*, 1637−1648.
(38) Nakamura, Y.; Yamamoto, N.; Sakai, K.; Okubo, A.; Yamazaki, S.; Takano, T. Purification and characterization of angiotensin I-converting enzyme inhibitors from sour milk. *J. Dairy Sci.* **1995**, *78*, 777−783.
(39) Escudero, E.; Mora, L.; Fraser, P. D.; Aristoy, M. C.; Arihara, K.; Toldrá, F. Purification and Identification of antihypertensive peptides in Spanish dry-cured ham. *J. Proteomics* **2013**, *78*, 499−507.
(40) Coates, D.; Isaac, R. E.; Cotton, J.; Siviter, R.; Williams, T. A.; Shirras, A.; Corvol, P.; Dive, V. Functional conservation of the active sites of human and *Drosophila* angiotensin I-converting enzyme. *Biochemistry* **2000**, *39*, 8963−8969.
(41) Corradi, H. R.; Schwager, S. L.; Nchinda, A. T.; Sturrock, E. D.; Acharya, K. R. Crystal structure of the N domain of human somatic angiotensin I-converting enzyme provides a structural basis for domain-specific inhibitor design. *J. Mol. Biol.* **2006**, *357*, 964−974.
(42) Yates, C. J.; Masuyer, G.; Schwager, S. L.; Akif, M.; Sturrock, E. D.; Acharya, K. R. Molecular and thermodynamic mechanisms of the chloride-dependent human angiotensin-I-converting enzyme (ACE). *J. Biol. Chem.* **2014**, *289*, 1798−1814.
(43) Cheung, H. S.; Wang, F. L.; Ondetti, M. A.; Sabo, E. F.; Cushman, D. W. Binding of peptide substrates and inhibitors of angiotensin-converting enzyme. Importance of the COOH-terminal dipeptide sequence. *J. Biol. Chem.* **1980**, *255*, 401−407.
(44) Fujita, H.; Yokoyama, K.; Yoshikawa, M. Classification and antihypertensive activity of angiotensin I-converting enzyme inhibitory peptides derived from food proteins. *J. Food Sci.* **2000**, *65*, 564−569.

DOI: 10.1021/acs.jafc.5b02303
J. Agric. Food Chem. 2015, 63, 6366−6375

Table 1. High-Resolution LC-MS Data of FKA Samples Using Positive and Negative Electrospray Ionization[a]

	detected metabolites of FKA					
		m/z $[M + H]^+$		m/z $[M - H]^-$		
	t_R (min)	found	calcd	found	calcd	M formula
FKA	6.18	315.1234	315.1227			$C_{18}H_{18}O_5$
phase I	4.02			285.0766	285.0768	$C_{16}H_{14}O_5$
	5.07	**301.1073**	**301.1071**	**299.0925**	**299.0925**	**$C_{17}H_{16}O_5$**
phase II	3.38	491.1150	491.1548	489.1402	489.1402	$C_{24}H_{26}O_{11}$
	3.50	**491.1151**	**491.1548**	**489.1405**	**489.1402**	**$C_{24}H_{26}O_{11}$**
phase I+II	2.81	477.1389	477.1391	475.1238	475.1246	$C_{23}H_{24}O_{11}$
	3.50	**491.1549**	**491.1548**	**489.1399**	**489.1402**	**$C_{24}H_{26}O_{11}$**
	3.71			505.1345	505.1351	$C_{24}H_{26}O_{12}$
	3.81			505.1345	505.1351	$C_{24}H_{26}O_{12}$
	3.87	477.1391	477.1391	475.1239	475.1246	$C_{23}H_{24}O_{11}$
	5.07	301.1072	301.1071	299.0920	299.0925	$C_{17}H_{16}O_5$

[a]Major metabolites are written in bold. Corresponding mass spectra can be found in the SI.

synthase and cyclooxygenase-2 in lipopolysaccharide-induced RAW 264.7 cells via inhibition of the NF-κB pathway.[28,29] Moreover, Mohamad et al. proposed a nociceptive activity of FKB in mice.[30,31]

Despite increasing data regarding bioactivity, to date there is no information about the metabolism of flavokawains. In the present study, we therefore analyzed the in vitro metabolism of flavokawains using human liver microsomes. Different microsomal incubation systems were applied to study phase I metabolism and phase II glucuronidation as well as combined phase I and II metabolism. Metabolites were identified by liquid chromatography–high-resolution electrospray ionization mass spectrometry (LC-HRESIMS) and nuclear magnetic resonance spectroscopy (NMR). A metabolic profile of flavokawains is proposed.

MATERIALS AND METHODS

Chemicals and Reagents. Glucose-6-phosphate sodium salt (G6P), glucose-6-phosphate dehydrogenase (G6PDH), nicotinamide adenine dinucleotide phosphate sodium salt hydrate (NADP), uridine 5′-diphosphoglucuronic acid trisodium salt (UDPGA), and alamethicin (Ala) from *Trichoderma viride* were obtained from Sigma-Aldrich (Taufkirchen, Germany). Acetonitrile (MeCN, LiChroSolv) and methanol (LiChroSolv) were obtained from Merck (Darmstadt, Germany). All other solvents used were of pro analysis quality and derived from Merck or Arcos.

Human Liver Microsomes. Frozen pooled liver microsomes (HMMC-PL, 0.5 mL) were purchased from Life Technologies (Darmstadt, Germany). They derived from 50 adult donors of mixed gender having a total protein concentration of 20 mg/mL and a cytochrome P450 content of 0.286 nmol/mg. Microsomes were stored at −80 °C until use. A detailed certificate of analysis of the used microsomes can be found on the provider's homepage.

Test Compounds. FKA, FKB, FKC, and cardamonin were synthesized during previous work at the Institute of Pharmacy, University of Regensburg, and showed no impurities in the HPLC runs.[7] For preparation of stock solutions, test compounds were first dissolved in DMSO at a concentration of 10 mM and then diluted with EtOH to a concentration of 1 mM.

Microsomal Incubation Systems for Phase I Metabolism and Phase II Glucuronidation. For phase I metabolism, a NADPH regeneration system was used. A typical 1 mL incubation mix consisted of 0.5 mg of liver microsomal protein, 3.3 mM $MgCl_2$, 3.3 mM G6P, 0.4 U/mL G6PDH, 1.3 mM NADP, and 10 μM flavokawain or cardamonin in 0.1 M potassium phosphate buffer.

For phase II glucuronidation, the 1 mL incubation mix was composed of 0.5 mg of microsomal protein, 3.3 mM $MgCl_2$, 2 mM UDPGA, 25 μg/mL Ala, and 10 μM flavokawain or cardamonin in 0.1 M potassium phosphate buffer.

Combined phase I and II metabolism was investigated using a 1 mL incubation system consisting of 0.5 mg of microsomal protein, 3.3 mM $MgCl_2$, 3.3 mM G6P, 0.4 U/mL G6PDH, 1.3 mM NADP, 2 mM UDPGA, 25 μg/mL Ala, and 10 μM flavokawain or cardamonin in 0.1 M potassium phosphate buffer.

The reaction was started by the addition of NADP and/or UDPGA. Incubation was carried out in a shaken water bath at 37 °C for 60 min. Negative control incubations were carried out without microsomes or without cofactors (NADP or UDPGA). Reactions were terminated by the addition of 1 mL of ice-cold EtOH. Samples were vortexed for 5 min and then centrifuged for 5 min at 14000 rpm and 4 °C. Supernatants were subjected to further analysis.

For NMR, sample size was increased to 5 mL and the concentration of chalcones was raised to 100 μM due to the lower sensitivity of NMR compared to MS. An incubation time of 4 h was chosen to maximize transformation rate. Metabolic reactions were stopped by the addition of ice-cold EtOH. To improve storage stability, EtOH was evaporated and samples were refilled with ultrapure water. Then samples were freeze-dried and stored at −20 °C until further analysis.

Liquid Chromatography–High-Resolution Electrospray Ionization Mass Spectrometry (LC-HRESIMS). Samples for LC-HRESIMS analysis were prepared after 0 and 60 min of incubation. Matrix samples without test compound were used as blank controls. Analysis was performed with UHPLC Agilent 1290 infinity, DAD G4212A, and MS Agilent 6540 UHD Q-TOF with negative electrospray ionization using dual ion source. Separation was performed on a Thermo Accucore aQ column (C18, 50 × 2.1 mm, 2.6 μm) using a gradient of 0.1% formic acid (solvent A) and 100% MeCN supplemented with 0.1% formic acid (solvent B). Gradient: 0–10 min, 0 → 98% B; 10–11 min, 98% B; 11–11.1 min, 98 → 0% B; 11.1–13 min, 0% B; flow rate, 0.6 mL/min; injection volume, 5 μL; oven temperature, 40 °C. Data analysis was performed with MassHunter software (B.05.00, Agilent) using automatic mass spectrum integration.

HRESIMS of 5,7-Dimethoxy-flavanone-4′-*O*-glucuronide. HRESIMS of FKC metabolite 5,7-dimethoxy-flavanone-4′-*O*-glucuronide was recorded on a LC-MS/MS system consisting of an Ultimate 3000 series RSLC (Dionex, Sunnyvale, CA, USA) system and an Orbitrap mass spectrometer (Thermo Fisher Scientific, Bremen, Germany). HRESIMS data were analyzed using XCALIBUR (Thermo Fisher Scientific, Waltham, MA, USA) software.

Isolation and Structure Elucidation of Metabolites. Samples were dissolved with a minimum amount of HPLC solvent, and HPLC

DOI: 10.1021/acs.jafc.5b01858
J. Agric. Food Chem. 2015, 63, 6376–6385

fractionation was performed using an Agilent HP1100 series HPLC system (Agilent Technologies, Waldbronn, Germany) equipped with a binary pump G1312A, degasser G1322A, autoinjector 1367A, column oven G1316, and G11315B diode array detector controlled with ChemStationRev.A.08.04 (1008) software. Separation was performed on a LiChrosphere RP-18 column (5 μm, 250 × 4 mm, Merck KGaA, Darmstadt, Germany) with a guard column (5 μm, 4 × 4 mm) using a linear binary gradient of ultrapure water containing 0.1% (v/v) trifluoroacetic acid (solvent A) and MeCN (solvent B) with a flow rate of 0.8 mL/min. The gradient profile was 0−30 min, 20% → 80% B; 30−35 min, 80% B; 35−37 min, 80% → 20% B; and column temperature was set at 30 °C.

NMR spectra were recorded in MeOH-d_4 with a Bruker Avance 500 NMR spectrometer (Bruker-Biospin, Karlsruhe, Germany) operating at 500.13 MHz for ^{1}H and 125.75 MHz for ^{13}C. The spectrometer was equipped with a 5 mm TCI cryoprobe, and capillary tubes (2 mm o.d.; 80 μL filling volume) were used for measuring NMR spectra with standard Bruker pulse sequences. Tetramethylsilane was used as internal chemical shift reference standard. The spectrometer was controlled by TopSpin 3.1 software, which was also used for processing of the NMR spectra. According to the limited amounts, only ^{1}H NMR spectra were recorded of FKA metabolites. In addition to ^{1}H NMR spectra of FKB and FKC metabolites, 2D NMR spectra (^{1}H,^{1}H−COSY; ^{1}H,^{13}C HMBC; ^{1}H,^{13}C HSQC) were recorded.

RESULTS

To gain insight into the metabolism of flavokawains, FKA, FKB, and FKC as well as cardamonin were subjected to different microsomal incubation systems providing phase I reactions or phase II glucuronidation. Furthermore, combined phase I and II metabolism was studied by activation of phase I enzymes and UDP-glucuronosyl transferases in one system. HPLC was used to confirm the stability of the test compounds in phosphate incubation buffer. In the control incubation systems without cofactors or microsomes, no nonspecific metabolism or degradation was observed (data not shown).

Metabolites of FKA. Two phase I metabolites were found for FKA. According to retention times (t_R) and LC-MS data (Table 1), they were identified as helichrysetin (Heli) (t_R = 4.02 min; m/z [M − H]$^-$ 285.0766) and FKC (t_R = 5.07 min; m/z [M − H]$^-$ 299.0920), with FKC being the major phase I metabolite.

Phase II metabolism resulted in glucuronidation of FKA. Despite only one available OH-group at C-2′, two FKA glucuronides (t_R = 3.38, m/z [M − H]$^-$ 489.1402 and t_R = 3.50 min, m/z [M − H]$^-$ 489.1405) were detected, which are suggested to be *E*/*Z*-isomers. Combined phase I and II metabolism led to the formation of a FKA glucuronide (t_R = 3.50 min, m/z [M − H]$^-$ 489.1402) as well as of two FKC glucuronides (t_R = 2.81, m/z [M − H]$^-$ 475.1238, and t_R = 3.87 min, m/z [M − H]$^-$ 475.1239). Additionally, hydroxylation and glucuronidation resulted in the generation of two OH-FKA glucuronides (t_R = 3.71, m/z [M − H]$^-$ 505.1345, and t_R = 3.81 min, m/z [M − H]$^-$ 505.1345) that were identified as minor metabolites. The exact positions of hydroxylation and glucuronidation of major metabolites were established by NMR but could not be determined for minor ones.

The aglycone part of the ^{1}H NMR spectrum of the FKA glucuronides revealed two sets of signals, which by means of the coupling constants and chemical shift differences of H-α and H-β (Table 2) were clearly assignable to the suggested (*E*)- and (*Z*)-isomers of the aglycone with $J_{H\alpha\text{-}H\beta}$ = 15.9 Hz indicating the (*E*)-form being the major one. The (*Z*)-form ($J_{H\alpha\text{-}H\beta}$ = 12.5 Hz) might constitute an artifact that is formed during incubation, sample processing, or isolation procedure because it was detected again after separation of the peak at t_R = 3.50 min by HPLC. Comparison of the ^{1}H NMR spectrum of the FKA glucuronides with the parent compound clearly shows a strong difference in the chemical shifts for H-3′ and H-5′ in ring B and for the two olefinic protons α/β, whereas the chemical shifts of the protons in ring A changed only slightly (Table 2). This constitutes evidence of the glucuronide moiety being attached to 2′-OH. According to the limited availability of the FKA metabolites and the resulting poor signal-to-noise ratio, ^{13}C chemical shifts could not be completely assigned from the HSQC and HMBC spectra, but the obtained data of FKA-2′-*O*-glucuronide ((*E*)-form: δ 95.3 (C-3′), 93.8 (C-5′), 131.8 (C-2/6), 115.6 (C-3/5), 55.7 (4′-OCH$_3$), 56.2 (6′-OCH$_3$), 56.0 (4-OCH$_3$), 164.2 (C-4 and C-4′), and 160.8 (C-6′)) supported the suggested structure. The resonances of the glucuronide moieties could not be completely assigned from the ^{1}H NMR and ^{1}H,^{1}H COSY spectrum of the mixtures of the (*E*)- and (*Z*)-isoform because of strong overlap of signals in the spectral region of carbohydrate signals. A metabolism scheme of FKA is proposed in Figure 2. Although, due to this overlap, the coupling constant of the H-1″ signal was invisible, the β-configuration was inferred from its chemical shift (δ 4.99) for both the (*E*)- and (*Z*)-isomers, whereas a corresponding α-H-1″ signal is expected at lower field.[32]

Table 2. ^{1}H NMR Data (500 MHz, MeOH-d_4) of FKA and (*E*)- and (*Z*)-FKA-2′-*O*-glucuronide

	FKA	FKA-2′-*O*-glucuronide	
		(*E*)-form (major)	(*Z*)-form (minor)
no.	^{1}H δ (m, int, *J* (Hz))	^{1}H δ (m, int, *J* (Hz))	^{1}H δ (m, int, *J* (Hz))
3′	6.11 (d, 1H, *J* = 2.3)	6.57 (d, 1H, *J* = 2.3)	6.48 (d, 1H, *J* = 2.3)
5′	6.09 (d, 1H, *J* = 2.3)	6.36 (d, 1H, *J* = 2.3)	6.15 (d, 1H, *J* = 2.3)
α	7.71 (d, 1H, *J* = 15.9)	6.96 (d, 1H, *J* = 15.9)	6.39 (d, 1H, *J* = 12.5)
β	7.81 (d, 1H, *J* = 15.9)	7.39 (d, 1H, *J* = 15.9)	6.88 (d, 1H, *J* = 12.5)
2/6	7.60 (d, 2H, *J* = 8.7)	7.58 (m, 2H)	7.56 (m, 2H)
3/5	6.98 (d, 2H, *J* = 8.7)	6.95 (m, 2H)	6.81 (m, 2H)
4′-OCH$_3$	3.95 (s, 3H)	3.83 (s, 3H)	3.79 (s, 3H)
6′-OCH$_3$	3.84 (s, 3H)	3.78 (s, 3H)	3.73 (s, 3H)
4-OCH$_3$	3.85 (s, 3H)	3.85 (s, 3H)	3.80 (s, 3H)
1″		4.99 (overlap with residual HDO signal)	nd (overlap with HDO signal)
2″		3.38	nd
3″		3.5−3.6 (m)	3.5−3.6 (m)
4″		nd	nd
5″		nd (overlap with OCH$_3$ signals)	nd (overlap with OCH$_3$ signals)

Metabolites of FKB. For FKB, also FKC (t_R = 5.07 min, m/z [M − H]$^-$ 299.0927) was detected as major phase I metabolite (Table 3). In addition, cardamonin (t_R = 5.17 min, m/z [M − H]$^-$ 269.0819) and 2′,4′,6′-trihydroxychalcone (t_R = 4.48 min, m/z [M − H]$^-$ 255.0659) were generated. The 2′-*O*-glucuronide of FKB (t_R = 3.46 min, m/z [M − H]$^-$ 459.1297) was found after phase II metabolism. Combined phase I and II metabolism also led to the formation of 2′-*O*-glucuronide of FKB and additionally to four further glucuronides. Two of them (t_R = 2.81 min, m/z [M − H]$^-$ 475.1239, and t_R = 3.87 min, m/z [M − H]$^-$ 475.1241) were identified as 2′- and 4-*O*-

DOI: 10.1021/acs.jafc.5b01858
J. Agric. Food Chem. 2015, 63, 6376−6385

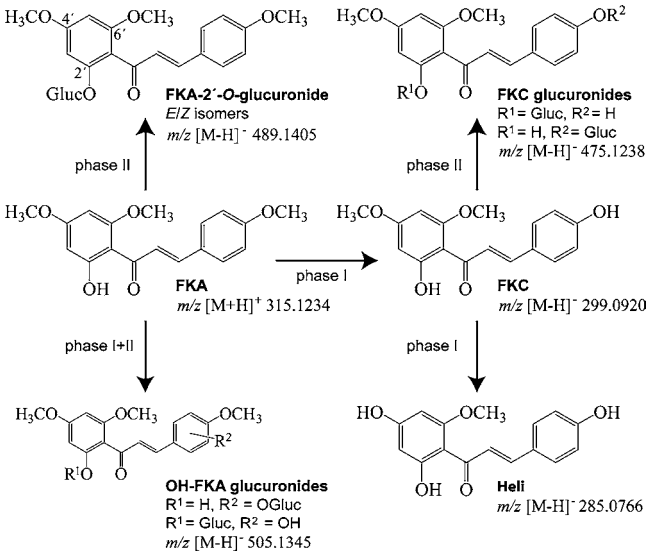

Figure 2. Proposed metabolic pathway of FKA by human liver microsomes. Structures of metabolites that could not be elucidated completely are depicted in smaller size.

glucuronide of FKC. As only two OH-groups are available on FKC, the other two generated glucuronides (t_R = 3.15 min, m/z $[M - H]^-$ 475.1239, and t_R = 3.75 min, m/z $[M - H]^-$ 475.1241) probably are *Z*-isoforms of those metabolites. Furthermore, the phase I metabolite cardamonin was glucuronidated (t_R = 3.95 min, m/z $[M - H]^-$ 445.1123) at either position C-2′ or C-4′.

(*E*)-FKB-2′-*O*-*β*-glucuronide constitutes the major metabolite of FKB, and its structure was unambiguously identified by ^{1}H NMR, COSY, HSQC, and HMBC. Comparison of the ^{1}H NMR spectrum of the major FKB metabolite with that of the parent compound clearly shows the slightly changed chemical shifts for the protons in ring B, whereas a strong change in the chemical shift position occurs for H-3′ and H-5′ and for the two olefinic protons *α*/*β* (Table 4), indicating structural modification near ring A. The large coupling constant $J_{H\alpha\text{-}H\beta}$ = 15.9 Hz indicated that the *E*-configuration at the *α*/*β* double bond has been retained in the metabolite. The signal of the proton (*δ* 5.02) at the anomeric C-1″ displays the coupling constant of $J_{H1''\text{-}H2''}$ = 7.8 Hz, typical of *β*-configuration. This signal also shows a reduced signal-to-noise ratio due to its proximity to the suppressed residual water signal. The ^{1}H NMR signal of H-5″ (*δ* 3.85) is overlapping with the 4′-methoxy signal (*δ* 3.85). The remaining signals of the *β*-glucuronide moiety were assigned by the COSY spectrum even if some signals overlapped. ^{13}C resonances were obtained from HSQC and HMBC spectra (Table 4). ^{13}C NMR chemical shifts of the quaternary C-2′ and the COOH carbon atom were not

Table 4. ^{1}H NMR Data (500 MHz, MeOH-d_4) of FKB and ^{1}H and ^{13}C NMR Data (500 MHz for ^{1}H and 125 MHz for ^{13}C, MeOH-d_4) of (*E*)-FKB-2′-*O*-glucuronide

	FKB	(*E*)-FKB-2′-*O*-glucuronide	
no.	^{1}H *δ* (m, int, *J* (Hz))	^{1}H *δ* (m, int, *J* (Hz))	^{13}C *δ*
1′			113.5
2′			nd
3′	6.12 (d, 1H, *J* = 2.3)	6.55 (d, 1H, *J* = 2.0)	95.3
4′			164.1
5′	6.10 (d, 1H, *J* = 2.3)	6.37 (d, 1H, *J* = 2.0)	93.8
6′			160.1
C=O			196.0
α	7.72 (d, 1H, *J* = 15.9)	7.09 (d, 1H, *J* = 15.9)	129.5
β	7.92 (d, 1H, *J* = 15.9)	7.42 (d, 1H, *J* = 15.9)	145.7
1			136.2
2/6	7.65 (m, 2H)	7.62 (m, 2H)	129.5
3/5	7.42 (m, 2H)	7.39 (m, 2H)	129.9
4			131.6
4′-OCH_3	3.95 (s, 3H)	3.85 (s, 3H)	55.8
6′-OCH_3	3.84 (s, 3H)	3.79 (s, 3H)	56.1
1″		5.02 (d, 1H, *J* = 7.8)	102.5
2″		3.38 (m, 1H)	74.6
3″		3.49 (m, 2H)	77.3
4″			73.3
5″		3.85 (overlap with OCH_3)	76.3
COOH			n.d.

Table 3. High-Resolution LC-MS Data of FKB Samples Using Positive and Negative Electrospray Ionization[a]

	detected metabolites of FKB					
		m/z $[M + H]^+$		m/z $[M - H]^-$		
	t_R (min)	found	calcd	found	calcd	M formula
FKB	6.26	285.1125	285.1121			$C_{17}H_{16}O_4$
phase I	4.48			255.0659	255.0663	$C_{15}H_{12}O_4$
	5.07	**301.1070**	**301.1071**	**299.0927**	**299.0925**	**$C_{17}H_{16}O_5$**
	5.17			269.0819	269.0819	$C_{16}H_{14}O_4$
phase II	**3.46**	**461.1445**	**461.1442**	**459.1297**	**459.1297**	**$C_{23}H_{24}O_{10}$**
phase I+II	2.81			475.1239	475.1246	$C_{23}H_{24}O_{11}$
	3.15			475.1239	475.1246	$C_{23}H_{24}O_{11}$
	3.46	**461.1441**	**461.1442**	**459.1293**	**459.1297**	**$C_{23}H_{24}O_{10}$**
	3.75	477.1388	477.1391	475.1241	475.1246	$C_{23}H_{24}O_{11}$
	3.87			475.1241	475.1246	$C_{23}H_{24}O_{11}$
	3.95			445.1123	445.1140	$C_{22}H_{22}O_{10}$
	5.07			299.0920	299.0925	$C_{17}H_{16}O_5$

[a]Major metabolites are written in bold. Corresponding mass spectra can be found in the SI.

DOI: 10.1021/acs.jafc.5b01858
J. Agric. Food Chem. 2015, 63, 6376−6385

detected (nd) because of the low signal-to-noise ratio of the HMBC spectrum. Again, signals of (*Z*)-FKB-2′-*O*-*β*-glucuronide (data not shown) were detected as a minor component accompanying the major (*E*)-form. A metabolism scheme of FKB is proposed in Figure 3.

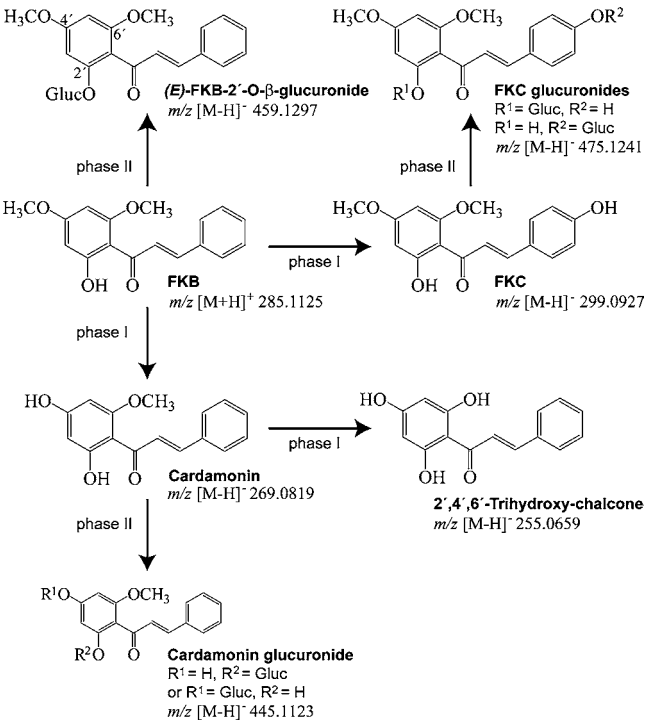

Figure 3. Proposed metabolic pathway of FKB by human liver microsomes. Structures of metabolites that could not be elucidated completely are depicted in smaller size.

Metabolites of FKC. LC-MS data of FKC metabolism samples revealed Heli (t_R = 4.03 min, m/z $[M - H]^-$ 285.0767) as the major phase I metabolite (Table 5). In addition, hydroxylation at undetermined positions generated two OH-FKC (t_R = 4.00 min, m/z $[M - H]^-$ 315.0872 and t_R = 4.52 min, m/z $[M - H]^-$ 315.871). Two major monoglucuronides (t_R = 2.81 min, m/z $[M - H]^-$ 475.1245, and t_R = 3.86 min, m/z $[M - H]^-$ 475.1248) and one minor glucuronide of FKC (t_R = 2.71 min, m/z $[M - H]^-$ 475.1244) were detected after phase II metabolism. Combined phase I and II metabolism resulted in the generation of one Heli-glucuronide (t_R = 3.03 min, m/z $[M - H]^-$ 461.1085) and three different glucuronides of OH-FKC (t_R = 2.83 min, m/z $[M - H]^-$ 491.1183; t_R = 3.18 min, m/z $[M - H]^-$ 491.1188; and t_R = 3.72 min, m/z $[M - H]^-$ 491.1187).

The two major monoglucuronides of FKC (t_R = 2.81 and 3.86 min) were identified by NMR spectroscopy as (*E*)-FKC-4-*O*-*β*-glucuronide and (*E*)-FKC-2′-*O*-*β*-glucuronide, and the minor glucuronide (t_R = 2.71 min) was identified as 5,7-dimethoxy-flavanone-4′-*O*-*β*-glucuronide (Figure 4). Comparing the ^{1}H NMR spectrum of FKC-4-*O*-*β*-glucuronide with that of the parent compound shows the slightly changed chemical shifts for H-3′ and H-5′ in ring A and the olefinic protons *α*/*β*. The chemical shifts of H-2/6 and H-3/5 changed strongly from *δ* 7.51 and 6.82 in the spectrum of FKC to *δ* 7.62 and 7.15 in the spectrum of the glucuronide, indicating a substitution in ring B (Table 6). The large coupling constant of $J_{H\alpha\text{-}H\beta}$ = 15.5 Hz indicated *E*-configuration of the *α*/*β* double bond. The signal of H-1″ (*δ* 5.05) shows a reduced signal-to-noise ratio due to its proximity to the suppressed residual water signal and a spin−spin coupling $J_{H1''\text{-}H2''}$ = 7.7 Hz characteristic of *β*-configuration at the anomeric center. The remaining signals of the *β*-glucuronide moiety were putatively assigned on the basis of ^{1}H NMR data matching with corresponding glucuronide signals of the other metabolites.

Different from FKC-4-*O*-*β*-glucuronide, comparison of the ^{1}H NMR spectrum of FKC-2′-*O*-*β*-glucuronide with that of the parent compound reveals only little chemical shift changes for H-2/6 and H-3/5 in ring B, whereas a strong change in the chemical shifts occurs for H-3′ and H-5′ and for the two olefinic protons *α*/*β* (Table 6). This finding resembles that of

Table 5. High-Resolution LC-MS Data of FKC Samples Using Positive and Negative Electrospray Ionization[a]

	detected metabolites of FKC					
		m/z $[M + H]^+$		m/z $[M - H]^-$		
	t_R (min)	found	calcd	found	calcd	M formula
FKC	5.07	301.1071	310.1070	299.0926	299.0925	$C_{17}H_{16}O_5$
phase I	4.00			315.0872	315.0874	$C_{17}H_{16}O_6$
	4.03	**287.0911**	**287.0914**	**285.0767**	**285.0768**	**$C_{16}H_{14}O_5$**
	4.52	317.1019	317.1019	315.0871	315.0874	$C_{17}H_{16}O_6$
phase II	2.71	477.1389	477.1391	475.1244	475.1246	$C_{23}H_{24}O_{11}$
	2.81	**477.1392**	**477.1391**	**475.1245**	**475.1246**	**$C_{23}H_{24}O_{11}$**
	3.86	**477.1395**	**477.1391**	**475.1248**	**475.1246**	**$C_{23}H_{24}O_{11}$**
phase I+II	2.71			475.1241	475.1241	$C_{23}H_{24}O_{11}$
	2.81	**477.1391**	**477.1391**	**475.1241**	**475.1241**	**$C_{23}H_{24}O_{11}$**
	2.83			491.1183	491.1195	$C_{23}H_{24}O_{12}$
	3.03	463.1234	463.1235	461.1085	461.1089	$C_{22}H_{22}O_{11}$
	3.18			491.1188	491.1195	$C_{23}H_{24}O_{12}$
	3.72			491.1187	491.1195	$C_{23}H_{24}O_{12}$
	3.86	**477.1390**	**477.1390**	**475.1241**	**475.1241**	**$C_{23}H_{24}O_{11}$**

[a]Major metabolites are written in bold. Corresponding mass spectra can be found in the SI.

DOI: 10.1021/acs.jafc.5b01858
J. Agric. Food Chem. 2015, 63, 6376−6385

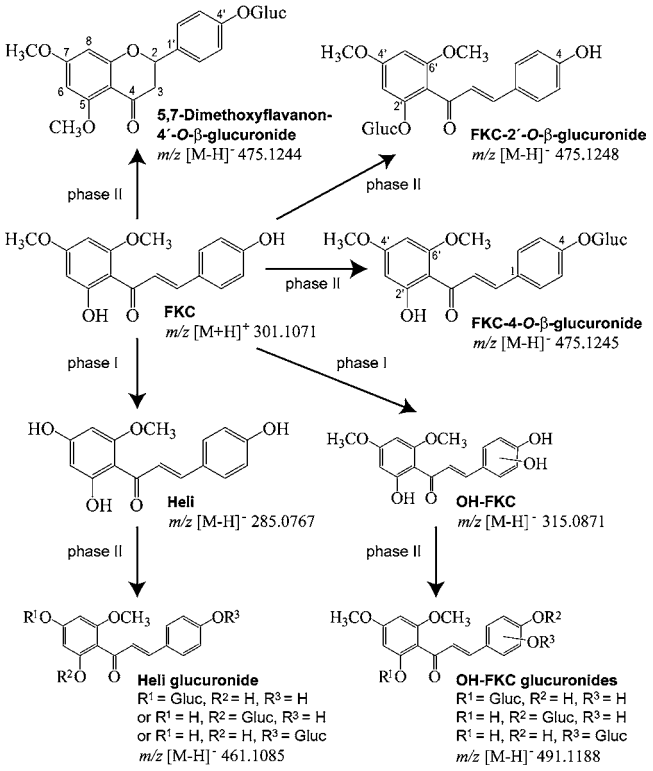

Figure 4. Proposed metabolic pathway of FKC by human liver microsomes. Structures of metabolites that could not be elucidated completely are depicted in smaller size.

major FKA- and FKB-2′-*O*-*β*-glucuronides described above. Thus, the substitution must have occurred in the 2′-position. Well resolved signals of the glucuronide moiety with very good signal-to-noise ratio were detected in the ^{1}H NMR spectrum of FKC-2′-*O*-*β*-glucuronide, allowing the precise determination of the J_{H-H} coupling constants. This included $J_{H1''\text{-}H2''}$ = 7.7 Hz, indicating *β*-configuration at the anomeric center of the sugar unit. In addition, the 2D NMR experiments (^{1}H,^{1}H COSY, HSQC, HMBC) enabled assignment of all ^{1}H and ^{13}C chemical shifts. An HMBC correlation between H-5″ (*δ* 3.97) and the ^{13}C signal at *δ* 171.9, a typical chemical shift for carboxylic carbons, proves the carbohydrate unit to be a glucuronide. The HMBC cross signal between H-1″ (*δ* 7.15) and C-2′ (*δ* 157.8) clearly proved the attachment of the carbohydrate to the 2′-*O*-position. HMBC also enabled assignment of ^{1}H resonances, such as those of the methoxy groups or protons H-3′ and H-5′, that would be otherwise potentially interchangeable.

For 5,7-dimethoxy-flavanone-4′-*O*-*β*-glucuronide, the disappearance of the signals of the olefinic *α*/*β* protons in the ^{1}H NMR spectrum together with the appearance of new resonances of H-2 (*δ* 5.43) and H-3 (*δ* 3.04/*δ* 2.72) enables the assignment of the aglycone skeleton as a flavanone (Figure 4). The molecule was fully identified by means of 1D and 2D NMR spectroscopic data. In addition to the aglycone signals (Table 7), the ^{1}H NMR spectrum displays signals of the glucuronide unit with some overlap of the signals of H-2″, H-3″, and H-4″ and a doublet of the *β*-configured H-1″ (*δ* 4.98; $J_{H1''\text{-}H2''}$ = 7.5 Hz). HMBC correlation between H-1″ and C-4′ (*δ* 158.9) assigned the *β*-glucuronide unit to the hydroxyl group in the para-position of ring B. Interestingly, the signals of H-3*β* (*δ* 2.72) appear as a two double doublets (dd) with integral values corresponding to 0.5 proton each. This could be explained by the assumption that the compound is a racemate, which consists of two diastereomers with opposite configuration at C-2. The signals of H-2 of the 2*R*- and the 2*S*-form as well as the signals of the H-3*α* at *δ* 3.04 are isochronic. Only the dd signals of H-3*β* appear at slightly different chemical shifts (Δ*δ* ∼ 0.01). If this assumption is correct, the 5,7-dimethoxy-flavanone-4′-*O*-*β*-glucuronide is probably generated by a nonenzymatic chemical reaction and therefore an artifact. The HRESIMS spectrum (positive ionization) confirmed the structure. In Figure 4 a metabolic pathway for FKC is proposed.

Table 6. ^{1}H NMR Data (500 MHz, MeOH-d_4) of FKC, FKC-4-*O*-glucuronide, and FKC-2′-*O*-glucuronide and ^{13}C NMR Data (125 MHz, MeOH-d_4) of FKC-2′-*O*-glucuronide

	FKC	FKC metabolites		
		(*E*)-FKC-4-*O*-glucuronide	(*E*)-FKC-2′-*O*-glucuronide	
no.	^{1}H *δ* (m, int, *J* (Hz))	^{1}H *δ* (m, int, *J* (Hz))	^{1}H *δ* (m, int, *J* (Hz))	^{13}C *δ*
1′				113.7
2′				157.8
3′	6.10 (d, 1H, *J* = 2.3)	6.12 (d, 1H, *J* = 2.3)	6.49 (d, 1H, *J* = 2.0)	95.1
4′				163.8
5′	6.09 (d, 1H, *J* = 2.3)	6.10 (d, 1H, *J* = 2.3)	6.38 (d, 1H, *J* = 2.0)	93.8
6′				160.0
C=O				196.4
α	7.71 (d, 1H, *J* = 15.6)	7.71 (d, 1H, *J* = 15.5)	6.89 (d, 1H, *J* = 16.0)	126.4
β	7.77 (d, 1H, *J* = 15.6)	7.84 (d, 1H, *J* = 15.5)	7.34 (d, 1H, *J* = 16.0)	147.4
1				127.2
2/6	7.51 (d, 2H, *J* = 8.7)	7.62 (d, 2H, *J* = 8.7)	7.48 (d, 2H, *J* = 8.9)	131.6
3/5	6.82 (d, 2H, *J* = 8.7)	7.15 (d, 2H, *J* = 8.7)	6.80 (d, 2H, *J* = 8.9)	116.6
4				161.5
4′-OCH_3	3.94 (s, 3H)	3.95 (s, 3H)	3.85 (s, 3H)	55.7
6′-OCH_3	3.84 (s, 3H)	3.85 (s, 3H)	3.78 (s, 3H)	56.1
1″		5.05 (d, 1H, *J* = 7.7)	5.05 (d, 1H, *J* = 7.7)	102.4
2″		3.52 (m, 2H)	3.37 (dd, 1H, *J* = 7.7, 9.1)	74.2
3″			3.46 (dd, 1H, *J* = 9.1, 9.1)	76.9
4″		3.65 (m)	3.56 (dd, 1H, *J* = 9.6, 9.1)	72.5
5″		3.93 (m)	3.97 (d, 1H *J* = 9.6)	76.3
COOH				171.9

Metabolites of Cardamonin. For additional information, also the chalcone cardamonin, which was found as a phase I metabolite of FKB, was subjected to phase I and II metabolism as well as combined phase I+II metabolism.

LC-MS data of cardamonin metabolism samples are depicted in Table 8. Three hydroxylated metabolites of cardamonin were found after phase I metabolism; one of them was identified as Heli (t_R = 4.03 min, *m*/*z* [M − H]$^-$ 285.0763). For the other two metabolites (t_R = 4.43 min, *m*/*z* [M − H]$^-$ 285.0763, and t_R = 4.52 min, *m*/*z* [M − H]$^-$ 285.0762), the exact positions for the OH-group could not be determined.

After phase II metabolism, three glucuronides of cardamonin (t_R = 2.67 min, *m*/*z* [M − H]$^-$ 445.1141; t_R = 3.01 min, *m*/*z* [M − H]$^-$ 445.1138; t_R = 3.95 min, *m*/*z* [M − H]$^-$ 445.1140)

DOI: 10.1021/acs.jafc.5b01858
J. Agric. Food Chem. 2015, 63, 6376−6385

Table 7. ^{1}H and ^{13}C NMR Data of 5,7-Dimethoxyflavanone-4′-*O*-glucuronide (500 MHz for ^{1}H and 125 MHz for ^{13}C, MeOH-d_4)

	5,7-dimethoxyflavanone-4′-*O*-glucuronide	
no.	^{1}H δ (m, int, J (Hz))	^{13}C δ
2	5.43 (dd, 1H, J = 12.8, 3.0)	79.9
3	3.04 (dd, 1H, J = 16.4, 12.8)	46.2
	2.72 (dd, 1H, J = 16.4, 3.0)[a]	
4		192.4
5		163.6
6	6.20 (d, 1H, J = 2.0)	93.7
7		168.3
8	6.22 (d, 1H, J = 2.0)	94.9
9		167.5
10		106.3
1′		134.2
2′/6′	7.44 (d, 2H, J = 8.7)	128.7
3′/5′	7.14 (d, 2H, J = 8.7)	117.8
4′		158.9
5- and 7-OCH$_3$	3.84 (s, 6H)	56.2
1″	4.98 (d, 1H, J = 7.5)	102.3
2″	3.51 (m, 2H)	74.6
3″		77.3
4″	3.59 (m, 1H)	73.1
5″	3.92 (d, 1H, J = 9.6)	76.3
COOH		173.5

[a]Two dd at δ 2.723 and 2.717 with identical coupling constants indicate (2*S*)- and (2*R*)-diastereomers.

were detected. As only two free OH-groups are available, a third corresponding mass suggests the presence or formation of isomers. Additionally to the cardamonin glucuronides, one glucuronide of OH-cardamonin (t_R = 3.58 min, m/z [M − H]$^-$ 461.1081) was found after combined metabolism. Figure 5 suggests a metabolic pathway of cardamonin.

DISCUSSION

In this study, we characterized the in vitro metabolism of FKA, FKB, FKC, and cardamonin using human liver microsomes. In phase I metabolism, demethylation in position C-4 or C-4′ and

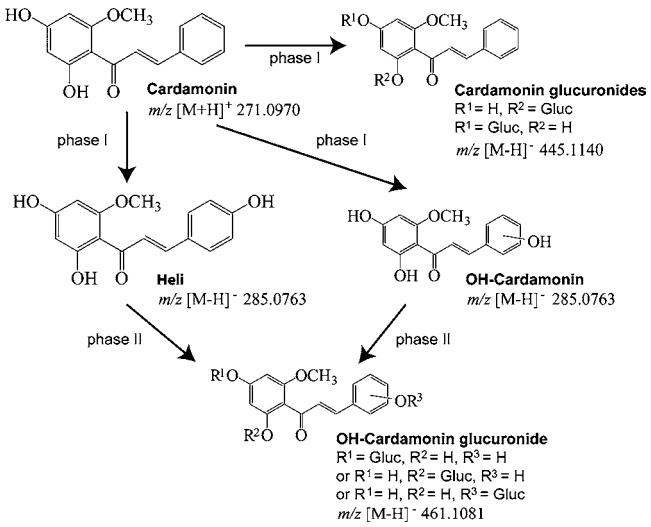

Figure 5. Proposed metabolic pathway of cardamonin by human liver microsomes. Structures of metabolites that could not be elucidated completely are depicted in smaller size.

hydroxylation predominantly in position C-4 occurred. Demethylation at C-4 on the B-ring of FKA as well as hydroxylation at C-4 of FKB leads to the formation of FKC, being the major phase I metabolite. Further demethylation of FKC at C-4′ on the A-ring generated Heli. Demethylation of FKB at C-4′ led to the generation of cardamonin and hydroxylation of cardamonin at C-4 to the formation of Heli. Moreover, other monohydroxylated minor metabolites of FKA and cardamonin were found, but the position of hydroxylation could not be determined by mass spectrometric methods.

He et al. investigated the CYP450-dependent metabolism of cardamonin previously.[33] They identified two monohydroxylated metabolites by MS fragmentation. The exact position of hydroxylation on the B-ring was not determined. However, the authors suggested C-4 being the most likely position. Kohno et al. already described this position as preferential for hydroxylation of chalcones.[34] According to this, in the study of He et al. 4-OH-cardamonin would correspond to Heli, which has also been found in our study. Furthermore, they suggested

Table 8. High-Resolution LC-MS Data of Cardamonin Samples Using Positive and Negative Electrospray Ionization[a]

	detected metabolites of cardamonin					
		m/z [M + H]$^+$		m/z [M − H]$^-$		
	t_R (min)	found	calcd	found	calcd	M formula
cardamonin	5.17	271.0970	271.0965	269.0820	269.0819	$C_{16}H_{14}O_4$
phase I	**4.03**	**287.0915**	**287.0914**	**285.0763**	**285.0768**	**$C_{16}H_{14}O_5$**
	4.43	287.0917	287.0914	285.0763	285.0768	$C_{16}H_{14}O_5$
	4.52	287.0917	287.0914	285.0762	285.0768	$C_{16}H_{14}O_5$
phase II	2.67	447.1286	447.1286	445.1141	445.1140	$C_{22}H_{22}O_{10}$
	3.01	447.1282	447.1286	445.1138	445.1140	$C_{22}H_{22}O_{10}$
	3.95	**447.1287**	**447.1286**	**445.1140**	**445.1140**	**$C_{22}H_{22}O_{10}$**
phase I+II	2.67	447.1284	447.1284	445.1135	445.1140	$C_{22}H_{22}O_{10}$
	3.00	447.1283	447.1283	445.1136	445.1140	$C_{22}H_{22}O_{10}$
	3.58	463.1232	463.1235	461.1081	461.1089	$C_{22}H_{22}O_{11}$
	3.95	**447.1287**	**447.1286**	**445.1135**	**445.1140**	**$C_{22}H_{22}O_{10}$**

[a]Major metabolites are written in bold. Corresponding mass spectra can be found in the SI.

DOI: 10.1021/acs.jafc.5b01858
J. Agric. Food Chem. 2015, 63, 6376−6385

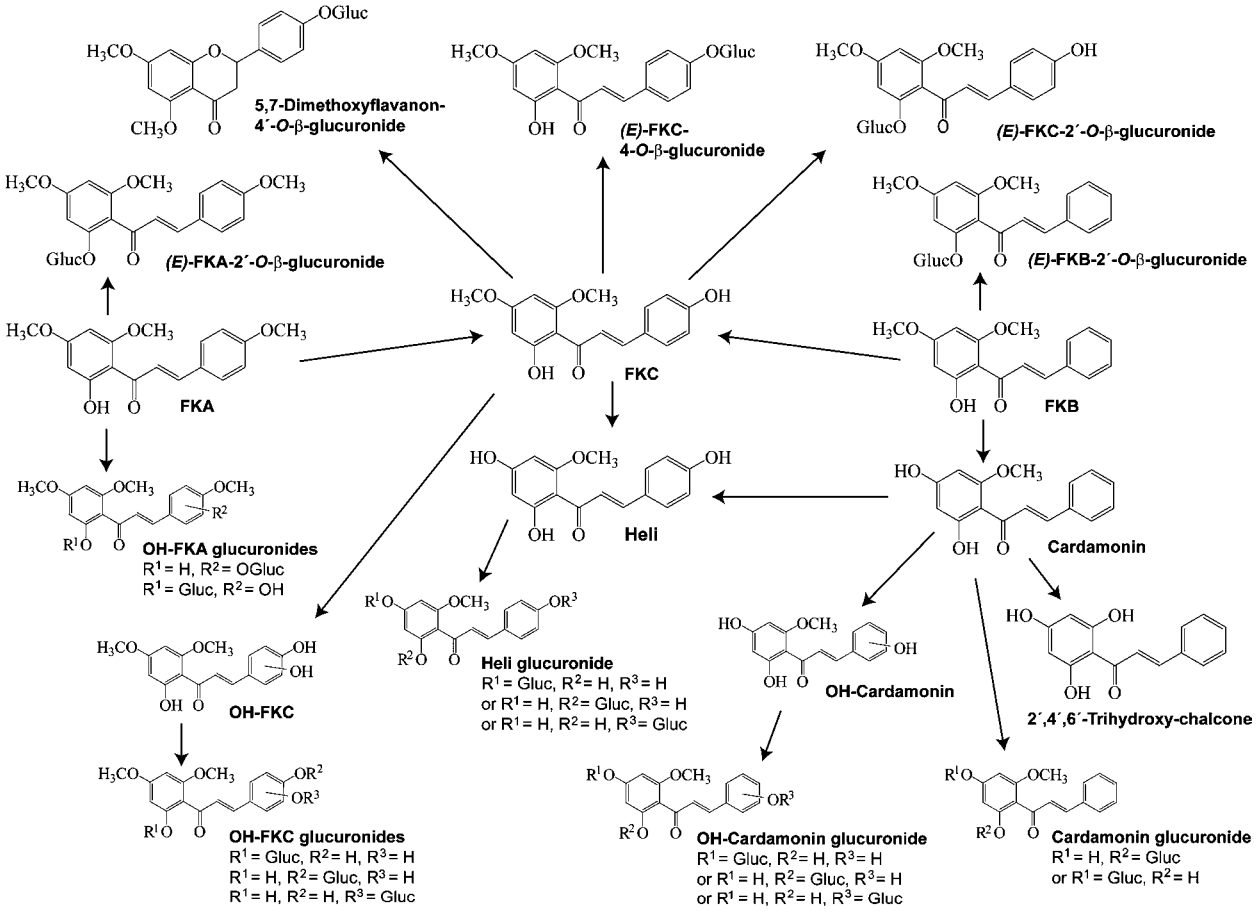

Figure 6. Proposed combined metabolism scheme for FKA, FKB, FKC, and cardamonin. Structures of metabolites that could not be elucidated completely are depicted in smaller size.

hydroxylation in the *β*-position of the unsaturated ketone, which might correspond to another hydroxylated derivative (t_R = 4.43 or 4.52 min) of our study. In contrast to our findings, no third hydroxylated metabolite of cardamonin was described.[33]

The compounds were even more extensively metabolized by microsomal UDP-glucuronosyl transferases in the presence of UDPGA in phase II samples. Corresponding monoglucuronides were detected for all test compounds as the major metabolites of phase II and combined metabolism. The structures of the major flavokawain glucuronides were elucidated by NMR.

After glucuronidation, two metabolite masses corresponding to FKA-glucuronides were detected, despite only one available OH-group at C-2′ of FKA. This can be explained by the occurrence of the major *E*- and the minor *Z*-isomer. For both, ^{1}H NMR signals were detected. The occurrence of three glucuronides of cardamonin, despite only two free OH groups, also suggests the formation of cardamonin *E*/*Z*-isomers.

In addition to the 2′-*O*- and 4-*O*-chalcone-mono-*β*-glucuronides of FKC, also the corresponding 5,7-dimethoxyflavanone-4′-*O*-*β*-glucuronide was identified by LC-NMR. The flavanone-glucuronide is most likely formed by a nonenzymatic chemical reaction and might be an artifact similar to the (*Z*)-isoforms of FKA, FKB, and cardamonin metabolites.

As FKC is a major phase I metabolite of FKA and FKB and Heli is a metabolite of FKC as well as of the FKB metabolite cardamonin, the metabolisms of all three flavokawains (and cardamonin) are closely linked to each other. Therefore, we propose a combined metabolism pathway for the flavokawains in Figure 6.

Although the metabolic conversions occurring in our in vitro system are very likely to also occur in vivo, it is likewise almost certain that they constitute only a part of the entire metabolization that is happening in the body. Therefore, the extent of formation of conjugated metabolites may even be underestimated by the use of microsomes, as phase II reactions in this system are limited to glucuronidation reactions only. As a result, the absolute amount of conjugated metabolites in vivo may be even higher than what we observed in vitro. To include all possible phase II metabolites, liver cell models and in vivo metabolism systems could be used for an additional metabolism analysis. However, the fact that glucuronides dominate over phase I metabolites emphasizes the important role of conjugated chalcone metabolites as presumable in vivo active principle. This was likewise shown for various flavonoids and chalcones, for example, xanthohumol.[35]

Nevertheless, as far as the biological activity or toxicity of chalcones is concerned, to date conjugated metabolites are not routinely included in testing.

Looking ahead, assessment of toxicity and pharmacological characterization of flavokawain glucuronides and other phase II metabolites is mandatory and will be conducted to evaluate their contribution and relevance for the bioactivity of the parent compounds.

DOI: 10.1021/acs.jafc.5b01858
J. Agric. Food Chem. 2015, 63, 6376−6385

■ ASSOCIATED CONTENT

Supporting Information

Corresponding MS and NMR spectra of the determined metabolites. The Supporting Information is available free of charge on the ACS Publications website at DOI: 10.1021/acs.jafc.5b01858.

■ AUTHOR INFORMATION

Corresponding Author

*(B.K.) Phone: +49 941 9434494. Fax: +49 941 9434990. E-mail: birgit1.kraus@chemie.uni-regensburg.de.

Notes

The authors declare no competing financial interest.

■ ACKNOWLEDGMENTS

We thank Jörg Heilmann (Institute of Pharmacy, University of Regensburg) for fruitful discussions and scientific support.

■ ABBREVIATIONS USED

Ala, alamethicin; EtOAc, ethyl acetate; FKA, flavokawain A; FKB, flavokawain B; FKC, flavokawain C; dd, double doublets; G6P, glucose-6-phosphate; G6PDH, glucose-6-phosphate dehydrogenase; Gluc, glucuronic acid; Heli, helichrysetin; NMR, nuclear magnetic resonance spectroscopy; LC-HRESIMS, liquid chromatography−high-resolution electrospray ionization mass spectrometry; MeCN, acetonitrile; NADP, nicotinamide adenine dinucleotide phosphate; NF-κB, nuclear factor kappa-B; t_R, retention time; UDP, uridine diphosphate; UDPGA, uridine 5′-diphosphoglucuronic acid

■ REFERENCES

(1) Gerhäuser, C.; Alt, A.; Heiss, E.; Gamal-Eldeen, A.; Klimo, K.; Knauft, J.; Neumann, I.; Scherf, H.-R.; Frank, N.; Bartsch, H.; et al. Cancer Chemopreventive Activity of Xanthohumol, A Natural Product Derived from Hop. *Mol. Cancer Ther.* **2002**, *1*, 959−969.

(2) Furusawa, J.; Funakoshi-Tago, M.; Mashino, T.; Tago, K.; Inoue, H.; Sonoda, Y.; Kasahara, T. *Glycyrrhiza inflata*-Derived Chalcones, Licochalcone A, Licochalcone B and Licochalcone D, Inhibit Phosphorylation of NF-κB p65 in LPS Signaling Pathway. *Int. Immunopharmacol.* **2009**, *9*, 499−507.

(3) Freischmidt, A.; Jürgenliemk, G.; Kraus, B.; Okpanyi, S. N.; Müller, J.; Kelber, O.; Weiser, D.; Heilmann, J. Contribution of Flavonoids and Catechol to the Reduction of ICAM-1 Expression in Endothelial Cells by a Standardised Willow Bark Extract. *Phytomedicine* **2012**, *19*, 245−252.

(4) Gaucher, M.; Dugé de Bernonville, T.; Lohou, D.; Guyot, S.; Guillemette, T.; Brisset, M.-N.; Dat, J. F. Histolocalization and Physico-Chemical Characterization of Dihydrochalcones: Insight into the Role of Apple Major Flavonoids. *Phytochemistry* **2013**, *90*, 78−89.

(5) Iwase, Y.; Takahashi, M.; Takemura, Y.; Ju-ichi, M.; Ito, C.; Furukawa, H.; Yano, M. Isolation and Identification of Two New Flavanones and a Chalcone from *Citrus kinokuni*. *Chem. Pharm. Bull.* **2001**, *49*, 1356−1358.

(6) Yamamoto, T.; Yoshimura, M.; Yamaguchi, F.; Kouchi, T.; Tsuji, R.; Saito, M.; Obata, A.; Kikuchi, M. Anti-Allergic Activity of Naringenin Chalcone from a Tomato Skin Extract. *Biosci., Biotechnol., Biochem.* **2004**, *68*, 1706−1711.

(7) Vogel, S.; Heilmann, J. Synthesis, Cytotoxicity, and Antioxidative Activity of Minor Prenylated Chalcones from *Humulus lupulus*. *J. Nat. Prod.* **2008**, *71*, 1237−1241.

(8) Vogel, S.; Ohmayer, S.; Brunner, G.; Heilmann, J. Natural and Non-Natural Prenylated Chalcones: Synthesis, Cytotoxicity and Anti-Oxidative Activity. *Bioorg. Med. Chem.* **2008**, *16*, 4286−4293.

(9) Ahmad, S.; Israf, D. A.; Lajis, N. H.; Shaari, K.; Mohamed, H.; Wahab, A. A.; Ariffin, K. T.; Hoo, W. Y.; Aziz, N. A.; Kadir, A. A.; et al. Cardamonin, Inhibits pro-Inflammatory Mediators in Activated RAW 264.7 Cells and Whole Blood. *Eur. J. Pharmacol.* **2006**, *538*, 188−194.

(10) Lee, I.-S.; Lim, J.; Gal, J.; Kang, J. C.; Kim, H. J.; Kang, B. Y.; Choi, H. J. Anti-Inflammatory Activity of Xanthohumol Involves Heme Oxygenase-1 Induction via NRF2-ARE Signaling in Microglial BV2 Cells. *Neurochem. Int.* **2011**, *58*, 153−160.

(11) Yadav, V. R.; Prasad, S.; Sung, B.; Aggarwal, B. B. The Role of Chalcones in Suppression of NF-κB-Mediated Inflammation and Cancer. *Int. Immunopharmacol.* **2011**, *11*, 295−309.

(12) Orlikova, B.; Tasdemir, D.; Golais, F.; Dicato, M.; Diederich, M. Dietary Chalcones with Chemopreventive and Chemotherapeutic Potential. *Genes Nutr.* **2011**, *6*, 125−147.

(13) Winter, E.; Locatelli, C.; Di Pietro, A.; Creczynski-Pasa, T. B. Recent Trends of Chalcones Potentialities as Antiproliferative and Antiresistance Agents. *Anticancer Agents Med. Chem.* **2015**, *15*, 592−604.

(14) Modzelewska, A.; Pettit, C.; Achanta, G.; Davidson, N. E.; Huang, P.; Khan, S. R. Anticancer Activities of Novel Chalcone and Bis-Chalcone Derivatives. *Bioorg. Med. Chem.* **2006**, *14*, 3491−3495.

(15) Gerhäuser, C. Broad Spectrum Anti-Infective Potential of Xanthohumol from Hop (*Humulus lupulus* L.) in Comparison with Activities of Other Hop Constituents and Xanthohumol Metabolites. *Mol. Nutr. Food Res.* **2005**, *49*, 827−831.

(16) Nowakowska, Z. A Review of Anti-Infective and Anti-Inflammatory Chalcones. *Eur. J. Med. Chem.* **2007**, *42*, 125−137.

(17) Batovska, D. I.; Todorova, I. T. Trends in Utilization of the Pharmacological Potential of Chalcones. *Curr. Clin. Pharmacol.* **2010**, *5*, 1−29.

(18) Meissner, O.; Häberlein, H. HPLC Analysis of Flavokavins and Kavapyrones from *Piper methysticum* Forst. *J. Chromatogr. B: Anal. Technol. Biomed. Life Sci.* **2005**, *826*, 46−49.

(19) He, X. G.; Lin, L. Z.; Lian, L. Z. Electrospray High Performance Liquid Chromatography-Mass Spectrometry in Phytochemical Analysis of Kava (*Piper methysticum*) Extract. *Planta Med.* **1997**, *63*, 70−74.

(20) Singh, Y. N. Kava: An Overview. *J. Ethnopharmacol.* **1992**, *37*, 13−45.

(21) Bilia, A. R.; Gallon, S.; Vincieri, F. F. Kava-Kava and Anxiety: Growing Knowledge about the Efficacy and Safety. *Life Sci.* **2002**, *70*, 2581−2597.

(22) Whitton, P. A.; Lau, A.; Salisbury, A.; Whitehouse, J.; Evans, C. S. Kava Lactones and the Kava-Kava Controversy. *Phytochemistry* **2003**, *64*, 673−679.

(23) Olsen, L. R.; Grillo, M. P.; Skonberg, C. Constituents in Kava Extracts Potentially Involved in Hepatotoxicity: A Review. *Chem. Res. Toxicol.* **2011**, *24*, 992−1002.

(24) Rowe, A.; Zhang, L. Y.; Ramzan, I. Toxicokinetics of Kava. *Adv. Pharmacol. Sci.* **2011**, *2011*, 326724.

(25) Kraft, K. Verwaltungsgericht Köln Kippt Das Kava-Verbot. *Z. Phytother.* **2014**, *35*, 186−189.

(26) Zi, X.; Simoneau, A. R.; Flavokawain, A. Flavokawain A, a Novel Chalcone from Kava Extract, Induces Apoptosis in Bladder Cancer Cells by Involvement of Bax Protein-Dependent and Mitochondria-Dependent Apoptotic Pathway and Suppresses Tumor Growth in Mice. *Cancer Res.* **2005**, *65*, 3479−3486.

(27) Tang, Y.; Simoneau, A. R.; Xie, J.; Shahandeh, B.; Zi, X. Effects of the Kava Chalcone Flavokawain A Differ in Bladder Cancer Cells with Wild-Type versus Mutant p53. *Cancer Prev. Res.* **2008**, *1*, 439−451.

(28) Lin, C.-T.; Senthil Kumar, K. J.; Tseng, Y.-H.; Wang, Z.-J.; Pan, M.-Y.; Xiao, J.-H.; Chien, S.-C.; Wang, S.-Y. Anti-Inflammatory Activity of Flavokawain B from *Alpinia pricei hayata*. *J. Agric. Food Chem.* **2009**, *57*, 6060−6065.

(29) Kwon, D.-J.; Ju, S. M.; Youn, G. S.; Choi, S. Y.; Park, J. Suppression of iNOS and COX-2 Expression by Flavokawain A via Blockade of NF-κB and AP-1 Activation in RAW 264.7 Macrophages. *Food Chem. Toxicol.* **2013**, *58*, 479−486.

(30) Mohamad, A. S.; Akhtar, M. N.; Khalivulla, S. I.; Perimal, E. K.; Khalid, M. H.; Ong, H. M.; Zareen, S.; Akira, A.; Israf, D. A.; Lajis, N.; et al. Possible Participation of Nitric Oxide/cyclic Guanosine

DOI: 10.1021/acs.jafc.5b01858
J. Agric. Food Chem. 2015, 63, 6376−6385

Monophosphate/protein Kinase C/ATP-Sensitive K(+) Channels Pathway in the Systemic Antinociception of Flavokawin B. *Basic Clin. Pharmacol. Toxicol.* **2011**, *108*, 400−405.
(31) Mohamad, A. S.; Akhtar, M. N.; Zakaria, Z. A.; Perimal, E. K.; Khalid, S.; Mohd, P. A.; Khalid, M. H.; Israf, D. A.; Lajis, N. H.; Sulaiman, M. R. Antinociceptive Activity of a Synthetic Chalcone, Flavokawin B on Chemical and Thermal Models of Nociception in Mice. *Eur. J. Pharmacol.* **2010**, *647*, 103−109.
(32) Yoshimoto, K.; Itatani, Y.; Shibata, K.; Tsuda, Y. Syntheses and ^{1}H- and ^{13}C-Nuclear Magnetic Resonance Spectra of All Positional Isomers of Methyl Mono-*O*-Tetradecanoyl-α- and β-D-Glucopyranosides. *Chem. Pharm. Bull.* **1980**, *28*, 208−219.
(33) He, Y.-Q.; Yang, L.; Liu, Y.; Zhang, J.-W.; Tang, J.; Su, J.; Li, Y.-Y.; Lu, Y.-L.; Wang, C.-H.; Yang, L.; et al. Characterization of Cardamonin Metabolism by P450 in Different Species via HPLC-ESI-Ion Trap and UPLC-ESI-Quadrupole Mass Spectrometry. *Acta Pharmacol. Sin.* **2009**, *30*, 1462−1470.
(34) Kohno, Y.; Kitamura, S.; Sanoh, S.; Sugihara, K.; Fujimoto, N.; Ohta, S. Metabolism of the α,β-Unsaturated Ketones, Chalcone and *trans*-4-Phenyl-3-buten-2-one, by Rat Liver Microsomes and Estrogenic Activity of the Metabolites. *Drug Metab. Dispos.* **2005**, *33*, 1115−1123.
(35) Jirásko, R.; Holcapek, M.; Vrublová, E.; Ulrichová, J.; Simánek, V. Identification of New Phase II Metabolites of Xanthohumol in Rat in Vivo Biotransformation of Hop Extracts Using High-Performance Liquid Chromatography Electrospray Ionization Tandem Mass Spectrometry. *J. Chromatogr A* **2010**, *1217*, 4100−4108.

DOI: 10.1021/acs.jafc.5b01858
J. Agric. Food Chem. 2015, 63, 6376−6385

(median lethal dose) was also evaluated to test the safety of the new formulation. In addition, we determined the pharmacokinetics and tissue distribution of SME-CA in comparison with CA suspension in rats after a single intravenous (iv) dose.

MATERIALS AND METHODS

Chemicals. CA (99.0% purity) was supplied by Yuancheng Pharmaceutical Co., Ltd. Acetonitrile (HPLC grade) was obtained from Honeywell (Muskegon, MI, USA). All other reagents were of analytical grade. Propiophenone was used as the internal standard (IS). Egg lecithin (Lipoid E80, 80% purity) was supplied by LIPOID Co. (Ludwigshafen, Germany). Soybean oil was purchased from AVIC (Tieling) Pharmaceutical Co., Ltd. (Tieling, China). Glycerol was purchased from Jiahe Biological Technology Co., Ltd. (Shantou, China). Sodium oleate was purchased from Xi'an Libang Pharmaceutical Co., Ltd. (Xi'an, China).

Animals and Cell Lines. Male Sprague−Dawley rats weighing 225−275 g and KM mice weighing 20−25 g were supplied by the Experimental Animal Research Center, Fourth Military Medical University (Xi'an, China). They were kept separately in an individually ventilated cage (IVC) system and fed standard laboratory food and water ad libitum for 5 days before the experiments. All rats were fasted (except for water) overnight and prepared for pharmacokinetic and toxicological study. Experimental procedures involving animals were reviewed and approved by the Institutional Animal Care and Use Committee of the Fourth Military Medical University (Approval 2014-1114-R).

The Eca-109, Hct-116, HepG2, HT-29, A549, Mkn-45, PANC-1, HeLa, SGC-7901, SW 620, and Tca-8113 cell lines were obtained from Xi'an Cell Engineering Center (Xi'an, China). Eca-109, HepG2, Mkn-45, HeLa, SGC-7901, SW 620, and Tca-8113 were cultured at a density of 5×10^4 cells/mL in RPMI 1640 medium; A549 and Panc-1 were cultured in DMEM; Hct-116 and HT-29 were cultured in Myco's medium. All of the cell lines were supplemented with 10% fetal bovine serum, penicillin (100 U/mL), and streptomycin (100 μg/mL) and incubated at 37 °C in a 5% CO_2 humidified atmosphere.

Preparation of SME-CA. SME-CA was prepared by using the following method. Step 1, preparation of the oil phase: 10% (w/v) soybean oil and 0.1% (w/v) vitamin E together with 1.2% (w/v) egg lecithin were heated until the egg lecithin was totally dissolved. Then, 0.5% CA was added into the mixture. Step 2, preparation of the water phase: 85.5% (w/v) water, 2.5% (w/v) glycerinum, and 0.2% sodium oleate were added in order. After that, the mixture was heated to 40 °C until all of the ingredients were dissolved. Step 3, preparation of the pre-emulsion: the oil phase was added into the water phase and homogenized with a high shear dispersing emulsifier (FLUKO FA25, FLUKO Co., Germany) under the condition of 2000 rpm shear force and 55 °C. After 10 min of shearing, a crude emulsion formed and was rapidly cooled to 15−30 °C. Fourth and final step, preparation of emulsion: the colostrum was homogenized with a high-pressure homogenizer (PandaPlus1000; Niro Soavi Co., Italy) at 800 bar under a pressure of 100 bar and then increased to 1280 bar eight times. Consequently, the SME-CA was successfully prepared with 25.6 mg/mL CA loaded into the emulsion.

Pharmacokinetic Study. *Intravenous Administration Study.* In the pharmacokinetic study CA was dissolved in solution with 1:1:8 (polyoxyethylenated castor oil/ethanol/water, by vol). A group of SD rats (n = 5, each group) was intravenously administered 20 mg/kg CA, and blood was collected at 2, 5, 10, 15, 30, 60, 90, 120, and 180 min. These time plots were selected on the basis of previous studies of CA. The blood samples were centrifuged at 3500g, and after 15 min, 200 μL of supernatant was extracted and stored at −80 °C until analysis.

Tissue Distribution Study. SD rats were randomly assigned to two groups (n = 6 per group). These two groups were intravenously administered a single dose of 20 mg/kg CA and SME-CA, respectively. Major tissue samples, such as heart, liver, spleen, lung, kidney, and brain, were collected at 15, 45, and 90 min after administration. Tissue samples were quickly rinsed with saline solution (0.9%) to remove the blood and content. After cleaning, samples were blotted by filter paper and weighed and then homogenized in a 2-fold weight saline solution (0.9%) for all tissue samples by a T10 Basic homogenizer (Staufen, Germany). Then the obtained homogenates were stored at −80 °C until analysis.

Sample Preparation. A liquid−liquid preparation method was utilized to extract target compounds and eliminate the interference of endogenous protein. We found that acetonitrile enhanced the sensitivity and selectivity, especially in minimizing endogenous interference and improving extraction recovery. Consequently, we chose acetonitrile as the optimized solvent for sample preparation. Fifty microliters of propiophenone as internal standard solution (2500 ng/mL) and 500 μL acetonitrile were sequentially added in every 200 μL of homogenate and plasma samples. Then, the solution was thoroughly vortex-mixed for 120 s. After centrifugation at 12000g for 10 min, 1 μL of supernatant was injected into GC-MS for analysis.

GC-MS Analysis. Chromatography was performed on a Trace ISQ Ultra (Thermo Fisher Scientific, Waltham, MA, USA) system combined with a Triplus atuosampler and injector. A DB-5 ms capillary column (30 m × 0.25 mm, 0.25 μm thickness, Agilent Technologies, Santa Clara, CA, USA) was used for separation. The initial oven temperature was set at 50 °C, held for 1 min, then increased to 160 °C at 10 °C/min for 1 min, then increased to 280 at 20 °C/min, and held at the final temperature for 1 min. High-purity helium was used as carrier gas at a constant flow rate of 1.0 mL/min.

The transfer line and ion source of the MS system were both operated at 250 °C. MS analysis was operated in the selected ion monitoring (SIM) mode with the ionization energy being 70 eV. Quantifying ion masses (m/z 131, 105, and 92) were selected for simultaneously investigating IS, CA, methyl cinnamate, and cinnamyl alcohol. The mass spectra of all analytes were analyzed by the NIST library (Shimadzu, Kyoto, Japan) and are shown in the Supporting Information.

Pharmacokinetics and Statistical Analysis. All of the pharmacokinetic data of CA were processed by the DAS 2.0 software supplied by the Anhui Provincial Center for Drug Clinical Evaluation. The different pharmacokinetic features of CA and SME-CA were assessed using the following parameters: area under the curve to termination time (AUC_{0-t}), mean residence time (MRT_{0-t}), half-life ($t_{1/2}$), time at maximum plasma concentration (t_{max}), maximum plasma concentration (C_{max}), plasma clearance (CLz), and volume of distribution (Vz). The data are presented as the mean ± SD, and Student's t test was used to analyze the difference between groups. A P value of <0.05 was considered to be statistically significant.

Antitumor Efficacy. The antitumor efficacy was determined using the MTT assay. All of the cell lines were seeded at a density of 1×10^5 cells/mL in 96-well plates at 37 °C with 5% (v/v) CO_2 for 24 h. After that, 10 μL of different concentrations of CA and SME-CA was added to test the cell viability. After 12 h of incubation, to each well was added 30 μL of MTT and incubated for 4 h. Then the supernatants were discarded, and 150 μL of dimethyl sulfoxide was added to each well to dissolve formazan crystals. The absorbance of formazan crystals was detected and quantified at 570 nm by a microplate reader (Bio-Rad 680, Hercules, CA, USA). The percentage of growth inhibition and the IC_{50} were estimated from a dose response curve. Averages from six replicate wells were used for each sample and control.

Acute Toxicity. The in vivo toxicity of the CA was evaluated using acute toxicity, which is usually expressed as LD_{50} (medium lethal concentration). One hundred KM mice (half males and half females) were randomly divided into 10 groups (n = 10). In the acute toxicity study CA was dissolved in solution with 1:1:8 (polyoxyethylenated castor oil/ethanol/water, by vol). Five groups received a single intravenous injection of CA of 96.0, 84.5, 74.3, 65.4, or 57.6 mg/kg. The other five groups received a single intravenous injection of SME-CA of 152.9, 143.3, 133.7, 124.2, or 114.7 mg/kg. After the treatment, the general behavior and death rate were surveyed for 3 h. For the dead mice, general organs were anatomized for macroscopic observation. Observation was continued for 14 days for behavioral changes and signs of toxicity or death.

DOI: 10.1021/acs.jafc.5b01883
J. Agric. Food Chem. 2015, 63, 6386−6392

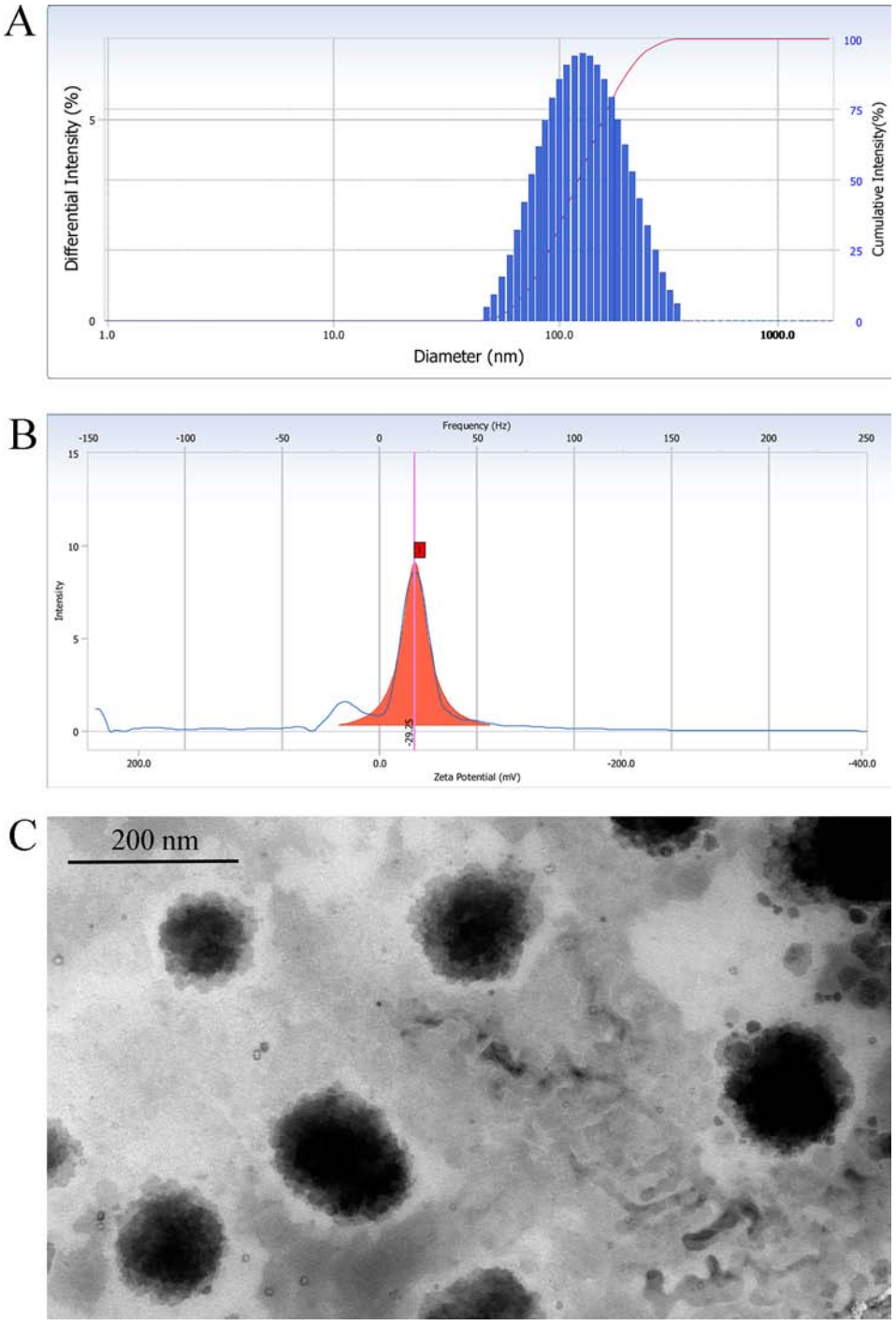

Figure 1. Particle size distribution (A), zeta potential (B), and transmission electron microscopic images of the SME-CA.

RESULTS AND DISCUSSION

Characterization of SME-CA. Previous studies found the size of SME-CA depended on the structure and the concentration of CA; other influential factors including molecular weight, electrical charge, and hydrophobicity of the polymers should also be considered.[24] Among them, the electrostatic properties are very important for emulsion stability as they can reduce or eliminate the influence of flocculation, enhancing the emulsion stability. Panels A and B of Figure 1 show the particle size distribution and zeta potential of the emulsion, measured by dynamic light scattering (DelsaNano Zeta, Beckman Coulter, USA), were 130 ± 5.92 nm and −25.7 ± 6.00 mv, respectively. Encapsulation efficiency was measured by HPLC. In Figure 1C, further morphology confirmation of particle size was performed by using a transmission electron microscope (Tecnai G2, FEI Co., Hillsboro, OR, USA), which demonstrated that the droplet diameter is around 130 ± 5.92 nm.

Long-Term Stability of SME-CA. Because the storage condition may affect the stability of SME-CA, resulting in collapse of membranes and release of encapsulated materials, the stability study was carried out. The particle size, zeta potential, pH value, and encapsulation efficiency of SME-CA were evaluated after 12 months to estimate the stability. The

DOI: 10.1021/acs.jafc.5b01883
J. Agric. Food Chem. 2015, 63, 6386−6392

results showed (Table 1) that SME-CA could maintain its characteristics without significant changes in particle size, zeta potential, pH value, and encapsulation efficiency after 12 months of storage at room temperature.

Table 1. Results of the Long-Term Stability Test for SME-CA (Mean ± SD, n = 3)

characterization of SME-CA	0 days	storage at room temperature for 12 months
appearance	milk white	milk white
particle size distribution (nm)	130 ± 5.92	135 ± 8.74
pH	8.32 ± 0.12	8.11 ± 0.09
zeta potential (mv)	−25.7 ± 6.00	−24.3 ± 7.81
encapsulation efficiency (%)	99.5 ± 0.25	99.4 ± 0.17

Antitumor Efficacy. The MTT assay showed a dose-dependent decrease in cell viability. As shown in Table 2, after 12 h of treatment, a significant decrease in the number of viable cells was observed in the cancer cell lines. The viability of most cell lines showed more reduction when added in SME-CA than in CA, whereas HT-29 and Eca-109 appeared reduction only with a high concentration of both SME-CA and CA. Among all of the results, HeLa and A549 showed relatively higher sensitivity to SME-CA, with the IC_{50} values reaching 0.003 and 0.001 mmol/L, respectively. The IC_{50} of CA was comparatively higher at the concentration of 0.024 mmol/L to HeLa and 0.011 mmol/L to A549. A similar study also demonstrated the antitumor activity can be improved by using a new formulation.[25] CA was also proved be effective in cervical cancer and lung cancer. Further exploration by using SME-CA should also be carried out.[26,27]

Table 2. Effects of CA and SME-CA on the Growth of 11 Kinds of Cancer Cells

	IC_{50} (mmol/L)	
tumor strain	CA	SME-CA
Eca-109	0.985	0.853
Hct-116	0.100	0.110
HepG-2	0.041	0.078
HT-29	1.73	0.867
A549	0.011	0.001
Mkn-45	0.057	0.070
PANC-1	0.321	0.118
HeLa	0.024	0.003
SGC-7901	0.022	0.067
SW 620	0.512	0.278
Tca-8113	0.328	0.272

Acute Toxicity. The results of the acute intoxication study after a single intravenous injection to KM mice were calculated; the LD_{50} values of CA and SME-CA were 74.8 and 125 mg/kg, respectively. Compared with the former formulation, there was a significant optimization in the acute toxicity by using SME-CA. This was mainly because the drug was loaded in a lipid emulsion vehicle, which controlled CA released into blood. Direct and severe irritation was avoided, which makes the body more tolerable to the high dose SME-CA. The main organs of dead mice were anatomized; general performance and macroscopic observation showed no special pathological changes. After 14 days, the behavior of living mice was normal without any changes.

Pharmacokinetic Study. The aim of the pharmacokinetic study was to investigate the different plasma parameters of CA and SME-CA including quantifying the concentration of CA and its metabolites in rats up to 3 h after iv administration. To compare the concentration of CA and its metabolites, the mean plasma concentration−time profiles for CA and SME-CA are shown in Figure 2. Figure 2A shows the AUC_{0-t} of SME-CA was significantly higher than that of CA (589 ± 59.2 vs 375 ± 83.5 ng h/L, $P < 0.01$). The mean peak plasma concentration of CA was 547 ± 142 ng/mL at 2 min after iv injection, whereas, in the case of SME-CA, a significantly higher peak plasma level

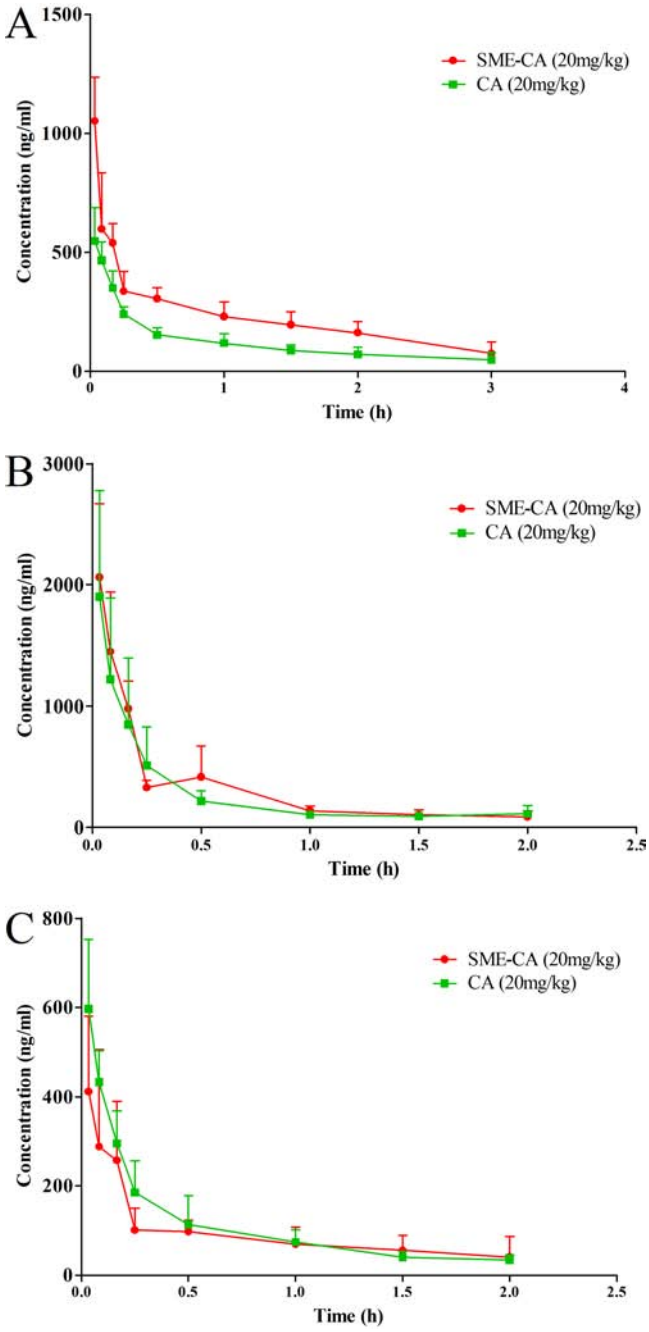

Figure 2. Compared mean plasma concentration−time profile of cinnamaldehyde (A), cinnamyl alcohol (B), and methyl cinamate (C) in rats after a single intravenous administration of SME-CA and CA of 20 mg/kg (mean ± SD, n = 5).

DOI: 10.1021/acs.jafc.5b01883
J. Agric. Food Chem. 2015, 63, 6386−6392

Table 3. Comparison of Main Pharmacokinetic Parameters for SME-CA and CA after 20 mg/kg Intravenous Injection (Mean ± SD, n = 5)

pharmacokinetic parameter[a]		SME-CA	CA	SME-cinnamyl alcohol	cinnamyl alcohol	SME-methyl cinnamate	methyl cinnamate
AUC_{0-t}	ng h/L	589 ± 59.2	375 ± 83.5	632 ± 138	537 ± 181	170 ± 55.6	225 ± 64.0
MRT_{0-t}	h	0.84 ± 0.14	0.96 ± 0.21	0.44 ± 0.12	0.47 ± 0.21	0.61 ± 0.14	0.50 ± 0.13
$t_{1/2}$	h	2.17 ± 0.96	3.26 ± 2.82	0.60 ± 0.26	0.96 ± 0.91	0.96 ± 0.44	0.68 ± 0.26
t_{max}	h	0.04 ± 0.02	0.04 ± 0.02	0.03 ± 0.00	0.03 ± 0.00	0.04 ± 0.02	0.03 ± 0.00
C_{max}	ng/mL	1052 ± 184	547 ± 142	2062 ± 605	1899 ± 878	440 ± 170	596 ± 156
CLz	L/h/kg	20.4 ± 2.19	36.3 ± 22.2	30.5 ± 9.24	32.0 ± 5.80	93.2 ± 44.2	81.9 ± 20.4
Vz	L/kg	62.0 ± 22.9	120 ± 31.0	25.4 ± 11.5	45.1 ± 45.0	115 ± 63.0	77.8 ± 30.1

[a] AUC_{0-t}, area under the curve to termination time; MRT_{0-t}, mean residence time; $t_{1/2}$, half-life; t_{max}, time at maximum plasma concentration; C_{max}, maximum plasma concentration; CLz, plasma clearance; Vz, volume of distribution.

(1052 ± 184 ng/mL, $P < 0.01$) appeared at the same time.[14] This might be related to the lecithin sphere, which creates a steric barrier at the oil/water interface so that the chemical stability of CA was significantly increased and the metabolism of CA was prolonged and changed. There is a similar behavior observed in the research of SME-nitrendipine after iv administration in rats.[28] For the metabolite cinnamyl alcohol, Figure 2B shows a similar concentration−time profile of both formulations. The pharmacokinetic parameters are shown in Table 3. The CLz and $t_{1/2}$ exhibted a slight decrease, but no significant difference was detected after the statistical analysis. Because CA showed a relatively high concentration in SME-CA, the aldehyde part is protected, indicating it can be more effective in the pharmacological area. It is exhibited in Table 3 that the SME-CA had a significant increase in AUC_{0-t} when compared to the previous CA solution. In addition, the Vz after administration of SME-CA was decreased to 62.0 ± 22.8 L/kg. On the other hand, the AUC_{0-t} of cinnamyl alcohol and methyl cinnamate experienced a slight increase and decrease when encapsulated into submicrometer emulsion. Figure 2C shows that the C_{max} of methyl cinnamate was decreased to 440 ± 170 ng/mL in the SME-CA group. It can be concluded that the change of CA in the pharmaceutical characterization has led to a pharmacokinetic change for both CA and its metabolites.

After intravenous injection of SME-CA, the result of tissue distribution is influenced by several variables, such as composition, particle size, and zeta potential. The concentration profiles of CA and its metabolites in various tissues, that is, heart, liver, spleen, lung, kidney, and brain, were quantified and are shown at 15, 45, and 90 min in Figure 3. Comparison of the new formulation with the former drug, improved concentration was found in kidney, liver, spleen, and brain in the SME group.[29] Significant accumulation of CA was detected in the liver and kidney, with the concentration increasing to 334 ± 60.1 and 459 ± 148 ng/g, respectively. This is mainly caused by the dramatic increase in the blood that needed to be metabolized and excreted. Higher concentration was also found for the metabolites of CA in the SME group. A similar phenomenon was exhibited in the previous study with a sharp increase in the liver.[30] To make CA easier to penetrate the endothelium cell barrier, the particle size was reduced to 130 ± 5.92 nm. As a result, 1.27-fold higher free CA (442 ± 180 ng/g) was detected in the brain compared with the former drug. Although the stability and penetrability were enhanced in the new formulation, there is no significant distribution difference found in the lung and heart. The aldehyde part of CA is very easily oxidized to cinnamic acid. However, when it was encapsulated in lecithin and other materials, the chemical stability were significantly enhanced, which resulted in the pharmacokinetic and distribution changes of CA.

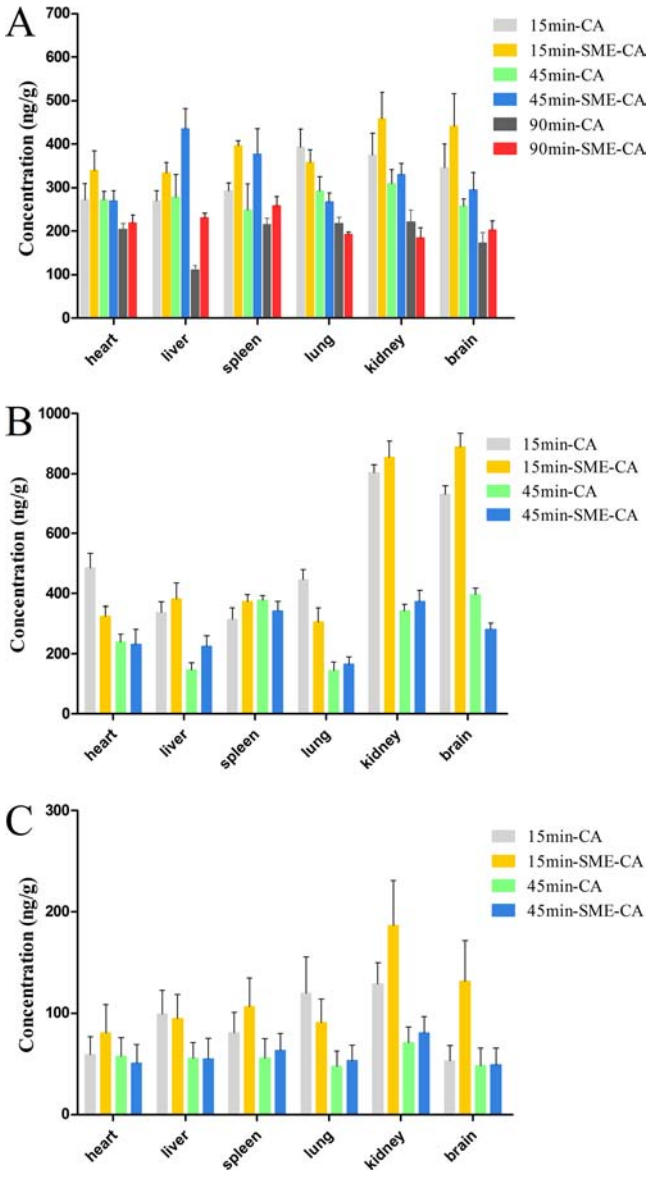

Figure 3. Compared tissue distribution profile of cinnamaldehyde (A), cinnamyl alcohol (B), and methyl cinamate (C) in rats after a single intravenous administration of SME-CA and CA of 20 mg/kg at 15, 45, 90 min (mean ± SD, n = 5).

DOI: 10.1021/acs.jafc.5b01883
J. Agric. Food Chem. 2015, 63, 6386−6392

In the present study, we have tested different excipients and conditions to prepare the submicrometer emulsion and finally exhibited optimal pharmacokinetic properties reported above. Moreover, the new formulation was more easily dissolved in water, which can be administered by various routes such as intragastrically or intraperitoneally. As CA was encapsulated in a submicrometer emulsion, it might affect the pharmacokinetic results when used in oral applications. We believe the development of the new formulation has laid a foundation for the future clinical application of CA.

■ ASSOCIATED CONTENT

Supporting Information

Typical GC-MS chromatograms of blank samples (1) and samples (2) at 1.5 h after iv administration: a, plasma; b, heart; c, liver; d, spleen; e, lung; f, kidney; g, brain. Peaks: 1, propiophenone; 2, cinnamaldehyde; 3, cinnamyl alcohol; 4, methyl cinnamate. The Supporting Information is available free of charge on the ACS Publications website at DOI: 10.1021/acs.jafc.5b01883.

■ AUTHOR INFORMATION

Corresponding Authors

*(W.C.) Phone: +86 29 84773752. Fax: +86 29 83224790. E-mail: caowei@fmmu.edu.cn.

*(S.W.) Phone: +86 29 84772519. Fax: +86 29 83224790. E-mail: wangsiw@fmmu.edu.cn.

Funding

This study was supported by NSFC (National Science Foundation of China) (No. 20872180).

Notes

The authors declare no competing financial interest.

■ REFERENCES

(1) Du, W. X.; Avena-Bustillos, R. J.; Woods, R.; Breksa, A. P.; McHugh, T. H.; Friedman, M.; Levin, C. E.; Mandrell, R. Sensory evaluation of baked chicken wrapped with antimicrobial apple and tomato edible films formulated with cinnamaldehyde and carvacrol. *J. Agric. Food Chem.* **2012**, *60*, 7799−7804.

(2) Gutierrez, L.; Escudero, A.; Batlle, R.; Nerin, C. Effect of mixed antimicrobial agents and flavors in active packaging films. *J. Agric. Food Chem.* **2009**, *57*, 8564−8571.

(3) Lin, L. T.; Tai, C. J.; Chang, S. P.; Chen, J. L.; Wu, S. J.; Lin, C. C. Cinnamaldehyde-induced apoptosis in human hepatoma PLC/PRF/5 cells involves the mitochondrial death pathway and is sensitive to inhibition by cyclosporin A and z-VAD-fmk. *Anticancer Agents Med. Chem.* **2013**, *13*, 1565−1574.

(4) Shin, S. Y.; Jung, H.; Ahn, S.; Hwang, D.; Yoon, H.; Hyun, J.; Yong, Y.; Cho, H. J.; Koh, D.; Lee, Y. H.; Lim, Y. Polyphenols bearing cinnamaldehyde scaffold showing cell growth inhibitory effects on the cisplatin-resistant A2780/Cis ovarian cancer cells. *Bioorg. Med. Chem.* **2014**, *22*, 1809−1820.

(5) Huang, T. C.; Chung, Y. L.; Wu, M. L.; Chuang, S. M. Cinnamaldehyde enhances Nrf2 nuclear translocation to upregulate phase II detoxifying enzyme expression in HepG2 cells. *J. Agric. Food Chem.* **2011**, *59*, 5164−5171.

(6) Matsuda, H.; Matsuda, R.; Fukuda, S.; Shiomoto, H.; Kubo, M. Anti-thrombic actions of 70% methanolic extract and cinnamic aldehyde from cinnamomi cortex. *Chem. Pharm. Bull.* **1987**, *35*, 1275−1280.

(7) Youn, H. S.; Lee, J. K.; Choi, Y. J.; Saitoh, S. I.; Miyake, K.; Hwang, D. H.; Lee, J. Y. Cinnamaldehyde suppresses toll-like receptor 4 activation mediated through the inhibition of receptor oligomerization. *Biochem. Pharmacol.* **2008**, *75*, 494−502.

(8) Ding, Y.; Qiu, L.; Zhao, G.; Xu, J.; Wang, S. Influence of cinnamaldehyde on viral myocarditis in mice. *Am. J. Med. Sci.* **2010**, *340*, 114−120.

(9) Huang, J.; Wang, S.; Luo, X.; Xie, Y.; Shi, X. Cinnamaldehyde reduction of platelet aggregation and thrombosis in rodents. *Thromb. Res.* **2007**, *119*, 337−342.

(10) Song, F.; Li, H.; Sun, J.; Wang, S. Protective effects of cinnamic acid and cinnamic aldehyde on isoproterenol-induced acute myocardial ischemia in rats. *J. Ethnopharmacol.* **2013**, *150*, 125−130.

(11) Zhang, Y.; Cao, W.; Xie, Y. H.; Yang, Q.; Li, X. Q.; Liu, X. X.; Wang, S. W. The comparison of alpha-bromo-4-chlorocinnamaldehyde and cinnamaldehyde on coxsackie virus B3-induced myocarditis and their mechanisms. *Int. Immunopharmacol.* **2012**, *14*, 107−113.

(12) *Synthetic Organic Chemicals, U.S. Production and Sales*; U.S. International Trade Commission; U.S. Government Printing Office: Washington, DC, USA, 1978.

(13) Belsito, D.; Bickers, D.; Bruze, M.; Calow, P.; Dagli, M.; Fryer, A. D.; Greim, H.; Miyachi, Y.; Saurat, J. H.; Sipes, I. G. A toxicologic and dermatologic assessment of cinnamyl phenylpropyl materials when used as fragrance ingredients. *Food Chem. Toxicol.* **2011**, *49* (Suppl. 2), S256−S267.

(14) Zhao, H.; Xie, Y.; Yang, Q.; Cao, Y.; Tu, H.; Cao, W.; Wang, S. Pharmacokinetic study of cinnamaldehyde in rats by GC-MS after oral and intravenous administration. *J. Pharm. Biomed. Anal.* **2014**, *89*, 150−157.

(15) Tian, Y.; Zhu, Y.; Bashari, M.; Hu, X.; Xu, X.; Jin, Z. Identification and releasing characteristics of high-amylose corn starch-cinnamaldehyde inclusion complex prepared using ultrasound treatment. *Carbohydr. Polym.* **2013**, *91*, 586−589.

(16) Ponce Cevallos, P. A.; Buera, M. P.; Elizalde, B. E. Encapsulation of cinnamon and thyme essential oils components (cinnamaldehyde and thymol) in β-cyclodextrin: effect of interactions with water on complex stability. *J. Food Eng.* **2010**, *99*, 70−75.

(17) Kim, I. H.; Han, J.; Na, J. H.; Chang, P. S.; Chung, M. S.; Park, K. H.; Min, S. C. Insect-resistant food packaging film development using cinnamon oil and microencapsulation technologies. *J. Food Sci.* **2013**, *78*, E229−E237.

(18) Faikoh, E. N.; Hong, Y. H.; Hu, S. Y. Liposome-encapsulated cinnamaldehyde enhances zebrafish (Danio rerio) immunity and survival when challenged with *Vibrio vulnificus* and *Streptococcus agalactiae*. *Fish Shellfish Immunol.* **2014**, *38*, 15−24.

(19) Chiu, T. C.; Lee, H. Y.; Li, P. H.; Chao, J. H.; Lin, C. H. Effects of interfacial charge and the particle size of titanate nanotube-supported Pt nanoparticles on the hydrogenation of cinnamaldehyde. *Nanotechnology* **2013**, *24*, 115601.

(20) Wang, Y.; Mesfin, G. M.; Rodriguez, C. A.; Slatter, J. G.; Schuette, M. R.; Cory, A. L.; Higgins, M. J. Venous irritation, pharmacokinetics, and tissue distribution of tirilazad in rats following intravenous administration of a novel supersaturated submicron lipid emulsion. *Pharm. Res.* **1999**, *16*, 930−938.

(21) Singh, M.; Ravin, L. J. Parenteral emulsions as drug carrier systems. *J. Parenter. Sci. Technol.* **1986**, *40*, 34−41.

(22) Zhang, T.; Zheng, Y.; Peng, Q.; Cao, X.; Gong, T.; Zhang, Z. A novel submicron emulsion system loaded with vincristine-oleic acid ion-pair complex with improved anticancer effect: in vitro and in vivo studies. *Int. J. Nanomed.* **2013**, *8*, 1185−1196.

(23) Singh, B.; Bandopadhyay, S.; Kapil, R.; Singh, R.; Katare, O. Self-emulsifying drug delivery systems (SEDDS): formulation development, characterization, and applications. *Crit. Rev. Ther. Drug Carrier Syst.* **2009**, *26*, 427−521.

(24) Cerpnjak, K.; Zvonar, A.; Gasperlin, M.; Vrecer, F. Lipid-based systems as a promising approach for enhancing the bioavailability of poorly water-soluble drugs. *Acta Pharm.* **2013**, *63*, 427−445.

(25) Sloat, B. R.; Sandoval, M. A.; Li, D.; Chung, W. G.; Lansakara, P. D.; Proteau, P. J.; Kiguchi, K.; DiGiovanni, J.; Cui, Z. In vitro and in vivo anti-tumor activities of a gemcitabine derivative carried by nanoparticles. *Int. J. Pharm.* **2011**, *409*, 278−288.

(26) Koppikar, S. J.; Choudhari, A. S.; Suryavanshi, S. A.; Kumari, S.; Chattopadhyay, S.; Kaul-Ghanekar, R. Aqueous cinnamon extract

DOI: 10.1021/acs.jafc.5b01883
J. Agric. Food Chem. 2015, 63, 6386−6392

(ACE-c) from the bark of Cinnamomum cassia causes apoptosis in human cervical cancer cell line (SiHa) through loss of mitochondrial membrane potential. *BMC Cancer* **2010**, *10*, 210.
(27) Imai, T.; Yasuhara, K.; Tamura, T.; Takizawa, T.; Ueda, M.; Hirose, M.; Mitsumori, K. Inhibitory effects of cinnamaldehyde on 4-(methylnitrosamino)-1-(3-pyridyl)-1-butanone-induced lung carcinogenesis in rasH2 mice. *Cancer Lett.* **2002**, *175*, 9−16.
(28) Guan, J.; Zhao, N.; Zhai, Y.; Chu, C.; Chen, H.; Zhang, T. Pharmacokinetic performance of the nitrendipine intravenous submicron emulsion in rats. *Asian J. Pharm. Sci.* **2014**, *9*, 330−335.
(29) Zhao, H.; Yang, Q.; Xie, Y.; Sun, J.; Tu, H.; Cao, W.; Wang, S. Simultaneous determination of cinnamaldehyde and its metabolite in rat tissues by gas chromatography-mass spectrometry. *Biomed. Chromatogr.* **2015**, *29*, 182−187.
(30) Zhao, Y. X.; Liu, D. X.; Liang, W. Q.; Ye, Z. W. In-vivo pharmacokinetics, tissue distribution and anti-tumour effect of hydroxycamptothecin delivered in oil-in-water submicron emulsions. *J. Pharm. Pharmacol.* **2012**, *64*, 783−791.

DOI: 10.1021/acs.jafc.5b01883
J. Agric. Food Chem. 2015, 63, 6386−6392

classified by the Endemic Species Research Institute, Council of Agriculture, Taiwan, as an endemic herb in Taiwan, and it has long been used in folk medicine for the treatment of hepatitis, jaundice, diarrhea, and arthritis.[12] It is reported that extracts or purified compounds from VTT exhibited several biological activities, including antihypertensive,[13,14] antiarthritis,[15,16] neuroprotective,[17] and hepatoprotective[18] activities. The active components were reported to be resveratrol, resveratrol oligomers,[14−16] and other polyphenols.[17,18] Moreover, the ethanolic extract of VTT has exhibited less lipid accumulation through regulation of the AMPK-ACC pathway in hypercholesterolemic rabbits.[19] Therefore, the purpose of this study was to investigate whether VTT could decrease lipid levels to improve glucose tolerances in diet-induced obese rats. In the present study, ethanol extracts (Et) and hot-water extracts (Hw) from the stem (S) and leaf (L) of VTT and their Et partitioned fractions, including ethyl acetate fraction (Et-EA), butanol fraction (E*t*-BuOH), and water fraction (Et-w), were used to investigate yeast α-glucosidase and porcine DPP-IV inhibitory activities. Later, a high-fat (HF) diet was used to induce Wistar rat obesity for 5 weeks. Then VTT-S-Et and VTT-L-Et (20 and 50 mg/kg) were used daily concurrently with the HF diet (HF + S-Et or HF + L-Et) from day 36 to day 68 and were then used to investigate improvements of the impaired glucose tolerances by OGTT. The isolated compounds from S-Et-EA were tested for yeast α-glucosidase and porcine DPP-IV inhibitory activities and related kinetic properties.

MATERIALS AND METHODS

Materials. α-Glucosidase (from *Saccharomyces cerevisiae*, type I, lyophilized powder, ≥10 units/mg protein), DPP-IV (from porcine kidney, lyophilized powder, ≥10 units/mg protein, D-7052), *p*-nitrophenyl α-D-glucopyranoside (pNPG), Gly-Pro-*p*-nitroanilide, dimethyl sulfoxide (DMSO), acarbose, and sitagliptin phosphate were purchased from Sigma Chemical Co. (St. Louis, MO, USA). The HF diet for diet-induced obesity (fat composition provided 60% of total calories, D12942) was purchased from Research Diets, Inc. (New Brunswick, NJ, USA). The standard mouse/rat chow (fat composition provided 12% of total calories, Prolab RMH2500, 5P14 Diet; PMI Nutrition International, St. Louis, MO, USA). The compositions of the standard chow and high-fat diets for providing total calories are listed in Supplementary Table S1 of the Supporting Information. Other chemicals were from Sigma Chemical Co. (St. Louis, MO, USA). For pure compound identifications, optical rotation measurements were measured with a JASCO DIP-180 digital spectropolarimeter, NMR spectra were analyzed in $CDCl_3$ at room temperature using a Varian Mercury plus 400 NMR spectrometer, and the solvent resonance was used as the internal shift reference [tetramethylsilane (TMS) as standard]; electrospray ionization mass was determined on a VG platform electrospray mass spectrometer. Thin-layer chromatography was performed on silica gel 60 F254 plates (Merck, Darmstadt, Germany). Silica gels (230−400 mesh ASTM, Merck) were used for column chromatography. Semipreparative HPLC was performed on a Hitachi L-7000 chromatograph with a Thermo Betasil C-18 column (5 μm, 250 × 10 mm).

Preparation of VTT Extracts and Fractions. VTT leaves and stems were collected in Taichung County, Taiwan, in July 2006. They were cultivated by Dr. Chi-Luan Wen (Taiwan Seed Improvement and Propagation Station, Council of Agriculture, Taichung, Taiwan) and identified by Dr. Tsai-Wen Hsu (Endemic Species Research Institute, Nantou, Taiwan). The specimens were kept in the laboratory of Dr. Chi-I Chang (National Pingtung University of Science and Technology, Pingtung, Taiwan) for reference. All plant materials were oven-dried at 50 °C for 3 days and mechanically ground to a fine powder passing through a 10-mesh sieve. The powder of the leaves and stems (10 kg each) was extracted with ethanol in a solid/solvent ratio of 1:5 at room temperature for 7 days. The combined ethanol extract was filtered through Whatman no. 1 filter paper and evaporated under reduced pressure to obtain the ethanol extracts (Et, 405 and 485 g, respectively), which were suspended in H_2O, and then partitioned sequentially using ethyl acetate (EA) and *n*-butanol (BuOH), to get the ethyl acetate fraction (Et-EA), butanol fraction (E*t*-BuOH), and water fraction (Et-w). For hot-water extraction, 100 g of leaf and stem powder was extracted with 1 L of distilled water in reflux for 3 h. Once cooled to room temperature, the extract was filtered through Whatman no. 1 filter paper and dried under reduced pressure below 45 °C using a rotary evaporator. It was then freeze-dried to obtain hot-water extracts (Hw 5.3 and 3.6 g, respectively) and was stored at −20 °C until further use.

Compounds Isolated from S-Et-EA. The S-Et-EA (39 g) was resolved by silica gel column chromatography (90 × 5 cm) using *n*-hexane−EA gradients as eluent. Twenty-four fractions were collected. Fraction 24 (6.2 g) was in turn passed through an RP-18 reversed phase column (60 × 3 cm) and eluted by using water−methanol gradients (1:1 to 0:1) to obtain seven subfractions (each 200 mL, fractions 24A−24G), among which fraction 24D was further purified by semipreparative HPLC (Thermo Betasil C-18 column; flow rate = 2 mL/min) by water/acetonitrile (9:1 to 1:1) gradients to afford (+)-hopeaphenol (**1**) (7.2 mg, t_R = 39.6 min) and (+)-vitisin A (**2**) (12.3 mg, t_R = 46.8 min), respectively; fraction 24E was finally purified by semipreparative HPLC by water/acetonitrile (9:1 to 5:5) to afford (−)-vitisin B (**3**) (17.2 mg, t_R = 48.7 min). The collections of appropriate sample amounts for studies were carried out by repeated injection under the above HPLC conditions.

α-Glucosidase Inhibitory Assays. The α-glucosidase inhibitory activity was assayed according to a previous study with modifications.[20] Each test sample was dissolved in DMSO. Ten microliters of VTT extracts and fractions (0.1 mg/mL) and different concentrations of purified compounds [(+)-hopeaphenol, 0.78, 1.56, 3.125, 6.25, 12.5, and 25 μM; (+)-vitisin A and (−)-vitisin B, 0.625, 1.25, 2.5, 5, and 10 μM] or acarbose (positive control, 1.67, 3.33, 5.0, 6.67, 8.3, 10, and 11.67 mM) were premixed with 10 μL of α-glucosidase (1 U/mL) at 37 °C for 10 min. Then, 50 μL of 10 mM pNPG (in 200 mM phosphate buffer, pH 6.8) and 50 μL of 200 mM phosphate buffer (pH 6.8) were added and incubated at 37 °C for 30 min. One hundred microliters of 200 mM sodium carbonate was added to stop reactions. DMSO was used instead of tested samples for the blank. For sample background interference determinations, each sample was added into the phosphate buffer only during reactions. The absorbance at 405 nm was measured by using an ELISA reader (TECAN Sunrise microplate reader; Männedorf, Switzerland). The α-glucosidase inhibition (%) was calculated as follows:

$$\frac{[A405_{\text{blank}} - (A405_{\text{sample}} - A405_{\text{background}})]}{A405_{\text{blank}}} \times 100\%$$

The 50% inhibition (IC_{50}) value was calculated as the concentration of samples that inhibited 50% of α-glucosidase activity under tested conditions.

DPP-IV Inhibitory Assays. The DPP-IV inhibitory activity was assayed according to a previous study with modifications.[21,22] The enzyme powder (lyophilized powder, ≥10 units/mg protein) was redissolved in 1 mL of 100 mM Tris buffer (pH 8.0) as a stock solution and a 50-fold dilution (~0.002 unit/mL) as a working solution. Each test sample was dissolved in DMSO. Fifty microliters of VTT extracts and fractions (0.5 mg/mL) and different concentrations of purified compounds [(+)-hopeaphenol, 100, 200, 300, 400, and 500 μM; (+)-vitisin A, 25, 50, 75, 100, 125, 150, and 200 μM; (−)-vitisin B, 2.5, 5, 10, 15, 20, 25, and 30 μM] or sitagliptin phosphate (positive control, 0.01, 0.025, 0.05, 0.1, and 0.2 μM) were premixed with 50 μL of DPP-IV working solution at 37 °C for 10 min. Then, 50 μL of 1 mM Gly-Pro-*p*-nitroanilide and 50 μL of 100 mM Tris buffer (pH 8.0) were added and incubated at 37 °C for 60 min. Fifty microliters of 3% acetic acid was added to stop reactions. DMSO was used instead of tested samples for the blank. To determine sample background

DOI: 10.1021/acs.jafc.5b02069
J. Agric. Food Chem. 2015, 63, 6393−6401

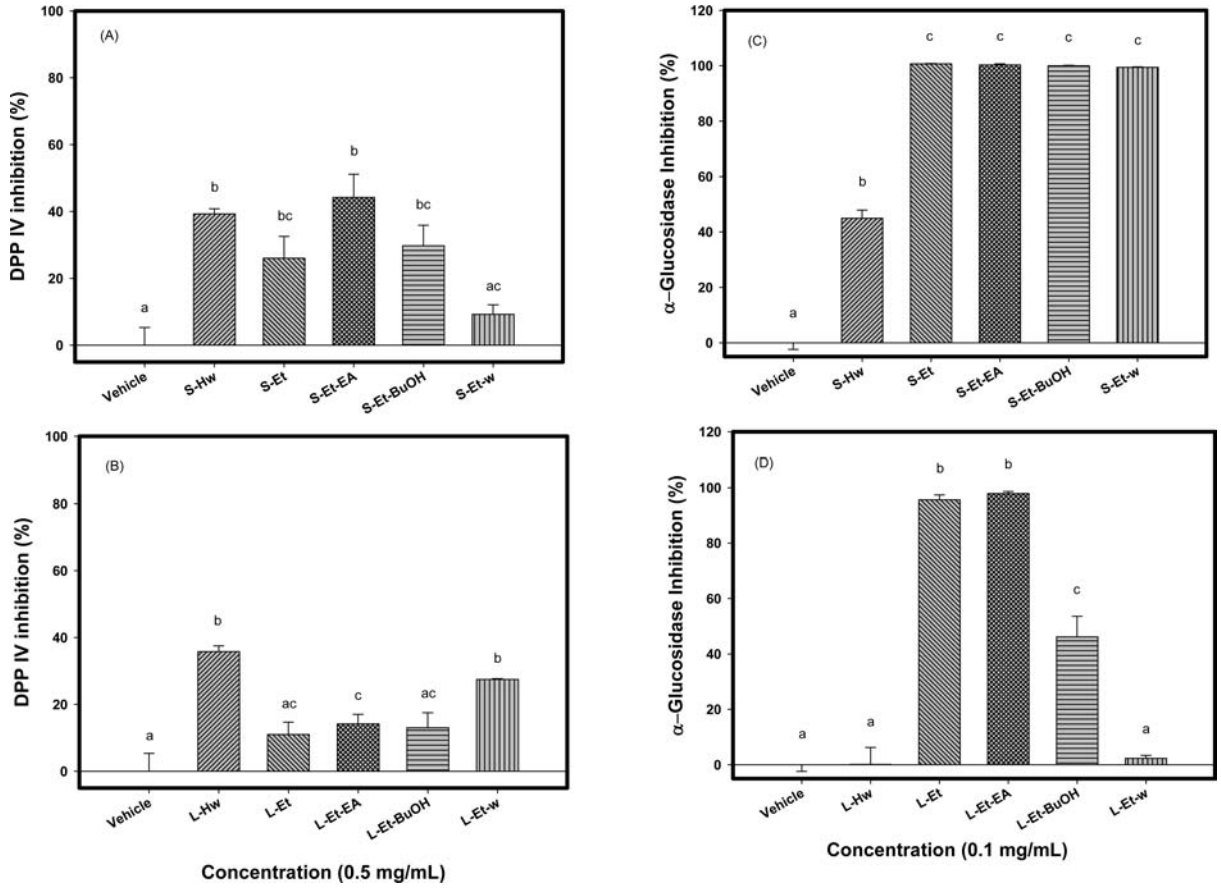

Figure 1. Effect of 0.5 mg/mL extracts and partitioned fractions on dipeptidyl peptidase-IV (DPP-IV) inhibitory activities from stem of *Vitis thunbergii* var. *taiwaniana* (A) and from leaf of *V. thunbergii* var. *taiwaniana* (B); effect of 0.1 mg/mL extracts and partitioned fractions on α-glucosidase inhibitory activities from stem of *V. thunbergii* var. *taiwaniana* (C) and from leaf of *V. thunbergii* var. *taiwaniana* (D). S, stem; L, leaf; Et, ethanol extracts; Hw, hot-water extracts; Et-EA, ethyl acetate partitioned fractions from Et; Et-BuOH, butanol partitioned fractions from Et; Et-w, Et partitioned water fractions. Triplicates were determined and expressed as the mean ± SD. Multiple group comparisons under the same treatment time were performed using one-way analysis of variance followed by the post hoc Tukey's test, and values that have not been marked with the same letter are significantly different ($P < 0.05$).

interference, each sample was added into the Tris buffer only during reactions. The absorbance at 405 nm was measured by using an ELISA reader (TECAN Sunrise microplate reader). The DPP-IV inhibition (%) was calculated as follows:

$$\frac{[A405_{\text{blank}} - (A405_{\text{sample}} - A405_{\text{background}})]}{A405_{\text{blank}}} \times 100\%$$

The 50% inhibition (IC_{50}) value was calculated as the concentration of sample that inhibited 50% of DPP-IV activity under tested conditions.

Kinetic Analyses of α-Glucosidase and DPP-IV. The kinetic properties of α-glucosidase (0.083 unit) without or with different concentrations of (+)-vitisin A (0.3125 and 1.25 μM) and (−)-vitisin B (0.3125 and 0.625 μM) were determined using different concentrations of pNPG as substrate (0.625, 1.25, 2.5, and 5 mM). The kinetic properties of DPP-IV (0.005 unit) without or with different concentrations of (−)-vitisin B (5, 15, and 25 μM) were determined using different concentrations of Gly-Pro-*p*-nitroanilide as substrate (0.1, 0.2, 0.4, 0.6, 0.8, and 1 mM). The K_m, K'_m, V_{max}, and V'_{max} were calculated from Lineweaver−Burk plots. The enzyme−inhibitor dissociation constant (K_i) was the intercept of the *x*-axis calculated (each line slope in the Lineweaver−Burk plot vs the tested inhibitor concentrations), and the inhibitor-enzyme−substrate dissociation constant (K_{is}) was the intercept of the *x*-axis calculated (each line *y*-axis intercept in the Lineweaver−Burk plot vs the tested inhibitor concentrations).

Impaired Glucose Tolerance in Obese Rat Models. Male 10-week-old Wistar rats ($N = 48$) were purchased from the National Laboratory Animal Center (Taipei, Taiwan) and housed in wire-bottomed stainless steel cages in a temperature- and humidity-controlled room (at 22 °C) with a 12-h light/dark cycle and had free access to feed and water. All animal experimental procedures were reviewed and approved by the Institutional Animal Care and Use Committee, Taipei Medical University (LAC-99-0136). After acclimation for 1 week, the rats were randomly divided into three groups ($N = 8$ for each group), including a normal diet (ND) group given standard mouse/rat chow and five HF diet-induced obese groups (one control as HF group, two VTT-S-Et intervened groups, and two VTT-L-Et intervened groups) for 68 days. The Wistar rats were subjected to diet-induced obesity during days 0−35 and then randomly divided into groups for further interventions at days 36−68. The HF was changed every 2 days to avoid oxidation. In the VTT-S-Et and VTT-L-Et intervened groups, S-Et or L-Et (20 and 50 mg/kg, respectively, Et20 and Et50) was orally administered daily by oral gavage together with HF diets (HF + S-Et20, HF + S-Et50; HF + L-Et20, HF + L-Et50) from days 36 to 68. The rat weights were recorded during experiments. The impaired glucose tolerances of HF diet-induced obese rats were measured by OGTT methods following a previous study.[22] Rats of each group at day 68 were fasted for 16 h, and glucose (1g/kg) was administered by oral gavage. Blood (0.1 mL) was obtained from the tail vein at 0 (basal level), 5, 30, 60, 90, and 120 min after the glucose loads. Plasma glucose was determined by using a

DOI: 10.1021/acs.jafc.5b02069
J. Agric. Food Chem. 2015, 63, 6393−6401

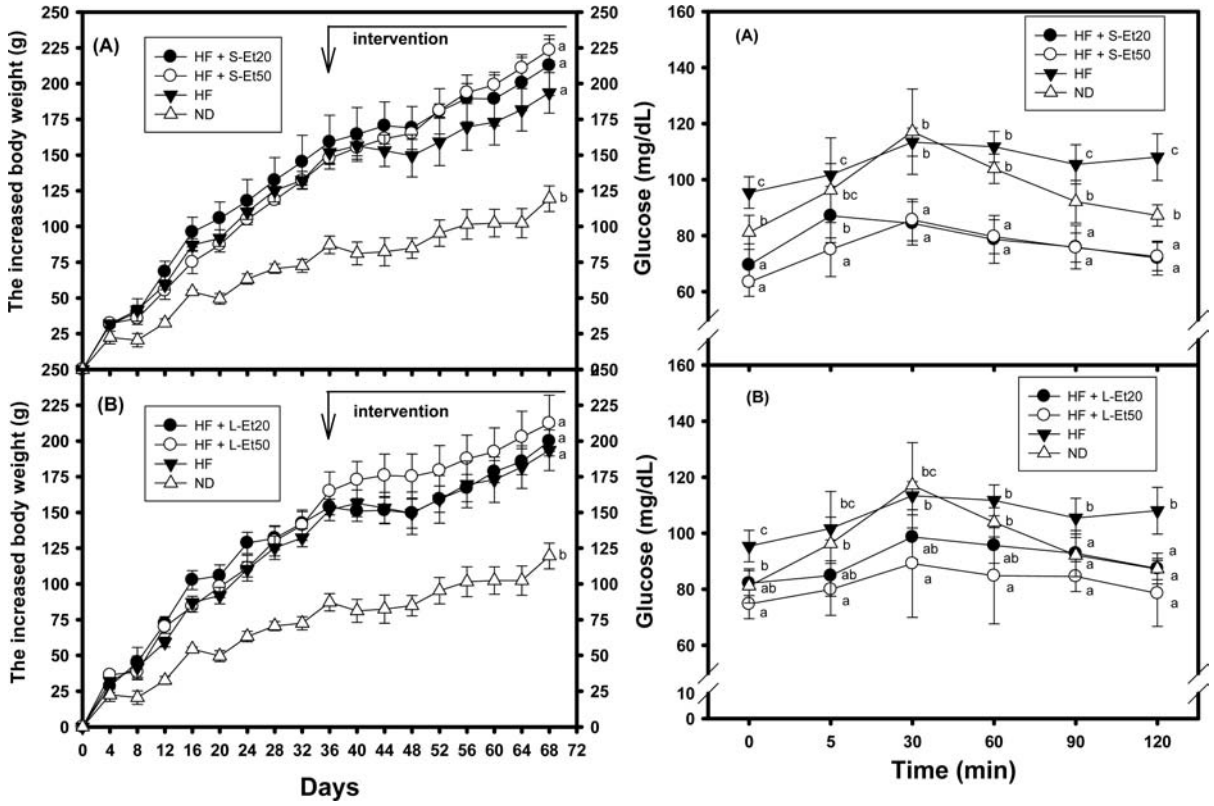

Figure 2. Effects of (A) stem ethanol extracts (S-Et) interventions (20 and 50 mg/kg) and (B) leaf ethanol extracts (L-Et) interventions (20 and 50 mg/kg) of *Vitis thunbergii* var. *taiwaniana* on the changes of increased body weight. Effects of (C) S-Et20 and S-Et50 and (D) L-Et20 and L-Et50 on impaired glucose intolerances of high fat-diet induced obese rats by oral glucose tolerance tests. The HF diet and normal diet (ND) were provided from day 1 to day 68. The arrow indicates the intervened periods from day 36 to day 68. Data are expressed as the mean ± SD. ND, normal diet; HF, high-fat diet; (HF + Et20 or HF + Et50), ethanol extracts (20 mg/kg, Et20; 50 mg/kg, Et50) were intervened daily concurrent with the HF diet. Multiple group comparisons at the end of experiment were performed using one-way analysis of variance (ANOVA) followed by the post hoc Tukey's test. Values that have not been marked with the same letter are significantly different ($P < 0.05$).

RANDOX glucose kit (Randox Laboratories-US, Ltd., Kearneysville, WV, USA).

Statistical Analyses. Data are expressed as the mean ± SD. Multiple group comparisons were performed using one-way analysis of variance (ANOVA) followed by the post hoc Tukey's test. The animal experiments were compared among groups on the day of the experiment end. Values that have not been marked with the same letter are significantly different ($P < 0.05$). Statistical analysis was performed using GraphPad Prism 5.0 software (San Diego, CA, USA).

RESULTS AND DISCUSSION

DPP-IV and α-Glucosidase Inhibitory Activities of VTT Extracts and Fractions. VTT was reported to have different biological activities depending on which plant portions (roots, stems, or leaves) were used in combination with different solvent extracts.[14−19] Therefore, the Et and Hw from S and L and their Et partitioned fractions, S-Et-EA and L-Et-EA, S-E*t*-BuOH and L-E*t*-BuOH, and S-Et-w and L-Et-w, were used to investigate inhibitory activities against DPP-IV (Figure 1A,B) and yeast α-glucosidase (Figure 1C,D). Generally, the VTT extracts and Et partitioned fractions exhibited higher yeast α-glucosidase inhibitory activities than those of the DPP-IV inhibitory ones. At the same concentration of 0.5 mg/mL, the order of VTT extracts for DPP-IV inhibitory activity was S-Hw ≥ L-Hw > S-Et ≫ L-Et; the order of Et partitioned fractions for DPP-IV inhibitory activity was S-Et-EA > S-E*t*-BuOH > L-Et-w ≫ L-Et-EA ≅ L-E*t*-BuOH ≅ S-Et-w, and the maximal DPP-IV inhibition was close to 40% (Figure 1A,B). At the same concentration of 0.1 mg/mL, the order of VTT extracts for α-glucosidase inhibitory activity weas S-Et ≥ L-Et ≫ S-Hw ≫ L-Hw; the order of Et partitioned fractions for α-glucosidase inhibitory activity was S-Et-EA ≅ S-E*t*-BuOH ≅ S-Et-w ≅ L-Et-EA ≫ L-E*t*-BuOH ≫ L-Et-w, and the maximal α-glucosidase inhibition was close to 100% (Figure 1C,D).

Impaired Glucose Tolerance Improvements of S-Et and L-Et in High-Fat (HF) Diet-Induced Obese Rats. HF diets are reported to induce an overweight condition, obesity, dyslipidemia, insulin resistance, and high blood pressure in rodents.[23] The α-glucosidase and DPP-IV inhibitions can reduce postprandial blood glucose levels and prolong GLP-1 and GIP biological activities. Therefore, a HF diet was used to preinduce obese rats, and then Et-S/Et-L was used together with HF to investigate the improved possibility of impaired glucose tolerance in obese rats. Figure 2 shows the increased body weights in Wistar rats fed normal diets (ND) or HF without or with S-Et (Figure 2A) or L-Et (Figure 2B) interventions at doses of 20 mg/kg (Et20) and 50 mg/kg (Et50). The increased body weight (g) at day 68 in HF groups was 212.73 ± 21.05, 223.47 ± 7.66, 199.93 ± 10.46, 212.37 ± 19.67, and 193.53 ± 14.19, respectively, for HF + S-Et20, HF + S-Et50, HF + L-Et20, HF + L-Et50, and HF. The rats in the HF groups without or with S-Et or L-Et interventions showed no significant difference ($P > 0.05$) in weight increases on the day of experiment end. The increased body weight (g) at day 68 in the ND group was only 119.35 ± 9.00. This was significantly

DOI: 10.1021/acs.jafc.5b02069
J. Agric. Food Chem. 2015, 63, 6393−6401

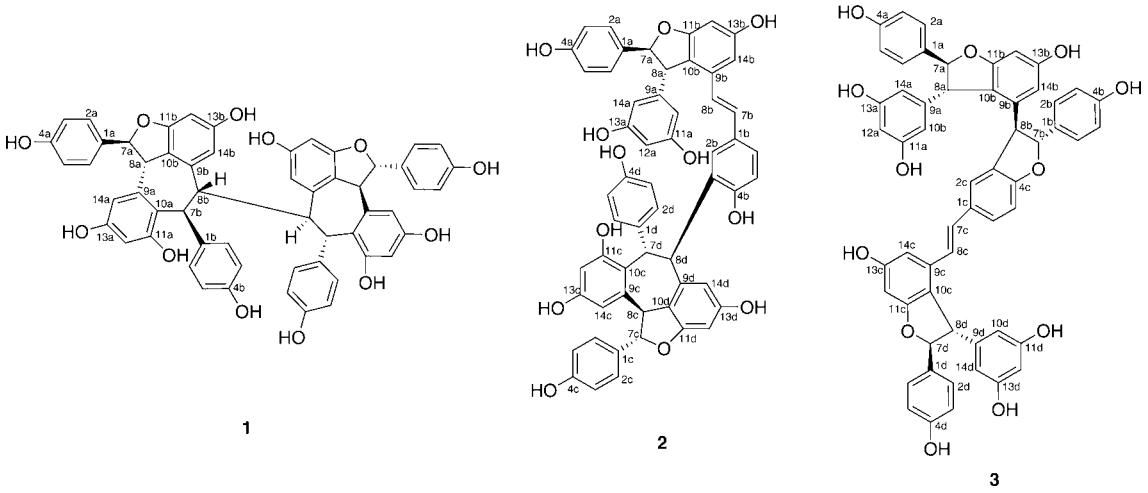

Figure 3. Chemical structures of three compounds, (+)-hopeaphenol (**1**), (+)-vitisin A (**2**), and (−)-vitisin B (**3**), isolated from the ethyl acetate fractions of stem ethanol extracts of *Vitis thunbergii* var. *taiwaniana*.

different ($P < 0.05$) compared to the HF group. The standard chow of normal diet (Table S1) in the present experiment was not a real low-fat diet control, and hence the protocol was not easy to compare to the efficiency of the normal diet group and the HF-induced groups in the increased rat body weights. From the present results, S-Et or L-Et interventions at 20 and 50 mg/kg for around 5 weeks showed no weight reduction in preobese rat models. Meanwhile, rats with similar weights in different HF groups and rats in the ND group were used to evaluate the impaired glucose tolerance by OGTT after fasting for 16 h (Figure 2C,D). Figure 2C shows the basal level (0 min) and plasma glucose concentrations (mg/dL) after glucose loads at 5, 30, 60, 90, and 120 min of HF + S-Et20, HF + S-Et50, HF, and the blank groups. After glucose loads for 120 min, the rats in the HF group still showed high plasma glucose concentrations, a symptom of impaired glucose tolerance. However, the rats in the S-Et intervened groups seemed to improve with respect to impaired glucose tolerance in OGTT profiles. The obese rats in the HF + S-Et20 and HF + S-Et50 groups showed the lowest plasma glucose concentrations at the basal level, and each time the intervals and significant differences ($P < 0.05$) were compared to those of the HF group and the ND group. Figure 2D shows the basal level (0 min) and plasma glucose concentrations (mg/dL) after glucose loads at 5, 30, 60, 90, and 120 min of HF + L-Et20, HF + L-Et50, and HF compared to the ND group. The rats in the L-Et intervened groups seemed to improve with respect to impaired glucose tolerance in OGTT profiles. The plasma glucose concentrations of obese rats in the intervened groups of HF + L-Et20 and HF + L-Et50 showed lower and significant differences ($P < 0.05$) compared to those of the HF group at the basal level and at each time interval. Rats in the L-Et50 intervened groups showed better and significant difference ($P < 0.05$) in OGTT profiles at 0, 5, 30, and 60 min after glucose loads and were comparable at 90 and 120 min time intervals compared to rats in the ND group. From the present OGTT data, S-Et and L-Et interventions showed improved activities against impaired glucose tolerance in obese rats, and S-Et interventions seemed to result in greater improvement than L-Et interventions. Lin et al.[15] reported that VTT-S-Et showed better than VTT-L-Et in angiotensin converting enzyme inhibitory activities, and the oral administration of VTT-S-Et exhibited antihypertensive activities in spontaneously hypertensive rats. The improved OGTT profiles in obese rats of VTT-S-Et or VTT-L-Et interventions together with antihypertensive activities[15] provided evidence that VTT extracts could be processed as health-promoting foods. The HF provides 20 and 60% of total calories, respectively, from carbohydrate and fat in the diets. S-Et and L-Et showed excellent yeast α-glucosidase inhibitory and partial DPP-IV inhibitory activities in vitro (Figure 1), which might correlate with the improvement of impaired glucose tolerance in obese rats (Figure 2C,D). The S-Et intervention showed better than L-Et in OGTT results (Figure 2B). The S-Et-EA fraction in vitro screening test showed good anti-α-glucosidase and DPP-IV inhibitory activities; therefore, the EA partitioned fraction from S-Et was selected to isolate the active compounds for further studies.

Compounds Isolated from S-Et-EA. Stilbenoid compounds are rich in *Vitis* genus plants and are considered as the active constituents in them. All 24 fractions were analyzed by HPLC method and monitored at the characteristic UV absorption wavelength of stilbenoids, 280 nm. Fraction 24 was found to contain the most abundant stilbenoid compounds and was thus selected for further purification. Three resveratrol tetramers, **1**−**3** (Figure 3), were isolated from the S-Et-EA and identified by comparing their physical and spectral data (specific rotation, MS, and NMR) with the available values in the literature. The chemical structures of these compounds were identified as (+)-hopeaphenol (**1**),[24] (+)-vitisin A (**2**),[25] and (−)-vitisin B (**3**),[26] and the spectral properties were as follows.

(+)-Hopeaphenol (**1**): brown-yellow powder; $[\alpha]_D^{25}$ +390.0° (*c* 0.35, MeOH); ESI-MS *m*/*z* 907 $[M + H]^+$; ^{1}H NMR (400 MHz, acetone-d_6) δ 7.12 (2H, d, *J* = 8.4 Hz, H-2a, 6a), 6.89 (2H, d, *J* = 8.4 Hz, H-2b, 6b), 6.77 (2H, d, *J* = 8.8 Hz, H-3a, 5a), 6.54 (2H, d, *J* = 8.8 Hz, H-3b, 5b), 6.28 (2H, d, *J* = 2.4 Hz, H-14a), 5.80 (1H, br s, H-7b), 5.73 (1H, d, *J* = 12.0 Hz, H-7a), 5.71 (1H, d, *J* = 2.0 Hz, H-12b), 5.15 (1H, d, *J* = 2.0 Hz, H-14b), 4.22 (1H, d, *J* = 12.0 Hz, H-8a), 3.93 (1H, d, *J* = 4.8 Hz, H-7b).

(+)-Vitisin A (**2**): brown solid; $[\alpha]_D^{25}$ +210.5° (*c* 0.4, MeOH); ESI-MS *m*/*z* 907$[M + H]^+$; ^{1}H NMR (400 MHz, acetone-d_6) δ 7.19 (2H, d, *J* = 8.5 Hz, H-2a, 6a), 7.14 (2H, d, *J* = 8.5 Hz, H-2c, H-6c), 7.02 (2H, d, *J* = 8.3 Hz, H-2d, H-6d), 6.87 (1H, dd, *J* = 8.4, 2.2 Hz, H-6b), 6.81 (2H, d, *J* = 8.5 Hz, H-

DOI: 10.1021/acs.jafc.5b02069
J. Agric. Food Chem. 2015, 63, 6393−6401

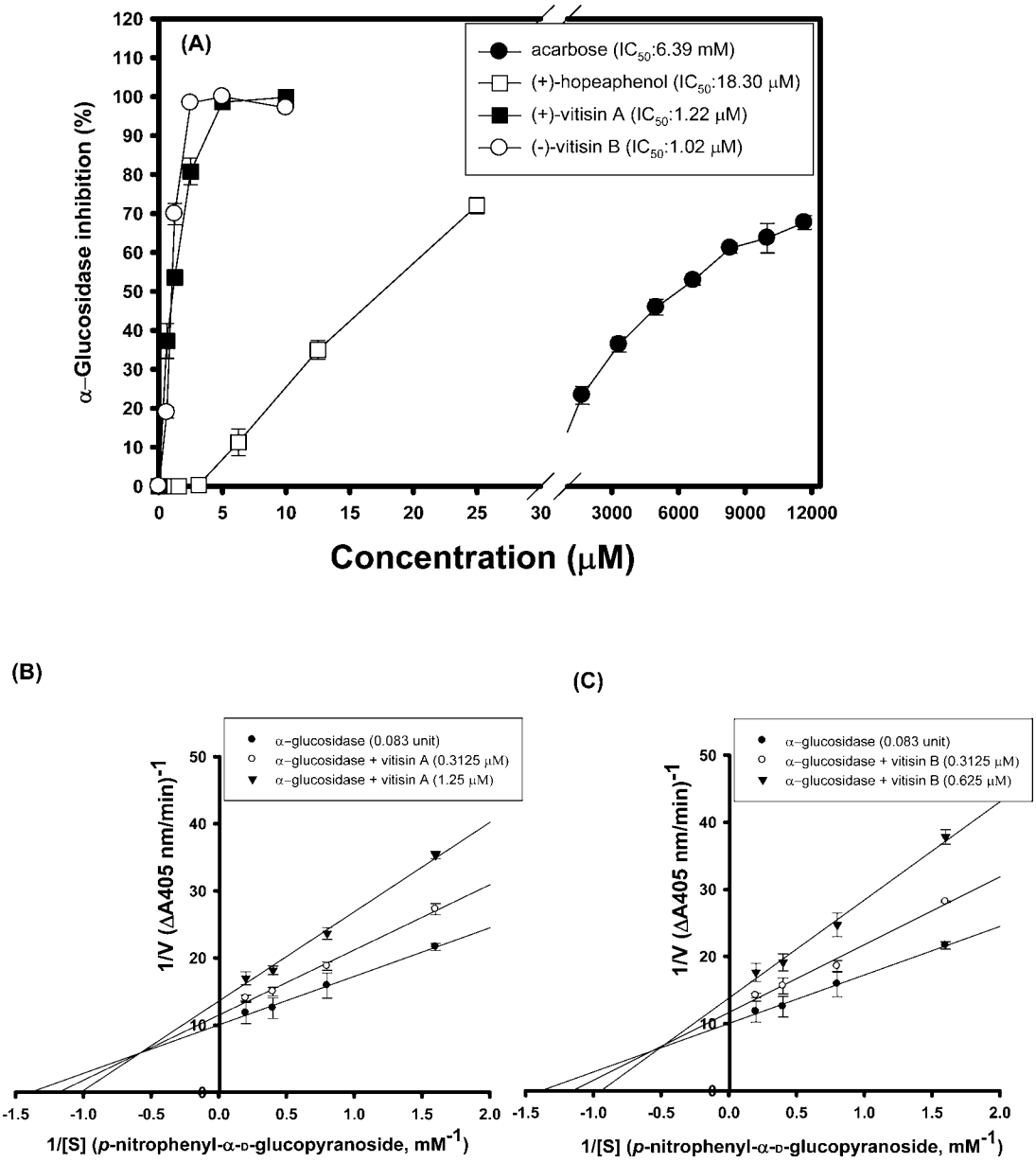

Figure 4. (A) Effect of different concentrations of (+)-hopeaphenol, (+)-vitisin A, and (−)-vitisin B on α-glucosidase inhibitory activities compared to the positive control of acarbose: Lineweaver−Burk plots of α-glucosidase (0.083 U) (B) without or with (+)-vitisin A (0.3125 and 1.25 μM) or (C) without or with (−)-vitisin B at the different concentrations of *p*-nitrophenyl α-D-glucopyranoside as substrates (0.625, 1.25, 2.5, and 5 mM). Fifty percent inhibition (IC_{50}) of α-glucosidase activity was calculated as the concentration of sample that inhibited 50% of α-glucosidase activity under tested conditions. Data are expressed as the mean ± SD (n = 3).

3a, 5a), 6.77 (2H, d, J = 8.5 Hz, H-3c, H-5c), 6.68 (1H, d, J = 8.4 Hz, H-5b), 6.65 (2H, d, J = 8.3 Hz, H-3d, H-5d), 6.50 (1H, d, J = 2.2 Hz, H-14b), 6.38 (2H, br s, H-7b, H-8b), 6.25 (1H, d, J = 2.2 Hz, H-12b), 6.23 (1H, d, J = 2.2 Hz, H-14c), 6.21 (1H, d, J = 2.2 Hz, H-12a), 6.16 (2H, d, J = 2.2 Hz, 10a, 14a), 6.08 (1H, d, J = 1.8 Hz, H-12d), 6.07 (1H, d, J = 2.2 Hz, H-2b), 6.04 (1H, d, J = 1.8 Hz, H-14d), 6.02 (1H, d, J = 2.2 Hz, H-12c), 5.87 (1H, d, J = 11.6 Hz, H-7c), 5.47 (1H, d, J = 3.3 Hz, H-8d), 5.38 (1H, d, J = 3.3 Hz, H-7d), 5.35 (1H, d, J = 5.3 Hz, H-7a), 4.40 (1H, d, J = 5.3 Hz, H-8a), 4.23 (1H, d, J = 11.6 Hz, H-8c).

(−)-Vitisin B (**3**): brown solid; $[\alpha]_D^{25}$ −112.4° (c 0.5, MeOH); ESI-MS m/z 907 $[M + H]^+$; ^{1}H NMR (400 MHz, acetone-d_6) δ 7.26 (2H, d, J = 8.6 Hz, H-2a, H-6a), 7.20 (2H, d, J = 8.5 Hz, H-2d, H-6d), 7.14 (1H, d, J = 8.3 Hz, H-6b), 6.92 (2H, d, J = 8.6 Hz, H-3a, H-5a), 6.83 (2H, d, J = 8.6 Hz, H-3d, H-5d), 6.76 (1H, d, J = 16.8 Hz, H-8b), 6.70−6.62 (5H, m, H-5b, H-2b, H-14b, H-2c, H-6c), 6.61 (1H, d, J = 16.8 Hz, H-7b), 6.59 (2H, d, J = 8.6 Hz, H-3c, H-5c), 6.33 (2H, br s, H-12c), 6.24−6.19 (5H, m, H-12b, H-10d, H-14d, H-12d, H-14c, H-12a), 6.13 (2H, d, J = 2.2 Hz, H-10a, H-14a), 5.55 (1H, d, J = 4.7 Hz, H-7c), 5.41 (2H, m, H-7d, H-7a), 4.53 (1H, d, J = 4.5 Hz, H-8a), 4.45 (1H, d, J = 5.4 Hz, H-8d), 4.33 (1H, d, J = 4.7 Hz, H-8c).

Anti-α-glucosidase Activities of (+)-Hopeaphenol, (+)-Vitisin A, and (−)-Vitisin B. Three isolated compounds were used to determine the α-glucosidase inhibitory activities compared to the positive control of acarbose (Figure 4A). Before the determinations of IC_{50} inhibitions, the same 10 μM was used for prescreening tests. For hopeaphenol, about 60% inhibition was found, and for vitisin A and vitisin B, almost

DOI: 10.1021/acs.jafc.5b02069
J. Agric. Food Chem. 2015, 63, 6393−6401

Table 1. Kinetic Parameters of α-Glucosidase and DPP-IV Inhibition in the Presence of (−)-Vitisin B or (+)-Vitisin A

	α-glucosidase inhibition					
	(+)-vitisin A			(−)-vitisin B		
	control	0.3125 μM	1.25 μM	control	0.3125 μM	0.625 μM
inhibition type		mixed noncompetitive			mixed noncompetitive	
K_m or K'_m[a] (mM)	0.719	0.845	0.981	0.719	0.866	1.058
V_{max} or V'_{max}[b]	0.095	0.0871	0.0737	0.095	0.086	0.072
K_i[c] (μM)		1.784			0.633	
K_{is}[d] (μM)		3.842			1.249	

	DPP-IV inhibition (−)-vitisin B			
	control	5 μM	15 μM	25 μM
inhibition type		mixed noncompetitive		
K_m or K'_m[a] (mM)	1.25	1.029	0.941	0.927
V_{max} or V'_{max}[b]	0.0208	0.0153	0.00878	0.00543
K_i[c] (μM)		7.661		
K_{is}[d] (μM)		11.361		

[a]K_m and K'_m are Michaelis constants in the absence and presence of inhibitor, respectively. [b]V_{max} and V'_{max} are maximal velocities in the absence and presence of inhibitor, respectively. [c]Enzyme−inhibitor dissociation constant. [d]Enzyme−substrate dissociation constant.

100% inhibition was found. Therefore, different dilutions and different concentrations for each purified compound were used to perform α-glucosidase inhibition. These three compounds, (+)-hopeaphenol, (+)-vitisin A, and (−)-vitisin B, showed dose-dependent inhibitions against α-glucosidase with IC_{50} values of 18.3, 1.22, and 1.02 μM, respectively, compared to the IC_{50} of acarbose of 6.39 mM. These three resveratrol tetramers with the same molecular mass showed much more significant α-glucosidase inhibitory activities than that of acarbose. (+)-Hopeaphenol, (+)-vitisin A, and (−)-vitisin B showed about 350-, 5340-, and 6265-fold better α-glucosidase inhibitions than acarbose. Therefore, the first two potent α-glucosidase inhibitors of (+)-vitisin A and (−)-vitisin B with similar IC_{50} values were selected for further kinetic analyses. It was found that (+)-vitisin A (Figure 4B) and (−)-vitisin B (Figure 4C) showed mixed-type noncompetitive inhibition against α-glucosidase with respect to pNPG (substrate) and pNPG−α-glucosidase (substrate−enzyme complex). In the absence of (+)-vitisin A, the K_m and V_{max} were 0.719 mM and 0.095 (Δ*A*405/min), respectively; whereas with the 0.3125 and 1.25 μM (+)-vitisin A additions, the K'_m was increased to 0.845 and 0.981 mM, and V'_{max} was decreased to 0.0871 and 0.0737 (Δ*A*405/min). The calculated K_i and K_{is} for (+)-vitisin A, respectively, were 1.784 and 3.842 μM (Table 1). In the absence of (−)-vitisin B, the K_m and V_{max} were 0.719 mM and 0.095 (Δ*A*405/min), respectively; with the 0.3125 μM and 0.625 μM (−)-vitisin B additions, the K'_m was increased to 0.866 and 1.058 mM and V'_{max} was decreased to 0.086 and 0.072 (Δ*A*405/min). The calculated K_i and K_{is} for (−)-vitisin B, respectively, were 0.633 and 1.249 μM (Table 1). Tadera et al.[27] tested 16 flavonoids against yeast α-glucosidase activity (IC_{50}, μM), among which epigallocatechin gallate (2 μM), cyanidin (4 μM), myricetin (5 μM), and quercetin and genistein (7 μM) showed excellent yeast α-glucosidase inhibition with IC_{50} values of <10 μM; however, none of them were active inhibitors against rat intestinal α-glucosidase. In fact, the current results for (+)-vitisin A and (−)-vitisin B exhibited better inhibitory activities than those reported by Tadera et al.[27] The low values of K_i and K_{is} represented less dissociation of the inhibitor−enzyme complex and inhibitor−enzyme−substrate complex, respectively, with high inhibitory potency. Tadera et al.[27] reported the potent flavonoids against yeast α-glucosidase activities in mixed noncompetitive patterns with K_i and K_{is} values of 3 and 7.6 μM for epigallocatechin gallate, 3 μM and 7.6 μM for myricetin, 3.4 μM and 14 μM for quercetin, and 52 μM and 4.2 μM for genistein, which were higher than those with (+)-vitisin A (1.784 and 3.842 μM) and (−)-vitisin B (0.633 and 1.249 μM) in the present study. The yeast α-glucosidase has been widely used to evaluate α-glucosidase inhibitory ability. However, Oki et al.[28] have indicated that the efficacy of α-glucosidase inhibition was greatly affected by different origins. Therefore, α-glucosidase from mammalian will be used for further investigations.

Anti-DPP-IV Activities of (+)-Hopeaphenol, (+)-Vitisin A, and (−)-Vitisin B. Three isolated compounds from S-Et-EA were used to determine the DPP-IV inhibitory activities compared to the positive control of sitagliptin (Figure 5A). Before the determinations of IC_{50} inhibitions, the same 25 μM was used for prescreening tests. For hopeaphenol, about 10% inhibition was found; for vitisin A, about 25% inhibition was found; and for vitisin B, about 80% inhibition was found. Therefore, different dilutions and different concentrations for each purified compound were used to perform DPP-IV inhibitions. These three compounds, (+)-hopeaphenol, (+)-vitisin A, and (−)-vitisin B, showed dose-dependent inhibitions against DPP-IV with IC_{50} values of 401, 90.75, and 15.3 μM, respectively, compared to sitagliptin (IC_{50} = 47.35 nM). (−)-Vitisin B showed about 26- and 6-fold better DPP-IV inhibitions than (+)-hopeaphenol and (+)-vitisin A and less than that of sitagliptin. Therefore, the potent DPP-IV inhibitor (−)-vitisin B was selected for further kinetic analyses. (−)-Vitisin B showed mixed noncompetitive type (close to noncompetitive type) inhibition against DPP-IV with respect to Gly-pNA (substrate) and Gly-pNAp−DPP-IV (substrate−enzyme complex) (Figure 5B). In the absence of (−)-vitisin B, the K_m and V_{max} were 1.25 mM and 0.0208 (Δ*A*405/min), respectively; with 5, 15, and 25 μM (−)-vitisin B additions, the K'_m was decreased to 1.029, 0.941, and 0.927 mM. However, the V'_{max} was also decreased to 0.0153, 0.00878, and 0.00543 (Δ*A*405/min). The calculated K_i and K_{is} for (−)-vitisin B, respectively, were 7.661 and 11.361 μM (Table 1). The DPP-IV inhibitory activities were frequently screened from protein

DOI: 10.1021/acs.jafc.5b02069
J. Agric. Food Chem. 2015, 63, 6393−6401

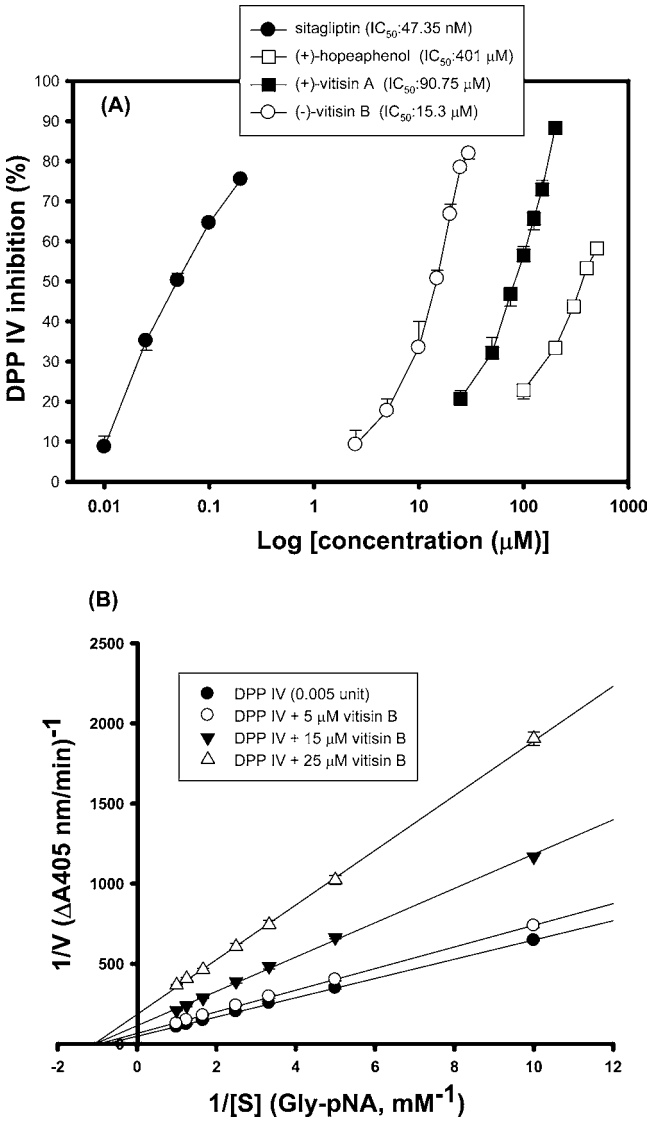

Figure 5. (A) Effect of different concentrations of (+)-hopeaphenol, (+)-vitisin A, and (−)-vitisin B on dipeptidyl peptidase-IV (DPP-IV) inhibitory activities compared to the positive control of sitagliptin. (B) Lineweaver−Burk plots of DPP-IV (0.005 U) without or with (−)-vitisin B at the different concentrations of Gly-Pro-*p*-nitroanilide as substrate (0.1, 0.2, 0.3, 0.4, 0.6, 0.8, and 1 mM). Fifty percent inhibition (IC_{50}) of DPP-IV activity was calculated as the concentration of sample that inhibited 50% of DPP-IV activity under tested conditions. Data are expressed as the mean ± SD (n = 3).

hydrolysates, such as pepsin-treated whey proteins[21] or pepsin-treated yam dioscorin.[22] Fan et al.[29] reported the DPP-IV inhibitory activities from flavonoids by using luciferase assay kits, among which luteolin, apigenin, and flavone for DPP-IV inhibition, respectively, were the noncompetitive type, non-competitive type, and competitive type. For the K_i from the Lineweaver−Burk plot, the results were 4.9, 7.9, and 18.6 μM, respectively. Saleem et al.[30] reported the potent DPP-IV inhibitory activities (expressed as IC_{50}) including quinovic acid (30.7 μM), quinovic acid-3*β*-*O*-*β*-D-glycopyranoside (57.9 μM), and quinovic acid-3*β*-*O*-*β*-D-glucopyranosyl-(28-1)-*β*-D-glucopyranosyl ester (23.5 μM) from *Fagonia cretica* and lupeol (31.6 μM) from *Hedera nepalensis*. It was suggested that the improved impaired glucose tolerance in HF-induced obese rats after S-Et interventions might be in part due to α-glucosidase and DPP-IV inhibitory activities. Interestingly, several results have indicated that VTT ethanol extracts showed an antiobesity effect and preferentially improved glucose and lipid dysregulation in developing obese mice.[31] Moreover, vitisin A could inhibit 3T3L1 adipocyte differentiations through p21-dependent and Rb-dependent cell cycle arrest, which resulted in suppressions of preadipocyte proliferation.[32] Taken together, these results suggested that VTT ethanol extract or vitisin A might reduce serum lipid levels and inhibition against preadipocyte differentiations to suppress the development of obesity. In the present study VTT-Et might act to inhibit α-glucosidase and DPP-IV activities to ameliorate impaired glucose tolerance rather than weight loss in obese rats. Therefore, the conflicting results could be due to different obesity stages.

In conclusion, the current results showed that the isolated compounds, resveratrol tetramers of (−)-vitisin B and (+)-vitisin A, effected excellent inhibitory activities against yeast α-glucosidase and DPP-IV, which might correlate with the VTT-Et interventions in improvements of impaired glucose tolerance in diet-induced obese rats. Therefore, on the basis of the observed biological functions of the current results, the development of VTT extracts as functional foods may be beneficial for blood glucose regulation and diabetic management.

■ ASSOCIATED CONTENT

Ⓢ Supporting Information

Supplementary Table S1. The Supporting Information is available free of charge on the ACS Publications website at DOI: 10.1021/acs.jafc.5b02069.

■ AUTHOR INFORMATION

Corresponding Authors

*(W.-C.H.) E-mail: wchou@tmu.edu.tw.
*(C.-I.C.) E-mail: changchii@mail.npust.edu.tw.

Funding

We thank Ministry of Science and Technology, Republic of China (NSC 100-2324-B-038-001), for financial support.

Notes

The authors declare no competing financial interest.

■ REFERENCES

(1) WHO Fact Sheet 311: Obesity and overweight.
(2) Chowdhury, T. Diabetes and cancer. *QJM* **2010**, *103*, 905−915.
(3) Kahn, B. B.; Flier, J. S. Obesity and insulin resistance. *J. Clin. Invest.* **2000**, *106*, 473−481.
(4) Kahn, S. E.; Hull, R. L.; Utzschneider, K. M. Mechanisms linking obesity to insulin resistance and type 2 diabetes. *Nature* **2006**, *444*, 840−846.
(5) Alberti, K. G. M. M.; Eckel, R. H.; Grundy, S. M.; Zimmet, P. Z.; Cleeman, J. I.; Donato, K. A.; Fruchart, J. C.; James, W. P. T.; Loria, C. M.; Smith, S. C. Harmonizing the metabolic syndrome: a joint interim statement of the International Diabetes Federation Task Force on Epidemiology and Prevention; National Heart, Lung, and Blood Institute. *Circulation* **2009**, *120*, 1640−1645.
(6) Day, C. Metabolic syndrome, or what you will: definitions and epidemiology. *Diabetes Vasc. Dis. Res.* **2007**, *4*, 32−38.
(7) Smyth, S.; Heron, A. Diabetes and obesity: the twin epidemics. *Nat. Med.* **2005**, *12*, 75−80.
(8) Balfour, J. A.; McTavish, D. Acarbose. An update of its pharmacology and therapeutic use in diabetes mellitus. *Drugs* **1993**, *46*, 1025−1054.
(9) Drucker, D.; Easley, C.; Kirkpatrick, P. Sitagliptin. *Nat. Rev. Drug Discovery* **2007**, *6*, 109−110.

DOI: 10.1021/acs.jafc.5b02069
J. Agric. Food Chem. 2015, 63, 6393−6401

(10) Idris, I.; Donnelly, R. Dipeptidyl peptidase-IV inhibitors: a major new class of oral antidiabetic drug. *Diabetes, Obes. Metab.* **2007**, *9*, 153−165.
(11) Drucker, D. J. The biology of incretin hormones. *Cell Metab.* **2006**, *3*, 153−165.
(12) Chiu, N. Y.; Chang, K. H. *The Illustrated Medicinal Plants of Taiwan*; SMC Publishing: Taipei, Taiwan, 1995; Vol. 4, 147 pp.
(13) Huang, C. Y.; Wen, C. L.; Lu, Y. L.; Lin, Y. S.; Chen, L. G.; Hou, W. C. Antihypertensive activities of extracts from tissue cultures of *Vitis thunbergii* var. *taiwaniana*. *Bot. Stud.* **2010**, *51*, 317−324.
(14) Lin, Y. S.; Lu, Y. L.; Wang, G. J.; Chen, L. G.; Wen, C. L.; Hou, W. C. Ethanolic extracts and isolated compounds from small-leaf grape (*Vitis thunbergii* var. *taiwaniana*) with antihypertensive activities. *J. Agric. Food Chem.* **2012**, *60*, 7435−7441.
(15) Wang, K. T.; Chen, L. G.; Tseng, S. H.; Huang, J. S.; Hsieh, M. S.; Wang, C. C. Anti-inflammatory effects of resveratrol and oligostilbenes from *Vitis thunbergii* var. *taiwaniana* against lipopolysaccharide-induced arthritis. *J. Agric. Food Chem.* **2011**, *59*, 3649−3656.
(16) Tsai, C. F.; Wang, K. T.; Chen, L. G.; Lee, C. J.; Tseng, S. H.; Wang, C. C. Anti-inflammatory effects of *Vitis thunbergii* var. *taiwaniana* on knee damage associated with arthritis. *J. Med. Food* **2014**, *17*, 479−486.
(17) Wang, C. K.; Chen, L. G.; Wen, C. L.; Hou, W. C.; Hung, L. F.; Yen, S. J.; Shen, Y. J.; Lin, S. Y.; Liang, Y. C. Neuroprotective activity of *Vitis thunbergii* var. *taiwaniana* extracts in vitro and in vivo. *J. Med. Food* **2010**, *13*, 170−178.
(18) Deng, J. S.; Chang, Y. C.; Wen, C. L.; Liao, J. C.; Hou, W. C.; Amagaya, S.; Huang, S. S.; Huang, G. J. Hepatoprotective effect of the ethanol extract of *Vitis thunbergii* on carbon tetrachloride-induced acute hepatotoxicity in rats through anti-oxidative activities. *J. Ethnopharmacol.* **2012**, *142*, 795−803.
(19) Pan, C.-H.; Tsai, C.-H.; Lin, W.-H.; Chen, G.-Y.; Wu, C.-H. Ethanolic extract of Vitis thunbergii exhibits lipid lowering properties via modulation of the AMPK-ACC pathway in hypercholesterolemic rabbits. *Evidence-Based Complement. Altern. Med.* **2012**, *2012*, 1.
(20) Liu, X.; Zhu, L.; Tan, J.; Zhou, X.; Xiao, L.; Yang, X.; Wang, B. Glucosidase inhibitory activity and antioxidant activity of flavonoid compound and triterpenoid compound from *Agrimonia pilosa* Ledeb. *BMC Complement. Altern. Med.* **2014**, *14*, 12.
(21) Lacroix, I. M. E.; Li-Chan, E. C. Y. Inhibition of dipeptidyl peptidase (DPP)-IV and α-glucosidase activities by pepsin-treated whey proteins. *J. Agric. Food Chem.* **2013**, *61*, 7500−7506.
(22) Shih, S. L.; Lin, Y. S.; Lin, S. Y.; Hou, W. C. Effects of yam dioscorin interventions on improvements of the metabolic syndrome in high-fat diet-induced obese rats. *Bot. Stud.* **2015**, *56*, 4.
(23) Woods, S. C.; Seeley, R. J.; Rushing, P. A.; D'Alessio, D.; Tso, P. A controlled high-fat diet induces an obese syndrome in rats. *J. Nutr.* **2003**, *133*, 1081−1087.
(24) Yan, K. X.; Terashima, K.; Takaya, Y.; Niwa, M. A novel oligostilbene named (+)-viniferol A from the stem of *Vitis vinifera* 'Kyohou'. *Tetrahedron* **2001**, *57*, 2711−2715.
(25) Ito, J.; Gobaru, K.; Shimamura, T.; Niwa, M.; Takaya, Y.; Oshima, Y. Absolute configurations of some oligostilbenes from *Vitis coignetiae* and *Vitis vinifera* 'Kyohou'. *Tetrahedron* **1998**, *54*, 6651−6660.
(26) Ito, J.; Niwa, M. Absolute structures of new hydroxystilbenoids, vitisin C and viniferal, from *Vitis vinifera* 'Kyohou'. *Tetrahedron* **1996**, *52*, 9991−9998.
(27) Tadera, K.; Minami, Y.; Takamatsu, K.; Matsuoka, T. Inhibition of α-glucosidase and α-amylase by flavonoids. *J. Nutr. Sci. Vitaminol.* **2006**, *52*, 149−153.
(28) Oki, T.; Matsui, T.; Osajima, Y. Inhibitory effect of α-glucosidase inhibitors varies according to its origin. *J. Agric. Food Chem.* **1999**, *47*, 550−553.
(29) Fan, J.; Johnson, M. H.; Lila, M. A.; Yousef, G.; de Mejia, E. G. Berry and citrus phenolic compounds inhibit dipeptidyl peptidase IV: implications in diabetes management. *Evidence-Based Complement. Altern. Med.* **2013**, *2013*, 479503.
(30) Saleem, S.; Jafri, L.; ul Haq, I.; Chang, L. C.; Calderwood, D.; Green, B. D.; Mirza, B. Plants *Fagonia cretica* L. and *Hedera nepalensis* K. Koch contain natural compounds with potent dipeptidylpeptidase-4 (DPP-4) inhibitory activity. *J. Ethnopharmacol.* **2014**, *156*, 26−32.
(31) Hsu, H. M.; Chen, W. Y.; Pan, P. H.; Mao, F. C. *Vitis thunbergii* supplementation demonstrates an anti-obesity effect in developing obese mice. *Eur. J. Integr. Med.* **2014**, *6*, 581−587.
(32) Kim, S. H.; Park, H. S.; Lee, M. S.; Cho, Y. J.; Kim, Y. S.; Hwang, J. T.; Sung, M. J.; Kim, M. S.; Kwon, D. Y. Vitisin A inhibits adipocyte differentiation through cell cycle arrest in 3T3-L1 cells. *Biochem. Biophys. Res. Commun.* **2008**, *372*, 108−113.

DOI: 10.1021/acs.jafc.5b02069
J. Agric. Food Chem. 2015, 63, 6393−6401

Table 1. Strains and Plasmids Used in This Study

bacterial strain or plasmid	characteristics[a]	source or reference	medium
Strains			
E. coli Rosetta (DE3)	gene expression studies	TranGens Biotech Co.	LB
*Trans*1-T1 phage resistant chemically competent *E. coli*	standard cloning procedures	TranGens Biotech Co.	LB
L. monocytogenes	the indicator strain	our laboratory	BHI
L. innocua	the indicator strain	our laboratory	BHI
Lactococcus lactis 1363	the indicator strain	17	M17
Lactobacillus casei 2	the indicator strain	17	M17
Streptococcus thermophilus	the indicator strain	our laboratory	M17
Pediococcus acidilactici	the indicator strain	17	M17
Lactobacillus rhamnosus	the indicator strain	17	M17
Bacillus licheniformis	the indicator strain	our laboratory	BHI
Staphylococcus aureus 1	the indicator strain	our laboratory	BHI
Staphylococcus aureus 2	the indicator strain	our laboratory	BHI
Bacillus subtilis 1	the indicator strain	our laboratory	BHI
Bacillus subtilis 2	the indicator strain	our laboratory	BHI
Enterococcus durans			
41D	Durancin GL producer	16	MRS
9EB8	the indicator strain	16	MRS
KLDS 6.0603	the indicator strain	our laboratory	M17
KLDS 6.0605	the indicator strain	our laboratory	M17
KLDS 6.0607	the indicator strain	our laboratory	M17
KLDS 6.0315	the indicator strain	our laboratory	M17
KLDS 6.0323	the indicator strain	our laboratory	M17
Enterococcus faecalis			
R612-Z1	the indicator strain	our laboratory	M17
ATCC 19433	the indicator strain	our laboratory	M17
Enterococcus faecium			
R615-Z1	the indicator strain	our laboratory	M17
ATCC 19434	the indicator strain	our laboratory	M17
Plasmids			
pEASY-Blunt	Amp^r, Kan^r; lacZ, cloning vector	TranGens Biotech Co.	
pEASY/durAB	Amp^r, Kan^r; durAB cloned into *pEASY*-Blunt simple cloning vector	this study	
pGEX/his-durAB	Amp^r, Kan^r; *Bam*H I-*Xho* I fragement harboring mature-durAB gene cloned into pGEX-6p-1	this study	
pGEX/his-durAB mutants	Forty different pGEX/his-durAB based plasmids with each carried only one single alanine mutagenesis	this study	
pGEX-6p-1	Amp^r, Kan^r; *E. coli* expression vector, with the N-terminal GST-tag	our laboratory	

[a] Amp^r, ampicillin resistant; Kan^r, kanamycin resistant;

products prone to *Listeria* infections because of its high antilisterial activity and narrow inhibitory spectrum. As information on the structure and underlying mechanisms of durancin GL remains limited at the molecular level, widespread functional screening of its residues must be developed.

In this study, we constructed an in vitro heterologous expression system to produce mature durancin GL in *Escherichia coli*. Alanine substitution was also performed through site-directed in vitro mutagenesis with the constructed expression vector. The effects of mutations on the potency or specificity of the peptide toward *L. monocytogenes* and other selected indicator strains were also determined.

MATERIALS AND METHODS

Bacterial Strains, Plasmids, and Culture Conditions. The strains and plasmids used in this study are listed in Table 1. *Trans1*-T1 phage-resistant chemically competent *E. coli* and *pEASY*-Blunt simple cloning vector (TransGen Biotech, Beijing, China) were used for standard cloning procedures. Chemically competent *E. coli* Rosetta (DE3) was prepared using a competent cell preparation kit (Takara) according to the manufacturer's recommendations. *E. durans* 41D, a bacteriocin-producing strain, and other LAB strains, such as *Lactococcus*, *E. durans*, *Enterococcus faecalis*, and *Enterococcus faecium*, were propagated at 37 °C without agitation in M17 broth (Becton, Dickinson Co. Ltd., Franklin Lakes, New Jersey, USA). *Listeria* spp., *Bacillus subtilis*, *Staphylococcus aureus*, and *Bacillus licheniformis* were propagated in brain heart infusion (BHI) medium (Land Bridge Co., Ltd., Beijing, China) under aerobic conditions at 37 °C. *E. coli* strains were grown in LB medium at 37 °C on a shaking incubator. When required, antibiotics (Ameresco Co., Ltd., USA) were added as selective agents with appropriate concentrations (ampicillin, 50 μg/mL; kanamycin, 50 μg/mL).

Construction of Recombinant Plasmid and DNA Transformation. The constructs used in this study are listed in Table 1. DNA cloning techniques, transformations, and restriction enzyme reactions were performed according to the standard protocols[18] or by following the recommendation of the manufacturers. Plasmids were isolated from *E. coli* by using a high-purity plasmid mini-prep kit (BioTeke, Beijing, China). Restriction enzymes and DNA ligation kit were obtained from Takara Biotech (Dalian, China) and Sangon Biotech Co., Ltd. (Shanghai, China), respectively. Primers were designed according to the plasmid pGL sequence (Accession no. HQ696461.1) and synthesized by Sangon Biotech (Shanghai, China). The *Trans*1-T1 phage-resistant chemically competent *E. coli* and *E. coli* Rosetta (DE3) were transformed using heat-shock method.[19]

DOI: 10.1021/acs.jafc.5b02114
J. Agric. Food Chem. 2015, 63, 6402−6409

The *durAB* genes were amplified using dur1 and dur2 primers and PrimeSTAR HS Premix (TaKaRa) with 1 μL of overnight broth containing fresh *E. durans* 41D as template. Amplification conditions were as follows: preheating at 95 °C for 3 min, 30 cycles of denaturation at 95 °C for 15 s, annealing at 55 °C for 20 s, extension at 72 °C for 40 s, and a final extension at 72 °C for 7 min. PCR-generated fragments were analyzed by agarose gel electrophoresis and purified using a DNA fragment purification recovery kit (Bioteke Corporation, Beijing, China). The DNA fragments were subcloned into a cloning vector by using a *pEASY*-blunt simple cloning kit (TransGen, Beijing, China) to produce the *pEASY*/durAB construct. The ligation mixture was transformed into *Trans*1-T1 phage-resistant chemically competent *E. coli*. The positive clones were screened through PCR using M13-F and M13-R primers and sequenced by Sangon Biotech.

The his-durAB fragment was amplified using GST1 and GST2 primers with *pEASY*/durAB plasmid as template. The amplified fragment was digested with *Bam*H I and *Xho* I before subcloning into the plasmid pGEX-6p-1 to construct the expression vector pGEX/his-durAB (Figure 1). Ligation was then performed with a DNA ligation

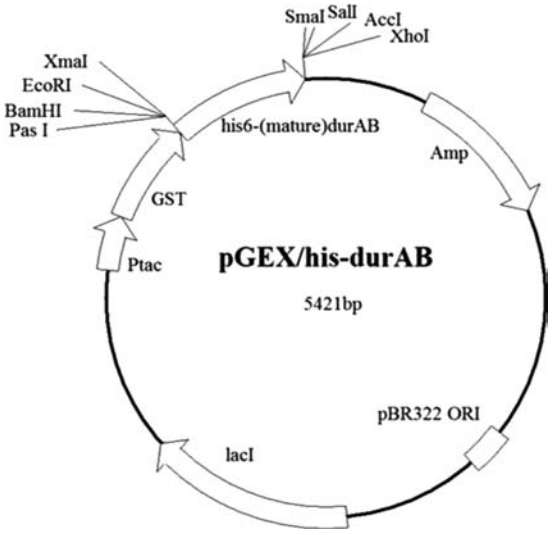

Figure 1. Map of the expression vector pGEX/his-*dur*AB with ORFs indicated by arrows.

kit (TaKaRa). Chimeric DNA was transformed into *Trans*1-T1 phage-resistant chemically competent *E. coli*. PCR analysis with pGEX-3 and pGEX-5 primers and DNA sequencing (Sangon Biotech Co) were used to confirm the correct construction of the plasmid. The correct pGEX/his-durAB plasmid was reisolated and transformed into *E. coli* Rosetta (DE3). By using the cloning strategy proposed in this work, we obtained the translational fusion protein of GST-His-durancin GL.

Site-Directed Mutagenesis and Construction of Variants. Durancin GL mutations were generated using a Mut Express II fast mutagenesis kit (Vazyme Biotech Co., Nanjing, China) with the pGEX/his-durAB plasmid as template. The mutant primers used are presented in Table 2 and Supporting Information Table S1. PCR reactions were established according to the manufacturer's recommendations. The PCR product was digested for 1 h at 37 °C with the restriction enzyme DpnI (Vazyme Biotech) to eliminate the original template and increase mutation efficiency. After homologous recombination and linear plasmid cyclization, the circular mutant plasmid was then transformed into *E. coli*. The proper orientation of the fragments was verified through PCR analysis using pGEX-3 and pGEX-5 primers, and the accuracy of mutagenesis was confirmed through DNA sequencing. After sequence confirmation, the plasmid was introduced into *E. coli* Rosetta (DE3) for protein expression.

Protein Expression and Purification. The fusion protein GST-His-durancin GL was purified by Ni-NTA and GST affinity purification system (GE Healthcare Co., USA) according to the manufacturer's instructions. The transformed plasmids encoding wild-type durancin GL and mutants were grown overnight in 25 mL of LB containing 50 μg/mL ampicillin at 37 °C. About 9 mL of the respective precultures were inoculated into 900 mL of LB, grown at 37 °C until OD_{600} = 0.6, and then induced with 1.0 mM IPTG (final concentration) for 5 h. Cells were collected through centrifugation at 8000*g* at 4 °C for 5 min. The cell pellets were resuspended in 90 mL of Ni−NTA binding buffer (20 mM sodium phosphate, 20 mM imidazole, 500 mM NaCl, pH 7.4) and sonicated in an ice bath (400 W, 400 cycles of 2 s pulses with a 9 s pause). The lysate was centrifuged at 4 °C for 30 min at 12000*g* to remove debris. The supernatant was filtered through a 0.22 μm filter (Sartorius; Goettingen, Germany) before loading onto a 1 mL nickel His-Trap chelating column (GE Healthcare, Beijing, China). After loading, the column was washed with 10 mL of Ni−NTA binding buffer. The bound His-tagged proteins were eluted from the Ni resin with 10 mL of elution buffer (20 mM sodium phosphate, 500 mM NaCl, 500 mM imidazole, pH 7.4). The eluent was dialyzed overnight at 4 °C against 2 L of GST binding buffer (140 mM NaCl, 2.7 mM KCl, 10 mM Na_2HPO_4, 2 mM KH_2PO_4, pH 7.3) by using 7 kDa MWCO dialysis membranes (Millipore, USA). After centrifugation (12000*g* for 20 min), the supernatant was loaded onto GSTrap 4B column (GE Healthcare). The column was washed with 10 mL of GST binding buffer and 10 mL of enterokinase cleavage buffer (25 mM Tris-HCl, 50 mM NaCl, 2 mM $CaCl_2$, pH 7.6). Enterokinase cleavage mixture (Sangon Biotech) was then loaded onto the column. The column was then incubated at 25 °C for 16 h and eluted with 5 mL of enterokinase cleavage buffer. The eluate was collected and verified through mass spectrometry (MoonBiochem Co., Ltd., Wuhan, China). Final concentration was adjusted to 20 μg/mL for subsequent usage.

Antibacterial Activity Assay of Durancin GL and Its Mutants. The overnight culture of *E. durans* 41D (propagated in MRS broth) was centrifuged at 12000*g* for 10 min to obtain cell-free supernatant, which was used as control. With *L. monocytogenes* and *Listeria innocua* as targets, antibacterial activity assay was performed using agar diffusion method with a peptide concentration of 20 μg/mL.[20] The diameter of each inhibition zone was measured and integrated into calculation for total activity.

For antimicrobial spectrum inspection, minimum inhibitory concentration (MIC) was determined using the method described by Pilet et al.[20] Briefly, 5 μL of 2-fold serially diluted purified peptide (20 μg/mL starting concentration) was spotted in duplicates on BHI agar plates seeded with 0.5% (v/v) of indicator strain cultured for 16 h. The plates were then air-dried and incubated at 37 °C for 10−14 h. The resulting inhibition zones were detected through inspection. MIC was determined as the lowest concentration that inhibited visible growth. The MIC results showed that the required concentration of durancin GL was 2.5 μg/mL, and this concentration was used for all the mutants for antibacterial activity assay.

RESULTS

Expression and Purification of the Fusion Protein of Durancin GL (GST-his-durancin GL) and Its Variants. The sequence of the recombinant plasmid pGEX/his-*dur*AB was consistent with the anticipated results (data not shown). The recombinant GST-His-durancin GL was then expressed in *E. coli* Rosetta (DE3). A clear band of about 31.0 kDa was observed after IPTG induction at 37 °C (Figure 2A), which was consistent with the expected molecular mass of GST-His-durancin GL. After purified through Ni−NTA metal affinity chromatography, GST affinity chromatography and then treated with the recombinant bovine enterokinase. The purity of the isolated peptides was checked through analytical reverse-phase chromatography to be higher than 95% (Figure 2A). As shown in Figure 2B, the expressed cleaved durancin GL was biologically active against the indicator strain *L. monocytogenes* and *L. innocua* as determined through agar diffusion method.

DOI: 10.1021/acs.jafc.5b02114
J. Agric. Food Chem. 2015, 63, 6402−6409

Table 2. Primers and PCR Products Used in This Study for Bacteriocin Expression

primer[a]	sequence (5′−3′); restriction site or description[b]	purpose or generated plasmid(s)
dur1	GGGAGGCAATTATATGAAGAAAAAATTTGTTAGTATT	amplification of durAB
dur2	CCA GTG CCC CCA TAA ACT ATA CAC CC	
GST1	ctgGGATCCCACCATCATCATCATCATGACGACGACGACAAGGCAACTTATTATGGAAATGGTGTTTATTG	amplification of inserts from *pEASY*/durAB; introduction cleavage sites and his-tag to mature durAB
GST2	aaaCTCGAGTTTAACTCCAAATACCGATAGACGCCCATCCCC	
M13-F	GTAAAACGACGGCCAGT	PCR identification
M13-R	CAGGAAACAGCTAT GAC	
pGEX-3	CCGGGAGCTGCATGTGTCAGAGG	PCR identification
pGEX-5	GGGCTGGCAAGCCACGTTTGGTG	
T02A-F	GACAAGGCA**GCT**TATTATGGAAATGGTGTTTATTGTAATA	introducing alanine to the sencond amino acid of Durancin GL
T02A-R	TCCATAATAAGCTGCCTTGTCGTCGTCGTCATGATGATGA	
PCR Products		
durAB	574-bp fragment containing the *dur*A and *dur*B genes	cloning in *pEASY*-Blunt vector; *pEASY*/durAB
His-durAB	485-bp *Bam*H I-*Xho* I fragement carrying the His-tag and enterokinase recognition sequences fused to the mature *dur*A and *dur*B genes	pGEX/his-durAB; bacteriocin expression

[a]Other primers used for site-directed mutagenesis are listed in the Supporting Information Table S1. [b]Cleavage sites for restriction enzymes are underlined in the primers. Lowercase letters indicate incorporated tag sequences.

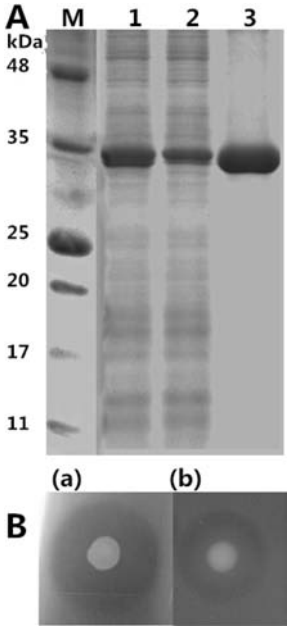

Figure 2. (A) SDS-PAGE analysis of the expression of GST-His-durancin GL and protein purification. Lane M, prestained protein standard; lanes 1 and 2, lysate of *E. coli* Rosetta (DE3) transformed with pGEX/his-*dur*AB; lane 3, GST-His-durancin GL purified with Ni-NTA and GST affinity columns. (B) Bacteriocin activity of the cleaved durancin GL after enterokinase treatment of GST-His-durancin GL; Activity was determined through agar diffusion method with *L. monocytogenes* (a) and *L. innocua* (b) as target microorganisms.

Durancin GL variants were expressed and purified using methods similar to those used for the wild-type. Sequencing of the mutated genes and analysis of the purified peptides through mass spectrometry revealed correct alterations in the primary structure in all samples (results not shown). Our results indicated that durancin GL can be readily subjected to mutagenesis, and large quantities (29.5 mg to 46.3 mg per L) of a desired mutant can be obtained through recombinant expression.

Determination of Antibacterial Activities. Each durancin GL residue was replaced with a hydrophobic small residue (alanine) through site-directed mutagenesis, and activity changes were calculated relative to that of wild-type durancin GL (Table 3). Overall, *L. monocytogenes* was more susceptible than *L. innocua* on the basis of the size of the inhibition zone of the corresponding bacteriocin (e.g., Figure 2B). Two other strains, namely, *E. durans* 9EB8 and *E. faecalis* 6.0603, were further used to detect general trends in mutational effects, and the activities measured using these two strains were in the same trend (data not shown).

As shown in Table 3, no activity was detected in G07A, C10A, and C15A mutants up to 20 μg/mL, indicating that these residues are essential for the antibacterial activity. Ten mutations (N06A, E14A, W16A, D18A, E25A, G27A, I29A, N32A, G33A, and G38A) demonstrated a detrimental effect on the activity (relative activities $\leq$80%), and seven mutations (K12A, K21A, K24A, K28A, I30A, H37A, and R43A) exhibited a relatively high activity (relative activities $\geq$110%). In addition, 21 other mutations were relatively tolerated, resulting in slight reduction or increase in the activity of mutants compared with wild-type durancin GL.

The MIC of all purified mutants was determined using two indicator strains, namely, *L. monocytogenes* and *L. innocua*, through microdilution method. Most mutants displayed antibacterial activity similar to the wild-type, whereas some mutants increased or decreased the activity for about 2-fold (MIC values in the Supporting Information S2). As the activities measured using *L. monocytogenes* and *L. innocua* were in the same trend based on the MIC results, the concentration for the inhibitory spectra determination of the durancin GL and its mutants was determined to be 2.5 μg/mL.

Determination of Inhibitory Spectra against Different Indicator Organisms. The antibacterial activity spectra of durancin GL analogues were assayed through agar diffusion

DOI: 10.1021/acs.jafc.5b02114
J. Agric. Food Chem. 2015, 63, 6402−6409

Table 3. Activities of the Purified Durancin GL and Its Derivatives[a]

	L. monocytogenes		*L. innocua*	
peptide	diameters of inhibition zone (mm)	relative to WT (%)	diameters of inhibition zone (mm)	relative to WT (%)
CFS	10.54 ± 0.45	–	8.18 ± 0.45	–
WT	17.12 ± 0.14	–	12.68 ± 0.21	–
T02A	15.18 ± 0.21	88.67	11.52 ± 0.36	90.85
Y03A	15.65 ± 0.18	91.42	11.93 ± 0.17	94.09
Y04A	14.32 ± 0.31	83.64	10.35 ± 0.16	81.62
G05A	14.46 ± 0.28	84.46	11.27 ± 0.18	88.88
N06A	11.15 ± 0.45	65.13	9.25 ± 0.22	72.95
G07A	–	–	–	–
V08A	14.52 ± 0.16	84.81	10.68 ± 0.09	84.23
Y09A	14.18 ± 0.32	82.83	10.52 ± 0.25	82.97
C10A	–	–	–	–
N11A	14.48 ± 0.22	84.58	11.68 ± 0.31	92.11
K12A	20.14 ± 0.58	117.64	14.84 ± 0.12	117.03
Q13A	15.78 ± 0.42	92.18	12.04 ± 0.15	94.95
E14A	11.68 ± 0.08	68.22	10.12 ± 0.09	79.81
C15A	–	–	–	–
W16A	13.28 ± 0.25	77.57	10.35 ± 0.34	81.62
V17A	14.32 ± 0.64	83.64	11.56 ± 0.09	91.17
D18A	9.24 ± 0.35	53.97	8.92 ± 0.12	70.35
W19A	16.94 ± 0.21	98.95	12.56 ± 0.48	99.06
N20A	13.64 ± 0.34	79.67	11.46 ± 0.25	90.38
K21A	20.44 ± 0.38	119.39	15.18 ± 0.62	119.72
S23A	13.54 ± 0.06	79.09	10.58 ± 0.18	83.44
K24A	20.22 ± 0.64	118.11	14.12 ± 0.23	111.36
E25A	11.12 ± 0.05	64.95	9.6 ± 0.26	75.71
I26A	17.48 ± 0.76	102.1	12.24 ± 0.67	96.53
G27A	13.00 ± 0.12	75.93	10.38 ± 0.31	81.86
K28A	20.72 ± 0.38	121.03	14.32 ± 0.27	112.93
I29A	12.86 ± 0.14	75.12	9.62 ± 0.17	75.87
I30A	21.00 ± 0.36	122.66	14.35 ± 0.44	113.17
V31A	17.76 ± 0.22	103.74	12.74 ± 35	100.47
N32A	11.24 ± 0.15	65.65	9.72 ± 0.15	76.66
G33A	11.46 ± 0.28	66.94	9.25 ± 0.18	72.95
W34A	17.68 ± 0.42	103.27	11.84 ± 0.16	93.38
V35A	15.12 ± 0.15	88.32	12.18 ± 0.17	96.06
Q36A	14.26 ± 0.21	83.29	12.04 ± 0.23	94.95
H37A	19.42 ± 0.36	113.43	14.56 ± 0.38	114.82
G38A	11.72 ± 0.64	68.46	9.42 ± 0.22	74.31
P39A	14.46 ± 0.28	84.46	10.74 ± 0.26	84.7
W40A	17.82 ± 0.26	104.09	10.68 ± 0.31	84.24
P42A	17.26 ± 0.35	100.82	12.32 ± 0.25	97.16
R43A	20.32 ± 0.28	118.69	13.86 ± 0.32	109.31

[a]Antibacterial activity was tested by agar diffusion method with a concentration of 20 μg/mL. Relative to WT (%) was defined as the ratio of the area (mm^2) of the inhibition zone formed by the wild type to that formed by the mutant, multiplied by 100%. –, no inhibition; CFS, cell-free culture supernatant; WT, wild-type; activity of the CFS was determined as control. Data are mean ± SD of three independent experiments.

method against a wide range of Gram-positive microorganisms (Table 4), including foodborne pathogens and probiotics of similar species and related strains. According to the size of the inhibition zones, *E. durans* showed the highest sensitivity to the purified durancin GL and its variants (Table 4). Only some *E. faecium* and *E. faecalis* strains also exhibited sensitivity to the purified durancin GL and its variants at a low level, which indicates that these bacteriocins displayed a relatively narrow spectrum of activity, which was mostly limited to *Enterococcus* (closely related to bacteriocin producer) and *Listeria* cultures.

The inhibitory spectra of durancin GL analogues differed from that of the wild-type. G07A, C10A, C15A, W16A, and N20A mutants showed no antimicrobial activity against any indicator strains at the concentration of 2.5 μg/mL, indicating these residues were important for the bacteriocin activity. D18A, K21A, G27A, and G38A mutants demonstrated a narrow antimicrobial spectrum compared with wild-type durancin GL, implying their importance for target specificity. K12A, Q13A, I30A, and V31A mutants presented a broader target cell spectrum and increased potency than wild-type durancin GL. These mutants also inhibited durancin GL resistant strains, namely, *L. lactis* 1363 and *E. faecium* R36. These results indicated that K12A, I30A, and V31A mutants were "activity enhancing" substitutions for all indicator strains, whereas Q13A mutant enhanced target specific activity against *L. lactis* 1363 and *E. faecium* R35. Therefore, position/orientation may be important to modulate the spectrum of target cells. A similar phenomenon was observed in N6A, V8A, E14A, V17A, S23A, E25A, P39A, and W40A mutants, which demonstrated enhanced specific activity against *E. faecium*. Several other mutants further exhibited activity against five *E. faecalis* strains, whereas some mutants showed a weaker activity against one or two indicators. Generally, most mutants presented no inhibitory activity against four *E. faecium* strains, except in cases with a low level of activity retention.

DISCUSSION

Durancin GL, a class IIa bacteriocin, is highly homologous to bacteriocin 31 and has been recently characterized.[16,17] Durancin GL belongs to the subgroup 4 of subclass IIa bacteriocins, which include bacteriocin 31, bacteriocin RC714, bacteriocin T8, penocin A, and enterocin SE-K4.[21] As durancin GL exhibits a high level of antilisterial activity with a relatively narrow spectrum limited to *Enterococcus* and *Listeria* cultures, it exhibits significant potential to be used as a food-grade preservative for LAB fermentations which are prone to *Listeria* infections. Nevertheless, data (available for durancin GL or even subgroup 4 of IIa bacteriocins) regarding bacteriocin structure and underlying mechanisms are limited at the molecular level; hence, each durancin GL residue must be subjected to systematic functional screening through site-directed mutagenesis. In this study, the recombinant durancin GL was expressed in *E. coli* Rosetta (DE3) fused after GST and His tag. All durancin GL residues were then subjected to systematic mutational analysis.

The fold changes in MIC values were not significant, except for G07A, C10A, and C15A mutants, which exhibited significant detrimental effect on the activity; these findings were consistent with the conservative residues of class IIa bacteriocins.[22] Replacement of Cys10 and Cys15 in durancin GL presented adverse effect on the activity; these highly conserved cysteines are essential for the stability of N-terminal β-sheet domain in all class IIa bacteriocins because of their role in formation of Cys10−Cys15 disulfide bonds.[8] Alanine alteration can disrupt the formation of Cys10−Cys15 disulfide bonds, thus resulting in antibacterial activity loss.

By contrast, mutations, such as Y04A, G05A, N06A, and V08A, at other positions of the conserved motif were well tolerated. The replacement of G7 with alanine triggered a functional loss. This result was in accordance with previous

DOI: 10.1021/acs.jafc.5b02114
J. Agric. Food Chem. 2015, 63, 6402−6409

Table 4. Inhibition Spectrum of Durancin GL and Its Derivatives Assayed against Different Susceptible Strains[a]

	E. faecalis					*E. durans*	*L. lactis*	*E. faecium*				
peptide	6.0315	6.2315	6.0323	6.0603	6.0607	9EB8	1363	R615−21	R612−21	R35	R36	other indicator strains[b]
CFS	+++	+++	+++	+++	+++	++	−	−	−	−	−	−
WT	+++	+++	+++	+++	+++	++	−	+	+	+	−	−
T02A	+++	+++	+++	+++	+++	−	−	+	−	+	−	−
Y03A	+++	+++	+++	+++	+++	−	−	+	+	+	+	−
Y04A	+++	+++	+++	+++	+++	−	−	++	−	−	−	−
G05A	++	+++	+++	+++	+++	−	−	−	−	−	−	−
N06A	+++	+++	+++	+++	+++	−	−	++	++	++	−	−
G07A	−	−	−	−	−	−	−	−	−	−	−	−
V08A	+++	+++	+++	+++	+++	−	−	++	−	++	+	−
Y09A	+	+	+++	+++	+++	−	−	−	−	−	−	−
C10A	−	−	−	−	−	−	−	−	−	−	−	−
N11A	+++	+++	+++	+++	+++	−	−	+	+	++	+	−
K12A	+++	+++	+++	+++	+++	++	++	++	++	+++	++	−
Q13A	+++	+++	+++	+++	+++	−	++	−	−	++	−	−
E14A	+++	+++	+++	+++	+++	−	−	++	++	+++	++	−
C15A	−	−	−	−	−	−	−	−	−	−	−	−
W16A	−	−	−	−	−	−	−	−	−	−	−	−
V17A	+++	+++	+++	+++	+++	−	−	++	++	++	++	−
D18A	+++	+++	−	−	−	−	−	−	−	−	−	−
W19A	+++	+++	+++	+++	+++	−	−	−	−	++	+	−
N20A	−	−	−	−	+	−	−	−	−	−	−	−
K21A	−	−	+	+++	+++	−	−	−	−	−	−	−
S23A	+++	+++	+++	+++	+++	−	−	++	++	+++	++	−
K24A	++	+	+++	+++	+++	−	−	−	−	−	−	−
E25A	+++	+++	+++	+++	+++	−	−	++	++	+++	+	−
I26A	+++	+++	+++	+++	+++	−	−	−	−	−	−	−
G27A	+++	+++	+++	+	+	−	−	+	++	−	−	−
K28A	+++	+++	+++	+++	+++	−	−	−	−	−	−	−
I29A	+++	+++	+++	+++	+++	−	−	+	−	−	−	−
I30A	+++	+++	+++	+++	+++	++	++	++	++	+++	+	−
V31A	+++	+++	+++	+++	+++	++	++	+++	++	+++	++	−
N32A	++	+	+++	+++	+++	−	−	−	−	−	−	−
G33A	+++	+++	+++	+	+++	−	−	−	−	−	−	−
W34A	+++	+++	+++	+++	+++	−	−	−	−	−	−	−
V35A	++	++	+++	+++	+++	−	−	−	−	−	−	−
Q36A	+++	+++	+++	+++	+++	−	−	−	−	−	−	−
H37A	+++	+++	+++	+++	+++	−	−	−	−	−	−	−
G38A	++	++	−	−	−	−	−	−	−	−	−	−
P39A	+++	+++	+++	+++	+++	−	−	++	++	++	−	−
W40A	+++	+++	+++	+++	+++	−	−	+	+	++	−	−
P42A	+++	+++	+++	+++	+++	−	−	−	−	−	−	−
R43A	+++	+++	+++	+++	+++	−	−	+	++	−	−	−

[a]Diameter of inhibition zone: −, no inhibition; +, ≤ 7 mm; ++, 7−10 mm; +++, ≥10 mm. [b]Other indicator strains are the indicator strains listed at Table 1.

studie on the corresponding glycine in position 6 of pediocin PA-1 and sakacin P.[23] These findings indicated that G7 in durancin GL plays an important role within the YGNGV motif. As GNGV may assume a β-sheet-like structure, alanine substitution at this position could destroy β-turn and lead to activity loss.[15,24]

In comparison with wild-type durancin GL, activities against *L. monocytogenes* and *L. innocua* were altered to different extents in all variants. The limited effect of most mutants could be attributed to conservative alanine substitution (small and nonpolar) relative to other amino acid replacements (with regard to size, polarity, and charge). However, several mutants, such as Q13A, I30A, and V31A, further displayed changes in their inhibition zones and inhibitory spectra, indicating their importance for durancin GL activity, but their contribution varied in terms of magnitude.

Most substitutions localized in the N-terminal moiety exhibited adverse effect on the activity, but antimicrobial activity was enhanced in K12A mutant. This finding was unforeseen because Lys12 is a highly conserved residue in subgroup 4 of class IIa bacteriocin;[25] moreover, positively charged residues at the N terminus are important for recognition and binding of the target bacterial membrane.[4] Bacteriocin mutants decrease the net positive charge of the N-terminal β-sheet-like domain by introducing a neutral polar residue, resulting in 2−100-fold reduction in activity.[24] In addition, K12 is the only positively charged residue in the N-terminal domain of durancin GL. The negatively charged

DOI: 10.1021/acs.jafc.5b02114
J. Agric. Food Chem. 2015, 63, 6402−6409

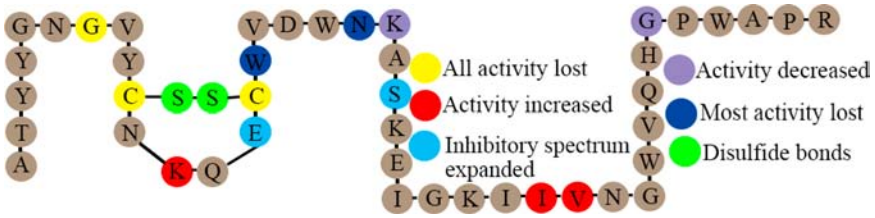

Figure 3. Most important residues unraveled by alanine-scanning method.

replacement E14A further showed a significant decrease in antibacterial activity, but these results were not isolated. Substitutions at K21, K24, K28, H37, R43 (positively charged), D18, and E25 (negatively charged) also exhibited an identical effect on the activity. Notably, D18A considerably decreased the value by approximately 50%, suggesting that this residue is critical for activity. Previous structural analysis of five pediocin-like bacteriocins (leucocin A, carnobacteriocin B2, curvacin A, sakacin P, and sakacin mutation) revealed a flexible hinge at the conserved Asp17/Asn17 in the peptides of subgroup 1; this hinge also possibly existed between the β-sheet N-terminal region and the hairpin-like C-terminal region in the peptides of subgroups 2, 3, and 4.[24] Hence, negative charge and residue position are important. These results may imply that the net charge of durancin GL is essential for its antilisterial activity, and peptides with a net charge of +2 are preferred for its initial interaction with the acidic membrane or receptor proteins of *Listeria*. However, the optimal net charge of bacteriocin to achieve maximum activity remains unknown and requires further mutation studies.

Replacement of the conserved or partially conserved asparagine residue (positions 6 and 32) with alanine reduced bacteriocin activity by more than 30%. By contrast, substitution of N11 or N20 residues, which are less conserved, minimally affected the activity. These results are in agreement with those reported by Gunnar Fimland;[24] in his study, the polar amide group in position 5 and its exact location in space are crucial for pediocin-like bacteriocins to be fully active. Hence, the amide group interacts in a structurally specified and restricted manner with the polar group(s) on target cells, possibly on a peptide receptor or docking site or on the peptide itself. Asn32 may also interact with target cells in a similar manner.

As residue Trp15 (corresponding to Trp16 in durancin GL) is typical in groups 3 and 4 bacteriocins,[21] its replacement abolished the antibacterial activity in the inhibitory spectrum assay; this finding indicated that aromaticity or hydrophilicity is important at this position. Tryptophan residues also play a determinant role in the adsorption and orientation of amphiphilic peptides and proteins in the membranes; these residues can form hydrogen and hydrophobic bonds with the polar and nonpolar groups of polar lipids.[26,27] In particular, Trp16 at the adjoining part of the N- and C-terminal domains could play a major role in the proper domain orientation within the membrane. Trp18 is conserved in groups 1, 2, and 4 bacteriocins, Trp33 is conserved in groups 3 and 4, and Trp39 is partially conserved in groups 1 and 4 (which correspond to Trp19, Trp34, and Trp40 in durancin GL, respectively).[21] However, W16A mutant exhibited negative effects compared with W19, W34, and W40 mutants, which had similar activity to the wild-type but limited effect because hydrophobic and aromatic residues were replaced with small and nonpolar residues. Two tryptophan residues (one in the middle of the peptide and one near the C-terminal end) play a critical role in stabilizing the hairpin-like structure of the C-terminal domain in subgroups 1 and 2 among bacteriocins with one disulfide bridge.[21,25,28] Hence, Trp19, Trp34, and Trp40 are not essential for helix promotion or helix stabilization in the membrane. These results could also be explained by the inability of durancin GL to create a hairpin structure or functional redundancy in tryptophan residues. These hypotheses must be verified in further work through nuclear magnetic resonance or circular dichroism spectral analyses of the mutants.

In conclusion, alanine-scanning results unraveled some of the most important residues in durancin GL as shown in Figure 3. They are G07A, C10A, C15A, W16A and N20A, which caused a loss in antimicrobial activity; K12A, I30A, and V31A, which caused increased inhibitory activity; K21A and G38A, which caused decreased activity; and furthermore, E14A and S23A, which showed expanded inhibitory spectrum. These results shed light on future design of bacteriocins with more activity and specific inhibitory spectrum.

■ ASSOCIATED CONTENT

Supporting Information

Primers used for the site-directed mutagenesis. The Supporting Information is available free of charge on the ACS Publications website at DOI: 10.1021/acs.jafc.5b02114.

■ AUTHOR INFORMATION

Corresponding Author

*Phone: +86-25-8671-8506. E-mail: ddabc_2000@163.com.

Funding

This project was financially supported by the National Natural Science Foundation of China (no. 31271930) and the Support Program for Science and Technology of Jiangsu Province (no. BE2014711). This study was also supported by a Project Funded by the Priority Academic Program Development of Jiangsu Higher Education Institutions (PAPD).

Notes

The authors declare no competing financial interest.

■ ACKNOWLEDGMENTS

Xinquan Chen is grateful for a scholarship of the Innovation of Graduate Culturing of Jiangsu Province (CXZZ13_0636).

■ REFERENCES

(1) Drider, D.; Fimland, G.; Héchard, Y.; McMullen, L. M.; Prévost, H. The continuing story of class IIa bacteriocins. *Microbiol. Mol. Biol. Rev.* **2006**, *70*, 564−582.

(2) Klaenhammer, T. R. Genetics of bacteriocins produced by lactic acid bacteria. *FEMS Microbiol. Rev.* **1993**, *12*, 39−85.

(3) Fimland, G.; Johnsen, L.; Dalhus, B.; Nissen-Meyer, J. Pediocin-like antimicrobial peptides (class IIa bacteriocins) and their immunity proteins: biosynthesis, structure, and mode of action. *J. Pept. Sci.* **2005**, *11*, 688−696.

DOI: 10.1021/acs.jafc.5b02114
J. Agric. Food Chem. 2015, 63, 6402−6409

(4) Cleveland, J.; Montville, T. J.; Nes, I. F.; Chikindas, M. L. Bacteriocins: safe, natural antimicrobials for food preservation. *Int. J. Food Microbiol.* **2001**, *71*, 1−20.
(5) Cotter, P. D.; Hill, C.; Ross, R. P. Bacteriocins: developing innate immunity for food. *Nat. Rev. Microbiol.* **2005**, *3*, 777−788.
(6) Corr, S. C.; Li, Y.; Riedel, C. U.; O'Toole, P. W.; Hill, C.; Gahan, C. G. Bacteriocin production as a mechanism for the antiinfective activity of *Lactobacillus salivarius* UCC118. *Proc. Natl. Acad. Sci. U. S. A.* **2007**, *104*, 7617−7621.
(7) Lohans, C. T.; Vederas, J. C. Development of class IIa bacteriocins as therapeutic agents. *Int. J. Microbiol.* **2012**, *2012*, 1−13.
(8) Cui, Y.; Zhang, C.; Wang, Y.; Shi, J.; Zhang, L.; Ding, Z.; Qu, X.; Cui, H. Class IIa bacteriocins: Diversity and new developments. *Int. J. Mol. Sci.* **2012**, *13*, 16668−16707.
(9) Fimland, G.; Blingsmo, O. R.; Sletten, K.; Jung, G.; Nes, I. F.; Nissen-Meyer, J. New biologically active hybrid bacteriocins constructed by combining regions from various pediocin-like bacteriocins: the C-terminal region is important for determining specificity. *Appl. Environ. Microbiol.* **1996**, *62*, 3313−3318.
(10) Miller, K. W.; Schamber, R.; Osmanagaoglu, O.; Ray, B. Isolation and characterization of pediocin AcH chimeric protein mutants with altered bactericidal activity. *Appl. Environ. Microbiol.* **1998**, *64*, 1997−2005.
(11) Fimland, G.; Eijsink, V. G.; Nissen-Meyer, J. Mutational analysis of the role of tryptophan residues in an antimicrobial peptide. *Biochemistry* **2002**, *41*, 9508−9515.
(12) Kazazic, M.; Nissen-Meyer, J.; Fimland, G. Mutational analysis of the role of charged residues in target-cell binding, potency and specificity of the pediocin-like bacteriocin sakacin P. *Microbiology* **2002**, *148*, 2019−2027.
(13) Morisset, D.; Berjeaud, J. M.; Marion, D.; Lacombe, C.; Frère, J. Mutational analysis of mesentericin Y105, an anti-Listeria bacteriocin, for determination of impact on bactericidal activity, in vitro secondary structure, and membrane interaction. *Appl. Environ. Microbiol.* **2004**, *70*, 4672−4680.
(14) Quadri, L. E.; Yan, L. Z.; Stiles, M. E.; Vederas, J. C. Effect of amino acid substitutions on the activity of carnobacteriocin B2 Overproduction of the antimicrobial peptide, its engineered variants, and its precursor in *Escherichia coli*. *J. Biol. Chem.* **1997**, *272*, 3384−3388.
(15) Tominaga, T.; Hatakeyama, Y. Determination of essential and variable residues in pediocin PA-1 by NNK scanning. *Appl. Environ. Microbiol.* **2006**, *72*, 1141−1147.
(16) Du, L.; Somkuti, G. A.; Renye, J. A., Jr. Molecular analysis of the bacteriocin-encoding plasmid pDGL1 from *Enterococcus durans* and genetic characterization of the Durancin GL locus. *Microbiology* **2012**, *158*, 1523−1532.
(17) Du, L.; Somkuti, G. A.; Renye, J. A., Jr.; Huo, G. Properties of Durancin GL, a new antilisterial bacteriocin produced by *Enterococcus durans* 41D. *J. Food Saf.* **2012**, *32*, 74−83.
(18) Sambrook, J.; Fritsch, E. F.; Maniatis, T. *Molecular Cloning: A Laboratory Manual*, 2nd ed.; Cold Spring Harbor Laboratory Press: Cold Spring Harbor, NY, 1989a.
(19) Sambrook, J.; Fritsch, E.; Maniatis, T. *Molecular Cloning: A Laboratory Manual*, 2nd ed. Cold Spring Harbor Laboratory Press: Cold Spring Harbor, NY, 1989b.
(20) Pilet, M. F.; Dousset, X.; Barré, R.; Novel, G.; Desmazeaud, M.; Piard, J. C. Evidence for two bacteriocins produced by *Carnobacterium piscicola* and *Carnobacterium divergens* isolated from fish and active against *Listeria monocytogenes*. *J. Food Protect.* **1995**, *58*, 256−262.
(21) Nissen-Meyer, J.; Rogne, P.; Oppegard, C.; Haugen, H.; Kristiansen, P. Structure-function relationships of the non-lanthionine-containing peptide (class II) bacteriocins produced by gram-positive bacteria. *Curr. Pharm. Biotechnol.* **2009**, *10*, 19−37.
(22) Eijsink, V. G.; Skeie, M.; Middelhoven, P. H.; Brurberg, M. B.; Nes, I. F. Comparative studies of class IIa bacteriocins of lactic acid bacteria. *Appl. Environ. Microbiol.* **1998**, *64*, 3275−3281.
(23) Chen, Y.; Shapira, R.; Eisenstein, M.; Montville, T. J. Functional characterization of pediocin PA-1 binding to liposomes in the absence of a protein receptor and its relationship to a predicted tertiary structure. *Appl. Environ. Microbiol.* **1997**, *63*, 524−531.
(24) Fimland, G.; Pirneskoski, J.; Kaewsrichan, J.; Jutila, A.; Kristiansen, P. E.; Kinnunen, P. K.; Nissen-Meyer, J. Mutational analysis and membrane-interactions of the β-sheet-like N-terminal domain of the pediocin-like antimicrobial peptide sakacin P. *Biochim. Biophys. Acta, Proteins Proteomics* **2006**, *1764*, 1132−1140.
(25) Haugen, H. S.; Fimland, G.; Nissen-Meyer, J. Mutational analysis of residues in the helical region of the class IIa bacteriocin pediocin PA-1. *Appl. Environ. Microbiol.* **2011**, *77* (6), 1966−1972.
(26) Hu, W.; Lazo, N.; Cross, T. Tryptophan dynamics and structural refinement in a lipid bilayer environment: solid state NMR of the gramicidin channel. *Biochemistry* **1995**, *34*, 14138−14146.
(27) Hu, W.; Cross, T. Tryptophan hydrogen bonding and electric dipole moments: functional roles in the gramicidin channel and implications for membrane proteins. *Biochemistry* **1995**, *34*, 14147−14155.
(28) Richard, C.; Canon, R.; Naghmouchi, K.; Bertrand, D.; Prevost, H.; Drider, D. Evidence on correlation between number of disulfide bridge and toxicity of class IIa bacteriocins. *Food Microbiol.* **2006**, *23*, 175−183.

DOI: 10.1021/acs.jafc.5b02114
J. Agric. Food Chem. 2015, 63, 6402−6409

which are set at different temperatures and with decreasing pressures.[22] This technique has been used for the separation of bioactive compounds from herbs, plants, and food industry byproducts as well as for samples for algae and microalgae with different ranges of bioactivities, including antibacterial, antifungal, antiviral, and antioxidant.[23]

With the aforementioned concepts in mind, we performed the bioguided optimization of the leaf extraction on three varieties of sunflower (Stella, Hillian, and Arianna) using CO_2 as a supercritical solvent in an effort to obtain an extract with the highest possible activity.[24−28]

The aims of the study presented here were to isolate and structurally characterize the components of this most active extract. Furthermore, the activities of these compounds were measured to identify those responsible for the activity. It was envisaged that this study would provide a better understanding of the bioactivity of sunflower extracts and indicate the possibility of their future use in applications such as weed control.

MATERIALS AND METHODS

General Experimental Procedures. Infrared (IR) spectra (KBr) were recorded on a Fourier transform infrared (FT-IR) Spectrum 1000 spectrophotometer (PerkinElmer, Waltham, MA, USA). Nuclear magnetic resonance (NMR) spectra were acquired on 400, 500, and 600 MHz spectrometers (Agilent, Palo Alto, CA, USA). Chemical shifts are given in parts per million with respect to residual ^{1}H signals of $CHCl_3$-d_1 (δ 7.25), and ^{13}C signals are referenced to the solvent signal (δ 77.00). Optical rotations were determined at room temperature on a model 241 polarimeter (PerkinElmer) (on the sodium D line). HRMS were obtained on a Synapt G2 UPLC-QTOF ESI mass spectrometer (Waters, Milford, MA, USA). Column chromatography was carried out on silica gel 0.060−0.200, 60A, from Acros Organics (Geel, Belgium). Thin layer chromatography was carried out on TLC silica gel 60 F245 aluminum sheets. Compounds were visualized under $UV_{254/366}$ light and by spraying with H_2SO_4/H_2O/HOAc (4:16:80 v/v/v) followed by heating at 80 °C. HPLC was carried on a HPLC chromatograph (Merck-Hitachi L, Tokyo, Japan), and solvents were eluted by four-channel pumps (Elite LaChrom L-2130) with flow rates of 1 mL/min for analytical columns and 3 mL/min for semipreparative columns and with IR detection (Elite LaChrom RI L-2490). The HPLC columns employed were a semipreparative column (Luna 10 μm, silica (2) 100 Å, 250 mm × 10 mm i.d., 10 μm, with a Security Guard SemiPrep Cartridge silica 10 × 10 mm; Phenomenex, Torrance, CA, USA) and an analytical column (Luna 5 μm, silica (2) 100 Å, 250 mm × 4.60 mm i.d., 5 μm, with an Analytical Security Guard Cartridge System; Phenomenex, Torrance, CA, USA). The extractions and fractionations for the supercritical fluid extraction with CO_2 (SFE) were carried out in equipment supplied by Thar Technology (model SF2000; Pittsburgh, PA, USA).

Chemicals. Chloroform, *n*-hexane, methanol, dichloromethane, ethyl acetate, and acetone (HPLC grade) Hipersolv Chromanorm for HPLC were obtained from VWR International (Radnor, PA, USA). Carbon dioxide (Abelló Linde, S.A., Barcelona, Spain) was used as the supercritical solvent. MagniSolv chloroform-d_1 (deuteration degree minimum 99.8%) for NMR spectroscopy was obtained from Merck (Darmstadt, Germany).

Plant Material. Leaves of *H. annuus* L. var. Arianna were collected manually in June 2009 during the third growth stage of the plant[29] (plants 1.2 m tall with flowers, 1 week before harvest), because it has been found that at this stage the plant shows greater phytotoxicity. These leaves were provided by Rancho de la Merced, Agricultural Research Station (CIFA), Junta de Andalucia, Jerez de la Frontera, Spain. The moisture of the leaves after harvesting was 65%. Samples were dried on blotting paper at room temperature (25 ± 1 °C) until a constant weight was reached.

Extraction Fractionation and Isolation. Dried and ground leaves (75.5 g) were extracted in equipment supplied by Thar Tecnology (model SF2000), and this included an extraction vessel (capacity of 2 L) and a high-pressure pump with a maximum flow rate of 200 g/min of carbon dioxide (P200 model). Two cyclonic separators (500 mL each) connected in series allowed the periodic discharge of extracted material during the SFE process. A pressure regulating valve allowed different conditions to be applied to the separators. The extractions (fractionation process) conducted under the best extraction conditions[28] gave the best results in terms of yield and bioactivities (cytotoxicity and phytotoxicity bioassays). The conditions used in the extractor were 55 °C and 400 bar and in the separators, 90 bar and 40 °C in the first separator S1 and atmospheric conditions in the second separator S2. The flow rate measured for the supercritical carbon dioxide was 20 g/min during 3 h. The extracts were collected in acetone and concentrated under vacuum at the same temperature as the extraction. The dried extract (7.0 g) obtained in the second separator S2 by the fractionation process (SFE), which was free of chlorophylls, was chromatographed on a column (116 cm × 15 cm i.d., 1300 g of silica gel 60 A) using *n*-hexane/ethyl acetate mixtures of increasing polarity from 5 to 100% in ethyl acetate with a 10% increase each time and finishing with 100% methanol (500 mL of each polarity). This procedure afforded seven fractions after comparison by TLC: A (95:5 v/v, 664.8 mg), B (90:10 v/v, 343 mg), C (80:20 v/v, 1.2 g), D (70:30 v/v, 349.6 mg), E (50:50 v/v, 2.5 g), F (20:80 v/v, 644.3 mg), G (100% ethyl acetate, 158 mg), and H (100% MeOH, 63.9 mg).

The data of fractionation and isolation of compounds from fractions B−F are presented in detail in the Supporting Information (Fractionation and Isolation S3).

Spectroscopic Data for the New Compounds. Heliannuol M (**31**): colorless oil; $[\alpha]^{25}_{D} = -11.0°$ (*c* 1.0, $CHCl_3$); IR ν_{max} (KBr) cm^{-1} 3350 (OH), 1620 (aromatic C═C), 1265 (C—O—C); ^{1}H NMR ($CDCl_3$ 400 MHz) data, see Table 1; ^{13}C NMR ($CDCl_3$ 125 MHz) data, see Table 1; HREIMS *m*/*z* (rel intensity) 266.1512 $[M]^+$ (calcd 266.1518); EIMS *m*/*z* 266 $[M]^+$, 248 $[M - H_2O]^+$, 235 $[M - CH_2 - OH]^+$.

Helivypolide K (**36**): colorless oil; $[\alpha]^{25}_{D} = -30.0°$ (*c* 1.0, $CHCl_3$); IR ν_{max} (KBr) cm^{-1} 3466 (OH), 1779 (α,β-unsaturated γ-lactone), 1710 (α,β-unsaturated ester); ^{1}H NMR ($CDCl_3$, 600 MHz) data, see Table 2; ^{13}C NMR ($CDCl_3$, 125 MHz) data, see Table 2; positive-ion HREITOFMS *m*/*z* 375.1441 $[M + H]^+$ (calcd for $[M + H]^+$, 375.1444); EIMS *m*/*z* (rel intensity) 375 $[M + H]^+$, 292 $[M - C_5H_7O + H]^+$, 83 $[C_4H_7O]^+$.

Table 1. ^{1}H NMR (600 MHz) and ^{13}C (125 MHz) Spectroscopic Data for Compound 31 in $CDCl_3$

no.	δ_H multi (*J* in Hz)	δ_C
1		138.0
2		151.5
3	6.70 s	123.5
4		122.1
5		149.8
6	6.53 s	115.9
7	2.90 ddq (7.2, 5.0, 3.0)	38.5
8α	1.86 dddd (13.5, 4.0 5.0, 3.6)	31.8
8β	1.72 dddd (13.5, 10.6, 3.0, 3.2)	
9α	2.02 dddd (13.2, 11.1, 10.6, 3.6)	25.2
9β	1.91 dddd (13.2, 3.2, 4.0, 1.5)	
10	3.48 dd (11.1, 1.5)	89.0
11		73.8
12	1.21 s	20.1
13	3.93 d (11.1)	67.3
13′	3.52 d (11.1)	
14	1.26 d (7.2)	18.6
15	2.17 s	15.3

DOI: 10.1021/acs.jafc.5b02261
J. Agric. Food Chem. 2015, 63, 6410−6421

Table 2. ^{1}H NMR (600 MHz) and ^{13}C (125 MHz) Spectroscopic Data for Compounds 36 and 37 and Helivypolide F[12] in $CDCl_3$

	36		37		helivypolide F[12]	
no.	δ_H multi (J in Hz)	δ_C	δ_H multi (J in Hz)	δ_C	δ_H multi (J in Hz)	δ_C
1	6.51 d (13.2)	151.6	6.34 d (12.8)	147.5	6.32 d (13.1)	150.0
2	6.05 d (13.2)	126.8	5.99 d (12.8)	127.4	5.99 d (13.1)	127.3
3		195.5		202.2		189.4
4		60.4		69.0		143.8
5	3.74 d (10.3)	80.4	3.73 d (10.2)	78.8	4.54 (9.8)	79.3
6	5.36 dd (10.3, 9.9)	74.8	5.47 dd (10.2, 9.9)	75.3	5.11 dd (9.8, 9.7)	76.2
7	3.42 dddd (9.9, 1.7, 3.2, 3.5)	47.2	3.37 dddd (9.9, 1.8, 3,1, 3.4)	45.2	3.41dddd (9.7, 1.7, 3.2, 3.4)	47.1
8	5.81 ddd (1.76, 3.5, 2.6)	65.3	5.78 ddd (1.8, 3.5, 2.5)	66.5	5.75 ddd (3.8, 2.8, 1.7)	65.4
9α	2.40 dd (3.5, 15.5)	46.8	2.34 dd (3.5, 15.3)	46.2	2.34 dd (2.8, 15.4)	46.8
9β	2.20 dd (2.6, 15.5)		2.23 dd (2.5, 15.3)		2.16 dd (3.8, 15.4)	
10		81.1		80.8		80.4
11		133.0		134.1		134.5
12		168.5		167.3		168.3
13a	5.68 d (3.2)	123.3	5.67 d (3.1)	122.6	5.62 d (3.2)	122.6
13b	6.36 d (3.5)		6.33 d (3.4)		6.35 d (3.4)	
14	1.50 s	32.9	1.41 s	29.9	1.40 s	32.9
15	3.30 d (6.5)	52.4	3.70 d (4.4)	64.2	5.60 d (1.5)	128.5
15′	3.13 d (6.5)		3.71 d (4.4)		6.40 d (1.5)	
1′		165.8		166.1		166.1
2′		125.8		126.4		122.4
3′	6.17 qq (7.2, 1.5)	141.6	6.16 qq (7.1, 1.5)	141.3	6.15 qq (7.2, 1.5)	141.3
4′	1.98 dq (1.5, 7.2)	15.3	1.97 dq (7.1, 1.5)	16.1	1.98 dq (7.2, 1.5)	15.5
5′	1.80 dq (1.5, 1.5)	20.5	1.82 dq (1.5, 1.5)	20.1	1.80 dq (1.5, 1.5)	20.5

Helivypolide L (**37**): colorless oil; $[\alpha]^{25}_D = -21.7°$ (c 1.0, $CHCl_3$); IR ν_{max} (KBr) cm^{-1} 3468 (OH), 1780 (α,β-unsaturated γ-lactone), 1710 (α,β-unsaturated ester); ^{1}H NMR ($CDCl_3$, 600 MHz) data, see Table 2; ^{13}C NMR ($CDCl_3$, 125 MHz) data, see Table 2; positive-ion HREITOFMS m/z 393.1544 $[M + H]^+$ (calcd for $[M + H]^+$, 393.1549); EIMS m/z (rel intensity) 393 $[M + H]^+$, 310 $[M - C_5H_7O + H]^+$, 83 $[C_4H_7O]^+$.

Helieudesmanolide B (**38**): colorless oil; $[\alpha]^{25}_D = -33.6°$ (c 1.0, $CHCl_3$); IR ν_{max} (KBr) cm^{-1} 3410 (OH), 1776 (α,β-unsaturated γ-lactone), 1700 (α,β-unsaturated ester); ^{1}H NMR ($CDCl_3$, 600 MHz) data, see Table 3; ^{13}C NMR ($CDCl_3$, 125 MHz) data, see Table 3; positive-ion HREITOFMS m/z 363.1806 $[M + H]^+$ (calcd for $[M + H]^+$, 363.1808).

Bioassays. Wheat coleoptile bioassays as well as phytotoxicity bioassays on tomato seeds were performed according to previously described procedures.[30]

Molecular Modeling. Three-dimensional models for the tested chemicals were obtained from PM3 calculations performed by Hyperchem 7.01 software (Hypercube Inc., Gainesville, FL, USA; 2000).

RESULTS AND DISCUSSION

The results indicated that the best extraction yields and activity profiles were obtained from the Arianna variety with an extraction pressure and temperature of 400 bar and 55 °C, respectively, at a flow rate of 20 g/min for 3 h. A cascade fractionation was carried out in an effort to increase the biological activity of the extract obtained under these conditions.[28] This process involved the stepwise precipitation of the extracts obtained in the process. This goal was achieved by modification of the density of CO_2 through changes in the pressure and temperature in the separators. In this way, the compounds that were least soluble in the supercritical solvent precipitated in the first separator, whereas more soluble materials remained in the second separator.

Table 3. ^{1}H NMR (600 MHz) and ^{13}C (125 MHz) Spectroscopic Data for Compound 38 in $CDCl_3$

no.	δ_H multi (J in Hz)	δ_C
1	3.70 dd (1.9, 11.6)	76.3
2α	2.74 dd (1.9, 12.1)	46.2
2β	2.55 dd (11.6, 12.1)	
3		207.5
4	2.58 dd (11.3, 6.7)	44.2
5	1.60 dd (11.3, 11.1)	50.6
6	4.46 dd (11.1, 10.8)	78.2
7	2.85 ddd (10.8, 1.8, 3.3)	52.9
8	5.82 dd (1.8, 2.5, 3.7)	65.1
9α	2.48 dd (2.5, 15.1)	40.9
9β	1.61 dd (3.7, 15.1)	
10		41.9
11		133.6
12		169.3
13a	5.50 d (2.9)	120.2
13b	6.19 d (3.3)	
14	1.27 s	13.8
15	1.31 d (6.7)	13.7
1′		166.7
2′		126.8
3′	6.12 qq (7.0, 1.5)	140.1
4′	1.99 dq (7.0, 1.5)	20.6
5′	1.86 dq (1.5, 1.5)	13.8

Better bioactivity profiles, yields, and separation of chlorophylls were obtained when the first separator was run at a pressure of 90 bar and a temperature of 40 °C with atmospheric conditions in the second separator. The extract obtained in the second separator (chlorophyll free) showed inhibition levels in the coleoptile bioassay of around 60% at the

DOI: 10.1021/acs.jafc.5b02261
J. Agric. Food Chem. 2015, 63, 6410−6421

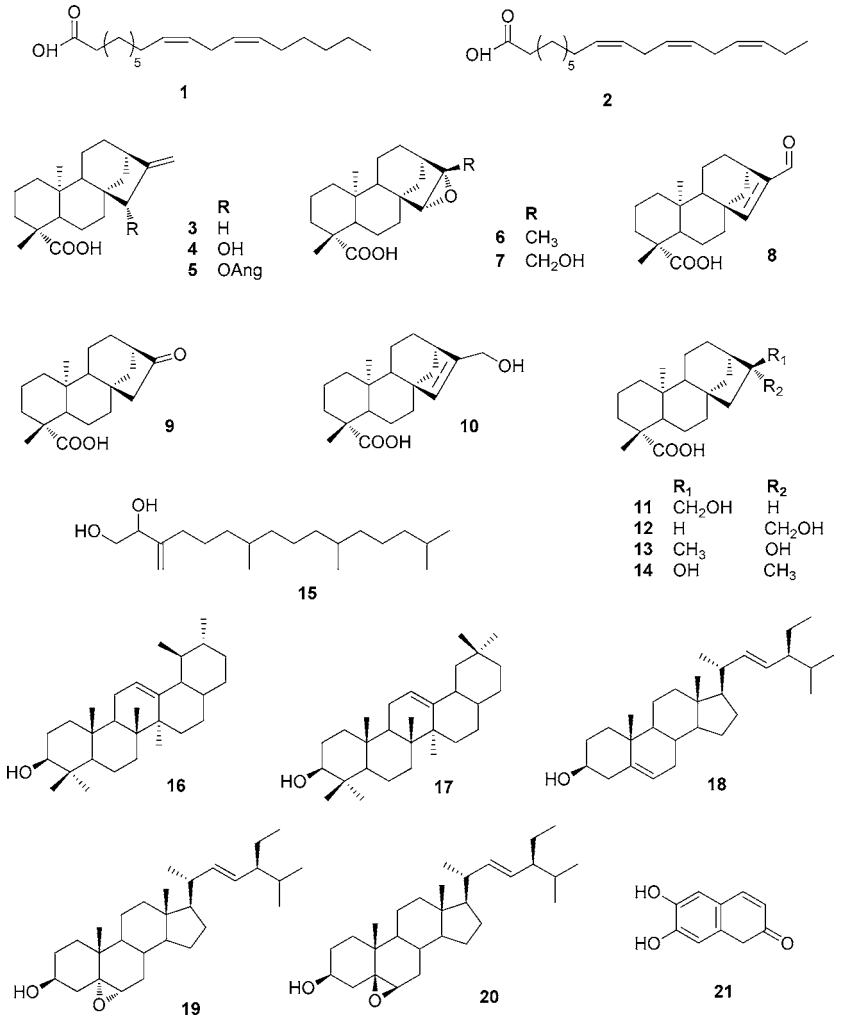

Figure 1. Compounds **1**–**21** isolated from dried leaves of *H. annuus* L. var. Arianna extracted with pure supercritical CO_2.

highest concentration tested (1.0 mg/mL) and 30% at the most dilute concentration (0.075 mg/mL). Phytotoxicity was also analyzed using two different bioassays, namely, a phytotoxicity bioassay carried out on tomato, lettuce, onion, and watercress seeds and a bioassay under hydroponic conditions on tomato.[28] The results were compared with those obtained with the commercial herbicide Logran. The data obtained on tomato showed the highest levels of activity. The extract showed root growth inhibitions of 70% at 0.8 mg/mL and 43% at 0.2 mg/mL (the limiting dilutions tested in this bioassay). Germination of tomato was also affected by this extract with values similar to the standard herbicide, that is, in the range of 78–57% for the three dilutions studied (0.8, 0.4, and 0.2 mg/mL). The bioassay under hydroponic conditions corroborated the activity observed in the Petri dish bioassay. Significant growth inhibition (>60%) of stems and roots of the tomato plants was obtained at 0.8 mg/mL.

Appropriate conditions for the fractionation of the bioactive extract (7 g) by CC and HPLC were identified. The chromatographic separation of fractions B–F led to the isolation of 52 compounds (Figures 1–3), and these were grouped together as 10 different chemical classes depending on their carbon skeleton: 2 fatty acids, 2 monoterpenes, 4 bisnorsesquiterpenes, 2 sesquiterpenes, 14 sesquiterpene lactones, 13 diterpenes, 2 triterpenes, 3 sterols, 8 flavonoids, 1 coumarin, and 1 lignan. The isolated compounds were identified from their spectroscopic data by comparison with the data reported in the literature as presented in the Supporting Information (Identified Compounds S8).

Compounds **6**, **11**, **19**–**21**, **23**, **41**, and **48** were isolated from *H. annuus* for the first time. Heliannuol M (**31**) was previously isolated by our research group from *H. annuus* variety SH-222,[31] and its spectral data are being reported for the first time. Helivypolide K (**36**), helivypolide L (**37**), and helieudesmanolide B (**38**) were characterized as new compounds.

Compound **31** was isolated as a colorless oil. The HRMS contained a peak at m/z 266.1512, which is consistent with a molecular formula of $C_{15}H_{22}O_4$. The ^{1}H NMR and ^{13}C NMR (Table 1) data are very similar to those previously reported for heliannuol D.[11] The only difference observed is the lack of the singlet assigned to one methyl group located on C-11 and the appearance of doublet signals with coupling constants of J = 11.1 Hz at δ 3.93 and 3.52, which are assigned to a hydroxymethylene group located on one of these carbons.

This assignment is fully supported by the ^{1}H NMR and ^{13}C NMR spectra as well as by COSY, HMBC, and HSQC experiments. The relative stereochemistries of C-7 and C-10 can be inferred by comparison with the chemical shifts and coupling constants of protons on the heterocycle of heliannuol D, which are established as 7*R* and 10*R*.[11] Thus, the similarities between the signals of these two compounds indicate that the

DOI: 10.1021/acs.jafc.5b02261
J. Agric. Food Chem. 2015, 63, 6410–6421

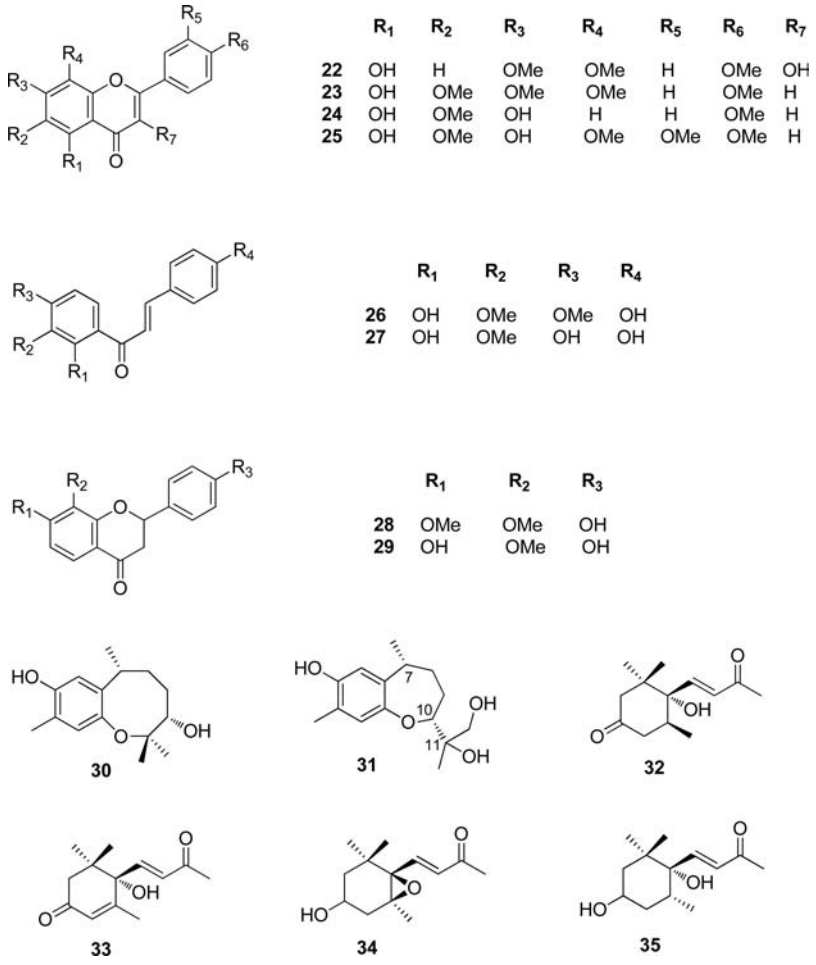

Figure 2. Compounds **22**−**35** isolated from dried leaves of *H. annuus* L. var. Arianna extracted with pure supercritical CO_2.

structure of **31** can be established as 5,11,13-trihydroxy-7*R*,10*R*-heliannane, which is named heliannuol M.[31]

Compound **36** was isolated as a colorless oil. The positive ion mode HREITOFMS contained a peak at *m*/*z* 375.1441 [M + H]$^+$. This result, together with the EIMS fragment ions at *m*/*z* 375 [M + H]$^+$, 292 [M − C_5H_7O + H]$^+$, and 83 [C_4H_7O]$^+$ and the ^{1}H and ^{13}C NMR data (Table 2), is consistent with the molecular formula $C_{20}H_{22}O_7$ (calcd for [M + H]$^+$, 375.1444). The ^{1}H NMR spectrum of this compound was very similar to that of helivypolide F[12] (Table 2), which was previously isolated from *H. annuus*, except for an upfield shift for H-15, which appears instead of the exocyclic-methylene signals. Comparison of the ^{1}H NMR and ^{13}C NMR spectra supports a structure very similar to that of helivypolide F with some modifications at C-4 and C-15.

The absence of a signal assignable to H-4, as well as the presence in the ^{1}H NMR spectrum of two isolated doublets at δ 3.30 and 3.13 (d, $J_{15\alpha,15\beta}$ = 6.5 Hz) for H-15α and H-15β, and the chemical shifts of the signals corresponding to C-4 (δ 60.4) and C-15 (δ 52.4) in the ^{13}C NMR spectrum indicated the presence of an epoxide between C-4 and C-15. This was confirmed by a g-HMBC experiment, in which the coupling of C-4 with H-2, H-5, H-15, and H-15′ was observed (Supporting Information S18). The α-orientation of H-5 was corroborated by an NOE effect observed in the corresponding bidimensional 2D-NOESY spectrum with H-15′ and with H-7 and H-8 (Figure 4). Thus, **36** was established as 8β-angeloyloxy-5β,10β-epoxy-4,15-epoxy-3-oxo-germacrane-1*Z*,11(13)-dien-6α,12-olide and was named helivypolide K.

Compound **37** was isolated as a colorless oil. The positive-ion HREITOFMS showed an *m*/*z* of 393.1544 [M + H]$^+$ which, in conjunction with the ^{1}H NMR data (Table 2), is consistent with the molecular formula $C_{20}H_{24}O_8$ (calcd for [M + H]$^+$, 393.1549). The ^{1}H NMR spectrum was essentially the same as that described above for compound **36** (Figure 5), but with slight differences in some of the chemical shifts. The differences are due to the shielding experienced by H-1 (δ 6.34; $\delta\Delta$ = 0.16) and H-2 (δ 5.99; $\delta\Delta$ = 0.15) and the deshielding of H-15′ (δ 3.71; $\delta\Delta$ = −0.41) and H-15 (δ 3.70; $\delta\Delta$ = −0.57). These findings indicate a modification of the methylene group at C-15 with respect to compound **36**, and once again the signal for H-4 was absent and two doublets were observed for H-15 and H-15′ at δ 3.70 and 3.71, (d, $J_{15,15'}$ = 4.4 Hz) in the ^{1}H NMR spectrum. On the other hand, the changes in the ^{13}C NMR spectrum for C-15 (δ 66.5) and C-4 (δ 69.0) (Table 2) indicated the presence of hydroxyl groups at C-15 and C-4, which correspond to the opened epoxide derivative of **36**. The g-HMBC experiment showed coupling between H-5 (δ 3.73) and C-15 (δ 66.5), and this confirmed the position of a hydroxyl group at C-15. This finding substantiates the significant hydrogen bond obtained in the minimum energy conformation calculations for this compound using PM3 (Figure 6). Thus, **37** was established as 8β-angeloyloxy-5β,10β-epoxy-4,15-dihydroxy-3-oxogermacrane-1*Z*,11(13)-dien-6α,12-olide, which was named helivypolide L.

DOI: 10.1021/acs.jafc.5b02261
J. Agric. Food Chem. 2015, 63, 6410−6421

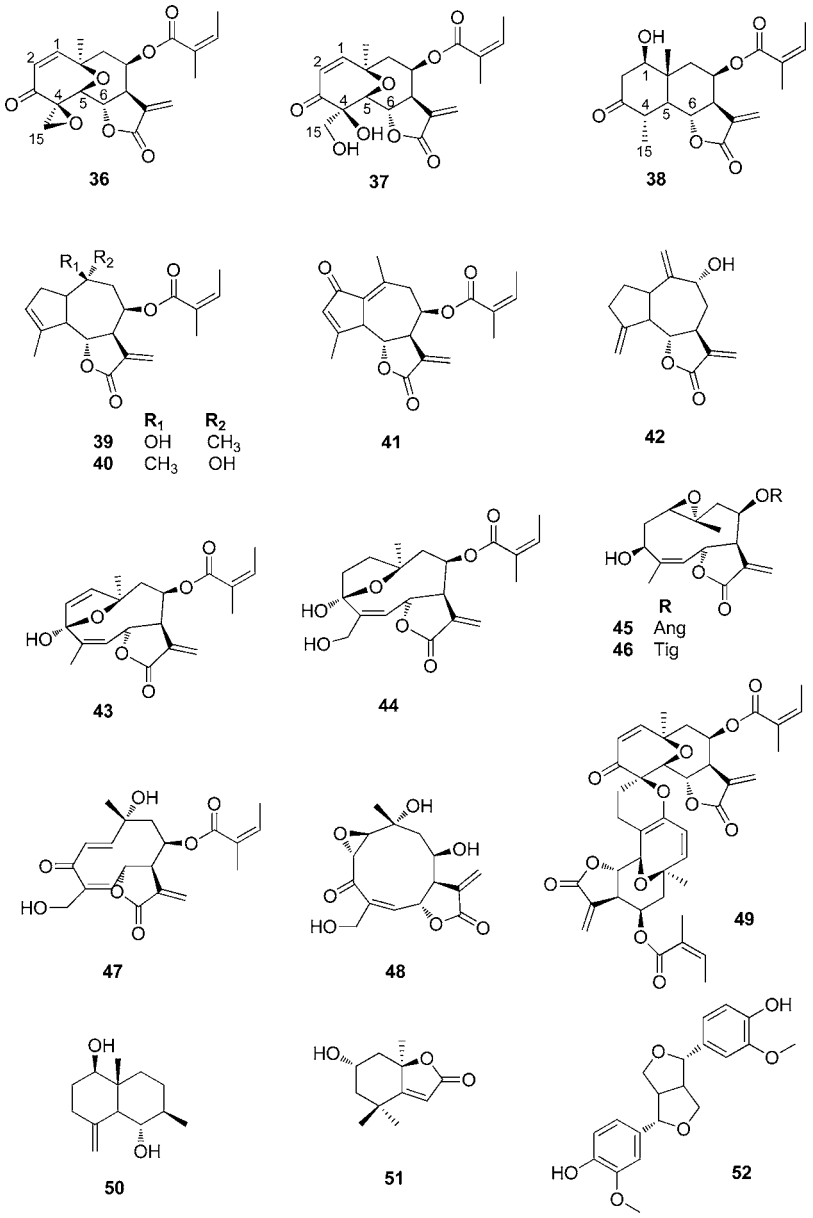

Figure 3. Compounds **36**–**52** isolated from dried leaves of *H. annuus* L. var. Arianna extracted with pure supercritical CO_2.

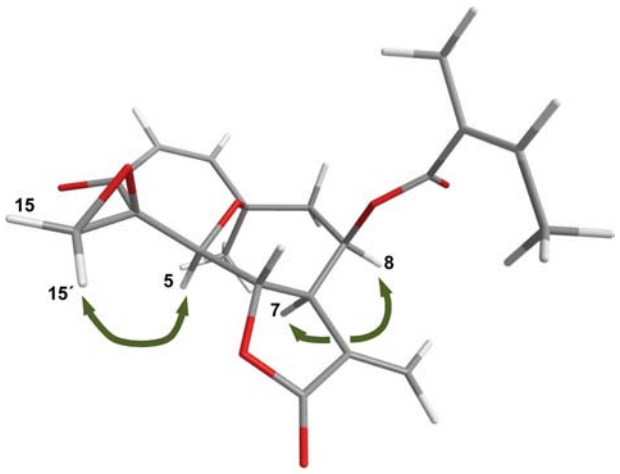

Figure 4. NOE effects observed for the most stable conformer of helivypolide K (**36**).

Compound **38** was isolated as a colorless oil. The positive ion mode HREITOFMS contained an $[M + H]^+$ ion at m/z 363.1806, which is consistent with the molecular formula $C_{20}H_{26}O_6$ (calcd for $[M + H]^+$, 363.1808). The ^{1}H NMR spectrum (Table 3) showed signals characteristic of a sesquiterpene lactone with a eudesmane skeleton very similar to that of helieudesmanolide A,[12] previously isolated from *H. annuus*, except for a doublet due to a methyl group at δ 1.31 ($J_{4,15}$ = 6.75 Hz) on C-4, corresponding to H-15, and the absence of a signal for H-3. In this case the eudesmane skeleton showed a typical methyl signal at δ 1.27 (H-14) and a doublet of doublets at δ 4.46 assigned to H-6 ($J_{5,6}$ = 11.1 Hz, $J_{6,7}$ = 10.8 Hz). The ^{1}H NMR–2D-COSY experiment showed that H-5 (δ 1.60) was coupled with H-4 (δ 2.58, dd, $J_{4,5}$ = 11.3 Hz) and H-15 (δ 1.31, d, $J_{4,15}$ = 6.7 Hz). Signals observed at δ 3.70 (dd, $J_{1,2\alpha}$ = 1.9 Hz, $J_{1,2\beta}$ = 11.6 Hz), δ 2.55 (dd, $J_{2\beta,2\alpha}$ = 12.1 Hz, $J_{1,2\beta}$ = 11.6 Hz), and δ 2.74 (dd, $J_{2\alpha,2\beta}$ = 12.1, $J_{1,2\alpha}$ = 1.9 Hz) were assigned to H-1, H-2β, and H-2α, respectively, and other proton coupling was not observed, which suggests that the C-3

DOI: 10.1021/acs.jafc.5b02261
J. Agric. Food Chem. 2015, 63, 6410–6421

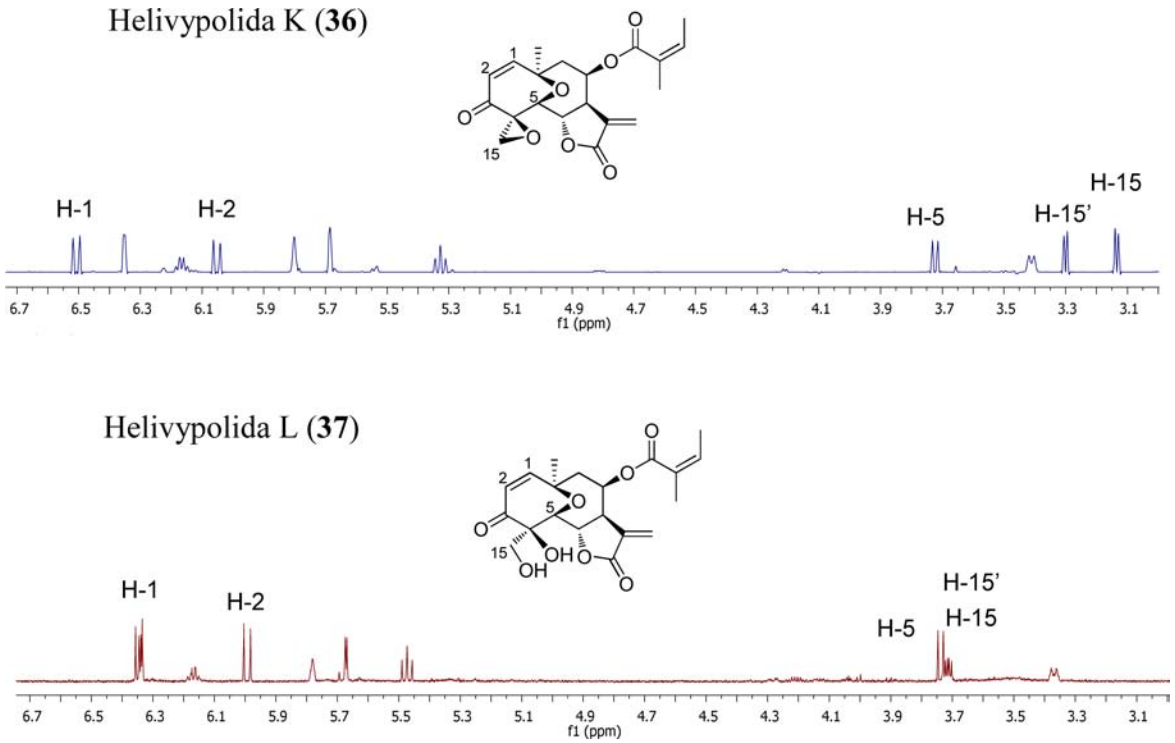

Figure 5. ^{1}H NMR comparison between helivypolide K (**36**) and helivypolide L (**37**).

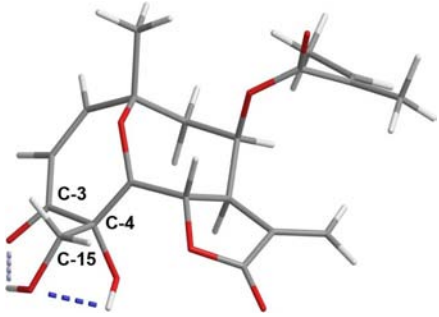

Figure 6. Significant hydrogen bond obtained in minimum energy calculations on the conformation of helivypolide L (**37**) using PM3.

position is occupied. The chemical shifts of C-1 and C-2 in the ^{13}C NMR spectrum at δ 76.3 (CH) and δ 46.2 (CH_2), respectively, indicate that there is a hydroxyl group bonded to C-1. The ^{13}C NMR spectrum (Table 3) contained 20 signals, and the signal at δ 207.5 confirmed the presence of a ketone group, which is located at C-3 due to the absence of a signal assignable to H-3 in the ^{1}H NMR spectrum and the correlations observed in the g-HMBC experiment between protons at δ 2.55 (H-2β), δ 2.74 (H-2α), δ 2.58 (H-4) δ 1.60 (H-5), and δ 1.31 (H-15) with the carbon at δ 207.5 (C-3) (Supporting Information S23).

The orientation of H-5 was established on the basis of the coupling constant with H-6 ($J_{5,6}$ = 11.1 Hz) and assuming a β-orientation for H-6 and an α-orientation for H-7 and H-8. The relative stereochemistry of the molecule was determined on the basis of NOE effects observed in the 2D-NOESY experiment. Thus, NOE effects were observed for proton H-5 with H-1 and H-8 and for H-14 with H-4 and H-6. The latter indicates an orientation α to the methyl at C-4 (H-15) (Figure 7). Thus, **38** was established as 8β-angeloyloxyl-1β-hydroxy-3-oxo-eudesmane-11(13)-en-6α,12-olide, and this compound was named helieudesmanolide B.

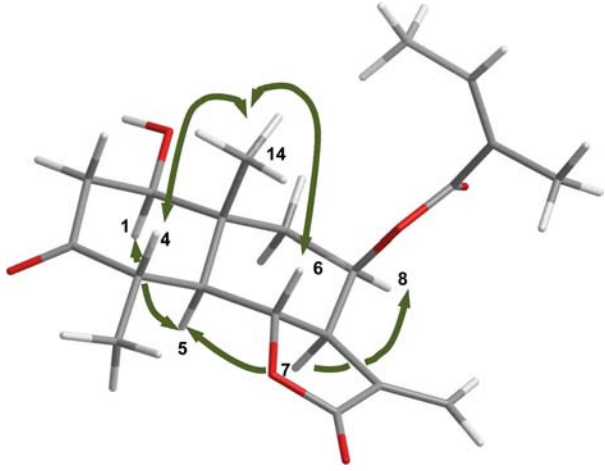

Figure 7. NOE effects observed for the most stable conformer of helieudesmanolide B (**38**) by PM3 calculations.

The bioactivities of 12 diterpenes (**3**−**14**), 1 coumarin (**21**), 8 flavonoids (**22**−**29**), 2 heliannuols (**30** and **31**), 4 bisnorsesquiterpenes (**32**−**35**), and 11 sesquiterpene lactones (**39**−**49**) were assessed in the wheat coleoptile bioassay in a concentration range from 10^{-3} to 10^{-5} M (except for compounds **13**, **27**, **31**, **43**, and **46**, which had a concentration limit of 3×10^{-4} M). The results obtained are summarized in Figures 8 and 9.

The remaining compounds, **15**, **18**, **36**−**38**, and **50**−**52**, were not tested due to the low amounts obtained. Compounds **16**, **17**, **19**, and **20** were not assessed because they were obtained as mixtures. The bioassay employed is rapid (24 h) and sensitive

DOI: 10.1021/acs.jafc.5b02261
J. Agric. Food Chem. 2015, 63, 6410−6421

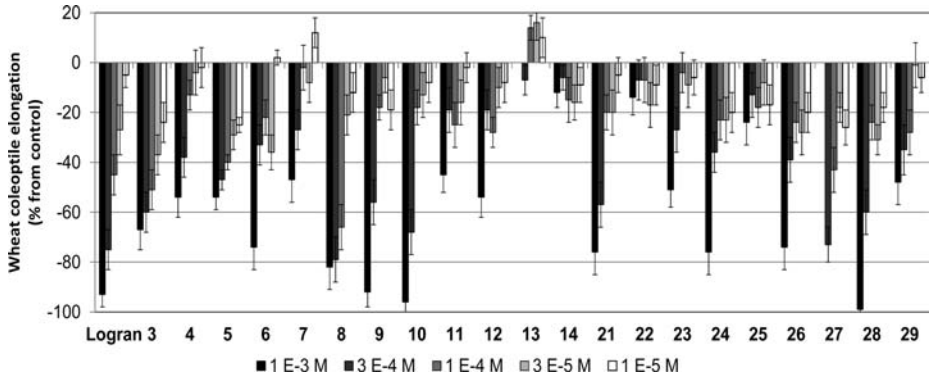

Figure 8. Effects of compounds **3**–**29** from the bioactive fraction of the extract of *H. annuus* L. var. Arianna on the elongation of etiolated wheat coleoptiles. Values are expressed as percentage difference from control.

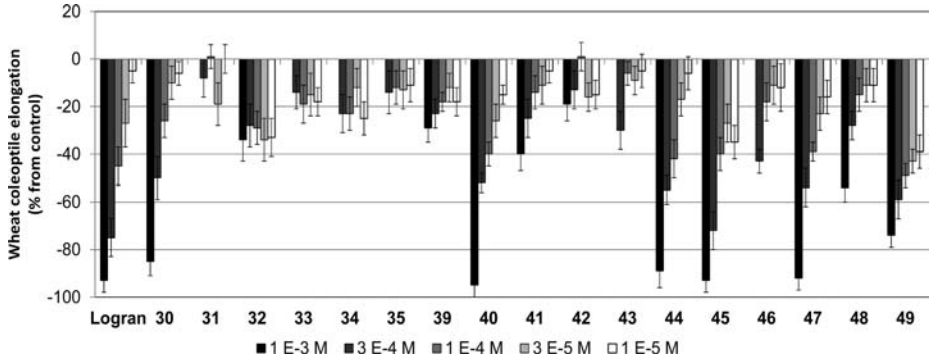

Figure 9. Effects of compounds **30**–**49** from the bioactive fraction of the extract of *H. annuus* L. var. Arianna on the elongation of etiolated wheat coleoptiles. Values are expressed as percentage difference from control.

to a wide range of bioactive substances including plant growth regulators, herbicides, antimicrobials, mycotoxins, and assorted pharmaceuticals.[32]

The activities of some of these compounds have been evaluated previously using the etiolated wheat coleoptile[33] and standard target species (STS)[34] bioassays in the concentration range of 10^{-4}–10^{-9} M.[8,35] To obtain a more complete picture of the compounds isolated in this work, we have reconsidered that, as better candidates for a natural herbicide model, the compounds should be tested in bioassays with a range of activities with the following dilutions: 10^{-3}, 3×10^{-4}, 10^{-4}, 3×10^{-5}, and 10^{-5} M for both bioassays. The commercial herbicide Logran was used as an internal reference.

Diterpene compounds **3**–**14** showed significant inhibitory activity on coleoptile elongation, except diterpenes **13** and **14**. The highest inhibitory activities of these diterpenes were shown by **8**, **9**, and **10**, with values >80% at 10^{-3} M (82, 92, and 96% inhibition, respectively). Some of these values are higher than that of the commercial herbicide Logran at this concentration (Figure 8). These compounds were also active at the second concentration (3×10^{-4} M) (79, 56, and 68% inhibition, respectively), and compound **8** was even active at the third (10^{-4} M with an inhibition of 66%), but these compounds had a little effect at the highest dilutions. Compounds **3** and **5** were less active than those outlined above, but they showed higher persistence with dilution and a better effect was observed at the high concentration for compound **3** (68%) in comparison to compound **5** (53%). On the other hand, compound **6** showed a high inhibition at 10^{-3} M (73%), but this decreased with dilution.

Coumarin **21** also showed high inhibitory activity at the two highest concentrations (10^{-3} and 3×10^{-4} M) (76 and 57% inhibition). Flavonoids **22**–**29** inhibited coleoptile elongation, and in this series, **24** and **26**–**28** had the highest values. These compounds showed high inhibitory activity at the highest concentration (10^{-3} M): **24** (76%), **26** (74%), **27** (73%), and **28** (99%). Even the least active compound had better activity than the commercial herbicide reference at this concentration (Figure 8).

Heliannuol A (**30**) showed high inhibitory activity on coleoptile elongation at 10^{-3} M, with a value of 85% (very close to the value value of Logran, 93%), and at 3×10^{-3} (50%), but the activity decreased significantly with dilution. In contrast, heliannuol M (**31**) had no effect on coleoptile elongation at any concentration (Figure 9). Bisnorsesquiterpene compounds **32**–**35** showed low inhibitory activities at all concentrations assayed (<30%).

Of all sesquiterpene lactones tested (**39**–**49**) compounds **40**, **44**, **45**, **47**, and **49** had the best activity profiles and the highest inhibitory activity on coleoptile elongation (Figure 9). These compounds showed values close to 90% inhibition at the highest concentration (10^{-3} M): **40** (95%), **45** (93%), **44** (89%), and **47** (92%). These values are similar to that of the commercial herbicide at the same concentration. Compound **49** showed the best inhibitory activity profile of all compounds evaluated and also showed the most persistence with dilution (73% at 10^{-3} M and 39% at 10^{-5} M).

Of all the compounds tested on the elongation of etiolated wheat coleoptile, compounds **8**–**10**, **21**, **24**, **26**–**28**, **30**, **40**, **44**, **45**, **47**, and **49** were the most active, and they were selected for the evaluation of phytotoxicity on tomato seed growth (except

DOI: 10.1021/acs.jafc.5b02261
J. Agric. Food Chem. 2015, 63, 6410–6421

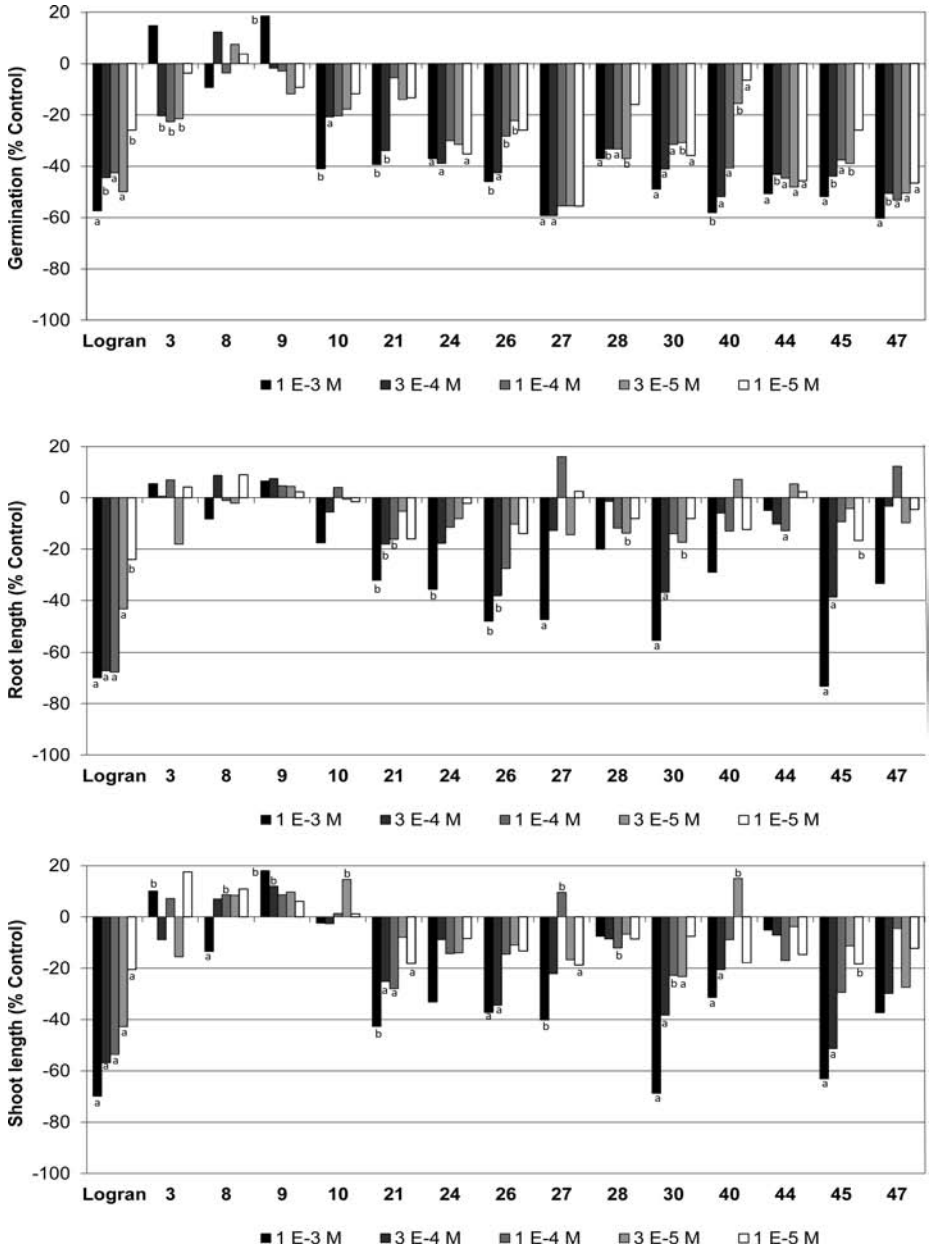

Figure 10. Effects of compounds **3**, **8**−**10**, **21**, **24**, **26**−**28**, **30**, **40**, **44**, **45**, and **47** from the bioactive fraction of the extract of sunflower (*H. annuus* L. var. Arianna) on *L. esculentum* seed growth. Values are expressed as percentage difference from control.

for **49**, due to the low amount available) as this was the most sensitive species in previous bioassays with the initial extract.[28] The commercial herbicide Logran was used as an internal standard.[34] The results of the bioassay are represented in Figure 10, where data are presented as percentage differences from the control. The concentrations tested were identical to those in the coleoptile bioassay.

In this phytotoxicity bioassay the most significantly affected parameter was the germination for all compounds assayed, except for diterpenes **3** and **8**−**10**. Coumarin **21**, flavonoids **24** and **26**−**28**, heliannuol **30**, and sesquiterpene lactones **40**, **44**, **45**, and **47** showed inhibition levels close to that of the herbicide Logran for most dilutions (between 40 and 60%).

Allelopathy is often demonstrated by testing allelochemical effects on germination. The germination process usually begins with water uptake by the seed (imbibition) and ends with the protrusion of the radicle through the testa. The seed germination test has been a widely used bioassay for the determination of allelopathic activity.[36] Another important point is that the observed effects varied with the seed tested. Tomato seeds were found to be more sensitive than other species evaluated. This may be due to differences in seed size, seed coat permeability, differential uptake, and metabolism.[37]

Root and shoot length were the variables that were most affected by heliannuol A (**30**) and the sesquiterpene lactone leptocarpin (**45**) at the first two concentrations (10^{-3} and 3×10^{-4} M), and they showed inhibitory activity similar to that of the commercial herbicide (70%).

Heliannuol A (**30**) was the most active compound on the shoot growth of tomato seeds at the first concentration (10^{-3} M) with 70% inhibition, that is, similar to that of the commercial herbicide. The inhibition of root growth at the same concentration was 56%. Furthermore, this compound had an inhibitory effect on germination at the highest concen-

DOI: 10.1021/acs.jafc.5b02261
J. Agric. Food Chem. 2015, 63, 6410−6421

trations, with values close to those of the standard herbicide (around 50%).

This compound belongs to the sesquiterpene family, which has a basic heliannane skeleton typical of such compounds isolated from sunflower,[11] and it has been reported to have plant growth regulatory activity.[10] The activity shown by this compound at the dilutions tested in both bioassays carried out in this work and the amount isolated from the extract indicate that its role may be related to the allelopathic behavior shown by this species.

The best results on root growth of tomato seeds at the highest concentration were shown by the sesquiterpene lactone leptocarpin (**45**) (10^{-3} M, 73% inhibition). For this compound, shoot inhibition at 10^{-3} M was 63%. The effect on germination of this seed also reached inhibition values similar to that of Logran at the highest concentrations (50%).

Sesquiterpene lactones bearing germacranolide and heliangolide backbones along with diterpenes are the most abundant compounds in the genus *Helianthus*. The activities of these compounds have been related to the presence of the α-methylene-γ-lactone moiety, the presence of an oxygenated group (mainly an angelate ester) at C-8, and/or the different special arrangements that the molecule can adopt.[38] It seems that the accessibility of groups that can be alkylated plays an important role in the activity of these compounds. Moreover, these compounds have shown a wide spectrum of activities: allelopathic, deterrent, cytotoxic, bacteriacidal, fungicidal, etc. Some of these activities can be correlated to the ecological roles of the compounds in the plant, but others are mainly characterized by their toxic properties and their ability to bind to important biomolecules.[39]

Furthermore, there are several studies concerning the regulatory activity of sesquiterpene lactones on germination and plant growth.[40] The observed activity of leptocarpin **45** on the germination and root growth inhibition of *Lycopersicon esculentum* seeds can be related to the flexibility that this molecule has in comparison to the other sesquiterpene lactones tested (**40**, **44**, and **47**) and to the presence of two electrophilic functions, namely, the α-methylene-γ-lactone moiety and the oxirane ring. It can be considered that leptocarpin **45** is another candidate that one would expect to be involved in defense mechanisms of *H. annuus*.

Annuolide G (**40**), niveusin B (**44**), and 15-hydroxy-3-dehydrodeoxytifruticin (**47**) showed low inhibitory effects on root and shoot growth of tomato seeds, but they showed high inhibitory activity on germination, as mentioned above, with values close to that of Logran (at 10^{-3} M: 58, 54, and 60% of inhibition for **40**, **44**, and **47**, respectively). For this parameter, **44** and **47** showed greater persistence as the activity was retained upon dilution, even at 10^{-5} M (50%), when compared to **40**, the activity of which decreased markedly in the last two dilutions. It is noteworthy that these heliangolides (**44** and **47**) have shown antibacterial properties against several organisms, such as *P. vulgaris*, *B. brevis*, *B. subtilis*, and *Streptomyces* sp.,[41] and they are highly active as fungicides, especially against *Eremothecium asbhbyi*,[42] along with leptocarpin **45**, which gave an MIC value as low as 1 ppm for several fungal species.[43]

The compounds that had the smallest effect on the germination and growth of tomato seeds were the diterpenes **3** and **8**−**10**, although these compounds did show good activity in the coleoptile bioassay. These diterpenoids are not usually reported as being phytotoxic agents despite the fact that they constitute a large group of compounds present in the genus *Helianthus*. The ecological role of these compounds has been associated more with antifeedant, insecticidal, and deterrent activity. Moreover, some diterpenoids, such as giberrellins, act as important plant hormones that are involved in growth regulation.[44]

Coumarins are defined as stress or defensive metabolites, and their synthesis is usually induced as a response to both biotic and abiotic stress-inducing agents.[45] The most significant values obtained on tomato seeds by coumarin sculetin (**21**) were found for the inhibition of germination (39%) and shoot length (42%) at a concentration of 10^{-3} M, although this compound did exhibit high levels of inhibition in the coleoptile bioassay at higher concentrations (10^{-3}, 3×10^{-3} M) with values of 77 and 58%, respectively.

Another large group of compounds that are widely distributed in *Helianthus* are the flavonoids, but very few of these have been implicated in allelopathy (some chalcones and dihydrochalcones).[46] These compounds (**24**, **26**−**28**) showed inhibitory effects on tomato seed growth, especially on germination, but they had intermediate effects on shoot and root growth. The structures of chalcones **26** and **27** are very similar as they differ only in the presence of an additional methyl group in **26**; however, their activities on germination are quite different. The reason for this variation could be related to the number and positions of free hydroxyl groups. Chalcone kukulkanin B (**27**) was the most active on germination of the flavonoids tested, and it also showed the best inhibitory activity profile with an average value of 60% from 10^{-3} M to 10^{-5} M (higher values than the commercial herbicide). The chalcone heliannone A (**26**) showed inhibition values of around 47% for the first concentrations (10^{-3} and 3×10^{-4} M). Compounds **26** and **27** both caused inhibition of shoot (around 40%) and root growth (50%) at the first concentration (10^{-3} M). It has been reported that flavonoids and flavones may act as insect attractants or repellents, either playing a defensive role or providing favorable interactions, among other activities.[47]

In conclusion, the results obtained in this study complement the current knowledge of allelopathic behavior shown by sunflower. The new extraction techniques used are environmentally clean and are more effective and selective for the extraction of bioactive natural products. Supercritical fluid extraction is one alternative to supplement or replace the conventional separation systems because the energy yields and separation efficiency are both good. In this study a bioactive extract of medium polarity was selectively obtained using CO_2 as the supercritical solvent. A total of 52 compounds were isolated from this extract, and these belong to 10 different chemical skeletons. Of these, the majority were sesquiterpene lactones (three of them are described for the first time in the literature), diterpenes, and flavonoids.

Because the initial extract showed good activity profiles in the coleoptile bioassay,[28] 38 pure compounds isolated from this fraction were again evaluated in the same bioassay, and >50% of these showed better results than the initial extract, with inhibition values in some cases >90%.

Good results were obtained for the initial extract in a previously reported phytotoxicity bioassay on tomato seeds in terms of percentage inhibition of germination and shoot and root length compared with Logran.[28] Good results were also obtained for the pure compounds, with a remarkable effect observed on germination in particular. The exceptions to this trend were the diterpene compounds. With regard to the development of this seed, sesquiterpene **30** (heliannuol A) and

DOI: 10.1021/acs.jafc.5b02261
J. Agric. Food Chem. 2015, 63, 6410−6421

sesquiterpene lactone **45** (leptocarpin) showed the strongest inhibitory effects, with activities similar to that of the commercial herbicide.

It is clear that allelopathic behavior is a very complex phenomenon and, hence, it cannot be assumed that a single compound, or even a small number of them, can be identified as being responsible for this behavior in all cases. The wide variety and activity of compounds found in the sunflower extract studied, both here and previously, makes, it conceivable that they are implicated in these interactions. Synergistic or additive interactions are usually not comparable to the activity of a single active compound, unless such a compound already participates in the combination. The specific structural factors that operate and determine the activity of a particular combination of compounds remains unclear. The same holds true for the combined effect; the character of such an effect cannot be predicted on the basis of an individual compound acting alone. In some cases, a noninhibitory concentration of a specific compound inhibits growth when this compound acts additively or synergistically with other allelochemicals that are present, and such joint action is the most common situation.

As a consequence, any studies that focus on the understanding of allelopathic interactions in *Helianthus* spp. should involve as many structures as be possible; otherwise, the study will be incomplete. On the other hand, the SFE technique has proven to be a useful tool to obtain bioactive extracts that contain a number of bioactive compounds from an agricultural byproduct. These extracts and compounds could be used in the future for weed control in an environmentally safe way within the context of sustainable agriculture.

■ ASSOCIATED CONTENT

Supporting Information

^{1}H, ^{13}C of new compounds, **31** and **36**−**38**; enlargement g-HMBC spectra of compounds **36** and **38**; additional information on fractionation, isolation and identification of compounds. The Supporting Information is available free of charge on the ACS Publications website at DOI: 10.1021/acs.jafc.5b02261.

■ AUTHOR INFORMATION

Corresponding Author

*(F.A.M.) Phone: +34 956012770. Fax: +34 956016193. E-mail: famacias@uca.es.

Funding

This research was supported by the Ministerio de Economía y Competitividad (MINECO) (Project AGL2013-42238-R) and Consejería de Economía Innovación y Ciencia, Junta de Andalucía (Project DP12-TEP-725).

Notes

The authors declare no competing financial interest.

■ ACKNOWLEDGMENTS

We gratefully acknowledge the staff at the Rancho de la Merced Research and Formation Center (Junta de Andalucia, Jerez de la Frontera, Spain) for providing the raw material.

■ DEDICATION

In memory of Professor George R. Waller, Jr.

■ ABBREVIATIONS USED

Ang, angelate; Tigl, tiglate

■ REFERENCES

(1) Macias, F. A. Allelopathy in the search for natural herbicide models. *ACS Symp. Ser.* **1995**, *No. 582*, 310−329.

(2) Macias, F. A.; Varela, R. M.; Torres, A.; Molinillo, J. M. G. Allelopathic studies on cultivar species. 3. Potential allelopathic guaianolides from cultivar sunflower leaves, var. SH-222. *Phytochemistry* **1993**, *34*, 669−674.

(3) Macias, F. A.; Molinillo, J. M. G.; Torres, A.; Varela, R. M.; Castellano, D. Allelopathic studies in cultivar species. Part 9. Bioactive flavonoids from *Helianthus annuus* cultivars. *Phytochemistry* **1997**, *45*, 683−687.

(4) Macias, F. A.; Varela, R. M.; Torres, A.; Oliva, R. M.; Molinillo, J. M. G. Allelopathic studies in cultivar. Part 10. Bioactive norsesquiterpenes from *Helianthus annuus* with potential allelopathic activity. *Phytochemistry* **1998**, *48*, 631−636.

(5) Macias, F. A.; Varela, R. M.; Torres, A.; Molinillo, J. M. G. Allelopathic studies in cultivar species. II. Heliespirone A. The first member of a novel family of bioactive sesquiterpenes. *Tetrahedron Lett.* **1998**, *39*, 427−430.

(6) Macias, F. A.; Varela, R. M.; Torres, A.; Molinillo, J. M. G. Allelopathic studies in cultivar species. 12. Heliannuol E. A novel bioactive sesquiterpene of the heliannane family. *Tetrahedron Lett.* **1999**, *40*, 4725−4728.

(7) Macias, F. A.; Varela, R. M.; Torres, A.; Molinillo, J. M. G. New bioactive plant heliannuols from cultivar sunflower leaves. *J. Nat. Prod.* **1999**, *62*, 1636−1639.

(8) Macias, F. A.; Oliva, R. M.; Varela, R. M.; Torres, A.; Molinillo, J. M. G. Allelopathic studies in cultivar species. 14. Allelochemicals from sunflower leaves cv. Peredovick. *Phytochemistry* **1999**, *52*, 613−621.

(9) Macias, F. A.; Lopez, A.; Varela, R. M.; Torres, A.; Molinillo, J. M. G. Bioactive lignans from a cultivar of *Helianthus annuus*. *J. Agric. Food Chem.* **2004**, *52*, 6443−6447.

(10) Macias, F. A.; Varela, R. M.; Torres, A.; Molinillo, J. M. G.; Fronczek, F. R. Allelopathic studies on cultivar species. 2. Novel sesquiterpene from bioactive fractions of cultivar sunflowers. *Tetrahedron Lett.* **1993**, *34*, 1999−2002.

(11) Macias, F. A.; Molinillo, J. M. G.; Varela, R. M.; Torres, A.; Fronczek, F. R. Structural elucidation and chemistry of a novel family of bioactive sesquiterpenes: heliannuols. *J. Org. Chem.* **1994**, *59*, 8261−8266.

(12) Macias, F. A.; Fernandez, A.; Varela, R. M.; Molinillo, J. M. G.; Torres, A.; Alves, P. L. C. A. Sesquiterpene lactones as allelochemicals. *J. Nat. Prod.* **2006**, *69*, 795−800.

(13) Mannila, M.; Koistinen, J.; Vartiainen, T. Comparison of SFE with Soxhlet in the analyses of PCDD/PCDFs and PCBs in sediment. *J. Environ. Monit.* **2002**, *4*, 1047−1053.

(14) Berg, B. E.; Lund, H. S.; Kringstad, A.; Kvernheim, A. L. Routine analysis of hydrocarbons, PCB and PAH in marine sediments using supercritical CO_2 extraction. *Chemosphere* **1998**, *38*, 587−599.

(15) Hartonen, K.; Bowadt, S.; Dybdahl, H. P.; Nylund, K.; Sporring, S.; Lund, H.; Oreld, F. Nordic laboratory intercomparison of supercritical fluid extraction for the determination of total petroleum hydrocarbon, polychlorinated biphenyls and polycyclic aromatic hydrocarbons in soil. *J. Chromatogr. A* **2002**, *958*, 239−248.

(16) Marr, R.; Gamse, T. Use of supercritical fluids for different processes including new developments − a review. *Chem. Eng. Process.* **2000**, *39*, 19−28.

(17) Beckman, E. J. Supercritical and near-critical CO_2 in green chemical synthesis and processing. *J. Supercrit. Fluids* **2004**, *28*, 121−191.

(18) Bravi, E.; Perretti, G.; Montanari, L.; Favati, F.; Fantozzi, P. Supercritical fluid extraction for quality control in beer industry. *J. Supercrit. Fluids* **2007**, *42*, 342−346.

(19) Bravi, M.; Bubbico, R.; Manna, F.; Verdone, N. Process optimization in sunflower oil extraction by supercritical CO_2. *Chem. Eng. Sci.* **2002**, *57*, 2753−2764.

(20) Mendiola, J. A.; Herrero, M.; Cifuentes, A.; Ibanez, E. Use of compressed fluids for sample preparation: food applications. *J. Chromatogr. A* **2007**, *1152*, 234−246.

DOI: 10.1021/acs.jafc.5b02261
J. Agric. Food Chem. 2015, 63, 6410−6421

(21) Valcarcel, M.; Tena, M. T. Applications of supercritical fluid extraction in food analysis. *Fresenius' J. Anal. Chem.* **1997**, *358*, 561−573.
(22) Fornari, T.; Vicente, G.; Vazquez, E.; Garcia-Risco, M. R.; Reglero, G. Isolation of essential oil from different plants and herbs by supercritical fluid extraction. *J. Chromatogr. A* **2012**, *1250*, 34−48.
(23) Herrero, M.; Cifuentes, A.; Ibanez, E. Sub- and supercritical fluid extraction of functional ingredients from different natural sources: plants, food-by-products, algae and microalgae. *Food Chem.* **2006**, *98*, 136−148.
(24) Casas, L.; Mantell, C.; Rodriguez, M.; Gordillo, M. D.; Torres, A.; Macias, F. A.; Martinez de la Ossa, E. Effect of the pre-treatment of the samples on the natural substances extraction from *Helianthus annuus* L. using supercritical carbon dioxide. *Talanta* **2005**, *67*, 175−181.
(25) Casas, L.; Mantell, C.; Rodriguez, M.; Torres, A.; Macias, F. A.; Martinez de la Ossa, E. J. Supercritical fluid extraction of bioactive compounds from sunflower leaves with carbon dioxide and water on a pilot plant scale. *J. Supercrit. Fluids* **2008**, *45*, 37−42.
(26) Casas, L.; Mantell, C.; Rodriguez, M.; Torres, A.; Macias, F. A.; Martinez de la Ossa, E. J. SFE kinetics of bioactive compounds from *Helianthus annuus* L. *J. Sep. Sci.* **2009**, *32*, 1445−1453.
(27) Casas, L.; Mantell, C.; Rodriguez, M.; Torres, A.; Macias, F. A.; Martinez de la Ossa, E. Extraction of natural compounds with biological activity from sunflower leaves using supercritical carbon dioxide. *Chem. Eng. J. (Amsterdam, Neth.)* **2009**, *152*, 301−306.
(28) El Marsni, Z.; Casas, L.; Mantell, C.; Rodriguez, M.; Torres, A.; Macias, F. A.; Martinez de la Ossa, E. J.; Molinillo, J. M. G.; Varela, R. M. Potential allelopathic of the fractions obtained from sunflower leaves using supercritical carbon dioxide. *J. Supercrit. Fluids* **2011**, *60*, 28−37.
(29) Macias, F. A.; Varela, R. M.; Torres, A.; Molinillo, J. M. G. In *Potential of Cultivar Sunflowers (Helianthus annuus L.) as a Source of Natural Herbicide Templates*; CRC: Boca Raton, FL, USA, 1999; pp 531−550.
(30) Rial, C.; Novaes, P.; Varela, R. M.; JM, G. M.; Macias, F. A. Phytotoxicity of cardoon (*Cynara cardunculus*) allelochemicals on standard target species and weeds. *J. Agric. Food Chem.* **2014**, *62*, 6699−6706.
(31) López, A. Estudios Alelopáticos de variedades Cultivadas de Girasol. SH-222 y Stella. Ph.D. dissertation, Universidad de Cádiz, Spain, 2003.
(32) Cutler, H. G.; Cutler, S. J.; Matesic, D. In *Mode of Action of Phytotoxic Fungal Metabolites*; CRC: Boca Raton, FL, USA, 2004; pp 253−270.
(33) Macias, F. A.; Torres, A.; Galindo, J. L. G.; Varela, R. M.; Alvarez, J. A.; Molinillo, J. M. G. Bioactive terpenoids from sunflower leaves cv. Peredovick. *Phytochemistry* **2002**, *61*, 687−692.
(34) Macias, F. A.; Castellano, D.; Molinillo, J. M. G. Search for a standard phytotoxic bioassay for allelochemicals. selection of standard target species. *J. Agric. Food Chem.* **2000**, *48*, 2512−2521.
(35) Macias, F. A.; Torres, A.; Molinillo, J. M. G.; Varela, R. M.; Castellano, D. Potential allelopathic sesquiterpene lactones from sunflower leaves. *Phytochemistry* **1996**, *43*, 1205−1215.
(36) Chiapusio, G.; Sanchez, A. M.; Reigosa, M. J.; Gonzalez, L.; Pellissier, F. Do germination indices adequately reflect allelochemical effects on the germination process? *J. Chem. Ecol.* **1997**, *23*, 2445−2453.
(37) Williams, R. D.; Hoagland, R. E. The effects of naturally occurring phenolic compounds on seed germination. *Weed Sci.* **1982**, *30*, 206−212.
(38) Macias, F. A.; Velasco, R. F.; Alvarez, J. A.; Castellano, D.; Galindo, J. C. G. Synthesis of melampolides and *cis*,*cis*-germacranolides as natural herbicide models. *Tetrahedron* **2004**, *60*, 8477−8488.
(39) Macias, F. A.; Galindo, J. C. G.; Molinillo, J. M. G.; Cutler, H. G. *Allelopathy: Chemistry and Mode of Action of Allelochemicals*; CRC: Boca Raton, FL, USA, 2004; p 372.
(40) Macias, F. A.; Galindo, J. C. G.; Molinillo, J. M. G.; Castellano, D. "Natural products as allelochemicals". 10. Dehydrozaluzanin C: a potent plant growth regulator with potential use as a natural herbicide template. *Phytochemistry* **2000**, *54*, 165−171.
(41) Spring, O.; Kupka, J.; Maier, B.; Hager, A. Biological activities of sesquiterpene lactones from *Helianthus annuus*: antimicrobial and cytotoxic properties; influence on DNA, RNA, and protein synthesis. *Z. Naturforsch. C* **1982**, *37*, 1087−1091.
(42) Kato, T.; Tsunakawa, M.; Sasaki, N.; Aizawa, H.; Fujita, K.; Kitahara, Y.; Takahashi, N. Growth and germination inhibitors in rice husks. *Phytochemistry* **1977**, *16*, 45−48.
(43) Picman, A. K.; Schneider, E. F. Inhibition of fungal growth by selected sesquiterpene lactones. *Biochem. Syst. Ecol.* **1993**, *21*, 307−314.
(44) Macias, F. A.; Marin, D.; Oliveros-Bastidas, A.; Castellano, D.; Simonet, A. M.; Molinillo, J. M. G. Structure-activity relationships (SAR) studies of benzoxazinones, their degradation products and analogues. phytotoxicity on standard target species (STS). *J. Agric. Food Chem.* **2005**, *53*, 538−548.
(45) Roseland, C. R.; Grosz, T. J. Induced responses of common annual sunflower *Helianthus annuus* L. from geographically diverse populations and deterrence to feeding by sunflower beetle. *J. Chem. Ecol.* **1997**, *23*, 517−542.
(46) Inderjit; Dakshini, K. M. M. Hesperetin 7-rutinoside (hesperidin) and taxifolin 3-arabinoside as germination and growth inhibitors in soils associated with the weed, *Pluchea lanceolata* (DC) C.B. Clarke (Asteraceae). *J. Chem. Ecol.* **1991**, *17*, 1585−1591.
(47) Harborne, J. B.; Smith, D. M. Anthochlors and other flavonoids as honey guides in the Compositae. *Biochem. Syst. Ecol.* **1978**, *6*, 287−291.

DOI: 10.1021/acs.jafc.5b02261
J. Agric. Food Chem. 2015, 63, 6410−6421

of the product. Each modified triglyceride molecule would now have two polar groups and two nonpolar groups, namely, the ester headgroup and the middle polar amino segment of each acyl chain compared to the virgin oil with a traditionally nonpolar tail. We envisioned this change would introduce better packing of the chains, leading to improved density with associated properties for the derivatives. The change in geometry and polarity of the chains would also enhance metal-binding capability in lubricating and chelating applications. It was also anticipated that such changes would find the product to be useful both as a neutralization agent and as a component in metal-working fluids application. Another potential application would be as an agent of sequestration of metal ions in waste effluents. Most amines currently in use for neutralizations or as pH adjusters are monoamines with short- to medium-sized alkyl chains and are generally milder than inorganic bases such as NaOH or KOH, which are at the top of the scale of neutralizing agents. However, the draw for amines as neutralizers is their less caustic nature on equipment, which leads to prolonged useful lifetimes for equipment. The polyamine triglyceride reported here is novel and initiates new characteristics and uses for the modified oil.

MATERIALS AND METHODS

Materials. Polyhydroxy triglycerides of milkweed oil were obtained from our in-house supply from previous work.[10] Initial Dess-Martin Periodinane (DMP), anhydrous $MgSO_4$, sulfuric acid, and anhydrous diethyl ether were obtained from Sigma-Aldrich (St. Louis, MO, USA). Dichloromethane, ethyl acetate, $NaHCO_3$, potassium bromate, 2-iodobenzoic acid, sodium borohydride, and acetic anhydride were obtained from ACROS ORGANICS (Vineland, NJ, USA) whereas $Na_2S_2O_3.5H_2O$ was from J.T. Baker Chemical Co. (Phillipsburg, NJ, USA).

Methods. *Instrumentation. (a) Fourier Transform Infrared (FT-IR) Spectrometry.* FT-IR spectra were measured on an Arid Zone FT-IR spectrometer (ABB MB-Series, Houston, TX, USA) equipped with a DTGS detector. Liquid derivatives were pressed between two NaCl disks (25 mm × 5 mm) to give thin transparent oil films for analysis by FT-IR spectrometry. Absorbance spectra were acquired at 4 cm^{-1} resolution and signal-averaged over 32 scans. Interferograms were Fourier transformed using cosine apodization for optimum linear response. Spectra were baseline corrected, scaled for mass differences, and normalized to the methylene peak at 2927 cm^{-1}.

(b) NMR Spectroscopy. ^1H and ^{13}C NMR spectra were acquired on a Bruker AV-500 MHz spectrometer with a dual 5 mm proton/carbon probe (Bruker, Billerica, MA, USA). The internal standard used was tetramethylsilane.

Refractive Index (RI). RI was measured as a function of temperature (30−80 °C) on a model Mark II Plus Abbe refractometer (Reichert Inc., Depew, NY, USA). The instrument provides data to four-digit precision. RI at 100 °C was obtained by extrapolation of data collected at ≤80 °C.

Density, Viscosity, and Viscosity Index (VI). Density and dynamic viscosity were measured as a function of temperature on a Stabinger SVM3000/G2 viscometer (Anton Paar GmbH, Graz, Austria). The instrument also provides the kinematic viscosity as a function of temperature by automatically manipulating the corresponding measured density and dynamic viscosity data. VI was calculated from kinematic viscosity data at 40 and 100 °C following the procedure outlined in ASTM D 2270-93.[17]

Pour Point (PP) and Cloud Point (CP). PP and CP were determined on a model PSA-70S automatic analyzer from Phase Technology (Richmond, BC, Canada) according to ASTM standard test method D 5949[18] and D 5773,[19] respectively.

Pressurized Differential Scanning Calorimetry (PDSC). PDSC tests were conducted on a Q20P pressure differential scanning calorimeter (TA Instruments − Waters LLC, New Castle, DE, USA) fitted with a computer and software to allow for automatic data acquisition and analysis. All tests were conducted with the cell pressurized with pure oxygen to 500 ± 25 psig in dynamic mode, with a positive oxygen flow rate of 100 ± 10 mL/min. Details of the experimental procedure have been given previously.[20] The resulting heat flow versus temperature data were analyzed using the instrument computer and software to determine onset temperature (OT) and peak temperature (PT). Duplicate runs were conducted on each sample, and average OT and PT values are reported.

Four-Ball Tribometer and Test Specimen. The four-ball tests were conducted on a model KTR-30L four-ball tribometer (Koehler Instruments, Bohemia, NY, USA). The instrument comprises a mechanical unit, an electronic unit, and a computer with TriboDATA software (Koehler Instruments) that allows for setting and controlling test parameters as well as for automatic data acquisition. A detailed description and specification of the instrument can be found elsewhere.[21] Test balls used in four-ball experiments were obtained from Falex Corp. (Aurora, IL, USA) and had the following specifications: material, chrome−steel alloy made from AISI E52100 standard steel; hardness, 64−66 R_c; diameter, 12.7 mm; finish, grade 25 extra polish. Test balls were degreased by two consecutive sonications in isopropyl alcohol and hexane solvents in an ultrasonic bath prior to use. The pot and spindle used for securing the balls were also thoroughly washed with isopropyl alcohol and hexane, wiped with Kimwipe (Kimberly-Clark Worldwide, Inc., Roswell, GA, USA), and allowed to air-dry prior to testing with a new lubricant.

Four-Ball Anti-Wear (AW) Test. The four-ball AW tests were conducted according to the procedure outlined in ASTM D 4172-94[22] under the following test conditions: load, 392 N; speed, 1200 rpm; lubricant temperature, 75 °C; test duration, 60 min. During the test, frictional torque and test conditions (load, speed, temperature) were automatically recorded as a function of time by the instrument computer at a rate up to 300 samples/min. The torque and load data were used to calculate the coefficient of friction (COF) for each test using the procedure outlined in ASTM D 5183.[23] At the end of the AW test, the wear scar diameters (WSD) of each of the three balls in the ball pot were measured parallel and across the wear direction using a wear scar measurement system supplied by Koehler Instrument Co., Inc. The system comprises hardware (for taking a digital image of the wear scar of the three balls without disassembling the ball pot) and software (Scar View, Koehler Instrument Co., Inc.). The WSD along and across the wear direction of the three balls were used to calculate the average WSD for the test. Each test lubricant was used in at least two AW measurements, and average COF and WSD values were reported.

Four-Ball Extreme Pressure (EP) Test. EP tests were conducted according to ASTM D 2783[24] under the following conditions: speed, 1760 ± 40 rpm; temperature, ambient; load, variable; test duration, 10 s. EP tests comprise a series of 10 s tests at increasing loads until welding of the four balls is observed. The load increments are selected on the basis of the expected weld point (WP) for the test lubricant, with finer increments being used close to the WP. The load at which welding is observed is the WP and is a characteristic EP property of the lubricant tested.

Synthesis of Milkweed Polyketone from Polyhydroxy Milkweed Oil. In a typical reaction, polyhydroxy milkweed oil (61.0 g, 57.72 mmol) previously derived from milkweed oil[10−13] was placed into a 500 mL dry round-bottom flask (RBF) containing a magnetic stir bar. Dry dichloromethane (150 mL) was then added and stirred to dissolve the oil. The stirred solution was cooled to −5 °C in an ice bath augmented with NaCl. Dess−Martin periodinane reagent (59.5 g, 140 mmol) was added quickly while stirring was continued. The reaction temperature was gradually allowed to warm to 0 °C over 3 h and then to room temperature overnight. A yellow solid formed, which later redissolved in the dichloromethane. The resulting mixture was then concentrated to dryness under reduced pressure, and the solid was triturated with anhydrous EtOEt (100 mL × 3) and filtered. The filtrate was washed with saturated $NaHCO_3$. The organic layer was rewashed with a mixture of $NaHCO_3$−$Na_2S_2O_3·5H_2O$. After separation of phases, the organic layer was rewashed with brine and

DOI: 10.1021/acs.jafc.5b00598
J. Agric. Food Chem. 2015, 63, 6422−6429

dried over $MgSO_4$ overnight.[14] The filtrate was then concentrated under reduced pressure to give 60.7 g (99.0%) yield of the polyketone triglyceride. The FT-IR spectrum of the product obtained was ν_{NCl} cm^{-1} 2927 vs (−CH_2− asym stretch), 2858 s (−CH_2− sym stretch), 1744 vs (second derivative C═O) ester; 1720 s-m (ketone C═O), 1463 m (CH_2 def), 1370 m (CH_3 def), 1235 m (C—OC−) stretch, 1166 s (−HC—O) stretch, 1097 m (−HCO−) stretch, 1020 m (−CH_2O−) stretch, 723 w (−CH_2−) wag. ^{13}C NMR: δ 213.6, 213.27, 209.7, 208.5, 206.6, 205.58, 205.52, 202.93, 202.8 (polyketone C═O).

Milkweed Schiff Base Formation from the Polyketone. Milkweed polyketone triglyceride (161.3 g, 156.5 mmol) was placed in a dry 1 L RBF) containing a magnetic stirrer. Dry dichloromethane (300 mL) was added and the mixture stirred and cooled to −1 °C in an ice bath; 2-propylamine (92.45 g, 1.564 mol) was then added dropwise to maintain the reaction temperature at 0 °C. After the amine had been added, the temperature was slowly allowed to warm to room temperature overnight. The solvent was removed under reduced pressure at 50 °C, and the crude product was diluted with EtOAc, dried over $MgSO_4$, filtered, and concentrated under reduced pressure followed by pump vacuum drying to give a yield of 158.8 g (70.6%) of the Schiff base. FT-IR cm^{-1}: 3366 w, 2959 sh, 2926 vs, 2874 sh, 2854s, 1741s, 1716 (C═O), 1686, 1588 (C═N of Schiff base), 1468 (−CH_2− def), 1381 (−CH_3 def), 1245, 1169,1018, 726. ^{13}C NMR δ 173.19, 172.77, 172.46, 171.15, (C═O ester), 160.69 (C═O formyl ester), 68.88 (−CH− glyceride backbone), 63.75 methine C of isopropyl), 62.06, 60.36(−CH_2O−glyceride backbone), 44.44, 43.72, 41.19, 40.30, 38.58 (−CH−isopropyl), 34.07− 21.71 (−CH_2−), 20.98−13.89 (−CH_3).

Conversion of the Schiff base (Imine) Triglyceride to the Polyamine Triglyceride. In a 1 L RBF containing a magnetic stir bar, the intermediate imine triglyceride (155.7 g, 0.1084 mmol) dissolved in 50:50 EtOH (300 mL)/1,4-dioxane (300 mL) was placed. Acetic acid (3 mL) was added to the solution and the mixture vigorously stirred and cooled to 0 °C in an ice bath. Powdered $NaBH_4$ (40.0 g) was added portion-wise to maintain the reaction temperature around 0 °C. At the end of the borohydride addition, the reaction was allowed to stir overnight, warming to room temperature. The mixture was then diluted to 1000 mL with 3% AcOH solution followed by extraction with dichloromethane. The extract was then washed with distilled water, dried over $MgSO_4$, and concentrated under reduced pressure at 48 °C followed by further drying at the pump to yield the polyamine product (160.2 g). Density at 24 °C was 1.072 g cm^{-3}; pH 8.09 (EtOH). FT-IR ($NaCl_{film}$) ν cm^{-1}: 3382 (−N—H stretch), 2962 (−CH_3 asym), 2929 (−CH_2− asym) vs, 2873 (−CH_3 sym), 2856 (−CH_2− sym) s, 1741 vs (C═O ester backbone), 1664 m, 1549 m-w (N—C), 1470 s (−CH_2− def), 1376 s (−CH_3 def), 1256, 1240 s (−C—O—C═O), 1167 s, 1109 s, 875, 722 (−CH_2−) wag. ^{13}C NMR DEPT ($CDCl_3$) δ 176.67 (C═O ester), 160.96 (−HC═O), 82.45, 81.54, 80.90, 80.11, 73.81, 71. 85, 68.88, 67.02, 65.80 (−CHN−), 62.05, 60.14 (−CH_2O−), 57.25, 43.55, 41.19, 40.28, 35.94−22.63 (−CH_2−), 21.08−14.19 (−CH_3).

RESULTS AND DISCUSSION

Synthesis and Identification of Milkweed Polyamine. The FT-IR spectrum of the unmodified milkweed oil is shown in Figure 1. This spectrum displays the olefinic −C═C—H absorption mode at around 3009 cm^{-1} as well as the breathing or puckering mode of the C═C bond at around 1658 cm^{-1}. In contrast, the starting material, polyhydroxy oil Figure 2, exhibits the characteristic broad (O−H) stretching band centered around 3448 cm^{-1}. This spectral region is transparent in the virgin oil. Substitution of the hydroxyl groups of polyhydroxy milkweed oil with nitrogen proceeded through an intermediate polyketone triglyceride of milkweed oil. An initial attempt at oxidation of the polyhydroxy oil (Figure 2) to the polyketone using the Jones reagent (chromic acid/H_2SO_4) resulted in an isolated product, which was characteristically not the desired material judging from the ^{13}C NMR spectrum obtained (not

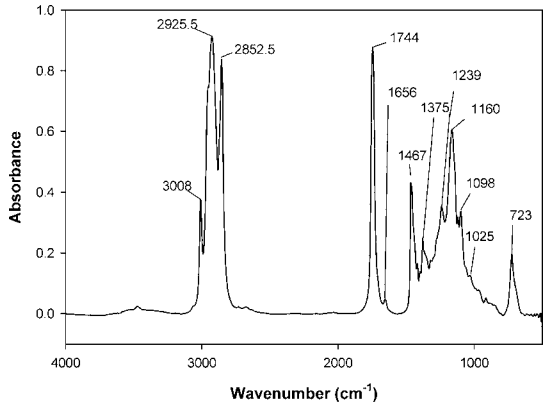

Figure 1. FT-IR spectrum of virgin milkweed oil.

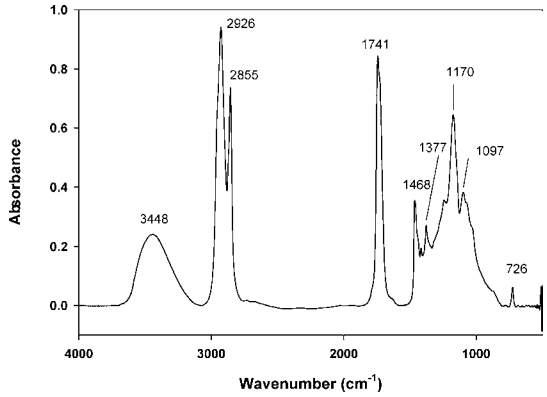

Figure 2. FT-IR spectrum of milkweed polyhydroxy triglyceride generated from hydration of the olefinic units of the virgin oil.

shown here). Use of the Dess−Martin periodinane oxidation technique for the polyhydroxy oil, on the other hand, gave an excellent, almost quantitative, yield of the polyketone triglyceride. Figure 3 shows the synthetic procedure used. Spectroscopic characterization of the polyketone is shown in Figures 4−6. Figures 4 and 5 are the FT-IR spectra of the polyketone. The second derivative of this FT-IR spectrum (Figure 5) shows the carbonyl region of the spectrum with three bands indicating the keto carbonyl absorbance at 1724 cm^{-1}, whereas the ester carbonyl absorption of the triglyceride is at 1746 cm^{-1} and there is a smaller higher frequency band at 1763 cm^{-1}. The ^{13}C NMR spectrum of this product (Figure 6) clearly shows the polyketo resonances (10 lines) from 202.8 to 213.6 ppm corresponding to about 10 keto groups expected in this intermediate from the 10 secondary hydroxyl groups of the polyhydroxy starting material. The arrangement of these carbonyl groups as shown in Figure 7 is such that on its own the polyketone would form a number of coordination spheres with metal ions. The operating principle is that when two keto groups are separated by a methylene species as in this structure (C10−C12 of the linoleyl chains), the two methylene protons at C-11 become more acidic by virtue of being sandwiched between C10 and C12 carbonyls. Enolization tends to be strong and is observed as shown in Figure 7 under appropriate conditions in the ^{13}C spectrum. Evidence are absorbances around 91 and 191 ppm for the enolic carbons in addition to the intact keto forms (spectrum not included here). Because of this enolization tendency, this polyketone bears a strong resemblance to the molecular structure of 2,4-pentanedione (acetyl acetone), which is a known chelating agent. This

DOI: 10.1021/acs.jafc.5b00598
J. Agric. Food Chem. 2015, 63, 6422−6429

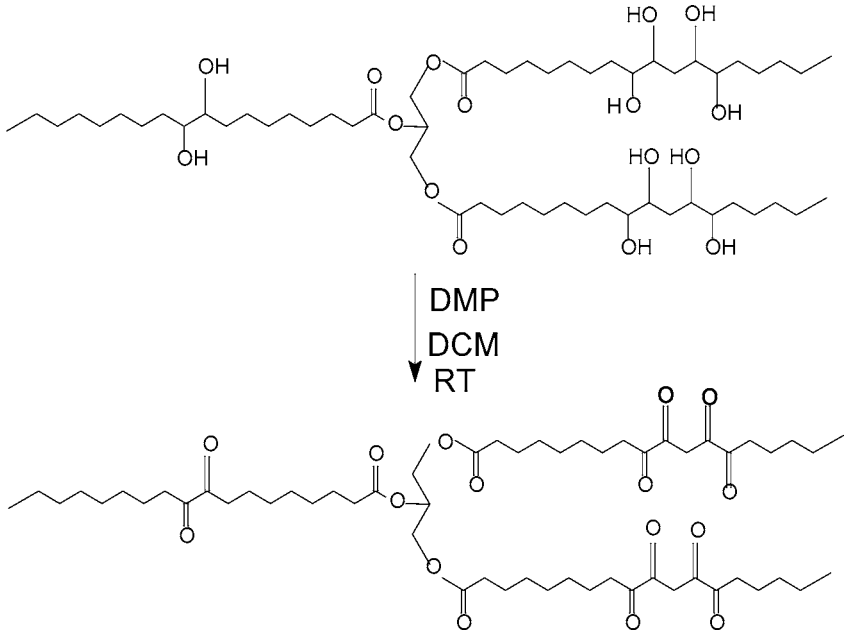

Figure 3. Generation of milkweed oil polyketone from Dess−Martin periodinane oxidation of the polyhydroxy milkweed oil.

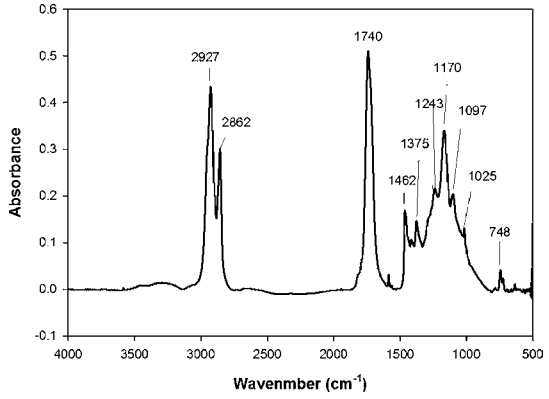

Figure 4. FT-IR spectrum of milkweed oil polyketone.

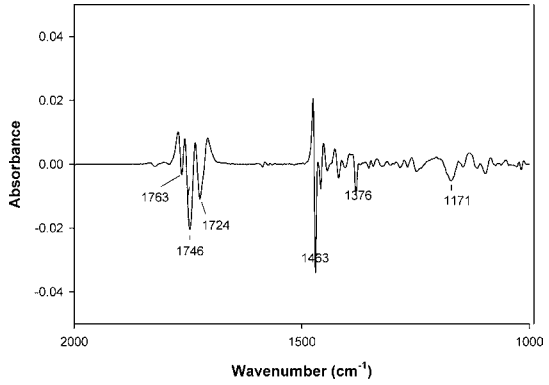

Figure 5. FT-IR carbonyl spectral region second-derivative 1763−1724 cm^{-1} showing keto carbonyl at 1724 and ester carbonyl absorption at 1746 cm^{-1}, respectively.

skeletal arrangement gives the polyketone intermediate the properties of a powerful chelating agent, and it may be pertinent to note that this is the first reported polyketo vegetable oil.

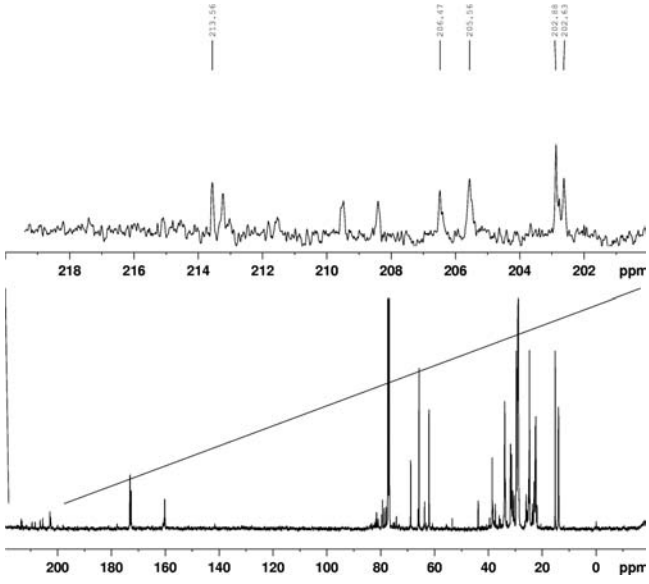

Figure 6. ^{13}C NMR spectrum of milkweed oil polyketone showing keto carbonyl resonances 202.63−213.56 ppm.

Conversion of the polyketone in dry dichloromethane at −1 °C with 2-propylamine as shown in Figure 8 gave the Schiff base (polyimines) in good yield. The polyimine adduct obtained was first characterized by FT-IR spectroscopy (Figure 9), followed by the ^{13}C NMR spectrum. The obtained ^{13}C NMR spectrum showed that the most downfield resonances observed were only those of the ester carbonyl absorbances at 173.19, 172.77, 172.46, and 171.15 ppm (C═O ester), which correspond to the polar headgroup ester functionalities of the triglyceride. The indication is that all of the keto carbonyl groups have undergone reaction with 2-propylamine. Reduction of this polyimine was achieved with sodium borohydride utilizing the method of Haire.[15,16] The polyamine isolated is a reddish viscous liquid. Its FT-IR spectrum (Figure 10) shows a prominent characteristic broad N−H stretching mode of secondary amines at 3384 cm^{-1} and C−N stretching bands at

DOI: 10.1021/acs.jafc.5b00598
J. Agric. Food Chem. 2015, 63, 6422−6429

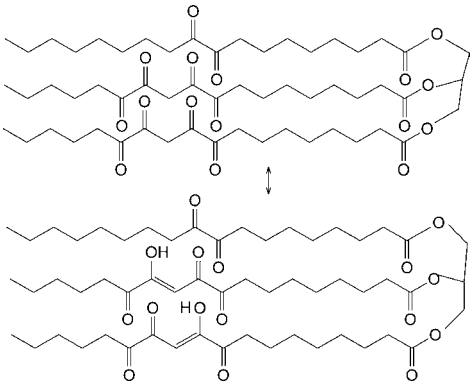

Figure 7. Schiff base formation from milkweed oil polyketone followed by borohydride reduction to the polyamine triglyceride.

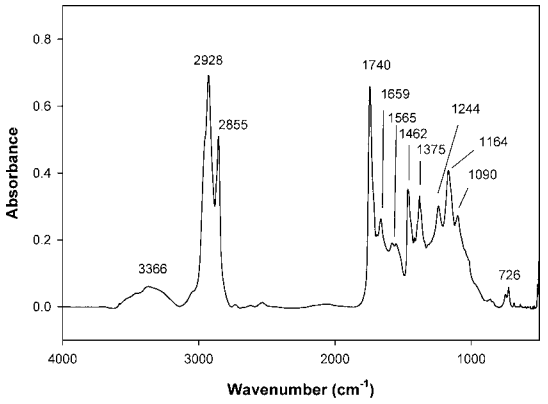

Figure 9. FT-IR spectrum of the polyimine (Schiff base).

1668 and 1551 cm^{-1}. The band broadening arose from hydrogen bonding. Figure 11 is the second derivative of Figure 10 and allows us to conclude that the only carbonyl absorption bands present are those of the glyceride backbone ester functional groups at 1755 cm^{-1}, the N−H stretch being around 3500 cm^{-1}.

Physical and Viscosity Properties of Milkweed Polyamine Oil. The effect of temperature on the density and RI of milkweed polyamine is summarized in Table 2. The polyamine is denser than water. Table 3 compares the kinematic viscosities of milkweed oil and its polyamine derivatives as a function of temperature. Also compared in Table 3 are the VIs of the two oils. As shown in this table, polyamination has considerably increased the viscosity of milkweed oil at all temperatures. At 40 °C, the viscosity displayed an almost 20-fold increase and an almost 6-fold increase at 100 °C. This means polyamination

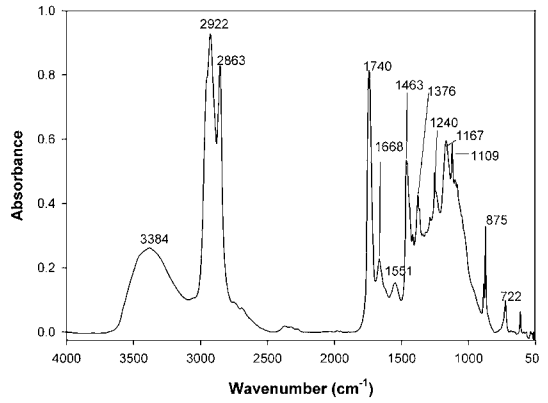

Figure 10. FT-IT spectrum of milkweed polyamine following reduction of Schiff base.

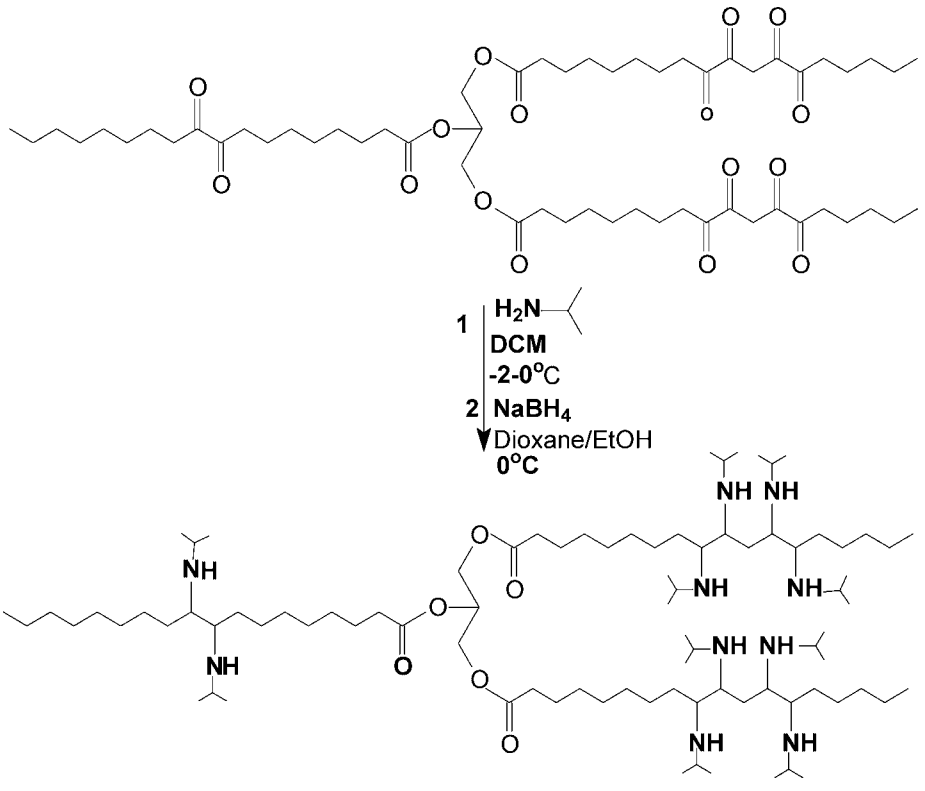

Figure 8. Schiff base formation from milkweed oil polyketone followed by borohydride reduction to the polyamine triglyceride.

DOI: 10.1021/acs.jafc.5b00598
J. Agric. Food Chem. 2015, 63, 6422−6429

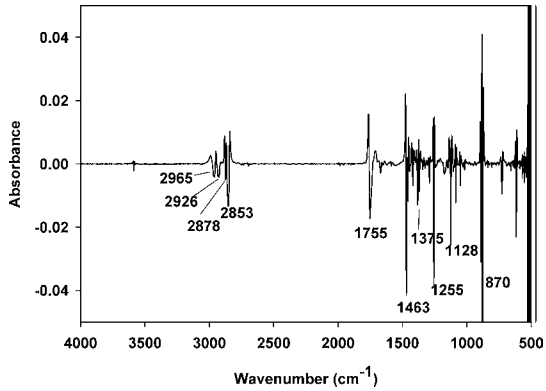

Figure 11. Second-derivative spectrum of Figure 9 milkweed polyamine.

Table 2. Density and Refractive Index of Milkweed Polyamine Oil[a]

T, °C	RI	density, g/cm^3
25		1.0209 ± 0.0001
30	1.4694 ± 0.0002	1.0171 ± 0.0001
40	1.4651 ± (9.6×10^{-5})	1.0093 ± 0.0002
75	1.4530 ± 0.0003	0.9820 ± 0.0003
100	1.4439 ± 0.0017[b]	0.9642 ± 0.0007

[a]All data from this work unless noted. [b]RI data at 10 °C is extrapolated from measured data at ≤80 °C.

Table 3. Kinematic Viscosity and Viscosity Index (VI) of Milkweed Oil (MWO) and Its Polyamine Derivative[a]

k_{Vis}, mm^2/s	MWO	MW polyamine
40 °C	33.8[b]	581.01 ± 16.69
75 °C		95.80 ± 0.05
100 °C	7.3[b]	41.60 ± 0.60
VI	210[b]	116

[a]All data from this work unless noted. [b]Data from ref 26.

will increase the viscosity range for the application of milkweed oil in lubrication. As expected, Table 3 also shows that although polyamination results in considerable reduction of the VI of the parent milkweed oil to almost half its value, its VI is double that of the polyhydroxy starting oil. Even though the VI of milkweed polyamine is considerably below those of unmodified vegetable oils, it is still comparable to petroleum-based oils widely used in lubrication.[25] Thus, milkweed polyamine can still be competitive with petroleum-based oils in lubrication applications.

Oxidation Stability and Cold Flow Properties of Milkweed Polyamine Oil. Table 4 summarizes the cold flow and oxidation stability data for milkweed polyamine oil.

Table 4. Cold Flow (Pour Point, Cloud Point) and Oxidation Stability (by PDSC) Properties of Milkweed Oil and Milkweed Polyamine[a]

cold flow	milkweed oil	milkweed polyamine oil
pour point, °C		−4.3 ± 0.6
cloud point, °C		not discernible
oxidation stability		
PDSC − OT, °C	136.78 ± 0.35	173.49 ± 0.79
PDSC − PT, °C	154.32 ± 0.47	194.18 ± 0.07

[a]All data from this work unless noted.

Cold flow properties are evaluated using pour point (PP) and cloud point (CP) data. As shown in Table 4, only PP data could be generated for milkweed polyamine oil because the oil was dark red and clouding could not be easily detected during the test. In general, oils with double-digit below zero PP values are preferred for lubrication applications. However, a PP of below freezing, such as that for milkweed polyamine oil, is not considered bad because it can be easily improved with the use of low concentrations of PP depressants.

Table 4 also shows the results of oxidation stability tests by the PDSC method. In this method, the temperatures at which oxidation of the oil under oxygen atmosphere begins (OT) and peaks (PT) are reported. The higher the values of OT and PT, the higher the oxidation stability of the oil. Table 4 compares the OT and PT of milkweed polyamine oil with those of milkweed oil. As seen in Table 4, polyamination has resuted in considerable improvement in the oxidation stability of milkweed oil. Both OT and PT have increased by almost 40 °C after polyamination. There could be many reasons for this improvement in oxidation stability due to polyamination. A major contributor to such an improvement is the elimination of unsaturation in the oil structure, which eliminates reactive allylic and bis-allylic protons, which are considered major contributors to oil oxidation.

Tribological Properties. Table 5 shows the results of AW and EP tests on milkweed polyamine oil. Also shown in Table 5 are similar AW data for three milkweed polyester derivatives from our previous work.[26] The data in Table 5 indicate that milkweed polyamine oil displays the lowest average COF and the second lowest WSD among the four derivatives. No EP measurements were done on the milkweed polyesters in the study cited. Milkweed polyamine oil showed an EP WP of 140 kgf, which indicates that the oil lacks any significant EP properties. This is consonant with the fact that none of the elements comprising milkweed polyamine oil (C, H, O, N) are expected to display EP characteristics.[26]

Effect of Chemical Structure. Table 6 compares available properties of milkweed oil and several of its derivatives, namely, polyepoxy, polyamine, acetate, butyrate, and valerate polyesters and the polyhydroxy. Table 6 compares the kinematic viscosity, VI, cold flow (PP, CP), and oxidation stability (OS) determined using PDSC (OT and PT) of MWO and the listed derivatives. In Table 6, the oil derivatives are arranged in order of increasing kinematic viscosity from left to right. As can be seen in Table 6, the kinematic viscosity of MWO increases dramatically due to derivatization. Kinematic viscosity increases in the order MWO < polyepoxy < polyvalerate < polyamine < polybutyrate < polyacetate < polyhydroxy. This trend can be explained in terms of intermolecular hydrogen bonding, which will be greatest for the polyhydroxy derivative. The order for the polyesters and polyepoxide could be due to intermolecular polar interactions, which is expected to increase in the order polyepoxy < polyvalerate < polybutyrate < polyacetate. It appears there was no significant hydrogen bonding in the polyamine, and any polar interactions were slightly better than the polyepoxide. On the basis of structural considerations, the polyamine should have shown significantly higher intermolecular interaction and, therefore, significantly higher viscosity than the polyesters. However, the fact that the viscosity of the polyamine was below those of the polyesters implies a different mechanism is at play. A possible explanation for the observed data may lie in the contrast between the linearity of the polyester substituents as against the branched alkyl group on

DOI: 10.1021/acs.jafc.5b00598
J. Agric. Food Chem. 2015, 63, 6422−6429

Table 5. Anti-wear (AW) and Extreme Pressure (EP) Properties of Milkweed Oil Derivatives[a]

		MW polyesters[b]		
anti-wear	MW polyamine	valerate	butyrate	acetate
COF	0.050 ± 0.001	0.055 ± 0.005	0.064 ± 0.014	0.059 ± 0.008
wsd, mm	0.593 ± 0.011	0.778 ± 0.058	0.622 ± 0.067	0.576 ± 0.030
EP				
weld point, kgf	140			

[a]All data from this work unless noted. [b]Data from ref 26.

Table 6. Selected Properties of Milkweed Oil (MWO) and Certain Derivatives[a]

				polyesters			
	MWO	polyepoxy	polyamine	valerate	butyrate	acetate	polyhydoxy
k_{Vis}, mm^2/s							
40 °C	33.8[b]	164.4[b]	581.01 ± 16.69	489.4[b]	926.2[b]	1733[b]	2332[b]
75 °C			95.80 ± 0.05				
100 °C	7.3[b]	19.22[b]	41.60 ± 0.60	42.2[b]	63.2[b]	78[b]	75.5[b]
VI	210[b]	133[b]	116	136[b]	131[b]	105[b]	85[b]
cold flow							
PP, °C			−4.3 ± 0.6	−18[b]	−18[b]	−3[b]	−15[b]
CP, °C				−28[b]	−30[b]	−25[b]	−7[b]
OS by PDSC							
OT, °C	136.78 ± 0.35		173.49 ± 0.79				
PT, °C	154.32 ± 0.47		194.18 ± 0.07				

[a]All data from this work unless noted. [b]Data from ref 26.

the nitrogen in the polyamine. It is well-known that increased branching tends to increase the bulkiness of a substrate rather than linearizing it, and this occurring in the middle aspect of the acyl chains of the triglyceride would make the molecule more spherical.[27−29] Such induced sphericity naturally would cause attenuation of the apparent sweep-width of the molecule and hence lower its viscosity as observed for the polyamine triglyceride.

Comparison of the VI of MWO and its derivatives in Table 6 shows an interesting correlation between the oil polarity and VI. MWO, which is the least polar of these substances, has the highest VI, whereas the polyhydroxy derivative, which is the most polar, has the lowest VI. The VI of the rest of the derivatives follows a similar trend and increases in the order polyacetate < polyamine < polybutyrate < polyvalerate < polyepoxy. This observation is similar to what is widely known about the effect of the polar hydroxyl groups on the VI of vegetable oils such as castor oil, which has a VI of ∼89, much lower than that for the nonpolar vegetable oils such as milkweed, soybean, etc., the VI of which is >200.[26] Examination of Table 6 also shows that the VI was a better predictor of polarity than kinematic viscosity, because it predicts the polarity of polyamine to be closer to polyacetate than to polyvalerate. Table 6 also shows the derivatization of MWO to polyamine and polyacetate was not an effective method for improving the PP of MWO, whereas conversion to polybutyrate or polyvalerate was more effective.

AUTHOR INFORMATION

Corresponding Author

*(R.E.H.-O.) Phone: (309) 681-6341. Fax: (309) 681-6524. E-mail: Rogers.HarryOkuru@ars.usda.gov.

Notes

Mention of trade names or commercial products in this publication is solely for the purpose of providing specific information and does not imply recommendation or endorsement by the U.S. Department of Agriculture.

The authors declare no competing financial interest.

ACKNOWLEDGMENTS

We are grateful to Dr. Karl Vermillion for the NMR spectra and Linda Cao and Mark Klokkenga for technical assistance.

REFERENCES

(1) Kalac, P.; Krizek, M.; Pelikanova, T.; Langova, M.; Veskrna, O. Contents of polyamines in selected foods. *Food Chem.* **2004**, *90*, 561−564.

(2) Kalac, P.; Krausova, P. A review of dietary polyamines: Formation, implications for growth and health and occurrence in foods. *Food Chem.* **2005**, *90*, 219−230.

(3) Seiler, N. Thirty years of polyamine-related approaches to cancer therapy. Retrospect and prospect. 1 Selected enzyme inhibitors. *Current Drug Targets* **2003**, *4*, 537−564.

(4) Seiler, N. Thirty years of polyamine-related approaches to cancer therapy. Retrospect and prospect. 2 Structural analogues and derivatives. *Current Drug Targets* **2003**, *4*, 565−585.

(5) Shalaby, A. R. Significance of biogenic amines to food safety and human health. *Food Res. Int.* **1996**, *29*, 675−690.

(6) Desury, G.; Moulinoux, J. P.; Delcros, J. G. Alteration of intestinal putrescine uptake in tumor-bearing rats. *Int. J. Oncol.* **2002**, *21*, 569−576.

(7) Catros-Quemener, V.; Chamaillard, L.; Bouet, F. *Les polyamines*: Role diagnostique et cible therapeutique en ccncerologie. *M/S − Medecine* **1999**, *15*, 1078−1085.

(8) Teti, D.; Visalli, M.; McNair, H. Analysis of polyamines as markers of (patho) physiological conditions. *J. Chromatogr. B: Anal. Technol. Biomed. Life Sci.* **2002**, *781*, 107−149.

(9) Larque, E.; Sabater-Molina, M.; Zamora, S. Biological significance of dietary polyamines. *Nutrition* **2007**, *23*, 87−95.

(10) Harry-O'kuru, R. E.; Holser, R. A.; Abbott, T. P.; Weisleder, D. Synthesis and characterization of polyhydroxy triglycerides from milkweed oil. *Ind. Crops Prod.* **2002**, *15*, 51−58.

DOI: 10.1021/acs.jafc.5b00598
J. Agric. Food Chem. 2015, 63, 6422−6429

(11) Harry-O'kuru, R. E.; Carriere, C. J. Synthesis, rheological characterization and constitutive modeling of polyhydroxy triglycerides derived from Milkweed oil. *J. Agric. Food Chem.* **2002**, *50*, 3214−3221.
(12) Harry-O'kuru, R. E.; Gordon, S. H.; Biswas, A. A facile synthesis of aminohydroxy triglycerides from new crop oils. *J. Am. Oil Chem. Soc.* **2005**, *82* (3), 207−212.
(13) Harry-O'kuru, R. E. 4-Hydroxy-3-methoxycinnamate esters of milkweed oil: Synthesis and Characterization. *Lipids* **2005**, *40* (11), 1179−1831.
(14) Harry-O'kuru, R. E.; Smith, J. M.; Wolfe, M. S. A short flexible route toward 2′- *C*-branched ribonucleosides. *J. Org. Chem.* **1997**, *62* (6), 1754−1759.
(15) Haire, M. J. Improved reduction of nitrimines to nitramines using sodium borohydride and acetic acid. *J. Org. Chem.* **1977**, *42* (21), 3446.
(16) Lustenberger, N.; Lange, H.; Hempel, K. Amino acid analysis on the picomole scale. *Angew. Chem., Int. Ed. Engl.* **1972**, *11* (3), 227.
(17) ASTM D 2270-93. Standard practice for calculating viscosity index from kinematic viscosity at 40 and 100 °C. *Annual Book of ASTM Standards*; American Society for Testing and Materials International: West Conshohocken, PA, USA, 2002; Vol. 05.01, pp 769−774.
(18) ASTM D5949-96. Standard Test Method for Pour Point of petroleum products (automatic pressure pulse method). *Annual Book of ASTM Standards*; American Society for Testing and Materials International: West Conshohocken, PA, USA, 2002; Vol. 5.03, pp 1051−1055.
(19) ASTM D5773-95. Standard test method for cloud point of petroleum products (constant cooling rate method). *Annual Book of ASTM Standards*; American Society for Testing and Materials International: West Conshohocken, PA, USA, 2002; Vol. 5.03, pp 811−816.
(20) Biresaw, G.; Bantchev, G. B. Tribological properties of biobased phosphonate derivatives. *J. Am. Oil Chem. Soc.* **2013**, *90*, 891−902.
(21) Asadauskas, S. J.; Biresaw, G.; McClure, T. G. Effects of chlorinated paraffin and ZDDP concentrations on boundary lubrication properties of mineral and soybean oils. *Tribol. Lett.* **2010**, *37* (2), 111−121.
(22) ASTM D 4172-94. Standard test method for wear preventive characteristics of lubricating fluid (four-ball method). *Annual Book of ASTM Standards*; American Society for Testing and Materials International: West Conshohocken, PA, USA, 2002; Vol. 05.02, pp 752−756.
(23) ASTM D 5183-95. Standard test method for determination of the coefficient of friction of lubricants using the four-ball wear test machine. *Annual Book of ASTM Standards*; American Society for Testing and Materials International: West Conshohocken, PA, USA, 2002; Vol. 05.03, pp 165−169.
(24) ASTM D 2783-88. Standard test method for measurement of extreme-pressure properties of lubricating fluids (four-ball method). *Annual Book of ASTM Standards*; American Society for Testing and Materials International: West Conshohocken, PA, USA, 2002; Vol. 05.02, pp 130−137.
(25) Brown, S. F. Base oil groups; manufacture, properties and performance. *Tribol. Lubrication Technol.* **2015**, *71* (4), 32−35.
(26) Harry-O'kuru, R.; Biresaw, S. C.; Cermak, S. C.; Gordon, S. H.; Vermillion, K. Investigation of the tribological properties of acylated derivatives of polyhydroxy milkweed Triglycerides. *J. Agric. Food Chem.* **2011**, *59* (9), 4725−4735.
(27) Jonsson, U. J. Lubrication of rolling element bearings with HFC polyester mixtures. *Wear* **1990**, *232*, 185−191.
(28) Wood-Adams, P. The effect of long chain branches on the shear flow behavior of polyethylene. *J. Rheol.* **2001**, *45*, 203−210.
(29) Lawate, S. S.; Lal, K.; Huang, C. Vegetable oils − structure and performance. In *Tribology Data Handbook*; Booser, E. R., Ed.; CRC Press: New York, 1997; pp 103−116.

DOI: 10.1021/acs.jafc.5b00598
J. Agric. Food Chem. 2015, 63, 6422−6429

Table 1. DNA Oligonucleotides Used in This Study

name	sequence (from 5′ to 3′ ends)	application
XynA-F1	TCAGGACCATGGGCAAGAGTATTGTAAACAGAGTTGTA	forward primer for the full-length of *xynA*
XynA-F2	CGTTCGGATCCATGGACGATACTAATACAAATCTGG	forward primer for the intracellular expression of *xynA* in *B. subtilis*
XynA-F3	CGGTTCCCATGGACGACACTAATACAAATCTGG	forward primer for the intracellular expression of NS-*xynA*ΔSLH in *E. coli*
sXynA-F1	GTATCGGATCCATGAAAAGCATTGTAAACAGAGTTG	forward primer for the secretion expression of *xynA* with its native signal sequence in *B. subtilis*
sXynA-F2	CGCTGGGATCCGATGATACTAATACAAATCTGG	forward primer for the secretion expression of *xynA* in *B. subtilis*
XynA-R1	TGGGACTCGAGAGAAGAGCCAAGATTGTTTGTTTTTTCTAATAAGCC	reverse primer for the full-length of *xynA*
XynA-R2	TTACGCTCGAGGCTGCTGCCAGATGGCTTACCTGTAAGCATCA	reverse primer for the truncated *xynA* gene
XynA-R3	AATACCTGCAGAGAAGGTTTACCTGTAAGCATCA	reverse primer for the expression of *xynA*ΔSLH in *B. subtilis*
His-1	TGTACGGATCCGGTGGTTCTCTGCAGCATCA	oligonucleotides used for C-terminal 6×His tag addition to pHT01
His-2	CCGATGACGTCTTAATGATGATGATGATGATGCTGCAGAGAACCAC	oligonucleotides used for C-terminal 6×His tag addition to pHT01
ssPhoD-F	GCGCTTGATCAATGGCATACGACAGTC	forward primer for the amplification of the signal sequence ss*phoD*
ssPhoD-R	CACGAGGATCCCGCAGCATTTACTTCAAAG	reverse primer for the amplification of the signal sequence ss*phoD*
ssBglS-F	CGACGTGATCAATGCCTTATCTGAAACGAGT	forward primer for the amplification of the signal sequence ss*bglS*
ssBglS-R	CGCACGGATCCCTGAGCAGAGGCAGTAGCA	reverse primer for the amplification of the signal sequence ss*bglS*
ssBpr-F	TCACCTGATCAATGCGTAAAAAAACTAAAAACAGACTC	forward primer the amplification of the signal sequence ss*bpr*
ssBpr-R	CCTTAGGATCCGCTTGCCCCGGCTGCTC	reverse primer the amplification of the signal sequence ss*bpr*
SamyQ1	TAGGCCTGATCAATGATTCAAAA	oligonucleotides used for the synthesis of ss*SamyQ*
SamyQ2	GAAACTGTCCGCTTTCGTTTTTGAATCATTGATCAGGCC	oligonucleotides used for the synthesis of ss*SamyQ*
SamyQ3	ACGAAAGCGGACAGTTTCGTTCAGACTTGTGCTTATGTG	oligonucleotides used for the synthesis of ss*SamyQ*
SamyQ4	AAACTGACAAATAACAGCGTGCACATAAGCACAAGTCTGAAC	oligonucleotides used for the synthesis of ss*SamyQ*
SamyQ5	CACGCTGTTATTTGTCAGTTTGCCGATTACAAAAACATCAGC	oligonucleotides used for the synthesis of ss*SamyQ*
SamyQ6	TAGGCCGGATCCTACGGCTGATGTTTTTGTAATCGGC	oligonucleotides used for the synthesis of ss*SamyQ*

[a]Restriction endonuclease recognition sites are underlined.

in the conversion of biomass into sugars, as high temperatures usually promote better enzyme penetration and cell wall disorganization of the raw materials.[9] *Thermoanaerobacterium aotearoense* SCUT27 is a thermophilic anaerobic bacterium isolated from a hot spring in China.[18] Previous studies have demonstrated that it can produce a multiple-enzyme mixture for xylan degradation, making it possible to utilize xylan as the sole carbon source.[19,20] We describe in this study the cloning and sequence analysis of the *xynA* gene from *T. aotearoense* SCUT27. We explore the possibility of the secretion of truncated *xynA*ΔSLH in *B. subtilis* using different signal peptides to increase the expression level of the multidomain xylanase. The recombinant *xynA*ΔSLH was purified and biochemically characterized.

MATERIALS AND METHODS

Chemicals, Reagents, and Materials. Oat spelt xylan and beechwood xylan were from Sigma-Aldrich Co. (St. Louis, MO, USA). Sodium carboxymethylcellulose (CMC-Na) was purchased from Aladdin (Shanghai, China). *T. aotearoense* SCUT27 was isolated by our group previously.[18] Cells were cultured in modified MTC medium. *Escherichia coli* DH5α (Invitrogen, San Diego, CA, USA), BL21(DE3) (Novagen, Madison, WI, USA), and *Bacillus subtilis* 1012wt (MoBiTec, Goettingen, Germany) were used for cloning and heterologous expression of xylanase. *E. coli* and *B. subtilis* were both cultured at 37 °C in Luria−Bertani (LB) medium. When necessary, 50 μg/mL of kanamycin, 100 μg/mL of ampicillin, or 5 μg/mL chloromycetin was added to the medium.

Molecular Techniques. DNA was manipulated using standard procedures. DNA polymerase of PrimeSTAR was purchased from TaKaRa (Dalian, China). FastDigest restriction enzymes were obtained from Fermentas (Thermo Scientific Ltd., Waltham, MA, USA). SanPrep Column Plasmid Mini-preps Kit and SanPrep Column PCR Product Purification Kit (Sangon, Shanghai, China) were used for the purification of plasmids and PCR products.

Xylanase gene (*xynA*) was amplified with the genomic DNA of *T. aotearoense* SCUT27 as the template and with primers of xynA-F1 and xynA-R1 (Table 1). Primers xynA-F1 and xynA-R1 were designed on the basis of the endoxylanase *xynA* gene sequence from *Thermoanaerobacterium* sp. (GenBank U27183.1). A truncated derivative of xylanase gene (x*ynA*ΔSLH) was obtained by PCR amplification with the primer pairs of xynA-F1 and xynA-R2, and the xylanase gene without its signal peptide (NS-*xynA*ΔSLH) was also generated similarly with the primer pairs of xynA-F3 and xynA-R2. The *xynA*, *xynA*ΔSLH, and NS-x*ynA*ΔSLH genes were digested and inserted between the *Nco*I and *Xho*I sites of pET28a vector (Novagen), yielding the plasmids of pET28a-*xynA*, pET28a-*xynA*ΔSLH, and pET28a-NS-*xynA*ΔSLH, respectively.

Preparation of Plasmid for Secretion Expression in *B. subtilis*. The construction of expression plasmids in *B. subtilis* is shown in Figure 1.

DNA fragments (AddHis) encoding the C-terminal 6×His tag were generated by overlapping extension PCR through combining two DNA fragments (His1 and His2) at a 1:1 ratio and inserted into pHT01 (MoBiTec) to obtain pHTHis (between the *Bam*HI and *Aat*II sites).

To generate secretion vectors, DNA fragments containing the signal sequences of ss*PhoD*, ss*BglS*, and ss*Bpr* from *B. subtilis* 168 were amplified by PCR using appropriate primers and genomic DNA isolated from *B. subtilis* 168 (Figure 1 and Table 1).[21] The amplified DNA fragments were digested with isocaudamer enzymes of *Bam*HI and *Bcl*I and inserted into pHTHis cleaved by the *Bam*HI restriction enzyme, generating pHTHisD, pHTHisS, and pHTHisR, respectively. By inputting the gene sequence of ss*SamyQ* (95 bp) into the free software DNAworks (http://helixweb.nih.gov/dnaworks/), six oligo sequences (from SamyQ1 to SamyQ6) were returned and synthesized accordingly (Table 1).[22] These oligos were assembled to *SamyQ* by standard overlapping procedure.[23] Then two flanking primers (SamyQ1 and SamyQ6) were used to amplify the full-length of ss*SamyQ* by standard PCR. Likewise, the ss*SamyQ* were inserted into pHTHis to obtain pHTHisQ.

DOI: 10.1021/acs.jafc.5b01259
J. Agric. Food Chem. 2015, 63, 6430−6439

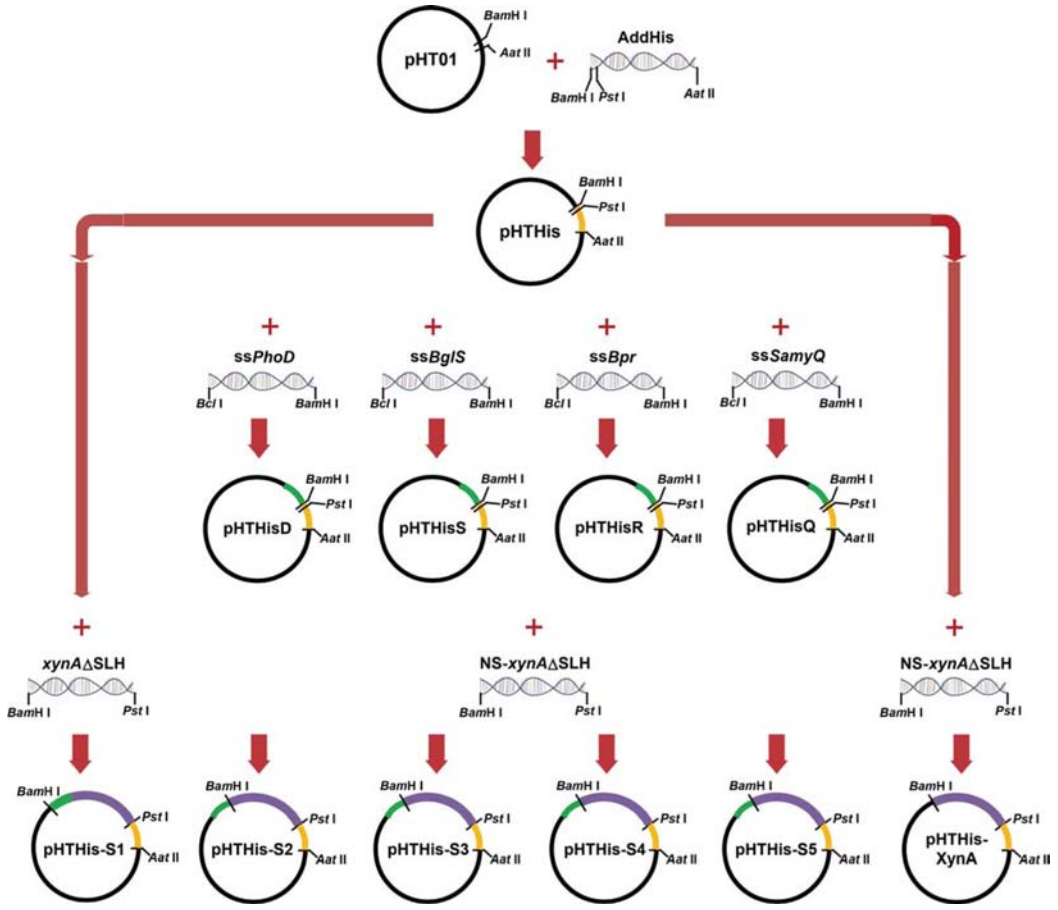

Figure 1. Heterologous expression vector construction for *B. subtilis* 1012wt. pHTHis-XynA is an intracellular expression plasmid derived from pHTHis with the deduced *xyn*AΔSLH. pHTHis-S1 is a secretion expression plasmid containing the deduced *xyn*AΔSLH and its native signal sequence. pHTHis-S2, pHTHis-S3, pHTHis-S4, and pHTHis-S5 are all secretion expression vectors with the deduced *xyn*AΔSLH.

In this study, six types of destination vectors carrying *xynA*ΔSLH expressed in *B. subtilis* were constructed. The *xynA*ΔSLH gene containing its native signal sequence was generated by PCR with primers sXynA-F1 and XynA-R3, then inserted between the *Bam*HI and *Pst*I sites of pHTHis, yielding pHTHis-S1. Similarly, another four secretion types of destination vectors containing different signal peptides were prepared as follows: the NS-*xynA*ΔSLH without its natural signal sequence was amplified by PCR with primers sXynA-F2 and XynA-R3 and inserted between the pHTHisD, pHTHisS, pHTHisR, and pHTHisQ (doubly digested with *Bam*HI and *Pst*I), generating pHTHis-S2, pHTHis-S3, pHTHis-S4, and pHTHis-S5. The vector pHTHis-XynA without signal sequence was constructed by inserting the NS-*xynA*ΔSLH between the *Bam*HI and *Pst*I sites of the plasmid pHTHis. Recombinant expression vectors were transformed into natural competent *B. subtilis* 1012wt as previously described.[24]

Heterologous Expression and Purification of Recombinant Xylanase. *E. coli* BL21(DE3) and *B. subtilis* 1012wt cells with various expression vectors were grown in Erlenmeyer flasks at 37 °C to the early exponential phase, followed by the addition of 1 mM IPTG to induce the expression of enzyme, and then incubated at 30 °C for 8 h for both *E. coli* and *B. subtilis*.

The cells were harvested by centrifugation at 13000*g* for 10 min and then resuspended in 20 mM Tris-HCl buffer (pH 7.5) containing 20 mM imidazole, 0.5 M NaCl, and 2 mg/mL lysozyme, followed by incubation at 45 °C for 1 h and sonication to release the intracellular proteins. The resulting clear supernatant was collected and loaded onto a HiTrap Chelating HP affinity column (GE Healthcare, Uppsala, Sweden) equilibrated with buffer (20 mM Tris-Cl, 20 mM imidazole, 0.5 M NaCl, pH 7.5). After binding, the column was washed with a linear gradient of 20−500 mM imidazole in 20 mM Tris-HCl buffer (pH 7.5) at a flow rate of 1 mL/min. Aliquots containing xylanase activity were pooled and loaded onto a HiPrep 26/10 desalting column (GE Healthcare). Fractions of the elute were stored in 100 mM Bis-Tris-HCl buffer (pH 6.5) containing 20% (v/v) glycerol at −20 °C.

Enzyme Characterization. Protein concentration was determined by a BCA Protein Assay Kit (Sangon, Shanghai, China) using bovine serum albumin (BSA; Sangon) as the standard. Protein homogeneity and molecular mass were estimated by sodium dodecyl sulfate−polyacrylamide gel electrophoresis (SDS-PAGE) in a 10 or 12% separating gel. Isolated proteins were visualized by staining with Coomassie Brilliant Blue R-250 (Sangon).

Xylanase activity was assayed by measuring the amount of reducing sugars released from beechwood xylan. The reaction mixtures contained 90 μL of 1% (w/v) beechwood xylan in 190 μL of 0.1 M Bis-Tris-HCl buffer (pH 6.5) and 20 μL of appropriately diluted enzyme. The catalytic reaction was carried out at 80 °C for 5 min and stopped on ice with the addition of 200 μL of 3,5-dinitrosalicylic acid (DNS) solution. The production of reducing sugars was measured at 540 nm as the literature reported.[25] One unit of xylanase activity was defined as the amount of enzyme required to release 1 μmol of reducing sugar equivalent per minute under assay conditions. All activity measurements were performed at least three times.

The pH profile of purified XynAΔSLH was determined by measuring the enzyme activity at 80 °C over the pH range from 3.5 to 9.0 using potassium acetate buffer (pH 3.5−6.0), Bis-Tris-HCl buffer (pH 6.0−7.0), and Tris-HCl buffer (pH 7.0−9.0). The enzyme activity obtained at the optimum pH was used to calculate the relative percentage of enzyme activity at other pH values. To estimate the pH stability, aliquots of purified enzymes were pre-incubated at 70 °C for 30 min at various pH values. Residual xylanase activities were

DOI: 10.1021/acs.jafc.5b01259
J. Agric. Food Chem. 2015, 63, 6430−6439

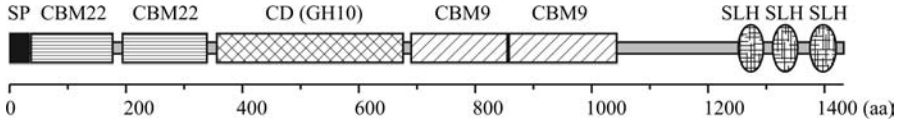

Figure 2. Schematic representation of full-length and truncated amino acid residues of xylanase. SP, signal peptide; CBM22, family 22 carbohydrate-binding module; CD, catalytic domain, GH10 family; CBM9, family 9 carbohydrate-binding module; SLH, S-layer-homology domain.

Table 2. Expression of Xylanase from *T. aotearoense* SCUT27 in *E. coli* BL21(DE3) and *B. subtilis* 1012wt[a]

no.	vector	expression host	OD_{600}	intracellular activity (U/mL)	extracellular activity (U/mL)	total activity (U/mL)	specific activity (U/mL/OD_{600})
1	pET28a-*xynA*	*E. coli*	2.12	2.87		2.87	1.35
2	pET28a-*xynA*ΔSLH	*E. coli*	2.08	2.91		2.91	1.40
3	pET28a-NS-*xynA*ΔSLH	*E. coli*	3.04	5.89		5.89	1.94
4	pHTHis-XynA	*B. subtilis*	1.56	11.93	0.38	12.31	7.89
5	pHTHis-S1	*B. subtilis*	5.34	0.35	0.21	0.56	0.10
6	pHTHis-S2	*B. subtilis*	5.97	7.13	1.67	8.80	1.47
7	pHTHis-S3	*B. subtilis*	6.15	0.62	4.03	4.65	0.76
8	pHTHis-S4	*B. subtilis*	6.03	0.95	3.42	4.37	0.72
9	pHTHis-S5	*B. subtilis*	6.42	0.70	4.28	4.98	0.78

[a]Experiments were performed in triplicate and expressed as the mean value. The relative standard deviations were all <5%.

determined under standard assay conditions and expressed as a percent of the initial activity of the enzyme.

To determine the optimum temperature, the enzyme activities were assayed in 0.1 M Bis-Tris-HCl buffer (pH 6.5) at various temperatures ranging from 45 to 90 °C. To evaluate the thermostability, XynAΔSLH was incubated at various temperatures (70, 75, and 80 °C). Aliquots were sampled at appropriate intervals to assay the residual enzyme activity under standard conditions. Furthermore, the remaining xylanase activities were also determined after incubation at a temperature of 75, 76, 77, 78, 79, or 80 °C for 30 min.

To investigate the effects of different metal ions and chemical reagents on the purified XynAΔSLH activity, 1 or 5 mM (final concentration) KCl, NaCl, $CaCl_2$, $MgCl_2$, $MnCl_2$, or $CuCl_2$ and 0.5 or 1 mM EDTA were individually added to the reaction mixture. Residual xylanase activities were determined under standard assay conditions.

The kinetic parameters of purified XynAΔSLH were obtained by measuring the rate of hydrolysis of beechwood xylan at various concentrations ranging from 1 to 8 mg/mL under optimum conditions. The enzymatic kinetic parameters K_m, V_{max}, and K_{cat} were determined graphically from Lineweaver−Burk plots.

Analysis of Xylan Hydrolysis Products. A 2.5 mg/mL solution of xylobiose (X2), xylotriose (X3), xylotetraose (X4), or xylopentaose (X5) or 1% of beechwood xylan was incubated with 60 μg/mL of purified XynAΔSLH in 50 mM potassium phosphate buffer (pH 6.5) at 55 °C. Hydrolysis products of xylooligosaccharides and beechwood xylan were sampled after 30 min and 6 h, respectively. The samples were then analyzed on silica gel plates (CF_{254}, 100 × 100 mm, Merck) with a mixture of chloroform/acetic acid/water (3:6:1) as the solvent system. The sugars on the plate were incubated at 105 °C for 15 min and visualized by spraying with an ethanol concentrated sulfuric acid mixture (95:5, v/v) followed by heating at 105 °C for another 5 min. A xylooligosaccharide mixture containing equal concentrations of xylose, xylobiose, xylotriose, xylotetraose, and xylopentaose (Megazyme, Bray, Ireland) was used as the standard.

Sugar Cane Bagasse Hydrolysis. Sugar cane bagasse obtained from the Guangzhou Sugar Cane Industry Research Institute (Guangzhou, China) was air-dried, milled, and screened through a 0.3 mm sieve.[20] Then 0.2 g of the sugar cane bagasse was hydrolyzed in 20 mL of 0.1 M Bis-Tris-HCl buffer (pH 6.5) containing (a) 10 U of XynAΔSLH (based on the activity toward beechwood xylan), (b) 10 U of XynAΔSLH with 0.2 FPU (filter paper unit) of Cellic Ctec2 (Novozyme, Denmark), or (c) 0.2 FPU Ctec2 only. The hydrolysis was carried out for 18 h at 55 °C. One milliliter of reaction mixture was taken at different time interval for the reducing sugar analysis by the DNS method using xylose as standard.

Nucleotide Sequence Accession Number. The nucleotide sequence of *xynA* has been deposited in the GenBank database under accession no. KP743979.

RESULTS AND DISCUSSION

Cloning and Sequence Analysis of XynA. A xylanase gene (*xynA*), encoding 1432 amino acids with a calculated p*I* of 4.47, was amplified from the strain of *T. aotearoense* SCUT27. A BLAST search showed that XynA shares highest amino acid sequence identities of 93 and 81% with GH10 xylanases from *Thermoanaerobacterium saccharolyticum* (Swiss-Prot P36917.1) and *Ruminiclostridium thermocellum* (Swiss-Prot P38535.1), respectively.

Analysis of the deduced amino acid sequence revealed that there was a putative 32 amino acid signal peptide identified by SignalP 4.0 (http://www.cbs.dtu.dk/services/SignalP/) (Figure 2). It contained a typical "Ala-X-Ala" motif at the −3 and −1 positions relative to the cleavage site (designated +1), which is expected to be in secreted proteins recognized by type I signal peptidase from Gram-positive bacteria.[26] The BLAST algorithm scan of the GenBank database indicated that the mature XynA is a modular protein containing several different domains: a carbohydrate-binding domain (CBM), a catalytic domain (CD), and a surface layer homology (SLH) domain. The CD (D324−G643) is flanked by duplicated noncatalytic domains and shows high homology to catalytic domains of GH10. The highest homology (48%) was found with XynC from *Bacillus* sp. (Swiss-Prot O69230.1).[27] The N-terminal noncatalytic region of XynA contains a duplicated sequence (T5−L144, G162−S306) identified as a carbohydrate-binding module (CBM, CBM22 family), homologous to noncatalytic thermostabilizing domains from other xylanases.[27−29] Bergquist et al. reported that the absence of the CBM22 family module in 1,4-β-xylanase from *Caldibacillus cellulovorans* resulted in a decrease in thermostability of the catalytic domain.[29] However, the previously designated thermostabilizing domains have subsequently been shown to promote binding to xylan.[2] Another two tandem family 9 carbohydrate-binding modules (CBM9)

DOI: 10.1021/acs.jafc.5b01259
J. Agric. Food Chem. 2015, 63, 6430−6439

are located at S658−K822 and I826−T1010 downstream of the CD, playing a role in the microbial degradation of cellulose and hemicellulose. Three SLH domains at the carboxy-terminal end of the cloned *xynA* have been identified. The SLH domains seemingly play a role in anchoring the enzyme to the cell surface in plant polysaccharide degradation.[30,31] Some studies have shown that SLH domains neither contribute to enzyme activity nor are required for substrate binding.[32] The CBM9 and SLH domains were found connected via a linker region of 209 amino acids, which likely provides a certain degree of flexibility, helping attack on the substrate.[31]

Recombinant Expression of XynA. To validate the contribution of the SLH domain and the linker region to the enzymatic activity, *xynA* gene with or without SLH and linker sequences was separately cloned into the pET28a vector and expressed in *E. coli* BL21(DE3). After 8 h of induction by 1 mM IPTG, the crude xylanase activities were measured as 1.35 ± 0.00 and 1.40 ± 0.01 U/mL/OD_{600} for XynA and XynAΔSLH, respectively (Table 2). Results indicated that the SLH domain and linker sequences did not contribute to enzyme activity, as previous research pointed out that the SLH at the C-terminal end of XynA from *T. saccharolyticum* NTOU1 mediated enzyme anchorage on the bacterial surface layer and had no effect on catalytic efficiency.[12] When the N-terminal signal peptide was deleted, the xylanase activity (NS-XynAΔSLH) was further increased by 38% compared with XynAΔSLH. These further demonstrated the fact that the xylanase activity expressed in *E. coli* was negatively influenced by the existence of signal sequence. In the subsequent study, the sequence of *xynA* without signal sequence and SLH domain coding sequence was used for expression and characterization. It was interesting to note that two new protein bands on SDS-PAGE were detected for pET28a-*xynA* compared to the control sample (Figure 3). The molecular weights for the two bands

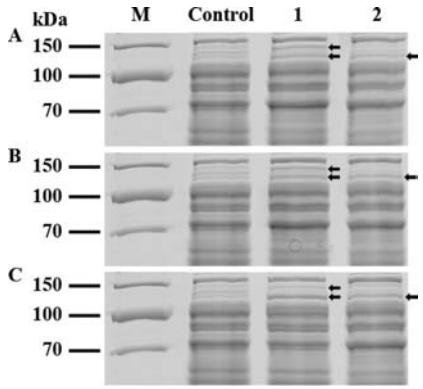

Figure 3. SDS-PAGE (12%) of XynA and XynAΔSLH expressed in *E. coli* BL21(DE3) for 4 h (A), 8 h (B), and 12 h (C). Lanes: control, *E. coli* BL21(DE3)/pET28a; 1, *E. coli* BL21(DE3)/pET28a-xynA; 2, *E. coli* BL21(DE3)/pET28a-xynAΔSLH; M, protein marker, broad range (PageRuler unstained protein ladder, Fermentas, Thermo).

were estimated to be 153 and 113 kDa, which agreed with the calculated molecular masses of XynA and XynAΔSLH from the amino sequence. Considering the fact that total xylanase activities for XynA and XynAΔSLH were nearly the same, we deduced that self-degradation or proteolytic degradation to XynAΔSLH would be occurred in the full-length XynA from *T. aotearoense* SCUT27 when it was expressed in *E. coli*.

Many heterologous protein expression systems have been developed to produce target proteins. Among them, *E. coli* is a valuable organism for the high-level production of recombinant proteins because of its many advantages. However, the application of *E. coli* in heterologous large protein expression is significantly limited, which may be caused by the lack of necessary control of the protein folding rates in the crowded *E. coli* cytoplasm.[33−35] Considered as a GRAS (generally recognized as safe) organism, *B. subtilis* has been developed as one of the best model bacteria for heterologous protein secretion. However, it is often impossible to predict whether a recombinant protein will be exported or to identify the suitable signal peptides for the target protein secretion.[36] To increase the expression level of XynAΔSLH, we constructed several versions of XynAΔSLH expression vectors in *B. subtilis* based on the pHT01 plasmid, including the Sec-dependent signal peptides of *ssBglS*, *ssBpr*, and *ssSamyQ* and the Tat signal peptide, *ssphoD* (Figure 1). The intracellular expression vector without any signal sequence in *B. subtilis* was also constructed.

To evaluate the expression level of XynAΔSLH, the extracellular and intracellular fractions of the recombinant *B. subtilis* were detected on SDS-PAGE (Figure 4) and the xylanase activities were determined (Table 2). Most of the total xylanase activities of XynAΔSLH were higher when expressed in *B. subtilis* than in *E. coli*, which was in part due to the enhanced cell density. Encouragingly, the total xylanase enzymatic activity increased dramatically from the basal level of 5.89 U/mL generated by *E. coli*/pET28a-NS-*xynA*ΔSLH to 11.93 U/mL by *B. subtilis*/pHTHis-XynA. The expression host change from *E. coli* to *B. subtilis* also resulted in a 4.1-fold increase of the specific xylanase activity, indicating that the increase of xylanase activity was due to the ability of a single cell. The results implied that *B. subtilis* 1012wt strain is a potential candidate to achieve a high-level expression of multidomain xylanase for industrial application. Many efforts have been made for high-level expression of xylanase through codon or medium optimization.[37−39] However, the molecular weights of these reported recombinant xylanases were <100 kDa. To our best knowledge, only a few studies focused on the expression level enhancement of multidomain xylanase.[14] Zhao et al. reported the recombinant *E. coli* harboring a multidomain xylanase gene showed a xylanase activity of 5.48 U/mL in shaker flasks.[17]

It should be mentioned that the secretion expression of the studied XynAΔSLH showed relatively much lower xylanase activity compared to the intracellular expression in *B. subtilis*. However, the attempts of secretion expression using *ssbglS*, *ssBpr*, or *ssSamyQ* as signal peptide indicated that the XynAΔSLH could be translocated in an unfolded state via the Sec-dependent pathway.[36] The reason for the inefficient exportation of the recombinant protein was complicated and ambiguous.[40] Tat-type signal peptide secretion system is an attractive alternative for the secretion of heterologous protein in *B. subtilis* because it dedicates the translocation of folded proteins across the bacterial cytoplasmic membrane. Unfortunately, the extracellular enzyme activities exported through this type of signal peptide originated from its native sequence (pHTHis-S1) and ss*phoD* (pHTHis-S2) were not satisfying. The reason might be attributed to the substrate specificity of the Tat-type translocases.[41,42] All these results implied that the secretion of XynAΔSLH from *T. aotearoense* SCUT27 in *B. subtilis* was preferably routed via a Sec-dependent pathway.

DOI: 10.1021/acs.jafc.5b01259
J. Agric. Food Chem. 2015, 63, 6430−6439

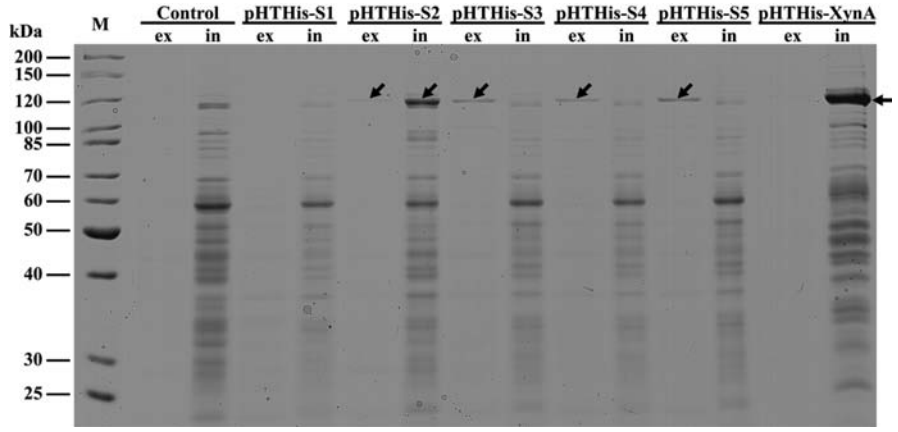

Figure 4. Expression of XynA in *B. subtilis* detected by Coomassie Brilliant Blue-stained 10% acrylamide SDS-PAGE using *B. subtilis* 1012wt as control (denoted "control"). Calculated molecular mass for mature xylanase XynAΔSLH was 113 kDa. Corresponding band positions are indicated by arrows. "ex" indicates extracellular fractions, and "in" denotes intracellular fraction of the cells. Lane M: protein marker, broad range (PageRuler unstained protein ladder, Fermentas, Thermo), the five largest bands of which were 200, 150, 120, 100, and 85 kDa, respectively.

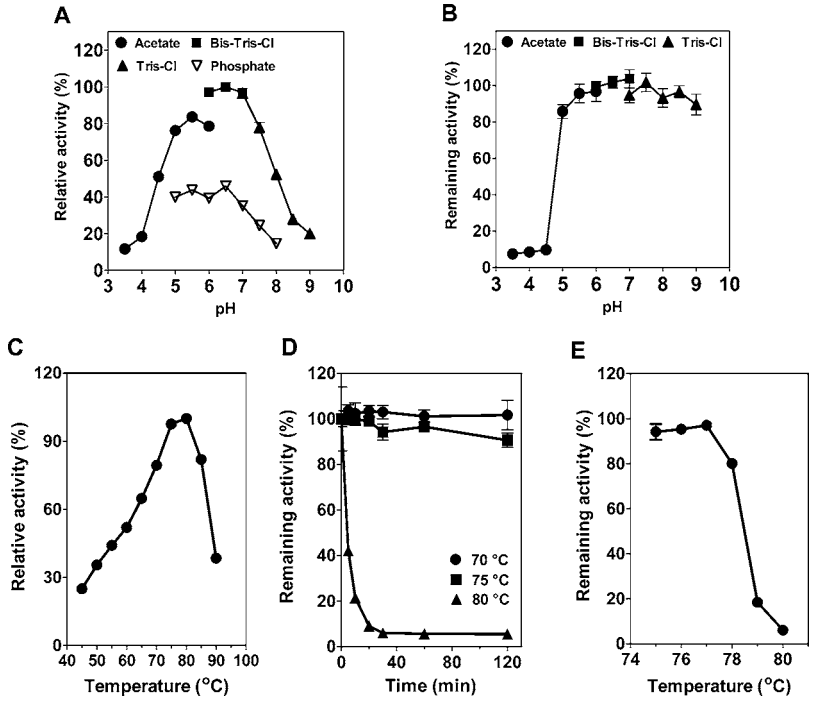

Figure 5. Effects of pH and temperature on the activity and stability of the recombinant XynAΔSLH expressed in *B. subtilis* 1012wt: (A) optimal pH; (B) pH stability (reaction buffers are potassium acetate buffer (pH 3.5−6.0, ●), Bis-Tris-HCl buffer (pH 6.0−7.0, ■), Tris-HCl buffer (pH 7.0−9.0, ▲), and potassium phosphate buffer (pH 5.0−8.0, ▽)); (C) optimal temperature; (D) thermostability of XynAΔSLH at 70 °C (●), 75 °C (■), and 80 °C (▲); (E) remaining activity of XynAΔSLH incubated at different temperatures ranging from 75 to 80 °C for 30 min. Values are the means and standard deviation of the average of three independent experiments.

Determination of Enzyme Activities and Properties. The XynAΔSLH expressed in *B. subtilis* (pHTHis-XynA) was purified by Ni-affinity chromatography and desalting. These procedures resulted in an 18.7-fold purification with a recovery yield of 79.2%, and a specific activity of 379.8 U/mg.

The influences of various buffers and pH on enzyme activities were studied using 100 mM potassium acetate buffer (pH 3.5−6.0), Bis-Tris-HCl buffer (pH 6.0−7.0), Tris-HCl buffer (pH 7.0−9.0) and potassium phosphate buffer (pH 5.0−8.0). Interestingly, XynAΔSLH exhibited relatively high activities in a rather broad pH range (pH 5.0−7.5) with an optimum activity in the Bis-Tris-HCl buffer at pH 6.5 (Figure 5A). At pH 5.0−8.0, the XynAΔSLH in phosphate buffers lost >50% of relative activity compared with the activity in the corresponding other buffers. At pH 6.0, XynAΔSLH was active in acetate and Bis-Tris-HCl buffers, but it was more significantly active in Bis-Tris-HCl buffer. The purified XynAΔSLH was stable between pH 5.0 and 9.0, retaining >80% of the initial enzyme activity after 30 min of incubation at 70 °C. However, it was rapidly irreversibly inactivated with pH <5.0 (Figure 5B).

The XynAΔSLH exhibited its optimal activity at 80 °C. At 85 °C, it showed about 80% of the optimum activity (Figure 5C). However, <40% of maximum activity was detected when the reaction temperature was increased to 90 °C. In contrast, it

DOI: 10.1021/acs.jafc.5b01259
J. Agric. Food Chem. 2015, 63, 6430−6439

displayed relatively low activities at lower temperatures, but sretained 25% of its highest activity at 45 °C.

The recombinant xylanase retained almost 100% of its initial activity when incubated at 70 °C, pH 7.0, for 2 h (Figure 5D) (data for temperatures below 70 °C are not shown). It remained about 90% of its activity after standing for 2 h at 75 °C, which indicated that the half-life of the recombinant xylanase was approximately 14.0 h at this temperature. Furthermore, it was interesting to find that the thermostability of the xylanase was sensitive in the range from 75 to 80 °C. The results showed that the XynAΔSLH lost its activity dramatically after incubation for 30 min at >79 °C. However, the recombinant xylanase retained about 80% of initial activity after being incubated at 78 °C for 30 min (Figure 5E).

With respect to kinetic parameters, the K_m, V_{max}, and K_{cat} of recombinant XynAΔSLH using beechwood xylan as the substrate were 4.10 mg/mL, 813.0 U/mg, and 1539.1 s^{-1}, respectively (Table 3). The K_{cat}/K_m ratio, reflecting the catalytic efficiency of enzyme, was 375.6 mL/mg·s, indicating that XynAΔSLH has great hydrolytic capacity for beechwood xylan. The specific activity of XynAΔSLH (379.8 U/mg) was much higher than that of other multidomain xylanases from *T. saccharolyticum* B6A-RI,[43] *T. saccharolyticum* JW/SL-YS485,[15] and *T. thermarum*.[16]

When various metal ions or EDTA was added into the reaction buffer separately, the activity of XynAΔSLH was not affected (100 ± 5%) by KCl (1 and 5 mM), NaCl (1 mM), or $MgCl_2$ (1 mM), but slightly affected (100 ± 25%) by $MnCl_2$ (1 mM), $CaCl_2$ (1 mM), NaCl (5 mM), and $MgCl_2$ (5 mM). However, its activity was strongly inhibited by $CaCl_2$ (5 mM) and $CuCl_2$ (1 mM). Besides that, EDTA (1 mM) addition in the reaction buffer reduced the activity of XynAΔSLH by 78% (Table 4). These findings suggested that some metal cations may serve to hold the enzyme in a catalytically active conformation. As a common trend, some metal ions are known to affect the xylanase activity. The enzymatic properties reported in this study are similar to those of other multidomain xylanases.[14,16] It should be mentioned that the activity of Xyn10A from *Thermotoga thermarum*, another multidomain xylanase, could be increased by >400% when the Ca^{2+} existed in the reaction mixture.[16]

Substrate Specificity and Products of Xylan Degradation. Experiments were carried out to study the specificity of XynAΔSLH to various substrates. The XynAΔSLH had the highest specific activity of 379.8 ± 3.2 U/mg toward beechwood xylan (defined as 100%), followed by oat spelt xylan (213.8 ± 1.6 U/mg, 56.3%). No obvious catalytic activity was detected when CMC-Na was used as substrate by XynAΔSLH (16.4 ± 0.4 U/mg). These results are contrary to other previously reported results; for example, the endoxylanases isolated from *T. thermarum*[16] and alkaline wastewater sludge[17] showed maximum activity on birchwood xylan, and xylanase from *G. thermoleovoranse* had maximum activity on oat spelt xylan.[13]

Using xylooligosaccharides or beechwood xylan as substrate, the purified XynAΔSLH showed relatively uniform hydrolysis capability (Figure 6). Xylotetraose and xylopentaose could be easily hydrolyzed to xylobiose with a trace of xylose by XynAΔSLH in 30 min of catalysis. However, much of xylotriose was not thoroughly degraded to xylobiose after being incubated at 55 °C for 30 min. Moreover, hydrolysis of xylobiose was not observed during the experiment. To ensure the maximum extent of degradation, the beechwood xylan was

Table 3. Comparison of the Enzymatic Properties of GH10 Multidomain Xylanases[a]

property	XynAΔSLH	XynA	XynA	Xyn10A	XynA	Xyn-b39	XynC	XynA	XynA
source	*T. aotearoense* SCUT27	*T. saccharolyticum* B6A-RI	*T. saccharolyticum* JW/SL-YS485	*T. thermarum*	*T. saccharolyticum* NTOU1	alkaline wastewater sludge	*Paenibacillus* sp. DG-22	*T. maritima*MSB8	*T. neapolitana*
molecular weight	113 kDa	130 kDa	150 kDa	130 kDa	154 kDa	158 kDa	159.5 kDa	120 kDa	119 kDa
optimum temperature	80 °C	70 °C	80 °C	95 °C	72 °C	60 °C	65 °C	92 °C	102 °C
optimum pH	6.5	5.5	6.3	7.0	5.5	7.0	6.5	6.2	5.5
thermostability[b]	75 °C for 2 h	NA	65 °C for 2 h	85 °C for 2 h	65 °C for 2 h	55 °C for 2 h	55 °C for 2 h	stable at 75 °C	90 °C for 200 min
pH stability	5.0–9.0	NA	NA	5.5–8.0	6.0–6.5	7.0–11.0	6.0–10.0	NA	NA
specific activity (U/mg)	379.8	227.4	NA	145.8	241	63.6	454.4	306	111.3
V_{max} (U/mg)	813.0	NA[c]	NA	325.3	NA	73.5	201.34	374	NA
K_m (mg/mL)	4.10	NA	NA	2.57	NA	1.01	3.49	1.1	NA
K_{cat} (1/s)	1539.1	NA	NA	710.2	NA	193.8[d]	535.2[d]	748	NA
K_{cat}/K_m (mL/mg·s)	375.6	NA	NA	276.4	NA	191.9[d]	153.4[d]	680	NA
reference	this study	Lee et al.[43]	Liu et al.[15]	Shi et al.[16]	Hung et al.[12]	Zhao et al.[17]	Lee et al.[14]	Winterhalter et al.[46]	Zerlov et al.[47]

[a]All data are based on the favorite substrates of the enzymes. [b]Thermostability was defined as >90% of enzyme activity being retained after incubation at the claimed conditions. [c]NA, not analyzed. [d]Calculated according to the data reported.

DOI: 10.1021/acs.jafc.5b01259
J. Agric. Food Chem. 2015, 63, 6430−6439

Table 4. Influence of Metals and EDTA on Enzyme Activity of XynAΔSLH[a]

	relative activity (%)	
compound	1 mM	5 mM
none	100.00 ± 0.43	
KCl	101.32 ± 4.16	98.69 ± 1.20
NaCl	97.75 ± 5.87	93.84 ± 0.77
$MgCl_2$	98.65 ± 0.53	75.86 ± 1.94
$MnCl_2$	92.72 ± 2.66	70.45 ± 1.56
$CaCl_2$	75.25 ± 1.31	32.47 ± 0.45
$CuCl_2$	11.59 ± 0.21	0.00
EDTA	37.00 ± 1.46 (0.5 mM)	22.29 ± 0.94 (1 mM)

[a]Enzyme activity was determined under standard conditions in the presence of each compound at concentrations of 1 and 5 mM if it is not annotated. Relative activity was calculated by taking the activity in the absence of metals as 100%. Experiments were performed in triplicate, and data were expressed as the mean ± SD.

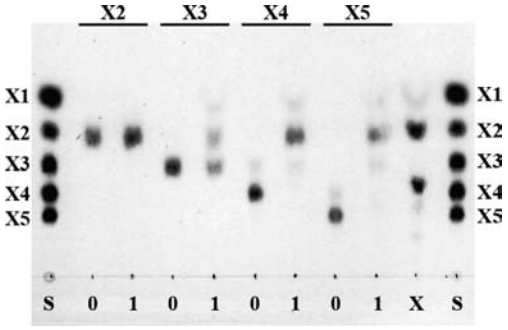

Figure 6. Thin-layer chromatography analysis of xylooligosaccharide or beechwood xylan hydrolysis products by the purified XynAΔSLH. 2.5 mg/mL of X2, X3, X4, or X5 was hydrolyzed by 60 μg/mL of XynAΔSLH in 50 mM potassium phosphate buffer (pH 6.5) at 55 °C for 0 (lane 0) and 30 min (lane 1). Lane X: 1% beechwood xylan hydrolysis was also carried out in 50 mM potassium phosphate buffer (pH 6.5) with 60 μg/mL of XynAΔSLH at 55 °C for 6 h. Lane S: standard mixture containing X1, X2, X3, X4, and X5.

incubated with XynAΔSLH for 6 h at 55 °C. Two major deposits were clearly shown on TLC. According to the mobility relative to the xylooligosaccharide standards, one of them was xylobiose, and the migration velocity of another deposit was a little faster than that of xylotetraose, indicating that it might be methylglucuronoxylotriose ($MeGlcAXyl_3$) according to previous research.[44] It was reported that $MeGlcAXyl_3$ might be the shortest aldouronic acid liberated from methylglucuronoxylan by the GH10 family of xylanases.[44,45] Depolymerization of beechwood xylan by XynAΔSLH also released a little xylose, which was found in the hydrolysis products of xylotriose, xylotetraose, or xylopentaose as well. All of the results suggested that although the middle subsites would be more specific, XynAΔSLH could attack the xylosidic linkage at the terminus while there was not a glucuronic acid as a substituted residue to block the cleavage.

Sugar Cane Bagasse Hydrolysis. Efficient hydrolysis of lignocellulosic biomass into fermentable sugars is the key step in the biofuel production. A combination of a commercial cellulase (Cellic Ctec2) from Novozyme with the purified XynAΔSLH was applied to the sugar cane bagasse hydrolysis. Results showed that XynAΔSLH supplementation in the reaction mixture led to an increase of up to 63.4% of reducing sugar production (Figure 7). After 78 h treatment with Cellic

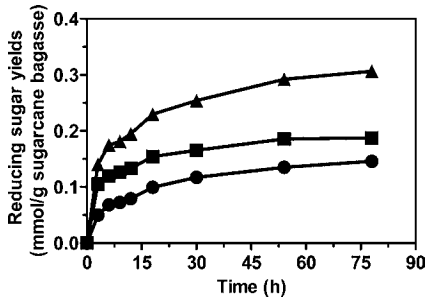

Figure 7. Hydrolysis of sugar cane bagasse by XynAΔSLH and Cellic Ctec2: ●, reaction with XynAΔSLH only; ■, reaction with Cellic Ctec2 only; ▲, reaction with XynAΔSLH and Cellic Ctec2. 0.2 g of sugar cane bagasse was hydrolyzed in 20 mL of 0.1 M Bis-Tris-HCl buffer (pH 6.5) containing 10 U of XynAΔSLH with or without Cellic Ctec2 (0.2 FPU). Experiments were carried out in triplicate, and all standard deviations were <5.0%.

Ctec2 and XynAΔSLH, about 0.3 mmol of reducing sugars per gram of sugar cane bagasse was released. Compared to the hydrolysis without XynAΔSLH, 0.19 mmol of reducing sugars was obtained per gram of sugar cane bagasse. When the purified XynAΔSLH was used as the sole hydrolyzing enzyme, it was also able to release reducing sugars with a final concentration of 0.15 mmol per gram sugar cane bagasse. The sugar cane bagasse contains about 40% of glucan and 20% of xylan.[20] Assuming that xylobiose was the only product by XynAΔSLH, 43.7 mg of xylobiose, accounting for 22.5% of the sugar cane bagasse, was produced. This indicated that almost all of the xylan in the sugar cane bagasse was converted into xylooligosaccharides. Adding XynAΔSLH with other glycosidic hydrolases in the degradation process of lignocellulosic biomass could efficiently enhance the conversion of polysaccharides.

A multidomain xylanase affiliated with the GH10 family from *T. aotearoense* SCUT27 was cloned, sequenced, and analyzed in this study. Successful improvement to the expression of the truncated XynAΔSLH was achieved in *B. subtilis*. Moreover, the wide pH stability, high temperature tolerance and thermostability, high specific activity value, and outstanding performance in the beechwood xylan or sugar cane bagasse hydrolysis make this endoxylanase a suitable candidate for biofuel and bioprocessing industries using cellulosic biomass as substrate.

AUTHOR INFORMATION

Corresponding Author

*(S.L.) Phone/fax: +86-20-39380629. E-mail: shuangli@scut.edu.cn.

Funding

This work was supported in part by the National Natural Science Foundation of China (NSFC 21276096), the Natural Science Foundation of Guangdong, China (2014A030313258), and the Open Project Program of Guangdong Key Laboratory of Fermentation and Enzyme Engineering, SCUT (FJ2013006). S. L. was funded by the Pearl River New-Star of Science & Technology supported by Guangzhou City (2012J2200012).

Notes

The authors declare no competing financial interest.

ABBREVIATIONS USED

CD, catalytic domain; CBM, carbohydrate-binding module; SLH, surface layer homology; GH, glycoside hydrolase; CMC-

DOI: 10.1021/acs.jafc.5b01259
J. Agric. Food Chem. 2015, 63, 6430−6439

Na, sodium carboxymethyl cellulose; LB, Luria−Bertani; BSA, bovine serum albumin; DNS, 3,5-dinitrosalicylic acid; GRAS, generally recognized as safe; X1, xylose; X2, xylobiose; X3, xylotriose; X4, xylotetraose; X5, xylopentaose

REFERENCES

(1) Collins, T.; Gerday, C.; Feller, G. Xylanases, xylanase families and extremophilic xylanases. *FEMS Microbiol. Rev.* **2005**, *29*, 3−23.

(2) Javier, P. F. I.; Óscar, G.; Sanz-Aparicio, J.; Díaz, P. Xylanases: Molecular properties and applications. In *Industrial Enzymes: Structure, Function and Applications*, 1st ed.; Polaina, J., MacCabe, A. P., Eds.; Springer: New York, 2007; pp 65−82.

(3) Valenzuela, S. V.; Díaz, P.; Javier Pastor, F. I. Recombinant expression of an alkali stable GH10 xylanase from *Paenibacillus barcinonensis*. *J. Agric. Food Chem.* **2010**, *58*, 4814−4818.

(4) Juturu, V.; Wu, J. C. Microbial exo-xylanases: a mini rview. *Appl. Biochem. Biotechnol.* **2014**, *174*, 81−92.

(5) Paes, G.; Berrin, J. G.; Beaugrand, J. GH11 xylanases: structure/function/properties relationships and applications. *Biotechnol. Adv.* **2012**, *30*, 564−592.

(6) Motta, F. L.; Andrade, C. C. P.; Santana, M. H. A. A review of xylanase production by the fermentation of xylan: classification, characterization and applications. In *Sustainable Degradation of Lignocellulosic Biomass − Techniques, Applications and Commercialization*; Chandel, A. K., Silva, S. S. d., Eds.; InTech: Rijeka, Croatia, 2013; pp 251−275.

(7) Collins, T.; Hoyoux, A.; Dutron, A.; Georis, J.; Genot, B.; Dauvrin, T.; Arnaut, F.; Gerday, C.; Feller, G. Use of glycoside hydrolase family 8 xylanases in baking. *J. Cereal Sci.* **2006**, *43*, 79−84.

(8) Shoseyov, O.; Shani, Z.; Levy, I. Carbohydrate binding modules: biochemical properties and novel applications. *Microbiol. Mol. Biol. Rev.* **2006**, *70*, 283−295.

(9) Ribeiro, L. F. C.; De Lucas, R. C.; Vitcosque, G. L.; Ribeiro, L. F.; Ward, R. J.; Rubio, M. V.; Damasio, A. R. L.; Squina, F. M.; Gregory, R. C.; Walton, P. H.; Jorge, J. A.; Prade, R. A.; Buckeridge, M. S.; Polizeli, M. d. L. T. M. A novel thermostable xylanase GH10 from *Malbranchea pulchella* expressed in *Aspergillus nidulans* with potential applications in biotechnology. *Biotechnol. Biofuels* **2014**, *7*, 115.

(10) Amoresano, A.; Andolfo, A.; Corsaro, M. M.; Zocchi, I.; Petrescu, I.; Gerday, C.; Marino, G. Structural characterization of a xylanase from psychrophilic yeast by mass spectrometry. *Glycobiology* **2000**, *10*, 451−458.

(11) Deesukon, W.; Nishimura, Y.; Sakamoto, T.; Sukhumsirichart, W. Purification, characterization of GH11 endo-β-1,4-xylanase from thermotolerant *Streptomyces* sp. SWU10 and overexpression in *Pichia pastoris* KM71H. *Mol. Biotechnol.* **2013**, *54*, 37−46.

(12) Hung, K. S.; Liu, S. M.; Fang, T. Y.; Tzou, W. S.; Lin, F. P.; Sun, K. H.; Tang, S. J. Characterization of a salt-tolerant xylanase from *Thermoanaerobacterium saccharolyticum* NTOU1. *Biotechnol. Lett.* **2011**, *33*, 1441−1447.

(13) Bhalla, A.; Bischoff, K. M.; Uppugundla, N.; Balan, V.; Sani, R. K. Novel thermostable endo-xylanase cloned and expressed from bacterium *Geobacillus* sp. WSUCF1. *Bioresour. Technol.* **2014**, *165*, 314−318.

(14) Lee, S. H.; Lee, Y. E. Cloning and characterization of a multidomain GH10 xylanase from *Paenibacillus* sp. DG-22. *J. Microbiol Biotechnol* **2014**, *24*, 1525−1535.

(15) Liu, S. Y.; Gherardini, F. C.; Matuschek, M.; Bahl, H.; Wiegel, J. Cloning, sequencing, and expression of the gene encoding a large S-layer-associated endoxylanase from *Thermoanaerobacterium* sp. strain JW/SL-YS 485 in *Escherichia coli*. *J. Bacteriol.* **1996**, *178*, 1539−1547.

(16) Shi, H.; Zhang, Y.; Li, X.; Huang, Y. J.; Wang, L. L.; Wang, Y.; Ding, H. H.; Wang, F. A novel highly thermostable xylanase stimulated by Ca^{2+} from *Thermotoga thermarum*: cloning, expression and characterization. *Biotechnol. Biofuels* **2013**, *6*, 26.

(17) Zhao, Y. Y.; Meng, K.; Luo, H. Y.; Huang, H. Q.; Yuan, T. Z.; Yang, P. L.; Yao, B. Molecular and biochemical characterization of a new alkaline active multidomain xylanase from alkaline wastewater sludge. *World J. Microbiol. Biotechnol.* **2013**, *29*, 327−334.

(18) Li, S.; Lai, C.; Cai, Y.; Yang, X.; Yang, S.; Zhu, M.; Wang, J.; Wang, X. High efficiency hydrogen production from glucose/xylose by the *ldh*-deleted *Thermoanaerobacterium* strain. *Bioresour. Technol.* **2010**, *101*, 8718−8724.

(19) Yang, X.; Lai, Z.; Lai, C.; Zhu, M.; Li, S.; Wang, J.; Wang, X. Efficient production of L-lactic acid by an engineered *Thermoanaerobacterium aotearoense* with broad substrate specificity. *Biotechnol. Biofuels* **2013**, *6*, 124.

(20) Lai, Z.; Zhu, M.; Yang, X.; Wang, J.; Li, S. Optimization of key factors affecting hydrogen production from sugarcane bagasse by a thermophilic anaerobic pure culture. *Biotechnol. Biofuels* **2014**, *7*, 119.

(21) Wang, G.; Chen, H.; Zhang, H.; Song, Y.; Chen, W. The secretion of an intrinsically disordered protein with different secretion signals in *Bacillus subtilis*. *Curr. Microbiol.* **2013**, *66*, 566−572.

(22) Hoover, D. M.; Lubkowski, J. DNAWorks: an automated method for designing oligonucleotides for PCR-based gene synthesis. *Nucleic Acids Res.* **2002**, *30*, e43.

(23) Joo, H.; Lin, Z. L.; Arnold, F. H. Laboratory evolution of peroxide-mediated cytochrome P450 hydroxylation. *Nature* **1999**, *399*, 670−673.

(24) Klein, C.; Kaletta, C.; Schnell, N.; Entian, K. D. Analysis of genes involved in biosynthesis of the lantibiotic subtilin. *Appl. Environ. Microbiol.* **1992**, *58*, 132−142.

(25) Miller, G. L. Use of dinitrosalicylic acid reagent for determination of ruducing sugar. *Anal. Chem.* **1959**, *31*, 426−428.

(26) Tuteja, R. Type I signal peptidase: an overview. *Arch. Biochem. Biophys.* **2005**, *441*, 107−111.

(27) Blanco, A.; Diaz, P.; Zueco, J.; Parascandola, P.; Pastor, F. I. J. A multidomain xylanase from a *Bacillus* sp. with a region homologous to thermostabilizing domains of thermophilic enzymes. *Microbiology* **1999**, *145*, 2163−2170.

(28) Meissner, K.; Wassenberg, D.; Liebl, W. The thermostabilizing domain of the modular xylanase XynA of *Thermotoga maritima* represents a novel type of binding domain with affinity for soluble xylan and mixed-linkage β-1,3/β-1,4-glucan. *Mol. Microbiol.* **2000**, *36*, 898−912.

(29) Sunna, A.; Gibbs, M. D.; Bergquist, P. L. A novel thermostable multidomain 1,4-β-xylanase from *Caldibacillus cellulovorans* and effect of its xylan-binding domain on enzyme activity. *Microbiology* **2000**, *146*, 2947−2955.

(30) Brechtel, E.; Bahl, H. *Thermoanaerobacterium thermosulfurigenes* EM1 S-layer homology domains do not attach to peptidoglycan. *J. Bacteriol.* **1999**, *181*, 5017−5023.

(31) Ozdemir, I.; Blumer-Schuette, S. E.; Kelly, R. M. S-Layer homology domain proteins Csac_0678 and Csac_2722 are implicated in plant polysaccharide deconstruction by the extremely thermophilic bacterium *Caldicellulosiruptor saccharolyticus*. *Appl. Environ. Microbiol.* **2012**, *78*, 768−777.

(32) Cann, I. K. O.; Kocherginskaya, S.; King, M. R.; White, B. A.; Mackie, R. I. Molecular cloning, sequencing, and expression of a novel multidomain mannanase gene from *Thermoanaerobacterium polysaccharolyticum*. *J. Bacteriol.* **1999**, *181*, 1643−1651.

(33) Zhao, Y.; He, W.; Liu, W. F.; Liu, C. C.; Feng, L. K.; Sun, L.; Yan, Y. B.; Hang, H. Y. Two distinct states of *Escherichia coli* cells that overexpress recombinant heterogeneous β-galactosidase. *J. Biol. Chem.* **2012**, *287*, 9259−9268.

(34) Schein, C. H. Production of soluble recombinant proteins in bacteria. *Nat. Biotechnol.* **1989**, *7*, 1141−1149.

(35) Peleg, Y.; Unger, T. Resolving bottlenecks for recombinant protein expression in *E. coli*. *Methods Mol. Biol.* **2012**, *800*, 173−186.

(36) Wang, G.; Chen, H.; Zhang, H.; Song, Y.; Chen, W. The secretion of an intrinsically disordered protein with different secretion signals in *Bacillus subtilis*. *Curr. Microbiol.* **2013**, *66*, 566−572.

(37) Jia, H.; Fan, G.; Yan, Q.; Liu, Y.; Yan, Y.; Jiang, Z. High-level expression of a hyperthermostable *Thermotoga maritima* xylanase in *Pichia pastoris* by codon optimization. *J. Mol. Catal. B: Enzym.* **2012**, *78*, 72−77.

DOI: 10.1021/acs.jafc.5b01259
J. Agric. Food Chem. 2015, 63, 6430−6439

(38) Damaso, M. C.; Almeida, M. S.; Kurtenbach, E.; Martins, O. B.; Pereira, N., Jr.; Andrade, C. M.; Albano, R. M. Optimized expression of a thermostable xylanase from *Thermomyces lanuginosus*. *Pichia pastoris*. *Appl. Environ. Microbiol.* **2003**, *69*, 6064−6072.
(39) Huang, Y. Attenuated secretion of the thermostable xylanase *xynB* from *Pichia pastoris* using synthesized sequences optimized from the preferred codon usage in yeast. *J. Microbiol. Biotechnol.* **2012**, *22*, 316−325.
(40) Li, W.; Zhou, X.; Lu, P. Bottlenecks in the expression and secretion of heterologous proteins in *Bacillus subtilis*. *Res. Microbiol.* **2004**, *155*, 605−610.
(41) Eijlander, R. T.; Jongbloed, J. D.; Kuipers, O. P. Relaxed specificity of the *Bacillus subtilis* TatAdCd translocase in Tat-dependent protein secretion. *J. Bacteriol.* **2009**, *191*, 196−202.
(42) Jongbloed, J. D.; Antelmann, H.; Hecker, M.; Nijland, R.; Bron, S.; Airaksinen, U.; Pries, F.; Quax, W. J.; van Dijl, J. M.; Braun, P. G. Selective contribution of the twin-arginine translocation pathway to protein secretion in *Bacillus subtilis*. *J. Biol. Chem.* **2002**, *277*, 44068−44078.
(43) Lee, Y. E.; Lowe, S. E.; Zeikus, J. G. Gene cloning, sequencing, and biochemical characterization of endoxylanase from *Thermoanaerobacterium saccharolyticum* B6A-RI. *Appl. Environ. Microbiol.* **1993**, *59*, 3134−3137.
(44) Gallardo, Ó.; Pastor, F. I. J.; Polaina, J.; Diaz, P.; Łysek, R.; Vogel, P.; Isorna, P.; González, B.; Sanz-Aparicio, J. Structural insights into the specificity of Xyn10B from *Paenibacillus barcinonensis* and its improved stability by forced protein evolution. *J. Biol. Chem.* **2010**, *285*, 2721−2733.
(45) Biely, P.; Vršanská, M.; Tenkanen, M.; Kluepfel, D. Endo-β-1,4-xylanase families: differences in catalytic properties. *J. Biotechnol.* **1997**, *57*, 151−166.
(46) Winterhalter, C.; Liebl, W. Two extremely thermostable xylanases of the hyperthermophilic bacterium *Thermotoga maritima* MSB8. *Appl. Environ. Microbiol.* **1995**, *61*, 1810−1815.
(47) Zverlov, V.; Piotukh, K.; Dakhova, O.; Velikodvorskaya, G.; Borriss, R. The multidomain xylanase A of the hyperthermophilic bacterium *Thermotoga neapolitana* is extremely thermoresistant. *Appl. Microbiol. Biotechnol.* **1996**, *45*, 245−247.

DOI: 10.1021/acs.jafc.5b01259
J. Agric. Food Chem. 2015, 63, 6430−6439

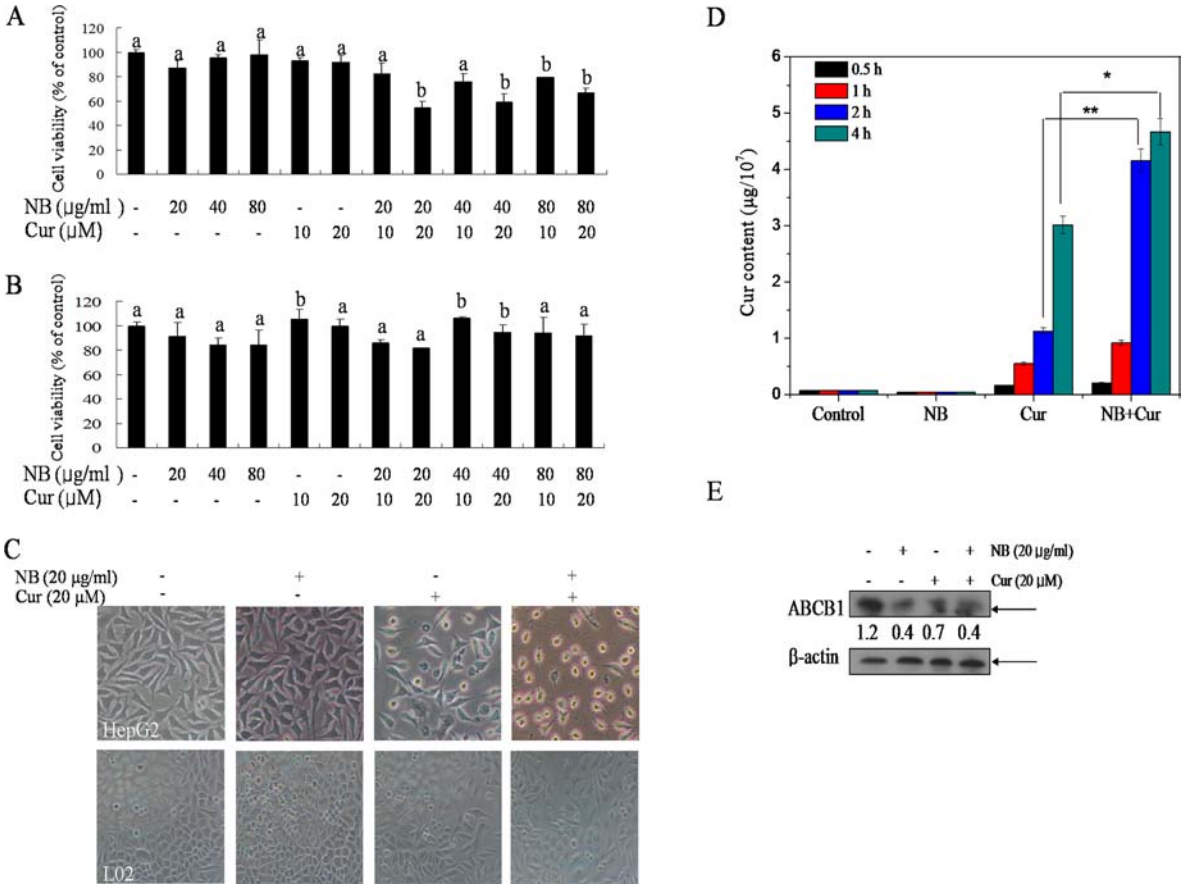

Figure 1. NB enhances the anticancer effects of Cur on HepG2 cells. (A) HepG2 cells were treated with different concentrations of NB (20, 40, 80 μg/mL) and Cur (10, 20 μM) alone and their combinations for 24 h. Bars with different characters are statistically different at the $P < 0.05$ level relative to control. (B) The human fetal liver cells L02 were exposed to different concentrations of NB (20, 40, 80 μg/mL) and Cur (10, 20 μM) alone and their combination for 72 h. Bars with different characters are statistically different at the $P < 0.05$ level relative to control. (C) MTT staining image of cells after treatments as examined by light microscopy (magnification 10×). HepG2 and LO2 cells growth inhibition induced by pretreatment of 20 μg/mL NB for 12 h then incubated with 20 μM Cur for 24 and 72 h, respectively. (D) NB enhances the cellular uptake of Cur. Quantitative analysis of Cur content in HepG2 cells exposed to NB and Cur alone and their combination for 0.5, 1.0, 2.0, 4.0 h, respectively. Bars between NB + Cur groups and Cur groups are significantly different at the $P < 0.05$ (*) or $P < 0.01$ (**) level. (E) Effects of NB on the expression levels of ABCB1 were detected by Western blotting assay. HepG2 cells were pretreated with or without 20 μg/mL NB for 12 h then incubated with or without 20 μM Cur for 24 h.

In the present study, two-dimensional polyacrylamide gel electrophoresis (2-DE) is used to investigate differentially expressed proteins in HepG2 cells under different treatment conditions and 2-DE integrated with matrix assisted laser desorption ionization time-of-flight mass spectrometry (MALDI-TOF-MS) has been used to further identify anticancer mechanism of NB and Cur in combination by a comparative proteomics approach.

MATERIALS AND METHODS

Materials. Curcumin (Cur), 3-(4,5-dimethylthiazol-2-yl)-2.5-diphenyltetrazolium bromide (MTT), propidium iodide (PI), and bicinchoninic acid (BCA) kit were bought from Sigma-Aldrich (Sigma-Aldrich, St. Louis, MO, USA). NB was obtained from the Natural Institute for the Control of Pharmaceuticals and Biological Products, Beijing, China. All reagents used in 2-DE were purchased from Bio-Rad Laboratories (Hercules, CA, USA). Antibodies against p53, p21, cdc2, and cyclin B1 were purchased from Cell Signaling Technology (Beverly, MA, USA).

Cell Culture. The human hepatocellular carcinoma cell line HepG2 was purchased from American Type Culture Collection (ATCC, Manassas, VA, USA). The human fetal liver cell line LO2 was obtained from Nanjing KeyGEN Biotech. CO., Ltd. (Nanjing, China). Both the cell lines were cultured in DMEM medium with 10% fetal bovine serum, 100 units/mL penicillin, and 50 units/mL streptomycin at 37 °C in a humidified (5% CO_2, 95% air) atmosphere.

Cell Viability Assay. The HepG2 cells with a density of 2×10^4 cells/well and LO2 cells with a density of 5×10^4 cells/well were seeded in 96-well culture plates for 24 h. The cells were pretreated with or without NB at different concentrations for 12 h and coincubated with or without Cur at different concentrations for different periods of time. Cell viability was determined by the MTT assay as previously described.[27]

Flow Cytometric Analysis. The HepG2 cells were harvested after treatment of NB (20 μg/mL)/Cur (20 μM) for 24 h, washed with PBS, and fixed with 70% cold ethanol at −20 °C overnight. The fixed cells were then stained with PI for 30 min in darkness. The cell cycle distribution was monitored by flow cytometric analysis as previously described by Chen et al.[28]

2-D SDS-PAGE Analysis. The HepG2 cells were treated with NB (20 μg/mL), Cur (20 μM), and NB (20 μg/mL)/Cur (20 μM) for 24 h, respectively. Then, the cells were washed with phosphate buffered saline (PBS) and were lysed with 1000 μL of alkylsis buffer including 20 mM Tris, 7 M urea, 2 M thiourea, 2% 3-[(3-cholamidopropyl)]-dimethylammonio-1-propanesulfonate (CHAPs), and 1 mM phenylmethanesulfonyl fluoride (PMSF). The cell lysates were treated with ultrasound to break nucleic acid and centrifuged at 12000 rpm/min for

DOI: 10.1021/acs.jafc.5b01773
J. Agric. Food Chem. 2015, 63, 6440−6449

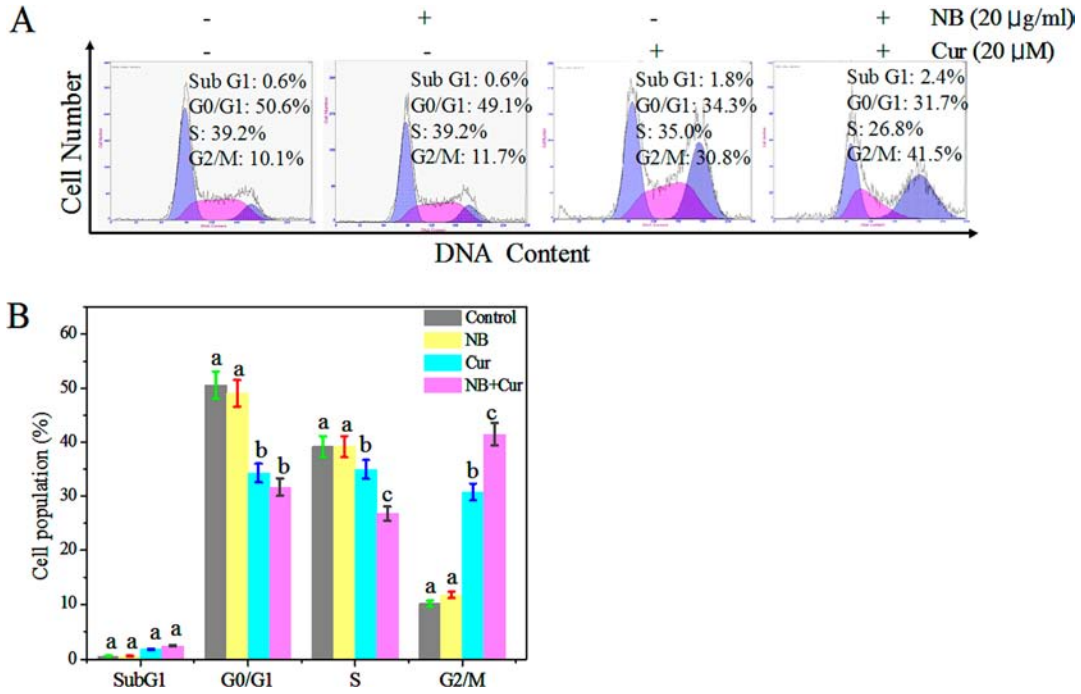

Figure 2. NB enhances Cur induces apoptosis in HepG2 cells. (A) NB/Cur induces G2/M-phase arrest in HepG2 cells. Cells after treatment were harvested and fixed with 70% ethanol before being stained with propidium iodide. (B) Quantitative analysis of NB/Cur induced cell cycle arrest in HepG2 cells by measuring the SubG1, G0/G1, S, and G2/M cell population. All data here are expressed as means ± SD of triplicates. Bars with different characters are statistically different at the $P < 0.05$ level. All images shown here are representative of three independent experiments with similar results.

20 min at 4 °C, and the supernatant was transferred into new EP tubes. Proteins from the supernatant were precipitated by acetone and then kept at −20 °C overnight. The protein concentration was measured using the Bradford assay with bovine serum albumin (BSA) as the standard sample for normalization. The protein samples were diluted to 450 μL rehydration buffer solution containing 7 M urea, 2 M thiourea, 4% CHAPs, 1% dithiothreitol (DTT), 1% immobilized pH gradient (IPG) buffer, and a trace of 1× bromophenol blue. Then, the samples were applied to immobilized dry IPG strips (linear pH gradient from pH 4−7, 24 cm) and rehydrated for 12 h. The samples were then focused for 30 min at 300 V, 30 min at 700 V, 90 min at 1500 V, 3 h gradient at 9000 V, and 4 h at 9000 V, for a total of 52 kV·h, using the Ettan IPGphor 3 isoelectric focusing (IEF) system (GE Health care, Little Chalfont, Buckinghamshire, UK). Focused IPG strips were equilibrated in 8 mL sodium dodecyl sulfonate (SDS) equilibration buffer I (6 M urea, 30% (v/v) glycerol, 2% (w/v) SDS, 50 mM Tris-HCl, pH 8.8, 0.002% bromophenol blue, and 100 mM DTT) for 15 min and then equilibrated for an additional 15 min in SDS equilibration buffer II (6 M urea, 30%(v/v) glycerol, 2% (w/v) SDS, 50 mM tris-HCl, pH 8.8, 0.002% bromophenol blue, and 250 mM iodoacetamide). After equilibration, 12.5% SDS-PAGE was performed on an Ettan DALTsix system (GE Health care, Little Chalfont, Buckinghamshire, UK). The 2-DE gel was then visualized using silver staining.

Protein Identification by MALDI-TOF-MS Analysis. The stained 2-DE gels were scanned with UMAX Powerlook1100 scanner (UMAX) and analyzed using ImageMaster 2D platinum 5.0 (GE Healthcare, Little Chalfont, Buckinghamshire, UK) according to the manufacturer's protocol. The spots of interest were manually excised from the silver-stained gel and subjected to in-gel trypsin digestion. After digestion, the peptides in gel pieces were then extracted using extraction buffer containing 2.5% trifluoroacetic acid (TFA) and 90% acetonitrile (ACN). The extracts were dried completely using a DZF-6020 vacuum drying system (Yiheng instrument Co., Ltd., Shanghai, China). The peptides were redissolved using 0.1% TFA in 30% ACN. Then, 0.5 μL of matrix (5 mg/mL α-cyano-4-hydroxycinnamic acid [CHCA] in 50% ACN and 0.1% TFA) was added into 0.8 μL of peptide solution before spotting on the target plate. Protein identification was carried out on an Ultraflex III MALDI-TOF mass spectrometric analysis (Bruker Dalton, Billerica, MA, USA). The peptides were detected in 355 nm UV wavelength and were accelerated with a 20000 V voltage. The peptides were scanned in the mass range of 700−3200 Da. Peptide masses were matched with the theoretical peptides of all proteins in the NCBI database using the BioTools (Bruker Dalton, Billerica, MA, USA) software. The following parameters were used for the database searching: peptides mass range of 800−4000 Da, first grade mass tolerance of 50 ppm, second grade mass tolerance of 0.5 Da, a maximum of one missed cleavage, monoisotopic masses, methionine oxsidation as a variable modification, cysteine iodoacetamide as a global modification.

Western Blot Analysis. Total cellular proteins were harvested by incubating the cells in the lysis buffer obtained from Cell Signaling Technology. The protein concentrations were determined by BCA kit (Sigma-Aldrich, St. Louis, MO, USA) according to the manufacturer's protocols. Equal amounts of protein (30 μg) loaded per lane were run on 10% SDS-PAGE, and transferred to nitrocellulose membrane at 110 V for 1 h. Following blocking with 5% nonfat milk in TBST buffer (20 mM Tris-HCl [pH 7.4], 137 mM NaCl, and 0.1% Tween-20) for 2 h, the membranes were then incubated with primary antibodies at 1:1000 dilution in 5% nonfat milk overnight at 4 °C and then incubated with secondary antibodies conjugated with horseradish peroxidase at 1:2000 dilution for 1 h at room temperature. Protein bands were visualized on X-ray film using an enhanced chemiluminescence system (Kodak, Rochester, NY, USA).

Measurement of ROS Generation. The intracellular production of reactive oxygen species (ROS) was measured by dihydroethidium (DHE) fluorescence assay according to the previously description.[20]

Statistical Analysis. Experiments were carried out at least in triplicate and repeated three times. All data were expressed as mean ± SD. Statistical analysis was performed using SPSS statistical package (SPSS 13.0 for Windows; SPSS, Inc. Chicago, IL, USA). The difference between two groups was analyzed by two-tailed Student's *t* test. The difference between three or more groups was analyzed by one-way analysis of variance multiple comparisons. Differences with *P*

DOI: 10.1021/acs.jafc.5b01773
J. Agric. Food Chem. 2015, 63, 6440−6449

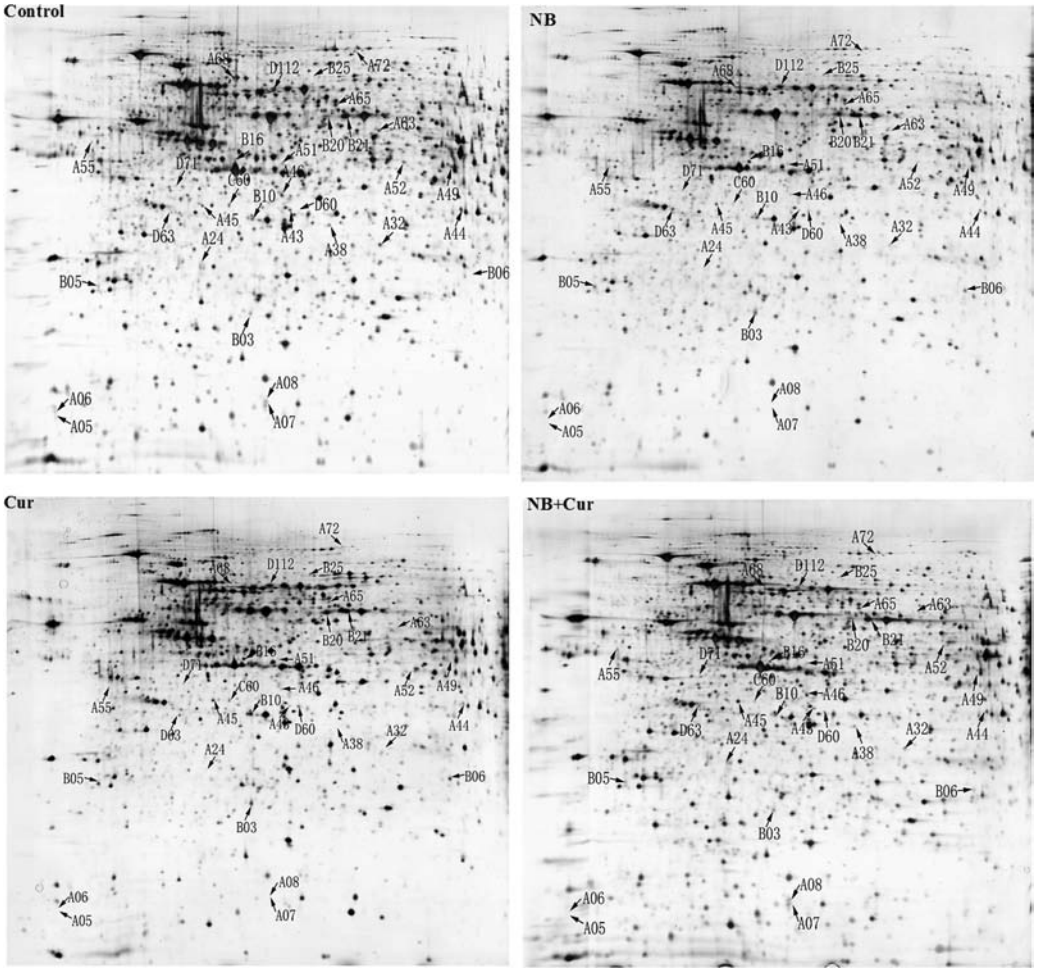

Figure 3. 2-DE analysis of protein expression in control, NB-, Cur-, and NB/Cur-treated HepG2 cells.

< 0.05 (*) or P < 0.01 (**) were considered statistically significant. Bars with different characters are statistically different at the P < 0.05 level.

RESULTS AND DISCUSSION

NB Enhances Cur-Induced the Growth Inhibition on HepG2 Cells through Enhancement of the Cellular Uptake of Cur. To determine the cytotoxicity effects of NB and Cur in combination on HepG2 cells, the cells were treated with different concentrations of NB (20, 40, 80 μg/mL) alone and Cur (10, 20 μM) alone and in their combinations for 24 h, while LO2 cells were exposed to NB alone and Cur alone and in their combination for 72 h. As shown in Figure 1A,B, NB not only induced negligible growth inhibition on HepG2 cells, but also slightly promoted cell growth. Meanwhile, Cur alone only demonstrated a slight inhibition of cancer cell growth. However, pretreatment of the cells with NB significantly enhanced the cells growth inhibitory effects of Cur on HepG2 cells. Interestingly, the combination of 20 μg/mL NB and 20 μM Cur exhibited the highest cytotoxicity against HepG2 melanoma cells with the cell viability at 54.3% (cells exposure to NB/Cur for 24 h), but showed the lower cytotoxicity toward LO2 cells with the cell viability at 81.5% (cells exposure to NB/Cur for 72 h). Therefore, we selected 20 μg/mL NB and 20 μM Cur for single or combination treatments in all subsequent experiments.

The above results were also confirmed by microscopic examination. As displayed in Figure 1C, the images showed that HepG2 cells treated with NB and Cur in combination had more cell shrinkage, cell rounding, and formation of apoptotic bodies than those treated with Cur alone and NB alone. In contrast, LO2 cells treated with NB alone and Cur alone and their combination remained intact with regularity in shape.

In order to determine whether NB enhanced the anticancer activity of Cur via the increase of Cur content, fluorescent spectrometry was employed to measure the cellular uptake of Cur. As shown in Figure 1D, compared with Cur treatment alone, HepG2 cells exposed to NB and Cur in combination significantly increased the Cur concentration in a time dependent manner. For instance, after 0.5, 1.0, 2.0, and 4.0 h incubation with NB and Cur in combination, the intracellular concentrations of Cur reached 0.2, 0.9, 4.2, and 4.7 $\mu g/10^7$ cells, which was about 1.2, 1.6, 3.5, and 1.5 times higher than Cur treatment alone (0.2, 0.6, 1.1, and 3.0 $\mu g/10^7$ cells), respectively. These results demonstrated that NB enhanced the cellular uptake of Cur in HepG2 cells.

To further investigate the mechanism of NB enhancement of cellular Cur uptake, we analyzed the expression of ABCB1 (a main multidrug resistance protein) protein by Western blotting assay. The results exhibited that pretreatment of HepG2 cells with NB markedly decreased the expression of ABCB1 compared with Cur treatment alone, which contributed to the enhancement of Cur content induced by NB (Figure 1E).

DOI: 10.1021/acs.jafc.5b01773
J. Agric. Food Chem. 2015, 63, 6440−6449

Table 1. MALDI-TOF-MS Identification of Differentially Expressed Protein Spots in NB-, Cur-, and NB/Cur-Treated HepG2 Cells

spot no.	protein name	gene name	accession no. (Swiss-Prot)	MW/PI	no. matched peptides	protein score	sequence coverage (%)	fold change NB/Cur/NB + Cur
A05	DNA-directed RNA polymerases I, II, and III subunit RPABC3	POLR2H	RPAB3_HUMAN	17189/4.5	7	288	55	0/0/1.7
A06	DNA-directed RNA polymerases I, II, and III subunit RPABC3	POLR2H	RPAB3_HUMAN	17189/4.5	2	58	19	0/0/1.6
A07	transmembrane protein 65	TMEM65	TMM65_HUMAN	25812/9.1	3	63	13	0.4/0.4/1.1
A08	ferritin heavy chain	FTH1	FRIH_HUMAN	25383/5.3	4	148	14	0/0.3/1.1
A24	cathepsin B	CTSB	CATB_HUMAN	38766/5.9	1	116	5	0.3/0.4/1.1
A32	Carbonic anhydrase 5B, mitochondrial	Ca5b	CAH5B_MOUSE	36999/6.9	11	246	38	0.5/0.4/0.5
A38	Serine/threonine-protein phosphatase 6 catalytic subunit	PPP6C	PPP6_HUMAN	35806/5.4	10	295	39	0.4/0.4/0.8
A43	2-oxoisovalerate dehydrogenase subunit beta, mitochondrial	BCKDHB	ODBB_HUMAN	43779/5.9	5	270	17	0.5/0.4/0.7
A44	39S ribosomal protein L39, mitochondrial	MRPL39	RM39_HUMAN	39210/7.6	7	202	21	0.5/0.4/0.7
A45	heterogeneous nuclear ribonucleoprotein U	HNRNPU	HNRPU_HUMAN	91269/5.8	1	42	1	0/0.3/0.4
A46	farnesyl pyrophosphate synthase	Fdps	FPPS_MOUSE	40898/5.5	13	412	45	0.3/0.4/0.9
A49	adenosylhomocysteinase	AHCY	SAHH_HUMAN	48255/5.9	14	121	22	0.4/0.4/0.6
A51	protein FAM185A	Fam185a	F185A_MOUSE	40651/6.0	8	176	35	0.3/0.3/0.7
A52	pyruvate dehydrogenase E1 component subunit alpha, somatic form, mitochondrial	PDHA1	ODPA_HUMAN	43952/8.4	16	270	30	0.4/0.3/0.8
A55	reticulocalbin-3	RCN3	RCN3_HUMAN	37470/4.7	5	74	17	0.5/0.4/0.9
A63	selenium-binding protein 1	SELENBP1	SBP1_HUMAN	52928/5.9	6	157	12	0/0.4/0.6
A65	prolyl 4-hydroxylase subunit alpha-1	P4HA1	P4HA1_HUMAN	61296/5.7	11	132	17	0.5/0.5/0.7
A68	NADH-ubiquinone oxidoreductase 75 kDa subunit, mitochondrial	NDUFS1	NDUS1_HUMAN	80443/5.9	24	297	30	0.5/0.6/0.9
A72	mitochondrial 10-formyltetrahydrofolate dehydrogenase	ALDH1L2	AL1L2_HUMAN	102365/6.1	6	59	10	0.3/0.4/0.6
B03	apolipoprotein A-I	APOA1	APOA1_BOVIN	30258/5.7	23	558	59	3.8/2.4/1.3
B05	proteasome subunit alpha type-5	PSMA5	PSA5_HUMAN	26565/4.7	8	304	41	3.7/3.3/1.5
B06	trypsin-1	PRSS1	TRY1_HUMAN	27111/6.1	1	34	8	3.2/4.8/1.2
B10	F-actin-capping protein subunit alpha-1	CAPZA1	CAZA1_HUMAN	33073/5.5	5	67	16	1.7/2.1/0.8
B16	probable ATP-dependent RNA helicase DDX56	DDX56	DDX56_HUMAN	62007/9.3	1	31	2	4.5/3.2/1.6
B20	protein disulfide-isomerase A3	PDIA3	PDIA3_HUMAN	57146/6.0	12	123	22	
B21	protein disulfide-isomerase A3	PDIA3	PDIA3_HUMAN	57146/6.0	11	109	18	2.5/2.6/1.0
B25	protein disulfide-isomerase A3	Pdia3	PDIA3_MOUSE	57099/5.9	7	100	17	4.0/3.0/0
C60	heterogeneous nuclear ribonucleoprotein U	HNRNPU	HNRPU_HUMAN	91296/5.8	4	152	6	0.5/0.5/0.4
D60	four and a half LIM domains protein 3	FHL3	FHL3_HUMAN	33166/-	10	151		3.4/2.7/1.9
D63	nucleophosmin	NPM1	NPM_HUMAN	32726/4.6	8	162	28	6.0/2.6/2.1
D71	heterogeneous nuclear ribonucleoproteins C1/C2	HNRNPC	HNRPC_HUMAN	33707/5.0	4	95	8	3.2/1.9/0.8
D112	stress-70 protein, mitochondrial	HSPA9	GRP75_HUMAN	73920/5.9	30	619	41	2.9/0.8/0.5

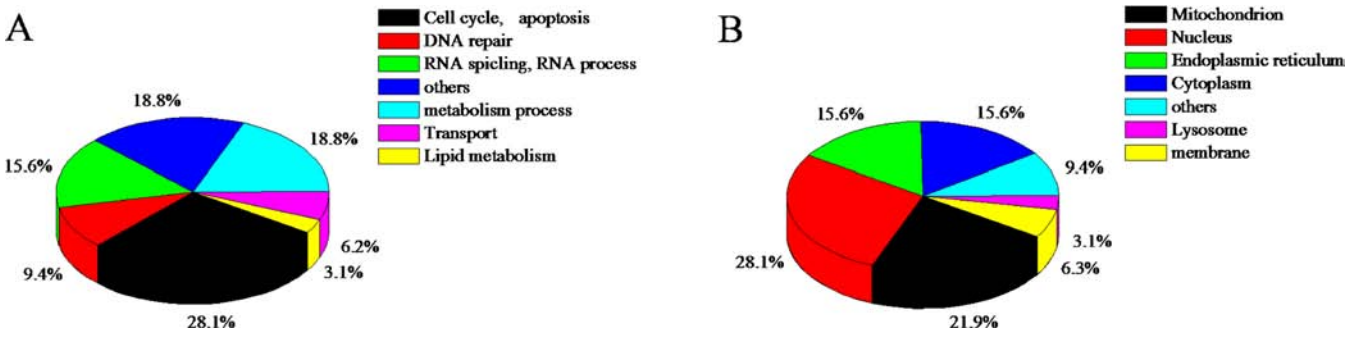

Figure 4. Classification of protein according to their biological progress (A) and subcellular localization (B).

The results clearly demonstrated that NB enhanced the cellular uptake of Cur to inhibit the cell viability of HepG2 cells.

NB Enhances Cur-Induced the Growth Inhibition on HepG2 Cells through Induction of G2/M Cell Cycle

DOI: 10.1021/acs.jafc.5b01773
J. Agric. Food Chem. 2015, 63, 6440−6449

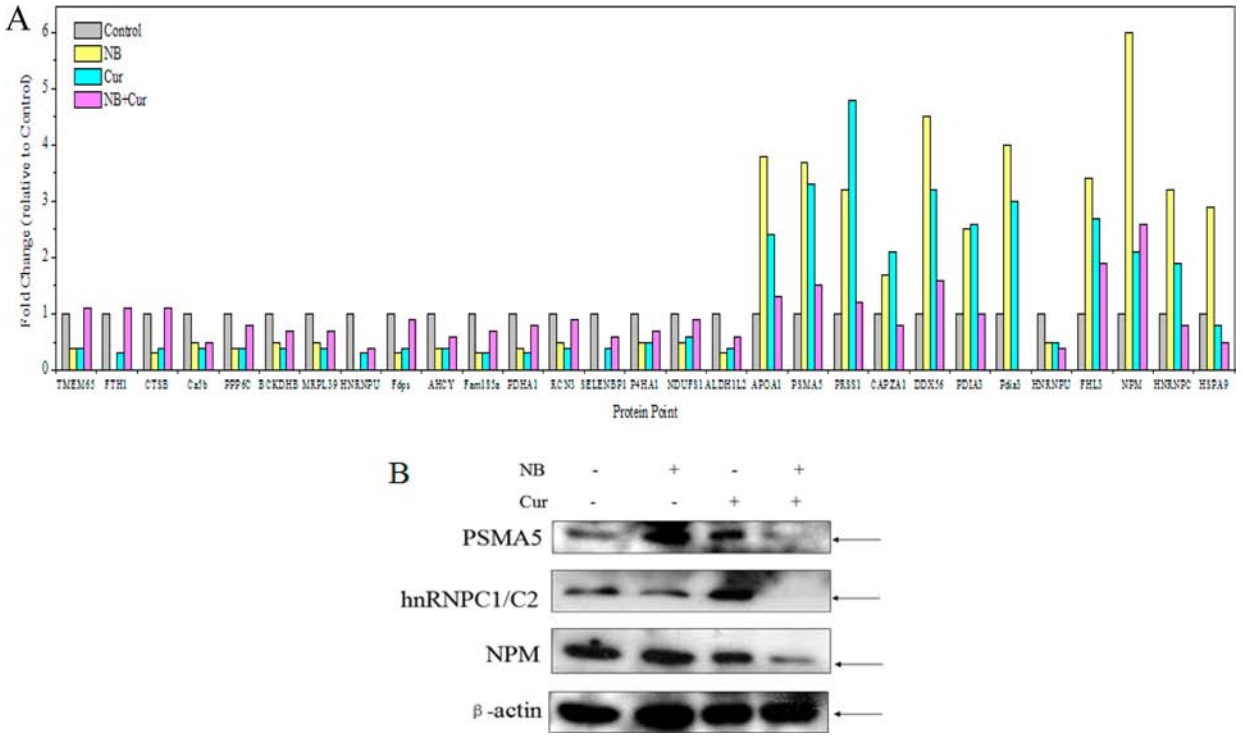

Figure 5. Results of proteomic analysis for alterations of proteins in NB-, Cur-, and NB/Cur-treated HepG2 cells (A) and the effects of NB/Cur on the expression levels of PSMA5, hnRNPC1/C2, and NPM (B). HepG2 cells were pretreated with 20 μg/mL NB for 12 h then incubated with 20 μM Cur for 24 h. The expression levels of PSMA5, hnRNPC1/C2, and NPM were detected by Western blotting assay.

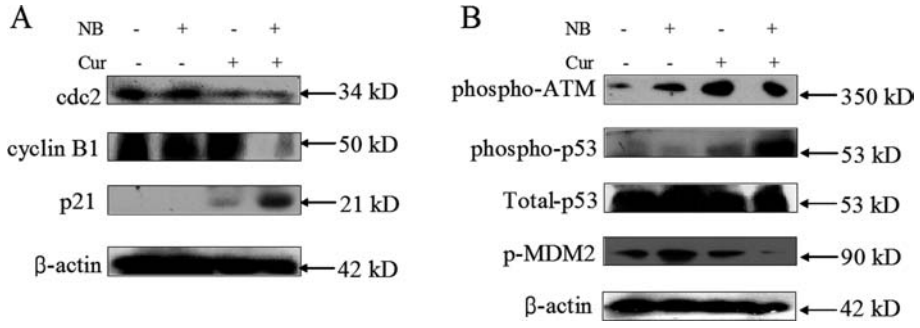

Figure 6. Effects of NB/Cur on the expression levels of cdc2, cyclin B1, and p21. HepG2 cells were pretreated with 20 μg/mL NB for 12 h then incubated with 20 μM Cur for 24 h. (A) The expression levels of cdc2, cyclin B1, and p21 were detected by Western blotting assay. (B) The phosphorylation status and expression levels of ATM, p53, MDM2 were examined by Western blotting analysis.

Arrest. Because of the significant proliferation inhibitory effect of NB and Cur in combination on HepG2 cells, we carried out the effects of NB/Cur on cell cycle distribution by flow cytometry. As shown in Figure 2A,B, the results showed that concomitant with the growth inhibitory effect, NB/Cur treatment induced a strong G2/M-phase arrest. For instance, cell populations in the G0/G1, S, and G2/M phases were 50.6, 39.2, and 10.1% in control HepG2 cells, respectively. No significant increase in the G2/M phase population was observed in cells exposed to NB (20 μg/mL) alone. Treatment of Cur alone increased the G2/M population from 10.1% (control) to 30.8%. However, compared with the treatment of Cur alone, after 24 h of incubation with the combination of NB (20 μg/mL) and Cur (20 μM), the G2/M population was noticeably enhanced by 10.7%. This increase in the G2/M phase cell population was accompanied by a concomitant decrease in the G0/G1 and S phase cell populations. Meanwhile, the sub-G1 population was slightly increased from 0.6% (control) to 2.4% in cells exposed to NB/Cur. The results demonstrated that NB/Cur inhibited the growth of HepG2 cells through induction of G2/M arrest.

Proteomic Analyses of the NB/Cur Effect on HepG2 Cells. To further confirm the induction of G2/M arrest and understand the toxicity of NB/Cur in HepG2 cells from a molecular perspective, the proteomic profile changes induced by NB/Cur were investigated by comparative 2DE proteomic analysis. A total of 32 protein spots were found to be differentially expressed proteins between Cur-treated groups and NB/Cur-treated groups. The position of each spot is shown in Figure 3. On this basis, all these 32 protein spots were further identified by MALDI-TOF-MS, and four protein spots were found to be repeated. Information about each spot is shown in Table 1. The identified proteins have been classified in terms of their biological process and subcellular localization. The proteins were divides into seven classes including proteins related to cell cycle and apoptosis (28.1%), DNA repair (9.4%),

DOI: 10.1021/acs.jafc.5b01773
J. Agric. Food Chem. 2015, 63, 6440−6449

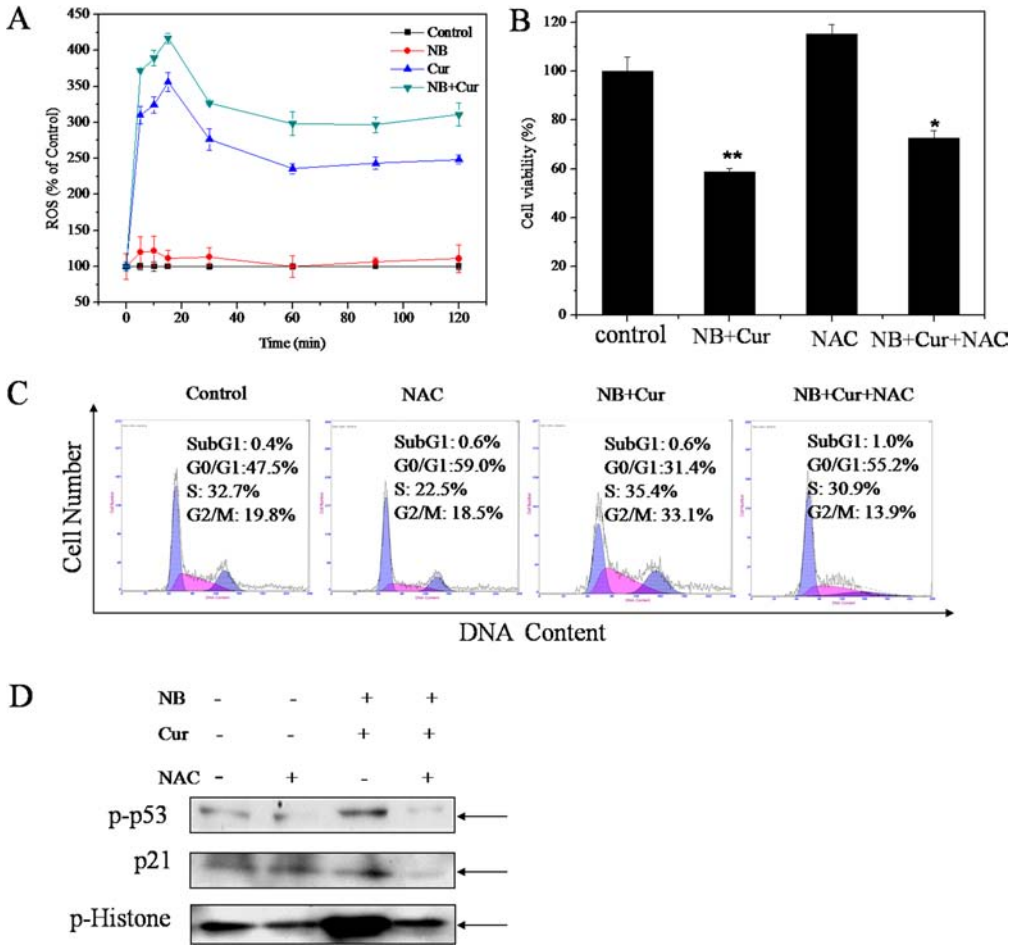

Figure 7. Role of intracellular ROS generation in G2/M cell cycle arrest induced by NB/Cur. (A) Cells were exposed to NB and Cur at indicated concentration for different times, and the levels of the intracellular ROS were analyzed by measuring the fluorescence intensity of an oxidation-sensitive fluorescein DHE. Cells were treated with 20 μg/mL NB with or without 20 μM Cur for different periods of time. (B) Effects of NAC on cell viability of NB/Cur-treated HepG2 cells. Cells were pretreated with 2 mM NAC or for 4 h prior to addition of NB and Cur. Cell viability was determined by MTT assay. All results were obtained from three independent experiments. Bars with a significant difference between treatment and control groups is indicated at the $P < 0.05$ (*) and $P < 0.01$ (**) levels. (C) Effects of NAC on G2/M cell population. Cells were pretreated with 2 mM NAC or for 4 h prior to addition of NB and Cur. Cell cycle was determined by flow cytometric analysis. All results were obtained from three independent experiments. (D) Effects of NAC on the expression levels of p21, p53, and p-histone. Cells were pretreated with 2 mM NAC or for 4 h prior to addition of 20 μg/mL NB and 20 μM Cur. The expression levels of p21, p53, and p-histone were detected by Western blotting assay.

RNA splicing and RNA process (15.6%), metabolism process (18.8%), transport (6.2%), lipid metabolism (3.1%), and others (18.8%) (Figure 4A). Subcellular localization of the detected proteins is illustrated. The majority of identified proteins fall in the nucleus (28.1%), mitochondrion (21.9%), endoplasmic reticulum (15.6%), cytoplasm (15.6%), membrane (6.3%), lysosome (3.1%), and others (9.4%) (Figure 4B). Among all identified proteins, 12 proteins were down-regulated and 17 proteins were up-regulated (Figure 5A). The down-regulated proteins are apolipoprotein A-I (APOA1), proteasome subunit alpha type-5 (PSMA5), DNA-directed RNA polymerases I, II, and III subunit RPABC3 (PRSS1), F-actin-capping protein subunit alpha-1 (CAPZA1), probable ATP-dependent RNA helicase DDX56 (DDX56), protein disulfide-isomerase A3 (PDIA3), protein disulfide-isomerase A3 (Pdia3), neterogeneous nuclear ribonucleoprotein U (HNRNPU), four and a half LIM domains protein 3 (FHL3), nucleophosmin (NPM1), heterogeneous nuclear ribonucleoproteins C1/C2 (HNRNPC), and stress-70 protein (HSPA9), while up-regulated proteins are transmembrane protein 65 (TMEM65), ferritin heavy chain (FTH1), cathepsin B (CTSB), carbonic anhydrase 5B (Ca5b), serine threonine protein phosphatase 6 catalytic subunit (PPP6C), 2-oxoisovalerate dehydrogenase subunit beta (BCKDHB), 39S ribosomal protein L39 (MRPL39), heterogeneous nuclear ribonucleoprotein U (HNRNPU), farnesyl pyrophosphate synthase (Fdps), adenosylhomocysteinase (AHCY), protein FAM185A (Fam185a), pyruvate dehydrogenase E1 component subunit alpha (PDHA1), reticulocalbin-3 (RCN3), selenium-binding protein 1 (SELENBP1), prolyl 4-hydroxylase subunit alpha-1 (P4HA1), NADH-ubiquinone oxidoreductase 75 kDa subunit (NDUFS1), and probable 10-formyltetrahydrofolate dehydrogenase ALDH1L2 (ALDH1L2). These proteins are involved in cell cycle and apoptosis, DNA repair, RNA splicing and RNA process, metabolism process, transport, and lipid metabolism in the anticancer activity of NB and Cur in combination.

Of these proteins, proteasome subunit alpha type-5 (PSMA5), heterogeneous nuclear ribonucleoproteins C1/C2 (hnRNPC1/C2), and nucleophosmin (NPM) were not reported in previous proteomic studies on NB/Cur exposure, which are of particular interest. These three proteins involved

DOI: 10.1021/acs.jafc.5b01773
J. Agric. Food Chem. 2015, 63, 6440−6449

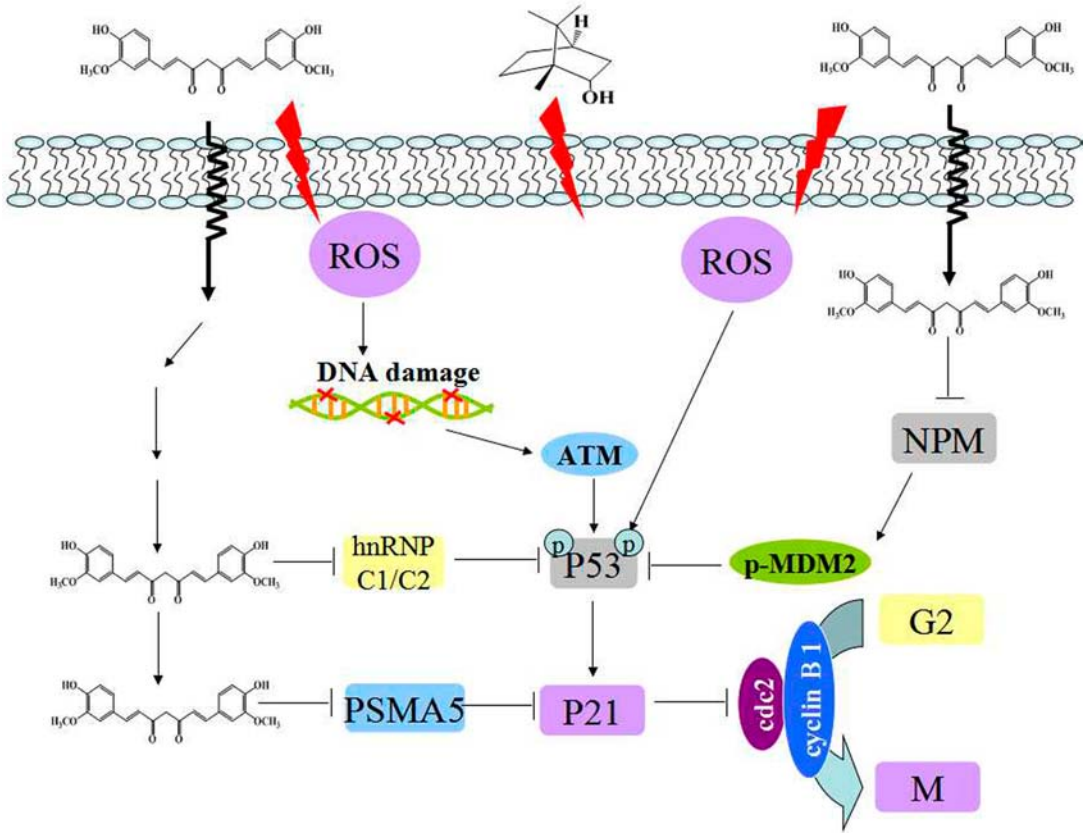

Figure 8. Proposed signaling pathway triggered by NB/Cur in HepG2 cells.

in RNA splicing, DNA repair and cell cycle and apoptosis in the anticancer activity of NB/Cur are discussed below.

Proteasome subunit alpha type-5 (PSMA5) is a subunit of 20S proteasome, which is a high molecular weight proteolytic enzyme and widely presents in the cytoplasm and the nucleus of eukaryotic cells.[29] Previous studies showed that protein degradation by the proteasome is the most regulatory mechanism in the cell, and inhibition of the proteasome activity can induce apoptosis and/or cell cycle arrest in cancer cells.[30−32] Our results indicated that compared with NB or Cur alone treatment, proteasome subunit alpha type-5 (PSMA5) could be down-regulated by NB/Cur. Moreover, further studies using Western blotting also exhibited that exposure of HepG2 cells to NB/Cur markedly down-regulated the expression level of PSMA5 (Figure 5B), which is consistent with the above results.

Heterogeneous nuclear ribonucleoprotein C1/C2 (hnRNP C1/C2), belonging to the hnRNP family, is a nuclear pre-mRNA binding protein that regulates pre-mRNA processing.[33] Studies demonstrated that hnRNP C1/C2 is involved in various biological processes, such as mRNA splicing,[34,35] cell cycle and apoptosis.[36,37] Nucleophosmin (NPM) is a vital player in the DNA-damage response and cell-cycle regulation, and it is an important regulator of p53 by modulating Mdm2.[39] Our results showed that compared to NB or Cur alone treatment, NB/Cur treatment resulted in a decrease in the expression levels of hnRNP C1/C2 and NPM (Figure 5A). These results were further confirmed by a Western blot assay. Indeed, as shown in Figure 5B, the expression levels of hnRNP C1/C2 and NPM were down-regulated when cells were exposed to NB/Cur (Figure 5B).

NB Enhances Cur-Induced G2/M Arrest in HepG2 Cells through Down- Regulation of the Expression of Cdc2 and Cyclin B1. Studies showed that hnRNP C1/C2 can regulate p53 expression and participate in DNA damage repair by the NHEJ pathway.[38,39] Moreover, NPM also can modulate Mdm2 to regulate p53 expression.[39] The enhancement of p53 could increase the expression of p21 protein in response to DNA damage, which in turn inhibits cyclin-dependent kinases activity.[40] p53, a nuclear transcription factor, regulates the G2/M transition by modulation of the cyclin dependent kinase cdc2, which is essential for the entry of cells into mitosis.[41] Therefore, to further confirm the results of proteomics, the effects of NB/Cur on the expression of cell-cycle regulatory protein and their upstream related protein were investigated using Western blot analysis. As shown in Figure 6A, compared with NB or Cur alone, NB and Cur in combination significantly decreased the expression levels of cyclin B1 and cdc2 and increased the expression levels of p21, which contributed to the inhibition of cdc2 activity. To confirm this hypothesis, the expression of phosphorylated p53, phosphorylated ATM, and phosphorylated MDM2 was detected by Western blot analysis. The results exhibited that exposure of HepG2 cells to NB/Cur markedly up-regulated the expression levels of phosphorylated p53 and phosphorylated ATM and down-regulated the expression levels of phosphorylated MDM2 (Figure 6B). These results clearly suggest that NB/Cur inhibited cell-cycle progression via down-regulation of the expression levels of cdc2 and cyclin B1.

NB Enhances Cur-Induced G2/M Arrest in HepG2 Cells through Activation of ROS Overproduction. It has been reported that ROS is involved in various cancer cells apoptosis, and our previous studies also showed that NB/Cur could

DOI: 10.1021/acs.jafc.5b01773
J. Agric. Food Chem. 2015, 63, 6440−6449

increase ROS to induce apoptosis in A375 cells.[20,42] Therefore, we investigated the effects of NB/Cur on ROS generation in HepG2 cells by measuring the DHE fluorescence intensity. As shown in Figure 7A, NB treatment alone exhibited no obvious change on ROS generation. Cur treatment alone resulted in significant ROS generation. NB/Cur treatment caused more ROS generation than Cur alone, indicating that NB/Cur increased ROS generation in HepG2 cells. To further confirm this hypothesis, NAC, a ROS inhibitor, was used to raise the intracellular glutathione levels to improve cell survival. The results showed that compared with the control group, NAC treatment alone had no significant change to the cell viability. HepG2 cell viability rate was 58.7 ± 1.5% when exposed only to NB/Cur, and the rate went up to 72.6 ± 3.1% when pretreated with NAC (Figure 7B). Consistent results are shown in Figure 7C, the G2/M rate was 33.1% when exposed only to NB/Cur, and the rates dropped to 13.9% when pretreated with NAC. Moreover, exposure of HepG2 cells to NAC down-regulated the expression level of p53, p21, and p-histone (Figure 7D), which is agreement with the above results. These results demonstrated that ROS might be upstream of the G2/M arrest signaling pathway.

On the basis of the above results, a signaling network for the synergistic action of NB/Cur was proposed. As depicted in Figure 8, NB/Cur treatment led to the accumulation of ROS, facilitating DNA damage and p53 activation. Moreover, down-regulation of hnRNPC1/C2 and NPM also contributed to the enhancement of p53. Activated p53 and down-regulation of PSMA5 resulted in an increase in p21, which bound and inactivated the cdc2-cyclin B1 complexes, and then led to cell cycle arrest in the G2/M phase.

In summary, the effect of NB/Cur on HepG2 was investigated by proteomic analysis. Our results found that NB/Cur down-regulated hnRNPC1/C2, NPM, and PSMA5 protein, which were associated with the p53 pathway. Moreover, NB/Cur also induced ROS generation, which caused oxidative stress and induced oxidative DNA damage. Both of the two explanations contributed to G2/M arrest induced by NB/Cur in HepG2 cells.

AUTHOR INFORMATION

Corresponding Authors

*(J.S.) Address: College of Light Industry and Food Sciences, South China University of Technology, Wu Shan Road 381, Guangzhou 510640, China. E-mail: jysu@scut.edu.cn. Tel: (+86) 20 87113252. Fax: (+86) 20 87113252.

*(T.C.) Address: Department of Chemistry, Jinan University, Guangzhou, 510632, China. E-mail: tchentf@jnu.edu.cn. Tel: (+86) 20 85225962. Fax: (+86) 20 85221263.

Funding

This work was supported by the 973-plan (2012CB720800), National Natural Science Foundation of China (31130042), the National Science and Technology Support Program (2012BAD37B01), Natural Science Foundation of Guangdong (2014A030313265), the YangFan Innovative & Entepreneurial Research Team Project (201312H05), the Science and Technology Planning Project of Guangdong province (2013B020311009, 2010A011200019, 2011B010600029), and the Fundamental Research Funds for the Central Universities of SCUT (2015ZZ0050).

Notes

The authors declare no competing financial interest.

REFERENCES

(1) Chirumbolo, S. Plant phytochemicals as new potential drugs for immune disorders and cancer therapy: really a promising path? *J. Sci. Food Agric.* **2012**, *92*, 1573−1577.

(2) Manikandan, R.; Beulaja, M.; Arulvasu, C.; Sellamuthu, S.; Dinesh, D.; Prabhu, D.; Babu, G.; Vaseeharan, B.; Prabhu, N. M. Synergistic anticancer activity of curcumin and catechin: An in vitro study using human cancer cell lines. *Microsc. Res. Technol.* **2012**, *75*, 112−116.

(3) Yang, C. S.; Landau, J. M.; Huang, M. T.; Newmark, H. L. Inhibition of carcinogenesis by dietary polyphenolic compounds. *Annu. Rev. Nutr.* **2001**, *21*, 381−406.

(4) Madden, K.; Flowers, L.; Salani, R.; Horowitz, I.; Logan, S.; Kowalski, K.; Xie, J.; Mohammed, S. I. Proteomics-based approach to elucidate the mechanism of antitumor effect of curcumin in cervical cancer. *Prostaglandins, Leukotrienes Essent. Fatty Acids* **2009**, *80*, 9−18.

(5) Liu, H.; Liu, Y. Z.; Zhang, F.; Wang, H. S.; Zhang, G.; Zhou, B. H.; Zuo, Y. L.; Cai, S. H.; Bu, X. Z.; Du, J. Identification of potential pathways involved in the induction of cell cycle arrest and apoptosis by a new 4-arylidene curcumin analogue T63 in lung cancer cells: a comparative proteomic analysis. *Mol. Biosyst.* **2014**, *10*, 1320−1331.

(6) Anto, R. J.; Mukhopadhyay, A.; Denning, K.; Aggarwal, B. B. Curcumin (diferuloylmethane) induces apoptosis through activation of caspase-8, BID cleavage and cytochrome c release: its suppression by ectopic expression of Bcl-2 and Bcl-xl. *Carcinogenesis* **2002**, *23*, 143−150.

(7) Chang, Z.; Xing, J.; Yu, X. Curcumin induces osteosarcoma MG63 cells apoptosis via ROS/Cyto-C/Caspase-3 pathway. *Tumour Biol.* **2014**, *35*, 753−758.

(8) Chan, W. H.; Wu, H. J.; Hsuuw, Y. D. Curcumin inhibits ROS formation and apoptosis in methylglyoxal-treated human hepatoma G2 cells. *Ann. N.Y. Acad. Sci.* **2005**, *1042*, 372−378.

(9) Chen, Q.; Lu, G.; Wang, Y.; Xu, Y.; Zheng, Y.; Yan, L.; Jiang, Z.; Yang, L.; Zhan, J.; Wu, Y.; Zhou, J. Cytoskeleton disorganization during apoptosis induced by curcumin in A549 lung adenocarcinoma cells. *Planta Med.* **2009**, *75*, 808−813.

(10) Chen, Q.; Wang, Y.; Xu, K.; Lu, G.; Ying, Z.; Wu, L.; Zhan, J.; Fang, R.; Wu, Y.; Zhou, J. Curcumin induces apoptosis in human lung adenocarcinoma A549 cells through a reactive oxygen species-dependent mitochondrial signaling pathway. *Oncol. Rep.* **2010**, *23*, 397−403.

(11) Chen, Q. Y.; Lu, G. H.; Wu, Y. Q.; Zheng, Y.; Xu, K.; Wu, L. J.; Jiang, Z. Y.; Feng, R.; Zhou, J. Y. Curcumin induces mitochondria pathway mediated cell apoptosis in A549 lung adenocarcinoma cells. *Oncol. Rep.* **2010**, *23*, 1285−1292.

(12) Deeb, D.; Jiang, H.; Gao, X.; Hafner, M. S.; Wong, H.; Divine, G.; Chapman, R. A.; Dulchavsky, S. A.; Gautam, S. C. Curcumin sensitizes prostate cancer cells to tumor necrosis factor-related apoptosis-inducing ligand/Apo2L by inhibiting nuclear factor-kappaB through suppression of IkappaBalpha phosphorylation. *Mol. Cancer Ther.* **2004**, *3*, 803−812.

(13) Deeb, D. D.; Jiang, H.; Gao, X.; Divine, G.; Dulchavsky, S. A.; Gautam, S. C. Chemosensitization of hormone-refractory prostate cancer cells by curcumin to TRAIL-induced apoptosis. *J. Exp. Ther. Oncol.* **2005**, *5*, 81−91.

(14) Wu, C.; Liao, Q.; Yao, M.; Xu, X.; Zhou, Y.; Hou, X.; Xie, Z. Effect of natural borneol on the pharmacokinetics and distribution of nimodipine in mice. *Eur. J. Drug Metab. Pharmacokinet.* **2014**, *39*, 17−24.

(15) Su, J. Y.; Chen, J. P.; Li, L.; Li, B.; Shi, L.; Zhang, H.; Ding, X. Preparation of natural borneol/2-hydroxypropyl-beta-cyclodextrin inclusion complex and its effect on the absorption of tetramethylpyrazine phosphate in mouse. *Chem. Pharm. Bull.* **2012**, *60*, 736−742.

(16) Lu, Y.; Du, S. Y.; Chen, X. L.; Wu, Q.; Song, X.; Xu, B.; Zhai, Y. S. Enhancing effect of natural borneol on the absorption of geniposide in rat via intranasal administration. *J. Zhejiang Univ. Sci. B* **2011**, *12*, 143−148.

(17) Chen, J. P.; Li, L.; Su, J. Y.; Chen, T. F. Natural borneol enhances bisdemethoxycurcumin-induced cell cycle arrest in the G2/

DOI: 10.1021/acs.jafc.5b01773
J. Agric. Food Chem. 2015, 63, 6440−6449

M phase through up-regualtion of intracellular ROS in HepG2 cells. *Food Funct.* **2015**, *6*, 740−748.
(18) Cai, Z.; Hou, S.; Li, Y.; Zhao, B.; Yang, Z.; Xu, S.; Pu, J. Effect of borneol on the distribution of gastrodin to the brain in mice via oral administration. *J. Drug Targeting* **2008**, *16*, 178−184.
(19) Yang, H.; Xun, Y.; Li, Z.; Hang, T.; Zhang, X.; Cui, H. Influence of borneol on in vitro corneal permeability and on in vivo and in vitro corneal toxicity. *J. Int. Med. Res.* **2009**, *37*, 791−802.
(20) Chen, J. P.; Li, L.; Su, J. Y.; Li, B.; Chen, T. F.; Wong, Y. S. Synergistic apoptosis-inducing effects on A375 human melanoma cells of natural borneol and curcumin. *PLoS One* **2014**, *9*, e101277.
(21) Schiess, R.; Wollscheid, B.; Aebersold, R. Targeted proteomic strategy for clinical biomarker discovery. *Mol. Oncol.* **2009**, *3*, 33−44.
(22) Lin, L. L.; Huang, H. C.; Juan, H. F. Discovery of biomarkers for gastric cancer: A proteomics approach. *J. Proteomics* **2012**, *75*, 3081−3097.
(23) Swami, M. PROTEOMICS A discovery strategy for novel cancer biomarkers. *Nat. Rev. Cancer* **2010**, *10*, 597.
(24) Fang, H. Y.; Chen, S. B.; Guo, D. J.; Pan, S. Y.; Yu, Z. L. Proteomic identification of differentially expressed proteins in curcumin-treated MCF-7 cells. *Phytomedicine* **2011**, *18*, 697−703.
(25) Rajcevic, U.; Niclou, S. P.; Jimenez, C. R. Proteomics strategies for target identification and biomarker discovery in cancer. *Front. Biosci.* **2009**, *14*, 3292−3303.
(26) D'Aguanno, S.; D'Agnano, I.; De Canio, M.; Rossi, C.; Bernardini, S.; Federici, G.; Urbani, A. Shotgun proteomics and network analysis of neuroblastoma cell lines treated with curcumin. *Mol. Biosyst.* **2012**, *8*, 1068−1077.
(27) Chen, T. F.; Zheng, W. J.; Wong, Y. S.; Yang, F. Mitochondria-mediated apoptosis in human breast carcinoma MCF-7 cells induced by a novel selenadiazole derivative. *Biomed. Pharmacother.* **2008**, *62*, 77−84.
(28) Chen, T. F.; Wong, Y. S. Selenocystine induces caspase-independent apoptosis in MCF-7 human breast carcinoma cells with involvement of p53 phosphorylation and reactive oxygen species generation. *Int. J. Biochem. Cell Biol.* **2009**, *41*, 666−676.
(29) Han, Y. G.; Liu, H. L.; Zheng, H. J.; Li, S. G.; Bi, R. C. Purification and refolding of human alpha 5-subunit (PSMA5) of the 20S proteasome, expressed as inclusion bodies in Escherichia coli. *Protein Expr. Purif.* **2004**, *35*, 360−365.
(30) Xu, H.; Ju, D.; Jarois, T.; Xie, Y. Diminished feedback regulation of proteasome expression and resistance to proteasome inhibitors in breast cancer cells. *Breast Cancer Res. Treat.* **2008**, *107*, 267−274.
(31) Liu, Q.; Shang, F.; Guo, W.; Hobbs, M.; Valverde, P.; Reddy, V.; Taylor, A. Regulation of the ubiquitin proteasome pathway in human lens epithelial cells during the cell cycle. *Exp. Eye Res.* **2004**, *78*, 197−205.
(32) Clarke, D. J. Proteolysis and the cell cycle. *Cell Cycle* **2002**, *1*, 233−234.
(33) Stone, J. R.; Maki, J. L.; Collins, T. Basal and hydrogen peroxide stimulated sites of phosphorylation in heterogeneous nuclear ribonucleoprotein C1/C2. *Biochemistry* **2003**, *42*, 1301−1308.
(34) Shetty, S. Regulation of urokinase receptor mRNA stability by hnRNP C in lung epithelial cells. *Mol. Cell. Biochem.* **2005**, *272*, 107−118.
(35) Rajagopalan, L. E.; Westmark, C. J.; Jarzembowski, J. A.; Malter, J. S. hnRNP C increases amyloid precursor protein (APP) production by stabilizing APP mRNA. *Nucleic Acids Res.* **1998**, *26*, 3418−3423.
(36) Kim, J. H.; Paek, K. Y.; Choi, K.; Kim, T. D.; Hahm, B.; Kim, K. T.; Jang, S. K. Heterogeneous nuclear ribonucleoprotein C modulates translation of c-myc mRNA in a cell cycle phase-dependent manner. *Mol. Cell. Biol.* **2003**, *23*, 708−720.
(37) Holcik, M.; Gordon, B. W.; Korneluk, R. G. The internal ribosome entry site-mediated translation of antiapoptotic protein XIAP is modulated by the heterogeneous nuclear ribonucleoproteins C1 and C2. *Mol. Cell. Biol.* **2003**, *23*, 280−288.
(38) Christian, K. J.; Lang, M. A.; Raffalli-Mathieu, F. Interaction of heterogeneous nuclear ribonucleoprotein C1/C2 with a novel cis-regulatory element within p53 mRNA as a response to cytostatic drug treatment. *Mol. Pharmacol.* **2008**, *73*, 1558−1567.
(39) Lee, S. Y.; Park, J. H.; Kim, S.; Park, E. J.; Yun, Y.; Kwon, J. A proteomics approach for the identification of nucleophosmin and heterogeneous nuclear ribonucleoprotein C1/C2 as chromatin-binding proteins in response to DNA double-strand breaks. *Biochem. J.* **2005**, *388*, 7−15.
(40) Boulaire, J.; Fotedar, A.; Fotedar, R. The functions of the cdk-cyclin kinase inhibitor p21(WAF1). *Pathol. Biol.* **2000**, *48*, 190−202.
(41) Naidu, K. A.; Fang, Q.; Cheng, J. Q.; Nicosia, S. V.; Coppola, D. P53 enhances ascorbyl stearate-induced G2/M arrest of human ovarian cancer cells. *Anticancer Res.* **2007**, *27*, 3927−3934.
(42) Du, Q.; Hu, B.; An, H. M.; Shen, K. P.; Xu, L.; Deng, S.; Wei, M. M. Synergistic anticancer effects of curcumin and resveratrol in Hepa1-6 hepatocellular carcinoma cells. *Oncol. Rep.* **2013**, *29*, 1851−1858.

DOI: 10.1021/acs.jafc.5b01773
J. Agric. Food Chem. 2015, 63, 6440−6449

well as poor solubility at a concentration of 10% (w/v) or higher.[16] In this work, the above α-D-glucan has been chosen as a model system to elucidate the advantage of endodextranase for modifying the structural and physicochemical properties. From the data, the mechanism of the chain hydrolysis reaction and solution properties have been revealed, which could lead to insights into the fundamental basis of the structure−function relationship and the development of potential industrial applications as a low-viscosity and soluble filler ingredient for designing novel carbohydrate-based foods.

MATERIALS AND METHODS

Materials. Endodextranase (catalog no. D0443, 500 U/mL) from *Chaetomium erraticum*, polyethylene glycol (average M_w 2000), and deuterium oxide (isotopic purity = 99.99 atom % D) were purchased from Sigma-Aldrich Co. (St. Louis, MO, USA). Arabic gum was kindly provided by Kerry Group (Shanghai, China). All other chemicals were of reagent grade and were obtained from Sinopharm Chemical Reagent Co., Ltd. (Shanghai, China).

L. citreum SK24.002, with high alternansucrase-producing ability, was obtained from Chinese traditional pickled vegetables. de Man−Rogosa−Sharpe (MRS) medium, composed of 40 g of sucrose, 10 g of yeast extract, 10 mL of Tween 80, 20 g of K_2HPO_4, 0.02 g of $CaCl_2$, 0.2 g of $MgSO_4·7H_2O$, 0.01 g of NaCl, 0.01 g of $MnSO_4·H_2O$, and 0.01 g of $FeSO_4·7H_2O$ per liter (pH 6.9), was used for alternansucrase production.[5]

Methods. *(1→3)(1→6)-α-D-Glucan Biosynthesis.* *L. citreum* SK24.002 was propagated in liquid MRS medium with shaking (160 rpm) at 30 °C for 48 h. Cells and other insoluble components were removed from the medium by centrifugation. Two-phase partition (water−polyethylene glycol) was used to extract the soluble alternansucrase from the supernatants, taking advantage of the dextranosyl−enzyme complex form in which the enzyme would be present in enriched precipitate. The harvested alternansucrase was washed and dissolved in sodium acetate buffer (50 mM, pH 4.5) for further measurements, and the activity was determined by measuring the initial rate of fructose production using the 3,5-dinitrosalicylic acid method.[17]

The alternansucrase solution was supplemented with 20% (w/w) sucrose in a final volume of 2 L. The biosynthesis of water-soluble α-D-glucan was carried out at 40 °C with 1 U/mL of enzyme for 48 h. The polysaccharide was then recovered from the precipitate by adding 1 volume of ethanol at 4 °C followed by centrifugation at 10000*g* for 10 min. The precipitate was resuspended in the deioinized water, and the above procedure was repeated three times and finally with 50% (v/v) ethanol precipitation to discard mono- and oligosaccharides, if any. The final product in supernatant was freeze-dried for further use.

Enzymatic Modification of (1→3)(1→6)-α-D-Glucan. One gram of glucan was dissolved in 20 mL of sodium acetate buffer solution (pH 4.5, 50 mM). The temperature was adjusted to 55 °C, and the endodextranase (0.2 mL) was added. The process with six different flasks was carried out for 10 or 30 min and 1, 2, 4, or 8 h, respectively. Subsequently, the reaction was stopped by heating the solution in the boiling water for 30 min, cooled to room temperature, and precipitated in 3 volumes of 90% ethanol (v/v). The material was centrifuged at 5000*g* for 10 min, resuspended in ethanol, filtered twice, and dried. It was then ground to fine powder (approximately 100 mesh) and stored in a desiccator for further analysis. These samples are designated DG1, DG2, DG3, DG4, DG5, and DG6, respectively, for brevity, in the rest of the paper.

UV Absorption Analysis. The method described by Kobayashi, Utsugi, and Matsuda[18] was adapted to measure the polysaccharide solution absorption using a UV−visible spectrophotometer (UV-2102PC, Unico Instrument Co., Ltd., Shanghai, China). The glucan exhibited a strong absorption at 220 nm, and thus the optical density (OD_{220}) was measured at 220 nm for estimating the extent of structural modification.

Solution Appearance Analysis. The glucan sample was dissolved in water with a concentration of 6% (w/v) at room temperature. The solution was stirred for 30 min until the polysaccharide was completely dissolved and then was transferred to a glass tube. The appearance of glucan solution was recorded using a digital camera (Canon, Shanghai, China).

Scanning Electron Microscopy (SEM). The surface morphology was examined by a Quanta-200 scanning electron microscopy (FEI Co., Eindhoven, The Netherlands). The dried sample was coated with a thin gold film (10 nm) and mounted on an aluminum stub using double-sided tape. The instrument was operated at an accelerating voltage of 5.0 kV.

Molecular Weight Distribution (MWD) Analysis. The sample (0.5 mg/mL) was passed through a cellulose acetate filter (0.45 μm, Whatman, Maidstone, UK) and injected into a high-performance size exclusion chromatography (HPSEC) system coupled with a DAWN HELEOS-II multiangle laser light scattering detector (MALLS) and an Optilab T-rEX refractive-index detector (RI, Wyatt Technology, Santa Barbara, CA, USA). The MALLS was equipped with a He−Ne laser of 658.0 nm. A Shodex OH-pak SB-806 HQ column (8 × 300 mm, Showa Denko K.K., Tokyo, Japan) with an OH-pak SB-G guard column was used at 25 °C. The mobile phase was 0.1 M $NaNO_3$ along with 0.02% of sodium azide, and a flow rate of 0.5 mL/min was used. The data were processed with Wyatt Astra software (version 5.3.4.14, Wyatt Technology).

Spectroscopic Characterization. The FT-IR spectrum was recorded using a Nicolet Nexus 470 FT-IR spectrometer (Thermo Electron Co., Waltham, MA, USA) at room temperature. The polysaccharide powder was blended with KBr at a ratio of 1:100 and pressed into tablets. Scanning was carried out in the region of 400−4000 cm^{-1} at 4 cm^{-1} resolution using 32 scans.

The ^1H NMR spectrum was recorded at 80 °C with an AVANCE III 400 MHz digital NMR spectrometer (Bruker Co., Billerica, MA, USA). The glucan sample (approximately 60 mg) was exchanged with deuterium by lyophilizing it three times with deuterium oxide and then dissolving it in 0.45 mL of 99.99% deuterium oxide. Chemical shifts (δ) were expressed in parts per million and referenced internally with acetone (δ_H 2.225).

Solution Properties. The viscosity was measured at 25 °C using the Brookfield digital viscometer (type DV-II+ Pro, Brookfield Engineering Laboratories, Inc., Middleboro, MA, USA), with an RV3 spindle. Shear thinning was analyzed using the stress-controlled rheometer (AR-G2, TA Instruments, New Castle, DE, USA). The instrument was equipped with a stainless steel cone of 40 mm diameter and 2° angle along with the solvent trap to minimize water evaporation during the analysis. The temperature was maintained at 25 °C using a circulating bath and controlled Peltier system. The apparent viscosity of the polysaccharide was estimated by using a range of shear rates of 0.01−100 1/s.

Statistical Analysis. Data were analyzed using the one-way analysis of variance (ANOVA) procedure using Origin 8.5 (OriginLab Inc., USA). A level of 0.05 was set to determine statistical significance. The results were expressed as the mean value ± standard deviation.

RESULTS AND DISCUSSION

Optical Density. According to Kobayashi, the UV absorbance profile of glucan solution exhibits a strong intensity at 220 nm, which reveals a quantitative determination method for the amount of high M_w glucan without any pretreatments or reagents.[18] The OD_{220} values of the glucan solution as a function of time of enzyme treatment are shown in Table 1. The bioengineered glucan solution exhibits a value of 2.52. Upon endodextranase hydrolysis, the OD_{220} decreased substantially to 1.51 during the first 60 min and then incrementally reached a final limiting OD_{220} of 1.03 after ≥480 min. Moreover, the observations of glucan solution appearance also confirmed the structural change, in which the control sample solution has a more opalescent, bluish-white

DOI: 10.1021/acs.jafc.5b00472
J. Agric. Food Chem. 2015, 63, 6450−6456

Table 1. UV Absorbance at 220 nm (OD_{220}), Molecular Weight (M_w), and Percentage of α-1,6 Linkages of the Enzyme-Treated (1→3)(1→6)-α-D-Glucan[a]

	OD_{220}	M_w (10^6 g/mol)	α-1,6 linkages (%)
control	2.52 ± 0.04	24.1 ± 1.51	59.5 ± 0.51
DG1	2.19 ± 0.12	17.5 ± 0.39	59.2 ± 1.64
DG2	1.92 ± 0.08	15.5 ± 0.04	58.1 ± 1.21
DG3	1.51 ± 0.02	10.2 ± 0.07	57.4 ± 0.91
DG4	1.27 ± 0.17	9.7 ± 0.11	57.0 ± 0.80
DG5	1.10 ± 0.06	8.6 ± 0.02	56.5 ± 1.42
DG6	1.03 ± 0.09	7.5 ± 0.08	56.3 ± 1.17

[a]Mean ± standard deviations of triplicate analyses.

color than the modified one, especially for DG 6 (see Figure S1 in the Supporting Information). The larger the molecular size, the deeper was the opalescent color of the glucan solution, revealing that the enzyme treatment affected the depth of solution color. A similar trend was also observed for alternan from *Leuconostoc mesenteroides* strain NRRLB-21297.[19] Those authors also reported that a rapid reduction of UV absorption at 225 nm after adding ≥5 U/mL enzyme solution. Overall, these results clearly highlight the significant role of enzyme treatment in reducing the M_w of polysaccharides. For this bioengineered (1→3)(1→6)-α-D-glucan, some α-1,6 linkages were speculated to be randomly hydrolyzed per endodextranase attack, resulting in a reduction of higher M_w fragment.

Surface Morphology. The scanning electron microscope is a potent tool to elucidate the surface morphology of polymer for predicting its physical properties as suggested by Wang and co-workers.[20] Figure 1 portrays the surface morphologies of the

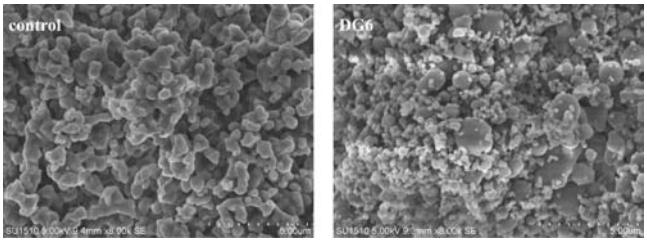

Figure 1. Surface morphology of the enzyme-treated (1→3)(1→6)-α-D-glucans.

(1→3)(1→6)-α-D-glucan after enzyme treatment. The native glucan appears like a cementitious material with a web-like network. The strong attractions between the surface functional groups appear to result in the aggregation of the glucan chains. This type of network arrangement also prevails in the purified exopolysaccharide made from *Leuconostoc dextranicum* NRRL B-1146[21] and *Lactobacillus plantarum* KF5.[20] After enzyme hydrolysis for 480 min, the modified glucan (DG6) had a looser structure with considerable small fragments. These results suggest that the bioengineered glucan after endodextranse modification might produce some particles with smaller size, in accord with the results of molecular weight analysis.

Molecular Weight Distribution. The MWD of the (1→3)(1→6)-α-D-glucan was measured by using HPSEC-MALLS-RI, and the related parameters are given in Table 1.Figure 2A highlights the HPSEC chromatogram of the native glucan appearing as a single symmetrical peak (2.41×10^7 g/mol), indicating that the bioengineered glucan was a homogeneous polysaccharide as suggested by our previous study.[5] Upon

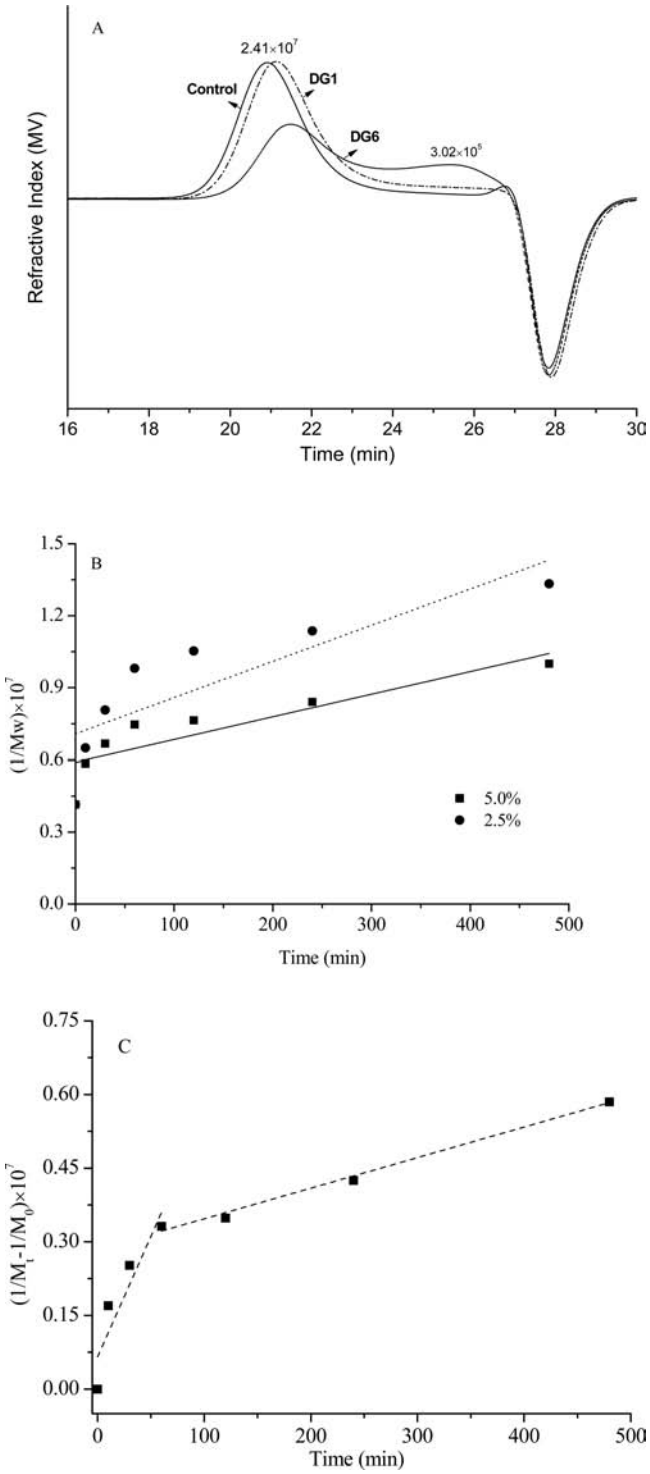

Figure 2. Molecular weight distribution profiles of the native and enzyme-treated glucans for 5% solution (A), comparison of M_w^{-1} as a function of hydrolysis time for 5 and 2.5% solution (B), and ($M_t^{-1} - M_0^{-1}$) as a function of hydrolysis time for 5% solution (C).

enzymatic hydrolysis of native glucan, the distribution gradually shifted to the smaller MWD region with a significant broadening. In addition, a low M_w peak (3.02×10^5 g/mol) appeared after the modification, for example, in DG6, indicating the heterodisperse characteristic of the treated sample. Leathers, Nunnally, and Côté also found a similar behavior in alternan, wherein the high peak of 10^6 −10^7 Da in the

DOI: 10.1021/acs.jafc.5b00472
J. Agric. Food Chem. 2015, 63, 6450−6456

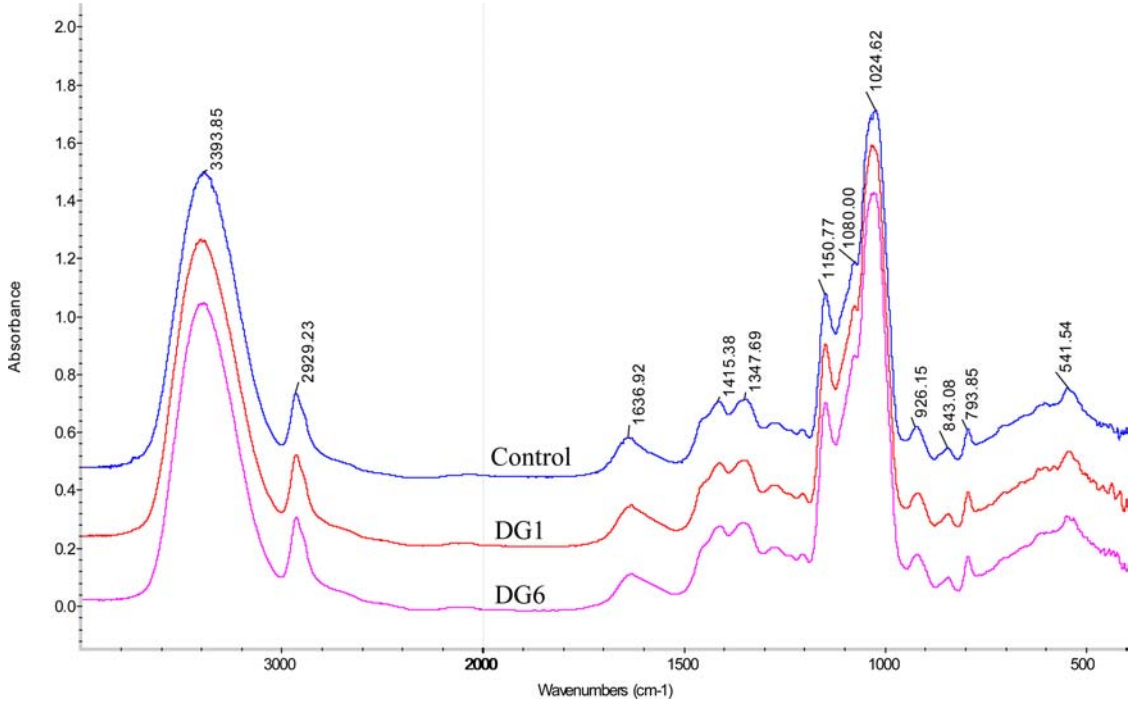

Figure 3. FT-IR spectra of the enzyme-treated (1→3)(1→6)-α-D-glucans.

bioengineered polysaccharide moves to peaks of (5−10) × 10^5 Da and (1−5) × 10^4 Da after modification.[22] Simultaneously, the peak at (1−5) × 10^4 Da) did not change over time, and only its relative proportion increased as the process took a long time, up to 24 h. Moreover, Tayal, Kelly, and Khan[23] observed significant reduction in molecular weight during the course of the enzymatic degradation of a water-soluble guar, with the peak maximum shifting by approximately 2 orders of magnitude, reflecting the scission of backbone linkage by enzyme, which was comparable with our results.

As shown in Table 1, the weight-average M_w decreased sharply from 24.1 × 10^6 (control) to 10.2 × 10^6 g/mol (DG3), and thereafter slowed and finally settled at 7.5 × 10^6 g/mol at 480 min (DG6). This trend is in congruence with the OD_{220} decrease. In particular, a considerable reduction in M_w (approximately 60% M_w reduction) took place at the initial short time, indicating enzymatic hydrolysis of the (1→3)(1→6)-α-D-glucan was a complex reaction for which mechanism analysis could be a combination of two or more reactions with diverse orders as described by Tayal et al.[23] To understand the degradation kinetics of enzymatic hydrolysis, the inverse M_w ($1/M_w$) as a function of process time has been analyzed and highlighted in Figure 2B. A nonlinear relationship between $1/M_w$ and time was observed for enzymatic hydrolysis of either 5.0 or 2.5% (w/v) α-D-glucan solution. The slope of $1/M_w$ versus time decreased as glucan concentration increased from 2.5 to 5.0%, which indicated that the apparent rate constant was dependent on the initial concentration, and the hydrolysis reaction appeared to be of the nth order.

According to Basedow, Ebert, and Ederer, the degradation reaction using enzyme belongs to an nth-order process: $dB/dt = -kB^n$, wherein B is the total number of hydrolyzable linkages, k is the rate constant, and n is the order of reaction.[24] Our data were rationalized as a combination of zeroth- and first-order processes, where the zeroth-order reaction preceded initially for time t', followed by a first-order reaction up to time t.

The two kinetic equations

$$\frac{1}{M'_{t'}} - \frac{1}{M_0} = \frac{k}{mN_0}t' \quad (1)$$

and

$$\frac{1}{M_t} - \frac{1}{M'_{i'}} = \frac{k_1}{m}(t - t') \quad (2)$$

were used to calculate the experimental kinetics of enzymatic hydrolysis, where M_0, M_t', and M_t were the M_w values at time 0, t', and t, respectively; k and k_1 were the rate constants for zeroth- and first-order reactions, respectively; m was the M_w of the monomer (glucose); and N_0 was the total number of molecules. The data in Figure 2C were modeled as a combination of two reactions using the above eqs 1 and 2. The analysis indicates the correlation coefficient (R^2) and rate constant (k) were 0.858 and 4.91 × 10^{-3} g/(mol·min) and 0.989 and 6.22 × 10^{-4} g/(mol·min) for zeroth- and first-order reactions of 5.0% glucan solution, respectively. In some previous papers, a linear relationship between $1/M_w$ and time was used to model the enzymatic degradation of natural polymer.[25−27] However, our data indicated zeroth- and first-order kinetics were better representations.

FT-IR Analysis. The FT-IR spectra of the native glucan and its derivatives are compared in Figure 3. The control and enzyme-treated samples essentially displayed similar spectra, indicating the intact chemical glucan structure and non-destructive nature of the enzyme treatment. In both samples, characteristic bands of ν(O−H) 3400 cm^{-1}, ν(C−H) 2930 cm^{-1}, δ(HOH) 1640 cm^{-1}, δ(O−H) 1420 cm^{-1}, and δ(C−H) 1370 cm^{-1} and a complex bands ν(C−O) and ν(C−C) 1200−1000 cm^{-1} and γ(C−H) 1000−700 cm^{-1} are observed. The broad peak at 3393 cm^{-1} indicates the presence of hydroxyl groups of glucan and water. The bands at 2929 and 1636 cm^{-1} are due to the C−H stretching and water-bending, respectively. The spectra also indicate C−H deformation at 1415 and 1347

DOI: 10.1021/acs.jafc.5b00472
J. Agric. Food Chem. 2015, 63, 6450−6456

cm^{-1}. In the fingerprint region (1200−1000 cm^{-1}), there are three characteristic peaks at 1150, 1080, and 1024 cm^{-1}. The wavenumbers 1150 and 1080 cm^{-1} are attributed to the C−O stretching of the anhydroglucose. The sharp peak at 1024 cm^{-1} could most likely be due to C−O stretching in the C−O−C linkage across the α-1,6-glucosidic bonds. The vibration bands at around 926, 843, and 793 cm^{-1} are attributed to the mixed C−C−H deformations coupled with C−C−O, O−C−O, and C−O−C bending. The peak at 793 cm^{-1} is from the skeletal mode vibrations of the α-1,3-glucosidic linkage.[28] All of these results clearly suggest that both the control and enzyme-treated glucans exhibit similar chemical structures composed of both α-1,3 and α-1,6 linkages. The similarities in the γ(C−H) range further suggest that there are no differences in the D-glucopyranose conformation that prefer $^4C_1$ chair conformation.[6]

NMR Analysis. The linkage changes in the (1→3)(1→6)-α-D-glucan after enzyme treatment are compared in Figure 4, and

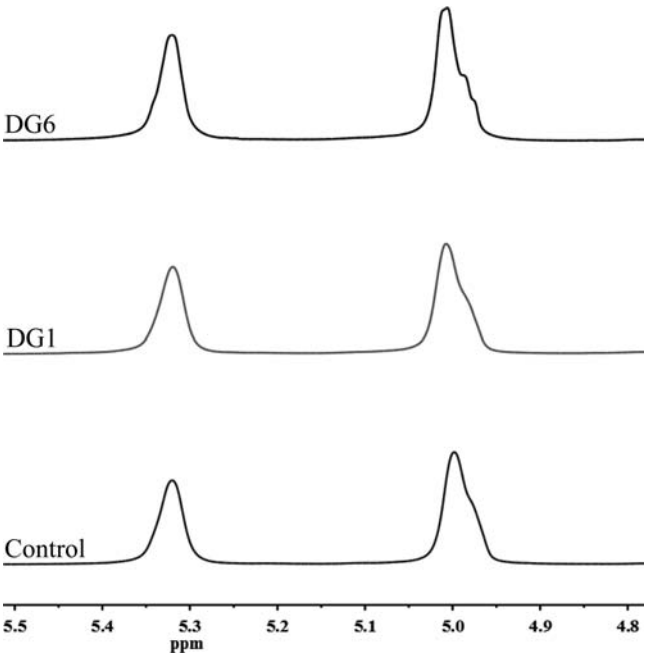

Figure 4. ^{1}H NMR spectra of the enzyme-treated (1→3)(1→6)-α-D-glucans.

the related data are presented in Table 1. In the anomeric proton region (4.5−5.4 ppm), the peaks at 4.98 and 5.32 ppm indicate the H-1 at α-1,6 and α-1,3 linkages, respectively.[29] The percentage of α-1,6 linkages in the control sample was approximately 60%, which agrees with previous observations.[5] As expected, after enzyme treatment this number decreased to 56.3% of DG6, suggesting that the chain fragments with α-1,6 linkages are partially broken.

The main domain of endodextranase is a right-handed parallel β helix connecting to a sandwich domain at the N terminus.[14] In the enzyme−glucan complex, the glycosidic oxygen of the glucose unit from the subsite +1 forms a hydrogen bond to the catalytic active site (Asp395) through a single displacement mechanism. Generally, glucans from *L. citreum* SK24.002 are considered to be resistant to the enzyme action.[5] However, the bioengineered glucan used in this study displayed some short stretches of consecutive α-1,6 linkages in the limited regions, which could be the primary factor for the observed structural changes. Overall, it can be concluded that the enzymatic treatment of (1→3)(1→6)-α-D-glucan is influenced by the unique biopolymer structure, and some specific α-1,6 linkages of the glucan chains were broken with enzyme treatment.

Rheological Analysis. Figure 5A shows the concentration dependence of solution viscosities for the control and its

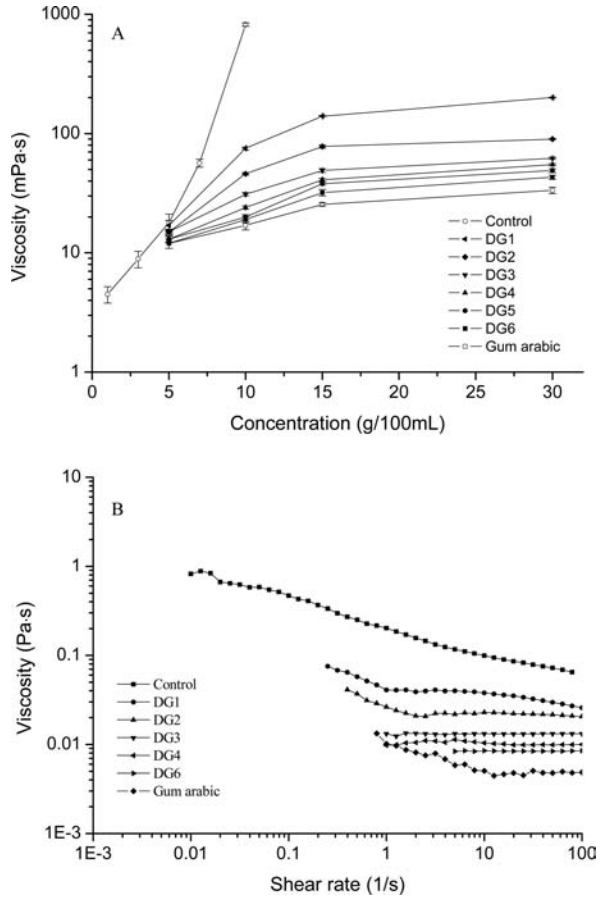

Figure 5. Comparison of the solution properties of the enzyme-treated glucans: (A) viscosity; (B) apparent viscosity.

enzymatic derivatives. The viscosity of bioengineered glucan at 5 g/100 mL concentration is around 18 mPa·s, suggesting a thin liquid for such a high M_w polymer. However, at the higher polymer concentrations, in the range of 5−10 g/100 mL, the viscosity increased exponentially and finally formed a gel-like dispersion. On the other hand, the viscosity of enzyme-treated glucans has decreased considerably, mainly due to the chain degradation, similar to solution behavior of the commercial gum arabic (9%, w/v), which could be dissolved in water to give solutions of ≥30 g/100 mL.

The profiles of viscosity versus shear rate are shown in Figure 5B. The bioengineered glucan displays a non-Newtonian pseudoplastic behavior (shear thinning) in the shear rate range of 0.01−100 1/s, indicating a branched nature of glucan as suggested by Majumder and Goyal.[21] The viscosity decreased with increasing shear rate, but with minimal changes at high shear rates. A similar behavior is noted for glucans synthesized by *Agrobacterium* sp. ZX09.[30] As shown in Figure 5B, the gum arabic (9%, w/v) showed a flat curve at high shear rates (10−100 1/s), indicating it more or less behaves like a Newtonian liquid. Interestingly, Newtonian plateaus are also

DOI: 10.1021/acs.jafc.5b00472
J. Agric. Food Chem. 2015, 63, 6450−6456

observed from the enzyme-treated glucan solutions. In general, polymer chains in solution could exhibit considerable stiffness, thus making themselves more susceptible to orient under suitable shear conditions.[30] The shear thinning property observed in our measurements appears to be the outcome of the orientation effect under shear. In other words, the long chains of (1→3)(1→6)-α-D-glucan after enzymatic hydrolysis became aligned in the direction of flow with increasing shear rate, resulting in less interaction between adjacent chains for modified glucan.

In summary, an environmentally friendly and reproducible enzymatic modification has been used to reduce the M_w and improve the solution properties of the high M_w (1→3)(1→6)-α-D-glucan from *L. citreum* SK24.002. The enzymatic degradation followed both zeroth- and first-order kinetics. Some specific α-1,6 linkages of glucan chains were cleaved with enzyme treatment. The viscosity of the modified glucan solution was markedly reduced, and Newtonian plateaus were also observed at high shear rates (10−100 1/s). The enzymatically modified glucans showed solution viscosity and shear thinning behavior comparable to those of commercial gum arabic, indicating that the modified (1→3)(1→6)-α-D-glucan as a substitute for gum arabic could find potential applications as low-viscosity biomaterials and soluble fillers in the design and development of novel carbohydrate-based foods. Optimizing the processing parameters for biosynthesis modification and glucan retrogradation during storage as well as assessing the bioavailability and bioefficency of the modified glucans will be the focus of future studies.

■ ASSOCIATED CONTENT

Supporting Information

Figure S1: Comparison of aqueous solutions of native and enzyme treated glucans. The Supporting Information is available free of charge on the ACS Publications website at DOI: 10.1021/acs.jafc.5b00472.

■ AUTHOR INFORMATION

Corresponding Author

*(M.M.) Phone: +86 (0)510 853 27859. Fax: +86 (0)510 859 19161. E-mail: miaoming@jiangnan.edu.cn.

Funding

The research was financially supported by the National Natural Science Foundation of China (31000764, 31230057), the International Cooperative Program of Jiangsu Province (BZ2012031), and the Science & Technology Pillar Program of Jiangsu Province (BE2013647, BE2014703).

Notes

The authors declare no competing financial interest.

■ REFERENCES

(1) Badel, S.; Bernardi, T.; Michaud, P. New perspectives for Lactobacilli exopolysaccharides. *Biotechnol. Adv.* **2011**, *29*, 54−66.

(2) Garai-Ibabe, G.; Areizaga, J.; Aznar, R.; Elizaquivel, P.; Prieto, A.; Irastorza, A.; Dueñas, M. T. Screening and selection of 2-branched (1,3)-β-D-glucan producing lactic acid bacteria and exopolysaccharide characterization. *J. Agric. Food Chem.* **2010**, *58*, 6149−6156.

(3) Galle, S.; Arendt, E. K. Exopolysaccharides from sourdough lactic acid bacteria. *Crit. Rev. Food Sci. Nutr.* **2014**, *54*, 891−901.

(4) Salazar, N.; Ruas-Madiedo, P.; Prieto, A.; Calle, L. P.; de los Reyes-Gavilán, C. G. Characterization of exopolysaccharides produced by *Bifidobacterium longum* NB667 and its cholate-resistant derivative strain IPLA B667dCo. *J. Agric. Food Chem.* **2012**, *60*, 1028−1035.

(5) Miao, M.; Bai, A.; Jiang, B.; Song, Y.; Cui, S. W.; Zhang, T. Characterisation of a novel water-soluble polysaccharide from *Leuconostoc citreum* SK24.002. *Food Hydrocolloids* **2014**, *36*, 265−272.

(6) Miao, M.; Ma, Y.; Jiang, B.; Huang, C.; Li, X.; Cui, S. W.; Zhang, T. Structural investigation of a neutral extracellular glucan from *Lactobacillus reuteri* SK24.003. *Carbohydr. Polym.* **2014**, *106*, 384−392.

(7) Cui, S. W. *Food Carbohydrates: Chemistry, Physical Properties, And Applications*; Taylor & Francis: Boca Raton, FL, USA, 2005.

(8) Basedow, M. A.; Ebert, H. K. Ultrasonic degradation of polymers in solution. *Adv. Polym. Sci.* **1977**, *22*, 83−148.

(9) Miao, M.; Xiong, S.; Jiang, B.; Jiang, H.; Cui, S. W.; Zhang, T. Dual-enzymatic modification of maize starch for increasing slow digestion property. *Food Hydrocolloids* **2014**, *38*, 180−185.

(10) Tao, Y.; Xu, W. Microwave-assisted solubilization and solution properties of hyperbranched polysaccharide. *Carbohydr. Res.* **2008**, *343*, 3071−3078.

(11) Tharanathan, R. N. Starch—value addition by modification. *Crit. Rev. Food Sci. Nutr.* **2005**, *45*, 371−384.

(12) BeMiller, J. N.; Whistler, R. L. *Starch: Chemistry and Technology*, 3rd ed.; Academic Press: New York, 2009.

(13) Bailey, R. W.; Clarke, R. T. J. A bacterial dextranase. *Biochem. J.* **1959**, *72*, 49−54.

(14) Larsson, A. M.; Andersson, R.; Ståhlberg, J.; Kenne, L.; Jones, T. A. Dextranase from *Penicillium minioluteum*: reaction course, crystal structure, and product complex. *Structure* **2003**, *11*, 1111−1121.

(15) Jiménez, E. R. Dextranase in sugar industry: a review. *Sugar Technol.* **2009**, *11*, 124−134.

(16) Miao, M.; Huang, C.; Jia, X.; Cui, S. W.; Jiang, B.; Zhang, T. Physicochemical characteristics of a high molecular weight bioengineered α-D-glucan from *Leuconostoc citreum* SK24.002. *Food Hydrocolloids* **2015**, *50*, 37−43.

(17) Musa, A.; Miao, M.; Zhang, T.; Jiang, B. Biotransformation of stevioside by *Leuconostoc citreum* SK24.002 alternansucrase acceptor reaction. *Food Chem.* **2014**, *146*, 23−29.

(18) Kobayashi, M.; Utsugi, H.; Matsuda, K. Intensive UV absorption of dextrans and its application to enzyme reactions. *Agric. Biol. Chem.* **1986**, *50*, 1051−1053.

(19) Leathers, T. D.; Nunnally, M. S.; Côté, G. L. Modification of alternan by dextranase. *Biotechnol. Lett.* **2009**, *31*, 289−293.

(20) Wang, Y.; Li, C.; Liu, P.; Ahmed, Z.; Xiao, P.; Bai, X. Physical characterization of exopolysaccharide produced by *Lactobacillus plantarum* KF5 isolated from Tibet kefir. *Carbohydr. Polym.* **2010**, *82*, 895−903.

(21) Majumder, A.; Goyal, A. Rheological and gelling properties of a novel glucan from *Leuconostoc dextranicum* NRRL B-1146. *Food Res. Int.* **2009**, *42*, 525−528.

(22) Leathers, T. D.; Nunnally, M. S.; Côté, G. L. Optimization of process conditions for enzymatic modification of alternan using dextranase from *Chaetomium erraticum*. *Carbohydr. Polym.* **2010**, *81*, 732−736.

(23) Tayal, A.; Kelly, R. M.; Khan, S. A. Rheology and molecular weight changes during enzymatic degradation of a water-soluble polymer. *Macromolecules* **1999**, *32*, 294−300.

(24) Basedow, A. M.; Ebert, K. H.; Ederer, H. J. Kinetic studies on the acid hydrolysis of dextran. *Macromolecules* **1978**, *11*, 774−781.

(25) Masson, C. R. The degradation of carrageenan I. Kinetics in aqueous solution at pH 7. *Can. J. Chem.* **1955**, *33*, 597−603.

(26) Vink, H. Degradation of some polymers in aqueous solutions. *Makromol. Chem.* **1963**, *67*, 105−123.

(27) Thoma, J. A. Models for depolymerizing enzymes. Application to α-amylases. *Biopolymers* **1976**, *15*, 729−746.

(28) Seymour, F. R.; Julian, R. L.; Jeanes, A.; Lamberts, B. L. Structural analysis of insoluble D-glucans by Fourier-transform, infrared difference-spectrometry: correlation between structures of dextrans from strains of *Leuconostoc mesenteroides* and of D-glucans from strains of *Streptococcus mutans*. *Carbohydr. Res.* **1980**, *86*, 227−246.

DOI: 10.1021/acs.jafc.5b00472
J. Agric. Food Chem. 2015, 63, 6450−6456

(29) Seymour, F. R.; Knapp, R. D.; Bishop, S. H. Correlation of the structure of dextrans to their ^{1}H-NMR spectra. *Carbohydr. Res.* **1979**, *74*, 77−92.
(30) Xiu, A.; Zhou, M.; Zhu, B.; Wang, S.; Zhang, J. Rheological properties of Salecan as a new source of thickening agent. *Food Hydrocolloids* **2011**, *25*, 1719−1725.

DOI: 10.1021/acs.jafc.5b00472
J. Agric. Food Chem. 2015, 63, 6450−6456

Syntheses. *D-Galacturonic Acid Methyl Ester.* (Trimethylsilyl)-diazomethane (TMSDM) was used for the esterification of D-galacturonic acid instead of explosive and toxic diazomethane[6] or methanolic hydrochloric acid[7,8] used in most other publications. Methylation of carboxylic acids with TMSDM is more specific and can take place under relatively mild conditions.[9] One hundred milligrams of D-galacturonic acid (0.5 mmol) was dried over phosphorus pentoxide and dissolved in 5 mL of absolute methanol. A solution of 0.2 M TMSDM diluted with diethyl ether was added dropwise until the yellow color of the reagent persisted. The reaction proceeded instantaneously and nearly quantitatively without any influence of other reactive groups. The reaction was easily monitored by the disappearance of the yellow color of TMSDM. The reaction mixture was stirred for 30 min at room temperature and concentrated under reduced pressure to give the corresponding methyl ester. The yellow syrup was purified by recrystallization from 1,4-dioxane and yielded after freeze-drying 83.1 mg (0.39 mmol) of a white powder, which was instantaneously used for model reactions. Purity was confirmed by GC-MS after derivatization with trifluoroacetic acid anhydride (TFAA). For this purpose aliquots of the freeze-dried substance were resolved in 325 μL of dichloromethane. One hundred and fifty microliters of TFAA and 25 μL of pyridine were added, and the sample was shaken for 30 s and afterward derivatized for 3 h at room temperature. After that, 500 μL of dichloromethane was added and the diluted derivatized sample subjected to GC-MS. For the GC-MS analysis of the D-galacturonic acid methyl ester the same setup was used as for pyrrole-2-carboxaldehyde (see below).

FPA. D-Galacturonic acid (10.345 g; 50 mmol) and L-alanine (4.595 g; 52 mmol) were dissolved in 100 mL of distilled water and stirred for 2 h under reflux. The resulting brown/black reaction mixture was extracted with 40 mL of ethyl acetate/diethyl ether (1:1) three times. The combined extracts were concentrated in a nitrogen stream and purified by silica gel flash chromatography (Merck silica gel 60, 0.040−0.063 mm, 230−400 mesh) with ethyl acetate/diethyl ether (1:1) as solvent. Removing the solvent at 30 °C in vacuo yielded 16.6 mg (0.1 mmol) of yellow crystals. Tentative identification and purity control were carried out by GC-MS (setup as described below) after derivatization with TMSDM. For this purpose 10 μL of *N*-methylpyrrole-2-carboxylic acid as internal standard (9 mM in methanol) was added to an aliquot of 10 μL of FPA in methanol (5.5 mM). After that, 150 μL of a TMSDM solution (20 mM) in methanol/diethyl ether was slowly added for derivatization. After 30 min at 25 °C in a reaction tube, the sample was subjected to GC-MS (see Figure 3). A purity of 98% was achieved.

Model Reaction. *D-Galacturonic Acid versus D-Glucuronic Acid and Reducing Sugars.* To investigate the degradation behavior and the formation of key intermediates and degradation products, D-galacturonic acid monohydrate (0.5 M) and L-alanine, L-aspartic acid, or GABA (0.05 M) were dissolved in water. The above-mentioned concentrations were chosen to adapt the model systems as close as possible to foods rich in uronic acids such as juices or jams in which the uronic acid compounds occur in a surplus. The pH value was adjusted to 3.0, 5.0, or 8.0 by adding thinned hydrochloric acid and sodium hydroxide solution. In this case, the application of buffer substances was avoided by choice, because buffers are known to cause unintended side reactions.[10] Aliquots of the model solution were filled into glass ampules and incubated in a heating block at 100 °C for 2 h. The reaction was stopped at various points in time and worked up as follows. Browning was measured as the absorption at 420 nm with a spectrophotometer (UV-1650 PC, Shimadzu, Duisburg, Germany) and the CIELab color with a reflectance attachment with Spectralon integrating sphere (Specord 40, Analytik Jena, Jena, Germany). pH values were measured after the sample had been cooled to room temperature with a pH-electrode (SenTix Mic, WTW, Weilheim, Germany; pH-meter CG 820, Schott, Mainz, Germany). For the analysis of the organic acids, aci-reductones, and pyridines, samples were diluted (1:10) with 1% metaphosphoric acid and 10 mM dithiothreitol and measured by HPLC-DAD. For the quantification of furans, furanones, and pyrroles, samples were diluted (1:100; v/v) with 10 mM phosphate buffer (pH 6.0) and subjected to HPLC-DAD. For α-dicarbonyl compounds, *o*-phenylenediamine hydrochloride (OPD; 20 mM) was added (1:1; v/v). Because advance tests had shown no further chemical change after 3 h of reaction time, the samples were reincubated for at least 3 h at room temperature to obtain UV-active quinoxalines and subsequently analyzed by HPLC-DAD. For identification and quantification of FPA the carboxyl group was methylated with (trimethylsilyl)diazomethane and subjected to GC-MS. Model solutions (0.5 M) of D-glucuronic acid, D-galactose, and D-arabinose with 0.05 M L-alanine were treated and analyzed as the model reactions of D-galacturonic acid.

D-Galacturonic Acid versus D-Galacturonic Acid Methyl Ester. The concentrations of the model reactions were 0.05 M of the carbonyl compound and 0.005 M of the amino acid L-alanine. The procedure and the measurements were the same as in the higher concentrated model systems of D-galacturonic acid.

All experiments were conducted in three independent replications, and the arithmetical mean of all quantified values was calculated. For quantification five-point calibration curves were determined from parent solutions of mixes of different pure reference compound groups.

Qualification and Quantification. *Organic Acids and Aci-reductones.* The diluted samples were analyzed by HPLC-DAD (degasser, Gastorr GT-103; pump, Shimadzu LC-9A; autosampler, Dionex GINA50; column oven, VDS optilab; guard column, YMC ODS-AQ 4.0 × 20 mm, 3 μm; column, YMC-Pack ODS-AQ 150 × 4.6 mm, 3 μm; detector, Gynkotek UVD340S; software, Chromeleon v6.00 build 435) using a phosphate buffer (20 mM, pH 2.8) as an isocratic eluent with a flow rate of 0.6 mL/min, an oven temperature of 25 °C, and an injection volume of 40 μL. The effluent was monitored at wavelengths of 214 nm for organic acids (formic acid (3.9 min), acetic acid (6.3 min), succinic acid (11.4 min), 2-ketoglutaric acid (6.9 min), malic acid (4.2 min)) and 254 nm for reductic acid (7.5 min) detection. Identification of the compounds was tentatively accomplished by comparing their retention times with those of authentic known commercially available references or pure authentic compounds isolated and elucidated from reaction mixtures in our working group.[3] For quantification pure reference compounds were used.

Furans and Furanones. The diluted samples were analyzed by HPLC-DAD (setup as described above; guard column, Macherey-Nagel CC 8/4 Nucleosil 120/3 C18; column, Macherey-Nagel EC 125/3 Nucleosil 120-3 C18) using a solvent gradient starting with a mixture (99:1; v/v) of phosphate buffer (5 mM, pH 6.0) and methanol and increasing the methanol content after 10 min to 20% within 5 min and after another 5 min to 99% within 5 min with a flow rate of 0.5 mL/min, an oven temperature of 40 °C, and an injection volume of 40 μL. By monitoring the effluent at a wavelength of 280 nm for furan-2-carboxaldehyde (6.7 min) and norfuraneol (3.6 min) and at a wavelength of 254 nm for 2-furanoic acid (8.5 min) the compounds were detected. Quantification was performed by external calibration with standard solutions containing known amounts of either commercially available references or pure authentic compounds isolated and elucidated from reaction mixtures in our working group.[3]

α-Dicarbonyl Compounds as Quinoxalines. The derivatized samples were analyzed by HPLC-DAD (setup as described above; guard column, Macherey-Nagel CC 8/4 Nucleosil 120/3 C18; column, Macherey-Nagel EC 250/4.6 Nucleosil 120-5 C18) using a solvent gradient starting with a mixture (95:5; v/v) of water and acetonitrile and increasing the acetonitrile content after 5 min to 10% within 3 min. After another 5 min, the content was increased to 20% within 7 min and after 5 min increased to 50% within 10 min with a flow rate of 1.0 mL/min, an oven temperature of 35 °C, and an injection volume of 40 μL. Quantification was performed by comparing the peak areas with those of a standard solution at 317 nm containing known amounts of each pure reference or pure authentic quinoxaline isolated and elucidated from reaction mixtures in our working group.[11] Identification of unknown quinoxalines was accomplished by LC-MS measurements in the total ion mode of the pre- and postderivatized and diluted samples. The gradient used for the separation was the same (Thermo Fischer Scientific pump Accela, CTC PAL autosampler) as for the HPLC-DAD measurements.

DOI: 10.1021/acs.jafc.5b01121
J. Agric. Food Chem. 2015, 63, 6457−6465

Ionization (TSQ Vantage System with Ion Max Source, H-ESI II Probe) in the ESI positive mode followed, using a spray voltage of 3 kV, a vaporizer temperature of 450 °C, a sheath gas pressure of 60 psi, and a capillary temperature of 270 °C. Spectra were obtained by setting the scan at m/z 50−1000. Software Thermo Excalibur 2.1.0.1139 was used for the identification of the substances.

Pyrroles and Hydroxypyridines. The diluted samples were analyzed by HPLC-DAD (see above) in the case of 3-hydroxypyridines using the same method as for organic acids, but monitoring the effluent at a wavelength of 280 nm and in the case of pyrrole-2-carboxaldehyde derivatives with the same method mentioned for furans but monitoring at a wavelength of 293 nm. Quantification was performed by external calibration with pure authentic compounds isolated and elucidated from reaction mixtures in our working group.

For the identification and quantification of FPA a GC-MS method was established. Therefore, the carboxyl group had to be methylated with (trimethylsilyl)diazomethane. For that, 100 μL of a model solution was spiked with 10 μL of *N*-methylpyrrole-2-carboxylic acid in methanol (2 mM) as internal standard in a 1 mL reaction tube. The sample mixture was dried under nitrogen stream and resolved in 100 μL of distilled water. After that, the sample was extracted five times with 100 μL of diethyl ether/ethyl acetate (1:1). The combined extracts were dried under nitrogen stream and resolved in 100 μL of methanol. For derivatization 300 μL of TMSDM (20 mM) was added, and after 30 min at 25 °C, the sample was subjected to GC-MS analysis (Shimadzu GC-2010, AOC-20i autosampler, GCMS-QP2010plus mass spectrometer, Duisburg, Germany) using a fused silica capillary column (Supelco SLB-5 ms, 30 m × 0.25 mm, 0.25 μm). The derivatized samples were applied by a split injection technique at an injection temperature of 250 °C and an oven temperature of 80 °C. The temperature was increased at a rate of 6 °C/min to 104 °C, held for 1 min, increased again at a rate of 10 °C/min to 164 °C, and then increased at a rate of 12 °C/min to 280 °C. Helium 5.0 was used as a carrier gas with a flow rate of 2 mL/min. Software Lab Solutions version 2.71 was used for the identification of the substances.

RESULTS AND DISCUSSION

Formation of Colored Compounds. Thermal treatment of unbuffered solutions of D-galacturonic acid and L-alanine at pH 5.0 and a temperature of 100 °C for 2 h led to a 6 times higher browning compared to L-arabinose, a 7 times higher browning compared to D-galactose, and an almost 3 times higher browning compared to D-galacturonic acid alone (see Figure 1). Its epimer D-glucuronic acid offers a decreased browning trend. More precisely, after a reaction time of 120 min at 100 °C, a D-galacturonic acid model solution exceeded twice the value of the absorption at 420 nm of an equimolar D-glucuronic acid reaction model (results not shown).

Figure 2 shows the influence of several amino acids on browning intensities of the D-galacturonic acid solutions

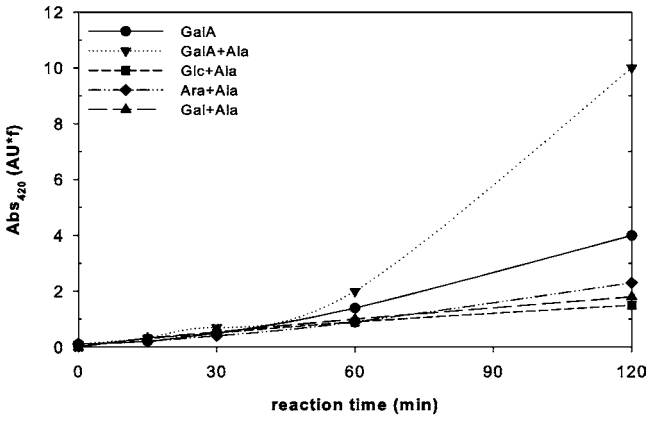

Figure 1. Nonenzymatic browning of D-galacturonic acid (GalA) solutions with and without L-alanine (Ala) compared to solutions of L-arabinose (Ara), D-glucose (Glc), and D-galactose (Gal) with L-alanine thermally treated at 100 °C and a starting pH value of 5.0, measured as absorption at 420 nm.

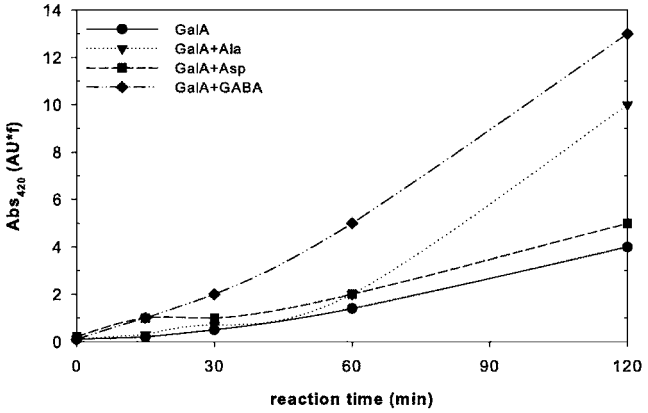

Figure 2. Nonenzymatic browning of D-galacturonic acid (GalA) solutions with L-alanine (Ala), L-aspartic acid (Asp), or γ-aminobutyric acid (GABA) after thermal treatment at 100 °C and a starting pH value of 5.0, measured as absorption at 420 nm.

(starting pH 5.0), which were heated at 100 °C for different time intervals. As expected, GABA promotes browning the most followed by Ala and Asp. Both might degrade more rapidly in the presence of dicarbonyl compounds (Strecker degradation), resulting in a loss of browning-fostering molecules. In comparison to a starting pH of 5.0, an initial pH value of 3.0 caused less absorption at 420 nm, whereas starting at pH 8.0 induced a higher absorption. Despite different browning intensities all starting pH values led to the same order of priority concerning the amino acid influence on color development (results not shown).

Not only the addition of amino acids but also the structure of the carbonyl compound can affect color formation, especially the presence of the carboxyl group on C-6 and the stereochemistry of a $^1C_4$-conformation in the pyranoic form. Eliminative decarboxylation gives a plausible explanation for the carboxyl group's strong influence. Eliminative decarboxylation preferably occurred in the presence of D-galacturonic acid with the substituents at C-4 and C-5 in *trans* position and at elevated temperatures under slightly acidic to neutral conditions.

Table 1 shows the browning values and the corresponding CIELab values for the thermally treated model solutions (2 h) and the calculated yellowness (YI), chroma (C), and saturation (S). Compared to the slightly yellow model solutions of the previously heated reducing sugars (Ara, Glc) the color of uronic acids Maillard reactions was reddish and CIELab measurements revealed that not only the lightness was considerably lower, but the $+a$ (red) as well as the $+b$ (yellow) values were higher in the thermally treated D-galacturonic acid solutions compared to reducing sugars. In the presence of amino acids (e.g., L-alanine) the lightness of the model solutions was lower than without an amino acid, the $+a$ value increased from +19 to +36, whereas the $+b$ value decreased from +54 to +44. Also, the structure of the amino acid influences color and browning intensity. The browning value was highest with GABA (13.1) and lowest with L-aspartic acid (4.5); the average value of L-alanine was (9.9).

DOI: 10.1021/acs.jafc.5b01121
J. Agric. Food Chem. 2015, 63, 6457−6465

Table 1. CIELab Values of Maillard Reaction Models of D-Galacturonic Acid (GalA) Alone or with L-Alanine (Ala), L-Aspartic Acid (Asp), or γ-Aminobutyric Acid (GABA) Compared to Model Solutions of L-Arabinose (Ara) and D-Glucose (Glc) with L-Alanine at a Reaction Temperature of 100 °C after 2 h and a pH Value of 5.0 at the Beginning of the Reaction[a]

	L	*a* (red)	*b* (yellow)	YI	*C*	*S* (%)	Abs_{420}
Ara + Ala	90	−1	22	35	22	24	2.3
Glc + Ala	98	−2	11	16	11	11	1.5
GalA	67	19	54	114	57	65	4.0
GalA + Ala	56	36	44	113	57	71	9.9
GalA + Asp	56	28	43	111	57	71	4.5
GalA + GABA	21	30	−13	90	33	84	13.1

[a]Yellowness (YI), chroma (*C*), and saturation (*S*) were calculated according to the method of Hunter and Harold.[22] Browning intensity (Abs_{420}) was measured as the absorption at 420 nm.

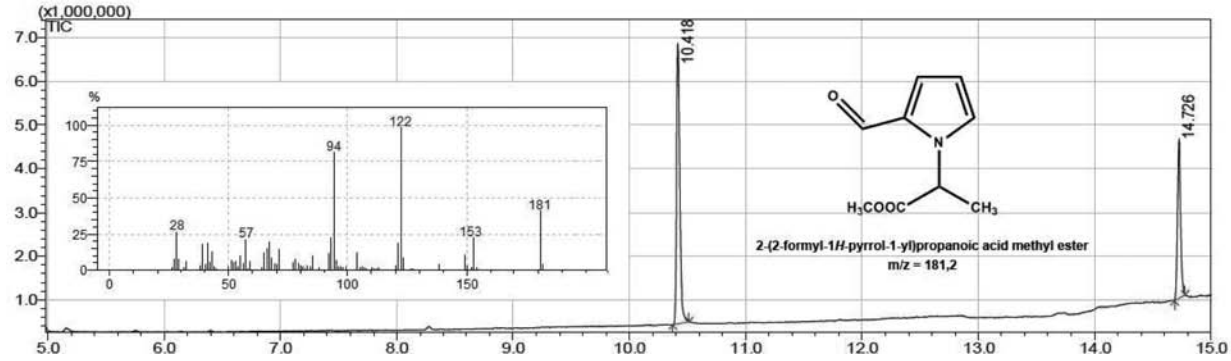

Figure 3. Total ion chromatogram of the FPA as a degradation product of D-galacturonic acid (GalA) and L-alanine by GC-MS after postderivatization with TMSDM and total ion chromatogram of the methylated FPA derivative (t_R 14.73 min) with its embedded fragmentation pattern and the internal standard *N*-methylpyrrole-2-carboxylic acid (t_R 10.42 min).

Furthermore, differences in yellowness, saturation, and chroma could be detected. These three parameters are much higher in thermally treated D-galacturonic acid solutions than in model solutions of reducing sugars as well. These findings emphasize the differences in browning behavior and in the formation of polymeric dyes between uronic acids and common reducing sugars. The browning of D-glucuronic acid was slower than that of D-galacturonic acid, but the characteristic red color of the model was equal (data not shown). Color formation by D-galacturonic acid methyl ester was also slower than that of the unesterified D-galacturonic acid and the browning index detectable after 2 h of heating at 100 °C without amino acid catalysis was only around half of the value of unesterified D-galacturonic acid (data not shown).

As described for the D-galacturonic acid model solutions without amino acid, the pH value of D-galacturonic acid solutions with L-alanine increased steadily from starting pH 5.0 until it reached 5.8 after 120 min (data not shown). Only in model solutions starting at pH 3.0 did the value not change with reaction progress. The pH increase may be caused by heterocyclic or carbocyclic compounds formed during thermally induced decomposition of D-galacturonic acid. These heterocyclic compounds are supposed to be less acidic than short-chained dicarbonyl cleavage products as formic or acetic acid. In addition, a loss of the carboxyl group of the uronic acid itself due to eliminative decarboxylation leads to a deacidification of the model system. In contrast to the almost colorless to slightly yellow color of the common reducing sugar solutions, the color of uronic acid model solutions treated under the same conditions was red-brown. This typical red-brown color of D-galacturonic acid solutions is caused by specific degradation products, such as reductic acid and the pyrroles discussed later, which are involved in the formation of polymeric dyes.[14] Higher pH values as well as the addition of amino compounds accelerated the degradation reaction of D-galacturonic acid and led to a higher absorption at 420 nm and an increase in the +*a* value.

Reactive Intermediates of D-Galacturonic Acid. Our earlier experiments confirmed that 2-ketoglutaraldehyde is a key intermediate in the formation of reductic acid, DHCP, and furan-2-carboxaldehyde.[3] This would support the eliminative decarboxylation mechanism being the main degradation pathway of D-galacturonic acid under slightly acidic to neutral conditions. A concerted mechanism involving a simultaneous dehydration at C-4 and decarboxylation at C-5 of GalA resulting in the formation of 4,5-unsaturated 4-deoxy-L-arabinose, as labile precursor for 2-ketoglutaraldehyde formation, can be assumed. After dehydration, the postulated 4,5-unsaturated 4-deoxypentose can yield the enol form of 2-ketoglutaraldehyde, which leads directly to the formation of reductic acid or, after isomerization, to DHCP and furan-2-carboxaldehyde. However, because Amadori compounds of D-uronic acids are unstable, the 4-deoxypentose can also react with the amino group to form imine intermediates, which then may cyclize to *N*-heterocyclic compounds such as pyrroles and pyridines. 3-Hydroxypyridinium compounds have already been found as degradation products of D-glucuronic acid and peptides by Horvat et al., who postulated a formation pathway that includes the intermediate formation of an Amadori compound.[12]

So far, pyrroles have not been identified as degradation products of thermally treated uronic acids. Figure 3 shows the total ion chromatogram of the GC-MS analysis of an unknown degradation product, which has been isolated from the model

DOI: 10.1021/acs.jafc.5b01121
J. Agric. Food Chem. 2015, 63, 6457−6465

solution of GalA and L-alanine by diethyl ether/ethyl acetate extraction. After methylation with TMSDM, this compound could be identified by GC-MS as FPA and thus also verified pyrroles in general as typical reaction products of D-galacturonic acid and amino acids for the first time. In addition, the formation of pyrrole-2-carboxaldehyde derivatives could also be confirmed in the reaction of D-galacturonic acid with other amino compounds such as L-glycine and GABA, but not with L-aspartic acid (data not shown). These pyrrole-2-carboxaldehydes are also formed during thermal treatment of D-galacturonic acid methyl ester (see Table 3).

The concentration of pyrrole-2-carboxaldehydes formed depends not only on the ratio of carbonyl to amino compound but also on the structure of the carbonyl used (see Figure 4), as well as on the reaction temperature, initial pH value, and reaction time of the model solution. The highest amounts were formed with ratios of uronic acid to amino acid between 2:1 and 1:1, pH values <5.0, and temperatures >100 °C (data not shown).

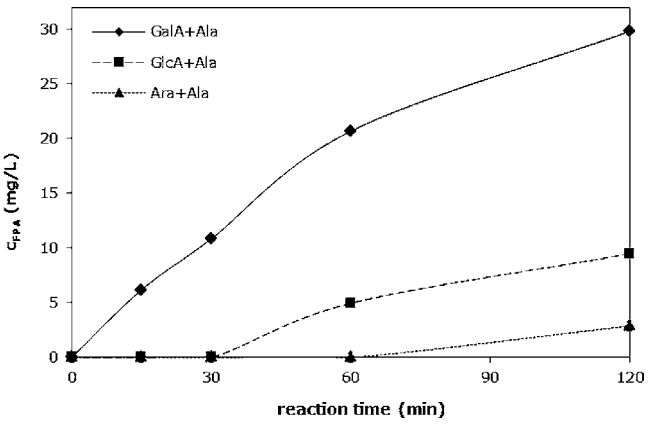

Figure 4. Comparison of FPA formation in model reactions between L-alanine (Ala) and D-galacturonic acid (GalA), D-glucuronic acid (GlcA), and L-arabinose (Ara) at 100 °C and a starting pH value of 8.0.

Table 2 gives an overview of the concentration of the most important products formed during thermal treatment of D-galacturonic acid compared to D-glucuronic acid solutions with and without the presence of L-alanine at 100 °C after 2 h. Relatively high concentrations of FPA **4** and HPA **5** in the reaction of both uronic acids with L-alanine cannot be explained via the formation of the Amadori compound **2c** shown in Figure 5 alone. Amadori compounds are not easily formed under these conditions, because the intermediate *N*-glucosides **2a**−**2c** are not stable and preferably cleaved back to the free uronic and amino acid **1**. A direct dehydration of the *N*-glycoside should lead to the formation of 3-deoxyhexosulosuronic acid **6**, which then preferably degrades to furan-2-carboxaldehyde and reductic acid.[3,5] Compared to the relatively high concentrations of FPA and HPA no furan-2-carboxaldehyde was found in the solutions and only traces of 3-deoxyhexosulosuronic acid could be detected by LC-MS after postderivatization of the solution with OPD (determined as quinoxaline). Thus, a formation pathway of pyrrole-2-carboxaldehyde derivatives and 3-hydroxypyridines distinct from the formation of furan-2-carboxaldehyde and 3-deoxyhexosulosuronic acid is postulated (see Figure 6). Due to eliminative decarboxylation of D-galacturonic acid, the 4,5-unsaturated 4-deoxy-L-arabinose is formed. In the presence of amino acids a nucleophilic addition reaction at C-5 followed by dehydration and cyclization reactions leads to the six-membered *N*-heterocyclic compound HPA. As a competitive reaction the nucleophilic addition at C-1 yields a Schiff base. A concerted cyclization dehydration reaction via a carbenium ion **10**, the (3*Z*)-configuration of which is mandatory for cyclization,[13] results in the five-membered *N*-heterocyclic compound FPA.

Besides pyrroles such as FPA that are formed via a breakdown of the carbohydrate backbone and the incorporation of amino compounds, another reaction pathway was postulated by De Kimpe et al. This pathway suggests pyrroles being built from smaller fragmentation products. Methylglyoxal was identified as an important precursor leading via condensation reactions to highly substituted pyrroles.[14]

3-Hydroxypyridine derivatives are known to be stable compounds and therefore not relevant as color precursors,[15] which was experimentally confirmed (data not shown). However, Tressl et al. identified certain pyrroles as important precursors of polymerization and color and postulated an acid-catalyzed formation of so-called type II polymers. Furan-2-carboxaldehyde could also take part in this polymerization, but decelerated the polymerization speed.[16] Type II polymers possess a red color, but after longer exposure to air, they turn black because of oxidation reactions. The higher the reaction temperature and the higher the amount of amino acids present in the model solutions of uronic acids, the higher was the

Table 2. Concentrations (Micromolar) of the Main Degradation Products Reductic Acid (RA), DHCP, Furan-2-carboxaldehyde (FF), Norfuraneol (Norf), FPA, HPA, and Glyoxal and the Sum of Short-Chain α-Dicarbonyl Compounds (DC) in Model Solutions of D-Glucuronic Acid (GlcA) with and without the Participation of L-Alanine (Ala) Compared to Model Reactions of D-Galacturonic Acid (GalA) after Thermal Treatment for 2 h at 100 °C and with Different Initial pH Values

	pH	RA	DHCP[a]	FF	Norf	FPA	HPA	glyoxal	DC[b]
GalA	5	150	40000	nd	260			69	110
	8	370	nd	nd	2200			110	170
GalA + Ala	5	610	12000	nd	290	840	230	40	71
	8	700	nd	nd	4400	180	130	100	160
GlcA	5	630	22000	nd	850			190	320
	8	330	5200	nd	200			280	460
GlcA + Ala	5	420	41000	nd	3900	360	180	110	430
	8	860	nd	nd	1900	59	nd	160	430

[a]quantified as malic acid equivalent. [b]Sum of glyoxal, 2-oxopropanal, diacetyl, and 3-deoxypentosulose.

DOI: 10.1021/acs.jafc.5b01121
J. Agric. Food Chem. 2015, 63, 6457−6465

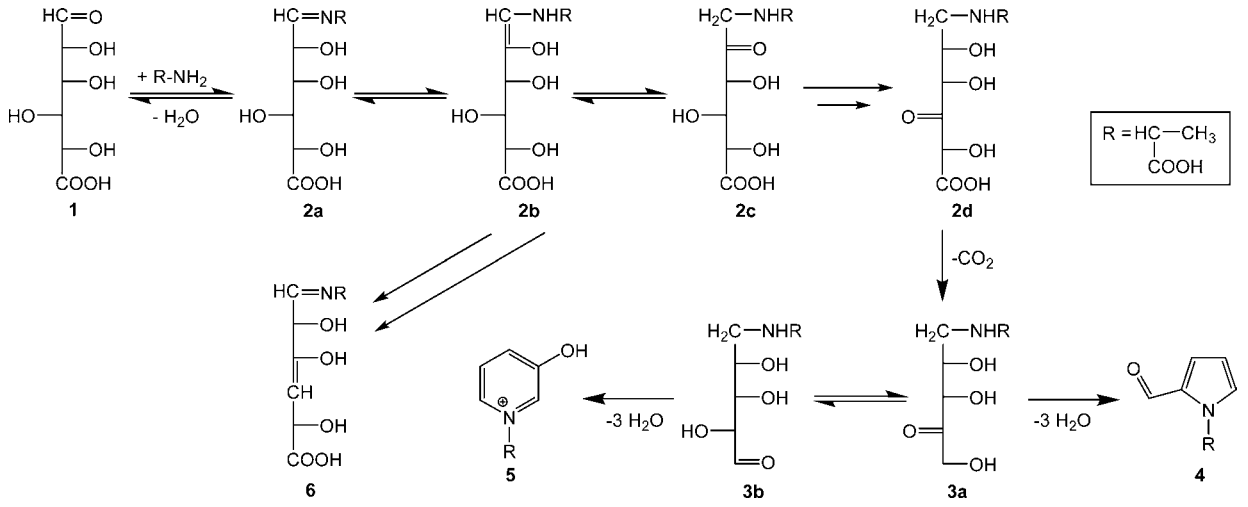

Figure 5. Formation of FPA **4** and HPA **5** via the Amadori reaction pathway. **2a**−**2c** formed of D-galacturonic acid **1** and L-alanine[12] by decarboxylation, cyclization. and dehydrations reactions. Direct dehydrations of the *N*-glycoside **2b** without the formation of an Amadori compounds led to the formation of 3-deoxyhexosulosuronic acid **6**.

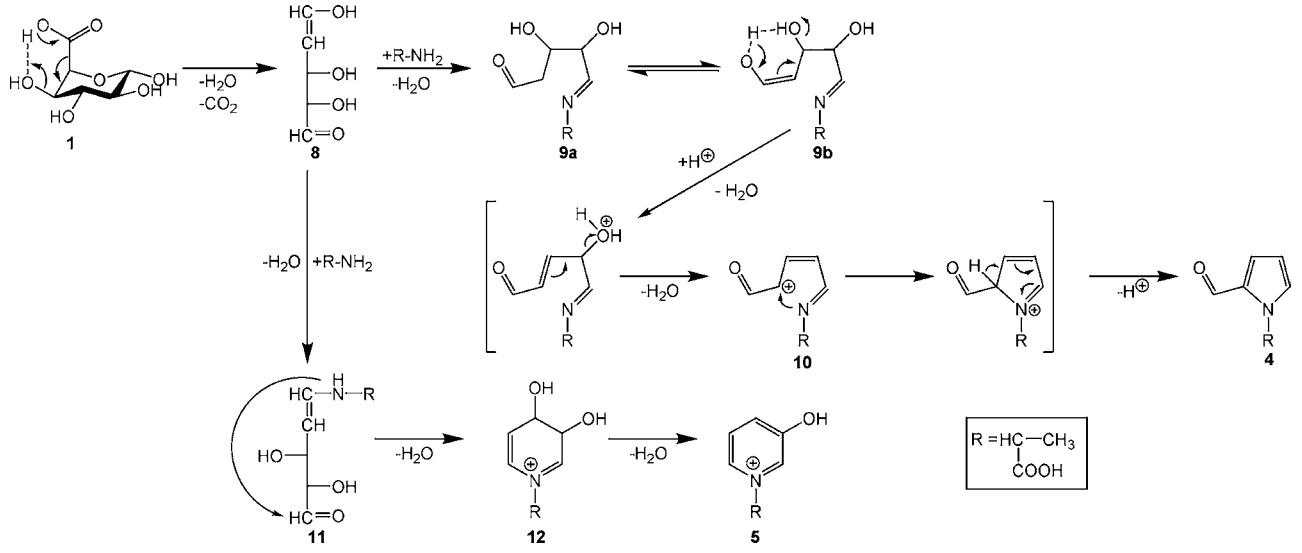

Figure 6. Alternative formation pathway of *N*-heterocyclic compounds due to imine formation on C-5 or C-1 of the 4,5-unsaturated 4-deoxy-L-arabinose **8** with L-alanine and further cyclization and dehydration to FPA **4** or HPA **5**.

concentration of pyrrole-2-carboxaldehyde derivatives and the darker was the color of the model solution (data not shown).

The polymerization speed along with the polymer's solubility depended on the structure of the amino acid. In equimolar solutions of D-galacturonic acid with L-alanine or GABA at a reaction temperature of 160 °C, the associated pyrrole-2-carboxaldehyde derivative (FPA, FPG) was the main degradation product. Figure 7 illustrates the pyrrole-2-carboxaldehyde derivative formation in relation to the browning of the respective model solutions measured at 420 nm. In the above-mentioned reaction with L-alanine the FPA formation was very fast and the maximum concentration was reached after 5 min. Afterward, it slightly decreased because D-galacturonic acid was probably degraded in large part, but because of the accumulated FPA, polymerization could still take place; only the polymerization speed slowed. In the case of L-alanine the polymers were still soluble in the aqueous solution after 2 h of continuous heating. With GABA, the polymerization was even faster than with L-alanine; insoluble black particles were formed

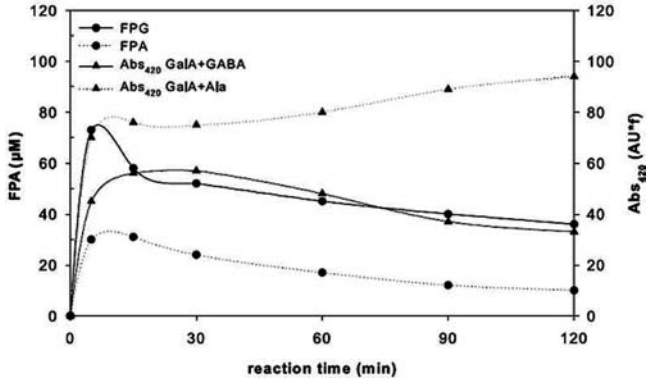

Figure 7. Nonenzymatic browning progress as the absorption at 420 nm and FPA and FPG concentrations of D-galacturonic acid (GalA) solutions with L-alanine (Ala) or γ-aminobutyric acid (GABA) at a reaction temperature of 160 °C, respectively.

DOI: 10.1021/acs.jafc.5b01121
J. Agric. Food Chem. 2015, 63, 6457−6465

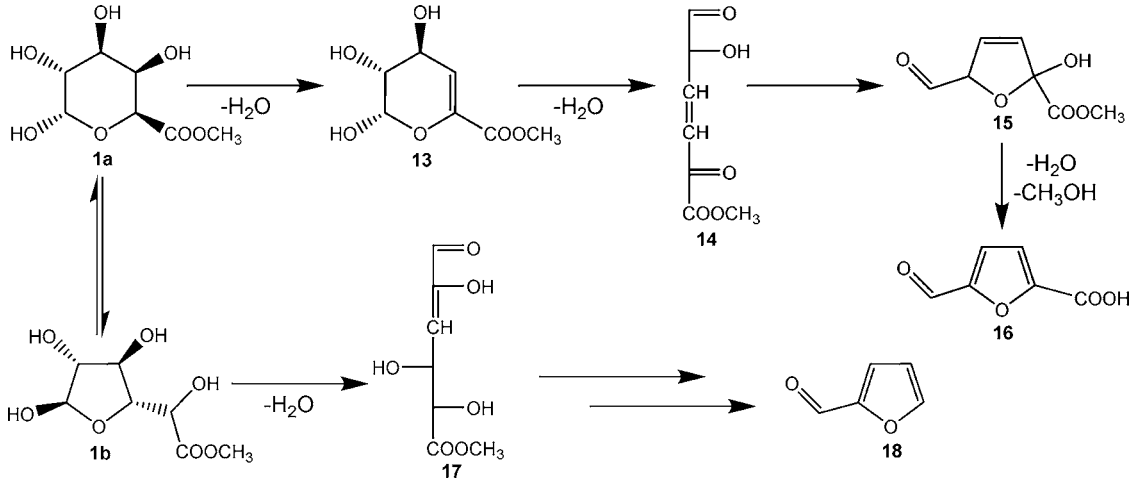

Figure 8. β-Elimination of the pyranoic and the furanoic forms of D-galacturonic acid methyl ester **1a**, **1b** and further degradation to 5-formyl-2-furanoic acid **16** and β-elimination of the furanoic form of the methyl ester **1b** leading to furan-2-carboxaldehyde **18**.

after about 20 min. After reaching an absorption plateau at 420 nm at about 5 min of reaction time, the absorption of the solution with GABA started to decrease again because of the formation of insoluble black particles.

Experiments with several uronic acid derivatives gave indication that the reason for the differences in browning behavior lies within the preferred ring structure of these compounds in aqueous solution. D-Galacturonic acid prefers the lowest energy $^1C_4$ chair conformation with the substituents at C-4 and C-5 in *trans* position.[17] This can be the reason for a relieved eliminative decarboxylation under neutral to slightly acidic conditions resulting in the formation of 2-ketoglutaraldehyde and its isomers and their secondary degradation products discussed recently.[3] D-Glucuronic acid mainly exists in the more labile furanoic hemiacetal form, which is stabilized by a γ-lactone ring under acidic conditions.[18] Due to this lactone ring the proton of the C-4 is acidified and can easily be withdrawn by a base in a β-elimination step at C-3. Dax et al. postulated a degradation pathway that leads to the formation of glyoxal and 3-formyl-2-oxopropanoic acid in acidic solutions of D-glucuronic acid and the formation of 2-ketoglutaraldehyde under more alkaline conditions.[19] This postulated pathway could be confirmed by our investigations, which proved glyoxal as the main α-dicarbonyl compound also formed by the degradation of D-galacturonic acid under slightly acidic conditions. 2-Ketoglutaraldehyde emerged as a key intermediate in browning and the formation of other typical degradation products such as reductic acid and DHCP. In addition, the furanoic compound norfuraneol could be verified as a main degradation product (see Table 2). In reactions with D-galacturonic acid it can especially be found under alkaline conditions, and in participation of L-alanine the amount formed is doubled.

In contrast, D-glucuronic acid model reactions yield only small portions of norfuraneol. Adding L-alanine increases the norfuraneol amount to the level found in alkaline D-galacturonic browning reactions. As mentioned above, this can be explained by D-glucuronic acid mainly existing as γ-lactone in aqueous solutions, which hinders a direct degradation. However, in the presence of amino compounds the degradation reaction toward norfuraneol is catalyzed to a high degree. Compared to model reactions with D-galacturonic acid, the total concentration of the short-chain α-dicarbonyl compounds glyoxal, 2-oxopropanal, diacetyl, and 3-deoxpentosulose, respectively, were 3−4 times higher in D-glucuronic acid models. On the other hand, cyclic nitrogen-containing products such as FPA and HPA are formed on a larger scale in D-galacturonic acid browning reactions. The most obvious reason for these differences in reaction behavior is their special cyclic conformation, as mentioned above. However, more structural elucidation is necessary to clarify this issue. A comparison of degradation products detected after thermal treatment of D-glucuronic and D-galacturonic acid model reactions with and without L-alanine, respectively, after 2 h of reaction at 100 °C and starting pH values of 5.0 and 8.0 can be found in Table 2.

Reactive Intermediates of D-Galacturonic Methyl Ester. The monomeric methyl ester of D-galacturonic acid prefers the furanoic form **1b** (shown in Figure 8) as well, and therefore β-elimination at C-3 is preferred.[20] Subsequent dehydration and elimination of the labile formic acid methyl ester group is supposed to lead to the formation of furan-2-carboxaldehyde (FF) **18** as the main degradation product. This pathway would give an explanation for the comparatively high amounts of FF detected for GalA methyl ester models compared to free D-galacturonic acid model reactions as mentioned above. When the reaction was started at pH 3.0, the pH value remained stable because neither alkaline hydrolysis leading to higher pH values nor acid ester cleavage can take place at these conditions (see Table 3).

Starting GalA methyl ester model reactions at pH 5.0, deesterification and β-elimination proceeded simultaneously and caused a decrease in the pH value from 5.0 to about 4.0. Except for DHCP, all other described degradation products of D-galacturonic acid were formed, but mostly in a lesser extent, with the exception of FF (Table 3). Concerning reductic acid, the thermal D-galacturonic methyl ester degradation yields only a small amount of it compared to its unesterified derivative. Methylation seems to prevent a β-ketoacid-like decarboxylation leading to reductic acid via 2-ketoglutaraldehyde. Starting thermal degradation at pH 3.0, the methyl ester was partially hydrolyzed to the free acid, which could be further converted into its typical and highly browning active degradation products such as reductic acid. In contrast, less acidic starting conditions (pH 5.0) caused a decrease in reductic acid. Under these conditions β-elimination of the relatively stable methyl ester

DOI: 10.1021/acs.jafc.5b01121
J. Agric. Food Chem. 2015, 63, 6457−6465

Table 3. Concentrations (Micromolar) of the Main Degradation Products Reductic Acid (RA), Furan-2-carboxaldehyde (FF), Norfuraneol (Norf), FPA, and HPA in Model Solutions of D-Galacturonic Acid Methyl Ester (GalA-Me) with and without L-Alanine (Ala) Compared with Model Reactions of D-Galacturonic Acid (GalA) with and without Ala after Thermal Treatment for 2 h at 100 °C and with Different Initial pH Values

	pH	RA	FF	Norf	FPA	HPA
GalA	3	7	9	nd		
	5	39	2	15		
GalA + Ala	3	38	2	29	50	203
	5	29	38	368	14	84
GalA-Me	3	12	17	nd		
	5	6	30	nd		
GalA-Me + Ala	3	2	43	nd	35	157
	5	2	58	nd	41	84

seemed to be preferred, leading via a 2,3-unsaturated intermediate to FF as already described.

In the presence of Ala a decrease of the browning active RA could be seen at all pH values, probably caused by amino−carbonyl reactions leading to colored polymers. However, the formation of other less reactive compounds such as FF, FPA, or HPA was strongly promoted. Concerning the pH influence, FPA formation seemed analogous to FF, whereas HPA was formed only after acidic ester hydrolysis to a greater extent.

Pectins are important biopolymers that naturally occur in the more ligneous parts of fruits and vegetables. Their backbone mainly consists of D-galacturonic acid methyl ester and D-galacturonic acid units, which are both present in $^4C_1$ chair conformation. When pectins are exposed to alkaline conditions, the methyl ester **1a** is particularly degraded by β-elimination at C-4. Therefrom unsaturated oligogalacturonides occur, which decompose to shortened saturated oligogalacturonides and further degrade via furan-typical dehydration rearomatization reactions to 5-formyl-2-furanoic acid **16**.[21] 2-Furanoic acid, which was also experimentally verified, is supposed to be formed in the same reaction pathway.

Neither furanoic acid could be detected during the degradation of monomeric D-galacturonic acid methyl ester alone, thus confirming the different degradation pathways preferred by the furanoic or pyranoic ring structure according to the constitution of the uronic acid derivative (see Figure 8).

In summary, it can be stated that D-galacturonic acid has emerged as a very potent browning active carbonyl compound within the Maillard reaction compared to other related carbonyl compounds such as D-glucuronic acid or L-arabinose. Model reactions of D-galacturonic acid and L-alanine provoke a >6 times higher browning intensity compared to similar reactions of Ara, Gal, and GalA, respectively. CIELab measurements revealed thereby a uronic acid specific red cast formed during the Maillard reaction.

Besides reductic acid, DHCP, furan-2-carboxaldehyde, and norfuraneol, pyrrole-2-carboxaldehyde and 3-hydroxypyridine-1-ium amino acid derivatives were identified as specific Maillard reaction products of uronic acids. The so-formed relatively high concentrations cannot likely be explained by the Amadori rearrangement pathway alone becaue uronic acid *N*-glucosides are not stable and easily decompose to their starting products. Thus, an alternative reaction pathway has been suggested. Due to eliminative decarboxylation of D-galacturonic acid and an associated carbonyl−amine condensation, Schiff bases of the 4,5-unsaturated 4-deoxy-L-arabinose are formed, which after cyclization and dehydrations lead to the corresponding *N*-heterocyclic compounds.

By comparison of results obtained for D-galacturonic acid model systems with those of the corresponding methyl ester, the ester compound shows less browning activity and degradation under equal reaction conditions. 5-Formyl-2-furanoic acid and 2-furanoic acid could not be identified as specific reaction products of monomeric esters even though thermal pectin decomposition is known to yield these acids. Further short-chain acidic cleavage products such as formic or acetic acid could not be verified as degradation products for both D-galacturonic acid and its methyl ester.

In conclusion, uronic acids are assumed to be responsible for color alteration processes in thermally treated pectin-containing foods. Especially some kinds of juices such as apple juice are susceptible to color change because amino−carbonyl reactions between the endogenous uronic and free amino acids can easily take place during industrial applied pasteurization and storage processes. In this case not only does the undesired color diminish quality but also a loss of free amino acids connected with a decline in nutritional quality is to be expected. For industrial use our findings may implicate changes in cultivation procedures resulting in a reduced free uronic acid content of respective fruits and vegetables and the consideration of negative effects caused by uronic acids during special engineering technologies. However, besides color effects uronic acids affect food quality in many other ways such as texture, taste, and scent, and thus more studies concerning their roles in foods and food technology and their influence on the end product are strongly recommended before a final evaluation.

AUTHOR INFORMATION

Corresponding Author

*(L.W.K.) E-mail: lothar.kroh@tu-berlin.de. Phone: +49 30 314 72 583. Fax: +49 30 314 72 585.

Notes

The authors declare no competing financial interest.

ABBREVIATIONS USED

Ara, L-arabinose; Ala, L-alanine; Asp, L-aspartic acid; DAD, diode array detector; DHCP, 4,5-dihydroxy-2-cyclopenten-1-one; DNPH, 2,4-dinitrophenylhydrazine; FF, furan-2-carboxaldehyde; FPA, (2-(2-formyl-1*H*-pyrrol-1-yl)propanoic acid; FPG, (4-(2-formyl-1*H*-pyrrol-1-yl)butanoic acid); GABA, γ-aminobutyric acid; Gal, D-galactose; GalA, D-galacturonic acid; GalA-Me, D-galacturonic acid methyl ester; GC, gas chromatography; GlcA, D-glucuronic acid; GPC, gel permeation chromatography; HPA, 1-(1-carboxyethyl)-3-hyroxypyridin-1-ium; HPLC, high-performance liquid chromatography; MS, mass spectrometry; OPD, *o*-phenylenediamine; Norf, norfuraneol; RA, reductic acid; TMSDM, (trimethylsilyl)-diazomethane

REFERENCES

(1) Yeom, H. W.; Streaker, C. B.; Zhang, Q. H.; Min, D. B. Effects of pulsed electric fields on the quality of orange juice and comparison with heat pasteurization. *J. Agric. Food Chem.* **2000**, *48*, 4597−4605.

(2) Scott, R. W.; Moore, W. W.; Effland, M. J.; Millett, M. A. Ultraviolet spectrophotometric determination of hexoses, pentoses,

DOI: 10.1021/acs.jafc.5b01121
J. Agric. Food Chem. 2015, 63, 6457−6465

and uronic acids after their reactions with concentrated sulfuric acid. *Anal. Biochem.* **1967**, *21*, 68−80.
(3) Bornik, M.-A.; Kroh, L. W. D-Galacturonic acid as a highly reactive compound in nonenzymatic browning. 1. Formation of browning active degradation products. *J. Agric. Food Chem.* **2013**, *61*, 3494−3500.
(4) Heyns, K.; Schulz, W. Die Umsetzung von D-Glucuronsäure und D-Galakturonsäure mit Aminosäuren zu 1-*N*-Aminosäure-1-desoxy-fructuronsäuren und 1-*N*-Aminosäure-1-desoxytagaturonsäuren. *Chem. Ber.* **1962**, *95*, 709−719.
(5) Eichner, K.; Ciner-Doruk, M. Bildung und Stabilität von Amadori-Verbindungen in wasserarmen Modellsystemen. *Z. Lebensm.-Unters. Forsch.* **1979**, *168*, 360−367.
(6) Sell, H. M.; Link, K. P. Derivatives of D-galacturonic acid IV. The preparation of the methyl ester of D-galacturonic acid. *J. Biol. Chem.* **1938**, 230−233.
(7) Jansen, E. F.; Jang, R. Esterification of galacturonic acid and polyuronides with methanol hydrogen. *J. Am. Chem. Soc.* **1946**, *68*, 1475−1477.
(8) Chanez, M.; Sag, G. Préparation du galacturonate de méthyle. *Bull. Soc. Chim. Fr.* **1959**, 1500−1501.
(9) Presser, A.; Hüfner, A. Trimethylsilydiazomethane − a mild and efficient reagent for the methylation of carboxylic acids and alcohols in natural products. *Monatsh. Chem.* **2004**, *135*, 1015−1022.
(10) Rizzi, G. P. Role of phosphate and carboxylate ions in Maillard browning. *J. Agric. Food Chem.* **2004**, *52*, 953−957.
(11) Pfeiffer, Y. V.; Kroh, L. W. Investigation of reactive α-dicarbonyl compounds generated from the Maillard reactions of L-methionine with reducing sugars via their stable quinoxaline derivatives. *J. Agric. Food Chem.* **2010**, *58*, 8293−8299.
(12) Horvat, Š.; Roščić, M.; Lemieux, C.; Nguyen, T. M. D.; Schiller, P. W. Formation pathway and opioid activity data for 3-hydroxypyridinium compounds derived from glucuronic acid and opioid peptides by Maillard processes. *Chem. Biol. Drug Des.* **2007**, *70*, 30−39.
(13) Owczarek-Fendor, A.; De Meulenaer, B.; Scholl, G.; Adams, A.; Van Lancker, F.; Eppe, G.; De Pauw, E.; Scippo, M.-L.; De Kimpe, N. Furan formation from lipids in starch-based model systems, as influenced by interactions with antioxidants and proteins. *J. Agric. Food Chem.* **2011**, *59*, 2368−2376.
(14) Adams, A.; Polizzi, V.; van Boekel, M.; De Kimpe, N. Formation of pyrazines and a novel pyrrole in Maillard model systems of 1,3-dihydoxyacetone and 2-oxopropanal. *J. Agric. Food Chem.* **2008**, *56*, 2147−2153.
(15) Soldo, S.; Frank, O.; Ottinger, H.; Hofmann, T. Systematic studies of structure and physiological activity of alapyridaine. A novel food-borne taste enhancer. *Mol. Nutr. Food Res.* **2004**, *48*, 270−281.
(16) Tressl, R.; Wondrak, G. T.; Garbe, L. A. Pentoses and hexoses as sources of new melanoidinlike Maillard polymers. *J. Agric. Food Chem.* **1998**, *46*, 1765−1776.
(17) BeMiller, J. N.; Kumari, G. V. β-Elimination in uronic acids: evidence for an E1cB mechanism. *Carbohydr. Res.* **1972**, *25*, 419−428.
(18) Heslop, D.; Smith, F. Lactones of glucosaccharic acid. Part IV. The enol of 5-keto-4-deoxyglucosaccharo-3:6-lactone, an analogue of ascorbic acid. *J. Chem. Soc.* **1944**, 637−642.
(19) Dax, K.; Gassner, N. A.; Weidmann, H. Eliminierungen an D-Glucofuranurono-6,3-lacton und seinen Derivaten. *Liebigs Ann. Chem.* **1977**, *1977*, 169−176.
(20) Schmidt, H. W. H.; Neukom, H. Zur säurekatalysierten Reaktion von Galakturonsäure mit Methanol. II. Isomerenverteilung und Isomerisierung der Galakturonoside. *Helv. Chim. Acta* **1966**, *49*, 510−517.
(21) Li, J.; Kisara, K.; Danielsson, S.; Lindström, M. E.; Gellerstedt, G. An improved methodology for the quantification of uronic acid units in xylans and other polysaccharides. *Carbohydr. Res.* **2007**, *342*, 1442−1449.
(22) Hunter, R. S., Harold, R. W., Eds. *The Measurement of Appearance*, 2nd ed.; Wiley: New York, 1987; pp 177−180.

DOI: 10.1021/acs.jafc.5b01121
J. Agric. Food Chem. 2015, 63, 6457−6465

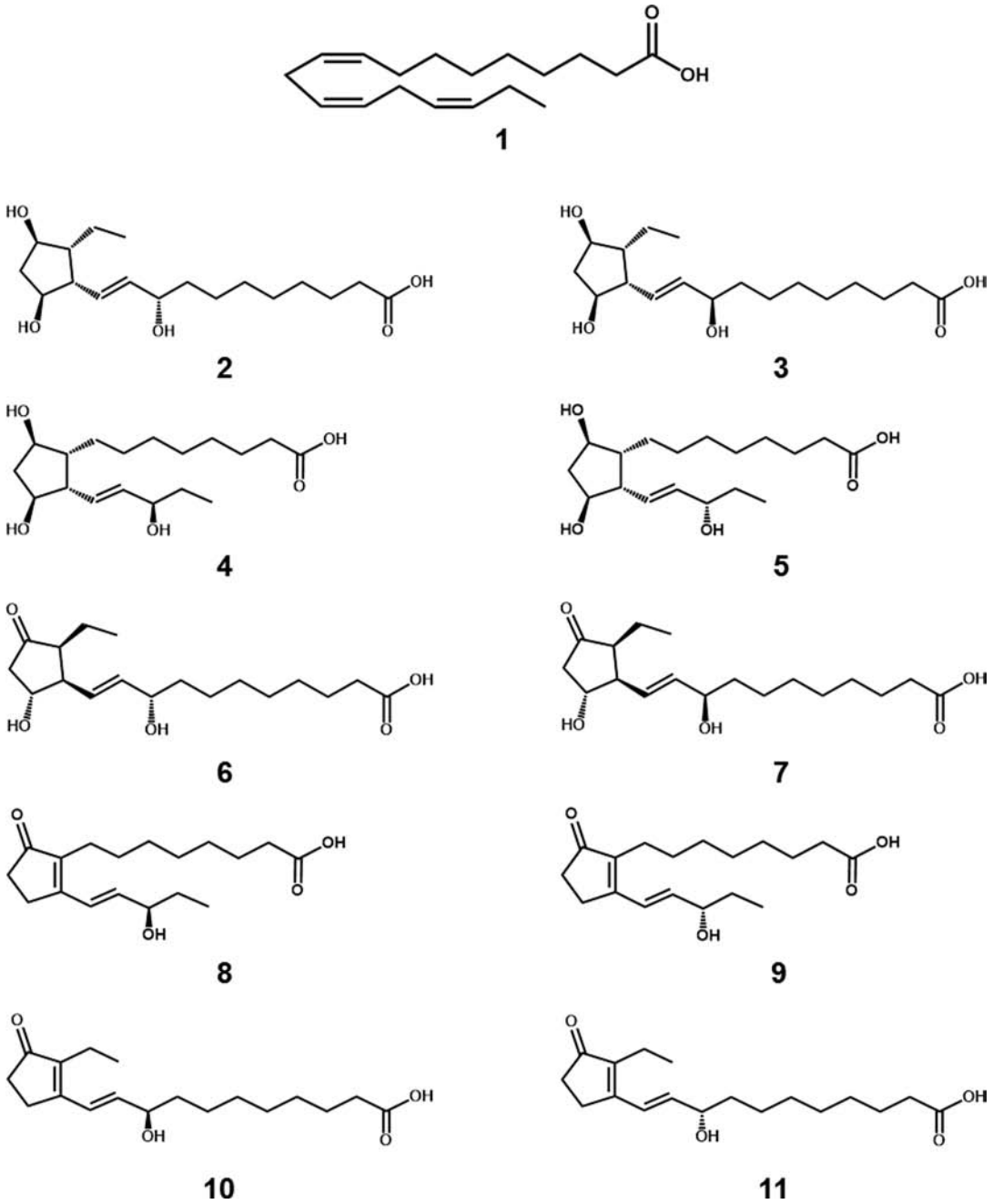

Figure 1. Chemical structures of α-linolenic acid (**1**) and of the studied phytoprostanes 9-F_{1t}-phytoprostane (**2**), 9-*epi*-9-F_{1t}-phytoprostane (**3**), *ent*-16-F_{1t}-phytoprostane (**4**), *ent*-16-*epi*-16-F_{1t}-phytoprostane (**5**), 9-D_{1t}-phytoprostane (**6**), 9-*epi*-9-D_{1t}-phytoprostane (**7**), 16-B_1-phytoprostane (**8**), *ent*-16-B_1-phytoprostane (**9**), 9-L_1-phytoprostane (**10**), and *ent*-9-L_1-phytoprostane (**11**).

according to the presence of specific pigments. These marine organisms are rich sources of bioactive compounds from both primary and secondary metabolism, among which fatty acids are highlighted.[14,15] Although marine algae present low lipid content (1−5% of dry matter), PUFA account for almost half of the lipid fraction.[15] Several studies have shown that despite PUFA profiles being highly variable between and within algal groups, linoleic (C18:2 ω6), linolenic (C18:3 ω3), arachidonic (C20:4 ω6), eicosapentaenoic (C20:5 ω3), and docosahexaenoic (C22:6 ω3) acids are predominant in macroalgae.[16−20]

The marine ecosystem is characterized by broad fluctuations of environmental conditions that can be strong stress inducers in macroalgae populations, including extreme temperatures, rapid salinity and nutrient changes, desiccation, and intense sunlight, among others.[21]

Taken together, these observations suggest that macroalgae can be valuable sources of phytoprostanes potentially used as biomarkers of oxidative stress and/or present important biological effects.[9,22] Due to the fact that macroalgae are an integral part of Asian cuisine and recently became a popular addition to some Western diets, our goal was to assess the occurrence of free phytoprostanes, readily bioavailable and absorbed by the human body, in 24 species of macroalgae belonging to Chlorophyta, Phaeophyta, and Rhodophyta. The reason for this characterization was based on the fact that humans do not possess significant esterase activity in the

DOI: 10.1021/acs.jafc.5b01904
J. Agric. Food Chem. 2015, 63, 6466−6474

Table 1. Characterization of Macroalga Samples

phylum	species	origin	location	date of collection
Chlorophyta				
	Codium tomentosum Stackhouse	Praia do Quebrado	N 39°22′0.91, W 9°22′25.86	April 2011
	Ulva lactuca Linnaeus	Praia do Quebrado	N 39°22′0.91, W 9°22′25.86	August 2011
	Ulva sp.	IMTA	N 41°27′11.20, W 8°46′28.29	July 2012
Rhodophyta				
	Asparagopsis armata Harvey	Praia do Quebrado	N 39°22′0.91, W 9°22′25.86	June 2010
	Gigartina sp.	Praia da Amorosa	N 41°38′51.44, W 8°49′32.53	December 2013
	Gracilaria vermiculophylla (Ohmi) Papenfuss	IMTA	N 41°27′11.20, W 8°46′28.29	July 2012
	Plocamium cartilagineum (Linnaeus) P. S. Dixo	Praia do Quebrado	N 39°22′0.91, W 9°22′25.86	July 2012
	Sphaerococcus coronopifolius Stackhouse	Praia do Quebrado	N 39°22′0.91, W 9°22′25.86	June 2010
Phaeophyta				
	Bifurcaria bifurcata R. Ross	Praia da Amorosa	N 41°38′51.44, W 8°49′32.53	December 2013
	Cladostephus spongiosus (Hudson) C. Agardh	Praia do Quebrado	N 39°22′0.91, W 9°22′25.86	June 2010
	Cystoseira tamariscifolia (Hudson) Papenfuss	Praia do Quebrado	N 39°22′0.91, W 9°22′25.86	July 2012
	Cystoseira usneoides (Linnaeus) M. Roberts	Praia do Quebrado	N 39°22′0.91, W 9°22′25.86	August 2011
	Fucus guiryi G. I. Zardi, K. R. Nicastro, E. S. Serrão & G. A. Pearson	Praia da Amorosa	N 41°38′51.44, W 8°49′32.53	December 2013
	Fucus serratus Linnaeus	Praia da Amorosa	N 41°38′51.44, W 8°49′32.53	December 2013
	Fucus spiralis Linnaeus	Praia da Amorosa	N 41°38′51.44, W 8°49′32.53	December 2013
	Halopteris filicina (Grateloup) Kützing	Praia do Quebrado	N 39°22′0.91, W 9°22′25.86	July 2012
	Laminaria ochroleuca Bachelot de la Pylaie	Praia da Amorosa	N 41°38′51.44, W 8°49′32.53	December 2013
	Padina pavonica (Linnaeus) Thivy	Praia do Quebrado	N 39°22′0.91, W 9°22′25.86	July 2012
	Pelvetia canaliculata (Linnaeus) Decaisne & Thuret	Praia do Norte	N 41°41′49.75, W 8°51′3.52	December 2013
	Saccharina latissima (Linnaeus) C. E. Lane, C. Mayes, Druehl & G. W. Saunders	IMTA	N 41°27′11.20, W 8°46′28.29	December 2013
	Saccorhiza polyschides (Lightfoot) Batters	Praia do Quebrado	N 39°22′0.91, W 9°22′25.86	September 2012
	Sargassum muticum (Yendo) Fensholt	Praia da Amorosa	N 41°38′51.44, W 8°49′32.53	December 2013
	Sargassum vulgare C. Agardh	Praia do Quebrado	N 39°22′0.91, W 9°22′25.86	August 2011
	Stypocaulon scoparium (Linnaeus) Kützing	Praia do Quebrado	N 39°22′0.91, W 9°22′25.86	June 2010

gastrointestinal tract, rendering impossible the absorption of the esterified form of phytoprostanes.[23]

A fast, selective, and robust ultrahigh-performance liquid chromatography coupled to triple-quadrupole mass spectrometry (UHPLC-QqQ-MS/MS) method, previously validated by Collado-González et al.,[24] was employed. Moreover, all macroalgae species selected for this work were characterized for their composition in α-linolenic acid (**1**) by gas chromatography−mass spectrometry (GC-MS) after alkaline hydrolysis and derivatization.

MATERIALS AND METHODS

Standards and Reagents. Ten phytoprostane standards (9-F_{1t}-phytoprostane (**2**), 9-*epi*-9-F_{1t}-phytoprostane (**3**), *ent*-16-F_{1t}-phytoprostane (**4**), *ent*-16-*epi*-16-F_{1t}-phytoprostane (**5**), 9-D_{1t}-phytoprostane (**6**), 9-*epi*-9-D_{1t}-phytoprostane (**7**), 16-B_1-phytoprostane (**8**), *ent*-16-B_1-phytoprostane (**9**), 9-L_1-phytoprostane (**10**), and *ent*-9-L_1-phytoprostane (**11**)) (Figure 1) were synthesized according to our previous procedures.[25−27] The d_4-15-F_{2t}-isoprostane (8-isoPGF$_{2\alpha}$-d_4) (containing four deuterium atoms at positions 3, 3′, 4, and 4′) was purchased from Cayman Chemicals (Ann Arbor, MI, USA). Authentic standards of fatty acids methyl esters (FAME) for GC-MS analysis were obtained from Supelco (Bellefonte, PA, USA).

Two types of solid-phase extraction (SPE) cartridges were used in this study: Chromabond C18 columns (1000 mg/6 mL) were

DOI: 10.1021/acs.jafc.5b01904
J. Agric. Food Chem. 2015, 63, 6466−6474

obtained from Macherey-Nagel (Düren, Germany) and Strata X-AW (500 mg/3 mL) columns from Phenomenex (Torrance, CA, USA). Butylated hydroxyanisole (BHA), bis(2-hydroxyethyl)-amino-tris-(hydroxymethyl)-methane (BIS-TRIS), chloroform, isooctane, and boron trifluoride (BF_3) were purchased from Sigma-Aldrich (St. Louis, MO, USA). Methanol was acquired from VWR (Fontenay-sous-Bois, France), acetonitrile was obtained from Merck (Darmstadt, Germany), and *n*-hexane was purchased from Panreac (Barcelona, Spain). All LC-MS grade solvents were obtained from J. T. Baker (Phillipsburg, NJ, USA). Water was treated in a Milli-Q water purification system from (Millipore, Bedford, MA, USA).

Macroalgae Samples. Macroalgae samples consisted of 3 Chlorophyta, 5 Rhodophyta, and 16 Phaeophyta species collected between 2010 and 2013 (Table 1). With the exceptions of *G. vermiculophylla*, *S. latissima*, and *Ulva* sp., which were cultivated in integrated multitrophic aquaculture (IMTA) systems and provided by CIIMAR/CIMAR − Centre for Marine and Environmental Research, all samples were randomly collected during low-tide periods from different places of the western coast of Portugal, each sample corresponding to a mixture of three to four individuals in the same stage of development. To prevent sample alterations, after collection they were immediately placed on ice and transported to the laboratory in insulated, sealed ice boxes to protect them from heat, air, and light exposure. Macroalgae were then carefully and quickly washed with NaCl aqueous solution (3.5%) to remove epiphytes and encrusting material, at room temperature, without exposure to direct light, and kept at −20 °C, prior to lyophilization. The dried material was powdered (<910 μm) and kept in the dark, in a desiccator, until it was subjected to extraction. No alteration (color, smell, humidity) of the samples was noted during storage.

α-Linolenic Acid and Extract Derivatization for GC-MS Analysis. The extraction of α-linolenic acid was performed as previously described, with slight modifications.[28] Briefly, 0.25 g of the dried macroalgae was extracted with 25 mL of chloroform/methanol (2:1), under magnetic stirring at 500 rpm, for 10 min, at 40 °C. The extraction procedure was repeated five times and the resulting extracts were pooled and concentrated to dryness under reduced pressure (40 °C). The residue was then hydrolyzed with 1 mL of KOH methanolic solution (11 g/L), at 90 °C, for 10 min. The free fatty acids originally present and those resulting from the alkaline hydrolysis were derivatized to their methyl esters with 1 mL of BF_3 methanolic solution (10%), at 90 °C, for 10 min. FAME were purified with 2 × 10 mL of isooctane, and anhydrous sodium sulfate was added to ensure the total absence of water. The resulting extract was evaporated to dryness under a stream of nitrogen and dissolved in 200 μL of isooctane. Each macroalga species was assayed in triplicate.

GC-MS Analysis of α-Linolenic Acid. GC-MS analysis was performed following a previously established method.[28] Derivatized extracts (1 μL) were analyzed using a Varian CP-3800 gas chromatograph (Walnut Creek, CA, USA) equipped with a Varian Saturn 4000 mass selective detector and a Saturn GC-MS workstation software version 6.8. The column used was a 30 × 0.25 mm, i.d., 0.25 μm, VF-5 ms (Varian). The injector port was heated to 250 °C. Injections were performed in split mode, with a ratio of 1:40. The carrier gas was helium C-60 (Gasin, Portugal), at a constant flow of 1 mL/min. The oven temperature was set at 40 °C for 1 min, then increased at 5 °C/min to 250 °C and at 3 °C/min to 300 °C, and held for 15 min. All mass spectra were acquired in EI mode. Ionization was maintained off during the first 4 min, to avoid solvent overloading. The ion trap detector was set as follows: transfer line, manifold, and trap temperatures were, respectively, 280, 50, and 180 °C. The mass ranged from m/z 50 to 600, with a scan rate of 6 scan/s. The emission current was 50 μA, and the electron multiplier was set in relative mode to autotune procedure. The maximum ionization time was 25000 μs, with an ionization storage level of m/z 35. The analysis was performed in full scan mode. Identification of α-linolenic acid was achieved by comparison of its retention index and mass spectra with those from pure standard injected under the same conditions and from NIST 05 MS Library Database. The amount of methyl ester of α-linolenic acid present in the samples was achieved from the calibration curve of the respective standard prepared in isooctane.

Phytoprostane Extraction. Each pulverized macroalga sample (1 g) was crushed in a mortar and pestle with 5 mL of methanol (0.1% BHA). The sample extracts were centrifuged at 2000*g* during 10 min, and the supernatants underwent SPE using a Chromabond C18 column. Briefly, 10 mL of *n*-hexane was added to 1 mL of the filtered sample and then rediluted in 2 mL of methanol and 2 mL of BIS-TRIS buffer.[24]

The emulsion of each macroalga sample was applied to a previously conditioned and equilibrated Strata-X-AW cartridge. After the column had been loaded with the emulsion, 2 mL of *n*-hexane, followed by 2 mL of Milli-Q water, 2 mL of methanol/Milli-Q water (1:3), and 2 mL of acetonitrile were applied for removing undesired compounds. Target compounds were eluted with 1 mL of methanol and dried under nitrogen stream. The dried residue of each macroalga sample was reconstituted with 200 μL of a mixture of A/B solvents (90:10, v/v), solvent A being Milli-Q water/0.01% acetic acid and solvent B being methanol/0.01% acetic acid. Reconstituted extracts were sonicated, filtered through a 0.45 μm filter (Millipore), and further injected and analyzed in an UHPLC-QqQ-MS/MS apparatus.

UHPLC-QqQ-MS/MS Analysis of Free Phytoprostanes. Separation of the phytoprostanes present in macroalga samples was performed using an UHPLC coupled to 6460 QqQ-MS/MS (Agilent Technologies, Waldbronn, Germany), as previously described.[24] The column used was a 50 × 2.1 mm i.d., 1.7 μm, BEH C18 (Waters, Milford, MA, USA). The column temperature was 6 °C. The mobile phases employed were solvent A (Milli-Q water/acetic acid (99.99:0.01, v/v)) and solvent B (methanol/acetic acid (99.99:0.01, v/v)). The elution was performed at a flow rate of 0.2 mL/min using the following gradient profile: 60% B at 0 min, 62% B at 2 min, 62.5% B at 4 min, reaching 65% B at 8 min, and returning to the initial conditions at 8.01 min. The MS analysis was applied in the multiple reaction monitoring (MRM) negative ESI mode. ESI conditions and ion optics were as previously described.[24] Data acquisition and processing were performed using MassHunter software version B.04.00 (Agilent Technologies). The quantitation of phytoprostanes detected in macroalgae was performed using authentic standards of compounds **2**, **3**, **8**, and **10**. The synthetic isoprostane d_4-15-F_{2t}-isoprostane (8-isoPGF$_{2\alpha}$-d_4) was used as internal standard.

Statistical Analysis. All of the analytical determinations were performed in triplicate, and the mean values were reported. All values obtained were compared using analysis of variance (one-way ANOVA, post hoc Tukey) and unpaired *t* test. Pearson correlations were calculated according to GraphPad Prism 6 Software, Inc. (San Diego, CA, USA). One-way ANOVA, unpaired *t* test, and principal component analysis (PCA) were performed using IBM SPSS Statistic for Windows version 22.0 (Armonk, NY, USA). Differences at $p < 0.05$ were considered statistically significant.

RESULTS AND DISCUSSION

The field of phytoprostanes was opened in 2000 and currently is still in its infancy. As far as we know, our work is the first report of different naturally occurring classes of free phytoprostanes in 24 macroalga species belonging to Chlorophyta, Phaeophyta, and Rhodophyta collected along the western coast of Portugal and from IMTA systems. Likewise, this is the first time a correlation between α-linolenic acid levels and its autoxidation products was ever tried in algae material.

Occurrence of α-Linolenic Acid in Macroalgae. Although the fatty acid profiles of some of the target species in this work have already been characterized, intraspecific variability is common in macroalgae from different geographical locations and/or with exposure to diverse abiotic factors, resulting in different PUFA profiles.[18] In this work we were able to identify and quantitate α-linolenic acid (**1**) in the 24 selected macroalga species (Table 2). The content of this compound

DOI: 10.1021/acs.jafc.5b01904
J. Agric. Food Chem. 2015, 63, 6466−6474

Table 2. α-Linolenic Acid and Phytoprostane Contents in the Analyzed Macroalga Species

species	α-linolenic acid (g/kg dry algae)	phytoprostanes[a] compound 2 (ng/100 g dry algae)	compound 3 (ng/100 g dry algae)	compound 8 (ng/100 g dry algae)	compound 10 (ng/100 g dry algae)	total (ng/100 g dry algae)
A. armata	0.96 (0.00)de	nd	nd	nd	nd	
B. bifurcata	3.57 (0.04)ef	nd	nd	5.68 (1.09)d	nd	5.68 (1.09)
C. spongiosus	4.09 (2.77)i	75.25 (3.71)de	38.05 (6.57)d	10.53 (2.32)bc	4.67 (1.17)a	128.49 (6.78)
C. tomentosum	3.77 (0.28)i	22.67 (3.38)e	32.49 (4.45)d	14.42 (2.10)a	6.36 (0.25)a	75.94 (9.22)
C. tamariscifolia	0.69 (0.01)b	nd	nd	nd	nd	
C. usneoides	2.62 (0.05)f	nd	nd	nd	nd	
F. guiryi	5.08 (0.06)b	nd	nd	nd	nd	
F. serratus	4.23 (0.06)cd	nd	nd	nd	nd	
F. spiralis	3.98 (0.14)de	18.61 (3.04)e	17.27 (1.32)d	nd	nd	35.87 (2.18)
Gigartina sp.	1.66 (0.02)h	nd	nd	nd	nd	
G. vermiculophylla	1.79 (0.03)h	54.46 (6.31)de	43.49 (2.14)d	nd	nd	97.96 (4.91)
H. filicina	3.43 (0.08)f	nd	nd	nd	nd	
L. ochroleuca	3.90 (0.13)de	36.42 (6.23)de	21.07 (5.54)d	nd	nd	57.48 (11.69)
P. pavonica	5.03 (0.08)a	26.33 (4.15)de	28.91 (3.60)d	6.39 (0.52)d	nd	61.36 (7.03)
P. canaliculata	4.40 (0.10)c	nd	nd	nd	nd	
P. cartilagineum	2.63 (0.01)g	nd	nd	nd	nd	
S. latissima	2.01 (0.07)h	700.94 (53.14)a	667.62 (51.34)a	12.33 (0.55)ab	nd	1380.90 (103.83)
S. polyschides	1.10 (0.03)i	413.35 (50.88)b	305.97 (39.56)b	nd	nd	719.62 (24.22)
S. muticum	3.94 (0.22)de	nd	nd	nd	nd	
S. vulgare	3.62 (0.12)ef	99.94 (17.63)d	39.54 (9.62)d	4.00 (0.86)d	nd	143.48 (26.92)
S. coronopifolius	0.78 (0.01)i	38.10 (4.91)de	36.80 (2.44)d	nd	nd	74.90 (4.93)
S. scoparium	0.80 (0.01)i	334.28 (44.67)c	170.23 (15.97)c	7.43 (0.37)cd	nd	511.94 (52.69)
U. lactuca	5.11 (0.01)b	74.95 (6.10)de	55.17 (4.04)d	nd	nd	130.13 (2.14)
Ulva sp.	3.49 (0.30)f	88.28 (23.82)de	64.98 (6.72)d	nd	nd	153.25 (25.44)

[a]9-F_{1t}-phytoprostane (**2**), 9-epi-9-F_{1t}-phytoprostane (**3**), 16-B_1-phytoprostane (**8**), and L_1-phytoprostane (**10**). Results are expressed as mean (standard deviation) of three determinations. nd, not detected. Different letters in the same column indicate significant differences ($p < 0.05$) between the reported values for each macroalga species.

ranged between ca. 0.7 and 5.6 g/kg of dry algae, *C. tamariscifolia* and *U. lactuca* presenting, respectively, the lowest and the highest amounts. Indeed, previous studies have reported that members of the order Ulvales presented compound **1** as the characteristic PUFA.[17,18] The presence of compound **1** in all of the analyzed species enables and emphasizes the importance of assessing the occurrence of its autoxidation products, the phytoprostanes.

Occurrence of Free Phytoprostanes in Macroalgae. The analysis of phytoprostanes in natural matrices is extremely challenging, requiring highly sensitive and specific tools for their profiling and characterization.[29] Moreover, the great diversity granted by the presence of racemic mixtures of phytoprostanes increases the complexity of these analyses. In this work, a fast, accurate, and robust UHPLC-QqQ-MS/MS method previously developed by Collado-González et al.[24] for the quantitative and qualitative determination of free phytoprostanes in foodstuffs was employed.

Among the 10 available phytoprostane standards, only 3 were detected in the analyzed macroalga samples (Table 2). Neither 16-series of F_{1t}-phytoprostanes nor 9-series of D_{1t}-phytoprostanes was detected in the studied species. Phytoprostane identity was confirmed according to their molecular masses, the precursor ions (m/z 327.2 and 307.2), the characteristic MS/MS fragmentation product ions, and the corresponding retention times. The mass spectrometric information on the phytoprostanes detected in one macroalga sample (*C. tomentosum*) is summarized in Figure 2. Compounds **2** and **3** (Figure 2A) showed the same transition from the precursor ion at m/z $[M - H]^-$ 327.2 to the product ion at m/z 171.2 (Figure 2B,C). Thus, their identification was only possible by the comparison of their retention times: compound **2** eluted at 1.75 min, whereas compound **3** eluted at 1.93 min (Figure 2A,B). Contrary to prostaglandins, phytoprostanes are non-enzymatically formed as regio- and stereoisomeric mixtures.[3] The analytical conditions employed in this study did not allow enantiomer separation. Therefore, compounds **8** and **10** (Figure 2A) were identified and quantitated according to their specific transitions from the precursor ion m/z $[M - H]^-$ 307.2 to the product ions m/z $[M - H]^-$ 235.2 and m/z $[M - H]^-$ 185.2, respectively (Figure 2D,E).

The qualitative profile of phytoprostanes found in the analyzed macroalgae samples showed great variability among the three phyla (Chlorophyta, Phaeophyta, and Rhodophyta) and even between species belonging to the same genus; that is, compounds **2** and **3** were detected in *F. spiralis*, but in *F. serratus* and *F. guiryi* none of the studied phytoprostanes was identified.

In the three studied green macroalgae (*C. tomentosum*, *U. lactuca*, and *Ulva* sp.), as well as in two of the red (*S. coronopifolius* and *G. vermiculophylla*) and eight of the brown species (*C. spongiosus*, *F. spiralis*, *L. ochroleuca*, *P. pavonica*, *S. latissima*, *S. polyschides*, *S. vulgare*, and *S. scoparium*), compounds **2** and **3** were identified. Also, compound **8** was detected in four of the brown species (*P. pavonica*, *S. latissima*, *S. vulgare*, and *S. scoparium*). The brown macroalgae *B. bifurcata* contained only compound **8**. None of the screened phytoprostanes were detected in 10 macroalga species (*A. armata*, *C. tamariscifolia*, *C. usneoides*, *F. guiryi*, *F. serratus*, *Gigartina* sp., *H. filicina*, *P. canaliculata*, *P. cartilagineum*, and *S.*

DOI: 10.1021/acs.jafc.5b01904
J. Agric. Food Chem. 2015, 63, 6466−6474

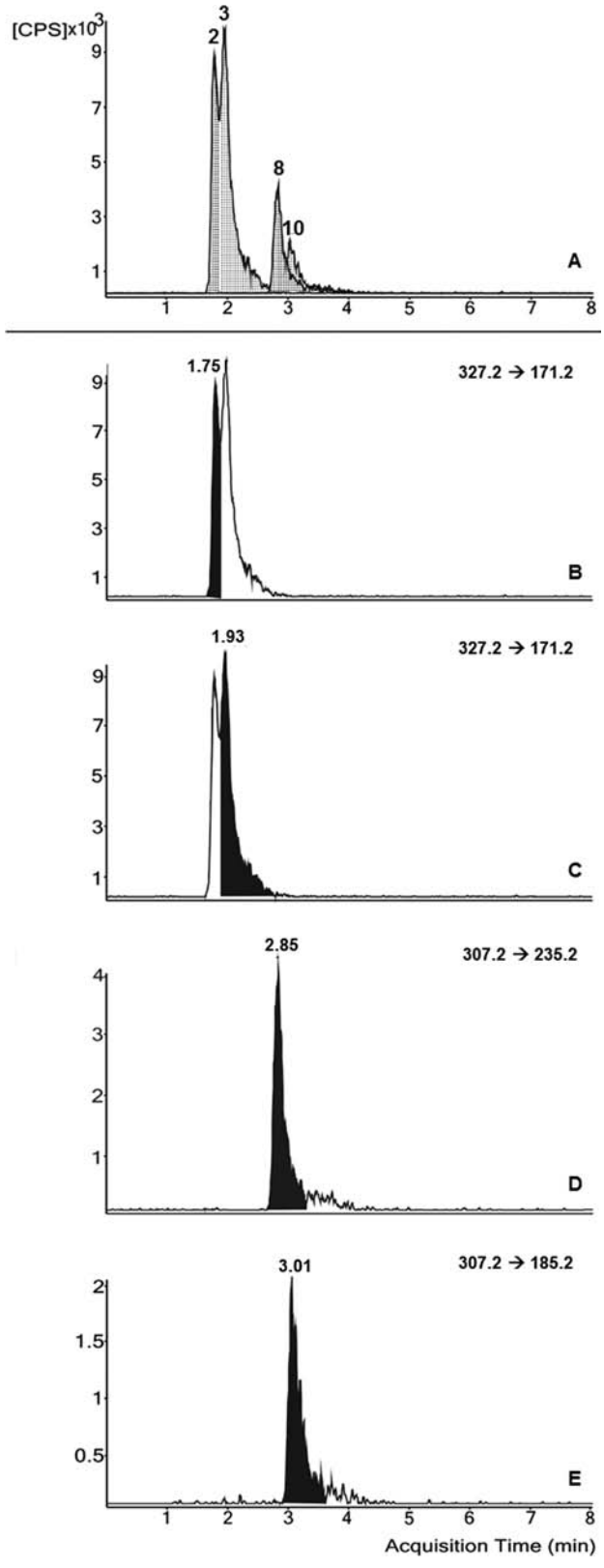

Figure 2. (A) Representative UHPLC-QqQ-MS/MS chromatogram of detected phytoprostanes (*C. tomentosum*) and MRM transitions for quantitation of (B) 9-F_{1t}-phytoprostane (**2**), (C) 9-epi-9-F_{1t}-phytoprostane (**3**), (D) 16-B_1-phytoprostane (**8**), and (E) 9-L_1-phytoprostane (**10**).

muticum). The species *C. spongiosus* and *C. tomentosum* exhibited higher diversity in phytoprostanes.

The determination of phytoprostane levels in macroalgae is of extreme importance, stimulating the exploitation and characterization of new natural dietary sources of these compounds.

The amount of phytoprostanes found in the analyzed samples is shown in Table 2. F_{1t}-phytoprostanes were the dominant class determined in this study, whereas L_1-phytoprostanes were detected in only two macroalga species and at very low levels. Concerning each phytoprostane class, both compounds **2** and **3** were found in higher concentration in the brown macroalgae *S. latissima* (ca. 701 and 668 ng/100 g of dry algae, respectively); *F. spiralis* exhibited the lowest amount of these phytoprostanes (ca. 19 and 17 ng/100 g of dry algae, respectively). The sample with the lowest content of compound **8** was *S. vulgare* (ca. 4 ng/100 g of dry algae), whereas *C. tomentosum* was found to have the highest amount (ca. 14 ng/100 g of dry algae). *C. spongiosus* and *C. tomentosum* were the only samples that presented compound **10** (ca. 5 and 6 ng/100 g of dry algae, respectively).

As observed with the qualitative profile, the quantitation of total phytoprostanes in the studied macroalgae species revealed significant variability. The total phytoprostane content ranged between ca. 6 and 1381 ng/100 g of dry algae. The macroalga species showing the highest amount of phytoprostanes (*S. latissima*) was from IMTA systems. However, no conclusions can be drawn regarding the advantages of IMTA for obtaining higher yields of phytoprostanes, as no marine counterpart of this species was analyzed.

To the best of our knowledge, no information has been published before on the content of naturally occurring free phytoprostanes in macroalgae. Therefore, the results obtained can be compared only with those of previous work performed on plant material and other foodstuffs. Karg et al.[9] found that either D_1- or F_{1t}-phytoprostanes were the dominant classes in vegetable oils, whereas B_1- and L_1-phytoprostanes, including their enantiomers, were minor components.[9] More recently, Collado-González et al.[24] reported that F_{1t}-phytoprostanes were the main class in the green table olive 'Manzanilla de Sevilla'.[24] Likewise, in macroalgae, F_{1t}-phytoprostanes were the main phytoprostanes detected. This class of compounds was also found to occur in the leaves, flowers, and roots of taxonomically distinct plant species, ranging from 43 to 1380 ng/g of dry weight.[30] Although we are aware structural differentiation in macroalgae is likely to be accompanied by variation in chemical composition, the present work used full alga individuals in the same stage of development, rendering it impossible to conclude about the presence and distribution of phytoprostanes in different morphological parts of the selected species.

Although it was theoretically expected to find both 9- and 16-series of F_1-phytoprostanes in equal amounts, we were not able to ensure this hypothetical relation in the studied macroalgae. In fact, previous studies reported only that 9- and 16-series (previously referred to as types II and I, respectively) of A_1-, B_1-, and E_1-phytoprostanes were of equal abundance in different plant tissues.[9] Moreover, Imbusch et al.[31] stated that due to the isomeric complexity of F_1-phytoprostanes, identification and quantitation of this class of compounds are technically difficult. Therefore, studies reporting the presence of F_1-phytoprostanes focused essentially on the differentiation between free and esterified isomers.[9,30−32] The analytical methodology employed in this work was able to differentiate 9-F_1-phytoprostane and 16-F_1-phytoprostane in previous

DOI: 10.1021/acs.jafc.5b01904
J. Agric. Food Chem. 2015, 63, 6466−6474

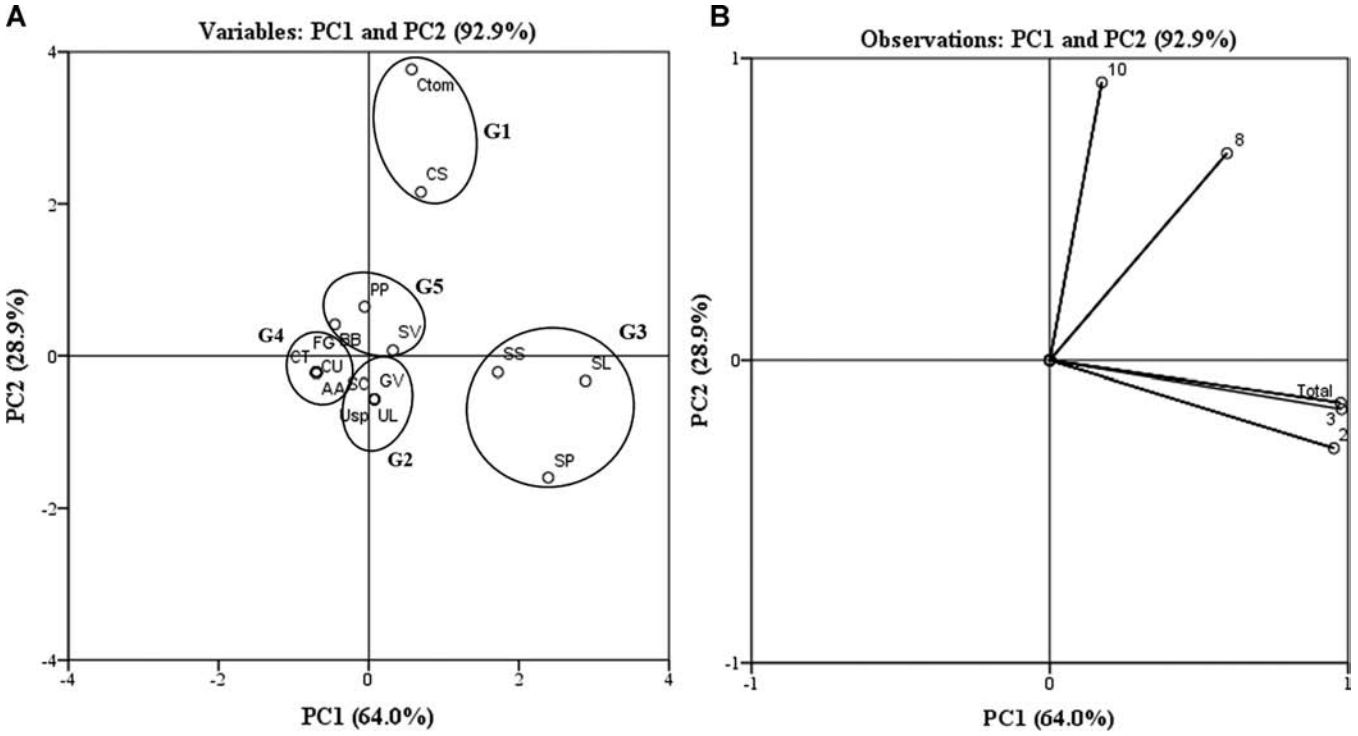

Figure 3. Projection of macroalgae (A) (variables: *A. armata* (AA), *B. bifurcata* (BB), *C. spongiosus* (CS), *C. tomentosum* (Ctom), *C. tamariscifolia* (CT), *C. usneoides* (CU), *F. guiryi* (FG), *F. serratus* (Fser), *F. spiralis* (Fspi), *Gigartina* sp. (Gsp), *G. vermiculophylla* (GV), *H. filicina* (HL), *L. ochroleuca* (LO), *P. pavonica* (PP), *P. canaliculata* (PC), *P. cartilagineum* (Pcart), *S. latissima* (SL), *S. polyschides* (SP), *S. muticum* (SM), *S. vulgare* (SV), *S. coronopfolius* (SC), *S. scoparium* (SS), *U. lactuca* (UL), and *Ulva* sp. (Usp)) and loadings (B) by phytoprostane composition (variables: **2**, **3**, **8**, and **10**) into the plane composed by principal components PC1 and PC2 containing 92.9% of the total variance.

studies using several natural matrices, such as olives and oils.[24] It was reported that the occurrence of these regioisomers was not of equal proportions: in refined sunflower oil the 9-F_1-phytoprostane was found in 44.48 ng/mL, whereas the 16-F_1-phytoprostane was found in 24.40 ng/mL of; in 0.8° and 0.4° extra virgin oil 9-F_1-phytoprostane were not detected, whereas 16-F_1-phytoprostane was found in 2.13 and 3.70 ng/mL, respectively.[24] The reason for these differences is still unclear, and more studies are needed to clarify the underlying response mechanisms of individual free phytoprostanes in natural products.

Statistical Analysis. Principal component analysis (PCA) was performed to determine possible distribution patterns of the identified and quantitated phytoprostanes (**2**, **3**, **8**, and **10**) in all of the analyzed macroalga samples. PCA of the normalized phytoprostane data set explained 92.9% of total variations, PC1 accounting for 64.0% of the variance and PC2 for 28.9%. Five groups were distinguished (Figure 3A). One group (**G1**) includes *C. spongiosus* and *C. tomentosum*, the only two macroalgae species in which compound **10** was identified. **G2** contains *G. vermiculophylla*, *S. coronopifolius*, *U. lactuca*, and *Ulva* sp., which presented similar amounts of both compounds **2** and **3**, whereas **G3** comprises the three macroalgae species that clearly stood out for their high levels in these exact phytoprostanes (*S. latissima*, *S. scoparium*, and *S. polyschides*). The low amounts of compounds **2** and **3** in *F. spiralis* and *L. ochroleuca* led to the inclusion of these two species in another group (**G4**), together with *A. armata*, *C. tamariscifolia*, *C. usneoides*, *F. guiryi*, *F. serratus*, *Gigartina* sp., *H. filicina*, *P. canaliculata*, *P. cartilagineum*, and *S. muticum*, in which none of the available phytoprostanes was identified. Finally, *B. bifurcata*, *P. pavonica*, and *S. vulgare* were grouped together (**G5**) due to their similar amounts of compound **8** (Figure 3). The total amount of phytoprostanes is visibly influenced by the levels of both compounds **2** and **3**, confirming that F_{1t}-phytoprostane is the dominant phytoprostane class in the analyzed samples (Figure 3B).

Pearson correlations were calculated to establish a potential relationship between the presence of α-linolenic acid (**1**) in alga material and phytoprostane composition. Our results showed a lack of correlation between the amount of compound **1** and total phytoprostane content ($r = -0.318$). However, the possibility of enzymatic oxidation of compound **1** cannot be ignored. Although this compound is prone to undergo autoxidation reactions, it can also be released from membrane lipids and metabolized by the enzymatic action of lipoxygenases (LOX).[33] In fact, several studies have already reported the presence of diverse structurally unique oxylipins from enzymatic routes in macroalgae.[34−39] Also recently, Barden et al.[40] conducted a clinical trial with healthy volunteers whose diet was supplemented with linseed oil. They detected high levels of phytoprostanes, but they were not able to assess whether phytoprostanes increased due to enhanced concentration of compound **1** or by direct intake from linseed oil.[40]

Altogether, these observations suggest that the large variations observed in phytoprostane composition can be partially explained by intrinsic factors (e.g., physiological variations within algae organs) and/or extrinsic factors (e.g., geographical origin or area of cultivation, seasonal, and environmental variations, time of harvest, water temperature, salinity levels, and processing methods).

At present, the interest in phytoprostanes comprises two general areas: as biomarkers of oxidative stress in plant-derived foodstuffs and as bioactive mediators with potential benefits in

DOI: 10.1021/acs.jafc.5b01904
J. Agric. Food Chem. 2015, 63, 6466−6474

human health. As an example, Collado-González et al.[41] have recently reported that some phytoprostanes could be considered as early candidate biomarkers of water stress in olive tree.[41] Concerning their biological potential, studies have been shown that certain phytoprostane classes were active in various experimental models.[9,22,42,43] However, further studies are required using different natural dietary sources of phytoprostanes to evaluate the real effect of these oxidized lipids on human health.

In this regard, our study represents a first approach in the assessment of different naturally occurring classes of free phytoprostanes in macroalgae. The rational exploitation of photosynthetic marine organisms as valuable sources of prominent oxidized lipids is encouraged for future application as substitutes of chemically synthesized oxylipins and as pharmaceuticals and/or nutraceuticals, providing a complementary treatment for chronic diseases, including neurodegenerative and inflammation-related pathologies.

AUTHOR INFORMATION

Corresponding Author

*(A.G.-I.) Phone: +34 968396363. Fax: +34 968396213. E-mail: angelgil@cebas.csic.es.

Funding

This work received financial support from the European Union (FEDER funds through COMPETE) and National Funds (FCT, Fundação para a Ciência e Tecnologia) through Project UID/QUI/50006/2013. The work also received financial support from Projects AGL2011-23690, AGL2013-45922-C2-1-R, and AGL2013-45922-C2-2-R (CICYT). We are greatly indebted to all financing sources. M.B. and J.C.-G. are indebted to FCT and MINECO (Ministerio de Economia y Competitividad Español) for their grants, SFRH/BD/95861/2013 and BES-2011-048401, respectively.

Notes

The authors declare no competing financial interest.

ABBREVIATIONS USED

BHA, butylated hydroxyanisole; BIS-TRIS, bis(2-hydroxyethyl)-amino-tris(hydroxymethyl)-methane); IMTA, integrated multitrophic aquaculture; MAPK, mitogen-activated protein kinase; MRM, multiple reaction monitoring; PCA, principal component analysis; ROS, reactive oxygen species; SPE, solid-phase extraction; UHPLC-QqQ-MS/MS, ultrahigh-performance liquid chromatography−triple-quadrupole mass spectrometry

REFERENCES

(1) Mueller, M. J. Archetype signals in plants: the phytoprostanes. *Curr. Opin. Plant Biol.* **2004**, *7*, 441−448.

(2) Durand, T.; Bultel-Poncé, V.; Guy, A.; Berger, S.; Mueller, M. J.; Galano, J.-M. New bioactive oxylipins formed by non-enzymatic free-radical-catalyzed pathways: the phytoprostanes. *Lipids* **2009**, *44*, 875−888.

(3) Jahn, U.; Galano, J.-M.; Durand, T. A cautionary note on the correct structure assignment of phytoprostanes and the emergence of a new prostane ring system. *Prostaglandins, Leukotrienes Essent. Fatty Acids* **2010**, *82*, 83−86.

(4) Porta, A.; Chiesa, F.; Quaroni, M.; Persico, M.; Moratti, R.; Zanoni, G.; Vidari, G. A divergent enantioselective synthesis of 9-J_1-phytoprostane and 9-A_1-phytoprostane methyl ester. *Eur. J. Org. Chem.* **2014**, *2014*, 2111−2119.

(5) Loeffler, C.; Berger, S.; Guy, A.; Durand, T.; Bringmann, G.; Dreyer, M.; von Rad, U.; Durner, J.; Mueller, M. B_1-phytoprostanes trigger plant defense and detoxification responses. *Plant Physiol.* **2005**, *137*, 328−340.

(6) Savchenko, T.; Zastrijnaja, O.; Klimov, V. Oxylipins and plant abiotic stress resistance. *Biochemistry (Moscow)* **2014**, *79*, 362−375.

(7) Thoma, I.; Loeffler, C.; Sinha, A.; Gupta, M.; Krischke, M.; Steffan, B.; Roitsch, T.; Mueller, M. Cyclopentenone isoprostanes induced by reactive oxygen species trigger defense gene activation and phytoalexin accumulation in plants. *Plant J.* **2003**, *34*, 363−375.

(8) Traidl-Hoffmann, C.; Mariani, V.; Hochrein, H.; Karg, K.; Wagner, H.; Ring, J.; Mueller, M. J.; Jakob, T.; Behrendt, H. Pollen-associated phytoprostanes inhibit dendritic cell interleukin-l2 production and augment T helper type 2 cell polarization. *J. Exp. Med.* **2005**, *201*, 627−636.

(9) Karg, K.; Dirsch, V.; Vollmar, A. M.; Cracowski, J.-L.; Laporte, F.; Mueller, M. J. Biologically active oxidized lipids (phytoprostanes) in the plant diet and parenteral lipid nutrition. *Free Radical Res.* **2007**, *41*, 25−37.

(10) Ritter, A.; Dittami, S. M.; Goulitquer, S.; Correa, J. A.; Boyen, C.; Potin, P.; Tonon, T. Transcriptomic and metabolomic analysis of copper stress acclimation in *Ectocarpus siliculosus* highlights signaling and tolerance mechanisms in brown algae. *BMC Plant Biol.* **2014**, *14*, 1−17.

(11) John, R. P.; Anisha, G. S.; Nampoothiri, K. M.; Pandey, A. Micro and macroalgal biomass: a renewable source for bioethanol. *Bioresour. Technol.* **2011**, *102*, 186−193.

(12) Leal, M. C.; Munro, M. H.; Blunt, J. W.; Puga, J.; Jesus, B.; Calado, R.; Rosa, R.; Madeira, C. Biogeography and biodiscovery hotspots of macroalgal marine natural products. *Nat. Prod. Rep.* **2013**, *30*, 1380−1390.

(13) Smit, A. J. Medicinal and pharmaceutical uses of seaweed natural products: a review. *J. Appl. Phycol.* **2004**, *16*, 245−262.

(14) Kadam, S. U.; Tiwari, B. K.; O'Donnell, C. P. Application of novel extraction technologies for bioactives from marine algae. *J. Agric. Food Chem.* **2013**, *61*, 4667−4675.

(15) Lordan, S.; Ross, R. P.; Stanton, C. Marine bioactives as functional food ingredients: potential to reduce the incidence of chronic diseases. *Mar. Drugs* **2011**, *9*, 1056−1100.

(16) Andrade, P. B.; Barbosa, M.; Matos, R. P.; Lopes, G.; Vinholes, J.; Mouga, T.; Valentão, P. Valuable compounds in macroalgae extracts. *Food Chem.* **2013**, *138*, 1819−1828.

(17) Kumari, P.; Bijo, A.; Mantri, V. A.; Reddy, C.; Jha, B. Fatty acid profiling of tropical marine macroalgae: an analysis from chemotaxonomic and nutritional perspectives. *Phytochemistry* **2013**, *86*, 44−56.

(18) Pereira, H.; Barreira, L.; Figueiredo, F.; Custódio, L.; Vizetto-Duarte, C.; Polo, C.; Rešek, E.; Engelen, A.; Varela, J. Polyunsaturated fatty acids of marine macroalgae: potential for nutritional and pharmaceutical applications. *Mar. Drugs* **2012**, *10*, 1920−1935.

(19) Schmid, M.; Guihéneuf, F.; Stengel, D. B. Fatty acid contents and profiles of 16 macroalgae collected from the Irish Coast at two seasons. *J. Appl. Phycol.* **2014**, *26*, 451−463.

(20) van Ginneken, V. J.; Helsper, J.; de Visser, W.; van Keulen, H.; Brandenburg, W. A. Polyunsaturated fatty acids in various macroalgal species from north Atlantic and tropical seas. *Lipids Health Dis.* **2011**, *10*, 104.

(21) Sudatti, D. B.; Fujii, M. T.; Rodrigues, S. V.; Turra, A.; Pereira, R. C. Effects of abiotic factors on growth and chemical defenses in cultivated clones of *Laurencia dendroidea* J. Agardh (Ceramiales, Rhodophyta). *Mar. Biol. (Heidelberg, Ger.)* **2011**, *158*, 1439−1446.

(22) Minghetti, L.; Salvi, R.; Lavinia Salvatori, M.; Ajmone-Cat, M. A.; De Nuccio, C.; Visentin, S.; Bultel-Poncé, V.; Oger, C.; Guy, A.; Galano, J.-M.; Greco, A.; Bernardo, A.; Durand, T. Nonenzymatic oxygenated metabolites of α-linolenic acid B1- and L1-phytoprostanes protect immature neurons from oxidant injury and promote differentiation of oligodendrocyte progenitors through PPAR-γ activation. *Free Radical Biol. Med.* **2014**, *73*, 41−50.

DOI: 10.1021/acs.jafc.5b01904
J. Agric. Food Chem. 2015, 63, 6466−6474

(23) Lafay, S.; Gil-Izquierdo, A.; Manach, C.; Morand, C.; Besson, C.; Scalbert, A. Chlorogenic acid is absorbed in its intact form in the stomach of rats. *J. Nutr.* **2006**, *136*, 1192−1197.
(24) Collado-González, J.; Medina, S.; Durand, T.; Guy, A.; Galano, J.-M.; Torrecillas, A.; Ferreres, F.; Gil-Izquierdo, A. New UHPLC-QqQ-MS/MS method for quantitative and qualitative determination of free phytoprostanes in foodstuffs of commercial olive and sunflower oils. *Food Chem.* **2015**, *178*, 212−220.
(25) El Fangour, S.; Guy, A.; Vidal, J.-P.; Rossi, J.-C.; Durand, T. Total synthesis of phytoprostane F_1 and its 16 epimer. *Tetrahedron Lett.* **2003**, *44*, 2105−2108.
(26) El Fangour, S.; Guy, A.; Despres, V.; Vidal, J.-P.; Rossi, J.-C.; Durand, T. Total syntheses of the eight diastereoisomers of the syn-anti-syn phytoprostanes F_1 types I and II. *J. Org. Chem.* **2004**, *69*, 2498−2503.
(27) Pinot, E.; Guy, A.; Fournial, A.; Balas, L.; Rossi, J.-C.; Durand, T. Total synthesis of the four enantiomerically pure diasteroisomers of the phytoprostanes E_1 type II and of the 15-E_{2t}-isoprostanes. *J. Org. Chem.* **2008**, *73*, 3063−3069.
(28) Ribeiro, B.; de Pinho, P. G.; Andrade, P. B.; Baptista, P.; Valentão, P. Fatty acid composition of wild edible mushrooms species: a comparative study. *Microchem. J.* **2009**, *93*, 29−35.
(29) Thoma, I.; Krischke, M.; Loeffler, C.; Mueller, M. The isoprostanoid pathway in plants. *Chem. Phys. Lipids* **2004**, *128*, 135−148.
(30) Imbusch, R.; Mueller, M. J. Formation of isoprostane F(2)-like compounds (phytoprostanes F(1)) from alpha-linolenic acid in plants. *Free Radical Biol. Med.* **2000**, *28*, 720−726.
(31) Imbusch, R.; Mueller, M. J. Analysis of oxidative stress and wound-inducible dinor isoprostanes F1 (phytoprostanes F1) in plants. *Plant Physiol.* **2000**, *124*, 1293−1303.
(32) Sattler, S. E.; Mène-Saffrané, L.; Farmer, E. E.; Krischke, M.; Mueller, M. J.; DellaPenna, D. Nonenzymatic lipid peroxidation reprograms gene expression and activates defense markers in *Arabidopsis* tocopherol-deficient mutants. *Plant Cell* **2006**, *18*, 3706−3720.
(33) Kumari, P.; Reddy, R.; Jha, B. Quantification of selected endogenous hydroxy-oxylipins from tropical marine macroalgae. *Mar. Biotechnol.* **2014**, *16*, 74−87.
(34) Gerwick, W. H.; Proteau, P. J.; Nagle, D. G.; Wise, M. L.; Jiang, Z. D.; Bernart, M. W.; Hamberg, M. Biologically active oxylipins from seaweeds. *Hydrobiologia* **1993**, *260*, 653−665.
(35) Proteau, P. J.; Gerwick, W. H. Divinyl ethers and hydroxy fatty acids from three species of *Laminaria* (brown algae). *Lipids* **1993**, *28*, 783−787.
(36) Todd, J. S.; Proteau, P. J.; Gerwick, W. H. The absolute configuration of ecklonialactones A, B, and E, novel oxylipins from brown algae of the genera *Ecklonia* and *Egregia*. *J. Nat. Prod.* **1994**, *57*, 171−174.
(37) Jiang, Z.-D.; Gerwick, W. H. Novel oxylipins from the temperate red alga *Polyneura latissima*: evidence for an arachidonate 9(*S*)-lipoxygenase. *Lipids* **1997**, *32*, 231−235.
(38) Kousaka, K.; Ogi, N.; Akazawa, Y.; Fujieda, M.; Yamamoto, Y.; Takada, Y.; Kimura, J. Novel oxylipin metabolites from the brown alga *Eisenia bicyclis*. *J. Nat. Prod.* **2003**, *66*, 1318−1323.
(39) Choi, H.; Proteau, P. J.; Byrum, T.; Gerwick, W. H. Cymatherelactone and cymatherols A− C, polycyclic oxylipins from the marine brown alga *Cymathere triplicata*. *Phytochemistry* **2012**, *73*, 134−141.
(40) Barden, A. E.; Croft, K. D.; Durand, T.; Guy, A.; Mueller, M. J.; Mori, T. A. Flaxseed oil supplementation increases plasma F_1-phytoprostanes in healthy men. *J. Nutr.* **2009**, *139*, 1890−1895.
(41) Collado-González, J.; Pérez-López, D.; Memmi, H.; Gijón, M. C.; Medina, S.; Durand, T.; Guy, A.; Galano, J.-M.; Ferreres, F.; Torrecillas, A.; Gil-Izquierdo, A. Water deficit during pit hardening enhances phytoprostanes content, a plant biomarker of oxidative stress, in extra virgin olive oil. *J. Agric. Food Chem.* **2015**, *63*, 3784−3792.
(42) Gutermuth, J.; Bewersdorff, M.; Traidl-Hoffmann, C.; Ring, J.; Mueller, M. J.; Behrendt, H.; Jakob, T. Immunomodulatory effects of aqueous birch pollen extracts and phytoprostanes on primary immune responses *in vivo*. *J. Allergy Clin. Immunol.* **2007**, *120*, 293−299.
(43) Barden, A.; Mas, E.; Henry, P.; Durand, T.; Galano, J.-M.; Roberts, L. J.; Croft, K. D.; Mori, T. A. The effects of oxidation products of arachidonic acid and n3 fatty acids on vascular and platelet function. *Free Radical Res.* **2011**, *45*, 469−476.

DOI: 10.1021/acs.jafc.5b01904
J. Agric. Food Chem. 2015, 63, 6466−6474

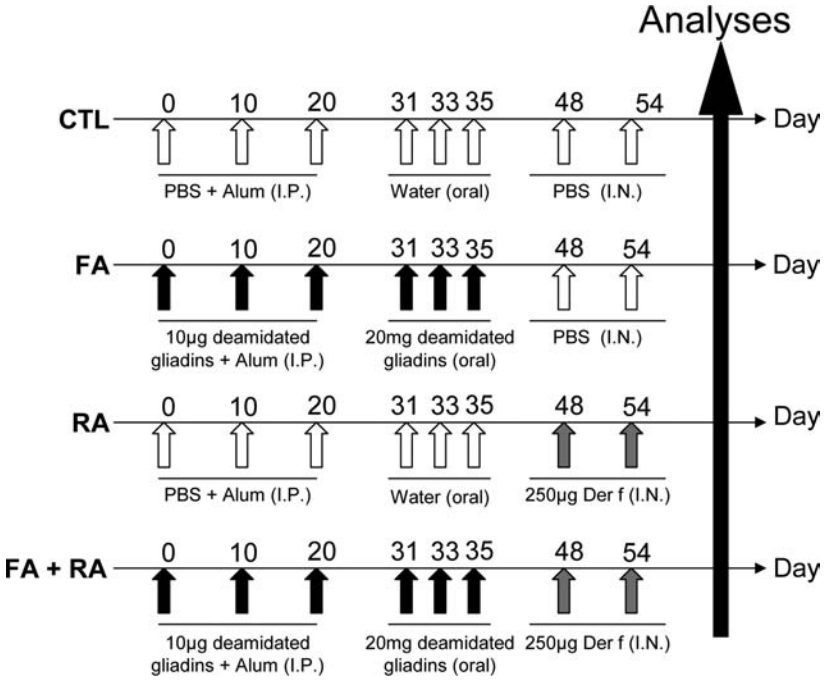

Figure 1. Study design. Mice were distributed into four groups: control (CTL), food allergy (FA), respiratory allergy (RA), and food and respiratory allergy (FA+RA).

MATERIALS AND METHODS

Animals. Balb/c mice (Charles River, France) were fed with an irradiated semisynthetic diet devoid of plant proteins (Safe, Augy, France). The Ethics Committee in Animal Experimentation of Pays de la Loire approved the protocol. (CEEA.2011.52; accreditation no. 4478), and all efforts were made to minimize suffering. All mice were maintained under specific pathogen-free conditions at the institutional animal facility. All animal procedures were conducted on mice between 8 and 12 weeks of age, in accordance with appropriate animal care. At the designated times, the animals were sacrificed according to institutional guidelines, and blood and tissues were collected for analyses.

Allergy Models. Freeze-dried deamidated gliadins were solubilized in 70% ethanol at 5 mg/mL and then diluted to 0.1 mg/mL in sterile PBS. Mice were intraperitoneally sensitized with 10 μg of deamidated gliadins absorbed on aluminum hydroxide (Sigma-Aldrich, Saint Quentin Fallavier, France) on days 0, 10, and 20. Challenge was performed by intragastric administration of 20 mg of deamidated gliadins on days 31, 33, and 35. For this mouse model of atopic march, a delay of 2 weeks was set between the last oral challenge and the first intranasal sensitization. Respiratory allergy was induced by intranasal exposure to 40 μL, containing 250 μg of HDM extract (*Dermatophagoides farinae*, Stallergenes, Antony, France) and approximately 1200 UE/ml of endotoxin, as measured by LAL test (Thermo, Waltham, MA, USA) on mice anesthetized with a 200 μL of mixture of ketamine (80 mg/kg)/xylazine (10 mg/kg) intraperitoneally injected on days 48 and 54. Mice were sacrificed 1 day after the last HDM extract challenge on day 55. As described (Figure 1), mice were then exposed to different protocols: food allergen alone (wheat, FA), respiratory allergen alone (HDM extract, RA), and successive exposure to allergens (wheat and HDM extract, FA+RA). Unexposed mice were used as controls (CTL).

Immunoglobulin Assays. Blood was removed on day 55 by cardiac puncture and centrifuged to collect serum. Sera were stored at −20 °C before immunoglobulin assays. Mouse IgE specific to deamidated gliadins was assayed by indirect F-ELISA as described by Gourbeyre et al.[21] Plates were coated with 5 μg/mL deamidated gliadins in carbonate buffer (30 mM Na_2CO_3 and 70 mM $NaHCO_3$, pH 9.6). Serum samples were diluted 1:50 in PBS with 0.1% Tween-20 and 0.5% gelatin. A detection rat antibody directed against mouse IgE (diluted 1/250 in PBS with 0.1% Tween-20 and 0.5% gelatin) and conjugated to alkaline phosphatase (Southern Biotechnology Associates Birmingham, AL, USA) was used. Fluorescence intensity was measured (at 440 nm after excitation at 360 nm) after incubation with an alkaline phosphatase substrate (4-methylumbeliferin, Sigma-Aldrich). Specific anti-Der f 1 IgE was assessed by indirect ELISA. Briefly, 96-well plates (Nunc) were coated with 100 μL of a solution of 50 μM sodium bicarbonate and 0.25 μg of purified Der f 1 (Indoor Biotechnologies, Cardiff, UK) in each well and left overnight at 4 °C. Then, wells were incubated with bovine serum albumin 1% in PBS for 12 h at 4 °C. Sera were diluted in Can Get Signal immunoreaction enhancer solution 1 (CGS1, Cosmo Bio, Tokyo, Japan), and 100 μL of this solution was incubated overnight at 4 °C. Specific immunoglobulins were detected after incubation at room temperature with an anti-mouse IgE (AbD serotec, Oxford, UK) antibody coupled to horseradish peroxidase and diluted in CGS 2 (Cosmo Bio). Substrate, 2,2′-azinobis[3-ethylbenzothiazoline-6-sulfonic acid] diammonium salt (ABTS, Roche, Basel, Switzerland), was added, and optical density was measured by spectrophotometry (PerkinElmer, Waltham, MA, USA).

Histamine Assay. Blood samples were collected on day 55, and histamine was measured by ELISA (Labor Diagnostika Nord, Nordhom, Germany), according to the manufacturer's recommendations.

Cell Proliferation. Organs were crushed using a tissue grinder (Wheaton, Rochdale, UK) after removal to obtain single-cell suspensions, and after red blood cell lysis, cells were suspended in supplemented RPMI. Cells from Peyer patches were transferred to HBSS/Hepes 1.5%. Fragments were incubated 1 h at 37 °C in HBSS/Hepes 1.5%/FBS 2%/Dispase/DNase (Sigma-Aldrich) solution. Cells were plated at 10^6 cells/well for 96 h at 37 °C in the presence of concanavalin A (1 μg/mL) (Sigma-Aldrich), and proliferation was measured by MTT assay.[21]

Flow Cytometry. Anti-mouse antibodies used were the following: CD3-APC, CD19 PE-Cy7, Ly6G-PerCP-Cy5.5, CD8 APC-H7, and CCR3-PE (BD Biosciences). Dead cells were excluded using DAPI. Stained cells resuspended in PBS-FCS 1% were acquired on a BD LSR II (BD Biosciences) and analyzed on BD FACSDiva software (BD Biosciences). The following cells were stained in the presence of Fc blocker (BD Biosciences): eosinophils (gated on SSC^{high}, $Ly6G^{int}$, and

DOI: 10.1021/acs.jafc.5b02338
J. Agric. Food Chem. 2015, 63, 6475−6483

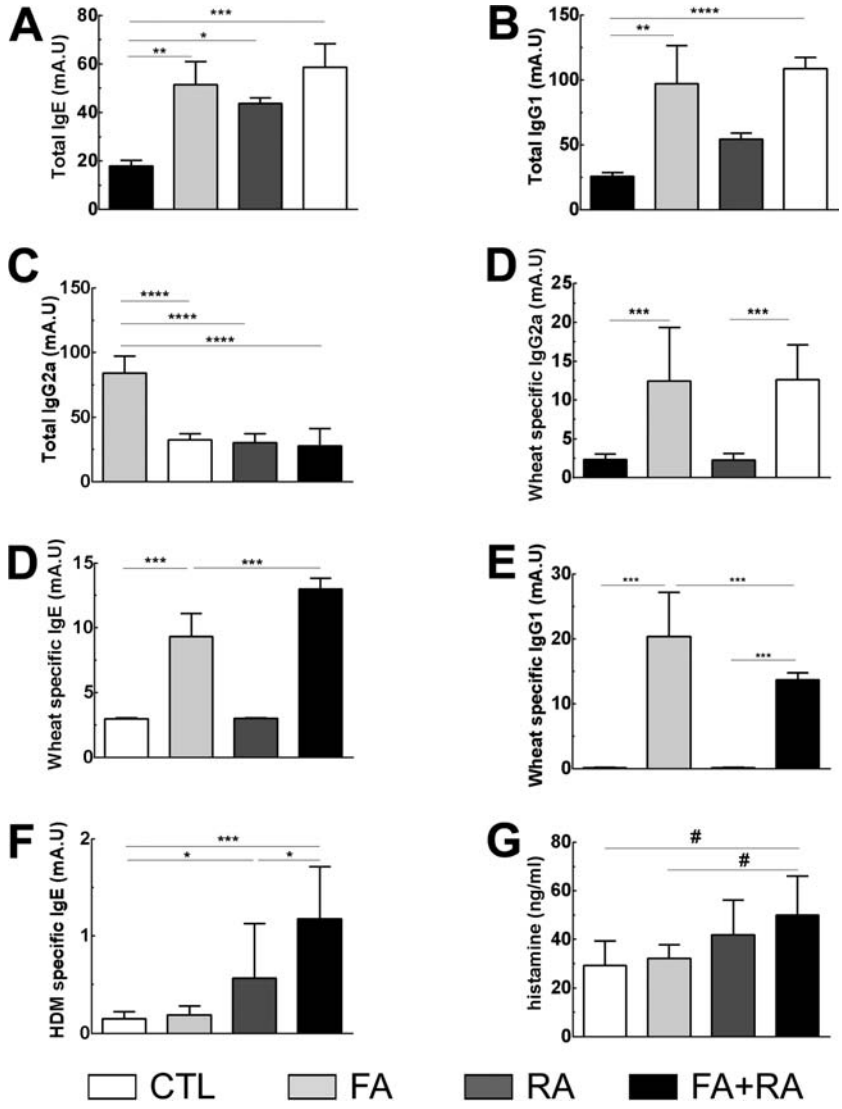

Figure 2. Ig and histamine levels are increased in food and respiratory allergy. Total and wheat-specific IgE (A, D), IgG1 (B, E), IgG2a (C, D), HDM-specific IgE (F), and histamine (G) were measured at day 54 in serum of mice after the last sensitization to HDM (n = 8 animals per group). Bonferroni multiple-comparison test: (*) $p < 0.05$, (**) $p < 0.01$, and (***) $p < 0.005$. Dunn's comparison test: (#) $p < 0.05$, (##) $p < 0.01$, and (###) $p < 0.005$.

CCR3$^+$), neutrophils (gated on SSC^{high} and Ly6G^{high}), and lymphocytes (gated on CD3$^+$).

Cytokine Measurements. In lymphoid organs and Peyer patches, cell culture supernatants IL-4 and IFN-γ were assayed using ELISA kits cytoset (Invitrogen, Paisley, UK), and IL-10, IL-17A, and TGF-β were assayed using ELISA Ready-Set-Go! Kits (eBioscience, Paris, France) according to the manufacturer's recommendations. Broncho-alveolar lavages (BAL) were performed by intratracheally administering 1 mL of PBS and gentle aspiration to collect the epithelial lining fluid. IL-4, IL-10, IFN-γ, and IL-17 were quantified by Luminex technology (BioPlex 200 system, Bio-Rad, Hercules, CA, USA) according to the manufacturer's instructions (Bio-Rad).

Histopathological Analysis. The jejunum and proximal colon were collected, formalin fixed, and paraffin embedded. Sections (5 μm thick) were stained with hematoxylin and eosin and inspected for the presence of mucosal inflammation. Histological analysis images were taken with an Axio Imager M1 microscope and an Axiocam HRc (Zeiss). Sections were analyzed using ImageScope for image acquisition (Aperio Technologies, Inc.), and a cell type count for goblet cells and leukocytes was performed on 10 villus/mouse. Grading of intestinal inflammation was determined in a blinded fashion, as previously described.[22] Briefly, sections of mouse jejunum were individually scored on the basis of three parameters. Inflammation was scored as follows: 0, rare inflammatory cells in the lamina propria; 1, increased numbers of cells in the lamina propria; 2, confluence of inflammatory cells extending into the submucosa; and 3, transmural extension of the inflammatory infiltrate. Crypt damage was scored as follows: 0, intact crypts; 1, loss of the basal one-third; 2, loss of the basal two-thirds; 3, entire crypt loss; 4, change of epithelial surface with erosion; and 5, confluent erosion. Ulceration was scored as follows: 0, absence of ulcer; 1, one or two foci of ulcerations; and 2, confluent or extensive ulceration. The total histological score represents the sum of all features evaluated and thus ranges from 0 to 10.

Evaluation of Gastrointestinal Functions. To assess permeability, the jejunum and proximal colon were removed and washed in cold Krebs solution, and segments were mounted in Ussing chambers (Physiological Instruments, San Diego, CA, USA). Paracellular and transcellular permeability were assayed by simultaneously measuring the flux of fluorescein−5.6 sulfonic acid (400 Da; 1 mg/mL, Invitrogen) and horseradish peroxidase (HRP) (44 kDa; 375 μg/mL; Sigma, Saint Quentin Fallavier, France), respectively, over 3 h.

Airway Hyper-reactivity (AHR) Measurement. Enhanced pause (Penh) was measured by whole body plethysmography (Emka

DOI: 10.1021/acs.jafc.5b02338
J. Agric. Food Chem. 2015, 63, 6475−6483

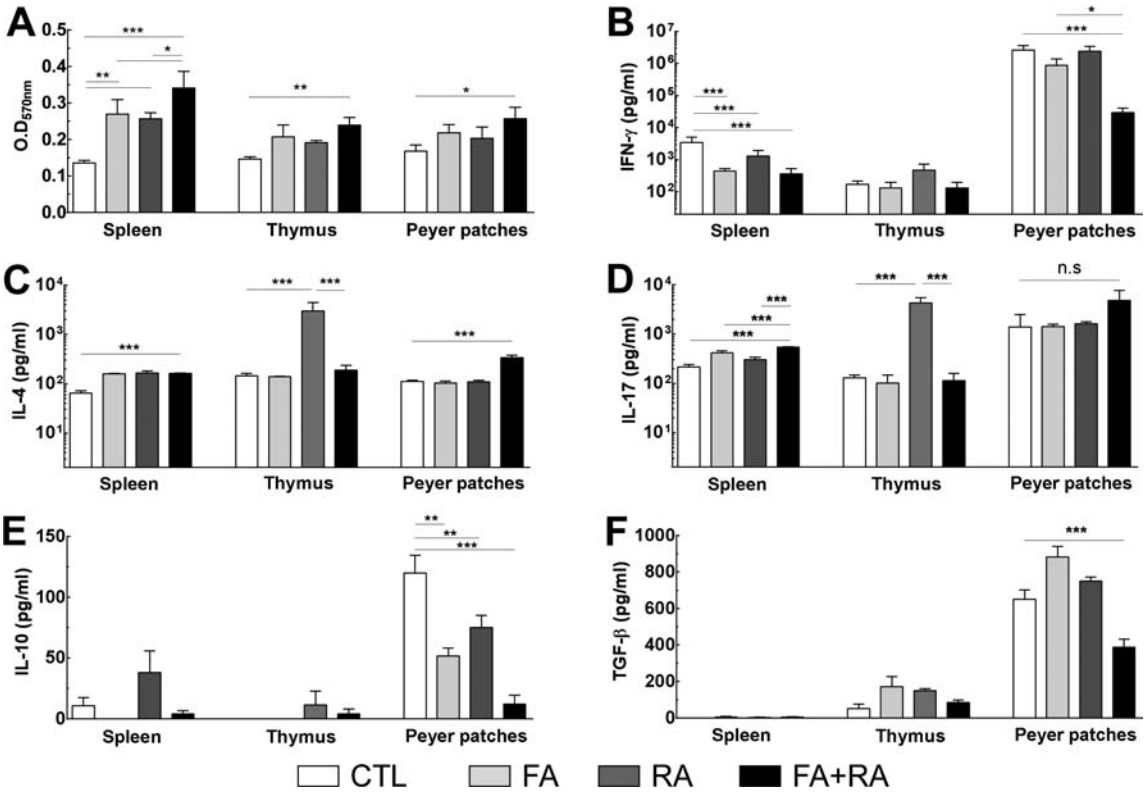

Figure 3. Allergens synergize to increase cell proliferation and cytokine secretion in lymphoid organs. Proliferation from spleen, thymus, and Peyer patch cells in response to ConA was measured (A) in control (white bar), food allergic (light gray bar), respiratory allergic (dark gray bar), and combined allergic (black bar) mice. IFN-γ (B), IL-4 (C), IL-17 (D), IL-10 (E), and TGF-β (F) from those cells were also measured by ELISA. The data represent the mean ± SEM (n = 8 animals per group). Bonferroni multiple comparison test: (*) $p < 0.05$, (**) $p < 0.01$, and (***) $p < 0.005$. Dunn's comparison test: (#) $p < 0.05$, (##) $p < 0.01$, and (###) $p < 0.005$.

Technologies, Paris, France) in response to nebulization of methacholine (Sigma-Aldrich) from 0 to 40 mg/mL, as described.[23] Because we previously ascertained in our mouse model using female Balb/c mice that Penh was similar to resistance or other measures determined by FLEXIVENT, intubation (not shown) and whole body plethysmography were determined to be sufficient to explore respiratory function.

Statistics. Values were expressed as the mean ± standard error (SEM). Statistical analysis was performed using GraphPad Prism (GraphPad Software, San Diego, CA, USA). Means were compared among groups using analysis of variance (ANOVA). In the case of positive ANOVA, means were compared by Mann−Whitney test. The results were corrected by a Bonferroni multiple-comparisons correction test. Statistically significant was marked as follow: (*) $p < 0.05$, (**)$p < 0.01$, and (***) $p < 0.001$. For data not following a normal distribution, a nonparametric Kruskal−Wallis test corrected using Dunn's test. Statistically significant was marked as follows: (#) $p < 0.05$, (##)$p < 0.01$, and (###) $p < 0.001$.

RESULTS

Peripheral Effects of Wheat and HDM Sensitization. After the induction of a wheat-induced food allergy and/or the HDM-induced asthma-like reaction protocol (Figure 1), total and specific Ig and histamine levels were assessed in control (CTL), food allergy (FA), respiratory allergy (RA), and combined allergy (FA+RA) mice. Total IgE was increased in allergic mice groups compared to CTL but remained unchanged when compared to the FA, RA, and FA+RA groups (Figure 2A). The level of total IgG1 was also increased in all groups of allergic mice compared to CTL but with no statistically significant difference between the single and double allergies (Figure 2B). Conversely, total IgG2a was decreased in the serum of all groups of allergic mice compared to CTL (Figure 2C). Wheat-specific IgG2a, IgE, and IgG1 were increased in the serum of FA mice (Figure 2D−F) compared to CTL mice. Conversely, they were at the threshold of detection in CTL and RA animals. In mice sensitized to both allergens, wheat-specific IgE and IgG1 levels were significantly increased compared to CTL or RA as well as the FA mice. Symmetrically, HDM-specific IgE was increased in the serum of RA mice (Figure 2F). In animals sensitized to both allergens, HDM-specific IgE levels were twice as high in mice sensitized to HDM only. FA+RA and RA sera but not FA displayed higher levels of histamine than CTL (Figure 2G). Specific IgE was therefore increased for each allergen by the sensitization to its counterpart, whereas histamine release increased only in mice sensitized to HDM, whether or not they were presensitized to wheat.

Cell Proliferation and Cytokine Secretion in Lymphoid Organs. Splenocyte proliferation in response to concanavalin A was evaluated by MTT in the spleen, thymus, and Peyer patches (Figure 3A). In FA+RA mice, immune cells from the spleen, thymus, or Peyer patches displayed increased proliferation by 2.52-, 1.63-, and 1.54-fold, respectively, compared to CTL mice. In FA and RA groups, increases of splenocyte proliferation of 2- and 1.9-fold, respectively, were also found. The proliferation was significantly higher in FA+RA mice compared to both single-sensitization groups only in the spleen.

To further detail the mechanisms linking both types of allergy, cytokine secretion by immune cells was measured in supernatants of spleen, thymus, and Peyer patches cells. After

DOI: 10.1021/acs.jafc.5b02338
J. Agric. Food Chem. 2015, 63, 6475−6483

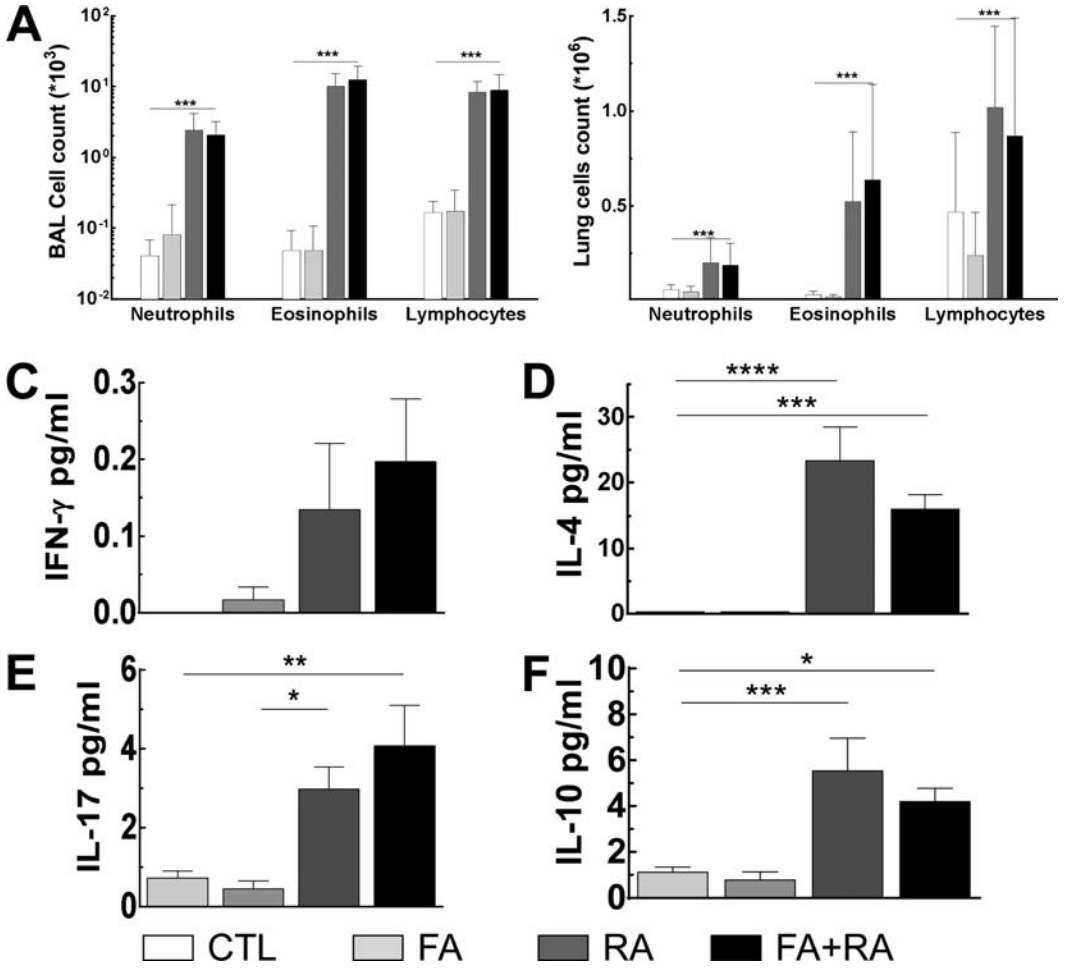

Figure 4. Successive allergies increase neither cell population nor cytokine secretion in the respiratory tract. Different cell populations from each group of mice were analyzed by flow cytometry in the broncho-alveolar lavage (BAL) (A, left panel) and lungs (A, right panel). Cell populations were polymorphonuclear neutrophil cells (neutrophils), polymorphonuclear eosinophil cells (eosinophils), and T lymphocytes (lymphocytes). IFN-γ (C), IL-4 (D), IL-17 (E), and IL-10 (F) were measured in parallel in BAL fluids after the last HDM intranasal challenge (day 54). The data represent the mean ± SEM (n = 8 animals per group). Bonferroni multiple-comparison test: (*) $p < 0.05$, (**$p < 0.01$, and (***) $p < 0.005$.

nonspecific activation by concanavalin A, IFN-γ secretion was reduced in spleen and Peyer patches cell supernatants from FA+RA mice compared to CTL mice. In single-allergy groups, this difference was observed in the spleen only. IFN-γ reduction was not observed in the thymus (Figure 3B). Then, Th2 polarization was evaluated by IL-4 production, which was found to be elevated in FA+RA compared to CTL in the spleen and Peyer patches (Figure 3C). In these compartments, no additive effects were observed, as IL-4 levels remained unchanged between RA or FA and FA+RA in the spleen, even though IL-4 levels were increased compared to controls. In Peyer patches, an effect was observed, as IL-4 levels were higher in FA+RA mice compared to other groups. In the thymus of RA mice, a clear increase in IL-4 secretion was observed (Figure 3C). To obtain a broader view of T-helper polarization, IL-17 production was also measured and shown to be significantly enhanced in the spleen but not in Peyer patches or in the thymus of FA+RA mice compared to CTL, FA, or RA mice (Figure 3D). In the thymus, only cells exposed to respiratory allergens produced elevated levels of IL-17 compared to controls. As a read-out of Treg cell activation, IL-10 and TGF-β levels were measured in the spleen, Peyer patches, and thymus cell supernatants. Low levels of TGF-β and IL-10 were detected in splenocyte and thymocyte supernatants from all groups, whereas in Peyer patches, as high levels of both cytokines were detected in CTL, a drastic reduction was observed in FA+RA mice, suggesting a defect in intestinal T-cell regulation (Figure 3E,F). Furthermore, IL-10 but not TGF-β cell secretion was also attenuated in the Peyer patches of FA or RA mice compared to controls but to a lesser extent than FA+RA.

Our data therefore revealed that in this mouse model of atopic march, the Th1/Th2-related cytokines leaned toward a Th2 response after unspecific activation. Then, inflammation was boosted by the development of Th17 and down-modulation of Treg differentiation and/or activation in lymphoid organs. However, we observed no major change in the thymus except in RA mice.

Cell Population and Cytokine Secretion in the Respiratory Tract. Because our results demonstrated an effect of a food allergy on lymphoid cell proliferation and cytokine secretion, we assayed cell populations and cytokine secretion in the respiratory tract of the mice, including broncho-alveolar lavage (BAL) fluid and lungs (Figure 4). Additionally, we measured cell numbers of different subsets in the BAL and the lungs from each group by flow cytometry. Total cell numbers, polymorphonuclear neutrophils, polymorphonuclear eosinophils, and T lymphocytes (either $CD8^+$ or

DOI: 10.1021/acs.jafc.5b02338
J. Agric. Food Chem. 2015, 63, 6475−6483

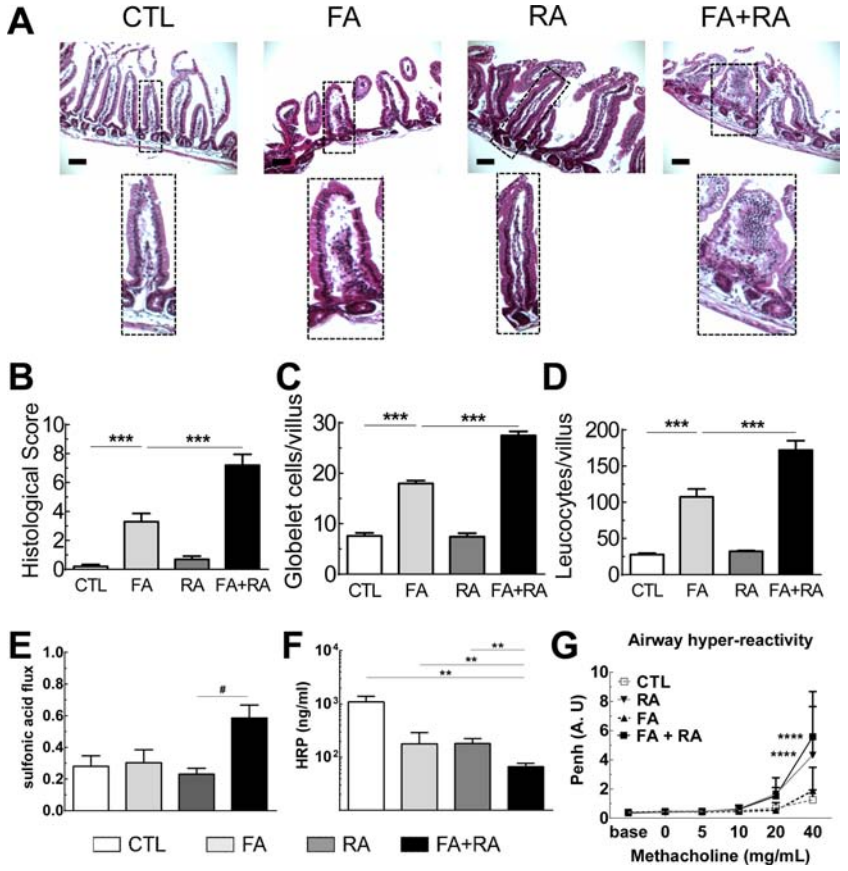

Figure 5. Successive exposure to allergens alters intestinal morphology and exacerbates symptoms without affecting respiratory parameters. At the end of the allergy-inducing protocol, gut segments were collected and processed for histopathology in jejunum (A), scored for inflammation (B), and counted for goblet cells (C) and leukocytes (D). As a critical feature of the gastrointestinal epithelium and function ex vivo paracellular permeability in proximal colon (E) and ex vivo transcellular permeability in jejunum (F) were evaluated in Ussing's chamber using intestine fragments. Respiratory function was determined by airway resistance measurements after methacholine nebulization (G). $n = 8$ animals per group. Bonferroni multiple-comparison test: (*) $p < 0.05$, (**) $p < 0.01$, and (***) $p < 0.005$. Dunn's comparison test: (#) $p < 0.05$, (##) $p < 0.01$, and (###) $p < 0.005$. Scale bar = 250 μm.

$CD4^+$) were increased in mice with respiratory or mixed allergy compared to FA or CTL in both the BAL and lungs (Figure 4A, left and right panels, respectively). However, the inflammatory cell counts were equivalent in mice with the mixed or the single-respiratory allergy. Cytokine secretion was also assayed in BAL fluids. As expected, lower levels of cytokines were observed in the BAL compared to cell culture after nonspecific activation. The levels of all cytokines were increased in both groups of HDM-induced asthma-like reaction mice compared to the two other groups (Figure 3C−F). However, no further increase was observed in FA+RA mice. Similar results were observed in the lungs (data not shown). Taken together, our results establish that double allergy impacts the systemic and intestinal but not lung immune response.

Effects of Wheat and HDM Sensitization on Intestinal and Respiratory Functions. Having shown the influence of a double exposure to allergens on immune cell homeostasis and cytokine production, we aimed to explore the morphologic and phenotypic impact linking observations on cell and cytokine levels to the development of allergic symptoms. Therefore, we first determined whether combined allergy was associated with intestinal histological alterations by evaluating the development of inflammation in the jejunum of mice. FA+RA mice developed intestinal inflammation characterized by epithelial ulceration, edema, and leukocyte infiltration in the lamina propria (Figure 5A). These lesions were, to a lesser extent, also present in FA mice. In contrast, in control or RA mice, no mucosal inflammation or edema was observed in the jejunum or proximal colon (Figure 5A and data not shown). Using histological inflammation semiquantitative scoring, we showed an absence of intestinal alterations in CTL and RA mice. In contrast, the inflammatory score was significantly larger in RA mice compared to CTL and even larger in FA+RA compared to FA mice (7.2 versus 3.3, respectively, $P < 0.05$). (Figure 5B). This inflammation is linked to an increase of goblet cells and leukocytes within the villus of the intestine in FA mice compared to CTL mice (Figure 5C,D). Moreover, in line with the histological score, the number of cells was increased in FA +RA mice compared to single-FA mice (Figure 5C,D).

Then, we measured jejunal and proximal colon paracellular and transcellular permeability ex vivo. Paracellular permeability was increased in the proximal colon of FA+RA mice compared to the other groups (Figure 5E). In contrast, HRP flux in the jejunum was significantly reduced in FA+RA compared to the other groups (70.3 versus 1078 and 179 ng/mL for FA+RA, CTL, and FA, respectively) (Figure 5F). No change in HRP flux was observed in the proximal colon (data not shown).

The effect of each allergy protocol on lung function was also evaluated by measuring mouse airway reactivity in response to methacholine. As expected, a gain in methacholine sensitivity

DOI: 10.1021/acs.jafc.5b02338
J. Agric. Food Chem. 2015, 63, 6475−6483

was noted in the RA and FA+RA groups compared to the CTL and FA groups (Figure 5G). However, airway hyperresponsiveness was not higher in RA allergic mice in cases of pre-existing food sensitization.

DISCUSSION

In this study, we aimed to establish that food sensitization primes the immune system to enhance the effects of a subsequent respiratory allergy. Contrasting results were obtained, with a clear effect observed on the systemic and gut hallmarks of allergy but without modification of respiratory inflammation and function.

Dual exposure to food and respiratory allergens exerted effects that can be considered at various levels: (1) the systemic compartment composed of blood, thymus, and spleen; (2) the intestinal mucosa; and (3) the lung mucosa. Exposure to FA and RA led to a higher production of specific IgE directed against each allergen that may cause blood basophils to degranulate and release higher levels of histamine, as observed. The marked secretion of IgE specific to each allergen might be enhanced by a dysregulation of the T-cell population balance, as suggested by the higher levels of IL-4 observed in spleen, whereas IFN-γ levels were moderated in FA+RA mice compared with mice allergic to a single substance. IL-17 was also elevated, suggesting that Th17 could act in synergy with Th2 cells to exacerbate the immune response. Interestingly, a role for Th17 cells in food allergy and asthma has been suggested.[4,5] In contrast, thymocyte cytokine production was much more related to respiratory allergy. In fact, cytokine secretion in the thymus was increased in respiratory allergic mice but not in food allergic mice. Because thymocyte analysis was carried out shortly after the intranasal challenge and at a distance from the gut sensitization, it cannot be excluded that the thymocytes lost their food allergy-related reactivity at the time of analysis. However, in combined allergic mice, the effect of respiratory allergy on thymocytes was no longer observed. Although a negative feedback of food allergy on thymocyte reactivity can be evoked as a potential explanation, it is more likely that the thymocytes may have become unreactive after the first food allergen stimulation.[24,25]

At the level of intestinal Peyer patches, a clear Th2 inflammatory profile was demonstrated in FA+RA mice, with higher IL-4 and lower IFN-γ, IL-10, and TGF-β production. IL-10 secretion by Peyer patch cells was already dampened in mice exposed to a single allergen. It is noteworthy that intranasal exposure to RA induced a decrease in the secretion of IL-10 in the small intestine. Thus, the intestinal mucosal immune system of allergic mice may be more vulnerable to novel allergenic sensitizations by locally dampening tolerance-related cytokines (IL-10 and TGF-β) and increasing Th2 commitment (IL-4). Numerous studies have addressed the role of gut-associated lymphoid tissues (GALT) for oral tolerance induction.[26−29] Notably, Peyer patch dendritic cells (DCs) were shown to produce much more IL-10 than spleen DCs.[26] In addition, gut DCs efficiently promote the differentiation of naïve Th0 cells into inducible Treg cells.[30] Furthermore, GALT were demonstrated to be a preferential site for the induction of the forkhead box P3$^+$ Treg.[26] In healthy animals, CD4$^+$ T cells activated by Peyer patch DCs produce much more IL-4 and IL-10 than CD4$^+$ T cells activated by spleen DCs and promote the differentiation of Th2 cells.[27] Thus, GALT appear to be highly involved in allergy induction through their capacity to induce Th2 cells.

The observed perturbations in T-cell homeostasis induced by FA and RA affected intestinal functions such as a reduced HRP flux observed in FA+RA mice. This reduced flux could reflect either a drop in lysosomal transcellular transport or an increase in the lysosomal activity of epithelial cells. Indeed, an increase in the lysosomal degradation of HRP was observed in cecum treated with toxin A from *Clostridium difficile*.[31] Under our experimental conditions, we could not determine the total amount of HRP that was transported across the epithelium, which could have been accomplished using [^{3}H]HRP. Reduced HRP flux could also be a consequence of villus atrophy (as less surface exchange), as was reported in FA and RA+FA. This discrepancy could be due to the measurement of intact protein but not total HRP in the latter. Proximal colon, but not small intestine, paracellular permeability was increased in FA+RA mice.

Hence, these mice displayed signs of gut permeability perturbation as well as altered intestine morphology linked with allergy pathophysiology.[13] Moreover, the stronger gut alteration in FA+RA mice may be due to a boost in local leucocytes after airway challenge. The mechanisms of intestinal modification under the action of RA are questionable. The ingestion of RA extract during intranasal challenge cannot be excluded. However, the huge pulmonary inflammation observed in lungs after intranasal challenge shows that most if not all of the extract is inhaled. Moreover, the absence of an effect in non-wheat-sensitized mice renders a direct local effect of HDM in the gut most unlikely. An effect of RA-induced systemic effect in wheat-sensitized mice is likely and is in accordance with the Ig and histamine results as well as the spleen data. A local priming by wheat sensitization of intestinal cells is also likely, as demonstrated by results in Peyer patches, and could account for the effects of HDM in wheat-sensitized mice. Interestingly, HDM exposure was necessary to obtain an effect on intestinal functional parameters that were not perturbed by the food allergy alone. However, the latter had a clear effect on intestinal architecture that was largely enhanced by subsequent HDM respiratory exposure.

By contrast, dual exposure did not exert any additive effects on the lung compartment, as all inflammatory parameters (cells and cytokines) were similarly increased in mice sensitized to HDM, regardless of the previous sensitization to gliadins. Moreover, in the lung, contrary to the results in the intestine, dual exposure increased IL-10 production in BAL. In addition, in the lungs, both Th2 and Th17 activation was observed in RA and FA+RA mice. In BAL fluids of asthmatic patients, this pattern of cytokine responses is frequently observed[32] and may be related to a particular property of the lung mucosa. Thus, it can be suggested that the allergy mechanism is much more related to the Th2 pathway in the intestine than in the lung. In accordance with cell and cytokine results, respiratory function was not modified by dual exposure to wheat and HDM allergens compared to HDM only. The absence of a supplementary effect of food allergy on lung inflammation of HDM-sensitized mice could be related to the insensitivity of the lung compartment to the previous wheat sensitization. Another hypothesis is that the second exposure influences only the compartment in which the first sensitization operated. To validate this hypothesis in a further study, it would be interesting to reverse the two sensitization phases with an RA +FA model. However, these views contradict the typical sequence observed in humans, in whom food allergy predisposes to subsequent asthma and in whom respiratory

DOI: 10.1021/acs.jafc.5b02338
J. Agric. Food Chem. 2015, 63, 6475−6483

allergy is not known to aggravate symptoms related to food allergy. It is therefore more likely that the huge inflammation due to the sole HDM sensitization cannot be further extended. Indeed, a synergy between the two processes is still very well documented in the periphery through the increase of specific IgE and histamine release when both allergies are present.

These results are complementary to those we obtained in a model of successive allergies using ovalbumin (OVA) as food allergen and HDM extract. In fact, Bihouée et al.[33] previously demonstrated that food allergy to OVA increases AHR, hypereosinophilia, and global hypercellularity in response to subsequent HDM challenges, although no further increase in OVA-specific IgE was observed. However, physiological intestinal parameters and intestinal architecture were not assessed in dual allergic mice, leaving a gap in the intestinal impact of prior food allergy after respiratory allergy. Moreover, the absence of AHR and lung immunology modification in our experiment could result from the respiratory allergic protocol, which consists of two intranasal doses of HDM. However, the results from Bihouée et al.[33] were obtained after four sensitizations and two intranasal challenges.

The possibility that cross-reaction between the food allergen and the airborne allergen generates IgE that recognizes both antigens has never previously been described. Although cross-reactivity between aero-allergens such as pollen or plant allergens and food allergens such as shrimp and apple has been described[34,35] cross-reactivity with wheat proteins, especially gliadin cross-reactivity with HDM, has not yet been described. Gliadin is known to cross-react with other foods such as milk or rice.

Our study demonstrates that sensitization to a first allergen imprints the immune response and enhances the effects of a novel subsequent sensitization. It therefore shows that multiple allergies observed in atopic subjects in the process of the atopic march are not independent events that occur within a common genetic background, but they synergize to mutually increase the effects of each allergen involved. Further studies are needed to decipher the mechanisms involved in this reciprocal intestine and lung allergic cross talk.

AUTHOR INFORMATION

Corresponding Author

*(M.B.) E-mail: marie.bodinier@nantes.inra.fr.

Author Contributions

‖G.B. and P.G. contributed equally to this work.

Notes

The authors declare no competing financial interest.

ACKNOWLEDGMENTS

We thank Manon Pietri for her technical assistance with the mouse model. We also thank the Cytocell Cytometry Facility in Nantes for expert technical assistance and the "Therassay platform and the UTE animal facility for animal welfare.

ABBREVIATIONS USED

Alum, aluminum hydroxide; ANOVA, analysis of variance; BAL, broncho-alveolar lavage; CTL, control group; *Der f*, *Dermatophagoides farinae*; DMSO, dimethyl sulfoxide; DNase, deoxyribonuclease; FA, food allergy; FA+RA, combined allergy group; F-ELISA, fluorometric enzyme-linked immunosorbent assay; FBS, fetal bovine serum; HBSS, Hank's balanced salt solution; HDM, house dust mite; HRP, horseradish peroxidase; IFN, interferon; Ig, immunoglobulin; IL, interleukin; MTT, 3-(4,5-dimethylthiazol-2-yl)-2,5-diphenyltetrasodium bromide; PBS, phosphate-buffered saline; RA, respiratory allergy; RPMI, Roswell Park Memorial Institute; SD, standard deviation; TGF, transforming growth factor; Treg, regulatory T cell; TSLP, thymic stromal lymphopoietin

REFERENCES

(1) Pawankar, R.; Canonica, G. W.; Holgate, S. T.; Lockey, R. F. *WAO White Book on Allergy 2011−2012: Executive Summary*; World Allergy Organization: Milwaukee, WI, USA, 2011.

(2) Prescott, S.; Nowak-Wegrzyn, A. Strategies to prevent or reduce allergic disease. *Ann. Nutr. Metab.* **2011**, *59* (Suppl. 1), 28−42.

(3) Agache, I.; Ciobanu, C.; Agache, C.; Anghel, M. Increased serum IL-17 is an independent risk factor for severe asthma. *Respir. Med.* **2010**, *104*, 1131−1137.

(4) Herberth, G.; Daegelmann, C.; Roder, S.; Behrendt, H.; Kramer, U.; Borte, M.; Heinrich, J.; Herbarth, O.; Lehmann, I. IL-17E but not IL-17A is associated with allergic sensitization: results from the LISA study. *Pediatr. Allergy Immunol.* **2010**, *21*, 1086−1090.

(5) Asher, M. I.; Montefort, S.; Bjorksten, B.; Lai, C. K.; Strachan, D. P.; Weiland, S. K.; Williams, H. Worldwide time trends in the prevalence of symptoms of asthma, allergic rhinoconjunctivitis, and eczema in childhood: ISAAC Phases One and Three repeat multicountry cross-sectional surveys. *Lancet* **2006**, *368*, 733−743.

(6) Bjorksten, B.; Clayton, T.; Ellwood, P.; Stewart, A.; Strachan, D. Worldwide time trends for symptoms of rhinitis and conjunctivitis: Phase III of the International Study of Asthma and Allergies in Childhood. *Pediatr. Allergy Immunol.* **2008**, *19*, 110−124.

(7) Strachan, D.; Sibbald, B.; Weiland, S.; Ait-Khaled, N.; Anabwani, G.; Anderson, H. R.; Asher, M. I.; Beasley, R.; Bjorksten, B.; Burr, M.; Clayton, T.; Crane, J.; Ellwood, P.; Keil, U.; Lai, C.; Mallol, J.; Martinez, F.; Mitchell, E.; Montefort, S.; Pearce, N.; Robertson, C.; Shah, J.; Stewart, A.; von Mutius, E.; Williams, H. Worldwide variations in prevalence of symptoms of allergic rhinoconjunctivitis in children: the International Study of Asthma and Allergies in Childhood (ISAAC). *Pediatr. Allergy Immunol.* **1997**, *8*, 161−176.

(8) Valovirta, E. *Respiratory Allergies: Raise Awareness, Relieve the Burden*; EFA: Brussels, Belgium, 2011

(9) Patrizi, A.; Pileri, A.; Bellini, F.; Raone, B.; Neri, I.; Ricci, G. Atopic dermatitis and the atopic march: what is new? *J. Allergy* **2011**, *2011*, 279425.

(10) Zheng, T.; Yu, J.; Oh, M. H.; Zhu, Z. The atopic march: progression from atopic dermatitis to allergic rhinitis and asthma. *Allergy, Asthma Immunol. Res.* **2011**, *3*, 67−73.

(11) Fuiano, N.; Incorvaia, C. Dissecting the causes of atopic dermatitis in children: less foods, more mites. *Allergol. Int.* **2012**, *61*, 231−243.

(12) Sampson, H. A. Update on food allergy. *J. Allergy Clin. Immunol.* **2004**, *113*, 805−819 quiz 820, .

(13) Hagel, A. F.; de Rossi, T. M.; Zopf, Y.; Lindner, A. S.; Dauth, W.; Neurath, M. F.; Raithel, M. Small-bowel capsule endoscopy in patients with gastrointestinal food allergy. *Allergy* **2012**, *67*, 286−292.

(14) Cingi, C.; Demirbas, D.; Songu, M. Allergic rhinitis caused by food allergies. *Eur. Arch. Otorhinolaryngol.* **2010**, *267*, 1327−1335.

(15) Malmberg, L. P.; Saarinen, K. M.; Pelkonen, A. S.; Savilahti, E.; Makela, M. J. Cow's milk allergy as a predictor of bronchial hyperresponsiveness and airway inflammation at school age. *Clin. Exp. Allergy* **2010**, *40*, 1491−1497.

(16) Allen, K. J.; Dharmage, S. C. The role of food allergy in the atopic march. *Clin. Exp. Allergy* **2010**, *40*, 1439−1441.

(17) Boralevi, F.; Hubiche, T.; Leaute-Labreze, C.; Saubusse, E.; Fayon, M.; Roul, S.; Maurice-Tison, S.; Taieb, A. Epicutaneous aeroallergen sensitization in atopic dermatitis infants − determining the role of epidermal barrier impairment. *Allergy* **2008**, *63*, 205−210.

(18) Bergmann, R. L.; Edenharter, G.; Bergmann, K. E.; Forster, J.; Bauer, C. P.; Wahn, V.; Zepp, F.; Wahn, U. Atopic dermatitis in early

DOI: 10.1021/acs.jafc.5b02338
J. Agric. Food Chem. 2015, 63, 6475−6483

infancy predicts allergic airway disease at 5 years. *Clin. Exp. Allergy* **1998**, *28*, 965−970.
(19) Host, A.; Halken, S.; Jacobsen, H. P.; Christensen, A. E.; Herskind, A. M.; Plesner, K. Clinical course of cow's milk protein allergy/intolerance and atopic diseases in childhood. *Pediatr. Allergy Immunol.* **2002**, *13* (Suppl. 15), 23−28.
(20) Simpson, A. B.; Glutting, J.; Yousef, E. Food allergy and asthma morbidity in children. *Pediatr. Pulmonol.* **2007**, *42*, 489−495.
(21) Gourbeyre, P.; Denery-Papini, S.; Larre, C.; Gaudin, J. C.; Brossard, C.; Bodinier, M. Wheat gliadins modified by deamidation are more efficient than native gliadins in inducing a Th2 response in Balb/c mice experimentally sensitized to wheat allergens. *Mol. Nutr. Food Res.* **2012**, *56*, 336−344.
(22) Wan, H.; Winton, H. L.; Soeller, C.; Taylor, G. W.; Gruenert, D. C.; Thompson, P. J.; Cannell, M. B.; Stewart, G. A.; Garrod, D. R.; Robinson, C. The transmembrane protein occludin of epithelial tight junctions is a functional target for serine peptidases from faecal pellets of *Dermatophagoides pteronyssinus*. *Clin. Exp. Allergy* **2001**, *31*, 279−294.
(23) Beilvert, F.; Tissot, A.; Langelot, M.; Mevel, M.; Chatin, B.; Lair, D.; Magnan, A.; Pitard, B. DNA/amphiphilic block copolymer nanospheres reduce asthmatic response in a mouse model of allergic asthma. *Hum. Gene Ther.* **2012**, *23*, 597−608.
(24) Konkel, J. E.; Jin, W.; Abbatiello, B.; Grainger, J. R.; Chen, W. Thymocyte apoptosis drives the intrathymic generation of regulatory T cells. *Proc. Natl. Acad. Sci. U. S. A.* **2014**, *111*, E465−473.
(25) Tepper, R. I.; Levinson, D. A.; Stanger, B. Z.; Campos-Torres, J.; Abbas, A. K.; Leder, P. IL-4 induces allergic-like inflammatory disease and alters T cell development in transgenic mice. *Cell* **1990**, *62*, 457−467.
(26) Coombes, J. L.; Powrie, F. Dendritic cells in intestinal immune regulation. *Nat. Rev. Immunol.* **2008**, *8*, 435−446.
(27) Mowat, A. M. Anatomical basis of tolerance and immunity to intestinal antigens. *Nat. Rev. Immunol.* **2003**, *3*, 331−341.
(28) Pabst, O.; Bernhardt, G.; Forster, R. The impact of cell-bound antigen transport on mucosal tolerance induction. *J. Leukocyte Biol.* **2007**, *82*, 795−800.
(29) Varol, C.; Zigmond, E.; Jung, S. Securing the immune tightrope: mononuclear phagocytes in the intestinal lamina propria. *Nat. Rev. Immunol.* **2010**, *10*, 415−426.
(30) Coombes, J. L.; Siddiqui, K. R.; Arancibia-Carcamo, C. V.; Hall, J.; Sun, C. M.; Belkaid, Y.; Powrie, F. A functionally specialized population of mucosal CD103+ DCs induces Foxp3+ regulatory T cells via a TGF-beta and retinoic acid-dependent mechanism. *J. Exp. Med.* **2007**, *204*, 1757−1764.
(31) Heyman, M.; Corthier, G.; Lucas, F.; Meslin, J. C.; Desjeux, J. F. Evolution of the caecal epithelial barrier during Clostridium difficile infection in the mouse. *Gut* **1989**, *30*, 1087−1093.
(32) Jang, M. H.; Sougawa, N.; Tanaka, T.; Hirata, T.; Hiroi, T.; Tohya, K.; Guo, Z.; Umemoto, E.; Ebisuno, Y.; Yang, B. G.; Seoh, J. Y.; Lipp, M.; Kiyono, H.; Miyasaka, M. CCR7 is critically important for migration of dendritic cells in intestinal lamina propria to mesenteric lymph nodes. *J. Immunol.* **2006**, *176*, 803−810.
(33) Bihouée, T.; Bouchaud, G.; Chesne, J.; Lair, D.; Rolland-Debord, C.; Braza, F.; Cheminant, M. A.; Aubert, P.; Mahay, G.; Sagan, C.; Neunlist, M.; Brouard, S.; Bodinier, M.; Magnan, A. Food allergy enhances allergic asthma in mice. *Respir Res.* **2014**, *15*, 142.
(34) Vieths, S.; Scheurer, S.; Ballmer-Weber, B. Current understanding of cross-reactivity of food allergens and pollen. *Ann. N. Y. Acad. Sci.* **2002**, *964*, 47−68.
(35) Klinglmayr, E.; Hauser, M.; Zimmermann, F.; Dissertori, O.; Lackner, P.; Wopfner, N.; Ferreira, F.; Wallner, M. Identification of B-cell epitopes of Bet v 1 involved in cross-reactivity with food allergens. *Allergy* **2009**, *64*, 647−651.

DOI: 10.1021/acs.jafc.5b02338
J. Agric. Food Chem. 2015, 63, 6475−6483

evaluate the effects of such supplementation on Se metabolism differ depending on studies. Schram et al.[17] determined total Se and Se speciation in muscle, Küçükbay et al.[15] measured total Se in both muscle and serum, as well as GPx activity in serum, and Rider et al.[16] quantified total Se in whole body of fish and also determined hepatic GPx and TRx activities. The two latter studies concluded on a beneficial effect of Se supplementation and on the superiority of the organic form of Se supplementation over supplementation with selenite.

In the present study, Se form supplementation was compared in two different types of feeds, based on either fish meal and fish oil (base M0) or plant ingredients and vegetable oils (V0). To be relevant to European regulation limiting Se supplementation at +200 μg kg^{-1} organic Se, supplementation levels were kept rather low (+300 μg kg^{-1}) compared to what is usually found in such studies (maximum supplementation levels were, respectively, +6650 and +6670 μg kg^{-1} in the studies of Schram et al.[17] and Rider et al.[16]). Also, taking into consideration that Se requirement/utilization might differ depending on the age of trout,[18] the study was undertaken with first-feeding swim-up fry of rainbow trout, whereas previously mentioned studies were undertaken with juvenile fish (20 g body mass). Given the uneven distribution of Se in the tissues/organs of fish,[19] it was chosen to measure total Se in the whole body. The objective of the study was hence to evaluate, on the basis of speciation analysis results, whether a plant-based diet may induce a different utilization and fate of Se in rainbow trout compared to the traditional FM-based diet. In addition, the potential benefit of a Se supplementation was investigated, together with the suitability of the chemical form used for supplementation.

MATERIALS AND METHODS

Chemicals and Reagents. All of the reagents used in this study were of analytical grade and purchased from Sigma-Aldrich (Saint-Quentin Fallavier, France). Water (18 MΩ cm) was obtained from a Milli-Q system (Millipore, Bedford, MA, USA). Selenium species standards were prepared from sodium selenite (>99%), sodium selenate (>98%), seleno-DL-methionine (>99%), and seleno-DL-cystine, all purchased from Sigma-Aldrich. Carbamidomethylated selenocysteine (SeCys-CAM) standard was prepared according to the method of Dernovics et al.;[20] briefly, selenocystine in TRIS-HCl buffer was reduced using dithiothreitol and carbamidomethylation was carried out by the addition of iodoacetamide; the excess of resulting iodoacetamide was further destroyed using dithiothreitol.

Instrumentation. Total Se measurements were carried out on an ICP QMS equipped with a collision/reaction cell (Agilent 7500ce, Agilent Technologies, Wilmington, DE, USA). H_2 was used as reaction gas; flow was kept close to 4 mL min^{-1} and optimized daily to achieve proper background signal.[21] Chromatographic separations were performed using an 1100 series HPLC pump (Agilent Technologies) with anion-exchange (PRP-X100, 10 μm, 4.1 × 250 mm; Hamilton Co., Reno, NV, USA) and reversed phase (C8 Altima column, 5 μm 150 × 4.6 mm; Alltech, Deerfield, IL, USA) HPLC columns. HPLC-ICP QMS analyses were achieved by connecting directly the exit of the HPLC column to the Meinhard nebulizer (Glass Expansion, Romainmotier, Switzerland) of the ICP QMS. The lyophilizer was a model LP3 (Jouan, Saint-Herblain, France).

Feeding Trial and Sample Collection. A 12-week feeding trial was carried out using either FM- or plant-based diets supplemented with two different forms of Se (six diets in total, two basal diets, M0 and P0, and four supplemented diets, MSeIV, MSeMet, PSeIV, and PSeMet), as summarized in Table 1. Basically, diets consisted of two groups, one based on marine ingredients (74%) and the other based on plant ingredients (88%). Each group of diets contained one control diet and two diets supplemented with either an inorganic (sodium selenite) or an organic form of Se (Se-enriched yeast Selsaf (Lesaffre, Marcq en Baroeul, France), containing 2200 ± 200 μg kg^{-1} Se with the following composition: SeMet, 63%; SeIV, <1%; SeVI, <0.02%). For both supplementations, diet formulation was made to achieve a supplementation of 300 μg kg^{-1} Se. The ingredient composition of the basal diets is described in Table 2. Diet preparation consisted first of grinding finely together mineral premix with the corresponding Se supplement and wheat. The fine powder obtained was then thoroughly mixed with other powder ingredients, and the mixture was extruded into pellets. Finally, oil was added in a final stage and diets were dried and ground again to reach a size suitable to feed the fry.

Table 1. Main Characteristics of the Diets Used in the Feeding Trial

diet	basal ingredient	supplementation form (amount)
M0	fish meal and fish oil	
MSeIV		Na_2SeO_3 (300 μg(Se) kg^{-1})
MSeMet		Selsaf (300 μg(Se) kg^{-1})
P0	plants	
PSeIV		Na_2SeO_3 (300 μg(Se) kg^{-1})
PSeMet		Selsaf (300 μg(Se) kg^{-1})

Table 2. Detailed Composition (Percent) of Basal Diets

ingredient	M0	P0
fish meal	62	
fish oil	12	5
whole wheat	25	22
corn		18
soy bean		23
other (rapeseed, lupin, pea)		14
vegetable oils (rapeseed, linseed, palm)		11
premix[a]	1	7

[a]Premix consisted of a mixture of vitamins, minerals, and crystalline amino acid blend.

Rainbow trout (*Oncorhynchus mykiss*) swim-up fry (initial average weight was approximately 91 mg) were stocked into 18 50-L tanks supplied with flow-through spring water at 17 °C at a density of 200 fish per tank. Diets were randomly assigned among the tanks, and each was offered to triplicate groups of fish. At the end of the feeding trial, fish were ethically euthanized and frozen in liquid nitrogen for further analysis. Growth (final average weight was approximately 8.1 g) and survival (86%) of rainbow trout fry were not significantly affected by dietary Se sources and levels. Experimental procedure for the feeding trial complied with the European Directive 010/63/EU for the protection of animals used for scientific purposes, as well as French Decree 2001-464 for animal experimentation.

Sample Preparation. Diets were extracted as, given to fish, they consisted of a relatively fine powder. For the analysis of Se species in fish, three whole fry from each tank were thoroughly ground with Milli-Q water using an Ultraturrax t25 (IKA, Staufen, Germany) until a homogeneous light slurry was obtained. Samples were then kept at −20 °C until further analysis.

Total Selenium Determination. For the determination of total Se in samples, a preliminary acid digestion step was conducted using a DigiPrep MS (SCP Science, Quebec, Canada). Nitric acid and hydrogen peroxide were added to the sample (respectively, 2.5 and 1 mL for 200 mg of diet or 1 and 0.5 mL for 100 mg of fish), and the temperature was kept at 85 °C for 6 h. After dilution with water to reach a HNO_3 concentration of 5%, samples were filtered through 0.45 μm cellulose acetate syringe filters (VWR International, Radnor, PA, USA), and total Se was measured using the ICP QMS. Isotopes 77 and 78 were monitored, and quantification for diet samples was achieved

DOI: 10.1021/acs.jafc.5b00768
J. Agric. Food Chem. 2015, 63, 6484−6492

Table 3. Total Selenium Concentrations in Diets and Mass Balance Verification for Sodium Hydroxide and Protease Extraction[a]

		sodium hydroxide extraction			protease extraction		
diet	total Se (μg kg^{-1})	total Se in extract[b] (μg kg^{-1})	total Se in residue[c] (μg kg^{-1})	mass balance (%)	total Se in extract[b] (μg kg^{-1})	total Se in residue[c] (μg kg^{-1})	mass balance (%)
M0	1222 ± 19	688 ± 9	338 ± 9	84 ± 2	1003 ± 23	183 ± 10	97 ± 3
MSeIV	1648 ± 36	965 ± 28	349 ± 8	80 ± 3	1259 ± 16	242 ± 15	91 ± 3
MSeMet	1703 ± 8	875 ± 7	438 ± 2	77 ± 1	1318 ± 8	159 ± 2	87 ± 1
P0	496 ± 26	352 ± 26	57 ± 8	82 ± 9	360 ± 9	65 ± 10	86 ± 6
PSeIV	915 ± 12	675 ± 7	42 ± 1	78 ± 2	741 ± 27	102 ± 8	92 ± 4
PSeMet	871 ± 3	547 ± 10	109 ± 2	75 ± 2	644 ± 11	91 ± 13	84 ± 3

[a]Values are the mean ± standard error of the mean, $n = 3$. [b]Calculated as (total Se in the extract × mass of extract)/(mass of diet). [c]Calculated as (total Se in the residue × mass of residue)/(mass of diet).

by external calibration using m/z 78. In the case of fish, internal calibration was used with gallium as internal standard.

Inorganic Selenium Species Determination in Diets. A 100-mg portion of feed was extracted with 5 mL of a 0.1 M sodium hydroxide solution, and the mixture was mechanically shaken with an elliptic table during 20 h at room temperature. After centrifugation (2600*g*, 10 min), supernatant was collected and diluted 2 times with HPLC mobile phase. Inorganic selenium species were then separated and detected by HPLC-ICP QMS. A 100-μL aliquot was injected on the anion-exchange chromatography column and eluted with 5 mM ammonium citrate solution (pH 5.3) containing 3% of methanol. Quantification of selenium species was achieved according to the method of standard additions.

Selenoamino Acid Determination. SeMet and SeCys determination was done on the basis of the work of Bierla et al.[22] For SeMet, 100 mg of sample (feeds or fish) was weighed in a polypropylene tube, and 5 mL of a solution of 0.1 M TRIS-HCl, pH 7.5, containing 10 mg of protease type XIV *Streptomyces griseous* was added. This mixture was incubated for 20 h at 37 °C and centrifuged (2600*g*, 10 min). The supernatant was collected and incubated twice with 10 mg of protease. Finally, the supernatant was diluted 2-fold, and 100 μL was injected on the previously mentioned anion-exchange column coupled to ICP QMS. SeCys concentration was determined only in fish samples, and a preliminary derivatization step was carried out using the following procedure. Two milliliters of a 7 M urea solution (in 0.1 M TRIS-HCl, pH 7.5) was added to 100 mg of fish, and the mixture was sonicated for 10 min using an ultrasound probe (VC 505 fitted with a tapered microtip, Sonics & Materials, Newtown, CT, USA) to denature proteins. Then, 30 μL of a dithiothreitol solution at 0.2 M (in 0.1 M TRIS-HCl, pH 7.5) was added, and the mixture was shaken during 1 h. Forty microliters of a 0.5 M iodoacetamide solution (in 0.1 M TRIS-HCl, pH 7.5) was added and the mixture shaken for an additional hour in the dark. Dithiothreitol (375 μL, 0.2 M) was finally added to destroy iodoacetamide excess. Fourteen milliliters of 0.1 M TRIS-HCl was added to decrease urea concentration, and proteolytic digestion was performed with protease as previously described. Sample was then frozen and freeze-dried, the residue was redissolved in 1.2 mL of Milli-Q water, and a 100 μL aliquot was injected on a Superdex Peptide column (300 × 10 mm, Pharmacia, Uppsala, Sweden) eluted with a 10 mM TRIS-HCl, pH 7.5, solution. The low molecular weight fraction was collected (25−35 min) and freeze-dried, and the obtained residue was redissolved and injected on a C8 and eluted with a 0.1% heptafluorobutyric acid solution containing 5% of methanol. For both SeMet and SeCys, m/z 77, 78, 79, and 80 were monitored, and quantification was achieved by using the method of standard additions.

Statistics. Statistical analyses were carried out using the software Statbox (Grimmer Logiciels, Paris, France). Total selenium, SeMet, and SeCys concentrations were analyzed using one-way ANOVA and Student−Newman−Keuls post hoc test ($p < 0.05$) to test the effect of the supplementation form.

RESULTS AND DISCUSSION

Optimization of Sample Preparation Conditions. Several extracting solutions were evaluated for their extraction efficiencies and compatibility with Se species preservation. For inorganic Se species in the diets, tested extractants were water, 50 mM TRIS-HCl buffer, pH 7.5,[17,23] and 0.1 M sodium hydroxide solution.[24] Water and TRIS buffer gave extraction yields of total Se below 20% with a rather large relative standard deviation (36−49%). Sodium hydroxide extraction yields were above 45% with more consistent results (RSD ranged from 6 to 27%). Moreover, the stability of Se species in NaOH extracting solution has been previously demonstrated;[25] it was therefore chosen for analysis of inorganic species in diets.

Determination of SeMet in diets was optimized with regard to the enzymatic digestion. With a single addition of 10 mg of protease XIV, it was found that SeMet concentration obtained in the extract was stable after 20 h of extraction, and extending digestion time to 48 h did not improve results. Defatting the sample with *n*-heptane prior to enzymatic digestion did not increase SeMet concentration in the extract. The use of an ultrasound probe[26] instead of an elliptic table was unsuccessful in improving protein digestion and did not increase extraction yields. Larger amounts of protease XIV (up to 20 mg) as a single addition were also ineffective; however, a second addition of 10 mg of protease in the supernatant resulting from a first digestion clearly improved SeMet concentration in the final extract. Finally, two further additions of 10 mg of protease were used, resulting in an increase of SeMet concentration in the final extract of around 50% compared to single-step digestion.

Se mass balances, determined by measuring total Se in both extract and residue after both extractions, are shown in Table 3. The lower mass balance values obtained in the case of NaOH extraction could be due to the difficulty of collecting residue after extraction because it took in this case the consistency of a very dense slurry.

For SeCys determination in fry, higher (2 and 4 times more) and lower (0.5 and 10 times less) concentrations of derivatization reagents were tested. Although the chromatographic peak height of selenocysteine was not affected with 2 and 4 times the conditions described above, several new minor Se-containing peaks were observed with higher reagent concentrations. It appeared that these new peaks were most likely derivatization products of SeMet and made the chromatogram more complex and not well resolved. Lower concentrations of derivatizing reagents did not increase SeCys peak height, which indicates that no overderivatization occurred in the conditions described above.

DOI: 10.1021/acs.jafc.5b00768
J. Agric. Food Chem. 2015, 63, 6484−6492

Table 4. SeIV, SeVI, and SeMet Concentrations Determined in Diets[a]

diet	SeIV (μg(Se) kg^{-1})	SeVI (μg(Se) kg^{-1})	SeMet (μg(Se) kg^{-1})	total calcd (μg(Se) kg^{-1})	identification (%)
M0	48 ± 5	ND[b]	288 ± 15	336 ± 19	28 ± 2
MSeIV	105 ± 6	ND	290 ± 3	395 ± 8	24 ± 1
MSeMet	53 ± 6	ND	390 ± 8	343 ± 13	26 ± 1
P0	55 ± 10	10 ± 2	98 ± 7	163 ± 17	33 ± 4
PSeIV	115 ± 14	11 ± 2	95 ± 2	221 ± 15	24 ± 2
PSeMet	55 ± 4	12 ± 1	196 ± 6	263 ± 9	31 ± 1

[a]Values are the mean ± standard error of the mean, n = 3. [b]Not detected.

Total Selenium in Fish Feeds. The comparison of the two basal diets, M0 and P0, shows that total Se concentration was much higher in the FM-based diet (Table 3). This is not surprising considering the fact that Se concentrations in animal tissues are generally higher than in plants;[27] thus, these concentrations reflect the Se content of the raw materials used for the production of these feeds. This also highlights the fact that plant-based diets may require a Se supplementation to compete with marine diets regarding total selenium content. In addition, these results confirmed that very similar Se levels were reached for both Se supplementations in each diet group. The Se concentrations found in the marine ingredient-based diets were in the same range as data from the literature.[17,28,29] For all feeds used in this experiment, the Se levels were high enough to avoid deficiency situation (<150 μg kg^{-1} of Se dry feed) and were below toxicity threshold (>3000 μg kg^{-1} of Se dry feed).[30]

Selenium Speciation in Fish Feeds. The concentration of SeIV in diet MSeIV was around twice those found in diets M0 and MSeMet (Table 4). Similarly, the concentration of SeIV in diet PSeIV was around 2 times higher compared to diets P0 or PSeMet. In both marine- and plant-based diets, the increase in SeIV concentration resulting from sodium selenite supplementation was close to 60 μg kg^{-1} (respectively, +57 and +60 μg kg^{-1} for diets MSeIV and PSeIV). An example of a chromatogram obtained in HPLC-ICP QMS for a sodium hydroxide extract of diet is given in Figure 1a; it can be observed that without protease, the amount of free SeMet is very low.

For SeMet concentrations, no differences were observed for diets M0 and MSeIV, whereas the SeMet level of diet MSeMet was increased by 102 μg kg^{-1}. For plant-based diets, a very similar increase (98 μg kg^{-1}) was found in diet PSeMet compared to diets P0 and PSeIV. Figure 1b shows an example chromatogram obtained for a protease extract, where it can be noted that inorganic selenium species are not well extracted in the pH condition of proteolytic digestion. All in all, the results of speciation analysis confirmed the supplementation desired in the experimental design, although no quantitative recovery of initial supplementation could be achieved. This could be explained by a potential nonreversible adsorption of Se on dietary ingredients during the feed preparation process (extrusion), which involves both heating and pressure. Nevertheless, supplementation levels for SeIV and SeMet were approximately the same for both plant and marine diets. SeVI was detected only in plant-based diets, which is in agreement with the fact that the main Se source for plants are selenium species found in soils, which are most often inorganic species such as selenite and selenate,[31] and the previously observed low metabolization of SeVI in plants.[32] The three plant-based diets also present the same SeVI level, which indicates that no species conversion of Se used for

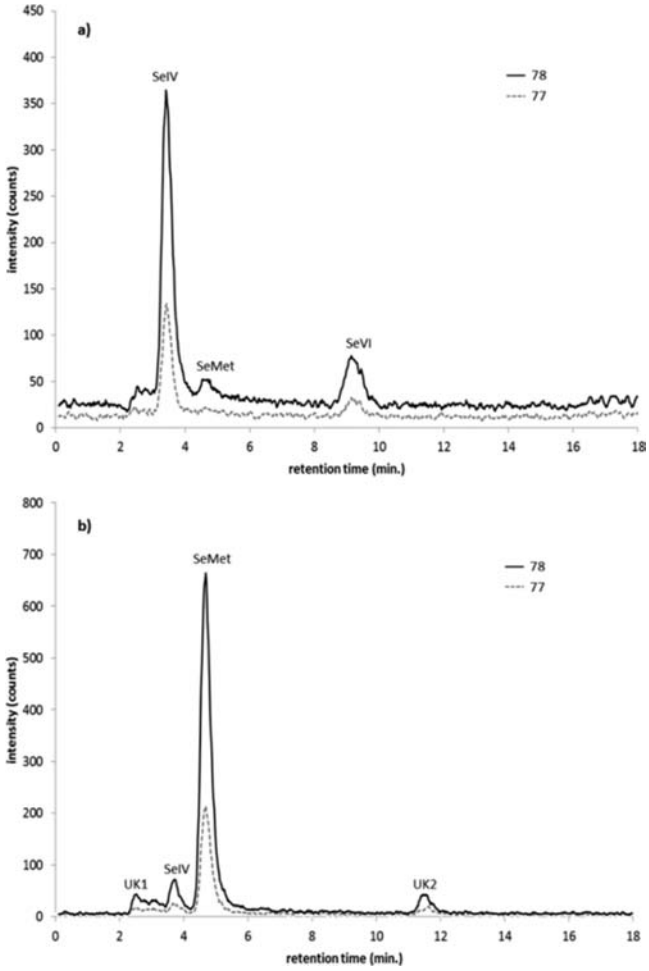

Figure 1. Example anion-exchange chromatograms (HPLC-ICP QMS) for diet (PSeMet) extracts: (a) sodium hydroxide extract; (b) protease extract. UK1 and UK2, unknown Se-containing peaks.

supplementation occurred during diet preparation. Although SeMet concentration found in the basal marine diet was around 3 times higher than in the basal plant diet, it should be noted that the SeMet/total Se ratios, 24 and 20%, respectively, for M0 and P0, were relatively close for these two kinds of feeds. These percentages appear to be rather low compared to values that can be found in the literature for the individual constituents of these diets; it is likely that the feed preparation process mentioned above (extrusion) may have induced transformations in the constituents of diets and thus made the proteolytic digestion not as efficient as the one observed for these constituents when analyzed separately. This is furthermore supported by several observations of the low digestibility of Se from fish meal.[33,34] The percentage of Se identification in diets

DOI: 10.1021/acs.jafc.5b00768
J. Agric. Food Chem. 2015, 63, 6484−6492

ranged from 28 to 33%, these results are similar to those previously reported by Schram et al.[17] This low identification percentage was obtained despite relatively good extraction yields obtained for sodium hydroxide and protease extraction (Table 5). Identification in sodium hydroxide extracts was very low, especially in FM-based diets, which is very likely due to Se being mainly present in proteins in these extracts and therefore not available for detection in this form. In the case of protease extracts, identification was close to 30% except for diet PSeIV, for which identification was 15%; this is relevant with SeIV being the major species found in this diet and the fact that inorganic species were not measured in these extracts because measured concentrations were found to be not repeatable under these pH conditions. A low column recovery was finally found to be responsible for the quite low percentage of identification in protease extracts.

Table 5. Extraction Yields and Percentage of Identification in Extracts for Diet Speciation Analysis[a]

diet	NaOH extraction yield (%)	identification in NaOH extract (%)	protease extraction yield (%)	identification in protease extract (%)
M0	56 ± 2	7 ± 1	82 ± 3	29 ± 2
MSeIV	58 ± 2	11 ± 1	76 ± 2	23 ± 1
MSeMet	51 ± 1	6 ± 1	77 ± 1	30 ± 1
P0	71 ± 7	18 ± 4	73 ± 5	27 ± 2
PSeIV	74 ± 2	19 ± 2	81 ± 3	13 ± 1
PSeMet	63 ± 2	12 ± 1	74 ± 2	30 ± 1

[a]Values are the mean ± standard error of the mean, $n = 3$.

Total Se in Whole Body of Fry. Total Se was determined in initial fry at the beginning of the feeding trial and was found to be 227 ± 2 μg kg^{-1}. Total Se levels in fry at the end of the trial are shown in Table 6; whole body Se was significantly ($p < 0.05$) increased for all groups fed the Se-supplemented diets. Increases of, respectively, +39 and +64 μg kg^{-1} were found for diets MSeIV and MSeMet compared to the basal diet M0. For the plant diets, increases of, respectively, +61 and +86 μg kg^{-1} were found for diets PSeIV and PSeMet compared to the basal diet P0. These results indicate that supplementation with Se yeast has a higher capacity to raise the whole body Se level in comparison to sodium selenite. This is in agreement with previously reported data by Rider et al. in a similar feeding trial using juvenile trouts and higher supplementation levels.[16] In addition, the increases observed were higher in the case of plant-based diets, and it was shown that dose response was almost linear until 2000 μg kg^{-1} regardless of supplementation form,[16] which suggests that Se supplementation is more effective with plant-based diets compared to diets based on fish meal. It can be assumed that this comes from the different speciation of selenium that can be found in diets depending on the basal ingredients; however, due to the low percentage of identification of selenium obtained in diets in this work, this cannot be firmly stated at this point. As previously observed,[17] a good correlation ($R^2 = 0.97$) was found between total Se in diets and total Se in the whole body of fry (Figure 2). The observation that whole body total Se was lower than initial state for fish fed diets P0 and PSeIV does not necessarily imply that these diets were Se deficient but emphasizes the necessity to supplement plant-based diets.

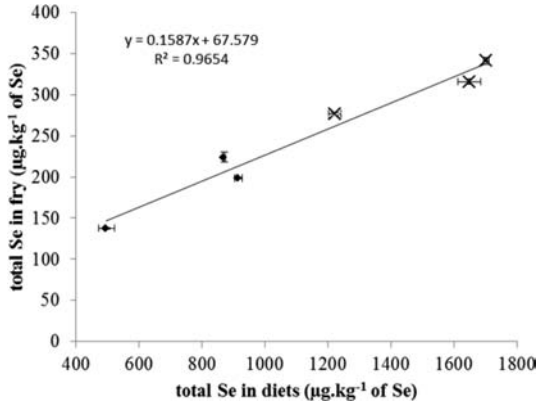

Figure 2. Linear regression between total Se in diets and total Se in whole body of fry: (◆) plant-based diets; (×) fish meal-based diets. Horizontal and vertical error bars are standard error of the mean.

Whole Body Selenomethionine and Selenocysteine Concentration in Fry. A typical chromatogram obtained in HPLC-ICP QMS for a proteolytic digest of fry is given in Figure 3. SeMet concentrations were statistically not changed with selenite supplementation of the basal diet for both marine and plant diets (Table 6), which is in agreement with the suggested metabolic pathway of Se in animals in which SeMet cannot be synthesized from selenite.[35] On the other hand, the two diets supplemented with Se yeast led to increased SeMet concentrations in fry, although this increase was significant only in the case of diet PSeMet ($p < 0.05$). There was a good correlation between SeMet concentrations in diets and SeMet levels in whole body of fry (Figure 4); this concurs with the conclusion of Whanger et al. on the biological significance of SeMet,[36] this selenoamino acid being mostly intact after ingestion, especially in the case of diets containing relatively

Table 6. Total Se, SeMet, and SeCys Concentrations, Ratio of SeMet and SeCys over Total Se, and Percentage of Identification in Whole Body Fry at the End of the Feeding Trial[a]

diet	total Se (μg(Se) kg^{-1}, fw)	SeMet (μg(Se) kg^{-1}, fw)	SeCys (μg(Se) kg^{-1}, fw)	SeMet/total Se	SeCys/total Se	identification[b]
M0	277 $^{\alpha}$ ± 3	123 $^{\alpha}$ ± 13	73 $^{\alpha}$ ± 1	44 $^{\alpha\beta}$ ± 8	26 $^{\alpha\beta}$ ± 1	71 ± 9
MSeIV	316 $^{\beta}$ ± 3	127 $^{\alpha}$ ± 10	70 $^{\alpha}$ ± 8	40 $^{\beta}$ ± 6	22 $^{\alpha\beta}$ ± 4	62 ± 10
MSeMet	341 $^{\gamma}$ ± 4	149 $^{\alpha}$ ± 16	69 $^{\alpha}$ ± 3	44 $^{\alpha\beta}$ ± 8	20 $^{\beta}$ ± 1	64 ± 9
P0	138 $^{\delta}$ ± 1	78 $^{\beta}$ ± 4	47 $^{\beta}$ ± 4	57 $^{\alpha\beta}$ ± 5	34 $^{\gamma}$ ± 5	91 ± 10
PSeIV	199 $^{\varepsilon}$ ± 2	75 $^{\beta}$ ± 3	59 $^{\alpha\beta}$ ± 4	38 $^{\beta}$ ± 3	30 $^{\alpha\gamma}$ ± 4	67 ± 6
PSeMet	224 $^{\eta}$ ± 6	111 $^{\alpha}$ ± 3	59 $^{\alpha\beta}$ ± 4	50 $^{\alpha\beta}$ ± 4	26 $^{\alpha\beta}$ ± 3	76 ± 7

[a]Values are the mean ± standard error of the mean, $n = 3$. Within columns, values with unlike Greek letters ($\alpha, \beta, \gamma, \delta, \varepsilon, \eta$) are significantly different (one-way ANOVA and Student−Newman−Keuls post hoc test, $p < 0.05$). [b]Not statistically processed.

DOI: 10.1021/acs.jafc.5b00768
J. Agric. Food Chem. 2015, 63, 6484−6492

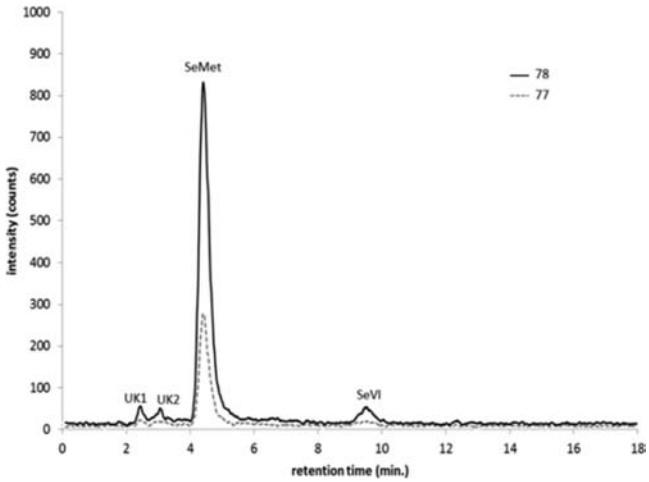

Figure 3. Typical anion-exchange chromatogram (HPLC-ICP QMS) for selenomethionine analysis in protease extract of fry. UK1 and UK2, unknowns.

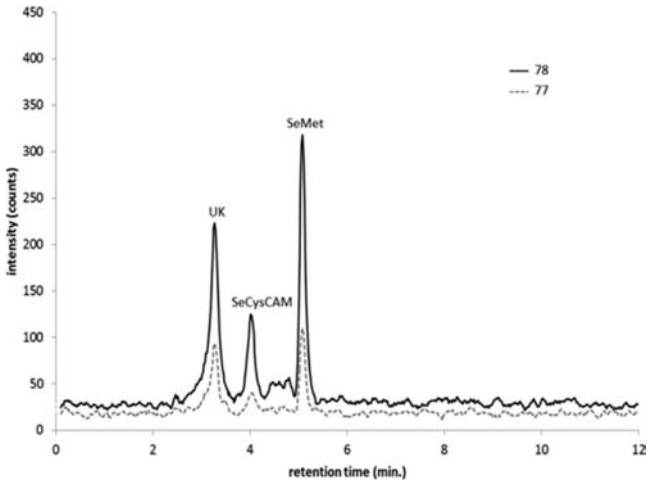

Figure 5. Typical reversed-phase chromatogram (HPLC-ICP QMS) for selenocysteine analysis in protease extract of fry after derivatization. SeCysCAM, carbamidomethyl-selenocysteine; UK, unknown.

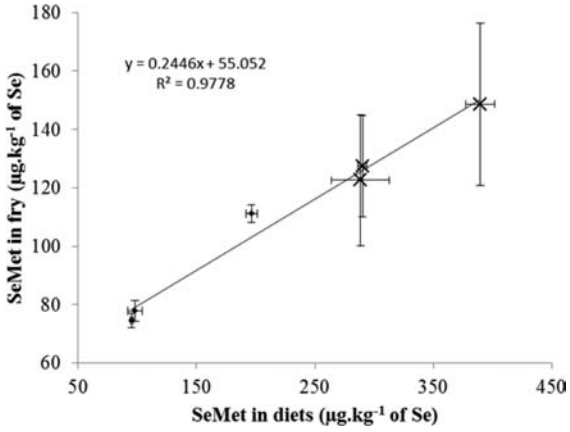

Figure 4. Linear regression between selenomethionine concentrations in diets and whole body of fry fry: (◆) plant-based diets; (×) fish meal-based diets. Horizontal and vertical error bars are standard error of the mean.

low methionine levels such as those based on plant ingredients.[37] With regard to SeCys, the three marine diets lead to the same SeCys concentration at the end of trial, suggesting that Se requirements for selenoprotein expression were already fulfilled with the basal diet M0. Conversely, plant diet P0 led to SeCys concentration in fry significantly ($p < 0.05$) lower than in the case of fry fed the FM-based diets. Both selenite and Se yeast supplementations of the basal diet P0 restored SeCys concentrations to levels similar to those obtained with the marine diets. Furthermore, there was no significant difference between SeCys levels reached for PSeIV and PSeMet diets. An example chromatogram obtained in reversed phase chromatography for a proteolytic extract of fry after SeCys derivatization is shown in Figure 5.

The ratios of SeMet and SeCys concentrations over total Se one were also calculated in fry to roughly estimate the selenium utilization of diets from the speciation point of view. Fry fed diet P0 showed ratios of SeMet/total Se significantly ($p < 0.05$) higher than those fed diet PSeIV, indicating that the major fate of the added selenite in PSeIV was not SeMet production. This is consistent with the inability of selenite to be metabolized in SeMet. Conversely, no significant difference was found for SeMet/total Se ratio between fry fed diets P0 and PSeMet, suggesting that the addition of Se yeast to P0 did not change the proportion of Se in the diet available for incorporation as SeMet in fry proteins. For fry fed FM-based diets, SeMet/total Se ratio was not significantly different for any diets, which could be due to the fact that the proportion of added Se through supplementation in these diets was much lower compared to plant diets (around +40% in FM-based diets versus +80% in plant-based diets), minimizing the effect of the supplementation. The SeCys/total Se ratio was found to be significantly ($p < 0.05$) higher in fry fed diet P0 compared with the ratio for fry fed diet M0, which indicates that Se from diet P0 is mainly transformed into selenoproteins and that the storage of Se in other forms is limited for this diet compared to other dietary treatments. Also, although no difference was found for this ratio between fry fed diets P0 and PSeIV, fry fed diet P0 were found to have a significantly ($p < 0.05$) higher SeCys/total Se ratio than fry fed the PSeMet diet; this seems to indicate that the major fate for added Se yeast was not SeCys synthesis. Nevertheless, no significant difference was found for SeCys/total Se ratio between fry fed diets PSeIV and PSeMet or between fry fed diets MSeIV and MSeMet, whereas all supplemented diets, either FM- or plant-based, increased total Se levels in fry. This confirms the similar abilities of supplemented Se yeast and selenite to be metabolized into SeCys.

Overall, these results indicate that the superiority of Se yeast in increasing Se levels of fry seems to lie in its ability to increase more efficiently SeMet levels. However, according to SeCys determination performed in this study, supplementation with selenite appears to be able to compete with Se yeast when it comes to raising selenoprotein expression. To our knowledge, such an observation has not been made in fish until now, but these results are in agreement with observations made in humans in a study performed by Thomson et al.,[38] where selenate and Se yeast supplementations of 32 New Zealand women were compared. This work demonstrated that higher total Se values in blood were obtained with Se yeast supplementation, but very close glutathione peroxidase activities were achieved with both types of supplementations. This is also in agreement with the fact that SeCys is considered to be the major selenium species formed after selenite

DOI: 10.1021/acs.jafc.5b00768
J. Agric. Food Chem. 2015, 63, 6484−6492

supplementation.[36] The percentage of identification of Se species was higher in fry fed plant-based diets, possibly due to a more complex selenium mixture present in the diets based on fish meal as a consequence of the more developed Se metabolism in fish in comparison to plants. Also, Se identification percentages in whole body were lower in fry fed Se-supplemented diets compared to fry fed basal diets. This may indicate that the part of Se brought through supplementation was transformed to selenium species other than SeMet or SeCys. Another explanation could be that degradation products of these two selenoamino acid were not determined in this study, and a buildup of these species such as presumably selenosugars[35,39] would have led to a drop in identification of Se in whole body of fry.

To our knowledge, such aspects of Se supplementation of fish were until now rather overlooked, principally due to the fact that conclusions of studies were mainly based on total Se observations. Moreover, Se utilization is often assessed through measurements of GPx or TRx activities.[40] Fish have one of the largest selenoproteomes known, with 30−37 selenoproteins versus 25 in humans, and several selenoproteins are specific to fish.[41] Besides, SeCys residues are more numerous in fish selenoproteins in comparison with those known in mammals; for instance, selenoprotein P (selP), which is principally believed to act as SeCys transporter,[42] contains 16−17 SeCys residues in fish, whereas it ranges from 7 to 15 in mammals.[41] Thus, SeCys determination may allow for full coverage of the selenoproteome assessment providing complementary information together with the measurement of activities of selenoenzymes. On the other hand, selenoproteins cannot be differentiated through SeCys determination, which can be troublesome when Se utilization is evaluated, taking into consideration that some selenoproteins are more essential than others and that selenium intake can affect selenoprotein expression pattern.[43] Also, information obtained through SeMet determination should not be disregarded because the transformation of SeMet into SeCys was found to be rather limited in rats; Waschulewski et al.[37] showed that after ingestion of SeMet incorporated in a low methionine containing diet during 21 days, GPx activity dropped close to 50% compared to the initial state. Switching to a Se-deficient diet, GPx activity was increased for a short time and then kept dropping while total Se in tissue also decreased; this short time increase was significantly affected by methionine content of the diet. Therefore, the availability of tissue SeMet for GPx synthesis seems to be related to protein turnover and was found to be quite low. SeMet determination could consequently allow determination of the part of incorporated selenium that is not directly available to the considered organism. Hence, due to the particular metabolism of selenium, attention should be paid to the utilization of this essential element by organisms when the forms of supplementation are compared. In this respect, selenium speciation analysis can provide useful information that cannot be retrieved from total Se analysis.

To conclude, the results obtained in this work showed the usefulness of performing selenium speciation in nutrition studies and the gain in terms of information on metabolic utilization of Se that can be collected. It was shown that the form of Se supplementation can lead to differences in incorporation of Se in both qualitative and quantitative terms. In agreement with previously published data, Se yeast and therefore organic Se showed an undisputably superior ability to increase Se levels in rainbow trout fry compared to inorganic Se. Speciation analyses showed that this is a consequence of the inability of selenite to be incorporated into general proteins under SeMet form and is a clear advantage of Se yeast when the aim is to produce Se-enriched food. On the other hand, the essentiality of Se as a micronutrient is related to its incorporation into selenoproteins, and results obtained here showed that inorganic Se has the ability to fortify this selenoprotein synthesis as organic Se does when supplied in similar amounts. Thus, the determination of SeMet and SeCys provides further knowledge in addition to monitoring selenoenzymes. Although the results in this study did not clearly indicate whether the nonsupplemented plant-based diet led to a Se deficiency situation in fish or not, selenoprotein levels were much lower in this diet compared to the one obtained with the traditional nonsupplemented fish meal-based one, and the increase in SeCys level induced by supplementation appears as a clear benefit for the plant-based diet.

AUTHOR INFORMATION

Corresponding Author

*(S.G.) Phone: + 33 559407762. Fax: + 33 559407674. E-mail: simon.godin@univ-pau.fr.

Funding

This work was supported by a grant from the French Ministry of Higher Education and Research. Financial support was also provided by the Conseil Régional d'Aquitaine (20071303002PFM).

Notes

The authors declare no competing financial interest.

ACKNOWLEDGMENTS

F. Terrier, F. Sandres, and Y. Hontang are acknowledged for the preparation of diets and care of fish.

ABBREVIATIONS USED

FM, fish meal; FO, fish oil; Se, selenium; GPx, glutathione peroxidase; TRx, thioredoxin reductase; SeMet, selenomethionine; SeCys, selenocysteine; SeIV, selenite; SeCys-CAM, carbamidomethylated selenocysteine; TRIS, tris(hydroxymethyl)aminomethane; ICP QMS, inductively coupled plasma quadrupole mass spectrometry; HPLC, high-performance liquid chromatography; M0, marine ingredients basal diet; P0, plant ingredients basal diet; MSeIV, M0 supplemented with 300 μg kg^{-1} of sodium selenite; MSeMet, M0 supplemented with 300 μg kg^{-1} of Se as Se yeast; PSeIV, P0 supplemented with 300 μg kg^{-1} of sodium selenite; PSeMet, M0 supplemented with 300 μg kg^{-1} of Se as Se yeast; selP, selenoprotein P

REFERENCES

(1) Food and Agriculture Organization of the United Nations. *Fishery and Aquaculture Statistics*; FAO: Rome, Italy, 2011.

(2) Food and Agriculture Organization of the United Nations. *The State of World Fisheries and Aquaculture*; FAO: Rome, Italy, 2014.

(3) Tacon, A. G. J.; Hasan, M. R.; Allan, G.; El-Sayed, A. F. M.; Jackson, A.; Kaushik, S. J.; Ng, W. K.; Suresh, V.; Viana, M. T. Aquaculture Feeds: Addressing the Long-Term Sustainability of the Sector. *Farming the Waters for People and Food, Proceedings of the Global Conference on Aquaculture*; Food and Agriculture Organization of the United Nations: Rome, Italy, 2010; pp 22−25

(4) Lobo, A. S.; Balmford, A.; Arthur, R.; Manica, A. Commercializing Bycatch Can Push a Fishery beyond Economic Extinction: Bycatch

DOI: 10.1021/acs.jafc.5b00768
J. Agric. Food Chem. 2015, 63, 6484−6492

Landing Drives Overfishing in India. *Conserv. Lett.* **2010**, *3* (4), 277−285.
(5) Subasinghe, R. P.; Arthur, J. R.; Bartley, J. M.; De Silva, S. S.; Halwart, M.; Hishamunda, C. V.; Mohan, C. V.; Sorgeloos, P. *Farming the Waters for People and Food*; Food and Agriculture Organization of the United Nations: Rome, Italy, 2012.
(6) Tacon, A. G. J. *Demand and Supply of Feed Ingredients for Farmed Fish and Crustaceans*; FAO Fisheries and Aquaculture Technical Paper; Food and Agriculture Organization of the United Nations: Rome, Italy, 2011.
(7) Trushenski, J. T.; Kasper, C. S.; Kohler, C. C. Challenges and Opportunities in Finfish Nutrition. *North Am. J. Aquac.* **2006**, *68* (2), 122−140.
(8) Watanabe, T.; Kiron, V.; Satoh, S. Trace Minerals in Fish Nutrition. *Aquaculture* **1997**, *151* (1), 185−207.
(9) Gammelgaard, B.; Gabel-Jensen, C.; Stürup, S.; Hansen, H. R. Complementary Use of Molecular and Element-Specific Mass Spectrometry for Identification of Selenium Compounds Related to Human Selenium Metabolism. *Anal. Bioanal. Chem.* **2008**, *390* (7), 1691−1706.
(10) Suzuki, K. T. Metabolomics of Selenium: Se Metabolites Based on Speciation Studies. *J. Health Sci.* **2005**, *51* (2), 107−114.
(11) Behne, D.; Hammel, C.; Pfeifer, H.; Röthlein, D.; Gessner, H.; Kyriakopoulos, A. Speciation of Selenium in the Mammalian Organism. *Analyst* **1998**, *123* (5), 871−873.
(12) Moreno, P.; Quijano, M. A.; Gutiérrez, A. M.; Pérez-Conde, M. C.; Cámara, C. Study of Selenium Species Distribution in Biological Tissues by Size Exclusion and Ion Exchange Chromatagraphy Inductively Coupled Plasma−Mass Spectrometry. *Anal. Chim. Acta* **2004**, *524* (1−2), 315−327.
(13) Hamilton, S. J. Review of Selenium Toxicity in the Aquatic Food Chain. *Sci. Total Environ.* **2004**, *326* (1−3), 1−31.
(14) Rayman, M. P. The Use of High-Selenium Yeast to Raise Selenium Status: How Does It Measure Up? *Br. J. Nutr.* **2004**, *92* (04), 557.
(15) KüçüKbay, F. Z.; Yazlak, H.; Karaca, I.; Sahin, N.; Tuzcu, M.; Cakmak, M. N.; Sahin, K. The Effects of Dietary Organic or Inorganic Selenium in Rainbow Trout (*Oncorhynchus mykiss*) under Crowding Conditions. *Aquacult. Nutr.* **2009**, *15* (6), 569−576.
(16) Rider, S. A.; Davies, S. J.; Jha, A. N.; Fisher, A. A.; Knight, J.; Sweetman, J. W. Supra-Nutritional Dietary Intake of Selenite and Selenium Yeast in Normal and Stressed Rainbow Trout (*Oncorhynchus mykiss*): Implications on Selenium Status and Health Responses. *Aquaculture* **2009**, *295* (3−4), 282−291.
(17) Schram, E.; Pedrero, Z.; Cámara, C.; van der Heul, J. W.; Luten, J. B. Enrichment of African Catfish with Functional Selenium Originating from Garlic. *Aquacult. Res.* **2008**, *39* (8), 850−860.
(18) Bell, J. G.; Cowey, C. B.; Adron, J. W.; Shanks, A. M. Some Effects of Vitamin E and Selenium Deprivation on Tissue Enzyme Levels and Indices of Tissue Peroxidation in Rainbow Trout (*Salmo gairdneri*). *Br. J. Nutr.* **1985**, *53* (01), 149−157.
(19) Misra, S.; Peak, D.; Chen, N.; Hamilton, C.; Niyogi, S. Tissue-Specific Accumulation and Speciation of Selenium in Rainbow Trout (*Oncorhynchus mykiss*) Exposed to Elevated Dietary Selenomethionine. *Comp. Biochem. Physiol., Part C: Toxicol. Pharmacol.* **2012**, *155* (4), 560−565.
(20) Dernovics, M.; Lobinski, R. Characterization of the Selenocysteine-Containing Metabolome in Selenium-Rich Yeast: Part II. On the Reliability of the Quantitative Determination of Selenocysteine. *J. Anal. At. Spectrom.* **2008**, *23* (5), 744−751.
(21) B'Hymer, C.; Caruso, J. A. Selenium Speciation Analysis Using Inductively Coupled Plasma-Mass Spectrometry. *J. Chromatogr. A* **2006**, *1114* (1), 1−20.
(22) Bierla, K.; Dernovics, M.; Vacchina, V.; Szpunar, J.; Bertin, G.; Lobinski, R. Determination of Selenocysteine and Selenomethionine in Edible Animal Tissues by 2D Size-Exclusion Reversed-Phase HPLC-ICP MS Following Carbamidomethylation and Proteolytic Extraction. *Anal. Bioanal. Chem.* **2008**, *390* (7), 1789−1798.
(23) Mazej, D.; Falnoga, I.; Veber, M.; Stibilj, V. Determination of Selenium Species in Plant Leaves by HPLC-UV-HG-AFS. *Talanta* **2006**, *68* (3), 558−568.
(24) Cutter, G. A. Determination of Selenium Speciation in Biogenic Particles and Sediments. *Anal. Chem.* **1985**, *57* (14), 2951−2955.
(25) Tolu, J.; Le Hécho, I.; Bueno, M.; Thiry, Y.; Potin-Gautier, M. Selenium Speciation Analysis at Trace Level in Soils. *Anal. Chim. Acta* **2011**, *684* (1−2), 126−133.
(26) Capelo, J. L.; Ximénez-Embún, P.; Madrid-Albarrán, Y.; Cámara, C. Enzymatic Probe Sonication: Enhancement of Protease-Catalyzed Hydrolysis of Selenium Bound to Proteins in Yeast. *Anal. Chem.* **2004**, *76* (1), 233−237.
(27) McNaughton, S. A.; Marks, G. C. Selenium Content of Australian Foods: A Review of Literature Values. *J. Food Compos. Anal.* **2002**, *15* (2), 169−182.
(28) Rider, S. A.; Davies, S. J.; Jha, A. N.; Clough, R.; Sweetman, J. W. Bioavailability of Co-Supplemented Organic and Inorganic Zinc and Selenium Sources in a White Fishmeal-Based Rainbow Trout (*Oncorhynchus mykiss*) Diet. *J. Anim. Physiol. Anim. Nutr.* **2010**, *94* (1), 99−110.
(29) Jesu Prabhu, P. A.; Schrama, J. W.; Mariojouls, C.; Godin, S.; Fontagné-Dicharry, S.; Geurden, I.; Surget, A.; Bouyssiere, B.; Kaushik, S. J. Post-Prandial Changes in Plasma Mineral Levels in Rainbow Trout Fed a Complete Plant Ingredient Based Diet and the Effect of Supplemental Di-Calcium Phosphate. *Aquaculture* **2014**, *430*, 34−43.
(30) Hilton, J. W.; Hodson, P. V.; Slinger, S. J. The Requirement and Toxicity of Selenium in Rainbow Trout (*Salmo gairdneri*). *J. Nutr.* **1980**, *110* (12), 2527−2535.
(31) Dumont, E.; Vanhaecke, F.; Cornelis, R. Selenium Speciation from Food Source to Metabolites: A Critical Review. *Anal. Bioanal. Chem.* **2006**, *385* (7), 1304−1323.
(32) Zayed, A.; Lytle, C. M.; Terry, N. Accumulation and Volatilization of Different Chemical Species of Selenium by Plants. *Planta* **1998**, *206* (2), 284−292.
(33) Bell, J. G.; Cowey, C. B. Digestibility and Bioavailability of Dietary Selenium from Fishmeal, Selenite, Selenomethionine and Selenocystine in Atlantic Salmon (*Salmo salar*). *Aquaculture* **1989**, *81* (1), 61−68.
(34) Le, K. T.; Fotedar, R. Bioavailability of Selenium from Different Dietary Sources in Yellowtail Kingfish (*Seriola lalandi*). *Aquaculture* **2014**, *s 420−421*, 57−62.
(35) Ogra, Y.; Anan, Y. Selenometabolomics: Identification of Selenometabolites and Specification of Their Biological Significance by Complementary Use of Elemental and Molecular Mass Spectrometry. *J. Anal. At. Spectrom.* **2009**, *24* (11), 1477−1488.
(36) Whanger, P. D. Selenocompounds in Plants and Animals and Their Biological Significance. *J. Am. Coll. Nutr.* **2002**, *21* (3), 223−232.
(37) Waschulewski, I.; Sunde, R. Effect of Dietary Methionine on Utilization of Tissue Selenium from Dietary Selenomethionine for Glutathione Peroxidase in the Rat. *J. Nutr. 118* (3), 367−374.
(38) Thomson, C. D.; Robinson, M. F.; Butler, J. A.; Whanger, P. D. Long-Term Supplementation with Selenate and Selenomethionine: Selenium and Glutathione Peroxidase (EC 1.11.1.9) in Blood Components of New Zealand Women. *Br. J. Nutr.* **1993**, *69* (2), 577−588.
(39) Kuehnelt, D.; Kienzl, N.; Traar, P.; Le, N. H.; Francesconi, K. A.; Ochi, T. Selenium Metabolites in Human Urine after Ingestion of Selenite, L-Selenomethionine, or DL-Selenomethionine: A Quantitative Case Study by HPLC/ICPMS. *Anal. Bioanal. Chem.* **2005**, *383* (2), 235−246.
(40) National Research Council. Nutrient Requirements of Fish and Shrimp, 2011.
(41) Lobanov, A. V.; Hatfield, D. L.; Gladyshev, V. N. Eukaryotic Selenoproteins and Selenoproteomes. *Biochim. Biophys. Acta, Gen. Subj.* **2009**, *1790* (11), 1424−1428.
(42) Pedrero, Z.; Madrid, Y. Novel Approaches for Selenium Speciation in Foodstuffs and Biological Specimens: A Review. *Anal. Chim. Acta* **2009**, *634* (2), 135−152.

DOI: 10.1021/acs.jafc.5b00768
J. Agric. Food Chem. 2015, 63, 6484−6492

(43) Schomburg, L.; Schweizer, U. Hierarchical Regulation of Selenoprotein Expression and Sex-Specific Effects of Selenium. *Biochim. Biophys. Acta, Gen. Subj.* **2009**, *1790* (11), 1453−1462.

DOI: 10.1021/acs.jafc.5b00768
J. Agric. Food Chem. 2015, 63, 6484−6492

The olive wood samples used in our past studies were collected from trees belonging to cultivar Picual. This olive cultivar is the most abundant in Spain (860,000 ha) and is extensively cultivated in the province of Jaén and partially in Córdoba and Granada provinces, southern Spain.[35] There are approximately 260 olive cultivars in Spain, of which 24 are the dominant cultivar (i.e., "main cultivar") in at least one region. In this paper, we report on the phenolic composition of olive wood samples from 10 Spanish olive cultivars, growing under the same environmental and agronomical conditions. Herein, we report on differences and similarities among olive cultivars. The chosen cultivars, in order of cultivated areas in Spain, were 'Cornicabra' (cv. Cor), 'Hojiblanca' (cv. Ho), 'Lechín de Sevilla' (cv. LS), 'Manzanilla de Sevilla' (cv. MS), 'Empeltre' (cv. Em), 'Arbequina' (cv. Ar), 'Farga' (cv. Far), 'Gordal sevillana' (cv. Gs), and 'Verdial de Badajoz' (cv. VB), along with 'Picual' (cv. Pi) for comparative purposes. Fruits from cv. MS and cv. Gs are used for the preparation of table olives, whereas fruits of the rest of the cultivars are utilized for olive oil production, with the exception of cv. Ho fruits, which are used for both purposes. These 10 olive cultivars are "main cultivars" and are representative of olives cultivated throughout Spain. No study encompassing the phenolics of these 10 cultivars has been reported.

MATERIALS AND METHODS

Chemicals. The solvents used for olive wood extraction (dichloromethane and ethyl acetate) were glass-distilled prior to use. Methanol used for radical-scavenging activity assays and HPLC analyses was of HPLC grade. Two reference compounds were obtained from commercial sources: oleoside 11-methyl ester (**3**) (PhytoLab GmbH & Co., Vestenbergsgreuth, Germany) and eriodictyol (**9**) (Extrasynthèse, Genay, France). Other identified compounds in this work were previously isolated in the authors' laboratory.[14,27,28] 2,2-Diphenyl-1-picrylhydrazyl radical (DPPH$^{\bullet}$) (95%, Sigma-Aldrich Chemie, Steinheim, Germany) was used for radical-scavenging assays.

Plant Material. The olive tree (*O. europaea* L.) wood samples used in this work were collected on March 28, 2014 (during an ordinary day of pruning work), in the "garden of olive cultivars" of the Centro IFAPA "Venta del Llano", Mengíbar (Jaén province), Spain. This experimental farm, located at 280 m above sea level (37° 56′ 26″ N; 3° 47′ 6″ O), consists of a collection of one-trunk olive trees (30 years old), growing at 7 × 7 m distance, under standard growing practices and without artificial irrigation. The farm comprises one or two individual trees per each olive cultivar (around 180 different olive cultivars from Spain and the rest of the world). Thus, a single tree per olive cultivar was chosen to take pruning material. The olive cultivars selected were 'Arbequina', 'Cornicabra', 'Empeltre', 'Farga', 'Gordal sevillana', 'Hojiblanca', 'Lechín de Sevilla', 'Manzanilla de Sevilla', 'Picual', and 'Verdial de Badajoz' (Table 1). Because only one or two old olive branches were cut per tree during the pruning work, it was necessary to take a single piece of wood (approximately 3−4 cm diameter and 50 cm length) from each olive cultivar as not all cultivars had two branches pruned from the south side. In all cases, one old branch was utilized having been pruned from the south-facing side of the tree to minimize microhabitat variation. Thus, all single wood pieces collected for this work were taken from the south side of the trees in order to make the selected pruning material as homogeneous as possible for comparative purposes. Every wood sample was stored for 3 months in a dry and dark place at room temperature with passive ventilation, prior to extraction. Just before the start of the extraction process, the wood piece was shaved in a local sawmill (wood shavings: length, 3−5 cm; thickness, 0.1−0.3 mm).

Extraction. Wood shavings (40 g) were extracted successively with dichloromethane (DCM) and ethyl acetate (EtOAc) (350 mL of each) for 2 h at reflux under nitrogen atmosphere, following a protocol previously optimized by the authors.[29] The solvents were evaporated under reduced pressure to give the corresponding DCM and EtOAc extracts (i.e., dry extracts). DCM dry extracts were discarded, whereas all EtOAc dry extracts were stored under argon in sealed vials at −20 °C until analysis. All of the extractions were carried out in duplicate. Extraction yields are reported in Table 2.

Table 1. Selection of Spanish Olive Cultivars (*Olea europaea* L.) Included in This Work

olive cv. name	abbrev[a]	surface[b] (×1.000 ha)	crop land (provinces)[b]	fruit destination[b]
Picual	Pi	860	Jaén, Córdoba, Sevilla	olive oil
Cornicabra	Cor	269	Ciudad Real, Toledo	olive oil
Hojiblanca	Ho	217	Córdoba, Málaga, Sevilla	olive oil, table olives
Lechín de Sevilla	LS	105	Sevilla, Cádiz	olive oil
Manzanilla de Sevilla	MS	85	Sevilla, Badajoz	table olives
Empeltre	Em	72	Zaragoza, Teruel, Baleares	olive oil
Arbequina	Ar	71	Lérida, Tarragona	olive oil
Farga	Far	45	Castellón, Tarragona	olive oil
Gordal sevillana	Gs	30	Sevilla	table olives
Verdial de Badajoz	VB	29	Badajoz, Cáceres	olive oil

[a]These abbreviations for olive cultivar names are used throughout the text. [b]Information included in this column has been taken from ref 35.

Table 2. Extraction Yields and Radical-Scavenging Percentages of Olive Wood Samples from 10 Spanish Olive Cultivars (*Olea europaea* L.)

olive cultivar[a]	DCM[b]	EtOAc[c]	RSP[d]
Pi	0.7	1.6	91.4 a
Cor	0.4	0.5	32.7 ab
Far	0.4	0.4	31.3 bc
LS	0.5	0.5	28.4 bcd
MS	0.4	0.5	26.4 cde
Ar	0.6	0.4	24.0 de
Gs	0.5	0.5	21.6 e
Em	0.5	0.3	21.0 e
Ho	0.5	0.3	21.0 e
VB	0.4	0.5	18.6 e

[a]Abbreviated olive cultivar names. See Table 1 for meaning. [b]Yields for dichloromethane extracts. Values are means of two replicates. [c]Yields for ethyl acetate extracts. Values are means of two replicates. [d]RSP (radical-scavenging percentage) values for the ethyl acetate extracts are expressed as DPPH$^{\bullet}$ scavenging (%). Values are means of three replicates, and the RSD is <1%. RSP data values followed by common letters are not significantly different (F = 230.0; P < 0.05).

HPLC-DAD Analysis. High-performance liquid chromatography (HPLC) analyses were performed by an analytical RP-HPLC (Spherisorb ODS-2 column, 250 mm × 3 mm i.d., 5 μm, Waters Chromatography Division, Milford, MA, USA) on a Waters 600E instrument (Waters Chromatography Division) equipped with a diode array detector, with a scan range of 190−800 nm (Waters CapLC 2996 photodiode array detector, Waters Chromatography Division) and operating at 30 °C. Samples for injection were prepared by dissolving each EtOAc dry extract in MeOH at a concentration of 10 mg/mL (injection volume, 5 μL). HPLC separations were achieved following a method previously used by the authors to analyze olive wood extracts:[14] H_2O/CH_3COOH, 99.8:0.2, v/v (solvent A) and CH_3OH/

DOI: 10.1021/acs.jafc.5b02979
J. Agric. Food Chem. 2015, 63, 6493−6500

Table 3. Chromatographic and Spectral Characteristics of the Phenolic Compounds Studied in 10 Spanish Olive Cultivars (*Olea europaea* L.)

compound	t_R, min	λ_{max}, nm	$[M - H]^-$	fragment ions
hydroxytyrosol (**1**)[a]	5.1	226, 280	152.8	123.1
tyrosol (**2**)[a]	6.6	224, 278	136.8	119.0
oleoside 11-methyl ester (**3**)[b]	10.0	239	402.7	332.7, 222.6
aldehydic form of oleuropein aglycone (**4**)[c]	10.5	226, 284, 346	–[d]	176.8
(−)-olivil 4-*O*-*β*-D-glucopyranoside (**5**)[c]	13.0	230, 279	537.1	375.2
(−)-olivil (**6**)[c]	19.4	230, 282	375.2	179.7
2″-hydroxyoleuropein (**7**)[e]	20.4	226, 279	555.1	539.0, 393.1
7-deoxyloganic acid (**8**)[a]	23.5	232	359.2	197.6
eriodictyol (**9**)[b]	28.3	288	286.7	150.6
(+)-1-hydroxypinoresinol 1-*O*-*β*-D-glucopyranoside (**10**)[c]	29.7	230, 280	535.1	355.1
oleuropein (**11**)[a]	34.1	230, 284	539.0	376.9
ligustroside (**12**)[a]	39.9	230, 279	522.8	361.2
jaspolyoside (**13**)[e]	44.6	233, 284	925.2	539.1
jaspolyoside isomer (**14**)[f]	49.2	233, 284	925.2	539.1
jaspolyanoside (**15**)[e]	49.6	228, 277	909.2	523.1
isojaspolyoside A (**16**)[e]	49.7	233, 283	925.2	539.1
jaspolyanoside isomer (**17**)[f]	50.0	228, 277	909.2	523.1

[a]An authentic sample of this compound was isolated by the authors from cv. Pi.[27] [b]This compound was identified by comparison with a commercial standard. [c]An authentic sample of this compound was isolated by the authors from cv. Pi.[14] [d]The $[M - H]^-$ ion for this compound was not observed. [e]An authentic sample of this compound was isolated by the authors from cv. Pi.[28] [f]This compound was tentatively identified on the basis of its UV−vis and MS spectra and MS fragmentation pattern.

CH_3COOH, 99.8:0.2, v/v (solvent B) at a flow rate of 0.7 mL/min: linear gradient from 20 to 70% B for 55 min and another 10 min to return to the initial conditions. Quantification of identified compounds in each EtOAc extract was carried out by the external-standard method, using HPLC peak areas at 230 nm (**5**−**7**, **10**−**17**), 239 nm (**3**, **8**), 280 nm (**1**, **2**), 288 nm (**9**), or 346 nm (**4**). The concentration of each compound was measured by comparing it with calibrations made with the pure compound analyzed under the same conditions. Two of them are commercial reference standards (**3** and **9**), and the remainder of the compounds were isolated and characterized previously by us.[14,27,28] Calibration curves were obtained for each standard in the following concentration ranges: hydroxytyrosol (**1**) in the range of 1.0−50.0 μg/mL; oleoside 11-methyl ester (**3**) in the range of 1.0−100.0 μg/mL; aldehydic form of oleuropein aglycone (**4**) in the range of 48.7−325.0 μg/mL; (−)-olivil 4-*O*-*β*-D-glucopyranoside (**5**) in the range of 47.5−316.6 μg/mL; (−)-olivil (**6**) in the range of 51.9−692.5 μg/mL; eriodictyol (**9**) in the range of 29.2−729.0 μg/mL; (+)-1-hydroxypinoresinol 1-*O*-*β*-D-glucopyranoside (**10**) in the range of 100.0−1000.0 μg/mL; oleuropein (**11**) in the range of 120.0−1000.0 μg/mL. Concentration values for compounds **1** and **2** were calculated by external calibration against hydroxytyrosol (**1**). Concentration values for compounds **3** and **8** were calculated by external calibration against oleoside 11-methyl ester (**3**). Concentration values for compounds **4**−**6**, **9**, and **10** were calculated by external calibration against the corresponding pure compounds. Concentration values for compounds **7** and **11**−**17** were calculated by external calibration against oleuropein (**11**). The results were expressed as milligrams of compound per gram of dry weight EtOAc extract.

Because the number of wood samples studied for each olive cultivar was limited (see discussion above), the concentration data were analyzed on the basis of two extraction replicates per cultivar for ANOVA and SNK multiple-range tests of significance.

HPLC-DAD/ESI-MS Analysis. Analyses were performed using an Agilent 1100 HPLC system (Agilent Technologies, Palo Alto, CA, USA) equipped with a diode array detector and an Esquire 6000 ion mass spectrometer (MS, Bruker Daltonics, Bremen, Germany) fitted with an electrospray ionization (ESI) interface, operating in negative mode. Chromatographic separation was achieved using an analytical reverse-phase column (Spherisorb ODS-2, 150 mm × 3 mm i.d., 5 μm, Waters Chromatography Division) using the same solvents and conditions as described above. Ionization and mass spectrometric conditions were optimized by infusing a solution of pure compounds. The nebulizer pressure was 40 psi; dry gas flow, 9 L/min; dry gas temperature, 350 °C; and capillary voltage, 4 kV. Analyses were performed using scans from m/z 50 to 1200.

DPPH Radical-Scavenging Activity Assay. The radical-scavenging activity of EtOAc dry extracts was determined spectrophotometrically with the stable DPPH radical.[36] Methanolic solutions (2.4 mL) of DPPH• (~7×10^{-5} M) with an absorbance at 515 nm of 0.80 ± 0.03 AU were mixed with methanolic solutions (1.2 mL) of EtOAc dry extracts at a concentration of 50 μg/mL. The resulting mixtures were shaken and kept in the dark for 15 min at room temperature. The decrease of absorbance was measured at 515 nm. Results are expressed as radical-scavenging percentage (RSP) and were calculated by using the formula[36]

$$\mathrm{RSP} = \left[\frac{A_B - A_A}{A_B}\right] \times 100$$

where A_B is the absorbance of the blank (t = 0 min) and A_A is the absorbance of tested sample solution (t = 15 min). The experiments were carried out in triplicate.

Statistical and Multivariate Analyses. Data were collected from two independent extractions from each olive cultivar. Thus, each compound (as mg/g DM) was compared among the cultivars (two replicates per cultivar) by one-way ANOVA SNK (Student−Newman−Keuls multiple-range test).[37] Gower or Manhattan metric similarities[38,39] were computed among all cultivars using character weighting of the square root ($F - 1$) (where F is the F ratio of variance among cultivars/variance within cultivars for each compound, taken from ANOVA). Using the square root of ($F - 1$) for character weighting factors places more importance on characters that vary more among the cultivars, thus improving their separation (see discussion in ref 39). Principal coordinate ordination (PCO) factored the association matrix using the formulations of Gower[40] and Veldman.[41]

RESULTS AND DISCUSSION

The olive cultivars included in this work were selected from the group of 24 main Spanish olive cultivars.[35] Table 1 presents information on the 10 olive cultivars, their cultivated areas in Spain, the Spanish provinces where they are mainly cultivated, and the use of their fruits. Each of the 10 olive varieties studied

DOI: 10.1021/acs.jafc.5b02979
J. Agric. Food Chem. 2015, 63, 6493−6500

are the dominant cultivar at least in one district. Thus, they represent all of the olive-growing areas of Spain, from the southern half to northeastern Spain. All of the olive wood samples were collected on the same day and location, so any differences in the phenolic compositions of the samples should be due to genetics rather than different environmental and/or agronomical conditions. The olive wood samples used in the work came from the pruning materials collected at an experimental farm, Jaén province, southern Spain.

Extraction of Olive Wood Samples and Radical-Scavenging Activity. Olive wood shavings were sequentially extracted with dichloromethane and ethyl acetate under reflux conditions. Dichloromethane extractions (0.4−0.7% yield) removed nonpolar components, which are known to have negligible antioxidant activities.[29] Hence, the dichloromethane extracts were discarded. Because it is known that ethyl acetate is an excellent solvent for the extraction of antioxidants,[29] the resulting ethyl acetate extracts (0.3−1.6% yield) were submitted to the DPPH assay. The DPPH assay is based on the ability of the antioxidants to scavenge the model free radical, DPPH$^{\bullet}$, and has been widely used due to its simplicity and worldwide acceptance for comparative purposes.[36] Table 2 presents the extraction yields from wood samples and the antioxidant activities of the ethyl acetate extracts expressed in terms of radical-scavenging percentage (RSP). The ethyl acetate yields for all olive cultivars were <1%, with the exception of cv. Pi (1.6%). ANOVA of antioxidant activities revealed a highly significant difference (F = 230.0, $P = 0.2 \times 10^{-5}$) between the RSP value of cv. Pi and the other cultivars (Table 2). The RSP value for cv. Pi was 91.4%, whereas the RSP of the other olive cultivars ranged from 18.6 to 32.7% (Table 2).

Identification and Quantitative Analysis of Phenolic Compounds. The 10 ethyl acetate extracts were submitted to HPLC-DAD and HPLC-DAD/ESI-MS analyses. The identifications of components were carried out by comparison of retention times and mass and UV spectra with those of authentic samples. Table 3 shows the phenolic compounds studied in order of elution from a C_{18} HPLC column, along with their chromatographic and spectral characteristics. Figure 1 shows the HPLC chromatograms (recorded at 230 nm) of cultivars Ar, Gs, and Pi, which typify the different component profiles of the selection of olive cultivars. Compounds **1**, **2**, **4**−**8**, **10**−**13**, **15**, and **16** have been previously isolated and fully characterized by our laboratory from ethyl acetate extracts of cv. Pi.[14,27,28] Compounds **3** and **9** were identified as oleoside 11-methyl ester and eriodictyol, respectively, by comparison with the corresponding commercial standards (Figure 2). On the other hand, compounds **14** and **17** have mass and UV spectra very similar to those of jaspolyoside (**13**) and jaspolyanoside (**15**), respectively, indicating they are isomers. The 17 compounds belong to five groups of phenolic compounds: (I) simple phenols (**1**, **2**); (II) lignans (**5**, **6**, **10**); (III) flavonoids (**9**); (IV) iridoids (**8**); and (V) secoiridoids (**3**, **4**, **7**, **11**−**17**). All of these compounds have previously been isolated or detected in different parts of the olive tree, although some of them (**5**−**9**, **13**, **15**, and **16**) have been described in *O. europaea* on rare occasions.[14,27,28,42,43] In contrast, it is the first time that compounds **3** and **9** have been described in olive tree wood. Several studies on the biological activities and potential applications of some of these compounds, especially focused on hydroxytyrosol or oleuropein, have been conducted.[44−46]

After identification of the HPLC peaks, the concentration of each compound in all ethyl acetate extracts was calculated by the external standard method, correlating the peak area for each component in a given HPLC chromatogram with the calibration curves obtained using our own standards (**1**, **2**, **4**−**8**, **10**−**13**, **15**, **16**) and those commercial ones (**3**, **9**) (Table 4). Significant differences, both quantitative and qualitative, were found among olive cultivars (Table 4). Compounds **1**, **2**, **4**−**7**, **9**, **10**, and **12** were present in all olive cultivars, whereas compounds **3**, **8**, and **13** were present in only five, three, and four cultivars, respectively (Table 4). In contrast, compounds **11** and **14**−**17** were absent in three cultivars (Table 4). Compound **10** was the major phenolic compound in all cultivars, except in cv. Far and cv. Pi, where it was the second most abundant component. Compound **9** was the second highest concentration component in four cultivars (Cor, Gs, MS, and VB) and the third highest in cv. Ho (Table 4). Compound **6** was also quite abundant, being the third highest concentration component in three cultivars (Em, Gs, and LS), the highest in cv. Far, and the second highest in cv. Ar and cv. Ho (Table 4). Other prominent constituents are compounds **4**, **7**, **12**, and **11**, the latter being the major component in cv. Pi. In

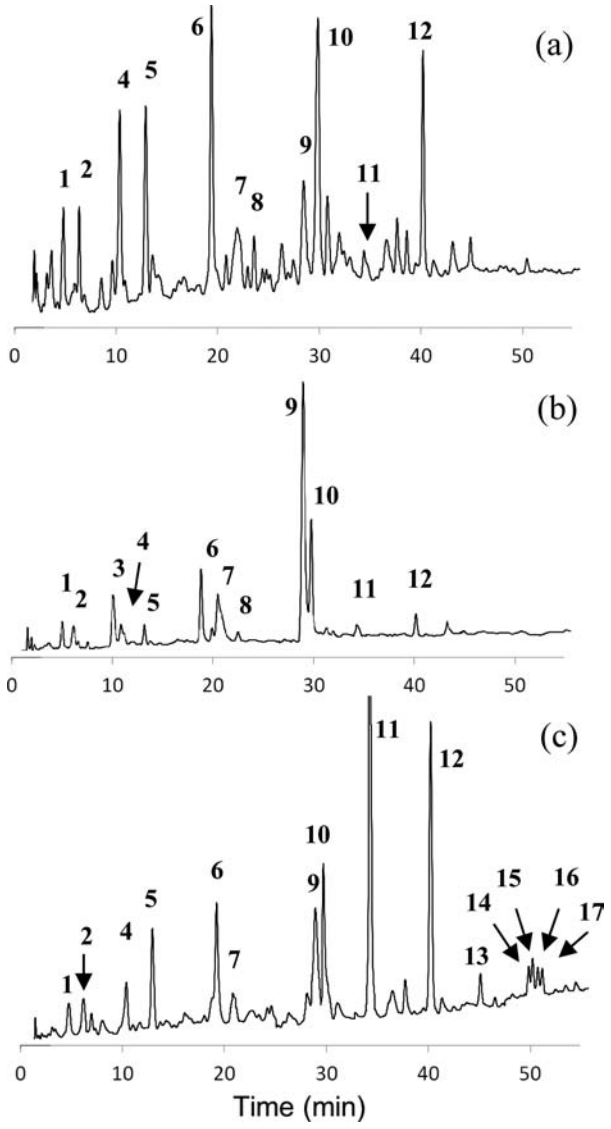

Figure 1. HPLC profiles of ethyl acetate extracts from olive tree wood at 230 nm: (a) cv. 'Arbequina'; (b) cv. 'Gordal sevillana'; (c) cv. 'Picual'. See Table 3 for compound names.

DOI: 10.1021/acs.jafc.5b02979
J. Agric. Food Chem. 2015, 63, 6493−6500

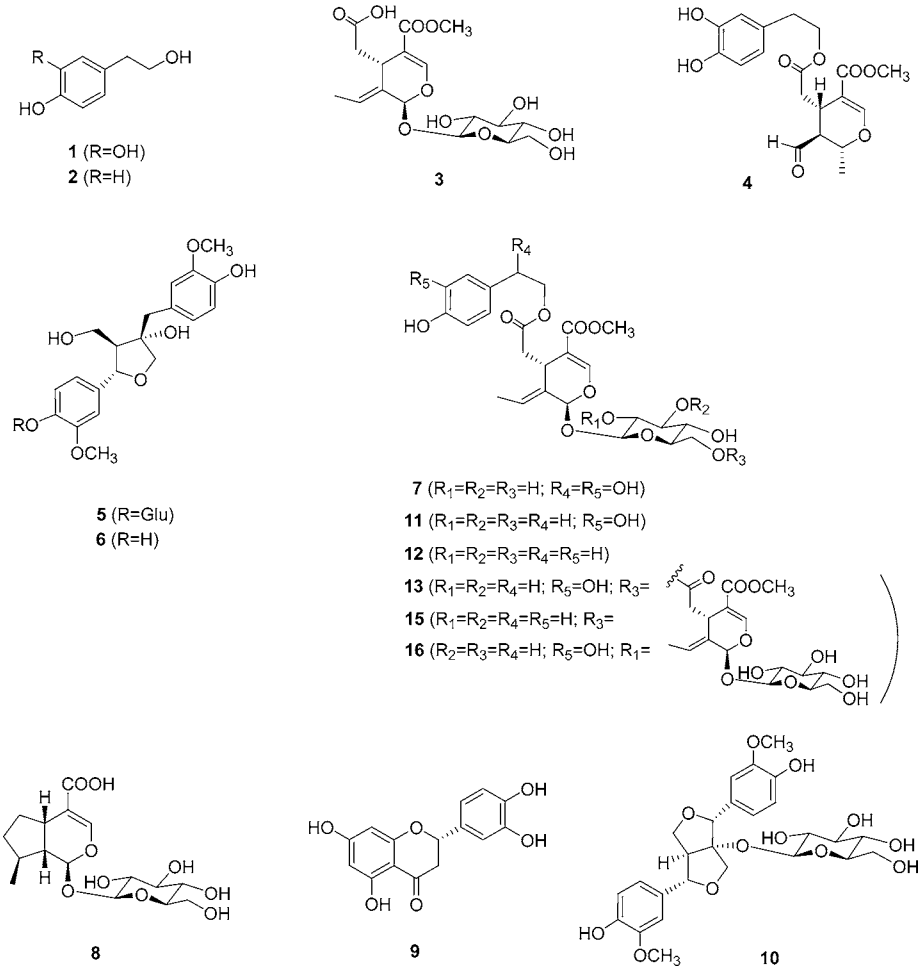

Figure 2. Compounds identified in this work from olive wood EtOAc extracts of 10 Spanish olive cultivars (*Olea europaea* L.).

Table 4. Composition of Olive Wood Ethyl Acetate Extracts from 10 Spanish Olive Cultivars (*Olea europaea* L.)

	olive cultivars[a]											
compd[b]	Ar	Cor	Em	Far	Gs	Ho	LS	MS	Pi	VB	*F* ratio[c]	*P*[d]
1	0.34 c	0.29 c	0.62 c	0.63 c	2.96 a	0.17 c	1.23 b	0.23 c	0.34 c	0.21 c	38.2	0.3×10^{-4}
2	1.46 a	0.64 bc	1.24 ab	1.10 ab	0.65 bc	1.25 ab	0.81 b	0.21 c	0.92 ab	0.62 bc	6.51	0.4×10^{-2}
3	– c	0.24 c	– c	– c	3.76 a	0.21 c	– c	0.73 b	– c	0.61 b	239.7	0.2×10^{-5}
4	17.71 c	18.68 b	20.29 b	26.81 a	26.74 a	15.37 c	25.74 a	14.91 c	17.92 bc	21.03 b	28.4	0.5×10^{-4}
5	13.33 cd	6.41 g	5.30 g	14.64 bc	15.98 b	11.37 e	9.26 f	8.38 f	19.20 a	11.98 de	66.6	0.1×10^{-4}
6	18.52 e	12.02 f	13.93 f	51.81 a	42.82 b	25.38 c	22.63 cd	18.13 e	20.70 de	20.69 de	192.7	0.2×10^{-5}
7	14.50 e	22.03 c	11.92 f	22.50 c	29.61 a	15.47 e	17.72 d	18.49 d	15.57 e	26.19 b	145.7	0.3×10^{-5}
8	1.62 b	– d	– d	1.88 a	0.62 c	– d	– d	– d	– d	– d	146.4	0.3×10^{-5}
9	5.67 e	23.19 c	3.00 f	13.94 d	71.03 a	21.62 c	15.92 d	22.20 c	7.42 e	27.61 b	779.8	0.8×10^{-6}
10	32.63 e	50.03 b	21.02 f	36.68 d	90.21 a	43.10 c	89.39 a	37.90 d	38.99 d	49.73 b	448.4	0.1×10^{-5}
11	13.11 b	12.92 b	– c	– c	11.88 b	– c	12.38 b	13.01 b	42.30 a	12.29 b	310.8	0.2×10^{-5}
12	16.68 c	20.40 b	13.28 d	16.52 c	15.97 c	17.53 c	16.52 c	17.09 c	35.00 a	21.45 b	94.1	0.6×10^{-5}
13	– c	– c	– c	– c	– c	11.22 b	11.20 b	– c	12.31 a	10.91 b	839.5	0.7×10^{-6}
14	– d	12.24 ab	– d	10.98 c	– d	13.40 a	12.13 ab	11.91 ab	13.11 a	12.09 ab	244.0	0.2×10^{-5}
15	– b	13.03 a	– b	12.13 a	– b	12.43 a	12.54 a	11.92 a	13.01 a	12.43 a	127.0	0.4×10^{-5}
16	– b	12.48 a	– b	11.41 a	– b	12.22 a	12.27 a	12.02 a	12.90 a	11.63 a	232.6	0.2×10^{-5}
17	– c	11.92 ab	– c	11.61 ab	– c	11.24 b	12.41 ab	12.13 ab	13.30 a	11.70 ab	183.1	0.3×10^{-5}

[a]See Table 1 for complete olive cultivar names. Concentration values are expressed as milligrams of compound per gram of dry weight EtOAc extract. Data values in the same row followed by common letters are not significantly different ($P < 0.05$). [b]See Table 3 for complete compound names. [c]*F* ratio = variance among cultivars/variance within cultivars, from ANOVA. [d]*P* = probability of significant difference among the cultivars. Sixteen compounds differ among cultivars at very highly significantly difference ($P < 0.001$) levels; compound **2** is highly significantly different among cultivars ($P < 0.01$).

DOI: 10.1021/acs.jafc.5b02979
J. Agric. Food Chem. 2015, 63, 6493−6500

contrast, compound **2**, with a concentration that ranged from 0.21 to 1.46 mg/g, was a very minor component (Table 4) as were compounds **8** (0−1.88 mg/g) and **1** (0.17−2.96 mg/g). With respect to the phenolics found in our past analyses on olive wood samples from cv. Pi[14,27,28] and those identified in the Picual wood sample analyzed in this work, some minor differences are found; the flavonoid **9** has been detected now for the first time, and the group of lignans (**5**, **6**, **10**) has increased its presence, representing now ca. 30% (in weight) of the reported components. However, oleuropein (**11**) still is the major component, and the group of secoiridoids (**4**, **7**, **11**−**17**) remains the most representative (ca. 70% in weight).

Multivariate Analysis. To investigate the pattern of the chemical relationships among the cultivars, PCO was performed. A similarity matrix was produced using the average values for each of the 17 compounds. Factoring the similarity matrix resulted in five eigenroots that appeared to asymptote after the fifth root. These eigenroots accounted for 43.91, 16.51, 13.68, 8.06, and 4.87% (87.03% total) of the variance among the 10 cultivars. Ordination of the cultivars onto the first three principal coordinates (Figure 3) reveals three major

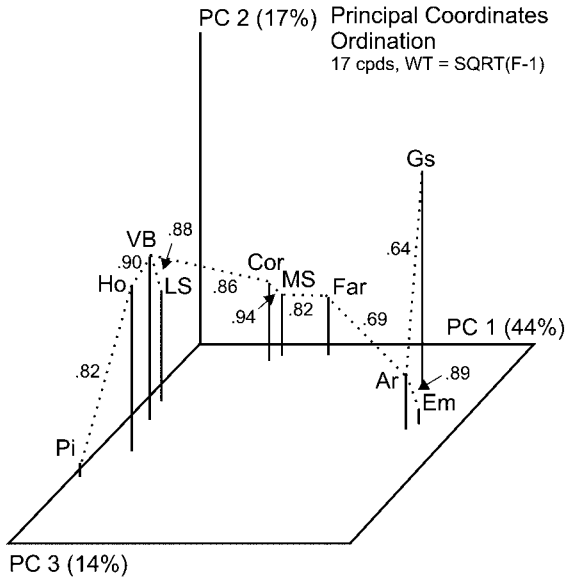

Figure 3. Principal coordinates ordination (PCO) of 10 olive cultivars based on 17 compounds with matches weighted by square root of (F − 1), where F is the F ratio from ANOVA (the dotted line is the minimum spanning network; the numbers next to the dotted line are the similarity between cultivars).

groups (cv. Ar-Em, Cor-MS, and Ho-VB-LS). Cultivar Gs has the most distinct chemical profile (being only 0.64 similar to cv. Ar), followed by cv. Pi (0.82 to cv. Ho) and cv. Far (0.82 to cv. MS) (Figure 3).

An alternative view of the chemical relationships among the cultivars is the minimum spanning network (Figure 4). Three sets of cultivars are very similar in their phenolics chemistry (cv. Cor-MS, Ho-VB, and Ar-Em) (Figure 4; Table 4). Cultivar Gs has the most distinct chemical profile (Figure 4; Table 4) with cv. Pi and Far being somewhat similar to cv. Ho and MS, respectively (Figure 4). It should be noted that the PCO and minimum spanning network reflect similarity in the cultivar's phenolics. This may or may not indicate their genetic relationships. Additional research utilizing DNA sequencing

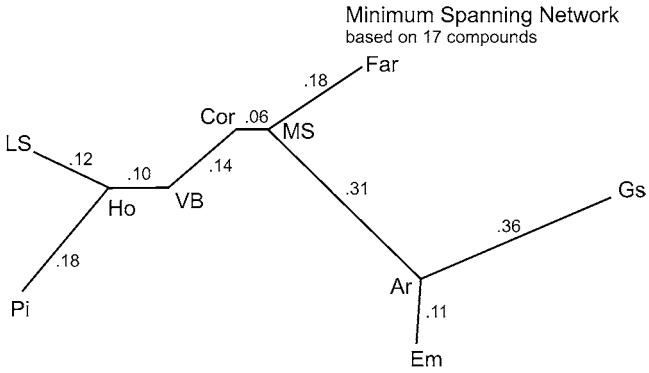

Figure 4. Minimum spanning network for 10 olive cultivars based on 17 compounds (the numbers next to the lines are distances (1 − similarity) between cultivars).

would be needed to more fully explore the overall genetic relationships among these cultivars.

In conclusion, 17 compounds were identified and quantified after analysis of the ethyl acetate extracts of 10 Spanish olive cultivars by HPLC-DAD and HPLC-DAD/ESI-MS. The lignan (+)-1-hydroxypinoresinol 1-*O*-*β*-D-glucopyranoside (**10**) (21.02−90.21 mg/g) and the flavonoid eriodictyol (**9**) (3.00−71.03 mg/g), together with compounds **6** (12.02−51.81 mg/g), **4** (14.91−26.81 mg/g), or **7** (11.92−29.61 mg/g), were prominent components in most cultivars. Multivariate analysis revealed significant quantitative and qualitative differences among the cultivars. The principal coordinates ordination and minimum spanning network established the chemical relationships among cultivars. Three sets of cultivars were found to be similar in their phenolic composition: (a) 'Cornicabra' and 'Manzanilla de Sevilla', (b) 'Hojiblanca' and 'Verdial de Badajoz', and (c) 'Arbequina' and 'Empeltre'. In contrast, cultivars 'Gordal sevillana', 'Picual', and 'Farga' had the most distinct chemical profiles. Despite having only two replicate extractions per cultivar, highly significant differences were found in ANOVA and SNK multiple-range comparisons of the chemical components among cultivars for this important biomass. Considering the abundance of this renewable agricultural byproduct and the influence of the cultivar genotype on the chemical composition, new opportunities for the industry are developing to recover diverse value-added products and explore potential applications from olive tree waste byproduct wood.

AUTHOR INFORMATION

Corresponding Author

*(J.A.) Phone: +34 953 212743. Fax: +34 953 211876. E-mail: jaltare@ujaen.es.

Funding

This study was supported by the Spanish Ministerio de Educación y Ciencia (R+D Project CTQ2005-07005/PPQ; partial financial support from the FEDER funds of the European Union). M.P.-B. was the recipient of a predoctoral fellowship granted by the Andalusian Government Junta de Andalucía. Part of the work was supported by the Centro de Instrumentación Científico-Técnica of the University of Jaén.

Notes

The authors declare no competing financial interest.

DOI: 10.1021/acs.jafc.5b02979
J. Agric. Food Chem. 2015, 63, 6493−6500

■ ACKNOWLEDGMENTS

We thank the Director and technical staff of Centro IFAPA "Venta del Llano", Mengíbar (Jaén province), Spain, for kindly providing all olive tree wood samples.

■ REFERENCES

(1) Grossman, S.; Dovrat, S.; Bergman, M. Natural antioxidants: just free radical scavengers or much more? *Trends Cancer Res.* **2011**, *7*, 57−73.

(2) Laitonjam, W. S. Natural antioxidants (NAO) of plants acting as scavengers of free radicals. In *Studies in Natural Products Chemistry*; Atta-ur-Rahman, Ed.; Elsevier: Amsterdam, The Netherlands, 2012; Vol. 37, pp 259−275.

(3) Kusumawati, I.; Indrayanto, G. Natural antioxidants in cosmetics. In *Studies in Natural Products Chemistry*; Atta-ur-Rahman, Ed.; Elsevier: Amsterdam, The Netherlands, 2013; Vol. 40, pp 485−505.

(4) Brewer, M. S. Natural antioxidants: sources, compounds, mechanisms of action, and potential applications. *Compr. Rev. Food Sci. Food Saf.* **2011**, *10*, 221−247.

(5) Kammerer, D. R.; Kammerer, J.; Valet, R.; Carle, R. Recovery of polyphenols from the by-products of plant food processing and application as valuable food ingredients. *Food Res. Int.* **2014**, *65*, 2−12.

(6) Ilarioni, L.; Proietti, P. Olive tree cultivars. In *The Extra-Virgin Olive Oil Handbook*; Peri, C., Ed.; Wiley Blackwell: Oxford, UK, 2014; pp 59−68.

(7) Martín-Peláez, S.; Covas, M. I.; Fito, M.; Kusar, A.; Pravst, I. Health effects of olive oil polyphenols: recent advances and possibilities for the use of health claims. *Mol. Nutr. Food Res.* **2013**, *57*, 760−771.

(8) Goulas, V.; Charisiadis, P.; Gerothanassis, I. P.; Manganaris, G. A. Classification, biotransformation and antioxidant activity of olive fruit biophenols: a review. *Curr. Bioact. Compds.* **2012**, *8*, 232−239.

(9) Bianco, A.; Ramunno, A. The chemistry of *Olea europaea*. In *Studies in Natural Products Chemistry*; Atta-ur-Rahman, Ed.; Elsevier: Amsterdam, The Netherlands, 2006; Vol. 33, pp 859−903.

(10) Ghanbari, R.; Anwar, F.; Alkharfy, K. M.; Gilani, A.-H.; Saari, N. Valuable nutrients and functional bioactives in different parts of olive (*Olea europaea* L.) − a review. *Int. J. Mol. Sci.* **2012**, *13*, 3291−3340.

(11) Japón-Luján, R.; Luque de Castro, M. D. Small branches of olive tree: a source of biophenols complementary to olive leaves. *J. Agric. Food Chem.* **2007**, *55*, 4584−4588.

(12) Ortega-García, F.; Peragón, J. HPLC analysis of oleuropein, hydroxytyrosol, and tyrosol in stems and roots of *Olea europaea* L. cv. Picual during ripening. *J. Sci. Food Agric.* **2010**, *90*, 2295−2300.

(13) Spizzirri, U. G.; Restuccia, D.; Parisi, O. I.; Cirillo, G.; Curcio, M.; Iemma, F.; Puoci, F.; Picci, N.; Chiricosta, S. Olive stones as a source of antioxidants for food industry (Bratislava). *J. Food Nutr. Res.* **2011**, *50*, 57−67 , http://www.vup.sk/en/index.php?mainID=2=34=2=50e=969.

(14) Pérez-Bonilla, M.; Salido, S.; van Beek, T. A.; Altarejos, J. Radical-scavenging compounds from olive tree (*Olea europaea* L.) wood. *J. Agric. Food Chem.* **2014**, *62*, 144−151.

(15) Talhaoui, N.; Gómez-Caravaca, A. M.; Roldán, C.; León, L.; De la Rosa, R.; Fernández-Gutiérrez, A.; Segura-Carretero, A. Chemometric analysis for the evaluation of phenolic patterns in olive leaves from six cultivars at different growth stages. *J. Agric. Food Chem.* **2015**, *63*, 1722−1729.

(16) Sabatini, N. Recent patents in olive oil industry: new technologies for the recovery of phenols compounds from olive oil, olive oil industrial by-products and waste waters. *Rec. Patents Food Nutr. Agric.* **2010**, *2*, 154−159.

(17) Gómez-Caravaca, A. M.; Verardo, V.; Bendini, A.; Toschi, T. G. From wastes to added value by-products: an overview on chemical composition and healthy properties of bioactive compounds of olive oil chain by-products. In *Virgin Olive Oil*; De Leonardis, A., Ed.; Nova Science Publishers: Hauppauge, NY, 2014; pp 301−334.

(18) Rubio-Senent, F.; Martos, S.; García, A.; Fernández-Bolaños, J. G.; Rodríguez-Gutiérrez, G.; Fernández-Bolaños, J. Isolation and characterization of a secoiridoid derivative from two-phase olive waste (alperujo). *J. Agric. Food Chem.* **2015**, *63*, 1151−1159.

(19) Romero-García, J. M.; Niño, L.; Martínez-Patiño, C.; Álvarez, C.; Castro, E.; Negro, M. J. Biorefinery based on olive biomass. State of the art and future trends. *Bioresour. Technol.* **2014**, *159*, 421−432.

(20) Ould-Idriss, A.; Stitou, M.; Cuerda-Correa, E. M.; Fernández-González, C.; Macías-García, A.; Alexandre-Franco, M. F.; Gómez-Serrano, V. Preparation of activated carbons from olive-tree wood revisited. I. Chemical activation with H_3PO_4. *Fuel Process. Technol.* **2010**, *92*, 261−265.

(21) Toledano, A.; Serrano, L.; Labidi, J. Process for olive tree pruning lignin revalorization. *Chem. Eng. J.* **2012**, *193*−*194*, 396−403.

(22) Moral, A.; Hernández, M. D.; de la Torre, M. J.; Torrecilla, J. S. Pulp and paper obtained from olive tree trimmings. *Adv. Environ. Res.* **2012**, *20*, 237−244.

(23) Ruiz, E.; Cara, C.; Ballesteros, M.; Manzanares, P.; Ballesteros, I.; Castro, E. Ethanol production from pretreated olive tree wood and sunflower stalks by an SSF process. *Appl. Biochem. Biotechnol.* **2006**, *130*, 631−643.

(24) Intini, F.; Kuhtz, S.; Rospi, G. Life cycle assessment (LCA) of an energy recovery plant in the olive oil industries. *Int. J. Energy Environ.* **2012**, *3*, 541−552.

(25) Salido, S.; Palomino, F. M.; Linares, P.; van Beek, T. A.; Altarejos, J.; Nogueras, M.; Sánchez, A. Antioxidant activity of olive wood extracts. 23rd IUPAC−International Symposium on the Chemistry of Natural Products, Florence, Italy, 2002; p 321.

(26) Altarejos, J.; Salido, S.; Pérez-Bonilla, M.; Linares-Palomino, P. J.; van Beek, T. A.; Nogueras, M.; Sánchez, A. Preliminary assay on the radical scavenging activity of olive wood extracts. *Fitoterapia* **2005**, *76*, 348−351.

(27) Pérez-Bonilla, M.; Salido, S.; van Beek, T. A.; Linares-Palomino, P. J.; Altarejos, J.; Nogueras, M.; Sánchez, A. Isolation and identification of radical scavengers in olive (*Olea europaea*) wood. *J. Chromatogr. A* **2006**, *1112*, 311−318.

(28) Pérez-Bonilla, M.; Salido, S.; van Beek, T. A.; de Waard, P.; Linares-Palomino, P. J.; Sánchez, A.; Altarejos, J. Isolation of antioxidative secoiridois from olive wood (*Olea europaea* L.) guided by on-line HPLC−DAD−radical scavenging detection. *Food Chem.* **2011**, *124*, 36−41.

(29) Pérez-Bonilla, M.; Salido, S.; Sánchez, A.; van Beek, T. A.; Altarejos, J. Effect of extraction conditions on the antioxidant activity of olive wood extracts. *Int. J. Food Sci.* **2013**, *1* (719593), 1−13.

(30) Koleva, I. I.; Niederländer, H. A. G.; van Beek, T. A. An on-line HPLC method for detection of radical scavenging compounds in complex mixtures. *Anal. Chem.* **2000**, *72*, 2323−2328.

(31) van Beek, T. A.; Tetala, K. K. R.; Koleva, I. I.; Dapkevicius, A.; Exarchou, V.; Jeurissen, S. M. F.; Claassen, F. W.; van der Klift, E. J. C. Recent developments in the rapid analysis of plants and tracking their bioactive constituents. *Phytochem. Rev.* **2009**, *8*, 387−399.

(32) Dahmani-Hamzaoui, N.; Salido, S.; Linares-Palomino, P. J.; Baaliouamer, A.; Altarejos, J. On-line radical scavenging detection and characterization of antioxidants from *Artemisia herba-alba*. *Helv. Chim. Acta* **2012**, *95*, 564−576.

(33) Argoti, J. C.; Linares-Palomino, P. J.; Salido, S.; Ramírez, B.; Insuasty, B.; Altarejos, J. On-line activity screening for radical scavengers from *Baccharis chilco*. *Chem. Biodiversity* **2013**, *10*, 189−197.

(34) Salido, S.; Pérez-Bonilla, M.; Linares-Palomino, P. J.; Nogueras, M.; Sánchez, A.; Altarejos, J. Procedimiento de extracción de madera de olivo y extractos enriquecidos en productos de interés alimentario. Span. Patent ES 2386860, 2012.

(35) Barranco, D. *El Cultivo del Olivo*. Ediciones Mundi-Prensa: Madrid, Spain, 2008.

(36) von Gadow, A.; Joubert, E.; Hansmann, C. F. Comparison of the antioxidant activity of aspalathin with that of other plant phenols of rooibos tea (*Aspalathus linearis*), α-tocopherol, BHT, and BHA. *J. Agric. Food Chem.* **1997**, *45*, 632−638.

(37) Steele, R. G. D.; Torrie, J. H. *Principles and Procedures of Statistics*; McGraw-Hill Book: New York, 1960.

DOI: 10.1021/acs.jafc.5b02979
J. Agric. Food Chem. 2015, 63, 6493−6500

(38) Gower, J. C. A general coefficient of similarity and some of its properties. *Biometrics* **1971**, *27*, 857−874.
(39) Adams, R. P. Statistical character weighting and similarity stability. *Brittonia* **1975**, *27*, 305−316.
(40) Gower, J. C. Some distance properties of latent root and vector methods used in multivariate analysis. *Biometrika* **1966**, *53*, 326−338.
(41) Veldman, D. J. *Fortran Programming for the Behavioral Sciences*; Holt, Rinehart and Winston Publishing: New York, 1967.
(42) Wang, X.; Li, C.; Zheng, Y.; Di, D. Polyphenols from leaves of *Olea europaea*. *Zhongcaoyao* **2011**, *42*, 848−851.
(43) Peralbo-Molina, A.; Priego-Capote, F.; Luque de Castro, M. D. Tentative identification of phenolic compounds in olive pomace extracts using liquid chromatography-tandem mass spectrometry with a quadrupole-quadrupole-time-of-flight mass detector. *J. Agric. Food Chem.* **2012**, *60*, 11542−11550.
(44) Granados-Principal, S.; Quiles, J. L.; Ramírez-Tortosa, C. L.; Sánchez-Rovira, P.; Ramírez-Tortosa, M. C. Hydroxytyrosol: from laboratory investigations to future clinical trials. *Nutr. Rev.* **2010**, *68*, 191−206.
(45) Hu, T.; He, X.-W.; Jiang, J.-G.; Xu, X.-L. Hydroxytyrosol and its potential therapeutic effects. *J. Agric. Food Chem.* **2014**, *62*, 1449−1455.
(46) Hassen, I.; Casabianca, H.; Hosni, K. Biological activities of the natural antioxidant oleuropein: exceeding the expectation − a mini-review. *J. Funct. Foods* **2014** (in press; DOI:10.1016/j.jff.2014.09.001).

DOI: 10.1021/acs.jafc.5b02979
J. Agric. Food Chem. 2015, 63, 6493−6500

crops worldwide.[14] To date, a number of studies have used two-dimensional electrophoresis (2-DE) to investigate gluten protein responses to high temperature, fertilizers, and drought[15−18] and reported changes in as few as 3[15] to as many as 107 2-DE spots;[17] moreover, most research focuses on metabolic wheat grain proteins,[19] whereas fewer studies focus on storage proteins. High temperature (and also water deficit) shortens the duration of grain filling and reduces the time taken to reach apoptosis and harvest maturity.[20] Consistent with these events, transcripts for α-, γ-, and ω-gliadins, HMW-GS, and LMW-GS accumulate and disappear earlier.[21] Yang et al.[17] applied both heat and water stress to a *T. aestivum* cultivar and found the highest gliadin contents at 19 DAA under heat treatment and at maturity under water stress conditions. Moreover, the authors found that high-temperature treatment resulted in higher glutenin and gliadin contents at maturity; this contrasts with the findings of other authors, who found that high temperature can induce synthesis of gliadins in wheat at the expense of glutenins.[22] In contrast to the gliadin fractions, multiple high-temperature or water-deficit events applied at both terminal spikelet and anthesis resulted in significantly higher glutenin contents at maturity than did the single-stress treatments.[17] Moreover, the same authors reported that some storage proteins, including α- and γ-gliadins, LMW-GS, and globulins, decreased and that one globulin and one specific LMW-GS increased in response to water deficit. It is fundamentally important to understand how environmental treatments affect the timing of grain developmental processes in order to pursue wheat quality, because protein synthesis of storage proteins occurs during this stage. However, most research has focused on the effects of high temperature, whereas fewer have focused on the effect of water stress on the accumulation on gluten proteins during grain filling, particularly in durum wheat.

The aim of the present study was to evaluate the effect of terminal drought stress on the gluten protein composition of durum wheat during grain filling by a proteomic approach. For this purpose two Italian cultivars characterized by different technological qualities were used.

MATERIALS AND METHODS

Plant Material and Growth Conditions. Two Italian durum wheat (*T. turgidum* spp. *durum*) cultivars, Ciccio and Svevo, were cultivated in a growth chamber under controlled conditions of temperature, humidity, and light during 2010. The two cultivars were chosen for their different technological performances, Ciccio showing a higher gluten index (84) than Svevo (39) in the seed batch used for sowing.[23] Both cultivars have almost the same growing, flowering, and maturation times. The plants were grown in pots (37 × 15 cm), using a completely randomized design with two replications and three factors (phonological stage, cultivar, and water regimen). Seeds were sown on February 8 with a seeding density of 150 seeds m^{-2} (8 seeds per pot); after emergence, seed density was standardized at 5 seeds per pot. Each pot contained a mixture of sandy clay loam soil, sand, and peat in a 6:3:1 ratio, with a field capacity of 26.9% and a wilting point of 16.4%. Temperature and photoperiod (hours of daylight) were modified during the plant life cycle from 8/6 °C and 10 h at sowing to 28/22 °C and 16 h at physiological maturity. Phosphorus was applied at sowing as diammonium phosphate at a rate of 9 g m^{-2}. Nitrogen was applied as ammonium nitrate at a rate of 3.5 g m^{-2} at sowing, at a rate of 6.5 g m^{-2} at tillering, and at preanthesis at a rate of 2 g m^{-2}. Before anthesis (73 days after sowing), all plants were well watered (WW) by replenishing soil to field capacity whenever the threshold of 50% of available soil water was reached; water stress (WS) was imposed since anthesis by replenishing soil up to 70% of available water, whereas for the control plants soil was replenished up to 100% of available water. Heads were collected at selected time points during grain development under the two water regimens. Under WW, heads were monitored at 2−5 day intervals from anthesis by visual inspection of cut endosperm. Because water stress shortened the grain developmental process, heads were monitored at 1−3 day intervals from anthesis under WS; on this basis the heads were collected at 10 and 14 DAA, at 18 and 21 DAA, and at 28 and 31 DAA in WS and WW, respectively, corresponding to medium milk (stage 75), soft dough (waxy) (stage 85), and physiological maturity (stage 92) of the Zadoks growth scale.[24] The following parameters were determined at physiological maturity: kernel number per spike, 1000 kernel weight (g) (TKW), and protein content (% dw) by using a micro-Kjeldahl.

Storage Protein Extraction. Five ears were harvested at each specific stage from the primary tillers of milk, waxy, and physiological sets of pots. Kernels harvested from the middle part of the ears were used for storage protein extraction. Milk and waxy samples were immediately frozen in liquid nitrogen. All of the samples were freeze-dried. Fifty milligrams of ground grain samples was suspended in 200 μL of KCl buffer solution (100 mM KCl, 50 mM Tris-HCl, pH 7.8, 5 mM EDTA). The suspension was incubated on ice for 5 min, with intermittent shaking, and centrifuged at 14500*g* for 15 min at 4 °C to separate the soluble (supernatant) from the insoluble fraction (pellet), which was mostly gliadins and glutenins. Storage proteins were then extracted from the pellet using 800 μL of SDS buffer (2% SDS, 10% glycerol, 50 mM DTT, 40 mM Tris-HCl, pH 6.8). Proteins were precipitated by adding 4 volumes of cold acetone (−20 °C) to remove the SDS, which interferes with protein determination and prevents separation of proteins by isoelectric focusing (IEF). After overnight incubation at −20 °C and double centrifugation at 16000 rpm for 10 min at room temperature, the acetone was removed. The pellet was suspended in urea buffer solution (8 M urea, 2% Triton X-100, 0.03% DTT, 0.04% BPB, 0.5% IPG buffer) and stored at −20 °C. Protein concentration was measured using the biuret method, with BSA as a standard.[25] Under WW and WS conditions the following results (expressed in mg mL^{-1}) were obtained in milk stage, waxy stage, and physiological maturity, respectively: Ciccio, 0.069 and 0.08, 0.098 and 0.114, and 0.116 and 0.134; Svevo, 0.076 and 0.093, 0.109 and 0.132, and 0.129 and 0.155.

2-DE Analysis. Storage proteins were separated by 2-DE, as reported in Pompa et al.[26] Briefly, IEF was performed by using the Ettan IPGphor 3 isoelectric focusing system (GE Healthcare Bio-Sciences AB, Uppsala, Sweden). Samples containing 200 μg of storage proteins were loaded onto each IEF gel. Immobiline DryStrips (pH 3−10, 13 cm length; GE Healthcare Bio-Sciences AB) were used. SDS-PAGE was carried out using an SE 600 apparatus (Hoefer, Inc., Holliston, MA, USA). Strips were equilibrated and then loaded onto 1 mm × 18 cm × 16 cm vertical polyacrylamide SDS-PAGE gels (T, 12%; C, 1.28%). Separation of both proteins and molecular weight markers (GE Healthcare Bio-Sciences AB) was performed at 30 mA per gel at 10 °C. Staining was performed by GBB 250 Coomassie Brilliant Blue and destaining in deionized water.

Two biological replications were taken into consideration, but these were pooled due to the scarcity of material, especially at the milk and waxy stages. Four replicates were performed on pooled samples for each of the two cultivars (Ciccio and Svevo), each of the two irrigation treatments (WS and WW), and each of the three developmental stages (milk, waxy, and physiological), for a total of 48 gels. 2-DE gels were digitized at 600 dpi by a scanner. ImageMaster 2D Platinum 6.0 software (GE Healthcare Bio-Sciences AB) was used for gel analysis, including spot detection, spot match, and spot and region volume quantification, and the expression levels of protein spots on 2-DE gels were determined by protein abundance (% vol). The 2-DE gels were subdivided into four regions on the basis of protein molecular weight, as reported also in Pompa et al.:[26] the high molecular weight (H) region (>60 kDa, mostly including the HMW-GS); the intermediate (I) region (60−48 kDa, including ω-gliadins and D subunits of LMW-GS); the low molecular weight (L48−35) region (48−35 kDa, including most of the typical LMW-GS, namely, LMW-s and LMW-m types); and the low molecular weight (L<35) region (<35 kDa, including α- and γ-gliadins and c-type LMW-GS).[27]

DOI: 10.1021/acs.jafc.5b01635
J. Agric. Food Chem. 2015, 63, 6501−6512

The gel region data from the four replicates were analyzed using the ANOVA procedure of the M-stat C statistical package (Crop Soil Sciences Department, Michigan State University). Significant differences between the mean values were calculated using Tukey's test. Moreover, the differences between spots were evaluated by the using *t* test.

In-Gel Digestion of Protein Spots and Mass Spectrometry Analyses. *Chemicals.* Unless otherwise indicated, all chemicals used in the preparation of buffers and solutions were of analytical reagent grade. 1,4-Dithiothreitol (DTT) was purchased from Sigma-Aldrich (St. Louis, MO, USA). Formic acid (≥98%), sodium hydroxide, calcium chloride (≥99%), and urea were purchased from Merck (Darmstadt, Germany). Water, methanol, and acetonitrile (LC-MS CHROMASOLV, ≥99.9%) were from Fluka. Chymotrypsin (bovine) was purchased from Princeton Separation (Adelphia, NJ, USA).

In-Gel Chymotrypsin Digestion. The protein spots excised from 2-DE gels were digested by an optimized in-gel chymotrypsin procedure.[26] Gel pieces (3 mm), thoroughly washed with 10 μL of deionized water and dried, were destained with 50 mM ammonium bicarbonate and acetonitrile (ACN) (50:50, v/v) (four times for 5 min). After liquid removal, the gel pieces were dehydrated for 0.5 h using 30 μL of ACN. The dehydrated gel pieces were incubated with 10 mM DTT at 56 °C for 45 min and then with 55 mM iodoacetamide (IoAA) at room temperature in the dark for 30 min; finally, they were washed with a solution of 50 mM ammonium bicarbonate/ACN (50:50, v/v) with gentle agitation for 10 min and briefly dehydrated with ACN. The washing step was repeated twice before the gel pieces were dried. Proteins in the gel pieces were digested with 5 μL of chymotrypsin (5 ng/μL) in 25 mM ammonium bicarbonate at 37 °C for 16 h. Five microliters of 1 M urea at pH 8, as the denaturing agent, and calcium chloride (1 mM) were added to the solution to promote enzyme action. After digestion, the peptides were extracted for 15 min with 5 μL of 50 mM ammonium bicarbonate and 5 μL of ACN/formic acid (FA; 1% in water) solution (50:50, v/v). The solution containing the extracted peptides was collected after 15 min.

Liquid Chromatography and Mass Spectrometry. Digested proteins were separated by a nanoLC apparatus, Ultimate 3000 (Dionex LC-Packings, Amsterdam, The Netherlands) consisting of an autosampler, a low-pressure gradient micropump series, equipped with flow managers, a column thermostat, and a UV detector set at 214 nm. The nanoLC-ESI-IT-MS/MS system was controlled by Chromeleon CHM-1 (Dionex) and Hystar 2.3 (Bruker Daltonics) software. A PepMapTM C18 nano trap column (300 μm i.d. × 5 mm, 5-μm particle size, LC Packings) was used for concentrating and desalting the injected sample. Chromatographic separations were carried out by a PepMap C18 analytical column (15 cm length × 75 μm i.d., 3-μm particle size, 100-Å pore diameter; LC Packings). The mobile phase consisted of ACN/0.1% formic acid (FA) in water (2:98 v/v) (eluent A) and ACN/0.1% FA in water (80:20 v/v) (eluent B). Sample elution through the analytical column was obtained at a flow rate of 0.300 μL/min. The optimized elution gradient was the following: 7 min isocratic step at 98% A and 2% B; 28 min linear gradient to 50% A and 50% B; 1 min linear gradient to 10% A and 90% B; 4 min isocratic step at 10% A and 90% B; 1 min to the initial mobile phase composition (98% A and 2% B), at which the system was re-equilibrated for 19 min; total run time was 60 min. Mass spectrometry analyses were performed by using a high-capacity ion trap, coupled to a nano-ESI source, operating in the positive ion mode. The following parameters were set: spray voltage, 4.5 kV; sheath gas (nitrogen) flow rate, 10 L/min; capillary voltage, 1.5 V; heated capillary temperature, 160 °C. A full scan MS acquisition in the m/z 100−1500 range was performed with the acquisition of base peak chromatogram (BPC) and total ion current (TIC) profiles. MS/MS analysis by collision-induced dissociation (CID) was performed using unattended data-dependent acquisition mode, and the auto-MS/MS event was carried out with a number of precursor ions of 3. The minimal signal required for precursor ion selection was set to an absolute threshold of 10000.

Data Analysis and Database Search. Extraction of mass spectra peak lists from chromatograms, mass annotation, and deconvolution were performed by using Data Analysis 4.0. The acquired MS and MS/MS data sets were submitted to database searches by using Biotools 3.2 and MASCOT search engine (Matrix Science, London, UK). To do further research taking into consideration the wide dynamic range of relative peptide abundance, in addition to the MS/MS spectra obtained along the entire chromatographic run, the TIC chromatogram was divided into a series of time segments corresponding to the main peaks. Each segment was composed of a sequence of MS/MS acquisitions, for a better identification by database search.

The data analysis files were used to search entries under the *other green plant* category of NCBI-nr and SwissProt databases. As variable modifications, the oxidation of methionine, the phosphorylation of serine, threonine, and tyrosine, and the deamination of glutamine and asparagine were set. A maximum number of three missed cleavages was allowed, and a peptide tolerance of 0.3 Da was set for both precursor peptide ion and MS/MS tolerance in the window of error for matching the peptide mass values.

As far as the enzyme selection is concerned, consecutive database searches were performed by setting chymotrypsin as protease.

RESULTS

Gluten Protein Composition during Grain Development. Different durations of grain development were observed for the two irrigation treatments (WW and WS). In particular, both cultivars reached the milk, waxy, and physiological stages earlier under WS than under WW (10 vs 14 DAA, 18 vs 21 DAA, and 28 vs 31 DAA, respectively).

At physiological maturity, the two cultivars presented a significantly lower TKW and higher protein content under water stress. In particular, Ciccio showed TKW values of 37 g in WW and 23 g in WS, whereas Svevo showed TKW values of 36 g in WW and 22 g in WS ($P \leq 0.05$). The protein concentration values were 14.5% in WW and 16.8% in WS for Ciccio and 16.1% in WW and 19.5% in WS for Svevo ($P \leq 0.05$).

The 2-DE gels were highly reproducible (SD range of the total spot volumes of the four technical replicates for each thesis = 4−13%) and presented well-defined spots without streaking (Figures 1 and 2). Under WW, the average numbers of spots at the milk, waxy, and physiological stages were 66, 107, and 99 for Ciccio and 65, 112, and 100 for Svevo; under WS, the average numbers were 57, 82, and 96 for Ciccio and 63, 87, and 107 for Svevo. The number of spots increased progressively in both cultivars from the milk stage to physiological maturity under WS conditions; under WW conditions, the highest number of spots was at the waxy stage, with a slight reduction at maturity (Figures 1 and 2).

During grain filling, some spots apparently changed their isoeletrical point. This was more evident in the waxy stage for HMW-GS that showed more acidic position with respect to the milky and physiological stages; we do not have any reliable explanation for this, since deamidation, which is a common artifact for gluten proteins because of the numerous glutamine residues,[28] should be excluded because this shift was not observed on the same proteins also at physiological stage.

Figure 3 reports the percentages of H, I, L48−35, and L<35 regions for the two cultivars and the two water regimens during grain development.

The H region percentage in Ciccio increased progressively to the maximum value at the physiological maturity, when similar values were observed between the two water regimens. In Svevo, the H region percentage was the same at both milk and waxy stages with a sharp increase at maturity, which was more marked under WS (Figure 3a).

The I region presented the highest percentages at physiological maturity and the lowest percentages at the waxy stage

DOI: 10.1021/acs.jafc.5b01635
J. Agric. Food Chem. 2015, 63, 6501−6512

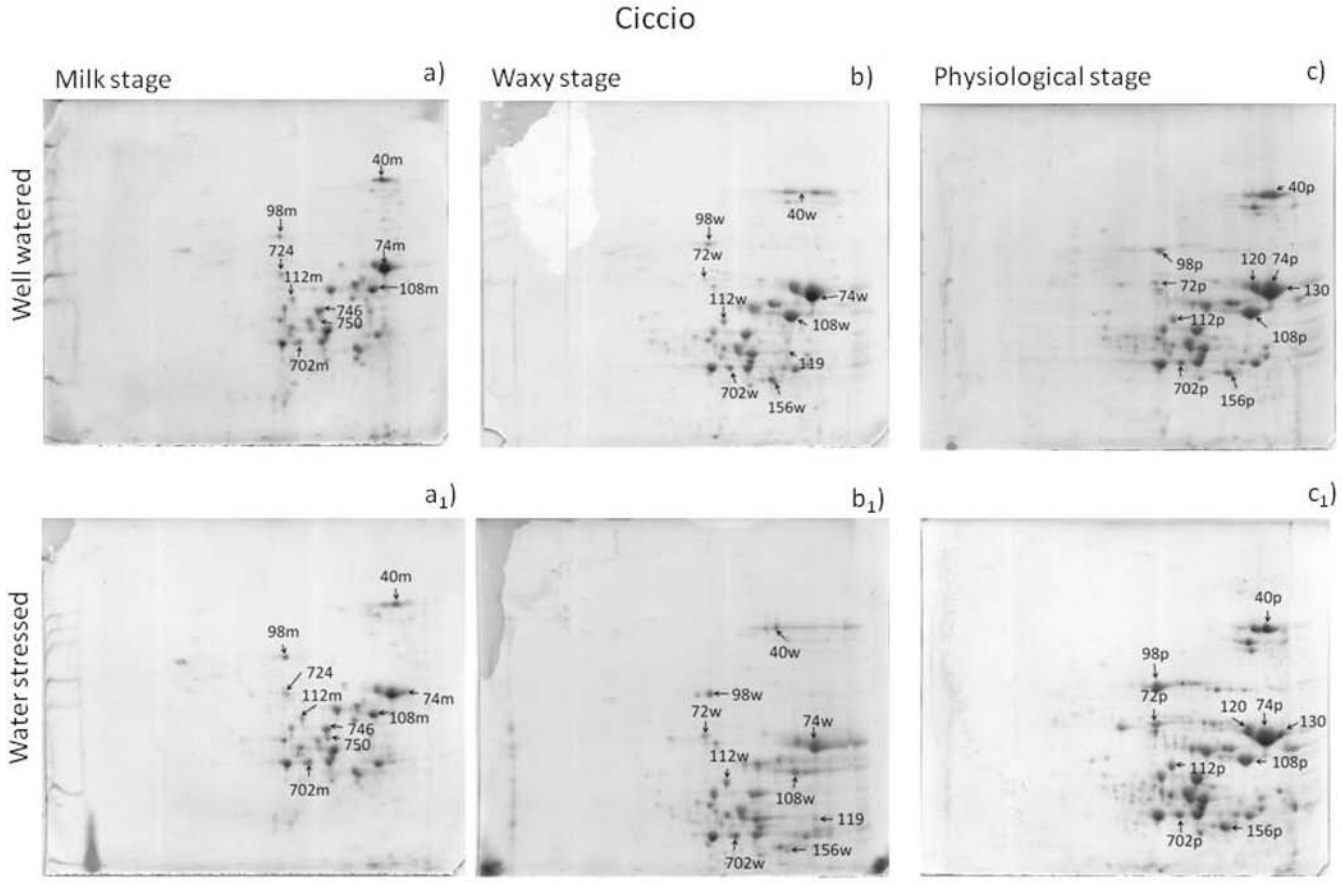

Figure 1. Gluten protein 2DE gels (IEF × SDS-PAGE) of the cultivar Ciccio cultivated under well-watered and water-stress conditions (a, a_1, b, b_1, c, and c_1 are milk, waxy, and physiological stages in WW and WS, respectively).

for both cultivars, generally showing higher values under WS (Figure 3b).

The L48−35 region in both cultivars showed a slight progressive increase during grain development, with lower values under WS (Figure 3c).

Finally, the L<35 region decreased slightly during grain development in both cultivars, with a general increase under WS (Figure 3d).

At physiological maturity, significant differences ($P \leq 0.05$) were found between the two cultivars in the different gel regions. In particular, H was significantly overexpressed in Svevo, especially under WS (11.8 vs 10.7% under WW and 13.5 vs 10.6% under WS); moreover, the L48−35 region was always significantly overexpressed in Ciccio (46.7 vs 43% under WW and 40 vs 35% under WS), and the L<35 region was always significantly overexpressed in Svevo (42.4 vs 36% under WW and 45.3 vs 39% under WS).

Differences in Protein Expression between Well-Watered and Water-Stressed Conditions (WW vs WS). Table 1 reports differentially expressed spots between the two water regimens for the two cultivars in the three grain developmental stages and their *P* levels, whereas Table 2 lists spot identification using nano-HPLC-ESI-IT/MS/MS.

H Region. At the milk stage, Ciccio presented spot 40m significantly down-expressed in WS (Table1). This spot matched spot 40w in the waxy stage, identified as the HMW-GS1Bx7 (Table 2), and spot 40p in the physiological maturity, both down-expressed under WS (Figure 1).

As for Svevo, spot 43m of the milk stage was slightly down-expressed under WS (Table 1). This spot matched spot 43w in the waxy stage, which did not differ between the two water regimens, and spot 43p at physiological maturity, which was overexpressed under WS (Table 1 and Figure 2); at physiological maturity, this spot was identified as the HMW-GS 1Bx (Table 2). Spot 66m, down-expressed under WS and identified as the HMW-GS 1By8 (Tables 1 and 2), matched spot 66p at physiological maturity with the same identification, but with an overexpression under WS (Figure 2 and Table 1). Finally, spot 38w at the waxy stage matched spot 38p at physiological maturity (Figure 2), identified as the HMW-GS 1Bx (allele *1Bx* Tdu-e) (Table 2). In both cases, the spots showed down-expression under WS (Table 1).

I Region. In both Ciccio and Svevo, 98m and 96m spots at the milk stage matched 98w and 96w spots at the waxy stage and 98p and 96p spots at physiological maturity (Figures 1 and 2), which were constantly overexpressed under WS (Table 1); at physiological maturity, these spots have been identified as an ω-5-gliadin (Table 2).

L48−35 Region. In this region, Ciccio significantly overexpressed spot 724 under WS in the milk stage and significantly down-expressed spots 120 and 130 under WS at physiological maturity (Table1); unfortunately, identification using nano-HPLC-ESI-IT/MS/MS was impossible for these spots. Spot 74m presented similar values under the two water regimens and matched spot 74w at waxy stage and spot 74p at physiological maturity, both significantly down-expressed under WS condition (Figure 1 and Table 1); at physiological maturity this spot was identified as a LMW-GS s-type (Table 2). Spot 108m did not present any differences between the two water

DOI: 10.1021/acs.jafc.5b01635
J. Agric. Food Chem. 2015, 63, 6501−6512

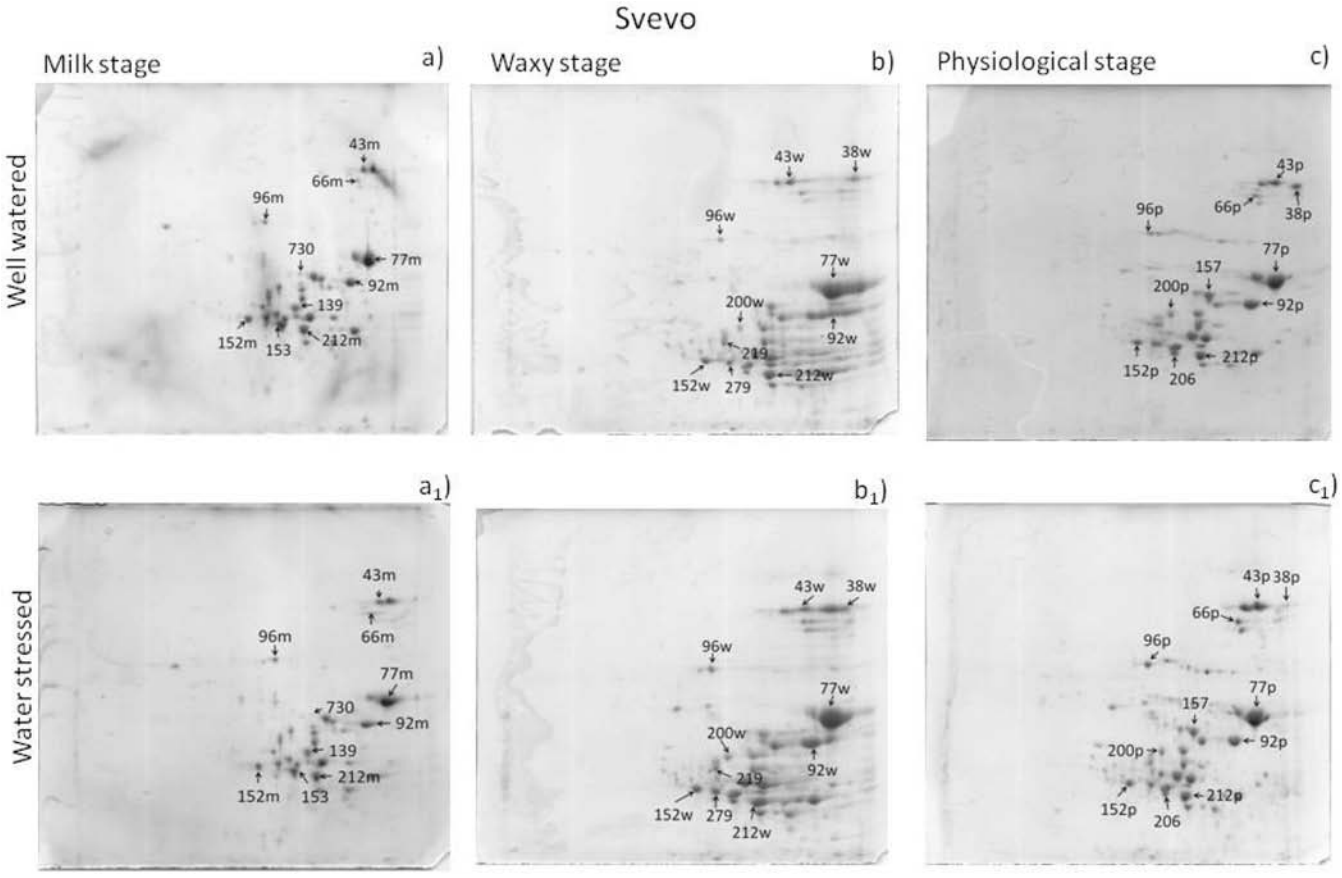

Figure 2. Gluten protein 2DE gels (IEF × SDS-PAGE) of the cultivar Svevo cultivated under well-watered (WW) and water-stress conditions (WS) (a, a_1, b, b_1, c, and c_1 are milk, waxy, and physiological stages in WW and WS, respectively).

regimens and matched spot 108w at the waxy stage and spot 108p at physiological maturity, both down-expressed under WS (Figure 1 and Table 1); spot 108p was identified as a LMW-GS m-type (Table 2). In the waxy stage, spot 72w, identified as a triticin (Table 2), matched spot 72p at physiological maturity (Figure 1), and in both cases an overexpression under WS was observed (Table 1).

As for Svevo, spot 730 at the milk stage and spot 157 at physiological maturity were down-expressed under WS (Table 1), but identification of these spots was unsuccessful. Spot 77m, generically identified as a LMW-GS type 2 (Table 2), matched spot 77w of the waxy stage and spot 77p at physiological maturity (Figure 2); this protein was down-expressed under WS in the milk and waxy stages, but no difference was observed between the two water regimens at physiological maturity (Table 1). Spot 92m, identified as a LMW-GS (Table 2), matched spot 92w at the waxy stage and spot 92p at physiological maturity (Figure 2); these spots were constantly down-expressed under WS (Table 1).

L<35 Region. As for Ciccio, at the milk stage spots 746 and 750 were down-expressed under WS (Table1); spot 746 was identified as an α-gliadin (Table 2). On the contrary, spot 119 at the waxy stage was overexpressed under WS (Table 1); for spots 750 and 119, no identification was possible. Spot 702m was significantly overexpressed under WS (Table 1) and was identified as an α-gliadin (Table 2). This spot matched spot 702w at the waxy stage, significantly overexpressed under WS, and spot 702p at physiological maturity, which did not present any significant differences between the two water regimens (Table 1 and Figure 1). Spot 112m matched spot 112w, identified as an α-gliadin precursor, and spot 112p at physiological maturity (Figure 1 and Table 2); for these spots, significant differences were found between the two water regimens only at the waxy stage, with an overexpression under WS (Table 1). Finally, at the waxy stage, spot 156 was slightly down-expressed under WS (Table 1) and matched spot 156p at physiological maturity, which was significantly down-expressed under WS (Figure 1 and Table 1) and identified as a γ-gliadin (Table 2).

As for Svevo, spots 139 and 153 at the milk stage were identified as α-gliadins (Table 2); both spots were overexpressed under WS (Table 1). Spot 152m has been identified as an α-gliadin (Table 2) and matched spot 152w at the waxy stage and spot 152p at physiological maturity (Figure 2), which were significantly overexpressed under WS at the milk and waxy stages (Table 1). Spot 212m matched spot 212w at the waxy stage and spot 212p at physiological maturity (Figure 2), identified as an α-gliadin constantly overexpressed under WS (Tables 1 and 2). At the waxy stage, spots 219 and 279 were overexpressed under WS (Table 1); no identification was possible for spot 219, whereas spot 279 was identified as an α-gliadin (Table 2). Spot 200w, identified as an α-gliadin precursor (Table 2) matched spot 200p at physiological maturity (Figure 2); in both cases the spots were overexpressed under WS (Table 1). Finally, at physiological maturity, spot 206, the only spot down-expressed under WS (Table 1), was identified as an α-gliadin (Table 2).

DISCUSSION

The shorter grain filling period observed in water stress conditions compared with well-watered conditions agrees with

DOI: 10.1021/acs.jafc.5b01635
J. Agric. Food Chem. 2015, 63, 6501−6512

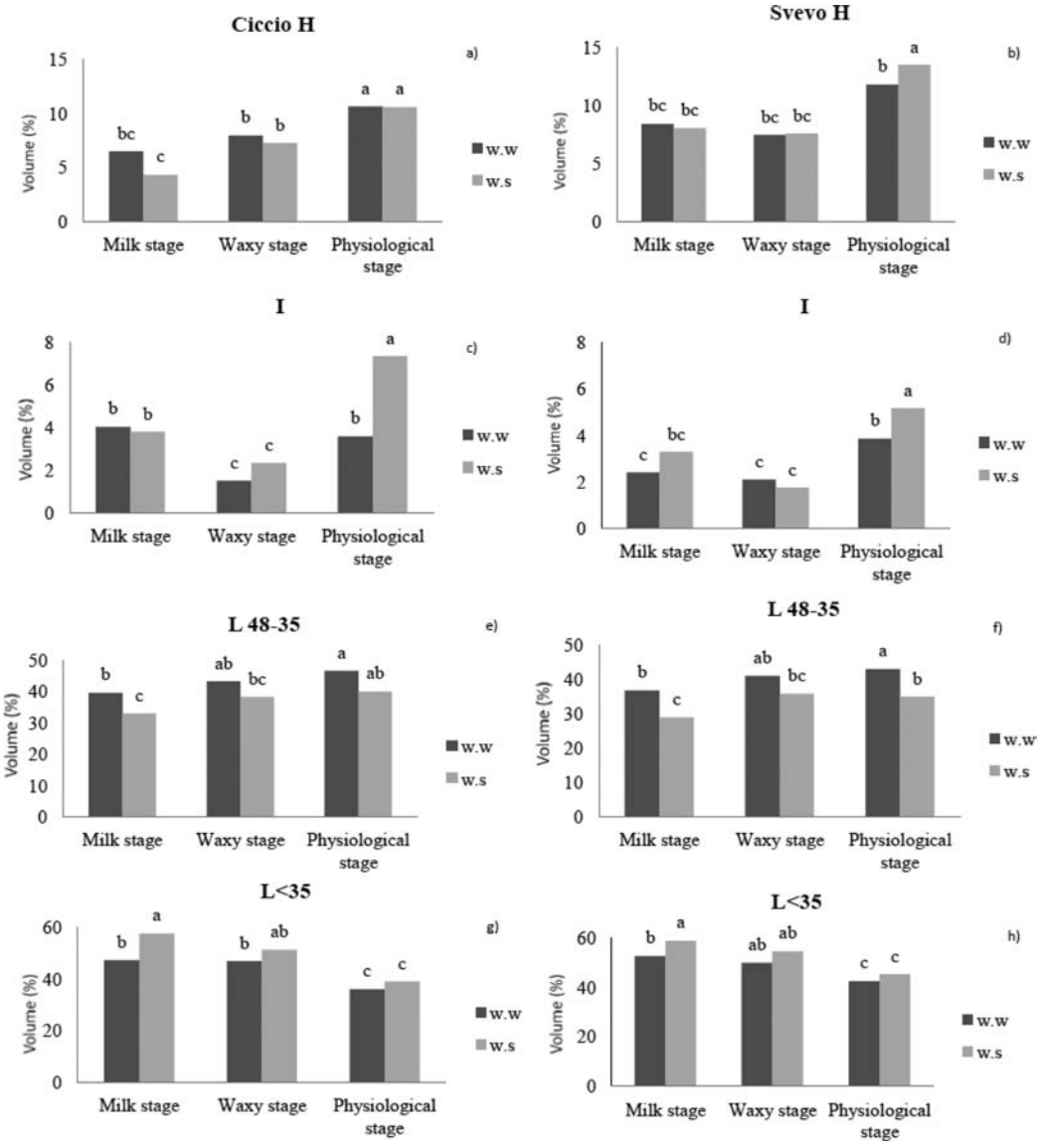

Figure 3. Percentage gel regions volume of the cultivars Ciccio and Svevo cultivated under well-watered (WW) and water-stress (WS) conditions during milk, waxy, and physiological stages (a, b, c, and d are high molecular weight (H), intermediate weight (I), low molecular weight 48−35 kDa, and low molecular weight <35 kDa regions, respectively). Different letters indicate significant differences at $P \leq 0.05$ according to Tukey's test.

several studies carried out in controlled environments, showing that high temperatures and drought accelerate grain development.[29] In addition, the reduced yield and increased protein content observed under WS confirmed what was already observed under the Mediterranean environment.[30,31] Storage protein composition showed significant changes during grain development, differing in relation to cultivar and water regimen in all of the gel regions considered (Figure 3).

H Region. The progressive increase in percentage of the high-molecular-weight region (H) during grain development observed for both cultivars and under both water regimens agrees with Shewry et al.,[10] who found that the HMW-GS belonging to the H gel region accumulated slowly during the early and midgrowth stages and continued to accumulate until maturity. Both Ciccio[32] and Svevo[33] cultivars have a HMW-GS composition consisting of the 1Bx7 and 1By8 subunits that have been associated with good dough properties.[26,33,34] During grain filling, both cultivars showed a differential expression of these proteins in relation to the water regimen. In particular, Ciccio showed a down-expression of HMW-GS1Bx7 under WS at the milk (spot 40m), waxy (spot 40w), and physiological stages (spot 40p), with fold variations of 0.56, 0.83, and 0.87, respectively. In Svevo, both HMW-GS 1Bx7 and HMW-GS 1By8 were down-expressed at the milk stage (spots 43m and 66m), but over-expression was observed at physiological maturity (spots 43p and 66p) under water stress. Thus, in Svevo water stress seems to slow protein synthesis during the milk stage but to promote it at maturity; on the contrary, the effect of water stress on Ciccio was evident only for the 1Bx7 subunit, with a down-expression during the whole period of grain filling, which became more evident at the milk stage. Furthermore, Svevo showed a specific spot, not present in Ciccio, identified as a HMW-GS glutenin subunit encoded at locus *Glu-1B* allele *1Bx* (Tdu-e)[14] detected both in the waxy (spot 38w) and physiological stages (spot 38p). This protein was always down-expressed under WS condition, showing an opposite behavior with respect to the 1Bx7 subunit. However, because Svevo has only the pair of HMW-GS 1Bx7−1By8, it is likely that this protein spot is a procedure artifact.

DOI: 10.1021/acs.jafc.5b01635
J. Agric. Food Chem. 2015, 63, 6501−6512

Table 1. Protein Spots of the Two Cultivars and the Two Water Regimens Detected in the Three Developmental Stages by Image Analysis

phenological stage	gel region	spot	well watered (% vol)	water stress (% vol)	fold variation[a]	*P*
			Cultivar Ciccio			
milk stage	H	40m	4.29	2.41	0.56	**
	I	98m	1.37	1.57	1.14	ns
	L48−35	724	0.85	1.05	1.23	*
	L48−35	74m	13.12	11.91	0.9	ns
	L48−35	108m	4.27	3.85	0.9	ns
	L<35	746	4.69	3.54	0.75	**
	L<35	750	2.11	1	0.47	**
	L<35	702m	2.76	3.16	1.14	*
	L<35	112m	1.32	1.33	1.01	ns
waxy stage	H	40w	1.87	1.56	0.83	*
	I	98w	1.00	1.46	1.46	**
	L48−35	74w	12.71	8.86	0.7	*
	L48−35	108w	6.6	3.6	0.54	**
	L48−35	72w	0.64	0.9	1.4	**
	L<35	119	0.80	1.05	1.31	*
	L<35	112w	1.01	1.34	1.32	*
	L<35	702w	1.39	1.78	1.28	*
	L<35	156w	0.58	0.52	0.89	ns
physiological maturity	H	40p	6.99	6.08	0.87	*
	I	98p	1.54	2.70	1.75	**
	L48−35	120	4.04	2.93	0.72	*
	L48−35	130	3.44	2.08	0.6	**
	L48−35	74p	14.1	11	0.78	*
	L48−35	108p	8.67	4.34	0.50	**
	L48−35	72p	0.73	1.08	1.48	**
	L<35	112p	1.10	1.31	1.19	ns
	L<35	156p	2.61	2.2	0.84	*
	L<35	702p	1.46	1.53	1.05	ns
			Cultivar Svevo			
milk stage	H	43m	5.92	5.12	0.86	*
	H	66m	1.18	0.55	0.46	**
	I	96m	0.88	1.27	1.44	**
	L48−35	730	0.67	0.4	0.6	**
	L48−35	77m	12.9	7.07	0.54	**
	L48−35	92m	4.9	3.4	0.69	*
	L<35	139	2.45	3.59	1.46	**
	L<35	153	3.62	4.17	1.15	*
	L 35	152m	2.14	2.72	1.27	*
	L<35	212m	3.95	5.48	1.39	**
waxy stage	H	43w	4.98	4.97	0.99	ns
	H	38w	1.73	0.79	0.46	**
	I	96w	0.85	0.95	1.11	ns
	L48−35	77w	11.24	9.15	0.81	*
	L48−35	92w	5.61	4.93	0.87	ns
	L<35	219	0.98	1.4	1.42	**
	L<35	279	1.58	2.7	1.7	**
	L<35	212w	3.27	4.11	1.26	*
	L<35	200w	0.96	1.08	1.12	ns
	L<35	152w	1.99	2.85	1.43	**
physiological maturity	H	43p	7.07	9.04	1.23	*
	H	66p	2.19	4.24	1.94	**
	H	38p	2.2	0.35	0.16	*
	I	96p	1.36	1.92	1.41	**
	L48−35	157	3.23	2.74	0.84	*
	L48−35	77p	14.26	12.93	0.9	ns

DOI: 10.1021/acs.jafc.5b01635
J. Agric. Food Chem. 2015, 63, 6501−6512

Table 1. continued

phenological stage	gel region	spot	well watered (% vol)	water stress (% vol)	fold variation[a]	P
			Cultivar Svevo			
	L48−35	92p	7.36	4.84	0.66	**
	L<35	206	2.49	2	0.8	*
	L<35	152p	1.89	2.19	1.16	ns
	L<35	200p	1.13	1.51	1.34	*
	L<35	212p	3.96	4.39	1.11	*

[a]Fold variation: ratio stressed/well-watered.

I Region. The I region, mainly characterized by ω-gliadins encoded by genes at *Gli-1* loci (*Gli-A1* and *Gli-B1* in tetraploid wheat) and by D subunits of LMW-GS that are modified ω-gliadins,[35] showed a marked increase under water stress at maturity. In this region, a protein spot was expressed in both cultivars during the whole grain filling period; a train of spots was also observed, being more evident at physiological maturity under WS (Figures 1c,c_1 and 2c,c_1). In both cultivars, the protein spots have been identified at physiological maturity (98p and 96p) as ω-5-gliadin, known as Tri a-19, one of the main allergens in wheat-dependent exercise-induced anaphylaxis.[36] This protein was always overexpressed in Ciccio under WS, with a progressively increasing fold variation during grain filling (1.14, 1.46, and 1.75 at the milk, waxy, and physiological stages, respectively). Likewise, it was always overexpressed under WS in Svevo, particularly at the milk stage and at physiological maturity, with a similar fold variation (1.44 and 1.41, respectively). Hurkman et al.[11] also reported an increase in ω-gliadins under different environmental stresses. However, in the same region, a previous study[26] identified a train of spots having the same molecular weight but different p*I* values (shifted toward basic pH) as the globulin 3 protein encoded by the *Glo3A* gene. Train spots can occur due to deamidation of asparagine and glutamine residues,[37] the latter being abundant in gluten proteins. This globulin train spot showed an up-regulation under high temperature, in agreement with Altenbach et al.[38] and Laino et al.,[39] who reported increased globulin during grain development under high temperatures in both *T. aestivum* and *T. durum*. Moreover, Yang et al.[17] found an increase in one globulin in response to water stress.

L48−35 Region. The slight increasing trend in L48−35 percentage region volume observed for both cultivars during grain development agrees with Hurkman et al.,[11] who reported that although the majority of LMW-GS attained their maximum level at 28 DAA, a small group of these gradually increased throughout development and attained their maximum level at 37 DAA.

Relative to the effect of water stress on the L48−35 region, the higher percent values observed in the control with respect to water stress for both cultivars and at all developmental stages, suggest an inhibition of some LMW subunit expression under water stress. This result agrees with Hurkman et al.[11] and also with our previous studies,[26] which showed that high-temperature stress induced a down-expression of LMW proteins.

The L48−35 region included most of the LMW-GS encoded at the *Glu-A3* and *Glu-B3* loci, which correspond to the typical LMW-GS. The *Glu-B3* locus is of particular interest in durum wheat, because the proteins encoded at this locus are involved in the viscoelastic characteristics of durum wheat flour.[40,41] Both s-type and m-type LMW-GS are encoded at this locus, with s-type generally having a greater molecular weight than m-type.[42] LMW-GS encoded at the *Glu-B3* locus have been identified in both Ciccio and Svevo (spot 74p for Ciccio and spot 77m, for Svevo). Spot 74p has been identified as s-type LMW-GS classified as 42 k-like LMW-GS protein;[41] spot 77m has also been identified as LMW-2,[43] reported to be a major component of the glutenin fraction in some good-quality common and durum wheat cultivars.[43,44] The spot volume of this protein increased in both cultivars from the milk to the physiological maturity, with values ranging from 8.9 to 14.1 for Ciccio and from 7.1 to 14.3 for Svevo. Moreover, the behavior of this protein in the two cultivars differed in relation to water stress. In Ciccio, this protein did not vary with the water regimen in the milk stage (spot 74m); however, in the waxy and physiological stages it showed a down-expression under drought conditions (spots 74w and 74p, respectively). This protein was also down-expressed under WS in Svevo, but this behavior was more evident at the milk stage (spot 77m; fold variation = 0.56) than at the waxy (spot 77w; fold variation = 0.81) and physiological stages (spot 77p; fold variation = 0.9). This protein seems to be sensitive to environmental stress, because it resulted in down-regulation under high temperatures.[26] Another LMW-GS identified in both cultivars was an m-type LMW-GS[42] encoded by locus *Glu-B3*. This protein was significantly down-expressed in WS at physiological maturity in both Ciccio (spots 108m, 108w, and 108p) and Svevo (spots 92m, 92w, and 92p). In particular, spot volume tends to increase more from the milk to the physiological maturity stages under WW than under WS (Table 1), allowing us to suppose that water stress inhibits the synthesis of this protein. The volume increase observed during grain filling in WW agrees with Hurkman et al.,[11] who reported that m-type protein gradually increased throughout development and attained maximum levels at physiological maturity. The LMW-GS spot volume was higher for Ciccio than for Svevo (8.67 vs 7.36) at physiological maturity.

Spot 72 detected in genotype Ciccio and identified as a triticin overexpressed under WS (spots 72w and 72p) also belongs to this gel region. This minor storage protein is thought to be involved in the determination of flour quality because of the thiol−disulfide interchange during grain maturation when subjected to dehydration.[45] The literature reports that there are greater accumulations of triticins in superior quality wheat varieties than in lower quality genotypes.[46]

L<35 Region. The L<35 region percentage decreased progressively during grain development in both cultivars and under both water regimens. This was consistent with an increase in the glutenin percentage during grain filling. This result agrees with Kawaura et al.,[47] who analyzed in *T. aestivum* the expression patterns of gene families for α-gliadins based on the frequencies of expressed sequence tags (ESTs). The authors reported that α-gliadin genes from the A genome showed the highest expression level at 20 DAA and then decreased until 30 DAA. Abonyi et al.[48] also found a decrease in gliadin quantity in the final period of ripening, explained as possible

DOI: 10.1021/acs.jafc.5b01635
J. Agric. Food Chem. 2015, 63, 6501−6512

Table 2. Protein Spot Identification Using Nano-HPLC-ESI-IT/MS/MS Analysis and Searching the NCBInr Database Using MASCOT (www.matrixscience.com)

spot	accession (NCBInr general index)	proteins	species	Mascot score	sequence coverage (%)	theor M_w (kDa); p*I*	no. of peptide matches	peptide sequence[a]
40w	71084277	HMW glutenin x-type subunit Bx7 (precursor)	*Triticum aestivum*	76	5	85.4; 8.68	2	YPISPQQSGQGQQPGQGQQGYYPTSPQQSGQGQQPGHEQQPGQW
43p	94315065	HMW glutenin subunit 1Bx	*Triticum aestivum*	67	4	84.5; 8.89	2	YPTSPQQPGQL; YPTSPQQSGQGQQPGHEQQPGQW
66m	29150726	HMW glutenin subunit 1By8	*Triticum turgidum* subsp. *durum*	75	3	77.69; 8.76	2	EQTVVPPKGGSF; QQVGQGQQIGQL
66p	29150726	HMW glutenin subunit 1By8	*Triticum turgidum* subsp. *durum*	445	27	77.6; 8.76	7	EQTVVPPKGGSFYPGETTPL; GTSSQTVQGYYPSVSSPQQGPYYPGQASPQQPGQGQQPGKWQELGQGQQGYYPTSLHQSGQGQQ-GYYPSSL; YPTSPQHPGQRQQPGQGQQIGQGQQ; LASQQQPGQGQQRHYPASL; TASLQQPGQGQQGHYPASL; SSSLQQPGQGLQGHYPASL; YPTSPQQPGQGKQLGQGQQGY
38p	409691237	HMW glutenin subunit	*Triticum turgidum* subsp. *durum*	321	25	86.05; 9.21	8	QQVVDQQLRDVSPGY; YPSVTSSQQGSY; YPTSPQQPGQGQQL; YPTSPQQSGQGQQPGQRQSGY; QLVYYPTSL; QLVYYPTSPQQPGQLQQPAQGQQGY; YPTSPQQSGQGQQPGQGQQPRQGQQGYYPISPQQSGQGQQTGQGQQGYYPTSPQQSGQGQQPR-HEQQPGQWLQPGQGQQGYYPTSSQQ; WQPGQGQQPGQRQQGYDSPY
96p	73912496	*ω*-5-gliadin	*Triticum aestivum*	72	4	52.9; 6.58	2	QQYPQQQPSGSDVISISGL
98p	73912496	*ω*-5-gliadin	*Triticum aestivum*	72	4	52.9; 6.58	2	QQYPQQQPSGSDVISISGL
74p	4584082	LMW glutenin subunit s-type	*Triticum turgidum* subsp. *durum*	199	19	42.6; 8.736	5	SHIPGLERPSQQQPLPPQQTL; QQQIPFVHPSILQQLNPCKVF; EAIRAIVY; GQQPQQQQLAHGTF; YRTTTRVPF
108p	485474672	LMW glutenin subunit m-type	*Triticum aestivum*	399	49	38.1; 8.47	5	METSHIPSLEKPLQQQPLPLQQILW; QQPPFSQHQQPVLPQQQIPSVQPSILQQLNPCKVFLQQQCSPVAMPQ; RQLPQIPEQSRYDAIRAIIYSIVLQEQQHGQGLNQPQQQQPQQSVQGVSQPQQQQKQLGQCSF; GQWPQQQQVPQGTL; RTLPTMCSVNVPVY
77m	4584082	LMW glutenin subunit type 2	*Triticum turgidum* subsp. *durum*	199	19	42.6; 8.736	5	SHIPGLERPSQQQPLPPQQTL; QQQIPFVHPSILQQLNPCKVF; EAIRAIVY; GQQPQQQQLAHGTF; YRTTTRVPF
92m	485474672	LMW glutenin subunit m-type	*Triticum aestivum*	399	49	38.1; 8.47	5	METSHIPSLEKPLQQQPLPLQQILW; QQPPFSQHQQPVLPQQQIPSVQPSILQQLNPCKVFLQQQCSPVAMPQ; RQLPQIPEQSRYDAIRAIIYSIVLQEQQHGQGLNQPQQQQPQQSVQGVSQPQQQQKQLGQCSF; GQWPQQQQVPQGTL; RTLPTMCSVNVPVY
72w	171027813	triticin	*Triticum aestivum*	109	7	65.2; 6.37	4	IIQGSGFAGLSFPGCPETF; RQGDVIALPAGIVHW; VFDVNNY
72p	171027813	triticin	*Triticum aestivum*	310	13	65.2; 6.37	4	IIQGSGFAGLSFPGCPETF; FYNDGDAPIVAIYVFDVNNY; SGFDVRLLAEALGTSGKIAQRL; LKPVFTQQREPESYPHTQY
746	90101517	*α*-gliadin Gli2-LM2−12	*Triticum aestivum*	64	18	36.3; 7.66	4	QQHNIAHASSQVLQQSTY; QQQRQQPSSQVSF; QQPQQQYPSSQVSF; IPPHCSTTIAPF
702m	1256791	*α*-gliadin	*Triticum aestivum*	158	23	33.67; 8.24	3	LQLQPFPQPQLPY; RPQQPYPQPQPQY; QQPLQQYPLGQGSFRPSQQN PQAQGSVQPQQLPQFEEIRNL
112w	283476402	*α*-gliadin precursor, partial	*Triticum aestivum*	66	6	32.9; 6.62	1	QQPNIAHASSQVSQQSY
156p	30141195	*γ*-gliadin	*Triticum turgidum* subsp. *durum*	231	15	32.7; 6.34	2	CEQPQRTIPQPHQTF; GIIQPQQPAQLEGIRSLVLKTLPTMCNVY
139	383210739	*α*-gliadin	*Triticum aestivum*	102	14	33.9; 7.64	1	QQPQQQYPSGQGFFQPSQQ NPQAQGFVQPQQLPQFEEIRNL
153	66393328	*α*-gliadin	*Triticum monococcum*	116	14	31.09; 7.14	3	LQLQPFPQPQLPY; RPQQPYPQPQPQY; QQPQQQYPLGQGSFRPSQQNPQA
152m	1304264	*α* -gliadin	*Triticum aestivum*	84	14	30.3; 6.18	3	VRVPVPQLQPQNPSQQQPQEQVPL; RPQQPYPQPQPQY
212p	72537616	*α*-type gliadin, partial	*Triticum dicoccoides*	324	28	31.8; 6.99	4	VRVPVPQLQPQNPSQQQPQEQVPL; RPQQPYPQPQPQY; QQPLQQYPLGQGSF; VQPQQLPQFEEIRNLA LQTLPAMCNVY
279	421932520	*α*-gliadin	*Triticum aestivum*	72	12	34.1; 6.56	3	RPQQPYPQPQPQY; HQQQQQQQQQQQQQQQQQPLSQVCF
200w	283476402	*α*-gliadin precursor, partial	*Triticum aestivum*	139	17	32.9; 6.62	3	VRVPVPQLQPQNPSQQQPQEQVPL; QQPQQQYPSGQGSFQPSQQNPQAQGF
206	7209259	*α*-gliadin	*Triticum aestivum*	301	29	31.8; 6.56	4	LQLQPFPQPQLPY; RPQQPYPQPQPQY; QPQQQYPLGQGSF; GSVQPQQLPQFEEIRNLALQTLPAMCNVYIPPYCTIAPF

[a]Peptide sequences identified in spots with the highest sequence coverage; underlined amino acids show a deamination.

J. Agric. Food Chem. 2015, 63, 6501−6512
DOI: 10.1021/acs.jafc.5b01635

changes in their solubility caused by aggregation with polar lipids.

With regard to the effects of the water regimen, a higher protein expression was generally observed under water stress, in agreement with the literature, which reports a higher gliadin and gliadin/glutenin ratio under environmental stress during grain filling.[11] In fact, in this region several α-gliadins have been identified, which behave differently in relation to the water regimen. The α-gliadin identified in Ciccio (spots 702m, 702w, and 702p) was significantly overexpressed under WS at the milk and waxy stages, whereas no significant difference was found between the two water regimens at physiological maturity, which showed an effect of water stress on the synthesis of this protein only in the early−mid stage. Finally, the α-gliadin identified in Svevo (spots 212m, 212w, and 212p) was always overexpressed under WS, with a fold variation that decreased from the milk to the physiological maturity stages (fold variation = 1.39, 1.26, and 1.11).

Moreover, several gliadins associated with the immunological potential of wheat changed their expression in relation to the water regimen, especially in Svevo. An α-gliadin involved in wheat allergy[49] was identified in Svevo (spots 152m, 152w, and 152p) as overexpressed under WS at all three stages, especially at the waxy stage (fold variation = 1.43), allowing us to suppose higher synthesis of this protein under water stress, especially in the mid-development stage. Another α-gliadin (partial), known to contain the celiac disease-related T-cell stimulatory epitopes glia-α9 and glia-α20,[50] was identified in Svevo at the milk stage (spot 153), showing a slight overexpression under WS. This protein seems to match spot 206 at physiological maturity, because the molecular weight and isolectric point of the two proteins were very similar in our gel (Figure 2a,c). However, a different identification resulted for spot 206 identified as an α-gliadin, which does not contain epitopes recognized by these T cells.[51] This gliadin was also slightly down-expressed under WS.

The α-gliadin precursor identified in both Ciccio (spots 112m, 112w, and 112p) and Svevo (spots 200w and 200p) was recognized as an allergen involved in baker's asthma.[52] Under WS this protein was significantly overexpressed only in the waxy stage for Ciccio and at physiological maturity for Svevo. Thus, this gliadin was overexpressed under drought conditions in the mid and late developmental stages of the two cultivars under study.

Finally, under WS, the γ-gliadin identified in Ciccio (spots 156w and 156p) was significantly down-expressed only at physiological maturity. In the literature it has been reported that this particular γ-gliadin, with an odd number of cysteine residues, is able to form an intermolecular disulfide bond, thus incorporating this protein into the glutenin polymer fraction. For this reason, it is called γ-type glutenin and likely acts as a terminator of growing polymer chains by causing the molecular weight distribution of the glutenin polymer system to shift downward.[53] Moreover, this protein seems to be sensitive to environmental changes because its down-regulation under high-temperature conditions has been reported.[26]

In summary, the two durum wheat cultivars showed significant differences in the gluten proteome during grain development in relation to the water regimen. The HMW-GS region percentage increased progressively in both cultivars, showing a sharp increase under water stress at maturity in Svevo. In particular, water stress caused a down-expression of HMW-GS 1Bx7 in Ciccio during the whole grain-filling period, whereas in Svevo it seemed to promote the synthesis of the HMW-GS 7 + 8 pair at maturity. Down-expression of the L48−35 region was always observed under water stress, although the reactions of the two cultivars were different. In particular, both m-type and s-type LMW were always down-expressed under water stress; for the s-type LMW belonging to class 2, related to good durum wheat quality, Svevo showed a down-expression in the early−mid period (milk and waxy stages) and Ciccio in the mid−late period (waxy and physiological stages). Instead, for the m-type LMW, both cultivars showed a down-expression under water stress at the waxy and physiological stages. Finally, with regard to the L<35 region, a general increase was observed under water stress; furthermore, several α-gliadins associated with the immunological potential of wheat increased their expression under water stress, especially for Svevo in the early−mid stage. When the two cultivars were compared at physiological maturity, the H region was overexpressed in Svevo; this might be related to its higher protein content, which in the literature was associated with a higher HMW-GS/LMW-GS ratio.[13] Furthermore, Svevo showed an overexpression in the L<35 region and Ciccio in the L48−35 region, which may be responsible for Ciccio's superior gluten quality.

On the basis of these results, it is possible to draw the general conclusion that water stress affects gluten protein accumulation in the two cultivars at all developmental stages by causing an increase in gliadins and gliadin-like proteins (such as C- and D-subunits of LMW-GS) and a reduction in typical LMW-GS. Both an increase in gliadins with respect to glutenins and a higher amount of chain terminators, like C- and D-subunits of LMW-GS are known to negatively affect rheological properties.[54,55] Moreover, typical LMW-GS, especially those coded at the *Glu-B3* locus, are the most important factors determining dough quality and are down-regulated after water stress.

Taken all together, these results suggest that although there was not enough material available to perform predictive technological tests on the collected seeds, it is likely that the observed modifications of protein composition in water-stressed materials have negative effects on gluten quality.

AUTHOR INFORMATION

Corresponding Author

*(Z.F.) E-mail: zina.flagella@unifg.it. Phone: +39 0881 589220. Fax: +39 0881 589507.

Notes

The authors declare no competing financial interest.

REFERENCES

(1) Wieser, H. Chemistry of gluten proteins. *Food Microbiol.* **2007**, *24*, 115−119.

(2) Mamone, G.; De Caro, S.; Di Luccia, A.; Addeo, F.; Ferranti, P. Proteomic-based analytical approach for the characterization of glutenin subunits in durum wheat. *J. Mass Spectrom.* **2009**, *44*, 1709−1723.

(3) Sissons, M. J.; Ames, N. P.; Hare, R. A.; Clarke, J. M. Relationship between glutenin subunit composition and gluten strength measurements in durum wheat. *J. Sci. Food Agric.* **2005**, *85*, 2445−2452.

(4) Pogna, N.; Lafiandra, D.; Feillet, P.; Autran, J. C. Evidence for a direct causal effect of low molecular weight subunits of glutenins on gluten viscoelasticity in durum wheat. *J. Cereal Sci.* **1988**, *7*, 211−214.

(5) Katagiri, M.; Masuda, T.; Tani, F.; Kitabatake, N. Expression and development of wheat proteins during maturation of wheat kernel and the rheological properties of dough prepared from the flour of mature and immature wheat. *Food Sci. Technol. Res.* **2011**, *17*, 111−120.

DOI: 10.1021/acs.jafc.5b01635
J. Agric. Food Chem. 2015, 63, 6501−6512

(6) Tosi, P.; Parker, M.; Carzaniga, R.; Martin, B.; Gritsch, C. S.; Shewry, P. R. Trafficking of storage proteins in developing grain of wheat. *J. Exp. Bot.* **2009**, *60*, 979−991.
(7) Hurkman, W. J.; Vensel, W. H.; Tanaka, C. K.; Whitehand, L.; Altenbach, S. B. Effect of high temperature on albumin and globulin accumulation in the endosperm proteome of the developing wheat grain. *J. Cereal Sci.* **2009**, *49*, 12−23.
(8) Iametti, S.; Bonomi, F.; Pagani, M. A.; Zardi, M.; Cecchini, C.; D'Egidio, M. G. Properties of the protein and carbohydrate fractions in immature wheat kernels. *J. Agric. Food Chem.* **2006**, *54*, 10239−10244.
(9) Naeem, H. A.; Paulon, D.; Irmak, S.; MacRitchie, F. Developmental and environmental effects on the assembly of glutenin polymers and the impact on grain quality of wheat. *J. Cereal Sci.* **2012**, *56*, 51−57.
(10) Shewry, P. R.; Underwood, C.; Wan, Y.; Lovegrove, A.; Bhandari, D.; Toole, G.; Mills, E. N. C.; Denyer, K.; Mitchell, R. A. C. Storage product synthesis and accumulation in developing grains of wheat. *J. Cereal Sci.* **2009**, *50*, 106−112.
(11) Hurkman, W. J.; Tanaka, C. K.; Vensel, W. H.; Thilmony, R.; Altenbach, S. B. Comparative proteomic analysis of the effect of temperature and fertilizer on gliadin and glutenin accumulation in the developing endosperm and flour from *Triticum aestivum* L. cv. Butte 86. *Proteome Sci.* **2013**, *11*, 8.
(12) Liu, W.; Zhang, Y.; Gao, X.; Wang, K.; Wang, S.; Zhang, Y.; He, Z.; Ma, W.; Yan, Y. Comparative proteome analysis of glutenin synthesis and accumulation in developing grains between superior and poor quality bread wheat cultivars. *J. Sci. Food Agric.* **2012**, *92*, 106−115.
(13) Flagella, Z.; Giuliani, M. M.; Giuzio, L.; Volpi, C.; Masci, S. Influence of water deficit on durum wheat storage protein composition and technological quality. *Eur. J. Agron.* **2010**, *33*, 197−207.
(14) Jiang, Q. T.; Ma, J.; Zhao, S.; Zhao, Q. Z.; Lan, X. J.; Dai, S. F.; Lu, Z. X.; Zheng, Y. L.; Yu-Ming Wei, Y. M. Characterization of HMW-GSs and their gene inaction in tetraploid wheat. *Genetica* **2012**, *140*, 325−335.
(15) DuPont, F. M.; Hurkman, W. J.; Vensel, W. H.; Chan, R.; Lopez, R.; Tanaka, C. K.; Altenbach, S. B. Differential accumulation of sulfur-rich and sulfur-poor wheat flour proteins is affected by temperature and mineral nutrition during grain development. *J. Cereal Sci.* **2006**, *44*, 101−112.
(16) Majoul, T.; Bancel, E.; Triboi, E.; Ben Hamida, J.; Branlard, G. Proteomic analysis of the effect of heat stress on hexaploid wheat grain: characterization of heatresponsive proteins from total endosperm. *Proteomics* **2003**, *3*, 175−183.
(17) Yang, F.; Jorgensen, A. D.; Li, H.; Sondergaard, I.; Finnie, C.; Svensson, B.; Jiang, D.; Wollenweber, B.; Jacobsen, S. Implications of high-temperature events and water deficits on protein profiles in wheat (*Triticum aestivum* L. cv. Vinjett) grain. *Proteomics* **2011**, *11*, 1684−1695.
(18) Zörb, C.; Steinfurth, D.; Seling, S.; Langenkämper, G.; Koehler, P.; Wieser, H.; Lindhauer, M. G.; Mühling, K. H. Quantitative protein composition and baking quality of winter wheat as affected by late sulfur fertilization. *J. Agric. Food Chem.* **2009**, *57*, 3877−3885.
(19) Kong, L.; Guo, H.; Sun, M. Signal transduction during wheat grain development. *Planta* **2015**, *241*, 789−801.
(20) Altenbach, S. B.; DuPont, F. M.; Kothari, K. M.; Chan, R.; Johnson, E. L.; Lieu, D. Temperature, water and fertilizer influence the timing of key events during grain development in a US spring wheat. *J. Cereal Sci.* **2003**, *37*, 9−20.
(21) Altenbach, S. B.; Kothari, K. M. Transcript profiles of genes expressed in endosperm tissue are altered by high temperature during wheat grain development. *J. Cereal Sci.* **2004**, *40*, 115−126.
(22) Daniel, C.; Triboi, E. Effects of temperature and nitrogen nutrition on the grain composition of winter wheat: effects on gliadin content and composition. *J. Cereal Sci.* **2000**, *32*, 45−56.
(23) Giuliani, M. M.; De Santis, M. A.; Pompa, M.; Giuzio, L.; Flagella, Z. Analysis of gluten proteins composition during grain filling in two durum wheat cultivars submitted to two water regimes. *Ital. J. Agron.* **2014**, *9*, 558.
(24) Zadoks, J. C.; Chang, T. T.; Konzac, C. F. A decimal code for the growth stages of cereals. *Weed Res.* **1974**, *14*, 415−421.
(25) Lawrence, M. S. Amino acids and proteins. In *Textbook of Clinical Chemistry*; Tietz, N. W., Ed.; W. B. Saunders Co.: Philadelphia, PA, USA, 1986; pp 519−618.
(26) Pompa, M.; Giuliani, M. M.; Palermo, C.; Agriesti, F.; Centonze, D.; Zina Flagella, Z. Comparative analysis of gluten proteins in three durum wheat cultivars by a proteomic approach. *J. Agric. Food Chem.* **2013**, *61*, 2606−2617.
(27) Muccilli, V.; Cunsolo, V.; Saletti, R.; Foti, S.; Margiotta, B.; Scossa, F.; Masci, M.; Lafiandra, D. Characterisation of a specific class of typical low molecular weight glutenin subunits of durum wheat by a proteomic approach. *J. Cereal Sci.* **2010**, *51*, 134−139.
(28) Egidi, E.; Sestili, F.; Janni, M.; D'Ovidio, R.; Lafiandra, D.; Ceriotti, A.; Vensel, W. H.; Kasarda, D. D.; Masci, S. An asparagine residue at the n-terminus affects the maturation process of low molecular weight glutenin subunits of wheat endosperm. *BMC Plant Biol.* **2014**, *14*, 64.
(29) Hurkman, W. J.; Wood, D. F. High temperature during grain fill alters the morphology of protein and starch deposits in the starchy endosperm cells of developing wheat (*Triticum aestivum* L.) grain. *J. Agric. Food Chem.* **2011**, *59*, 4938−4946.
(30) Giuliani, M. M.; Giuzio, L.; De Caro, A.; Flagella, Z. Relationships between nitrogen utilization and grain technological quality in durum wheat: I. Nitrogen translocation and nitrogen use efficiency for protein. *Agron. J.* **2011**, *103*, 1487−1494.
(31) Giuliani, M. M.; Giuzio, L.; De Caro, A.; Flagella, Z. Relationships between nitrogen utilization and grain technological quality in durum wheat: II. Grain yield and quality. *Agron. J.* **2011**, *103*, 1668−1675.
(32) Chňapek, M.; Tomka, M.; Peroutokova, R.; Gàlova, Z. Polymorphism of HMW-GS in collection of wheat genotypes. *Int. J. Biol., Biomol., Agric., Food Biotechnol. Eng.* **2014**, *8*, 7.
(33) Muccilli, V.; Lo Bianco, M.; Cunsolo, V.; Saletti, R.; Gallo, G.; Foti, S. High molecular weight glutenin subunits in some durum wheat cultivars investigated by means of mass spectrometric techniques. *J. Agric. Food Chem.* **2011**, *59*, 12226−12237.
(34) De Vita, P.; Li Destri Nicosia, O.; Nigro, F.; Platani, C.; Riefolo, C.; Di Fonzo, N.; Cattivelli, L. Breeding progress in morpho-physiological, agronomical and qualitative traits of durum wheat cultivars released in Italy during the 20th century. *Eur. J. Agron.* **2007**, *26*, 39−53.
(35) D'Ovidio, R.; Masci, S. The wheat low-molecular-weight glutenin subunits. *J. Cereal Sci.* **2004**, *39*, 321−339.
(36) Matsuo, H.; Kohno, K.; Niihara, H.; Morita, E. Specific IgE determination to epitope peptides of omega-5 gliadin and high molecular weight glutenin subunit is a useful tool for diagnosis of wheat-dependent exercise-induced anaphylaxis. *J. Immunol.* **2005**, *175*, 8116−8122.
(37) Righetti, P. G. Real and imaginary artefacts in proteome analysis via two-dimensional maps. *J. Chromatogr. B: Anal. Technol. Biomed. Life Sci.* **2006**, *841*, 14−22.
(38) Altenbach, S. B.; Tanaka, C. K.; Hurkman, W. J.; Vensel, W. H. Expression of globulin-2, a member of the cupin superfamily of proteins with similarity to known food allergens, is increased under high temperature regimens during wheat grain development. *J. Cereal Sci.* **2009**, *49*, 47−54.
(39) Laino, P.; Shelton, D.; Finnie, C.; De Leonardis, A. M.; Mastrangelo, A. M.; Svensson, B.; Lafiandra, D.; Masci, S. Comparative proteome analysis of metabolic proteins from seeds of durum wheat (cv. Svevo) subjected to heat stress. *Proteomics* **2010**, *10*, 2359−2368.
(40) D'Ovidio, R.; Simeone, M.; Masci, S.; Porceddu, E. Molecular characterization of a LMW-GS gene located on chromosome 1B and the development of primers specific for the Glu-B3 complex locus in durum wheat. *Theor. Appl. Genet.* **1997**, *95*, 1119−1126.
(41) Ikeda, T. M.; Nagamine, T.; Fukuoka, H.; Yano, H. Identification of new low-molecular-weight glutenin subunit genes in wheat. *Theor. Appl. Genet.* **2002**, *104*, 680−687.

DOI: 10.1021/acs.jafc.5b01635
J. Agric. Food Chem. 2015, 63, 6501−6512

(42) Zhang, X.; Liu, D.; Zhang, J.; Wei Jiang, W.; Luo, G.; Yang, W.; Sun, J.; Tong, Y.; Cui, D.; Zhang, A. Novel insights into the composition, variation, organization, and expression of the low-molecular-weight glutenin subunit gene family in common wheat. *J. Exp. Bot.* **2013**, *64*, 2027−2040.
(43) D'Ovidio, R.; Marchitelli, C.; Ercoli Cardelli, L.; Porceddu, E. Sequence similarity between allelic Glu-B3 genes related to quality properties of durum wheat. *Theor. Appl. Genet.* **1999**, *98*, 455−461.
(44) Masci, S.; D'Ovidio, R.; Lafiandra, D.; Kasarda, D. D. A 1B-coded low-molecular-weight glutenin subunit associated with quality in durum wheats shows strong similarity to a subunit present in some bread wheat cultivars. *Theor. Appl. Genet.* **2000**, *100*, 396−400.
(45) Singh, N. K.; Donovan, G. R.; Carpenter, H. C.; Skerritt, J. H.; Langridge, P. Isolation and characterization of wheat triticin cDNA revealing a unique lysine-rich repetitive domain. *Plant Mol. Biol.* **1993**, *22*, 227−237.
(46) Kim, K. H.; Mostafa Kamal, A. H.; Shin, K. H.; Choi, J. S.; Heo, H. Y.; Woo, S. H. Large-scale proteome investigation in wild relatives (A, B, and D genomes) of wheat. *Acta Biochim. Biophys. Sin.* **2010**, *42*, 709−716.
(47) Kawaura, K.; Mochida, K.; Ogihara, Y. Expression profile of two storage-protein gene families in hexaploid wheat revealed by large-scale analysis of expressed sequence tags. *Plant Physiol.* **2005**, *139*, 1870−1880.
(48) Abonyi, T.; Kiraly, I.; Tomoskozi, S.; Baticz, O.; Guoth, A.; Gergely, E. S.; Lasztity, D.; Lasztity, R. Synthesis of gluten-forming polypeptides. 1. Biosynthesis of gliadins and glutenins subunits. *J. Agric. Food Chem.* **2007**, *55*, 3655−3660.
(49) Maruyama, N.; Ichise, K.; Katsube, T.; Kishimoto, T.; Kawase, S. I.; Matsumura, Y.; Takeuchi, Y.; Sawada, T.; Utsumi, S. Identification of major wheat allergens by means of the *Escherichia coli* expression system. *Eur. J. Biochem.* **1998**, *255*, 739−745.
(50) van Herpen, T. W.; Goryunova, S. V.; van der Schoot, J.; Mitreva, M.; Salentijn, E.; Vorst, O.; Schenk, M. F.; van Veelen, P. A.; Koning, F.; van Soest, L. J. M.; Vosman, B.; Bosch, D.; Hamer, R. J.; Gilissen, L. J. W. J.; Smulders, M. J.M. α-Gliadin genes from the A, B, and D genomes of wheat contain different sets of celiac disease epitopes. *BMC Genomics* **2006**, *7*, 1.
(51) Arentz-Hansen, E. H.; McAdam, S. N.; Molberg, Ø.; Kristiansen, C.; Sollid, L. M. Production of a panel of recombinant gliadins for the characterisation of T cell reactivity in celiac disease. *Gut* **2000**, *46*, 46−51.
(52) Sander, I.; Rozynek, P.; Rihs, H.- P.; van Kampen, V. F.; Chew, T.; Lee, W. S.; Kotschy-Lang, N.; Merget, R.; Brüning, T.; Raulf-Heimsoth, M. Multiple wheat flour allergens and cross-reactive carbohydrate determinants bind IgE in baker's asthma. *Allergy* **2011**, *66*, 1208−1215.
(53) D'Ovidio, R.; Simeone, M.; Masci, S.; Porceddu, E.; Kasarda, D. D. Nucleotide sequence of a γ-type glutenin gene from a durum wheat: correlation with a γ-type glutenin subunit from the same biotype. *Cereal Chem.* **1995**, *72*, 443−449.
(54) MacRitchie, F. Evaluation of contribution from wheat protein fractions to dough mixing and breadmaking. *J. Cereal Sci.* **1987**, *6*, 259−268.
(55) Kasarda, D. D. Glutenin structure in relation to wheat quality. In *Wheat Is Unique*; Pomeranz, Y., Ed.; American Association of Cereal Chemists: St. Paul, MN, USA, 1989; pp 277−302.

DOI: 10.1021/acs.jafc.5b01635
J. Agric. Food Chem. 2015, 63, 6501−6512

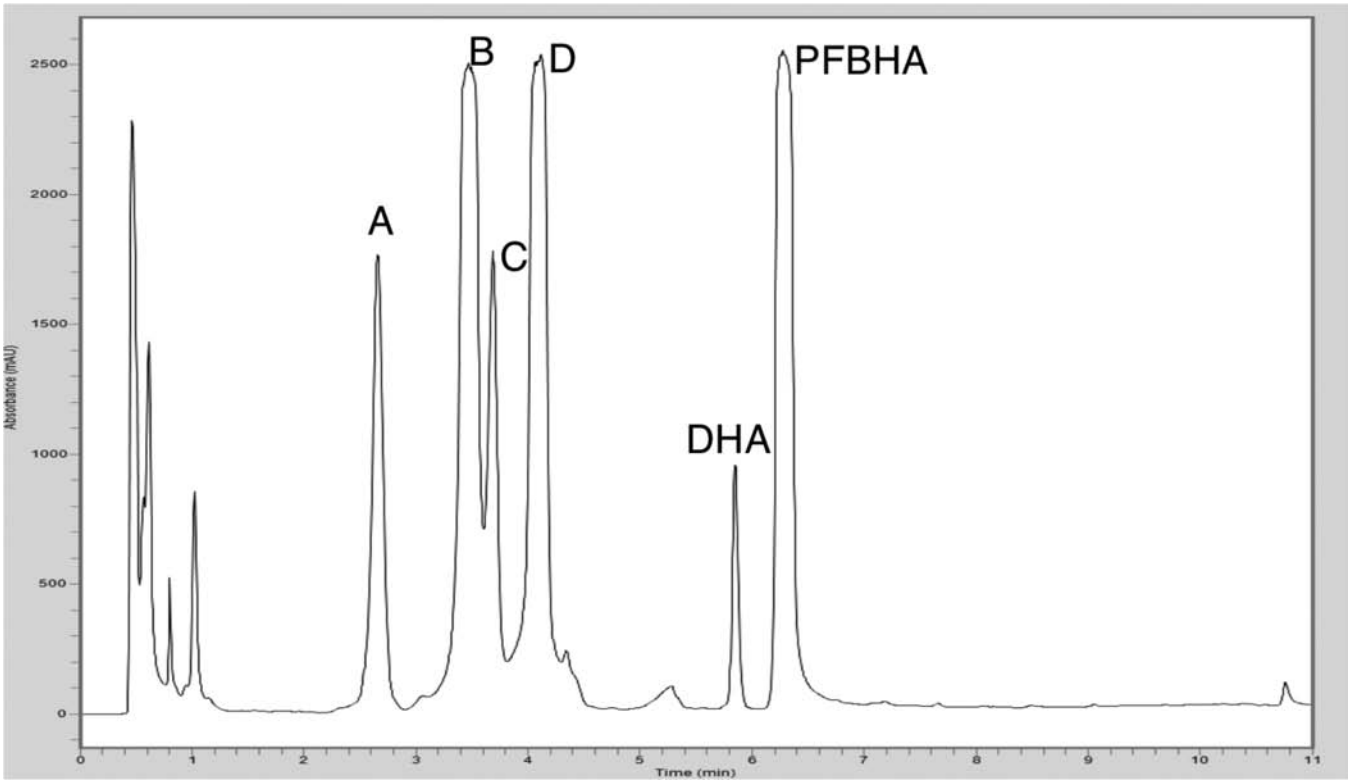

Figure 1. RP-HPLC chromatogram at λ = 200 nm of a *Leptospermum polygalifolium* sample obtained from the Sunshine Coast. The chromatogram shows a sharp peak for DHA derivative at 5.8 min. In contrast, sugar derivatives (A−D) showed high sensitivity and were unable to be accurately quantitated.

Herbarium Depository. Flower and shoot morphology were used to identify wild specimens to species level. Specimens were deposited in the Queensland Herbarium, Toowong, and identified by a chief botanist.

Chemicals. HPLC grade Milli-Q water was used in all analyses. HPLC Chromasolv gradient grade acetonitrile (ACN) was purchased from Merck (Kilsyth, Australia). *o*-(2,3,4,5,6-Pentafluorobenzyl) hydroxylamine hydrochloride (PFBHA) was purchased from Bio-Scientific (Gymea, Australia). Reagent grade citric acid, 1,3-dihydroxyacetone (DHA) (dimer, 97%), D-fructose 99+%, and β-D(+)-glucose 99+% were purchased from Sigma-Aldrich (Ryde, Australia).

HPLC Conditions. Analysis was conducted from an adapted Windsor et al.[20] method, via reverse-phase high-performance liquid chromatography (RP-HPLC) on a PerkinElmer series 200 HPLC with a Phenomenex Synergi Fusion column (75 mm × 4.6 mm, 4 μm particle size) and a Flexar photodiode array. Detection was set for 200 and 243 nm. Mobile phase A (MPA) was water 90%/ACN 10% (v/v), and mobile phase B (MPB) was ACN 100%. The pump program had a flow rate of 1.5 mL/min, with an injection volume of 20 μL. A gradient elution was employed: MPA/MPB = 95:5 (isocratic 0.5 min), 60:40 (gradient 4.0 min), 50:50 (gradient 2.0 min), 10:90 (gradient 2.0 min), 10:90 (isocratic 1.0 min), 95:5 (gradient 0.5 min), and 95:5 (isocratic over 1.0 min).

Preparation of Standards. Standard aqueous solutions of sugars or DHA were prepared with D-fructose (0.500 g) and D-glucose (0.500 g) dissolved in 50.0 mL of water and 0.050 g of DHA in 50.0 mL of water. DHA standards (0, 1, 2, 5, 10, 20, and 40 μL) were added to seven sugar standard solutions (200 μL), which gave DHA/total sugar mass ratios of 0, 250, 500, 1000, 2000, 5000, and 10000 ppm, respectively.

A PFBHA buffer solution was made with 0.20 g of PFBHA dissolved in 10. mL of 0.10 M citric acid buffer (pH 4). The DHA and sugar standards were derivatized quantitatively with 600 μL of PFBHA buffer solution at 65 °C for 2 h, prior to analysis via RP-HPLC as above. A calibration curve was constructed, whereby the known mass ratios (DHA/sugar ppm) were plotted against the peak area ratios of the DHA derivative (λ = 200 nm) to total sugar derivatives (λ = 243 nm).

Sample Preparation. Prior to analysis, thawed nectar samples were derivatized with 400 μL of PFBHA buffer solution and heated at 65 °C for 2 h. RP-HPLC analysis was performed as above, and peak area ratios of DHA (λ = 200 nm) to total sugars (λ = 243 nm) were obtained. The DHA/sugar ppm of individual samples was determined against the calibration curve by linear regression.

Statistical Analysis. The DHA/sugar ratio (ppm) for an individual tree (n) was the calculated mean of the replicated vials per tree. Differences in DHA/sugar concentration between species were analyzed with a Mann−Whitney U test with IBM SPSS (v.22).

RESULTS

Under the derivatization conditions, DHA formed a single compound, eluting at 5.8 min in Figure 1. The fructose and glucose formed four partially resolved derivatives by HPLC, 2.4−4.4 min in Figure 1. The multiple peaks were likely due to cis/trans isomers of the derivative oximes. Hence, total peak area measurements of sugars were used. Initial analysis of PFBHA derivatized sugars and DHA within nectar was performed at 259 nm. At this wavelength neither DHA nor sugars could be accurately quantitated as DHA had low sensitivity and sugars had high sensitivity. Peak sensitivity of DHA was increased 10-fold at 200 nm; however, the sugar peaks were saturated and unable to be accurately quantitated as shown by peaks A−D in Figure 1. In contrast, optimal sensitivity of the sugars was obtained at 243 nm, yet DHA showed poor sensitivity. Optimal sensitivity for both components was achieved when the peak area values were obtained at 200 nm for DHA and at 243 nm for sugars. The

DOI: 10.1021/acs.jafc.5b01930
J. Agric. Food Chem. 2015, 63, 6513−6517

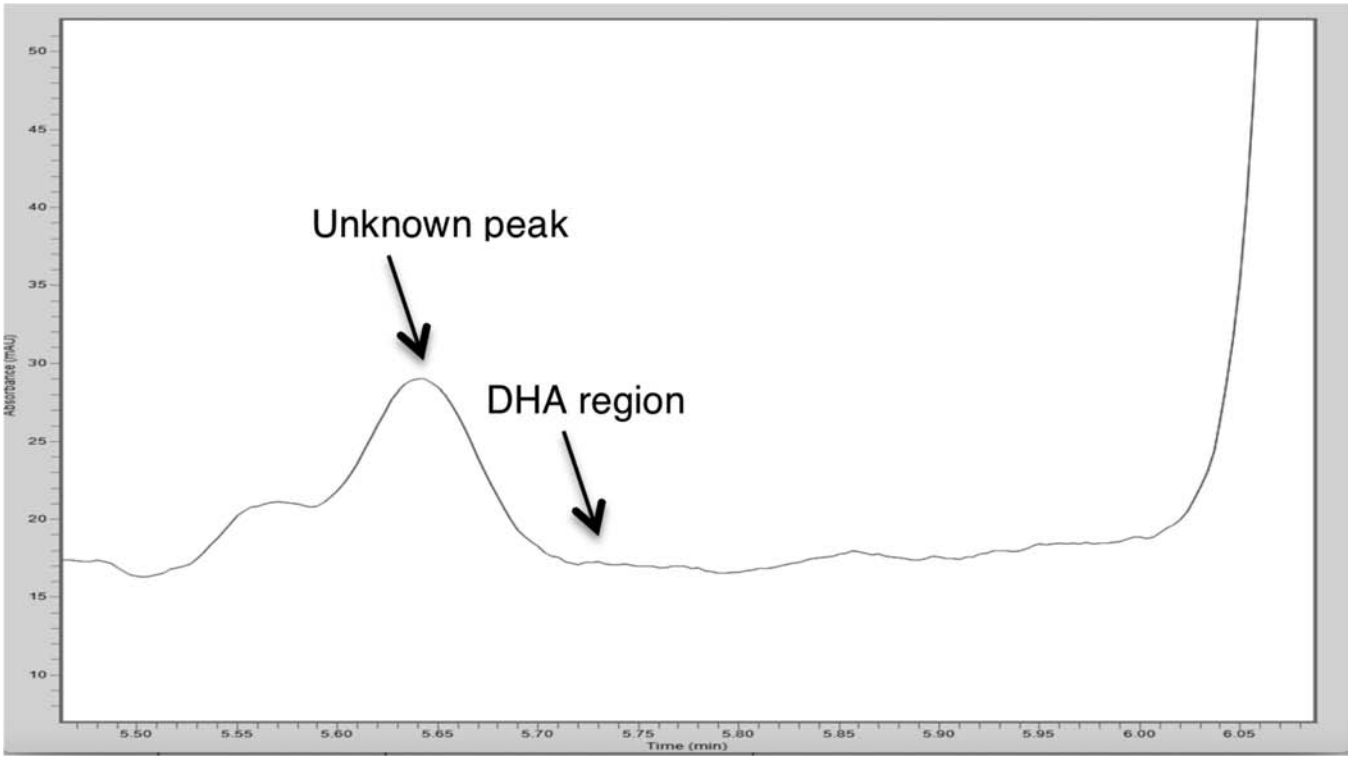

Figure 2. RP-HPLC chromatogram at λ = 200 nm of a *Leptospermum laevigatum* sample obtained from Northern Rivers. The chromatogram shows a broad peak of unknown 5.64 min, which eluted earlier than expected for DHA in relation to the sugars and derivative. No peak was observed in the DHA region.

Table 1. *Leptospermum* Nectar Samples Collected in Replicate from Individual Trees (n) between September and November 2014

	L. laevigatum		*L. polygalifolium*			*L. trinervium*		*L. whitei*	
	NR region	NWT region	NR region	SC region	NR region	SC region	PS region	NR region	SC region
trees (n)	37	1	22	4	22	2	1	10	3

seven standards showed a linear relationship between peak area ratio of DHA/sugar, at 200 and 243 nm, respectively against the known mass ratios of DHA/sugar (R^2 = 0.9982). Therefore, the mass ratio of DHA/sugar in individual samples was determined against the calibration curve by linear regression, as displayed by eq 1:

$$\text{DHA/sugar (ppm)} = \text{DHA/sugar (peak area ratio)} \times 11021 \quad (1)$$

DHA was present in all *L. polygalifolium* and *L. whitei* samples (Figure 1). In contrast, NR *L. laevigatum* samples showed a broad unknown peak with low absorbance at approximately 5.64 min, which eluted earlier than expected for DHA (Figure 2). To confirm whether the unknown peak was DHA, four *L. laevigatum* samples were spiked with 1 μL of DHA standard and analyzed again by RP-HPLC. A sharp DHA peak at 5.72 min was observed in the spiked runs, which verified that the unknown peak was not DHA (data not shown). To determine the identity of the source of the unknown peak, 400 μL of PFBHA buffer solution was analyzed via RP-HPLC alone. The unknown was observed on the chromatogram at 5.62 min, which suggested the unknown was a component within the derivatizing reagent (data not shown). DHA was not detected in any of the *L. laevigatum* samples collected from NR or NWT, nor was DHA detected in any of the *L. trinervium* samples collected from NR, SC, or PS (Table 1).

The DHA/sugar ratio in *L. polygalifolium* and *L. whitei* nectar samples varied between species (Table 2; Figure 3). The highest nectar activity levels were observed in the *L. whitei* samples, where the DHA/sugar ratio ranged from 10169 to 24199 ppm. In comparison, the nectar activity of *L. polygalifolium* ranged from 9321 to 20174 ppm. The data were not normally distributed; therefore, statistical analysis was performed with a nonparametric test. Differences in nectar activity between species were analyzed with a Mann−Whitney U test, which showed that there was a statistically significant difference between the DHA/sugar ratio of *L. polygalifolium* and that of *L. whitei* (U = 270; n_1 = 26, n_2 = 13; $P < 0.05$).

Table 2. Comparison of DHA/Sugar Concentration (ppm) between *Leptospermum polygalifolium* and *Leptospermum whitei* Nectar Collected at Sunshine Coast and Northern Rivers Sites

species	n	min	max	median	IQR
L. polygalifolium	26	9321	20174	12182	4741
L. whitei	13	10169	24199	15625	6909

DOI: 10.1021/acs.jafc.5b01930
J. Agric. Food Chem. 2015, 63, 6513−6517

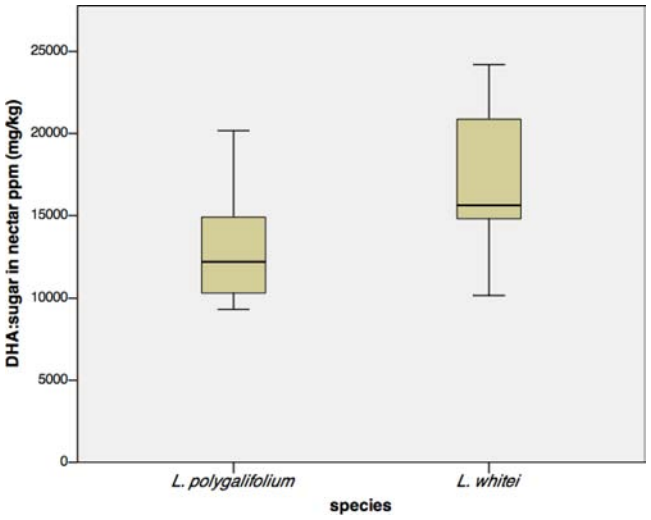

Figure 3. Box-plot comparison of the range of DHA/sugar in nectar from individual *Leptospermum polygalifolium* (n = 26) and *Leptospermum whitei* (n = 13) trees sampled at both Sunshine Coast and Northern Rivers sites.

DISCUSSION

The novel nectar extraction technique developed in this study has not to our knowledge been previously reported. Windsor et al.[20] reported successful analysis of PFBHA derivatized DHA and MGO in Australian *Leptospermum* honeys via RP-HPLC; hence, a modified version of this procedure was used to quantitatively derivatize the sugars and DHA in nectar. The PFBHA derivatization of DHA and sugars improved the chromatographic separation and detection of compounds. The method developed in this study was both rapid and convenient. The nectar solution extracted in situ was derivatized with PFBHA buffer solution upon analysis, and after 2 h at 65 °C, samples were analyzed directly with RP-HPLC and photodiode array detection. In addition, total sugars and DHA were analyzed within the one sample, via detection at two wavelengths. In contrast, the method described by Williams et al.,[15] which analyzed DHA/sugar in New Zealand *L. scoparium* by GC-FID and in Australian *Leptospermum* samples by GC-MS, had increased complexity and involved two separate procedures to detect DHA and sugars. Furthermore, Williams et al.[15] found that approximately 4% of DHA was transferred to the sample bag during flower collection. The method described in this study eliminates such loss, as nectar is deposited directly to the HPLC vial at the time of collection.

The results of this study indicated that perhaps not all species within the *Leptospermum* genus produce DHA within their nectar and, consequently, will not produce non-peroxide active honeys. The results showed that DHA was not detected in any of the *L. laevigatum* nectar samples, as illustrated by the sharp DHA peak when samples were spiked with 1 μL of DHA (data not shown). It was calculated that 1 μL of DHA standard was equivalent to approximately 300 ppm of DHA/sugar in nectar; therefore, it was conservatively estimated that all of the *L. laevigatum* nectar samples had a DHA activity level <100 ppm. No prior studies within the available literature have analyzed *L. laevigatum* nectar, apart from one sample analyzed by Williams et al.,[15] who were also unable to detect DHA. As DHA was also undetectable in the replicated NWT *L. laevigatum* samples, it appeared unlikely that lack of nectar activity was a result of environmental factors, as the NR and NWT samples were separated by approximately 1500 km. Moreover, this suggested that lack of bioactivity in *L. laevigatum* nectar is species wide. Similarly, DHA was not detected in any of the *L. trinervium* samples collected from the SC, NR, and PS regions. As a result, it was concluded that *L. trinervium* samples also had an activity level <100 ppm. No prior studies were found to have previously analyzed monofloral *L. trinervium* honey.

As *L. laevigatum*, *L. polygalifolium*, *L. trinervium*, and *L. whitei* flower at similar times of the year, beekeepers in NNSW target all four species to produce active honey. The results indicated that honey produced from *L. laevigatum* and *L. trinervium* nectar has a high probability of being inactive. Therefore, the findings suggested that beekeepers should avoid both species if they intend to produce active honey. Windsor et al.[20] detected DHA and MGO in *L. leavigatum* and blended *L. trinervium*/*Guioa semiglauca* honey, at low activity levels of <750 and <150 ppm, respectively. However, the presence of DHA may have been attributed to bees collecting nectar from other active *Leptospemum* species in flower at the same time, such as *L. polygalifolium* or *L. whitei*.

DHA was present in all *L. polygalifolium* and *L. whitei* nectar samples, yet nectar activity significantly varied between species. The *L. whitei* samples had the highest nectar activity (Table 2). No previous studies within the available literature have analyzed the DHA/MGO concentration or antibacterial activity of monofloral *L. whitei* honey. The environmental conditions at the sample sites were not quantitatively measured within this study. However, the *L. polygalifolium* and *L. whitei* trees sampled at SC and NR were believed to be wild populations in sandy, low-nutrient soils. It is possible that environmental factors, such as nutrient availability, may have contributed to the variation in nectar activity observed between species. Williams et al.[15] measured soil type, yet no correlation was found between soil type and nectar activity.

Williams et al.[15] classified nectar activity into three categories: low (<1000 ppm), moderate (1000−2000 ppm), and high (>2000 ppm). The study reported that the majority of nectar samples collected from *L. scoparium* trees over a two-year period had a moderate to low activity level. The highest observation was <9000 ppm from a garden cultivar from the Waikato region. In contrast, the lowest observations for *L. polygalifolium* and *L. whitei* in this study were >9000 ppm (Table 2). The high DHA/sugar ratios found in this study suggested that perhaps honey derived purely from *L. polygalifolium* or *L. whitei* may have higher bioactivity than mānuka honey. Research into the antibacterial activity of *L. polygalifolium* and *L. whitei* honey is recommended. In addition, it is possible that the results of this study may not be comparable to the values reported by Williams et al.,[15] due to method-related differences. Overall, the findings of the study have implications for beekeepers and the honey industry. Active honey is of high commercial value; therefore, the findings of this study indicated that Australian beekeepers should target *L. polygalifolium* and *L. whitei* if they intend to produce active honeys.

AUTHOR INFORMATION

Corresponding Author

*(P.R.B.) E-mail: pbrooks@usc.edu.au. Phone: +61 75430 2828.

Notes

The authors declare no competing financial interest.

DOI: 10.1021/acs.jafc.5b01930
J. Agric. Food Chem. 2015, 63, 6513−6517

■ ACKNOWLEDGMENTS

We thank Michael Howes of Tyagarah Apiaries for access to field sites.

■ ABBREVIATIONS USED

ACN, acetonitrile; DHA, dihydroxyacetone; GC-MS, gas chromatography−mass spectrometry; IQR, interquartile range; MGO, methylglyoxal; NNSW, northern New South Wales; NR, Northern Rivers; NWT, northwestern Tasmania; PFBHA, *o*-(2,3,4,5,6-pentafluorobenzyl) hydrochloride; PS, Port Stephens, NSW; RP-HPLC, reverse-phase high-performance liquid chromatography; SC, Sunshine Coast; SEQ, southeastern Queensland

■ REFERENCES

(1) Lusby, P. E.; Coombes, A. L.; Wilkinson, J. M. Bactericidal activity of different honeys against pathogenic bacteria. *Arch. Med. Res.* **2005**, *36*, 464−467.

(2) French, V.; Cooper, R.; Molan, P. C. The antibacterial activity of honey against coagulase-negative *Staphylococci*. *J. Antimicrob. Chemother.* **2005**, *56*, 228−231.

(3) Blair, S.; Cokcetin, N.; Harry, E.; Carter, D. The unusual antibacterial activity of medical-grade *Leptospermum* honey: antibacterial spectrum, resistance and transcriptome analysis. *Eur. J. Clin. Microbiol. Infect. Dis.* **2009**, *28*, 1199−1208.

(4) Cooper, R.; Jenkins, L.; Henriques, A.; Duggan, R.; Burton, N. Absence of bacterial resistance to medical-grade manuka honey. *Eur. J. Clin. Microbiol. Infect. Dis.* **2010**, *29*, 1237−1241.

(5) Henle, T. Golden opportunities. *Chem. Ind.* **2012**, *76*, 32−35.

(6) Mandal, M. D.; Mandal, S. Honey: its medicinal property and antibacterial activity. *Asian Pac. J. Trop. Biomed.* **2011**, *1*, 154−160.

(7) Molan, P. C. The role of honey in the management of wounds. *J. Wound Care* **1999**, *8*, 415−418.

(8) Adams, C. J.; Boult, C. H.; Deadman, B. J.; Farr, J. M.; Grainger, M. N.; Manley-Harris, M.; Snow, M. J. Isolation by HPLC and characterisation of the bioactive fraction of New Zealand manuka (*Leptospermum scoparium*) honey. *Carbohydr. Res.* **2008**, *343*, 651−659.

(9) Atrott, J.; Henle, T. Methylglyoxal in manuka honey − correlation with antibacterial properties. *Czech J. Food Sci.* **2009**, *27*, 163−165.

(10) Kwakman, P. H.; Te Velde, A. A.; De Boer, L.; Vandenbroucke-Grauls, C. M.; Zaat, S. A. Two major medicinal honeys have different mechanisms of bactericidal activity. *PLoS One* **2011**, *6*, 1−7.

(11) Kwakman, P. H.; Zaat, S. A. Antibacterial components of honey. *IUBMB Life* **2012**, *64*, 48−55.

(12) Henriques, A.; Jenkins, R.; Burton, N.; Cooper, R. The intracellular effects of manuka honey on *Staphylococcus aureus*. *Eur. J. Clin. Microbiol. Infect. Dis.* **2010**, *29*, 45−50.

(13) Adams, C. J.; Manley-Harris, M.; Molan, P. C. The origin of methylglyoxal in New Zealand manuka (*Leptospermum scoparium*) honey. *Carbohydr. Res.* **2009**, *344*, 1050−1053.

(14) Atrott, J.; Haberlau, S.; Henle, T. Studies on the formation of methylglyoxal from dihydroxyacetone in manuka (*Leptospermum scoparium*) honey. *Carbohydr. Res.* **2012**, *361*, 7−11.

(15) Williams, S.; King, J.; Revell, M.; Manley-Harris, M.; Balks, M.; Janusch, F.; Kiefer, M.; Clearwater, M.; Brooks, P.; Dawson, M. Regional, annual and individual variation in the dihydroxyacetone content of the nectar of manuka (*Leptospermum scoparium*) in New Zealand. *J. Agric. Food Chem.* **2014**, *62*, 10332−10340.

(16) Price, J. N.; Morgan, J. W. Variability in plant fitness influences range expansion of *Leptospermum scoparium*. *Ecography* **2006**, *29*, 623−631.

(17) Stephens, J.; Molan, P. C.; Clarkson, B. D. A review of *Leptospermum scoparium* (Myrtaceae) in New Zealand. *N. Z. J. Bot.* **2005**, *43*, 431−449.

(18) Thompson, J. *A Revision of the Genus Leptospermum (Myrtaceae)*. *Telopea* **1989**, *3*, 301−448.

(19) Wrigley, J. W.; Fagg, M. *Australian Native Plants - Cultivation, Use in Landscaping and Propagation*; New Holland Publishers: Sydney, Australia, 2007.

(20) Windsor, S.; Pappalardo, M.; Brooks, P.; Williams, S.; Manley-Harris, M. A convenient new analysis of dihydroxyacetone and methylglyoxal applied to Australian *Leptospermum* honeys. *J. Pharmacogn. Phytother.* **2012**, *4*, 6−11.

■ NOTE ADDED AFTER ASAP PUBLICATION

This paper was published ASAP on July 17, 2015, with an error to equation 1. The corrected version reposted on July 21, 2015.

DOI: 10.1021/acs.jafc.5b01930
J. Agric. Food Chem. 2015, 63, 6513−6517

Table 1. Chemical Composition and Nutrient Profiles of Tested Feedstuffs (± Standard Deviation)

	samples[a]							
chemical composition[b]	barley	corn	wheat	triticale	SBM	SFM	CSM	CM
DM (g/kg)	894 ± 11	878 ± 7	874 ± 9	882 ± 10	932 ± 9	912 ± 8	917 ± 13	942 ± 7
CP (g/kg DM)	112 ± 3	91 ± 2	123 ± 3	103 ± 2	432 ± 4	301 ± 3	322 ± 4	398 ± 4
EE (g/kg DM)	17 ± 3	34 ± 2	17 ± 2	12 ± 1	19 ± 3	56 ± 2	65 ± 2	77 ± 3
ash (g/kg DM)	24 ± 4	17 ± 3	21 ± 4	24 ± 4	70 ± 6	77 ± 8	66 ± 4	62 ± 3
NDF (g/kg DM)	215 ± 4	112 ± 6	154 ± 7	118 ± 5	155 ± 5	403 ± 13	305 ± 9	273 ± 10
ADF (g/kg DM)	54 ± 6	34 ± 6	21 ± 8	33 ± 5	101 ± 7	311 ± 10	213 ± 7	176 ± 6
starch (g/kg DM)	564 ± 17	652 ± 21	566 ± 20	614 ± 13	47 ± 14	nd	nd	nd
RNSP (g/kg DM)	50 ± 24	79 ± 22	91 ± 27	104 ± 21	278 ± 22	163 ± 18	242 ± 13	191 ± 17
NFC (g/kg DM)	632 ± 13	746 ± 11	685 ± 15	743 ± 10	324 ± 16	163 ± 21	242 ± 17	191 ± 18
NDICP (g/kg CP)	169 ± 7	80 ± 6	144 ± 7	142 ± 11	17 ± 9	219 ± 17	106 ± 10	165 ± 8
ADICP (g/kg CP)	46 ± 4	35 ± 6	17 ± 5	20 ± 7	10 ± 5	42 ± 4	59 ± 3	63 ± 5
$TDN_{1\times}$ (g/kg DM)	883 ± 17	952 ± 21	902 ± 23	905 ± 19	886 ± 17	756 ± 18	816 ± 21	847 ± 24
FOM2010 (g/kg DM)	701 ± 9	652 ± 11	742 ± 8	818 ± 11	618 ± 10	571 ± 5	435 ± 7	483 ± 12
FOM1994 (g/kg DM)	670 ± 8	698 ± 8	687 ± 6	733 ± 9	398 ± 7	266 ± 6	298 ± 5	346 ± 8

[a]SBM, soybean meal; SFM, sunflower meal; CSM, cottonseed meal; CM, canola meal. [b]ADF, acid detergent fiber; ADICP, acid detergent insoluble crude protein; CP, crude protein; DM, dry matter; EE, ether extract; FOM, fermented organic matter; NDF, neutral detergent fiber; NDICP, neutral detergent insoluble crude protein; NFC, nonfiber carbohydrate; RNSP, residual nonstarch polysaccharides.

especially in quantifying calculations.[7,8] For instance, DVE1994 uses fermentable organic matter for these calculations, whereas DVE2010 uses a more complex approach considering a more detailed fractionation of feeds and differences in efficiency of microbial protein synthesis for different types of bacteria and different type of substrates for the rumen microbiota. The objective of the present study was to compare the DVE1994, DVE2010, and NRC-2001 systems in the prediction of truly absorbed microbial protein synthesis, rumen bypass protein, and endogenous protein loss, as well as total metabolizable protein from starchy and protein-rich raw feed materials.

MATERIALS AND METHODS

Chemicals. All chemicals used in this study were of commercial and analytical reagent grade. Sodium hydroxide (purity = 99%), sulfuric acid (purity = 98%), ethyl ether (purity = 99%), sodium borate ($Na_2B_4O_7{\cdot}10H_2O$; purity = 99.5%), sodium phosphate ($NaH_2PO_4{\cdot}H_2O$; purity = 95.5%), copper sulfate (purity = 99%), potassium sulfate (purity = 99%), acetone (purity ≥ 99.5%), thermostable α-amylase (180000 u/ML), ethylenediaminetetraacetic acid (purity = 99.4%), sodium borate (purity = 99%), disodium hydrogen phosphate anhydrous (purity = 99%), and triethylene glycol (purity = 99%) were purchased from Fardan Shimi (Mashhad, Iran).

Starchy and Protein Feedstuffs. Commonly used grains and protein-rich raw feed materials for dairy cattle, including barley, corn, triticale, wheat, soybean meal (SBM), sunflower meal (SFM), cottonseed meal (CSM), and canola meal (CM), were investigated. Samples from these feeds were provided by local distributers (Marvdasht, Fars province, Iran). Half of each sample was ground for laboratory analysis, and the half was stored as backup at −20 °C.

In Situ Incubations. The degradation characteristics of the feedstuffs were estimated with the in situ technique of Ørskov and McDonald,[9] as adapted by CVB (Netherlands Centraal Veevoeder Bureau),[10] but with 96 h instead of 336 h as the prolonged incubation time point. This study was conducted in two experimental runs and, in each run, the treatments were randomly assigned among the three Holstein dairy cows (weight = 605 ± 15.6 kg and 27 ± 2.5 kg/day milk production) fitted with a large rumen cannula with an internal diameter of 10 cm used for measuring rumen degradation characteristics. Cows were housed individually in the Dairy Research building at the Ferdowsi University of Mashhad, during in situ rumen incubation time. Cows were fed according to NRC 2001 recommendations for their milk production level. Ration was based upon corn silage, alfalfa hay, and mixed concentrate consisting of barley grain, corn grain, soybean meal, canola meal, cottonseed meal, micromineral premix, vitamin premixes A and D, limestone, and salt. Animals were fed in the form of TMR daily at 6:00 a.m., 2:00 p.m., and 10:00 p.m. right after milking. The incubation time points were 0, 2, 4, 8, 12, 24, 48, 72, and 96 h. The "gradual addition/all out" method was followed.[8] The 0-h samples were treated in the laboratory according to the procedure of Azarfar et al.[11] to determine the soluble and insoluble washable fractions. After incubation, bags were removed from the rumen and washed in a bucket with cold tap water to remove excess ruminal contents. Subsequently, bags were dried at 70 °C for 48 h. Dried samples were stored in a refrigerated cool room (4 °C) until analysis. The in situ data were fitted to the modified first-order kinetic equation[9,12,13]

$$R(t) = U + D \times e^{-K_d \times t}$$

where $R(t)$ = residue at t h of incubation (%), U = undegradable fraction (%), D = potentially degradable fraction (%), t = time of incubation (h), and K_d = degradation rate of potentially degradable fraction (%/h). In situ parameters were calculated with the NLIN (nonlinear) procedure of SAS.[14]

Chemical Analysis. Laboratory samples of the feedstuffs and rumen residues were prepared by grinding to pass a 1-mm screen. The dry matter (DM; AOAC official method 930.15), ash (AOAC official method 942.05), crude fat (EE; AOAC official method 954.02), and crude protein (CP; AOAC official method 984.13) contents were analyzed according to the procedures of AOAC.[15] The acid detergent fiber (ADF) and neutral detergent fiber (NDF) values were analyzed according to the procedures of Van Soest et al.[16] Neutral detergent fiber was determined without sodium sulfite.[16] The chemical composition and characteristics of these samples are provided in Table 1.

NRC-2001 Model. Calculating metabolizable protein is a summative approach based upon (1) digestible rumen undegradable protein (ARUP), (2) digestible microbial crude protein (AMCP), and (3) rumen endogenous CP (ECP) calculated as

$$MP = ARUP + AMCP + ECP$$

The amount of ruminally (un)degraded feed protein was calculated from crude protein content and ruminally (un)degraded feed protein proportion derived from in situ incubations as

$$RDP = S + D \times K_d/(K_p + K_d)$$

where S = soluble fraction (%), D = potentially degradable fraction (%), K_d = degradation rate of D fraction; and K_p = passage rate; a K_p of 6%/h was adopted.[3] The amount of ruminally synthesized microbial

DOI: 10.1021/jf505961e
J. Agric. Food Chem. 2015, 63, 6518−6524

protein (MCP) was calculated conditionally as 130 g/kg TDN. When RDP exceeded 1.18 × TDN-predicted MCP and was calculated as 0.85 of RDP, the RDP was <1.18 × TDN-predicted MCP. The amount of truly absorbed MCP was estimated assuming that true protein content and digestibility of rumen microbial protein both are 80%; therefore, the amount of truly absorbed MCP was estimated as

$$\mathrm{AMCP_{NRC}} = 0.80 \times 0.80 \times \mathrm{MCP}$$

For feed ingredients, truly absorbed rumen undegraded feed protein in the small intestine (ARUP) was calculated as the amount of RUP multiplied by the intestinal digestibility of RUP (dRUP), and rumen endogenous CP was calculated as

$$\mathrm{ECP} = 6.25 \times 1.9 \times \mathrm{DM}/1000$$

where DM is in g kg^{-1}. Assuming that 50% of rumen endogenous CP passes to the duodenum and 80% of rumen endogenous CP is true protein, the truly absorbed endogenous protein in the small intestine (AECP) was estimated as

$$\mathrm{AECP} = 0.50 \times 0.80 \times \mathrm{ECP}$$

Detailed information about the model is provided by NRC.[2]

DVE1994 System. Truly digested and absorbed protein in the small intestine (DVE1994) is contributed by (1) feed protein escaping rumen degradation (RUP), (2) microbial protein synthesized in the rumen (MCP), and (3) a correction for endogenous protein losses in the digestive tract (EPL). Therefore, the DVE value was estimated as

$$\mathrm{DVE} = \mathrm{ARUP} + \mathrm{AMCP} - \mathrm{EPL}$$

Rumen-undegraded protein from feedstuff (RUP) was calculated as

$$\mathrm{RUP} = 1.11 \times \mathrm{CP} \times \mathrm{RUP_{fraction}}$$

where

$$\mathrm{RUP_{fraction}} = U + D \times K_p/(K_p + K_d)$$

where U = undegraded fraction (%), D = potentially degradable fraction (%), K_d = degradation rate of D fraction, K_p = passage rate, which was assumed to be 6%/h. For feed ingredients, the content of truly absorbed bypass feed protein in the small intestine (ARUP) was calculated as

$$\mathrm{ARUP} = \mathrm{dRUP} \times \mathrm{RUP}$$

Microbial protein synthesized in the rumen (MCP) is considered to be 150 g/kg of organic matter fermented in rumen (FOM). The content of FOM was estimated from digestible organic matter minus the sum of ether extract, $\mathrm{RUP_{DVE}}$, undegradable feed starch in the rumen and fermentation products (not relevant for concentrated feedstuffs). Assuming that 25% of microbial protein N is in the form of nucleic acids, 75% of MCP was added to the undegraded feed protein (RUP) with assumed digestibility of 85%; therefore, the amount of rumen synthesized microbial protein truly absorbed in the small intestine (AMCP) was estimated as

$$\mathrm{AMCP} = 0.85 \times 0.75 \times \mathrm{MCP}$$

A correction is needed for protein losses due to incomplete digestion and from endogenous secretions.

The amount of undigested DM (UDM) that is excreted in the feces was used to calculate losses regarding digestive tract secretions, epithelial cells, and other endogenous protein sources which occur during the digestion process (EPL), calculated as

$$\mathrm{EPL} = 0.075 \times \mathrm{UDM}$$

where UDM was calculated as undigested organic matter (UOM) plus undigested ash (UASH).

More detailed information about the DVE1994 system is provided by Tamminga et al.[3]

DVE2010 System. As with the DVE1994 system, the DVE2010 system calculates the amount of digested true protein in the small intestine from various sources, and dairy cow requirements for protein are represented in DVE units. Several facets of the DVE1994 system such as feed components ruminal degradation, feedstuff fractionation, degradation rates of non-wash-out fraction, and efficiency of microbial protein synthesis were reappraised in the DVE2010 system. Detailed descriptions on concepts and formulas are presented by Van Duinkerken et al.,[6] and a brief explanation on calculation rules follows.

$$\mathrm{DVE} = \mathrm{ARUP} + \mathrm{AMCP} - \mathrm{EPL}$$

The quantity of feed protein not degraded in the rumen (RUP) and the intestinal digestibility of this rumen undegraded feed protein (dRUP) were used to estimate ARUP. ARUP is calculated as

$$\mathrm{ARUP} = \mathrm{CP} \times \%\mathrm{RUP}/100 \times \%\mathrm{dRUP}/100$$

The relative amount of RUP (%RUP) was calculated as

$$\%\mathrm{RUP} = K_{p,S}/(K_{d,S} + K_{p,S}) \times S + K_{p,W\text{-}S}/(K_{p,W\text{-}S} + k_{d,D}) \times (W\text{-}S) + K_{p,D}/(K_{p,D} + K_{d,D}))D + U$$

where S = crude protein soluble fraction (%); (W-S) = crude protein in washable but not soluble fraction, W = washable crude protein fraction (%); D = potentially degradable CP fraction (%) (D = 100 − W − U); U = undegradable crude protein fraction (%); $K_{p,S}$ = passage rate of the S fraction, assuming 11%/h; $K_{p,W\text{-}S}$ = passage rate of the W-S fraction, assuming 8%/h; $K_{p,D}$ = rate of passage from the rumen of the D fraction, assuming 6%/h for concentrates; $K_{d,S}$ = rate of degradation of CP in the S fraction in the rumen, assuming 200%/h; $K_{d,D}$ = rate of degradation of CP in the D and W-S fractions in the rumen (%/h).

Calculation of AMCP in the DVE2010 system is rather sophisticated and complex. It is assumed that within each chemical component, degradation and passage rates of different fractions determine how that component is degraded in the rumen as

$$\mathrm{FCOMP} = \mathrm{COMP} \times (S \times k_{d,S}/(k_{d,S} + k_{p,S}) + (W\text{-}S) \times k_{d,(7W\text{-}S)}/(k_{d,(W\text{-}S)} + k_{(p,W\text{-}S)}) + D \times k_{d,D}/(k_{d,D} + k_{p,D}))$$

where FCOMP is a component fermented in the rumen (g/g DM), COMP is the content of the relevant component (g/g DM), S represents the soluble fraction (g/g), $k_{d,S}$ is the fractional degradation rate of fraction S (/h), $k_{p,S}$ is the fractional rate of passage of fraction S (/h), W is the fraction that leaves nylon bags by washing (g/g), (W-S) is the insoluble portion in washout fraction (g/g), $k_{d,(W\text{-}S)}$ is the fractional degradation rate of fraction (W-S) (/h), $k_{p,(W\text{-}S)}$ is the fractional rate of passage of fraction (W-S) (/h), D is the non-wash-out potentially degradable fraction (g/g), $k_{d,D}$ is the fractional rate of degradation of fraction D (/h), and $k_{p,D}$ is the fractional rate of passage of fraction D (/h).

For each fraction in the FCOMP formula, DVE2010 considers a specific microbial protein yield. So the fermentable organic matter and MCP were calculated as the sum of FCOMP and its related microbial protein yield, respectively. It is assumed that 85% of microbial protein is truly digested, and therefore the amount of truly absorbed rumen synthesized microbial protein in the small intestine (AMCP) was estimated as

$$\mathrm{AMCP} = 0.85 \times 0.75 \times \mathrm{MCP}$$

A correction is needed for protein losses due to incomplete digestion and from endogenous secretions. For calculating endogenous protein losses during the digestion process (EPL), undigested ash (UASH) was added to undigested organic matter (UOM), which represents the amount of undigested DM (UDM) excreted in the feces, and EPL was calculated as

$$\mathrm{EPL} = 0.075 \times \mathrm{UDM}$$

Degraded Protein Balance. Degraded protein balance (RDPB) indicates the balance between microbial protein synthesis potentially possible from rumen degraded feed protein and available energy from total digestible nutrient, calculated as

$$\mathrm{RDPB} = \mathrm{RDP} - 1.18\mathrm{MCP}$$

DOI: 10.1021/jf505961e
J. Agric. Food Chem. 2015, 63, 6518−6524

Rumen degraded protein balance (OEB) in the DVE system (in Dutch, Onbestendig Eiwit Balans) represents the difference (at rumen level) between the maximum possible microbial protein synthesis, based on the available amount of degradable protein, on the one hand, and the maximum possible microbial protein synthesis, based on the available amount of energy, on the other.

$$\text{RDPB} = \text{MCPn} - \text{MCPe}$$

where MCPn = the maximum possible microbial protein synthesis based on available nitrogen and MCPe = the maximum possible microbial protein synthesis based on available energy.

Statistical Analysis. Statistical analyses were performed using the MIXED procedure of SAS 9.3 (SAS Institute, Inc., Cary, NC, USA) using the following model: $Y_{ij} = \mu + \alpha_i + e_{ij}$, in which Y_{ij} was an observation of the dependent variable ij, μ was the population mean for the variable, α_i was the effect of the treatments, and e_{ij} was the random error associated with observation of ij. The significance level for all statistical analyses was declared at $P < 0.05$ and trends at $P < 0.10$. Treatment means were compared using the Tukey test.

RESULTS AND DISCUSSION

The predictions of the potential protein supply (g kg^{-1} DM) to dairy cows from starchy and protein concentrates, using the DVE1994 system, NRC-2001 dairy model, and DVE2010 system are presented in Tables 2 and 3. DVE1994 predictions for ARUP for starchy and concentrates were higher than those of the NRC-2001 model (Table 4), which is in agreement with several previous studies.[17−20] In the DVE1994 system, a

Table 2. Predictions of the Potential Protein Supply (Grams per Kilogram DM) to Dairy Cows from Starchy Concentrates, Using the DVE1994 System, NRC-2001 Dairy Model, and DVE2010 System

		model			
feed	parameter[a]	DVE1994	NRC-2001	DVE2010	SEM[b]
barley	ARUP	29	20	27	1.8
	AMCP	64	47	88	7.5
	ECP (EPL)	19	4	19	3.2
	MP (DVE)	74	71	96	5.0
	RDPB	−24	−61	−59	7.6
corn	ARUP	25	20	22	0.8
	AMCP	67	37	88	9.4
	ECP (EPL)	17	4	17	2.6
	MP (DVE)	75	61	94	6.0
	RDPB	−42	−44	−73	6.2
triticale	ARUP	20	11	15	1.6
	AMCP	70	48	100	9.6
	ECP (EPL)	16	4	16	2.4
	MP (DVE)	74	63	99	6.8
	RDPB	−32	−72	−73	8.6
wheat	ARUP	33	21	27	2.2
	AMCP	66	52	91	7.1
	ECP (EPL)	18	4	18	2.9
	MP (DVE)	81	78	99	4.3
	RDPB	−19	−69	−52	9.7

[a]AMCP, truly absorbed microbial protein in the small intestine; ARUP, truly absorbed rumen undegraded protein in the small intestine; RDPB, rumen degraded protein balance; DVE, truly digested protein in the small intestine (DVE system); ECP, rumen endogenous protein; MP, metabolizable protein. [b]Standard error of the mean.

Table 3. Predictions of the Potential Protein Supply (Grams per Kilogram DM) to Dairy Cows from Protein Concentrates, Using the DVE1994 System, NRC-2001 Dairy Model, and DVE2010 System

		model			
feed[a]	parameter[b]	DVE1994	NRC-2001	DVE2010	SEM[c]
CM	ARUP	148	117	134	5.7
	AMCP	33	70	43	7.1
	ECP (EPL)	26	11	26	4.5
	MP (DVE)	155	192	152	8.1
	RDPB	157	24	159	28.3
CSM	ARUP	120	94	109	4.8
	AMCP	28	68	40	7.4
	ECP (EPL)	34	11	34	6.2
	MP (DVE)	115	166	115	10.8
	RDPB	140	−15	134	32.0
SBM	ARUP	215	184	194	5.9
	AMCP	38	74	58	6.5
	ECP (EPL)	23	11	23	4.0
	MP (DVE)	230	262	229	6.9
	RDPB	150	54	141	19.3
SFM	ARUP	101	77	88	4.4
	AMCP	25	63	54	7.3
	ECP (EPL)	38	11	38	7.2
	MP (DVE)	88	145	103	10.8
	RDPB	152	−32	121	36.0

[a]SBM, soybean meal; SFM, sunflower meal; CSM, cottonseed meal; CM, canola meal. [b]AMCP, truly absorbed microbial protein in the small intestine; ARUP, truly absorbed rumen undegraded protein in the small intestine; RDPB, rumen degraded protein balance; DVE, truly digested protein in the small intestine (DVE system); ECP, rumen endogenous protein; MP, metabolizable protein. [c]Standard error of the mean.

Table 4. Means of Predictions of the Potential Protein Supply (Grams per Kilogram DM) to Dairy Cows from Pooled Data for Starchy and Protein Concentrates, Using the DVE1994 System, NRC-2001 Dairy Model, and DVE2010 System

		model[a]			
feed	parameter[b]	DVE1994	NRC-2001	DVE2010	SEM[c]
starchy	ARUP	27 a	18 b	23 ab	1.2
	AMCP	67 b	46 c	92 a	4.0
	ECP (EPL)	17 a	10 b	17 a	1.3
	MP (DVE)	76 b	68 c	97 a	2.7
	RDPB	−29 a	−62 b	−64 b	3.9
protein	ARUP	146	131	118	8.9
	AMCP	31 c	69 a	49 b	3.4
	ECP (EPL)	30 a	10 b	30 a	2.7
	MP (DVE)	147 b	191 a	150 b	11.1
	RDPB	150 a	139 a	9 b	14.2

[a]Means within the same row with different letters are different ($P < 0.05$). [b]AMC, truly absorbed microbial protein in the small intestine; ARUP, truly absorbed rumen undegraded protein in the small intestine; RDPB, rumen degraded protein balance; DVE, truly digested protein in the small intestine (DVE system); ECP, rumen endogenous protein; MP, metabolizable protein. [c]Standard error of the mean.

DOI: 10.1021/jf505961e
J. Agric. Food Chem. 2015, 63, 6518−6524

correction factor of 1.11 (as in the French Protein System) was used for ARUP,[4] which represents the regression coefficient of in vivo on in situ degradation data, and in NRC model there is no correction for the difference between in vivo and in situ results.

Instead of this correction factor, in the DVE2010 system the wash-out fraction is divided into two fractions of soluble (*S*) and insoluble (*W-S*). It is assumed that a part of the soluble fraction (5%/h)[6] and the *W-S* fraction (not constant) escape degradation in the rumen and add up to the calculated amount of RUP.[6] The DVE2010 system and NRC-2001 model predicted more intestinally digestible microbial protein (AMCP) for both starchy and protein concentrates. Our results are in agreement with Yu,[21] who reported higher MP and lower protein degraded balance (PDB) estimation from NRC-2001 in comparison to DVE1994 lupin seeds, Damiran et al.[17] and Yu et al.,[8] who reported higher MP and lower protein degraded balance (PDB), predicted by NRC-2001 comparison to DVE 1994 for barley grain and Peng et al.,[18] who reported the same for camelina seeds. Gamage and Yu[22] compared the DVE2010 system with NRC-2001 in modeling metabolic characteristics of proteins in dairy cattle from wheat and wheat distillers dried grain and concluded that the DVE2010 system predicted higher truly absorbed rumen synthesized microbial protein, higher truly absorbed rumen undegraded feed protein, higher endogenous protein, higher total truly absorbed protein in the small intestine, and lower degraded protein balance in comparison with the NRC-2001 model. In the DVE1994 system, it is assumed that 100% of RDP is available for microbial protein synthesis in the presence of enough fermentable energy, whereas in the NRC-2001 model, it is assumed that only 85% of ruminally degraded feed protein could be potentially converted to microbial protein. This indicates assumed conversion rates from rumen degraded protein to microbial protein are different between NRC and DVE. Although the DVE2010 system also assumes that all of the RDP in the presence of sufficient energy could potentially form microbial protein, as mentioned earlier parts of the *S* and *W-S* fractions are considered to leave the rumen. Another source for differences is that NRC-2001 and DVE1994 use constant coefficients for prediction of microbial protein synthesis based on fermentable organic matter or TDN (150 g/kg fermentable organic matter vs 120 g microbial protein synthesis/kg TDN), whereas DVE2010 is a sophisticated model that uses a more dynamic approach for the prediction of microbial protein synthesis based on ATP.[6] This approach is based on the nature of the feed (concentrate vs forage), its components (crude protein, neutral detergent fiber, and etc.), fractions of each component (soluble, wash-out, etc.) and different microbial protein synthesis efficiency for different rumen bacteria (liquid associated bacteria vs particle associated bacteria).[6] Estimations based on the NRC-2001 model for ECP are lower than DVE system predictions of EPL for starchy and protein concentrates. There is a big difference in how endogenous protein loss is taken into account by the NRC-2001 model and DVE systems.

Estimations for endogenous protein loss by the NRC-2001 model for protein concentrates are less than DVE estimations, which is in agreement with several previous studies.[17,19,20,23] Endogenous protein loss is considered as a source of protein that partially can be used by animals in the NRC-2001 model, whereas the DVE system considers the endogenous protein loss as a total waste, which is replaced by a part of available protein in the small intestine, and considers the total balance of available protein.

The proportion of endogenous protein loss is very small compared to other contributors, and overall DVE (MP) estimations, especially in protein concentrates and DVE (MP), do not differ among the models for this type of feedstuff. Predictions for degradable protein balance (RDPB) from the NRC-2001 model are close to RDPB using DVE2010 for starchy concentrates and close to RDPB using DVE1994 for protein concentrates. The RDPB (OEB) value shows the (im)balance between microbial protein synthesis from available rumen degradable CP and potential energy from anaerobic fermentation in the rumen. When the OEB value is positive, it indicates the N-loss from the rumen. When negative, microbial protein synthesis is predicted to be impaired because of a shortage of N in the rumen. The optimum OEB value in a ration is therefore zero or slightly above.[3] The margin for safety is to allow for asynchrony—a factor important in feeding supplements to grazing animal or feeding an ingredient separately from the main basal feed.[8] The present study showed that all starchy feedstuffs had a negative (R)RDPB value predicted by all of the models, which indicates an imbalance between feed N degradation and utilization and indicates a potential shortage of N in the rumen. On the other hand, all of the protein concentrates, except CSM, had positive (R) rumen degraded protein balance (RDPB), which shows excess amounts of N in the rumen compared to ruminally available energy. In the case of CSM, the DVE system predicts a positive RDPB, whereas NRC-2001 estimates a negative RDPB. This is because energy estimations in NRC-2001 are based on TDN instead of fermentable organic matter and CSM contains relatively high amounts of digestible NDF and low amounts of RDP. Because the NRC-2001 model does not fully address many of the potential limitations in diets or management conditions, more complex models are needed to identify why some herds appear to underperform.[5] The DVE2010 system is a mechanistical model that incorporates data and concepts from fundamental research over past decades into a previous model (DVE1994) to overcome shortages in protein evaluation systems. It should be mentioned that, as quoted,[5] besides the advantages of mechanistic models, increased complexity may increase the risk of misuse. As complexity increases there is a potential for users to lose sight of the most important issues, and "hired" relationships may not be properly represented. Furthermore, more complex models require more time and money to specify the required variables.

In conclusion, predictions of the potential protein supply to dairy cows from starchy and protein concentrates are widely different among the tested models. The extent of differences in model predictions is not equal among different types of concentrates. Incorporation of new concepts into the DVE2010 model has a potential to improve predictions, although comparable direct measurements are needed to evaluate the actual ability of different models in predicting the potential protein supply to dairy cows from different feedstuffs.

AUTHOR INFORMATION

Corresponding Authors

*(A.V.) Phone: +98-511-8795620. E-mail: savakili@um.ac.ir.
*(P.Y.) Phone: (306) 966-4132. E-mail: peiqiang.yu@usask.ca.

Notes

The authors declare no competing financial interest.

DOI: 10.1021/jf505961e
J. Agric. Food Chem. 2015, 63, 6518−6524

■ ACKNOWLEDGMENTS

Ehsan Parand was a joint training PhD student. This work was conducted with the financial support of Ferdowsi University of Mashhad, Iran. Financial support for SRP Research Chair (Professor Dr. Peiqiang Yu) from the Ministry of Agriculture Strategic Research Chair Program, the Natural Sciences and Engineering Research Council of Canada (NSERC), the Thousand-Talent People Research Program and University Innovation Team "Veterinary Biotechnology" (TD12-5019, Tianjin), the Saskatchewan Agriculture Development Fund (ADF), the SaskCanola, the SaskMilk, the SPG, the Saskatchewan Forage Network (SNK), and Western Grain Research Foundation (WGRF) etc is acknowledged.

■ ABBREVIATIONS USED

ADF	acid detergent fiber
ADICP	acid detergent insoluble crude protein
AECP	truly absorbed rumen endogenous protein in the small intestine
AMCP	truly absorbed microbial protein in the small intestine
ARUP	truly absorbed rumen undegraded protein in the small intestine
CP	crude protein
DM	dry matter
dRUP	digestible rumen undegraded protein in the small intestine
DVE	truly digested protein in the small intestine (DVE system)
ECP	rumen endogenous protein
EE	ether extract
EPL	endogenous protein loss
FOM	fermented organic matter
MCPe	microbial protein synthesized in the rumen based on available energy
MCPn	microbial protein synthesized in the rumen based on available nitrogen
MP	metabolizable protein
NDF	neutral detergent fiber
NDICP	neutral detergent insoluble crude protein
NFC	nonfiber carbohydrates
OEB	rumen degraded protein balance
PDB	protein degraded balance in NRC-2001
RDP	rumen degraded feed protein
RDPB	rumen degradable protein balance
RNSP	residual nonstarch polysaccharides
TDN	total digestible nutrient
UASH	undigestible ash
UDM	undigestible dry matter
UOM	undigestible organic matter

■ REFERENCES

(1) Hvelplund, T.; Madsen, J. Protein systems for ruminants. *Icel. Agric. Sci.* **1993**, *7*, 21−36.

(2) NRC. *National Research Council (U.S.). Subcommittee on Dairy Cattle Nutrition, Nutrient Requirements of Dairy Cattle*, 7th rev. ed.; National Academy Press: Washington, DC, USA, 2001; p *xxi*, 381 po.

(3) Tamminga, S.; Vanstraalen, W. M.; Subnel, A. P. J.; Meijer, R. G. M.; Steg, A.; Wever, C. J. G.; Blok, M. C. The Dutch Protein Evaluation System − the Dve/Oeb-system. *Livest. Prod. Sci.* **1994**, *40*, 139−155.

(4) Verite, R. Present situation of protein evaluation for ruminants in France: the PDI system. *Feed Evaluation and Protein Requirements Systems for Ruminants. Report*; Commission of the European CommunitiesL Luxembourg, 1987.

(5) Kohn, R.; Kalscheur, K.; Hanigan, M. Evaluation of models for balancing the protein requirements of dairy cows. *J. Dairy Sci.* **1998**, *81*, 3402−3414.

(6) Van Duinkerken, G.; Blok, M.; Bannink, A.; Cone, J.; Dijkstra, J.; Van Vuuren, A.; Tamminga, S. Update of the Dutch protein evaluation system for ruminants: the DVE/OEB2010 system. *J. Agric. Sci.* **2011**, *149*, 351−367.

(7) Yu, P. Prediction of protein supply to ruminants from concentrates: comparison of the NRC-2001 model with the DVE/OEB system. *J. Sci. Food Agric.* **2005**, *85*, 527−538.

(8) Yu, P.; Meier, J.; Christensen, D.; Rossnagel, B.; McKinnon, J. Using the NRC-2001 model and the DVE/OEB system to evaluate nutritive values of Harrington (malting-type) and Valier (feed-type) barley for ruminants. *Anim. Feed Sci. Technol.* **2003**, *107*, 45−60.

(9) Ørskov, E.; McDonald, I. The estimation of protein degradability in the rumen from incubation measurements weighted according to rate of passage. *J. Agric. Sci.* **1979**, *92*, 499−503.

(10) CVB. *Protocol voor in situ pensincubatie: bepaling van afbraaksnelheid en uitwasbare fracties van eiwit, zetmeel, celwanden en organische restfractie [Protocol for in situ Rumen Incubations: Determination of Degradation Rate and Washable Fractions of Protein, Starch, Cell Walls and Organic Residual Fraction]*; Centraal Veevoeder Bureau: Lelystad, The Netherlands, 2003.

(11) Azarfar, A.; Tamminga, S.; Boer, H. Effects of washing procedure, particle size and dilution on the distribution between non-washable, insoluble washable and soluble washable fractions in concentrate ingredients. *J. Sci. Food Agric.* **2007**, *87*, 2390−2398.

(12) Dhanoa, M. On the analysis of dacron bag data for low degradability feeds. *Grass Forage Sci.* **1988**, *43*, 441−444.

(13) Robinson, P.; Fadel, J.; Tamminga, S. Evaluation of mathematical models to describe neutral detergent residue in terms of its susceptibility to degradation in the rumen. *Anim. Feed Sci. Technol.* **1986**, *15*, 249−271.

(14) SAS Institute Inc. *Base SAS® 9.3 Procedures Guide*; SAS Institute Inc.: Cary, NC, USA, 2011.

(15) AOAC. *Official Methods of Analysis of the Association of Official Analytical Chemists*, 15th ed.; Arlington, VA, USA, 1990.

(16) Van Soest, P.; Robertson, J.; Lewis, B. Methods for dietary fiber, neutral detergent fiber and non-starch polysaccharides in relation to animal nutrition. *J. Dairy Sci.* **1991**, *74*, 3583−3597.

(17) Damiran, D.; Zhang, X.; Yu, P. Optimized utilization of the co-products from bioethanol processing and oat grain: effect of blending on biochemical, biodegradation, and nutritional profiles. *J. Agric. Food Chem.* **2013**, *61*, 11517−11523.

(18) Peng, Q.; Khan, N. A.; Wang, Z.; Zhang, X.; Yu, P. Effect of thermal processing on estimated metabolizable protein supply to dairy cattle from camelina seeds: relationship with protein molecular structural changes. *J. Agric. Food Chem.* **2014**, *62*, 8263−8273.

(19) Liu, B.; McKinnon, J. J.; Thacker, P.; Yu, P. Molecular structure and metabolic characteristics of the proteins and energy in triticale grains and dried distillers grains with solubles for dairy cattle. *J. Agric. Food Chem.* **2012**, *60*, 10064−10074.

(20) Damiran, D.; Jonker, A.; Zhang, X.; Yari, M.; McKinnon, J. J.; McAllister, T.; Abeysekara, S.; Yu, P. Evaluation of the feed value for ruminants of blends of corn and wheat distillers dried grains. *J. Agric. Food Chem.* **2013**, *61*, 4387−4395.

(21) Yu, P. Modeling nutrient supply to dairy cattle from a feedstuff using NRC-2001 (a TDN-based model) with inputs based on in situ and mobile bag technique measurements. *Can. Vet. J.* **2005**, *85*, 513−519.

(22) Gamage, I. H.; Yu, P. Short communication: Comparison of the newly developed DVE/OEB (2010) system and the National Research Council (2001) model in modeling metabolic characteristics of proteins in dairy cattle. *J. Dairy Sci.* **2013**, *96*, 5908−5913.

(23) Theodoridou, K.; Yu, P. Metabolic characteristics of the proteins in yellow-seeded and brown-seeded canola meal and presscake in dairy cattle: comparison of three systems (PDI, DVE, and NRC) in nutrient

DOI: 10.1021/jf505961e
J. Agric. Food Chem. 2015, 63, 6518−6524

supply and feed milk value (FMV). *J. Agric. Food Chem.* **2013**, *61*, 2820−2830.

DOI: 10.1021/jf505961e
J. Agric. Food Chem. 2015, 63, 6518−6524

MATERIALS AND METHODS

Chemicals. The fruiting body of *D. indusiata* was obtained from Zhijin, Guizhou Province, China. Ascorbic acid, sodium selenite (Na_2SeO_3), 5,5′,6,6′-tetraethylimida-carbocyanine iodide (JC-1), 2′,7′-dichlorofluorescein diacetate (DCFH-DA), 4′,6-diamidino-2-phenylindole (DAPI), diethyl pyrocarbonate (DEPC), thiazolyl blue tetrazolium bromide (MTT), bicinchoninic acid, and BCA kit were purchased from Sigma Co. (St. Louis, MO, USA). Human hepatocarcinoma HepG2 cell line, human pulmonary carcinoma A549 cell line, human cervical carcinoma HeLa cell line, human breast carcinoma MCF-7 cell line, and human prostate carcinoma PC3 cell line were obtained from American Type Culture Collection (ATCC, Rockville, MD, USA). Another two cell lines, human normal liver HL-7702 (L02) and human gastric carcinoma SGC-7901 cell line, were purchased from the Medical College of Sun Yat-Sen University (Guangzhou, Guangdong, China). Phosphate-buffered saline (PBS, pH 7.4), streptomycin and penicillin, heat-inactivated fetal bovine serum (FBS), and Dulbecco's modified Eagle's medium (DMEM) were purchased from Gibco Life Technologies (Grand Island, NY, USA). Substrates of caspase-3/7 (Ac-DEVD-AMC), caspase-8 (Ac-IETD-AFC), and caspase-9 (Ac-LEHD-AFC) were purchased from Calbiochem (La Jolla, CA, USA). The 6-well plate and 96-well plate were obtained from Corning Inc. (Corning, NY, USA). Sephadex G-200 and diethylaminoethyl (DEAE)-52 cellulose were purchased from GE Healthcare Life Science (Piscataway, NJ, USA). Ultrapure water was obtained from a Milli-Q water purification system (Millipore, Bedford, MA, USA). All other chemical reagents used in the present study were of analytical grade.

Preparation of DP1. The polysaccharide (DP1) was prepared according to our previous study.[21] Briefly, the natural polysaccharide (DP1) was extracted from the fruiting body of *D. indusiata* using water extraction at 100 °C for 2 h. Then the obtained crude extractions were deproteinated using the Sevage method and precipitated by 75% ethanol. The obtained sample was then sequentially purified by DEAE-52 anion-exchange chromatography and Sephadex G-200 column chromatography.

Preparation of DP1−Zn. Zinc chloride ($ZnCl_2$) was dissolved in distilled water (2 mg/mL). The pH value of the solution was adjusted to 2.0−3.0 by adding 400 μL of 0.3 M HCl solution until the solute was fully dissolved. Then the $ZnCl_2$ solution was mixed with DP1 solution (5 mg/mL) at the ratio of 1:1 (w/w) using a vortex mixer, and the pH value of the mixture was adjusted to 8.0 by NaOH (0.5 mol/L). The prepared mixture was incubated for 48 h at 50 °C in a reciprocating shaker bath. After incubation, the pH of the mixture was adjusted to 3.0, and the crude DP1−Zn chelating product was obtained. It was then subjected to purification by 3000 Da dialysis bag (Spectrum Medical Industries, Inc., Los Angeles, CA, USA) and then freeze-dried using vacuum freeze-dryer (R2L-100 KPS, Kyowa Vacuum Engineering, Tokyo, Japan) for 36 h to the DP1−Zn complex.

Characterization of DP1−Zn. The obtained DP1−Zn was characterized by SEM, model 1530VP, LEO, Oberkochen, Germany). SEM samples were prepared by drawing DP1−Zn solution and dropping on the slides. Then, samples were sputter-coated with gold and observed by SEM. EDX was taken on an EX-250 system (Horiba Ltd., Kyoto, Japan) to examine the elemental composition of DP1−Zn. The infrared spectra of DP1−Zn were analyzed on a FT-IR spectrophotometer (Bruker, Ettlingen, Germany) in the range of 400−4000 cm^{-1}. The synthesized DP1−Zn was further characterized by UV−vis spectrophotomtry (Cary 219 UV−vis double-beam spectrophotometer) for comparison ranging from 200 to 800 nm.

Cell Lines and Cell Culture. The human cell lines used in the present study were maintained in DMEM supplemented with penicillin (100 units/mL), fetal bovine serum (10%), and streptomycin (50 units/mL) at 37 °C in a humidified incubator with 5% CO_2 atmosphere.

Analysis of Cell Viability Using MTT Assay. The antiproliferative activity of DP1−Zn on the selected human cell lines (HepG2, MCF-7, SCG-7901, A549, HeLa, PC3, and L02) was analyzed using the MTT assay.[22] Cells were seeded in 96-well plates at a density of 3×10^3 cells/well. After incubation for 24 h, each well was treated with different concentrations of DP1−Zn (62.5, 125, and 250 μg/mL) and then incubated for 48 h. Cells without treatment of DP1−Zn was used as the control group. The medium was then replaced by MTT (0.5 μg/mL, 200 μL, in PBS) and cultured for 4 h, the supernatant fluid was removed, and the formazan was dissolved in DMSO (100 μL). The plates were placed on a multiplate reader using a test wavelength at 570 nm by Versasax microplatereader (Molecular Devices, Sunnyvale, CA, USA). The cytotoxicity of DP1−Zn was demonstrated by percentage of cell viability (absorbance) of treated cell (A) to the control cell (B), as the following formula:

$$\text{cell viability}\ (\%) = A/B \times 100\%$$

Analysis of Nuclear Morphology Using the Hoechst 33258 Assay. MCF-7 cells were seeded in a 6-well culture plate at 37 °C. The supernatant was removed after 24 h, and the cells were treated with DP1−Zn (62.5, 125, and 250 μg/mL) for 48 h. Then the cells were harvested by centrifugation, washed twice with PBS, and fixed with methanol (4%) at 4 °C for 10 min. After that, the cells were centrifuged, washed, resuspended, and smeared on a glass slide. Staining was performed with Hoechst 33258 for 10 min at room temperature in the dark. Slides were then washed with deionized water and observed under a fluorescence microscope (Nikon Eclipse 80i) with the excitation and emission wavelengths at 345 and 460 nm, respectively.

Analysis of DNA Fragmentation. After the treatment with DP1−Zn (62.5, 125, and 250 μg/mL) for 48 h, MCF-7 cells were accumulated, washed with PBS, and then lysed in lysis buffer (10 mM Tris-HCl, pH 7.5, 10 mM EDTA, 0.5% Triton X-100, 500 μL) . The cell lysates were then dissolved in RNaseA (200 mg/mL) for 1 h at 37 °C and treated with proteinase K (200 mg/mL) for 1 h at 55 °C. DNA was extracted by ethanol from samples and isolated in isopropyl alcohol, and then sodium acetate (0.3M, in 2 volumes of ethonal) was add to precipitate the DNA at −20 °C. Finally, the ethidium bromide (1 mg/mL) stained DNA fragmentations were analyzed via examination of electrophoretic mobility on 2% agarose gel, and the results were visualized by UV transilluminator (Tanon 1600; Tanon, Shanghai, China).

Analysis of Apoptosis and Cell Cycle Arrest Using Flow Cytometry. The apoptosis of MCF-7 was analyzed by flow cytometry using an annexin V-FITC/PI apoptosis detection kit. Cells treated with or without DP1−Zn (62.5, 125, and 250 μg/mL) for 48 h were harvested by trypsinization and washed with PBS three times. Then the cells were resuspended by binding buffer and divided into two groups. Annexin V conjugated with FITC was added to one group of cell suspension, and the suspensions were incubated for 15 min in the dark. The other group of the cell suspension was used as the blank control. Then propidium iodide (PI) was added into each sample, and the stained cells were analyzed by flow cytometry under 488 nm excitation wavelength. The signal from FITC was read at 516 nm, whereas the signal from PI was read at 560 nm. The data were collected and analyzed by the Cell Quest Research Software (Becton Dickinson).

The cell cycle distribution of MCF-7 was monitored in flow cytometry by PI staining method. MCF-7 cells treated with DP1−Zn (62.5, 125, and 250 μg/mL) for 48 h were harvested by trypsinization and washed with PBS three times. The treated cells were stained with PI contained with RNase in the dark after fixation by 70% alcohol solution (−20 °C, overnight). Labeled cells were washed twice with PBS and analyzed by flow cytometry. For each sample, 10000 events were recorded. Cell cycle distribution was determined by the amount of PI intercalated to DNA and analyzed by Cell Quest Research Software.

Analysis of Mitochondrial Membrane Potential (ΔΨm). The ΔΨm of MCF-7 cells was determined by JC-1. JC-1 is a lipophilic and cationic fluorescence probe, which exists as a monomer (green) at low membrane potential or forms red fluorescent aggregates at higher potential. MCF-7 cells were seeded in 6-well plates (1×10^5 cells/well), followed by a 48 h treatment with DP1−Zn at different

DOI: 10.1021/acs.jafc.5b00614
J. Agric. Food Chem. 2015, 63, 6525−6534

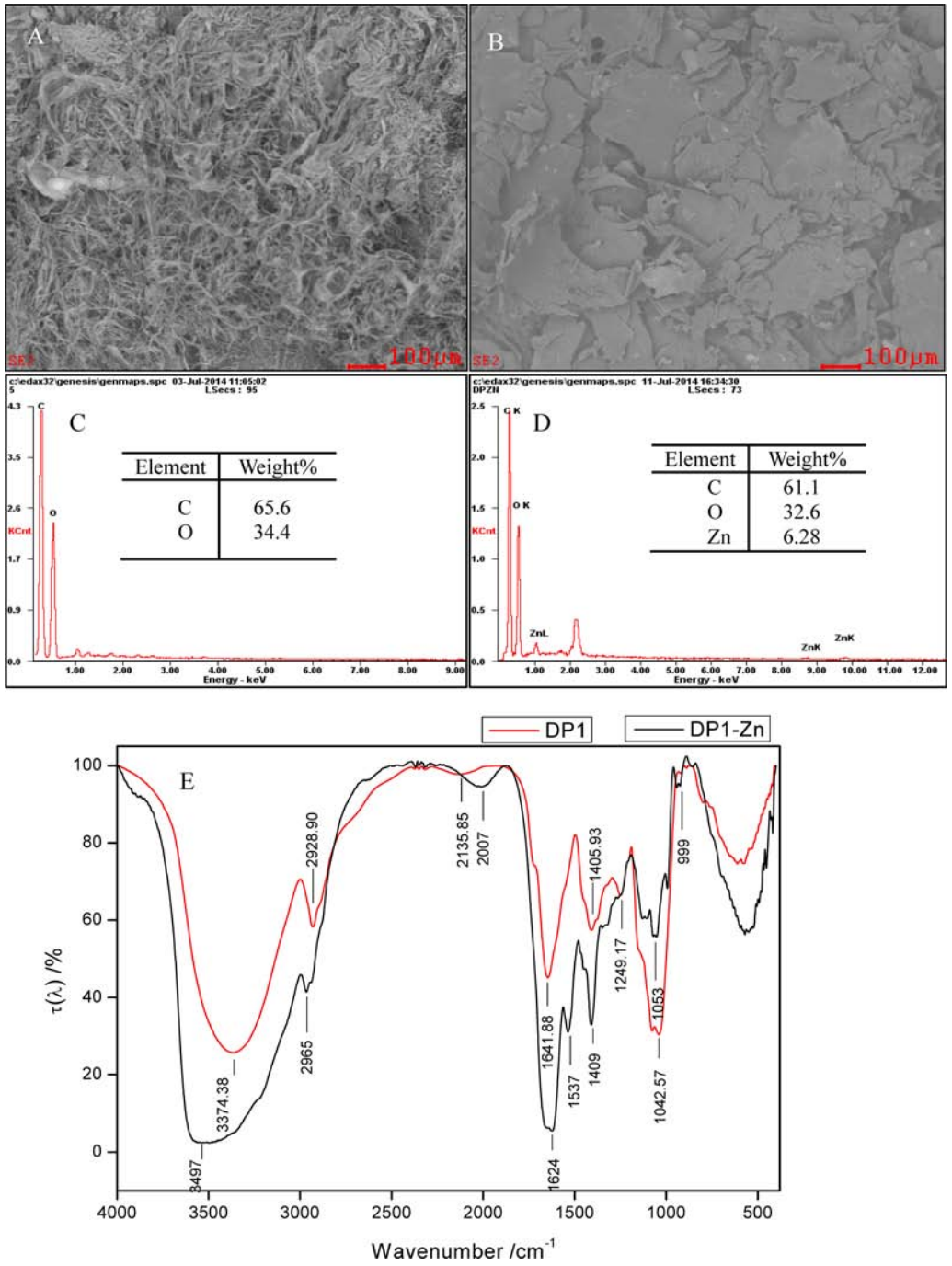

Figure 1. SEM images of DP1 (A) and DP1−Zn (B); EDX analysis of DP1 (C) and DP1−Zn (D); FT-IR analysis of DP1 and DP1−Zn (E).

concentrations (62.5, 125, and 250 μg/mL). Then the cells were trypsinized, suspended, and dyed in PBS buffer containing JC-1 dye (20 μg/mL) at 37 °C for 15 min in the dark. After removal of JC-1 dye, the cells were washed with PBS and resuspended in PBS (0.5 mL). The percentages of pure red and green fluorescence intensity were tested by flow cytometry analysis. The excitation was set at 488 nm, with the emission at 525 nm for green fluorescence detection and the other emission at 590 nm for red fluorescence. The fluorescence intensity of JC-1 stained was determined using a fluorometer (Thermo Electron Corp., Vantaa, Finland). Finally, the stained cells were also observed using a fluorescence microscope with argon-ion 488 nm laser excitation (Nikon Eclipse 80i, Nikon, Tokyo, Japan).

Assay of Reactive Oxygen Species (ROS) Generation. The effect of the DP1−Zn on ROS generation was determined by using DCFH-DA method reported by Wang and Joseph[23] with some modifications. In the method, the stable nonfluorescent DCFH-DA is hydrolyzed by esterases in cells to nonfluorescent DCFH, and the product is rapidly oxidized by peroxy radicals to highly fluorescent 2′,7′-dichlorofluorescein (DCF), which provides a quantitative assay of ROS formation with fluorometric analysis and microscopic fluorescence. In the current study, MCF-7 cells, which were treated with different concentrations of DP1−Zn (62.5, 125, and 250 μg/mL) for 48 h in advance, were seeded in 6-well plates (1×10^5 cells/well), and then they were washed with PBS and incubated with DCFH-DA (10 μM) in a 37 °C non-CO_2 incubator for 30 min. After being incubated with DCFH-DA, the cells were washed with PBS, lysed, and centrifuged (3000*g*, 10 min) in turn, and then a 200 μL supernatant was harvested and transferred to a 96-well plate. For fluorometric analysis, fluorescence of the MCF-7 cells was determined by using a fluorometer with the excitation and emission wavelengths at 485 and

DOI: 10.1021/acs.jafc.5b00614
J. Agric. Food Chem. 2015, 63, 6525−6534

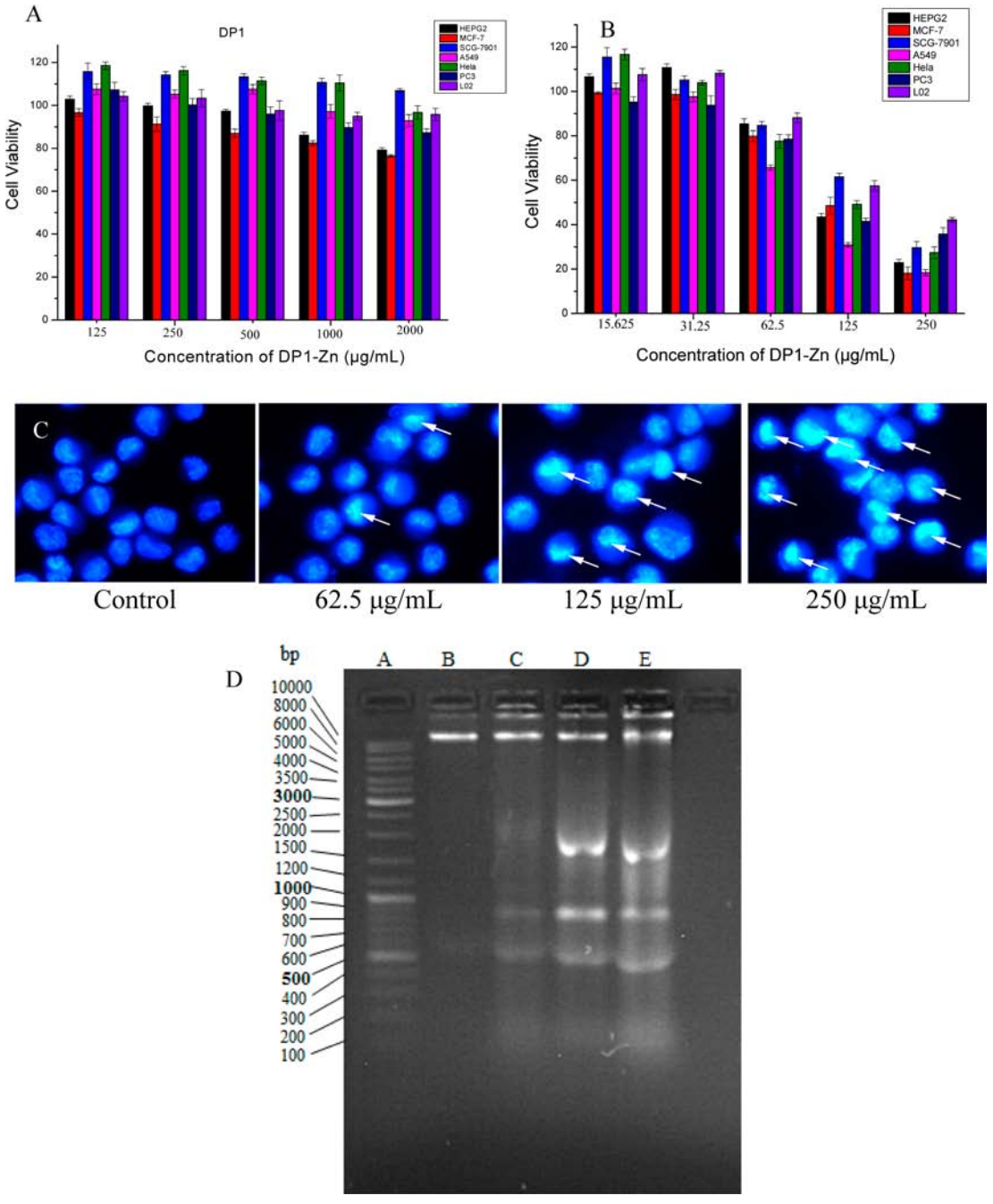

Figure 2. Growth inhibition of DP1 (A) and DP1−Zn (B) on human cell lines (HepG2, MCF-7, SCG-7901, A549, HeLa, PC3, and L02 cells). Cells were treated with different concentrations of DP1 or DP1−Zn for 48 h. (C, D) DNA fragmentation of MCF-7 cells induced by different concentrations of DP1−Zn (62.5, 125, and 250 μg/mL) for 48 h. Lanes: A, DNA maker; B, control group; C, 62.5 μg/mL; D, 125 μg/mL; E, 250 μg/mL exposed group.

520 nm, respectively; for the visual image of ROS generation, the fluorescence was visualized by using a fluorescence microscope (Nikon Eclipse 80i) with the excitation and emission wavelengths at 485 and 520 nm.

Caspase Activity Assay. Caspase activity was use to confirm the existing of caspase-dependent apotosis in cell induced by DP1−Zn, and it was monitored by fluorometric method. MCF-7 cells were treated with different concentrations of DP1−Zn (62.5, 125, and 250 μg/mL) for 48 h and harvested as mentioned above. Harvested cell pellets were suspended in cell lysis buffer and incubated on ice for 1 h. After centrifugation (11000*g*, 30 min), supernatants were isolated, collected, and measured for protein concentration immediately by a BCA kit. For caspase activity assay, the cell lysates were placed in 96-well plates and mixed with the specific caspase substrates (Ac-DEVD-AMC for caspase-3/7, Ac-IETD-AMC for caspase-8, and Ac-LEHD-AMC for caspase-9). Plates were then incubated at 37 °C for 1 h, and the caspase activity was determined by fluorescence intensity with the excitation and emission wavelengths at 380 and 440 nm, respectively.

Statistical Analysis. The preparation of DP1−Zn was repeated three times, and the structure and bioactivity assays were done in triplicate for each sample. Results were expressed as the mean with standard deviation. Statistical analysis was performed using SPSS 19.0 software (IBM Corp., Armonk, NY, USA). The difference between the control and the experimental groups was analyzed by two-tailed Student's *t* test. Differences with $P < 0.05$ were considered statistically

DOI: 10.1021/acs.jafc.5b00614
J. Agric. Food Chem. 2015, 63, 6525−6534

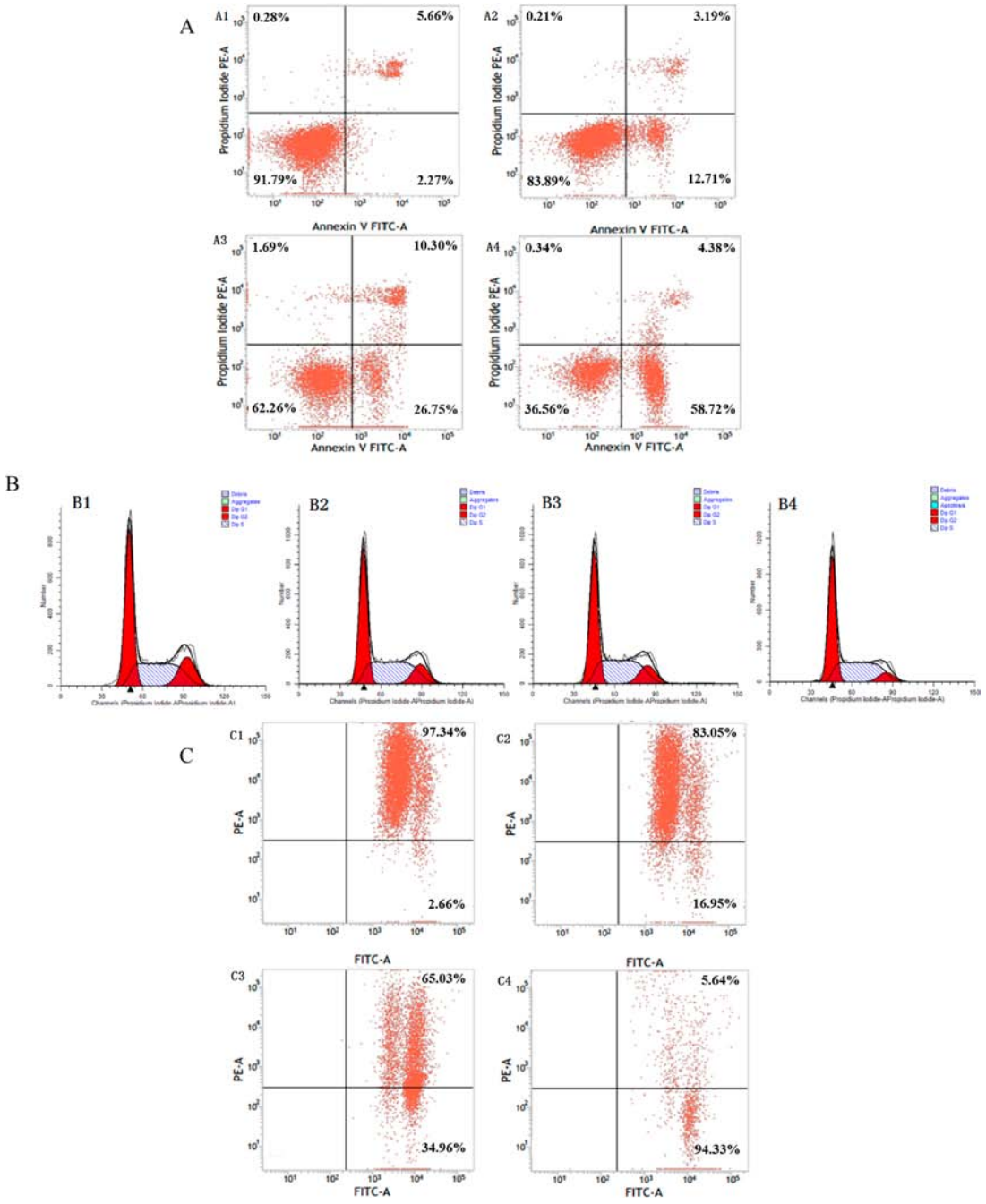

Figure 3. (A1−A4) Induction of apoptosis by DP1−Zn: (A1) control group; (A2) cells treated with 62.5 μg/mL DP1−Zn; (A3) cells treated with 125 μg/mL DP1−Zn; (A4) cells treated with 250 μg/mL DP1−Zn. The lower left (LL) quadrant represents the proportion of normal cells, the lower right (LR) quadrant represents the proportion of early apoptotic cells, and the upper left (UL) and upper right (UR) quadrants represent proportion of necrosis and late apoptosis cells, respectively. (B1−B4) Effect of DP1−Zn on cell cycle distribution of MCF-7 cells: (B1) control group; (B2) cells treated with 62.5 μg/mL DP1−Zn; (B3) cells treated with 125 μg/mL DP1−Zn; (B4) cells treated with 250 μg/mL DP1−Zn. (C1−C4) Loss of mitochondrial membrane potential of MCF-7 cells induced by DP1−Zn: (C1) control group; (C2) cells treated with 62.5 μg/mL DP1−Zn; (C3) cells treated with 125 μg/mL DP1−Zn; (C4) cells treated with 250 μg/mL DP1−Zn. The upper right (UR) and lower right (LR) quadrants represent the proportion of red fluorescence and green fluorescence, respectively.

significant. The differences among three or more groups were analyzed by one-way ANOVA multiple comparisons.

RESULTS AND DISCUSSION

Preparation and Characterization of DP1−Zn Complexes. In this study, DP1−Zn complexes were successfully synthesized by the reaction of polysaccharide DP1 and zinc chloride. As can be seen from the SEM images, the polysaccharide DP1 showed flocculent and filamentous structure (Figure 1A), whereas after a Zn atom was coupled to the polysaccharide, the formed DP1−Zn complexes exhibited a totally different blocky structure (Figure 1B). The elemental compositions of DP1 and DP1−Zn were investigated using EDX. As compared with DP1 (Figure 1C), a certain level of Zn atoms (6.28%) was observed in the DP1−Zn sample, together with the other two elements, C (61.09%) and O

DOI: 10.1021/acs.jafc.5b00614
J. Agric. Food Chem. 2015, 63, 6525−6534

(32.63%) (Figure 1D). This indicated that Zn has been successfully conjugated to DP1 with a conjugation rate of 6.28%.

The chemical binding of DP1 and Zn atom was further characterized by FT-IR (Figure 1E). It was found that the chelation of Zn with DP1 mainly through the additional absorptions at 1537 and 2007 cm^{-1} corresponded to a nitro group and an aromatic ring. Additionally, the peaks correspond to the stretching vibrations of hydroxyl groups shifted from 3374 to 3497 cm^{-1}, and the absorptions at 2928−2965 cm^{-1} correspond to the vibrations of CH bonds. All of these changes could be due to the formation of Zn−O bonds and physical absorption in the complexes.

Antiproliferative Activity of DP1−Zn. The antiproliferative activity of the DP1−Zn complex on the selected human cells was evaluated by MTT assay. As shown in Figure 2A, DP1 itself had no cytotoxicity on normal cells (human normal hepatocyte L02). Also, most of the cancer cells tested in this study, for example, SCG-7901, A549, HeLa, and PC3, were not sensitive to DP1. As a comparison, MCF-7 cells were more susceptible to DP1 treatment in a dose-dependent manner. As for DP1−Zn (Figure 2B), it was found that a low concentration (62.5 μg/mL) of DP1−Zn had no significant effect on all kinds of cells, but further increase of its concentration to 250 μg/mL could noticeably inhibit MCF-7 cell growth in a dose-dependent manner. Among all of the under-tested cancer cells, the lowest cell viability (18.13%) was observed for MCF-7 cell treated by 250 μg/mL DP1−Zn. For human normal cell line L02, the treatment of DP1−Zn (250 μg/mL) did cause a certain level of cell apoptosis, but it was much safer as compared to the cytotoxicity on cancer cells. Hence, the result suggested that the cytotoxicity of DP1−Zn was cancer-specific. On the basis of the above results, MCF-7 cells were chosen as the targeted cell line to further evaluate the antitumor activity of DP1−Zn.

Induction of Apoptosis by DP1−Zn. Apoptosis is genetically regulated cell demise in living tissues that can be induced by many specific stimuli. Pro-apoptosis is thought to be the key mechanism for antiproliferative action of drugs against cancer cells.[24−26] The process of apoptosis is generally characterized by some distinct morphological characteristics including cytoplasmic and nuclear condensation, DNA breakage, membrane dysfunction, cell cycle arrest, and loss of microvilli. In the present study, the inner changes of the cell nucleus induced by DP1−Zn were analyzed using a DNA-specific fluorochrome (Hoechst 33258). The fluorescence intensity was proportional to the degree of nuclear chromatin condensation. As indicated in Figure 2C, MCF-7 cells treated with DP1−Zn exhibited an increase of fluorescent brightness in a dose-dependent manner. At the concentration of 250 μg/mL, some highlight dyeing areas were found (see the white arrows in Figure 2C), which was an indication of the late-stage apoptosis of cancer cells. These results suggested that apoptosis was involved in the antiproliferative action of DP1−Zn.

DNA fragmentation is one of the hallmarks of apoptosis. The chromosomal DNA was cleaved by specific DNases when the cells suffered apoptotic stimuli. The pro-apoptosis action of DP1−Zn was further confirmed by DNA fragmentation. The total DNA of MCF-7 cells treated with or without DP1−Zn (62.5, 125, and 250 μg/mL) was extracted and analyzed by 2% agarose gel electrophoresis. As shown in Figure 2D, "DNA ladders" were found in the lanes of the samples treated with DP1−Zn. The tail intensity and tail migration of the DNA ladders were significantly aggravated with the increment of DP1−Zn concentration, which indicated that DP1−Zn triggered DNA damage in a dose-dependent manner.

The apoptosis rates and apoptosis period of MCF-7 cells induced by DP1−Zn were investigated using flow cytometric analysis. The results of annexin V-FITC/PI staining assay are shown in Figure 3A; DP1−Zn showed a noticeable effect on the proportion of early apoptotic cells. MCF-7 cells treated with DP1−Zn (62.5 μg/mL) had a significant increase in the proportion of early-stage apoptosis cells (12.71%) compared with the control group (2.27%). A more obvious enhancement was obtained for cells treated by 125 μg/mL DP1−Zn (26.75%) and 250 μg/mL DP1−Zn (58.72%), respectively. Additionally, the ratio of late apoptosis in MCF-7 cells did not show distinct changes. These results proved that the inhibitory effect of DP1−Zn on MCF-7 cell proliferation was mainly in early-stage apoptosis, manifesting the potential application of DP1−Zn as effective anticancer supplements or drugs.

Effects of DP1−Zn on Cell Cycle Arrest. Cell cycle is a repeated round of cell duplication and growth; it is thought that cell proliferation is mainly regulated by cell cycle arrest and apoptosis.[27,28] The effects of DP1−Zn on cell cycle arrest were investigated by PI-flow cytometric analysis. The cell cycle distribution histograms of MCF-7 cells are shown in Figure 3B and Table 1. The results demonstrated an increase in the proportion of S phase arrest of MCF-7 cells with the increment of DP1−Zn concentration. It was 37.28% in the control group and increased to 43.93% after 250 μg/mL DP1−Zn treatment. Besides, no significant change in G0/G1 phase was observed in the treated cells, whereas the percentage of G2/M phase arrested cells was decreased accompanied by the increase of S phase arrested cells. Thus, the antiproliferative effect of DP1−Zn was regulated mainly by S phase cell cycle arrest.

Table 1. Effect of DP1−Zn on MCF-7 Cells in Cell Cycle Pattern

		DP1−Zn		
dip of MCF-7 cells (%)	control	62.5 μg/mL	125 μg/mL	250 μg/mL
G0/G1	45.9	45.1	45.5	48.8
S	37.3	42.0	42.1	43.9
G2/M	16.8	12.9	12.4	7.27

DP1−Zn Induced Cell Apoptosis via Mitochondrial Dysfunction. Mitochondrial dysfunction has been shown to play a central role in the induction of apoptosis. Loss of mitochondrial membrane potential (ΔΨm) is an early event in the apoptotic process.[29] In this study, the changes of mitochondrial membrane potential in MCF-7 cells were analyzed by flow cytometry analysis via JC-1 staining. The mitochondrial stain JC-1 can spontaneously aggregate as J-aggregates, which will emit red fluorescence at high membrane potential in healthy cells, whereas in the apoptotic cells, JC-1 would remain green fluorescent monomers due to mitochondrial membrane depolarization.[30] The changes of ΔΨm in MCF-7 cells induced by DP1−Zn are shown in Figure 3C. The mitochondrial membrane potential of MCF-7 cells was remarkably reduced with the increment of DP1−Zn concentration. Compared with the control group, the proportion of the green fluorescence of cells treated with 62.5 μg/mL DP1−Zn increased from 2.66 to 16.95%, and it further increased to 34.96% (125 μg/mL) and 94.33% (250 μg/mL), respectively. The reduction of ΔΨm was further confirmed by a fluorescence

DOI: 10.1021/acs.jafc.5b00614
J. Agric. Food Chem. 2015, 63, 6525−6534

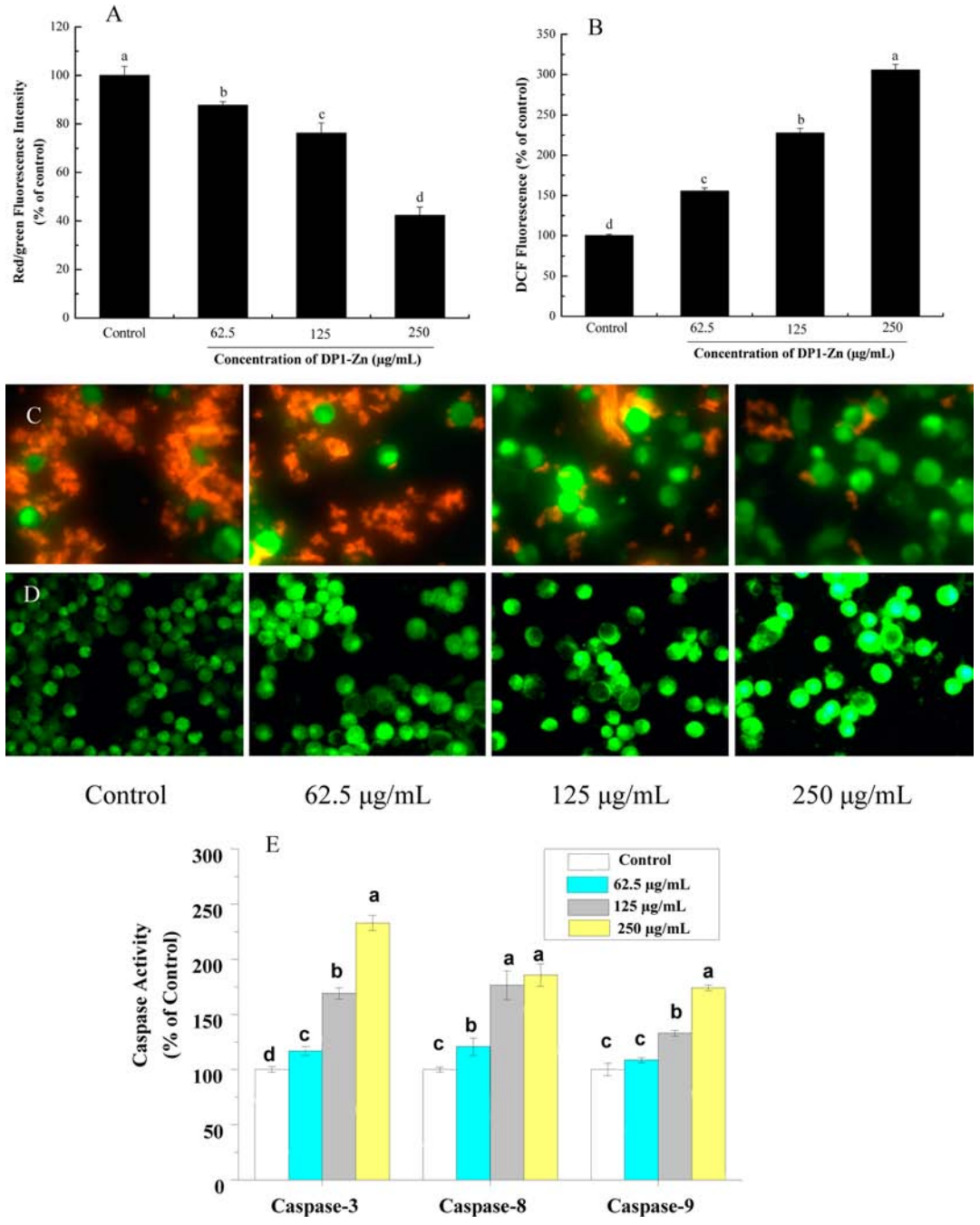

Figure 4. (A) Red/green fluorescence intensity of JC-1 stained MCF-7 cells induced by DP1−Zn. MCF-7 cells were treated with different concentrations of DP1−Zn (62.5, 125, and 250 μg/mL) for 48 h and stained by JC-1. (B) Intracellular ROS level of MCF-7 cells after treatment with DP1−Zn (62.5, 125, and 250 μg/mL) for 48 h. (C) JC-1 staining images after treatment with DP1−Zn (62.5, 125, and 250 μg/mL) for 48 h. (D) ROS generation images under a fluorescence microscope after treatment with DP1−Zn (62.5, 125, and 250 μg/mL) for 2 h. (E) Activation of caspase-3, -8, and -9 in MCF-7 cells incubated with DP-Zn for 24 h.

microscope, as shown in Figure 4C; an increment of green fluorescence and decrement of red fluorescence in MCF-7 cells were clearly observed after treatment with DP1−Zn. The red/green fluorescence intensity ratios decreased by 87.10, 76.18, and 42.22% after treatment with 62.5, 125, and 250 μg/mL DP1−Zn, respectively (Figure 4A). These results indicated that treatment of DP1−Zn induced the reduction of mitochondrial membrane potential, which facilitated the apoptosis of MCF-7 cells.

DP1−Zn Induce Cell Apoptosis Due to ROS Overproduction. Intracellular ROS, such as superoxide anion, singlet oxygen, hydroxyl radical, and hydrogen peroxide, are generated as byproducts in the process of aerobic metabolism. Overproduction of ROS may result in oxidative damage of DNA and mitochondrial dysfunction and eventually lead to cell apoptosis.[21,31] The intracellular ROS level of MCF-7 cells was measured using DCFH-DA (a fluorescein-labeled dye). DCFH can be oxidized into a highly fluorescent compound, DCF, with the presence of ROS. The fluorescence intensity of oxidized DCF was proportional to the level of ROS. As shown in Figure 4D, the fluorescence intensity increased in a dose-dependent manner after treatment with DP1−Zn (62.5, 125, and 250 μg/

DOI: 10.1021/acs.jafc.5b00614
J. Agric. Food Chem. 2015, 63, 6525−6534

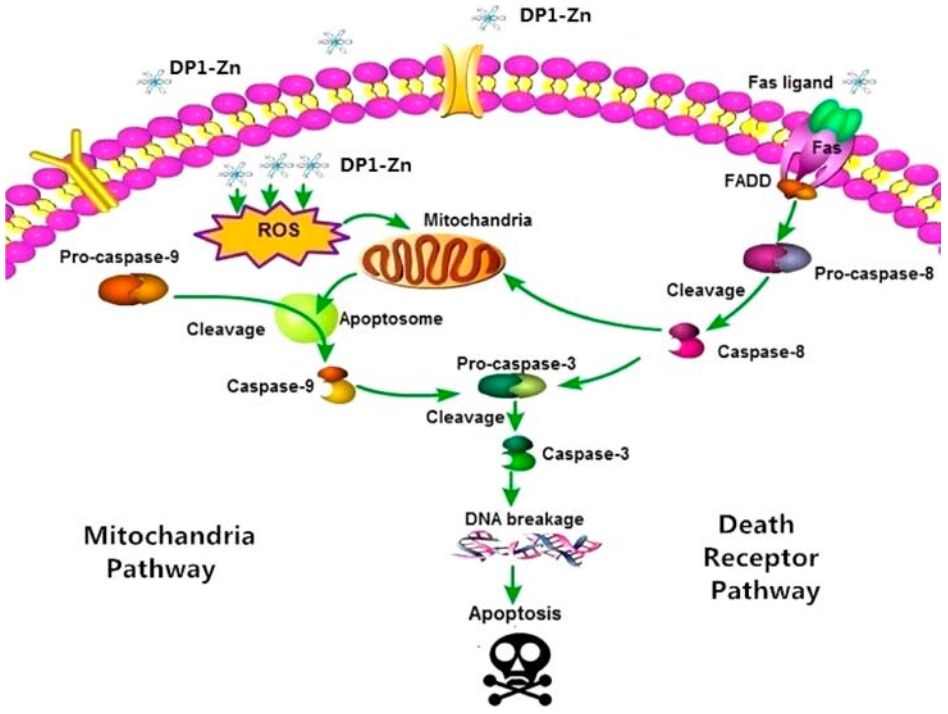

Figure 5. Possible pro-apoptotic mechanisms of DP1−Zn in MCF-7 cells.

mL). Compared with the control group, the DCF fluorescence intensity was increased by 155.04, 226.98, and 305.10% after exposure to 62.5, 125, and 250 μg/mL DP1−Zn, respectively (Figure 4B). Thus, ROS overproduction induced by DP1−Zn might directly lead to DNA breakage, mitochondrial dysfunction, and apoptosis in MCF-7 cells.

Caspase Activation Was Involved in the DP1−Zn-Induced Apoptosis. Caspases are a group of cysteine proteases that are specifically activated in the process of cell apoptosis. They are suggested to be the central executioners of apoptosis. Caspases involved in apoptosis can be divided into initiator caspases (caspases-2, -8, -9, and -10) and effector caspases (caspases-3, -6, and -7). To determine whether caspase activation was involved in the DP1−Zn-induced apoptosis, the activities of initiator caspases (caspases-8 and -9) and the effector caspase-3 were examined by fluorometric assays. As shown in Figure 4E, the activities of caspases-3, -8, and -9 in MCF-7 cells were significantly increased after treatment with DP1−Zn (62.5, 125, and 250 μg/mL, respectively). These enzymes were triggered in response to proapoptotic signals and culminate in cleavage of a set of proteins, resulting in disassembly of the cell.[32] The upstream caspases-8 and -9 are activated via recruitment of signaling complexes that are known as the initiator caspases; they provide a link between cell signaling and apoptotic execution.[33] The activation of downstream caspase-3 depends on the activition of initiator caspases-8 and -9 by transprocessing. These caspases act as the executioner of apoptosis due to the processes of their substrates leading to morphological changes associated with apoptosis, such as DNA degradation, chromatin condensation, and membrane blebbing.[34,35] As a result, the activation of caspases-3, -8, and -9 plays a crucial role in the apoptosis of MCF-7 induced by DP1−Zn.

Zinc is an essential trace element with various physiological functions. Recent evidence has shown that the main chemical forms of zinc in the human body are organic zinc complexes. The organic zinc exhibits higher bioavailability and fewer toxic side effects as compared with inorganic zinc. In this study, a novel organic zinc complex DP1−Zn was successfully prepared by using the chelation of *D. indusiata* polysaccharide (DP1) with zinc chloride, to achieve enhanced bioavailability and reduced toxicity.

The obtained DP1−Zn complexes showed notable antiproliferative effect on the selected human cancer cells through the induction of apoptosis. The DP1−Zn-induced apoptosis was associated with nuclei condensation, DNA fragmentation, S phase cell cycle arrest, and mitochondrial dysfunction. Further study found that the activation of caspases-3, -8, and -9 and ROS overproduction were also involved in the process of DP1−Zn-induced apoptosis. Therefore, the antiproliferative activity of DP1−Zn was via both caspase-dependent and mitochondria-mediated apoptotic pathways, as illustrated in Figure 5. We can infer that the possible molecular mechanism of DP1−Zn-mediated apoptosis may be mainly through two signaling pathways: One is through the extrinsic apoptotic pathway, because DP1−Zn treatment promotes the activation of caspase-8, which consequently activates the downstream caspase-3. Another way is via the intrinsic apoptotic pathway, as DP1−Zn treatment induced the dysfunction of mitochondrion, leading to the activation of caspases-9 and -3. Ultimately, these pathways resulted in the induction of apoptosis.

Overall, the design of DP1−Zn complexes gave a new idea and a new theoretical basis for the synergistic effects of DP1 and Zn as anticancer factors. This antiproliferative activity on cancer cells could be considered as a first screening, and further in vivo animal tests could be taken into consideration for the actual effectiveness of DP1−Zn on cancer prophylaxis and therapy.

DOI: 10.1021/acs.jafc.5b00614
J. Agric. Food Chem. 2015, 63, 6525−6534

AUTHOR INFORMATION

Corresponding Authors

*(J.Y.) Phone: (+86)20-87112594. Fax: (+86) 20-38897117. E-mail: yangjg@scut.edu.cn.

*(J.R.) Phone: (+86)20-87112594. Fax: (+86) 20-38897117. E-mail: jyren@scut.edu.cn.

Funding

This study was supported by the National Key Technology R&D Program of China in the 12th five-year period (No. 2012BAD33B11), Guangdong Natural Science Funds for Distinguished Young Scholars (No. S2013050013954), Program for New Century Excellent Talents in University (NCET-13-0213), and the Fundamental Research Funds for the Central Universities, SCUT (2014ZZ0058 and 2014ZZ0063).

Notes

The authors declare no competing financial interest.

REFERENCES

(1) Xu, W.; Zhang, F.; Luo, Y.; Ma, L.; Kou, X.; Huang, K. Antioxidant activity of a water-soluble polysaccharide purified from Pteridium aquilinum. *Carbohydr. Res.* **2009**, *344*, 217−222.

(2) Khan, M. T. H.; Ather, A.; Thompson, K. D.; Gambari, R. Extracts and molecules from medicinal plants against herpes simplex viruses. *Antiviral Res.* **2005**, *67*, 107−119.

(3) Yang, T.; Jia, M.; Meng, J.; Wu, H.; Mei, Q. Immunomodulatory activity of polysaccharide isolated from *Angelica sinensis*. *Int. J. Biol. Macromol.* **2006**, *39*, 179−184.

(4) Yang, X.; Guo, D.; Zhang, J.; Wu, M. Characterization and anti-tumor activity of pollen polysaccharide. *Int. Immunopharmacol.* **2007**, *7*, 401−408.

(5) Wu, S.-B.; Pang, F.; Wen, Y.; Zhang, H.-F.; Zhao, Z.; Hu, J.-F. Antiproliferative and apoptotic activities of linear furocoumarins from *Notopterygium incisum* on cancer cell lines. *Planta Med.* **2010**, *76*, 82−85.

(6) Yang, B.; Jiang, Y.; Zhao, M.; Chen, F.; Wang, R.; Chen, Y.; Zhang, D. Structural characterisation of polysaccharides purified from longan (*Dimocarpus longan* Lour.) fruit pericarp. *Food Chem.* **2009**, *115*, 609−614.

(7) Ooi, V. E. C.; Liu, F. Immunomodulation and anti-cancer activity of polysaccharide-protein complexes. *Curr. Med. Chem.* **2000**, *7*, 715−729.

(8) Falchuk, K. H. The molecular basis for the role of zinc in developmental biology. *Mol. Cell. Biochem.* **1998**, *188*, 41−48.

(9) Vallee, B. L.; Falchuk, K. H. The biochemical basis of zinc physiology. *Physiol. Rev.* **1993**, *73*, 79−118.

(10) Sharma, V.; Anderson, D.; Dhawan, A. Zinc oxide nanoparticles induce oxidative DNA damage and ROS-triggered mitochondria mediated apoptosis in human liver cells (HepG2). *Apoptosis* **2012**, *17*, 852−870.

(11) D'Orazi, G.; Givol, D. p53 reactivation: the link to zinc. *Cell Cycle* **2012**, *11*, 2581−2582.

(12) Ricci, M. S.; Zong, W.-X. Chemotherapeutic approaches for targeting cell death pathways. *Oncologist* **2006**, *11*, 342−357.

(13) Yu, X.; Vazquez, A.; Levine, A. J.; Carpizo, D. R. Allele-specific p53 mutant reactivation. *Cancer Cell* **2012**, *21*, 614−625.

(14) Bolfarini, G. C.; Siqueira-Moura, M. P.; Demets, G. J. F.; Morais, P. C.; Tedesco, A. C. In vitro evaluation of combined hyperthermia and photodynamic effects using magnetoliposomes loaded with cucurbituril zinc phthalocyanine complex on melanoma. *J. Photochem. Photobiol., B* **2012**, *115*, 1−4.

(15) Nagy, E. M.; Sitran, S.; Montopoli, M.; Favaro, M.; Marchio, L.; Caparrotta, L.; Fregona, D. Zinc(II) complexes with dithiocarbamato derivatives: structural characterisation and biological assays on cancerous cell lines. *J. Inorg. Biochem.* **2012**, *117*, 131−139.

(16) Sweigert, P.; Xu, Z.; Hong, Y.; Swavey, S. Nickel, copper, and zinc centered ruthenium-substituted porphyrins: effect of transition metals on photoinduced DNA cleavage and photoinduced melanoma cell toxicity. *Dalton Trans.* **2012**, *41*, 5201−5208.

(17) Tabassum, S.; Asim, A.; Arjmand, F.; Afzal, M.; Bagchi, V. Synthesis and characterization of copper(II) and zinc(II)-based potential chemotherapeutic compounds: their biological evaluation viz. DNA binding profile, cleavage and antimicrobial activity. *Eur. J. Med. Chem.* **2012**, *58*, 308−316.

(18) Pucci, D.; Bellini, T.; Crispini, A.; D'Agnano, I.; Liguori, P. F.; Garcia-Orduna, P.; Pirillo, S.; Valentini, A.; Zanchetta, G. DNA binding and cytotoxicity of fluorescent curcumin-based Zn(II) complexes. *MedChemComm* **2012**, *3*, 462−468.

(19) Abramkin, S. *Synthesis and Characterization of Novel Oxaliplatin Analogs*. Ph.D. dissertation, Universitat Wien, Austria, 2012.

(20) Anbu, S.; Kamalraj, S.; Varghese, B.; Muthumary, J.; Kandaswamy, M. A series of oxyimine-based macrocyclic dinuclear zinc(II) complexes enhances phosphate ester hydrolysis, DNA binding, DNA hydrolysis, and lactate dehydrogenase inhibition and induces apoptosis. *Inorg. Chem.* **2012**, *51*, 5580−5592.

(21) Liao, W.; Luo, Z.; Liu, D.; Ning, Z.; Yang, J.; Ren, J. Structure characterization of a novel polysaccharide from *Dictyophora indusiata* and its macrophage immunomodulatory activities. *J. Agric. Food Chem.* **2015**, *63*, 535−544.

(22) Costa-Lotufo, L. V.; Khan, M. T. H.; Ather, A.; Wilke, D. V.; Jimenez, P. C.; Pessoa, C.; de Moraes, M. E. A.; de Moraes, M. O. Studies of the anticancer potential of plants used in Bangladeshi folk medicine. *J. Ethnopharmacol.* **2005**, *99*, 21−30.

(23) Wang, H.; Joseph, J. A. Quantifying cellular oxidative stress by dichlorofluorescein assay using microplate reader. *Free Radical Biol. Med.* **1999**, *27*, 612−616.

(24) Hu, T.; He, X.-W.; Jiang, J.-G. Functional analyses on antioxidant, anti-inflammatory, and antiproliferative effects of extracts and compounds from *Ilex latifolia* Thunb., a Chinese bitter tea. *J. Agric. Food Chem.* **2014**, *62*, 8608−8615.

(25) Zhao, L.; Chen, J.; Su, J.; Li, L.; Hu, S.; Li, B.; Zhang, X.; Xu, Z.; Chen, T. In vitro antioxidant and antiproliferative activities of 5-hydroxymethylfurfural. *J. Agric. Food Chem.* **2013**, *61*, 10604−10611.

(26) Zheng, Z.-P.; Xu, Y.; Qin, C.; Zhang, S.; Gu, X.; Lin, Y.; Xie, G.; Wang, M.; Chen, J. Characterization of antiproliferative activity constituents from *Artocarpus heterophyllus*. *J. Agric. Food Chem.* **2014**, *62*, 5519−5527.

(27) Ong, R. C. Y.; Lei, J.; Lee, R. K. Y.; Cheung, J. Y. N.; Fung, K. P.; Lin, C.; Ho, H. P.; Yu, B.; Li, M.; Kong, S. K. Polyphyllin D induces mitochondrial fragmentation and acts directly on the mitochondria to induce apoptosis in drug-resistant HepG2 cells. *Cancer Lett.* **2008**, *261*, 158−164.

(28) Luo, H.; Wang, F.; Bai, Y.; Chen, T.; Zheng, W. Selenium nanoparticles inhibit the growth of HeLa and MDA-MB-231 cells through induction of S phase arrest. *Colloids Surf., B* **2012**, *94*, 304−308.

(29) Zheng, S.; Li, X.; Zhang, Y.; Xie, Q.; Wong, Y.-S.; Zheng, W.; Chen, T. PEG-nanolized ultrasmall selenium nanoparticles overcome drug resistance in hepatocellular carcinoma HepG2 cells through induction of mitochondria dysfunction. *Int. J. Nanomed.* **2012**, *7*, 3939.

(30) Sharma, S.; Chockalingam, S.; Sanpui, P.; Chattopadhyay, A.; Ghosh, S. S. Silver nanoparticles impregnated alginate-chitosan-blended nanocarrier induces apoptosis in human glioblastoma cells. *Adv. Healthcare Mater.* **2014**, *3*, 106−114.

(31) Liao, W.; Ning, Z.; Chen, L.; Wei, Q.; Yuan, E.; Yang, J.; Ren, J. Intracellular antioxidant detoxifying effects of diosmetin on 2,2-azobis(2-amidinopropane) dihydrochloride (AAPH)-induced oxidative stress through inhibition of reactive oxygen species generation. *J. Agric. Food Chem.* **2014**, *62*, 8648−8654.

(32) Thornberry, N. A.; Lazebnik, Y. Caspases: enemies within. *Science* **1998**, *281*, 1312−1316.

(33) Kumar, S. Caspase function in programmed cell death. *Cell Death Differ.* **2007**, *14*, 32−43.

(34) Danial, N. N.; Korsmeyer, S. J. Cell death: Critical control points. *Cell* **2004**, *116*, 205−219.

DOI: 10.1021/acs.jafc.5b00614
J. Agric. Food Chem. 2015, 63, 6525−6534

(35) Lakhani, S. A.; Masud, A.; Kuida, K.; Porter, G. A.; Booth, C. J.; Mehal, W. Z.; Inayat, I.; Flavell, R. A. Caspases 3 and 7: key mediators of mitochondrial events of apoptosis. *Science* **2006**, *311*, 847−851.

DOI: 10.1021/acs.jafc.5b00614
J. Agric. Food Chem. 2015, 63, 6525−6534

involved in the development of coronary heart disease, by 10% at 25 μM.[11] R3S, R3G, and R4G could be shown to reduce colon cancer cell growth at 10−50 μM.[10] Also, as recently shown by Walker et al.,[12] R3S, at a concentration as low as 1 μM, lowered IL-6 expression by 57.8% in an in vitro model of stimulated human macrophages after 6 h of co-incubation with *Escherichia coli* lipopolysaccharides (1 μg/mL). Lipolysaccharide (LPS) from the outer membrane of bacteria is widely used for in vitro studies on inflammation because it activates the NF-κB signaling cascade in the host tissue.[13] Down-stream of NF-κB activation, the CC motif chemokines monocyte chemotactic protein-1 (MCP-1 = CCL2) and macrophage inflammatory protein 1 beta (MIP-1b = CCL4) and the CXC motif chemokine interleukin 8 (IL-8 = CXCL8) and chemokine receptors CXCR2 (transcript variants 1 and 2, CXCR2var1/2), CCR1, and CCR2 are important factors in triggering immune cell trafficking and infiltration from the bloodstream into tissues via chemotaxis, but also enhance local cell activation and proliferation of inflamed tissue and immune competent cells, leading to disease progression.[14,15] Another factor involved in inflammatory processes is the deacetylase Sirtuin-1 (SIRT1), a member of the silent mating type information regulation 2 enzyme family. SIRT1 inhibits NF-κB transcription and is down-regulated in response to LPS.[16] Thus, an up-regulation of SIRT1 results in decreased levels of pro-inflammatory cytokines.[16]

The ability of phenolic dietary compounds to inhibit immune cell migration has been shown in vivo, in a model of allergic airway inflammation in mice, where intraperitoneal epigallocatechin-3-gallate (10 mg/kg body weight for 4 days) potently reduced infiltration of immune cells and was able to inhibit migration of Th1 cells in vitro by 30−50% at a concentration of 1 μM via direct interaction with CXC motif chemokines.[17] RES has also been demonstrated to inhibit monocyte recruitment into endothelium via inhibition of adhesion over a concentration range 0.3−10 μM in vitro.[18] Furthermore, RES inhibited mRNA expression of CCR2 in THP-1 monocytes by 12% after 6 h of treatment and blunted monocyte recruitment on vascular endothelia at a concentration of 10 μM.[19] As for RES metabolites, in an enzymatic study, SIRT1 was activated to the same extent by RES, R3S, and RES-4′-*O*-sulfate over a concentration range from 10 to 500 μM, resulting in attenuated cytokine levels in vitro.[20] In a mouse model of colitis, in which a dose of 100 mg RES/kg body weight was administered for 7 days, the induction of SIRT1 has been linked with attenuated cytokine levels in vivo.[21] Considering the low bioavailability of free RES in vivo, those effects could very likely be caused by present metabolites. Therefore, this in vitro study investigates the effect of RES and its main physiological metabolites on immune chemotactic genes and proteins, as well as SIRT1, in differentiated human U-937 macrophages (U-937 Mϕ). Macrophages were activated with LPS from *Porphyromonas gingivalis* (pgLPS), an oral pathogen responsible for disease progression in periodontitis.[22] Macrophages are exposed to dietary substances either directly during ingestion or via the bloodstream. As the parent compound RES is barely bioavailable after dietary intake, we aimed to identify the potential of RES metabolites, each of which may have the same or higher benefit than the parent compound. Considering plasma metabolite concentrations after intake of dietary-scale doses, in this study, we deliberately used compounds at only 1 μM. The glucocorticoid dexamethasone (DEX), which is known to suppress inflammation via the NF-κB pathway, was used as anti-inflammatory control at 100 nM.[23] Here, we show for the first time the attenuating impact of main physiological RES metabolites on genes involved in macrophage activation and recruitment (chemokines IL-8, MIP-1b, MCP-1, and chemokine receptors CXCR2var2, CCR1, and CCR2) on mRNA and protein levels, as well as their effects on SIRT1 gene expression. Our findings may contribute to the development of more potent nutraceuticals and adjuvants in local and systemic inflammatory diseases containing RES and/or conjugates thereof.

MATERIALS AND METHODS

Chemicals. Methanol (MeOH) of HPLC and LC-MS grade was purchased from Carl Roth (Karlsruhe, Germany). FBS was obtained from Invitrogen (Karlsruhe, Germany) and pgLPS from InvivoGen (San Diego, CA, USA); peqGOLD total RNA isolation kit, peqGOLD Ultra Low Range DNA-Ladder II, and qPCR plates were purchased from Peqlab (Erlangen, Germany); a high-capacity cDNA reverse transcription kit and fast SYBR green Mastermix for PCR experiments were from LifeTechnologies (Carlsbad, CA, USA). ELISA kits for IL-8, MIP-1b, and MCP-1 were obtained from Merck (Vienna, Austria), RayBiotech (Norcross, GA, USA), and LifeTechnologies, respectively. For flow cytometry, fluorescein-labeled CXCR2 and labeled isotype control antibodies (both R&D Systems, Minneapolis, MN, USA) and rabbit anti-human CCR-1 pAb (PromoCell, Heidelberg, Germany) and isotype control rabbit mAb IgG (New England Biolabs, Ipswich, MA, USA) were used. CCR1 and isotype control were labeled with AlexaFluor488 (Abcam, Cambridge, UK). All other chemicals were from Sigma-Aldrich (Vienna, Austria).

Synthesis and Purification of RES Metabolites. The method for synthesis of RES glucuronides was adapted from an already published method,[24] with the following modifications: 1 equiv of RES-phenolate was conjugated with 2 equiv of acetobromo-α-D-glucuronic acid methyl ester, and after 1 h of stirring at 40 °C, the reaction flask was put on ice and adjusted to pH 8−9 with 16.7 mM sodium carbonate solution. The mixture of RES conjugates was evaporated to dryness and kept at −80 °C prior to purification. Metabolites were purified on a Dionex Ultimate 3000 semipreparative LC system (Thermo Fisher Scientific, Vienna, Austria) with the UV detector set to 300 nm. After dissolution of the synthesis product in MeOH/water (1:1, v/v), the first purification step was done on an RP18 column (Synergi Fusion, 250 × 10 mm, 4 μm, Phenomenex, Aschaffenburg, Germany) at a flow rate of 1.5 mL/min, by gradient elution with 10 mM ammonium formate buffer at pH 8.2 and MeOH. LC gradient (*t* (min), % MeOH) was (0, 20), (20, 70), (25, 100), (30, 20), and the column was equilibrated for 10 min after each run. The major peak (retention time of 20.5 min) was collected and subjected to a second purification on an RP18 column (XTerra Prep MS C18, 100 × 50 mm, 5 μm, Waters, Eschborn, Germany). The flow rate was set at 11 mL/min, gradient elution was done with the eluents already mentioned, and the following gradient (*t* (min), % MeOH) was used: (0, 25), (23, 60), (26, 25). Again, the column was equilibrated for 10 min after each run. Five peaks were collected and subjected to LC-MS (LCMS-2020, Shimadzu, Columbia, MD, USA, with LabSolutions software) analysis with an MS detector with ESI source and quadrupole analyzer recording positive and negative total ion current (TIC(±)) and negative single ion monitoring (SIM(−)), with the following MS interface settings: heatblock temperature, 300 °C; desolvation line temperature, 200 °C; nebulizing gas flow, 1.5 L/min; drying gas flow, 15 L/min; gas flows were obtained from a nitrogen generator, scanning speed, 682 u/s. After evaluation of TIC(−) and SIM(−) for *m*/*z* 227 (RES), *m*/*z* 403 (RES glucuronides), and *m*/*z* 589 (RES diglucuronides), structure identification for two fractions of RES monoglucuronides was done by 1D and 2D NMR on a Bruker Avance III 500 MHz instrument (^{1}H, ^{1}H^{1}H, ^{1}H^{13}C, ^{13}C) at the NMR center of the Faculty of Chemistry, Vienna, Austria. NMR spectra were analyzed with SpinWorks 3.1.8.1 software, and chemical shifts and coupling constants were compared to published data sets.[25]

DOI: 10.1021/acs.jafc.5b01830
J. Agric. Food Chem. 2015, 63, 6535−6545

Table 1. Forward and Reverse Primer Pair Sequences and Number of Cycles per Run[a]

target	direction	sequence (5′−3′)	cycles	C_T
IL-8	forward	ACCGGAAGGAACCATCTCAC	40	15.4 ± 0.4
	reverse	GGCAAAACTGCACCTTCACAC		
MIP-1b	forward	CATGAAGCTCTGCGTGACTG	45	19.0 ± 1.2
	reverse	CCACAAAGTTGCGAGGAAGC		
MCP-1	forward	CCGAGAGGCTGAGACTAACC	40	15.9 ± 0.8
	reverse	CTTTCATGCTGGAGGCGAGA		
CCR1	forward	AACCAGAGAGAAGCCGGGATG	45	21.3 ± 0.7
	reverse	ACGGAGTTGCATCCCCATAG		
CCR2	forward	GAGCGGTGAAGAAGTCACCA	55	31.0 ± 1.2
	reverse	GCAGTTTATTAAGATGAGGACGAC		
CXCR2var1	forward	TGTTCCTCTGTGGGAATACCTCCCC	55	32.0 ± 1.7
	reverse	GCTGTGACCTGCTGTTATTGGAGT		
CXCR2var2	forward	TCTGCCTAGAGCTCTGACTACCA	55	30.0 ± 0.3
	reverse	TGGGCTTTTCACCTGTAGGAC		
SIRT1	forward	AGTAGGCGGCTTGATGGTAA	45	24.6 ± 0.8
	reverse	CCTCAGCGCCATGGAAAATG		

[a] C_T is the cycle when amplification of a target is first detected. C_T values represent the mean ± SD for 6 h incubations with pgLPS (n = 3−4).

Compounds were dissolved in DMSO at 10 mM and stored in aliquots at −80 °C.

Cell Culture. U-937 cell line was obtained from the American Type Culture Collection and cultured in Roswell Park Memorial Institute 1640 (RPMI) medium supplemented with 10% FBS, 100 U/mL penicillin, 0.1 mg/mL streptomycin, and 2 mM glutamine in a humidified incubator with 5% CO_2 at 37 °C and were split every 2−3 days. Differentiation was achieved by incubation with PMA (10 ng/mL) over 48 h, as already published by our group.[12] Incubations were done with complete medium, and DMSO concentration was 0.1% in all experiments.

Cellular Uptake. Uptake of RES and R4G into U-937 Mϕ was tested at 1 μM and, subsequently, 10 μM. Time points chosen were 10 and 30 min and 1, 1.5, 2, 2.5, and 3 h. For R3S, uptake was only measured after 3 h of treatment. Cells were seeded in 24-well plates at a density of 0.2 × 10^6 cells/well and, after differentiation, incubated with compounds at 37 °C. Cell culture plates were then immediately put on ice, and supernatants were removed. For protein precipitation, MeOH (−20 °C) was added to the supernatant (3:1) and centrifuged for 10 min at 4 °C and 16000g. Immediately after removal of the supernatant, cells were washed once with ice-cold PBS and taken up in 300 μL of distilled water, and two freeze−thaw cycles were done by immersing the plates in liquid N_2 and thawing them at ambient temperature. Lysed cells were then centrifuged under the conditions already mentioned. Both supernatants of precipitated incubation medium and lysed cells were filtered through a 0.45 μM PVDF filter and quantified by LC-MS. Limit of detection (LOD, S/N ratio 3.3:1) and limit of quantification (LOQ, S/N ratio 10:1) were calculated by LabSolutions software to be 3.15 and 10.5 nM for RES, 21.3 and 64.5 nM for R3S, and 15.1 and 50.2 nM for R4G, as determined by calibration curve from 0.039 to 10 μM at 300 nm UV detector wavelength. Recoveries for supernatant were 79, 76, and 73% for RES, R3S, and R4G, respectively. Recoveries for cell lysate were 84, 90, and 66% for RES, R3S, and R4G, respectively.

RT-qPCR. For gene expression analysis, cells were seeded in the same manner as for uptake experiments. Compounds were co-incubated in triplicate for 3 and 6 h with 1 μg/mL pgLPS and either DEX (100 nM) or compounds at 1 μM. mRNA of three wells was pooled and isolated and, subsequently, 2 μg, as measured by spectrophotometry at 260/280 nm (TecanInfinite200, Groedig, Austria), was reverse transcribed, following the instructions provided by the manufacturer. RT-qPCR experiments were carried out in triplicate on a StepOnePlus device (AppliedBiosystems, Carlsbad, CA, USA). Primers were designed using PrimerBlast, and data were normalized to PPIA (primer sequences already published).[12] Primers were used at 100 nM, and qPCR cycles were adapted to the number of cycles when amplification of a target is first detected (C_T values) to reach fluorescent plateau phases, with 40 cycles for IL-8 and MCP-1, 45 cycles for MIP-1b, CCR1, and SIRT1, and 55 cycles for CCR2, CXCR2var1, and CXCR2var2 (Table 1). For data analysis, LinRegPCR2012.3 was used, and baseline-corrected starting concentrations (N_0 values) were used for normalization over PPIA. Four independent experiments with three technical replicates were conducted. To confirm PCR product lengths and purities, gene copies were run on a 3.5% agarose gel, with a DNA ladder ranging from 25 to 700 bp. All PCR products showed single bands, and product lengths corresponded to DNA ladder within 10 ± 3 bp.

ELISA. Incubations for the measurement of chemokines in cell culture supernatant were done as described for qPCR experiments. The supernatants of three wells were pooled and centrifuged for 10 min at 4 °C and 16000g, and aliquots were stored at −80 °C. Samples were diluted with complete medium, if necessary. ELISA measurements for IL-8 (Merck, Vienna, Austria), MIP-1b (RayBiotech, Norcross, GA, USA), and MCP-1 (LifeTechnologies, Carlsbad, CA, USA) were completed following the manufacturers' protocols. Four independent experiments were conducted.

Flow Cytometry (FC). For FC measurements, cells were seeded in 6-well plates 48 h prior to experiments at 1 × 10^6 cells/well. After 6 h of incubation, the medium was removed, cells were scraped and taken up in ice-cold FC buffer, consisting of PBS (170 mM NaCl, 3.4 mM KCl, 10.0 mM Na_2HPO_4, 1.8 mM KH_2PO_4, pH 7.4), 10% FBS, and 0.5% sodium azide. All staining and washing steps were done in Eppendorf tubes, centrifugation conditions were 5 min at 4 °C and 400g. The use of sodium azide and working at 4 °C are common strategies to impede further metabolism and prevent membrane proteins from being internalized.[26] Aliquots of 0.2 × 10^6 cells were incubated with antibodies in 200 μL of FC buffer, 30 min for CXCR2 antibody (1:100) and 15 min for CCR1 pAb (1:400), followed by 15

DOI: 10.1021/acs.jafc.5b01830
J. Agric. Food Chem. 2015, 63, 6535−6545

min AlexaFluor488 (1:2000). Subsequently, samples were washed twice with 1 mL of FC buffer and resuspended in Hank's balanced salt solution (Sigma-Aldrich). Samples were transferred to a 96-well plate in duplicate and measured with a Guava easyCyte 8HT flow cytometer (Millipore, Darmstadt, Germany). Geometric mean fluorescence intensity (MFI) was used for effect calculation (treated over pgLPS (%)). Four independent experiments with two technical replicates were conducted.

Statistical Analysis. Data represent means ± SD and were analyzed using SigmaPlot 11.0 (SystatSoftware, USA). Prior to comparative testing, all sets were normality tested (Shapiro–Wilk). If normality was passed, values were *t* tested (*, $p < 0.05$) against pgLPS-control; if equal variance testing failed, a Wilcoxon–Mann–Whitney rank sum test was performed. For comparison of compounds to DEX, ANOVA was used with a post hoc Holm–Sidak test; if prior normality testing failed, a Kruskal–Wallis one-way analysis of variance on ranks followed by Dunn's test for multiple comparisons was performed.

RESULTS AND DISCUSSION

Purification and Structure Elucidation of RES-Metabolites. Compounds in Figure 1 were drawn with ChemBioDraw Ultra 12.0 (Cambridgesoft, Cambridge, MA, USA). R3S and a mixture of RES-3,5-*O*- and -3,4′-*O*-disulfate (59:41, RdS) were synthesized and purified as reported previously.[27] The synthesis of RES-glucuronides resulted in a collection of five peaks after the second purification step, with retention times (Rt, min) of 10.9 ± 0.38 (1), 17.4 ± 0.77 (2), 20.9 ± 1.28 (3), 27.3 ± 1.62 (4), and 30.9 ± 0.27 (5) (averages of 12 measurements; for a representative HPLC chromatogram, see Supplemental Figure A). As TIC(−) and SIM(−) chromatograms for *m*/*z* 403 of peaks 2 and 3 showed only slight impurities (see Supplemental Figure B for MS chromatograms), NMR spectra of those two fractions were taken.

NMR Data. NMR shifts and coupling constants corresponded to data already published for R3G and R4G.[25] Peak 2 (Rt = 17.4 ± 0.77 min) was therefore identified as R4G with a purity of 87.8%, and peak 3 (Rt = 20.9 ± 1.28 min) corresponded to NMR and MS data for R3G, with a purity of 95.0%. Impurities consisted mainly of the other isomer and traces of solvent.

Cellular Uptake. A previously published study on the uptake kinetics of 3–100 μM labeled RES by human hepatic cells showed that RES is taken up in a concentration-dependent manner through a combination of passive diffusion and carrier-mediated transport.[28] In this study, we measured the uptake of RES and R4G into U-937 Mϕ time-dependently over 3 h (Table 2) and of R3S after 3 h of incubation at 37 °C to determine the amount of compound available for biological effects. At the concentration of 1 μM none of the substances could be detected in the cells. To exclude limitations due to LOD (3.15, 21.3, and 15.1 nM for RES, R3S, and R4G, respectively), uptake was repeated at a concentration of 10 μM. At the 10-fold concentration, an uptake at all measured time points could be observed for RES with a maximum of 0.12 ± 0.001 μM (1.37 ± 0.31% of the applied concentration), after 3 h. Following an incubation with 10 μM R3S, this compound could not be detected in the cells; however, after 3 h, its concentration in the supernatant showed a decrease of −1.22 ± 0.82 μM compared to the concentration in the incubation medium ($p = 0.017$), indicating an uptake. Table 2 shows an uptake of R4G at 10 μM into cells only at time points of 10 min (0.023 ± 0.001 μM) and 30 min (0.028 ± 0.003 μM), and the supernatant at 1 and 10 μM showed no differences from the incubation medium at any measured time point, indicating no further uptake into cells. Riha et al.[29] identified RES and R3S as substrates for organic anion transporting polypeptides in Chinese hamster ovary cells, whereas R4G was not taken up at concentrations between 12.5 and 400 μM, partially confirming our results obtained in U-937 cells. The uptake patterns of RES, R3S, and R4G in macrophages could be due to efflux transporters, such as breast cancer resistance protein 1 (BCRP1) and multidrug resistance protein 3 (MRP3), both of which can be found on macrophages.[30] As shown in a study by van de Wetering et al.,[31] RES, R3S, and R3G are substrates for those two ABC transporters. In said study, it was shown that the transport kinetics of RES and R3S for the efflux transporters BCRP1 and MRP3 were similar; therefore, studies for R3S were limited to 3 h of uptake. The glucuronated metabolite, on the other hand, had a much higher affinity to MRP3, leading to a higher efflux rate, as compared to RES and R3S, further confirming our results for RES and R4G.[31] Another point to be considered is the high plasma protein binding of RES (nearly 100%) and metabolites (approximately 50%), reducing the amount of free compound susceptible to transport.[9] In this uptake study in U-937 Mϕ, no further metabolism of substances such as degradation, dehydrogenation, or dimer formation could be observed.

Despite the very limited uptake, our data show effects on gene and protein expression (see following chapters). It is possible that the amounts of the here tested substances in the cells suffice for our observed effects via the already reported interaction with the NF-κB pathway.[1] Another possibility for the observed effects is the interaction of RES with the estrogen receptor α. RES has been shown to be an agonist for the

Table 2. Time-Dependent Uptake of (A) RES and (B) R4G into U-937 Mϕ[a]

(A) RES				
	1 μM RES (mean ± SD)		10 μM RES (mean ± SD)	
time (min)	supernatant (μM)	cells (μM)	supernatant (μM)	cells (μM)
10	1.05 ± 0.13	nd	9.79 ± 1.04	0.08 ± 0.02
30	1.03 ± 0.14	nd	9.98 ± 1.21	0.10 ± 0.01
60	0.79 ± 0.07a	nd	8.80 ± 1.24a	0.11 ± 0.03
90	0.65 ± 0.10a	nd	9.18 ± 1.16	0.10 ± 0.01
120	0.78 ± 0.46a	nd	9.07 ± 1.02	0.120 ± 0.001b
150	0.43 ± 0.09a	nd	7.73 ± 1.16a	0.120 ± 0.001b
180	0.41 ± 0.09a	nd	8.86 ± 1.25	0.120 ± 0.001b
(B) R4G				
	1 μM R4G (mean ± SD)		10 μM R4G (mean ± SD)	
time (min)	supernatant (μM)	cells (μM)	supernatant (μM)	cells (μM)
10	1.05 ± 0.30	nd	9.24 ± 0.46	0.023 ± 0.001
30	1.18 ± 0.12	nd	9.31 ± 0.70	0.028 ± 0.003
60	1.05 ± 0.19	nd	8.87 ± 0.71	nd
90	0.84 ± 0.23	nd	8.62 ± 1.30	nd
120	1.07 ± 0.06	nd	8.95 ± 0.89	nd
150	0.90 ± 0.21	nd	9.12 ± 1.03	nd
180	0.98 ± 0.09	nd	8.64 ± 1.21	nd

[a]Data are depicted as the mean ± SD ($n = 3$, tr = 2). Data for supernatant were compared to the incubation medium by ANOVA; differences from incubation medium are marked with "a" ($p < 0.05$). Data for cells were compared by all-pairwise ANOVA, and according to ANOVA results, calculated differences to 10 min measurements are marked with "b" ($p < 0.05$).

DOI: 10.1021/acs.jafc.5b01830
J. Agric. Food Chem. 2015, 63, 6535–6545

estrogen receptor α,[32] albeit at concentrations of 3−10 μM, which are higher than the concentration used in this study. The activation of this receptor has been associated with the suppression of the inflammatory response in a model of arthritis in rats.[33]

Activation of U-937 Mϕ with pgLPS. As a control study for the activation of U-937 Mϕ, the effects on gene and protein expression of cells treated with or without 1 μg/mL pgLPS were compared at various time points. As shown in Figure 2, pgLPS significantly up-regulated mRNA levels of IL-8, MIP-1b, and MCP-1 at 3 and 6 h (Figure 2B), the largest effect was measured for MIP-1b at 3 h, with a (59.4 ± 6.98)-fold increase. The corresponding proteins (with the exception of MCP-1 at 3 h) also showed elevated levels, with the highest protein expression for MIP-1b after treatment for 6 h ((53.6 ± 12.1)-fold, Figure 2C). Gene expression of chemokine receptors and SIRT1 (Figure 2A) was down-regulated by pgLPS with maximum decreases for CXCR2var2 (6 h) and CCR1 (3 h) of −74.9 ± 8.20 and −64.6 ± 5.05%, respectively, and −22.4 ± 4.16% for SIRT1 (3 h). A similar decrease in mRNA expression for CXC and CC receptors was published for activated human leucocytes ex vivo and for rats in vivo, as well as down-regulation of SIRT1 deacetylase after incubation with *Escherichia coli* LPS in vitro in RAW264.7 macrophages.[34−36] In U-937 Mϕ, in contrast to decreased receptor mRNA expression (Figure 2A), flow cytometric measurements of CXCR2 and CCR1 after 6 h of treatment with pgLPS showed an increase in surface protein compared to control of 7.70 ± 0.13% for CXCR2 (p = 0.03) and 0.7 ± 0.01% for CCR1 (p = 0.02). Keller et al.[37] reported time-dependent changes in cytokine gene and protein expression in cultured LPS-activated mouse macrophages. In their study, the gene and protein expression of transcription factors of inflammatory pathways underwent repeated oscillating changes over 48 h. Those changes were attributed to an "intrinsic clockwork" in macrophages. Thus, we hypothesize that this oscillation might have contributed to our differential findings for mRNA and protein levels. Also, as shown by Daigneault et al.,[38] the PMA-induced differentiation process of monocytes into macrophages might have caused our here observed elevated levels of membrane receptor proteins.

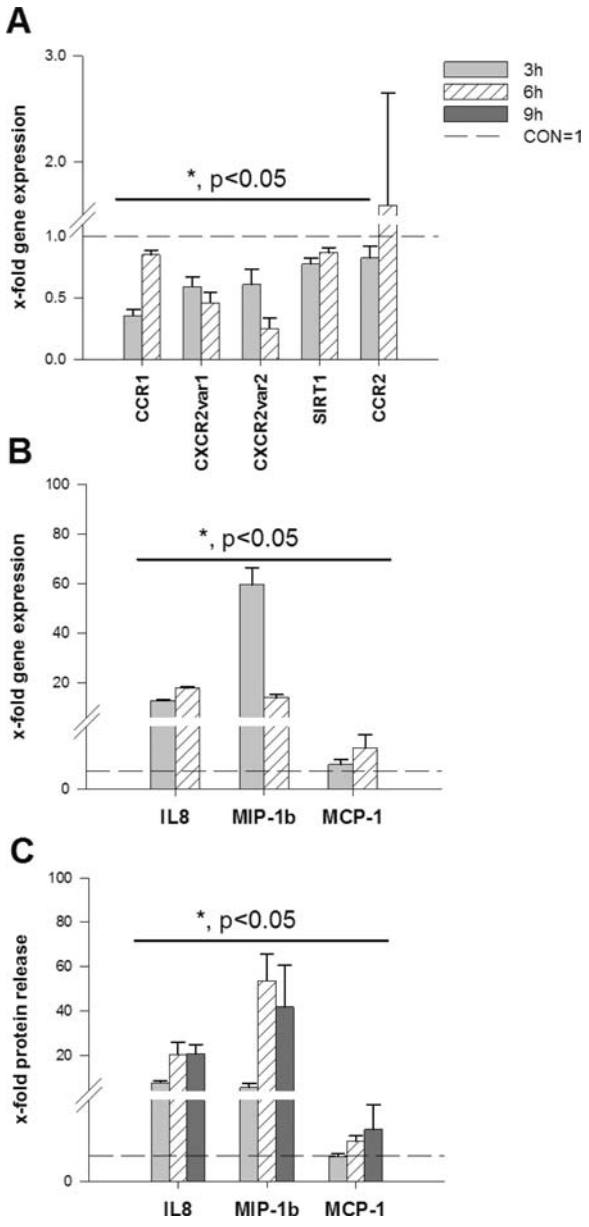

Figure 2. Control data for (A, B) mRNA and (C) protein expression of CCR1, CXCR2var1/2, SIRT1, CCR2, IL8, MIP-1b, and MCP-1 in U-937 Mϕ after treatment with 1 μg/mL pgLPS for indicated time points (see legend). x-Fold changes in pgLPS treated cells were compared to DMSO-control (dashed line = 1-fold). Data represent means ± SD (n = 3−4, tr = 2−3). (*) $p < 0.05$ compared to untreated control.

Gene Expression and Protein Release of Chemokines. Glucocorticoids inhibit inflammation by direct interaction with the NF-κB-pathway.[23] Accordingly, in our experiments, the anti-inflammatory control DEX inhibited mRNA expression and protein expression of all chemokines at 100 nM (Figure 3). As recently reviewed by Joven et al.,[39] especially CC motif chemokines present a promising target for polyphenols in the prevention and treatment of a multitude of inflammatory diseases. In our study, qPCR analysis of MIP-1b and MCP-1 confirmed these results only partially, by showing that mean mRNA levels of MCP-1 (CCL2, Figure 3E), but not MIP-1b (CCL4, Figure 3C), after 3 h of incubation are comparably decreased after treatment with pgLPS and RES, R3S, and RdS by −24.3 ± 11.1, −24.7 ± 5.51, and −28.7 ± 19.2%, respectively. For RES, a similar effect has been shown in adipocytes at a concentration of 10 μM.[40] Yang et al.[41] obtained similar results for human pulmonary artery endothelial cells and reported an attenuating effect on cytokine-induced eotaxin (CCL11) for RES, but not for R3G and R4G at 25 μM. Although IL-8 and MCP-1 are regulated by the same transcription factor in U-937 cells, NF-κB,[42] the here tested compounds had no apparent effect on IL-8 gene expression at the chosen time points (Figure 3A). Interestingly, though, in our experiments, RES, RdS, and R3G did show an inhibiting effect on IL-8 protein release after 9 h (−12.7 ± 7.65, −22.9 ± 3.57, and −16.5 ± 6.04%, Figure 3B). RES, R3S, RdS, and R3G also inhibited protein release for MIP-1b, with the highest inhibiting value of −20.1 ± 7.00% for RdS followed by R3S with −15.4 ± 8.68% (both 9 h of treatment, Figure 3D). An inhibition of MCP-1 protein was measured for RdS after 3 and 9 h treatments (−25.7 ± 8.29 and −23.0 ± 10.1%), RES (9 h, −21.8 ± 16.2%), and R3S (3 h, −20.8 ± 13.9%), as shown in Figure 3F. In contrast to sulfated metabolites and R3G, R4G showed a differential effect on MIP-1b, with an mRNA increase of 24.5 ± 14.8% after 6 h. In our test system, sulfated

DOI: 10.1021/acs.jafc.5b01830
J. Agric. Food Chem. 2015, 63, 6535−6545

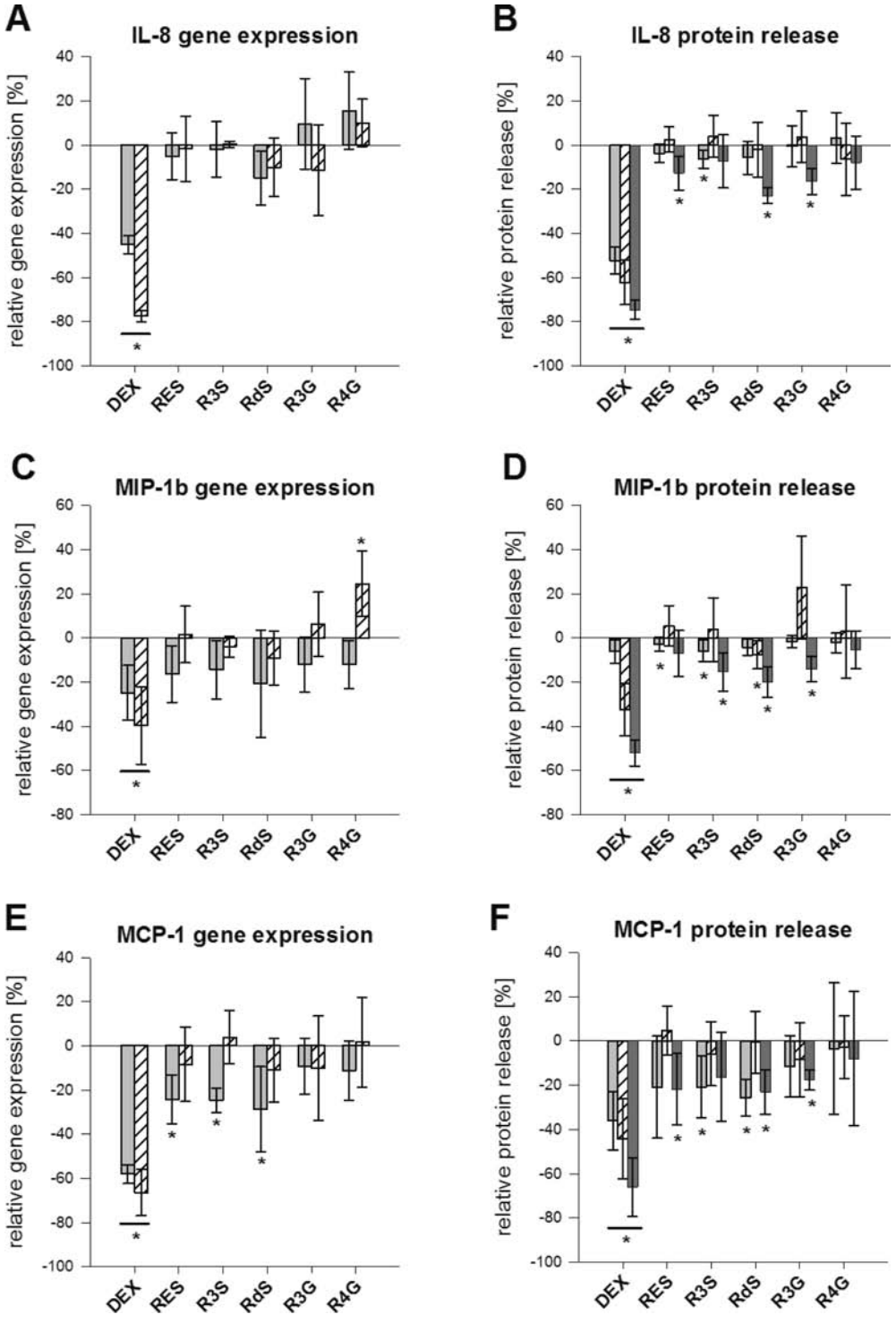

Figure 3. Changes in (A, C, E) mRNA expression and (B, D, F) protein release after 3 (light gray bars), 6 (slashed bars), and 9 h (dark gray bars) of co-incubation with pgLPS (1 μg/mL) and substances at 1 μM and 100 nM (DEX), respectively. pgLPS-control was set at 0% change; values are differences from pgLPS-control in percent. Data represent means ± SD (n = 3−4, tr = 2−3). (*) $p < 0.05$ compared to pgLPS-control.

metabolites were more anti-inflammatory active than glucuronated metabolites, which is in accordance with previously published work by our group, studying concentrations of 1−10 μM RES, R3S, RdS, R3G, and R4G, where RES and sulfated, but not glucuronated, conjugates inhibited IL-6 and TNF-α protein release.[12] Similarly, in an in vitro study on colon cancer cell progression by Aires et al.,[43] R3S showed inhibiting effects at 30 μM in contrast to R3G and R4G. Considering the results of our uptake experiments, RES and R3S did indeed have effects on gene and protein expression, whereas R4G showed an uptake only at early time points at 10 μM and no changes indicating any further uptake in the concentration of the supernatant at 1 or 10 μM. The pro-inflammatory effect of R4G on MIP-1b could be an indication of the inflammatory properties of glucuronated phenolic metabolites, as reported by Liao and Lin for quercetin-3-glucuronide in isolated mouse

DOI: 10.1021/acs.jafc.5b01830
J. Agric. Food Chem. 2015, 63, 6535−6545

Table 3. Gene Expression Levels of CCR2 and CXCR2var1 at Various Incubation Times after Co-incubation with Compounds[a]

CCR2	3 h	6 h	CXCR2var1	3 h	6 h
DEX	97 (63)	170 (87)	DEX	111 (101)	100 (61)
RES	81 (105)	142 (74)	RES	106 (137)	121 (117)
R3S	103 (100)	132 (61)	R3S	111 (129)	122 (91)
RdS	98 (196)	101 (13)	RdS	109 (167)	102 (72)
R3G	85 (110)	131 (94)	R3G	110 (95)	102 (113)
R4G	108 (89)	224 (49)*	R4G	104 (127)	175 (110)

[a]Data are median and percent range (%); (*) $p < 0.05$ compared to pgLPS-treated control set at 100%.

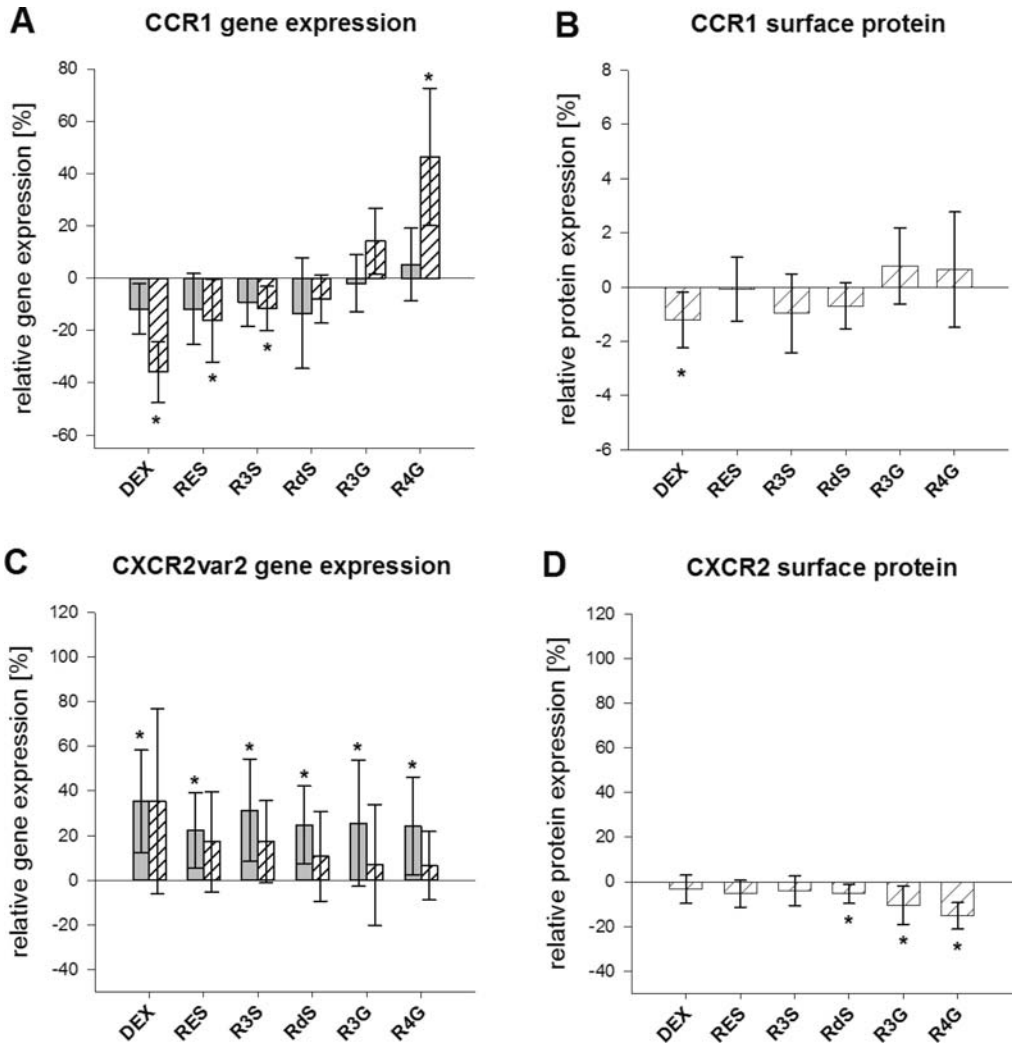

Figure 4. Changes in (A, C) mRNA and (B, D) surface protein expression after 3 (gray bars) and 6 h (slashed bars) of co-incubation with pgLPS (1 μg/mL) and substances at 1 μM and 100 nM (DEX), respectively. pgLPS-control was set at 0% change; values are differences from pgLPS-control in percent. Data represent means ± SD (n = 3–4, tr = 2–3). (*) $p < 0.05$ compared to pgLPS-control.

macrophages.[44] In our study, treatment with sulfated metabolites showed no significant difference (ANOVA) to treatment with the parent compound, as also found for COX-1 and iNOS inhibition at a compound concentration of 34 μM.[45] Considering the aggravated inflammatory profile in patients with rheumatoid arthritis, after application of a monoclonal MCP-1 antibody,[46] our results also support the hypothesis that sulfated RES metabolites could prove beneficial in inflammatory diseases, especially targeting MCP-1 and MIP-1b. Additionally, our results show that the impact of compounds should preferably be assessed on both gene and protein levels. Our data provide an interesting insight into the functional impact of minute amounts of RES and the metabolites formed upon ingestion on inflammatory processes. The long-lasting and pronounced effects of sulfated metabolites in macrophages, especially on MCP-1, may be worth further investigation in animal or human studies.

Gene and Surface Protein Expression of Chemokine Receptors. Treatment with pgLPS led to down-regulation of chemokine receptor mRNA (Figure 2A); co-incubation with pgLPS and compounds/DEX for 3 and 6 h did not influence mRNA levels of CXCR2var1 (Table 3). Interestingly, only R4G showed an up-regulation of CCR2 by 224% with a percent range of 48.5% after 6 h (Table 3), suggesting an anti-

DOI: 10.1021/acs.jafc.5b01830
J. Agric. Food Chem. 2015, 63, 6535–6545

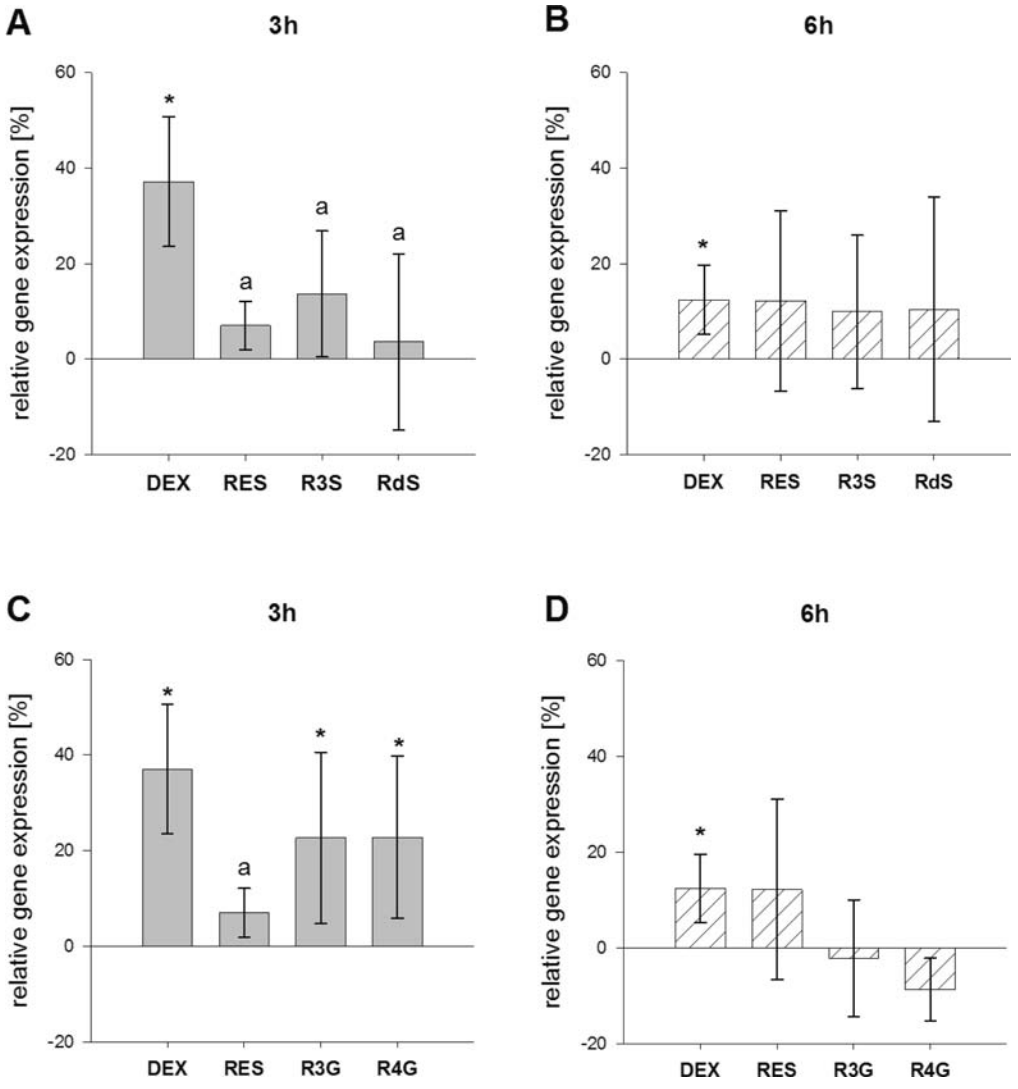

Figure 5. Impact of compounds at 1 μM or 100 nM (DEX) in co-incubation with pgLPS (1 μg/mL) on SIRT1 mRNA expression for (A, B) DEX, RES, R3S, and RdS after 3 and 6 h and for (C, D) DEX, RES, R3G, and R4G after 3 and 6 h. pgLPS-control was set at 0% change; values are differences from pgLPS-control in percent. Data represent means ± SD (n = 3−4, tr = 2−3). The asterisk (∗) indicates statistically significant differences compared to pgLPS-treated control ($p < 0.05$). Letter "a" indicates results for one-way ANOVA versus anti-inflammatory control DEX.

inflammatory activity of this compound. It should be noted that our PCR results show high standard deviations, likely due to low abundances of mRNA in U-937 Mϕ for both genes, which resulted in very high CT values. Hence, we cannot exclude that the here tested compounds could elicit effects on CXCR2var1 mRNA expression in other immune cells. The same applies for CCR2 mRNA expression, as, for example, RES at 10 μM has been shown to inhibit CCR2 expression in THP-1 monocytes.[19]

mRNA levels of chemokine receptors CCR1 and CXCR2var2 were differentially affected by RES metabolites (Figure 4). After 6 h, RES and R3S decreased CCR1 gene expression to the same extent as DEX, whereas R4G (46.3 ± 26.2%) showed the opposite effect (Figure 4A), as also reported for MIP-1b and CCR2 mRNA in this study (Figure 3C; Table 3). CCR1 receptor surface expression after 6 h of co-incubation with pgLPS was not affected by treatments, except for DEX, which down-regulated surface protein levels (Figure 4B). mRNA of CXCR2var2 was up-regulated to the same extent by all treatments, after 3 h of incubation, as tested by ANOVA (Figure 4C), showing that R4G affected the CXC motif receptor differently from the CC motif receptors. After 6 h, no effect for RES and its metabolites on CXCR2var2 mRNA expression could be observed (Figure 4C). An up-regulation of chemokine receptors previously down-regulated by an inflammatory stimulus (Figure 2A) was also demonstrated in cytokine-induced rat synovial fibroblasts treated with green tea extract containing polyphenols (2.5−40 μg/mL catechins).[34] However, it should be noted, that, in our study, the mRNA levels for two different transcript variants of CXCR2 (var1 and var2) were measured separately, with the CXCR2 antibody not being specific for a certain transcript variant, which could account for the differential effects on mRNA and surface protein levels.

In the here presented study, despite the up-regulation of mRNA compared to LPS, CXCR2 surface protein was down-regulated by RdS, R3G, and R4G by −5.33 ± 4.18, −10.6 ± 8.49, and −15.2 ± 5.99%, respectively (Figure 4D). This effect could be due to internalization of CXCR2 receptor proteins upon exposure to inflammatory stimuli.[15,47] Another possibility for the differential effects on CXC-motif gene and protein expression would be the post-transcriptional influence of

DOI: 10.1021/acs.jafc.5b01830
J. Agric. Food Chem. 2015, 63, 6535−6545

microRNAs on CXC-motif receptors, as shown for microRNA146a and the CXC motif receptor 4 (CXCR4).[48] Considering our results on mRNA expression of chemokine receptors CCR1, CCR2, and CXCR2var2, we find it difficult to definitely attribute effects on receptors to be pro- or anti-inflammatory (Figure 4A). Further studies are needed to elucidate the complex mechanisms underlying chemokine receptor regulation.

Sirtuin-1 Gene Expression. High levels of SIRT1 have been demonstrated to exert protective effects in numerous inflammatory diseases.[16,36] SIRT1 is an active inhibitor of NF-κB, leading to reduced levels of chemokines and cytokines.[21] As our data in Figure 5 show, after 3 h of treatment (Figure 5A,C), at 1 μM, up-regulated SIRT1 gene expression for R3G and R4G was comparable to DEX (ANOVA versus DEX, p = 0.392), but not for RES or the sulfated metabolites (ANOVA versus DEX, p = 0.017). R3G and R4G even overcompensated the down-regulation of SIRT1 by pgLPS (Figure 2A) by 22.7 ± 17.9 and 22.8 ± 16.9%, respectively. A similar up-regulation could be shown in HEPG2 cells, after treatment with 10 μM RES and glucuronated conjugates.[49] Further confirming our in vitro results, in an in vivo study in mice, after ingestion of high doses of RES (440 μM/kg bw per day for 2 weeks), an increase of SIRT1 expression of about 25% has been shown in lymphocytes from inflamed colon lamina propria.[21] RES glucuronides are mainly formed and absorbed in the small intestine,[25,50] but as glucuronides are transported via the bloodstream and are substrates for BCRP1 and MRP1,[31] they could affect SIRT1 expression in colon mucosa and other tissues. In our study, in contrast to glucuronated metabolites, at 1 μM, RES and the sulfated conjugates did not show effects on SIRT1 expression after 3 and 6 h of co-incubation with pgLPS (Figure 5A,B) and for glucuronated metabolites, no up-regulation could be measured after 6 h (Figure 5D).

The mRNA of SIRT1 and CXCR2var2, both being important factors in the development and progression of inflammatory diseases, was regulated comparably to the anti-inflammatory control DEX. The effects of sulfated and glucuronated metabolites, as well as DEX, on CC and CXC motif receptors on mRNA and protein levels are ambiguous and require further studies, as mentioned above. With regard to CC and CXC motif chemokines (IL-8, MCP-1, MIP-1b), the sulfated RES metabolites R3S and RdS were more potent than the tested RES glucuronates in inhibiting LPS-induced gene expression and protein expression in immune-competent macrophages. In summary, resveratrol metabolites formed in vivo, at concentrations reached after dietary-scale doses, were demonstrated to influence genes and proteins involved in inflammatory immune processes in immune-competent macrophages.

■ ASSOCIATED CONTENT

Ⓢ Supporting Information

Supplemental Figures A and B. The Supporting Information is available free of charge on the ACS Publications website at DOI: 10.1021/acs.jafc.5b01830.

■ AUTHOR INFORMATION

Corresponding Author

*(V.S.) E-mail: veronika.somoza@univie.ac.at. Phone: +43-1-4277-70610. Fax: +43-1-4277-970610.

Funding

This work was funded by the University of Vienna via the doctoral program *BioProMotion*.

Notes

The authors declare no competing financial interest.

■ ACKNOWLEDGMENTS

We thank Prof. Dr. Klaus Stolze from the University of Veterinary Medicine (Vienna, Austria) for letting us use the XTerra column for glucuronide purification and Prof. Dr. Markus Galanski from the Faculty of Chemistry (University of Vienna, Austria) for conducting the NMR experiments.

■ ABBREVIATIONS USED

BCRP1, breast cancer resistance protein 1; CCR, CC motif chemokine receptor; COX, cyclo-oxygenase; C_T, number of qPCR cycles when amplification of a target is first detected; CXCR, CXC motif chemokine receptor; DEX, dexamethasone; FC, flow cytometry; IL, interleukin; iNOS, inducible nitric oxide synthase; LOD, limit of detection; LOQ, limit of quantification; MCP-1, monocyte chemotactic protein-1; MeOH, methanol; MIP-1b, macrophage inflammatory protein 1 beta; MRP3, multidrug resistance protein 3; pgLPS, *Porphyromonas gingivalis* LPS; R3G, *trans*-RES-3-*O*-glucuronide; R4G, *trans*-RES-4′-*O*-glucuronide; R3S, *trans*-RES-3-*O*-sulfate; RdS, *trans*-RES-disulfates; RES, *trans*-resveratrol; Rt, retention time; SIM, single ion monitoring; SIRT1, Sirtuin-1; TIC, total ion current; TNF-α, tumor necrosis factor alpha; U-937 Mφ, U-937 macrophages

■ REFERENCES

(1) Alarcón, C.; Villegas, I. Resveratrol as an anti-inflammatory and anti-aging agent: Mechanisms and clinical implications. *Mol. Nutr. Food Res.* **2005**, *49*, 405−430.

(2) Martinez, J.; Moreno, J. Effect of resveratrol, a natural polyphenolic compound, on reactive oxygen species and prostaglandin production. *Biochem. Pharmacol.* **2000**, *59*, 865−870.

(3) Moreno, J. Resveratrol modulates arachidonic acid release, prostaglandin synthesis, and 3t6 fibroblast growth. *J. Pharmacol. Exp. Ther.* **2000**, *294*, 333−338.

(4) Tili, E.; Michaille, J. J. Resveratrol, microRNAs, inflammation, and cancer. *J. Nucleic Acids* **2011**, *2011*, 1−9.

(5) Walle, T.; Hsieh, F.; DeLegge, M. H.; Oatis, J. E.; Walle, U. K. High absorption but very low bioavailability of oral resveratrol in humans. *Drug Metab. Dispos.* **2004**, *32*, 1377.

(6) Wenzel, E.; Somoza, V. Metabolism and bioavailability of trans-resveratrol. *Mol. Nutr. Food Res.* **2005**, *49*, 472−481.

(7) Andres-Lacueva, C.; Macarulla, M. T.; Rotches-Ribalta, M.; Boto-Ordonez, M.; Urpi-Sarda, M.; Rodriguez, V. M.; Portillo, M. P. Distribution of resveratrol metabolites in liver, adipose tissue, and skeletal muscle in rats fed different doses of this polyphenol. *J. Agric. Food Chem.* **2012**, *60*, 4833−40.

(8) Brown, V. A.; Patel, K. R.; Viskaduraki, M.; Crowell, J. A.; Perloff, M.; Booth, T. D.; Vasilinin, G.; Sen, A.; Schinas, A. M.; Piccirilli, G.; Brown, K.; Steward, W. P.; Gescher, A. J.; Brenner, D. E. Repeat dose study of the cancer chemopreventive agent resveratrol in healthy volunteers: Safety, pharmacokinetics, and effect on the insulin-like growth factor axis. *Cancer Res.* **2010**, *70*, 9003−9011.

(9) Burkon, A.; Somoza, V. Quantification of free and proteine-bound trans-resveratrol metabolites and identification of trans-resveratrol-c/o-conjugated diglucuronides-two novel resveratrol metabolites in human plasma. *Mol. Nutr. Food Res.* **2008**, *52*, 549−557.

(10) Storniolo, C. E.; Moreno, J. J. Resveratrol metabolites have an antiproliferative effect on intestinal epithelial cancer cells. *Food Chem.* **2012**, *134*, 1385−1391.

(11) Wu, J. M.; Hsieh, T.-c.; Yang, C.-J.; Olson, S. C. Resveratrol and its metabolites modulate cytokine-mediated induction of eotaxin-1 in human pulmonary artery endothelial cells. *Ann. N. Y. Acad. Sci.* **2013**, *1290*, 30−36.
(12) Walker, J.; Schueller, K.; Schaefer, L.-M.; Pignitter, M.; Esefelder, L.; Somoza, V. Resveratrol and its metabolites inhibit pro-inflammatory effects of lipopolysaccharides in U-937 macrophages in plasma-representative concentrations. *Food Funct.* **2013**, *5*, 74−84.
(13) Cianciulli, A.; Calvello, R.; Cavallo, P.; Dragone, T.; Carofiglio, V.; Panaro, M. A. Modulation of NF-kappa b activation by resveratrol in LPS treated human intestinal cells results in downregulation of PGE(2) production and COX-2 expression. *Toxicol. In Vitro* **2012**, *26*, 1122−1128.
(14) D'Amico, G.; Frascaroli, G.; Bianchi, G.; Transidico, P.; Doni, A.; Vecchi, A.; Sozzani, S.; Allavena, P.; Mantovani, A. Uncoupling of inflammatory chemokine receptors by IL-10: Generation of functional decoys. *Nat. Immunol.* **2000**, *1*, 387−391.
(15) Raghuwanshi, S. K.; Su, Y.; Singh, V.; Haynes, K.; Richmond, A.; Richardson, R. M. The chemokine receptors CXCR1 and CXCR2 couple to distinct G protein-coupled receptor kinases to mediate and regulate leukocyte functions. *J. Immunol.* **2012**, *189*, 2824−32.
(16) Michan, S.; Sinclair, D. Sirtuins in mammals: Insights into their biological function. *Biochem. J.* **2007**, *404*, 1−13.
(17) Qin, S.; Alcorn, J. F.; Craigo, J. K.; Tjoeng, C.; Tarwater, P. M.; Kolls, J. K.; Reinhart, T. A. Epigallocatechin-3-gallate reduces airway inflammation in mice through binding to proinflammatory chemokines and inhibiting inflammatory cell recruitment. *J. Immunol.* **2011**, *186*, 3693−3700.
(18) Deng, Y.-H.; Alex, D.; Huang, H.-Q.; Wang, N.; Yu, N.; Wang, Y.-T.; Leung, G. P. H.; Lee, S. M.-Y. Inhibition of TNF-alpha mediated endothelial cell-monocyte cell adhesion and adhesion molecules expression by the resveratrol derivative, trans-3,5,4′-trimethoxystilbene. *Phytother. Res.* **2011**, *25*, 451−457.
(19) Cullen, J. P.; Morrow, D.; Jin, Y.; von Offenberg Sweeney, N.; Sitzmann, J. V.; Cahill, P. A.; Redmond, E. M. Resveratrol inhibits expression and binding activity of the monocyte chemotactic protein-1 receptor, CCR2, on THP-1 monocytes. *Atherosclerosis* **2007**, *195*, e125−e133.
(20) Calamini, B.; Ratia, K.; Malkowski, M. G.; Cuendet, M.; Pezzuto, J. M.; Santarsiero, B. D.; Mesecar, A. D. Pleiotropic mechanisms facilitated by resveratrol and its metabolites. *Biochem. J.* **2010**, *429*, 273−282.
(21) Singh, U. P.; Singh, N. P.; Singh, B.; Hofseth, L. J.; Price, R. L.; Nagarkatti, M.; Nagarkatti, P. S. Resveratrol (trans-3,5,4′-trihydroxystilbene) induces silent mating type information regulation-1 and down-regulates nuclear transcription factor-kB activation to abrogate dextran sulfate sodium-induced colitis. *J. Pharmacol. Exp. Ther.* **2010**, *332*, 829−839.
(22) Darveau, R. P. Periodontitis: A polymicrobial disruption of host homeostasis. *Nat. Rev. Microbiol.* **2010**, *8*, 481−90.
(23) De Bosscher, K.; Berghe, W. V.; Vermeulen, L.; Plaisance, S.; Boone, E.; Haegeman, G. Glucocorticoids repress nf-kb-driven genes by disturbing the interaction of p65 with the basal transcription machinery, irrespective of coactivator levels in the cell. *Proc. Natl. Acad. Sci. U. S. A.* **2000**, *97*, 3919−3924.
(24) Brandolini, V.; Maietti, A.; Tedeschi, P.; Durini, E.; Vertuani, S.; Manfredini, S. Capillary electrophoresis determination, synthesis, and stability of resveratrol and related 3-*O*-*β*-D-glucopyranosides. *J. Agric. Food Chem.* **2002**, *50*, 7407.
(25) Wenzel, E.; Soldo, T.; Erbersdobler, H.; Somoza, V. Bioactivity and metabolism of trans-resveratrol orally administered to wistar rats. *Mol. Nutr. Food Res.* **2005**, *49*, 482−494.
(26) Luttmann, W.; Bratke, K.; Küpper, M.; Myrtek, D. *Der Experimentator: Immunologie*, 3 ed.; Springer Spektrum: Berlin, Germany, 2009.
(27) Ladurner, A.; Schachner, D.; Schueller, K.; Pignitter, M.; Heiss, E. H.; Somoza, V.; Dirsch, V. M. Impact of trans-resveratrol-sulfates and -glucuronides on endothelial nitric oxide synthase activity, nitric oxide release and intracellular reactive oxygen species. *Molecules* **2014**, *19*, 16724−36.
(28) Lancon, A.; Delma, D.; Osman, H.; Thénot, J. P.; Jannin, B.; Latruffe, N.; Osman, N.; Thénot, N. Human hepatic cell uptake of resveratrol: Involvement of both passive diffusion and carrier-mediated process. *Biochem. Biophys. Res. Commun.* **2004**, *316*, 1132−1137.
(29) Riha, J.; Brenner, S.; Böhmdorfer, M.; Giessrigl, B.; Jäger, W.; Pignitter, M.; Schueller, K.; Somoza, V.; Thalhammer, T.; Stieger, B.; Szekeres, T. Resveratrol and its major sulfated conjugates are substrates of organic anion transporting polypeptides (OAPTs): Impact on growth of ZR-75−1 breast cancer cells. *Mol. Nutr. Food Res.* **2014**, *58*, 1830−1842.
(30) Vallet, C. M.; Marquez, B.; Nhiri, N.; Anantharajah, A.; Mingeot-Leclercq, M.-P.; Tulkens, P. M.; Lallemand, J.-Y.; Jacquet, E.; Van Bambeke, F. Modulation of the expression of ABC transporters in murine (j774) macrophages exposed to large concentrations of the fluoroquinolone antibiotic moxifloxacin. *Toxicology* **2011**, *290*, 178−186.
(31) van de Wetering, K.; Burkon, A.; Feddema, W.; Bot, A.; de Jonge, H.; Somoza, V.; Borst, P. Intestinal breast cancer resistance protein (BCRP)/BCRP1 and multidrug resistance protein 3 (MRP3)/MRP3 are involved in the pharmacokinetics of resveratrol. *Mol. Pharmacol.* **2009**, *75*, 876−885.
(32) Gehm, B. D.; McAndrews, J. M.; Chien, P. Y.; Jameson, J. L. Resveratrol, a polyphenolic compound found in grapes and wine, is an agonist for the estrogen receptor. *Proc. Natl. Acad. Sci. U. S. A.* **1997**, *94*, 14138−14143.
(33) Dulos, J.; Vijn, P.; van Doorn, C.; Hofstra, C. L.; Veening-Griffioen, D.; de Graaf, J.; Dijcks, F. A.; Boots, A. M. H. Suppression of the inflammatory response in experimental arthritis is mediated via estrogen receptor alpha but not estrogen receptor beta. *Arthritis Res. Ther.* **2009**, *12*, R101−R101.
(34) Marotte, H.; Ruth, J. H.; Campbell, P. L.; Koch, A. E.; Ahmed, S. Green tea extract inhibits chemokine production, but up-regulates chemokine receptor expression, in rheumatoid arthritis synovial fibroblasts and rat adjuvant-induced arthritis. *Rheumatology* **2010**, *49*, 467−479.
(35) Asagoe, K.; Yamamoto, K.; Takahashi, A.; Suzuki, K.; Maeda, A.; Nohgawa, M.; Harakawa, N.; Takano, K.; Mukaida, N.; Matsushima, K.; Okuma, M.; Sasada, M. Down-regulation of CXCR2 expression on human polymorphonuclear leukocytes by TNF alpha. *J. Immunol.* **1998**, *160*, 4518−4525.
(36) Ye, J.; Liu, Z.; Wei, J.; Lu, L.; Huang, Y.; Luo, L.; Xie, H. Protective effect of SIRT1 on toxicity of microglial-derived factors induced by LPS to PC12 cells via the p53-caspase-3-dependent apoptotic pathway. *Neurosci. Lett.* **2013**, *553*, 72−77.
(37) Keller, M.; Mazuch, J.; Abraham, U.; Eom, G.; Herzog, E.; Volk, H. D.; Kramer, A.; Maier, B. A circadian clock in macrophages controls inflammatory immune responses. *Proc. Natl. Acad. Sci. U. S. A.* **2009**, *106*, 21407−21412.
(38) Daigneault, M.; Preston, J. A.; Marriott, H. M.; Whyte, M. K. B.; Dockrell, D. H. The identification of markers of macrophage differentiation in PMA-stimulated THP-1 cells and monocyte-derived macrophages (macrophage differentiation). *PLoS One* **2010**, *5*, e8668.
(39) Joven, J.; Rull, A.; Rodriguez-Gallego, E.; Camps, J.; Riera-Borrull, M.; Hernández-Aguilera, A.; Martin-Paredero, V.; Segura-Carretero, A.; Micol, V.; Alonso-Villaverde, C.; Menéndez, J. A. Multifunctional targets of dietary polyphenols in disease: A case for the chemokine network and energy metabolism. *Food Chem. Toxicol.* **2013**, *51*, 267−279.
(40) Zhu, J.; Yong, W.; Wu, X.; Yu, Y.; Lv, J.; Liu, C.; Mao, X.; Zhu, Y.; Xu, K.; Han, X. Anti-inflammatory effect of resveratrol onTNFa-induced MCP-1 expression in adipocytes. *Biochem. Biophys. Res. Commun.* **2008**, *369*, 471−477.
(41) Yang, C. J.; Lin, C. Y.; Hsieh, T. C.; Olson, S. C.; Wu, J. M. Control of eotaxin-1 expression and release by resveratrol and its metabolites in culture human pulmonary artery endothelial cells. *Am. J. Cardiovasc. Dis.* **2011**, *1*, 16−30.

DOI: 10.1021/acs.jafc.5b01830
J. Agric. Food Chem. 2015, 63, 6535−6545

(42) Jang, S. I.; Kim, Y.-J.; Kim, H. J.; Lee, J.-C.; Kim, H.-Y.; Kim, Y.-C.; Yun, Y.-g.; Yu, H.-H.; You, Y.-O. Scoparone inhibits PMA-induced IL-8 and MCP-1 production through suppression of NF-κB activation in U937 cells. *Life Sci.* **2006**, *78*, 2937−2943.
(43) Aires, V.; Limagne, E.; Cotte, A. K.; Latruffe, N.; Ghiringhelli, F.; Delmas, D. Resveratrol metabolites inhibit human metastatic colon cancer cells progression and synergize with chemotherapeutic drugs to induce cell death. *Mol. Nutr. Food Res.* **2013**, *57*, 1170−1181.
(44) Liao, Y.; Lin, J. Quercetin, but not its metabolite quercetin-3-glucuronide, exerts prophylactic immunostimulatory activity and therapeutic antiinflammatory effects on lipopolysaccharide-treated mouse peritoneal macrophages ex vivo. *J. Agric. Food Chem.* **2014**, *62*, 2872−2880.
(45) Hoshino, J.; Park, E. J.; Kondratyuk, T. P.; Marler, L.; Pezzuto, J. M.; Van Breemen, R. B.; Mo, S.; Li, Y.; Cushman, M. Selective synthesis and biological evaluation of sulfate-conjugated resveratrol metabolites. *J. Med. Chem.* **2010**, *53*, 5033−5043.
(46) Haringman, J. J.; Gerlag, D. M.; Smeets, T. J. M.; Baeten, D.; Van Den Bosch, F.; Bresnihan, B.; Breedveld, F. C.; Dinant, H. J.; Legay, F.; Gram, H.; Loetscher, P.; Schmouder, R.; Woodworth, T.; Tak, P. P. A randomized controlled trial with an anti-CCL2 (anti-monocyte chemotactic protein 1) monoclonal antibody in patients with rheumatoid arthritis. *Arthritis Rheum.* **2006**, *54*, 2387.
(47) Richardson, R. M.; Pridgen, B. C.; Haribabu, B.; Ali, H.; Snyderman, R. Differential cross-regulation of the human chemokine receptors CXCR1 and CXCR2. Evidence for time-dependent signal generation. *J. Biol. Chem.* **1998**, *273*, 23826−23830.
(48) Pilakka-Kanthikeel, S.; Napuri, J.; Nair, M. P. N. Cocaine down regulates microRNA-146a with a reciprocal up-regulation of CXCR-4: Implications in HIV immunopathogenesis. *J. Neuroimmune Pharm.* **2012**, *7*, S49.
(49) Andersen, G.; Burkon, A.; Sulzmaier, F. J.; Walker, J. M.; Leckband, G.; Fuhst, R.; Erbersdobler, H. F.; Somoza, V. High dose of dietary resveratrol enhances insulin sensitivity in healthy rats but does not lead to metabolite concentrations effective for SIRT1 expression. *Mol. Nutr. Food Res.* **2011**, *55*, 1197−1206.
(50) Kuhnle, G.; Spencer, J. P. E.; Chowrimootoo, G.; Schroeter, H.; Debnam, E. S.; Srai, S. K. S.; Rice-Evans, C.; Hahn, U. Resveratrol is absorbed in the small intestine as resveratrol glucuronide. *Biochem. Biophys. Res. Commun.* **2000**, *272*, 212−217.

DOI: 10.1021/acs.jafc.5b01830
J. Agric. Food Chem. 2015, 63, 6535−6545

proteins provide an alternative method. Some recombinant prolamin allergens have already been produced and characterized.[20,21,27−31] Well-defined protein fragments can also be produced by heterologous expression, and such recombinant fragments have been valuable for studying the antigenicity of LMW glutenin subunits and their two domains[30] as well as fragments of high-molecular-weight (HMW) glutenins.[27]

The present work aims to further characterize the structural features linked to allergenicity of proteins belonging to the prolamin superfamily by focusing on two members: α- and γ-gliadins. Different forms (natural/recombinant; native/reduced-alkylated) and fragments (Nt- and Ct-) of α- and γ-gliadins were produced to study the contribution of their structural domains and disulfide bonds to IgE binding. Their secondary structure was determined using synchrotron radiation circular dichroism (SRCD); sera from patients with food allergies to wheat (FAW) or baker's asthma (BA) were used to analyze IgE binding.

MATERIALS AND METHODS

PCR Cloning of Whole Gliadins cDNA and of Their Moieties. rAG has been previously cloned.[29] The same procedure was used for cloning recombinant γ-gliadin. Briefly, total RNA was extracted from immature (14 days before anthesis) wheat grains (Neepawa cultivar). α-Gliadin (rAG) and γ-gliadin (rGG) cDNA were cloned by RT-PCR. First-strand cDNA was synthesized with using Superscript II system (Invitrogen, Carlsbad, CA, USA) containing an oligo-dT and adapter primers. PCR was done using primers described in ref 29 chosen according to dETS sequences found in databases or already cloned γ-gliadin (ID Q94G94) cDNA.[32] Their Nt- and Ct-moieties (rNt-AG, rAG-Ct, rNt-GG, and rGG-Ct) were cloned by PCR using full-length α- and γ-gliadin cDNA clones as templates. The DNA polymerase used was AccuPrime Pfx (Life Technologies). Fragments were cloned with restriction enzymes into a pET28b (Novagen) plasmid in frame with a sequence encoding the hexahistidine Tag (His-Tag). The sequences of the specific primers used in the cloning procedure are described in Supporting Information Table S.1 and in ref 29.

Production and Purification of Natural or Recombinant Gliadins and Fragments. Natural α- and γ-gliadins (nAG and nGG) were prepared from wheat flour (cultivar Recital) by several steps of chromatography.[15] The γ-gliadin corresponded to the γ46 fraction described in ref 33. When indicated, natural proteins were used after reduction/alkylation. After solubilization in 0.5 M Tris-HCl, pH 8.5, containing 8 M urea and 0.01 M EDTA, they were reduced with 0.1 M dithiothreitol (DTT) for 2 h at 37 °C and then alkylated with iodoacetamide in 0.5 M NaOH for 30 min in the dark. *Escherichia coli* strain Rosetta (Novagen) was used for recombinant protein production. Bacteria were transformed with a plasmid encoding rAG or rGG or their domains. Protein production and purification were performed as described in ref 30 with standard culture and IPTG induction, lysis with lysozyme in the presence of RNase A and DNase I (Qiagen), and precipitation steps. Proteins were reduced with DTT and alkylated with iodoacetamide during purification to increase extraction yields except when native full-length proteins were produced.

The purity of materials was checked by SDS-PAGE on a 15% w/w gel; 5 μg of proteins was loaded on the gel, and the proteins were stained with Coomassie Brilliant Blue R250. The presence of Nt-histidines in recombinant proteins was confirmed by Western blot using an anti-HisTag antibody.

Natural α-Gliadin Identification by Mass Spectrometry. nAG (3 mg/mL) was hydrolyzed at 37 °C for 6 h using porcine trypsin (Sigma T8253) and chymotrypsin (Sigma C 4879) in 25 mM NH_4HCO_3 at an enzyme/substrate ratio of 1:100 w/w. The resulting hydrolysate was reduced by mixing with 10 mM DTT and 10% acetonitrile at 45 °C for 1 h in the dark with gentle stirring. After the sample had cooled to room temperature, 0.5 M iodoacetamide was added, and the sample was incubated for 30 min in the dark. Following reduction/alkylation, the peptides were diluted 10 times in water; subsequently, 50 μL of the solution was eluted on C18 resin pipet tips (ZipTip, Millipore Corp, Billerica, MA, USA), cleaned, and finally extracted from the Zip Tip with 30 μL of 1:1 acetonitrile/water containing 0.05% formic acid. The acetonitrile was then evaporated on a Speed Vac, and the sample was stored for mass spectrometry analysis.

Nanoscale capillary liquid chromatography−tandem mass spectrometry (LC-MS/MS) analyses were performed using an Ultimate U3000 RSLC system (Dionex) coupled with an LTQ-Orbitrap VELOS mass spectrometer (Thermo Fisher). Chromatographic separation and mass data acquisition were performed as described in ref 34. Protein identification was performed using the Mascot database search engine and the UniProt databank, which was restricted to *Triticum aestivum* sequences (release 2015_01). Mass tolerance for peptide precursors was set at 5 ppm, with the fragment mass tolerance set at 0.5 Da. Enzyme specificity was set to trypsin and chymotrypsin with a maximum of one missed cleavage. Proteins were identified with at least three peptides according to the above specifications.

Synchrotron Radiation Circular Dichroism (SRCD). Measurements were taken using the DISCO beamline at Soleil synchrotron (Gif-sur-Yvette, France). The samples were prepared in 50 mM sodium phosphate buffer, pH 8, containing 2% SDS and 10 mM sodium sulfate (typical range = 0.5−1.5 g/L). Data acquisition and processing were recorded as previously described.[35] Ratios of secondary structures were determined using the ContinLL program[36] in Dichroweb[37] and SP175 or Set5 as reference sets on the mean spectra from five measurements. Normalized root-mean-square deviation (NRMSD) indicated the most accurate fit for each spectrum; values <0.25 were considered significant.

Sera from Allergic Patients. Sera from 25 patients with FAW and from 5 patients with baker's asthma (BA) were selected on the basis of the presence of gliadin (nAG or nGG) specific IgE as determined by ELISA (Supporting Information Table S.2). All patients with BA were adults and presented rhinitis and asthma. Except for one adult, all patients with FAW were children. Their symptoms included atopic eczema dermatitis syndrome, anaphylaxis, asthma, urticaria, or gastrointestinal disorders. Sensitization to wheat proteins was assessed in patients using skin prick tests (SPT) to wheat flour (Moulins Soufflet), gluten (ALK-Abello), and natural gliadins and/or using specific IgE assays to wheat flour or gluten (Phadia ImmunoCAP). A wheat allergy was confirmed by a positive challenge or evident effect of wheat avoidance. The double-blind placebo-controlled food challenge and the inhalation challenge with wheat flour are described in refs38 and 4, respectively. Blood collection, SPT, and challenges were performed with the informed consent of the patients or their parents and after receiving approval from the biomedical research by the Ethics Committee of Ile de France III and AFSSAPS (Authorization 2008-A01565-50).

IgE Binding to Gliadins and Their Domains. Specific IgE concentrations toward the different forms of AG and GG (natural/recombinant; native/reduced-alkylated) and their Nt- or Ct-domains were determined by F-ELISA as described in ref 39 using alkaline phosphatase-conjugated goat anti-human IgE and 4-MUP as a substrate (Sigma A3525 and A3168, respectively, Saint-Quentin Fallavier, France). Proteins solubilized in PBS were coated at 5 mg/L in carbonate buffer on white 384-well plates (NUNC 460372, Fischer Scientific).

IgE Binding to Solid-Phase Synthetic Peptides (Pepscan). Sera containing high levels of specific IgE toward the gliadins and their domains (n = 6 for AG and n = 5 for GG) and three control sera from nonatopic subjects were used in the Pepscan analysis as described in ref 39. Decapeptides, overlapping on eight amino acid residues, spanned the full-length sequences of α- and γ-gliadins (UniProt ID P04725 and P08453, respectively), which were already used in previous Pescan analysis.[4,22]

Activation of RBL Cells by α-Gliadins and Their Domains. Rat basophil leukemia (RBL SX38) cell degranulation was expressed as the percentage of β-hexosaminidase release with a positive threshold set at

DOI: 10.1021/acs.jafc.5b01922
J. Agric. Food Chem. 2015, 63, 6546−6554

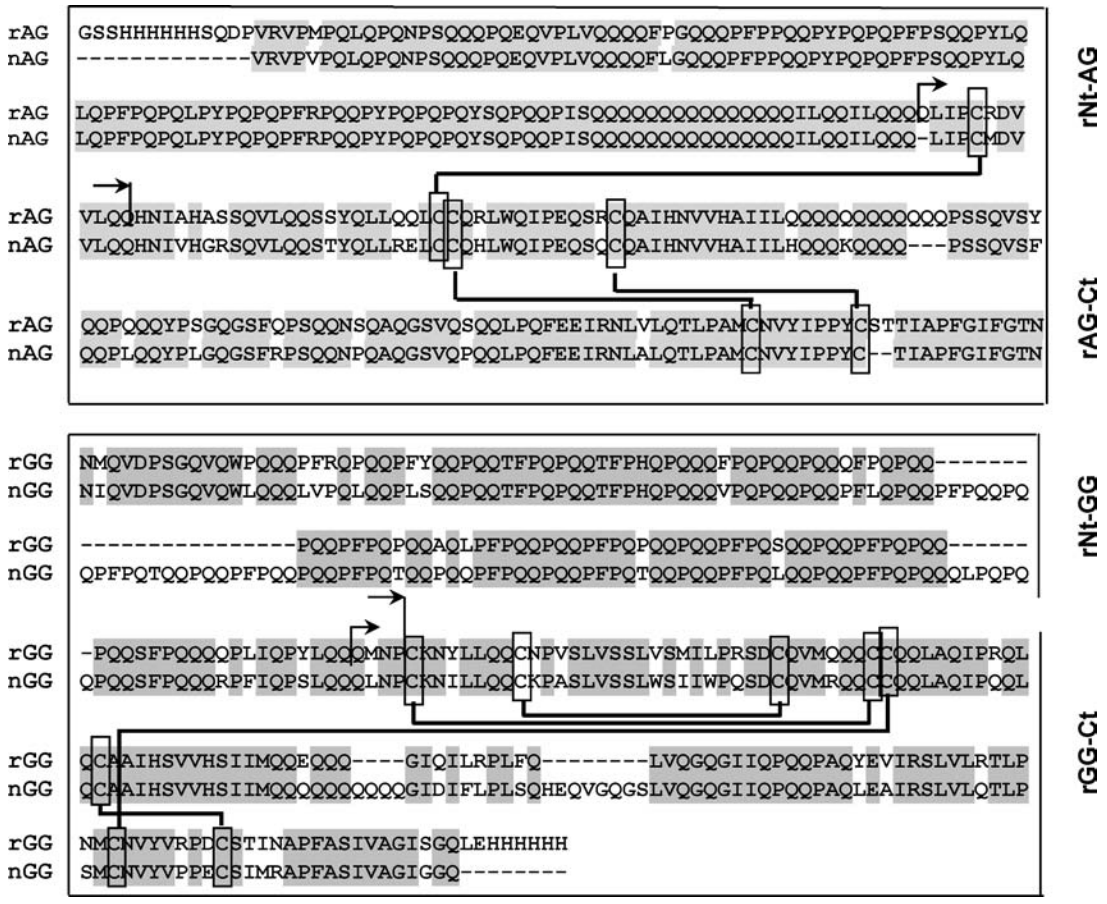

Figure 1. Comparison of the sequences of the recombinant proteins, α-gliadin (rAG) and γ-gliadin (rGG), and of the natural proteins, Uniprot ID Q3S4 V7 for α-gliadin and P08453 for γ-gliadin. The connections correspond to disulfide bonds between surrounded cysteine residues. The end of rNt-domains and the beginning of rCt-domains, (rNt-AG, rAG-Ct) and (rNt-GG, GG-Ct), are indicated by arrows. Identical amino acid residues are highlighted in gray.

11% as described in ref 39. Gliadin samples were tested at 2, 20, 200, and 2000 ng/mL with a pool of two sera (899 + 907) diluted 1:10.

Statistical Analysis. Statistical analyses were performed using GraphPad Prism version 5.04 for Windows (GraphPad Software, San Diego, CA, USA). For the ELISA results, paired tests were performed, and each pairing was confirmed to be significantly effective. Both specific IgE distributions and their paired differences failed the d'Agostino−Pearson omnibus normality test. Wilcoxon signed rank tests or Friedman tests with Dunn's multiple comparisons were then performed to compare the medians ; p values <0.05 were considered significant.

RESULTS

Characterization of Natural and Recombinant Gliadins and Their Domains. The full-length sequences of the recombinant and natural gliadins are shown in Figure 1. The recombinant α-gliadin (rAG) sequence (ID 1834759) shares 96% identity with the protein that was recorded under UniProt ID P02863.2. MS analysis of the natural α-gliadin (nAG) indicated that it contained in majority the α-gliadin ID Q3S4 V7, in addition to several minor isoforms of this protein. Sequence alignment revealed 95% similarity between rAG and nAG. In SDS-PAGE under reducing conditions, rAG migrated to approximately 45 kDa, whereas the nAG migrated to approximately 40 kDa (Figure 2). The sequence of recombinant protein rGG was deduced from its cloned cDNA sequence. It is identical to UniProt ID Q94G94.[32] The natural protein nGG corresponded to a γ46-gliadin type

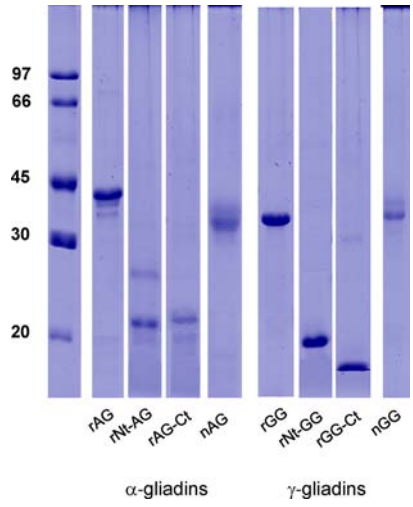

Figure 2. SDS-PAGE analysis of the proteins under reducing conditions colored with Coomassie Brilliant Blue R250. rAG and rGG, recombinant α-gliadin and γ-gliadin; rNt-AG, rNt-GG, rAG-Ct, and rGG-Ct, recombinant Nt- and Ct-domains of α-gliadin and γ-gliadin; nAG and nGG, natural α-gliadin and γ-gliadin.

according to its electrophoretic mobility in acid-PAGE and was previously described as P08453.[33] The rGG and nGG sequences displayed 80% similarity. Their mobility in SDS-PAGE was approximately 40 kDa. The Nt- and Ct-recombinant

DOI: 10.1021/acs.jafc.5b01922
J. Agric. Food Chem. 2015, 63, 6546−6554

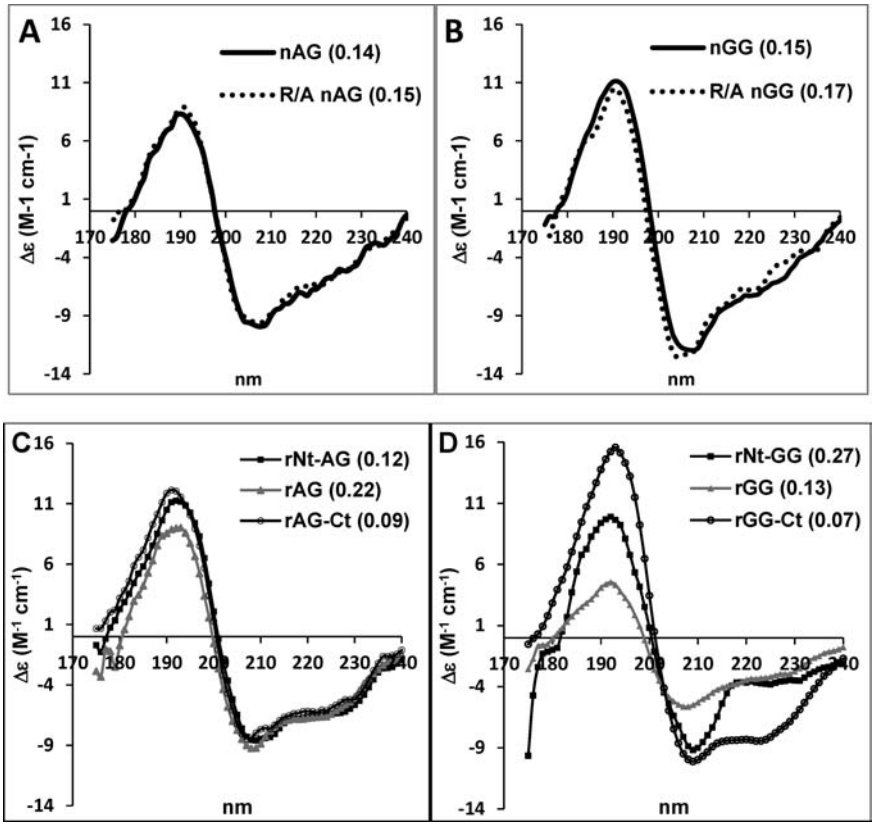

Figure 3. SRCD on natural and recombinant gliadins: spectra of native and reduced alkylated (R/A) natural α-gliadin (nAG) (A) and natural γ-gliadin (nGG) (B); spectra of recombinant full-length, N-terminal (Nt) and C-terminal (Ct) domains, (C) rAG and (D) rGG. NRMSDs are indicated in parentheses.

domains each constitute approximately half of a gliadin protein and migrated approximately 15−22 kDa. Despite their similar sizes, the mobility of the rNt-GG fragment (133 residues) differed that of the rGG-Ct fragment (136 residues). The molecular weights of the prolamins are often overestimated by SDS-PAGE, which has been attributed to the high content of proline in their Nt-repetitive domains.[10]

Secondary Structures of Natural and Recombinant Gliadins and Their Domains. The secondary structure contents of gliadins and of their domains were calculated after the deconvolution of the CD spectra. Low NRMSD values were obtained except for the rNt-GG domain (0.27).

The CD spectra of α-gliadins presented minimal values in the 206−208 and 220−224 nm regions, which reflects the α-helical structures. nAG contained approximately 35% α-helix, 18% turns, and a low level of β-strand. Reduction/alkylation of the protein did not affect the dichroic signal (Figure 3A). rAG and its domains displayed similar dichroic signals (Figure 3C) corresponding to a higher level of α-helix (52−58%) and a lower level of turn structures (11%) compared with nAG.

The secondary structure contents of nGG were approximately 25% α-helix and 16% β-strand and turns, and the reduction/alkylation of nGG did not change the CD spectrum (Figure 3B). The recombinant rGG contained slightly more α-helix (37%) and fewer strands (11%) than did nGG. Unlike rAG, full-length rGG and its Nt- and Ct-domains displayed different spectra (Figure 3D). The rGG-Ct domain is notably folded in α-helices (67%). The CD spectrum of the repetitive rNt-GG domain showed an unusual negative peak at 210 nm, which is characteristic of turn structures. This spectrum could be only poorly deconvoluted with the currently available sets (NRMSD >0.25); hence, its secondary structure was not evaluated.

IgE Binding to Natural and Recombinant Gliadins and the Involvement of Disulfide Bonds. Sera from 28 patients with FAW or BA were used to compare IgE reactivity toward different forms of α-gliadins in an ELISA. As shown in Figure 4 (top), compared with nAG, the IgE binding to rAG was significantly reduced. The mean of the specific IgE concentration was reduced by 60%, but 25 of the 28 sera retained binding to rAG. Reduction/alkylation highly decreased the IgE binding to nAG: the mean reduction was approximately 70%, and 67% of the sera exhibited a reduction of >70%. Reduction/alkylation had a lower but significant impact on IgE binding to rAG, with a 30% reduction.

Sera from 20 patients with FAW were used to compare IgE reactivity toward γ-gliadins. The sera from the five patients with BA had no or very weak IgE reactivity toward nGG. As shown in Figure 4 (bottom), compared with nGG, IgE binding to rGG was reduced. The reduction in the mean specific IgE concentration was approximately 30%, and 18 of the 20 sera retained IgE binding after nGG had been replaced with rGG. The decrease in the mean specific IgE concentration induced by the reduction/alkylation of nGG was approximately 60%, and 37% of the sera exhibited a reduction >70%. In the case of rGG, a significant decrease of approximately 60% was also observed.

Involvement of Nt- and Ct-Domains in IgE Binding to Gliadins. The involvement of the two structural domains of gliadins in IgE binding was analyzed with recombinant

DOI: 10.1021/acs.jafc.5b01922
J. Agric. Food Chem. 2015, 63, 6546−6554

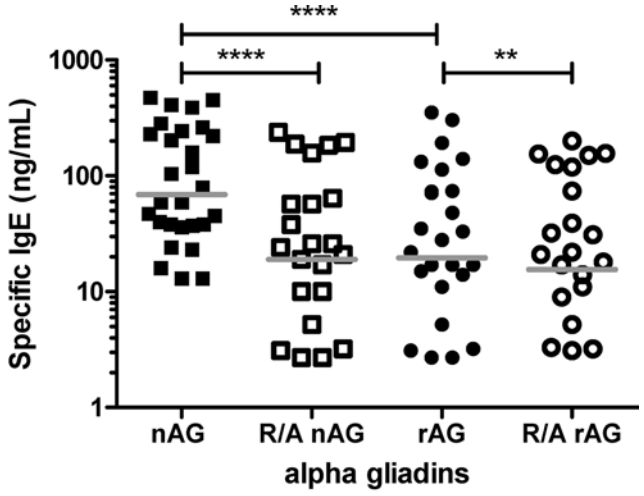

Mean	147	50	62	43
Median	69	19	20	16

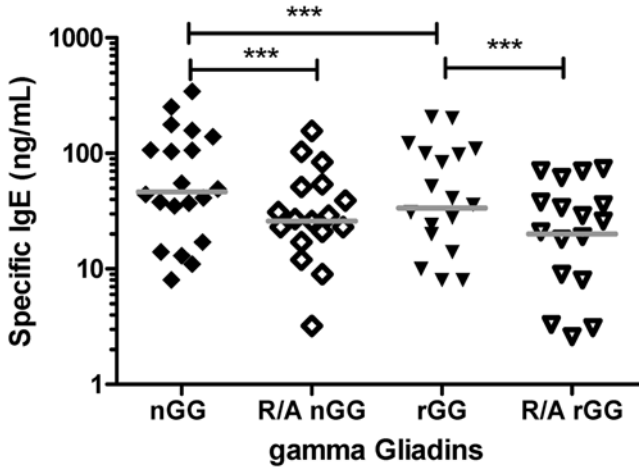

Mean	88	37	60	26
Median	47	26	34	20

Figure 4. Effect of heterologous expression and reduction/alkylation of natural and recombinant α-gliadins (top) and γ-gliadins (bottom) on IgE binding measured by ELISA. Means and medians per sample are indicated under the graph. Medians, plotted as gray bars, are significantly different (**, $0.001 < p < 0.01$; ***, $0.0001 < p < 0.001$; ****, $p < 0.0001$; Wilcoxon signed rank test, $n = 28$ for AG and $n = 20$ for GG). Fifteen data points (5 for R/A nAG, 3 for rAG, 7 for R/A rAG) and seven data points (2 for R/A nGG, 2 for rGG, 3 for R/A rGG) were below the detection limit and not included on the graphs.

repetitive domains (rNt) and nonrepetitive domains (rCt). rCt domains were extracted after the reduction/alkylation of cysteines. Because it was shown above that reduction/alkylation affected IgE binding to gliadins, comparisons were then performed with reduced/alkylated full-length recombinant gliadins, and only sera with positive IgE binding to R/A recombinant gliadins were considered (Figure 5). The IgE binding data were analyzed by a Friedman test, which indicated significant difference among full-length gliadins and their fragments ($p < 0.0001$; $F = 19.4$, $n = 21$ for AG and $F = 26.8$, $n = 17$ for GG). For both gliadins, a subsequent Dunn's comparison test comparing the domains with the full-length protein revealed that the differences for the Ct-domain (difference in rank sum = 28.0 for AG, 20.0 for GG) were significant but that the differences were not significant ($p > 0.05$) for the Nt-domain.

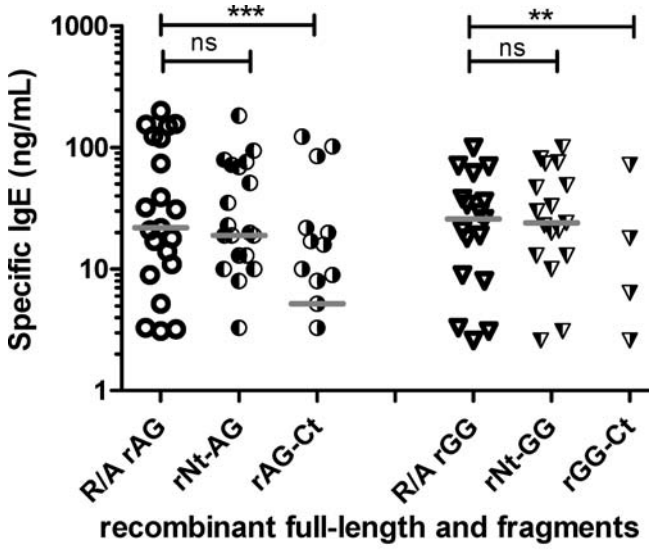

Mean	57	39	20	32	36	6
Median	22	19	5	26	24	0

Figure 5. Comparison of IgE binding to the full-length gliadins and to their N-terminal (Nt) or C-terminal (Ct) domains measured by ELISA. Means and medians per sample are indicated under the graph. Statistical differences between medians of specified groups using Friedman and Dunn's multiple comparison post test are indicated. Medians, plotted as gray bars, are significantly different (**, $0.001 < p < 0.01$; ***, $p < 0.001$; $n = 21$ for AG and 17 for GG) or not (ns, $p > 0.05$). Twenty-four data points (2 for rNt-AG, 9 for rAG-Ct, 13 for rGG-Ct) were below the detection limit and not included in the graph.

For the α-gliadins, the mean specific IgE concentration was twice as high for the rNt-AG as it was for rAG-Ct (39 and 20 ng/mL, respectively); IgE from 43% of sera did not bind the Ct-domain, whereas most sera reacted the Nt-domain. The sum of the mean specific IgE concentrations for the two domains was equivalent to the mean concentration for the full-length recombinant gliadin after reduction/alkylation (57 ng/mL). For the γ-gliadins, the rGG-Ct domain was rarely bound by specific IgE (only 25% of the sera). Conversely, all sera displayed IgE binding to the rNt-GG. The mean concentrations of specific IgE for rNt-GG and R/A rGG binding were equivalent (36 and 32 ng/mL).

The involvement of the two structural gliadin domains in IgE binding was also analyzed by searching for continuous epitopes within these sequences. As shown in Supporting Information Table S3, IgE from all six tested sera bound sequences belonging to the Nt-domain of α-gliadin, whereas two sera (no. 451 and 590) did not bind any sequence located in the Ct-domain. Generally, more spots were detected in the Nt-domain than in the Ct-domain. Stretches of peptides were detected by several sera: the sequences ^{1}VRVPVPQLQP^{10}, ^{25}VQQQQFPG^{32}, ^{53}QPYLQLQPFPQQPFPPQLP^{72}, and ^{77}QSFPPQQPYPQQ^{88} in the Nt-domain and the sequence ^{219}QQQPSSQVSFQQ^{230} in the Ct-domain.

DOI: 10.1021/acs.jafc.5b01922
J. Agric. Food Chem. 2015, 63, 6546−6554

The five sera tested on the γ-gliadin sequence displayed IgE binding to several peptides located in the Nt-domain, whereas only one serum (no. 899) displayed IgE binding to a sequence in the Ct-domain. The numerous epitopes in the Nt-domain corresponding to the consensus sequences PQQPFPQQPQ, LSQQPQQTFP, or QPQQ(S/T)FPQ were found with all sera, reflecting a higher homogeneity of repetition in γ-gliadin than in α-gliadin. There is no relationship between the number of peptides detected by Pepscan analysis and the IgE binding measured by ELISA toward the respective domains.

Triggering Potential of Natural, Recombinant, and Nt- and Ct-Fragments of α-Gliadin. The triggering potential of α-gliadin samples was assessed in an RBL assay using a pool of two sera that displayed high levels of specific IgE toward nAG (approximately 400 ng/mL), rAG (approximately 250 ng/mL), R/A nAG (approximately 200 ng/mL), R/A rAG (approximately 150 ng/mL), and the gliadin domains (70 ng/mL for rNt-AG and 100 ng/mL for rAG-Ct). Both nAG and rAG were able to induce cell degranulation in the presence of the pool of sera (Figure 6). However, maximum degranulation (approximately 35%) was obtained at a lower protein concentration for nAG (20 ng/mL) than for rAG (200 ng/mL). Reduced/alkylated nAG or rAG induced low degranulation at similar concentration (200 ng/mL), and none of the recombinant domains were able to induce degranulation above the positive threshold.

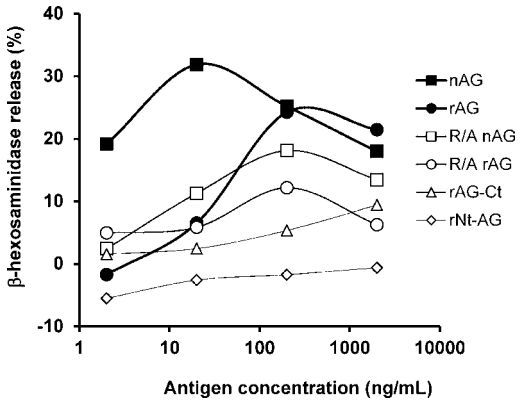

Figure 6. Triggering potential of natural and recombinant α-gliadins and domains tested in an RBL assay with a pool of two sera. Duplicate measurements were performed, and means are represented on the graph.

DISCUSSION

Wheat gliadins are frequently involved in FAW and occasionally involved in BA. This work aimed to elucidate the molecular structures responsible for IgE binding to α- and γ-gliadins by using a collection of sera from patients with FAW and BA and different preparations of gliadin proteins: natural and recombinant full-length proteins (native or reduced), recombinant fragments corresponding to the structural Nt- and Ct-domains, and synthetic peptides.

Like all wheat storage proteins, α- and γ-gliadins are polymorphic and have closely related sequences. The recombinant gliadins rAG and rGG displayed good sequence homology to the isoforms present in the natural AG and GG purified fractions. These recombinant proteins displayed higher contents in α-helical secondary structure (52% for rAG and 36% for rGG) compared with the natural fractions (36% for nAG and 25% for nGG). The results from SRCD are in accordance with the published data indicating that nAG contains primarily α-helical structure,[8,9,29] whereas nGG contains large amounts of α-helical and turn structures.[10,40]

The recombinant α-gliadin rAG showed reduced IgE binding compared with natural α-gliadin nAG, but 90% of the sera were still reactive. We also observed that rAG retained the capacity to induce basophil activation. A smaller reduction in IgE binding was observed for rGG compared to nGG. It is unlikely that these differences arise from the presence of post-translational modifications such as glycosylation, as no evidence of significant levels of glycosylation was found on the natural gliadins.[41] Different folding and a possibly incorrect formation of disulfide bonds by the heterologous expression in *E. coli* may be partly responsible for the different IgE reactivity. The small differences in sequences between the recombinant and natural isoforms (Figure 1) may also partly explain the difference in IgE reactivity. However, recombinant gliadins maintained the IgE reactivity for most sera, as recently reported for recombinant LMW glutenins.[28,30]

The disruption of disulfide bonds in AG and GG led to reduced IgE binding to these allergens for many sera. This disruption also reduced the degranulation potency of AG. Disulfide bonds are located in the Ct-domain of both proteins. Protein reduction likely disrupted some of the conformational epitopes. Only one sera (no. 901) bound to a cysteine-containing peptide of AG by Pepscan analysis. However, reduction may have an indirect but drastic effect on the global folding of the protein. When the proteins were reduced/alkylated, no significant effect was observed on the secondary structures of natural AG and GG. Reduction/alkylation likely modified the tertiary structures of these proteins but, unfortunately, all attempts to crystallize them failed. These results indicate that gliadins with their disulfide bonds are more IgE-reactive for many sera than are gliadins without disulfide bonds. The importance of disulfide bonds for IgE binding has already been shown for other allergens of the prolamin superfamily. For example, wheat LTP and peanut allergen Ara h 6 were poorly recognized by patient IgE after reduction of their disulfide bonds.[4,5] However, in the case of LTP and Ara h 6, secondary structures were also greatly affected by disulfide bond disruption, whereas in the present study, the CD spectra of α and γ-gliadins were not affected by this modification.

IgE binding to peptides and recombinant domains of AG indicated the presence of epitopic regions in both domains of this protein. Nevertheless, stronger binding to the Nt-domain compared with the Ct-domain was observed both by the Pepscan technique and using the recombinant domains. The secondary structure contents of the Nt- and Ct-domains were equivalent, with the high level of α-helix most likely due to the clusters of 13−15 glutamines present in both domains. Recombinant rNt-AG polypeptide and synthetic peptides may represent, to a certain extent, the natural Nt-domain folding, allowing IgE to cross-react with these different entities. Conversely, IgE cross-reactions between the natural Ct-domain and the corresponding (reduced) recombinant domain and synthetic peptides should be less likely. In the case of GG, this phenomenon was more pronounced because very low binding to the Ct-domain was observed by both Pepscan and ELISA using the recombinant domain, whereas numerous continuous epitopes were detected in the Nt-domain. The CD spectra clearly indicated that the two domains have different secondary

DOI: 10.1021/acs.jafc.5b01922
J. Agric. Food Chem. 2015, 63, 6546−6554

structures: the rNt-GG primarily contains turn structures, whereas the rGG-Ct contains a very high content of α-helix.

Despite sequence homologies and similarities in their organization, differences were observed in patients' reactivity toward α- and γ-gliadins: allergenicity of GG was less affected by the reduction of disulfide bridges and more pronounced toward its Nt-domain than in the case of AG. This could be linked to differences in the number and homogeneity of repeated motifs between gliadins.

The continuous epitopes identified in this study by Pepscan in AG confirmed some of the epitopes identified in previous works: PLVVQQQQFPGQQQQ, YLQLQPFPQP, and PAMCNVYIPP.[4,22] The present work supports the hypothesis that AG appears to contain both types of epitopes, with continuous epitopes primarily located in the repetitive sequence domain and discontinuous epitopes most likely in the Ct-domain.[4] Nt-repetitive domains were previously shown to be highly resistant to pepsin hydrolysis;[42] they could more efficiently stimulate the production of specific IgEs compared with the nonrepetitive domains. However, both domains and correctly formed disulfide bonds in the Ct-domain appeared to be required for AG to induce basophil degranulation. This result differs from the reported presence of continuous repetitive IgE epitopes in deamidated ω2-gliadins or fragments from the repetitive domain of HMW glutenin that could induce basophil degranulation.[27,43]

Using recombinant domains of gliadins is a complementary approach to synthetic peptides and expands the possibilities of epitope research by accounting, to a certain extent, for protein folding. The proteins in their native form should be preferentially used for IgE reactivity detection. As for other allergens of the prolamin superfamily, disulfide bond formation appears to be of importance for IgE binding to α- and γ-gliadins. Disulfide bonds in the Ct-domain most likely play a role in generating conformational epitopes within this domain or formed by a combination of residues from both domains. Indeed, studies with Nt- and Ct-fragments of LMW glutenin subunits demonstrated interactions between both parts and their significance in IgE binding.[30]

■ ASSOCIATED CONTENT

Supporting Information

Tables S1−S3. The Supporting Information is available free of charge on the ACS Publications website at DOI: 10.1021/acs.jafc.5b01922.

■ AUTHOR INFORMATION

Corresponding Author

*(S.D.-P.) Mail: INRA, UR1268 BIA, Rue de la Géraudière, B.P. 71627, 44316 Nantes cedex 3, France. Phone: (+33) 2 40 67 51 37. Fax: (+33) 2 40 67 50 25. E-mail: Sandra.denery@nantes.inra.fr.

Author Contributions

S.D.-P. conceived and coordinated the study; S.D.-P., H.M., J.-C.G., and J.S. participated in the design of the study; E.P., E.B., D.-A.M.-V., and M.D. recruited patients and performed clinical tests; H.M. carried out the experiments; V.S. and C.L. participated in the production/characterization of natural proteins; R.L. performed RBL studies; Y.G. and F.W. supervised CD studies; C.B. analyzed Pepscan results and performed the statistical analysis; S.D.-P., H.M., and C.B. wrote the manuscript. All authors helped to revise the manuscript and concur with the submission.

Funding

This work and H.M.'s fellowship was supported by the French grant ANR ALIA program Predexpitope (ANR-08ALIA-014).

Notes

The authors declare no competing financial interest.

■ ACKNOWLEDGMENTS

We thank Florence Pineau and Laurence Lavenant for their technical assistance, G. Branlard, INRA, UMR ASP-UBP, Clermont-Ferrand, and B. Rolland and J. P. Lemonnier, INRA, UMR IGEPP, Rennes, France, for providing wheat grains, H. Rogniaux (INRA, UR BIA BIBS platform) for MS analysis, and T. Mothes (University Hospital, Leipzig, Germany) for the supply of Pepscan membranes. CD measurements on DISCO beamline at the SOLEIL synchrotron facility were performed under proposal 20110666.

■ ABBREVIATIONS USED

AG, α-gliadin; GG, γ-gliadin; nAG, natural α-gliadin; rAG, recombinant α-gliadin; nGG, natural γ-gliadin; rGG, recombinant γ-gliadin; Nt, N-terminal; Ct, C-terminal; rNt-AG, N-terminal domain of α-gliadin; rNt-GG, N-terminal domain of γ-gliadin; rAG-Ct, C-terminal domain of α-gliadin; rGG-Ct, C-terminal domain of γ-gliadin; ATI, α-amylase/trypsin inhibitors; LTP, nonspecific lipid transfer proteins; SRCD, circular dichroism synchrotron radiation; FAW, food allergy to wheat; BA, baker's asthma; RBL cells, rat basophil leukemia cells; LMW or HMW, low or high molecular weight; SPT, skin prick test; R/A, reduced and alkylated

■ REFERENCES

(1) Radauer, C.; Breiteneder, H. Evolutionary biology of plant food allergens. *J. Allergy Clin. Immunol.* **2007**, *120* (3), 518−525.

(2) Radauer, C.; Bublin, M.; Wagner, S.; Mari, A.; Breiteneder, H. Allergens are distributed into few protein families and possess a restricted number of biochemical functions. *J. Allergy Clin. Immunol.* **2008**, *121* (4), 847−852.e7.

(3) Tatham, A. S.; Shewry, P. R. The conformation of wheat gluten proteins. The secondary structures and thermal stabilities of α-, β-, γ- and ω-gliadins. *J. Cereal Sci.* **1985**, *3* (2), 103−113.

(4) Denery-Papini, S.; Bodinier, M.; Pineau, F.; Triballeau, S.; Tranquet, O.; Adel-Patient, K.; Moneret-Vautrin, D. A.; Bakan, B.; Marion, D.; Mothes, T.; Mameri, H.; Kasarda, D. Immunoglobulin-E-binding epitopes of wheat allergens in patients with food allergy to wheat and in mice experimentally sensitized to wheat proteins. *Clin. Exp. Allergy* **2011**, *41* (10), 1478−1492.

(5) Hazebrouck, S.; Guillon, B.; Drumare, M. F.; Paty, E.; Wal, J. M.; Bernard, H. Trypsin resistance of the major peanut allergen Ara h 6 and allergenicity of the digestion products are abolished after selective disruption of disulfide bonds. *Mol. Nutr. Food Res.* **2012**, *56* (4), 548−557.

(6) Wijesinha-Bettoni, R.; Alexeev, Y.; Johnson, P.; Marsh, J.; Sancho, A. I.; Abdullah, S. U.; Mackie, A. R.; Shewry, P. R.; Smith, L. J.; Mills, E. N. C. The structural characteristics of nonspecific lipid transfer proteins explain their resistance to gastroduodenal proteolysis. *Biochemistry* **2010**, *49* (10), 2130−2139.

(7) Ang, S.; Kogulanathan, J.; Morris, G. A.; Kok, M. S.; Shewry, P. R.; Tatham, A. S.; Adams, G. G.; Rowe, A. J.; Harding, S. E. Structure and heterogeneity of gliadin: a hydrodynamic evaluation. *Eur. Biophys. J.* **2010**, *39* (2), 255−261.

(8) Blanch, E. W.; Kasarda, D. D.; Hecht, L.; Nielsen, K.; Barron, L. D. New insight into the solution structures of wheat gluten proteins from Raman optical activity. *Biochemistry* **2003**, *42* (19), 5665−5673.

DOI: 10.1021/acs.jafc.5b01922
J. Agric. Food Chem. 2015, 63, 6546−6554

(9) Wong, B. T.; Zhai, J.; Hoffmann, S. r. V.; Aguilar, M.-I.; Augustin, M.; Wooster, T. J.; Day, L. Conformational changes to deamidated wheat gliadins and β-casein upon adsorption to oil-water emulsion interfaces. *Food Hydrocolloids* **2012**, *27* (1), 91−101.
(10) Tatham, A. S.; Masson, P.; Popineau, Y. Conformational studies of peptides derived by the enzymic hydrolysis of a gamma-type gliadin. *J. Cereal Sci.* **1990**, *11* (1), 1−13.
(11) Camarca, A.; Anderson, R. P.; Mamone, G.; Fierro, O.; Facchiano, A.; Costantini, S.; Zanzi, D.; Sidney, J.; Auricchio, S.; Sette, A.; Troncone, R.; Gianfrani, C. Intestinal T Cell Responses to gluten peptides are largely heterogeneous: implications for a peptide-based therapy in celiac disease. *J. Immunol.* **2009**, *182* (7), 4158−4166.
(12) Jacquenet, S.; Morisset, M.; Battais, F.; Denery-Papini, S.; Croizier, A.; Baudouin, E.; Bihain, B.; Moneret-Vautrin, D. A. Interest of ImmunoCAP system to recombinant omega-5 gliadin for the diagnosis of exercise-induced wheat allergy. *Int. Arch. Allergy Immunol.* **2009**, *149* (1), 74−80.
(13) Matsuo, H.; Dahlstrom, J.; Tanaka, A.; Kohno, K.; Takahashi, H.; Furumura, M.; Morita, E. Sensitivity and specificity of recombinant omega-5 gliadin-specific IgE measurement for the diagnosis of wheat-dependent exercise-induced anaphylaxis. *Allergy* **2008**, *63* (2), 233−236.
(14) Shibata, R.; Nishima, S.; Tanaka, A.; Borres, M. P.; Morita, E. Usefulness of specific IgE antibodies to omega-5 gliadin in the diagnosis and follow-up of Japanese children with wheat allergy. *Ann. Allergy, Asthma, Immunol.* **2011**, *107* (4), 337−343.
(15) Battais, F.; Courcoux, P.; Popineau, Y.; Kanny, G.; Moneret-Vautrin, D. A.; Denery-Papini, S. Food allergy to wheat: differences in IgE-Binding proteins as a function of age and symptoms. *J. Cereal Sci.* **2005**, *42*, 109−117.
(16) Battais, F.; Pineau, F.; Popineau, Y.; Aparicio, C.; Kanny, G.; Guerin, L.; Moneret-Vautrin, D. A.; Denery-Papini, S. Food allergy to wheat: identification of immunogloglin E and immunoglobulin G-binding proteins with sequential extracts and purified proteins from wheat flour. *Clin. Exp. Allergy* **2003**, *33* (7), 962−970.
(17) Hofmann, S. C.; Fischer, J.; Eriksson, C.; Bengtsson Gref, O.; Biedermann, T.; Jakob, T. IgE detection to $\alpha/\beta/\gamma$-gliadin and its clinical relevance in wheat-dependent exercise-induced anaphylaxis. *Allergy* **2012**, *67* (11), 1457−1460.
(18) Mäkelä, M. J.; Eriksson, C.; Kotaniemi-Syrjänen, A.; Palosuo, K.; Marsh, J.; Borres, M.; Kuitunen, M.; Pelkonen, A. S. Wheat allergy in children − new tools for diagnostics. *Clin. Exp. Allergy* **2014**, *44* (11), 1420−1430.
(19) Waga, J.; Obtulowicz, K.; Zientarski, J. B. B.; Czarnobilska, E.; Stachowicz, M. Purified wheat gliadin proteins as immunoglobulin E binding factors in wheat mediated allergies. *Am. J. Plant Sci.* **2011**, *2*, 476−483.
(20) Bittner, C.; Grassau, B.; Frenzel, K.; Baur, X. Identification of wheat gliadins as an allergen family related to baker's asthma. *J. Allergy Clin. Immunol.* **2008**, *121* (3), 744−749.
(21) Sander, I.; Rozynek, P.; Rihs, H.-P.; van Kampen, V.; Chew, F. T.; Lee, W. S.; Kotschy-Lang, N.; Merget, R.; Brüning, T.; Raulf-Heimsoth, M. Multiple wheat flour allergens and cross-reactive carbohydrate determinants bind IgE in baker's asthma. *Allergy* **2011**, *66* (9), 1208−1215.
(22) Battais, F.; Mothes, T.; Moneret-Vautrin, D. A.; Pineau, F.; Kanny, G.; Popineau, Y.; Bodinier, M.; Denery-Papini, S. Identification of IgE-binding epitopes on gliadins for patients with food allergy to wheat. *Allergy* **2005**, *60*, 815−821.
(23) Matsuo, H.; Morita, E.; Tatham, A. S.; Morimoto, K.; Horikawa, T.; Osuna, H.; Ikezawa, Z.; Kaneko, S.; Kohno, K.; Dekio, S. Identification of the IgE-binding epitope in omega-5 gliadin, a major allergen in wheat-dependent exercise-induced anaphylaxis. *J. Biol. Chem.* **2004**, *279* (13), 12135−12140.
(24) Tanabe, S. IgE-binding abilities of pentapeptides, QQPFP and PQQPF, in wheat gliadin. *J. Nutr. Sci. Vitaminol.* **2004**, *50* (5), 367−370.
(25) Dupont, F. M.; Vensel, W. H.; Tanaka, C. K.; Hurkman, W. J.; Altenbach, S. B. Deciphering the complexities of the wheat flour proteome using quantitative two-dimensional electrophoresis, three proteases and tandem mass spectrometry. *Proteome Sci.* **2011**, *9*, 10.
(26) Metakovsky, E. V. Gliadin allele identification in common wheat II. Catalogue of gliadin alleles in common wheat. *J. Genet. Breed* **1991**, *45*, 325−344.
(27) Baar, A.; Pahr, S.; Constantin, C.; Giavi, S.; Papadopoulos, N. G.; Pelkonen, A. S.; Makela, M.; Scheiblhofer, S.; Thalhamer, J.; Weber, M.; Ebner, C.; Mari, A.; Vrtala, S.; Valenta, R. The high molecular weight glutenin subunit Bx7 allergen from wheat contains repetitive IgE epitopes. *Allergy* **2014**, *69* (10), 1316−1323.
(28) Baar, A.; Pahr, S.; Constantin, C.; Scheiblhofer, S.; Thalhamer, J.; Giavi, S.; Papadopoulos, N. G.; Ebner, C.; Mari, A.; Vrtala, S.; Valenta, R. Molecular and immunological characterization of Tri a 36, a low molecular weight glutenin, as a novel major wheat food allergen. *J. Immunol.* **2012**, *189* (6), 3018−3025.
(29) Mameri, H.; Bouchez, I.; Pecquet, C.; Raison-Peyron, N.; Choudat, D.; Chabane, H.; Kerre, S.; Denery-Papini, S.; Gohon, Y.; Briozzo, P.; Laurière, M.; Snégaroff, J. A Recombinant ω-gliadin-like D-type glutenin and an α-gliadin from wheat (*Triticum aestivum*): two immunoglobulin E binding proteins, useful for the diagnosis of wheat-dependent allergies. *J. Agric. Food Chem.* **2012**, *60* (32), 8059−8068.
(30) Mameri, H.; Snégaroff, J.; Gohon, Y.; Pecquet, C.; Choudat, D.; Raison-Peyron, N.; Denery-Papini, S.; Wien, F.; Briozzo, P. Immunoglobulin-E reactivity and structural analysis of wheat low-molecular-weight glutenin subunits and their repetitive and non-repetitive halves. *J. Agric. Food Chem.* **2012**, *60* (30), 7538−7547.
(31) Matsuo, H.; Kohno, K.; Morita, E. Molecular cloning, recombinant expression and IgE-binding epitope of ω-5 gliadin, a major allergen in wheat-dependent exercise-induced anaphylaxis. *FEBS J.* **2005**, *272* (17), 4431−4438.
(32) Arentz-Hansen, H.; Körner, R.; Molberg, Ø.; Quarsten, H.; Vader, W.; Kooy, Y. M. C.; Lundin, K. E. A.; Koning, F.; Roepstorff, P.; Sollid, L. M.; McAdam, S. N. The intestinal T cell response to α-gliadin in adult celiac disease is focused on a single deamidated glutamine targeted by tissue transglutaminase. *J. Exp. Med.* **2000**, *191* (4), 603−612.
(33) Egorov, T.; Odintsova, T.; Musolyamov, A.; Barbashov, S.; Pustobaev, V.; Andersen, J.; Roepstorff, P.; Popineau, Y. Partial amino acid sequence of γ-46 gliadin. *Biokhimia* **1998**, *63* (9), 1061−1067.
(34) Lupi, R.; Masci, S.; Rogniaux, H.; Tranquet, O.; Brossard, C.; Lafiandra, D.; Moneret-Vautrin, D. A.; Denery-Papini, S.; Larré, C. Assessment of the allergenicity of soluble fractions from GM and commercial genotypes of wheats. *J. Cereal Sci.* **2014**, *60*, 179−186.
(35) Vindigni, J.-D.; Wien, F.; Giuliani, A.; Erpapazoglou, Z.; Tache, R.; Jagic, F.; Chardot, T.; Gohon, Y.; Froissard, M. Fold of an oleosin targeted to cellular oil bodies. *Biochim. Biophys. Acta, Biomembr.* **2013**, *1828* (8), 1881−1888.
(36) Van Stokkum, I.; Spoelder, H.; Bloemendal, M.; Van Grondelle, R.; Groen, F. Estimation of protein secondary structure and error analysis from CD spectra. *Anal. Biochem.* **1990**, *191*, 110−118.
(37) Whitmore, L.; Wallace, B. A. DICHROWEB, an online server for protein secondary structure analyses from circular dichroism spectroscopic data. *Nucleic Acids Res.* **2004**, *32*, W668−W6773.
(38) Bensefa, L.; Villette, C.; Tabka, F.; Causse-Sounillac, E.; Fabries, J. F.; Choudat, D. Rye flour induces a stronger early bronchial response than wheat flour in occupational asthma. *Allergy* **2004**, *59* (8), 833−838.
(39) Mameri, H.; Denery-Papini, S.; Pietri, M.; Tranquet, O.; Larré, C.; Drouet, M.; Paty, E.; Jonathan, A.-M.; Beaudouin, E.; Moneret-Vautrin, D.-A.; Moreau, T.; Briozzo, P.; Gaudin, J.-C. Molecular and immunological characterization of wheat serpin (Tri a 33). *Mol. Nutr. Food Res.* **2012**, *56* (12), 1874−1883.
(40) Lullien-Pellerin, V.; Popineau, Y.; Meersman, F.; Morel, M. H.; Heremans, K.; Lange, R.; Balny, C. Reversible changes of the wheat gamma 46 gliadin conformation submitted to high pressures and temperatures. *Eur. J. Biochem./FEBS* **2001**, *268* (22), 5705−5712.
(41) Turner, J. B.; Garner, G. V.; Gordon, D. B.; Brookes, S. J.; Smith, C. A. Are α-gliadins glycosylated. *Protein Pept. Lett.* **2002**, *9* (1), 23−29.

DOI: 10.1021/acs.jafc.5b01922
J. Agric. Food Chem. 2015, 63, 6546−6554

(42) Masson, P.; Popineau, Y.; Pineau, F. Limited hydrolysis of γ-gliadin by pepsin: fractionation and partial characterisation of large polypeptides. *Lebensm.−Wiss. −Technology* **1989**, *22*, 157−163.
(43) Denery-Papini, S.; Bodinier, M.; Larré, C.; Brossard, C.; Pineau, F.; Triballeau, S.; Pietri, M.; Battais, F.; Mothes, T.; Paty, E.; Moneret-Vautrin, D.-A. Allergy to gluten isolates in patients tolerant to wheat: specific epitopes linked to deamidation. *Allergy* **2012**, *67* (8), 1023−1032.

DOI: 10.1021/acs.jafc.5b01922
J. Agric. Food Chem. 2015, 63, 6546−6554

reaction of gallic acid or ellagic acid with different reagents, were widely used.[15] Although these methods are simple and fast, they generally do not provide accurate quantitative data. Different high-performance liquid chromatography (HPLC) methods have been reported in the literature for the determination of phenolic compounds in pomegranate samples and related products.[14,16−18] However, most of them refer to compounds extracted in aqueous and hydroalcoholic extracts (extractable polyphenols), but ellagitannins can also remain unextracted in the extraction residue, as they can be partly soluble or insoluble in the extraction solvent or remain covalently bound to cell walls and other macromolecules of the fruit.[19,20]

In some fruits, ETs were previously quantified as total ellagic acid on the basis of the fact that when these compounds are exposed to acids or bases release hexahydroxydiphenic (HHDP) acid, which undergoes spontaneous lactonization to ellagic acid. Many authors have reported the total ellagic acid content after acid hydrolysis, mainly in berries and nuts.[21−24] Most of the existing procedures rely solely on the quantification of released ellagic acid, and only some of them[25] consider other compounds formed during hydrolysis, which may provide helpful information on the chemical structure of the naturally occurring ETs. Despite the numerous methods for acid hydrolysis described in the literature, an optimized and validated method for the determination of total ellagic acid and other reaction products in pomegranates after hydrolysis is still lacking.

The objectives of this study were (1) to optimize a method for a more complete characterization of pomegranate ETs by quantitating the ellagic acid and other reaction products released after acid hydrolysis, (2) to carry out an interlaboratory trial to examine the reproducibility of the method, and (3) to demonstrate the applicability of this method in pomegranate extracts and different parts of pomegranate fruits and juices.

MATERIALS AND METHODS

Chemicals and Samples. Standards of ellagic acid, punicalagin (≥98% HPLC purity), and gallic acid were obtained from Sigma-Aldrich (St. Louis, MO, USA). Vescalagin was kindly supplied by Prof. Stéphane Quideau, Université de Bordeaux, France. Methanol (MeOH) and acetonitrile were purchased from J. T. Baker (Deventer, The Netherlands), and dimethyl sulfoxide (DMSO) was from Labscan (Dublin, Ireland). Formic acid 98% and HCl 37% were obtained from Panreac (Barcelona, Spain). Ultrapure water from a Milli-Q system (Millipore Corp., Bedford, MA, USA) was used throughout this experiment. All chemicals and reagents were of analytical grade.

Eleven pomegranate extracts were supplied by Laboratorios Admira (Alcantarilla, Murcia, Spain). Pomegranate juice was provided by a juice processor (AMC, Murcia, Spain). Pomegranates of the cultivar 'Mollar' (Elche, Spain) were purchased in a supermarket. The fruits were manually separated into husk (pericarp), peels (membranes/mesocarp), and arils (containing the seeds) and then were freeze-dried and ground with a mixer grinder. The powders and extracts were kept in a desiccator prior to analyses.

Stock solutions of punicalagin (1 mM), vescalagin (0.5 mM), and gallic acid (10 mM) were prepared in MeOH, and ellagic acid (3 mM) was dissolved in DMSO. Calibration curves were prepared by appropriate dilutions of the stock solutions in methanol at 10 different concentration levels from 1 to 500 μM for punicalagin and vescalagin and from 1 to 1000 μM for ellagic acid and gallic acid.

Polyphenol Extraction from Pomegranate Samples. The homogenized powder of pomegranate samples (extracts and freeze-dried pomegranate fruit parts) were weighed (75 mg) and dissolved with 5 mL of a mixture of MeOH/DMSO/H_2O (40:40:20, v/v/v) containing 0.1% HCl. Samples were vortexed for 10 min and centrifuged at 3500*g* (Eppendorf 5804R) for 10 min. The supernatant was filtered through a 0.45 μm polyvinylidene difluoride (PVDF) filter (Millipore) and measured with HPLC-ESI-UV-MS/MS.

Acid Hydrolysis Optimization of Pomegranate Samples. Optimal acid hydrolysis of ETs was completed using the following protocol: Accurately weighed freeze-dried samples (50 mg) were placed in 10 mL Pyrex screw-cap tubes, and 3.34 mL of water and 1.66 mL of 37% HCl (final concentration of 4 M) were added. Samples were vortexed for 1 min and incubated in an oven at 90 °C for 24 h. After incubation, the samples were allowed to cool to room temperature and the pH was adjusted to 2.5 with 10 and 5 M NaOH. The tubes were centrifuged for 10 min at 3500*g* (Eppendorf 5804R). The supernatant was recovered, and the volume was adjusted to 10 mL with ultrapure water. The supernatant was filtered through a 0.45 μm PVDF filter before injection onto the HPLC column. The resulting pellets, containing the majority of water-insoluble compounds, were dissolved into 10 mL of DMSO/MeOH (50:50, v/v) by vortexing for 2 min, and, after centrifugation as above, the supernatants were filtered through a 0.45 μm PVDF filter. When the concentration in the pellet was high, as in the case of pomegranate extracts, the samples were diluted 1:10 with DMSO/MeOH (50:50 v/v) before injection onto the HPLC column. Hydrolysis experiments were carried out in triplicate.

For juice samples, 3.34 mL of juice was mixed with 1.66 mL of 37% HCl (final concentration of 4 M HCl), vortexed for 1 min, and incubated in an oven at 90 °C for 24 h. The hydrolysis and analysis was performed as described above for solid samples.

HPLC-ESI-UV/MS/MS (IT) Analysis. The analyses of hydrolyzed and nonhydrolyzed samples were carried out on an Agilent 1100 HPLC system equipped with a photodiode array detector and an ion-trap mass spectrometer detector (Agilent Technologies, Waldbronn, Germany). Chromatographic separation was performed on a reverse phase Pursuit XRs C18 column (250 mm × 4 mm, 5 μm particle size) (Agilent Technologies, Waldbronn, Germany). The mobile phases were water with 1% formic acid (A) and acetonitrile (B) following a gradient profile of 0−20 min, 5−30% B; 20−30 min, 30−55% B; 30−38 min, 55−90% B; 38−40 min, 90% B; and then returned to the initial conditions. A volume of 10 μL of sample was injected onto the column operating at room temperature at a flow rate of 1 mL/min. Scan wavelength was performed in DAD at 200−600 nm with scan rate of 2.5 Hz (2 s response) and scan step of 2 nm. UV chromatograms were recorded at 280 and 360 nm with a bandwidth of 8 nm. The ion trap (IT) mass spectrometer was equipped with an electrospray interface (ESI). Nitrogen was used as drying gas with a flow of 11 L/min at a temperature of 350 °C and nebulizing gas at pressure of 65 psi. The capillary voltage was set at 4 kV. Mass scan (MS) and daughter (MS/MS) spectra were recorded in negative mode in the range of m/z 100−1500 with target mass of 500. Maximum accumulation time of ion trap and the number of MS repetitions to obtain the MS average spectra were set at 200 ms and 3, respectively. Compound stability was set at 75%.

Peak identification was performed by comparison with authentic reference standards, and, when they were not available, by using the diode array spectral characteristics, molecular mass, and fragmentation pattern of the compounds. Ellagic acid (360 nm), punicalagin (360 nm), vescalagin (280 nm), and gallic acid (280 nm) were used as external standards to quantify compounds in nonhydrolyzed samples. In the hydrolyzed samples a calibration curve of ellagic acid at 360 nm was used to quantify all of the hydrolysis products except gallic acid, which was quantified with its own standard at 280 nm.

Hydrolysis Method Validation. The limits of detection (LODs) were determined on the basis of a signal-to-noise ratio (S/N) of 3, and a S/N of 10 was used for the limit of quantification (LOQ).

Due to the lack of available standards for most of the hydrolysis products, except for ellagic acid, and the absence of pomegranate matrices free of these compounds, recoveries for each compound after the hydrolysis protocol were calculated as follows: recovery % = (quantity of compound obtained after the optimized protocol/total quantity of compound after adding two more extractions of the pellet with DMSO) × 100. After the optimized protocol (hydrolysis in water

DOI: 10.1021/acs.jafc.5b02062
J. Agric. Food Chem. 2015, 63, 6555−6566

and extraction of the pellet with DMSO/MeOH (50:50, v/v)) the resulting pellet was extracted two more times with pure DMSO to ensure the complete extraction of all hydrolysis products. DMSO has been reported to be adequate for the solubilization of ellagic acid, highly insoluble in water and other solvents.[26] The quantity recovered by applying the optimized protocol was expressed as a percentage of the total amount calculated in the sample.

The effectiveness of the optimized protocol and the effect of acid hydrolysis on pure ellagic acid were checked by hydrolysis of known amounts of punicalagin (225 μM) and ellagic acid (200 μM), respectively. The optimized protocol (hydrolysis in water and extraction of the pellet with DMSO/MeOH (50:50, v/v)) was applied to both standards.

Precision was evaluated by determining repeatability (intraday), intermediate precision (interday and different instruments/analysts), and reproducibility (interlaboratory). Repeatability was evaluated by analyzing data from three measurements of the same hydrolyzed sample three times in the same day. For the intermediate precision the same sample was analyzed on three different days and the method was also applied by 10 different analysts in the same laboratory using the same instrumentation (HPLC DAD equipment as above) and by the same analyst on different equipment (Agilent 1100, Agilent 1200 Infinity Series, Agilent 1220 Infinity series and Hitachi Elite LaChrom HPLC). In addition, a large interlaboratory reproducibility study was conducted analyzing the same pomegranate extract by six European laboratories using different instruments and chromatographic columns (see below).

RESULTS AND DISCUSSION

Identification of Ellagitannins in Pomegranate Extracts. To choose the most appropriate extract to be used in the optimization of the hydrolysis protocol (i.e., the one with the highest/most diverse hydrolyzable tannin content), different pomegranate extracts were analyzed by HPLC-DAD-ESI-MS/MS. The HPLC-UV chromatograms at 280 and 360 nm of the pomegranate peel extract selected for the hydrolysis optimization trial are shown in Figure 1. Twenty-three hydrolyzable tannins and ellagic acid conjugates were tentatively identified by their retention time, molecular mass, fragments obtained by MS/MS experiments, and UV spectra (Table 1). These compounds had been previously described[2,17,18] and include free ellagic acid, ellagic acid glycosides, gallagyl esters, and more complex ETs comprising combinations of hexahydroxydiphenic acid, gallic acid, and glucose. Due to the large number of ETs and isomers, complex chromatograms with many unresolved peaks were obtained, especially at 280 nm (Figure 1B). The complexity of the chromatograms, together with the absence of commercial standards, hampers the correct identification and quantification of pomegranate ellagitannins. Therefore, acid hydrolysis of the samples and quantification of the reaction products could be a good alternative method for ET characterization and quantification.

Acid Hydrolysis Optimization. Several methodologies for the acid hydrolysis of ETs, especially from berries and nuts, have previously been reported.[22−24] In most of these methods, a primary extraction of the polyphenols with hydro-organic mixtures, usually acetone/water or MeOH/water, was applied. After evaporation, the extracts were usually dissolved in MeOH (methanolysis) or in MeOH/water prior to hydrolysis.[22] This extraction process, however, does not allow the quantification of nonextractable ellagitannins, leading to an underestimation of these polyphenols. Studies by Vrhovsek et al.[25] and Da Silva Pinto et al.[21] concluded that acetone/water was the best solvent for the initial extraction and that 2 N trifluoroacetic acid (TFA)

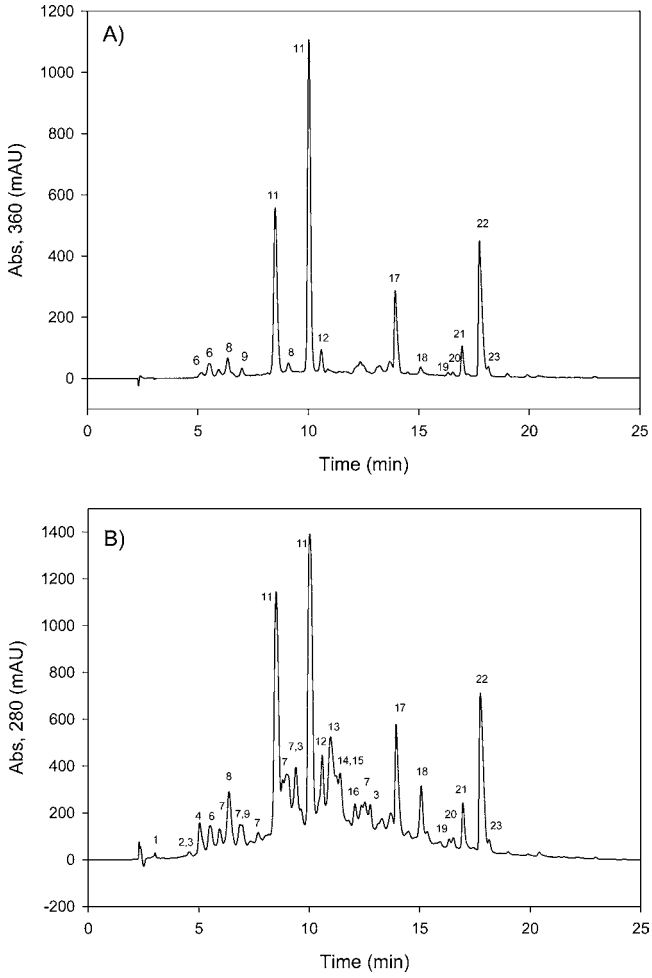

Figure 1. HPLC-UV chromatograms at 360 nm (A) and 280 nm (B) of the nonhydrolyzed pomegranate peel extract. This sample was chosen for the hydrolysis optimization. Numbers refer to compounds described in Table 1.

for 1 h at 120 °C in water and 4 M HCl for 6 h at 90 °C in MeOH were the best hydrolysis conditions for the determination of total ellagic acid in strawberries and raspberries, respectively. As a first step in the optimization process these two hydrolytic conditions were tested in the selected pomegranate extract in both MeOH and water. The freeze-dried samples were hydrolyzed after an initial extraction with acetone/water (0.6 g of pomegranate sample with 25 mL of acetone/water) and also a direct hydrolysis was tested. Figure 2 shows the reaction compounds produced during the hydrolysis of pomegranate samples and the ETs from which they have been formed (described in detail in the next section). The content of the main compounds detected after the different hydrolysis conditions, original ETs (punicalagin and two isomers of punicalin), and reaction products (gallic acid, gallagic acid dilactone, ellagic acid, sanguisorbic acid dilactone, and valoneic acid dilactone) is shown in Table 2. Although similar results were obtained for most of the compounds with and without previous extraction, direct hydrolysis was chosen as the preferred approach as it required less time and solvents and allowed quantification of both the extractable and nonextractable compounds. In general, larger amounts of reaction products were obtained after 6 h of hydrolysis with 4 M HCl at 90 °C. The reaction was better carried out in water as the

DOI: 10.1021/acs.jafc.5b02062
J. Agric. Food Chem. 2015, 63, 6555−6566

Table 1. Characterization of the Main Tannins Present in the Pomegranate Extract Selected for Hydrolysis Optimization

no.[a]	compound[b]	retention time (min)	$[M-H]^-$	fragments	λ_{max}[c]
1	HHDP-hexoside	2.33−3.35	481	463, 421, 301, 275, 191	238
2	galloyl-HHDP-glucuronide	4.45/6.15	649	605, 497, 361, 301	238, 270
3	galloyl-HHDP- hexoside	4.58/5.76/7.79/8.85/9.30/10.97/12.78	633	615, 463, 301, 275, 229[d]	236, 270
4	digalloyl-hexoside	4.88/6.45	483	331, 313, 169	270
5	gallagyl derivative	5.11	1101	1083, 1057, 781, 601	nd
6	gallagyl-hexoside (punicalin)	5.48	781	721, 601, 299	262, 378
7	bis-HHDP-hexoside (pedunculagin I)	5.99/6.84/7.63/8.95/9.30/11.26/12.48	783	765, 481, 301, 275[d]	242, 262sh
8	ellagitannin 1	6.46/8.21/9.30	707	1113, 783, 633, 613, 481, 301	260, 378
9	galloyl-gallagyl-hexoside (pedunculagin III)	6.62/6.97	933	915, 781, 721, 601	260, 378
10	vescalagin/castalagin	8.15	933	631, 451, 301	nd
11	punicalagin	8.42/10.02	1083	781, 721, 601, 299	268, 378
12	digalloyl-gallagyl-hexoside	9.09/10.65	1085	933, 783, 631, 601, 451	258, 378
13	ellagitanin 2	10.97	799	781, 479, 301	242, 268
14	galloyl-bisHHDP-hexoside (casuarin)	11.36	935	783, 633, 301	242, 278sh
15	digalloyl HHDP-glucuronide (punigluconin)	11.46	801	781, 649, 499, 347, 301	242, 278sh
16	digalloyl- HHDP-hexoside (pedunculagin II)	12.09/14.18/15.93	785	685, 633, 483, 301[d]	262
17	ellagic acid hexoside	13.95	463	301	254, 365
18	galloyl-HHDP-DHHDP-hexoside (granatin B)	15.05	951	933, 613, 631, 301	367, 378
19	galloyl-ellagic acid hexoside	16.35	615	463, 301	265, 365
20	ellagic acid pentoside	16.56	433	301	255, 360
21	ellagic acid-deoxyhexoside	17.00	447	299	255, 364
22	ellagic acid	17.79	301	229, 185	255, 370
23	dimethyl EA hexoside	18.17	491	328, 313, 298	250, 370

[a]Compounds numbers are as in Figure 1. [b]DHHDP, dehydro-hexahydroxydiphenic acid; HHDP, hexahydroxydiphenic acid. [c]nd, below the limit of detection; sh, shoulder. [d]Not all fragments are present in the isomers detected at different times

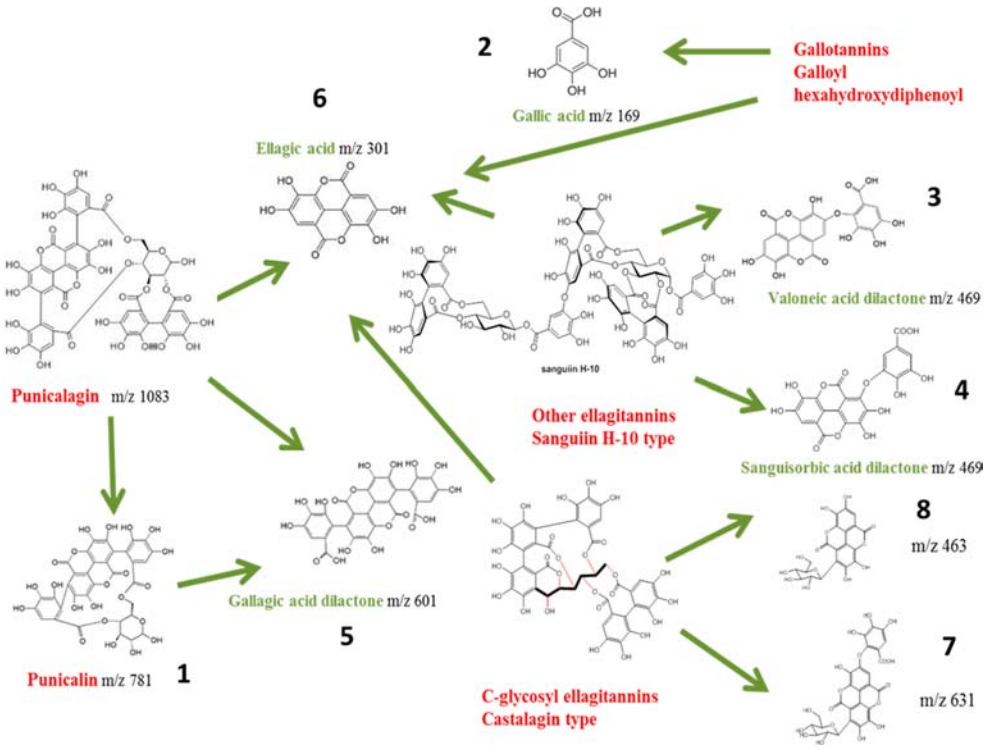

Figure 2. Structures of the hydrolysis products (in green) of pomegranate samples and the original ETs (in red) from which they may have been formed.

hydrolysis in MeOH generated methylated derivatives (methyl gallate, methyl valoneic acid dilactone, and methyl punicalin, among others), preventing the correct quantification due to the lack of authentic standards.[22,24] Although there was a drawback of using water, namely, the very low solubility of ellagic acid in aqueous media,[27] which caused some of the hydrolysis products to remain precipitated in the pellet, re-extraction of the pellet with DMSO/MeOH (50:50, v/v) proved to be very efficient at dissolving highly insoluble compounds such as ellagic acid, gallagic acid dilactone, and valoneic acid dilactone, and these

DOI: 10.1021/acs.jafc.5b02062
J. Agric. Food Chem. 2015, 63, 6555−6566

Table 2. Total Content (mg of Compound/g dw) of the Original Ellagitannins and Hydrolysis Products Obtained under Different Hydrolysis Conditions during the Protocol Optimization (N = 3)

	punicalin 1[a,b]	punicalin 2[a,b]	punicalagin[b]	gallic acid[a,c]	valoneic acid dilactone 1[a,d]	sanguisorbic acid dilactone[a,d]	gallagic acid dilactone[d]	ellagic acid[d]
previous extraction with acetone/water								
2 M TFA, 120 °C, 1 h in MeOH	1.4[a]	32.3[a]	178.5	11.3[a]	0[a]	5.1[a]	0	14.4
2 M TFA, 120 °C, 1 h in water	13.8	126.4	17.3	35.3	9.1	14.5	0	19.8
4 M HCl, 90 °C, 6 h in MeOH	13.6[a]	37.1[a]	0	11.9[a]	3.4[a]	6.2[a]	0	13.9
4 M HCl, 90 °C, 6 h in water	39.6	22.8	0	44.9	4.0	7.2	0	41.0
direct hydrolysis								
2 M TFA, 120 °C, 1 h in MeOH	1.4[a]	31.3[a]	217.6	13.1[a]	0[a]	5.1[a]	0	11.1
2 M TFA, 120 °C, 1 h in water	15.5	126.5	17.7	36.6	12.3	15.6	0	16.2
4 M HCl, 90 °C, 6 h in MeOH	14.2[a]	48.7[a]	0	13.8[a]	5.8[a]	8.8[a]	0	12.6
4 M HCl, 90 °C, 6 h in water	38.3	24.7	0	23.6	8.1	20.0	0	49.4
pellet re-extracted with MeOH/DMSO								
4 M HCl, 90 °C, 6 h (water) + pellet (total amount)	38.3 + 0 (38.3)	24.7 + 0 (24.7)	0 + 0 (0)	23.6 + 1.3 (24.9)	8.1 + 2.2 (10.3)	20.0 + 50.0 (70.0)	0 + 189.1 (189.1)	49.4 + 190.6 (239.9)
4 M HCl, 90 °C, 24 h (water) + pellet (total amount)	6.4 + 0 (6.4)	0 + 0 (0)	0 + 0 (0)	34.5 + 2.4 (36.9)	10.1 + 4.2 (14.3)	15.1 + 61.0 (76.1)	0 + 338.0 (338.0)	45.4 + 215.4 (260.8)

[a]Methylated derivatives of these compounds were not quantified and appeared in the chromatograms of the samples hydrolyzed in MeOH. [b]Quantified at 360 nm with punicalagin. [c]Quantified at 280 nm with gallic acid. [d]Quantified at 360 nm with ellagic acid.

DOI: 10.1021/acs.jafc.5b02062
J. Agric. Food Chem. 2015, 63, 6555−6566

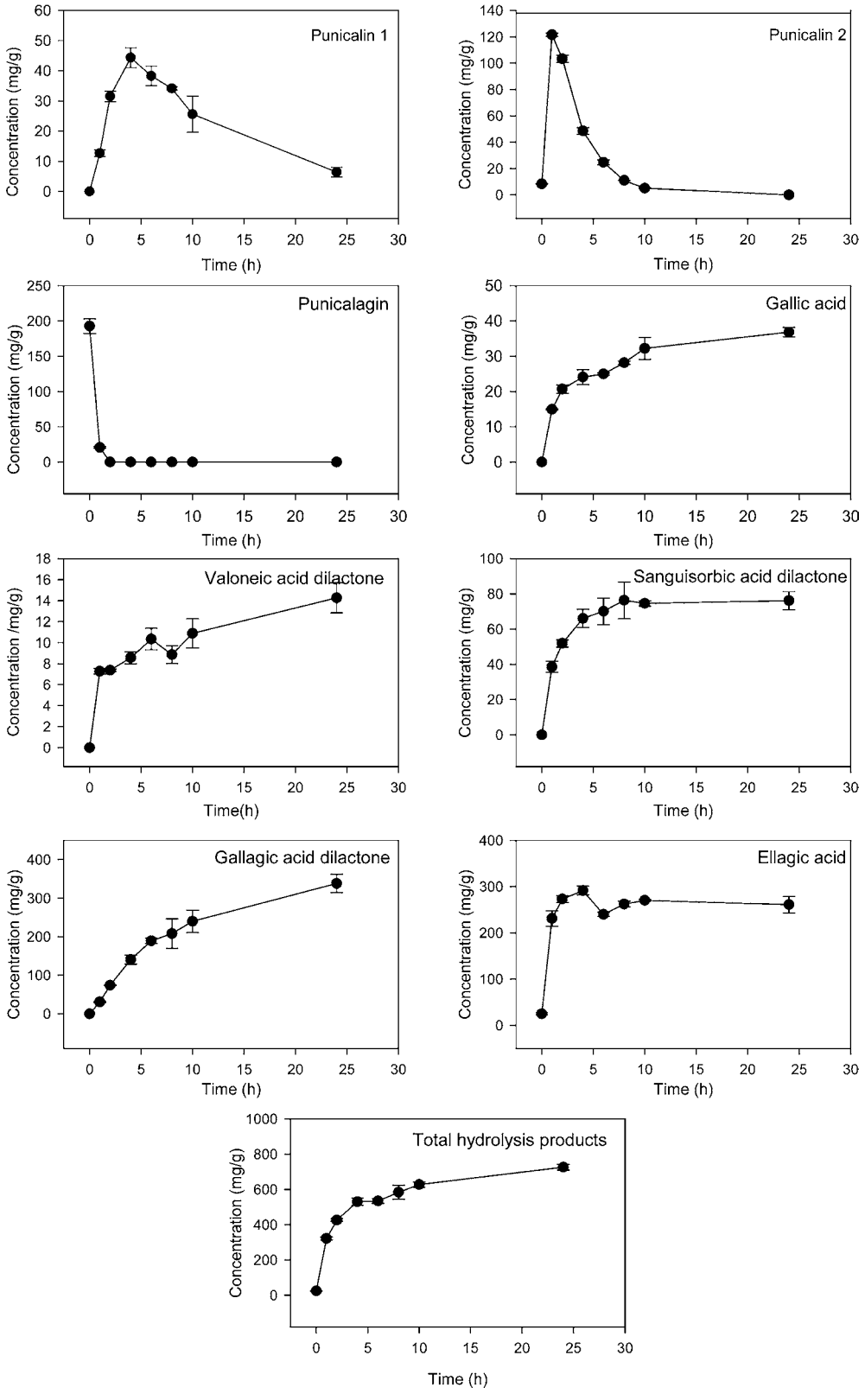

Figure 3. Evolution of punicalagin and reaction products after direct hydrolysis of pomegranate peel extract with 4 M HCl at 90 °C in water and subsequent extraction of the pellet with MeOH/DMSO (50:50, v/v). Total hydrolysis products refer to the addition of gallic acid, valoneic acid dilactone, sanguisorbic acid dilactone, gallagic acid dilactone, and ellagic acid. Results are expressed as the mean ± SD (n = 3).

were subsequently recovered completely from the pellet (Table 2).

Hydrolysis of freeze-dried samples with 4 M HCl at 90 °C in water and subsequent extraction of the pellet with DMSO/MeOH (50:50, v/v) were finally selected as the best conditions for maximum hydrolysis and recovery. However, 6 h was not sufficient to complete the hydrolysis as punicalin and other ETs were still present (Table 2). To find the most efficient

DOI: 10.1021/acs.jafc.5b02062
J. Agric. Food Chem. 2015, 63, 6555−6566

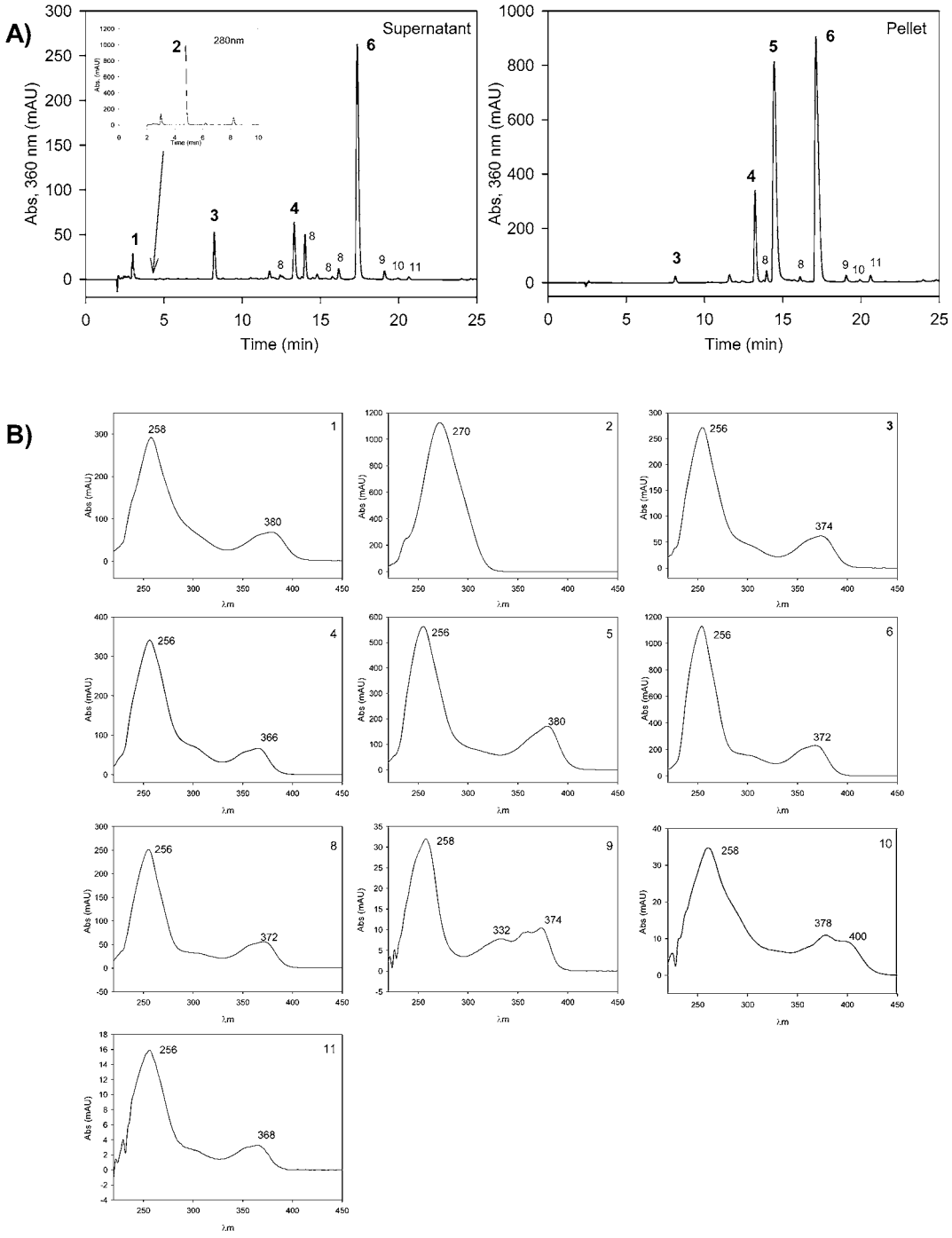

Figure 4. (A) HPLC-UV chromatograms of the supernatant (360 and 280 nm) and pellet (360 nm) of a pomegranate peel extract after 24 h of hydrolysis. (B) UV spectrum of the reaction products detected after the hydrolysis of pomegranate samples. Numbers refer to compounds described in Table 3.

hydrolysis of pomegranate ETs, different hydrolysis times (0, 1, 2, 4, 6, 8, 10, 12, and 24 h) were tested. Figure 3 shows the evolution of punicalagin and the main reaction products after the hydrolysis of the pomegranate extract (three replicates).

The kinetics showed the fast hydrolysis of punicalagin that disappeared after 2 h of incubation and the much slower hydrolysis of the punicalin produced, taking 24 h to reach a complete hydrolysis. Two punicalin isomers were detected; punicalin 2 was already present in the original extract, whereas punicalin 1 was detected only after acid hydrolysis. The punicalins were hydrolyzed at different rates, punicalin 2 being hydrolyzed more rapidly than punicalin 1. Both punicalins increased gradually during acid hydrolysis as a product of the release of ellagic acid from punicalagin, and then decreased when gallagic acid dilactone was released (Figure 3). This shows that the release of ellagic acid from punicalagin by acid hydrolysis is much more favored than the hydrolysis of the gallagyl ester to release gallagic acid dilactone, as it needs up to 24 h to be completed. Ellagic acid reached a maximum after 4 h because of the fast hydrolysis of punicalagin, and this value was maintained up to 24 h. Longer periods of treatment with HCl did not release more ellagic acid. Gallagic acid dilactone,

DOI: 10.1021/acs.jafc.5b02062
J. Agric. Food Chem. 2015, 63, 6555−6566

Table 3. Compounds Identified in HPLC-UV-MS after 24 h of Hydrolysis of Pomegranate Extracts

		retention time (min)	$[M-H]^-$	MS/MS[a]	λ_{max}
main compounds[b]					
1	punicalin	3.00	781	721, **601**, 299	258, 380
2	gallic acid	4.77	169	**125**	272
3	valoneic acid dilactone	8.22	469	425 → **407**, 397, 300, 271	256, 308sh, 374
4	sanguisorbic acid dilactone	13.32	469	425 → **301**, 299, 271	256, 308sh, 366
5	gallagic acid dilactone	14.45	601		256, 308sh, 380
6	ellagic acid	17.35	301	**271**, 229	256, 310sh, 372
minor compounds[b]					
7	valoneic acid dilactone *C*-glucoside	7.701	631	571, 541, 511, 469, **451**, 425	nd
8	ellagic acid *C*-glucoside	12.39/**13.98**/15.28/15.75/16.14	463	**445**, 403, **373**, **343**, 313, 300	256, 310sh, 372
9	unknown 2	19.09	427	409, 367, **355**, 337, 325, 300	258, 332sh, 360sh, 374
10	unknown 3	19.94	451	433, 407, 379, 338	260, 378, 400sh
11	unknown 4	20.61	425	301, **299**, 285, 271	256, 308sh, 368

[a]The main fragments in MS^2 are given in boldface. [b]Compounds with numbers as in Figure 4.

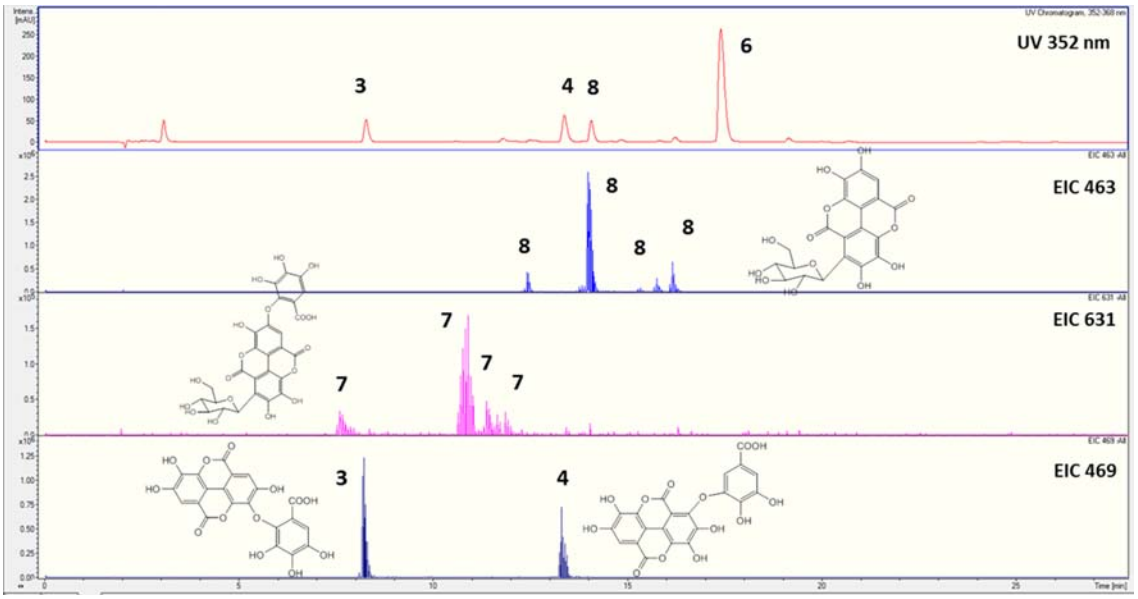

Figure 5. HPLC-DAD-MS-MS analysis of the supernatant obtained after acid hydrolysis of the pomegranate extract; UV chromatogram at 352 nm; extracted ion chromatograms (EIC) at *m/z* 631, 463, and 469. Numbers refer to the compound described in Table 3.

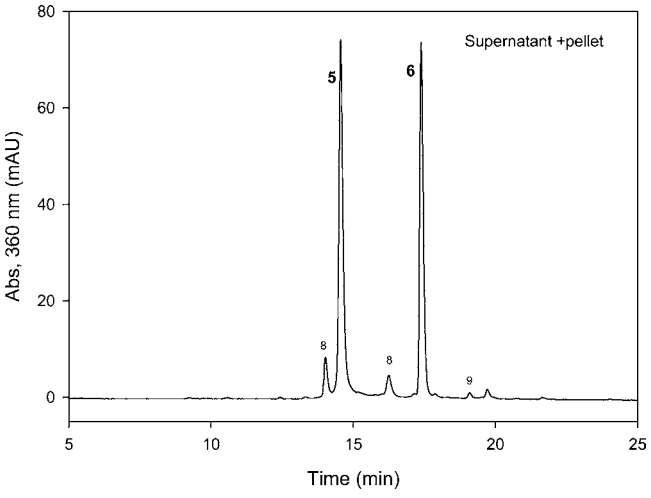

Figure 6. HPLC-UV chromatogram at 360 nm of the mixture of supernatant and pellet obtained after the hydrolysis of punicalagin standard. Numbers refer to the compound described in Table 3.

originating from punicalagin and punicalin, increased over time, reaching the maximum concentration after 24 h, as well as gallic acid and valoneic acid dilactone. Sanguisorbic acid dilactone reached steady-state concentration between 6 and 10 h.

Finally, hydrolysis for 24 h with 4 M HCl at 90 °C in water and subsequent extraction of the pellet with DMSO/MeOH (50:50, v/v) was selected as the most suitable pretreatment to yield maximum recovery for the main hydrolysis products of pomegranate ETs (see graph of total hydrolysis products in Figure 3).

Reaction Products Obtained after the Hydrolysis. Several reaction products were detected after acid hydrolysis of pomegranate extracts. Figure 4A shows the HPLC-UV chromatograms of the supernatant (360 and 280 nm) and pellet (360 nm) of a pomegranate extract after acid hydrolysis. All of these compounds were identified by their retention time, molecular mass, fragmentation pattern, and the spectral properties shown in Table 3. The UV spectrum for each compound (Figure 4B) is also useful for the identification of the hydrolysis products when only HPLC with UV diode array detectors is available for analysis. All compounds (except gallic

DOI: 10.1021/acs.jafc.5b02062
J. Agric. Food Chem. 2015, 63, 6555−6566

Table 4. Interlaboratory Study for the Determination of the Hydrolysis Products of Ellagitannins in Pomegranate Extracts after Acid Hydrolysis[a]

laboratory	LC instrument	column	valoneic acid dilactone	sanguisorbic acid dilactone	gallagic acid dilactone	ellagic acid	total
CEBAS	Agilent 1100 HPLC, DAD	Agilent Pursuit XRs C18 (250 × 4 mm, 5 μm)	14.3 ± 1.4	76.2 ± 5.1	338.0 ± 23.9	260.9 ± 37.7	689.3 ± 24.3
VITO	Waters Acquity UPLC PDA	Alltima C18 (250 × 4.6 mm, 5 μm)	11.7 ± 0.4	80.3 ± 1.5	250.4 ± 11.8	245.1 ± 8.4	587.5 ± 21.5
NOFIMA	Agilent 1100 HPLC, DAD	Betasil C18 (250 × 2.1 mm, 5 μm)	12.3 ± 2.1	84.7 ± 6.7	285.4 ± 18.1	240.3 ± 10.5	622.7 ± 36.9
TUBITAK	Shimadzu SPD-M20A Prominence HPLC PDA	Zivak C18 (250 × 4.6 mm, 5 μm)	7.9 ± 0.6	72.1 ± 0.9	283.5 ± 11.9	230.4 ± 6.3	593.9 ± 18.5
Helsinki	Waters Acquity UPLC, PDA	Acquity UPLC HSS T3 C18 (150 × 2.1 mm, 1.8 μm)	7.1 ± 2.4	53.0 ± 5.7	259.2 ± 33.9	209.9 ± 15.4	529.2 ± 59.4
IFR	Agilent 1100 HPLC, DAD	Luna C18 (250 × 4.6 mm, 5 μm)	17.5 ± 1.8	73.8 ± 0.4	300.0 ± 6.3	292.1 ± 8.6	683.4 ± 12.8
av			11.8	73.3	286.1	246.4	631.3
SD			3.9	110	31.3	28.0	59.2
RSD (%)			33.1	14.9	10.9	11.4	9.4

[a]Final concentrations of the hydrolysis products are expressed as the mean ± SD of three replicates in mg of compound/g dw. Hydrolysis products were quantified with calibration curve of ellagic acid at 360 nm.

acid) exhibit two major absorption maxima. The first one was around 256 nm and the second one in the region of 350−400 nm with slight differences in the UV maxima depending on the compound. As indicated before, the main reaction products identified and quantified were ellagic acid, gallagic acid dilactone, gallic acid, and two compounds with m/z 469 consistent with ellagic acid derivatives in which an additional gallic acid is linked to the ellagic acid molecule through an ether bond (Figure 5). Traces of punicalin (<1%) were also observed and indicated that the hydrolysis of this compound was incomplete. In general, the main hydrolysis products were ellagic acid and gallagic acid dilactone. In particular, the detection of gallagic acid dilactone could be considered as an unequivocal signal of the presence of pomegranate, as it was produced by hydrolysis of the unique and characteristic ETs (gallagyl esters) of pomegranate, punicalagin and punicalin. After acid hydrolysis, one molecule of punicalagin releases one molecule of ellagic acid and one of gallagic acid dilactone. This last compound could also be released from punicalin (Figure 2). The detection of gallic acid was indicative of the presence of gallotannins and other gallic acid-containing products. The two compounds with m/z^- 469 showed different fragmentation patterns and UV spectra (Table 3; Figures 4 and 5). In both cases, the presence of an M − 44 fragment (m/z 425) was observed, this being consistent with the loss of CO_2 as could be expected for phenolic with a free carboxylic group. According to the literature these isomers could be consistent with valoneic acid dilactone and sanguisorbic acid dilactone. The only structural difference between these two isomers is that the hydroxyl that links the hexahydroxydiphenoyl group (HHDP) to the galloyl group belongs either to the HHDP group or to the galloyl group (Figure 2). According to the literature[25] the hydrolysis of strawberry ellagitannins produces sanguisorbic acid dilactone in addition to ellagic acid. Thus, to identify both isomers the optimized hydrolysis protocol was applied to a strawberry sample. One peak with m/z 469 was detected at 13.46 min, the same retention time of the compound **4** that was tentatively identified as sanguisorbic acid dilactone. The detection of both isomers after hydrolysis of the pomegranate extract indicates the occurrence of other complex ETs with linkages in their structure involving an additional galloyl group linked to the HHDP ester.

Apart from the major compounds, other minor analytes with UV−vis absorbance spectra similar to the spectrum of ellagic acid were detected after the hydrolysis. Two of them with m/z^- 631 and 463 exhibited fragmentation profiles characteristic of *C*-glycosidic compounds with typical losses of 60, 90, 120, and 150 mu, often accompanied by an additional loss of water (−m/z 18 mu). Several isomers for each compound were detected in the MS-MS analysis (Figure 5). Different isomers of ellagic acid *C*-glucoside (**8**) were identified. These could be produced after the hydrolysis of *C*-glycosidic ellagitannins. The occurrence of different isomers indicates that the original HHDP-*C*-glucoside can be cycled in different conformations after the hydrolysis. The presence of these reaction products suggests that *C*-glycosidic ETs such as casuariin, punicacortein, and vescalagin/castalagin could be present in the extract. The identification of compounds **9** and **10** was not possible with the instrumentation used in this experiment, although information about fragmentation patterns and UV spectra is provided in Table 3. Ellagic acid *C*-glucosides represented <3% of the total hydrolysis products, indicating that, in general, *C*-glycosidic ellagitannins were minor constituents of pomegranate samples.

Method Validation. For the quantitation of ETs in nonhydrolyzed samples, the LOD and LOQ, considering the whole protocol, were estimated at 0.06 and 0.20 mg/g for vescalagin, 0.07 and 0.24 mg/g for punicalagin, and 0.01 and 0.03 mg/g for both ellagic acid and gallic acid. For the quantitation of hydrolyzed samples the LOD and LOQ, considering the whole protocol, were 0.03 and 0.10 mg/g for both ellagic acid and gallic acid.

The effectiveness of the optimized hydrolysis protocol was checked by hydrolysis of a known amount of punicalagin standard (225 μM). Complete hydrolysis of punicalagin was observed after 24 h with the presence of two main peaks: ellagic acid and gallagic acid dilactone (Figure 6). Other minor compounds were observed (representing <5%), probably due to the presence of trace amounts of other ETs in the punicalagin standard (standard purity ≥ 98% HPLC isolated from pomegranate). Hydrolysis of punicalagin would theoret-

DOI: 10.1021/acs.jafc.5b02062
J. Agric. Food Chem. 2015, 63, 6555−6566

Table 5. Compounds Quantified in the Pomegranate Peel Extract (Extract 1 in Figure 7) Used for Method Optimization: (A) Without Hydrolysis (Expressed as mg/g dw) and the Calculated Equivalents of Ellagic, Gallagic, and Gallic Acids (Expressed as mg/g dw) Present in the Quantified Compounds; (B) After Acid Hydrolysis (Expressed as mg/g dw)

			calcd equiv (mg/g dw)		
no.	compound	quantified (mg/g dw)	ellagic acid	gallagic acid dilactone	gallic acid
(A) without hydrolysis (extractable compounds)					
1	HHDP-hexoside[a]	2.4	1.5		
3	galloyl-HHDP-hexoside[a]	13.8	6.6		3.7
4	digalloyl-hexoside[b]	17.4			12.2
6	punicalin[c]	8.3		6.4	
7	bis-HHDP-hexoside[a]	67.3	51.9		
8	ellagitannin 1[c]	14.9			
9	galloyl-gallagyl-hexoside[c]	2.7		1.7	0.5
11	punicalagin[c]	192.7	53.7	107.0	
12	digalloyl-gallagyl-hexoside[c]	7.2		3.6	2.0
13	ellagitannin 2[a]	86.4			
15	digalloyl-HHDP-glucu[b]	35.4	13.3		15.0
16	digalloyl- HHDP-hexoside[a]	11.4	4.4		4.9
17	ellagic acid-hexoside[d]	18.8	12.2		
18	galloyl-HHDP-DHHDP-hexoside[a]	38.3	12.2		6.8
19	galloyl-ellagic acid-hexoside[d]	0.8	0.4		0.2
20	ellagic acid- pentoside[d]	0.8	0.5		
21	ellagic acid-deoxyhexoside[d]	5.7	3.8		
22	ellagic acid[d]	24.9	24.9		
	total	549.1	185.3	118.7	45.3
(B) after acid hydrolysis (extractable + nonextracatable)					
	punicalin[d]	6.4			
	gallic acid[b]	36.9			
	gallagic acid dilactone[d]	338.0			
	ellagic acid[d]	260.9			
	total	635.8 (640.7 considering punicalin)			
	valoneic acid dilactone[d]	14.3			
	sanguisorbic acid dilactone[d]	76.2			
	ellagic acid *C*-glucoside[d]	18.0			
	grand total	750.6			

[a]Quantified at 280 nm with vescalagin. [b]Quantified at 280 nm with gallic acid. [c]Quantified at 360 nm with punicalagin. [d]Quantified at 360 nm with ellagic acid.

ically yield 1 mol of ellagic acid and 1 mol of gallagic acid dilactone per mole of punicalagin. UV response factors were similar for both compounds, indicating that the ellagic acid calibration curve can be used as a good proxy for the accurate quantitation of gallagic acid dilactone as no standard was available of the latter compound.

Recoveries of hydrolysis products in pomegranate extracts after hydrolysis were between 97 and 99%, and no decomposition of ellagic acid was observed up to 24 h.

Method precision was evaluated by determining repeatability, intermediate precision, and reproducibility. The optimized method has a high precision with a relative standard deviation (RSD) of peak areas below 5.6% for intraday precision and below 7.5% for interday precision. The intermediate precision assessed by means of using different instruments or having various analysts prepare the samples was estimated at 9.5 and 14%, respectively. Finally, reproducibility of the method was assessed by means of an interlaboratory study conducted by six European laboratories. Reproducibility of the method for most of the main compounds was <15% (Table 4). Only valoneic acid dilactone showed higher values (33%), probably due to its low intensity as this compound is usually present in low concentrations (around 2% of the total hydrolysis products).

Comparison with the Conventional Quantitation (without Hydrolysis). The quantitative results obtained with the new hydrolysis method were compared with those produced with a conventional method (Table 5). The conventional method for pomegranate ETs quantitation involves the individual assessment of each compound after a hydro-organic extraction of the samples. Due to the lack of available standards, each compound was quantified with the most appropriate calibration curve (indicated in Table 5). Direct quantification of extractable ellagitannins using HPLC-DAD and external standards (punicalagin, vescalagin, ellagic acid, gallic acid) yielded 549.1 mg/g dw extract (Table 5A). When the corresponding equivalents of ellagic acid, gallagic acid dilactone and gallic acid, were calculated, the total amount of the equivalents that should be released after hydrolysis of the

DOI: 10.1021/acs.jafc.5b02062
J. Agric. Food Chem. 2015, 63, 6555−6566

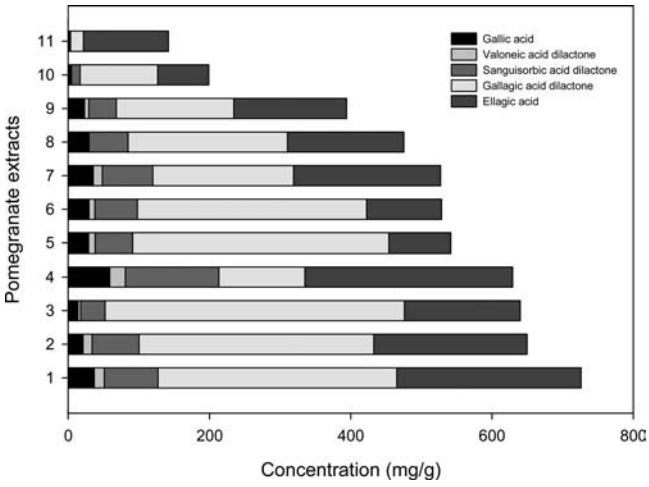

Figure 7. Content of the main hydrolysis products in different pomegranate extracts, expressed as mg of compound/g dw.

extractable ellagitannins reached 349.3 mg/g, and this value should be compared with that obtained after direct hydrolysis without hydroalcoholic extraction that amounted to 635.8 mg/g dw (Table 5B). The results show that around 300 mg/g of the hydrolysis products corresponded to nonextractable ellagitannins (either nonextracted or not quantifiable with the direct HPLC-DAD analysis). Other minor compounds (those with valoneic acid bilactone, sanguisorbic acid bilactone, and *C*-glycosyl ellagitannins) were not quantified in the conventional analysis without hydrolysis (Table 5A), as their quantification in the chromatograms of the nonhydrolyzed extracts was not possible. After hydrolysis, a small amount of these compounds was detected (90.5 mg/g of the valoneic and sanguisorbic acid dilactones and 18 mg/g of ellagic acid *C*-glucoside), therefore increasing even more the content of ETs in the analyzed extract (750.6 mg/g dw) (Table 5B).

As indicated before, the presence of a high background and unresolved peaks in the chromatograms (especially at 280 nm, see Figure 2), together with the absence of available standards for most of the compounds, could lead to an underestimation when using the conventional method. The hydrolysis method has shown to be a good alternative for quantitation purposes.

Application of the Method to Different Pomegranate Samples. The optimized method was successfully applied to different pomegranate extracts, finding large differences in the ellagitannin content (Figure 7). Pomegranate peel extracts have recently attracted interest because of their potential use as natural food preservatives and nutraceuticals.[28,29] Industrial scale extraction of phenolic compounds from pomegranate peel is carried out by using solvents such as water and ethanol or their mixtures. The content of hydrolysis products ranged from 150 mg/g to 750 mg/g extract, showing that different plant materials and different extraction and purification processes had been applied for extract preparation. In addition, highly significant chemical differences ($p < 0.01$) in the ellagitannin composition were observed.

The high variability observed among the different pomegranate extracts was especially important in the amount and ratio of ellagic acid and gallagic acid dilactone, indicating large differences in the presence of the gallagyl esters punicalagin and punicalin. One pomegranate extract containing mainly punicalagin should have a gallagic acid dilactone/ellagic acid ratio around 2. Ratios above 2 indicate that the extract is richer in punicalin, and ratios below 2 indicate that the extracts are richer in ellagitannins based on ellagic acid or extracts with larger amounts of free ellagic acid. Thus, extracts 2, 3, and 10 (Figure 7) show gallagic acid dilactone/ellagic acid ratios that indicate that punicalagin was the main ellagitannin, whereas extracts 5 and 6 contain mainly punicalin and extracts 4 and 11 contain mainly ellagic acid-based ellagitannins. Furthermore, the presence or absence of other hydrolysis products is indicative of other ET content. This variability is in agreement with the literature, where the use of different solvents for peel phenolic extraction is reported to yield different phenolic content ratios and associated different antioxidant activity.[28] Previous studies for the analysis of extractable ETs in pomegranate extracts using HPLC had reported ET contents of 330 mg/g dw[30] and 220 mg/g dw,[31] values that are smaller than those found in the present study, particularly after hydrolysis that takes into account the nonextractable ETs.

The applicability of the method was also tested on different parts of a pomegranate fruit: husk (pericarp), peels and membranes (mesocarp), arils, and commercial juices. Quantitative results are shown in Table 6. The highest concentration of ellagic acid and other hydrolysis products occurred in the husk, followed by the peels, and only traces were present in the arils. This is in agreement with previous studies in which individual quantitations of ETs with conventional extraction methods were assayed.[2,5]

Further research will be conducted to apply this methodology to other ellagitannin-rich food products including berries and nuts and to extrapolate the present findings to a simplified method that can be easily used for the routine analysis of pomegranate ETs in all laboratories and industry.

Table 6. Quantification of Hydrolysis Products in Different Parts of Pomegranate Fruit (mg/g dw) and in Pomegranate Juice (mg/L)[a]

	extract	husk (pericarp)	peels mesocarp	arils	juice
punicalin	6.4 ± 0.1	0.7 ± 0.1	0.5 ± 0.1		
gallic acid	36.9 ± 1.3	3.3 ± 0.6	2.1 ± 0.1		
valoneic acid dilactone	14.3 ± 1.4	1.3 ± 0.5	1.4 ± 01		11.0 ± 1.6
sanguisorbic acid dilactone	76.2 ± 5.1	11.8 ± 0.4	10.7 ± 0.2	0.3 ± 0.0	109.4 ± 2.0
gallagic acid dilactone	338.0 ± 23.9	86.6 ± 1.4	73.8 ± 1.2	0.5 ± 0.1	438.9 ± 12.4
ellagic acid	260.9 ± 37.7	62.6 ± 0.2	38.7 ± 2.1	0.7 ± 0.1	811.1 ± 24.5
total	732.6 ± 23.2	166.0 ± 3.6	126.6 ± 3.1	1.5 ± 0.2	1370.4 ± 40.1

[a]Results are expressed as the mean ± SD of three replicates.

DOI: 10.1021/acs.jafc.5b02062
J. Agric. Food Chem. 2015, 63, 6555−6566

AUTHOR INFORMATION

Corresponding Author

*(F.A.T.-B.) E-mail: fatomas@cebas.csic.es. Fax: +34-968-396213.

Funding

The research reported in this paper has been supported by the Projects BACCHUS (FP7 European Commission Grant Agreement, 312090), CICYT-AGL2011-22447 (MINECO, Spain), and CSIC 201370E068. R.G.V. was the holder of a JAE-DOC contract from CSIC (Spain) cofunded by the European Social Fund (ESF).

Notes

The authors declare no competing financial interest.

REFERENCES

(1) Seeram, M.; Zhang, Y.; Reed, J. D.; Krueger, C. G.; Vaya, J. Pomegranate phytochemicals. In *Pomegranate: Ancient Roots to Modern Medicine*; Seeram, N. P., Schulman, R., Heber, D., Eds.; CRC Taylor and Francis: New York, 2006; pp 3−29.

(2) Fischer, U. A.; Carle, R.; Kammerer, D. R. Identification and quantification of phenolic compounds from pomegranate (*Punica granatum L.*) peel, mesocarp, aril and differently produced juices by HPLC-DAD−ESI/MS^n. *Food Chem.* **2011**, *127*, 807−821.

(3) Vrhovsek, U.; Giongo, L.; Mattivi, F.; Viola, R. A survey of ellagitannin content in raspberry and blackberry cultivars grown in Trentino (Italy). *Eur. Food Res. Technol.* **2008**, *226*, 817−824.

(4) Xie, L.; Roto, A. V.; Bolling, B. W. Characterization of ETs, gallotannins and bound proanthocyanidins from California almond (*Prunus dulcis*) varieties. *J. Agric. Food Chem.* **2012**, *60*, 12151−12156.

(5) Gil, M. I.; Tomás-Barberán, F. A.; Hess-Pierce, B.; Holcroft, D. M.; Kader, A. A. Antioxidant activity of pomegranate juice and its relationship with phenolic composition and processing. *J. Agric. Food Chem.* **2000**, *48*, 4581−4589.

(6) Qu, W.; Breksa, A. P., III; Pan, Z.; Ma, H. Quantitative determination of major polyphenols constituents in pomegranate products. *Food Chem.* **2012**, *132*, 1585−1591.

(7) Viuda-Martos, M.; Fernández-López, J.; Pérez-Alvarez, J. A. Pomegranate and its many functional components as related to human health: a review. *Compr. Rev. Food Sci. Food Saf.* **2010**, *9*, 635−654.

(8) Faria, A.; Conceição, C. The bioactivity of pomegranate: impact on health and disease. *Crit. Rev. Food Sci. Nutr.* **2011**, *51*, 626−634.

(9) Ismail, T.; Sestili, P.; Akhtar, S. Pomegranate peel and fruit extracts: a review of potential anti-inflammatory and anti-infective effects. *J. Ethnopharmacol.* **2012**, *143*, 397−405.

(10) Larrosa, M.; García-Conesa, M. T.; Espín, J. C.; Tomás-Barberán, F. A. ETs, ellagic acid and vascular health. *Mol. Aspects Med.* **2010**, *31*, 513−539.

(11) Zahin, M.; Ahmad, I.; Gupta, R. C.; Aqil, F. Punicalagin and ellagic acid demonstrate antimutagenic activity and inhibition of benzo[a]pyrene induced DNA adducts. *BioMed Res. Int.* **2014**, *2014*, 1−10.

(12) Cerdá, B.; Periago, P.; Espín, J. C.; Tomás-Barberán, F. A. Identification of urolithin A as a metabolite produced by human colon microflora from ellagic acid and related compounds. *J. Agric. Food Chem.* **2005**, *53*, 5571−5576.

(13) Espín, J. C.; Larrosa, M.; García-Conesa, M. T.; Tomás-Barberán, F. Biological significance of urolithins, the gut microbial ellagic acid-derived metabolites: the evidence so far. *Evidence-Based Complement. Altern. Med.* **2013**, DOI: 10.1155/2013/270418.

(14) Arapitsas, P. Hydrolyzable tannin analysis in food. *Food Chem.* **2012**, *135*, 1708−1717.

(15) Mueller-Harvey, I. Analysis of hydrolysable tannins. *Anim. Feed Sci. Technol.* **2001**, *91*, 3−20.

(16) Nuncio-Jáuregui, N.; Nowicka, P.; Munera-Picazo, S.; Hernández, F.; Carbonell-Barrachina, A. A.; Wojdylo, A. Identification and quantification of major derivatives of ellagic acid and antioxidant properties of thining and ripe Spanish pomegranates. *J. Funct. Foods* **2015**, *12*, 354−364.

(17) Gómez-Caravaca, A. M.; Verardo, V.; Toselli, M.; Segura-Carretero, A.; Fernández-Gutiérrez, A.; Caboni, M. F. Determination of the major phenolic compounds in pomegranate juices by HPLC-DAD-ESI-MS. *J. Agric. Food Chem.* **2013**, *61*, 5328−5337.

(18) Calani, L.; Beghé, D.; Mena, P.; Del Rio, D.; Bruni, R.; Fabbri, A.; Dall'Asta, C.; Galaverna, G. Ultra-HPLC-MSn (poly)phenolic profiling and chemometric analysis of juices from ancient *Punica granatum* L. cultivars: a nontargeted approach. *J. Agric. Food Chem.* **2013**, *61*, 5600−5609.

(19) Arranz, S.; Saura-Calixto, F.; Shaha, S.; Kroon, P. A. High contents of nonextractable polyphenols in fruits suggest that polyphenol contents of plant foods have been underestimated. *J. Agric. Food Chem.* **2009**, *57*, 7298−7303.

(20) Tarascou, I.; Souquet, J. M.; Mazauric, J. P.; Carrillo, S.; Coq, S.; Canon, F.; Fulcrand, H.; Cheynier, V. The hidden face of food phenolic composition. *Arch. Biochem. Biophys.* **2010**, *501*, 16−22.

(21) Da Silva Pinto, M.; Lajolo, F. M.; Genovese, M. I. Bioactive compounds and quantification of total ellagic acid in strawberries (*Fragaria* × *ananassa* Duch). *Food Chem.* **2008**, *107*, 1629−1635.

(22) Lei, Z.; Jervis, J.; Helm, R. F. Use of methanolysis for the determination of total ellagic and gallic acid contents of wood and food products. *J. Agric. Food Chem.* **2001**, *49*, 1165−1168.

(23) Theocharis, G.; Andlauer, W. Innovative microwave-assisted hydrolysis of ETs and quantification as ellagic acid equivalents. *Food Chem.* **2013**, *138*, 2430−2434.

(24) Häkkinen, S. H.; Kärenlampi, S. O.; Mykkänen, H. M.; Heinonen, I. M.; Törrönen, A. R. Ellagic acid content in berries: Influence of domestic processing and storage. *Eur. Food Res. Technol.* **2000**, *212*, 75−80.

(25) Vrhovsek, U.; Palchetti, A.; Reniero, F.; Guillou, C.; Masuero, D.; Mattivi, F. Concentration and mean degree of polymerization of *Rubus* ETs evaluated by optimized acid methanolysis. *J. Agric. Food Chem.* **2006**, *54*, 4469−4475.

(26) Bala, I.; Bhardwaj, V.; Hariharan, S.; Ravi Kumar, M. N. V. Analytical methods for assay of ellagic acid and its solubility studies. *J. Pharm. Biomed. Anal.* **2006**, *23*, 206−210.

(27) Li, B.; Harich, K.; Wegiel, L.; Taylor, L. S.; Edgar, K. J. Stability and solubility enhancement of ellagic acid in cellulose ester soli dispersions. *Carbohydr. Polym.* **2013**, *92*, 1443−1450.

(28) Ismail, T.; Sestili, P.; Akhatar, S. Pomegranate peel and fruit extracts: a review of potential anti-inflammatory and anti-infective effects. *J. Ethnopharmacol.* **2012**, *143*, 397−405.

(29) Akhtar, S.; Ismail, T.; Fraternale, D.; Sestili, P. Pomegranate peel and peel extracts: chemistry and food features. *Food Chem.* **2015**, *174*, 417−425.

(30) Mertens-Talcott, S. U.; Jilma-Sothlawetz, P. J.; Rios, J.; Hingorani, L.; Dorendorf, H. Absorption, metabolism, and antioxidant effects of pomegranate (*Punica granatum*, L.) polyphenols after ingestion of a standardized extract in healthy human volunteers. *J. Agric. Food Chem.* **2006**, *54*, 8956−8961.

(31) Madrigal-Carballo, S.; Rodriguez, G.; Krueger, C. G.; Dreter, M.; Reed, J. D. Pomegranate (*Punica granatum*) supplements: Authenticity, antioxidant and polyphenol composition. *J. Funct. Foods* **2009**, *1*, 324−329.

DOI: 10.1021/acs.jafc.5b02062
J. Agric. Food Chem. 2015, 63, 6555−6566

in in vivo tests. In addition to IgE antibodies, a significant percentage of subjects, both kiwifruit allergic and tolerant, were also reported to produce kiwellin-specific IgG4.[7] The subjects positive to kiwellin in IgE-immunoblotting were also positive to KiTH, purified from the natural source, thus suggesting that at least the linear sequence epitopes recognized by IgE antibodies could be located on the kiwellin C-terminal domain.[2] The immunological properties, especially those correlated with the conformational epitopes, were reported to be modulated by the physicochemical features of the environment/experimental conditions, such as solvent pH and polarity.[5]

The effects of kiwellin on human health have so far received more attention than the physiological role of this protein in the natural source. The few papers describing putative homologues from other species provide only vague information on the possible implications of kiwellin in complex plant processes without any attribution of a specific function. For instance, in grape berries, a kiwellin homologue was classified as a "ripening-related protein" because of a marked increase in the mRNA levels associated with the fruit ripening.[8] A DIGE-based quantitative proteomic analysis of the grape berry suggested kiwellin's involvement in fruit development and stress response.[9] In addition, a pathogenesis-related function was hypothesized following experiments in potato leaves showing a strong up-regulation of kiwellin mRNA transcription after infection with *Phytophthora infestans*, an oomycete that causes late blight in *Solanum* spp.[10] It is worth noting that a clear orthologue of kiwellin is not present in *Arabidopsis thaliana*,[11] the model plant for which the entire genome is described. This observation suggests that kiwellin might have a specialized function associated with physiological processes particular to some plant species/families, rather than a basic function found ubiquitously throughout the plant kingdom.

In summary, the biochemical function of kiwellin, as well as its physiological role in kiwifruit, is still unknown. However, the available literature indicates that kiwellin, and its disjoined domains kissper and KiTH, may have some effects on human health, including intriguing pharmacological activities. Very recently, the partial (about 83%) crystal structure of kiwellin from the golden kiwifruit species, registered as allergen Act c 5, was reported.[12] Here we describe an investigation of the structure of kiwellin from green kiwifruit, allergen Act d 5, determined using X-ray crystallography and refined to 2.1 Å. Additionally, attempts to correlate the structural features with possible biological and immunological activities were performed.

MATERIALS AND METHODS

Protein Purification. Kiwellin was purified from the pulp of green kiwifruit (*A. deliciosa* cv. Hayward) following the already described procedure.[13] As a final purification step, the protein was subjected to size exclusion chromatography on a Superdex 75 HR10/30 column (Amersham Biosciences, Uppsala, Sweden), equilibrated and eluted with 10 mM Tris-HCl, pH 7.5, containing 0.25 M NaCl. The protein fractions were pooled and used for crystallization experiments. The protein concentration was estimated on the basis of the molar extinction coefficient at 280 nm (23335 M^{-1} cm^{-1}). The purity of the protein preparation was checked by SDS-PAGE, RP-HPLC, and N-terminal amino acid sequencing, as previously reported.[13]

Crystallization, Data Collection, and Processing. Crystallization experiments were performed at room temperature using the hanging-drop vapor diffusion method and NeXtal plates (Qiagen, Chatsworth, CA, USA). A solution of purified Act d 5 was mixed with glucose such that the final protein and glucose concentrations were 3.5 mg/mL and 50 mM, respectively. The Act d 5−glucose solution was mixed with mother liquor [0.1 M HEPES, pH 7.5, 25% (w/v) polyethylene glycol (PEG) 3350] in a 1:1 ratio and was hung over a reservoir of 26% PEG 400. The crystals were cryo-protected with PEG 400 and cooled in liquid N_2. Data were collected from a single crystal at 100 K at SER-CAT 22ID beamline at the Advanced Photon Source (APS), Argonne National Laboratory (ANL). The crystal belonged to the $P2_1$ spacegroup with two subunits per asymmetric part of the unit cell. The data were processed with the HKL-2000 software package.[14] The data collection statistics are reported in Table 1.

Table 1. Crystallographic Data and Refinement Statistics for Act d 5[a]

PDB code	4X9U
data collection	
wavelength (Å)	1.00
unit cell (a, b, c; β) (Å; °)	52.4, 60.42, 55.60; 95.9
space group	$P2_1$
solvent content (%)	43.0
protein chains in AU	2
resolution range (Å)	50.0−2.10
highest resolution shell (Å)	2.14−2.10
unique reflections	20290
redundancy	5.9 (4.3)
completeness (%)	99.8 (96.6)
R_{merge} (%)	13.0 (75.0)
average $I/\sigma(I)$	15.3 (2.1)
CC1/2	0.94(0.83)
refinement	
R (%)	16.8 (18.4)
R_{free} (%)	22.3 (26.1)
mean B value (Å^2)	39.0
B from Wilson plot (Å^2)	25.2
RMS deviation bond lengths (Å)	0.02
RMS deviation bond angles (deg)	1.80
no. of amino acid residues	326 residues total subunit A: 183 residues subunit B: 143 residues
no. of water molecules	245
Ramachandran plot	
most favored regions (%)	95.0
additional allowed regions (%)	5.0

[a]Values in parentheses refer to the highest resolution shell. AU, asymmetric unit.

Structure Determination and Refinement. The Act d 5 structure was solved by molecular replacement using a truncated version (residues 176−263) of *Achromobacter lyticus* protease I (PDB ID 1ARB) as a starting model. The starting model was identified after a BLAST[15] search with a sequence of Act d 5 against sequences of proteins with their structures determined experimentally, as reported in the Protein Data Bank.[16] Molecular replacement was performed with HKL-3000[17] integrated with MOLREP[18] and selected programs from the CCP4 package.[19] Models were rebuilt using COOT,[20] Buccaneer,[21] and ARP/wARP[22] and refined with REFMAC.[23] MOLPROBITY[24] and ADIT[25] were used for structure validation. The refinement statistics are summarized in Table 1.

Analysis of Protein Molecular Weight by Size Exclusion Chromatography. The entire molecule, kiwellin, and the C-terminal domain, KiTH, were loaded on a gel filtration column Superdex 75 HR10/30 (Amersham Biosciences), eluted with 10 mM Tris-HCl, pH

DOI: 10.1021/acs.jafc.5b02159
J. Agric. Food Chem. 2015, 63, 6567−6576

7.5, 0.25 M NaCl. Fractions of 0.5 mL were collected, and the absorbance at 280 and 230 nm was recorded.

Circular Dichroism (CD) Experiments. CD spectra were recorded on a JASCO J-810 spectropolarimeter (Easton, MD, USA) as already reported.[5] A quartz cell of 0.1 cm path length was used to record the spectra over the wavelength range of 260−190 nm with a bandwidth of 1.0 nm. The purified protein was first extensively dialyzed against 0.2 M NaCl to eliminate Tris-HCl contained in the solution and then against 2 mM NaCl. After that, the protein solution was concentrated to 1 mg/mL by ultrafiltration. For CD experiments, the protein solution was diluted 10-fold in the appropriate buffer and left for 2 h at 25 °C before acquisition of the spectra. Measurements were performed in 5 mM sodium phosphate, pH 7.4, and 5 mM sodium acetate, pH 4.5, at SDS concentrations from 0 to 100 mM, at 25 °C. The protein concentration was 0.10 mg/mL. Each spectrum was baseline corrected for the contribution of the solvent.

Endoglucanase Activity Assay. Endo-1,4-β-D-glucanase activity was assayed using dyed soluble azo-carboxymethylcellulose (AZO-CMC) as the substrate, according to the manufacturer's protocol (Megazyme, Intl., Bray, Ireland). Five, 20 and 50 μg of kiwellin were incubated overnight, at 37 °C, in the presence of 2% AZO-CMC, at pH 4.0, 5.0, 6.0, and 7.4, in 100 mM sodium acetate or sodium phosphate buffer, in a final volume of 1 mL. The reaction was stopped by adding 96% ethanol. Then, the mixture was centrifuged, and the supernatant absorbance was measured at 590 nm.

3,5-Dinitrosalicylic Acid (DNS) Assay for Reducing Sugars. Kiwellin's capacity to hydrolyze different polysaccharides made of glucose or mannose was analyzed by using the DNS colorimetric method, allowing for a quantitative estimation of released reducing sugars.[26] The substrates used were cellobiose, cellotetraose, mannan, laminarin, curdlan, and lichenan. Each one was analyzed in the following buffers: sodium phosphate, pH 4.0 and 7.4; sodium acetate, pH 5.0; MES, pH 6.0. Amounts of kiwellin corresponding to 12.5, 25, and 50 μg were added to the incubation mixture containing 100 μg of a substrate in 0.1 M buffer, in a final volume of 125 μL. Incubations were carried out at 37 °C for 1 and 3 h and overnight. Then, after 10 min at room temperature, 0.1 mL of DNS reagent was added to the samples, and the mixtures were incubated for 5 min in a boiling water bath. After cooling in an ice bath, the absorbance at 546 nm was measured. Standard curves with glucose as reducing sugar were used as a reference. All assays were carried out in duplicate.

Analysis of Released Glucose by HPLC. To assess the possible hydrolytic activity of kiwellin on cellobiose, the release of glucose was analyzed by chromatographic separation. Twenty-five micrograms of kiwellin was incubated at 37 °C in 50 mM sodium acetate, pH 5.0, in the presence of 100 μg of cellobiose, in a final volume of 0.3 mL. Fifty-microliter aliquots were removed at incubation times of 0, 3, 24, and 72 h and analyzed by an HPLC (Dionex, Sunnyvale, CA, USA), equipped with an anionic exchange column (Carbopac PA-100). Monosaccharides were separated by isocratic elution with 16 mM NaOH at a flow rate of 0.25 mL/min. Glucose was used as an internal standard.

Glycan Array Analysis. Biotinylated Act d 5 was diluted to 0.5 mg/mL in 100 mM Na_2HPO_4, 20 mM NaCl, pH 7.6, and sent to the Consortium for Functional Genomics (CFG) at Emory University to determine if protein−glycan interactions occur. The CFG facility ran the mammalian glycan array assay (version 5.1), testing 610 glycans in replicates of 6 with bacterial lectin as the positive control. The protein was directly labeled with a fluorescent tag for detection. This CFG mammalian glycan array contains glycans of potential interest for the biological effects of kiwellin in human being. It does not include plant cell wall glycans such as cellulose, xyloglucan, and pectins, but recent results indicate kiwellin has negligible affinity for these plant components.[12]

Cell Wall Creep Analysis. Cucumber seedlings were grown in the dark, and hypocotyls were harvested, frozen, abraded, and prepared for wall extension assays as described previously.[27] Seeds of wheat (*Triticum aestivum* L. cv. Pennmore) were germinated on Kimpak Seed Germination Paper K-22 (Seedburo Equipment Co., Chicago, IL, USA) soaked with distilled water, in flats, 50 × 25 × 6 cm, with lids of the same dimensions. Seedlings were grown in the dark for 4 days at 28 °C. Coleoptiles from etiolated grass seedlings were cut, gently abraded by rubbing them between two fingers coated with a slurry of well washed carborundum (320 grit, Fisher Scientific Inc., Fair Lawn, NJ, USA), separated from primary leaves, and then stored at −80 °C before use.

Etiolated wheat coleoptiles and cucumber hypocotyls were inactivated by a 15 s dip in boiling water and clamped in a constant-force extensometer[28] with 5 mm between clamps, a 20-g force, in 200 μL of 20 mM sodium acetate buffer, pH 5.5. To increase the wall sensitivity to wall-loosening agents, the buffer was exchanged at 15 min for 50 mM NaOH for ∼35 min (for coleoptile walls) or 50 mM CDTA (for cucumber walls) and then rinsed in 20 mM sodium acetate buffer. Finally, the buffer was replaced with fresh buffer containing 500 μg/mL kiwellin. All experiments were performed in replicates of four.

Protein Sequencing. Protein direct sequencing was carried out by automated Edman degradation on a Procise 492 automatic sequencer, connected with an online phenyl thiohydantoin (PTH) amino acid analyzer (Applied Biosystems, Foster City, CA, USA). Amino acids were separated by RP-HPLC and identified, as their PTH derivatives, on the basis of coelution with appropriate standards (20 PTH-amino acid standard solution, PerkinElmer Life Sciences).

Immunological Data Collection, Storing, Processing, and Statistics. Act d 5 IgE reactivity, as well as IgE reactivity toward other food and inhaled allergens, was collected by routinely testing 30836 allergics using a molecule-based microarray (ImunoCAP ISAC 103, Phadia Multiplexing Diagnostics, PMD, Vienna, Austria) bearing 103 allergenic proteins. All diagnostic data were stored during testing by online connectivity to the InterAll e-record (Allergy Data Laboratories, Italy). The study was approved by the Institutional Review board (35/IDI-CE/2006).

To understand the immunological behavior of Act d 5, a new statistical procedure was applied to this IgE data set. Act d 5 IgE reactivity was compared to the other 102 allergens using an aggregative hierarchical clustering algorithm with Ward's linkage method. The distance between two allergens was built as a dissimilarity for the categorical value (0 = patient IgE negative to the allergen, 1 = patient IgE positive to the allergen). The chosen dissimilarity was

$$d = \frac{n01 + n10}{n11 + n01 + n10}$$

where $n11$ is the number of patients positive to both allergens, $n10$ the number of patients positive to the first allergen, and $n01$ the number of patients positive to the second allergen, respectively. To remove the effect of the frequency of IgE positive patients, the allergens were divided into four frequency classes, broadly dispersed in a range from 33 for Bla g 5.0101 to 8774 patients for Phl p 1.0101 (Table S1). The results of the analysis are shown in cluster dendrogram graphics. The approximately unbiased (AU) p values for the cluster dendrograms were calculated via multiscale bootstrap resampling (pvclust package in R). To understand whether the findings obtained with the newly applied data analysis were reliable, the same analytical method was applied to a second green kiwifruit molecule, namely Act d 1, actinidin, which is known to have cysteine protease activity.[29] The IgE binding frequency of this allergen was evaluated in comparison with that of other three cysteine proteases, Der p 1, Der f 1, and Ana c 2, immobilized on the same ISAC system, usually grouped together with Act d 1 on the basis of their similar biochemical features.[30] The statistical analysis and graphical visualization of the data were performed using the R software (www.r-project.org). The statistically significant level was set at a p value <0.05.

Other Computational Calculations. The SSM algorithm[31] in COOT was used to superpose protein models. All figures containing protein structures were prepared with PyMOL[32] or Chimera.[33] PDBePISA was used to calculate the possibility of quaternary structure.[34] The Dali server was used to identify structurally similar proteins.[35] The ConSurf server was used to map sequence conservation on the Act d 5 structure.[36] An omit map was calculated with SFCHECK[37] from the CCP4 package.

DOI: 10.1021/acs.jafc.5b02159
J. Agric. Food Chem. 2015, 63, 6567−6576

RESULTS

Structural Analysis of Kiwellin. The Act d 5 molecule is composed of 189 residues (residues 2−41 and 47−189 are visible in the electron density map of subunit A, whereas residues 47−189 are visible in the electron density map of subunit B) that form two domains: the N-terminal kissper domain (residues 1−39) and the C-terminal KiTH domain (residues 40−189). Although Act d 5 crystallized with two subunits per asymmetric unit, PDBePISA indicates that this protein is more than likely monomeric, which is in line with the results from size exclusion chromatography (see below).

The kissper domain is composed of 39 residues, 6 of which are cysteines that form three disulfide bonds between residues 4 and 36, 8 and 20, and 14 and 25. This domain was run through the Dali server, and no significant matches were found. This finding could possibly indicate that kissper forms a new, previously unobserved, structural motif. The electron density for this domain is significantly worse than that of the KiTH domain, and the average *B* factors are 95 Å^2 (Figures S1 and S2). The kissper domain from chain A (Figures S1 and S2), that we were able to trace forms crystal contacts with two other symmetry-related molecules. Therefore, the conformation of the Act d 5 that we observed corresponds to a protein state that was "trapped" by crystal lattice. Most likely, the kissper domain of chain B did not form any stable crystal contacts and was relatively free to move in the crystal. Therefore, there is no well-defined electron density that corresponds to this fragment of the structure.

The KiTH domain, however, is composed 150 residues arranged as a six-stranded β-barrel with two extended loops (residues 81−105 and 144−159) that form a "pincher-like" structure (Figure 1). An additional loop is found at the N-terminal portion of this domain and is stabilized to the core of the KiTH module by two disulfide bridges. KiTH contains eight cysteines in total, all of which participate in disulfide bonds: residues 48 and 66, 56 and 148, 95 and 120, and 142 and 158 (Figure 2). It also has more complete density than the kissper domain, and the average *B* factors of subunits A and B are 34 and 33 Å^2, respectively.

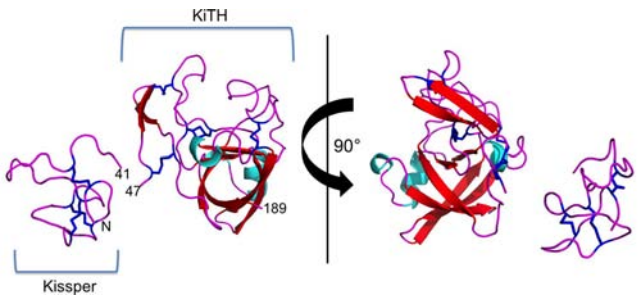

Figure 1. Overall structure of kiwellin. Secondary structural elements are colored separately where α-helices are colored cyan, β-sheets are colored red, loops are colored magenta, and disulfide bonds are colored blue. The N-terminal kissper domain and the C-terminal KiTH domain are labeled.

After performing a search of the KiTH domain using the Dali server, Dali identified kiwellin (PDB code 4PMK) as the most closely related structure. A superposition of 4PMK on our structure results in a root-mean-square deviation (RMSD) of 0.3 Å over 142 aligned Cα atoms. Hamiaux and colleagues recently determined this structure,[12] and although the RMSD is 0.3 Å between the two structures, there are some structural differences. One evident difference between the two structures is seen at the N terminus. Kiwellin from golden kiwifruit has a short fragment of the kissper domain modeled, which contains residues 24−39. Our structure, however, contains a more complete N-terminal domain spanning from residues 2 to 39. With this more complete model, we were able to properly establish which C-terminal (KiTH) domain corresponds to the proper kissper (N-terminal) domain, which was improperly done in the case of the kiwellin from golden kiwifruit.[12] The correct domain organization of the Act d 5 molecule was determined on the basis of the analysis of the crystal packing and the distance from residue 42 to 47 (where there is a gap in electron density); all other subunits, other than the one chosen for our model, were located at a distance that was too far away and therefore could not be correct. With an incomplete model it is not obvious how to correctly match domains. Once this was established, the second protein chain in the asymmetric unit was properly assigned.

Dali also identified the N-terminal (double-ψ β-barrel) domain of several expansin proteins, including one from *Clavibacter michiganensis* (for example, PDB code 4JJO, RMSD value 1.6 Å over 92 aligned Cα atoms, sequence identity of 25%); several expansin−yoaj proteins from *Bacillus subtilis* (for example, PDB code 4FFT, RMSD value 1.6 Å over 91 aligned Cα atoms, sequence identity of 13%); maize allergen Zea m 1 (PDB code 2HCZ, RMSD value 2.0 Å over 101 aligned Cα atoms, sequence identity of 15%); and pollen allergen Phl p 1 (PDB code 1N10, RMSD value 1.4 Å over 89 aligned Cα atoms, sequence identity of 18%) as having the most similar structures to Act d 5. Act d 5 and the previously mentioned similar structures align through the core, β-barrel, domain of the protein, confirming the observations of Hamiaux et al.[12] The differences between the other similar structures and Act d 5 are seen outside the core structure. Mainly, the kissper domain of Act d 5 does not align with any of the similar structures. Furthermore, the N-terminal loop of the KiTH domain (residues 47−72) and the two loops that form the "pincher-like" structure (residues 81−105 and 114−159) do not align with any of the similar structures. These three structural elements, the kissper domain, and the positions of loops 47−72, 81−105 and 114−159, are unique to Act d 5.

Figure 2 also shows surface and ribbon representations of the Act d 5 molecule, indicating conservation among 150 Act d 5-related protein sequences selected by ConSurf. It also includes the sequence of kiwellin, where the most and least conserved residues are indicated, broken down into domains, and disulfide linkages are indicated. Even though the Dali server did not find any structurally significant matches for the kissper domain, the protein sequence is conserved, especially when compared to proteins with uncharacterized function. Electrostatic potentials were calculated using Chimera[33] and are mapped out on the surface of kiwellin, shown in Figure 3. It is interesting to note that a large portion of the KiTH domain is negatively charged, thus suggesting that Act d 5 can bind positively charged ligands and cations.

Identification of Residues 41 and 43 of Kiwellin as Hydroxyproline (Hyp). The primary structure of kiwellin had been elucidated by direct sequencing of the N-terminal region of the native protein and of the peptides obtained by proteolytic digestion of the denatured and alkylated protein.[13] Residues at positions 41 and 43 were interpreted to be histidine (UniProtKB, accession no. P84527). Later it was observed that,

DOI: 10.1021/acs.jafc.5b02159
J. Agric. Food Chem. 2015, 63, 6567−6576

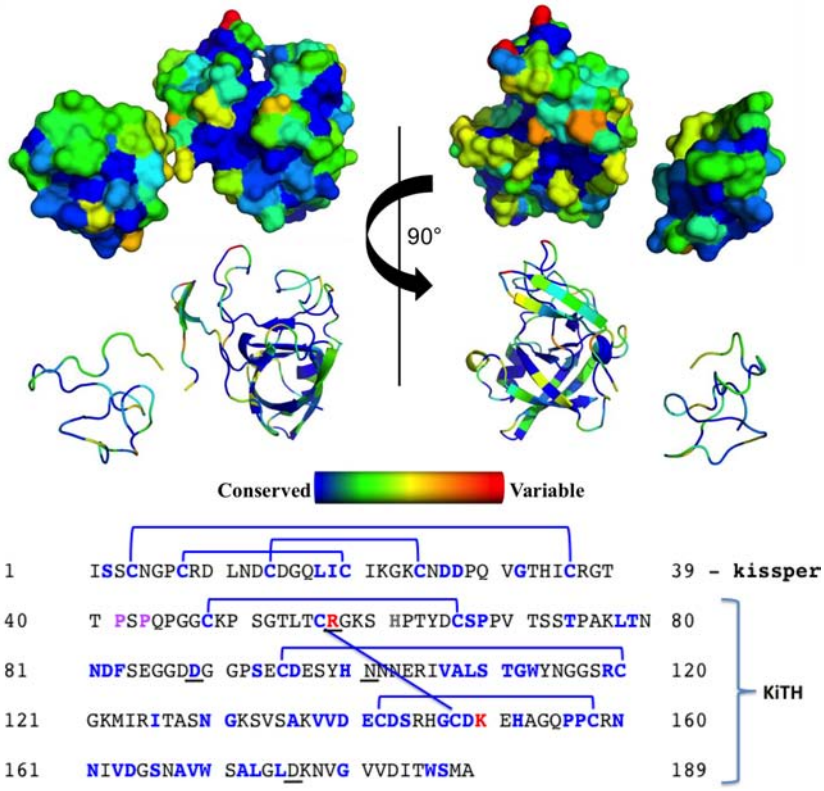

Figure 2. (Top) Surface and ribbon representation of Act d 5 showing conserved residues derived from an alignment of 150 Act d 5-related protein sequences selected by ConSurf. The most conserved residues are shown in blue, whereas the most variable residues are shown in red. (Bottom) Sequence of Act d 5, where the kissper and KiTH domains are separated. The most conserved residues are shown in blue and the most variable residues are shown in red. Residues 41 and 43, shown in purple, are hydroxyprolines. A mutation in residue 61 is seen in the natural variants of the protein where a tyrosine is substituted for a histidine. Due to kiwellin being purified from a natural source, residue 61, shown in gray, is a histidine. The four residues that are different between Act d 5 and Act c 5 are underlined.

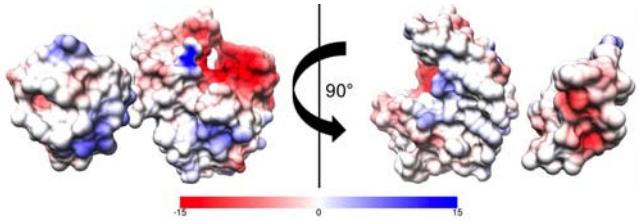

Figure 3. Surface representation of Act d 5 with electrostatic potentials, where blue indicates positive charge and red indicates negative charge in units of kcal/(mol·*e*).

during the sequencing procedure, both residues 41 and 43 were reproducibly eluted by RP-HPLC as two peaks, one almost coeluting with histidine and the other was eluted near alanine, in a peak ratio of about 3:5. This observation, together with literature reports, strongly suggested that residues 41 and 43 are Hyp, as an isomeric mixture,[38] rather than histidine. Nevertheless, no standards used as a reference were available to confirm it. Then, the publication of the DNA-derived protein sequence of kiwellin confirmed that the gene-coded amino acid present in positions 41 and 43 is proline.[11] It was initially confused with histidine because of the post-translational modification, consisting of the hydroxylation of proline residues and affecting their chromatographic behavior during the protein sequencing procedure.

Analysis of Protein Molecular Weight in Solution. On the basis of the elution volume by gel filtration chromatography on a precalibrated Superdex 75, the molecular weight estimated for the entire molecule kiwellin and that for KiTH correspond to 22 and 16 kDa, respectively (Figure 4). These values are in agreement with the size calculated on the basis of the amino acid sequence and indicate that both molecules are monomeric in the conditions of the size exclusion chromatography.

Effect of pH and Hydrophobic Environments on the Structure of Kiwellin, Kissper, and KiTH. SDS was used to

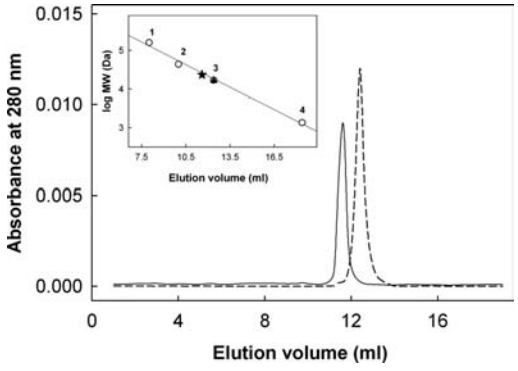

Figure 4. Gel filtration profile on a Superdex 75 column of kiwellin (solid line) and KiTH (dashed line). (Inset) Plot of the elution volume versus log molecular weight of kiwellin (star) and KiTH (triangle). The marker proteins (empty circle) are (1) γ-globulin (158 kDa), (2) ovalbumin (45 kDa), (3) myoglobin (17 kDa), and (4) vitamin B12 (1.3 kDa).

DOI: 10.1021/acs.jafc.5b02159
J. Agric. Food Chem. 2015, 63, 6567−6576

mimic hydrophobic environments in buffer solutions. Overlapping CD spectra were obtained with kiwellin in neutral and acidic buffer solution (Figure 5). The presence of SDS causes

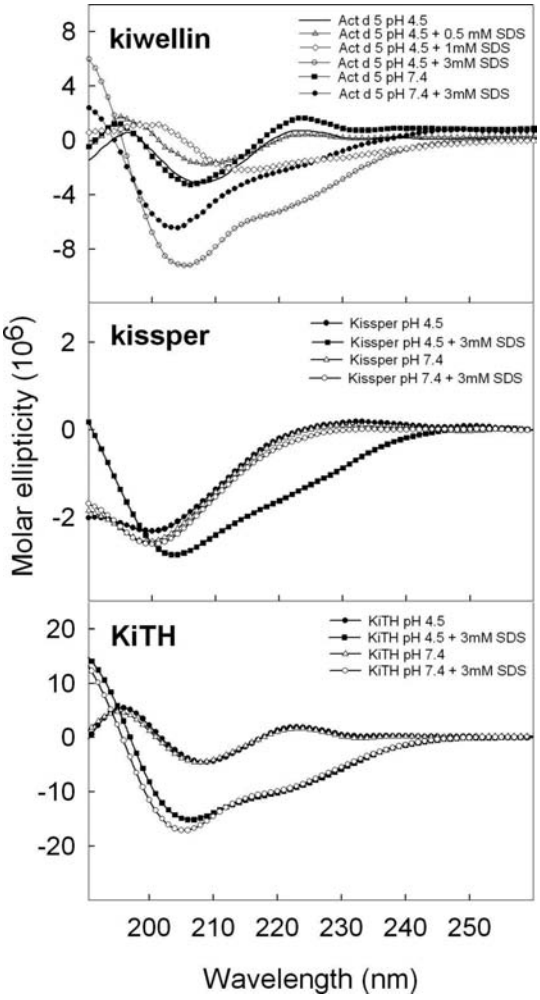

Figure 5. CD spectra of kiwellin, kissper, and KiTH, at pH 7.4 and 4.5, and in the presence of SDS.

significant variation of the structural features. SDS concentrations lower than 3 mM cause a decrease in the structure content. In contrast, at concentrations higher than 3 mM, corresponding to the critical micellar concentration (CMC), SDS induces an increase in secondary structure content, as shown by the large increase in negative ellipticity of the spectra. Spectra at 10 and 100 mM SDS overlap with the spectra at 3 mM and therefore have not been shown in Figure 5. Overall, the shapes of spectra suggest mixed secondary structure content in all of the assayed conditions. In the 3−100 mM SDS range, the presence in the curves of minima at about 208 and 222 nm suggests an increase in the helical content in these experimental conditions.

Kissper displays the typical spectrum of unstructured proteins in both buffers, at neutral and acidic pH. At neutral pH, the addition of 3 mM SDS does not change the spectrum shape. Conversely, the presence of both SDS and acidic pH is the only condition under which kissper shows the spectrum of a structured protein. Unlike kissper, KiTH does not show pH dependence, both in the presence and in the absence of SDS. However, its structure is affected by the presence of SDS that causes an increase in the secondary structure content. The shape of the KiTH spectra suggests a higher content of helical structure in the hydrophobic environment mimicked by SDS.

Attempts To Identify the Biological Function of Act d 5. Assays of glycosidase activity by kiwellin were negative. Results obtained using cellobiose, cellotetraose, mannan, laminarin, curdlan, lichenan, and carboxymethylcellulose as substrates suggest that kiwellin does not have hydrolytic activity on linear and branched glucose chains bearing β-1,3, β-1,4, and β-1,6 glycosidic bonds, as well on oligosaccharides made of mannose units. Indeed, the DNS assay showed a weak positive response when cellobiose was used as a substrate. However, the analysis of the reaction products by a Dionex HPLC revealed the absence of monosaccharidic glucose, thus suggesting the weak positive response observed by DNS assay was attributable to an artifact. Attempts to assess glycan binding to kiwellin likewise gave negative results. The glycan array, completed by the CFG, did not indicate any binding between Act d 5 and any of the 610 different carbohydrates tested.

The cell wall creep assay was performed in 4−8 replicate experiments with two different types of cell wall (cucumber hypocotyl, representing dicot walls, and wheat coleoptile, representing grass walls) and at a high kiwellin concentration of 500 μg/mL. This assay is a very sensitive assay (detection of less than 10 ng/mL of alpha-expansin is possible), but no sign of activity was detected upon kiwellin application (Figure S3). Thus, there was no sign of classical expansin activity in kiwellin.

Attempts To Identify Act d 5 IgE Binding Activity Shared with 102 Other Allergens. Table S1 reports the list of the 103 allergens spotted on the ISAC microarray used in this study and the frequency with which they were recognized by specific IgE of a population composed of 30836 random allergic subjects. On the basis of the frequency of detected IgE positivities, allergens have been divided in four groups. Table S1 shows that Act d 5 is included in the group of "low-frequency allergens", due to the low percentage of subjects having IgE recognizing this molecule. In contrast, the two allergens belonging to the expansin biochemical family, Phl p 1 and Cyn d 1, are included in the group of "high-frequency allergens". The large difference between the relative frequency of positive subjects, ranging from 0.49% for Act d 5 to 28.45% for Phl p 1 and 24.3% for Cyn d 1, emphasizes the different immunological behavior of the kiwifruit allergen when compared to the two expansins. In particular, Act d 5 appears much less allergenic than Phl p 1 and Cyn d 1.

The immunological behavior of Act d 5 was further investigated using a statistical procedure. The analysis of Act d 5 toward the four data sets of Table S1 produced the results shown in Figure S4. The dendrograms of Figure S4 show that no Act d 5 IgE reactivity clustering reaching statistical significance could be obtained with any of the other 102 analyzed allergens, including the two expansins Phl p 1 and Cyn d 1. Conversely, statistically significant clustering was obtained for more closely related allergens, such as the expansins Phl p 1 and Cyn d 1, the LTP Pru p 3 and Art v 3, the cysteine proteases Der p 1 and Der f 1, and so on. The real immunological correlation between the clustered allergens is supported by literature data reporting IgE corecognition.[39] All together, the clustering results and the reported IgE corecognition data highlight that allergenic proteins having similar folds and amino acid sequences generally display similar immunological features, reasonably correlated to a common set of antigenic epitopes. Act d 5 does not show immunological

DOI: 10.1021/acs.jafc.5b02159
J. Agric. Food Chem. 2015, 63, 6567−6576

correlation with expansins or with any of the other analyzed allergens. This observation suggests that, despite the observed folding similarities with expansins, Act d 5 does not bear on its surface the structural determinants of IgE epitopes found in Phl p 1 and Cyn d 1, and more in general that the molecular surface of the kiwifruit allergen is significantly different from that of the two expansins.

As a control, the same statistical procedure was applied to the analysis of another kiwifruit allergen, Act d 1. Act d 1 is a cysteine protease that is reported to be structurally similar to other allergens, including the three spotted on the ISAC 103 microarray, namely, Ana c 2, Der p 1, and Der f 1.[30] In line with the absence of any data attesting immunological cross-reaction with the three homologous cysteine proteases,[30] no Act d 1 IgE reactivity clustering was observed (Figure S5).

DISCUSSION

Here we report the crystal structure of green kiwifruit kiwellin, Act d 5, obtained by X-ray diffraction analysis. This study supplements the very recently reported results for the homologous protein from golden kiwifruit, Act c 5.[12] In fact, the published structure included 158 amino acids, which is approximately 83% of the overall molecule, including residues 24−39 and 48−189 and the four disulfide bridges inside the C-terminal domain, KiTH. The analysis of the electron density maps of green kiwifruit kiwellin, described in this paper, has allowed for the elucidation of additional portions of the structure. Overall, about 97% of the three-dimensional structure of the green kiwifruit allergen has been resolved, and it includes residues 2−42 and 47−189; only five residues, Ile,[1] Hyp,[43] Gln[44], Pro[45], and Gly[46], remain unresolved, which correspond to a flexible linker between the two protein domains. In addition, we report here the description of the post-translational modification occurring on residues 41 and 43 that undergo hydroxylation, producing Hyp. The correction of the sequence data provides useful information that better describes the site recognized by actinidin in the in vivo proteolytic processing of kiwellin. It was previously reported that actinidin cleaves between residues 39−40 and 41−42 of the kiwellin sequence.[2] It is also known that the kiwifruit protease hydrolyzes different types of collagen,[40] which are Hyp-containing proteins. These observations suggest that the two Hyp residues, which are located in the flexible linker region connecting kissper to KiTH, are involved in the formation of kiwellin's proteolytic sites recognized by actinidin. This site is formed by the sequence Thr/Ser-Hyp, where the kiwifruit protease cleaves at the N-terminal side of this motif having Hyp at the P2′ position.

The sequence of green kiwifruit kiwellin was reported to contain heterogeneity in position 61, where Y is sometimes substituted by H. Similar to golden kiwellin, the isoform used in this study had H in position 61. Green and golden kiwifruit kiwellin (accession no. P84527 and L7TT83) share about 98% sequence identity. In fact, only the following residues of the green kiwifruit molecule are substituted in the golden species: R57 with Q, D89 with G, N101 with S, and D176 with N. In line with the very high sequence identity, some major structural features described for the golden kiwifruit kiwellin have been observed in the homologous molecule from the green species. The best defined example is the C-terminal domain, KiTH, characterized by a six-stranded β-barrel with two extended loops forming a "pincher-like" structure and an additional loop found at the N-terminal portion that is connected to the core of this domain by two disulfide bridges.

The structure of the entire N-terminal domain, kissper, has also been determined, and the connectivity of the six cysteine residues, previously suggested on the basis of NMR studies,[3] has been confirmed by the crystal structure analysis. In the structure, kissper appears devoid of clearly defined secondary structural elements such as α-helix or β-sheet. Previous NMR studies indicated that in aqueous solution, at pH 3.5, kissper was characterized by the presence of multiple conformations. Nevertheless, in the experimental conditions of NMR, short regions of regular structure, described as a short antiparallel β-sheet encompassing residues 19−21/24−26 and a short helix spanning residues 32−35, were detected. Therefore, the kissper domain, in solution at low pH, showed some structural features different from those of the crystallized molecule. In line with the crystal structure results, in the conditions of CD experiments, kissper appears completely unstructured in buffer solutions, at both neutral and acidic pH values. Only the combination of acidic pH and SDS, used to mimic the hydrophobic environment of cell membranes, was effective in inducing the peptide folding. This behavior is in line with the reported functional properties. In fact, functional studies showed that kissper displays pore-forming and ion-channeling activities in lipid bilayers, and the efficiency increases at low pH.[3] These data suggest that the N-terminal domain of kiwellin performs its physiological function by interacting with cell membranes in the acidic environment of kiwifruit. It is then conceivable that kissper adopts the native structure, likely corresponding to the most structured conformation, in the cell membranes of the natural source or in experimental conditions mimicking those of kiwifruit membranes. Unfortunately, these conditions could not be used for protein crystallization. Therefore, we speculate that kissper, which is devoid of secondary structural elements in the conditions used for crystallization, may adopt a different conformation in the physiological environment. Unlike kissper, the kiwellin C-terminal domain has well-defined secondary structural elements both in the crystal and in solution. In addition, CD data suggest that the KiTH conformation is not dependent on pH, whereas it is influenced by the hydrophobic environment that causes an increase in secondary structure content. The amount of secondary structure in the entire kiwellin molecule seems to be correlated to the individual contribution of the two independent domains. A higher content of secondary structure when incubated at acidic pH in low-polarity media, namely fluorinated alcohols, had already been reported.[5] Specifically, higher amounts of α-helical structure were detected and the strongest increase in secondary structure was obtained in the environments where low pH was combined with high hydrophobicity. In line with those results, in this paper we show that the amount of kiwellin's secondary structure increases in SDS.

Additionally, it was reported that the immunological properties of kiwellin are also affected by the physicochemical features of the experimental conditions.[5] In fact, protein solubilized in acidic solvent caused positive skin tests in patients that tested negative at neutral pH, and vice versa. This observation therefore indicates that the assay conditions influence the protein conformation and/or surface charge, thus affecting the results of the diagnostic systems by modulating the pattern of exposed IgE-binding epitopes. Intriguingly, some patients allergic to kiwifruit and positive in

DOI: 10.1021/acs.jafc.5b02159
J. Agric. Food Chem. 2015, 63, 6567−6576

skin prick test were negative when tested for IgE binding by serological tests. The above-described structural properties, which are strongly dependent on the features of the environment, support the concept that the discrepant immunological results, obtained using different allergy test systems, can be correlated to different combinations of IgE epitopes exposed on the protein surface as a function of the specific experimental conditions, affecting the kiwellin conformation or surface charge. Due to the changing structure, the definition of immunological properties of kiwellin and patient sensitivity to this molecule becomes a tricky matter. It is worth noting that the behavior of other allergens is also unknown. In fact, the state of the solid phases is not known for either kiwellin or for any other tested protein. Furthermore, the overall conditions of the testing system might generate alterations of the state of any molecule, altering some conformational epitopes and leading to the loss of some IgE reactivity. Therefore, the observations deriving from the study of kiwellin highlight a concept that probably is of general meaning and could cover any protein.

Similarity searches revealed several expansins, including the maize allergen Zea m 1 and the pollen allergen Phl p 1, as the proteins having structures most similar to kiwellin, specifically to the KiTH domain. However, attempts to detect expansin activity (plant cell wall loosening) proved negative for kiwellin. Likewise, kiwellin lacked lytic activity and binding activity toward wall-related polysaccharides (our results and those of Hamiaux et al.[12]). These results are consistent with what we know about expansins:[41] the N-terminal domain of expansin (which is structurally related to KiTH) is not sufficient to cause cell creep; it has negligible affinity for wall polysaccharides, and it lacks wall lytic activity. It is notable that kiwellin has an Asp−Thr pair (D164, T79) that superposes closely with two highly conserved residues in expansins and other structurally related proteins,[42] but it lacks a Tyr residue corresponding to the highly conserved Tyr that makes up the part of the presumptive active site of expansin. Another major difference is that expansin forms an open structure surrounding the conserved Asp−Thr pair, whereas kiwellin has two loops (S84−P92 and S144−C158) that form a tunnel-like/pincher-like structure with D164−T79 at the base of the tunnel. The tunnel is likely able to accommodate a single glycan chain.

An attempt to assess the binding of kiwellin to the 610 different mammalian carbohydrates immobilized on the test system of the Consortium for Functional Genomics indicated negligible binding under the test conditions. In view of the tunnel-like structure of the kiwellin, Figure 6, it is possible that immobilization of the carbohydrates would interfere with their ability to fit into the tunnel. In addition to these structural and functions comparisons, IgE-based immunological data also seem to confirm the absence of similarities of kiwellin with expansins and other carbohydrate-binding allergens. In fact, the analysis performed using a newly adopted statistical procedure shows no Act d 5 IgE reactivity clustering with any of the other 102 tested allergens, thus suggesting the absence of epitope sharing.

In summary, attempts to find a correlation between structural and functional properties of kiwellin indicate important similarities and differences with expansins, but have not revealed a specific function or saccharide ligand that binds tightly. Expansin's N-terminal domain, as well as kiwellin, resembles a protein named barwin.[43] Although barwin's biological function is uncertain, it binds weakly (K_d = 5 mM) to chitin oligosaccharide, and it may be involved in defense mechanisms. Such a role for kiwellin, that is, as an antifungal agent, might be consistent with its high expression in ripening fruit and should be considered in future studies.

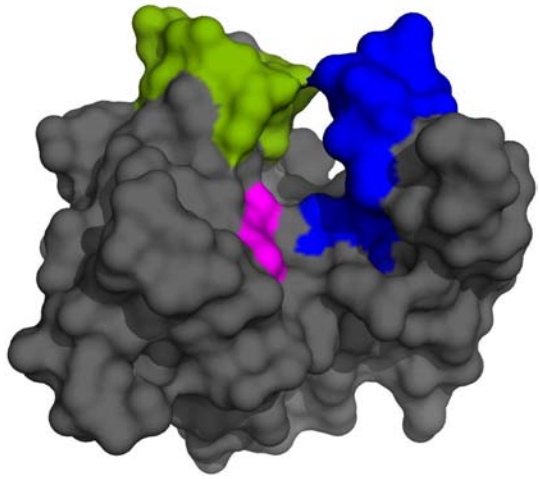

Figure 6. Space-filling model of KiTH domain showing the surface formed by conserved D164−T79 (magenta) at the bottom of a tunnel formed by loops S84−P92 (green) and S144−C158 (blue).

A notable feature of our results is the strong dependence of kiwellin properties on the environmental/experimental conditions. It is not known if the conformation found in the crystal is the same conformation that is exhibited in some tissues of the human body, where it works as an allergen. It is also unclear how the physiological fold of kiwellin is different from that observed in the crystal. However, we do know from the CD experiments in low-polarity media that kiwellin is capable of significant structural changes as a function of the environmental conditions. The results reported in this paper can be considered a collection of valuable data to better design targeted future studies with the aim to understand the structure of the molecule working in the physiological environment and also the structure of the molecule that causes allergic reactions. In fact, it is not obvious that the same fold is correlated with the function in the natural source and also with the allergenic properties.

■ ASSOCIATED CONTENT

Ⓢ Supporting Information

Additional table and figures. The Supporting Information is available free of charge on the ACS Publications website at DOI: 10.1021/acs.jafc.5b02159.

Accession Codes

Coordinates and structure factors have been deposited to the PDB with the following accession code 4X9U.

■ AUTHOR INFORMATION

Corresponding Authors

*(M. A. Ciardiello) Phone: +39 081 6132573. Fax: +39 081 6132646. E-mail: mariaantonietta.ciardiello@ibbr.cnr.it.

*(M. Chruszcz) Phone: (803) 777-7399. Fax: (803) 777-9521. E-mail: chruszcz@mailbox.sc.edu.

Funding

Use of the Advanced Photon Source was supported by the U.S. Department of Energy, Office of Science, Office of Basic Energy Sciences, under Contract W-31-109-Eng-38. This work is

DOI: 10.1021/acs.jafc.5b02159
J. Agric. Food Chem. 2015, 63, 6567−6576

partially supported by an ASPIRE grant from the Office of the Vice President of Research at the University of South Carolina. We acknowledge the participation of the Protein-glycan Interaction Resource of the CFG and the supporting grant R24 GM098791. The Italian Ministry of Economy and Finance (MEF) Project, CISIA-Conoscenze Integrate per la Sostenibilità e l'Innovazione del made in Italy Agroalimentare, also contributed to this study. We acknowledge the contribution of the Italian Ministry of Health, Current Research Program 2009−2010, and the partial financial support to I.G. by the International Fund for Advanced Research in Allergy and Immunology Onlus (Italy). The cell wall creep assays were carried out by Edward Wagner and supported by U.S. Department of Energy Grant DE-FG02-84ER13179 to D.J.C. from the Office of Basic Energy Sciences.

Notes

The authors declare no competing financial interest.

■ ACKNOWLEDGMENTS

Data were collected at Southeast Regional Collaborative Access Team (SER-CAT) 22-ID beamline at the Advanced Photon Source, Argonne National Laboratory. Supporting institutions may be found at www.ser-cat.org/members.html. Use of the Allergome-InterAll software was generously made available for free by Allergy Data Laboratories s.c., Italy. We thank members of the Center for Molecular Allergology who contributed to laboratory data collection. We acknowledge Consortium for Functional Glycomics Grant GM62116 for glycan array screening.

■ ABBREVIATIONS USED

PDB, Protein Data Bank; APS, advanced photon source; ANL, Argonne National Laboratory; RMSD, root-mean-square deviation; AU, approximately unbiased; CD, circular dichroism; SDS, sodium dodecyl sulfate

■ REFERENCES

(1) Ciardiello, M. A.; Giangrieco, I.; Tuppo, L.; Tamburrini, M.; Buccheri, M.; Palazzo, P.; Bernardi, M. L.; Ferrara, R.; Mari, A. Influence of the natural ripening stage, cold storage, and ethylene treatment on the protein and IgE-binding profiles of green and gold kiwi fruit extracts. *J. Agric. Food Chem.* **2009**, *57*, 1565.

(2) Tuppo, L.; Giangrieco, I.; Palazzo, P.; Bernardi, M. L.; Scala, E.; Carratore, V.; Tamburrini, M.; Mari, A.; Ciardiello, M. A. Kiwellin, a modular protein from green and gold kiwi fruits: evidence of in vivo and in vitro processing and IgE binding. *J. Agric. Food Chem.* **2008**, *56*, 3812.

(3) Ciardiello, M. A.; Meleleo, D.; Saviano, G.; Crescenzo, R.; Carratore, V.; Camardella, L.; Gallucci, E.; Micelli, S.; Tancredi, T.; Picone, D.; Tamburrini, M. Kissper, a kiwi fruit peptide with channel-like activity: structural and functional features. *J. Pept. Sci.* **2008**, *14*, 742.

(4) Ciacci, C.; Russo, I.; Bucci, C.; Iovino, P.; Pellegrini, L.; Giangrieco, I.; Tamburrini, M.; Ciardiello, M. A. The kiwi fruit peptide kissper displays anti-inflammatory and anti-oxidant effects in in-vitro and ex-vivo human intestinal models. *Clin. Exp. Immunol.* **2014**, *175*, 476.

(5) Bernardi, M. L.; Picone, D.; Tuppo, L.; Giangrieco, I.; Petrella, G.; Palazzo, P.; Ferrara, R.; Tamburrini, M.; Mari, A.; Ciardiello, M. A. Physico-chemical features of the environment affect the protein conformation and the immunoglobulin E reactivity of kiwellin (Act d 5). *Clin. Exp. Allergy* **2010**, *40*, 1819.

(6) Palazzo, P.; Tuppo, L.; Giangrieco, I.; Bernardi, M. L.; Rafaiani, C.; Crescenzo, R.; Tamburrini, M.; Zuzzi, S.; Alessandri, C.; Mari, A.; Ciardiello, M. A. Prevalence and peculiarities of IgE reactivity to kiwifruit pectin methylesterase and its inhibitor, Act d 7 and Act d 6, in subjects allergic to kiwifruit. *Food Res. Int.* **2013**, *53*, 24.

(7) Bublin, M.; Dennstedt, S.; Buchegger, M.; Ciardiello, M. A.; Bernardi, M. L.; Tuppo, L.; Harwanegg, C.; Hafner, C.; Ebner, C.; Ballmer-Weber, B. K.; Knulst, A.; Hoffmann-Sommergruber, K.; Radauer, C.; Mari, A.; Breiteneder, H. The performance of a component-based allergen microarray for the diagnosis of kiwifruit allergy. *Clin. Exp. Allergy* **2011**, *41*, 129.

(8) Davies, C.; Robinson, S. P. Differential screening indicates a dramatic change in mRNA profiles during grape berry ripening. Cloning and characterization of cDNAs encoding putative cell wall and stress response proteins. *Plant Physiol.* **2000**, *122*, 803.

(9) Martinez-Esteso, M. J.; Selles-Marchart, S.; Lijavetzky, D.; Pedreno, M. A.; Bru-Martinez, R. A DIGE-based quantitative proteomic analysis of grape berry flesh development and ripening reveals key events in sugar and organic acid metabolism. *J. Exp. Bot.* **2011**, *62*, 2521.

(10) Draffehn, A. M.; Li, L.; Krezdorn, N.; Ding, J.; Lubeck, J.; Strahwald, J.; Muktar, M. S.; Walkemeier, B.; Rotter, B.; Gebhardt, C. Comparative transcript profiling by SuperSAGE identifies novel candidate genes for controlling potato quantitative resistance to late blight not compromised by late maturity. *Front. Plant Sci.* **2013**, *4*, 423.

(11) Crowhurst, R. N.; Gleave, A. P.; MacRae, E. A.; Ampomah-Dwamena, C.; Atkinson, R. G.; Beuning, L. L.; Bulley, S. M.; Chagne, D.; Marsh, K. B.; Matich, A. J.; Montefiori, M.; Newcomb, R. D.; Schaffer, R. J.; Usadel, B.; Allan, A. C.; Boldingh, H. L.; Bowen, J. H.; Davy, M. W.; Eckloff, R.; Ferguson, A. R.; Fraser, L. G.; Gera, E.; Hellens, R. P.; Janssen, B. J.; Klages, K.; Lo, K. R.; MacDiarmid, R. M.; Nain, B.; McNeilage, M. A.; Rassam, M.; Richardson, A. C.; Rikkerink, E. H. A.; Ross, G. S.; Schroder, R.; Snowden, K. C.; Souleyre, E. J. F.; Templeton, M. D.; Walton, E. F.; Wang, D.; Wang, M. Y.; Wang, Y. Y.; Wood, M.; Wu, R. M.; Yauk, Y. K.; Laing, W. A. Analysis of expressed sequence tags from *Actinidia*: applications of a cross species EST database for gene discovery in the areas of flavor, health, color and ripening. *BMC Genomics* **2008**, *9*, 351.

(12) Hamiaux, C.; Maddumage, R.; Middleditch, M. J.; Prakash, R.; Brummell, D. A.; Baker, E. N.; Atkinson, R. G. Crystal structure of kiwellin, a major cell-wall protein from kiwifruit. *J. Struct. Biol.* **2014**, *187*, 276.

(13) Tamburrini, M.; Cerasuolo, I.; Carratore, V.; Stanziola, A. A.; Zofra, S.; Romano, L.; Camardella, L.; Ciardiello, M. A. Kiwellin, a novel protein from kiwi fruit. Purification, biochemical characterization and identification as an allergen. *Protein J.* **2005**, *24*, 423.

(14) Otwinowski, Z., Minor, W. Processing of X-ray diffraction data collected in oscillation mode. In *Methods in Enzymology: Macromolecular Crystallography, Part A*; Academic Press: New York, 1997; Vol. 276, pp 307.

(15) Altschul, S. F.; Madden, T. L.; Schaffer, A. A.; Zhang, J.; Zhang, Z.; Miller, W.; Lipman, D. J. Gapped BLAST and PSI-BLAST: a new generation of protein database search programs. *Nucleic Acids Res.* **1997**, *25*, 3389.

(16) Berman, H. M.; Battistuz, T.; Bhat, T. N.; Bluhm, W. F.; Bourne, P. E.; Burkhardt, K.; Feng, Z.; Gilliland, G. L.; Iype, L.; Jain, S.; Fagan, P.; Marvin, J.; Padilla, D.; Ravichandran, V.; Schneider, B.; Thanki, N.; Weissig, H.; Westbrook, J. D.; Zardecki, C. The Protein Data Bank. *Acta Crystallogr., Sect. D: Biol. Crystallogr.* **2002**, *58*, 899.

(17) Minor, W.; Cymborowski, M.; Otwinowski, Z.; Chruszcz, M. HKL-3000: the integration of data reduction and structure solution − from diffraction images to an initial model in minutes. *Acta Crystallogr., Sect. D: Biol. Crystallogr.* **2006**, *62*, 859.

(18) Vagin, A.; Teplyakov, A. MOLREP: an automated program for molecular replacement. *J. Appl. Crystallogr.* **1997**, *30*, 1022.

(19) Winn, M. D.; Ballard, C. C.; Cowtan, K. D.; Dodson, E. J.; Emsley, P.; Evans, P. R.; Keegan, R. M.; Krissinel, E. B.; Leslie, A. G. W.; McCoy, A.; McNicholas, S. J.; Murshudov, G. N.; Pannu, N. S.; Potterton, E. A.; Powell, H. R.; Read, R. J.; Vagin, A.; Wilson, K. S. Overview of the CCP4 suite and current developments. *Acta Crystallogr., Sect. D: Biol. Crystallogr.* **2011**, *67*, 235.

DOI: 10.1021/acs.jafc.5b02159
J. Agric. Food Chem. 2015, 63, 6567−6576

(20) Emsley, P.; Cowtan, K. Coot: model-building tools for molecular graphics. *Acta Crystallogr., Sect. D: Biol. Crystallogr.* **2004**, *60*, 2126.
(21) Cowtan, K. The Buccaneer software for automated model building. 1. Tracing protein chains. *Acta Crystallogr., Sect. D: Biol. Crystallogr.* **2006**, *62*, 1002.
(22) Perrakis, A.; Morris, R.; Lamzin, V. S. Automated protein model building combined with iterative structure refinement. *Nat. Struct. Biol.* **1999**, *6*, 458.
(23) Murshudov, G. N.; Skubak, P.; Lebedev, A. A.; Pannu, N. S.; Steiner, R. A.; Nicholls, R. A.; Winn, M. D.; Long, F.; Vagin, A. A. REFMAC5 for the refinement of macromolecular crystal structures. *Acta Crystallogr., Sect. D: Biol. Crystallogr.* **2011**, *67*, 355.
(24) Davis, I. W.; Leaver-Fay, A.; Chen, V. B.; Block, J. N.; Kapral, G. J.; Wang, X.; Murray, L. W.; Arendall, W. B., 3rd; Snoeyink, J.; Richardson, J. S.; Richardson, D. C. MolProbity: all-atom contacts and structure validation for proteins and nucleic acids. *Nucleic Acids Res.* **2007**, *35*, W375.
(25) Yang, H.; Guranovic, V.; Dutta, S.; Feng, Z.; Berman, H. M.; Westbrook, J. D. Automated and accurate deposition of structures solved by X-ray diffraction to the Protein Data Bank. *Acta Crystallogr. Acta Crystallogr., Sect. D: Biol. Crystallogr.* **2004**, *60*, 1833.
(26) Miller, G. L. Use of dinitrosalicylic acid reagent for determination of reducing sugar. *Anal. Chem.* **1959**, *31*, 426.
(27) Mcqueen-Mason, S.; Durachko, D. M.; Cosgrove, D. J. Two endogenous proteins that induce cell-wall extension in plants. *Plant Cell* **1992**, *4*, 1425.
(28) Cosgrove, D. J. Characterization of long-term extension of isolated cell-walls from growing cucumber hypocotyls. *Planta* **1989**, *177*, 121.
(29) Baker, E. N.; Boland, M. J.; Calder, P. C.; Hardman, M. J. The specificity of actinidin and its relationship to the structure of the enzyme. *Biochim. Biophys. Acta* **1980**, *616*, 30.
(30) Dall'Antonia, F.; Pavkov-Keller, T.; Zangger, K.; Keller, W. Structure of allergens and structure based epitope predictions. *Methods* **2014**, *66*, 3.
(31) Krissinel, E.; Henrick, K. Secondary-structure matching (SSM), a new tool for fast protein structure alignment in three dimensions. *Acta Crystallogr., Sect. D: Biol. Crystallogr.* **2004**, *60*, 2256.
(32) DeLano, W. S. *PyMOL Molecular Graphics System*; Schrödinger LLC, 2002
(33) Pettersen, E. F.; Goddard, T. D.; Huang, C. C.; Couch, G. S.; Greenblatt, D. M.; Meng, E. C.; Ferrin, T. E. UCSF chimera − a visualization system for exploratory research and analysis. *J. Comput. Chem.* **2004**, *25*, 1605.
(34) Krissinel, E.; Henrick, K. Inference of macromolecular assemblies from crystalline state. *J. Mol. Biol.* **2007**, *372*, 774.
(35) Holm, L.; Rosenstrom, P. Dali server: conservation mapping in 3D. *Nucleic Acids Res.* **2010**, *38*, W545.
(36) Ashkenazy, H.; Erez, E.; Martz, E.; Pupko, T.; Ben-Tal, N. ConSurf 2010: calculating evolutionary conservation in sequence and structure of proteins and nucleic acids. *Nucleic Acids Res.* **2010**, *38*, W529.
(37) Vaguine, A. A.; Richelle, J.; Wodak, S. J. SFCHECK: a unified set of procedures for evaluating the quality of macromolecular structure-factor data and their agreement with the atomic model. *Acta Crystallogr., Sect. D: Biol. Crystallogr.* **1999**, *55*, 191.
(38) (a) Grant, G. A.; Crankshaw, M. W. Identification of PTH-amino acids by HPLC. *Methods Mol. Biol.* **2003**, *211*, 247. (b) Orsomando, G.; Lorenzi, M.; Raffaelli, N.; Dalla Rizza, M.; Mezzetti, B.; Ruggieri, S. Phytotoxic protein PcF, purification, characterization, and cDNA sequencing of a novel hydroxyproline-containing factor secreted by the strawberry pathogen *Phytophthora cactorum*. *J. Biol. Chem.* **2001**, *276*, 21578.
(39) Ferreira, F.; Hawranek, T.; Gruber, P.; Wopfner, N.; Mari, A. Allergic cross-reactivity: from gene to the clinic. *Allergy* **2004**, *59*, 243.
(40) Kunii, S.; Morimoto, K.; Nagai, K.; Saito, T.; Sato, K.; Tonomura, B. Actinidain-hydrolyzed type I collagen reveals a crucial amino acid sequence in fibril formation. *J. Biol. Chem.* **2010**, *285*, 17465.
(41) Georgelis, N.; Nikolaidis, N.; Cosgrove, D. J. Bacterial expansins and related proteins from the world of microbes. *Appl. Microbiol. Biotechnol.* **2015**, *99*, 3807.
(42) Kerff, F.; Amoroso, A.; Herman, R.; Sauvage, E.; Petrella, S.; Filee, P.; Charlier, P.; Joris, B.; Tabuchi, A.; Nikolaidis, N.; Cosgrove, D. J. Crystal structure and activity of Bacillus subtilis YoaJ (EXLX1), a bacterial expansin that promotes root colonization. *Proc. Natl. Acad. Sci. U. S. A.* **2008**, *105*, 16876.
(43) Ludvigsen, S.; Poulsen, F. M. Three-dimensional structure in solution of barwin, a protein from barley seed. *Biochemistry* **1992**, *31*, 8783.

DOI: 10.1021/acs.jafc.5b02159
J. Agric. Food Chem. 2015, 63, 6567−6576

Table 1. Seventeen Isolates of *Pochonia chlamydosporia* and Results for Chemical Analysis and Nematicidal Activities

strain	source[b]	field	aurovertins[a] TLC	aurovertins[a] HPLC	mortality of *Caenorhabditis elegans* L1 at 24 h (%)
YMF 1.00107	RKN egg	Yuxi	−	−	8.33 ± 1.77
YMF 1.00111	RKN female	Xiangyun	+	+	100 ± 0.00
YMF 1.00113	soil	Tengchong	−	−	10.63 ± 2.97
YMF 1.00130	soil	Yuxi	−	−	6.27 ± 0.30
YMF 1.00603	RKN egg	Xiangyun	−	−	18.13 ± 4.22
YMF 1.00606	RKN female	Jianshui	−	−	10.15 ± 3.16
YMF 1.00613	RKN female	Songming	+	+	100 ± 0.00
YMF 1.00615	RKN female	Jianshui	+	+	100 ± 0.00
YMF 1.00617	RKN female	Jianshui	−	−	16.45 ± 2.15
YMF 1.00618	RKN female	Jianshui	−	−	17.61 ± 2.91
YMF 1.00619	RKN female	Jianshui	−	−	17.45 ± 2.65
YMF 1.00620	RKN female	Jianshui	−	−	18.82 ± 3.0 5
YMF 1.00804	RKN egg	Jianshui	−	−	10.45 ± 1.21
YMF 1.00832	RKN egg	Mengzi	−	−	6.8 ± 0.44
YMF 1.00901	soil	Kunming	−	−	17.29 ± 2.55
YMF 1.00928	RKN juvenile	Shilin	−	−	10.62 ± 2.01
YMF 1.01301	RKN female	Mengzi	−	−	8.39 ± 1.00

[a]+, aurovertins were detected in the culture medium; −, no aurovertins were detected in the culture medium. [b]RNK, root-knot nematode.

the F_1-ATPase found on the inner membrane of mitochondria, inhibiting the ATPase and thereby uncoupling oxidative phosphorylation in in vitro bioassays.[17] Furthermore, aurovertin B strongly inhibits the proliferation of breast cancer cell lines and arrests cell cycles at the G0/G1 phase.[18]

However, despite these findings, information on the natural functions of aurovertins in fungi remains scarce. This study has four major goals: (1) to establish the role of fungal aurovertin metabolites in nematodes such as the root-knot nematode *Meloidogyne incognita* and the model species *Caenorhabditis elegans*; (2) to recognize the relationship between different ecological niches such as nematode eggs and worm bodies and the production of the class of fungal aurovertin metabolites; (3) to evaluate whether the aurovertins work on the β subunit of F_1-ATPase in nematodes; and (4) to study the nematode response reaction to this class of fungal metabolites.

Several studies provide evidence that the functions of the secondary metabolites produced by pathogenic fungi in the host may vary according to their concentrations.[19−21] Considering the possibility that the production of aurovertins by *P. chlamydosporia* could lead to the generation of metabolite concentration gradients in the environment and thus potentially exposing nematodes to subinhibitory concentrations of fungal nematicidal aurovertins, we characterized the main effects of aurovertin at subinhibitory concentrations (SICs) on the nematode and tested several different end points including lethality, lifespan, brood size, overall development, and pharyngeal pumping rate. Increasing evidence suggests that frequent exposure to nonlethal (that is, subinhibitory) concentrations of antibiotics plays an important role in the evolution of antibiotic resistance.[19] The well-established model organism *C. elegans*[22] was used as an alternative system for the investigation of the mode of action of the aurovertins in nematodes and aurovertin-induced host responses.

MATERIALS AND METHODS

Fungal Strains and Fermentation. Isolation of *P. chlamydosporia* strains from nematode worms was performed according to the modified method.[23] Tobacco roots infected by *M. incognita* were collected from different fields in Yunnan Province, People's Republic of China. The infected juveniles of *M. incognita* were collected from the roots using the Baermann funnel technique. Three hundred grams of galled roots with lengths of 3−5 cm was collected and placed on a Baermann funnel apparatus. A length of rubber tubing and a collecting tube were attached to the funnel and filled with water. In the funnel, the nematodes moved out of the root tissue and sank to the bottom of the funnel due to gravity. After 24 h, a pinch clamp was applied on the rubber tubing, allowing the collecting tubing containing infected nematodes to be removed. The nematode suspension was concentrated to 1 mL by centrifuge at 8000 rpm, and then 0.2 mL of the resulting suspension containing about 200 juveniles was poured onto each of five Petri dishes containing 2% (w/v) of agar in water. After incubation for 10−20 days at 28 °C, mycelial tips that emerged from naturally infected juveniles were transferred to fresh Petri dishes containing potato dextrose agar (PDA medium consisting of 20% peeled potato, 2% glucose, and 2% agar) and recultured at least three times to obtain genetically identical fungal cultures. Collection of *P. chlamydosporia* strains from nematode eggs was performed according to a procedure described previously.[15]

To identify these fungal isolates, the general fungal primers ITS4 (5′ TCCTCCGCTTATTGATATGC) and ITS5 (5′ GGAAGTAAAAGTCGTAACAAGG) were used for amplifying internal transcribed spacer (ITS) 1, 2, and 5.8s rDNA regions of all the strains. The PCR products were purified followed by sequence analysis. The obtained ITS data were compared to those in the NCBI using a BLAST search. The nucleotide sequences were aligned manually using ClustalX. Phylogenetic analyses were completed using MEGA (ver. 6.06) to construct the neighbor-joining tree (Figure S1). The stability of clades was evaluated using bootstrap tests with 1000 replications. On the basis of the phylogenetic analyses of internal transcribed spacer (ITS) sequences, as well as the macroscopic and microscopic characteristics,[24] 17 fungal strains, including 4 from nematode eggs, 3 from soils, and 10 from nematode worms, were identified as *P. chlamydosporia* and are listed in Table 1. All of the isolates were deposited in the strain collection of the Laboratory for Conservation and Utilization of Bio-Resources & Key Laboratory for Microbial Resources of the Ministry of Education, Yunnan University, Kunming, People's Republic of China.

After the conidia had developed on PDA slants in test tubes at 25 °C, the strains were kept at −30 °C as stock cultures. The *P. chlamydosporia* strains were cultured on a PDA medium for a week and then inoculated into 500 mL flasks each containing 250 mL of medium potato dextrose broth (PDB) consisting of 20% peeled potato and 2%

DOI: 10.1021/acs.jafc.5b02595
J. Agric. Food Chem. 2015, 63, 6577−6587

glucose. The inoculated flasks were incubated at 28 °C for 12 days with shaking at 180 rpm.

Standards and Reagents. Dimethyl sulfoxide (DMSO), juglone (Ju), and oligomycin A (OA) were purchased from Sigma-Aldrich China Inc. Water was obtained from a Milli-Q system (Millipore, Bedford, MA, USA). Acetonitrile (Merck KGaA, Darmstadt, Germany) and formic acid (Roe Scientific Inc., USA) were of HPLC grade. Methanol (Guangdong Xilong Chemical Co., Ltd., Guandong, People's Republic of China) was analytical-reagent grade.

Isolation of Aurovertin Standards. The aurovertins were isolated from *P. chlamydosporia* according to the modified method described in the literature.[15] A 12-day-old fermentation broth of strain *P. chlamydosporia* YMF 1.00613 was filtered to separate the mycelia from the culture. The culture filtrate was concentrated in vacuo and partitioned with acetyl acetate, and the organic part was evaporated to dryness to give an oily residue. The residue was dissolved in $CHCl_3$/MeOH and subjected to a Sephadex LH-20 column, developing with $CHCl_3$/MeOH (1:1, v/v) to give five fractions. Fractions were monitored by TLC, and spots were visualized by spraying with 10% H_2SO_4 in EtOH. Fraction 2 was chromatographed with a silica gel column, eluting with $CHCl_3$/MeOH (7:1, v/v, 1 L) to afford six subfractions. Subfraction 2 was repeatedly subjected to a silica gel column eluting with $CHCl_3$/MeOH (50:1) to yield aurovertin D. Subfraction 4 was rechromatographed over a silica gel column eluting with $CHCl_3$/MeOH (30:1, v/v) to give aurovertin F. Subfraction 3 was repeatedly chromatographed over a silica gel column washing with $CHCl_3$/MeOH (40:1) to obtain aurovertins E and I. All of the purified aurovertins were elucidated and confirmed with ^{1}H NMR data.[17]

TLC Analysis. To determine the presence of aurovertins in the fermentation broths of *P. chlamydosporia* strains, 17 *P. chlamydosporia* strains were cultivated in PD broth medium for 12 days and then filtered to separate the mycelia from the culture. The culture filtrates were dried in vacuo and then were extracted with 10 mL of acetone three times. The extracts were combined and concentrated to 1 mL. About 5 μL of each extract was spotted onto a 10 × 5 cm silica gel 60 F254 layer, and the developing solvent $CHCl_3$/MeOH (13:1, v/v) was used. After treatment with 10% H_2SO_4 in ethanol followed by heating at 120 °C, purple color spots were visualized.

HPLC Analysis. To confirm the presence of aurovertins and determine the contents of aurovertins in the fermentation broths of *P. chlamydosporia* strains, 17 *P. chlamydosporia* strains were cultivated in PDB medium, and then 1 mL of the broths was filtered to separate the mycelia from the culture. The culture filtrate (300 μL) was filtered through a 0.22 μm hydrophilic PVDF membrane (Millipore) for HPLC analysis. HPLC analysis was carried out using an HP 1200 (Agilent, Waldbronn, Germany) unit, employing the following instrumental conditions: column, CAPCELL PAK C18, 5 μm; 4.6 × 250 mm (Shiseido); flow rate, 1 mL/min; mobile phase A, 0.1% formic acid in water; mobile phase B, 0.1% formic acid in acetonitrile. The column temperature was maintained at 40 °C, and the injection volume for the culture filtrates was 25 μL. The HPLC conditions were manually optimized on the basis of separation patterns of the aurovertins and were as follows: gradient program of B (gradient, 0 min, 25% B; 2 min, 25% B; 29 min, 40% B; 31 min, 95% B; 34 min, 95% B; 35 min, 25% B; 45 min, 25% B). Detection was performed at 365 nm. The parameters of the regression equations and the limits of detection (LOD) and quantification (LOQ) were obtained with standard aurovertins D, E, F, and I. All of the aurovertins showed good linearity over the concentration range studied and five points of each calibration curve ($R^2 \geq 0.9992$). LOD and LOQ were determined to evaluate the sensitivity of the method.

Worm Strains and Maintenance Conditions. Root-knot nematode *M. incognita* (race 3) was reared on tomato for about 2 months in a glasshouse at 25 ± 2 °C. Batches of mature egg masses (averaging 4000 eggs/batch) were obtained from infected tomato roots. Batches were collected on 2 cm diameter sieves (74 μm mesh) and placed on a 6 cm diameter sterile Petri dish, and then 15 mL of distilled water was added to promote hatching. Batches were then incubated at 28 °C in the dark. Emerging juveniles J2 (24 h) were removed and collected for the acute toxicity experiments.

Live specimens of the model nematode *C. elegans* Bristol N2 (wild type) were obtained from the Institute of Genetics and Developmental Biology, Chinese Academy of Sciences. Strains CF1308 *daf-16(mu86) I*, CB1370 *daf-2(e1370) III*, VC2255 *atp-2(ok3002) III/hT2 [bli-4(e937) let-?(q782) qIs48] (I;III)*, and TJ356 *zls356[daf-16p::daf-16a/b::gfp; rol-6] IV* were obtained from the *Caenorhabditis* Genetics Center at the University of Minnesota (Minneapolis, MN, USA). All strains were routinely propagated at 20 °C with 42% relative humidity in the dark on nematode growth medium (NGM) plates using *Escherichia coli* strain OP50 as a food source. Synchronization of worm culture was achieved by treating gravid hermaphrodites with hypochlorite bleaching. The hatched L1 arrested worms were age-synchronous and were transferred onto NGM plates with *E. coli* OP50 containing either one of a range of different concentrations of aurovertin D (25, 50, and 100 μg/mL) or DMSO until they reached the desired stages.[25] An Olympus CX31 microscope was used to observe nematodes.

Acute Toxicity Assay. An acute toxicity test was performed according to a procedure described previously.[15] About 300 age-synchronous *C. elegans* wild type N2 L1 were dispensed into 3.5 cm plates containing 1 mL of fungal culture broth. PDB medium was used as a negative control. About 300 age-synchronous root-knot nematode *M. incognita* juveniles J2, model species *C. elegans* wild type N2 L1, *C. elegans* mutant *daf-16(mu86)* L1, *C. elegans* mutant *daf-2(e1370)* L1, and *C. elegans* mutant *atp-2(ok3002)/hT2[bli-4(e937) let-?(q782) qIs48]* L1 were dispensed into 3.5 cm plates containing 1 mL of M9 buffer with variable amounts of aurovertin D (dissolved in DMSO) per plate (0, 12.5, 25, 50, and 100 μg/mL). Control groups were prepared with the same volume of DMSO (0.5% DMSO, v/v). Worms were exposed for 24 h at 20 °C, and the number of dead or live worms was determined by the absence/presence of touch-provoked movement when probed with a platinum wire. The median lethal concentration (LC_{50}) value was calculated using the probit method. All treatments were conducted in triplicate.

Development Assay. Synchronized L1 nematodes [wild type N2, *daf-16(mu86)*, and *daf-2(e1370)*] treated with or without aurovertin D were cultured for 60 h. Then the numbers of nematodes in each stage including L1, L2, L3, L4, and adult were counted at 40× magnification. The development of 50 worms was assessed for each treatment. All treatments were conducted in triplicate.

Pharyngeal Pumping, Lifespan, and Brood Size Assay. Synchronized L4 worms of wild type N2, *daf-16(mu86)*, and *daf-2(e1370)* treated with or without aurovertin D were manually assessed for the pharyngeal pumping rates. The pharyngeal pumping experiments were carried out in triplicate. For lifespan assay, these worms were counted and scored as live or dead, and live worms were transferred to fresh plates every day until no new progeny was generated in a 24-h period and no live worms remained.[26] The brood sizes of nematodes were counted 2 days after the removal of the parents, and the progeny of at least 30 parental nematodes was counted. The lifespan and brood size experiments were carried out in quadruplicate.

Reactive Oxygen Species (ROS) Assay. Cellular ROS levels were quantified by the dihydroethidium (DHE) assay using fluorescence microscopy.[27] Synchronized L2 larvae of wild type N2 were incubated for 24 h at 20 °C in M9 buffer containing DMSO, aurovertin D (100 μg/mL), or juglone (3483 μg/mL, 20 mM). Worms were then allowed to recuperate on NGM plates with *E. coli* OP50 for about 20 h before their viability was determined by touch-provoked movement. After recovery, worms were washed with M9 buffer and then incubated in M9 buffer containing 3 μM DHE for 30 min in the dark. DHE is a fluorogenic probe that is highly selective for superoxide anion radical detection. DHE is cell-permeable and reacts with intracellular ROS to form ethidium, which, in turn, intercalates with DNA, thereby exhibiting a red fluorescence. Recording of the DHE fluorescence intensity was used as an index of the individual intracellular levels of ROS in individual worms. Fluorescence from worms exposed to DMSO as negative control and juglone as positive control was also measured. Three independent experiments were performed per treatment, and in each experiment ROS measurement

DOI: 10.1021/acs.jafc.5b02595
J. Agric. Food Chem. 2015, 63, 6577−6587

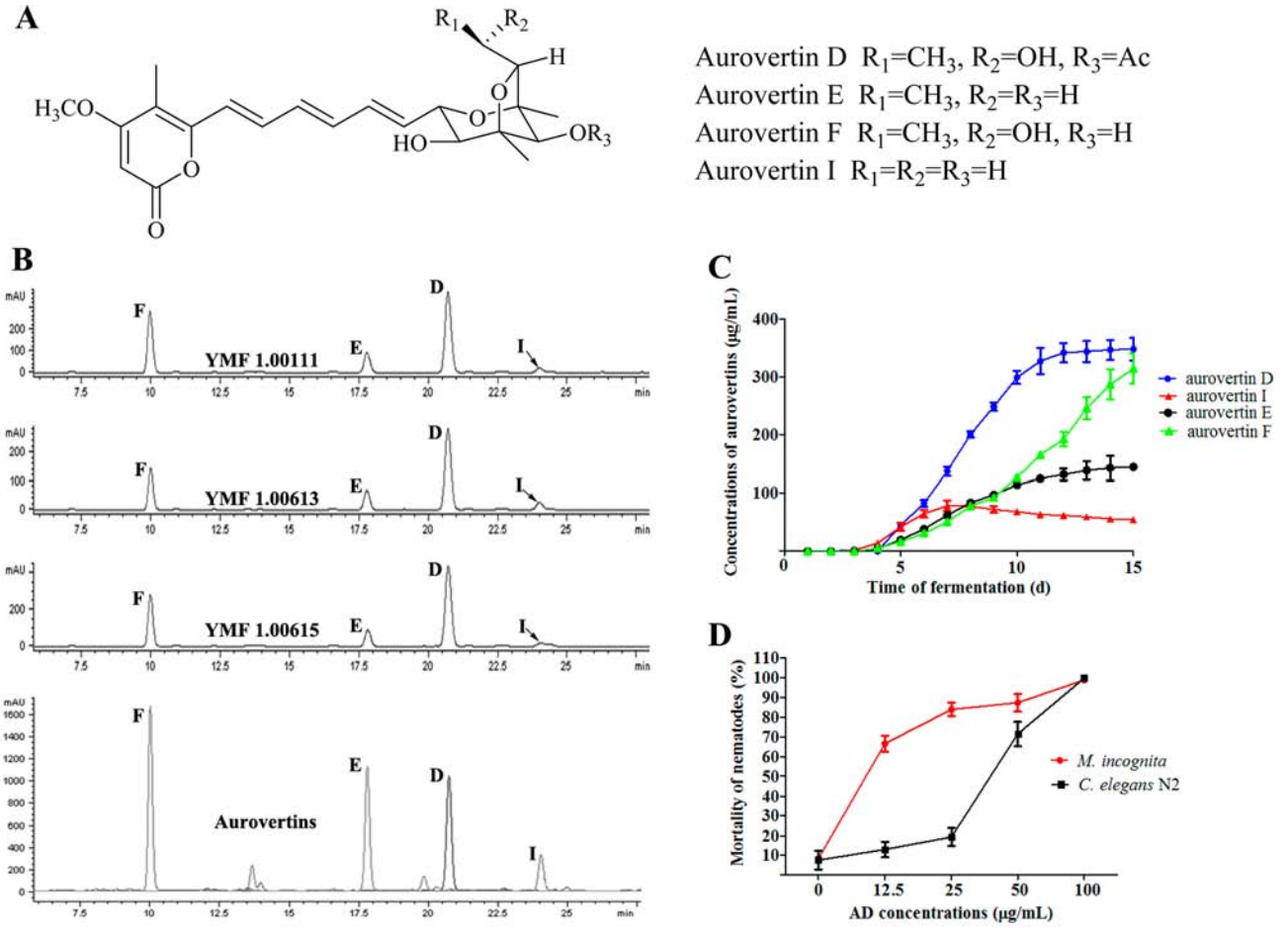

Figure 1. (A) Structures of aurovertins D, E, F, and I. (B) HPLC-DAD profiles of aurovertins in fermentation broths of *Pochonia chlamydosporia* strains YMF 1.00111, YMF 1.00613, and YMF 1.00615, and standard aurovertins. (C) Contents of aurovertins in the fermentation broth of aurovertin-producing *P. chlamydosporia* strain YMF 1.00613 in 15 days. (D) Effects of aurovertin D (AD) on the mortality of *Meloidogyne incognita* J2 and *Caenorhabditis elegans* N2 L1 nematodes in the acute toxicity assay.

was made in at least 36 worms. A Zeiss Axioskop 2 plus microscope was used for the imaging of the red fluorescence of worms. These images were analyzed using Axiovision V4.5 (Zeiss) line tool to determine the mean relative fluorescence intensity of the nematodes. All treatments were conducted in triplicate.

RNA Interference (RNAi). RNAi was administered by feeding worms strains of *E. coli* engineered to transcribe double-stranded RNA homologous to a target gene.[28] Bacteria (HT115) with empty plasmid pPD129.36 were used as a negative control for nonspecific RNAi effects, whereas bacteria expressing *fasn-1* dsRNA were utilized as positive control. Approximately 300 synchronized wild type N2 L1 worms were plated onto 6 cm NGM plates supplemented with 1 mM IPTG and 100 μg/mL ampicillin. The plates were seeded with different RNAi bacteria targeting each subunit of F_1F_O-ATPase, including *asb-1*, *asb-2*, *atp-5*, R04F11.2, R53.4, *asg-1*, *asg-2*, *atp-3*, H28O16.1, T26E3.7, *atp-2*, F58F12.1, *hpo-18*, R05D3.6, and ZC262.5, or with bacteria containing control vectors. Worms matured into adults in 3 days at 20 °C. Following a synchronization of the knockdown adult worms, the growth of L1 worms on NGM plates containing 100 μg/mL aurovertin D or DMSO for 60 h was monitored. Three independent RNAi experiments were performed for each gene tested. All treatments were done in triplicate.

DAF-16::GFP Nuclear Localization. Synchronized L1 worms of the transgenic strain TJ356, which expresses a DAF-16::GFP fusion protein, were fed on NGM plates with or without 50 or 100 μg/mL aurovertin D for 60 h. DAF-16::GFP localization was monitored using a Zeiss M2BIO stereo dissecting microscope fitted with an Axiocam MRC DAGE-MTI CCD-100 camera. Images were acquired at 100× and 400× magnifications in compound mode.

Statistical Analyses. All experiments were performed in either triplicate or quadruplicate. Replicated trials had similar outcomes. Data were analyzed using the software SPSS (SPSS Inc., Chicago, IL, USA), and the results were presented as the mean ± SD. The LC_{50} was calculated using the probit analysis. Statistical significance was determined by Student's *t* test for comparison between the means of two groups or by a one-way analysis of variance (ANOVA) followed by Tukey's honest significant difference tests for equal variances and Dunnett's T3 tests for unequal variances at the $\alpha = 0.05$ level of significance among multiple groups. Differences were considered as significant when $P < 0.05$. Lifespan survival curve data were compared by the log-rank test of the Kaplan−Meier survival function. The relative average/maximal lifespan of worms was calculated according to the following formula:

$$\text{rel av (max) lifespan} = \frac{\text{av (max) lifespan of worms treated with aurovertins}}{\text{av (max) lifespan of worms treated without aurovertins}}$$

RESULTS

Non-nematicidal Activity of Most *P. chlamydosporia* Strains. Seventeen *P. chlamydosporia* strains collected from three different ecological niches, including nematode worms and eggs, and soil, were evaluated for the nematicidal activity of

DOI: 10.1021/acs.jafc.5b02595
J. Agric. Food Chem. 2015, 63, 6577−6587

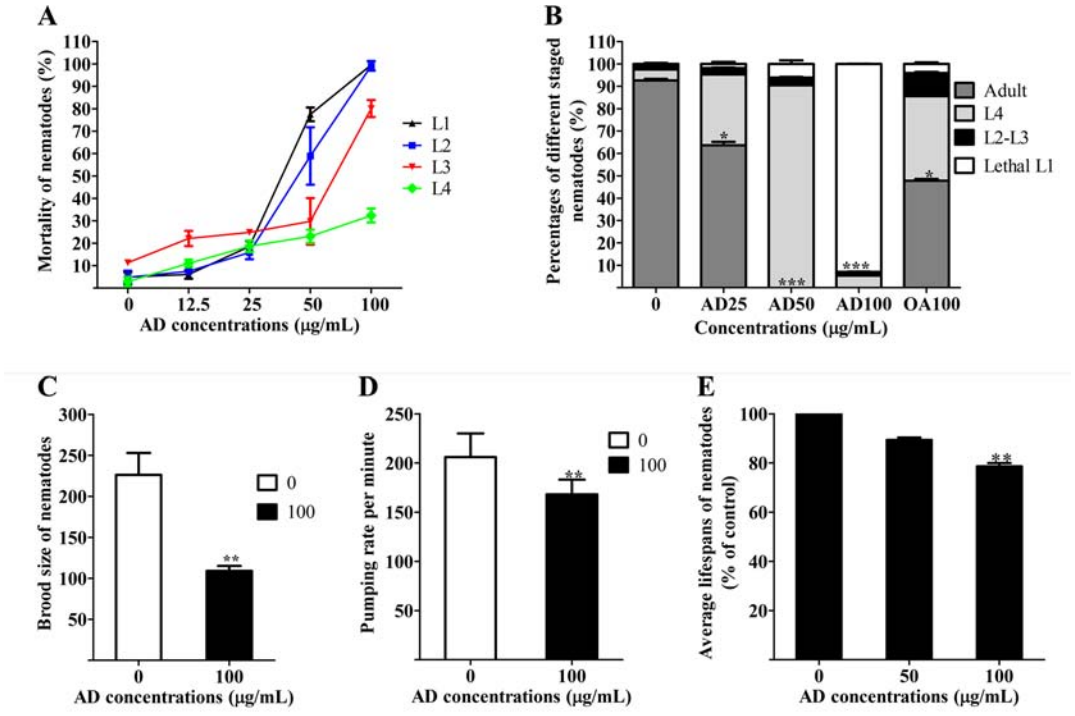

Figure 2. Toxicity effects of aurovertin D on the viability of *Caenorhabditis elegans* wild type N2: (A) effects of aurovertin D (AD) (0, 12.5, 50, and 100 μg/mL) on the mortality of different-staged larvae; (B) effects of aurovertin D (AD) (0, 25, 50, and 100 μg/mL) and oligomycin A (OA) (100 μg/mL) on the developments of L1 nematodes; (C) effects of 100 μg/mL aurovertin D (AD) on brood size of nematodes; (D) effects of 100 μg/mL aurovertin D (AD) on pumping rates of nematodes; (E) effects of aurovertin D (AD) (50 and 100 μg/mL) on the average lifespan of nematodes. (∗) $P < 0.05$; (∗∗) $P < 0.01$; (∗∗∗) $P < 0.001$.

their culture broths toward larval nematodes (Table 1). Among them, three strains, YMF 1.00111, YMF 1.00613, and YMF 1.00615, yielded distinctive luminous yellow in their fermentation broths. Nematicidal bioassays displayed that only these three strains showed 100% inhibitory rates toward the free-living nematode *C. elegans* L1 larvae nematodes, whereas those strains without yellow pigments exhibited no more than 19% inhibitory rates (Table 1).

Aurovertins in the Nematicidal *P. chlamydosporia* Strains. All 17 *P. chlamydosporia* strains were examined for aurovertin production (Table 1; Figure 1A). Analysis with TLC and HPLC revealed that the aurovertins were abundant in the luminous yellow culture broths of the three bioactive strains YMF 1.00111, YMF 1.00613, and YMF 1.00615 (Table 1; Figure 1B). HPLC analysis of the three aurovertin-producing *P. chlamydosporia* strains indicated that these strains grown for ≥4 days yielded a total aurovertin production with contents ranging from 500 to 900 μg/mL (Figure 1C), exceeding the inhibitory concentration of aurovertins during nematicidal bioassays (Figure 1D).

Aurovertin D as the Major Component in the Yellow Pigment Metabolite Profiles of Nematicidal *P. chlamydosporia*. Four major pigment metabolites, aurovertins D (348 μg/mL), E (144.5 μg/mL), F (314.2 μg/mL), and I (54.6 μg/mL), were isolated from the 15-day yellow culture broths of the *P. chlamydosporia* strains and identified with ^{1}H NMR data and confirmed using comparisons with the retention times of the aurovertin standards. HPLC analysis of the aurovertin compositions of all three *P. chlamydosporia* strains YMF 1.00111, YMF 1.00613, and YMF 1.00615 grown between 1 and 15 days revealed that aurovertin D was the major pigment metabolite in the aurovertin-producing *P. chlamydosporia* strains grown for ≥5 days (Figure 1C).

Stronger Toxicity of Aurovertin D toward Root-Knot Nematodes than Free-Living Nematodes. The effects of aurovertin D on the plant-parasitic nematode *M. incognita* J2 and the model species *C. elegans* were evaluated. A dose−response relationship was established. Within 24 h, aurovertin D caused significant death of *M. incognita* J2 with an LC_{50} value of 16.45 μg/mL and inhibited *C. elegans* with an LC_{50} value of 33.50 μg/mL, indicating a stronger inhibitory activity toward root-knot nematodes than free-living nematodes ($P < 0.01$, Figure 1D).

Profound Effects of Aurovertin D on the Viability of Model Species *C. elegans* at a Subinhibitory Concentration. Dose−response curves were generated for different-staged larvae in the acute toxicity assay. The percentage of dead worms was defined as the mortality rate. Aurovertin D was most toxic to the earliest larval stage L1 (Figure 2A). The percentages of different-staged worms indicated that the development of wild type N2 L1 worms treated with various concentrations of aurovertin D was altered in a dose-dependent manner (Figure 2B). When exposed to aurovertin D at concentrations of 50 or 100 μg/mL, none of the worms reached adult stage, and only 5.4% of the worms treated with 100 μg/mL aurovertin D grew into L4 larval stage, whereas 92.6% of the worms in the negative control group grew into adult stage in 60 h (Figure 2B). This indicated that 100 μg/mL aurovertin D significantly inhibited the development of worms ($P < 0.05$). Additionally, aurovertin D displayed stronger inhibitory activity than the positive control oligomycin A (an F_O-ATPase inhibitor, OA) toward larval development because 47.8% of worms exposed to 100 μg/mL oligomycin A grew into

DOI: 10.1021/acs.jafc.5b02595
J. Agric. Food Chem. 2015, 63, 6577−6587

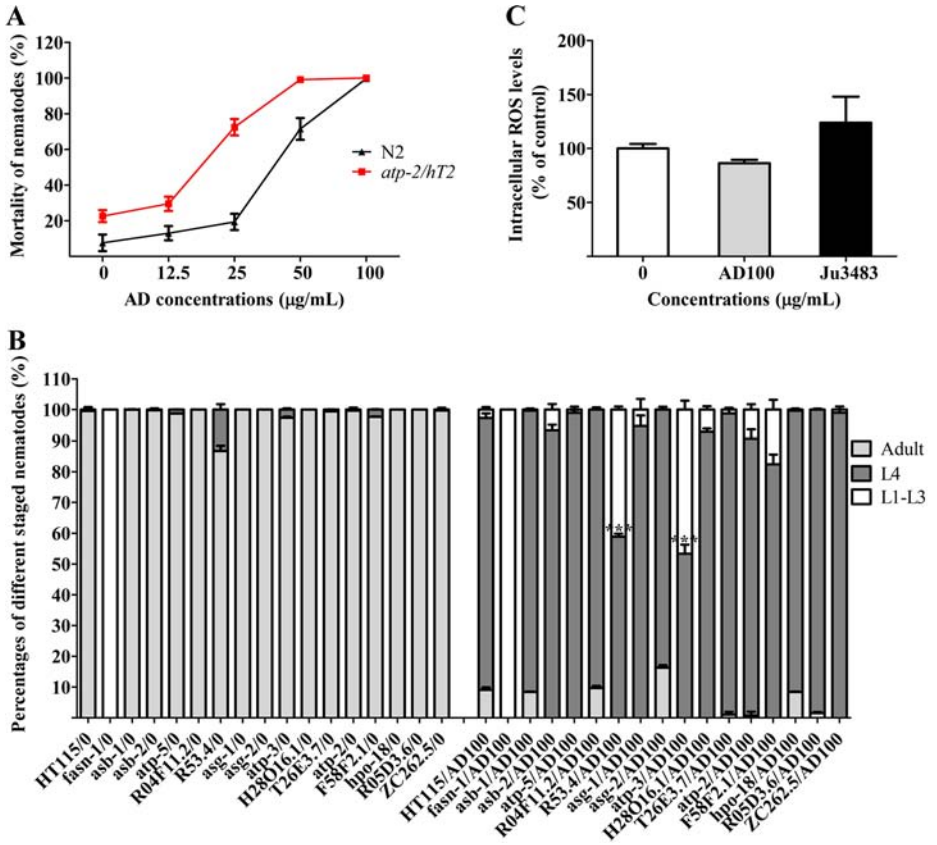

Figure 3. (A) Effects of aurovertin D on the mortality of *Caenorhabditis elegans* wild type N2 and mutant VC2255 (*atp-2/hT2*) L1 nematodes. (B) Effects of 100 μg/mL aurovertin D (AD100) on the development of L1 nematodes fed different RNAi bacteria targeting each subunit of F_1F_O-ATPase, including *asb-1*, *asb-2*, *atp-5*, R04F11.2, R53.4, *asg-1*, *asg-2*, *atp-3*, H28O16.1, T26E3.7, *atp-2*, F58F12.1, *hpo-18*, R05D3.6, and ZC262.5. HT115 was used as negative control, and *fasn-1(RNAi)* was used as positive control for RNAi experiments. The percentages of L4 nematodes fed RNAi bacteria targeting each subunit of F_1F_O-ATPase were compared with that fed control vector (HT115) using a one-way ANOVA with Tukey's honest significant difference test for equal variances and Dunnett's T3 tests for unequal variances post-test following 100 μg/mL aurovertin D treatment. (***) $P < 0.001$. (C) Intracellular ROS levels of wild type N2 nematodes treated with 100 μg/mL aurovertin D (AD100) or 3483 μg/mL (20 mM) juglone (Ju3483) at L2 stage for 24 h.

adult stage. In measuring brood size, L4 worms treated with aurovertin D had a significantly decreased brood size of 51.8% less than those of worms without aurovertin D treatment ($P < 0.01$, Figure 2C). Pharyngeal pumping rates of worms treated with 100 μg/mL aurovertin D were significantly decreased with 17.6% less than those in the negative control ($P < 0.01$, Figure 2D). The relative average lifespan of wild type N2 worms exposed to aurovertin D at a concentration of 100 μg/mL was significantly shortened by 21.5% less than that of the negative control ($P < 0.01$, Figure 2E).

Toxicity of Aurovertin D to β Subunit-Deficient Nematode Mutant. Aurovertin B was regarded as a potent inhibitor of ATP synthesis and ATP hydrolysis catalyzed by mitochondria1 enzyme systems, because it could bind to and inhibit mitochondrial ATPase, thereby uncoupling oxidative phosphorylation.[17] To check if the β subunit of F_1-ATPase was involved in the mode of action of aurovertin D in vivo, we tested the mortality of loss-of-function mutant *atp-2(ok3002)* by exposing the worms to aurovertin D. *C. elegans atp-2* encodes the active site of the β subunit in the F_1F_O-ATPase in *C. elegans*. Unexpectedly, all L1 worms of β subunit-deficient mutant *atp-2/hT2* died when exposed to 100 μg/mL of aurovertin D (Figure 3A). Moreover, the mortality of *atp-2/hT2* was even higher than that of wild type N2, and LC_{50} values of aurovertin D for wild type N2 and *atp-2/hT2* were 33.50 and 17.53 μg/mL ($P < 0.05$), respectively. The results suggested that β subunit-deficient nematode mutant did not display significant resistance to aurovertin D.

Toxicity of Aurovertin D to Nematode Mutants by RNAi Silencing of Each Subunit of F_1F_O-ATPase. RNAi studies were performed to determine whether aurovertin D exerted its effects in *C. elegans* by interfering with the functions of each subunit of F_1F_O-ATPase. Animals in the positive control group with *fasn-1* RNAi were arrested in either the L2 or L3 larval stage and could not reach the L4 stage, indicating the efficiency of this RNAi experiment.[29] Animals treated with strain HT115 with the empty vector were used as negative control. The right-hand panel in Figure 3B displays the developmental stages of each RNAi nematode exposed to 100 μg/mL aurovertin D treatment, and the left-hand panel demonstrates that of each RNAi nematode without aurovertin D. The results indicated that RNAi silencing of the β subunit did not significantly increase the percentage of L4 worms compared to the negative control ($P > 0.05$, Figure 3B). Overall, none of the RNAi worms displayed significant improvement in larval development, and the R53.4 and *hpo-18* nematodes even displayed significant delays (sensitivity, $P < 0.001$) in larval development compared with those in negative control. The results suggested that RNAi silencing of each subunit of F_1F_O-ATPase of nematode did not result in

DOI: 10.1021/acs.jafc.5b02595
J. Agric. Food Chem. 2015, 63, 6577−6587

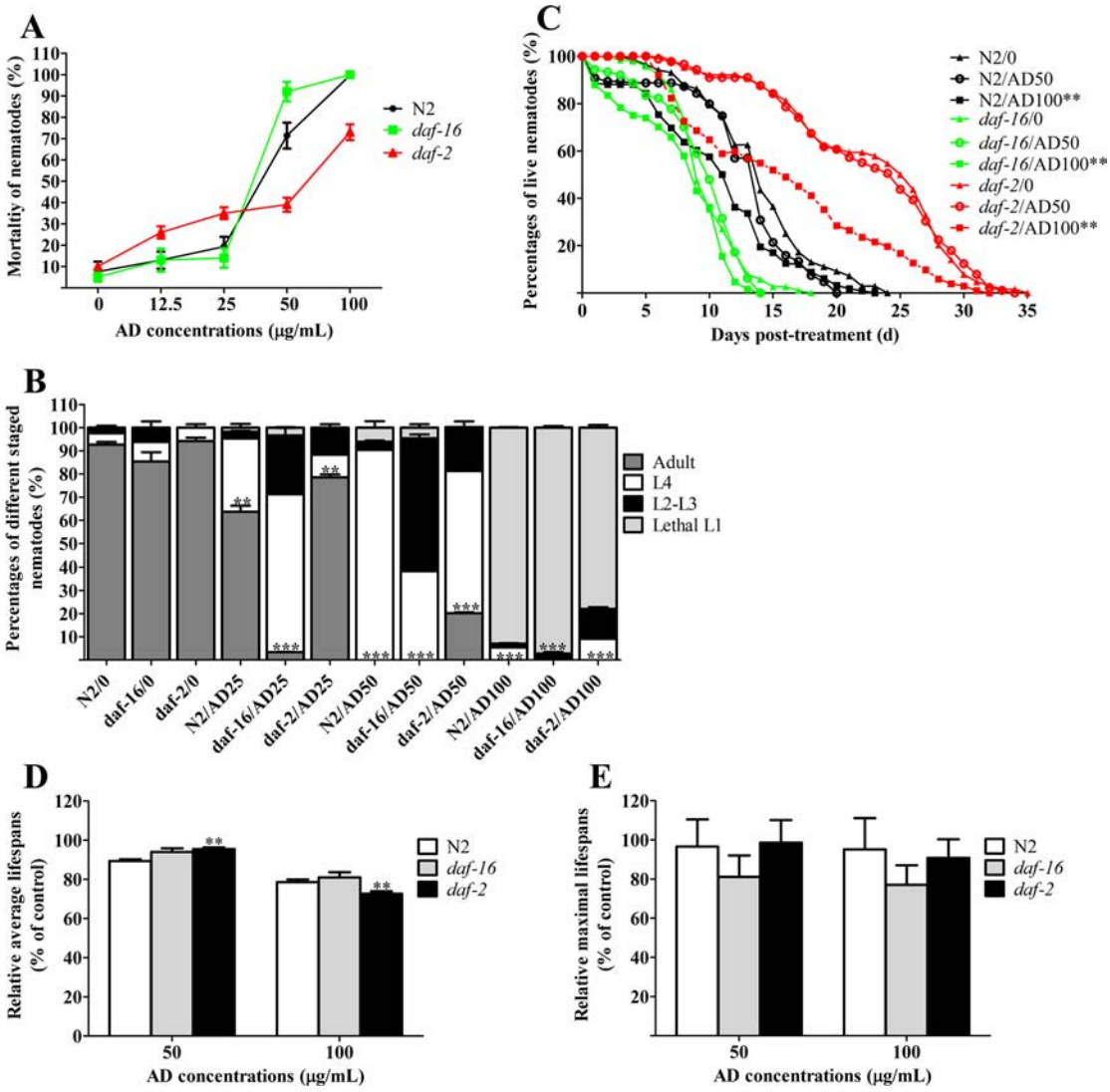

Figure 4. Effects of aurovertin D on the mortality, larval development, and lifespan of *Caenorhabditis elegans* wild type N2, *daf-2(e1370)*, and *daf-16(mu86)*: (A) Effects of aurovertin D (AD) (0, 12.5, 25, 50, and 100 μg/mL) on the mortality of L1 nematodes of wild type N2, *daf-2(e1370)*, and *daf-16(mu86)* L1 nematodes; (B) effects of aurovertin D (AD) (0, 25, 50, and 100 μg/mL) on the development of wild type N2, *daf-2(e1370)*, and *daf-16(mu86)* L1 nematodes [(**) $P < 0.01$; (***) $P < 0.001$]; (C) effects of aurovertin D (AD) (0, 50, and 100 μg/mL) on the lifespans of wild type N2, *daf-2(e1370)*, and *daf-16(mu86)* [(**) $P < 0.01$]; (D) effects of aurovertin D (AD) (0, 50, and 100 μg/mL) on the relative average lifespans (% of control) of wild type N2, *daf-2(e1370)*, and *daf-16(mu86)* nematodes [(**) $P < 0.01$]; (E) effects of aurovertin D (AD) (0, 50, and 100 μg/mL) on the relative maximal lifespans (% of control) of wild type N2, *daf-2(e1370)*, and *daf-16(mu86)*. A one-way ANOVA followed by Tukey's honest significant tests for equal variances and Dunnett's T3 Tests for unequal variances were used to compare the relative average/maximal lifespans between mutants and wild type N2.

significant resistance of nematode mutants against aurovertin D.

ROS Levels in Nematodes Treated with Aurovertin D. The levels of ROS with important roles in cell signaling and homeostasis in nematodes can increase dramatically under environmental stresses including xenobiotics.[30] We tested whether aurovertin D could increase the ROS level in worms. However, aurovertin D did not alter ROS level in nemtaodes compared to negative control treatments (Figure 3C).

Increased Sensitivity of *daf-16* Nematode Mutant to Aurovertin D. DAF-16 is a *C. elegans* FOXO transcription factor and a key mediator involved in multiple stress responses.[31] Experiments were carried out to test whether DAF-16 in nematodes is required for the aurovertin D-induced response. The acute toxicity assay showed that the mortality of *daf-16(mu86)* mutant treated with aurovertin D at a subinhibitory concentration of 50 μg/mL was significantly increased with 26.7% compared to that of wild type N2 ($P < 0.05$) under the same treatment (Figure 4A). The larval growth rates of wild type N2 and the *daf-16(mu86)* mutant synchronized L1 worms exposed to various concentrations of aurovertin D are shown in Figure 4B. When exposed to aurovertin D at a concentration of 25 μg/mL, only 67.9% of *daf-16(mu86)* mutants developed into the L4 larval stage and no *daf-16(mu86)* mutants reached adult stage, whereas 63.6% of wild type N2 reached adult stage (Figure 4B), indicating that the development of *daf-16(mu86)* mutants was significantly inhibited compared to wild type N2 worms. For *daf-16(mu86)* mutant worms grown on medium with aurovertin D at concentrations of 0, 50, and 100 μg/mL, longevity including both average and maximum lifespans correlated with exposure doses (Figure 4C). Both the average lifespans and the

DOI: 10.1021/acs.jafc.5b02595
J. Agric. Food Chem. 2015, 63, 6577−6587

maximum lifespans of *daf-16(mu86)* mutant treated with aurovertin D at a concentration of 100 μg/mL were significantly reduced, with 19.4% ($P < 0.05$) and 23.5% ($P < 0.01$), respectively, less than those of the worms without aurovertin D treatment. However, the relative average lifespan and relative maximal lifespans of the treated *daf-16(mu86)* and wild type N2 worms were not significantly different (Figure 4D,E).

Decreased Sensitivity of *daf-2* Nematode Mutant to Aurovertin D. DAF-2 is the only insulin/IGF-1-like receptor in *C. elegans*, and insulin/IGF-1-like signaling is evolutionarily conserved across the animal kingdom, from single-celled organisms to mammals.[32] To clarify the involvement of DAF-2 in aurovertin D-induced toxicity, we tested the response of *daf-2(e1370)* mutants to aurovertin D exposure. The mortality percentages of *daf-2(e1370)* mutant L1 worms exposed to aurovertin D at concentrations of 50 and 100 μg/mL were significantly decreased at 44.4 and 26.3%, respectively, lower than those of wild type N2 ($P < 0.05$, Student's *t* test) (Figure 4A). Because DAF-2 activity is required for larval developmental timing, maturation of *daf-2(e1370)* mutants to adulthood was delayed compared to wild type N2. In the bioassay, the larval growth development of N2 worms was evaluated at 60 h, whereas *daf-2(e1370)* mutant worms were assessed at 84 h after the synchronized L1 stage worms were exposed to aurovertin D at concentrations of 0, 25, 50, and 100 μg/mL. The result showed that the percentage of *daf-2(e1370)* mutants which reached adulthood was significantly increased at 23.4% higher than that of wild type N2 nematodes following 25 μg/mL aurovertin D treatment ($P < 0.01$, Figure 4B). After exposure to 100 μg/mL aurovertin D, the average lifespan of *daf-2(e1370)* mutant was 56.7% longer than that of the wild type N2, whereas the average lifespan of *daf-2(e1370)* mutant was 69% longer than that of the wild type N2 when exposed to DMSO. The average lifespan of *daf-2(e1370)* mutant treated with 100 μg/mL of aurovertin D was significantly decreased at 27.2% less than the worms without aurovertin D treatment ($P < 0.01$, Figure 4C). Meanwhile, the maximal lifespan of *daf-2(e1370)* mutant was not significantly different when exposed to aurovertin D at concentrations of 50 and 100 μg/mL (Figure 4C). Exposed to aurovertin D treatment, the relative average lifespan of *daf-2(e1370)* mutant was significantly extended at 19.2% higher than that of wild type N2 ($P < 0.01$, Figure 4D). No significant difference was observed for the relative maximal lifespan between *daf-2(e1370)* mutants and wild type N2 upon aurovertin D exposure (Figure 4E).

DAF-16 Nuclear Localization in Nematodes Induced by Aurovertin D. DAF-16 is activated by translocation from the cytoplasm to the nucleus.[31] To determine the contribution of DAF-16/FOXO to the aurovertin D-induced host response, the influence of aurovertin D on the subcellular distribution of DAF-16 was examined using the transgenic strain TJ356. Worms of this strain carry a DAF-16::GFP fusion construct as a reporter gene, allowing the observation of the subcellular localization of DAF-16. The location of the transcription factor of DAF-16 in the cytosol, the nucleus, or an intermediate localization was observed after TJ356 L1 worms were treated with or without 50 and 100 μg/mL of aurovertin D for 60 h. Worms in the control group predominantly revealed a cytosolic localization (83 ± 5%) of DAF-16 (Figure 5A). Only a small fraction of the control worms showed a nuclear (12 ± 4%) or intermediate (5 ± 1%) localization phenotype (Figure 5A). A greater proportion of DAF-16::GFP was translocated to the nuclei in the intestine and other cells in the aurovertin D-treated worms in comparison to the control population. The fraction of worms showing cytosolic localization decreased to 22 ± 3%, and the percentage of worms with nuclear localization increased to 77 ± 6% (Figure 5B,C). Thus, a translocation of DAF-16 from the cytosol to the nucleus was observed in nematodes in response to aurovertin D (Figure 5).

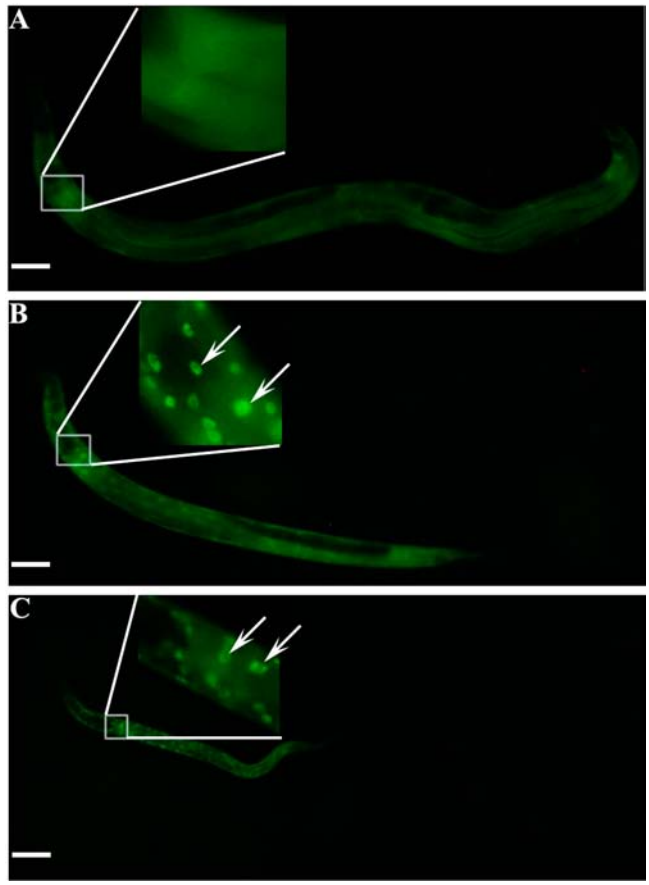

Figure 5. Effects of aurovertin D on nuclear localization of DAF-16::GFP in TJ356: (A) expression of DAF-16::GFP in TJ356 grown on the NGM Petri dishes containing 0.5% DMSO as negative control; (B) expression of DAF-16::GFP in TJ356 grown on the NGM Petri dishes containing 50 μg/mL aurovertin D; (C) expression of DAF-16::GFP in TJ356 grown on the NGM Petri dishes containing 100 μg/mL aurovertin D. The development of TJ356 nematodes was inhibited and nuclear localization of DAF-16 was induced by aurovertin D. Three independent experiments with at least 20 nematodes per group were performed. White arrows indicate nuclear enrichment of DAF-16::GFP. Scale bar = 50 μm.

DISCUSSION

P. chlamydosporia has a great capacity to infect and destroy the eggs and kill females of plant-parasitic nematodes. Increasing numbers of worldwide reports of *P. chlamydosporia* native isolates have been published.[33] Our recent study demonstrated that a *P. chlamydosporia* strain collected from root-knot nematode could produce a class of yellow pigment metabolites that showed nematicidal activity toward the free-living nematode *Panagrellus redivivus*.[15] This study hinted at the potential natural functions of fungal secondary metabolites in the pathosystem of nematode-parasitic fungi. Here we investigated 17 *P. chlamydosporia* isolates obtained from root-knot nematode worms, root-knot nematode eggs, or soils to

DOI: 10.1021/acs.jafc.5b02595
J. Agric. Food Chem. 2015, 63, 6577−6587

evaluate the effects of the ecological niches on the fungal nematicidal activity and the production of nematicidal metabolites in *P. redivevus* strains. Among the 17 *P. chlamydosporia* strains, only three culture broths of the fungal strains showed strong inhibitory activities toward larval nematodes (Table 1), suggesting that only a small portion of the fungal strains might be nematicidal. One of the possible reasons might be the fact that the fungus *P. chlamydosporia* can survive as a saprophyte in the soil in the absence of both plant and nematode hosts, and many strains may thus survive in the soil despite not possessing toxic metabolites toward nematode worms.[33]

Interestingly, all three *P. chlamydosporia* strains with strong nematicidal activities yielded distinctive luminous yellow fermentation broths (Figure 1) and were obtained from the nematode female worms instead of nematode eggs (Table 1). Chemical investigation of the three *P. chlamydosporia* strains demonstrated that the yellow pigment metabolites consisted of polyketide metabolite aurovertins (Figure 1A,B). Among them, four aurovertins, D, E, F, and I, were identified from all three *P. chlamydosporia* strains with distinctive luminous yellow fermentation broths. Further HPLC-DAD analysis of the aurovertin metabolite profiles of the *P. chlamydosporia* strains indicated that aurovertin D became the main component among the yellow pigment metabolites of the aurovertin-producing *P. chlamydosporia* strains grown for ≥5 days. Together with our previous study that among these aurovertins, aurovertin D showed the strongest nematodetoxic activity, more than double that of the second strongest metabolite, aurovertin F, which lacked only one acetyl group compared with the aurovertin D structure,[15] aurovertin D was chosen to be the representative of aurovertin-type metabolites to evaluate the effect of the aurovertins on nematodes and to study the nematode response reaction to this class of fungal metabolites.

Bioassay results revealed that aurovertin D showed stronger toxicity toward root-knot nematode *M. incognita* than toward free-living nematode *C. elegans*. The LC_{50} value of aurovertin D for root-knot nematode *M. incognita* is 16.45 μg/mL, only half of the LC_{50} value for *C. elegans*. These results indicated that the class of aurovertins could be involved in the pathosystem of the nematode-parasitic fungus, and the major aurovertin played a key role in the nematode-killing process of the aurovertin-producing *P. chlamydosporia* strains. The *P. chlamydosporia* strains that colonized the nematode worms tended to produce the nematicidal yellow pigment aurovertins compared to the strains obtained from nematode eggs. This might be attributable to the fact that aurovertins did not affect the nematode egg hatch.[15] From the above results, it could be deduced that some of nematode-parasitic *P. chlamydosporia* strains isolated from nematode body ecological niches instead of nematode eggs tended to produce a highly conserved class of nematicidal yellow metabolites to attack and kill the larval nematode.

Our results demonstrated that exposure to aurovertin D at subinhibitory concentrations led to decreases in brood size, lifespan, and pharyngeal pumping rates and to a retardation in larval development of nematode *C. elegans*. In addition, aurovertin D was more toxic to the younger than to the older individuals. This could be attributed to the immaturity of detoxifying systems in L1 stage larvae of *C. elegans*,[34] which might function better in the L4 larvae, as was observed for the antimicrotubule agent hemiasterlin.[35]

ATPase is a molecular target for various diseases and the regulation of energy metabolism.[36] The enzyme comprises a soluble globular F_1 (subunit composition $\alpha_3\beta_3\gamma_1\delta_1\varepsilon_1$) catalytic sector and a membrane-bound F_O proton-translocating sector.[37] *C. elegans atp-2* encodes the β subunit of the soluble catalytic F_1 portion of ATP synthase and is required for nematode larval development, as well as for normal mobility, pharyngeal pumping, defecation, and growth rate.[36,37] Aurovertins were found to inhibit both membrane-bound and soluble mitochondrial F_1F_O-ATPase of the protozoan *Trypanosoma cruzi*.[38] An aurovertin-resistant mutant of *Saccharomyces cerevisiae* contained an altered nuclear gene that specifies the structure of the β subunit of F_1 portion of ATP synthase.[39] To evaluate whether aurovertin D exerts its toxicity by targeting the β subunit of F_1-ATPase in nematodes, the resistance of nematode mutants deficient in the β subunit to aurovertins was assessed. However, no significant difference between these mutants and wild type N2 nematodes was observed after aurovertin D treatments. Because the catalytic β subunit of F_1-ATPase is required for mitochondrial ATP synthesis, the knockout of the entire β subunit is lethal to nematodes, so the mutants used in this part of study contained *ok3002* allele that had a deletion of only about 500 bp in the third exon of the β subunit encoding gene *atp-2*.[27] Previous study revealed that the change of one base G in the gene *unc D* in *E. coli* resulted in the change of the amino acid β-398Arg of the β subunit of F_1-ATPase and conferred resistance to aurovertins in bacteria.[40,41] It is possible that the mutation in *atp-2/ht2* in *C. elegans* might not occur at the gene fragment which encodes the amino acid target equivalent to that of β-398Arg of the β subunit of F_1-ATPase in *E. coli*. In addition, nematode mutant *atp-2(ok3002)* can develop only through two larval stages and arrest at the L3 stage due to the deficiency in the β subunit,[42] which might lead to greater sensitivity of the impaired mutants to aurovertin D than that of the wild type N2 as shown in Figure 3A.

Further RNAi experiments were performed to evaluate the responses of the mutants deficient in each subunit of F_1F_O-ATPase of *C. elegans* to aurovertin D. The silencing of the β subunit of F_1-ATPase by RNAi did not significantly increase the resistance of worms to aurovertin D compared to the wild type N2. In fact, none of the RNAi worms showed a significant difference in larval development except for those nematodes grown on bacteria expressing double-stranded RNAs (dsRNA) R53.4 and *hpo-18*, respectively, which showed much greater sensitivity to aurovertin D than did the negative control. R53.4 encodes a mitochondrial ATP synthase subunit f homologue and is assumed to be required for the expression of antimicrobial peptides in response to infection,[43] whereas *hpo-18* encodes the *C. elegans* homologue of the oligomycin sensitivity-conferring protein (OSCP) subunit of mitochondrial ATP synthase (complex V), which is crucial for transmitting the energy of AGH+ to the catalytic sector.[44] A previous study revealed that aurovertin inhibited ATPase considerably in the absence of F_O and found that some protective action occurred in the presence of F_O.[45] Furthermore, the gene encoding OSCP is involved in controlling respiration and regulates growth rate and body size, aging, and rates of behaviors such as pharyngeal pumping, defecation, and locomotion. Our results that the RNAi mutants in R53.4 or *hpo-18* caused the nematodes to be more sensitive to aurovertin D were consistent with previous reports.

Previous studies reported that the ATPase inhibitor oligomycin could promote mitochondrial hyperpolarization,

DOI: 10.1021/acs.jafc.5b02595
J. Agric. Food Chem. 2015, 63, 6577−6587

which leads to variation of ROS.[46] ROS not only plays important roles in apoptosis (programmed cell death) but also displays positive effects such as the induction of host defense.[46] The toxicity of aurovertins in nematodes might be partially attributable to varied production of ROS in nematodes, so we checked the ROS levels in nematodes exposed to aurovertin D. However, no significant alteration of ROS levels in nematodes upon aurovertin D exposure was observed, indicating that the *C. elegans* response system might possess alternative mechanisms for dealing with this toxin.

The *C. elegans* FOXO transcription factor DAF-16 represents the end point of several key signaling cascades controlling the stress response, the process of aging, and other important biological functions in *C. elegans* in parallel to FOXO transcription factors in mammals.[31] As DAF-16 is thought to be the main target of the DAF-2 pathway and DAF-2 is negatively correlated with DAF-16 activity and longevity, the mutants *daf-16(mu86)* and *daf-2(e1370)* were used to investigate the signaling pathways involved in the aurovertin D-elicited stress response of nematodes. The higher sensitivity of mutant *daf-16(mu86)* deficient in *daf-16* to aurovertin D indicated that DAF-16 was involved in protecting the nematodes from the effects of aurovertin D. We noted that mutant *daf-16(mu86)* was also significantly more sensitive than the wild type N2 to avermectin and oligomycin B, suggesting that *daf-16* may be involved in a general resistance mechanism in nematodes exposed to outside toxins. At the same time, our results demonstrated decreased sensitivity of *daf-2(e1370)* mutants to aurovertin, just opposite that of *daf-16(mu86)*. The reduced sensitivity of *daf-2(e1370)* to aurovertin D might be attributed to the activation of DAF-16 due to the reduced DAF-2 signal.

Because DAF-16 in *C. elegans* is partially activated by nuclear translocation, the transgenic worm strain TJ356 with DAF-16::GFP fusion reporter protein was utilized to further evaluate the involvement of DAF-16 proteins in aurovertin resistance. Our result revealed DAF-16 nuclear localization in aurovertin-treated worms, confirming the activation of the transcription factor DAF-16/FOXO in nematodes by aurovertin D. A previous study indicated that the absence of food for >1 h resulted in nuclear translocation of DAF-16.[36] It is likely that the aurovertin D-induced DAF-16 nuclear localization was triggered by starvation due to the reduced pharyngeal pumping rate caused by aurovertin D.

In summary, some strains of the nematode-parasitic fungus *P. chlamydosporia* isolated from the worm bodies developed a highly conserved class of yellow chemical compounds capable of inducing the death of the host. The yellow pigment metabolites consisted of polyketide pigment aurovertins. The aurovertin-producing *P. chlamydosporia* strains, when cultured in broth for ≥5 days, yielded a total aurovertin production exceeding the inhibitory concentration of aurovertins. The major aurovertin produced in the broth is more toxic to root-knot nematode than to the model species *C. elegans*. Aurovertins play important roles in reducing the population of nematodes and delaying their growth. Investigation of the mode of action of the major aurovertin in the nematode model *C. elegans* revealed that the β subunit of F_1-ATPase might not be the specific target in nematodes as previously reported. On the other hand, nematodes triggered the DAF-16/FOXO transcription factor to cope with the attack from fungal nematicidal aurovertin metabolites.

■ ASSOCIATED CONTENT

Supporting Information

Figures S1 and S2. The Supporting Information is available free of charge on the ACS Publications website at DOI: 10.1021/acs.jafc.5b02595.

■ AUTHOR INFORMATION

Corresponding Authors

*(K.Z.) Phone: 86-871-65032538. Fax: 86-871-65034838. E-mail: kqzhang@ynu.edu.cn.

*(X.N.) E-mail: xmniu@ynu.edu.cn.

Funding

This work was sponsored by grants from the National Basic Research Program of China (973 Program) on Biological Control of Key Crop Pathogenic Nematodes (2013CB127505), the National High Technology Research and Development Program of China (2011AA10A205), the National Natural Science Foundation of China (U1036602 and 31070051), and the Yunnan University Program for Excellent Young Talents awarded to X.N. (XT412003).

Notes

The authors declare no competing financial interest.

■ ACKNOWLEDGMENTS

We thank Dr. Mei Ding (Institute of Genetics and Developmental Biology, Chinese Academy of Sciences) for worms and Dr. Cheng-Gang Zou and Xiao-Wei Huang for helpful discussions and technical support.

■ REFERENCES

(1) Nordbring-Hertz, B.; Jansson, H.; Tunlid, A. Nematophagous fungi. In *Encyclopedia of Life Sciences*; Wiley: Chichester, UK, 2006; pp 1−11.

(2) Schmidt, A.; Dörfelt, H.; Perrichot, V. Carnivorous fungi from Cretaceous amber. *Science* **2007**, *318*, 1743.

(3) Li, G.; Zhang, K. Nematode-toxic fungi and their nematicidal metabolites. In *Nematode-Trapping Fungi*; Zhang, K., Hyde, K., Eds.; Springer: Dordrecht, The Netherlands, 2014; pp 313−375.

(4) Olthof, T. H. A.; Estey, R. H. A nematotoxin produced by the nematophagous fungus *Arthrobotrys oligospora* Fresenius. *Nature* **1963**, *197*, 514−515.

(5) Larriba, E.; Jaime, M. D.; Carbonell-Caballero, J.; Conesa, A.; Dopazo, J.; Nislow, C.; Martín-Nieto, J.; Lopez-Llorca, L. V. Sequencing and functional analysis of the genome of a nematode egg-parasitic fungus. *Fungal Genet. Biol.* **2014**, *65*, 69−80.

(6) Lopez-Llorca, L. V.; Gómez-Vidal, S.; Monfort, E.; Larriba, E.; Casado-Vela, J.; Elortza, F.; Jansson, H. B.; Salinas, J.; Martín-Nieto, J. Expression of serine proteases in egg-parasitic nematophagous fungi during barley root colonization. *Fungal Genet. Biol.* **2010**, *47*, 342−351.

(7) Hellwig, V.; Mayer-Bartschmid, A.; Muller, H.; Greif, G.; Kleymann, G.; Zitzmann, W.; Tichy, H. V.; Stadler, M. Pochonins A−F, new antiviral and antiparasitic resorcylic acid lactones from *Pochonia chlamydosporia* var. *catenulata*. *J. Nat. Prod.* **2003**, *66*, 829−837.

(8) Khambay, B. P. S.; Bourne, J. M.; Cameron, S.; Kerry, B. R.; Zaki, M. A nematicidal metabolite from *Verticillium chlamydosporium*. *Pest Manage. Sci.* **2000**, *56*, 1098−1099.

(9) Shinonaga, H.; Kawamura, Y.; Ikeda, A.; Aoki, M.; Sakai, N.; Fujimoto, N.; Kawashima, A. Pochonins K−P: new radicicol analogues from *Pochonia chlamydosporia* var. *chlamydosporia* and their WNT-5A expression inhibitory activities. *Tetrahedron* **2009**, *65*, 3446−3453.

(10) Shinonaga, H.; Kawamura, Y.; Ikeda, A.; Aoki, M.; Sakai, N.; Fujimoto, N.; Kawashima, A. The search for a hair-growth stimulant: new radicicol analogues as WNT-5A expression inhibitors from

DOI: 10.1021/acs.jafc.5b02595
J. Agric. Food Chem. 2015, 63, 6577−6587

Pochonia chlamydosporia var. *chlamydosporia*. *Tetrahedron Lett.* **2009**, *50*, 108−110.
(11) Zhou, H.; Qiao, K.; Gao, Z.; Vederas, J. C.; Tang, Y. Insights into radicicol biosynthesis via heterologous synthesis of intermediates and analogs. *J. Biol. Chem.* **2010**, *285*, 41412−41421.
(12) Baldwin, C.; Weaver, L.; Brooker, R.; Jacobsen, T.; Osborne, C. J.; Nash, H. Biological and chemical properties of aurovertin, a metabolic product of *Calcarisporium abuscula*. *Lloydia* **1964**, *27*, 88−95.
(13) Wang, F.; Luo, D. Q.; Liu, J. K. Aurovertin E, a new polyene pyrone from the basidiomycete *Albatrellus confluens*. *J. Antibiot.* **2005**, *58*, 412−415.
(14) Azumi, M.; Ishidoh, K.; Kinoshita, H.; Nihira, T.; Ihara, F.; Fujita, T.; Igarashi, Y. Aurovertins F−H from the entomopathogenic fungus *Metarhizium anisopliae*. *J. Nat. Prod.* **2008**, *71*, 278−280.
(15) Niu, X. M.; Wang, Y. L.; Chu, Y. S.; Xue, H. X.; Li, N.; Wei, L. X.; Mo, M. H.; Zhang, K. Q. Nematodetoxic aurovertin-type metabolites from a root-knot nematode parasitic fungus *Pochonia chlamydosporia*. *J. Agric. Food Chem.* **2010**, *58*, 828−834.
(16) Guo, H.; Feng, T.; Li, Z. H.; Liu, J. K. Ten new aurovertins from cultures of the basidiomycete *Albatrellus confluens*. *Nat. Prod. Bioprospect.* **2013**, *3*, 8−13.
(17) van Raaij, M. J.; Abrahams, J. P.; Leslie, A. G.; Walker, J. E. The structure of bovine F_1-ATPase complexed with the antibiotic inhibitor aurovertin B. *Proc. Natl. Acad. Sci. U. S. A.* **1996**, *93*, 6913−6917.
(18) Huang, T. C.; Chang, H. Y.; Hsu, C. H.; Kuo, W. H.; Chang, K. J.; Juan, H. F. Targeting therapy for breast carcinoma by ATP synthase inhibitor aurovertin B. *J. Proteome Res.* **2008**, *7*, 1433−1444.
(19) Andersson, D. I.; Hughes, D. Microbiological effects of sublethal levels of antibiotics. *Nat. Rev. Microbiol.* **2014**, *12*, 465−478.
(20) Wu, D. K.; Zhang, C. P.; Zhu, C. Y.; Wang, Y. L.; Guo, L. L.; Zhang, K. Q.; Niu, X. M. Metabolites from carnivorous fungus *Arthrobotrys entomopaga* and their functional roles in fungal predatory ability. *J. Agric. Food Chem.* **2013**, *61*, 4108−4113.
(21) Wu, H. Y.; Wang, Y. L.; Tan, J. L.; Zhu, C. Y.; Li, D. X.; Huang, R.; Zhang, K. Q.; Niu, X. M. Regulation of the growth of cotton bollworms by metabolites from an entomopathogenic fungus *Paecilomyces cateniobliquus*. *J. Agric. Food Chem.* **2012**, *60*, 5604−5608.
(22) Hulme, S. E.; Whitesides, G. M. Chemistry and the worm: *Caenorhabditis elegans* as a platform for integrating chemical and biological research. *Angew. Chem., Int. Ed.* **2011**, *50*, 4774−4807.
(23) Mauchline, T. H.; Kerry, B. R.; Hirsch, P. R. Quantification in soil and the rhizosphere of the nematophagous fungus *Verticillium chlamydosporium* by competitive PCR and comparison with selective plating. *Appl. Environ. Microbiol.* **2002**, *68*, 1846−1853.
(24) White, T. J.; Bruns, T; Lee, S. Amplification and direct sequencing of fungal ribosomal RNA genes for phylogenetics. In *PCR Protocols: A Guide to Methods and Applications*; Innis, M. A., Gelfand, D. H., Sninsky, J. J., White, T. J., Eds.; Academic Press: San Diego, CA, USA, 1990; pp 315−322.
(25) Stiernagle, T. Maintenance of *Caenorhabditis elegans*. *WormBook* **2006**, 1−11.
(26) Chen, W.; Müller, D.; Richling, E.; Wink, M. Anthocyanin-rich purple wheat prolongs the life span of *Caenorhabditis elegans* probably by activating the DAF-16/FOXO transcription factor. *J. Agric. Food Chem.* **2013**, *61*, 3047−3053.
(27) Lee, S. J.; Hwang, A. B.; Kenyon, C. Inhibition of respiration extends *C. elegans*' life span via reactive oxygen species that increase HIF-1 activity. *Curr. Biol.* **2010**, *20*, 2131−2316.
(28) Timmons, L.; Court, D. L.; Fire, A. Ingestion of bacterially expressed dsRNAs can produce specific and potent genetic interference in *Caenorhabditis elegans*. *Gene* **2001**, *263*, 103−112.
(29) Greer, E. R.; Perez, C. L.; Van Gilst, M. R.; Lee, B. H.; Ashrafi, K. Neural and molecular dissection of a *Caenorhabditis elegans* sensory circuit that regulates fat and feeding. *Cell Metab.* **2008**, *8*, 118−131.
(30) Martorell, P.; Forment, J. V.; de Llanos, R.; Montón, F.; Llopis, S.; González, N.; Genovés, S.; Cienfuegos, E.; Monzó, H.; Ramón, D. Use of *Saccharomyces cerevisiae* and *Caenorhabditis elegans* as model organisms to study the effect of cocoa polyphenols in the resistance to oxidative stress. *J. Agric. Food Chem.* **2011**, *59*, 2077−2085.
(31) Henderson, S. T.; Johnson, T. E. *daf-16* integrates developmental and environmental inputs to mediate aging in the nematode *Caenorhabditis elegans*. *Curr. Biol.* **2001**, *11*, 1975−1980.
(32) Lee, R. Y.; Hench, J.; Ruvkun, G. Regulation of *C. elegans* DAF-16 and its human ortholog FKHRL1 by the *daf-2* insulin-like signaling pathway. *Curr. Biol.* **2001**, *11*, 1950−1957.
(33) Manzanilla-López, R. H.; Esteves, I.; Finetti-Sialer, M. M.; Hirsch, P. R.; Ward, E.; Devonshire, J.; Hidalgo-Díaz, L. *Pochonia chlamydosporia*: advances and challenges to improve its performance as a biological control agent of sedentary endo-parasitic nematodes. *J. Nematol.* **2013**, *45*, 1−7.
(34) Lindblom, T. H.; Dodd, A. K. Xenobiotic detoxification in the nematode *Caenorhabditis elegans*. *J. Exp. Zool. A: Comp. Exp. Biol.* **2006**, *305*, 720−730.
(35) Zubovych, I.; Doundoulakis, T.; Harran, P. G.; Roth, M. G. A missense mutation in *Caenorhabditis elegans* prohibitin 2 confers an atypical multidrug resistance. *Proc. Natl. Acad. Sci. U. S. A.* **2006**, *103*, 15523−15528.
(36) Berger, K.; Sivars, U.; Winzell, M. S.; Johansson, P.; Hellman, U.; Rippe, C.; Erlanson-Albertsson, C. Mitochondrial ATP synthase-a possible target protein in the regulation of energy metabolism *in vitro* and *in vivo*. *Nutr. Neurosci.* **2002**, *5*, 201−210.
(37) Pedersen, P. L.; Ko, Y. H.; Hong, S. ATP synthases in the year 2000: evolving views about the structures of these remarkable enzyme complexes. *J. Bioenerg. Biomembr.* **2000**, *32*, 325−332.
(38) Cataldi de Flombaum, M. A.; Stoppani, A. O. Influence of efrapeptin, aurovertin and citreoviridin on the mitochondrial adenosine triphosphatase from *Trypanosoma cruzi*. *Mol. Biochem. Parasitol.* **1981**, *3*, 143−155.
(39) Douglas, M. G.; Koh, Y.; Ebner, E.; Agsteribbe, E.; Schatz, G. A nuclear mutation conferring aurovertin resistance to yeast mitochondrial adenosine triphosphatase. *J. Biol. Chem.* **1979**, *254*, 1135−1139.
(40) Lee, R. S.; Pagan, J.; Satre, M.; Vignais, P. V.; Senior, A. E. Identification of a mutation in *Escherichia coli* F_1-ATPase beta-subunit conferring resistance to aurovertin. *FEBS Lett.* **1989**, *253*, 269−272.
(41) Lee, R. S.; Pagan, J.; Wilke-Mounts, S.; Senior, A. E. Characterization of *Escherichia coli* ATP synthase beta-subunit mutations using a chromosomal deletion strain. *Biochemistry* **1991**, *30*, 6842−6847.
(42) Tsang, W. Y.; Lemire, B. D. The role of mitochondria in the life of the nematode. *Biochim. Biophys. Acta, Mol. Basis Dis.* **2003**, *1638*, 91−105.
(43) Couillault, C.; Pujol, N.; Reboul, J.; Sabatier, L.; Guichou, J. F.; Kohara, Y.; Ewbank, J. J. TLR-independent control of innate immunity in *Caenorhabditis elegans* by the TIR domain adaptor protein TIR-1, an ortholog of human SARM. *Nat. Immunol.* **2004**, *5*, 488−494.
(44) Weber, J. ATP synthase: subunit-subunit interactions in the stator stalk. *Biochim. Biophys. Acta, Bioenerg.* **2006**, *1757*, 1162−1170.
(45) Johnson, K. M.; Swenson, L.; Opipari, A. W., Jr.; Reuter, R.; Zarrabi, N.; Fierke, C. A.; Borsch, M.; Glick, G. D. Mechanistic basis for differential inhibition of the F_1F_O-ATPase by aurovertin. *Biopolymers* **2009**, *91*, 830−840.
(46) Formentini, L.; Sanchez-Aragó, M.; Sánchez-Cenizo, L.; Cuezva, J. M. The mitochondrial ATPase inhibitory factor 1 triggers a ROS-mediated retrograde prosurvival and proliferative response. *Mol. Cell* **2012**, *45*, 731−742.

DOI: 10.1021/acs.jafc.5b02595
J. Agric. Food Chem. 2015, 63, 6577−6587

tion for optimal linear response. Spectra were baseline corrected, adjusted for mass differences, and normalized to the methylene peak at 2927 cm^{-1}. FTIR spectra of the oils (crude, refined, and products) are shown in Figures 1−3, 5, and 6.

(b) Thin Layer Chromatography (TLC). TLC of the reaction mixtures was carried out using precoated silica gel plates (0.2 mm, 5 × 20 cm; EM Science, Darmstadt, Germany). The solvent system used was (hexane/ethyl acetate/acetic acid 10:5:2). The developed chromatogram was visualized by methanol−sulfuric acid spray and heated to 100−110 °C.

(c) Viscosity Measurements. Kinematic viscosity was determined using a Cannon-Fenske viscometer for transparent liquids (Cannon Instrument Co., State College, PA, USA) in accordance with AOCS Official Method Tq 1a-64. The tube number was 400. The cleaned dry tube was loaded with the sample oil at room temperature and placed in its holder in the constant-temperature bath. The sample was allowed to equilibrate for 10 min at 40 °C or for 15 min at 100 °C before the sample was suctioned into the lower bulb until the meniscus just overshot the mark above the lower bulb. The suction was removed and the meniscus adjusted to the mark. The sample was allowed to flow at the same time the stop clock was started. The time (in seconds) it took for the meniscus to reach the mark below the bulb multiplied by the tube constant gave the viscosity of the sample. The measurement was replicated and averaged to obtain the viscosity.

(d) Nuclear Magnetic Resonance Spectroscopy. ^{13}C NMR spectra were acquired on a Bruker AV-500 MHz spectrometer with a dual 5 mm proton/carbon probe (Bruker, Ballerica, MA, USA). The internal standard was tetramethylsilane.

(e) Density. Sample density measurements were carried out using a pycnometer or Kimble specific gravity bottle (10 mL) equipped with a thermometer and a side arm cap (Kimble Glass Inc., Vineland, NJ, USA). The pycnometer was cleaned with hexane and acetone and dried with an air jet. The reassembled unit was weighed empty and then carefully loaded with the sample, cleaned of excess sample, and reweighed. The process was replicated so that sample masses could be averaged.

(f) Oil Extraction and Degumming. Osage orange oil was extracted from 3 kg of ground seed using a Retsch mill. The seeds were preconditioned in powdered dry ice for several minutes before milling to facilitate particle size reduction. The obtained seed meal was extracted in approximately 1 kg batches in a Soxhlet extractor using hexane. The hexane extract was decolorized with activated carbon before solvent removal to yield the crude oil. The oil content of the seed was calculated to be 30−35% by weight of the dry seed. Portions of the crude oil were chilled (5 °C) and centrifuged (10000*g*) at the same temperature for 30 min to remove phospholipids and waxy content. The free fatty acid component was removed from the degummed oil (Figure 1) by dissolving it in hexane, and the solution

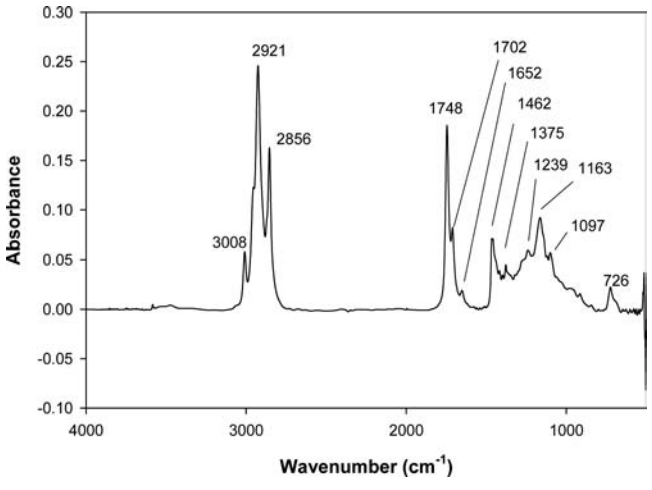

Figure 1. FTIR spectrum of degummed crude Osage orange oil.

was shaken with cold aqueous (0.1 M) ammonium hydroxide solution in a separatory funnel. The separated organic phase was then washed with deionized water until the washings were neutral to litmus. The organic layer was dried over $MgSO_4$, filtered, and concentrated under reduced pressure at 67 °C to give the Osage orange triglyceride (Figure 2); density = 0.979 g mL^{-1} at 23 °C. The free fatty acids were

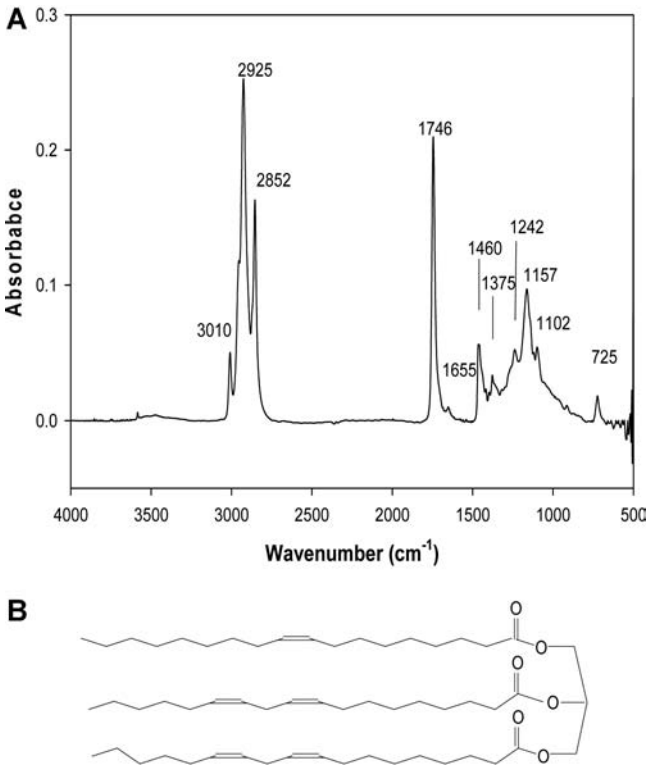

Figure 2. (A) FTIR spectrum of cleaned Osage orange triglyceride and (B) structural representation of the triglyceride molecule.

recovered by acidulation of the combined aqueous layer and washings with dilute HCl followed by extraction with hexane. The hexane extract was dried over $MgSO_4$ and concentrated to give the free fatty acids, which were set aside from the intact triglyceride.

Synthesis of Osage Orange Oxirane. In a 1 L jacketed three-necked reaction flask equipped with an overhead stirrer at a starting temperature of 40 °C was placed Osage orange oil (280.90 g, 320.8 mmol) to which formic acid (88%, 30.50 g, 25.0 mL, 663 mmol, i.e., 0.4 equiv/−C═C−) was added in one portion. On stirring to homogeneity, H_2O_2 (50%, 200 mL, 7.05 mol) was added dropwise, and at the end of peroxide addition the reaction temperature was raised to 70 °C. Progress of the reaction was monitored in 30 min intervals by FTIR spectral analysis of withdrawn samples of the reaction mixture for disappearance of the 3008 and 1648 cm^{-1} bands of the olefin with the concomitant formation of a doublet observable at 822−845 cm^{-1} for the oxirane. After 2 h, the reaction was judged complete; the heat source was then withdrawn and the product mixture allowed to cool to near room temperature, when it was transferred into a separatory funnel with ethyl acetate as diluent and allowed to separate into two layers. The aqueous layer was removed and discarded. The organic phase was washed with a mixture of saturated NaCl and Na_2CO_3 solution followed by drying over $MgSO_4$ overnight. Filtering and concentration of the filtrate gave a quantitative yield, 316.0 g, of the oxirane of Osage orange oil, $d^{22.3}$ 1.067 g mL^{-1}. FTIR spectral features of its film on NaCl disk are given in cm^{-1}: 2928 vs (−CH_2− sym stretch), 2859 s (−CH_2− asym stretch), 1743 vs (−C═O stretch), 1461 s (−CH_2− deform), 1377 m-s (−CH_3 deform), 1236 m-s (−O—C═O), 1160 s (−CH—O− stretch), 1045 (−CH_2O− stretch), 845−824 doublet m (−C—O—C− oxirane asym stretch), 725 (−CH_2− wag). ^{13}C NMR ($CDCl_3$): δ 173.17,

DOI: 10.1021/acs.jafc.5b01625
J. Agric. Food Chem. 2015, 63, 6588−6595

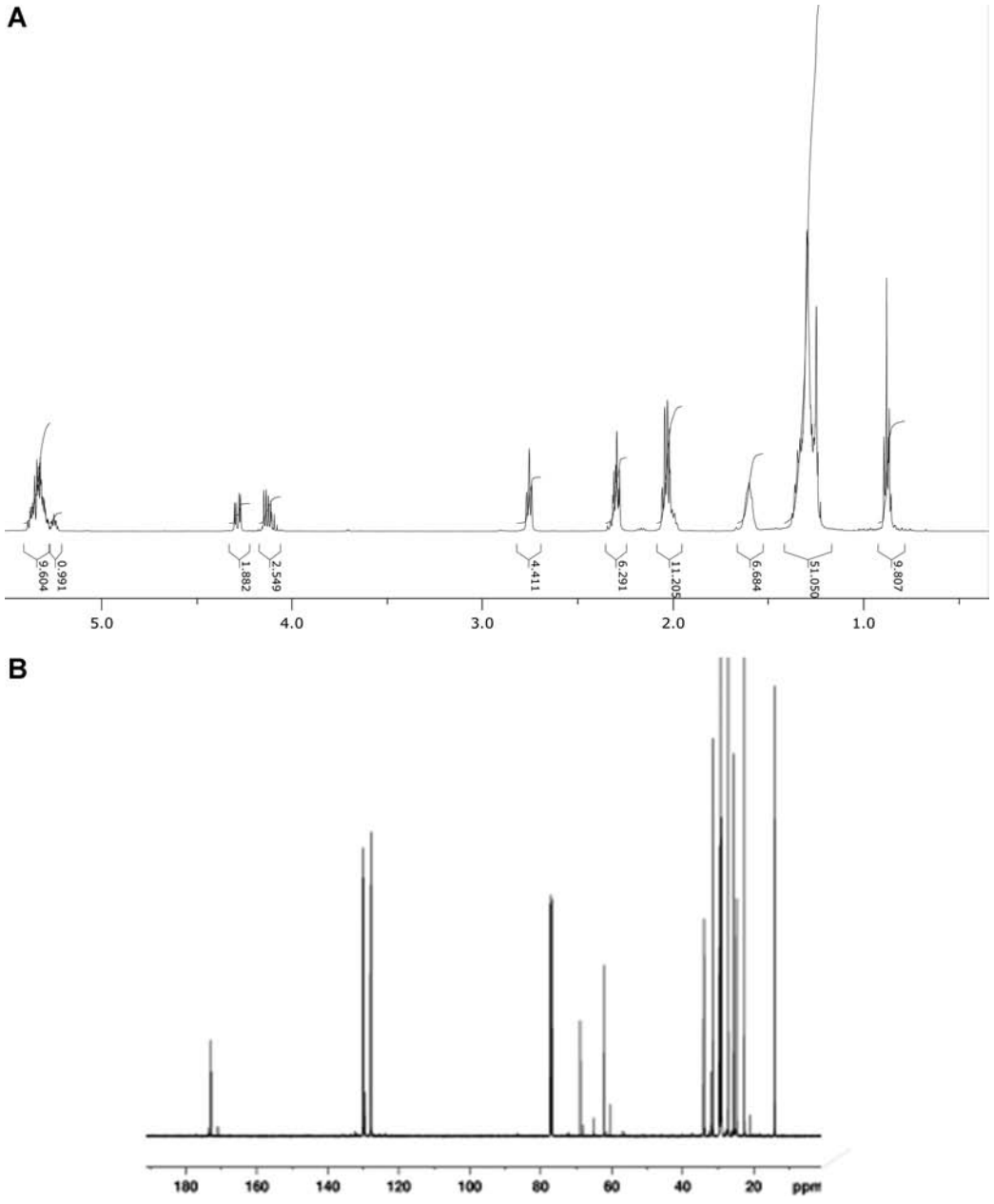

Figure 3. (A) ^{1}H NMR spectrum of the cleaned triglyceride and (B) its ^{13}C NMR spectrum.

173.1, 172.7 (ester carbonyls); 68.9 (−H**C**O−) glyceryl, 62.0, 60.3 (−**C**H$_2$O−) glyceryl; 57.2, 57.1, 56.9, 56.88, 56.7, 56.6, 54.3, 54.27, 54.1 (oxirane carbons); 34.1, 34.0, 33.9 (C-2), 31.8, 31.77, 31.6 (C-11), 29.6, 29.57, 29.5 (C-8), 29.46, 29.45, 29.4 (C-14), 29.27, 29.25, 29.21 (C-3), 29.18, 29.13, 29.10 (C-7), 29.08, 29.0, 28.9, 28.87, 27.81, 27.8, 27.74, 27.72, 27.1, 26.8, 26.5, 26.5, 26.48, 26.4, 26.36, 26.33, 26.2, 26.1, 24.8, 24.73, 24.70 (−CH$_2$−); 22.6 (C-18), 14. 0 (C-18). ^{1}H NMR (CDCl$_3$): δ 5.20 (m, **H**CO− glyceryl); 4.23 (m, C**H**$_2$O glyceryl), 4.1 (m 3H, CH$_2$O glyceryl); 3.05 (m, 3H), 2.91 (m, 6H, epoxy methine protons); 2.82 (bs, 1H), 2.26 (t, J = 7.4 Hz, 7.3 Hz, C11 protons), 1.6 (m, 7H), 1.56 (bs, 8H), 1.43 (m, 13H), 1.28 (bs, 7H), 1.26 (s 38H), 1.18 (s, 9H), 0.83 (t, 9H, terminal C**H**$_3$). The kinematic viscosity was 131.6 cSt (40 °C) and 19.2 cSt (100 °C); that is, a viscosity index (VI) = 166.

Synthesis of Osage Orange Poly(α-hydroxydibutylamine) Triglyceride. In a dry 250 mL round-bottom reaction flask equipped with an overhead stirrer as above was placed epoxy Osage orange oil (59.5 g, 62.26 mmol), and anhydrous ZnCl$_2$ (1.0 g) was added followed with *N*,*N*-dibutylamine (43.41g, 56.6 mL, 336 mmol, i.e., 5.4 equiv) introduced dropwise into the stirred reaction mixture. A reflux condenser was attached, and the reaction mixture was stirred and heated to gentle reflux. The reaction was monitored by sampling the mixture at 1 h intervals to observe diminution of the 820−845 cm^{-1} band of the oxirane in the FTIR spectrum as ring-opening progressed. The reaction was stopped when no trace of the 820−845 cm^{-1} band was visible, ca. 2.5 h. TLC (hexane/EtAc/AcOH 10:5:2) was a second mode of tracking reaction progress, confirming the absence of starting epoxide. The reaction product was cooled to room temperature, diluted with ethyl acetate, and washed with saturated NaCl solution. The organic phase was dried over MgSO$_4$ and filtered, and the solvent was removed by rotary evaporation under reduced pressure, giving 93.3 g, (i.e., 93.3%) yield of the poly(α-hydroxydibutylamine); $d^{22.6}$ = 0.9985 g mL^{-1}. FTIR film on NaCl disk: ν cm^{-1} 3431 (br OH stretch, second deriv 3586), 2952 s (−CH$_3$ asym stretch, second deriv 2956), 2929 vs (−CH$_2$− sym stretch, second deriv 2931), 2853 s (−CH$_2$− asym stretch, second deriv 2876), 2857 (−CH$_3$ asym stretch), 1739 vs (−C═O stretch, second deriv 1741), 1667 w (−N—C, 1575 vw), 1463 s (−CH$_2$− deform, second deriv 1468), 1378 m-s (−CH$_3$

DOI: 10.1021/acs.jafc.5b01625
J. Agric. Food Chem. 2015, 63, 6588−6595

deform), 1244 m (−O—C═O), 1164 m-s (−CHO− stretch), 1101 m-s (−CHO− stretch), 1035 sh (−CH_2O− stretch), 726 (−CH_2− wag). The kinematic viscosity was 410.54 cSt (40 °C) and 38.57 cSt (100 °C); VI = 141.

RESULTS AND DISCUSSION

Efficient solvent extraction of the fat content of the seed depends on the extent to which particle size of the ground seed could be reduced, especially in a seed of higher fat content. To maximize the particle surface area of the grind, experience suggested that chilling of the dry seed before milling would give the best results. Therefore, at near dry ice temperature the seed was easily ground to a reasonably fine powder without clumping, as would otherwise be experienced. This condition of the meal greatly facilitated hexane extraction of each kilogram batch of the seed meal. This was evidenced by the result that at the end of each 24 h extraction interval, the residual pool of solvent below the extraction thimble was colorless. Concentration of the resulting extract by rotary evaporation gave a crude dark Osage orange oil. Decolorization of the crude was by redissolution in hexane and treatment with activated carbon. The decolorized crude triglyceride obtained after solvent removal was then winterized followed by centrifugation at low temperature (5 °C) to separate the phospholipid and waxy components. Although purification of the degummed crude oil could have been achieved by fractional distillation, we chose the wet chemistry approach for economic reasons. Cold storage of the seed seemed to have slowed the metabolic release of free fatty acids in the oil as seen in Figure 1. The free fatty acid level in the extracted oil was reasonably low judging from the lower intensity of the 1702 cm^{-1} carbonyl absorption band of the free fatty acids compared to that of the intact ester functionality of the triglyceride at 1748 cm^{-1}. Consequently, we opted for the wet chemistry approach, which successfully separated the intact triglycerides (Figure 2A) from the admixture in Figure1. Interpretation of the FTIR spectral features of the cleaned triglyceride (Figure 2A) in relation to the structural representation of the oil (Figure 2B) is as follows. The absorption band at 3010 cm^{-1} is the olefinic (**H—C═**) stretch, whereas the 2956 and 2925 cm^{-1} bands are respectively the terminal methyl (H_3C−) and the methylene (−CH_2−) groups asymmetric stretching modes of the alkyl chains. The symmetric stretching bands of the terminal methyl and that of the methylene groups are seen around 2855 cm^{-1}. The 2855 cm^{-1} band is a composite of the more preponderant methylene groups at 2855 cm^{-1}, whereas the smaller population of methyl symmetric absorption band is at 2865 cm^{-1}. The other prominent diagnostic absorption band of the oil is the very strong carbonyl (**−C═O**) of the ester groups at 1746 cm^{-1}. It should be noted here that the 1740 cm^{-1} region of the spectrum is devoid of any free fatty acid absorption, hence the absence of the 1702−1713 cm^{-1} band as exists in the admixture (Figure 1). The methylene and the terminal methyl deformation bands of the chain are seen at 1460 and 1375 cm^{-1}, respectively. The small band at 1655 cm^{-1} indicates the puckering or breathing mode of the vinylic (**−C═C−**) bonds of the triglyceride. The FTIR absorbance at 1242 cm^{-1} represents the (**−O—C═O**) stretching mode of the ester head groups of the triglyceride, whereas the 1157 and 1102 cm^{-1} bands are those of the glyceryl (HCO). A feature that seems to be missing is the 1050 cm^{-1} band of the (CH_2O) of the glyceryl absorbance, which is here overlapped by the 1102 cm^{-1} band. Finally, the IR band at 725 cm^{-1} is the wagging mode of the long methylene skeleton. The ^1H and ^{13}C NMR spectra of the cleaned triglyceride are shown in Figure 3, panels A and B, respectively. From the chemical shift values, the most downfield protons are the vinylic multiplet at 5.4 ppm (9−10H), immediately followed by a multiplet at 5.3 ppm (1H), which is the glyceryl methine proton by virtue of coupling from the two neighboring methylene groups. A doublet of doublets at 4.3 ppm (J = 4.3 Hz, 2H) and multiplet centered at 4.1 (2H)

Table 1. Fatty Acid Composition of Osage Orange Seed Oil[16]

fatty acid	area %
C 14:0	0.1
C 16:0	7.0
C 16:1 Δ^9	0.1
C 18:0	2.4
C 18:1 Δ^9	11.9
C 18:1 Δ^{11}	0.8
C 18:2 $\Delta^{9,12}$	76.4
C 18:3 $\Delta^{9,12,15}$	0.4
C 20:0	0.6
unknown (sum)	0.3
Σsaturated	10.1
Σmonounsaturated	12.8
Σpolyunsaturated	76.8

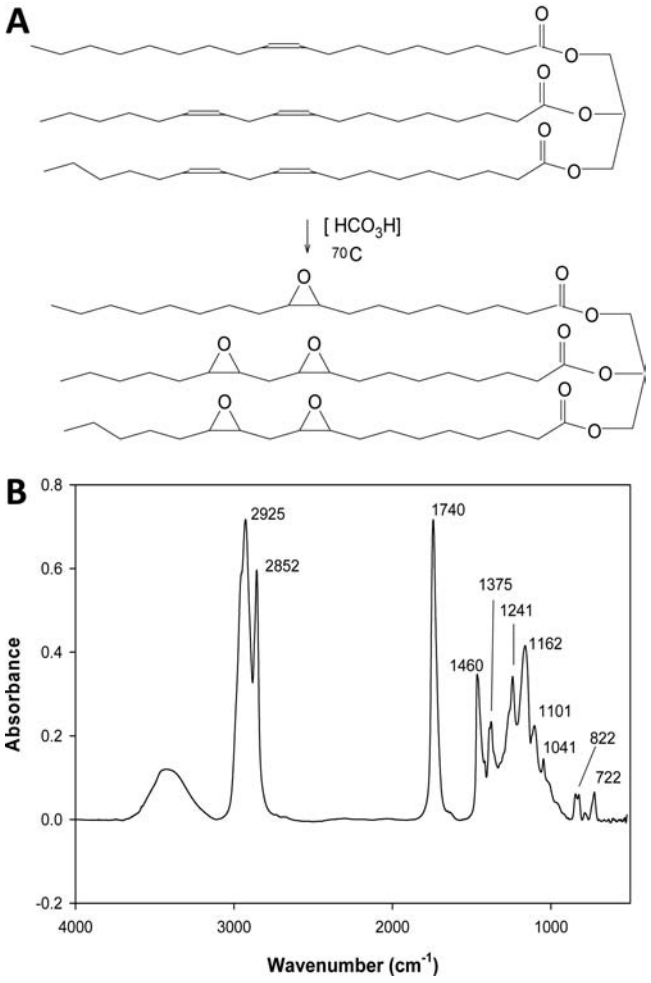

Figure 4. (A) Epoxidation scheme for the cleaned Osage orange oil; (B) FTIR spectrum of epoxidized Osage orange triglyceride.

DOI: 10.1021/acs.jafc.5b01625
J. Agric. Food Chem. 2015, 63, 6588−6595

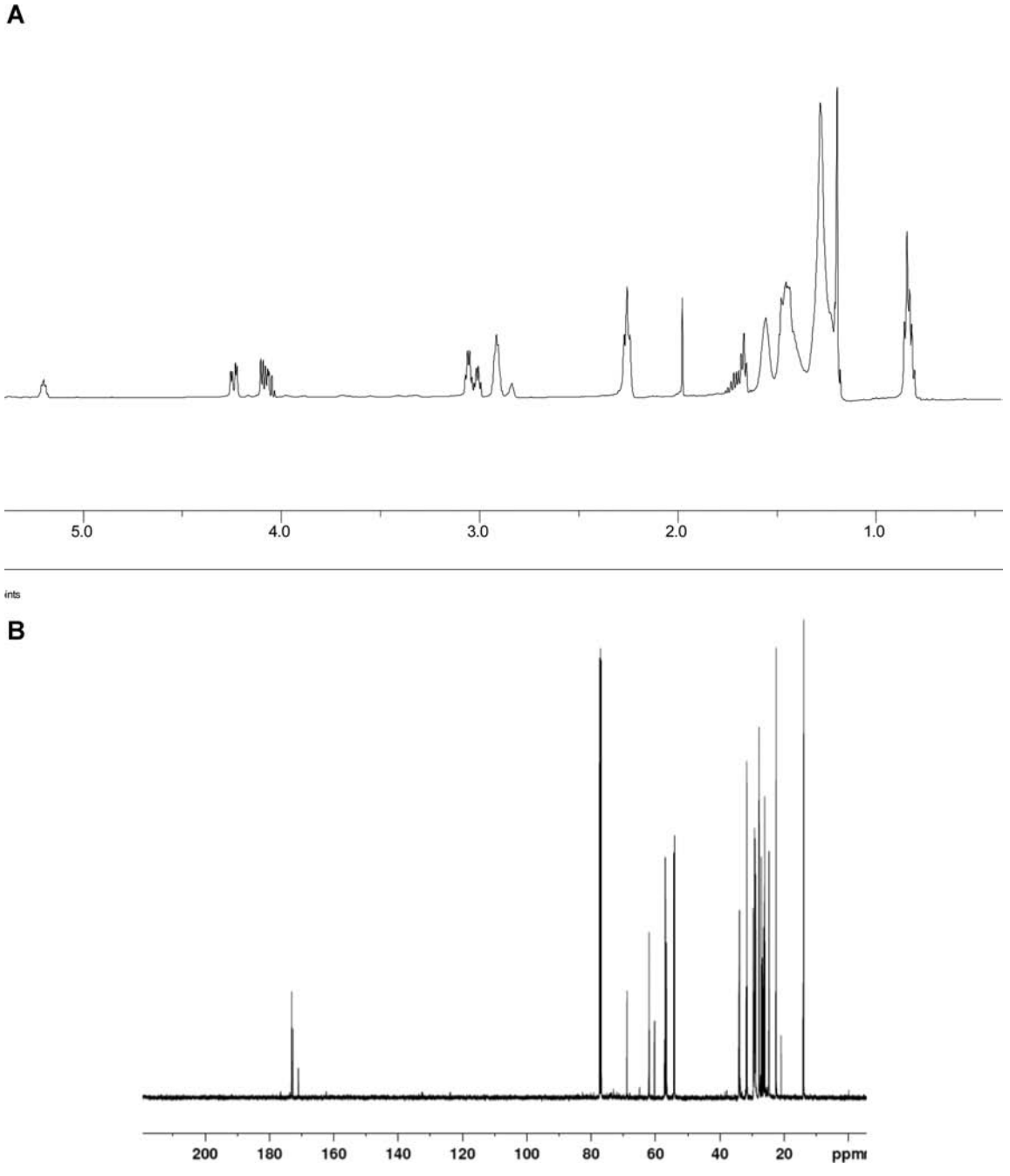

Figure 5. (A) ^{1}H and (B) ^{13}C NMR spectra of the oxirane of Osage orange oil showing resonances of the epoxy methine protons around 3.3 ppm and of the methine carbons from 57.15 to 54.13 ppm.

Table 2. Densities and Kinematic Viscosities of Derivatives

compound	density (g cm^{-3})	kinematic viscosity (cSt)	viscosity index
unmodified triglyceride	0.979 (23 °C)		>200
oxirane	1.067 (22.3 °C)	131.6 (40 °C) 19.6 (100 °C)	166
poly(α-hydroxydibutylamine)	0.998 (22.6 °C)	410.54 (40 °C) 38.57 (100 °C)	141

are the glyceryl CH_2s. The clean triplet centered at 2.75 ppm (J = 6.6 Hz, 6.5 Hz, 4H) represents the methylene groups contiguous to the ester carbonyl, whereas the multiplet at 2.30 ppm represents the 6H of C11 sandwiched between C10, C12, and C14 vinylic carbons of linoleic acid moieties. The multiplet at 2.03 ppm (11H) is the C3 and C4 protons, and the broad multiplet at 1.6 ppm (6H) accounts for C8 protons. The huge multiplet at 1.29 ppm is assigned to the remaining methylene protons, whereas the terminal methyl protons are the overlapping triplets (multiplet) at 0.87 ppm. A profile of the fatty acid methyl esters of Osage orange oil (Table 1) shows the fatty acid composition of this oil.[16]

Epoxidation of the cleaned triglyceride was smooth and high yielding.[17−20] Figure 4A depicts the epoxidation reaction scheme transforming the olefinic units of this oil to the polyoxirane derivative, and Figure 4B is the FTIR spectrum of

DOI: 10.1021/acs.jafc.5b01625
J. Agric. Food Chem. 2015, 63, 6588−6595

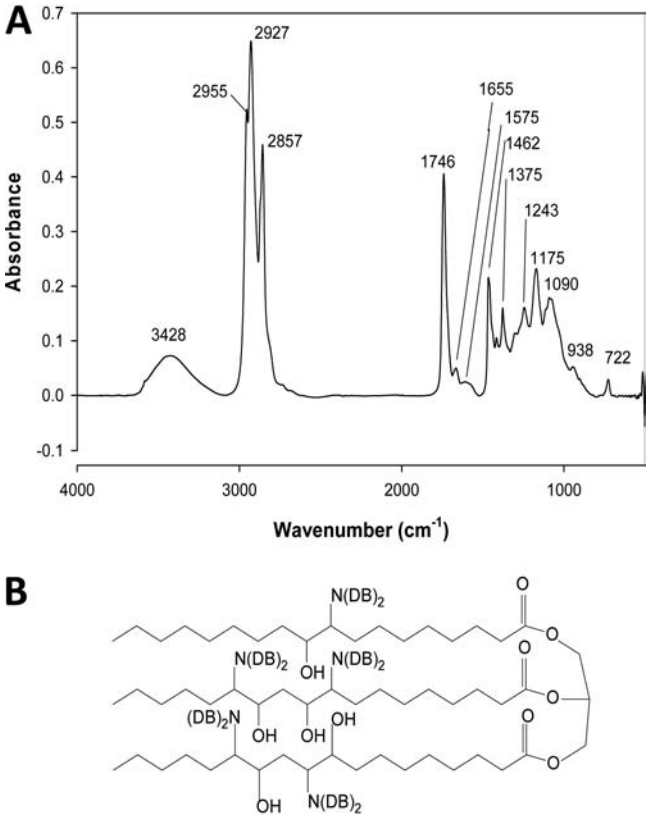

Figure 6. (A) FTIR spectrum of poly(α-hydroxy-*N*,*N*-dibutylamine) triglyceride of Osage orange oil and (B) proposed structure of this derivative.

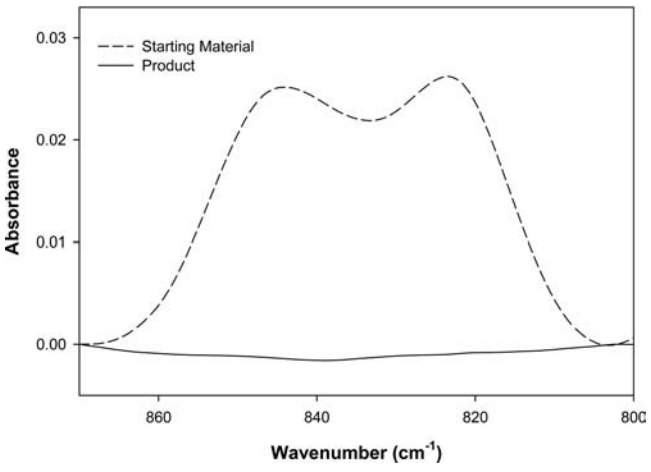

Figure 7. FTIR spectral difference between the epoxy band region before and after reaction with *N*,*N*-dibutylamine.

the polyoxirane of Osage orange oil. The glaring diagnostic spectral feature of the oxirane is the characteristic doublet at 824−845 cm^{-1} for the (−**C**—**O**—**C**−) asymmetric stretching mode of the three-membered ring. A not so obvious absorption band of the oxirane, however, is the methine (**H**—**C**—O—**C**—**H**) band of the three-membered ring that is buried under the strong $-CH_3$ asymmetric stretching mode close to 3000 cm^{-1}. This band is only obvious in the second derivative of the epoxy spectrum at 2994 cm^{-1}. The ^{13}C NMR of the oxirane is shown in Figure 5. The essential diagnostic features observed here are the 10 resonance lines starting from 57.2 to 54.1 ppm

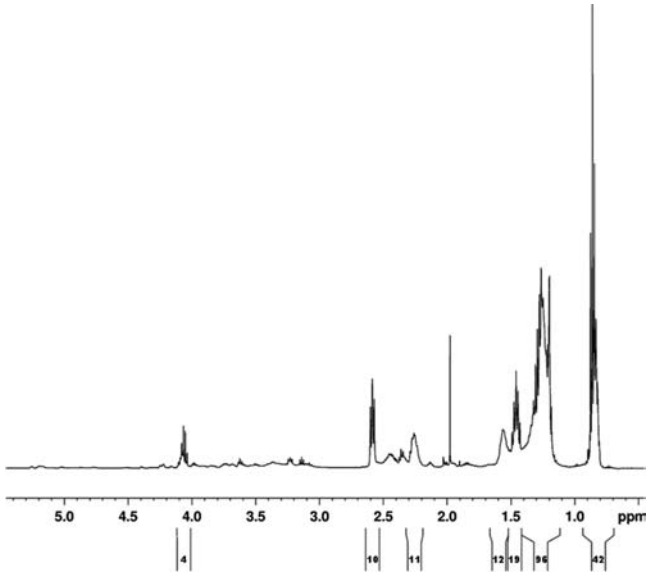

Figure 8. ^1H NMR spectrum of poly(α-hydroxydibutylamine).

resulting from the methine carbons (−**C**—O—**C**−) of the ring. This spectral region is featureless in the parent triglyceride (Figure 3B) and in subsequent derivatives from the oxirane. What is also noticeable from this epoxy spectrum is the complete disappearance or absence of signals of the olefinic moieties (140−120 ppm) in the ^{13}C. In other words, epoxidation of the olefin was complete. The first upfield methylene resonances from the oxirane methine carbons are the three methylene carbons that are proximal to the ester carbonyl at 34.1−33.9 ppm. These are followed by the C-11 carbons sandwiched between the oxirane C-10 and C-12 species at 31.8−31.6 ppm, whereas the six (−**C**H_2−) contiguous to epoxy carbons are observed at 29.6−29.4 ppm. The remaining methylene carbon resonances gradually tend upfield as distance from heteroatoms increases. Thus, some 21 (−CH_2−) invariantly resonate between 29.02 and 24.70 ppm as their location tends toward the alkyl termini. The terminal methyl groups are upfield around 14 ppm. The other spectral features of the ^{13}C NMR are the low-field ester carbonyl resonances at 173.2, 173.1, and 172.7 ppm, whereas the glyceryl methine carbon (−CH−O−) is at 68.9 ppm and its methyleneoxy carbons (−**C**H_2O−) are observed at 62.0 and 60.3 ppm, respectively.

Aminolysis of the oxirane was more sluggish compared to the oxirane formation even as catalyzed by anhydrous $ZnCl_2$ under gentle reflux irrespective of the lower scale of reactants used. The reaction was sometimes run overnight to give the poly-α-hydroxydibutylamine triglyceride derivative in excellent yield.[17,20] This was consistent with earlier observation in amidation ring-opening of other vegetable oxiranes (Milkglyde, Saliglyde, and Soyglyde).[18,19,21] TLC monitoring of the ring-opening of the oxirane showed several discrete spots (R_f = 0.56, 0.52, and 0.48) for the starting epoxide lane in relation to the solvent front when migration was stopped about halfway up the plate height. The polyhydroxydibutylamine tended to smear a bit on the stationary phase even though migrating more slowly with an R_f = 0.26 compared to the oxirane starting material. When development of the loaded plate was allowed to run close to the top of the 5 × 20 cm plate, the developed chromatogram shows up to eight discrete spots in the oxirane lane (R_f = 0.77, 0.74, 0.67, 0.55, 0.48, 0.35, 0.29, and 0.19) as

DOI: 10.1021/acs.jafc.5b01625
J. Agric. Food Chem. 2015, 63, 6588−6595

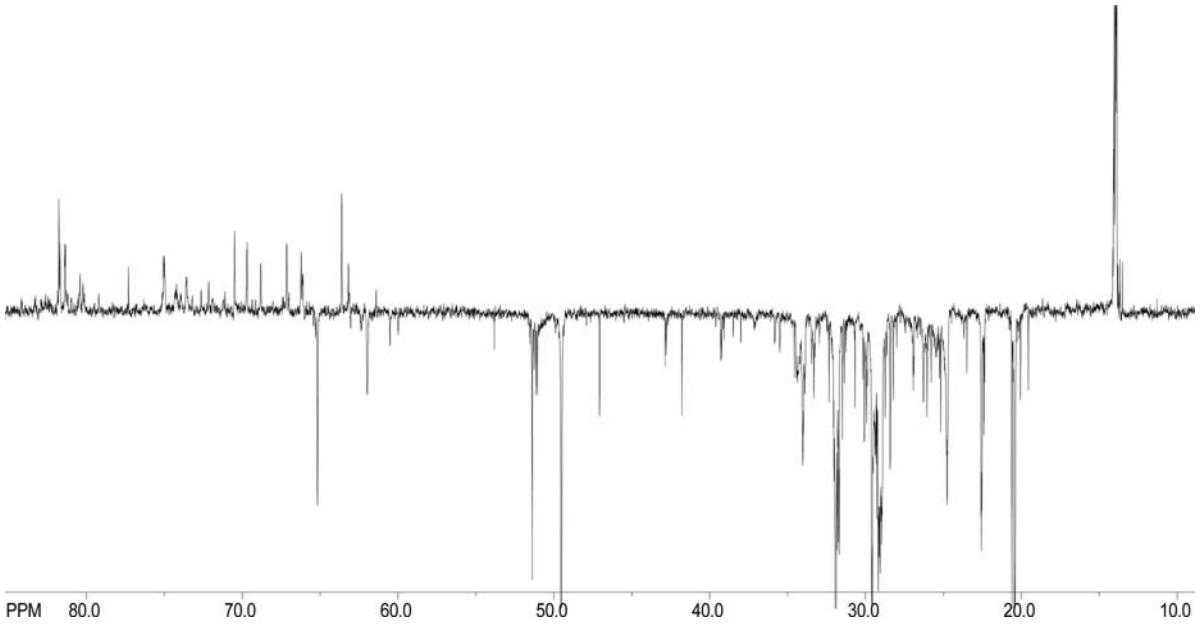

Figure 9. ^{13}C NMR DEPT spectrum poly(α-hydroxydibutylamine).

contrasted to R_f = 0.13 for the product. For an understanding of the TLC data, the cleaned natural oil is a mixture of various C-18 triglycerides and so the epoxidized oil should of necessity contain those permutations. Hence, the species are shown by the TLC spots on the developed plate. The aminolysis seemed to have tamped down the conformational differences into one through streamlining of the structures from the semi sp^2 hybrid in the three-membered rings to full sp^3 configurations that would allow better packing of the chains except for the disrupting influence of the *N*,*N*-dibutylamine substituents. Aminohydration of the chains introduces both higher polarity to the midsection of each acyl chain of the triglyceride and greater sphericity or bulkiness induced by branching of the triglyceride chains. One of the resulting effects of branching in the triglyceride caused by insertion of *N*,*N*-dibutylamine is lowering of the density of the derivatized triglyceride as observed in Table 2. This table also shows enhanced viscosity of the derivative relative to the oxirane. The corresponding FTIR spectrum of the product confirmed complete replacement of the characteristic 820−845 cm^{-1} band of the epoxide with the α-hydroxyl dibutylamine groups.

Figure 7 is an overlay of the FTIR spectra of the starting oxirane over that of the poly-α-hydroxydibutyl amine product in the 800−870 cm^{-1} region, that is, before and after reaction of the starting polyoxirane. This convincingly shows the extent of the ring-opening aminolysis reaction. The broad IR band centered around 3428 cm^{-1} in Figure 6A is the stretching mode of the α-hydroxyl (O−H) groups of the hydroxydibutylamine triglyceride (Figure 6B). The tertiary polyamine generated in the epoxy ring-opening aminolysis reaction is spectroscopically transparent in this region under the product isolation conditions. Inspection of Figure 6A shows attenuation of the ester carbonyl absorption as compared to the strong carbonyl absorption band in the oxirane triglyceride. The explanation lies in the major contribution resulting from the mass effect of adding over 600 mass units of alkyl side chains to the alkyl component of the triglyceride molecule without a corresponding increase in carbonyl moiety contribution. A second but minor contributing factor also is the very weak IR band at 1655 cm^{-1}, which is assignable to a −C−N absorption from the small amount of competing amidation process on the ester head groups. This band is assignable to an "amide I" C−N stretching mode especially as it is accompanied by an unresolved but much smaller band around 1575 cm^{-1} for the "amide II" absorption mode. This phenomenon has been observed in an earlier study of aminolysis ring-opening of new crop epoxy oils.[21] Figure 8 is the ^{1}H NMR spectrum of the poly(α-hydroxydibutylamine). The theoretical total proton count in the product is 194, and the proton integration values when normalized to the spectral resonances of Figure 8 are consistent with characteristics of the desired compound. Figure 9 is the ^{13}C distortionless enhancement proton transfer (DEPT) spectrum of the product. The methylene carbons bound to nitrogen atoms in the product resonate downfield starting at 42.0, 47.1, 49.5, 51.4, and 65.0 ppm, whereas the methine oxygen-bonded carbons are farther downfield from those bonded to nitrogen atoms and are observed between 81.1 and 66.0 ppm. This derivatized vegetable oil is in the exploratory stage for a non-food use in lubricant and related applications, where oxidative stability of the oil is of value. We intend to further modify the hydroxyl units of this tree oil derivative to both lower its polarity and enhance its oxidative stability so as to potentiate its lubricity character.

AUTHOR INFORMATION

Corresponding Author

*(R.E.H.-O.) Phone: (309) 681-6341. Fax: (309) 681-6524. E-mail: Rogers.HarryOkuru@ars.usda.gov.

Notes

Mention of trade names or commercial products in this publication is solely for the purpose of providing specific information and does not imply recommendation or endorsement by the U.S. Department of Agriculture.

The authors declare no competing financial interest.

ACKNOWLEDGMENTS

We express gratitude to Dr. Karl Vermillion for the NMR spectra and to Mark Klokkenga for technical assistance.

DOI: 10.1021/acs.jafc.5b01625
J. Agric. Food Chem. 2015, 63, 6588−6595

REFERENCES

(1) Smith, J. L.; Perino, J. V. Osage orange (*Maclura pomifera*): history and economic uses. *Econ. Bot.* **1981**, *35* (1), 24−41.

(2) Akhmedkhodzhaeva, N. M.; Khazanovich, R. L. Triterpene compounds of *Maclura aurantiaca* grown in Uzbekistan, Mater, Ubileinoi Res. *Nauchu, Knof. Farm, Posvyashch 50-Letyes Obraz.* **1972**, 105−107.

(3) Aliev, R. K.; Yuzbashinskaya, P. A.; Rakhimova, A. Kh. Chemical composition of the fruit of Maclura, cultivated in Azeraidzhan and the pharmacological properties of its medicinal forms and drugs. *Ucen. Zap. Azerb. Gosud. Univ., Ser. Biol. Nauk.* **1961**, *3*, 59−66.

(4) Barnes, R. A.; Gerbern, N. N. The antifungal agent from Osage orange wood. *J. Am. Chem. Soc.* **1955**, *77*, 3259−3262.

(5) Baumgardt, J. P. The Osage orange. *Hort* **1972**, *50* (26), 47.

(6) Betts, H. S. *The Strength of North American Woods*; Miscellaneous Publication 46; U.S. Department of Agriculture: Washington, DC, USA, 1929.

(7) Bonner, F. T.; Ferguson, E. R. *Maclura pomifera* (Raf.) Schneid Osage-Orange. In *Seeds of Woody Plants in the United States*; Handbook 450; Schopmeyer, C. S., Ed.; Forest Service, U.S. Department of Agriculture: Washington, DC, USA, 1974; pp 525−526.

(8) Clopton, J. R. Antioxidant material from Osage orange (bois d'arc) fruit. *J. Am. Oil Chem. Soc.* **1953**, *30*, 156−159.

(9) Collingwood, G. H. Osage orange. *Am. Forests* **1939**, *45*, 508−510.

(10) Hart, J. H. Morphological and chemical differences between sapwood, discolored sapwood and heartwood in black locust and Osage orange. *For. Sci.* **1968**, *14*, 334−338.

(11) Wagner, J. G.; Harris, L. E. Phytochemical investigation of the fruit of *Maclura pomifera* I. *J. Am. Pharm. Assoc., Sci. Ed.* **1952**, *41*, 497−499.

(12) Wagner, J. G.; Harris, L. E. Isolation of a new triterpene. *J. Am. Pharm. Assoc., Sci. Ed.* **1952**, *41*, 497−499.

(13) Wolfrom, M. L.; Benton, F. L.; Gregory, A. S.; Hess, W. W.; Mahan, J. E.; Morgan, P. W. Osage orange pigments II. Isolation of a new pigment, pomiferin. *J. Am. Chem. Soc.* **1939**, *61*, 32−36.

(14) Wolfrom, M. L.; Benton, F. L.; Gregory, A. S.; Hess, W. W.; Mahan, J. E.; Morgan, P. W. Osage orange pigments. V. Isomerization. *J. Am. Chem. Soc.* **1941**, *63*, 422−426.

(15) Tsao, R.; Yang, R.; Young, J. C. Antioxidant isoflavones in Osage orange, *Maclura pomifera* (Raf.) Schneid. *J. Agric. Food Chem.* **2003**, *51*, 6445−6451.

(16) Moser, B. R.; Eller, F. J.; Tisserat, B. H.; Gravett, A. Preparation of fatty acid methyl ester from Osage orange (*Maclura pomifera*) oil and evaluation as biodiesel. *Energy Fuels* **2011**, *25*, 1869−1877.

(17) Harry-O'kuru, R. E.; Mohamed, A.; Gordon, S. H.; Xu, J. Syntheses of novel protein products (milkglyde, saliglyde and soyglyde) from vegetable epoxy oils and gliadin. *J. Agric. Food Chem.* **2012**, *60*, 1688−1694.

(18) Harry-O'kuru, R. E.; Mohamed, A.; Gordon, S. H.; Xu, J. Elastomer product from epoxidized vegetable oil and gliadin. U.S. Patent 8,575,289, Nov 5, 2013.

(19) Harry-O'kuru, R. E.; Mohamed, A.; Xu, J.; Sharma, B. K. Synthesis and characterization of Corn oil polyhydroxy fatty acids designed as additive agent for many applications. *J. Am. Oil Chem. Soc.* **2011**, *88*, 1211−1221.

(20) French, W. H. Ashland Oil & Refining Co. Epoxidation process using peracetic acid produced *in situ*. U.S. Patent 3,360,531, 1967.

(21) Harry-O'kuru, R. E.; Gordon, S. H.; Biswas. A facile synthesis of aminohydroxy triglycerides from new crop oils. *J. Am. Oil Chem. Soc.* **2005**, *82*, 207−212.

DOI: 10.1021/acs.jafc.5b01625
J. Agric. Food Chem. 2015, 63, 6588−6595

ward and efficient approach to make large amounts of rubrosterone available for biological testing is urgently required.

It has been well documented that in the sterol-degrading microorganisms, the ring nucleus and side chain are metabolized by different enzyme systems simultaneously and independently.[25] According to previous papers, the microorganism *Mycobacterium* sp. (NRRL B-3805) was a mutant for the selective cleavage of the sterol side chain to generate C_{19} and other useful steroid intermediates.[26] The microorganism *Fusarium lini* (ATCC 9593) was also capable of oxidatively catabolizing the 20*R*,22*R*-dihydroxy side chain in ponasterone A to yield rubrosterone; incubation of β-ecdysone yielded rubrosterone, as well.[27] Nevertheless, this type conversion using *F. lini* was relatively less efficient (15% of ponasterone A and <5% of β-ecdysone).[27]

Previous studies have revealed that some botanical medicines from the genus *Asparagus* (Liliaceae), such as *Asparagus cochinchinensis*, *Asparagus officinalis*, and *Asparagus filicinus* Buch.-Ham, have been widely used in China for a long time.[28] Particularly, the dried roots of *A. filicinus* under the name "Xiao-Bai-Bu" are used as a folk medicine for the treatment of tracheitis, cough, pneumonia, hemoptysis, acariasis, phthisis, and lung cancer.[28] According to the previous studies, 37 compounds, including 8 ecdysteroids, have been extracted from *A. filicinus* so far.[29] In particular, 20-hydroxyecdysone, an analogue of ponasterone A, has been shown to be a predominant constituent in the roots of *A. filicinus*. Therefore, Xiao-Bai-Bu could be an extremely suitable material for the accumulation of rubrosterone.

In the present study, *A. filicinus* was inoculated with 10 plant pathogenic fungi by solid fermentation. Interestingly, the anticipated compound, rubrosterone, was produced in large quantities by *Fusarium oxysporum*, a fungus from the same genus as *F. lini*. To confirm that rubrosterone was transformed from 20-hydroxyecdysone, pure 20-hydroxyecdysone was used in the biotransformation experiment with *F. oxysporum*. The results confirmed the microbial transformation between the two chemical compounds. This study addresses the accumulation of rubrosterone by the solid-state fermentation of *A. filicinus* with *F. oxysporum*.

MATERIALS AND METHODS

Chemicals and Instruments. Acetonitrile and methanol of HPLC grade were supplied by Fisher Scientific (Fair Lawn, NJ, USA). The silica gel used of 200−300 and 300−400 mesh and Sephadex LH-20 for column chromatography (CC) were obtained from the Qingdao Marine Chemical Corp. (Qingdao, China) and GE Amersham Biosciences (Piscataway, NJ, USA), respectively. RP-C18 silica gel of 40−60 μm was provided by Merck KGaA (Darmstadt, Germany). Pyridine-d_5 (99.5 atom % D) was purchased from Qingdao Tenglong Weibo Technology Co., Ltd. (Qingdao, China). The water (resistivity ≥ 18.25 MΩ/cm) was purified with a purity water system. All other chemicals used were of analytical grade.

The ^{1}H NMR and ^{13}C NMR spectra were recorded on a Bruker DRX-400 (the chemical shift was referred to the solvent peak) at 298 K with tetramethylsilane (TMS) as an internal standard. The HR-ESI-MS spectrum data of the two isolated compounds were recorded by a G3250AA LC/MSD TOF spectrometer (Agilent Technologies, Santa Clara, CA, USA). The HPLC system, equipped with a Delta 600 quaternary pump and 2487 dual wavelength absorbance detector (Waters Corp., Milford, MA, USA) was used for the identification and quantitation of the compounds. The HPLC column used was a 250 mm × 4.6 mm i.d., 5 μm, Zorbax SB-C18 (Agilent). The HPLC-MS were recorded on an Agilent 1100 HPLC system and G3250AA (Agilent) mass spectrometer.

Plant Material. *A. filicinus* was collected in Kunming City, Yunnan Province, of China in November 2013 and authenticated by Prof. Shugang Lu of the School of Life Sciences at Yunnan University. A voucher specimen (No. YNU-XBB01) is deposited in the Key Laboratory of Medicinal Chemistry for Natural Resources at Yunnan University.

Microorganisms and Fermentation. The plant pathogen fungus *F. oxysporum* was obtained from the Stains Collection of Yunnan Institute of Microbiology, Yunnan Institute of Microbiology, Yunnan Province, China. *F. oxysporum* was then activated in PDA (1 L of water, 200 g of potato, 20 g of dextrose, and 15 g of agar) slant culture medium in a constant-temperature incubator at 28 °C for 5 days. The mature plant pathogen fungus was added to the fermentation culture medium containing 5.00 g of *A. filicinus* powder that had been dampened with 8 mL of water, sterilized at 121 °C for 30 min, and then incubated at 28 °C for 30 days. The blank fermented *A. filicinus* was treated the same as the microorganism-fermented *A. filicinus* in the absence of plant pathogen fungus. The nonfermented *A. filicinus* was the original material of the herb.

Extraction and Isolation. The nonfermented *A. filicinus* (5.00 g), blank fermented *A. filicinus* (5.00 g), and microorganism-fermented *A. filicinus* (5.00 g) were immersed with 80% methanol/H_2O (v/v) at a ratio of 1:10 (w/v) for 24 h at room temperature and then exhaustively extracted ultrasonically three times for 30 min each. The extracts were decanted, filtered through Whatman no. 1 filter paper, and concentrated under a rotary evaporator. The nonfermented, blank fermented, and *F. oxysporum*-fermented *A. filicinus* extracts were obtained as E1 (3.41 g), E2 (3.07 g), and E3 (0.56 g), respectively. E3 was then chromatographed on a silica gel column (column, 200 mm × 20 mm) eluted with chloroform/methanol (30:1, 600 mL) to yield fraction A. Fraction A (42.6 mg) was further subjected to silica gel CC (column, 200 mm × 10 mm) with petroleum ether/acetone (3:1, 200 mL) to yield compound **1** (25.1 mg). E1 was passed through a macroporous resin and then isolated by a combination of RP-C18 silica gel (column, 450 mm × 40 mm) and silica gel CC (column, 200 mm × 20 mm) with a gradient elution mixture of chloroform/methanol (10:1, 500 mL) for the acquisition of compound **2** (24.7 mg).

Structure Elucidation of Rubrosterone and 20-Hydroxyecdysone. Rubrosterone, **1**: white crystal (methanol/H_2O); mp 245.0−247.0 °C; HR-ESI-MS *m*/*z* 357.1683 $[M + Na]^+$ (calcd for $C_{19}H_{26}O_5Na$ $[M + Na]^+$, 357.1672); ^{1}H NMR (400 MHz, pyridine-d_5) δ_H 0.85 (3H, s, H-18), 1.04 (3H, s, H-19), 1.58 (1H, dd, *J* = 12.0, 4.8 Hz, H-11), 1.94 (1H, t, *J* = 12.4 Hz, H-1), 2.28 (2H, m, H-15), 3.05 (1H, dd, *J* = 13.2, 3.6 Hz, H-5), 3.54 (1H, m, H-9), 4.15 (1H, dt, *J* = 11.2, 3.2 Hz, H-2), 4.26 (1H, br s, H-3), 6.29 (1H, s, H-7); ^{13}C NMR (100 MHz, pyridine-d_5) δ_C 37.6 (C-1), 67.8 (C-2), 67.8 (C-3), 32.2 (C-4), 51.3 (C-5), 203.1 (C-6), 121.8 (C-7), 162.7 (C-8), 34.8 (C-9), 38.6 (C-10), 19.9 (C-11), 28.7 (C-12), 53.0 (C-13), 79.3 (C-14), 33.4 (C-15), 24.5 (C-16), 217.1 (C-17), 17.0 (C-18), 24.3 (C-19). The NMR data were compared with the literature,[14,15] and compound **1** was determined to be rubrosterone (Figure 1).

20-Hydroxyecdysone, **2**: white amorphous powder; HR-ESI-MS *m*/*z* 481.3137 $[M + H]^+$ (calcd for $C_{27}H_{45}O_7$ $[M + H]^+$, 481.3165), 503.2962 $[M + Na]^+$ (calcd for $C_{27}H_{44}O_7Na$ $[M + Na]^+$, 503.2985), 983.6036 $[2M+Na]^+$ (calcd for $C_{54}H_{88}O_{14}Na$ $[2M + Na]^+$, 983.6072); ^{1}H NMR (400 MHz, pyridine-d_5) δ_H 0.97 (3H, s, H-19), 1.11 (3H, s, H-18), 1.30 (6H, br s, H-26, 27), 1.55 (3H, s, H-21), 2.18 (1H, m, H-24), 2.87 (2H, br s, H-5, 17), 3.47 (1H, br s, H-9), 3.75 (1H, d, *J* = 6.4 Hz, H-22), 4.12 (2H, m, H-2, 3), 6.14 (1H, s, H-7); ^{13}C NMR (100 MHz, pyridine-d_5) δ_C 37.2 (C-1), 67.5 (C-2), 67.6 (C-3), 31.8 (C-4), 50.7 (C-5), 203.3 (C-6), 121.1 (C-7), 165.8 (C-8), 33.8 (C-9), 38.1 (C-10), 20.9 (C-11), 31.4 (C-12), 47.5 (C-13), 83.7 (C-14), 31.1 (C-15), 20.5 (C-16), 49.5 (C-17), 17.3 (C-18), 23.9 (C-19), 76.4 (C-20), 21.1 (C-21), 77.0 (C-22), 26.8 (C-23), 41.9 (C-24), 69.3 (C-25), 29.5 (C-26), 29.4 (C-27). The evidence reported above, combined with the data reported in the literature,[30] led to the assignment of the structure of 20-hydroxyecdysone, **2**, as shown in Figure 1.

HPLC and HPLC-MS Analysis. The identification and quantitation of crude extracts of nonfermented *A. filicinus*, blank fermented *A.*

DOI: 10.1021/acs.jafc.5b02570
J. Agric. Food Chem. 2015, 63, 6596−6602

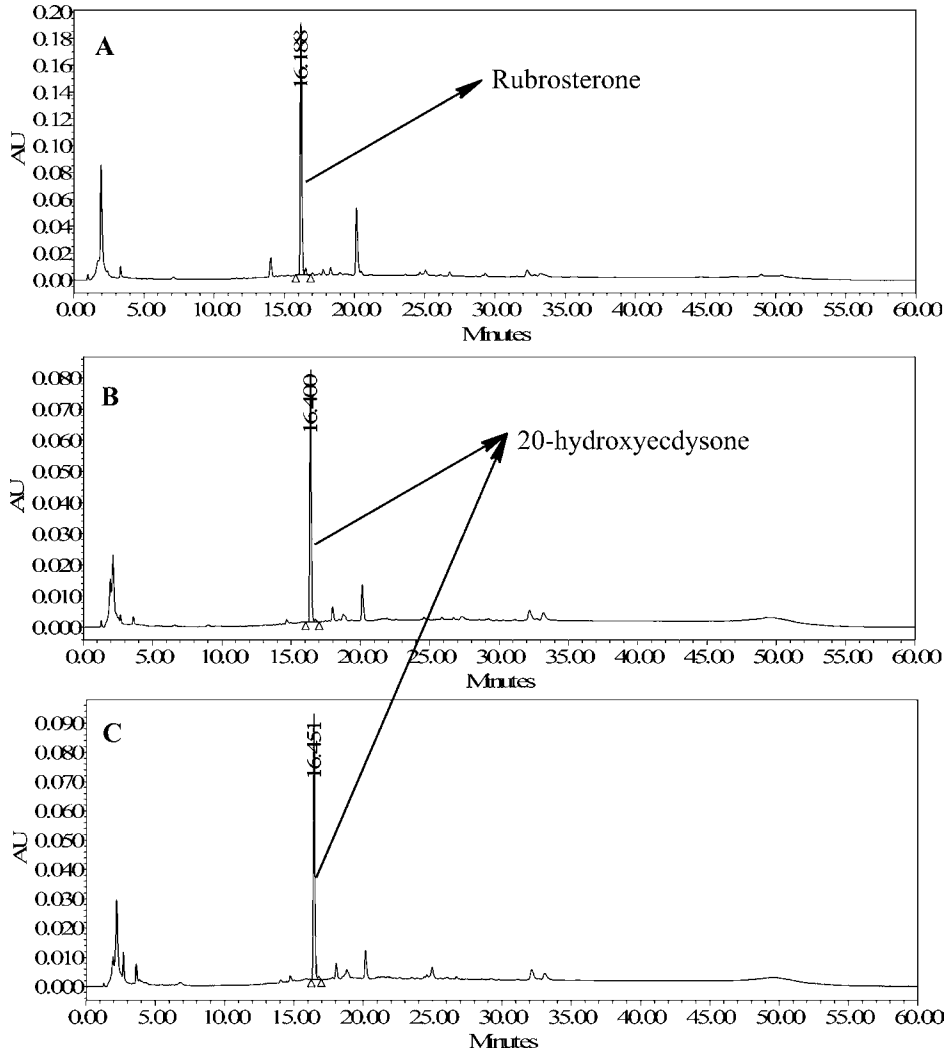

Figure 2. HPLC chromatograms of (A) *F. oxysporum*-fermented *A. filicinus*, (B) nonfermented *A. filicinus*, amd (C) blank fermented *A. filicinus*.

filicinus, and *F. oxysporum*-fermented *A. filicinus* were carried out by an HPLC system. Samples or standards were dissolved with methanol/H_2O and filtered through a 0.45 μm filter before injection into the HPLC system. Mobile phase A was water, mobile phase B was methanol, and mobile phase C was acetonitrile. HPLC fingerprints were obtained by following a linear gradient program: 0−5 min, 5−10% (v/v) solvent B, 5−10% solvent C; 5−10 min, 10−30% solvent B, 10−20% solvent C; 10−20 min, 30−48% solvent B, 20−32% solvent C; 20−40 min, 48% solvent B, 32% solvent C; 40−43 min, 48−40% solvent B, 32−60% solvent C; 43−50 min, 40−5% solvent B, 60−5% solvent C. The peaks were confirmed by the UV absorptions at 245 nm and the retention times, while the flow rate was 1.0 mL/min. The column temperature was maintained at 25 °C, and the injection volume was 10 μL for *F. oxysporum*-fermented *A. filicinus* and 20 μL for nonfermented *A. filicinus* and blank fermented *A. filicinus*, respectively. The standard addition method was used for the identification of ecdysteroids, and an external standard method was applied for quantitation. The limits of detection (LOD) and quantitation (LOQ) of the ecdysteroids were as follows [ecdysteroid compound, LOD (LOQ)]: 20-hydroxyecdysone, 0.00712 μg (0.0200 μg); rubrosterone, 0.01558 μg (0.0400 μg). The accuracy of the method was determined by recovery experiments. The recoveries of two ecdysteroid compounds for quantitation analysis ranged from 95 to 105%. The determination conditions of the HPLC-MS analysis were similar to those of the HPLC assay except for the flow rate, which was 0.6 mL/min.

Fermentation of 20-Hydroxyecdysone with *F. oxysporum*. The archetypal ecdysteroid 20-hydroxyecdysone, which was the most representative compound in *A. filicinus*, was involved in the biotransformation experiment with *F. oxysporum*. The activation process of *F. oxysporum* was the same as that mentioned above. Specifically, chopped potatoes (30 g), potato dextrose broth (PDB) medium (1 L of water, 200 g of potato, and 20 g of dextrose), and Czapek's medium (1 L of water, 3 g of $NaNO_3$, 1 g of K_2HPO_4, 0.5 g of $MgSO_4{\cdot}7H_2O$, 0.5 g of KCl, 0.01 g of $FeSO_4$, 30 g of sucrose) were, respectively, autoclaved at 121 °C for 30 min as fermentation culture media. Afterward, 20 mg 20-hydroxyecdysone isolated from the *A. filicinus* was inoculated with the plant pathogen fungus and cultivated for 20 days (potato medium) and 7 days (PDB medium, Czapek's medium) at 28 °C. The chopped potatoes, PDB medium, and Czapek's medium were autoclaved and inoculated under the same conditions as the blank control groups.

Statistical Analysis. All measurements were performed in triplicate and reported as the mean ± standard deviation (SD).

RESULTS AND DISCUSSION

Transformation from 20-Hydroxyecdysone to Rubrosterone with *F. oxysporum*. In previous studies, our team had emphasized that plant pathogenic fungi fermentation was effective in improving the total phenolic content and antioxidant activities of *Bletilla formosana*[31] and *Bletilla striata*,[32] which might be considered as a novel strategy for processing

DOI: 10.1021/acs.jafc.5b02570
J. Agric. Food Chem. 2015, 63, 6596−6602

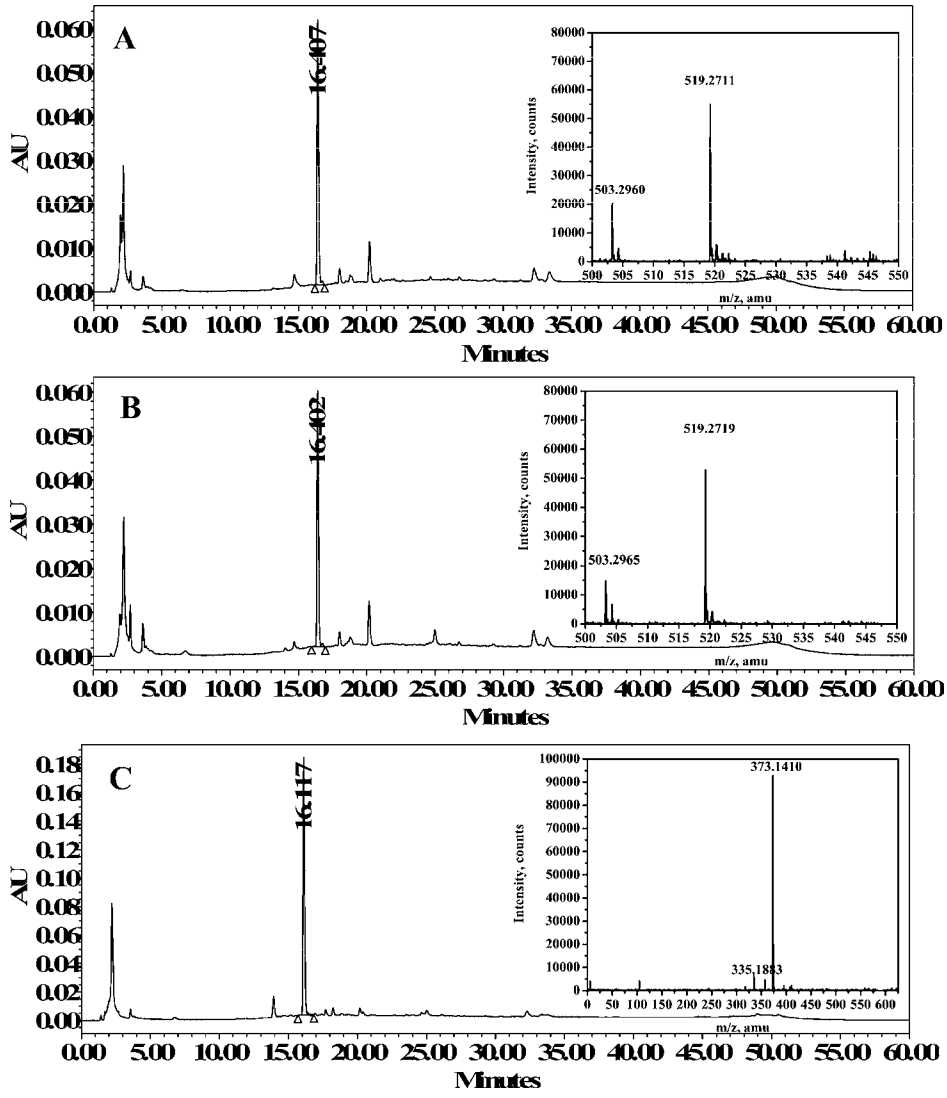

Figure 3. Chromatograms at 245 nm obtained from the HPLC-MS of the extracts of (A) nonfermented *A. filicinus*, (B) blank fermented *A. filicinus*, and (C) *F. oxysporum*-fermented *A. filicinus*.

traditional Chinese medicines. In the present study, *A. filicinus* was fermented with *F. oxysporum* to accumulate rubrosterone. The major plant extract components were determined using HPLC. The results (Figure 2) revealed that the main peak of 20-hydroxyecdysone, with retention time at 16.40 and 16.45 min in E1 (Figure 2B) and E2 (Figure 2C), disappeared in E3. The peak of rubrosterone, which was not present in E1 and E2, was obvious in E3 with a retention time at 16.19 min (Figure 2A). These two compounds were further isolated by silica gel CC from E1 and E3 and identified as 20-hydroxyecdysone and rubrosterone on the basis of extensive spectroscopic methods. Combining all of the above studies, it could be speculated that there might be a transformation between 20-hydroxyecdysone and rubrosterone.

To determine whether other ecdysteroids that share the same skeleton with 20-hydroxyecdysone participate in the accumulation of rubrosterone, HPLC-MS analysis of the extracts of E1, E2, and E3 was conducted. The HPLC-MS analysis results (Figure 3) showed that there were no obvious signals of other possible rubrosterone precursors (Figures 3A, B), such as ecdysone and stachysterone C, which have been reported to be isolated from *A. filicinus*. However, from the previous paper about the constituent study of *A. filicinus*,[33] it could be inferred that 20-hydroxyecdysone was the main precursor in the conversion. It is possible that other compounds were present in quantities too low to detect.

In consideration of the substantial decrease of the weight of the crude extract of E3 (0.56 g) compared with E1 (3.41 g) and E2 (3.07 g), the ^{1}H NMR spectra of all of the crude extracts were recorded to evaluate the specific constituent variations. As observed in Figure 4, the proton signals of saccharides ranging from 3.0 to 3.7 ppm in E1 (Figure 4C) and E2 (Figure 4B) were significantly diminished in E3 (Figure 4A), which implies that a large amount of saccharides was consumed during fermentation of *A. filicinus* with *F. oxysporum*; this is the best explanation for why the weights of the crude extracts of E3 were greatly decreased and why the extraction process was much easier after fermentation. Therefore, fermentation of *A. filicinus* with plant pathogen fungus is also a convenient and simple method to make the process of production and extraction much easier in industry.

Microbiological Transformation of Pure 20-Hydroxyecdysone. To further demonstrate the conclusion that rubrosterone was transformed from 20-hydroxyecdysone, pure

DOI: 10.1021/acs.jafc.5b02570
J. Agric. Food Chem. 2015, 63, 6596−6602

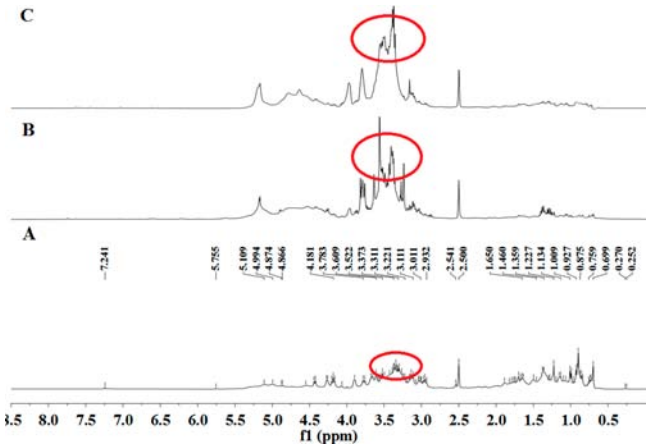

Figure 4. ^{1}H NMR spectra of all crude extracts: (A) *F. oxysporum*-fermented *A. filicinus*; (B) blank fermented *A. filicinus*; (C) nonfermented *A. filicinus*. The red circles ranging from 3.0 to 3.7 ppm indicate the proton signals of saccharides.

20-hydroxyecdysone was used in the biotransformation. Potatoes, PDB medium, and Czapek's medium, containing no rubrosterone and 20-hydroxyecdysone, were used as fermentation culture media, respectively. Similar to what we show in Figure 5, the peak of rubrosterone with retention time at 16.12 min was distinctly detected by HPLC after solid fermentation of 20-hydroxyecdysone with potato medium (Figure 5A). The peak of the initial 20-hydroxyecdysone completely disappeared. This experiment confirmed the microbial transformation between these two chemical compounds.

However, the biotransformations with the PDB and Czapek's media were not successful. The peaks with retention time at 16.39 min (Figure 5C) and 16.45 min (Figure 5E) indicated the obvious presence of 20-hydroxyecdysone. Therefore, liquid culture media are inefficient for the microbial transformation between 20-hydroxyecdysone and rubrosterone, which was consistent with the results obtained previously.[27] The key reason for this problem might be the lower solubility of 20-hydroxyecdysone in the liquid medium. Previous studies have also demonstrated that the steroidal invertase is an intracellular enzyme, and only intracellular substrates (exogenous or endogenous) that have a contact with the enzyme system can participate in the bioconversion reactions. However, steroidal compounds are fat-soluble compounds, which results in a low concentration of substrates in the liquid culture media and low sterol-transforming activity.[34−38] Additionally, the shorter growth cycle of liquid suspension culture might be another reason for the reduced transformation rate. Therefore, as the most commonly occurring and the most abundant resource in both arthropods and plants,[39−43] **2** is a suitable starting material to produce rubrosterone efficiently in solid culture medium.

Content of Rubrosterone in Fermented *A. filicinus*. HPLC was further used to assess the content of rubrosterone in fermented *A. filicinus*. The content of rubrosterone was 3.497 ± 0.007 μg/mg *A. filicinus* sample in *F. oxysporum*-fermented *A. filicinus* (Table 1), which was almost equal to 20-hydroxyecdysone in the original material (4.352 ± 0.008 μg/mg *A. filicinus* sample) and blank fermented *A. filicinus* (4.453 ± 0.011 μg/mg *A. filicinus* sample) ($n_{\text{20-hydroxyecdysone}}/n_{\text{rubrosterone}}$ = 1.1:1.0). Therefore, we could conclude that the transformation from 20-hydroxyecdysone in *A. filicinus* to rubrosterone could be put into practice at a conversion ratio close to 100%. The high conversion rate, which had never been achieved, demonstrated that it was indeed an efficient, simple, prospective, and straightforward approach to produce rubrosterone. These results also indicate that an effective, specific steroidal invertase in the fungus, which could transform 20-hydroxyecdysone into rubrosterone during the process of microbial fermentation, must exist. Furthermore, it also

Table 1. Contents of Rubrosterone, 1, and 20-Hydroxyecdysone, 2[a]

sample	20-hydroxyecdysone	rubrosterone
E1	4.352 ± 0.008	
E2	4.453 ± 0.011	
E3		3.497 ± 0.007

[a]Each value is presented as the mean ± SD (n = 3). Values of contents were expressed as μg compound/mg *A. filicinus*.

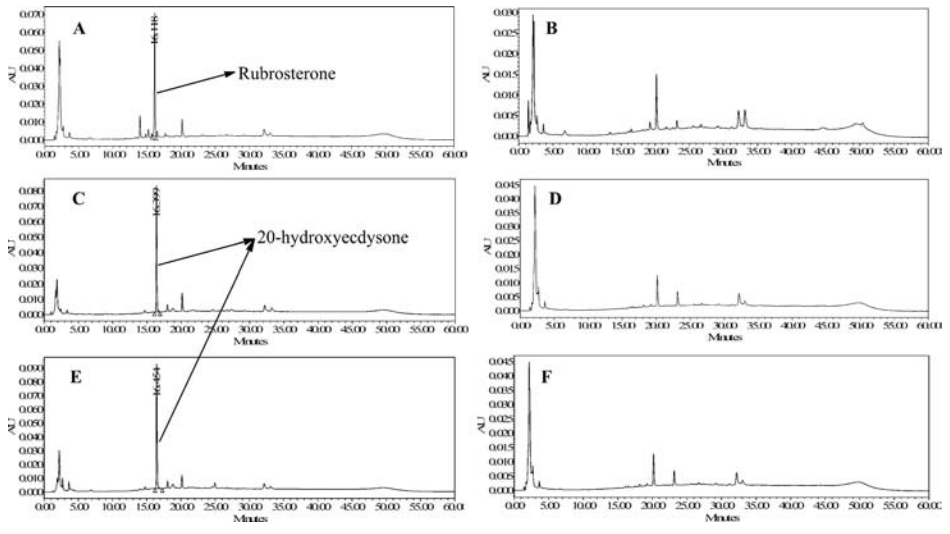

Figure 5. HPLC chromatograms of the microbiological transformation of 20-hydroxyecdysone with three different media: (A) chopped potatoes; (C) PDB medium; (E) Czapek's medium. Blank control trials: (B) potato culture medium; (D) PDB medium; (F) Czapek's medium.

DOI: 10.1021/acs.jafc.5b02570
J. Agric. Food Chem. 2015, 63, 6596−6602

provided us a creative means by which to generate some inaccessible and rare substances.

In summary, there are a few reports of the production of rubrosterone by the use of microbial transformation. However, there are no papers to date regarding the use of the solid-state bioprocess of *A. filicinus* by *F. oxysporum* to obtain rubrosterone. Furthermore, the unique method described herein could generate rubrosterone at the highest conversion ratio reported to date, which was not achieved in other reported methods. Fermentation of *A. filicinus* with *F. oxysporum* also led to a substantial decrease of saccharides, which further results in an easier extraction process. Consequently, the solid-state bioprocessing strategy could be an effective, innovative, and expedient approach to accumulate rubrosterone.

■ ASSOCIATED CONTENT

Ⓢ Supporting Information

Figures S1−S11. The Supporting Information is available free of charge on the ACS Publications website at DOI: 10.1021/acs.jafc.5b02570.

■ AUTHOR INFORMATION

Corresponding Author

*(Z.-T.D.) E-mail: ztding@ynu.edu.cn. Phone/fax: +86 871 65033910.

Funding

This work was financially supported by a grant from the Natural Science Foundation of China (No. 81460648) and a grant from the Program for Changjiang Scholars and Innovative Research Team in University (No. IRT13095).

Notes

The authors declare no competing financial interest.

■ ACKNOWLEDGMENTS

We are grateful to Associate Professor Li-Xing Zhao from the Yunnan Institute of Microbiology for providing microbial strains.

■ ABBREVIATIONS USED

CC, column chromatography; LOD, limit of detection; LOQ, limit of quantitation; PDB, potato dextrose broth; SD, standard deviation; TMS, tetramethylsilane

■ REFERENCES

(1) Lin, Y. W.; Mou, Y. C.; Su, C. C.; Chiang, B. H. Antihepatocarcinoma activity of lactic acid bacteria fermented *Panax notoginseng*. *J. Agric. Food Chem.* **2010**, *58*, 8528−8534.

(2) Manosroi, J.; Abe, M.; Manosroi, A. Biotransformation of steroidal drugs using microorganisms screened from various sites in Chiang Mai, Thailand. *Bioresour. Technol.* **1999**, *69*, 67−73.

(3) Tripathi, C. M.; Agarwal, S. C.; Basu, S. K. Production of L-phenylacetylcarbinol by fermentation. *J. Ferment. Bioeng.* **1997**, *84*, 487−492.

(4) Faramarzi, M. A.; Badiee, M.; Yazdi, M. T.; Amini, M.; Torshabi, M. Formation of hydroxysteroid derivatives from androst-4-en-3,17-dione by the filamentous fungus *Mucor racemosus*. *J. Mol. Catal. B: Enzym.* **2008**, *50*, 7−12.

(5) Rasor, J. P.; Voss, E. Enzyme-catalyzed processes in pharmaceutical industry. *Appl. Catal., A* **2001**, *221*, 145−158.

(6) Choi, H. S.; Kim, J. H.; Park, Y.; Ra, K. S.; Imm, J. Y.; Suh, H. J. Radical-scavenging activities of cactus cladodes (*Opuntia humifusa* Raf.) in a submerged culture. *J. Food Biochem.* **2014**, *38*, 491−497.

(7) Vaněk, T.; Valterová, I.; Vaisar, T. Biotransformation of (*S*)-(−)- and (*R*)-(+)-limonene using *Solanum aviculare* and *Dioscorea deltoidea* plant cells. *Phytochemistry* **1999**, *50*, 1347−1351.

(8) Bae, E. A.; Han, M. J.; Kim, E. J.; Kim, D. H. Transformation of ginseng saponins to ginsenoside Rh2 by acids and human intestinal bacteria and biological activities of their transformants. *Arch. Pharmacal Res.* **2004**, *27*, 61−67.

(9) Hubert, J.; Berger, M.; Nepveu, F.; Paul, F.; Daydé, J. Effects of fermentation on the phytochemical composition and antioxidant properties of soy germ. *Food Chem.* **2008**, *109*, 709−721.

(10) Katina, K.; Laitila, A.; Juvonen, R.; Liukkonen, K. H.; Kariluoto, S.; Piironen, V.; Landberg, R.; Åman, P.; Poutanen, K. Bran fermentation as a means to enhance technological properties and bioactivity of rye. *Food Microbiol.* **2007**, *24*, 175−186.

(11) Philip, K.; Sinniah, S. K.; Muniandy, S. Antimicrobial peptides in aqueous and ethanolic extracts from microbial, plant and fermented sources. *Biotechnology* **2009**, *8*, 248−253.

(12) Haridy, M. S.; Ahmed, A. A.; Doe, M. Microbiological transformation of two labdane diterpenes, the main constituents of *Madia* species, by two fungi. *Phytochemistry* **2006**, *67*, 1455−1459.

(13) Takemoto, T.; Hikino, Y.; Hikino, H.; Ogawa, S.; Nishimoto, N. Structure of rubrosterone, a novel C_{19} metabolite of insect-moulting substances from *Achyranthes rubrofusca*. *Tetrahedron Lett.* **1968**, *9*, 3053−3056.

(14) Rudel, D.; Bathori, M.; Gharbi, J.; Girault, J. P.; Racz, I.; Melis, K.; Szendrei, K.; Lafont, R. New ecdysteroids from *Serratula tinctoria*. *Planta Med.* **1992**, *58*, 358−364.

(15) Tan, C. Y.; Wang, J. H.; Li, X. Phytoecdysteroid constituents from *Cyanotis arachnoidea*. *J. Asian Nat. Prod. Res.* **2003**, *5*, 237−240.

(16) Li, S. H.; Zhan, H. J.; Yao, P.; Niu, X. M.; Xiang, W.; Sun, H. D. Non-taxane compounds from the bark of *Taxus yunnanensis*. *J. Asian Nat. Prod. Res.* **2002**, *4*, 147−154.

(17) Takemoto, T.; Hikino, H. Rubrosterone and acylated compounds thereof. Japanese Patent JP48042872B, 19731214.

(18) Agui, N.; Fukaya, M. Effects of molting hormones and prothoracic glands on the development of wing disks of the cabbage armyworm (*Mamestra brassicae*) *in vitro* (Lepidoptera, Noctuidae). *Appl. Entomol. Zool.* **1973**, *8*, 73−82.

(19) Takeda, N. Effect of some phytoecdysones on the spermatogenesis of the slug moth prepupa, *Monema flavescens* Walker (Lepidoptera: Heterogeneidae) Short communication. *Appl. Entomol. Zool.* **1972**, *7*, 37−39.

(20) Chihara, C. J.; Petri, W. H.; Fristrom, J. W.; King, D. S. Assay of ecdysones and juvenile hormones on *Drosophila* imaginal disks *in vitro*. *J. Insect Physiol.* **1972**, *18*, 1115−1123.

(21) Hikino, H.; Hikino, Y.; Takemoto, T. Rubrosterone, a metabolite of insect metamorphosing substance from *Achyranthes rubrofusca*: synthesis. *Tetrahedron* **1969**, *25*, 3389−3394.

(22) Otaka, T.; Uchiyama, M.; Okui, S.; Takemoto, T.; Hikino, H.; Muniandy, S.; Nishimoto, N. Stimulatory effect of insect-metamorphosing steroids from *Achuranthes* and *Cyathula* on protein synthesis in mouse liver. *Chem. Pharm. Bull.* **1968**, *16*, 2426−2429.

(23) Shibata, K.; Mori, H. Synthetic studies on insect molting hormones, synthesis of rubrosterone. *Tetrahedron* **1971**, *27*, 1149−1155.

(24) VanBever, W.; Kohen, F.; Ranade, V. V.; Counsell, R. E. Synthesis of the steroid rubrosterone. *J. Chem. Soc. D* **1970**, 758.

(25) Kieslich, K. Microbial side-chain degradion of sterols. *J. Basic Microbiol.* **1985**, *25*, 461−474.

(26) Marsheck, W. J.; Krachy, S.; Muir, R. D. Microbial degradation of sterols. *Appl. Microbiol.* **1972**, *23*, 72−77.

(27) Tom, W. M.; Abul-Hajj, Y. J.; Koreeda, M. Microbial oxidation of ecdysones. A convenient preparation of rubrosterone. *J. Chem. Soc., Chem. Commun.* **1975**, 24−25.

(28) Wu, J. J.; Cheng, K. W.; Zuo, X. F.; Wang, M. F.; Li, P.; Zhang, L. Y.; Wang, H.; Ye, W. C. Steroidal saponins and ecdysterone from *Asparagus filicinus* and their cytotoxic activities. *Steroids* **2010**, *75*, 734−739.

DOI: 10.1021/acs.jafc.5b02570
J. Agric. Food Chem. 2015, 63, 6596−6602

(29) Tao, H. M., The chemical constituents of the roots of *Ephedra sinica* Stapf and *Asparagus filicinus* Buch.-Ham. Ph.D. Thesis, Ji Lin University, 2009.
(30) Ling, T. J.; Ma, W. Z.; Wei, X. Y. Ecdysteroids from the roots of *serratula chinensis*. *J. Trop. Subtrop. Bot.* **2003**, *11*, 143−147.
(31) Dong, J. W.; Zhao, L. X.; Cai, L.; Fang, H. X.; Chen, X. H.; Ding, Z. T. Antioxidant activities and phenolics of fermented *Bletilla formosana* with eight plant pathogen fungi. *J. Biosci. Bioeng.* **2014**, *118*, 396−399.
(32) Dong, J. W.; Cai, L.; Xiong, J.; Chen, X. H.; Wang, W. Y.; Shen, N.; Liu, B. L.; Ding, Z. T. Improving the antioxidant and antibacterial activities of fermented *Bletilla striata* with *Fusarium avenaceum* and *Fusarium oxysporum*. *Process Biochem.* **2015**, *50*, 8−13.
(33) Tao, H. M.; Wang, L. S.; Zhao, D. Q.; Zhu, Q. H.; Yin, Y. G.; Liu, Y. H. Steroids from tubers of *Asparagus filicinus*. *Chin. Tradit. Herbal Drugs* **2012**, *43*, 1716−1720.
(34) Goetschel, R.; Bar, R. Formation of mixed crystals in microbial conversion of sterols and steroids. *Enzyme Microb. Technol.* **1992**, *14*, 462−469.
(35) Donova, M. V.; Nikolayeva, V. M.; Dovbnya, D. V.; Gulevskaya, S. A.; Suzina, N. E. Methyl-β-cyclodextrin alters growth, activity and cell envelope features of sterol-transforming mycobacteria. *Microbiology* **2007**, *153*, 1981−1992.
(36) Smith, M.; Zahnley, J.; Pfeifer, D.; Goff, D. Growth and cholesterol oxidation by Mycobacterium species in Tween 80 medium. *Appl. Environ. Microbiol.* **1993**, *59*, 1425−1429.
(37) Rumijowska, A.; Lisowska, K.; Ziolkowski, A.; Sedlaczek, L. Transformation of sterols by *Mycobacterium vaccae*: effect of lecithin on the permeability of cell envelopes to sterols. *World J. Microbiol. Biotechnol.* **1997**, *13*, 89−95.
(38) Hesselink, P. G. M.; Vliet, S. V.; Vries, H. D.; Witholt, B. Optimization of steroid side chain cleavage by *Mycobacterium* sp. in the presence of cyclodextrins. *Enzyme Microb. Technol.* **1989**, *11*, 398−404.
(39) Festucci, B. R. A.; Contim, L. A. S.; Barbosa, L. C. A.; Stuart, J.; Otoni, W. C. Biosynthesis and potential functions of the ecdysteroid 20-hydroxyecdysone − a review. *Botany* **2008**, *86*, 978−987.
(40) Fang, X.; Di, Y. T.; He, H. P.; Hu, G. W.; Li, S. L.; Hao, X. J. Chemical constituents of *Toona microcarpa* (C. DC.) Harms in Engl. (Meliaceae). *Biochem. Syst. Ecol.* **2010**, *38*, 128−130.
(41) Ben Nejma, A.; Nguir, A.; Ben Jannet, H.; Hamza, M. A.; Daïch, A.; Othman, M.; Lawson, A. M. New septanoside and 20-hydroxyecdysone septanoside derivative from *Atriplex portulacoides* roots with preliminary biological activities. *Bioorg. Med. Chem. Lett.* **2015**, *25*, 1665−1670.
(42) Wu, P.; Xie, H. H.; Tao, W. Q.; Miao, S. Y.; Wei, X. Y. Phytoecdysteroids from the rhizomes of *Brainea insignis*. *Phytochemistry* **2010**, *71*, 975−981.
(43) Li, J.; Jadhav, A. N.; Khan, I. A. Triterpenoids from Brazilian ginseng. *Planta Med.* **2010**, *76*, 635−638.

DOI: 10.1021/acs.jafc.5b02570
J. Agric. Food Chem. 2015, 63, 6596−6602

In general, the results available in the literature on the formation of solid−gas type clathrates based on CDs are limited. Therefore, the present work aims at studying the possibilities for synthesizing this type of clathrate, using α-, β-, and γ-CDs and different gases (CO_2, N_2, N_2O, Ar). To realize this goal, a number of experimental conditions (temperature, gas pressure, CD concentration, and time) were varied over a relatively large range and a physicochemical characterization of the clathrates' morphology, crystal size distribution, growth rate, and amount and stability of the entrapped gas was performed.

EXPERIMENTAL PROCEDURES

The "CD-gas" type clathrates in this study have been prepared by crystallization from water solution of CDs under the pressure of the gas to be entrapped into the CD molecules. To realize the clathrate syntheses under controlled conditions, two types of reactors were designed and constructed: one from stainless steel for higher pressures (up to 100 atm) and a transparent one from Plexiglas (up to 15−20 atm)). The molar concentrations of α-CD water solutions were 5, 7, 10, and 14%, and the gas pressure was kept constant in the range of 5−40 atm (5, 10, 15, and 40 atm). After the gas was added to the reactor with the solution, the reactor was sealed and remained at room temperature or 5 °C from an hour to a few days (depending on the type of the cyclodextrin and the gas used) to form clathrates. The water solutions of β- and γ-CD were 10 and 20% for both cyclodextrins, as the gas pressure and temperature were varied in the same ranges as for the α-CD; the crystallization process took place again for about a few hours to a few days. The formed clathrates were filtered and washed with ice water to remove the unreacted CD. The purity of the CDs was ≥98%, and the gases were 99.999% pure.

To determine how much gas is trapped in the cavity of the cyclodextrin, thermogravimetry (TG-MS) was applied. The quantity of the trapped gas has also been measured by using a simple foam rise method,[55] where a known amount of clathrate (0.5 g) was added into a hot mixture of 15 wt % skimmed milk powder and 0.5 wt % xanthan gum. The proteins in skimmed milk powder are needed to stabilize the interface of newly formed gas babbles, due to clathrates' dissociation, whereas xanthan gam was added to provide yield stress to the mixture, which will prevent bubbles from fast creaming. The amount of captured gas was measured from the difference of the volume of the mix, before and after addition of the clathrates. It is important to realize that this method measures only the volume of the gas captured and not the total volume of the released gas.

To choose the optimal synthesis conditions, different experimental parameters have been varied (pressure, temperature, time, concentration, nucleation initiators, and additives) as well as clathrates' crystal growth kinetics has been studied. The crystal morphology and size of the clathrates formed under different conditions were characterized by optical and scanning electron microscopy (SEM, JEOL JSM-5510). The structure and microstructure were studied by X-ray diffraction (XRD, TUR-62) of both clathrates and cyclodextrins. The ultrasound treatment of some of the CD water solutions was performed with a 20 kHz probe (with a vibrating titanium tip) for 10 min.

RESULTS AND DISCUSSION

The main synthetic parameters varied in the present investigation were the concentration of the CDs (from undersaturated to saturated at room temperature), temperature (5 and 20 °C), and gas pressure (5−40 atm.). Under the conditions applied in this study clathrate formation (crystallization) was observed with all used gases (N_2, N_2O, CO_2, Ar) only for α-CD; β- and γ-CDs formed clathrates only with N_2 (Table 1). N_2O and N_2 were preferred for our study for technological reasons. Studies report the use of high-pressure N_2O in food technology in pasteurization over CO_2, thus avoiding the pH problems resulting from the formation of carbonic acid.[55,56] Also, CO_2 has a bitter taste and it is not preferred for sweets. With this in mind we focused our study on the comprehensive investigation of CDs with N_2 and N_2O clathrates. By comparing the yield of the α-CD-N_2O and α-CD-N_2 clathrates it was found that it is noticeably higher for α-CD-N_2O, which determined the more emphasized interest to its study. Due to the very low yield of the α-CD-Ar clathrate, it will not be considered further in the study.

Table 1. Clathrates Formation from CDs with Gases

gas	α-cyclodextrin	β-cyclodextrin	γ-cyclodextrin
N_2	yes	yes	yes
N_2O	yes	no	no
CO_2	yes	no	no
Ar	yes (low yield)	no	no

Table 2. Clathrate Synthesis Conditions and Corresponding Average Crystal Size and Clathrate Yield

	pressure (atm)	temperature (°C)	yield (%)	size (μm)
α-CD	5 N_2O	5	20	200−300
α-CD	5 N_2O	20	21	250−300
α-CD	15 N_2O	5	20	130−150
α-CD	15 N_2O	20	20	150−200
α-CD	40 N_2O	5	30	50−60
α-CD	40 N_2O	20	35	100−150

The clathrates' crystal growth kinetics were studied, first, to elucidate some important crystallization parameters (e.g., growth rates, mean crystal size) at different synthetic conditions and, second, to investigate the influence of the crystal morphology and size on the amount and stability of the entrapped gas.

Clathrates Based on α-CD. As already mentioned, under the applied conditions α-CD forms clathrates with all gases used in the study. Table 2 presents the experimental parameters used for these syntheses.

SEM micrographs (Figure 1) show the morphology and crystal size of the clathrates formed by crystallization of α-CD and different gases. Depending on the conditions of crystallization, the clathrates' average crystal size changes from 50 to 300 μm (Table 2) and the crystals' shape from cubic to needle- and plate-like form. For the needle-like crystals their length was measured and used for the crystal size distribution curves.

It was found that α-CD-N_2O clathrates can be formed even at 5 atm of N_2O gas pressure and room temperature (20−25 °C). However, optimization of the pressure and temperature was necessary to achieve the best properties of the clathrate: yield, crystal size and kinetics of crystallization, amount of entrapped gas. For comparison, Figure 2 shows SEM micrographs (including size distribution−crystal length) of some of the clathrates crystallized at fairly different conditions and as a result having noticeable difference in their size. Generally, at higher pressures (40 atm) and lower temperatures (5 °C) the clathrate crystals reveal the smallest size (average size of 50−60 μm) (Figure 3).

At the optimum conditions, with respect to smaller clathrate crystal size (40 atm of N_2O and 5 °C), kinetic analysis of the clathrate growth has been carried out as well. It has to be mentioned that under these conditions the clathrate crystallization starts almost immediately. Ten minutes is sufficient to reach about 20% clathrate yield, whereas for 1 h we obtained around 30% yield. The crystal size distribution curves at different crystallization times are shown in Figure 4. Plotting the average crystal size as a function of time, a linear growth rate of about 100 μm/h can be determined (Figure 4).

DOI: 10.1021/acs.jafc.5b01357
J. Agric. Food Chem. 2015, 63, 6603−6613

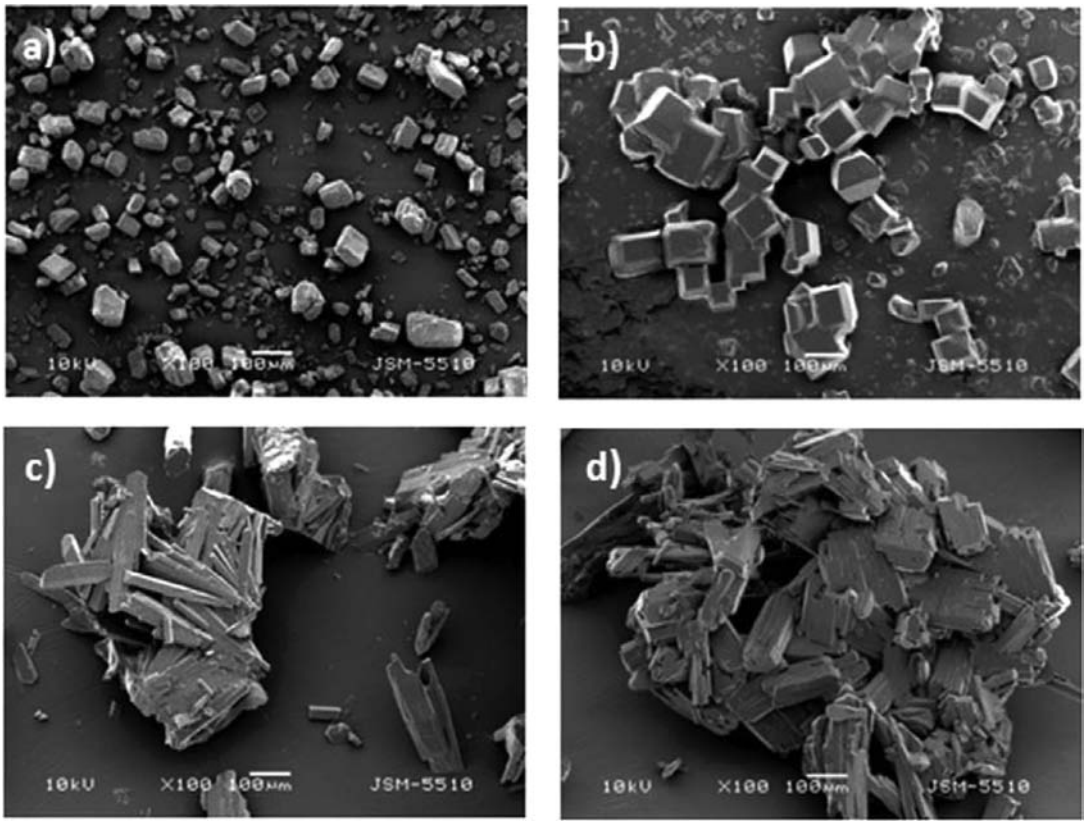

Figure 1. SEM images of α-cyclodextrin-based clathrates: (a) α-CD; (b) clathrate of α-CD and N_2 at 15 atm, 5 °C; (c) clathrate of α-CD and CO_2 at 10 atm, 5 °C; (d) clathrate of α-CD and N_2O at 40 atm, 5 °C.

As mentioned above, α-CD forms crystalline clathrates with CO_2 and N_2 as well, as the synthetic conditions (15−40 atm and 5−20 °C) are almost the same compared to those for the α-CD-N_2O clathrates. Highest yield of about 30−35% is obtained at lower temperatures and higher pressures. The crystal growth kinetics analysis of α-CD-CO_2 clathrates is presented in Figure 5. Linear crystal growth has been observed with growth rates of about 60 μm/h for α-CD-CO_2, which is about 2 times lower than that for α-CD-N_2O. The growth rate for the clathrate α-CD-N_2 is comparable to that for α-CD-CO_2.

From a practical point of view, one of the clathrates' crucial characteristics to be determined is the amount of gas entrapped in the CD molecules. For this purpose both thermogravimetry (PerkinElmer TGS-2, PerkinElmer Diamond SII TG/DTA) and "foam rise method" have been applied. Figure 6 reveals typical thermogravimetric (TG) curves of α-CD and of its clathrate with N_2O (α-CD-N_2O). Two main weight decrease steps for the pure α-CD can be distinguished; the first one starting at about 45−50 °C is associated with the release of weakly bonded water, and the second in the range of 65−90 °C has to be connected with the desorption of water having stronger interaction with the CD molecules.[2] The total amount of water embedded in the α-CD is about 10 wt %, as this quantity is repeated for all measured samples of pure α-CD. Unlike at T = 45−50 °C, the weight of the clathrate is already reduced by about 1−2 wt %, obviously connected with the release of the entrapped gas (N_2O). This result is also confirmed by TG-MS. The amount of N_2O released before 50 °C depends on the conditions of the clathrate formation. Besides, if one considers the final difference in the weight decrease during heating between the α-CD and its clathrate at about 140 °C, it can be seen that it is larger than the weight difference at about 50 °C. Hence, assuming that the differences between the weight reduction of the CD and its clathrate during heating are due to the release of the entrapped gas (N_2O), it could be supposed that there exist weaker and stronger bonded N_2O molecules. Additionally, it is interesting to report that after a stay of 120 days at 25−30 °C, the low-temperature TG step (usually 1−1.5 wt %), observed only for the clathrate, preserves its magnitude even when the total weight decreases during heating of the CD and its clathrate are equal. To prove that the low-temperature weight loss is due to the entrapped gas, the foam rise method has also been applied. The amount of gas determined by this method gives a value of about 7−10 mL gas/g clathrate, which corresponds to the amount determined by TG. Moreover, we cannot claim that the amount of water molecules embedded in the CD is the same in the clathrates compared to the pure α-CD. It is possible that a larger part of the water molecules included in the CD molecules is replaced by the N_2O molecules. In this way the differences in the weight decrease steps measured by TG for the CDs and clathrates cannot directly be used for the determination of the entrapped gas amount, and therefore additional methods (e.g., TG-MS) are necessary for obtaining the accurate gas quantity.

Differential scanning calorimetry (DSC; PerkinElmer DSC-2C) analysis of the CDs and of the corresponding clathrates based on them confirmed the effects observed by TG, both as temperature range of their appearance as well as relative magnitude. Figure 7 shows example calorimetric curves of pure α-CD and of the α-CD-N_2O clathrate. It is clearly seen that the first endothermic DSC peak of the clathrate is shifted to lower temperatures compared to the pure α-CD. It has a maximum

DOI: 10.1021/acs.jafc.5b01357
J. Agric. Food Chem. 2015, 63, 6603−6613

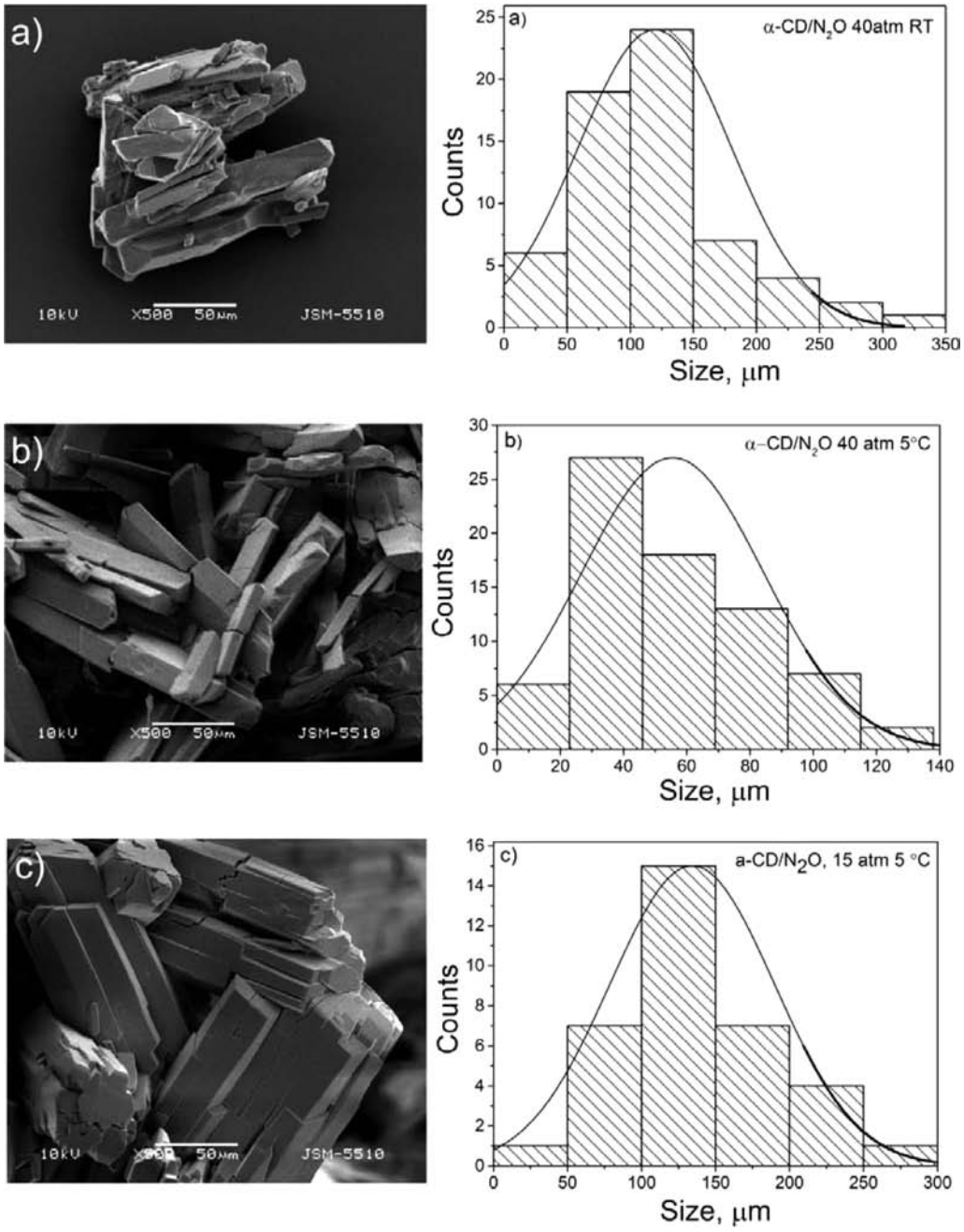

Figure 2. SEM micrographs and crystal size distribution of the clathrates formed from α-CD and N_2O at different conditions: (a) 40 atm gas pressure at room temperature; (b) 40 atm gas pressure at 5 °C; (c) 15 atm gas pressure at 5 °C.

exactly at the temperature of the inflex point of the TG curve. Moreover, the peak is complex with a low-temperature shoulder, indicating overlapping of two endothermic effects. It can be assumed that the low-temperature fraction of the complex peak is due to the evolution of N_2O. To determine, however, the enthalpy (heat) of the N_2O release, deconvolution of the first DSC peak is necessary, which in this case is connected with a large uncertainty. A very rough estimation gives a value of about 20 kJ/mol for the enthalpy of N_2O release.

Another important characteristic of the clathrates is the stability of entrapped gas (N_2O) at room and slightly higher temperatures (25−30 °C). After 30 days at 30 °C, only some of the gas is released (Figure 6b). A continuous stay at 30 °C (120 days) leads to reduction of the amount of entrapped gas, but still about 1−1.5 wt % is desorbing in the temperature

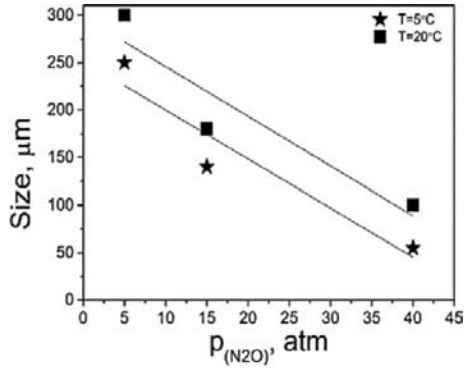

Figure 3. Relationship between gas pressure and the size of the clathrate crystals at 5 and 20 °C.

DOI: 10.1021/acs.jafc.5b01357
J. Agric. Food Chem. 2015, 63, 6603−6613

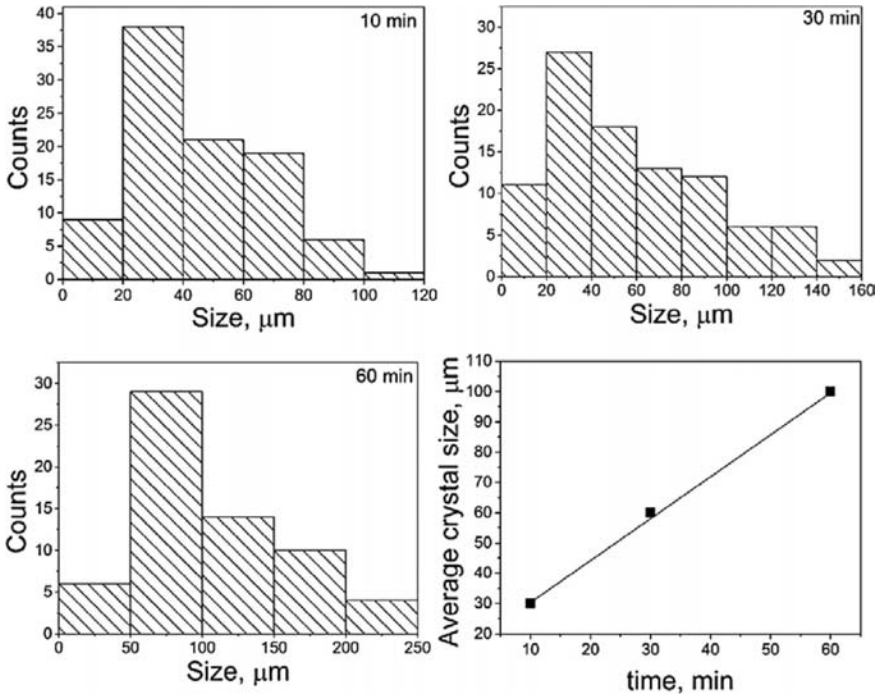

Figure 4. Crystal growth kinetics of the clathrate formed by α-CD and N_2O (40 atm, 5 °C).

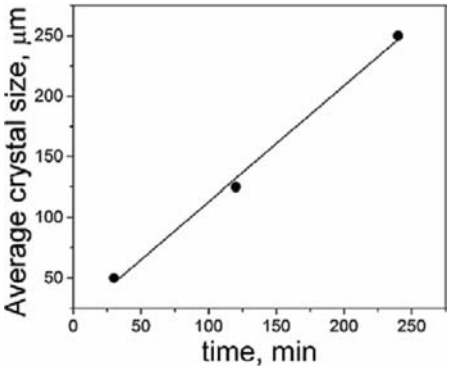

Figure 5. Crystal growth kinetics of the clathrate formed by α-CD and CO_2.

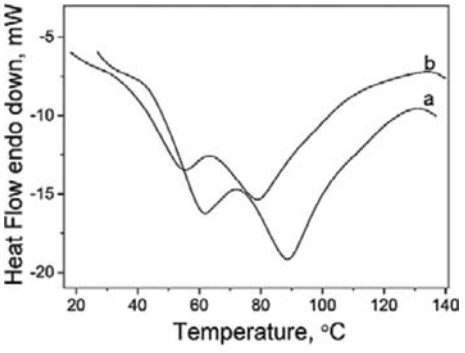

Figure 7. DSC of α-CD (curve a) and its clathrate with N_2O (after 120 days at room temperature) (curve b).

range of 40−60 °C. A similar amount of about 7−8 mL N_2O/g clathrate has been determined by the foam rise method as well.

Similar to the case of α-CD-N_2O clathrates, for α-CD-N_2 and α-CD-CO_2 the direct determination of the gas content by TG analysis was also connected with some uncertainty (Figure 8). For proving the result obtained by TG for the amount of entrapped gas, the foam rise method was applied, and values of about 5−7 mL CO_2/g clathrate and 4−5 mL N_2/g clathrate

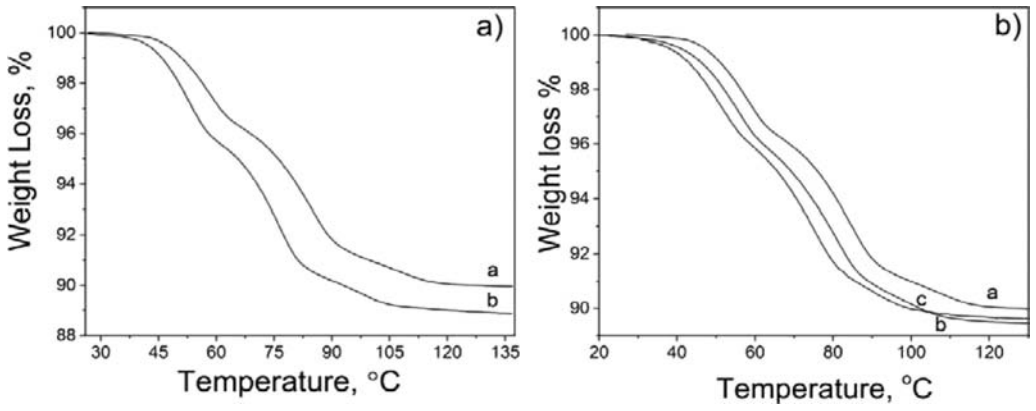

Figure 6. (a) TG analyses of α-cyclodextrin (curve a) and its clathrate formed with N_2O at 40 atm (curve b); (b) TG of α-CD-N_2O clathrates after a stay at 30 °C for different times: (curve a) pure α-CD; (curve b) clathrate after 30 days; (curve c) clathrate after 120 days.

DOI: 10.1021/acs.jafc.5b01357
J. Agric. Food Chem. 2015, 63, 6603−6613

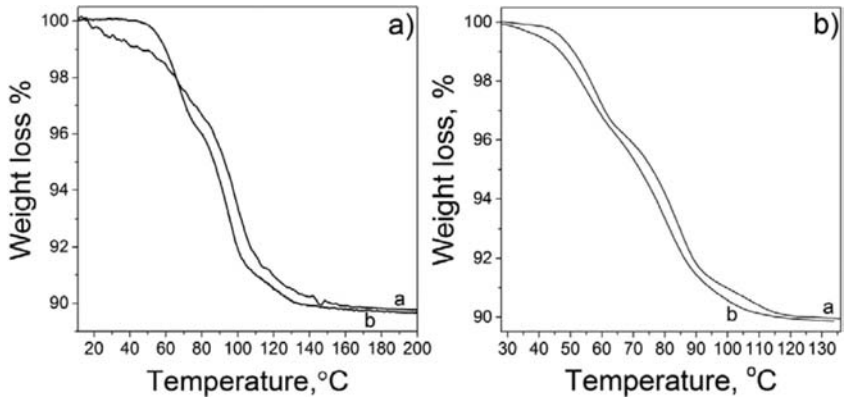

Figure 8. (a) TG curves of α-CD (curve b) and its clathrate with CO_2 (curve a); (b) α-CD (curve a) and its clathrate with N_2 (curve b).

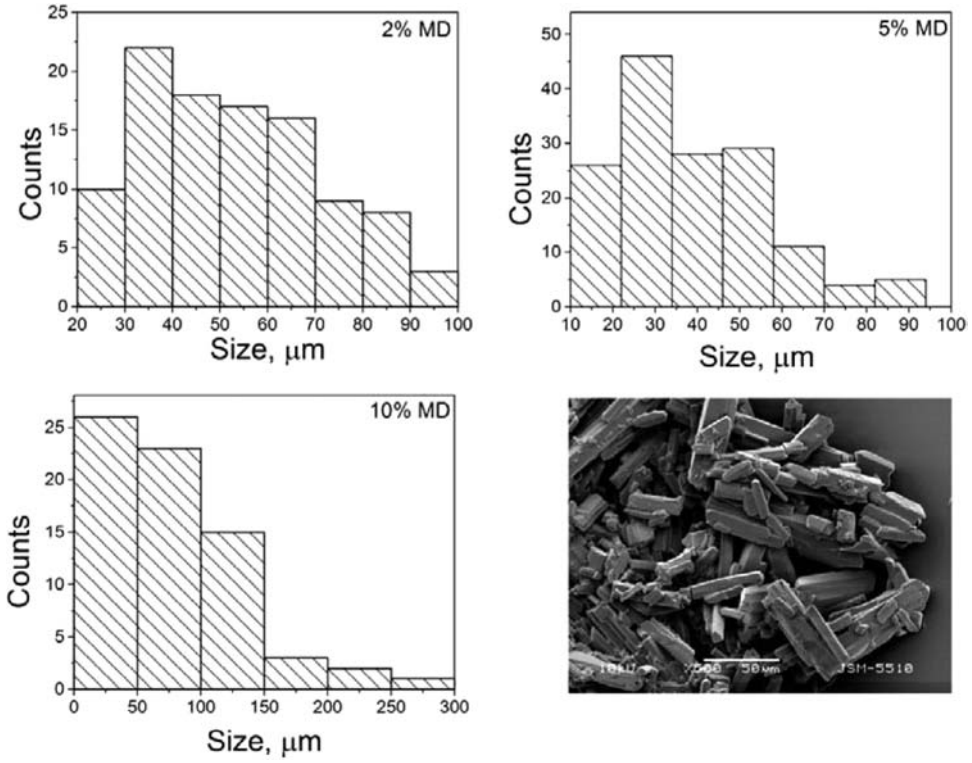

Figure 9. SEM and crystal size distribution of the clathrate formed by α-CD-N_2O with maltodextrin (MD) as nucleation initiator (at different concentrations: 2, 5, 10%).

were determined, which actually correspond quite well with the low-temperature weight decrease steps for the two clathrates, before any mass reduction for the α-CD to be observed (Figure 8). Nevertheless, complete correspondence of the weight decrease detected by TG and the amount of gas obtained by the foam rise method should not be expected, because the amount of water in the CD cavity can be different for the initial CD and for the clathrate formed on its base.

Undoubtedly, one of the important goals of our study was to increase the amount of gas incorporated into the α-CD molecules. For this reason different approaches have been applied: additions of maltodextrin (MD) as nucleation and crystal growth modifier, ultrasound treatment, and precrystallization of the CD. Different amounts of MD (2, 5, and 10 wt %) were added to the CD solution as a nucleation initiator and crystal habit modifier. The clathrate crystal size and morphology

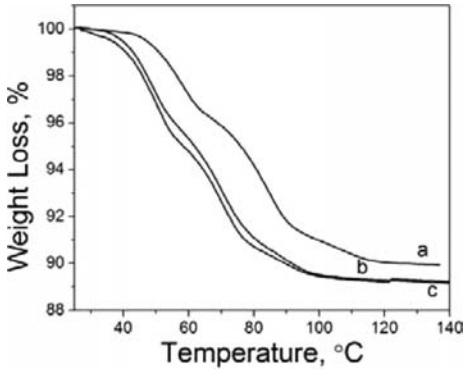

Figure 10. TG curves of α-CD (curve a) and of the clathrates α-CD-N_2O with 2% MD as initiator of the crystal growth, without (curve b) and with (curve c) ultrasound treatment.

DOI: 10.1021/acs.jafc.5b01357
J. Agric. Food Chem. 2015, 63, 6603−6613

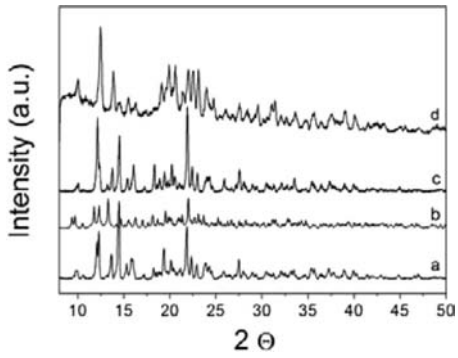

Figure 11. XRD of α-CD (diffractogram a), its theoretical/calculated diffractogram (diffractogram b), and of the clathrates formed with N_2O (diffractogram c) and CO_2 (diffractogram d).

are presented in Figure 9, and the thermogravimetric curve is shown in Figure 10. The ultrasound treatment was applied to the water solution of CD (10 min at 20 kHz) as well as to the CD+MD with the aim to accelerate α-CD solubility. The influence of the ultrasound treatment on the later clathrate crystal formation could also be expected. In general, it is revealed that the amount of the entrapped gas does not differ very much for the samples treated in a different way. This amount varies in the range of 1−1.5 wt %, and it is stable with the time of stay at room temperature. The smallest clathrate crystal size of about 40 μm was obtained with the addition of 5 wt % MD. However, a distinct influence of the clathrate crystal size on the amount and stability of the gas included in the α-CD molecules was not found.

For the amount of entrapped N_2O in α-CD, it can be calculated that if one molecule of N_2O is bonded to one molecule of α-CD, the maximum quantity of N_2O could be about 20−22 mL gas/g clathrate. This result was, however, not obtained experimentally. High-level quantum-mechanical calculations (Dudev and Spassov, unpublished work) reveal that in the *gas-phase* α-CD forms favorably 1:1 complexes with N_2O. Binding of a second N_2O to the host molecule (either inside the hydrophobic cavity or at the larger or smaller hydroxylate rim), however, does not seem energetically favorable as the binding free energies are positive. Note that the present experiments in *condensed* phase support smaller than 1:1 ratios of N_2O to α-CD (see above). The source of discrepancy between the gas-phase quantum mechanical results and experimental observations in condensed phase is intriguing and is the subject of current investigation.

To prove the crystalline state of the clathrates and to get additional information about the average crystal size and possible influence of the included gas on the crystal lattice parameters, X-ray diffraction analyses (XRD) were performed as well. Figure 11 reveals the X-ray diffractograms of α-CD used for the clathrate formation and of the corresponding clathrates with different gases. In the same figure the simulated diffractogram using α-CD structural data (lattice parameters) available in the literature is also plotted. It is seen that the position of the diffraction peaks of the clathrates and the initial α-CD used for their formation are the same, but some of them have different intensities—an indication for a preferred crystal growth in certain crystallographic directions. In addition, the peaks of the clathrates are slightly broader—an indication for smaller crystal size. Moreover, the diffractogram for the α-CD-CO_2 clathrate reveals the presence of an amorphous phase together with the crystalline one.

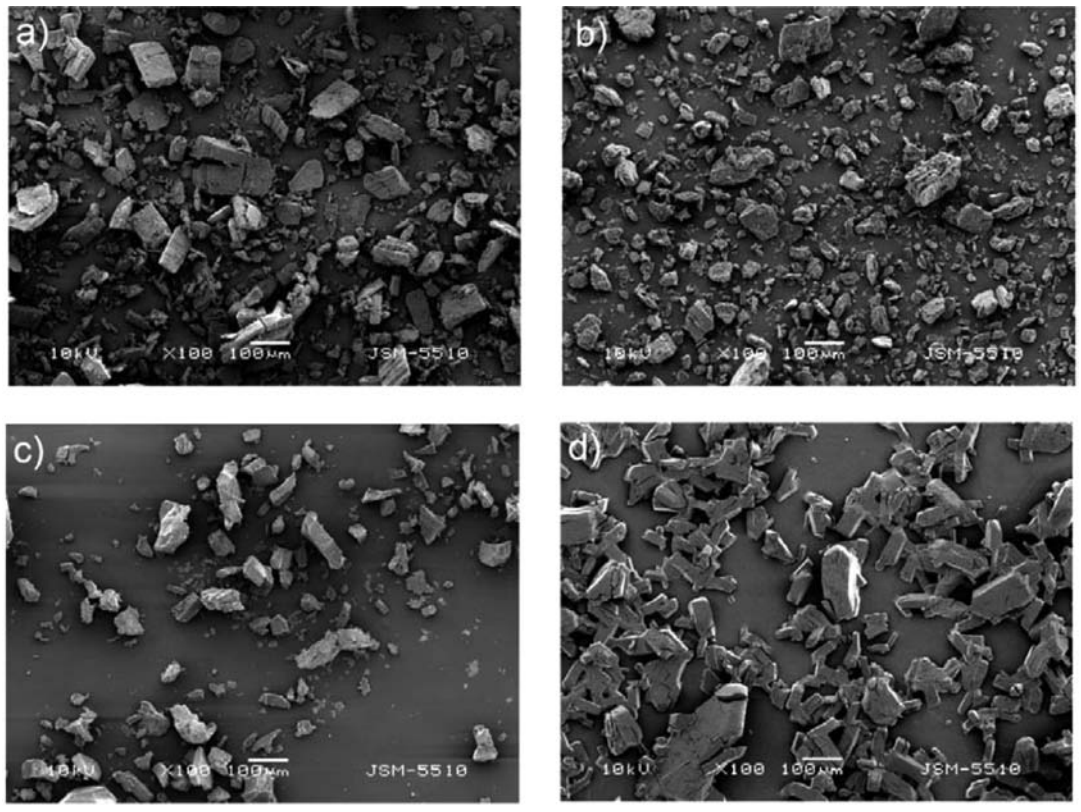

Figure 12. Morphology of β-CD (a), γ-CD (b), β-CD-N_2 (c), and γ-CD-N_2 (d) clathrate crystals.

DOI: 10.1021/acs.jafc.5b01357
J. Agric. Food Chem. 2015, 63, 6603−6613

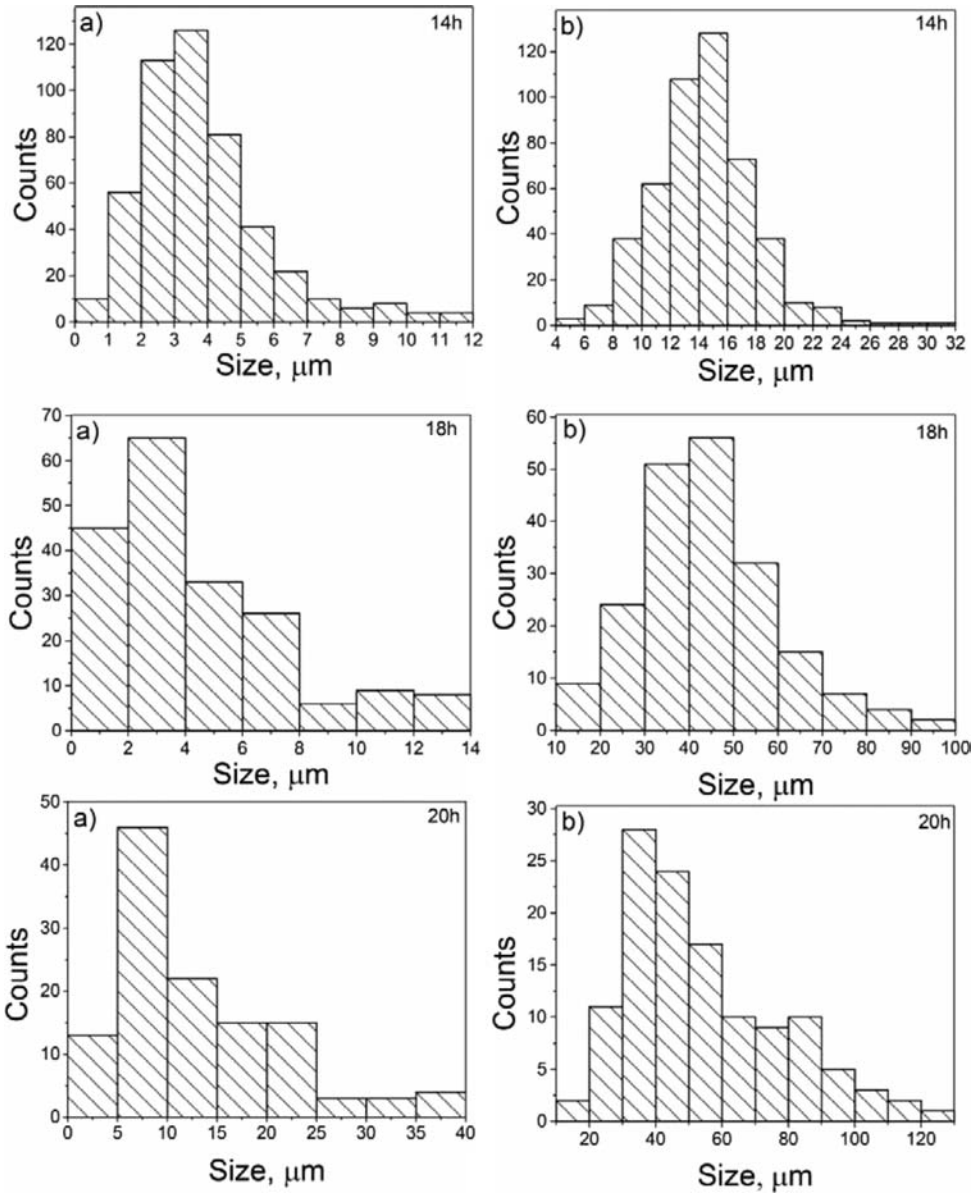

Figure 13. Crystal size distribution histograms of the clathrate of γ-CD-N_2 (taking into account the crystals' width (a) and length (b)).

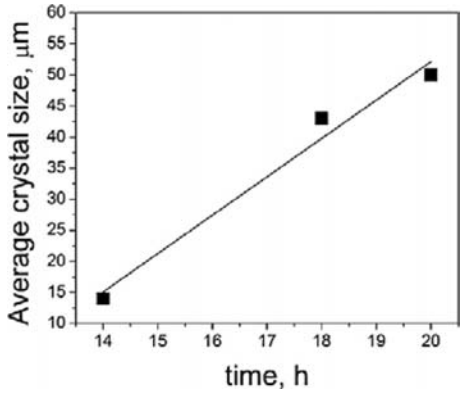

Figure 14. Kinetics of the crystal growth of the clathrate formed by γ-CD and N_2 (length).

Clathrates of β- and γ-CD with N_2. For β- and γ-CDs it was proven that in the gas pressure range of 5−40 atm and temperature range of 5−20 °C they form crystalline clathrates only with N_2 as guest molecule. The synthetic conditions were optimized with respect to the clathrates' yield (∼40−50%), the amount of N_2 trapped in the CD molecules (5−10 mL gas/g clathrate), crystallization kinetics, and crystal size distribution. The following optimal synthetic parameters were determined: nitrogen gas pressure, >10 atm; temperature, ∼5 °C; crystallization time, 10−15 h; saturated water solution at eoom temperature of γ-CD (20 wt %) and β-CD (1 wt %).

Figure12 shows the typical morphology of the β-CD-N_2 and γ-CD-N_2 clathrate crystals. Most of the crystals are elongated with polyhedral shape. From the constructed crystal size distribution diagrams the average crystal size has been determined, and information about the crystal growth kinetics was obtained. To study the nucleation and crystal growth kinetics, the clathrate crystal size distribution was analyzed at different crystallization times, keeping all other synthetic parameters constant (Figure 13). For γ-CD-N_2 two types of size distribution histograms have been obtained: the first one accounts for the distribution of the crystal size considering the width of the crystals, and the second

DOI: 10.1021/acs.jafc.5b01357
J. Agric. Food Chem. 2015, 63, 6603−6613

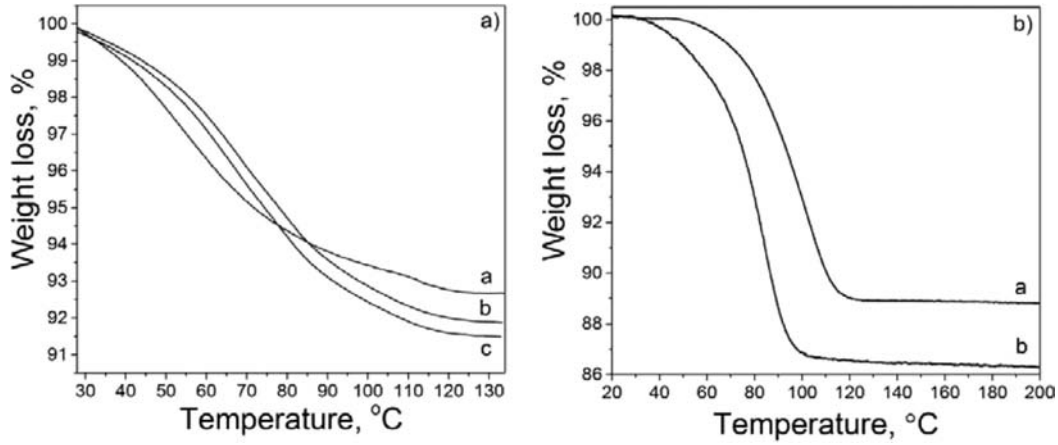

Figure 15. (a) TG curves of γ-CD (curve a) and its clathrate formed with N_2 (curve b); (b) TG curves of β-CD (curve a) and its clathrate with N_2 (curve b).

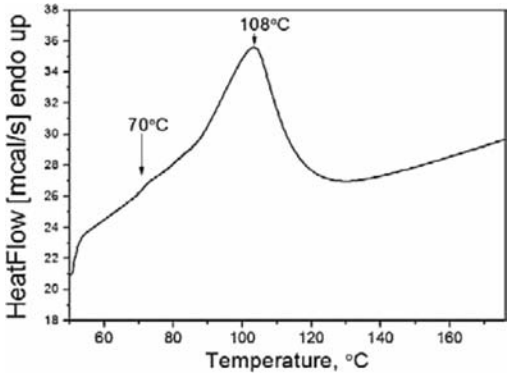

Figure 16. DSC curve of clathrate β-CD-N_2.

takes into account the length of the crystals. An interesting observation for this clathrate crystallization is the long incubation time, about 10 h, before any noticeable clathrate crystals can be detected microscopically. Both the unimodal crystal size distribution and the long incubation time indicate a homogeneous nucleation mechanism. A rough estimation of the nucleation rate gives a value in the range of $(6-8) \times 10^6$ m^{-2} h^{-1}. Figure14 shows the dependence of the mean clathrate crystal size as a function of time. An almost linear rate of crystal growth of about 5−6 μm/h can be detected, which is substantially lower than that of the α-CD-N_2O, α-CD-N_2, and α-CD-CO_2 crystal formations. Analogous crystal size distribution analysis of β-CD-N_2 clathrates gives a mean crystal size of about 60−70 μm and a linear growth rate of 4−5 μm/min.

In summary, with regard to the clathrates' crystallization kinetics it was found that α-CD-N_2O and α-CD-CO_2 crystals grow much faster than those of β- and γ-CD-N_2, most probably due to the larger driving force of the crystallization process for the α-CD-based clathrates.

By TG and foam raise method the amount of the gas trapped in the β- and γ-CDs was determined, and values in the range of 5−15 mL of gas in 1 g of clathrate were found (maximum values of about 15 mL N_2/g clathrate for β-CD-N_2 and about 7−8 mL N_2/g for γ-CD-N_2). Figure 15 presents the TG curves for γ-CD and β-CD and their clathrates with N_2. The DSC analysis of the clathrates confirms the release of N_2 at temperatures of about 60−80 °C, expressed by a broad peak overlapped with the main one (T_{max} = 108 °C) due to water release (Figure 16).

Figure 17 reveals the X-ray diffractograms of β-CD and γ-CD and their clathrates with N_2. The position of the diffraction peaks of the clathrates and the initial CDs used for their formation are the same with some small differences in the peak intensities. The diffraction peaks of the clathrates are slightly broader, due to their smaller crystal size. The presence of some amorphous phase can also be seen from the diffractograms of the clathrates.

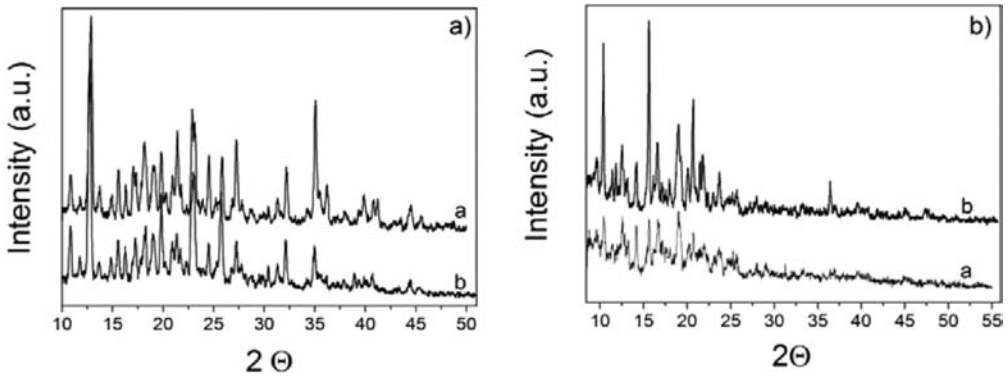

Figure 17. (a) XRD of β-CD (diffractogram a) and the β-CD-N_2 clathrate (diffractogramb); (b) XRD of γ-CD (diffractogram a) and the γ-CD-N_2 clathrate (diffractogram b).

DOI: 10.1021/acs.jafc.5b01357
J. Agric. Food Chem. 2015, 63, 6603−6613

AUTHOR INFORMATION

Corresponding Author

*(T.S.) tspassov@chem.uni-sofia.bg.

Funding

We acknowledge the financial support of EU Project FP7-REGPOT-2011-1, "Beyond Everest", and EU COST Actions FA1001, MP1305, and MP1106. This work has also been financially supported by Unilever R&D, The Netherlands.

Notes

The authors declare no competing financial interest.

REFERENCES

(1) Manakker, F.; Vermonden, T.; Nostrum, C.; Hennink, W. Cyclodextrin-based polymeric materials: synthesis, properties, and pharmaceutical/biomedical applications. *Biomacromolecules* **2009**, *10* (12), 3157.

(2) Bilensoy, E.; Duchene, D.; Ahuja, A.; Baboota, S.; Ali, J.; Mustafa, G.; Acartürk, F.; Celebi, N. Part 1, Chapter 1: Cyclodextrins and their inclusion complexes. Chapter 2: Cyclodextrins as potential excipients in pharmaceutical formulations: solubilizing and stabilizing effects. Chapter 3: Cyclodextrins as bioavailability enhancers. *Cyclodextrins in Pharmaceutics, Cosmetics and Biomedicine*, 1st ed.; Wiley: Hoboken, NJ, USA, 2011; pp 3−43.

(3) Loftsson, T.; Duchene, D. Cyclodextrins and their pharmaceutical applications. *Int. J. Pharm.* **2007**, *329*, 1.

(4) Loftsson, T.; Brewster, M. E. Pharmaceutical applications of cyclodextrins. 1. Drug solubilization and stabilization. *J. Pharm. Sci.* **1996**, *85*, 10.

(5) Liu, L.; Guo, Q. X. J. The driving forces in the inclusion complexation of cyclodextrins. *J. Inclusion Phenom. Mol. Recognit. Chem.* **2002**, *42*, 1.

(6) Harries, D.; Rau, D. C.; Parsegian, V. A. Solutes probe hydration in specific association of cyclodextrin and adamantane. *J. Am. Chem. Soc.* **2005**, *127*, 2184.

(7) Davis, M. E.; Brewster, M. E. Cyclodextrin-based pharmaceutics: past, present and future. *Nat. Rev. Drug Discovery* **2004**, *3*, 1023.

(8) Stella, V. J.; Rao, V. M.; Zannou, E. A.; Zia, V. V. Mechanisms of drug release from cyclodextrin complexes. *Adv. Drug Delivery Rev.* **1999**, *36*, 3.

(9) Ribeiro, A.; Figueiras, A.; Santos, D.; Veiga, F. Preparation and solid state characterization on inclusion complexes formed between miconazole and methyl-β-cyclodextrin. *AAPS PharmSciTech* **2008**, *9*, 1102.

(10) Irie, T.; Uekama, K. Pharmaceutical applications of cyclodextrins: III. Toxicological issues and safety evaluation. *J. Pharm. Sci.* **1997**, *86*, 147.

(11) Frank, D. W.; Gray, J. E.; Weaver, R. N. Cyclodextrin nephrosis in the rat. *Am. J. Pathol.* **1976**, *83*, 367.

(12) Frijlink, H. W.; Eissens, A. C.; Hefting, N. R.; Poelstra, K.; Lerk, C. F.; Meijer, D. K. F. The effect of parenterally administered cyclodextrins on cholesterol levels in the rat. *Pharm. Res.* **1991**, *8*, 9.

(13) Szejtli, J. Introduction and general overview of cyclodextrin chemistry. *Chem. Rev.* **1998**, *98*, 1743.

(14) Brewster, M. E.; Loftsson, T. Cyclodextrins as pharmaccutical solubilizers. *Adv. Drug Delivery Rev.* **2007**, *59*, 645.

(15) Uekama, K. Design and evaluation of cyclodextrinbased drug formulation. *Chem. Pharm. Bull.* **2004**, *52*, 900.

(16) Uekama, K.; Hirayama, F.; Irie, T. Cyclodextrin drug carrier systems. *Chem. Rev.* **1998**, *98*, 2045.

(17) Fenyvesi, E. Cyclodextrin polymers in the pharmaceutical industry. *J. Inclusion Phenom.* **1988**, *5*, 537.

(18) Trotta, F.; Cavalli, R.; Martina, K.; Biasizzo, M.; Vitillo, J.; Bordiga, S.; Vavia, P.; Ansari, K. Cyclodextrin nanosponges as effective gas carriers. *J. Inclusion Phenom. Mol. Recognit. Chem.* **2011**, *71*, 189.

(19) Buschmann, H.; Schollmeyer, E. Applications of cyclodextrins in cosmetic products: a review. *J. Cosmet. Sci.* **2002**, *53*, 185.

(20) Kohler, P.; Peterseann, R.-D.; Botcher, S. Stabilization of tea tree oil. *SÖFW J.* **1999**, *125*, 10.

(21) Kock, J. Storage of stable, powdered detergent and cleaning agent containing perfume. *DE* **1981**, *30*, 20−269.

(22) Bacon, D. R.; Trinh, T. Detergent compositions containing enduring perfume. U.S. Patent 5 500 154, 1996.

(23) Kubota, M.; Komaki, R. Long-lasting perfume compositions containing (−)muscone. *Jpn. Kokai, Tokkyo Koho JP* **1995**, *07* (324), 196.

(24) Astray, G.; Gonzalez-Barreiro, C.; Mejuto, J. C.; Rial-Otero, R.; Simal-Gándara, J. A review on the use of cyclodextrins in foods. *Food Hydrocolloids* **2009**, *23*, 1631−1640.

(25) Kitahata, S.; Okada, S.; Fukui, T. Acceptor specificity of the trans-glycosylation catalyzed by cyclodextrin glycosyltransferase. *Agric. Biol. Chem.* **1978**, *42*, 2369−2374.

(26) U.S. FR 3 425 910, 1980.

(27) Yamamoto, M.; Horikoshi, K.; Wako-shi. Isolation and purification of α-cyclodextrin by synthetic adsorption polymer. *Starch* **1981**, *3*, 244−246.

(28) Horikoshi, K. Production and industrial applications of β-cyclodextrin. *Process Biochem.* **1979**, *14*, 26−30.

(29) Nakamura, N.; Horikoshi, K. Production of schardinger β-dextrin by soluble and immobilized cyclodextrin glycosyltransferase of an alkalophilic *Bacillus* sp. *Biotechnol. Bioeng.* **1977**, *19*, 87−99.

(30) Flaschel, E.; Landert, J. P.; Spiesser, D.; Renken, A. The production of α-cyclodextrin by enzymatic degradation of starch. *Ann. N. Y. Acad. Sci.* **1984**, *434*, 70−77.

(31) Kobayashi, S.; Kainuma, K.; French, D. Effect of surfactants on cyclization of *Bacillus macerans* cyclodextrin glucanotransferase. *Denpun Kagaku* **1983**, *30* (1), 62−68.

(32) Kobayashi, S.; Kainuma, K. Cyclodextrins. Production and utilization of α-cyclodextrin. *Denpun Kagaku* **1981**, *28* (2), 132−141.

(33) Bender, H. An improved method for the preparation of cyclooctaamylose, using starches and the cyclodextrin glycosyltransferase of *Klebsiella pneumoniae* M 5 al. *Carbohydr. Res.* **1983**, *124*, 225−233.

(34) Lubbers, S.; Landy, P.; Voilley, A. Retention and release of aroma compounds in foods containing proteins. *Food Technol.* **1998**, *52*, 68−74.

(35) Jouquand, C.; Ducruet, V.; Giampaoli, P. Partition coefficients of aroma compounds in polysaccharide solutions by the phase ratio variation method. *Food Chem.* **2004**, *85*, 467−474.

(36) Pagington, J. S. β-Cyclodextrin and its uses in the flavour industry. In *Developments in Food Flavours*; Birch, G. G., Lindley, M. G., Eds.; Elsevier Applied Science: London, UK, 1986.

(37) Szente, L.; Szejtli, J. Cyclodextrins as food ingredients. *Trends Food Sci. Technol.* **2004**, *15*, 137−142.

(38) Bhandari, B.; D'Arcy, B.; Young, G. Flavour retention during high temperature short time extrusion cooking process: a review. *Int. J. Food Sci. Technol.* **2001**, *36*, 453−461.

(39) Irwin, P. L.; Pfeffer, P. E.; Doner, L. W.; Sapers, G. M.; Brewster, J. D.; Nagahashi, G. Binding geometry, stoichimetry, and thermodynamics of cyclomaltoligosaccharide (cyclodextrin) inclusion complex formation with chlorogenic acid, the major substrate of apple polyphenol oxidase. *Carbohydr. Res.* **1994**, *256*, 13−27.

(40) Lopez-Nicolas, J. M.; Garcıa-Carmona, F. Use of cyclodextrins as secondary antioxidants to improve the color of fresh pear juice. *J. Agric. Food Chem.* **2007**, *55*, 6330−6338.

(41) Lopez-Nicolas, J. M.; Nuñez-Delicado, E.; Sanchez-Ferrer, A.; Garcıa-Carmona, F. Kinetic model of apple juice enzymatic browning in the presence of cyclodextrins: the use of maltosyl-β-cyclodextrin as secondary antioxidant. *Food Chem.* **2007**, *101* (3), 1164−1171.

(42) Lopez-Nicolas, J. M.; Perez-Lopez, A. J.; Carbonell-Barrachina, A.; Garcıa-Carmona, F. Use of natural and modified cyclodextrins as inhibiting agents of peach juice enzymatic browning. *J. Agric. Food Chem.* **2007**, *55*, 5312−5319.

(43) Lopez-Nicolas, J. M.; Perez-Lopez, A. J.; Carbonell-Barrachina, A.; Garcıa-Carmona, F. Kinetic study of the activation of banana juice

DOI: 10.1021/acs.jafc.5b01357
J. Agric. Food Chem. 2015, 63, 6603−6613

enzymatic browning by the addition of maltosyl-β-cyclodextrin. *J. Agric. Food Chem.* **2007**, *55*, 9655−9662.
(44) Vaidya, S. Clathrates — an exploration of the chemistry of caged compounds. *Resonance* **2004**, *9*, 18−31.
(45) Johari, G. P. On the origin of the heat capacity feature of the annealed ices and ice clathrates, and interpreting water's diffusivity in term of the entropy. *Chem. Phys.* **2000**, *258*, 277.
(46) Ho, B. T.; Joyce, D. C.; Bhandari, B. R. Encapsulation of ethylene gas into α-cyclodextrin and characterization of the inclusion complexes. *Food Chem.* **2011**, *127*, 572−580.
(47) Mohammadi, A.; Manteghian, M.; Mirzaei, M. Effect of β-cyclodextrin on dissolution of methane in water. *Chem. Eng. Res. Des.* **2011**, *89*, 421−427.
(48) Steiner, T.; Koellner, G. Crystalline β-cyclodextrin hydrate at various humidities. Fast, continuous, and reversible dehydration studied by X-ray diffraction. *J. Am. Chem. Soc.* **1994**, *116*, 5122.
(49) Chacko, K. K.; Saenger, W. Topography of cyclodextrin inclusion complexes. 15. Crystal and molecular structure of the cyclohexaamylose-7.57 water complex, form III. Four- and six-membered circular hydrogen bonds. *J. Am. Chem. Soc.* **1981**, *103*, 1708.
(50) Klar, B.; Hingerty, B.; Saenger, W. Topography of cyclodextrin inclusion complexes. XII. Hydrogen bonding in the crystal structure of α-cyclodextrin hexahydrate: the use of a multicounter detector in neutron diffraction. *Acta Crystallogr., Sect. B: Struct. Crystallogr. Cryst. Chem.* **1980**, *B36*, 1154.
(51) Lindner, K.; Saenger, W. Topography of cyclodextrin inclusion complexes. XVI. Cyclic system of hydrogen bonds: structure of α-cyclodextrin hexahydrate, form (II): comparison with form (I). *Acta Crystallogr., Sect. B: Struct. Crystallogr. Cryst. Chem.* **1982**, *B38*, 203.
(52) Damodharan, L.; Pattabhi, V.; Nagarajan, K. Solvent interactions with β-cyclodextrin as observed in crystal structures. *Mol. Cryst. Liq. Cryst.* **2004**, *423*, 17.
(53) Ivanova, B.; Spiteller, M. Macromolecular ensembles of cyclodextrin crystallohydrates and clathrates − experimental and theoretical gas − and condense phase study. *Int. J. Biol. Macromol.* **2014**, *64*, 383.
(54) WO, 036744, 2008. U.S. PCT, 078897, 2007.
(55) Bickerman, J. J.; Perri, J. M.; Booth, R. B.; Currie, C. C. *Foams: Theory and Industrial Applications*; Reinhold Publishing: New York, 1953; p 9.
(56) Spilimbergo, S.; Matthews, M. A.; Cinquemani, C. Chapter 4: Supercritical fluid pasteurization and food safety: process based on gases other than CO_2. In *Alternatives to Conventional Food Processing*, 1st ed.; Proctor, A., Ed.; Royal Society of Chemistry: Cambridge, UK, 2010; RSC Green Chemistry (Book 10), p 162.

DOI: 10.1021/acs.jafc.5b01357
J. Agric. Food Chem. 2015, 63, 6603−6613

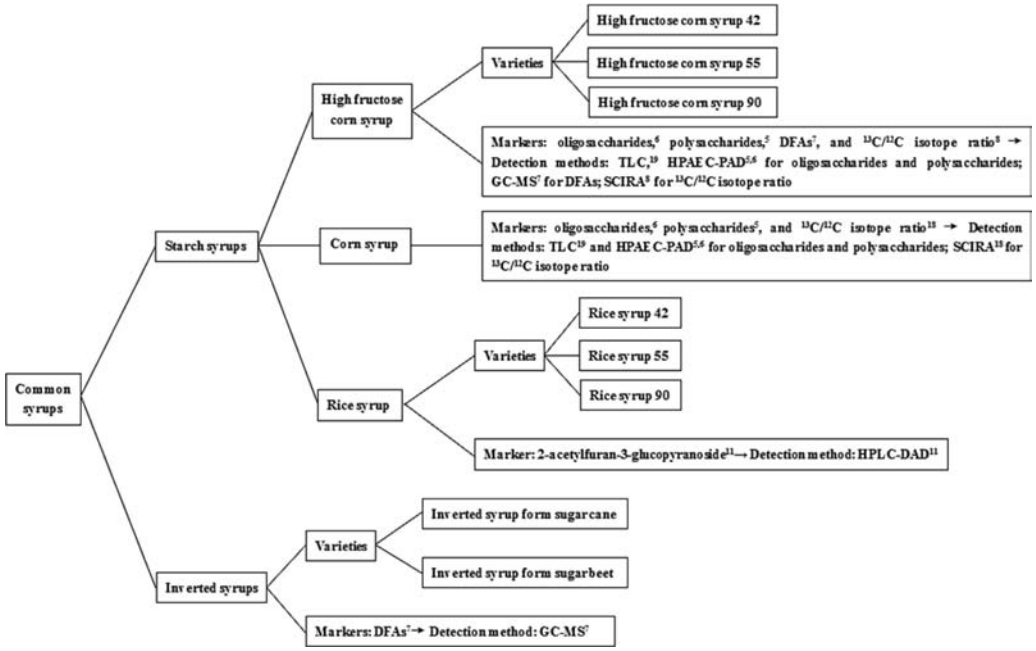

Figure 1. Sugar syrup markers and detection methods.

Quadrupole time-of-flight mass spectrometry (Q-TOF-MS) is a novel detection method that provides accurate mass measurements of full-product ions, thereby ensuring sensitive and accurate analyte identification. Apart from the application in target compound analyses, the identification of nontarget compounds is another advantage of Q-TOF-MS. Q-TOF-MS has been successfully used in the detection of pesticides[27,28] in foods, animal medications[29,30] in feeds, bioactive compounds in healthy foods[31,32] and pharmaceutical drugs,[33,34] and organic contaminants and their nontarget byproducts in water.[35,36] However, there is little information on the application of Q-TOF-MS in honey, especially in honey authenticity.

In this study, a Q-TOF-MS method coupled with UHPLC was developed to detect the presence of sugar syrups in honey samples using polysaccharides, DFAs, and AFGP as markers. This method is simple, rapid, and effective and allows the simultaneous detection of several syrups. Additionally, we evaluated the effects of honeybee feeding on several syrups for 3 days in the winter; the resulting honeys were detected by our developed method to evaluate whether syrups remain in them.

MATERIALS AND METHODS

Samples. In this study, 106 honey samples were used: 20 acacia honey samples (A1−A20), 20 rape honey samples (R1−R20), 20 linden honey samples (L1−L20), 20 jujube honey samples (J1−J20), and 20 multifloral honey samples (MF1−MF20) were obtained from 24 cooperative beekeepers located in Hebei and Henan, Sichuan, Heilongjiang and Jilin, Shaanxi, and Shandong and Xinjiang, respectively. Six manuka honey samples (M1−M6) were obtained from a supermarket in New Zealand. The honey samples were selected on the basis of strict quality criteria to ensure their authenticity.

Forty-five sugar syrup samples were purchased from different markets, including five corn syrups (CS1−CS5), five rice syrups 42 (RS-42-1−RS-42-5), five rice syrups 55 (RS-55-1−RS-55-5), five rice syrups 90 (RS-90-1−RS-90-5), five inverted syrups from sugar beet (IB1−IB5), five inverted syrups from sugar cane (IC1−IC5), five high-fructose corn syrups 42 (HFCS-42-1−HFCS-42-5), five high-fructose corn syrups 55 (HFCS-55-1−HFCS-55-5), and five high-fructose corn syrups 90 (HFCS-90-1−HFCS-90-5). CS, RS-42, RS-55, RS-90, IB, IC, HFCS-42, HFCS-55, and HFCS-90 were added in different concentrations (10, 20, or 30%, w/w) to pure honey samples for analysis.

Two hundred market honey samples (sam1−sam200) were randomly purchased from different Chinese markets in Beijing, Hebei, Henan, Shaanxi, Jilin, and Shandong and analyzed for adulteration of sugar syrups.

Reagents and Standards. An analytical standard of difructose anhydride III (DFA III) was purchased from Sigma Chemical Co. (St. Louis, MO, USA). AFGP (≥95% purity) was obtained by preparative high-performance liquid chromatography (PHPLC) and lyophilization from our previous study.[11] Crude polysaccharide extracts (DP 3−19, ≥90% purity) were purchased from Beijing Langlin Co. Acetonitrile of HPLC grade was purchased from Fisher Chemicals (Fair Lawn, NJ, USA). Deionized water was prepared using a Millipore Milli-Q Plus system (Millipore, Bedford, MA, USA).

Bee-Feeding Experiments. A bee-feeding experiment was conducted in a Ping Hu apiary to evaluate the effects of commercial sugar syrups such as RS (RS-42, RS-55, and RS-90), HFCS (HFCS-42, HFCS-55, and HFCS-90), CS, IB, and IC on the resulting honey. In this experiment, 2 kg of each syrup was fed to each honeybee colony for 3 days during the winter nectar dearth. The resulting honey was analyzed.

Sample Preparation. Sample (1 g) was dissolved in 10 mL of acetonitrile/deionized water (50:50, v/v) and mixed in a vortex for 2 min. The mixture was passed through two 0.22 μm PVDF membranes.

UHPLC/Q-TOF-MS. UHPLC was performed in an Agilent 1260 series UHPLC (Agilent, Palo Alto, CA, USA) equipped with an autoinjector and a quaternary UHPLC pump. An Acquity UPLC BEH Amide column (2.1 mm × 100 mm, 1.7 μm) was used. The mobile phase gradient consisted of 30% water (solvent A) and 70% acetonitrile (solvent B) for the first 5 min. Solvent B was reduced to 45% acetonitrile over 5 min and held at this concentration for 5 min. Subsequently, solvent B was adjusted to 70% over 0.1 min and held at this concentration for 2.9 min to clean the column. The total run time was 18 min, with the flow rate of 0.3 mL/min, and the injection volume was 5 μL. The column temperature was maintained at 50 °C.

MS was performed in an Agilent 6530 ESI-Q-TOF. The optimum MS conditions consisted of a capillary voltage of 3.0 kV in negative ionization mode, a skimmer voltage of 65 V, and a segmented fragmentor at 135 V for the first 5 min and at 200 V for the remaining run. The gas temperature, drying gas flow rate, and nebulizer pressure

DOI: 10.1021/acs.jafc.5b01410
J. Agric. Food Chem. 2015, 63, 6614−6623

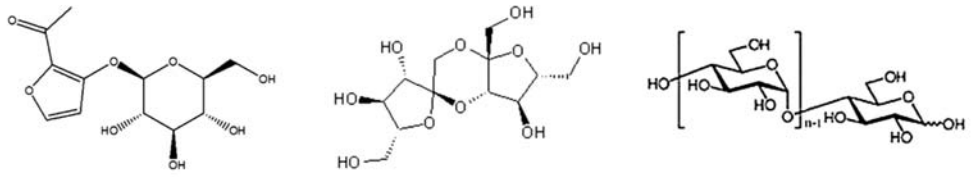

Figure 2. Chemical structures of markers: (a) 2-acetylfuran-3-glucopyranoside (AFGP); (b) difructose anhydride III (DFA III); (c) polysaccharides (DP 12−19).

were 325 °C, 7 L/min, and 30 psi, respectively. Nitrogen was used as the collision, drying, and nebulizer gas. MS spectra were acquired at m/z 100−3200 using an extended dynamic range and a scan rate of 1.5 spectra/s by varying collision energy with mass. A reference mass solution containing reference ions (301.998139, 1033.988109, 1633.948689, and 1933.930624) was used to maintain mass accuracy during the run. Data were acquired with MassHunter Acquisition B.06.00 (Build 4033.1, 1 Patch) and processed with MassHunter Qualitative Analysis B.06.00 (Build 4.0.479.9, Service Pack 2) and Microsoft Excel 2007. A database was generated using PCDL Manager B.04.00 (Build 92.0).

RESULTS AND DISCUSSION

Sugar Syrup Markers. In general, two main detection methods for honey adulteration were approached: one based on the composition of honey and the other based on the presence of a specific adulterant component, that is, a marker.[37] The latter approach is commonly used as honey composition varies considerably by type and geographic location. The most common sugar syrup markers and their detection methods are summarized in Figure 1. Oligosaccharides and polysaccharides have been used as markers for corn-based syrups in TLC,[19] and HPACE-PAD.[5,6] AFGP is a marker of honey adulterated with RS.[11] DFAs, which are pseudodisaccharides formed during caramelization, consist of two fructose molecules,[38,39] and there are 14 DFA isomers.[38,40] As shown in Figure 1, DFAs have been utilized as markers of HFCS and IS.[7] In this study, polysaccharides, AFGP, and DFAs were used as markers of adulterated honey.

Optimization of UHPLC/Q-TOF-MS Conditions. As shown in Figure 2, the molecular sizes and polarities of these markers were significantly different from each other. Therefore, it was crucial to select an analytical column that could effectively separate the makers. Several commercial columns including a ZORBAX SB-C_{18} column (2.1 mm × 100 mm, 3.5 μm, Phenomenex), a HILIC Analytical Column (2.1 mm × 100 mm, 3.5 μm, Agilent), and an Acquity UPLC BEH Amide column (2.1 mm × 100 mm, 1.7 μm, Waters) were evaluated. The results revealed that, among the three markers, DFAs and polysaccharides could not be reserved on the C_{18} column due to their high polarity. AFGP and polysaccharides were not thoroughly separated by the HILIC column. Additionally, separation of markers by the HILIC column was very low. The Acquity UPLC BEH Amide column (2.1 mm × 100 mm, 1.7 μm) was therefore selected due to its high resolution and adequate signal-to-noise performance. Even though the BEH Amide column has been extensively used in the separation for saccharides,[41,42] there is less information about its application in DFAs and AFGP separation. In this study, the suitability of the BEH Amide column for DFA and AFGP separation was evaluated. The results revealed that an adequate marker separation was achieved with the Acquity UPLC BEH Amide column (Figure 3a). Peaks 1−19 correspond to AFGP, difructose anhydride III (DFA III), oligosaccharides (DP 3−11), and polysaccharides (DP 12−19).

Two mobile phases (water + acetonitrile and water + ammonia + acetonitrile) were evaluated. No significant differences in signal intensities or peak shapes between the two mobile phases were observed. To protect the column, water with acetonitrile and without ammonia was chosen as the mobile phase; 2 mM NH_4COOH was added to the mobile phase to form adducts of $[M + COOH]^-$. Other LC conditions were also evaluated. The most suitable UHPLC conditions consisted of a column temperature of 50 °C and a flow rate of 0.3 mL/min, with an injection volume of 5 μL.

In Q-TOF-MS, the fragmentor is the most influential parameter. A suitable fragmentor contributes to an efficient transmission of parent ions with few fragments. The signal intensities of parent ions with low mass values increase with increasing fragmentor voltage. Once the threshold is surpassed, the signal intensities decrease because the parent ions are fragmented. Parent ions of high mass values require higher voltage. To improve the sensitivity and validity of the method, a segmented fragmentor was utilized: 135 V for the first 5 min and for low mass values (DFAs and AFGP) and 200 V for the remaining run and for high mass values (polysaccharides with DP 12−19). Furthermore, a negative mode was selected for Q-TOF-MS due to the saccharide characteristics. The optimization of other key parameters (capillary voltage, skimmer voltage, gas temperature, drying gas flow rate, and nebulizer pressure) of Q-TOF-MS was performed by injecting a mixture of standard solutions (1 μg/mL) into the MS. To increase accuracy, real time reference mass corrections were performed during each run by applying reference ions having mass values similar to those of the markers.

Database Generation. Databases are useful for searching markers.[43] In this study, a small-scale database was generated for the automatic screening of sugar syrup markers on the basis of their retention time, accurate mass, characteristic ions (i.e., m/z, $[M - H]^-$, $[2M - H]^-$, or $[M - 2H]^{2-}$), and possible adducts (e.g., with $HCOO^-$).

An Excel spreadsheet (Table 1), compatible with the automatic screening software, was generated containing information on the sugar syrup markers, for example, molecular formula, retention time, accurate mass, and m/z values of characteristic ions. As shown in Table 1, AFGP, DFA III, and polysaccharides with DP 12−19 were selected as markers. AFGP, which has lower polarity than the other markers, was present as singly charged ions $[M - H]^-$ and $[2M - H]^-$ with m/z values of 287.0772 and 575.1618, respectively. AFGP was prone to form $HCOO^-$ adducts; therefore, $[M + COOH]^-$ (m/z 333.0822) was used as another characteristic ion. DFA III was used as all DFAs have similar m/z values and exist as long as DFA III is present, which has been certified by GC-MS.[7] The ability of TOF to identify nontarget compounds also guarantees

DOI: 10.1021/acs.jafc.5b01410
J. Agric. Food Chem. 2015, 63, 6614−6623

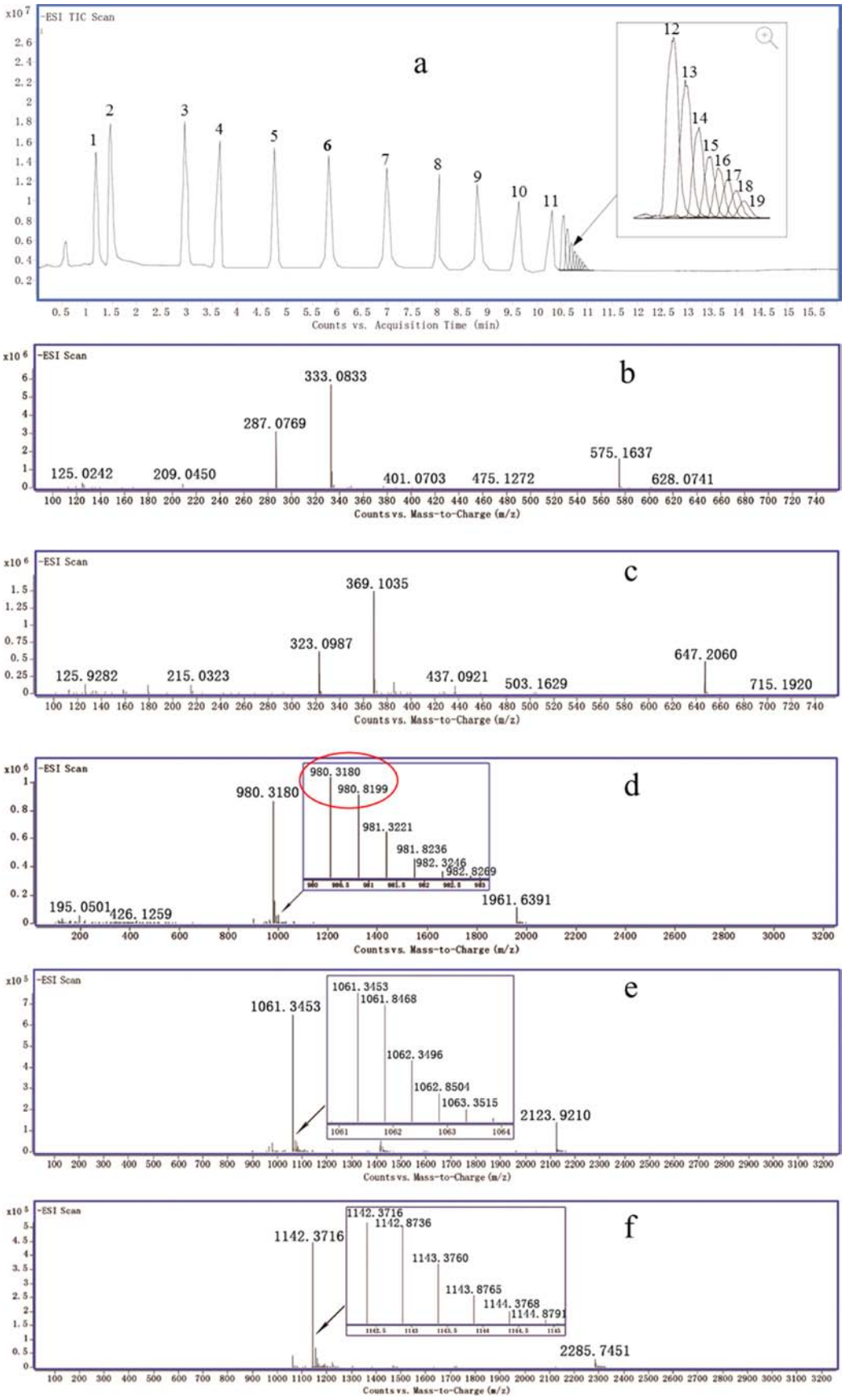

Figure 3. continued

DOI: 10.1021/acs.jafc.5b01410
J. Agric. Food Chem. 2015, 63, 6614−6623

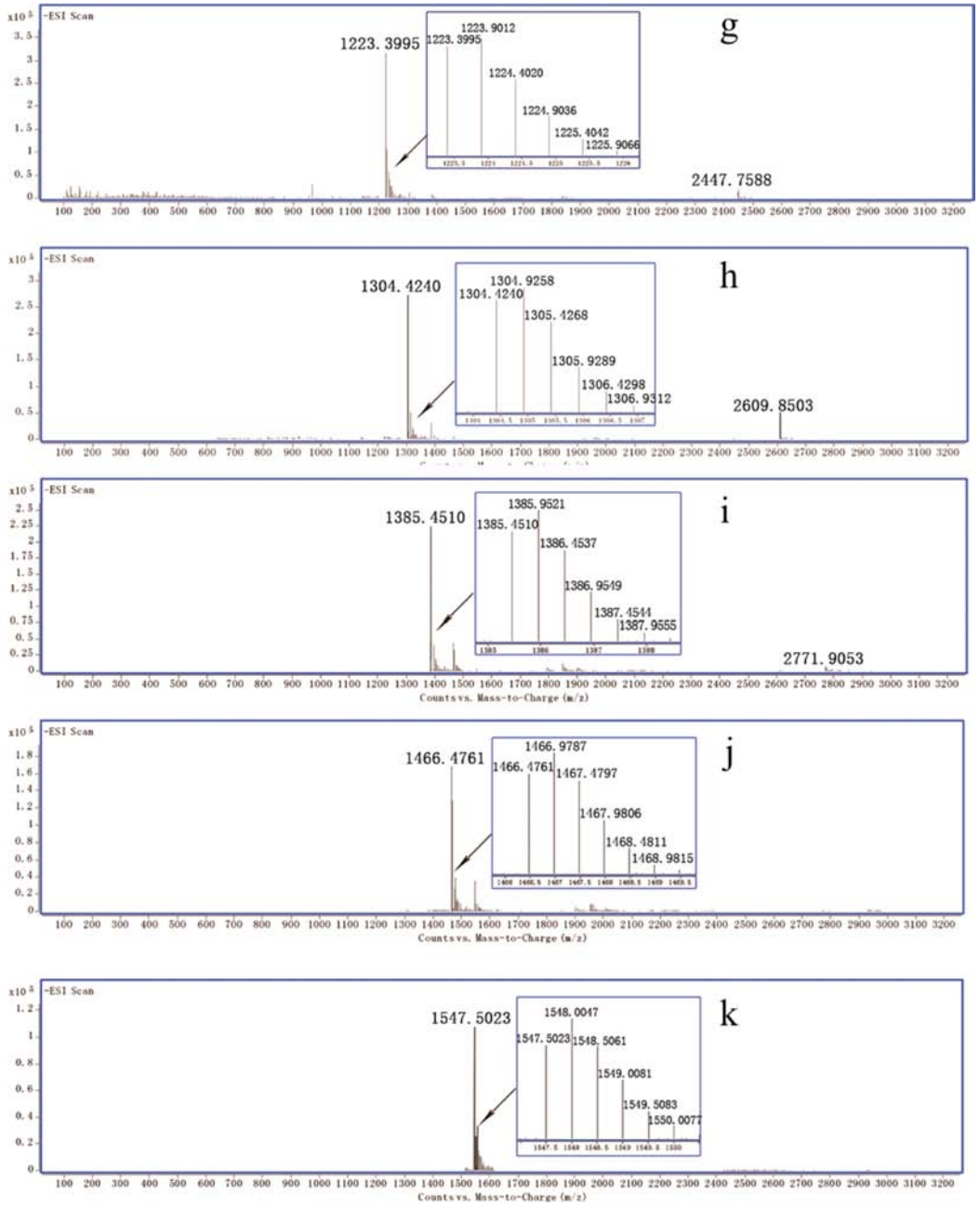

Figure 3. Chromatograms of standards (a), and mass spectra of 2-acetylfuran-3-glucopyranoside (AFGP) (b), difructose anhydride III (DFA III) (c), and polysaccharides (DP 12−19) (d−k). Peaks 1−19 in panel a are 2-acetylfuran-3-glucopyranoside (AFGP), difructose anhydride III (DFA III), oligosaccharides (DP 3−11), and polysaccharides (DP 12−19). The peaks highlighted are two isotope peaks.

the feasibility of DFA III in representing all DFAs. Similar to AFGP, DFA III was deprotonated, resulting in singly charged ions $[M - H]^-$ and $[2M - H]^-$ with m/z values of 323.0984 and 647.204, respectively; $[M + COOH]^-$ with an m/z value of 369.1033 was another characteristic ion of DFA III. Polysaccharides with DP 12−19 were chosen as markers because oligosaccharides with DPs between 3 and 6 have been detected in pure honey.[6,44] In our experiments, the detection of oligosaccharides (DP 7−11) in some honey samples was affected. On the other hand, Megherbiet al.[5] have successfully used polysaccharides (DP > 11) as markers of honey adulteration. The chromatographic profile of polysaccharides (DP 12−19) is shown in Figure 3a. Polysaccharides exist in the form of multicharged ions. In our experiments, polysaccharides (DP 12−19) were deprotonated, forming doubly charged ions $[M - 2H]^{2-}$ and $[M - H]^-$ detected in polysaccharides with DPs between 12 and 17. Isotope peaks were observed when polysaccharides (DP 12−19) were extracted. In the extraction of polysaccharides with DP 12, mass values of 980.3180 and 980.8199 were obtained (Figure 3d). The deviation of 0.5 confirmed the doubly charged form of the polysaccharides ($[M - 2H]^{2-}$). Polysaccharides with DP 13−19 had the same behavior as polysaccharides with DP 12. Polysaccharides with DP 20−25 can be detected using this method with less sensitivity. Therefore, they cannot be used as markers.

Analyses of Sugar Syrups and Honey Samples. The chromatographic profiles and mass spectra of standards, which include AFGP, DFA III, and polysaccharides (DP 12−19), are

DOI: 10.1021/acs.jafc.5b01410
J. Agric. Food Chem. 2015, 63, 6614−6623

Table 1. Characteristics of Sugar Syrup Markers

target compound	molecular formula	retention time (min)	mass	m/z values of characteristic ions	allowance error (ppm)
2-acetylfuran-3-glucopyranoside (AFGP)	$C_{12}H_{16}O_8$	1.188	288.0845	287.0772 $[M - H]^-$, 575.1618 $[2M - H]^-$, 333.0822 $[M + HCOO]^-$	<5
difructose anhydride III (DFA III)[a]	$C_{12}H_{20}O_{10}$	1.522	324.1056	323.0984 $[M - H]^-$, 647.204 $[2M - H]^-$, 369.1033 $[M + HCOO]^-$	<5
maltododecaose (DP 12)	$C_{72}H_{122}O_{61}$	10.523	1962.6444	1961.6372 $[M - H]^-$, 980.3149 $[M - 2H]^{2-}$	<5
maltotridecaose (DP 13)	$C_{78}H_{132}O_{66}$	10.596	2124.6973	2123.69 $[M - H]^-$, 1061.3414 $[M - 2H]^{2-}$	<5
maltotetradecaose (DP 14)	$C_{84}H_{142}O_{71}$	10.664	2286.7501	2285.7428 $[M - H]^-$, 1142.3678 $[M - 2H]^{2-}$	<5
maltopentadecaose (DP 15)	$C_{90}H_{152}O_{76}$	10.738	2448.8029	2447.7956 $[M - H]^-$, 1223.3942 $[M - 2H]^{2-}$	<5
maltohexadecaose (DP 16)	$C_{96}H_{162}O_{81}$	10.802	2610.8557	2609.8485 $[M - H]^-$, 1304.4206 $[M - 2H]^{2-}$	<5
maltoheptadecaose (DP 17)	$C_{102}H_{172}O_{86}$	10.875	2772.9086	2771.9013 $[M - H]^-$, 1385.447 $[M - 2H]^{2-}$	<5
maltooctadecaose (DP 18)	$C_{108}H_{182}O_{91}$	10.946	2934.9614	1466.4734 $[M - 2H]^{2-}$	<5
maltononadecaose (DP 19)	$C_{114}H_{192}O_{96}$	11.012	3097.0142	1547.4998 $[M - 2H]^{2-}$	<5

[a]CAS Registry No. 81129-73-9.

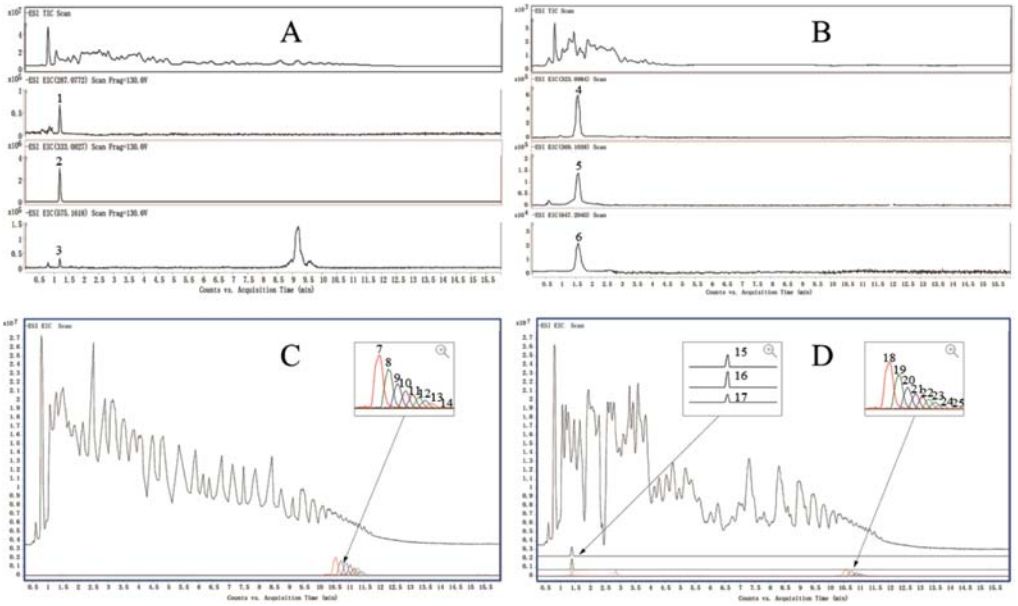

Figure 4. Chromatograms of rice syrup (A), inverted syrup from sugar beet (B), corn syrup (C), and high-fructose corn syrup (D). Peaks 1, 2, and 3 correspond to $[M - H]^-$, $[M + COOH]^-$, and $[2M - H]^-$ of 2-acetylfuran-3-glucopyranoside (AFGP), respectively; peaks 4–6 and 15–17 correspond to $[M - H]^-$, $[M + COOH]^-$, and $[2M - H]^-$ of DFAs; peaks 7–14 and 18–25 correspond to $[M - 2H]^{2-}$ of polysaccharides (DP 12–19).

shown in Figure 3. Peaks 1 and 2 corresponded to AFGP and DFA III, respectively (Figure 3a). Peaks 3–11 were oligosaccharides with DP 3–11, and peaks 12–19 were polysaccharides with DP 12–19. The mass spectrogram of AFGP is shown in Figure 3b; 287.0769, 333.0833, and 575.1637 were the m/z values of $[M - H]^-$, $[M + COOH]^-$, and $[2M - H]^-$, respectively. Figure 3c shows the mass spectrogram of DFA III; 323.0987, 369.1035, and 647.2060 were the m/z values of $[M - H]^-$, $[M + COOH]^-$, and $[2M - H]^-$, respectively. Panels d–k of Figure 3 show the mass spectrograms of polysaccharides with DP 12–19; 980.3180 corresponded to $[M - 2H]^{2-}$ and 1961.6391 corresponded to $[M - H]^-$. Polysaccharides with DP 13–19 have the same characteristic ions as polysaccharides with DP 12, with the exception of $[M - H]^-$, which cannot be detected in the mass spectrograms of polysaccharides with DP 18 or 19.

Sugar syrups including RS, IB, IC, CS, and HFCS were analyzed by UHPLC/Q-TOF-MS. One representative sample was selected from each type of syrup for the chromatographic profile (Figure 4). Figure 4A shows the chromatogram of RS. Peaks 1–3 were identified as characteristic ions of AFGP, the marker of RS. These three peaks correspond to $[M - H]^-$, $[M + COOH]^-$, and $[2M - H]^-$ based on mass spectra. Figure 4B shows the chromatogram of IB. Peaks 4–6 correspond to DFAs, markers of IS. On the basis of mass spectra, the three peaks (retention time: 1.522 min) correspond to $[M - H]^-$, $[M + COOH]^-$, and $[2M - H]^-$. The chromatogram of IC was similar to that of IB. Figure 4C shows the chromatogram of CS. Peaks 7–14 were identified as $[M - 2H]^{2-}$ of polysaccharides with DP 12–19 on the basis of the retention time and mass spectra of the standards. The chromatogram of HFCS is shown in Figure 4D. Peaks 15–17 correspond to $[M - H]^-$, $[M + COOH]^-$, and $[2M - H]^-$ of DFAs based on the DFA III standard. Peaks 18–25 were $[M - 2H]^{2-}$ of polysaccharides with DP 12–19. Therefore, AFGP appeared in RS and polysaccharides with DP 12–19 were detected in RS-42 and RS-55; DFAs were present in IS (from sugar cane and beet) and HFCS (HFCS-42, HFCS-55, and HFCS-90). Polysaccharides with DP 12–19 were present in CS and HFCS except in HFCS-90 because of its high degree of hydrolysis.

DOI: 10.1021/acs.jafc.5b01410
J. Agric. Food Chem. 2015, 63, 6614–6623

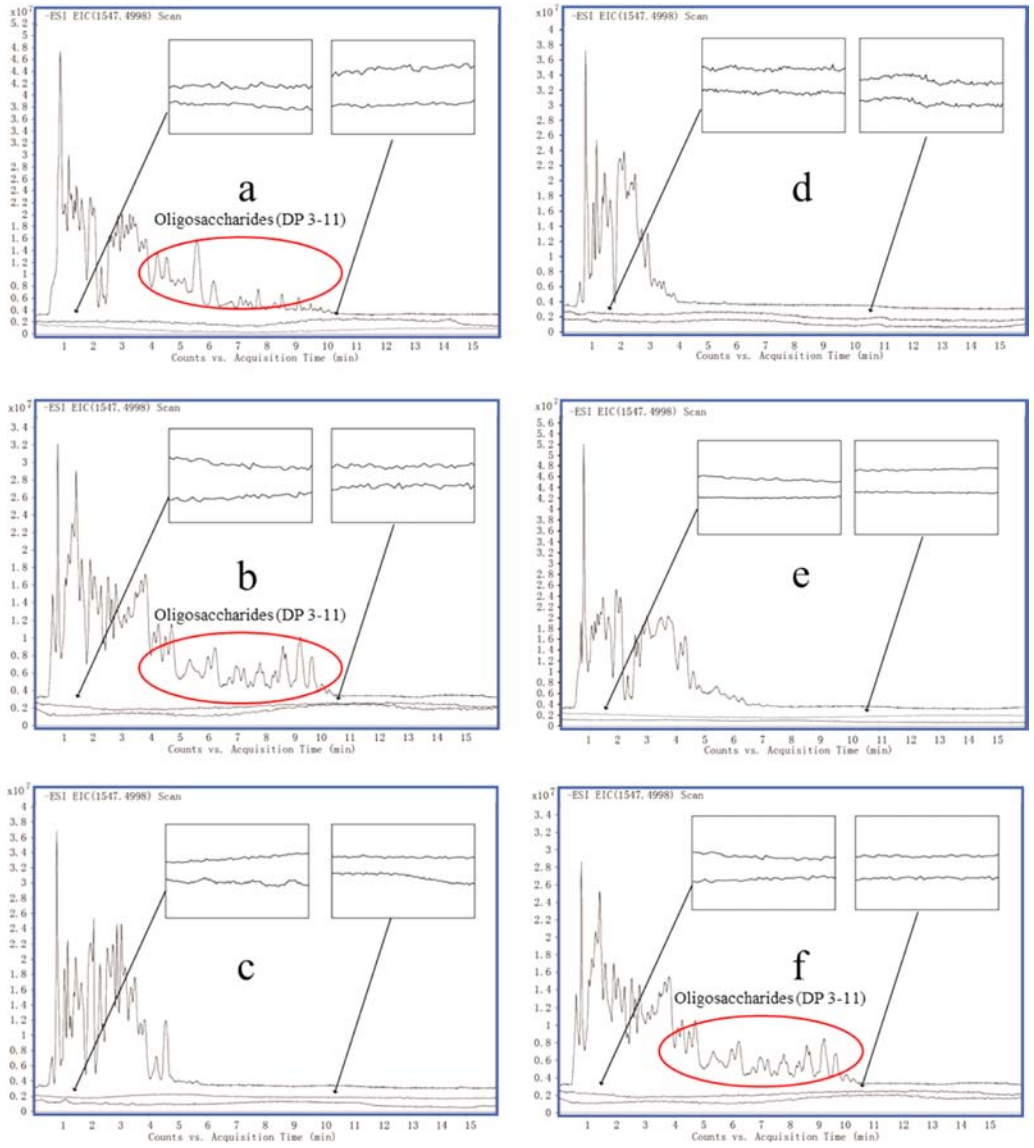

Figure 5. Chromatograms of linden honey (a), manuka honey (b), rape honey (c), jujube honey (d), acacia honey (e), and multifloral honey (f). The highlighted regions correspond to oligosaccharides (DP 3−11).

In addition, 120 pure honey samples were analyzed. The chromatographic profiles of six representative pure honey samples are shown in Figure 5. AFGP, DFAs, and polysaccharides (DP 12−19) were absent in these samples. However, oligosaccharides (DP 3−6) were detected in some honey samples, including linden honey (Figure 5a), manuka honey (Figure 5b), and multifloral honey (Figure 5f), in agreement with previous study findings.[6,44]

Analysis of Spiked Honey Samples. To assess the validity of the method, six pure honey samples including one jujube honey (J 1), one acacia honey (A 1), one rape honey (R 1), one linden honey (L 1), one manuka honey (M 1), and one multifloral honey (MF 1) were selected as representative samples. Mixed syrups composed of equal amounts of CS, RS (RS-42, RS-55, and RS-90), HFCS (HFCS-42, HFCS-55, and HFCS-90), and IS (from sugar cane and beet) were prepared. The amount of marker in each of the individual syrups was low. These six honey samples were spiked with different percentages (10, 20, or 30%, w/w) of the mixed syrups and analyzed by our developed method. The chromatographic profile of rape honey with 10% adulterants is shown in Figure 6. There were characteristic peaks in the chromatographic profile of spiked rape honey: peaks 1−4 correspond to $[M - H]^-$ and $[M + COOH]^-$ of AFGP and DFAs. The amount of dipolymer $[2M - H]^-$ was too low to be detected. Peaks 5−12 were identified as polysaccharides with DP 12−19 ($[M - 2H]^{2-}$). The signal-to-noise ratio of the peak with the lowest response (maltononadecaose, DP 19) was 27:1, which confirmed the feasibility, simplicity, and validity of our developed method. It is noteworthy that the presence of <10% adulterants in honey is nonsignificant.

Analyses of Market Honey Samples. In this study, 200 random honey samples from markets were analyzed. The results were compared with the database to assess whether the honey samples had been adulterated. AFGP was detected in 16 of 200 market honey samples; therefore, 16 samples had been adulterated with RS. DFA III was detected in 28 of 200 market honey samples; therefore, 28 samples had been adulterated with HFCS or IS. Polysaccharides (DP 12−19) were detected in 18 of 200 market honey samples; therefore, 18 samples had

DOI: 10.1021/acs.jafc.5b01410
J. Agric. Food Chem. 2015, 63, 6614−6623

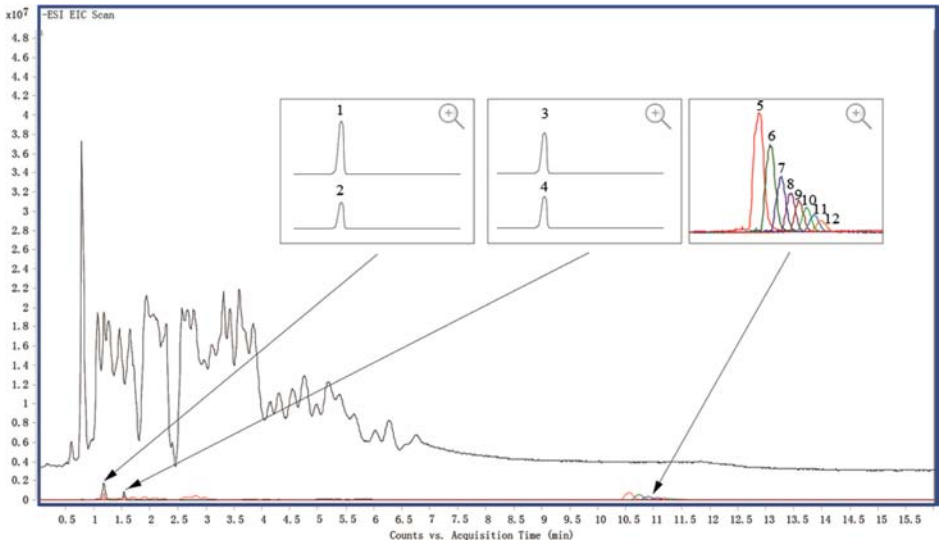

Figure 6. Chromatogram of rape honey with 10% mixed syrups. Peaks 1 and 2 correspond to $[M - H]^-$ and $[M + COOH]^-$ of 2-acetylfuran-3-glucopyranoside (AFGP), respectively; peaks 3 and 4 correspond to $[M - H]^-$ and $[M + COOH]^-$ of DFAs, respectively; and peaks 5−12 correspond to $[M - 2H]^{2-}$of polysaccharides (DP 12−19).

Table 2. Detection of 10 Positive Honey Samples by UHPLC/Q-TOF-MS and Other Traditional Methods

	detection method[a]					
sample	UHPLC/Q-TOF-MS	SCIRA[8,17,18]	TLC[19]	HPAEC-PAD[5,6]	GC-MS for DFAs[7]	HPLC-DAD for 2-acetylfuran-3-glucopyranoside[11]
Sam9	+	−	−	−	−	+
Sam18	+	−	−	−	−	+
Sam37	+	+	+	+	+	−
Sam49	+	+	+	+	+	−
Sam103	+	+	+	+	+	−
Sam129	+	+	+	+	+	−
Sam147	+	+	−	−	+	−
Sam189	+	+	−	−	+	−
Sam192	+	−	−	−	+	−
Sam196	+	+	+	+	−	−

[a]+, detected; −, not detected.

been adulterated with HFCS, CS, or RS. More than one marker was present in the adulterated samples, suggesting that the honeys had been adulterated with more than one sugar syrup. All adulterated honeys were marked as positive samples. The proportion of adulterated honeys ranged from 50 to 100% based on the peak areas corresponding to 10% adulterated honey.

Comparisons with Traditional Analytical Methods. To validate the developed method, 10 positive samples were evaluated by traditional analytical methods (Table 2). AFGPs in positive samples 9 and 18 were successfully detected by HPLC-DAD, suggesting that these two honey samples were adulterated with RS. Positive samples 37, 49, 103, and 129 were successfully detected by SCIRA and GC-MS, suggesting that the syrups used as adulterants were produced from C_4 plants and contained DFAs. Additionally, oligosaccharides and polysaccharides were detected by TLC and HPAEC-PAD in these four samples, suggesting the adulteration with HFCS. Adulterants produced from C_4 plants and DFAs in positive samples 147 and 189 were detected by SCIRA and GC-MS, respectively, suggesting they were adulterated with IS from sugar cane. Positive sample 192 was detected only by GC-MS, which suggested that the sample contained DFAs and had been adulterated with IS from sugar beet. Positive sample 196 was successfully detected by SCIRA, suggesting that the syrups were produced from C_4 plants. Oligosaccharides and polysaccharides were also detected in positive sample 196 by TLC and HPAEC-PAD, indicating adulteration with CS. All positive samples were successfully detected by UHPLC/Q-TOF-MS, revealing that our developed method can simultaneously detect multiclass sugar syrups. Therefore, UHPLC/Q-TOF-MS is a feasible, effective, simple, and rapid detection method of multiclass syrups.

Bee-Feeding Experiment. A bee-feeding experiment in a Ping Hu apiary was performed to evaluate the effects of supplementary sugar syrups on honey quality. Sugar syrups can be used to feed honeybees during the winter, when honeybees produce hardly any honey. Even though HFCS is commonly used by beekeepers, scientists have suggested that all syrups should be tried with bee colonies.[12] Cordella et al.[15] reported that the consequences of overfeeding honeybees with syrups were similar to directly adding sugar syrups to honey. HFCS can affect the quality of the resulting honey.[15] Furthermore, some honeybees die following the consumption of HFCS because of its high levels of hydroxymethylfurfural.[45] Therefore, the resulting honey produced by honeybees for the first time after being fed syrup are not allowed to enter the market because it is considered as another form of honey adulteration.

DOI: 10.1021/acs.jafc.5b01410
J. Agric. Food Chem. 2015, 63, 6614−6623

However, some of these adulterated honeys inevitably enter the market. Therefore, the detection of indirect honey adulteration is important; however, few detection methods have been successfully applied in this field. Guler et al.[13] reported that official analytical methods (e.g., AOAC 978.17, 1995; AOAC 991.41, 1995; AOAC 998.12, 2005) and SCIRA could not effectively detect indirect adulteration of honey. In this study, the results of a simple bee-feeding experiment revealed that our developed UHPLC/Q-TOF-MS method can effectively detect residual syrups in honeys produced by honeybees after being fed syrups for 3 days. The amounts of syrup markers in the resulting honeys were >60% based on peak area variations.

In conclusion, a simple, rapid, and effective method was developed to assess honey adulteration with multiclass sugar syrups. A syrup marker database was generated. Our developed method is simple, rapid, and less time-consuming compared to other published methods. Additionally, UHPLC/Q-TOF-MS allows the simultaneous detection of several sugar syrups. The validity and applicability of the proposed method have been confirmed by comparisons with traditional methods. UHPLC/Q-TOF-MS has broad applications in honey acquisition and honey quality control.

AUTHOR INFORMATION

Corresponding Authors

*(X.X.) Phone/fax: +86 1062594643. E-mail: xuebqsitc@126.com.

*(W.C.) E-mail: caowei@nwu,edu.cn.

Funding

This study was supported by the National Natural Science Foundation of China (No. 31472155), a special fund (NYCYTX-43), the Agricultural Science and Technology Innovation Program (CAAS-ASTIP-2015-IAR) from the Apicultural Industry Technology System, and the National Natural Science Foundation of China (No. 31272510).

Notes

The authors declare no competing financial interest.

ACKNOWLEDGMENTS

We are grateful to Professor Jianzhong Li from Agilent (Beijing) for his assistance in structure identification and database development.

ABBREVIATIONS USED

UHPLC/Q-TOF-MS, ultrahigh-performance liquid chromatography−quadrupole time-of-flight mass spectrometry; PHPLC, preparative high-performance liquid chromatography; SCIRA, stable carbon isotopic ratio analysis; TLC, thin-layer chromatography; HPAEC-PAD, high-performance anion exchange chromatography with pulsed amperometric detection; GC-MS, gas chromatography−mass spectrometry; AFGP, 2-acetylfuran-3-glucopyranoside; DFA, difructose anhydride; CS, corn syrups; HFCS, high-fructose corn syrups; IS, inverted syrups; RS, rice syrup; IB, inverted syrups from sugar beet; IC, inverted syrups from sugar cane

REFERENCES

(1) Cimpoiu, C.; Hosu, A.; Miclaus, V.; Puscas, A. Determination of the floral origin of some Romanian honeys on the basis of physical and biochemical properties. *Spectrochim. Acta, Part A* **2013**, *100*, 149−154.

(2) Cheng, N.; Du, B.; Wang, Y.; Gao, H.; Cao, W.; Zheng, J. B.; Feng, F. Antioxidant properties of jujube honey and its protective effects against chronic alcohol-induced liver damage in mice. *Food Funct.* **2014**, *5*, 900−908.

(3) Isidorov, V. A.; Bagan, R.; Bakier, S.; Swiecicka, I. Chemical composition and antimicrobial activity of Polish herb honeys. *Food Chem.* **2015**, *171*, 84−88.

(4) Gheldof, N.; Engeseth, N. J. Antioxidant capacity of honeys from various floral sources based on the determination of oxygen radical absorbance capacity and inhibition of vitro lipoprotein oxidation in human serum samples. *J. Agric. Food Chem.* **2002**, *50*, 3050−3055.

(5) Megherbi, M.; Herbreteau, B.; Faure, R.; Salvador, A. Polysaccharides as a marker for detection of corn sugarsyrup addition in honey. *J. Agric. Food Chem.* **2009**, *57*, 2105−2111.

(6) Morales, V.; Corzo, N.; Sanz, M. L. HPAEC-PAD oligosaccharide analysis to detect adulterations of honey with sugar syrups. *Food Chem.* **2008**, *107*, 922−928.

(7) Ruiz-Matute, A. I.; Soria, A. C.; Martínez-Castro, I.; Sanz, M. L. A new methodology based on GC−MS to detect honey adulteration with commercial syrups. *J. Agric. Food Chem.* **2007**, *55*, 7264−7269.

(8) Cinar, S. B.; Eksi, A.; Coskun, I. Carbon isotope ratio ($^{13}C/^{12}C$) of pine honey and detection of HFCS adulteration. *Food Chem.* **2014**, *157*, 10−13.

(9) Paradkar, M. M.; Irudayaraj, J. Discrimination and classification of beet and cane inverts in honey by FT-Raman spectroscopy. *Food Chem.* **2001**, *76*, 231−239.

(10) Sivakesava, S.; Irudayaraj, J. Detection of inverted beet sugar adulteration of honey by FTIR spectroscopy. *J. Sci. Food Agric.* **2001**, *81*, 683−690.

(11) Xue, X. F.; Wang, Q.; Li, Y.; Wu, L. M.; Chen, L. Z.; Zhao, J.; Liu, F. M. 2-Acetylfuran-3-glucopyranoside as a novel marker for the detection of honey adulterated with rice syrup. *J. Agric. Food Chem.* **2013**, *61*, 7488−7493.

(12) Ruiz-Matute, A. I.; Weiss, M.; Sammataro, D.; Finely, J.; Sanz, M. L. Carbohydrate composition of high-fructose corn syrups (HFCS) used for bee feeding: effect on honey composition. *J. Agric. Food Chem.* **2010**, *58*, 7317−7322.

(13) Guler, A.; Kocaokutgen, H.; Garipoglu, A. V.; Onder, H.; Ekinci, D.; Biyik, S. Detection of adulterated honey produced by honeybee (*Apis mellifera* L.) colonies fed with different levels of commercial industrial sugar (C_3 and C_4 plants) syrups by the carbon isotope ratio analysis. *Food Chem.* **2014**, *155*, 155−160.

(14) Wheeler, M. M.; Robinson, G. E. Diet-dependent gene expression in honey bees: honey vs. sucrose or high fructose corn syrup. *Sci. Rep.* **2014**, *4*, 5726.

(15) Cordella, C.; Militão, J. S. L. T.; Clément, M. C.; Drajnudel, P.; Cabrol-Bass, D. Detection and quantification of honey adulteration via direct incorporation of sugar syrups or bee-feeding: preliminary study using high-performance anion exchange chromatography with pulsed amperometric detection (HPAEC-PAD) and chemometrics. *Anal. Chim. Acta* **2005**, *531*, 239−248.

(16) Cotte, J. F.; Casabianca, H.; Chardon, S.; Lheritier, J.; Grenier-Loustalot, M. F. Application of carbohydrate analysis to verify honey authenticity. *J. Chromatogr., A* **2003**, *1021*, 145−155.

(17) Padovan, G. Detection of adulteration of commercial honey samples by the $^{13}C/^{12}C$ isotopic ratio. *Food Chem.* **2003**, *82*, 633−636.

(18) Tosun, M. Detection of adulteration in honey samples added various sugar syrups with $^{13}C/^{12}C$ isotope ratio analysis method. *Food Chem.* **2013**, *138*, 1629−1632.

(19) Kushnir, I. Sensitive thin-layer chromatographic detection of high fructose corn syrup and other adulterants in honey. *J. Assoc. Off. Anal. Chem.* **1979**, *62* (4), 917−920.

(20) Puscas, A.; Hosu, A.; Cimpoiu, C. Application of a newly developed and validated high-performance thin-layer chromatographic method to control honey adulteration. *J. Chromatogr., A* **2013**, *1272*, 132−135.

(21) Wang, J. M.; Xue, X. F.; Du, X. J.; Cheng, N.; Chen, L. Z.; Zhao, J.; Zheng, J. B.; Cao, W. Identification of acacia honey adulteration with rape honey using liquid chromatography−electrochemical detection and chemometrics. *Food Anal. Methods* **2014**, *7*, 2003−2012.

DOI: 10.1021/acs.jafc.5b01410
J. Agric. Food Chem. 2015, 63, 6614−6623

(22) Wang, S. Q.; Guo, Q. L.; Wang, L. L.; Lin, L.; Shi, H. L.; Cao, H.; Cao, B. S. Detection of honey adulteration with starch syrup by high performance liquid chromatography. *Food Chem.* **2015**, *172*, 669−674.
(23) Cabañero, A. I.; Recio, J. L.; Rupérez, M. Liquid chromatography coupled to isotope ratio mass spectrometry: a new perspective on honey adulteration detection. *J. Agric. Food Chem.* **2006**, *54*, 9719−9727.
(24) Bertelli, D.; Lolli, M.; Papotti, G.; Bortolotti, L.; Serra, G.; Plessi, M. Detection of honey adulteration by sugar syrups using one-dimensional and two-dimensional high-resolution nuclear magnetic resonance. *J. Agric. Food Chem.* **2010**, *58*, 8495−8501.
(25) De Ribeiro, R. O. R.; Mársico, E. T.; Da Carneiro, C. S.; Monteiro, M. L. G.; Júnior, C. C.; De Jesus, E. F. O. Detection of honey adulteration of high fructose corn syrup by Low field nuclear magnetic resonance (LF ^{1}H NMR). *J. Food Eng.* **2014**, *135*, 39−43.
(26) Kelly, J. F. D.; Downey, G.; Fouratier, V. Initial study of honey adulteration by sugar solutions using midinfrared (MIR) spectroscopy and chemometrics. *J. Agric. Food Chem.* **2004**, *52*, 33−39.
(27) Sobhanzadeh, E.; Bakar, N. K. A.; Abas, M. R. B.; Nemati, K. Low temperature followed by matrix solid-phase dispersion-sonication procedure for the determination of multiclass pesticides in palm oil using LC-TOF-MS. *J. Hazard. Mater.* **2011**, *186*, 1308−1313.
(28) Sivaperumal, P.; Anand, P.; Riddhi, L. Rapid determination of pesticide residues in fruits and vegetables, using ultra-high-performance liquid chromatography/time-of-flight mass spectrometry. *Food Chem.* **2015**, *168*, 356−365.
(29) Wang, J.; Sporns, P. MALDI-TOF MS quantification of coccidiostats in poultry feeds. *J. Agric. Food Chem.* **2000**, *48*, 2807−2811.
(30) Boix, C.; Ibanez, M.; Sancho, J. V.; Leon, N.; Yusa, V.; Hernandez, F. Qualitative screening of 116 veterinary drugs in feed by liquid chromatography-high resolution mass spectrometry: potential application to quantitative analysis. *Food Chem.* **2014**, *160*, 313−320.
(31) López-Cobo, A.; Gómez-Caravaca, A. M.; Cerretani, L.; Segura-Carretero, A.; Fernández-Gutiérrez, A. Distribution of phenolic compounds and other polar compounds in the tuber of *Solanum tuberosum* L. by HPLC-DAD-q-TOF and study of their antioxidant activity. *J. Food Compos. Anal.* **2014**, *36*, 1−11.
(32) Collins, T. S.; Zweigenbaum, J.; Ebeler, S. E. Profiling of nonvolatiles in whiskeys using ultra high pressure liquid chromatography quadrupole time-of-flight mass spectrometry (UHPLC-QTOF MS). *Food Chem.* **2014**, *163*, 186−196.
(33) Wang, J.; Yue, Y. D.; Tang, F.; Sun, J. Screening and analysis of the potential bioactive components in rabbit plasma after oral administration of hot-water extracts from leaves of *Bambusa textilis* McClure. *Molecules* **2012**, *17*, 8872−8885.
(34) Lv, D.; Cao, Y.; Dong, X.; Chen, X. F.; Lou, Z. Y.; Chai, Y. F. Analysis and pharmacokinetic study of curdione in Rhizoma Curcumae by UPLC/QTOF/MS. *Biomed. Chromatogr.* **2014**, *28*, 782−787.
(35) Sirtori, C.; Aguera, A.; Carra, I.; Sanchez Perez, J. A. Identification and monitoring of thiabendazole transformation products in water during Fenton degradation by LC-QTOF-MS. *Anal. Bioanal. Chem.* **2014**, *406*, 5323−5337.
(36) Wang, H. X.; Zhou, Y.; Jiang, Q. W. Simultaneous screening of estrogens, progestogens, and phenols and their metabolites in potable water and river water by ultra-performance liquid chromatography coupled with quadrupole time-of-flight mass spectrometry. *Microchem. J.* **2012**, *100*, 83−94.
(37) Swallow, K. W.; Low, N. H. Analysis and quantitation of the carbohydrates in honey using HPLC. *J. Agric. Food Chem.* **1990**, *38*, 1828−1832.
(38) Ratsimba, V.; Fernández, J. M. G.; Defaye, J.; Nigay, H.; Voilley, A. Qualitative and quantitative evaluation of mono- and disaccharides in D-fructose, D-glucose and sucrose caramels by gas-liquid chromatography-mass spectrometry di-D-fructose dianhydrides as tracers of caramel authenticity. *J. Chromatogr., A* **1999**, *844*, 283−293.
(39) Saito, K.; Tomita, F. Difructose anhydrides: their mass-production and physiological functions. *Biosci., Biotechnol., Biochem.* **2000**, *64* (7), 1321−1327.
(40) Manley-Harris, M.; Richards, G. N. Di-D-fructose dianhydrides and related oligomers from thermal treatments of inulin and sucrose. *Carbohydr. Res.* **1996**, *287*, 183−202.
(41) Li, J.; Hu, D. J.; Zong, W. R.; Lv, G. P.; Zhao, J.; Li, S. P. Determination of inulin-type fructooligosaccharides in edible plants by high-performance liquid chromatography with charged aerosol detector. *J. Agric. Food Chem.* **2014**, *62*, 7707−7713.
(42) Westereng, B.; Agger, J. W.; Horn, S. J.; Vaaje-Kolstad, G.; Aachmann, F. L.; Stenstrom, Y. H.; Eijsink, V. G. Efficient separation of oxidized cello-oligosaccharides generated by cellulose degrading lytic polysaccharide monooxygenases. *J. Chromatogr., A* **2013**, *1271*, 144−152.
(43) Gómez-Pérez, M. L.; Plaza-Bolaños, P.; Romero-González, R.; Martínez-Vidal, J. L.; Garrido-Frenich, A. Comprehensive qualitative and quantitative determination of pesticides and veterinary drugs in honey using liquid chromatography-Orbitrap high resolution mass spectrometry. *J. Chromatogr., A* **2012**, *1248*, 130−138.
(44) Morales, V.; Sanz, M. L.; Olano, A.; Corzo, N. Rapid separation on activated charcoal of high oligosaccharides in honey. *Chromatographia* **2006**, *64*, 233−238.
(45) LeBlanc, B. W.; Eggleston, G.; Sammataro, D.; Cornett, C.; Dufault, R.; Deeby, T.; St. Cyr, E. Formation of hydroxymethylfurfural in domestic high-fructose corn syrup and its toxicity to the honey bee (*Apis mellifera*). *J. Agric. Food Chem.* **2009**, *57*, 7369−7376.

DOI: 10.1021/acs.jafc.5b01410
J. Agric. Food Chem. 2015, 63, 6614−6623

diffusion have been reported for a range of applications.[11,22,25−27] Furthermore, a number of researchers have studied the interactions between various solutes in systems based on casein micelles: small polyphenol compounds,[28−31] positively charged proteins such as lactoferrin and lysozyme,[32,33] and polysaccharides in mixed systems.[34,35] However, the specific interactions between casein micelles, which are negatively charged at neutral pH, and other macromolecules, in particular, negatively charged proteins, have not been studied in detail. Moreover, the influence of these interactions on the diffusion of solutes as a function of their physicochemical characteristics has rarely been explored in casein systems.[18] In a previous work, we have shown that the diffusion of rigid and negatively charged proteins (α-lactalbumin (α-LA), β-lactoglobulin (β-LG), and bovine serum albumin (BSA)) was hindered more than that of flexible and neutral dextrans with similar hydrodynamic radius when diffusing through a model cheese; in this case, the cheese had a casein concentration below close-packing (estimated as 178 g/L).[18] It was concluded that solute−matrix interactions had hindered the diffusing proteins. However, the nature of these interactions was not clearly identified and was related to the molecule flexibility and/or its charge.

The question thus arises of how the diffusion of solutes is specifically affected by their physicochemical characteristics in casein systems. The study carried out considered the effect of the flexibility and charge of solutes on diffusion and subsequently evaluated the nature of the solute−matrix interactions implied. Diffusion coefficients of a selected group of solutes were measured in casein systems. The solutes studied were dextrans (neutral or charged, flexible solutes), proteins (charged, rigid solutes), and peptides (charged, flexible solutes). The casein systems presented different microstructures (suspension versus gel), but their casein concentration and water activity were kept constant. A casein concentration lower than that for the close-packing of the micelles was chosen to specifically highlight solute−matrix interactions. The casein gels had different pH values (5.2 and 6.6), which enabled a modification in the net charge of the diffusing proteins to explore the effect of the solute charge on diffusion. The technique of fluorescence recovery after photobleaching (FRAP) was chosen because it allows a nondestructive and fast measurement of the solute diffusion coefficient. This technique has been recently successfully applied to study diffusion properties of solutes in casein systems.[17,18] Furthermore, it enables an estimation of the proportion of the solute present that is immobile (i.e., the fraction of molecules that are locked in place and prevented from diffusing), which can provide relevant information about solute−matrix interactions.[36−38]

MATERIALS AND METHODS

FITC-Labeled Solutes. *Dextrans and Poly-L-lysines.* Neutral fluorescein isothiocyanate (FITC)-dextrans of five different average molecular weights (M_w = 4, 10, 20, 40, and 70 kDa, denoted FITC-D4, FITC-D10, FITC-D20, FITC-D40, and FITC-D70, respectively) were used in this study (Sigma-Aldrich, St. Louis, MO, USA). Product specification declared that all of the FITC-dextrans contained between 0.003 and 0.02 mol of FITC per glucose unit. One anionic FITC-dextran with an average molecular weight of 70 kDa was purchased from Molecular Probes (Eugene, OR, USA). Product specification in this case stipulated that the anionic FITC-dextran contained from 0.01 to 0.02 mol of FITC per glucose unit. Two FITC-labeled poly-L-lysines (FITC-PLLs) with molecular weight ranges of 15−30 and 30−70 kDa were purchased from Sigma-Aldrich. According to the supplier, the average molecular weights of the FITC-PLLs of 15−30 and 30−70 kDa were 23 and 32 kDa, respectively, and will be denoted FITC-PLL23 and FITC-PLL32. Both FITC-PLLs contained between 0.003 and 0.1 mol of FITC per lysine monomer.

Globular Proteins. The studied set of solutes was completed with three globular proteins. The first was FITC-labeled bovine serum albumin (denoted FITC-BSA) (Sigma-Aldrich). The second and third globular proteins were α-LA and hen egg white lysozyme (LYS) (Liot, Pleumartin, France), which were labeled separately using FITC (Sigma-Aldrich) as previously reported.[18] The procedure was as follows. Proteins were first dissolved at a concentration of 0.27 mM in a 10 mM phosphate buffer solution (pH 8.0). They were covalently labeled with FITC by mixing 1.8 mL of a FITC solution (38 mM FITC) with 100 mL of the protein solution for 90 min at room temperature and protected from light. The solutions of FITC-α-LA and FITC-LYS were then dialyzed with cellulose membranes with a nominal cutoff of 6−8 kDa (Spectrum Laboratories, Canada) against 10 mM Tris/0.6 M NaCl buffer (pH 7.33) for 2 days to eliminate any remaining free FITC. A final dialysis was made by using deionized water. The two solutions from the α-LA and LYS proteins were lyophilized, and labeling efficiencies were determined by mass spectrometry analyses. Following this procedure, the α-LA and LYS proteins were mainly monolabeled (10 and 43%, respectively) with FITC. The mass spectrometry analyses were carried out on a hybrid quadrupole time-of-flight (Q-TOF) mass spectrometer QStar XL (MDS Sciex, Toronto, ON, Canada). Measurements were performed by direct infusion electrospray ionization mass spectrometry (ESI-MS) using a nano ESI sample source. Data were collected in the selected mass range of m/z 1000−3000 for MS spectra and processed using Analyst QS 1.1 Sciex software. The deconvolution of spectra was carried out using Bioanalyst 1.1.5.

Preparation of FITC-Labeled Solutes. All of the FITC-dextrans and FITC-α-LA were dissolved in a 0.1 M BisTris buffer at pH 6.8 (called buffered water hereafter) to a concentration of 50 g/L, FITC-BSA and FITC-LYS to 25 g/L, and FITC-PLLs to 5 g/L. For the FRAP measurements, all of the FITC-labeled solutes were diluted to 1/100 (v/v) in the different media (i.e., buffered water, permeate, and casein systems). These solute concentrations were chosen because they fell in the concentration range where fluorescence intensity and solute concentration are related linearly. The diffusion coefficients of the FITC-labeled solutes were measured by using trace amounts, thus approaching the condition of infinite dilution with respect to the FITC-labeled solute concentration to avoid solute−solute interactions.

Physicochemical Characteristics of FITC-Labeled Solutes. The physicochemical characteristics of the described set of FITC-labeled solutes such as size (molecular weight and hydrodynamic radius), flexibility, and charge are summarized in Table 1. The hydrodynamic

Table 1. Physicochemical Characteristics of FITC-Labeled Solutes

FITC-labeled solute	M_w (kDa)	R_h (nm)	flexibility	net charge at neutral pH
FITC-D4[a]	4	1.4	flexible	neutral
FITC-D10[a]	10	2.3	flexible	neutral
FITC-D20[a]	20	3.3	flexible	neutral
FITC-D40[a]	40	4.5	flexible	neutral
FITC-D70[a]	70	6.0	flexible	neutral
anionic FITC-D70[a]	70	6.0	flexible	negative
FITC-PLL23[a]	23		flexible	positive
FITC-PLL32[a]	32		flexible	positive
FITC-α-LA[b]	14.2	2.1	rigid	negative
FITC-BSA[b]	66.3	3.6	rigid	negative
FITC-LYS[c]	14.3	2.5	rigid	positive

[a]Supplier information. [b]Bouhallab and Croguennec[39] and Johnson et al.[10] [c]Bouhallab and Croguennec[39] and Parmar and Muschol.[40]

DOI: 10.1021/acs.jafc.5b02401
J. Agric. Food Chem. 2015, 63, 6624−6632

radii given were taken from the literature. The molecular weights of the globular proteins are well-known and were taken from literature. The molecular weights of the FITC-dextrans and of the FITC-PLLs come from the supplier and correspond to average values from a distribution of molecular weights. On the basis of information from the supplier, the mole proportion of FITC per glucose and lysine (for FITC-dextrans and FITC-PLLs, respectively) was very low, and the negative charge contribution of the FITC for these solutes was not taken into account. The net charge of each FITC-labeled protein at the pH of the casein systems studied in the present work (pH 6.6 and 5.2) was calculated by using simulated titration curves for the unlabeled proteins, which took their 3D structure and the dosage of the label into account to adjust the contribution of the carboxyl group of the FITC.[41−44] These values are presented in Table 2.

Table 2. Simulated Net Charge of FITC-Labeled Proteins at pH 6.6 and 5.2

		net charge at pH 6.6[a]			net charge at pH 5.2[a]		
solute	p*I*	protein	FITC	FITC-protein	protein	FITC	FITC-protein
α-LA	5.0	−4.6	−0.06	−4.7	−0.7	−0.005	−0.7
BSA	5.8	−9.5	−7.2	−16.7	+11.3	−0.6	+10.7
LYS	10.9	+8.8	−0.2	+8.6	+10.1	−0.02	+10.1

[a]The given net charge values were calculated by using simulated titration curves obtained from PROPKA[41−44] for the unlabeled proteins and the dosage of labeled protein to adjust the contribution of the carboxyl group of the FITC.

Preparation of Casein Systems. A casein concentrate was prepared following a previously described procedure.[45] The process allowed the concentration of the total proteins of milk by a factor of 4.3. Neither NaCl nor cream was added, leaving a salt-free and fat-free concentrate. The final composition of the casein concentrate was as follows: dry matter, 196.4 g/kg; casein, 130.3 g/kg; whey proteins, 4.4 g/kg; lactose and minerals, 60.1 g/kg; and 1.6 g/kg of all other components. Sodium azide was added (0.05% w/w) to prevent bacteria growth.

Prior to the FRAP measurements, each FITC-labeled solute was added to the casein concentrate (1:100 v/v) to obtain the casein suspensions. For the casein gels, the coagulant agent Maxiren 180 (DSM Food Specialties, France) was added to the casein concentrate (at a dosage of 0.03% v/v) after the FITC-labeled solute addition. To obtain the acid casein gels, glucono-δ-lactone (GdL) (Merck, Darmstadt, Germany) was added simultaneously with the coagulant agent Maxiren 180 at a dosage of 24 g/L.

The use of gel cassette systems[46,47] (IFR, Norwich, UK) enabled nondestructive and microscopic examinations as discussed previously.[17,18] The gel cassette systems were filled with 1 mL of the previously prepared mixture and then incubated at 30 °C for 1 h before being held at 19 °C for 2 h to obtain both casein suspension or gel. The final pH for these two systems was 6.6 ± 0.05. The "gel time" of the casein gel, that is, the time at which the storage modulus (G') and the loss modulus (G'') are equal, was about 16 min (determined using an AR2000 rheometer (TA Instruments, Guyancourt, France) equipped with a coaxial cylindrical geometry using the oscillatory mode at a frequency of 1 Hz and 0.1% strain; data not shown). Therefore, the time of 2 h after coagulation was chosen for FRAP experiments because both G' and G'' values had by then reached a plateau. Beyond this time, the gel microstructure was not expected to develop further, and measurements could thus be performed under stable conditions. For the acid casein gel, the gel cassette systems were also incubated at 30 °C for 1 h, but this time held at 19 °C for 4 h to obtain the stable pH of 5.2. The final pH of the acid casein gel was 5.2 ± 0.05. No gel shrinkage was observed during the experiments for both gels (casein gel or acid casein gel).

The water activity of casein systems was determined using a water activity meter (FA-st lab, GBX Instrumentation Scientific, Bourg de Peage, France), which involved placing about 5 mL of sample in a small cylinder container. This apparatus uses chilled dew point technology to measure water activity. Condensation occurred on a gold mirror cooled by the Peltier effect. This technique involved the measurement of the relative humidity in an enclosed chamber containing the sample being studied. The measurement was done in triplicate on each sample. The water activity values did not differ significantly between the three casein systems studied ($a_w \sim 0.979 \pm 0.003$).

Fluorescence Recovery after Photobleaching. Diffusion coefficients of FITC-labeled solutes in the casein systems were measured using the FRAP protocol described by Floury et al.[17] and adapted by Silva et al.[18] Measurements were carried out using an inverted confocal laser scanning microscope (CLSM) (Nikon, Champigny-sur-Marne, France). Samples were observed using a 40× objective lens (oil immersion) with a numerical aperture of 1.30. The FITC-labeled solutes were excited using a 50 mW sapphire laser system with a wavelength of 488 nm and detected on the 500−530 nm spectral bandwidth. All diffusion measurements were performed at 19 °C in an air-conditioned room to avoid any temperature effects on the diffusion coefficient values. The procedure used is summarized as follows: three prebleach images were taken at 0.1% of the maximum laser intensity. Five images were then scanned at 100% laser intensity to bleach a small circular region of interest (ROI) of 5.2 μm radius. A series of 100−150 single-section images (depending on the solute) were then collected to follow the recovery process at 0.1% of the maximum laser intensity. The FRAP measurements were also carried out in the same way in buffered water (0.1 M, pH 6.8) and in the permeate (∼0.1 M, according to the methods of Jenness and Koops[48] and Bouchoux et al.,[49] and pH 6.8). The permeate is mainly made up by water, lactose, minerals, and free amino acids and corresponds to the aqueous phase filling the voids of the structure of the casein systems. Measured diffusion coefficients of the FITC-labeled solutes in both the buffered water and the permeate were used to calculate the hydrodynamic radii of the solute molecules. About 100 μL of the fluorescent buffered water or permeate was used for the measurement, being placed between a glass slide and a coverslip sealed with an adhesive frame (Gene Frame, ABgene House, UK). About 10 repetitions of the FRAP measurements were done on each sample. Results were separately modeled to obtain an average diffusion coefficient for the FITC-labeled solutes in each of the media and to test the repeatability of the method. Two different sets of casein systems (i.e., suspension, gel or acid gel) were prepared for the FRAP measurements of the charged solutes to test the reproducibility of the method.

FRAP Data Analysis. Diffusion coefficients of FITC-labeled solutes in the different systems were calculated according to the method of Silva et al.[18] By assuming a homogeneous medium and considering that the diffusion is the only relevant transport process, the system behaves according to the classical diffusion equation after photobleaching as follows:

$$\frac{\partial}{\partial t}C(\vec{r},t) = D\nabla^2 C(\vec{r},t) \quad (1)$$

$C(\vec{r},t)$ is the solute concentration at position $\vec{r}$ at time t.

The effective diffusion coefficient (D_{eff}) of the diffusing fluorescent solute was calculated using eq 2:

$$D_{eff} = \frac{w_M^2}{4\tau_D} \quad (2)$$

Data analysis was performed by the EZ-C1 FreeViewer software, Gold Version 3.2, Nikon Corp.

It has been proposed that only a fraction of the solutes is mobile (f_m) and that the rest ($1 - f_m$) remains immobile and does not diffuse during the diffusion measurements.[36−38] The mobile fraction is related to the measured fluorescence before (F_i) and immediately after photobleaching (F_0) and at "infinite" time after recovery (F_∞) by the following expression:

DOI: 10.1021/acs.jafc.5b02401
J. Agric. Food Chem. 2015, 63, 6624−6632

$$f_m = \frac{F_\infty - F_0}{F_i - F_0} \quad (3)$$

Statistical Analysis. One-way analysis of variance (ANOVA) and Tukey's paired comparison test were applied to the diffusion coefficient data of the three casein systems (i.e., casein suspension, casein gel, and acid casein gel) to determine which mean values were significantly different from one another at the 95% confidence level. Results are presented with the mean value and standard deviation. The mean values of diffusion coefficients obtained were statistically compared using R software (version R i386 3.0.2) (R Foundation for Statistical Computing, Vienna, Austria).

RESULTS

Diffusion of FITC-Labeled Solutes in the Permeate. It was important to first check if there were interactions between the solutes and the components present in the permeate. This was tested by comparing diffusion behavior of solutes in the permeate with that in a buffered water with a similar ionic strength and pH.

Diffusion coefficient values of FITC-labeled solutes in the buffered water (D_∞) and in the permeate (D_{aq}) at 19 °C are given in Table 3. The hydrodynamic radii of the FITC-labeled solutes (Table 3) were calculated from diffusion coefficient values using the Stokes−Einstein equation

$$R_h = \frac{k_B T}{6\pi\eta D} \quad (4)$$

where k_B is the Boltzmann constant (1.38×10^{-23} J/K), T is the absolute temperature (K), and η is the viscosity of water (1×10^{-3} Pa s) or of the permeate (1.2×10^{-3} Pa s, according to Bouchoux et al.[49]).

The hydrodynamic radii of FITC-labeled solutes calculated from experimental diffusion coefficient values (Table 3) in buffered water were found to be in very good agreement with those found in the literature (Table 1). Moreover, the calculated hydrodynamic radii whether in the permeate or in the buffered water were very similar in all cases. These results showed that interactions between FITC-labeled solutes and the components present in the permeate (i.e., lactose, minerals, and free amino acids) can be considered as negligible, as previously reported for neutral FITC-dextrans and negatively charged FITC-labeled proteins.[17,18]

Table 3. Diffusion Coefficients of the Studied FITC-Labeled Solutes (Obtained by Using the FRAP Technique at 19 °C) and Their Hydrodynamic Radii in the Buffered Water and in the Permeate

FITC-labeled solute	D_∞[a] (μm^2/s)	D_{aq}[a] (μm^2/s)	R_h in water[b] (nm)	R_h in permeate[b] (nm)
FITC-D4	102 ± 5	94 ± 8	2.1 ± 0.1	1.9 ± 0.2
FITC-D10	66 ± 2	60 ± 4	3.2 ± 0.1	3.0 ± 0.2
FITC-D20	44 ± 3	40 ± 3	4.9 ± 0.3	4.5 ± 0.3
FITC-D40	43 ± 2	34 ± 2	5.0 ± 0.2	5.2 ± 0.3
FITC-D70	33 ± 2	26 ± 2	6.5 ± 0.2	6.9 ± 0.4
anionic FITC-D70	30 ± 2	25 ± 2	7.1 ± 0.1	7.1 ± 0.1
FITC-PLL23	46 ± 8	50 ± 10	4.7 ± 0.8	3.6 ± 0.7
FITC-PLL32	38 ± 5	32 ± 9	5.6 ± 0.8	5.6 ± 1.6
FITC-α-LA	102 ± 7	82 ± 8	2.1 ± 0.1	2.2 ± 0.2
FITC-BSA	59 ± 9	41 ± 5	3.7 ± 0.5	4.3 ± 0.5
FITC-LYS	86 ± 4	81 ± 6	2.5 ± 0.1	2.2 ± 0.2

[a]Diffusion coefficients of FITC-labeled solutes in the buffered water (D_∞) and in the permeate (D_{aq}) determined by FRAP at 19 °C. The diffusion coefficient values of neutral FITC-dextrans, FITC-α-LA, and FITC-BSA were taken from a previous study.[18] Diffusion coefficients are given as the mean ± one standard deviation for 10 measurements. [b]Hydrodynamic radii of solutes calculated from the Stokes−Einstein eq (eq 4) and given as the mean value ± one standard deviation for 10 diffusion coefficient measurements.

Diffusion of FITC-Labeled Solutes in Casein Systems at pH 6.6. *FITC-Labeled Globular Proteins Are More Hindered than FITC-Dextrans.* Figure 1 shows the diffusion coefficients of (i) flexible and neutral FITC-dextrans (results from Silva et al.[50]), (ii) two rigid and negatively charged FITC-labeled proteins (FITC-α-LA and FITC-BSA), and (iii) one rigid and positively charged FITC-labeled protein (FITC-LYS) in both casein suspension and gel at pH 6.6. All values are presented as a function of the hydrodynamic radius of the FITC-labeled solutes. The net charge of each protein at the same pH (Table 2) is also given.

A key finding emerging from Figure 1 is that the FITC-labeled proteins were much more hindered in both casein suspension and gel than FITC-dextrans of a similar hydrodynamic radius. More specifically, the FITC-α-LA was 3 and 2 times more hindered (than the dextran of similar size) in the casein suspension and gel, respectively. For the FITC-BSA, diffusion was retarded by factors of 10 and 3 times in casein suspension and gel, respectively. The FITC-LYS was also more hindered (than the dextran of similar size) in both casein systems, being even more hindered than the FITC-α-LA and FITC-BSA proteins. These results show that the diffusion of rigid and charged proteins was more hindered than that of flexible and neutral dextrans in the casein suspension or gel.

Figure 1 also shows that the FITC-dextrans (FITC-D4, FITC-D10, and FITC-D20) as a group presented similar diffusion behaviors whether in the casein suspension or in the gel. Diffusion coefficients for both FITC-D4 and FITC-D10 are superposed in casein suspension and gel, and thus results are not distinguishable. On the other hand, the FITC-labeled proteins (FITC-α-LA, FITC-LYS, and FITC-BSA) were more hindered (by factors of 1.4, 3.4, and 2.5, respectively) in the casein suspension than in gel.

Cationic FITC-Poly-L-lysines and Anionic FITC-Dextrans Present the Same Diffusion Behavior as Neutral FITC-Dextrans. To study the influence of the charge of flexible solutes on their diffusion in casein systems, the diffusion coefficients of both neutral and charged flexible solutes were compared in the casein suspension and in the gel.

Table 4 sets out the diffusion coefficients in both casein suspension and gel (pH 6.6) of the charged flexible solutes (cationic FITC-PLL23, cationic FITC-PLL32, and anionic FITC-D70) and the neutral FITC-dextrans with a similar hydrodynamic radius.

The diffusion coefficients of both FITC-PLLs (FITC-PLL23 and FITC-PLL32) presented higher standard deviation values than for the other solutes. This fact could be related to the distribution of molecular weights of the FITC-PLLs.

Despite the variability, Table 4 shows that the diffusion coefficients of the positively charged solutes (FITC-PLL23 and FITC-PLL32) and that of the negatively charged one (anionic FITC-D70) are very similar when compared with those of neutral FITC-dextrans of similar hydrodynamic radius in both casein suspension and gel (Table 4).

Charged FITC-Labeled Solutes Present Higher Immobile Fractions than the Neutral Ones. Figure 2 shows that the

DOI: 10.1021/acs.jafc.5b02401
J. Agric. Food Chem. 2015, 63, 6624−6632

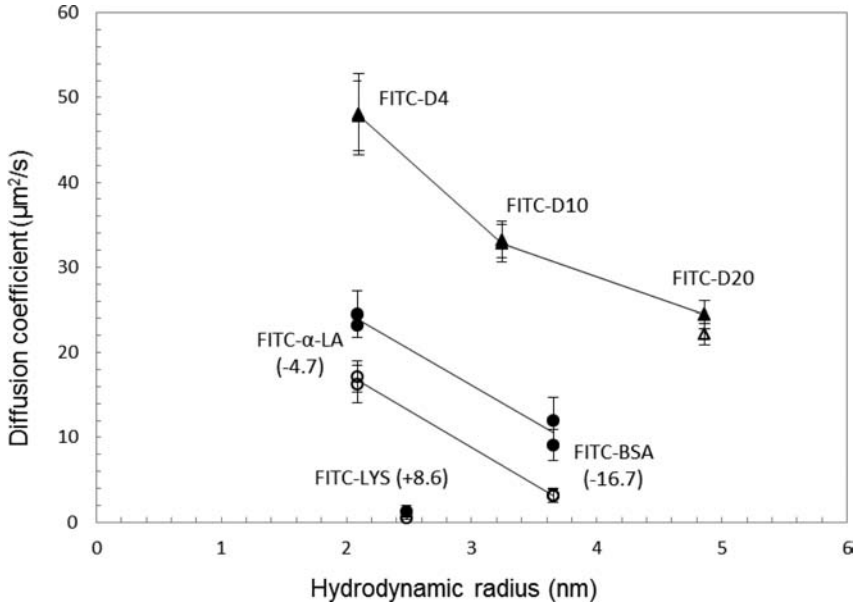

Figure 1. Diffusion coefficients of FITC-dextrans (△ in casein suspension and ▲ in casein gel) and FITC-labeled proteins (FITC-α-LA, FITC-LYS, and FITC-BSA) (○ in casein suspension and ● in casein gel) plotted as a function of their hydrodynamic radii. The diffusion coefficients of FITC-dextrans in these casein systems were taken from a previous work.[50] The net charge values at pH 6.6 were taken from Table 2. The solid lines are only guides to the eyes.

Table 4. Diffusion Coefficients of the Flexible FITC-Labeled Solutes in Casein Suspension and Gel (pH 6.6)

solute	R_h in water (nm)	D (μm^2/s) in casein suspension	D (μm^2/s) in casein gel
neutral solutes[a]			
FITC-D20	4.9 ± 0.3	22 ± 1	24 ± 2
FITC-D40	5.0 ± 0.2	13 ± 1	17 ± 1
FITC-D70	6.5 ± 0.2	9 ± 1	12 ± 1
charged solutes			
FITC-PLL23	4.7 ± 0.8	22 ± 8	22 ± 7
FITC-PLL32	5.6 ± 0.8	12 ± 8	13 ± 4
anionic FITC-D70	7.1 ± 0.1	9 ± 1	11 ± 1

[a]The diffusion coefficients of the neutral FITC-dextrans were taken from a previous study.[50] For the charged solutes, the diffusion measurements were carried out on two different samples of each casein system. Diffusion coefficients are given as the mean ± one standard deviation for 10 measurements.

immobile fractions of neutral FITC-dextrans are close to zero, irrespective of their molecular weight (over a range of 4−70 kDa). This observation was expected because neutral FITC-dextrans are not supposed to bind to the casein matrix in dairy systems.[17,18] However, the immobile fraction of all the charged solutes was >10% (except for the anionic FITC-dextran). Moreover, all of the positively charged solutes (FITC-PLL23, FITC-PLL32, and FITC-LYS) presented much higher immobile fraction values when compared with the negatively charged ones for diffusion in both casein suspension and gel.

Diffusion of FITC-Labeled Solutes in an Acid Casein Gel (pH 5.2). *FITC-Labeled Globular Proteins Are More Hindered than FITC-Dextrans.* To explore the charge effect of rigid solutes on diffusion in casein systems, the diffusion of the FITC-labeled proteins was also studied in an acid gel system at pH 5.2.

Table 2 lists the variation of the net charge of the FITC-labeled proteins as a function of the pH of the system. FITC-α-LA is less negatively charged at pH 5.2 than at pH 6.6. FITC-BSA is negatively charged at pH 6.6 and positively charged at pH 5.2. FITC-LYS is less positively charged at pH 6.6 than at pH 5.2.

Figure 3a shows that, in the acid casein gel, the diffusion of the FITC-labeled proteins was much more hindered (2.5 times for both FITC-α-LA and FITC-BSA and 14 times for FITC-LYS) than that of the FITC-dextrans of a similar hydrodynamic radius. These results are in agreement with findings in the casein suspension and gel (both at pH 6.6) discussed above and also with findings for a model cheese discussed in ref 18.

The diffusion coefficient of FITC-α-LA did not differ significantly in the casein gel (Figure 1) from that in the acid casein gel (Figure 3a), whereas the net charge of this protein was changed from −4.7 to −0.7. On the other hand, a slight increase of the diffusion coefficients values of FITC-BSA in the acid casein gel (protein charge = +10.7) compared with those in the casein gel (protein charge = −16.7) was observed. Furthermore, in the case of the positively charged FITC-LYS, an increase of the diffusion coefficient was observed in the acid casein gel.

Figure 3b shows that, as for the casein systems at pH 6.6 (Figure 2), FITC-labeled proteins present higher immobile fractions than FITC-dextrans of similar size in the acid casein gel. The immobile fractions of both FITC-α-LA and FITC-BSA were higher in the acid casein gel than in the casein gel at pH 6.6. On the other hand, the immobile fraction of FITC-LYS was lower in the acid casein gel.

■ DISCUSSION

Dextrans Diffuse More Rapidly than Proteins in Casein Suspensions and Gels. The present results highlighted that the diffusion of rigid and charged solutes (FITC-labeled proteins) was more hindered than that of flexible and neutral solutes (FITC-dextrans) in both casein suspension and gel at pH 6.6. This fact suggests that interactions between the

DOI: 10.1021/acs.jafc.5b02401
J. Agric. Food Chem. 2015, 63, 6624−6632

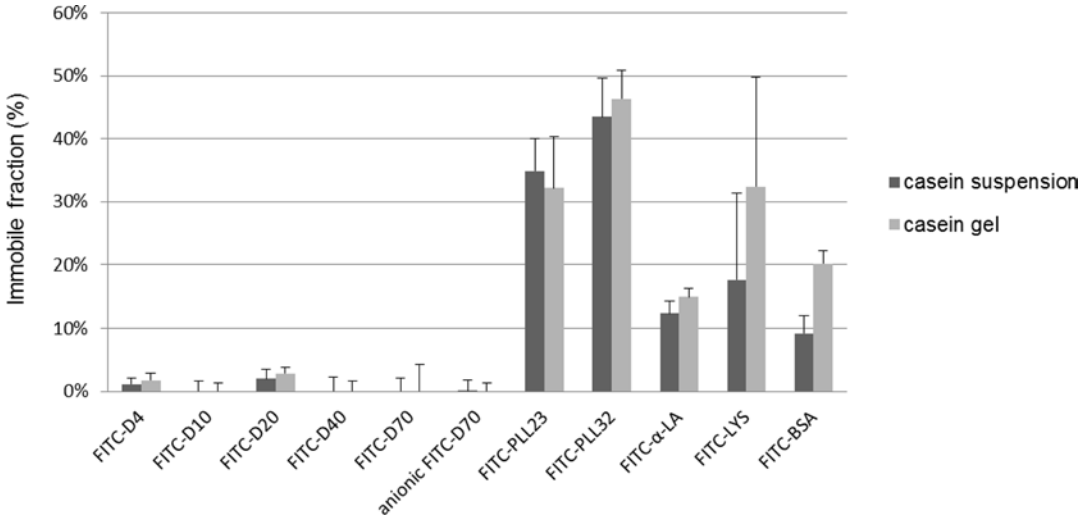

Figure 2. Calculated immobile fractions $(1 - f_m)$ of the diffusing FITC-labeled solutes in both casein suspension and gel (pH 6.6).

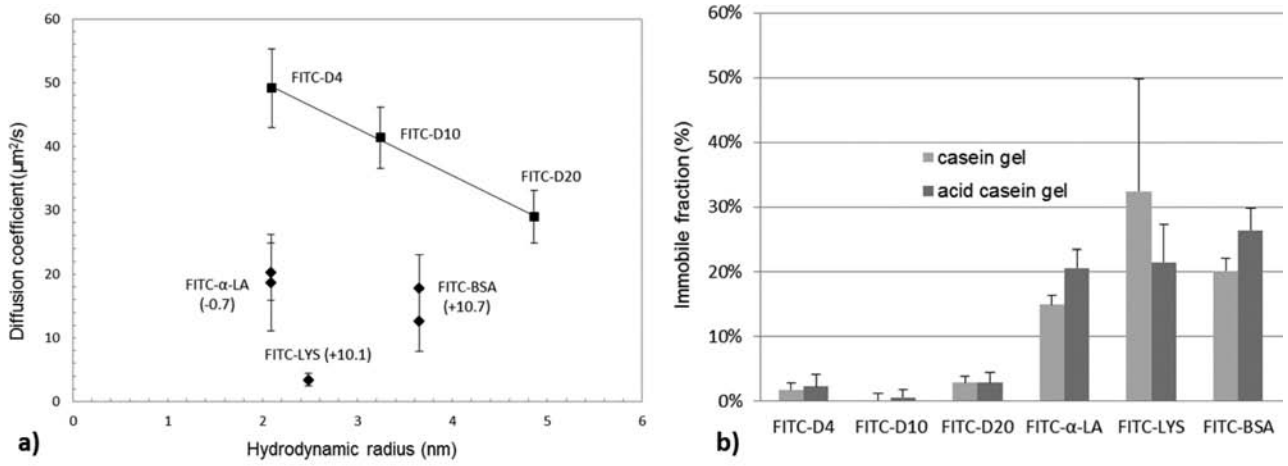

Figure 3. (a) Diffusion coefficients of FITC-labeled proteins (FITC-α-LA, FITC-LYS, and FITC-BSA) (◆) and FITC-dextrans (■) of similar hydrodynamic radius (FITC-D4, FITC-D10, and FITC-D20) in acid casein gel (pH 5.2). The solid line is only a guide to the eyes. (b) Immobile fractions $(1 - f_m)$ of FITC-labeled proteins and FITC-dextrans of similar size calculated from eq 3 in both casein gel (pH 6.6) and acid casein gel (pH 5.2).

diffusing proteins and the casein matrix exist. We will now discuss the possible nature of these interactions.

First, it is important to point out that any molecular interaction of hydrophobic origin was excluded by comparing the diffusion behavior of three different FITC-labeled proteins in two kinds of milk protein suspensions (see Figure SI-1 in the Supporting Information (SI)). The first suspension corresponds to the native casein suspension described under Material and Methods. The second suspension (UF-suspension in SI) corresponds to a heat-treated protein concentrate where whey proteins were also present. At temperatures >60 °C, whey proteins are known to denature and interact with themselves and with casein micelles, forming aggregates via hydrophobic interactions and disulfide bridging.[30] Consequently, these interactions can modify the surface hydrophobicity of the casein micelles in the heat-treated protein concentrate and should affect hydrophobic interactions between the matrix and the diffusing proteins. However, as shown in Figure SI-1, diffusion coefficients of the three FITC-labeled proteins did not differ significantly ($p < 0.05$) in both suspensions presenting casein micelles with different surface hydrophobicities. Moreover, it is unlikely that other types of forces such as van der Waals and London forces are involved because they are very short ranged.

Therefore, in the present study, we will discuss the different diffusion behaviors between dextrans and proteins on the basis of their specific physicochemical characteristics, such as the molecule charge (which could be responsible to electrostatic interactions) and/or molecule flexibility.

Immobile Fractions Are Related to Attractive Electrostatic Interactions between the Charged Solutes and the Casein Matrix. Higher immobile fractions were associated with electrostatic interactions between charged solutes and the casein matrix. The casein matrix is overall negatively charged in both casein suspension and gel at pH 6.6. In both systems, the immobile fraction of the charged solutes was higher compared with that of the neutral solutes, except for the anionic FITC-dextran. The anionic FITC-dextran, the only charged solute that has no positively charged groups in its structure, had an immobile fraction close to zero, as the neutral FITC-dextrans. The other charged solutes, even if their net charge is negative at pH 6.6 (such as FITC-α-LA and FITC-BSA), have positively

DOI: 10.1021/acs.jafc.5b02401
J. Agric. Food Chem. 2015, 63, 6624−6632

charged groups in their structure, which can then interact with the negatively charged casein matrix by electrostatic forces.

Moreover, the increase of the immobile fraction values for both FITC-α-LA and FITC-BSA in the acid casein gel compared with the casein gel strengthens the hypothesis of the existence of attractive electrostatic interactions between these diffusing proteins and the matrix. Electrostatic attractions were higher in the acid casein gel because these diffusing proteins are respectively less negatively charged and positively charged at pH 5.2 than at pH 6.6.

The higher immobile fractions of charged FITC-labeled proteins compared with neutral FITC-dextrans showed the existence of attractive forces due to electrostatic interactions between the positive charges of the diffusing proteins and the negative charges of the casein matrix. It is now important to investigate if this higher immobile fraction of the FITC-labeled proteins also accounts for the diffusion hindrance of these diffusing proteins (compared with dextrans) in both casein suspension and gel.

Electrostatic Interactions Are Not the Main Factor Hindering the Diffusion of Charged Solutes in Casein Systems. The initial hypothesis was that the diffusion of FITC-labeled proteins was more hindered in casein systems than that of FITC-dextrans because of electrostatic interactions between these charged diffusing proteins and the casein matrix, rather than because of the solute flexibility. This hypothesis was supported by recent results of Salami et al.,[51] who concluded that the solute flexibility did not influence their diffusion behavior in casein suspensions below the close-packing of casein micelles (estimated as 178 g/L).[49] They measured, using pulsed field gradient-NMR (PFG-NMR), that flexible PEGs and rigid dendrimers (both neutral) of similar size (R_h) presented similar diffusion behaviors in such suspensions.

The casein concentration of the casein systems studied here was also below the close-packing limit. This fact was confirmed in a previous work[45] in which we determined by image analysis of TEM observations that the mean pore sizes were around 120 and 150 nm in the casein suspension and gel, respectively. Thus, the spaces in which diffusion takes place are much larger than the diameter of the FITC-labeled solutes (largest solute ~14 nm of diameter).

We observed that the charge of flexible solutes did not modify their diffusion behavior either in the casein suspension or in the gel. We have shown that electrostatic interactions between these flexible charged solutes and the casein matrix exist, because a non-negligible fraction of FITC-PLLs solutes was shown to be immobile. However, even if a certain proportion of these solutes could not diffuse in the casein systems because of these interactions, their global diffusion rates were no more affected than those of the neutral solutes. This can be explained by the high ionic strength of the casein systems, which screened the electrostatic interactions between the charged solutes and the charged matrix.[25,26] Indeed, due to their mineral contents, the ionic strength of the aqueous phase of the casein systems is relatively high, around 0.1 M. At this ionic strength, the Debye screening length (κ^{-1}) is around 1 nm, which reflects the short-range of electrostatic interactions under these conditions.

If solute charge determined diffusion rate, it might be expected that FITC-α-LA, which is almost neutral (−0.7) at pH 5.2, has the same or similar diffusion behavior as the neutral FITC-dextran of similar size (FITC-D4) in the acid casein gel. FITC-α-LA was, however, 2.5 times more hindered compared with the FITC-D4 in this system.

To confirm this, we also compared the diffusion behaviors of solutes in both casein gel and acid casein gel, acidified to modify the net charge of the diffusing proteins. The microstructure of both gels, and not only the net charge of the diffusing proteins, is expected to be different, which could also influence the diffusion behavior of solutes.[50] Nevertheless, in the present study, the diffusion coefficient of FITC-D4 did not differ between these two casein systems, and the diffusion coefficients of both FITC-D10 and FITC-D20 were only 1.2 times greater in the acid casein gel when compared with the casein gel. Moreover, the diffusion coefficients of much larger FITC-dextrans ranging from 40 to 2000 kDa did not differ significantly ($p < 0.05$) between the casein gel and the acid casein gel (see Figure SI-2 in the SI). Therefore, the physicochemical characteristics of solutes influenced more the diffusion than the microstructure of the casein system itself.

The diffusion behavior of FITC-α-LA did not differ significantly between the casein gel and the acid casein gel. If diffusion were predominantly influenced by the solute charge, greater differences in the diffusion coefficients should be observed for FITC-α-LA when its charge changed from −4.7 (at pH 6.6) to −0.7 (at pH 5.2). Furthermore, at pH 5.2 the casein matrix itself is also less negatively charged than at pH 6.6. We expected that the FITC-α-LA was less hindered in the acid casein gel when compared with the casein gel because of the reduced interactions of electrostatic nature. The high ionic strength of the aqueous phase screened electrostatic interactions (see above), so this kind of interaction (due to the solute and matrix charge) is insufficient to explain diffusion behavior. Thus, the solute charge seems to influence less the diffusion than the solute flexibility in these casein systems.

The solute charge had no major influence on the diffusion in a high ionic strength. However, this effect can be pronounced when a rigid solute undergoes a major change on its charge or when specific electrostatic interactions are present. Indeed, in contrast to FITC-α-LA, which was negatively charged at both pH values, the effect of the pH change on the FITC-BSA charge was substantial, its net charge changing from −16.7 to +10.7. The slight increase of the diffusion coefficient values of FITC-BSA in the acid casein system (compared with the casein gel) was due to this major variation of its net charge. Similar results were found when diffusion coefficients of myoglobin (pI 6.8) were measured in agarose (neutral) and κ-carrageenan (negatively charged) at three pH values (2.0, 6.8, and 9.0).[25] These authors proposed that when the matrix repels the diffusing protein, the effective accessible space for the protein in the medium voids decreases.

Moreover, we observed that the diffusion of the positively charged FITC-LYS was much more hindered when compared with that of the negatively charged proteins in the casein systems. This fact is explained by the existence of specific interactions between the lysozyme and casein micelles as reported.[32,33] In a recent study, Anema and de Kruif[33] showed that in skim milk lysozyme penetrates the casein micelles (similar ionic strength compared with the casein systems in the current study) and binds to the more charged α_s-casein and β-casein. They showed that because lysozyme is a small protein (with a radius of about 2 nm), it diffuses into the casein micelle and effectively replaces counterions inside the micelles. This hypothesis was established by knowing the average mesh size of micelles, calculated to be 4.5 nm, which is comparable to the

DOI: 10.1021/acs.jafc.5b02401
J. Agric. Food Chem. 2015, 63, 6624−6632

diameter of the lysozyme. In the present study, the FITC-LYS diffused significantly more quickly in the acid casein gel (3.4 ± 1.0 $\mu m^2/s$) than in the casein suspension (0.5 ± 0.3 $\mu m^2/s$) and casein gel (1.2 ± 0.6 $\mu m^2/s$). It has been shown that the binding between the lysozyme and the casein micelles is less pronounced in acid conditions as a consequence of a reduced electrostatic interaction between the NH_3 group of lysines in the lysozyme and the ionized phosphate groups of the caseins in the casein micelles at low pH.[52]

Solute Flexibility Facilitates the Diffusion in Casein Systems. We showed that rigid solutes were more hindered than flexible solutes in casein systems. In agreement with our results, different diffusion behaviors were found for flexible and rigid solutes in other polymer systems even when the solute size was smaller than the pore size of the system.[24] This fact has been related by Seiffert and Oppermann[24] to solute dynamics; that is, flexible solutes present a high internal flexibility and dynamics compared with the rigid ones. When comparing the diffusion of solutes in casein suspension versus gel, we showed that flexible solutes had the same diffusion behavior, whereas the rigid ones were more hindered in the suspension compared to the gel. This fact is explained by the inherent dynamics of the casein system itself that influenced the diffusion of rigid solutes. The friction to diffusion caused by the motionless or immobile structure of the gel is less than the friction caused by the mobile structure of the suspension, as previously observed for larger FITC-dextrans ranging from 40 to 2000 kDa in casein systems,[50] in κ-carrageenan,[9] and in heat-set globular protein systems.[53] Seiffert and Opperman[24] suggest that the mobility of rigid solutes is solely determined by the structure and dynamics of the surrounding matrix, whereas for flexible solutes, their internal flexibility and dynamics will have a major and decisive influence. Therefore, the flexibility of solutes facilitates their diffusion in casein systems and represents the limiting factor of the solute diffusion in these systems. This factor was more important than electrostatic interactions between charged proteins and the casein matrix.

■ ASSOCIATED CONTENT

Ⓢ Supporting Information

Diffusion of FITC-labeled proteins in an UF suspension obtained by heat treatment of the UF concentrate and in the acid casein gel. The Supporting Information is available free of charge on the ACS Publications website at DOI: 10.1021/acs.jafc.5b02401.

■ AUTHOR INFORMATION

Corresponding Author

*(J.F.) Phone: +33 (0)2 23 48 54 52. Fax: +33 (0)2 23 48 55 78. E-mail: juliane.floury@agrocampus-ouest.fr.

Funding

We acknowledge with thanks the financial support received both from the Brittany Regional Council and from INRA Rennes (France).

Notes

The authors declare no competing financial interest.

■ ACKNOWLEDGMENTS

We thank Saïd Bouhallab, Valérie Gagnaire, Thomas Croguennec, and Rachel Boutrou (INRA, Rennes, France) for their helpful discussions and suggestions during the preparation of this paper.

■ REFERENCES

(1) Gehrke, S. H.; Fisher, J. P.; Palasis, M. A. R. I.; Lund, M. E. Factors determining hydrogel permeability. *Ann. N. Y. Acad. Sci.* **1997**, *831*, 179−184.

(2) Amsden, B. Solute diffusion in hydrogels. Mechanisms and models. *Macromolecules* **1998**, *31*, 8382−8395.

(3) Masaro, L.; Zhu, X. X. Physical models of diffusion for polymer solutions, gels and solids. *Prog. Polym. Sci.* **1999**, *24*, 731−775.

(4) Burke, M. D.; Park, J. O.; Srinivasarao, M.; Khan, S. A. Diffusion of macromolecules in polymer solutions and gels: A laser scanning confocal microscopy study. *Macromolecules* **2000**, *33*, 7500−7507.

(5) Amsden, B. Modeling solute diffusion in aqueous polymer solutions. *Polymer* **2002**, *43*, 1623−1630.

(6) Loren, N.; Nyden, M.; Hermansson, A. M. Determination of local diffusion properties in heterogeneous biomaterials. *Adv. Colloid Interface Sci.* **2009**, *150*, 5−15.

(7) Cai, L. H.; Panyukov, S.; Rubinstein, M. Mobility of nonsticky nanoparticles in polymer liquids. *Macromolecules* **2011**, *44*, 7853−7863.

(8) Schuster, E.; Eckardt, J.; Hermansson, A. M.; Larsson, A.; Loren, N.; Altskar, A.; Strom, A. Microstructural, mechanical and mass transport properties of isotropic and capillary alginate gels. *Soft Matter* **2014**, *10*, 357−366.

(9) Johansson, L.; Skantze, U.; Löfroth, J.-E. Diffusion and interaction in gels and solutions. 2. Experimental results on the obstruction effect. *Macromolecules* **1991**, *24*, 6019−6023.

(10) Johnson, E. M.; Berk, D. A.; Jain, R. K.; Deen, W. M. Hindered diffusion in agarose gels: test of effective medium model. *Biophys. J.* **1996**, *70*, 1017−1023.

(11) Fatin-Rouge, N.; Milon, A.; Buffle, J.; Goulet, R. R.; Tessier, A. Diffusion and partitioning of solutes in agarose hydrogels: the relative influence of electrostatic and specific interactions. *J. Phys. Chem. B* **2003**, *107*, 12126−12137.

(12) Hagel, V.; Haraszti, T.; Boehm, H. Diffusion and interaction in PEG-DA hydrogels. *Biointerphases* **2013**, *8*, 1−9.

(13) Morris, G. A.; Foster, T. J.; Harding, S. E. Further observations on the size, shape, and hydration of casein micelles from novel analytical ultracentrifuge and capillary viscometry approaches. *Biomacromolecules* **2000**, *1*, 764−767.

(14) Fox, P. F.; Brodkorb, A. The casein micelle: historical aspects, current concepts and significance. *Int. Dairy J.* **2008**, *18*, 677−684.

(15) Fox, P. F. Milk: an overview. In *Milk Proteins: From Expression to Food*; Thompson, A., Boland, M., Singh, H., Eds.; Elsevier: Amsterdam, The Netherlands, 2009; pp 1−54.

(16) Aly, S.; Floury, J.; Famelart, M. H.; Madec, M. N.; Dupont, D.; Le Gouar, Y.; Lortal, S.; Jeanson, S. Nisin quantification by ELISA allows the modeling of its apparent diffusion coefficient in model cheeses. *J. Agric. Food Chem.* **2011**, *59*, 9484−9490.

(17) Floury, J.; Madec, M. N.; Waharte, F.; Jeanson, S.; Lortal, S. First assessment of diffusion coefficients in model cheese by fluorescence recovery after photobleaching (FRAP). *Food Chem.* **2012**, *133*, 551−556.

(18) Silva, J. V. C.; Peixoto, P. D. S.; Lortal, S.; Floury, J. Transport phenomena in a model cheese: the influence of the charge and shape of solutes on diffusion. *J. Dairy Sci.* **2013**, *96*, 6186−6198.

(19) Tolstoguzov, V. Some thermodynamic considerations in food formulation. *Food Hydrocolloids* **2003**, *17*, 1−23.

(20) Saltzman, W. M.; Radomsky, M. L. Drugs released from polymers: diffusion and elimination in brain tissue. *Chem. Eng. Sci.* **1991**, *46*, 2429−2444.

(21) Pluen, A.; Netti, P. A.; Jain, R. K.; Berk, D. A. Diffusion of macromolecules in agarose gels: Comparison of linear and globular configurations. *Biophys. J.* **1999**, *77*, 542−552.

(22) Arends, F.; Baumgartel, R.; Lieleg, O. Ion-specific effects modulate the diffusive mobility of colloids in an extracellular matrix gel. *Langmuir* **2013**, *29*, 15965−15973.

(23) Johansson, L.; Elvingson, C.; Löfroth, J.-E. Diffusion and interaction in gels and solutions. 3. Theoretical results on the obstruction effect. *Macromolecules* **1991**, *24*, 6024−6029.

DOI: 10.1021/acs.jafc.5b02401
J. Agric. Food Chem. 2015, 63, 6624−6632

(24) Seiffert, S.; Oppermann, W. Diffusion of linear macromolecules and spherical particles in semidilute polymer solutions and polymer networks. *Polymer* **2008**, *49*, 4115−4126.
(25) Hirota, N.; Kumaki, Y.; Narita, T.; Gong, J. P.; Osada, Y. Effect of charge on protein diffusion in hydrogels. *J. Phys. Chem. B* **2000**, *104*, 9898−9903.
(26) Johnson, E. M.; Berk, D. A.; Jain, R. K.; Deen, W. M. Diffusion and partitioning of proteins in charged agarose gels. *Biophys. J.* **1995**, *68*, 1561−1568.
(27) Mun, E. A.; Hannell, C.; Rogers, S. E.; Hole, P.; Williams, A. C.; Khutoryanskiy, V. V. On the role of specific interactions in the diffusion of nanoparticles in aqueous polymer solutions. *Langmuir* **2013**, *30*, 308−317.
(28) Shukla, A.; Narayanan, T.; Zanchi, D. Structure of casein micelles and their complexation with tannins. *Soft Matter* **2009**, *5*, 2884−2888.
(29) Esmaili, M.; Ghaffari, S. M.; Moosavi-Movahedi, Z.; Atri, M. S.; Sharifizadeh, A.; Farhadi, M.; Yousefi, R.; Chobert, J. M.; Haertlé, T.; Moosavi-Movahedi, A. A. Beta casein-micelle as a nano vehicle for solubility enhancement of curcumin; food industry application. *LWT−Food Sci. Technol.* **2011**, *44*, 2166−2172.
(30) Rahimi Yazdi, S.; Corredig, M. Heating of milk alters the binding of curcumin to casein micelles. A fluorescence spectroscopy study. *Food Chem.* **2012**, *132*, 1143−1149.
(31) Haratifar, S.; Corredig, M. Interactions between tea catechins and casein micelles and their impact on renneting functionality. *Food Chem.* **2014**, *143*, 27−32.
(32) Anema, S. G.; de Kruif, C. G. Interaction of lactoferrin and lysozyme with casein micelles. *Biomacromolecules* **2011**, *12*, 3970−3976.
(33) Anema, S. G.; de Kruif, C. G. Protein composition of different sized casein micelles in milk after the binding of lactoferrin or lysozyme. *J. Agric. Food Chem.* **2013**, *61*, 7142−7149.
(34) Doublier, J. L.; Garnier, C.; Renard, D.; Sanchez, C. Protein-polysaccharide interactions. *Curr. Opin. Colloid Interface Sci.* **2000**, *5*, 202−214.
(35) de Kruif, C. G.; Tuinier, R. Polysaccharide protein interactions. *Food Hydrocolloids* **2001**, *15*, 555−563.
(36) Goehring, N. W.; Chowdhury, D.; Hyman, A. A.; Grill, S. W. FRAP analysis of membrane-associated proteins: Lateral diffusion and membrane-cytoplasmic exchange. *Biophys. J.* **2010**, *99*, 2443−2452.
(37) Sukhorukov, V. M.; Dikov, D.; Busch, K.; Strecker, V.; Wittig, I.; Bereiter-Hahn, J. Determination of protein mobility in mitochondrial membranes of living cells. *Biochim. Biophys. Acta, Biomembr.* **2010**, *1798*, 2022−2032.
(38) Paës, G.; Chabbert, B. Characterization of arabinoxylan/cellulose nanocrystals gels to investigate fluorescent probes mobility in bioinspired models of plant secondary cell wall. *Biomacromolecules* **2011**, *13*, 206−214.
(39) Bouhallab, S.; Croguennec, T. Spontaneous assembly and induced aggregation of food proteins. In *Polyelectrolyte Complexes in the Dispersed and Solid State II*, 256th ed.; Müller, M., Ed.; Springer: Berlin Germany, 2014; pp 67−101.
(40) Parmar, A. S.; Muschol, M. Hydration and hydrodynamic interactions of lysozyme: Effects of chaotropic versus kosmotropic ions. *Biophys. J.* **2009**, *97*, 590−598.
(41) Li, H.; Robertson, A. D.; Jensen, J. H. Very fast empirical prediction and rationalization of protein pKa values. *Proteins: Struct., Funct., Genet.* **2005**, *61*, 704−721.
(42) Bas, D. C.; Rogers, D. M.; Jensen, J. H. Very fast prediction and rationalization of pKa values for protein-ligand complexes. *Proteins: Struct., Funct., Genet.* **2008**, *73*, 765−783.
(43) Olsson, M. H. M.; Sondergaard, C. R.; Rostkowski, M.; Jensen, J. H. PROPKA3: Consistent treatment of internal and surface residues in empirical pKa predictions. *J. Chem. Theory Comput.* **2011**, *7*, 525−537.
(44) Sondergaard, C. R.; Olsson, M. H. M.; Rostkowski, M.; Jensen, J. H. Improved treatment of ligands and coupling effects in empirical calculation and rationalization of pKa values. *J. Chem. Theory Comput.* **2011**, *7*, 2284−2295.
(45) Silva, J. V. C.; Legland, D.; Cauty, C.; Kolotuev, I.; Floury, J. Characterization of the microstructure of dairy systems using automated image analysis. *Food Hydrocolloids* **2015**, *44*, 360−371.
(46) Brocklehurst, T. F.; Mackie, A. R.; Steer, D. C.; Wilson, D. R. Detection of microbial growth. U.K. Patent 9313052.4, 1995.
(47) Brocklehurst, T. F.; Piggott, R. B.; Smith, A. C.; Steer, D. C. An apparatus for studying the effect of transient temperature on growth of bacteria in a gel matrix. *Food Microbiol.* **1996**, *13*, 109−114.
(48) Jenness, R.; Koops, J. Preparation and properties of salt solution which simulates milk ultra-filtrate. *Neth. Milk Dairy J.* **1962**, *16*, 153.
(49) Bouchoux, A.; Debbou, B.; Gésan-Guiziou, G.; Famelart, M.-H.; Doublier, J.-L. Rheology and phase behavior of dense casein micelle dispersions. *J. Chem. Phys.* **2009**, *131*.16510610.1063/1.3245956
(50) Silva, J. V. C.; Lortal, S.; Floury, J. Diffusion behavior of dextrans in dairy systems of different microstructures. *Food Res. Int.* **2015**, *71*, 1−8.
(51) Salami, S.; Rondeau-Mouro, C.; van Duynhoven, J.; Mariette, F. Probe mobility in native phosphocaseinate suspensions and in a concentrated rennet gel: Effects of probe flexibility and size. *J. Agric. Food Chem.* **2013**, *61*, 5870−5879.
(52) Thapon, J.; Brulé, G. Effets du pH et de la forme ionique sur l'affinité lysozyme-caséines. *Lait* **1986**, *66*, 19−30.
(53) Croguennoc, P.; Nicolai, T.; Kuil, M. E.; Hollander, J. G. Self-diffusion of native proteins and dextran in heat-set globular protein gels. *J. Phys. Chem. B* **2001**, *105*, 5782−5788.

DOI: 10.1021/acs.jafc.5b02401
J. Agric. Food Chem. 2015, 63, 6624−6632

by more than one mycotoxin, mostly by AFs, T-2, and ZEN together.[10] An extensive study investigating the content of 35 mycotoxins in traditional Chinese medicines found 83% of the 60 tested, commercially available supplements to be positive and contain mainly AFs, trichothecenes, and ochratoxins (OTs), usually at levels of units or tens of micrograms per kilogram.[11] Different types of botanical-based dietary supplements were investigated by Di Mavungu et al., who analyzed set of samples containing mainly garlic, soy, radish, and maca.[12] From the 23 investigated mycotoxins, only FBs and OTA were detected in 10% of samples. Mycotoxin contamination has been also evaluated in dietary supplements made from green coffee, red rice, and ginkgo biloba. The following mycotoxin concentration ranges were determined in a study testing 34 mycotoxins in 50 commercially available green coffee supplement products: OTA, 2.7−136.9 μg/kg; ochratoxin B (OTB), 3.5−20.2 μg/kg; fumonisin B1 (FB1), 110.0−415.0 μg/kg; and mycophenolic acid (MPA), 43.1−395.0 μg/kg.[13] As concerns the red rice, Li et al. investigated the content of CIT in 109 samples, where 31 were positive, with CIT ranging from 16.6 to 5 253 μg/kg.[14] A study by Martinez-Dominguez et al. focused on gikgo biloba-based dietary supplements and investigated a set of 9 samples for 10 mycotoxins.[15] Six samples were contaminated with mycotoxins as follows: aflatoxin B1 (AFB1), 5−54 μg/kg; aflatoxin B2 (AFB2), 4−300 μg/kg; and T-2, 18−20 μg/kg. The details about all of the mentioned studies are summarized in the Supporting Information

Various conditions influencing the final quality of botanical-based dietary supplements are thoroughly discussed in a study of Sanzini et al.[16] In addition to potential contamination by mycotoxins, pesticide residues, and other environmental contaminants, other issues, such as addition of pharmacologically/psychotropically active compounds or adulteration with plants of different species, could potential threaten health of various herbal dietary supplements.

The aim of this study was to assess mycotoxin contamination in a unique set of botanical-based dietary supplements using ultrahigh performance liquid chromatography coupled to tandem mass spectrometry (U-HPLC-MS/MS) for the analysis of 57 mycotoxins. The evaluated products included dietary supplements supporting liver function (based on milk thistle); reducing menopause effects (red clover, flax seed, and soya); and supporting health in general (green barley, nettle, goji berries, yucca, etc.).

This pilot study provides interesting results about the co-occurrence of multiple toxins in these preparations and discusses the health risk associated with this phenomenon. Moreover, important questions related to the quality of the botanicals used in dietary supplements have been raised in this study, which could help to increase the quality requirements for the raw materials entering the dietary supplements production chain.

MATERIALS AND METHODS

Analytical Standards and Chemicals. Analytical standards of mycotoxins 3- and 15-acetyldeoxynivalenol (3- and 15-ADON); beauvericin (BEA); DON, deoxynivalenol-3-glucoside (DON-3-Glc); diacetoxyscirpenol (DAS); enniatins A, A1, B, B1 (ENN-A, ENN-A1, ENN-B, ENN-B1); fumonisins B1, B2, B3 (FB1, FB2, FB3); fusarenon X (FUS-X); T-2; HT-2; neosolaniol (NEO); nivalenol (NIV); ZEN; α- and β-zearalenol (α-ZEL, β-ZEL); tentoxin (TEN); agroclavine (A-clavine); ergocornine (E-cornine); ergocorninine (E-corninine); ergocristine (E-cristine); ergocristinine (E-cristinine); ergocryptine (E-cryptine); ergocryptinine (E-cryptinine); ergometrine (E-metrine); ergosine (E-sine); ergosinine (E-sinine); ergotamine (E-amine); ergotaminine (E-aminine); aflatoxins B1, B2, G1, G2 (AFB1, AFB2, AFG1, AFG2); altenuene (ATE); gliotoxin (GLIO); sterigmatocystin (STER); cyclopiazonic acid (CPA); CIT; meleagrin (MEL); MPA; OTA; patulin (PAT); paxilline (PAX); penicillic acid (PEN-Ac); penitrem A (PEN-A); roquefortine C (ROQ-C); verruculogen (Verruc); and stachybotrylactam (STACH) were purchased from Romer Labs (Austria). Analytical standards of mycotoxins alternariol (AOH), alternariol-methyl ether (AME), tenuazonic acid (TeA), and verrucarol (VER) were purchased from Sigma-Aldrich (United States). All the used analytical standards were certified by the manufacturers with defined purity (95.0−99.8%).

HPLC grade acetonitrile, ammonium acetate (≥99.0%), ammonium formate (≥99.0%), sodium chloride (>99.5%), and magnesium sulfate (>99.5%) were obtained from Sigma-Aldrich (United States). HPLC grade methanol and hexane were purchased from Merck (Germany), formic acid from Penta Chrudim (Czech Republic), and Bondesil-C18 sorbent from Varian (United States). Water was purified by a Milli-Q water system (Millipore, Germany).

Samples. Samples of dietary supplements based on various herbs or plants were collected from Czech and US retail markets. The detailed description of the preparations (matrix characterization, application form, recommended dosage, and the country of origin) is provided in the Supporting Information. Generally, the samples can be divided into three main groups: (i) 32 samples based on milk thistle, containing silymarin, intended to treat and maintain the health of liver; (ii) 9 samples based on red clover, soy, flax, and black cohosh, containing phytoestrogens and intended for reduction of menopausal effects; (iii) 28 samples based on other herbs and plants, e.g., green barley/wheat, nettle, goji, yucca, acerola, magnolia, guarana, orange peel, turmeric, black cohosh, bacopa monnieri, Chinese jujube, green tea leaf, boswellia serrate, containing various antioxidants and intended for general health improvement (immunity, vitality, cardiovascular system, brain functions, etc.).

Sample Preparation. Prior to the extraction procedure, the tested samples were properly homogenized. Seeds, dried leaves, and uncoated tablets were homogenized directly using a mill Grindomix GM200 (Retsch, Germany). In the case of wrapped capsules, only the inside part containing the herbal extract was used for the analysis (the empty capsule was removed and weighed for the purposes of follow-up results recalculation). Samples were processed by the QuEChERS-based (quick, easy, cheap, effective, rugged, safe) method published by Dzuman et al.[17] Representative sample (1.00 ± 0.01 g) was weighed into a 50 mL polytetrafluorethylene (PTFE) centrifuge tube (Merci, Czech Republic) and mixed with 10.0 mL of 1% aqueous formic acid. Matrix was allowed to soak for 30 min, followed by a 30 min extraction by shaking with 10.0 mL of acetonitrile using an automatic shaker HS 250 basic (IKA Labortechnik, Germany). After that, 1.00 g of sodium chloride and 4.00 g of magnesium sulfate were added and the tube was shaken again for 1 min by hand. After centrifugation (5 min at 15 800*g* using ROTINA 35R, Hettich, Germany), a 2.00 mL aliquot of the upper acetonitrile layer was taken for dispersive solid phase extraction (d-SPE) cleanup in a smaller PTFE centrifuge tube (15 mL) containing 100 mg of Bondesil-C18 sorbent and 300 mg of magnesium sulfate. The d-SPE tube was shaken by hand for 1 min and then centrifuged for 5 min (15 800g). An aliquot of the upper acetonitrile layer was microfiltered (0.2 μm PTFE microfilter, Alltech, United States) and transferred into a 2 mL PTFE autosampler vial (MicroSolv, United States).

For solid samples with high amount of fat (preparations formed as encapsulated oily paste), the sample (1.00 g) was first shaken for 5 min with 3.00 mL of hexane to solubilize the samples. After this step, the procedure described above was followed (i.e., addition of 1% aqueous formic acid and acetonitrile, shaking, addition of inorganic salts, shaking again, and d-SPE cleanup with Bondesil-C18).

Separation and Detection. Analyte separation and detection were performed using an U-HPLC-MS/MS system consisting of an ultrahigh performance liquid chromatograph (Acquity UPLC System, Waters, United States) coupled to a highly sensitive tandem mass spectrometer QTRAP 5500 (AB SCIEX, Canada). The chromato-

DOI: 10.1021/acs.jafc.5b02105
J. Agric. Food Chem. 2015, 63, 6633−6643

Table 1. Validation Results of the Used QuEChERS-Based U-HPLC-MS/MS Multianalyte Method[a]

matrix	milk thistle powder (no. 16)				oil-based milk thistle matrix (no. 9)				tea (no. 10, dry nettle)			
analyte	recovery (%)	RSD (%)	LOQ (μg/kg)	SSE (%)	recovery (%)	RSD (%)	LOQ (μg/kg)	SSE (%)	recovery (%)	RSD (%)	LOQ (μg/kg)	SSE (%)
15-acetyldeoxynivalenol	92	5.9	20	78	88	3.4	50	101	82	7.3	50	88
3-acetyldeoxynivalenol	98	5.7	10	91	89	2.9	50	96	82	7.3	50	97
agroclavine	94	4.6	5	71	105	7.0	5	82	82	7.3	10	65
aflatoxin B1	106	3.0	5	65	91	2.6	5	72	97	4.4	5	71
aflatoxin B2	99	5.9	5	69	90	1.5	10	85	93	9.0	10	80
aflatoxin G1	99	4.0	5	58	88	2.0	5	69	96	7.3	5	71
aflatoxin G2	89	2.6	10	47	84	5.9	10	71	97	10.2	20	56
altenuene	79	2.4	5	39	85	8.1	5	48	84	10.6	10	44
alternariol	76	3.7	5	79	88	2.7	5	81	91	4.3	5	92
alternariol-methyl ether	74	1.5	5	75	91	2.6	5	74	88	7.5	5	81
beauvericin	100	2.7	5	91	97	8.3	5	105	97	6.4	5	110
citrinin	76	4.4	50	51	75	10.1	100	65	85	7.1	250	64
cyclopiazonic acid	96	7.5	500	41	–	–	1000	45	–	–	1000	50
deoxynivalenol	95	1.8	50	62	78	7.2	50	65	83	6.8	100	71
deoxynivalenol-3-glucoside	65	4.9	100	40	40	10.9	100	47	44	7.2	250	41
diacetoxyscirpenol	85	3.2	10	95	102	6.6	10	110	92	7.2	10	91
enniatin A	64	2.0	5	95	89	7.8	5	100	86	9.6	5	95
enniatin A1	68	2.8	5	101	88	8.6	5	95	90	4.3	5	96
enniatin B	62	5.7	5	96	91	6.7	5	90	88	3.8	5	89
enniatin B1	61	6.4	5	110	87	7.1	5	105	91	2.2	5	101
ergocornine	90	4.9	10	74	89	8.6	10	78	89	7.1	50	81
ergocorninine	89	3.2	5	68	105	12.9	10	81	97	4.1	20	82
ergocristine	91	6.1	5	49	90	15.9	10	52	92	8.9	50	60
ergocristinine	86	3.2	5	55	98	17.7	10	49	90	7.1	20	58
ergocryptine	91	6.2	5	52	99	6.4	10	52	91	6.0	20	61
ergocryptinine	92	7.0	5	60	110	19.9	10	59	97	10.2	20	65
ergometrine	95	4.6	5	39	79	5.2	10	45	78	6.1	20	49
ergosine	91	6.3	10	34	85	11.1	10	49	93	7.0	20	52
ergosinine	78	3.0	10	39	95	10.8	10	51	92	2.9	20	38
ergotamine	93	7.6	5	48	87	10.3	10	41	93	7.1	50	60
ergotaminine	85	8.1	5	47	103	12.4	10	45	98	4.1	50	55
fusarenon X	108	6.7	20	50	86	10.2	50	55	80	9.2	100	62
fumonisin B1	71	4.8	50	89	79	12.4	100	85	92	6.9	250	105
fumonisin B2	93	9.7	10	100	82	8.7	50	84	103	9.9	100	100
fumonisin B3	95	11	10	105	81	6.5	50	92	99	7.0	100	110
gliotoxin	92	18	250	80	91	8.7	500	85	–	–	1000	82
HT-2 toxin	97	5.0	50	92	122	6.3	100	91	99	11.8	100	105
meleagrin	92	4.1	5	78	95	2.1	5	79	98	6.4	5	82
mycophenolic acid	106	6.2	5	84	94	1.8	10	92	103	6.7	10	98
neosolaniol	95	4.4	10	71	78	5.5	20	69	98	2.7	20	82
nivalenol	94	11	200	55	73	9.6	200	78	–	–	1000	61
ochratoxin A	98	3.0	10	90	99	6.5	10	105	97	10.1	10	99
patulin	82	11	50	90	71	15.4	100	120	89	9.2	250	104
paxilline	91	5.2	50	80	83	6.7	50	79	89	7.3	100	75
penicillic acid	98	9.3	100	74	74	7.5	250	82	99	3.3	500	80
penitrem A	106	4.1	20	58	107	5.8	50	72	98	5.2	250	74
roquefortine C	110	4.7	10	79	103	3.2	10	85	108	3.0	20	70
stachybotrylactam	97	4.6	10	92	88	8.1	20	88	90	6.4	20	101
sterigmatocysin	106	1.6	5	79	89	2.7	5	85	97	7.3	5	91
T-2 toxin	88	2.4	10	82	96	6.3	20	89	96	5.0	20	79
tentoxin	95	3.2	10	105	93	6.4	20	98	93	4.2	20	115
tenuazonic acid	89	5.6	100	70	75	10.3	250	80	82	5.4	500	69
verrucarol	98	6.5	250	74	78	8.7	250	74	76	5.7	500	65
verruculogen	80	4.9	100	84	79	3.7	250	88	88	6.4	500	124
zearalenone	92	3.2	10	84	97	3.5	10	89	97	9.1	10	85
α-zearalenol	91	3.8	20	87	87	4.5	20	96	92	5.4	20	87
β-zearalenol	90	2.8	20	90	89	3.0	50	95	97	9.4	50	97

[a]Analysis of spiked samples at 500 μg/kg was performed in 7 replicates.

DOI: 10.1021/acs.jafc.5b02105
J. Agric. Food Chem. 2015, 63, 6633−6643

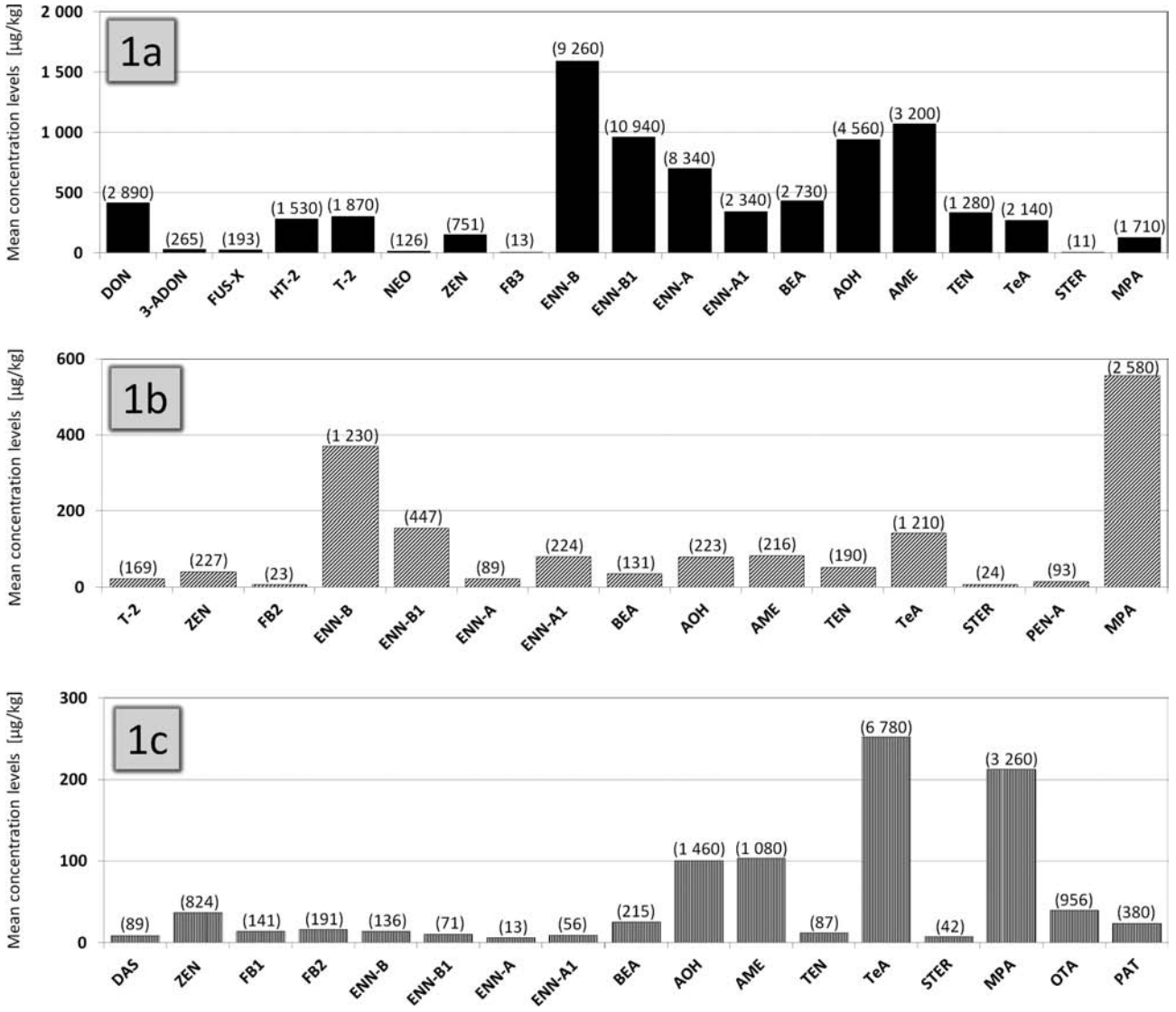

Figure 1. Mean concentrations of mycotoxins (µg/kg) determined in the tested dietary supplements: (a) milk thistle-based supplements, $n = 32$; (b) supplements for menopause effects treatment, $n = 9$; (c) supplements for the general health improvement, $n = 28$. Maximum concentrations are noted in brackets. 1/2LOQ of analytes was used for samples without findings. Abbreviations used: 3-ADON, 3-acetyldeoxynivalenol; AME, alternariol-methyl ether; AOH, alternariol; BEA, beauvericin; DAS, diacetoxyscirpenol; DON, deoxynivalenol; ENN-A, enniatin A; ENN-A1, enniatin A1; ENN-B, enniatin B; ENN-B1, enniatin B1; FB1, fumonisin B1; FB2, fumonisin B2; FB3, fumonisin B3; FUS-X, fusarenon X; HT-2, HT-2 toxin; MPA, mycophenolic acid; NEO, neosolaniol; OTA, ochratoxin A; PAT, patulin; PEN-A, penitrem A; STER, sterigmatocystin; T-2, T-2 toxin; TeA, tenuazonic acid; TEN, tentoxin; ZEN, zearalenone.

graphic separation was carried out with an Acquity UPLC HSS T3 column (100 × 2.1 mm i.d., 1.8 µm; Waters, United States). The working parameters of the separation−detection method were set according to Dzuman et al.:[17] column temperature, 40 °C; injection volume, 2.0 µL; and autosampler temperature, 10 °C. The mobile phases were different for ESI(+) and ESI(−) analyses. ESI(+) employed 5 mM ammonium formate and 0.2% (v/v) formic acid in Milli-Q water and in MeOH as mobile phases A1 and B1, respectively. In ESI(−), 5 mM ammonium acetate in Milli-Q water was used as the mobile phase A2 and pure MeOH as B2. The gradient was different in ESI(−) and ESI(+). In ESI(+), the initial composition of mobile phases was 10% (v/v) of B1 at 0.35 mL/min followed by a linear change to 50% B1 in 1 min, a slower linear gradient from to 100% of B1 in 8.5 min followed, simultaneously with flow change to 0.55 mL/min. The column was then washed for 2 min at 0.7 mL/min with 100% organic solvent and reconditioned for 2 min with 10% of B1 (0.35 mL/min). In ESI(−), the initial mobile phase composition was 10% of B2 at 0.35 mL/min followed by a linear change to 50% of B2 in 1 min. A linear gradient to 100% of B2 with linear increase of the flow rate to 0.5 mL/min in 6.5 min was followed by a column wash with 100% of B2 for 2 min at 0.7 mL/min. The column was then reconditioned for 2 min using the starting composition of the mobile phases at 0.35 mL/min.

The mass spectrometric detection was performed by QTRAP 5500 tandem mass spectrometer equipped with an electrospray (ESI) ion source operated in both positive and negative modes. The ESI(+) ion source parameters were as follows: needle voltage 4 500 V and turbo gas temperature, 500 °C. In ESI(−): needle voltage −4 500 V and turbo gas temperature 450 °C. Gas pressures were the same for both ESI(+) and ESI(−): curtain gas 241 kPa (35 psi), nebulizer and turbo gases 379 kPa (55 psi). Scheduled multiple reaction monitoring (MRM) methods were used in both ESI(+) and ESI(−) with the cycle time 0.6 and 1 s, respectively. Declustering potential (DP), collision energy (CE), collision cell exit potential (CXP), and particular MRM transitions of mycotoxins and all analyte-dependent parameters are summarized in the Supporting Information.

Method Validation. For validation of the method performance characteristics (recoveries, repeatabilities, and limits of quantitation,

DOI: 10.1021/acs.jafc.5b02105
J. Agric. Food Chem. 2015, 63, 6633−6643

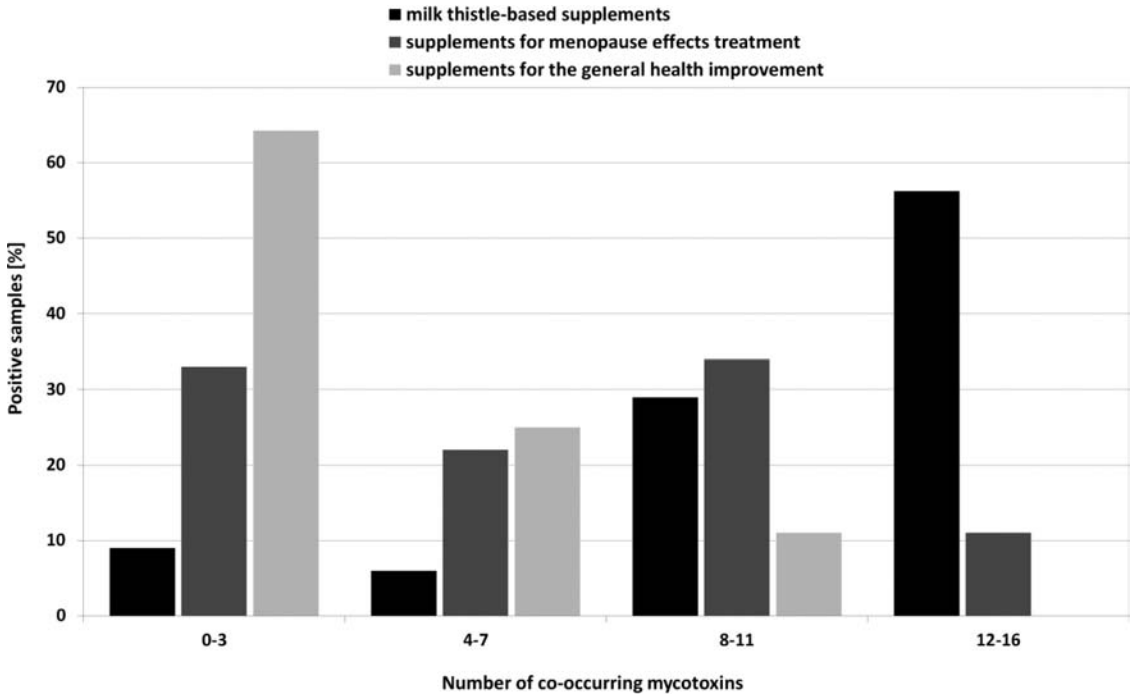

Figure 2. Histogram showing co-occurrence of mycotoxins in analyzed samples (black, milk thistle-based supplements, n = 32; dark gray, supplements for menopause effects treatment, n = 9; light gray, supplements for general health improvement, n = 28).

LOQs) we selected "blank" matrices with very low or no mycotoxin content, which also represented matrices with different chemical composition to verify the method rugedness. Based on these considerations, powdered milk thistle extract (sample 16), oil-based milk thistle preparation (sample 9), and dry nettle tea (sample 10) were used. The external matrix-matched calibration standards at levels 0.5, 1, 2, 5, 10, 25, 50, 100, and 200 μg/L (corresponding to 5−2 000 μg/kg in the sample) were prepared. The repeatability of the method expressed as a relative standard deviation (RSD) was assessed by analysis of spiked samples (mixed standard was added to the "blank" matrix before extraction at 500 μg/kg in seven replicates). LOQs were estimated as the lowest matrix-matched calibration standard levels which provided signal-to-noise ratio (S/N) higher than 10 at the quantifier and 3 at the qualifier ion transitions. For calculation of SSE (signal suppression/enhancement), matrix-matched calibration standards and solvent standards (acetonitrile) at 100 μg/L were used. Validation results are summarized in Table 1.

Quantitation of Mycotoxins in Real Samples. Because medical plant-based extracts used for dietary supplements production represent very diverse matrices, also the matrix induced ionization suppression/enhancement can be different for various mycotoxin/matrix combinations. To minimize potential bias in calculated results, the standard addition approach was chosen for quantitation, to compensate for matrix effects. The practical realization of the standard addition method was as follows. First, the set of samples was preliminarily screened and detected mycotoxins quantitated using generic matrix-matched standards (prepared using the "blank" matrix employed in the method validation). Then, the standard addition was performed by spiking the sample after extraction at three different concentration levels (referring to approximately 1 times, 3 times, and 5 times of the estimated concentration).

A calibration curve was created by plotting the added concentrations (x-axis) against the peak areas measured in samples with standard addition after extraction (y-axis). The native extract (without any standard addition) was included in the regression using a concentration of zero. The analyte concentration in the sample was calculated from the linear regression formula according to eq 1, where the "k" is the calibration curve slope.

$$c\ (\mu g/kg) = \mathrm{Area(sample)}/k \quad (1)$$

All the results were corrected for recovery calculated based on the standard added before and after the extraction procedure.

Arithmetic means of mycotoxins concentrations (presented in Figure 1 and the Supporting Information) were calculated using determined mycotoxin concentrations and, in the case of no detection, 1/2 of LOQ value (micrograms per kilogram) for a given mycotoxin (LOQs derived from the milk thistle powder matrix were used for capsules with dried powder and for tablets; LOQs derived from nettle tea matrix were employed for herbal teas; and LOQs derived from the oil-based milk thistle matrix were utilized for capsules with oil-based content).

Dietary Intake Calculation. Tolerable daily intake (TDI) values are set by the Health and Consumer Protection Directorate General of the European Commission for the following mycotoxins: 1 μg/kg body weight (bw) for DON, 0.1 μg/kg bw for the sum of HT-2 and T-2, 0.25 μg/kg bw for ZEN, 2 μg/kg bw for sum of FB1 and FB2, 0.12 μg/kg bw for OTA, and 0.4 μg/kg bw for PAT.[18] Overview of the above-mentioned TDIs is stated in Commission Regulation 1881/2006. For these mycotoxins, the percentage of TDI obtained by consumption of the tested dietary supplements was calculated. For the mycotoxin exposure calculation (in micrograms of the mycotoxin per kilogram of human bw), the average adult body weight (70 kg) and the recommended dosage of the particular dietary supplement declared by the manufacturer were considered.

RESULTS AND DISCUSSION

As dicussed in the Introduction, beside health-promoting biologically active components, also various contaminants, such as mycotoxins, may occur in botanical-based dietary supplements. Until now, only limitted information has been available on their presence. To get more comprehensive information on the mycotoxins pattern in this commodity, multianalyte method targeting altogether 57 toxic secondary fungal metabolites was employed for analysis of 69 samples obtained in the Czech and US market. Rather unexpectedly, almost 96% of all samples (66 of the 69) contained detectable mycotoxins. As shown in Figure 1 and the Supporting Information, 25 of 57 mycotoxins involved in the method scope were quantitated.

DOI: 10.1021/acs.jafc.5b02105
J. Agric. Food Chem. 2015, 63, 6633−6643

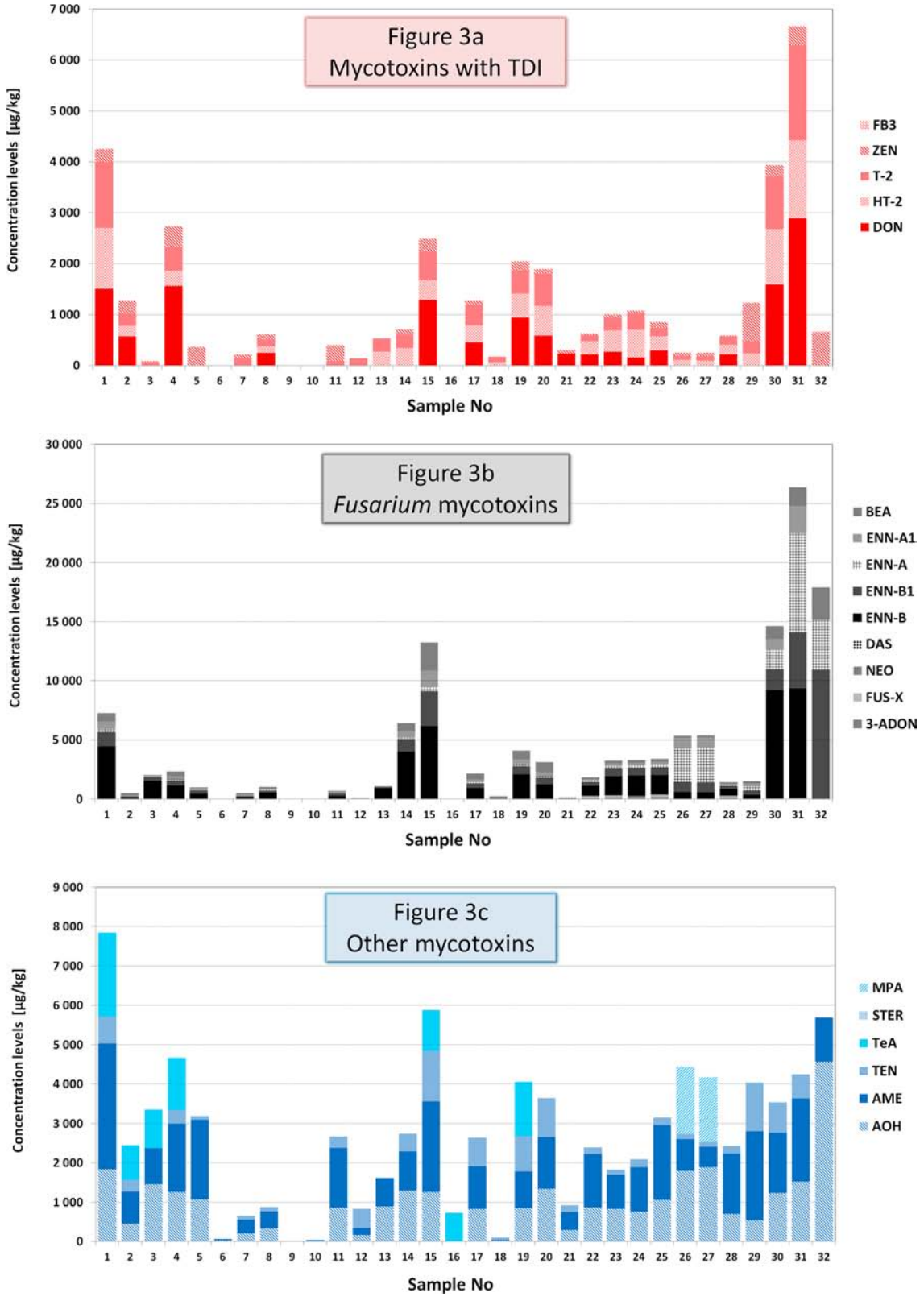

Figure 3. Concentration of mycotoxins (micrograms per kilogram) found in dietary supplements made from milk thistle: *Fusarium* mycotoxins for which the TDI has been established (a); other *Fusarium* mycotoxins (b); other *Alternaria*, *Aspergillus*, and *Penicillium* mycotoxins (c). Abbreviations used: 3-ADON, 3-acetyldeoxynivalenol; AME, alternariol-methyl ether; AOH, alternariol; BEA, beauvericin; DAS, diacetoxyscirpenol; DON, deoxynivalenol; ENN-A, enniatin A; ENN-A1, enniatin A1; ENN-B, enniatin B; ENN-B1, enniatin B1; FB3, fumonisin B3; FUS-X, fusarenon X; HT-2, HT-2 toxin; MPA, mycophenolic acid; NEO, neosolaniol; STER, sterigmatocystin; T-2, T-2 toxin; TDI, tolerable daily intake; TeA, tenuazonic acid; TEN, tentoxin; ZEN, zearalenone.

DOI: 10.1021/acs.jafc.5b02105
J. Agric. Food Chem. 2015, 63, 6633−6643

The highest incidence and concentrations were observed for *Fusarium* mycotoxins (DON, HT-2/T-2, ZEN, and enniatins, ENNs); *Alternaria* mycotoxins (AOH, AME, TEN); and MPA. The comments on the contamination of particular sample groups are discussed in detail below.

Milk Thistle-Based Dietary Supplements. Dietary supplements derived from the milk thistle were clearly the most contaminated samples from all three sample groups. As shown in Figure 1a and in the Supporting Information, in all of 32 tested samples at least one mycotoxin was present, and also the co-occurrence of more than one mycotoxin was very frequent as shown in Figure 2. The majority of the samples contained mycotoxins DON, ZEN, HT-2, and T-2. Moreover, a wide range of the newly emerging mycotoxins (other *Fusarium* mycotoxins such as 3-ADON, FUS-X, DAS; and NEO, ENNs, BEA; *Alternaria* mycotoxins such as AOH, AME, TEN; TeA; and several *Penicillium* and *Aspergillus* mycotoxins, from which the MPA was the most concentrated) were present. The frequency of occurrence of the highly abundant mycotoxins was 13−78% for trichothecenes, 78% for ZEN, 84−91% for ENNs, and 22−97% for *Alternaria* toxins. The average concentrations of trichothecene mycotoxins, ENNs, and *Alternaria* toxins were occurring typically in order of units of milligrams per kilogram (see Figure 3a−c and the Supporting Information). The highest concentration levels were observed for ENNs (2 340−10 900 μg/kg in samples 31 and 32), DON (2 890 μg/kg in sample 31), and AOH (4 560 μg/kg in sample 32).

As mentioned in the Introduction, high levels of mycotoxins in dietary supplements can be associated with the use of low-quality raw materials for their production. The low quality of the raw material could relate to nonoptimal or unsuitable conditions during plant growing, harvesting, and storage. On the basis of the results of mycotoxins in milk thistle-based dietary supplements determined in our study, we contacted several Czech and European milk thistle producers to communicate the potential health risk and possible reasons for such high contamination of milk thistle-based products. As we have learned, the critical point influencing the spreading of fungi on the milk thistle heads and seeds is the humidity during harvesting. Wet and humid weather is needed during the harvest because, under these conditions, the milk thistle heads are closed, and losses of achens (seeds) are thereby prevented. After the harvest, the proper drying to 12% humidity should be performed. The weather during the harvest and the postharvest drying were assessed as the critical parameters in several studies.[4,19,20] The truth is that only a small percentage of milk thistle intended for dietary supplements production is grown in Europe; the majority of the current commercial milk thistle production comes from Argentina and China. The European pharmaceutical companies or dietary supplements producers often purchase the "ready-to-use", dried ethanolic extracts.

Phytoestrogenic Dietary Supplements. Regarding the dietary supplements based on soy, red clover, flax seed, and black cohosh intended for menopause effects treatment, all of the nine examined samples were contaminated with at least one mycotoxin. The most frequently found mycotoxins included ENNs, *Alternaria* toxins, and MPA. Their incidence was 67−78% for ENNs, 11−67% for *Alternaria* toxins, 67% for MPA. However, the average concentrations of *Fusarium* and *Alternaria* mycotoxins in these preparations were approximately one or two orders of magnitude lower than those found in milk thistle-based preparations. The average concentrations of T-2, ENNs, AOH, AME, and TEN were in order of tens to hundreds of micrograms per kilogram. The mean concentration of TeA (143 μg/kg) exceeded the mean concentrations of other *Alternaria* mycotoxins 2-fold. Also, the *Penicillium* mycotoxins, PEN-A and MPA, were determined in the discussed supplements at average concentrations of 15 and 557 μg/kg, respectively. The highest concentration were detected for MPA (2 580 μg/kg, sample 6), ENN-B (1 230 μg/kg, sample 6), and TeA (1 200 μg/kg, sample 9). For detailed information about the sample contamination, see the Supporting Information.

As in the case of other plants and agricultural commodities, also the soy, red clover, flax seed, and black cohosh can be affected by fungi in the field, as well as during the storage, when the appropriate agricultural and manufacturing practices are not followed. The most important factors probably include application of fungicides, air humidity, and temperature during the harvest and water activity during the storage.

Other Dietary Supplements Intended for General Health Improvement. The last group of investigated samples included dietary supplements containing various antioxidants, based on a large number of different herbs and plants (green barley/wheat, nettle (*Urtica dioica* L.), goji (*Lycium barbarum* Mill.), yucca (*Yucca spp*. L.), boswellia (*Boswellia serrata* Roxb. ex Colebr.), acerola (*Malpighia glabra* L.), magnolia (*Magnolia* L.), guarana (*Paullinia cupana* Kunth ex H.B.K.), orange peel, turmeric root, black cohosh (*Actaea racemosa* L.), bacopa monnieri (*Bacopa monnieri* L.), Chinese jujube, and green tea leaves). From a total number of 28 samples, 25 of them were positive for at least one mycotoxin. Dietary supplements with a very low or no mycotoxin contamination were made of green wheat, green barley, acerola, and boswellia. Preparations based on nettle contained predominantly ENNs, BEA, AOH, TEN, and MPA at concentrations of tens up to hundreds of micrograms per kilogram (with the exception of nettle tea, sample 9, which was almost mycotoxin free). One sample of dried goji berry tea contained an extremely high concentration of TeA (6 780 μg/kg, sample 12), whereas no mycotoxins were detected in another sample of goji berry tea (sample 11). Regarding yucca-based preparations, only one sample from four investigated (sample 16) contained mycotoxins, ENNs (5−37 μg/kg) and *Alternaria* toxins (191−261 μg/kg). In the black cohosh sample (sample 18), rather high concentrations of FBs (110 and 101 μg/kg for FB1 and FB2, respectively), ZEN (45 μg/kg), and *Alternaria* toxins (123 and 129 μg/kg for AOH and AME, respectively) were determined. The main mycotoxins in an orange peel extract sample (sample 20) were FBs (141 and 191 μg/kg for FB1 and FB2, respectively). Turmeric powder samples (samples 24 and 25) contained mainly BEA (up to 215 μg/kg), FB2 (29 μg/kg), AME (27 μg/kg), ENN-B (5 μg/kg), NEO (8 μg/kg), and STE (11 μg/kg). In guarana bark powder (sample 26), BEA (21 μg/kg) and *Alternaria* toxins were found (169 and 106 μg/kg for AOH and AME, respectively). In the sample of Chinese jujube, magnolia bark, and green tea (samples No 23, 27, and 28, respectively), high concentrations of MPA were present (3 260, 1 380, and 304 μg/kg, respectively), and also very high levels of *Alternaria* toxins in the first two samples (samples 23 and 27). Magnolia bark (sample 27) contained 1 460 and 1 080 μg/kg of AOH and AME, and in Chinese jujube (sample 23), these two mycotoxins reached the concentration of 692 and 889 μg/kg, respectively. In bacopa monnieri-based sample (sample 21), 824 μg/kg of ZEN, 218 μg/kg of AME, and 956 μg/kg of OTA were determined.

DOI: 10.1021/acs.jafc.5b02105
J. Agric. Food Chem. 2015, 63, 6633−6643

Table 2. Percent Values of TDI[a] for Particular Dietary Supplements

main health effect declared	sample	recommended dosage	*m* (g)	TDI DON (%)	TDI SUM T-2, HT-2 (%)	TDI ZEA (%)	PMTDI SUM[b] FUMs (%)	TWI[c] OTA (%)	PMTDI[b] PAT (%)
liver treatment	1	2 capsules	1.1	2.3	39.2	1.5	–	–	–
	2	1 capsule	0.4	0.3	2.6	0.6	–	–	–
	3	2 tea bags	4.0	–	3.9	0.4	–	–	–
	4	1 tablet	0.7	1.6	8.1	1.7	–	–	–
	5	1 tablet	0.9	–	–	1.9	–	–	–
	6	14 g	14	–	–	–	–	–	–
	7	1 capsule	0.6	–	1.3	0.2	–	–	–
	8	2 capsules	1.9	0.7	7.0	1.0	–	–	–
	9	1 capsule	0.4	–	–	–	–	–	–
	10	3 small spoons	19	–	–	–	–	–	–
	11	1 capsule	1.4	–	1.7	2.4	–	–	–
	12	1 tablet	1.0	–	2.0	–	–	–	–
	13	1 capsule	0.5	–	3.7	–	–	–	–
	14	1 capsule	0.7	–	6.1	0.4	–	–	–
	15	10 capsules	3.8	7.0	52.1	5.3	–	–	–
	16	not provided	0.5	–	–	–	–	–	–
	17	1 capsule	0.4	0.3	4.3	0.2	–	–	–
	18	2 spoons of seeds	19	–	44.6	–	–	–	–
	19	1 tablet	0.4	0.5	5.5	0.4	–	–	–
	20	1 tablet	0.3	0.2	4.5	0.1	–	–	–
	21	1 tablet	0.9	0.3	–	0.4	–	–	–
	22	1 small spoon of seeds	6.0	1.8	32.6	1.0	–	–	–
	23	1 small spoon of seeds	6.0	2.3	57.3	2.3	–	–	–
	24	1 small spoon of seeds	6.0	1.3	74.8	1.6	–	–	–
	25	1 small spoon of seeds	6.0	2.5	37.9	3.8	–	–	–
	26	2 capsules	1.0	–	2.6	0.3	–	–	–
	27	2 capsules	1.0	–	2.6	0.3	–	–	–
	28	2 capsules	1.0	0.3	5.1	0.1	–	–	–
	29	2 capsules	1.0	–	6.8	4.3	–	–	–
	30	2 capsules	1.0	2.3	30.4	1.2	–	–	–
	31	2 capsules	1.0	4.1	48.5	2.1	–	–	–
	32	2 capsules	1.0	–	–	3.7	0.01	–	–
menopause effects treatment	1	2 tablets	1.1	–	–	–	–	–	–
	2	2 tablets	1.2	–	–	0.2	–	–	–
	3	1 capsule	0.4	–	–	–	0.01	–	–
	4	2 capsules	1.0	–	2.5	1.3	–	–	–
	5	2 tablets	1.2	–	–	–	–	–	–
	6	2 tablets	1.8	–	–	0.9	–	–	–
	7	2 capsules	0.9	–	–	–	–	–	–
	8	1 tablet	0.7	–	–	–	–	–	–
	9	3 tablets	1.5	–	–	–	–	–	–
general health improvement	1	10 g	10.0	–	–	–	–	–	–
	2	10 g	10.0	–	–	–	–	–	–
	3	4 g	4.0	–	–	–	–	–	–
	4	4 g	4.0	–	–	0.1	–	–	–
	5	4 g	4.0	–	–	–	–	–	–
	6	2 tea bags	6.0	–	–	–	–	–	–
	7	6 tablets	3.0	–	–	0.1	–	–	–
	8	1 capsule	0.5	–	–	0.0	–	–	–
	9	10 g	50	–	–	1.7	–	–	–
	10	1 tea bag	3.0	–	–	0.2	–	–	–
	11	60 g	60	–	–	–	–	–	–
	12	20 g	20	–	–	–	–	–	–
	13	2 tablets	1.0	–	–	–	–	–	–
	14	3 capsules	1.5	–	–	–	–	–	–
	15	2 capsules	1.0	–	–	–	–	–	–
	16	6 tablets	3.0	–	–	–	–	–	–

DOI: 10.1021/acs.jafc.5b02105
J. Agric. Food Chem. 2015, 63, 6633−6643

Table 2. continued

main health effect declared	sample	recommended dosage	*m* (g)	TDI DON (%)	TDI SUM T-2, HT-2 (%)	TDI ZEA (%)	PMTDI SUM[b] FUMs (%)	TWI[c] OTA (%)	PMTDI[b] PAT (%)
	17	2 capsules	1.0	–	–	–	–	–	–
	18	3 tablets	1.5	–	–	0.3	0.2	–	–
	19	3 tablets	1.5	–	–	–	0.01	–	–
	20	2 tablets	1	–	–	–	0.2	–	–
	21	4 tablets	2	–	–	–	0.04	–	–
	22	2 tablets	1	–	–	4.7	–	11.4	–
	23	2 tablets	1	–	–	–	–	–	–
	24	2 tablets	1	–	–	0.1	–	–	–
	25	2 tablets	1	–	–	–	–	–	–
	26	2 tablets	1	–	–	–	–	–	–
	27	2 tablets	1	–	–	–	–	–	1.4
	28	2 tea bags	6	–	–	–	–	–	–

[a]Values are calculated for a 70 kg person. [b]Provisional maximum TDI. [c]Tolerable weekly intake.

There are probably similar reasons for the mycotoxin contamination of raw materials used for production of these dietary supplements as in the previously described cases (i.e., weather conditions in the field and agricultural and storage management). The recommendation on keeping the good agricultural and manufacturing practices should be commonly applied.

Co-occurrence of Mycotoxins. We would like to emphasize that most of the samples were contaminated with multiple mycotoxins, i.e., more than one mycotoxin occurred in one sample. Figure 2 shows a histogram of multiply contaminated samples and demonstrates the relationship between the number of co-occurring mycotoxins and the dietary supplement type. For example, approximately 58% of milk thistle-based samples contained a "cocktail" of more than 12 mycotoxins together. On the other hand, a low number of co-occurring mycotoxins was determined for supplements made from green barley/wheat, nettle, goji, yucca, acerola, magnolia, guarana, orange peel, turmeric, black cohosh, bacopa monnieri, Chinese jujube, green tea leaf, and boswellia. Quite a high number of co-occurring mycotoxins was observed for supplements made from red clover, soy, flax, and black cohosh (preparations containing phytoestrogens); 22% of samples contained 4−7 mycotoxins, 33% of samples contained 8−11 mycotoxins, and 10.5% of samples contained more than 12 mycotoxins together in one sample. Interestingly, co-occurrence of mycotoxins representing various toxin classes was very common. The most frequent combination was *Fusarium* mycotoxins ENNs, HT-2/T-2, and *Alternaria* toxins (AOH, AME, TEN). The next very frequent combination was ENNs and *Alternaria* toxins (AOH, AME, TEN) and MPA. As discussed in several previous studies, the toxic effects resulting from the co-occurrence of multiple mycotoxins can be both additive and even synergistic, i.e., the overall toxicity might be even higher than the sum of individual toxicities.[21−23] From this point of view, the co-occurrence of mycotoxins may pose an underestimated toxicological hazard because the impact of mycotoxin "cocktails" on human health is currently unknown.

Mycotoxins and Legislation. As regards mycotoxins included in the EU legislation, OTA, PAT, DON, ZEA, FBs, HT-2, and T-2 were found in many samples in various combinations (for details see the discussion above).[18,24−27] AFs were not detected in the investigated samples. There are no maximum limits established for mycotoxins in dietary supplements in the EU. Nevertheless, when considering the concentrations determined in our study, we can point out that they often dramatically exceeded even the highest maximum limits established for other food commodities. For example, in the bacopa-based tablets, 956 μg/kg of OTA was found (see the Supporting Information). The highest maximum regulatory limit for OTA, which is set for the liquorice extract, is 80 μg/kg.[25] Therefore, the bacopa-based sample exceeded this level more than 10-fold. The other example can be given for the sum of HT-2 and T-2. The legislatively recommended maximum concentration level in cereals intended for human consumption is 200 μg/kg.[27] As shown in the Supporting Information, the sum of HT-2 and T-2 in 56% of the investigated milk thistle-based preparations exceeded this value up to 17-times. Of course, this comparison of the mycotoxin concentrations determined in dietary supplements with the maximum limits set for other food commodities is meant as approximate only because the maximum limits consider not only the toxicity but also the quantities of the food which is usually consumed. The best way to express the risk associated with the mycotoxins occurrence in this commodity is to calculate the daily exposure based on the recommended dosage of the particular dietary supplement and compare the calculated value with the tolerable daily intake (TDI) given by the regulations.[18] This exposure assessment is discussed in detail in the paragraph below.

Exposure Assessment. To assess possible health risk associated with mycotoxins occurrence, the mycotoxin daily intake, calculated based on the recommended dosage of the respective dietary supplement, should be considered. Table 2 provides the information about fulfilling the TDI (in %) for mycotoxins, for which the TDI level (in micrograms per kilogram of body weight) have been set.[18] The highest consumer exposure to mycotoxins occurs through the milk thistle-based preparations. Administration of the dose recommended by the manufacturers (usually, two capsules or tablets can cause fulfilling of up to approximately 50% of the TDI for the sum of HT-2 and T-2 (e.g., samples 1, 15, 18, 23, and 24 fulfilled the TDI of HT-2 and T-2 from 39, 52, 45, 57, and 75%, respectively). Considering the fact that the milk thistle preparations are mainly used by people who suffer from a liver disease, such high intake of immunotoxic, genotoxic, and hepatotoxic mycotoxins from the "health beneficial" preparations are of concern. Moreover, when taking into account high concentrations of mycotoxins co-occurring in cocktails, the toxicological impact might be even more serious.

On the basis of the results obtained from the analysis of mycotoxins in the set of botanical-based dietary supplements,

DOI: 10.1021/acs.jafc.5b02105
J. Agric. Food Chem. 2015, 63, 6633−6643

we can conclude that the preparations made from milk thistle were of the highest contamination; mycotoxin concentrations in the sum reached up to milligrams per kilogram. Effective communication of this topic with dietary supplement manufacturers and increased requirements on the quality of botanical-based raw material would be very helpful. The toxicological impact of many emerging mycotoxins is still unknown (especially when present in cocktails), and research focused on this topic should be performed. Nevertheless, considering the 75% fulfillment of the TDI for HT-2 and T-2 toxins at the recommended dosage of milk thistle preparations, it is obvious that the health risk problem should not be marginalized (especially for people who suffer from a liver disease).

■ ASSOCIATED CONTENT

Supporting Information

Tables S1−S5: (S1) overview of studies dealing with analysis of mycotoxins in dietary supplements, (S2) description of the analyzed samples, (S3) analyte-dependent MS/MS parameters in the used U-HPLC-MS/MS method, (S4) concentrations of the mycotoxins in the sample groups, and (S5) concentrations of the detected mycotoxins in individual samples. The Supporting Information is available free of charge on the ACS Publications website at DOI: 10.1021/acs.jafc.5b02105.

■ AUTHOR INFORMATION

Corresponding Author

*E-mail: milena.zachariasova@vscht.cz. Tel.: +420 220 443 142. Fax: +420 220 443 184. University of Chemistry and Technology, Prague, Faculty of Food and Biochemical Technology, Department of Food Analysis and Nutrition, Technicka 3, Prague, Czech Republic, 166 28.

Notes

The authors declare no competing financial interest.

■ ACKNOWLEDGMENTS

The financial support of the European Union Seventh Framework Programme (EP7/CSA/KBBE.2010.2.6-01) under Grant Agreement 266061, Safe Food for Europe − Coordination of research activities and dissemination of research results of EC funded research on food safety (FOODSEG), is gratefully acknowledged. The work was also supported by "Operational Program Prague − Competitivness" (CZ.2.16/3.1.00/22197), "National Program of Sustainability" (NPU I (LO) MSMT − 34870/2013), and Ministry of Education, Youth and Sports of the Czech Republic (Project AMVIS LH11059).

■ ABBREVIATIONS USED

15-ADON, 15-acetyldeoxynivalenol; 3-ADON, 3-acetyldeoxynivalenol; A-clavine, agroclavine; AFB1/B2/G1/G2, aflatoxin B1/B2/G1/G2; AFs, aflatoxins; AME, alternariol-methyl ether; AOH, alternariol; ATE, altenuene; BEA, beauvericin; CE, collision energy; CIT, citrinin; CPA, cyclopiazonic acid; CXP, collision cell exit potential; DAS, diacetoxyscirpenol; DON, deoxynivalenol; DON-3-Glc, deoxynivalenol-3-glucoside; DP, declustering potential; d-SPE, dispersive solid phase extraction; EC, European Commission; EFSA, European Food Safety Authority; ENN-A, enniatin A; ENN-A1, enniatin A1; ENN-B, enniatin B; ENN-B1, enniatin B1; ENNs, enniatins; EP, entrance potential; ESI, electrospray; E-cornine, ergocornine; E-corninine, ergocorninine; E-cristine, ergocristine; E-cristinine, ergocristinine; E-cryptine, ergocryptine; E-cryptinine, ergocryptinine; E-metrine, ergometrine; E-sine, ergosine; E-sinine, ergosinine; E-tamine, ergotamine; E-taminine, ergotaminine; FB1/B2/B3, fumonisin B1/B2/B3 FBs, fumonisins; FUS-X, fusarenon X; GLIO, gliotoxin; HT-2, HT-2 toxin; LOQ, limit of quantitation; MEL, meleagrin; MPA, mycophenolic acid; MRM, multiple reaction monitoring; MS/MS, tandem mass spectrometry; NEO, neosolaniol; NIV, nivalenol; OTA, ochratoxin A; OTB, ochratoxin B; OTs, ochratoxins; PAT, patulin; PAX, paxilline; PEN-Ac, penicillic acid; PEN-A, penitrem A; PTFE, polytetrafluorethylene; QuEChERS, quick, easy, cheap, effective, rugged, safe; ROQ-C, roquefortine C; RSD, relative standard deviation; S/N, signal-to-noise; SSE, signal suppression/enhancement; STACH, stachybotrylactam; STER, sterigmatocystin; T-2, T-2 toxin; TDI, tolerable daily intake; TEN, tentoxin; TeA, tenuazonic acid; U-HPLC, ultrahigh performance liquid chromatography; VER, verrucarol; Verruc, verruculogen; ZEN, zearalenone; α-ZEL, alpha-zearalenol; β-ZEL, beta-zearalenol

■ REFERENCES

(1) Mehta, A. Pharmacology of medicinal plants with antioxidant activity. In *Plants as a Source of Natural Antioxidants*; Dubey, N. K., Ed.; CABI Publishing: Boston, MA,, 2015; pp 225−244.

(2) Vargas-Mendoza, N.; Madrigal-Santillan, E.; Morales-Gonzales, A.; Esquivel-Soto, J.; Esquivel-Chirino, C.; Garcia-Luna, Y.; Gonzales-Rubio, M.; Gayosso-de-Lucio, J. A.; Morales-Gonzales, J. A. Hepatoprotextive effect of silymarin. *World J. Hepatol.* **2014**, *6*, 144−149.

(3) European Food Safety Authority (2010). Scientific Opinion on the substantiation of a health claim related to silymatin BIO-C® and increase in production of breast milk after delivery pursuant to Article 13(5) of Regulation (EC) No 1924/2006. *EFSA Journal*, *8* (9), 1774, 1−9. URL (http://www.efsa.europa.eu/en/topics/topic/article13.htm). Accessed February 25, **2015**.

(4) Stevic, T.; Pavlovic, S.; Stankovic, S.; Savikin, K. Pathogenic microorganisms of medicinal herbal drugs. *Arch. Biol. Sci.* **2012**, *64* (1), 49−58.

(5) Zhang, J.; Wider, B.; Shang, H.; Li, X.; Ernst, E. Quality of herbal medicines: challenges and solutions. *Complement. Ther. Med.* **2012**, *20* (1−2), 100−106.

(6) Efuntoye, M. O. Mycotoxins of fungal strains from stored herbal plants and mycotoxin contents of Nigerian crude herbal drugs. *Mycopathologia* **1999**, *147* (1), 43−48.

(7) Tournas, V. H.; Rivera Calo, J.; Sapp, C. Fungal profiles in various milk thistle botanicals from US retail. *Int. J. Food Microbiol.* **2013**, *164*, 87−91.

(8) Tournas, V. H.; Sapp, C.; Trucksess, M. W. Occurrence of aflatoxins in milk thistle herbal supplements. *Food Addit. Contam., Part A* **2012**, *29* (6), 994−999.

(9) Arroyo-Manzanares, N.; Garcia-Campana, A. M.; Gamiz-Gracia, L. Multiclass mycotoxin analysis in *Silybum marianum* by ultra high performance liquid chromatography-tandem mass spectrometry using a procedure based on QuEChERS and dispersive liquid-liquid microextraction. *J. Chromatogr. A* **2013**, *1282*, 11−19.

(10) Santos, L.; Marin, S.; Sanchis, V.; Ramos, A. J. Screening of mycotoxin multicontamination in medicinal and aromatic herbs sampled in Spain. *J. Sci. Food Agric.* **2009**, *89* (10), 1802−1807.

(11) Han, Z.; Ren, Y. P.; Zhu, J. F.; Cai, Z. X.; Chen, Y.; Luan, L. J.; Wu, Y. J. Multianalysis of 35 mycotoxins in traditional Chinese medicines by ultra-high-performance liquid chromatography−tandem mass spectrometry coupled with accelerated solvent extraction. *J. Agric. Food Chem.* **2012**, *60* (33), 8233−8247.

(12) Di Mavungu, J. D.; Monbaliu, S.; Scippo, M. L.; Maghuin-Rogister, G.; Schneider, Y. J.; Larondelle, Y.; Callebaut, A.; Robbens, J.; Van Petergmen, C.; De Saeger, S. LC-MS/MS multi-analyte method

DOI: 10.1021/acs.jafc.5b02105
J. Agric. Food Chem. 2015, 63, 6633−6643

for mycotoxin determination in food supplements. *Food Addit. Contam., Part A* **2009**, *26* (6), 885−895.
(13) Vaclavik, L.; Vaclavikova, M.; Begley, T. H.; Krynitsky, A. J.; Rader, J. I. Determination of multiple mycotoxins in dietary supplements containing green coffee bean extracts using ultrahigh-performance liquid chromatography−tandem mass spectrometry (UHPLC-MS/MS). *J. Agric. Food Chem.* **2013**, *61* (20), 4822−4830.
(14) Li, Y.; Zhou, Y. C.; Yang, M. H.; Ou-Yank, Z. Natural occurrence of citrinin in widely consumed traditional Chinese food red yeast rice, medicinal plants and their related products. *Food Chem.* **2012**, *132* (2), 1040−1045.
(15) Martinez-Dominguez, G.; Romero-Gonzalez, R.; Garrido Frenich, A. Determination of toxic substances, pesticides and mycotoxins, in ginkgo biloba nutraceutical products by liquid chromatography orbitrap-mass spectrometry. *Microchem. J.* **2015**, *118*, 124−130.
(16) Sanzini, E.; Badea, M.; Dos Santos, A.; Restani, P.; Sievers, H. Quality control of plant food supplements. *Food Funct.* **2011**, *2* (12), 740−746.
(17) Dzuman, Z.; Zachariasova, M.; Lacina, O.; Veprikova, Z.; Slavikova, P.; Hajslova, J. A rugged high-throughput analytical approach for the determination and quantification of multiple mycotoxins in complex feed matrices. *Talanta* **2014**, *121*, 263−272.
(18) European Commission. Commission Regulation (EC) No. 1881/2006 of 19 December 2006 setting maximum levels for certain contaminants in foodstuffs. *Off. J. Eur. Union* 2006, *L364*, 5−24.
(19) Efuntoye, M. O. Fungi associated with herbal drug plants during storage. *Mycopathologia* **1996**, *136* (2), 115−118.
(20) Ashiq, S.; Hussain, M.; Ahmad, B. Natural occurrence of mycotoxins in medicinal plants: A review. *Fungal Genet. Biol.* **2014**, *66* (2014), 1−10.
(21) D'Mello, J. P. F.; Placinta, C. M.; Macdonald, A. M. C. Fusarium mycotoxins: a review of global implications for animal health, welfare and productivity. *Anim. Feed Sci. Technol.* **1999**, *80* (3−4), 183−205.
(22) Grenier, B.; Oswald, I. P. Mycotoxin co-contamination of food and feed: Meta-analysis of publications describing toxicological interactions. *World Mycotoxin J.* **2011**, *4* (3), 285−313.
(23) Zachariasova, M.; Dzuman, Z.; Veprikova, Z.; Hajkova, K.; Jiru, M.; Vaclavikova, M.; Zachariasova, A.; Pospichalova, M.; Florian, M.; Hajslova, J. Occurrence of multiple mycotoxins in European feedingstuffs, assessment of dietary intake by farm animals. *Anim. Feed Sci. Technol.* **2014**, *193*, 124−140.
(24) European Commission. Commission Regulation (EC) No. 1126/2007 of 28 September 2007 amending Regulation (EC) No. 1881/2006 setting maximum levels for certain contaminants in foodstuffs as regards Fusarium toxins in maize and maize products. *Off. J. Eur. Union* 2007, *L 255*, 14−17.
(25) European Commission. Commission Regulation (EU) No 105/2010 of 5 February 2010 amending regulation (EC) No 1881/2006 setting maximum levels for certain contaminants in foodstuffs as regards ochratoxin A. *Off. J. Eur. Union* 2010, *L 35*, 7−8.
(26) European Commission. Commission Regulation (EU) No 165/2010 of February 2010 amending regulation (EC) No 1881/2006 setting maximum levels for certain contaminants in foodstuffs as regards aflatoxins. *Off. J. Eur. Union* 2010, *L 50*, 8−12.
(27) European Commission. Commission recommendation (2013/165/EU) of 27 March 2013 on the presence of T-2 and HT-2 toxin in cereals and cereal products. *Off. J. Eur. Union* 2013, *L 91*, 12−15.

DOI: 10.1021/acs.jafc.5b02105
J. Agric. Food Chem. 2015, 63, 6633−6643

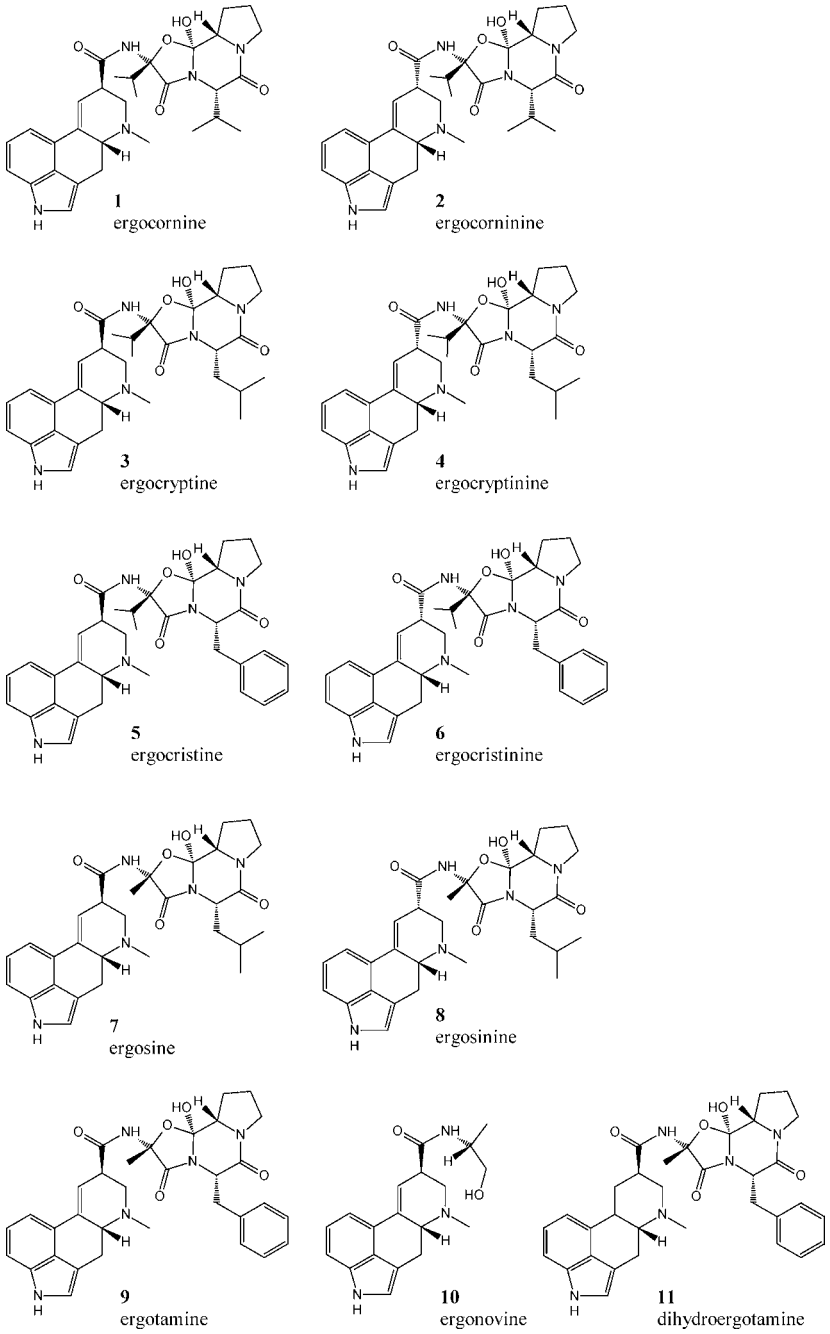

Figure 1. Structures of ergot alkaloid analytes and internal standard.

fine enough that ≥85% of mass passed through a U.S. 50 sieve (nominal sieve openings of 300 μm).

In addition, samples from shipments of western Canadian cereals were provided by CGC Industry Services inspectors. Grains sampled included wheat (n = 117), durum (n = 46), barley (n = 25), and rye (n = 1). These samples represented randomly selected export shipments of cereal grains that occurred between August 1, 2010, and July 31, 2012. It should be noted that the year of transport does not necessarily correspond to the year in which grain was grown and harvested. During the loading of the shipments, moving grain was sampled according to standardized procedures at a constant interval using CGC-approved automated cross-stream sample diverters and dividers.[12] The increments obtained during loading of a lot were combined into a composite sample that was considered to be representative of the entire lot. A Boerner divider (Seedburo Equipment Co.) was used to divide the composite sample into 10 kg laboratory samples. The 10 kg laboratory samples were stored at room temperature in canvas bags for up to 5 weeks until further preparation.

Test portions of the shipment samples were prepared from the 10 kg laboratory sample of whole grain according to the process described previously.[13] The 10 kg laboratory sample of whole grain was comminuted using a Retsch SR 300 rotor beater mill fitted with a 750 μm screen and coupled with a Retsch DR 100 vibratory feeder. After comminution, the entire mass of ground grain was homogenized and divided into 10 × 1 kg portions on a rotary sample divider (Materials Sampling Solutions, Southport, Australia). After the first division into 10 × 1 kg, all 10 portions were recombined in the RSD hopper and divided into 10 × 1 kg again. One 1 kg portion of ground grain was randomly selected and further divided on another RSD into 10 subsamples of 100 g of ground grain. Subsamples of 100 g were stored at room temperature in closed high-density polyethylene or polypropylene containers. The containers were not airtight, but were sealed to prevent the possibility of insects entering the samples.

DOI: 10.1021/acs.jafc.5b02977
J. Agric. Food Chem. 2015, 63, 6644−6650

Analysis of Ergot Alkaloids. Ten ergot alkaloids were included in the analytical method (Figure 1). Standards of individual analytes were obtained as crystals (Sigma-Aldrich, Oakville, Canada; Novartis, Dorval, Canada; Biopure, Tulln, Austria); purities ranged from 97 to 99%. Four of the alkaloids were *S* epimers of *R* enantiomers. The two epimers that were not included in the method were not easily obtained at the time of analysis. Dihydroergotamine (**11**, Fluka, analytical standard grade) was used as an internal standard for the analytical method.

A method based on that of Krska et al.[4] was developed for the extraction and ultrahigh-pressure liquid chromatographic−tandem mass spectrometric (UPLC-MS/MS) analysis of the 10 ergot alkaloids. Ground sample (10 g) was extracted with 50 mL of a 84:16 (v/v) acetonitrile/3.03 mM aqueous ammonium carbonate in 250 mL polyethylene centrifuge bottles. This mixture was shaken on a flatbed shaker for 30 min and then centrifuged at 2450*g* for 10 min at room temperature. A 464 μL aliquot of the supernatant was transferred to a glass test tube and mixed with 20 μL of internal standard solution (4 ng/μL dihydroergotamine in acetonitrile) and 1536 μL of 3.03 mM aqueous ammonium carbonate. Samples were vortexed to mix well and filtered using a disposable plastic syringe and PTFE syringe filter prior to injection.

Final extracts were autoinjected, with the autosampler tray held at 15 °C, and chromatographed on a 2.1 × 100 mm i.d., 1.7 μm, BEH C_{18} column (Waters) held at 30 °C on a Waters Acquity I-class UPLC. A gradient of two solutions (A = 3.03 mM ammonium carbonate and B = acetonitrile) was used to resolve the analytes. The mobile phase began at 80% A, changed to 20% A over 5 min, and returned to 80% A after a further 1 min. Analysis was performed using a Waters Xevo MS/MS in the positive electrospray ionization mode using multiple reaction monitoring. The source and desolvation temperatures were held at 150 and 500 °C, respectively, with the capillary at 0.50 kV and the extractor at 3.0 V. The cone, desolvation, and collision gas flows were 100 L/h, 700 L/h, and 0.15 mL/min, respectively.

To avoid epimerization of analytes, diluted standard mixes were dried down and kept in a freezer until needed. The dried mixes were reconstituted in acetonitrile just prior to instrumental analysis. Exposure to light was minimized, and samples and extracts were kept covered during processing and were placed in the UPLC sample manager with the illumination option turned off once diluted.

Analytes were considered to be positively identified and quantitated if their retention times were within 0.1 min of the average retention time of the corresponding analyte in the external calibration standards; the peak had a signal-to-noise ratio >9:1, and the ratio of qualification to quantitation ions was within acceptable tolerances.[14] The analyte responses were normalized to the dihydroergotamine responses during calculation of concentrations.

Blank samples fortified with a solution of standards and an in-house reference material were analyzed with each batch of samples and were used to monitor the performance of the analytical method.

RESULTS AND DISCUSSION

Validation and Method Performance. Validation of the analytical method was performed using fortified wheat and rye. Blank wheat and rye were created by hand-cleaning grain samples to remove ergot sclerotia. Even with this extra cleaning, some ergot alkaloids were still present in the blanks; therefore, during method validation concentrations of ergot alkaloids in the fortified samples were corrected by subtracting the concentration of analyte in the blanks prior to calculation of recoveries. Blank samples were fortified at three different concentrations and extracted and analyzed on multiple days. Seven replicates were fortified and extracted for each day/concentration combination: low (2 μg/kg ergonovine and 10 μg/kg other analytes), medium (41 μg/kg ergonovine and 200 μg/kg other analytes), and high (407 μg/kg ergonovine and 2000 μg/kg other analytes). To conserve standards, the *S* ergot alkaloid analytes were fortified only at the medium concentration.

During validation, separate sets of blanks were fortified with *R* and *S* ergot alkaloid analytes because a low amount of *S* enantiomers was found in the *R* enantiomer standard solutions. Ergosinine, ergocorninine, ergocryptinine, and ergocristinine were present at approximately 6% of the concentration of their analogues in the *R* enantiomer standard mix. Ergosine, ergocornine, ergocryptine, and ergocristine were also present in the *S* enantiomer standard mix, although at only about 2% of the concentration of their analogues. It was not clear if this was due to impurities in the analytical standards or due to epimerization during handling and use of the standard solutions over time. Both of these possibilities have been noted in the literature.[15] Because of this apparent "contamination", separate calibration standards were made for *R* and *S* enantiomers, and these were used in the validation and in all subsequent samples analyses.

The method produced good results with recoveries from individual ergot alkaloids in individual fortified samples ranging from 60 to 132%. The overall mean recovery ± standard deviation for all ergot alkaloids over all fortification concentrations and days was 83 ± 12% for wheat and 88 ± 15% for rye.

A comparison of individual ergot alkaloid peak areas from standard solutions prepared in solvent to postextraction fortified wheat and rye matrix matched standards indicated some enhancement of ergocorninine, ergocryptinine, and ergocristinine occurred due to matrix effects. The enhancement was somewhat higher for the rye matrix as compared to the wheat matrix (Table 1). The average ratio of ergot alkaloid peak area in matrix to solvent was 1.13 for wheat and 1.22 for rye. These averages are very close to the ratios observed for the internal standard dihydroergotamine in wheat (1.12) and rye (1.23). This similarity indicates that normalization of individual ergot alkaloid responses to the dihydroergotamine internal standard would mitigate matrix effects on the measurement of the sum total concentration of all 10 ergot alkaloids analyzed.

Table 1. Ratios of Responses for Ergot Alkaloids and Internal Standard in Wheat and Rye Matrix Extract As Compared to Solvent

	wheat	rye
ergonovine	1.05	1.05
ergosine	0.94	0.82
ergotamine	1.09	1.10
ergocornine	0.99	1.07
ergocryptine	1.05	1.12
ergocristine	1.07	1.19
dihydroergotamine	1.12	1.23
ergosinine	1.05	1.08
ergocorninine	1.28	1.40
ergocryptinine	1.34	1.55
ergocristinine	1.43	1.83

Limits of quantitation (LOQs) were 2 μg/kg for ergonovine and 10 μg/kg for the nine other ergot alkaloids. The LOQs were estimated as the lowest concentration to produce a chromatographic peak with a signal-to-noise ratio of at least 9:1 having an area that could be measured with good precision (i.e., a relative standard deviation of ≤20% for seven replicate injections).

DOI: 10.1021/acs.jafc.5b02977
J. Agric. Food Chem. 2015, 63, 6644−6650

Stability of Ergot Alkaloids during Sample Storage. An additional Canadian western rye sample was provided by CGC grain inspectors for use as an in-house reference material. This sample was ground and homogenized following the procedure used for the shipment samples described above.

The ground and homogenized sample was stored, and test portions were weighed prior to each run and analyzed to monitor for changes in ergot alkaloid concentrations during storage.

Portions of the in-house reference material were analyzed 27 times over a 10 month period. There was variation in the sum total ergot alkaloid concentrations over this period, but no overall decreasing or increasing tendency in sum total ergot alkaloid concentration was apparent. There were also no visible trends in individual ergot alkaloid concentrations or as fractions of the sum total ergot alkaloid concentrations over the storage period. The absence of trends in ergot alkaloid concentrations supports the appropriateness of storage at room temperature for ergot alkaloids in ground cereals.

Ergot Alkaloids in Harvest Samples and Grain Shipments. The amounts of ergot sclerotia determined in all 2011 CWAD and CWRS submitted to the CGC Harvest Sample Program are shown in Figure 2, along with results from other harvests between 2002 and 2013 for context. The number of samples inspected for the presence of ergot sclerotia each year ranged from approximately 3200 to 5000 for CWRS and from 820 to 2000 for CWAD. Figure 2 shows that the occurrence and severity of ergot infection (as shown by the percentage of samples downgraded due to ergot and the mean percentage of ergot in submitted samples, respectively) vary from year to year in both CWRS and CWAD. The mean percentages of ergot in 2011 were 0.030 and 0.026 for CWAD and CWRS, respectively. These means were both lower than in 2010; however, for CWRS the percentage of samples submitted to the CGC Harvest Sample Program that were downgraded due to the presence of ergot in 2011 was the highest between 2002 and 2013; for CWAD the second highest percentage of samples was downgraded in 2011. These data indicate that ergot was more widespread in 2011, even though the levels of infection in CGC Harvest Sample Program submitted grain were not the most serious that had been observed between 2002 and 2013.

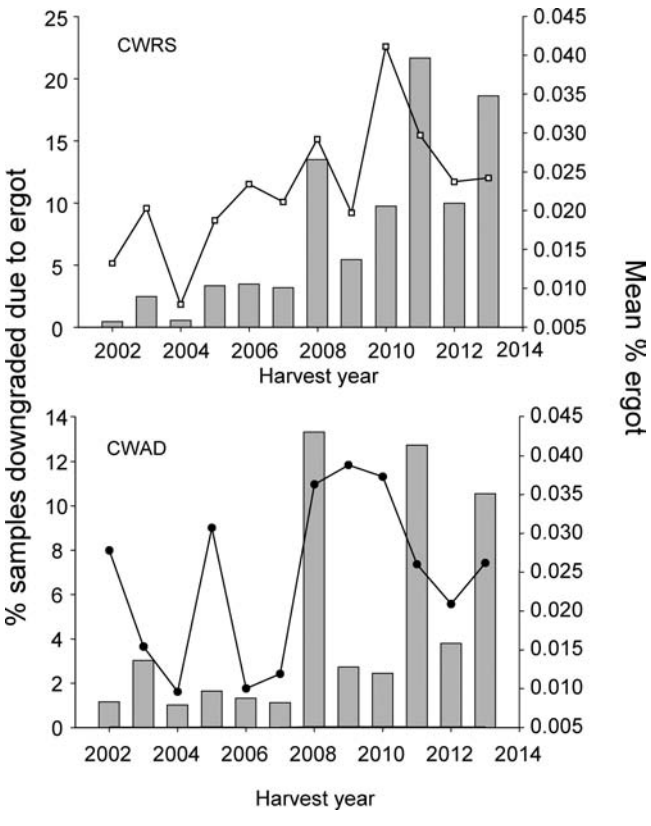

Figure 2. Occurrence of ergot in wheat (CWRS) and durum (CWAD) samples submitted to the Canadian Grain Commission Harvest Sample Program. The percentage of samples downgraded due to ergot is provided by the vertical bars, and the mean percent ergot observed in the samples is indicated by the line graph. Samples with no ergot sclerotia were set to 0 for the calculation of the annual mean percent ergot.

Overall, the data illustrated in Figure 2 suggest that the occurrence and severity of ergot infection in CWRS and CWAD have increased over the time period from 2002 to 2013. The incidence of ergot in the United Kingdom also increased during the mid-2000s.[16]

Changes in agronomical practices, such as the use of grass field margins and zero-tillage treatment of fields, have been implicated as factors contributing to the increase of ergot. Because burying ergot sclerotia prevents the release of ascopores and subsequent infection of flowering cereal plants,[17] zero-tillage practices result in more inoculum on the field. The adoption of zero tillage in the Canadian Prairie provinces grew during the 2000s. From 2002 to 2008, the percentage of area in zero tillage increased from about 35% to 55%.[18] Field margins act not only as a reservoir for *C. purpurea* inoculum but as a local source of secondary inoculum as well. Bayles et al.[16] reported a higher risk of ergot infection to wheat mainly at the edges of wheat fields due to secondary inoculum from infected grasses in field margins. These practices would affect the presence of ergot in addition to environmental factors such as precipitation, temperature, and soil conditions,[19] which have also been implicated as affecting ergot in cereals.

Total concentrations of ergot alkaloids in CWAD and CWRS harvest samples from 2011 are shown in Figure 3. Concentrations of sum total ergot alkaloids in the harvest

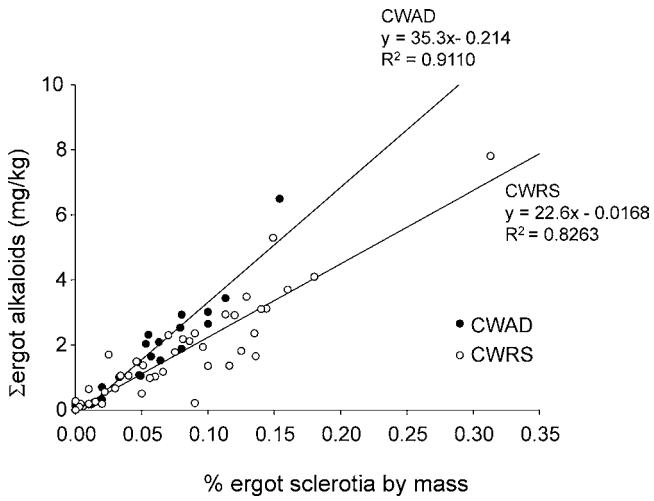

Figure 3. Relationship between the amount of ergot sclerotia and ergot alkaloids in Canada Western Amber Durum (CWAD) and Canada Western Red Spring (CWRS) samples from the 2011 harvest.

DOI: 10.1021/acs.jafc.5b02977
J. Agric. Food Chem. 2015, 63, 6644−6650

Table 2. Total Concentration of 10 Ergot Alkaloids Quantitated in Cereals Shipped between August 1, 2010, and July 31, 2012

grain	n	n > LOQ[a]	mean ΣEA (mg/kg)	median ΣEA (mg/kg)	range ΣEA (mg/kg)	90th percentile ΣEA (mg/kg)
wheat	117	117	0.229	0.195	0.012−0.666	0.399
durum	46	46	0.225	0.193	0.040−0.584	0.406
barley	25	21	0.065	0.047	<0.002−0.149	0.149
rye	1	1	1.138			

[a]Limit of quantitation of most sensitive analyte ergonovine, 2 μg/kg.

samples ranged from < LOQ to 7.81 mg/kg and were generally higher than the sum total ergot alkaloids observed in cereal shipments (Table 2). The maximum sum total ergot alkaloids in cereal shipments was in the rye sample at 1.14 mg/kg. The higher concentration in rye is not unexpected because it is particularly susceptible to infection by *C. purpurea* as it is a cross-pollinator with large open florets.[5]

The lowest mean sum total ergot alkaloid concentration was in barley shipments, which mainly represented grain selected for malting. It is not clear from these results if the low sum total ergot alkaloid concentrations observed are due to less ergot infection in barley or to a more thorough cleaning of barley prior to export for use as malt. There were no significant differences between the sum total ergot alkaloid concentrations measured in wheat and durum.

The wider range of sum total ergot alkaloid concentrations in the harvest samples is not unexpected, due to the nature of the samples and the design of the research. The 2011 harvest samples were not cleaned to remove contaminants such as ergot sclerotia prior to analysis. They were also selected to include grain with high levels of ergot infection to examine the relationship between sum total ergot alkaloid concentrations and percent ergot sclerotia, whereas the cereal shipments analyzed represent grain that had been graded and cleaned. The use of color sorters or mechanical methods including sieving[5] in grain-handling facilities can remove contaminants such as ergot sclerotia.

There are few studies in the literature regarding ergot alkaloids in raw grain. Two studies that do present data on the occurrence of ergot alkaloids in unprocessed cereal grains did not analyze the same 10 analytes that were included in this study; therefore, an in-depth comparison of results is not possible. Martos et al.[20] reported the presence of ergocornine and ergotamine in only 10% of eastern Canadian wheat samples analyzed. However, total concentrations of these two ergot alkaloids ranged from 0.076 to 0.638 mg/kg. Considering that the analysis did not include the predominant alkaloids ergocristine and ergocristinine, and assuming the pattern of occurrence of individual ergot alkaloids is consistent, the eastern wheat samples appear to contain higher levels of ergot alkaloids than in the western grain shipments, but the levels are consistent with the harvest samples analyzed in the current study. Uhlig et al.[21] reported lower average concentrations of 0.058 and 0.049 mg/kg for the sum of eight ergot alkaloids in Norwegian wheat and barley delivered to mills.

Ergot Alkaloid Patterns in Grain. The relative amounts of individual ergot alkaloids present in the wheat and durum shipments, as well as the harvest samples, are shown in Figure 4. The relative amounts were calculated as the fraction of an individual alkaloid concentration as compared to the sum total ergot alkaloid concentration. For the shipments, ergocristinine was the predominant alkaloid at a fraction of 0.39, followed by ergocristine (0.28) and ergotamine (0.10). The ergocristine/inine and ergotamine/inine pairs were the most abundant

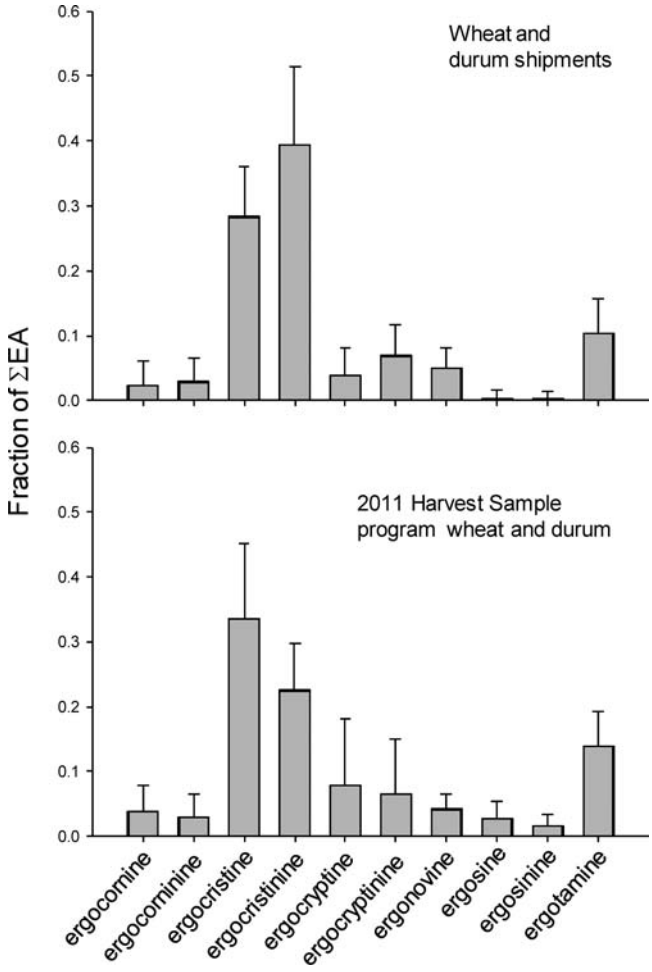

Figure 4. Ergot alkaloid patterns observed in shipments (n = 163) and harvest samples (n = 65) of wheat and durum. Bars represent the mean of each alkaloid as a fraction of the total concentration of ergot alkaloids (ΣEA); error bars indicate the standard deviation. Results less than the limit of quantitation were set to 0 for calculations.

alkaloids observed in sclerotia from Canadian wheat.[22] The pattern observed for the wheat and durum shipments was also very similar to those for barley and rye shipments (data not shown). Young and Chen[23] also noted a similarity in ergot alkaloid patterns among rye, wheat, and barley ergot sclerotia from grains grown in western Canada.

The pattern observed in the harvest samples differed slightly from the grain shipments. In the harvest samples for all *R* and *S* enantiomeric pairs, the *R* enantiomers were present at higher mean fractions of total ergot alkaloid than their epimers. Most noticeably, ergocristine rather than ergocristinine was the predominant alkaloid at a fraction of 0.32. The second most abundant alkaloid was ergocristinine (0.23). In the grain shipment samples, ergocornine, ergocristinine, and ergocrypti-

DOI: 10.1021/acs.jafc.5b02977
J. Agric. Food Chem. 2015, 63, 6644−6650

nine were all at higher mean fractions than their corresponding enantiomers.

The harvest samples can be considered to be "fresher" samples, as they were not stored as long prior to analysis as compared to the shipment samples. The shipment samples were stored for at least a year prior to analysis. In addition, the grain in the shipment samples would have been stored for an additional period on the farm and in grain-handling facilities prior to shipment. Potentially, a number of years could have passed between harvest and analysis of the grain in the shipment samples. During this time, epimerization could have occurred, thereby transforming the *R* enantiomers into *S* enantiomers. Such a change has been observed for sclerotia stored for several years; older sclerotia contained a higher percentage of *S* enantiomers as compared to sclerotia stored for a few months (36 vs 20%).[24]

The predominance of ergocristine/inine in the Canadian cereal samples and the consistency of the predominance across the various cereal grains differ from reports of ergot alkaloid patterns observed in other studies. In cereal-based food and feed in Europe, ergocryptine was reported as the predominant ergot alkaloid in rye and wheat-based food and rye feed, whereas ergosine was the most abundant compound in wheat feed.[25] Ergotamine was predominant in rye sclerotia from Australia,[24] and ergocornine and ergosine were predominant in wheat sclerotia from England.[16] The differences observed in ergot alkaloid patterns likely reflect variation in production by *C. purpurea* strains among host plants,[5,16] epimerization, and other transformations under field, storage, and processing conditions.

Relationship between the Presence of Ergot Sclerotia and Ergot Alkaloids in Grain. Figure 3 illustrates the relationship observed between the percentage of ergot sclerotia and sum total ergot alkaloid concentration in CWAD and CWRS samples from one growing season. The sum total ergot alkaloid concentrations increase with an increase in the percentage of ergot sclerotia present in a sample, with the relationship for CWRS significantly different from CWAD (parallel lines analysis; $p = 0.005$). The steeper slope of the CWAD relationship may indicate that durum is more susceptible to infection or production of ergot alkaloids when infected or that it is grown in areas with more virulent and/or toxigenic strains of *C. purpurea* as compared to CWRS. Differences in host resistance to ergot sclerotia production, as well as differences in the ability of various *C. purpurea* strains to elicit production of sclerotia, have been reported for wheat.[5,16] Variation in total ergot alkaloid concentrations in wheat sclerotia are also seen among fields and broader geographic regions.[22,26]

Even though studies have reported variation in sum total ergot alkaloid concentrations in sclerotia, the relationships observed between percentage of ergot sclerotia and sum total ergot alkaloid in CWAD and CWRS are strong. The relationships support the use of ergot sclerotia percentage as a tool to manage the presence of ergot alkaloids in wheat and durum. Figure 5 illustrates a comparison of sum total ergot alkaloid concentrations among wheat and durum shipments of various grades. Even though these grades were based on a number of grading factors and not just the presence of ergot sclerotia, the median sum total ergot alkaloid concentration of the lowest quality shipments (feed) was significantly higher than that of the highest quality grades (1 and 2). Changes to the Canadian grading tolerances for ergot are not expected to result in sizable changes to ergot alkaloid concentrations in future shipments, as the new grading tolerances are the same as those recently used for CWAD and CWRS grades 3 and 4.

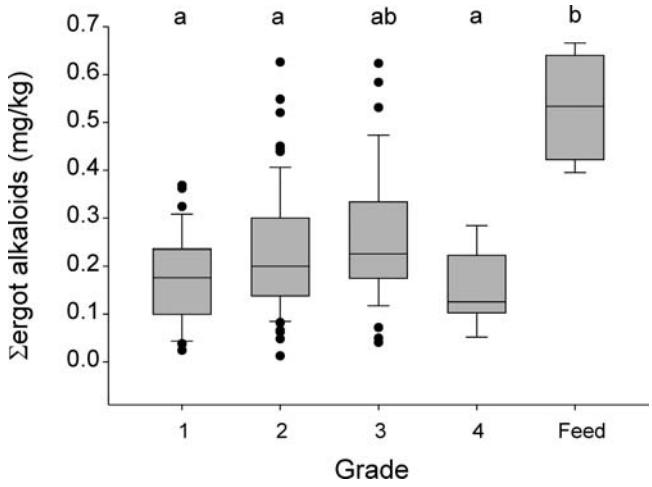

Figure 5. Sum of 10 ergot alkaloids in various grades of wheat and durum shipments. Median concentrations are indicated by horizontal lines in the boxes encompassing the 25th−75th percentiles. Whiskers indicate the 90th and 10th percentiles. Outliers in the 95th and 5th percentiles are indicated by dots. Unique letters indicate that median concentrations are significantly different among grades (Kruskal−Wallis one-way analysis of variance on ranks).

■ ASSOCIATED CONTENT

Supporting Information

Supplementary Table 1: Ergot alkaloids analyzed by the liquid chromatography-tandem mass spectrometry method. Supplementary Table 2: Summary of ergot alkaloid method validation results. Mean ± standard deviation ($n = 7$) percent recoveries are listed for fortified wheat and rye. Supplementary Figure 1: Total concentrations of 10 ergot alkaloids quantified in a sample of rye over 10 months. The Supporting Information is available free of charge on the ACS Publications website at DOI: 10.1021/acs.jafc.5b02977.

■ AUTHOR INFORMATION

Corresponding Author

*(S.A.T.) Phone: (204) 984-3456. Fax: (204) 983-0724. E-mail: sheryl.tittlemier@grainscanada.gc.ca.

Notes

Contribution 1090 from the Grain Research Laboratory of the Canadian Grain Commission.

The authors declare no competing financial interest.

■ ACKNOWLEDGMENTS

Sampling by Canadian Grain Commission inspectors was essential in the monitoring of harvest samples and grain shipments. Wes Harnden assisted with sample handling and processing.

■ REFERENCES

(1) Schiff, P. L. Ergot and its alkaloids. *Am. J. Pharm. Educ.* **2006**, *70*, 1−10.

(2) Bryden, W. L. Mycotoxin contamination of the feed supply chain: Implications for animal productivity and feed security. *Anim. Feed Sci. Technol.* **2012**, *173*, 134−158.

DOI: 10.1021/acs.jafc.5b02977
J. Agric. Food Chem. 2015, 63, 6644−6650

(3) Stoll, A.; Hoffmann, A. The chemistry of the ergot alkaloids. In *Chemistry of the Alkaloids*; Pelletier, S. W., Ed.; Van Nostrand Reinhold: New York, 1970; pp 267−301.
(4) Krska, R.; Stubbings, G.; Macarthur, R.; Crews, C. Simultaneous determination of six major ergot alkaloids and their epimers in cereals and foodstuffs by LC−MS−MS. *Anal. Bioanal. Chem.* **2008**, *391*, 563−576.
(5) Lorenz, K.; Hoseney, R. C. Ergot on cereal grains. *CRC Crit. Rev. Food Sci. Nutr.* **1979**, *11*, 311−354.
(6) European Food Safety Authority. Scientific opinion on ergot alkaloids in food and feed. *EFSA J.* **2012**, *10*, 2798−2956.
(7) Canadian Grain Commission. *Official Grain Grading Guide*; Winnipeg, MB, Canada, 2013.
(8) Codex Alimentarius. Codex standard for wheat and durum wheat, Codex Standard 199-1995; 1995.
(9) Grain Inspection, Packers & Stockyards Administration, U.S. Department of Agriculture. United States standards for wheat; 2006.
(10) European Commission. Commission regulation (EU) No. 1272/2009 of December 11, 2009 laying down common detailed rules for the implementation of Council Regulation (EC) No. 1234/2007 as regards buying-in and selling of agricultural products under public intervention; 2009.
(11) Gräfenhan, T.; Patrick, S. K.; Roscoe, M.; Trelka, R.; Gaba, D.; Chan, J. M.; McKendry, T.; Clear, R. M.; Tittlemier, S. A. Fusarium damage in cereal grains from western Canada. 1. Phylogenetic analysis of moniliformin producing *Fusarium* species and their natural occurrence in mycotoxin contaminated wheat, oats, and rye. *J. Agric. Food Chem.* **2013**, *61*, 5425−5437.
(12) Canadian Grain Commission. *Sampling Systems Handbook and Approval Guide*; Aug 1, 2013.
(13) Tittlemier, S. A.; Roscoe, M.; Kobialka, C.; Blagden, R. Considerations in the preparation of laboratory samples for the analysis of ochratoxin A in wheat. *World Mycotoxin J.* **2012**, *5*, 107−116.
(14) European Commission. Commission decision implementing Council Directive 96/23/EC concerning the performance of analytical methods and the interpretation of results. *Off. J. Eur. Communities* **2002**, *L221*, 8−36.
(15) Krska, R.; Berthiller, F.; Schuhmacher, R.; Nielsen, K. F.; Crews, C. Determination of ergot alkaloids: purity and stability assessment of standards and optimization of extraction conditions for cereal samples. *J. AOAC Int.* **2008**, *91*, 1363−1371.
(16) Bayles, R.; Fletcher, M.; Gladders, P.; Hall, R.; Hollins, W.; Kenyon, D.; Thomas, J. *Towards a Sustinable Whole-Farm Approach to the Control of Ergot*; Report 456; Home Grown Cereals Authority: Warwickshire, UK, 2009.
(17) Bretag, T. W.; Merriman, P. R. Effect of burial on survival of sclerotia and production of stromata by *Claviceps purpurea*. *Trans. Br. Mycol. Soc.* **1981**, *77*, 658−660.
(18) Nagy, C.; Gray, R. *Rate of Return to the Research and Development Expenditure on Zero Tillage Technology Development in Western Canada (1960−2010)*; Department of Bioresource Policy, Business and Economics, University of Saskatchewan: Saskatoon, SK, Canada, Jan 11, 2012.
(19) Evans, I.; Solberg, E.; Huber, D. M., Copper and plant disease. In *Mineral Nutrition and Plant Disease*; Datnoff, L. E., Elmer, W. H., Huber, D. M., Eds.; The American Phytopathological Society: St. Paul, MN, USA, 2007; pp 177−188.
(20) Martos, P. A.; Thompson, W.; Diaz, G. J. Multiresidue mycotoxin analysis in wheat, barley, oats, rye and maize grain by high performance liquid chormatography-tandem mass spectrometry. *World Mycotoxin J.* **2010**, *3*, 205−223.
(21) Uhlig, S.; Eriksen, G. S.; Hofgaard, I. S.; Krska, R.; Beltrán, E.; Sulyok, M. Faces of a changing climate: Semi-quantitative multi-mycotoxin analysis of grain grown in exceptional climatic conditions in Norway. *Toxins* **2013**, *5*, 1682−1697.
(22) Young, J. C. Variability in the content and composition of alkaloids found in Canadian ergot. II. Wheat. *J. Environ. Sci. Health, Part B* **1981**, *16*, 381−393.
(23) Young, J. C.; Chen, Z. Variability in the content and composition of alkaloid found in Canadian ergot. III. Triticale and barley. *J. Environ. Sci. Health, Part B* **1982**, *17*, 93−107.
(24) Blaney, B. J.; Molloy, J. B.; Brock, I. J. Alkaloids in Australian rye ergot (*Claviceps purpurea*) sclerotia: implications for food and stockfeed regulations. *Anim. Prod. Sci.* **2009**, *49*, 975−982.
(25) Diana Di Mavunga, J.; Larionova, D. A.; Malysheva, S. V.; Van Peteghem, C.; De Saeger, S. *Survey on Ergot Alkaloids in Cereals Intended for Human Consumption and Animal Feeding*; submitted to European Food Safety Authority, 2011.
(26) Mainka, S.; Dänicke, S.; Böhme, H.; Ueberschär, K. H.; Liebert, F. On the composition of ergot and the effects of feeding two different ergot sources on piglets. *Anim. Feed Sci. Technol.* **2007**, *139*, 52−68.

DOI: 10.1021/acs.jafc.5b02977
J. Agric. Food Chem. 2015, 63, 6644−6650

JOURNAL OF AGRICULTURAL AND FOOD CHEMISTRY

Addition/Correction

pubs.acs.org/JAFC

Correction to Neutral Pectin Side Chains of Amaranth (*Amaranthus hypochondriacus*) Contain Long, Partially Branched Arabinans and Short Galactans, Both with Terminal Arabinopyranoses

Daniel Wefers, Catrin E. Tyl, and Mirko Bunzel*

J. Agric. Food Chem. **2015** (2), 707−715. DOI: 10.1021/jf505283x

From our previous experiments, we assigned α-L-arabinopyranose as the terminal sugar unit of disaccharide **A-II2**. However, further purification of compound **A-II2** for its use as an analytical standard compound, followed by HPAEC monosaccharide analysis, yielded xylose and arabinose in equal amounts. Determination of the D/L configuration confirmed the presence of D-xylose. Because the NMR data are in good agreement with values obtained for terminal β-D-xylose, we now conclude that compound **A-II2** contains β-D-xylopyranose and not α-L-arabinopyranose. However, because this oligosaccharide was released due to *endo*-arabinanase treatment, it may be a new structural element of arabinans with similar impact as the originally published structure.

A more appropriate title for this publication would be "Neutral Pectin Side Chains of Amaranth (*Amaranthus hypochondriacus*) Contain Long, Partially Branched Arabinans and Short Galactans with Terminal Arabinopyranoses".

Most of the sections referring to substitution of arabinans by arabinopyranoses are also correct for xylopyranoses; the more specific discussions about the arabinopyranoses are irrelevant now.

A revised version of Figure 1 is provided below.

Published: July 15, 2015

ACS Publications © 2015 American Chemical Society

DOI: 10.1021/acs.jafc.5b03233
J. Agric. Food Chem. 2015, 63, 6651−6652

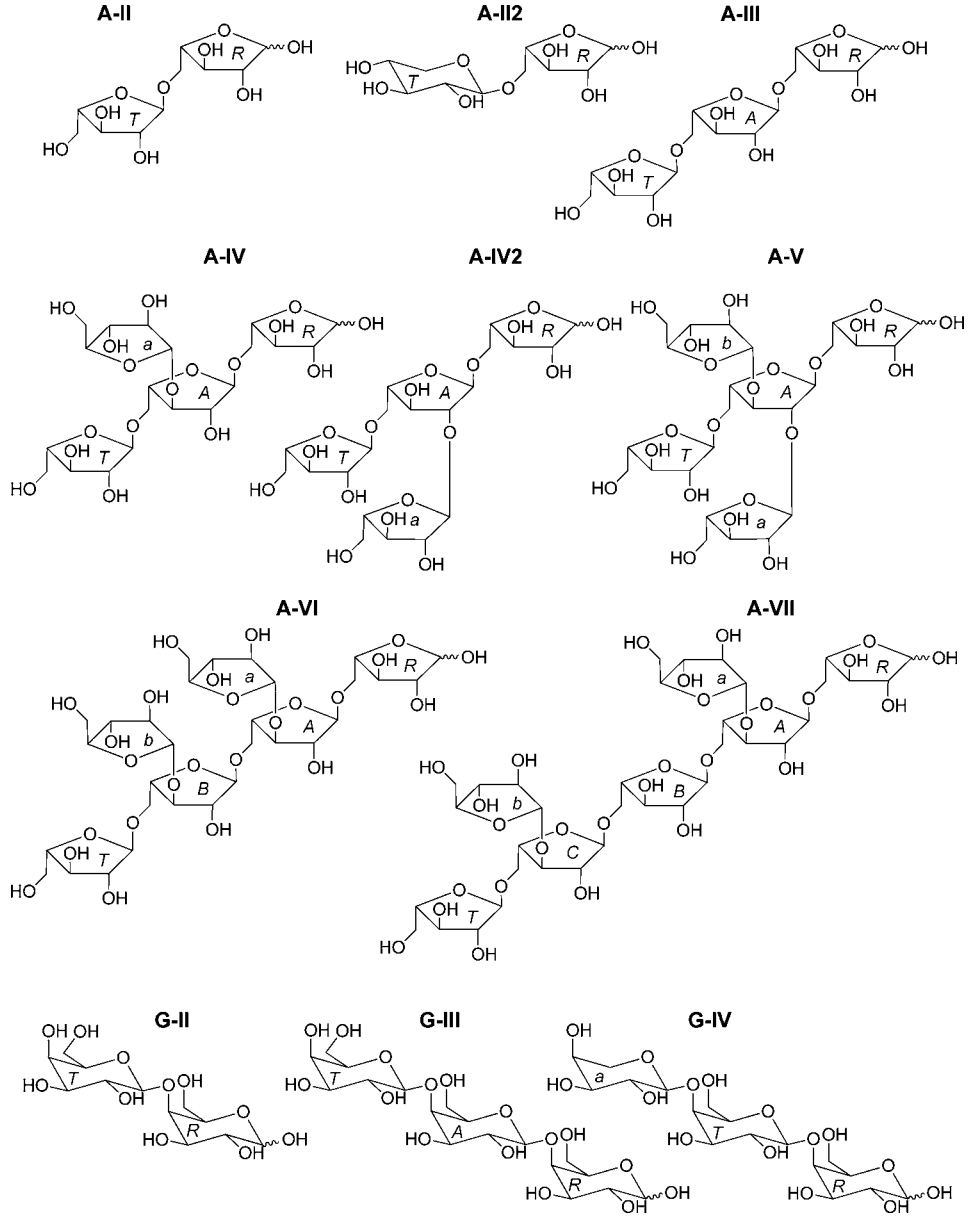

Figure 1. Structures of arabino-oligosaccharides isolated from sugar beet arabinan (**A-II**−**A-VII**), amaranth (**A-II2**), and red clover sprouts (**A-IV2**) and structures of galacto-oligosaccharides isolated from potato galactan (**G-II**−**G-IV**). Letters R, A, B, C, T, a, and b are used to describe the sugar units for the NMR spectroscopic assignment (see Table 2 and Supporting Information).

DOI: 10.1021/acs.jafc.5b03233
J. Agric. Food Chem. 2015, 63, 6651−6652

Table 1. Sequences of Gene-Specific Primers Used for Quantitative Real-Time RT-PCR[a]

gene family	specific class	accession no.	5′ primer	3′ primer	T_m (°C)	PCR fragment size (bp)
PR1	PR1a, acidic PR1	X12485.1	TGCTAAGGCTGTTGAGATGTGGGTC	ACTGAACCCTAGCACATCCAACACG	58	143
PR2	PR2a, basic glucanase	EU867448.1	CGTTTAGGAACGATGCTAGG	GAACCATCTTGTACCACCAC	55	175
PR3	endochitinase	X16939.1	GCCATAGGAGTGGACCTCTAAAC	AAAAGACCTCTGGTTGCCGC	59	335
PR5	osmotin	DQ403158.1	TGCAACTTTGATGGTGCTGG	CCGTGACATTTTCCAGG ACC	58	215
EF	elongation factor-1α	AF120093	ATTGGTGGAATTGGTACTGTCC	CCGCAACATTCTTGACATTAAA	58	184

[a]PR, pathogenesis-related protein.

dual effect of GME (i.e., antimicrobial and PDI) could be involved in tobacco plant protection against *Ppn*.

MATERIALS AND METHODS

Biological Compounds and Chemicals. The GME is a *Vitis vinifera* L. extract provided by Grap'Sud (Cruviers-Lascours, France). Its pesticide (<1 ppm), heavy metal (<3 ppm), and bacterial (*Escherichia coli*-free, *Salmonella*-free, and total coliform-free) contents were certified by the manufacturer. Lot LPb123281703 used in our experiments was produced by water extraction containing SO_2 followed by concentration. The aqueous end-product contains 23.6% DW with <1000 ppm of SO_2. GME is produced from the postharvest grape marc of several red wine varieties (e.g., Merlot, Syrah, Carignan, Grenache, Cabernet, and Alicante) cultivated in southern France. The partial characterization of GME indicated that the winery byproducts from red grapes consist mainly of polyphenols (PP) including anthocyanins, a low amount of soluble sugars, and no detectable salicylic acid, jasmonic acid, or *trans*-resveratrol.[11,14] The GME used here came from the 2012 grape harvest, and the water-extracted product contains 35% PP of the dry matter with 2% anthocyanins (as specified by Grap'Sud). GME diluted in ultrapure water to reach 0.19% PP concentration is an acidic solution at pH 3.2. Salicylic acid (SA) was purchased from Sigma (St-Quentin-Fallavier, France).

Plant Material and Treatments. The biological activity of GME was assayed on 8-week-old wild-type tobacco plants (*N. tabacum* L. var. Samsun NN) and NahG transgenic plants (NahG8 line[16]) carrying the *NahG* gene, which encodes a bacterial salicylate hydroxylase. NahG seeds were generously provided by M. Ponchet (INRA, Sophia Antipolis, France). Plants were grown in a growth chamber at 22 °± 5 °C with a 16 h photoperiod. GME was infiltrated as an aqueous solution on foliar tissue using a plastic syringe. As routine protocol, 50 μL was infiltrated until the solution was spread across a 1−2 cm^2 leaf area. Three leaves per tobacco plant were infiltrated with GME at 0.19% PP, and GME was serially diluted prior to use for dose-dependent experiments. Leaves were infiltrated with 2 mM SA for the positive control and with acidic water (pH adjusted to 3.5 with acetic acid) for the negative control. Macroscopic symptoms were examined under bright-field (white light from 60 W bulb) or UV light (at 312 nm). Fluorescent areas were measured using Optimas 6.1 software.

Quantitative Real-Time RT-PCR. Leaf tissue was collected from whole limb infiltrated in 20 areas covering the whole limb of the three most basal leaves without chlorotic symptoms. Total RNA was extracted from 200 mg of leaves using CTAB extraction buffer as described by Chang et al.[17] The purified total RNAs were treated with 1 U of DNase I solution (Euromedex, France) containing 40 U of RNase inhibitor (Euromedex, France) to remove DNA contamination. RNA purity and concentration were measured at 260/280 nm using a NanoDrop-1000 spectrophotometer (Thermo Scientific, Villebon-sur-Yvette, France). RNA integrity was verified on a 1% agarose gel by detecting rRNAs. First-strand cDNA was synthesized from 1 μg of total RNA using Euroscript Reverse Transcriptase (Eurogentec, France) according to the manufacturer's instructions. PCR reactions were prepared using the qPCR Mastermix kit for SYBR green (Eurogentec, France) following the manufacturer's protocol. Reaction mix consisted of SYBR green-containing buffer (7.5 μL), forward primer (1 μL, 100 nM), reverse primer (1 μL, 100 nM), and template (2.5 μL, 0.1 ng). The three-step protocol PCR conditions were as follows: initial denaturing at 94 °C for 5 min, followed by 40 cycles of denaturing at 94 °C for 20 s, annealing at 55/59 °C for 20 s and polymerization at 72 °C for 20 s. Quantitative assessment of mRNA levels was performed using an iCycler iQ5 (Bio-Rad, France). The cDNA concentration used yielded a threshold cycle value (C_T) between 15 and 30 cycles. Amplification specificity was checked by melting-curve analysis. Elongation factor EF-1α was used as internal control.[18] The relative quantity of transcripts was calculated with the delta−delta method mathematical model developed by Pfaffl.[19] For every experiment, the abundance of targeted gene transcripts was set relative to control plants (no GME exposure). The relative quantities of targeted gene transcripts in controls take then always the value of 1. We analyzed transcript accumulation on three infiltrated leaves per plant and at least two independent experiments. Every run was carried out in triplicate. Primers and amplicon sizes are given in Table 1. Efficiencies of all primer sets were routinely checked (data not shown). Bars give means ± standard error (SEM).

Oomycete Material and Culture Conditions. The model pathosystem *Phytophthora*/tobacco was used for the pathogenesis experiments. *Ppn* isolate 329 was obtained from the INRA (Sophia-Antipolis, France) *Phytophthora* collection[20] and cultivated on V8 juice agar (V8A) plates (1 L of V8A contains 200 mL of commercial V-8, 2 g of $CaCO_3$, 17 g of agar, and 800 mL of distilled water) at 24 °C in the dark and then transferred to fresh medium every week. GME was used at concentrations of 0.95% PP, 0.19% PP, 0.038% PP, and 0.0076% PP.

In Vitro Antifungal Activity Assays. *Mycelial Growth.* Individual agar disks (6 mm in diameter) were removed from the edge of an actively growing culture of *Ppn* and placed at the middle of a fresh V8A plate (90 mm in diameter) amended or not with GME. GME was added to the prewarmed V8A to adjust the required final PP concentrations. GME was replaced by acidic water (pH 3.5) for the control. After a 5-day incubation period at 24 °C in darkness, radial growth of mycelia was measured by using ImageJ 1.48 software.

Sporangium Formation. Sporangia were produced by growing *Ppn* on V8A plates as above. Four agar disks (6 mm in diameter) and attached mycelia were removed from the edge of an actively growing culture and placed in a series of plastic Petri dishes (60 mm in diameter) containing 7 mL of sterile water supplemented or not (negative control) with GME. Following a 4-day incubation period at 24 °C in darkness, the liquid was decanted from the Petri dishes, and the agar disks were stained and fixed with acid fuchsin in 85% lactic acid. The number of sporangia along the margins of each agar disk was counted under a microscope (Olympus CX41, Japan).

Zoospore Motility and Cyst Germination. Zoospores were released from *Ppn* sporangia. *Ppn* mycelia were used, macerated and incubated for 4 days on agar plates (2% agar in water) to produce sporangia. Zoospores were released by heat shock treatment with chilling first at 4 °C for 20 min and then heating by adding 10 mL of prewarmed water (37 °C) followed by incubation at 37 °C for 30 min. Aqueous mixtures of GME were added to equal volumes of the zoospore suspensions, leading to final concentrations of 0.95, 0.19, 0.038, and 0.0076% PP. Control zoospore suspensions received an equal volume

DOI: 10.1021/acs.jafc.5b01740
J. Agric. Food Chem. 2015, 63, 6653−6659

of water only. Zoospore suspensions were held at 25 °C and observed microscopically at 10× magnification to determine the maximum elapsed time for complete cessation of motility. Observations were made at 1 min intervals for the first 15 min, then at 15-min intervals for the next 45 min, and finally at 1-h intervals until there was no detectable zoospore movement. To determine cyst germination, equal volumes of the encysted zoospore suspensions were deposited on Petri dishes containing V8A amended with GME. The encysted zoospores were incubated at 24 °C for 6 h and examined for mycelial growth arising from germinating cysts. Every cyst with a germ tube was counted as germinated.

In Vivo Protection Test. Experiments were performed on 8-week-old tobacco leaves from wild-type and NahG transgenic plants. Nonsenescent leaves were first sprayed with GME containing 0.19% PP or 2 mM SA (positive control) or acidic water (negative control) onto the adaxial face using a fine atomizer (2 mL per leaf). Sprayed leaves were detached from the plant at 0, 2, and 4 days after treatment (dpt), and two leaf disks (8-cm diameter) were punched out from every sprayed leaf. *Ppn* was then inoculated into distinct areas with 100 μL of zoospore suspension containing 200 zoospores. Leaf disks were placed on agar plates (17 g of agar in water) and incubated at 24 °C in the dark. Level of protection was evaluated 3 days after inoculation by measuring the *Ppn*-infected areas. The infection areas were measured by using Optimas 6.1 software. In each experiment at least four consecutive mature leaves received *Ppn* inoculations. All experiments were performed at least with duplicates of plants.

Statistical Analysis. All experiments were performed in biological and technical triplicates. Results were expressed as means ± standard error of the mean (SEM). Letters above bars indicate statistically significant differences between samples, according to one-way ANOVA followed by LSD significant test ($p \leq 0.05$) using JMP 11.2.0 software. Significant changes in gene expression were determined using Fisher's least significant differences (**, $0.001 < P < 0.01$; ***, $P < 0.001$).

RESULTS

GME-Induced Macroscopic Symptoms. To investigate the involvement of SA in the GME-induced HR-like response, we first looked at the deployment of macroscopic symptoms on tobacco plants. Wild-type and NahG transgenic tobacco plants were infiltrated with 5 GME concentrations ranging from 0.19% PP (dilution 1) to the 4-, 8-, 16-, and 32- fold diluted GME concentrations (Figure 1). The 0.19% PP concentration produced a high level of defense in tobacco.[11] At 4 days postinfiltration (dpi), the 0.19% GME concentration generated microlesions on leaf tissues in both tobacco lines (Figure 1A–C,E) in a dose-dependent manner. The wild-type leaves developed topical lesions with large and marked chlorotic zones when GME was infiltrated at the 0.19% or 4-fold diluted level. The NahG leaves were less sensitive to GME, and lesions appeared when the concentrated GME (0.19% PP) was applied. The diluted GME failed to generate tissue injury in the tobacco mutant. Examination of the macroscopic changes under UV light ($\lambda_{312\ nm}$) revealed the expected sharp fluorescence surrounding the necrotic zone, with an estimated area value near 8.5 cm^2 indicative of high phenolic compound accumulation on wild-type leaves (Figure 1D). Transgenic leaves were less affected by GME, with only weak production of autofluorescent compounds (estimated area value near 0.5 cm^2) (Figure 1F).

GME-Induced PR Transcript Accumulation. The ability of GME to induce defense-related gene expression was investigated in tobacco plants. Transcript accumulation of four *PR* genes in response to GME treatment was assayed by quantitative real-time PCR. Figure 2A shows the ratio of transcript levels in treated leaf tissues versus negative control (acidic water-infiltrated tissues) of the antimicrobial *PR1*, β-1,3-glucanase *PR2*, endochitinase *PR3*, and osmotin-like *PR5* target genes in wild-type and NahG transgenic plants. Total RNA was extracted at 4 dpi from leaves infiltrated with GME containing 0.19% PP.

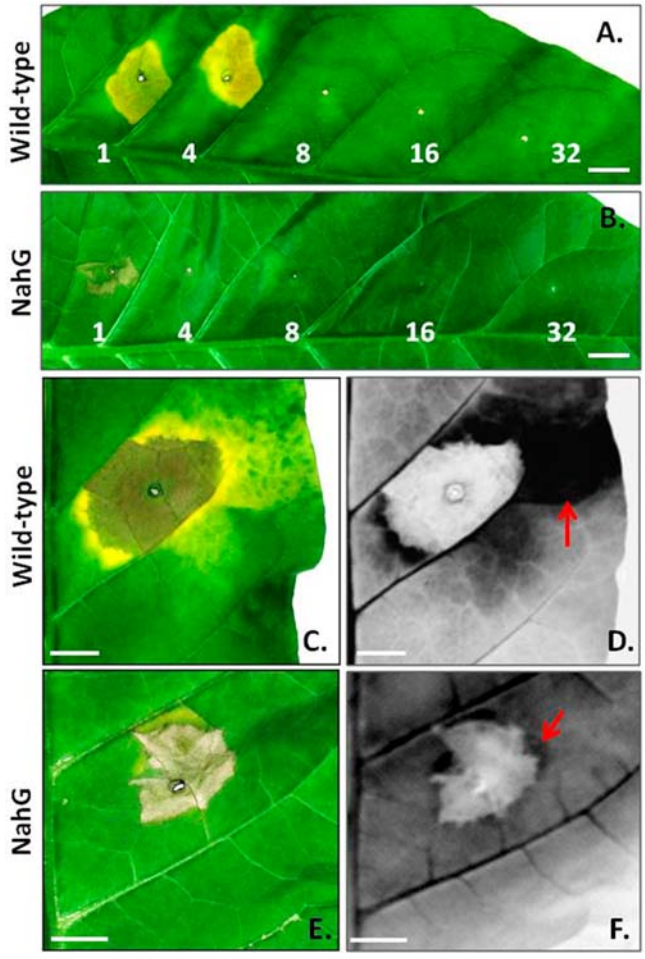

Figure 1. Macroscopic symptoms induced on tobacco leaves of wild-type plants (A, C, D) and NahG transgenic plants (B, E, F) by GME infiltration observed at 4 dpi under bright light (A, B, C, E) and UV light (D, F). GME was infiltrated at 0.19% PP in panels C–F and serially diluted: no dilution (1), 4-fold (4), 8-fold (8), 16-fold (16), and 32-fold (32) in panels A and B. Bars, 1 cm. Arrows point to fluorescent areas.

The transcripts for the four defense genes were over-accumulated in wild-type GME-treated tobacco plants, with 12-, 127-, 55-, and 186-fold inductions for *PR1*, *PR2*, *PR3*, and *PR5*, respectively, compared to water treatment. The accumulation profile of the defense markers was dramatically lower in NahG transgenic plants. *PR1* transcript accumulation was impaired (ratio below 1) and *PR2*, *PR3*, and *PR5* transcripts accumulated to ratios reaching 6–16-fold the water control. These data showing reduced sensitivity of the NahG transgenic plants carrying the salicylate hydroxylase gene point to the involvement of SA pathways in GME-induced defense marker gene expression. To validate the experimental plant system, *PR1* transcripts were quantified in wild-type and NahG tansgenic plants treated with exogeneous SA (Figure 2B). As expected, treatment with 2 mM SA induced strong *PR1* transcript accumulation in wild-type tobacco leaves (60-fold the water treatment). In contrast, application of SA on NahG leaves induced lower *PR1* transcript accumulation than wild-type

DOI: 10.1021/acs.jafc.5b01740
J. Agric. Food Chem. 2015, 63, 6653–6659

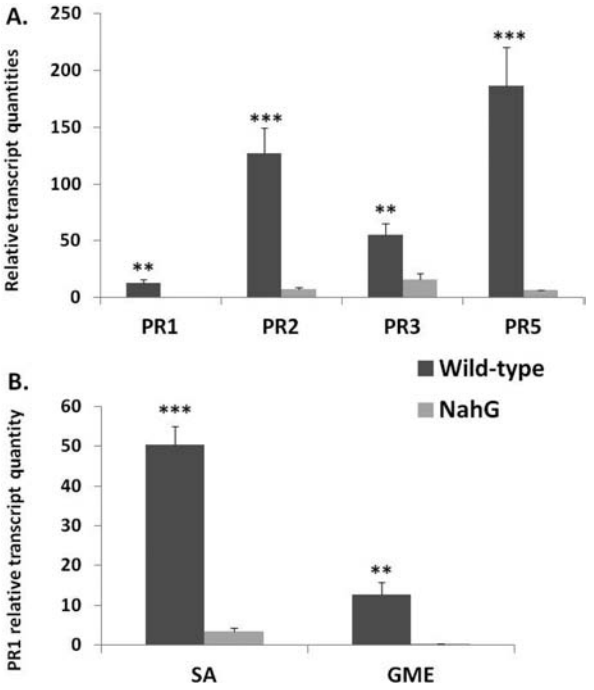

Figure 2. *PR* transcript accumulation in wild-type and NahG transgenic tobacco plant leaves infiltrated with 0.19% PP of GME or SA (2 mM). Transcripts encoding the *PR1*, *PR2*, *PR3*, and *PR5* (A) and *PR1* (B) genes were quantified by real-time RT-PCR in the infiltrated leaves. Values are expressed relative to control (acidic water treatment) values. Three leaves per plant were treated for each experiment. Statistics were generated from at least two independent experiments. Bars represent means ± SEM. Asterisks indicate significant differences compared with the wild-type: (**) $0.001 < P < 0.01$; (***) $P < 0.001$.

leaves with nevertheless residual expression level (3.5-fold the water treatment) (Figure 2B).

Antimicrobial Effect of GME on *Ppn*. The potential antimicrobial properties of GME were investigated on *Ppn* via a series of in vitro tests studying mycelia growth, sporangium formation, zoospore motility, and cyst germination of the oomycete. GME effect was assayed at different PP concentrations ranging from 0.0076 to 0.95%. Figure 3, panels A and B, shows the in vitro impact of GME on mycelial growth and germ hyphae elongation of *Ppn* on V8A medium. GME inhibited both developmental stages of *Ppn* in a dose-dependent manner. The radial surface of the *Ppn* mycelium was inversely proportional to GME concentration. The length of cyst germ tubes observed under microscope 24 h after treatments was highly affected proportionally to GME concentration.

Figure 3C shows the quantified inhibitory effects of GME over the water control. GME dramatically affected both sporangium formation and zoospore motility, with marked inhibition (82%) at 0.0076% PP. The complete inhibitory effect was achieved at 0.038% PP. Cyst germination was less affected by the lowest concentrations of GME (19% inhibition at 0.0076% PP and 44% inhibition at 0.038% PP), and full inhibition was reached at 0.19% PP. Higher GME concentrations were required to inhibit mycelial growth of *Ppn*. GME at 0.19% PP induced a 60% inhibition of mycelial growth, and only GME 0.95% PP was able to generate full inhibition.

Taken together, all of the GME concentrations tested were found to have inhibitory effects with various degrees of sensitivity according to asexual developmental stage of *Ppn*. The GME concentrations with inhibitory activity in spore experiments did not significantly affect the mycelial growth of *Ppn*. The GME at 0.038% PP, which had fully inhibited sporangium formation and zoospore motility, led to only an 8% inhibition of radial growth. These results indicate that spores are likely more sensitive than mycelium to the antimicrobial effect of GME.

GME-Induced Protection against *Ppn* Infection. We further determined how far the GME-induced protection of tobacco plants against *Ppn* was SA-dependent. Both wild-type and NahG transgenic plants were sprayed with GME, and then leaves were detached from the plant at 0, 2, and 4 days for zoospore inoculation. Figure 4 shows the lesion areas measured 3 days after *Ppn* inoculation relative to water treatment. SA-induced protection was also measured on leaves treated with 2 mM exogenous SA.

In wild-type tobacco plants, GME induced a significant reduction of infected areas translating to a high level of protection against *Ppn*. The local lesion areas induced by *Ppn* were reduced in size by 33, 45, and 46% at 0, 2, and 4 dpt, respectively. The 33% protection level was the result of GME biocide action because GME treatment was applied right before inoculation (0 dpt). Lesion areas of the NahG leaves were reduced to similar extents as in wild-type tobacco plants at 0 dpt. Protection level decreased radically in the NahG leaves when GME had been sprayed previously (at 2 and 4 dpt), with local lesion sizes mirroring those measured in control leaves infiltrated with water. This demonstrates that NahG transgenic plants lacking endogenous SA accumulation had lost GME-induced protection against *Ppn* at 2 or 4 dpt. The data clearly demonstrate that GME induced efficient protection against *Ppn* in wild-type leaves and suggest that endogenous SA may well be involved in GME-induced protection.

Exogenously supplied SA could protect tobacco leaves from *Ppn* with the reduction in size of infected areas in the wild-type (Figure 4). The SA treatment also induced a degree of protection at 0 dpt (32%), 2 dpt (20%), and 4 dpt (36%). Either SA might act as biocide agent or the NahG plants were still sensitive to SA in our experimental conditions.

DISCUSSION

The elicitor activity of GME has been largely demonstrated in previous work. This PP-rich extract activates a cascade of chemical defenses in tomato, *Arabidopsis*, and tobacco with local tissue injury, biochemical changes, and systemic molecular responses.[11,13] We predicted that SA may be involved in the plant defense reactions deployed after GME application to tobacco tissues. GME elicited molecular responses leading to up-regulation of the acidic *PR1*, *PR2*, *PR3*, and *PR5* genes in treated tobacco tissues. The expression of this array of PR protein genes occurs via an SA-dependent signaling pathway during elicitor-induced LAR and SAR in tobacco.[21] Here, the use of NahG transgenic plants expressing the salicylate hydroxylase gene allowed us to dissect the role of SA in GME-induced PDI events.

NahG transgenic plants expressing the bacterial salicylate hydroxylase gene did not exhibit the full spectrum of defense responses. The necrotic lesion was dramatically abolished, and the surrounding fluorescent zone in the NahG tissue was reduced by about 95% compared to the wild-type tissue at the HR-dose of GME containing 0.19% PP. Necrosis is the result of topical cell death together with the surrounding phytoalexin

DOI: 10.1021/acs.jafc.5b01740
J. Agric. Food Chem. 2015, 63, 6653−6659

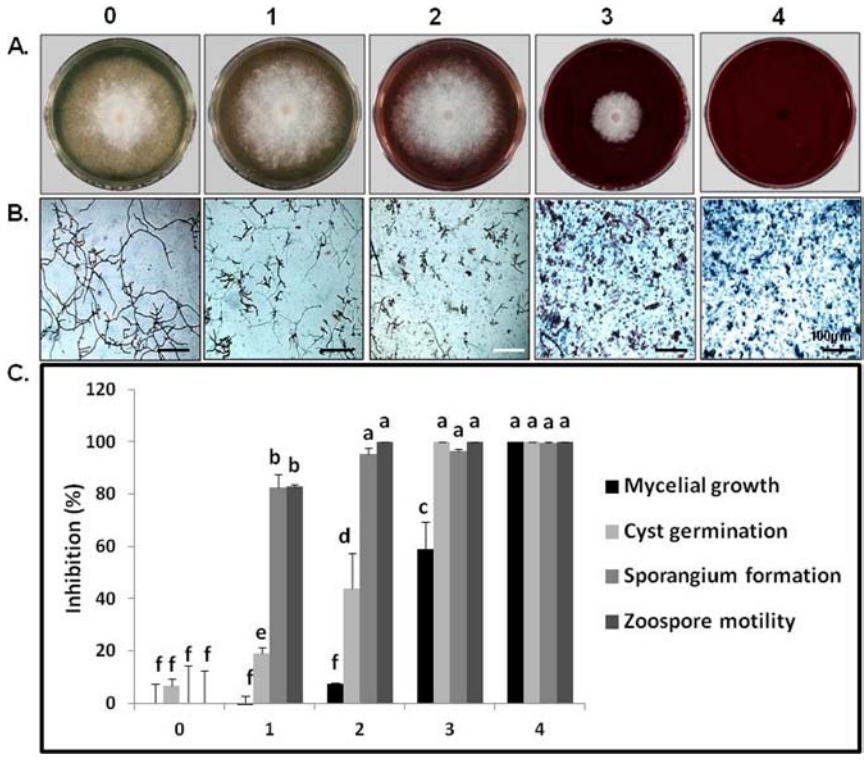

Figure 3. Antipathogenic activity of GME against *Ppn*. GME was serially diluted and used at different concentrations: no GME (0); 0.0076% PP (1); 0.038% PP (2); 0.19% PP (3); 0.95% PP (4). The impact of GME on (A) mycelial radial growth and (B) germ hyphae elongation of *Ppn* was observed in V8 medium amended with GME. The germ elongation and radial growth of *Ppn* were observed 24 h and 5 days postculture, respectively. (C) Quantification of the inhibitory effect of GME on several asexual developmental stages of *Ppn*. The in vitro antifungal assays were repeated in triplicate. Statistics were generated from at least two independent experiments. Results are expressed as means ± SEM. Letters next to bars indicate significant differences between treated and control samples according to one-way ANOVA followed by LSD test ($p \leq 0.05$).

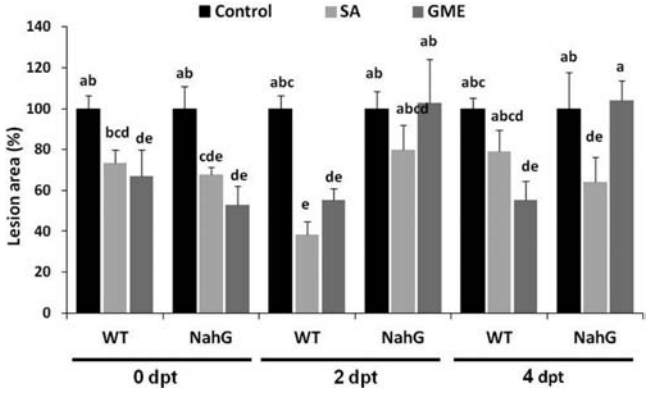

Figure 4. Induction of protection against *Ppn* in tobacco leaves. Leaves from 8-week-old wild-type (WT) and NahG transgenic plants were sprayed with water (control), 0.19% PP GME, or 2 mM SA and detached from the plant. At 0, 2, or 4 days post-treatment (dpt), *Ppn* zoospores were inoculated on the treated leaves. The pathogen-invaded areas were measured 3 days after *Ppn* inoculation. Bars represent standard error of four replicates from two independent experiments. Letters next to bars indicate statistically significant differences between treated and control samples according to one-way ANOVA followed by LSD test ($p \leq 0.05$).

production. SA has been previously demonstrated to be involved in phenomena modulating both HR cell death and phytoalexin accumulation.[22] Cell death is believed to occur before SA accumulation, but feedback mechanisms may mediate the regulation of cell death by an SA-dependent pathway.[23,24] In our GME/tobacco system, NahG transgenic plants showed dramatically compromised signs of GME-induced HR. These data serve as evidence that SA is required to mount the GME-induced HR in tobacco plants.

Treatment of NahG transgenic plants with the HR dose of GME also demonstrated the involvement of SA in later molecular defense events. The whole treated leaves were taken into account for molecular analysis, meaning that both LAR and SAR zones were indifferently pooled.[21] The LAR/SAR reactions were largely affected, with a dramatic down-regulation of *PR* genes in the NahG transgenic plants. This suggests that SA likely orchestrates *PR* transcript accumulation. Interestingly, a coordinated regulation was observed in the NahG plants with down-regulation of all four *PR* transcript accumulations. Nevertheless, the amount of acidic *PR1* transcripts was clearly suppressed and the amounts of *PR2*, *PR3*, and *PR5* transcripts were partially reduced in GME-treated NahG transgenic plants. As posited by Friedrich et al.,[25] residual SA levels might occur in NahG plants. The accumulation profile of the acidic isoforms would reflect their differential sensitivity to SA in the GME-treated plants.

Here we demonstrated the antifungal activity of GME against the oomycete *Ppn*. Polyphenols are groups of compounds serving as plant defense mechanisms against pathogenic microorganisms.[7] The many defensive functions of these bioactive phytochemicals enable cell strengthening and repair (lignin and suberin), antimicrobial activity (isoflavonoid phytoalexins), and signaling (SA). The largest and best studied polyphenols are extracted from grapes. Their direct antimicrobial activity has been demonstrated for bacteria and fungi (reviewed by Yu and Ahmedna[26]), although with various

DOI: 10.1021/acs.jafc.5b01740
J. Agric. Food Chem. 2015, 63, 6653−6659

sensitivities according to microbe species.[27] The relationship between compound structure and antimicrobial activity has been established.[28] Position(s) and numbers of hydroxyl groups and the degree of polymerization might be pivotal to the antimicrobial activity of phenolics. The different parts of grapes are rich sources of potentially bioactive polyphenols that vary in content between grape varieties.[29,30] The *V. vinefera* extract used here is produced from the marc of grapes harvested from various red wine varieties and showed potential antifungal activity in vitro with an inhibitory effect on the four asexual developmental stages of *Ppn*. The 0.19% PP concentration fully suppressed sporangium formation, cyst germination, and motility and partially suppressed mycelial growth.

The antipathogenic activity of GME could also induce in vivo protection against *Ppn* in tobacco leaves. Indeed, the GME treatment right before *Ppn* inoculation (at 0 dpt) in the wild-type and NahG transgenic plants led to 30−45% reduction in infection area. The involvement of PDI activity in GME-induced protection level was demonstrated by experiments led on NahG plants at 2 and 4 dpt. GME-induced accumulation of *PR1*−5 transcripts was highly reduced in the NahG tissues 4 days after infiltration, and the SA-depleted tissues did not show any GME-induced protection effect at 2 and 4 dpt compared to wild-type tissues. These results suggest that the in situ PR antimicrobial action might not have been high enough to provide protection against *Ppn* at 2 and 4 dpt. They also demonstrate that SA-dependent defense reactions play a primary role in GME-induced protection level. Interestingly, the *Ppn* infection areas at 2 and 4 dpt were significantly identical in control and GME-sprayed NahG tissues (100% infection areas), suggesting that the direct antimicrobial impact of GME was nonfunctional from day 2 postspraying. In the wild-type tobacco plants, PDI activity would play a preponderant role at 2 and 4 dpt, leading to 45% protection against *Ppn*. This suggests that the GME-induced *PR1*−5 transcript accumulation was high enough to provide the protection.

The impact of SA was concomitantly analyzed in our *Ppn*/tobacco pathosystem to rule out the possibility that NahG transgenic plants could respond to SA. Exogenous application of SA provided significant antifungal effect against *Ppn* at 0 dpt, leading to an average 30% protection level in both wild-type and NahG transgenic tissues. Treatment of wild-type plants with 2 mM SA provided clear protection against *Ppn* (62%) at 2 dpt, whereas exogenous SA treatment of SA-depleted NahG tissues led to at least partial loss of the high protection level. The phytohormone SA plays a central role in regulating defense response in plants, and its accumulation leads to resistance against pathogens.[5] At the dose tested (2 mM), the phytohormone was able to induce an accumulation of *PR* transcripts in wild-type tobacco plants and potentiate their resistance against the oomycete *Ppn*. The phenolic compound sprayed on tobacco leaves also led to a direct antifungal effect against *Ppn* that could match its antipathogenicity properties evidenced for plant pathogens.[31,32]

Taken together, our data provide key insights into the mode of action of GME. The dual antifungal and PDI activities of GME could induce high levels of protection against *Ppn*. This natural grape extract is geared to meet current plant protection product criteria and can be regarded as a promising biocontrol agent appropriate for more environmentally friendly crop protection schemes. We have so far investigated GME-induced disease resistance under controlled laboratory conditions, but the critical factor that will decide the real-world value of GME will be its potential effectiveness on crops in open fields. Field trials are currently in progress.

AUTHOR INFORMATION

Corresponding Author

*(P.G.) E-mail: Pascale.Goupil@univ-bpclermont.fr. Phone: (33) 04 73 40 79 40. Fax: (33) 04 73 40 79 51.

Funding

This work had financial support provided by grants from FUI: Fonds Unique Interministériel.

Notes

The authors declare no competing financial interest.

ACKNOWLEDGMENTS

We thank Céline Sac for her help in growing the tobacco plants and Dominique Marcon for the tobacco leaf images.

REFERENCES

(1) Abdul Latif, N.; Wake, G.; Reglinski, T.; Elmer, P. Modelling induced resistance to plant diseases. *J. Theor. Biol.* **2014**, *347*, 144−150.

(2) Conrath, U.; Corné, M. J-P.; Mauch-Mani, B. Priming in plant-pathogen interactions. *Trends Plant Sci.* **2002**, *7*, 210−216.

(3) Fu, Z. Q.; Dong, X. Systemic acquired resistance: turning local infection into global defense. *Annu. Rev. Plant Biol.* **2013**, *64*, 839−863.

(4) Durrant, W. E.; Dong, X. Systemic acquired resistance. *Annu. Rev. Phytopathol.* **2004**, *42*, 185−209.

(5) Vlot, A. C.; Dempsey, M. A.; Klessig, D. F. Salicylic acid, a multifaceted hormone to combat disease. *Annu. Rev. Phytopathol.* **2009**, *47*, 177−206.

(6) Walters, D. R.; Ratsep, J.; Havis, N. D. Controlling crop diseases using induced resistance: challenges for the future. *J. Exp. Bot.* **2013**, *64*, 1263−1280.

(7) Gurjar, M.; Ali, S.; Akhtar, M.; Singh, K. Efficacy of plant extracts in plant disease management. *Agric. Sci.* **2012**, *3*, 425−433.

(8) Gozzo, F.; Faoro, F. Systemic acquired resistance (50 years after discovery): moving from the lab to the field. *J. Agric. Food Chem.* **2013**, *61*, 12473−12491.

(9) Delaunois, B.; Farace, G.; Jeandet, P.; Clément, C.; Baillieul, F.; Dorey, S.; Cordelier, S. Elicitors as alternative strategy to pesticides in grapevine? Current knowledge on their mode of action from controlled conditions to vineyard. *Environ. Sci. Pollut. Res.* **2014**, *21*, 4837−4846.

(10) Lyon, G. Agents that can elicit induced resistance. In *Induced Resistance for Plant Defense: A Sustainable Approach to Crop Protection*; Walters, D. R., Newton, A. C., Lyon, G., Eds.; Wiley-Blackwell: Oxford, UK, 2014; pp 11−40.

(11) Goupil, P.; Benouaret, R.; Charrier, O.; ter Halle, A.; Richard, C.; Eyheraguibel, B.; Thiery, D.; Ledoigt, G. Grape marc extract acts as elicitor of plant defence responses. *Ecotoxicology* **2012**, *21*, 1541−1549.

(12) Benouaret, R.; Goujon, E.; Goupil, P. Plant defence inducer properties of grape marc extract. *IOBC-WPRS Bull.* **2013**, *89*, 95−97.

(13) Benouaret, R.; Goujon, E.; Goupil, P. Grape marc extract causes early perception events, defence reactions and hypersensitive response in cultured tobacco cells. *Plant Physiol. Biochem.* **2014**, *77*, 84−89.

(14) Benouaret, R.; Goujon, E.; Trivella, A.; Richard, C.; Ledoigt, G.; Joubert, J.-M.; Mery-Bernardon, A.; Goupil, P. Water extracts from winery by-products as tobacco defense inducers. *Ecotoxicology* **2014**, *23*, 1574−1581.

(15) Eyheraguibel, B.; Richard, C.; Ledoigt, G.; Ter Halle, A. Photoprotection by plant extracts: a new ecological means to reduce pesticide photodegradation. *J. Agric. Food Chem.* **2010**, *58*, 9692−9696.

(16) Gaffney, T.; Friedrich, L.; Vernooij, B.; Negrotto, D.; Nye, G.; Uknes, S.; Ward, E.; Kessmann, H.; Ryals, J. Requirement of salicylic

DOI: 10.1021/acs.jafc.5b01740
J. Agric. Food Chem. 2015, 63, 6653−6659

acid for the induction of systemic acquired resistance. *Science* **1993**, *261*, 754−766.
(17) Chang, S.; Pur Year, J.; Carney, J. A simple and efficient method for isolating RNA from pine trees. *Plant Mol. Biol. Rep.* **1993**, *11*, 113−116.
(18) Peng, J.-L.; Bao, Z.-L.; Ren, H.-Y.; Wang, J.-S.; Dong, H.-S. Expression of harpin$_{Xoo}$ in transgenic tobacco induces pathogen defense in the absence of hypersensitive cell death. *Phytopathology* **2004**, *94*, 1048−1055.
(19) Pfaffl, M. W. A new mathematical model for relative quantification in real-time RT-PCR. *Nucleic Acids Res.* **2001**, *29*, 2002−2007.
(20) Lacourt, I.; Panabières, F.; Marais, A.; Venard, P.; Ricci, P. Intraspecific polymorphism of *Phytophthora parasitica* revealed by analysis of mitochondrial DNA restriction fragment length polymorphism. *Mycol. Res.* **1994**, *98*, 562−568.
(21) Cordelier, S.; de Ruffray, P.; Fritig, B.; Kauffmann, S. Biological and molecular comparison between localized and systemic acquired resistance induced in tobacco by a *Phytophthora megasperma* glycoprotein elicitin. *Plant Mol. Biol.* **2003**, *51*, 109−118.
(22) Nawrath, C.; Métreaux, J. P. Salicylic acid induction-deficient mutants of *Arabidopsis* express PR-2 and PR-5 and accumulate high levels of camalexin after pathogen inoculation. *Plant Cell* **1999**, *11*, 1393−1404.
(23) Alvarez, M. E. Salicylic acid in the machinery of hypersensitive cell death and disease resistance. *Plant Mol. Biol.* **2000**, *44*, 429−442.
(24) Lam, E. Controlled cell death, plant survival and development. *Nat. Rev. Mol. Cell Biol.* **2004**, *5*, 305−315.
(25) Friedrich, L.; Vernooij, B.; Gaffney, T.; Morse, A.; Ryals, J. Characterization of tobacco plants expressing a bacterial salicylate hydroxylase gene. *Plant Mol. Biol.* **1995**, *29*, 959−968.
(26) Yu, J.; Ahmedna, M. Functional components of grape pomace: their composition, biological properties and potential applications. *Int. J. Food Sci. Technol.* **2013**, *48*, 221−237.
(27) Katalinić, V.; Možina, S. S.; Skroza, D.; Generalić, I.; Abramović, H.; Miloš, M.; Ljubenkov, I.; Piskernik, S.; Pezo, I.; Terpinc, P.; Bodan, M. Polyphenolic profile, antioxidant properties and antimicrobial activity of grape skin extracts of 14 *Vitis vinifera* varieties frown in Dalmatia (Croatia). *Food Chem.* **2010**, *119*, 715−723.
(28) Taguri, T.; Tanaka, T.; Kouno, I. Antimicrobial activity of 10 different plant polyphenols against bacteria causing food-borne disease. *Biol. Pharm. Bull.* **2004**, *27*, 1965−1969.
(29) Xia, E.-Q.; Deng, G.-F.; Guo, Y.-J.; Li, H.-B. Biological activities of polyphenols from grapes. *Int. J. Mol. Sci.* **2010**, *11*, 622−646.
(30) Friedman, M. Antibacterial, antiviral, and antifungal properties of wines and winery byproducts in relation to their flavonoid content. *J. Agric. Food Chem.* **2014**, *62*, 6025−6042.
(31) Amborabé, B.-E.; Fleurat-Lessard, P.; Chollet, J.-F.; Roblin, G. Antifungal effects of salicylic acid and other benzoic acid derivatives towards *Eutypa lata*: structure-activity relationship. *Plant Physiol. Biochem.* **2002**, *40*, 1051−1060.
(32) Qi, P.-F.; Johnston, A.; Balcerzak, M.; Rocheleau, H.; Harris, L. J.; Long, X.-Y.; Wei, Y.-M.; Zheng, Y.-L.; Ouellet, T. Effect of salicylic acid on *Fusarium graminearum*, the major causal agent of fusarium head blight in wheat. *Fungal Biol.* **2012**, *116*, 413−426.

DOI: 10.1021/acs.jafc.5b01740
J. Agric. Food Chem. 2015, 63, 6653−6659

germination was not significantly affected by biochars made from a range of organic sources. Solaiman et al.[17] showed that biochars generally increased germination at low application rates (10−50 t/ha), whereas higher application rates of 100 t/ha had no effect or decreased germination rate. Alburquerque et al.[27] observed that different biochars exerted a positive effect on seed germination also at high application rates.

Recent studies have also suggested different methods for reducing the toxicity of biochar.[28,29] Washing biochar with water or an organic solvent has been successfully tested to reduce the phytotoxicity of biochar.[21,28,30] Meanwhile, Kołtowski and Oleszczuk[31] demonstrated significant reduction in the toxicity of biochars by drying them at various temperatures (100−300 °C) for 24 h.

Although the published and ongoing investigations are providing increasing data helpful to understanding the relationships between biochar characteristics and seed germination,[28,31] further studies are needed to better clarify the role played by the chemical properties in determining the toxicity effect on plants in order to forecast strategies in biochar synthesis or post-treatments. Biochars from different feedstock and process conditions may exhibit a wide range of plant response, from growth inhibition to stimulation. The relatively simple seed germination test is a valid and fast tool to compare several biochars obtained from different starting materials and under different pyrolysis conditions. Because the test is performed in a short time and without the buffering effect of soil, it could be considered a kind of precautionary procedure that highlights the intrinsic phytotoxicity of the tested materials.

The aim of this study was to evaluate the phytotoxicity of biochar from poultry litter by means of standard germination tests and to identify possible relationships with its chemical characteristics. To this purpose, germination tests with cress (*Lepidium sativum* L.) were conducted with poultry litter biochars synthesized under different pyrolysis conditions. Besides manure, poultry litter typically contains bedding such as sawdust, wood shavings, rice hulls, and straw.[8,12] Therefore, a comparison was made with biochars produced from a lignocellulosic material, prepared under the same conditions, to better discriminate the contributions of lipids/proteins and (hemi)cellulose/lignin. The effect of solvent extraction and biological conditioning on seed germination was tested on a selected poultry litter biochar prepared upon pyrolysis at 400 °C (PL400). The chemical composition of mobile constituents in this sample capable of being potentially released in water and air compartments was investigated by solvent extraction and solid-phase microextraction (SPME).

MATERIALS AND METHODS

Biochar Synthesis. Cornstalk was described in a previous study.[32] Granular poultry litter was a marketed organic fertilizer obtained after processing raw poultry litter collected from local broiler farms by pasteurizing at 80−110 °C, milling, and pelletizing. Biomass was air-dried at 60 °C, milled, and sieved at 2 mm before pyrolysis.

Batch pyrolysis experiments were conducted under nitrogen flow with a fixed bed tubular quartz reactor placed into a refractory furnace (see Conti et al.[33] for details) with about 20 g of cornstalk or 35 g of poultry litter exactly weighed and uniformly placed onto a sliding quartz boat; nitrogen flow was set at 1500 cm^3/min, and when the temperature inside the reactor, measured with a thermocouple, reached the selected value, the boat was pushed into the oven and left for a given residence time before it was pulled back into the unheated part of the reactor. Pyrolysis was performed under three different conditions based on a previous study[33] of temperature/residence time: 400 °C/20 min, 500 °C/10 min, and 600 °C/5 min. In accordance with the original biomass (cornstalk, CS; poultry litter, PL) and pyrolysis temperature, the obtained biochar samples were named CS400, CS500, CS600, PL400, PL500, and PL600. Chemicals were purchased from Sigma-Aldrich. SPME Carboxen-PDMS fibers and the fiber holder were purchased from Supelco.

Biochar Characterization. Elemental composition (HCNS) was determined by combustion using a Thermo Scientific Flash 2000 series analyzer. Ash was determined as the residual mass left after exposure at 600 °C for 5 h. The oxygen content was calculated from the mass balance, O% = 100 − (C + H + N + ash)%.

Analytical pyrolysis (Py-GC-MS) was conducted at 900 °C for 100 s with a CDS 5250 pyroprobe interfaced to a Varian 3400 GC-Saturn 2000 MS. GC-MS conditions and the determination of indicators of carbonization percent charred and the toluene/naphthalene ratio were described in Conti et al.[33]

The content of the 16 EPA priority PAHs was measured in triplicate as described in Fabbri et al.[34] Briefly, about 0.5 g of biochar was spiked with 0.1 mL of surrogate PAH mix (Supelco for EPA 525 containing acenaphthene-d_{10}, phenanthrene-d_{10}, and chrysene-d_{12}, 5 μg/mL each in acetonitrile) and Soxhlet extracted with acetone/cyclohexane (1:1, v/v) for 36 h. The solution was filtered, added to 1 mL of *n*-nonane (keeper), carefully evaporated by rotatory vacuum evaporation at 40 °C, and cleaned up by solid phase extraction onto a silica gel cartridge before analysis with an Agilent HP 6850 GC coupled to an Agilent HP 5975 quadrupole mass spectrometer; GC-MS conditions were those detailed in Fabbri et al.[34] Recovery of surrogate PAHs was determined with respect to the internal standard tri-*tert*-butylbenzene added prior to GC-MS analysis.

Volatile fatty acids (VFAs) were determined by the single-drop extraction procedure as described in Torri et al.[35] About 200 mg of biochar exactly weighed was added to 0.1 mL of internal standard solution (1 g/L 2-ethylbutyrate in deionized water) and thoroughly mixed with 0.2 mL of saturated aqueous $KHSO_4$. After centrifugation, a drop of dimethyl carbonate (1.2 μL) from a 10 μL chromatography microsyringe was exposed into the supernatant aqueous solution. After 20 min of exposure, the drop was retracted and injected into a GC-FID (injection temperature = 250 °C) equipped with a polar GC column (Agilent Q7221J&W nitroterephthalic acid-modified polyethylene glycol DB-FFAP 222 30 m, 0.25 mm, 0.2 μm) with the following thermal program: 80 °C for 5 min, then 10 °C/min to 250 °C. Calibration was performed by applying the same procedure to standard solutions containing known concentrations of each VFA (namely, acetic, propionic, isobutyric, butyric, isovaleric, and valeric acids).

For the determination of N-NH_4^+, about 10 g of biochar was placed in an end-to-end shaker for 2 h with 1 N KCl (1:10 dw/v) followed by centrifuging at 4500*g* for 20 min and passing through a 0.45 μm paper filter.

SPME of Mobile Compounds. An aliquot (1 mL) of the aqueous extract solution was introduced into a vial mixed with 0.5 mL of KH_2PO_4/Na_2HPO_4 phosphate buffer 2 M at pH 5.3 and then spiked with 1 μg/mL *o*-eugenol and 5 μg/mL 2-ethylbutyric acid as internal standards. SPME analyses were performed by directly exposing the Carboxen-PDMS fiber into the test solution under magnetic stirring. After 30 min of exposure, the fiber was inserted into the injector of an Agilent 5977 gas chromatograph, and analytes were thermally desorbed at 250 °C for 10 min and analyzed as described for VFAs with a DB-FFAP polar column (30 m length, 0.25 mm i.d, 0.25 μm film thickness). Detection was made with a quadrupole mass spectrometer Agilent 7820A operating under electron ionization at 70 eV with acquisition at 1 scan/s in the m/z 35 and 450 range. Mass spectra were acquired in full scan mode with a gain factor of 5. Prior to sample analysis, blanks were performed first with a thermal desorption of the fiber alone and then after a 30 min exposure to a solution of deionized water with 0.67 M phosphate buffer.

Headspace (HS) analysis was performed following the procedure described by Spokas et al.[36] (150 °C, 30 min) but using SPME instead of syringe sampling. Poultry litter biochar was weighed (0.5 g) into 20 mL headspace vials. The vials were spiked with 1 μg of *o*-eugenol

DOI: 10.1021/acs.jafc.5b01540
J. Agric. Food Chem. 2015, 63, 6660−6667

Table 1. Yield, Water-Holding Capacity, Elemental Analysis, Ash (Mean Values ± SD, n = 4), and Elemental Molar Ratios of Biochars from the Pyrolysis of Corn Stalk (CS) and Poultry Litter (PL) at Different Conditions (400 °C/20 min, 500 °C/10 min, and 600 °C/5 min)

			elemental content (%)						
biochar	yield (% wt)	water-holding capacity (%)	C	H	N	O	S	ash (% dry wt)	molar ratio H/C
CS400	38.3 ± 0.9	69.5	50 ± 2.1	3.3 ± 0.1	0.96 ± 0.03	15 ± 1.9	0.07 ± 0.01	28.95 ± 0.01	0.79
CS500	33 ± 1.6	81.1	51 ± 1.6	2.7 ± 0.1	0.91 ± 0.04	14.9 ± 0.1	0.03 ± 0.04	30.14 ± 0.02	0.63
CS600	31.4 ± 0.5	73.7	50.7 ± 0.3	2.4 ± 0.1	0.81 ± 0.03	13 ± 1.6		32.30 ± 0.02	0.57
PL400	49 ± 3.4	88.6	33 ± 4.7	2.7 ± 0.5	3.6 ± 0.8	11 ± 2.1	1.7 ± 0.5	46.64 ± 0.01	0.98
PL500	41.4 ± 0.9	94.1	33 ± 1.0	2.1 ± 0.1	3.4 ± 0.1	6.5 ± 0.9	2.2 ± 0.1	52.29 ± 0.04	0.76
PL600	39.5 ± 0.5	92.3	31.4 ± 0.5	1.7 ± 0.1	3.2 ± 0.5	4.6 ± 0.3	2.3 ± 0.1	56.82 ± 0.01	0.65

(1000 μg/mL solution in methanol) and then sealed. HS-SPME was carried out by placing the fiber holder at the top of the vial and exposing the Carboxen-PDMS fiber to the headspace close to the cap (30 min) while the bottom of the vial was put on a heating plate at 150 °C. GC-MS analysis was carried out as described above but with the GC oven starting from 36 °C held for 5 min. Prior to sample analysis, blanks were carried out first with a thermal desorption of the fiber alone and a sealed vial with empty headspace.

Biochar Post-treatments. *Aqueous Extraction.* About 2 g of PL400 was extracted with 50 mL of deionized water in a 100 mL flask at room temperature for 12 h with mechanical shaking. The aqueous phase was separated by filtration through a 0.22 μm paper filter and used as such for the germination test, whereas an aliquot was kept at −20 °C for SPME-GC-MS analysis (see above). The solid biochar residue left after water extraction was further extracted with 50 mL of methanol under reflux for 12 h. The methanol was separated by filtration, and an aliquot corresponding to the 40 g/L suspension of biochar was poured into Petri dishes and dried overnight at 70 °C under vacuum to remove all of the methanol. Thereafter, deionized water was added to perform germination tests. The final solid biochar residue left after water and methanol extraction was dried overnight at 100 °C under vacuum and utilized for germination tests.

Biological Treatment. Microbial treatment of PL400 was conducted with an activated sludge obtained from a municipal wastewater treatment plant located in Ravenna after centrifugation at 6000 rpm (20% w/w volatile suspended solids). A suspension containing 0.5 g of the concentrated sludge and 250 mL of 40 g/L PL400 in deionized water was thoroughly mixed under laminar shaking at 120 rpm overnight. An aliquot of 10 mL of this suspension was added in Petri dishes and stored for 14 days at 25 °C as shown above before germination tests were performed.

Germination Tests. The germination tests were conducted in four replicates by incubating 50 seeds of cress (*L. sativum* L.) with 5 g of a mixture containing biochar and deionized water onto sterilized cellulose filter paper (Whatman no. 1) placed in a Petri dish sealed with paraffin film. Three levels of biochar concentration were tested, 2, 5, and 40 g/L. These rates were equivalent to 2, 5, and 40 t/ha on an area basis of 10 cm soil depth and a dry bulk density of 1.5 kg/m^3. Germination tests were also performed on the fractions obtained from the chemical and biological post-treatments of PL400 described above. The quantity of these fractions was adjusted to correspond to the concentration level of 40 g/L of the original biochar. Before incubation, the samples were shaken at 150 rpm on a platform shaker at room temperature for 24 h. pH and electrical conductivity (EC) were both determined. The pH was directly measured by placing the glass electrode into the suspension with a Mettler Toledo SG 2-ELK pH-meter. The EC was measured with a Delta OHM HD 8706 conductimeter in the supernatant obtained by centrifuging the suspension and filtered at 0.45 μm.

Phytotoxicity tests were performed on biochar/deionized water mixtures (wetted biochar) according to the procedure described in UNI 11357:2010. The experiments were conducted with 50 seeds of cress, which were incubated with 10 g of biochar saturated with deionized water according to value of the water-holding capacity (Table 1) on sterilized cellulose filter paper placed in a Petri dish. All Petri dishes were covered and incubated at room temperature, 25 ± 2 °C, for 72 ± 0.5 h in the dark. Similarly, a control was prepared with deionized water.

After 72 h of exposure, visible root development was used as the operational definition of seed germination. Data were reported as relative seed germination (RSG) percentage with respect to the control (deionized water):

$$\text{RSG} = (\text{no. of germinated seeds in the sample}/\text{no. of germinated seeds in control}) \times 100$$

Statistical Analysis. All of the experiments were conducted at least in duplicate. Results of germination tests were evaluated statistically using analysis of variance (ANOVA) performed with R software version 3.1.2 (http://www.r-project.org) followed by Student−Newman−Keuls post hoc tests. The difference between the treated groups and the control group was evaluated with Dunnett's t test ($p < 0.05$).

RESULTS AND DISCUSSION

Characterization of Biochar. *Bulk Analysis.* The yields and characteristics of biochars obtained from the pyrolysis of poultry litter (PL400, PL500, PL600) under three different pyrolysis conditions are reported in Table 1 and compared with those of biochar from corn stalk (CS400, CS500, CS600). As expected, the chemical characteristics of the biochars were dependent on the original biomass and the pyrolysis conditions. In particular, the H/C and O/C ratios decreased with increasing pyrolysis temperature, whereas the content of ash increased as observed with the same pyrolysis unit under the same conditions.[33] Biochar from poultry litter contained higher levels of nitrogen, sulfur, and ash, derived from the manure fraction, as demonstrated by comparative studies on manure and lignocellulosic biochars.[9] In general, the elemental composition, ash content, and the trends with pyrolysis conditions of the investigated poultry litter chars were comparable to those reported in the literature.[7,8,37]

Extractable Compounds. The concentrations of specific potentially toxic extractable compounds, namely PAHs, VFAs, and ammonium, are reported in Table 2. Solvent-extractable PAHs occurred within the range of 0.7−1.7 mg/kg, values that were typical of biochars from different origins.[34,38,39] PAH concentration can be considered negligible for acute effect and comparable to typical values in soils.[40] Generally, naphthalene was the most abundant PAH followed by phenanthrene and fluorene; the level of benzo[a]pyrene was in the 5−65 ng/g range.

DOI: 10.1021/acs.jafc.5b01540
J. Agric. Food Chem. 2015, 63, 6660−6667

Table 2. Molecular Analysis of Extractable Compounds and Volatile Matter by Py-GC-MS of Biochar from Corn Stalk (CS) and Poultry Litter (PS) (Mean Values ± SD from Two Replicates)

	extractable			Py-GC-MS	
biochar	PAHs (mg/kg)	VFAs (mg/g)	NH_4^+ (mg/kg)	% charred	T/N[a]
CS400	0.72 ± 0.06	3.8 ± 1.2		53 ± 3	8.5 ± 0.7
CS500	1.09 ± 0.05	0.9 ± 0.3		80 ± 3	5.4 ± 1.5
CS600	0.84 ± 0.01	2.6 ± 0.1		92 ± 3	3.0 ± 1.7
PL400	1.7 ± 0.2	9.3 ± 0.3	45	88 ± 9	13 ± 10
PL500	0.88 ± 0.05	4.3 ± 2.0	25	90 ± 3	12 ± 6
PL600	0.79 ± 0.01	6.8 ± 1.8	14	88 ± 3	11 ± 2

[a]T/N, toluene/naphthalene ratio.

The concentration of VFAs was significantly higher in poultry litter biochars (4−9 mg/g) in comparison to those from cornstalk (1−4 mg/g). Acetic acid was always the most abundant VFA and could be derived from the thermal degradation of hemicellulose.[41] VFAs could also be derived from the thermal degradation of triacylglycerols[42] and free fatty acids.[43]

Ammonium was not detected in cornstalk biochar, whereas it was abundant in biochars from poultry litter with higher concentrations in the less carbonized biochars.

Py-GC-MS. Thermolabile Fraction. The molecular composition of the thermally labile fraction could be inferred from the structural identification of the compounds identified in the pyrolysates.[33,34,44] The pyrolysate of CS400 was characterized by a complex pattern of compounds dominated by phenols and methoxyphenols associated with the presence of partially charred lignin, whereas the pyrolysate of CS600 contained few peaks due to the hydrocarbons associated with more heavily charred fraction (Figure 1). Proxies of the degree of carbonization established in previous studies[33] for lignocellulosic biomass were confirmed in this study for corn stalk biochar: the toluene/naphthalene ratio and the relative abundance of compounds representative of the charred fraction (% charred) exhibited a clear trend with H/C ratios (Table 2). However, biochar samples from poultry litter did not exhibit significant changes with the H/C ratios, and the variability was higher. This finding would suggest that the pyrolysis proxies developed for lignocellulosic biochar could not be valid for biochar containing charred proteins and lipids.

The occurrence of partially charred components from proteins and lipids was clearly evidenced in the pyrolysates of biochar. Phenols and methoxyphenols were detected in PL400 as well as in CS400 in accordance with the fact that the original substrates contained a lignocellulosic component. The distinctive signature of PL pyrolysate was the occurrence of nitrogen-containing compounds (NCCs) from proteins and a pattern of *n*-alkanes/*n*-alk-1-enes assigned to the thermal cracking of bound or free fatty acids (Figure 1). The occurrence of saturated alkyl domains was confirmed by ^{13}C NMR studies on poultry manure biochars that disappear after carbonization and may play a role in the availability of sorbed compounds.[37] Among the tentatively identified NCCs, pyrrole, pyridine, (iso)quinoline, and carbazole along with their alkyl derivatives are indicative of partially charred proteinaceous matter. It is worth noting that NCCs were also identified in the volatile fraction by SPME as described in the next section.

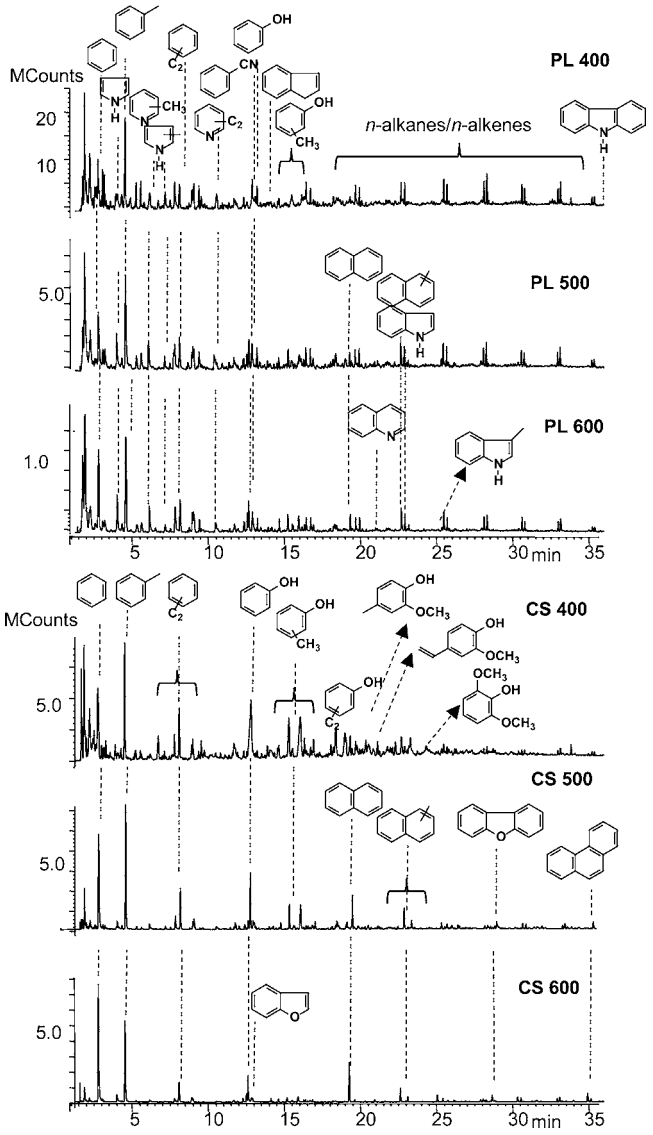

Figure 1. Total ion chromatograms from Py-GC-MS of poultry litter (PL) and cornstalk (CS) biochars.

SPME-GC-MS. Volatile and Water-Soluble Compounds. Information on the molecular characteristics of the mobile fraction was gathered by HS-SPME (volatile) and DI-SPME (water-soluble). Poultry litter contains heavy metals that may end up in the resulting biochar.[45] However, our attention was specifically focused on organic compounds, it having been reported that heavy metals are generally present below the limits causing adverse effects and loosely bioavailable.[46] Moreover, Bastos et al.[16] argued that in aqueous extracts PAHs and metals might occur at concentrations below the level to pose detrimental effects, at least for woody biochar up to 80 t/ha; however, it has to be remarked that the biological response depends on the organisms selected in the bioassay,[16] and the content of metals depends on pyrolysis conditions;[45] thus, the influence of inorganic constituents cannot be always excluded.

SPME was applied to sample PL400 that was utilized in post-treatment studies. The results are shown in Figure 2 for the analysis of volatile organic compounds (VOCs) by HS-SPME (Figure 2A) and DI-SPME of aqueous extracts (Figure 2B), respectively. The VOCs were characterized by the presence of a

DOI: 10.1021/acs.jafc.5b01540
J. Agric. Food Chem. 2015, 63, 6660−6667

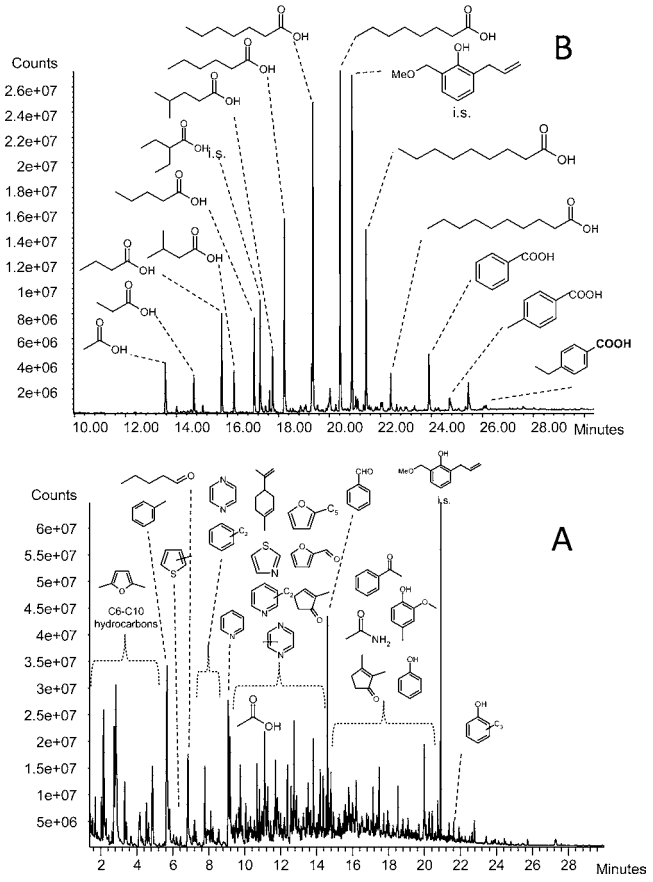

Figure 2. Total ion chromatograms obtained after (A) HS-SPME of volatile organic compounds and (B) DI-SPME of water extract of poultry litter biochar (PL400).

wide array of compounds deriving from the thermal degradation of polysaccharides (e.g., cyclopentenones, furans), lignin (e.g., 4-vinylphenol, guaiacol), proteins (e.g., pyrroles, pyridines, indole), lipids (e.g., VFAs; acetic acid is also derived from hemicellulose). Alkylated pyrazines and acetamide were probably derived from Maillard reactions between carbohydrates and proteins.

Notably, a suite of short-chain *n*-alkanes/alkenes were identified, supporting Py-GC-MS results and literature data about the occurrence of aliphatic components in poultry litter biochar.[37] It is expected that the polar fraction of VOCs will be preferentially distributed into the aqueous phase in comparison to nonpolar constituents. In fact, the SPME-GC-MS analysis of the PL400 water extract showed a predominance of organic acids, including C_2-C_{10} aliphatic and C_7-C_9 aromatic acids (Figure 2B).

Effect of Biochar on Seed Germination. The pH and EC of the biochar/water suspensions utilized in germination tests are reported in Table 3. The pH values were higher for the suspensions, from the same feedstock, with the more carbonized biochars and increased, for each biochar type, with increasing concentration. Under the same conditions, the pH was higher in the suspensions with poultry litter biochar, in accordance with previous studies.[9]

The EC values of the suspensions increased with increasing biochar concentration and, at the same concentrations, the biochar from poultry litter had much higher (from 4 to 40 times for the same condition) EC values than the CS suspensions. Salinity can have a detrimental effect on seed germination and plant growth, especially in the seedling stage, although the response of various plant species to salinity differs considerably.[47] In general, salinity effects are mostly negligible in extracts with EC readings of ≤2000 μS/cm.[48] This critical level was exceeded in poultry litter biochar at 40 g/L. The toxicity of inorganic nitrogen results mainly from ammonia (NH_3), which affects plant growth and metabolism at low concentration levels at which NH_4^+ is not harmful.[47] At concentrations of 0.15−0.20 mM, which are comparable to those calculated in the 40 g/L biochar/water mixtures, NH_3 could be toxic.[49]

Table 3. Results from Chemical Analysis of Biochar Water Suspensions

	pH			electrical conductivity (μS/cm)		
biochar	2 g/L	5 g/L	40 g/L	2 g/L	5 g/L	40 g/L
CS400	7.6	8.0	8.5	16	75	1.8×10^3
CS500	8.2	8.5	9.3	72	76	1.9×10^3
CS600	8.4	8.9	10.1	1.9×10^2	3.5×10^2	1.9×10^3
PL400	8.0	9.0	9.7	7.1×10^2	1.3×10^3	7.3×10^3
PL500	8.4	9.3	10.2	8.7×10^2	1.5×10^3	7.7×10^3
PL600	9.4	9.8	10.3	9.3×10^2	2.0×10^3	8.1×10^3

The effect of the biochar suspensions on seed germination of cress (*L. sativum* L.) is presented in Table 4 in terms of relative seed germination percentage with respect to control (deionized water only).

Table 4. Relative Seed Germination (% of Control) of Cress (*Lepidium sativum* L.) in Biochar/Deionized Water Suspensions (2, 5, and 40 g/L) and Phytotoxicity Tests (% Seed Germination with Respect to Control) according to UNI 11357:2010 (Mean Values and SD from Four Replicates)[a]

	germination (%)			
biochar ID	2 g/L	5 g/L	40 g/L	UNI
control	96 ± 2	97 ± 2	98 ± 2	94 ± 2
CS400	98 ± 2	93 ± 1*	96 ± 4	81 ± 3*
CS500	97 ± 5	98 ± 1	96 ± 2	41 ± 3*
CS600	95 ± 4	95 ± 2	96 ± 1	14 ± 4*
control	92 ± 2	92 ± 2	92 ± 2	94 ± 1
PL400	83 ± 4*	74 ± 3*	52 ± 19*	no germination
PL500	77 ± 2*	73 ± 2*	47 ± 10*	no germination
PL600	77 ± 3*	74 ± 3*	53 ± 7*	no germination

[a]The percent seed germination in pure deionized water (control) is also reported. * indicates differences at the 0.05 level compared with the control by Dunnett's tests.

The assay results in this work suggested that all of the cornstalk biochar suspensions had little impact on seed germination as one-way ANOVA showed no significant difference between control group and test groups ($p > 0.05$). Notably, CS400 was almost nontoxic to germination even if used as the growth substrate (UNI test, Table 4).

On the contrary, all of the biochar samples from poultry litter significantly inhibited seed germination at the highest level of 40 g/L in water suspensions. At the harsh conditions of the UNI test the germination was totally suppressed.

DOI: 10.1021/acs.jafc.5b01540
J. Agric. Food Chem. 2015, 63, 6660−6667

The comparison with cornstalk suggested that the toxicity of biochar from poultry litter could be explained by some distinctive chemical components originated from this feedstock. Compounds derived from lignin and cellulose/hemicellulose could be excluded on the grounds that biochar samples from corn stalk did not suppress seed germination in water suspensions. The biochar suspensions from both substrates presented similar pH values; thus, this parameter is not involved in toxicity. This is in accordance with the findings of Gell et al.,[50] who found no evidence of clear trends of pH and short-term phytotoxicity in biochars of different origins, at least under neutral/basic conditions. Similarly, the solvent-extractable PAH concentrations were similar in PL and CS biochars; thus, PAHs cannot be responsible for the observed toxicity. The calculated concentrations of VFAs in biochar suspensions (from data of Table 2) are at levels that may cause detrimental effects; for instance, the calculated PL400 VFAs at 40 g/L (374 μg/g) was higher than 252 μg/g EC_{50} values for plant growth.[46] However, different factors govern the physiological response of VFAs, including pH and bioavailability.[51,52] Acetic acid was present in all of the biochars, partly due to the decomposition of cellulose/hemicellulose. In addition, the occurrence of benzoic acid and other aromatic acids was identified by DI-SPME along with VFAs. Benzoic acid is reported to inhibit hydraulic conductivity and nutrient uptake by plant roots, thus resulting in growth inhibition.[53] However, no significant effect of benzoic acid on *Orobanche crenata* seed germination was observed by Fernández-Aparicio et al.[54]

The suite of alkanes/alkenes characterizing the Py-GC-MS pyrolysates of poultry litter biochar samples would suggest the presence of a lipid fraction producing shorter chain fatty acids by thermal degradation as confirmed by SPME-GC-MS on PL400.

The main differences between the CS and PL biochars were the higher content of elemental nitrogen (Table 1) and ammonium (Table 2) and the presence of a thermally labile fraction derived from proteins and lipids (Py-GC-MS data).

Germination Tests after Biochar Post-treatment. A selected sample of poultry litter biochar (PL400) was extracted with water followed by methanol extraction; the extracts and the residue were utilized in germination tests. Germination tests were also performed on PL400 after treatment with sewage sludge to assess the effect of biodegradation. The quantity of extracts and the residues corresponded to the biochar loading level of 40 g/L. The results are presented in Figure 3. The cress germination rate in the water extracts was similar to that of the original biochar suspensions, indicating inhibition due to some components in the water extracts. The germination rates increased significantly to values similar to the control when the suspension was made with the biochar left after solvent extraction. These observations are supported by the results of Rogovska et al.,[21] who showed that growth inhibition no longer occurred when biochars were washed prior to germination.

Biochar suspensions treated with an active sludge for almost 2 weeks displayed a germination rate similar to that of the extracted biochar (Figure 3). The reduced toxicity could be ascribed to microbial degradation of some noxious components as suggested by Bargmann et al.[28]

The results shown in Figure 3 indicated that the relative seed germination of water extracts is low and comparable to that of the original biochar, strongly supporting the hypothesis that the polar/ionic constituents ending up in water are responsible for the observed biochar toxicity. Similarly, Bargmann et al.,[28] applying germination tests to hydrochars from various origins, demonstrated that the inhibiting effects were caused by some water-soluble substances. These authors hypothesized that organic acids could be possibly responsible for the water-extractable fractions' toxicity. The potential of microbial detoxification was evidenced by Busch et al.,[26] who observed that the genotoxicity of hydrochar mixed with compost became lower than that of pure hydrochar.

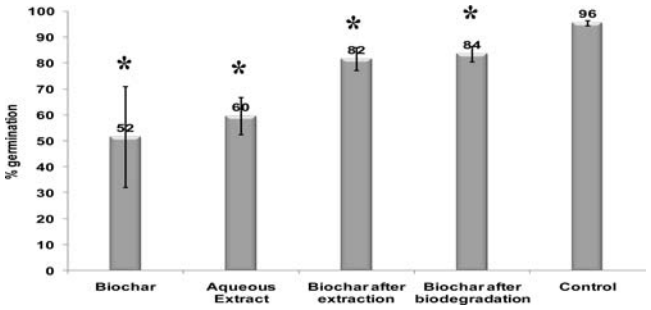

Figure 3. Seed germination rates relative to control of original poultry litter biochar (PL400), water extracts, and PL400 after post-treatments (solvent extraction and treatment with active sludge). Germination tests referred to a biochar load of 40 g/L. The germination rate of control (water only) is reported for comparison. * indicates differences at the 0.05 level compared with the control by Dunnett's tests.

Gell et al.[50] showed that the short-term phytotoxicity of biochar is dependent on the feedstock and is probably associated with ionic water-soluble constituents rather than the less polar organic compounds' composing tars. Accordingly, the methanolic extract of biochar after water extraction exhibited a seed germination rate of 93% (not reported in Figure 3), higher than that measured in the water extracts. Interestingly, among the various biochars investigated by Gell et al.,[50] those obtained from poultry biochar exhibited positive effects (radish root elongation) and acted to decrease the phytotoxicity of digestates.

The results of this study suggested that toxic compounds responsible for the toxicity of PL400 were water extractable and biodegradable. The SPME analysis of the water extracts (Figure 2) evidenced that aliphatic and aromatic carboxylic acids were the dominant compounds. Py-GC-MS and HS-SPME analyses evidenced the presence of NCCs that seemingly were not partitioned into the water phase.

Biochar has potential as a soil amendment for improving soil quality, decreasing fertilizer losses, and storing carbon in the soil. Nevertheless, as a soil additive, the absence of phytotoxicity is the minimal requirement. Biochar from poultry litter may exert a negative effect at least at the relatively high level of soil amendment (40 t/ha) due to the presence of water-soluble and biodegradable components, probably derived from the thermal decomposition of proteins and lipids. However, the toxicity can be drastically reduced by means of washing with water or mixing with biologically active material. Whereas leaching (accompanied by wastewater generation) would be not an applicable option, biological treatment (e.g., composting or mixing with activated sludge) of phytotoxic biochars could be a simple and economic solution for increasing the agronomic performance of biochar characterized by toxicity issues. The results obtained show that biochars are not an "intrinsically safe" material, and every biochar (from different processes and/or feedstocks) has to be evaluated, checked, and eventually treated before agronomic application.

DOI: 10.1021/acs.jafc.5b01540
J. Agric. Food Chem. 2015, 63, 6660−6667

AUTHOR INFORMATION

Corresponding Author

*(A.G.R.) Fax: +39 0544 937411. E-mail: alessandro.rombola@unibo.it.

Funding

This study was partly conducted within the framework of the APQ Ricerca Intervento a "Sostegno dello sviluppo dei Laboratori di ricerca nei campi della nautica e dell'energia per il Tecnopolo di Ravenna" "Energia, parte Biomasse" between Università di Bologna and Regione Emilia Romagna (Italy). The SPME study was conducted within the framework of the Fraunhofer UMSICHT − University of Bologna Collaboration Agreement.

Notes

The authors declare no competing financial interest.

ACKNOWLEDGMENTS

We acknowledge Denis Zannoni, University of Bologna, for ammonium analysis. Part of this study was based on the Master's thesis by G.M. at the University of Bologna Ravenna Campus.

REFERENCES

(1) Glaser, B.; Lehmann, J.; Zech, W. Ameliorating physical and chemical properties of highly weathered soils in the tropics with charcoal e a review. *Biol. Fertil. Soils* **2002**, *35*, 219−230.

(2) Lehmann, J.; Gaunt, J.; Rondon, M. Bio-char sequestration in terrestrial ecosystems − a review. *Mitigation Adapt. Strat. Glob. Change* **2006**, *11*, 403−427.

(3) Sohi, S. P.; Krull, E.; Lopez-Capel, E.; Bol, R. A review of biochar and its use and function in soil. *Adv. Agron.* **2010**, *105*, 47−82.

(4) Manyà, J. J. Pyrolysis for biochar purposes: a review to establish current knowledge gaps and research needs. *Environ. Sci. Technol.* **2012**, *46*, 7939−7954.

(5) Jeffery, S.; Verheijen, F. G. A.; van der Velde, M.; Bastos, A. C. A quantitative review of the effects of biochar application to soils on crop productivity using meta-analysis. *Agric., Ecosyst. Environ.* **2011**, *144*, 175−187.

(6) Mukherjee, A.; Lal, R.; Zimmerman, A. R. Effects of biochar and other amendments on the physical properties and greenhouse gas emissions of an artificially degraded soil. *Sci. Total Environ.* **2014**, *487*, 26−36.

(7) Chan, K. Y.; Van Zwieten, L.; Meszaros, I.; Downie, A.; Joseph, S. Using poultry litter biochars as soil amendments. *Aust. J. Soil Res.* **2008**, *46*, 437−444.

(8) Van Zwieten, L.; Kimber, S. W. L.; Morris, S. G.; Singh, B. P.; Grace, P. R.; Scheer, C.; Downie, A. E.; Cowie, A. L.; Rust, J. Pyrolysing poultry litter reduces N_2O and CO_2 fluxes. *Sci. Total Environ.* **2013**, *465*, 279−287.

(9) Novak, J. M.; Cantrell, K. B.; Watts, D. W.; Busscher, W. J.; Johnson, M. G. Designing relevant biochars as soil amendments using lignocellulosic-based and manure-based feedstocks. *J. Soils Sediments* **2014**, *14*, 330−343.

(10) Ameloot, N.; Sleutel, S.; Das, K. C.; Kanagaratnam, J.; De Neve, S. Biochar amendment to soils with contrasting organic matter level: effects on N mineralization and biological soil properties. *GCB Bioenergy* **2015**, *7*, 135−144.

(11) Hosseini Bai, S.; Xu, C.-Y.; Xu, Z.; Blumfield, T. J.; Zhao, H.; Wallace, H.; Reverchon, F.; Van Zwieten, L. Soil and foliar nutrient and nitrogen isotope composition ($\delta^{15}N$) at 5 years after poultry litter and green waste biochar amendment in a macadamia orchard. *Environ. Sci. Pollut. Res.* **2015**, *22*, 3803−3809.

(12) Huang, Y.; Anderson, M.; McIlveen-Wright, D.; Lyons, G. A.; McRoberts, W. C.; Wang, Y. D.; Roskilly, A. P.; Hewitt, N. J. Biochar and renewable energy generation from poultry litter waste: a technical and economic analysis based on computational simulations. *Appl. Energy* **2015**, DOI: 10.1016/j.apenergy.2015.01.029.

(13) Wang, Y.; Lin, Y.; Chiu, P. C.; Imhoff, P. T.; Guo, M. Phosphorus release behaviors of poultry litter biochar as a soil amendment. *Sci. Total Environ.* **2015**, *512−513*, 454−463.

(14) Oleszczuk, P.; Hale, S. E.; Lehmann, J.; Cornelissen, G. Activated carbon and biochar amendments decrease pore-water concentrations of polycyclic aromatic hydrocarbons (PAHs) in sewage sludge. *Bioresour. Technol.* **2012**, *111*, 84−91.

(15) Smith, C. R.; Sleighter, R. L.; Hatcher, P. G.; Lee, J. W. Molecular characterization of inhibiting biochar water extractable substances using electrospray ionization Fourier transform ion cyclotron resonance mass spectrometry. *Environ. Sci. Technol.* **2013**, *47*, 13294−13302.

(16) Bastos, A. C.; Keizer, J. J.; Prodana, M.; Abrantes, N.; Soares, A. M. V. M.; Loureiro, S. Potential risk of biochar-amended soil to aquatic systems: an evaluation based on aquatic bioassays. *Ecotoxicology* **2014**, *23*, 1784−1793.

(17) Solaiman, Z. M.; Murphy, D. V.; Abbott, L. K. Biochars influence seed germination and early growth of seedlings. *Plant Soil* **2012**, *353*, 273−287.

(18) Zimmerman, A. R.; Gao, B.; Ahn, M. Y. Positive and negative carbon mineralization priming effects among a variety of biochar-amended soils. *Soil Biol. Biochem.* **2011**, *43*, 1169−1179.

(19) Kuriakose, S. V.; Prasad, M. N. V. Cadmium stress affects seed germination and seedling growth in *Sorghum bicolor* L. Moench by changing the activities of hydrolyzing enzymes. *Plant Growth Regul.* **2008**, *54*, 143−156.

(20) Wollan, E.; Davis, R. D.; Jenner, S. Effects of sewage sludge on seed germination. *Environ. Pollut.* **1978**, *17*, 195−205.

(21) Rogovska, N.; Laird, D.; Cruse, R. M.; Trabue, S.; Heaton, E. Germination tests for assessing biochar quality. *J. Environ. Qual.* **2012**, *41*, 1014−1022.

(22) Wong, M. H.; Cheung, Y. H.; Cheung, C. L. The effects of ammonia and ethylene oxide in animal manure and sewage sludge on the seed germination and root elongation of *Brassica parachinensis*. *Environ. Pollut., Ser. A* **1983**, *30*, 109−123.

(23) Adriano, D. C.; Chang, A. C.; Pratt, P. F.; Sharpless, R. Effect of soil application of dairy manure on germination and emergence of some selected crops. *J. Environ. Qual.* **1973**, *2*, 396−399.

(24) Zucconi, F.; Monaco, A.; Forte, M.; De Bertoldi, M. Phytotoxins during the stabilization of organic matter. In *Composting of Agricultural and Other Wastes*; Gasser, J. K. R., Ed.; Elsevier: London, UK, 1985; pp 73−86.

(25) Free, H. F.; McGill, C. R.; Rowarth, J. S.; Hedley, M. J. The effect of biochars on maize (*Zea mays*) germination. *N. Z. J. Agric. Res.* **2010**, *53*, 1−4.

(26) Busch, D.; Stark, A.; Kammann, C. I.; Glaser, B. Genotoxic and phytotoxic risk assessment of fresh and treated hydrochar from hydrothermal carbonization compared to biochar from pyrolysis. *Ecotoxicol. Environ. Saf.* **2013**, *97*, 59−66.

(27) Alburquerque, J. A.; Calero, J. M.; Barrón, V.; Torrent, J.; del Campillo, M. C.; Gallardo, A.; Villar, R. Effects of biochars produced from different feedstocks on soil properties and sunflower growth. *J. Plant Nutr. Soil Sci.* **2014**, *177*, 16−25.

(28) Bargmann, I.; Rillig, M. C.; Buss, W.; Kruse, A.; Kuecke, M. Hydrochar and biochar effects on germination of spring barley. *J. Agron. Crop Sci.* **2013**, *199*, 360−373.

(29) Buss, W.; Masek, O. Mobile organic compounds in biochar − a potential source of contamination − phytotoxic effects on cress seed (*Lepidium sativum*) germination. *J. Environ. Manage.* **2014**, *137*, 111−119.

(30) Bernardo, M.; Lapa, N.; Gonçalves, M.; Barbosa, R.; Mendes, B.; Pinto, F.; Gulyurtlu, I. Toxicity of char residues produced in the co-pyrolysis of different wastes. *Waste Manage.* **2010**, *30*, 628−635.

(31) Kołtowski, M.; Oleszczuk, P. Toxicity of biochars after polycyclic aromatic hydrocarbons removal by thermal treatment. *Ecol. Eng.* **2015**, *75*, 79−85.

DOI: 10.1021/acs.jafc.5b01540
J. Agric. Food Chem. 2015, 63, 6660−6667

(32) Cordella, M.; Torri, C.; Adamiano, A.; Fabbri, D.; Barontini, F.; Cozzani, V. Bio-oils from biomass slow pyrolysis: a chemical and toxicological screening. *J. Hazard. Mater.* **2012**, *231*−*232*, 26−35.
(33) Conti, R.; Rombolà, A. G.; Modelli, A.; Torri, C.; Fabbri, D. Evaluation of the thermal and environmental stability of switchgrass biochars by Py-GC-MS. *J. Anal. Appl. Pyrolysis* **2014**, *110*, 239−247.
(34) Fabbri, D.; Rombolà, A. G.; Torri, C.; Spokas, K. A. Determination of polycyclic aromatic hydrocarbons in biochar and biochar amended soil. *J. Anal. Appl. Pyrolysis* **2013**, *103*, 60−67.
(35) Torri, C.; Fabbri, D. Biochar enables anaerobic digestion of aqueous phase from intermediate pyrolysis of biomass. *Bioresour. Technol.* **2014**, *172*, 335−341.
(36) Spokas, K.; Novak, J.; Stewart, C.; Cantrell, K.; Uchimiya, M.; DuSaire, M.; Ro, K. Qualitative analysis of volatile organic compounds on biochar. *Chemosphere* **2011**, *85*, 869−882.
(37) Cimo', G.; Kucerik, J.; Berns, A. E.; Schaumann, G. E.; Alonzo, G.; Conte, P. Effect of heating time and temperature on the chemical characteristics of biochar from poultry manure. *J. Agric. Food Chem.* **2014**, *62*, 1912−1918.
(38) Hale, S. E.; Lehmann, J.; Rutherford, D.; Zimmerman, A. R.; Bachmann, R. T.; Shitumbanuma, V.; O'Toole, A.; Sundqvist, K. L.; Arp, H. P. H.; Cornelissen, G. Quantifying the total and bioavailable polycyclic aromatic hydrocarbons and dioxins in biochars. *Environ. Sci. Technol.* **2012**, *46*, 2830−2838.
(39) Hilber, I.; Blum, F.; Leifeld, J.; Schmidt, H. P.; Bucheli, T. D. Quantitative determination of PAHs in biochar: a prerequisite to ensure its quality and safe application. *J. Agric. Food Chem.* **2012**, *60*, 3042−3050.
(40) Bucheli, T. D.; Blum, F.; Desaules, A.; Gustafsson, O. Polycyclic aromatic hydrocarbons, black carbon, and molecular markers in soils of Switzerland. *Chemosphere* **2004**, *56*, 1061−1076.
(41) Mante, O. D.; Babu, S. P.; Amidon, T. E. A comprehensive study on relating cell-wall components of lignocellulosic biomass to oxygenated species formed during pyrolysis. *J. Anal. Appl. Pyrolysis* **2014**, *108*, 56−67.
(42) Higman, E. B.; Schmeltz, I.; Higman, H. C.; Chortyk, O. T. Studies on thermal degradation of naturally occurring materials. II. Products from pyrolysis of triglycerides at 400 degrees. *J. Agric. Food Chem.* **1973**, *21* (2), 202−204.
(43) Asomaning, J.; Mussone, P.; Bressler, D. C. Thermal deoxygenation and pyrolysis of oleic acid. *J. Anal. Appl. Pyrolysis* **2014**, *105*, 1−7.
(44) Kaal, J.; Rumpel, C. Can pyrolysis-GC/MS be used to estimate the degree of thermal alteration of black carbon? *Org. Geochem.* **2009**, *40*, 1179−1187.
(45) Song, W. P.; Guo, M. X. Quality variations of poultry litter biochar generated at different pyrolysis temperatures. *J. Anal. Appl. Pyrolysis* **2012**, *94*, 138−145.
(46) Cely, P.; Gascó, G.; Paz-Ferreiro, J.; Méndez, A. Agronomic properties of biochars from different manure wastes. *J. Anal. Appl. Pyrolysis* **2015**, *111*, 173−182.
(47) Mengel, K.; Kirkby, E. A. *Principles of Plant Nutrition*, 4th ed.; International Potash Institute: Bern, Switzerland, 1987; p 745.
(48) Hoekstra, N. J.; Bosker, T.; Lantinga, E. A. Effects of cattle dung from farms with different feeding strategies on germination and initial root growth of cress (*Lepidium sativum* L.). *Agric., Ecosyst. Environ.* **2002**, *93*, 189−196.
(49) Bennet, A. C.; Adams, F. Concentration of NH_3(aq) required for incipient NH_3 toxicity to seedlings. *Soil Sci. Soc. Am. Proc.* **1970**, *34*, 259−263.
(50) Gell, K.; van Groenigen, J. W.; Cayuela, M. L. Residues of bioenergy production chains as soil amendments: Immediate and temporal phytotoxicity. *J. Hazard. Mater.* **2011**, *186*, 2017−2025.
(51) Himanen, M.; Prochazka, P.; Hänninen, K.; Oikari, A. Phytotoxicity of low-weight carboxylic acids. *Chemosphere* **2012**, *88*, 426−431.
(52) Paavola, T.; Rintala, J. Effects of storage on characteristics and hygienic quality of digestates from four co-digestion concepts of manure and biowaste. *Bioresour. Technol.* **2008**, *99*, 7041−7051.
(53) Blum, U. The value of model plant−microbe−soil systems for understanding processes associated with allelopathic interactions: one example. In *Allelopathy: Organisms, Processes, and Applications*; Inderjit, K. M. M., Dakshini, F. A., Eds.; American Chemical Society, Washington, DC, USA, 1995; pp 127−131.
(54) Fernández-Aparicio, M.; Cimmino, A.; Evidente, A.; Rubiales, D. Inhibition of *Orobanche crenata* seed germination and radicle growth by allelochemicals identified in cereals. *J. Agric. Food Chem.* **2013**, *61*, 9797−9803.

DOI: 10.1021/acs.jafc.5b01540
J. Agric. Food Chem. 2015, 63, 6660−6667

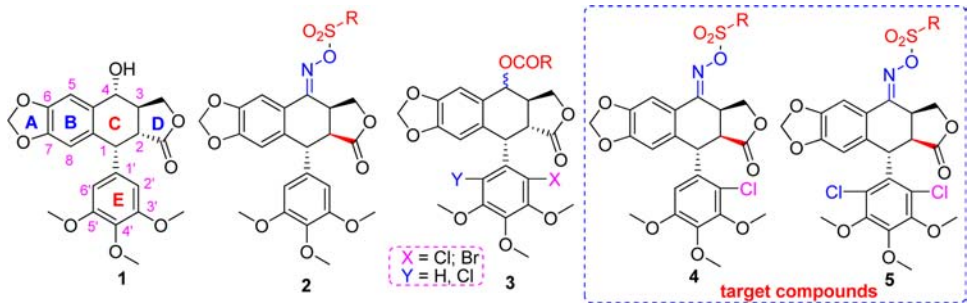

Figure 1. Chemical structures of podophyllotoxin (**1**) and its derivatives (**2**−**5**).

Scheme 1. Synthesis of Oxime Sulfonate Derivatives of 2′(2′,6′)-(Di)chloropicropodophyllotoxins (4a−4j, 5c, 5d, and 5f−5k)

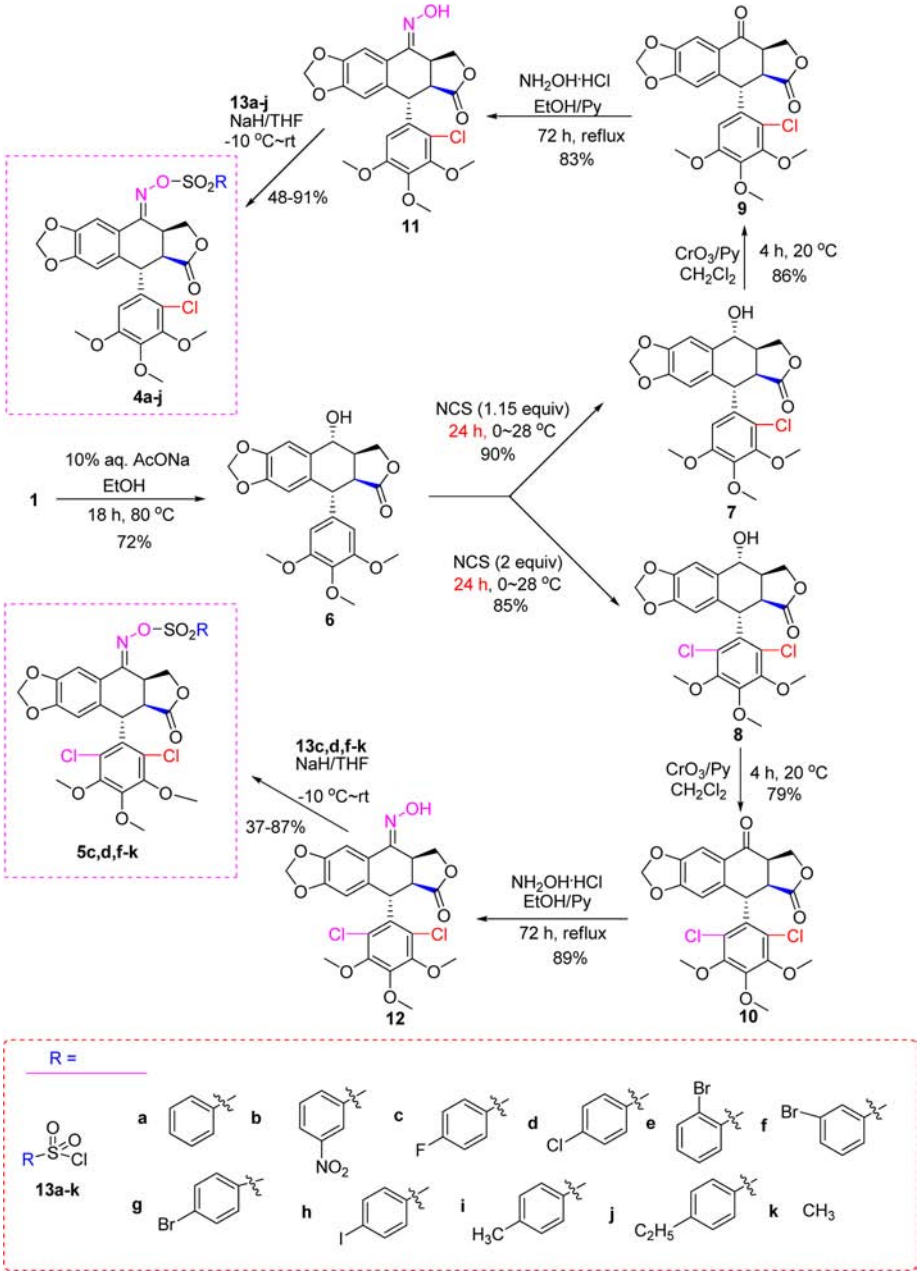

Instrumentation. Melting points (mp) were determined on a XT-4 digital melting point apparatus (Beijing Tech Instrument Co., Ltd., Beijing, China) and were uncorrected. Optical rotation was measured on a Rudolph Research Analytical Autopol III automatic polarimeter. Proton nuclear magnetic resonance spectra (^{1}H NMR) were recorded in $CDCl_3$ on a Bruker Avance III 500 MHz instrument using tetramethylsilane (TMS) as the internal standard. High-resolution mass spectrometry (HRMS) was carried out with an IonSpec 4.7 T FTMS instrument.

DOI: 10.1021/acs.jafc.5b02036
J. Agric. Food Chem. 2015, 63, 6668−6674

General Procedure for Synthesis of 2′-Chloropicropodophyllotoxin (7) and 2′,6′-Dichloropicropodophyllotoxin (8). To a solution of compound **6** (2 mmol) in dry DMF (5 mL) at 0 °C, a solution of NCS (1.15 or 2.0 equiv) in dry DMF (4 mL) was added dropwise for 10 min. During 1 h, the solution was allowed to warm slowly from 0 to 28 °C. When the reaction was complete checked by TLC analysis, the reaction mixture was diluted with water (15 mL) and extracted with ethyl acetate (30 mL × 3). Subsequently, the combined organic phase was washed by saturated aqueous Na_2CO_3 (30 mL × 3) and brine (30 mL), dried over anhydrous Na_2SO_4, concentrated *in vacuo*, and purified by silica gel column chromatography eluting with petroleum ether/ethyl acetate (1:1, v/v) to afford compound **7** (747 mg, 90% yield) or compound **8** (705 mg, 85% yield).

*Data for Compound **7**.* CAS Registry Number: 1458601-21-2. Yield: 90%, white solid. mp: 115−117 °C (literature value of 116−117 °C).[21] $[\alpha]_D^{20}$ = 5 (*c* 3.2 mg/mL, acetone). ^{1}H NMR (500 MHz, $CDCl_3$) δ: 7.09 (s, 1H, H-5), 6.61 (s, 1H, H-8), 6.18 (s, 1H, H-6′), 5.94 (s, 2H, OCH_2O), 4.66 (d, *J* = 9.5 Hz, 1H, H-11), 4.47 (d, *J* = 9.5 Hz, 1H, H-4), 4.40−4.43 (m, 1H, H-11), 4.38 (d, *J* = 5.0 Hz, 1H, H-1), 3.92 (s, 3H, 3′-OCH_3), 3.91 (s, 3H, 5′-OCH_3), 3.80 (s, 3H, 4′-OCH_3), 3.27−3.30 (m, 1H, H-2), 2.90 (s, 1H, 4-OH), 2.60−2.65 (m, 1H, H-3). HRMS (ESI): calcd for $C_{22}H_{25}ClNO_8$ ($[M + NH_4]^+$), 466.1263; found, 466.1271.

*Data for Compound **8**.* CAS Registry Number: 1458601-23-4. Yield: 85%, pale yellow solid. mp: 155−157 °C (literature value of 159−160 °C).[21] $[\alpha]_D^{20}$ = 29 (*c* 3.8 mg/mL, acetone). ^{1}H NMR (500 MHz, $CDCl_3$) δ: 7.15 (s, 1H, H-5), 6.05 (s, 1H, H-8), 5.93 (s, 2H, OCH_2O), 5.01 (d, *J* = 6.5 Hz, 1H, H-1), 4.77 (d, *J* = 10.0 Hz, 1H, H-4), 4.44−4.46 (m, 2H, H-11), 3.99 (s, 3H, 3′-OCH_3), 3.96 (s, 3H, 5′-OCH_3), 3.89 (s, 3H, 4′-OCH_3), 3.49 (dd, *J* = 9.0 and 6.5 Hz, 1H, H-2), 2.59−2.64 (m, 1H, H-3). HRMS (ESI): calcd for $C_{22}H_{24}Cl_2NO_8$ ($[M + NH_4]^+$), 500.0873; found, 500.0876.

General Procedure for Synthesis of 2′-Chloropicropodophyllone (9) and 2′,6′-Dichloropicropodophyllone (10). A mixture of compound **7** or **8** (1 mmol), chromium trioxide (CrO_3, 5 mmol), and pyridine (10 mmol) in dry dichloromethane (20 mL) was stirred at room temperature. When the reaction was complete after 4 h and checked by TLC analysis, the mixture was diluted by dichloromethane (60 mL), washed by saturated aqueous $NaHSO_3$ (30 mL) and brine (30 mL), dried over anhydrous Na_2SO_4, concentrated under reduced pressure, and purified by silica gel column chromatography eluting with petroleum ether/ethyl acetate (1:1, v/v) to afford compound **9** (386 mg, 86% yield) or compound **10** (383 mg, 79% yield).

*Data for Compound **9**.* Yield: 86%, yellow solid. mp: 105−107 °C. $[\alpha]_D^{20}$ = −30 (*c* 3.4 mg/mL, acetone). ^{1}H NMR (500 MHz, $CDCl_3$) δ: 7.51 (s, 1H, H-5), 6.68 (s, 1H, H-8), 6.07 (d, *J* = 1.0 Hz, 2H, OCH_2O), 5.85 (s, 1H, H-6′), 5.21 (d, *J* = 1.5 Hz, 1H, H-1), 4.75 (d, *J* = 9.0 Hz, 1H, H-11), 4.32−4.35 (m, 1H, H-11), 3.95 (s, 3H, 3′-OCH_3), 3,85 (s, 3H, 5′-OCH_3), 3.54 (s, 3H, 4′-OCH_3), 3.42 (dd, *J* = 8.0 and 2.0 Hz, 1H, H-2), 3.15−3.18 (m, 1H, H-3). HRMS (ESI): calcd for $C_{22}H_{20}O_8Cl$ ($[M + H]^+$), 447.0841; found, 447.0835.

*Data for Compound **10**.* Yield: 79%, yellow solid. mp: 90−92 °C. $[\alpha]_D^{20}$ = −67 (*c* 3.3 mg/mL, acetone). ^{1}H NMR (500 MHz, $CDCl_3$) δ: 7.48 (s, 1H, H-5), 6.32 (s, 1H, H-8), 6.01 (s, 2H, OCH_2O), 5.68 (d, *J* = 4.5 Hz, 1H, H-1), 4.91 (dd, *J* = 9.0 and 3.5 Hz, 1H, H-11), 4.50 (dd, *J* = 9.5 and 7.0 Hz, 1H, H-11), 3.97 (s, 3H, 3′-OCH_3), 3.96 (s, 3H, 5′-OCH_3), 3.86 (s, 3H, 4′-OCH_3), 3.65−3.69 (m, 1H, H-2), 3.43−3.45 (m, 1H, H-3). HRMS (ESI): calcd for $C_{22}H_{19}O_8Cl_2$ ($[M + H]^+$), 481.0451; found, 481.0455.

General Procedure for Synthesis of Oximes of 2′-Chloropicropodophyllone and 2′,6′-Dichloropicropodophyllone (11 and 12). A mixture of compound **9** or **10** (0.5 mmol), hydroxylamine hydrochloride (0.75 mmol), and pyridine (2 mmol) in absolute ethanol (20 mL) was refluxed. When the reaction was complete after 72 h and checked by TLC analysis, the solvent was removed under reduced pressure and saturated aqueous $NaHCO_3$ (15 mL) was added to the residue, which was extracted with ethyl acetate (3 × 30 mL). The combined organic phase was dried over anhydrous Na_2SO_4, filtered, concentrated under reduced pressure, and purified by silica gel column chromatography eluting with petroleum ether/ethyl acetate (1:1, v/v) to afford compound **11** (193 mg, 83% yield) or compound **12** (214 mg, 89% yield).

*Data for Compound **11**.* Yield: 83%, pale yellow solid. mp: 106−107 °C. $[\alpha]_D^{20}$ = −27 (*c* 3.4 mg/mL, acetone). ^{1}H NMR (500 MHz, $CDCl_3$) δ: 7.27 (s, 1H, H-5), 6.70 (s, 1H, H-8), 5.99 (s, 2H, OCH_2O), 5.95 (s, 1H, H-6′), 5.07 (d, *J* = 2.0 Hz, 1H, H-1), 4.47−4.53 (m, 2H, H-11), 3.93 (s, 3H, 3′-OCH_3), 3.83−3.86 (m, 4H, H-3, 5′-OCH_3), 3.52 (s, 3H, 4′-OCH_3), 3.43 (dd, *J* = 8.5, 2.5 Hz, 1H, H-2). HRMS (ESI): calcd for $C_{22}H_{21}O_8NCl$ ($[M + H]^+$), 462.0950; found, 462.0949.

*Data for Compound **12**.* Yield: 89%, white solid. mp: 118−120 °C. $[\alpha]_D^{20}$ = 54 (*c* 5.3 mg/mL, acetone). ^{1}H NMR (500 MHz, $CDCl_3$) δ: 8.63 (s, 1H, OH), 7.41 (s, 1H, H-5), 6.21 (s, 1H, H-8), 5.93 (s, 2H, OCH_2O), 5.24 (d, *J* = 10.5 Hz, 1H, H-1), 5.02−5.08 (m, 1H, H-11), 4.28−4.33 (m, 2H, H-11, H-3), 3.99 (s, 3H, 4′-OCH_3), 3.93 (s, 3H, 3′-OCH_3), 3.90 (s, 3H, 5′-OCH_3), 3.59 (dd, *J* = 10.5 and 6.5 Hz, 1H, H-2). HRMS (ESI): calcd for $C_{22}H_{20}O_8NCl_2$ ($[M + H]^+$), 496.0560; found, 496.0555.

General Procedure for Synthesis of Oxime Sulfonate Derivatives of 2′(2′,6′)-(Di)chloropicropodophyllotoxins (4a−4j, 5c, 5d, and 5f−5k). To a stirred solution of NaH (1.4 mmol) in dry THF (8 mL) at −10 °C was slowly added compound **11** or **12** (0.2 mmol). After the completion of addition, the reaction mixture was stirred at −10 °C for 0.5 h. Then, the corresponding sulfonyl chlorides RSO_2Cl (**13**, 0.8 mmol) were added to the above mixture. The reaction process was checked by TLC analysis. When the reaction mixture was stirred for 3 h at −10 °C (for methanesulfonyl chloride, the reaction mixture was stirred at room temperature for 48 h), saturated aqueous $NaHCO_3$ (15 mL) was added to the mixture, which was extracted with dichloromethane (3 × 30 mL). The combined organic phase was dried over anhydrous Na_2SO_4, filtered, concentrated under reduced pressure, and purified by preparative thin-layer chromatography (PTLC) to give target products compounds **4a−4j**, **5c**, **5d**, and **5f−5k** in 37−91% yields. The example data of compounds **4a−4e**, **5c**, and **5d** are described as follows, whereas the data of compounds **4f−4j** and **5f−5k** are shown in the Supporting Information.

*Data for Compound **4a**.* Yield: 82%, white solid. mp: 102−104 °C. $[\alpha]_D^{20}$ = 4 (*c* 4.2 mg/mL, acetone). ^{1}H NMR (500 MHz, $CDCl_3$) δ: 8.02−8.04 (m, 2H, H-2″, H-6″), 7.73 (t, *J* = 7.5 Hz, 1H, H-4″), 7.59−7.62 (m, 2H, H-3″, H-5″), 7.14 (s, 1H, H-5), 6.71 (s, 1H, H-8), 6.02 (s, 2H, OCH_2O), 5.77 (s, 1H, H-6′), 5.08 (d, *J* = 2.0 Hz, 1H, H-1), 4.54 (dd, *J* = 10.0 and 7.0 Hz, 1H, H-11), 4.31 (d, *J* = 10.0 Hz, 1H, H-11), 3.92 (s, 3H, 3′-OCH_3), 3.89−3.91 (m, 1H, H-3), 3.84 (s, 3H, 5′-OCH_3), 3.40 (dd, *J* = 8.5 and 2.5 Hz, 1H, H-2), 3.36 (s, 3H, 4′-OCH_3). HRMS (ESI): calcd for $C_{28}H_{25}O_{10}NClS$ ($[M + H]^+$), 602.0882; found, 602.0885.

*Data for Compound **4b**.* Yield: 48%, yellow solid. mp: 112−114 °C. $[\alpha]_D^{20}$ = 6 (*c* 4.0 mg/mL, acetone). ^{1}H NMR (500 MHz, $CDCl_3$) δ: 8.90 (s, 1H, H-2″), 8.59 (d, *J* = 7.5 Hz, 1H, H-6″), 8.36 (d, *J* = 7.5 Hz, 1H, H-4″), 7.87 (t, *J* = 7.5 Hz, 1H, H-5″), 7.09 (s, 1H, H-5), 6.73 (s, 1H, H-8), 6.03 (s, 2H, OCH_2O), 5.77 (s, 1H, H-6′), 5.09 (s, 1H, H-1), 4.54−4.57 (m, 1H, H-11), 4.31 (d, *J* = 10.0 Hz, 1H, H-11), 3.93 (s, 3H, 3′-OCH_3), 3.89−3.90 (m, 1H, H-3), 3.85 (s, 3H, 5′-OCH_3), 3.42−3.46 (m, 4H, 4′-OCH_3, H-2). HRMS (ESI): calcd for $C_{28}H_{24}O_{12}N_2ClS$ ($[M + H]^+$), 647.07; found, 647.07.

*Data for Compound **4c**.* Yield: 75%, yellow solid. mp: 106−108 °C. $[\alpha]_D^{20}$ = 10 (*c* 3.6 mg/mL, acetone). ^{1}H NMR (500 MHz, $CDCl_3$) δ: 8.04−8.07 (m, 2H, H-2″, H-6″), 7.27−7.30 (m, 2H, H-3″, H-5″), 7.12 (s, 1H, H-5), 6.72 (s, 1H, H-8), 6.03 (s, 2H, OCH_2O), 5.77 (s, 1H, H-6′), 5.08 (d, *J* = 2.0 Hz, 1H, H-1), 4.55 (dd, *J* = 10.0 and 7.0 Hz, 1H, H-11), 4.32 (d, *J* = 9.5 Hz, 1H, H-11), 3.92 (s, 3H, 3′-OCH_3), 3.90 (m, 1H, H-3), 3.84 (s, 3H, 5′-OCH_3), 3.39−3.41 (m, 4H, 4′-OCH_3, H-2). HRMS (ESI): calcd for $C_{28}H_{24}O_{10}NClFS$ ($[M + H]^+$), 620.0788; found, 620.0784.

*Data for Compound **4d**.* Yield: 82%, white solid. mp: 88−90 °C. $[\alpha]_D^{20}$ = 15 (*c* 4.0 mg/mL, acetone). ^{1}H NMR (500 MHz, $CDCl_3$) δ: 7.96 (d, *J* = 7.0 Hz, 2H, H-2″, H-6″), 7.59 (dd, *J* = 6.5 and 2.0 Hz, 2H, H-3″, H-5″), 7.13 (s, 1H, H-5), 6.72 (s, 1H, H-8), 6.03 (s, 2H, OCH_2O), 5.75 (s, 1H, H-6′), 5.08 (d, *J* = 2.5 Hz, 1H, H-1), 4.55 (dd, *J* = 9.5 and 7.0 Hz, 1H, H-11), 4.30−4.32 (m, 1H, H-11), 3.92 (s, 3H, 3′-OCH_3), 3.87−3.90 (m, 1H, H-3), 3.84 (s, 3H, 5′-OCH_3), 3.41 (dd, *J* = 8.5 and 2.5 Hz, 1H, H-2), 3.38 (s, 3H, 4′-OCH_3). HRMS (ESI): calcd for $C_{28}H_{24}O_{10}NCl_2S$ ($[M + H]^+$), 636.0492; found, 636.0498.

*Data for Compound **4e**.* Yield: 57%, yellow solid. mp: 116−118 °C. $[\alpha]_D^{20}$ = 21 (*c* 3.0 mg/mL, acetone). ^{1}H NMR (500 MHz, $CDCl_3$)

DOI: 10.1021/acs.jafc.5b02036
J. Agric. Food Chem. 2015, 63, 6668−6674

δ: 8.22−8.24 (m, 1H, H-6″), 7.79−7.81 (m, 1H, H-3″), 7.52−7.59 (m, 2H, H-4″, H-5″), 7.00 (s, 1H, H-5), 6.71 (s, 1H, H-8), 5.99 (d, J = 3.5 Hz, 2H, OCH_2O), 5.76 (s, 1H, H-6′), 5.07 (d, J = 2.0 Hz, 1H, H-1), 4.52−4.61 (m, 2H, H-11), 3.94 (s, 3H, 3′-OCH_3), 3.89−3.92 (m, 1H, H-3), 3.87 (s, 3H, 5′-OCH_3), 3.44−3.47 (m, 1H, H-2), 3.40 (s, 3H, 4′-OCH_3). HRMS (ESI): calcd for $C_{28}H_{24}O_{10}NBrClS$ ([M + H]$^+$), 679.9987; found, 679.9985.

Data for Compound ***5c***. Yield: 42%, yellow solid. mp: 98−100 °C. $[\alpha]_D^{20}$ = 16 (c 3.0 mg/mL, acetone). ^{1}H NMR (500 MHz, $CDCl_3$) δ: 8.07−8.09 (m, 2H, H-2″, H-6″), 7.29−7.30 (m, 2H, H-3″, H-5″), 7.27 (s, 1H, H-5), 6.22 (s, 1H, H-8), 5.99 (d, J = 10.0 Hz, 2H, OCH_2O), 5.25 (d, J = 10.5 Hz, 1H, H-1), 4.92−4.97 (m, 1H, H-11), 4.21−4.27 (m, 2H, H-11, H-3), 3.97 (s, 3H, 4′-OCH_3), 3.91 (s, 3H, 3′-OCH_3), 3.87 (s, 3H, 5′-OCH_3), 3.48−3.52 (m, 1H, H-2). HRMS (ESI): calcd for $C_{28}H_{23}O_{10}NCl_2FS$ ([M + H]$^+$), 654.0398; found, 654.0407.

Data for Compound ***5d***. Yield: 44%, yellow solid. mp: 96−98 °C. $[\alpha]_D^{20}$ = 20 (c 3.8 mg/mL, acetone). ^{1}H NMR (500 MHz, $CDCl_3$) δ: 7.98−8.00 (m, 2H, H-2″, H-6″), 7.58−7.59 (m, 2H, H-3″, H-5″), 7.30 (s, 1H, H-5), 6.22 (s, 1H, H-8), 5.99 (d, J = 9.5 Hz, 2H, OCH_2O), 5.25 (d, J = 10.0 Hz, 1H, H-1), 4.91−4.97 (m, 1H, H-11), 4.24−4.27 (m, 2H, H-11, H-3), 3.97 (s, 3H, 4′-OCH_3), 3.92 (s, 3H, 3′-OCH_3), 3.87 (s, 3H, 5′-OCH_3), 3.48−3.51 (m, 1H, H-2). HRMS (ESI): calcd for $C_{28}H_{23}O_{10}NCl_3S$ ([M + H]$^+$), 670.0103; found, 670.0100.

Biological Assay. The insecticidal activity of compounds **1**, **4a**−**4j**, **5c**, **5d**, **5f**−**5k**, and **6**−**12** was evaluated as the mortality rate values by the leaf-dipping method, as described previously,[19] against the pre-third-instar larvae of oriental armyworm (*M. separata* Walker). For each compound, 30 pre-third-instar larvae (10 larvae per group) were used. Acetone solutions of compounds **1**, **4a**−**4j**, **5c**, **5d**, **5f**−**5k**, and **6**−**12** and toosendanin (a positive control) were prepared at 1 mg/mL. Fresh wheat leaf discs (1 × 1 cm) were dipped into the corresponding solution for 3 s, then taken out, and dried. Leaf discs treated with acetone alone were used as a blank control group. Several pieces of treated leaf discs were kept in each dish (10 larvae were raised in each dish), which was then placed in a conditioned room [25 ± 2 °C, 65−80% relative humidity (RH), and 12/12 h (light/dark) photoperiod]. If the treated leaf discs were consumed, additional treated leaf discs were added to the dish. After 48 h, compound-soaked leaves were removed and the larvae were fed with untreated fresh wheat leaves thereafter until adult emergence. The corrected mortality rate values were obtained by the formula

$$\text{corrected mortality rate } (\%) = (T - C) \times 100/(100\% - C)$$

where T is the mortality rate in the tested compound group and C is the mortality rate in the blank control group (T and C were expressed as percentages).

RESULTS AND DISCUSSION

Synthesis. As described in Scheme 1, 2′-chloropicropodophyllotoxin (**7**) and 2′,6′-dichloropicropodophyllotoxin (**8**) were smoothly prepared by reaction of compound **6** with different amounts of NCS. Further oxidation of the hydroxy group at the C-4 position of compound **7** or **8** in the presence of CrO_3 and pyridine gave 2′-chloropicropodophyllone (**9**) and 2′,6′-dichloropicropodophyllone (**10**), respectively. Subsequently, oximes of 2′-chloropicropodophyllone and 2′,6′-dichloropicropodophyllone (**11** and **12**) were obtained by reaction of hydroxylamine hydrochloride with compounds **9** and **10**, respectively. Finally, oxime sulfonate derivatives of 2′(2′,6′)-(Di)chloropicropodophyllotoxins (**4a**−**4j**, **5c**, **5d**, and **5f**−**5k**) were afforded by reaction of sulfonyl chlorides with compounds **11** and **12**, respectively. The structures of all target compounds were well-characterized by ^{1}H NMR, HRMS, optical rotation, and melting point. Moreover, the single-crystal structure of compound **5f** was further confirmed by X-ray crystallography (Figure 2). It clearly demonstrated that the substituents on the C═N double bond of compound **5f** were present in *trans* configuration; two hydrogen atoms at the C-2 and C-3 positions all adopted α configuration (that is, the configuration of lactone (D ring) of compound **5f** was *cis*), and two chlorine atoms were at the C-2′ and C-6′ positions of compound **5f**. Crystallographic data (excluding structure factors) for the structure of compound **5f** have been deposited with the Cambridge Crystallographic Data Centre (CCDC) as supplementary publication number CCDC 1055791. Copies of the data can be obtained, free of charge, on application to CCDC, 12 Union Road, Cambridge CB2 1EZ, U.K. (fax, +44-0-1223-336033; e-mail, deposit@ccdc.cam.ac.uk).

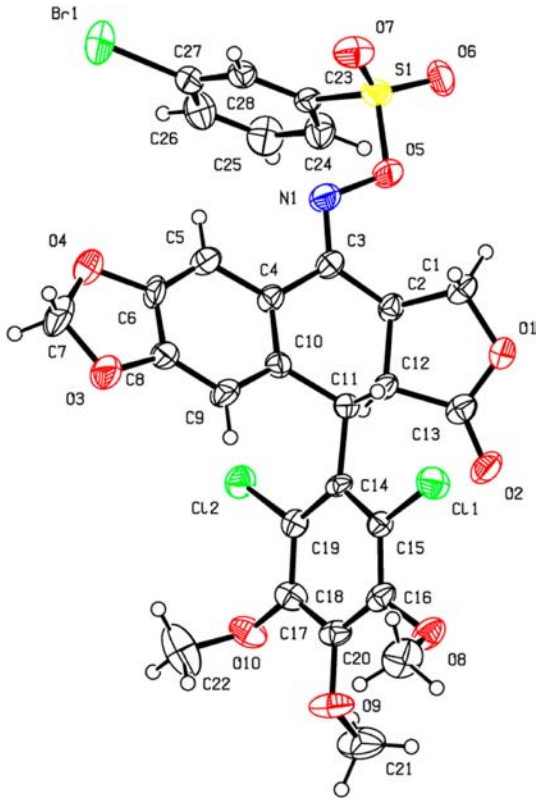

Figure 2. X-ray crystal structure of compound **5f**.

Insecticidal Activity. As shown in Table 1, the insecticidal activity of compounds **1**, **4a**−**4j**, **5c**, **5d**, **5f**−**5k**, and **6**−**12** against the pre-third-instar larvae of *M. separata in vivo* was evaluated as the mortality rates at 1 mg/mL. Toosendanin was used as a positive control at 1 mg/mL, and leaves treated with acetone alone were used as a blank control group. The corresponding mortality rates of the treated groups after 35 days were higher than those after 5, 10, 15, 20, and 25 days, as we reported in our previous papers.[19−21] As described in Figure 3, the lethal times for 50% mortality of compounds **8**, **4c**−**4g**, **5c**, **5d**, **5f**, and **5g** were 32, 23, 26, 31, 29, 29, 24, 25, 27, and 28 days, respectively. In addition, the symptoms of *M. separata* in the treated groups were characterized as follows: some larvae with the slim and wrinkled bodies died at the larval stage because of feeding too much treated leaves during the first 48 h (Figure 4); some larvae molted to malformed pupae or died during the pupation period (Figure 5), and it was noteworthy that more than half of the final mortality rates were generally occupied by the mortality rates at this stage; malformed moths also appeared with imperfect wings (Figure 6). It suggested that the podophyllotoxin derivatives possibly exhibited the anti-molting hormone effect. Among all derivatives, compounds **7**, **8**, **4c**−**4g**, **5c**, **5d**, **5f**, and **5g** exhibited insecticidal activity equal to or higher than that of the positive control

DOI: 10.1021/acs.jafc.5b02036
J. Agric. Food Chem. 2015, 63, 6668−6674

Table 1. Insecticidal Activity of Oxime Sulfonate Derivatives of 2′(2′,6′)-(Di)chloropicropodophyllotoxins (4a−4j, 5c, 5d, and 5f−5k) against *M. separata* on Leaves Treated with a Concentration of 1 mg/mL

	corrected mortality rate (%)		
compound	10 days	20 days	35 days
1	13.3 ± 3.3	16.7 ± 3.3	37.9 ± 0
6	10.0 ± 0	16.7 ± 3.3	34.5 ± 3.3
7	16.7 ± 3.3	33.3 ± 3.3	48.3 ± 0
8	20.0 ± 0	30.0 ± 0	51.7 ± 3.3
9	13.3 ± 3.3	20.0 ± 0	37.9 ± 5.8
10	10.0 ± 0	16.7 ± 3.3	34.5 ± 3.3
11	13.3 ± 3.3	20.0 ± 0	34.5 ± 3.3
12	6.7 ± 3.3	13.3 ± 3.3	31.0 ± 3.3
4a	3.3 ± 3.3	16.7 ± 3.3	37.9 ± 5.8
4b	13.3 ± 3.3	26.7 ± 3.3	41.4 ± 3.3
4c	16.7 ± 3.3	40.0 ± 0	62.1 ± 3.3
4d	20.0 ± 0	33.3 ± 3.3	58.6 ± 5.8
4e	16.7 ± 3.3	30.0 ± 0	51.7 ± 3.3
4f	20.0 ± 0	26.7 ± 3.3	55.2 ± 3.3
4g	16.7 ± 3.3	30.0 ± 0	55.2 ± 3.3
4h	16.7 ± 3.3	30.0 ± 0	44.8 ± 3.3
4i	13.3 ± 3.3	20.0 ± 0	41.4 ± 3.3
4j	6.7 ± 3.3	13.3 ± 3.3	37.9 ± 0
5c	16.7 ± 3.3	46.7 ± 3.3	65.5 ± 3.3
5d	16.7 ± 3.3	36.7 ± 3.3	62.1 ± 3.3
5f	20.0 ± 0	33.3 ± 3.3	58.6 ± 5.8
5g	16.7 ± 3.3	33.3 ± 3.3	58.6 ± 0
5h	16.7 ± 3.3	23.3 ± 3.3	44.8 ± 3.3
5i	16.7 ± 3.3	23.3 ± 3.3	44.8 ± 3.3
5j	16.7 ± 3.3	23.3 ± 3.3	41.4 ± 3.3
5k	10.0 ± 0	20.0 ± 0	44.8 ± 3.3
toosendanin	13.3 ± 3.3	20.0 ± 0	48.3 ± 0
blank control	0 ± 0	0 ± 0	3.3 ± 3.3

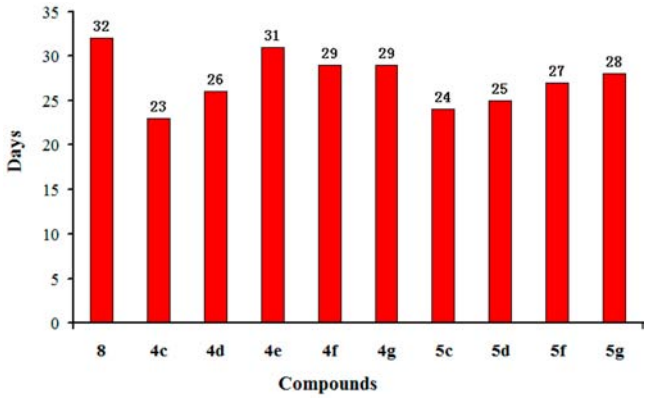

Figure 3. Lethal time for 50% mortality of compounds **8**, **4c**−**4g**, **5c**, **5d**, **5f**, and **5g**.

toosendanin. Especially compounds **4c**, **5c**, and **5d** exhibited more promising insecticidal activity, with the final mortality rates greater than 60%. For example, the final mortality rates of compounds **4c**, **5c** and **5d** were 62.1, 65.5, and 62.1%, respectively, whereas the final mortality rates of the precursor **1** and toosendanin were 37.9 and 48.3%, respectively. Introduction of the chlorine atom at the C-2′ or C-2′,6′ position on the E ring of compound **6** afforded the potent compounds **7** and **8** (48.3% for compound **7** and 51.7% for compound **8**, while 34.5% for compound **6**). Similarly, introduction of the chlorine atom at the

Figure 4. Representative abnormal larvae pictures of compounds **4g** (WR-015), **4d** (WR-026), **4c** (WR-039), **5g** (WR-022), **5j** (WR-043), **5d** (WR-038), and **5c** (WR-041) during the larval period (CK = blank control group).

Figure 5. Representative malformed pupae pictures of compounds **4g** (WR-015), **4d** (WR-026), **4f** (WR-046), **5j** (WR-043), **5g** (WR-022), **5d** (WR-038), and **5c** (WR-041) during the pupation period (CK = blank control group).

C-2′ or C-2′,6′ position on the E ring of oxime sulfonate derivatives of picropodophyllotoxin (**2**) could also produce more potent compounds compared to compound **2**.[19] For example, the final mortality rates of compounds **4a**, **4b**, **4d**, **4g**, **4i**, and **4j** were 37.9, 41.4, 58.6, 55.2, 41.4, and 37.9%, respectively, whereas the final mortality rates of the corresponding oxime sulfonate derivatives of picropodophyllotoxin were 24.1, 13.8, 55.2, 27.6, 44.8, and 27.6%, respectively.[19] To oxime sulfonate derivatives of 2′-chloropicropodophyllotoxins (**4a**−**4j**), introduction of a halogen atom (such as a fluorine, chlorine, or bromine atom) on the phenylsulfonyl group of compound **4a** resulted in more promising compounds **4c**−**4g**. The final mortality rates of compounds **4c**−**4g** were 62.1, 58.6, 51.7, 55.2, and 55.2%, respectively, whereas the final mortality rate of compound **4a** was only 37.9%. Interestingly, to oxime sulfonate derivatives of

DOI: 10.1021/acs.jafc.5b02036
J. Agric. Food Chem. 2015, 63, 6668−6674

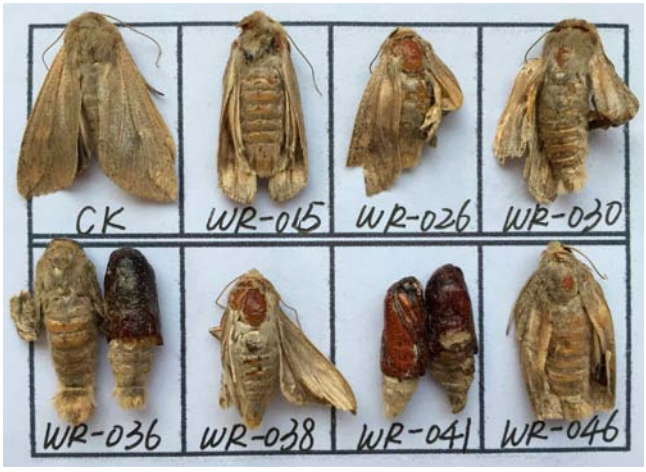

Figure 6. Representative malformed moth pictures of compounds **4g** (WR-015), **4d** (WR-026), **4a** (WR-030), **5k** (WR-036), **5d** (WR-038), **5c** (WR-041), and **4f** (WR-046) during the stage of adult emergence (CK = blank control group).

2′,6′-dichloropicropodophyllotoxins (**5c**, **5d**, and **5f**–**5k**), introduction of a fluorine, chlorine, or bromine atom on the phenylsulfonyl group could also give potent compounds **5c**, **5d**, **5f**, and **5g**, the final mortality rates of which were 65.5, 62.1, 58.6, and 58.6%, respectively. On the contrary, compounds **4a**–**4j**, **5c**, **5d**, and **5f**–**5k**, whether introduction of a nitro group (electron-withdrawing group) or methyl/ethyl group (electron-donating group) on the phenylsulfonyl fragment, all afforded less potent compounds **4b**, **4i**, **4j**, **5i**, and **5j**. When the methylsulfonyl group was introduced at the oxime fragment of compound **12**, the corresponding compound **5k** showed less potent insecticidal activity compared to compound **5c** (44.8% for compound **5k** and 65.5% for compound **5c**).

In conclusion, a series of oxime sulfonate derivatives of 2′(2′,6′)-(Di)chloropicropodophyllotoxins were prepared by structural modification of podophyllotoxin. Their insecticidal activity was evaluated at 1 mg/mL against the pre-third-instar larvae of *M. separata*. The key steric structure of compound **5f** was unambiguously determined by single-crystal X-ray diffraction. Among all derivatives, compounds **4c**, **5c**, and **5d** exhibited more potent insecticidal activity, with the final mortality rates greater than 60%. It demonstrated that introduction of the chlorine atom at the C-2′ or C-2′,6′ position on the E ring of picropodophyllotoxin or oxime sulfonate derivatives of picropodophyllotoxin was necessary for the insecticidal activity and introduction of a halogen (e.g., fluorine, chlorine, or bromine) atom-substituted phenylsulfonyl group on the oxime fragment of 2′(2′,6′)-(di)chloropicropodophyllones led to more promising compounds. It will pave the way for further design and chemical modification of podophyllotoxin as botanical insecticidal agents.

■ ASSOCIATED CONTENT

Supporting Information

Data on ^{1}H NMR, HRMS, optical rotation, and melting point for the target compounds (PDF). The Supporting Information is available free of charge on the ACS Publications website at DOI: 10.1021/acs.jafc.5b02036.

■ AUTHOR INFORMATION

Corresponding Author

*Telephone/Fax: +86-0-29-87091952. E-mail: orgxuhui@nwsuaf.edu.cn.

Funding

The present research was supported by the Special Funds of Central Colleges Basic Scientific Research Operating Expenses (2452015096) and the National Natural Science Foundation of China (31071737).

Notes

The authors declare no competing financial interest.

■ REFERENCES

(1) Han, E.; Gatehouse, A. G. Genetics of precalling period in the oriental armyworm, *Mythimna separata* (Walker) (Lepidoptera: Noctuidae), and implications for migration. *Evolution* **1991**, *45*, 1502–1510.

(2) Zeng, J.; Jiang, Y.; Liu, J. Analysis of the armyworm outbreak in 2012 and suggestions of monitoring and forecasting. *Plant Prot.* **2013**, *39*, 117–121.

(3) Sun, J. Y.; Liang, P.; Gao, X. W. Cross-resistance patterns and fitness in fufenozide-resistant diamondback moth, *Plutella xylostella* (Lepidoptera: Plutellidae). *Pest Manage. Sci.* **2012**, *68*, 285–289.

(4) Saddiq, B.; Shad, S. A.; Khan, H. A. A.; Aslam, M.; Ejaz, M.; Afzal, M. B. S. Resistance in the mealybug *Phenacoccus solenopsis* Tinsley (Homoptera: Pseudococcidae) in Pakistan to selected organophosphate and pyrethroid insecticides. *Crop Prot.* **2014**, *66*, 29–33.

(5) Ferreira, C. B. S.; Andrade, F. H. N.; Rodrigues, A. R. S.; Siqueira, H. A. A.; Gondim, M. G. C. Resistance in field populations of *Tetranychus urticae* to acaricides and characterization of the inheritance of abamectin resistance. *Crop Prot.* **2015**, *67*, 77–83.

(6) Guillette, L. J., Jr.; Iguchi, T. Life in a contaminated world. *Science* **2012**, *337*, 1614–1615.

(7) Xu, H. Comments to "Insecticide resistance after *Silent Spring*". 2013; http://comments.sciencemag.org/content/10.1126/science.1226994.

(8) Chu, S. S.; Jiang, G. H.; Liu, Z. L. Insecticidal compounds from the essential oil of Chinese medicinal herb *Atractylodes chinensis*. *Pest Manage. Sci.* **2011**, *67*, 1253–1257.

(9) Cheng, S. S.; Lin, C. Y.; Chen, Y. J.; Chung, M. J.; Chang, S. T. Insecticidal activities of *Cunninghamia konishii* Hayata against Formosan subterranean termite, *Coptotermes formosanus* (Isoptera: Rhinotermitidae). *Pest Manage. Sci.* **2014**, *70*, 1215–1219.

(10) Lin, L.; Mulholland, N.; Wu, Q.; Beattie, D.; Huang, S.; Irwin, D.; Clough, J.; Gu, Y.; Yang, G. F. Synthesis and antifungal activity of novel sclerotiorin analogues. *J. Agric. Food Chem.* **2012**, *60*, 4480–4491.

(11) Sousa, R. M. O. F.; Rosa, J. S.; Oliveira, L.; Cunha, A.; Fernandes-Ferreira, M. Activities of Apiaceae essential oils against armyworm, *Pseudaletia unipuncta* (Lepidoptera: Noctuidae). *J. Agric. Food Chem.* **2013**, *61*, 7661–7672.

(12) Diao, W. R.; Hu, Q. P.; Feng, S. S.; Li, W. Q.; Xu, J. G. Chemical composition and antibacterial activity of the essential oil from Green Huajiao (*Zanthoxylum schinifolium*) against selected foodborne pathogens. *J. Agric. Food Chem.* **2013**, *61*, 6044–6049.

(13) Zhang, Y.; Wang, J. S.; Wang, X. B.; Gu, Y. C.; Wei, D. D.; Guo, C.; Yang, M. H.; Kong, L. Y. Limonoids from the fruits of *Aphanamixis polystachya* (Meliaceae) and their biological activities. *J. Agric. Food Chem.* **2013**, *61*, 2171–2182.

(14) Wu, M.; Han, G. F.; Wang, Z. W.; Liu, Y. X.; Wang, Q. M. Synthesis and antiviral activities of antofine analogues with different C-6 substituent groups. *J. Agric. Food Chem.* **2013**, *61*, 1030–1035.

(15) Fan, L. L.; Guo, Y.; Zhi, X. Y.; Yu, X.; Xu, H. Stereoselective synthesis of 2α-chloropicropodophyllotoxins and insecticidal activity of their esters against oriental armyworm, *Mythimna separata* Walker. *J. Agric. Food Chem.* **2014**, *62*, 3726–3733.

(16) Seiber, J. N.; Coats, J.; Duke, S. O.; Gross, A. D. Biopesticides: state of the art and future opportunities. *J. Agric. Food Chem.* **2014**, *62*, 11613–11619.

(17) Lv, M.; Xu, H. Recent advances in semisynthesis, biosynthesis, biological activities, mode of action, and structure–activity relationship of podophyllotoxins: An update (2008–2010). *Mini-Rev. Med. Chem.* **2011**, *11*, 901–909.

DOI: 10.1021/acs.jafc.5b02036
J. Agric. Food Chem. 2015, 63, 6668–6674

(18) Hu, H.; Liu, S. Y.; Cheng, Y. C.; Lee, K. H.; Wang, Z. Q. Antitumor agents. 123. Synthesis and human DNA topoisomerase II inhibitory activity of 2′-chloro derivatives of etoposide and 4.beta.-(arylamino)-4′-O-demethylpodophyllotoxins. *J. Med. Chem.* **1992**, *35*, 866−871.

(19) Wang, Y.; Shao, Y. H.; Wang, Y. Y.; Fan, L. L.; Yu, X.; Zhi, X. Y.; Yang, C.; Qu, H.; Yao, X. J.; Xu, H. Synthesis and quantitative structure-activity relationship (QSAR) study of novel isoxazoline and oxime derivatives of podophyllotoxin as insecticidal agents. *J. Agric. Food Chem.* **2012**, *60*, 8435−8443.

(20) Che, Z. P.; Yu, X.; Zhi, X. Y.; Fan, L. L.; Yao, X.; Xu, H. Synthesis of novel 4α-(acyloxy)-2′(2′,6′)-(di)halogenopodophyllotoxin derivatives as insecticidal agents. *J. Agric. Food Chem.* **2013**, *61*, 8148−8155.

(21) Che, Z. P.; Yu, X.; Fan, L. L.; Xu, H. Insight into dihalogenation of E-ring of podophyllotoxins, and their acyloxyation derivatives at the C4 position as insecticidal agents. *Bioorg. Med. Chem. Lett.* **2013**, *23*, 5592−5598.

DOI: 10.1021/acs.jafc.5b02036
J. Agric. Food Chem. 2015, 63, 6668−6674

The spring onion (*Allium fistulosum*) is widely used throughout southeast Asia as well as in the north in China, Korea, and Japan. It is used raw as a herb to give flavor and a touch of bright green color to many soups, noodles, and other dishes. Dried spring onion is used for seasonings or condiments to improve the flavor and pungency of food, which have some potential benefits for human health.[7,8]

Because pesticides are a toxic compound used to kill pests in crops, when it remains on treated crops, the presence of harmful pesticide residues in food has caused a great concern among consumers. Food safety is an area of growing worldwide concern on account of its direct bearing on human health. Food processing treatment such as washing, peeling, canning, or cooking leads to a significant reduction of pesticide residues.[9]

There are no publications on the dissipation of etofenprox in spring onion and residue removal during processing. In this paper, we report residue decline in green onion after treatment of etofenprox with two different application rates and reduction of residual etofenprox on spring onion by various washing and drying processes with a heating oven or a freeze dryer.

MATERIALS AND METHODS

Chemicals and Reagents. The analytical standard of etofenprox (97.7%) was purchased from Fluka (Switzerland). The etofenprox formulation with 20% emulsifiable concentrate (EC) (Kyung Nong Co., Ltd., Korea) was purchased from a local market. Acetonitrile, dichloromethane, ethyl acetate, *n*-hexane, and methanol were high-performance liquid chromatography (HPLC)-grade (Burdick and Jackson, Ulsan, Korea). Sodium chloride [Extra Pure (EP) grade] and sodium sulfate (EP grade) were from Samchun Pure Chemical Co., Ltd. (Pyeongtaek, Korea). Florisil (0.15−0.250 mm) was purchased from Merck KGaA (Germany) and activated by drying at 130 °C for over 5 h. Filter papers (GF/A) were from Whatman International, Ltd. (Maidstone, U.K.). The vacuum rotary evaporator was from Heidolph (Germany). The Waring blender was from Zymark (Germany). A FO-600M drying oven was from Jeio Tech, Korea. The PVTFD20R freeze dryer was from ilShin Biobase, Korea.

Field Experiment. The field trial on spring onion (Jeju Island variety) was carried out in a greenhouse located in Cheong-ju, Republic of Korea. Treatment (control, single application, and double application) was made in triplicate of 30 m^2 plot size with a total of 90 m^2 for each treatment. Each randomized plot was separated by a buffering area of 5 m^2 to avoid cross-contamination by drift, etc. The first application was sprayed to onions 20 days after germination, and the second application was performed after 7 days. The planting density of spring onion was 15 × 15 cm, and over 1300 bunches of onions were evenly distributed for each test plot (30 m^2). The temperature and relative humidity in the greenhouse were continuously measured during the spring onion cultivation period using an electric data logger (Lascar, China).

Pesticide Application and Sample Collection. Etofenprox with 20% EC with the product name of "Severo" (Gyung Nong Co., Ltd., Korea) was sprayed at a standard rate (20 mL/20 L) 1 time or 2 times with a 7 day interval using a pressurized hand-held sprayer. The total volume of spray solution applied to each 30 m^2 plot was 10 L, which is equivalent to 200 mg of etofenprox per plot. To study the dissipation pattern, 2 kg of spring onion samples was collected randomly from each treated plot as well as from the untreated plot at 0, 1, 4, 6, 8, 10, 12, and 14 days after final treatment (DAT). Immediately after picking, the samples were put into polyethylene bags and transported with ice to the laboratory, where the samples were homogenized. The homogenate of each sample was then placed into polyethylene bottles and frozen at −20 °C until analysis. For the processing experiment, 12 DAT samples were collected and processed with washing or drying.

Growth Condition during Cultivation. During spring onion cultivation, the greenhouse air temperature range was 12.5−20.8 °C and humidity was 63.6−90.5%. The weights of collected spring onion were gradually increased from 25.5 g at 0 DAT to 45.5 g at 14 DAT (Figure 1).

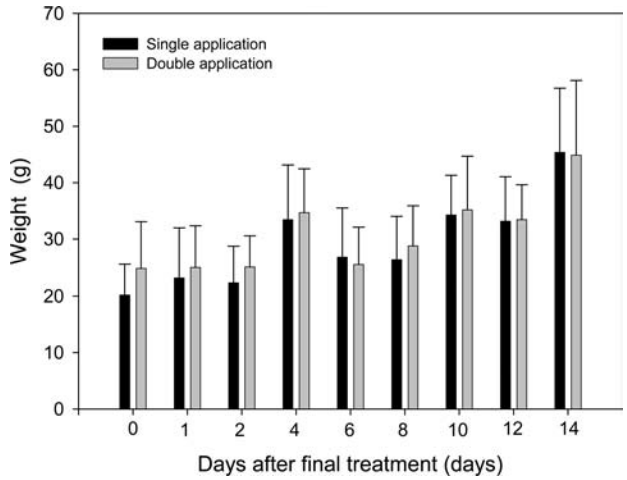

Figure 1. Growth rate of spring onion during cultivation [means ± standard deviation (SD); n = 10].

Measurement of Instrumental Sensitivity and Calibration Curve Linearity. The etofenprox analytical standard (97.7%, 10.24 mg) was dissolved in 100 mL of acetonirile to make stock 100 mg/L solution. From this stock solution, a working standard solution (50 mg/L) was prepared by dilution with acetonirile and then serially diluted to obtain a standard solution of 10, 5, 2.5, 1.0, 0.5, and 0.25 mg/L. An aliquot of 10 μL was analyzed using HPLC, and a standard calibration curve was prepared on the basis of the peak area.

HPLC Analysis Condition. HPLC was performed using a HP1200 system (Hewlett-Packard, Palo Alto, CA) with a Phenomenex Gemini-NX C_{18} (4.6 × 150 mm, 3 μm, Phenomenex, Torrance, CA) column. Mobile phases consisted of water (A) and acetonitrile (B) acidified with 0.1% acetic acid. The gradient condition used was from 70:30 (A/B, at 0−3 min) to 15:85 (at 12−17 min) and 70:30 (at 18−20 min). The flow rate was 0.8 mL/min. The injected sample (10 μL) was monitored at the wavelength of 235 nm.

Recovery Test of Etofenprox from Samples. To a sample (20 g) of homogenized spring onion, a standard solution of etofenprox was spiked at 0.5, 1.0, and 10 mg/kg. Then, the sample was extracted with 100 mL of acetone by homogenation in a Waring blender for 2 min, followed by filtering into a round-bottom flask of 500 mL capacity under vacuum through a Whatman filter paper no. 2. The container and filter cakes were washed twice with 50 mL of acetone, and the combined extracts were collected in a 500 mL flask. The filtrate was redissolved in 100 mL of dichloromethane (DCM). Then, 10 mL of saturated NaCl solution and 90 mL of water were added in the separatory funnel, and the funnel was shaken. After shaking, the lower DCM layer was drained into a 500 mL flask through anhydrous sodium sulfate supported on a prewashed glass wool in the conical funnel. This procedure was repeated with 100 mL of DCM. Then, extracts were collected, pooled, and concentrated to dryness using a vacuum evaporator at 40 °C. Then, the residue was redissolved in 10 mL of hexane. The concentrated extract was transferred to a chromatographic glass column, which was packed with 10 g of florisil in the bottom and 3 g of sodium sulfate in the top, with hexane as the packing solvent. The packed column was washed with 50 mL of hexane prior to use, and the concentrated extract was loaded on the top of the column and washed with 100 mL of hexane. Then, etofenprox was eluted with 100 mL of 5% ethyl acetate in hexane. Eluate was concentrated using a rotary vacuum evaporator, and the residue was redissolve in 4 mL of acetonitrile for analysis. Spring onion samples collected from the treated field were prepared with the method described above and analyzed using HPLC.

DOI: 10.1021/acs.jafc.5b02345
J. Agric. Food Chem. 2015, 63, 6675−6680

Dissipation and Biological Half-Life on Spring Onion. Dissipation of pesticide on spring onion was determined by first-order kinetic regression analysis with the following model:

$$C_t = C_0 e^{-kt}$$

where C_t is the concentration of pesticide at any time t, C_0 is the initial concentration, and k is the rate of constant in day^{-1}.

The biological half-life (DT_{50}), which is the time at which the concentration of initial deposits reaches the 50% level, was determined by the following equation:

$$DT_{50} = \ln 2k^{-1} = 0.693/k$$

Washing Process with Running Tap Water. The spring onion samples (1 kg) at 12 DAT were washed with running tap water for 1 min. The flow rate of the running tap water was regulated to 1 L/10 s. Then, the spring onion was air-dried under room temperature.

Tap Water Bath. The spring onions (1 kg) at 12 DAT were rinsed in a 6 L of tap water for 1 min, after which the onions were removed, the water was allowed to drain, and the onions were allowed to dry at room temperature for approximately 30 min.

Neutral Detergent Solution. The spring onion samples (1 kg) at 12 DAT were dipped at stagnant tap water containing 1% neutral detergent for 1 min. Afterward, they were washed with running tap water (the flow rate of the water was 1 L/10 s) for 30 s 2 times. Then, the spring onion was air-dried under room conditions.

Drying Process. Spring onion samples from a treated field were dried in the oven at 80 °C for 24 h or freeze-dried in the freeze dryer for 3 days. The compensated residue level (CRL) was expressed as fresh sample weight based on using the weight loss during the dry process. Weight reduction ratio (WRR) was calculated by dividing the weight before dry by the weight after dry. The CRL and removal rate was derived from the following formulation:

$$\text{WRR} = \frac{\text{weight before dry (g)}}{\text{weight after dry (g)}}$$

$$\text{CRL (mg/kg)} = \frac{\text{residue after dry (mg/kg)}}{\text{WRR}}$$

$$\text{removal rate (\%)} = \left(1 - \frac{\text{CRL}}{\text{residue before dry}}\right) \times 100$$

RESULTS AND DISCUSSION

Validation of the Analytical Method. Method validation is a set of procedures to evaluate the performance characteristics, such as recovery, reproducibility, linearity, range of calibration, limit of detection (LOD), and quantitation of a method for specific analyte and sample types.[10]

Quantification was accomplished by preparation of an external standard calibration curve after the dilution of the stock standard solution with acetonitrile. The calibration curve of etofenprox was linear from 0.25 to 50 mg/kg, covering the whole range of concentrations in the samples. The regression equation was $y = 20.60396x + 9.97170$, with the correlation coefficient (R^2) of 0.9995.

Instrumental LOD and limit of quantitation (LOQ) express the sensitivity of analytical instruments.[11,12] On the basis of the analysis of several concentrations, 1.0 and 2.5 ng were determined as the LOD and LOQ, respectively, which were satisfactory for sensitive analysis of etofenprox residue.

The method limit of quantitation (MLOQ) is not an instrumental LOQ but, instead, is a practical LOQ for the total analytical method. It is calculated using LOQ, injection volume, final solution volume, and sample weight in the analytical method.[13]

$$\text{MLOQ (mg/kg)} = (\text{LOQ} \times \text{final solution volume}) / (\text{injection volume} \times \text{sample weight})$$

$$\text{MLOQ (mg/kg)} = (2.5\ \text{ng} \times 4\ \text{mL})/(10\ \mu\text{L} \times 20\ \text{g}) = 0.05\ \text{mg/kg}$$

The MLOQ value for etofenprox calculated using the equation was 0.05 mg/kg. This value satisfied the criteria of the Korea Food and Drug Administration (KFDA), which are below 0.05 mg/kg or half of the maximum residue limit (MRL).[14]

The recovery was validated to estimate the efficiency of extraction and purification procedure before the determination of quantities of pesticides on collected samples. The untreated samples were fortified with etofenprox standard solution at three different levels and were analyzed after pretreatment. Average recovery ranged from 92.0 to 107.7% (Table 2), with the coefficient of variation (CV) less than 7.9%. According to the methods and criterion of pesticide registration tests, a typical recovery range should be from 75 to 120%, and the CV (standard deviation/average × 100) should be below 20%.[14] The HPLC chromatograms of the spring onion sample were shown in Figure 2. The retention time of etofenprox was 17.4 min, and no chromatographic interferences in the untreated sample of spring onion were observed. Thus, the developed method is applicable to analysis of the etofenprox residue in spring onion.

Table 2. Recovery and MLOQ for Etofenprox in Spring Onion

fortified level (mg/kg)	recovery ± CV[a]	MLOQ (mg/kg)[b]
0.5	97.0 ± 7.9	0.05
1	92.0 ± 6.3	
10	107.7 ± 4.3	

[a]Coefficient of variation = standard deviation/average × 100. [b]Method limit of quantification.

Biological Half-Lives of Etofenprox on Spring Onion. Under field conditions, various environmental conditions, such as temperature, moisture, and microbial activity, result in different degradation kinetics during the experimental period.[15] Decline of the pesticide residue during crop cultivation may be attributed primarily to physical chemistry characteristics of the pesticide as well as conditions of the cultivation, weathering, heat decomposition, methods for application, pre-harvest interval, or other complex conditions.[16−18] The etofenprox residue on the spring onion on the day of application under a standard application rate was 9.0 mg/kg and decreased to 3.1 mg/kg after 14 days after final treatment, while the initial concentration of etofenprox with 2 times application with a 7 day interval was 10.6 mg/kg and decreased to 2.7 mg/kg after the same period (Table 3). The MRL of etofenprox was set as 2.0 mg/kg in spring onion in Korea, but the residue at 14 DAT was higher than the MRL. To find the method to reduce the residue below the MRL, we conducted a removal experiment by washing and drying.

The biological half-life of etofenprox at 1 time application determined from the first-order kinetics was 9.5 days, and degradations could be described by following equation $C = 8.8197e^{-0.073t}$, with a correlation coefficient R^2 of 0.8792. At 2 times application, the half-life was 7.9 days and degradations

DOI: 10.1021/acs.jafc.5b02345
J. Agric. Food Chem. 2015, 63, 6675−6680

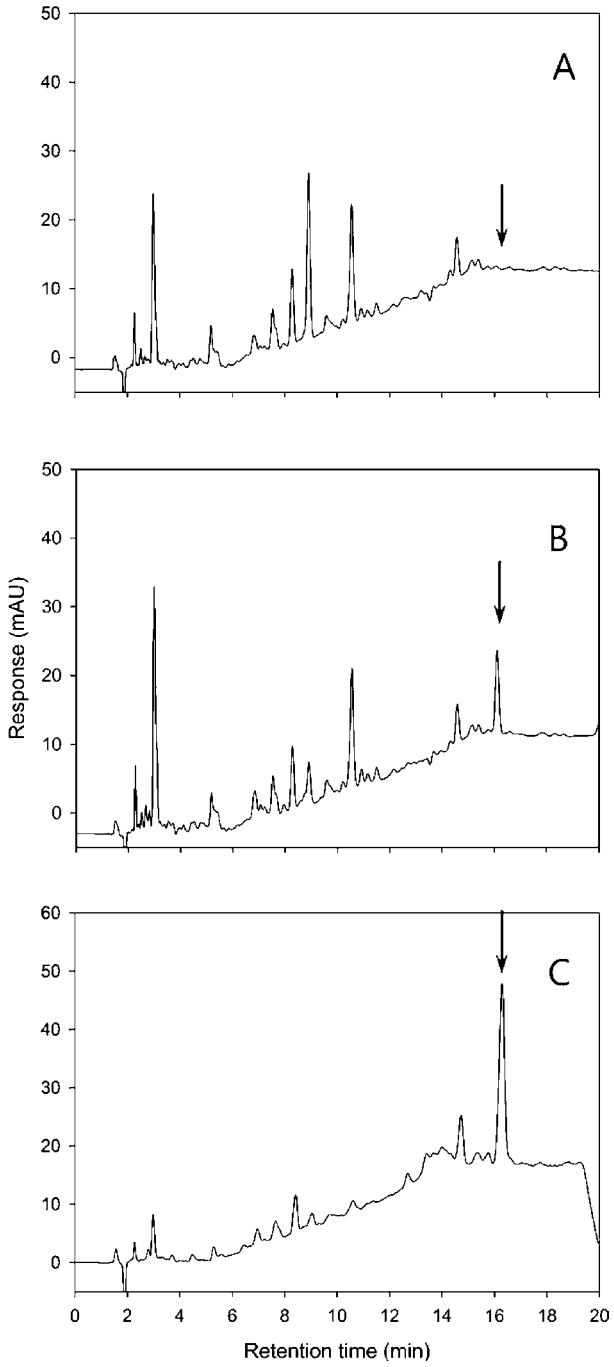

Figure 2. HPLC chromatograms of etofenprox in spring onion extract (A, untreated; B, 1.0 mg/kg level fortified; and C, 12 DAT sample of one time application).

could be described by following equation $C = 10.368e^{-0.088t}$, with $R^2 = 0.9611$ (Table 4).

The biological half-lives of etofenprox in Chinese cabbage under the greenhouse condition were 3.2 and 2.7 days at the recommended rate and the double rate of recommendation, respectively.[19] The half-lives of etofenprox in green onion are longer than in Chinese cabbage. The weight and growth rate of Chinese cabbage were higher than those of spring onion. Spring onion had a more specific surface area per unit weight than Chinese cabbage, which made a higher deposition of pesticide on the surface, and a slow growth rate resulted in slower dissipation of residues. The greenhouse temperature during the experiment with Chinese cabbage ranged from 16.47 to 39.26 °C; this was higher than the greenhouse temperature of spring onion, which was 12.5−20.8 °C. Because a higher temperature accelerates the degradation of etofenprox, the half-lives of Chinese cabbage were less than those of spring onion.[20] Photodegradation half-lives of etofenprox on the flooded soil surface and the air-dried surface under 300 nm ultraviolet (UV) light were 3.0 and 19 days, respectively.[21] Etofenprox degradation occurred relatively quickly on a glass surface with the half-life of 0.23 days compared to both flooded and air-dried soil layers.[21] From the microbial degradation experiment, the overall anaerobic half-lives ranged from 49.1 to 100 days at 22 °C compared to 27 days at 40 °C, whereas they were 27.5 days at 22 °C and 10−26.5 days at 40 °C under aerobic conditions. Etofenprox was stable for 56 days of the incubation period in the sterilized control soil.[22]

Table 3. Decline of Etofenprox Residues (mg/kg) on Spring Onion after 1 and 2 Times Application (n = 3)

		residue level (mg/kg)			
application	DAT[a]	replicate			average ± SD[b]
1	0	8.8	9.1	9.0	9.0 ± 0.1
	1	9.0	8.9	9.0	9.0 ± 0.1
	2	8.9	9.0	8.8	8.9 ± 0.1
	4	5.4	5.6	5.7	5.6 ± 0.1
	6	4.9	4.8	4.6	4.8 ± 0.1
	8	4.2	4.9	4	4.4 ± 0.4
	10	4.6	4.4	4.3	4.4 ± 0.1
	12	4.7	4.5	4.1	4.4 ± 0.3
	14	3.1	3.2	2.9	3.1 ± 0.1
2	0	10.6	10.9	10.2	10.6 ± 0.3
	1	9.3	10	9.7	9.7 ± 0.4
	2	8.8	8.5	8.1	8.5 ± 0.4
	4	7.4	7.7	7.5	7.5 ± 0.1
	6	5.5	5.4	5.7	5.5 ± 0.2
	8	5.2	4.8	4.7	4.9 ± 0.3
	10	4.7	4.6	5.1	4.8 ± 0.3
	12	4.0	4.1	4.4	4.2 ± 0.2
	14	2.7	2.7	2.7	2.7 ± 0.0

[a]Days after final treatment. [b]Standard deviation.

Table 4. Biological Half-Lives of Etofenprox on Spring Onion 1 and 2 Times Application

application	application dose	equation	R^2	half-life (day)
1	20 mL/20 L	$C = 8.8197e^{-0.073t}$	0.8792	9.5
2	20 mL/20 L × 2	$C = 10.368e^{-0.088t}$	0.9611	7.9

Removal Efficiency of Etofenprox by Washing. Washing is generally the first step in various types of processes of food commodities in combination with cooking, drying, peeling, and juicing, to allow for effective decontamination from pesticide.[9]

The average residue of etofenprox on spring onion at 12 days after treatment was 4.44 mg/kg. The washing of treated spring onion in the water bath, running tap water, and 1% neutral detergent solution reduced the residue level to 3.48, 2.49, and 3.18 mg/kg, respectively, with a corresponding removal percentage of 21.6, 43.9, and 28.5, respectively (Figure 3). The running tap water washing was more effective than tap water bath washing in removal of etofenprox in spring onion. The water solubility of etofenprox is very low and non-

DOI: 10.1021/acs.jafc.5b02345
J. Agric. Food Chem. 2015, 63, 6675−6680

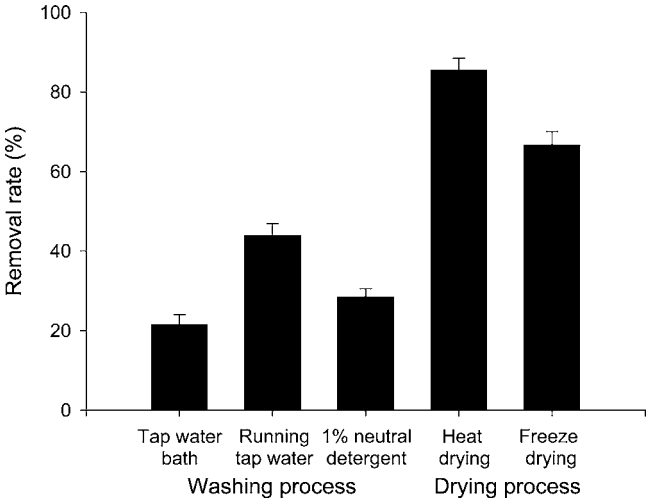

Figure 3. Removal efficiency of etofenprox on spring onion by different washing and drying processes (n = 3).

systemic. Most etofenprox will be deposited on the surface of the crop, and loosely attached residues could be effectively removed by a gentle running stream of water, which also results in a low removal rate of detergent solution in a bath. Running water was effective to remove diazinon and procymidone residues in cucumber and tomatoes, respectively.[23,24]

Washing is the most common process, which is the preliminary step in both household and commercial preparations. Loosely held residues of several pesticides are removed with reasonable efficiency by various types of washing processes in many agricultural commodities, such as green bean, bitter gourd, rice, eggplant, mango, apple, peach, and tomatoes.[25−34] In this study, the running water washing is the most effective to remove etofenpox by 43.9%, but another paper reported that tap water was least effective in reducing the pesticide residues and removed them by only 10−12%.[35] Washing with water and/or detergent solution was necessary to decrease the intake of the pesticide residue. The acidic detergent solution was more effective in the removal of organochlorine under investigation than alkaline and neutral solutions.[35]

Removal Efficiency of Etofenprox by Drying. Drying is the oldest and quite a simple method of preserving food compared to other methods. Several methods of drying by sun or in an oven or a freeze dryer can be used. The residue of etofenprox on spring onion 12 days after treatment was 4.44 mg/kg on average. The residue level increased to 12.04 and 30.29 mg/kg after heat dry and freeze dry, respectively. The residue could be concentrated by mass reduction during the dry process because of water evaporation. The CRL calculated was 0.64 by heat dry, while it was 1.48 mg/kg by freeze dry, corresponding to a removal rate of 85.5 and 66.6%, respectively (Figure 3 and Table 5). The heating drying was more effective than freeze drying in removal of etofenprox in spring onion, because the pesticide degraded by heat.[36] Drying has been reported to reduce the pesticide residues considerably. Sun drying of raisin decreased the dimethoate residue by 81%, while oven drying after washing lead to a 73% decline in the residue. The decrease in dimethoate was attributed to heat, which could cause evaporation and degradation.[36] For sunlight drying in raisin processing, the residue level of vinclozolin and dimethoate was reduced to one-third and one-fifth of the fresh fruits, respectively. While the oven drying after washing caused residue decreases for iprodione and procdymidone of 57 and 47%, respectively. However, oven drying increased the phosalone residue level compared to sunlight drying, which could be attributed to photodegradation.[36] Drying of grape leads to 64.2−71.9% losses of methamidophos possibly because of evaporation of the pesticide during the process.[37]

Table 5. Pesticide Residue and Removal Rate from Spring Onion Dried in an Oven and a Freeze Dryer (n = 3)

		after drying	
	before drying	heat	freeze
residue (mg/kg)	4.4 ± 0.2	12.0 ± 2.5	30.1 ± 3.1
weight reduction ratio		18.7 ± 0.2	20.4 ± 0.1
compensated residue (mg/kg)		0.6 ± 0.1	1.5 ± 0.2
removal rate (%)		85.5 ± 3.0	66.6 ± 3.4

In conclusion, the biological half-lives of etofenprox in spring onion were found to be 9.5 and 7.9 days, at the single or double application rates and most residues of etofenpox in spring onion could be removed by oven drying after washing with running tap water.

AUTHOR INFORMATION

Corresponding Author

*Telephone: +82-31-670-5083. Fax: 82-31-670-5089. E-mail: jkmoon@hknu.ac.kr.

Author Contributions

†Kyu-Won Hwang and Woo-Suk Bang contributed equally to this work.

Funding

This work was supported by the 2013(213A380059) Yeungnam University Research Grant.

Notes

The authors declare no competing financial interest.

REFERENCES

(1) Krol, W. J.; Arsenault, T. L.; Pylypiw, H. M.; Incorvia Mattina, M. J. Reduction of pesticide residues on produce by rinsing. *J. Agric. Food Chem.* **2000**, *48*, 4666−4670.

(2) Clark, J. M.; Symington, S. B. Advances in the mode of action of pyrethroids. *Top. Curr. Chem.* **2012**, *314*, 48−72.

(3) Jia, G.; Bi, C.; Wang, Q.; Qiu, J.; Zhou, W.; Zhou, Z. Determination of etofenprox in environmental samples by HPLC after anionic surfactant micelle-mediated extraction (coacervation extraction). *Anal. Bioanal. Chem.* **2006**, *384*, 1423−1427.

(4) Tomlin, C. D. C. *The Pesticide Manual*, 15th ed.; British Crop Protection Council: Hamlshire, U.K., 2009; pp 454−455.

(5) Becker, N.; Petric, D.; Zgomba, M.; Boase, C. *Mosquito and Their Control*, 2nd ed.; Springer: New York, 2010; p 463.

(6) Korean Crop Protection Association (KCPA). *Pesticide Handbook*; KCPA: Seoul, Korea, 2014; pp 606−609.

(7) Amagase, H.; Petesh, B. L.; Matsuura, H. Intake of garlic and its bioactive components. *J. Nutr.* **2001**, *131*, 955S−962S.

(8) Liu, S.; He, H.; Feng, G.; Chen, Q. Effect of nitrogen and sulfur interaction on growth and pungency of different pseudostem types of Chinese spring onion (*Allium fistulosum* L.). *Sci. Hortic.* **2009**, *121*, 12−18.

(9) Kaushik, G.; Satya, S.; Naik, S. N. Food processing a tool to pesticide residue dissipation − a review. *Food Res. Int.* **2009**, *42*, 26−40.

(10) Lee, H.; Kim, E.; Moon, J. K.; Zhu, Y. Z.; Do, J. A.; Oh, J. H.; Kwon, K. S.; Lee, Y. D.; Kim, J. H. Establishment of analytical method for cyazofamid residue in apple, mandarin, Korean cabbage, green pepper, potato and soybean. *J. Korean Soc. Appl. Biol. Chem.* **2012**, *55*, 241−247.

DOI: 10.1021/acs.jafc.5b02345
J. Agric. Food Chem. 2015, 63, 6675−6680

(11) Fong, W. G.; Moye, H. A.; Seiber, J. N.; Toth, J. P. *Pesticide Residues in Foods: Methods, Technologies, and Regulations*; John Wiley & Sons, Inc.: New York, 1999.
(12) Miller, J. M. *Chromatography: Concepts and Contrasts*; Wiley: Hoboken, NJ, 2005.
(13) Lee, J. H.; Park, H. W.; Keum, Y. S.; Kwon, C. H.; Lee, Y. D.; Kim, J. H. Dissipation pattern of boscalid in cucumber under greenhouse condition. *Korean J. Pest. Sci.* **2008**, *12*, 67−73.
(14) Lee, Y. D. *Practical Guide for Food Code Pesticide Residue Analysis*; Korea Food and Drug Administration: Osong, Korea, 2013.
(15) Gupta, S.; Gajbhiye, V. T.; Gupta, R. K. Soil dissipation and leaching behavior of a neonicotinoid insecticide thiamethoxam. *Bull. Environ. Contam. Toxicol.* **2008**, *80*, 431−437.
(16) Kanazawa, J. *Environmental Sciences of Pesticide*; Cooperative Publication: Japan, 1992; pp 55−56.
(17) Walash, M. I.; Metwally, M. E.; Hefnawy, M. M. Spectrophotometric determination of maneb, zineb, and their decomposition products in some vegetables and its application to kinetic studies after greenhouse treatment. *Food Chem.* **1993**, *47*, 411−416.
(18) Valverde-Garcia, A. G. P. E.; Aguilera-Del Real, A.; Ureña-Amate, M. D.; Camacho-Ferre, F. Determination and degradation study of chlorothalolnil residues in cucumber, peppers, and cherry tomatoes. *Anal. Chim. Acta* **1993**, *276*, 15−23.
(19) Lee, E. Y.; Noh, H. H.; Park, Y. S.; Kanf, K. W.; Kim, J. K.; Jin, Y. D.; Yun, S. S.; Jin, C. W.; Han, S. K.; Kyung, K. S. Residual characteristics of etofenprox and methoxyfenozide in Chinese cabbage. *Korean J. Pestic. Sci.* **2009**, *13*, 13−20.
(20) European Food Safety Authority (EFSA). Opinion on a request from EFSA related to the default Q10 value used to describe the temperature effect on transformation rates of pesticide in soil. *EFSA J.* **2007**, *62*, 1−32.
(21) Vasquez, M.; Cahill, T.; Tjeerdema, R. Soil and glass surface photodegradation of etofenprox under simulated California rice growing condition. *J. Agric. Food Chem.* **2011**, *59*, 7874−7881.
(22) Vasquez, M.; Holstege, D. M.; Tjeerdema, R. Aerobic versus anaerobic microbial degradation of etofenprox in a California rice field soil. *J. Agric. Food Chem.* **2011**, *59*, 2486−2492.
(23) Cengiz, M. F.; Certel, M.; Karakas, B.; Gocmen, H. Residue contents of DDVP(Dichlorvos) and diazinon applied on cucumbers grown in greenhouses and their reduction by duration of a pre-harvest interval and post-harvest culinary applications. *Food Chem.* **2006**, *98*, 127−135.
(24) Cengiz, M. F.; Certel, M.; Karakas, B.; Gocmen, H. Residue contents of captan and procymidone applied on tomatoes grown in greenhouses and their reduction by duration of a pre-harvest interval and post-harvest culinary applications. *Food Chem.* **2007**, *100*, 1611−1619.
(25) Cabras, P.; Angioni, A.; Garau, V. L.; Melis, M.; Pirisi, F. M.; Karim, M.; Minelli, E. V. Persistence of insecticide residues in olives and olive oil. *J. Agric. Food Chem.* **1997**, *45*, 2244−2247.
(26) Street, J. C. Methods of removal of pesticide residues. *Can. Med. Assoc. J.* **1969**, *100*, 154−160.
(27) Marshall, W. D. Preprocessing oxidative washes with alkaline hypochlorite to remove ethylenebis(dithiocarbamate) fungicide residues from tomatoes and green beans. *J. Agric. Food Chem.* **1982**, *30*, 649−652.
(28) Nath, G.; Agnihotri, S. Removal of endosulfan from bitter gourds by home processing. *Pesticides* **1984**, *18*, 13−15.
(29) Lee, S. R.; Mourer, C. R.; Shibamoto, T. Analysis before and after cooking processes of a trace chlorpyrifos spiked in polished rice. *J. Agric. Food Chem.* **1991**, *39*, 906−908.
(30) Kumar, U.; Agarwal, H. C. Degradation of dithane M-45 residues in brinjals during cooking. *Bull. Environ. Contam. Toxicol.* **1991**, *47*, 725−731.
(31) Awasthi, M. D. Decontamination of insecticide residues on mango by washing and peeling. *J. Food Sci. Technol.* **1993**, *30*, 132−133.
(32) Mergnat, T.; Fritsch, P.; Saint-Joly, C.; Truchot, E.; Saint-Blanquat, G. Reduction in phosalone residue levels during industrial dehydration of apples. *Food Addit. Contam.* **1995**, *12*, 759−767.
(33) Ong, K. C.; Cash, J. N.; Zabik, M.; Siddiq, M.; Jones, A. L. Chlorine and ozone washes for pesticide removal from apples and processed apple sauce. *Food Chem.* **1996**, *55*, 153−160.
(34) Abou-Arab, A. A. K. Behavior of pesticides in tomatoes during commercial and home preparation. *Food Chem.* **1999**, *65*, 509−514.
(35) Zohair, A. Behaviour of some organophophorus and organo-chlorine pesticides in potatoes during soaking in different solutions. *Food Chem. Toxicol.* **2001**, *39*, 751−755.
(36) Cabras, P.; Angioni, A.; Garau, V. L.; Melis, M.; Pirisi, F. M.; Cabitza, F.; Pala, M. Pesticide Residues in raisin processing. *J. Agric. Food Chem.* **1998**, *46*, 2309−2311.
(37) Athanasopoulos, P. E.; Pappas, C.; Kyriakidis, N. V.; Thanos, A. Degradation of methamidophos on soultanian grapes on the vines and during refrigerated storage. *Food Chem.* **2005**, *91*, 235−240.

DOI: 10.1021/acs.jafc.5b02345
J. Agric. Food Chem. 2015, 63, 6675−6680

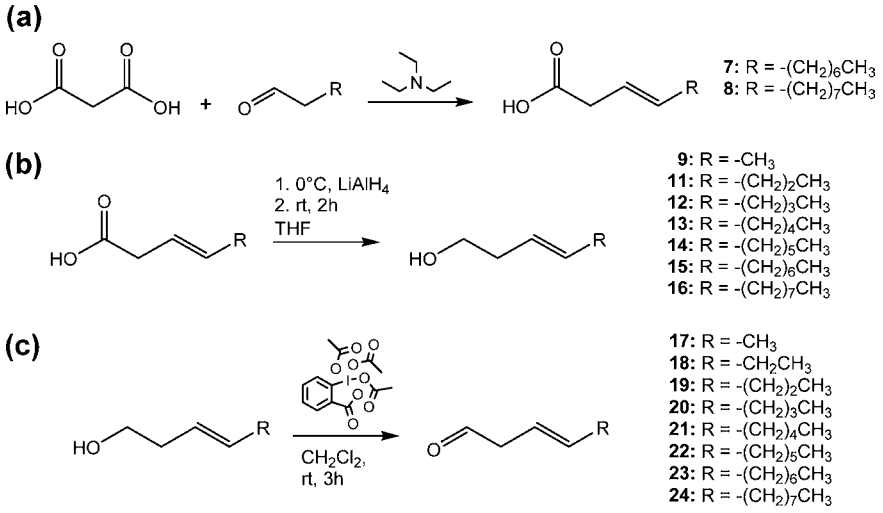

Figure 1. Synthetic routes leading to (a) the (*E*)-3-alkenoic acids, (b) the (*E*)-3-alken-1-ols, and (c) the (*E*)-3-alkenals.

Table 1. Retention Indices (RI), Odor Thresholds (OT), and Odor Qualities of (a) (*E*)-3-Alkenoic Acids, (b) (*E*)-3-Alken-1-ols, and (c) (*E*)-3-Alkenals

odorant	RI[a] DB5	RI[a] FFAP	OT (ng/L_{air}) median	OT (ng/L_{air}) range	odor qualities[b,c]	previously identified in[d]
(a) (*E*)-3-Alkenoic Acids						
(*E*)-3-pentenoic acid	988	1842	28	3.6−56	**sweaty**, sweet	nr
(*E*)-3-hexenoic acid	1075	1928	4.13	0.27−17	**sweaty**, cheesy, sweet	rhubarb,[5] soy sauce,[6] guava leaves,[45] snake fruit,[46] fish sauce,[47] breadfruit[7]
(*E*)-3-heptenoic acid	1153	2026	3.60	0.49−14	**plastic-like**, waxy, **pungent**	nr
(*E*)-3-octenoic acid	1245	2134	34	7.7−138	**plastic-like**, waxy	nr
(*E*)-3-nonenoic acid	1335	2237	68	8.6−137	waxy, sweaty, **plastic-like**	nr
(*E*)-3-decenoic acid	1422	2341	66	3.9−132	sweaty, **plastic-like**, pungent	*Siraitia grosvenorii*[8]
(*E*)-3-undecenoic acid	1525	2461	24	4.6−94	**waxy**, pungent, acidic, **sweaty**	black tea[9]
(*E*)-3-dodecenoic acid	1627	2565	34	3.3−68	**waxy**, plastic-like, vomit-like	nr
(b) (*E*)-3-Alken-1-ols						
(*E*)-3-penten-1-ol	645	1274	414	26−1655	grassy, **green** fresh	Parmigiano Reggiano cheese[10]
(*E*)-3-hexen-1-ol	777	1355	69	9.0−138	**green**, **musty**, grassy, clover-like	yellow passion fruit,[11] rose,[48] olive oil,[49] oyster leaf[15]
(*E*)-3-hepten-1-ol	865	1445	114	28−227	**citrus-like**, cleanser	South African red wine[50]
(*E*)-3-octen-1-ol	958	1548	62	8.0−124	**citrus-like**, **cleanser-like**, fresh	yellow passion fruit[11]
(*E*)-3-nonen-1-ol	1058	1647	57	7.0−459	**citrus-like**, soapy, **cleanser-like**	pepper[12]
(*E*)-3-decen-1-ol	1156	1750	61	30−484	citrus-like, green, **cleanser-like**	yellow passion fruit[11]
(*E*)-3-undecen-1-ol	1257	1859	23	11−181	**cleanser-like**, fresh	nr
(*E*)-3-dodecen-1-ol	1350	1954	104	52−207	fresh, green, **cleanser-like**	nr
(c) (*E*)-3-Alkenals						
(*E*)-3-pentenal	716	1056	3.03	3.0−48	grassy, **green**, cheesy	nr
(*E*)-3-hexenal	805	1135	4.96	0.62−10	fresh, **green**, soapy	yellow passion fruit,[11] pink guava,[13] jostaberry,[51] gooseberry,[52] baked potato[14]
(*E*)-3-heptenal	899	1224	14	3.5−14	citrus-like, **soapy**, fatty, green	nr
(*E*)-3-octenal	998	1327	12	2.9−12	**citrus-like**, soapy, fatty	roasted chickpeas[53]
(*E*)-3-nonenal	1097	1429	12	6.2−25	**fatty**, fresh, coriander-like	oyster leaf[15]
(*E*)-3-decenal	1199	1530	9.05	4.5−36	fatty, soapy, **coriander-like**	nr
(*E*)-3-undecenal	1301	1636	11	2.8−23	**coriander-like**, fatty, green	nr
(*E*)-3-dodecenal	1396	1737	8.33	4.2−17	**coriander-like**, soapy	nr

[a]Retention indices were determined as described by Van den Dool and Kratz.[19] [b]Odor qualities as perceived at the sniffing port. [c]Boldfaced attributes are the main odor qualities. These were named by the majority of the panel. [d]nr, compound has not been reported previously.

(Normasil 60, 40−63 μm), dichloromethane, and ethyl acetate were from VWR International GmbH (Darmstadt, Germany). (*E*)-3-Pentenoic acid (entry 1), (*E*)-3-hexenoic acid (entry 2), and (*E*)-3-hexen-1-ol (entry 10) were purchased from Sigma-Aldrich (Steinheim, Germany); (*E*)-3-heptenoic acid (entry 3), (*E*)-3-octenoic acid (entry 4), (*E*)-3-nonenoic acid (entry 5), and (*E*)-3-decenoic acid (entry 6)

DOI: 10.1021/acs.jafc.5b02169
J. Agric. Food Chem. 2015, 63, 6681−6688

were from TCI Europe (Zwijndrecht, Belgium). All chemicals were used without further purification.

Nuclear Magnetic Resonance (NMR) Spectra. ^{1}H and ^{13}C NMR spectra were recorded in $CDCl_3$ on an Avance 360 spectrometer, 360 MHz, and an Avance 600, 600 MHz (Bruker Biospin, Rheinstetten, Germany) at room temperature operating at 360 or 600 MHz (^{1}H) and 90 or 150 MHz (^{13}C), with tetramethylsilane (TMS) as internal standard.

GC-FID, GC−Olfactrometry (GC-O), and GC−Electron Impact−Mass Spectrometry (GC-EI-MS). GC-FID and GC-O analyses were performed with a Trace GC Ultra (Thermo Fisher Scientific GmbH, Dreieich, Germany) by using the following capillaries: FFAP (30 m × 0.32 mm fused silica capillary, free fatty acid phase, 0.25 μm; Chrompack, Mühlheim, Germany) and DB5 (30 m × 0.32 mm fused silica capillary, 0.25 μm; J&W Scientific, Fisons Instruments). The samples were applied by the cool-on-column injection technique at 40 °C. After 2 min, the temperature of the oven was raised at 10 °C/min to 240 °C, then raised at 40 °C/min to 280 °C (DB5) or at 10 °C/min to 240 °C (FFAP), respectively, and held for 5 min. The flow rate of the carrier gas helium was 2.5 mL/min. At the end of the capillary, the effluent was split in a ratio 1:1 (by volume) into an FID and a sniffing port using two deactivated but uncoated fused silica capillaries (50 cm × 0.32 mm). The FID and the sniffing port were held at 250 °C, respectively. GC-EI-MS analyses were performed with an Agilent MSD 5975C (Agilent Technologies, Waldbronn, Germany) and a Thermo ITQ 900 (Thermo Fisher Scientific, Dreieich, Germany) with the capillaries described above. Mass spectra in the electron impact mode (EI-MS) were generated at 70 eV.

Retention Indices (RI). Retention indices were determined according to the method previously described by Van den Dool and Kratz.[19]

Panelists. Panelists were trained volunteers from the University of Erlangen (Erlangen, Germany), exhibiting no known illness at the time of examination and with audited olfactory function. In preceding weekly training sessions the assessors were trained for at least half a year in recognizing orthonasally about 90 selected known odorants at different concentrations according to their odor qualities and in naming these according to an in-house developed flavor language. Furthermore, the panel was trained every 2 weeks on specific attributes with the help of specifically developed sniffing sticks; in the course of this training, all panelists also had to fill out the same questionnaire (hedonic, intensity) to obtain insights into their specific sensitivities or insensitivities, which were systematically recorded. On the basis of these tests, panelists were tested regularly for compliance with the established flavor language.

Odor Threshold Values. Thresholds in air were determined by GC-O with (*E*)-2-decenal as internal standard.[1,20,21] Of every dilution, 2 μL were applied for injection into the GC system. The thresholds were determined by five panelists (one male, four females), with each experiment being conducted once. GC analyses were performed on capillary FFAP as already described. The purity of all commercially available and synthesized compounds was taken into account in the GC-O experiments. All synthesized compounds were further checked for potential olfactorily active impurities by sniffing each substance on both capillaries of different polarity, to exclude interferences.

Odor Quality Determination. The odor qualities, determined during GC-O evaluation, were related to odor qualities of commercially available reference compounds. Panelists were asked to freely choose the respective odor quality descriptors based on the in-house developed flavor language (cf. Panelists). No additional descriptors were supplied to the panelists. The panelists determined the qualities during sniffing of FD 1 solution (injection of 2 μL). The panelists were instructed to record any changes in odor qualities in all following dilutions.

Syntheses, General Procedures. *(E)-3-Alkenoic Acids (**7** and **8**, Figure 1a).* Malonic acid (1 equiv) was dissolved in triethylamine (1.5 equiv) in a round-bottom flask fitted with a reflux condenser, a dropping funnel, and a nitrogen inlet tube. The corresponding aldehyde (1 equiv) was added slowly over a period of 0.5 h under continuous stirring at room temperature. The contents were then heated to 80 °C and maintained at this temperature for 3 h. The product was then acidified with dilute HCl (1 mL/mmol malonic acid) and extracted with diethyl ether (1 mL/mmol malonic acid) three times. The ether extracts were thoroughly washed with distilled water and dried over anhydrous magnesium sulfate. After evaporation of the solvent, the residue was purified by column chromatography (silica gel; eluent, hexane/EtOAc = 4:1) to give the pure product.[22]

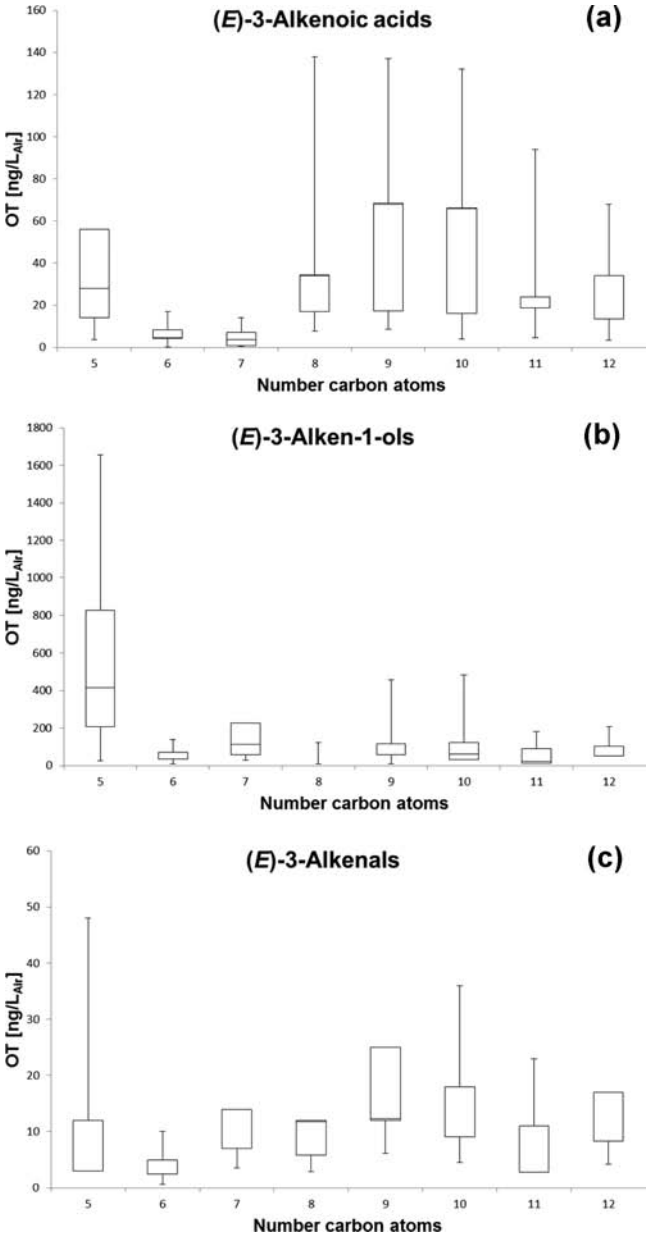

Figure 2. Influence of the chain length on the odor thresholds of (a) (*E*)-3-alkenoic acids, (b) (*E*)-3-alken-1-ols, and (c) (*E*)-3-alkenals (mean value (±SD), markers at minimum and maximum OT, box percentage 25−75%).

The mechanism follows a Linstead modification of the Knoevenagel reaction.[22−26]

*(E)-3-Alken-1-ols (**9** and **11−16**, Figure 1b).* Under a nitrogen atmosphere $LiAlH_4$ (1 equiv, 1 M THF) was added to an ice-cold solution of (*E*)-3-alkenoic acid (1 equiv) in THF (3 mL/mmol acid). The reaction was allowed to warm to room temperature. After 2 h, the reaction mixture was cooled in an ice bath, and water (4 mL/mmol acid) was added slowly. NaOH (3 M) and water (4 mL/mmol acid each) were added, and the resulting mixture was extracted with CH_2Cl_2 (8 mL/mmol acid) three times. The combined organic layer was washed with brine (8 mL/mmol acid) and then dried over $MgSO_4$, filtered, and evaporated to get the corresponding (*E*)-3-alken-1-ol as an oily substance.[27]

DOI: 10.1021/acs.jafc.5b02169
J. Agric. Food Chem. 2015, 63, 6681−6688

Table 2. Odor Thresholds (OT, GC-O) of All Five Panelists (P1−P5) of (a) (*E*)-3-Alkenoic Acids, (b) (*E*)-3-Alken-1-ols, and (c) (*E*)-3-Alkenals

		OT in air[a] (ng/L_{Air})						
entry	odorant	geometric mean	P1	P2	P3	P4	P5	literature[b]
			(a) (*E*)-3-Alkenoic Acids					
1	(*E*)-3-pentenoic acid	21	14	28	56	3.6	56	nr
2	(*E*)-3-hexenoic acid	3.6	4.1	8.3	4.1	0.27	17	nr
3	(*E*)-3-heptenoic acid	2.7	3.6	7.2	0.9	0.49	14	nr
4	(*E*)-3-octenoic acid	29	34	34	17	7.7	138	nr
5	(*E*)-3-nonenoic acid	40	68	68	8.6	17	137	nr
6	(*E*)-3-decenoic acid	32	66	132	16	3.9	66	nr
7	(*E*)-3-undecenoic acid	20	12	24	24	4.6	94	nr
8	(*E*)-3-dodecenoic acid	18	8.5	34	34	3.3	68	nr
			(b) (*E*)-3-Alken-1-ols					
9	(*E*)-3-penten-1-ol	314	827	1655	26	207	414	nr
10	(*E*)-3-hexen-1-ol	46	69	138	9.0	35	69	nr
11	(*E*)-3-hepten-1-ol	99	227	57	28	114	227	nr
12	(*E*)-3-octen-1-ol	47	124	62	8.0	62	62	nr
13	(*E*)-3-nonen-1-ol	65	459	57	7.0	57	115	nr
14	(*E*)-3-decen-1-ol	80	484	61	30	30	121	nr
15	(*E*)-3-undecen-1-ol	34	181	23	11	11	90	nr
16	(*E*)-3-dodecen-1-ol	90	207	104	52	52	104	nr
			(c) (*E*)-3-Alkenals					
17	(*E*)-3-pentenal	6.9	48	3.0	12	3.0	3.0	n.r.
18	(*E*)-3-hexenal	3.3	5.0	5.0	0.62	10	2.5	n.r.
19	(*E*)-3-heptenal	9.3	14	14	3.5	14	7.0	n.r.
20	(*E*)-3-octenal	7.8	12	12	5.9	12	2.9	n.r.
21	(*E*)-3-nonenal	14	12	25	25	6.2	12	n.r.
22	(*E*)-3-decenal	12	36	9.1	4.5	9.1	18	n.r.
23	(*E*)-3-undecenal	7.4	23	11	2.8	2.8	11	n.r.
24	(*E*)-3-dodecenal	9.6	17	17	4.2	8.3	8.3	n.r.

[a]Odor thresholds in air were determined as described by Ullrich and Grosch.[1] [b]nr, OT (determined as in this study) has not been reported previously, to the best of our knowledge.

(E)-3-Alkenals (17−24, Figure 1c). A solution of (*E*)-3-alken-1-ol (1 equiv) in CH_2Cl_2 (1 mL/mmol alcohol) was added dropwise to a suspension of Dess−Martin periodinane (1.1 equiv) in CH_2Cl_2 (2 mL/mmol Dess−Martin periodinane). After a few minutes, in some cases the reaction mixture started to boil and was allowed to do so for about 5 min. After that, the obtained suspension was stirred for 3 h at room temperature. It was then filtered through a glass frit, and the filtrate was washed with saturated aqueous $NaHCO_3$ solution containing $Na_2S_2O_3$ (25%) (3.5 mL/mmol alcohol). The resulting clear solution was dried over $MgSO_4$ and filtered, and the CH_2Cl_2 was removed by using a rotary evaporator to give the corresponding (*E*)-3-alkenal as a colorless to pale yellow oil.[28]

RESULTS AND DISCUSSION

The median odor threshold values in air, the odor threshold range, and the main odor qualities of the homologues (*E*)-3-alkenoic acids, (*E*)-3-alken-1-ols, and (*E*)-3-alkenals are given in Table 1 and Figure 2. For the interested reader, besides the median odor threshold values, the geometric mean values are given in Table 2. In the following, only the median values are discussed, because they appear to be the more representative ones: In this study, the number of single values is limited, and some of these single values more strongly deviate from those of the other panelists. Such deviations would influence the geometric mean more significantly than the median. Nevertheless, when the geometric mean and the corresponding median values are compared, it becomes evident that both values show the same overall tendencies, and, if compared with each other, the differences are quite low, with only a few exceptions (e.g., (*E*)-3-decenoic or (*E*)-3-dodecenoic acid).

Regarding the median odor thresholds, the lowest can be found for (*E*)-3-pentenal with 3.03 ng/L_{Air}, followed by (*E*)-3-heptenoic acid with 3.6 ng/L_{Air} and (*E*)-3-hexenoic acid with 4.13 ng/L_{Air}. Due to the, at times, quite broad spreading of the individual threshold values, no clear insights about potential minima in the OT values can be deduced. Thereby, clustering or, on the other hand, broad spreading of the OT values of individual panelists is not evenly distributed among substances. As can be seen in Table 1a and Figure 2a, the OT range of (*E*)-3-pentenoic acid is much higher than for the homologously related (*E*)-3-hexenoic acid and (*E*)-3-heptenoic acid. Clustering of the OT values for these six- and seven-carbon atom compounds is also much narrower than that of the OTs of the substances of the same series with longer chain lengths. The widest clustering was observed for (*E*)-3-octenoic acid, followed by (*E*)-3-nonenoic and (*E*)-3-decenoic acid. From 11 and 12 carbon atoms onward, the broadness of the clustering decreases again. A similar pattern was observable in the case of the homologous series of the (*E*)-3-alken-1-ols (Table 1b and Figure 2b). However, despite the wide spreading of the odor threshold for (*E*)-3-penten-1-ol, the clustering range of the alkenols was not as wide as in the case of the (*E*)-3-alkenoic acids. Table 1c and Figure 2c present the values for the (*E*)-3-alkenals. Again, there is a comparable pattern to the (*E*)-3-alkenoic acids and (*E*)-3-alken-1-ols, with a quite wide spreading of the OT ranges for each substance in this homologous series. However, it needs to be kept in mind that a

DOI: 10.1021/acs.jafc.5b02169
J. Agric. Food Chem. 2015, 63, 6681−6688

Table 3. Odor Qualities (GC-O) of All Five Panelists (P1−P5) of (a) (*E*)-3-Alkenoic Acids, (b) (*E*)-3-Alken-1-ols, and (c) (*E*)-3-Alkenals

		odor qualities				
entry	odorant	P1	P2	P3	P4	P5
			(a) (*E*)-3-Alkenoic Acids			
1	(*E*)-3-pentenoic acid	sweet, flowery	sweaty	sweaty	pungent, plastic-like	sweaty, moldy
2	(*E*)-3-hexenoic acid	sweet, flowery	sweaty	sweaty, cheesy	pungent, plastic-like, sweaty	sweaty, moldy, musty
3	(*E*)-3-heptenoic acid	pungent, musty, cheesy	sweaty	plastic-like, green	pungent, plastic-like	waxy, moldy
4	(*E*)-3-octenoic acid	cheesy, plastic-like	plastic-like, waxy	plastic-like	pungent, plastic-like	waxy, paraffin-like
5	(*E*)-3-nonenoic acid	pungent, sweaty	plastic-like, waxy	plastic-like, sweaty	plastic-like, burned rubber	Waxy
6	(*E*)-3-decenoic acid	pungent, cheesy, musty	sweaty, waxy, plastic-like,	plastic-like	plastic-like, burned rubber	waxy, black tea
7	(*E*)-3-undecenoic acid	acidic, vomit-like	sweaty, waxy, plastic-like,	sweaty, waxy	sweaty, cheesy, plastic-like	pungent, waxy, old wood-like,
8	(*E*)-3-dodecenoic acid	vomit-like	plastic-like, waxy	waxy	burned rubber, pungent	waxy, burned
			(b) (*E*)-3-Alken-1-ols			
9	(*E*)-3-penten-1-ol	fresh, green, sweet	green, grassy	grassy, green	green, grassy	soapy, green
10	(*E*)-3-hexen-1-ol	green, fresh, flowery	musty, green, sweaty	green, grassy, musty	grassy, musty	musty, putrid
11	(*E*)-3-hepten-1-ol	green, plastic-like	musty, green, cleanser-like	citrus-like, cleanser-like	musty, citrus-like	citrus-like, soapy
12	(*E*)-3-octen-1-ol	green, sweet, fatty	musty, cleanser-like	citrus-like, cleanser-like	citrus-like, sweet	citrus-like, fresh, cleanser-like
13	(*E*)-3-nonen-1-ol	fatty, fresh	musty, citrus-like, cleanser-like	citrus-like, cleanser-like	citrus-like, cleanser-like	citrus-like, cleanser-like
14	(*E*)-3-decen-1-ol	sweet, green, flowery	musty, cleanser-like, green, citrus-like	citrus-like, cleanser-like, pungent	cleanser-like	soapy
15	(*E*)-3-undecen-1-ol	sweet	cleanser-like	cleanser-like, citrus-like	cleanser-like, sebum-like	cleanser-like, musty
16	(*E*)-3-dodecen-1-ol	citrus-like, fresh, green	musty, cleanser-like	cleanser-like, green	cleanser-like, sebum-like	herb-like, citrus-like
			(c) (*E*)-3-Alkenals			
17	(*E*)-3-pentenal	flowery, cheesy	green, grassy	green	green	musty
18	(*E*)-3-hexenal	fresh, green, cabbage-like	green, musty, sweaty	green, soapy	green, honey-like	grassy, fatty, metallic
19	(*E*)-3-heptenal	sweet, flowery, musty	green, cleanser-like, citrus-like	soapy, green	soapy, green	citrus-like, fatty, soapy
20	(*E*)-3-octenal	fresh, citrus-like	green, fatty, citrus-like	soapy, fatty	soapy, citrus-like	citrus-like, soapy, fresh
21	(*E*)-3-nonenal	fatty, fresh, cucumber-like	fatty, green, soapy	coriander-like, soapy, fatty	fatty, coriander-like	fatty, green, fresh
22	(*E*)-3-decenal	fresh, citrus-like, fatty	coriander-like, soapy	coriander-like, soapy	coriander-like, fatty	citrus-like, balmy, woody
23	(*E*)-3-undecenal	sweet, flowery	coriander-like	green, fatty	coriander-like	citrus-like, eucalyptus, ethereous, balmy
24	(*E*)-3-dodecenal	citrus-like, fresh	soapy, coriander-like, cucumber-like	coriander-like, soapy	coriander-like, soapy	ethereous, fresh, rancid, cedar-like

larger panel number, or an untrained panel, might lead to changes in the order of threshold ranking and might lead to a distinct change of the spreading and clustering.[2,29−33]

When all three homologue series were compared, the series with the lowest median odor thresholds was the series of (*E*)-3-alkenals, followed by the (*E*)-3-alkenoic acids. However, when the single odor thresholds of all five panelists were viewed independently (Table 1, OT range; Table 2) enormous differences between the respective values of the individual panelists can be observed. Especially with regard to the series of (*E*)-3-alkenoic acids, huge variances between individual values can be found. The lowest OT of 0.27 ng/L_{Air} for (*E*)-3-hexenoic acid and the highest of 17 ng/L_{Air} span a threshold range with a factor of 63. An analogously broadly distributed pattern can be found for (*E*)-3-penten-1-ol with a threshold range from 26 to 1655 ng/L_{Air}, which corresponds to a factor of 64, and for (*E*)-3-nonen-1-ol with a range from 7 to 459 ng/L_{Air}, which relates to a factor of 66 between the most extreme values. Nevertheless, despite these huge differences, the ranking of the thresholds of the single panelists of a homologous series was in many cases comparable (cf. Table 2). For instance, for four of five panelists, the lowest individual OT of the (*E*)-3-alkenoic acids was that of (*E*)-3-heptenoic acid. On the other hand, the highest individual OT in the case of the (*E*)-3-alken-1-ols was that of (*E*)-3-penten-1-ol, again for four of the five panelists.

Compared with other studies, such as that of Czerny et al.,[21] in which the odor thresholds range "only" from a factor of 2 to 8, the differences between the odor thresholds of the individual panelists in this study might seem very huge. However, in the case of Czerny et al., it needs to be highlighted that only two panelists participated in the experiments. Furthermore, only aromatic compounds, and, more precisely, phenol derivatives, were investigated, and not open-chained substances as in the present study.[21] Accordingly, a satisfactory comparison would be hard to achieve.

DOI: 10.1021/acs.jafc.5b02169
J. Agric. Food Chem. 2015, 63, 6681−6688

The main odor quality in the series of (*E*)-3-alkenoic acids changes noticeably with increasing chain length from sweaty for (*E*)-3-pentenoic acid and (*E*)-3-hexenoic acid, to plastic-like for (*E*)-3-heptenoic acid to (*E*)-3-decenoic acid, to waxy for (*E*)-3-undecenoic acid and (*E*)-3-dodecenoic acid. (*E*)-3-Penten-1-ol and (*E*)-3-hexen-1-ol of the homologous series of (*E*)-3-alken-1-ols show a green odor, changing with increasing chain length to citrus-like and cleanser-like for (*E*)-3-hepten-1-ol to (*E*)-3-nonen-1-ol, ending in a cleanser-like smell for (*E*)-3-decen-1-ol to (*E*)-3-dodecen-1-ol. The (*E*)-3-alkenals start also with a green odor quality for the short-chain (*E*)-3-pentenal to (*E*)-3-heptenal, shifting to citrus-like for (*E*)-3-octenal, to fatty for (*E*)-3-nonenal, and finally to coriander-like for (*E*)-3-decenal to (*E*)-3-dodecenal. With regard to the individual odor qualities named by each panelist (Table 3), there are similarly broadly distributed patterns in the individual naming of the odor characters as observed for the individual odor thresholds, and they vary enormously. The odor quality descriptions of (*E*)-3-pentenoic acid range from sweet and flowery to sweaty to pungent and plastic-like. (*E*)-3-Dodecen-1-ol is described either as citrus-like, musty from another, or herb-like, depending on the evaluating panelist. Only in the case of the (*E*)-3-alkenals was the variety not that broad, with most panelists having reported the terms green for (*E*)-3-pentenal and (*E*)-3-hexenal, soapy for (*E*)-3-heptenal and (*E*)-3-octenal, soapy and coriander-like for (*E*)-3-nonenal, and coriander-like for (*E*)-3-decenal, (*E*)-3-undecenal, and (*E*)-3-dodecenal.

One explanation for these discrepancies in the odor thresholds and odor qualities between the single panelists could be the interindividual interaction of the respective odorant with the receptors. There are reports on interindividual differences in receptor expression in humans that might be related to the observed differences.[34,35] It also needs to be kept in mind that numerous odorants activate not only one receptor but a number of them and that receptors can also be activated by a range of odorants.[36,37] The interindividual patterns in activation resulting from that coding might also be divergent between different subjects. However, apart from the direct binding of an odorant to the respective receptors in the olfactory system, there might also be interindividually different effects related to the so-called peri-receptor events, meaning that odorants may be biotransformed, for example, by cytochrome P 450 metabolization, prior to interacting with the target receptor sites. This biotransformation of aroma compounds can alter the quality and quantity of the substances and might lead to differences in odor threshold as well as odor quality.[38−43] Accordingly, the investigated compounds, bearing, for example, double-bond moieties, might be prone to metabolic attack as has been previously shown for other unsaturated compounds by Schilling et al.[38,39,43,44]

Here, it might be worth drawing some comparison between the substances investigated within this study and other related substance groups differing in degree of saturation. Table 4 provides a compilation of literature data and our own data of the present study for direct comparison of the impact of the double-bond configuration (either *E* or *Z*) or the impact of saturation of the double bond on the respective OT values. Unfortunately, available data for a straightforward comparison are not comprehensive. Nevertheless, from the few reported (*Z*)-3-compound values it becomes clear that the (*Z*)-3-configuration obviously represents a very favorable moiety in terms of high odor impact. In contrast to this, the (*E*)-3-configuration obviously does not impart the same effect, and is even, in several cases, to be regarded as less odoriferous than even the saturated analogue. Nevertheless, these conclusions would need to be further substantiated by future studies, filling in the missing data of Table 4.

Table 4. Odor Thresholds in Air (OT in Air) of (a) (*E*)-3-Alkenoic Acids Compared to (*Z*)-3-Alkenoic Acids and Saturated Carboxylic Acids, (b) (*E*)-3-Alken-1-ols Compared to (*Z*)-3-Alken-1-ols and 1-Alkanols, and (c) (*E*)-3-Alkenals Compared to (*Z*)-3-Alkenals and 1-Alkanals Obtained from the Literature

(a) (*E*)-3-Alkenoic Acids Compared to (*Z*)-3-Alkenoic Acids and Saturated Carboxylic Acids

	OT in air (ng/L_{Air})[a]		
no. carbon atoms	(*E*)-3-alkenoic acids[a,b]	(*Z*)-3-alkenoic acids[c]	saturated carboxylic acids[c]
5	28	nr	4.6[54]
6	4.13	nr	nr
7	3.60	nr	nr
8	34	nr	nr
9	68	nr	nr
10	66	nr	nr
11	24	nr	nr
12	34	nr	nr

(b) (*E*)-3-Alken-1-ols Compared to (*Z*)-3-Alken-1-ols and 1-Alkanols

	OT in air (ng/L_{Air})[a]		
no. of carbon atoms	(*E*)-3-alken-1-ols[a,b]	(*Z*)-3-alken-1-ols[c]	1-alkanols[c]
5	414	nr	150[55]
6	69	4−16[56]	nr
7	114	nr	nr
8	62	nr	nr
9	57	nr	22[55]
10	61	nr	18[55]
11	23	nr	nr
12	104	nr	nr

(c) (*E*)-3-Alkenals Compared to (*Z*)-3-Alkenals and 1-Alkanals

	OT in air[a] (ng/L_{Air})		
no. carbon atoms	(*E*)-3-alkenals[a,b]	(*Z*)-3-alkenals	1-alkanals[c]
5	414	nr	nr
6	69	0.09−0.36[56]	1.1[55]
7	114	nr	0.9[55]
8	62	nr	0.4[55]
9	57	nr	2.6[55]
10	61	nr	2.6[55]
11	23	nr	nr
12	104	nr	nr

[a]Odor thresholds in air were determined as described by Ullrich and Grosch.[1] [b]In this study determined median odor threshold values. [c]nr, OT (determined as in this study) has not been reported previously, to the best of our knowledge.

To sum up, our study demonstrates that some of the investigated compounds in the series of the (*E*)-3-alkenoic acids, (*E*)-3-alken-1-ols, and (*E*)-3-alkenals show low odor thresholds or high odor potencies and interesting odor qualities. In consideration of the fact that many of the 24 investigated substances have already been identified in food, or generally in nature, some of the currently unreported substances may be also promising candidates to be discovered as natural compounds in future studies. The analytical data compiled in this study, such as retention indices, mass spectra, odor thresholds in air, or odor qualities can aid in their future discovery. Moreover, this study aims at raising future attention to this substance class, not only in

DOI: 10.1021/acs.jafc.5b02169
J. Agric. Food Chem. 2015, 63, 6681−6688

terms of some of the compounds being potentially important odorants in food but also with regard to other biological meaning that has not been investigated comprehensively to date.

In view of this, one needs to keep in mind that chemosensorically active compounds can serve a number of purposes in nature such as communication between and across species, resulting, for example, in chemo-attraction or -repulsion. As an example, another interesting field of research is the potential biological meaning of the target compounds investigated within the present study in relation to entomology. As mentioned in the introduction, some of the investigated compounds have already been shown to function as pheromones, attractants, or repellents in insects. Accordingly, it would be of high interest to have a closer look at such possible functionalities of the compounds of the current study and to also establish the respective structure−response relationships in view of insect behavior. Comprehensive substance libraries as generated in the current study will aid the targeted and systematic discovery of such effects in future investigations.

■ ASSOCIATED CONTENT

Supporting Information

Spectroscopic data (MS-EI, NMR), yield and purity of all synthesized compounds as well as a table with the concentrations of the FD1 solutions and figures of the individual odor thresholds are documented separately. The Supporting Information is available free of charge on the ACS Publications website at DOI: 10.1021/acs.jafc.5b02169.

■ AUTHOR INFORMATION

Corresponding Author

*(A.B.) Phone: +49-9131-85 22739. E-mail: andrea.buettner@fau.de.

Notes

The authors declare no competing financial interest.

■ ACKNOWLEDGMENTS

We thank all members of our working group for their participation in the sensory analyses, although the odors were not always pleasant.

■ REFERENCES

(1) Ullrich, F.; Grosch, W. Identification of the most intense volatile flavor compounds formed during autoxidation of linoleic acid. *Z. Lebensm.-Unters. Forsch.* **1987**, *184*, 277−282.

(2) Schieberle, P.; Buettner, A. Influence of the chain length on the aroma properties of homologous epoxy-aldehydes, ketones, and alcohols. In *Aroma Active Compounds in Foods*; American Chemical Society: Washington, DC, USA, 2001; Vol. 794, pp 109−118.

(3) Chang, S.; Peterson, R.; Ho, C.-T. Chemical reactions involved in the deep-fat frying of foods. 1. *J. Am. Oil Chem. Soc.* **1978**, *55*, 718−727.

(4) Bock, G.; Benda, I.; Schreier, P. Reduction of cinnamaldehyde and unsaturated acids by *Botrytis cinerea*. *Z. Lebensm.-Unters. Forsch.* **1988**, *186*, 33−35.

(5) Dregus, M.; Engel, K.-H. Volatile constituents of uncooked rhubarb (*Rheum rhabarbarum* L.) stalks. *J. Agric. Food Chem.* **2003**, *51*, 6530−6536.

(6) Sun, S. Y.; Jiang, W. G.; Zhao, Y. P. Profile of volatile compounds in 12 Chinese soy sauces produced by a high-salt-diluted state fermentation. *J. Inst. Brew.* **2010**, *116*, 316−328.

(7) Iwaoka, W.; Hagi, Y.; Umano, K.; Shibamoto, T. Volatile chemicals identified in fresh and cooked breadfruit. *J. Agric. Food Chem.* **1994**, *42*, 975−976.

(8) Chen, H.-y.; Luo, L.-h.; Wang, Z.-b.; Lin, C.-w.; Qin, J.-k. Analysis of volatile oil from seedless fruits of Siraitia grosvenorii by gas chromatography-mass spectrometry. *Guangxi Daxue Xuebao, Ziran Kexueban* **2011**, *36*, 489−492.

(9) Mick, W.; Goetz, E. M.; Schreier, P. Volatile acids of black tea aroma. *Lebensm.-Wiss. Technol.* **1984**, *17*, 104−106.

(10) Meinhart, E.; Schreier, P. Study of flavor compounds from Parmigiano Reggiano cheese. *Milchwissenschaft* **1986**, *41*, 689−691.

(11) Werkhoff, P.; Guentert, M.; Krammer, G.; Sommer, H.; Kaulen, J. Vacuum headspace method in aroma research: flavor chemistry of yellow passion fruits. *J. Agric. Food Chem.* **1998**, *46*, 1076−1093.

(12) Cardeal, Z. L.; Gomes da Silva, M. D. R.; Marriott, P. J. Comprehensive two-dimensional gas chromatography/mass spectrometric analysis of pepper volatiles. *Rapid Commun. Mass Spectrom.* **2006**, *20*, 2823−2836.

(13) Steinhaus, M.; Sinuco, D.; Polster, J.; Osorio, C.; Schieberle, P. Characterization of the aroma-active compounds in pink guava (*Psidium guajava*, L.) by application of the aroma extract dilution analysis. *J. Agric. Food Chem.* **2008**, *56*, 4120−4127.

(14) Coleman, E. C.; Ho, C.-T.; Chang, S. S. Isolation and identification of volatile compounds from baked potatoes. *J. Agric. Food Chem.* **1981**, *29*, 42−48.

(15) Delort, E.; Jaquier, A.; Chapuis, C.; Rubin, M.; Starkenmann, C. Volatile composition of oyster leaf (*Mertensia maritima* (L.) Gray. *J. Agric. Food Chem.* **2012**, *60*, 11681−11690.

(16) Light, D.; Jang, E.; Dickens, J. Electroantennogram responses of the Mediterranean fruit fly, *Ceratitis capitata*, to a spectrum of plant volatiles. *J. Chem. Ecol.* **1988**, *14*, 159−180.

(17) Suzuki, T.; Haga, K.; Tsutsumi, T.; Matsuyama, S. Analysis of anal secretions from phlaeothripine thrips. *J. Chem. Ecol.* **2004**, *30*, 409−423.

(18) Farine, J.-P.; Everaerts, C.; Le Quere, J.-L.; Semon, E.; Henry, R.; Brossut, R. The defensive secretion of *Eurycotis floridana* (Dictyoptera, Blattidae, Polyzosteriinae): chemical identification and evidence of an alarm function. *Insect Biochem. Mol. Biol.* **1997**, *27*, 577−586.

(19) Van den Dool, H.; Kratz, P. D. A generalization of the retention index system including linear temperature programmed gas-liquid partition chromatography. *J. Chromatogr.* **1963**, *11*, 463−471.

(20) Boelens, M. H.; Van Gemert, L. J. In *Physicochemical Parameters Related to Organoleptic Properties of Flavor Components*; Elsevier Applied Science: Amsterdam, The Netherlands, 1986; pp 23−49.

(21) Czerny, M.; Brueckner, R.; Kirchhoff, E.; Schmitt, R.; Buettner, A. The influence of molecular structure on odor qualities and odor detection thresholds of volatile alkylated phenols. *Chem. Senses* **2011**, *36*, 539−553.

(22) Rao, B.; Vijayalakshmi, P.; Subbarao, R. Synthesis of long-chain (*E*)-3-alkenoic acids by the Knoevenagel condensation of aliphatic aldehydes with malonic acid. *J. Am. Oil Chem. Soc.* **1993**, *70*, 297−299.

(23) Boxer, S. E.; Linstead, R. P. Olefinic acids. V. Influence of bases on the condensation of aldehydes and malonic acid and a note on the Knoevenagel reaction. *J. Chem. Soc.* **1931**, 740−751.

(24) Corey, E. J. The mechanism of the decarboxylation of α,β- and β,γ-unsaturated malonic acid derivatives and the course of decarboxylative condensation reactions in pyridine. *J. Am. Chem. Soc.* **1952**, *74*, 5897−5905.

(25) Corey, E. J. The decarboxylation of α,β-unsaturated malonic acid derivatives via β,γ-unsaturated intermediates. II. The effect of α-substituents upon product composition and rate. *J. Am. Chem. Soc.* **1953**, *75*, 1163−1167.

(26) Ragoussis, N. Modified knoevenagel condensations. Synthesis of (*E*)-3-alkenoic acids. *Tetrahedron Lett.* **1987**, *28*, 93−96.

(27) Donde, Y.; Nguyen, J. H.; Burk, R. M. Preparation of substituted cyclopentanes having prostaglandin activity for the treatment of glaucoma. WO2009061811A1, 2009.

(28) van den Nieuwendijk, A. M. C. H.; Kriek, N. M. A. J.; Brussee, J.; van Boom, J. H.; van der Gen, A. Stereoselective synthesis of (2*R*,5*R*)- and (2*S*,5*R*)-5-hydroxylysine. *Eur. J. Org. Chem.* **2000**, *2000*, 3683−3691.

(29) Boerger, D.; Buettner, A.; Schieberle, P. In Structure/odour relationships in homologous series of aroma-active allylalcohols and allylketones. In *The 10th Weurman Flavour Research Symposium*, Beaune, France, 2002.

DOI: 10.1021/acs.jafc.5b02169
J. Agric. Food Chem. 2015, 63, 6681−6688

(30) Boerger, D.; Buettner, A.; Schieberle, P. *State-of-the-Art in Flavour Chemistry and Biology*; Deutsche Forschungsanstalt für Lebensmittelchemie: Eisenach, Germany, 2005.
(31) Buettner, A.; Schieberle, P. Aroma properties of a homologous series of 2,3-epoxyalkanals and *trans*-4,5-epoxyalk-2-enals. *J. Agric. Food Chem.* **2001**, *49*, 3881−3884.
(32) Leonardos, G.; Kendall, D.; Barnard, N. Odor threshold determinations of 53 odorant chemicals. *J. Air Pollut. Control Assoc.* **1969**, *19*, 91−95.
(33) Hoshika, Y.; Imamura, T.; Muto, G.; Van Gemert, L. J.; Don, J. A.; Walpot, J. I. International comparison of odor threshold values of several odorants in Japan and in the Netherlands. *Environ. Res.* **1993**, *61*, 78−83.
(34) Keller, A.; Zhuang, H.; Chi, Q.; Vosshall, L. B.; Matsunami, H. Genetic variation in a human odorant receptor alters odour perception. *Nature* **2007**, *449*, 468−472.
(35) Mombaerts, P. The human repertoire of odorant receptor genes and pseudogenes. *Annu. Rev. Genomics Hum. Genet.* **2001**, *2*, 493−510.
(36) Katada, S.; Hirokawa, T.; Oka, Y.; Suwa, M.; Touhara, K. Structural basis for a broad but selective ligand spectrum of a mouse olfactory receptor: mapping the odorant-binding site. *J. Neurosci.* **2005**, *25*, 1806−1815.
(37) Araneda, R. C.; Kini, A. D.; Stuart, F. The molecular receptive range of an odorant receptor. *Nat. Neurosci.* **2000**, *3*, 1248−1255.
(38) List of abstracts from the 28th Annual Meeting of the Association for Chemoreception Sciences. *Chem. Senses* **2006**, *31*, 479−493.10.1093/chemse/bjj055
(39) Schilling, B.; Kaiser, R.; Natsch, A.; Gautschi, M. Investigation of odors in the fragrance industry. *Chemoecology* **2010**, *20*, 135−147.
(40) Nagashima, A.; Touhara, K. Enzymatic conversion of odorants in nasal mucus affects olfactory glomerular activation patterns and odor perception. *J. Neurosci.* **2010**, *30*, 16391−16398.
(41) Chougnet, A.; Woggon, W.-D.; Locher, E.; Schilling, B. Synthesis and in vitro activity of heterocyclic inhibitors of CYP2A6 and CYP2A13, two cytochrome P450 enzymes present in the respiratory tract. *ChemBioChem* **2009**, *10*, 1562−1567.
(42) Zhang, X.; Zhang, Q.-Y.; Liu, D.; Su, T.; Weng, Y.; Ling, G.; Chen, Y.; Gu, J.; Schilling, B.; Ding, X. Expression of cytochrome P450 and other biotransformation genes in fetal and adult human nasal mucosa. *Drug Metab. Dispos.* **2005**, *33*, 1423−1428.
(43) Granier, T.; Schilling, B. Preparation of amides, carbamates, and ureas which inhibit cytochrome P450 for use as modulators of fragrance compositions. WO2010037244A2, 2010.
(44) Schilling, B. Perireceptor processes in the nose − biochemical events beyond olfactory receptor activation. In *Springer Handbook of Odor*; Büttner, A., Ed.; Springer-Verlag: Berlin, Germany, 2016 (in press).
(45) García, M.; Quijano, C. E. Free and glycosidically bound volatiles in guava leaves (*Psidium guajava* L.) Palmira ICA-I cultivar. *J. Essent. Oil Res.* **2009**, *21*, 131−134.
(46) Wijaya, C. H.; Ulrich, D.; Lestari, R.; Schippel, K.; Ebert, G. Identification of potent odorants in different cultivars of snake fruit [*Salacca zalacca* (Gaert.) Voss] using gas chromatography−olfactometry. *J. Agric. Food Chem.* **2005**, *53*, 1637−1641.
(47) Peralta, R. R.; Shimoda, M.; Osajima, Y. Further identification of volatile compounds in fish sauce. *J. Agric. Food Chem.* **1996**, *44*, 3606−3610.
(48) Mannschreck, A.; von Angerer, E. The scent of roses and beyond: molecular structures, analysis, and practical applications of odorants. *J. Chem. Educ.* **2011**, *88*, 1501−1506.
(49) Garcia-Gonzalez, D. L.; Vivancos, J.; Aparicio, R. Mapping brain activity induced by olfaction of virgin olive oil aroma. *J. Agric. Food Chem.* **2011**, *59*, 10200−10210.
(50) Weldegergis, B. T.; Crouch, A. M.; Gorecki, T.; de Villiers, A. Solid phase extraction in combination with comprehensive two-dimensional gas chromatography coupled to time-of-flight mass spectrometry for the detailed investigation of volatiles in South African red wines. *Anal. Chim. Acta* **2011**, *701*, 98−111.
(51) Hempfling, K.; Fastowski, O.; Celik, J.; Engel, K.-H. Analysis and sensory evaluation of jostaberry (*Ribes* × *nidigrolaria* Bauer) volatiles. *J. Agric. Food Chem.* **2013**, *61*, 9067−9075.
(52) Hempfling, K.; Fastowski, O.; Kopp, M.; Pour Nikfardjam, M.; Engel, K.-H. Analysis and sensory evaluation of gooseberry (*Ribes uva crispa* L.) volatiles. *J. Agric. Food Chem.* **2013**, *61*, 6240−6249.
(53) Lasekan, O.; Juhari, N. H.; Pattiram, P. D. Headspace solid-phase microextraction analysis of the volatile flavour compounds of roasted chickpea (*Cicer arietinum* L). *J. Food Process. Technol.* **2011**, *2*, 1000112.
(54) Christlbauer, M. R. *Evaluation of Odours from Agricultural Sources by Methods of Molecular Sensory*. Ph.D. thesis, TU Munich, Garching, Germany, 2006.
(55) Yang, D. S.; Shewfelt, R. L.; Lee, K.-S.; Kays, S. J. Comparison of odor-active compounds from six distinctly different rice flavor types. *J. Agric. Food Chem.* **2008**, *56*, 2780−2787.
(56) Guth, H.; Grosch, W. A comparative study of the potent odorants of different virgin olive oils. *Lipid/Fett* **1991**, *93*, 335−339.

DOI: 10.1021/acs.jafc.5b02169
J. Agric. Food Chem. 2015, 63, 6681−6688

Additionally, matrix effects, which can significantly interfere with the accuracy of an analytical method,[28] were not studied in the previous literatures.

A liquid chromatography−mass spectrometry (LC-MS) technique has been developed to measure QACs in both environmental media and food products.[25−27,29,30] However, a gas chromatography−mass spectrometry (GC-MS) technique has only been developed to measure QACs in environmental media without food products.[5,9,31,32] GC-MS is available in ordinary laboratories much more commonly than LC-MS because of the cost. Furthermore, GC-MS performs higher chromatographic resolution than LC-MS because it possesses a long capillary column where analytes can be effectively separated, which is beneficial to improve the accuracy of an analytical method.[31,32] Therefore, we believe that the GC-MS technique is more appropriate, cost-effective, and practical to be developed for routine determination of QACs in vegetables.

Dodecyltrimethylammonium chloride (DTAC), cetyltrimethylammonium chloride (CTAC), and didodecyldimethylammonium chloride (DDAC) (Figure 1), the representatives of

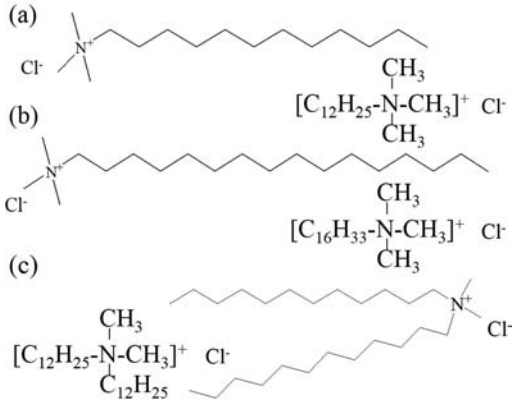

Figure 1. Structure of the three tested QACs: (a) dodecyltrimethylammonium chloride (DTAC), (b) cetyltrimethylammonium chloride (CTAC), and (c) didodecyldimethylammonium chloride (DDAC).

alkyl QACs with shorter alkyl chain lengths [C12−C16] as well as higher mobility and toxicity than other homologues [C18−C22],[11,13,33] have been detected in both agricultural soils and irrigation water as mentioned above.[5,9] Therefore, these QACs are most likely to be taken up by vegetables and consequently exhibit a health risk to humans through the food chain.[26,27,34]

The aim of the present study was to develop a reliable, sensitive, and cost-effective analytical method for routinely determining the three typical QACs (DTAC, CTAC, and DDAC) in various vegetables using ultrasonic-assisted extraction and GC-MS. This method is composed of sample pretreatment procedures optimized and reliable methodologies validated with linearity, matrix effect, precision, and accuracy. Acceptable results were obtained using this method to determine QACs in various real vegetables. To the best of our knowledge, this is the first study for the quantitation of QACs in various vegetables using GC-MS technique, and we believe it will effectively promote further research on QACs in soil−plant systems.

MATERIALS AND METHODS

Reagents. Standards DDAC (99%, purity) and CTAC (99%, purity) were purchased from Adamas (Emeryville, USA), and DTAC (99%, purity) was obtained from Aladdin (Seattle, USA). HPLC-grade solvents (including methanol, methyl trichloride, dichloromethane, and *n*-hexane) were purchased from Sigma-Aldrich (Steinheim, Germany). Neutral silica gel (200 mesh), neutral alumina oxide (200 mesh), and hydrochloric acid bought from Guangzhou Chemical Reagent Co., Ltd. (Guangzhou, China) were all of analytical grade.

Mixture stock solution (100 mg/L) of the three QACs (DTAC, DDAC, and CTAC) was prepared in methanol, which was kept in a refrigerator at 4 °C in the dark and used within one month. Standard working solutions of the three tested compounds at 20, 50, 100, 200, 500, 1000, and 2000 μg/L were prepared by diluting the stock solution with methanol when they would be used. Because matrix components in vegetables can influence detector responses, and the same vegetable species should have similar matrix effects,[28] nine vegetables including leafy vegetables (Chinese flowering cabbage, water spinach, and lettuce), root vegetables (white radish, potato, and carrot), and fruit vegetables (cucumber, pumpkin, and eggplant) were chosen to evaluate the matrix effects on the determination of QACs in vegetables. Correspondingly, matrice-matched standard solutions (20, 50, 100, 200, 500, 1000, and 2000 μg/L) were obtained by adding a blank vegetable sample extract to each diluted standard solution. All of these nine blank vegetables without the target QAC pollution were purchased from an organic vegetable farm where clean water and fertilizer without QAC residues were used.[28]

Sample Treatment. Approximately, 5 kg of each fresh vegetable sample was chopped and homogenized using a crusher (Jiu Yang Co., Ltd., China). An aliquot of about 1000 g of the sample was weighed and then lyophilized in a vacuum freeze drier (Jiangsu Hengfeng Equipment Manufacture Co., Ltd., China). Compared to the fresh vegetable sample, using a lyophilized vegetable sample was beneficial not only to minimize the sample volume and the reagent volume but also to shorten the extraction time.[28] The lyophilized samples were ground to a powder (0.45 mm) in a mill and stored in brown glass bottles. The spiked samples at three concentration levels (50, 200, and 1000 μg/kg) were obtained by adding 1 mL of mixture standard working solutions at 50, 200, and 1000 μg/L in methanol to 1.0 g of lyophilized blank vegetable sample powder, respectively. Afterward, the spiked samples were shaken continually to be homogenized and left for 12 h under a fume hood to evaporate the solvent at room temperature before analysis.

One gram aliquot of each lyophilized vegetable sample powder was weighed into 50 mL of Teflon centrifuge tube. Then, 10 mL of 0.1% acidified methanol (hydrochloric acid/methanol, v/v) was added into each tube. The tubes were shaken vigorously for 10 min with a constant temperature vibrator and then ultrasounicated for 10 min in a 100 W ultrasonic instrument (Kunshan Ultrasonic Instrument, Co., Ltd., China). The supernatant of each sample was collected after centrifugation at 8000 rpm for 5 min. The extraction was repeated twice again. All of the supernatants of each sample were combined and concentrated to almost 2 mL using a rotator vacuum evaporator (Shanghai Optical Instrument Factory, China) with 200 rpm at 40 °C. In order to remove interfering matrix components and other contaminants, neutral alumina oxide sorbent presoaked in methanol overnight was loaded into a glass column (30 cm height, 1 cm diameter) coupled with a flow control valve and filter cartridge until 8 cm height. The extracts were separately passed through the glass columns and eluted with 7 mL of methanol. The resulting elutes were collected and evaporated to near dryness, and then were redissolved with methanol, strained through 0.22 μm nylon filters, and transferred to sampler vials for GC-MS analysis.

Instrument and Apparatus. Analysis of the three QACs was conducted on a Shimadzu-QP2010 Plus series gas chromatograph equipped with a triple quadrupole mass spectrometry (GC-MS). According to the optimized conditions of GC-MS, the three QACs were separated with a DB-5MS fused silica capillary column (30 m length × 0.25 mm diameter, 0.1 μm film thickness). Samples were injected in splitless mode with 1 μL volume. The carrier gas was high purity helium (99.9999%) at a flow rate of 1.0 mL/min. The temperatures of injector, detector, and ion source were set at 280 °C, 250 °C, and 250 °C separately. The column oven temperature program was set as follows: start at 100 °C for 2 min, increase to 200

DOI: 10.1021/acs.jafc.5b01828
J. Agric. Food Chem. 2015, 63, 6689−6697

Table 1. Comparison of Matrix-Matched Calibrations and Solvent Calibration at Seven Concentrations Ranging from 20 to 2000 μg/L

QAC	matrix	regression equation	R^2	linear range (μg/L)	slope ratio (matrix/methanol)	LOD (μg/kg)	LOQ (μg/kg)
DTAC	methanol	$Y^a = 1387477x^b + 30491$	0.999	20−2000	-	-	-
	Chinese cabbage	$Y = 1428112x - 61689$	0.998	20−2000	1.03	5.8	19.2
	water spinach	$Y = 1431568x - 60351$	0.997	20−2000	1.03	5.6	18.6
	lettuce	$Y = 1557865x - 8820$	0.995	20−2000	1.12	3.7	12.3
	pumpkin	$Y = 1629247x - 38187$	0.998	20−2000	1.17	5.8	19.4
	cucumber	$Y = 1763182x - 79974$	0.998	20−2000	1.27	3.3	11.0
	eggplant	$Y = 1227865x - 123104$	0.998	20−2000	0.88	3.8	12.7
	potato	$Y = 1432219x - 34051$	0.998	20−2000	1.03	5.5	18.4
	white radish	$Y = 1503215x - 82402$	0.999	20−2000	1.08	3.3	11.0
	carrot	$Y = 1772079x - 43264$	0.999	20−2000	1.28	4.5	15.1
CTAC	methanol	$Y = 1397583x + 25275$	0.999	20−2000	-	-	-
	Chinese cabbage	$Y = 1408233x + 12586$	0.999	20−2000	1.01	3.7	12.4
	water spinach	$Y = 1512305x + 8929$	0.997	20−2000	1.08	3.8	12.8
	lettuce	$Y = 1475279x + 82068$	0.992	20−2000	1.06	5.5	18.2
	pumpkin	$Y = 1484901x - 33443$	0.999	20−2000	1.06	3.3	11.0
	cucumber	$Y = 1725138x - 62511$	0.999	20−2000	1.23	1.3	4.4
	eggplant	$Y = 1396822x - 89874$	0.999	20−2000	1.00	1.3	4.2
	potato	$Y = 1719931x - 26713$	0.999	20−2000	1.23	2.4	8.0
	white radish	$Y = 1600135x - 68794$	0.999	20−2000	1.14	2.7	8.9
	carrot	$Y = 1955302x - 6349$	0.999	20−2000	1.40	6.0	20.0
DDAC	methanol	$Y = 620569x + 9729.4$	0.999	20−2000	-	-	-
	Chinese cabbage	$Y = 616255x - 18161$	0.999	20−2000	0.99	4.0	13.5
	water spinach	$Y = 598534x - 616$	0.995	20−2000	0.96	1.3	4.3
	lettuce	$Y = 671015x - 6623$	0.998	20−2000	1.08	1.2	3.9
	pumpkin	$Y = 616238x - 17129$	0.999	20−2000	0.99	1.6	5.4
	cucumber	$Y = 771454x - 30101$	0.999	20−2000	1.24	0.7	2.4
	eggplant	$Y = 592653x - 43187$	0.999	20−2000	0.96	0.8	2.7
	potato	$Y = 691922x - 5736$	0.996	20−2000	1.11	0.7	2.4
	white radish	$Y = 773358x - 45449$	0.999	20−2000	1.25	0.7	2.3
	carrot	$Y = 745671x - 11858$	0.999	20−2000	1.20	3.0	10.0

[a]Peak area produced by the standard QACs in a concentration. [b]Concentration of the standard QACs.

°C at a rate of 30 °C/min, and increase to 280 °C at a rate of 40 °C (held 4 min), in a total run time of 11.33 min. The mass spectrometer was operated using electron-impact (EI) mode (70 eV) in the selective ion monitoring (SIM) mode in order to improve detection limits of the three QACs. The target ions of DTAC, CTAC, and DDAC were 58, 58, and 212 m/z, respectively,[31] and their retention time in this analytical procedure was 5.31, 6.85, and 8.67 min, respectively.

Validation Study. Validation of the developed method was performed in terms of linearity, limit of detection (LOD), limit of quantitation (LOQ), specificity, accuracy, and precision using the nine vegetables (Chinese flowering cabbage, water spinach, lettuce, pumpkin, cucumber, eggplant, potato, white radish, and carrot). The linearity was studied for each of the tested three QACs by spiking their standards in methanol and the nine vegetable matrices, respectively, in triplicate at seven concentration levels (20, 50, 100, 200, 500, 1000, and 2000 μg/L). The calculated parameters of the linear regression equations (slope, determination coefficient (R^2), and intercept) are presented in Table 1. Matrix effects were determined by calculating the slope ratios of matrix-matched calibration curves to solvent one. The matrix dependent LOD and LOQ were determined using the blank and calibration standards of the tested nine vegetable matrixes. The LOD of the each QAC is the concentration that produces a signal-to-noise (S/N) ratio of three, whereas the LOQ is estimated based on the S/N ratio of 10. Specificity of the developed method was analyzed based on the absence of interfering peaks at the retention time of the three QACs in the nine blank sample matrices. Accuracy and precision of the developed method were tested using recovery assays performed on samples spiked at three concentrations (50, 200, 1000 μg/kg). Five replicates for each spiked sample were prepared on three different days. The precision of the developed method was expressed as the intraday (repeatability) and interday (reproducibility) relative standard deviation (RSD^a and RSD^b) for 5 and 15 replicates, respectively.

Statistical Analysis. QAC concentrations from GC-MS analysis were calculated using postrun software of a Shimadzu-QP2010 plus series gas chromatograph. The data were exported to SPSS 21.0 (International Business Machines Co, USA) to determine the means and relative standard deviations (RSDs). Microsoft Excel 2010 was used to draw tables and figures.

RESULTS AND DISCUSSION

GC-MS Condition Optimization. The GC-MS conditions were optimized using the single and the mixture standard solutions of the three typical QACs (DTAC, CTAC, and DDAC) at 1000 μg/L. First, the mass spectral fragmentation pattern of each QAC was evaluated by analyzing the standard working solutions using EI mode at full-scan mode with the mass range of 50−300 m/z and at a rate of 3 scan/s. The three QACs were effectively converted into the corresponding tertiary amines by demethylation in the injection port at 280 °C as previously reported.[31,32] Then the tertiary amines were separated on a capillary column, depending on their alkyl chain lengths.[31] The target ions of DTAC, CTAC, and DDAC under the EI mode were 58, 58, and 212 m/z, respectively (Figure 2). Both the target ions at m/z = 58 ($[CH_2{=}N(CH_3)_2]^+$) and m/z = 212 ($[CH_2{=}N(CH_3)(C_{12}H_{25})]^+$) were derived from the α-cleavage of the carbon−carbon bond with respect to nitrogen.[31] In order to obtain an optimized separation of the tested QACs, three capillary columns (30 m × 0.25 mm × 0.25 μm) with

DOI: 10.1021/acs.jafc.5b01828
J. Agric. Food Chem. 2015, 63, 6689−6697

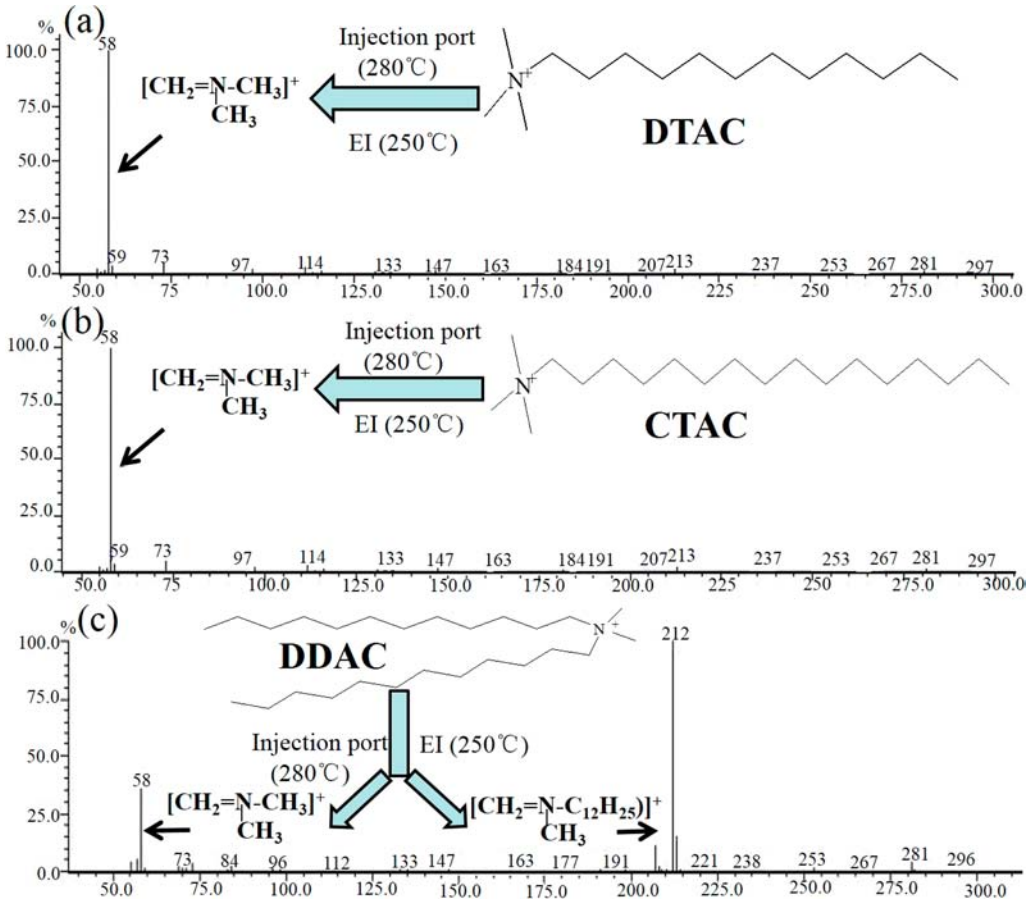

Figure 2. Product ion spectra of the three tested QACs: (a) DTAC, (b), CTAC, and (c) DDAC.

different stationary phases (i.e., DB-5MS consisted of 5% phenyl and 95% dimethylpolysiloxane, HP-1MS consisted of 100% dimethylpolysiloxane, and Rtx-35 consisted of 35% phenyl and 65% dimethylpolysiloxane) were compared. The best separation was obtained at the DB-5MS column with the appropriate proportion of phenyl and dimethylpolysiloxane. So the DB-5MS column was selected for the subsequent analysis. Furthermore, various temperature programs were investigated in order to achieve the best separation in the minimal time. By monitoring the target ions of the three QACs under the optimized GC-MS conditions, high response, remarkable selectivity, and excellent peak shape were obtained in a suitable analytical time (11.33 min), which are presented in Supporting Information, Figure S1.

Sample Extraction Optimization. To obtain an optimized sample extraction procedure, recovery tests for each single-variable (variety and acidity of extraction solvents, extraction times, and cleanup solvent) using QAC-spiked lettuce samples at 1000 μg/kg were carried out. Sequentially, the obtained procedure was evaluated in the other eight vegetable samples. First, four commonly used solvents (methanol, dichloromethane, methyl trichloride, and *n*-hexane) were separately investigated in recovery tests to get a satisfied extraction solvent for the three QACs. As the results exhibit in Figure 3 a, both recoveries (60%−77%) and RSD (<10%) of the three QACs were satisfied when methanol was used as the extraction solvent, while low recoveries of QACs were observed when using methyl trichloride and *n*-hexane as extraction solvent. QACs are cationic compounds tending to be extracted by polar solvents according to the similarity−intermiscibility theory.[9] Therefore, the highest recovery was obtained when using methanol with the strongest polarity among the four tested solvents in the present study.

As reported in the literature, the acidity of the extraction solvent significantly influences the extraction efficiency of QACs in the sample matrix (water and sediment).[29,30] So, recovery experiments using methanol as the extraction solvent with acidity ranging from 0.05% to 0.5% (hydrochloric acid/methanol, v/v) were conducted. Results showed that recoveries of the three QACs increased with increasing acidity of methanol under lower acidity (<0.1%, v/v) (Figure 3b). However, lower recoveries were observed with further increase in acidity from 0.2% (v/v) to 0.5% (v/v). Appropriate increase in acidity of methanol promoted the transfer of QACs from the sample matrix to the methanol phase because this approach not only improved methanol's polarity but also increased the concentration of hydrogen ion (H^+) which competed with the cationic compounds (i.e., QACs) in activated sorption sites of the sample matrix.[9,32] However, excessive increase in the acidity of methanol decreased recoveries of the three QACs because additional water entered the methanol solvent with the addition of hydrochloric acid, which heavily interfered with separation and extraction of the three QACs from the sample matrix.[9] So, methanol acidified with 0.1% of hydrochloric acid (v/v) was selected as the extraction solvent for subsequent experiments.

The influences of extraction times (once to three times) on recoveries of the three QACs were also investigated. As shown in Figure 3c, recoveries of all of the three QACs increased with increasing extraction times, and three times of extraction gained recoveries up to 96%−100%.

DOI: 10.1021/acs.jafc.5b01828
J. Agric. Food Chem. 2015, 63, 6689−6697

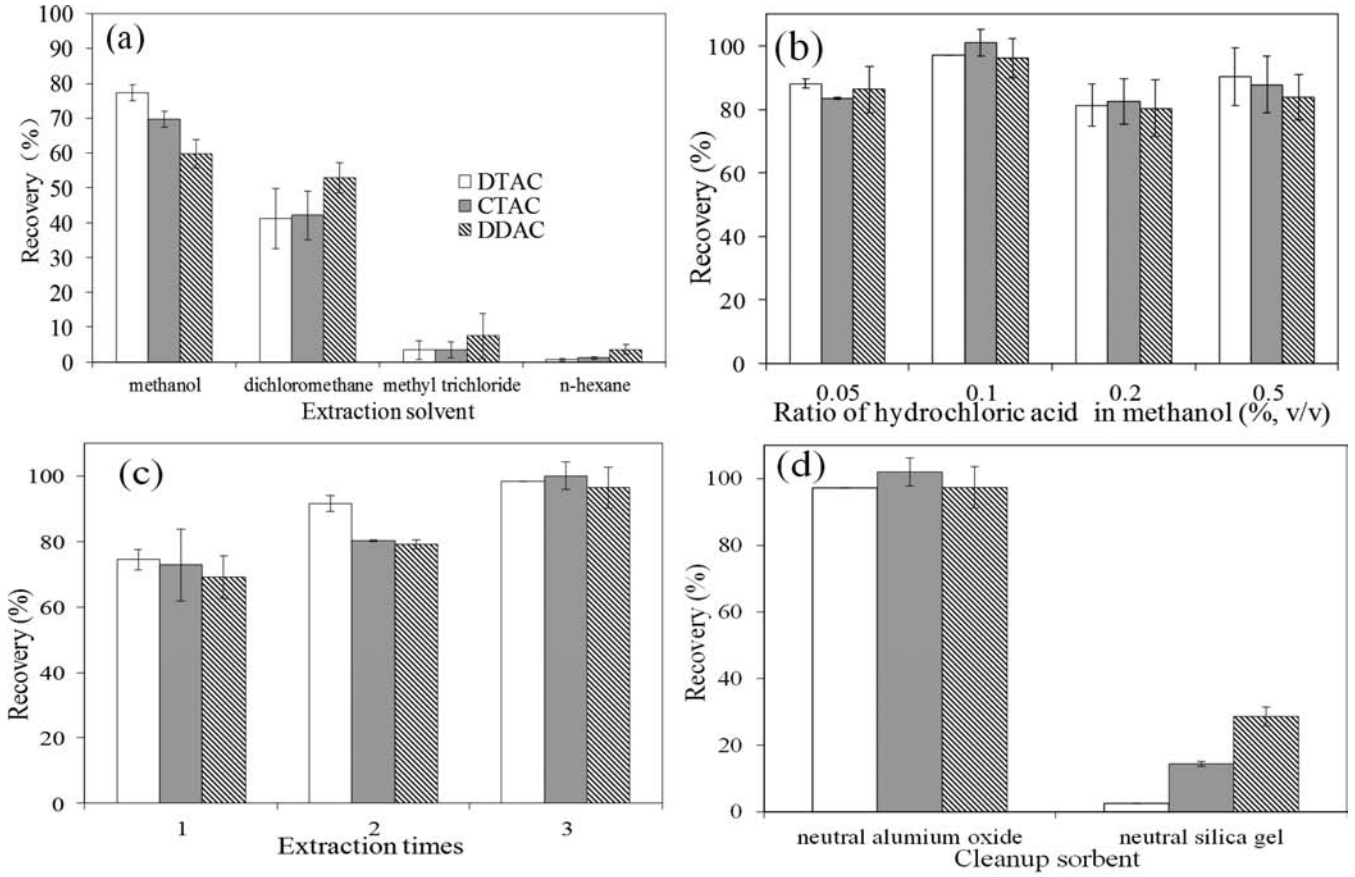

Figure 3. Effects of extractant (a), extractant acidity (b), extraction time (c), and cleanup sorbent (d) on the recovery of QACs in lettuce sample spiked with 1000 μg/kg.

In the cleanup procedure, two commonly used sorbents, neutral silica gel and neutral aluminum oxide filled to 8 cm height in a glass column (30 cm height, 1 cm diameter), were separately tested to obtain a satisfactory cleanup effect for the vegetable matrix. Unfortunately, as shown in Figure 3d, neutral silica gel used as the cleanup sorbent presented low recoveries for the three QACs (<30%). However, when neutral aluminum oxide was used, satisfactory recoveries (97%−102%) of the three QACs were observed. As we know, the negative polar silanol group (Si−OH), which is the main functional group of neutral silica gel, could be strongly bonded to positive polar chemicals especially cationic compounds.[9,35] Furthermore, the positive polarity of the three QACs decreased in the order of DTAC > CTAC > DDAC because increasing length and branch structure of the carbon chain remarkably decreases the polarity of QACs.[11] Thereby, the QACs with positive charges were more difficult to elute from neutral silica gel, and recoveries decreased with increasing polarity of the three QACs when using neutral silica gel as cleanup sorbent. Conversely, neutral aluminum oxide is suitable to separate positive polar chemicals from the sample matrix because the active-sites of aluminum oxide with the positive functional aluminum−oxygen group (Al−O) can hardly retain positive polar chemicals but can remove matrix compounds like lipid and chlorophyll via sorption.[9] Therefore, neutral aluminum oxide was selected as the cleanup sorbent in the present study.

Once the pretreatment procedure of the three QACs in lettuce had been optimized, it was used to determine the analytes in other eight vegetable samples including Chinese flowering cabbage, water spinach, pumpkin, cucumber, eggplant, potato, white radish, and carrot. Satisfactory recoveries between 72% and 108% were obtained in Chinese flowering cabbage, cucumber, potato, white radish, and carrot. However, lower recoveries (52%−70%) in water spinach, pumpkin, and eggplant were observed, but they were still acceptable as to the complex vegetable matrix.[28] Especially, when the eluant volume of the cleanup procedure was adjusted from 6 to 7 mL, satisfactory recoveries were obtained for the three QACs in all of the vegetables.

Method Validation. *Linearity, LOD, and LOQ.* The peak areas of the QACs target ions obtained from MS mode were applied to achieve the linearity, LOD, and LOQ. The linearity was estimated by preparing different calibration curves (methanol, and various vegetable matrixes including Chinese flowering cabbage, water spinach, lettuce, pumpkin, cucumber, eggplant, potato, white radish, and carrot) at seven concentrations ranging from 20 to 2000 μg/L for each compound. The regression equations and coefficients of determinations (R^2) of the standard solution curves and the nine matrix-matched curves are presented in Table 1. Good linearities (R^2 > 0.992) of the three QACs were obtained in all cases. The LODs and LOQs of the three compounds ranged from 0.7 to 6.0 μg/kg (dw) and 2.3 to 20.0 μg/kg (dw), respectively. As for specificity, no responses were observed in the procedure blank and the vegetable blank, indicating a high specificity of MS determination (Supporting Information, Figure S2).

Matrix Effect. The presence of matrix effects in the analysis of trace organic pollutants in complex samples by GC-MS is

DOI: 10.1021/acs.jafc.5b01828
J. Agric. Food Chem. 2015, 63, 6689−6697

Table 2. Recoveries (n = 15), RSD[a](%), and RSD[b](%) for the Three Tested QACs from Various Matrices at Three Spiked Levels

		DTAC			CTAC			DDAC		
matrix	spiked level (μg/kg)	recovery	RSD[a]	RSD[b]	recovery	RSD[a]	RSD[b]	recovery	RSD[a]	RSD[b]
Chinese cabbage	50	76.6	5.2	5.3	78.0	7.9	9.7	81.1	5.8	5.7
	200	73.4	4.9	4.5	85.6	8.4	12.6	91.9	5.8	6.3
	1000	102.8	7.0	7.8	93.9	9.8	9.8	94.6	7.6	6.9
water spinach	50	73.6	6.3	5.6	71.8	7.9	7.4	72.0	7.0	7.8
	200	79.4	5.8	5.3	76.9	8.4	9.5	75.1	4.8	4.3
	1000	89.8	5.5	4.7	81.1	3.4	3.9	90.6	3.6	5.1
lettuce	50	82.3	7.6	8.3	79.7	8.7	8.5	73.6	9.0	8.5
	200	75.8	3.8	4.1	82.1	2.1	2.2	73.1	2.2	2.6
	1000	97.1	6.1	6.7	101.2	9.2	8.9	96.2	9.5	8.5
pumpkin	50	88.8	9.1	8.4	82.7	9.8	9.9	84.0	10.9	10.2
	200	106.2	7.6	7.1	107.9	9.9	10.4	100.5	8.1	7.8
	1000	98.1	6.0	5.5	82.4	4.8	4.4	92.6	8.2	7.5
cucumber	50	73.3	6.0	7.7	70.5	9.0	8.6	79.7	9.2	8.4
	200	74.3	3.2	6.4	72.5	6.9	6.3	85.3	5.5	4.8
	1000	72.3	5.8	5.1	82.7	6.6	6.6	98.1	8.3	7.8
eggplant	50	73.0	5.9	6.2	72.1	6.0	6.9	71.2	5.1	5.3
	200	81.1	4.3	4.5	71.3	2.9	5.2	77.8	2.4	2.6
	1000	72.3	4.6	4.8	72.9	4.3	5.1	70.5	3.7	3.8
potato	50	86.2	7.2	6.2	73.3	5.1	4.2	75.5	8.8	9.0
	200	90.2	4.1	3.8	77.1	3.2	3.4	87.0	5.9	6.9
	1000	108.0	4.5	4.2	84.1	4.5	4.1	86.7	7.3	6.6
white radish	50	80.8	4.9	4.8	81.3	8.7	8.5	79.1	8.1	7.5
	200	91.4	5.0	4.9	90.4	7.7	7.5	85.3	5.4	5.0
	1000	94.5	2.4	2.3	96.5	5.3	5.3	96.6	6.7	6.3
carrot	50	80.8	6.2	4.5	79.2	13.0	15.3	82.2	10.4	14.1
	200	77.3	3.5	2.2	85.2	18.0	15.7	81.2	11.3	11.3
	1000	100.4	3.9	3.7	89.1	7.9	7.3	99.7	7.5	7.0

[a]Intraday precision (n = 5). [b]Interday precision (n = 15).

well-known, which may exert a strong impact on the precision and accuracy of analyte quantitation.[36,37] As referred to in previous research, the matrix effects can suppress or enhance detector response compared with the standard response in pure solvent.[36−39] Usually, the extent of matrix effect depends on the analytes, type and amount of matrix, and sample preparation procedure, etc.[40] Therefore, in the present study, various matrix effects were evaluated by calculating the slope ratio of the matrix-matched standard calibration curves to the solvent one. An accepted ranking criterion was applied according to Zhu et al., i.e., at the slope ratio value under 0.9, the matrix effect suppressed detector response; at the slope ratio value between 0.9 and 1.1, the matrix effect was negligible; at the slope ratio value above 1.1, the matrix effect enhanced the detector response.[38] Dada in Table 1 indicated that matrix effects on all of the three QACs in two matrices (Chinese flowering cabbage and water spinach) was negligible since the slope ratios of the matrix/methanol ranged from 0.96 to 1.08. However, matrix effects slightly enhanced the detector response of DTAC in lettuce, pumpkin, cucumber, and carrot but slightly suppressed that in eggplant. Matrix effects on CTAC and DDAC were negligible in five matrices (Chinese flowering cabbage, water spinach, lettuce, pumpkin, and cucumber) but enhanced the detector response to various extents in the other four matrices (cucumber, carrot, potato, and white radish). Generally, matrix effects originate from insufficient removal of the interfering constituents such as fatty acids, pigments, and phospholipids in the sample matrix.[40,41] However, the mechanism underlying these matrix-effects are still not completely understood and need to be further investigated.[38] Therefore, in order to obtain more realistic results in various samples in the present study, matrix-matched standard calibrations were applied to eliminate the matrix effects.

Precision and Accuracy. The recovery and RSD of the three QACs were measured to evaluate the precision and accuracy of the proposed method by spiking with the QACs at three different concentrations (50, 200, and 1000 μg/kg) in the blank sample and then analyzing them in quintuplicate (Table 2). The precision of the method expressed as RSD was determined by both repeatability and reproducibility experiments. The repeatability RSD[a] (intraday precision, n = 5) was obtained by calculating the standard deviation of the recoveries for the spiked samples run during the same day. The reproducibility RSD[b] (interday precision n = 5, for three distinct days) was also measured by analyzing the spiked samples. Detailed recovery, RSD[a], and RSD[b] data of the three QACs analyzed in nine vegetable samples are presented in Table 2. The recoveries in various vegetable matrices at three spiked concentrations (50, 200, and 1000 μg/kg) were between 70.5% and 108.0% (n = 15), and the RSD[a] (n = 5) and RSD[b] (n = 15) for the proposed method ranged from 2.1% to 18.0%, and 2.2% to 15.7%, respectively, which meet DG SANCO/12459/2011 guidelines (recovery at the range of 70% to 120%, and RSD lower than 20%).[37] These results indicated that the proposed method achieved satisfactory precision and accuracy.

The determination methods of QACs in food stuffs using LC-MS/MS have been recently developed.[25−27] Compared with these methods (recoveries, 72%−112%; RSDs, 1.4%−

DOI: 10.1021/acs.jafc.5b01828
J. Agric. Food Chem. 2015, 63, 6689−6697

Table 3. Concentrations of the Three QAC Variants in Real Vegetables

		DTAC		CTAC		DDAC		∑QACs	
vegetable[a]	water content (%)	detection rate (%)	range (dw[b]/fw[c]) (μg/kg)	detection rate (%)	average ± SD (dw/fw, μg/kg)	detection rate (%)	average ± SD (dw/fw, μg/kg)	detection rate (%)	average ± SD (dw/fw, μg/kg)
Chinese cabbage	94.8	100	25 ± 16/ 1.3 ± 0.8	100	67 ± 27/3.5 ± 1.4	100	15 ± 11/0.8 ± 0.5	100	107 ± 36/ 5.6 ± 1.9
water spinach	91.2	0	ND[d]	100	23 ± 16/2.0 ± 1.4	0	ND	100	23 ± 16/2.0 ± 1.4
lettuce	95.0	0	ND	100	29 ± 17/1.3 ± 0.8	100	5 ± 4/0.2 ± 0.2	100	34 ± 19/1.6 ± 0.9
pumpkin	88.5	0	ND	100	25 ± 12/2.9 ± 1.4	100	9 ± 6/1.0 ± 0.7	100	34 ± 16/3.9 ± 1.8
cucumber	83.2	100	18 ± 10/ 3.0 ± 1.8	100	23 ± 11/3.9 ± 1.8	100	4 ± 3/0.7 ± 0.4	100	45 ± 21/7.6 ± 3.4
eggplant	93.2	0	ND	100	28 ± 8/1.9 ± 0.5	100	6 ± 2/0.4 ± 0.1	100	34 ± 9/2.3 ± 0.6
potato	80.1	0	ND	100	41 ± 12/8.2 ± 2.3	100	15 ± 6/3.0 ± 1.1	100	56 ± 14/ 11.1 ± 2.8
white radish	92.8	100	30 ± 13/ 2.2 ± 0.9	100	122 ± 29/ 8.8 ± 2.1	100	28 ± 15/2.0 ± 1.0	100	180 ± 41/ 13.0 ± 3.0
carrot	90.1	0	ND	0	ND	0	ND	0	ND

[a] $n = 3$ for each vegetable. [b] Dry weight. [c] Fresh weight. [d] Not detected.

17%; LODs, 0.4−6 μg/kg), the present method for determining QACs in vegetables using GC-MS provided the comparable precision and accuracy as well as the LODs (recoveries, 70.5%−108%; RSDs, 2.1%−18.0%; LODs, 0.7−6 μg/kg). Furthermore, the sample amount used (1 g) and analytical time (11.33 min) in the present method were smaller than those of previous methods (sample amount, 2−10 g; analytical time, 14−16 min). In addition, the GC-MS instrument used in the present study is available more commonly in ordinary laboratories than LC-MS. Therefore, the developed method is more cost-effective and practical for routine determination of the three QACs in vegetables.

Method Application. To estimate its practicality, the developed method was applied to measure the real vegetable samples ($n = 27$; Supporting Information, Figure S3) including Chinese flowering cabbages, water spinaches, lettuces, pumpkins, cucumbers, eggplants, potatoes, white radishes, and carrots. These samples with water contents between 80.1% (potato) and 95.4% (lettuce) were collected from several local markets in Guangzhou, southern China, a metropolitan city with high daily consumption of vegetables. Three quality controls at 50, 200, and 1000 μg/kg were performed for each sample in the analysis procedure.

As shown in Table 3, the three QAC compounds were detected in all of the tested vegetable samples (except carrot) with a concentration of 23−180 μg/kg (dry weight, dw). The detection frequency and concentration range (dw) of the three QACs were 33.3% and ND-30 μg/kg for DTAC, 88.9% and ND-122 μg/kg for CTAC, and 77.8% and ND-28 μg/kg for DDAC, respectively. CTAC was one of the dominant varieties of industrial QAC products and was frequently detected in sludge and agricultural soil,[8,9] which likely explained the highest frequency and concentration in the vegetable samples among the three tested QACs. As for the tested vegetable samples, all of the three QACs were detected in cucumber and white radish at concentrations of 4 to 122 μg/kg (dw). Both CTAC and DDAC were detected in lettuce, pumpkin, eggplant, and potato with concentrations of 5 to 41 μg/kg (dw). Only CTAC was detected in water spinach at concentrations of 23 μg/kg (dw). However, the concentration of all of the three QACs in carrot was lower than LOQs.

In conclusion, a reliable, sensitive, and cost-effective method was developed for routine determination of trace QACs (DTAC, CTAC, and DDAC) in vegetables using ultrasonic-assisted extraction and GC-MS. This method performed an accurate determination of the three QACs in a short time (11.33 min) with excellent specificity. Using a simple procedure consuming only 1 g of lyophilized sample for ultrasonic-assisted extraction, neutral aluminum oxide cleanup, and GC-MS analysis, the method can be applied to simultaneously analyze the three common QACs in various vegetable samples at μg/kg level with recoveries ranging from 70.5% to 108.0% and RSDs below 18.0%. The proposed method was used to successfully determine QACs in real vegetable samples collected from several markets in a metropolitan city of southern China. QACs were detected in almost all of the samples with a concentration of 23−180 μg/kg (dw). More studies are needed to further estimate human health risk of exposure to QACs through edible terrestrial plants, particularly vegetables, in the future.

■ ASSOCIATED CONTENT

Supporting Information

Typical GC-MS chromatograms of the three tested QACs in methanol standard solution (1000 μg/L), in blank vegetable samples and spiked vegetable samples (1000 μg/L), and in real vegetable samples. The Supporting Information is available free of charge on the ACS Publications website at DOI: 10.1021/acs.jafc.5b01828.

■ AUTHOR INFORMATION

Corresponding Authors

*(Y.-W.L.) Tel: +86 020 85221844. Fax: +86 020 85226615. E-mail: edou6033@163.com.

*(C.-H.M.) Tel: +86 020 85220564. Fax: +86 020 85226615. E-mail: tchmo@jnu.edu.cn.

Funding

This work was supported by the National Natural Science Foundation of China (41071211, 41173101, 41301337, and 41273113), the project of Guangdong Natural Science Foundation (S2011010001083 and 2011020003196), the project on the Integration of Industry, Education and Research of Guangdong Province (2013B0906001), and the High-Level Talents Program of Guangdong Higher Education Institutions granted to C.H.M.

DOI: 10.1021/acs.jafc.5b01828
J. Agric. Food Chem. 2015, 63, 6689−6697

Notes

The authors declare no competing financial interest.

REFERENCES

(1) Jing, G. H.; Zhou, Z. M.; Zhuo, J. Quantitative structure-activity relationship (QSAR) study of toxicity of quaternary ammonium compounds on *Chlorella pyrenoidosa* and *Scenedesmus quadricauda*. *Chemosphere* **2012**, *86*, 76−82.

(2) Ismail, Z. Z.; Tezel, U.; Pavlostathis, S. G. Sorption of quaternary ammonium compounds to municipal sludge. *Water Res.* **2010**, *44*, 2303−2313.

(3) Zhu, M.; Ge, F.; Zhu, R.; Wang, X.; Zheng, X. A DFT-based QSAR study of the toxicity of quaternary ammonium compounds on *Chlorella vulgaris*. *Chemosphere* **2010**, *80*, 46−52.

(4) Peng, X. T.; Shi, Z. G.; Feng, Y. Q. Rapid and high-throughput determination of cationic surfactants in environmental water samples by automated on-line polymer monolith microextraction coupled to high performance liquid chromatography-mass spectrometry. *J. Chromatogr., A* **2011**, *1218*, 3588−3594.

(5) Zheng, M.-J.; Xiang, L.; Li, Y.-W.; Mo, C.-H.; Cai, Q.-Y.; Huang, X.-P.; Wu, X.-L.; Zhao, H.-M. Simultaneous extraction and determination of three quaternary ammonium compounds in water using liquid-liquid exaction and gas chromatography-mass spectrometry. *Chin. J. Anal. Chem.* **2014**, *42*, 735−740.

(6) Lara-Martin, P. A.; Li, X. L.; Bopp, R. F.; Brownawell, B. J. Occurrence of alkyltrimethylammonium compounds in urban estuarine sediments: behentrimonium as a new emerging contaminant. *Environ. Sci. Technol.* **2010**, *44*, 7569−7575.

(7) Li, X. L.; Brownawell, B. J. Quaternary ammonium compounds in urban estuarine sediment environments - a class of contaminants in need of increased attention? *Environ. Sci. Technol.* **2010**, *44*, 7561−7568.

(8) Ruan, T.; Song, S. J.; Wang, T.; Liu, R. Z.; Lin, Y. F.; Jiang, G. B. Identification and composition of emerging quaternary ammonium compounds in municipal sewage sludge in China. *Environ. Sci. Technol.* **2014**, *48*, 4289−4297.

(9) Xiang, L.; Zheng, M.-J.; Wang, X.-K.; Li, Y.-W.; Mo, C.-H.; Cai, Q.-Y.; Huang, X.-P.; Wu, X.-L.; Zhao, H.-M. Simultaneous extraction and determination of three quaternary ammonium compounds in soil by ultrasonic exaction and gas chromatography-mass spectrometry. *Chin. J. Anal. Chem.* **2014**, *42*, 1459−1464.

(10) Li, X. L.; Luo, X. J.; Mai, B. X.; Liu, J. Q.; Chen, L.; Lin, S. S. Occurrence of quaternary ammonium compounds (QACs) and their application as a tracer for sewage derived pollution in urban estuarine sediments. *Environ. Pollut.* **2014**, *185*, 127−133.

(11) Berthelsen, P.; Beltoft, V.; Thorup, I.; Søborg, I.; Nielsen, E. *Toxicological Evaluation and Limit Values for 2-Ethylhexyl Acryate, Propylene Carbonate, Quaternary Ammonium Compounds, Triglycidyl Isocyanurate and Tripropyleneglycol Diacrylate*; Danish Veterinary and Food Administration: Glostrup, Denmark, 2000.

(12) Nalecz-Jawecki, G.; Grabinska-Sota, E.; Narkiewicz, P. The toxicity of cationic surfactants in four bioassays. *Ecotoxicol. Environ. Saf.* **2003**, *54*, 87−91.

(13) Zhang, C.; Cui, F.; Zeng, G. M.; Jiang, M.; Yang, Z.-Z.; Yu, Z.-G.; Zhu, M. Y.; Shen, L.-Q. Quaternary ammonium compounds (QACs): A review on occurrence, fate and toxicity in the environment. *Sci. Total Environ.* **2015**, *518*−*519*, 352−362.

(14) Ferk, F.; Misik, M.; Hoelzl, C.; Uhl, M.; Fuerhacker, M.; Grillitsch, B.; Parzefall, W.; Nersesyan, A.; Micieta, K.; Grummt, T.; Ehrlich, V.; Knasmüller, S. Benzalkonium chloride (BAC) and dimethyldioctadecyl-ammonium bromide (DDAB), two common quaternary ammonium compounds, cause genotoxic effects in mammalian and plant cells at environmentally relevant concentrations. *Mutagenesis* **2007**, *22* (6), 363−370.

(15) Lu, L.; Zhu, L. Z. Reducing plant uptake of PAHs by cationic surfactant-enhanced soil retention. *Environ. Pollut.* **2009**, *157*, 1794−1799.

(16) Liang, Z. J.; Ge, F.; Zeng, H.; Xu, Y.; Peng, F.; Wong, M. H. Influence of cetyltrimethyl ammonium bromide on nutrient uptake and cell responses of Chlorella vulgaris. *Aquat. Toxicol.* **2013**, *138*, 81−87.

(17) Jin, F.; Hu, J. Y.; Yang, M.; Jin, X. H.; He, W. J.; Han, H. D. Determination of diallyldimethylammonium chloride in drinking water by reversed-phase ion-pair chromatography-electrospray ionization mass spectrometry. *J. Chromatogr., A* **2006**, *1101*, 222−225.

(18) Ventura, S. P.; e Silva, F. A.; Goncalves, A. M.; Pereira, J. L.; Goncalves, F.; Coutinho, J. A. Ecotoxicity analysis of cholinium-based ionic liquids to *Vibrio fischeri* marine bacteria. *Ecotoxicol. Environ. Saf.* **2014**, *102*, 48−54.

(19) Grillitsch, B.; Gans, O.; Kreuzinger, N.; Scharf, S.; Uhl, M.; Fuerhacker, M. Environmental risk assessment for quaternary ammonium compounds: a case study from Austria. *Water Sci. Technol.* **2006**, *54*, 111−118.

(20) Grabinska-Sota, E. Genotoxicity and biodegradation of quaternary ammonium salts in aquatic environments. *J. Hazard. Mater.* **2011**, *195*, 182−187.

(21) Hong, J. L.; Tezel, U.; Tas, D. O.; Pavlostathis, S. G. Influence of quaternary ammonium compounds on the microbial reductive dechlorination of pentachloroaniline. *Water Res.* **2013**, *47*, 6780−6789.

(22) Cumming, J.; Hawker, D.; Chapman, H.; Nugent, K. The Fate of polymeric quaternary ammonium salts from cosmetics in wastewater treatment plants. *Water, Air, Soil Pollut.* **2011**, *216*, 441−450.

(23) Pateiro-Moure, M.; Arias-Estevez, M.; Simal-Gandara, J. Critical review on the environmental fate of quaternary ammonium herbicides in soils devoted to vineyards. *Environ. Sci. Technol.* **2013**, *47*, 4984−4998.

(24) Warren, C. R. Quaternary ammonium compounds can be abundant in some soils and are taken up as intact molecules by plants. *New Phytol.* **2013**, *198*, 476−485.

(25) Cao, H. W.; Kang, M. Q.; Chen, Z.; Li, L.; Cui, M. H.; Chen, M. Y.; Zhang, H. Q.; Wang, Y. H. Determination of five quaternary ammonium compounds in foodstuffs using high performance liquid chromatography-tandem mass spectrometry. *Anal. Methods* **2014**, *6*, 4790−4796.

(26) Arrebola-Liébanas, F. J.; Abdo, M. A. H.; Moreno, J. L. F; Martínez-Vidal, J. L.; Frenich, A. G. Determination of quaternary ammonium compounds in oranges and cucumbers using QuEChERS extraction and ultra-performance liquid chromatography/tandem mass spectrometry. *J. AOAC Int.* **2014**, *97*, 1021−1026.

(27) Fríedle, A.; Nitsopoulos A.; Lach, G.; Bruns, S. Determination of Quaternary Ammonium Compounds (QACs) in Food Products. http://www.iib.org.tr/les/downloads/PageFiles/%7B6089aa41-ac9f-4d71-8fe9-8621a6851e4d%7D/Files/4_Notice%20Labor.pdf.

(28) Li, Y. W.; Zhan, X. J.; Xiang, L.; Deng, Z. S.; Huang, B. H.; Wen, H. F.; Sun, T. F.; Cai, Q. Y.; Li, H.; Mo, C. H. Analysis of trace microcystins in vegetables using solid-phase extraction followed by high performance liquid chromatography triple-quadrupole mass spectrometry. *J. Agric. Food Chem.* **2014**, *62*, 11831−11839.

(29) Martinez-Carballo, E.; Sitka, A.; Gonzalez-Barreiro, C.; Kreuzinger, N.; Fürhacker, M.; Scharf, S.; Gans, O. Determination of selected quaternary ammonium compounds by liquid chromatography with mass spectrometry. Part I. Application to surface,) waste and indirect discharge water samples in Austria. *Environ. Pollut.* **2007**, *145*, 489−496.

(30) Martinez-Carballo, E.; Gonzalez-Barreiro, C.; Sitka, A.; Kreuzinger, N.; Scharf, S.; Gans, O. Determination of selected quaternary ammonium compounds by liquid chromatography with mass spectrometry. Part II. Application to sediment and sludge samples in Austria. *Environ. Pollut.* **2007**, *146*, 543−547.

(31) Ding, W. H.; Tsai, P. C. Determination of alkyltrimethylammonium chlorides in river water by gas chromatography/ion trap mass spectrometry with electron impact and chemical ionization. *Anal. Chem.* **2003**, *75*, 1792−1797.

(32) Tsai, P. C.; Ding, W. H. Determination of alkyltrimethylammonium surfactants in hair conditioners and fabric softeners by gas chromatography-mass spectrometry with electron-impact and chemical ionization. *J. Chromatogr., A* **2004**, *1027* (1−2), 103−108.

DOI: 10.1021/acs.jafc.5b01828
J. Agric. Food Chem. 2015, 63, 6689−6697

(33) Zhu, M.; Ge, F.; Zhu, R.; Wang, X. Y.; Zheng, X. Y. A DFT-based QSAR study of the toxicity of quaternary ammonium compounds on Chlorella vulgaris. *Chemosphere* **2010**, *80*, 46−52.
(34) Larsen, S. T.; Verder, H.; Nielsen, G. D. Airway effects of inhaled quaternary ammonium compounds in mice. *Basic Clin. Pharmacol. Toxicol.* **2012**, *110*, 537−543.
(35) Garcia Falcon, M. S.; Gonzalez Amigo, S.; Lage Yusty, M. A.; Simal Lozano, J. Determination of benzo[a]pyrene in some Spanish commercial smoked products by HPLC-FL. *Food Addit. Contam.* **1999**, *16*, 9−14.
(36) Belmonte Valles, N.; Retamal, M.; Mezcua, M.; Fernandez-Alba, A. R. A sensitive and selective method for the determination of selected pesticides in fruit by gas chromatography/mass spectrometry with negative chemical ionization. *J. Chromatogr., A* **2012**, *1264*, 110−116.
(37) Lagunas-Allue, L.; Sanz-Asensio, J.; Martinez-Soria, M. T. Comparison of four extraction methods for the determination of fungicide residues in grapes through gas chromatography-mass spectrometry. *J. Chromatogr., A* **2012**, *1270*, 62−71.
(38) Zhu, Y.; Liu, X.; Xu, J.; Dong, F.; Liang, X.; Li, M.; Duan, L.; Zheng, Y. Simultaneous determination of spirotetramat and its four metabolites in fruits and vegetables using a modified quick, easy, cheap, effective, rugged, and safe method and liquid chromatography/tandem mass spectrometry. *J. Chromatogr., A* **2013**, *1299*, 71−77.
(39) Zhang, Q.; Tian, M.; Wang, M.; Shi, H.; Wang, M. Simultaneous enantioselective determination of triazole fungicide flutriafol in vegetables, fruits, wheat, soil, and water by reversed-phase high-performance liquid chromatography. *J. Agric. Food Chem.* **2014**, *62*, 2809−2815.
(40) Dong, F.; Chen, X.; Liu, X.; Xu, J.; Li, Y.; Shan, W.; Zheng, Y. Simultaneous determination of five pyrazole fungicides in cereals, vegetables and fruits using liquid chromatography/tandem mass spectrometry. *J. Chromatogr., A* **2012**, *1262*, 98−106.
(41) Wu, X.; Xu, J.; Dong, F.; Liu, X.; Li, Y.; Zheng, Y. Simultaneous determination of oxathiapiprolin and two metabolites in fruits, vegetables and cereal using a modified quick, easy, cheap, effective, rugged, and safe method and liquid chromatography coupled to tandem mass spectrometry. *J. Chromatogr., A* **2014**, *1329*, 30−37.

DOI: 10.1021/acs.jafc.5b01828
J. Agric. Food Chem. 2015, 63, 6689−6697

similar to that of solid-phase microextraction (SPME) and allows for extraction and concentration in a single step, followed by thermal desorption of the entire extracted fraction into a GC system. These capabilities greatly simplify the sample preparation process and minimize any risk of contamination. Moreover, the enrichment factor for SBSE, which is determined by the analyte recovery in the extraction phase, is much higher than that of SPME using the same extraction phase, i.e., polydimethylsiloxane (PDMS), because of the 50−250 times larger volume of the extraction phase on the stir bar. SBSE can also be used in combination with a derivatization step similar to SPME. For polar solutes with low octanol−water distribution coefficient (K_{ow}) values, the corresponding derivatives generally have higher K_{ow} values, resulting in higher recovery and sensitivity.[18] Also, higher molecular weights of derivatives provide higher selectivity in GC−MS analysis. In this regard, SBSE with *in situ* derivatization (der−SBSE) using pentafluorobenzylhydroxylamine (PFBHA), followed by thermal desorption (TD)−GC−MS, was demonstrated for the analysis of stale-flavor carbonyl compounds, including *E*-2-nonenal, in beer.[21]

In this study, we developed a simple and solvent-less method for the quantitation of hop-derived thiols (4S4M2Pone, 3SHol, and 3SHA) in the three different sample matrices of beer, hop water extract, and wort at nanogram per liter levels by der−SBSE using ETP, followed by TD−GC−tandem mass spectrometry (MS/MS). Although the ETP derivatives (thioacrylates) of thiols (4S4M2Pone-ETP, 3SHol-ETP, and 3SHA-ETP) increase both log K_{ow} values (from 1.07−2.70 to 1.83−3.45) and molecular weights (from 132−176 to 230−274), the selectivity and sensitivity of conventional GC−single-quadrupole MS in selected ion monitoring (SIM) mode were not sufficient for real samples, which include very complex matrices. Therefore, GC−triple-quadrupole (QQQ) MS with selected reaction monitoring (SRM) mode was used for both increased selectivity and sensitivity.

MATERIALS AND METHODS

Chemicals. 4S4M2Pone, 3SHol, and 3SHA were purchased from Penta Manufacturing Co. (Livingston, NJ). d_{10}-4-Sulfanyl-4-methylpentan-2-one (d_{10}-4S4M2Pone) was purchased from aromaLAB AG (Freising, Germany). d_2-3-Sulfanylhexan-1-ol (d_2-3SHol) was purchased from NARD Institute, Ltd. (Hyogo, Japan). ETP and Tris(hydroxymethyl)-aminomethane hydrochloride (Tris−HCl) solution (1 M, pH 9.0) were purchased from Wako Pure Chemicals (Osaka, Japan). Sodium hydroxide (NaOH) solution (1 N) and ethanol (pesticide residue analysis grade) were purchased from Kanto Kagaku (Tokyo, Japan).

Hops. The hop cultivars investigated were Cascade, Citra, and Nelson Sauvin. Cascade (6.4% α-acid pellets, 2013 crop) was purchased from John I. Haas, Inc. (Yakima, WA). Citra (12.8% α-acid pellets, 2013 crop) was purchased from Yakima Chief (Sunnyside, WA). Nelson Sauvin (11.2% α-acid pellets, 2013 crop) was purchased from New Zealand Hops, Ltd. (Nelson, New Zealand).

Brewing Processes. Pellets of the hop cultivars Cascade, Citra, and Nelson Sauvin were used in the brewing process. For the evaluation of each cultivar, the wort from each hop cultivar was prepared to contain equal amounts of α acid. A 20 L volume of wort without hops was boiled for 60 min in a wort kettle. An amount of the hop pellet with 130 mg of α acid was then added to 1 L of hot wort (85 °C) in a glass vessel, and the wort was cooled promptly to 5 °C. The yeast was pitched at a rate of 20 × 10^6 cells/mL into the wort (12.5 °P), and static fermentations were carried out while stirring at 14.0 °C for 7 days in the 1 L glass vessel. The finished beer was obtained by cooling to −1 °C for 5 days and then centrifuging at 7000 rpm for 30 min.

Hop Water Extract. The water extract of each hop cultivar was prepared to contain the same amount of α acid as the corresponding wort. The amount of each hop pellet containing 130 mg of α acid was added to 1 L of hot water (85 °C) to extract the water-soluble aroma components and then cooled promptly. The hop water extracts were obtained by centrifuging at 7000 rpm for 30 min at −1 °C.

Stir Bar Sorptive Extraction with *in Situ* Derivatization (der−SBSE). Stir bars (Twister) coated with 24 μL of PDMS were obtained from GERSTEL (Mülheim an der Ruhr, Germany). For SBSE, 20 mL headspace vials with a metal screw cap containing polytetrafluoroethylene (PTFE)-coated silicon septa (GERSTEL) and a multiple-position

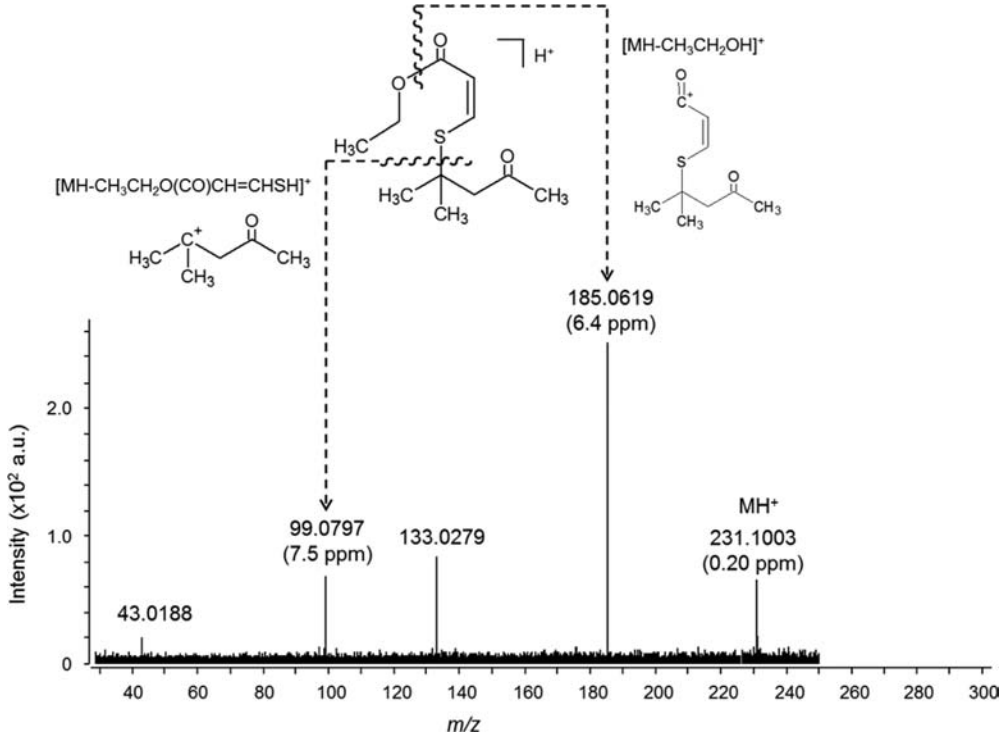

Figure 1. CAD mass spectrum of the *cis*-ETP derivative of 4S4M2Pone obtained from der−SBSE−TD−GC−Q−TOF−MS/SCD of spiked water at 10 ng/L. Mass errors from the theoretical formula are also shown in parentheses.

DOI: 10.1021/acs.jafc.5b02298
J. Agric. Food Chem. 2015, 63, 6698−6706

magnetic stirrer (20 positions) from Global Change (Tokyo, Japan) were used. Prior to use, the stir bars were conditioned for 20 min at 250 °C in a flow of helium. Before der−SBSE, beer and wort samples were adjusted to pH 9 using NaOH solution (1 M). Hop water extract was adjusted to pH 9 using 5 mM Tris−HCl to give buffer capacity. A total of 10 mL of sample containing 35 mM ETP, internal standards (20 ng/L d_{10}-4S4M2Pone and 200 ng/L d_2-3SHol), and the PDMS stir bar was transferred to 20 mL headspace vials. The vial was sealed with the metal screw cap, and the PDMS stir bar was first stirred at room temperature (25 °C) for 10 min at 500 rpm for the ETP derivatization step.[17] After 10 min of initial stirring, 30% NaCl was added and the vial was sealed again. To prevent damage to the glass jacket of the stir bar when dissolving NaCl, the PDMS stir bar was first attached to the inside of the metal screw cap with magnetic attraction. Then, the vial was gently shaken for a few minutes (horizontally). Finally, the PDMS stir bar was dropped to the bottom of the vial, and SBSE was performed for 180 min while stirring at 1500 rpm. After extraction, the stir bars were removed with forceps, dipped briefly in ultrapure water, dried with a lint-free tissue, and placed in a glass thermal desorption liner. The glass liner was placed in the thermal desorption unit. No further sample preparation was necessary. No carry-over was observed for concentrations up to 1000 ng/L after analysis. Reconditioning of stir bars was performed after use by soaking each consecutively in ultrapure water and acetonitrile for 1−2 h. Stir bars were then removed from the solvent and dried on a clean surface at room temperature for 1 h. Finally, the stir bars were thermally conditioned for 20 min at 250 °C in a flow of helium. Typically, the same PDMS stir bar could be used more than 50 times.

Thermal Desorption−Gas Chromatography−Quadrupole Time-of-Flight Mass Spectrometry with Parallel Sulfur Chemiluminescence Detection (TD−GC−Q−TOF−MS/SCD). For the identification of the ETP derivatives of thiols, the TD−GC−Q−TOF−MS/SCD analysis was performed with a thermal desorption unit (TDU) equipped with a MPS 2 autosampler and a Peltier-cooled CIS 4 programmed temperature vaporization (PTV) inlet (GERSTEL) installed on an Agilent 7890A gas chromatograph with a 7200 Q−TOF−MS and a SCD (Agilent Technologies, Santa Clara, CA). The GC−Q−TOF−MS/SCD configuration was equipped with an Agilent capillary flow technology (CFT) three-way splitter (with makeup gas line), which was controlled with a pressure control module (PCM).

The stir bars were thermally desorbed by programming the TDU from 30 °C (held for 0.5 min) to 200 °C (held for 3 min) at 720 °C/min with 50 mL/min desorption flow. Desorbed compounds were focused at 10 °C on a liner packed with quartz wool in the Peltier-cooled PTV inlet for subsequent GC−Q−TOF−MS/SCD analysis. After desorption, the PTV inlet was programmed from 10 to 240 °C (held for GC run time) at 720 °C/min to inject trapped compounds onto the analytical column. The injection was performed in the splitless mode, and the split valve was closed for 3 min. Separations were performed on a 30 m × 0.25 mm inner diameter, 0.25 μm film thickness DB-Wax column (Agilent). The column temperature for the DB-Wax was programmed from 40 °C (held for 3 min) to 250 °C (held for 20 min) at 10 °C/min. After the retention time of 33 min, the capillary column was back-flushed. The inlet pressure was 362 kPa, and the pressure of the PCM for the three-way splitter was 25 kPa. The constant pressure mode was used with helium carrier gas. A deactivated fused silica capillary with 1.1 m × 0.25 mm inner diameter was used for connecting from the splitter to the SCD, and a deactivated fused silica capillary with 1.1 m × 0.20 mm inner diameter was used for connecting from the splitter to the Q−TOF−MS. These pressures and transfer-line capillaries allow for parallel MS and SCD with minimum delay time (typically less than 0.1 s) at a constant split ratio of 1:2.

The Q−TOF−MS was operated at a mass range of m/z 29−500 with dual gain mode {resolution was approximately 7000 full width at half maximum [(fwhm)]}. The data acquisition speed was 5 Hz. The electron accelerating voltage of the electron ionization (EI) was 70 eV. Methane was used as a reagent gas at 1.0 mL/min in the positive chemical ionization (PCI) mode. Nitrogen was used as collision gas at 1.5 mL/min, and a collision energy of 2.5−10 V was used for MS/MS

Table 1. Mass Spectral Information for *cis*-ETP Derivatives of 4S4M2Pone, 3SHol, and 3SHA

	GC−EI−TOF−MS			GC−PCI−TOF−MS							GC−PCI−Q−TOF−MS		
	M^+			MH^+			$[M + C_2H_5]^+$			$[M + C_3H_5]^+$			
compound	formula	m/z	mass error (ppm)	formula	m/z	mass error (ppm)	formula	m/z	mass error (ppm)	formula	m/z	mass error (ppm)	MS/MS fragment ion, MH^+ fragment ion[a]	m/z	mass error (ppm)
cis-4S4M2Pone−ETP	$C_{11}H_{18}O_3S$	230.0963	4.1	$C_{11}H_{19}O_3S$	231.1033	6.5	$C_{13}H_{23}O_3S$	259.1345	4.8	$C_{14}H_{23}O_3S$	271.1343	6.6	$[MH - CH_3CH_2O(CO)CH{=}CHSH]^+$	99.0797	7.5
													$[MH - CH_3CH_2OH]^+$	185.0619	6.4
													MH^+	231.1003	2.0
cis-3SHol−ETP	$C_{11}H_{20}O_3S$	232.1140	−5.4	$C_{11}H_{21}O_3S$	233.1193	4.2	$C_{13}H_{25}O_3S$	261.1524	6.3	$C_{14}H_{25}O_3S$	273.1496	9.3	$[MH - CH_3CH_2O(CO)CH{=}CHSH]^+$	101.0941	20
													$[MH - CH_3CH_2OH]^+$	187.0762	13
cis-3SHA−ETP	$C_{13}H_{22}O_4S$	274.1232	0.51	$C_{13}H_{23}O_4S$	275.1299	2.5	$C_{15}H_{27}O_4S$	303.1614	3.7	$C_{16}H_{27}O_4S$	315.1606	3.6	$[MH - CH_3CH_2O(CO)CH{=}CHSH]^+$	143.1056	7.4
													$[MH - CH_3(CO)OCH_3]^+$	187.0770	4.4
													$[MH - CH_3CH_2OH]^+$	229.0881	5.2
													MH^+	275.2797	−10

[a]Collision energy of 2.5 V was used for *cis*-4S4M2Pone−ETP and *cis*-3SHA−ETP, and collision energy of 10 V was used for *cis*-3SHol−ETP.

DOI: 10.1021/acs.jafc.5b02298
J. Agric. Food Chem. 2015, 63, 6698−6706

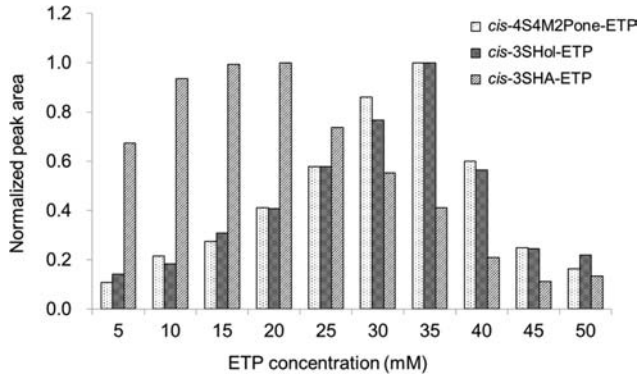

Figure 2. Comparison of the normalized responses of *cis*-ETP derivatives of thiols in spiked beer as a function of the ETP concentrations (5−50 mM).

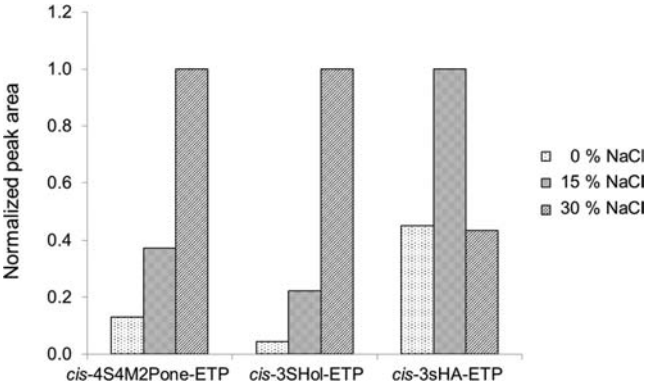

Figure 3. Comparison of the normalized responses of *cis*-ETP derivatives of thiols in spiked beer as a function of the NaCl concentrations (0, 15, and 30%).

experiments. Alternate MS mode was used in the MS/MS measurement for simultaneous TOF−MS and Q−TOF−MS (MS/MS) detection. TOF−MS calibration was performed with perfluorotributylamine (PFTBA) for EI and perfluoro-5,8-dimethyl-3,6,9-decane trioxide (PFDTD) for PCI, respectively, in every sequence.

Thermal Desorption−Gas Chromatography−Triple-Quadrupole Mass Spectrometry (TD−GC−QQQ−MS). For the optimization of the method parameters and the determination of the ETP derivatives of thiols, TD−GC−MS/MS in the SRM mode using the GERSTEL MPS2/TDU/CIS system installed on the Agilent 7890GC combined with a 7000B triple-quadrupole (QQQ) MS was used. GC−QQQ−MS was equipped with the PCM and a purge tee option for back-flush capability.

The same TD condition described in the previous section but with the liquid nitrogen cooling for the PTV inlet (because of the higher GC initial temperature of 100 °C) was used for the TD−GC−QQQ−MS analysis. Separations were performed on a 15 m × 0.25 mm inner diameter, 0.25 μm film thickness DB-Wax column (Agilent). A 0.75 m × 0.15 mm inner diameter uncoated deactivated post-column (Agilent) was used and connected between the purge tee and the QQQ−MS. Column flow was set at a constant helium flow of 1.2 mL/min. The column temperature for the DB-Wax was programmed from 100 °C (held for 3 min) to 250 °C (held for 11 min) at 10 °C/min. After the retention time of 19 min, the capillary column was back-flushed.

The QQQ−MS was operated in three acquisition modes: (1) scan mode at a mass range of m/z 29−500, (2) product ion scan mode at a mass range of m/z 29−500, and (3) SRM mode with the selected transitions (precursor to product ion). Transitions of the analytes are listed in Tables 2 and 3. The electron accelerating voltage of the EI was 70 eV. Methane was used as a reagent gas at 1.0 mL/min in the

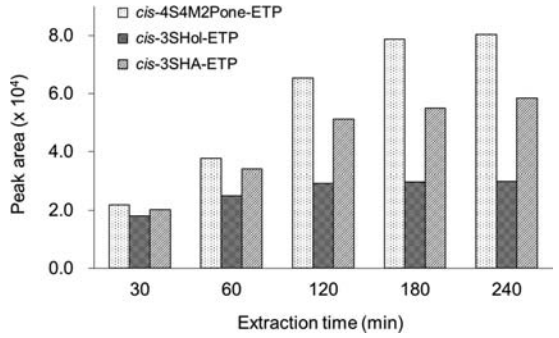

Figure 4. Extraction time profiles for *cis*-ETP derivatives of thiols in spiked beer by der−SBSE. The peak area for 3SHol is multiplied by 30.

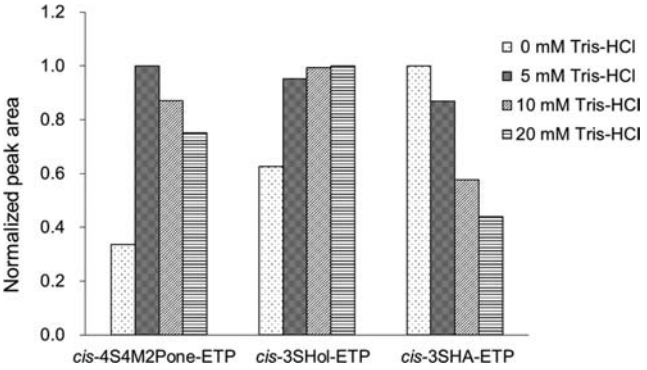

Figure 5. Comparison of the normalized responses of *cis*-ETP derivatives of thiols in spiked hop as a function of the Tris−HCl concentrations (0, 5, 10, and 20 mM).

PCI mode. Nitrogen was used as collision gas at 1.5 mL/min, and a collision energy of 2.5−10 V was used for MS/MS experiments.

Data Analysis. MassHunter qualitative analysis version B.06.00633 (Agilent) and MassHunter Quantitative Analysis version B.06.00388 (Agilent) were used for data analysis. The log K_{ow} values are calculated with a SRC-KOWWIN version 1.68 software package (Syracuse Research, Syracuse, NY).

RESULTS AND DISCUSSION

Identification of ETP Derivatives of Thiols. Because reference compounds of the ETP derivatives of the target thiols are not commercially available, identification of the ETP derivatives was first investigated. der−SBSE of spiked water at 10 ng/mL (adjusted at pH 9 and containing 5% ethanol and 10 mM ETP) was performed for 60 min with the PDMS stir bar. After extraction, the PDMS stir bar was analyzed with TD−GC−Q−TOF−MS/SCD. The peaks in the SCD chromatogram clearly indicate the presence of sulfur compounds. From the corresponding peaks in a total ion chromatogram (TIC), EI mass spectra of ETP derivatives of thiols (4S4M2Pone-ETP, 3SHol-ETP, and 3SHA-ETP) were obtained for both *cis* and *trans* stereoisomers. Previous studies[22] reported that the major isomer is likely to be *cis* form. Although molecular ions were observed for all analytes with mass errors of less than 1.3 mDa (5.4 ppm), the relative abundances of those ions were very small (especially for 3SHol). To determine the molecular mass of these compounds, PCI was also performed. The protonated molecule (MH^+) and adduct ions ($[M + C_2H_5]^+$ and $[M + C_3H_5]^+$) from PCI with methane could be observed for all analytes, with the mass errors in the range of 0.69−2.55 mDa (2.5−9.3 ppm). Finally, structure elucidation was performed with collision-induced dissociation (CID) [also known as collisionally activated

DOI: 10.1021/acs.jafc.5b02298
J. Agric. Food Chem. 2015, 63, 6698−6706

Table 2. Selectivity and Sensitivity in GC−EI−MS/MS Analysis for *cis*-ETP Derivatives of 4S4M2Pone, 3SHol, and 3SHA

	EI									
	M^+ precursor					fragment ion precursor[a]				
compound	precursor ion[b,c]	collision energy (V)	product ion[b,c]	selectivity[d]	sensitivity (S/N ratio)[e]	precursor ion[b,c]	collision energy (V)	product ion[b,c]	selectivity[d]	sensitivity (S/N ratio)[e]
cis-4S4M2Pone−ETP	**230**	2.5	**132**	○	64	195	5.0	195	×	n/a
	230	2.5	**99**	○	28	195	5.0	167	×	n/a
cis-3SHol−ETP	**232**	2.5	**152**	○	18	214	5.0	185	×	n/a
	232	2.5	**141**	○	33	214	5.0	141	×	n/a
						214	5.0	**127**	○	29
cis-3SHA−ETP	**274**	2.5	**241**	○	27	241	5.0	181	×	n/a
	274	2.5	**214**	○	41	241	5.0	135	×	n/a
						241	5.0	107	△	18

[a]The highest intensity ion as well as having higher m/z than that of the molecular ion of the non-derivative form. [b]The ions shown in bold were used for SRM transitions. [c]The ions shown in underline were used for quantification. [d]Selectivity was shown as follows: ○, targeted peak (*cis* form) was separated from interferences; △, targeted peak was co-eluted with interferences, but the targeted peak in the spiked beer was clearly higher than those in the non-spiked beer; and ×, targeted peak was co-eluted with interferences. [e]Sensitivity was shown by the signal-to-noise ratio of the targeted peak in the spiked beer.

dissociation (CAD)[23]] of the protonated molecule (MH^+ ± 0.5 mDa). It is known that fragmentation of the protonated molecule generally occurs in the protonated part (function) of a compound,[24,25] resulting in a simple bond cleavage process compared to the more extensive EI fragmentation. Therefore, CAD of the protonated molecule in accurate mass measurement can significantly help structure elucidation. Figure 1 demonstrates the CAD mass spectra of the protonated molecule of 4S4M2Pone−ETP using the collision energy of 2.5 V. Also, structures and bond cleavages of the analytes are shown in Figure 1. Considerable information concerning the structures of ETP derivatives of thiols can be derived from the fragment ions in the CAD mass spectra. For 4S4M2Pone−ETP [$CH_3CH_2O(CO)$-$CH{=}CHSC(CH_3)_2CH_2(CO)CH_3 + H]^+$], the mass error of the protonated molecule (m/z 231.1003) was 0.46 mDa (2.0 ppm). The most abundant ion at m/z 185.0619 corresponds to the bond cleavage 1 and [$MH - CH_3CH_2OH]^+$, with a mass error of 1.2 mDa/6.4 ppm, and the ion at m/z 99.0797 corresponds to the bond cleavage 2 and [$MH - CH_3CH_2O(CO)CH{=}CHSH]^+$, with a mass error of 0.74 mDa/7.5 ppm. The neutral loss of $CH_3CH_2O(CO)CH{=}CHSH$ demonstrates the derivatization of the mercapto function of thiols with ETP ($CH_3CH_2O(CO)$-$CH{\equiv}CH$). These ions clearly demonstrate that the structures, such as CH_3CH_2O- and $CH_3CH_2O(CO)CH{=}CHS-$, are involved. The neutral loss of $CH_3CH_2O(CO)CH{=}CHSH$ and CH_3CH_2OH is also observed for 3SHol−ETP (m/z 101.0941, mass error of 2.0 mDa/20 ppm; m/z 187.0762, mass error of 2.4 mDa/13 ppm) and 3SHA−ETP (m/z 143.1056, mass error of 1.1 mDa/7.4 ppm; m/z 229.0881, mass error of 1.2 mDa/5.2 ppm). Consequently, the ETP derivatives of three thiols could be identified with molecular mass determination, formula calculation, and structure elucidation. The mass spectral information used for the identification of the ETP derivatives is summarized in Table 1.

Optimization of der−SBSE Conditions for the Beer Sample. To optimize der−SBSE of thiols with ETP in beer matrices, the influence of varying concentration of ETP was first examined with the spiked beer. The pH of the spiked beer was adjusted to 9, and the spiked concentration of thiols was 10 ng/mL each. The concentration of ETP was varied with the addition of a 50% ethanol solution of ETP. SBSE with 60 min extraction was performed in duplicate for 10 concentrations of ETP between 5 and 50 mM. Figure 2 demonstrates a comparison of normalized responses of the *cis*-ETP derivatives as a function of ETP concentrations. For 3SHA−ETP, which has the highest log K_{ow} of 3.45 (the most hydrophobic of the analytes), the ETP concentrations of 20 mM showed the largest response and the ETP concentrations of 10 and 15 mM also showed a similar large response (94 and 99% of the largest response, respectively). However, the responses decreased with ETP concentrations of more than 25 mM. For 4S4M2Pone−ETP (log K_{ow} of 1.83) and 3SHol−ETP (log K_{ow} of 2.45), the normalized responses gradually increased with increasing ETP concentrations from 5 to 35 mM and the ETP concentration of 35 mM showed the largest response. However, the responses dramatically decreased with the ETP concentrations of more than 40 mM. It was observed that the ETP concentrations of more than 40 mM induced a visible "droplet" of ETP in beer matrices. This "oil effect" might influence the reaction and/or the kinetics between thiols, ETP, ETP derivatives (thioacrylates), beer matrices, and the PDMS coating of the stir bar in der−SBSE, even before the appearance of the visible droplet. This relationship is quite complex, but it is clear that the solubility of ETP in sample matrices is a critical parameter. This parameter should be considered when the method is applied for non-alcoholic sample matrices, such as hop water extract and wort, which might have low ETP solubility without percent levels of ethanol. Because 4S4M2Pone has the lowest odor threshold level in beer at 1.5 ng/L[4] compared to those of 3SHol at 55 ng/L[4] and 3SHA at 5.0 ng/L,[5] the parameters should be optimized for the condition that gives the best sensitivity of 4S4M2Pone. Therefore, the ETP concentration of 35 mM was selected for further study.

Previous studies have shown that salt addition increases the recovery of polar solutes with low log K_{ow} values (e.g., log K_{ow} < 2.5).[19,20] Therefore, the effect of salt addition was examined with the spiked beer at 10 ng/mL containing 35 mM ETP. der−SBSE was performed for 50 min in duplicate. Figure 3 demonstrates a comparison of normalized responses of the *cis*-ETP derivatives as a function of the NaCl concentrations (0, 15, and 30%). As expected, the responses for 4S4M2Pone−ETP (log K_{ow} of 1.83) and 3SHol−ETP (log K_{ow} of 2.45) significantly increased with the salt addition and the 30% salt addition gives the largest responses. However, 3SHA−ETP (log K_{ow} of 3.45)

DOI: 10.1021/acs.jafc.5b02298
J. Agric. Food Chem. 2015, 63, 6698−6706

shows the largest response with the 15% salt addition, and the 30% salt addition results in nearly the same response as with the non-salt addition. It is known that the salt addition decreases the recovery of more hydrophobic solutes (e.g., log K_{ow} > 4.0) in SBSE.[19,20] Although the log K_{ow} value of 3SHA−ETP is lower than 4.0, the oil effect of ETP might be promoted with the 30% salt addition, resulting in the reduced response of 3SHA−ETP (in comparison to the 15% salt addition). To obtain the best sensitivity for 4S4M2Pone, which has the lowest odor threshold level, the 30% salt addition was selected for further study. Finally, the extraction time profile was examined with five extraction times between 30 and 240 min. Duplicate analyses were performed for each extraction time. Figure 4 shows the extraction time profiles of the *cis*-ETP derivatives in the spiked beer. Equilibrium was nearly reached at 120 min for 3SHol−ETP and 180 min for 4S4M2Pone−ETP and 3SHA−ETP. Although it is necessary to have 180 min extraction for the maximum recovery for 4S4M2Pone (and 3SHA), the der−SBSE method can be performed in parallel (up to 20 samples on one stir plate) and does not require any additional manual steps after extraction (before TD−GC analysis). Therefore, the extraction time of 180 min was selected for further study.

Optimization of der−SBSE Conditions for Hop Water Extracts and Wort Samples. The optimized der−SBSE condition with the spiked beer in the previous section was applied to the spiked beer, hop water extract, and wort at 1 ng/mL (except for 3SHol at 10 ng/mL) in duplicate. All samples were adjusted to pH 9 using NaOH solution (1 M). In comparison to the spiked beer, ETP derivatives of all target thiols were, however, much more weakly detected in the hop water extract and were not detected in the wort. This is due to the low ETP solubility of both hop water extract and wort, which do not contain percent level ethanol, resulting in the "oil effect" (visible "droplet") of ETP in the samples. To give a similar ETP solubility with beer, hop water extract and wort were 2-fold diluted with 10% ethanol solution (resulting in 5% ethanol in the diluted sample). Then, the same der−SBSE conditions were applied to the spiked hop water extract and wort again. For the spiked wort, ETP derivatives of all target thiols were detected with nearly the same abundance as the spiked beer. However, for the spiked hop water extract, 4S4M2Pone−ETP and 3SHol−ETP were still lower than those of the spiked beer and wort. This might be due to lack of buffer capacity of hop water extract, which leads to changes in pH during the derivatization. It is known that both beer and wort have relatively similar buffer capacities that resist changes in pH on the addition of acids or bases.[25] To examine the effect of buffer in the hop extract, Tris−HCl (1 M, pH 9) was added to the spiked hop water extract. Figure 5 shows a comparison of normalized responses of *cis*-ETP derivatives as a function of the Tris−HCl concentrations (0, 5, 10, and 20 mM). The response for 4S4M2Pone−ETP notably increased with the buffer addition, and 5 mM gives the largest response. The response for 3SHol−ETP also increased with the buffer addition, and similar responses are seen with all buffered conditions. However, the response for 3SHA−ETP decreased with the buffer addition, especially for 10 and 20 mM. Therefore, the 5 mM Tris−HCl addition was selected for the hop extract sample.

Selectivity and Sensitivity in GC−MS/MS Analysis. To evaluate the selectivity and sensitivity of the method, the spiked water at 1−10 ng/mL and non-spiked and spiked beer at 10−100 pg/mL were analyzed with several GC−MS/MS conditions, including different ionization modes (EI and PCI), collision energies, and SRM transitions. We selected the following

Table 3. Selectivity and Sensitivity in GC−PCI−MS/MS Analysis for *cis*-ETP Derivatives of 4S4M2Pone, 3SHol, and 3SHA

	PCI															
	MH^+ precursor						$[M + C_2H_5]^+$ precursor						fragment ion precursor[a]			
compound	precursor ion[b,c]	collision energy (V)	product ion[b,c]	selectivity[d]	sensitivity (S/N ratio)[e]	precursor ion[b,c]	collision energy (V)	product ion[b,c]	selectivity[d]	sensitivity (S/N ratio)[e]	precursor ion[b,c]	collision energy (V)	product ion[b,c]	selectivity[d]	sensitivity (S/N ratio)[e]
cis-4S4M2Pone−ETP	231	2.5	231	×	n/a	259	5.0	259	×	n/a	185	2.5	185	×	n/a
	231	2.5	185	×	n/a	259	5.0	161	×	n/a	185	2.5	99	△	11
	231	2.5	133	△	3.7	259	5.0	133	×	n/a	185	2.5	87	△	49
	231	2.5	99	△	0.60										
cis-3SHol−ETP	233	2.5	233	×	n/a	261	5.0	261	×	n/a	187	2.5	187	×	n/a
	233	2.5	187	×	n/a	261	5.0	187	△	0.80	187	2.5	103	○	22
	233	2.5	135	×	n/a	261	5.0	115	×	n/a	187	2.5	83	×	n/a
cis-3SHA−ETP	275	5.0	229	×	n/a	303	5.0	303	×	n/a	229	2.5	229	×	n/a
	275	5.0	187	×	n/a	303	5.0	215	△	3.6	229	2.5	187	○	53
	275	5.0	143	×	n/a						229	2.5	143	○	55
											229	2.5	83	○	87

[a]The highest intensity ion as well as having higher *m/z* than that of the molecular ion of the non-derivative form. [b]The ions shown in bold were used for SRM transitions. [c]The ions shown in underline were used for quantification. [d]Selectivity was shown as follows: ○, targeted peak (*cis* form) was separated from interferences; △, targeted peak was co-eluted with interferences, but the targeted peak in the spiked beer was clearly higher than those in the non-spiked beer; and ×, targeted peak was co-eluted with interferences. [e]Sensitivity was shown by the signal-to-noise ratio of the targeted peak in the spiked beer.

DOI: 10.1021/acs.jafc.5b02298
J. Agric. Food Chem. 2015, 63, 6698−6706

Table 4. Linearity, LOD, and Apparent Recovery of *cis*-ETP Derivatives of 4S4M2Pone, 3SHol, and 3SHA

	SRM transitions				apparent recovery	
compound	target	qualification	r^2	LOD (ng/L)	recovery (%)	RSD (%) (n = 6)
cis-4S4M2Pone−ETP	230 > 132	230 > 99	0.9999	0.20	99	2.8
cis-3SHol−ETP	232 > 141	232 > 152, 214 > 127	0.9976	27	101	1.3
cis-3SHA−ETP	274 > 214	274 > 241	0.9943	0.19	101	7.2

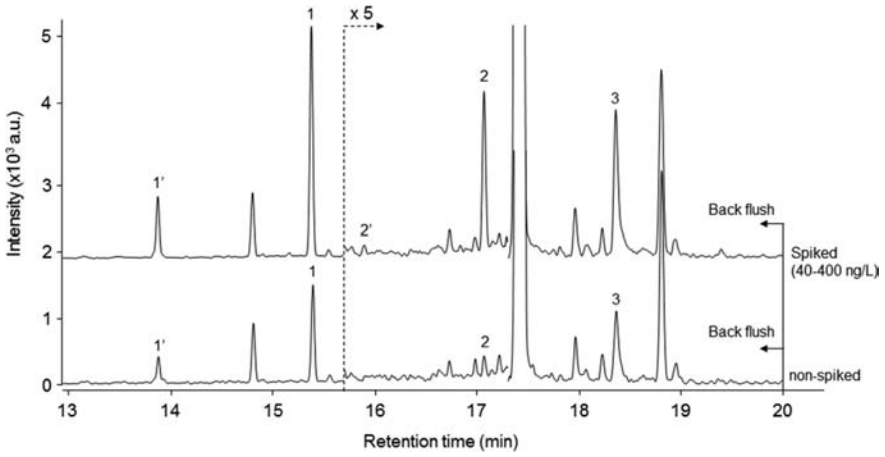

Figure 6. SRM chromatograms obtained by der−SBSE−TD−GC−QQQ−MS of spiked and non-spiked beer hopped with Citra hop: (1′) *trans*-4S4M2Pone−ETP, (1) *cis*-4S4M2Pone−ETP, (2′) *trans*-3SHA−ETP, (2) *cis*-3SHA−ETP, (3′) *trans*-3SHol−ETP, and (3) *cis*-3SHol−ETP. Spiked concentrations are 40 ng/L for 4S4M2Pone and 3SHA and 400 ng/L for 3SHol.

precursor ions for SRM: (1) molecular ion, (2) fragment ion that shows the highest intensity as well as having higher m/z than that of the molecular ion of the non-derivative form (e.g., m/z > 132 for 4S4M2Pone), (3) protonated molecule (PCI), and (4) adduct ion (PCI). Product ion scan with EI and PCI for the precursor ions was first performed with collision energies of 2.5, 5, 10, and 20 V for the spiked water, and the collision energies that give the largest sum of the ion intensities were selected for SRM of each precursor ion. SRM with EI and PCI was then performed with the selected collision energies for non-spiked and spiked beer. The selectivity of SRM conditions was evaluated with the following criteria: (1) the targeted peaks (*cis* form) should be separated from the interferences, and (2) the targeted peaks in the spiked beer should be clearly higher than those in the non-spiked beer (if detected). The sensitivity of SRM conditions was evaluated with a signal-to-noise (S/N) ratio of the targeted thiols in the spiked beer. More than two acceptable transitions could be obtained for all targeted thiols, with SRM using the molecular ion or fragment ion as the precursor ion in the EI. However, no acceptable transitions and only one transition were obtained for 4S4M2Pone−ETP and 3SHol−ETP, respectively, with all SRM conditions in the PCI. Therefore, SRM transitions that give the highest S/N ratio in the EI mode were selected for quantitation. Additionally one or two SRM transitions in the EI were selected as qualifiers. The relative ratios of transition intensities (e.g., 230 > 132/230 > 99 for 4S4M2Pone−ETP) were compared to those in the spiked water, and those were less than 20%. Finally, the selection of SRM transitions for the internal standards (d_{10}-4S4M2Pone and d_2-3SHol) was performed with the same procedure but with the EI only. Tables 2 and 3 summarize the parameters used for the selectivity and sensitivity in GC−MS/MS analysis.

Analytical Performance. We evaluated linearity, limit of detection (LOD), and apparent recovery (the quantity of observed value/reference value, obtained using an analytical procedure that involves a calibration graph[26]) of the method. The standard addition calibration method and the spiked beer sample were used for the evaluation. The peak area of the selected ion from the *cis*-ETP derivative was used for both calibration and determination. Linearity was assessed at six concentration levels between 1 and 100 ng/L for 4S4M2Pone and 3SHA in the beer sample, which contains these compounds at non-detectable levels (below sub-nanogram per liter) with the proposed method. Because detectable levels of 3SHol (>20 ng/L) are present in most beer samples, the linearity between 20 and 1000 ng/L for 3SHol was evaluated. For each level, duplicate analyses were performed. For all compounds, good linearity was achieved with r^2 above 0.9943. The LOD for 4S4M2Pone and 3SHA was estimated using low-concentration spikes (at 1 ng/L) in the same beer samples used for the linearity study and calculating the standard deviation of the determination. The LOD is then defined as 3 times the standard deviation (for six replicates) obtained for the analyte concentration not greater than 10 times the LOD.[27] The LOD for 3SHol was estimated using the blank determination procedure[28] because of the presence of 3SHol at the detectable levels in the beer samples. The LOD for 3SHol is then expressed as the analyte concentration corresponding to the sample blank value plus 3 times the standard deviation.[28] For all analytes, the LODs were below their odor threshold levels in the range of 0.19−27 ng/L. The apparent recovery was assessed by six replicate analyses of the spiked beer samples. The spiked levels were 10 ng/L for 4S4M2Pone and 3SHA and 100 ng/L for 3SHol. The apparent recoveries were good for all analytes in the range of 99−101% [relative standard deviation (RSD) of 1.3−7.2%; n = 6]. The linearity, LOD, and apparent recovery of the method are summarized in Table 4.

Analysis of Beer, Hop Water Extract, and Wort Samples. To demonstrate the applicability of the method, quantitation of the targeted thiols was performed for three kinds of beer hopped with Cascade, Citra, and Nelson Sauvin hop cultivars.

DOI: 10.1021/acs.jafc.5b02298
J. Agric. Food Chem. 2015, 63, 6698−6706

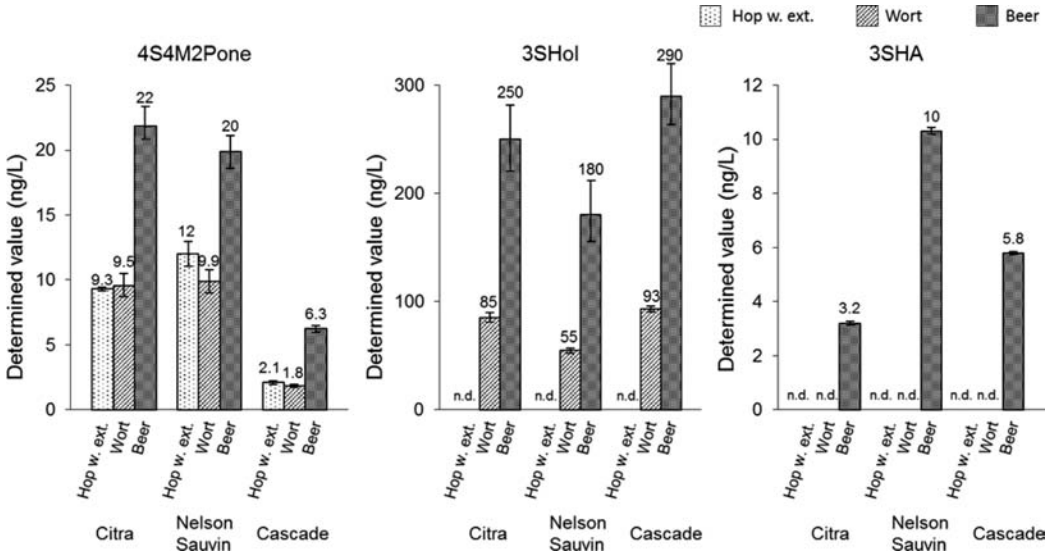

Figure 7. Determined values obtained by der−SBSE−TD−GC−QQQ−MS of beer samples hopped with Cascade, Citra, and Nelson Sauvin hop cultivars and the corresponding hop water extracts and wort sample.

The corresponding hop water extract and (hopped) wort were also analyzed. Triplicate analyses with a three-point standard addition calibration method using internal standards (d_{10}-4S4M2Pone for 4S4M2Pone and 3SHA and d_2-3SHol for 3SHol) were performed for each sample. The peak area of the selected ion from the *cis*-ETP derivative was used for both calibration and determination. Figure 6 illustrates the sum of SRM chromatograms obtained from beer hopped with Citra hop cultivar. The determined values are shown in Figure 7. For 4S4M2Pone, Citra hop and Nelson Sauvin hop show higher values (9.3−12 ng/L; RSD of 3.0−5.2%; n = 3) than that of Cascade hop (2.1 ng/L; RSD of 4.1%; n = 3). The corresponding hopped wort and beer also show a similar trend, and the increased values of all beer samples (6.3−22 ng/L; RSD of 5.1−8.2%; n = 3) indicate the formation of 4S4M2Pone during fermentation from precursors.[6] Although 3SHol was not detected in all hop water extract samples, the determined values of 3SHol in hopped wort and beer are in the range of 55−93 ng/L (RSD of 11−12%; n = 3) and 180−290 ng/L (RSD of 7.5−12%; n = 3), respectively. Again, the increased values of all beer samples illustrate the effect of precursors during fermentation. As a previous study reported,[10] the determined values of 3SHol between hopped wort and beer show a linear correlation with r^2 of 0.9477. 3SHA was not detected in hop water extract and hopped wort and was only detected in beer (3.2−10 ng/L; RSD of 4.6−9.8%; n = 3). It is known that some yeasts have high capability of converting 3SHol into 3SHA during fermentation.[29,30] However, the order of the determined values of 3SHA in beer (Nelson Sauvin > Cascade > Citra) did not reflect those of 3SHol in hopped wort and beer (Cascade > Citra > Nelson Sauvin).

AUTHOR INFORMATION

Corresponding Author

*Telephone: +81-3-5731-5321. Fax: +81-3-5731-5322. E-mail: nobuo_ochiai@gerstel.co.jp.

Notes

The authors declare no competing financial interest.

ACKNOWLEDGMENTS

The authors thank Kevin MacNamara (Dublin, Ireland) and Shigeki Daishima of Agilent Technologies Japan, Ltd. for their kind support.

ABBREVIATIONS USED

3SHol, 3-sulfanylhexan-1-ol; 3SHA, 3-sulfanylhexyl acetate; 4S4M2Pone, 4-sulfanyl-4-methylpentan-2-one; CAD, collision-ally activated dissociation; ETP, ethyl propiolate; LOD, limit of detection; PDMS, polydimethylsiloxane; Q−TOF−MS, quadrupole time-of-flight mass spectrometer; RSD, relative standard deviation; SRM, selected reaction monitoring; der−SBSE, stir bar sorptive extraction with *in situ* derivatization; SCD, sulfur chemiluminescence detector; MS/MS, tandem mass spectrometry; TD, thermal desorption; QQQ−MS, triple-quadrupole mass spectrometer

REFERENCES

(1) McGorrin, R. J. The significance of volatile sulfur compounds in food flavors. An overview. In *Volatile Sulfur Compounds in Food*; Qian, M. C., Fan, X., Mahattanatawee, K., Eds.; American Chemical Society (ACS): Washington, D.C., 2011; ACS Symposium Series, Vol. *1068*, Chapter 1, pp 10−14.

(2) Tominaga, T.; Murat, M.-L.; Dubourdieu, D. Development of a method for analyzing the volatile thiols involved in the characteristic aroma of wines made from *Vitis vinifera* L. Cv. Sauvignon Blanc. *J. Agric. Food Chem.* **1998**, *46*, 1044−1048.

(3) Roland, A.; Schneider, R.; Razungles, A.; Cavelier, F. Varietal thiols in wine: discovery, analysis and applications. *Chem. Rev.* **2011**, *111*, 7355−7376.

(4) Kishimoto, T.; Wanikawa, A.; Kono, K.; Shibata, K. Comparison of the odor-active compounds in unhopped beer and beers hopped with different hop varieties. *J. Agric. Food Chem.* **2006**, *54*, 8855−8861.

(5) Kishimoto, T.; Morimoto, M.; Kobayashi, M.; Yako, N.; Wanikawa, A. Behaviors of 3-mercaptohexan-1-ol and 3-mercaptohexyl acetate during brewing processes. *J. Am. Soc. Brew. Chem.* **2008**, *66*, 192−196.

(6) Kishimoto, T.; Kobayashi, M.; Yako, N.; Iida, A.; Wanikawa, A. Comparison of 4-mercapto-4-methylpentan-2-one contents in hop cultivars from different growing regions. *J. Agric. Food Chem.* **2008**, *56*, 1051−1057.

DOI: 10.1021/acs.jafc.5b02298
J. Agric. Food Chem. 2015, 63, 6698−6706

(7) Steinhaus, M.; Wilhelm, W.; Schieberle, P. Comparison of the most odor-active volatiles in different hop varieties by application of a comparative aroma extract dilution analysis. *Eur. Food Res. Technol.* **2007**, *226*, 45−55.
(8) Steinhaus, M.; Schieberle, P. Transfer of the potent hop odorants linalool, geraniol, and 4-methyl-4-sulfanyl-2-pentanone from hops into beer. *Proceedings of the 31st European Breweries Convention Congress*; Venice, Italy; May 6−10, 2007; pp 1004−1011.
(9) Gros, J.; Nizet, S.; Collin, S. Occurance of odorant polyfunctional thiols in the Super Alpha Tomahawk hop cultivar. Comparison with the thiol-rich Nelson Sauvin bitter variety. *J. Agric. Food Chem.* **2011**, *59*, 8853−8865.
(10) Gros, J.; Peeters, F.; Collin, S. Occurance of odorant polyfunctional thiols in beers hopped with different cultivars. First evidence of an S-cysteine conjugate in hop (*Humulus lupulus L.*). *J. Agric. Food Chem.* **2012**, *60*, 7805−7816.
(11) Tominaga, T.; Dubourdieu, D. A novel method for quantification of 2-methyl-3-furanthiol and 2-furanmethanethiol in wines made from *Vitis vinifera* grape varieties. *J. Agric. Food Chem.* **2006**, *54*, 29−33.
(12) Mateo-Vivaracho, L.; Ferreira, V.; Cacho, J. Automated analysis of 2-methyl-3-furanthiol and 3-mercaptohexyl acetate at ng L^{-1} level by headspace solid-phase microextracion with on-fibre derivatisation and gas chromatography−negative chemical ionization mass spectrometric determination. *J. Chromatogr. A* **2006**, *1121*, 1−9.
(13) Mateo-Vivaracho, L.; Cacho, J.; Ferreira, V. Quantitative determination of wine polyfunctional mercaptans at nanogram per liter level by gas chromatography−negative ion mass spectrometric analysis of their pentafluorobenzyl derivatives. *J. Chromatogr. A* **2007**, *1146*, 242−250.
(14) Mateo-Vivaracho, L.; Cacho, J.; Ferreira, V. Improved solid-phase extraction procedure for the isolation and in-sorbent pentafluorobenzyl alkylation of polyfunctional mercaptans, Optimized procedure and analytical applications. *J. Chromatogr. A* **2008**, *1185*, 9−18.
(15) Owen, T. C. Thiol detection, derivatization and tagging at micromole to nanomole levels using propiolates. *Bioorg. Chem.* **2008**, *36*, 156−160.
(16) Zacharis, C. K.; Tzanavaras, P. D.; Themelis, D. G. Ethyl-propiolate as a novel and promising analytical reagent for the derivatization of thiols: Study of the reaction under flow conditions. *J. Pharm. Biomed. Anal.* **2009**, *50*, 384−391.
(17) Herbst-Johnstone, M.; Piano, F.; Duhamel, N.; Barker, D.; Fedrizzi, B. Ethyl propiolate derivatisation for the analysis of varietal thiols in wine. *J. Chromatogr. A* **2013**, *1312*, 104−110.
(18) David, F.; Sandra, P. Star bar sorptive extraction for trace analysis. *J. Chromatogr. A* **2007**, *1152*, 54−69.
(19) Prieto, A.; Basauri, O.; Rodil, R.; Usobiaga, A.; Fernández, L. A.; Etxebarria, N.; Zuloaga, O. Stir-bar sorptive extraction: A view on method optimization, novel applications, limitations and potential solutions. *J. Chromatogr. A* **2010**, *1217*, 2642−2666.
(20) Kawaguchi, M.; Ito, R.; Nakazawa, H.; Takatsu, A. Applications of stir-bar sorptive extraction to food analysis. *TrAC, Trends Anal. Chem.* **2013**, *45*, 280−293.
(21) Ochiai, N.; Sasamoto, K.; Daishima, S.; Heiden, A. C.; Hoffmann, A. Determination of stale-flavor carbonyl compounds in beer by stir bar sorptive extraction with in-situ derivatization and thermal desorption−gas chromatography−mass spectrometry. *J. Chromatogr. A* **2003**, *986*, 101−110.
(22) Halphen, P. D.; Owen, T. C. Carboxyalkylthioacrylates. *J. Org. Chem.* **1973**, *38*, 3507−3510.
(23) Cooks, R. G. Collision-induced dissociation: Readings and commentary. *J. Mass Spectrom.* **1995**, *30*, 1215−1221.
(24) Nakata, H.; Suzuki, Y.; Shibata, M.; Takahashi, K.; Konishi, H.; Takeda, N.; Tatematsu, A. Chemical Ionization Mass Spectrometry of Bifunctional Compounds. The Behaviour of Bifunctional Compounds on Protonation. *Org. Mass Spectrom.* **1990**, *25*, 649−654.
(25) Nakata, H. A fundamental aspect of the structure and fragmentations of organic ions in mass spectrometry, Protonation of organic compounds and the behavior of resulting protonated molecules. *J. Mass Spectrom. Soc. Jpn.* **2000**, *48*, 79−93 (in Japanese) .
(26) Burns, D. T.; Danzer, K.; Townshend, A. Use of the terms "recovery" and "apparent recovery" in analytical procedures (IUPAC Recommendations). *Pure Appl. Chem.* **2002**, *74*, 2201−2205.
(27) Pawliszyn, J. Method development. In *Solid Phase Micro-extraction—Theory and Practice*, 1st ed.; Pawliszyn, J., Eds.; Wiley-VCH: New York, 1997; p 1037.
(28) Shrivastava, A.; Gupta, V. B. Methods for the determination of limit of detection and limit of quantification of the analytical methods. *Chronicles of Young Scientists* **2011**, *2*, 21−25.
(29) Swiegers, J. H.; Francis, I. L.; Herderich, M. J.; Pretorius, I. S. Meeting consumer expectations through management in vineyard and winery: The choice of yeast for fermentation offers great potential to adjust the aroma of Sauvignon Blanc wine. *Aust. N. Z. Wine Ind. J.* **2006**, *21*, 34−42.
(30) Swiegers, J. H.; Capone, D. L.; Pardon, K. H.; Elsey, G. M.; Sefton, M. A.; Francis, I. L.; Pretorius, I. S. Engineering volatile thiol release in Saccharomyces cerevisiae for improved wine aroma. *Yeast* **2007**, *24*, 561−57.

DOI: 10.1021/acs.jafc.5b02298
J. Agric. Food Chem. 2015, 63, 6698−6706

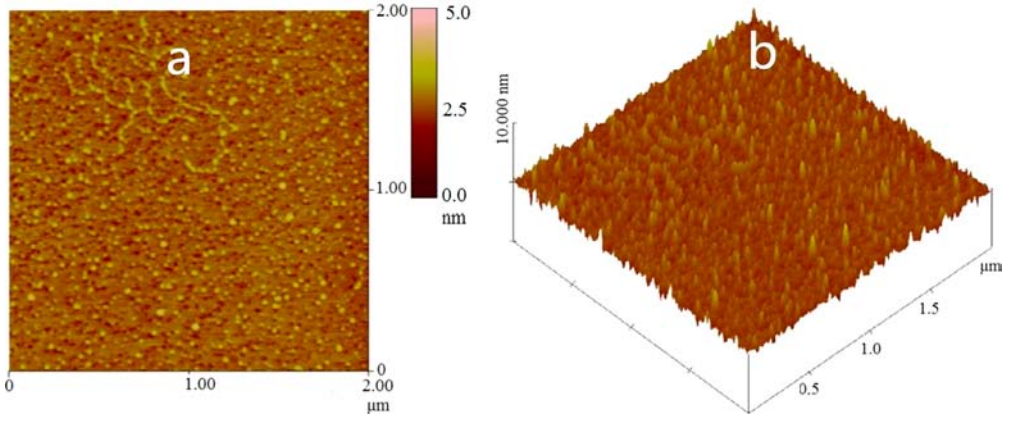

Figure 1. AFM images of the C-dots.

EXPERIMENTAL PROCEDURES

Materials. Aloe was obtained from potted plants in our laboratory and washed with water for further use. Dichloromethane (CH_2Cl_2, 99.5%) was purchased from Aladdin Industrial Corp. (Shanghai, China). Tartrazine ($C_{16}H_9N_4Na_3O_9S_2$, 87%), sunset yellow ($C_{16}H_{10}N_2Na_2O_7S_2$, 85%), erioglaucine disodium salt ($C_{37}H_{34}Na_2N_2O_9S_3$, 85%), and amaranth ($C_{20}H_{11}N_2Na_3O_{10}S_3$, 85%) were received from Aladdin Chemistry Co. Ltd. (Shanghai, China). Sodium dihydrogen phosphate ($NaH_2PO_4{\cdot}H_2O$) and disodium hydrogen phosphate dodecahydrate ($Na_2HPO_4{\cdot}12H_2O$) were obtained from Tianjin Fuchen Chemical Reagents Co., Ltd. (Tianjin, China). All chemicals were of analytical reagent grade and used without further purification. The ultrapure water used throughout the experiments was purified through an UPH-II-20T up water purification system (Chengdu Ultrapure Technology Co. Ltd., Chengdu, China).

Apparatus and Characterization. The AFM analysis was carried out on a Multimode/Nanoscope (Veeco Corp., USA) on a tapping mode with a RTESP-Veeco cantilever on a platinum-coated mica substrate. All absorption spectra were recorded on a Shimadzu UV-2550 UV−vis absorption spectrophotometer (Kyoto, Japan). Fluorescence measurements were conducted with a Cary Eclipse fluorescence spectrophotometer (Varian, Palo Alto, CA, USA). The infrared spectra were obtained on a Nicolet 6700 Fourier transform infrared (FTIR) spectrometer (Thermo Electron Corp., USA) with passed KBr pellet at room temperature.

Synthesis of Fluorescent C-Dots. The C-dots were prepared by hydrothermal treatment of fresh aloe in water. In a typical procedure, 5 g of aloe was added into 25 mL of water, and then the mixture was transferred into a 50 mL Teflon-lined autoclave and was heated at 180 °C for 11 h. After heating, the autoclaves were allowed to naturally cool in a fume hood on a heat-resistant plate and the resulting yellow solution was filtered with a 0.22 μm membrane followed by washing with dichloromethane to remove the unreacted organic moieties. Finally, the upper light yellow aqueous solution containing C-dots was collected and stored at 4 °C for further characterization and use.

Quantum Yield Measurements. The quantum yield of the as-synthesized C-dots was measured on the basis of a procedure described previously.[25] Rhodamine 6G aqueous solution was used as a reference standard, for which the quantum yield was 0.95 at 488 nm reported by the literature. Absolute values of the quantum yield were calculated according to the equation

$$\Phi_x = \Phi_{std}\frac{I_x}{A_x}\frac{A_{std}}{I_{std}}\frac{\eta_x^2}{\eta_{std}^2}$$

where Φ is the quantum yield of the as-prepared C-dots, A is the absorbance, I is the corrected emission intensity at the excitation wavelength, and η is the refractive index of the solvent. The subscripts "std" and "x" refer to reference standard with known quantum yield and the C-dots solution, respectively. For the sake of reducing effects of reabsorption within the sample on the observed emission spectrum, the absorbance values (A) of all solutions in the 10 mm cuvette were always controlled under 0.1.

Sample Pretreatment. Candy, steamed buns made of corn, and honey were selected as test samples because tartrazine may be added as a colorant into them. All samples were obtained from a local supermarket in Nanchong, China. The candy or honey sample (10.0 g) was crushed and subsequently dissolved in hot water (~60 °C). The resulting solution was transferred and diluted to a 50 mL volumetric flask. The diluted solution was filtered through a 0.45 μm filter membrane for subsequent use. Ten grams of steamed buns and a certain amount of water were added into a 100 mL beaker, and then the mixture was blended by electric mixer and extracted with ultrasonic for 15 min, respectively. After extraction, the mixture was centrifuged at 12000 rpm for 10 min followed by transferring the supernatant and diluting to 50 mL. The diluted solution was also filtered through a 0.45 μm filter membrane for subsequent use. The above sample pretreatment method is referenced to the literature with some minor modifications.[26]

Detection of Tartrazine in Food Samples. The tartrazine detection procedure was carried out in phosphate buffer (PB) (30 mM, pH 6.0) at 5 °C. In a typical run, 450 μL of C-dots solution was added into 500 μL of PB, followed by the addition of 1000 μL of sample solution and thorough mixing. The resulting mixture was reconstituted to 4 mL with water. After a reaction time of 5 min at 5 °C, the spectra were recorded under excitation at 441 nm with slit widths setting at 10/10 nm. All of the recoveries were calculated according to the equation below:

$$\text{recovery} = (C_{measured} - C_{initial})/C_{added}$$

RESULTS AND DISCUSSION

Optimization of the Synthesis Conditions. To ensure excellent performance of the synthesized C-dots, we have optimized the time and temperature of the synthesis simply, and results are shown in Figures S1 and S2. From Figure S1 we can see clearly that the fluorescence intensity gradually increased with the reaction time up to 11 h but decreased when the time exceeded 11 h. Therefore, 11 h was chosen as the optimal reaction time. Simultaneously, as displayed in Figure S2, the fluorescence intensity increased with the reaction temperature rise. We finally chose 180 °C as the optimal temperature because when the temperature exceeded 180 °C, the fluorescence intensity increase was not obvious.

Characterization. Figure 1 shows the typical AFM image of the as-synthesized C-dots solution. It reveals that the C-dots are well dispersed in solution with spherical shape and have an average size of 5 nm approximately. Similarly, Figure S3 shows the typical TEM image of the C-dots. It can be seen that the C-

DOI: 10.1021/acs.jafc.5b02319
J. Agric. Food Chem. 2015, 63, 6707−6714

dots are in the monodispersion state and their size is consistent with the results of AFM.

The absorption (black line) and emission spectra (green line) of the as-synthesized C-dots are shown in Figure 2. A peak

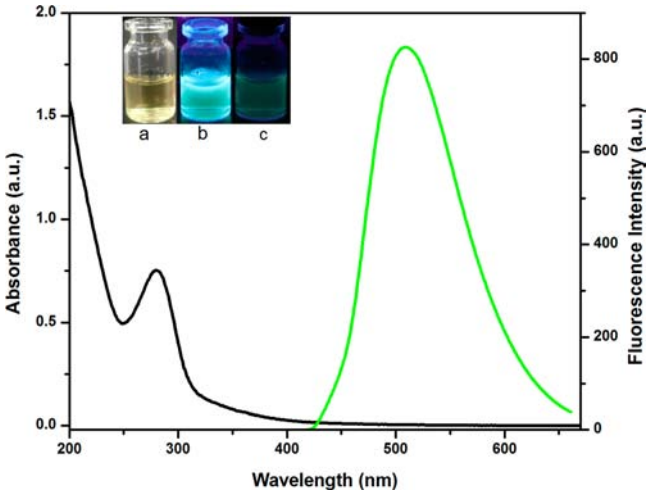

Figure 2. UV−vis absorption (black line) and fluorescence emission (green line) spectra of the C-dots. (Inset) Photographic images of C-dots under (a) visible light, (b) ultraviolet light, and (c) ultraviolet light with tartrazine (22.5 μM).

at 278 nm is exhibited in the UV−vis absorption spectrum, which was attributed to n−π* transition of C═O and π−π* transition of C═C.[27] The photoluminescent (PL) spectrum shows an optimal emission peak at about 503 nm when excited at 441 nm. The inset photograph in Figure 2 indicates the C-dots aqueous solution under visible (a) and UV illumination at 365 nm (b). The bright yellow PL of the C-dots under UV light is strong enough to be seen with the naked eye, but when tartrazine was added, the fluorescence was obviously quenched (c). The full width at half-maximum (fwhm) is 100 nm, suggesting a relatively small size distribution of C-dots, which was consistent with AFM and TEM data and approximately equal to that of most reported C-dots.[28,29] The strong fluorescence can be caused by the surface energy traps in the C-dots that become emissive upon stabilization.[17]

To further investigate the optical properties, the PL emission spectrum of the C-dots was recorded at progressively increasing excitation wavelengths (Figure 3). It can be observed that a red shift was attributed in the emission spectra of C-dots from 443 to 525 nm with increasing excitation wavelengths, accompanied by a decrease of the fluorescence intensity, revealing that the fluorescence of C-dots is strongly dependent on the excitation wavelength. This finding is substantially in agreement with that of Vaibhavkumar.[30,31] To investigate the components, surface groups, and structure of the as-synthesized C-dots, EDS and FT-IR have been carried out. Figure S4 shows the as-prepared C-dots are mainly composed of C, H, O, and N. As shown in Figure 4, characteristic absorption bands of the −OH stretching vibration mode at about 3400 and 1073 cm^{-1} could be observed. The band at 2923 cm^{-1} corresponds to the C−H stretching mode.[32] In addition, the peaks appearing at 1590 and 1400 cm^{-1} may be caused by the asymmetric and symmetric stretching vibration of COO^{-}, respectively. These findings provide evidence that both the hydroxyl and carboxylic groups originated from carbohydrates in the aloe.

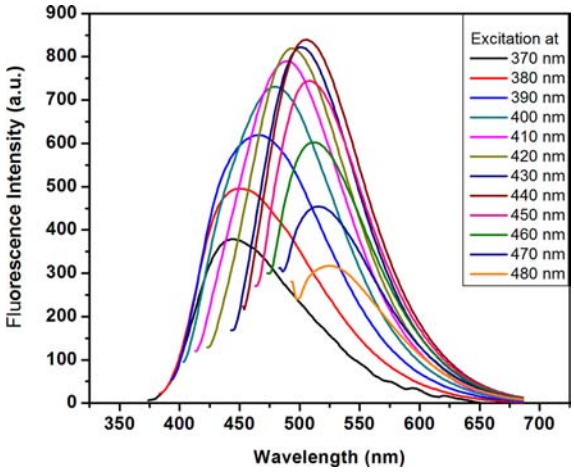

Figure 3. Fluorescence emission spectra of C-dots obtained at different excitation wavelengths progressively increasing from 370 to 480 nm in 10 nm increments.

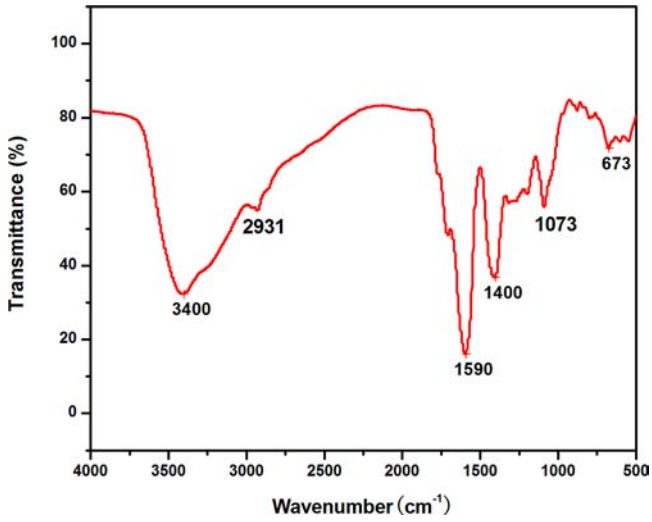

Figure 4. FT-IR spectrum of C-dots.

It is well-known that the photostability of C-dots plays a key role in sensitive fluorescence detection. In this connection, we studied the emission behavior of the C-dots under continuous UV light illumination at 365 nm for 120 min. It was also noted that as shown in Figure S5 the photobleaching of C-dots is not observed and the fluorescence intensity of C-dots remained constant even after 120 min of continuous UV light illumination, indicating the good photostability of C-dots. Using rhodamine 6G as a reference, a PL quantum yield (QY) of 10.37% was measured. Table S1 shows the comparison of the optical properties and applications of the C-dots derived from aloe with the reported methods. It can be seen that the present method is green and simple and has a relatively high quantum yield. At the same time, it is worth mentioning that the as-prepared C-dots emit strong yellow fluorescence, whereas most reported carbon dots are blue, and they can be a sensitive fluorescent probe for colorant detention.

Design Principle of the Sensor. Under the same experimental conditions, the fluorescence spectra of the C-dots alone and the system of C-dots with tartrazine were recorded, respectively. As shown in Figure S6, the C-dots presented strong fluorescence at 503 nm when excited at 441

DOI: 10.1021/acs.jafc.5b02319
J. Agric. Food Chem. 2015, 63, 6707−6714

Scheme 1. Scheme of the Synthetic Strategy for C-Dots and the Principle of Tartrazine Sensing

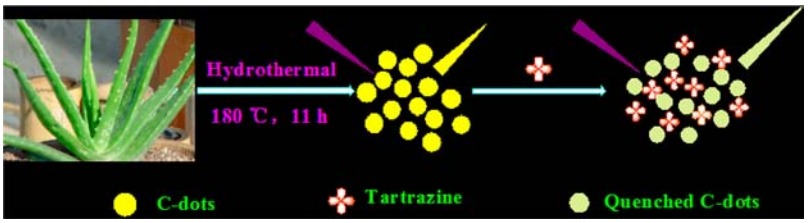

nm. Upon the addition of tartrazine, the fluorescence intensity of the prepared C-dots decreased significantly. On the basis of the fluorescence quenching, we speculated that a facile fluorescence sensor for the determination of tartrazine could be constructed. The synthetic strategy for C-dots and the principle of tartrazine sensing are schematically presented in Scheme 1.

Mechanism of Fluorescence Quenching. Broadly speaking, various kinds of molecular interactions with the quencher molecule can reduce the fluorescence quantum yield, such as electron or energy transfer, collisional quenching, excited-state reaction, and ground-state complex formation The quenching mechanisms are usually divided into dynamic quenching, which results from collision, and static quenching, resulting from the formation of a ground-state complex between the fluorescence material and quencher. On the other hand, they could be distinguished by some additional formations such as the relationship between the quenching and viscosity, temperature, and lifetime measurements.[33] In general, the dynamic fluorescence quenching constants will increase with the rise of the system temperature due to the energy transfer efficiency, and the effective collision times between molecules will also increase. On the contrary, the values of the static fluorescence quenching constants will decrease with the rise of temperature. Let us suppose that the mechanism is dynamic quenching; it can be described by the Stern–Volmer equation[34]

$$F_0/F = 1 + K_{SV}[Q] = 1 + K_q\tau_0[Q]$$

where F_0 and F are the C-dots fluorescence intensities at 503 nm in the absence and presence of tartrazine, respectively; K_{SV} and K_q are the Stern–Volmer quenching constant and the bimolecular quenching constant, respectively; [Q] is the concentration of tartrazine; and τ_0 is the average lifetime of the C-dots without any other fluorescence quencher, with a general value of 10^{-8} s. Figure 5 shows the fluorescence intensities of the C-dots analyzed by plotting F_0/F versus [Q] at 278, 288, 298, and 308 K. Table 1 summarizes the calculated K_{SV} and K_q values for each temperature. As shown, the K_{SV} is inversely correlated with temperature, and the value of K_q is far larger than 2.0×10^{10} L mol^{-1} s^{-1}, which is the maximum scatter collision quenching constant. These findings indicate that the quenching process may be caused by static quenching. Additionally, the UV–vis spectra of the prepared C-dots alone and the system of the C-dots with tartrazine are illustrated in Figure S7. As can be seen from this figure, with the addition of tartrazine, the absorbance intensity of the C-dots at 280 nm increases, with a blue shift. This observation indicates that the formation of ground-state complexes is generated due to the interaction between tartrazine and C-dots.

Optimization of Experimental Conditions. With the purpose of investigating the sensitivity, precision, and selectivity of the analytical method, parameters including the medium pH, dosage of C-dots, reaction temperature, and incubation time were systematically optimized for the system.

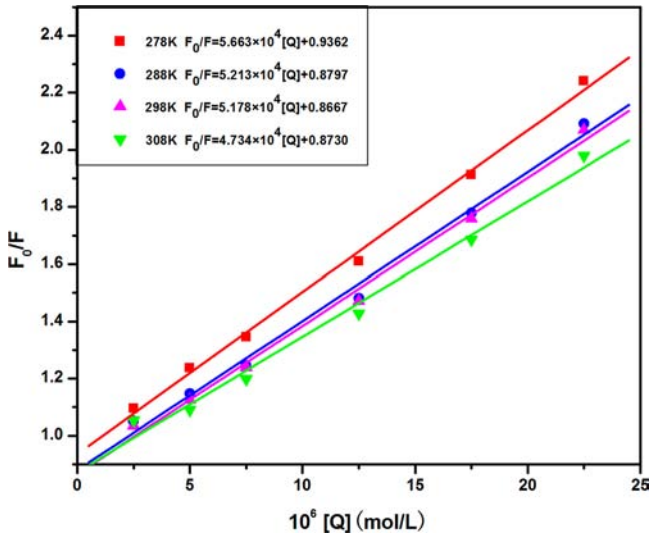

Figure 5. Stern–Volmer plots for the system of C-dots–tartrazine under temperatures of 278, 288, 298, and 308 K, respectively. F_0 and F are the fluorescence intensity of C-dots in the absence and presence of tartrazine, respectively. Conditions: C-dots, 450 μL; PB, 30 mM, pH 6.0.

Table 1. Stern–Volmer Quenching Constants for the Interaction of C-Dots and Tartrazine at Different Temperatures

pH	T (K)	K_{SV} (L mol^{-1})	K_q (L mol^{-1} s^{-1})	R	SD
6.0	278	5.663×10^4	5.663×10^{12}	0.9984	0.0278
6.0	288	5.213×10^4	5.213×10^{12}	0.9960	0.0402
6.0	298	5.178×10^4	5.178×10^{12}	0.9967	0.0361
6.0	308	4.734×10^4	4.734×10^{12}	0.9939	0.0452

The effect of the solution pH on the fluorescence quenching of C-dots in the presence of tartrazine is shown in Figure 6a. An increase in pH from 4.0 to 6.0 results in the increased fluorescence quenching efficiency (represented as F_0/F, where F_0 and F are the fluorescence intensities of the C-dots at 503 nm before and after the addition of tartrazine, respectively.) whereas a further increase in pH from 6 to 7.5 leads to a gradual decrease. Such an observation suggests that the fluorescence intensity of the C-dots strongly depends on the pH value of the system. Our results are consistent with those of C-dots functioned with hydroxyl and carboxylic/carbonyl moieties.[10,19,32] Consequently, we selected 6.0 as the optimal pH for our study.

The effect of the dosage of C-dots on the fluorescence quenching efficiency is presented in Figure 6b. The fluorescence quenching efficiency gradually increased with the dosage of C-dots up to 450 μL. When the dosage of C-dots

DOI: 10.1021/acs.jafc.5b02319
J. Agric. Food Chem. 2015, 63, 6707–6714

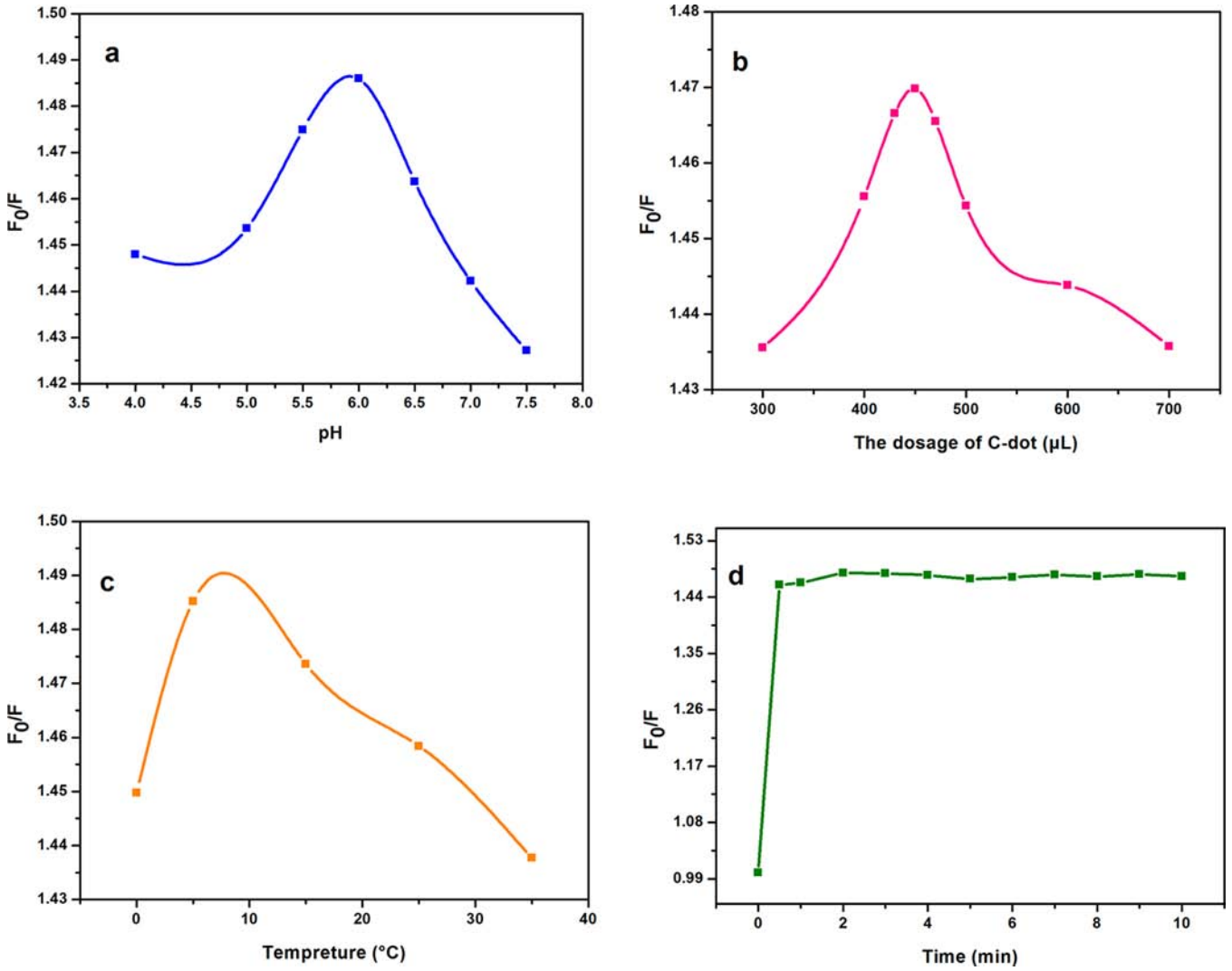

Figure 6. Effect of (a) pH of buffer solution, (b) dosage of C-dots, (c) reaction temperature, and (d) reaction time on fluorescence quenching efficiency of the C-dots−tartrazine system. F_0 and F are the fluorescence intensity of C-dots in the absence and presence of tartrazine, respectively. Conditions: PB, 30 mM; tartrazine, 10 μM.

exceeded 450 μL, the fluorescence quenching efficiency decreased. Therefore, 450 μL was used as the optimal dosage for further performance

Figure 6c shows the fluorescence curves of the system at different temperatures. As the temperature increased from 5 to 35 °C, the fluorescence quenching efficiency decreased gradually. Among the temperatures studied, the maximum fluorescence intensity efficiency was achived at 5 °C. Hence, 5 °C is selected as the optimum reaction temperature.

The effect of incubation time on the fluorescence intensity of the system is shown in Figure 6d. No significant changes in F_0/F were observed after an incubation time of 1 min. To ensure the consistency of the whole experiment, it is important to record the stable fluorescence signal. Thus, 5 min is conservatively chosen as the optimum incubation time.

Analytical Performance for Tartrazine Sensing. *Sensitivity.* The dependence of F_0/F on the different concentrations of tartrazine under the identical conditions is shown in Figure 7. As displayed, the fluorescence quenching efficiency of C-dots gradually decreases with an increase in the concentration of tartrazine. As shown in the upper right inset of Figure 7, the decrease in fluorescence quenching efficiency exhibited a linear response to the tartrazine concentration in the range of 0.25−32.50 μM, which was consistent with the photograph of the solutions under UV light. The calibration curve can be depicted as $F_0/F = 0.9604 + 0.0577X$ (X is the concentration of tartrazine, μM) with a correlation coefficient of 0.9986. The relative standard deviation (RSD) was 0.25% through five parallel determinations ($n = 5$) at a fixed tartrazine concentration of 10.00 μM, indicating the excellent reliability of this sensor. The detection limit is estimated to be 73 nM at a signal-to-noise ratio of 3.

In Table 2, we compare the experimental results with those for reported methods of tartrazine detection. As shown in Table 2, our developed assay exhibits a wider linear range and lower RSD compared to some methods. Our method can be an alternative to others for the determination of tartrazine in samples, although the limit of detection (LOD) our method is not the smallest in Table 2. It is worth mentioning that almost all of the reported sensors need special equipment, a sophisticated technique, or complicated operations. By contrast, the sensor we developed here has its own features, including low instrumentation cost, simplicity of operation, and fast

DOI: 10.1021/acs.jafc.5b02319
J. Agric. Food Chem. 2015, 63, 6707−6714

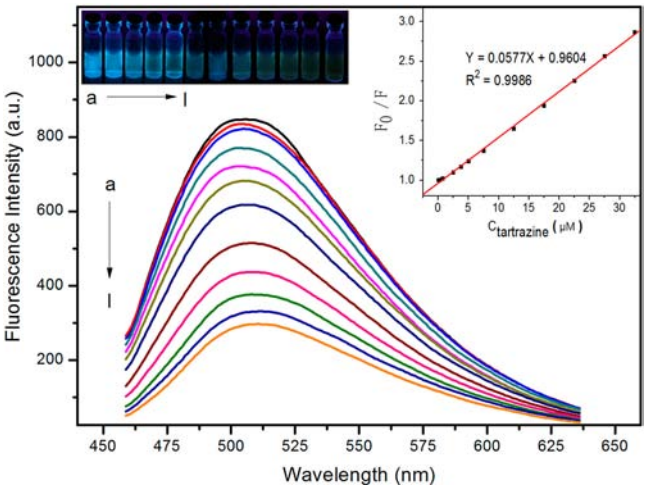

Figure 7. Fluorescence emission spectra of C-dots in the presence of different concentrations of tartrazine in 30 mM PB (pH 6.0). From a to l: 0.00, 0.25, 0.75, 2.50, 3.75, 5.00, 7.50, 12.50, 17.50, 22.50, 27.50, 32.50 μM, respectively. C-dots, 450 μL. (Inset) Photographic images of the corresponding solutions under UV light and the relationship curve between F_0/F and concentration of tartrazine.

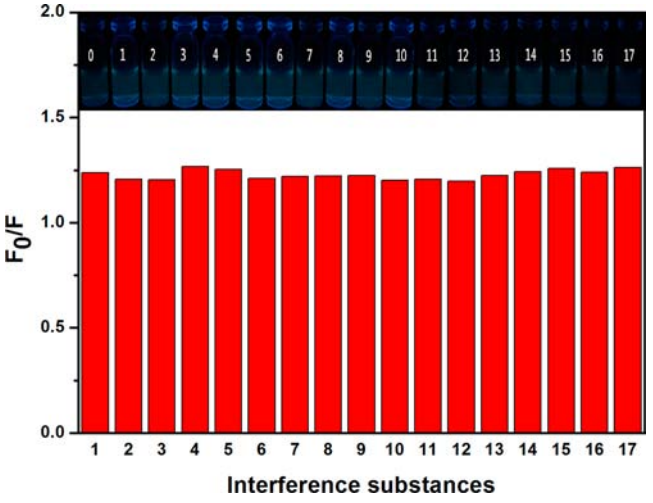

Figure 8. Effects of potentially interfering substances: (0) non-interference; (1) glucose, 500 μM; (2) lactose, 500 μM; (3) starch, 500 μM; (4) citric acid, 500 μM; (5) tartaric acid, 500 μM; (6) ascorbic acid, 500 μM; (7) glutamic acid, 250 μM; (8) phenylalmine, 250 μM; (9) NO_2^-, 500 μM; (10) HCO_3^-, 500 μM; (11) Ca^{2+}, 500 μM; (12) Zn^{2+}, 500 μM; (13) K^+, 500 μM; (14) Fe^{3+}, 25 μM; (15) sunset yellow, 5.0 μM; (16) erioglaucine disodium salt, 25 μM; (17) amaranth, 5.0 μM. Conditions: C-dots, 450 μL; PB, 30 mM, pH 6.0; tartrazine, 5.0 μM.

response, which makes it more applicable for routine analysis of tartrazine in foods.

Selectivity. To evaluate the selectivity of this sensing system, we examined the fluorescence response of the system to tartrazine at a concentration of 5.0 μM with the presence of coexisting foreign substances such as K^+, Ca^{2+}, Zn^{2+}, Fe^{3+}, HCO_3^-, NO_2^-, glutamic acid, glutathione (GSH), citric acid, phenylalanine, starch, tartaric acid, vitamin C, glucose, lactose, sunset yellow, erioglaucine disodium salt, and amaranth under the same conditions. As shown in Figure 8, for the present study, various different substances were added in the test solution at the amount of 100 times tartrazine initially, and the ratio would be gradually reduced when the interference presented. It was found that some of the materials, such as Fe^{3+}, sunset yellow, erioglaucine disodium salt, and amaranth, could be only allowed at relatively lower levels. Nevertheless, the concentrations of these substances were much lower than the allowed levels in food samples. Meanwhile, most of the common excipients in foods could be tolerated at high concentrations up to 100 times. That is to say the established strategy possesses a high selectivity toward tartrazine detection.

Application in Food Samples. The developed approach was employed to detect the trace level of tartrazine in some food samples. The results for the pretreated food samples spiked with known amounts of standard tartrazine are shown in Table 3. The intraday and interday recoveries ranged from 88.6 to 103.4% and from 87.3 to 106.6%, respectively. All of these results indicate that the accuracy and reliability of the proposed method can be applied to the determination of tartrazine in food samples.

In summary, C-dots based on aloe were synthesized via a simple and green method. Without further chemical modification, the synthesized C-dots have been applied to the sensitive and selective detection of tartrazine in some food samples. The new C-dots described here may extend their great potential for cell imaging and drug delivery applications due to

Table 2. Comparison of the Proposed Method with Other Methods for Determination of Tartrazine

method	linear range (μM)	R^2	LOD (nM)	RSD%	ref
graphene and mesoporous TiO_2 electrochemical sensor	0.02−1.18	0.994	8	2.70	26
spectrophotometry method	0.00131−0.67	0.992	0.56	0.98	23
electrochemical detection	0.11−56		56	3.12	17
electrochemical detection	0.05−20		14.3		18
electrochemical sensor	0.00936−0.37	0.994	2.8	4.3	22
high-performance liquid chromatography	0.0934−9.34	0.999	18.5	4.3	35
alumina microfibers-based electrochemical sensor	0.005−0.14	0.998	2.0	4.7	36
gold nanoparticles carbon paste electrode	0.05−1.6	0.997	2	1.1	37
differential pulse polarography	0.19−19	0.999	30		38
multiwalled carbon nanotubes film-modified electrode	0.37−74.8	0.990	187	5.2	39
solid phase spectrophotometry	0.094−1.22	0.998		4.00	40
capillary zone electrophoresis	5.6−178	0.995	2430		41
thin-layer chromatography	74.9−356	0.992		0.03	5
reversed-phase high-performance liquid chromatography	0.011−39.3	0.999	3.5		42
fluorescence analysis	0.25−32.5	0.998	73	0.25	this work

DOI: 10.1021/acs.jafc.5b02319
J. Agric. Food Chem. 2015, 63, 6707−6714

Table 3. Recovery Test and Precision of the Analysis of Tartrazine in Food Samples

			intraday			interday		
food sample	detected (μM)	spiked (μM)	found[a] (μM)	recovery (%)	RSD (%)	found[a] (μM)	recovery (%)	RSD (%)
steamed buns	ND[b]	1.00	1.00 ± 0.07	99.9	2.8	1.06 ± 0.09	106.6	4.2
		5.00	4.96 ± 0.07	99.2	0.6	4.99 ± 0.07	99.8	0.6
		7.00	7.00 ± 0.05	100.0	0.3	7.02 ± 0.13	100.3	0.7
honey	ND	1.00	1.04 ± 0.11	103.4	3.9	1.05 ± 0.15	105.4	5.8
		5.00	4.96 ± 0.03	99.1	0.2	5.00 ± 0.07	99.9	0.6
		7.00	7.04 ± 0.10	100.6	0.7	7.00 ± 0.18	100.0	1.0
candy	4.80	3.00	7.48 ± 0.15	88.6	0.8	7.44 ± 0.08	87.3	0.4
		5.00	9.44 ± 0.06	92.3	0.2	9.51 ± 0.12	93.6	0.5
		7.00	11.12 ± 0.12	90.0	0.5	11.16 ± 0.10	90.4	0.4

[a]Value = mean ± SD (n = 5). [b]Not detectable.

the simplicity of their synthesis procedure and the use of affordable and environmentally friendly aloe as carbon source.

■ ASSOCIATED CONTENT

Supporting Information

Experimental procedures for EDS, supplementary figures of EDS, fluorescence spectra, and absorbance spectra of the C-dots and the system of C-dots−tartrazine. The Supporting Information is available free of charge on the ACS Publications website at DOI: 10.1021/acs.jafc.5b02319.

■ AUTHOR INFORMATION

Corresponding Authors

*(X.Y.) Phone/fax: +86-817-2568081. E-mail: xiupeiyang@163.com.

*(X.L.) Phone/fax: (613) 415-2098. E-mail: xiangjun.liao@mail.mcgill.ca.

Funding

We thank the Natural Science Foundation of China (21277109) and the Program for Young Scientific and Technological Innovative Research Team in Sichuan Province (2014TD0020) for research grants.

Notes

The authors declare no competing financial interest.

■ ACKNOWLEDGMENTS

We thank Prof. Martin M. F. Choi of the Department of Chemistry, Hong Kong Baptist University, for valuable suggestions and fluorescence spectra study.

■ ABBREVIATIONS USED

C-dots, carbon quantum dots; TEM, transmission electron microscopy; AFM, atomic force microscope; FTIR, Fourier transform infrared spectroscopy; EDS, energy dispersive spectrometry; TLC, thin-layer chromatography; HPLC, high performance liquid chromatograph; fwhm, full width at half-maximum; PB, phosphate buffer; PL, photoluminescent; QY, quantum yield; LOD, limit of detection; RSD, relative standard deviation; GSH, glutathione

■ REFERENCES

(1) Gan, T.; Sun, J. Y.; Cao, S. Q.; Gao, F. X.; Zhang, Y. X.; Yang, Y. Q. One-step electrochemical approach for the preparation of graphene wrapped-phosphotungstic acid hybrid and its application for simultaneous determination of sunset yellow and tartrazine. *Electrochim. Acta* **2012**, *74*, 151−157.

(2) Ye, X. L.; Du, Y. L.; Lu, D. B.; Wang, C. M. Fabrication of beta-cyclodextrin-coated poly (diallyldimethylammonium chloride)-functionalized graphene composite film modified glassy carbon-rotating disk electrode and its application for simultaneous electrochemical determination colorants of sunset yellow and tartrazine. *Anal. Chim. Acta* **2013**, *779*, 22−34.

(3) Amin, K. A.; Hameid, H. A.; Abd Elsttar, A. H. Effect of food azo dyes tartrazine and carmoisine on biochemical parameters related to renal, hepatic function and oxidative stress biomarkers in young male rats. *Food Chem. Toxicol.* **2010**, *48*, 2994−2999.

(4) Tanaka, T. Reproductive and neurobehavioural toxicity study of tartrazine administered to mice in the diet. *Food Chem. Toxicol.* **2006**, *44*, 179−187.

(5) Soponar, F.; Moţ, A. C.; Sărbu, C. Quantitative determination of some food dyes using digital processing of images obtained by thin-layer chromatography. *J. Chromatogr. A* **2008**, *1188*, 295−300.

(6) Song, X. J.; Shi, Z.; Tan, X. H.; Zhang, S. H.; Liu, G. S.; Wu, K. B. One-step solvent exfoliation of graphite to produce a highly-sensitive electrochemical sensor for tartrazine. *Sens. Actuators, B* **2014**, *197*, 104−108.

(7) Sahraei, R.; Farmany, A.; Mortazavi, S. S. A nanosilver-based spectrophotometry method for sensitive determination of tartrazine in food samples. *Food Chem.* **2013**, *138*, 1239−1242.

(8) Culzoni, M. J.; Schenone, A. V.; Llamas, N. E.; Garrido, M.; Di Nezio, M. S.; Fernández Band, B. S.; Goicoechea, H. C. Fast chromatographic method for the determination of dyes in beverages by using high performance liquid chromatography—diode array detection data and second order algorithms. *J. Chromatogr. A* **2009**, *1216*, 7063−7070.

(9) Baker, S. N.; Baker, G. A. Luminescent carbon nanodots: emergent nanolights. *Angew. Chem., Int. Ed.* **2010**, *49*, 6726−6744.

(10) Liu, H. P.; Ye, T.; Mao, C. D. Fluorescent carbon nanoparticles derived from candle soot. *Angew. Chem., Int. Ed.* **2007**, *46*, 6473−6475.

(11) Ding, C. Q.; Zhu, A. W.; Tian, Y. Functional surface engineering of C-dots for fluorescent biosensing and in vivo bioimaging. *Acc. Chem. Res.* **2014**, *47*, 20−30.

(12) Greenshields, M. W. C. C.; Mamo, M. A.; Coville, N. J.; Spina, A. P.; Rosso, D. F.; Latocheski, E. C.; Destro, J. G.; Pimentel, I. C.; Hümmelgen, I. A. Electronic detection of *Drechslera* sp. fungi in charentais melon (*Cucumis melo* Naudin) using carbon-nanostructure-based sensors. *J. Agric. Food Chem.* **2012**, *60*, 10420−10425.

(13) Purkayastha, M. D.; Manhar, A. K.; Das, V. K.; Borah, A.; Mandal, M.; Thakur, A. J.; Mahanta, C. L. Antioxidative, hemocompatible, fluorescent carbon nanodots from an " end-of-pipe" agricultural waste: exploring its new horizon in the food-packaging domain. *J. Agric. Food Chem.* **2014**, *62*, 4509−4520.

DOI: 10.1021/acs.jafc.5b02319
J. Agric. Food Chem. 2015, 63, 6707−6714

(14) Shen, J. H.; Zhu, Y. H.; Yang, X. L.; Li, C. Z. Graphene quantum dots: emergent nanolights for bioimaging, sensors, catalysis and photovoltaic devices. *Chem. Commun.* **2012**, *48*, 3686−3699.
(15) Hu, L. M.; Sun, Y.; Li, S. L.; Wang, X. L.; Hu, K. L.; Wang, L. R.; Liang, X. J.; Wu, Y. Multifunctional carbon dots with high quantum yield for imaging and gene delivery. *Carbon* **2014**, *67*, 508−513.
(16) Xu, X. Y.; Ray, R.; Gu, Y. L.; Ploehn, H. J.; Gearheart, L.; Raker, K.; Scrivens, W. A. Electrophoretic analysis and purification of fluorescent single-walled carbon nanotube fragments. *J. Am. Chem. Soc.* **2004**, *126*, 12736−12737.
(17) Sun, Y. P.; Zhou, B.; Lin, Y.; Wang, W.; Shiral Fernando, K. A.; Pathak, P.; Mohammed, J. M.; Harruff, B. A.; Wang, X.; Wang, H. F.; Luo, P. J. G.; Yang, H.; Kose, M. E.; Chen, B. L.; Veca, L. M.; Xie, S. Y. Quantum-sized carbon dots for bright and colorful photoluminescence. *J. Am. Chem. Soc.* **2006**, *128*, 7756−7757.
(18) Wang, J.; Wang, C. F.; Chen, S. Amphiphilic egg-derived carbon dots: rapid plasma fabrication, pyrolysis process, and multicolor printing patterns. *Angew. Chem., Int. Ed.* **2012**, *51*, 9297−9301.
(19) Zhao, Q. L.; Zhang, Z. L.; Huang, B. H.; Peng, J.; Zhang, M.; Pang, D. W. Facile preparation of low cytotoxicity fluorescent carbon nanocrystals by electrooxidation of graphite. *Chem. Commun.* **2008**, 5116−5118.
(20) Liu, J. M.; Lin, L. P.; Wang, X. X.; Lin, S. Q.; Cai, W. L.; Zhang, L. H.; Zheng, Z. Y. Highly selective and sensitive detection of Cu2+ with lysine enhancing bovine serum albumin modified-carbon dots fluorescent probe. *Analyst* **2012**, *137*, 2637−2642.
(21) Yang, Y. H.; Cui, J. H.; Zheng, M. T.; Hu, C. F.; Tan, S. Z.; Xiao, Y.; Yang, Q.; Liu, Y. L. One-step synthesis of amino-functionalized fluorescent carbon nanoparticles by hydrothermal carbonization of chitosan. *Chem. Commun.* **2012**, *48*, 380−382.
(22) Prasannan, A.; Imae, T. One-pot synthesis of fluorescent carbon dots from orange waste peels. *Ind. Eng. Chem. Res.* **2013**, *52*, 15673−15678.
(23) Hsu, P. C.; Shih, Z. H.; Lee, C. H.; Chang, H. T. Synthesis and analytical applications of photoluminescent carbon nanodots. *Green Chem.* **2012**, *14*, 917−920.
(24) Liu, S.; Tian, J. Q.; Wang, L.; Zhang, Y. W.; Qin, X. Y.; Luo, Y. L.; Asiri, A. M.; Al-Youbi, A. O.; Sun, X. P. Hydrothermal treatment of grass: a low-cost, green route to nitrogen-doped, carbon-rich, photoluminescent polymer nanodots as an effective fluorescent sensing platform for label-free detection of Cu(II) ions. *Adv. Mater.* **2012**, *24*, 2037−2041.
(25) Dai, H. C.; Shi, Y.; Wang, Y. L.; Sun, Y. J.; Hu, J. T.; Ni, P. J.; Li, Z. A carbon dot based biosensor for melamine detection by fluorescence resonance energy transfer. *Sens. Actuators, B* **2014**, *202*, 201−208.
(26) Gan, T.; Sun, J. Y.; Meng, W.; Song, L.; Zhang, Y. X. Electrochemical sensor based on graphene and mesoporous TiO_2 for the simultaneous determination of trace colourants in food. *Food Chem.* **2013**, *141*, 3731−3737.
(27) Yang, X. M.; Zhuo, Y.; Zhu, S. S.; Luo, Y. W.; Feng, Y. J.; Dou, Y. Novel and green synthesis of high-fluorescent carbon dots originated from honey for sensing and imaging. *Biosens. Bioelectron.* **2014**, *60*, 292−298.
(28) Wang, X.; Cao, L.; Yang, S. T.; Lu, F. S.; Meziani, M. J.; Tian, L. L.; Sun, K. W.; Bloodgood, M. A.; Sun, Y. P. Bandgap-like strong fluorescence in functionalized carbon nanoparticles. *Angew. Chem., Int. Ed.* **2010**, *49*, 5310−5314.
(29) Fan, R. J.; Sun, Q.; Zhang, L.; Zhang, Y.; Lu, A. H. Photoluminescent carbon dots directly derived from polyethylene glycol and their application for cellular imaging. *Carbon* **2014**, *71*, 87−93.
(30) Vaibhavkumar, N. M.; Sanjay, J.; Hirakendu, B.; Rakesh, K. S.; Suresh, K. K. One-step hydrothermal approach to fabricate carbon dots from apple juice for imaging of mycobacterium and fungal cells. *Sens. Actuators, B* **2015**, *213*, 434−443.
(31) Vaibhavkumar, N. M.; Sanjay, J.; Rakesh, K. S.; Suresh, K. K. Preparation of multicolor emitting carbon dots for HeLa cell imaging. *New J. Chem.* **2014**, *38*, 6152−6160.
(32) Lu, W. B.; Qin, X. Y.; Liu, S.; Chang, G. H.; Zhang, Y. W.; Luo, Y. L.; Asiri, A. M.; Al-Youbi, A. O.; Sun, X. P. Economical, green synthesis of fluorescent carbon nanoparticles and their use as probes for sensitive and selective detection of mercury(II) ions. *Anal. Chem.* **2012**, *84*, 5351−5357.
(33) Paramaguru, G.; Kathiravan, A.; Selvaraj, S.; Venuvanalingam, P.; Renganathan, R. Interaction of anthraquinone dyes with lysozyme: evidences from spectroscopic and docking studies. *J. Hazard. Mater.* **2010**, *175*, 985−991.
(34) Papadopoulou, A.; Green, R. J.; Frazier, R. A. Interaction of flavonoids with bovine serum albumin: a fluorescence quenching study. *J. Agric. Food Chem.* **2005**, *53*, 158−163.
(35) Li, W. J.; Zhou, X.; Tong, S. S.; Jia, Q. Poly(*N*-isopropylacrylamide-*co*-*N*,*N*′-methylene bisacrylamide) monolithic column embedded with g-alumina nanoparticles microextraction coupled with high-performance liquid chromatography for the determination of synthetic food dyes in soft drink samples. *Talanta* **2013**, *105*, 386−392.
(36) Zhang, Y. Y.; Hu, L. T.; Liu, X.; Liu, B. F.; Wu, K. B. Highly-sensitive and rapid detection of ponceau 4R and tartrazine in drinks using alumina microfibers-based electrochemical sensor. *Food Chem.* **2015**, *166*, 352−357.
(37) Ghoreishi, S. M.; Behpour, M.; Golestaneh, M. Simultaneous determination of Sunset yellow and tartrazine in soft drinks using gold nanoparticles carbon paste electrode. *Food Chem.* **2012**, *132*, 637−641.
(38) Dominguez, F. B.; Diego, F. G.; Mendez, J. H. Determination of sunset yellow and tartrazine by differential pulse polarography. *Talanta* **1990**, *37*, 655−658.
(39) Zhang, W. K.; Liu, T.; Zheng, X. J.; Huang, W. S.; Chidan Wan, C. D. Surface-enhanced oxidation and detection of Sunset Yellow and tartrazine using multi-walled carbon nanotubes film-modified electrode. *Colloids Surf., B* **2009**, *74*, 28−31.
(40) Capitan-Vallvey, L. F.; Fernandez, M. D.; Orbe, I. D.; Avidad, R. Simultaneous determination of the colorants tartrazine, ponceau 4R and sunset yellow FCF in foodstuffs by solid phase spectrophotometry using partial least squares multivariate calibration. *Talanta* **1998**, *47*, 861−868.
(41) Pérez-Urquiza, M.; Beltrán, J. L. Determination of dyes in foodstuffs by capillary zone electrophoresis. *J. Chromatogr. A* **2000**, *898*, 271−275.
(42) Minioti, K. S.; Sakellariou, C. F.; Thomaidis, N. S. Determination of 13 synthetic food colorants in water-soluble foods by reversed-phase high-performance liquid chromatography coupled with diode-array detector. *Anal. Chim. Acta* **2007**, *583*, 103−110.

DOI: 10.1021/acs.jafc.5b02319
J. Agric. Food Chem. 2015, 63, 6707−6714

leaves, has several pharmacological activities, including antioxidant, anti-inflammatory, and antimicrobial activities.[16] As oleuropein exhibits potent antioxidant activity *in vitro*,[17] it is speculated to be the main component responsible for the potentially beneficial effects of olive leaves on various diseases.[18] In fact, previous studies have indicated that oleuropein ameliorates hepatic steatosis,[19] cardiovascular diseases,[20] and neurodegenerative diseases.[21] In addition, hyperglycemia in type 1 diabetes model animals[22] and metabolic abnormalities in high-carbohydrate and high-fat diet rats[20] were partially attenuated by feeding oleuropein-rich extracts. However, it is unknown whether an oleuropein-rich diet is efficacious against type 2 diabetic phenotypes, including chronic hyperglycemia and impaired glucose tolerance.

In the present study, we investigated the effect of the oleuropein-containing supplement OPIACE, an olive leaf extract whose oleuropein content exceeds 35% (w/w), on the diabetic phenotypes in type 2 diabetes model TSOD mice. We found that OPIACE attenuated hyperglycemia and impaired glucose tolerance over the long-term but had no effect on obesity in TSOD mice. Furthermore, we demonstrated that OPIACE mildly reduced oxidative stress in TSOD mice when feeding duration was extended. Interestingly, OPIACE also attenuated anxiety-like behavioral abnormality in aged TSOD mice. Our findings suggest that the oleuropein-rich diet has beneficial effects on the progression of type 2 diabetes and behavioral disorder that is likely related to diabetes.

MATERIALS AND METHODS

Chemicals. 13-Hydroxy-9*Z*,11*E*-octadecadienoic acid [13-(*Z*,*E*)-HODE], 9-hydroxy-10*E*,12*Z*-octadecadienoic acid [9-(*Z*,*E*)-HODE], and 13*S*-hydroxy-10*E*,12*Z*-octadecadienoic-9,10,12,13-d_4 acid (13-HODE-d_4) were obtained from Cayman Chemical Company (MI, USA). 9-Hydroxy-10*E*,12*E*-octadecadienoic acid (9-(*E*,*E*)-HODE) and 13-hydroxy-9*E*,11*E*-octadecadienoic acid (13-(*E*,*E*)-HODE) were purchased from Larodan Fine Chemicals AB (Malmo, Sweden). OPIACE was provided by Eisai Food & Chemical Co., Ltd. (Tokyo, Japan). The nutrient composition in OPIACE was measured by high performance liquid chromatography (HPLC). OPIACE was dissolved in methanol/water (60:40, v/v) and subjected to HPLC analysis. Other materials were of the highest grade commercially available.

Animals. Male TSOD mice and male Tsumura Suzuki Non Obesity (TSNO) (control) were obtained from the Institute for Animal Reproduction (Ibaraki, Japan). The animals were housed individually and had free access to food (CE-2; Clea Japan Inc., Tokyo, Japan) and water. The animal room was maintained at 23 ± 2 °C and 50 ± 10% humidity under a 12 h light (8:00−20:00) and dark (20:00−8:00) cycle. The animals were acclimated to the laboratory environment for at least 1 week before the experiment. TSOD mice were divided into two weight-matched groups (n = 12 each), the control diet group and OPIACE-containing diet group. The OPIACE-containing diet was prepared by mixing the control diet (CE-2) with 0.2% (w/w) OPIACE, and began to feed TSOD mice from 4 weeks of age. The experimental protocols were approved by the Institutional Animal Care and Use Committee of the National Institute of Advanced Industrial Science and Technology.

Measurements of Body Weight, Food Intake, and Biochemical Parameters. Body weight, food intake, and nonfasting blood glucose levels were measured once a week. Nonfasting blood glucose level was measured with the same method as that described previously.[4] For the measurement of plasma triglyceride levels, mice at 5, 8, 11, and 13 weeks of age were sacrificed after fasting for 16 h. Blood was collected from the vena cava and gently mixed with heparin. The obtained plasma samples were stored at −30 °C until use. Plasma triglyceride levels were measured with a LabAssay Triglyceride kit (Wako Pure Chemical Industries, Ltd., Osaka, Japan) according to the manufacturer's instructions. The weight of epididymal white adipose tissue (WAT), a type of visceral fat, in mice was measured at 5, 8, 11, and 13 weeks of age.

Oral Glucose Tolerance Test (OGTT). After fasting for 16 h, glucose solution at the dose of 1.5 g/kg body weight was administered orally with a gavage needle to mice at 5, 8, 11, 13, 15, and 24 weeks of age. For the measurement of blood glucose level, mice were placed in a mouse restrainer, and their tail tips were resected with surgical scissors. Glucose level in effused blood (approximately 1 μL) was measured with a glucose meter (Life Check; EIDIA Co., Ltd., Tokyo, Japan). Measurement of blood glucose levels in the tail was performed at 0 (preadministration), 15, 30, 60, and 120 min after glucose administration. The area under the curve (AUC) after OGTT was calculated using the trapezoidal method.

Analysis of Hydroxyoctadecadienoic Acid by Liquid Chromatography−Mass/Mass Spectrometry (LC-MS/MS). Hydroxyoctadecadienoic acids (HODEs) were measured with a previously described method.[23] Briefly, the mouse plasma sample was mixed with the internal standard, 13-HODE-d_4, and then butylated hydroxytoluene and triphenylphosphine were added to reduce hydroperoxides in the sample. The reduced sample was saponified by adding KOH in methanol. The mixture was acidified with 10% (v/v) acetic acid in water and extracted with chloroform/ethyl acetate (4:1, v/v). The chloroform/ethyl acetate layer was concentrated and divided equally into two portions, and each portion was evaporated to dryness under nitrogen. One portion of the derivatized sample was reconstituted with methanol/water (70:30, v/v) and subjected to LC-MS/MS analysis of HODEs. The precursor, the product ions, and the collision energies were determined after the optimization of MS/MS conditions as follows: m/z = 295.0 and 194.6−195.6 at 21 eV for 13-(*E*,*E*)-HODE; m/z = 295.0 and 170.5−171.5 at 24 eV for 9-(*E*,*E*)-HODE; m/z = 295.0 and 182.6−183.6 at 22 eV for both 10-(*Z*,*E*)-HODE and 12-(*Z*,*E*)-HODE; and m/z = 299.0 and 197.6−198.6 at 15 eV for 13-HODE-d_4. Plasma total hydroxyoctadecadienoic acid (tHODE) levels were determined from the total amount of the products of the free-radical-mediated oxidation of the four isomers: 13-(*Z*,*E*)-HODE, 13-(*E*,*E*)-HODE, 9-(*Z*,*E*)-HODE, and 9-(*E*,*E*)-HODE.

Open Field Test. The open field test was performed according to a modified version of the test described previously.[24] The open field apparatus was constructed by a square box with a black wall (35 × 35 × 20 cm^3). The field was divided two areas: the central and peripheral zones. A central square (15 × 15 cm^2) was set in the middle of the open field, and another square was set in the peripheral area. A mouse was placed in one corner of the field and allowed to explore for 10 min. Locomotor activity (movement distance, line crossing, and movement rate) and anxiety-related parameters (freezing, entry into central area, and latency of entry into central area) were measured with the ANY-maze video tracking system (Brain Science Idea Co., Ltd., Osaka, Japan). The field was cleaned before the start of each session.

Statistics. The results were expressed as the means ± standard error. Outliers were omitted by the Smirnov-Grubbs' outlier test. Statistical analysis was performed by using analysis of variance (ANOVA) followed by Tukey's test for multiple comparisons with Ekuseru-Toukei 2012 (Social Survey Research Information Co., Ltd., Tokyo, Japan). Differences with a probability of 5% or less were considered significant.

RESULTS

Effect of OPIACE on Obesity-Related Parameters in the TSOD Mice. We investigated the effect of OPIACE (the nutrient composition indicated in Table 1) on obesity, which is a major risk factor for the development of type 2 diabetes, in TSOD mice. As shown in Figure 2A and B, body weight and food intake of TSOD mice (black circle) were significantly higher than those of control TSNO mice (white circle) throughout the experiments. However, there were no significant differences in body weight and food intake between

DOI: 10.1021/acs.jafc.5b00556
J. Agric. Food Chem. 2015, 63, 6715−6722

Table 1. Nutrient Composition of OPIACE[a]

nutrient composition	(%)
oleuropein	35
phenolic compounds	7
saccharides	54
ignition residue	2
moisture	2

[a]Phenolic compounds consist of 0.08% caffeic acid, 0.06% vanillic acid, 0.04% vanillin, 0.26% rutin, 1.89% luteolin-7-glucoside, 1.04% apigenin-7-glucoside, and 3.8% oleuroside.

TSOD and OPIACE-fed TSOD (gray triangle) mice (Figure 2A and B). Whereas plasma triglyceride level and epididymal WAT weight, which are related to obesity, were significantly higher in TSOD mice (black bar) than in TSNO mice (white bar), these parameters were not significantly different between TSOD mice and OPIACE-fed TSOD mice (gray bar) (Figure 2C and D). The results indicate that OPIACE has no effect on obesity in TSOD mice.

Effect of OPIACE on Blood Glucose Level in TSOD Mice. Next, we investigated the effect of OPIACE on the diabetic phenotypes in TSOD mice. As shown in Figure 3, nonfasting blood glucose levels in TSOD mice (black circle) gradually increased with age, and a significant increase was noted from 6 weeks of age compared with that of age-matched TSNO mice (white circle). Whereas nonfasting blood glucose levels in OPIACE-fed TSOD mice (gray triangle) were comparable to those in TSOD mice until 9 weeks of age,

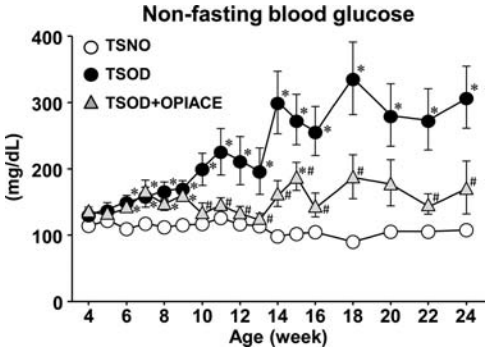

Figure 3. Effect of OPIACE on blood glucose level. Time course of changes in nonfasting blood glucose level in TSNO (white circle), TSOD (black circle), and 0.2% (w/w) OPIACE-fed TSOD (gray triangle) mice. Results are expressed as the means ± standard error (n = 11−12). Statistical analyses were carried out using ANOVA (Tukey's *posthoc* test). *Significant difference from age-matched TSNO mice (p < 0.05). #Significant difference from age-matched TSOD mice (p < 0.05).

glucose levels in the OPIACE-fed TSOD mice were significantly lower than those in the TSOD mice up to 24 weeks of age (Figure 3). The results indicate that OPIACE partially attenuates blood glucose elevation in TSOD mice over the long-term.

Effect of OPIACE on Glucose Tolerance in TSOD Mice. To evaluate the effect of OPIACE on glucose tolerance, we performed OGTT in TSOD mice at 5, 8, 11, 13, 15, and 24

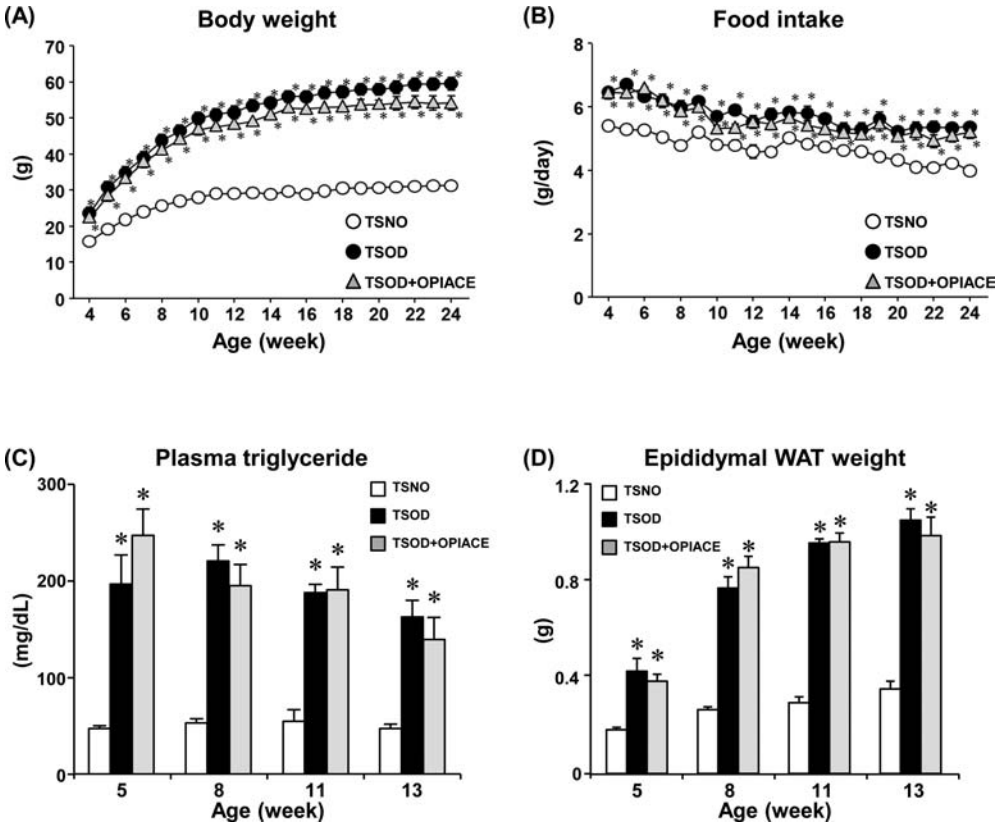

Figure 2. Effects of OPIACE on obesity-related parameters. Time course of changes in body weight (A), food intake (B), plasma triglyceride level (C), and epididymal WAT weight (D) in TSNO (white), TSOD (black), and 0.2% (w/w) OPIACE-fed TSOD (gray) mice. Results are expressed as the means ± standard error (n = 6−12). Statistical analyses were carried out using ANOVA (Tukey's *posthoc* test). *Significant difference from age-matched TSNO mice (p < 0.05).

DOI: 10.1021/acs.jafc.5b00556
J. Agric. Food Chem. 2015, 63, 6715−6722

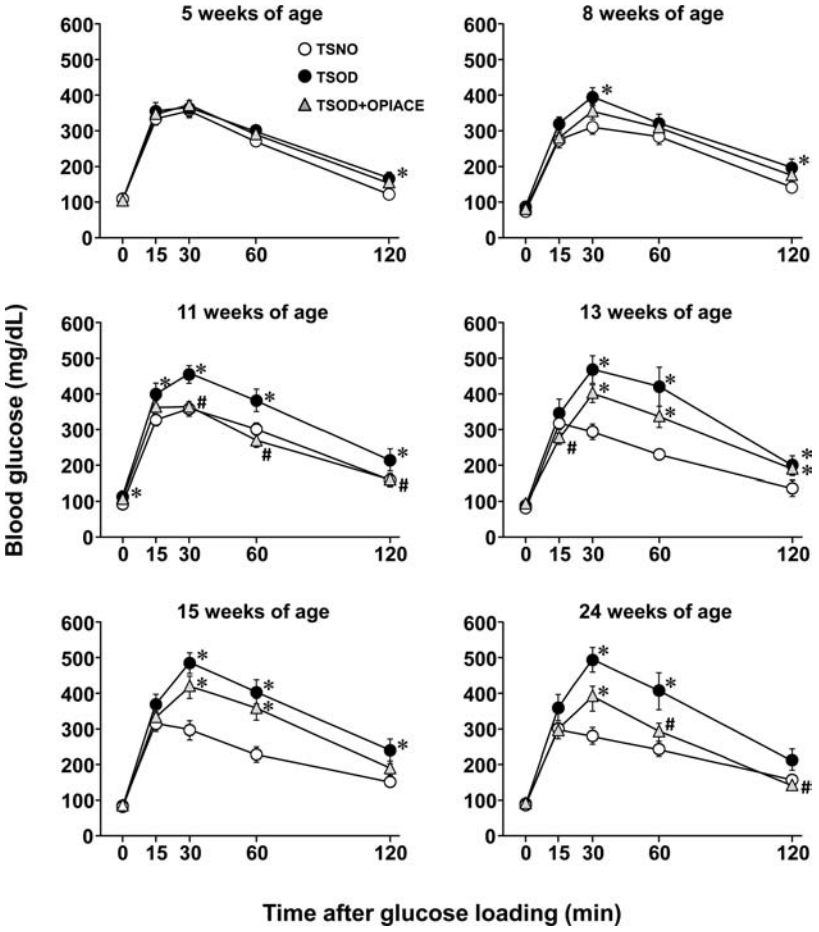

Figure 4. Effect of OPIACE on glucose tolerance. Time course of changes in glucose tolerance in TSNO (white circle), TSOD (black circle), and 0.2% (w/w) OPIACE-fed TSOD (gray triangle) mice at 5, 8, 11, 13, 15, and 24 weeks of age. Results are expressed as the means ± standard error (n = 11−12). Statistical analyses were carried out using ANOVA (Tukey's *posthoc* test). *Significant difference from age-matched TSNO mice (p < 0.05). #Significant difference from age-matched TSOD mice (p < 0.05).

weeks of age. At 5 weeks of age, there was no obvious abnormality in glucose tolerance of TSOD mice (black circle) compared with that of age-matched TSNO mice (white circle) (Figure 4). However, glucose levels after glucose loading in TSOD mice increased with age, and a significant increase was noted from 8 weeks of age compared with that of age-matched TSNO mice (Figure 4), indicating that glucose tolerance in TSOD mice was impaired from around 8 weeks of age, consistent with our previous report.[25] Glucose tolerance in TSOD mice was markedly impaired after 11 weeks of age. However, the impaired glucose tolerance in TSOD mice at 11 and 24 weeks of age was almost completely attenuated by OPIACE (gray triangle). Glucose levels after glucose loading in OPIACE-fed TSOD mice at 13 and 15 weeks of age tended to be lower than those of age-matched TSOD mice, although there were no significant differences between those glucose levels (Figure 4). Those findings indicate that the impaired glucose tolerance in TSOD mice is partially inhibited by OPIACE.

Effect of OPIACE on Oxidative Stress in TSOD Mice. It is known that oxidative stress induces insulin resistance that in turn leads to the progression of type 2 diabetes.[5] To investigate the effect of OPIACE on oxidative stress *in vivo*, we examined plasma levels of tHODE, which has been used as a biomarker for the evaluation of oxidative stress,[23] in TSNO and TSOD mice. tHODE were determined from the total amount of the four isomers: 13-(*Z*,*E*)-HODE, 13-(*E*,*E*)-HODE, 9-(*Z*,*E*)-HODE, and 9-(*E*,*E*)-HODE, which were measured with LC-MS/MS as reported previously[23](Figure 5A; also see Materials and Methods). As shown in Figure 5B, plasma tHODE levels in TSOD mice (black bar) were significantly higher than those in TSNO mice (white bar), consistent with our previous report,[4] and the levels were maintained during the measurements. Plasma tHODE levels in OPIACE-fed TSOD mice (gray bar) tended to decrease with feeding duration and significantly decreased at 13 weeks of age compared with those in TSOD mice. The results indicate that OPIACE mildly attenuates oxidative stress in TSOD mice by long-term feeding.

Effect of OPIACE on Locomotor Activity and Anxiety-Like Behavior in TSOD Mice. It has been reported that locomotor activity is reduced in type 2 diabetes model animals, including the db/db mouse,[24] Akita mouse,[26] and high-fat fed rat.[27] The behavioral abnormality is more clearly observed in older animals with diabetes than younger animals.[24,27] In addition, repeated hyperglycemia was found to reduce locomotor activity in an open field test,[28] which is used to assess general locomotor activity and as an initial screen for anxiety-related behavior in rodents.[29] To investigate the long-term effects of OPIACE on the behavioral traits of TSOD mice, we performed an open field test in TSOD mice at 36 weeks of age (Figure 6). We found that the differences in body weight and food intake between TSNO and TSOD mice remained

DOI: 10.1021/acs.jafc.5b00556
J. Agric. Food Chem. 2015, 63, 6715−6722

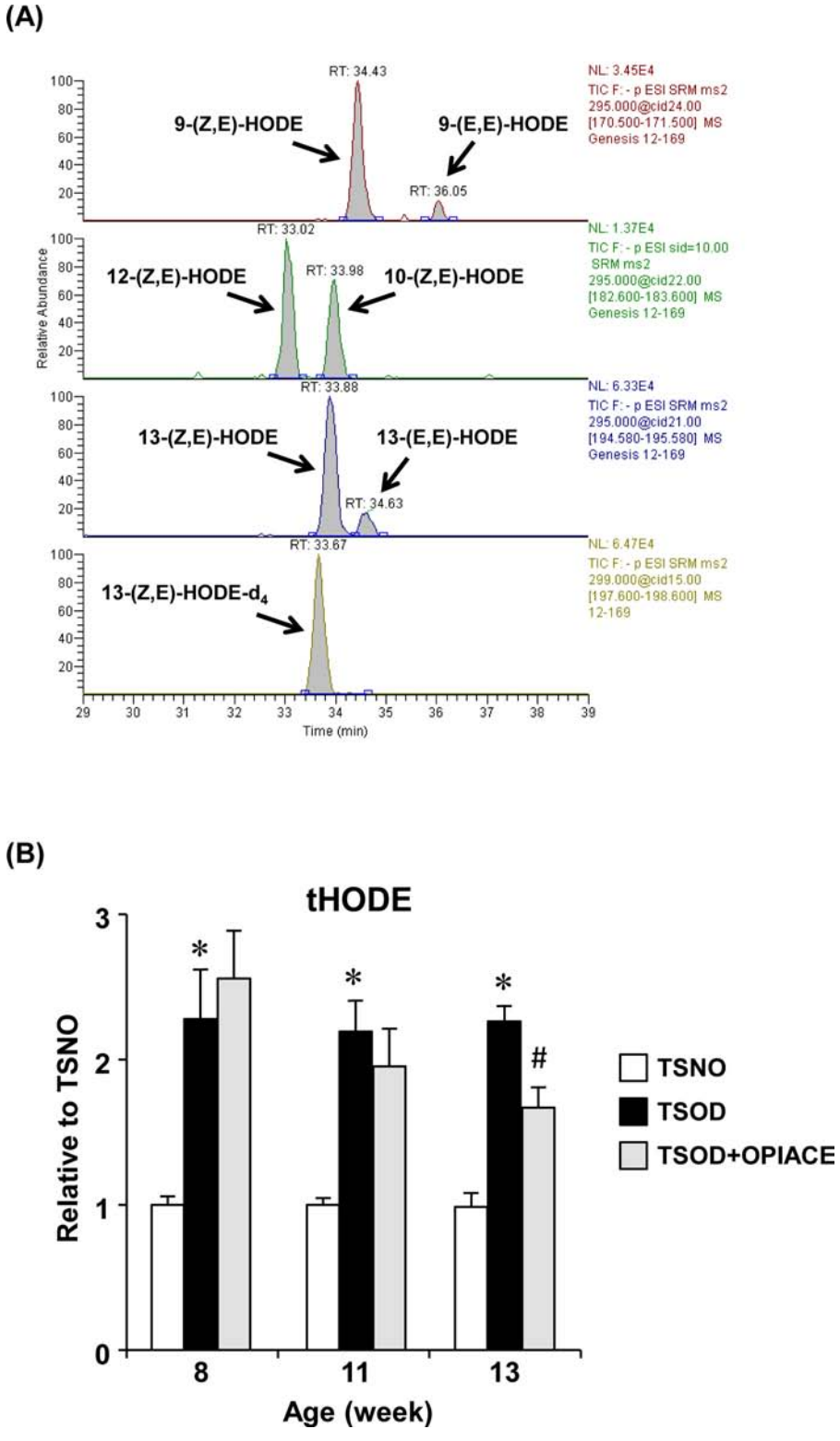

Figure 5. Effects of OPIACE on plasma levels of lipid oxidation products. (A) Typical chromatograms obtained from LC-MS/MS of mouse plasma samples measured in this study. (B) Time course of changes in the plasma levels of lipid oxidation products in TSNO (white bar), TSOD (black bar), and 0.2% (w/w) OPIACE-fed TSOD (gray bar) mice. Values in age-matched TSNO mice are set to 1. Results are expressed as the means ± standard error (n = 4–6). Statistical analyses were carried out using ANOVA (Tukey's *posthoc* test). *Significant difference from age-matched TSNO mice ($p < 0.05$). #Significant difference from age-matched TSOD mice ($p < 0.05$).

unchanged at 36 weeks of age (body weights of TSNO and TSOD mice were 37.8 ± 0.88 and 64.6 ± 1.24 g, respectively; food intake in TSNO and TSOD mice was 3.42 ± 0.13 and 4.64 ± 0.18 g/day, respectively) and that there were no significant differences in nonfasting blood glucose level and glucose tolerance between TSNO and TSOD mice (nonfasting blood glucose levels in TSNO and TSOD mice were 120 ± 0.85 and 136 ± 9.45 mg/dL, respectively; OGTT AUCs in

DOI: 10.1021/acs.jafc.5b00556
J. Agric. Food Chem. 2015, 63, 6715–6722

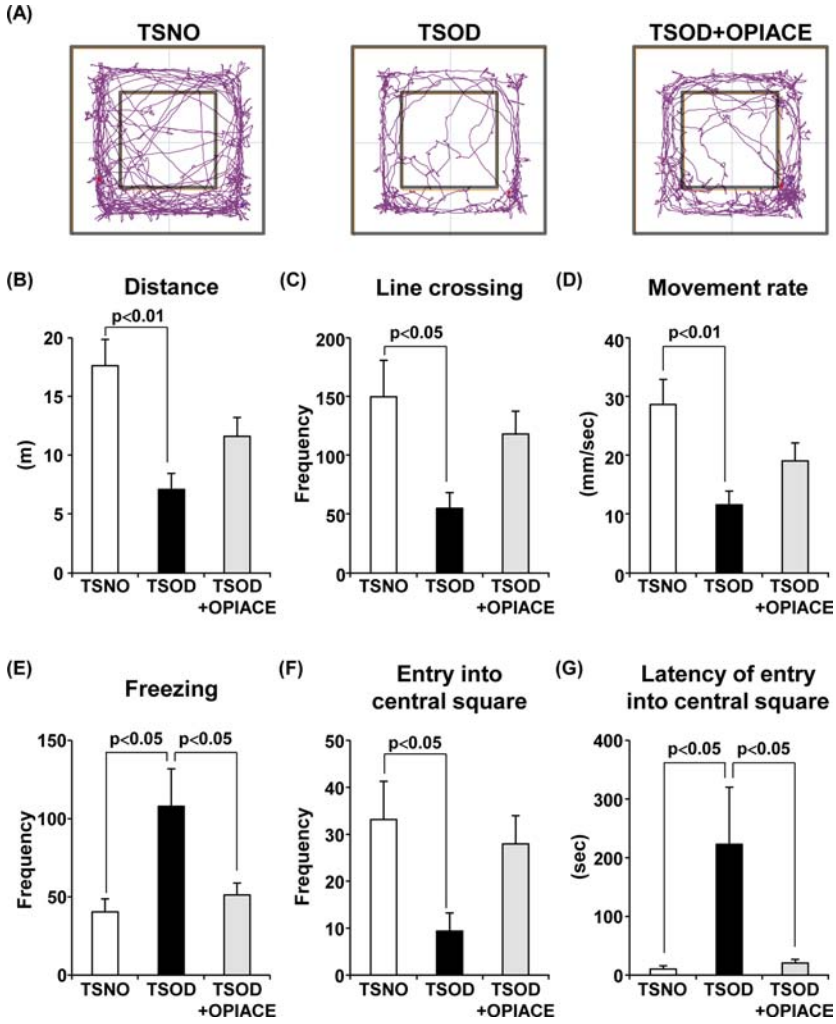

Figure 6. Effect of OPIACE on locomotor activity and anxiety-like behavior. (A) Representative trajectories of TSNO, TSOD, and 0.2% (w/w) OPIACE-fed TSOD mice in the open field test. Movement distance (B), line crossing (C), movement rate (D), freezing (E), entry into the central square (F), and latency of entry into the central square (G) were measured for 10 min. Results are expressed as the means ± standard error (n = 6 each). Statistical analyses were carried out using ANOVA (Tukey's *posthoc* test).

TSNO and TSOD mice were 2.53 ± 0.09 and 3.08 ± 0.71 arbitrary units, respectively) (Table 2), as observed in other diabetic model ob/ob mice of a similar age.[30] Movement distance (Figure 6B), line crossing (Figure 6C), and movement rate (Figure 6D) were significantly decreased in TSOD mice (black bar) compared with those in TSNO mice (white bar), indicating that TSOD mice have low locomotor activity.

Table 2. Body Weight, Food Intake, Nonfasting Blood Glucose Level, and OGTT AUC in TSNO, TSOD, and OPIACE-Fed TSOD Mice at 36 Weeks of Age[a]

	TSNO	TSOD	TSOD + OPIACE
body weight (g)	37.8 ± 0.88	64.6 ± 1.24[b]	65.2 ± 0.68[b]
food intake (g/day)	3.42 ± 0.13	4.64 ± 0.18[b]	5.19 ± 0.20[b]
nonfasting blood glucose (mg/dL)	120 ± 0.85	136 ± 9.45	152 ± 32.5
OGTT AUC (× 10^4, arbitrary unit)	2.53 ± 0.09	3.08 ± 0.71	2.69 ± 0.42

[a]Results are expressed as the means ± standard error (n = 6 each). Statistical analyses were carried out using ANOVA (Tukey's *posthoc* test). [b]Significant difference from age-matched TSNO mice ($p < 0.05$).

OPIACE-fed TSOD mice (gray bar) tended to attenuate the decreases in locomotor activity compared with that of TSOD mice (Figure 6B–D), although there were no significant differences in the results. TSOD mice showed increased freezing (Figure 6E), decreased frequency of entry into the central square (Figure 6F), and longer latency of entry into the central square (Figure 6G) compared with those of TSNO mice, indicating that TSOD mice have anxiety-like phenotypes. Interestingly, the anxiety-like phenotypes in free-fed TSOD mice were significantly attenuated by the feeding of OPIACE (Figure 6E and G). Thus, long-term feeding of OPIACE has a preventive effect on the anxiety-like symptoms in the type 2 diabetes model mouse.

DISCUSSION

Our results indicated that OPIACE attenuated chronic hyperglycemia (Figure 3) and impaired glucose tolerance (Figure 4) in TSOD mice. Those effects are likely to be due to oleuropein because it is the major component in OPIACE (Table 1). It has been demonstrated that an oleuropein-containing diet improved insulin sensitivity in middle-aged overweight men[31] and decreased homeostasis model assessment as an index of insulin resistance (HOMA-IR) in high-fat

DOI: 10.1021/acs.jafc.5b00556
J. Agric. Food Chem. 2015, 63, 6715–6722

diet fed mice.[32] In addition, plasma insulin levels were unchanged between TSOD mice and OPIACE-fed TSOD mice from 5 to 13 weeks of age (data not shown). These findings suggest that the improvement effects of OPIACE on blood glucose level are due to not the acceleration of insulin secretion but the improvement of insulin resistance.

As oleuropein has potent antioxidative activity *in vitro*,[17] we expected that the preventive effects of an oleuropein-rich diet on blood glucose elevation in TSOD mice would be partly due to the antioxidative capacity of oleuropein. However, OPIACE did not clearly reduce plasma tHODE levels in TSOD mice even at 11 weeks of age, which is the age when OPIACE exerted a preventive effect on the diabetic phenotypes (Figure 5B). Furthermore, OPIACE had no effect on obesity in TSOD mice (Figure 2). It was reported that potent antioxidants resveratrol[33] and epigallocatechin-3[34] suppressed high-fat diet induced obesity and hyperglycemia. In addition, in a previous DNA microarray analysis, oleuropein was found to have beneficial effects on nonalcoholic fatty liver disease by exerting multiple effects, including antilipogenesis, anti-inflammation, and anti-insulin resistance,[35] and the multiple effects of oleuropein are likely to contribute to the improvement of the diabetic phenotypes. Therefore, our results suggest that an oleuropein-rich diet exerts not only a mild antioxidant effect but also other effects for the attenuation of the increased glucose levels in TSOD mice.

A recent meta-analysis indicated that diabetes is associated with the increased possibility of having anxiety disorders.[36] In fact, our results indicated that TSOD mice exhibited anxiety-like behavior (Figure 6) consistent with other diabetic models, including the ob/ob mouse,[37] Akita mouse,[26] and high-fat fed mouse.[38] Some reports suggest that this central nervous system disorder is a kind of diabetic complication.[9] It is easily presumed that the comorbidity of diabetes and anxiety disorder may lead to a lower quality of life than the morbidity of those diseases separately.[39] In addition, it was recently suggested that the treatment of anxiety disorder may exacerbate the symptoms of diabetes, as selective serotonin reuptake inhibitors, which are used for the treatment of mood and anxiety disorders, promote insulin resistance and insulin secretion in Min6 cells.[40] Thus, as shown in Figure 6, our results suggested that OPIACE may be a valuable supplement for reducing diabetes-related anxiety, although the mechanism for attenuating the anxiety-like behavior in TSOD mice is unknown. Blood glucose levels in TSOD mice and OPIACE-fed TSOD mice at 36 weeks of age were not significantly increased compared with those in TSNO mice, probably because food intake in TSOD mice tended to decrease with age (Table 2). The improvement of blood glucose levels in TSOD mice over the long-term might contribute to the antianxiety effect of OPIACE.

In conclusion, we demonstrated that OPIACE attenuated chronic hyperglycemia and impaired glucose tolerance in TSOD mice over the long-term. Furthermore, OPIACE attenuated the anxiety-like behavior in aged TSOD mice. Our results suggest that an oleuropein-rich diet has the potential to inhibit the progression of type 2 diabetes and diabetes-related behavioral disorders.

AUTHOR INFORMATION

Corresponding Author

*Tel: +81-87-869-4207. Fax: +81-87-869-4178. E-mail: k-murotomi@aist.go.jp.

Funding

This work was supported by a Grant-in-Aid for Young Scientist (B) (Grant Number 25860183) to K.M. from the Japan Society for the Promotion of Science (JSPS) and by a donation from Eisai Food and Chemical Co., Ltd. to Y.N.

Notes

The authors declare no competing financial interest.

ACKNOWLEDGMENTS

We thank Y. Fujita of AIST for technical assistance; Y. Senba of JAC Co., Ltd. for supporting animal care; and Dr. W. Suzuki of Tsumura Co., Ltd., and Dr. K. Ohwada of AIST for valuable suggestions and discussion.

ABBREVIATIONS USED

OPIACE, olive leaf extract with more than 35% (w/w) oleuropein content; TSOD, Tsumura Suzuki obese diabetes; TSNO, Tsumura Suzuki nonobesity; WAT, white adipose tissue; OGTT, oral glucose tolerance test; AUC, area under the curve; HPLC, high performance liquid chromatography; HODE, hydroxyoctadecadienoic acid; LC-MS/MS, liquid chromatography−mass/mass spectrometry; ANOVA, analysis of variance

REFERENCES

(1) Lin, Y.; Sun, Z. Current views on type 2 diabetes. *J. Endocrinol.* **2010**, *204*, 1−11.

(2) Matsuzawa-Nagata, N.; Takamura, T.; Ando, H.; Nakamura, S.; Kurita, S.; Misu, H.; Ota, T.; Yokoyama, M.; Honda, M.; Miyamoto, K.; Kaneko, S. Increased oxidative stress precedes the onset of high-fat diet-induced insulin resistance and obesity. *Metab., Clin. Exp.* **2008**, *57*, 1071−1077.

(3) Suzuki, W.; Iizuka, S.; Tabuchi, M.; Funo, S.; Yanagisawa, T.; Kimura, M.; Sato, T.; Endo, T.; Kawamura, H. A new mouse model of spontaneous diabetes derived from ddY strain. *Exp. Anim.* **1999**, *48*, 181−189.

(4) Murotomi, K.; Umeno, A.; Yasunaga, M.; Shichiri, M.; Ishida, N.; Abe, H.; Yoshida, Y.; Nakajima, Y. Type 2 diabetes model TSOD mouse is exposed to oxidative stress at young age. *J. Clin. Biochem. Nutr.* **2014**, *55*, 216−220.

(5) Evans, J. L.; Goldfine, I. D.; Maddux, B. A.; Grodsky, G. M. Are oxidative stress-activated signaling pathways mediators of insulin resistance and beta-cell dysfunction? *Diabetes* **2003**, *52*, 1−8.

(6) Krentz, A. J.; Clough, G.; Byrne, C. D. Interactions between microvascular and macrovascular disease in diabetes: pathophysiology and therapeutic implications. *Diabetes, Obes. Metab.* **2007**, *9*, 781−791.

(7) De Felice, F. G.; Ferreira, S. T. Inflammation, defective insulin signaling, and mitochondrial dysfunction as common molecular denominators connecting type 2 diabetes to Alzheimer disease. *Diabetes* **2014**, *63*, 2262−2272.

(8) Santiago, J. A.; Potashkin, J. A. System-based approaches to decode the molecular links in Parkinson's disease and diabetes. *Neurobiol. Dis.* **2014**, *72*, 84−91.

(9) Siddiqui, S. Depression in type 2 diabetes mellitus–a brief review. *Diabetes Metab. Syndr.* **2014**, *8*, 62−65.

(10) Collins, M. M.; Corcoran, P.; Perry, I. J. Anxiety and depression symptoms in patients with diabetes. *Diabetic Med.* **2009**, *26*, 153−161.

(11) The Diabetes Control and Complications Trial Research Group. The effect of intensive treatment of diabetes on the development and progression of long-term complications in insulin-dependent diabetes mellitus. *N. Engl. J. Med.* **1993**, *329*, 977−986.

(12) Geijselaers, S. L.; Sep, S. J.; Stehouwer, C. D.; Biessels, G. J. Glucose regulation, cognition, and brain MRI in type 2 diabetes: a systematic review. *Lancet Diabetes Endocrinol.* **2015**, *3*, 75−89.

(13) Wu, S. B.; Yue, G. G.; To, M. H.; Keller, A. C.; Lau, C. B.; Kennelly, E. J. Transport in Caco-2 cell monolayers of antidiabetic

DOI: 10.1021/acs.jafc.5b00556
J. Agric. Food Chem. 2015, 63, 6715−6722

cucurbitane triterpenoids from Momordica charantia fruits. *Planta Med.* **2014**, *80*, 907−911.
(14) Bhathena, S. J.; Velasquez, M. T. Beneficial role of dietary phytoestrogens in obesity and diabetes. *Am. J. Clin. Nutr.* **2002**, *76*, 1191−1201.
(15) Servili, M.; Sordini, B.; Esposto, S.; Urbani, S.; Veneziani, G.; Maio, I. D.; Selvaggini, R.; Taticchi, A. Biological Activities of Phenolic Compounds of Extra Virgin Olive Oil. *Antioxidants* **2014**, *3*, 1−23.
(16) Omar, S. H. Oleuropein in olive and its pharmacological effects. *Sci. Pharm.* **2010**, *78*, 133−154.
(17) Lee, O. H.; Lee, B. Y.; Lee, J.; Lee, H. B.; Son, J. Y.; Park, C. S.; Shetty, K.; Kim, Y. C. Assessment of phenolics-enriched extract and fractions of olive leaves and their antioxidant activities. *Bioresour. Technol.* **2009**, *100*, 6107−6113.
(18) El, S. N.; Karakaya, S. Olive tree (Olea europaea) leaves: potential beneficial effects on human health. *Nutr. Rev.* **2009**, *67*, 632−638.
(19) Park, S.; Choi, Y.; Um, S. J.; Yoon, S. K.; Park, T. Oleuropein attenuates hepatic steatosis induced by high-fat diet in mice. *J. Hepatol.* **2011**, *54*, 984−993.
(20) Poudyal, H.; Campbell, F.; Brown, L. Olive leaf extract attenuates cardiac, hepatic, and metabolic changes in high carbohydrate-, high fat-fed rats. *J. Nutr.* **2010**, *140*, 946−953.
(21) Grossi, C.; Rigacci, S.; Ambrosini, S.; Dami, T. E.; Luccarini, I.; Traini, C.; Failli, P.; Berti, A.; Casamenti, F.; Stefani, M. The polyphenol oleuropein aglycone protects TgCRND8 mice against Ass plaque pathology. *PLoS One* **2013**, *8*, e71702.
(22) Jemai, H.; El Feki, A.; Sayadi, S. Antidiabetic and antioxidant effects of hydroxytyrosol and oleuropein from olive leaves in alloxan-diabetic rats. *J. Agric. Food Chem.* **2009**, *57*, 8798−8804.
(23) Yoshida, Y.; Kodai, S.; Takemura, S.; Minamiyama, Y.; Niki, E. Simultaneous measurement of F2-isoprostane, hydroxyoctadecadienoic acid, hydroxyeicosatetraenoic acid, and hydroxycholesterols from physiological samples. *Anal. Biochem.* **2008**, *379*, 105−115.
(24) Sharma, A. N.; Elased, K. M.; Garrett, T. L.; Lucot, J. B. Neurobehavioral deficits in db/db diabetic mice. *Physiol. Behav.* **2010**, *101*, 381−388.
(25) Murotomi, K.; Umeno, A.; Yasunaga, M.; Shichiri, M.; Ishida, N.; Abe, H.; Yoshida, Y.; Nakajima, Y. Switching from singlet-oxygen-mediated oxidation to free-radical-mediated oxidation in the pathogenesis of type 2 diabetes in model mouse. *Free Radical Res.* **2014**, *49*, 133.
(26) Maher, P.; Dargusch, R.; Ehren, J. L.; Okada, S.; Sharma, K.; Schubert, D. Fisetin lowers methylglyoxal dependent protein glycation and limits the complications of diabetes. *PLoS One* **2011**, *6*, e21226.
(27) Erdos, B.; Kirichenko, N.; Whidden, M.; Basgut, B.; Woods, M.; Cudykier, I.; Tawil, R.; Scarpace, P. J.; Tumer, N. Effect of age on high-fat diet-induced hypertension. *Am. J. Physiol. Heart Circ. Physiol.* **2011**, *301*, H164−172.
(28) Moghadami, M.; Moghimi, A.; Ahangar, E.; Jalal, R.; Rassouli, M. B.; Shahri, N. M. Effects of infantile repeated hyperglycemia on behavioral alterations in adult male and female rats. *Basic. Clin. Neurosci.* **2012**, *3*, 60−67.
(29) Prut, L.; Belzung, C. The open field as a paradigm to measure the effects of drugs on anxiety-like behaviors: a review. *Eur. J. Pharmacol.* **2003**, *463*, 3−33.
(30) Genuth, S. M.; Przybylski, R. J.; Rosenberg, D. M. Insulin resistance in genetically obese, hyperglycemic mice. *Endocrinology* **1971**, *88*, 1230−1238.
(31) de Bock, M.; Derraik, J. G.; Brennan, C. M.; Biggs, J. B.; Morgan, P. E.; Hodgkinson, S. C.; Hofman, P. L.; Cutfield, W. S. Olive (Olea europaea L.) leaf polyphenols improve insulin sensitivity in middle-aged overweight men: a randomized, placebo-controlled, crossover trial. *PLoS One* **2013**, *8*, e57622.
(32) Kim, S. W.; Hur, W.; Li, T. Z.; Lee, Y. K.; Choi, J. E.; Hong, S. W.; Lyoo, K. S.; You, C. R.; Jung, E. S.; Jung, C. K.; Park, T.; Um, S. J.; Yoon, S. K. Oleuropein prevents the progression of steatohepatitis to hepatic fibrosis induced by a high-fat diet in mice. *Exp. Mol. Med.* **2014**, *46*, e92.
(33) Kim, S.; Jin, Y.; Choi, Y.; Park, T. Resveratrol exerts anti-obesity effects via mechanisms involving down-regulation of adipogenic and inflammatory processes in mice. *Biochem. Pharmacol.* **2011**, *81*, 1343−1351.
(34) Bose, M.; Lambert, J. D.; Ju, J.; Reuhl, K. R.; Shapses, S. A.; Yang, C. S. The major green tea polyphenol, (−)-epigallocatechin-3-gallate, inhibits obesity, metabolic syndrome, and fatty liver disease in high-fat-fed mice. *J. Nutr.* **2008**, *138*, 1677−1683.
(35) Kim, Y.; Choi, Y.; Park, T. Hepatoprotective effect of oleuropein in mice: mechanisms uncovered by gene expression profiling. *Biotechnol. J.* **2010**, *5*, 950−960.
(36) Smith, K. J.; Beland, M.; Clyde, M.; Gariepy, G.; Page, V.; Badawi, G.; Rabasa-Lhoret, R.; Schmitz, N. Association of diabetes with anxiety: a systematic review and meta-analysis. *J. Psychosom. Res.* **2013**, *74*, 89−99.
(37) Asakawa, A.; Inui, A.; Inui, T.; Katsuura, G.; Fujino, M. A.; Kasuga, M. Leptin treatment ameliorates anxiety in ob/ob obese mice. *J. Diabetes Complications* **2003**, *17*, 105−107.
(38) Kaczmarczyk, M. M.; Machaj, A. S.; Chiu, G. S.; Lawson, M. A.; Gainey, S. J.; York, J. M.; Meling, D. D.; Martin, S. A.; Kwakwa, K. A.; Newman, A. F.; Woods, J. A.; Kelley, K. W.; Wang, Y.; Miller, M. J.; Freund, G. G. Methylphenidate prevents high-fat diet (HFD)-induced learning/memory impairment in juvenile mice. *Psychoneuroendocrinology* **2013**, *38*, 1553−1564.
(39) Santos, M. A.; Ceretta, L. B.; Reus, G. Z.; Abelaira, H. M.; Jornada, L. K.; Schwalm, M. T.; Neotti, M. V.; Tomazzi, C. D.; Gulbis, K. G.; Ceretta, R. A.; Quevedo, J. Anxiety disorders are associated with quality of life impairment in patients with insulin-dependent type 2 diabetes: a case-control study. *Rev. Bras. Psiquiatr.* **2014**, *36*, 298−304.
(40) Isaac, R.; Boura-Halfon, S.; Gurevitch, D.; Shainskaya, A.; Levkovitz, Y.; Zick, Y. Selective serotonin reuptake inhibitors (SSRIs) inhibit insulin secretion and action in pancreatic beta cells. *J. Biol. Chem.* **2013**, *288*, 5682−5693.

DOI: 10.1021/acs.jafc.5b00556
J. Agric. Food Chem. 2015, 63, 6715−6722

The formation of these lysine derivatives ("lysine blockage") implicates a decrease of the nutritional value of proteins.[12,13] Moreover, the accessibility by intestinal peptidases is impaired; thus, the release also of other proteinogenic amino acids into absorbable units is hampered.[14,15] However, at levels of lysine modification that are relevant in food (8−15%), the digestibility of casein is not significantly lowered.[16,17] Individual Maillard reaction products (MRPs) can be released from glycated proteins as small peptides and free amino acids, similarly to the proteinogenic amino acids,[16,17] but they cannot be transported across the intestinal membrane via amino acid carriers. Bound in small peptides, some MRPs can be translocated into epithelial cells via the di- and tripeptide transporter PEPT1. After intracellular peptidolysis, glycated amino acids with polar or charged side chains (e.g., CML) are "trapped" inside the cells, whereas those with unpolar side chains (e.g., PYR and MAL) can pass the basolateral membrane.[18−20] It has been shown in several human studies that dietary FL can pass into the circulation only to a very small extent, whereas 50−100% of dietary PYR must be absorbed as it appears in the urine after oral administration.[7,21,22]

Unabsorbed amino acids and peptides, as well as intracellularly accumulated amino acids released during desquamation, will pass into the colon. A passage of approximately 13 g per day of protein (endogenous protein from intestinal peptidases and mucins, as well as recalcitrant dietary protein) has been estimated.[23] The distal colonic microbiota can degrade large peptides and proteins, and all proteinogenic amino acids can then be fermented by anaerobic bacteria.[24] The predominant products are ammonia, carbon dioxide, hydrogen, and short-chain fatty acids (SCFA; acetic, propionic, and butyric acids). Branched-chain amino acids are degraded to branched-chain fatty acids (e.g., isobutyrate, isovalerate, and 2-methylbutyrate), which can serve as urinary markers of colonic protein fermentation. Products such as phenol, cresol, indole, and substituted acetic and propionic acids mainly result from the fermentation of aromatic amino acids. Due to the toxicological properties of some of these products, protein fermentation in the colon is often regarded as detrimental.[24,23,25] Glycated proteins passing into the colon can have specific effects on the composition of the colonic microbiota: On incubation with glycated bovine serum albumin, the amount of clostridia, sulfate-reducing bacteria, and *Bacteroides* in the microbiota from humans suffering from ulcerative colitis, but not that from healthy subjects, increased, whereas the amount of eubacteria and bifidobacteria decreased.[26] An inhibitory effect on the growth of lactobacilli was also found in the colonic microbiota of adolescents consuming a diet rich in MRPs (bread with crust, grilled meat), compared to a diet low in MRPs (bread without crust, baked meat).[27] Protein glycated with different sugars (galactose, lactulose, and galacto-oligosaccharides), however, can induce a bifidogenic effect on the human microbiota in vitro.[28,29] The structural basis of these findings remains unclear. In particular, the stability of individual MRPs in the colon has been only poorly investigated.

FL is the only MRP that was found to be unstable in the presence of rat and human intestinal microbiota in vitro and in vivo.[7,21,30] Several enzymatic degradation mechanisms have been described.[31,32] It has also been postulated that CML is degraded by the human colonic microbiota, because the recovery of the substance in urine and feces after oral administration never reaches 100%, either in human or in rat studies.[33,34]

As the human colonic microbiota has the ability to metabolize all proteinogenic amino acids,[24] and because it is continuously exposed to substantial amounts of unabsorbed dietary MRPs, we hypothesized that the human colonic microbiota is able to degrade MRPs. Four individual MRPs were synthesized and incubated in the presence of fecal suspensions from eight human volunteers. The stability of the MRPs was measured by HPLC with UV or MS/MS detection.

MATERIALS AND METHODS

Chemicals. Nonafluoropentanoic acid (NFPA), resazurin sodium salt, and cysteine hydrochloride monohydrate were from Sigma (Steinheim, Germany). Acetic acid for HPLC was obtained from Merck (Darmstadt, Germany). HPLC grade methanol and acetonitrile were from VWR Prolabo (Darmstadt, Germany). [$^2H_2$]CML was obtained from PolyPeptide (Strasbourg, France). The synthesis of the following MRPs was performed according to the literature stated: FL,[35] [$^{13}C_6$,$^{15}N_2$]FL,[36] CML,[20] PYR,[18] and MAL.[19]

Brain−heart infusion (BHI) medium was used for anaerobic cultivation and prepared as follows: 18.5 g of brain−heart infusion broth (Merck) and 0.28 g of cysteine hydrochloride monohydrate were dissolved in distilled water, and 50 μL of an aqueous resazurin solution (1%, w/v) was added. The pH was adjusted to 7.6 with 5 M sodium hydroxide, and water was added to a final volume of 500 mL. The required volume of medium was filled into Hungate tubes. The filled Hungate tubes were subjected to three cycles of first vacuum and then N_2 overpressure application to remove oxygen. The media were autoclaved (121 °C, 15 min). The medium needed for the preparation of fecal suspensions was allowed to equilibrate overnight under oxygen-free conditions in an anaerobic workstation (MG 500, Don Whitley, Shipley, UK).

Incubation of MRPs in the Presence or Absence of Human Fecal Inocula. Feces samples were obtained from eight healthy volunteers (6 males, 2 females) aged between 25 and 55 years who consumed a Western diet (no vegetarians). The volunteers had not taken antibiotics in the previous 3 months. One experiment with a feces sample from one volunteer was performed per week.

The preparation of fecal suspensions was performed as described previously[37] in an anaerobic workstation under an atmosphere consisting of $N_2/CO_2/H_2$ (80:10:10, v/v/v). Feces samples were suspended in BHI medium to a concentration of 25% (w/v). The suspensions were shaken (10 min, 180 rpm) and then centrifuged (10 min, 300*g*). The supernatants were removed carefully and directly utilized for the incubations as the native fecal suspension. In addition, an aliquot (20 mL) of the suspension was autoclaved (121 °C, 20 min).

Aqueous solutions (5 mM) of the MRPs were prepared and sterile-filtered (0.2 μm). The stability of the MRPs in the presence of BHI medium was assessed by adding 0.5 mL of the 5 mM MRP solutions to 9.5 mL of autoclaved oxygen-free BHI medium in a Hungate tube (V = 16 mL). The stability of the MRPs in the presence of an autoclaved feces sample was assessed by adding 0.5 mL of the 5 mM MRP solutions and 1.0 mL of autoclaved fecal suspension to 8.5 mL of autoclaved, oxygen-free BHI medium. These controls were done in a single determination in parallel to each experiment. The stability of the MRPs in the presence of native feces samples was analyzed by adding 0.5 mL of the 5 mM MRP solutions and 1.0 mL of native fecal suspension to 8.5 mL of autoclaved oxygen-free BHI medium. The latter incubation was performed in triplicate for each feces sample. All MRPs were incubated separately. The stability of medium components was analyzed by mixing 1.0 mL of native fecal suspension and 9.0 mL of autoclaved oxygen-free BHI medium.

Samples were withdrawn directly after the addition of the fecal suspension (0 h) and then after 4, 24, 48, and 72 h. A portion of sterilized gas was injected, and 1.0 mL of the suspension was removed. All samples were then frozen and stored at −80 °C.

Preparation of Samples for Analysis. For the analysis of PYR and MAL, 50 μL of the samples was mixed with 950 μL of 0.1% acetic acid in 5% aqueous methanol. The mixture was shaken vigorously and

DOI: 10.1021/acs.jafc.5b01391
J. Agric. Food Chem. 2015, 63, 6723−6730

Table 1. Transitions Recorded during Measurement of FL and CML in the MRM Mode[a]

analyte	transition	fragmentor voltage (V)	collision energy (eV)	Q/q[b]
FL	m/z 309 → m/z 84	125	36	Q
	m/z 309 → m/z 225	125	13	q
[$^{13}C_6$,$^{15}N_2$]FL	m/z 317 → m/z 233	70	13	Q
	m/z 317 → m/z 129	70	15	q
CML	m/z 205 → m/z 130	100	9	Q
	m/z 205 → m/z 142	100	9	q
[$^{2}H_2$]CML	m/z 207 → m/z 130	80	5	Q
	m/z 207 → m/z 144	80	12	q

[a]General conditions: positive mode; dwell time, 120 ms. [b]Q, transition used for quantification; q, transition used to confirm the presence of the analyte.

centrifuged (10 min, 13000 rpm). The supernatant was transferred to an HPLC vial. For the analysis of FL and CML, 50 μL of the samples was mixed first with 50 μL of methanol and shaken vigorously. After 45 min, 900 μL of 0.1% acetic acid was added; the mixture was shaken and frozen. After the mixture had been thawed and centrifuged (10 min, 13000 rpm), 180 μL of the supernatant was mixed with 20 μL of the internal standard solution containing 0.121 mM [$^{2}H_2$]CML and 0.656 mM [$^{13}C_6$,$^{15}N_2$]FL in water.

Pellet extraction followed a protocol employed for the extraction of water-soluble metabolites from *Escherichia coli*.[38] An aliquot of 500 μL of the above samples was centrifuged (10 min, 13000 rpm) and the supernatant removed. A 300 μL aliquot of 5 mM NFPA in 80% aqueous acetonitrile was then added to the pellet. After vigorous shaking, the suspension was stored at −80 °C for 30 min. After the suspension had been thawed and centrifuged (2 min, 13000 rpm), the supernatant was transferred to another tube and the pellet was extracted two more times. The supernatants were combined, and 300 μL of water was added. From these solutions, 200 μL was mixed with 800 μL of a solution of 0.1% acetic acid in 5% aqueous methanol. The mixtures were centrifuged (10 min, 13000 rpm) and the supernatants transferred to HPLC vials.

High-Pressure Liquid Chromatography with UV Detection. HPLC-DAD analyses were performed on a LaChrom Elite system consisting of a pump L-2130, an autosampler L-2200, a column oven L-2300, and a diode array detector L-2450 (all from VWR Hitachi, Darmstadt, Germany). A stainless steel column (150 mm × 4.6 mm, 5 μm) filled with Eurospher 100 C-18 material with an integrated guard column (5 × 4 mm) of the same material (Knauer, Berlin, Germany) was used for the analysis of PYR.[18] For the analysis of MAL, a polymer-based RP-18-column (PLRP-S, 100 Å, 250 mm × 4.6 mm, 8 μm, Polymer Laboratories, Darmstadt, Germany) with a guard column of the same material (5 × 4 mm) was used.[19] Eluent A was a solution of 5 mM NFPA in water; eluent B was a solution of 5 mM NFPA in a mixture of 80% methanol and 20% water. During the analysis of PYR, a linear gradient from 13% B to 100% B in 20 min was applied at a flow rate of 0.8 mL/min, whereas during the analysis of MAL, a linear gradient was mixed from 20 to 80% B in 20 min at a flow rate of 1.0 mL/min. During all analyses, the temperature of the autosampler was maintained at 10 °C, and the temperature of the column oven was set at 35 °C. The injection volume was 50 μL. UV spectra were recorded between 200 and 350 nm, and the quantification was performed with the chromatograms extracted at 280 nm (MAL) and 297 nm (PYR), respectively. External calibration was performed with the isolated MRP standards.

High-Pressure Liquid Chromatography with Mass Spectrometric Detection. Chromatography was performed with the high-pressure gradient system 1200 series (Agilent Technologies, Böblingen, Germany), consisting of a binary pump, an online degasser, a column oven, and an autosampler. A stainless steel column (Zorbax 300 SB-C18, 50 mm × 2.1 mm, 3.5 μm, Agilent Technologies) was used for the analysis of FL and CML. The eluents used were a solution of 10 mM NFPA in bidistilled water (solvent A) and a solution of 10 mM NFPA in acetonitrile (solvent B). A linear gradient from 5 to 29% B in 8 min was applied at a flow rate of 0.25 mL/min. The column temperature was maintained at 35 °C. The injection volume was 10 μL. The chromatographic system was connected to the mass spectrometer 6410 triple-quad (Agilent Technologies), working in the positive mode with a capillary voltage of 4000 V and a source temperature of 350 °C. FL and CML were quantified by MS detection in the multiple reaction monitoring (MRM) mode using the stable isotope dilution technique. The transitions used for the quantification of the analytes (quantifier, Q) and for the confirmation of the presence of the analytes (qualifier, q) are compiled in Table 1. All transitions were recorded between 1 and 9 min after injection. Data acquisition and evaluation were performed with the software MassHunter B.02.00 (Agilent). The same HPLC system was also used during metabolite analysis. Selected samples were measured first in the scan mode (m/z 90−500) and then in the product ion scan mode. For the latter approach, protonated molecular ions ([M + H]$^+$) of possible metabolites (e.g., biogenic amines, oxidized/reduced species) were stabilized in the first quadrupole and fragmented in the second quadrupole (fragmentor voltage, 100 V; collision energy, 20 eV), and spectra (m/z 50−250) were recorded with the third quadrupole.

Statistical Treatment. Comparisons of mean MRP concentrations between inoculated and non-inoculated media were performed using Student's t test. P values ≤0.05 were considered significant using the software PASW Statistics 18.

RESULTS AND DISCUSSION

Incubation Conditions. Significant amounts of protein-bound glycated amino acids are taken up with the daily diet. Unabsorbed glycated amino acids or those positioned at recalcitrant sites of heat-damaged proteins and not released during gastrointestinal digestion can pass into the colon. Although the microbial metabolism of FL has been investigated in vitro and in vivo,[7,13,21,22,30] no knowledge has yet been gained about the stability of other MRPs in the presence of the colonic microbiota, especially the human microbiota. Smith and Macfarlane have performed such investigations with the proteinogenic amino acids.[24] These authors had worked with a minimal medium and a final feces concentration of 20%. In our study, we wanted to conserve the metabolic variability of the gut microbiota as much as possible, and therefore chose brain−heart infusion broth, which is recommended for fastidious microorganisms, as in earlier investigations.[37] Unfortunately, due to the abundance of other amino acids from peptones in the medium, the analysis of SCFA as typical products of microbial amino acid metabolism was not possible.

DOI: 10.1021/acs.jafc.5b01391
J. Agric. Food Chem. 2015, 63, 6723−6730

In vitro experiments on the digestion of protein-bound MRPs show that FL and PYR are released during luminal digestion bound in short-chain peptides (<1 kDa) or as the free amino acids, whereas CML remains in longer peptides (1−4 kDa).[16,17] Dipeptides incorporating MRPs can be cleaved by membrane-bound peptidases of intestinal cells. Thus, a major portion of unabsorbed MRPs should enter the colon as the free amino acids. Considering a passage of the whole daily amount of 500−1000 mg of ARPs into the colon and a mean daily feces mass of 124 g,[10,39] an incubation of 250 μM of the free amino acid FL in the presence of a 2.5% (w/v) fecal suspension was chosen. This concentration was also applied to the other MRPs.

Stability of MRPs in the Absence of a Viable Microbiota. The incubation conditions chosen in this study comprised an elevated incubation temperature of 37 °C, a particularly low redox potential, and high concentrations of amino acids and phosphate from the medium, as well as a slightly alkaline pH. Under such conditions, it cannot be excluded that FL is degraded nonenzymatically. The formation of MRPs such as FL and CML from medium components is possible as well.[40] Therefore, the non-inoculated medium was incubated at 37 °C for up to 72 h without MRPs added. Samples were taken regularly up to 72 h of incubation and analyzed by RP-HPLC-MS/MS. The medium itself contained measurable amounts of FL and CML (Figure 2), but the formation of additional FL or CML from medium components could be excluded. PYR and MAL were not detected in the autoclaved medium. The MRPs were then added to non-inoculated BHI medium at a concentration of 250 μM and incubated at 37 °C. The concentrations of FL and MAL decreased slightly during 72 h of incubation, whereas the concentrations of CML and PYR remained constant (Figure 3). To assess a possible influence of the feces matrix on the recovery of MRPs, the compounds were incubated in the presence of autoclaved fecal suspension without a viable microbiota. No loss of compounds that could have been traced back to adsorption to feces matrix components could be measured; there were no significant differences in the time courses of MRP concentrations after the addition to non-inoculated medium or medium with added autoclaved feces matrix, respectively.

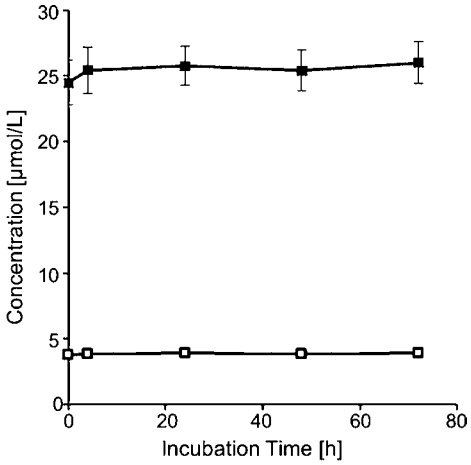

Figure 2. Development of the concentrations of FL (solid squares) and CML (open squares) in the non-inoculated BHI medium during anaerobic incubation at 37 °C for 72 h (no MRPs added). Data are given as means ± SD.

Stability of MRPs in the Presence of a Viable Microbiota. The four MRPs at a concentration of 250 μM were then added to 2.5% (w/v) fecal suspensions obtained from eight healthy volunteers. The analysis of FL by HPLC-MS/MS allowed quantification of at least 0.2 μM in the undiluted samples, equivalent to 0.08% of the initial FL concentration. Likewise, as low as 2.7 μM CML, corresponding to 1.1% of the initial amount, could be quantified in the undiluted samples. The recoveries of FL and CML, respectively, after addition to the non-inoculated medium, were 94.2 ± 5.1 and 92.1 ± 2.7%, respectively. For data evaluation, the MRP concentration measured in the non-inoculated medium was regarded as 100%, and all other values were expressed as percentages of this concentration.

As could be expected from the literature,[7,21,30] the concentration of FL declined very quickly in the presence of the viable microbiota (Figure 3A; Table S1). In some cases, >80% of the initial amount had already disappeared in the sample taken directly after the addition to the fecal suspension. The time between sampling inside the anaerobic chamber and deep-freezing (approximately 30−45 min) must have been sufficient for the degradation of the substance. This short time could probably point to metabolism of the substance by extracellular enzymes, as already proposed by Griffiths and Pridham.[41] After 4 h of incubation, FL was in each case not detectable anymore. The separation by centrifugation of the samples taken from the inocula and the independent analysis of supernatants and pellets after extraction did not lead to a higher recovery of FL; that is, at no time was FL detectable in the cell pellet extract. Our data therefore suggest that the low recovery of orally administered FL in urine and feces[21,22] can at least in part be explained by metabolism of the compound by the intestinal microbiota.

CML was also degraded in the presence of all fecal samples, but to a lesser extent than FL. After 4 and 24 h, average amounts of 84.6% (range of 45−98%) and 36.2% (range of 0−59%) remained, respectively (Figure 3B; Table S2). Only about 1% of the initial CML amount was detectable in the pellet extract for samples taken at different incubation times. The interindividual differences of CML degradation were very pronounced. After 24 h of incubation, CML was degraded to <15% of the initial concentration in the presence of the fecal microbiota of three of the eight volunteers, whereas for the other five, the remaining CML concentration ranged between 53 and 59%. The first group could thus be tentatively classified as "fast CML metabolizers" and the second as "slow CML metabolizers". On average, the relative standard deviation of the CML concentration between the triplicate stability measurements performed for each of the subjects was 3−5%. The differences that appeared between subjects can thus not be explained by insufficient precision. Further studies will have to show the microbiological background of these findings and whether this difference is of any (patho)physiological importance. Because the volunteers during the duration of this study consumed their usual diet, food matrix components might also be causative for the observed differences, and further studies should be performed with volunteers on controlled diets.

For both FL and CML samples, MS/SCAN experiments were performed for m/z 90−500. However, no significant changes in the extracted ion chromatograms became apparent when samples of viable microbiota incubated with or without the MRPs were compared. Owing to the free lysine content of

DOI: 10.1021/acs.jafc.5b01391
J. Agric. Food Chem. 2015, 63, 6723−6730

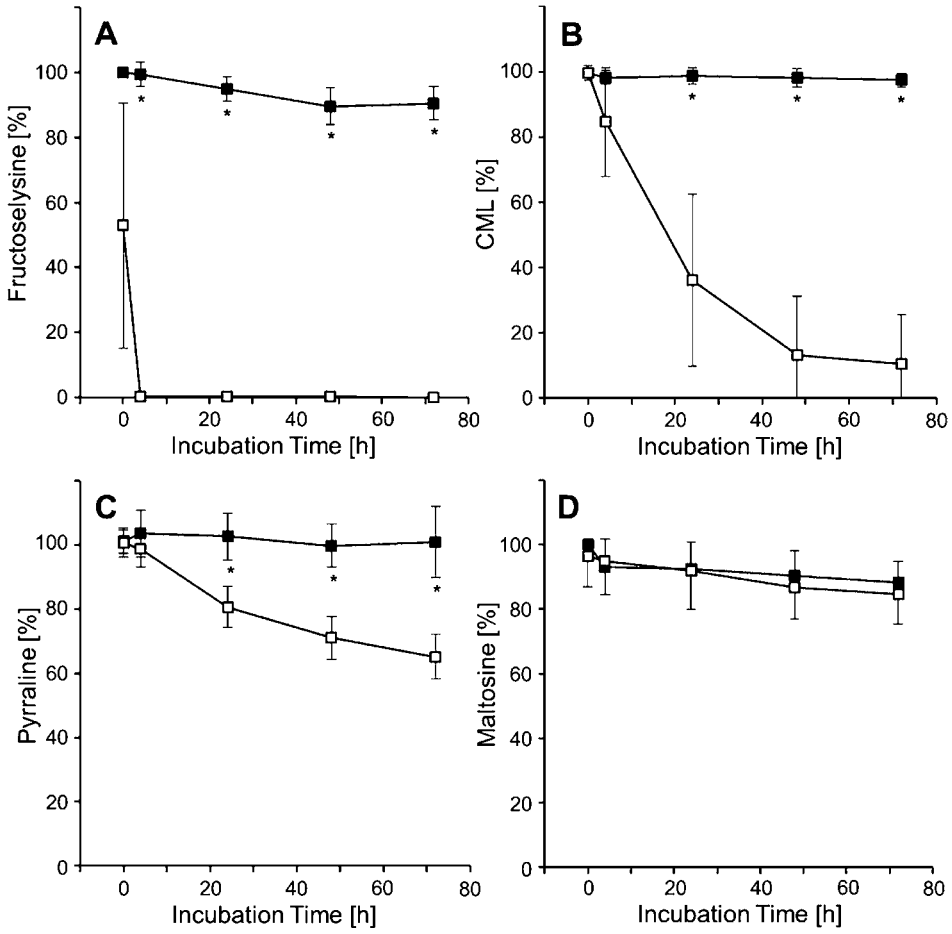

Figure 3. Time course of the concentrations of (A) fructoselysine, (B) carboxymethyllysine, (C) pyrraline, and (D) maltosine in fecal suspensions (2.5%, w/v) in BHI medium (open squares) and in non-inoculated BHI medium (solid squares) at an initial concentration of 250 μM MRP (eight human volunteers, eight separate trials). MRPs were quantified by HPLC with mass spectrometric detection (FL, CML) or UV detection (PYR, MAL) as described under Materials and Methods. Data are given as the percentage of the initial concentration of each MRP in the non-inoculated medium as means ± SD. Significant differences ($P < 0.05$) between means are indicated by asterisks (*).

the medium and the concomitant release from peptides and proteins, it was not possible to assess whether lysine might be a, possibly even an extracellular,[41] metabolite of FL. A qualitative analysis was performed for typical products of the amino acid metabolism, for example, the corresponding biogenic amines[42] or organic acids,[24] by selected ion monitoring and product ion scanning; however, no verification of the presence of these products was possible. We therefore conclude that FL and CML enter microbial amino acid degradation pathways and that the concentration of intermediates is too low to be detected by the mass spectrometric techniques applied.

PYR and MAL were quantified by RP-HPLC with UV detection. As for FL and CML, this technique still allowed quantification of the analytes at concentrations corresponding to 1% of the initial amount. PYR was degraded by the fecal microbiota of all individuals (Figure 3C; Table S3), but again to a lesser extent than CML. Tryptophan could be detected besides PYR with our method (Figure 4). The degradation of tryptophan, which is known from the literature,[24] was corroborated qualitatively in our experiments. A small portion of PYR (3.5% of the initial amount) was detected in the pellet extract in samples taken after 24 h, but this small portion cannot fully explain the decrease of PYR in the course of fermentation. HPLC-DAD allowed generation of extracted wavelength chromatograms between 200 and 400 nm; however,

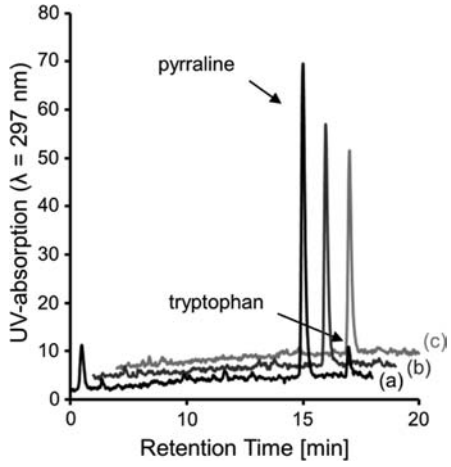

Figure 4. RP-HPLC with UV detection of fecal suspensions (2.5%, w/v) in BHI medium supplemented with 250 μM pyrraline measured after 0 h (a), 24 h (b), and 72 h (c) of incubation.

neither with this approach nor with the MS experiments performed as for FL and CML samples was it possible to detect potential metabolites. It is most probable that the metabolism of PYR starts with a modification of the pyrrole ring, possibly a

DOI: 10.1021/acs.jafc.5b01391
J. Agric. Food Chem. 2015, 63, 6723−6730

reduction, leading to a decline in the UV absorbability rendering the metabolite(s) undetectable by UV detection.

The concentration of MAL slightly declined in the presence of the viable microbiota; however, this was not significantly different from the decline in the non-inoculated medium (Figure 3D; Table S4). We thus conclude that MAL is not degraded by the intestinal microbiota.

In conclusion, we have shown that the human fecal microbiota is able to degrade the MRPs FL, CML, and PYR, but not MAL, when cultivated anaerobically in a nutrient-rich medium. Our data, especially those showing strong differences in the extent of degradation of individual substances, provide an experimental basis for some new questions concerning the metabolism of MRPs. First, is the higher degradability of products appearing earlier in the Maillard reaction cascade due to the lower chemical stability compared to the advanced products (secondary amines vs chemically more stable *N*-substituted heterocycles)? The investigation of further Amadori products (*N*-ε-tagatosyllysine, *N*-ε-lactulosyllysine, *N*-ε-maltulosyllysine) should reveal whether the intestinal microbiota is generally able to metabolize such products or whether this is specific only for FL. Moreover, because PYR and MAL can be transported across the small-intestinal membrane whereas FL and CML cannot,[20] a further question to be answered is whether the higher degradability of FL and CML is due to their higher concentrations in the ileal chyme and, thus, whether the human gut microbiota has accommodated to using glycated amino acids as a source of energy, nitrogen, or carbon. With regard to the passage of protein into the colon of 13 g per day,[23] an intake of ca. 500−1000 mg of ARPs represents an important part of the colonic nitrogen supply. Studies on the metabolism of FL in *E. coli* consistently show an induction period needed to induce the necessary enzyme systems.[41,43] In the present study, a similar induction period was not observed, possibly because the enzyme systems are permanently induced in the microbiota of human subjects due to permanent exposure to ARPs such as FL. Recent experiments with tagatosylated proteins reveal the possibility of generating bifidogenic substances from non-bifidogenic precursors.[28] Further studies have to show whether such a bifidogenic effect might also result from dietary ARPs such as FL. Whether degrading FL is a general capability of microorganisms or whether there are "specialists" that even might have had an evolutionary benefit remains to be elucidated. Experiments using *E. coli* indicate a pronounced strain specificity of FL degradation, because some authors report degradation of the compound,[32,41] whereas others do not.[40]

Interestingly, the influence on the amino acid supply to the colonic microbiota by intestinal transport phenomena is not restricted to glycated amino acids. Diets high in protein can generally give rise to increasing amino acid fermentation in the colon and the production of the respective metabolites, some of which are discussed as being toxicologically relevant.[44,45] Moreover, metabolic diseases based on impaired intestinal transporter activity, such as Hartnup disease, lead to significant increases in the concentrations of tryptophan metabolites in the blood.[46] Some of these products, for example, phenylacetic and indoleacetic acids, are classified as uremic toxins for patients suffering from uremia.[47] Links between MRPs and their negative effects in disease states such as uremia[10] and ulcerative colitis[26] can likely be explained by adverse actions not necessarily of glycated amino acids themselves but of their microbial metabolites. Therefore, it would be of high interest to determine whether MRPs can enter into microbial amino acid metabolism. Further studies concerning the identity of microbial metabolites of individual MRPs and the identification of the metabolizing species are urgently needed.

■ ASSOCIATED CONTENT

Ⓢ Supporting Information

Concentrations of MRPs during incubation in the presence of human fecal suspensions of FL (Table S1), CML (Table S2), PYR (Table S3), and MAL (Table S4) individualized for all study participants. The Supporting Information is available free of charge on the ACS Publications website at DOI: 10.1021/acs.jafc.5b01391.

■ AUTHOR INFORMATION

Corresponding Author

*(T.H.) Phone: +49-351-463-34647. Fax: +49-351-463-34138. E-mail: Thomas.Henle@chemie.tu-dresden.de.

Present Address

#(C.M.A.P.F.) Department of Microbiology and Biotechnology, Max Rubner-Institut, Federal Research Institute of Nutrition and Food, Hermann-Weigmann-Straße 1, 24103 Kiel, Germany.

Funding

M. Hellwig is indebted to the Josef-Schormüller-Gedächtnisstiftung (Berlin, Germany) for their financial support of the study.

Notes

The authors declare no competing financial interest.

■ ACKNOWLEDGMENTS

We thank all of the study participants for their support. We are grateful to Luisa Martinez and Alexander Hanak (MRI, Karlsruhe) for their help during microbiological works.

■ ABBREVIATIONS USED

ARP, Amadori rearrangement product; BHI, brain−heart infusion; CML, *N*-ε-carboxymetyllysine; DAD, diode array detection; FL, *N*-ε-fructosyllysine; HPLC, high-pressure liquid chromatography; MAL, maltosine; MRM, multiple reaction monitoring; MRP, Maillard reaction product; MS, mass spectrometry; NFPA, nonafluoropentanoic acid; PYR, pyrraline; RP, reversed-phase; SCFA, short-chain fatty acid; t_R, retention time; UV, ultraviolet

■ REFERENCES

(1) Ledl, F.; Schleicher, E. New aspects of the Maillard reaction in foods and in the human body. *Angew. Chem., Int. Ed. Engl.* **1990**, *29*, 565−594.

(2) Hellwig, M.; Henle, T. Baking, ageing, diabetes: a short history of the Maillard reaction. *Angew. Chem., Int. Ed.* **2014**, *53*, 10316−10329.

(3) Smuda, M.; Glomb, M. Novel insights into the Maillard catalyzed degradation of maltose. *J. Agric. Food Chem.* **2011**, *59*, 13254−13264.

(4) Hellwig, M.; Löbmann, K.; Orywol, T.; Voigt, A. Model studies on the oxidation of benzoyl methionine in a carbohydrate degradation system. *J. Agric. Food Chem.* **2014**, *62*, 4425−4433.

(5) Nakayama, T.; Hayase, F.; Kato, H. Formation of ε-(2-formyl-5-hydroxymethylpyrrol-1-yl)-L-norleucine in the Maillard reaction between D-glucose and L-lysine. *Agric. Biol. Chem.* **1980**, *44*, 1201−1202.

(6) Ledl, F.; Osiander, H.; Pachmayr, O.; Severin, T. Formation of maltosine, a product of the Maillard reaction with a pyridone structure. *Z. Lebensm.-Unters. Forsch.* **1989**, *188*, 207−211.

DOI: 10.1021/acs.jafc.5b01391
J. Agric. Food Chem. 2015, 63, 6723−6730

(7) Erbersdobler, H. F.; Faist, V. Metabolic transit of Amadori products. *Nahrung* **2001**, *45*, 177−181.
(8) Assar, S. H.; Moloney, C.; Lima, M.; Magee, R.; Ames, J. M. Determination of *N*-ε-(carboxymethyl)lysine in food systems by ultra-performance liquid chromatography-mass spectrometry. *Amino Acids* **2009**, *36*, 317−326.
(9) Hellwig, M.; Henle, T. Quantification of the Maillard reaction product 6-(2-formyl-1-pyrrolyl)-L-norleucine in food. *Eur. Food Res. Technol.* **2012**, *235*, 99−106.
(10) Henle, T. AGEs in foods: do they play a role in uremia? *Kidney Int.* **2003**, *63*, S145−S147.
(11) Henle, T.; Walter, A. W.; Klostermeyer, H. Simultaneous determination of protein-bound Maillard products by ion-exchange chromatography and photodiode array detection. In *Maillard Reactions in Chemistry, Food, and Health*; Labuza, T. P., Ed.; The Royal Society of Chemistry: Cambridge, UK, 1994; pp 195−200.
(12) Henry, K. M.; Kon, S. K.; Lea, C. H.; Smith, J. A. B.; White, J. C. D. Deterioration on storage of skim milk. *Nature* **1946**, *158*, 348−349.
(13) Finot, P. A.; Bujard, E.; Mottu, F.; Mauron, J. Availability of the true Schiff's base of lysine. Chemical evaluation of the Schiff's base between lysine and lactose in milk. *Adv. Exp. Med. Biol.* **1977**, *86B*, 343−365.
(14) Chung, S. Y.; Swaisgood, H. E.; Catignani, G. L. Effects of alkali treatment and heat-treatment in the presence of fructose on digestibility of food proteins as determined by an immobilized digestive enzyme assay (IDEA). *J. Agric. Food Chem.* **1986**, *34*, 579−584.
(15) Rérat, A.; Calmes, R.; Vaissade, P.; Finot, P. A. Nutritional and metabolic consequences of the early Maillard reaction of heat-treated milk in the pig. Significance for man. *Eur. J. Nutr.* **2002**, *41*, 1−11.
(16) Hellwig, M.; Matthes, R.; Peto, A.; Löbner, J.; Henle, T. *N*-ε-fructosyllysine and *N*-ε-carboxymethyllysine, but not lysinoalanine, are available for absorption after simulated gastrointestinal digestion. *Amino Acids* **2014**, *46*, 289−299.
(17) Hellwig, M.; Henle, T. Release of pyrraline in absorbable peptides during simulated gastrointestinal digestion of casein glycated by 3-deoxyglucosone. *Eur. Food Res. Technol.* **2013**, *237*, 47−55.
(18) Hellwig, M.; Geissler, S.; Peto, A.; Knütter, I.; Brandsch, M.; Henle, T. Transport of free and peptide-bound pyrraline at intestinal and renal epithelial cells. *J. Agric. Food Chem.* **2009**, *57*, 6474−6480.
(19) Geissler, S.; Hellwig, M.; Markwardt, F.; Henle, T.; Brandsch, M. Synthesis and intestinal transport of the iron chelator maltosine in free and dipeptide form. *Eur. J. Pharm. Biopharm.* **2011**, *78*, 75−82.
(20) Hellwig, M.; Geissler, S.; Matthes, R.; Peto, A.; Silow, C.; Brandsch, M.; Henle, T. Transport of free and peptide-bound glycated amino acids: synthesis, transepithelial flux at Caco-2 cell monolayers, and interaction with apical membrane transport proteins. *ChemBioChem* **2011**, *12*, 1270−1279.
(21) Lee, K.; Erbersdobler, H. F. Balance experiments on human volunteers with ε-fructoselysine (FL) and lysinoalanine (LAL). In *Maillard Reactions in Chemistry, Food, and Health*; Labuza, T. P., et al., Eds.; The Royal Society of Chemistry: Cambridge, UK, 1994; 358−363.
(22) Förster, A.; Kühne, Y.; Henle, T. Studies on absorption and elimination of dietary Maillard reaction products. *Ann. N. Y. Acad. Sci.* **2005**, *1043*, 474−481.
(23) Tuohy, K. M.; Hinton, D. J. S.; Davies, S. J.; Crabbe, M. J. C.; Gibson, G. R.; Ames, J. M. Metabolism of Maillard reaction products by the human gut microbiota − implications for health. *Mol. Nutr. Food Res.* **2006**, *50*, 847−857.
(24) Smith, E. A.; Macfarlane, G. T. Dissimilatory amino acid metabolism in human colonic bacteria. *Anaerobe* **1997**, *3*, 327−337.
(25) Russell, W. R.; Gratz, S. W.; Duncan, S. H.; Holtrop, G.; Ince, J.; Scobbie, L.; Duncan, G.; Johnstone, A. M.; Lobley, G. E.; Wallace, R. J.; Duthie, G. D.; Flint, H. J. High-protein, reduced-carbohydrate weight-loss diets promote metabolite profiles likely to be detrimental to colonic health. *Am. J. Clin. Nutr.* **2011**, *93*, 1062−1072.
(26) Mills, D. J. S.; Tuohy, K. M.; Booth, J.; Buck, M.; Crabbe, M. J. C.; Gibson, G. R.; Ames, J. M. Dietary glycated protein modulates the colonic microbiota towards a more detrimental composition in ulcerative colitis patients and non-ulcerative colitis subjects. *J. Appl. Microbiol.* **2008**, *105*, 706−714.
(27) Seiquer, I.; Rubio, L. A.; Peinado, M. J.; Delgado-Andrade, C.; Navarro, M. P. Maillard reaction products modulate gut microbiota composition in adolescents. *Mol. Nutr. Food Res.* **2014**, *58*, 1552−1560.
(28) Corzo-Martínez, M.; Hernandez-Hernandez, O.; Villamiel, M.; Rastall, R. A.; Moreno, F. J. In vitro bifidogenic effect of Maillard-type milk protein-galactose conjugates on the human intestinal microbiota. *Int. Dairy J.* **2013**, *31*, 127−131.
(29) Hernandez-Hernandez, O.; Sans, M. L.; Kolida, S.; Rastall, R. A.; Moreno, F. J. In vitro fermentation by human gut bacteria of proteolytically digested caseinomacropeptide nonenzymatically glycosylated with prebiotic carbohydrates. *J. Agric. Food Chem.* **2011**, *59*, 11949−11955.
(30) Erbersdobler, H.; Gunsser, I.; Weber, G. Abbau von Fruktoselysin durch die Darmflora. *Zentralbl. Veterinaermed.* **1970**, *17*, 573−575.
(31) Deppe, V. M.; Bongaerts, J.; O'Connell, T.; Maurer, K.-H.; Meinhardt, F. Enzymatic deglycation of Amadori products in bacteria: mechanisms, occurrence and physiological functions. *Appl. Microbiol. Biotechnol.* **2011**, *90*, 399−406.
(32) Van Schaftingen, E.; Collard, F.; Wiame, E.; Veiga-da-Cunha, M. Enzymatic repair of Amadori products. *Amino Acids* **2011**, *42*, 1143−1150.
(33) Delgado-Andrade, C.; Tessier, F. J.; Niquet-Leridon, C.; Seiquer, I.; Navarro, M. P. Study of the urinary and faecal excretion on N^{ε}-carboxymethyllysine in young human volunteers. *Amino Acids* **2012**, *43*, 595−602.
(34) Alamir, I.; Niquet-Leridon, C.; Jacolot, P.; Rodriguez, C.; Orosco, M.; Anton, P. M.; Tessier, F. J. Digestibility of extruded proteins and metabolic transit of *N*-ε-carboxymethyllysine in rats. *Amino Acids* **2013**, *44*, 1441−1449.
(35) Krause, R.; Knoll, K.; Henle, T. Studies on the formation of furosine and pyridosine during acid hydrolysis of different Amadori products of lysine. *Eur. Food Res. Technol.* **2003**, *216*, 277−283.
(36) Hegele, J.; Parisod, V.; Richoz, J.; Förster, A.; Maurer, S.; Krause, R.; Henle, T.; Buetler, T.; Delatour, T. Evaluating the extent of protein damage in dairy products. Simultaneous determination of early and advanced glycation induced lysine modifications. *Ann. N. Y. Acad. Sci.* **2008**, *1126*, 300−306.
(37) Bode, L. M.; Bunzel, D.; Huch, M.; Cho, G.-S.; Ruhland, D.; Bunzel, M.; Bub, A.; Franz, C. M. A. P.; Kulling, S. E. In vivo and in vitro metabolism of *trans*-resveratrol by human gut microbiota. *Am. J. Clin. Nutr.* **2013**, *97*, 295−309.
(38) Rabinowitz, J. D.; Kimball, E. Acidic acetonitrile for cellular metabolome extraction from *Escherichia coli*. *Anal. Chem.* **2007**, *79*, 6167−6173.
(39) Rendtorff, R. C.; Kashgarian, M. Stool patterns of healthy adult males. *Dis. Colon Rectum* **1967**, *10*, 222−228.
(40) Helou, C.; Marier, D.; Jacolot, P.; Abdennebi-Najar, L.; Niquet-Léridon, C.; Tessier, F. J.; Gadonna-Widehem, P. Microorganisms and Maillard reaction products: a review of the literature and recent findings. *Amino Acids* **2014**, *46*, 267−277.
(41) Griffiths, D. R.; Pridham, J. B. The metabolism of 1-(ε-*N*-lysyl)-1-deoxy-D-fructose by *Escherichia coli*. *J. Sci. Food Agric.* **1980**, *31*, 1214−1220.
(42) Smith, E. A.; Macfarlane, G. T. Studies on amine production in the human colon: enumeration of amine forming bacteria and physiological effects of carbohydrate and pH. *Anaerobe* **1996**, *2*, 285−297.
(43) Wiame, E.; Delpierre, G.; Collard, F.; van Schaftingen, E. Identification of a pathway for the utilization of the Amadori product fructoselysine in *Escherichia coli*. *J. Biol. Chem.* **2002**, *277*, 42523−42529.
(44) Russell, W. R.; Duncan, S. H.; Scobbie, L.; Duncan, G.; Cantlay, L.; Calder, A. G.; Anderson, S. E.; Flint, H. J. Major phenylpropanoid-

DOI: 10.1021/acs.jafc.5b01391
J. Agric. Food Chem. 2015, 63, 6723−6730

derived metabolites in the human gut can arise from microbial fermentation of protein. *Mol. Nutr. Food Res.* **2013**, *57*, 523−535.
(45) Russell, W. R.; Hoyles, L.; Flint, H. J.; Dumas, M.-E. Colonic bacterial metabolites and human health. *Curr. Opin. Microbiol.* **2013**, *16*, 246−254.
(46) Smith, H. G.; Smith, W. R. D.; Jepson, J. B. Interconversions of indolic acids by bacteria and rat tissue − possible relevance to Hartnup disorder. *Clin. Sci.* **1968**, *34*, 333−342.
(47) Evenepoel, P.; Meijers, B. K. I.; Bammens, B. R. M.; Verbeke, K. Uremic toxins originating from colonic microbial metabolism. *Kidney Int.* **2009**, *76*, S12−S19.

DOI: 10.1021/acs.jafc.5b01391
J. Agric. Food Chem. 2015, 63, 6723−6730

populations, including those derived from the human monocyte cell line THP-1,[17−19] and, furthermore, without need of further oxidation.[20]

The FA composition of CMR influences their uptake and lipid accumulation in macrophages.[12,21] De Pascale et al.[12] studied the effects of CMR-like particles (CRLP) enriched in saturated fatty acids (SFA), monounsaturated fatty acids (MUFA), n-6 polyunsaturated fatty acids (PUFA), and n-3 PUFA, obtained by incorporating TAG from palm, olive, corn, and fish oils, respectively, on THP-1 macrophage foam cell formation. They reported that CRLP enriched in SFA or MUFAs were taken up more rapidly than those enriched in n-6 or n-3 PUFA and that SFA-rich particles showed the greatest lipid accumulation.

Accordingly, the FA composition of CMR may be determinant for the accumulation of cholesterol and TAG in the macrophages, affecting their metabolism and modulating their atherogenicity.[19,22] However, the effect of different FA profiles of monovarietal oils on foam cell formation from macrophages has not been addressed so far. Therefore, in the present study we investigated the effect of the fatty acid composition of EVOO from five olive cultivars on foam cell formation by THP-1 macrophages.

MATERIALS AND METHODS

Chemicals. Cholesterol and cholesteryl esters (CE) were supplied by Larodan Inc. (Malmö, Sweden). Phospholipids (PL) (phosphatidylcholine, lysophosphatidylcholine, phosphatidylethanolamine, phosphatidylinositol, phosphatidylserine, and sphingomyelin), Trypan Blue, albumin (BSA), and Oil Red O were obtained from Sigma-Aldrich (St. Louis, MO, USA). Human serum was supplied by VWR International Eurolab, S.L (Spain). The THP-1 monocyte−macrophage cell line was provided by the European Collection of Cell Cultures (ECACC, UK). RPMI 1640 medium with L-glutamine (L-alanyl-glutamine) and fetal bovine serum (FBS) were purchased from Biowest SAS (France). Penicillin−streptomycin (5000 U/mL) was obtained from Gibco (Paisley, UK). Phorbol 12-myristate 13-acetate (PMA) and phosphate-buffered saline (PBS) were supplied by Fisher Scientific (USA). All other chemicals were of analytical reagent grade.

Plant Material and Virgin Olive Oil Extraction. 'Picual', 'Buidiego', 'Blanqueta', 'Galega', and 'Chetoui' (*Olea europaea* L.) olive cultivars were selected according to differences in their FA composition. The trees were spaced 7 × 7 m and grown in the experimental orchard of Centro IFAPA "Venta Del Llano", Mengibar, Jaen, Spain, using standard growing techniques. The study was carried out during the 2013/2014 crop year. Olives were harvested separately from two olive trees per cultivar.

EVOO extraction was performed using an Abencor laboratory oil mill (Comercial Abengoa, S.A., Seville, Spain) equipped with a hammer mill, a thermobeater, and a paste centrifuge; it simulates at laboratory scale the industrial process of EVOO production. The extraction was carried out for each cultivar and tree separately. The milling of olive fruits was performed using a stainless steel hammer mill operating at 3000 rpm provided with a 5 mm sieve. The olive paste malaxation was carried out at 28 °C with kneading at 50 rpm for 45 min. Centrifugation of the kneaded olive paste was performed in a basket centrifuge at 3500 rpm for 1 min. After centrifugation, the obtained oil was decanted, filtered, and stored in glass bottles at −20 °C in the dark without headspace and under N_2 until analysis.

Fatty Acid Composition of Virgin Olive Oil. Fatty acid methyl esters (FAME) were prepared as described by EU Regulation 2568/91.[23] The chromatographic separation was carried out on a Perkin-Elmer Autosystem gas chromatograph (Perkin-Elmer, Spain) equipped with an autosampler, split/splitless injector, flame ionization detector (FID), and fused silica capillary BPX70 column of 50 m length × 0.25 mm i.d. and 0.25 μm of film thickness (SGE Scientific Pty. Ltd., Australia). Helium was used as carrier gas, and the oven temperature was maintained at 198 °C throughout the analysis. The injector and detector temperatures were 235 and 245 °C, respectively. The results were expressed as relative area percent of the total.

Preparation of Chylomicron Remnant-like Particles (CRLP). TAG were isolated from 'Chetoui', 'Buidiego', 'Galega', 'Blanqueta', and 'Picual' EVOO by solid-phase extraction (SPE) using diol cartridges (Supercleane LC-Diol; Supelco, Bellefonte, PA, USA) and hexane/methylene choride (9:1, v/v) as eluent. The eluate containing TAG was evaporated to dryness under a stream of nitrogen and redissolved in hexane. CRLP were prepared using a lipid mixture containing 70% TAG from EVOO, 2% cholesterol, 3% cholesteryl esters (CE)/ and 25% PL as described previously.[24] The composition of the initial PL moieties was phosphatidylcholine, 70.50%; lysophosphatidylcholine, 6.88%; phosphatidylethanolamine, 11.00%; phosphatidylinositol, 2.58%; phosphatidylserine, 2.58%; and sphingomyelin, 6.54%.

Lipids were sonicated by immersing a clean ultrasonic probe (Bandelin Electronics, Berlin, Germany) directly into the lipid mixture in 0.9% NaCl in tricine buffer (20 mM, pH 7.4) and supplying the probe with 50 W for 20 min (5 min bursts with 5 min rest periods to allow for cooling) at 56 °C. The resulting emulsion was brought to a density of 1.21 g/mL with KBr, layered under a stepwise density gradient (2.5 mL, d = 1.065 g/mL; 2.5 mL, d = 1.020 g/mL; 3 mL, d = 1.006 g/mL) as described previously,[24] and centrifuged at 17000g for 20 min at 20 °C (Beckman Optima L-90K centrifuge; Beckman Coulter, Palo Alto, CA, USA) in a SW41Ti swing-out rotor. The upper layer, which was an uneven emulsion of lipids, was discarded. The removed layer was replaced with an equal volume of NaCl solution (d = 1.006 g/mL), and tubes were centrifuged at 70000g for 1 h (20 °C) in a SW41Ti swing-out rotor. The upper layer was then collected and stored at 4 °C until use (maximum of 2 days).

Apolipoprotein E Transfer to CRLP. The apolipoprotein transfer was achieved by incubation of the lipid emulsion with a fraction of human serum (1:2, vol/vol), prepared by ultracentrifugation and dialyzed before use[24] (5 h, 4 °C). After incubation, the particles were ultracentrifuged (154000g, 16 h, 12 °C) under a NaCl solution (d = 1.006 g/mL). The upper layer was collected and recentrifuged (254000g, 5 h, 12 °C) under a NaCl solution (d = 1.006 g/mL) to isolate the CRLP fraction. CRLP were dialyzed before use (2 h, 4 °C) and stored a 4 °C. All preparations were used within 1 week.

Culture of THP-1 Macrophages. THP-1 monocytes were maintained in suspension at a density of (3−8) × 10^5 cells/mL in RPMI 1640 culture medium containing 10% fetal bovine serum (previously inactivated at 56 °C, 30 min), 2 mM L-alanyl-glutamine, 100 U/mL penicillin, and 100 μg/mL streptomycin at 37 °C in 95% air/5% CO_2.

The cells at a 1 × 10^6/mL concentration were induced to differentiate into macrophages by incubation with phorbol myristate acetate (PMA) (200 ng/mL) for 72 h at 37 °C in 95% air/5% CO_2. After this time, the cells adhering to the culture dishes were washed with RPMI 1640 culture medium without FBS (3 × 2 mL) to remove any undifferentiated cells and traces of PMA. The viability of the THP-1 monocytes, as assessed by Trypan Blue exclusion, was >90% in all experiments. The adherent cell was 70−80%, and cell viability was unaffected with incubation with CRLPs.

Lipid Accumulation Studies. Cells adhering to the culture dishes were added to 2 mL of RPMI 1640 culture medium without fetal bovine serum and were incubated with CRLP (0.15 μmol TAG/mL medium) for 24 h at 37 °C in 95% air/5% CO_2. For Oil Red O staining, cells were washed with PBS 1× (3 × 2 mL) and 60% propan-2-ol, and then 1 mL of Oil Red O (0.15% w/v) in 40% propan-2-ol/H_2O v/v was added. After 10 min, the stain was removed and cells were washed with 3 mL of PBS 1× as many times as necessary to remove traces of the solution. Then, 2 mL of glycerol (30%) was added, and images were captured using a microscope-mounted Canon digital camera.

For intracellular lipid analysis, cells were washed with PBS (3 × 3 mL), harvested in 0.7 μL of PBS, and kept on a bed of ice. Cells were then disrupted by sonication for 5 s (× 2, 50 W), and a sample was taken for protein determination (preserved at −70 °C); the rest were

DOI: 10.1021/acs.jafc.5b01626
J. Agric. Food Chem. 2015, 63, 6731−6738

Table 1. Fatty Acid Composition of EVOO from 'Chetoui', 'Buidiego', 'Galega', 'Blanqueta', and 'Picual' Cultivars and of TAG in CRLP, Which Were Prepared Using the TAG from the Same Oils[a]

	'Chetoui'		'Buidiego'		'Galega'		'Blanqueta'		'Picual'	
	EVOO	CRLP	EVOO	CRLP	EVOO	CRLP	EVOO	CRLP	EVOO	CRLP
16:0	13.5 ± 0.05	13.8 ± 0.22 a	13.4 ± 0.10	13.8 ± 0.3 a	15.8 ± 0.21	15.3 ± 0.30 b	16.4 ± 0.21	16.6 ± 1.20 c	12.3 ± 0.04	12.5 ± 0.46 d
16:1	0.37 ± 0.01	0.76 ± 0.05 a	0.71 ± 0.02	1.36 ± 0.23 ab	2.13 ± 0.03	2.62 ± 0.05 b	1.39 ± 0.05	1.40 ± 0.78 ab	1.01 ± 0.02	1.37 ± 0.10 ab
17:0	0.05 ± 0.01	0.07 ± 0.02	0.06 ± 0.01	0.11 ± 0.04	0.11 ± 0.01	0.15 ± 0.04	0.12 ± 0.01	0.14 ± 0.10	0.03 ± 0.01	0.07 ± 0.03
17:1	0.08 ± 0.01	0.10 ± 0.02	0.07 ± 0.01	0.25 ± 0.24	0.26 ± 0.01	0.28 ± 0.02	0.25 ± 0.02	0.14 ± 0.16	0.07 ± 0.02	0.14 ± 0.04
18:0	2.55 ± 0.02	3.52 ± 0.15 ab	2.87 ± 0.02	4.12 ± 0.83 a	1.83 ± 0.01	2.46 ± 0.24 b	2.11 ± 0.03	2.80 ± 0.26 b	2.56 ± 0.02	3.44 ± 0.22 a,b
18:1	62.5 ± 0.08	60.9 ± 0.17 a	75.4 ± 0.19	70.6 ± 1.24 b	74.6 ± 0.23	71.7 ± 0.60 c	64.1 ± 0.23	62.9 ± 0.63 d	79.9 ± 0.06	76.6 ± 1.28 e
18:2	19.7 ± 0.01	18.9 ± 0.19 a	6.22 ± 0.04	7.33 ± 1.25 b	4.29 ± 0.02	5.69 ± 0.45 c	14.3 ± 0.01	14.3 ± 0.29 d	3.06 ± 0.03	4.11 ± 0.56 e
18:3	0.55 ± 0.04	1.06 ± 0.03	0.57 ± 0.05	1.04 ± 0.18	0.51 ± 0.03	0.88 ± 0.05	0.59 ± 0.02	1.05 ± 0.05	0.55 ± 0.01	0.93 ± 0.03
20:0	0.34 ± 0.03	0.47 ± 0.03	0.34 ± 0.01	0.49 ± 0.24	0.24 ± 0.02	0.35 ± 0.02	0.38 ± 0.03	0.35 ± 0.02	0.31 ± 0.02	0.31 ± 0.01
20:1	0.29 ± 0.01	0.13 ± 0.03	0.22 ± 0.02	0.24 ± 0.16	0.17 ± 0.01	0.11 ± 0.04	0.19 ± 0.01	0.11 ± 0.04	0.17 ± 0.01	0.13 ± 0.07
22:0	0.09 ± 0.01	0.22 ± 0.03	0.08 ± 0.00	0.31 ± 0.07	0.05 ± 0.01	0.27 ± 0.08	0.10 ± 0.01	0.25 ± 0.03	0.05 ± 0.01	0.25 ± 0.08
others		0.19 ± 0.12		0.39 ± 0.35		0.13 ± 0.03		0.09 ± 0.02		0.14 ± 0.05
total SFA	16.6 ± 0.02	17.9 ± 0.09 a	16.8 ± 0.03	18.8 ± 0.30 a	18.0 ± 0.05	18.6 ± 0.14 a	19.1 ± 0.06	20.1 ± 0.32 b	15.3 ± 0.02	16.6 ± 0.16 c
total MUFA	63.2 ± 0.10	61.9 ± 0.25 a	76.4 ± 0.23	72.4 ± 1.75 b	77.1 ± 0.27	74.7 ± 0.68 c	65.9 ± 0.30	64.5 ± 1.58 d	81.1 ± 0.10	78.3 ± 1.44 e
total PUFA	20.24 ± 0.03	19.97 ± 0.21 a	6.79 ± 0.07	8.37 ± 1.34 b	4.80 ± 0.04	6.57 ± 0.48 c	14.90 ± 0.02	15.33 ± 0.32 d	3.61 ± 0.04	5.04 ± 0.58 e
unsaturated/SFA	5.04 ± 0.05	4.56 ± 0.18	4.96 ± 0.11	4.29 ± 1.13	4.54 ± 0.12	4.38 ± 0.43	4.22 ± 0.13	3.97 ± 0.74	5.54 ± 0.05	5.03 ± 0.72
18:1/18:2	3.17 ± 0.09	3.22 ± 0.27 a	12.13 ± 0.21	9.63 ± 1.87 b	17.38 ± 0.24	12.60 ± 0.83 c	4.48 ± 0.24	4.40 ± 0.78 d	26.09 ± 0.08	18.65 ± 1.56 e

[a]Data are expressed as area percent and are the mean ± SD from three separate preparations ($n = 3$). Different letters in value of CRLP within a row are different ($p < 0.05$) by two-way ANOVA analysis.

DOI: 10.1021/acs.jafc.5b01626
J. Agric. Food Chem. 2015, 63, 6731−6738

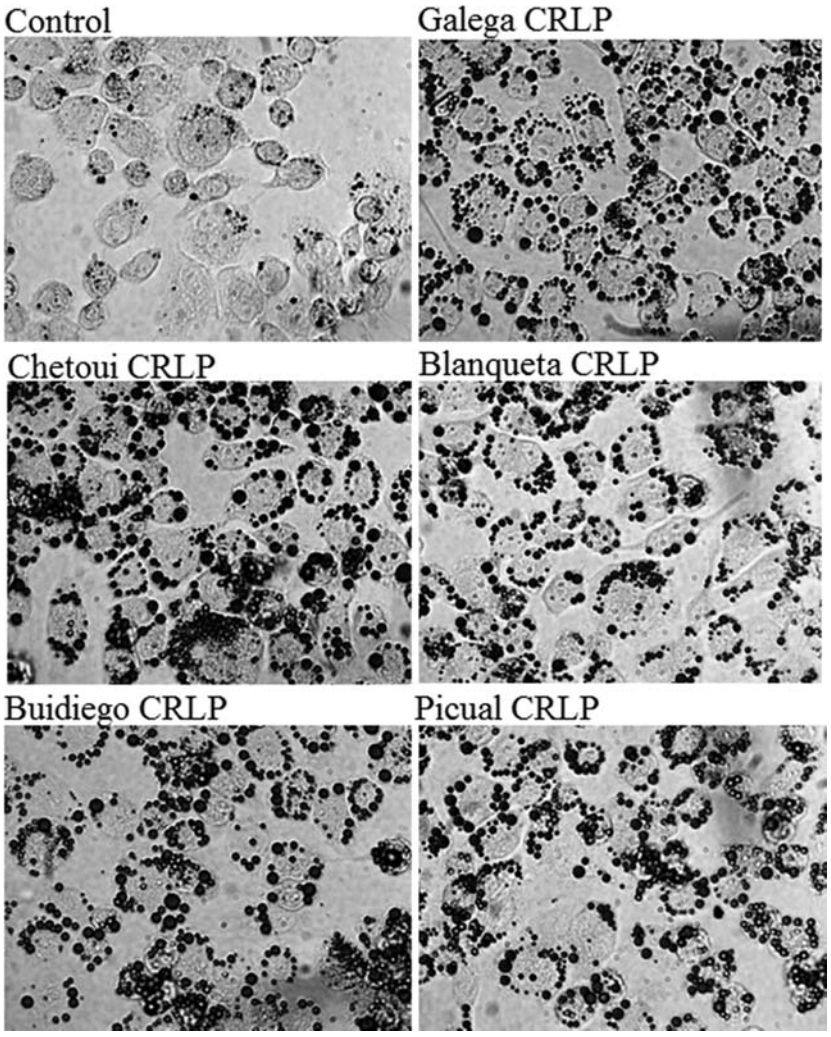

Figure 1. Lipid accumulation in cell THP-1 macrophagues incubated with CRLP containing TAG from 'Chetoui', 'Buidiego', 'Galega', 'Blanqueta', and 'Picual' EVOO cultivars. THP-1 macrophages were incubated with CRLP (final concentration = 0.15 μmol TAG/mL) for 24 h and stained with Oil Red O.

kept at −20 °C for subsequent total TAG determination and FA composition.

Triacylglycerol and Fatty Acid Composition. Total TAG in CRLP and cells were determined by enzymatic analysis using a commercial enzymatic reagent colorimetric/fluorometric kit (BioVision Inc., Milpitas, CA, USA). For the determination of CRLP FA composition, TAG were isolated by SPE diol columns as described above and were transmethylated using sodium metoxide in methanol (0.5%). For the analysis of FA composition in the cells, intracellular TAG were directly transmethylated using a methylation mixture (MeOH/toluene/DMP/H_2SO_4) and heptane. The resulting FAME of CRLP and cells were analyzed by GC, using a model 5890 series II GC (Hewlett-Packard Co, Avondale, AZ, USA) equipped with a flame ionization detector and a capillary silica column Supelcowax 10 (Supelco Co., Bellefonte, PA, USA) of 60 m length and 025 mm internal diameter. FAME were identified by comparison of their retention times against those of standards and quantified by external standard using peak area integration; results were expressed as relative area percentage. CRLP and cell protein content were measured according to the method of Bradford using BSA as standard.

Statistical Analysis. Results are expressed as means ± SD, unless otherwise stated. Statistical analyses were conducted using the GraphPad Prism v.5 statistical package (GraphPad Software, Inc.). Statistical significance was assessed by one- or two-way ANOVA, followed by Bonferroni's multiple-comparison tests. Correlations between variables were assessed using Pearson's correlation coefficients. Differences were considered statistically significant at $p < 0.05$.

RESULTS

CRLP TAG Content and FA Composition. The TAG contents were similar in all five types of CRLP (μmol/mL, n = 3): 'Chetoui' CRLP, 2.38 ± 0.4; 'Buidiego' CRLP, 1.99 ± 0.62; 'Galega' CRLP, 2.76 ± 0.17; 'Blanqueta' CRLP, 1.93 ± 0.10; 'Picual' CRLP, 1.83 ± 0.53.

Overall, the FA profiles CRLP-TAG and EVOO of all cultivars studied were similar (Table 1). However, significant differences were observed among cultivars, which resulted in differences in CRLP-TAG. Oleic acid content was the main FA in all CRLP, accounting for 60−76% of all FA, with significant differences among cultivars. Likewise, linoleic acid ranged from 4 to 18%. 'Picual' CRLP showed the highest oleic acid content (76.6%) and the lowest linoleic acid content (4.1%), whereas 'Chetoui' CRLP had the lowest oleic acid content (60.9%) and the greatest linoleic acid content (18.9%). As a consequence, the MUFA concentration was highest in 'Picual' CRLP and PUFA concentration in 'Chetoui' CRLP. SFA content was higher in 'Blanqueta' CRLP.

DOI: 10.1021/acs.jafc.5b01626
J. Agric. Food Chem. 2015, 63, 6731−6738

Intracellular Lipid Accumulation in THP-1 Macrophages. THP-1 macrophages were treated with 'Chetoui', 'Buidiego', 'Galega', 'Blanqueta', and 'Picual' CRLP (0.15 μmol TAG/mL) for 24 h. Incubation of macrophages with all CRLP resulted in increased intracellular accumulation of lipids as assessed by Oil Red O staining (Figure 1). Images revealed a light staining in control cells and a strong red staining in cells incubated with CRLP, confirming the intracellular lipid incorporation.

Intracellular TAG concentrations differed according to the type of CRLP used. There was a significantly higher accumulation of TAG in cells incubated with 'Chetoui' and 'Blanqueta' CRLP than with 'Buidiego' and 'Picual' CRLP (Figure 2).

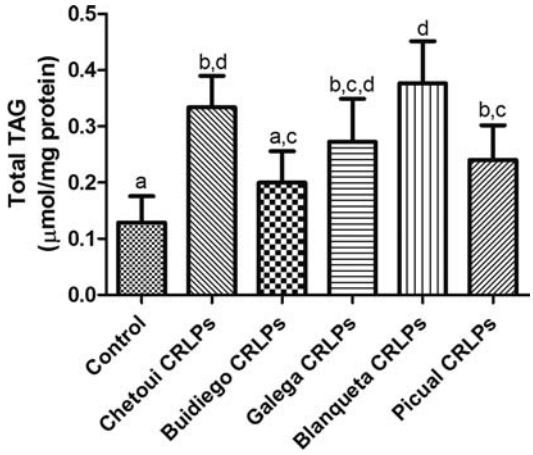

Figure 2. Total TAG accumulated after 24 h in THP-1 macrophages incubated with 'Chetoui', 'Buidiego', 'Galega', 'Blanqueta', and 'Picual' CRLP. Data are the mean from three separate experiments, and error bars show the SD. Different letters indicate significant difference ($p < 0.05$) by one-way ANOVA analysis and Bonferroni's post hoc test.

The TAG fraction of THP-1 macrophages showed significant differences for the main FA, namely, palmitic, palmitoleic, stearic, oleic, linoleic, and arachidonic (20:4 n-6) acids and, therefore, for the SFA, MUFA, and PUFA contents (Table 2). Control cells presented a higher SFA proportion compared with cells incubated with CRLP. Among cells incubated with CRLP, SFA accumulation was enhanced in cells incubated with 'Galega' CRLP (29%), whereas MUFA concentration was higher in those incubated with 'Picual' (62%) and 'Buidiego' (61%) CRLP and lower with 'Chetoui' CRLP (51%). Finally, PUFA content was increased in cells treated with 'Chetoui' CRLP (22%) and decreased with 'Picual' CRLP (11%). As well as in CRLP, palmitic, stearic, oleic, and linoleic acids were found with the highest proportions in the intracellular TAG fraction. It was observed that oils with the greatest oleic and linoleic acid contents led to cells engorged with TAG rich in those FA. Oleic acid was found at higher concentration in cells incubated with 'Picual' CRLP (59%) and at lowest concentrations in those treated with 'Chetoui' (48%) and 'Galega' CRLP (50%). Conversely, linoleic acid was found at greater amounts in cells incubated with 'Chetoui' CRLP (13%) and at lower concentration in cells incubated with 'Picual' CRLP (4%).

The oleic acid to linoleic acid ratio (18:1/18:2 ratio) of the EVOO was plotted against TAG accumulation in cells to determine the relationship between oleic and linoleic acid content in the parent oils and lipid intracellular accumulation (Figure 3A) and the FA composition in intracellular TAG (Figure 3B). A higher 18:1/18:2 ratio was associated with lower TG accumulation in the cells and very strongly with the intracellular 18:1/18:2 ratio.

DISCUSSION

Dietary fats enter the blood as CM that undergo lipolysis in extrahepatic capillary beds. The resulting CMR particles contain about 30% of TAG and most of the cholesterol mass of the parent lipoproteins and are considered atherogenic lipoproteins. CMR are taken by several types of macrophages[13] and give rise to foam cells by inducing accumulation of cholesterol, TAG, or both.[12,13,17,25−27]

A number of epidemiologic studies developed in different countries constitute a firm and reliable experimental base supporting the beneficial effects of the Mediterranean diet, rich in olive oil, with regard to the reduction of cardiovascular disease.[28,29] Although the benefits of EVOO against cardiovascular disease cannot be attributed solely to oleic acid,[30] the protective effects have been ascribed to higher intakes of oleic and α-linolenic acid (18:3 n-3) acids and lower intakes of SFA and linoleic acid (18:2 n-6).[31−34]

The FA composition of EVOO depends on the zone of production, the latitude, the climate, the variety, and the stage of maturity of the fruit.[4−6] For instance, Greek, Italian, and Spanish EVOO are, in general terms, low in linoleic and palmitic acids, and they have a high percentage of oleic acid. In contrast, Tunisian EVOO are high in linoleic and palmitic acids and lower in oleic acid.[4] Given these differences, we evaluated the uptake of CRLP prepared with TAG obtained from five EVOO cultivars and the induction of lipid accumulation in macrophages derived from the human monocyte cell line THP-1. Because it is difficult to obtain CMR uncontaminated with lipoproteins of a similar density, such as CM and very-low-density lipoproteins, from human blood, we used CRLP as an experimental model.[24] CRLP have been used previously by a number authors to study lipid metabolism[12,26,35−38] as their composition can be easily manipulated, providing a suitable and convenient model.

We obtained EVOO from 'Chetoui', 'Buidiego', 'Galega', 'Blanqueta', and 'Picual' cultivars, which presented differences in their FA composition, and we used their TAG to prepare CRLP that did not differ in their TAG content and having FA composition similar to that of the parent oils (Table 1). These findings are consistent with previous works using palm, olive, corn, or fish oils.[37,38]

The exposure of human THP-1 cells to EVOO-CRLP caused intracellular lipid accumulation and thus provided evidence of CRLP uptake by macrophages and foam cell formation. It has been reported that not all CMR are equally taken up by macrophages, and the particle size and lipid composition may have a significant influence on the process of uptake and lipid accumulation.[39] Batt et al.[17] studied the effect of LDL and CRLP on lipid accumulation in human monocyte-derived macrophages (HMDMs) and in THP-1 cells. They found that CRLP, without prior oxidation, caused lipid accumulation in human macrophages to an extent comparable to that caused by oxidized LDL. They also reported a greater proportion lipid accumulation in response to CRLP in the form of TAG and in the form of CE in response to oxidized LDL.

Our experiments showed that 'Blanqueta' and 'Chetoui' CRLP caused the greatest TAG accumulation in THP-1 cells.

DOI: 10.1021/acs.jafc.5b01626
J. Agric. Food Chem. 2015, 63, 6731−6738

Table 2. Fatty Acid Composition of THP-1 Macrophages Incubated with 'Chetoui', 'Buidiego', 'Galega', 'Blanqueta', and 'Picual' CRLP for 24 h[a]

	control	'Chetoui' CRLP	'Buidiego' CRLP	'Galega' CRLP	'Blanqueta' CRLP	'Picual' CRLP
14:0	0.74 ± 0.38	0.28 ± 0.06	0.10 ± 0.03	0.22 ± 0.22	0.32 ± 0.03	0.17 ± 0.07
14:1 n-5	0.13 ± 0.07	0.31 ± 0.03	1.14 ± 0.31	0.95 ± 1.33	0.06 ± 0.02	0.06 ± 0.03
16:0	25.4 ± 1.89 a	17.3 ± 1.51 b	17.2 ± 0.50 b	19.9 ± 0.96 c	18.6 ± 0.65 b	16.6 ± 0.76 b
16:1 n-9	6.14 ± 0.30 ad	2.04 ± 0.35 b	7.20 ± 2.49 ac	4.48 ± 0.17 d	2.59 ± 0.10 b	2.59 ± 0.27 b
16:1 n-7	0.33 ± 0.06	0.35 ± 0.04	0.11 ± 0.02	0.19 ± 0.05	0.28 ± 0.02	0.12 ± 0.01
16:1 n-5	0.51 ± 0.14	0.66 ± 0.00	1.80 ± 0.10	0.34 ± 0.04	0.34 ± 0.07	0.21 ± 0.05
18:0	14.5 ± 0.50 a	7.94 ± 0.37 bd	7.27 ± 0.18 b	8.58 ± 0.64 bd	6.69 ± 0.98 bc	9.55 ± 0.88 d
18:1 n-9	32.0 ± 0.33 a	48.3 ± 1.79 b	51.4 ± 0.86 c	49.9 ± 6.21 bc	51.5 ± 1.38 cd	59.3 ± 4.07 de
18:2 n-6	3.38 ± 0.38 a	13.3 ± 0.91 b	5.92 ± 1.28 c	6.07 ± 0.89 c	11.6 ± 0.28 b	4.43 ± 0.15 ac
18:3 n-6	0.44 ± 0.10	0.90 ± 0.15	0.70 ± 0.09	0.52 ± 0.02	0.90 ± 0.01	0.73 ± 0.08
18:3 n-3	1.21 ± 0.11	1.27 ± 0.12	1.20 ± 0.01	0.38 ± 0.13	0.97 ± 0.13	1.24 ± 0.07
20:0	1.58 ± 0.01	0.41 ± 0.06	0.20 ± 0.02	0.45 ± 0.04	0.38 ± 0.00	0.24 ± 0.07
20:1 n-9	0.56 ± 0.07	0.22 ± 0.05	0.09 ± 0.05	0.12 ± 0.03	0.18 ± 0.03	0.11 ± 0.02
20:2 n-6	1.22 ± 0.10	0.53 ± 0.02	1.03 ± 0.13	0.67 ± 0.07	0.50 ± 0.04	0.39 ± 0.05
20:4 n-6	4.63 ± 0.15 a	1.79 ± 0.06 b	1.89 ± 0.06 b	2.52 ± 0.64 b	1.80 ± 0.14 b	1.42 ± 0.23 b
20:5 n-3	1.37 ± 0.19	0.72 ± 0.09	0.40 ± 0.08	0.74 ± 0.05	0.68 ± 0.05	0.46 ± 0.28
22:4 n-6	0.39 ± 0.00	0.47 ± 0.15	0.63 ± 0.06	0.94 ± 0.04	0.61 ± 0.10	0.50 ± 0.08
22:5 n-6	1.21 ± 0.22	0.53 ± 0.18	0.23 ± 0.03	0.85 ± 0.06	0.75 ± 0.04	0.76 ± 0.01
22:5 n-3	1.64 ± 0.31	0.49 ± 0.10	0.36 ± 0.01	0.87 ± 0.10	0.42 ± 0.03	0.40 ± 0.07
22:6 n-3	2.45 ± 0.29	2.16 ± 0.41	1.15 ± 0.58	1.30 ± 0.56	0.81 ± 0.11	0.75 ± 0.09
total SFA	42.4 ± 0.70 a	26.0 ± 0.50 b	24.7 ± 0.18 b	29.2 ± 0.46 c	26.0 ± 0.42 b	26.5 ± 0.45 b
total MUFA	39.7 ± 0.16 a	51.8 ± 0.38 b	61.8 ± 0.64 c	56.0 ± 1.31 d	54.9 ± 0.27 d	62.4 ± 0.74 c
total PUFA	17.9 ± 0.19 ad	22.2 ± 0.22 b	13.5 ± 0.23 c	14.9 ± 0.26c	19.0 ± 0.09 d	11.1 ± 0.11 e
unsaturated/SFA	1.36 ± 0.35	2.85 ± 0.36	3.04 ± 0.35	2.43 ± 0.68	2.84 ± 0.26	2.77 ± 0.43
18:1/18:2	9.48 ± 0.35 a	3.62 ± 1.35 b	8.69 ± 1.07 a	8.22 ± 3.55 a	4.44 ± 0.83 b	13.4 ± 2.11 c

[a]Data are expressed as area percent and are the mean ± SD from three separate preparations (n = 3). Different letters within a row are different (p < 0.05) by two-way ANOVA analysis.

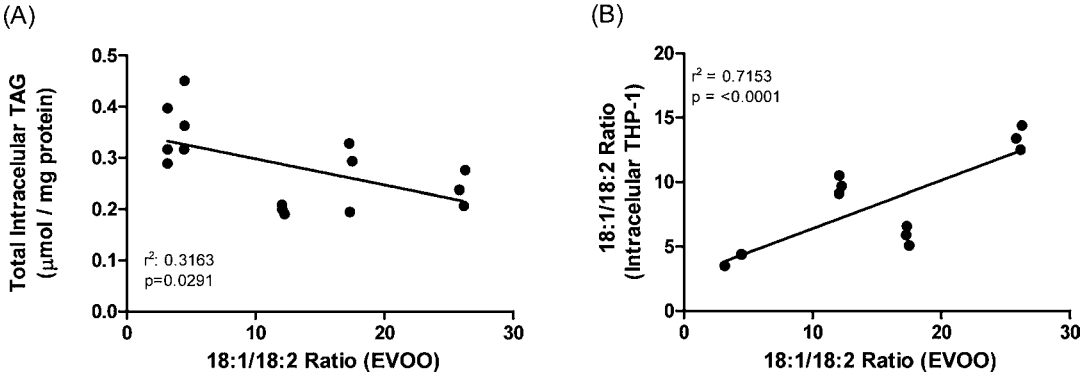

Figure 3. Correlation of oleic acid to linoleic acid ratio (18:1/18:2) of EVOO with (A) TAG accumulated in THP-1 macrophages and (B) oleic acid to linoleic acid ratio (18:1/18:2) in intracellular THP-1 macrophages after incubation with 'Chetoui', 'Buidiego', 'Galega', 'Blanqueta', and 'Picual' CRLPs.

'Blanqueta' CRLP were characterized by higher SFA content and 'Chetoui' CRLP by higher linoleic acid and PUFA content. This result is comparable with previous works by De Pascale et al.[12] and Song et al.,[27] who added SFA, MUFA, and n-6 or n-3 PUFA to THP-1 macrophages in the form of CRLP or nonesterified FA, respectively. Both confirmed that SFA are taken up more rapidly and result in greater lipid accumulation in cells, although they observed that PUFA-rich particles caused the lowest lipid accumulation. In contrast, our results showed the CRLP with greater PUFA content caused more lipid accumulation in cells than MUFA rich-CRLP. In this sense Song et al.[27] described differences between incubation with oleic or linoleic acids only for cholesterol and not for TAG. Likewise, De Pascale et al.[12] employed CRLP, reporting significant differences in intracellular TAG accumulation only between palm-CRLP and corn-CRLP, although differences between corn-CRLP and olive-CRLP were not observed. Interestingly, in that study the 18:1/18:2 ratio in CRLP (7.65) was similar to that obtained when we prepared CRLP from the 'Buidiego' cultivar (9.63), which caused the lowest TAG accumulation in the cells.

When the FA composition of intracellular TAG was compared with that of CRLP, we observed that it was highly preserved; that is, cells treated with CRLP with the highest concentrations of 18:1, 18:2, or 16:0 also exhibited the highest levels of these FA intracellularly. In fact, the 18:1/18:2 ratio in the oils correlated positively and very strongly with the same ratio in cell TAG. Also, we found that the 18:1/18:2 ratio also

DOI: 10.1021/acs.jafc.5b01626
J. Agric. Food Chem. 2015, 63, 6731−6738

correlated with TAG concentration in the cells, although a negative relationship was obtained. Napolitano and Bravo[40] studied the influence of the TAG source (trilinolein or triolein) in CRLP in human macrophages. Their results were in close agreement with ours, finding that particles enriched with both trilinolein and triolein induced a pattern of increase in intracellular TAG synthesis, but which was higher after incubation with trilinolein. However, an important point to consider is that although all of the CRLP employed here were rich in oleic acid, they differed in every other minor FA. Slight differences in the FA can lead to a highly different TAG molecular species composition, which may have important effects in the metabolic fate of lipoproteins, as observed in elderly individuals.[41]

Although the mechanisms by which TRL are taken up by macrophages have not been studied extensively, CMR are believed to be incorporated into macrophages by two main pathways: uptake of whole particles via membrane receptors and hydrolysis by macrophage-secreted LPL.[40] Extracellular lipolysis seems particularly important for internalization of dietary fatty acids.[40] It has been suggested that the V_{max} of LPL in the adipose tissue decreases with increasing chain length and unsaturation degree of monoacid CM-TAG due to decreased fluidity of the particle.[42] However, differences between oleic acid- and linoleic acid-rich seem to be significant only for large CM and not for VLDL.[43] On the other hand, studies carried out in THP-1 cells have proposed that oleic acid-rich dietary fats may prevent excessive lipid accumulation in monocyte/macrophage cells by down-regulating the gene expression of apolipoprotein B48 receptor[44] and that linoleic acid stimulates CD36 receptor, promoting intracellular TAG accumulation.[45]

In conclusion, the results of this study demonstrated that the effect of differences in the FA composition of EVOO is similar to the effect caused by the same FA when forming part of other dietary oils. In fact, linoleic acid-rich EVOO induced higher TAG incorporation into THP-1 macrophages compared to oleic acid-rich EVOO, the 18:1/18:2 ratio being consistently correlated with intracellular TAG accumulation. In this regard, the ratio between 18:1 and 18:2 could be used as a helpful marker to identify EVOO with possible cardioprotective effects. Because EVOO oleic and linoleic acid composition is cultivar dependent, among other agronomical factors, this marker could be independent of these factors.

Although the results presented here may be a starting point to indicate the possibility of selecting VOO cultivars for specific nutritional uses according to their FA composition, it is certainly too early to give recommendations to the population. Apart from the fatty acid composition, there are many other factors to consider that may have direct or indirect influence on health.

AUTHOR INFORMATION

Corresponding Author

*(A.Q.-F.) Phone: (34) 671532221. E-mail: angelica.quintero@juntadeandalucia.es.

Funding

This work was supported by Project FEDER-P10-AGR6099 of Junta de Andalucía, Grant CAICEM 12-79 from Interprofessional del Aceite de Oliva Español, and FEDER-INIA RTA 2010-00013-C02-01.

Notes

The authors declare no competing financial interest.

ABBREVIATIONS USED

CRLP, chylomicron remnant-like particles; VOO, virgin olive oil; EVOO, extra virgin olive oil; TAG, triacylglycerols; CM, chylomicrons; TRL, TAG-rich lipoproteins; SFA, saturated fatty acids; MUFA, monounsaturated fatty acids; PUFA, polyunsaturated fatty acids; CE, cholesteryl esters; CMR, chylomicron remnants; FA, fatty acid

REFERENCES

(1) López-Miranda, J.; Pérez-Jiménez, F.; Ros, E.; De Caterina, R.; Badimón, L.; Covas, M. I.; Escrich, E.; Ordovás, J. M.; Soriguer, F.; Abiá, R.; Alarcón de la Lastra, C.; Battino, M.; Corella, D.; Chamorro-Quirós, J.; Delgado-Lista, J.; Giugliano, D.; Esposito, K.; Estruch, R.; Fernandez-Real, J. M.; Gaforio, J. J.; La Vecchia, C.; Lairon, D.; López-Segura, F.; Mata, P.; Menéndez, J. A.; Muriana, F. J.; Osada, J.; Panagiotakos, D. B.; Paniagua, J. A.; Pérez-Martinez, P.; Perona, J.; Peinado, M. A.; Pineda-Priego, M.; Poulsen, H. E.; Quiles, J. L.; Ramírez-Tortosa, M. C.; Ruano, J.; Serra-Majem, L.; Solá, R.; Solanas, M.; Solfrizzi, V.; de la Torre-Fornell, R.; Trichopoulou, A.; Uceda, M.; Villalba-Montoro, J. M.; Villar-Ortiz, J. R.; Visioli, F.; Yiannakouris, N. Olive oil and health: summary of the II international conference on olive oil and health consensus report, Jaén and Córdoba (Spain) 2008. *Nutr., Metab. Cardiovasc. Dis.* **2010**, *20*, 284−294.

(2) Frankel, E. N. Nutritional and biological properties of extra virgin olive oil. *J. Agric. Food Chem.* **2011**, *59*, 785−792.

(3) International Olive Conucil. Trade standard applying to olive oils and olive-pomace oils (February 2015). COI 2015, T.15/NC No. 3/REV.8 2015.

(4) Boskou, D.; Blekas, G.; Tsimidou, M. Olive oil composition. In *Olive Oil: Chemistry and Technology*, 2nd ed.; Boskou, D., Ed.; AOCS Publishing: Champaign, IL, USA, 2006; pp 41−72.

(5) Beltrán, G.; del Rio, C.; Sánchez, S.; Martínez, L. Influence of harvest date and crop yield on the fatty acid composition of virgin olive oils from cv. Picual. *J. Agric. Food Chem.* **2004**, *52*, 3434−3440.

(6) Mousa, Y.; Gerasopoulos, D.; Metzidakis, I.; Kiritsakis, A. Effect of altitude on fruit and oil quality characteristics of 'Mastoides' olives. *J. Sci. Food Agric.* **1996**, *71*, 345−350.

(7) Kaliora, A. C.; Artemiou, A.; Giogios, I.; Kalogeropoulos, N. The impact of fruit maturation on bioactive microconstituents, inhibition of serum oxidation and inflammatory markers in stimulated PBMCs and sensory characteristics of Koroneiki virgin olive oils from Messenia, Greece. *Food Funct.* **2013**, *4*, 1185−1194.

(8) Fabiani, R.; Sepporta, M. V.; Mazza, T.; Rosignoli, P.; Fuccelli, R.; De Bartolomeo, A.; Crescimanno, M.; Taticchi, A.; Esposto, S.; Servili, M.; Morozzi, G. Influence of cultivar and concentration of selected phenolic constituents on the in vitro chemiopreventive potential of olive oil extracts. *J. Agric. Food Chem.* **2011**, *59*, 8167−8174.

(9) Uceda, M.; Hermoso, M.; Aguilera, M. P. La calidad del aceite de oliva. In *El Cultivo del Olivo*, 6th ed.; Barranco, D., Ed.; Mundi-Prensa: Madrid, Spain, 2008; pp 699−727.

(10) Pérez-Jiménez, F.; López-Miranda, J.; Mata, P. Protective effect of dietary monounsaturated fat on arteriosclerosis: beyond cholesterol. *Atherosclerosis* **2002**, *163*, 385−398.

(11) Abia, R.; Pacheco, Y. M.; Perona, J. S.; Montero, E.; Muriana, F. J. G.; Ruiz-Gutiérrez, V. The metabolic availability of dietary triacylglycerols from two high oleic oils during the postprandial period does not depend on the amount of oleic acid ingested by healthy men. *J. Nutr.* **2001**, *131*, 59−65.

(12) De Pascale, C.; Avella, M.; Perona, J. S.; Ruiz-Gutierrez, V.; Wheeler-Jones, C. P. D.; Botham, K. M. Fatty acid composition of chylomicron remnant-like particles influences their uptake and induction of lipid accumulation in macrophages. *FEBS J.* **2006**, *273*, 5632−5640.

(13) Yu, K. C.; Mamo, J. C. L. Chylomicron-remnant-induced foam cell formation and cytotoxicity: a possible mechanism of cell death in atherosclerosis. *Clin. Sci.* **2000**, *98*, 183−192.

(14) Redgrave, T. G.; Ly, H. I.; Quintao, E. C. R.; Ramberg, C. F.; Boston, R. C. Clearance from plasma of triacylglycerol and cholesteryl

DOI: 10.1021/acs.jafc.5b01626
J. Agric. Food Chem. 2015, 63, 6731−6738

ester after intravenous injection of chylomicron-like lipid emulsions in rats and man. *Biochem. J.* **1993**, *290*, 843−847.
(15) Proctor, S. D.; Mamo, J. C. L. Intimal retention of cholesterol derived from apolipoprotein B100- and apolipoprotein B48-containing lipoproteins in carotid arteries of Watanabe heritable hyperlipidemic rabbits. *Arterioscler., Thromb., Vasc. Biol.* **2003**, *23*, 1595−1600.
(16) Proctor, S. D.; Vine, D. F.; Mamo, J. C. L. Arterial retention of apolipoprotein B48- and B100-containing lipoproteins in atherogenesis. *Curr. Opin. Lipidol.* **2002**, *13*, 461−470.
(17) Batt, K. V.; Avella, M.; Moore, E. H.; Jackson, B.; Suckling, K. E.; Botham, K. M. Differential effects of low-density lipoprotein and chylomicron remnants on lipid accumulation in human macrophages. *Exp. Biol. Med.* **2004**, *229*, 528−537.
(18) Moore, E. H.; Bejta, F.; Avella, M.; Suckling, K. E.; Botham, K. M. Efflux of lipid from macrophages after induction of lipid accumulation by chylomicron remnants. *Biochim. Biophys. Acta, Mol. Cell Biol. Lipids* **2005**, *1735*, 20−29.
(19) Moore, E. H.; Napolitano, M.; Avella, M.; Bejta, F.; Suckling, K. E.; Bravo, E.; Botham, K. M. Protection of chylomicron remnants from oxidation by incorporation of probucol into the particles enhances their uptake by human macrophages and increases lipid accumulation in the cells. *Eur. J. Biochem.* **2004**, *271*, 2417−2427.
(20) Napolitano, M.; Avella, M.; Botham, K. M.; Bravo, E. Chylomicron remnant induction of lipid accumulation in J774 macrophages is associated with up-regulation of triacylglycerol synthesis which is not dependent on oxidation of the particles. *Biochim. Biophys. Acta, Mol. Cell Biol. Lipids* **2003**, *1631*, 255−264.
(21) Hunter, K. A.; Crosbie, L. C.; Horgan, G. W.; Miller, G. J.; Dutta-Roy, A. K. Effect of diets rich in oleic acid, stearic acid and linoleic acid on postprandial haemostatic factors in young healthy men. *Br. J. Nutr.* **2001**, *86*, 207−215.
(22) Cabello-Moruno, R.; Perona, J. S.; Ruiz-Gutierrez, V. Influence of minor components of olive oils on the composition and size of TRLs and on macrophage receptors involved in foam cell formation. *Biochem. Soc. Trans.* **2007**, *35*, 470−471.
(23) European Community Regulation. Characteristics of olive and pomace oils and on their analytical methods. *Off. J. Eur. Communities* **1991**, *2568/91*, L248, 1−82.
(24) Antelo, A.; Perona, J. S. Evaluation of a method of preparation of lipid emulsions as a model for chylomicron-like particles. *J. Liposome Res.* **2013**, *23*, 126−133.
(25) Botham, K. M.; Bravo, E.; Elliott, J.; Wheeler-Jones, C. P. D. Direct interaction of dietary lipids carried in chylomicron remnants with cells of the artery wall: implications for atherosclerosis development. *Curr. Pharm. Des.* **2005**, *11*, 3681−3695.
(26) Napolitano, M.; Batt, K. V.; Avella, M.; Bravo, E.; Botham, K. M. Lipid synthesis in macrophages derived from the human cell line THP-I: modulation of the effects of native and oxidized chylomicronremnant-like particles by oestrogen. *Clin. Sci.* **2001**, *101*, 403−413.
(27) Song, Y.; Zhang, L.; Li, H.; Gu, Y.; Li, F.; Jiang, L.; Liu, F.; Ye, J.; Li, Q. Polyunsaturated fatty acid relatively decreases cholesterol content in THP-1 macrophage-derived foam cell: partly correlates with expression profile of CIDE and PAT members. *Lipids Health Dis.* **2013**, *12*, 111.
(28) Wahrburg, U.; Kratz, M.; Cullen, P. Mediterranean diet, olive oil and health. *Eur. J. Lipid Sci. Technol.* **2002**, *104*, 698−705.
(29) Guasch-Ferré, M.; Hu, F. B.; Martínez-González, M. A.; Fitó, M.; Bulló, M.; Estruch, R.; Ros, E.; Corella, D.; Recondo, J.; Gómez-Gracia, E.; Fiol, M.; Lapetra, J.; Serra-Majem, L.; Muñoz, M. A.; Pintó, X.; Lamuela-Raventós, R. M.; Basora, J.; Buil-Cosiales, P.; Sorlí, J. V.; Ruiz-Gutiérrez, V.; Martínez, J. A.; Salas-Salvadó, J. Olive oil intake and risk of cardiovascular disease and mortality in the PREDIMED Study. *BMC Med.* **2014**, *12*, 78−78.
(30) Perona, J. S.; Cabello-Moruno, R.; Ruiz-Gutierrez, V. The role of virgin olive oil components in the modulation of endothelial function. *J. Nutr. Biochem.* **2006**, *17*, 429−445.
(31) Hu, F. B. The Mediterranean diet and mortality − olive oil and beyond. *N. Engl. J. Med.* **2003**, *348*, 2595−2596.
(32) De Lorgeril, M.; Renaud, S.; Mamelle, N.; Salen, P.; Martin, J.; Monjaud, I.; Guidollet, J.; Touboul, P.; Delaye, J. Mediterranean α-linolenic acid-rich diet in secondary prevention of coronary heart disease. *Lancet* **1994**, *343*, 1454−1459.
(33) Mensink, R. P.; Katan, M. B. Effect of dietary fatty acids on serum lipids and lipoproteins: a meta- analysis of 27 trials. *Arterioscler., Thromb., Vasc. Biol.* **1992**, *12*, 911−919.
(34) Gardner, C. D.; Kraemer, H. C. Monounsaturated versus polyunsaturated dietary fat and serum lipids: a meta-analysis. *Arterioscler., Thromb., Vasc. Biol.* **1995**, *15*, 1917−1927.
(35) Maranhão, R. C.; Feres, M. C.; Martins, M. T.; Mesquita, C. H.; Toffoletto, O.; Vinagre, C. G. C.; Gianinni, S. D.; Pileggi, F. Plasma kinetics of a chylomicron-like emulsion in patients with coronary artery disease. *Atherosclerosis* **1996**, *126*, 15−25.
(36) Bentley, C.; Hathaway, N.; Widdows, J.; Bejta, F.; De Pascale, C.; Avella, M.; Wheeler-Jones, C. P. D.; Botham, K. M.; Lawson, C. Influence of chylomicron remnants on human monocyte activation in vitro. *Nutr., Metab. Cardiovasc. Dis.* **2011**, *21*, 871−878.
(37) López-Soldado, I.; Avella, M.; Botham, K. M. Differential influence of different dietary fatty acids on very low-density lipoprotein secretion when delivered to hepatocytes in chylomicron remnants. *Metab., Clin. Exp.* **2009**, *58*, 186−195.
(38) Lopez-Soldado, I.; Avella, M.; Botham, K. M. Comparison of the effects of dietary saturated, mono-unsaturated and polyunsaturated fatty acids on very-low-density lipoprotein secretion when delivered to hepatocytes in chylomicron remnant-like particles. *Biochem. Soc. Trans.* **2007**, *35*, 440−441.
(39) Botham, K. M.; Wheeler-Jones, C. P. D. Postprandial lipoproteins and the molecular regulation of vascular homeostasis. *Prog. Lipid Res.* **2013**, *52*, 446−464.
(40) Napolitano, M.; Bravo, E. Evidence of dual pathways for lipid uptake during chylomicron remnant-like particle processing by human macrophages. *J. Vasc. Res.* **2006**, *43*, 355−366.
(41) Perona, J. S.; Cañizares, J.; Montero, E.; Sánchez-Domínguez, J. M.; Pacheco, Y. M.; Ruiz-Gutierrez, V. Dietary virgin olive oil triacylglycerols as an independent determinant of very low-density lipoprotein composition. *Nutrition* **2004**, *20*, 509−514.
(42) Sato, K.; Takahashi, T.; Takahashi, Y.; Shiono, H.; Katoh, N.; Akiba, Y.; Akiba, Y. Preparation of chylomicrons and VLDL with monoacid-rich triacylglycerol and characterization of kinetic parameters in lipoprotein lipase-mediated hydrolysis in chickens. *J. Nutr.* **1999**, *129*, 126−131.
(43) Sato, K.; Takahashi, Y.; Takahashi, T.; Katoh, N.; Akiba, Y. Identification of factors regulating lipoprotein lipase catalyzed hydrolysis in rats with the aid of monoacid-rich lipoprotein preparations (1). *J. Nutr. Biochem.* **2002**, *13*, 528−538.
(44) Varela, L. M.; Ortega-Gomez, A.; Lopez, S.; Abia, R.; Muriana, F. J. G.; Bermudez, B. The effects of dietary fatty acids on the postprandial triglyceride-rich lipoprotein/apoB48 receptor axis in human monocyte/macrophage cells. *J. Nutr. Biochem.* **2013**, *24*, 2031−2039.
(45) Vallvé, J.; Uliaque, K.; Girona, J.; Cabré, A.; Ribalta, J.; Heras, M.; Masana, L. Unsaturated fatty acids and their oxidation products stimulate CD36 gene expression in human macrophages. *Atherosclerosis* **2002**, *164*, 45−56.

DOI: 10.1021/acs.jafc.5b01626
J. Agric. Food Chem. 2015, 63, 6731−6738

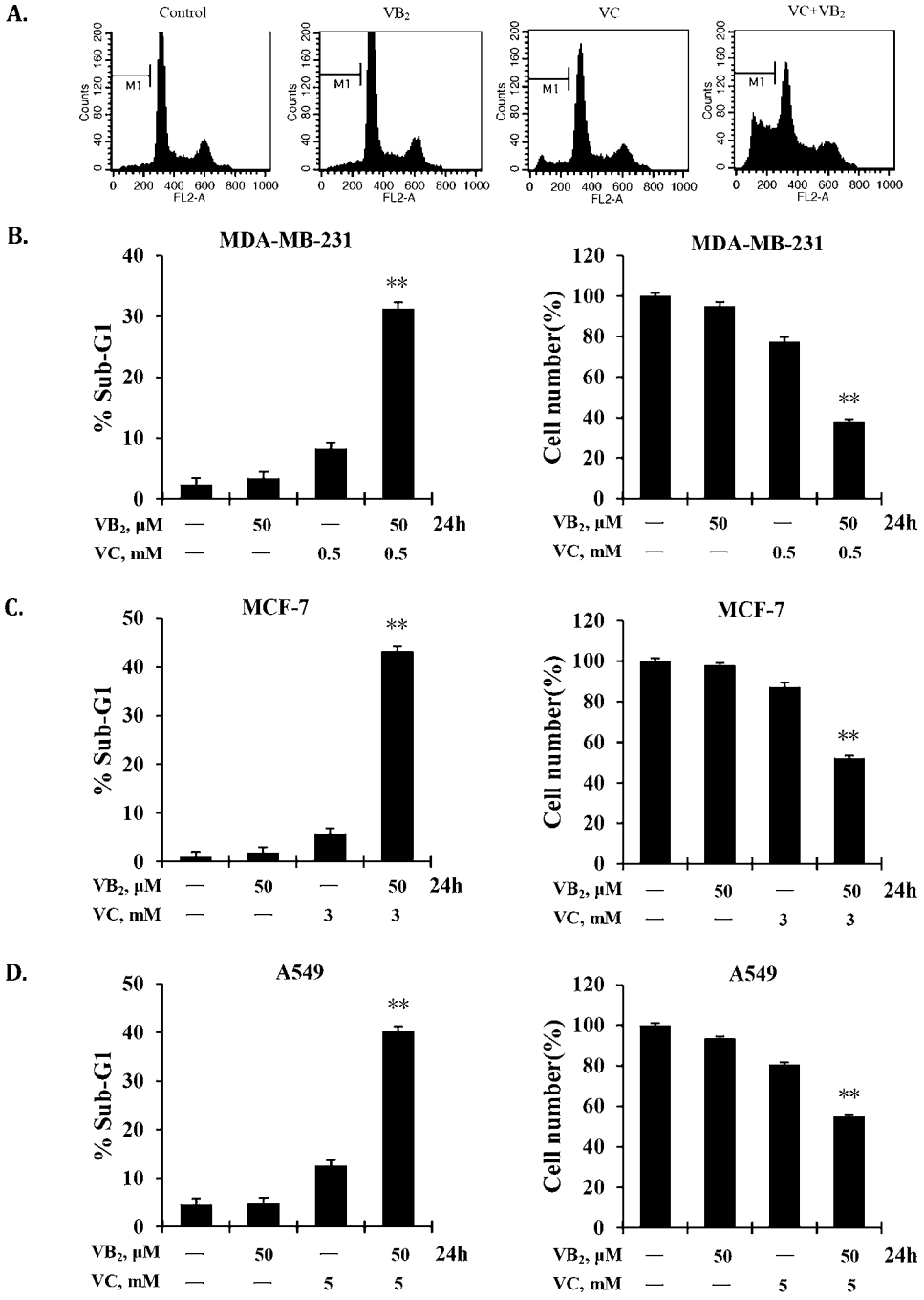

Figure 1. Combining vitamin C with vitamin B_2 resulted in enhanced cytotoxicity in MDA-MB-231 and MCF-7 breast cancer cells and A549 lung cancer cells. The cells were exposed to vitamins C and/or B_2 for 24 h, and apoptosis induction and overall inhibitory effects were measured by sub-G1 analysis and crystal violet staining, respectively: (A and B) MDA-MB-231 cells, (C) MCF-7 cells, and (D) A549 cells (**, $p < 0.01$).

agent alone or the combination on cell proliferation and survival. Briefly, the cells were exposed to vitamins C and/or B_2 for the indicated time, and then 1% glutaraldehyde was used to fix the cells for 15 min. After fixation, 0.02% crystal violet dye was added to stain the cells for 30 min. After staining, 70% ethanol was used to solubilize crystal violet dye bound to the cells. An enzyme-linked immunosorbent assay (ELISA) reader (Thermo, MA) was used to measure the absorbance at a wavelength of 570 nm, with the reference wavelength at 405 nm.

Determination of the Combination Index (*CI*). The nature of the combinatory effects of vitamins C and B_2 was quantitatively evaluated by the Chou−Talalay method.[17,18] The cells were exposed to varying doses of vitamins C and/or B_2. The overall suppressive actions were used to calculate the *CI* using the following formula:

$$CI = \frac{CA, x}{ICx, A} + \frac{CB, x}{ICx, B}$$

where *CA,x* and *CB,x* are the doses of each compound alone used in combination to produce *x*% inhibitory action and *ICx,A* and *ICx,B* are the doses for each compound alone to produce the same action. $CI < 1$ indicates a synergistic effect by the combination, whereas $CI = 1$ means an additive effect. If *CI* is greater than 1, it suggests antagonism produced by the combination.

Immunoblotting Assay. The cell was lysed with radioimmunoprecipitation assay (RIPA) buffer. An equal amount of proteins of the samples was loaded onto the gel. After electrophoretic separation, the proteins were transferred to a nitrocellulose membrane. The membrane was subsequently incubated with primary antibodies,

DOI: 10.1021/acs.jafc.5b01909
J. Agric. Food Chem. 2015, 63, 6739−6748

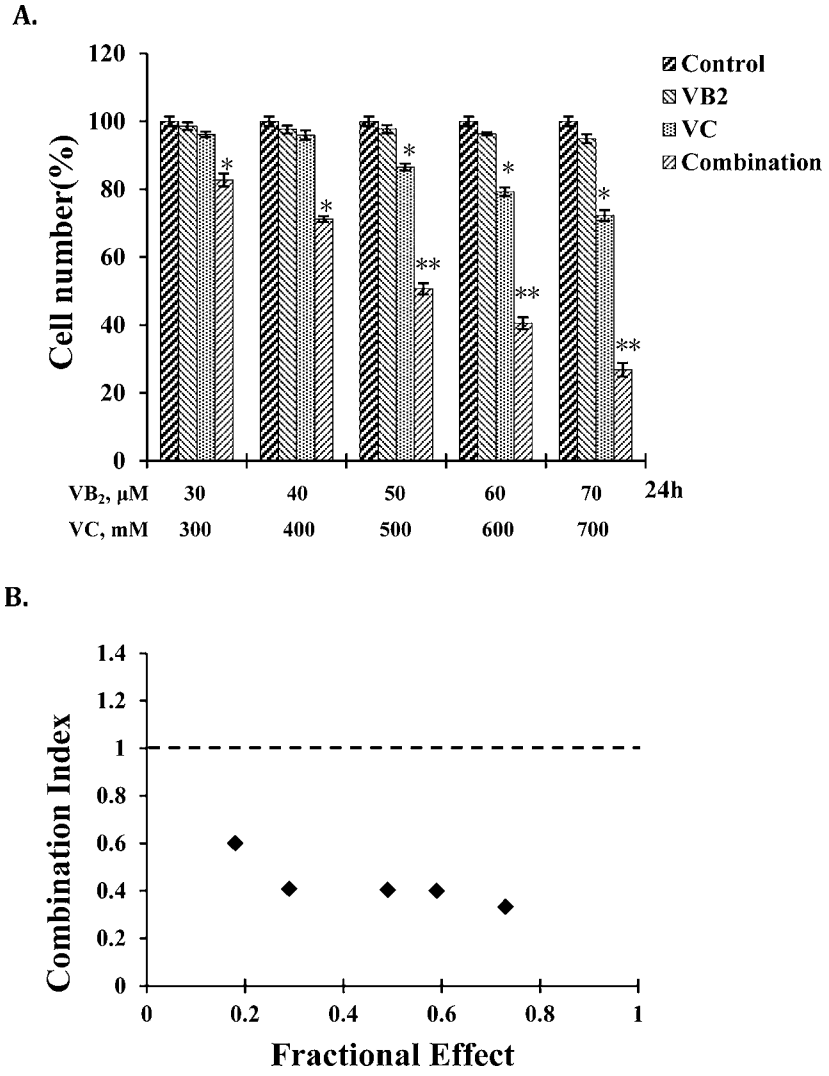

Figure 2. Enhanced inhibitory effect of vitamins C/B_2 combination is a synergistic action. (A) MDA-MB-231 cells were treated with each agent alone and combinations in a fixed ratio of 1:10 (vitamins B_2/C) for 24 h, and overall inhibitory effects of each agent alone or combinations on cell number were determined by crystal violet staining. (B) *CI* charts for the vitamins C/B_2 combination were plotted on the basis of data generated in panel A (∗, $p < 0.01$).

followed by recognition with corresponsive secondary antibody. The immunoreactive bands were detected using enhanced chemiluminescence.

Detection of AIF Translocation. The cells were exposed to vitamins C and/or B_2 for 12 h. After the treatment, the cells were fixed with 4% paraformaldehyde for 15 min, followed by permeabilization with Triton X-100 (0.25%) for 10 min. After blocking with 1% bovine serum albumin (BSA), the cells were probed with the antibody of AIF for 2 h, followed by incubation with fluorescein isothiocyanate (FITC)-conjugated secondary antibody for 1 h. DAPI was employed to counterstain the nuclei. The fluorescence was detected using confocal microscopy.

Preparation of Nuclear Extraction. A nuclear extraction kit (Thermo Scientific, catalog number P78835) was used to isolate nuclear fractions following the instructions of the manufacturer. Briefly, cells were exposed to vitamins C and/or B_2 for the indicated time, harvested with trypsin−ethylenediaminetetraacetic acid (EDTA), and centrifuged at 4 °C and 500*g*. Cells were washed by suspending the cell pellet with PBS and centrifuged to obtain the cell pellet. Three lysis buffers (CER I, CER II, and NER) were used sequentially following the protocol to isolate cytoplasmic and nuclear fractions.

Measurement of Mitochondrial Membrane Potential. The cells were exposed to vitamins C and/or B_2 the indicated time. After treatment, the cells were stained with 5,5′,6,6′-tetrachloro-1,1′,3,3′-tetraethylbenzimidazolocarbocyanine iodide (JC-1 dye) for 20 min. The fluorescence conversion from red to green was measured by flow cytometry.

RNA Interference. Bim siRNA and non-targeting siRNA were synthesized by Ambion (Austin, TX). To knockdown Bim, 50 nm of Bim siRNA was transfected into the cells using siPORT NeoFX. At 24 h post-transfection, the cells were used for subsequent experiments.

Statistical Analysis. The data shown represent the mean ± standard deviation (SD) for triplicates. A one-way analysis of variation (ANOVA) was used determine differences among multiple groups. The difference between two groups was assessed by the Student's *t* test using SPSS 18.0 for Microsoft Windows.

RESULTS

Combination of Vitamin C and B_2 Achieved a Significant Increase of Cell Death Induction in MDA-MB-231 and MCF-7 Breast Cancer Cells and A549 Lung Cancer Cells. To evaluate the combined actions of vitamins C and B_2 on cell death, MDA-MB-231 cells were treated with a mild toxic dose (around 10% cell death) of each single agent (on the basis of dose-finding experiments and literature[15,19,20]) or the combination for the indicated time. Cell death was

DOI: 10.1021/acs.jafc.5b01909
J. Agric. Food Chem. 2015, 63, 6739−6748

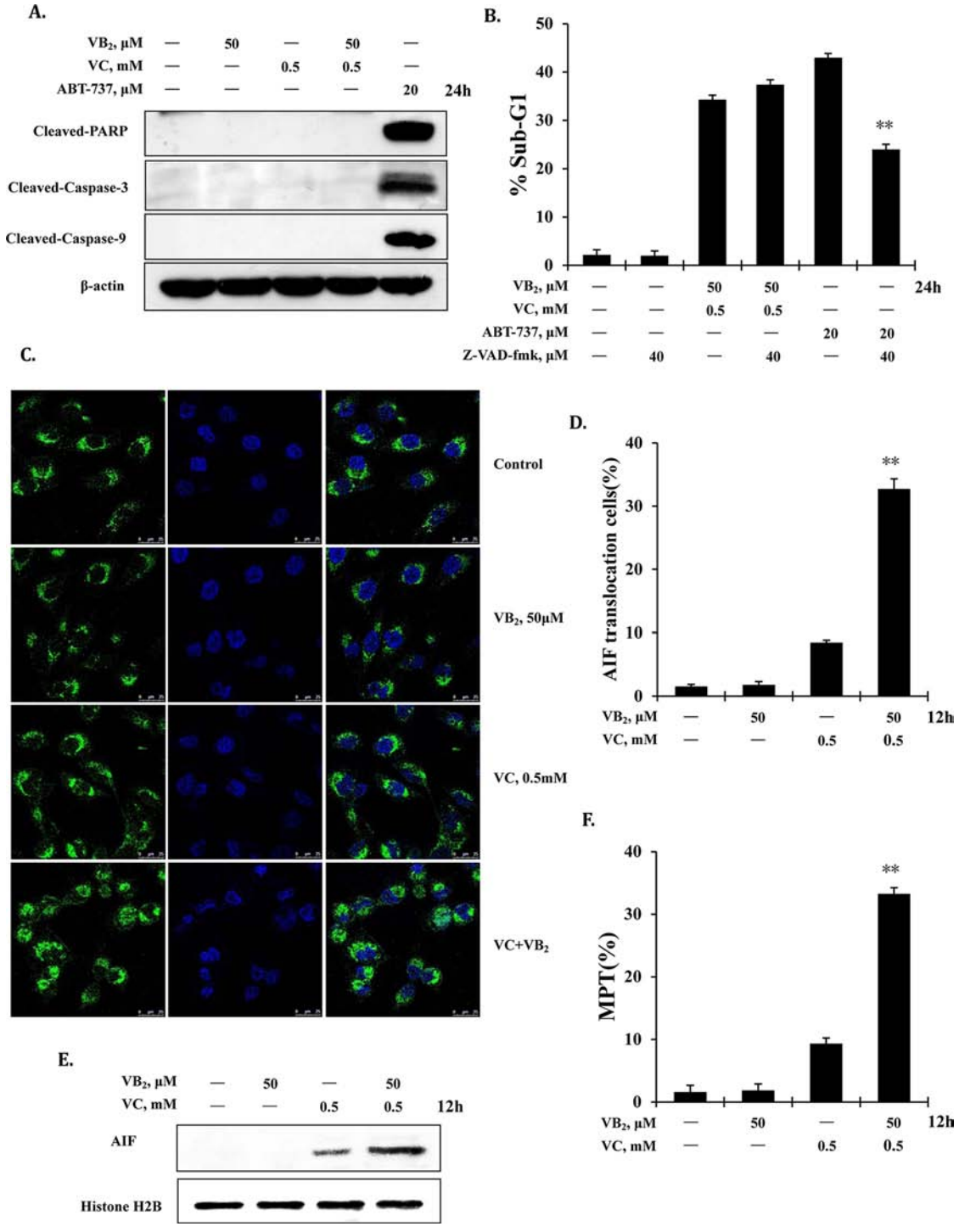

Figure 3. Caspase-independent apoptosis was involved in the combination-induced cytotoxicity in MDA-MB-231 cells. (A) Effects of the combination on caspase activation. The cells were exposed to vitamins C and/or B_2 for 24 h, and cleavages of caspases and PARP were analyzed by western blotting. (B) Effects of a pan-caspase inhibitor on the combination-induced cell death. Cell death was estimated by sub-G1 analysis after 24 h of treatment with vitamins C/B_2 and/or caspase inhibitor. (C) Caspase-independent apoptosis by the combination was associated with an enhanced AIF nuclear translocation. The cells were treated with vitamins C and/or B_2 for 12 h, and localization of AIF was detected using immunofluorescence staining. (D) Quantitative analysis of AIF nuclear translocation. (E) Nuclear content of AIF was detected by western blotting. (F) Vitamins C/B_2 combination induced an enhanced MPT measured by flow cytometry, following JC-1 staining.

assessed using sub-G1 analysis. As shown in panel A and the left panel in panel B of Figure 1, 50 μM vitamin B_2 alone caused 3.44% cell death, whereas 8.27% cell death was induced by 0.5 mM vitamin C alone. In contrast, the combination resulted in significantlly increased cytotoxicity (31.33%; $p < 0.01$). To further validate these enhanced actions, we next measured the overall suppressive action induced by vitamin C, vitamin B_2, or their combination using crystal violet staining, and results are presented in the right panel of Figure 1B. Each agent alone caused a marginally or slightly suppressive effect, but the combination resulted in a much stronger inhibitory action, further supporting the enhanced effects achieved by combining

DOI: 10.1021/acs.jafc.5b01909
J. Agric. Food Chem. 2015, 63, 6739−6748

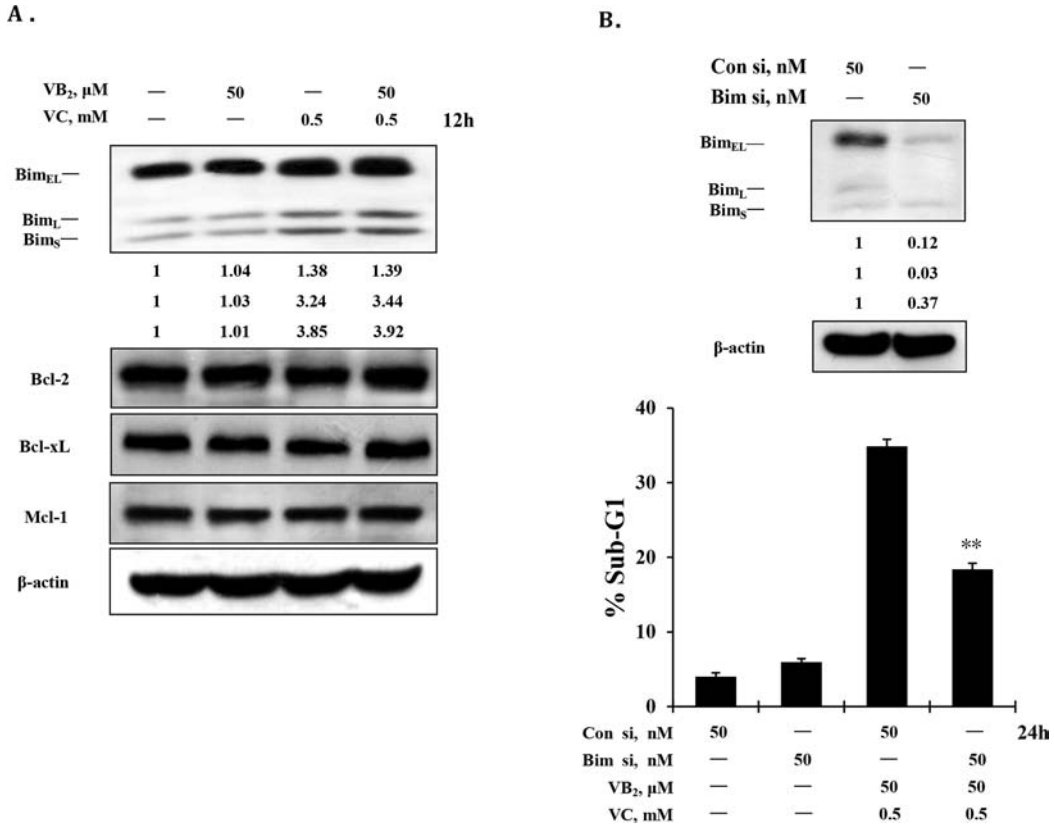

Figure 4. Activation of Bim was required for the combination-induced apoptosis in MDA-MB-231 cells. (A) Effects of vitamins C and/or B_2 on expression of Bcl-2 family proteins. The cells were treated with each agent alone or the combination for 12 h, and expression of Bim, Bcl-2, Bcl-x1, and Mcl-1 was analyzed by western blotting. Relative protein levels were quantitated and indicated below each band. (B) Effects of Bim knockdown on the combination-induced apoptosis. Knockdown efficiency was validated by western blotting, and apoptosis was assessed by sub-G1 analysis.

vitamin C with vitamin B_2. To determine whether the enhanced effect is specific for MDA-MB-231 cells, vitamins C/B_2-induced cell death and overall inhibitory effects in two additional cell lines were investigated by sub-G1 analysis and crystal violet staining, respectively. The data are shown in panels C and D of Figure 1. Similar increased cell death and overall inhibitory effects of the combination were also observed in MCF-7 breast cancer cells (Figure 1C) and A549 lung cancer cells (Figure 1D).

Enhanced Inhibitory Effect of Vitamins C/B_2 Combination Is a Synergistic Action. To evaluate critically whether the enhancement effect by vitamins C/B_2 combination is a synergism, we assessed the combinatory actions of varying combinations in a fixed ratio of 10:1 (vitamins C/B_2) by crystal violet staining. As shown in Figure 2A, vitamin B_2 (30−70 μM) or vitamin C (300−700 μM) induced a dose-dependent suppressive effect, whereas the combinations resulted in significantly further increased suppressive actions. These data were used to calculate the *CI* based on the Chou−Talalay method.[17,18] As shown in Figure 2B, *CI* values were less than 1 at all combinations tested, supporting a synergism achieved by combining vitamin B_2 with vitamin C.

Enhanced Effect by Vitamins B_2/C Combination Was Not Associated with Caspase Activation. To investigate if increased caspase activation contributed to the cell death induction by the combination, we analyzed active forms of caspase-9 and caspase-3 and substrate of caspase PARP cleavage by western blotting, and the results are shown in Figure 3A. Cleavages of caspase-9, caspase-3, and PARP (positive control ABT-737 induced significantly increased cleavages of these three proteins) were not detected with all of the treatments, suggesting that caspase activation might not play a role in this enhanced action. To further confirm this notion, we examined the influence of caspase inhibition on cell death examined using sub-G1 analysis. Caspase inactivation by its inhibitor did not influence the combination-induced cell death (but dramatically decreased apoptosis induction by positive control ABT-737; Figure 3B), further supporting the enhanced cytotoxic effect by the combination not associated with activation of caspases.

AIF plays a critical role in caspase-independent cell death.[21] A previous study has shown that vitamin C causes AIF-triggered caspase-independent cell death in SK-BR3 and Hs578T breast cancer cells.[9] We then questioned if this enhanced caspase-independent cell death by the combination was attributed to promoting nuclear relocation of AIF. The AIF localization was examined using the immunofluorescence assay, and the results are presented in Figure 3C. A clear AIF cytoplasmic distribution was observed in the control cells. Vitamin B_2 did not change AIF cytoplasmic distribution, whereas vitamin C induced a slight increase of AIF nuclear relocation, and the percentage of the cells with AIF nuclear staining was 8.46% (Figure 3D). Vitamins C/B_2 combination led to a significantly further enhanced AIF nuclear relocation (32.72%; $p < 0.01$, as compared to vitamin C treatment alone). The enhanced AIF nuclear translocation was further validated by western blotting analysis of the nuclear content of AIF (Figure 3E). These results clearly indicate that vitamin B_2 facilitated vitamin-C-induced AIF nuclear translocation. The

DOI: 10.1021/acs.jafc.5b01909
J. Agric. Food Chem. 2015, 63, 6739−6748

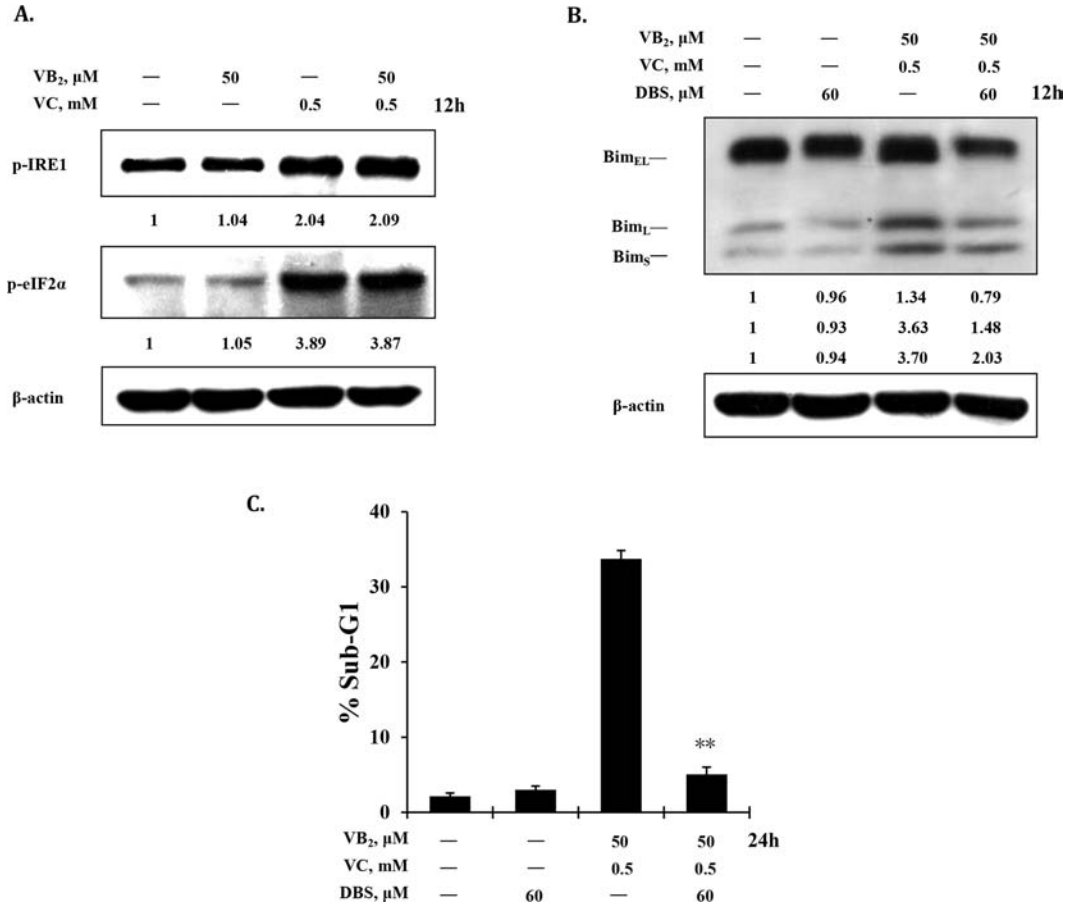

Figure 5. Activation of Bim was attributed to ER stress of MDA-MB-231 cells. (A) Influences of vitamins C and/or B_2 on ER stress. The cells were treated with vitamins C and/or B_2 for 12 h, and changes of ER stress markers were analyzed by western blotting. (b) Effects of IRE1 inhibition by its inhibitor DBS on Bim expression analyzed by western blotting. Relative protein levels were quantitated and indicated below each band. (C) Effects of IRE1 inhibition by its inhibitor on apoptosis induction by the combination measured by sub-G1 analysis.

AIF release from mitochondria suggested that mitochondrial membrane potential was reduced in response to the combination. We next examined the changes of mitochondrial membrane potential by flow cytometry, following JC-1 staining. As expected, the combination treatment caused a significantly enhanced disruption of mitochondrial membrane potential. Together, these results suggested that combining vitamin C with vitamin B_2 induced an enhanced mitochondrial permeability transition (MPT), which, in turn, led to a synergistic AIF-mediated caspase-independent cell death.

Activation of Bim Was Required for the Combination-Induced Cell Death in MDA-MB-231 Cells. Mitochondrial membrane potential is tightly regulated by Bcl-2 family members.[22] Having found the enhancement action of the combination on mitochondria, we next investigated the mechanisms of mitochondrial activation by Bcl-2 family members in response to vitamins C/B_2 exposure. The changes of key Bcl-2 proteins were analyzed by western blotting. As shown in Figure 4A, a significant upregulation of Bim was observed in vitamin-C-treated cells, but the combination failed to induce a further increase of Bim expression. No obvious changes of Bcl-2, Bcl-xl, and Mcl-1 were found in response to either each agent alone or the combination. To assess the role of Bim in cell death induction by vitamins C/B_2, we tested the influence of Bim inactivation by the RNA interference (RNAi) approach on the combination-induced cell death. As shown in Figure 4B, under the condition that Bim was silenced by its siRNA, cell death induction by the combination was significantly reduced in comparison to that found with control siRNA/combination. These data suggested that Bim induction by vitamin C played an important role in vitamins C/B_2-induced cell death, but the synergistic effect of vitamins C/B_2 combination did not happen at the Bim activation level.

Endoplasmic Reticulum (ER) Stress Was Responsible for Bim Upregulation. It has been shown that Bim can be activated by ER stress in a certain model of systems.[23] To decipher the mechanisms involved in the upregulation of Bim, we first evaluated the changes of the key ER stress markers in response to each agent alone or the combination by western blotting. As shown in Figure 5A, phosphorylation of IRE1 and eIF2α was significantly increased in response to vitamin C but not vitamin B_2, whereas the combination caused a comparable level of phosphorylation of these two ER stress markers with vitamin C alone. To determine the role of ER stress activation on the upregulation of Bim, we next tested the effect of IRE1 inhibition by its inhibitor DBS[24] on the combination-induced Bim expression. As shown in Figure 5B, when IRE1 was blocked by its inhibitor, the expression of Bim was significantly decreased. Consistent with Bim reduction, the combination-induced cell death was dramatically attenuated under the condition of IRE1 inactivation (Figure 5C). These results supported a critical role of ER stress, especially IRE1 activation, in the combination-induced Bim upregulation and cell death induction.

DOI: 10.1021/acs.jafc.5b01909
J. Agric. Food Chem. 2015, 63, 6739−6748

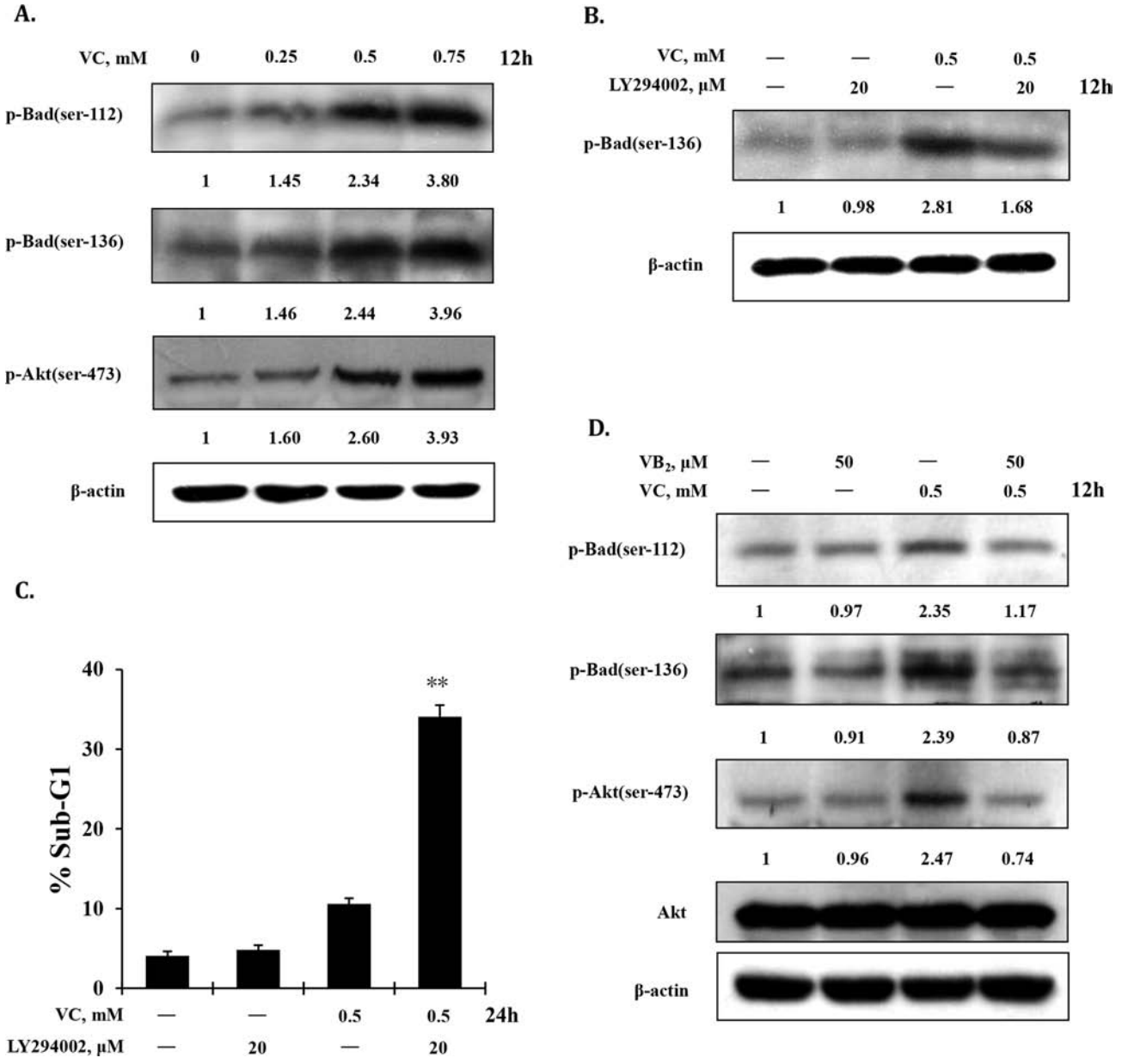

Figure 6. Vitamin B_2 sensitized cancer cells to vitamin-C-induced apoptosis via modulation of Akt activation and Bad inactivation. (A) Vitamin C induced a concentration-dependent increase of Bad and Akt phosphorylation. (B) Effects of Akt inactivation by its inhibitor LY294002 on vitamin-C-induced Bad serine 136 phosphorylation. (C) Effects of Akt inactivation by its inhibitor LY294002 on vitamin-C-induced apoptosis. (D) Influences of vitamin B_2 on phosphorylation of Akt and Bad induced by vitamin C. Relative protein levels were quantitated and indicated below each band.

Vitamin B_2 Sensitized Cancer Cells to Vitamin-C-Induced Cell Death via Modulation of Akt Activation and Bad Inactivation. Bad is a member of BH3-only pro-apoptotic Bcl-2 family proteins. It has been shown that the phosphorylation status of Bad plays a key role in the regulation of its apoptotic activity.[25,26] To further investigate the mechanisms by which vitamin B_2 potentiated cancer cells to vitamin-C-induced cell death, we assessed influences of vitamins C and/or B_2 on Bad phosphotylation by western blotting. As shown in Figure 6A, phosphorylation of Bad at serine 136 and serine 112 was significantly increased in response to vitamin C. Because Akt could phosphorylate Bad at serine 136,[27] we then asked if vitamin-C-induced Bad serine 136 phosphorylation could be due to activation of Akt. As shown in Figure 6A, vitamin C increased phosphorylation of Akt at serine 473, which was consistent with phosphorylation of Bad at serine 136. To determine the relationship between phosphorylation of Akt and Bad and the effect of Akt phosphorylation on cell death induced by vitamin C, we measured influences of Akt inhibition by LY294002 on these events. As shown in Figure 6B, under condition of Akt inactivation, phosphorylation of Bad at serine 136 by vitamin C was dramatically suppressed. Consistent with Bad dephosphorylation, inactivation of Akt resulted in a significant enhanced cell death in response to vitamin C exposure (Figure 6C). These results suggested that Akt activation by vitamin C compromised its cytotoxic activity via phosphorylating Bad at serine 136. We next examined whether vitamin B_2 could prevent phosphorylation of Akt/Bad by vitamin C, and the results are shown in Figure 6D. The combination of vitamins C/B_2 significantly inhibited vitamin-C-induced phosphorylation

DOI: 10.1021/acs.jafc.5b01909
J. Agric. Food Chem. 2015, 63, 6739−6748

of Akt/Bad, which was consistent with the enhanced cell death induction by the combination.

DISCUSSION

Combinatory therapy is considered to be an attractive approach to improve the efficacy of cancer chemotherapy. MDA-MB-231 is a representative of triple-negative breast cancer that lacks effective targeted therapy.[28] The present study demonstrated that combining serum achievable level of vitamins C and B_2 can achieve a synergistic cytotoxic effect on multiple types of cancer cells, including a cell line of triple-negative breast cancer, providing an additional support for combination as a practical approach for improving the chemotherapeutic outcome. Findings of the present study may have important clinical implications for vitamin-C-based combinatorial therapy, especially for the management of triple-negative breast cancer.

As mentioned above, Bad is member of a BH3-only pro-apoptotic Bcl-2 family. A previous study has revealed that phosphorylation of Bad at serine 112 and serine 136 could inhibit its apoptotic function.[25] Indeed, such a mechanism has been reported to contribute cancer cells resistant to several anticancer compounds.[29−32] The findings of the present study, for the first time, demonstrated that Bad was phosphorylated by vitamin C at serine 136 and serine 112 (Figure 6A), which suppressed cytotoxic action of vitamin C. Moreover, we revealed that Bad phosphorylation at serine 136 was attributed to phosphorylation of Akt (Figure 6A), an important anti-apoptotic kinase contributed to drug resistance. Akt inactivation led to a significant dephosphorylation of Bad and increase of cell death (panels B and C of Figure 6). The results supported an important mechanism of cancer cells resistant to vitamin C through activation of Akt and inactivation of Bad. We further revealed that vitamin B_2 was able to significantly suppress Akt and Bad phosphorylation in response to vitamin C exposure. Thus, Akt/Bad axis is a reasonable target for sensitizing cancer cells to vitamin-C-induced cell death. Our data show that vitamin B_2 effectively blocked vitamin-C-induced Akt phosphorylation. Because PI3K/PDK1 are the key upstream kinases that are responsible for Akt phosphorylation,[33] we speculated that inhibition of Akt phosphorylation by vitamin B_2 is probably through regulation of the PI3K/PDK1 axis.

Bim is another BH3-only protein contributing to apoptosis by direct binding and inactivation of pro-survival Bcl-2 family proteins or direct activation of the downstream death mediator Bax and Bak.[34,35] The functional role of Bim in vitamin-C-induced apoptosis has not been established. Our current study showed that vitamin C was able to increase Bim expression and inhibition of Bim expression by the RNAi approach resulted in a significant reduction of cell death by vitamins C/B_2 combination, suggesting that activation of Bim is required for the combination-induced cell death. However, a further enhanced Bim expression by the combination was not observed in comparison to that found in vitamin C treatment alone, suggesting that the synergistic cell death induction by the combination was not due to further increased activation of Bim. With regard to upstream mediator of Bim activation in response to vitamin C exposure, our data revealed that activation of ER stress was responsible for the upregulation of Bim. However, combining vitamin C with vitamin B_2 did not cause further enhanced induction of ER stress compared to vitamin C alone, which was consistent with the changes of Bim expression. Together, these data suggested that activation of ER stress of the Bim axis was only attributed to vitamin C and functioned as an important pro-death signal, contributing to the combination-induced cell death. ER stress is a well-established activator of autophagy.[36] We have tested the role of autophagy in this synergistic action by vitamins C/B_2 and found that autophagy was indeed activated in response to the combination. However, inhibition of autophagy by the genetic approach did not influence the cell death level (data not shown), ruling out the possible involvement of autophagy in the combination-induced cell death.

Several studies have showed that an increased apoptosis or cytotoxicity was observed by a combination of vitamins C and B_{12b}[37] or K3,[38−41] which was associated with augment of oxidative stress. To determine whether this mechanism was also involved in cell death induction by vitamins C/B_2 combination in our current system, we measured the levels of reactive oxygen species (ROS) with flow cytometry, following staining with 2′,7′-dichlorodihydrofluorescein diacetate (H2DCFDA). An enhanced ROS level by combining vitamin C with vitamin B_2 was not detected (data not shown), suggesting that vitamin B_2 sensitized cancer cells to vitamin-C-induced cell death was not due to the boost of ROS.

In summary, vitamin B_2 was capable of sensitizing breast cancer cells to vitamin-C-induced cell death via dephosphorylation of vitamin-C-mediated Akt active and Bad inhibitory phosphorylation. The findings of the present study suggest that vitamin B_2 has great potential as a sensitizer for improving therapeutic efficacy of vitamin C against triple-negative breast cancer.

AUTHOR INFORMATION

Corresponding Author

*Telephone/Fax: 86-10-6273-8653. E-mail: hongbo@cau.edu.cn.

Author Contributions

†(N.C. and S.Y.) Ni Chen and Shutao Yin contributed equally to this work.

Funding

This work was supported by grants from the Ministry of Science and Technology of China (2012BAD33B09) and the National Natural Science Foundation of China (NSFC, 31371752).

Notes

The authors declare no competing financial interest.

ABBREVIATIONS USED

AIF, apoptosis-inducing factor; PI, propidium iodide; DAPI, 4′,6′-diamidin-2-phenylindole; FITC, fluorescein isothiocyanate; MPT, mitochondrial permeability transition; ER, endoplasmic reticulum; ROS, reactive oxygen species; H2DCFDA, 2′,7′-dichlorodihydrofluorescein diacetate; RNAi, RNA interference; DBS, 3-ethoxy-5,6-dibromosalicylaldehyde

REFERENCES

(1) Grosso, G.; Bei, R.; Mistretta, A.; Marventano, S.; Calabrese, G.; Masuelli, L.; Giganti, M. G.; Modesti, A.; Galvano, F.; Gazzol, D. Effects of vitamin C on health: A review of evidence. *Front. Biosci., Landmark Ed.* **2013**, *18*, 1017−1029.

(2) Vollbracht, C.; Schneider, B.; Leendert, V.; Weiss, G.; Auerbach, L.; Beuth, J. Intravenous vitamin C administration improves quality of life in breast cancer patients during chemo-/radiotherapy and aftercare: Results of a retrospective, multicentre, epidemiological cohort study in Germany. *In Vivo* **2011**, *25*, 983−990.

DOI: 10.1021/acs.jafc.5b01909
J. Agric. Food Chem. 2015, 63, 6739−6748

(3) Harris, H. R.; Bergkvist, L.; Wolk, A. Vitamin C intake and breast cancer mortality in a cohort of Swedish women. *Br. J. Cancer* **2013**, *109*, 257−264.
(4) Ullah, M. F.; Bhat, S. H.; Hussain, E.; Abu-Duhier, F.; Ahmad, A.; Hadi, S. M. Ascorbic acid in cancer chemoprevention: Translational perspectives and efficacy. *Curr. Drug Targets* **2012**, *13*, 1757−1771.
(5) Gao, Z.; Spilk, S.; Momen, A.; Muller, M. D.; Leuenberger, U. A.; Sinoway, L. I. Vitamin C prevents hyperoxia-mediated coronary vasoconstriction and impairment of myocardial function in healthy subjects. *Eur. J. Appl. Physiol.* **2012**, *112*, 483−492.
(6) Kawanaka, M.; Nishino, K.; Nakamura, J.; Suehiro, M.; Goto, D.; Urata, N.; Oka, T.; Kawamoto, H.; Nakamura, H.; Yodoi, J.; Hino, K.; Yamada, G. Treatment of nonalcoholic steatohepatitis with vitamins E and C: a pilot study. *Hepatic Med.* **2013**, *5*, 11−16.
(7) Mikirova, N. A.; Hunninghake, R. Effect of high dose vitamin C on Epstein-Barr viral infection. *Med. Sci. Monit.* **2014**, *20*, 725−732.
(8) Casciari, J. J.; Riordan, N. H.; Schmidt, T. L.; Meng, X. L.; Jackson, J. A.; Riordan, H. D. Cytotoxicity of ascorbate, lipoic acid, and other antioxidants in hollow fibre in vitro tumours. *Br. J. Cancer* **2001**, *84*, 1544−1550.
(9) Hong, S. W.; Jin, D. H.; Hahm, E. S.; Yim, S. H.; Lim, J. S.; Kim, K. I.; Yang, Y.; Lee, S. S.; Kang, J. S.; Lee, W. J.; Lee, W. K.; Lee, M. S. Ascorbate (vitamin C) induces cell death through the apoptosis-inducing factor in human breast cancer cells. *Oncol. Rep.* **2007**, *18*, 811−815.
(10) Chen, P.; Yu, J.; Chalmers, B.; Drisko, J.; Yang, J.; Li, B.; Chen, Q. Pharmacological ascorbate induces cytotoxicity in prostate cancer cells through ATP depletion and induction of autophagy. *Anti-Cancer Drugs* **2012**, *23*, 437−444.
(11) Fritz, H.; Flower, G.; Weeks, L.; Cooley, K.; Callachan, M.; McGowan, J.; Skidmore, B.; Kirchner, L.; Seely, D. Intravenous Vitamin C and Cancer: A Systematic Review. *Integr. Cancer Ther.* **2014**, *13*, 280−300.
(12) Chen, P.; Li, C.; Li, X.; Li, J.; Chu, R.; Wang, H. Higher dietary folate intake reduces the breast cancer risk: a systematic review and meta-analysis. *Br. J. Cancer* **2014**, *110*, 2327−2338.
(13) Powers, H. J. Riboflavin (vitamin B-2) and health. *Am. J. Clin. Nutr.* **2003**, *77* (6), 1352−1360.
(14) Liu, Y.; Yu, Q. Y.; Zhu, Z. L.; Tang, P. Y.; Li, K. Vitamin B_2 intake and the risk of colorectal cancer: a meta-analysis of observational studies. *Asian Pac. J. Cancer Prev.* **2015**, *16* (3), 909−913.
(15) de Souza, A. C.; Kodach, L.; Gadelha, F. R.; Bos, C. L.; Cavagis, A. D.; Aoyama, H.; Peppelenbosch, M. P.; Ferreira, C. V. A promising action of riboflavin as a mediator of leukaemia cell death. *Apoptosis* **2006**, *11* (10), 1761−1771.
(16) Bouzari, A.; Holstege, D.; Barrett, D. M. Vitamin retention in eight fruits and vegetables: a comparison of refrigerated and frozen storage. *J. Agric. Food Chem.* **2015**, *63*, 957−962.
(17) Chou, T. C.; Talalay, P. Quantitative analysis of dose effect relationships: the combined effects of multiple drugs or enzyme inhibitors. *Adv. Enzyme Regul.* **1984**, *22*, 27−55.
(18) Bhat, U. G.; Pandit, B.; Gartel, A. L. ARC synergizes with ABT 737 to induce apoptosis in human cancer cells. *Mol. Cancer Ther.* **2010**, *9*, 1688−1696.
(19) Padayatty, S. J.; Sun, H.; Wang, Y.; Riordan, H. D.; Hewitt, S. M.; Katz, A.; Wesley, R. A.; Levine, M. Vitamin C pharmacokinetics: Implications for oral and intravenous use. *Ann. Intern. Med.* **2004**, *140* (7), 533−537.
(20) Vuyyuri, S. B.; Rinkinen, J.; Worden, E.; Shim, H.; Lee, S.; Davis, K. R. Ascorbic acid and a cytostatic inhibitor of glycolysis synergistically induce apoptosis in non-small cell lung cancer cells. *PLoS One* **2013**, *8* (6), e67081.
(21) Lorenzo, H. K.; Susin, S. A.; Penninger, J.; Kroemer, G. Apoptosis inducing factor (AIF): A phylogenetically old, caspase-independent effector of cell *death*. *Cell Death Differ.* **1999**, *6*, 516−524.
(22) Kroemer, G.; Galluzzi, L.; Brenner, C. Mitochondrial membrane permeabilization in cell death. *Physiol. Rev.* **2007**, *87*, 99−163.
(23) Zhang, L.; Lopez, H.; George, N. M.; Liu, X.; Pang, X.; Luo, X. Selective involvement of BH3-only proteins and differential targets of Noxa in diverse apoptotic pathways. *Cell Death Differ.* **2011**, *18*, 864−873.
(24) Volkmann, K.; Lucas, J. L.; Vuga, D.; Wang, X.; Brumm, D.; Stiles, C.; Kriebel, D.; Der-Sarkissian, A.; Krishnan, K.; Schweitzer, C.; Liu, Z.; Malyankar, U. M.; Chiovitti, D.; Canny, M.; Durocher, D.; Sicheri, F.; Patterson, J. B. Potent and selective inhibitors of the inositol-requiring enzyme 1 endoribonuclease. *J. Biol. Chem.* **2011**, *286*, 12743−12755.
(25) Zha, J.; Harada, H.; Yang, E.; Jockel, J.; Korsmeyer, S. J. Serine phosphorylation of death agonist BAD in response to survival factor results in binding to 14−3-3 not BCL-X(L). *Cell* **1996**, *87*, 619−628.
(26) Datta, S. R.; Ranger, A. M.; Lin, M. Z.; Sturgill, J. F.; Ma, Y. C.; Cowan, C. W.; Dikkes, P.; Korsmeyer, S. J.; Greenberg, M. E. Survival factormediated BAD phosphorylation raises the mitochondrial threshold for apoptosis. *Dev. Cell* **2002**, *3*, 631−643.
(27) Datta, S. R.; Brunet, A.; Greenberg, M. E. Cellular survival: a play in three Akts. *Genes Dev.* **1999**, *13*, 2905−2927.
(28) Chai, Y.; Lee, H. J.; Shaik, A. A.; Nkhata, K.; Xing, C.; Zhang, J.; Jeong, S. J.; Kim, S. H.; Lu, J. Penta-O-galloyl-beta-D-glucose induces G1 arrest and DNA replicative S-phase arrest independently of cyclin-dependent kinase inhibitor 1A, cyclin-dependent kinase inhibitor 1B and P53 in human breast cancer cells and is orally active against triple negative xenograft growth. *Breast Cancer Res.* **2010**, *12*, R67.
(29) Yamaguchi, K.; Uzzo, R. G.; Pimkina, J.; Makhov, P.; Golovine, K.; Crispen, P.; Kolenko, V. M. Methylseleninic acid sensitizes prostate cancer cells to TRAIL-mediated apoptosis. *Oncogene* **2005**, *24*, 5868−5877.
(30) Kraus, A. C.; Ferber, I.; Bachmann, S. O.; Specht, H.; Wimmel, A.; Gross, M. W.; Schlegel, J.; Suske, G.; Schuermann, M. In vitro chemoand radio-resistance in small cell lung cancer correlates with cell adhesion and constitutive activation of AKT and MAP kinase pathways. *Oncogene* **2002**, *21*, 8683−8695.
(31) Grund, K.; Ahmadi, R.; Jung, F.; Funke, V.; Gdynia, G.; Benner, A.; Sykora, J.; Walczak, H.; Joos, S.; Felsberg, J.; Reifenberger, G.; Wiestler, O. D.; Herold-Mende, C.; Roth, W. Troglitazone-mediated sensitization to TRAIL-induced apoptosis is regulated by proteasome-dependent degradation of FLIP and ERK1/2-dependent phosphorylation of BAD. *Cancer Biol. Ther.* **2008**, *7*, 1982−1990.
(32) Yin, S.; Dong, Y.; Li, J.; Fan, L.; Wang, L.; Lu, J.; Vang, O.; Hu, H. Methylseleninic acid potentiates multiple types of cancer cells to ABT-737-induced apoptosis by targeting Mcl-1 and Bad. *Apoptosis* **2012**, *17*, 388−399.
(33) Vanhaesebroeck, B.; Alessi, D. R. The PI3K-PDK1 connection: more than just a road to PKB. *Biochem. J.* **2000**, *346* (Part 3), 561−576.
(34) Kim, H.; Rafiuddin-Shah, M.; Tu, H. C.; Jeffers, J. R.; Zambetti, G. P.; Hsieh, J. J.; Cheng, E. H. Hierarchical regulation of mitochondrion-dependent apoptosis by BCL-2 subfamilies. *Nat. Cell Biol.* **2006**, *8*, 1348−1358.
(35) Chipuk, J. E.; Green, D. R. How do BCL-2 proteins induce mitochondrial outer membrane permeabilization? *Trends Cell Biol.* **2008**, *18*, 157−164.
(36) Moretti, L.; Cha, Y. I.; Niermann, K. J.; Lu, B. Switch between apoptosis and autophagy: radiation-induced endoplasmic reticulum stress? *Cell Cycle* **2007**, *6* (7), 793−798.
(37) Solovieva, M. E.; Soloviev, V. V.; Akatov, V. S. Vitamin B12b increases the cytotoxicity of short-time exposure to ascorbic acid, inducing oxidative burst and iron-dependent DNA damage. *Eur. J. Pharmacol.* **2007**, *566*, 206−214.
(38) Noto, V.; Taper, H. S.; Jiang, Y. H.; Janssens, J.; Bonte, J.; De Loecker, W. Effects of sodium ascorbate (vitamin C) and 2-methyl-1,4-naphthoquinone (vitamin K3) treatment on human tumor cell growth in vitro. I. Synergism of combined vitamin C and K3 action. *Cancer* **1989**, *63* (5), 901−906.
(39) Venugopal, M.; Jamison, J. M.; Gilloteaux, J.; Koch, J. A.; Summers, M.; Giammar, D.; Sowick, C.; Summers, J. L. Synergistic antitumor activity of vitamins C and K3 on human urologic tumor cell lines. *Life Sci.* **1996**, *59* (17), 1389−1400.

DOI: 10.1021/acs.jafc.5b01909
J. Agric. Food Chem. 2015, 63, 6739−6748

(40) Zhang, W.; Negoro, T.; Satoh, K.; Jiang, Y.; Hashimoto, K.; Kikuchi, H.; Nishikawa, H.; Miyata, T.; Yamamoto, Y.; Nakano, K.; Yasumoto, E.; Nakayachi, T.; Mineno, K.; Satoh, T.; Sakagami, H. Synergistic cytotoxic action of vitamin C and vitamin K3. *Anticancer Res.* **2001**, *21* (5), 3439−3444.
(41) Bonilla-Porras, A. R.; Jimenez-Del-Rio, M.; Velez-Pardo, C. Vitamin K3 and vitamin C alone or in combination induced apoptosis in leukemia cells by a similar oxidative stress signalling mechanism. *Cancer Cell Int.* **2011**, *11*, 19.

DOI: 10.1021/acs.jafc.5b01909
J. Agric. Food Chem. 2015, 63, 6739−6748

biological activity. Altogether, three natural compounds, xanthohumol (**14**), isoxanthohumol (**6**), and naringenin (**5**), and 11 synthetic derivatives with various structural modifications were examined for aphid-deterrent activity.

Usually, antifeedants are natural compounds with a lactone ring,[29−31] but they may also belong to terpenes[32,33] or phenolic compounds.[34] Many plants have strong repellent properties, and for this reason they have been used for a long time to repel the wheat weevil, the major pest of stored cereal grains. This group of plants includes field mint (*Mentha arvensis*), common yarrow (*Achillea millefolium*), and several other common plant species.[35] Obtained by extraction, preparations of lavender (*Lavandula luisieri*) and rough cocklebur (*Xanthium sibiricum*) demonstrated insecticidal activity, among others, against the peach-potato aphid (*Myzus persicae*).[36,37] Tropical plants are a very rich source of antifeedants. Among them, Indian neem (*Azadirachta indica*) is one of the best known, because it contains the strongest of known feeding repellents, azadirachtin. Nawrot et al. in 2013 proved the strong deterrent activity of ionic liquids toward wheat weevil beetles (*Sitophilus granarius* L.), confused flour beetle larvae (*Tribolium confusum* Duv.), and khapra beetle larvae (*Trogoderma granarium* Ev.).[38] This activity was equal to or stronger than that of azadirachtin. There is increasing application of microbial agents, so-called bioinsecticides, that contain live bacterial cultures, mostly of the genus *Bacillus* (*Bacillus thuringiensis*).[39] Another large group of biopreparations that inhibit plant pest development is based on viruses and nematodes.[40] Apart from interacting with insect chemoreceptors of taste, preparations of antifeeding activity may inhibit the fertility of insects, prolong their larval development, or inhibit the transmission of some viruses.[41,42]

According to literature data, biological methods constitute only a small fraction of plant protection management. One reason is that there have been no effective biological methods of crop protection developed, especially concerning control of diseases and pests of cereals and plants of the families Fabaceae and Brassicaceae, which are essential for the production of organic food.[43] Gökçe et al. in 2011 proved antifeedant activity of the extract from hop cones (*H. lupulus*) against the Colorado potato beetle (*Leptinotarsa decemlineata*).[44]

In our previously published study, we found that one of the hop extracts examined significantly deterred *M. persicae* settling on treated leaves, and the effect was relatively stable and lasted at least 24 h.[45] However, aphid probing and phloem sap consumption were not impeded. Therefore, we hypothesized that the extract contained a component that could reach sieve elements using the symplastic or apoplastic pathway and produce a delayed, postingestional metabolic detrrent effect without evoking the rejection behavior based on gustatory stimuli. Consequently, we decided that there was a need for a more detailed study to find which components of the hop extract were responsible for the deterrent activity. Exogenously applied hop chemicals, α- and β-hop acids and colupulone, had an antifeedant effect on the grain aphid (*Sitobion avenae*) and bird cherry-oat aphid *Rhopalosiphum padi*.[46] However, to the best of our knowledge, there is no information about the deterrent activity of hop flavonoids toward plant pests, especially aphids. There is also no study on the antifeedant activity of chalcone (**10**) and its structural analogues toward the peach-potato aphid (*M. persicae*).

The aim of our research was to evaluate the deterrent activity of natural flavonoid compounds found in hop (*H. lupulus*): xanthohumol (**14**) and isoxanthohumol (**6**). The settling behavior of the peach-potato aphid (*M. persicae* [Sulz.]) was evaluated. We investigated also the effect of structural modifications of these flavonoid molecules on aphid behavior. We selected compounds of diverse chemical structures, belonging to three flavonoid groups, compounds with 4-chromanone (**1**), chromone (**7**), or *trans*-chalcone (**10**) skeletons.

MATERIALS AND METHODS

Reagents. Chemical reagents were purchased from Sigma-Aldrich, Merck, Chempur, and Alfa Aesar. For the study we used commercially available 4-chromanone (**1**) (Sigma-Aldrich), flavanone (**4**) (Alfa Aesar), naringenin (**5**), chromone (**7**) (Sigma-Aldrich), flavone (**8**) (Sigma-Aldrich), 7-aminoflavone (**9**) (Sigma-Aldrich), *trans*-chalcone (**10**) (Sigma-Aldrich), and 4-methoxychalcone (**12**) (Sigma-Aldrich).

General Procedures. The structures of products obtained were determined by spectroscopic methods (^{1}H NMR, ^{13}C NMR, IR, and HR ESI-MS). The purity of compounds **2**, **3**, **11**, and **13** was established by gas chromatography (GC) using an HP-5 capillary column, whereas, for compounds **6** and **14**, high-performance liquid chromatography (HPLC) was employed, with the help of the reversed-phase C-18 column as described perviously.[19] For the biological tests we used the compounds with the purity >95%.

Synthesis of Compounds. 7-Hydroxy-2,2-dimethylchroman-4-one (**2**) was obtained in the reaction of 1,3-dihydroxybenzene with dimethylacrylic acid (DMAA) in the presence of zinc chloride in phosphorus oxychloride, followed by isomerization of the intermediate product according to a modified method of Alizadeh et al.[47] (80% of isolated yield). The spectroscopic data were consistent with those reported in the literature.[47,48] In the next step the purified product (**2**) was subjected to the Williamson ether synthesis with methyl iodide to give 7-methoxy-2,2-dimethylchroman-4-one (**3**), the spectroscopic data of which matched those reported by An et al.[49] The synthesis of 4-hydroxychalcone (**11**) and 4-ethyl-4′-methoxychalcone (**13**) was carried out according to the literature method[50] under strongly basic conditions (KOH), using methanol as a solvent. Xanthohumol (**14**) was isolated using the earlier described method[51] from spent hops, the residue of supercritical carbon dioxide hop extraction, which was delivered by the Supercritical Extraction Department of the New Chemical Syntheses Institute in Puławy, Poland. The second prenylated hop flavonoid, isoxanthohumol (**6**), was obtained by the alkaline isomerization of xanthohumol (**14**) according to the method of Wilhelm and Wessjohann.[52]

Cultures of Aphids and Plants. Aphids (*M. persicae*) and plants (Chinese cabbage *Brassica pekinensis*) were reared in the laboratory at 20 °C, 65% realtive humidity, and a 16/8 h light/dark photoperiod. All experiments were carried out under the same conditions.

Aphid Settling. This bioassay allows aphid host preferences to be studied under seminatural conditions. In this bioassay, aphids are given free choice between control and treated leaves. The standard leaf-dip method[53] was applied for the evaluation of activities of xanthohumol (**14**), isoxanthohumol (**6**), and their derivatives. The compounds studied were applied by immersing a leaf in 0.1% ethanolic solution of a given compound for 30 s. Control leaves of similar size were immersed in 70% ethanol, which was used as a solvent for the tested compounds. Treated and control leaves were placed in a Petri dish and allowed to air-dry for 1 h before being offered to the insects. Next, aphids were placed in the dish along the line that divided the area into two halves so that aphids could choose between treated (on half of a Petri dish) and control leaves (on the other half of the dish). Aphids that settled, that is, they did not move and the position of their antennae indicated feeding, on each leaf were counted at 1, 2, and 24 h intervals after access to the leaf (8 replicates, 20 viviparous apterous females/replicate). Aphids that were moving or out of any of the leaves were not counted.

The data were analyzed using one-way ANOVA (Statistica 6.1. package). If aphids showed a clear preference for the leaves treated with the tested compound ($P < 0.05$), the compound was described as having **attractant** properties. If aphids settled mainly on the control

DOI: 10.1021/acs.jafc.5b02025
J. Agric. Food Chem. 2015, 63, 6749−6756

Table 1. Deterrent Activity of Selected Derivatives of 4-Chromanone (1) to the Peach-Potato Aphid *M. persicae* (Sulz.)[a]

Compound number	Chemical structure		Time from the start of the experiment [h]		
			1	2	24
(1)		T	1.3 ± 0.4	0.9 ± 0.4	0.9 ± 0.5
		C	3.9 ±0.7	4.5 ± 0.9	3.0 ± 1.3
		p	**0.0050**	**0.0022**	0.1392
		DI	0.51	0.67	0.55
(2)	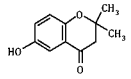	T	2.3 ± 0.6	1.9 ± 0.5	4.3 ±1.3
		C	2.5 ±0.5	3.0 ± 0.8	4.8 ± 0.8
		p	0.7356	0.2748	0.7428
		DI	0.05	0.23	0.06
(3)	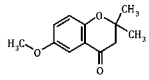	T	5.6 ± 0.4	5.0 ± 0.7	3,0 ± 1,0
		C	8.0 ± 1.0	6.6 ± 0.9	9.9 ± 1.8
		p	**0.0403**	0.1678	**0,0047**
		DI	0.17	0.14	0.53
(4)	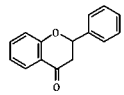	T	7.5 ± 1.4	7.9 ± 1.2	7.6 ± 1.8
		C	4.6 ± 1.3	4.0 ± 1.2	3.8 ± 1.1
		p	0.1597	0.0383	0.0922
		DI	0.24	0.33	0.34
(5)	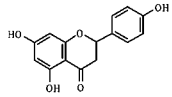	T	4.6 ± 1.5	4.1 ± 1.2	4.8 ± 0.9
		C	5.3 ± 1.1	5,3 ± 1.3	5.9 ± 1.4
		p	0.7501	0.5474	0.4979
		DI	0.06	0.12	0.11
(6)	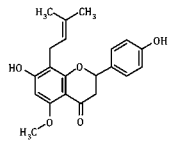	T	4.5 ± 1.3	2.6 ± 0.8	3.1 ± 0.8
		C	6.3 ± 1.5	6.4 ± 1.8	12.4 ± 1.4
		p	0.3853	0.0768	**0.0000**
		DI	0.16	0.42	0.60

[a]Numbers for T, test, and C, control, represent mean number of aphids settled on test or control leaves (choice test); *p*, significance level (ANOVA); significant differences (Student's *t* test, $p < 0.05$) between number of aphids settled on either half of the Petri dish are in bold; DI, indices of deterrence.

half of the Petri dish ($p < 0.05$), the compound tested in the respective choice test was labeled a **deterrent**. From the data thus obtained the indices of deterrence (DI) were calculated (DI_1, DI_2, and DI_{24} corresponding with 1, 2, and 24 h after exposure monitoring, respectively):

$$DI = (C - T/C + T)$$

C is the number of aphids settled on control leaves, and *T* is the number of aphids settled on the leaves treated with the tested compound. The value of DI ranged between 1 (ideal deterrent) and −1 (ideal attractant).

RESULTS AND DISCUSSION

Aphid Settling. On the basis of the bioassay, we found that the natural hop flavanone, isoxanthohumol (**6**), has deterrent properties toward the peach-potato aphid. In comparison, xanthohumol (**14**) did not demonstrate such an activity. In contrast, xanthohumol (**14**) was a weak attractant. However, strong deterrent properties of isoxanthohumol (**6**) were expressed with a delay, that is, at least 2 h after treatment ($DI_{24} = 0.6$, $p = 0.0000$) (Tables 1 and 3).

The compounds with strongly polar groups in the aromatic ring, such as hydroxyl ones, were inactive, as opposed to their methoxy derivatives with a 4-chromanone skeleton (**2** and **3**) and to chalcones (**11** and **12**).

Comparing the activity of ketones (**7**) and (**1**), we observed that hydrogenation of the C_2−C_3 double bond in compound **7** resulted in a switch from attractant to deterrent activity. However, the effect on aphid behavior was of various potencies

DOI: 10.1021/acs.jafc.5b02025
J. Agric. Food Chem. 2015, 63, 6749−6756

Table 2. Deterrent Activity of Selected Derivatives of Chromone (7) to the Peach-Potato Aphid *M. persicae* (Sulz.)[a]

Compound number	Chemical structure		Time from the start of the experiment [h]		
			1	2	24
(7)		T	7.4 ± 1.3	4.9 ± 1.0	4.1 ± 1.3
		C	3.1 ± 0.7	4.0 ± 1.1	4.0 ± 1.9
		p	**0.0147**	0.5544	0.9573
		DI	-0.40	-0.10	-0.02
(8)	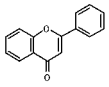	T	3.4 ± 1.0	3.5 ± 1.1	3.1 ± 0.6
		C	9.3 ± 0.9	7.9 ± 0.9	7.1 ± 1.9
		p	**0.0006**	**0.0090**	0.0609
		DI	0.47	0.38	0.39
(9)	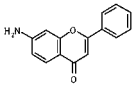	T	1.5 ± 0.5	2.4 ± 1.0	2.3 ± 0.8
		C	8.6 ± 1.3	9.0 ± 1.2	6.9 ± 1.5
		p	**0.0002**	**0.0008**	**0.0167**
		DI	0.70	0.58	0.51

[a]Numbers for T, test, and C, control, represent mean number of aphids settled on test or control leaves (choice test); *p*, significance level (ANOVA); significant differences (Student's *t* test, $p < 0.05$) between number of aphids settled on either half of the Petri dish are in bold; DI, indices of deterrence.

and durabilities. For 4-chromanone (**1**), strong deterrent activity was noted until the second hour of the experiment, whereas chromone (**7**) proved to be a weak attractant to the peach-potato aphid. The opposite situation was observed for the derivatives with a phenyl substituent at C-2, where flavone (**8**) ($DI_1 = 0.5$, $p = 0.0006$) was more active than flavanone (**4**), which proved to be inactive: the relative index of deterrence was within the range from $DI_1 = 0.2$ ($p = 0.1597$) to $DI_2 = DI_{24} = 0.3$ ($p = 0.0383$ and $p = 0.0922$, respectively (Tables 1 and 2).

In the case of the derivatives with a chromone system, the presence of a phenyl group at C-2 resulted in an increase in the deterrent activity; during the initial 2 h after treatment later on, the deterrent effect ceased (flavone (**8**): $DI_1 = 0.5$, $p = 0.0006$; $DI_2 = 0.4$, $p = 0.0090$; $DI_{24} = 0.4$, $p = 0.0609$). The introduction of an amine group at C-7 in the flavanone led to a considerable increase of the antifeedant activity, which was observed during the whole time of the experiment. The relative coefficient of deterrence values from DI = 0.7 after 1 h ($p = 0.0002$) to DI = 0.5 after 24 h ($p = 0.0167$) determined for compound **9** proved its high deterrent properties (Table 2).

It was observed that in the case of chalcone derivatives, the compound that caused the strongest reduction of aphid settling on treated leaves was 4-methoxychalcone (**12**). It was proved by the values of the relative coefficient of deterrence ($DI_1 = 0.5$, $p = 0.0086$; $DI_2 = 0.5$, $p = 0.0386$). However, the effect of 4-methoxychalcone (**12**) on inhibition of aphid settling was short-lived. 4′-Methoxy-4-ethylchalcone (**13**) proved to be also an active deterrent, which additionally reduced aphid settling during the whole experiment time (Table 3). The relative index of deterrence value (DI) was within the range from $DI_1 = 0.25$ to $DI_{24} = 0.30$ at $p < 0.05$. The deterrent activity at 2 h after application was also observed for *trans*-chalcone (**10**) ($DI_2 = 0.3$, $p = 0.0406$; $DI_{24} = 0.4$, $p = 0.0216$) (Table 3).

Differences in the durability of deterrent effects of compounds examined in the present study, for example, isoxanthohumol (**6**), and changes in their activity over time may be caused by changing conditions of their action. Presumably, it may be related to altered concentration of a tested substance in the phloem juice and changes in the pH, arising from metabolic transformations in a plant.[45] Additionally, aphids may decompose some substances with the help of their saliva enzymes. The important factors may be also aphid endogenous enzymes and symbiotic microbes, which can perform detoxification of tested compounds.[54] Xanthohumol (**14**), the most important hop prenylated chalcone, in the in vitro study was transformed into isoxanthohumol (**6**) and 8-prenylnaringenin.[55] Biotransformations of isoxanthohumol (**6**) using human liver cells[56] and fungi[57] led to the product of *O*-demethylation, 8-prenylnaringenin, which is the strongest phytoestrogen known so far. An aphid attack may induce synthesis of some organic compounds in *B. pekinensis* as a defense response to feeding. In response to the oxidative stress caused by aphids, a plant may activate a very efficient production of certain enzymes (for example, antioxidative ones, such as superoxide dismutase or catalase), hormones, and signaling molecules, which are part of plant defense against invading insect herbivores (e.g., H_2O_2 and NO).[58] These may also cause transformations of tested compounds into their derivatives.[59]

Structure–Activity Aspects. The current state of the art in antifeedant activity of flavonoid compounds relates to plant extracts, pure compounds, products of their metabolism, and also their synthetic analogues.[60,61] Russel et al.[62] came to the conclusion that the lack of substituents in ring C of flavanone as well as the lack of 3-oxo groups (−OH, $-OCH_3$) at C-3 led to an increase in antifeeding activity of the compounds toward larvae of *Ctenopsteustis obliquana*, which feed on avocado leaf

DOI: 10.1021/acs.jafc.5b02025
J. Agric. Food Chem. 2015, 63, 6749−6756

Table 3. Deterrent Activity of Selected Derivatives of Chalcone (10) to the Peach-Potato Aphid *M. persicae* (Sulz.)[a]

Compound number	Chemical structure		Time from the start of the experiment [h]		
			1	2	24
(10)	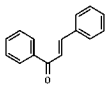	T	2.0 ± 0.5	2.5 ± 0.6	2.6 ± 0.8
		C	4.1 ± 0.9	4.5 ± 0.7	6.1 ± 1.1
		p	0.05348	**0.0406**	**0.0216**
		DI	0.35	0.29	0.40
(11)	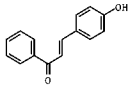	T	4.6 ± 1.1	4.9 ± 1.3	3.9 ± 1.3
		K	4.3 ± 0.9	4.8 ± 0.8	5.6 ± 1.7
		p	0.7977	0.9338	0.4344
		DI	-0.04	-0.13	0.18
(12)	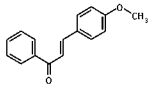	T	2.5 ± 0.6	1.9 ± 0.4	1.9 ± 0.7
		C	7.5 ± 1.5	5.3 ± 1.4	4.9 ± 1.9
		p	**0.0086**	**0.0386**	0.1691
		DI	0.50	0.47	0.44
(13)	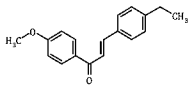	T	4.3 ± 0.8	4.3 ± 0.6	3.9 ± 0.7
		C	7.1 ± 1.0	7.9 ± 0.8	7.3 ± 1.3
		p	**0.0345**	**0.0028**	**0.0413**
		DI	0.25	0.30	0.30
(14)	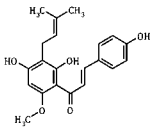	T	4.4 ± 1.6	4.0 ± 1.5	4.8 ± 1.1
		C	7.9 ± 1.6	8.4 ± 1.7	8.8 ± 2.0
		p	0.1519	0.0715	0.0990
		DI	0.29	0.35	0.30

[a]Numbers for T, test and C, control, represent mean number of aphids settled on test or control leaves (choice test); *p*, significance level (ANOVA); significant differences (Student's *t* test, $p < 0.05$) between number of aphids settled on either half of the Petri dish are in bold; DI, indices of deterrence.

shoots and young fruitlets. It is an advantage for antifeedant activity to have an ether linkage such as a pyran moiety in the chemical structure. Among the prenyl flavanones isolated from *Tephrosia apollinea* L., the most active antifeedants proved to be compounds with a dihydrofuran ring.[63] According to the literature, good antifeeding activity was also observed for compounds with a naphthalene substituent[64] and chalcones with electron acceptor groups in ring A.[65,66]

The objective of our work was to obtain hop flavonoid compounds and their derivatives of diverse relatively simple chemical structures and to evaluate their antifeedant activity. For the biological tests we have chosen two major prenylated hop flavonoids, xanthohumol (**14**) and isoxanthohumol (**6**), and an isoxanthohumol derivative without the prenyl and methyl groups, naringenin (**5**), a flavonoid that is commonly found in citrus fruits. As model compounds for this study, flavone and flavanone derivatives were used without the phenyl substituent, containing either a chromone or 4-chromanone skeleton obtained by chemical synthesis and also flavones and flavanones, which are structural analogues of natural phytoestrogens and their derivatives. To the group of compounds described in the earlier works[67,68] and also for comparison, we decided to expand our group of tested substrates by adding a flavone derivative with an amino group at C-7 in ring A. The antifeedant activity of synthetic aminoflavones toward plant pests, especially aphids, has not been investigated, so far. We expected that comparing the results of antifeedant activity of chromones, chromanones, and the selected flavanones and chalcones, which are precursors of flavonoids, would allow us to determine which structural elements of the compounds are necessary for subsequent reduced aphid settling.

The antifeedant activity of hop compounds, selected synthetic chalcone derivatives, and chromones against the peach-potato aphid (*M. persicae* [Sulz.]) was evaluated. Synthetic pesticides, which are used against agricultural pests, are highly toxic to humans and the environment. However, these natural compounds were regarded as one of the plant's defensive systems against phytophagous insects along with the peach potato plant surface. Our results showed that deterrent properties changed depending on their structure, cyclic or not. Isoxanthohumol (**6**), obtained by cyclization of xanthohumol (**14**), had strong deterrent activity against the peach-potato aphid, whereas its derivative, xanthohumol (**14**), was inactive. As we have already mentioned, the presence of a 2′-OH group

DOI: 10.1021/acs.jafc.5b02025
J. Agric. Food Chem. 2015, 63, 6749−6756

in chalcones facilitates their cyclization to their isomeric forms, flavones. The second major difference likely to affect the activity is the existence in compound **14** of a strong intramolecular hydrogen bond between the carbonyl group and the hydroxyl group. On the ^{1}H NMR spectrum it is evidenced by the presence of a signal at δ 14.7 for the proton of the 2′-OH group involved in a strong intramolecular hydrogen bond.[18] The carbonyl group of isoxanthohumol (**6**) for obvious reasons is not involved in such binding. According to the literature, the observed differences in activity may also arise from inhibition of the activity of the enzymes involved in the detoxification of xenobiotics, for example, cytochrome P450 enzymes.[69] The compounds selected for the study showed various degrees of feeding detterent activity. In our study, flavanones, chromanones, and chalcones having hydroxyl groups did not show any insect antifeedant activity. The most inactive was a 4-hydroxychalcone (**11**), which was an attractant. An additional substituent of a hydroxyl group at the *para* position in ring B of a chalcone decreased the antifeedant activity, compared to the unsubstituted chalcone (**10**). The structure−activity analysis led to the conclusion that acylation of the hydroxyl group in ring B of chalcone **11** results in an increase of the antifeedant activity, compared to the molecule with the free OH group. The presence of hydroxyl groups in the molecule of naringenin (**5**) had a considerable influence on the antifeedant activity, compared to the unsubstituted flavanone (**4**), which was only weakly active. As in the case of other biological activity, moderate deterrent properties of polyphenolic compounds, including naringenin (**5**), stem from the presence of the reactive hydroxyl groups, which facilitate binding to enzyme active sites as well as formation of hydrogen bonding with enzyme system in aphids. These result in a change of their metabolism. Flavonoids **4**, **8**, and **9**, especially, have no hydroxy substituent on the A-ring. Recent research confirming the antifeedant activity of naringenin (**5**) and its derivatives indicates that generalizations concerning the structure−activity relationships of the mentioned compounds cannot be applied to a wide range of pests[34,70,71] because the above-mentioned compounds stimulated feeding behavior of the insects, whereas another was the best feeding deterrent. As describe in the literature, cleavage of the ether linkage of the pyran ring of flavanoids[67] and the hydrogenation of the α,β-unsaturated bond in chalcones decrease the antifeedant activity.[72] Ohmura et al. reported that a dihydrochalcone, phloretin, has the same structure as naringenin, except for the absence of the pyran ring, and showed less antifeedant activity against the subterranean termite *Coptotermes formosanus* than naringenin (**5**). As was reported by Morimoto et al.,[67] although the decrease in the activity and the number of hydroxyl groups were correlated, it was attributable to the penetrability toward the receptor in the insect taste-sensitive organ. The substitution of the flavonoid ring system with the prenyl unit and a $-OCH_3$ group increases the lipophilicity and confers to the molecule a strong affinity for biological membranes, which play an important role in biomolecule transport, distribution, action, and selectivity. The hop compounds intercalate into the lipid bilayer, influencing its glycerol backbone region, hydrocarbon chain region, and, to a lesser extent, polar headgroup region. The calculation of log *P* values identified xanthohumol (4.38 ± 0.78) as a more lipophilic molecule compared to isoxanthohumol (3.82 ± 0.86).[73] However, looking at the structures of our tested compounds it is difficult to predict whether their interactions with the lipid membrane will exert any impact on the antifeedant activity. Our results indicate that the prenyl group, and flavanones, rather than the flavonols and chalcones, might make predominant contributions to antifeedant inhibition. Therefore, prenylated flavonoids possessing lipophilic moieties may be potent candidates for antifeedants. Our results suggested that the antifeedant activity required not only the important 2-position substituent but also the substituent pattern on the A-ring and the hydrogenation of the C_2-C_3 double bond of these insect antifeedants, flavonoids and chromones. Similar results were reported by Morimoto et al.[67] In our study the introduction of an additional amino group at C-7 to flavone (**9**) caused an increase in antifeedant activity against the peach-potato aphid. This is a first report about the feeding deterrent activity of aminoflavones in the literature. Significant correlations were found between biological activity and molecular size of the derivatives with a chromone system. The presence of a phenyl group at C-2 of chromone (**7**) and the introduction of an amino group at C-7 in the flavone (**8**) resulted in an increase in the deterrent activity, which was observed during the longer time. The relationship between physicochemical properties and insect antifeedant activity of compounds has been reported by Morimoto et al.[74]

Among several pest control strategies (comprising mechanical, agrotechnical, and chemical methods), biological methods of crop protection that employ compounds of plant origin (including flavonoids) are best accepted in organic food production. Therefore, this biological method of plant protection should be recommended, which is confirmed by the results of laboratory tests.

In the next step of the research an optimization of the chemical structure of these compounds is needed. This will involve computational methods such as QSAR models that relate experimentally measured biological activities of compounds to their molecular structure.[67] Natural plant compounds, such as hop flavonoids, may be applied as models or substrates for the synthesis of highly specific substances that inhibit feeding of pests.

AUTHOR INFORMATION

Corresponding Author

*(M.S.) Phone: +48 71 320 5468. Fax: +48 71 320 7744. E-mail: monika.stompor@gmail.com.

Funding

This work was financially supported by the National Science Centre (Grant 2011/01/B/NZ9/02890), 2011−2014.

Notes

The authors declare no competing financial interest.

REFERENCES

(1) Ogah, O.; Watkins, C. S.; Ulbi, B. E.; Oraguzie, N. C. Phenolic compounds in Rosaceae fruits and nut crops. *J. Agric. Food Chem.* **2014**, *62*, 9369−9386.

(2) Shahidi, F.; Naczk, M. Phenolic in cereals, fruit and vegetables: occurence, extraction and analysis. *J. Pharm. Biomed. Anal.* **2006**, *41*, 1523−1542.

(3) Ceylan, M.; Karaman; Gezegen, I. H.; Gürdere, M. B.; Dingil, A. Screening of biological activities of series of chalcone derivatives against human pathogenic microorganisms. *Chem. Biodiversity* **2010**, *7*, 400−408.

(4) Shin, S. Y.; Lee, Y. H. 3-Hydroxyflavanone induced apoptosis in HeLa cells. *Han'guk Eungyong Sangmyong Hwahakhoeji* **2013**, *56*, 113−116.

(5) Dresel, M.; Dunkel, A.; Hofmann, T. Sensomics analysis of key bitter compounds in the hard resin of hops (*Humulus lupulus* L.) and

DOI: 10.1021/acs.jafc.5b02025
J. Agric. Food Chem. 2015, 63, 6749−6756

their contribution to the bitter profile of pilsner-type beer. *J. Agric. Food Chem.* **2015**, *63*, 3402−3418.
(6) Gorjanović, S.; Pastor, F. T.; Vasić, R.; Novaković, M.; Simonović, M.; Milić, S.; Sužnjević, D. Electrochemical versus spectrophotometric assessment of antioxidant activity of hop (*Humulus lupulus* L.) products and individual compounds. *J. Agric. Food Chem.* **2013**, *61*, 9089−9096.
(7) Potaniec, B.; Grabarczyk, M.; Stompor, M.; Szumny, A.; Zieliński, P.; Żołnierczyk, A.; Anioł, M. Antioxidant activity and spectroscopic data of isoxanthohomol oxime and related compounds. *Spectrochim. Acta, Part A* **2014**, *118*, 716−723.
(8) Liu, M.; Yin, H.; Liu, G.; Dong, J.; Qian, Z.; Miao, J. Xanthohumol, a prenylated chalcone from beer hops, acts as an α-glucosidase inhibitor in vitro. *J. Agric. Food Chem.* **2014**, *62*, 5548−5554.
(9) Yu, L.; Zhang, F.; Hu, Z.; Ding, H.; Tang, H.; Ma, H.; Ma, Z.; Zhao, X. Novel prenylated bichalcone and chalcone from *Humulus lupulus* and their quinine reductase induction activities. *Fitoterapia* **2014**, *93*, 115−120.
(10) Wang, Q.; Ding, Z.; Liu, J.; Zheng, Y. Xanthohumol, a novel anti-HIV-1 agent purified from hops *Humulus lupulus*. *Antiviral Res.* **2004**, *64*, 189−194.
(11) Cho, Y.-C.; You, S.-K.; Kim, H. J.; Cho, C.-W.; Lee, I.-S.; Kang, B. Y. Xanthohumol inhibits IL-12 production and reduces chronic allergic contact dermatitis. *Int. Immunopharmacol.* **2010**, *10*, 556−561.
(12) Miranda, C. L.; Stevens, J. F.; Helmrich, A.; Henderson, M. C.; Rodriguez, R. J.; Yang, Y.-H.; Deinzer, M. L.; Barnes, D. W.; Buhler, D. R. Antiproliferative and cytotoxic effects of prenylated flavonoids from hops (*Humulus lupulus*) in human cancer cell lines. *Food Chem. Toxicol.* **1999**, *37*, 271−285.
(13) Gerhauser, C.; Alt, A.; Heiss, E.; Gamal-Eldeen, A.; Klimo, K.; Knauft, J.; Neumann, I.; Scherf, H.-R.; Frank, N.; Bartsch, H.; Becker, H. Cancer chemopreventive activity of xanthohumol, a natural product derived from hop. *Mol. Cancer Ther.* **2002**, *1*, 959−969.
(14) Vanhoecke, B.; Derycke, L.; Marck, V. V.; Depypere, H.; Keukeleire, D. D.; Bracke, M. Antiinvasive effect of xanthohumol, a prenylated chalcone present in hops (*Humulus lupulus* L.) and beer. *Int. J. Cancer* **2005**, *117*, 889−895.
(15) Monteiro, R.; Faria, A.; Azevedo, I.; Calhau, C. Modulation of breast cancer cell survival by aromatase inhibiting hop (*Humulus lupulus* L.) flavonoids. *J. Steroid Biochem. Mol. Biol.* **2007**, *105*, 124−130.
(16) Ho, Y.-C.; Liu, C.-H.; Chen, C.-N.; Duan, K.-J.; Lin, M.-T. Inhibitory effects of xanthohumol from hops (*Humulus lupulus* L.) on human hepatocellular carcinoma cell lines. *Phytother. Res.* **2008**, *22*, 1465−1468.
(17) Stevens, J. F.; Taylor, A. W.; Nickerson, G. B.; Ivancic, M.; Henning, J.; Haunold, A.; Deinzer, M. L. Prenylflavonoid variation in *Humulus lupulus*: distribution and taxonomic significance of xanthogalenol and 4′-*O*-methylxanthohumol. *Phytochemistry* **2000**, *53*, 759−775.
(18) Stompor, M.; Potaniec, B.; Szumny, A.; Zieliński, P.; Żołnierczyk, A.; Anioł, M. Microbiological reduction of xanthohumol and 4-methoxychalcone. *Przem. Chem.* **2013**, *92*, 574−578.
(19) Stompor, M.; Potaniec, B.; Szumny, A.; Zieliński, P.; Żołnierczyk, A.; Anioł, M. Microbial synthesis of dihydrochalcones using *Rhodococcus* and *Gordonia* species. *J. Mol. Catal. B: Enzym.* **2013**, *97*, 283−288.
(20) Bartmańska, A.; Tronina, T.; Popłoński, J.; Huszcza, E. Biotransformation of prenylated hop flavonoids for drug discovery and production. *Curr. Drug Metab.* **2013**, *14*, 1083−1097.
(21) Wyns, C.; Derycke, L.; Soenen, B.; Bolca, S.; Deforce, D.; Bracke, M.; Heyerick, A. Production of monoclonal antibodies against hop-derived (*Humulus lupulus* L.) prenylflavonoids and the development of immunoassays. *Talanta* **2011**, *85*, 197−205.
(22) Mitić, S. S.; Paunović, D. D.; Pavlović, A. N.; Tošić, S. B.; Stojković, M. B.; Mitić, M. N. Phenolic profiles and total antioxidant capacity of marketed beers in Serbia. *Int. J. Food Prop.* **2014**, *17*, 908−922.
(23) Toboła, D.; Stompor, M.; Błażewicz, J.; Anioł, M. Xanthohumol content in Polish beers. *Przem. Chem.* **2014**, *93*, 1447−1450.
(24) Krause, E.; Yuan, Y.; Hajirahimkhan, A.; Dong, H.; Dietz, B. M.; Nikolic, D.; Pauli, G. F.; Bolton, J. L.; Breemen, B. B. Biological and chemical standardization of a hop (*Humulus lupulus*) botanical dietary supplement. *Biomed. Chromatogr.* **2014**, *28*, 729−734.
(25) Anioł, M.; Świderska, A.; Stompor, M.; Żołnierczyk, A. K. Antiproliferative activity and synthesis of 8-prenylnaringenin derivatives by demethylation of 7-*O*- and 4′-*O*-substituted isoxanthohumols. *Med. Chem. Res.* **2012**, *21*, 4230−4238.
(26) Abbas, A.; Naseer, M. M.; Hasan, A.; Hadda, T. B. Synthesis and cytotoxicity studies of 4-alkoxychalcones as new antitumor agents. *J. Mater. Environ. Sci.* **2014**, *5*, 281−292.
(27) Batagin-Neto, A.; Lavarda, F. C. The correlation between electronic structure and antimalarial activity of alkoxylated and hydroxylated chalcones. *Med. Chem. Res.* **2014**, *23*, 580−586.
(28) Nawrot, J.; Dams, I.; Wawrzeńczyk, C. Feeding detergent activity of terpenoid lactones with *p*-menthane system against stored product pest. *J. Stored Prod. Res.* **2009**, *45*, 221−225.
(29) Grudniewska, A.; Dancewicz, K.; Białońska, A.; Ciunik, Z.; Gabryś, B.; Wawrzeńczyk, C. Synthesis of piperitone-derived halogenated lactones and their effect on aphid probing, feeding, and settling behavior. *RSC Adv.* **2011**, *1*, 498−510.
(30) Dancewicz, K.; Gabryś, B.; Dams, I.; Wawrzeńczyk, C. Enantiospecific effect of pulegone and pulegone−derived lactones on settling and feeding of *Myzus persicae* (Sulz.). *J. Chem. Ecol.* **2008**, *34*, 530−538.
(31) Grudniewska, A.; Dancewicz, K.; Białońska, A.; Wawrzeńczyk, C.; Gabryś, B. Piperitone-derived saturated lactones: synthesis and aphid behavior-modifying activity. *J. Agric. Food Chem.* **2013**, *61*, 3364−3372.
(32) Gabryś, B.; Dancewicz, K.; Gliszczyńska, A.; Kordan, B.; Wawrzeńczyk, C. Systemic deterrence of aphid probing and feeding by β-damascone analogues. *J. Pest Sci.* **2014**, DOI: 10.1007/s10340-014-0635-x.
(33) Dancewicz, K.; Gliszczyńska, A.; Wróblewska, A.; Wawrzeńczyk, C.; Gabryś, B. Deterrent activity of (+)-nootkatone and its derivatives towards the peach potato aphid (*Myzus persicae* Sulzer). *Prog. Plant Prot.* **2012**, *52*, 221−225.
(34) Goławska, S.; Sprawka, I.; Łukasik, I.; Goławski, A. Are naringenin and quercetin useful chemicals in pest-management strategies? *J. Pest Sci.* **2014**, *87*, 173−180.
(35) Akhtar, Y.; Pages, E.; Stevens, A.; Bradbury, R.; da Camara, C. A. G.; Isman, M. B. Effect of chemical complexity of essential oils on feeding deterrence in larvae of the cabbage looper. *Physiol. Entomol.* **2012**, *37*, 81−91.
(36) Zhou, Q.; Wei, M. C.; Ou, X. M.; Zhong, Y. H.; Wang, W. X. Antifeedant and deterrent effect of active fractions in *Xanthium sibiricum* leaf against insect pests and its chemical component. *J. Plant Res. Environ.* **2009**, *18*, 74−79.
(37) Julio, L. F.; Martin, L.; Muñoz, R.; Mainar, A. M.; Urieta, J. S.; Sanz, J.; Burillo, J.; González-Coloma, A. Comparative chemistry and insect antifeedant effects of conventional (Clevenger and Soxhlet) and supercritical extracts (CO_2) of two *Lavandula luisieri* populations. *Ind. Crops Prod.* **2014**, *58*, 25−30.
(38) Nawrot, J.; Klejdysz, T. Ionic liquids as feeding deterrents for stored product pests. *Przem. Chem.* **2013**, *92*, 1643−1645.
(39) Palma, L.; Muñoz, D.; Berry, C.; Murillo, J.; Caballero, P. Draft genome sequences of two *Bacillus thuringiensis* strains and characterization of a putative 41.9-kDa insecticidal toxin. *Toxins* **2014**, *6*, 1490−1504.
(40) Jóźwicka, K.; Donskow-Łysoniewska, K.; Doligalska, M. *Caenorhabditis elegans* nematode − convenient for the study anthelmintic activity in plant saponins. *Med. Wet.* **2011**, *67*, 829−834.
(41) Fraizer, J. L.; Chyb, S. Use of feeding inhibitors in insect control. In *Regulatory Mechanisms of Insect Feeding*; de Boer, G., Chapman, R. F., Eds.; Chapman and Hall: New York, 1995.
(42) Halder, J.; Srivastava, C.; Dhingra, S.; Dureja, P. Effect of essential oils on feeding, survival, growth and development of third

DOI: 10.1021/acs.jafc.5b02025
J. Agric. Food Chem. 2015, 63, 6749−6756

instar larvae of *Helicoverpa armigera* Hubner. *Natl. Acad. Sci. Lett.* **2012**, *35*, 271−276.
(43) Ahmad, S.; Khan, I. A.; Hussain, Z.; Shah, S. I. A.; Ahmad, M. Comparison of a biopesticide with some synthetic pesticides against aphid in rapeseed crop. *Sarhad J. Agric.* **2007**, *23*, 1117−1120.
(44) Gökçe, A.; Isaacs, R.; Whalon, M. E. Dose−response relationship for the antifeedant effects of *Humulus lupulus* extracts against larvae and adults of the Colorado potato beetle. *Pest Manage. Sci.* **2012**, *68*, 476−481.
(45) Dancewicz, K.; Wiśniewska, E.; Lagiera, M.; Anioł, M.; Gabryś, B. Effect of spent hop extracts on the probing and setting behaviour of *Myzus persicae* (Sulzer, 1776), Aphids and other hemipterous insects. *Hemipterol. Sect. Polish Entomol. Soc.* **2011**, *17*, 121−127.
(46) Powell, G.; Hardie, J.; Pickett, J. A. Laboratory evaluation of antifeedant compounds for inhibiting settling by cereal aphids. *Entomol. Exp. Appl.* **1997**, *84*, 189−193.
(47) Alizadeh, B. H.; Foroumadi, A.; Shafiee, A. New synthetic route towards 2,2-dimethylchromene and synthesis of substituted 7-(dimethylpropargyl) chromene. *J. Heterocycl. Chem.* **2008**, *45*, 909−912.
(48) Garazd, Y. L.; Garazd, M. M.; Khilya, V. P. Modified coumarins. 13. Synthesis of cyclopentane-annelated pyranocoumarins. *Chem. Nat. Compd.* **2004**, *40*, 427−433.
(49) An, H.; Eum, S.-J.; Koh, M.; Lee, S. K.; Park, S. B. Diversity-oriented synthesis of privileged benzopyranyl heterocycles from *s-cis*-enones. *J. Org. Chem.* **2008**, *73*, 1752−1761.
(50) Tran, T.-D.; Park, H.; Kim, H. P.; Ecker, G. F.; Thai, K.-M. Inhibitory activity of prostaglandin E_2 production by the syntetic 2′-hydroxychalcone analogues: synthesis and SAR study. *Bioorg. Med. Chem. Lett.* **2009**, *19*, 1650−1653.
(51) Anioł, M.; Szymańska, K.; Żołnierczyk, A. K. An effecient synthesis of the phytoestrogen 8-prenylnaringenin from isoxanthohumol with magnesium iodide etherate. *Tetrahedron* **2008**, *64*, 9544−9547.
(52) Wilhelm, H.; Wessjohann, L. A. An efficient synthesis of the phytoestrogen 8-prenylnaringenin from xanthohumol by a novel demethylation process. *Tetrahedron* **2006**, *62*, 6961−6966.
(53) Cuthbertson, A. G. S.; Blackburn, L. F.; Northing, P.; Luo, W.; Cannon, R. J. C.; Walters, K. F. A. Leaf dipping as an environmental screening measure to test chemical efficacy against *Bemisia tabaci* on poinsettia plants. *Int. J. Environ. Sci. Technol.* **2009**, *6*, 347−352.
(54) Hanske, L.; Loh, G.; Szczęsny, S.; Blaut, M.; Braune, A. Recovery and metabolism of xanthohumol in germ-free and human microbiota-associated rats. *Mol. Nutr. Food Res.* **2010**, *54*, 1405−1413.
(55) Yilmazer, M.; Stevens, J. F.; Deinzer, M. L.; Buhler, D. R. In vitro biotransformation of xanthohumol, a flavonoid from hops (*Humulus lupulus*), by rat liver microsomes. *Drug. Metab. Dispos.* **2001**, *29*, 223−231.
(56) Guo, J.; Nicolic, D.; Chadwic, L. R.; Guido, F. P.; Van Breemen, R. B. Identification of human hepatic cytochrome P450 enzymes involved in the metabolism of 8-prenylnaringenin and isoxanthohumol from hops (*Humulus lupulus* L.). *Drug. Metab. Dispos.* **2006**, *34*, 1152−1159.
(57) Fu, M.-L.; Wang, W.; Chen, F.; Dong, Y.-C.; Liu, X.-J.; Ni, H.; Chen, Q.-H. Production of 8-prenylnaringenin from isoxanthohumol through biotransformation by fungi cells. *J. Agric. Food Chem.* **2011**, *59*, 7419−7426.
(58) Mai, V. C.; Drzewiecka, K.; Jeleń, H.; Narożna, D.; Rucińska-Sobkowiak, R.; Kęsy, J.; Floryszak-Wieczorek, J.; Gabryś, B.; Morkunas, I. Differential induction of *Pisum sativum* defense signaling molecules in response to pea aphid infestation. *Plant Sci.* **2014**, *221−222*, 1−12.
(59) Dietz, B. M.; Hagos, G. K.; Eskra, J. N.; Wijewickrama, G. T.; Anderson, J. R.; Nikolic, D.; Guo, J.; Wright, B.; Chem, S.-N.; Pauli, G. F.; Breemen, R. B.; Bolton, J. L. Differential regulation of detoxification enzymes in hepatic and mammary tissue by hops (*Humulus lupulus*) in vitro and in vivo. *Mol. Nutr. Food Res.* **2013**, *57*, 1055−1066.
(60) Thoison, O.; Sevenet, T.; Niemeyer, H. M.; Russell, G. B. Insect antifeedant compounds from *Nothofagus dombeyi* and *N. pumilio*. *Phytochemistry* **2004**, *65*, 2173−2176.
(61) Napal, G. N. D.; Defago, M. T.; Valladares, G. R.; Palacios, S. M. Response of *Epilachna paenulata* to two flavonoids, pinocembrin and quercetin, in a comparative study. *J. Chem. Ecol.* **2010**, *36*, 898−904.
(62) Russel, G. B.; Bowers, W. S.; Keesing, V.; Niemeyer, H. M.; Sevenet, T.; Vasanthaverini, S.; Wratten, S. D. Patterns of bioactivity and herbivory on *Nothofagus* species from Chile and New Zealand. *J. Chem. Ecol.* **2000**, *26*, 41−56.
(63) Nenaah, G. E. Toxic and antifeedant activities of prenylated flavonoids isolated from *Tephrosia apollinea* L. against three major coleopteran pests of stored grains with reference to their structure-activity relationship. *Nat. Prod. Res.* **2014**, *28*, 2245−2252.
(64) Nalwar, Y. S.; Sayyed, M. A.; Mokle, S. S.; Zanwar, P. R.; Vibhute, Y. B. Synthesis and insect antifeedant activity of some new chalcones against *Phenacoccus solanopsis*. *World J. Chem.* **2009**, *4*, 123−126.
(65) Kumar, R.; Sharma, P.; Shard, A.; Tewary, D. K.; Nadda, G.; Sinha, A. K. Chalcones as promising pesticidal agents against diamondback moth (*Plutella xylostella*): microwave-assisted synthesis and structure−activity relationship. *Med. Chem. Res.* **2012**, *21*, 922−931.
(66) Sundararajan, R.; Arulkumaran, R.; Kamalakkannan, D.; Suresh, R.; Joseph, S. J.; Ranganathan, K.; Sakthinathan, S. P.; Vanangamudi, G.; Vijayakumar, S.; Thirunarayanan, G. Insect antifeedant potent halogen substituted phenyl chalcones. *Int. Lett. Chem., Phys. Astron.* **2014**, *1*, 67−73.
(67) Morimoto, M.; Kumeda, S.; Komai, K. Insect antifeedant flavonoids from *Gnaphalium affine* D. Don. *J. Agric. Food Chem.* **2000**, *48*, 1888−1891.
(68) Morimoto, M.; Tanimoto, K.; Nakano, S.; Ozaki, T.; Nakano, A.; Komai, K. Insect antifeedant activity of flavones and chromones against *Spodoptera litura*. *J. Agric. Food Chem.* **2003**, *51*, 389−393.
(69) Yuan, Y.; Qiu, X.; Nikolić, D.; Chen, S.-N.; Huang, K.; Li, G.; Pauli, G. F.; van Breemen, R. B. Inhibition of human cytochrome P450 enzymes by hops (*Humulus lupulus*) and hop prenylphenols. *Eur. J. Pharm. Sci.* **2014**, *53*, 55−61.
(70) Goławska, S.; Łukasik, I. Antifeedant activity of luteolin and genistein against the pea aphid *Acyrthosiphon pisum*. *J. Pest Sci.* **2012**, *85*, 443−450.
(71) Fulcher, A. F.; Ranney, T. G.; Burton, J. D.; Walgenbach, J. F.; Danehower, D. A. Role of foliar phenolics in host plant resistance of *Malus* taxa to adult Japanese beetles. *HortScience* **1998**, *33*, 862−865.
(72) Ohmura, W.; Doi, S.; Aoyama, M.; Ohara, S. Antifeedant activity of flavonoids and related compounds against the subterranean termite *Coptotermes formosanus* Shiraki. *J. Wood Sci.* **2000**, *46*, 149−153.
(73) Wesołowska, O.; Gąsiorowska, J.; Petrus, J.; Czarnik-Matusewicz, B.; Michalak, K. Interaction of prenylated chalcones and flavanones from common hop with phosphatidylcholine model membranes. *Biochim. Biophys. Acta, Biomembr.* **2014**, *1838*, 173−184.
(74) Morimoto, M.; Fukumoto, H.; Nozoe, T.; Hagiwara, A.; Komai, K. Synthesis and insect antifeedant activity of aurones against *Spodoptera litura* larvae. *J. Agric. Food Chem.* **2007**, *55*, 700−705.

DOI: 10.1021/acs.jafc.5b02025
J. Agric. Food Chem. 2015, 63, 6749−6756

Because we observed no improvement in ferritin content in Caco-2 cells after addition of the same CPPs pools (α-CPPs and β-CPPs) as those used in the present study,[29] the latter were designed to complete these studies in hepatic cell lines by evaluating the effect of CPPs isolated from α_s- or β-CN upon iron uptake markers, specifically ferritin and soluble transferrin receptor in HuH7 cells.

MATERIALS AND METHODS

Reagents. *Digestion.* Porcine pepsin, pancreatin, and bile extract were purchased from Sigma Chemical Co. (St. Louis, MO, USA). The working dissolutions of these enzymes were prepared immediately before use. Water of cellular grade (Aqua B Braun, Braun Medical, Barcelona, Spain) or Milli-Q water (18.2 MΩ cm resistivity) was used for the preparation of all reagents.

Trifluoroacetic acid (TFA), absolute ethanol, and acetonitrile were purchased from Merck (Darmstadt, Germany), and all of these reagents were of analytical grade. $CaCl_2$ was purchased from Panreac (Barcelona, Spain).

Iron−calcein complex in 20 mM HEPES buffer (*N*-2-hydroxyethylpiperazine-*N*-2-ethanesulfonic acid, pH 7.3) contained 0.1 μM calcein from Molecular Probes (Leiden, The Netherlands) and 1 μM $FeCl_3$ from Analytical Carlo Erba (Barcelona, Spain) .

Preparation of α-CPPs and β-CPPs Pools. Two pools of α-CPPs and β-CPPs were obtained from α_s- and β-CN (Sigma Chemical Co.) and respectively subjected to simulated gastrointestinal digestion according to the method of García-Nebot et al.[11] Briefly, both samples were digested using two demineralized enzymatic solutions (pepsin solution in the gastric stage at pH 2 for 2 h at 37 °C and pancreatin−bile solution in the intestinal stage at pH 6.5 for 2 h at 37 °C). Samples were centrifuged (3500*g*, 60 min at 4 °C) after their pH was adjusted to 7.2. The undigested casein in the supernatants was precipitated at pH 4.6, and then the CPPs were selectively precipitated with $CaCl_2$ and absolute ethanol at pH 8. The preparation was then centrifuged at 12000*g* for 10 min at 10 °C. The precipitate was washed with 50% (v/v) ethanol, lyophilized, and stored at −20 °C.

Analysis of CPPs by Online RP-HPLC-ESI-MS/MS. The analysis of the α-CPPs and β-CPPs pools was carried out according to the method of García-Nebot et al.[11] Solvent A was a mixture of water/TFA (1000:0.37, v/v), and solvent B contained water/acetonitrile/TFA (200:800:0.27, v/v/v). The gradient was 60% of solvent B during 90 min, after which the percentage of solvent B increased to 90% in 5 min and remained constant at 90% for 5 min.

The m/z spectral data were processed and transformed to spectra representing mass values using Data Analysis version 3 (Bruker Daltonik). BioTools version 2.1 (Bruker Daltonik) was used to process the MS(n) spectra and perform peptide sequencing.

Iron Binding to α-CPPs and β-CPPs: Calcein Assay. The cellular labile iron pool (LIP) consists of chelatable and redox-active iron, which plays a key role as a crossroads in cell iron metabolism. The ability of iron chelators to mobilize this temporary iron pool bound to low-molecular-weight and low-iron affinity chelators (citrate, ascorbate, phosphate, and adenosine triphosphate) is an essential factor influencing their biological efficiency. According to previous work, the calcein test can predict the iron-chelating efficiency of chelators.[30−32]

Thus, an acellular calcein test was performed to compare the potential ability of CPPs to chelate this labile iron pool at physiological pH, at concentrations used for the assays with α-CPPs and β-CPPs pools in HuH7 cells. The fluorescence of this metallosensor dye is quenched during its interaction with iron and conversely is restored during removal of iron from the calcein−iron complex by various chelators. The rate and extent of fluorescence recovery depend on the chelator concentration, the kinetics and stoichiometry of iron binding, and the relative binding affinity. The calcein test is qualitative, but the concentration of the chelator for which 50% of the fluorescence is restored is indicative of chelator affinity (RC_{50}).

Twenty microliters of the α-CPPs and β-CPPs pools in HEPES buffer (20 mM HEPES, 150 mM NaCl, pH 7.3), in a final concentration interval between 0 and 74.07 μM, was added in a microplate and mixed with 250 μL of the complex iron−calcein (containing 0.1 μM calcein and 1 μM $FeCl_3$). Then, the microplate was subjected to shaking at room temperature in darkness for 4 h, and the fluorescence (λ_{exc} = 485 nm, λ_{em} = 520 nm) of calcein was measured with a microplate fluorescence reader (Packard, Fusion). Three independent replicates were performed for each experiment, and each experiment was repeated twice.

HuH7 Cells. The human hepatoma cell line HuH7 was a gift from Dr. Ferry (Centre Anticancéreux, Hôpital Ponchaillou, Rennes, France). The cell cultures were maintained in complete culture Dulbecco's Modified Eagle Medium (DMEM+GlutaMAX), containing 10% (v/v) fetal bovine serum, 1% (v/v) nonessential amino acids, 1% (v/v) antibiotic solution, and 1% (v/v) HEPES (Gibco BRL Life Technologies, Scotland) and were used between passages 13 and 16. The cells were seeded at a density of 21000 cells/cm^2 onto 96-well plates for the cytotoxicity assays or onto 6-well plates for iron bioavailability assays.

Cytotoxicity. Before the iron bioavailability assay, we analyzed the potential cytotoxicity of the Fe−CPPs complexes in the CPP concentration range from 0 to 25 μM (Fe:CPPs ratio 4:1). The binding of iron to α-CPPs and β-CPPs pools was performed by mixing them with $FeCl_3$ solution for 30 min at 37 °C. This interval was selected by taking into account the concentration of iron and β-CN(1−25)4P already used in iron bioavailability studies in Caco-2 cells.[16,17,29,33]

Cytotoxicity was evaluated at 4 days postseeding and 24 h of incubation by measuring extracellular lactate dehydrogenase (cytotoxicity detection kit LDH, Roche, Penzberg, Germany), according to the manufacturer, on a 20 μL aliquot of cell-free medium (supernatants) at 485 nm.[28] An LDH standard curve (0−4000 mU/mL) was used to quantify enzyme (L-lactate dehydrogenase, Sigma Chemical Co.). Extracellular LDH was reported as a percentage of the control value.

Ferritin and Soluble Transferrin Receptor Contents. Five samples were analyzed: iron control (50 μM $FeCl_3$), CPPs control (α-CPPs and β-CPPs) at 12.5 μM, and the Fe−CPPs complexes (Fe−α-CPPs and Fe−β-CPPs) obtained by mixing α-CPPs and β-CPPs with $FeCl_3$ solution for 30 min at 37 °C, final pH 7.4.

At 7 days from initial seeding, 2 mL of the sample was added to the cell monolayer, and cell cultures were incubated for 2 h at 37 °C in 5% CO_2 with 95% relative humidity. Cell supernatants containing the sample were then removed and replaced by culture medium. After 22 h of incubation at 37 °C, the cell supernatants were collected and concentrated 10-fold by ultrafiltration on Vivaspin spin columns with a membrane cutoff value of 3000 Da (Vivascience, France) for sTfR measurements. sTfR was quantified by immunonephelometry (BNII analyzer, Dade Behring, Paris) using the "N latex STFR" kit (Siemens Healthcare Diagnostics, Marburg, Germany).[32]

Finally, the cells were washed twice with 50 mM sodium phosphate buffer (PBS), pH 7, and were scraped and collected in 1 mL of PBS and centrifuged for 10 min at 1500*g*. The cell pellets were sonicated for 30 s at 4 °C in 600 μL of a homogenization buffer containing 25 mM Tris-HCl (pH 7.5), dithiothreitol (1 mM), ethylenediaminetetraacetic acid (EDTA) (0.1 mM), and Brij 35 (0.02%). These cell lysates were centrifuged at 10000*g* for 10 min prior to biochemical analysis, including protein levels and ferritin concentration measurements.

The ferritin content was quantified in the cell lysates by immunoturbidimetry (Olympus analyzer AU2700, Olympus Diagnostics GmbH), using commercial Olympus kits (Olympus OSR61138).[34]

Cell protein content was determined using Kit BC Assay, a colorimetric protein assay using bicinchoninic acid[35] for expressing ferritin content and soluble transferrin receptor as micrograms of ferritin per milligram of protein and nanograms of sTfR per milligram of protein and to check reproducibility among cell cultures.

Statistical Analysis. One-way ANOVA and the Tukey test for determining significant differences ($p < 0.05$) were used for calcein and cytotoxicity assays. The results referred to ferritin content and sTfR were analyzed by two-factorial ANOVA (pool of CPPs with three levels (control, α-CPPs, and β-CPPs); iron content with two levels

DOI: 10.1021/acs.jafc.5b02424
J. Agric. Food Chem. 2015, 63, 6757−6763

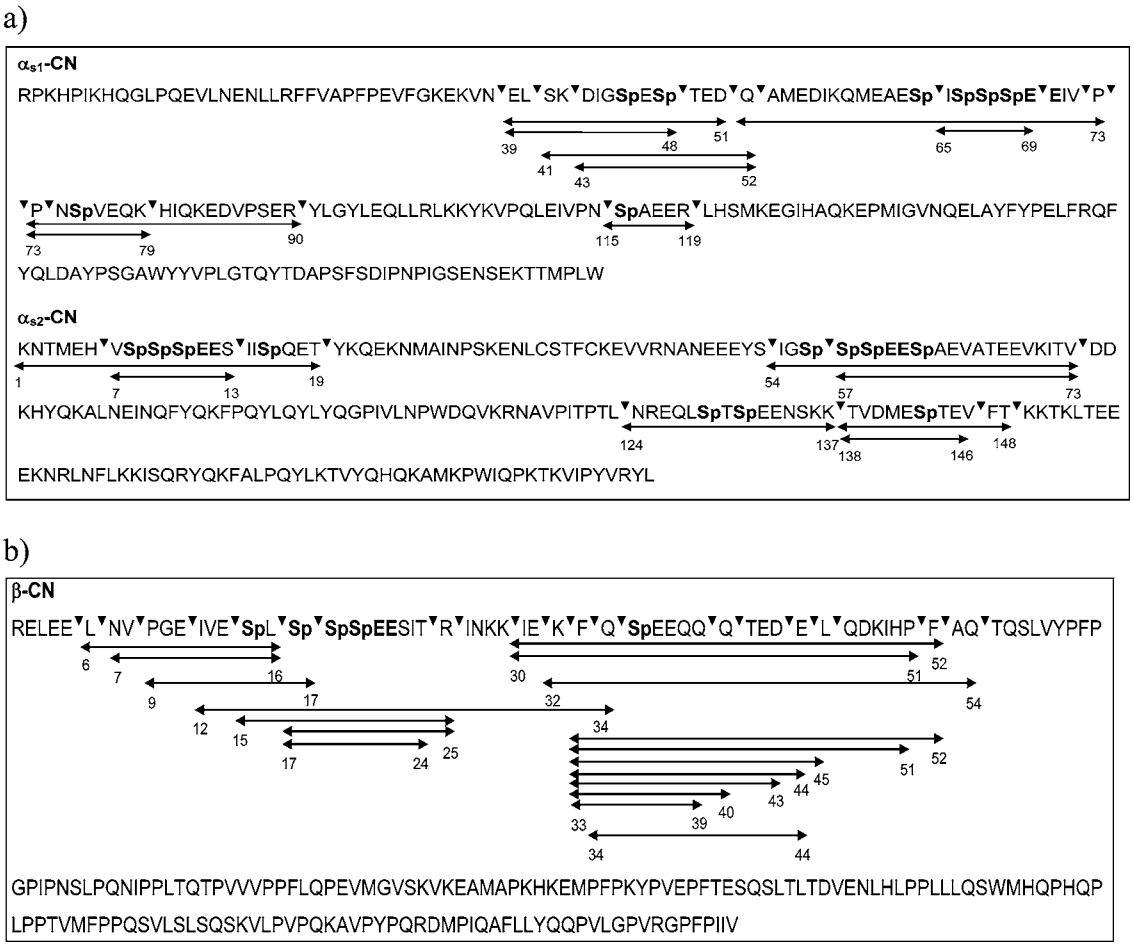

Figure 1. Caseinophosphopeptide sequences identified in α-CPPs (a) and β-CPPs (b), obtained from α-CN and β-CN subjected to simulated gastrointestinal digestion. ▼Cleavage sites; **Sp**: phosphoseryls; **SpSpSpEE**: sequence of three phosphoseryls residues followed by two glutamic acid residues.

(with/without iron)), and the Tukey test was used to determine significant differences ($p < 0.05$), with a view to evaluating the influence of the addition of different pools of CPPs and determining whether this effect is greater than when iron is added as chloride (Statgraphics Plus v. 5.1, Warrenton, VA, USA).

RESULTS AND DISCUSSION

CPPs Identified from α-CPPs and β-CPPs Pools. The main CPPs sequences identified in α-CPPs and β-CPPs pools, obtained from α- and β-CN, respectively, subjected to simulated gastrointestinal digestion and selective precipitation, are shown in Figure 1. The CPPs identified in our study contained R, T, S, V, P, K, L, E, Q, D, and F at the C-terminus, which matched with cleavages by the action of pancreatin and/or pepsin used during the simulated gastrointestinal digestion process.[1,36,37]

A total of 16 CPPs were identified in the α-CPPs pool; 9 of them corresponded to α_{s1}-CN and 7 to α_{s2}-CN. It should be noted that four CPPs contain the cluster (SpSpSpEE), which is observed in the sequences α_{s1}-CN(66−70), α_{s2}-CN(8−12), and α_{s2}-CN(55−60) (Figure 1a). From α_{s2}-CN subjected to simulated gastrointestinal digestion similar to that used in this study, Miquel et al.[5] identified peptides including the cluster (SpSpSpEE), such as α_{s2}-CN(14−73)5P and α_{s2}-CN(54−87)4P, which partially coincide with the CPPs identified in this study, that is, α_{s2}-CN(57−73)3P and α_{s2}-CN(54−73)4P. Moreover, α_{s2}-CN(137−154)1P identified by these authors has amino acid sequences common to α_{s2}-CN(138−148)1P, identified in this work.

Different digested substrates (α-CN, a commercial mixture of α_{s1}- and α_{s2}-CN used in this study versus α_{s2}-CN obtained from CN subjected to precipitation used in the above-mentioned study) and/or different experimental conditions during simulated gastrointestinal digestion (intestinal pH of 6.5 used in this study versus 5.2 in the above study) could explain the differences found in the identified product.

The peptides α_{s2}-CN(53−70)4P, α_{s2}-CN(126−137)2P, and α_{s2}-CN(138−149)1P identified by Tauzin et al.[3] from α_{s2}-CN subjected to tryptic hydrolysis partially coincide with the peptides α_{s2}-CN(54−73)4P, α_{s2}-CN(57−73)4P, α_{s2}-CN(124−137)2P, α_{s2}-CN(138−146)4P, and α_{s2}-CN(138−148)1P identified in this work. In the same way, CN subjected to simulated gastrointestinal digestion with two stages, pepsin and trypsin[8] or pepsin and a mixture of trypsin, chymotrypsin, elastase, carboxypeptidase, and intestinal brush border membrane enzymes,[9] released CPPs that totally or partially coincide with the peptides α_{s2}-CN(52−73)5P, α_{s1}-CN(115−119)1P, and α_{s2}-CN(138−146)1P identified in this study. On the other hand, some studies conducted in rats[38] or minipigs[39,40] fed CN have identified CPPs from feces or intestinal content, respectively, fully containing the cluster sequence present in the α_{s1}-CN fraction, α_{s1}-CN(66−70); thus, they partially

DOI: 10.1021/acs.jafc.5b02424
J. Agric. Food Chem. 2015, 63, 6757−6763

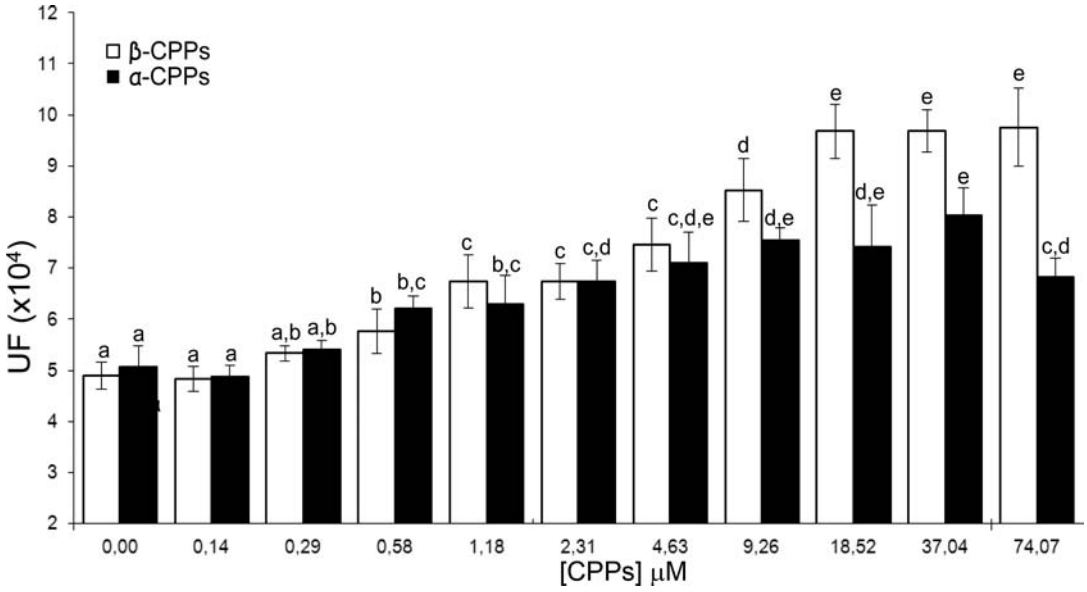

Figure 2. Iron binding to α-CPPs and β-CPPs as assessed by calcein assay. Fluorescence recovery from calcein/iron complex (contained 0.1 μM calcein and 1 μM $FeCl_3$). UF: Fluorescence units (mean ± standard deviation, $n = 6$). Different letter (a−e) in the same pool indicates statistically significant differences ($p < 0.05$) for the same pool.

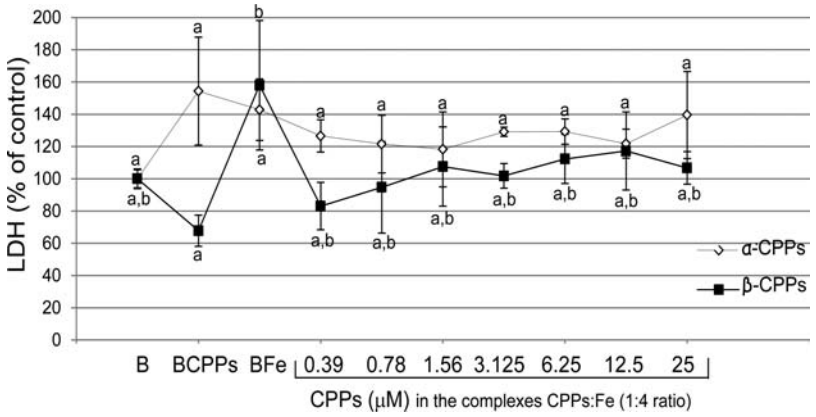

Figure 3. Cytoxicity test of α-CPPs and β-CPPs on HuH7 cells (CPP concentration range from 0 to 25 μM, Fe:CPPs ratio 4:1). B: control cells; BCPPs; control CPPs (at 25 μM); BFe: control iron (at 100 μM). LDH:lactate dehydrogenase. Different letter (a, b) in the same pool indicates statistically significant differences ($p < 0.05$) (mean ± standard deviation, $n = 3$).

coincide with some of the CPPs molecules identified in our work.

A total of 18 CPPs were identified in the β-CPPs pool, and 4 of them contained the same cluster (SpSpSpEE) present in the sequence β-CN(17−21) (Figure 1b). All peptidic fragments of CPPs identified in this sample are contained in peptide β-CN(1−52)5P, a CPP identified from the β-CN subjected to simulated gastrointestinal digestion similar to that used in this study.[7] The peptides β-CN(1−25)4P and β-CN(33−48)1P released from β-CN subjected to tryptic hydrolysis[4,41,42] partially coincide with the peptides found in this study. In this sense, Picariello et al.[9] identified the peptides β-CN(33−40)1P, β-CN(33−43)1P, β-CN(33−51)1P, and β-CN(33−52)1P from CN subjected to simulated gastrointestinal digestion with pepsin and a mixture of trypsin, chymotrypsin, elastase, carboxypeptidase, and intestinal brush border membrane enzymes, which totally coincide with some of the peptides found in this study.

Iron Binding to α-CPPs and β-CPPs: Calcein Assay. The qualitative calcein fluorescence assay was used to compare the iron-binding capacity of the α-CPPs and β-CPPs pools. For the α-CPPs pool, no statistically significant differences were recorded ($p > 0.05$) over concentrations ranging from 0.29 to 1.18 μM, this fluorescence being lower than that obtained over the concentration interval from 9.26 to 74.07 μM. No statistically significant differences were recorded ($p > 0.05$) versus this latter interval (Figure 2).

For the β-CPPs pools, a significantly greater fluorescence recovery ($p < 0.05$) was observed over concentrations ranging from 0.14 to 1.18 μM, but no statistically significant differences were obtained over concentrations from 1.18 to 4.63 μM. The fluorescence intensity obtained for this latter concentration range was lower than the fluorescence obtained over the concentration interval from 9.26 to 74.07 μM.

With these results taken into account, the β-CPPs pool showed greater fluorescence recovery from calcein/iron complexes than the α-CPPs pool over the concentration interval from 9.26 to 74.07 μM (Figure 2), thus suggesting that the β-CPPs pool could show greater iron-binding capacity

DOI: 10.1021/acs.jafc.5b02424
J. Agric. Food Chem. 2015, 63, 6757−6763

compared to the α-CPPs pool at the concentration used in the iron bioavailability assays (12.5 μM CPPs).

Cytotoxicity in HuH7 Cells from α-CPPs and β-CPPs Pools. No statistically significant differences were observed ($p > 0.05$) in extracellular LDH, indicating the absence of a cytotoxic effect of the α-CPPs and β-CPPs pools over a CPPs concentration range from 0 to 25 μM (Fe:CPPs ratio 4:1) (Figure 3).

After confirmation of the lack of a cytotoxic effect of the α-CPPs and β-CPPs pools at the assayed concentrations, the concentrations of 12.5 and 50 μM for CPPs and iron, respectively, were chosen for subsequent assays in HuH7 cells.

Ferritin and Soluble Transferrin Receptor Contents. The cell ferritin content and sTfR in supernatants in HuH7 cells are shown in Table 1. Treatment of the HuH7 cells with the pools of α-CPPs and β-CPPs at a concentration of 12.5 μM did not significantly improve ($p > 0.05$) either ferritin or sTfR contents versus control cells, taking into account the pool of CPPs factor (Figure 4a). The results obtained in the calcein assay are unable to justify these latter results, because the β-CPPs pool showed greater iron-binding capacity than the α-CPPs pool over a concentration range from 9.26 to 74.07 μM (Figure 2), a fact that would imply greater ferritin content due to treatment with β-CPPs than with α-CPPs.

Table 1. Ferritin Synthesis and Soluble Receptor Transferrin in HuH7 Cells[a]

sample		ng ferritin/mg protein	ng sTfR/mg protein
without iron	control	0.23 ± 0.03	0.99 ± 0.05
	α-CPPs	0.21 ± 0.02	1.11 ± 0.06
	β-CPPs	0.40 ± 0.13	1.12 ± 0.19
with iron	Fe control	0.66 ± 0.07	0.88 ± 0.18
	Fe-α-CPPs	0.66 ± 0.11	0.97 ± 0.01
	Fe-β-CPPs	0.57 ± 0.11	0.82 ± 0.05

[a]Control Fe, iron as chloride (mean ± standard deviation, $n = 2$ for soluble receptor transferrin (sTfR), and $n = 4$ for ferritin content). α-CPPs and β-CPPs at 12.5 μM and iron at 50 μM.

To our knowledge, no studies have evaluated the influence of CPPs upon iron bioavailability in HuH7 cells. The addition of a pool of CPPs obtained from CN (containing a mixture of both α_s-CN and β-CPPs) to fruit beverages subjected to simulated human gastrointestinal digestion did not increase iron uptake in Caco-2 cells.[19] These results were attributed to a greater proportion of CPPs proceeding from α_s-CN versus the β-CN fraction.[11] Consequently, the efficiency of various CPPs preparations in relation to iron bioavailability depends on their origin and structural properties, as previously reported by other authors. Besides, in Caco-2 cells, iron bound to a mixture of α_s-CN (α_{s1}-CN(59−79)5P and α_{s2}-CN(2−21)4P)[16] or to α_{s1}-CN(59−79)5P[17] decreased iron retention, transport, and uptake versus iron bound to β-CN(1−25)4P and iron gluconate or sulfate. Comparisons between these results and our own observations are difficult to establish, because the above-mentioned studies were performed in Caco-2 cells and the experimental conditions were different. These differences included the iron solution used (gluconate or sulfate versus chloride used in our study), the phosphopeptide concentration (25 versus 12.5 μM), and the use of a specific CPP (β-CN(1−25)4P, α_{s1}-CN(59−79)5P, or a mixture of α_{s1}-CN(59−79)5P and α_{s2}-CN(2−21)4P versus a pool of CPPs obtained from α-

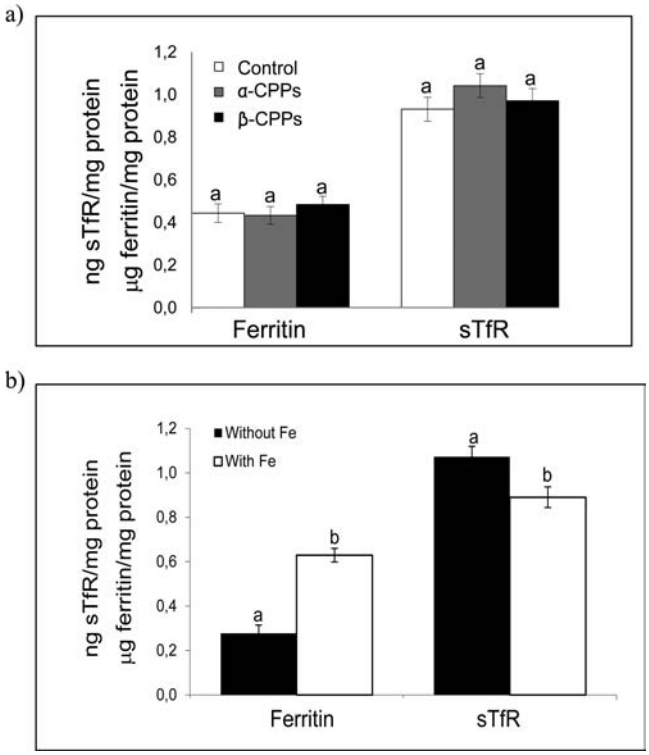

Figure 4. Influence of α-CPPs and β-CPPs on ferritin content and soluble transferrin receptor and in HuH7 cells taking into account the (a) pool of CPPs and (b) iron content (samples with/without iron). sTfR: soluble receptor transferrin. Different letter (a−b) in the same parameter indicates statistically significant differences ($p < 0.05$).

or β-CN, in which 16 or 18 CPPs have been identified, respectively).

The addition of exogenous iron significantly increased ($p > 0.05$) the ferritin content in HuH7 cells, with the iron content factor (samples with or without iron) taken into account (Figure 4b), this being consistent with the results reported by Trinder and Morgan.[23] These authors showed an increase in iron uptake in HuH7 cells after the addition of iron as ferric citrate for 2 h. This iron uptake was also demonstrated to be a saturable process from 1 to 16 μM iron, thus suggesting that it is mediated by an iron carrier.[23] In this context, in HepaRG cells isolated from a human hepatocellular carcinoma, an increase in ferritin content was reported due to the incubation of the cell line for 72 h with iron at 20 μM as ferric chloride.[32]

Treatment with ferric ammonium citrate (10 μg/mL) for 2 or 16 h resulted in a 1.3- or 5.6-fold increase in ferritin content versus the controls in the human hepatoma cell line HepG2.[26] When the same cell line was exposed to a different concentration of ferric ammonium citrate for 24 h, an increase was observed in iron uptake from 20 to 50 μg/mL iron, whereas a decrease was recorded at higher concentrations.[27] This fact was attributed to the capacity of the HepG2 cells to regulate their iron needs with the ability to limit uptake at concentrations >40 μg/mL of iron. However, no change was detected in the expression of ferritin from 20 to 120 μg/mL of iron in the medium under the same conditions.[27]

Concomitantly to the ferritin increase, the addition of exogenous iron was seen to significantly decrease ($p < 0.05$) sTfR in HuH7 cells, taking into account the iron content factor (samples with/without iron) (Figure 4b). These results indicate an inverse relationship between ferritin content and sTfR, in

DOI: 10.1021/acs.jafc.5b02424
J. Agric. Food Chem. 2015, 63, 6757−6763

agreement with the observations of other authors[28] and with Iron Regulatory Protein/Iron-Responsive Element regulation. A decrease in the expression of membrane transferrin receptor (TfR) in HuH7 cells was found to result from ferric ammonium citrate addition at 30 μg/mL for 24 h,[25] and in HepG2 cells over a range from 20 to 120 μg/mL during 24 h.[27] Furthermore, in HepaRG cells exposed to 20 μM ferric chloride for 72 h, a decrease in soluble transferrin receptor (TfR) in proliferating cells (assays performed at 4 days from initial seeding) has been reported, whereas the levels remained unchanged in differentiated cells (21 days from initial seeding).[32] These results have been attributed to the very low sTfR levels observed in the differentiated cells, which reflects the detection limit of this parameter under this condition.

On the basis of the ferritin and soluble transferrin receptor contents, used as markers, the treatment of HuH7 cells with iron complexed to phosphopeptides from either α_s-casein or β-casein did not improve iron bioavailability. Compared to already published works involving various CPPs preparations and different cell models, we confirm that the influence of different CPPs upon iron bioavailability depends on their structural properties and on the conformation which the complex can acquire when iron is bound to CPPs. Further research with CPPs proceeding from α_s- and β-CN fractions and purified CPP sequences, containing the sequence SpSpSpEE, such as the β-CN(1−25)4P, for which the positive influence upon iron bioavailability is known, are needed to evaluate their positive effects and compare their influence upon iron bioavailability, with a view to relating their structural properties to their influence upon iron bioavailability. Because no difference was detected, it will be also interesting to test smaller CPPs−iron complexes obtained after in vitro gastrointestinal digestion of CPPs−Fe complexes used in the present work.

■ ASSOCIATED CONTENT

Supporting Information

Additional tables. The Supporting Information is available free of charge on the ACS Publications website at DOI: 10.1021/acs.jafc.5b02424.

■ AUTHOR INFORMATION

Corresponding Author

*(A.A.) Phone: +34-963544907. Fax: +34-963544954. E-mail: amparo.alegria@uv.es.

Funding

M.J.G.-N. is the holder of a grant from the Generalitat Valenciana (Spain). This study has been partially funded by the Consolider Fun-C-Food CSD 2007-00063 (Fun-C-Food).

Notes

The authors declare no competing financial interest.

■ ACKNOWLEDGMENTS

We thank the Laboratoire de Biologie Générale et Enzymologie, CHRU Pontchaillou, Université de Rennes 1, for performing ferritin and sTfR analysis and quantification.

■ ABBREVIATIONS USED

CN, casein; CPPs, caseinophosphopeptides; DMEM, Dulbecco's Modified Eagle Medium; ESI-MS/MS, electrospray ionization tandem mass spectrometry; FBS, fetal bovine serum; LDH, lactate dehydrogenase; PBS, phosphate-buffered saline; RP-HPLC, reverse-phase high-performance liquid chromatography; sTfR, soluble receptor transferrin; TFA, trifluoroacetic acid

■ REFERENCES

(1) Adamson, N. J.; Reynolds, E. C. Characterization of multiply phosphorylated peptides selectively precipitated from a pancreatic casein digest. *J. Dairy Sci.* **1995**, *78*, 2653−2659.

(2) Adamson, N. J.; Reynolds, E. C. Relationship between degree of casein hydrolysis and phosphopeptide release. *J. Dairy Res.* **1997**, *64*, 505−514.

(3) Tauzin, J.; Miclo, L.; Roth, S.; Mollé, D.; Gaillard, J. L. Tryptic hydrolysis of bovine α_{s2}-casein: identification and release kinetics of peptides. *Int. Dairy J.* **2003**, *13*, 15−27.

(4) Visser, S.; Slangen, C. J.; Lagerwerf, F. M.; Vandongen, W. D.; Haverkamp, J. Identification of a new genetic variant of bovine β-casein using reversed-phase high-performance liquid-chromatography and mass-spectrometric analysis. *J. Chromatogr. A* **1995**, *711*, 141−150.

(5) Miquel, E.; Alegría, A.; Barberá, R.; Farré, R. Identification of novel phosphopeptides after simulated digestion of α_{s2}-casein by tandem mass spectrometry. *Food Sci. Technol. Int.* **2006**, *12*, 531−537.

(6) Miquel, E.; Gómez, J. A.; Alegría, A.; Barberá, R.; Farré, R.; Recio, I. Identification of casein phosphopeptides after simulated gastrointestinal digestion by tandem mass spectrometry. *Eur. Food Res. Technol.* **2006**, *222*, 48−53.

(7) Miquel, E.; Gómez, J. A.; Alegría, A.; Barberá, R.; Farré, R.; Recio, I. Identification of casein phosphopeptides in β-casein and commercial hydrolysed casein by mass spectrometry. *Food Sci. Technol. Int.* **2006**, *12*, 379−384.

(8) Ono, T.; Takagi, Y.; Kunishi, I. Casein phosphopeptides from casein micelles by successive digestion with pepsin and trypsin. *Biosci., Biotechnol., Biochem.* **1998**, *62*, 16−21.

(9) Picariello, G.; Ferranti, P.; Fierro, O.; Mamone, G.; Caira, S.; Di Luccia, A.; Monica, S.; Addeo, F. Peptides surviving the simulated gastrointestinal digestion of milk proteins: biological and toxicological implications. *J. Chromatogr. B: Anal. Technol. Biomed. Life Sci.* **2010**, *878*, 295−308.

(10) Meisel, H.; FitzGerald, R. J. Biofunctional peptides from milk proteins: mineral binding and cytomodulatory effects. *Curr. Pharm. Des.* **2003**, *9*, 1289−1295.

(11) García-Nebot, M. J.; Alegría, A.; Barberá, R.; Contreras, M. M.; Recio, I. Milk versus caseinophosphopeptides added to fruit beverage: Resistance and release from simulated gastrointestinal digestion. *Peptides* **2010**, *31*, 555−561.

(12) Yeung, A. C.; Glahn, R. P.; Miller, D. D. Dephosphorylation of sodium caseinate, enzymatically hydrolyzed casein and casein phosphopeptides by intestinal alkaline phosphatase: implications for iron availability. *J. Nutr. Biochem.* **2001**, *12*, 292−299.

(13) Yeung, A. C.; Glahn, R. P.; Miller, D. D. Effects of iron source on iron bioavailability from casein and casein phosphopeptides. *J. Food Sci.* **2002**, *67*, 1271−1275.

(14) Etcheverry, P.; Wallingford, J. C.; Miller, D. D.; Glahn, R. P. Calcium, zinc, and iron bioavailabilities from a commercial human milk fortifier: a comparison study. *J. Dairy Sci.* **2004**, *87*, 3629−3637.

(15) Bouhallab, S.; Cinga, V.; Aït-Oukhatar, N.; Bureau, F.; Neuville, D.; Arhan, P.; Maubois, J. L.; Bouglé, D. Influence of various phosphopeptides of caseins on iron absorption. *J. Agric. Food Chem.* **2002**, *50*, 7127−7130.

(16) Kibagou, I. B.; Bouhallab, S.; Henry, G.; Bureau, F.; Allouche, S.; Blais, A.; Guérin, P.; Arhan, P.; Bouglé, D. L. Milk proteins and iron absorption: contrasting effects of different caseinophosphopeptides. *Pediatr. Res.* **2005**, *58*, 731−734.

(17) Kibangou, I. B.; Bouhallab, S.; Bureau, F.; Guerin, P.; Allouche, S.; Arhan, P.; Bouglé, D. Influence of two forms of caseinophosphopeptide on iron bioavailability. In *Early Nutrition and Its Later Consequences: New Opportunities*; 1st ed.;Koletzko, B., Dodds, O., Akerblom, H., Ashwell, M., Eds.; Springer: Dordrecht, The Netherlands, 2005; Vol. 569, pp 221−222.

DOI: 10.1021/acs.jafc.5b02424
J. Agric. Food Chem. 2015, 63, 6757−6763

(18) Miquel, E.; Alegría, A.; Barberá, R.; Farré, R. Speciation analysis of calcium, iron, and zinc in casein phosphopeptide fractions from toddler milk-based formula by anion exchange and reversed-phase high-performance liquid chromatography-mass spectrometry/flame atomic-absorption spectroscopy. *Anal. Bioanal. Chem.* **2005**, *381*, 1082−1088.
(19) García-Nebot, M. J.; Alegría, A.; Barberá, R.; Clemente, G.; Romero, F. Addition of milk or caseinophosphopeptides to fruit beverages to improve iron bioavailability. *Food Chem.* **2010**, *119*, 141−148.
(20) García-Nebot, M. J.; Cilla, A.; Alegría, A.; Barberá, R.; Lagarda, M. J.; Clemente, G. Effect of caseinophosphopeptides added to fruit beverages upon ferritin synthesis in Caco-2 cells. *Food Chem.* **1010**, *122*, 92−97.
(21) Nakabayashi, H.; Taketa, K.; Miyano, K.; Yamane, T.; Sato, J. Growth of human hepatoma cell lines with differentiated functions in chemically defined medium. *Cancer Res.* **1982**, *42*, 3858−3863.
(22) Trinder, D.; Morgan, E. Inhibition of uptake of transferrin-bound iron by human hepatoma cells by nontransferrin-bound iron. *Hepatology* **1997**, *26*, 691−698.
(23) Trinder, D.; Morgan, E. Mechanisms of ferric citrate uptake by human hepatoma cells. *Am. J. Physiol.* **1998**, *275*, G279−G286.
(24) Trinder, D.; Zak, O.; Aisen, P. Transferrin receptor-independent uptake of differic transferrin by human hepatoma cells with antisense inhibition of receptor expression. *Hepatology* **1996**, *23*, 1512−1520.
(25) Herbison, C. E.; Thorstensen, K.; Chua, A. C. G.; Graham, R. M.; Leedman, P.; Olynyk, J. K.; Trinder, D. The role of transferrin receptor 1 and 2 in transferrin-bound iron uptake in human hepatoma cells. *Am. J. Physiol. Cell Physiol.* **2009**, *297*, C1567−C1575.
(26) Toth, I.; Rogers, J. T.; McPhee, J. A.; Elliot, S. Z.; Abramson, S. L.; Bridges, K. B. Ascorbic acid enhances iron-induced ferritin translation in human leukemia and hepatoma cells. *J. Biol. Chem.* **1995**, *270*, 2846−2852.
(27) Popovic, Z.; Templeton, D. Iron accumulation and iron-regulatory protein activity in human hepatoma (HepG2) cells. *Mol. Cell. Biochem.* **2004**, *265*, 37−45.
(28) Beguin, Y. Soluble transferrin receptor for the evaluation of erythropoiesis and iron status. *Clin. Chim. Acta* **2003**, *329*, 9−22.
(29) García-Nebot, M. J.; Alegría, A.; Barberá, R. Iron and zinc bioavailability in Caco-2 cells: influence of caseinophosphopeptides. *Food Chem.* **2013**, *138*, 1298−1303.
(30) Lescoat, G.; Léonce, S.; Pierré, A.; Gouffier, L.; Gaboriau, F. Antiproliferative and iron chelating efficiency of the new bis-8-hydroxyquinoline benzylamine chelator S1 in hepatocyte cultures. *Chem.−Biol. Interact.* **2012**, *195*, 165−172.
(31) Rodriguez-Lucena, D.; Gaboriau, F.; Rivault, F.; Schalk, I. J.; Lescoat, G.; Mislin, G. L. A. Synthesis and biological properties of iron chelators based on a bis-2-(2-hydroxy-phenyl)-thiazole-4-carboxamide or -thiocarboxamide (BHPTC) scaffold. *Bioorg. Med. Chem.* **2010**, *18*, 689−695.
(32) Gaboriau, F.; Leray, A. M.; Ropert, M.; Gouffier, L.; Cannie, I.; Troadec, M. B.; Loréal, O.; Brissot, P.; Lescoat, G. Effects of deferasirox and deferiprone on cellular iron load in the human hepatoma cell line HepaRG. *BioMetals* **2010**, *23*, 231−245.
(33) Kibangou, I.; Bouhallab, S.; Bureau, F.; Allouche, S.; Thouvenin, G.; Bouglé, D. Caseinophosphopeptide-bound iron: protective effect against gut peroxidation. *Ann. Nutr. Metab.* **2008**, *52*, 177−180.
(34) Do, T. H. T.; Gaboriau, F.; Ropert, M.; Moirand, R.; Cannie, I.; Brissot, P.; Loréal, O.; Lescoat, G. Ethanol effect on cell proliferation in the human hepatoma HepaRG cell line: relationship with iron metabolim. *Alcohol.: Clin. Exp. Res.* **2011**, *35*, 408−419.
(35) Smith, P. K.; Krohn, R. I.; Hermanson, G. T.; Mallia, A. K.; Gartner, F. H.; Provenzano, M. D.; Fujimoto, E. K.; Goeke, N. M.; Olson, B. J.; Klenk, D. C. Measurement of protein using bicinchoninic acid. *Anal. Biochem.* **1985**, *150*, 76−85.
(36) Schmelzer, C. E. H.; Schöps, R.; Ulbrich-Hofmann, R.; Neubert, R. H. H.; Raith, K. Mass spectrometric characterization of peptides derived by peptic cleavage of bovine β-casein. *J. Chromatogr.* **2004**, *1055*, 87−92.
(37) Su, R.; Qi, W.; He, Z.; Yuan, S.; Zhang, Y. Pancreatic hydrolysis of bovine casein: identification and release kinetics of phosphopeptides. *Food Chem.* **2007**, *104*, 276−286.
(38) Kasai, T.; Honda, T.; Kiriyama, S. Caseinphosphopeptides (CPP) in feces of rats fed casein diet. *Biosci., Biotechnol., Biochem.* **1992**, *56*, 1150−1151.
(39) Meisel, H.; Frister, H. Chemical characterization of a caseinophosphopeptide isolated from in vivo digests of a casein diet. *Biol. Chem. Hoppe−Seyler* **1998**, *369*, 1275−1279.
(40) Meisel, H.; Frister, H. Chemical characterization of bioactive peptides from in vivo digests of casein. *J. Dairy Res.* **1989**, *56*, 343−349.
(41) Carles, C.; Ribadeau-Dumas, B. Determination of gradient elution conditions for the separation of peptides mixture by reversed-phase high-performance liquid chromatography: bovine β-casein tryptic digest. *J. Dairy Res.* **1986**, *53*, 595−560.
(42) Leadbeater, L.; Ward, F. B. Analysis of tryptic digests of bovine β-casein by reversed phase high-performance liquid chromatography. *J. Chromatogr.* **1987**, *397*, 435−345.

DOI: 10.1021/acs.jafc.5b02424
J. Agric. Food Chem. 2015, 63, 6757−6763

Table 1. Accurate Mass Measurements of Pseudo-molecular and Fragment Ions of Seven Standards

compound	t_R (min)	formula	measured mass (Da)	calculated mass (Da)	error (mDa)	MS/MS fragment ions (Da)
echinacoside	3.02	$C_{35}H_{45}O_{20}$	785.2505	785.2504	0.1	623, 477, 461, 315, 179, 161, 153, 135
acteoside	3.78	$C_{29}H_{35}O_{15}$	623.1971	623.1976	−0.5	461, 315, 179, 161, 135
hydroxytyrosol	1.57	$C_8H_9O_3$	153.0562	153.0552	1.0	123
caffeic acid	2.33	$C_9H_7O_4$	179.0344	179.0344	0.0	135
3,4-dihydroxybenzenepropionic acid	2.26	$C_9H_9O_4$	181.0509	181.0501	0.8	137
3-hydroxyphenylpropionic	3.39	$C_9H_9O_3$	165.0560	165.0552	0.8	121
3-phenylpropionic acid	5.71	$C_9H_9O_2$	149.0612	149.0603	0.9	105

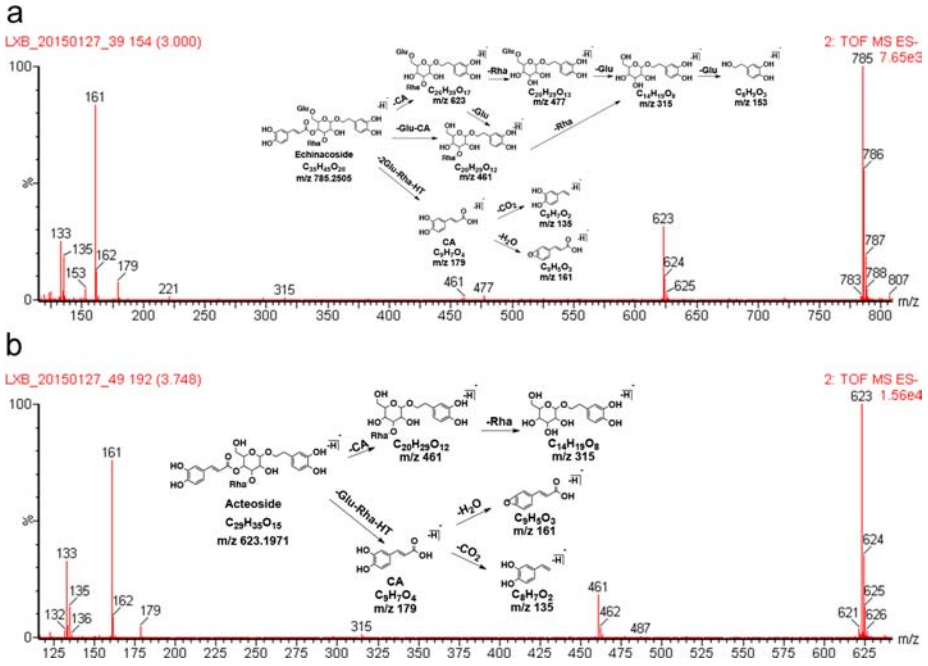

Figure 1. UPLC-MS/MS spectra and proposed fragmentation pathways of echinacoside (a) and acteoside (b).

Echinacoside was kindly provided by Dr. Pengfei Tu's laboratory from Peking University (Beijing, China). Acteoside was purchased from Sichuan Weikeqi Biological Technology Co., Ltd. (Chengdu, China). Hydroxytyrosol (HT), caffeic acid (CA), 3,4-dihydroxybenzenepropionic acid, 3-hydroxyphenylpropionic acid (3-HPP), and 3-phenylpropionic acid were purchased from Aladdin Industrial Inc. (Shanghai, China). The purity of each compound was determined to be >95% by HPLC-UV.

Stability Study of ECH in Simulated Gastric Juice and Intestinal Juice. One milligram of ECH was placed in 10 mL of simulated gastric juice (0.08 M HCl containing 50 mg of pepsin, pH 1.5) and incubated at 37 °C for 0, 1, 2, or 4 h, respectively. The reactions were quenched by water-saturated *n*-butanol immediately. The mixture was centrifuged at 4800 rpm for 20 min, and then the supernatant was evaporated. The residue was dissolved in 0.5 mL of methanol and centrifuged at 12000 rpm for 10 min at 4 °C, and the supernatant was analyzed by HPLC.

One milligram of ECH was placed in 10 mL of simulated intestinal juice (0.05 M KH_2PO_4 containing 50 mg of pancreatin, pH 6.8) and incubated at 37 °C for 0, 2, 4, or 6 h, respectively. The sample processing was the same as that for ECH in simulated gastric juice.

HPLC Analysis. The HPLC system (Agilent 1200, USA) consisted of a multisolvent delivery pump equipped with a quaternary solvent delivery system, an autosampler, and a DAD detector, which was used to analyze the stability of ECH in simulated gastric juice and intestinal juice. A ZORBAX Eclipse XDB-C18 column (250 mm × 4.6 mm i.d., 5 μm, Agilent Ltd., USA) was used. The chromatographic condition was acetonitrile (A) and water (B) with gradient elution, 0−30 min (A, 10−30%) and 30−35 min (A, 30−100%). UV absorption was monitored at 330 nm. The column temperature was set at 35 °C. The flow rate was 1.0 mL/min, and the sample injection volume was 10 μL.

Metabolism Study of ECH by Human Intestinal Bacteria. Fresh human fecal samples were obtained from six healthy volunteers (three males and three females, 22−50 years of age) who had no history of gastrointestinal disorders or antibiotics usage for at least 3 months prior to the study. The fresh fecal samples were mixed and immediately homogenized with 25 times volume of GAM broth. The sediments were removed by filtration through three pieces of gauze. The suspension was incubated at 37 °C in an anaerobic incubator in which the air had been replaced by a gas mixture (H_2 5%, CO_2 10%, N_2 85%). Three milligrams of ECH was placed in 10 mL of human fecal suspension, and the suspension was incubated at 37 °C for 48 h. The cultured mixture was removed and extracted with water-saturated *n*-butanol at time points of 1, 3, 6, 9, 12, 24, and 48 h. The mixture was centrifuged at 4800 rpm for 20 min, and the supernatant was then evaporated. The residue was dissolved in 0.5 mL of methanol and centrifuged at 12000 rpm for 10 min at 4 °C, and the supernatant was analyzed by UPLC-Q-TOF-MS.

UPLC-MS Analysis. UPLC-Q-TOF-MS analysis was performed on a Waters ACQUITY UPLC system (Waters Corp., Milford, MA, USA) using an ACQUITY UPLC BEH C18 column (100 mm × 2.1 mm i.d., 1.7 μm, Waters Corp., USA) by gradient elution using acetonitrile (A) and water (B) at a flow rate of 0.4 mL/min. The gradient profile was 0−3 min (A, 5−20%), 3−6 min (A, 20−30%), 6−9 min (A, 30−70%), and 9−10.5 min (A, 70−99%), then held for 2 min. The gradient was recycled back to 5% in 2.5 min for the next run. The injection volume was 3 μL. The temperature of the column oven was set to 35 °C.

DOI: 10.1021/acs.jafc.5b02881
J. Agric. Food Chem. 2015, 63, 6764−6771

Table 2. Echinacoside (M0) and Its Metabolites (M1−M13) Identified in the Samples Incubated with Human Intestinal Bacteria for 24 h Using UPLC-Q-TOF/MS

no.	t_R (min)	measured mass (Da)	error (mDa)	formula	MS/MS fragment ions (Da)	identification
M0	3.02	785.2482	−2.2	$C_{35}H_{45}O_{20}$	623, 477, 461, 315, 179, 161, 153, 135	parent
M1	1.57	153.0567	1.5	$C_8H_9O_3$	123	HT
M2	2.26	181.0505	0.4	$C_9H_9O_4$	137	3,4-dihydroxyphenylpropionic acid
M3	2.33	179.0372	2.8	$C_9H_7O_4$	135	CA
M4	2.44	801.2433	−2.1	$C_{35}H_{45}O_{21}$	783, 179, 161, 135	hydroxylated echinacoside
M5	2.95	639.1900	−2.5	$C_{29}H_{35}O_{16}$	477, 179, 135	M0-Rha
M6	3.19	787.2650	−1.1	$C_{35}H_{47}O_{20}$	623, 181, 153	reduction of echinacoside
M7	3.35	769.2546	−0.9	$C_{35}H_{45}O_{19}$	179, 161, 135	dehydroxylated echinasoside
M8	3.39	165.0563	1.1	$C_9H_9O_3$	121	3-HPP
M9	3.46	479.1549	−0.5	$C_{23}H_{27}O_{11}$	315, 181, 153, 137	M10-Rha
M10	3.66	625.2124	−0.9	$C_{29}H_{37}O_{15}$	461, 315, 181, 153, 137	reduction of acteoside
M11	3.72	827.2624	1.4	$C_{37}H_{47}O_{21}$	623, 179, 161, 153, 135	acetylated echinacoside
M12	3.77	623.1945	−3.1	$C_{29}H_{35}O_{15}$	461, 315, 179, 161, 135	acteoside
M13	5.72	149.0623	2.0	$C_9H_9O_2$	105	3-phenylpropionic acid

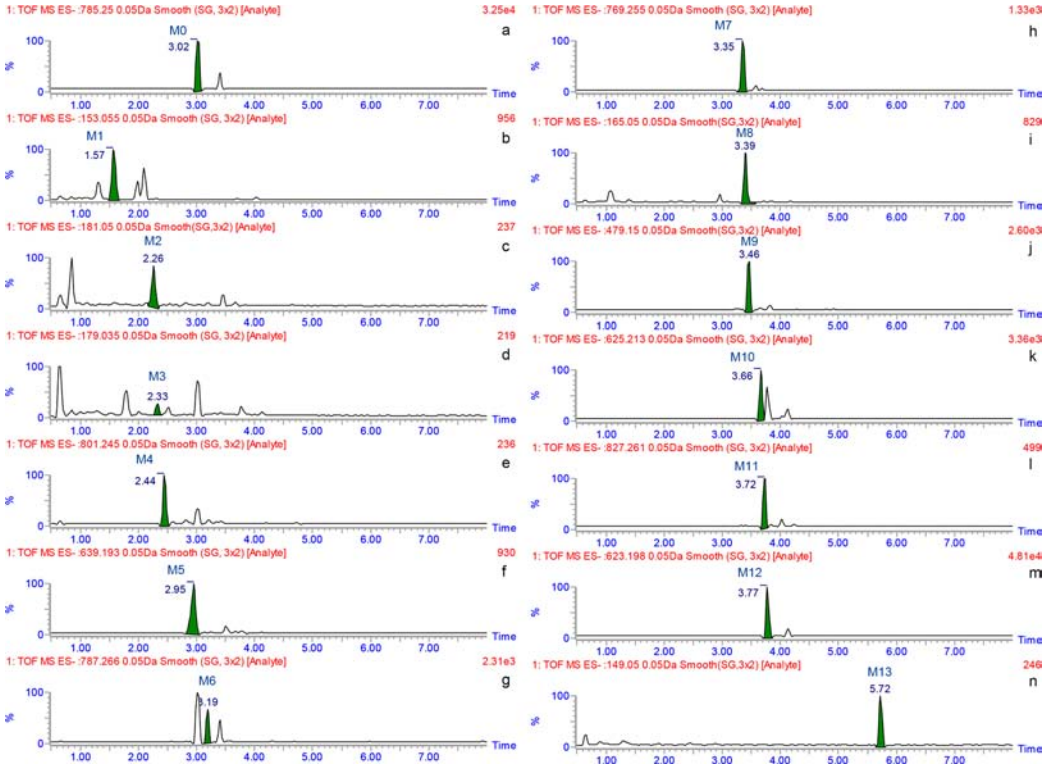

Figure 2. UPLC-MS extracted ion chromatograms (XICs) of echinacoside and its metabolites: (a) **M0**; (b) **M1**; (c) **M2**; (d) **M3**; (e) **M4**; (f) **M5**; (g) **M6**; (h) **M7**; (i) **M8**; (j) **M9**; (k) **M10**; (l) **M11**; (m) **M12**; (n) **M13**.

Mass spectrometry was carried out using a Waters Synapt mass spectrometer (Waters Corp., Milford, MA, USA). Ionization was performed in the negative electrospray (ESI) mode. The MS parameters were as follows: capillary voltage, 2.8 kV; cone voltage, 35 V; source temperature, 115 °C; desolvation temperature, 350 °C; gas flows of cone and desolvation, 50 and 700 L/h, respectively. For accurate mass measurement, leucine-enkephalin was used as the lock mass. The MS^E experiment in two scan functions was carried out as follows: function 1 (low energy), m/z 50−1000, 0.25 s scan time, 0.02 s interscan delay, 4 eV collision energy; function 2 (high energy), m/z 50−1000, 0.25 s scan time, 0.02 s interscan delay, collision energy ramp of 55−70 eV. The data were processed using MassLynx 4.1 software (Waters Corp.).

Data Analysis. Data analysis was performed using MetaboLynx software (Waters Corp.) that employs an expected list of potential biotransformation reactions such as deglycosylation, dehydroxylation, and acetylation. This software automates the detection and identification of metabolites by comparing the sample with the control to eliminate the interfering peaks in the sample that also appear in the control. The mass defect filter was set as 25 mDa. Results were filtered on the basis of the mass fractional deviation from the parent compound and the expected metabolites of the parent compound. The mass window of 0.05 Da was set for both expected and unexpected metabolite mass chromatograms. Apex track peak integration was used for peak detection, and the response threshold of the absolute peak height was set to 20 units.

RESULTS

Stability of ECH in Simulated Gastric Juice and Intestinal Juice. ECH was found to be stable in simulated gastric juice and intestinal juice. After incubation with artificial

DOI: 10.1021/acs.jafc.5b02881
J. Agric. Food Chem. 2015, 63, 6764−6771

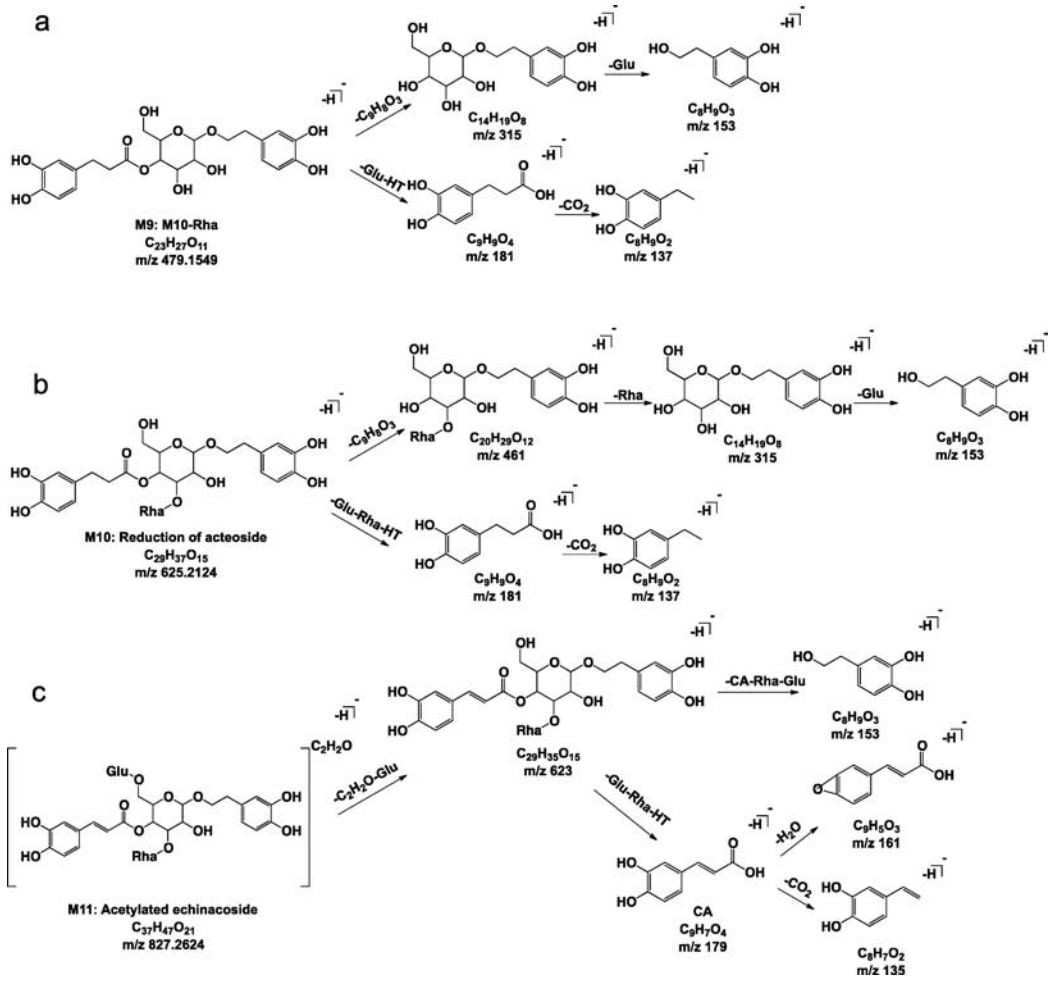

Figure 3. Proposed fragmentation pathways: (a) **M9** (m/z 479); (b) **M10** (m/z 625); (c) **M11** (m/z 827).

juices, the content of ECH did not change significantly over time according to the peak areas during the course of incubation (RSD < 3.0%).

Fragmentation Studies. Solutions of ECH, acteoside, HT, CA, 3,4-dihydroxybenzenepropionic acid, 3-HPP, and 3-phenylpropionic acid prepared in methanol were used for the fragmentation pattern study to support metabolite characterizations. The above seven standard compounds were eluted at 3.02 min (ECH), 3.78 min (acteoside), 1.57 min (HT), 2.33 min (CA), 2.26 min (3,4-dihydroxybenzenepropionic acid), 3.39 min (3-HPP), and 5.71 min (3-phenylpropionic acid), respectively (Table 1).

The fragmentation patterns of ECH and acteoside were described as followed. As shown in Figure 1a, ECH (m/z 785.2505) produced a fragment at m/z 623 by loss of a CA moiety, and then the sequential losses of rhamnose (Rha), glucose (Glu), and Glu moieties yielded the respective fragment ions at m/z 477, 315, and 153. The fragment at m/z 461 was generated through the loss of Glu and CA moieties from the precursor ion. The product ion at m/z 179, which was one of the major fragments, corresponded to the CA moiety and then produced ions at m/z 135 and 161 by the further loss of CO_2 and H_2O, respectively. Acteoside (m/z 623.1971) displayed a similar fragmentation pattern in the spectrum of ECH (Figure 1b). It produced the fragment ion at m/z 461 by losing the CA moiety and then produced the ion at m/z 315 by the further loss of a Rha moiety. The CA moiety was also found at m/z 179 that produced ions at m/z 135 and 161 by the loss of CO_2 and H_2O, respectively. HT (m/z 153.0562) produced a fragment at m/z 123, which was probably through the loss of a CH_2O moiety. Similarly, CA (m/z 179.0344) yielded a product ion at m/z 135 by the loss of CO_2. 3,4-Dihydroxybenzenepropionic acid (m/z 181.0509) produced the ion at m/z 137 by the loss of CO_2. CO_2 was lost from 3-HPP (m/z 165.0560) to form the ion at m/z 121. 3-Phenylpropionic acid (m/z 149.0612) produced m/z 105 by the loss of CO_2 as well.

Identification of ECH Metabolites by Human Intestinal Bacteria. Compared with the blank sample, the parent compound ECH (**M0**) and its 13 metabolites (**M1**−**M13**), including the metabolites of parent compound (**M4**−**M7**, **M9**−**M12**) and degradation products (**M1**−**M3**, **M8**, **M13**), were identified in human intestinal bacteria samples. Detailed information on these metabolites is listed in Table 2. Deglycosylation, dehydroxylation, reduction, hydroxylation, and acetylation were considered as the main metabolic pathways for the parent compound.

The extracted ion chromatograms (XICs) of the parent compound (**M0**) and its metabolites (**M1**−**M13**) from the total UPLC-MS chromatograms are shown in Figure 2. In addition, **M9**, **M10**, and **M11** were selected as the representative metabolites, and their proposed fragmentation pathways are shown in Figure 3.

Parent Compound (M0). ECH (**M0**) was identified by comparing the UPLC retention time (3.02 min), accurate MS

DOI: 10.1021/acs.jafc.5b02881
J. Agric. Food Chem. 2015, 63, 6764−6771

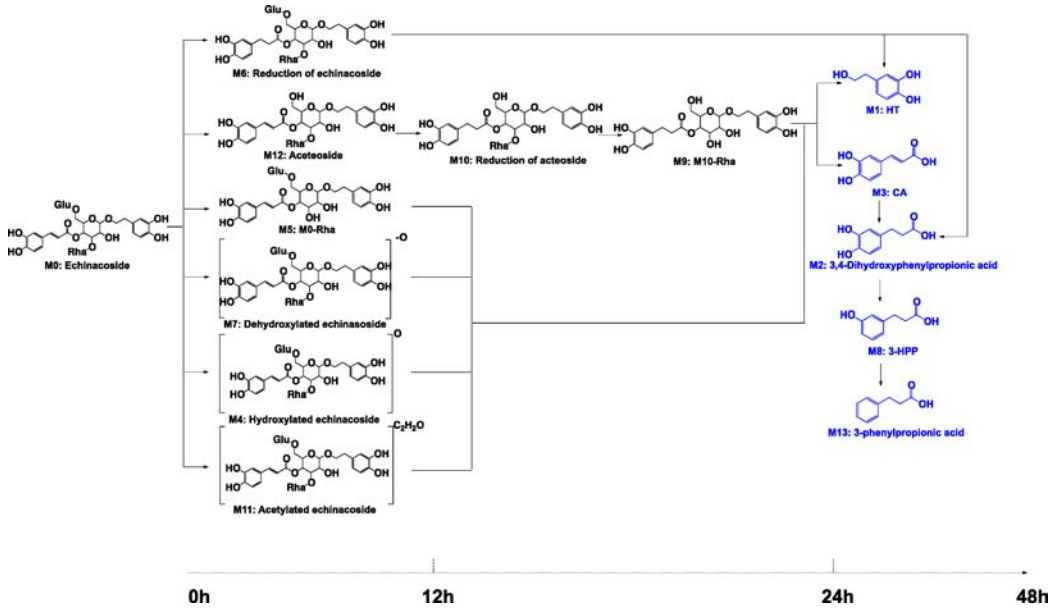

Figure 4. Proposed metabolic pathways of echinacoside by human intestinal bacteria.

at m/z 785.2482, and MS/MS spectra with those of the authentic reference standard. Characteristic product ions at m/z 623, 477, 461, 315, 179, 161, 153, and 135 were also found in the MS^2 fragmentation.

Metabolites of Parent Compound (M4−M7, M9−M12). In this study, the direct metabolites of parent compound were identified by the distinctive fragmentations when compared with the parent compound.

M12 (m/z 623.1945, $C_{29}H_{35}O_{15}$, 3.77 min), a loss of Glu (162 Da) from ECH (**M0**), was identified as acteoside through comparison of the UPLC retention time, accurate MS, and MS/MS spectra with the authentic reference standard. **M10** (m/z 625.2124, $C_{29}H_{37}O_{15}$, 3.66 min) was 2 Da (2H) higher than **M12**, which indicated that **M10** was the reduced product of **M12**. In the MS/MS spectrum of this metabolite, the presence of a diagnostic fragment ion at m/z 181 implied that reduction occurred on the α',β'-double bond of the CA moiety. Additionally, other fragment ions from **M10** were consistent with the product ions of **M12**. The previous study on caffeic acid metabolism by bacteria from the human gastrointestinal tract indicated that CA could be reduced to dihydro-CA by human intestinal bacteria,[19,20] which implied this reduction route might occur in the metabolic process of phenylethanoid glycoside and caffeoyl-containing compound. **M9** (m/z 479.1549, $C_{23}H_{27}O_{11}$, 3.46 min) was 146 Da (Rha) lower than **M10** in molecular weight and was considered as the de-Rha product of **M10**. **M9** produced signals at m/z 315, 181, 153, and 137, which were similar to the generated ions of **M10**. The proposed fragmentation pathways of **M9** and **M10** are shown in Figure 3.

M4 (m/z 801.2433, $C_{35}H_{45}O_{21}$, 2.44 min), a hydroxylated product of ECH, was 16 Da (O) higher than ECH in molecular weight. The characteristic product ion at m/z 783 was generated by a H_2O loss from the quasi-molecular ion. Moreover, caffeic acid related fragment ions were found at m/z 179, 161, and 135, which were the same as the fragment ions of ECH (**M0**), suggesting that the hydroxylation position was not on the CA moiety. A previous study proposed that the hydroxylation is more likely to occur on the HT moiety to form a benzenetriol structure.[21]

M5 (m/z 639.1900, $C_{29}H_{35}O_{16}$, 2.95 min) was 146 Da (Rha) lower than ECH (**M0**) in molecular weight and was identified as the de-Rha product of **M0**. The characteristic product ion at m/z 477 was shaped by the elimination of CA moiety (162 Da). The CA moiety was also found at m/z 179 and produced the ion at m/z 135 through the loss of CO_2.

M6 (m/z 787.2650, $C_{35}H_{47}O_{20}$, 3.19 min) was 2 Da (2H) higher than **M0** in molecular weight, which indicated that **M6** was the reduced product of **M0**. The characteristic fragments produced by **M6** at m/z 623, 181, and 153, were similar to those of **M10**. These results suggested that **M6** was generated by the reduction of ECH, which occurred on the α',β'-double bond of the CA moiety.

M7 (m/z 769.2546, $C_{35}H_{45}O_{19}$, 3.35 min) was 16 Da (O) lower than the protonated ion of ECH, which indicated that it was a metabolite of ECH after the loss of oxygen. In the MS/MS spectrum of **M7**, fragment ions associated with CA were found at m/z 179, 161, and 135. Therefore, the dehydroxylated site of **M7** was not at the CA moiety. However, the exact dehydroxylated site of **M7** could not be confirmed due to the limited information obtained in our study.

M11 (m/z 827.2624, $C_{37}H_{47}O_{21}$, 3.72 min) was 42 Da (C_2H_2O) higher than the protonated ion of ECH, suggesting a possible conjugation of an acetyl group on ECH. In addition, the characteristic MS/MS fragment ions of **M11** at m/z 623, 179, 161, 153, and 135 were observed. The proposed fragmentation pathways of **M11** are shown in Figure 3c. According to the previous research, the C-2′ position might be one of the acetyl conjugation sites of **M11**.[20]

Metabolites of Degradation Products (M1−M3, M8, M13). In this study, five degradation metabolites were identified using the authentic reference standard. ECH first degraded to HT (**M1**) and CA (**M3**), and CA underwent further metabolism to its major microbial metabolite, 3-HPP (**M8**).

M1 (m/z 153.0567, $C_8H_9O_3$, 1.57 min), **M2** (m/z 181.0505, $C_9H_9O_4$, 2.26 min), **M3** (m/z 179.0372, $C_9H_7O_4$, 2.33 min), **M8** (m/z 165.0563, $C_9H_9O_3$, 3.39 min), and **M13** (m/z 149.0623, $C_9H_9O_2$, 5.72 min) were identified as HT, 3,4-dihydroxyphenylpropionic acid, CA, 3-HPP, and 3-phenyl-

DOI: 10.1021/acs.jafc.5b02881
J. Agric. Food Chem. 2015, 63, 6764−6771

Table 3. Percentage of Relative Content and the Area of Each Metabolite at Different Time Points

no.	1 h (%) (area abs)	3 h (%) (area abs)	6 h (%) (area abs)	9 h (%) (area abs)	12 h (%) (area abs)	24 h (%) (area abs)	48 h (%) (area abs)
M0	78.84 (3008.20)	74.19 (3172.60)	73.04 (3066.50)	65.51 (3096.80)	52.71 (2388.60)	36.08 (2259.00)	1.64 (18.80)
M1		0.08 (3.40)	0.17 (7.00)	0.18 (8.60)	0.16 (7.10)	1.25 (76.70)	35.97 (412.90)
M2	0.43 (16.50)	0.37 (15.90)	0.28 (11.90)	0.17 (8.20)	0.08 (3.60)	0.20 (12.20)	0.36 (4.10)
M3					0.03 (1.40)	0.06 (3.50)	0.77 (8.80)
M4	0.53 (20.40)	0.54 (23.10)	0.54 (22.60)	0.45 (21.20)	0.31 (14.00)	0.27 (16.30)	
M5	1.75 (66.90)	1.81 (77.20)	1.59 (66.70)	1.57 (74.30)	1.20 (54.50)	1.43 (87.60)	
M6	0.33 (12.60)	0.77 (32.80)	0.92 (38.50)	0.48 (22.50)	0.43 (19.60)	1.49 (91.20)	
M7	3.18 (121.30)	3.20 (136.90)	3.04 (127.50)	2.70 (127.50)	1.85 (83.90)	1.44 (88.10)	
M8						0.91 (55.80)	38.21 (438.60)
M9						2.61 (160.00)	0.13 (1.50)
M10		0.09 (3.70)		0.15 (7.30)	0.15 (6.60)	3.21 (197.00)	0.62 (7.10)
M11	2.51 (95.70)	2.42 (103.40)	2.02 (85.00)	1.84 (86.90)	1.23 (55.80)	0.49 (29.80)	
M12	12.42 (473.80)	16.48 (704.80)	18.29 (767.70)	26.82 (1267.80)	41.72 (1890.40)	49.60 (3044.30)	19.61 (225.10)
M13		0.06 (2.70)	0.12 (5.00)	0.13 (6.00)	0.13 (5.90)	0.27 (16.60)	2.70 (31.00)
sum	100.00 (3815.40)	100.00 (4276.50)	100.00 (4198.40)	100.00 (4727.10)	100.00 (4531.40)	100.00 (6138.10)	100.00 (1147.90)

propionic acid, respectively, after analysis of the UPLC retention time, accurate MS, and MS/MS spectra of the authentic reference standards.

Analysis of the Metabolic Pathways of ECH by Human Intestinal Bacteria. According to the results of our experiment, the proposed metabolic pathways of ECH by human intestinal bacteria are displayed in Figure 4. After incubation with human intestinal bacteria, ECH was metabolized to **M4**, **M5**, **M6**, **M7**, **M11**, and **M12**. Additionally, **M12** was metabolized to **M10** and **M9** sequentially. After the degradation metabolites **M1** and **M3** emerged, **M3** was further metabolized to **M2**, **M8**, and **M13**.

Analysis of Relative Content of Metabolites by Human Intestinal Bacteria. The relative contents of parent compound ECH (**M0**) and its metabolites (**M1**−**M13**) by human intestinal bacteria were determined at 1, 3, 6, 9, 12, 24, and 48 h, respectively, by the percentage of each metabolite peak area accounted for in the total peak area of the determined metabolites (Table 3). According to our experimental results, ECH (**M0**) was metabolized to 50% in 24 h and was completely metabolized after 48 h. The major metabolites in the first 12 h were **M4**, **M5**, **M6**, **M7**, and **M11**, which decreased significantly from 24 h until the complete disappearance. Metabolites **M9**, **M10**, and **M12** generated the maximum level of their relative contents at 24 h, which then declined significantly afterward. The results above indicated that metabolites **M4**−**M7** and **M9**−**M12** were the intermediates of ECH metabolism by human intestinal bacteria, which were also susceptible to further metabolism. In contrast, the relative contents of metabolites **M1**, **M2**, **M3**, **M8**, and **M13**, especially **M1** and **M8**, were increased remarkably at 48 h. Therefore, these metabolites might be assumed to be the bioactive constituents of ECH that were formed before being absorbed into the blood.

DISCUSSION

In this study, we established an approach to analyze the metabolites of ECH produced by human intestinal bacteria and studied the relevant metabolic pathways. The combination of UPLC-Q-TOF-MS, MS^E technology, and MetaboLynx software was used to determine the metabolic profile and to detect the metabolites of ECH. Both precursor and fragment ions could be simultaneously obtained from a single analytical run through the application of the highly selective MS^E technique,[18] which provides a great advantage for the rapid investigation of multiple structures. MetaboLynx is an automated software[22,23] that can detect trace level of metabolites from biological samples and is a powerful tool for metabolic characterization.

Previous research found that the poor membrane permeability and the extensive presystemic metabolism of ECH might be the cause of its low oral bioavailability in rats.[21,24,25] Therefore, it is not surprising that the presence of bacteria and acidic/alkaline conditions in gastrointestinal ducts could initiate the hydrolysis of ECH. However, these previous studies did not provide detailed information about the metabolism of ECH in gastrointestinal ducts. Thus, we assessed whether gastric juice, intestinal juice, or intestinal microorganisms of gastrointestinal system could metabolize ECH. In our study, ECH was found to be stable in simulated gastric juice and intestinal juice, whereas it could be metabolized to HT and 3-HPP by intestinal bacteria. 3-HPP has been reported as a major microbial metabolite of CA by human intestinal bacteria in vitro,[26,27] which is in agreement with our findings. Additionally, reported evidence has shown that HT and 3-HPP possess bioactivities such as antioxidant,[28,29] neuroprotective,[30,31] and anti-inflammatory functions.[32,33] Therefore, we conclude that ECH acts as a prodrug that is transformed to bioactive compounds (HT and 3-HPP) by intestinal bacteria after oral administration, and the released compounds then exert biological activities.

In conclusion, a highly selective and sensitive approach using MS^E and MetaboLynx combined UPLC-Q-TOF-MS was applied to the screening and identification of ECH metabolites produced by human intestinal bacteria in vitro. Among the 13 metabolites (**M1**−**M13**) identified in this study, **M5**, **M6**, and **M11** have not been previously reported to our knowledge. Deglycosylation, dehydroxylation, reduction, hydroxylation, and acetylation were the five possible metabolic pathways that led to the generation of these metabolites. The observation of human intestinal bacteria produced HT and 3-HPP, which possess biological functions similar to those of ECH, could potentially explain the fact that ECH has prominent bioactivity but poor bioavailability. This study further explored the role of intestinal bacteria in the metabolism of natural products and improved the current understanding of ECH metabolism.

DOI: 10.1021/acs.jafc.5b02881
J. Agric. Food Chem. 2015, 63, 6764−6771

AUTHOR INFORMATION

Corresponding Author

*(X.L.) Phone: +86-21-3420-4806. Fax: +86-21-3420-4804. E-mail: xbli@sjtu.edu.cn.

Notes

The authors declare no competing financial interest.

ACKNOWLEDGMENTS

We thank Lei Feng for all of her help with UPLC-Q-TOF-MS.

REFERENCES

(1) Jimenez, C.; Riguera, R. Phenylethanoid glycosides in plants: structure and biological activity. *Nat. Prod. Rep.* **1994**, *11*, 591−606.

(2) Fu, G.; Pang, H.; Wong, Y. H. Naturally occurring phenylethanoid glycosides: potential leads for new therapeutics. *Curr. Med. Chem.* **2008**, *15*, 2592−2613.

(3) Perry, N. B.; Burgess, E. J.; Glennie, V. L. *Echinacea* standardization: analytical methods for phenolic compounds and typical levels in medicinal species. *J. Agric. Food Chem.* **2001**, *49*, 1702−1706.

(4) Cervellati, R.; Renzulli, C.; Guerra, M. C.; Speroni, E. Evaluation of antioxidant activity of some natural polyphenolic compounds using the Briggs-Rauscher reaction method. *J. Agric. Food Chem.* **2002**, *50*, 7504−7509.

(5) Hu, C.; Kitts, D. D. Studies on the antioxidant activity of *Echinacea* root extract. *J. Agric. Food Chem.* **2000**, *48*, 1466−1472.

(6) Speroni, E.; Govoni, P.; Guizzardi, S.; Renzulli, C.; Guerra, M. C. Anti-inflammatory and cicatrizing activity of *Echinacea pallida* Nutt. root extract. *J. Ethnopharmacol.* **2002**, *79*, 265−272.

(7) Zhao, Q.; Gao, J.; Li, W.; Cai, D. Neurotrophic and neurorescue effects of Echinacoside in the subacute MPTP mouse model of Parkinson's disease. *Brain Res.* **2010**, *1346*, 224−236.

(8) Geng, X.; Tian, X.; Tu, P.; Pu, X. Neuroprotective effects of echinacoside in the mouse MPTP model of Parkinson's disease. *Eur. J. Pharmacol.* **2007**, *564*, 66−74.

(9) Thomsen, M. O.; Fretté, X. C.; Christensen, K. B.; Christensen, L. P.; Grevsen, K. Seasonal variations in the concentrations of lipophilic compounds and phenolic acids in the roots of *Echinacea purpurea* and *Echinacea pallida*. *J. Agric. Food Chem.* **2012**, *60*, 12131−12141.

(10) Luo, W.; Ang, C. Y. W.; Gehring, T. A.; Heinze, T. M.; Lin, L. J.; Mattia, A. Determination of phenolic compounds in dietary supplements and tea blends containing *Echinacea* by liquid chromatography with coulometric electrochemical detection. *J. AOAC Int.* **2003**, *86*, 202−208.

(11) Xiong, W. T.; Gu, L.; Wang, C.; Sun, H. X.; Liu, X. Anti-hyperglycemic and hypolipidemic effects of *Cistanche tubulosa* in type 2 diabetic db/db mice. *J. Ethnopharmacol.* **2013**, *150*, 935−945.

(12) Kim, D. H.; Jung, E. A.; Sohng, I. S.; Han, J. A.; Kim, T. H.; Han, M. J. Intestinal bacterial metabolism of flavonoids and its relation to some biological activities. *Arch. Pharmacal Res.* **1998**, *21*, 17−23.

(13) Akao, T.; Hayashi, T.; Kobashi, K.; Kanaoka, M.; Kato, H.; Kobayashi, M.; Takeda, S.; Oyama, T. Intestinal bacterial hydrolysis is indispensable to absorption of 18β-glycyrrhetic acid after oral administration of glycyrrhizin in rats. *J. Pharm. Pharmacol.* **1994**, *46*, 135−137.

(14) Xing, S.; Peng, Y.; Wang, M.; Chen, D.; Li, X. In vitro human fecal microbial metabolism of forsythoside A and biological activities of its metabolites. *Fitoterapia* **2014**, *99*, 159−165.

(15) Jia, C.; Shi, H.; Wu, X.; Li, Y.; Chen, J.; Tu, P. Determination of echinacoside in rat serum by reversed-phase high-performance liquid chromatography with ultraviolet detection and its application to pharmacokinetics and bioavailability. *J. Chromatogr. B: Anal. Technol. Biomed. Life Sci.* **2006**, *844*, 308−313.

(16) Hurst, S.; Loi, C. M.; Brodfuehrer, J.; El-Kattan, A. Impact of physiological, physicochemical and biopharmaceutical factors in absorption and metabolism mechanisms on the drug oral bioavailability of rats and humans. *Expert Opin. Drug Metab. Toxicol.* **2007**, *3*, 469−489.

(17) Morikawa, T.; Ninomiya, K.; Imamura, M.; Akaki, J.; Fujikura, S.; Pan, Y.; Yuan, D.; Yoshikawa, M.; Jia, X.; Li, Z. Acylated phenylethanoid glycosides, echinacoside and acteoside from *Cistanche tubulosa*, improve glucose tolerance in mice. *J. Nat. Med.* **2014**, *68*, 561−566.

(18) Plumb, R. S.; Johnson, K. A.; Rainville, P.; Smith, B. W.; Wilson, I. D.; Castro-Perez, J. M.; Nicholson, J. K. UPLC/MS(E); a new approach for generating molecular fragment information for biomarker structure elucidation. *Rapid Commun. Mass Spectrom.* **2006**, *20*, 1989−1994.

(19) Peppercorn, M. A.; Goldman, P. Caffeic acid metabolism by bacteria of the human gastrointestinal tract. *J. Bacteriol.* **1971**, *108*, 996−1000.

(20) Deng, R.; Xu, Y.; Feng, F.; Liu, W. Identification of poliumoside metabolites in rat feces by high performance liquid chromatography coupled with quadrupole time-of-flight tandem mass spectrometry. *J. Chromatogr. B: Anal. Technol. Biomed. Life Sci.* **2014**, *969*, 285−296.

(21) Wang, Y.; Hao, H.; Wang, G.; Tu, P.; Jiang, Y.; Liang, Y.; Dai, L.; Yang, H.; Lai, L.; Zheng, C. An approach to identifying sequential metabolites of a typical phenylethanoid glycoside, echinacoside, based on liquid chromatography-ion trap-time of flight mass spectrometry analysis. *Talanta* **2009**, *80*, 572−580.

(22) Yan, G.; Sun, H.; Sun, W.; Zhao, L.; Meng, X.; Wang, X. Rapid and global detection and characterization of *aconitum* alkaloids in Yin Chen Si Ni Tang, a traditional Chinese medical formula, by ultra performance liquid chromatography-high resolution mass spectrometry and automated data analysis. *J. Pharm. Biomed. Anal.* **2010**, *53*, 421−431.

(23) Yang, S.; Shi, W.; Hu, D.; Zhang, S.; Zhang, H.; Wang, Z.; Cheng, L.; Sun, F.; Shen, J.; Cao, X. In vitro and in vivo metabolite profiling of valnemulin using ultraperformance liquid chromatography-quadrupole/time-of-flight hybrid mass spectrometry. *J. Agric. Food Chem.* **2014**, *62*, 9201−9210.

(24) Gao, Y.; Zong, C.; Liu, F.; Fang, L.; Cai, R.; Shi, Y.; Chen, X.; Qi, Y. Evaluation of the intestinal transport of a phenylethanoid glycoside-rich extract from *Cistanche deserticola* across the Caco-2 cell monolayer model. *PLoS One* **2015**, *10*, e0116490.

(25) Matthias, A.; Blanchfield, J. T.; Penman, K. G.; Toth, I.; Lang, C. S.; Voss, J. J.; Lehmann, R. P. Permeability studies of alkylamides and caffeic acid conjugates from echinacea using a Caco-2 cell monolayer model. *J. Clin. Pharm. Ther.* **2004**, *29*, 7−13.

(26) Gonthier, M. P.; Remesy, C.; Scalbert, A.; Cheynier, V.; Souquet, J. M.; Poutanen, K.; Aura, A. M. Microbial metabolism of caffeic acid and its esters chlorogenic and caftaric acids by human faecal microbiota in vitro. *Biomed. Pharmacother.* **2006**, *60*, 536−540.

(27) Parkar, S. G.; Trower, T. M.; Stevenson, D. E. Fecal microbial metabolism of polyphenols and its effects on human gut microbiota. *Anaerobe* **2013**, *23*, 12−19.

(28) Gordon, M. H.; Paiva-Martins, F.; Almeida, M. Antioxidant activity of hydroxytyrosol acetate compared with that of other olive oil polyphenols. *J. Agric. Food Chem.* **2001**, *49*, 2480−2485.

(29) Gómez-Ruiz, J. Á.; Leake, D. S.; Ames, J. M. In vitro antioxidant activity of coffee compounds and their metabolites. *J. Agric. Food Chem.* **2007**, *55*, 6962−6969.

(30) Schaffer, S.; Podstawa, M.; Visioli, F.; Bogani, P.; Müller, W. E.; Eckert, G. P. Hydroxytyrosol-rich olive mill wastewater extract protects brain cells in vitro and ex vivo. *J. Agric. Food Chem.* **2007**, *55*, 5043−5049.

(31) Wang, D.; Ho, L.; Faith, J.; Ono, K.; Janle, E. M.; Lachcik, P. J.; Cooper, B. R.; Jannasch, A. H.; D'Arcy, B. R.; Williams, B. A. Role of intestinal microbiota in the generation of polyphenol-derived phenolic acid mediated attenuation of Alzheimer's disease β-amyloid oligomerization. *Mol. Nutr. Food Res.* **2015**, *59*, 1025−1040.

(32) Richard, N.; Arnold, S.; Hoeller, U.; Kilpert, C.; Wertz, K.; Schwager, J. Hydroxytyrosol is the major anti-inflammatory compound in aqueous olive extracts and impairs cytokine and chemokine production in macrophages. *Planta Med.* **2011**, *77*, 1890−1897.

DOI: 10.1021/acs.jafc.5b02881
J. Agric. Food Chem. 2015, 63, 6764−6771

(33) Larrosa, M.; Luceri, C.; Vivoli, E.; Pagliuca, C.; Lodovici, M.; Moneti, G.; Dolara, P. Polyphenol metabolites from colonic microbiota exert anti-inflammatory activity on different inflammation models. *Mol. Nutr. Food Res.* **2009**, *53*, 1044−1054.

DOI: 10.1021/acs.jafc.5b02881
J. Agric. Food Chem. 2015, 63, 6764−6771

analyzed the expression of genes involved in the biosynthetic pathways of phenolic compounds during different light irradiations and investigated the distribution of the compounds in the various organs of adult plants. Chinese cabbage is an important source of beneficial nutrients, such as carotenoids, fibers, vitamins, minerals, glucosinolates (GSLs), and phenolics, and it is widely consumed in East Asia and, in particular, in Korea, where both the adult and sprouting plant parts are an important ingredient of kimchi and salad. Our results in this study provide useful information for improving the nutritional quality of Chinese cabbage as well as for improving horticultural practice.

MATERIALS AND METHODS

Plant Materials. Chinese cabbage (*B. rapa* ssp. *pekinensis* var. 'Bulam No. 3') was grown under field conditions at the experimental farm of the National Institute of Horticultural and Herbal Science, Rural Development Administration (Suwon, Korea). Different organs (flowers, stems, leaves, and roots) were separately harvested from at least than five 85-day-old field-grown plants. For white, blue, and red LED light irradiation, germinated seeds were sown onto vermiculate and cultivated in a growth chamber at 25 °C under a 16 h photoperiod with different LED light irradiation (380 nm for white, 470 nm for blue, and 660 nm for red) over a 12-day period. Whole seedlings were harvested at 6, 9, and 12 days after irradiation (DAI). All samples were immediately frozen in liquid nitrogen and then stored at −80 °C and/or freeze-dried for RNA isolation and/or high-performance liquid chromatography−ultraviolet (HPLC-UV) analysis. Whole cultivations and irradiations were repeated three times, and the samples from each set of cultures were used for biological repeats.

Identification of Phenylpropanoid Biosynthesis-Related Genes in Chinese Cabbage. Phenylpropanoid biosynthetic genes of *Arabidopsis thaliana* were searched and downloaded from The *Arabidopsis* Information Resource (TAIR) database.[12] The collected genes were subjected to a TBLASTX search against the genome of the *B. rapa* line Chiifu-401,[13] which was downloaded from the *Brassica* database (BRAD) to identify their homologues in the *B. rapa* genome. Only resultant sequences with *e* values <0 and identities >85% were considered as potentially orthologous, and among these we selected for further use only the ones that had the highest identities with each phenylpropanoid biosynthetic gene of *Arabidopsis*. A total of 11 Chinese cabbage phenylpropanoid biosynthetic genes were selected, and gene-specific primers for the 11 genes were designed with GenScript Real-Time PCR (TaqMan) Primer Design (https://www.genscript.com/ssl-bin/app/primer) software and used for quantitative real-time polymerase chain reaction (qRT-PCR) analysis. The accession numbers of the genes and primer sets used in this study are listed in Table 1.

Total RNA Extraction and Quantitative Real Time-PCR. Total RNA was isolated by an Easy BLUE Total RNA Kit (iNtRON, Seongnam, Korea). The quantity of RNA was measured on a NanoVue Plus spectrophotometer (GE Healthcare Life Sciences), and its quality was confirmed by running 1 μg of the RNA on 1.2% formaldehyde RNA agarose gel. Then, 1 μg of total RNA was reverse-transcribed by a ReverTra Ace-α Kit (Toyobo) and oligo $(dT)_{20}$ primers, according to the manufacturer's protocol. The cDNA was diluted 20-fold for qRT-PCR. qRT-PCR was performed in a 20-μL reaction volume containing 0.5 μM primers and 2× Real-Time PCR Smart mix (SolGent; Daejeon, Korea). The qRT-PCR program was as follows: initial denaturation at 95 °C for 15 min followed by 40 cycles of denaturation at 95 °C for 20 s, annealing at 55 °C for 40 s, and extension at 72 °C for 20 s. The qRT-PCR results were obtained as the mean of three replicates. *BrEF-1-α* (GO479260) was used as a reference gene because it was previously determined to be the most suitable reference gene among several Chinese cabbage genes.[14]

Extraction and Analysis of Phenylpropanoids in Chinese Cabbage. HPLC-UV analysis of the phenylpropanoids was carried out according to previously described methods with some modification.[15] Samples were freeze-dried and ground into a fine powder. A total of 100 mg of sample was transferred to 6 mL of 62.5% methanol containing 2 g/L *tert*-butylhydroquinone as an antioxidant. To hydrolyze, 1.5 mL of 6 N HCl was then added and incubated at 90 °C for 2 h. After centrifugation at 1000*g* for 5 min, the supernatant was passed through a 0.22 μm PTFE syringe filter prior to HPLC. External standards were purchased from Extrasynthese (Genay, France). MeOH and HCl were purchased from Wako Pure Chemical Industries (Osaka, Japan) and Sigma-Aldrich Co., Ltd. (St. Louis, MO, USA), respectively. The extract was diluted 2-fold with MeOH prior to HPLC-UV analysis. Samples were identified using a Futecs model NS-4000 HPLC apparatus (Daejeon, Korea) with an UV−vis detector and autosampler. The analysis was monitored at 280 nm and performed using a C18 column (250 × 4.6 mm, 5 μm; RStech; Daejeon, Korea). The mobile phase consisted of a mixture of (A) MeOH/water/acetic acid (5:92.5:2.5, v/v/v) and (B) MeOH/water/acetic acid (95:2.5:2.5, v/v/v), as described previously.[16] The initial mobile phase composition was 0% solvent B, followed by a linear gradient from 0 to 80% of solvent B in 48 min, then holding at 0% solvent B for an additional 10 min; the column was then maintained at 30 °C. The flow rate was set at 1.0 mL min^{-1}, and the injection volume was 20 μL. Quantification of the different compounds was based on peak areas and calculated as the equivalents of representative standard compounds. All contents are expressed as micrograms per milligram DW and were analyzed by ANOVA and Tukey's post hoc test using R software (ver. 3.1.0).

Table 1. qRT-PCR Primers Used in This Study

primer	sequence (5′ → 3′)	size (bp)
BrPAL-RT (F)	AAGCCGGAGTTCACCGATCA	100
BrPAL-RT (R)	ACGAGCTCCCGTCGAGAATG	
BrC4H-RT (F)	ATCCTGGTCAACGCCTGGTG	145
BrC4H-RT (R)	GTCCAACACCAAACGGCACA	
Br4CL1-RT (F)	CCCAATCACCTCCCTCTCCAC	133
Br4CL1-RT (R)	GCGACATGGACGTCGGAGTAA	
Br4CL2-RT (F)	ATGTCCACACGAGAAGAGACGGTC	150
Br4CL2-RT (R)	TGATCAAGCAAGGCTTTGCG	
Br4CL3-RT (F)	GGCCAAGAACCCAACTGTTA	179
Br4CL3-RT (R)	ACCCAAGGCTCATTGACAAC	
BrCHS-RT (F)	AGGAAACGCCACATGCACCT	114
BrCHS-RT (R)	AGGGACTTCGACCACCACGA	
BrCHI-RT (F)	TCTCCGTCCCGTCACTCTCC	133
BrCHI-RT (R)	AACGGCAGCTTCATCGTCACTT	
BrF3H-RT (F)	CAAGCCACACGAGACGATGG	110
BrF3H-RT (R)	TTGAACCTCCCGTTGCTCAGA	
BrF3′H-RT (F)	GCCGGAGAAGCTGAACATGG	117
BrF3′H-RT (R)	TAAGCCGACCCGAGTCCGTA	
BrFLS-RT (F)	TCCTTCCGCCGTCATTGTTC	141
BrFLS-RT (R)	TCACGGTGTGGCTCCAAGAA	
BrDFR-RT (F)	GGACAAAGTTCCGGGCAGTG	140
BrDFR-RT (R)	TCTGCTGTGCCGACATGTGA	
BrEF-1-α (F)	ATACCAGGCTTGAGCATACCG	117
BrEF-1-α (R)	GCCAAAGAGGCCATCAGACAA	

RESULTS AND DISCUSSION

Expression of Phenylpropanoid Biosynthetic Genes in Chinese Cabbage Irradiated with White, Blue, and Red Lights. The biosynthetic pathways for the phenolic compounds and genes responsible for those biosyntheses analyzed in this study are illustrated in Figure 1. The transcripts of the phenylpropanoid biosynthetic genes of *B. rapa* ssp. *pekinensis* were investigated by qRT-PCR in the whole seedlings of Chinese cabbage at 6, 9, and 12 DAI with white, blue, and red LED lights (Figure 2). Under white light, the expression levels of *BrDFR* noticeably increased at 9 DAI, whereas those of

DOI: 10.1021/acs.jafc.5b02086
J. Agric. Food Chem. 2015, 63, 6772−6778

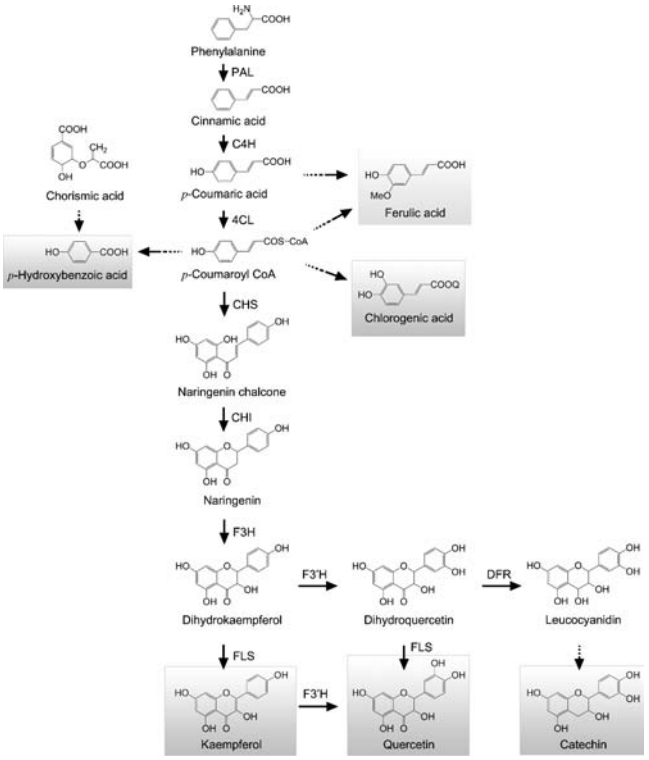

Figure 1. Proposed phenylpropanoid biosynthetic pathway in Chinese cabbage. PAL, phenylalanine ammonia-lyase; C4H, cinnamate 4-hydroxylase; 4CL, 4-coumaroyl CoA ligase; CHS, chalcone synthase; CHI, chalcone isomerase; F3H, flavanone 3-hydroxylase; F3′H, flavonoid 3′-hydroxylase; FLS, flavonol synthase; DFR, dihydroflavonol-4 reductase. The shaded boxes indicate the compounds analyzed in this study. The dashed arrow indicates the process catalyzed by unidentified enzymes in the Brassicaceae family.

BrPAL, *Br4CL1*, *Br4CL3*, *BrCHS*, *BrCHI*, *BrF3H*, *BrF3′H*, and *BrFLS* declined after peaking at 9 DAI. The expressions of *BrC4H* and *Br4CL2* did not significantly change during white light irradiation. Compared to white light, blue light had a more noticeable effect on the change in the expression patterns of phenylpropanoid biosynthetic genes. The transcript levels of *BrF3H*, *BrF3′H*, *BrFLS*, and *BrDFR* dramatically increased at 12 DAI. In particular, the expressions of *BrF3′H* and *BrFLS* peaked when compared with the white and red light treatments. Red light caused the expression of many phenylpropanoid genes to increase, including *Br4CL2*, *Br4CL3*,*BrCHS*, *BrCHI*, *BrF3H*, and *BrFLS* at 6 DAI. However, red light had no effect on the expression of *BrPAL*, *BrC4H*, *BrF3′H*, and *BrDFR* during irradiation. The transcript level of *Br4CL1* was noticeably up-regulated by red light at 12 DAI, unlike other genes, implying that the machinery for the transcription of *Br4CL1* might be regulated differently from other genes. Our results on the expressions of phenylpropanoid biosynthetic genes showed difference with results in similar studies with different crops. For example, similar light irradiation in buckwheat resulted in gradually reduced expression of most orthologous genes after 2 days of all LED light irradiation.[10] Basil leaves grown over yellow and green plastic mulches had higher phenolics content than those grown over white and blue covers.[17] Along with our study, these results indicate crops have diverse responses to light irradiation in terms of phenylpropanoid biosynthesis.

Accumulation of Phenylpropanoids in Chinese Cabbage Irradiated with White, Blue, and Red Lights. Previous studies have reported that abundant flavonol aglycones in Chinese cabbage pak choi (*B. rapa* L. ssp. *chinensis* L. (Hanelt.)) included quercetin, kaempferol, and isorhamnetin, as found for other species in the Brassicaceae family.[18] Studies analyzing hydroxycinnamic acid derivatives in various cultivars of pak choi demonstrated that phenolic

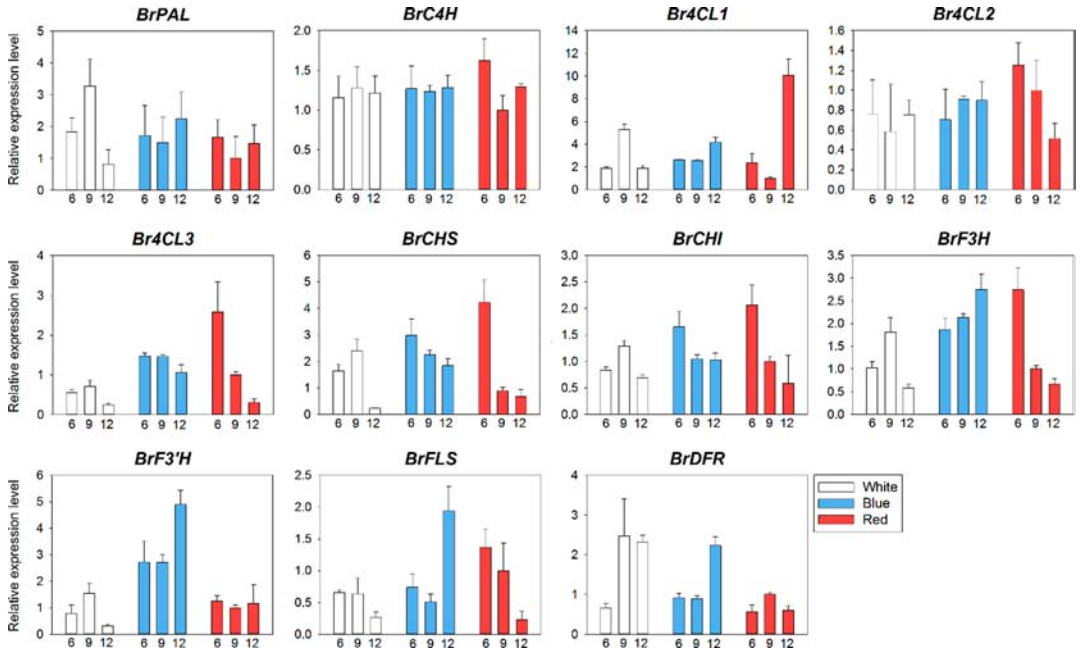

Figure 2. Expression levels of phenylpropanoid biosynthetic genes in the seedlings of Chinese cabbage irradiated with white, blue, and red LED lights. Total RNA was extracted from whole seedlings sampled at 6, 9, and 12 days after irradiation and used for qRT-PCR analysis. The relative expression ratio of transcripts was shown to be calibrated with expression of *BrEF-1-α*. The height of each bar and the error bars indicate the mean and standard error, respectively, from three independent measurements.

DOI: 10.1021/acs.jafc.5b02086
J. Agric. Food Chem. 2015, 63, 6772−6778

Table 2. Accumulation ($\mu g\ g^{-1}$) of Phenolic Compounds in the Seedlings of Chinese Cabbage Irradiated with White, Blue, and Red LED Light[a]

light		*p*-hydroxybenzoic acid	chlorogenic acid	ferulic acid	quercetin	kaempferol
white	6 days	22.1 ± 0.96 a	23.3 ± 0.74 a	4.37 ± 0.01 ab	1.36 ± 0.26 ac	3.2 ± 0.96 ab
	9 days	3.17 ± 0.13 c	23.84 ± 0.34 a	3.35 ± 0.13 a	0 ± 0 a	1.94 ± 0.23 a
	12 days	9.14 ± 2.74 c	29.13 ± 6.38 a	4.53 ± 1.4 ab	0 ± 0 a	7.71 ± 1.23 b
blue	6 days	26.02 ± 1.99 a	25.41 ± 0.33 a	5.51 ± 0.49 ab	0 ± 0 a	1.7 ± 0.28 a
	9 days	37.13 ± 0.81 b	26.93 ± 0.16 a	5.34 ± 2.63 ab	0 ± 0 a	4.53 ± 0.01 ab
	12 days	49.06 ± 2.15 d	27.34 ± 2.35 a	10.6 ± 2.01 b	4.8 ± 0.59 b	7.48 ± 0.91 b
red	6 days	4.03 ± 1.34 c	26.57 ± 1.2 a	7.11 ± 1.91 ab	2.61 ± 0.87 c	2.57 ± 1.03 ab
	9 days	3.69 ± 1.09 c	27.61 ± 0.04 a	6.42 ± 2.83 ab	2.43 ± 0.08 c	4.42 ± 3.20 ab
	12 days	3.48 ± 1.41 c	26.69 ± 0.01 a	19.52 ± 1.47 c	4.51 ± 0.14 b	4.25 ± 0.86 ab

[a]Whole seedlings were sampled at 6, 9, and 12 days after irradiation and used for HPLC-UV analysis. The means and standard deviations were obtained from three independent experiments. Letters a–c indicate significant differences ($P < 0.05$).

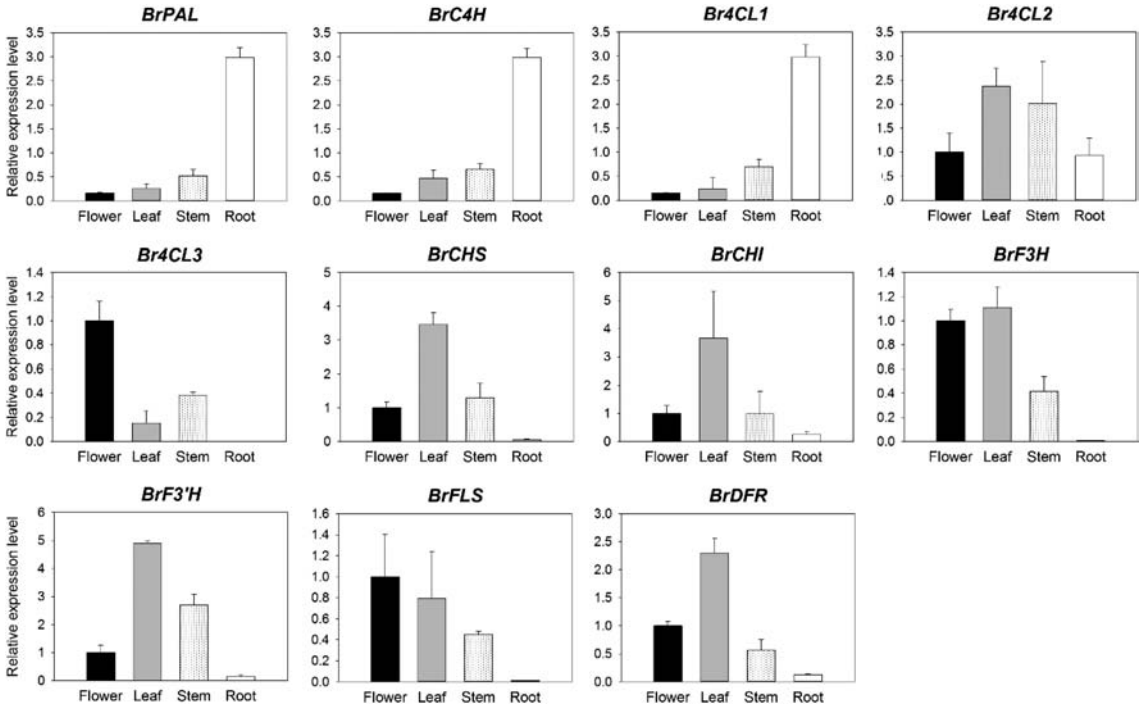

Figure 3. Expression profiles of phenylpropanoid biosynthetic genes in different organs of adult Chinese cabbage plants. Total RNA was extracted from the flowers, leaves, stems, and roots of 85-day-old plants and used for qRT-PCR analysis. The relative expression ratio of the transcripts was shown to be calibrated with expression of *BrEF-1-α*. The height of each bar and the error bars indicate the mean and standard error, respectively, from three independent measurements.

compounds, including chlorogenic acid, are also present in Chinese cabbage.[19] In our HPLC-UV analysis, *p*-hydroxybenzoic acid, ferulic acid, chlorogenic acid, quercetin, and kaempferol were detected in the seedlings of Chinese cabbage (Table 2). The phenolics found at the highest quantities were *p*-hydroxybenzoic acid (up to 49.06 ± 2.15 $\mu g\ g^{-1}$), followed by cholorogenic acid.

The effects of light irradiation on the accumulation of phenolic compounds appeared to differ with different light conditions. White light irradiation led to the accumulation of kaempferol (up to 7.71 ± 1.23 $\mu g\ g^{-1}$) and the reduction of *p*-hydroxybenzoic acid and quercetin content. Chlorogenic acid content remained unchanged during white light irradiation. Blue light led to the accumulation of all detected phenolic compounds at 6 DAI. In particular, *p*-hydroxybenzoic acid content was noticeably raised (up to 49.06 ± 2.15 $\mu g\ g^{-1}$) under blue light irradiation compared to other light conditions. In addition, quercetin and kaempferol content increased by >4-fold (up to 4.8 ± 0.59 and 7.48 ± 0.91 $\mu g\ g^{-1}$, respectively). Ferulic acid content increased by roughly 2-fold (up to 10.6 ± 2.01 $\mu g\ g^{-1}$) during blue light irradiation. The maximum *p*-hydroxybenzoic acid, ferulic acid, and quercetin content was obtained by blue light irradiation at 12 DAI, at which time the chlorogenic acid, benzoic acid, and quercetin contents almost reached their highest levels. This highest accumulation of phenylpropanoids by blue light irradiation coincided with the increased expression of *BrF3H*, *BrF3′H*, *BrFLS*, and *BrDFR* during irradiation. On the other hand, red light irradiation had a noticeable effect on ferulic acid accumulation. Ferulic acid content increased by about 2.7-fold to its highest level (19.52 ± 1.47 $\mu g\ g^{-1}$) under red light irradiation. Quercetin and kaempferol content only slightly increased. *Br4CL2*, *Br4CL3*,

DOI: 10.1021/acs.jafc.5b02086
J. Agric. Food Chem. 2015, 63, 6772–6778

Table 3. Accumulation ($\mu g\ g^{-1}$) of Phenolic Compounds in the Different Organs of Adult Chinese Cabbage Plants[a]

	flower	leaf	stem	root
p-hydroxybenzoic acid	32.79 ± 2.03 c	253.25 ± 4.82 a	0 ± 0 b	0 ± 0 b
chlorogenic acid	23.51 ± 6.38 ab	20.48 ± 0.32 ab	15.79 ± 0.64 b	28.97 ± 0.63 a
ferulic acid	272.52 ± 2.06 d	407.27 ± 15.24 a	95.12 ± 0.4 c	25.97 ± 0.48 b
quercetin	339.19 ± 18.87 b	15.13 ± 5.74 a	0 ± 0 a	0 ± 0 a
kaempferol	678.57 ± 3.05 c	0 ± 0 a	0 ± 0 a	26.21 ± 4.53 b
catechin	0 ± 0 d	46.64 ± 0.83 a	18.23 ± 1.18 c	8.67 ± 1.1 b

[a]The flowers, leaves, stems, and roots were collected from more than three 85-day-old plants and used for HPLC-UV analysis. The means and standard deviations were obtained from three independent experiments. Letters a–c indicate significant differences among organs ($P < 0.05$).

BrCHS, *BrCHI*, *BrF3H*, and *BrFLS* were highly expressed at initial stage during red light irradiation, but this did not lead to high accumulation of quercetin and kaempferol. Under all light conditions, chlorogenic acid content remained unchanged.

When combined with the gene expression results of this study, this finding indicates that blue light may induce the phenylpropanoid biosynthetic pathway, leading to an increase of many phenolic compounds in Chinese cabbage seedlings. In previous studies, blue light irradiation was effective in increasing rutin and cyanidin 3-*O*-rutinoside levels in buckwheat and total ploy phenol content in lettuce. Many previous studies have revealed environmental factors that act as abiotic stresses inducing phenylpropanoids in plants, for example, excessive light, UV, pathogen attack, elicitation, wounding, heat and cold stress, nutrient deficiency, and heavy metal stress.[2,20] It may be possible to employ the environmental factors as strategies to enhance phenylpropanoid biosynthesis in Chinese cabbage. However, they have some disadvantages, such as plant growth retardation, quality deterioration, and soil contamination, whereas the short-term LED light irradiation used in this study can be applied as a suitable method to increase phenylpropanoid content in seedlings of Chinese cabbage without negative effects on plant growth and quality and the environment. Although further studies are needed to apply this practice to Chinese cabbage grown in the field, the results in this study might be utilized as useful information to improve the nutritional quality of Chinese cabbage.

Expression Profiles of Phenylpropanoid Biosynthetic Genes in Different Organs. The expression patterns of *BrPAL*, *BrC4H*, *Br4CLs*, *BrCHS*, *BrCHI*, *BrF3H*, *BrF3Ls*, *BrFLS*, *BrDFR*, and *BrANS* were analyzed in the flower, leaf, stem, and root of adult Chinese cabbage plants (Figure 3). *BrPAL*, *BrC4H*, and *Br4CL1* were specifically expressed at the highest levels in the roots. The expression patterns of the three genes were fairly similar, with the highest transcript levels being recorded in the root, followed by the stem and leaf, and finally the flower. *Br4CL1*, *Br4CL2*, and *Br4CL3* are the paralogous genes of 4-coumarate:coenzyme A ligase and showed different expression profiles according to the plant organs. The highest expression was detected in the root, leaf and stem, and flower, respectively. *BrCHS*, *BrCHI*, *BrF3H*, *BrF3′H*, and *BrDFR* displayed the highest transcription levels in the leaf and the lowest transcription levels in the root. High transcript levels of *BrF3H* and *BrFLS* were also detected in the flowers. In summary, the upstream genes of *BrPAL*, *BrC4H*, and *Br4CL1* were highly expressed in the root, whereas all other genes were expressed at relatively abundant levels in the leaf or flower.

Accumulation of Phenylpropanoids in Different Organs of Chinese Cabbage. The phenylpropanoid contents in different organs of adult Chinese cabbage plants were analyzed by HPLC-UV (Table 3). Along with the phenolic compounds detected in seedlings, catechin was found in the leaves, stems, and roots, which is the flavonoid that is highly abundant in fruits and legumes.[21] The highest phenolic compound content was obtained for kaempferol (up to 678.57 ± 3.05 $\mu g\ g^{-1}$), whereas quercetin, ferulic acid, and *p*-hydroxybenzoic acid were also detected in great quantities.

Among detected nonflavonoids, considerable levels of *p*-hydroxybenzoic acid were detected in the leaf (253.25 ± 4.82 $\mu g\ g^{-1}$), whereas lower quantities were detected in the flower (32.79 ± 2.03 $\mu g\ g^{-1}$). *p*-Hydroxybenzoic acid was not detected in the stem and root. The highest ferulic acid content was detected in the leaf (407.27 ± 15.24 $\mu g\ g^{-1}$), followed by the flower (272.52 ± 2.06 $\mu g\ g^{-1}$), stem (95.12 ± 0.40 $\mu g\ g^{-1}$), and root (25.97 ± 0.48 $\mu g\ g^{-1}$). Chlorogenic acid contents were similar among the different organs: root (28.97 ± 0.63 $\mu g\ g^{-1}$), flower (23.51 ± 6.38 $\mu g\ g^{-1}$), leaf (20.48 ± 0.32 $\mu g\ g^{-1}$), and stem (15.79 ± 0.64 $\mu g\ g^{-1}$). Interestingly, there was no significant difference in chlorogenic acid content in the different organs at the adult stages or in seedlings grown under different light conditions.

High amounts of quercetin accumulated in the flower (339.19 ± 18.87 $\mu g\ g^{-1}$), whereas only small amounts were detected in the leaf (15.13 ± 5.74 $\mu g\ g^{-1}$). No quercetin was detected in the stem or root. Of note, high quantities of kaempferol were present in the flower (678.57 ± 3.05 $\mu g\ g^{-1}$), with 25.9 times more kaempferol being present in the flower than in the root. The antioxidant effect of *Brassica* species may be attributed to those phenolic compounds, because phenolics, including quercetin and kaempferol, have higher antioxidant activities than vitamins and carotenoids.[22] In the present study, quercetin and kaempferol specifically accumulated in the flowers of Chinese cabbage, indicating that greater nutritional benefits may be obtained from Chinese cabbage when the flowers are used. Relatively lower catechin content was detected compared to those of other flavonoids. Catechin content in the leaf (46.64 ± 0.38 $\mu g\ g^{-1}$) was 2.5- and 5.4-fold higher than that in the stem (18.23 ± 1.18 $\mu g\ g^{-1}$) and root (8.67 ± 3.05 $\mu g\ g^{-1}$), respectively. Catechin was not detected in the flower.

Many previous studies have revealed that the organ distribution of the phenylpropanoids was correlated with the expression patterns of *PAL*, *C4H*, and *4CL*.[23−25] However, in our results, the accumulation patterns of *p*-hydroxybenzoic acid and ferulic acid did not coincide with the expression patterns of *BrPAL*, *BrC4H*, *Br4CL1*, and *Br4CL3*, which are the genes responsible for their biosynthesis. It is well-known that phenylpropanoid metabolism in plants is an intricate network in which many enzymes are implicated. Multiple isoforms and paralogous genes might have redundant functions, and those synergistic regulations might complicate elucidating phenylpropanoid metabolism.[26−28] In addition, the biosynthesis of nonflavonoids yet unidentified in *Brassica* species might also

DOI: 10.1021/acs.jafc.5b02086
J. Agric. Food Chem. 2015, 63, 6772−6778

affect their accumulation. Further studies can be performed to elucidate the genes corresponding to the organ-specific distribution of phenylpropanoids in Chinese cabbage.

The organ-specific accumulation of quercetin, kaempferol, and catechin could be explained by the expression patterns of *Br4CL3*, *BrF3H*, and *BrFLS*, which were relatively high in the flower. Previous studies have revealed distinct functions and substrate specificities of the *4CL* gene family for phenylpropanoid biosynthesis[28−30] and the major role of FLS, which directs flux into flavonols such as quecertin and kaempferol,[31,32] indicating these genes may be key regulators in flavonoid biosynthesis. Although we did not investigate expression profiles of all of the genes responsible for phenylpropanoids biosynthesis, our results revealed organ-specific distribution of phenylpropanoids and corresponding expression patterns of key biosynthetic genes in Chinese cabbage.

In this study, we aimed to investigate light conditions that lead to accumulation of phenylpropanoids in Chinese cabbage and organ-specific distribution of the phenylpropanoids. The results of this study demonstrate that blue light is an effective light source to lead to enhancement of phenylpropanoid biosynthesis, and leaves and flowers are suitable organs from which to obtain specific phenylpropanoids from Chinese cabbage. Our results are expected to provide useful information for developing a strategy to enhance phenylpropanoid biosynthesis in Chinese cabbage.

AUTHOR INFORMATION

Corresponding Author

*(S.U.P.) Phone: +82-42-821-5730. Fax: +82-42-822-2631. E-mail: supark@cnu.ac.kr.

Funding

This research was supported by Golden Seed Project funded by the Ministry of Agriculture, Food and Rural Affairs (MAFRA), Ministry of Oceans and Fisheries (MOF), Rural Development Administration (RDA), and Korea Forest Service (KFS).

Notes

The authors declare no competing financial interest.

REFERENCES

(1) Cheynier, V. Polyphenols in foods are more complex than often thought. *Am. J. Clin. Nutr.* **2005**, *81*, 223−229.

(2) Dixon, R. A.; Paiva, N. L. Stress-induced phenylpropanoid metabolism. *Plant Cell* **1995**, *7*, 1085−1097.

(3) Bennett, R. N.; Wallsgrove, R. M. Secondary metabolites in plant defence mechanisms. *New Phytol.* **1994**, *127*, 617−633.

(4) Middleton, E., Jr.; Kandaswami, C.; Theoharides, T. C. The effects of plant flavonoids on mammalian cells: implications for inflammation, heart disease, and cancer. *Pharmacol. Rev.* **2000**, *52*, 673−751.

(5) Havsteen, B. H. The biochemistry and medical significance of the flavonoids. *Pharmacol. Ther.* **2002**, *96*, 67−202.

(6) Borevitz, J. O.; Xia, Y.; Blount, J.; Dixon, R. A.; Lamb, C. Activation tagging identifies a conserved MYB regulator of phenylpropanoid biosynthesis. *Plant Cell* **2000**, *12*, 2383−2393.

(7) Johkan, M.; Shoji, K.; Goto, F.; Hashida, S.-n.; Yoshihara, T. Blue light-emitting diode light irradiation of seedlings improves seedling quality and growth after transplanting in red leaf lettuce. *HortScience* **2010**, *45*, 1809−1814.

(8) Jeong, S. W.; Park, S.; Jin, J. S.; Seo, O. N.; Kim, G.-S.; Kim, Y.-H.; Bae, H.; Lee, G.; Kim, S. T.; Lee, W. S.; Shin, S. C. Influences of four different light-emitting diode lights on flowering and polyphenol variations in the leaves of chrysanthemum (*Chrysanthemum morifolium*). *J. Agric. Food Chem.* **2012**, *60*, 9793−9800.

(9) Hossen, M. Z. Light emitting diodes increase phenolics of buckwheat (*Fagopyrum esculentum*) sprouts. *J. Plant Interact.* **2007**, *2*, 71−78.

(10) Thwe, A. A.; Kim, Y. B.; Li, X.; Seo, J. M.; Kim, S.-J.; Suzuki, T.; Chung, S.-O.; Park, S. U. Effects of light-emitting diodes on expression of phenylpropanoid biosynthetic genes and accumulation of phenylpropanoids in *Fagopyrum tataricum* Sprouts. *J. Agric. Food Chem.* **2014**, *62*, 4839−4845.

(11) Li, Q.; Kubota, C. Effects of supplemental light quality on growth and phytochemicals of baby leaf lettuce. *Environ. Exp. Bot.* **2009**, *67*, 59−64.

(12) Garcia-Hernandez, M.; Berardini, T.; Chen, G.; Crist, D.; Doyle, A.; Huala, E.; Knee, E.; Lambrecht, M.; Miller, N.; Mueller, L.; Mundodi, S.; Reiser, L.; Rhee, S.; Scholl, R.; Tacklind, J.; Weems, D.; Wu, Y.; Xu, I.; Yoo, D.; Yoon, J.; Zhang, P. TAIR: a resource for integrated *Arabidopsis* data. *Funct. Integr. Genomics* **2002**, *2*, 239−253.

(13) Xu, F.; Li, L.; Zhang, W.; Cheng, H.; Sun, N.; Cheng, S.; Wang, Y. Isolation, characterization, and function analysis of a flavonol synthase gene from *Ginkgo biloba*. *Mol. Biol. Rep.* **2012**, *39*, 2285−2296.

(14) Qi, J.; Yu, S.; Zhang, F.; Shen, X.; Zhao, X.; Yu, Y.; Zhang, D. Reference gene selection for real-time quantitative polymerase chain reaction of mrna transcript levels in Chinese cabbage (*Brassica rapa* L. ssp. *pekinensis*). *Plant Mol. Biol. Rep.* **2010**, *28*, 597−604.

(15) Li, X.; Kim, J. K.; Park, S.-Y.; Zhao, S.; Kim, Y. B.; Lee, S.; Park, S. U. Comparative analysis of flavonoids and polar metabolite profiling of tanno-original and tanno-high rutin buckwheat. *J. Agric. Food Chem.* **2014**, *62*, 2701−2708.

(16) Li, X.; Thwe, A. A.; Park, N. I.; Suzuki, T.; Kim, S. J.; Park, S. U. Accumulation of phenylpropanoids and correlated gene expression during the development of tartary buckwheat sprouts. *J. Agric. Food Chem.* **2012**, *60*, 5629−5635.

(17) Loughrin, J. H.; Kasperbauer, M. J. Light reflected from colored mulches affects aroma and phenol content of sweet basil (*Ocimum basilicum* L.) leaves. *J. Agric. Food Chem.* **2001**, *49*, 1331−1335.

(18) Rochfort, S. J.; Imsic, M.; Jones, R.; Trenerry, V. C.; Tomkins, B. Characterization of flavonol conjugates in immature leaves of pak choi [*Brassica rapa* L. ssp. *chinensis* L. (Hanelt.)] by HPLC-DAD and LC-MS/MS. *J. Agric. Food Chem.* **2006**, *54*, 4855−4860.

(19) Harbaum, B.; Hubbermann, E. M.; Wolff, C.; Herges, R.; Zhu, Z.; Schwarz, K. Identification of flavonoids and hydroxycinnamic acids in pak choi varieties (*Brassica campestris* L. ssp. *chinensis* var. *communis*) by HPLC-ESI-MS*n* and NMR and their quantification by HPLC-DAD. *J. Agric. Food Chem.* **2007**, *55*, 8251−8260.

(20) Winkel-Shirley, B. Biosynthesis of flavonoids and effects of stress. *Curr. Opin. Plant Biol.* **2002**, *5*, 218−223.

(21) Arts, I. C. W.; van de Putte, B.; Hollman, P. C. H. Catechin contents of foods commonly consumed in The Netherlands. 1. Fruits, vegetables, staple foods, and processed foods. *J. Agric. Food Chem.* **2000**, *48*, 1746−1751.

(22) Cartea, M. E.; Francisco, M.; Soengas, P.; Velasco, P. Phenolic compounds in *Brassica* vegetables. *Molecules* **2010**, *16*, 251−280.

(23) Xu, F.; Cai, R.; Cheng, S.; Du, H.; Wang, Y. Molecular cloning, characterization and expression of phenylalanine ammonia-lyase gene from *Ginkgo biloba*. *Biologia* **2008**, *7*, 939.

(24) Singh, K.; Kumar, S.; Rani, A.; Gulati, A.; Ahuja, P. S. Phenylalanine ammonia-lyase (PAL) and cinnamate 4-hydroxylase (C4H) and catechins (flavan-3-ols) accumulation in tea. *Funct. Integr. Genomics* **2009**, *9*, 125−134.

(25) Rani, A.; Singh, K.; Sood, P.; Kumar, S.; Ahuja, P. S. *p*-Coumarate:CoA ligase as a key gene in the yield of catechins in tea [*Camellia sinensis* (L.) O. Kuntze]. *Funct. Integr. Genomics* **2009**, *9*, 271−275.

(26) Cochrane, F. C.; Davin, L. B.; Lewis, N. G. The *Arabidopsis* phenylalanine ammonia lyase gene family: kinetic characterization of the four PAL isoforms. *Phytochemistry* **2004**, *65*, 1557−1564.

(27) Zhou, B.; Wang, Y.; Zhan, Y.; Li, Y.; Kawabata, S. Chalcone synthase family genes have redundant roles in anthocyanin biosyn-

DOI: 10.1021/acs.jafc.5b02086
J. Agric. Food Chem. 2015, 63, 6772−6778

thesis and in response to blue/UV-A light in turnip (*Brassica rapa*; Brassicaceae). *Am. J. Bot.* **2013**, *100*, 2458−2467.
(28) Hamberger, B.; Hahlbrock, K. The 4-coumarate:CoA ligase gene family in *Arabidopsis thaliana* comprises one rare, sinapate-activating and three commonly occurring isoenzymes. *Proc. Natl. Acad. Sci. U. S. A.* **2004**, *101*, 2209−2214.
(29) Gui, J.; Shen, J.; Li, L. Functional characterization of evolutionarily divergent 4-coumarate:coenzyme A ligases in rice. *Plant Physiol.* **2011**, *157*, 574−586.
(30) Lu, S.; Zhou, Y.; Li, L.; Chiang, V. L. Distinct roles of cinnamate 4-hydroxylase genes in *Populus*. *Plant Cell Physiol.* **2006**, *47*, 905−914.
(31) Davies, K.; Schwinn, K.; Deroles, S.; Manson, D.; Lewis, D.; Bloor, S.; Bradley, J. M. Enhancing anthocyanin production by altering competition for substrate between flavonol synthase and dihydroflavonol 4-reductase. *Euphytica* **2003**, *131*, 259−268.
(32) Colliver, S.; Bovy, A.; Collins, G.; Muir, S.; Robinson, S.; de Vos, C. H. R.; Verhoeyen, M. E. Improving the nutritional content of tomatoes through reprogramming their flavonoid biosynthetic pathway. *Phytochem. Rev.* **2002**, *1*, 113−123.

DOI: 10.1021/acs.jafc.5b02086
J. Agric. Food Chem. 2015, 63, 6772−6778

Table 1. Initial Oxidation Rate (as Unit/Week Increase in Peroxide Value (PV) and K_{232} and K_{270} Extinction Coefficients) in Four Varieties of Virgin Olive Oil Stored at Different Temperatures

	closed bottle				open bottle			
	Chétoui	El Hor	Oueslati	Chemlali	Chétoui	El Hor	Oueslati	Chemlali
PV								
5 °C	0.104	0.094	0.063	0.063	0.250	0.167	0.167	0.115
15 °C	0.188	0.167	0.115	0.177	0.313	0.219	0.198	0.208
25 °C	0.229	0.385	0.156	0.302	1.542	1.073	0.542	1.469
50 °C	0.705	1.136	0.182	1.273	11.932	10.955	3.432	12.227
K_{232}								
5 °C	12.7	7.2	8.0	4.3	15.5	15.5	15.7	15.8
15 °C	15.7	8.8	11.2	7.0	17.4	18.4	20.2	18.4
25 °C	20.3	15.5	13.1	19.1	23.6	24.6	28.4	24.3
50 °C	66.9	63.0	55.3	83.4	128.1	138.5	140.2	134.6
K_{270}								
5 °C	0.9	1.4	0.3	0.4	0.9	2.0	0.8	2.1
15 °C	1.8	1.3	0.5	0.7	3.1	2.4	1.1	2.1
25 °C	2.2	2.6	1.6	1.8	4.0	5.6	2.6	8.3
50 °C	23.5	15.7	14.6	22.8	71.0	53.8	30.3	54.6

Virgin Olive Oil and Oxidation Experiments. Four Tunisian monovarietal extra virgin olive oil samples (Chemlali, Chétoui, Oueslati, and El Hor cultivars) that differed mainly in terms of their natural antioxidant content, phenolic compounds, and tocopherols were collected from quality-assured industrial oil mills in the 2011−2012 crop season. Olive oil samples (100 mL) were stored in 250 mL amber glass bottles. Half the samples were kept in open bottles (OB; internal diameter (i.d.) = 5.5 cm; surface area exposed to the atmosphere = 23.74 cm^2) to avoid oxygen limitation and therefore favor the autoxidation process. To compare the effect of oxygen availability during conservation, the other half of the olive oil samples were stored in closed 250 mL amber glass bottles (CB) with 10% headspace. All samples were stored in the dark, in a refrigerator set at 5 ± 1 °C or one of three other incubators set at 15 ± 1, 25 ± 1, or 50 ± 1 °C. Samples were periodically withdrawn from the incubator for scheduled analyses (0, 3, 6, 9, 12, and 18 months at 5−25 °C and 0, 0.75, 1.5, 3, 4.25, and 6.5 months at 50 °C).

Quality and Oxidation Indices. Free acidity was expressed as percentage of oleic acid; peroxide value (PV) was expressed as milliequivalents of active oxygen per kilogram of oil (mequiv O_2/kg), and K_{232} and K_{270} extinction coefficients, calculated from absorption at 232 and 270 nm, were measured following the analytical methods described in European Commission Regulation EEC 2568/91 (1991) and later amendments (the latest being EU 1348/2013).[18] Initial oxidation rates (for oxidation indices) and initial degradation rates (for phenolic compounds) are used to define the behavior at the beginning of the degradation or oxidation process, because the change in the value of the variable during storage could modify the observed rate. They are calculated by the slope of the tangent to the concentration/value versus time curve at time zero.

Phenolic Compounds. Phenolic compounds were identified and quantified at 280 nm using syringic acid as the internal standard according to the method of Mateos et al.[19] A 2.5 g sample of filtered VOO was weighed, and 250 μL of a solution of the internal standard (15 mg/L of syringic acid in methanol) was added. The solvent was evaporated in a rotary evaporator at 35 °C under vacuum, and then the oil was dissolved in 6 mL of *n*-hexane. A diol-bonded phase cartridge (bed wt = 500 mg, volume = 3 mL; Supelco Co., Bellefonte, PA, USA) was placed in a vacuum elution apparatus and conditioned by the consecutive addition of 6 mL of methanol and 6 mL of *n*-hexane. The vacuum was then released to prevent drying of the column. The oil solution was applied to the column, and the solvent was pulled through, leaving the sample and the standard on the solid phase. The sample container was washed with 6 mL of *n*-hexane (2 × 3 mL), which was run out of the cartridge. The sample container was washed again with 4 mL of *n*-hexane/ethyl acetate (85:15, v/v), which was run out of the cartridge and discarded. The column was eluted with 15 mL of methanol, and the solvent was evaporated in a rotary evaporator at room temperature and low speed under vacuum until dry. The phenolic residue was dissolved in 250 μL of methanol/water (1:1, v/v).[19]

High-performance liquid chromatography (HPLC) analysis was performed using an Agilent Technologies series 1100 system equipped with an automatic injector, a column oven, and a diode array UV detector. A Spherisorb S3 ODS2 column (250 × 4.6 mm i.d., 5 μm particle size) (Waters Co., Milford, MA, USA) was used, maintained at 30 °C, with an injection volume of 20 μL and a flow rate of 1.0 mL/min. The mobile phase was a mixture of water/acetic acid (95:5, v/v) (solvent A), methanol (B), and acetonitrile (C). The elution gradient was from 95% (A), 2.5% (B), 2.5% (C) to 34% (A), 33% (B), 33% (C) over 50 min, followed by 100% (B) for 15 min to clean the column.

Tocopherols. Tocopherols were measured following AOCS Method Ce 8-89.[20] A solution of oil in *n*-hexane was analyzed by HPLC (Agilent Technologies series 1100) on a silica gel Lichrosorb Si-60 column (particle size = 5 μm, 250 × 4.6 mm i.d.; Sugerlabor, Madrid, Spain), which was eluted with *n*-hexane/2-propanol (98.5:1.5, v/v) at a flow rate of 1 mL/min. A fluorescence detector (Thermo-Finnigan FL3000, San Jose, CA, USA) was used with excitation and emission wavelengths set at 290 and 330 nm, respectively.

Statistical Analysis. The experimental data set consisted of two individual batches of samples for each of four cultivars and for each of the two oxidation conditions studied (open and closed bottles). Moreover, duplicate measurements were carried out for each sample taken at scheduled time intervals. The standard deviation of the mean values of the analyzed concentration of phenolic and tocopherol compounds was generally <10%; if a higher value was obtained, a new analysis was performed. Statistical analysis was performed using IBM SPSS 22 statistical software (Chicago, IL, USA). Least-squares linear regression analyses were performed, and the best equations were selected on the basis of statistical parameters of the fit (r, p).

RESULTS AND DISCUSSION

The monovarietal VOOs studied in this assay, Chemlali, Chétoui, El Hor, and Oueslati, represent the most common olive cultivars grown in Tunisia, especially in the northern and central parts of the country. An initial characterization of their properties was reported by Krichene et al.[21]

Evolution of the Oxidation Process. The VOO samples stored at different temperatures (5, 15, 25, and 50 °C) in both CB and OB conditions were studied for their oxidative stability over a storage period of 18 months. The progress of the oxidation

DOI: 10.1021/acs.jafc.5b02187
J. Agric. Food Chem. 2015, 63, 6779−6786

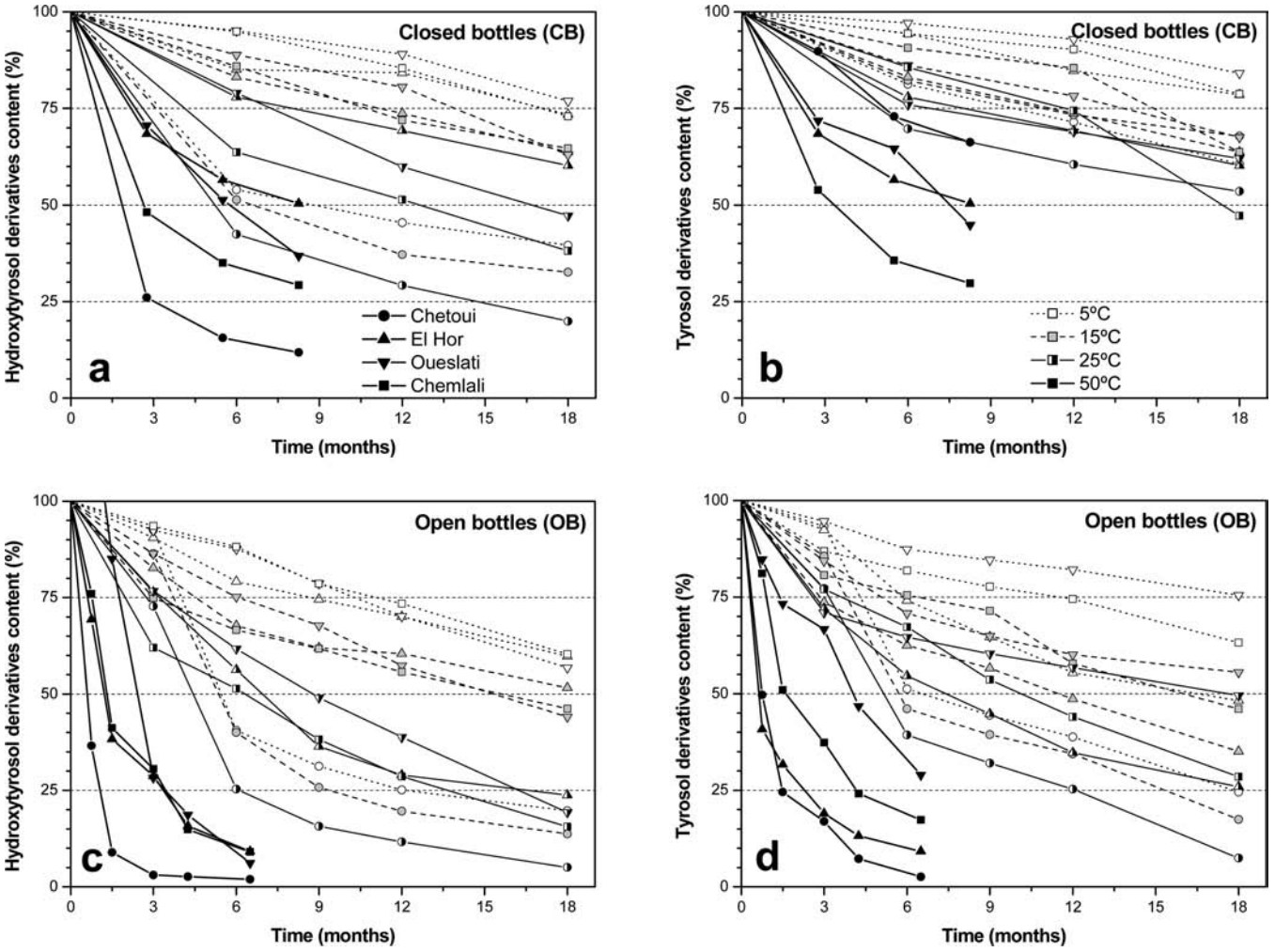

Figure 1. Stability of hydroxytyrosol and tyrosol derivative compounds at different storage temperatures (5−50 °C) and under closed (CB) and open bottle (OB) conditions. VOO variety: ●, Chétoui; ▲, El Hor; ▼, Oueslati; ■, Chemlali. Storage temperature: 5 °C (open symbols); 15 °C (gray symbols); 25 °C (half-solid symbols); 50 °C (solid symbols).

Table 2. Initial Degradation Rate (μmol/kg/month) of Selected Secoiridoid Phenolics under Open Bottle Conditions in Four Varieties of Virgin Olive Oil Stored at Different Temperatures[a]

	DOA				AOA			
	Chétoui	El Hor	Oueslati	Chemlali	Chétoui	El Hor	Oueslati	Chemlali
initial concn (μmol/kg)	351	26	38	15	432	34	46	48
5 °C	33.8	1.47	2.15	0.65	172	1.49	1.45	1.90
15 °C	35.7	2.52	2.98	0.87	178	2.20	2.36	4.22
25 °C	55.2	3.97	4.39	1.31	153	3.84	3.86	6.68
50 °C	505	17.5	15.5	3.19	510	15.2	20.5	31.4
	DLA				ALA			
	Chétoui	El Hor	Oueslati	Chemlali	Chétoui	El Hor	Oueslati	Chemlali
initial concn (μmol/kg)	210	242	60	54	188	21	7	19
5 °C	7.88	13.3	1.19	2.26	5.36	0.94	0.32	0.44
15 °C	8.14	20.0	3.90	2.66	7.27	0.81	0.80	0.46
25 °C	11.24	24.8	6.50	3.93	14.7	2.58	1.03	1.18
50 °C	141.5	266	10.7	25.3	160	8.75		5.63

[a]DOA and AOA, hydroxytyrosol secoiridoid derivatives: dialdehydic and aldehydic form of elenolic acid linked to hydroxytyrosol, (also known as 3,4-DHPEA-EDA and 3,4-DHPEA-EA). DLA and ALA, tyrosol secoiridoid derivatives: dialdehydic and aldehydic form of elenolic acid linked to tyrosol (aka p-HPEA-EDA and p-HPEA-EA).

process was monitored by measuring PV, acidity, and UV characteristics (K_{232} and K_{270}), which are indicators of oil stability and its oxidation level.[18−22]

Initial oxidation rates, expressed as the weekly increase in PV, K_{232}, and K_{270}, are reported in Table 1. As expected, the oxidation rate was faster in OB compared to CB due to oxygen limitation.

DOI: 10.1021/acs.jafc.5b02187
J. Agric. Food Chem. 2015, 63, 6779−6786

For example, PV-based rates of 1.073 mequiv O_2/kg/week in OB versus 0.385 mequiv O_2/kg/week in CB were found for El Hor VOO at 25 °C. The storage temperature also greatly affected the oxidation process. For example, the initial oxidation rate increased from 0.313 mequiv O_2/kg/week at 15 °C to 1.542 mequiv O_2/kg/week at 25 °C and up to 11.93 mequiv O_2/kg/week at 50 °C for Chétoui oil in OB conditions. The effect of the oil variety is also noteworthy; however, as previously reported,[21] no clear relationship between composition (mainly fatty acid profile and natural antioxidant content) and initial oxidation rate could be established. Nevertheless, the observed oxidation based on the evolution of K_{232} is very similar for all of the VOO varieties studied (Table 1).

The shelf life of VOO considerably increased at reduced storage temperature. For example, the shelf life of Chétoui olive oil in CB (based on PV = 20, the maximum value for edible VOO as established by EEC 2568/91 and later amendments) increased from 48 weeks at 25 °C to 57 weeks at 15 °C, due to a reduction of 22% in its oxidation rate, from 0.229 to 0.188 mequiv O_2/kg/week (Table 1). The increased shelf life of Oueslati VOO in CB (at PV = 20) was even greater: from 26 weeks at 25 °C to 44 weeks at 15 °C, associated with a reduction of 36% in its oxidation rate, from 0.156 mequiv O_2/kg/week at 25 °C to 0.115 mequiv O_2/kg/week at 15 °C (Table 1). In storage at 5 °C none of the VOOs studied reached PV > 20 during the 72-week experimental period.

Stability of Phenolic Compounds. The two main families of complex phenolic compounds in VOO (secoiridoids) are the derivatives of hydroxytyrosol (dialdehydic and aldehydic forms of elenolic acid linked to hydroxytyrosol, DOA and AOA, respectively) and of tyrosol (dialdehydic and aldehydic forms of elenolic acid linked to tyrosol, DLA and ALA, respectively). DOA and AOA are also known as 3,4-DHPEA-EDA and 3,4-DHPEA-EA, and DLA and ALA are also known as p-HPEA-EDA and p-HPEA-EA. The stability of secoiridoids, expressed as reduction in concentration over 18 months, is depicted in Figure 1.

As expected, the stability of phenolic compounds was higher under closed bottle storage conditions (Figure 1a,b) compared to OB conditions (Figure 1c,d) due to oxygen limitation. However, the observed difference was not great and the general behaviors of these two phenolic families were quite similar. For example, in Chemlali VOO (square symbols in figures) the residual content of hydroxytyrosol secoiridoid derivatives after 6 months of storage at 25 °C was 63% in CB and 52% in OB and the residual contents of tyrosol derivatives were 85 and 67% in CB and OB, respectively. In El Hor olive oil (up triangles in figures) after 12 months at 15 °C the content of hydroxytyrosol derivatives was maintained at 73% in CB and at 62% in OB and tyrosol derivative content remained at 73 and 49% in CB and OB, respectively (Figure 1).

The stability of the tyrosol secoiridoid compounds (Figure 1b,d) appeared to be greater than that of hydroxytyrosol derivatives (Figure 1a,c), especially in CB conditions, in agreement with previous studies.[13,17]

It is remarkable that in all cases the stability of the phenolic compounds in the Chétoui VOO (circles in figures) was considerably lower than in the other three varieties. El Hor, Oueslati, and Chemlali VOOs behaved similarly. Chétoui VOO had much higher phenolic secoiridoid content (DOA, AOA, DLA, and ALA) than the other varieties (Table 2). This may be the cause of the observed difference.

As expected, an increase in storage temperature increased the degradation of phenolic compounds, particularly at 50 °C

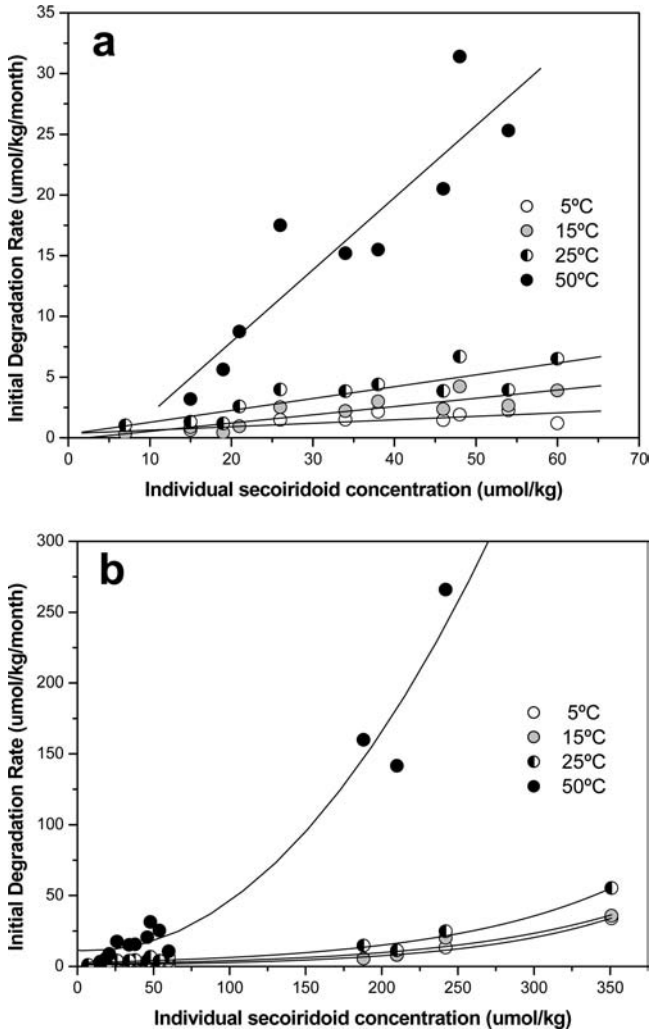

Figure 2. Effect of the concentration of individual secoiridoids (DOA, AOA, DLA, ALA) on their initial degradation rate. Storage temperature: 5 °C (open symbols); 15 °C (gray symbols); 25 °C (half-solid symbols); 50 °C (solid symbols). DOA and AOA, hydroxytyrosol secoiridoid derivatives: dialdehydic and aldehydic form of elenolic acid linked to hydroxytyrosol (also known as 3,4-DHPEA-EDA and 3,4-DHPEA-EA). DLA and ALA, tyrosol secoiridoid derivatives: dialdehydic and aldehydic form of elenolic acid linked to tyrosol (also known as p-HPEA-EDA and p-HPEA-EA).

(Figure 1). For example, in Oueslati oil (down triangle in figures) the residual content of hydroxytyrosol secoiridoid derivatives after 3 months of storage in OB was much lower at higher temperatures: 77% at 25 °C, but 28% at 50 °C. Similarly, the residual content of tyrosol derivatives after 6 months was 51% at 25 °C but 29% at 50 °C (Figure 1).

Only Chétoui VOO contained >250 mg/kg (5 mg/20 g) of the sum of hydroxytyrosol and its derivatives (Table 2), as established by European health claims for olive oil phenolics.[10] This minimum required amount was maintained for 10 months at 25 °C but for up to 18 months in storage at 15 °C. The initial content of total phenolics (hydroxytyrosol and tyrosol and their derivatives) in El Hor oil was 317 mg/kg;[21] this total amount was reduced to 250 mg/kg in just 4.5 months in storage at 25 °C but maintained for up to 7 months at 15 °C. The effect of storage temperature on the stability of phenolic compounds is therefore of great interest in regard to the nutritional and biological value of VOO, because lower storage temperatures considerably increase

DOI: 10.1021/acs.jafc.5b02187
J. Agric. Food Chem. 2015, 63, 6779−6786

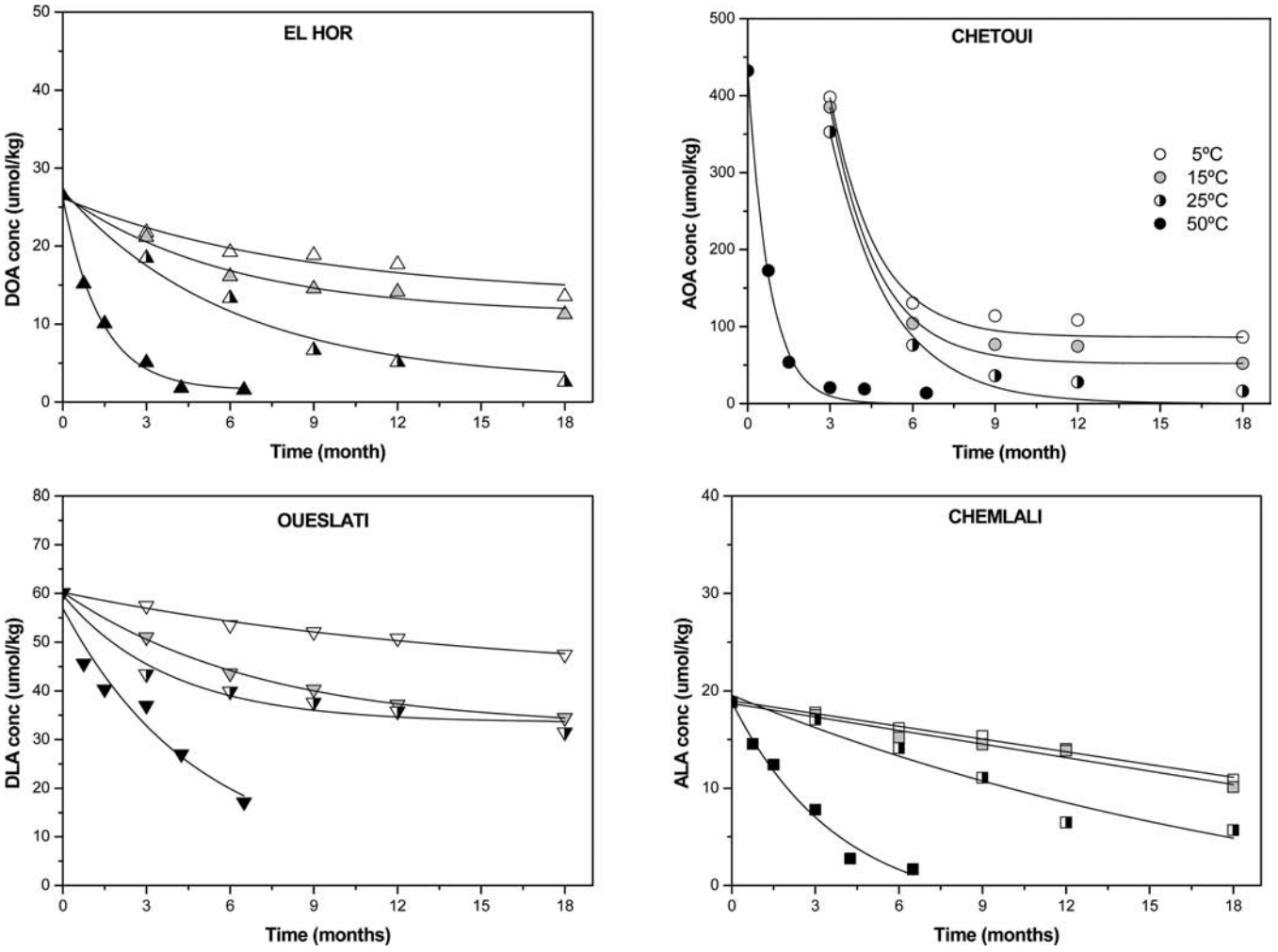

Figure 3. Stability of phenolic secoiridoids during storage at different temperatures (5−50 °C). VOO variety: ●, Chétoui; ▲, El Hor; ▼, Oueslati; ■, Chemlali. Storage temperature: 5 °C (open symbols); 15 °C (gray symbols); 25 °C (half-solid symbols); 50 °C (solid symbols). DOA and AOA, hydroxytyrosol secoiridoid derivatives: dialdehydic and aldehydic form of elenolic acid linked to hydroxytyrosol (also known as 3,4-DHPEA-EDA and 3,4-DHPEA-EA). DLA and ALA, tyrosol secoiridoid derivatives: dialdehydic and aldehydic form of elenolic acid linked to tyrosol (also known as p-HPEA-EDA and p-HPEA-EA). Standard deviation of the mean value of the phenolic compound concentrations was <10%.

the length of time for which the health claim is valid. This finding is particularly relevant for high-added-value products, sometimes defined as premium or superior VOO.

Kinetics of Degradation of Phenolic Compounds. The degradation of secoiridoid phenolics during storage fit a pseudo-first-order kinetics equation reasonably well ($r > 0.96$ and $p < 0.005$) at all of the temperatures and for all of the VOO varieties studied, as previously reported.[13] The reaction equation was $\ln(C_t/C_0) = kt$, where C_0 is the initial concentration and C_t the residual concentration at time t. The stability of tyrosol secoiridoid derivatives was greater than that of hydroxytyrosol derivatives as demonstrated by the lower slope of the degradation kinetics, especially at higher storage temperatures (i.e., -0.099 ± 0.005 as compared to -0.068 ± 0.002 for hydroxytyrosol and tyrosol derivatives at 25 °C in Chemlali oils; or -0.452 ± 0.046 vs -0.184 ± 0.015 for hydroxytyrosol and tyrosol derivatives at 50 °C in Oueslati oils), in agreement with other studies.[13,17]

The initial degradation rate was generally similar at storage temperatures of 5 and 15 °C but increased considerably at 25 °C and was even faster at 50 °C (Table 2). For example, in El Hor olive oil, the degradation rate of DOA increased from 2.52 μmol/kg/month at 15 °C to 3.97 μmol/kg/month at 25 °C and to 17.5 μmol/kg/month at 50 °C. Similarly, ALA in Chemlali VOO increased from 0.44 and 0.46 μmol/kg/month at 5 and 15 °C, respectively, to 1.18 μmol/kg/month at 25 °C and to 5.63 μmol/kg/month at 50 °C.

Both storage temperature and oil variety affected degradation rates (Table 2). The observed differences in the initial degradation rate of the secoiridoid compounds in the different VOO varieties studied (Table 2) may be explained by the difference in their initial phenolic contents.[21] Figure 2 plots the concentration of each of the main complex phenolic compounds (DOA, AOA, DLA, and ALA) versus their initial degradation rate (16 data points of four oil varieties for each of the four secoiridoids for each temperature). An approximately linear relationship ($r > 0.98$, and at 50 °C, $r = 0.91$, $p < 0.01$) between initial degradation rate and initial phenolic concentrations is observed at phenolic concentrations <100 μmol/kg at all storage temperatures assayed (Figure 2a). Moreover, with the higher phenolic content observed in this study (350 μmol/kg) also taken into account, the initial degradation rate fits an exponential growth curve $C_t = C_0(1 + r)^t$, where r is the growth rate (Figure 2b). Therefore, the effect of the oil variety on the stability of the phenolic compounds may be explained simply by their

DOI: 10.1021/acs.jafc.5b02187
J. Agric. Food Chem. 2015, 63, 6779−6786

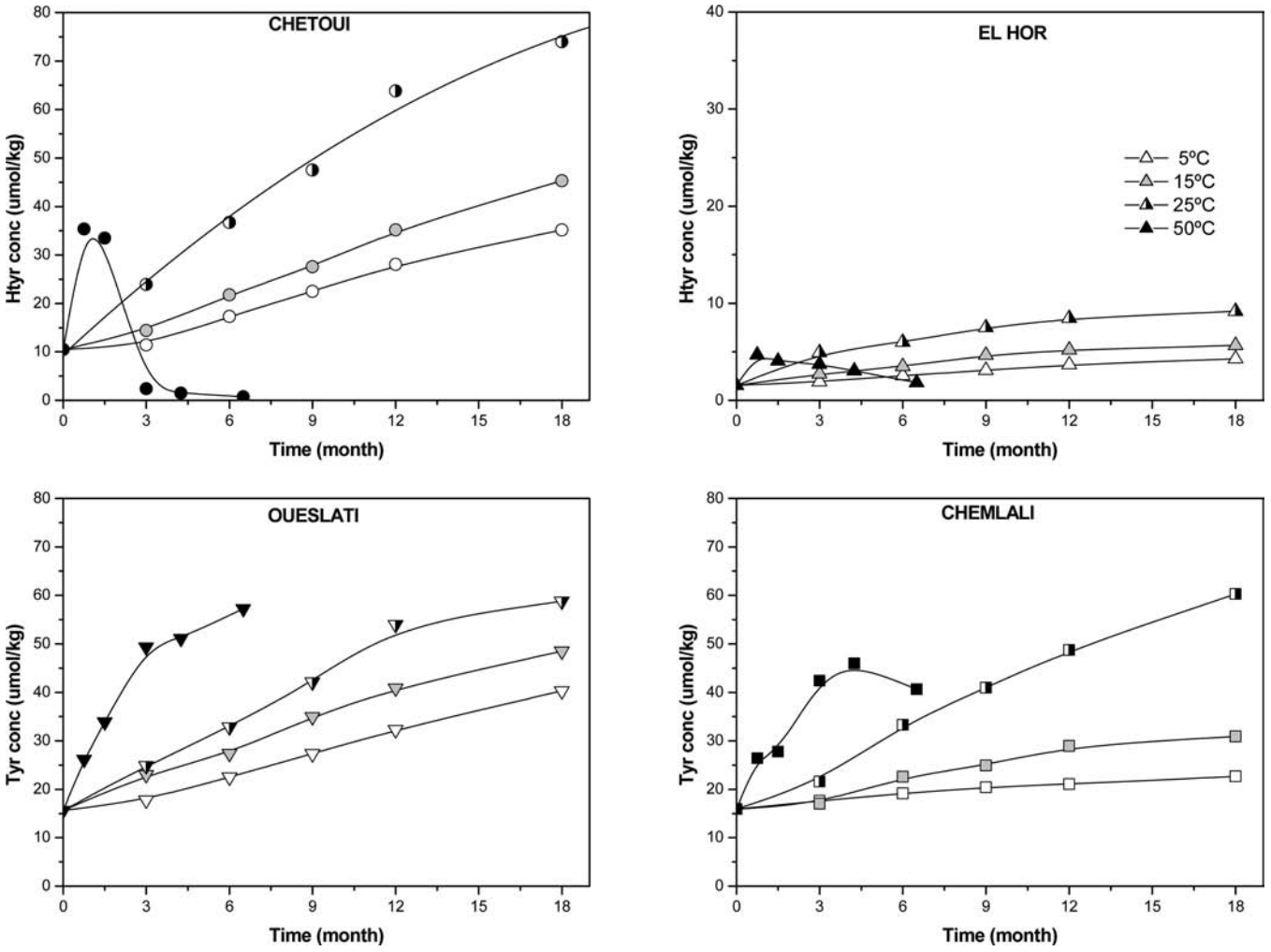

Figure 4. Evolution of hydroxytyrosol and tyrosol during storage at different temperatures (5−50 °C). VOO variety: ●, Chétoui; ▲, El Hor; ▼, Oueslati; ■, Chemlali. Storage temperature: 5 °C (open symbols); 15 °C (gray symbols); 25 °C (half-solid symbols); 50 °C (solid symbols). Htyr, hydroxytyrosol; Tyr, tyrosol. Standard deviation of the mean value of the phenolic compound concentrations was <10%.

different initial concentrations. Furthermore, the relationship between initial degradation rate and initial concentration of phenolics was very similar for all four main complex phenolic compounds, and therefore their stability should also be similar.

The stability of the main phenolic secoiridoid compounds (DOA, AOA, DLA, and ALA) is depicted in Figure 3; their behavior over time fit an exponential decay curve well ($r^2 > 0.96$). As discussed above, the different initial phenolic compound concentrations in different oil varieties and the different storage temperatures explained the different behaviors of the varieties.

It is of interest that in Chétoui olive oil, the variety with the greatest initial concentration of phenolic compounds (Table 2), a lag phase is apparent for AOA and ALA, but not for DOA or DLA (data not shown). In contrast, the behavior of the other three varieties was similar, taking into account the different initial concentrations of the individual phenolic compounds and the effect of the temperature.

Behavior of Simple Phenolics. The content of simple phenolics such as hydroxytyrosol and tyrosol, in fresh VOO is very low (e.g., Gomez-Rico et al.[23]). During storage there was an increase in the content of these simple phenolics due to the degradation of their complex derivatives (Figure 4), as observed in other studies.[14,24,25] The behavior of simple phenolics was similar and clearly related to the storage temperature and the initial concentration of their complex forms that determined the rate of the degradation of their complex derivatives. For example, a small amount of hydroxytyrosol was formed in El Hor olive oil (Figure 4; 8.4 μmol/kg after 12 months at 25 °C) because only a small initial amount of its derivatives was present (Table 2): a total of 60 μmol/kg, made up of 26 μmol/kg of DOA and 34 μmol/kg of AOA that had individual initial degradation rates at 25 °C of 3.97 and 3.84 μmol/kg/month, respectively (Table 2). In contrast, tyrosol was formed in greater amounts under the same conditions (48 μmol/kg after 12 months at 25 °C), because the concentration of its derivatives was initially higher: a total of 258 μmol/kg, made up of 242 μmol/kg of DLA and 21 μmol/kg of ALA (degradation rates of 24.8 and 2.58 μmol/kg/month, respectively).

In all cases a plateau was apparently reached probably because these compounds were also degraded during storage. Indeed, at 50 °C a decrease in hydroxytyrosol was clearly visible in all VOO varieties studied after reaching a maximum value.

The increase in the content of simple phenolics, the decrease in their secoiridoid derivatives, or the ratio of simple to secoiridoid phenolics can be used as indices of the oxidative and hydrolytic degradation of VOO phenolics[25,26] and may be used as freshness or aging indices of the VOO during its shelf life.

DOI: 10.1021/acs.jafc.5b02187
J. Agric. Food Chem. 2015, 63, 6779−6786

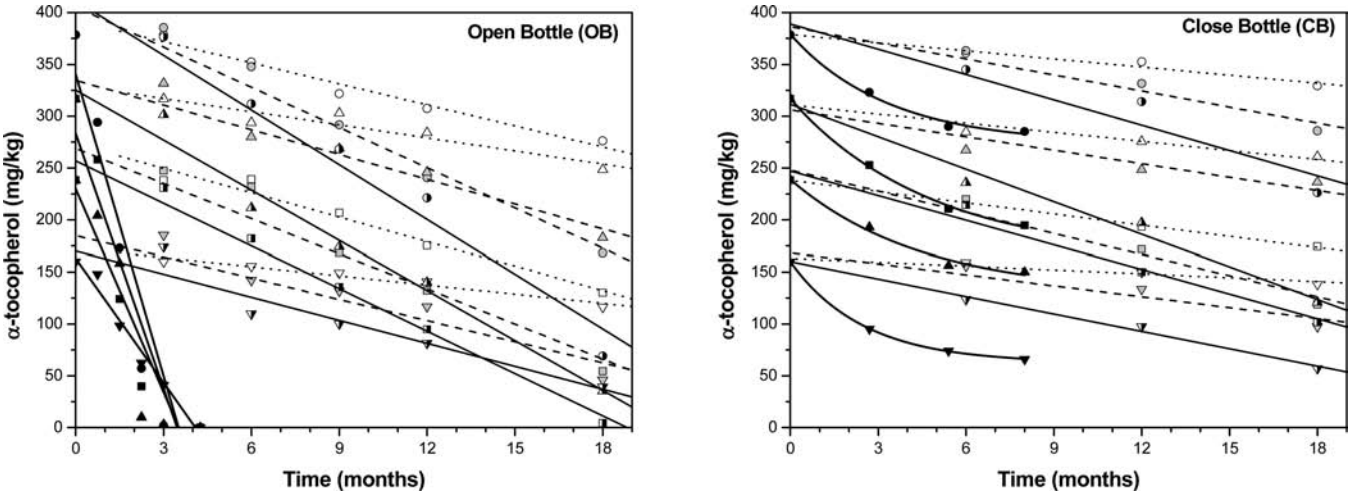

Figure 5. Evolution of tocopherol during storage at different temperatures (5−50 °C) in closed (CB) and open bottles (OB). VOO variety: ●, Chétoui; ▲, El Hor; ▼, Oueslati; ■, Chemlali. Storage temperature: 5 °C (open symbols); 15 °C (gray symbols); 25 °C (half-solid symbols); 50 °C (solid symbols). Standard deviation of the mean value of the tocopherol content was <10%.

Stability of Tocopherols. The most important tocopherol in VOO by far is α-tocopherol (e.g., Cunha et al.[27]); therefore, the other isomers were not investigated in this study.

In contrast to complex phenolics, α-tocopherol degradation apparently followed a simpler zero-order kinetic ($C_t = C_0 + kt$; $r > 0.97$ and $p < 0.01$; Figure 5).

A lag phase of a few months may be hidden, because the decrease from the initial concentration of α-tocopherol was very small up to 3 months in storage at all temperatures studied except at 50 °C storage conditions.

As observed for phenolics, the degradation in CB conditions was less due to the limited oxygen availability, as clearly noticeable at 50 °C when a plateau was reached (Figure 5).

AUTHOR INFORMATION

Corresponding Author

*(G.F.) E-mail: giuseppe.fregapane@uclm.es.

Funding

This work was supported by the Spanish Junta de Comunidades de Castilla-La Mancha (PBI 05-047), the Tunisian Ministry of Higher Education, Scientific Research and Technology, and the Agencia Española de Cooperación Internacional (AECI PCI España-Túnez A6675/06).

Notes

The authors declare no competing financial interest.

REFERENCES

(1) Boskou, D. *Olive Oil: Chemistry and Technology*; AOCS Press: Champaign, IL, USA, 1996.

(2) Psomiadou, E.; Tsimidou, M. Stability of virgin olive oil. 1. Autoxidation studies. *J. Agric. Food Chem.* **2002**, *50*, 716−721.

(3) Psomiadou, E.; Tsimidou, M. Stability of virgin olive oil. 2. Photoxidation studies. *J. Agric. Food Chem.* **2002**, *50*, 722−727.

(4) Gomez-Alonso, S.; Mancebo-Cambos, V.; Salvador, M. D.; Fregapane, G. Oxidation kinetics in olive oil triacylglycerols under accelerated shelf-life testing (25−75°C). *Eur. J. Lipid Sci. Technol.* **2004**, *106*, 369−375.

(5) Mancebo-Campos, V.; Salvador, M. D.; Fregapane, G. Comparative study of virgin olive oil behaviour under Rancimat accelerated oxidation conditions and long-term room temperature storage. *J. Agric. Food Chem.* **2007**, *55*, 8231−8236.

(6) Bendini, A.; Cerretani, L.; Salvador, M. D.; Fregapane, G.; Lercker, G. Stability of the sensory quality of virgin olive oil during storage: an overview. *Ital. J. Food Sci.* **2009**, *21*, 389−406.

(7) Angerosa, F. Influence of volatile compounds on virgin olive oil quality evaluated by analytical approaches and sensor panels. *Eur. J. Lipid Sci. Technol.* **2002**, *104*, 639−660.

(8) Aparicio, R.; Luna, G. Characterisation of monovarietal virgin olive oils. *Eur. J. Lipid Sci. Technol.* **2002**, *104*, 614−627.

(9) Visioli, F.; Galli, C. Olive oil phenols and their potential effects on human health. *J. Agric. Food Chem.* **1998**, *46*, 4292−4296.

(10) European Union Commission Regulation (EU) No 432/2012 of 16 May 2012 establishing a list of 199 permitted health claims made on foods, other than those referring to the 200 reduction of disease risk and to children's development and health.

(11) Okogeri, O.; Tasioula-Margari, M. Changes occurring in phenolic compounds and r-tocopherol of virgin olive oil during storage. *J. Agric. Food Chem.* **2002**, *50*, 1077−1080.

(12) Rastrelli, L.; Passi, S.; Ippolito, F.; Vacca, G.; De Simone, F. Rate of degradation of r-tocopherol, squalene, phenolics, and polyunsaturated fatty acids in olive oil during different storage conditions. *J. Agric. Food Chem.* **2002**, *50*, 5566−5570.

(13) Lavelli, V.; Fregapane, G.; Salvador, M. D. Effect of storage on secoiridoid and tocopherol contents and antioxidant activity of monovarietal extra virgin olive oils. *J. Agric. Food Chem.* **2006**, *54*, 3002−3007.

(14) Li, X.; Hanjiang, Z.; Shoemaker, C. F.; Wang, S. C. The effect of different cold storage conditions on the compositions of extra virgin olive oil. *J. Am. Oil Chem. Soc.* **2014**, *91*, 1559−1570.

(15) Brenes, M.; García, A.; Dobarganes, M. C.; Velasco, J.; Romero, C. Influence of thermal treatments simulating cooking processes on the polyphenol content in virgin olive oil. *J. Agric. Food Chem.* **2002**, *50*, 5962−5967.

(16) Carrasco-Pancorbo, A.; Cerretani, L.; Bendini, A.; Segura-Carretero, A.; Lercker, G.; Fernandez-Gutiérrez, A. Evaluation of the influence of thermal oxidation on the phenolic composition and on the antioxidant activity of extra-virgin olive. *J. Agric. Food Chem.* **2007**, *55*, 4771−4780.

(17) Daskalaki, D.; Kefi, G.; Kotsiou, K.; Tasioula-Margari, M. Evaluation of phenolic compounds degradation in virgin olive oil during storage and heating. *J. Food Nutr. Res.* **2009**, *48*, 31−41.

(18) European Union Commission Regulation EEC/2568/91. On the characteristics of olive and olive pomace oils and their analytical methods. *Off. J. Eur. Communities* **1991**, *L248*, 6−36, and later amendments, the latest being Commission Regulation (EU) No. 1348/2013 of 16 December 2013.

DOI: 10.1021/acs.jafc.5b02187
J. Agric. Food Chem. 2015, 63, 6779−6786

(19) Mateos, R.; Espartero, J. L.; Trujillo, M.; Rios, J. J.; Leon-Camacho, M.; Alcudia, F. Determination of phenols, flavones and lignans in virgin olive oils by solid-phase extraction and high-performance liquid chromatography with diode array ultraviolet detection. *J. Agric. Food Chem.* **2001**, *49*, 2185−2192.
(20) Determination of tocopherols and tocotrienols in vegetable oils and fats by HPLC. *AOCS Official Methods*; AOCS: Champaign, IL, USA, 1989; Ce 8-89.
(21) Krichene, D.; Allalout, A.; Mancebo-Campos, V.; Salvador, M. D.; Zarrouk, M.; Fregapane, G. Stability of virgin olive oil and behaviour of its natural antioxidants under medium temperature accelerated storage conditions. *Food Chem.* **2010**, *121*, 171−177.
(22) Frankel, E. N. *Lipid Oxidation*, 2nd ed.; The Oily Press: Dundee, Scotland, 2005.
(23) Gomez-Rico, A.; Fregapane, G.; Salvador, M. D. Effect of cultivar and ripening on minor components in Spanish olive fruits and their corresponding virgin olive oils. *Food Res. Int.* **2008**, *41*, 433−440.
(24) Fregapane, G.; Lavelli, V.; León, S.; Kapuralin, J.; Salvador, M. D. Effect of filtration on virgin olive oil stability during storage. *Eur. J. Lipid Sci. Technol.* **2006**, *108*, 134−142.
(25) Migliorini, M.; Cherubini, C.; Cecchi, L.; Zanoni, B. Degradazione dei composti fenolici durante la conservazione dell'olio extra vergine di olive − degradation of phenolic compounds during extra virgin olive oil shelf-life. *Riv. Ital. Sostanze Grasse* **2013**, *90*, 71−80.
(26) Fregapane, G.; Gómez-Rico, A.; Inarejos, A. I.; Salvador, M. D. Relevance of minor components stability in comercial olive oil quality during the market period. *Eur. J. Lipid Sci. Technol.* **2013**, *115*, 541−548.
(27) Cunha, S. C.; Amaral, J. S.; Fernandes, J. O.; Oliveira, M. B. Quantification of tocopherols and tocotrienols in portuguese olive oils using HPLC with three different detection systems. *J. Agric. Food Chem.* **2006**, *54*, 3351−3356.

DOI: 10.1021/acs.jafc.5b02187
J. Agric. Food Chem. 2015, 63, 6779−6786

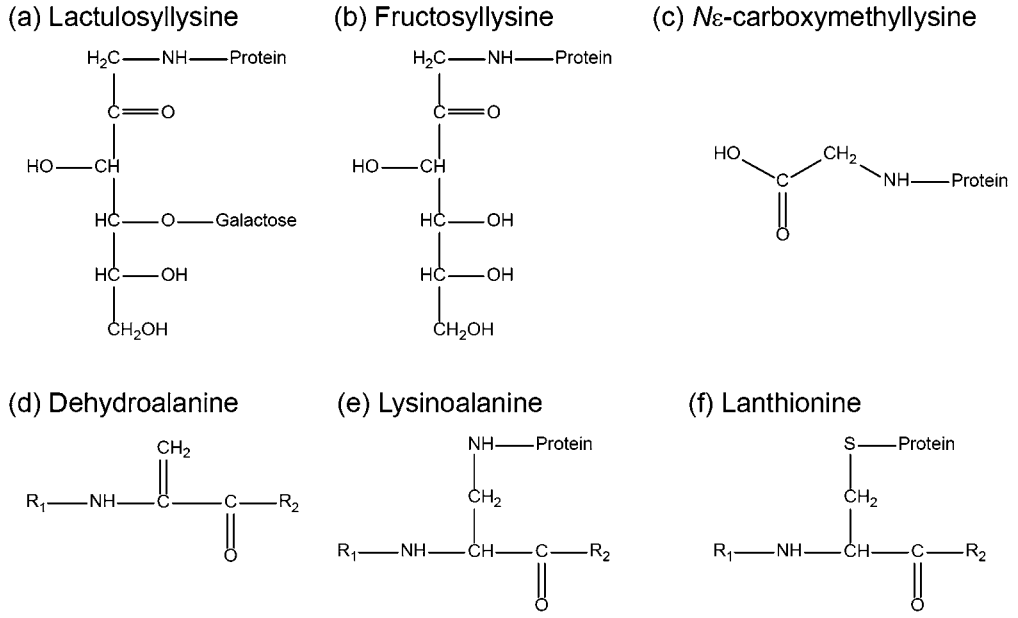

Figure 1. Chemical structures of heat-derived protein modifications. Lactulosyllysine (a) and fructosyllysine (b) are early Maillard reaction products, which are subsequently oxidized to N^{ε}-carboxymethyllysine (CML; c) as an advanced Maillard reaction product. Dehydroalanine (d) is the precursor of cross-linked products, lysinoalanine (e), and lanthionine (f).

analysis and in vitro/in vivo digestion as done previously,[12] and the relationship between protein modifications and protein digestibility is discussed.

MATERIALS AND METHODS

Milk Samples. Milk-based liquid formulas, simulating enteral formulas, were manufactured at the pilot plant of Morinaga Milk Industry (Zama, Japan) with ingredients such as high-heat skim milk powder, sodium caseinate, vegetable fat, maltodextrin, vitamins, minerals, and emulsifiers. The ratio of casein (CN) to whey protein was approximately 7:1. The heating conditions were set to mimic those for the manufacturer's enteral formula products (Table 1).

Table 1. Heat Treatment of Milk-Based Liquid Formulas[a]

treatment	holding temp/time	F_0 value
steam injection	151 °C for 4 s	65
in-can sterilization[b]	123 °C for 8 min	20

[a]Heating conditions were set by reference to those of the manufacturer's commercial products. [b]This heat treatment involves slow rates of temperature rise/fall, which also contributed to the F_0 value.

The heated formulas were homogenized at 30 MPa, followed by lyophilization. The lyophilized formula powders were stored at 4 °C until use. Nutrient composition of the products was determined by the Analytical Research Center of Morinaga Milk Industry (Table 2).

Table 2. Nutrient Composition of Lyophilized Enteral Formulas

component	g/100 g
protein	18.1
fat	12.3
carbohydrate	65.5
ash	3.2
water	0.9

Sodium Dodecyl Sulfate–Polyacrylamide Gel Electrophoresis (SDS-PAGE) of Milk Samples. Six grams of lyophilized formulas were reconstituted with 24 mL of Milli-Q water (Millipore, Billerica, MA), subjected to centrifugation at 8500*g* for 30 min twice, and the upper fat layer was removed. The tiny pellet, formed after centrifugation, was thoroughly mixed with the defatted supernatant. We confirmed, using a Dumas method (Sumigraph NC-220F, Sumica Chemical Analytic Center, Tokyo, Japan) that no notable loss in protein content (as measured by nitrogen (N) amount) was accompanied by removal of fat layer.

Protein concentrations were determined by the Bradford method,[18] and were adjusted to 7.5 g/L with Milli-Q water. Sodium dodecyl sulfate–polyacrylamide gel electrophoresis (SDS-PAGE) was performed under reducing/nonreducing conditions to separate the proteins (Bio-Rad, Hercules, CA). Fifty micrograms of protein was loaded for each sample onto Mini-PROTEAN TGX Any kD gel (Bio-Rad). Electrophoresis was run at 120 V for 50 min, and gels were stained with Bio-Safe Coommassie Stain (Bio-Rad).

Proteomic Analysis. Proteomic analysis was conducted at the Proteomic Core Facility at the University of California, Davis, as described previously,[12] in order to site-specifically semiquantify lactulosyllysine, fructosyllysine, CML, dehydroalanine formed from phosphoserine and Cys, and phosphorylation of serine (Ser) residues in major milk proteins such as α-lactalbumin (α-LA), β-lactoglobulin (β-LG), and CNs.

In-Gel Digestion. In-gel reduction, alkylation, and tryptic digestion were done using similar protocols as published previously.[19] Briefly, lyophilized formulas were reconstituted with Fisher Optima water (Fisher Scientific, Pittsburgh, PA), loaded onto a Novex 10% Tris-glycine gel (Life Technologies, Grand Island, NY), and applied to electrophoresis at 80 V for 20 min. The fraction containing the entire protein band was excised, and the gel piece was washed twice with 100 mM ammonium bicarbonate (AmBic) and dehydrated twice with 100% acetonitrile (ACN). The gel piece was reduced using 10 mM dithiothreitol (in 100 mM AmBic) at 56 °C for 30 min. The gel piece was then alkylated using 55 mM iodoacetamide (in 100 mM AmBic) at room temperature (RT) for 20 min in the dark. The gel piece was washed twice with 100 mM AmBic, dehydrated twice with 100% ACN, and then mechanically dried using vacuum centrifugation. Finally, sequencing grade modified trypsin (Promega, Madison, WI; in 50 mM AmBic) was added in a 1:30 ratio (trypsin:protein) to rehydrate the gel. After replacing the excess solution with 50 mM Ambic, the gel piece was incubated overnight at 37 °C. While the supernatant was collected into a new tube, 60% ACN (in 0.1% trifluoroacetic acid) was added to the remaining gel piece, which was then sonicated and centrifuged for collecting another supernatant. The supernatants were then dried by vacuum centrifugation.

DOI: 10.1021/acs.jafc.5b02189
J. Agric. Food Chem. 2015, 63, 6787–6798

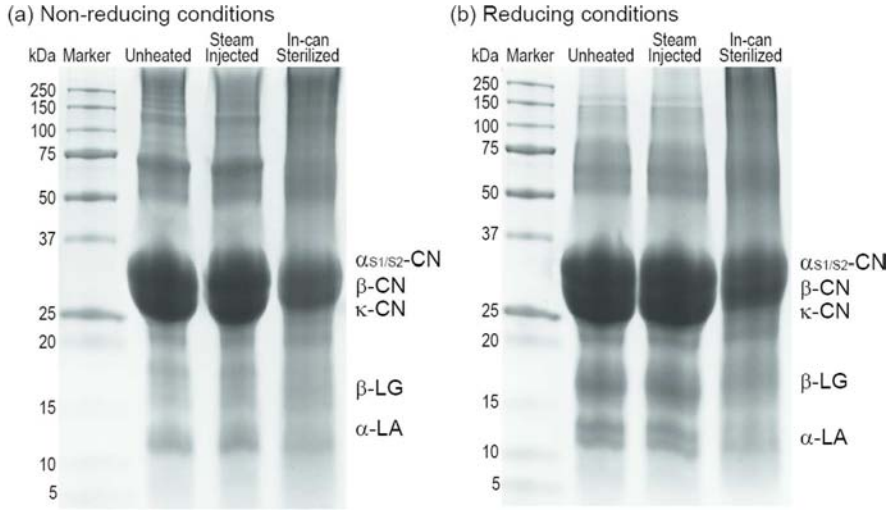

Figure 2. Electrophoresis of proteins in milk-based enteral formulas. Formula samples were applied to SDS-PAGE analysis under (a) nonreducing and (b) reducing conditions. Fifty micrograms of protein was loaded on a gel, and the gel was stained with Bio-Safe Coommassie Stain.

Liquid Chromatography coupled with tandem mass spectrometry (LC-MS/MS). Digested peptides were analyzed by a Thermo Scientific Q Exactive Orbitrap mass spectrometer in conjunction with a Paradigm MG4 HPLC (Michrom Bio Resources, Auburn, CA). The digested peptides were loaded onto a Michrom C18 trap and desalted before they were separated using a Michrom 200 μm × 150 mm Magic C18 AQ reverse phase column. A flow rate of 2 μL/min was used. Peptides were eluted using a 90 min gradient composed of buffer A (0.1% formic acid) and B (100% ACN), with 2% B to 35% B over 70 min, 35% B to 80% B for 5 min, 80% B for 2 min, and then a decrease from 80% to 2% B in 1 min, and held at 2% B for 12 min. A spray voltage of 2.2 kV was used with a transfer capillary temperature of 200 °C. A MS survey scan was obtained for the m/z range of 300–1600. MS/MS spectra were acquired using a top 15 method, where the top 15 ions in the MS spectra were subjected to high energy collisional dissociation. An isolation mass window of 2.0 m/z was used for the precursor ion selection, and normalized collision energy of 27% was used for fragmentation. A 5 s duration was used for the dynamic exclusion.

Data Analysis. All MS/MS samples were analyzed using X! Tandem (The GPM, thegpm.org; version TORNADO (2010.01.01.4)). X! Tandem was set up to search the digestion enzyme trypsin. Iodoacetamide derivative of Cys was specified in X! Tandem as a fixed modification. One of the targeted modifications [lactulosyllysine (+324.105647), fructosyllysine (+162.052824), CML (+58.005479), phosphorylation on Ser, threonine and tyrosine (+79.966331), dehydration of Ser (−18.010565), or dehydroalanine on Cys (−33.987721)], as well as acetylation of the N-terminus, ammonia-loss of the N-terminus, *pyro*-glutamination of the N-terminus, and oxidation of methionine and tryptophan were specified in X! Tandem as variable modifications. Scaffold (version Scaffold_4.1.1, Proteome Software Inc., Portland, OR) and Skyline (version 1.4.0.4421, MacCoss Lab, Department of Genome Science, University of Washington) were used to validate MS/MS based peptide and protein identifications,[20−22] and to determine retention time and peak areas of peptides with targeted modifications, respectively. Three different monoisotopic peak areas (M, M + 1, M + 2) were integrated for each specified peptide with Xcalibur (version 2.2 SP1.48, Thermo Scientific, Waltham, MA), and they were summed up to obtain higher confidence. For normalization between samples, the summed peak area was normalized by dividing it with the exclusive spectrum counts of all modified and nonmodified peptides derived from the parental protein, in Scaffold.

In Vitro Digestion. Powdered formulas were reconstituted with Milli-Q water and defatted, and protein concentration was adjusted to 7.5 g/L as above. Six mL of samples were aliquoted into 15 mL centrifuge tubes. Samples were subjected to in vitro digestion as described previously.[12] Conditions for the in vitro digestion in general,[23] the digestion times,[24] and pH of the gastric digestion,[24−28] had been reviewed carefully and selected accordingly.

Simulated gastric digestion was started with adjusting the pH to 2.0 (adult model) or 4.0 (infant model) with 1 M HCl. Porcine pepsin (Sigma-Aldrich; 2% in 1 mM HCl) was added to the sample in a 1:12.5 ratio (pepsin:protein). Samples were placed in a water bath equipped with an incubation shaker (Yamato Scientific, Tokyo, Japan) in the dark at 140 rpm at 37 °C for 30 min. After incubation, pH of the samples was adjusted to 7.0 with 0.1 mol/L $NaHCO_3$.

Simulated intestinal digestion was performed following the gastric digestion (at pH 2.0 or 4.0). After the pH was adjusted to 7.0, pancreatin (Sigma-Aldrich; 0.4% in 0.1 mol/L $NaHCO_3$) was added to the samples in a 1:62.5 ratio (pancreatin:protein). Samples were placed in a water bath equipped with an incubation shaker in the dark at 140 rpm at 37 °C for 60 and 240 min. After incubation, the enzymes were inactivated in a water bath at 85 °C for 3 min.

The digested samples were applied to reducing SDS-PAGE as described above, and each lane was loaded with the equivalent of 50 μg of protein before digestion. Protein digestibility of the samples subjected to digestion assays was determined using a Dumas method (Sumigraph NC-220F) and with a procedure as described previously.[29] Briefly, total N and nonprotein N [NPN; soluble fraction after trichloroacetic acid (TCA; 12% final concentration[30]) precipitation] were measured in milk samples before/after the digestion. Protein digestibility was defined as the ratio of ($NPN_{after\ digestion} - NPN_{before\ digestion}$)/(total $N_{before\ digestion} - NPN_{before\ digestion}$). Protein digestibility was analyzed six times for each pH condition/time period tested (i.e., pepsin digestion at pH 2.0/4.0 for 30 min, and pepsin digestion at 2.0/4.0 for 30 min + pancreatin digestion at pH 7.0 for 60 min).

In Vivo Digestion. A suckling rat pup model was used to investigate in vivo digestion of milk samples as described previously.[12,31] The study was approved by the Animal Research Committee of Morinaga Milk Industry (protocol no. 14-006). Sprague–Dawley rats with litters of 12 pups (6 males + 6 females) were obtained commercially (Charles River Japan, Yokohama, Japan), maintained in polycarbonate cages with wood shavings in a temperature-, humidity-, and light-controlled facility (24 °C, humidity 55%, and 12 h light/dark circle), and allowed to consume water and standard rat chow diet (F-2, Funabashi Farm, Funabashi, Japan) ad libitum. Pups were randomly assigned as 3 males + 3 females/formula sample/time point. After acclimation to facility conditions, on day 14 postpartum, pups were separated from their dams for 6 h and then intubated with unheated, steam-injected, or in-can sterilized formula (reconstituted and defatted as above; protein concentration was adjusted to 30 g/L), in a 1:36 v/w ratio (formula (mL)/body weight (g)), as done in our previous cow's milk study.[12] Pups were euthanized with CO_2 asphyxiation at 0.5, 1, or 2 h after intubation. As experiment control, 3 male pups + 2 female pups

DOI: 10.1021/acs.jafc.5b02189
J. Agric. Food Chem. 2015, 63, 6787−6798

Table 3. Lactulosyllysine in Milk Proteins[a]

protein	residue	amino acid	charge	steam injected[b]	in-can sterilized[b]
α-LA	59−79	Lys62	[3+]	0.9	1.3
			[4+]	1.0	1.6
	109−122	Lys114	[2+]	1.1	0.8
			[3+]	0.8	0.7
β-LG	1−14	Lys8	[2+]	2.2	1.0
			[3+]	6.5	2.9
	41−60	Lys47	[3+]	9.4	6.1
	76−83	Lys77	[2+]	1.1	0.9
	76−91	Lys83	[2+]	1.0	0.3
			[3+]	0.7	0.4
			[4+]	0.9	0.5
	78−91	Lys83	[3+]	2.3	1.8
	84−101	Lys91	[3+]	1.0	0.4
			[4+]	1.1	0.6
	125−138	Lys135	[2+]	1.4	0.8
			[3+]	1.1	0.7
	139−148	Lys141	[2+]	3.6	1.8
			[3+]	3.7	1.9
α_{s1}-CN	3−22	Lys7	[4+]	6.0	30.3
	35−42	Lys36	[2+]	1.2	1.5
			[3+]	1.8	1.7
	80−90	Lys82	[2+]	1.8	1.1
			[3+]	2.2	0.8
	104−119	Lys105	[2+]	4.2	14.8
			[3+]	2.1	8.1
	120−132	Lys124	[2+]	1.6	1.7
α_{s2}-CN	22−32	Lys24	[3+]	2.4	1.7
	25−41	Lys33	[3+]	1.9	0.9
	151−160	Lys152	[3+]	1.5	1.3
	171−181	Lys173	[2+]	2.5	2.4
			[3+]	6.1	5.7
	172−181	Lys173	[2+]	2.3	0.8
	198−205	Lys199	[2+]	1.4	1.3
			[3+]	1.2	1.2
β-CN	170−183	Lys176	[2+]	1.5	2.1
			[3+]	1.6	2.2
κ-CN	22−34	Lys24	[2+]	1.0[c]	1.1[c]
			[3+]	1.0[c]	1.0[c]
	61−68	Lys63	[2+]	1.8	2.0
	69−97	Lys86	[3+]	5.9	2.2

[a]Formula samples were treated with trypsin, followed by LC-MS/MS analysis for identifying and semiquantifying trypic peptides containing lactullosyllysine in major milk proteins. [b]Peak areas of the specific peptides are normalized to unheated formula. [c]Peak areas are normalized to steam-injected formula because those of unheated formula were below the detection limit.

were separated from their dams for 6 h and euthanized with CO_2 asphyxiation without formula samples administered.

Coagulates in the stomach were collected and weighed. Small intestine was cut into upper and lower parts, and each part was perfused twice with 0.2 mL of phosphate buffered saline (PBS) containing protease inhibitor cocktail (P2714, Sigma-Aldrich). Collected perfusates were stored at −80 °C until analysis. The perfusates underwent Western blotting. β-LG was set as an index of in vivo protein digestibility, as done previously.[12] The perfusates

Table 4. Fructosyllysine in Milk Proteins[a]

protein	residue	amino acid	charge	steam injected[b]	in-can sterilized[b]
β-LG	1−14	Lys8	[2+]	2.1	0.5
	40−60	Lys47	[3+]	4.4	3.8
	41−60	Lys47	[3+]	2.7	2.7
α_{s1}-CN	3−22	Lys3 and 7	[4+]	6.2	29.8
	4−22	Lys7	[3+]	3.3	3.0
	6−22	Lys7	[2+]	3.3	1.6
	80−90	Lys83	[2+]	1.4	2.1
			[3+]	1.7	2.1
	104−119	Lys105	[2+]	1.0[c]	5.4[c]
			[3+]	1.0[c]	0.9[c]
	120−132	Lys124	[3+]	2.4	1.6
			[4+]	1.4	1.0
α_{s2}-CN	79−91	Lys80	[2+]	6.0	2.4
	113−125	Lys113	[2+]	23.5	14.5
	151−160	Lys152	[3+]	1.6	1.2
	198−205	Lys199	[2+]	5.8	1.2
β-CN	28−40	Lys30	[3+]	2.3	7.6
			[4+]	3.0	15.0
	170−183	Lys176	[2+]	20.4	22.6
κ-CN	23−34	Lys24	[2+]	3.1	1.9

[a]Formula samples were treated with trypsin, followed by LC-MS/MS analysis for identifying and semiquantifying tryptic peptides containing fructosyllysine in major milk proteins. [b]Peak areas of the specific peptides are normalized to unheated formula. [c]Peak areas are normalized to steam-injected formula because those of unheated formula were below the detection limit.

(5 μg of protein) were applied to reducing SDS-PAGE, and proteins were transferred to a Trans-Blot Turbo PVDF membrane (Bio-Rad). The membrane was blocked with 2% bovine serum albumin (in PBS containing 0.05% Tween-20 (PBST)) for 45 min at RT. After the membrane was washed three times with PBST, it was probed with rabbit anti-bovine β-LG antibody (Bethyl Laboratories Inc., Montogomery, TX) in a 1:20000 dilution (antibody:blocking buffer) at RT for 45 min. After washing three times with PBST, the membrane was probed with donkey anti-rabbit IgG antibody conjugated with horseradish peroxidase (GE Healthcare, Pewaukee, WI) in a 1:20000 dilution (antibody:blocking buffer) at RT for 45 min. After washing three times with PBST, β-LG was detected by Pierce ECL Western Blotting Substrate (Thermo Scientific), with the chemiluminescence signal imaged by a ChemiDoc XRS+ (Bio-Rad).

Blood samples were taken by cardiac puncture using syringes treated with ethylenediaminetetraacetic acid disodium (Sigma-Aldrich). They were subjected to centrifugation at 1700*g* for 10 min, and upper plasma layers were collected and stored at −80 °C until analysis. Amino acid patterns were analyzed for the plasma samples. The samples were subjected to TCA (5% final concentration) precipitation, and soluble fractions were filtrated through 0.2 μm PVDF filters (Thomson Instrument Company, Oceanside, CA). The filtrates were applied to an amino acid analyzer (L-8900, Hitachi High-Technologies, Tokyo, Japan).

Statistical Analysis. Data on in vitro protein digestibility and coagulates in stomach (weight and pH) and plasma amino acid concentrations obtained from in vivo digestion assays were analyzed by one-way ANOVA and post-tested by Tukey test using JMP software (version 5.1.1, SAS Institute, Cary, NC), and significance was demonstrated at $p < 0.05$.

RESULTS

Electrophoresis of Milk Proteins. Formula samples were applied to SDS-PAGE, and the band patterns were compared

DOI: 10.1021/acs.jafc.5b02189
J. Agric. Food Chem. 2015, 63, 6787−6798

(Figure 2). Proteins smeared in a wide range of molecular weight for all three formulas under reducing/nonreducing conditions. While band patterns of unheated and steam injected formulas were similar, in-can sterilized formula showed a notably different band pattern; bands of intact major milk proteins such as α-LA, β-LG, and CNs decreased and a smear band above 37 kDa increased. All three formulas exhibited strong smear bands around 250 kDa under nonreducing conditions, during which disulfide bonds are kept intact. In contrast, under reducing conditions, a smear band at the high molecular weight fraction was observed only for in-can sterilized formula. These results suggest that milk proteins are associated prior to heat treatment, and that in-can sterilization caused newly formed protein modifications that are considered noncovalent interactions other than disulfide bonds.

Proteomic Analysis. Formula samples were applied to LC-MS/MS analysis following in-gel tryptic digestion for identifying and semiquantifying modifications involved in protein digestibility. It should be noted that some peptides containing the specified modifications were identified but could not be quantified probably due to low quantity.

Formation of lactulosyllysine and fructosylysine was targeted as early Maillard reaction products (Tables 3 and 4) because raw materials include skim milk powder and maltodextrin, which contain reducing sugars such as lactose and glucose. Formation of CML was also targeted as an advanced Maillard reaction product (Table 5). Maillard reaction products could be semiquantified in all the major milk proteins. Steam injected and in-can sterilized formulas had higher signals for lactulosyllysine and fructosyllysine than unheated formula at many modified sites in major milk proteins, but no clear trend was observed between steam injected formula and in-can sterilized formula. Similarly, steam injected and in-can sterilized formulas had higher signals for CML at most of the modified sites in CNs in comparison with unheated formula, but the signals were principally higher in in-can sterilized formula than in steam-injected formula.

As for targeting cross-linked structures, lysinoalanine and lanthionine are not compatible with the analysis of Maillard reaction products, and therefore their precursor, dehydroalanine on Ser and Cys residues, was analyzed instead (Table 6).

Table 5. N^{ε}-Carboxymethyllysine in Milk Proteins[a]

protein	residue	amino acid	charge	steam injected[b]	in-can sterilized[b]
α-LA	1−10	Lys5	[2+]	0.7	0.8
	59−79	Lys62	[3+]	0.9	0.5
β-LG	1−14	Lys8	[2+]	1.8	1.8
	125−138	Lys135	[3+]	0.8	0.5
α_{s1}-CN	4−22	Lys7	[3+]	3.4	5.1
			[4+]	2.3	2.6
	23−36	Lys34	[2+]	25.1	81.6
			[3+]	32.8	72.0
	80−90	Lys83	[2+]	0.7	0.6
			[3+]	1.0	0.8
	120−132	Lys124	[2+]	1.4	2.4
			[3+]	1.8	1.1
α_{s2}-CN	33−45	Lys41	[2+]	2.2	3.1
			[3+]	2.0	2.6
	171−181	Lys173	[2+]	2.1	4.7
	198−205	Lys199	[2+]	1.9	3.5
β-CN	168−176	Lys169	[3+]	0.8	5.1
	170−183	Lys176	[2+]	1.8	2.3
			[3+]	1.4	1.1
κ-CN	22−34	Lys24	[2+]	2.6	4.0
			[3+]	1.8	2.7

[a]Formula samples were treated with trypsin, followed by LC-MS/MS analysis for identifying and semiquantifying tryptic peptides containing N^{ε}-carboxymethyllsine in major milk proteins. [b]Peak areas of the specific peptides are normalized to unheated formula.

Table 6. Dehydroalanine Derivatives on Ser and Cys Residues in Milk Proteins[a]

protein	residue	amino acid	charge	steam injected[b]	in-can sterilized[b]
α-LA	63−79	Ser69	[2+]	1.2	0.6
	63−79	Cys77	[3+]	2.8	5.7
β-LG	145−162	Ser150	[2+]	0.8	0.4
α_{s1}-CN	80−90	Ser88	[2+]	3.4	2.2
			[3+]	4.6	2.8
	106−119	Ser115	[2+]	3.3	2.5
α_{s2}-CN	25−41	Ser31	[2+]	1.7	1.1
	33−45	Cys36	[2+]	0.6	1.2
			[3+]	1.4	2.4
β-CN	168−176	Ser168	[3+]	3.2	4.3
κ-CN	64−86	Ser69	[2+]	0.7	0.4
	69−83	Ser82	[2+]	1.2	0.6

[a]Formula samples were treated with trypsin, followed by LC-MS/MS analysis for identifying and semiquantifying tryptic peptides containing dehydroalanine in major milk proteins. [b]Peak areas of the specific peptides are normalized to unheated formula.

Formation of dehydroalanine has been reported to reflect thermal history to a considerable extent.[32] It was identified at 18 Ser/Cys residues in major milk proteins and could be quantified at 11 of these sites. Steam-injected and in-can sterilized formulas had higher signals than unheated formula at about half of the identified sites. No clear trend was observed between steam injected formula and in-can sterilized formula.

In addition to the above-mentioned modifications, phosphorylation of Ser was semiquantified (Table 7), as it may provide further information in the context of heat treatment of proteins.[33] In-can sterilized formula had the lowest signals at all the modified sites of CNs, while steam injection did not appear to have any significant effects on phosphorylation. Thus, dephosphorylation of CNs was caused only by in-can sterilization.

In Vitro Digestion of Formula Samples. SDS-PAGE analysis of formula samples after in vitro digestion is shown in Figure 3. While proteins were digested to a limited extent by pepsin at pH 4.0, peptic digestion proceeded at pH 2.0 and digestion patterns were quite similar for the three formulas except for smear bands resisting digestion in in-can sterilized formula. Protein digestion was facilitated extensively by pancreatin treatment. However, undigested smear bands remained more pronounced in in-can sterilized formula compared with the other

DOI: 10.1021/acs.jafc.5b02189
J. Agric. Food Chem. 2015, 63, 6787−6798

Table 7. Phosphorylation of Ser in Milk Proteins[a]

protein	residue	amino acid	charge	steam injected[b]	in-can sterilized[b]
α_{s1}-CN	35−58	Ser41, 46, and 48	[3+]	1.2	0.4
	37−58	Ser41, 46, and 48	[2+]	0.9	0.3
			[3+]	0.8	0.3
	43−58	Ser46 and 48	[2+]	1.7	0.7
	103−119	Ser115	[3+]	1.0	0.5
	104−119	Ser115	[2+]	1.4	0.7
			[3+]	1.4	0.7
	106−119	Ser115	[2+]	1.3	1.0
			[3+]	1.5	1.1
α_{s2}-CN	25−41	Ser31	[2+]	1.2	0.3
			[3+]	1.3	0.3
	126−137	Ser129 and 131	[2+]	1.1	0.5
			[3+]	1.5	0.6
	137−150	Ser143	[2+]	1.2	0.2
	138−149	Ser143	[2+]	1.1	0.5
β-CN	30−48	Ser35	[2+]	0.7	0.4
			[3+]	1.2	0.9

[a]Formula samples were treated with trypsin, followed by LC-MS/MS analysis for identifying and semiquantifying tryptic peptides containing phosphoserine in major milk proteins. [b]Peak areas of the specific peptides are normalized to unheated formula.

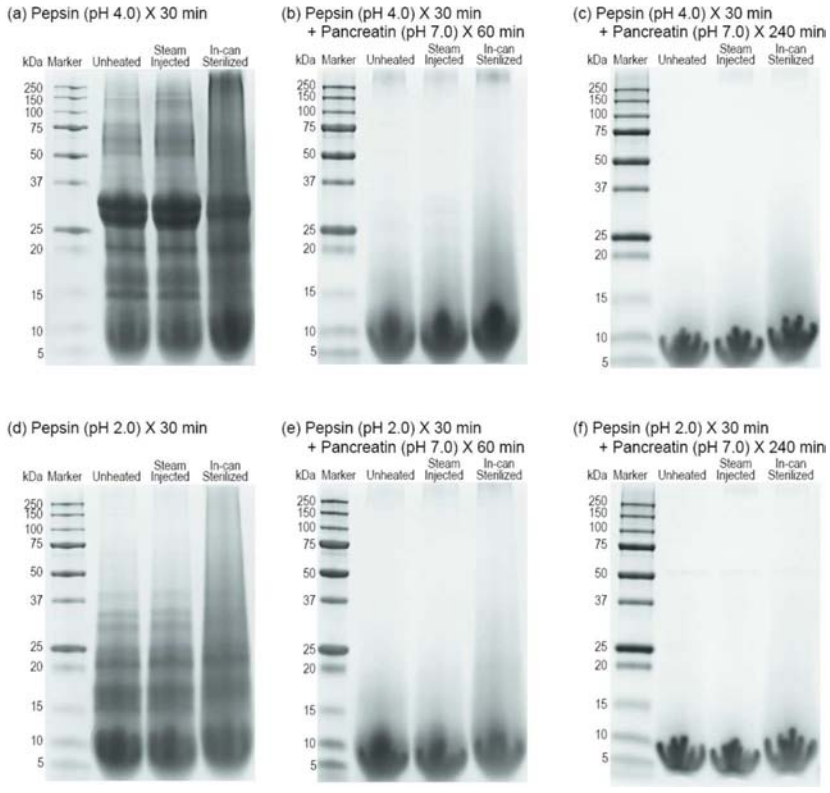

Figure 3. Electrophoresis of proteins in milk-based enteral formulas after in vitro digestion. Formula samples were subjected to in vitro digestion using pepsin and pancreatin. Both infant (a-c) and adult (d-f) digestion conditions were simulated by adopting different pH values during the peptic digestion. Fifty micrograms of protein (before digestion) was loaded on a gel, and the gel was stained with Bio-Safe Coommassie Stain. Pep and Pan denote pepsin and pancreatin, respectively.

two formulas, which could be recognized even after digestion for 240 min. In vitro protein digestibility was determined for some of the digestion conditions using a Dumas method in combination with TCA precipitation (Figure 4). Steam-injected formula showed the highest protein digestibility for all the digestion conditions, although the differences did not reach statistical significance.

In Vivo Digestion of Milk Samples. White coagulates, likely acid-precipitated CNs, were observed in stomachs of the rat pups after intubation with the formula samples. Weights of the coagulates decreased over time (Figure 5a), but we observed no significant difference, at any time point, among the groups fed the three formulas. The pHs were also quite similar

DOI: 10.1021/acs.jafc.5b02189
J. Agric. Food Chem. 2015, 63, 6787−6798

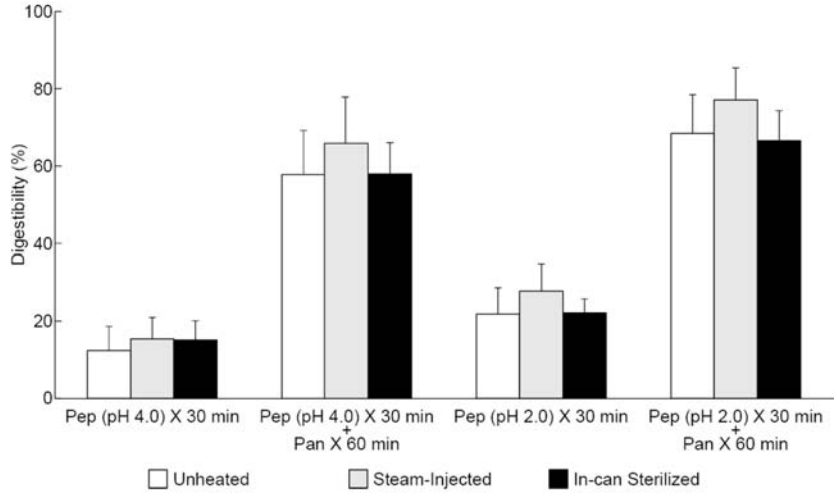

Figure 4. Digestibility of proteins in milk-based enteral formulas after in vitro digestion. Protein digestibility was defined as the increase in NPN after in vitro digestion, which was determined by a combination of TCA precipitation and a Dumas method. Each digestion and the subsequent procedures were conducted six times. No significant difference was observed among the formulas for the same digestion conditions. Pep and Pan denote pepsin and pancreatin, respectively.

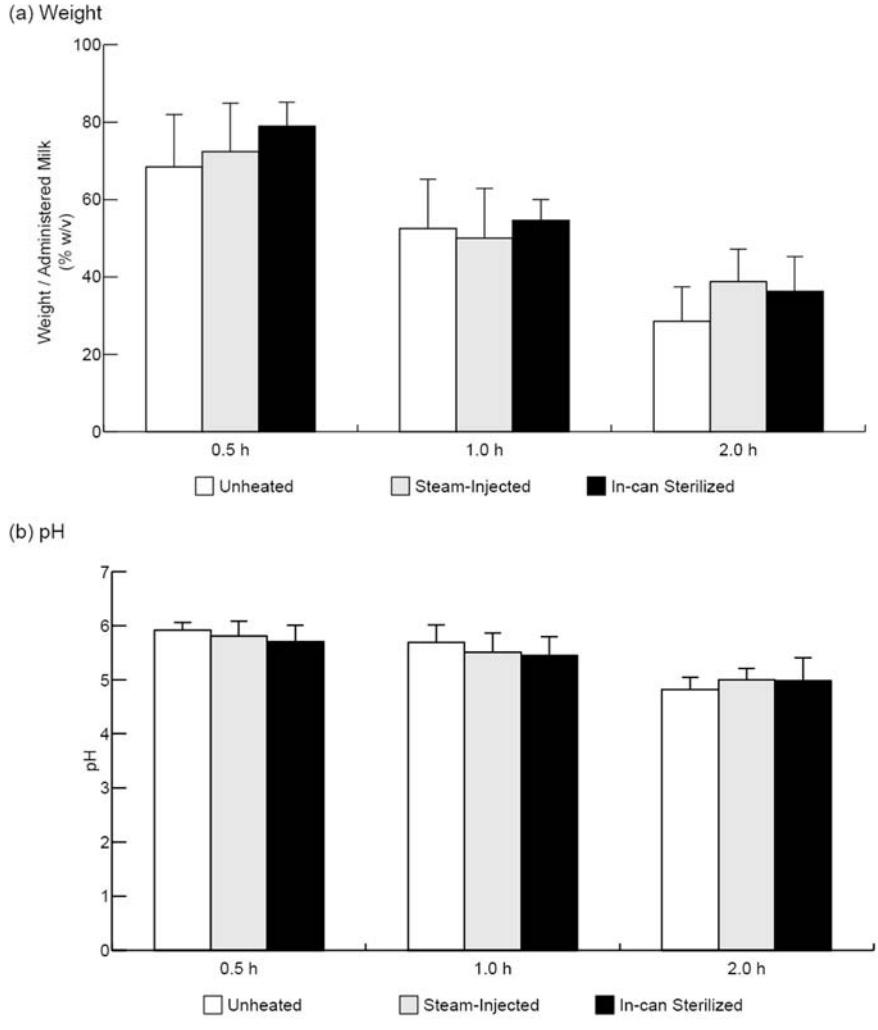

Figure 5. Coagulates in stomach of suckling rat pups. Rat pups fed different formula samples were killed at 0.5, 1, and 2 h after intubation, and coagulates in the stomach were obtained. Weight (a) and pH (b) were measured, and data are expressed as means ± SD (n = 3 males + 3 females). No significant difference was observed among the formula-fed pups at any time point.

DOI: 10.1021/acs.jafc.5b02189
J. Agric. Food Chem. 2015, 63, 6787−6798

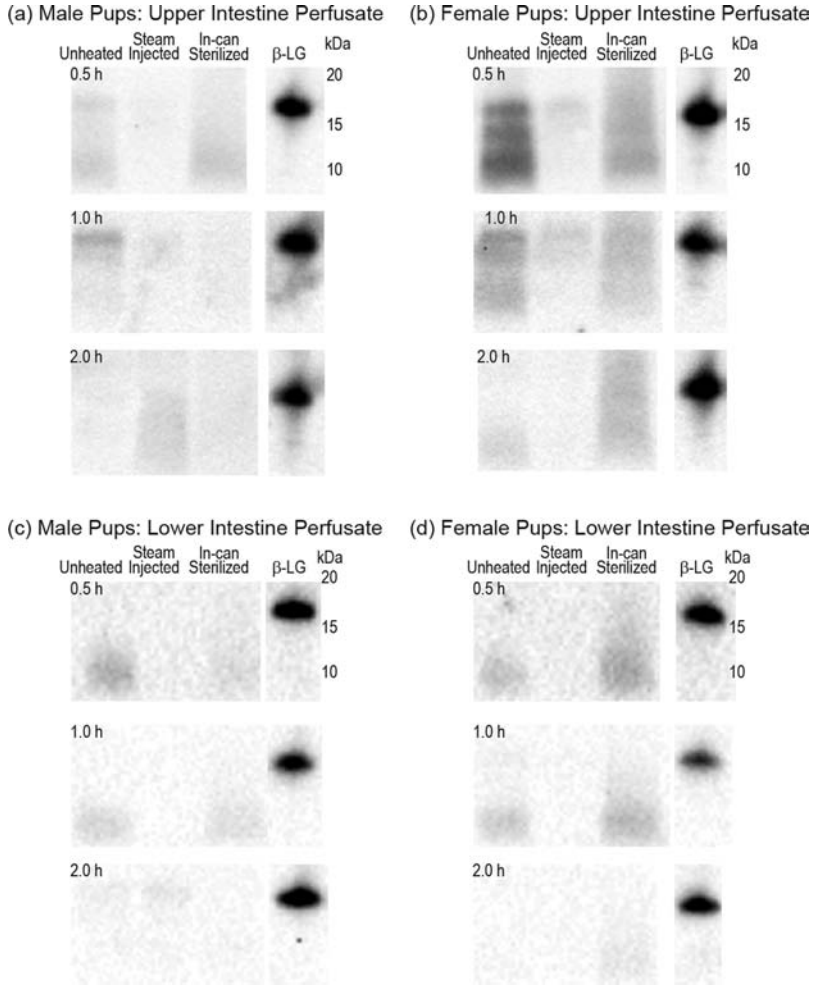

Figure 6. Western blotting of β-LG in upper/lower intestine perfusates from suckling rat pups. Rat pups fed different formula samples were killed at 0.5, 1, and 2 h after intubation, and the upper intestines (a) and lower intestines (b) were perfused with PBS containing protease inhbitor. Five micrograms of protein was loaded and β-LG was detected by Western blotting as an index of in vivo protein digestibility.

among the three formulas and decreased only slightly over time (Figure 5b).

Western blotting of β-LG was conducted for upper intestine perfusates (Figure 6a,b) in order to assess in vivo digestibility as done previously.[12] Each time point was assayed six times, using three male and three female pups per sample, and we observed no trend in terms of sex difference. While β-LG was barely observed in intact form in the perfusates obtained, fragmented forms and/or smear bands, supposedly degradation products from β-LG, were detected at fractions with molecular weights lower than that of β-LG. The smear bands generally became weaker over time. At 0.5 and 1.0 h, smear bands were weaker for the steam-injected formula-fed pups in 5 out of the 6 pups assayed. In contrast, at 2.0 h, results were inconsistent and the trend observed at 0.5 and 1.0 h was not confirmed. Western blotting of β-LG was also conducted for lower intestine perfusates. Like upper intestine perfusates, bands were observed principally in smear forms (Figure 6c,d). Bands were less intense than those in upper intestine perfusates, and they also became weaker over time. The bands for steam-injected formula were the weakest in all the six assays at 0.5 and 1.0 h, while the bands were hardly recognized and the trend was not observed at 2.0 h. Further, western blotting of CNs was conducted using a commercial anti-CN antibody that recognizes α_s- and β-CNs because they dominate proteins in the formulas. However, the antibody appeared to react with endogenous proteins in rats as well as partially digested CNs (data not shown), which hindered interpretation of the results and no conclusion could be drawn from the assays.

To further explore protein quality, as part of evaluating amino acid bioavailability, plasma amino acid patterns were analyzed. In pups fed unheated formula, total and essential plasma amino acids increased at 0.5 h, decreased at 1.0 h, and stayed at the similar level at 2.0 h (Figure 7). This trend held true for most of the respective amino acids (Table 8). In pups fed steam-injected and in-can sterilized formulas, the increases in total and essential plasma amino acid levels were less responsive and the concentrations were also lower for most of the respective amino acids than those in unheated formula-fed pups at 0.5 h; the differences were significant for leucine in steam-injected formula-fed pups and isoleucine in in-can sterilized formula-fed pups. When it comes to Lys, the amino acid of major interest in the context of proteomic analysis, the unheated formula-fed pups exhibited the highest plasma level, followed by steam-injected and in-can sterilized formula-fed pups. However, the differences did not reach statistical significance.

DISCUSSION

Aiming to elucidate the relationship between protein modifications and protein digestibility of milk-based infant/enteral

DOI: 10.1021/acs.jafc.5b02189
J. Agric. Food Chem. 2015, 63, 6787−6798

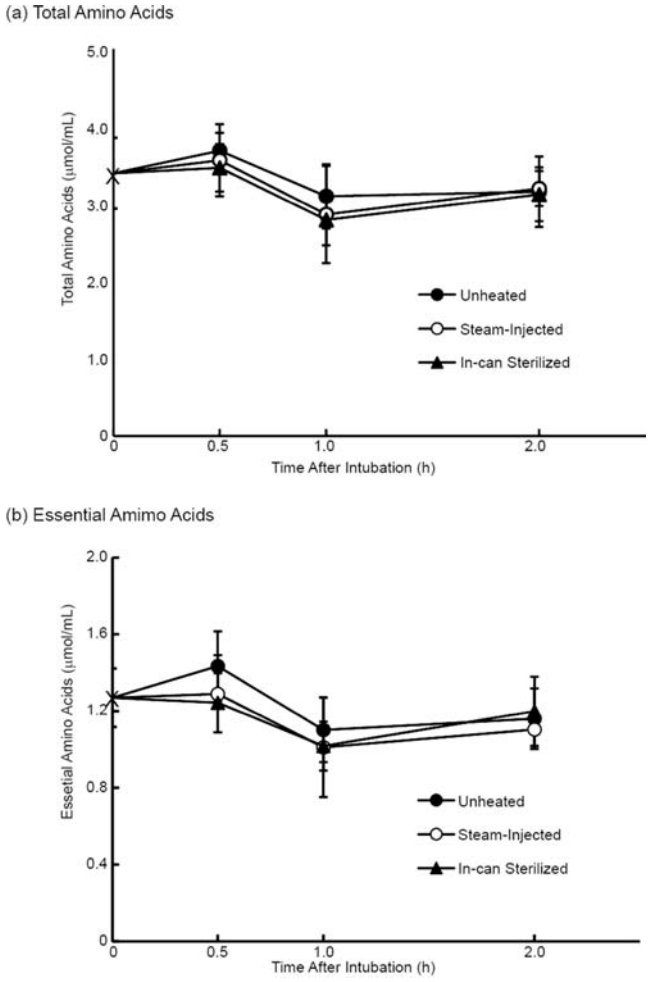

Figure 7. Plasma total and essential amino acid concentration in suckling rat pups. Rat pups fed different formula samples were killed at 0.5, 1, and 2 h after intubation, and blood was collected by cardiac puncture. Plasma was separated by centrifugation and applied to amino acid analysis. Total and essential amino acid levels are expressed as means ± SD (n = 3 males + 3 females) except for baseline, where it is shown as means ± SD (n = 3 male + 2 female pups). No significant difference was observed among the formula-fed pups at any time point.

formulas, enteral formulas with two types of industrial heating processes were industrially prepared, and these formulas as well as unheated formula were investigated as we did previously for cow's milk.[12]

Electrophoresis of the three formulas showed that in-can sterilization greatly influenced protein associations, while steam injection did not exert any significant effects. This observation was partly in disagreement with our previous study,[12] where both in-can sterilization and steam injection of raw milk affected protein band patterns (although the former had greater effects). This discrepancy may partly be attributed to protein damage potentially present in raw materials for enteral formulas; proteins are generally heat-treated and sometimes subjected to long terms of storage as raw materials. In the case of CN ingredients, industrial isolation involves isoelectric precipitation followed by neutralization at alkaline pH. These processes/conditions facilitate protein modifications such as formation of Amadori products and cross-linked products.[34,35] Proteomic analysis is also likely to unravel protein damage in raw materials; dehydroalanine formation could be identified and quantifiable at 8 Ser and 2 Cys residues in proteins of unheated enteral formula, while it was quantifiable only at 3 Ser residues in raw milk proteins of our previous study,[12] although some caution is needed for making a direct comparison between the two independent studies. Thus, proteins were associated with each other to a considerable extent in ingredients of enteral formulas, which may obscure the existence of newly formed aggregates caused by subsequent industrial heating (especially by steam injection) as shown in our electrophoretic analysis. Proteomic analysis further elucidated effects of heat treatment on proteins. Both steam injection and in-can sterilization progressed the Maillard reaction in major milk proteins, and the highest signals for CML were observed at many Lys residues of CNs in in-can sterilized formula. These results indicate that in-can sterilization facilitates the reaction to a greater extent, resulting from its more severe thermal history including slow rates of temperature rise/fall and longer hold time at high temperature. The severity of the in-can sterilization process is also likely to be manifested as a progression of dephosphorylation of CNs in the formula, while this was not found in steam-injected formula. This notion may also be supported by a study of Birlouez-Argon et al.; they reported higher CML amounts in sterilized infant formula than in UHT formula.[17] In contrast to CML and dephosphorylation, formation of lactulosyllysine, fructosyllysine, and dehydroalanine generally proceeded after both steam injection and in-can sterilization, and we observed only minor and inconsistent difference between the two heat treatments. Both lactulosyl/fructosyllysine and dehydroalanine are intermediates of CML and cross-linked products, respectively.[3,6,36] Rufián-Henares et al. formulated an infant/enteral formula-resembling mixture, dissolving whey protein isolate and lactose/maltodextrin in phosphate buffer, and they reported a time-induced increase and subsequent decrease in furosine contents after heating the mixture at 140 °C. They concluded that formation of Amadori products would first be facilitated, which is followed by degradation into advanced Maillard reaction products.[37] van Boekel reported that dehydroalanine formation paralleled heating time in β-CN solutions at 110 and 120 °C, but the amounts got saturated over time when heated at 130 and 140 °C,[32] suggesting its conversion into cross-linked products. Thus, formation of these intermediate structures may not always parallel intensity of the heat treatment.

Electrophoretic analyses of in vitro digestion assays demonstrated that in-can sterilized formula had smeared bands that persistently resisted pepsin/pancreatin digestion. Protein digestibility determined by a Dumas method in combination with TCA precipitation showed that steam-injected formula exhibited higher digestibility than unheated formula, while milk proteins in in-can sterilized formula were digested to an extent similar to those in unheated formula. Similarly, although it was only assessed by immuno-reactive materials for β-LG in in vivo digestion assays, β-LG in steam-injected formula showed more extensive digestion than in unheated formula, while β-LG in in-can sterilized formula was digested to an extent similar to that in unheated formula. Thus, as reported previously,[13] UHT treatment appears superior to in-can sterilization in terms of protein digestibility; steam injection principally improved protein digestibility, possibly by denaturation, but the heat-induced improvement in protein digestibility may be overwhelmed by adverse effects caused by formation of proteolytic-resistant aggregates to a greater extent in in-can sterilized formula. In contrast, it seems that both steam injection treatment and in-can sterilization equally had negative impact on amino acid bioavailability, as manifested by lower levels in plasma amino acids

DOI: 10.1021/acs.jafc.5b02189
J. Agric. Food Chem. 2015, 63, 6787−6798

Table 8. Mean Concentration of Plasma Amino Acids of Suckling Rat Pups[a]

		0.5 h (μmol/mL[c])			1.0 h (μmol/mL[c])			2.0 h (μmol/mL[c])		
	baseline (μmol/mL[b])	unheated	steam injected	in-can sterilized	unheated	steam injected	in-can sterilized	unheated	steam injected	in-can sterilized
Essential										
Val	0.143	0.168	0.146	0.139	0.119	0.115	0.109	0.130	0.119	0.131
Leu	0.118	0.126	0.097[d]	0.104	0.069	0.074	0.063	0.085	0.081	0.090
Ile	0.079	0.088	0.074	0.069[e]	0.052	0.055	0.051	0.064	0.059	0.067
Lys	0.422	0.479	0.425	0.393	0.350	0.326	0.334	0.364	0.330	0.407
Met	0.049	0.054	0.054	0.057	0.048	0.043	0.045	0.054	0.052	0.054
Phe	0.073	0.085	0.072	0.081	0.073	0.061	0.062	0.087	0.079	0.089
Trp	0.059	0.075	0.067	0.082	0.071	0.055	0.062	0.078	0.069	0.065
His	0.113	0.126	0.117	0.114	0.112	0.100	0.102	0.107	0.124	0.106
Thr	0.214	0.234	0.239	0.204	0.206	0.182	0.189	0.191	0.191	0.190
Nonessential										
Tyr	0.229	0.254	0.233	0.228	0.233	0.180	0.188	0.210	0.216	0.196
Asp	0.017	0.014	0.012	0.013	0.012	0.017	0.012	0.016	0.014	0.016
Asn	0.057	0.059	0.057	0.057	0.044	0.044	0.042	0.051	0.048	0.049
Ser	0.270	0.256	0.286	0.251	0.240	0.226	0.214	0.241	0.247	0.224
Glu	0.117	0.110	0.118	0.118	0.115	0.129	0.107	0.105	0.126	0.115
Gln	0.538	0.600	0.545	0.592	0.467	0.437	0.429	0.499	0.467	0.479
Pro	0.087	0.105	0.121	0.100	0.084	0.079	0.073	0.078	0.072	0.071
Gly	0.384	0.334	0.385	0.344	0.372	0.319	0.326	0.387	0.498	0.366
Ala	0.256	0.324	0.342	0.356	0.288	0.273	0.244	0.272	0.275	0.260
Arg	0.167	0.193	0.169	0.159	0.136	0.143	0.134	0.132	0.128	0.143

[a]Three-letter codes are used for all the amino acids. Note that cysteine (measured as cystine) were below the detection limit in all the plasma samples. [b]Each amino acid concentration is expressed as mean value (n = 3 male + 2 female pups). [c]Each amino acid concentration is expressed as mean value (n = 3 male + 3 female pups). [d]$P < 0.05$ (vs unheated formula-fed pups at 0.5 h). [e]$P < 0.05$ (vs unheated formula-fed pups at 0.5 h).

of rat pups fed these heated formulas at a specific time point compared with those of unheated formula-fed pups. Further, this trend was the case for most of the amino acids (but not for specific amino acids), and an involvement of decreased protein digestibility, rather than damage/modifications of specific amino acids, is therefore suggested. One possible explanation may be that digesta from steam-injected formula, as well as those from in-can sterilized formula, may contain large amounts of small proteolytic-resistant peptides that cannot be detected by SDS-PAGE/Western blotting nor be precipitated by TCA (12% final concentration), which would significantly compromise amino acid absorption. However, amino acid bioavailability discussed here was evaluated only by amino acid levels at a single time point, warranting further investigation with expanded experimental conditions. In a proteomic context, the extent of CML formation and dephosphorylation of Ser residues implicates the greatest protein damage in in-can sterilized formula, followed by in steam-injected formula. Progressed formation of proteolytic-resistant structures can therefore be suggested, as previously discussed by Cattaneo et al.,[34] but it should be remembered that protein modifications such as lysinoalanine and lanthionine per se could not be measured due to technical limitations.

When it comes to comparisons between our two studies,[12] protein digestibility of milk-based enteral formulas may be inferior to that of cow's milk, although there are some differences in milk protein composition and experimental procedures. Values for in vitro protein digestibility determined for unheated, steam-injected, and in-can sterilized formulas were principally lower than those for raw, steam-injected, and in-can sterilized cow's milk. In our in vivo study, rats fed enteral formulas exhibited a slower decrease in weights of coagulates in stomach and insignificant changes in their pH over time in comparison with cow's milk-fed rats, indirectly suggesting slower gastric emptying rates for enteral formulas caused by their poorer protein digestibility. Even though experimental settings for the Western blots were somewhat different, immuno-reactive materials from β-LG could be detected in lower small intestine of formula-fed rats, but not in cow's milk-fed rats, further supporting the inferiority in protein digestibility of enteral formulas. Differences in protein digestibility between cow's milk and enteral formulas are further supported by some studies,[13,16] and these may be explained by protein damage in raw materials as discussed above[34,35] and the fact that proteins are further damaged by subsequent heating in production of formula products.

In conclusion, heat treatment of milk protein-based enteral formulas facilitates protein modifications and apparently attenuates protein digestibility and amino acid bioavailability. These adverse effects are more likely to be prominent in enteral formulas in comparison with our previous study on cow's milk. In-can sterilization may have greater impact on protein modifications and digestibility than steam injection treatment, but the differences might be of limited significance in terms of amino acid bioavailability. It should be noted that the conditions for heat treatments used here may not be representative of UHT treatment and in-can sterilization in general, and the observations reported here may not always be applicable to other similar products. Still, raw materials and types of heat treatment should be carefully selected in terms of protein quality, for achieving better nutritional potential of milk-based enteral formulas.

AUTHOR INFORMATION

Corresponding Author

*Phone: +1-530-752-8347. Fax: +1-530-752-3564. E-mail: bllonnerdal@ucdavis.edu.

DOI: 10.1021/acs.jafc.5b02189
J. Agric. Food Chem. 2015, 63, 6787−6798

Notes

The authors declare no competing financial interest.

■ ACKNOWLEDGMENTS

We are grateful to Keisuke Miyazaki, Junichi Hashimoto, Hiroyoshi Yabuki, and Yuki Hayakawa, Morinaga Milk Industry, for preparing for the milk samples. We also want to thank Dr. Brett Phinney and Darren Weber, the University of California, Davis, for performing the proteomic analysis.

■ ABBREVIATIONS USED

UHT, ultra-high-temperature; Lys, lysine; CML, N^{ε}-carboxymethyllysine; Cys, cysteine; CN, casein; N, nitrogen; SDS-PAGE, sodium dodecyl sulfate−polyacrylamide gel electrophoresis; Ser, serine; α-LA, α-lactalbumin; β-LG, β-lactoglobulin; AmBic, ammonium bicarborate; ACN, acetonitrile; RT, room temperature; LC-MS/MS, liquid chromatography coupled with tandem mass spectrometry; NPN, nonprotein N; TCA, trichloroacetic acid; PBS, phosphate buffered saline; PBST, PBS containing 0.05% Tween-20

■ REFERENCES

(1) Sarwar Gilani, G.; Chao, W. X.; Cockell, K. A. Impact of antinutritional factors in food proteins on the digestibility of protein and the bioavailability of amino acids and on protein quality. *Br. J. Nutr.* **2012**, *108* (Suppl 2), S315−S332.

(2) Kim, S. B.; Ki, K. S.; Khan, M. A.; Lee, W. S.; Lee, H. J.; Ahn, B. S.; Kim, H. S. Peptic and tryptic hydrolysis of native and heated whey protein to reduce its antigenicity. *J. Dairy Sci.* **2007**, *90*, 4043−50.

(3) van Boekel, M. A. J. S. Effect of heating on Maillard reactions in milk. *Food Chem.* **1998**, *62*, 403−414.

(4) Rérat, A.; Calmes, R.; Vaissade, P.; Finot, P. A. Nutritional and metabolic consequences of the early Maillard reaction of heat treated milk in the pig. Significance for man. *Eur. J. Nutr.* **2002**, *41*, 1−11.

(5) Hellwig, M.; Matthes, R.; Peto, A.; Löbner, J.; Henle, T. *N*-ε-fructosyllysine and *N*-ε-carboxymethyllysine, but not lysinoalanine, are available for absorption after simulated gastrointestinal digestion. *Amino Acids* **2014**, *46*, 289−99.

(6) Friedman, M. Chemistry, biochemistry, nutrition, and microbiology of lysinoalanine, lanthionine, and histidinoalanine in food and other proteins. *J. Agric. Food Chem.* **1999**, *47*, 1295−1319.

(7) Patel, H. A.; Singh, H.; Anema, S. G.; Creamer, L. K. Effects of heat and high hydrostatic pressure treatments on disulfide bonding interchanges among the proteins in skim milk. *J. Agric. Food Chem.* **2006**, *54*, 3409−20.

(8) Peram, M. R.; Loveday, S. M.; Ye, A.; Singh, H. In vitro gastric digestion of heat-induced aggregates of beta-lactoglobulin. *J. Dairy Sci.* **2013**, *96*, 63−74.

(9) Fenaille, F.; Morgan, F.; Parisod, V.; Tabet, J. C.; Guy, P. A. Solid-state glycation of β-lactoglobulin monitored by electrospray ionisation mass spectrometry and gel electrophoresis techniques. *Rapid Commun. Mass Spectrom.* **2003**, *17*, 1483−1492.

(10) Meltretter, J.; Becker, C. M.; Pischetsrieder, M. Identification and site-specific relative quantification of β-lactoglobulin modifications in heated milk and dairy products. *J. Agric. Food Chem.* **2008**, *56*, 5165−5171.

(11) Meltretter, J.; Seeber, S.; Humeny, A.; Becker, C. M.; Pischetsrieder, M. Site-specific formation of Maillard, oxidation, and condensation products from whey proteins during reaction with lactose. *J. Agric. Food Chem.* **2007**, *55*, 6096−6103.

(12) Wada, Y.; Lönnerdal, B. Effects of different industrial heating processes of milk on site-specific protein modifications and their relationship to in vitro and in vivo digestibility. *J. Agric. Food Chem.* **2014**, *62*, 4175−85.

(13) Rudloff, S.; Lönnerdal, B. Solubility and digestibility of milk proteins in infant formulas exposed to different heat treatments. *J. Pediatr. Gastroenterol. Nutr.* **1992**, *15*, 25−33.

(14) Sarwar, G.; Peace, R. W.; Botting, H. G. Differences in protein digestibility and quality of liquid concentrate and powder forms of milk-based infant formulas fed to rats. *Am. J. Clin. Nutr.* **1989**, *49*, 806−813.

(15) Sarwar, G.; Peace, R. W. The protein quality of some enteral products is inferior to that of casein as assessed by rat growth methods and digestibility-corrected amino acid scores. *J. Nutr.* **1994**, *124*, 2223−2232.

(16) Rutherfurd, S. M.; Moughan, P. J. Digestible reactive lysine in selected milk-based products. *J. Dairy Sci.* **2005**, *88*, 40−48.

(17) Birlouez-Aragon, I.; Pischetsrieder, M.; Leclère, J.; Morales, F. J.; Hasenkopf, K.; Kientsch-Engel, R.; Ducauze, C. J.; Rutledge, D. Assessment of protein glycation markers in infant formulas. *Food Chem.* **2004**, *87*, 253−259.

(18) Bradford, M. M. A rapid and sensitive method for the quantitation of microgram quantities of protein utilizing the principle of protein-dye binding. *Anal. Biochem.* **1976**, *72*, 248−254.

(19) Alvarado, R.; Tran, D.; Ching, B.; Phinney, B. S. A comparative study of in-gel digestions using microwave and pressure-accelerated technologies. *J. Biomol. Tech.* **2010**, *21*, 148−155.

(20) Keller, A.; Nesvizhskii, A. I.; Kolker, E.; Aebersold, R. Empirical statistical model to estimate the accuracy of peptide identifications made by MS/MS and database search. *Anal. Chem.* **2002**, *74*, 5383−5392.

(21) Nesvizhskii, A. I.; Keller, A.; Kolker, E.; Aebersold, R. A statistical model for identifying proteins by tandem mass spectrometry. *Anal. Chem.* **2003**, *75*, 4646−4658.

(22) Elias, J. E.; Gygi, S. P. Target-decoy search strategy for mass spectrometry-based proteomics. *Methods Mol. Biol.* **2010**, *604*, 55−71.

(23) Bourlieu, C.; Ménard, O.; Bouzerzour, K.; Mandalari, G.; Macierzanka, A.; Mackie, A. R.; Dupont, D. Specificity of infant digestive conditions: some clues for developing relevant in vitro models. *Crit. Rev. Food Sci. Nutr.* **2014**, *54*, 1427−57.

(24) Armand, M.; Hamosh, M.; Mehta, N. R.; Angelus, P. A.; Philpott, J. R.; Henderson, T. R.; Dwyer, N. K.; Lairon, D.; Hamosh, P. Effect of human milk or formula on gastric function and fat digestion in the premature infant. *Pediatr. Res.* **1996**, *40*, 429−37.

(25) Simonian, H. P.; Vo, L.; Doma, S.; Fisher, R. S.; Parkman, H. P. Regional postprandial differences in pH within the stomach and gastroesophageal junction. *Dig. Dis. Sci.* **2005**, *50*, 2276−85.

(26) Kalantzi, L.; Goumas, K.; Kalioras, V.; Abrahamsson, B.; Dressman, J. B.; Reppas, C. Characterization of the human upper gastrointestinal contents under conditions simulating bioavailability/bioequivalence studies. *Pharm. Res.* **2006**, *23*, 165−76.

(27) Fredrikzon, B.; Hernell, O. Role of feeding on lipase activity in gastric contents. *Acta Paediatr.* **1977**, *66*, 479−84.

(28) Fink, C. S.; Hamosh, P.; Hamosh, M. Fat digestion in the stomach: stability of lingual lipase in the gastric environment. *Pediatr. Res.* **1984**, *18*, 248−54.

(29) Hambraeus, L.; Forsum, E.; Abrahamsson, L.; Lönnerdal, B. Automatic total nitrogen analysis in nutritional evaluations using a block digestor. *Anal. Biochem.* **1976**, *72*, 78−85.

(30) Yvon, M.; Chabanet, C.; Pélissier, J. P. Solubility of peptides in trichloroacetic acid (TCA) solutions. Hypothesis on the precipitation mechanism. *Int. J. Pept. Protein Res.* **1989**, *34*, 166−76.

(31) Lönnerdal, B.; Mendoza, C.; Brown, K. H.; Rutger, J. N.; Raboy, V. Zinc absorption from low phytic acid genotypes of maize (*Zea mays* L.), Barley (*Hordeum vulgare* L.), and Rice (*Oryza sativa* L.) assessed in a suckling rat pup model. *J. Agric. Food Chem.* **2011**, *59*, 4755−4762.

(32) van Boekel, M. A. J. S. Heat-induced deamidation, dephosphorylation and breakdown of caseinate. *Int. Dairy J.* **1999**, *9*, 237−241.

(33) Singh, H. Heat stability of milk. *Int. J. Dairy Technol.* **2004**, *57*, 111−119.

DOI: 10.1021/acs.jafc.5b02189
J. Agric. Food Chem. 2015, 63, 6787−6798

(34) Cattaneo, S.; Masotti, F.; Pellegrino, L. Liquid infant formulas: technological tools for limiting heat damage. *J. Agric. Food Chem.* **2009**, *57*, 10689−94.
(35) Friedman, M.; Zahnley, J. C.; Masters, P. M. Relationship between in vitro digestibility of casein and its content of lysinoalanine and D-amino acids. *J. Food Sci.* **1981**, *46*, 127−134.
(36) Swaisgood, H. E.; Catignani, G. L. Digestibility of modified milk proteins: nutritional implications. *J. Dairy Sci.* **1985**, *68*, 2782−2790.
(37) Rufián-Henares, J. A.; García-Villanova, B.; Guerra-Hernández, E. Generation of furosine and color in infant/enteral formula-resembling systems. *J. Agric. Food Chem.* **2004**, *52*, 5354−8.

DOI: 10.1021/acs.jafc.5b02189
J. Agric. Food Chem. 2015, 63, 6787−6798

d'Aquitaine (BA) breed, characterized by good muscle development, producing tender meat[20] but with a relatively pale color.

MATERIALS AND METHODS

Animals and Sampling. This study was part of the European ProSafeBeef project (FOOD-CT-2006-36241). Twenty-one Blond d'Aquitaine (BA) young bulls reared under intensive conditions and finished over two consecutive years (two replicated groups) were used. At 12 months of age, they were subjected to a 105 day finishing period until slaughter. Diets consisted of concentrate (75%) and straw (25%). Before slaughter, all animals were food deprived for 24 h and had free access to water. The animals at a live weight of 635 ± 52 kg were slaughtered at the experimental abattoir of the INRA Research center in compliance with the current ethical guidelines for animal welfare. Bulls were directly transported (4.5 ± 0.1 min) in a lorry (3 × 2 m livestock compartment) from the experimental farm to the experimental abattoir situated 2 km from the rearing building, with two bulls of the same home pen per transport to avoid social isolation stress. After unloading, they were slaughtered within 3 min.[21] The mean hot carcass weight was 410 ± 42 kg (range from 337 to 500 kg). The carcasses were not electrically stimulated, and they were chilled and stored at 4 °C from 1 h until 24 h post-mortem. *Longissimus thoracis* (LT, mixed fast oxido-glycolytic) muscle samples were excised from the left side of the sixth rib 30 min post-mortem and frozen in liquid nitrogen before storage at −80 °C until protein extractions for Dot-Blot analysis or myosin heavy chain (MyHC) quantification.

pH Measurements. For $pH_{45\ min}$ measurement, biopsies were made from the carcasses (10th rib), whereas $pH_{3\ h}$ and ultimate pH (30 h; pH_u) were measured directly on the carcass (right side). pH was determined as in Bourguet et al.[21] Briefly, 2 g of each LT sample excised 45 min after slaughter was immediately homogenized in 18 mL of 5 mM sodium iodoacetate and stored at 4 °C. The pH of the homogenate was measured the following day at 6 °C. For $pH_{3\ h}$ and pH_u, the pH was recorded directly on the carcass between the sixth and seventh rib using a pH meter (Hanna Instruments, HI9025) equipped with a glass electrode suitable for meat penetration. For each time point, five measurements were made (positioned on a horizontal line with about 1.5 cm between two measurements).

Meat Color. The LT muscle was excised from the stored carcass at the level of the sixth rib *thoracis* vertebra 24 h post-mortem to determine color attributes. Instrumental meat color measurements were recorded for lightness (L^* = measures light reflected), redness (a^* = measures positive red and negative green), and yellowness (b^* = measures positive yellow and negative blue) directly on the tissue of the muscle using a Minolta CR-300 chromameter (Minolta Co., Ltd., Osaka, Japan), with a 0° viewing angle, C illuminant, and 8 mm measurement aperture. Fresh-cut slices of muscle of not less than 2.5 cm thick and overwrapped were left on a polystyrene tray to refrigerate at 1 °C for 1 h to allow blooming. Calibration was performed by using standard white tiles (Y = 93.58, x = 0.3150, and y = 0.3217) prior to color determination. Three replicate measurements were taken, and an average value was used for analysis. Color coordinates were expressed as L^*, a^*, b^* following the CIE-$L^*a^*b^*$ system.

Protein Extractions. Total protein extractions were performed to use subsequently the soluble fractions for Dot-Blot analysis according to the method of Bouley et al.[22] Briefly, 80 mg of muscle was homogenized in a denaturation/extraction buffer containing 8.3 M urea, 2 M thiourea, 1% DTT, and 2% CHAPS. After 30 min of centrifugation at 10000*g* at 8 °C, the supernatant was stored at −20 °C until use. The protein concentrations of the extracts were determined according to the Bradford method[23] using the Bio-Rad protein assay. Bovine serum albumin (BSA) at a concentration of 1 mg/mL was used as standard.

Dot-Blot Analysis. The abundances of 18 proteins (including intact molecules and their fragments) corresponding to five different biological functions (Table 1), muscle fiber structure (actin, MyBP-H, CapZ-β, and MyLC-1F), metabolism (ENO3, LDHB, and MDH1), proteolysis (μ-calpain), oxidative resistance (DJ-1, Prdx6, and SOD1), and heat shock proteins (αB-crystallin, Hsp20, Hsp27, Hsp40, Hsp70-1A/B, Hsp70-8, and Hsp70-Grp75), were determined using the Dot-Blot technique.[14,15] Compared to Western blot, Dot-Blot is a fast technique, but with a similar coefficient of variation inter- and intra-assay (10%). Optimal dilution ratios of the antibodies were determined, using the conditions indicated by the supplier and adapted to bovine muscle samples (Table 1). For that, Western blots were used to check the specificity of all antibodies. An antibody was considered specific against the studied protein when only one band at the expected molecular weight was detected by Western blot. Western blots with all primary antibodies show that all of the antibodies used bound specifically to the bovine protein with the expected theoretical molecular weight.

Conditions retained and suppliers for all primary antibodies dilutions are summarized in Table 1. Protein extracts (15 μg) of each of the 21 muscle samples were spotted (four replications per muscle sample) on a nitrocellulose membrane with the Minifold I Dot-Blot apparatus from Schleicher & Schuell Biosciences (Germany) in a random order on the 96-spots membrane. In addition, a mixed standard sample (15 μg) was deposited for data normalization as reported by Guillemin et al.[15] The Dot-Blot membrane was air-dried for 5 min, blocked in 10% milk blocking buffer at 37 °C for 20 min, and then hybridized and incubated with the specific primary antibody of each protein (Table 1). Infrared

Table 1. Eighteen Protein Biomarkers Quantified Using the Dot-Blot Technique[a]

protein biomarker name (*gene*)[b]	UniProtKB ID	monoclonal (Mo) or polyclonal (Po) antibody ref	antibody dilution
heat shock proteins			
αB-crystallin (*CRYAB*)	P02511	Mo anti-bovine Assay Designs SPA-222	1/500
Hsp20 (*HSPB6*)	O14558	Mo anti-human Santa Cruz HSP20-11:SC51955	1/200
Hsp27 (*HSPB1*)	P04792	Mo anti-human Santa Cruz HSP27 (F-4):SC13132	1/3000
Hsp40 (*DNAJA1*)	P31689	Mo anti-human Santa Cruz HSP40-4 (SPM251): SC-56400	1/250
Hsp70-1A/B (*HSPA1B*)	P08107	Mo anti-human Abnova HSPA1B (M02), clone 3B7	1/2000
Hsp70-8 (*HSPA8*)	P11142	Mo anti-bovine Santa Cruz HSC70 (BRM22):SC-59572	1/250
Hsp70-Grp75 (*HSPA9*)	P38646	Mo anti-human RD Systems clone 419612	1/250
metabolism			
enolase 3 (*ENO3*)	P13929	Mo anti-human Abnova Eno3 (M01), clone 5D1	1/45000
LDH-B (*LDHB*)	P07195	Mo anti-human Novus LDHB NB110−57160	1/50000
MDH1 (*MDH1*)	P40925	Mo anti-pig Rockland 100-601-145	1/1000
structure			
CapZ-β (*CAPZB*)	P47756	Mo anti-human Abnova CAPZB (M03), clone 4H8	1/250
α-actin (*ACTA1*)	P68133	Mo anti-rabbit Santa Cruz α-actin (5C5):SC-58670	1/1000
MyLC-1F (*MYL1*)	P05976	Po anti-human Abnova MYL1 (A01)	1/1000
MyBP-H (*MYBPH*)	Q13203	Mo anti-human Abnova MYBPH (M01), clone 1F11	1/4000
oxidative resistance			
DJ-1 (*PARK7*)	Q99497	Po anti-human Santa Cruz DJ-1 (FL-189):SC-32874	1/250
Prdx6 (*PRDX6*)	P30041	Mo anti-human Abnova PRDX6 (M01), clone 3A10-2A11	1/500
SOD1 (*SOD1*)	P00441	Po anti-rat Acris SOD1 APO3021PU-N	1/1000
proteolysis			
μ-calpain (*CAPN1*)	P07384	Mo anti-bovine Alexis μ-calpain 9A4H8D3	1/1000

[a]The suppliers and conditions for each primary antibody used in this study are given. [b]For protein marker abbreviations see Table 2.

DOI: 10.1021/acs.jafc.5b02615
J. Agric. Food Chem. 2015, 63, 6799−6809

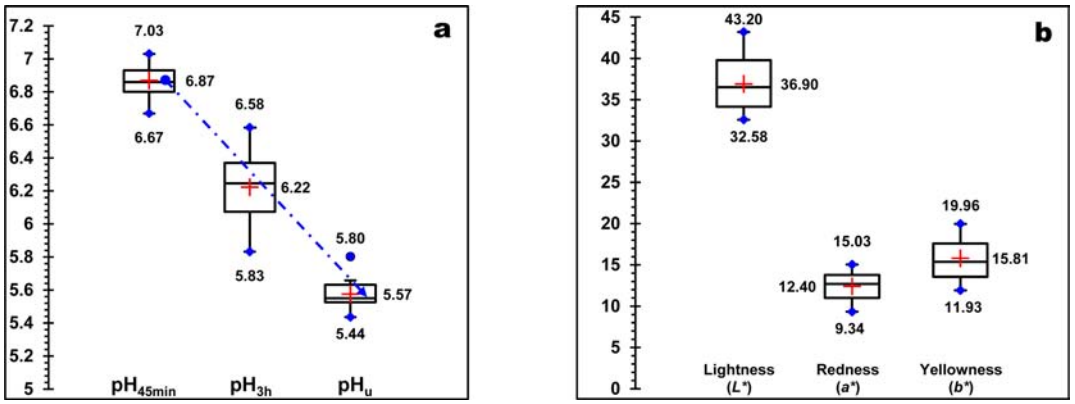

Figure 1. Average means of (a) pH (45 min, 3 h, and ultimate (u)) and (b) $L^*a^*b^*$ meat color parameters of *Longissimus thoracis* muscle of Blond d'Aquitaine young bulls (n = 21). The parameters are presented as box−whiskers plots: for each variable independently, the central point represents the average value calculated over all of the observations. The box represents the average value ± one standard deviation; the bar represents the minimum and maximum values.

fluorescence detection was then used for quantification of the relative protein abundances. Subsequently, the membranes were scanned by the Odyssey scanner (LI-COR Biosciences) at 800 nm. The relative protein abundances for each sample are given in arbitrary units.

Electrophoresis and Quantification of Myosin Heavy Chain Isoforms. Three other biomarkers corresponded to MyHC and were determined according to the method of Picard et al.[24] using an adequate SDS-PAGE and expressed in percentage. Briefly, 100 mg of frozen muscle was ground in 5 mL of extraction buffer solution containing 0.5 M NaCl, 20 mM sodium pyrophosphate, 50 mM Tris, 1 mM EDTA, and 1 mM dithiothreitol. After 10 min at 4 °C on ice, the sample was centrifuged for 5 min at 5000*g*. Following centrifugation, the supernatant was diluted 1:1 (v/w) with glycerol at 87% and stored at −20 °C until use. The samples were then mixed with an equal volume of loading buffer containing 4% SDS (w/v), 125 mM Tris, pH 6.8, 20% glycerol (v/v), 10% β-mercaptoethanol (v/v), and 0.02% pyronin Y (w/v). The proteins were separated using 9.2% polyacrylamide gels. After staining, the gels were scanned, and the proportions of the different MyHCs bands were quantified by densitometry with ImageQuant Software 5500 (Amersham Biosciences/GE Healthcare). The band quantification revealed the existence of MyHC-IIb isoforms in only some animals (4 animals of 21). Consequently, MyHC-IIb percentages were totaled with those of MyHC-IIx, creating a new variable "MyHC-IIx+b" (fast glycolytic fibers).

Statistical Analysis. For descriptive statistics, raw data were used. For statistical analyses all data were standardized for replicate using the Proc Standard of SAS 9.2 to obtain Z scores. A Z score represents the number of standard deviations each observation is relative to the mean of the corresponding animal: $Z = ((x - \mu)/\sigma)$, where x is the raw value, μ is the mean of the population, and σ is the standard deviation of the same population.

The PROC CORR of SAS was used to determine the Pearson's correlation coefficients between the 21 biomarkers with pH and CIE-$L^*a^*b^*$ color coordinates. Correlation values were considered significant at $P < 0.05$.

For each pH value and each color coordinate, a principal component analysis (PCA) was carried out using PROC PRINCOMP of SAS, using only the correlated biomarkers. PCA aimed to illustrate visually the correlated biomarkers with pH and color coordinates. The overall Kaiser's measures of sampling adequacies of the performed PCAs were >0.68 for pH parameters and >0.80 for $L^*a^*b^*$ color coordinates.

Multiple regression analyses were performed using PROC REG of SAS to create best models (maximal adjusted R^2) for pH and color coordinates (as dependent variables) using the 21 protein biomarkers (as independent variables). Partial R-squares and significance of each retained variable are given for the models. Regression analyses were further conducted on L^*, a^*, and b^* color coordinates to study specifically the relationships with pH values and muscle fiber type composition.

The absence of collinearity was systematically verified for each model, by producing condition indices and variance proportions using the COLLIN procedure of SAS. Variables were identified as collinear if they possessed both a high condition index >10 and a proportion of variation >0.5 for two or more traits.

RESULTS

pH Parameters, Color Traits, and Biomarker Abundances. Average means of pH and color parameters are shown in Figure 1. pH measured 45 min post-mortem was 6.87 (±0.10) and declined to 6.22 (±0.20) 3 h post-mortem, reaching 5.57 (±0.08) 30 h post-mortem (Figure 1a). Mean color coordinates were 36.9 (±3.32) for lightness (L^*), 12.40 (±1.74) for redness (a^*), and 15.81 (±2.65) for yellowness (b^*) (Figure 1b). Relative abundances of biomarkers expressed in arbitrary units or in percentage (MyHC) are summarized in Table 2. The LT muscle was characterized by 19.2% (±3.6) of type I fibers, 3.9% (±4.3) of IIa, and 56.9% (±4.0) of IIx/b.

Relationships between Biomarkers and pH Parameters. pHu was correlated with $pH_{45\ min}$ (r = 0.47; $P < 0.05$) and $pH_{3\ h}$ (r = 0.59, $P < 0.01$). $pH_{45\ min}$ was correlated with $pH_{3\ h}$ (r = 0.47, $P < 0.05$). pH was further correlated with 11 biomarkers (Figure 2a). Prdx6 was negatively correlated with $pH_{45\ min}$ (r = −0.49, $P < 0.05$), $pH_{3\ h}$ (r = −0.47, $P < 0.05$), and pH_u (r = −0.66, $P < 0.01$). Hsp70-Grp75 and DJ-1 were negatively correlated with both $pH_{3\ h}$ (r = −0.45 and −0.56, $P < 0.05$, respectively) and pH_u (r = −0.45 and −0.43, $P < 0.05$, respectively). Actin was negatively correlated with $pH_{45\ min}$ and pH_u (r = −0.40, $P < 0.05$). MDH1 was negatively correlated (r = −0.48, $P < 0.05$) with $pH_{45\ min}$ only. MyBP-H (r = −0.43), ENO3 (r = −0.46), LDH-B (r = −0.43), and Hsp20 (r = −0.50) were significantly ($P < 0.05$) and negatively correlated with $pH_{3\ h}$. MyHC-IIx/b (positively) and CapZ-β (negatively) were correlated with ultimate pH only (r = 0.40 and −0.55, $P < 0.05$, respectively). The biomarkers that were significantly correlated with pH were introduced into PCAs (Figure 3). The first two PCA axes explained 80.7, 69.4, and 73.2% of the variability between animals of $pH_{45\ min}$ (Figure 3a), $pH_{3\ h}$ (Figure 3b), and pH_u (Figure 3c), respectively.

Regression Analyses of pH Parameters. The multiple linear regression analyses, using pH parameters as dependent and biomarker abundances as independent variables, revealed significant relationships (Table 3; Figure 4). For $pH_{45\ min}$, 47% of the variability ($P < 0.01$) was explained by MDH1 and actin

DOI: 10.1021/acs.jafc.5b02615
J. Agric. Food Chem. 2015, 63, 6799−6809

Table 2. Mean and Standard Deviation (SD) of the 21 Protein Biomarkers Quantified in *Longissimus thoracis* Muscle of Blond d'Aquitaine Young Bulls

variable	mean	SD
heat shock proteins		
αB-crystallin	15.61	4.23
Hsp20	17.39	3.55
Hsp27	19.04	5.33
Hsp40	17.40	2.47
Hsp70-1A/B	17.40	3.10
Hsp70-8	17.85	1.64
Hsp70-Grp75	17.16	1.90
metabolism		
enolase 3	14.51	5.28
LDHB: lactate dehydrogenase chain B	19.69	3.89
MDH1: malate dehydrogenase 1	15.71	3.67
oxidative resistance		
DJ-1: Parkinson's disease protein 7	16.13	2.78
Prdx6: *cis*-peroxiredoxin	13.69	1.34
SOD1: superoxide dismutase Cu/Zn	16.26	1.36
proteolysis		
μ-calpain	16.50	1.99
structure		
CapZ-β: F-actin-capping protein subunit β	15.90	2.33
actin	19.45	3.58
MyBP-H: myosin binding protein H	15.18	2.94
MyLC-1F: myosin light chain 1F	15.74	1.47
MyHC-I: myosin heavy chain-I (%)	19.21	3.65
MyHC-IIA: myosin heavy chain-IIa (%)	23.85	4.34
MyHC-IIx/b: myosin heavy chain-IIx/b (%)	56.94	3.98

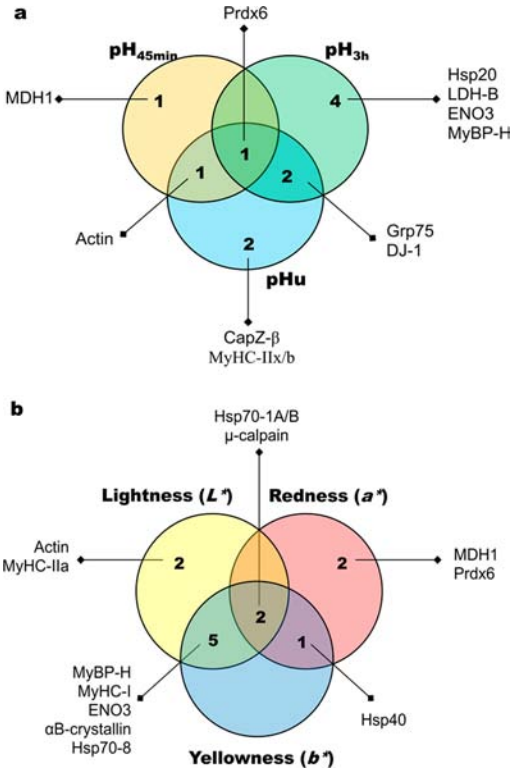

Figure 2. Venn diagrams depicting a summary of the number of biomarkers found significantly ($P < 0.05$) correlated with (a) pH parameters and (b) color coordinates. The directions of the correlations are presented in PCAs (Figures 3 and 5).

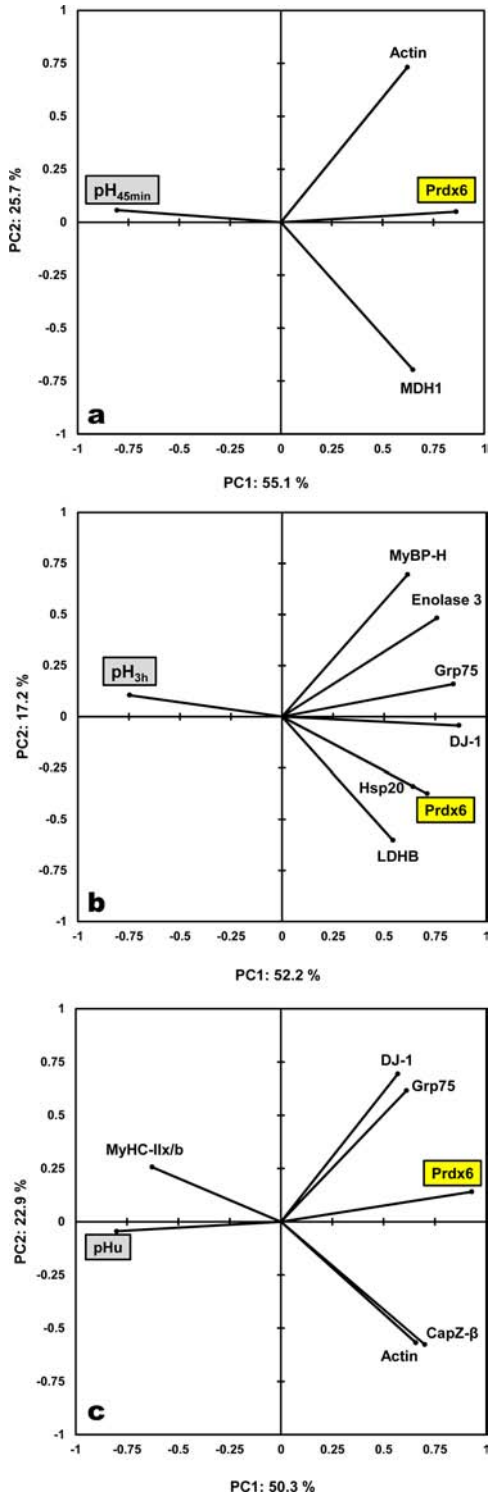

Figure 3. Principal component analyses showing relationships between (a) $pH_{45\ min}$, (b) $pH_{3\ h}$, and (c) pH_u and the correlated biomarkers.

(negative) and Hsp70-8 (positive). For $pH_{3\ h}$, the model was almost similar to the $pH_{45\ min}$ model and explained 59% of the variability ($P < 0.001$) in terms of LDH-B and actin (negative) and Hsp70-8 (positive). If included, Hsp27 (negative) was retained ($P < 0.05$) in the model, which then explains 67% of the variability. For ultimate pH, it was not possible to construct a significant model with three variables. Hence, a fourth variable was included, producing a model explaining 58% of the variability

DOI: 10.1021/acs.jafc.5b02615
J. Agric. Food Chem. 2015, 63, 6799−6809

Table 3. Regression Equations of $pH_{45\ min}$, $pH_{3\ h}$, and Ultimate pH of *Longissimus thoracis* Muscle of Blond d'Aquitaine Young Bulls Using Protein Biomarkers

dependent variable	adj-R^{2a}	SE	entered independent variable[b]	partial R^2	regression coefficient	t value	P value
$pH_{45\ min}$	0.47**	0.17	MDH1	0.11	−0.55	−3.22	0.005
		0.20	actin	0.12	−0.65	−3.25	0.005
		0.20	Hsp70-8	0.25	+0.58	+2.86	0.011
$pH_{3\ h}$	0.59***	0.15	LDHB	0.06	−0.66	−4.37	0.000
		0.18	Hsp70-8	0.29	+0.87	+4.74	0.000
		0.17	actin	0.25	−0.57	−3.24	0.005
pH_u	0.58***	0.19	Prdx6	0.31	−0.69	−3.72	0.002
		0.23	Hsp70-1A/B	0.08	+0.68	+3.00	0.008
		0.33	Hsp40	0.04	−0.86	−2.58	0.020
		0.24	MyLC-1F	0.15	+0.58	+2.41	0.028

[a]Significance of the models: **, $P < 0.01$; ***, $P < 0.001$. [b]Variables are shown in order of their entrance in the prediction models.

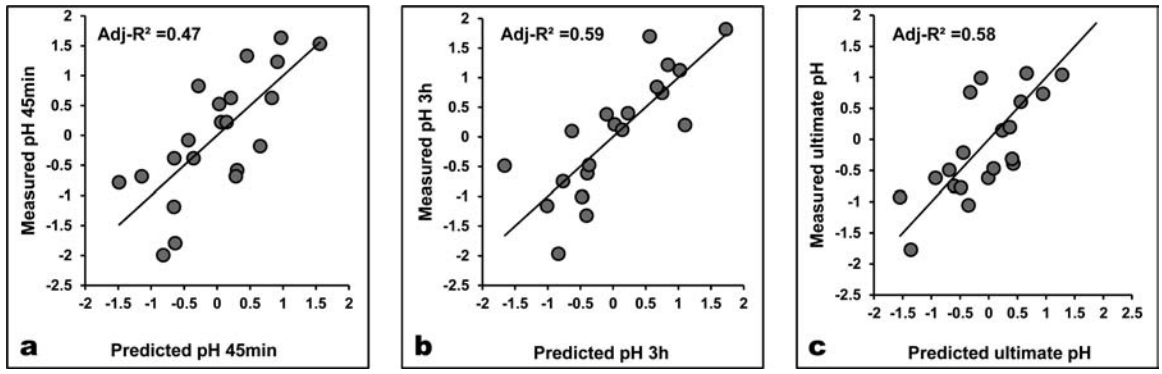

Figure 4. Correlations between measured and predicted $pH_{45\ min}$, $pH_{3\ h}$, and ultimate pH parameters using the best models. Adjusted R-squares corresponding to the prediction equations given in Table 3 for each parameter are shown.

($P < 0.001$): Prdx6 and Hsp40 (negatively) and Hsp70-1A/B and MyLC-1F (positively).

Relationships between Biomarkers and Meat Color Traits. Pearson correlation analyses revealed that the three measured color parameters were not correlated ($r < 0.29$). L^*, a^*, and b^* values were correlated with 12 biomarker abundances ($P < 0.05$; in Figure 2b). Hsp70-1A/B and μ-calpain were correlated with all color coordinates: negatively with L^* and positively with a^* and b^* (Figures 5 and Figure 6). These two proteins were correlated together ($r = 0.69$, $P < 0.001$). Five common correlations were found for L^* and b^*, although directions differed. L^* and b^* were correlated with αB-crystallin ($r = -0.56$ and 0.55, $P < 0.05$, respectively), Hsp70-8 ($r = -0.68$ and 0.41, $P < 0.05$; respectively), MyHC-I ($r = -0.53$ and 0.50, $P < 0.05$, respectively), ENO3 ($r = 0.73$ and -0.55, $P < 0.01$, respectively), and MyBP-H ($r = 0.44$ and -0.53, $P < 0.05$, respectively). Hsp40 was positively correlated with both a^* and b^* ($r = 0.65$ and 0.45, $P < 0.01$, respectively). Actin (negatively) and MyHC-IIa (positively) were correlated with L^* only ($r = -0.51$ and 0.46, $P < 0.05$, respectively). MDH1 and Prdx6 were positively correlated with a^* only ($r = 0.63$ and 0.46, $P < 0.01$, respectively). These two proteins were closely related ($r = 0.50$, $P < 0.05$). PCAs were carried out for each color coordinate, introducing only the correlated biomarkers. The first two axes of the PCA explained 68.8, 77.2, and 75.5% of the variability between animals of L^* (Figure 5a), a^* (Figure 5b), and b^* (Figure 5c), respectively.

Regression Models for Meat Color Traits. Simple correlations between pH values and color coordinates were not significant ($-0.34 < r < 0.10$; $p > 0.13$). The regression models using $L^*a^*b^*$ coordinates as dependent and pH and fiber types as independent variables found a significant model only for L^*, explaining 37.9% of the variability with pH_u (13.5%; $P < 0.05$) and MyHC-I (24.4%; $P < 0.01$): $L^* = -0.4^*\ pH_u - 0.7^*$ MyHC-I. The regression models using $L^*a^*b^*$ color traits as dependent and biomarker abundances as independent variables are presented in Table 4 and Figure 7. The models were significant and explained between 47 and 65% of variability. The model of L^* explained 65% of the variability between animals ($P < 0.0001$) by ENO3 (positive) and Hsp70-Grp75 (negative). The model of a^* explained 62% of the variability ($P < 0.001$) by Hsp40 (positive) and SOD1 and Hsp70-8 (both negative). The model of b^* explained 47% of the variability ($P < 0.01$) by μ-calpain (positive) and Hsp70-Grp75 (negative). Both L^* and b^* models included Hsp70-Grp75, explaining 17 and 24%, respectively. All of the L^*a^* b^* color coordinate models included heat shock proteins, which explained between 17 and 50% of the variability.

DISCUSSION

Results indicate that L^*, a^*, and b^* color coordinates were unrelated among themselves and that only L^* was weakly correlated with ultimate pH. Earlier studies on pork and cattle found correlations between ultimate pH, L^*, and b^*.[4] The absence of strong correlations with ultimate pH in the present study can be explained by the fact that ultimate pH values were within the normal range.[5] Redness (a^*) is generally more influenced by early post-mortem pH. Particularly, at least in

DOI: 10.1021/acs.jafc.5b02615
J. Agric. Food Chem. 2015, 63, 6799−6809

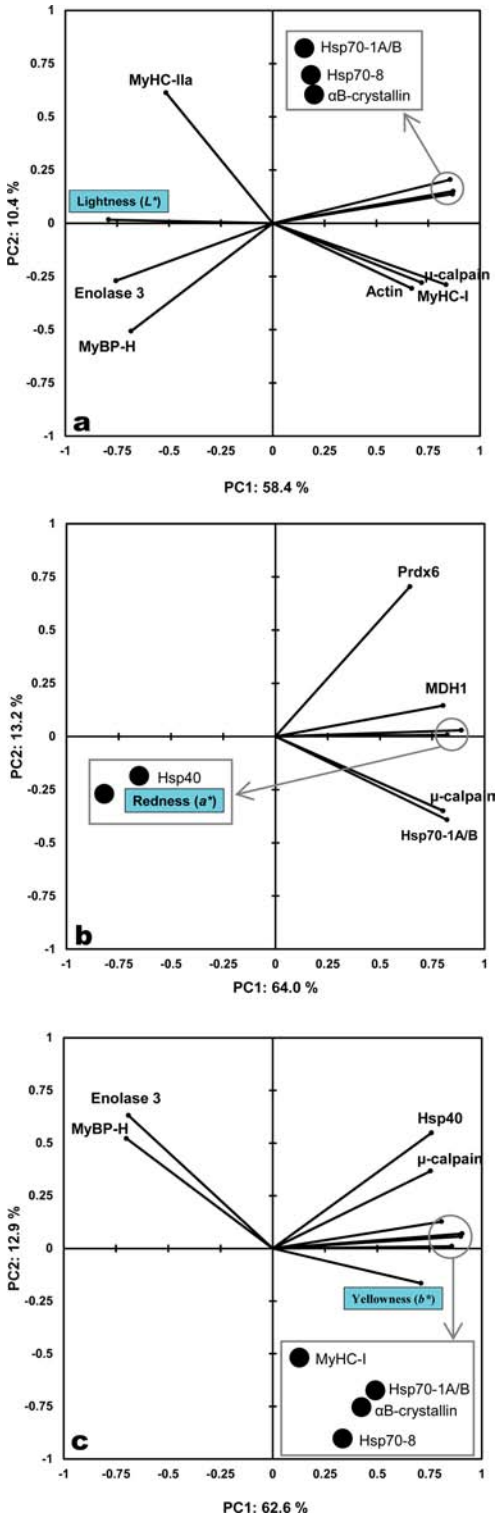

Figure 5. Principal component analyses showing relationships between (a) lightness (L^*), (b) redness (a^*), and (c) yellowness (b^*) and the correlated biomarkers.

pork, the combination of low early post-mortem thigh muscle temperature results in protein denaturation that leads to early inactivation of oxygen-consuming enzymes.[5] This promotes formation of MbO_2, leading to higher a^* values.[25] The absence of a correlation in the present study may be due to the use of cattle rather than pigs and/or the narrow range of early post-mortem pH values, compared to the study by Lindahl et al.[5]

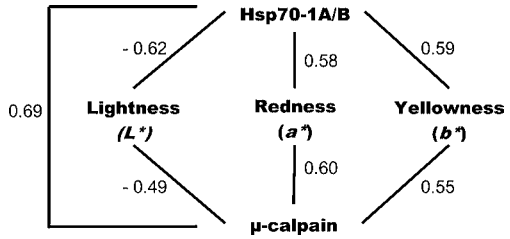

Figure 6. Pearson correlation analysis showing significant correlations ($P < 0.05$) between $L^*a^*b^*$ color coordinates and both Hsp70-1A/B and μ-calpain.

To increase our understanding of the biochemical mechanisms underlying post-mortem pH decline and color development in young Blond d'Aquitaine bulls, the following sections will discuss the relationships between these variables and the proteins (biomarkers) measured in the present study using the Dot-Bot technique.

Relationship between Biomarkers in the Early Post-Mortem Period and Post-Mortem pH Decline. *$pH_{45\ min}$.* PCA and regression analyses show that $pH_{45\ min}$ was correlated with four proteins (Actin, MDH1, Prdx6, and Hsp70-8), all implicated in apoptosis. Apoptosis is considered to start a few minutes after bleeding and to play a major role in the conversion of muscle to meat.[12,26] Apoptosis is initiated due to the hypoxic state of the muscle cells resulting in changes in the inner mitochondrial cell membrane that cause the release of pro-apoptotic proteins into the cytoplasm.[26] These events activate the caspase cascade, which is central in the apoptotic process. Actin is the first protein targeted by caspases. Actin fragments can induce morphological changes resembling apoptotic cells and may be used as a probe for apoptosis detection.[12,27] In coherence with our findings, proteomic studies found that in the early post-mortem period, actin fragments are released and that pH decline and actin degradation were closely related.[12,28,29]

In the early post-mortem period, as long as glycolytic enzymes are not inhibited by low pH, glycolysis will continue, thus contributing to the acidification process. MDH1 plays a pivotal role in the malate−aspartate shuttle operating between cytosol and mitochondria, which may explain the correlation between MDH1 and $pH_{45\ min}$.[30] MDH1 may also be implicated in apoptosis, as in response to glucose deprivation, MDH1 regulates p53-dependent cell-cycle arrest and apoptosis.[31]

In our study, low $pH_{45\ min}$ was also associated with higher Prdx6, a bifunctional protein with both glutathione peroxidase (GPx, antioxidative) and phospholipase A2 (PLA_2) activities.[32] The relationship between Prdx6 and pH decline may be partly explained by the activity of the PLA_2 group. This group plays a significant role in the hydrolysis of phosphatidylcholine (PC), which is a basic phospholipid present in cell membranes.[33] Phosphatidylserine (PS) is the acid phospholipid present in cell membranes. At the early stages of apoptosis, the phospholipid distribution in the cell membranes is inverted: PS switches to the external and PC to the internal leaflet of the membrane by a flip-flop process.[26,34] Due to this inversion, protons generated by glycolysis may be partly absorbed and the acidification process may be slowed. Due to PLA_2 activity, PC will be hydrolyzed, reducing its buffering capacity and thus enhancing the rate of pH decline in the cytosol.

Hsp70-8, a member of the Hsp70 kDa family, was positively related to early post-mortem pH. This Hsp is constitutively expressed in most tissues and essential for survival. It has many

DOI: 10.1021/acs.jafc.5b02615
J. Agric. Food Chem. 2015, 63, 6799−6809

Table 4. Regression Equations of *L*a*b Meat Color Traits of *Longissimus thoracis* Muscle of Blond d'Aquitaine Young Bulls Using Protein Biomarkers**

dependent variable	adj-R^{2a}	SE	entered independent variable[b]	partial R^2	regression coefficient	t value	P value
lightness (L^*)	0.65***	0.17	ENO 3	0.48	+1.05	+6.14	0.0001
		0.17	Hsp70-Grp75	0.17	−0.51	−2.99	0.008
redness (a^*)	0.62***	0.22	Hsp40	0.33	+1.22	+5.60	0.0001
		0.17	SOD1	0.12	−0.56	−3.38	0.004
		0.20	Hsp70-8	0.17	−0.57	−2.78	0.013
yellowness (b^*)	0.47**	0.17	μ-calpain	0.23	+0.64	+3.86	0.001
		0.17	Hsp70-Grp75	0.24	−0.48	−2.92	0.009

[a]Significance of the models: **, $P < 0.01$; ***, $P < 0.001$. [b]Variables are shown in order of their entrance in the prediction models.

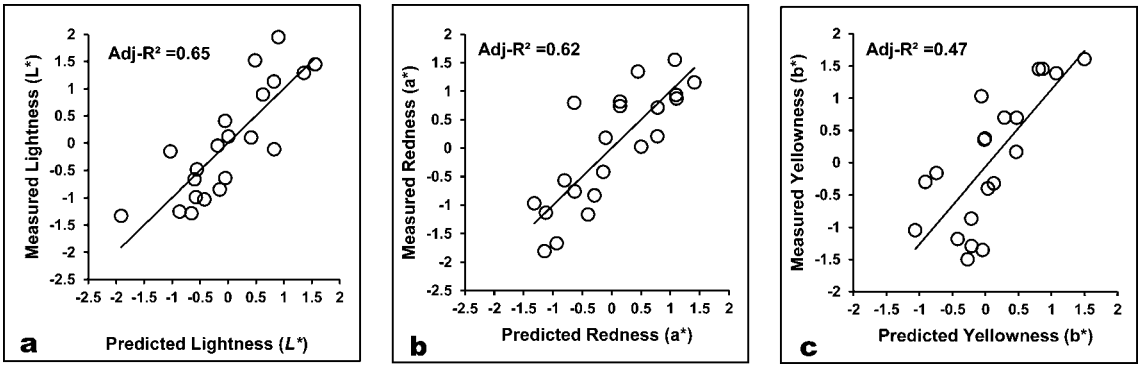

Figure 7. Correlations between predicted and measured (a) lightness (L^*), (b) redness (a^*), and (c) yellowness (b^*) color traits using the best models. Adjusted R-squares corresponding to the prediction equations given in Table 4 for each parameter are shown.

housekeeping chaperoning functions including folding of nascent polypeptides, protein translocation across membranes, chaperone-mediated autophagy, and prevention of protein aggregation under stress conditions.[35] Due to its protective functions, increased metabolic activity may have led to increased levels and vice versa, explaining its relationship with early post-mortem pH.

$pH_{3\ h}$. PCA and regression analyses show that 3 h post-mortem, the biological pathways appear partly similar to those involved in $pH_{45\ min}$. Several other proteins are also involved, and these new relationships become apparent due to the greater time span during which protons have been able to accumulate. The correlated proteins are implicated in glycolysis (ENO3 and LDH-B), heat stress (Hsp20, Hsp70-Grp75, and Hsp70-8), oxidative resistance (Prdx6 and DJ-1), and structure (actin and MyBP-H). Results show that high levels of these biomarkers 45 min post-mortem predict low pH about 2 h later. ENO3 and LDH-B are glycolytic enzymes, and their negative association with $pH_{3\ h}$ is undoubtedly explained by a faster energy metabolism resulting in a faster pH decline.

High levels of MyBP-H proteins at 45 min post-mortem predicted also low $pH_{3\ h}$ post-mortem. MyBP-H is a cytoskeletal protein interacting with myosin thick filaments in the A-band.[36] Its relationship with $pH_{3\ h}$ may have been indirect as higher MyBP-H levels were associated with higher levels of ENO3 and LDH-B. The Dot-Blot protocol used in the present study allowed revealing both intact and fragmented protein molecules in the soluble fraction. Higher MyBP-H levels in the early post-mortem period would suggest a faster fragmentation of these structural proteins, which may result from a faster early post-mortem metabolism.

Higher Hsp20 levels may occur in response to metabolic activity and pH decline, to stabilize myofibrillar proteins.[37] For example, Lomiwes et al.[38] demonstrated that a slight decrease in post-mortem muscle pH induces a rapid binding of another small Hsp of the same family, αB-crystallin, to the myofibril. Higher Hsp20 levels 45 min post-mortem may thus have been indicative of a faster metabolism and consequently be predictive of lower $pH_{3\ h}$.

Hsp70-Grp75 was related to $pH_{3\ h}$, pH_u, and L^* and b^* color coordinates. Hsp70-Grp75 is a cytoprotective chaperone present in nearly all cellular compartments and induced by glucose deprivation, Ca^{2+} influx, or agents perturbing glycolysis.[39] It assists in the import and folding of mitochondrial proteins and protects cells from glucose deprivation and ROS accumulation.[40] Its protective function may explain the relationship between its higher levels at 45 min post-mortem and the subsequent faster pH decline. Hsp70-Grp75 sequesters and inactivates p53, preventing its nuclear translocation and apoptosis.[41] Hsp70-Grp75 may thus slow apoptotic and other processes involved in the conversion of muscle to meat. In addition, Hsp70-Grp75 links the inositol 1,4,5-trisphosphate receptor of the endoplasmic reticulum to the mitochondrial voltage-dependent anion channels, presumably enhancing Ca^{2+} trafficking from the endoplasmic reticulum toward the mitochondria.[12] This mechanism may also contribute to the relationship between Hsp70-Grp75 and pH decline as Ca^{2+} exerts regulatory effects on many enzymes and proteins involved in metabolic and apoptotic processes including in the post-mortem muscle.[12,42]

The different functions of Prdx6 have been discussed above. Hence, increased Prdx6 levels 45 min post-mortem predicted low pH 3 h post-mortem probably partly due to its PLA_2 activity on pH decline. In addition, 3 h post-mortem pH was around 6.2 and less unfavorable for the activity of the GPx group of Prdx6.[32] Thus, approaching 3 h post-mortem, Prdx6 may have acted as an antioxidant, thereby protecting metabolic activity.

DOI: 10.1021/acs.jafc.5b02615
J. Agric. Food Chem. 2015, 63, 6799−6809

DJ-1 is another antioxidant protein present in the cytoplasm as well as in intracellular organelles and scavenges H_2O_2 through oxidation of Cys-106.[43] DJ-1 is further believed to promote the expression of a number of mitochondrial enzymes involved in reactive oxygen species (ROS) removal.[44] Its association with increased levels of glycolytic enzymes and Prdx6 is coherent with its association with a faster early post-mortem pH decline.

Ultimate pH. Ultimate pH was earlier found to be correlated with levels of various muscle proteins present in beef and pork muscles 45 min post-mortem.[11] In the present study, high levels of structural proteins (actin, CapZ-β, MyLC-1F, and MyHC-IIx/b), chaperones (Hsp70-Grp75, Hsp70-1A/B, and Hsp40), and oxidative resistance (DJ-1 and Prdx6) proteins 45 min post-mortem predicted low pH_u. In contrast to $pH_{45\ min}$ and $pH_{3\ h}$, low pH_u was not predicted by high levels of glycolytic enzymes, although pH values at different post-mortem intervals were correlated. This is coherent with the knowledge that the glycolytic rate is not the sole determining factor for pH_u. The extent of pH decline may be reduced if glycogen reserves are limiting. In the present experiment, preslaughter stress levels were low and glycogen levels were not the limiting factor as we have recently showed that 24 h post-mortem the muscles of the same BA bulls contained residual glycogen.[21] If glycogen content is not the limiting factor, glycolysis stops due to other factors, probably related to the disappearance of AMP and the inactivation of glycolytic enzymes.[45]

High actin and CapZ-β contents 45 min post-mortem predicted low pH_u. CapZ-β is located in the Z band of the muscle sarcomere and caps the barbed (plus) end of actin filaments, inhibiting polymerization.[46] A proteomic study found that CapZ-β was retained in the insoluble fraction of the protein extraction and that levels declined during the 48 h following slaughter,[10] indicative of progressive CapZ-β fragmentation or detachment from the Z band. As for MyBP-H (cf. above), the higher levels of actin and CapZ-β in the early post-mortem period would suggest a relatively fast fragmentation of these structural proteins. The association between faster structural protein degradation and higher levels of protective proteins (Prdx6, DJ-1, Hsp70-Grp75) 45 min post-mortem may thus express a faster metabolism. The association between higher levels of protective proteins and lower pH_u suggests that these pathways effectively protected the cell against adverse events such as oxidative stress, presumably retarding apoptosis and preserving energy metabolism. The association between high MyHC-IIx/b content and high ultimate pH may seem unexpected. A higher MyHC-IIx/b content is usually associated with higher glycogen content and a potential for a faster metabolism, which, depending on the slaughter conditions, may result in a lower, rather than a higher, pH_u.[3]

Meat Color Traits. Mean L^* values of the meat samples of the BA breed were within the range of normal values.[47] The redness (a^*) values were lower and yellowness (b^*) values were higher than those reported in the literature.[48] This may be partly due to the relatively high content of glycolytic fibers of the LT muscle of the BA breed.[20] These fibers contain less myoglobin, resulting in lower redness, and are less efficient in oxygen exchange compared to oxidative fibers, resulting in a less reductive environment and thus promoting MbO_2 formation with a net result of greater yellowness.[25]

Relationships between Biomarkers and Meat Color Traits. PCA and regression analyses showed that L^*, a^*, and b^* values were correlated with 10, 7, and 10 biomarker abundances, respectively. L^* and b^* showed seven correlations with the same proteins but in the opposite direction. The present study used proteins related to various beef sensory qualities including tenderness.[14] Although proteomic studies on pork, beef, and fish found relationships between color and proteins involved in muscle contraction, metabolism, heat stress, signaling, and other functions,[16−19] little information exists on the relationships between beef color and biomarkers validated for other meat qualities.[49]

In the present study, μ-calpain and Hsp70-1A/B were correlated with the three color coordinates. Similarly, Joseph et al.[18] identified three overabundant chaperone proteins that were related to beef meat color stability, including a Hsp-1B of 70 kDa. Kwasiborski et al.[11] found a negative correlation between abundance of an Hsp70 isoform (Hsp72 or Hsp70-1A/B) 45 min post-mortem and L^* in pig LT muscles. Hsp70-1A/B is a member of the inducible Hsp70 family and is abundantly induced in response to cellular stress, possibly due to its function to preserve proteins.[40] One hypothesis is that inducible Hsp70s and μ-calpain influence certain meat color coordinates interactively. First, post-mortem ROS damage of the endoplasmic reticulum of the cells leads to the liberation of Ca^{2+} in the cytosol, which activates μ-calpain. Structural proteins are a major substrate of μ-calpain, and their characteristics influence meat color aspects. Second, inducible Hsp70s may interfere in this process. Post-mortem, oxidative stress induced by a product of lipid peroxidation, 4-hydroxy-2-nonenal (4-HNE), an α,β-unsaturated aldehyde,[8] causes carbonylation of Hsp70,[50] thus inactivating it. It was recently reported that in monkey hippocampal CA1 neurons, carbonylated Hsp70s are key substrates of μ-calpain.[51] If this pathway exists also in muscle, the carbonylated forms of inducible Hsp70 may be hydrolyzed by μ-calpain.[51] 4-HNE may also contribute to the phenomenon as it may cause disruption of Ca^{2+} homeostasis, membrane and structure damage, and cell death.[52] In support of this hypothesis, 4-HNE was reported to affect meat color by formation of several adducts with muscle proteins, thus modifying protein functionality.[53,54] Thus, increased levels of carbonylated Hsp70s will protect structural proteins against μ-calpain activity, thereby deferring changes in the structure of pigment and myofibrillar proteins, influencing hence reflectance and other aspects of meat color. Inducible Hsp70 binds also with membrane phospholipids[55] and interacts with PLA2 activity[56] and may thus participate in reactions involving phospholipids, pH decline, and apoptosis onset.

Other Hsps were also correlated with color coordinates. Hsp70-8 and αB-crystallin were negatively and positively correlated with L^* and b^*, respectively. Hsp40 was positively correlated with a^*. Other studies found also relationships between Hsp contents of the early post-mortem muscle and color coordinates. Zhang et al.[57] reported opposite relationships between Hsp90 contents in the early post-mortem muscle and L^* and b^* in pigs. The involvement of Hsps in meat color may be in part related to their protective role against protein denaturation known to affect the reflectance of meat aspects.[19] Overall, these relationships indicate that inducible and constitutively expressed Hsps may play a major role in the determination of meat color.

The association between slow twitch oxidative fibers (type I) and L^* and b^* coordinates may be related to their relatively high content of myoglobin, which explains part of the variation in meat color.[25] In addition, they contain high levels of inducible Hsp70, of which the potential role has been described above.

The positive correlation between redness (a^*) and Prdx6 can be explained by the involvement of the GPx group, which has antioxidative properties. Tang et al.[58] reported that adding glutathione to bovine muscle cytosol improved MbO_2 redox stability, allowing increased redness. The present study found

DOI: 10.1021/acs.jafc.5b02615
J. Agric. Food Chem. 2015, 63, 6799−6809

also a positive correlation between MDH1 and a^* values. Glycolytic enzymes were earlier found to be positively correlated with redness (a^*) in beef.[16,18] In the presence of a reductor, MetMb can be converted back into Mb. The reduction process is primarily enzymatic in nature with NADH as cofactor and can take place under anaerobic or aerobic conditions.[1] The glycolytic pathway allows the production of NADH,[1,59] which may explain the correlation between a^* and MDH1.

While many studies have shown relationships between beef color and protein biomarkers after ≥24 h post-mortem, the present study shows that protein biomarkers present in the early post-mortem period may predict subsequent pH decline and color development. Overall, the results show that correlations between pH decline, meat color coordinates, and protein biomarkers reflect existing knowledge on post-mortem muscle processes involved in pH decline and meat color determinism. The role of the distribution of muscle fibers is probably due to their myoglobin content, directly influencing color, and mitochondria content, involved in the initiation of the apoptosis process. The involvement of Hsps and oxidative proteins is explained by their protective functions, thereby preserving metabolism and retarding proteolysis and apoptosis onset. Antioxidants maintain further the redox state, thus stabilizing myoglobin. Prdx6 plays an important role, probably due to its dual functions of antioxidant and phospholipase activities. Enzymes of the glycolytic pathways influence pH decline and thus, indirectly, color stability, but deliver also energy and cofactors (NADH) allowing reduction of MetMb. The degree of fragmentation of structural proteins reveals the proteolytic and apoptotic status of the cell, and being substrates that may also enhance these processes. pH plays an important role as it influences the activity of at least part of the proteins (e.g., sHsps and Prdx6).

Thus, several of the tested biomarkers have been identified as being relevant for the traits of interest, and their relationships with the traits have been discussed in terms of possible underlying biochemical mechanisms. Before these biomarkers can be used as an industrial tool, further developments are needed. For example, the robustness of the relationship, in terms of breed, gender, feeding regimen, and muscle, should be investigated. The knowledge presented here should allow a greater understanding of similarities but also of differences that may exist with other animal types than the one studied. In addition, techniques for routine measurements must be developed (for example, Dot-Blot or antibody microarray techniques[13,60]). Once developed, the meat industry may benefit from the use of biomarkers as a tool for investigation, monitoring, or decision/management. In addition, knowledge of the biochemical pathways involved in meat color development and stability may be used to control or improve meat aspects under field conditions. As indicated above, addition of pyruvate to beef cuts improved meat color, as pyruvate regenerates NADH through the TCA cycle, leading to MetMb reduction.[8] Similar results were obtained for the addition of NAD^+, lactate, or LDH.

AUTHOR INFORMATION

Corresponding Author

*(B.P.) Phone: 33 4 73 62 40 56. Fax: 33 4 73 62 46 39. E-mail: brigitte.picard@clermont.inra.fr.

Funding

This work was part of the EU FP6 Integrated Project ProSafeBeef, Contract FOODCT-2006-36241 (INRA Quality Assurance AQ284). Funding by the European Union is gratefully acknowledged with respect to animal production and laboratory analyses. We are further thankful to the Franco-Algerian PROFAS B+ program for the financial support given to M.G. (Ph.D.).

Notes

The authors declare no competing financial interest.

ACKNOWLEDGMENTS

We thank INRA UERT (Theix) for animal management and slaughter.

REFERENCES

(1) Mancini, R. A.; Hunt, M. C. Current research in meat color. *Meat Sci.* **2005**, *71*, 100−121.

(2) Mancini, R. A. 4 − Meat color. In *Improving the Sensory and Nutritional Quality of Fresh Meat*; Kerry, J. P., Ledward, D., Eds.; Woodhead Publishing: Cambridge, UK, 2009; pp 89−110.

(3) Renerre, M.; Anton, M.; Gatellier, P. Autoxidation of purified myoglobin from two bovine muscles. *Meat Sci.* **1992**, *32*, 331−342.

(4) Abril, M.; Campo, M. M.; Önenç, A.; Sañudo, C.; Albertí, P.; Negueruela, A. I. Beef colour evolution as a function of ultimate pH. *Meat Sci.* **2001**, *58*, 69−78.

(5) Lindahl, G.; Henckel, P.; Karlsson, A. H.; Andersen, H. J. Significance of early postmortem temperature and pH decline on colour characteristics of pork loin from different crossbreeds. *Meat Sci.* **2006**, *72*, 613−623.

(6) Boudjellal, A.; Becila, S.; Coulis, G.; Herrera-Mendez, C. H.; Aubry, L.; Lepetit, J.; Harhoura, K.; Sentandreu, M. A.; Ait-Amar, H.; Ouali, A. Is the pH drop profile curvilinear and either monophasic or polyphasic? Consequences on the ultimate bovine meat texture. *Afr. J. Agric. Res.* **2008**, *3*, 195−204.

(7) Suman, S. P.; Joseph, P. Myoglobin chemistry and meat color. *Annu. Rev. Food Sci. Technol.* **2013**, *4*, 79−99.

(8) Joseph, P.; Nair, M. N.; Suman, S. P. Application of proteomics to characterize and improve color and oxidative stability of muscle foods. *Food Res. Int.* **2015**, DOI: 10.1016/j.foodres.2015.05.041.

(9) Faustman, C.; Liebler, D. C.; McClure, T. D.; Sun, Q. α,β-Unsaturated aldehydes accelerate oxymyoglobin oxidation. *J. Agric. Food Chem.* **1999**, *47*, 3140−3144.

(10) Bjarnadottir, S. G.; Hollung, K.; Faergestad, E. M.; Veiseth-Kent, E. Proteome changes in bovine longissimus thoracis muscle during the first 48 h postmortem: shifts in energy status and myofibrillar stability. *J. Agric. Food Chem.* **2010**, *58*, 7408−7414.

(11) Kwasiborski, A.; Sayd, T.; Chambon, C.; Sante-Lhoutellier, V.; Rocha, D.; Terlouw, C. Pig Longissimus lumborum proteome: Part II: Relationships between protein content and meat quality. *Meat Sci.* **2008**, *80*, 982−996.

(12) Ouali, A.; Gagaoua, M.; Boudida, Y.; Becila, S.; Boudjellal, A.; Herrera-Mendez, C. H.; Sentandreu, M. A. Biomarkers of meat tenderness: present knowledge and perspectives in regards to our current understanding of the mechanisms involved. *Meat Sci.* **2013**, *95*, 854−870.

(13) Picard, B.; Lebret, B.; Cassar-Malek, I.; Liaubet, L.; Berri, C.; Le Bihan-Duval, E.; Hocquette, J. F.; Renand, G. Recent advances in omic technologies for meat quality management. *Meat Sci.* **2015**, DOI: 10.1016/j.meatsci.2015.05.003.

(14) Picard, B.; Gagaoua, M.; Micol, D.; Cassar-Malek, I.; Hocquette, J. F.; Terlouw, C. E. Inverse relationships between biomarkers and beef tenderness according to contractile and metabolic properties of the muscle. *J. Agric. Food Chem.* **2014**, *62*, 9808−9818.

(15) Guillemin, N.; Meunier, B.; Jurie, C.; Cassar-Malek, I.; Hocquette, J. F.; Leveziel, H.; Picard, B. Validation of a Dot-Blot quantitative technique for large scale analysis of beef tenderness biomarkers. *J. Physiol. Pharmacol.* **2009**, *60* (Suppl. 3), 91−97.

(16) Canto, A. C.; Suman, S. P.; Nair, M. N.; Li, S.; Rentfrow, G.; Beach, C. M.; Silva, T. J.; Wheeler, T. L.; Shackelford, S. D.; Grayson, A.; McKeith, R. O.; King, D. A. Differential abundance of sarcoplasmic proteome explains animal effect on beef Longissimus lumborum color stability. *Meat Sci.* **2015**, *102*, 90−98.

DOI: 10.1021/acs.jafc.5b02615
J. Agric. Food Chem. 2015, 63, 6799−6809

(17) Desai, M. A.; Joseph, P.; Suman, S. P.; Silva, J. L.; Kim, T.; Schilling, M. W. Proteome basis of red color defect in channel catfish (*Ictalurus punctatus*) fillets. *LWT − Food Sci. Techno.* **2014**, *57*, 141−148.
(18) Joseph, P.; Suman, S. P.; Rentfrow, G.; Li, S.; Beach, C. M. Proteomics of muscle-specific beef color stability. *J. Agric. Food Chem.* **2012**, *60*, 3196−3203.
(19) Sayd, T.; Morzel, M.; Chambon, C.; Franck, M.; Figwer, P.; Larzul, C.; Le Roy, P.; Monin, G.; Cherel, P.; Laville, E. Proteome analysis of the sarcoplasmic fraction of pig semimembranosus muscle: implications on meat color development. *J. Agric. Food Chem.* **2006**, *54*, 2732−2737.
(20) Listrat, A.; Picard, B.; Jailler, R.; Collignon, H.; Peccatte, J.-R.; Micol, D.; Geay, Y.; Dozias, D. Grass valorisation and muscular characteristics of blonde d'Aquitaine steers. *Ann. Zootech.* **2001**, *50*, 105−118.
(21) Bourguet, C.; Deiss, V.; Boissy, A.; Terlouw, E. M. C. Young Blond d'Aquitaine, Angus and Limousin bulls differ in emotional reactivity: relationships with animal traits, stress reactions at slaughter and post-mortem muscle metabolism. *Appl. Anim. Behav. Sci.* **2015**, *164*, 41−55.
(22) Bouley, J.; Chambon, C.; Picard, B. Mapping of bovine skeletal muscle proteins using two-dimensional gel electrophoresis and mass spectrometry. *Proteomics* **2004**, *4*, 1811−1824.
(23) Bradford, M. M. A rapid and sensitive method for the quantitation of microgram quantities of protein utilizing the principle of protein-dye binding. *Anal. Biochem.* **1976**, *72*, 248−254.
(24) Picard, B.; Barboiron, C.; Chadeyron, D.; Jurie, C. Protocol for high-resolution electrophoresis separation of myosin heavy chain isoforms in bovine skeletal muscle. *Electrophoresis* **2011**, *32*, 1804−1806.
(25) Lindahl, G.; Lundstrom, K.; Tornberg, E. Contribution of pigment content, myoglobin forms and internal reflectance to the colour of pork loin and ham from pure breed pigs. *Meat Sci.* **2001**, *59*, 141−151.
(26) Ouali, A.; Herrera-Mendez, C. H.; Coulis, G.; Becila, S.; Boudjellal, A.; Aubry, L.; Sentandreu, M. A. Revisiting the conversion of muscle into meat and the underlying mechanisms. *Meat Sci.* **2006**, *74*, 44−58.
(27) Mashima, T.; Naito, M.; Tsuruo, T. Caspase-mediated cleavage of cytoskeletal actin plays a positive role in the process of morphological apoptosis. *Oncogene* **1999**, *18*, 2423−2430.
(28) Morzel, M.; Terlouw, C.; Chambon, C.; Micol, D.; Picard, B. Muscle proteome and meat eating qualities of Longissimus thoracis of "Blonde d'Aquitaine" young bulls: a central role of HSP27 isoforms. *Meat Sci.* **2008**, *78*, 297−304.
(29) Rasolofoharitseheno, H.; Mompi, W.; Boudida, Y.; Gagaoua, M. Highlighting the degradation of actin in *Longissimus dorsi* muscle of different species: bovine, ovine, caprine, poultry and freshwater fish. *Br. Biotechnol. J.* **2015**, *7*, 169−176.
(30) Birktoft, J. J.; Fernley, R. T.; Bradshaw, R. A.; Banaszak, L. J. Amino acid sequence homology among the 2-hydroxy acid dehydrogenases: mitochondrial and cytoplasmic malate dehydrogenases form a homologous system with lactate dehydrogenase. *Proc. Natl. Acad. Sci. U. S. A.* **1982**, *79*, 6166−6170.
(31) Lee, S. M.; Kim, J. H.; Cho, E. J.; Youn, H. D. A nucleocytoplasmic malate dehydrogenase regulates p53 transcriptional activity in response to metabolic stress. *Cell Death Differ.* **2009**, *16*, 738−748.
(32) Fisher, A. B. Peroxiredoxin 6: a bifunctional enzyme with glutathione peroxidase and phospholipase A(2) activities. *Antioxid. Redox Signal.* **2011**, *15*, 831−844.
(33) Manevich, Y.; Shuvaeva, T.; Dodia, C.; Kazi, A.; Feinstein, S. I.; Fisher, A. B. Binding of peroxiredoxin 6 to substrate determines differential phospholipid hydroperoxide peroxidase and phospholipase A(2) activities. *Arch. Biochem. Biophys.* **2009**, *485*, 139−149.
(34) Martin, S. J.; Reutelingsperger, C. P.; McGahon, A. J.; Rader, J. A.; van Schie, R. C.; LaFace, D. M.; Green, D. R. Early redistribution of plasma membrane phosphatidylserine is a general feature of apoptosis regardless of the initiating stimulus: inhibition by overexpression of Bcl-2 and Abl. *J. Exp. Med.* **1995**, *182*, 1545−1556.
(35) Daugaard, M.; Rohde, M.; Jaattela, M. The heat shock protein 70 family: highly homologous proteins with overlapping and distinct functions. *FEBS Lett.* **2007**, *581*, 3702−3710.
(36) Vaughan, K. T.; Weber, F. E.; Ried, T.; Ward, D. C.; Reinach, F. C.; Fischman, D. A. Human myosin-binding protein H (MyBP-H): complete primary sequence, genomic organization, and chromospinal localization. *Genomics* **1993**, *16*, 34−40.
(37) Golenhofen, N.; Perng, M. D.; Quinlan, R. A.; Drenckhahn, D. Comparison of the small heat shock proteins αB-crystallin, MKBP, HSP25, HSP20, and cvHSP in heart and skeletal muscle. *Histochem. Cell Biol.* **2000**, *122*, 415−425.
(38) Lomiwes, D.; Hurst, S. M.; Dobbie, P.; Frost, D. A.; Hurst, R. D.; Young, O. A.; Farouk, M. M. The protection of bovine skeletal myofibrils from proteolytic damage post mortem by small heat shock proteins. *Meat Sci.* **2014**, *97*, 548−557.
(39) Wiedemann, N.; Frazier, A. E.; Pfanner, N. The protein import machinery of mitochondria. *J. Biol. Chem.* **2004**, *279*, 14473−14476.
(40) Mayer, M. P. Hsp70 chaperone dynamics and molecular mechanism. *Trends Biochem. Sci.* **2013**, *38*, 507−514.
(41) Kaul, S. C.; Deocaris, C. C.; Wadhwa, R. Three faces of mortalin: a housekeeper, guardian and killer. *Exp. Gerontol.* **2007**, *42*, 263−274.
(42) Glancy, B.; Balaban, R. S. Role of mitochondrial Ca^{2+} in the regulation of cellular energetics. *Biochemistry* **2012**, *51*, 2959−2973.
(43) Kinumi, T.; Kimata, J.; Taira, T.; Ariga, H.; Niki, E. Cysteine-106 of DJ-1 is the most sensitive cysteine residue to hydrogen peroxide-mediated oxidation in vivo in human umbilical vein endothelial cells. *Biochem. Biophys. Res. Commun.* **2004**, *317*, 722−728.
(44) Clements, C. M.; McNally, R. S.; Conti, B. J.; Mak, T. W.; Ting, J. P. DJ-1, a cancer- and Parkinson's disease-associated protein, stabilizes the antioxidant transcriptional master regulator Nrf2. *Proc. Natl. Acad. Sci. U. S. A.* **2006**, *103*, 15091−15096.
(45) Sales, J.; Mellett, F. D. Post-mortem pH decline in different ostrich muscles. *Meat Sci.* **1996**, *42*, 235−238.
(46) Zigmond, S. H. Beginning and ending an actin filament: control at the barbed end. In *Current Topics in Developmental Biology*; Academic Press: San Diego, CA, USA, 2004; Vol. 63, pp 145−188.
(47) Priolo, A.; Micol, D.; Agabriel, J. Effects of grass feeding systems on ruminant meat colour and flavour. A review. *Ann. Zootech.* **2001**, *50*, 185−200.
(48) Gil, M.; Serra, X.; Gispert, M.; Angels Oliver, M.; Sanudo, C.; Panea, B.; Olleta, J. L.; Campo, M.; Olivan, M.; Osoro, K.; Garcia-Cachan, M. D.; Cruz-Sagredo, R.; Izquierdo, M.; Espejo, M.; Martin, M.; Piedrafita, J. The effect of breed-production systems on the myosin heavy chain 1, the biochemical characteristics and the colour variables of Longissimus thoracis from seven Spanish beef cattle breeds. *Meat Sci.* **2001**, *58*, 181−188.
(49) Gagaoua, M.; Durand, D.; Micol, D.; Santé-Lhoutellier, V.; Terlouw, C.; Ellies-Oury, M. P.; Boudjellal, A.; Hocquette, J. F.; Picard, B. Biomarkers of meat sensory qualities of Angus beef breed: towards the development of prediction equations. In *15èmes JSMTV*; Viandes & Produits Carnés: Clermont-Ferrand, France, 2014; pp 137−138.
(50) Carbone, D. L.; Doorn, J. A.; Kiebler, Z.; Sampey, B. P.; Petersen, D. R. Inhibition of Hsp72-mediated protein refolding by 4-hydroxy-2-nonenal. *Chem. Res. Toxicol.* **2004**, *17*, 1459−1467.
(51) Sahara, S.; Yamashima, T. Calpain-mediated Hsp70.1 cleavage in hippocampal CA1 neuronal death. *Biochem. Biophys. Res. Commun.* **2010**, *393*, 806−811.
(52) Esterbauer, H.; Schaur, R. J.; Zollner, H. Chemistry and biochemistry of 4-hydroxynonenal, malonaldehyde and related aldehydes. *Free Radical Biol. Med.* **1991**, *11*, 81−128.
(53) Suman, S. P.; Faustman, C.; Stamer, S. L.; Liebler, D. C. Redox instability induced by 4-hydroxy-2-nonenal in porcine and bovine myoglobins at pH 5.6 and 4 degrees C. *J. Agric. Food Chem.* **2006**, *54*, 3402−3408.
(54) Ramanathan, R.; Mancini, R. A.; Suman, S. P.; Beach, C. M. Covalent binding of 4-hydroxy-2-nonenal to lactate dehydrogenase

DOI: 10.1021/acs.jafc.5b02615
J. Agric. Food Chem. 2015, 63, 6799−6809

decreases NADH formation and metmyoglobin reducing activity. *J. Agric. Food Chem.* **2014**, *62*, 2112−2117.
(55) Harada, Y.; Sato, C.; Kitajima, K. Complex formation of 70-kDa heat shock protein with acidic glycolipids and phospholipids. *Biochem. Biophys. Res. Commun.* **2007**, *353*, 655−660.
(56) Mahalka, A. K.; Code, C.; Jahromi, B. R.; Kirkegaard, T.; Jaattela, M.; Kinnunen, P. K. Activation of phospholipase A2 by Hsp70 in vitro. *Biochim. Biophys. Acta, Biomembr.* **2011**, *1808*, 2569−2572.
(57) Zhang, M.; Wang, D.; Geng, Z.; Bian, H.; Liu, F.; Zhu, Y.; Xu, W. The level of heat shock protein 90 in pig Longissimus dorsi muscle and its relationship with meat pH and quality. *Food Chem.* **2014**, *165*, 337−341.
(58) Tang, J.; Faustman, C.; Lee, S.; Hoagland, T. A. Effect of glutathione on oxymyoglobin oxidation. *J. Agric. Food Chem.* **2003**, *51*, 1691−1695.
(59) Renerre, M.; Labas, R. Biochemical factors influencing metmyoglobin formation in beef muscles. *Meat Sci.* **1987**, *19*, 151−165.
(60) Picard, B.; Meunier, B.; Barboiron, C.; Dunoyer, N.; Guillemin, N.; Micol, D. From protein markers to phenotyping tools for evaluation of beef tenderness. In *Farm Animal Proteomics*; Rodrigues, P., Eckersall, D., Almeida, A., Eds.; Wageningen Academic Publishers: Wageningen, The Netherlands, 2012; pp 165−168.

DOI: 10.1021/acs.jafc.5b02615
J. Agric. Food Chem. 2015, 63, 6799−6809

Table 1. Potato Cultivars for Metabolite Profiling Studies

cultivar	flesh	periderm russeting	skin
Norkotah Russet	white	russeted and netted	dark tan
Atlantic	white	lightly netted to heavily scaled	white
Chipeta	white	small russeted areas	light to buff
Yukon Gold	light yellow	smooth, finely flaked, yellowish white	yellowish

comprehensive chemical picture of the wound-healing process and its dependence on potato variety, the current study draws on a concurrent partitioning strategy to add cultivar-specific differences in the metabolite profiles and scavenging abilities of nonpolar extracts as well as chemical compositions of the corresponding insoluble material that remains after polar and nonpolar metabolite extraction. Contrasts are also drawn between the metabolites and solid materials present at early (day 3) vs late (day 7) time points after wounding, representing formation of the suberized closing layer as an initial healing response and when the nascent wound periderm is developing, respectively.[9,10,12] The nonpolar compounds signifying those metabolites that distinguish the two wound-healing time points (day 3 vs day 7 in all cultivars) or that discriminate among the four cultivars (at a given time point) are referred to as potential wound-healing and potential cultivar markers, respectively. These compounds were detected using multivariate statistical analysis, then identified and elucidated by matching their GC/MS data with suitable databases. Knowledge of the marker compounds involved in the wound healing process can guide the design of methods to expedite this process, thus improving crop protection during growth and after harvesting. Taken together, these studies can promote the development of food staples possessing beneficial antioxidant capabilities, robust wound healing, and reduced agricultural waste.

MATERIALS AND METHODS

Reagents. The following chemicals were used for extraction and GC/MS analysis: HPLC−MS grade water, methanol, and chloroform (J. T. Baker, Phillipsburg, NJ); hexadecyl hexadecanoate, C_7−C_{40} saturated alkane standards, and formic acid (Sigma-Aldrich, St. Louis, MO); GC/MS grade *N*-methyl-*N*-(trimethylsilyl)trifluoroacetamide (MSTFA) + 1% trimethylchlorosilane (TMCS) (Thermo Scientific, Bellefonte, PA); pyridine (EMD Millipore Corporation, Billerica, MA). Potassium peroxosulfate (Sigma-Aldrich), 2,2′-azinobis (3-ethylbenzothiazoline-6-sulfonic acid ammonium salt) (ABTS), and 6-hydroxy-2,5,7,8 tetramethylchromane-2-carboxylic acid (TCI, Tokyo, Japan) were used for the antioxidant assay.

Plant Material. Potato tuber cultivars from the 2011 crop year were provided by Joe Nuñez, University of California Cooperative Extension (Davis, CA). Differences in their overall phenotypic characteristics are summarized in Table 1.

Sample Preparation. The dormant freshly harvested potato tubers were peeled, sectioned, and allowed to heal as described previously.[12] Briefly, internal flesh tissues were sectioned longitudinally with a mandolin slicer to obtain disks about 5 mm thick. Healing in the dark at 25 °C was accomplished by placing the slices on wet cellulose filter paper inside closed humidified plastic boxes equipped with wire netting supports. The new brown surface layer of wound-healing tissue is identifiable because it is easily excoriated and detached, then removed by sweeping a flat spatula under the layer. During tissue collection, flesh (parenchyma) contamination under the wound healing surface was avoided to the extent possible. The samples were harvested at 3 and 7 days after wounding, corresponding to early healing in which the suberized closing layer had formed and to the developing wound periderm, respectively. Samples were frozen immediately in liquid nitrogen and stored at −80 °C. Processing involved grinding under liquid nitrogen, freeze-drying, and again storing at −80 °C.

For chemical analysis, concurrent extraction and partitioning of polar and nonpolar constituents were carried out using a slightly modified version of the method introduced by Choi et al.[13] for metabolomics of plant materials.[14] Extraction of 10 mg samples by 1 min of pan ultrasonication (Branson Ultrasonics, Danbury, CT) in 2 mL of 60% (v/v) methanol−water was followed by addition of 2 mL of chloroform and an additional 1 min of sonication in a 4-mL glass vial. Extracts were then incubated in a shaker at room temperature for 10 min, followed by tabletop centrifugation (Beckman Coulter, Fullerton, CA) at 1089*g* and 25 °C to produce three phases: upper soluble polar, lower soluble nonpolar, and an interphase of suspended particulates. After removal of the liquid polar and nonpolar extracts with a glass Pasteur pipet, the remaining residue of interfacial particulate solids was filtered, washed, and dried under a flow of nitrogen. Six biological replicates per cultivar were extracted in parallel for each of the day-3 and day-7 time points.

GC/MS Analysis. The samples were prepared according to Yang et al.[8] For metabolite separation and identification, a 500-μL aliquot of each nonpolar extract was placed in a glass vial and evaporated. Each sample was then reconstituted with 50 μL of pyridine and derivatized using 50 μL of *N*-methyl-*N*-(trimethylsilyl) trifluoroacetamide (MSTFA) + 1% trimethylchlorosilane (TMCS) at 50 °C for 1 h. Samples were analyzed with a QP2010 GC/MS (Shimadzu USA, Canby, RI) spectrometer with the injector oven set at 250 °C. The injection mode was splitless, and the volume injected for each sample was 1 μL. A Durabond-5 column (30 m × 0.25 mm i.d., film thickness 0.25 μm; Agilent Technologies, Santa Clara, CA) was used. The temperature program was based on the published method of Yang et al.[8] with minor modifications. After an initial delay of 5 min at 70 °C for the solvent to clear the system, the oven temperature was raised to 310 °C at a rate of 5 °C/min. The oven was kept at this temperature for 11 min and allowed to cool afterward to 70 °C. A 1-μL injection of 0.3 μM hexadecyl hexadecanoate provided a reference standard.

Preprocessing of GC/MS Data. The GC/MS data with a .qgd extension were converted to ANDI (CDFNET) format. MZmine version 2.4 (VTT Technical Research Center, Helsinki, Finland and Turku Center for Biotechnology, Turku, Finland) that included filtration, deconvolution, peak alignment, and data normalization was used for processing.[15] The region between 0 and 15 min, which contains peaks from derivatization artifacts, was excluded from the analysis. These peaks were also observed in blanks consisting of the solvent, pyridine, and derivatization reagent.

Multivariate Statistical Analysis. Simca-P+ software version 13.0 (Umetricas, Umea, Sweden) was used to carry out principal component analysis (PCA) of GC/MS data processed with MZ Mine using Pareto scaling.[16] This method organizes the data by relating the observations, cultivar types, and variables of the LC−MS data. The method tests the consistency of each set of biological replicates and discriminates among the different sample types.

Orthogonal partial least-squares discriminate analysis (OPLS-DA) of the data followed by the generation of S-plots helped to identify compounds that account for the differences among cultivars and between different wounding time points, which were designated as potential cultivar and potential wound-healing markers, respectively (Supporting Information, Figure S1). OPLS-DA is a regression and prediction method that finds information in the X data (e.g., variables from the LC−MS experiments) that is related to information in the Y data (e.g., discrete variables specifying cultivar type or wound-healing time point). This method shows how these two sets of information vary together and if they are dependent on each other, facilitating classification studies and potential marker identification. The S-plot serves to visualize OPLS-DA results in a scatter plot.[17] The variables (e.g., MS ions) at the extreme ends of the S-plot had $p(\mathrm{corr})[1] > 0.8$, indicating high reliability;[17] they were further examined using a variable line plot to check how specific they were to the sample type and if they qualified as potential marker ions (Supporting Information, Figure S1).

DOI: 10.1021/acs.jafc.5b03206
J. Agric. Food Chem. 2015, 63, 6810−6822

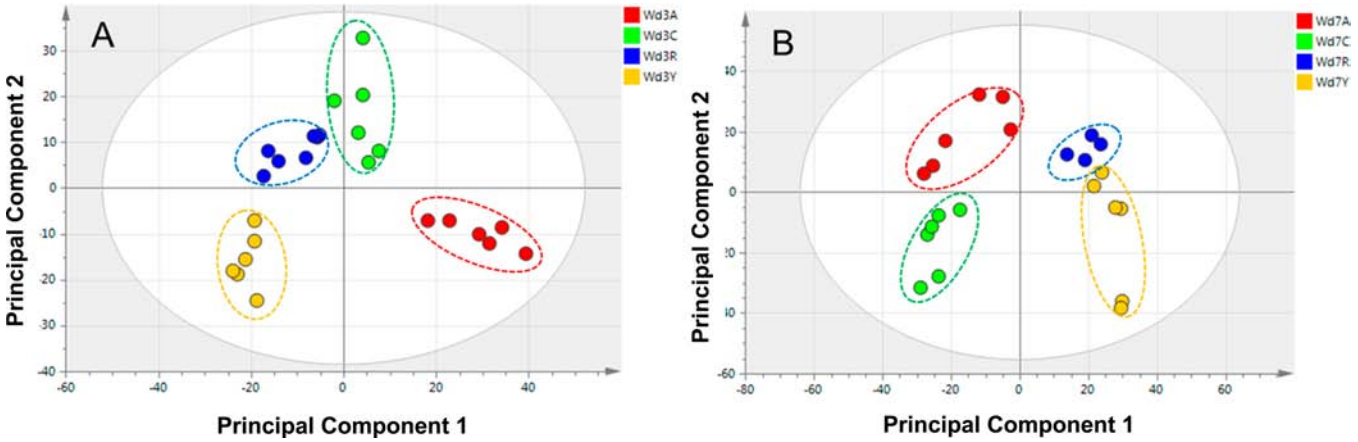

Figure 1. PCA score plot of GC/MS data from nonpolar extracts, showing consistency of each set of biological replicates and discrimination among the differently russeted cultivars at each of two time points after wounding. Included are wound-healing samples at day 3 (Wd3, A), and day 7 (Wd7, B), designated as Atlantic (red, A), Chipeta (green, G), Norkotah Russet (blue, R), and Yukon Gold (gold, Y) cultivars. The *x* and *y* axes of the plots represent the score values of principal components 1 and 2, respectively.

The PCA model was validated by calculating the values of R^2 and Q^2, which indicate fitness and predictive ability, respectively.[16] The Q^2 value, which is reported as a result of cross validation of the model, exceeded 0.5.[17] Cross validation using SIMCA-P+ divided the data into seven groups, one of which was removed. The model was then generated with the remaining groups, and the deleted group was predicted by the model. The partial predictive residual sum of squares (PRESS) was calculated. This procedure was repeated seven times to sum the partial PRESS values, obtain the overall PRESS, and calculate the Q^2 value. R^2 was larger than Q^2, but the difference between R^2 and Q^2 was small, as recommended.[17] For OPLS-DA, in addition to Q^2, the model diagnostics included R^2X and R^2Y values calculated for the X and Y variables, respectively.[17]

Metabolite Structural Identification. The ions corresponding to markers and other metabolites were identified using the Wiley Library (9th edition/NIST 2008). The ionic spectrum of each metabolite was matched against the spectra of known compounds from the library using a similarity index to identify hits. In addition, the observed spectra were compared with those of the known compounds for the ratio of ion intensities. C7−C40 saturated alkane standards (Sigma-Aldrich, St. Louis, MO) were injected. On the basis of their retention times and m/z values and using the NIST library peaks, they were assigned to standard reference compounds. There is a direct correlation between retention time and chain length.

ABTS$^{\bullet+}$ Scavenging. Antioxidant assessment of the nonpolar extracts was conducted using an ABTS$^{\bullet+}$ scavenging assay essentially as described by Dastmalchi et al.[12] Reaction of an aqueous ABTS solution (7 mM) with $K_2S_2O_8$ (2.45 mM) in the dark for 12−16 h at room temperature yielded ABTS$^{\bullet+}$, for which the absorbance at 734 nm was adjusted to 0.70 (±0.02) with ethanol. To a 2-μL aliquot of the extract of interest was added 198 μL of the ABTS$^{\bullet+}$ reagent; the absorbance at 734 nm was monitored after initial mixing and at 5 min intervals up to 45 min using a Spectra$_{max}$ M5 microplate reader (Molecular Devices, Sunnyvale, CA). Each percentage inhibition value was calculated as

$$\frac{\mathrm{Abs}_{\mathrm{control}} - \mathrm{Abs}_{\mathrm{sample}}}{\mathrm{Abs}_{\mathrm{control}}} \times 100$$

A calibration plot of percentage inhibition versus concentration was made for the reference standard, 6-hydroxy-2,5,7,8-tetramethylchroman-2-carboxylic acid (Trolox), permitting calculation of the Trolox equivalent antioxidant capacity (TEAC, mmol Trolox/g dried sample) for each extract.

Isolation of Suberin-Enriched Tissues. The interfacial solid from the partitioned mixture was passed through a Whatman no. 4 filter paper and then washed with distilled water. To remove unsuberized cell-wall materials, the sample was treated with 0.1% (w/v) *Aspergillus niger* cellulase (MP Biomedicals, Illkirch, France) in a 50 mM pH 5.0 acetate buffer for 48 h each at 37 and 44 °C, respectively. The residue was then treated with 0.4% (v/v) *A. niger* pectinase (Sigma-Aldrich) in a 50 mM pH 4.0 acetate buffer for 24 h each at 28 and 31 °C, respectively. After the enzyme treatments, the sample was filtered, washed with deionized water, and dried at 50 °C. Soxhlet extraction was conducted under reflux conditions to remove any remaining waxes and soluble lipids, using a succession of solvents of varying polarity: methanol, chloroform, and hexane for 48 h each. The resulting solid suberin-enriched samples were reserved for solid-state NMR analysis.

Solid-State NMR Analysis. The chemical moieties present in the suberin-enriched materials were identified and quantitated using cross-polarization and direct polarization magic-angle spinning ^{13}C NMR experiments (CPMAS, DPMAS) on 3−4 mg powdered samples. A four-channel Agilent (Varian) DirectDrive I (VNMRS) NMR spectrometer (Agilent Technologies, Santa Clara, CA, USA) operating at a ^1H frequency of 600 MHz (^{13}C at 150 MHz) and equipped with a 1.6 mm HXY FastMAS probe operating at a spinning rate of 10.00 kHz (±20 Hz) was used. The spectral data were typically processed with 100 Hz line broadening and analyzed in parallel using VNMRJ (version 2.2C; Agilent) and ACD/NMR Processor Academic Edition (version 12; Advanced Chemistry Development, Inc., Toronto, ON, Canada). Chemical shifts were referenced externally to the methylene ($-CH_2-$) group of adamantane (Sigma-Aldrich) at 38.48 ppm.

For typical CPMAS experiments used to identify the carbon-containing functional groups via their respective chemical shifts, conditions included 90° pulse durations of 1.3 and 1.2 μs for ^1H and ^{13}C, respectively, a contact time of 1.5 ms, acquisition delay of 4 μs, and recycle delay of 3 s between successive acquisitions. Heteronuclear decoupling was applied with a ^1H field strength of 204 kHz using the SPINAL method.[18] The spectral width was 46296 Hz, and the number of transients was 21500. For DPMAS experiments used to estimate the relative proportions of each carbon type, a 100-s recycle delay was used to collect 2600 transients.[19] Alternatively, quantitatively reliable ^{13}C NMR spectra of suberized cell walls were obtained by acquiring 100 transients with the multiple-CPMAS method[20] after validation with a *t*-BOC alanine standard (Sigma-Aldrich) and through DPMAS measurements for the Norkotah Russet day-7 wound suberin. Radiofrequency (rf) fields of ω_{1H} = 204 kHz and ω_{1C} = 189 kHz were used for all 90° pulses. Transfer of polarization from ^1H to ^{13}C nuclei was achieved via the condition $\omega_{1C} - \omega_{1H} = \omega_{\mathrm{rotation}}$, with rf frequencies of ω_{1H} = 53.3 kHz and ω_{1C} = 63.4 kHz; a 10% linear ramp of the ^1H radiofrequency power was used during the CP period. Recycle times between successive cross-polarizations were 1.0 s; 11 contact times of 1.0 ms were used to acquire each transient. SPINAL

DOI: 10.1021/acs.jafc.5b03206
J. Agric. Food Chem. 2015, 63, 6810−6822

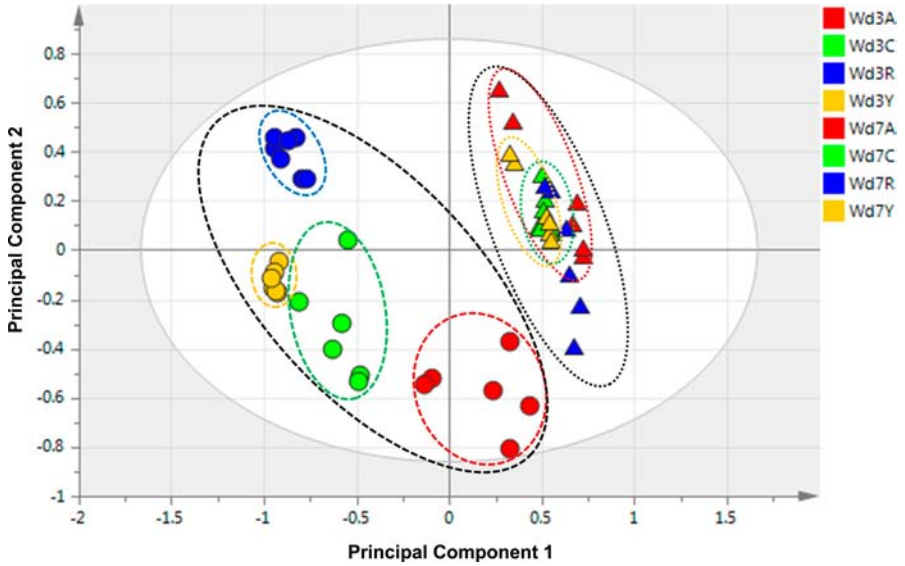

Figure 2. PCA score plot of GC/MS data from nonpolar extracts, showing overall differences among the metabolite profiles for wound-healing samples of four cultivars at day 3 (circles) and day 7 (triangles). The samples are color-coded as Atlantic (red, A), Chipeta (green, C), Norkotah Russet (blue, R), and Yukon Gold (gold, Y) cultivars. The *x* and *y* axes of the plots represent the score values of principal components 1 and 2, respectively.

heteronuclear decoupling[18] with ω_{1H} = 204 kHz was applied during an acquisition period of 22 μs.

The 3-day wound healing samples required 5000 transients (~20 h), whereas 7-day samples required only 1500 transients (~6 h). Integrated signal intensities were measured by counting pixels with the image manipulation software GIMP (www.gimp.org) and using the following chemical shift ranges to denote major structural components of suberin: carboxyl and amide groups (168−180 ppm, region 1); arenes and alkenes (115−160 ppm, region 2); alkoxy groups (96−108, 80−92, 67−80, 59−67 ppm; regions 3−6); methoxy groups (45−59 ppm, region 7); alkyl chain methylenes (15−45 ppm, region 8). Each chemical shift range was extended by ±1 ppm to ensure that the regions were not truncated in the middle of a resonance. Each quoted quantitative estimate was the result of measurements on two biological replicates, quoted as mean ± standard error.

Statistical Analysis. The antioxidant and solid-state NMR data were presented as mean values ± standard error. Significant differences between the values were determined using Tukey's pairwise comparison[21] at a level of $P < 0.05$, assessed with JMP software version 12 (http://www.jmp.com).

RESULTS AND DISCUSSION

GC/MS Multivariate Analysis Reveals Distinctive Metabolite Profiles for the Four Cultivars. The PCA score plots derived from GC/MS of the day-3 nonpolar samples show clear, nonoverlapping clusters representing the respective metabolite profiles of the four cultivars (Figure 1A), but those differences are less distinct for the day-7 time point (Figure 1B). For the GC/MS data considered collectively from both time points, the PCA plot of Figure 2 clearly shows that the cluster corresponding to all of the day-7 extracts is more compact compared with the overall day-3 cluster. This trend, which was also reported for the corresponding polar extracts[12] and for Russet Burbank wound-healing samples,[8] is likely to reflect a common biosynthetic pathway induced by wounding in each of the four cultivars. Thus, similar phytochemicals associated with wound healing are expected to become increasingly dominant with respect to the initially distinct metabolite pools of each cultivar. For the Atlantic extracts, the similar values of the first principal component (PC1) observed for day-3 and day-7 clusters (Figure 2) indicate that its nonpolar metabolites change more modestly, or at a slower rate, in response to wounding.

The nonpolar compounds that distinguish the two wound-healing time points (3-day vs 7-day for all cultivars) or the four cultivars at a particular time point can be considered as potential wound-healing and cultivar markers, respectively. These compounds were identified from the "wings" of S-plots generated by OPLS-DA[12] (Supporting Information, Figure S1) and elucidated structurally by matching their GC/MS data against the spectra of known compounds from the Wiley Library as described above. A total of 28 identified potential marker compounds were detected from the S-plots and variable line plots as noted above.

These compounds were classified as alkanes, α,ω-fatty diacids, α,ω-hydroxyfatty diacids, fatty acids, hydroxyfatty acids, fatty alcohols and aldehydes, and glyceryl esters (Table 2, **1**−**28**). Seven compounds that distinguish the day-7 time point (hentriacontane (**3**, 31:0), 2-hydroxysebacic acid (**8**, 10:0), tetradecanoic (myristic) acid (**10**, 14:0), hexadecanoic (palmitic) acid (**12**, 16:0), heneicosanoic acid (**19**, 21:0), tetracosanoic acid (**21**, 24:0), and pentacosanoic acid (**22**, 25:0)) are referred to as potential wound-healing markers. These compounds, which include an alkane, an α,ω-hydroxyfatty diacid, and several fatty acids, are more abundant at day 7 in all cultivars. Hentriacontane (**3**) has been reported to be cytotoxic to in vitro L5178Y-R lymphoma murine model.[22] Tetradecanoic (**10**, 14:0) and hexadecanoic (**12**, 16:0) acids have been reported to inhibit the growth of phytopathogenic fungi.[23]

By plotting the number of nonpolar potential marker compounds in each structural class by cultivar type and time point (Figure 3), it was possible to discern additional trends and lay the groundwork to align our metabolite findings for the extracts with the solid interfacial layers described below. Whereas most potential cultivar markers are found at day 7 postwounding, when suberin biosynthesis is well underway, nine of the markers are found in day-3 extracts of the various

DOI: 10.1021/acs.jafc.5b03206
J. Agric. Food Chem. 2015, 63, 6810−6822

Table 2. Potential Marker Compounds for Nonpolar Extracts from Potato Wound Tissues of Four Cultivars

Compound Number	Metabolite	C:D[a]	Potential Cultivar Marker[b]	Potential Wound-Healing Marker[c]	Molecular Structure[d]
			Alkanes		
1	Heneicosane[e-g]	21:0	Wd7A Wd7C		
2	Triacontane[f,h]	30:0	Wd7Y		
3	Hentriacontane	31:0	Wd7Y	+	
			α,ω-Fatty Diacids		
4	Butanedioic acid	4:0	Wd7A Wd7C		
5	Octanedioic acid	8:0	Wd7A		
6	Azelaic acid[e]	9:0	Wd7C Wd7R		
7	Sebacic acid[f]	10:0	Wd7C		
			α,ω-Hydroxyfatty Diacids		
8	2-Hydroxysebacic acid[h]	10:0	Wd3C Wd7Y	+	
			Fatty Acids		
9	Undecanoic acid	11:0	Wd7A Wd7C		
10	Myristic acid/Tetradecanoic acid[f,h]	14:0	Wd7C Wd7R	+	
11	Pentadecanoic acid[f]	15:0	Wd3Y Wd7C Wd7R		
12	Palmitic acid/Hexadecanoic acid[f-h]	16:0	Wd3A Wd3Y Wd7C Wd7Y		
13	Heptadecanoic acid[f,h]	17:0	Wd7A Wd7C		
14	Stearic acid/Octadecanoic acid[f-h]	18:0	Wd3Y Wd7C		
15	Oleic acid/cis-9-octadecanoic acid[f-h]	18:1	Wd7R Wd3C		
16	17-Octadecynoic acid[f]	18:1	Wd3A		
17	9,12-Octadecadienoic acid/Linoleic acid[f-h]	18:2	Wd3R		
18	Eicosanoic acid[f-h]	20:0	Wd7C Wd7R		
19	Heneicosanoic acid[f,g]	21:0		+	
20	Docosanoic acid[f-h]	22:0	Wd7A Wd7C		
21	Tetracosanoic acid[f,g]	24:0	Wd3Y	+	
22	Pentacosanic acid[f]	25:0		+	
			Hydroxyfatty Acids		
23	12-hydroxystearic acid	18:0	Wd3C Wd7C		
			Fatty Alcohols and Aldehydes		
24	cis-hexanedecanal	16:0	Wd7A		
25	Hexadecane-1,2 diol[e-g]	16:0	Wd7C		
26	Oleoyl alcohol/cis-9-octadecenol	18:1	Wd7C		
			Glyceryl Esters		
27	Glycerol monopalmitate/monopalmitin[f,h]	19:0	Wd7C Wd7Y		
28	Glycerol monostearate[f,h]	21:0	Wd7R Wd7Y		

[a]Alkyl or acyl chain specification, where *C* is the number of carbon atoms and *D* is the number of double bonds. [b]The wounding time points are denoted by Wd3 and Wd7; entries are color coded according to the cultivar for which the potential marker is specific: Atlantic (red), Chipeta (green), Norkotah Russet (blue), and Yukon Gold (gold). For instance, **Wd7Y** for Hentriacontane (**3**, 31:0) designates that compound as a Yukon Gold potential marker in the day-7 nonpolar extract. [c]These entries denote the potential marker compounds that are more abundant in all the four cultivars at day 7, which is associated with the development of the wound periderm. For instance, '+' for Hentriacontane (**3**, 31:0) designates that compound as notably abundant at day 7 for all four cultivars. [d]From the Wiley Library (9th edition/NIST 2008) unless noted otherwise. [e]Detected among the marker compounds identified in native periderms of these four cultivars (Huang et al., unpublished). [f]Yang, W.-L.; Bernards, M. A. Metabolite profiling of potato (*Solanum tuberosum* L.) tubers during wound-induced suberization. *Metabolomics* **2007**, *3*, 147−159. [g]Yang, W.-L.; Bernards, M. A. Wound-induced metabolism in potato (*Solanum tuberosum*) tubers. *Plant Sig. Behav.* **2006**, *1*, 59−66. [h]Detected among the metabolites identified in native periderms of these four cultivars (Huang et al., unpublished).

cultivars. All four Yukon Gold day-3 markers are fatty acids, three of which appear later as day-7 Chipeta markers (Table 2). The largest numbers of fatty acid markers are present at day 3 for Yukon Gold and at day 7 for Chipeta, followed by Norkotah Russet, respectively (Figure 3A). Fatty acids, which can be substrates for subsequent elongation, hydroxylation, or esterification steps during suberin biosynthesis, comprise nearly 40% of the nonpolar potential markers overall. Therefore, we

DOI: 10.1021/acs.jafc.5b03206
J. Agric. Food Chem. 2015, 63, 6810−6822

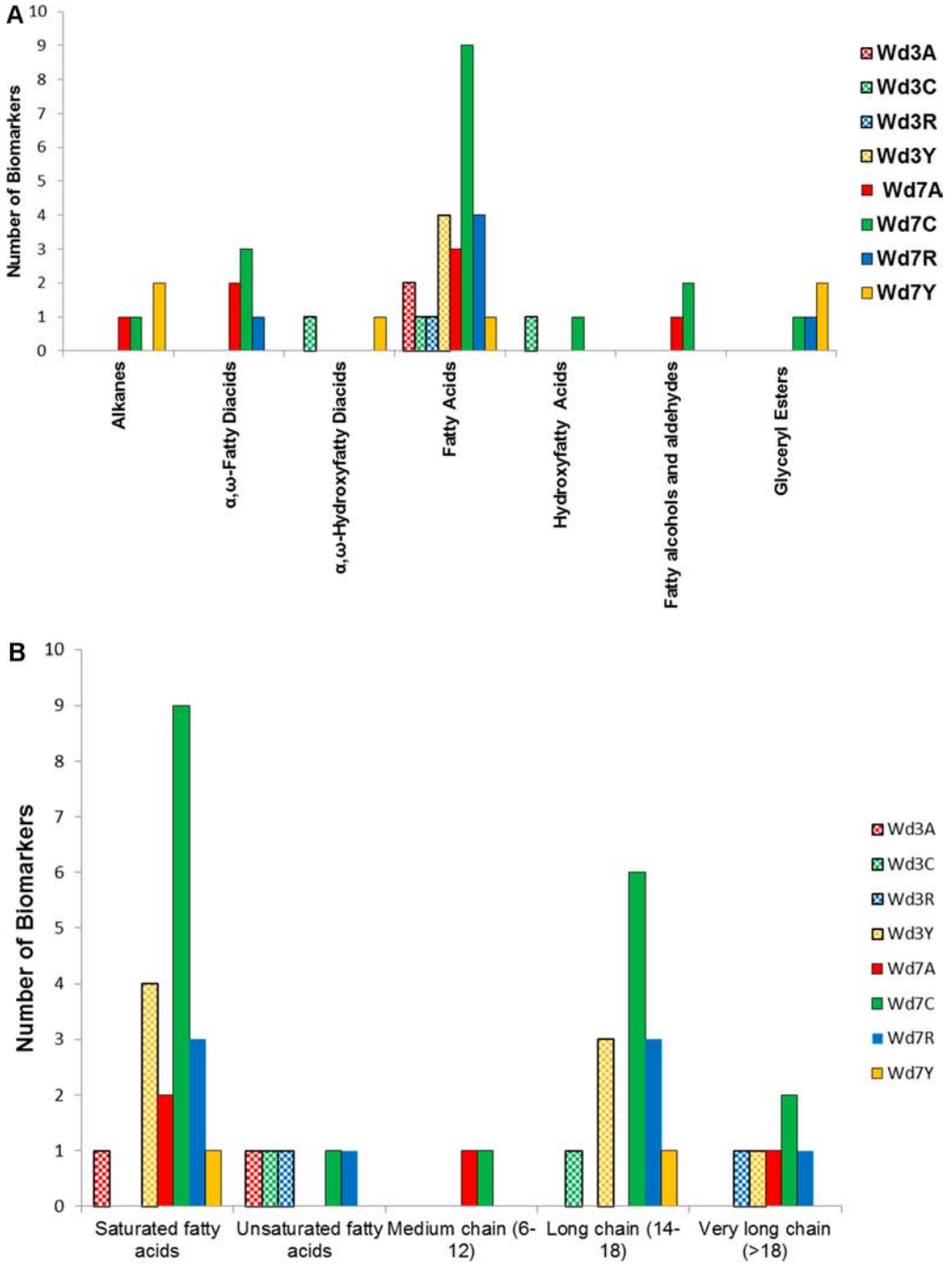

Figure 3. Accumulation of nonpolar marker compounds as a function of chemical class and time point after tissue wounding. (A) Nonpolar markers of day-3 and day-7 potato periderm extracts; (B) a detailed view of the fatty acid potential marker class. The samples are coded for Atlantic (red, A), Chipeta (green, C), Norkotah Russet (blue, R), and Yukon Gold (gold, Y), using checkerboards for day-3 and solid colors for day-7 markers, respectively.

examined this chemical class of markers in greater detail (Figure 3B), finding a significant portion (21%) of unsaturated homologues overall, although none in the Yukon Gold extracts. The fatty acid markers exhibit a broad distribution of chain lengths (11−25), with the majority in the range of 14 to 18 but no clear correlations of length according to healing time point.

The Chipeta cultivar contains nearly all potential marker classes (specifically at the day-7 time point), but a progressively diminished range of these abundant nonpolar metabolites is observed for Yukon Gold, Norkotah Russet, and Atlantic varieties. All Yukon Gold markers are saturated. Each of the less numerous marker classes is absent in one or more cultivars; hydroxyfatty acid and fatty alcohol markers are unique to the Chipeta cultivar at the day-7 time point. The absence of glyceryl ester, hydroxyfatty acid, and α,ω-hydroxyfatty diacid markers in the Atlantic cultivar is notable: the paucity of these key building blocks of suberin[2] could indicate limited development of its protective suberin polymer, particularly if the trend is confirmed in the solid biopolymer (see below).

Given that aliphatic compounds in general and free fatty acids in particular offer protection against fungal (*Fusarium sambucinum*) infections,[10,24] these compounds that have been

DOI: 10.1021/acs.jafc.5b03206
J. Agric. Food Chem. 2015, 63, 6810−6822

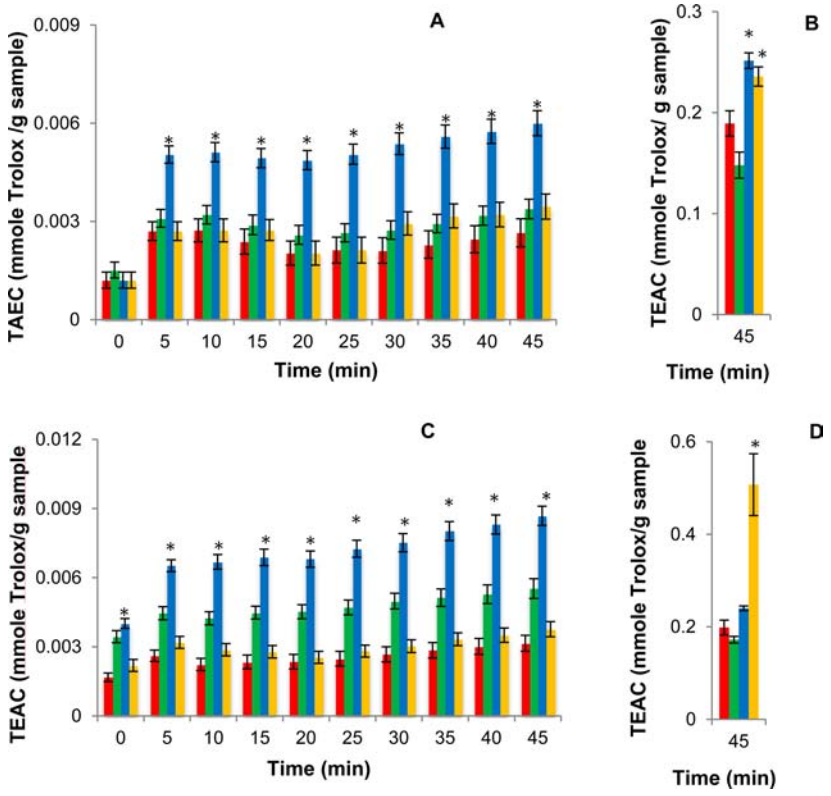

Figure 4. Antioxidant activity throughout the 45 min ABTS assay period for wound-healing potato extracts from Atlantic (red), Chipeta (green), Norkotah Russet (blue), and Yukon Gold (gold) cultivars, showing activities at day-3 post wounding for nonpolar (A) and polar (B) extracts; day-7 postwounding for nonpolar (C) and polar (D) extracts revealing diminished radical scavenging for nonpolar extracts (~50-fold at the 45 min assay time illustrated herein, ~100-fold at the 0 min assay time based on our prior report[12]). Scavenging activities for the nonpolar extracts were examined herein; polar extracts have been reported previously.[12] The data represent the mean ± standard error of the mean of six biological replicates for each cultivar. The highest significant scavenging activity ($P < 0.05$) at each time interval, calculated by means of Tukey pairwise comparisons, is denoted by an asterisk (*).[21]

found abundantly in all cultivars could provide strong protection against fungal infection. Unsaturated fatty acid markers such as 9-octadecenoic acid (oleic acid) (**15**, 18:1) and 9,12-octadecadienoic acid (linoleic acid) (**17**, 18:2) have also been implicated as active compounds against plant pathogenic fungi[25] and may contribute to the antioxidant activities described below.

Diacids such as markers **4**–**8** provide potential sites for the developing suberin biopolymer: for attachment to glycerol forming glyceryl esters, for esterification with long-chain alcohols forming linear esters, or for covalent linkages at either end.[6] Thus, these metabolites can build cross-links within the suberin polyester.[4] All fatty diacid markers emerge in day-7 extracts; namely, at a later time point in the healing process when the wound periderm is developing. Moreover, it is striking that these diacids have relatively short acyl chains compared with native periderm constituents (Huang et al., unpublished). However, medium-chain (C8–C12) species with saturated aliphatic chains have also been reported in wound-healing potato tissues as suberin triglyceride degradation products,[26] in contrast to the typical C16, C18, and longer chain lengths found as suberin monomers.[4,6] One of the diacid markers, 2-hydroxysebacic acid (**8**, 10:0), is up-regulated in all cultivars at day 7 (Table 2). Among the diacid markers, azelaic acid (**6**, 9:0) has been implicated in the plant immune system of *Arabidopsis*, offering protection against pathogens.[27]

Some of the potential markers identified in the current study (Table 2) have been reported previously as metabolites in wound tissue extracts[8] of potato tubers. Those marker compounds reported for the first time in the nonpolar extracts from potato wound tissues included α,ω-fatty diacids (**4**–**7**), an α,ω-hydroxyfatty diacid (**8**, 10:0), a fatty acid (**9**, 11:0), a hydroxyfatty acid (**23**, 18:0), an alcohol (**26**), an aldehyde (**24**, 16:1), and an alkane (**3**, 31:0). Conversely, some longer-chain fatty acid (28:0–30:0) and alcohol (20:0–27:0 and 29:0) metabolites reported previously[8] were not detected in the current study (Supporting Information Table 1). Since our GC/MS protocol successfully detects long-chain metabolites, we attribute this discrepancy to cultivar differences or unintended variations in tissue preparation procedures. Longer chain fatty acids, fatty alcohols, and alkanes have also been found previously in native potato periderms[5,7] (Huang et al., unpublished), but their absence in wound-healing tissues is sensible in light of their well-established anatomical and physiological differences.[28] The identified fatty acids included odd-numbered homologues, which have also been reported previously in the wound tissues of potato tubers[8] and are known elsewhere in the plant kingdom.[29] Some polar compounds, such as phenolic acids, sugars, and amino acids, were found in the nonpolar extracts, presumably as a result of bleed-through effects during the partitioning of the soluble layers.

ABTS$^{\bullet+}$ Scavenging Varies with Cultivar, Time Point, and Extract Polarity. It has been proposed that wounding of potato tubers contributes to the formation of reactive oxygen species and subsequent oxidative stress.[30] Nonetheless, both

DOI: 10.1021/acs.jafc.5b03206
J. Agric. Food Chem. 2015, 63, 6810–6822

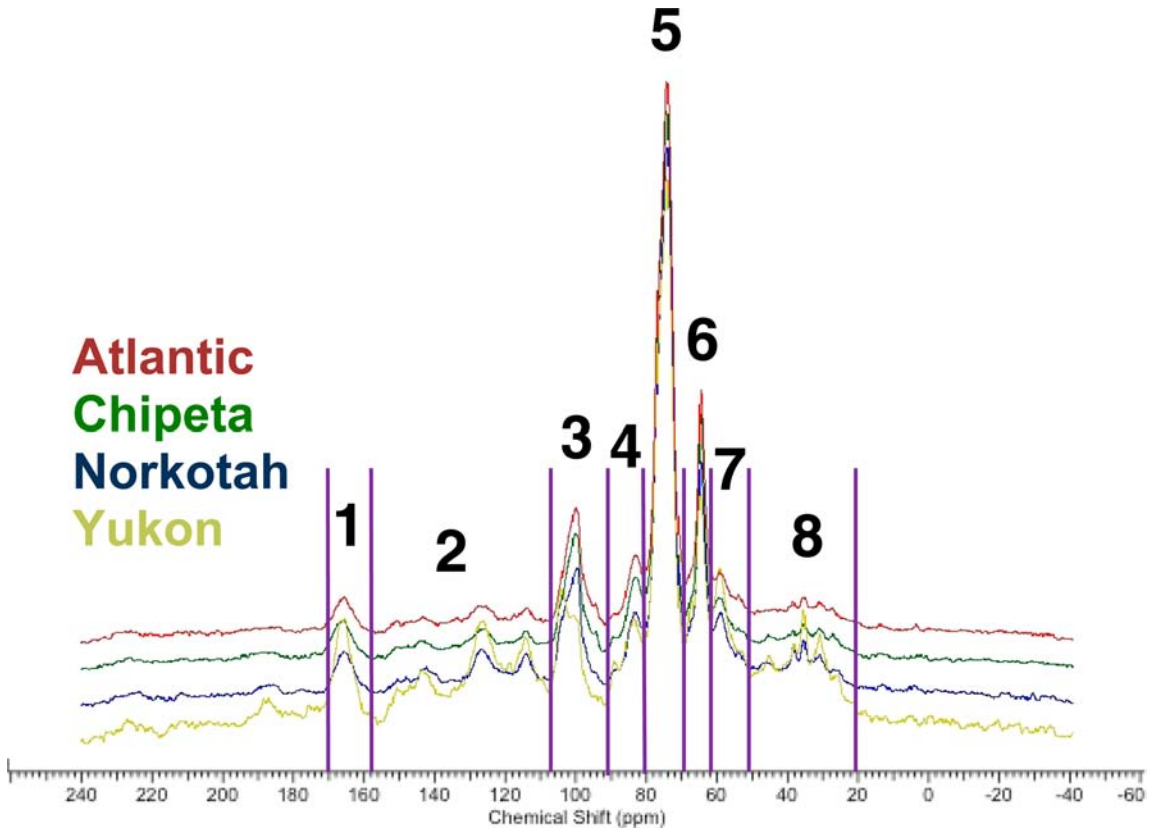

Figure 5. Stacked multi-CP solid-state ^{13}C NMR spectra of representative suberin-enriched tissue samples from each of the four cultivars at the day-7 post wounding time point, showing the chemical moieties present in the solid interfacial layer. The separated regions in the spectra are carboxyl and amide groups (168−180 ppm, region 1); arenes and alkenes (115−160 ppm, region 2); alkoxy groups (96−108, 80−92, 67−80, 59−67 ppm; regions 3−6); methoxy groups (45−59 ppm, region 7); and alkyl chain methylenes (15−45 ppm, region 8). Each spectrum was normalized by setting the largest peak to full scale.

increasing and decreasing stress responses of potato tissues by production of antioxidant chemical compounds have been reported by the same authors in response to wounding.[30,31] To avoid the established limitations of the diphenylpicrylhydrazyl free radical scavenging assay used in prior studies (narrow pH range, steric hindrance, spectral interference),[32,33] we selected an $ABTS^{\bullet+}$ assay. The latter method also permits clean comparisons with our previous investigation[12] of antioxidant activity in polar extracts derived concurrently from the same potato tissue samples. The end result is a more comprehensive picture of antioxidant activity in the potato wound tissues from these four cultivars.

Figure 4 shows that the activities of nonpolar extracts at day 7 postwounding (Figure 4C) are significantly higher than at day 3 postwounding (Figure 4A), supporting an accumulation of antioxidant constituents during the wound-healing process. The order of activity for day-3 nonpolar samples is Norkotah Russet > Chipeta ~ Yukon Gold > Atlantic, whereas at day 7 the trend changes slightly to Norkotah Russet > Chipeta > Yukon Gold ~ Atlantic. Thus, the heavily russeted Norkotah Russet cultivar exhibits the highest scavenging activity for both day-3 and day-7 nonpolar extracts.

As noted above, the applicability of the $ABTS^{\bullet+}$ scavenging assay for antioxidant activity of both polar and nonpolar compounds[32,33] makes it possible to compare the respective data directly. As a group, the antioxidant activities after 45 min of free radical scavenging reaction for both day-3 and day-7 extracts are 50- to 100-fold smaller for the nonpolar samples (Figure 4), reflecting the relative dearth of phenolic and other unsaturated molecular moieties among the nonpolar metabolites. Conversely, it can be deduced that the majority of the antioxidant compounds produced within the healing tissues in response to wounding stress are polar in nature, consistent with prior reports that resistance to infection directly after tuber wounding is related to the appearance of phenolic monomers that subsequently serve as substrates for suberin polyphenolic biosynthesis.[34] The increase in antioxidant activity for nonpolar extracts as healing progresses from day 3 to 7 is in contrast with our observations for the polar portions, which tend to maintain their antioxidant activity levels, except for the Yukon Gold cultivar (Figures 4B and D).[4]

In addition, the $ABTS^{\bullet+}$ assay allows us to evaluate the capacity of both fast- and slow-acting antioxidants.[32] The TEAC values displayed in Figure 4 for both 3- and 7-day time points show overall increases in antioxidant activity throughout the assay period (0−45 min). This trend, which parallels observations made for the corresponding polar tissue extracts,[12] demonstrates the presence of both fast- and slow-acting antioxidants. Finally, the absence of steric hindrance in the $ABTS^{\bullet+}$ assay allows sampling of the scavenging activity of substances with diverse molecular weights and architectural features.[32,33]

Solid-State NMR Tracks Postwounding Development of Suberin Biopolymers. A stacked plot of the quantitatively reliable multi-CP MAS ^{13}C NMR spectra for solid interfacial layers from the four day-7 wound-healing tissues shows largely

DOI: 10.1021/acs.jafc.5b03206
J. Agric. Food Chem. 2015, 63, 6810−6822

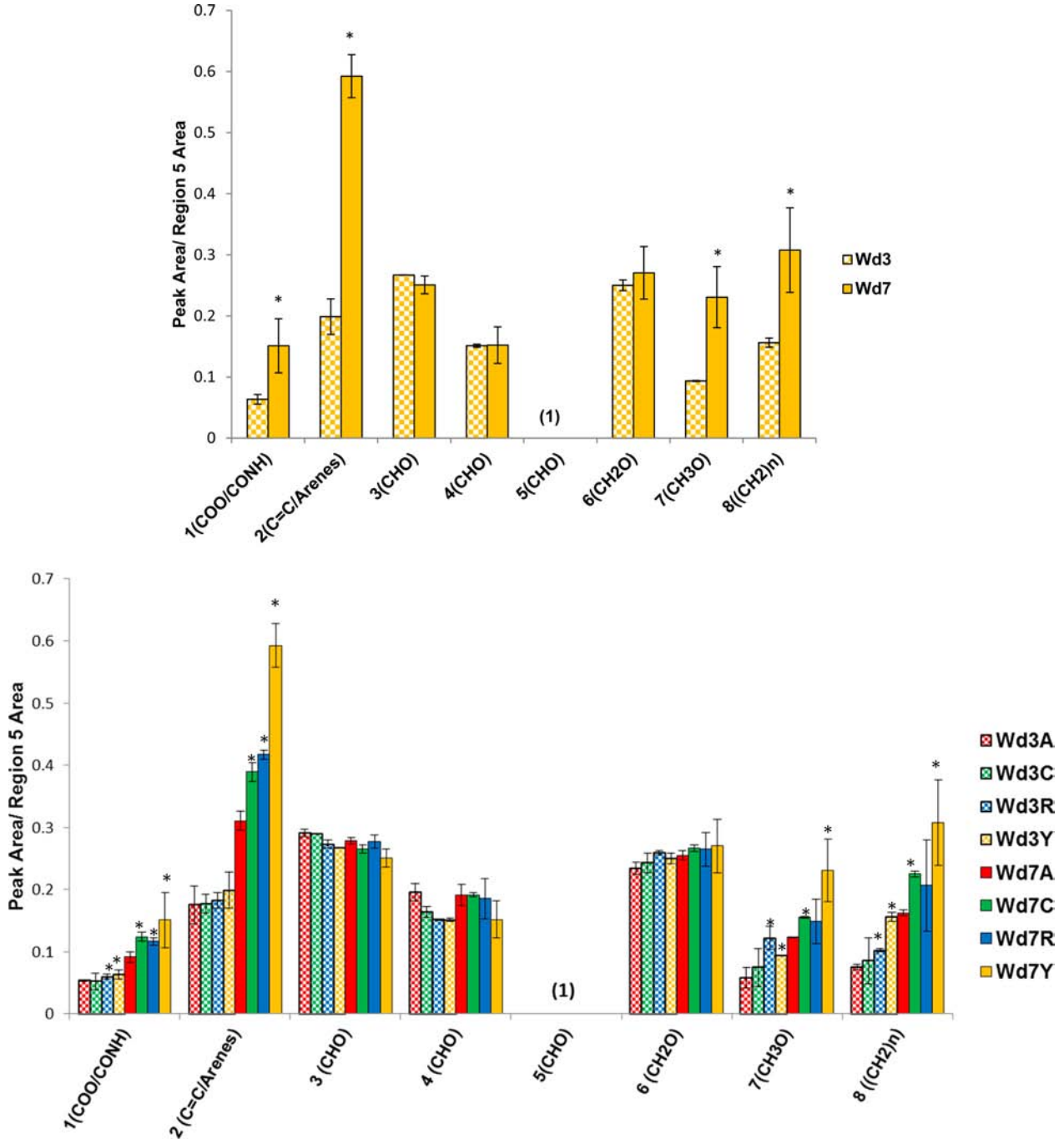

Figure 6. Peak ratios from 150 MHz multi-CP MAS ^{13}C NMR spectra for the solid interfacial layer from suberin-enriched potato wound-healing samples of the Yukon Gold cultivar (top) and all four cultivars (bottom) at days 3 (Wd3) and 7 (Wd7) postwounding, calculated with respect to the major polysaccharide CHO peaks in region 5 (67−80 ppm). The samples are coded for Atlantic (red, A), Chipeta (green, C), Norkotah Russet (blue, R), and Yukon Gold (gold, Y). The data represent the mean ± standard error of the mean of two biological replicates. Asterisks (*) are used to denote the most significant differences in peak area ratio with respect to day 3 (top) and with respect to Atlantic at any wounding time point (bottom) ($P < 0.05$, from Tukey pairwise comparisons).[21]

concordant chemical shifts but clear differences in relative peak intensities (Figure 5). The spectra of the suberin samples at day 7 are similar in appearance to those obtained from the day-7 wound periderm in prior studies of potato tubers.[19,35] (A unique peak at 198 ppm in the Yukon day-7 sample is attributable to a carbonyl within an aldehyde group.) Because quantitative comparisons *between* spectra of different plant materials can be skewed by inconsistencies in mass and instrumental conditions,[36] relative peak ratios *within* each spectrum were used to make compositional comparisons of the interfacial solids at each time point after wounding; the resulting trends were then interpreted in conjunction with metabolomic analyses of the soluble periderm extracts. Illustrative comparisons were made with respect to the major polysaccharide CHO group (region 5; Figure 6) and to the suberin carboxyl/amide groups (region 1; Figure 7).

With respect to the Yukon Gold polysaccharides (region 5), the integrated peak areas of the carboxyl/amide (region 1),

DOI: 10.1021/acs.jafc.5b03206
J. Agric. Food Chem. 2015, 63, 6810−6822

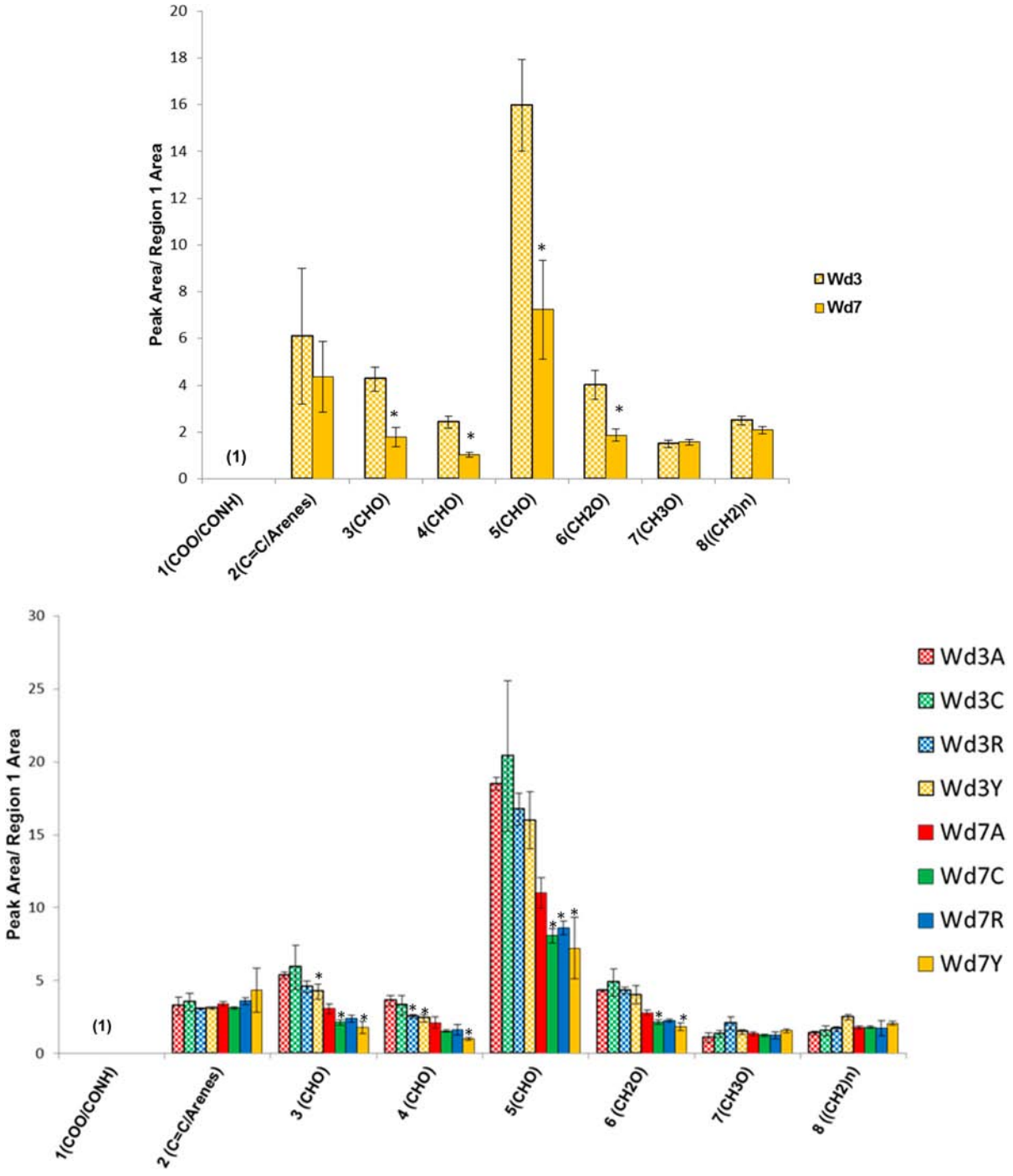

Figure 7. Peak ratios from 150 MHz multi-CP MAS ^{13}C NMR spectra for the solid interfacial layer from suberin-enriched potato wound-healing samples of the Yukon Gold cultivar (top) and all four cultivars (bottom) at days 3 (Wd3) and 7 (Wd7) postwounding, calculated with respect to the carbonyl peak in region 1 (168−180 ppm). The samples are coded for Atlantic (red, A), Chipeta (green, C), Norkotah Russet (blue, R), and Yukon Gold (gold, Y). The data represent the mean ± standard error of the mean of two biological replicates. Asterisks (*) are used to denote the most significant differences in peak area ratio with respect to day 3 (top) and with respect to Atlantic at any wounding time point (bottom) ($P < 0.05$, from Tukey pairwise comparisons).[21]

aromatic/alkene (region 2), methoxy (region 7), and chain methylene groups (region 8) increase significantly at day 7 compared with day 3 postwounding (Figure 6, top). Similar trends are observed for all cultivars (Figure 6, bottom). The relative increase in methylene peak areas for the interfacial layers at day 7 indicates increased hydrophobicity of the wound tissue, which should result in better protection against water loss. The increase in the ratio of methylene chain compounds ($(CH_2)_n$, region 8) is also in accord with the potential marker compounds identified above primarily in day-7 nonpolar extracts, which are mostly compounds containing long-chain aliphatic moieties. Analogously, the increases in peak area ratios involving the carboxyls/amides (COO/CONH, region 1), aromatics (C═C/arenes, region 2), and methoxy groups (CH_3O, region 7) align with the findings of amide-, methoxy-, and carboxyl-containing phenolic markers in our polar wound-

DOI: 10.1021/acs.jafc.5b03206
J. Agric. Food Chem. 2015, 63, 6810−6822

healing tissue extracts.[12] These latter markers include phenolic acids and phenolic amines, including derivatives of ferulic acid that become more abundant at day 7. Moreover, the larger aromatic-to-CHO ratios observed in day-7 Yukon Gold suberin samples (Figures 6) fit with trends observed for the marker compounds in the polar extracts: an increased number of aromatic markers is detected for this cultivar.[12] Together, these correlations suggest that both nonpolar and polar[4] soluble compounds can be viewed as precursors of the suberized cell wall layer that is being formed during the healing process.

At the day-7 time point, when the wound periderm layer is forming, peak area ratios for carboxyl/amide (COO/CONH, region 1), aromatic/alkene (C═C/arenes, region 2), methoxy (CH_3O, region 7), and chain methylene ($(CH_2)_n$, region 8) groups are found to be the highest in Yukon Gold and lowest in Atlantic (Figure 6, bottom, and Figure S2). This observation suggests that the suberin formed in Yukon Gold at day 7 has a higher proportion of long-chain aliphatic compounds, which can provide increased hydrophobicity and lead to decreased water permeability. The small ratio of COO/CONH groups with respect to polysaccharides observed for Atlantic also supports the hypothesis of diminished suberization that was proposed from analysis of the nonpolar soluble marker compounds.

When measured with respect to the carboxyl/amide signals (region 1), the integrated peak areas for oxygenated aliphatic compounds in regions 3−6 are found to decrease for all cultivars between day 3 and day 7 (Figure 7). This trend supports and extends the ratios outlined above: whereas (region 5)/(region 1) is just the inverse of the carbonyl-to-CHO ratio, additional polysaccharide peak areas in regions 3, 4, and 6 also decrease with respect to the suberin esters and amides that contribute to region 1 of the spectrum. Thus, these latter results reinforce the conclusion that deposition of the aliphatic-aromatic suberin polyester within the phellem cell-wall tissues during development of the wound periderm diminishes the polysaccharide-to-fatty acyl ester ratio. As noted above, the relative increase in carbonyl, aromatic, and olefinic groups can be related to both soluble polar and nonpolar potential marker compounds, many of which contain these functional groups. At day 7, Yukon has the lowest and Atlantic the highest peak area ratios for each of the oxygenated aliphatics in regions 3−6 (Figure 7 and Figure S3).

It is also notable that, among the suberin-associated groups, the aromatic/alkene moieties (C═C/arenes, region 2) show the most dramatic increase in relative intensity with respect to the polysaccharide carbons (Figure 6). This finding suggests that the majority of the compounds being deposited in the polyphenolic domain of suberin during the 3-to-7 day time frame originate from the polar extracts, as this is the layer that is rich in aromatic and olefinic structures (phenolic amines, flavonoids, and phenolic acids).[4]

Coordinated Measurements Provide a Chemical Picture of Potato Tuber Wound Healing. GC/MS multivariate analysis shows convergence of the nonpolar soluble metabolite composition at the day-7 time point after wounding of the potato tubers, suggesting induction of a common biosynthetic pathway as a result of wounding and suberization in all four cultivars. A similar trend was observed among the potential polar markers.[12] Analysis of the GC/MS data leads to the identification of 28 potential cultivar-specific and wound-healing marker compounds that discriminate among cultivar types and between wound healing time points day 3 and 7, during closing layer and periderm development. The distribution of nonpolar soluble markers (Figure 3) dovetails with the trends observed in the solid suberin composition of the cultivars at the same time point (Figures 6 and 7). That is, at day 7, Yukon Gold has the highest and Atlantic has the lowest relative amount of solid chain methylene-containing compounds in their respective suberin samples. This observation parallels the trend among the soluble nonpolar fatty acid markers (Figure 3B, Table 2), which at day 3 display the highest number of long-chain and very-long-chain homologues for Yukon Gold but at day 7 are diminished and putatively undergoing incorporation into the solid suberin biopolymer. It is sensible to propose, then, that the hydrocarbon chains of the fatty acid compounds contribute to the solid-state ^{13}C NMR resonance corresponding to the long-chain aliphatic suberin constituents. Conversely, the nonpolar extracts from the Atlantic cultivar exhibit no day-3 markers from these two classes or from glyceryl esters. The paucity of glyceryl esters, dioic acids, and hydroxyfatty acids in nonpolar Atlantic extracts, when considered in conjunction with the lowered proportions of COO/CONH groups in the interfacial solids, suggest a diminished extent of suberization.

For the solid suberized tissues (Figure 7), elevated ratios of methylene chain-containing compounds in the wound-healing tissues of all cultivars at day 7 can increase the periderm hydrophobicity, thereby offering the potential for more protection against water loss. The presence of flavonoid, phenolic acid, and phenolic amine marker compounds, all of which contain carboxyl or amide groups, in the polar extracts at both day-3 and day-7 time points, could also correlate with the deposition of such carbonyl-containing compounds in the Yukon Gold suberin at both time points.[12] The most vigorous deposition of alkenes and arenes at day 7, which is observed for Yukon Gold suberin samples (Figures 6 and 7), is in accord with trends observed among the aromatic markers found in the polar extracts of this cultivar.[12] Nonetheless, we note that rigorous validation of the metabolite profiling and solid-state NMR results for various cultivars at different wound-healing time points would require consideration of cultural, environmental, and geographic factors. A large-scale study including additional earlier and later wound-healing time points would also provide greater insight into these dynamic changes.

The antioxidant results show definitively that the scavenging activities of the nonpolar wound tissue extracts are 50−100 times smaller than those of the corresponding polar extracts, for each time point and for all four cultivars (Figure 4). Therefore, it can be concluded that the majority of the antioxidant compounds produced in the wound tissues are polar compounds, such as phenolic acids and flavonoids. At both day 3 and day 7, the nonpolar extract of Norkotah Russet demonstrated the highest antioxidant activity, an observation that can be attributed to the presence of unsaturated fatty acids among its potential markers. Among the nonpolar metabolite markers are compounds that may offer protection against invasion by plant pathogens based on their previous antimicrobial activity reported in vitro. They include unsaturated fatty acids, oleic acid (**15**, 18:1) and linoleic acid (**17**, 18:2); saturated fatty acids, tetradecanoic acid (**14**, 14:0) and hexadecanoic acid (**12**, 16:0); and the diacid azaleic acid (**5**, 9:0). In addition, we have previously identified marker compounds in polar extracts of the wound tissues that include phenolic amines, glycoalkaloids, flavonoids and phenolic acids, for which in vitro antimicrobial, insecticidal, and antioxidant

DOI: 10.1021/acs.jafc.5b03206
J. Agric. Food Chem. 2015, 63, 6810−6822

properties have been reported and which might offer protection to the wounded tuber surface.[12,37,38] Thus, the chemical picture of the defensive armor of the potato tuber that emerges from the current study encompasses both polar and nonpolar metabolites that may possess antimicrobial, antioxidant, and insecticidal properties and also the solid suberin biopolymer, which can provide robust defensive barriers in diverse cultivars.

■ ASSOCIATED CONTENT

Supporting Information

Table of metabolites, statistical analysis results. The Supporting Information is available free of charge on the ACS Publications website at DOI: 10.1021/acs.jafc.5b03206.

■ AUTHOR INFORMATION

Corresponding Author

*Phone: +1 212 650 8916. E-mail: stark@sci.ccny.cuny.edu.

Funding

Financial support for this work was obtained from the U.S. National Science Foundation (NSF MCB-0843627, 1411984, and 0741914 to R.E.S.), a PSC−CUNY Grant from the City University of New York (TradA-45-367 to V.C.P.), and a mobility grant from the Spanish Ministry of Education (JC2010-0147 to O.S.). The NMR resources were supported by The City College of New York (CCNY) and the CUNY Institute of Macromolecular Assemblies, with infrastructural assistance provided by the National Institutes of Health through the National Center for Research Resources (2G12RR03060) and National Institute on Minority Health and Health Disparities (8G12 MD007603). The GC/MS instrument was supported by NSF (CHE-0840498).

Notes

The authors declare no competing financial interest.

■ ACKNOWLEDGMENTS

Joe Nuñez (University of California Cooperative Extension) supplied the potato tubers for analysis. The authors would like to acknowledge Dr. Hsin Wang, Cristina Veresmortean, and Boris Kalmatsky for their valuable technical assistance with the NMR and GC/MS instruments. We thank Oseloka Chira for his diligent work in processing the NMR data. Professor David Jeruzalmi provided generous access to the microplate reader.

■ ABBREVIATIONS USED

ABTS$^{\bullet+}$, 2,2′-azinobis (3-ethylbenzothiazoline-6-sulfonic acid ammonium salt) free radical; CPMAS, cross-polarization magic-angle spinning; DPMAS, direct polarization magic-angle spinning; MSTFA, *N*-methyl-*N*-(trimethylsilyl)-trifluoroacetamide; OPLS-DA, orthogonal partial least-squares discriminate analysis; PCA, principal component analysis; TMCS, trimethylchlorosilane

■ REFERENCES

(1) Varns, J. L.; Schaper, L. A.; Preston, D. A. Potato losses during the first three months of storgae for processing. *Am. Potato J.* **1985**, *62*, 91−99.

(2) Franke, R.; Schreiber, L. Suberin- a biopolyester forming apoplastic plant interfaces. *Curr. Opin. Plant Biol.* **2007**, *10*, 252−259.

(3) Beisson, F.; Li-Beisson, Y.; Pollard, M. Solving the puzzles of cutin and suberin polymer biosynthesis. *Curr. Opin. Plant Biol.* **2012**, *15*, 329−337.

(4) Bernards, M. A. Demystifying suberin. *Can. J. Bot.* **2002**, *80*, 227−240.

(5) Mattinen, M.-L.; Filpponen, I.; Järvinen, R.; Li, B.; Kallio, H.; Lehtinen, P.; Argyropoulos, D. Structure of the polyphenolic component of suberin isolated from potato (*Solanum tuberosum* var. Nikola). *J. Agric. Food Chem.* **2009**, *57*, 9747−9753.

(6) Graça, J.; Santos, S. Suberin: A biopolyester of plant's skin. *Macromol. Biosci.* **2007**, *7*, 128−135.

(7) Järvinen, R.; Silvestre, A. J. D.; Holopainen, U.; Kaimainen, M.; Nyyssölä, A.; Gil, A. M.; Pascoal Neto, C.; Lehtinen, P.; Buchert, J.; Kallio, H. Suberin of potato (Solanum tuberosum var. Nikola): Comparison of the effect of cutinase CcCut1 with chemical depolymerization. *J. Agric. Food Chem.* **2009**, *57*, 9016−9027.

(8) Yang, W.-L.; Bernards, M. A. Metabolite profiling of potato (*Solanum tuberosum* L.) tubers during wound-induced suberization. *Metabolomics* **2007**, *3*, 147−159.

(9) Neubauer, J. D.; Lulai, E. C.; Thompson, A. L.; Suttle, J. C.; Bolton, M. D. Wounding coordinately induces cell wall protein, cell cycle and pectin methyl esterase genes involved in tuber closing layer and wounding periderm development. *J. Plant Physiol.* **2012**, *169*, 586−595.

(10) Lulai, E. C.; Corsini, D. L. Differential deposition of suberin phenolic and aliphatic domains and their roles in resistance to infection during potato tuber (*Solanum tuberosum* L.) wound healing. *Physiol. Mol. Plant Pathol.* **1998**, *53*, 209−222.

(11) Yang, W.-L.; Bernards, M. A. Wound-induced metabolism in potato (*Solanum tuberosum*) tubers. *Plant Signaling Behav.* **2006**, *1*, 59−66.

(12) Dastmalchi, K.; Cai, Q.; Zhou, K.; Huang, W.; Serra, O.; Stark, R. E. Solving the Jigsaw puzzle of wound-healing potato cultivars: Metabolite profiling and antioxidant activity of polar extracts. *J. Agric. Food Chem.* **2014**, *62*, 7963−7975.

(13) Choi, H.-K.; Choi, Y. H.; Verberne, M.; Lefeber, A. W. M.; Erkelens, C.; Verpoorte, R. Metabolic fingerprinting of wild type and transgenic tobacco plants by ^{1}H NMR and multivariate analysis technique. *Phytochemistry* **2004**, *65*, 857−864.

(14) Kim, H. K. C.; Choi, Y. H.; Verpoorte, R. NMR-based metabolomic analysis of plants. *Nat. Protoc.* **2010**, *5*, 536−549.

(15) Katajamaa, M.; Miettinen, J.; Orešič, M. MZmine: Toolbox for processing and visualization of mass spectrometry based molecular profile data. *Bioinformatics* **2006**, *22*, 634−636.

(16) Worley, B.; Powers, R. Multivariate analysis in metabolomics. *Curr. Metabol.* **2013**, *1*, 92−107.

(17) Wiklund, S., Multivariate Data Analysis and Modelling in "Omics". Umetrics AB: San Jose, CA, 2008.

(18) Fung, B. M.; Khitrin, A. K.; Ermolaev, K. An improved broadband decoupling sequence for liquid crystals and solid. *J. Magn. Reson.* **2000**, *142*, 97−101.

(19) Serra, O.; Chatterjee, S.; Figueras, M.; Molinas, M.; Stark, R. E. Deconstructing a plant macromolecular assembly: Chemical architecture, molecular flexibility, and mechanical performance of natural and engineered potato suberins. *Biomacromolecules* **2014**, *15*, 799−811.

(20) Johnson, R. L.; Schmidt-Rohr, K. Quantitative solid-state ^{13}C NMR with signal enhancement by multiple cross polarization. *J. Magn. Reson.* **2014**, *239*, 44−49.

(21) Jackson, S. *Research methods: A modular approach*; Cengage Learning: Stamford, CT, 2014; p 316−317.

(22) Quintanilla-Licea, R.; Morado-Castillo, R.; Gomez-Flores, R.; Laatsch, H.; Verde-Star, M. J.; Hernández-Martínez, H.; Tamez-Guerra, P.; Tamez-Guerra, R.; Rodríguez-Padilla, C. Bioassay-guided isolation and identification of cytotoxic compounds from *Gymnospera glutinosum* leaves. *Molecules* **2012**, *17*, 11229−11241.

(23) Liu, S.; Ruan, W.; Li, J.; Xu, H.; Wang, J.; Gao, Y.; Wang, J. Biological control of phytopathogenic fungi by fatty acids. *Mycopathologia* **2008**, *166*, 93−102.

(24) Ginzberg, I. Wound-periderm formation. In *Induced plant resistance to Herbivory*, Schaller, A., Ed. Springer: Berlin, 2008.

(25) Walters, D.; Raynor, L.; Mitchell, A.; Walker, R.; Walker, K. Antifungal activities of four fatty acids against plant pathogenic fungi. *Mycopathologia* **2004**, *157*, 87−90.

DOI: 10.1021/acs.jafc.5b03206
J. Agric. Food Chem. 2015, 63, 6810−6822

(26) Wang, W.; Tian, S.; Stark, R. E. Isolation and identification of triglycerides and ester oligomers from partial degradation of potato suberin. *J. Agric. Food Chem.* **2010**, *58*, 1040−1045.
(27) Jung, H. W.; Tschaplinski, T. J.; Wang, L.; Glazebrook, J.; Greenberg, J. T. Priming in systemic plant immunity. *Science* **2009**, *324*, 89−91.
(28) Schreiber, L.; Franke, R.; Hartmann, K. Wax and suberin development of native and wound periderm of potato (*Solanum tuberosum*) and its relation to peridermal transpiration. *Planta* **2005**, *220*, 520−530.
(29) Řezanka, T.; Sigler, K. Odd-numbered very-long-chain fatty acids from the microbial, animal and plant kingdoms. *Prog. Lipid Res.* **2009**, *48*, 206−238.
(30) Reyes, L. F.; Villarreal, J. E.; Cisneros-Zevallos, L. The increase in antioxidant capacity after wounding depends on the type of fruit or vegetable tissue. *Food Chem.* **2007**, *101*, 1254−1262.
(31) Reyes, L. F.; Cisneros-Zevallos, L. Wounding stress increases the phenolic content and antioxidant capacity of purple-flesh potatoes (*Solanum tuberosum* L.). *J. Agric. Food Chem.* **2003**, *51*, 5296−5300.
(32) Prior, R. L.; Wu, X.; Schaich, K. Standardized methods for the determination of antioxidant capacity and phenolics in foods and dietary supplements. *J. Agric. Food Chem.* **2005**, *53*, 4290−4302.
(33) Magalhães, L. M.; Segundo, M. A.; Reis, S.; Lima, J. L. F. C. Methodological aspects about in vitro evaluation of antioxidant properties. *Anal. Chim. Acta* **2008**, *613*, 1−19.
(34) Lulai, E. C., Skin-set, wound-healing, and related defects. In *Potato biology and biotechnology. Advances and Perspectives*, 1st ed.; Vreugdenhil, D.; Bradshaw, J.; Gebhardt, C.; Govers, F.; Mackerron, D. K. L.; Taylor, M. A.; Ross, H. A., Eds.; Elsevier: Oxford, UK, 2007; pp 471−500.
(35) Yan, B.; Stark, R. E. Biosynthesis, molecular structure, and domain architecture of potato suberin: A ^{13}C NMR study using isotopically labeled precursors. *J. Agric. Food Chem.* **2000**, *48*, 3298−3304.
(36) Kolodziejski, W.; Klinowski, J. Kinetics of cross-polarization in solid-state NMR: A guide for chemists. *Chem. Rev.* **2002**, *102*, 613−628.
(37) Back, K. Hydroxycinnamic acid amides and their possible utilization for enhancing agronomic traits. *Plant Pathology J.* **2001**, *17*, 123−127.
(38) Milner, S. E.; Brunton, N. P.; Jones, P. W.; O' Brien, N. M.; Collins, S. G.; Maguire, A. R. Bioactivities of glycoalkaloids and their aglycones from *Solanum tuberosum*. *J. Agric. Food Chem.* **2011**, *59*, 3454−3484.

DOI: 10.1021/acs.jafc.5b03206
J. Agric. Food Chem. 2015, 63, 6810−6822

Table 1. Names of Samples Used in This Experiment[a]

accession name	abbrev	original pedigree	species	class	country of origin
Merlot	MER	Magdeleine noire des Charentes × Cabernet Franc	*V. vinifera*	vinifera	France
Moscato Rosa	MOR	unknown	*V. vinifera*	vinifera	Greece
Gewuerztraminer	GWT	unknown	*V. vinifera*	vinifera	Italy
Moscato Ottonel	MOT	Chasselas × Muscat d'Eisenstadt	*V. vinifera*	vinifera	France
Iasma Eco 3*	ECO	Moscato Ottonel × Malvasia Bianca di Candia	*V. vinifera*	vinifera	Italy
Riesling	RIE	(*V. sylvestris* × Traminer) (?) × Heunisch weiss	*V. vinifera*	vinifera	Germany
Sauvignon Blanc	SAU	unknown	*V. vinifera*	vinifera	France
Nero	NER	Eger 2 × Gardonyi Geza	Seibel derivative hybrid	hybrid	Hungary
Isabella	ISA	*V. vinifera* × *V. labrusca*	American/European hybrid	hybrid	USA
Millardet et Grasset 41 B	41B	Chasselas × *V. berlandieri*	American/European hybrid	hybrid	France
V. cinerea	VCI	*V. cinerea* Engelmann	*V. cinerea*	American	USA
V. californica	VCA	*V. californica*	*V. californica*	American	USA
V. arizonica Texas	VAT	*V. arizonica* Engelmann	*V. arizonica* Texas	American	USA
Kober 5 BB	K5BB	*V. berlandieri* × *V. riparia*	American hybrid	American	Germany

[a]All samples were collected at 18 °Brix during the 2013 season. Sample names are from the *Vitis International Variety Catalogue* website www.vivc.de; the FEM collection is reported at the website with the number ITA362.

Conversely, explorative untargeted analysis of the metabolomes of wild American grapes is lacking. From our point of view, it is necessary to extend the analytical coverage of the metabolites present in wild grape berries and try to understand which undesirable (and desirable) traits are present in these species. It may be the case that wild American grapes have metabolic pathways not present in *V. vinifera*, producing "interesting" classes of metabolites. For example, hydrolyzable tannins are present in *Vitis rotundifolia*,[16] and lignans are accumulated in *Vitis thunbergii*.[17] These classes of metabolites might be present in other species, or different classes might be accumulated in unstudied *Vitis*. The transfer of such desirable traits to new hybrids could be worth considering.

All of the grapes used in this study are from the Fondazione Edmund Mach, where this research was carried out; here we maintain a large collection of grape varieties, including interspecific hybrids, rootstocks, and wild American grapes, recently genotyped[11] and uploaded to the *Vitis International Variety Catalogue* repository (www.vivc.de, institute no. ITA362). In this "proof of principle" study, the aim was to study comparatively the metabolic profiles of the berry tissues of four different wild American grapes as compared to seven commonly used *V. vinifera* cultivars, through untargeted LC-MS analysis, with two different goals: (1) to find differences in the metabolomes of the American *Vitis* and *V. vinifera* and (2) to discuss their importance in terms of grape quality (especially for wine production). Three interspecific hybrids were also included in the study. Two of them are first-generation inbreeds (41B and Isabella), whereas the third, Nero, is a PIWI variety obtained after numerous backcrosses with *vinifera* material. The inclusion of these three varieties aimed at understanding how the differences found between the two groups can be transferred to the hybrids. The inclusion of Nero, a variety registered for vinification in 1993, made it possible to understand, for this case study, whether the selection performed without the use of molecular markers was able to eliminate all of the undesirable traits and keep the desirable ones.

MATERIALS AND METHODS

Reagents. Acetonitrile, methanol, and formic acid of LC-MS grade were purchased from Sigma-Aldrich (Milan, Italy). Water was of Milli-Q grade obtained from a Millipore system (Millipore, Billerica, MA, USA). Phloroglucinol was purchased from Sigma-Aldrich. We built a standard set of around 600 common grape and wine metabolites, purchased from Sigma-Aldrich or Extrasynthese, and they were injected under the conditions described by Theodoridis et al.[18] Each standard spectrum was manually extracted and used to automatically assign the name to the compounds from the sample analysis.[22] The whole standard set used in this experiment has already been reported by Shahaf et al.[19]

Sample Preparation. One kilogram of each grape at technical maturity (using criteria similar to those of Liang et al.[14]) was harvested from the germplasm collection of the Fondazione Edmund Mach at San Michele all'Adige (TN), Italy. The skin, pulp, and seeds of fresh berries were manually separated, ground under liquid nitrogen, and stored at −80 °C until analysis. A list of the grapes analyzed in this work is available in Table 1.

Extraction for untargeted analysis was performed according to the optimized method of Theodoridis et al.,[18] slightly modified. Briefly, 1 g of ground tissue was extracted with methanol/water/chloroform 2:1:2 and 0.1% formic acid, vortexed, sonicated for 10 min, further agitated in an orbital shaker for 15 min, and then centrifuged at 5000 rpm for 5 min. The upper organic phase was collected and filtered through 0.22 μm PVDF Millipore Millex-GV filters before injection. Three replicates per variety, each from a different bunch of grapes, were selected for the analysis. Only healthy berries have been chosen.

Sample preparation for the quantification of the condensed tannin fraction by phloroglucinolysis was performed using a validated protocol.[20] Briefly, 1 g of ground tissue was extracted with 5 mL of methanol for 24 h, dried in a Rotavapor, and reconstituted with 10 mL of water. The water extract was loaded onto a C18 Sep-pak, washed with 40 mL of water, and eluted with 30 mL of methanol. The elute was dried in a Rotavapor and reconstituted with 1 mL of methanol. Nine hundred microliters of this extract was diluted 1:1 with methanol, filtered, and injected into the LC-MS system. The remaining 100 μL of the elute was added to 100 μL of phloroglucinol (100 g/L) at a reaction temperature of 50 °C. After 20 min, the reaction was stopped with 1 mL of sodium acetate (40 mM), diluted 1:5 with water/methanol, and injected for targeted condensed tannins analysis.

LC-MS Workflow, Analysis and Data Treatment. Untargeted LC-MS analysis was performed using a UPLC, interfaced through the ESI source to a "Synapt" (UHPLC-ESI-Q-TOF-MS), supplied by Waters (Manchester, UK). We used our standard LC method recently published.[21] Briefly, starting with 100% eluent A (0.1% formic acid in water), switching at 1.5 min to 10% of eluent B (0.1% formic acid in methanol) up to 3 min, then a gradient of up to 40% eluent B in 18 min, passing to 100% eluent B in 21 min, holding for up to 25 min, and then re-equilibrating back to 100% eluent A for a total run of 28 min. The MS settings were kept the same as the ones used for the standard set injection.[18]

All of the samples of the three different tissues were injected in the same injection sequence. The analysis workflow consisted of a starting

DOI: 10.1021/acs.jafc.5b01999
J. Agric. Food Chem. 2015, 63, 6823−6834

queue of one blank, one standard mix (a mixture of 15 common grape metabolites, STDmix), three "quality controls" (QCs), which consisted of three pooled samples specific for each tissue (one for the skin, one for the flesh, and one for the seeds from all of the grapes), and one pooled sample containing all of the tissues (the whole berry). During the analysis we injected a standard mix every 20 analyses and a QC representative for each tissue after every 8 sample injections. The acquired spectra were directly converted to NetCDF files using Databridge software (Waters). Peak picking, alignment, and principal component analysis (PCA) were performed using the automated data analysis pipeline MetaDB, developed at our institution.[22] This package supports the execution of experiment compatible with the concept of interoperable bioscience data, including both the production of a validated experimental data set with the relevant metadata in ISA-Tab format. The workflow of MetaDB consists of six different steps: (1) upload of metadata in ISA-Tab format; (2) preparation of MS acquisition sequence, including sample randomization; (3) upload of raw and derived spectral data files; (4) data processing for feature alignment and detection with metaMS (http://www.bioconductor.org/packages/release/bioc/html/metaMS.html); (5) visualization of data for quality assessment; (6) preparation of data for upload to public repositories (Metabolights).

Targeted LC-MS/MS analysis was performed using a UPLC-adapted version of the method described by Fortes Gris et al.[20] The samples were injected into a UPLC chromatograph, interfaced to a TQ mass spectrometer (UHPLC-ESI-QqQ-MS, Waters, Manchester, UK) through an ESI source. The eluents used were water with 0.1% formic acid (eluent A) and acetonitrile with 0.1% FA (eluent B). The gradient was as follows: starting from 95% of A, to 20% of B in 3 min; isocratic flow to 4.3 min, and then ramping to 45% of B at 9 min. Then 100% of B at 11 min, holding up to 13 min, and returning to the initial conditions of 95% of A for a total run of 17 min. The quantification of catechin, epicatechin, procyanidins B1 and B2, gallocatechin, epigallocatechin, and epicatechin gallate was done using a linear regression curve built on the injection of pure chemical standards, in the same analytical conditions through MRM. Quantification of phloroglucinol-bound flavanols was done as for epicatechin, epigallocatechin, and epicatechin gallate equivalents, respectively.

Statistical Analysis. The stability of the untargeted analysis was assured during the workflow, checking the repeatability of the QCs and STDmix injections manually by integrating representative peaks and through PCA. We also checked that the CV percentage of the internal standards (gentisic acid, 3-indole-propionic acid, and 4-stilbenol) was below 25%. The metabolic differences between the *V. vinifera* varieties and the wild American *Vitis* was obtained using two statistical tests: (1) univariate *t*-test analysis with corrected *p* values using the "fdr" function setting 0.05 corrected *p* value and 10-fold change as thresholds in R environment;[23] (2) multivariate statistical analysis using SIMCA-P +12.0 software performing OPLS-DA analysis, using 1 VIP value as threshold.[24] The boxplots on the procyanidin content have been created using Statistica 9.1 software (Statsoft, 2010).

Database Matching. The identification of compounds is one of the main bottlenecks in untargeted LC-MS analysis, due to the multiple signals from the same metabolite in the MS spectrum. An automatic identification pipeline based on injected standards has been established in our institution,[22] but the whole standard set was injected in a chromatographic gradient that we did not use in this experiment. To overcome this problem, we aligned the two chromatographic runs using standards injected in both, and we performed retention time prediction using the Web site predret.org.[25] The list of biomarkers was matched against the peak table using the db.comp.assign function in the R package "Chemhelper" (github.com/stanstrup/chemhelper), with 30 ppm mass accuracy and a 1 min retention time window. The biomarkers spotted by the Chemhelper package were further manually verified for correctness against pure chemical standards injected under the same chromatographic conditions. This allowed us to unambiguously assign MSI identification level 1 to all matching biomarkers.[26]

The remaining biomarkers not present in our standard database were considered as unknowns and underwent further identification steps summarized under Compound Identification Strategy below.

MS/MS Analysis. All of the analysis was done in V mode (improved sensitivity, nominal resolution 10000); precursor ions were selected in the quadrupole and fragmented in the collision cell through a collision energy profile ranging from 20 to 35 eV, with leucine enkephaline as internal calibrant. Collected MS/MS spectra were queried in MetFrag[27] and MetFusion[28] using KEGG, Chemspider, or PubChem as compound databases and MassBank-EU as the spectral database.

Isotopic Pattern Recognition and Formula Assignment. The isotopic patterns of all biomarkers were obtained using a strategy already published,[29] based on intensity-weighted means of the isotopes automatically identified by CAMERA.[54] Putative chemical formulas were obtained using these isotopic patterns through the getFormula function of the Rdisop package in the R environment.[30]

Compound Characteristics Comparison. An important identification step was "Compounds Characteristics Comparison" (CCC): This method was established in our group, and it is currently being prepared for publication. The idea behind the method is that the characteristics (RT, *m*/*z*, isotopic pattern, etc.) of the pseudomolecular ion of a compound detected in LC-MS are typical of its structure, so comparing the characteristics of the standards in our database with those from the unknown biomarkers allows us to reduce the number of possible structures to just a few plausible structures (L.N., Ph.D. thesis, chapter 6). It is a multivariate regression model built on retention time, *m*/*z*, and the isotopic intensities of standard collection that predicts the main substructures present in the compounds. Therefore, the values of these parameters are used together to validate the prediction properties of the model and estimate the presence of particular substructures in the compound (phenolic groups, aliphatic chains, acidic groups, glycosides, and so on). From the predicted substructures, the structure is further rebuilt and makes it possible to exclude all of the nonmatching structures proposed by the in silico analysis of the MS/MS spectra. It aids both formula calculation and structure elucidation.

Nonetheless, this method is a supplementary step in the common identification strategy described by Stanstrup et al.;[29] the method only helps to filter out improbable candidates, but it is not a stand-alone method, and the final identifications still rely on the common MS/MS analysis (Supplementary Figure 1).

Compound Identification Strategy. The following identification strategy is schematically summarized in Supplementary Figure 1. After database matching, the remaining unknown markers were subjected to MS/MS analysis. The acquired spectra were queried against MetFrag/MetFusion, and the chemical structure list obtained was compared to the putative chemical formula and the CCC method and manually verified for correctness. If any of the structure matched all of the characteristics, this biomarker was considered to have been identified at MSI level 2. Otherwise, if no match was found, a tentative structure was sketched, based on the putative class predicted by the CCC method, the putative formula calculated by both Rdisop and CCC methods, and the losses and neutral losses observed in MS/MS analysis. The putative structure was queried again against MetFrag; when a higher score was found for the sketched structure in comparison to the previous ones, the biomarker was labeled as MSI level 2 or 3, depending on how likely the spectral matching was.

Data Mining. Heatmaps were drawn using the heatmap.2 function of the gplots package in the R environment. The data were scaled to unit variance prior to calculation of the dendrograms. The dendrograms were constructed by hierarchical clustering analysis using "Canberra" as the distance function and Ward.D2 as the hierarchical clustering function.

Data Sharing. The whole experimental data set is available in the Metabolights repository under the code MTBLS209.

RESULTS AND DISCUSSION

Statistical Analysis. In the data analysis, we used both univariate and multivariate statistical tests. The tests are not mutually exclusive, whereas their combined use is suggested especially when the "curse of dimensionality" arises.[23,31] Tens to hundreds of "features" were recognized as markers in the different tissues. The marker lists were merged, and duplicates were excluded. Features in the same CAMERA[54] group were

DOI: 10.1021/acs.jafc.5b01999
J. Agric. Food Chem. 2015, 63, 6823−6834

excluded, keeping only the supposed pseudomolecular ions. The pseudomolecular ions were subsequently integrated using Targetlynx to manually supervise the data and eliminate false positives and incorrect peak-picking. The results of statistical analysis are shown in Table 2.

Table 2. Markers and Identified Pseudomolecular Ions: Number of Total Features Detected, Total Biomarkers in Each Tissue, Total Pseudomolecular Ions, and Identified Compounds[a]

			marker features		pseudomolecular ions		identified	
tissue	ionization mode	features	Vv	AV	Vv	AV	Vv	AV
flesh	positive	7726	20	117	6	24	3	21
flesh	negative	8906	14	88	8	18	5	14
seeds	positive	12607	32	44	12	10	10	9
seeds	negative	12624	57	52	23	5	23	2
skin	positive	13332	44	106	9	37	7	35
skin	negative	15826	36	280	13	29	12	29

[a]Vv, *Vitis vinifera*; AV, American *Vitis*.

Identified Compounds. The biomarkers underwent all of the identification steps described under Materials and Methods. In total, we were able to identify 32 biomarker metabolites in the flesh, 26 in the seeds, and 44 in the skin at MSI level 1 (Supplementary Table 1). The rest of the markers were considered "unknowns" and underwent compound identification strategy.

The whole identification strategy is described in Supplementary Figure 1. In total we could identify 13 compounds as MSI level 2 in the flesh, 13 compounds as MSI level 2, and 6 as MSI level 3 in the seeds as well as 42 compounds as MSI level 2 and 1 as MSI level 3 in the skin (Supplementary Table 1).

Comparative Analysis. All of the identified metabolites were grouped according to their biosynthetic pathway, and the hierarchical clustering analysis was performed on all of the samples using this information. The results are shown in Figures 1 and 2 (skin and seeds, respectively) and in Supplementary Figure 2 (flesh). Procyanidins, hydrolyzable tannins, aroma precursors, polar lipids, sugars, organic acids, anthocyanins, flavonols, and stilbenoids showed different accumulations in the two groups. The latter three compound classes have already been

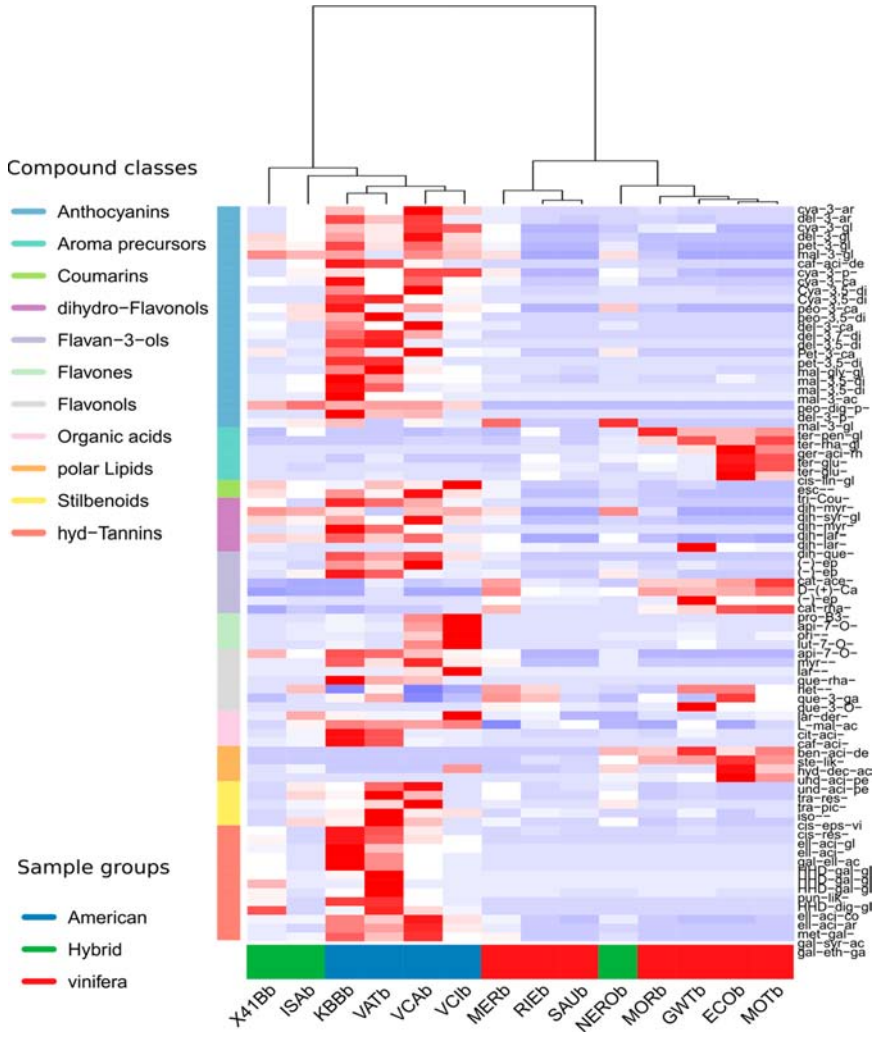

Figure 1. Heatmap of biomarkers from the skin. The legend on the left indicates the biosynthetic class of the compounds. The full names of the compounds shown in the right border can be found in Supplementary Table 1. The legend on the bottom indicates the sample groups. The values have been mean-centered and scaled to unit variance prior to the analysis, using as limits ±3 standard deviations. Red color indicates higher concentration; blue color indicates lower concentration.

DOI: 10.1021/acs.jafc.5b01999
J. Agric. Food Chem. 2015, 63, 6823−6834

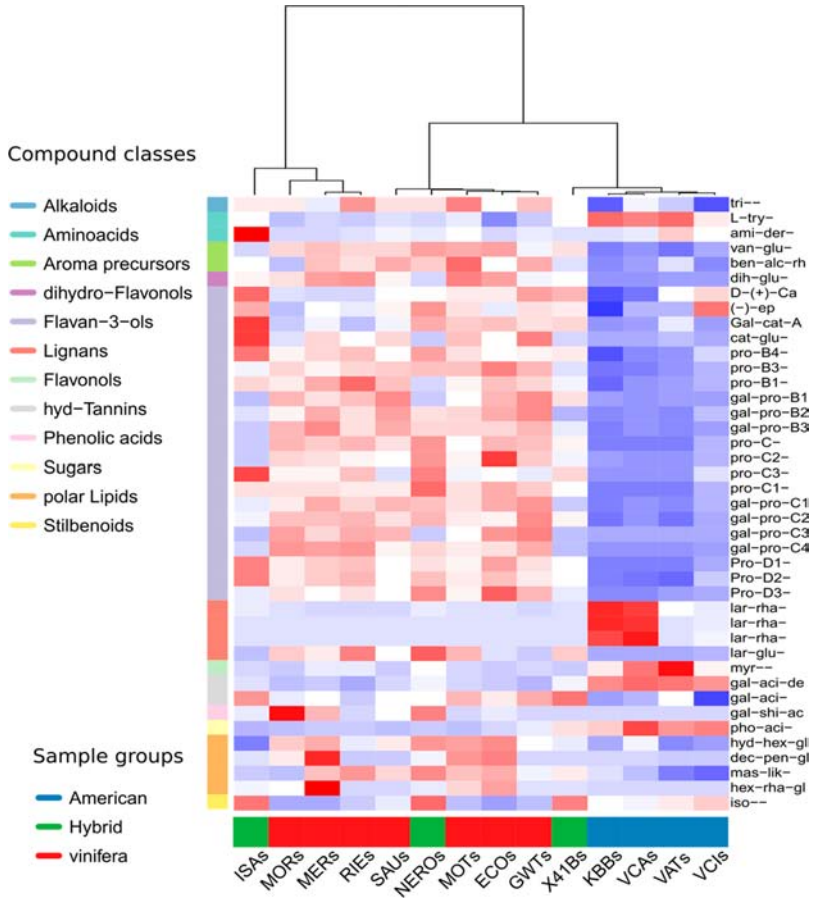

Figure 2. Heatmap of biomarkers from the seeds. The legend on the left indicates the biosynthetic class of the compounds. Full names of the compounds shown in the right border can be found in Supplementary Table 1. The legend on the bottom indicates the sample groups. The values have been mean-centered and scaled to unit variance prior to the analysis, using as limits ±3 standard deviations. Red color indicates higher concentration; blue color indicates lower concentration.

reported to be differently accumulated in *V. vinifera* and wild American grapes in previous papers[14,32,33] and will be discussed only briefly below. In the following section, we focus in particular on the first three compound classes, because their behavior has not been reported previously and it is very interesting from both enological and biological points of view.

Flavan-3-ols and Procyanidins. Flavan-3-ols are a very important class of polyphenols in grape and wine production, especially in their polymeric forms, that is, procyanidins. Procyanidins are a type of condensed tannins responsible for the astringency in wine and constitute the body of the wine, together with the alcohol and some lipids. Their content is very important, especially in red wine production: lack of procyanidins means poor-quality red wines.[55] The procyanidins are also recognized as the main antioxidants accumulated in grapes, and they have multiple health-related characteristics.[34,35] Unfortunately, the whole accumulation and polymerization pathway of procyanidins is still unknown, as reported in the KEGG repository in the map http://www.kegg.jp/pathway/map01061+C06562.

Flavan-3-ols via Untargeted Metabolomics. Differences were found in the accumulation of flavan-3-ols and procyanidins in the skin and seeds of the two groups. In the skin, *V. vinifera* was richer in catechin, epicatechin, catechin-rhamnoside, and procyanidin B3 (Figure 1). It is also richer in other dimeric, trimeric, and tetrameric forms of procyanidins, but this difference did not exceed the selected threshold (10-fold). Surprisingly, American *Vitis* accumulated higher levels of catechin-gallate and epicatechin-gallate. *V. vinifera* seeds were richer in all of the flavan-3-ols and procyanidins that we identified directly in untargeted analysis (Figure 2). A recent paper[15] reported a similar result: in this study, *V. vinifera* contained a higher level of monomeric, dimeric, and trimeric procyanidins in the seeds, in comparison to many different *Vitis* species except for *Vitis palmata*. Another study[36] obtained a similar result when comparing *V. vinifera* with *Vitis labrusca* seeds.

Procyanidins via Targeted Protocols. As stated earlier, the accumulation of procyanidins is related with many desirable characteristics; we therefore decided to perform targeted analysis of procyanidins, to quantify the difference between the two groups precisely, using a validated method.[20] The results obtained from targeted analysis are summarized in Figure 3. *V. vinifera* varieties showed a higher accumulation of both free flavanols and polymeric procyanidins, especially the latter, in the skin. The amount of procyanidins accumulated in *V. vinifera* skin was on average 30 times higher (from 5500 to 17000 mg/kg) in comparison to wild American grapes (200−650 mg/kg). The difference in free flavanols was about 8 times higher in *V. vinifera*, whereas American grapes accumulated a higher percentage (≈3%) of galloylated forms in comparison to *vinifera* grapes (≈1%) (reported in supplementary tables—skin procyanidins). As expected, the mean degree of polymerization (mDP) was higher in *V. vinifera* (25−52 units), in comparison to wild American grapes (4−17 units). The hybrid varieties showed a

DOI: 10.1021/acs.jafc.5b01999
J. Agric. Food Chem. 2015, 63, 6823−6834

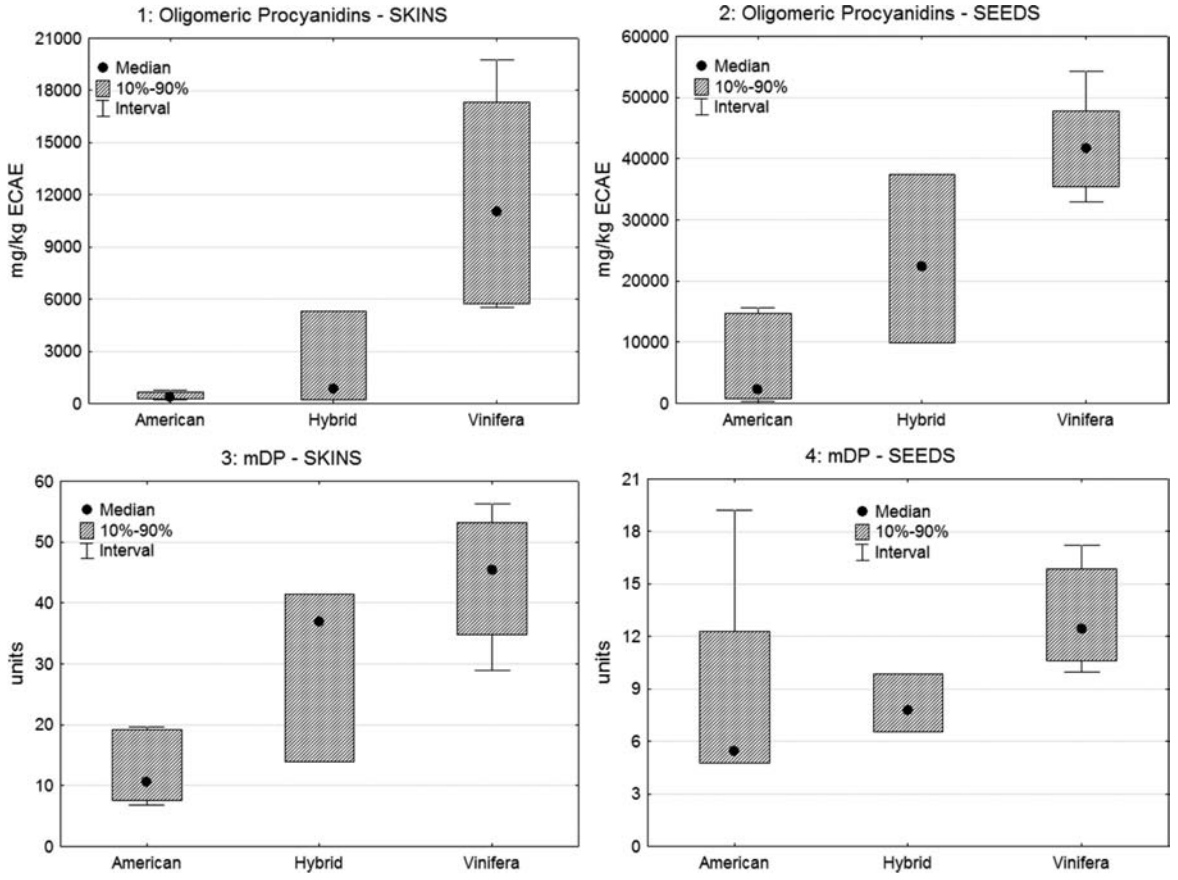

Figure 3. Box plots of oligomeric procyanidins content in the skin and seeds of different classes of grapes (1, 2) and mean degree of polymerization (mDP) of procyanidins (3, 4). Procyanidin content is expressed as epicatechin equivalents (ECAE), whereas mDP is expressed as average units.

different pattern: Isabella and 41B had a higher percentage of galloylated units (5−7%) in comparison to all other samples. Nero had slightly higher levels of free flavanols and polymeric procyanidins comparable to those of Sauvignon blanc (5000 mg/kg) and a mDP similar to that of the *V. vinifera* group. Isabella had an mDP superior to that of Nero (around 39 units on average).

V. vinifera varieties accumulated more flavanols and polymeric procyanidins in the seeds, but the difference was not as large as in the skin. Indeed, *Vitis cinerea* accumulated levels of catechin and epicatechin comparable to those of the *vinifera* varieties, whereas it had a lower amount of dimeric forms. The level of polymeric procyanidins in *V. cinerea* (10000 mg/kg) was lower than the level in *V. vinifera* (40000 mg/kg), but not so low as the rest of the American grapes (2000 mg/kg). These data indicate that the accumulation of procyanidins in the seeds may vary considerably between different species. Among the hybrids, Nero showed an accumulation pattern similar to those of the *vinifera* varieties, whereas 41B and Isabella both had levels of polymerization degree and accumulation intermediate between the two groups.

Wines produced from French−American hybrids were reported to be poor in terms of mouthfeel, due to a lack of astringency, indicating the scarcity of condensed tannins.[37] Previous authors have attributed the scarcity of condensed tannins in wines to their low availability and solubility,[7,37] due to the procyanidin-binding properties of pectin and proteins from the cell wall materials. Procyanidins have been demonstrated to be present inside the tonoplast and in the cell wall of grape cells, bound to proteins or pectins,[37−39] and their binding to the cell wall material is resistant to ultrasound and solvents.[40,41] Therefore, the differences reported in this work might depend on both availability and solubility of the procyanidins in the American grapes, especially in the skin. The American grapes might have stronger and wider procyanidin binding properties than *V. vinifera*. This would explain also why the American grapes had a lower polymerization degree in comparison to the *vinifera* grapes.[42] From a biological point of view, we must also consider that studying multiple plants of the Tracheophyta phylum, Bindon et al[40] proposed a single model for procyanidin production in the chloroplasts and a further transport of the procyanidins into the vacuole through vesicles structures. These authors concluded that all of the studied plants showed a similar model.[40] Therefore, production and accumulation must be similar inside the lone genus *Vitis*. As the polymerization process is still unknown, and their localization and binding in the tonoplast are only partially explained, it is impossible to discern whether the difference is due to different concentration, different binding or both. A more in-depth study into the reasons for such a marked difference between the two groups (especially in the skin) was beyond the aim of this study, and it was not investigated further.

It was very interesting to note that the procyanidin accumulation level in Nero (a recent hybrid variety) was more similar to that of *V. vinifera* than those of 41B and Isabella (old hybrid varieties), indicating that multiple backcrosses with *V. vinifera* increased the extractability and availability of procyanidins and that their availability is a characteristic likely controlled by multiple factors.

Hydrolyzable Tannins, Precursors, and Their Derivatives. Hydrolyzable tannins are polymeric compounds constituted by gallic acid subunits bound through a glycosidic

DOI: 10.1021/acs.jafc.5b01999
J. Agric. Food Chem. 2015, 63, 6823−6834

Table 3. MS/MS Spectra of Hydrolyzable Tannins[a]

compound	*m/z*	RT	MS/MS spectra	intensity	MS/MS interpretation
HHDP-galloyl-glucose	633.073	4.5	300.999 [$C_{14}H_6O_8$ − H]− (−11.0 ppm)	13900.00	ellagic acid − H
			275.0197 [$C_{13}H_8O_7$ −H]− (−11.6 ppm)	7814.00	ellagic acid fragment − H
			169.0142 [$C_7H_5O_5$]− (−13.0 ppm)	5512.00	gallic acid − H
			302.0068 [$C_{14}H_8O_8$ − 2H]− (−3.6 ppm)	2254.00	ellagic acid
			249.0405 [$C_{12}H_9O_6$]− (−12.0 ppm)	1721.00	ellagic acid fragment
			463.0518 [$C_{20}H_{17}O_{13}$ − 2H]− (−19.4 ppm)	1325.00	ellagic acid + glucose − H_2O − H
			481.0624 [$C_{20}H_{17}O_{14}$]− (−13.1 ppm)	1203.00	ellagic acid + glucose − H
HHDP-galloyl-glucose	633.073	5.3	300.999 [$C_{14}H_6O_8$ − H]− (−11.0 ppm)	13900.00	ellagic acid − H
			275.0197 [$C_{13}H_8O_7$ −H]− (−11.6 ppm)	6650.00	ellagic acid fragment
			169.0142 [$C_7H_5O_5$]− (−13.0 ppm)	5154.00	gallic acid − H
			302.0068 [$C_{14}H_8O_8$ − 2H]− (−3.6 ppm)	2254.00	ellagic acid
			463.0518 [$C_{20}H_{17}O_{13}$ − 2H]− (−19.4 ppm)	1971.00	ellagic acid + glucose − H_2O − H
			481.0624 [$C_{20}H_{17}O_{14}$]− (−13.1 ppm)	1600.00	ellagic acid + glucose − H
HHDP-galloyl-glucose	633.073	9.07	300.999 [$C_{14}H_6O_8$ − H]− (−9.6 ppm)	7825.00	ellagic acid − H
			275.0197 [$C_{13}H_8O_7$ − H]− (−11.3 ppm)	7311.00	ellagic acid fragment
			463.0518 [$C_{20}H_{17}O_{13}$ − 2H]− (−6.0 ppm)	2209.00	ellagic acid + glucose − H_2O − H
			302.0068 [$C_{14}H_8O_8$ − 2H]− (−3.3 ppm)	1244.00	ellagic acid
			481.0624 [$C_{20}H_{17}O_{14}$]− (−1.7 ppm)	685.30	ellagic acid + glucose − H
tellimangradin I	785.089	10.47	300.999 [$C_{14}H_6O_8$ − H]− (+3.6 ppm)	1896.00	ellagic acid − H
			275.0197 [$C_{13}H_8O_7$ − H]− (+10.4 ppm)	565.40	ellagic acid fragment
			463.0518 [$C_{20}H_{17}O_{13}$ − 2H]− (−6.0 ppm)	284.60	ellagic acid + glucose − H_2O − H
punicalin	781.0551	11.53	463.0518 [$C_{20}H_{16}O_{13}$ − H]− (−7.3 ppm)	27040.00	ellagic acid + glucose − H_2O − H
			754.0659 [$C_{33}H_{22}O_{21}$]− (9.0 ppm)	23640.00	M − H_2O
			737.0632 [$C_{33}H_{22}O_{20}$ − H]− (9.5 ppm)	10060.00	M − CO_2 − H
			299.9912 [$C_{14}H_4O_8$]− (−34.3 ppm)	9511.00	ellagic acid − 2H
			719.0526 [$C_{33}H_{20}O_{19}$ −H]− (−2.5 ppm)	8817.00	M − H_2O − O − H_2O
			736.0553 [$C_{33}H_{20}O_{20}$]− (5.2 ppm)	7156.00	M − CO_2 − 2H
			753.0581 [$C_{33}H_{22}O_{21}$ − H]− (0.1 ppm)	5405.00	M − H_2O − H
			735.0475 [$C_{33}H_{20}O_{20}$ − H]− (−1.0 ppm)	3091.00	M − CO_2 − 3H
			746.0397 [$C_{34}H_{19}O_{20}$ − H]− (6.0 ppm)	2499.00	M − H_2O − H_2O
			745.0319 [$C_{34}H_{19}O_{20}$ − 2H]− (3.2 ppm)	2017.00	M − H_2O − H_2O − H
			763.0424 [$C_{34}H_{21}O_{21}$ − 2H]− (3.8 ppm)	1964.00	M − H_2O − H
ellagic acid-arabinoside	433.0403	19.16	300.999 [$C_{14}H_5O_8$]− (−5.6 ppm)	47720.00	ellagic acid − H
			299.9912 [$C_{14}H_5O_8$ − H]− (−5.3 ppm)	37940.00	ellagic acid − 2H
ellagic acid-glucoside	463.0514	15.9	299.9912 [$C_{14}H_5O_8$ − H]− (−1.3 ppm)	121100.00	ellagic acid − 2H
			300.999 [$C_{14}H_5O_8$]− (2.3 ppm)	120600.00	ellagic acid − H
			89.0244 [$C_3H_6O_3$ − H]− (−14.6 ppm)	2690.00	
			275.0197 [$C_{13}H_8O_7$ − H]− (+2.8 ppm)	1789.00	ellagic acid fragment
galloyl-ellagic acid	469.005	13.97	300.999 [$C_{14}H_5O_8$]− (−8.3 ppm)	7047	ellagic acid − H
			299.9912 [$C_{14}H_5O_8$ − H]− (−7.3 ppm)	4859	ellagic acid − 2H
			298.9833 [$C_{14}H_5O_8$ − 2H]− (−31.4 ppm)	919.3	ellagic acid − 3H
			271.9963 [$C_{13}H_5O_7$ − H]− (−10.7 ppm)	802	ellagic acid − CO − 2H
			270.9884 [$C_{13}H_5O_7$ − 2H]− (−9.6 ppm)	775	ellagic acid − CO − 3H
			425.015 [$C_{20}H_9O_{11}$]− (5.9 ppm)	641.6	M − CO_2 − H
			273.0041 [$C_{13}H_5O_7$]− (9.9 ppm)	166.4	ellagic acid fragment

[a]The MS/MS spectra from *Vitis arizonica* Texas skin are shown. Only ions identified by MetFrag are reported in this table.

moiety. The gallic acid unit can create C−C bonds joined to each other to create hexahydroxydiphenic acid (HHDP) subunits and/or hydrolyze their acidic moiety to form ellagic acid subunits. The different combinations of gallic acid, HHDP, ellagic acid, and glycosides create diverse hydrolyzable tannins. The accumulation and degradation pathways of these metabolites are still unknown.

From an enological point of view, hydrolyzable tannins are desirable markers of quality. These metabolites are not found naturally in red wines from *V. vinifera*. Indeed, red wines are often aged in oak (or different woods) barrels, where the wine's alcohol

DOI: 10.1021/acs.jafc.5b01999
J. Agric. Food Chem. 2015, 63, 6823−6834

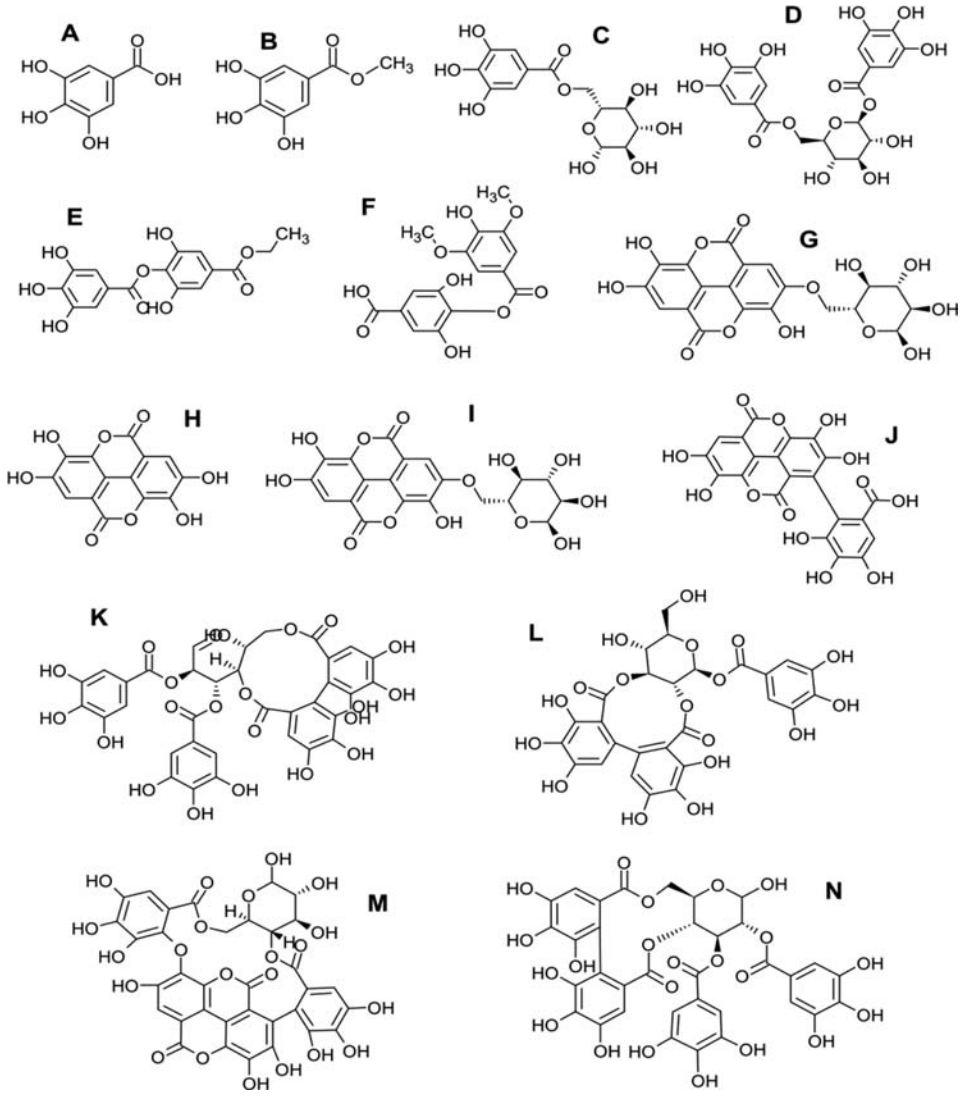

Figure 4. Structures of the hydrolyzable tannins identified in this study: (A) gallic acid; (B) methyl-gallate; (C) galloyl-glucose; (D) digalloyl-glucose; (E) galloyl-ethyl-gallate; (F) galloyl-syringic acid; (G) ellagic acid-arabinoside; (H) ellagic acid; (I) ellagic acid-glucoside; (J) galloyl-ellagic acid (valoneic acid dilactone); (K) digalloyl-HHDP-glucose (isoform 1); (L) galloyl-HHDP-glucose; (M) punicalin; (N) tellimangradin I (isoform 2).

extracts lignans and hydrolyzable tannins from the wood, improving wine body.[55] Furthermore, hydrolyzable tannins and their catabolic derivatives (ellagic acid and its conjugates) have many health-related properties.[41] For these reasons, their accumulation is welcome in the wines. To our knowledge, only gallic acid, galloyl-glucose, digalloyl-glucose, and ellagic acid have been reported in *V. vinifera* grapes. Of the *Vitis* germplasm, only *Vitis rotundifolia* has been reported to accumulate some hydrolyzable tannins and derivatives in its skin and seeds.[16,17]

In our experiment, we found that American grapes accumulated many hydrolyzable tannin precursors, such as gallic acid, galloyl-glucose, digalloyl-glucose, ellagic acid, methyl-gallate, galloyl-syringic acid, and galloyl-ethyl-gallate in the skin (Figure 1). Oligomeric hydrolyzable tannins were also found in the skin of American grapes, especially K5BB and *Vitis arizonica* Texas. They accumulated a total of eight oligomeric compounds in this class, reported here: ellagic acid-arabinoside, ellagic acid-glucoside, galloyl-ellagic acid, three different isomers of HHDP-galloyl-glucose, a punicalin-like compound, and HHDP-digalloyl-glucose (MSMS spectra in Table 3). We did not observe any hydrolyzable tannin, precursor, or derivative signal in *V. vinifera* skins, except for those already reported in the literature (gallic acid, galloyl-glucose, digalloyl-glucose, and ellagic acid). Moreover, the American grapes showed a concentration of ellagic acid around 1000 times higher than *vinifera* grape skin. Ellagic acid is the catabolic product of the hydrolyzable tannins. The putative structures of all identified hydrolyzable tannins are shown in Figure 4.

The lack of commercial standards available for this class of compounds did not allow us to confirm the identifications to MSI level 1. The presence of many putative compounds in the same class makes us confident about the identification. Interestingly, when looking selectively for previously reported ellagitannins, we observed that K5BB and *V. arizonica* Texas also had an m/z of 933.0692, the same mass of castalagin and vescalagin. Many fragments in the MS/MS spectrum corresponded as well, but they had different relative intensities and different retention times (5 and 6 min versus 12 min, data not shown). In this experiment, the signal for this ion was too low and was excluded from the statistical analysis, due to the intensity threshold selected, but it was clearly present in the chromatograms of K5BB and *V. arizonica* Texas. As shown in Figure 1, among the

DOI: 10.1021/acs.jafc.5b01999
J. Agric. Food Chem. 2015, 63, 6823−6834

hybrids, only 41B showed some accumulation of these compounds in the skin, whereas Nero and Isabella did not accumulate it, as for *vinifera* grapes. The genetic basis of hydrolyzable tannin accumulation is still unknown, so it is difficult to understand why there is a different behavior in the hybrids.

The situation became more complex when the accumulation of these compounds was observed in the seeds. All of the American grapes also showed accumulation of this class of compounds in the seeds but in lower intensities in comparison to the skin. Of the *vinifera* grapes, only Moscato Rosa showed a signal for many hydrolyzable types of tannin, usually higher than that from wild American grapes. This is extremely interesting, because no other *vinifera* showed any clear signal. These hydrotannic units were also observed in a preliminary pilot experiment (data not shown). In that experiment, Moscato Rosa and an intraspecific hybrid Pinot × Merlot showed a clear accumulation of such compounds. Their presence in Moscato Rosa's seeds is why this class of compounds was not recognized as a marker for American grapes in seeds.

Hydrolyzable tannins have been reported in numerous fruits and plants,[44] but this is the first time that they have been reported in species other than *V. rotundifolia* within the *Vitis* genus.

Aroma Precursors. Aroma precursors are all of the volatile metabolites stored in the vacuole through glycosylation, and they are supposed to serve as a reservoir for biotic and abiotic stress response. Many of these glycosylated volatiles undergo hydrolysis during vinification and wine aging, determining most of the wine's aroma.[43] For this reason, is important to study the intact aroma precursors found in the berries to understand the aroma potential of grapes. These metabolites are mostly accumulated in the skin and, to a lesser extent, in the flesh. Our group recently reported an untargeted LC-HRMS method to identify and semiquantify aroma precursors in grape.[53]

The American grapes are often reported to have a different range of aromas, including the undesirable "foxy" taste[5] and some herbaceous flavors.[5,6] The goal was to establish whether the putative precursors of these volatiles can be found in any of the tissues of the American grapes. Surprisingly, none of the markers obtained in this work corresponded to a putative precursor of this kind of metabolite.

It was interesting to see whether *V. vinifera* accumulates precursors with a pleasant aroma, such as terpenols, differentially (Figure 1). Our experiment showed that *vinifera* grapes accumulated a high amount of glycosylated-terpenoids in the skin, whereas the American grapes included in our experiment did not accumulate any. Nevertheless, high concentrations were found in Iasma Eco 3, Moscato Ottonel, Gewürztraminer, and Moscato Rosa, which are commonly recognized as aromatic varieties. Aromatic is a phenotypic definition: a fruity-smelling variety of grape is "aromatic". Recently, a single locus (VvDXS) encoding for a 1-deoxy-D-xylulose-5-phosphate enzyme has been found to be responsible for the aromatic qualities of grapes.[44] This locus is involved in the accumulation of isoprenoid precursors; isoprenoids are the building blocks for the monoterpenoids. The remaining *vinifera* varieties showed a lower accumulation of these aroma precursor volatiles, similar to those of American grapes. We assume that this difference is likely due more to the locus VvDXS, as reported in the literature, than to a difference between species. On the other hand, this locus was not derived from the natural evolution, but human-selected during the domestication of *V. vinifera*:[44] so it has been reproduced and is presently common in the *vinifera* grapes, whereas it is probably very rare in wild American grapes.

We noted the same aroma precursors' accumulation pattern in the flesh, with a lower concentration in comparison to the skin, as reported in previous works[45] (Supplementary Figure 2). The hybrids showed a level of accumulation of these metabolites similar to that shown by nonaromatic *vinifera* and wild American grapes, indicating that they probably do not have the active allele of the *VvDXS* gene. In the seeds (Figure 2), we were able to identify two aroma precursors with accumulations 10 times higher in *vinifera* seeds than in American seeds: vanillyl-glucoside and benzyl-alcohol-rhamnosyl-glucoside. Both compounds are catabolic derivatives of the lignin's production pathway. In this tissue, the hybrid grapes showed similar levels to the *vinifera* grapes. The putative structures of the identified volatile precursors are shown in Supplementary Figure 3.

Anthocyanins and Stilbenoids. Anthocyanins are the main pigments found in grapes, determining the visual impact of both grapes and wines. Anthocyanins are accumulated in the vacuole of the cells after glycosylation and are believed, inter alia, to defend the cells from oxidative damage caused by exposure to sunlight.[46] Anthocyanidins (i.e., the aglycones) cannot be found in grapes, because the aglycone form is very reactive and unstable. They share most of their metabolic pathway with flavan-3-ols, and probably they compete for the substrates during the accumulation process.

A differential accumulation of anthocyanins in wild American grapes and *V. vinifera* has been reported since the 1950, and it has been used historically to determine whenever a wine has been blended with non-*vinifera*/hybrid grapes. The wild American grapes tend to accumulate mostly diglycosidic anthocyanins, whereas *V. vinifera* contains most exclusively monoglycosidic anthocyanins.[47] Recently, it has been reported that the gene encoding for a 5-*O*-uridil-diphosphate-glycosyl-transferase (5-UFGT) has different alleles in *V. vinifera* and wild American grapes.[48] The alleles present in the *vinifera* grape are almost all nonfunctional; they do not produce the 5-UFGT enzyme able to bind the glycosides to the 5-terminal end of anthocyanins.

In our experiment, five different basic units of anthocyanins were found to be differently accumulated in the skin and in the flesh of the two groups (Figure 1 and Supplementary Figure 2): cyanidin, peonidin, petunidin, delphinidin, and malvidin. In the skin, berries from *vinifera* accumulated only anthocyanins glycosylated at position 3, sometimes with a *p*-coumaroyl or caffeoyl moiety attached to the glucoside. American *Vitis* was richer, from tens to hundreds of times, than *vinifera* in all of the anthocyanins identified, including 3-glucosylated forms. Furthermore, the American *Vitis* accumulated anthocyanins diglycosylated in positions 3 and 5, as shown in Figure 1. As expected, all of the hybrids showed lower accumulation of diglycosylated anthocyanins than the wild American grapes.

The flesh of the *vinifera* grapes did not accumulate anthocyanins, whereas all the American *Vitis* showed the typical red color in their flesh, indicating the presence of a high number of anthocyanins (Supplementary Figure 2). Tenturier (red-fleshed) *vinifera* do exist, but they are a minority in its germplasm, whereas white-fleshed American grapes exist only in *Vitis riparia* and *Vitis berlandieri*. The anthocyanin accumulation pattern seems to be similar in the flesh and skin of wild American grapes, but the relative amount was lower in the flesh. Among the hybrids, only Nero showed a certain degree of accumulation of anthocyanins in the flesh, due to a red layer on the external part of

DOI: 10.1021/acs.jafc.5b01999
J. Agric. Food Chem. 2015, 63, 6823−6834

the flesh, but this was likely due to the cold storage effect more than a physiological accumulation.

The stilbenoids are polyphenolic compounds that have a strong antifungal activity in plants and possess health-related characteristics (e.g., resveratrol belongs to this class). Their accumulation is reported to be directly correlated with the accumulation of anthocyanins during ripening stages. As expected, due to the high concentration of anthocyanins in the skin and flesh of American grape berries, these were also richer in stilbenoids, especially *V. arizonica* Texas and *V. californica*. We found larger amounts of isorhapontin, *cis*-ε-viniferin, *trans*-resveratrol, *trans*-piceid, and *cis*-resveratrol in the skin (Figure 1). Higher amounts of *trans*-resveratrol, *trans*-piceid, and *cis*-resveratrol were also found in the flesh. As hybrid flesh is colorless (without anthocyanins), 41B, Nero, and Isabella showed small amounts of stilbenoids in the flesh. Despite the strong anthocyanin color in their skins, the accumulation of stilbenoids in the skin of 41B and Isabella was poor, whereas Nero skin had a pattern similar to that of *V. cinerea*, which contains the lowest amount of the American grapes investigated.

Flavonols and Dihydro-flavonols. Flavonols are very strong antioxidants and have health-related properties.[49] Flavonols are yellow pigments and may contribute to the color of white grapes and white wines. In plants, they are believed to defend the tissues from oxidative damage by UV-B rays.[46]

In our experiment, we were able to identify four basic units of flavonols differently accumulated between the two groups: quercetin, myricetin, laricitrin, and syringetin. These were present in glucosylated or rutinosylated forms. The main differences were found in the skin, where *vinifera* tended to accumulate more quercetin-glucoside and galactoside than American grapes, whereas American grapes accumulated more myricetin, laricitrin, and syringetin-glucoside. Nevertheless, considering grape color and comparing the American varieties with only Merlot and Moscato Rosa, the differences were not so big, being only 2.5 times more concentrated. White grapes do not accumulate flavonols trihydroxylated in the B ring[50] (myricetin, laricitrin, and syringetin), whereas red ones do accumulate triydroxylated flavonols, so this difference seems to be due mostly to grape color rather than to grape species.

Interestingly, we could observe a similar pattern for dihydro-flavonols. This class of compounds has only recently been reported in grapes,[51] and, in our experiment, it seemed to follow the same pattern as flavonols' accumulation; American grapes, Merlot, and Moscato Rosa accumulated the trihydroxylated forms (dihydro-syringetin, dihydro-laricitrin, and dihydro-myricetin), whereas the remaining *vinifera* had only dihydro-quercetin. The dihydro-flavonols are the direct precursors of flavonols, and considering that the hydroxylation of the B ring happens earlier in the metabolic pathway,[52] a similar pattern for dihydro-flavonols and flavonols would seem to be legitimate. Nevertheless, further investigations, considering a wider population of red and white grapes (similar to the experiment performed by Mattivi et al.,[50]), are necessary to confirm these important results.

Other Identified Metabolites. Many other classes of metabolites were found to accumulate differently in wild American grapes and *V. vinifera*. Some sugar precursors, polar lipids, (putative) lignans, flavones, and some organic acids showed a different accumulation in the two groups. Nevertheless, it was not possible to determine the difference found in these classes of metabolites, because many of the identifications were putative and under-represented and had a nonunique accumulation pattern.

The putative identified polar lipids were all accumulated in larger amounts in *vinifera* tissues. Hydroxy-hexanoate-glucoside, decyl-pentosyl-glucoside, mascaroside-like, and hexyl-rhamnosyl-glucoside accumulated more in the seeds of the *vinifera* group than in the wild American grapes seeds; Nero had levels similar to those of the *vinifera* group. A similar pattern was observed in the skin for the compounds hydroxy-decanoic acid-pentosyl-glucoside, undecanoic acid-pentosyl-glucoside, and undecadioic acid-pentosyl-glucoside, with Nero again having levels similar to those of *vinifera*.

Among the remaining classes, lignans stand out as an interesting class: two signals, *m*/*z* 505.2080 and 491.1940, were found exclusively in the American group, specifically in . *arizonica* Texas and *V. cinerea*. Their identification is merely putative, but their fragmentation spectra were very similar to the spectrum of lariciresinol with a xyloside and rhamnoside moiety, respectively (data not shown). These metabolites have been previously identified in *V. thunbergii*,[17] and they are considered to be a very desirable marker because of health benefits related to lignans.

Potential and Limits of the American Grapes and Interspecific Hybrids in Wine Production. The aim of this work was to determine the chemical and metabolic differences that make *vinifera* suitable for wine production, in comparison to some American *Vitis* that are not ideal in quality wine production. The results clearly show that the method adopted (untargeted analysis) allowed us to have a broad picture on many metabolites involved in grape quality. We found that the American grapes considered in our study are poor in some important components of the wine, such as procyanidins and volatiles precursors (especially terpenols-glycosides). These differences were known and reported in previous papers,[5,6,37−39] but they were never comparatively studied against *V. vinifera* and never stated clearly in a single work. Breeders producing interspecific hybrids between *V. vinifera* and wild American grapes have to take in account these limitations and obtain an extensive characterization of the chemical phenotype of the parents to be used in the crosses and of the progeny in order to import the positive characteristics from the *V. vinifera* progenitors.

The American grapes, interestingly, showed accumulation of metabolites not commonly present in *V. vinifera*, such as hydrolyzable tannins and (likely) lignans. These characteristics represent the positive heritage of the American progenitors, and they might be the target of future breeding programs (for example, to obtain wines rich in hydrolyzable tannins without oak aging). Moreover, these compounds, if retained in the progeny, could be useful markers to identify the wines produced from the new varieties. Complementary analytical tools able to analyze in depth the primary metabolites, the lipids, and the volatiles may help in the description of other characteristics that differentiate the wild American grapes from the *V. vinifera*. Moreover, a wider number of accessions from the *Vitis* germplasm might be analyzed using the same approach.

The analysis of three hybrid varieties showed how the different characteristics are inherited from the progenies. All of the hybrids investigated showed a low content in procyanidins, a variable content of volatile precursors, anthocyanin content similar to that of the American grapes, and absence of hydrolyzable tannins. These observations indicate the need for targeted breeding programs to transfer the desired characteristics to the progenies. Phenotypic evaluation of the hybrid (as in Nero) has not been

DOI: 10.1021/acs.jafc.5b01999
J. Agric. Food Chem. 2015, 63, 6823−6834

sufficient to obtain a variety comparable to *V. vinifera*. Extensive coverage of the chemical phenotype should become an essential part of future breeding studies, and support for future research on the factors that limit the heritage of positive characteristics to the hybrid progeny is needed to facilitate breeders' work and shorten breeding programs.

■ ASSOCIATED CONTENT

Supporting Information

Supplementary Figures 1−3 and tables of biomarkers identified divided by tissue and quantification of procyanidins in the skin and seeds of grape samples. The Supporting Information is available free of charge on the ACS Publications website at DOI: 10.1021/acs.jafc.5b01999.

■ AUTHOR INFORMATION

Corresponding Author

*(F.M.) E-mail: fulvio.mattivi@fmach.it.

Notes

The authors declare no competing financial interest.

■ ACKNOWLEDGMENTS

We thank Monica Dalla Serra and Marco Stefanini for providing grape materials and Daniele Perenzoni for technical support during the targeted analysis.

■ ABBREVIATIONS USED

LC-MS	liquid chromatography−mass spectrometry
UHPLC-ESI-Q-TOF-MS	ultrahigh-performance liquid chromatography−electrospray ionization−time-of-flight mass spectrometer
QCs	quality controls
UHPLC-ESI-QqQ-MS	ultrahigh-performance liquid chromatography−electrospray ionization−triple-quadrupole mass spectrometer
STDmix	standard mix
PCA	principal component analysis
CV	coefficient of variation
OPLS-DA	orthogonal partial least-squares-discriminant analysis
CCC	compounds characteristics comparison (method)
MS/MS	tandem mass spectrometry
mDP	mean degree of polymerization
HHDP	hexahydroxydiphenic acid
VvDXS	*Vitis vinifera* 1-deoxy-D-xylulose 5-phosphate synthase
5-UFGT	5-*O*-uridil-diphosphate-glycosyltransferase
ECAE	epicatechin equivalents

■ REFERENCES

(1) Myles, S.; Boyko, A. R.; Owens, C. L.; Brown, P. J.; Grassi, F.; Aradhya, M. K. Genetic structure and domestication history of the grape. *Proc. Natl. Acad. Sci. U. S. A.* **2011**, *108* (9), 3530−3535.

(2) This, P.; Lacombe, T.; Thomas, M. R. Historical origins and genetic diversity of wine grapes. *Trends Genet.* **2006**, *22* (9), 511−519.

(3) Gadoury, D. M.; Cadle-Davidson, L.; Wilcox, W. F.; Dry, I. B.; Seem, R. C.; Milgroom, M. G. Grapevine powdery mildew (*Erysiphe necator*): a fascinating system for the study of the biology, ecology and epidemiology of an obligate biotroph. *Mol. Plant Pathol.* **2012**, *13* (1), 1−16.

(4) Levadoux, L. In *La Vigne et sa Culture*, 10th ed.; Presses universitaires de France, 1966.

(5) Rapp, A. Natural flavours of wine: correlation between instrumental analysis and sensory perception. *Fresenius' J. Anal. Chem.* **1990**, *337*, 777−785.

(6) Sun, Q.; Gates, M. J.; Lavin, E. H.; Acree, T. E.; Sacks, G. L. Comparison of odor-active compounds in grapes and wines from vitis vinifera and non-foxy American grape species. *J. Agric. Food Chem.* **2011**, *59*, 10657−10664.

(7) Harbertson, J. F.; Hodgins, R. E.; Thurston, L. N.; Schaffer, L. J.; Reid, M. S.; Landon, J. L.; Ross, C. F.; Adams, D. O. Variability of tannin concentration in red wines. *Am. J. Enol. Vitic.* **2008**, *59*, 210−214.

(8) Myles, S. Improving fruit and wine: what does genomics have to offer? *Trends Genet.* **2013**, *29* (4), 190−196.

(9) Borneman, A. R.; Schmidt, S. A.; Pretorius, I. S. At the cutting-edge of grape and wine biotechnology. *Trends Genet.* **2013**, *29* (4), 263−271.

(10) Blondon, A.; Martinez-Zapater, J. M.; Kole, C. *Genetics, Genomics and Breeding of Grapes*, 1st ed.; Science Publishers, an imprint of Edenbridge Ltd.: Enfield, NH, USA, 2011.

(11) Emanuelli, F.; Lorenzi, S.; Grzeskowiak, L.; Catalano, V.; Stefanini, M.; Troggio, M.; Myles, S.; Martinez-Zapater, J. M.; Zyprian, E.; Moreira, F. M.; et al. Genetic diversity and population structure assessed by SSR and SNP markers in a large germplasm collection of grape. *BMC Plant Biol.* **2013**, *13* (39), 1−17.

(12) Galet, P. In *Precis de Ampelographie Pratique. Cepables and Vignobles de France*; Impr. P. Dehan: Montpellier,1952.

(13) Goto-Yamamoto, N.; Azuma, A.; Mitani, N.; Kobayashi, S. SSR genotyping of wild grape species and grape cultivars of *Vitis vinifera* and *V. vinifera* × *V. labrusca*. *J. Jpn. Soc. Hortic. Sci.* **2013**, *82* (2), 125−130.

(14) Liang, Z.; Yang, Y.; Cheng, L.; Zhong, G. Y. Polyphenolic composition and content in the ripe berries of wild *Vitis* species. *Food Chem.* **2012**, *132* (2), 730−738.

(15) Liang, Z.; Yang, Y.; Cheng, L.; Zhong, G. Characterization of polyphenolic metabolites in the seeds of *Vitis* germplasm. *J. Agric. Food Chem.* **2012**, *60*, 1291−1299.

(16) Lee, J.-H.; Johnson, J. V.; Talcott, S. T. Identification of ellagic acid conjugates and other polyphenolics in muscadine grapes by HPLC-ESI-MS. *J. Agric. Food Chem.* **2005**, *53*, 6003−6010.

(17) Tung, Y. T.; Cheng, K. C.; Ho, S. T.; Chen, Y. L.; Wu, T. L.; Hung, K. C.; Wu, J. H. Comparison and characterization of the antioxidant potential of 3 wild grapes − *Vitis thunbergii*, *V. flexuosa*, and *V. kelungeusis*. *J. Food Sci.* **2011**, *76* (5), 701−706.

(18) Theodoridis, G.; Gika, H.; Franceschi, P.; Caputi, L.; Arapitsas, P.; Scholz, M.; Masuero, D.; Wehrens, R.; Vrhovsek, U.; Mattivi, F. LC-MS based global metabolite profiling of grapes: solvent extraction protocol optimization. *Metabolomics* **2012**, *8* (2), 175−185.

(19) Shahaf, N.; Franceschi, P.; Arapitsas, P.; Rogachev, I.; Vrhovsek, U.; Wehrens, R. Constructing a mass measurement error surface to improve automatic annotations in liquid chromatography/mass spectrometry based metabolomics. *Rapid Commun. Mass Spectrom.* **2013**, *27* (21), 2425−2431.

(20) Fortes Gris, E.; Mattivi, F.; Ferreira, E. A.; Vrhovsek, U.; Pedrosa, R. C.; Bordignon-Luiz, M. T. Proanthocyanidin profile and antioxidant capacity of Brazilian *Vitis vinifera* red wines. *Food Chem.* **2011**, *126* (1), 213−220.

(21) Arapitsas, P.; Speri, G.; Angeli, A.; Perenzoni, D.; Mattivi, F. The influence of storage on the "chemical age" of red wines. *Metabolomics* **2014**, *10* (5), 816−832.

(22) Franceschi, P.; Mylonas, R.; Shahaf, N.; Scholz, M.; Arapitsas, P.; Masuero, D.; Weingart, G.; Carlin, S.; Vrhovsek, U.; Mattivi, F.; et al. MetaDB a data processing workflow in untargeted MS-based metabolomics experiments. *Front. Bioeng. Biotechnol.* **2014**, *2* (December), 1−12.

(23) Vinaixa, M.; Samino, S.; Saez, I.; Duran, J.; Guinovart, J. J.; Yanes, O. A guideline to univariate statistical analysis for LC/MS-based untargeted metabolomics-derived data. *Metabolites* **2012**, *2* (4), 775−795.

DOI: 10.1021/acs.jafc.5b01999
J. Agric. Food Chem. 2015, 63, 6823−6834

(24) Wold, S.; Sjostrom, M.; Eriksson, L. PLS-regression: a basic tool of chemometrics. *Chemom. Intell. Lab. Syst.* **2001**, *58*, 109−130.
(25) Stanstrup, J.; Vrhovšek, U. [Conference poster]. AISBM 2014 − Challenges in annotation and de novo identification of small molecules. Gif-sur-Yvette, France, 2014.
(26) Sumner, L. W.; Amberg, A.; Barrett, D.; Beale, M. H.; Beger, R.; Daykin, C. A.; Fan, T. W.-M.; Fiehn, O.; Goodacre, R.; Griffin, J. L.; et al. Proposed minimum reporting standards for chemical analysis. *Metabolomics* **2007**, *3* (3), 211−221.
(27) Wolf, S.; Schmidt, S.; Müller-Hannemann, M.; Neumann, S. In silico fragmentation for computer assisted identification of metabolite mass spectra. *BMC Bioinf.* **2010**, *11*, 148.
(28) Gerlich, M.; Neumann, S. MetFusion: integration of compound identification strategies. *J. Mass Spectrom.* **2013**, *48* (3), 291−298.
(29) Stanstrup, J.; Gerlich, M.; Dragsted, L. O.; Neumann, S. Metabolite profiling and beyond: approaches for the rapid processing and annotation of human blood serum mass spectrometry data. *Anal. Bioanal. Chem.* **2013**, *405* (15), 5037−5048.
(30) Böcker, S.; Liptak, Z. Algorithmica, a fast and simple algorithm for the money changing problem 1. *Algorithmica* **2007**, *48*, 413−432.
(31) Goodacre, R.; Broadhurst, D.; Smilde, A. K.; Kristal, B. S.; Baker, J. D.; Beger, R.; Bessant, C.; Connor, S.; Capuani, G.; Craig, A.; et al. Proposed minimum reporting standards for data analysis in metabolomics. *Metabolomics* **2007**, *3* (3), 231−241.
(32) Poudel, P. R.; Tamura, H.; Kataoka, I.; Mochioka, R. Phenolic compounds and antioxidant activities of skins and seeds of five wild grapes and two hybrids native to Japan. *J. Food Compos. Anal.* **2008**, *21*, 622−625.
(33) Hilbert, G.; Temsamani, H.; Bordenave, L.; Pedrot, E.; Chaher, N.; Cluzet, S.; Delaunay, J.-C.; Ollat, N.; Delrot, S.; Mérillon, J.-M.; et al. Flavonol profiles in berries of wild *Vitis* accessions using liquid chromatography coupled to mass spectrometry and nuclear magnetic resonance spectrometry. *Food Chem.* **2015**, *169*, 49−58.
(34) Chung, K. T.; Wei, C. I.; Johnson, M. G. Are tannins a double-edged sword in biology and health? *Trends Food Sci. Technol.* **1998**, *9*, 168−175.
(35) Bak, M. J.; Jun, M.; Jeong, W. S. Procyanidins from wild grape (*Vitis amurensis*) seeds regulate ARE-mediated enzyme expression via Nrf2 coupled with p38 and PI3K/Akt pathway in HepG2 cells. *Int. J. Mol. Sci.* **2012**, *13*, 801−818.
(36) Fuleki, T.; da Silva, J. M. R. Catechin and procyanidin composition of seeds from grape cultivars grown in Ontario. *J. Agric. Food Chem.* **1997**, *45*, 1156−1160.
(37) Springer, L. F.; Sacks, G. L. Protein-precipitable tannin in wines from *Vitis vinifera* and interspecific hybrid grapes (*Vitis* ssp.): differences in concentration, extractability, and cell wall binding. *J. Agric. Food Chem.* **2014**, *62*, 7515−7523.
(38) Brillouet, J. M.; Romieu, C.; Schoefs, B.; Solymosi, K.; Cheynier, V.; Fulcrand, H.; Verdeil, J. L.; Conéjéro, G. The tannosome is an organelle forming condensed tannins in the chlorophyllous organs of Tracheophyta. *Ann. Bot.* **2013**, *112* (1962), 1003−1014.
(39) Amrani, J.; Glories, Y.; Mercier, M. Localisation des tanins dans la pellicule de baie de raisin. *Vitis* **1994**, *33*, 133−138.
(40) Bindon, K. A.; Smith, P. A.; Kennedy, J. A. Interaction between grape-derived proanthocyanidins and cell wall material. 1. Effect on proanthocyanidin composition and molecular mass. *J. Agric. Food Chem.* **2010**, *58*, 2520−2528.
(41) Landete, J. M. Ellagitannins, ellagic acid and their derived metabolites: a review about source, metabolism, functions and health. *Food Res. Int.* **2011**, *44* (5), 1150−1160.
(42) Arapitsas, P. Hydrolyzable tannin analysis in food. *Food Chem.* **2012**, *135* (3), 1708−1717.
(43) Fernández-González, M.; Di Stefano, R. Fractionation of glycoside aroma precursors in neutral grapes. Hydrolysis and conversion by *Saccharomyces cerevisiae*. *LWT − Food Sci. Technol.* **2004**, *37* (4), 467−473.
(44) Battilana, J.; Emanuelli, F.; Gambino, G.; Gribaudo, I.; Gasperi, F.; Boss, P. K.; Grando, M. S. Functional effect of grapevine 1-deoxy-D-xylulose 5-phosphate synthase substitution K284N on Muscat flavour formation. *J. Exp. Bot.* **2011**, *62* (15), 5497−5508.
(45) Luan, F.; Wüst, M. Differential incorporation of 1-deoxy-D-xylulose into (3*S*)-linalool and geraniol in grape berry exocarp and mesocarp. *Phytochemistry* **2002**, *60*, 451−459.
(46) Matus, J. T.; Loyola, R.; Vega, A.; Peña-Neira, A.; Bordeu, E.; Arce-Johnson, P.; Alcalde, J. A. Post-veraison sunlight exposure induces MYB-mediated transcriptional regulation of anthocyanin and flavonol synthesis in berry skins of Vitis vinifera. *J. Exp. Bot.* **2009**, *60* (3), 853−867.
(47) Burns, J.; Mullen, W.; Landrault, N.; Teissedre, P. L.; Lean, M. E. J.; Crozier, A. Variations in the profile and content of anthocyanins in wines made from Cabernet Sauvignon and hybrid grapes. *J. Agric. Food Chem.* **2002**, *50*, 4096−4102.
(48) Yang, Y.; Labate, J. A.; Liang, Z.; Cousins, P.; Prins, B.; Preece, J. E.; Aradhya, M.; Zhong, G.-Y. Multiple loss-of-function 5-*O*-glucosyltransferase alleles revealed in *Vitis vinifera*, but not in other *Vitis* species. *Theor. Appl. Genet.* **2014**, *127* (11), 2433−2451.
(49) de Pascual-Teresa, S.; Moreno, D. A.; García-Viguera, C. Flavanols and anthocyanins in cardiovascular health: a review of current evidence. *Int. J. Mol. Sci.* **2010**, *11* (4), 1679−1703.
(50) Mattivi, F.; Guzzon, R.; Vrhosek, U.; Stefanini, M.; Velasco, R. Metabolite profiling of grape: flavonols and anthocyanins. *J. Agric. Food Chem.* **2006**, *54* (54), 7692−7702.
(51) De Rosso, M.; Tonidandel, L.; Larcher, R.; Nicolini, G.; Dalla Vedova, A.; De Marchi, F.; Gardiman, M.; Giust, M.; Flamini, R. Identification of new flavonols in hybrid grapes by combined liquid chromatography-mass spectrometry approaches. *Food Chem.* **2014**, *163*, 244−251.
(52) Winkel-Shirley, B. Flavonoid biosynthesis. A colorful model for genetics, biochemistry, cell biology, and biotechnology 1. *Plant Physiol.* **2001**, *126* (January 2015), 485−493.
(53) Ghaste, M.; Narduzzi, L.; Carlin, S.; Vrhovsek, U.; Shulaev, V.; Mattivi, F. Chemical composition of volatile aroma metabolites and their glycosylated precursors that can uniquely differentiate individual grape cultivars. *Food Chem.* **2015**, *188*, 309−319.
(54) Kuhl, C.; Tautenhahn, R.; Bo, C.; Larson, T. R.; Neumann, S. CAMERA: an integrated strategy for compound spectra extraction and annotation of liquid chromatography/mass spectrometry data sets. *Anal. Chem.* **2012**, *84*, 283−289.
(55) Puech, J. L.; Feuillat, F.; Mosedale, J. R. The Tannins of Oak Heartwood: Structure, Properties, and Their Influence on Wine Flavor. *Symp. A Q. J. Mod. Foreign Lit.* **1999**, *50* (4), 469−478.

DOI: 10.1021/acs.jafc.5b01999
J. Agric. Food Chem. 2015, 63, 6823−6834

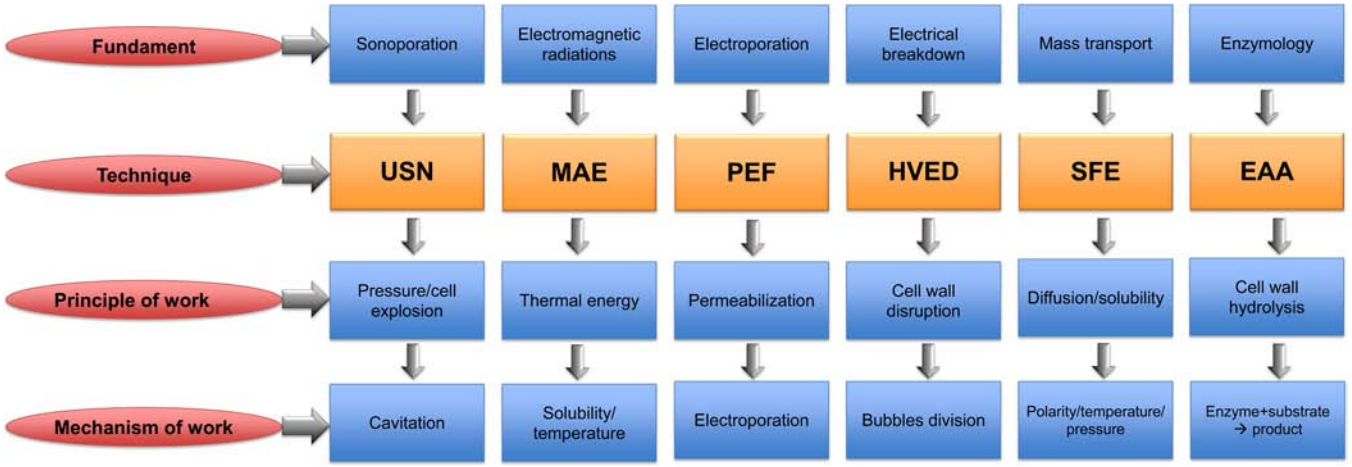

Figure 1. Chart of the nonconventional technologies described in this review for the extraction of high added value compounds from *Stevia rebaudiana* leaves. USN, ultrasounds; MAE, microwave assisted extraction; PEF, pulsed electric fields; HVED, high voltage electrical discharges; SFE, supercritical fluid extraction; EAA, enzyme assisted extraction.

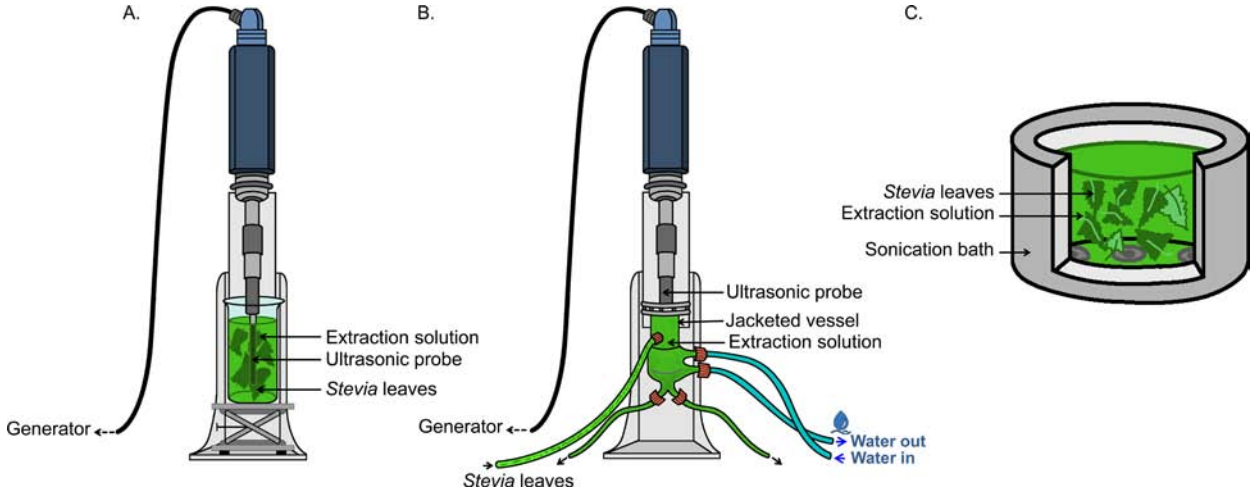

Figure 2. Schematic representations of the main ultrasonic systems. (A) Batch type probe system. (B) Continuous probe system used for liquid food processing. (C) Ultrasonic bath.

production of sound waves that create cavitation bubbles near the sample tissue, which break down to disrupt the cell walls, thereby releasing cell contents.[22−24] Probe and bath systems are the two most common ways of applying ultrasound waves to the sample (Figure 2). Probe sonicators are constantly in contact with the sample and make reproducibility and repeatability difficult.[25]

Recently, an overview of some novel technologies to extract valuable compounds from plant materials concluding that UAE is a promising technique with various benefits was given.[26] In fact, it could be applied with small volumes of organic solvents (1−15 mL) at atmospheric pressure, ambient temperature, and during a very short time of extraction compared to conventional solvent extraction. Additionally, UAE is harmless for operators, safe to use, and has low maintenance costs. Compared to conventional methods, UAE is one of the most simple, inexpensive extraction systems, and can be operated rapidly in a broad range of solvents for large-scale preparations suited for industrial purposes.[27,28]

Possible industrial scale up of UAE has been reported in the literature for the extraction of polyphenols from apple pomace. The process appeared to be a relevant, rapid and sustainable alternative to the conventional procedure.[29,30]

Nevertheless, it has been reported that the exposure of the product to ultrasound may involve compound degradation. In fact, the impact of ultrasound treatment on sunflower oil during ultrasound processing was studied.[31] The authors reported the detection of some off-flavors, which can incite depreciation by consumers. This behavior has been reviewed, describing component degradation, especially for high lipid containing products.[32] For instance, UAE has been used to recover antioxidant compounds and especially steviol glycosides from *Stevia rebaudiana* leaves. Some of the main findings are described below and in Table 1.

Steviol Glycosides. In a recent work, the authors investigated the most appropriate procedure to maximize the yield of steviol glycosides, total phenolic compounds, and flavonoids as well as antioxidant activity in *Stevia* extracts.[33] Authors compared UAE with the conventional solvent one. Conventional extraction was carried out with water (100 °C/24 h) and 70% of ethanol (70 °C/30 min) as solvent. UAE was conducted with directly immersed sonotrodes of maximum nominal power of 400 W with 7 and 22 mm in diameter, and 2,

DOI: 10.1021/acs.jafc.5b01994
J. Agric. Food Chem. 2015, 63, 6835−6846

Table 1. Impact of Ultrasound and Microwave Assisted Extraction on the Recovery of High-Added Value Compounds from *Stevia rebaudiana* Bertoni Leaves

treatment conditions	solvent(s)	major findings	ref
		Ultrasound Assisted Extraction (UAE)	
400 W/7 and 22 mm sonotrodes/2−10 min	water	maximum recovery found using 22 mm probe and 10 min; 96.48 and 36.92 mg/g of extract, for stevioside and rebaudioside A, respectively; 77.89 mg/g of extract for total phenolic compounds (TPC); 62.48 and 15.41 mg/g of extract for flavonoids and non-flavonoids, respectively	33
20−100 W/40−80 °C/10−60 min	water	optimal ultrasound treatment (60 W/68 °C/32 min) using RSM; significant increase of 19 and 43% in rebaudioside A and stevioside yields, respectively, compared to conventional values	34
2 mm ultrasonic horn transducer (30 kHz and 50 W) and an ultrasonic bath (40 kHz and 100 W), 60−100% nominal power, 20−80% pulsed range	water/ethanol	significant increase of stevioside recovery, almost 7 times higher than conventional extraction at the same treatment time; higher extraction solvent leads to higher extraction yield	35
20 kHz/360 W/6−24 min	water	maximum extraction yield of soluble molecules (18%) after 24 min of treatment time; maximum recovery of rebaudioside A (28.72 g/100 g) after 24 min of treatment time	36
24 kHz/480 W/30 °C/18 min	water, ethanol, isopropyl alcohol	maximum recovery of rebaudioside A: 37.10 g/100 g; shorter extraction time, lower energy consumption	37
1st phase: 25 kHz/10−30 min/30 °C 2nd phase: 25 and 50% *Stevia*-based osmotic solution, then drying step	water	partial removal of sucrose, fructose, and glucose from the strawberries; incorporation of stevioside and rebaudioside as low caloric sweeteners	38
0 and 25 kHz frequency/30 °C/10−60 min	water	sugar substitution in Malay apples by stevia-derived natural sweetener; the highest water loss (22.48%) and the greatest sweetener gain (9.8%), using 50% (w/w) stevia-based solution for 45 min	39
20 kHz/400 W/20 °C/0−2 min	water	recovery of phenolic compounds, chlorophylls, and carotenoids; significant improvement in the recovery of phenolic compounds, compared to conventional extraction	21
ultrasonic bath (160 W)/50 mL extraction solvent/25 °C/25 min	acetonitrile/water	maximum DPPH inhibition of 89.94% for the extracted high added value compounds	40
		Microwave Assisted Extraction (MAE)	
2.45 GHz/0−400 W/70−110 °C/1−5 min	water	extraction rate increased and the stevioside content reached a maximum value in <5 min; significant relationship among stevioside concentration, temperature increase, and type of waves used to intensify the mass transfer	50
2.45 GHz/20−160 W/10−90 °C/0.5−5 min	water/methanol	MAE yielded 8.64 and 2.34% of stevioside and rebaudioside A, respectively	51

4, 6, 8, and 10 min of treatment time. Full duty cycle of ultrasonic propagation was applied with maximum amplitude and without cooling the system. The authors also concluded how UAE is an environmental friendly technique for the extraction of functional compounds out of *Stevia* leaves due to the significantly shortened treatment time and lower energy consumption compared with those of conventional extraction.

Response surface methodology (RSM) was used to optimize the UAE of steviol glycosides from *Stevia rebaudiana* Bertoni.[34] Experiments were done at different extraction temperatures (40−80 °C with water circulation system), sonication power (20−100 W), and extraction times (10−60 min in increments of 10 min). The authors found a significant increase of 19 and 43% in rebaudioside A and stevioside yields, respectively, under the optimal ultrasound treatment (60 W/68 °C/32 min) in comparison to that of classic treatment with boiling water. Moreover, extraction time was substantially shortened compared to that in classical extraction. They attributed this effect to the mechanical action of ultrasound waves on cell walls, thus increasing the accessibility and extractability of the molecules.

In another study, the potential of UAE to recover steviol glycosides from *Stevia* was evaluated.[35] Two types of ultrasound assisted extractors were employed: an extractor equipped with a 2 mm ultrasonic horn transducer (30 kHz and 50 W) and an ultrasonic bath (40 kHz and 100 W). The yields obtained by UAE after 20 min were comparable with those achieved after maceration during 24 h. The same behavior was noticed with an ultrasound bath (the process is almost completed after 20 min). The optimum parameters for UAE were water as solvent, 1/10 (g/L) as solid concentration in extraction media, and 20 min for extraction time.

Moreover, the influence of UAE on steviol glycoside recovery was also investigated.[36] Ultrasound was used by immersing a sonotrode (20 mm diameter, 300 mm length) into the treated samples with processing conditions of 20 kHz frequency and 1200 W maximum power. The effect of ultrasound treatment on the extraction yield of rebaudioside A (g/100 g) and total soluble solids (%) was mainly due to both prolonged treatment time and particle size reduction. The experimental conditions for UAE were carried out using 20 kHz frequency, 360 W power, and 6−24 min of ultrasound propagation time. Results showed a significant increase of the total soluble compounds with 11.16, 12.23, 13.37, and 18% at 6, 12, 18, and 24 min of extraction time, respectively. The yield of rebaudioside A, however, decreased with increasing US treatment time, giving thus 32.79, 30.45, 28.66, and 28.72 g/100g at the same time range. The authors also compared their results with conventional extraction studies showing significant advantages of UAE as an innovative and emerging technology. In addition, they reported that *Stevia* leaves represent an important source of carbohydrates and fibers.

Special emphasis was also dedicated to rebaudioside A and its extraction yields from *Stevia* leaves using various concentrations (10−60% w/w) of 3 different solvents (water, ethanol, and isopropyl alcohol) using UAE.[37] The optimal extraction conditions were found using 60% (w/w) isopropyl alcohol and 24 kHz/18 min/480 W/30 °C, leading to 37.10 g/100 g of rebaudioside A recovery yield. Furthermore, after the comparison of conventional extraction technologies and UAE, the authors concluded that UAE could be successfully incorporated into existing industrial plants for more sustainable and eco-friendly processing. Many issues like shortening the processing time, safer environment for operators, increased

DOI: 10.1021/acs.jafc.5b01994
J. Agric. Food Chem. 2015, 63, 6835−6846

yield and lower energy consumption have been taken into consideration.

In addition, other authors studied the possibility of inducing the substitution of sweeteners in strawberries by replacing the high caloric sugars in the fruit with low caloric ones but without losing the well-known sweetness of the fruits.[38] The process was performed using UAE and was compared to conventional extraction. Experiments were carried out in two separate phases with first the partial removal of sucrose, fructose, and glucose from the strawberries and second the incorporation of stevioside and rebaudioside as low caloric sweeteners. Strawberry slices were first pretreated to remove the high caloric sugars by immersion in an ultrasonic bath filled with distilled water (25 kHz/10−30 min/30 °C). The second step consisted of immersing the pretreated samples into *Stevia* powder (25% and 50% *Stevia*-based osmotic solution) as a natural and low caloric sweetener with/without sonication, followed by an air-drying step. The authors showed that the application of utltrasound for sugar removal provides better results compared to that of the untreated samples. It was also found that the samples treated with 50% w/w *Stevia* osmotic solution had the highest values of water loss and soluble solid gain response. For the second stage, low caloric sugar incorporation was conducted using 20 min of sonication time, thus leading to the maximum gain response of soluble solids.

In the same manner, the feasibility of sugar's substitution in Malay apples by *Stevia*-derived natural sweetener using ultrasonic pretreatments in osmotic solutions was studied.[39] The first stage of pretreatment consisted of removing sugars by ultrasound, performed using an ultrasonic bath (25 kHz and 30 °C). The second stage consisted of sugar substitution by a *Stevia*-based natural sweetener structured in five time intervals (10−60 min); three solutions (distilled water and two osmotic concentrations (25% and 50%, w/w)); and two frequency levels (0 and 25 kHz). The highest water loss (22.48%) was observed in Malay apple subjected to ultrasonic energy in both stages of the process (sugar removal stage and sweetener incorporation stage) and immersed in the 50% (w/w) *Stevia*-based solution for 45 min. The first pretreatment stage (sugar removal stage) showed high soluble solid loss from Malay apples immersed for 20 min in distilled water at an ultrasound frequency of 25 kHz. The process resulting in the greatest sweetener gain (9.8%) was also observed for Malay apples subjected to ultrasound in the sugar removal stage followed by immersion in the 50% w/w *Stevia*-based osmotic solution for 45 min subjected to ultrasonic application.

Antioxidant Compounds. The influence of UAE on the recovery of phenolic compounds, chlorophylls, and carotenoids from *Stevia* leaves at room temperature and using only water as solvent, making the extraction process more environmentally friendly, was recently investigated.[21] When comparing with the conventional method, the authors observed a significant improvement in the recovery of phenolic compounds after using UAE with the highest energy input conditions. However, no significant changes in chlorophylls a and b, as well as in carotenoid content, were observed after US treatment compared to those of control samples at equivalent diffusion times.

In another study, the recovery of stevioside, rebaudioside A, total phenolic compounds, and flavonoids from *Stevia* leaves, using UAE, were evaluated and compared to conventional extraction.[33] The obtained results showed that the compound recovery yields using UAE were 96.5, 36.9, 77.9, and 62.5 mg/g, respectively. However, with conventional extraction, the yields for stevioside, rebaudioside A, total phenolic compounds, and flavonoids were 74.7, 22.3, 53.9, and 35.8 mg/g, using water, and 82.68, 24.39, 56.72, and 37.94 mg/g, using ethanol, respectively. In addition, the antioxidant activity (ABTS values) was also higher when using UAE (2.58 ± 1.84 mM Trolox) than that obtained for conventional hot water extraction (2.10 ± 1.06 mM Trolox) and ethanolic extraction (2.24 ± 1.11 mM Trolox).

The recovery of valuable compounds from 10 plant matrices, including *Stevia*, using UAE and pressurized fluid extraction (PFE) was investigated.[40] The UAE method was carried out in an ultrasonic bath (160 W) using 50 mL of extraction solvent (30% acetonitrile in water), at 25 °C and during 25 min. For all extracts, the antioxidant capacity based on the reduction of free DPPH (2,2-diphenyl-1-picrylhydrazyl) radical was determined. Results ranged from 82.04 to 94.43% of DPPH radical inhibition for the PFE method and from 76.01 to 89.94% when using the UAE method.

MICROWAVE ASSISTED EXTRACTION (MAE)

Microwaves are nonionizing radiation with frequencies between 300 MHz and 300 GHz. The advantages of microwave assisted extraction (MAE) techniques compared to conventional methods (such as maceration and heat reflux) include reduced use of organic solvents, reduced extraction time (generally less than 30 min), and increased extraction yields.[41] The hot solvents generated in MAE penetrate easily into the matrix and extract compounds from the lysed plant cells. Figure 3 shows a schematic representation of the MAE system used at a laboratory scale.

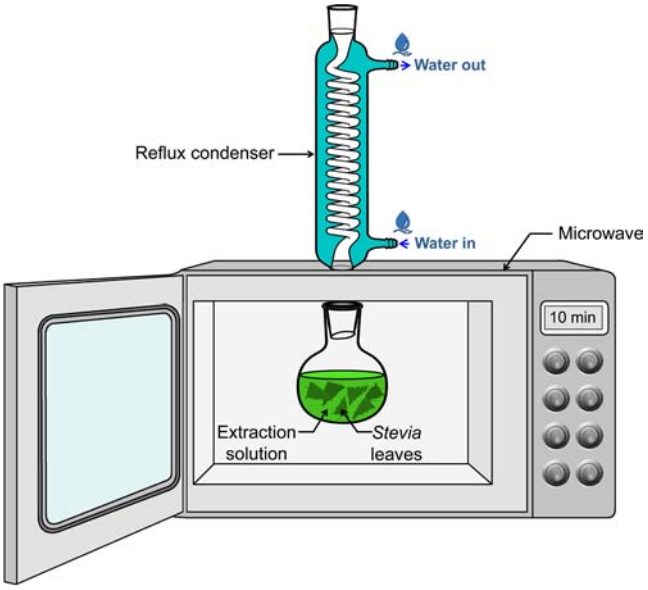

Figure 3. Laboratory scale equipment for microwave assisted extraction.

Some other benefits of MAE, compared to those of conventional extraction methodologies, were overviewed.[42] This method could be applied to a wide variety of plant matrices due to its minimal degradation of aimed and targeted functional and valuable compounds and increased selectivity.

DOI: 10.1021/acs.jafc.5b01994
J. Agric. Food Chem. 2015, 63, 6835−6846

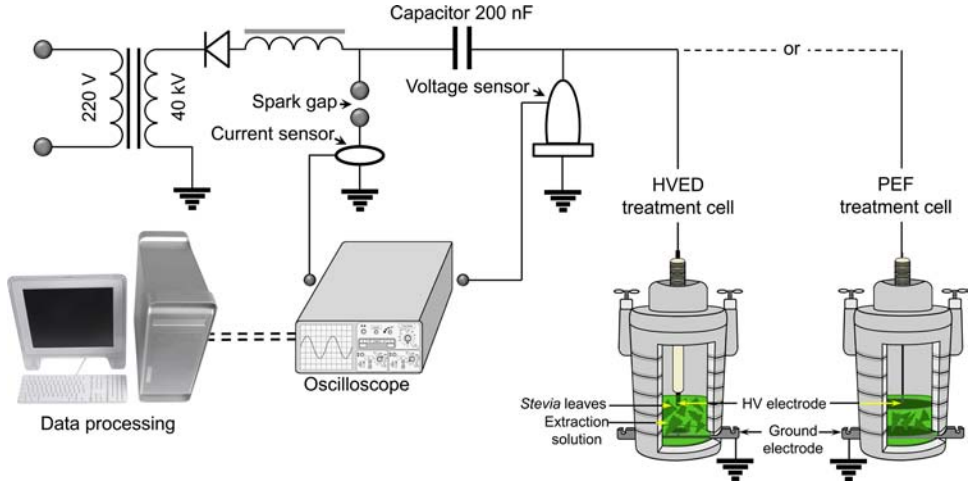

Figure 4. Typical scheme used for high voltage electrical discharges (HVED) and pulsed electric field (PEF) units.

Special emphasis was reported in the available literature regarding the feasibility of MAE process industrialization for green extraction of high-added value compounds from plant matrices and industrial byproducts.[43−46] Among the proposed processes for possible industrialization, solvent-free microwave extraction of essential oil from aromatic herbs[47] and the separation of volatile and nonvolatile organic compounds of boldo leaves[48] were discussed.

Despite the encouraging reports concerning the possible industrialization of the MAE process and even more the effective antimicrobial properties of microwaves for pasteurization and sterilization, this technique is facing numerous obstacles limiting its industrial uses. One of these limitations, is the high cost of industrial microwave heating-based equipment.[49] The potential of MAE to recover high-added value compounds from *Stevia rebaudiana* Bertoni was tested by several research groups, and Table 1 summarizes the main obtained results.

Steviol Glycosides. The effects of UAE, MAE, and conventional heat extraction on the recovery of stevioside from *Stevia* were evaluated and compared.[50] UAE was done using ultrasonic horn transducer (20 kHz and 750 W), sample temperature (up to 100 °C), and a microwave enclosed extractor (2.45 GHz), in the range of powers from 0 to 400 W and temperatures between 40 and 250 °C. UAE was conducted for 1−5 min at 50−100% amplitude of output power, without stirring. MAE was done for 1−5 min at 70−110 °C, with stirring. When using ultrasound and microwave fields, the extraction rate increased, and the stevioside content reached a maximum value in less than 5 min. The increase in stevioside content was observed when ultrasound treatment was applied using 50, 80, and 100% amplitude and an input power of 750 W. Compared to thermal extraction, these two techniques ensured high purity values of active substances. Moreover, they justified the use of ultrasound as an alternative extraction technology for steviol glycoside recovery as this technology can have economic benefits (relatively low-cost method) in comparison to conventional methods as well as for its simple use and significant efficiency. In addition, the authors observed a significant relationship between stevioside concentration, temperature increase, and type of waves used to intensify the mass transfer.

In the same manner, Jaitak, Bandna, and Kaul extracted stevioside and rebaudioside A from *Stevia* using dried and powdered leaves by conventional, UAE, and MAE techniques, using methanol, ethanol, and water as single solvents as well as in binary mixtures.[51] Conventional cold extraction was performed at 25 °C for 12 h, UAE was carried out at 35 ± 5 °C for 30 min, and MAE was carried out at 80 W power level, for 1 min at 50 °C. MAE yielded 8.64 and 2.34% of stevioside and rebaudioside A, respectively, while conventional and UAE yielded 6.54 and 1.20%, and 4.20 and 1.98% of stevioside and rebaudioside A, respectively.

Other authors developed a feasible and cost-effective system for the regeneration of *Stevia rebaudiana* with enhanced steviol glycosides production.[52] They used two different agar concentrations (3.5 and 7.0 g/L) and added plant growth regulators (PGRs) in the medium, adjusted pH, and boiled the media in a microwave oven. Media were placed in a growth room (25 °C) following a 16 h/8 h photoperiod. The results showed that lower agar concentrations are more effective for callus cultures and root induction, while higher agar concentration influences the shoot's organogenesis.

Moreover, the effects of pressurized hot water and microwave assisted water extractions were compared,[53,54] observing either similar or higher steviol glycoside recovery compared to that of conventional heating treatment.

Antioxidant Compounds. An artificial neural network (ANN) model was proposed to predict the extraction yields and rates for the recovery of bioactive molecules (the polyphenolic acids and flavonoids content) from three medicinal plants: *Stevia rebaudiana* leaves, *Cynara scolymus* leaves, and *Arctium lappa* roots.[55] MAE was done in a closed vessel system, in a temperature range of 40−250 °C, a power range of 0−400 W, and a pressure range of 0−20 bar.

PULSED ELECTRIC TECHNOLOGY ASSISTED EXTRACTION

Over the last years, the use of pulsed electric technologies, especially pulsed electric fields (PEF) and high voltage electrical discharges (HVED), have been shown as a potential tool to recover valuable compounds from plant food, from a green and sustainable point of view.[21,56] PEF consists of an electrical treatment for a short time (from several nanoseconds to several milliseconds) with pulse amplitude from 100−300 V/cm to 20−80 kV/cm. Under the effect of PEF, the biological membrane is electrically pierced and losses its semipermeability temporarily or permanently.[27,57] Scale-up of PEF food

DOI: 10.1021/acs.jafc.5b01994
J. Agric. Food Chem. 2015, 63, 6835−6846

Table 2. Impact of Pulsed Electric Technologies and Supercritical Fluid Extraction (SFE) on the Recovery of High-Added Value Compounds from *Stevia rebaudiana* Bertoni Leaves

treatment conditions	solvent	stevio glycosides yield	ref
		Pulsed Electric Technologies	
		Pulsed Electric Field	
20 kV/cm/0.5−2 ms/20 °C/60 min of diffusion	water	increase of 11−17% in total soluble solids compared to control samples	65 and 66
13.3 kV/cm/0−300 pulses/room temperature	water	polyphenol's recovery after PEF treatments was significantly higher compared to control samples; TPC were increased when energy input was augmented	21
		High Voltage Electrical Discharges	
40 kV/cm/0.5−2 ms/20 °C/60 min of diffusion	water	increase of 4−7% in total soluble solids compared to control samples	93
40 kV/cm/0−300 pulses/room temperature	water	significant increase in polyphenol, protein, chlorophyll, and carotenoid recovery after HVED compared to control, ultrasound, and PEF-treated samples; the increase in these compounds was proportional to energy input	21
		Supercritical Fluid Extraction (SFE)	
CO_2−SFE 200−250 bar/30 °C/12 h) CO_2+water-SFE (120−250 bar/10−16 °C/12 h)	CO_2 as solvent and water and/or ethanol as cosolvent	3% total glycosides when SFE was used as pretreatment and 3.4% after 120 bar, 16 °C, and 9.5% (molar) water	70
CO_2−SFE 200−250 bar/30 °C/12 h) CO_2+water-SFE (120−250 bar/10−16 °C/12 h)	CO_2 and water as cosolvent	yields of 50% and 72% for stevioside and rebaudioside A, respectively	71
150−350 bar/40−80 °C/60 min	CO_2 and ethanol−water mixture (70:30) as cosolvent (0−20%)	under the optimal conditions (211 bar, 80 °C, and 17.4% ethanol−water), yields of 36.66 mg/g and 17.79 mg/g for stevioside and rebaudioside A, respectively	72
		Subcritical Fluid Extraction (SubFE)	
244−372 bar/40 °C/0−90 min	20% MeOH-modified CO_2	increase in the extraction efficiency of stevioside, rebaudioside A, rebaudioside C, and dulcoside A when pressure was augmented; optimum extraction conditions of steviol glycosides at 372 bar pressure and 90 min extraction time	75
230 bar/100−150 °C/30−60 min/2−6 mL/min	water	yields of 38.67 mg/g stevioside, 35.68 mg/g rebaudioside, 48.63 mg gallic acid/g, and 29.81 mg quercetin/g under the optimal extraction conditions (230 bar/125 °C/45 min/4 mL/min)	76

DOI: 10.1021/acs.jafc.5b01994
J. Agric. Food Chem. 2015, 63, 6835−6846

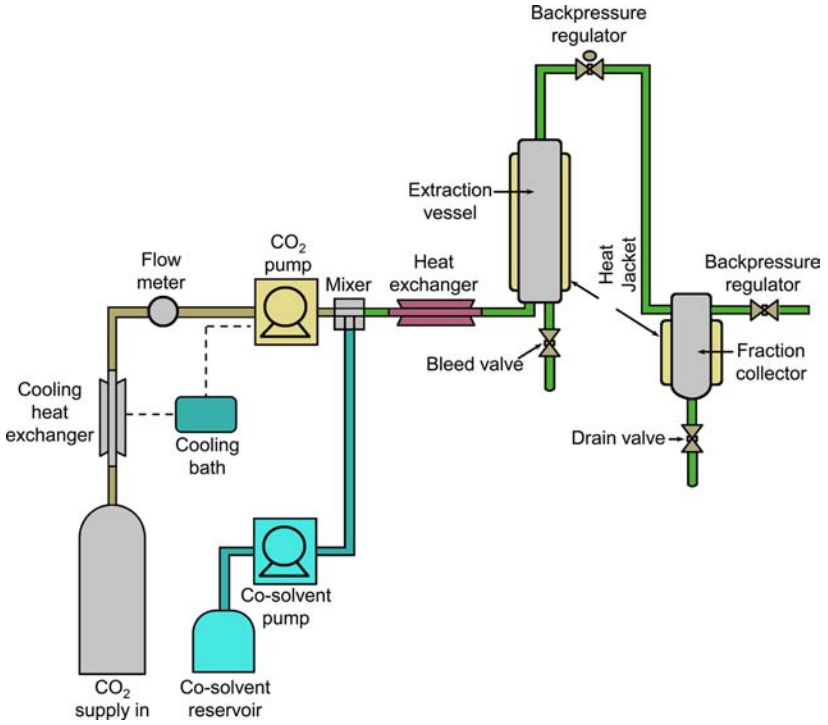

Figure 5. Schematic presentation of a supercritical carbone dioxide extraction system coupled with cosolvents and used at the laboratory scale.

processing as well as equipment design is already acquired by numerous food industries.[58,59] Regarding the field homogeneity as well as cleanability and flow behavior, several treatment chamber configurations were used, and equipment with 5, 30, and 80 kW average power levels was developed to process up to 10.000 l/h capacity.[60] The down side effects of using PEF treatment for industrial purposes are mainly the high industrial cost. In fact, the price for a PEF unit processor for inducing cell disintegration was estimated to be around $197,000, for a processing flow rate of 10 t/h, with an energy input of 10 kJ/kg, and an average output power of 30 kW.[61]

However, HVED is based on both chemical reactions and physical processes. When HVED is produced directly in water, it injects energy directly into an aqueous solution through a plasma channel formed by a high-current/high-voltage electrical discharge (>40 kV; >10 kA) between two submersed electrodes.[27,62−64] This technique, although more efficient for cell disintegration than PEF, requires a high investment too and produces free radicals in the submerging medium that reduce the total antioxidant activity of the extract. Nowadays, the performance of the industrial application of HVED treatment was not evaluated, thus requiring more research developments, but in any case, it is important that new steps be taken to help build a more rational use of our natural resources.

For instance, some authors have evaluated the potential of these technologies to recover nutritionally valuable compounds from *Stevia rebaudiana* leaves. Figure 4 shows a schematic representation of PEF and HVED processing systems. Moreover, some of the most important findings are listed below and in Table 2.

Steviol Glycosides. The impact of PEF assisted extraction on steviol glycosides recovery from *Stevia rebaudiana* leaves was previously studied.[65] It was found that PEF pretreatment (20 kV/cm and 0.5−2 ms) prior to conventional water extraction at ambient temperature (20 °C) improved both the kinetics and extraction yield of steviol glycosides from *Stevia*. A significant reduction in extraction time was also obtained (9 folds less) for achieving the maximum of steviol glycosides extraction compared to that of untreated samples at equivalent diffusion times and at 20 °C. In another study, it was observed that the effect of PEF-pretreatment can be observed at moderate (60 °C) and high (80 °C) extraction temperatures.[66]

Antioxidant Compounds. The potential of electrotechnologies to recover polyphenols from *Stevia rebaudiana* Bertoni has been recently evaluated.[21] These authors compared the effects of PEF and HVED on polyphenol's recovery at equivalent energy inputs (0, 24, 47, 71, 94, 118, and 141 kJ/kg). They found that HVED and PEF treatments enhanced the polyphenol's content of the obtained *Stevia* water extracts compared to that of control diffusion samples at equivalent treatment times. It was also found that the content of total polyphenolics increased proportionally to the energy input.

Moreover, the authors reported that HVED was the most effective technology to recover polyphenols (14.22−29.14 mg/g GAE DM), especially caffeic and chlorogenic acids, in terms of energy input and treatment time, compared to that of PEF (10.28−20.85 mg/g GAE DM) treatments. They justified the higher recovery of polyphenols after HVED treatments to the electric and mechanical disruption of *Stevia* leaves, thus facilitating the extraction of soluble biomolecules.

The recovery of coloring and antioxidant pigments (carotenoids and chlorophylls) from *Stevia rebaudiana* Bertoni leaves induced by pulsed electric technologies (PEF and HVED) at equivalent energy inputs was also investigated.[21] Increase of chlorophylls a and b contents in *Stevia* water extracts obtained from HVED-treated samples was observed and compared to the control. However, they did not find significant differences in chlorophylls a and b content in PEF-treated *Stevia* samples compared to those of the control at the same diffusion time.

Proteins. The effects of PEF and HVED on the recovery of proteins from *Stevia* at equivalent energy inputs (0, 24, 47, 71,

DOI: 10.1021/acs.jafc.5b01994
J. Agric. Food Chem. 2015, 63, 6835−6846

94, 118, and 141 kJ/kg) were also evaluated.[21] In this study, a significant improvement in protein yield was found after applying HVED treatment compared to that of control samples, obtaining the higher protein yield (1.127 g/100 g) when HVED was used at the highest energy input. Moreover, they also found a significant increase in protein yield, proportionally to HVED energy input.

SUB- AND SUPERCRITICAL FLUID EXTRACTION

The supercritical fluid state is reached when the pressure and the temperature of the system are above its critical point. At this state, the fluid could be considered either as expanded liquid or compressed gas. Supercritical fluids have relatively high density and therefore exhibit high solvation power that enables them to be used as solvents. Supercritical carbon dioxide ($SC-CO_2$), having a critical point of 7.38 MPa and 304.2 K, is the most widely used supercritical fluid. In fact, it has a low critical temperature, thus allowing operations near room temperature and a mild critical pressure. Furthermore, this fluid is nontoxic, nonflammable, nonexpensive, and readily available at good purity. $SC-CO_2$ has the feature to be used for hydrophobic or slightly hydrophilic compound extraction. Generally, when the pressure inside the extraction vessel increased, additional hydrophilic compounds could be extracted. When more hydrophilic compound extraction is targeted, the solvent's polarity has to be changed by using more polar organic solvents (i.e., ethanol, methanol, and ethyl acetate), mixed or not with water, and known as cosolvents or modifiers (Figure 5).

Although there are a few industrial applications for SFE (e.g., extraction of nicotine from tobacco, caffeine from coffee, theine from tea leaves, and few other examples),[67] the use of SFE in the food industry remains limited by its high equipment and installation costs.[68] The other major negative impact of applying SFE in the food industry is the processing cost, mainly related to the high CO_2 consumption, which is in most of the cases being lost at the end of the extraction and not recycled. One of the challenging solutions recently proposed to reduce the extraction time and the CO_2 consumption, consists of using continuous gas assisted mechanical expression (GAME) equipment.[69] Such equipment was successfully tested for oil extraction from oilseeds, paving the way toward possible large-scale continuous flow industrial applications of SFE. The current applications of SFE technology to recover high-added value compounds from *Stevia* are described below.

Steviol Glycosides. The impact of SFE, using CO_2 and either water or different mixtures of ethanol−water as cosolvents, on the recovery of steviol glycosides from *Stevia* has been studied by several research groups (Table 2). For instance, an increase in steviol glycoside's recovery was found after applying SFE (3−3.4%), in two steps, (a) the pretreatment of the leaves by SFE; (b) the extraction of the *Stevia* glycosides by SFE using CO_2 as solvent and water and/or ethanol as cosolvent, compared to that of the conventional extraction process.[70] In this line, other authors also obtained 50% and 72% recovery of the original stevioside and rebaudioside A, respectively, when using a two-step SFE process: (1) CO_2 extraction and (2) CO_2 + water extraction.[71]

In another study, a similar steviol glycoside yield was obtained when comparing SFE and conventional water extraction, concluding that SFE can be an alternative technique to conventional solvent extraction mainly due to the reduction extraction time of steviol glycosides.[72] The optimized conditions through this work were used later to obtain glycosides from *Stevia* leaves, then the raffinate was used to produce bioethanol. The operational conditions applied were 211 bar pressure, 80 °C temperature, 17.4% cosolvent, and a solvent/feed ratio of 30.[73]

Similarly, the effects of conventional organic extraction and SFE to extract steviol glycosides from *Stevia* were compared.[74] The authors found a 150% increase in steviol glycosides content when SFE was used compared to that in conventional extraction.

The use of subcritical fluids for the extraction of high-added value compounds from *Stevia rebaudiana* was also investigated. For instance, the extraction of steviol glycosides from *Stevia rebaudiana*, including stevioside, rebaudioside A, rebaudioside C, and dulcoside A by subcritical fluid extraction (SubFE) was studied.[75] The authors reported that the extraction efficiency increased proportionally to the pressure, at 40 °C, when using a 20% methanolic aqueous solution. The maximum recovery of steviol glycosides was ≈88% at 368 atm pressure, after 90 min of extraction time.

The potential of subcritical water extraction to recover steviol glucosides from *Stevia rebaudiana* leaves was also studied.[76] A Box-Bhenken experimental design was used to evaluate the effects of temperature (100−150 °C), extraction time (30−60 min), and flow rate (2−6 mL/min) at 230 bar pressure, and using a solid/liquid ratio of 1/10 (m/v). The optimal extraction conditions were found at 125 °C, 45 min, and 4 mL/min flow rate. At these conditions, the yields of stevioside and rebaudioside A were 38.67 mg/g and 35.68 mg/g, respectively.

Antioxidant Compounds. The total phenolic, flavonoid contents, and DPPH free radical scavenging activity were followed after the extraction of steviol glucosides using subcritical water. The authors found 48.63 mg of gallic acid equivalent/g extract for TPC, 29.81 mg of quercetin equivalent/g extract for flavonoids, and 92.50% for DPPH inhibition.[76]

ENZYME ASSISTED EXTRACTION

The use of enzyme assisted extraction constitutes another attractive "green" alternative to conventional methods in order to recover valuable compounds from plant food materials and, in particular from *Stevia rebaudiana* Bertoni leaves, thus reducing the consumption of organic solvents. In this line, some recent studies have shown the ability of enzyme assisted extraction to promote the breakdown of the plant cell wall, thus facilitating the recovery of intracellular compounds.[77]

For instance, the effects of enzyme assisted extraction (cellulase, pectinase, and hemicellulase) at different enzyme concentration, incubation time, and temperature to recover stevioside from *Stevia* leaves were evaluated, and the optimal conditions were evaluated.[77] The authors reported the high efficiency of this method compared to that of conventional solvent extraction. Moreover, they found that hemicellulose led to higher steviose yield (369 μg) after 60 min of extraction compared to cellulase (359 μg) and pectinases (333 μg), thus showing the importance of selecting the most appropriate enzyme.

GREEN IMPACT OF NONCONVENTIONAL TECHNOLOGIES

Developing new nonconventional technologies (UAE, MAE, SFE, EAE, etc.) to recover high-added value compounds from

DOI: 10.1021/acs.jafc.5b01994
J. Agric. Food Chem. 2015, 63, 6835−6846

agricultural resources and industrial byproducts has received increased interest compared to conventional methods. These emerging technologies may allow reducing extraction time, processing temperature, and solvent consumption, thus resulting in increasing the extraction yield and decreasing the energy cost.[67,78] In fact, thermal extraction processes, although considered as safe, require high-energy input and are not suitable for thermolabile compound extraction, being thus degraded.

The use of UAE brings many benefits such as shorter analysis time, simplified manipulation, and higher purity of the final product.[79] This technology has been widely applied to extract bioactive compounds (e.g., essential oils, antioxidants, and colorants) from plant matrices and industrial byproducts.[67] The green impact of UAE for the intensification of extraction of natural products has been reviewed by Shirsath and co-workers.[80]

When comparing conventional heating to emerging technologies, the heat transfer induced by microwaves remains cheaper, thus requiring moderate investment in equipment.[68] Moreover, it has been reported that when coupling conventional methods (e.g., hydrodistillation) with microwaves, the energy cost is reduced by almost 2-fold (compared to hydrodistillation alone); decreasing thus from 0.12 kWh/kg (430 kJ/kg, $6/t) to 0.07 kWh/kg (270 kJ/kg, $3.5/t).[81] In addition to the energy cost, the heat transfer generated by microwaves is much faster than the conventional one. This fact is due only to the dependence of the rate of heat loss and power applied and not limited to thermal conduction or convection currents.[82]

PEF technology represents a useful tool to recover selectively valuable compounds from different plant matrices from an economical and sustainable point of view.[83−85] This characteristic is mainly due to its ability to permeabilize the cell membrane, thus releasing the intracellular compounds,[21,56,57,86] although the rise of temperature during PEF treatment remains far lower than that reached during conventional thermal processing. PEF assisted drying and dehydration processes have been used for drying food products (vegetables and fruits), demonstrating not only higher drying rates but also great nutritional quality compared to that of conventional drying methods.[49] PEF treatment was able to produce the highest drying rate of okra, compared to that of both microwave heating and blanching.[87] It has also shown better mass transfer during osmotic dehydration of apples.[88] The drying character of PEF as well as nutritional quality retention were reported in other food products such as potato,[89,90] carrot,[91] beetroots,[92] and others. Morevover, the combination of nonconventional processes (i.e., PEF + US and PEF + HVED) with traditional extraction technologies (i.e., US/PEF/HVED + hot water extraction at mild temperatures or US/PEF/PEF + hydroethanolic extraction) could lead to the development of new and optimized extraction processes, thus shortening the extraction times, reducing the temperature, and minimizing the solvent consumption as well as the use of toxic solvents.

On the other hand, SFE has received great interest as a green technology to decrease or replace the consumption of toxic solvents, involving health and environmental related issues. Supercritical fluids have liquid-like solvent power and gas-like diffusivity, giving them great properties as ideal clean solvents for valuable compound recovery from plant matrices, thus having a green impact on the environment. In fact, green chemistry is mainly dominated by three aspects, which are waste, hazards (health, environmental, and safety), and energy.[68] Using nongreen organic solvents (e.g., hexane, diethyl ether, or chloroform) during food processing has a rising impact on human awareness as they must be removed from the extracts before being used as food additives. These impacts on both environment and health led to the use of emerging technologies, such as SFE.

AUTHOR INFORMATION

Corresponding Author

*Tel: +34-963544972. Fax: +34-963544954. E-mail: Francisco.Barba@uv.es.

Present Address

⊥Department of Agricultural Technology, Storage and Transport, Faculty of Agriculture, University of Zagreb, Svetošimunska cesta 25, 10000 Zagreb, Croatia.

Funding

F.J.B. thanks the Valencian Autonomous Government (Conselleria dEducació, Cultura i Esport. Generalitat Valenciana) for the postdoctoral fellowship of the VALi+d program "Programa VALi+d per a investigadors en fase postdoctoral 2013" (APOSTD/2013/092).

Notes

The authors declare no competing financial interest.

REFERENCES

(1) Barba, F. J.; Criado, M. N.; Belda-Galbis, C. M.; Esteve, M. J.; Rodrigo, D. *Stevia rebaudiana* Bertoni as a natural antioxidant/antimicrobial for high pressure processed fruit extract: Processing parameter optimization. *Food Chem.* **2014**, *148*, 261−267.

(2) Carbonell-Capella, J. M.; Barba, F. J.; Esteve, M. J.; Frígola, A. High pressure processing of fruit juice mixture sweetened with *Stevia rebaudiana* Bertoni: Optimal retention of physical and nutritional quality. *Innovative Food Sci. Emerging Technol.* **2013**, *18*, 48−56.

(3) Criado, M. N.; Barba, F. J.; Frígola, A.; Rodrigo, D. Effect of *Stevia rebaudiana* on oxidative enzyme activity and its correlation with antioxidant capacity and bioactive compounds. *Food Bioprocess Technol.* **2014**, 7 (5), 1518−1525.

(4) Lemus-Mondaca, R.; Vega-Gálvez, A.; Zura-Bravo, L.; Ah-Hen, K. *Stevia rebaudiana* Bertoni, source of a high-potency natural sweetener: A comprehensive review on the biochemical, nutritional and functional aspects. *Food Chem.* **2012**, *132* (3), 1121−1132.

(5) Abou-Arab, E. A.; Abu-Salem, H. Evaluation of bioactive compounds of *Stevia rebaudiana* leaves and callus. *Afr. J. Food Sci.* **2010**, *4* (10), 627−634.

(6) Kim, I.-S.; Yang, M.; Lee, O.-H.; Kang, S.-N. The antioxidant activity and the bioactive compound content of *Stevia rebaudiana* water extracts. *LWT - Food Sci. Technol.* **2011**, *44* (5), 1328−1332.

(7) Muanda, F. N.; Soulimani, R.; Diop, B.; Dicko, A. Study on chemical composition and biological activities of essential oil and extracts from *Stevia rebaudiana* Bertoni leaves. *LWT - Food Sci. Technol.* **2011**, *44* (9), 1865−1872.

(8) Tadhani, M. B.; Patel, V. H.; Subhash, R. In vitro antioxidant activities of *Stevia rebaudiana* leaves and callus. *J. Food Compos. Anal.* **2007**, *20* (3−4), 323−329.

(9) Barba, F. J.; Esteve, M. J.; Frígola, A. Bioactive Components from Leaf Vegetable Products. In *Studies in Natural Products Chemistry*; Atta-ur-Rahman, Ed.; Elsevier: New York, 2014; Vol. *41*, pp 321−346.

(10) Goyal, S. K.; Samsher; Goyal, R. K. Stevia (*Stevia rebaudiana*) a bio-sweetener: A review. *Int. J. Food Sci. Nutr.* **2010**, *61* (1), 1−10.

(11) Koyama, E.; Kitazawa, K.; Ohori, Y.; Izawa, O.; Kakegawa, K.; Fujino, A.; Ui, M. In vitro metabolism of the glycosidic sweeteners, stevia mixture and enzymatically modified stevia in human intestinal microflora. *Food Chem. Toxicol.* **2003**, *41* (3), 359−374.

DOI: 10.1021/acs.jafc.5b01994
J. Agric. Food Chem. 2015, 63, 6835−6846

(12) Puri, M.; Sharma, D.; Tiwari, A. K. Downstream processing of stevioside and its potential applications. *Biotechnol. Adv.* **2011**, *29* (6), 781−791.
(13) Lailerd, N.; Saengsirisuwan, V.; Sloniger, J. A.; Toskulkao, C.; Henriksen, E. J. Effects of stevioside on glucose transport activity in insulin-sensitive and insulin-resistant rat skeletal muscle. *Metab., Clin. Exp.* **2004**, *53* (1), 101−107.
(14) Anton, S. D.; Martin, C. K.; Han, H.; Coulon, S.; Cefalu, W. T.; Geiselman, P.; Williamson, D. A. Effects of stevia, aspartame, and sucrose on food intake, satiety, and postprandial glucose and insulin levels. *Appetite* **2010**, *55* (1), 37−43.
(15) Chan, P.; Tomlinson, B.; Chen, Y.-J.; Liu, J.-C.; Hsieh, M.-H.; Cheng, J.-T. A double-blind placebo-controlled study of the effectiveness and tolerability of oral stevioside in human hypertension. *Br. J. Clin. Pharmacol.* **2000**, *50* (3), 215−220.
(16) Nunes, A. P. M.; Ferreira-Machado, S. C.; Nunes, R. M.; Dantas, F. J. S.; De Mattos, J. C. P.; Caldeira-de-Araujo, A. Analysis of genotoxic potentiality of stevioside by comet assay. *Food Chem. Toxicol.* **2007**, *45* (4), 662−666.
(17) Rajab, R.; Mohankumar, C.; Murugan, K.; Harish, M.; Mohanan, P. V. Purification and toxicity studies of stevioside from *Stevia rebaudiana* Bertoni. *Toxicol. Int.* **2009**, *16* (1), 49−54.
(18) Da Porto, C.; Porretto, E.; Decorti, D. Comparison of ultrasound-assisted extraction with conventional extraction methods of oil and polyphenols from grape (*Vitis vinifera* L.) seeds. *Ultrason. Sonochem.* **2013**, *20* (4), 1076−1080.
(19) Šic Žlabur, J.; Brnčić, M. New Sweetener- *Stevia rebaudiana* Bertoni: Chemical Characteristics and Comparison of Classic and Ultrasound Assisted Extraction Techniques. In *Leaf Sweeteners: Resources, Processing and Health Effects*; Wu, W., Ed.; Food and Beverage Consumption and Health; Nova Science Publishers, Inc.: New York, 2014.
(20) Dent, M.; Dragović-Uzelac, V.; Penić, M.; Brnčić, M.; Bosiljkov, T.; Levaj, B. The effect of extraction solvents, temperature and time on the composition and mass fraction of polyphenols of dalmatian wild sage (*Salvia officinalis* L.). *Food Technol. Biotechnol.* **2013**, *51* (1), 84−91.
(21) Barba, F. J.; Grimi, N.; Vorobiev, E. Evaluating the potential of cell disruption technologies for green selective extraction of antioxidant compounds from *Stevia rebaudiana* Bertoni leaves. *J. Food Eng.* **2015**, *149*, 222−228.
(22) Barba, F. J.; Grimi, N.; Negm, M.; Quilez, F.; Vorobiev, E. Leaf Sweeteners: Resources, *Processing and Health Effects*. In; Wu, W., Ed.; Nova Science Publishers: New York, 2014; pp 41−57.
(23) Bubalo, M. C.; Sabotin, I.; Radoš, I.; Valentinčič, J.; Bosiljkov, T.; Brnčić, M.; Žnidaršič-Plazl, P. A comparative study of ultrasound-, microwave-, and microreactor-assisted imidazolium-based ionic liquid synthesis. *Green Process. Synth.* **2013**, *2* (6), 579−590.
(24) Roselló-Soto, E.; Galanakis, C. M.; Brnčić, M.; Orlien, V.; Trujillo, F. J.; Mawson, R.; Knoerzer, K.; Tiwari, B. K.; Barba, F. J. Clean recovery of antioxidant compounds from plant foods, by-products and algae assisted by ultrasounds processing. Modeling approaches to optimize processing conditions. *Trends Food Sci. Technol.* **2015**, *42*, 134−149.
(25) Režek Jambrak, A.; Herceg, Z. Application of Ultrasonics in Food Preservation and Processing. In *Conventional and Advanced Food Processing Technologies*; Bhattacharya, S., Ed.; John Wiley & Sons, Ltd.: New York, 2014; pp 515−536.
(26) Heng, M. Y.; Tan, S. N.; Yong, J. W. H.; Ong, E. S. Emerging green technologies for the chemical standardization of botanicals and herbal preparations. *TrAC, Trends Anal. Chem.* **2013**, *50*, 1−10.
(27) Barba, F. J.; Grimi, N.; Vorobiev, E. New approaches for the use of non-conventional cell disruption technologies to extract potential food additives and nutraceuticals from microalgae. *Food Eng. Rev.* **2015**, *7* (1), 45−62.
(28) Khoddami, A.; Wilkes, M. A.; Roberts, T. H. Techniques for analysis of plant phenolic compounds. *Molecules* **2013**, *18* (2), 2328−2375.
(29) Virot, M.; Tomao, V.; Le Bourvellec, C.; Renard, C. M. C. G.; Chemat, F. Towards the industrial production of antioxidants from food processing by-products with ultrasound-assisted extraction. *Ultrason. Sonochem.* **2010**, *17* (6), 1066−1074.
(30) Pingret, D.; Fabiano-Tixier, A.-S.; Bourvellec, C. L.; Renard, C. M. G. C.; Chemat, F. Lab and pilot-scale ultrasound-assisted water extraction of polyphenols from apple pomace. *J. Food Eng.* **2012**, *111* (1), 73−81.
(31) Pingret, D.; Durand, G.; Fabiano-Tixier, A.-S.; Rockenbauer, A.; Ginies, C.; Chemat, F. Degradation of edible oil during food processing by ultrasound: electron paramagnetic resonance, physicochemical, and sensory appreciation. *J. Agric. Food Chem.* **2012**, *60* (31), 7761−7768.
(32) Pingret, D.; Fabiano-Tixier, A.-S.; Chemat, F. Degradation during application of ultrasound in food processing: A review. *Food Control* **2013**, *31* (2), 593−606.
(33) Šic Žlabur, J.; Voća, S.; Dobričević, N.; Brnčić, M.; Dujmić, F.; Rimac Brnčić, S. Optimization of ultrasound assisted extraction of functional ingredients from *Stevia rebaudiana* bertoni leaves. *Int. Agrophysics* **2015**, *29* (2), 231−237.
(34) Liu, J.; Li, J.-W.; Tang, J. Ultrasonically assisted extraction of total carbohydrates from *Stevia rebaudiana* Bertoni and identification of extracts. *Food Bioprod. Process.* **2010**, *88* (2−3), 215−221.
(35) Alupului, A.; Lavric, V. Extraction intensification using ultrasounds case study: Glycosides from *Stevia rebaudiana* Bert. *Rev. Chim.* **2009**, *60* (5), 497−500.
(36) Gasmalla, M. A. A.; Yang, R.; Abubakr, M.; Xiao, H.; Zhang, W. Physico-chemical assessment and rebauidioside A. Productively of natural sweeteners (*Stevia rebaudiana* Bertoni). *J. Food Nutr. Res.* **2014**, *2* (5), 209−214.
(37) Gasmalla, M. A. A.; Yang, R.; Musa, A.; Hua, X.; Ye, F. Influence of sonication process parameters to the state of liquid concentration of extracted rebaudioside A from Stevia (*Stevia rebaudiana* bertoni) leaves. *Arabian J. Chem.* **2014**, DOI: 10.1016/j.arabjc.2014.06.012.
(38) Garcia-Noguera, J.; Weller, C. L.; Oliveira, F. I. P.; Rodrigues, S.; Fernandes, F. A. N. Dual-stage sugar substitution in strawberries with a Stevia-based sweetener. *Innovative Food Sci. Emerging Technol.* **2010**, *11* (1), 225−230.
(39) Oliveira, F. I. P.; Rodrigues, S.; Fernandes, F. A. N. Production of low calorie Malay apples by dual stage sugar substitution with Stevia-based sweetener. *Food Bioprod. Process.* **2012**, *90* (4), 713−718.
(40) Dobiáš, P.; Pavlíková, P.; Adam, M.; Eisner, A.; Beňová, B.; Ventura, K. Comparison of pressurised fluid and ultrasonic extraction methods for analysis of plant antioxidants and their antioxidant capacity. *Cent. Eur. J. Chem.* **2010**, *8* (1), 87−95.
(41) Chemat, F.; Cravotto, G. In *Microwave-Assisted Extraction for Bioactive Compound*; Chemat, F., Cravotto, G., Eds.; Springer: New York, 2013.
(42) Teo, C. C.; Tan, S. N.; Yong, J. W. H.; Hew, C. S.; Ong, E. S. Validation of green-solvent extraction combined with chromatographic chemical fingerprint to evaluate quality of *Stevia rebaudiana* Bertoni. *J. Sep. Sci.* **2009**, *32* (4), 613−622.
(43) Li, Y.; Radoiu, M.; Fabiano-Tixier, A.-S.; Chemat, F. From Laboratory to Industry: Scale-up, Quality, and Safety Consideration for Microwave-Assisted Extraction. In *Microwave-Assisted Extraction for Bioactive Compounds*; Chemat, F., Cravotto, G., Eds.; Food Engineering Series; Springer: New York, 2012; pp 207−229.
(44) Díaz-Ortiz, A.; de la Hoz, A.; Alcázar, J.; Carrillo, J. R.; Antonia Herrero, M.; Fontana, A.; de Mata Muñoz, J. Reproducibility and scalability of solvent-free microwave-assisted reactions: from domestic ovens to controllable parallel applications. *Comb. Chem. High Throughput Screen.* **2007**, *10* (3), 163−169.
(45) Tatke, P.; Jaiswal, Y. An overview of microwave assisted extraction and its applications in herbal drug research. *Res. J. Med. Plant* **2011**, *5* (1), 21−31.
(46) Mason, T. J.; Chemat, F.; Vinatoru, M. The extraction of natural products using ultrasound or microwaves. *Curr. Org. Chem.* **2011**, *15* (2), 237−247.

DOI: 10.1021/acs.jafc.5b01994
J. Agric. Food Chem. 2015, 63, 6835−6846

(47) Filly, A.; Fernandez, X.; Minuti, M.; Visinoni, F.; Cravotto, G.; Chemat, F. Solvent-free microwave extraction of essential oil from aromatic herbs: from laboratory to pilot and industrial scale. *Food Chem.* **2014**, *150*, 193−198.
(48) Petigny, L.; Périno, S.; Minuti, M.; Visinoni, F.; Wajsman, J.; Chemat, F. Simultaneous microwave extraction and separation of volatile and non-volatile organic compounds of boldo leaves. from lab to industrial scale. *Int. J. Mol. Sci.* **2014**, *15* (5), 7183−7198.
(49) Boye, J. I.; Arcand, Y. *Green Technologies in Food Production and Processing*; Springer Science+Business Media, LLC: New York, 2012.
(50) Alupului, A.; Calinescu, I.; Lavric, V. Ultrasonic *vs.* microwave extraction intensification of active principles from medicinal plants. *AIDIC Conference Series* **2009**, *09*, 1−8.
(51) Jaitak, V.; Bandna, B. S.; Kaul, V. K. An efficient microwave-assisted extraction process of stevioside and rebaudioside-A from *Stevia rebaudiana* (Bertoni). *Phytochem. Anal.* **2009**, *20* (3), 240−245.
(52) Aman, N.; Hadi, F.; Khalil, S. A.; Zamir, R.; Ahmad, N. Efficient regeneration for enhanced steviol glycosides production in *Stevia rebaudiana* (Bertoni). *C. R. Biol.* **2013**, *336* (10), 486−492.
(53) Pól, J.; Varadová Ostrá, E.; Karásek, P.; Roth, M.; Benesová, K.; Kotlaríková, P.; Cáslavský, J. Comparison of two different solvents employed for pressurised fluid extraction of stevioside from *Stevia rebaudiana*: methanol versus water. *Anal. Bioanal. Chem.* **2007**, *388* (8), 1847−1857.
(54) Teo, C. C.; Tan, S. N.; Yong, J. W. H.; Hew, C. S.; Ong, E. S. Pressurized hot water extraction (PHWE). *J. Chromatogr. A* **2010**, *1217* (16), 2484−2494.
(55) Alupului, A.; Lavric, V. Artificial neural network modelling of ultrasound and microwave extraction of bioactive constituents from medicinal plants. *Rev. Chim.* **2012**, *63* (7), 743−748.
(56) Parniakov, O.; Barba, F. J.; Grimi, N.; Lebovka, N.; Vorobiev, E. Impact of pulsed electric fields and high voltage electrical discharges on extraction of high-added value compounds from papaya peels. *Food Res. Int.* **2014**, *65* (Part C), 337−343.
(57) Deng, Q.; Zinoviadou, K. G.; Galanakis, C. M.; Orlien, V.; Grimi, N.; Vorobiev, E.; Lebovka, N.; Barba, F. J. The effects of conventional and non-conventional processing on glucosinolates and its derived forms, isothiocyanates: Extraction, degradation, and applications. *Food Eng. Rev.* **2014**, 1−25.
(58) Jaeger, H.; Balasa, A.; Knorr, D. Food Industry Applications for Pulsed Electric Fields. In *Electrotechnologies for Extraction from Food Plants and Biomaterials*; Food Engineering Series; Springer: New York, 2009; pp 181−216.
(59) Mohamed, M. E. A.; Amer Eiss, A. H. Pulsed Electric Fields for Food Processing Technology. In *Structure and Function of Food Engineering*; Amer Eissa, A., Ed.; InTech: Rijeka, Croatia, 2012.
(60) Töpfl, S. Pulsed Electric Field food treatment - scale up from lab to industrial scale. *Procedia Food Sci.* **2011**, *1*, 776−779.
(61) Töpfl, S. *Pulsed Electric Fields (PEF) for Permeabilization of Cell Membranes in Food- and Bioprocessing Applications, Process and Equipment Design and Cost Analysis*; Berlin University of Technology: Berlin, 2006.
(62) Boussetta, N.; Lesaint, O.; Vorobiev, E. A study of mechanisms involved during the extraction of polyphenols from grape seeds by pulsed electrical discharges. *Innovative Food Sci. Emerging Technol.* **2013**, *19*, 124−132.
(63) Boussetta, N.; Vorobiev, E. Extraction of valuable biocompounds assisted by high voltage electrical discharges: A review. *C. R. Chim.* **2014**, *17* (3), 197−203.
(64) Touya, G.; Reess, T.; Pécastaing, L.; Gibert, A.; Domens, P. Development of subsonic electrical discharges in water and measurements of the associated pressure waves. *J. Phys. D: Appl. Phys.* **2006**, *39* (24), 5236−5244.
(65) Duval, Q.; Grimi, N.; Vorobiev, E. Intensification d'un procédé de production du stevioside à partir des feuilles de stevia. *Rapp. PTV* **2011**, *50*.
(66) Negm, M.; Grimi, N.; Vorobiev, E. Pulsed Electric Field Pretreatment Assisted the Green Solvent Extraction of Sweet Glycosides from *Stevia rebaudiana*. In *International Congress on Green Extraction of Natural Products*; GENP Avignon: France, 2013.
(67) Rombaut, N.; Tixier, A.-S.; Bily, A.; Chemat, F. Green extraction processes of natural products as tools for biorefinery. *Biofuels, Bioprod. Biorefin.* **2014**, *8* (4), 530−544.
(68) Galanakis, C. M.; Barba, F. J.; Prasad, K. N. Cost and Safety Issues of Emerging Technologies against Conventional Techniques. In *Food Waste Recovery Processing Technologies and Industrial Techniques*; Elsevier - Academic Press: London, 2015; pp 323−338.
(69) Müller, M.; Eggers, R. Gas-assisted oilseed pressing on an industrial scale. *J. Am. Oil Chem. Soc.* **2014**, *91* (9), 1633−1641.
(70) Pasquel, A.; Meireles, M. A. A.; Marques, M. O. M.; Petenate, A. J. Extraction of stevia glycosides with CO_2 + water, CO_2 + ethanol, and CO_2 + water + ethanol. *Braz. J. Chem. Eng.* **2000**, *17*, 271−282.
(71) Yoda, S. K.; Marques, M. O. M.; Petenate, A. J.; Meireles, M. A. A. Supercritical fluid extraction from *Stevia rebaudiana* Bertoni using CO_2 and CO_2 + water: Extraction kinetics and identification of extracted components. *J. Food Eng.* **2003**, *57* (2), 125−134.
(72) Erkucuk, A.; Akgun, I. H.; Yesil-Celiktas, O. Supercritical CO_2 extraction of glycosides from *Stevia rebaudiana* leaves: Identification and optimization. *J. Supercrit. Fluids* **2009**, *51* (1), 29−35.
(73) Coban, I.; Sargin, S.; Celiktas, M. S.; Yesil-Celiktas, O. Bioethanol production from raffinate phase of supercritical CO_2 extracted *Stevia rebaudiana* leaves. *Bioresour. Technol.* **2012**, *120*, 52−59.
(74) Choi, Y. H.; Kim, I.; Yoon, K. D.; Lee, S. J.; Kim, C. Y.; Yoo, K.-P.; Choi, Y.-H.; Kim, J. Supercritical fluid extraction and liquid chromatographic-electrospray mass spectrometric analysis of stevioside from *Stevia rebaudiana* leaves. *Chromatographia* **2002**, *55* (9−10), 617−620.
(75) Liu, J.; Ong, C. P.; Li, S. F. Y. Subcritical Fluid Extraction of Stevia Sweeteners from *Stevia rebaudiana*. *J. Chromatogr. Sci.* **1997**, *35* (9), 446−450.
(76) Yildiz-Ozturk, E.; Tag, O.; Yesil-Celiktas, O. Subcritical water extraction of steviol glycosides from *Stevia rebaudiana* leaves and characterization of the raffinate phase. *J. Supercrit. Fluids* **2014**, *95*, 422−430.
(77) Puri, M.; Sharma, D.; Barrow, C. J.; Tiwary, A. K. Optimisation of novel method for the extraction of steviosides from *Stevia rebaudiana* leaves. *Food Chem.* **2012**, *132* (3), 1113−1120.
(78) Chemat, F.; Vian, M. A.; Cravotto, G. Green extraction of natural products: Concept and principles. *Int. J. Mol. Sci.* **2012**, *13* (7), 8615−8627.
(79) Chemat, S.; Lagha, A.; Ait Amar, H.; Chemat, F. Ultrasound assisted microwave digestion. *Ultrason. Sonochem.* **2004**, *11* (1), 5−8.
(80) Shirsath, S. R.; Sonawane, S. H.; Gogate, P. R. Intensification of extraction of natural products using ultrasonic irradiations—A review of current status. *Chem. Eng. Process.* **2012**, *53*, 10−23.
(81) Golmakani, M.-T.; Rezaei, K. Comparison of microwave-assisted hydrodistillation withthe traditional hydrodistillation method in the extractionof essential oils from *Thymus vulgaris* L. *Food Chem.* **2008**, *109* (4), 925−930.
(82) Proctor, A. *Alternatives to Conventional Food Processing*; Springer: New York, 2010.
(83) Abenoza, M.; Benito, M.; Saldana, G.; Alvarez, I.; Raso, J.; Sanchez-Gimeno, A. C. Effects of pulsed electric field on yield extraction and quality of olive oil. *Food Bioprocess Technol.* **2013**, *6* (6), 1367−1373.
(84) Vorobiev, E.; Lebovka, N. *Electrotechnologies for Extraction from Food Plants and Biomaterials*; Springer: New York, 2008; pp 39−81.
(85) Vorobiev, E. I.; Lebovka, N. I. Enhancing Extraction Processes in the Food Industry Series: Contemporary Food Engineering. In *Enhancing Extraction Processes in the Food Industry*; Lebovka, N., Vorobiev, E., Chemat, F., Eds.; Contemporary Food Engineering; CRC Press, Boca Raton, FL, 2011; pp 25−83.
(86) Puertolas, E.; Luengo, E.; Alvarez, I.; Raso, J. Improving mass transfer to soften tissues by pulsed electric fields: Fundamentals and applications. *Annu. Rev. Food Sci. Technol.* **2012**, *3* (1), 263−282.

DOI: 10.1021/acs.jafc.5b01994
J. Agric. Food Chem. 2015, 63, 6835−6846

(87) Adedeji, A. A.; Gachovska, T. K.; Ngadi, M. O.; Raghavan, G. S. V. Effect of Pretreatments on drying characteristics of okra. *Drying Technol.* **2008**, *26* (10), 1251−1256.
(88) Amami, E.; Vorobiev, E.; Kechaou, N. Effect of Pulsed Electric Field on the Osmotic dehydration and mass transfer kinetics of apple tissue. *Drying Technol.* **2005**, *23* (3), 581−595.
(89) Arevalo, P.; Ngadi, M. O.; Bazhal, M. I.; Raghavan, G. S. V. Impact of pulsed electric fields on the dehydration and physical properties of apple and potato slices. *Drying Technol.* **2004**, *22* (5), 1233−1246.
(90) Lebovka, N. I.; Shynkaryk, N. V.; Vorobiev, E. Pulsed electric field enhanced drying of potato tissue. *J. Food Eng.* **2007**, *78* (2), 606−613.
(91) Gachovska, T. K.; Adedeji, A. A.; Ngadi, M.; Raghavan, G. V. S. Drying characteristics of pulsed electric field-treated carrot. *Drying Technol.* **2008**, *26* (10), 1244−1250.
(92) Shynkaryk, M. V.; Lebovka, N. I.; Vorobiev, E. Pulsed electric fields and temperature effects on drying and rehydration of red beetroots. *Drying Technol.* **2008**, *26* (6), 695−704.
(93) Negm, M. S. PhD. Thesis. Technological and Biochemical Studies on the Natural Sweetener Stevioside. Zagazig University, Egypt, 2010.

DOI: 10.1021/acs.jafc.5b01994
J. Agric. Food Chem. 2015, 63, 6835−6846

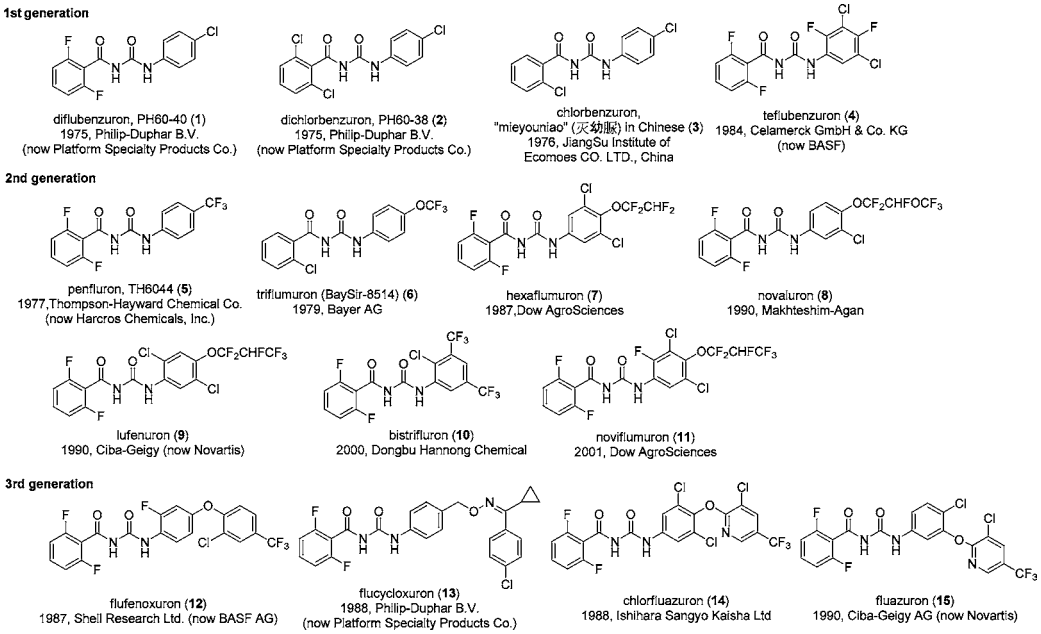

Figure 1. Chemical structures of commercial benzoylphenylurea chitin synthesis inhibitors.

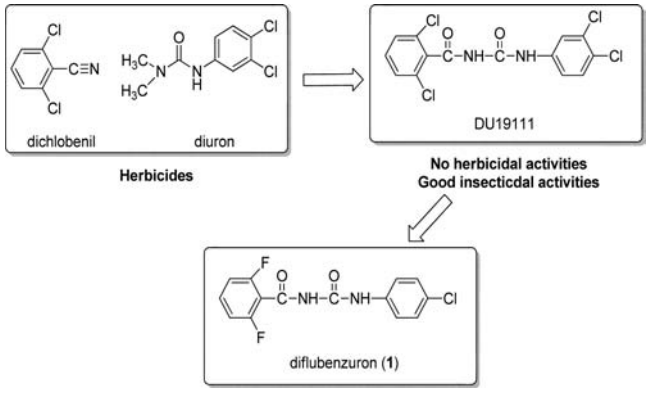

Figure 2. Discovery of benzoylphenylurea chitin synthesis inhibitor diflubenzuron (**1**).

introduced to the market with the trade name Dimilini in 1975.[7]

By virtue of the unique action mechanism and low toxicity for bees, birds, and humans along with their high biological activity against pests, many companies focused on the research of benzoylurea chitin synthesis inhibitors. Then dichlorbenzuron (PH60-38, **2**) and penfluoron (TH6044, **5**) were developed commercially as insecticides at Philip-Duphar B.V. Co. and Thompson-Hayward Chemical Co. Penfluoron (TH6044, **5**) was found to possess a high larvicidal activity, about 3 times as active as diflubenzuron (**1**) when tested against *P. brassicae* in laboratory tests. At the same time, chlorbenzuron (**3**) was discovered at JiangSu Institute of Ecomoes and Soochow University, China (Figure 2). Teflubenzuron (**4**) is a multihalo-substituted BPU and was introduced in Thailand by Celamerck GmbH & Co. KG (now BASF). Teflubenzuron (**4**) exhibited better ovicidal and larvicidal activities against the African armyworm (*Spodoptera exempta*) than diflubenzuron (**1**).[8]

The most successful benzoylurea compound after diflubenzuron (**1**) is triflumuron (**6**), which was discovered by Bayer (now Bayer AG) and it is the first commercial product of the second generation BPUs. Triflumuron (BaySir-8514, **6**) exhibited higher ovicidal and broad-spectrum larvicidal activity in comparison with the first-generation BPUs; for example, triflumuron (**6**) had larvicidal activity against cotton bollworm (*Helicoverpa armigera*), whereas teflubenzuron (**4**) and diflubenzuron (**1**) were inactive.[9] Hexaflumuron (**7**) was intended to be used in products to control termites at Dow AgroSciences. Dow AgroSciences was recognized by the U.S. EPA with the U.S. Presidential Green Chemistry Challenge Award in 2000 for the Sentricon System (active ingredient, hexaflumuron).[10] In the following years, novaluron (**8**), lufenuron (**9**), and noviflumuron (**11**) were developed successively at Makhteshim-Agan, Ciba-Geigy (now Novartis), and Dow AgroSciences, respectively. In 2011, the sale amounts of lufenuron (**9**, U.S. $165 million) and novaluron (**8**, U.S. $80.4 million) were the first and third of all commercial BPUs. Bistrifluoron (**10**) was obtained from more than 2000 BPUs at DongbuHannong Chemical Co., Korea. It is active against lepidopteran pests and especially whitefly as an insect growth regulator.

The third-generation BPUs exhibit stronger topical insecticidal activity and broader spectrum larvicidal activity (such as high acaricidal activity). Flufenoxuron (**12**) was developed at Shell Research Ltd. (now BASF AG). It is a broad-spectrum acaricide and insecticide that is effective against Lepidoptera, Homoptera, Diptera, and Hemiptera pests and *Tetranychus urticae*.[11,12] Flucycloxuron combines a high insecticidal activity with a high acaricidal activity against both tetranychid and eriophyid mites. It is the result of an optimization program with benzoylphenylureas on acaricidal activity at Philip-Duphar B.V. (now Platform Specialty Products Co.).[13] Chlorfluazuron (**14**) was launched in 1989, which was discovered and developed by Ishihara Sangyo Kaisha Ltd. It was very effective against oriental leafworm moth (*Spodoptera litura*) and diamondback moth (*Plutella xylostella*) larvae and was 10-fold more inhibitory than diflubenzuron (**1**).[14] Fluazuron (**15**) was discovered and developed at Ciba-Geigy AG (now Novartis). The chemical structure of fluazuron (**15**) is very similar to that of chlorfluazuron (**14**), but the insecticidal spectrum is different.

DOI: 10.1021/acs.jafc.5b02460
J. Agric. Food Chem. 2015, 63, 6847−6865

Scheme 1. Synthetic Routes of Benzoylphenylureas

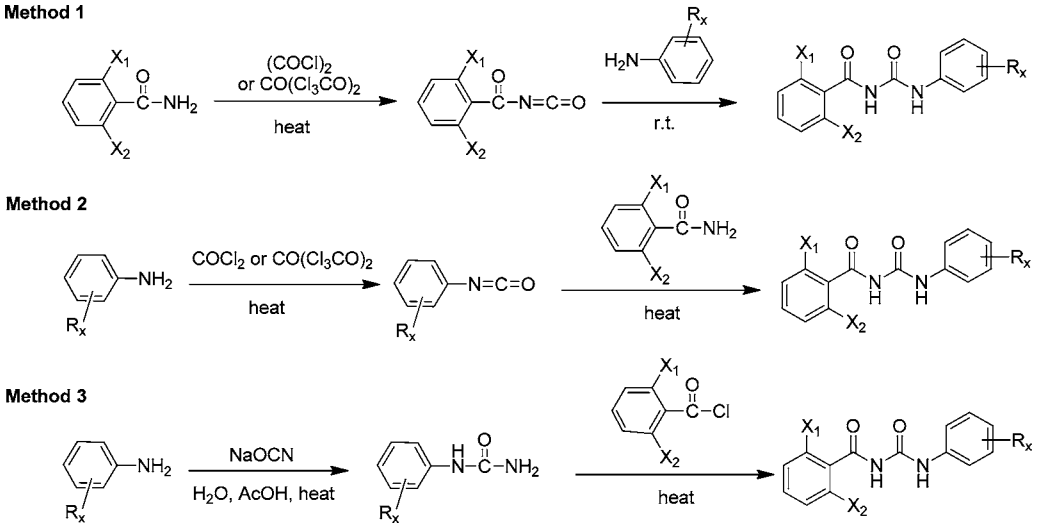

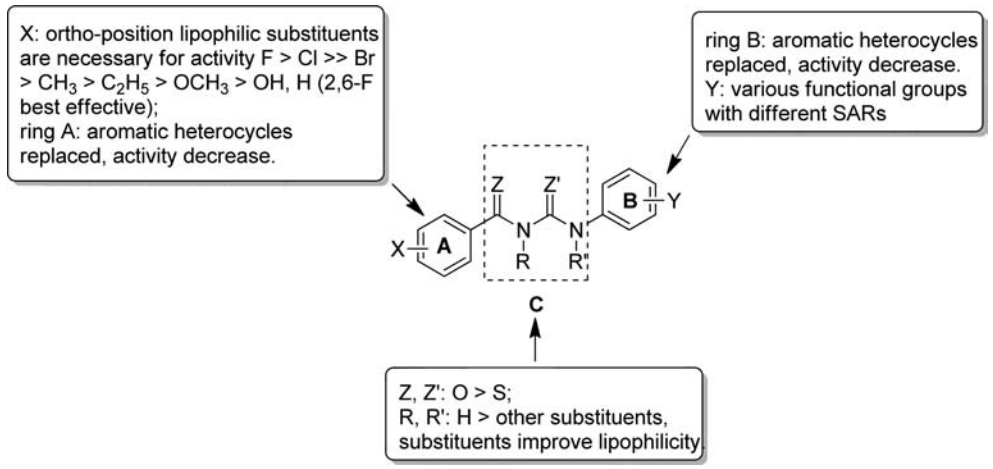

Figure 3. Molecular skeleton and SARs of BPU chitin synthesis inhibitors.

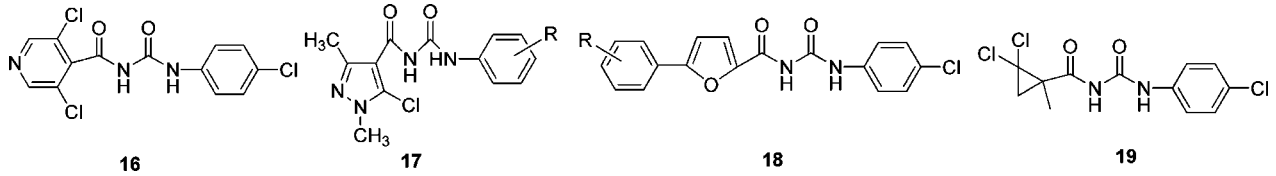

Figure 4. Chemical structures of benzoylphenylurea analogues.

Fluazuron is a tick development inhibitor, which controls the cattle tick (*Boophilus microplus*).[15]

SYNTHETIC METHODS OF BENZOYLPHENYLUREAS

The three synthetic approaches shown in Scheme 1 have been employed most widely in the construction of the typical benzoylphenylurea bridge.[5b] In all of the methods listed in Scheme 1, method 1 is the most commonly used for the laboratory synthesis of benzoylphenylureas. The reaction is both high-yield and highly atom efficient. In addition, the required benzoylisocyanates are readily accessed from the corresponding benzoylamides by reaction with oxalyl chloride (phosgene or triphosgene) under several conditions. The disadvantage of this method is that benzoylisocyanates are easily polymerized at room temperature. Method 2 is the most commonly used for the industrial production of benzoylphenylureas. The arylisocyanates are readily prepared by the reaction between the corresponding arylamines and phosgene (or triphosgene) and then combined with the benzoylamides under heating to give benzoylphenylureas. The disadvantage of this method is that the synthetic procedure needs high temperature. The advantage of method 3 is low environmental pollution along with cheap raw materials and high yields.

STRUCTURE–ACTIVITY RELATIONSHIPS (SARs)

The benzoylphenylureas can be separated into three parts for analysis of the SARs, namely, the benzoyl ring (**A**), aniline ring (**B**), and urea bridge (**C**) (Figure 3). Each part can be examined independently, as they appear to play distinct and different

DOI: 10.1021/acs.jafc.5b02460
J. Agric. Food Chem. 2015, 63, 6847–6865

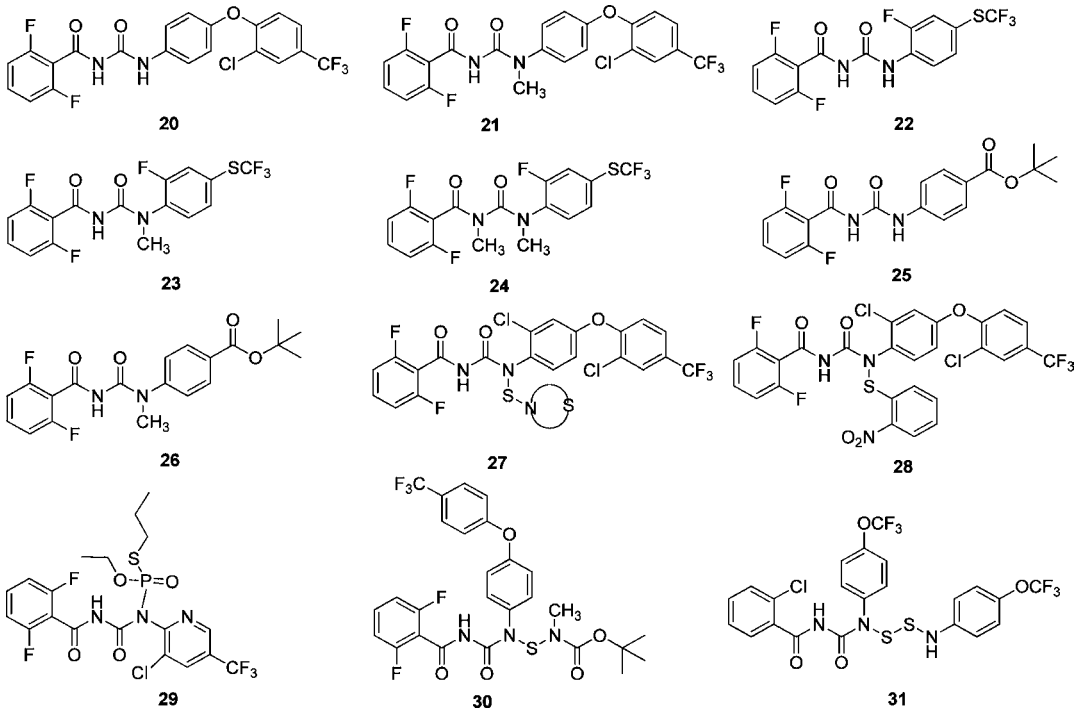

Figure 5. Chemical structures of *N*,*N*′-substituted benzoylphenylureas.

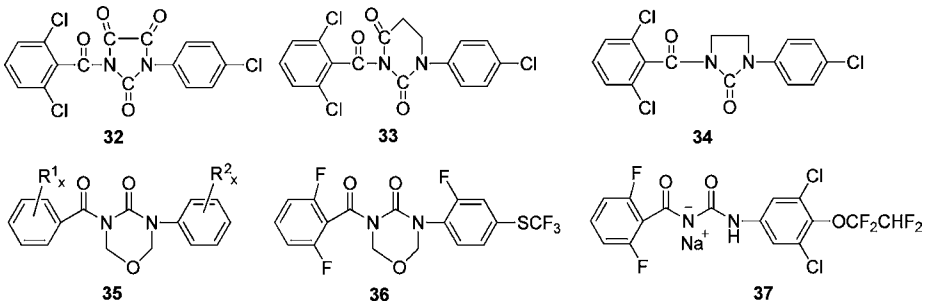

Figure 6. Chemical structures of benzoylphenylureas containing a cyclic urea structure.

roles in the overall expression of larvicidal activities. Nakagawa et al. have reported a series of the quantitative SAR studies of BPUs.[16] At the beginning of BPU research, it was established that a 2-Cl, 2,6-diCl, or 2,6-diF substitution pattern on the benzoyl moiety (**A**) was required for optimal activity, with the 2,6-diF substitution pattern being most effective.[17] The larvicidal activities against *P. brassicae* of the 2,6-difluorobenzoylphenylureas were about 20 times higher than the activities of the 2,6-dichlorobenzoylphenylureas. These results suggested that the conformation having an angle of 30° between the −CO(NH)− moiety and the benzoyl ring (**A**) has optimum larvicidal activity.[18] After more than 40 years of BPU research, this original optimal substitution pattern still seems to be valid, based on the analysis of published patents and the structure of commercial products (Figure 1). According to the bioisosterism principles, the benzoyl ring (**A**) of BPUs could be replaced by the aromatic heterocycles or cyclic alkylsubstituents (such as pyridine, pyrazole, furan, and cyclopropyl groups, Figure 4),[19] but the larvicidal activities decreased significantly, for example, the larvicidal activity against *A. aegypti* of dichlorbenzuron (**2**) was about 10 times higher than the activity of compound **16**.[17a]

In terms of the urea bridge (**C**) moiety (Figure 3), the larvicidal activity of thiourea derivatives with the same substructure was worse than that of the urea derivatives.[20] Research has shown that *N*′-substituted benzoylureas can improve the poor solubility of BPUs in organic solvents. Generally, *N*′-alkyl products displayed better solubility but worse larvicidal activity in comparison with their parent structure.[21] However, *N*′-methyl BPUs exhibited the same (or better) larvicdial activity as the parent structure but low toxicity to aquatic macroinvertebrates.[22] For example, the larvicidal activity of compound **21** was equivalent to that of compound **20**, whereas the toxicity of compound **21** against *Daphnia magna* (EC_{50} < 0.4 ppb) was reduced significantly (EC_{50} = 150 ppb) (Figure 5).[22a] Compounds **23**, **24**, and **26** exhibited 80−100% larvicidal activity against second-instar larvae of *Plutella xyllostella* at 25 mg L^{-1}; on the other hand, the comparative compounds **22** and **25** displayed only 5 and 0% larvicidal activity, respectively, at 25 mg L^{-1}.[22b] When *N*′-substituted groups at the urea bridge (**C**) moiety may be easily released in vivo, compounds **27**, **28**, and **29** displayed better solubility and almost the same level of larvicidal activity as their parent structure (Figure 5).[23] According to the literature, several series of novel *N*′-carbamylosulfenyl, *N*′-alkylaminothio, *N*′-arylaminothio (or dithio), and *N*′,*N*′-thio (or dithio) derivatives of benzoylphenylureas were designed and synthesized in our

DOI: 10.1021/acs.jafc.5b02460
J. Agric. Food Chem. 2015, 63, 6847−6865

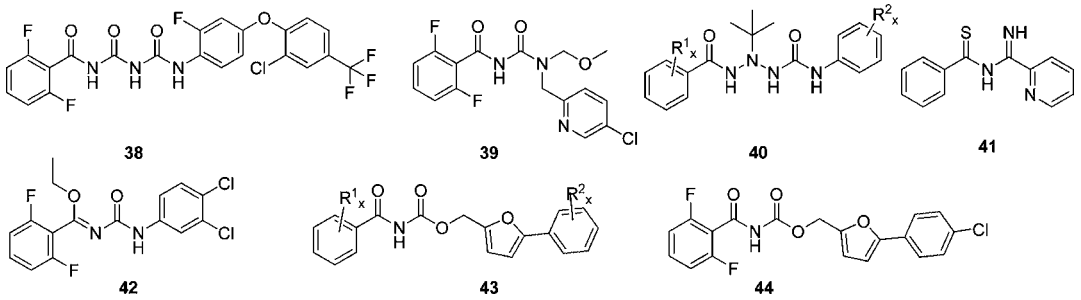

Figure 7. Chemical structures of benzoylurea analogues.

laboratory, and all compounds showed better solubility compared to their corresponding parent BPUs, which should make them easier to apply in the field (Figure 5, compounds **30** and **31**).[24] A series of novel BPUs containing a cyclic urea structure were first designed and synthesized by Philips-Duphar B.V. Co.[25] For example, compound **32** exhibited 90−100% larvicidal activity against second-instar larvae of *P. brassicae* at 0.1 mg L^{-1}, but compounds **33** and **34** did not display larvicidal activity under the same test conditions (Figure 6).[17a] As we know, BPUs are not plant systemic and do not penetrate the plant tissue. To our delight, a series of benzoylurea derivatives (Figure 6, compound **35**) containing a cyclic urea structure were discovered by researchers at Sumitomo Chemical Co., Ltd., and these compounds displayed excellent systemic activities with stomach action.[26] For example, compound **36** exhibited 100% systemic activities in roots against second-instar larvae of *P. xylostella* and *Spodoptera littoralis* at 25 mg L^{-1} and at the same time exhibited 96 and 100% systemic activity against second-instar larvae of *P. xylostella* in soil with 20 mg/plant and seeds with 1 mg/seed, respectively.[26] Therefore, these compounds can be used for soil and seed treatment, which will make a huge contribution to reducing the labor in agriculture and improve the insecticide safety of workers and the environment. Drabek et al. synthesized the benzoylurea salts (such as compound **37**) to improve their water solubility, and this compound exhibited good insecticidal activity against *M. domestica*.[27] The change of acylurea group into other functional groups will reduce the larvicdal activities, such as compounds **38**−**44** (Figure 7).[28] Interestingly, compound **43** (Figure 7) exhibited good fungicidal activities against *Corynespora cassiicola*, *Thanatephorus cucumeris*, *Botrytis cinerea*, and *Fusarium oxysporum*. The morphological result suggested that compound **44** (Figure 7) had disturbed the cell wall formation of *C. cassiicola*.[28d]

The structural optimization of the aniline moiety (**B** ring, Figure 4) is the focus for most researchers, and various functional groups on the aniline (**B** ring) produced three generations of commercial benzoylphenylureas (Figure 1). Research on the QSARs of BPUs has shown that different functional groups and pests have different SARs.[16] In general, bulky groups at the 2,6-position of the aniline moiety (**B** ring) are adverse to the larvicidal activities, and electron-withdrawing groups at the 4-positon of the aniline moiety (**B** ring) are helpful to the insecticidal effects (Figure 4). When the aniline moiety is replaced with other aromatic heterocycles, the insecticidal activities were kept the same or reduced in most conditions.

The earliest research was halo-substitutioon at the aniline moiety (**B** ring, Figure 3) after the discovery of DU19111, and the results of bioassay showed that 3,4-diCl- or 4-Cl-substituted BPUs exhibited the best larvicidal activity, whereas a 4-I substituted compound had little larvicidal activity, which can increase sharply by introducing a 2-F or 3-F group on the aniline (compound **45**, Figure 8).[17a] Mutihalo-substituted

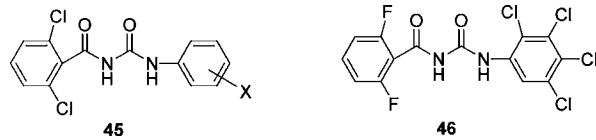

Figure 8. Chemical structures of halo-substituted benzoylphenylureas.

BPUs always exhibited better larvicidal activity, for example, compound **46** (Figure 8) exhibited 10 times higher larvicidal activity against *A. aegypti* and *S. littoralis* than that of diflubenzuron (**1**).[29]

It was found that the larvicidal activity of alkyl-substituted BPUs was worse than that of halo-substituted compounds, and 4-alkyl-substituted BPUs displayed better larvicidal activity than multialkyl-substituted derivatives.[17a] Many companies were engaged in the research of multihaloalkyl BPUs, especially multifluoroalkyl derivatives since penfluoron (TH6044, **5**, Figure 1) was introduced to the market by Thompson-Hayward Chemical Co. in 1977. Compound **47** exhibited 100% larvicidal activity against second-instar larvae of *S. littoralis* at 0.5 mg L^{-1}, but penfluoron (**5**) and teflubenzuron (**4**) displayed only 5 and 20% larvicidal activity, respectively, at the same concentration.[30a] The larvicidal activities of compound **48** (Figure 9) against *S. littoralis* and *A. aegypti* were at the same level as diflubenzuron (**1**).[30b] Bistrifluoron (**10**), which was active against the lepidopteran pest and especially whitefly, was developed and commercialized by DongbuHannong Chemical Co.[30c] Recently, Qian et al. designed and synthesized a series of heptafluoroisopropyl-containing benzoylphenylureas (**50**) inspired by the structure of flubendiamide (**49**) (Figure 9).[31a] These compounds showed excellent insecticidal effect, and their activity resembled that of diflubenzuron (**1**). Compound **50** (Figure 9) showed nearly the same larvicidal activity as novaluron (**8**) on African cotton leafworm (*S. littoralis*). Furthermore, results from a field trial indicated that 5% EC of TXH09 (**51**) (Figure 9) exhibited similar efficacy in comparison with chlorfluazuron (**14**) and hexaflumuron (**7**) against cabbage worm (*Pieris rapae*) and diamondback moth (*P. xylostella*).[31a] Due to the high price of heptafluoroiodopropane, which was the starting material to prepare TXH09 (**51**), a series of 2′-chloro-hexafluoroisopropyl-containing benzoylphenylureas were obtained using hexafluoroacetone with lower price as the starting material.[31b] These compounds showed excellent insecticidal effect. For example, the results from fields trial indicated that the efficacies of 5%

DOI: 10.1021/acs.jafc.5b02460
J. Agric. Food Chem. 2015, 63, 6847−6865

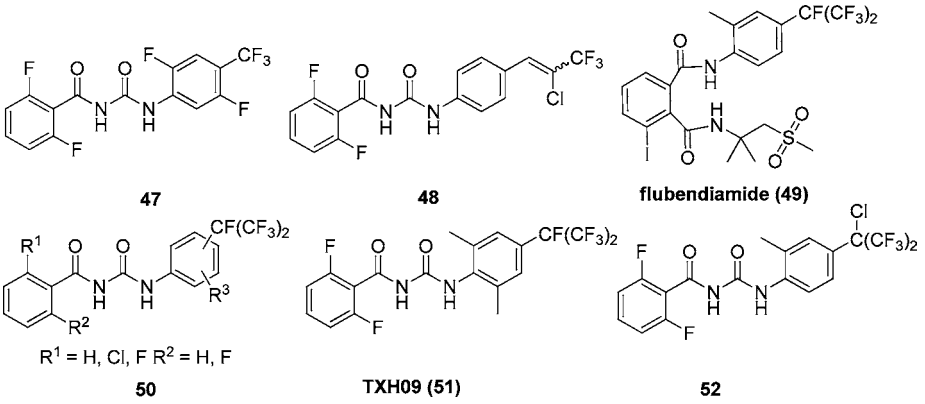

Figure 9. Chemical structures of multihaloalkyl-substituted benzoylphenylureas.

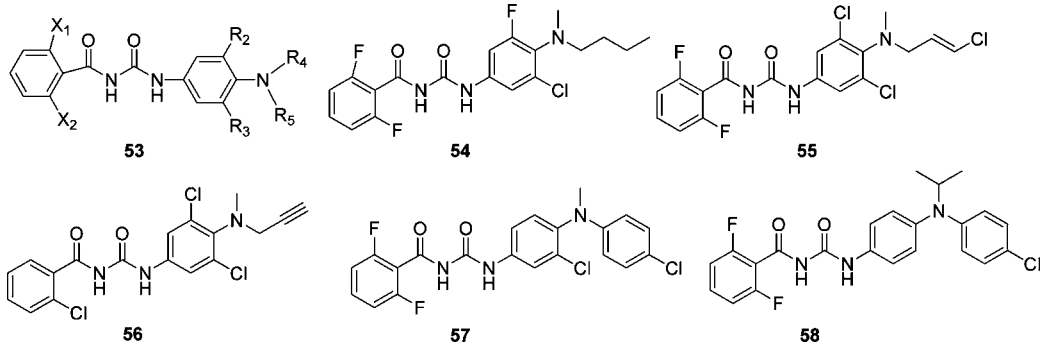

Figure 10. Chemical structures of alkyl(aryl)amino-substituted benzoylphenylureas.

EC **52** (Figure 9) against *S. littoralis* in capsicum and *S. littoralis* in vegetables were 76.7 and 69.0%, respectively. The efficacy of 5% EC **52** was higher than that of hexaflumuron (**7**) and a little lower than that of flubendiamide (**49**) at the same concentration.[31b]

The larvicidal activities of alkyl(aryl)amino-substituted benzoylphenylureas (compound **53**, Figure 10) were first studied by Ciba-Geigy Corp. (now Novartis).[32a] Most of these compounds exhibited both larvicidal and ovicidal activities against lepidopteran pests, and arylamino-substituted derivatives displayed unexpectedly high acaricidal activity.[32] For example, compound **54** (Figure 10) exhibited 80−100% larvicidal activity against *S. littoralis* (at 3 mg L^{-1}) and *Laspeyresia pomonella* (at 0.75 mg L^{-1}).[32a] Compounds **55** and **56** displayed 80−100% larvicidal activity against *S. littoralis* at 0.75 and 3 mg L^{-1}, respectively (Figure 10), and both possessed 80−100% ovicidal activity against *L. pomonella* at 12.5 mg L^{-1}.[32b,c] The researchers at Duphar International Research B.V. Co. found that arylamino-substituted derivative **57** (Figure 10) had 90−100% larvicidal activity against *P. brassicae* at 0.3 mg L^{-1}, whereas compound **58** (Figure 10) displayed 90−100% acaricidal activity against *Tetranychus cinnabarinus* at 1 mg L^{-1}.[32e]

Dow Chemical Co. Ltd. provided a series of 4-phenyldiazene-substituted benzoylphenylureas (compound **59**, Figure 11) that could be used as insecticides or acaricides.[33] The results of bioassay showed that when R^1, R^2, and R^5 were halogen atoms and R^3 and R^4 were methyl groups, compounds exhibited the best insecticidal activity, but CF_3, CN, and NO_2 groups were adverse to the insecticidal activity. For example, both compounds **60** and **61** (Figure 11) displayed 90−100% larvicidal and ovicidal activities against *S. littoralis* at 10 mg L^{-1},

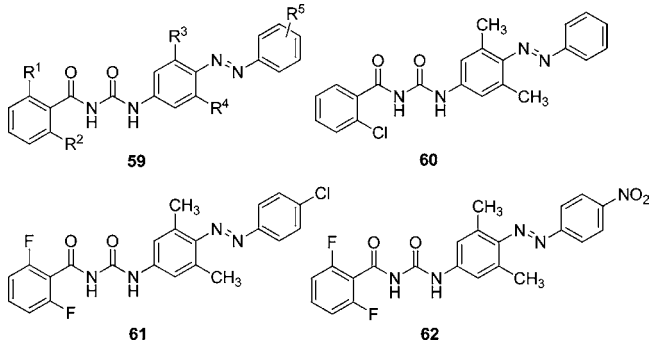

Figure 11. Chemical structures of phenyldiazenyl-substituted benzoylphenylureas.

whereas compound **62** had less than 24% larvicidal and 74% ovicidal activities in the same conditions.[33]

The insecticidal activities of alkoxyl(multihaloalkoxyl)phenyl benzoylureas (compound **63**, Figure 12) were studied mainly at Bayer AG Co., Ciba-Geigy Co. (now Novartis), and Dow Chemical Co.[34] These benzoylphenylureas (such as first commercial product, triflumuron (**6**, Figure 1) display both larvicidal and ovicidal activities and have a broader spectrum of effectiveness than the first generation of benzoylphenylureas. The SARs showed that multihaloalkoxy-substituted BPUs were much more effective than alkoxy-substituted BPUs and that 3,5-diCl substitutions at aniline moiety (compound **63**) were important to the insecticidal effects. For example, compounds **64** and **65** (Figure 12) and triflumuron (**6**) had 100% insecticidal activity against *Phaedon cochleariae* (at 10 mg L^{-1}) and *Laphygma exigua* (at 0.1 mg L^{-1}), but diflubenzuron (**1**) and DU19111 had no inhibition in the same conditions.[34a]

DOI: 10.1021/acs.jafc.5b02460
J. Agric. Food Chem. 2015, 63, 6847−6865

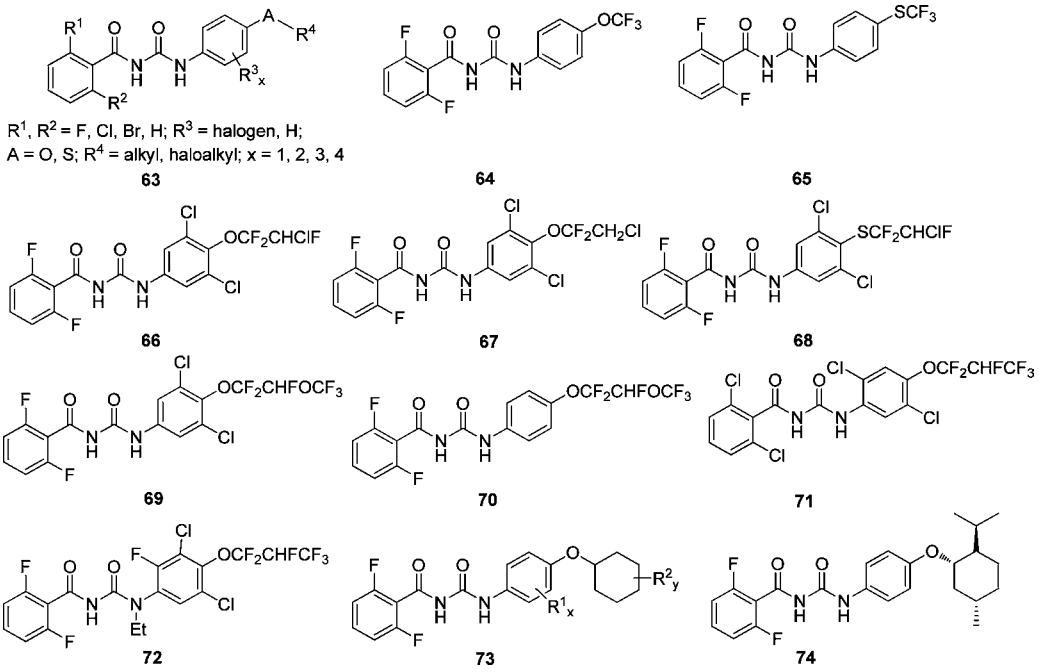

Figure 12. Chemical structures of alkoxy(mutihaloalkoxy)-substituted benzoylphenylureas.

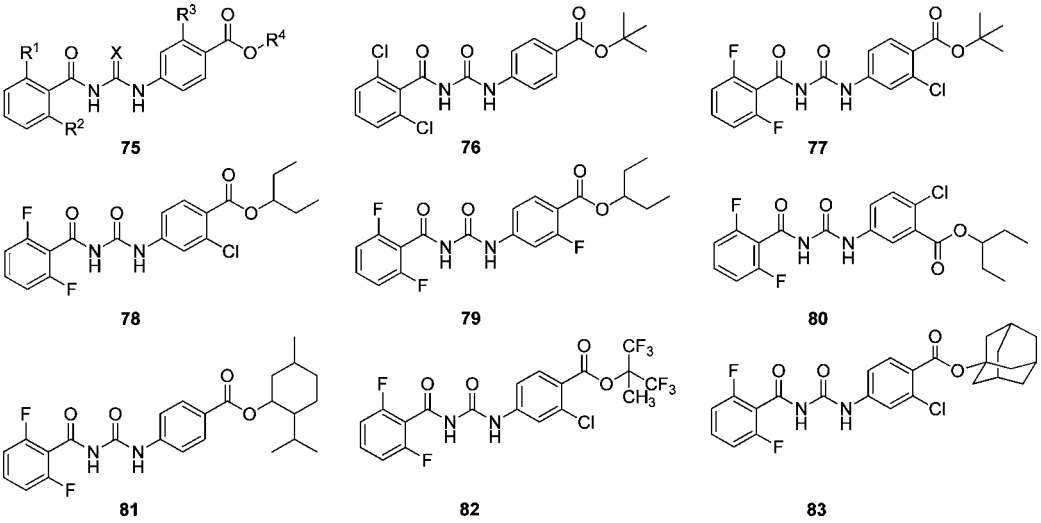

Figure 13. Chemical structures of alkoxycarbonyl-substituted benzoylphenylureas.

Compound **66** (Figure 12, LD_{90} = 1.2 mg L^{-1}, 1.2 mg L^{-1}) and hexaflumuron (**7**, LD_{90} = 1.6 mg L^{-1}, 1.6 mg L^{-1}) exhibited similar larvicidal activity against *Spodoptera exigua* and *Heliothis virescens*, whereas the inhibitory effects of compounds **67** (Figure 12, LD_{90} = 100 mg L^{-1}, 100 mg L^{-1}) and **68** (Figure 12, LD_{90} = 200 mg L^{-1}, >400 mg L^{-1}) possessing a slight structural difference from compound **66** reduced significantly.[34c] Compounds **69**, and **70** (Figure 12) and novaluron (**8**) had 96, 40, and 0% larvicidal activity against *S. littoralis*, respectively, at 0.05 mg L^{-1}; at the same time, they displayed 100, 0, and 0% larvicidal activity against *A. aegypti* at 0.002 mg L^{-1} and 100, 95, and 17% larvicidal activity against *Leptinotarsa decemelineata* at 5 mg L^{-1}, respectively.[34d] Lufenuron (**9**) effected 80−100% mortality against *S. exigua* larvae and *H. virescens* larvae at 0.75 mg L^{-1}, and compound **71** (Figure 12) effected 80−100% mortality against *S. exigua* larvae at 12.5 mg L^{-1} and against *H. virescens* larvae at 100 mg L^{-1}.[34e] Recently, lufenuron (**9**) has been put forward as an effective treatment for dermatophytosis in dogs and cats.[34f] A study indicated good efficacy at a single oral dose of 54−68.3 mg/kg orally in dogs and 51.2−266 mg/kg in cats.[34g] Under continuous exposure, noviflumuron (**11**, LC_{50} < 2.2 mg L^{-1} at 21 days and LC_{50} < 0.78 mg L^{-1} at 42 days) and compound **72** (Figure 12, LC_{50} = 0.35 mg L^{-1} at 21 days and LC_{50} = 0.26 mg L^{-1} at 42 days) were far more active than hexaflumuron (**7**, LC_{50} > 200 mg L^{-1} at 21 and 42 days) against German cockroach (*Blattella germanica*) second instars. Under limited exposure (48 h), noviflumuron (**11**, LC_{50} < 22.2 mg L^{-1} at 21 days and LC_{50} < 9.1 mg L^{-1} at 42 days) and compound **72** (Figure 12, LC_{50} = 21.1 mg L^{-1} at 21 days and LC_{50} = 12.8 mg L^{-1} at 42 days) were more potent than hexaflumuron (**7**, LC_{50} > 10000 mg L^{-1} at 21 and 42 days).[21] Generally, electron-donating groups at the aniline moiety (Figure 3, ring B) are unfavorable to the insecticidal activity; however, compound **73** (Figure 12)

DOI: 10.1021/acs.jafc.5b02460
J. Agric. Food Chem. 2015, 63, 6847−6865

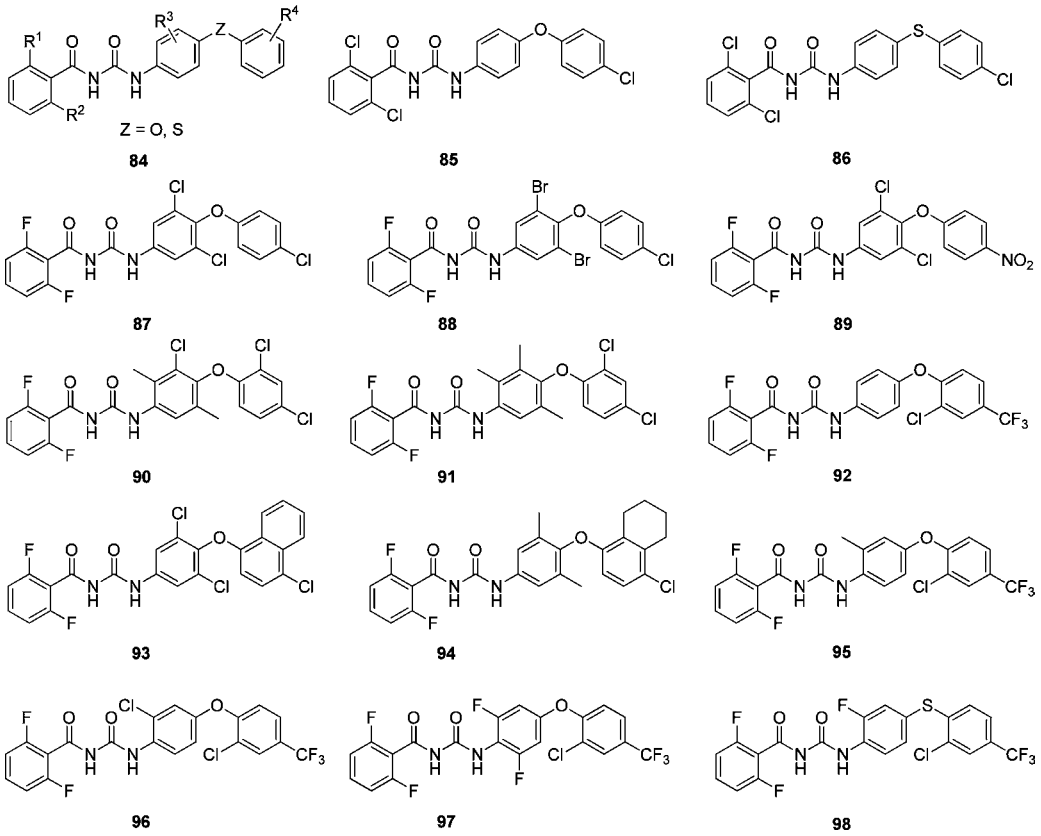

Figure 14. Chemical structures of phenoxyphenylbenzoylureas.

showed a broad spectrum of insecticidal activity. For instance, compound **74** (Figure 12) displayed 90−100% larvicdal activity against *P. brassicae* (at 0.1 mg L^{-1}), *A. aegypti* (at 0.003 mg L^{-1}), *S. littoralis* (at 3 mg L^{-1}), and *Leptinotarsa decemlineata* (at 10 mg L^{-1}).[34i]

The insecticidal activities of alkoxycarbonyl-substituted benzoylphenylureas (Figure 13, compound **75**) were reported at Bayer AG Co. for the first time,[35a] and the following research were conducted at BASF[35b,c] and Duphar International Research B.V. Co.[35d] These compounds could be used as pesticides to control Lepidoptera, Hemiptera, and Coleoptera pests. A survey of the patent literature[35] suggested that 3-Cl or 3-F substitution (compound **75**, R^3 = Cl, F) and certain bulky 4-alkoxycarbonyl (especially fluoroalkoxycarbonyl) groups (compound **75**, R^4) were favorable for the larvicidal activity. For example, compounds **76** and **77** had more effective larvicidal activity against *Plutella maculipennis* than DU19111 (Figure 13).[35a] Compound **78** showed better action against *Dysdercus intermedius* than compounds **77**, **79**, and **80** (Figure 13) at 10% active ingredient.[35b] The insecticidal activity improved greatly when a fluoroalkoxycarbonyl group was introduced, for example, compound **82** (Figure 13) had 100% mortality against *A. aegypti* at 0.004 mg L^{-1}, which exhibited the same level insecticidal activity as diflubenzuron (**1**) and much better activity than compound **77**.[35c] Compound **81** (Figure 13) reported by BASF exhibited 90−100% larvicdal activity against *P. brassicae* (at 0.3 mg L^{-1}), *S. littoralis* (at 1 mg L^{-1}), and *L. decemlineata* (at 3 mg L^{-1}),[35d] but compound **83** had poor insecticidal effects, probably because the group it contained was too bulky.[35b]

The phenoxyphenyl and phenthiophenylbenzoylureas (compound **84**, Figure 14) were first reported by Wellinga et al. at Phlip-Duphar B.V. Co., and only seven compounds were disclosed in the paper.[17a] These compounds had poor larvicidal activity in the bioassay except compound **86** (Figure 14), which exhibited 90−100% larvicidal activity against *A. aegypti*, *S. littoralis*, and *L. decemlineata* at 0.003, 10, and 100 mg L^{-1}, respectively, whereas compound **85** (Figure 14) had no insecticidal effects in the same conditions.[17a] Bayer AG, Ishihara Sangyo Kaisha, Ltd., BASF AG, Union Carbide Corp., Sumitomo Chemical Co., Ltd., and Shell International Research M.B.V. published 56 patents in the following years.[36] On the basis of an analysis of the published patents, it was established that 2,6-F or Cl substituents at the benzoyl moiety (Figure 14, compound **84**, R^1, R^2 = F, Cl), 3,5-Cl or CH_3 substituents at the aniline moiety (R^3 = 3,5-diCl, 3,5-diCH_3, 3-Cl-5-CH_3), and 4-Cl, CF_3, or NO_2 substituents at the phenoxy moiety (R^4 = 4-Cl, CF_3, NO_2) were required for optimal insecticidal activity. For example, compound **87** (Figure 14, LC_{50} = 0.0046 mg L^{-1}) exhibited excellent larvicidal activity against *S. littoralis*, which was much better than those of compound **86**, diflubenzuron (**1**, LC_{50} = 0.018 mg L^{-1}), and compound **88** (Figure 14, LC_{50} = 0.015 mg L^{-1}).[36a] Compound **90** had 100% larvicidal activity against *Spodoptera eridania* at 0.125 mg L^{-1} and atainst *Ephilachna varivestis* at 0.25 mg L^{-1}; on the other hand, compound **89** (Figure 14) exhibited only 10% larvicidal activity against *S. eridania* at 0.125 m $\cdot L^{-1}$ and 30% larvicdal activity against *E. varivestis* at 0.5 mg L^{-1}, whereas compound **92** had no larvicidal effect at the same concentration.[36b] Compound **91** (Figure 14) had 100% mortality against *S. eridania* at 0.4 mg L^{-1} and *E. varivestis* at 1.6 mg L^{-1}.[36b] Compounds **93** and **94** (Figure 14) had 100% mortality against *E. varivestis* at 8 mg L^{-1}, but diflubenzuron (**1**) had 60% mortality using the same bioassay process.[36c] The

DOI: 10.1021/acs.jafc.5b02460
J. Agric. Food Chem. 2015, 63, 6847−6865

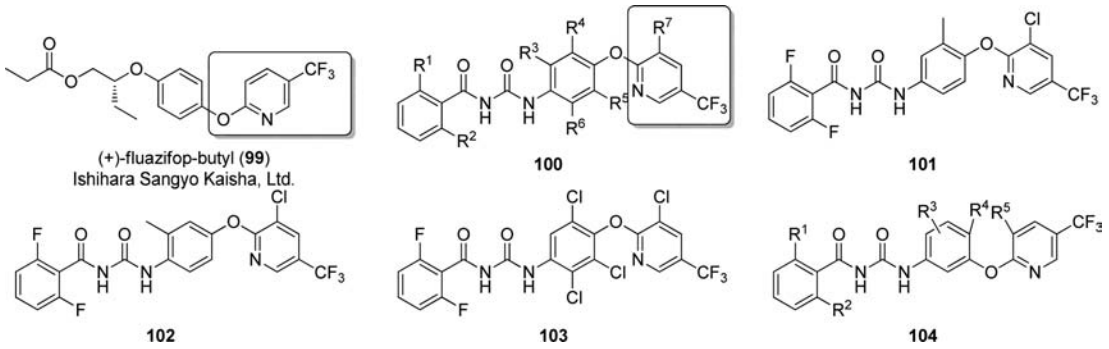

Figure 15. Chemical structures of pyridyloxyphenylbenzoylureas.

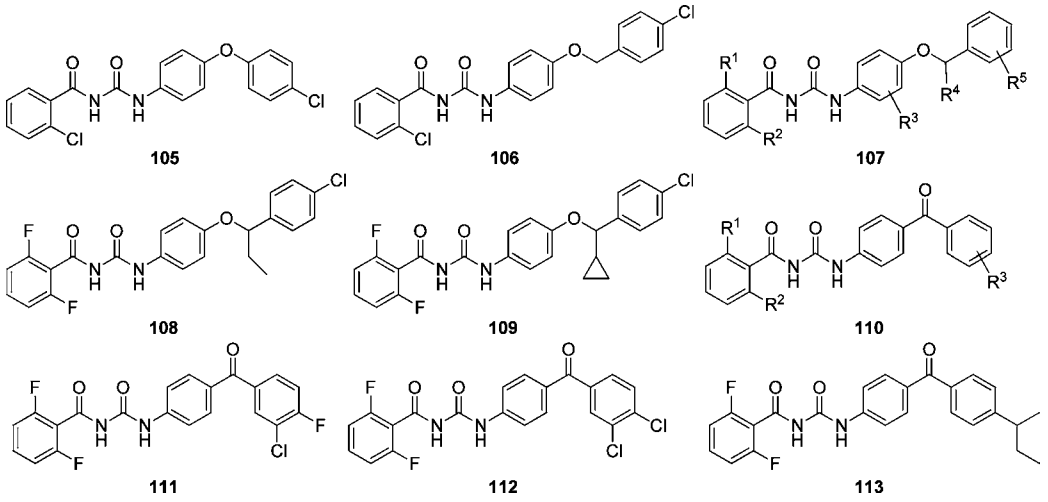

Figure 16. Chemical structures of benzyloxyphenyl and benzoylphenylbenzoylureas.

LC_{50} values of compounds **95**, **96**, and **97** (Figure 14) and flufenoxuron (**12**) against *Tetranicus urticae* were 32, 6.9, 1.5, and 1.3 mg L^{-1}, respectively.[36d] The adult emergence inhibitory ratio, sterilization ratio, and ovicidal ratio of compound **98** (Figure 14) against *T. cinnabarinus* were 100, 95, and 100%, respectively, at 100 mg L^{-1}, and those of flufenoxuron (**12**) were 60, 0, and 10%.[36e]

In the research of phenoxyphenylbenzoylureas (Figure 14, compound **84**) and SAR of fluazifop-butyl (Figure 15, **99**) at Ishihara Sangyo Kaisha, Ltd., a 5-trifluoromethyl-2-pyridinyloxy group was introduced into the structure of benzoylphenylureas and a series of novel pyridyloxyphenyl-benzoylureas (Figure 15, compound **100**) were designed and synthesized.[37] The results of bioassay showed that these compounds exhibited far surpassing insecticidal activity against specific target insects such as Lepidoptera, Diptera, and Orthoptera at their larval stages.[37a] From the literature, it was established that 2,6-F substituents at the benzoyl moiety (Figure 15, compound **100**, R^1, R^2 = F), 3,5-Cl, 2,6-H substituents at aniline moiety (R^3, R^6 = H, R^4 = Cl, CH_3, R^5= Cl, H) and 3-Cl or Br substituents at the phenoxy moiety (R^7 = Cl, Br) were required for optimal insecticidal activity. For example, compound **101** (Figure 15) had 100% larvicidal activity against *P. xylostella* (at 50 mg L^{-1}) and *Culex pipens molestus* (at 50 mg L^{-1}), but compound **102** (Figure 15) had no insecticidal activity in the same condition. Chlorfluazuron (**14**) has much more larvicidal activity against specific target insects such as Lepidoptera than the lead diflubenzuron (**1**). The LC_{50} values of chlorfluazuron (**14**) against *P. xylostella*, *S. littoralis*, and *S. exigua* were 0.021, 0.028, and 0.043 mg L^{-1}, respectively;[37a] however, compound **103** (Figure 15) exhibited no larvicidal activity against *P. xylostella* at 50 mg L^{-1}.[37b] The movement of the 3-chloro-5-trifluoromethyl-2-pyridinyloxy group in chlorfluazuron (**14**) from the *para*-position to the *meta*-position resulted in a series of novel benzoylphenylureas (Figure 15, compound **104**) at Ciba-Geigy Corp. (now Novartis).[38] These compounds displayed worse insecticidal activity against Lepidoptera and Diptera larvae than chlorfluazuron (**14**), however, the anthelmintic activity had an unexpected significant improvement. For example, the anthelmintic activity of fluazuron (**15**) was much more effective against *Hemonchus contortus* than chlorfluazuron (**14**) at 10 mg kg^{-1} day^{-1}.[38c]

As we have known that phenoxyphenylbenzoylureas (Figure 14, compound **84**) had excellent larvicidal activity against *S. littoralis*, for example, compound **105** (Figure 16) had 90−100% mortality against *P. brassicae* at 10 mg L^{-1}, it was surprisingly found that the corresponding benzyloxy compound **106** (Figure 16) had the same insecticidal effect against the larvae of *P. brassicae* at 0.3 mg L^{-1} at Duphar International Research B.V. Co.[39a] Then a series of novel benzyloxyphenylbenzoylureas (Figure 16, compound **107**) were obtained, and they found compound **108** (Figure 16) had 90−100% mortality against *P. brassicae* at 0.03 mg L^{-1} and compound **109** (Figure 16) had 90−100% insecticidal activities against *Panonychus ulmi*, *T. cinnabarinus*, *T. urticae*, and *Trialeurodes vaporariorum* at 10 mg L^{-1}.[39b] Carmellino et al. synthesized a series of benzoylphenylbenzoylureas that had a highly effective activity against *A. aegypti* larvae (Figure 16, compound **110**).[39c]

DOI: 10.1021/acs.jafc.5b02460
J. Agric. Food Chem. 2015, 63, 6847−6865

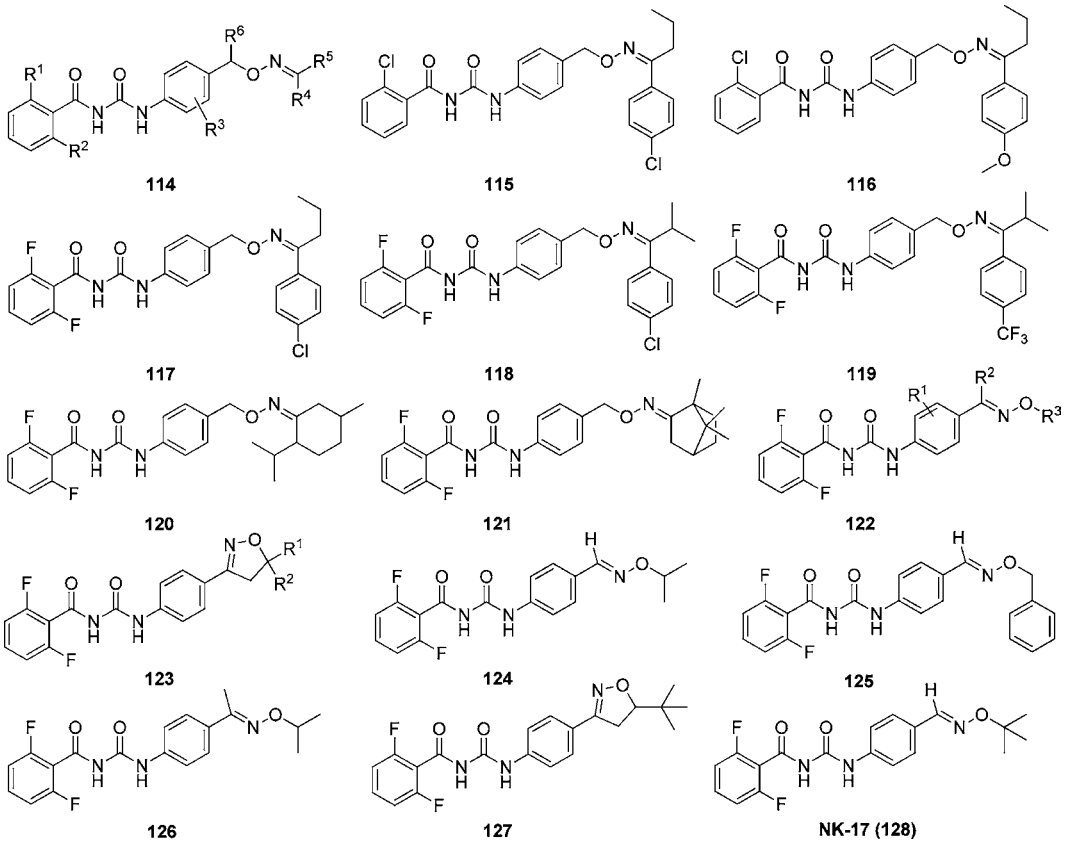

Figure 17. Chemical structures of benzoylphenylureas containing an oxime ether group.

With regard to the substituents on the benzophenone unit, generally the activity of halo derivatives was much higher than that of alkyl derivatives. In particular, with the dihalo-substituted compounds, especially a fluorine atom such as compound **111**(Figure 16), 100% mortality of *A. aegypti* larvae was achieved at very low doses (2×10^{-6} mg L^{-1}), whereas compound **112** (Figure 16) had a lower insecticidal activity (12% mortality achieved at 2×10^{-5} mg L^{-1}). Alkyl derivatives had much lower insecticidal activity, such as compound **113** (Figure 16), which exhibited 69% mortality at 2×10^{-3} mg L^{-1}.[39c]

During the research of benzyloxyphenylbenzoylureas (Figure 16, compound **107**), it was found that some of these compounds had good acaricidal activity such as compound **109**.[39b] Therefore, a series of novel benzoylphenylureas containing an oxime ether group (Figure 17, compound **114**) were first developed by Philip-Duphar B.V. Co., and flucycloxuron (**13**) was introduced to the market in 1988.[40a−c] On the basis of the SAR analysis from the literature, when R^1 and R^2 were F or Cl and R^3 and R^6 were H, compound **114** had the optimal activity. When R^4 was an alkyl group and R^5 was a substituted phenyl group, a 4-chlorophenyl group was the optimal group for insecticidal activity, and electron-withdrawing or electron-donating group are adverse to the activity. For example, compound **115** had 90−100% mortality against *P. brassicae* at 0.3 mg L^{-1}, and compound **116** exhibited the same insecticidal effects at 1 mg L^{-1} (Figure 17). Furthermore, compounds **117** and **118** had 90−100% mortality against *P. brassicae* at 0.1 mg L^{-1}, whereas compound **119** had no inhibitory activity at 0.1 mg L^{-1} (Figure 17).[40b] Compound **120** had 90−100% mortality against *T. urticae* at 0.1 mg $L^{-1}$and *L. decemlineata* at 5 mg L^{-1}, but compound **121** showed no insecticidal effect in the test (Figure 17).[40c] Inspired by the literature of alkoxycarbonyl substituted benzoylphenylureas (compound **75**, Figure 13), which exhibited high larvicidal activity against Lepidoptera and Hemiptera pests, a series of novel benzoylphenylureas containing an oxime ether group (compound **122**) and isoxazoline group (compound **123**) were designed and synthesized in our laboratories (Figure 17).[40d−f] The results of bioassay indicated that most compounds had excellent larvicidal activity against *M. separata* and that some compounds exhibited higher larvicidal activity than flucycloxuron (**13**).[40d] In general, R^2 is hydrogen, R^1 is fluorine, chlorine, or hydrogen, and R^3 is bulky alkyl groups, which are favorable for insecticidal effects. For example, compound **124** had 100% mortality against *M. separata* at 1.0 mg L^{-1}; on the other hand, compound **125** had 40% mortality at 200.0 mg L^{-1} and compound **126** had only 10% mortality at 1.0 mg L^{-1} (Figure 17).[40d,e] Compound **127** had 100% mortality against *Mythimna separata* and *P. xylostella* at 10 and *X* mg L^{-1}, respectively[1] (Figure 17).[40f] NK-17 (compound **128**) was chosen as an insecticide candidate through conventional screening. The toxicity against *M. separata* of compound NK-17 (LC_{50} = 0.017 mg L^{-1}) is about 18 times as active as hexaflumuron (LC_{50} = 0.31 mg L^{-1}). The field trial showed that the effects of 5% NK-17 EC (60 g ai ha^{-1}) on controlling *P. xylostella* and *S. exigua* were 88 and 89%, respectively, after 7 days of spraying, which were better than that of chlorfluazuron (**14**) and as active as hexaflumuron (**7**).[40g] In addition, NK-17 has the following features: novel skeleton structure, high insecticidal activity, simple synthesis (only four steps, each step accomplished under mild conditions, 82% overall yield), fewer fluorine atoms, and far better solubility than most commercial benzoylurea pesticides (20 °C in acetone, 168 g L^{-1}), which is

DOI: 10.1021/acs.jafc.5b02460
J. Agric. Food Chem. 2015, 63, 6847−6865

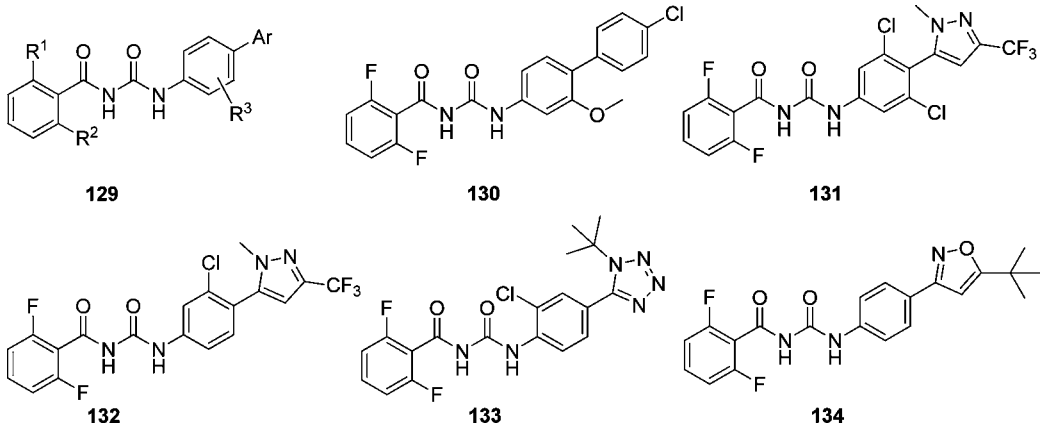

Figure 18. Chemical structures of arylphenylbenzoylphenylureas.

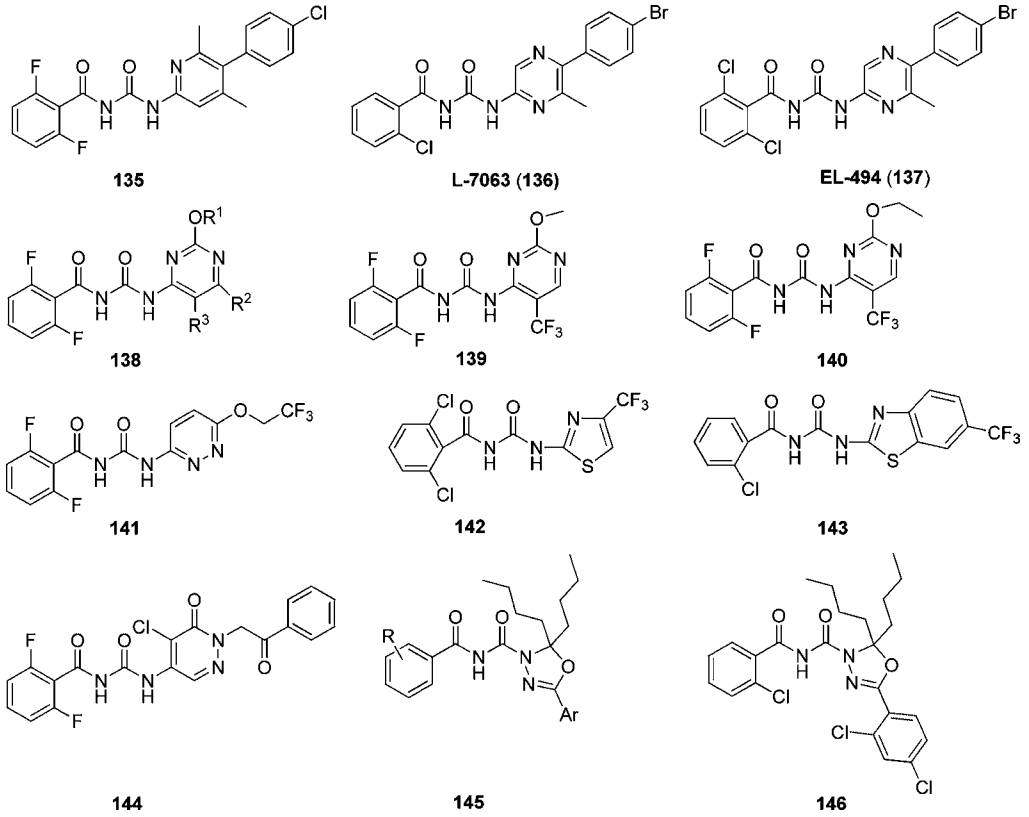

Figure 19. Chemical structures of aromatic heterocyclic benzoylureas.

more favorable for formulation process and application. NK-17 is being developed by Jiangsu Lanfeng Biochemical Co., Ltd., China.[40h]

The insecticidal activities of arylphenylbenzoylureas (Figure 18, compound **129**) were studied by some companies.[41] For example, diphenyl-benzoylurea derivative **130** exhibited 100% mortality against *S. eridania* and *Trichoplusiani* larvae at 2.0 mg L^{-1}.[41a] Pyrazolphenyl-benzoylurea derivative **131** (Figure 18) reported by Korea Research of Chemical Technology displayed better insecticidal effects against *P. xylostella* (LC_{50} = 0.15 mg L^{-1}) than diflubenzuron (**1**), and compound **132** (Figure 18) had better insecticidal activity against *S. litura* (LC_{50} = 0.04 mg L^{-1}) larvae than diflubenzuron (**1**) as well.[41b,c] Tetrazoylphenylbenzoylureas were prepared and used as pesticides at Bayer Cropscience. For instance, compound **33** (Figure 18) exhibited 100% insecticidal activity against *Heliothis virescens*, *P. cochleariae* larvae, *P. xylostella* larvae, *Spodoptera frugiperda* larvae, and *Diabrotica balteata* larvae at 1000 mg L^{-1}.[41d] Compound **134** (Figure 18), which had 60% mortality against *P. xylostella* at 0.2 mg L^{-1}, has been synthesized in our laboratories, and when the 5-*tert*-butyl group of the isoxazole moiety was changed to other alkyl groups, the insecticidal reduced significantly.[40f]

The phenyl ring of the aniline moiety (Figure 4, ring **B**) has been replaced by aromatic heterocycles, such as pyridine,[42a−e] pyrimidine,[42f−k] diazine,[42k,l] thiazole,[42m] and benzothiazole.[42n] The results of bioassay showed that most of these compounds had the same or worse activity in comparison with the corresponding benzoylphenylureas. The pyridinyl and pyrimidinylbenzoylurea derivatives were mainly studied at Eli Lilly and Co.; for example, compound **135** exhibited 100% mortality against *S. eridania* larvae at 0.125 mg L^{-1} (Figure 19). L-7063

DOI: 10.1021/acs.jafc.5b02460
J. Agric. Food Chem. 2015, 63, 6847−6865

Table 1. Physicochemical Properties and Environmental Fate for Commercial Benzoylphenylureas

compd	solubility (mg L^{-1})at 20 °C	melting point (°C)	log P[a]	soil degradation DT_{50}[b] (days)	aqueous photolysis DT_{50}[c] (days)	aqueous hydrolysis DT_{50}[d] (days)
diflubenzuron	0.08 (water),[e] 63 (hexane), 290 (toluene), 6980 (acetone), 1100 (methanol)	227.6	3.89[f]	3[g]	80[h]	96[i]
dichlorbenzuron	–[j]	236.0	4.27[k]	–	–	–
chlorbenzuron	10000 (acetone)	200.0	4.36[k]	–	–	–
teflubenzuron	0.01 (water), 10 (heptane), 740 (toluene), 1060 (methanol), 8850 (acetone)	225.0	4.30	92	10	stable[l]
penfluoron	–	211.5	4.36[k]	–	–	–
triflumuron	0.04 (water), 100 (heptane), 26600 (acetone), 23300 (ethyl acetate), 11700 (dichloromethane)	194.0	4.90	22	32.8	stable[m]
hexaflumuron	0.027 (water), 5 (heptane), 2000 (octanol), 162000 (acetone), 100000 (ethyl acetate)	203.5	5.68	57	6.3	stable[n]
novaluron	0.003 (water), 1880 (xylene), 8.39 (heptane), 2850 (dichloroethane), 113000 (ethyl acetate)	177	4.30	72	stable[o]	stable[p]
lufenuron	0.046 (water), 100 (hexane), 66000 (toluene), 460000 (acetone), 330000 (ethyl acetate)	169.1	5.12	16.3	0.75	stable[q]
bistrifluoron	0.03 (water), 3500 (hexane), 33000 (methanol), 64000 (dichloroethane)	171.5	5.74	80.5	10	stable[r]
noviflumuron	0.194 (water), 68 (heptane), 48900 (methanol), 425000 (acetone), 290000 (ethyl acetate)	156.2	4.94	250	–	stable[s]
flufenoxuron	0.0043 (water), 6000 (xylene), 83000 (acetone), 3500 (toluene), 16000 (dichloroethane)	167.0	5.11	42	6	267
flucycloxuron	0.001 (water), 3300 (xylene), 3800 (ethanol), 200 (cyclohexanone)	143.6	6.97	208	18	28
chlorfluazuron	0.016 (water), 4670 (xylene), 1000 (octanol), 2680 (methanol)	222.6	5.80	90	stable	stable[t]
fluazuron	0.02 (water), 700 (octanol), 30000 (hexane), 2400 (methanol), 900 (isopropanol)	219.0	5.10	–	–	–

[a]Octanol–water partition coefficient (P) at pH 7, 20 °C. [b]Aerobic. [c]At pH 7. [d]At 20 °C and pH 7. [e]≤ 50, low; 50–500, moderate; >500, high. [f]<2.7, low bioaccumulation; 2.7–3, moderate; >3.0, high. [g]<30, nonpersistent; 30–100, moderately persistent; 100–365, persistent; >365, very persistent. [h]<1, fast; 1–14, moderately fast; 14–30, slow; >30, stable. [i]<30, nonpersistent; 30–100, moderately persistent; 100–365, persistent; >365, very persistent. [j]–, no data. [k]Calculated ClogP value by ChemBioDraw Ultra 12.0. [l]pH sensitive: stable at pH 5; 8.7 days at pH 9; at pH 7 95% of substance remained after 30 days. [m]Stable at pH 5 and 7, DT_{50} = 57 days at pH 9, all at 25 °C. [n]Stable at pH 5. [o]DT_{50} = 139 days, natural light, 40 deg N. [p]pH sensitive: stable pH 5–7, DT_{50} = 101 days at pH 9, 25 °C. [q]Stable pH 5–9. [r]Stable pH 5–9, 20 °C. [s]pH sensitive: stable in acid and neutral media, DT_{50} = 19 days at pH 9. [t]Not sensitive to pH.

(**136**) and EL-494 (**137**) both showed a high degree of biological activity against mosquito larvae, the LC_{50} values of L-7063 and EL-494 against *Lymantria dispar* third-larvae were 0.176 and 0.76 mg L^{-1}, respectively (Figure 19).[42p,q] Compound **138** was reported by Yang et al. and compounds **139** and **140** showed 100% larvicidal activity against *Mythimna sepatara* at 100 mg L^{-1}(Figure 19).[42j] Compound **141** was synthesized in our laboratory, and it had 80% mortality against *M. separata* at 10.0 mg L^{-1} (Figure 19).[42k] Compound **142** had 100% mortality against *S. eridania* larvae at 8.0 mg L^{-1},[42m] and compound **143** had 100% mortality against *S. litura* larvae at 2.0 mg L^{-1} (Figure 19).[42n] Yang et al. reported a series of 5-benzoylphenylurea-3(2*H*)-pyridazinones that had good activity against the third-instar nymphs of locusts (*Locusta migratoria manilensis*) at 200.0 mg L^{-1}; for example, compound **144** displayed 65.5% mortality at 200.0 mg L^{-1} (Figure 19).[42l] Qian et al. reported two series of 1,3,4-oxadiazoline heterocycle derivatives **145**, and bioactivity assays showed that all synthesized compounds inhibited chitin synthesis in yeast, suggesting they might be a novel class of potential inhibitors against chitin biosynthesis; for example, compound **146** exhibited the highest inhibitory activity (about 86%) on chitin biosynthesis at 250 μM (Figure 19).

■ ACTION MECHANISM

Research on the mechanism of benzoylurea insecticides has been a focus of concern to scientists since the appearance of the first benzoylureainsecticide diflubenzuron (**1**) in 1975.[43−53]

DOI: 10.1021/acs.jafc.5b02460
J. Agric. Food Chem. 2015, 63, 6847−6865

Table 2. Ecotoxicology for Commercial Benzoylphenylureas

		acute toxicity						
compd	BCF[a]	mammals oral LD_{50} (mg kg^{-1}) (rat)	birds LD_{50} (mg kg^{-1}) (*Colinus virginianus*)	fish LC_{50} (96 h) (mg L^{-1}) (*Oncorhynchus mykiss*)	aquatic invertebrates EC_{50} (48 h) (mg L^{-1}) (*Daphnia magna*)	aquatic crustaceans LC_{50} (96 h) (mg L^{-1})	earthworms LC_{50} (14 days) (mg kg^{-1}) (*Eisenia fetida*)	honybees LD_{50} (48 h) (μg bee^{-1})
diflubenzuron	320[b]	>4640[c]	>5000[d]	>0.13[e]	0.0026[f]	0.0021[g] (*Americamysis bahia*)	>500[h]	>25[i] (oral)
dichlorbenzuron	–[j]	>3160	–	–	–	–	–	–
chlorbenzuron	–	>10000	>5000	126.8[k]	–	0.01 (*Macrobrachim nipponense*)	–	>17 (contact)
teflubenzuron	640	>5038	>2250	>0.0065[l]	0.0028	0.00059[m]	>500	>72 (oral)
penfluoron	–	–	–	–	–	–	–	–
triflumuron	612	>5000	561	>0.021[l]	0.0016	0.00021[m]	>500	>200 (contact)
hexaflumuron	4700	>5000	2000	100[l]	0.0001	0.00069 (*Penaeus aztecus*)	880	0.1 (oral)
novaluron	2091	>5000	>2000[n]	>1.0	0.058	–	>1000	>100 (oral)
lufenuron	5300	>2000	2000[n]	>29[l]	0.0013	0.008 (*Mysidopsis*)	>500	>197 (oral)
bistrifluoron	2414	>5000	>2250	>0.5[o]	>1.2	–	>1000	>100 (contact)
noviflumuron	3000	>5000	>2000	1.8	3.11	–	>10000	>100 (contact)
flufenoxuron	33856	>3000	>2000	>0.0049	0.000043	–	>500	>100 (contact)
flucycloxuron	–	>5000	>2000[n]	>100	>0.00027	–	1000	>100 (contact)
chlorfluazuron	–	>8500	>2510[n]	>300[o]	0.000908	–	>1000	>100 (oral)
fluazuron	–	>5000	>2000[n]	15	0.0006	–	1000	–

[a]Bioconcentration factor. [b]<100, low potential; 100–5000, threshold for concern; >5000, High potential. [c]>2000, low; 100–2000, moderate; <100, high. [d]>2000, low; 100–2000, moderate; <100, high. [e]>100, low; 0.1–100, moderate; <0.1, high. [f]>100, low; 0.1–100, moderate; <0.1, high. [g]>100, low; 0.1–100, moderate; <0.1, high. [h]>1000, low; 10–1000, moderate; <10, high. [i]>100, low; 1–100, moderate; <1, high. [j]–, no data. [k]*Cyprinus carpio*. [l]*Lepomis macrochirus*. [m]48-h acute toxicity (EC_{50}) of *Streptocephalus sudanicus* [n]*Anas platyrhynchos*. [o]*Cyprinidae*.

Matsumura gave a review of studies on the action mechanism of diflubenzuron in 2010.[54] From the review, we know that it has been identified that diflubenzuron indeed inhibits the process of incorporation of *N*-acetylglucosamine into insect chitin in vivo, but there are no direct biochemical effects on enzymes, receptors, or intracellular organelles under a cell-free system. In addition, benzoylphenylureas show no inhibitory actions on fungal systems in vivo as well as in cell-free systems, which have roughly equivalent chitin synthesis pathways as insects. As diflubenzuron does not compromise chitin synthesis when vesicles are mechanically destroyed, a direct effect of diflubenzuron on chitin synthases can be excluded. There was a breakthrough in the action site of BPUs when a sulfonylurea receptor (SUR) was identified in *D. melanogaster* by Matsumura's research group, and it was established that insect SUR in the above intracellular vesicles preparation from *P. americana* as well as *B. germanica* was likely the actual target site of diflubenzuron to cause inhibition of chitin synthesis. The role of SUR in this case was determined, by using glibenclamide, a typical SUR specific inhibitor as an aid, to be helping the exocytotic movement of these vesicles as was the case of other members of the group of ABC-transporters to which insect SUR belongs. In this case both diflubenzuron and glibenclamide have been shown to cause the depolarization of the vesicle membrane through inhibition of the K^+ channel, which leads to their inhibition of chitin synthesis. The assays of competitive binding of [^{3}H]-glibenclamide in *B. germanica* cuticular vesicles indicated that all unlabeled compounds were capable of completely displacing the radioligand, but among them glibenclamide appeared to be most potent, followed by diflubenzuron and then dechloro-diflubenzuron, a much less active analogue of diflubenzuron.[52d] NK-17 (compound **128**, Figure 17) was chosen as a novel and potent insecticide for further development. It is very important that the evaluation of insecticidal activity is a critical step to a new insecticide candidate with independent intellectual property right before it is introduced to the market. Matsumura et al. have established a method of studying the action mechanism of diflubenzuron on SUR proteins by utilizing isotope labeling technology.[52d] Due to the restriction on the level of laboratory condition and for the safety of the researchers, the isotope labeling technology cannot be quickly and easily used in a regular laboratory. Hence, the fluorescence polarization method was explored for the first time in our laboratories to be used in studying the insecticidal mechanism of NK-17.[40g] The results showed that NK-17 could bind to the SUR of *B. germanica* with stronger affinity compared to diflubenzuron and glibenclamide, which suggested that NK-17 may also act on the site of the SUR to inhibit the chitin synthesis in insect body, and the result can well explain that NK-17 exhibited stronger toxicity against *B. germanica* than diflubenzuron and glibenclamide in vivo. Although the above results indeed support the hypothesis that SUR protein is the major target of DFB in causing disruption of chitin synthesis in *D. melanogaster* and *B. germanica*, there are many questions to answer, and the most important one is the functional relationship between SUR and chitin synthesis. Recently, Moussian et al. found that cuticle architecture is normal and chitin amounts are not diminished in the cuticle of *D. melanogaster* larvae, which had been made of the phenotype suffering complete elimination of the SUR function.[53] The results indicated that SUR was dispensable for chitin synthesis. They concluded that there must be another sulfonylurea-sensitive ABC-transporter that either instead of SUR was the true sulfonylurea-sensitive transporter involved in chitin synthesis or was able to substitute SUR function during cuticle formation. In fact, Nasonkin et al. who studied the

DOI: 10.1021/acs.jafc.5b02460
J. Agric. Food Chem. 2015, 63, 6847–6865

expression of D_{SUR} in *Drosophila* egg development up to stage 16, showed the expression of D_{SUR} only in the tracheal system, salivary gland, and dorsal vessels in the early stages of development, not in the cuticle of developing embryos of *D. melanogaster*.[55] Therefore, the exact action site of benzoylurea insecticides has not been identified, and more efforts are needed for further research.

■ ENVIRONMENTAL FATE AND ECOTOXICOLOGY

The pesticide physicochemical and ecotoxicological data of commercial benzoylphenylureas are obtained from the Pesticide Properties Database (PPDB), U.S. Environmental Protection Agency (EPA), TOXNET Databases, Google Web Search, and Web of Science.

Benzoylurea insecticides possess favorable environmental properties and low acute toxicology to mammals and birds as well as crop pollinators such as bees (Tables 1 and 2). These specific features usually provide a large margin of safety with regard to ecological and toxicological effects. There are several processes steering pesticides in the environment, such as adsorption, transfer, breakdown, and degradation. Transfer is a process in which pesticides move away from the target site, such as "volatilization, spray drift, runoff, leaching, absorption and crop removal" (Ministry of Agriculture and Land, British Columbia http://www.agf.gov.bc.ca/pesticides/c_2.htm). Decomposition is the breakdown of the pesticide molecules. Such a process leads to their total or partial degradation. Complete degradation of complex molecules is known as mineralization, which generates molecules of water, CO_2 and other small molecules depending on the pesticide chemical composition. Breakdown processes are the routes of degradation undergone by pesticides. Such degradation can be due to microbes, chemical reactions (hydrolysis, oxidation, and others), and photodegradation. As such processes depend on the chemical properties of the pesticides, such as susceptibility to oxidation, reduction, hydrolysis, photolysis, and substitution, these processes may have different timings, from hours or days to years. Besides, physical properties also influence pesticide breakdown, such as solubility in water, dissociation constant, partition coefficient, and sorption to soil. Different degradation rates occur in a diverse range of environmental conditions, as it also depends on climatic conditions, clay/silt/sand ratio in soil and sediments, water content, organic matter, pH, microbial biomass, and temperature. Metabolism in aerobic soils and water represents a significant dissipation mechanism for pesticides in the environment. Most BPUs suffer a rapid degradation in both soil and water by photolysis and hydrolysis (Table 1). The half-life of benzoylureas in the environment varies by type of medium such as soil, water, or sunlight.[56] The half-life of diflubenzuron ranges from hours to months, that of novaluron in tropical soils ranges from 11 to 59 days,[56j] and noviflumuron and chlorfluazuron do not readily break down in the environment.[57] The metabolites of BPUs may have adverse effects to humans. For example, diflubenzuron is quickly degraded in the environment mainly by hydrolysis and photodegradation, producing as major metabolites 2,6-difluorobenzamide, 4-chlorophenylurea, 4-chloroacetanilide, 4-chloroaniline, and *N*-methyl-4-chloroaniline, the latter three being classified as mutagens.[58]

Bioconcentration is the accumulation of a chemical in or on an organism when the source of the chemical is solely water.[59] Bioconcentration is a term that was created for use in the field of aquatic toxicology.[59] Bioconcentration can also be defined as the process by which a chemical concentration in an aquatic organism exceeds that in water as a result of exposure to a waterborne chemical. Bioconcentration factor (BCF) can be expressed as the ratio of the concentration of a chemical in an organism to the concentration of the chemical in the surrounding environment. The BCF is a measure of the extent of chemical sharing between an organism and the surrounding environment.[59] All of the commercial BPUs have a threshold of concern for bioconcentration potential (BCF > 100), and lufenuron (BCF = 5300) and flufenoxuron (BCF = 33856) have high bioconcentration potentials (Table 2). Flufenoxuron was banned in the European Union in 2011 due to its high potential for bioaccumulation in the food chain and high risk to aquatic organisms.[60] Flufenoxuron is marketed as having "high persistence" in the environment, and the product data-sheet states that it does not biodegrade easily.[61]

Most BPUs have low to moderate toxicity to fish; however, BPUs exhibit high toxicity to aquatic invertebrates and crustaceans because these chitin synthesis inhibitors may adversely affect nontarget organisms including beneficial insect species and crustaceans with chitin as a component of the exoskeleton (Table 2).[62−68] For example, flufenoxuron, hexaflumuron, teflubenzuron, and chlorfluazuron have very high toxicity against *Daphnia magna*, and their EC_{50} values are 0.000043, 0.0001, 0.0028, and 0.000908 mg L^{-1}, respectively (Table 2). Some studies show that several BPUs may affect nontarget arthropods, such as teflubenzuron, hexaflumuron, and flufenoxuron, at concentrations that are probably environmentally relevant. Hexaflumuron application had significant effects on *C. septempunctata* end points in the 33-day test, including effects on development duration (no observed effect application rate, NOER, 1.52 g ai ha^{-1}), hatching (NOER 3.04 g ai ha^{-1}), pupation (NOER 3.04 g ai ha^{-1}), and survival (NOER 1.52 g ai ha^{-1}). These NOERs are lower than the reported maximum field application rate of hexaflumuron (135 g ai ha^{-1}) in cotton cultivation, suggesting potential risks to beneficial arthropods.[69]

■ FUTURE PROSPECTS OF BENZYLPHENYLUREAS

Benzoylphenylurea chitin synthesis inhibitors possess the valuable property of having a non-neurotoxic mode of action at a target site that is absent in vertebrates, which means in turn that they are generally safe to mammals. The availability of a target site that is distinct from that of the more commonly employed neurotoxic insecticides also allows these molecules to be used as important tools in insecticide resistance management (IRM) programs.[70] In addition, the low contact activity of benzophenylureas reduces their impact on predatory insects, which in turn promotes their use in IRM programs. Resistance to the benzoylphenylureas has been measured both in the field and in the laboratory, but is usually correlated with insects acquiring an increased capacity to metabolize and eliminate the compound,[71,72] as opposed to the generation of target-site resistance. Typically, the onset of action of the benzoylphenylureas is slow, with several days being required before any reduction is observed in larval numbers, although cessation of larval feeding often occurs much earlier. This slow activity has resulted in a need to educate farmers and growers, who are accustomed to the rapid knockdown activity of neurotoxic pesticides, regarding the correct application timing of these compounds and the time required to observe their full activity. The lack of or limited contact activity of the benzoylphenylur-

DOI: 10.1021/acs.jafc.5b02460
J. Agric. Food Chem. 2015, 63, 6847−6865

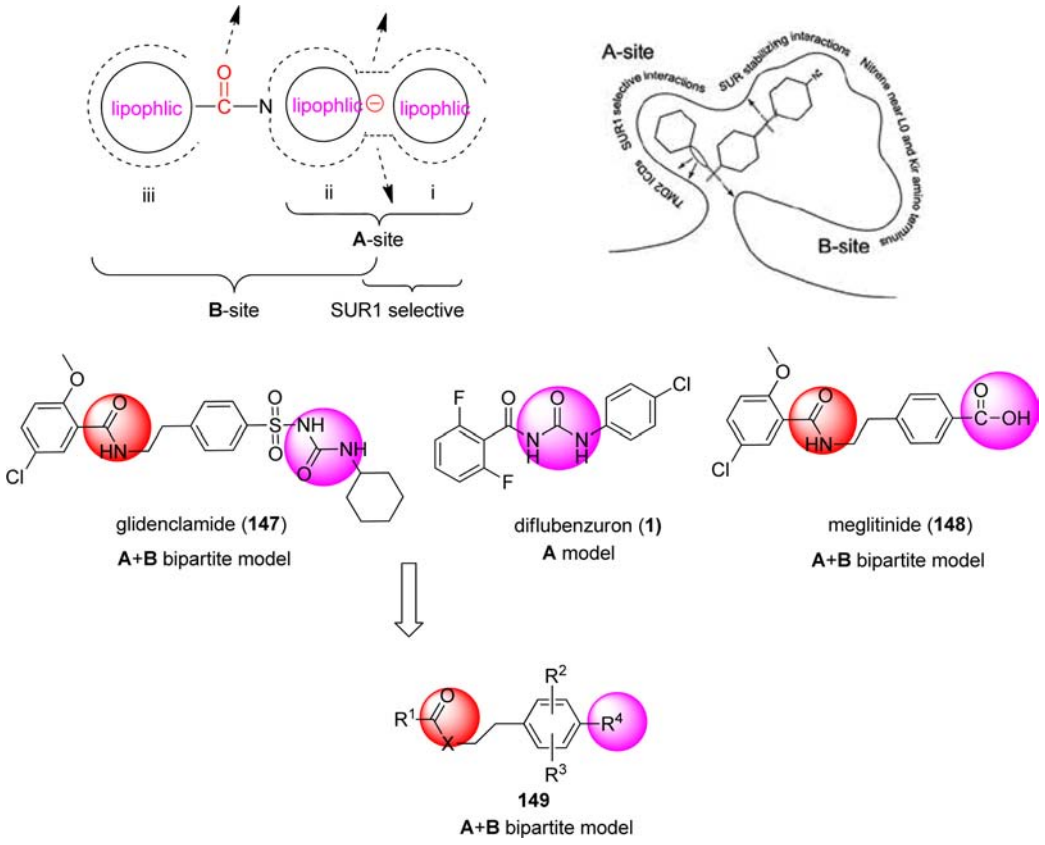

Figure 20. Sulfonylurea bipartite model and design strategy of bipartite BPU analogues.

eas has also limited their use against insects that are hidden feeders.[73]

Although the exact action site of diflubenzuron is in dispute,[52,53] glibenclamide (**147**) really can disrupt chitin synthesis in isolated cuticular integuments in both *B. germanica* and *D. melanogaster* at the same low concentration, and both compounds showed high competitive affinity binding with SUR isolated from *Drosophila* larvae as well.[52d] As we know, the urea bridge moiety (**C**, Figure 3) is essential to the insecticidal activity of BPUs and may be the functional group in binding the target protein. On the basis of an analysis of the literature and SAR of BPUs, we propose that the *para*-substituent at the anilide (**B**, Figure 3) of benzoylphenylureas should be the functional group. Vila-Carriles et al. found the substitution of lipophilic aromatic or heterocyclic groups at position iii (Figure 20) increased the potency of compounds such as glibenclamide (**147**, Figure 20) by 100−1000-fold in accord with their affinities for SUR1, 50 μM versus 0.5 nM. Studies with half-molecules such as meglitinide (**148**, Figure 20) suggested that the increase in affinity was a result of interactions with two overlapping binding sites, termed the A and B sites (Figure 20).[74−76] According to these facts, BPU analogues (**149**, Figure 20) with a bipartite model could be designed and synthesized (Figure 20) and may lead to novel insecticides through bioassay screening.

AUTHOR INFORMATION

Corresponding Authors

*(R.S.) Phone/fax: +86-471-4993227. E-mail: sunranfeng@yahoo.com, srf18@imu.edu.cn.

*(Q.W.) Phone/fax: +86-22-23503952. E-mail: wang98h@263.net, wangqm@nankai.edu.cn.

Funding

This work was financially supported by the National Science Foundation of China (21132003, 21421062, 21202079, 21462028, 21364005), Startup Foundation for Outstanding Young Scientists of Inner Mongolia University (Z20080213, No. 115110), and the "111" Project of the Ministry of Education of China (B06005).

Notes

The authors declare no competing financial interest.

REFERENCES

(1) Ortiz-Urquiza, A.; Luo, Z.; Keyhani, N. O. Improving mycoinsecticides for insect biological control. *Appl. Microbiol. Biotechnol.* **2015**, *99*, 1057−1068.

(2) Sechser, B.; Reber, B. Using a sequential testing scheme under laboratory and field conditions with the bumble bee Bombus terrestris to evaluate the safety of different groups of insecticides. In *Ecotoxicology*; Haskell, P., McEwen, P., Eds.; Springer: New York, 1998; pp 166−174.

(3) Doucet, D.; Retnakaran, A. Insect chitin: metabolism, genomics and pest management. In *Advances in Insect Physiology, Vol. 43: Insect Growth Disruptors*; Dhadialla, T. S., Ed.; Elsevier: Amsterdam, The Netherlands, 2012; Chapter 6, pp 437−511.10.1016/B978-0-12-391500-9.00006-1

(4) (a) Yang, G. F.; Yuan, J. W.; Liu, S.; Liu, Z. J. Research development of studies on inhibitors of chitin biosynthesis: benzoylurea derivatives. *J. Central China Normal Univ. (Nat. Sci.)* **1999**, *33*, 528−535. (b) Mao, D. S.; Lin, J.; Liu, F. C. Recent development of benzoyl urea chitin synthesis inhibitors. *Nongyao* **2001**, *40*, 6−12. (c) Liang, Y.; He, H. W.; Yang, Z. W. Progresses on research and development of the benzoylurea derivatives. *Nongyao* **2009**, *48*, 625−628,632. (d) Mi, N.; Wang, H.; Fan, Z. J.; Zhang, H. K.; Belskaia, N. P.; Bakulev, V. A. Study progress of BPUs insecticides.

DOI: 10.1021/acs.jafc.5b02460
J. Agric. Food Chem. 2015, 63, 6847−6865

Shijienongyao **2009**, *48*, 24−26. (e) Merzendorfer, H. Chitin synthesis inhibitors: old molecules and new developments. *Insect Sci.* **2013**, *20*, 121−138. (f) Huang, Z. Q.; Lue, L. J.; Zhu, H. L.; Liu, B.; Wei, Z.; Shang, Z. Q.; Shi, J. Application of drug design in benzoylurea insecticides. *Nongyao* **2014**, *53*, 157−163.

(5) (a) Qian, X. H. Quantitative studies on structure−activity relationship of sulfonylurea and benzoylphenylurea type pesticides and their substituents' bioisosterism using synthons' activity contribution. *J. Agric. Food Chem.* **1999**, *47*, 4415−4418. (b) Nakagawa, Y. Molecular mechanism of the molting and the structure-activity relationship for molting inhibitor. *J. Pestic. Sci.* **2011**, *36*, 300−303.

(6) Van Daalen, J. J.; Meltzer, J.; Mulder, R.; Willinga, K. A selective insecticide with a novel mode of action. *Naturwissenschaften* **1972**, *59*, 312−313.

(7) Sheets, J. J. Chitin synthesis. In *Modern Crop Protection Compounds, Vol. 3: Insecticide*; Kramer, W., Schirmer, U., Eds.; Wiley-VCH Verlag: Weinheim, Germany, 2012; Vol. 3, pp 999−1011.

(8) Degheele, D.; Yi, S. X.; Bai, C. Toxicity of benzoylphenylureas to the African armyworm *Spodoptera exempta* (Walker). *Crop Prot.* **1993**, *12*, 35−38.

(9) Ascher, K. R. S.; Eliyahu, M.; Nemny, N. E. Inherent toxicity of the acylureas hexaflumuron and chlorfluazuron against larvae of the cotton bollworm, *Helicoverpa armigera* (Huebner) (Lepidoptera: Noctuidae). *Z. Pflanzenkr. Pflanzenschutz* **1991**, *98*, 391−397.

(10) Kirchhoff, M. M. Promoting sustainability through green chemistry. *Resour., Conservation Recycl.* **2005**, *44*, 237−243.

(11) Karimzadeh, R.; Hejazi, M. J.; Khoei, F. R.; Moghaddam, M. Laboratory evaluation of five chitin synthesis inhibitors against the Colorado potato beetle *Leptinotarsa decemlineata*. *J. Insect Sci.* **2007**, *7*, 1−6.

(12) (a) Anderson, M.; Fisher, J. P.; Robinson, J.; Debray, P. H. Flufenoxuron − an acylurea acaricide/insecticide with novel properties. *Proc.−Brighton Crop Prot. Conf−-Pests Dis.* **1986**, *1*, 89−96. (b) Perugia, G.; Ingelsfield, C.; Tipton, J. D. The evaluation of a novel acylurea (flufenoxuron) on top fruit and citrus in Italy. *Proc.−Brighton Crop Prot. Conf.−Pests Dis.* **1986**, *1*, 315−322. (c) Easterbrook, M. A.; Buss, D. S. Tests of acaricides against apple rust mite (*Aculus schlechtendali*). *Ann. Appl. Biol.* **1988**, *112* (Suppl.), 2−3. (d) McGhie, R. A.; Tomkins, A. R. Laboratory evaluations of insect growth regulators against lightbrown apple moth. *Proc. N. Z. Weed Pest Control Conf.* **1988**, *41*, 243−248.

(13) (a) Grosscurt, A. C.; Ter Haar, M.; Jongsma, B.; Stoker, A. PH 70-23: a new acaricide and insecticide interfering with chitin deposition. *Pestic. Sci.* **1988**, *22*, 51−59. (b) Scheltes, P.; Hofman, T. W.; Grosscurt, A. C. Field data on PH 70-23, a novel benzoylphenylurea controlling mites and insects in a range of crops. *Brighton Crop Prot. Conf.−Pests Dis.* **1988**, *2*, 559−566. (c) Blair, B. W. Laboratory screening of acaricides against Tetranychus evansi Baker & Pritchard. *Crop Prot.* **1989**, *8*, 212−16. (d) Tabozada, E. K.; El-Arnaouty, S. A.; Sayed, S. M. Effectiveness of two chitin synthesis inhibitors; flufenoxuron and lufenuron on *Spodoptera littoralis* (Lepidoptera: Noctuidae) and side effects of sublethal concentrations of them on two hymenopteran parasitoids. *Life Sci. J.* **2014**, *11*, 239−245.

(14) (a) Nakagawa, Y.; Fujita, T. Insecticides with inhibitory effect of the ecdysis of insects. *Kagaku (Kyoto)* **1986**, *41*, 194−195. (b) Dayaoen, C. L. Toxicity of some insecticides and insecticide combinations of *Plutella xylostella* (Linn.). *Philipp. Entomol.* **1987**, *7*, 159−166. (c) Perng, F. S.; Sun, C. N. Susceptibility of diamondback moths (Lepidoptera: Plutellidae) resistant to conventional insecticides to chitin synthesis inhibitors. *J. Econ. Entomol.* **1987**, *80*, 29−31.

(15) de Oliveira, P. R.; Calligaris, I. B.; Roma, G. C.; Bechara, G. H.; Pizano, M. A.; Camargo Mathias, M. I. Potential of the insect growth regulator, fluazuron, in the control of *Rhipicephalus sanguineus* nymphs (Latreille, 1806) (Acari: Ixodidae): determination of the LD_{95} and LD_{50}. *Exp. Parasitol.* **2012**, *131*, 35−39.

(16) (a) Nakagawa, Y.; Kitahara, K.; Nishioka, T.; Iwamura, H.; Fujita, T. Quantitative structure-activity studies of benzoylphenylurea larvicides: I. Effect of substituents at aniline moiety against *Chilo suppressalis walker*. *Pestic. Biochem. Physiol.* **1984**, *21*, 309−325. (b) Nakagawa, Y.; Iwamura, H.; Fujita, T. Quantitative structure-activity studies of benzoylphenylurea larvicides: II. Effect of benzyloxy substituents at aniline moiety against *Chilo suppressalis* Walker. *Pestic. Biochem. Physiol.* **1985**, *23*, 7−12. (c) Nakagawa, Y.; Sotomatsu, T.; Irie, K.; Kitahara, K.; Iwamura, H.; Fujita, T. Quantitative structure-activity studies of benzoylphenylurea larvicides: III. Effects of substituents at the benzoyl moiety. *Pestic. Biochem. Physiol.* **1987**, *27*, 143−155. (d) Sotomatsu, T.; Nakagawa, Y.; Fujita, T. Quantitative structure-activity studies of benzoylphenylurea larvicides: IV. Benzoyl ortho substituent effects and molecular conformation. *Pestic. Biochem. Physiol.* **1987**, *27*, 156−164. (e) Nakagawa, Y.; Akagi, T.; Iwamura, H.; Fujita, T. Quantitative structure-activity studies of benzoylphenylurea larvicides: V. Substituted pyridyloxyphenyl and related derivatives. *Pestic. Biochem. Physiol.* **1988**, *30*, 67−78. (f) Nakagawa, Y.; Akagi, T.; Iwamura, H.; Fujita, T. Quantitative structure-activity studies of benzoylphenylurea larvicides: VI. Comparison of substituent effects among activities against different insect species. *Pestic. Biochem. Physiol.* **1989**, *33*, 144−157. (g) Nakagawa, Y.; Izumi, K.; Oikawa, N.; Kurozumi, A.; Iwamura, H.; Fujita, T. Quantitative structure-activity relationships of benzoylphenylurea larvicides: VII. Separation of effects of substituents in the multisubstituted anilide moiety on the larvicidal activity against *Chilo suppressalis*. *Pestic. Biochem. Physiol.* **1991**, *40*, 12−26. (h) Nakagawa, Y.; Matsutani, M.; Kurihara, N.; Nishimura, K.; Fujita, T. Quantitative structure-activity studies of benzoylphenylurea larvicides: VIII. Inhibition of N-acetylglucosamine incorporation into the cultured integument of *Chilo suppressalis* Walker. *Pestic. Biochem. Physiol.* **1992**, *43*, 141−151.

(17) (a) Wellinga, K.; Mulder, R.; van Daalen, J. J. Synthesis and laboratory evaluation of 1-(2,6-disubstituted benzoyl)-3-phenylureas, a new class of insecticides. I. 1-(2,6-Dichlorobenzoyl)-3-phenylureas. *J. Agric. Food Chem.* **1973**, *21*, 348−354. (b) Wellinga, K.; Mulder, R.; van Daalen, J. J. Synthesis and laboratory evaluation of 1-(2,6-disubstituted benzoyl)-3-phenylureas, a new class of insecticides. II. Influence of the acyl moiety on insecticidal activity. *J. Agric. Food Chem.* **1973**, *21*, 993−998. (c) Hajjar, N. P.; Casida, J. E. Insecticidal benzoylphenyl ureas: structure-activity relationships as chitin synthesis inhibitors. *Science* **1978**, *200*, 1499−1500.

(18) Luteijn, J. M.; Tipker, J. A note on the effects of fluorine substituents on the biological activity and environmental chemistry of benzoylphenylureas. *Pestic. Sci.* **1986**, *17*, 456−458.

(19) (a) Raymond, H. R. *N*-{8-(optionally substituted phenylamino)-carbonyl}pyridine carboxamides and insecticidal use thereof. U.S. 4148902, April 10, 1979. (b) Wade, L. L.; McDermott, M. Method of controlling manure-breeding insects.U.S. 4092421, May 30, 1978. (c) Liu, C. L.; Lei, X.; Liu, W. C.; Zhao, R. J. Synthesis of novel pyrazolecarbonylureas and their biological activities. *Hecheng Huaxue* **1997**, *5*, 394−398. (d) Huang, W. Y.; Yang, X. L.; Zhang, Z. N. Review on the synthesis of *E*-*β*-farnesene. *Huaxue Tongbao* **2002**, *65*, 157−161. (e) Baraldi, P. G.; Guarmeri, M. S.; Simoni, D.; Zanirato, V. Synthesis and evaluation of the antifungal activity of a new series of *N*-acylureas. *Farmaco* **1989**, *44*, 391−398.

(20) (a) Kaugars, G. Compounds, compositions and methods of combatting pest employing thioureas. U.S. 4160037, July 3, 1979. (b) Wellinga, K.; Mulder, R. Insecticidal use of ureas and thioureas. U.S. 4607044, August 19, 1986. (c) Drabek, J.; Boeger, M. Benzoylphenylureas, their preparation, intermediates for their preparation, and pesticides containing these compounds. DE 3628864, March 5, 1987. (d) Sirrenberg, W.; Becker, B. Benzoyl-(thio)ureas. DE 3640175, June 1, 1988. (e) Samoto, N.; Mori, T.; Ohsumi, T. A benzoylurea derivative and its production and use. EP 285428, October 5, 1988.

(21) Sbragia, R. J.; Johnson, G. W.; Karr, L. L.; Edwards, J. M.; Schneider, B. M. Benzoylphenylurea insecticides and methods of using certain benzoylphenylureas to control cockroaches, ants, fleas, and termites. U.S. 5886221, March 23, 1999.

(22) (a) Haga, T.; Toki, T.; Koyanagi, T.; Fujii, Y.; Yoshida, K.; Imai, O. Benzoylurea compounds, process for their production and pesticides containing them. EP 263438, April 13, 1988. (b) Konobe,

DOI: 10.1021/acs.jafc.5b02460
J. Agric. Food Chem. 2015, 63, 6847−6865

M.; Itoh, S.; Sakamoto, N.; Araki, T.; Tohyama, Y. A New benzoylurea derivatives useful for controlling pests for protecting plants, crops and vegetables. WO 2007046513, August 16, 2007.

(23) (a) Anderson, M. Insecticidal *N*-benzoyl-*N*′-phenyl-*N*′-(R-thio)ureas. U.S. 4497822, February 5, 1985. (b) Anderson, M. Pesticidal benzoylurea compounds. U.S. 4666942, May 19, 1987;. (c) Anderson, M.; Brinnand, A. G. Pesticidal benzoylurea compounds, compositions and use. U.S. 4745113, May 17, 1988. (d) Anderson, M.; Brinnand, A. G. Pesticidal benzoylurea compounds EP 216423, May 17, 1989.

(24) (a) Chen, L.; Wang, Q. M.; Huang, R. Q.; Mao, C. H.; Shang, J.; Bi, F. C. Synthesis and insecticidal evaluation of propesticides of benzoylphenylureas. *J. Agric. Food Chem.* **2005**, *53*, 38−41. (b) Chen, L.; Huang, Z. Q.; Wang, Q. M.; Shang, J.; Huang, R. Q.; Bi, F. C. Insecticidal benzoylphenylurea-*S*-carbamate: a new propesticide with two effects of both benzoylphenylureas and carbamates. *J. Agric. Food Chem.* **2007**, *55*, 2659−2663. (c) Sun, R. F.; Zhang, Y. L.; Chen, L.; Li, Y. Q.; Li, Q. S.; Song, H. B.; Huang, R. Q.; Bi, F. C.; Wang, Q. M. Design, synthesis, and insecticidal activities of new *N*-benzoyl-*N*′-phenyl-*N*′-sulfenylureas. *J. Agric. Food Chem.* **2009**, *57*, 3661−3668.

(25) (a) Wellinga, K.; Mulder, R. Substitued benzoyl ureas. U.S. 3748356, July 24, 1973;. (b) Richter, S. B.; Stach, L. J.; Wilke, R. N. Insecticidal 2-phenyl-4-benzoyl-1,2,4-oxadiazolidine-3,5-diones. U.S. 3959478, May 25, 1976.

(26) Ito, S.; Konobe, M.; Sakamoto, N. Preparation of heterocyclic compounds as pesticides. WO 2003074498, September 12, 2003.

(27) Drabek, J.; Boeger, M. Benzoyl urea salts. EP 221847, May 13, 1987.

(28) (a) Anderson, M.; Brinnand, A. G.; Verbrugge, P. A. Benzamide compounds, their preparation and their use as pesticides. U.S. 5155135, October 13, 1992. (b) Hu, H. X.; Chen, W. D.; Qian, X. H. Synthesis and quantitative structure-activity relationship of 1-aroyl-4-aryl-2-t-butyl semicarbazides. *Nongyaoxue Xuebao* **1999**, *1*, 20−25. (c) Huff, R. K.; Evans, D. D.; Anderson, N. H. Substituted benzoylimidates, their preparation and compositions comprising them for insecticidal use. EP 5944, December 12, 1979. (d) Li, Y.; Li, B. J.; Ling, Y.; Miao, H. J.; Shi, Y. X.; Yang, X. L. Synthesis and fungicidal activity of aryl carbamic acid-5-aryl-2-furanmethyl ester. *J. Agric. Food Chem.* **2010**, *58*, 3037−3042.

(29) Manfred, B. H. *N*-(2*H*-Difluoro-3,5-dichloro-phenyl)-*N*′-(2,6-difluorobenzoyl) urea derivative and pesticidal compositions containing same. U.S. 4457943, July 3, 1984.

(30) (a) Yoo, T.; Tadashi, O.; Toshihiko, Y.; Yoji, T. A benzoylurea derivative and its production and use. EP 246061, November 19, 1987. (b) Pietro, M.; Franco, B.; Gabriele, G.; Paol, P.; Franca, R.; Vincenzo, C.; Angelo, L. Benzoyl-ureas exerting an insecticide activity. EP 123302, October 31, 1984. (c) Kim, J. H.; Woo, J. W.; Shin, Y. W.; Heo, J. N.; Kim, E. D.; Park, J. S. Aryl benzoyl urea derivative and pesticidal composition comprising the same. U.S. 6051737, April 18, 2000.

(31) (a) Zhang, J.; Tang, X. H.; Ishaaya, I.; Cao, S.; Wu, J. J.; Yu, J. L.; Li, H.; Qian, X. H. Synthesis and insecticidal activity of heptafluoroisopropyl-containing benzoylphenylurea structures. *J. Agric. Food Chem.* **2010**, *58*, 2736−2740. (b) Cao, S.; Cheng, J. H.; Xiong, Y.; Jin, G. Y.; Xiao, J. 1,2′-Chloro-hexafluoroisopropylbenzoylurea compound and use thereof. CN 102702031, October 3, 2012.

(32) (a) Josef, E. Insecticidal *N*-(*p*-aminophenyl)-*N*′-benzoylureas. U.S. 4323579, April 6, 1982. (b) Josef, E. Insecticidal *N*-[4-(3′-haloprop-2′-en-1′-yl)-aminophenyl]-*N*′-benzoylureas. U.S. 4353925, October 12, 1982. (c) Josef, E. Phenylureas. DE 3233383, March 24, 1983. (d) Josef, E. Phenylureas. U.S. 4431671, February 14, 1984. (e) Brouwer, M. S.; Grosscurt, A. C. Benzoylurea compounds and pesticidal compositions comprisingsame. EP 116729, August 29, 1984. (f) Tetasuya, M.; Hiroaki, F. Noriyasu, S.; Izumi, F.; Tadashi, O. A benzoylurea derivative and its production and use. EP 278672, August 17, 1988.

(33) Burgess, M. J.; Clifford, D. P. Novel substituted *N*-phenyl-*N*′-benzoylureas and their use as insecticides and acaricides. EP 109172, May 23,1984.

(34) (a) Sirenberg, W.; Klauker, E.; Hammann, I.; Stendel, W. Substituierte *N*-phenyl-*N*′-benzoyl-harnstoffe, verfahren zu ihrer herstellung und ihre verwendung als insektizide. DE2601780, July 21, 1977. (b) Wade, L. L.; Mcdermott, M. Method of controlling manure-breeding insects. U.S. 4089975, May 16, 1978. (c) Rigterink, R. H.; Sbragia, R. J. Substituted *N*-aroyl-*N*′-phenyl urea compounds. U.S. 4468405, August 28, 1984. (d) Massardo, P.; Rama, F.; Piccardi, P.; Caprioli, V. *N*-(2,6-Difluorobenzoyl)-*N*′-3-chloro-4-[1,1,2-trifluoro-2-(trifluoromethoxy) ethoxy] phenyl urea having insecticidal activity. EP 271923, October 22, 1990. (e) Drabek, J.; Boger, M. Benzoylphenylureas. U.S. 4798837, January 17, 1989. (f) Rochette, F.; Engelen, M.; Vanden Bossche, H. Antifungal agents of use in animal health-practical applications. *J. Vet. Pharmacol. Ther.* **2003**, *26*, 31−53. (g) Zur, G.; Elad, D. In vitro and in vivo effects of lufenuron on dermatophytes isolated from cases of canine and feline dermatophytoses. *J. Vet. Med., Ser. B* **2006**, *53*, 122−125. (h) Yair, B. Z.; Boaz, A. Fungicide composition comprising a benzoylurea. WO 9944425, September 10, 1999. (i) Brouwer, M. S.; Grosscurt, A. C.; Van Hes, R. Benzoyl urea compounds, a composition with insecticidal and acaricidal activity, a pharmaceutical composition, and controlling insects and/or mites and combating live tumors. BR 8400235, August 28, 1984.

(35) (a) Sirrenberg, W.; Hammann, I.; Stendel, W.; Klauke, E. Insecticidal substituted *N*-benzoyl-*N*′-*tert*-alkoxycarbonylphenyl(thio)-ureas. U.S. 4234600, November 18, 1980. (b) Lange, A.; Kiehs, K.; Adolphi, H. *N*-Benzoyl-*N*′-phenylureas and their use as insecticides. EP 56124, July 21, 1982. (c) Neubauer, H. J.; Hofmeister, P.; Kuenast, C. Preparation of 4-(benzoylureido)-2-halobenzoates as insecticides. DE 3722155, January, 12, 1989. (d) Brouwer, M. S.; Grosscurt, A. C.; Van, H. R. Insecticidal and acaricidal benzoylurea compounds. EP 167197, January 8, 1986.

(36) (a) Hofmeister, P.; Kuenast, C.; Lange, A. *N*-Benzoyl-*N*′-phenoxyphenylureas and *N*-benzoyl-*N*′-carboxyphenylureas: a review of their chemical synthesis and biological profiles. *Pestic. Sci.* **1988**, *22*, 221−230. (b) Chou, D. T. W.; Cain, P. A. Pesticidal 1-(4-phenoxyphenyl)-3-benzoyl urea compounds. WO 8605780, October 9, 1986. (c) Cain, P. A. Insecticidal bicyclooxyphenyl ureas. U.S. 4426385, January 17,1984. (d) Anderson, M. Pesticidal benzoylurea compounds. EP 161019, January 25, 1989. (e) Sakamoto, N.; Mori, T.; Ohsumi, T.; Fujimoto, H.; Fujimoto, I. Preparation *N*-benzoyl-*N*′-[(phenylthio)phenyl]ureas as acaricides and insecticides. EP 285428, October 5, 1988. (f) Kisida, H.; Nishida, S.; Yano, T. Benzoylureas and their use. EP140590, September 28, 1985. (g) Kisida, H.; Nishida, S.; Yano, T. Benzoylureas and their use. EP140590, August 5, 1985. (h) Sirrenberg, W.; Schramm, J.; Klauke, E.; Hammann, I. Insecticidal benzoylureidodiphenyl ethers. DE 2537413, March 3, 1977. (i) Sirrenberg, W.; Schramm, J.; Klauke, E.; Hammann, I.; Stendel, W. Insecticidal 2′,3,6′-trichloro-4-cyano-4′-benzoylureidodiphenyl ethers. DE 2531743, February 3, 1977. (j) Nishama, R.; Haga, T.; Nasu, R.; Toki, T. Phenoxyphenylurea insecticides. JP 55038357, March 17, 1980. (k) Sirrenberg, W.; Schramm, J.; Klauke, E.; Hammann, I.; Stendel, W. Insecticidal (benzoylureido)phenyl nitrophenyl ethers. DE 2504983, August 19, 1976. (m) Sirrenberg, W.; Klauke, E.; Becker, B.; Krehan, I.; Stendel, W. Benzoylureas DE3309987, September 20, 1984. (l) Brouwer, M. S.; Grosscurt, A. C. Substituted benzoyl ureas as insecticides. U.S. 4399152, August 16, 1983.

(37) (a) Haga, T.; Toki, T.; Tsujii, Y.; Nishiyama, R. Development of an insect growth regulator, chlorfluazuron. *J. Pestic. Sci.* **1992**, *17*, S103−S113. (b) Nishiyama, R.; Haga, T.; Toki, T.; Koyanagi, T.; Murai, S. *N*-Benzoyl-*N*′-(pyridyloxyphenyl) urea. U.S. 4310530, January 12, 1982. (c) Nishiyama, R.; Haga, T.; Toki, T.; Koyanagi, T.; Murai, S. *N*-Benzoyl-*N*′-(pyridyloxyphenyl) urea. U.S. 4344951, August 17, 1982. (d) Nishiyama, R.; Fujikawa, K.; Nasu, R.; Toki, T.; Yamamoto, T. N-Benzoyl-N′-pyridyloxyphenylurea. DE 2748636, May 3, 1978. (e) Nishiyama, R.; Fujikawa, K.; Nasu, R.; Toki, T. N-pyridyloxyphenylureas as insecticides. JP 54106475, August 21, 1979. (f) Maeda, K.; Kaeriyama, M.; Matsui, T.; Ishikawa, N.; Yamada, S.; Okunuki, S. Pyridyloxyphenylurea insecticides. JP 55038356, March

DOI: 10.1021/acs.jafc.5b02460
J. Agric. Food Chem. 2015, 63, 6847−6865

17, 1980. (g) Nishiyama, R.; Haga, T.; Toki, T.; Koyanagi, T.; Murai, S. *N*-Benzoyl-*N*′-(pyridyloxyphenyl)urea. DE 3033512, March 26, 1981.

(38) (a) Boeger, M. Phenylbenzoylureas as pesticides. EP 79311, 1983. (b) Drabek, J.; Boger, M. Preparation of benzoylurea salts as pesticides. EP 221847A2, 1987. (c) Hausermann, W.; Maurer, M.; Friedel, T. Preparation of *N*-3-[[5-(trifluoromethyl)-2-pyridyl]oxy]-phenyl-*N*′-benzoylureas for combating helminths in livestock. U.S. 4977169, December 11, 1990.

(39) (a) Marius, S. B.; Arnoldus, C. G. Urea and thiourea compounds and insecticidal compositions. U.S. 4350706, September 21, 1982. (b) Brouwer, M. S.; Grosscurt, A. C. Composition active against mites, whitefly and thrips, pharmaceutical composition, and new benzoylureau compounds. EP 116728, August 29, 1984. (c) Carmellino, M. L.; Pagani, G.; Pregnolato, M.; Terreni, M.; Caprioli, V.; Zani, F. Studies on the insecticidal activities of some new *N*-benzoyl-*N*′-arylureas. *Pestic. Sci.* **1995**, *45*, 227−236.

(40) (a) Dekeyser, M. A. Acaricide mode of action. *Pest Manage. Sci.* **2005**, *61*, 103−110. (b) Brouwer, M. S.; Grosscurt, A. C. Benzoylurea compounds, and pesticidal and pharmaceutical compositions comprising same. U.S. 4609676, September 2, 1986. (c) Daniele, B.; Pletro, M.; Giovanni, M.; Franco, R.; Vincenzo, C. Benzoyl-ureas having acaricide and insecticide activity. EP 211665, February 25, 1987. (d) Sun, R. F.; Lue, M. Y.; Chen, L.; Li, Q. S.; Song, H. B.; Bi, F. C.; Huang, R. Q.; Wang, Q. M. Design, synthesis, bioactivity, and structure-activity relationship (SAR) studies of novel benzoylphenylureas containing oxime ether group. *J. Agric. Food Chem.* **2008**, *56*, 11376−11391. (e) Sun, R. F.; Li, Y. Q.; Lue, M. Y.; Xiong, L. X.; Wang, Q. M. Synthesis, larvicidal activity, and SAR studies of new benzoylphenylureas containing oxime ether and oxime ester group. *Bioorg. Med. Chem. Lett.* **2010**, *20*, 4693−4699. (f) Sun, R. F.; Li, Y. Q.; Xiong, L. X.; Liu, Y. X.; Wang, Q. M. Design, synthesis, and insecticidal evaluation of new benzoylureas containing isoxazoline and isoxazole group. *J. Agric. Food Chem.* **2011**, *59*, 4851−4859. (g) Li, Y. Q.; Qin, Y. G.; Yang, N.; Sun, Y. F.; Yang, X. L.; Sun, R. F.; Wang, Q. M.; Ling, Y. Studies on insecticidal activities and action mechanism of novel benzoylphenylurea candidate NK-17. *PLoS One* **2013**, *8* (6), e66251. (h) Liang, H. Z.; Xu, X. Z.; Li, G. P.; Gong, X. G.; Wen, J.; Wang, Q. M.; Yan, C. E.; Tong, L.; Zhou, Q. Y. NK-17 emulsifiable concentrate and its preparation method and field application in control of *Plutella xylostella* and *Spodoptera exigua*. CN 103960265, August 6, 2014.

(41) (a) Plummer, E. L. Inseciticidal substituted biphenyl benzoylureas. WO 8501047, March 14, 1985. (b) Ki, J. H.; Kyung, H. P. Pyrazole derivatives. U.S. 5430158, July 4, 1995. (c) Ki, J. H.; Kyung, H. P. Pyrazole containing benzoyl urea derivatives, and compositions. U.S. 5389667, February 14, 1995. (d) Maurer, F.; Erdelen, C. Preparation of tetrazolylbenzoylureas as pesticides and herbicides. WO 2001085705, November 15, 2001.

(42) (a) John, L. M. 1-Benzoyl-3-(arylphyridyl)urea compounds. U.S. 4405552, September 20, 1983. (b) Missel, J. L. 1-(2,6-Dichlorobenzoyl)-3-(5-substituted-2-pyridinyl)ureas, their preparation, formulations and use as insecticides. EP 8880, March 19, 1980. (c) Suhr, R. G. 1-Benzoyl-3-(alkoxy-or alkylthiopyridinyl)ureas. U.S. 4173639, November 6, 1979. (d) Missel, J. L. 1-(2,6-Dihalobenzoyl)-3-(5-substituted-2-pyridinyl)urea insecticides and insecticidal method. U.S. 4281003, July 28, 1981. (e) Missel, J. L. Improvements in or relating to 1-benzoyl-3-(arylpyridyl)urea compounds. EP 60071, September 15, 1982. (f) Missel, J. L. 1-(Substituted benzoyl)-3-(substituted pyrazinyl)ureas. GB 1521714, August 16, 1978. (g) Missel, J. L. Novel insecticidal 1-(substituted benzoyl)-3-(substituted pyrazinyl)-ureas. U.S. 4083977, April 11, 1978. (h) Missel, J. L. 1-(Substituted benzoyl)-3-(substituted pyrazinyl)ureas. U.S. 4160834, July 10, 1979. (i) Missel J. L. Novel 1-(mono-o-substituted benzoyl)-3-(substituted pyrazinyl) ureas. U.S. 4293552, October 6, 1981. (j) Wei, Z.-Z.; Pang, H.-L.; Liu, A.-P.; Cheng, H.; Ling, L.-Z.; Liu, Y.; Hu, C.-H.; Yang, G.-F. Synthesis and biological activity of 1-(pyrimidin-4-yl)-3-(2,6-difluorobenzoyl)urea derivatives. *Chin. J. Org. Chem.* **2006**, *26*, 1120−1124. (k) Sun, R. F.; Zhang, Y. L.; Bi, F. C.; Wang, Q. M. Design, synthesis, and bioactivity study of novel benzoylpyridazyl ureas. *J. Agric. Food Chem.* **2009**, *57*, 6356−6361. (l) Ling, Y.; Zhu, W. W.; Shi, W. P.; Li, X. C.; Qiu, L. H.; Sun, Y. F.; Yang, X. L. Synthesis and insect growth regulating activity of 5-benzoylphenyl urea 3(2H)-pyridazinone. *Nongyaoxue Xuebao* **2008**, *10*, 141−146. (m) Gibbs, C. G. 1-(2,6-Dichlorobenzoyl)-3-(4-trifluoromethyl-2-thiazolyl)urea and use as insecticide. U.S. 4164581, August 14, 1979. (n) Kume, T.; Tsuboi, S.; Isono, K.; Sasaki, S.; Hattori, Y. Benzoyl ureas. EP 198244, October 22, 1986. (o) Ke, S. Y.; Liu, F. Y.; Wang, N.; Yang, Q.; Qian, X. H. 1,3,4-Oxadiazoline derivatives as novel potential inhibitors targeting chitin biosynthesis: design, synthesis and biological evaluation. *Bioorg. Med. Chem. Lett.* **2009**, *19*, 332−335. (p) Abdelmonem, A. H.; Mumma, R. O. Comparative toxicity of some molt-inhibiting insecticides to the Gypsy. *J. Econ. Entomol.* **1981**, *74*, 176−179. (q) Abdel-Monem, A. H.; Cameron, E. A.; Mumma, R. O. Toxicological studies on the molt inhibiting insecticide EL-494 against the gypsy moth lymantria dispar and effect on chitin biosynthesis. *J. Econ. Entomol.* **1980**, *73*, 22−25.

(43) Post, L. C.; Vincent, W. R. A new insecticide inhibits chitin synthesis. *Naturwissenschaften* **1973**, *60*, 431−432.

(44) Ishaaya, I.; Casida, J. E. Dietary TH 6040 alters composition and enzyme activity of housefly larval cuticle. *Pestic. Biochem. Physiol.* **1974**, *4*, 484−490.

(45) Grosscurt, A. C. Effects of diflubenzuron on mechanical penetrability, chitin formation, and structure of the elytra of *Leptinotarsa decemlineata*. *J. Insect Physiol.* **1978**, *24*, 827−831.

(46) van Eck, W. H. Mode of action of two benzoylphenyl ureas as inhibitors of chitin synthesis in insects. *Insect Biochem.* **1979**, *9*, 295−300.

(47) Cohen, E.; Casida, J. E. Inhibition of *Tribolium* gut chitin synthetase. *Pestic. Biochem. Physiol.* **1980**, *13*, 129−136.

(48) Meola, S. M.; Mayer, R. T. Inhibition of cellular proliferation of imaginal epidermal cells by diflubenzuron in pupae of the stable fly. *Science* **1980**, *207*, 985−987.

(49) Deloach, J. R.; Meola, S. M.; Mayer, R. T.; Thompson, J. M. Inhibition of DNA synthesis by diflubenzuron in pupae of the stable fly *Stomoxys calcitrans* (L.). *Pestic. Biochem. Physiol.* **1981**, *15*, 172−180.

(50) Cohen, E.; Casida, J. E. Properties and inhibition of insect integumental chitin synthetase. *Pestic. Biochem. Physiol.* **1982**, *17*, 301−306.

(51) Merzendorfer, H.; Zimoch, L. Chitin metabolism in insects: structure, function and regulation of chitin synthases and chitinases. *J. Exp. Biol.* **2004**, *206*, 4393−4412.

(52) (a) Ishii, S.; Matsumura, F. Diflubenzuron-induced changes in activities of the cAMP-dependent protein kinase in the newly molted integument of American cockroach in situ and in cell free conditions. *Insect Biochem. Mol. Biol.* **1992**, *22*, 69−79. (b) Nakagawa, Y.; Matsumura, F. Diflubenzuron affects gamma-thioGTP stimulated Ca^{2+} transport *in vitro* in intracellular vesicles from the integument of the newly molted American cockroach. *Insect Biochem. Mol. Biol.* **1994**, *24*, 1009−1015. (c) Nakagawa, Y.; Ishii, S.; Matsumura, F. Diflubenzuron stimulates phosphorylation of a 39 kDa integumental protein from newly molted American cockroach (*Periplaneta americana*). *Insect Biochem. Mol. Biol.* **1996**, *26*, 891−898. (d) Abo-Elghar, G. E.; Fujiyoshi, P.; Matsumura, F. Significance of the sulfonylurea receptor (SUR) as the target of diflubenzuron in chitin synthesis inhibition in *Drosophila melanogaster* and *Blattella germanica*. *Insect Biochem. Mol. Biol.* **2004**, *34*, 743−752.

(53) Meyer, F.; Flotenmeyer, M.; Moussian, B. The sulfonylurea receptor Sur is dispensable for chitin synthesis in *Drosophila melanogaster* embryos. *Pest Manage. Sci.* **2013**, *69*, 1136−1140.

(54) Matsumura, F. Studies on the action mechanism of benzoylurea insecticides to inhibit the process of chitin synthesis in insects: a review on the status of research activities in the past, the present and the future prospects. *Pestic. Biochem. Physiol.* **2010**, *97*, 133−139.

(55) Nasonkin, I.; Alikasifoglu, A.; Ambrose, C.; Cahill, P.; Cheng, M.; Sarniak, A.; Egan, M.; Thomas, P. M. A novel sulfonylurea receptor family member expressed in the embryonic *Drosophila* dorsal vessel and tracheal system. *J. Biol. Chem.* **1999**, *274*, 29420−29425.

DOI: 10.1021/acs.jafc.5b02460
J. Agric. Food Chem. 2015, 63, 6847−6865

(56) (a) Mansager, E. R.; Still, G. G.; Frear, D. S.Fate of [^{14}C]diflubenzuron on cotton and in soil. *Pestic. Biochem. Physiol.* **1979**, *12*, 172−182. (b) Ivie, G. W.; Bull, D. L.; Veech, J. A. Fate of diflubenzuron in water. *J. Agric. Food Chem.* **1980**, *28*, 330−337. (c) Nimmo, W. B.; Willems, A. G. M.; Joustra, K. D.; Verloop, A. The degradation of diflubenzuron and its chief metabolites in soils. Part II: Fate of 4-chlorophenylurea. *Pestic. Sci.* **1986**, *17*, 403−411. (d) Nimmo, W. B.; Joustra, K. D.; Willems, A. G. M. The degradation of diflubenzuron and its chief metabolites in soils. Part III. Fate of 2,6-difluorobenzoic acid. *Pestic. Sci.* **1990**, *29*, 39−46. (e) Nohl-Weiler, C.; Dorn, E. On the fate of diflubenzuron in soil and water. In *Communications from the Federal Biological Institute for Agriculture and Forestry Berlin-Dahlem; Mass Outbreaks of Caterpillars in Forests*; 1997; pp 211−218. (f) Marsella, A. M.; Jaskolka, M.; Mabury, S. A. Aqueous solubilities, photolysis rates and partition coefficients of benzoylphenylurea insecticides. *Pest Manage. Sci.* **2000**, *56*, 789−794. (g) Huang, F.; Guo, Z. Y.; Chen, L.; Xu, Z.; Liu, Y.; Yang, C. M. Dissipation and evaluation of hexaflumuron residues in Chinese cabbage grown in open fields. *J. Agric. Food Chem.* **2010**, *58*, 4839−4843. (h) Sun, C. X.; Zhang, H.; Tang, T.; Qian, M. R.; Yuan, Y. W.; Zhang, Z. H. Comparison of greenhouse and field degradation behaviour of isoprocarb, hexaflumuron and difenoconazole in *Perilla frutescens*. *Bull. Environ. Contam. Toxicol.* **2012**, *89*, 868−872. (i) Chen, L.; ShangGuan, L. M.; Wu, Y. N.; Xu, L. J.; Fu, F. F. Study on the residue and degradation of fluorine-containing pesticides in olong tea by using gas chromatography-mass spectrometry. *Food Control* **2012**, *25*, 433−440. (j) Hsiao, Y.-L.; Ho, W.-H.; Yen, J.-H. Vertical distribution in soil column and dissipation in soil of benzoylurea insecticides diflubenzuron, flufenoxuron and novaluron and effect on the bacterial community. *Chemosphere* **2013**, *90*, 380−386. (k) Zhou, Q. X.; Lin, H. Y. Influence of surfactants on degradation of 1-(2-chlorobenzoyl)-3-(4-chlorophenyl) urea by nanoscale zerovalent iron. *Clean: Soil, Air, Water* **2013**, *41*, 128−133. (l) Davies, L. O.; Bramke, I.; France, E.; Marshall, S.; Oliver, R.; Nichols, C.; Schaefer, H.; Bending, G. D. Non-UV light influences the degradation rate of crop protection. *Environ. Sci. Technol.* **2013**, *47*, 8229−8237. (m) Lu, C. Y.; Yin, X.; Liu, X. F.; Wang, M. H. Study of the photodegradation kinetics and pathways of hexaflumuron in liquid media. *Photochem. Photobiol.* **2014**, *90*, 1219−1223.

(57) Eger, J. E.; Hamm, R. L.; Demark, J. J.; Chin-Heady, E.; Tolley, M. P.; Benson, E. P.; Zungoli, P. A.; Smith, M. S.; Spomer, N. A. Durability of a novel durable bait for control of subterranean termites (Isoptera: Rhinotermitidae): results of five-year field aging studies. *J. Econ. Entomol.* **2014**, *107*, 1201−1205.

(58) Rodriguez, E.; Barrio, R. J.; Goicolea, A.; de Balugera, Z. G. Determination of diflubenzuron and its main metabolites in forestry matrices by liquid chromatography with on-line diode-array and electrochemical detection. *Anal. Chim. Acta* **1999**, *384*, 63−70.

(59) (a) Frank, A. P. C. G.; Heather, A. M. Bioconcentration and biomagnification in the aquatic environment. In *Handbook of Property Estimation Methods for Chemicals*; CRC Press: Boca Raton, FL, USA, 2000. (b) Arnot, J. A.; Gobas, F. A. P. C. A review of bioconcentration factor (BCF) and bioaccumulation factor (BAF) assessments for organic chemicals in aquatic organisms. *Environ. Rev.* **2006**, *14*, 257−297. (c) Katagi, T. Bioconcentration, bioaccumulation, and metabolism of pesticides in aquatic organisms. *Rev. Environ. Contam. Toxicol.* **2010**, *204*, 1−132.

(60) Commission Implementing Regulation (EU). No. 942/2011, concerning the non-approval of the active substance flufenoxuron. September 22, 2011.

(61) BASF Cascade Product Details.

(62) (a) Ali, A.; Kok-Yokomi, M. L. Field studies on the impact of a new benzoylphenylurea insect growth regulator (UC-84572) on selected aquatic nontarget invertebrates. *Bull. Environ. Contam. Toxicol.* **1989**, *42*, 134−141. (b) Soltani, N.; Lechekhab, H.; Smagghe, G. Impact of the insect growth regulator diflubenzuron on biochemical composition of cuticle of the shrimp *Penaeus kerathurus*. *Commun. Agric. Appl. Biol. Sci.* **2009**, *74*, 137−41.

(63) Evans, T. A.; Main, B. Y. Attraction between social crab spiders: silk pheromones in *Diaea socialis*. *Behav. Ecol.* **1993**, *4*, 99−105.

(64) (a) Lahr, J.; Badji, A.; Marquenie, S.; Schuiling, E.; Ndour, K. B.; Diallo, A. O.; Everts, J. W. Acute toxicity of locust insecticides to two indigenous invertebrates from Sahelian temporary ponds. *Ecotoxicol. Environ. Saf.* **2001**, *48*, 66−75. (b) Langford, K. H.; Oxnevad, S.; Schoyen, M.; Thomas, K. V. Do antiparasitic medicines used in aquaculture pose a risk to the Norwegian aquatic environment? *Environ. Sci. Technol.* **2014**, *48*, 7774−7780. (c) Medeiros, L. S.; Souza, J. P.; Winkaler, E. U.; Carraschi, S. P.; Cruz, C.; Souza-Junior, S. C.; Machado-Neto, J. G. Acute toxicity and environmental risk of teflubenzuron to *Daphnia magna*, *Poecilia reticulata* and *Lemna minor* in the absence and presence of sediment. *J. Environ. Sci. Health, Part B* **2013**, *48*, 600−606. (d) Samuelsen, O. B.; Lunestad, B. T.; Farestveit, E.; Grefsrud, E. S.; Hannisdal, R.; Holmelid, B.; Tjensvoll, T.; Agnalt, A.-L. Mortality and deformities in European lobster (*Homarus gammarus*) juveniles exposed to the anti-parasitic drug teflubenzuron. *Aquat. Toxicol.* **2014**, *149*, 8−15.

(65) Grigarick, A. A.; Webster, R. K.; Meyer, R. P.; Zalom, F. G.; Smith, K. A. Effect of pesticide treatments on nontarget organisms in California rice paddies: I. Impact of triphenyltin hydroxide. *Hilgardia* **1990**, *58*, 1−36.

(66) (a) Cheng, Y.; Zhou, J.-Y.; Shan, Z.-J. Aquatic eco-risk and health risk assessment of application of pesticide in rice paddy in Dongtiaoxi watershed-based on modified RICEWQ EXAMS mode. *J. Ecol. Rural Environ.* **2012**, *28*, 579−586. (b) Koyanagi, T.; Morita, M.; Fujii, Y. Synthesis and insecticidal activity of alkylated *N*-benzoyl-*N*′-phenylureas and their toxicity to aquatic invertebrate. *J. Pestic. Sci.* **1998**, *23*, 250−254.

(67) Woodward, K. *Veterinary Products Containing Pesticide Active Ingredients*; 2013; Vol. 14, pp 150−243.

(68) Zaidi, N.; Soltani, N. Environmental risks of two chitin synthesis inhibitors on *Gambusia affinis*: chronic effects on growth and recovery of biological responses. *Biol. Control* **2011**, *59*, 106−113.

(69) Yu, C. H.; Fu, M. R.; Lin, R. H.; Zhang, Y.; Liu, Y. Q.; Jiang, H.; Brock, T. C. M. Toxic effects of hexaflumuron on the development of *Coccinella septempunctata*. *Environ. Sci. Pollut. Res.* **2014**, *21*, 1418−1424.

(70) (a) Ishaaya, I.; Kontsedalov, S.; Horowitz, A. R. Novaluron (Rimon), a novel IGR: Potency and cross-resistance. *Arch. Insect Biochem. Physiol.* **2003**, *54*, 157−164. (b) Perng, F. S.; Sun, C. N. Susceptibility of diamondback moths (Lepidoptera: Plutellidae) resistant to conventional insecticides to chitin synthesis inhibitors. *J. Econ. Entomol.* **1987**, *80*, 29−31.

(71) Kotze, A. C.; Sales, N.; Barchia, I. M. Diflubenzuron tolerance associated with monooxygenase activity in field strain larvae of the Australian sheep blowfly (Diptera: Calliphoridae). *J. Econ. Entomol.* **1997**, *90*, 15−20.

(72) (a) Lin, J. G.; Hung, C. F.; Sun, C. N. Teflubenzuron resistance and microsomal monooxygenases in larvae of the diamondback moth. *Pestic. Biochem. Physiol.* **1989**, *35*, 20−25. (b) Perng, F. S.; Yao, M. C.; Hung, C. F.; Sun, C. N. Teflubenzuron resistance in diamondback moth *Lepidoptera plutellidae*. *J. Econ. Entomol.* **1988**, *81*, 1277−1282.

(73) Sheets, J. J. Chitin synthesis inhibitors. In *Modern Crop Protection Compounds*; Kramer, W., Schirmer, U., Jeschke, P., Witschel, M., Eds.; Wiley-VCH: Weinheim, Germany, 2010; Vol. 3, pp 999−1011.

(74) Bryan, J.; Vila-Carriles, W. H.; Babenko, A. P.; Aguilar-Bryan, L. Insulin secretagogues, sulfonylurea receptors and K-ATP channels. *Curr. Pharm. Des.* **2005**, *11*, 2699−2716.

(75) Winkler, M.; Stephan, D.; Bieger, S.; Kuehner, P.; Wolff, F.; Quast, U. Testing the bipartite model of the sulfonylurea receptor binding site: binding of A-, B-, and A+B-site ligands. *J. Pharmacol. Exp. Ther.* **2007**, *322*, 701−708.

(76) Vila-Carriles, W. H.; Zhao, G.; Bryan, J. Defining a binding pocket for sulfonylureas in ATP-sensitive potassium channels. *FASEB J.* **2007**, *21*, 18−25.

DOI: 10.1021/acs.jafc.5b02460
J. Agric. Food Chem. 2015, 63, 6847−6865

Table 1. Calculated Vapor Pressures and Amounts of AF Components in the Tested EC Formulations

component	VP (Pa) at 25 °C	VP (Pa) at 20 °C	EC1 concentration (g in 4 L of solution)	EC2 concentration (g in 4 L of solution)
naphthalene	11	6.76	8.94	17.87
C2 indanes	23.85	16.68	2.88	5.76
C5/C6 benzene	24.05	18.01	5.36	10.72
C1 naphthalenes	9.08	6.62	41.31	82.62
C2 naphthalenes	3.9	2.19	22.74	45.48
C3 naphthalenes	0.645	0.416	8.34	16.68
C2−C4 biphenyls	0.471	0.337	9.73	19.46
hexachlorobenzene[a]	0.000616	0.000424	1.08	2.18

[a]Not present in commercial AFs but intentionally spiked to serve as a tracer in this study.

In 2012, 192 counties in the United States were designated as not attaining the 2008 ozone standard of 75 ppb over an 8 h averaging period.[4] Proposed revisions would further reduce this standard.[5] Given the Clean Air Act mandate to achieve attainment with the ozone standard, states must develop plans to meet this air quality objective. A key component of plans to reduce ground-level ozone often involves limiting VOC emissions from various sources, although oxides of nitrogen are precursors that can limit ozone formation. Understanding the nature and magnitude of VOC emissions is of particular concern in agricultural areas of California.[6] In such regions, VOCs are evolved naturally from plants, from the use of farm equipment, and from the use of pesticides. To address this challenge, California has developed a framework to assess and manage the potential ozone formation associated with pesticide formulations.[7]

The ozone formation potential (OFP) of a pesticide formulation allows the reactivity weighted emissions to be estimated in terms of ozone equivalents. The OFP is calculated as

$$\mathrm{OFP} = M \times \mathrm{EF} \times \mathrm{AMAF} \times \mathrm{IR} \quad (1)$$

where OFP = ozone formation potential of pesticide formulation (kg ozone/day), M = mass of product applied (kg product applied/day), EF = mass emission fraction of product (kg VOC in product/kg product applied), AMAF = application method adjustment factor (kg VOC emitted/kg VOC in product), and IR = incremental reactivity (kg ozone formed/kg VOC emitted).

The EF term is based on a thermogravimetric analysis (TGA) laboratory test, which involves heating a sample from 35 to 115 °C at a rate of 5 °C/min. The sample is then held at a final temperature of 115 °C to facilitate volatilization and loss of water in the formulation until the rate of sample mass loss drops below a defined threshold. The mean of three replicate loss measurements is used to estimate a product's EF. When TGA data are not available, the EF can be estimated given the weight composition and estimated vapor pressure (VP) of ingredients having VP at 25 °C of ≥0.05 Pa.[8] However, this vapor pressure cutoff is considerably lower than the value of 10 Pa that is commonly applied to define VOCs internationally[9] as adopted by IUPAC.[10] A key disadvantage of the TGA method is that the temperatures that the sample is exposed to are not representative of any naturally occurring environment; also, no chemical emission information is collected, and recent studies have shown that TGA can overestimate emissions quantified using GC-MS analysis.[11] A more direct approach is to use evaporation data measured under standard test conditions or to estimate this rate from a simple linear correlation with vapor pressure.[12] Furthermore, fate modeling has shown that partitioning to soil and water decreases the mobility of substances with vapor pressures below approximately 10 Pa, thus lowering the fraction of the emitted mass available to react in the atmosphere and serve as ozone precursors.[13] Nevertheless, the results of TGA or application of the calculation method yields a conservative EF estimate.

The IR term reflects the differential reactivity of formulation components in producing ozone under set assumptions. Although this parameter depends on the reactivity scale selected, the intent is to provide a consistent basis for comparing relative ozone formation potentials of different products on a mass basis. The AMAF term has been included to account for the fact that not all VOCs associated with the product will necessarily be emitted to air. Application of multimedia fate models suggests other fate processes such as sorption and biodegradation may reduce VOC losses following spray application. However, because quantitative data are generally lacking, use of adjustment factors is often not considered. Thus, in the case of aromatic fluids with VP ≥ 0.05 Pa, a worst-case scenario is applied in which all of the mass that is applied in pesticide formulation is assumed to be VOCs (EF = 1) that are emitted to air and available to contribute to ozone formation (AMAF = 1). Further research is therefore needed to assess the validity of this assumption and incorporate refinements if justified.

The objective of this study is to provide a model framework to estimate AMAF in spray application of aromatic fluid (AF) used in ECs. This objective is accomplished by (1) conducting spray chamber studies that simulate the fate of an EC containing aromatic fluid under field conditions and (2) using the resulting data to calibrate a predictive fate model, the agrochemical derived volatile organic compound air transfer evaluation (ADVOCATE) tool, to estimate VOC emissions that incorporates salient fate processes (volatilization, soil partitioning, and biodegradation) of constituents that comprise this fluid.

MATERIALS AND METHODS

Test Materials. Two ECs without an active ingredient were prepared from the following substances. A sample of AF (CAS Registry No. 64742-94-5) was obtained from ExxonMobil Chemical, Houston, TX, USA. This substance contains aromatic hydrocarbons predominantly with 10−13 carbons. TOXIMUL 3473, which is a blend of calcium sulfonate and nonionic surfactant, and TOXIMUL 3474, which is surfactant mixed with aromatic solvent, was obtained from the Stepan Co., Northfield, IL, USA. Hexachlorobenezene (CAS Registry No. 118-74-1) with a purity of 99% was purchased from Sigma-Aldrich and spiked into test EC formulations to serve as a conserved, involatile tracer. A fluorometric tracer dye was also included to determine spray recoveries. EC1 was prepared by mixing the above ingredients in water to yield the following composition on a

DOI: 10.1021/acs.jafc.5b01076
J. Agric. Food Chem. 2015, 63, 6866−6875

volumetric basis; AF (2.5%); TOXIMUL 3473 (0.095%); TOXIMUL 3474 (0.12%); HCB (0.025%); and tracer dye (0.0125%). EC2 was prepared using twice these volumetric concentrations for all components.

The two key substance properties determining the dissipation of ECs are vapor pressure (VP) and biodegradation rates in soil. The vapor pressures of the EC constituents were characterized using EPISuite MPBPWin v. 1.43 module[14] and were then temperature corrected using the Clausius−Claperyon equation at 20 °C and study temperatures (Appendix S1). Predicted biodegradation half-lives were calculated using EPISuite BioHCWin v. 1.01a[15] and compared to empirical estimates generated in this study. Table 1 shows the pertinent physical−chemical properties and amounts of EC constituents in the two spray formulations.

Spray Chamber Studies. The fate study was performed in collaboration with the U.S. Department of Agriculture, Agricultural Research Service (USDA-ARS), in College Station, TX. Researchers at the USDA-ARS have expertise in aerial application of pesticide formulations and have developed a spray chamber used to mimic agricultural spray applications. The methodology is described in detail[16] and is intended to simulate EC spraying under scenarios that are typical of ground application conditions. An agricultural sandy-loam soil with an organic matter content of 1.2% collected from the Central Valley of California near Fresno, CA, USA, was used in these studies. Soil was placed in six aluminum containment boxes (0.61 L × 0.91 W × 0.15 H m^3) with holes drilled in the bottom to allow for drainage. The filled boxes were placed in a greenhouse and watered over a 3 week period to return soil to conditions found in agricultural fields. Soil boxes were then placed on a table in a chamber that was equipped with automated spray nozzles that traverse the entire length of the chamber 1.4 m above the soil surface at a speed of 2.7 m/s. Air temperature at the time of spray application ranged from 16 to 19 °C.

Two different spray nozzles were employed to deliver a high volume (188 L/ha of EC1) spray with larger droplets (volume median diameter of 227 μm) representative of residual soil applications and a lower volume spray (94 L/ha of EC2) that gave smaller droplets (volume median diameter of 166 μm) representative of foliar and insecticidal treatment applications. Both nozzles were operated at 30 psi and provided average nozzle flow rates for larger and smaller droplet spray of 25 and 14.3 mL/s, respectively. Good spray recoveries ranging from 93 to 99% were reported on deposition samplers that were previously reported as part of this study.[16]

Six soil containment boxes were sprayed with each of the two selected nozzles (three boxes for each nozzle). Four of the boxes were sprayed with each nozzle (1, 2) in duplicate (A, B) for a short-term study to quantify volatilization losses of AF after spraying. The remaining two boxes were used to provide a single replicate for each spray nozzle to investigate longer term losses of AF due to soil biodegradation (designated boxes C1 and C2).

Soil samples were obtained from each location using a sharpened 1.6 cm diameter plug cutter inserted through the soil surface to a depth of 2.5 cm. The soil sample was then placed into a labeled 40 mL glass vial with an airtight screw-cap lid. The plug cutter was cleaned by rinsing with hexane between each sampling point. Four replicate soil samples were randomly collected from 20 gridded box locations at 0, 1, 4, 12, and 36 h for the volatilization study. Samples were frozen after collection to prevent biodegradation and then shipped for analysis. For the biodegradation study, samples were collected and frozen as above to serve as the day 0 time point. For the remaining samples, soil was collected immediately after spraying, placed in capped vials and shipped to the laboratory at ambient temperature to allow biodegradation to proceed in sealed vials. Samples were then analyzed after 0, 2, 4, 7, and 14 days of incubation taking into account elapsed transit time. Five replicates were included at time 0 and three replicates for subsequent sampling times. Control soil samples that were not sprayed were also collected and sent for analysis to determine background concentrations of AF components and HCB. All t = 0 samples were obtained while the containment boxes were on the spray table. Following initial soil sampling, the boxes were then moved to an adjacent greenhouse for subsequent sampling. Air temperature in the greenhouse during each soil sampling period ranged from 21 to 29 °C.[16]

Hydrocarbon Analysis. Two separate aliquots, equivalent in concentration, of emulsifiable concentrate (EC) amended with 1% HCB were received from USDA-ARS by the analytical chemistry laboratory of ExxonMobil Biomedical Sciences, Inc., Annandale, NJ, USA. Equal volumes of these EC aliquots were combined and diluted in acetone, yielding a single stock analytical standard solution. This stock solution was subsequently diluted in 1:1 methylene chloride/acetone providing a series of analytical standards used for subsequent GC-MS analysis of treated soil extracts. The concentrations of the total AF in the standards were 89, 356, 890, and 3560 ng/mL. The corresponding HCB concentrations in the standards were 1, 4, 10, and 40 ng/mL. Each analytical standard also contained a constant 209 ng/mL concentration of deuterated (d_8) dichlorobenzene as an internal standard.

Treated soil samples were extracted and analyzed by GC-MS. Briefly, 5 g samples of soil were dried with an approximately equal amount of Hydromatrix (Varian) and extracted on a Dionex Accelerated Solvent Extractor 200 at 1500 psi and 100 °C with a solvent 1:1 mixture of methylene chloride and acetone. The extracts were adjusted to a final volume of 20 mL of which a 1.0 mL aliquot was spiked with the equivalent of 209 ng/mL d_8 dichlorobenzene internal standard prior to analysis.

GC-MS analysis was performed in the selective ion monitoring mode (SIM) using an Agilent HP6890N GC and 5975 MSD with Gerstel MPS2 autosampler. A 30 m × 0.25 mm id Rtx-5Sil MS capillary column (Restek) with 0.25 μm film thickness preceded by an uncoated 10 m Integra guard column was used. Thirty microliter injections were made in the solvent vent mode into a Gerstel CIS 4 inlet. The inlet liner was packed with 10 mm of PDMS to trap the more volatile hydrocarbon components during the solvent vent process of the large-volume injections.

The AF consists of one- and two-ring aromatic compounds with various methyl or other alkyl substitutions. Using constituent analysis provided by ExxonMobil Chemical Co., structures were assigned to component groups (e.g., methyl and dimethyl (C5/C6) benzenes, dimethylindanes (C2), naphthalene, methyl (C1) naphthalenes, dimethyl and ethyl (C2) naphthalenes, C3 naphthalenes, C2−C4 biphenyl) comprising the AF. The concentration in the analytical standard for each group accounted for the fact that the AF comprised only 90% of the EC with the balance comprising other formulation components, including surfactants and HCB. Specific retention time and SIM windows were established for each of the individual groups plus the HCB conserved marker and deuterated dichlorobenzene internal standard. This technique permitted internal standard normalized calibration curves for each component group and subsequent quantification in soil extracts.

Data Analyses. The volatilization loss of each hydrocarbon component during spraying was estimated from the ratio of the measured concentrations of the AF components relative to HCB in the spray formulation and in the soil samples assuming that the relatively involatile and stable HCB (Table 1) is conserved. Direct measurement of the quantity of hydrocarbon sprayed and measured in soil samples is less accurate because of spray heterogeneity and possible spray drift. However, preliminary spray trials using the spray chamber and nozzle applied in this study indicated measured loss by spray drift was small (only 1−7%)[16] and would not likley affect the hydrocarbon/HCB ratio.

The predicted concentration of chemical in the soil at t = 0 and the fraction of the component volatilized X_i% can be estimated from eqs 2 and 3. The "predicted" concentrations assume the same ratio of hydrocarbon/HCB reaches the soil as is in the sprayed solution. The "observed" ratios are lower as a result of volatilization of the hydrocarbon components.

$$C_{\text{soil pred},i} = C_{\text{soil obs, HCB}} \times C_{\text{ECi}}/C_{\text{ECHCB}} \quad (2)$$

$$X_i = (C_{\text{soil pred},i} - C_{\text{soil obs},i})/C_{\text{soil pred},i} \times 100\% \quad (3)$$

DOI: 10.1021/acs.jafc.5b01076
J. Agric. Food Chem. 2015, 63, 6866−6875

Table 2. Average Measured Cumulative Mass Percent (X_i) ± the Standard Deviation of Each Hydrocarbon Component Lost during the Volatilization Study[a]

component	VP (Pa) at 20 °C	0 h, n = 26	1 h, n = 16	4 h, n = 16	12 h, n = 16	36 h, n = 16
C5/C6 benzenes	18.01	62.9 ± 16.4	79.3 ± 6.6	89.5 ± 5.6	92.7 ± 2.6	95.6 ± 2.6
C2 indanes	16.68	57.4 ± 13.2	74.3 ± 8.2	89 ± 5.3	92.8 ± 2.6	95.1 ± 1.9
naphthalene	6.76	46.1 ± 20.5	66.2 ± 9.1	83.9 ± 6.8	86.8 ± 3.9	89 ± 3.9
C1 naphthalenes	6.62	38.3 ± 14.1	57.1 ± 11	77.7 ± 9.7	83.7 ± 5.1	87.8 ± 4.3
C2 naphthalenes	2.19	16.2 ± 12.4	26.5 ± 15.5	47.1 ± 20.5	59.8 ± 11.8	70.4 ± 11.9
C3 naphthalenes	0.42	−2.5 ± 9.6	−0.8 ± 15.6	7.4 ± 21.4	20 ± 15.8	25.4 ± 20.1
C2−C4 biphenyls	0.34	−10.9 ± 8	−11.4 ± 13.5	−13.2 ± 17.2	−2.8 ± 15	−5.6 ± 18.7
AF (total)		28.3 ± 12	41.6 ± 11.7	57.6 ± 12.9	65.6 ± 7.8	70.4 ± 8.4

[a] n is the number of analytical measurements taken from the sample boxes and used in analysis; for calculations at time zero, all six boxes were used; for subsequent times, analyses for boxes A1, A2, B1, and B2 were used.

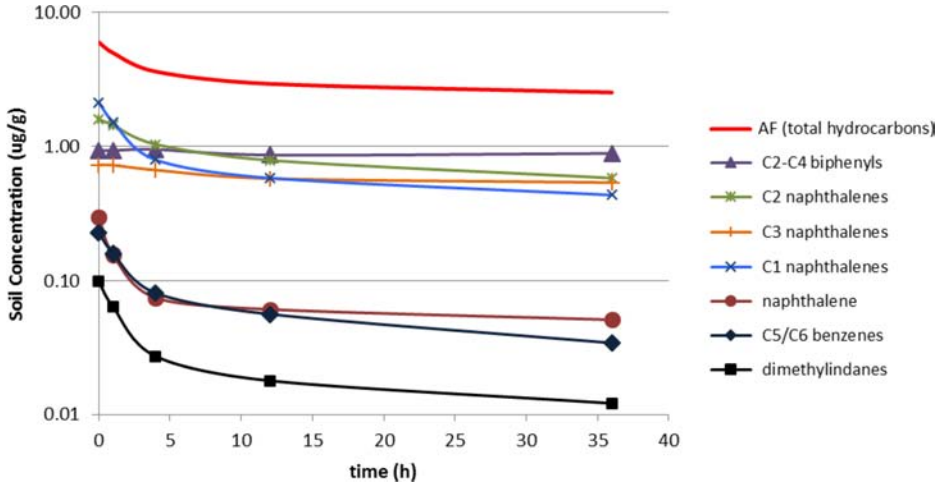

Figure 1. HCB-normalized soil concentrations of hydrocarbon components in the short-term volatilization study, showing the initial fast loss during the first 12 h followed by a slower rate of loss.

$C_{soil\ pred,i}$ is the predicted soil concentration (μg/g dry wt) of component i, where i can be the selected hydrocarbon component or the sum of all AF components, $C_{soil\ obs,HCB}$ is the measured HCB soil concentration (μg/g dry wt), and $C_{EC,i}/C_{EC,HCB}$ is the concentration ratio of component i to HCB in the EC formulation, which is known on the basis of analytical characterization of the EC formulation (unitless).

Biodegradation rates were estimated by measuring concentration ratios in samples from box C maintained in closed vials to prevent volatilization, again assuming HCB is conserved. The use of HCB as a nondegradable benchmark chemical that facilitates derivation of biodegradation half-lives has been reported in previous studies.[17] The rate constant k_{bio} was estimated by fitting the observed concentration ratios of component(s) to HCB over time using eq 4:

$$\ln[(C_{soil\ obs,i}/C_{soil\ obs,HCB}) = -k_{bio} \times t \quad (4)$$

Corresponding half-lives were calculated as $\tau_{1/2bio} = 0.693/k_{bio}$.

RESULTS

HCB Concentrations in Soil. The initial concentrations of HCB in soil were found to be close to the expected concentration in soil based on mass balance calculations assuming no losses. Furthermore, whereas absolute concentrations were variable over time, no significant decline in measured HCB soil concentrations was observed over the study period (Figure S1). These data support the assumption that HCB served as a conserved tracer in this study. On the basis of mass balance calculations described in Appendix S2, the quantity of AF sprayed is sufficient to saturate only a fraction of a millimeter depth of soil. Thus, subsaturation conditions must exist in the 2.5 cm deep soil samples, indicating that component concentrations are not homogeneously distributed in the soil compartment.

Volatilization Study. HCB-normalized concentrations for total AF hydrocarbons as well as component groups were used to calculate cumulative percent losses from 0 to 36 h for each spray nozzle using eq 3 (Table S1). Given limited data and lack of clear differences in calculated losses between the two nozzle types (Tables S2−S7), average values were determined as summarized in Table 2 and plotted in Figure 1. For t = 0, all six boxes were used; for subsequent times only the four boxes (A and B) comprising the volatilization study were used.

At time 0, immediately after spraying, a significant fraction of the AF is lost into the air by volatilization (Table 2). Most of this loss is attributable to the more volatile, higher vapor pressure components. Following this loss there appears to be a further initial fast drop in concentration within the first 12 h followed by a slower reduction to 36 h (Figure 1). This behavior suggests a change in loss mechanism over time and indicates that a simple first-order volatilization model cannot be used to adequately simulate this empirical loss profile. This observation casts doubt on the practice of assigning a single half-life to pesticides and carrier fluids that are applied to soil by spraying. Figure 1 also shows that the HCB-normalized concentrations of C3 naphthalenes and C2−C4 biphenyls

DOI: 10.1021/acs.jafc.5b01076
J. Agric. Food Chem. 2015, 63, 6866−6875

appear to increase at t = 1 h, then level out, showing very little loss over the entire 36 h of the volatilization study. The apparent increase in concentration results in negative calculated losses and is likely an artifact of the small changes observed (±1−14% as per Table 2) and the large variation within those observations in comparison to the lighter hydrocarbons.

Biodegradation Study. As the microbial community becomes acclimated to the presence of the AF hydrocarbons in soil, biodegradation processes are expected to contribute to observed losses. Figure 2 shows the decline in total AF

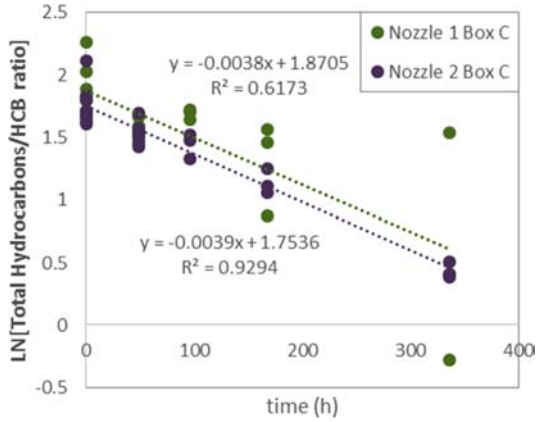

Figure 2. Regression of HCB-normalized soil concentrations of total hydrocarbons with time for the two spray nozzles in replicate boxes during biodegradation study.

hydrocarbons normalized to HCB over the 14 day (330 h) test period. The source of the increased variability in normalized values at the end of the test in nozzle 2 box C is not known. However, exclusion of these data in the analysis has little influence on the regression analysis results. The average half-life for total AF hydrocarbons derived from results with both spray nozzles was 180 h (7.5 days), corresponding to a mean biodegradation rate constant (k_{bio}) of 0.00385 h^{-1}.

For model calibration, the biodegradation rate of each component is required. Analogous plots and observed regressions for each of the AF components are included in Figure S2. Data for C5/C6 benzenes were highly variable, and estimated biodegradation rates are less certain. As the estimated biodegradation rates derived from tests with the two nozzles were similar across the different constituents as indicated by the individual regression equations included in Figure S2, values were averaged for input to model simulations as summarized in Table 3. Measured half-lives varied by a factor of 5 across the different components. The soil biodegradation half-lives

Table 3. Estimated Biodegradation Rates from Tests with Both Spray Nozzles and Corresponding Measured and Predicted Half-Lives Using HCBioWin

component	measured k_{bio} (h^{-1})	measured $t_{1/2}$ (h)	predicted $t_{1/2}$ (h)	ratio
C5/C6 benzenes	0.0020	355	128	2.77
C2 indanes	0.0040	173	48	3.62
naphthalene	0.0077	90	133	0.67
C1 naphthalenes	0.0085	82	213	0.38
C2 naphthalenes	0.0044	159	341	0.47
C3 naphthalenes	0.0014	495	233	2.12
C2−C4 biphenyls	0.0023	308	718	0.43

reported in this study are up to an order of magnitude lower (i.e., faster rates) than assumed in earlier modeling studies predicting the multimedia fate of hydrocarbons.[18,19] However, past laboratory studies have reported shorter, measured biodegradation half-lives for naphthalene and methyl naphthalene in agricultural soil of 1−2 days,[20,21] which is in agreement with values observed in this study. A modest agreement between empirical and predicted half-lives is observed. Differences of about a factor of 4 indicate HCBioWin predictions are within the correct order of magnitude but less precise in discriminating between hydrocarbon structures.

Model Formulation. It is hypothesized that volatilization of AF components during and after spraying is best treated in three distinct stages: stage 1, during the spray application (ending at t = 0 h); stage 2, volatilization of EC coating the surface of the soil (t = 0−12 h); and stage 3, combined transport into soil vapor from chemical sorbed to soil solids with subsequent volatilization and biodegradation (t = 12−36 h and beyond).

Stage 1: Volatilization during Spraying. During the spray event, a fraction of the AF evaporates or drifts to a downwind location. This fraction is likely dependent on the vapor pressure of the component and the dynamics of the spray process. The relationship of the percent loss of chemical with its vapor pressure can be determined and used to predict the percent mass lost to the air during such spray events.

We assume a spray droplet to contain V mol of hydrocarbon, each individual component having an initial mole fraction concentration x_0. As the droplet falls some of the hydrocarbon evaporates and the mole fraction x falls according to

$$dx/dt = -k_V \times A \times C_A \text{mol/h} \quad (5)$$

where k_V is a mass transfer coefficient, A is the surface area of the droplet, and C_A is the equilibrium concentration in the air intimately in contact with the drop. C_A can be estimated as xPM/RT, where P is the component's vapor pressure (Pa) and R, T, and M are the gas constant (8.314 m^3·Pa/mol·K), temperature (K), and molar mass (g/mol), respectively. This assumes that Raoult's law applies and that the partial pressure of each component is proportional to its mole fraction in a fluid of constant volume and composition; thus, the prediction may not be highly accurate, but the structure of the correlation equation is believed to be satisfactory. A rigorous equation would represent the batch or Rayleigh volatilization of a multicomponent mixture of changing volume and would be excessively complex for the present purposes.

Integration from $x = x_0$ at t = 0 gives

$$x = x_0 \cdot \exp[-Y \cdot P] \quad (6)$$

where

$$Y = k_V \cdot A \cdot M \cdot t/(V \cdot R \cdot T)$$

Because of the complexity of the mass transfer process, it is impossible to estimate the parameter Y a priori, but it can be estimated from empirical data quantifying losses during spraying. Furthermore, the process is more complex than is assumed here because V changes with time and there is a spectrum of droplet sizes. Thus, the parameter Y consolidates this information on droplet size, dynamics, and spray time into a single fitted parameter. It is preferable to express the percentage of the original mass remaining in the soil at each stage as M_{it}/M_{i0}.

DOI: 10.1021/acs.jafc.5b01076
J. Agric. Food Chem. 2015, 63, 6866−6875

The percentage loss (L_1) of a specific hydrocarbon during spraying is

$$L_1 = 100[1 - M_{i1}/M_{i0}] = 100[1 - \exp(-YP)] \quad (7)$$

Specifically M_{i0} is the original mass of component i. M_{i1} is the mass deposited by the spray; thus, the spray loss is $M_{i0} - M_{i1}$. Similarly M_{i2} is the mass after volatilization during stage 2, and M_{i3} is the mass after volatilization and biodegradation during stage 3. It follows that

$$M_{i1} = M_{i0} \exp(-YP) = (1 - L/100) \text{ or } YP = -\ln(M_{i1}/M_{i0}) \quad (8)$$

In this study, the HCB normalized data are used to reduce the noise associated with spatial variation in the spray pattern. The most reliable data are those of the five most volatile components for which Y is shown to average 0.066 Pa^{-1} (Figure 3). There is no significant difference in losses between

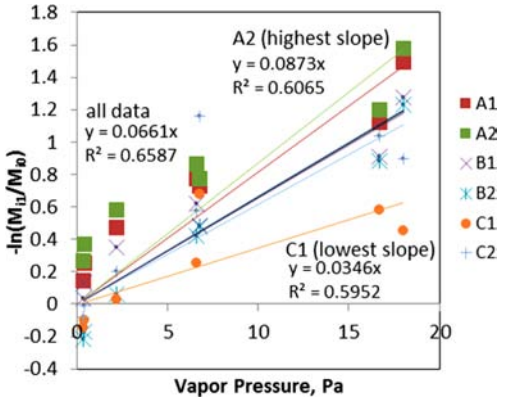

Figure 3. Regression of $-\ln(M_{i1}/M_{i0})$ against vapor pressure at 20 °C for the two spray nozzles in replicate boxes during spray loss for the five most volatile EC components. Differences are within the standard errors. The highest and lowest rates of loss were observed for A2 and C2.

the nozzles during stage 1. Box A2 shows the largest value of Y (0.0873 Pa^{-1}), and C1 shows the smallest value (0.0346 Pa^{-1}). The box C results from the degradation study for both nozzles are less consistent with boxes A and B from the volatilization study than they are within that study, but are included in the t = 0 spray loss analysis to increase the degrees of freedom in the analysis from $n - 1 = 15$ to $n - 1 = 25$.

Because AF is a mixture, it is impossible to assign a single vapor pressure; however, assuming Y to be 0.066 Pa^{-1}, a mean effective vapor pressure of the AF used in this study during spraying is 4.96 Pa. The model provides a simple method for predicting percent loss following spraying, as a function of vapor pressure during the stage 1 spray event.

Volatilization during Stage 2. When the sprayed fluid reaches the soil surface, it coats the soil particles and may not homogeneously distribute over the surface area depending on the nature of the spraying process. Volatilization then occurs directly from the deposited fluid to the atmosphere. In their studies of pesticide volatilization, Woodrow and Seiber[22] and Woodrow et al.[23] have suggested that this period may last up to 24 h, but it is observed here to be shorter, for example, 8–12 h for some of the more volatile hydrocarbons present in the EC applied. During stage 2 when free or pure phase hydrocarbon is present at the surface, the volatilization rate will likely be controlled by diffusive mass transport of the near-saturated vapor from the fluid surface and is best expressed as being first order in hydrocarbon concentration and will be proportional to the vapor pressure. It is assumed that there is no biodegradation during this stage.

During the 12 h following spraying the concentration of AF fell from ~6 to ~3.2 μg/g, that is, a loss of 47%, suggesting an overall half-life of approximately 13 h. Figure 4 shows that

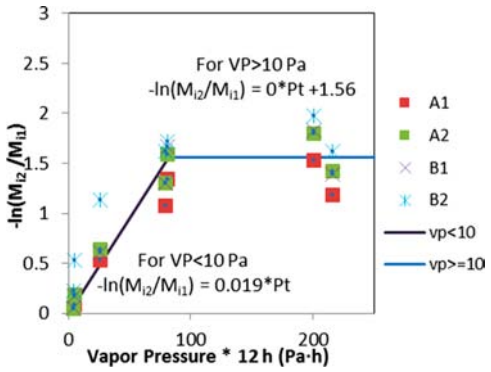

Figure 4. Regression of $-\ln(M_{i2}/M_{i1})$ against the product of vapor pressure at 20 °C and 12 h for the two nozzles tested in duplicate spray boxes during stage 2.

dependence of the total rate of loss is stronger for the less volatile components during stage 2; components with vapor pressures of >10 Pa are likely to volatilize quickly during the first stage, thus showing less dectectable loss by stage 2.

Assuming that volatilization rates are first order, the volatilization loss during stage 2 (L_2) for the less volatile components (VP < 10 Pa at 25 C) can be expressed as a function of vapor pressure P (Pa), time period of the stage, t (h), and a volatilization rate parameter that is common to all components, k_{v2} ($h^{-1}\cdot Pa^{-1}$), as follows:

$$L_2 = 100[1 - M_{i2}/M_{i1}] = 100[1 - \exp(-k_{v2} \times P \times t)] \quad (9)$$

$k_{v2} \times P$ is the rate constant (h^{-1}) for volatilization. This volatilization rate constant for stage 2 was deduced as for stage 1 as 0.019 and can be used to predict the volatilization of chemical as a function of vapor pressures up to 10 Pa (commonly used to define substances as VOCs) and for times up to 12 h postspray, assuming there is limited sorption of the AF to the soil. At a VP of 10 Pa the rate of change with vapor pressure levels off. Components with VP > 10 Pa at 25 °C exhibit a 36–70% loss during stage 1 and have much lower concentrations prior to stage 2. During stage 2 (between 0 and 12 h postspray), these more volatile components experience a 69–86% loss with an average of 79%, independent of vapor pressure (Figure 4). Because the y-intercept is constant at 1.56, the predicted percent stage 2 loss for hydrocarbons with VP > 10 Pa simplifies to $100[1 - \exp(-1.56)]$. The y-intercept of 1.56 can be prorated for a time to estimate losses between 0 and 12 h. For example, at 1 h, the y-intercept is $1.56 \times 1/12 = 0.13$, which corresponds to a stage 2 loss of $100[1 - \exp(-0.13)]$ or 12%.

Thus, 100 g of an AF component with a vapor pressure 10 Pa (6.8 Pa at 20 °C) will experience a 40 g loss during stage 1 and a further 47 g loss during stage 2, making a total cumulative loss of 87 g. One hundred grams of a hydrocarbon with a vapor pressure of 0.05 Pa (0.034 Pa at 20 °C) will experience a loss of

DOI: 10.1021/acs.jafc.5b01076
J. Agric. Food Chem. 2015, 63, 6866–6875

0.25 g during stage 1 and a further 0.77 g loss during stage 2, thus making the total cumulative loss about 1 g by 12 h.

Volatilization and Biodegradation in Stage 3. The volatilization study results provide an estimate of the rate of volatilization during stage 3 from approximately 12 to 36 h. During stage 3, the fluid increasingly sorbs into the soil particles and diffuses into the soil matrix, especially into the soil organic matter. Volatilization then occurs as a result of transport of soil vapor in equilibrium with the fluid present primarily in a sorbed state through the pore air space and a boundary layer to the atmosphere. The partial pressure or fugacity of the fluid component in stage 2 likely corresponds to that of the sprayed fluid, but in stage 3 it drops to a lower value corresponding to that of the sorbed state. In addition, as the hydrocarbon penetrates more deeply into the soil matrix the rate of mass transfer slows because of the increased path length for diffusion. The net result is relatively fast stage 2 volatilization, followed by a slower rate in stage 3 that is also assumed to be first-order in chemical concentration. During these periods the rates are controlled by the different air−fluid equilibrium relationships of the components and kinetic or mass transport terms.

Estimating Volatilization and Biodegradation in Stage 3. During stage 3, an attempt was made to regress the total loss (which includes both volatilization and biodegradation) against the product of vapor pressure and the 24 h duration (12−36 h) to obtain a total loss rate constant. However, no discernible pattern of loss during stage 3 was observed for spray nozzle 2. In fact, data show an increase in concentration for many components (evidenced by points below the *x*-axis), so results cannot be reliably modeled (Figure 5). In contrast, a decrease in concentration was observed for all components with nozzle 1. Further observed losses showed a positive relationship with vapor pressure. These findings suggest AF sprayed at a lower spray rate and smaller droplet size is better retained by the soil after 36 h; that is, there is less volatilization. To provide a conservative model parametrization of stage 3 losses an estimate of k_{3total} was derived using only nozzle 1 data. The biodegradation rate constant was then subtracted from this value to give the rate constant for volatilization (that depends on vapor pressure). The stage 3 volatilization rate parameter k_{v3} common to all components in the EC for spray nozzle 1 is then estimated to be 0.0023 Pa^{-1} h^{-1} (Figure 5). The rate constant for volatilization is then $k_{v3}P$ h^{-1} and the half-time is $0.693/(k_{v3}P)$ h. This is an order of magnitude slower rate than applies to stage 2. The total loss for stage 3, L_3, is then calculated as

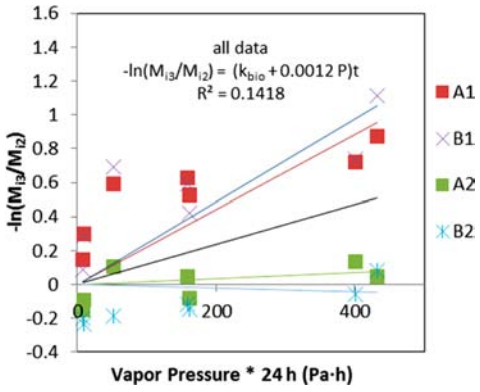

Figure 5. Regression of $-\ln(M_{i3}/M_{i2})$ against vapor pressure at 20 °C for both nozzles in replicate spray boxes during stage 3. A1, k_v = 0.0022 and R^2 = −0.239; B1, k_v = 0.0024 and R^2 = 0.2602; A2, k_v = 0.0002 and R^2 = 0.1696; B2, k_v = −0.0001 and R^2 = −1.481.

$$L_3 = 100[1 - M_{i3}/M_{i2}] = 100[1 - \exp(-(k_{bio} + k_{v3} \times P)t)] \quad (10)$$

where t is the length of time (24 h) between sampling at the beginning and end of stage 3 (12−36 h). It is likely that this rate constant for volatilization, k_{v3}, decreases with time as the AF components becomes more deeply sorbed into the soil matrix.

The relative contribution of volatilization to the total loss of the AF during stage 3 can be determined. The ratio of rates of biodegradation to volatilization is $k_{bio}/k_{v3}P$; thus, the total quantities of hydrocarbon components after 12 h, M_{i2}, that are volatilized and biodegraded can be estimated as respectively $M_{i2} \times (k_{v3}P/(k_{v3}P + k_{bio}))$ and $M_{i2} \times (k_{bio}/(k_{v3}P + k_{bio}))$. The losses of low-volatility chemicals are dominated by biodegradation, and the ratio $k_{bio}/k_{v3}P$ is >1. This ratio is quite small for the two most volatile components; thus, volatilization dominates the overall loss processes. Table 4 shows that biodegradation is more significant for the more methylated naphthalenes and the predominant loss process for the biphenyls. Clearly biodegradation occurs and it is likely responsible for long-term removal of the less volatile hydrocarbons, but it is inconsequential for the more volatile components because for these components the rate of biodegradation cannot effectively compete with volatilization. To a first approximation, the biodegradation half-lives of the components are similar in magnitude, but the volatilization rates differ by almost 2 orders of magnitude depending on component vapor pressure.

Table 4. Relative Importance of Biodegradation and Volatilization to Overall Loss of Components during Stage 3

component	biodegradation k_{bio} (h^{-1})	volatilization $k_{v3}P$ (h^{-1})	ratio $k_{bio}/k_{v3}P$
C5/C6 benzenes	0.0020	0.0418	0.05
C2 indanes	0.0040	0.0388	0.10
naphthalene	0.0077	0.0157	0.49
C1 naphthalenes	0.0085	0.0154	0.55
C2 naphthalenes	0.0044	0.0051	0.86
C3 naphthalenes	0.0014	0.0010	1.40
C2−C4 biphenyls	0.0023	0.0008	2.88

Combined Model of All Three Stages. The regressions described above have been combined in a spreadsheet model that estimates the fate of the hydrocarbon components and the AF for the sequence of stages 1, 2, and 3. It can be used, with appropriate caution, to provide a conservative estimate of the cumulative quantity of hydrocarbon lost and remaining for longer times on the order of weeks using eqs 7, 9, and 10 as shown in eqs 11 and 12.

For VP < 10 Pa at 25 °C

$$L_T = 100 \times [1 - \exp(-0.066 \times P) \times \exp(-0.019P \times 12) \times \exp(-(k_{bio} + 0.0023 \times P) \times t)] \quad (11)$$

For $P \geq 10$ Pa at 25 °C

$$L_T = 100 \times [1 - \exp(-0.066) \times \exp(-1.56) \times \exp(-(k_{bio} + 0.0023 \times P) \times t))] \quad (12)$$

DOI: 10.1021/acs.jafc.5b01076
J. Agric. Food Chem. 2015, 63, 6866−6875

Table 5. Estimated Cumulative Percent Dissipated (Volatilized and Degraded) Using the Three-Stage Model for t = 0−14 Days (336 h)[a]

	stage 1	stage 2			stage 3			
component	0 h	1 h	4 h	12 h	36 h	120 h	168 h	336 h
C5/C6 benzenes	69.61	73.33	81.96	93.64	97.78 (0.18)	99.94 (0.28)	99.99 (0.28)	100 (0.28)
naphthalene	66.82	70.88	80.30	93.05	97.51 (0.42)	99.93 (0.64)	99.99 (0.65)	100 (0.65)
C2 indanes	36.03	43.85	62.02	86.61	92.34 (1.87)	98.92 (4.02)	99.65 (4.25)	99.99 (4.37)
C1 naphthalenes	35.44	43.08	60.98	85.75	91.61 (1.78)	98.69 (3.93)	99.55 (4.2)	99.99 (4.33)
C2 naphthalenes	13.47	17.00	26.74	47.49	58.12 (4.9)	81.03 (15.45)	87.93 (18.63)	97.52 (23.05)
C3 naphthalenes	2.72	3.48	5.75	11.54	16.43 (2.9)	31.53 (11.84)	38.9 (16.21)	58.99 (28.1)
C2−C4 biphenyls	2.21	2.83	4.69	9.46	15.74 (4.64)	34.49 (**18.48**)	43.27 (**24.96**)	65.71 (**41.53**)
total AF	27.21	32.34	44.77	63.99	70.76 (2.75)	82.84 (8.38)	86.32 (10.24)	92.62 (13.94)

[a]Cumulative percent degraded in parentheses for stage 3. Bold values indicate cumulative percent degraded is greater than the cumulative percent volatilized.

where P is VP in Pa at 20 C, t is time in hours during stage 3 (i.e., time from spraying minus 12 h), and k_{bio} is the first-order substance-specific soil biodegrdation rate constant in h^{-1} (Table 3).

The model input is the AF composition treated as seven groups or "pseudo-components". Other hydrocarbon groups can be included as desired. For each group a temperature-dependent vapor pressure is assigned and used to estimate rate constants for all stages. The biodegradation half-life in Table 3 is assigned and used in stage 3. The model calculates masses remaining after stages 1 (spray loss), 2 (12 h), and 3 (36 h) as described earlier. It also estimates the masses remaining in soil for up to 2 weeks. The masses volatilized and biodegraded are also calculated. The altered AF compositions are calculated at all stages. The spreadsheet is "open"; thus, any desired times and hydrocarbon properties can be input and simulated and can be accessed in Appendix S3 as an MSExcel spreadsheet.

Table 5 gives the mass balance estimated by the model for the test conditions and comparison with the experimental data (given below in parentheses). For the AF, 27% is predicted to be lost in stage 1 (28%). After stage 2, a loss of 64% is predicted (66%). After 36 h, the predicted loss is 71% (70%). After 1 week, the predicted percentage lost is 86%, and at 2 weeks the loss is >92% as biodegradation removes the residual hydrocarbons. It is shown that for C2−4 biphenyls, biodegradation becomes the dominant loss process by 120 h (5 days).

Figure 6 shows the measured versus the modeled predicted soil concentrations for each of the AF components for 0−36 h.

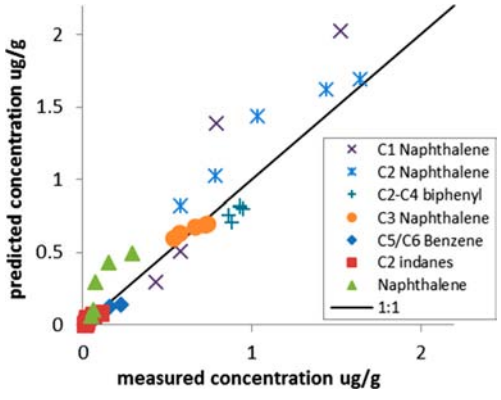

Figure 6. Comparison of measured and model-predicted soil concentrations for all sampling times during volatilization study (0, 1, 4, 12, 36 h). R^2 = 0.92.

The C2−C4 biphenyls and C3 naphthalenes experience the least loss (lowest spread) in the mid-concentration range. The lighter C1 and C2 naphthalenes experience relatively fast loss, mainly through volatilization. The model appears to overpredict soil concentrations in the beginning of stage 2 by approximately 25%, but then brings the predictions closer to measured values by stage 3 (Appendix S4). The R^2 obtained by regressing the predicted against the observed losses for all components and sampling times of 0.92 is regarded as an indication of satisfactory model performance.

DISCUSSION

On the basis of the model framework presented, it is instructive to consider how different conditions will influence the potential for AFs included in ECs to be emitted to air and potentially contribute to ozone formation.

Application Rate Per Unit Area. In this study the EC application rate was 4.7 kg/ha or 0.47 g/m^2. The model estimates the fraction of the mass of hydrocarbon sprayed that volatilizes, not the actual volatilization rate, although this can be calculated from the results. To a first approximation, an increase in application rate by, for example, a factor of 2 should not affect the volatilized fraction in stage 1, and it should have little effect on the fractions in stage 2, although the duration of the stage 2 period may be prolonged as more hydrocarbon must volatilize from a thicker coating on the soil before the onset of stage 3. The spray rates (L/Ha) were varied in this study, but the EC application rates (kg/Ha) were the same (the higher EC concentration solution was sprayed at a lower rate).

Variations in Organic Matter (OM) Content of the Soil. The OM content of the tested soil was 1.2%. No experimental determinations of the effect of OM content were performed; however, there is little doubt that increasing OM content may reduce volatilization rates. Doubling the OM content to 2.4% may not have an effect on stage 2, but the increased sorptive capacity of the soil is likely to reduce the volatilization rate in stage 3 and subsequently at longer times, probably by a factor of approximately 2. The model can thus directionally simulate the effect of soil OM content.

Other Hydrocarbon Components. The volatilization characteristics of other hydrocarbon components or groups can be estimated by input of the appropriate vapor pressure and biodegradation half-lives obtained experimentally or from estimation methods.

Relative Losses of Hydrocarbons. The model tends to overpredict the volatilization of the more volatile hydrocarbons. This can be accounted for in part by reducing the volatilization

DOI: 10.1021/acs.jafc.5b01076
J. Agric. Food Chem. 2015, 63, 6866−6875

Table 6. Estimated AMAF (Cumulative Percent Volatilized) for Hypothetical Chemicals Using the Three-Stage Model for t = 0−14 Days (336 h)

	stage 1	stage2			stage 3			
chemical VP (Pa)	0 h	1 h	4 h	12 h	36 h	120 h	168 h	336 h
30	74.31	77.45	84.74	94.62	98.05	99.31	99.32	99.32
20	59.58	64.52	76.00	91.54	95.75	98.38	98.47	98.49
10	36.43	44.19	62.25	86.69	90.60	95.18	95.70	95.96
5	20.27	25.30	38.56	63.52	69.38	79.11	81.11	82.86
1	4.43	5.67	9.28	18.26	21.09	27.45	29.49	32.56
0.5	2.24	2.87	4.75	9.59	11.17	14.86	16.11	18.14
0.1	0.45	0.58	0.97	2.00	2.34	3.17	3.47	3.98
0.05	0.23	0.29	0.49	1.00	1.18	1.60	1.75	2.01
0.01	0.05	0.06	0.10	0.20	0.24	0.32	0.35	0.41

rate constant as was done between stages 2 and 3. It appears that the most volatile hydrocarbons fail to achieve the expected losses at longer exposures. It is believed that this is due to some of the volatile hydrocarbons being "trapped" in the bulk of the EC mixture and being less available for volatilization. Essentially there appears to be a diffusive resistance to mass transfer when concentrations are low. The model inherently assumes well-mixed conditions in the EC mixture. In reality, there is likely extensive volatilization of water and AF components, thereby increasing the density and viscosity of the mixture. There may be some phase separation of the solid hydrocarbons as the "solvent effects" of the more volatile components are dissipated. To accommodate such effects would greatly increase the complexity of the model; thus, the simple and conservative assumptions used here are regarded as justified.

Implications for Estimating the AMAF. Table 5 shows that for hydrocarbons with vapor pressures of 0.337−18 Pa at 20 °C, 38.9−99.99% of the applied substance is predicted to be volatilized by 7 days postapplication. Several hypothetical components with 0.01−30 Pa vapor pressures (at 25 °C, adjusted to 20 °C for modeling predicted losses) and a degradation half-life of 100 h were also simulated to estimate the cumulative percent volatilized over time (Table 6). This model provides a practical method to quantify the application method adjustment factor (AMAF, kg VOC volatilized/kg VOC in product) term in the calculation of the ozone formation potential (OFP) included in eq 1.

This work shows that the regulatory assumption that AMAF is 1 for all hydrocarbons with a vapor pressure >0.05 Pa is overly conservative as only about 2% is predicted to have volatilized by 2 weeks postspray for a hypothetical chemical of a vapor pressure of 0.05 Pa and a degradation half-life of 100 h. Factors such as the degradation rate constant and the time post application as well as the vapor pressure are influential in determining the magnitude of the AMAF. For example, 7 days after application, only 18% of C2−4 biphenyl (VP = 0.34 Pa) losses are attributed to volatilization and 25% to degradation; after 14 days, only 24% is lost to volatilization, and the majority of the loss, 41%, to biodegradation. The model was used for determining cutoff values reflecting 67% losses by volatilization after 12, 24, 96, and 168 h, based on a typical biodegradation half-life of 100 h. The resulting cutoff values range between 2 and 3.5 Pa, nearly 2 orders of magnitude larger than the proposed cutoff (Appendix S5).

Summary and Future Work. After spraying, three stages of AF loss in an EC formulation can be characterized: initial loss during the spray event, which is related to the component vapor pressure; then loss from the pure phase of fluid coating the soil directly after the spray event; and, third, the volatilization and biodegradation of the remaining fluid that has been absorbed by the soil beyond 12 h postapplication. The mechanisms of volatilization and the corresponding models developed here give an adequate quantitative description of the fate processes of the seven components comprising the AF investigated during the complex series of events that occur following spraying. The model is simple, robust, and consistent with the experimental results and is intuitively in accord with expectations based on conventional descriptions of the salient equilibrium and kinetic processes; uncertainty analysis could further refine and add confidence to the framework. This model has practical utility in refining current default regulatory assumptions for estimating the ozone formation potential of ECs used in agricultural sprays.

A logical focus of future modeling work would be incorporation of photodegradation process at the soil surface and one or more vegetation compartments to account for substance bioaccumulation and degradation by plants as these processes are known to influence fate behavior of substances released to soil.[24−27] The present study also provides an initial model framework that can potentially be extended to other applications such as evaluating substances used in dust suppression control or petroleum substance spills to soils.

■ ASSOCIATED CONTENT

Supporting Information

Supplementary appendices, tables, and figures. The Supporting Information is available free of charge on the ACS Publications website at DOI: 10.1021/acs.jafc.5b01076.

■ AUTHOR INFORMATION

Corresponding Author

*(T.P.) E-mail: thomas.f.parkerton@exxonmobil.com.

Notes

The authors declare no competing financial interest.

■ ACKNOWLEDGMENTS

The authors would like to thank Pierre-Yves Guyomar, ExxonMobil Chemical Europe, for a critical review and helpful comments for improving an early draft of this paper.

■ REFERENCES

(1) Knowles, D. *Chemistry and Technology of Agricultural Formulations*; Kluwer Academic: London, UK, 1998.

(2) Krenek, M.; Rohde, W. Pesticide formulations and application systems. In *An Overview − Solvents for Agricultural Chemicals*; Hovde,

DOI: 10.1021/acs.jafc.5b01076
J. Agric. Food Chem. 2015, 63, 6866−6875

D., Beestman, G., Eds.; American Society for Testing and Materials: Philadelphia, PA, USA, 1989; Vol. 8, pp 113−127.
(3) Kumar, A.; Howard, C.; Derrick, D.; Malkina, I.; Mitloehner, F.; Kleeman, M.; Alaimo, C.; Flocchini, R.; Green, P. Determination of volatile organic compound emissions and ozone formation from spraying solvent-based pesticides. *J. Environ. Qual.* . **2001**, *40*, 1423−1431.
(4) U.S. EPA. Nonattainment Designations for the 2008 Ozone Standards − Counties by State. U.S. Evironmental Protection Agency − Area Designations for 2008 Ground-Level Ozone Standards, 2012.
(5) U.S. EPA. Regulatory Actions. U.S. Environmental Protection Agency − Ground-Level Ozone, 2011.
(6) CARB. Area Designations for the Federal 8-h Ozone Standard, California Environmental Protection Agency Air Resources Board, 2013.
(7) CPDR. Pilot Project Proposal: Estimating Pesticide Product Volatile Organic Compound Emission Speciation and Reactivity Based on Product, California Department of Pesticide Regulations, 2011.
(8) CPDR. Estimating the Pesticide Product volatile Organic Compounds Ozone Reactivity, Part 2 Reactivity Based Emissions, California Department of Pesticide Regulations, 2011.
(9) CEC. Proposal for a Council Directive on limitation of emissions of volatile organic compounds due to the use of organic solvents in certain industrial activities, article 2, 96/0276 (SYN); Commission of the European Communities, 1996.
(10) Heinrich-Ramm, R.; Jakubowski, M.; Heinzow, B.; Christensen, J.; Olsen, E.; Hertel, O. Biological monitoring for exposure to volatile organic compounds (VOCs). *Pure Appl. Chem.* **2000**, *72*, 385−436.
(11) Zeinali, M.; McConnell, L. L.; Hapeman, C. J.; Nguyen, A.; Schmidt, W. F.; Howard, C. J. Volatile organic compounds in pesticide formulations: methods to estimate ozone formation potential. *Atmos. Environ.* **2011**, *45*, 2404−2412.
(12) Mackay, D.; van Wesenbeeck, I. Correlation of chemical evaporation rate with vapor pressure. *Environ. Sci. Technol.* **2014**, *48*, 10259−10263.
(13) Foster, K.; Sharpe, S.; Webster, E.; Mackay, D.; Maddalena, R. The role of multimedia mass balance models for assessing the effects of volatile organic compound emissions on urban air quality. *Atmos. Environ.* **2006**, *40*, 2986−2994.
(14) U.S. EPA. EPiSuite MPBPWin v1.43, 1.43, 2000.
(15) U.S. EPA. EpiSuite BioHCWin v 1.01a, 2008.
(16) Fritz, B. K.; Hoffmann, W. C.; Rohde, A.; Warren, C.; Faulkner, W. B. Simulating and characterizing agricultural ground applications for soil VOC deposition studies. *J. ASTM Int.* **2010**, 7.10277610.1520/JAI102776
(17) Prince, R.; Haitmanek, C.; Lee, C. The primary aerobic biodegradation of biodiesel B20. *Chemosphere* **2008**, *71*, 1446−1451.
(18) Foster, K. L.; Mackay, D.; Parkerton, T. F.; Webster, E.; Milford, L. Five-Stage Environmental exposure assessment strategy for mixtures: gasoline as a case study. *Environ. Sci. Technol.* **2005**, *39*, 2711−2718.
(19) Coulon, F.; Whelan, M.; Patton, G.; Semple, K.; Villa, R.; Pollard, S. Multimedia fate of petroleum hydrocarbons in the soil: oil matrix of constructed biopiles. *Chemosphere* **2010**, *81*, 1454−1462.
(20) Park, K. S.; Sims, R. C.; DuPont, R.; Doucette, W. J.; Matthews, J. E. Fate of PAH compounds in two soil types: Influence of volatilization, abiotic loss and biological activity. *Environ. Toxicol. Chem.* **1990**, *9*, 187−195.
(21) Wang, C.; Wang, F.; Wang, T.; Tao; Bian, Y.; Jiang, X. PAHs biodegradation potential of indigenous consortia from agricultural soil and contaminated soil in two-liquid-phase bioreactor (TLPB). *J. Hazard. Mater.* **2010**, *176*, 41−47.
(22) Woodrow, J. E.; Seiber, J. N.; Baker, L. W. Correlation techniques for estimating pesticide volatilization flux and downwind concentrations. *Environ. Sci. Technol.* **1997**, *31*, 523−529.
(23) Woodrow, J. E.; Seiber, J. N.; Dary, C. Predicting pesticide emissions and downwind concentrations using correlations with estimated vapor pressures. *J. Agric. Food Chem.* **2001**, *49*, 3841−3846.
(24) Wang, D.; Chen, J.; Xu, Z.; Qiao, X.; Huang, L. Disappearance of polycyclic aromatic hydrocarbons sorbed on surfaces of pine [*Pinua thunbergii*] needles under irradiation of sunlight: volatilization and photolysis. *Atmos. Environ.* **2005**, *39*, 4583−4591.
(25) Steyaert, N. L.; Hauck, M.; Van Hulle, S.; Hendricks, A. Modelling bioaccumulation of semi-volatile organic compounds (SOCs) from air in plants based on allometric principles. *Chemosphere* **2009**, *77*, 727−732.
(26) Cropp, R. A.; Hawker, D. W.; Boonsaner, M. Predicting the accumulation of organic contaminants from soil by plants. *Bull. Environ. Contam. Toxicol.* **2010**, *85*, 525−529.
(27) Xu, C.; Dong, D.; Meng, X.; Su, X.; Zheng, X.; Li, Y. Photolysis of polycyclic aromatic hydrocarbons on soil surfaces under UV irradiation. *J. Environ. Sci.* **2013**, *25*, 569−575.

DOI: 10.1021/acs.jafc.5b01076
J. Agric. Food Chem. 2015, 63, 6866−6875

the soil bacterial communities. However, these values are very high compared to the treatments used in the present study. There exists a need to explore engineered nanoparticle effects on the rhizophere microbiome[19] and their possible role in nutrient management in agricultural soils.

In plant nutrition, NPs are not often considered as a factor affecting phytoavailable P. However, a recent study reported increased accumulation of P (3686 mg kg^{-1}) in roots of wheat at 250 mg kg^{-1} of CeO_2 NP treatment compared to the control (2417 mg kg^{-1}), while CeO_2 NPs at 500 mg kg^{-1} improved plant growth, shoot biomass, and grain yield by 9.0, 12.7, and 36.6%, respectively.[20] In another work, Al_2O_3 NP-bound P was reported to enhance P uptake by plants in aqueous solutions at a very low concentration of even 10 mg L^{-1}.[21] Pradhan et al.[22] studied the effects of Mn NPs on nitrogen uptake, assimilation, and metabolism in mung bean plants. The majority of these studies are short period assays up to 2 weeks and, in rare cases, up to months. In this context, the objectives of the present study were (1) effects of TiO_2 and Fe_3O_4 NP application on phytoavailability of P to *L. sativa* and plant growth, (2) rhizosphere changes in response to NP applications in soil, and (3) localization of metallic NPs in plants. To the best of our knowledge, this is the first report on P availability trends over an extended contact period (90 days) with different kinds of NPs under soil conditions.

MATERIALS AND METHODS

Synthesis of TiO_2 NPs by the Sol−Gel Method. TiO_2 NPs were synthesized using a slightly modified sol−gel method that was developed earlier for synthesis of molecularly imprinted titania.[23] The titania precursor was added in 0.5 M acidic solution. As $TiCl_4$ was added, the color of the solution turned yellowish. When the solution became transparent, it was neutralized with 0.5 M NH_4OH until pH became 7.0, followed by stirring until the gel-like network formed. The gel was allowed to settle. The supernatant was discarded, and the rest of the sol was dried in a vacuum oven at 105 °C. Dry gel was ground and calcined at 400 °C for 6 h.

Synthesis of Fe_3O_4 NPs by the Co-precipitation Method. For preparation of Fe_3O_4 NPs, $FeCl_2$ (0.1 M) was mixed with $FeCl_3$ (0.2 M) and NaOH (0.1 M) was added to the mixture. The solution turned black and was placed upon heating until a slurry was left. It was washed several times with distilled water until pH 7.0 was achieved. The slurry was dried in an oven at 80 °C. The dried magnetite clusters were ground to obtain NPs.[24]

Characterization of Synthesized NPs. The phase composition, crystal structure, and crystallite size measurements for the TiO_2 and Fe_3O_4 NPs were performed by X-ray diffraction (XRD, Theta/Theta STOE, Germany) at 40 keV and 40 mA. Processing of XRD results was performed with the X'Pert High Score software package (PANalytical B.V., Almelo, Netherland). The surface morphology of TiO_2 and Fe_3O_4 NPs was analyzed using scanning electron microscopy (SEM, Jeol, JSM 6490 A, Japan) equipped with energy-dispersive X-ray spectroscopy (EDX, Jeol, JED 2300) and an ion-sputtering device (Jeol, JFC 1500). Suspensions of TiO_2 and Fe_3O_4 NPs in ethanol were made-up on quartz slides. The sputtering technique was used to evaporate the volatile substances or moisture and stabilize the NPs on the substrate to avoid interference or prevent contamination. The technique can be used for several conductive materials.[25] Then, the slides were observed under SEM.

Soil Preparation. For the present study, sandy loam soil was selected. The air-dried soil was ground by ball mill and passed through a mechanical sieve (<2 mm) shaker to remove roots, shoots, and other materials. For the plant culture experiments, 300 g of soil was amended individually with NP suspensions to achieve 0, 50, 100, 150, 200, and 250 mg kg^{-1} levels, and it was filled in plastic pots (10 cm diameter and 9 cm height). Each treatment had four replicates, and the experiment was repeated twice.

Plant Culture and Growth Response. *L. sativa* seeds were sown in control soil to prepare the nursery. The 2 week old seedlings were uprooted and washed carefully with distilled water. These seedlings were then transferred to pots (one plant per pot) containing soil amended with TiO_2 and Fe_3O_4 NPs at 0, 50, 100, 150, 200, and 250 mg kg^{-1}. There were four replicates for each concentration level. Plants were watered as per requirement. At harvesting, roots and shoots of the plants were collected separately and their lengths were measured. The fresh weight of *L. sativa* roots and shoots was recorded. The plant material was placed in an oven at 70 °C for 48 h and then weighed to find out the dry weight. The moisture content was calculated using fresh and dry weight. The dried plant material was ground with a mortar and pestle separately and stored in airtight sampling bags for further analysis.

Soil and Plant Analysis. At harvesting, the plants were uprooted from the pots carefully and shaken gently to remove the loosely bound soil from the roots. The soil adhered to the roots, and the rhizosphere soil in this study was separated from the roots with gentle washing in 100 mL of distilled water taken in a glass beaker. The pH of rhizosphere soil solutions was immediately determined, and the solutions were filtered. The filtrate was placed at 4 °C for Raman spectroscopy analysis of plant primary metabolites in it. The filter papers containing humid rhizosphere soil were air-dried, and the soil collected was used for the phytoavailable P concentration using Olsen's method.[26]

For plant analysis, 100 mg of plant samples was taken and 5 mL of acid mixture (2:1 $HNO_3/HClO_4$) was added. The mixture was heated on a hot plate to obtain clear aliquots. These aliquots were filtered with Whatmann filter paper no. 42 and subjected to P analysis using the vanadomolybdophosphoric acid colorimetric method.[27] The P uptake per plant was calculated using the following equation:

$$\text{P uptake per plant (mg)} = [(\text{shoot dry weight} \times \text{shoot [P]}) + (\text{root dry weight} \times \text{root [P]})] \quad (1)$$

Microscopic and Spectroscopic Analyses of Soil and Plant Material. To find out the possible entry of NPs in *L. sativa* plants, shoots and roots were cut and washed with distilled water to remove electrolytes and dirt from the surfaces. The plant material was oven-dried at 70 °C for 48 h. The sputtering technique was used to coat fine pieces of shoots and roots to avoid the charge effect during SEM analysis. The plant material was then observed under SEM coupled with EDX to illustrate the elemental composition of the sample. Raman spectra of rhizosphere soil extracts were obtained from Micro Ramboss using a diode laser (532 nm λ) as an excitation source to determine the presence/absence of plant primary metabolites. Fourier transform infrared spectroscopy (FTIR) was performed with Nicolet 6700 (Thermo Corporation) to identify functional groups in the control and treated samples. The powdered plant samples of *L. sativa* shoots were scanned at room temperature (25 ± 2 °C) within a spectral range of 800−3600 cm^{-1}.

Statistical Data Analysis. The statistical significance of results was checked using Student's *t* test and standard deviation (SD). Statistically significant differences were reported when the probability of the result assuming the null hypothesis was $p \leq 0.05$.

RESULTS AND DISCUSSION

Synthesized NP Characteristics. The XRD analysis of TiO_2 NPs indicated the crystalline form and peak with the anatase phase at the (101) plane. The average crystallite size calculated by the Scherer formula was 15 nm with a tetragonal crystal system. While the XRD pattern of Fe_3O_4 showed a peak at the (311) plane with a crystallite size of 14.9 nm having a cubic crystal structure. The surface morphology of TiO_2 and Fe_3O_4 NPs analyzed through SEM confirmed the size of these NPs in the 12−20 nm range (Figure S1).

DOI: 10.1021/acs.jafc.5b01611
J. Agric. Food Chem. 2015, 63, 6876−6882

Growth Response of *L. sativa*. Results regarding plant length and biomass of *L. sativa* grown on soil amended with TiO_2 and Fe_3O_4 NPs have been presented in Table 1. Shoot length showed maximum values of 14.2 and 13.0 cm when treated with Fe_3O_4 (200 mg kg^{-1}) and TiO_2 (250 mg kg^{-1}) NPs, respectively, while the minimum value of 9.5 cm was observed in the control. This resulted in a 49 and 36% increase in shoot growth by Fe_3O_4 and TiO_2 NPs, respectively, relative to the control. In the case of root length, maximum values of 21.4 and 18.1 cm were observed in TiO_2 and Fe_3O_4 NP-treated groups, respectively, at 250 mg kg^{-1}, whereas the minimum value of 15.9 cm was observed in the control. Similarly, the shoot and root dry weight increased 1.2- and 1.6-fold at 250 mg kg^{-1} in TiO_2 and Fe_3O_4 NP-treated groups compared to the untreated group. As shown in Table 1, the values of plant biomass for TiO_2 and Fe_3O_4 NPs were 2450 and 2437 mg, respectively, and 1728 mg in the control. Therefore, the total biomass of *L. sativa* was significantly ($p \leq 0.05$) increased up to 1.4-fold of the control at the highest concentration (250 mg kg^{-1}) of both NPs applied. Application of NPs can affect various physiological processes within a plant. In our case, nutrient uptake, particularly that of P_i, was probably the main driver for improved plant growth and biomass of *L. sativa*, as supported by the results presented later. In the literature, TiO_2 NPs (with the anatase phase) applied to spinach improved the chlorophyll content (37.48%), fresh and dry biomass (91 and 99%), and total nitrogen concentration (23.35%) compared to the control.[28] In another study, 2.5% TiO_2 NPs were reported to increase the fresh and dry weight of spinach by 63 and 76%, respectively, compared to the control.[6] Our results (Table 1) are well in accordance with the reports in the literature.

Table 1. Influence of TiO_2 and Fe_3O_4 NP Concentrations on Plant Length and Biomass of *L. sativa*[a]

concentration (mg kg^{-1})	shoot length (cm)	root length (cm)	shoot dry weight (mg)	root dry weight (mg)	total biomass (mg)
control	9.5	15.9	969.7	758.3	1728.0
			TiO_2		
50	10.0[b]	17.3	1015.3[b]	964.3	1979.7
100	11.5	17.6	1037.7	1087.0	2124.7
150	12.0	19.6	1123.3	1223.0	2329.0
200	12.6	19.2	1106.0	1213.0	2319.0
250	13.0	21.4	1210.7	1239.7	2450.3
			Fe_3O_4		
50	10.6[b]	17.3	1026.7[b]	994.7	2021.3
100	10.9[b]	18.0	1073.3	980.3	2053.7
150	13.5	17.8	1065.7	1124.0	2189.7
200	14.2	17.8	1190.3	1196.3	2386.7
250	14.2	18.1	1225.7	1211.3	2437.0

[a]Values represent means of four replicates. [b]Means, in each column, followed by similar values are not significantly different at the 0.05% probability level (*t* test).

Root and Shoot P Concentrations and Moisture Content. Results in Figure 1 are the effects of TiO_2 and Fe_3O_4 NPs on P concentrations in plant parts (shoot and root) of *L. sativa*. Higher P concentrations of 2272 and 2648 mg kg^{-1} were found in *L. sativa* shoots treated with 250 mg kg^{-1} TiO_2 and Fe_3O_4 NPs, respectively, compared to the control, i.e., 1371 mg kg^{-1}. In the case of all TiO_2 NP treatments, i.e., 50, 100, 150, 200, and 250 mg kg^{-1}, a relative increase of 14, 25, 74, 42, and 66% was observed, respectively, while 26, 51, 89, 77, and 93% improvement was observed by Fe_3O_4 treatments, respectively, compared to the control. These differences are statistically significant ($p \leq 0.05$). In roots, the values of 2904 and 2439 mg kg^{-1} of P concentrations were observed in TiO_2 and Fe_3O_4 NP-treated groups, respectively, which were 2−2.5 times higher than the control (1162 mg kg^{-1}). Differential trends were observed in the case of both NP-treated groups, such as the P concentrations being 0.9 times higher in roots compared to shoots in response to TiO_2 treatment. In the case of Fe_3O_4 NPs, P concentrations in shoots were 0.1 times higher compared to those in roots. Although the P concentration increased at all of the tested levels of both NP-treated groups, the minimum feasible concentration is considered to be 150 mg kg^{-1} for TiO_2 NPs. In the case of Fe_3O_4 NPs, apparently, there is no difference between 150 and 250 mg kg^{-1}, but with respect to NP application, the preferred value will be 150 mg kg^{-1}. Besides these NP concentration levels, the P uptake also depends upon a number of factors, such as the soil type, nutrient availability in soil, properties of NPs, and plant species. In the literature, studies have suggested that TiO_2 NPs may have some similar effects of plant hormones, such as cytokinins,[29] that affect the P uptake. Our results are in conformity with those reported by Servin et al.,[13] who observed an increased concentration of 34% P and 35% K in cucumber fruit of plants treated with 500 mg kg^{-1} of TiO_2 NPs. Lopez-Moreno et al.[30] reported an increase of 62% fruit yield from *Capsicum annuum* L. as a result of TiO_2 application when grown under the lowest P feed.

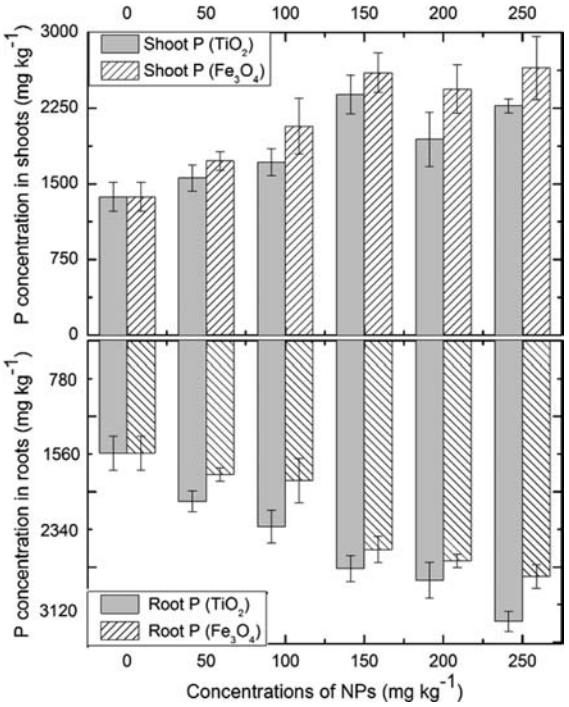

Figure 1. Concentrations of P in shoots and roots of *L. sativa* cultivated for 90 days on soil amended with TiO_2 and Fe_3O_4 NPs up to 250 mg kg^{-1}. Error bars stand for SD.

Figure 2 shows results regarding the NP effects to mobilize soil P for plant uptake. The minimum value of 14.2 mg kg^{-1} of P was observed in soil without NP treatment, whereas values of 31.7 and 24.5 mg kg^{-1} were observed in the rhizosphere soil amended with 250 mg kg^{-1} of TiO_2 and Fe_3O_4 NPs. Therefore, this significant ($p \leq 0.05$) increase in phytoavailable P in soil

DOI: 10.1021/acs.jafc.5b01611
J. Agric. Food Chem. 2015, 63, 6876−6882

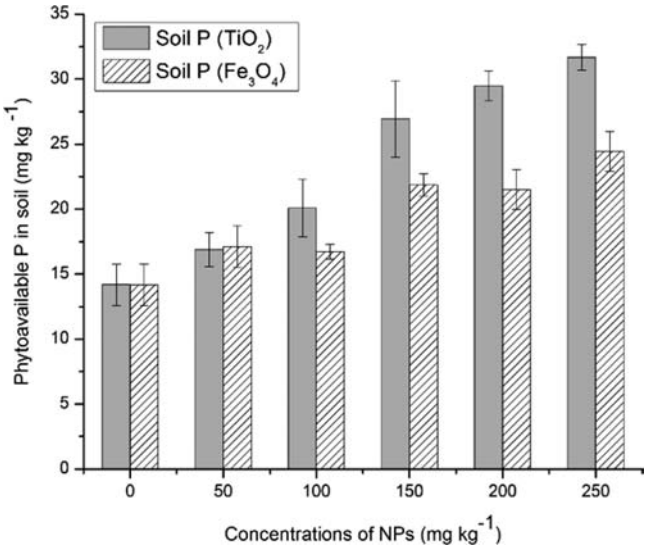

Figure 2. Concentrations of phytoavailable P in soil treated with 0–250 mg of TiO_2 and Fe_3O_4 NPs kg^{-1} of soil. Data are means of four replicates ± SD.

also enhanced the shoot and root P concentrations at different NP treatment levels, as discussed earlier. This effect may occur as a result of the increased absorption of P (converted from fixed to orthophosphate P_i form) because of applied NPs and especially their small size that favored the diffusion into the root structure and induced its positive functions during the phase of plant development.

Figure 3 shows that moisture contents increased up to 3.5 and 3.8% at 150 mg kg^{-1} of TiO_2 and Fe_3O_4 NP treatments,

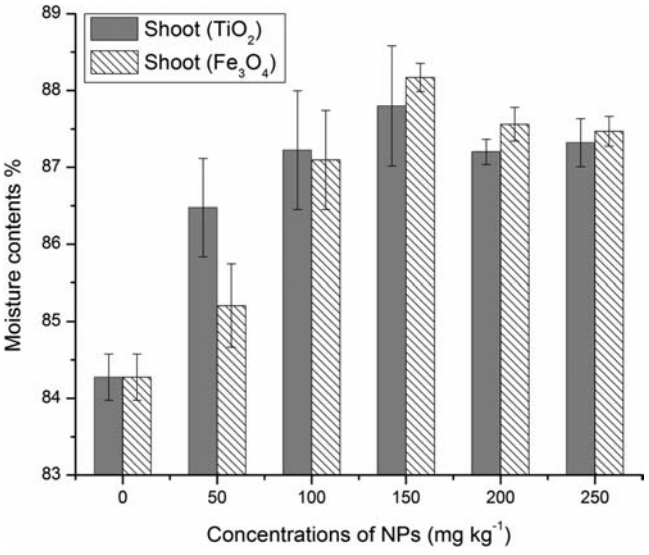

Figure 3. Effect of TiO_2 and Fe_3O_4 NPs on the moisture contents (%) of *L. sativa* shoots.

respectively, compared to the control. Because of the size of these particles (12–20 nm), they could easily be absorbed by the plant roots and translocated to the aerial parts of the plant. With these NPs having photocatalyzed attributes, they could trigger photosynthetic activity and ultimately increase the water uptake from soil. In another study, because of nano-anatase TiO_2 treatment, the photosynthetic rate in spinach was reported to improve by 31.87% compared to the control.[31] Similarly, the translocation of these NPs to shoots could result in improved chlorophyll formation[13] and increased root exudation (plant metabolites). Therefore, we hypothesized that this increased water movement and photosynthetic activity also favored the increased nutrient (P) uptake in the present study. Consequently, an increased moisture content percentage in *L. sativa* shoots was observed, which was also verified by the FTIR spectra (Figure 5b).

Rhizosphere Changes and P Uptake. Phosphorus uptake per plant and changes in rhizosphere soil pH plotted in response to NP treatments has been presented in Figure 4.

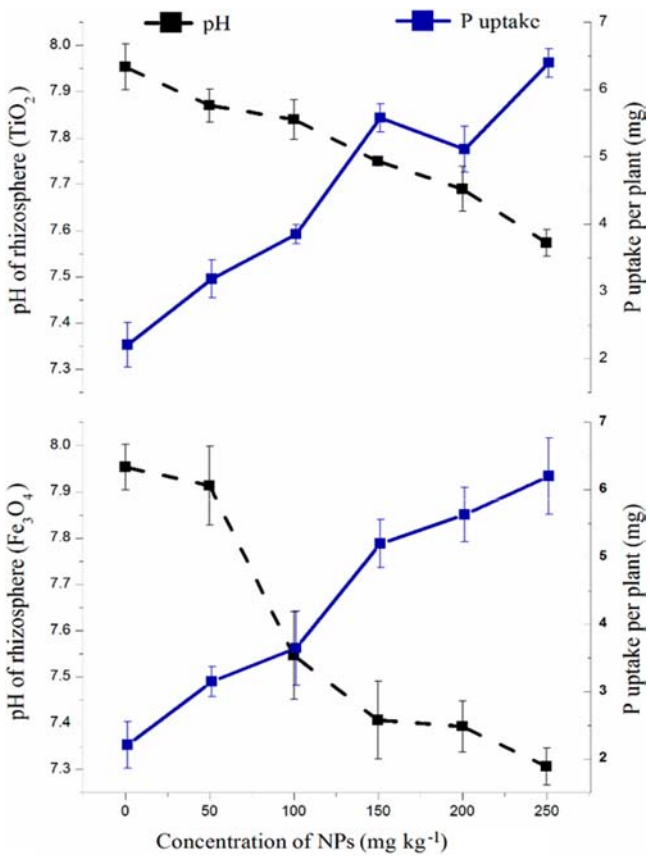

Figure 4. P uptake per plant and changes in rhizosphere pH in soil amended with 0–250 mg kg^{-1} of TiO_2 and Fe_3O_4 NPs for 90 days. Each data point represents the mean of four replicates ± SD. Error bars show SD.

Total P uptake was calculated from the P concentration and dry biomass using eq 1 mentioned earlier. The pH changes observed in the rhizosphere soil were dependent upon NP treatments and modified the P uptake in plants. The negative values of pH changes indicate the acidification of rhizosphere soil. The pH of rhizosphere soil without NP treatments was 7.95. A change of up to −0.38 pH units was observed in response to TiO_2 NPs, with a significant ($p \leq 0.05$) increase of 2.9-fold in P uptake. In a similar manner, Fe_3O_4 NP treatments also changed the pH up to −0.64 units, with a significant ($p \leq 0.05$) increase of 2.8-fold in P uptake per plant. In another study, Al_2O_3 NPs bound P at a very low concentration of 10 mg L^{-1} increased plant P uptake in hydroponics.[21] The P availability is mainly dependent upon (a) pH, (b) concentrations of metallic cations, such as Ca^{2+}, Fe^{3+}, and Al^{3+}, (c) release of competing inorganic (bicarbonate and sulfate) and

DOI: 10.1021/acs.jafc.5b01611
J. Agric. Food Chem. 2015, 63, 6876–6882

organic ligands (carboxylic anions) and gaseous (O_2/CO_2) exchanges. Therefore, the bioavailability of P_i in soil could be enhanced by modifying these factors.[32] Separate experiments with buffer solution were performed, and no significant change was found on pH in response to both TiO_2 and Fe_3O_4 NPs. Similarly, in soil medium without plant culture, both kinds of NPs at all concentration levels were unable to change the pH but increased the P availability (data not shown). In the present study, pH of rhizophere soil without NP treatment was slightly alkaline (7.95); therefore, the dominant cations would be Ca^{2+} and Mg^{2+}. The introduction of TiO_2 and Fe_3O_4 NPs in soil provided more adsorption sites to the PO_4^{3-} ions because of the increased polarizing power of Fe^{3+} (9.9 C/m^2) and Ti^{3+} (6.7 C/m^2) compared to Ca^{2+} (2.2 C/m^2) and made covalent bonds with the PO_4^{3-} groups. Because NPs had no direct influence on soil pH, the pH variations can be attributed to enhanced root exudation upon improved P uptake as a result of more available P fractions and TiO_2 and Fe_3O_4 NP entry into the plants triggering physiological mechanisms to cope with the stress through exudation. However, further research is required to explore this possible mechanism in detail.

In the literature, it is reported that adsorption of phosphate (PO_4^{3-}) on the solid phase of the soil could be the primary mechanism regulating P availability.[33] On the other hand, desorption of sorbed PO_4^{3-} mostly occurred through a ligand-exchange reaction as a result of plant root exudation that could alter the adsorption−desorption equilibrium toward improved desorption. This could occur because of either an decrease in the concentration of PO_4^{3-} ions in the soil or an increase in the concentration of competing anions produced.[32] In another study, the availability of trace metals in soil affected by organic ligands was also observed.[34] Mihajlovic et al. reported that charged zeolites that interacted in the plant rhizosphere induced the gradual release of nutrients as a result of chemical dissolution and ion-exchange reaction.[35] Wang et al. also reported the increased exudation of organic acids in response to Al treatments in the wheat root zone.[36] It is therefore suggested that the exudation by *L. sativa* roots resulted in solubilization of Fe- and Ti-bound phosphates in the rhizosphere, consequently improving the uptake of P per plant.

Translocation of NPs in *L. sativa*. SEM−secondary electron imaging (SEI) and −backscattering electron (BSE) images and EDX spectra illustrating the elemental composition of *L. sativa* shoots are provided in Figures S2 and S3. In the control group (Figures S2 and S3a), the SEM images of the shoot showed clear surfaces, whereas the aggregates of TiO_2 and Fe_3O_4 NPs are visible in NP-treated groups (Figure S2 and panels b and c of Figure S3). The EDX spectra confirmed the translocation of NPs into shoots of *L. sativa*. EDX analysis (Figure S2) revealed that major elemental variations, such as P, Ca, Mg, and Al levels, were modified in response to NP treatments. The root apex sections of *L. sativa* were also analyzed through a SEM−BSE detector and EDX (Figure S4). Both kinds of NPs dispersed in the soil were able to cover root epidermis and formed nanostructured agglomerates. NPs can be transported by capillary action to distinct sites where the passage was wider than their size. When they reached a point where the passage was narrow, NPs became accumulated in the form of aggregates. The uptake of ultra-small nano-anatase TiO_2 has been reported in *Arabidopsis thaliana* by Kurepa et al.[37] Larue et al. reported the presence of TiO_2 NPs into roots and shoots of hydroponically grown wheat (*Triticum aestivum*), confirmed through SEM.[38] Fe oxide NPs have been reported as facilitators for iron and photosynthate transfer to the leaves of the peanut plant.[39] In another study, no significant accumulation of Ti in plant tissues was observed in soil-grown wheat.[40] Diverse results could be seen using the same species with reference to the effects of NPs. NPs could behave differently depending upon their size, shape, and phase but also the concentration levels applied, experimental conditions, and plant species as well as their mechanisms of uptake.[41]

Primary Metabolites and P Speciation. Figure 5a shows Raman spectra of rhizosphere soil extracts, which were used to identify plant metabolites. The individual contents of primary metabolites, such as cystine and methionine, were found to increase in extract with NP application by the appearance of Raman peaks at 510 and 630 cm^{-1}. Cystine and methionine possess particular amino acid structures, such as S−S and S−H, act as growth regulators, and ultimately improve nutritional composition of crop plants.

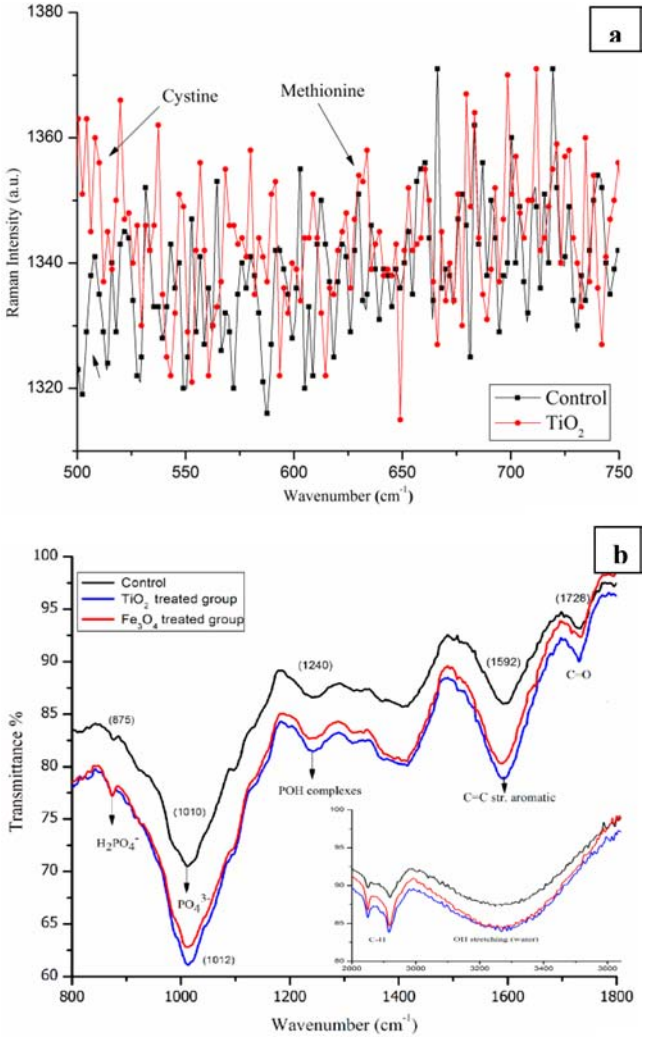

Figure 5. Spectroscopic analysis of rhizopshere soil and shoots: (a) Raman spectra of rhizosphere soil extract treated with 0 and 250 mg kg^{-1} of TiO_2 NPs and (b) FTIR spectra of *L. sativa* shoots treated with 0 and 250 mg kg^{-1} of TiO_2 and Fe_3O_4 NPs.

The results of FTIR spectral data presented in Figure 5b verified the above-mentioned results. The target species, i.e., PO_4^{3-}, showed high similarity in both of the NP-treated groups compared to the control. At the *x* axis, a slight shift in the

DOI: 10.1021/acs.jafc.5b01611
J. Agric. Food Chem. 2015, 63, 6876−6882

stretching vibration of the PO_4^{3-} group was observed from 1010 to 1012 cm^{-1} in both of NP-treated groups, indicating the strength of PO_4^{3-} bonds in TiO_2- and Fe_3O_4-treated groups compared to the control. The three phosphate species, including $H_2PO_4^-$, PO_4^{3-}, and POH, complexes and the functional groups (C−C and C═O) showed intense peaks in NP-treated groups that indicate their increased presence. These results are consistent with the above-mentioned results of P uptake by plant. In the literature, results of increased PO_4^{3-} complexes with acidification have been reported.[42] In another study, FTIR analysis of cucumber fruit from TiO_2 NP (250−750 mg kg^{-1}) treated plants showed significant modifications in lipids, amide, lignin, and carbohydrates.[13] Similarly, in the present study, NP-treated groups showed stronger OH bonds (water) relative to the control. These findings are relevant to the results of the moisture content percentage in shoots (Figure 3). Thus, *L. sativa* shoots with TiO_2 and Fe_3O_4 treatments contained more phosphate, hydroxyl, and carbonyl groups. Overall, results of Raman and FTIR support the findings presented in different sections and validate the accuracy of the experiments.

In conclusion, the application of TiO_2 and Fe_3O_4 NPs increased phytoavailability of P, growth, biomass, and moisture content of *L. sativa* at all tested concentrations compared to the control. The best feasible concentration of both TiO_2 and Fe_3O_4 NPs that increased the P uptake by 74 and 89%, respectively, was 150 mg kg^{-1}. In nutrient-uptake mechanisms, the affinities of NPs to adsorb PO_4^{3-} ions affected by the speciation of P, which made it phytoavailable, and their subsequent release through acidification caused by root exudation are the traits that could increase the solubility of soil-bound P_i in the rhizosphere. The findings suggest developing an innovative strategy of using NPs for improved nutrient management to ensure food security.

■ ASSOCIATED CONTENT

Supporting Information

The Supporting Information is available free of charge on the ACS Publications website at DOI: 10.1021/acs.jafc.5b01611.

Figures related to SEM images of NPs and their translocation in *L. sativa* shoots and roots (PDF)

■ AUTHOR INFORMATION

Corresponding Author

*Telephone: +92-51-9085-4309. E-mail: marshad@iese.nust.edu.pk.

Funding

Financial support was provided by Mega S&T Fund, National University of Sciences and Technology, Islamabad, Pakistan, to carry out this work.

Notes

The authors declare no competing financial interest.

■ ACKNOWLEDGMENTS

The authors acknowledge Hira Fatima and Farheen Mustafa for their valuable help during the research work. The authors are thankful to Muhammad Arif Ali and Kiran Hina for critical review and their valuable suggestions to improve this manuscript.

■ ABBREVIATIONS USED

P, phosphorus; NPs, nanoparticles; SEM, scanning electron microscopy; FTIR, Fourier transform infrared spectroscopy; XRD, X-ray diffraction; EDX, energy-dispersive X-ray spectroscopy

■ REFERENCES

(1) Armstrong, D. L. Functions of phosphorus in plant. In *Better Crops Plant Food*, 1st ed.; Potash & Phosphate Institute (PPI): Norcross, GA, 1999; Vol. *83*, pp 6−7.

(2) Scholz, R. W.; Roy, A. H.; Hellums, D. T. Sustainable phosphorus management: A transdisciplinary challenge. In *Sustainable Phosphorus Management—A Global Transdisciplinary Roadmap*, 1st ed.; Springer: New York, 2014; pp 1−256.

(3) Vance, C. P.; Uhde-Stone, C.; Allan, D. L. Phosphorus acquisition and use: Critical adaptations by plants for securing a nonrenewable resource. *New Phytol.* **2003**, *157* (3), 423−447.

(4) Vassilev, N.; Vassileva, M. Biotechnological solubilization of rock phosphate on media containing agro-industrial wastes. *Appl. Microbiol. Biotechnol.* **2003**, *61*, 435−440.

(5) Lambers, H.; Shane, M. W.; Cramer, M. D.; Pearse, S. J.; Veneklaas, E. J. Root structure and functioning for efficient acquisition of phosphorus: Matching morphological and physiological traits. *Ann. Bot.* **2006**, *98*, 693−713.

(6) Zheng, L.; Hong, F.; Lu, S.; Liu, C. Effect of nano-TiO_2 on strength of naturally aged seeds and growth of spinach. *Biol. Trace Elem. Res.* **2005**, *104* (1), 083−092.

(7) Lopez-Moreno, M. L.; de la Rosa, G.; Hernandez-Viezcas, J. A.; Peralta-Videa, J. R.; Gardea-Torresdey, J. L. X-ray absorption spectroscopy (XAS) corroboration of the uptake and storage of CeO_2 nanoparticles and assessment of their differential toxicity in four edible plant species. *J. Agric. Food Chem.* **2010**, *58* (6), 3689−3693.

(8) Morales, M. I.; Rico, C. M.; Hernandez-Viezcas, J. A.; Nunez, J. E.; Barrios, A. C.; Tafoya, A.; Flores-Marges, J. P.; Peralta-Videa, J. R.; Gardea-Torresdey, J. L. Toxicity assessment of cerium oxide nanoparticles in cilantro (*Coriandrum sativum* L.) plants grown in organic soil. *J. Agric. Food Chem.* **2013**, *61* (26), 6224−6230.

(9) Coria-Cayupán, Y. S.; Sánchez de Pinto, M. I.; Nazareno, M. A. Variations in bioactive substance contents and crop yields of lettuce (*Lactuca sativa* L.) cultivated in soils with different fertilization treatments. *J. Agric. Food Chem.* **2009**, *57*, 10122−10129.

(10) World Health Organization (WHO). *GEMS/Food Cluster Diets*; WHO: Geneva, Switzerland, 2013.

(11) Food and Agriculture Organization of the United Nations (FAO). *FAOSTAT*; FAO: Rome, Italy, 2011.

(12) Piccinno, F.; Gottschalk, F.; Seeger, S.; Nowack, B. Industrial production quantities and uses of ten engineered nanomaterials in Europe and the world. *J. Nanopart. Res.* **2012**, *14*, 1109−1120.

(13) Servin, A. D.; Morales, M. I.; Castillo-Michel, H.; Hernandez-Viezcas, J. A.; Munoz, B.; Zhao, L.; Nunez, J. E.; Peralta-Videa, J. R.; Gardea-Torresdey, J. L. Synchrotron verification of TiO_2 accumulation in cucumber fruit: a possible pathway of TiO_2 nanoparticle transfer from soil into the food chain. *Environ. Sci. Technol.* **2013**, *47* (20), 11592−11598.

(14) Ze, Y.; Liu, C.; Wang, L.; Hong, M.; Hong, F. The regulation of TiO_2 nanoparticles on the expression of light-harvesting complex II and photosynthesis of chloroplasts of Arabidopsis thaliana. *Biol. Trace Elem. Res.* **2011**, *143* (2), 1131−1141.

(15) Wang, H.; Kou, X.; Pei, Z.; Xiao, J. Q.; Shan, X.; Xing, B. Physiological effects of magnetite (Fe_3O_4) nanoparticles on perennial ryegrass (*Lolium perenne* L.) and pumpkin (*Cucurbita mixta*) plants. *Nanotoxicology* **2011**, *5* (1), 30−42.

(16) Monica, R. C.; Cremonini, R. Nanoparticles and higher plants. *Caryologia* **2009**, *62* (2), 161−165.

(17) He, S.; Feng, Y.; Ren, H.; Zhang, Y.; Gu, N.; Lin, X. The impact of iron oxide magnetic nanoparticles on the soil bacterial community. *J. Soils Sediments* **2011**, *11*, 1408−1417.

DOI: 10.1021/acs.jafc.5b01611
J. Agric. Food Chem. 2015, 63, 6876−6882

(18) Ge, Y.; Schimel, J. P.; Holden, P. A. Evidence for negative effects of TiO_2 and ZnO nanoparticles on soil bacterial communities. *Environ. Sci. Technol.* **2011**, *45* (4), 1659−1664.
(19) Judy, J. D.; Mcnear, D. H.; Chen, C.; Lewis, R. W.; Tsyusko, O. V.; Bertsch, P. M.; Rao, W.; Stegemeier, J. P.; Lowry, G. V.; Mcgrath, S. P.; Durenkamp, M.; Unrine, J. M. Nanomaterials in biosolids inhibit nodulation, shift microbial community composition, and result in increased metal uptake relative to bulk/dissolved metals. *Environ. Sci. Technol.* **2015**, *49*, 8751.
(20) Rico, C. M.; Lee, S. C.; Rubenecia, R.; Mukherjee, A.; Hong, J.; Peralta-Videa, J. R.; Gardea-Torresdey, J. L. Cerium oxide nanoparticles impact yield and modify nutritional parameters in wheat (*Triticum aestivum* L.). *J. Agric. Food Chem.* **2014**, *62* (40), 9669−9675.
(21) Santner, J.; Smolders, E.; Wenzel, W. W.; Degryse, F. First observation of diffusion-limited plant root phosphorus uptake from nutrient solution. *Plant, Cell Environ.* **2012**, *35* (9), 1558−1566.
(22) Pradhan, S.; Patra, P.; Mitra, S.; Dey, K. K.; Jain, S.; Sarkar, S.; Roy, S.; Palit, P.; Goswami, A. Manganese nanoparticles: impact on non-nodulated plant as a potent enhancer in nitrogen metabolism and toxicity study both in vivo and in vitro. *J. Agric. Food Chem.* **2014**, *62* (35), 8777−8785.
(23) Lieberzeit, P. A.; Afzal, A.; Glanzing, G.; Dickert, F. L. Molecularly imprinted sol-gel nanoparticles for mass-sensitive engine oil degradation sensing. *Anal. Bioanal. Chem.* **2007**, *389* (2), 441−446.
(24) Ahn, T.; Kim, J. H.; Yang, H.-M.; Lee, J. W.; Kim, J. D. Formation pathways of magnetite nanoparticles by coprecipitation method. *J. Phys. Chem. C* **2012**, *116* (10), 6069−6076.
(25) Sumi, T.; Motono, S.; Ishida, Y.; Shirahata, N.; Yonezawa, T. Formation and optical properties of fluorescent gold nanoparticles obtained by matrix sputtering method with volatile mercaptan molecules in the vacuum chamber and consideration of their structures. *Langmuir* **2015**, *31*, 4323−4329.
(26) Olsen, S. R.; Cole, C. V.; Watanabe, F. S.; Dean, L. A. *Estimation of Available Phosphorus in Soil by Extraction with Sodium Bicarbonate*; United States Department of Agriculture: Washington, D.C., 1954; Vol. *939*, pp 18−19.
(27) Ryan, J.; Estefan, G.; Rashid, A. *Soil and Plant Analysis: Laboratory Manual*, 2nd ed.; International Center for Agricultural Research in the Dry Areas (ICARDA): Aleppo, Syria, 2001; pp 131−134.
(28) Yang, F.; Liu, C.; Gao, F.; Su, M.; Wu, X.; Zheng, L.; Hong, F.; Yang, P. The improvement of spinach growth by nano-anatase TiO_2 treatment is related to nitrogen photoreduction. *Biol. Trace Elem. Res.* **2007**, *119* (1), 77−88.
(29) Mandeh, M.; Omidi, M.; Rahaie, M. In vitro influences of TiO_2 nanoparticles on barley (*Hordeum vulgare* L.) tissue culture. *Biol. Trace Elem. Res.* **2012**, *150* (1−3), 376−380.
(30) Lopez-Moreno, J. L.; Giménez, J. L.; Moreno, A.; Fuentes, J. L.; Alcaraz, C. F. Plant biomass and fruit yield induction by Ti(IV) in P stressed pepper crops. *Fert. Res.* **1996**, *43*, 131−136.
(31) Gao, F.; Hong, F.; Liu, C.; Zheng, L.; Su, M.; Wu, X.; Yang, F.; Wu, C.; Yang, P. Mechanism of nano-anatase TiO_2 on promoting photosynthetic carbon reaction of spinach: inducing complex of rubisco-rubisco activase. *Biol. Trace Elem. Res.* **2006**, *111*, 239−253.
(32) Hinsinger, P. Bioavailability of soil inorganic P in the rhizosphere as affected by root-induced chemical changes: a review. *Plant Soil* **2001**, *237*, 173−195.
(33) Duputel, M.; Devau, N.; Brossard, M.; Jaillard, B.; Jones, D. L.; Hinsinger, P.; Gerard, F. Citrate adsorption can decrease soluble phosphate concentration in soils: Results of theoretical modeling. *Appl. Geochem.* **2013**, *35*, 120−131.
(34) Gramlich, A.; Tandy, S.; Frossard, E.; Eikenberg, J.; Schulin, R. Availability of zinc and the ligands citrate and histidine to wheat: does uptake of entire complexes play a role? *J. Agric. Food Chem.* **2013**, *61* (44), 10409−10417.
(35) Mihajlovic, M.; Perisic, N.; Pezo, L.; Stojanovic, M.; Milojkovic, J.; Lopicic, Z.; Petrovic, M. Utilization of phosphate rock from lisina for direct application: release of plant nutrients in the exchange-fertilizer mixtures. *J. Agric. Food Chem.* **2014**, *62* (41), 9965−9973.
(36) Wang, P.; Bi, S.; Wang, S.; Ding, Q. Variation of wheat root exudates under aluminum stress. *J. Agric. Food Chem.* **2006**, *54* (26), 10040−10046.
(37) Kurepa, J.; Paunesku, T.; Vogt, S.; Arora, H.; Rabatic, B. M.; Lu, J.; Wanzer, M. B.; Woloschak, G. E.; Smalle, J. A. Uptake and distribution of ultrasmall anatase TiO_2 Alizarin red S nanoconjugates in *Arabidopsis thaliana*. *Nano Lett.* **2010**, *10* (7), 2296−2302.
(38) Larue, C.; Laurette, J.; Herlin-Boime, N.; Khodja, H.; Fayard, B.; Flank, A. M.; Brisset, F.; Carriere, M. Accumulation, translocation and impact of TiO_2 nanoparticles in wheat (*Triticum aestivum* spp.): influence of diameter and crystal phase. *Sci. Total Environ.* **2012**, *431*, 197−208.
(39) Liu, X. M.; Zhang, F. D.; Zhang, S. Q.; He, X. S.; Fang, R.; Feng, Z.; Wang, Y. J. Effects of nano-ferric oxide on the growth and nutrients absorption of peanut. *J. Plant Nutr. Fert.* **2010**, *11*, 14−18.
(40) Du, W.; Sun, Y.; Ji, R.; Zhu, J.; Wu, J.; Guo, H. TiO_2 and ZnO nanoparticles negatively affect wheat growth and soil enzyme activities in agricultural soil. *J. Environ. Monit.* **2011**, *13* (4), 822−828.
(41) Ruffini Castiglione, M.; Giorgetti, L.; Geri, C.; Cremonini, R. The effects of nano-TiO_2 on seed germination, development and mitosis of root tip cells of *Vicia narbonensis* L. and *Zea mays* L. *J. Nanopart. Res.* **2011**, *13* (6), 2443−2449.
(42) Elzinga, E. J.; Sparks, D. L. Phosphate adsorption onto hematite: an *in situ* ATR-FTIR investigation of the effects of pH and loading level on the mode of phosphate surface complexation. *J. Colloid Interface Sci.* **2007**, *308* (1), 53−70.

DOI: 10.1021/acs.jafc.5b01611
J. Agric. Food Chem. 2015, 63, 6876−6882

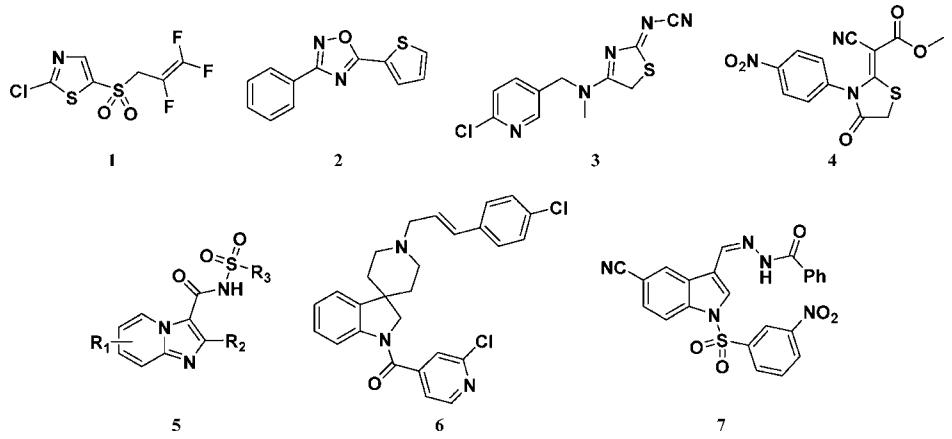

Figure 1. Nematicidal chemicals developed in recent years.

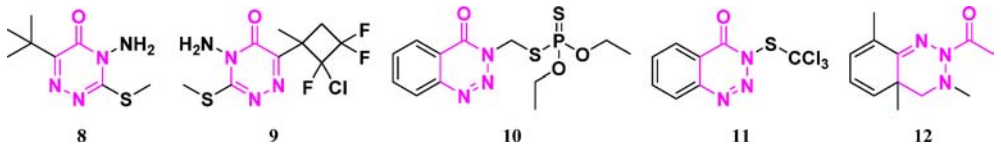

Figure 2. Bioactive agrochemicals containing triazinone skeletons.

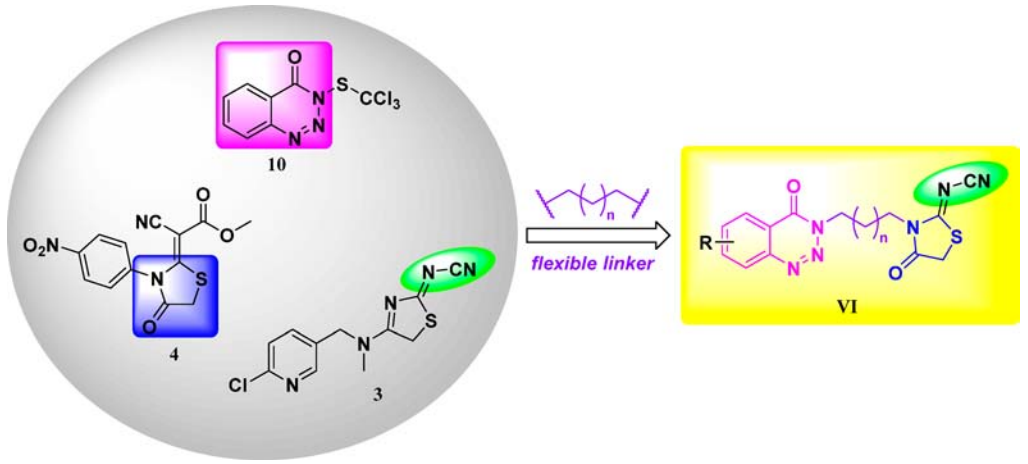

Figure 3. Design of title compounds (**VI-1**–**VI-23**).

and compound **12** had certain nematicidal activity against *Caenorhabditis elegans*.[31] However, little work has been performed on nematicidal 1,2,3-benzotriazin-4-one derivatives against plant-parasitic nematodes.

During the design of 1,2,3-benzotriazin-4-one derivatives, we found that thiazolidin-4-one compounds exhibited good inhibitory activities against *M. incognita*,[20] and the neonicotinoid derivative **3** had significant nematicidal activity against *M. incognita* at the concentration of 20.0 mg L^{-1}.[19] Hence, we attempted to introduce 2-cyanoiminothiazolidin-4-one moieties into the 1,2,3-benzotriazin-4-one structure, while the active fragment of compound **3** was also considered, aiming to obtain more active compounds against *M. incognita* (Figure 3).

In the present study, we reported for the first time 1,2,3-benzotriazin-4-one derivatives containing 2-cyanoiminothiazolidin-4-one moieties and their *in vivo* and *in vitro* biological activities against *M. incognita*. We also discussed the relationship between structure and nematicidal activity preliminarily and tried to illuminate the mechanism of our compounds against nematodes.

MATERIALS AND METHODS

Chemicals. Anthranilic acids (**I-1**–**I-13**) and triphosgene were purchased from Shanghai Darui Fine Chemicals Co., Ltd. Ammonium carbonate, sodium nitrite, hydrochloric acid, potassium hydroxide, potassium carbonate, anhydrous sodium sulfate, and all solvents were purchased from Shanghai Lingfeng Chemical Reagent Co., Ltd. *N*-Cyanodithiocarbonimidate, 1,2-dibromoethane, 1,3-dibromopropane, 1,4-dibromobutane, 1,5-dibromopentane, 1,6-dibromohexane, and potassium iodide were purchased from Shanghai Aladdin Chemistry Co., Ltd. All reagents and solvents were of reagent grade without further purification.

Instrumental Analysis. Analytical thin-layer chromatography (TLC) was performed on precoated glass plates (silica gel 60 F_{254}), visualizing the spots by an ultraviolet (UV) lamp (254 nm). All melting points were determined on a Büchi melting point B540 apparatus (Büchi Labortechnik AG, Flawil, Switzerland) and are uncorrected. ^{1}H, ^{13}C, and ^{19}F nuclear magnetic resonance (NMR) spectra were recorded in DMSO-d_6 on a Bruker AM-400 (400 MHz) spectrometer at ambient temperature. Chemical shifts are reported in δ (parts per million) values, with tetramethylsilane (TMS) as the internal standard. Coupling constants (J) are reported in hertz. High-resolution mass spectra (HRMS) were recorded under an electrospray

DOI: 10.1021/acs.jafc.5b01762
J. Agric. Food Chem. 2015, 63, 6883−6889

ionization condition on a Waters Micromass liquid chromatography−time of flight (LC−TOF) spectrometer.

General Procedures. *Synthesis of Isatoic Anhydrides*[32] ***(II-1−II-13)***. A mixture of anthranilic acid (**I-1−I-13**, 40 mmol) and tetrahydrofuran (THF, 100 mL) was stirred at −10 °C for 30 min. Then, a solution of triphosgene (BTC, 40 mmol) in THF (20 mL) was added dropwise to the above mixture. After that, the mixture was stirred for 1 h from −10 to −5 °C, followed by 18 h at room temperature. The solvent was removed under reduced pressure, and anhydrous ether (150 mL) was added to the obtained residue with vigorous stirring. The precipitate was collected by filtration, washed with anhydrous ether, and dried to afford compounds **II-1−II-13** in yields of 85−95%.

Synthesis of Anthranilamides[33] ***(III-1−III-13)***. A suspension of isatoic anhydride (**II-1−II-13**, 35 mmol), ammonium carbonate (140 mmol), and 1,4-dioxane (150 mL) was heated at 60 °C. After stirring for 5−8 h, the reaction mixture was cooled to room temperature and evaporated under reduced pressure, and then water (200 mL) was added to the residue, which was extracted with EtOAc (80 mL × 3). The organic layer was washed with brine (80 mL), dried over anhydrous Na_2SO_4, and concentrated to give compounds **III-1−III-13** in yields of above 73−94%.

Synthesis of 1,2,3-Benzotriazin-4-ones[34] ***(IV-1−IV-13)***. A solution of sodium nitrite (4.14 g, 60 mmol) in 0.5 N HCl (240 mL) was stirred at 0 °C for 20 min. Then, anthranilamide (**III-1−III-13**, 30 mmol) dissolved in *N*,*N*-dimethylformamide (DMF, 15 mL) was added dropwise to the above solution for 40 min. After another 1 h of stirring at 0 °C, 30% aqueous ammonia was added slowly to adjust the pH to 10.0. The reaction mixture was allowed to stir vigorously for 15 min and then reacidified to pH 2.0. After stirring for 30 min, the precipitated product was filtered off with suction, washed with water (200 mL), and dried to afford compounds **IV-1−IV-13** in yields of 84−92%.

Synthesis of Potassium Salt of 2-Cyanoimino-4-oxothiazolidine.[35] A stirring mixture of dimethyl *N*-cyanodithiocarbonimidate (11.68 g, 80 mmol), ammonium carbonate (4.22 g, 44 mmol), and EtOH (120 mL) was heated at 60 °C for 3 h. To this, methyl thioglycolate (7.15 mL, 80 mmol) and 50% KOH (aqueous, 8.96 g, 80 mmol) were added separately in one portion. The reaction mixture was heated to reflux for 5 h and then cooled to room temperature. The precipitate was collected by filtration, washed with cold EtOH, and dried to give the desirable potassium salt as a light yellow solid, with a yield of 73%.

Synthesis of 3-Bromoalkyl-1,2,3-benzotriazin-4-ones[36] ***(V-1−V-23)***. A stirring suspension of 1,2,3-benzotriazin-4-one (**IV-1−IV-13**, 6 mmol), dibromoalkane (30 mmol), potassium carbonate (1.66 g, 12 mmol), and acetone (50 mL) was refluxed for 5−8 h and then cooled to room temperature. The reaction mixture was evaporated under reduced pressure, and water (100 mL) was added to the residue, which was extracted with CH_2Cl_2 (50 mL × 2). The organic layer was dried over anhydrous Na_2SO_4, concentrated, and purified with flash chromatography on silica gel, eluting with petroleum ether (60−90 °C)/EtOAc to afford compounds **V-1−V-23** in yields of 46−62%.

General Synthetic Procedure for Title Compounds ***(VI-1−VI-23)***. To a mixture of compound **V** (2 mmol), potassium iodide (0.332 g, 2 mmol), and DMF (10 mL) was added potassium salt of 2-cyanoimino-4-oxothiazolidine (0.358 g, 2 mmol), and then the mixture was stirred at 100 °C. The reaction process was monitored by TLC. After the complete consumption of compound **V**, the reaction was cooled to room temperature. The solvent was removed under reduced pressure, and water (50 mL) was added to the residue, which was extracted with CH_2Cl_2 (30 mL × 2). The organic layer was dried over anhydrous Na_2SO_4, concentrated and purified with flash chromatography on silica gel, eluting with petroleum ether (60−90 °C)/EtOAc to afford compounds **VI-1−VI-23**. The data of compounds **VI-1−VI-10** are shown as follows, whereas data of compounds **VI-11−VI-23** are deposited in the Supporting Information.

N-(4-Oxo-3-(3-(4-oxobenzo[d][1,2,3]triazin-3(4H)-yl)propyl)-thiazolidin-2-ylidene)cyanamide ***(VI-1)***. Yield: 41%. Melting point (Mp): 156.9−157.6 °C. ^{1}H NMR (400 MHz, DMSO-d_6) δ: 8.26 (d, J = 7.6 Hz, 1H), 8.21 (d, J = 8.0 Hz, 1H), 8.10 (t, J = 7.6 Hz, 1H), 7.94 (t, J = 7.6 Hz, 1H), 4.41 (t, J = 7.2 Hz, 2H), 4.30 (s, 2H), 3.74 (t, J = 7.2 Hz, 2H), 2.21−2.09 (m, 2H). ^{13}C NMR (100 MHz, DMSO-d_6) δ: 179.6, 173.0, 155.3, 144.1, 135.9, 133.4, 128.5, 125.0, 119.7, 114.1, 47.1, 40.8, 36.1, 26.1. HRMS (ES+) calcd for $C_{14}H_{13}N_4O_2S$ (M + H)$^+$, 329.0821; found, 329.0823.

N-(3-(3-(7-Chloro-4-oxobenzo[d][1,2,3]triazin-3(4H)-yl)propyl)-4-oxothiazolidin-2-ylidene)cyanamide ***(VI-2)***. Yield: 52%. Mp: 163.4−164.2 °C. ^{1}H NMR (400 MHz, DMSO-d_6) δ: 8.35 (d, J = 2.0 Hz, 1H), 8.25 (dd, J_1 = 8.4 Hz, J_2 = 2.0 Hz, 1H), 7.97 (dd, J_1 = 8.4 Hz, J_2 = 2.0 Hz, 1H), 4.40 (t, J = 7.2 Hz, 2H), 4.29 (s, 2H), 3.74 (t, J = 7.2 Hz, 2H), 2.20−2.09 (m, 2H). ^{13}C NMR (100 MHz, DMSO-d_6) δ: 179.6, 172.9, 154.8, 144.9, 140.3, 133.6, 127.7, 127.3, 118.6, 114.0, 47.3, 40.8, 36.1, 26.0. HRMS (ES+) calcd for $C_{14}H_{11}N_6O_2NaS^{35}Cl$ (M + Na)$^+$, 385.0250; found, 385.0258. HRMS (ES+) calcd for $C_{14}H_{11}N_6O_2NaS^{37}Cl$ (M + Na)$^+$, 387.0221; found, 387.0232.

N-(3-(3-(8-Bromo-4-oxobenzo[d][1,2,3]triazin-3(4H)-yl)propyl)-4-oxothiazolidin-2-ylidene)cyanamide ***(VI-3)***. Yield: 35%. Mp: 159.7−160.6 °C. ^{1}H NMR (400 MHz, DMSO-d_6) δ: 8.38 (d, J = 7.6 Hz, 1H), 8.24 (d, J = 7.6 Hz, 1H), 7.82 (t, J = 7.6 Hz, 1H), 4.41 (t, J = 6.8 Hz, 2H), 4.30 (s, 2H), 3.75 (t, J = 6.8 Hz, 2H), 2.26−2.07 (m, 2H). ^{13}C NMR (100 MHz, DMSO-d_6) δ: 179.6, 173.0, 154.5, 141.4, 139.4, 134.2, 124.9, 122.9, 121.8, 114.1, 47.5, 40.8, 36.1, 26.0. HRMS (ES+) calcd for $C_{14}H_{12}N_6O_2S^{79}Br$ (M + H)$^+$, 406.9926; found, 406.9927. HRMS (ES+) calcd for $C_{14}H_{12}N_6O_2S^{81}Br$ (M + H)$^+$, 408.9905; found, 408.9908.

N-(3-(3-(7-Fluoro-4-oxobenzo[d][1,2,3]triazin-3(4H)-yl)propyl)-4-oxothiazolidin-2-ylidene)cyanamide ***(VI-4)***. Yield: 32%. Mp: 171.1−171.6 °C. ^{1}H NMR (400 MHz, DMSO-d_6) δ: 8.34 (dd, J_1 = 8.8 Hz, J_2 = 6.0 Hz, 1H), 8.09 (dd, J_1 = 9.2 Hz, J_2 = 2.4 Hz, 1H), 7.82 (td, J_1 = 8.8 Hz, J_2 = 2.4 Hz, 1H), 4.41 (t, J = 7.2 Hz, 2H), 4.29 (s, 2H), 3.74 (t, J = 7.2 Hz, 2H), 2.23−2.07 (m, 2H). ^{19}F NMR (376 MHz, DMSO-d_6) δ: −101.8 (td, J_1 = 9.0 Hz, J_2 = 5.6 Hz). HRMS (ES−) calcd for $C_{14}H_{10}N_6O_2FS$ (M − H)$^-$, 345.0570; found, 345.0570.

N-(3-(3-(6-(Trifluoromethyl)-4-oxobenzo[d][1,2,3]triazin-3(4H)-yl)propyl)-4-oxothiazolidin-2-ylidene)cyanamide ***(VI-5)***. Yield: 31%. Mp: 174.6−175.4 °C. ^{1}H NMR (400 MHz, DMSO-d_6) δ: 8.50 (s, 1H), 8.46−8.38 (m, 2H), 4.44 (t, J = 7.2 Hz, 2H), 4.30 (s, 2H), 3.75 (t, J = 7.2 Hz, 2H), 2.23−2.11 (m, 2H). ^{19}F NMR (376 MHz, DMSO-d_6) δ: −61.5 (s). HRMS (ES+) calcd for $C_{15}H_{11}N_6O_2F_3NaS$ (M + Na)$^+$, 419.0514; found, 419.0519.

N-(3-(3-(8-Methyl-4-oxobenzo[d][1,2,3]triazin-3(4H)-yl)propyl)-4-oxothiazolidin-2-ylidene)cyanamide ***(VI-6)***. Yield: 34%. Mp: 166.5−167.3 °C. ^{1}H NMR (400 MHz, DMSO-d_6) δ: 8.07 (d, J = 7.6 Hz, 1H), 7.91 (d, J = 7.2 Hz, 1H), 7.80 (t, J = 7.6 Hz, 1H), 4.41 (t, J = 7.2 Hz, 2H), 4.29 (s, 2H), 3.73 (t, J = 7.2 Hz, 2H), 2.77 (s, 3H), 2.23−2.09 (m, 2H). ^{13}C NMR (100 MHz, DMSO-d_6) δ: 179.6, 172.9, 155.4, 142.4, 137.7, 136.5, 133.1, 122.6, 119.8, 114.0, 47.1, 40.9, 36.1, 26.1, 17.1. HRMS (ES+) calcd for $C_{15}H_{15}N_6O_2S$ (M + H)$^+$, 343.0977; found, 343.0979.

N-(3-(3-(8-Methoxy-4-oxobenzo[d][1,2,3]triazin-3(4H)-yl)propyl)-4-oxothiazolidin-2-ylidene)cyanamide ***(VI-7)***. Yield: 40%. Mp: 190.0−190.9 °C. ^{1}H NMR (400 MHz, DMSO-d_6) δ: 7.86 (t, J = 8.0 Hz, 1H), 7.75 (d, J = 7.6 Hz, 1H), 7.63 (d, J = 8.0 Hz, 1H), 4.39 (t, J = 7.2 Hz, 2H), 4.29 (s, 2H), 4.04 (s, 3H), 3.72 (t, J = 7.2 Hz, 2H), 2.22−2.04 (m, 2H). ^{13}C NMR (100 MHz, DMSO-d_6) δ: 179.6, 172.9, 155.9, 155.1, 134.5, 134.4, 120.8, 116.8, 115.5, 114.1, 57.0, 47.1, 40.8, 36.1, 26.1. HRMS (ES−) calcd for $C_{15}H_{13}N_6O_3S$ (M − H)$^-$, 357.0770; found, 357.0769.

N-(3-(3-(5-Bromo-4-oxobenzo[d][1,2,3]triazin-3(4H)-yl)propyl)-4-oxothiazolidin-2-ylidene)cyanamide ***(VI-8)***. Yield: 39%. Mp: 201.5−202.5 °C. ^{1}H NMR (400 MHz, DMSO-d_6) δ: 8.18 (d, J = 8.0 Hz, 1H), 8.14 (d, J = 7.2 Hz, 1H), 7.91 (t, J = 8.0 Hz, 1H), 4.35 (t, J = 7.2 Hz, 2H), 4.31 (s, 2H), 3.75 (t, J = 7.2 Hz, 2H), 2.22−2.07 (m, 2H). ^{13}C NMR (100 MHz, DMSO-d_6) δ: 179.6, 173.0, 153.5, 145.7, 138.7, 136.1, 128.7, 119.2, 118.1, 114.1, 47.6, 40.9, 36.1, 25.9. HRMS (ES−) calcd for $C_{14}H_{10}N_6O_2S^{79}Br$ (M − H)$^-$, 404.9769; found, 404.9773. HRMS (ES−) calcd for $C_{14}H_{10}N_6O_2S^{81}Br$ (M − H)$^-$, 406.9749; found, 406.9753.

N-(3-(3-(6-Nitro-4-oxobenzo[d][1,2,3]triazin-3(4H)-yl)propyl)-4-oxothiazolidin-2-ylidene)cyanamide ***(VI-9)***. Yield: 46%. Mp: 186.0−

DOI: 10.1021/acs.jafc.5b01762
J. Agric. Food Chem. 2015, 63, 6883−6889

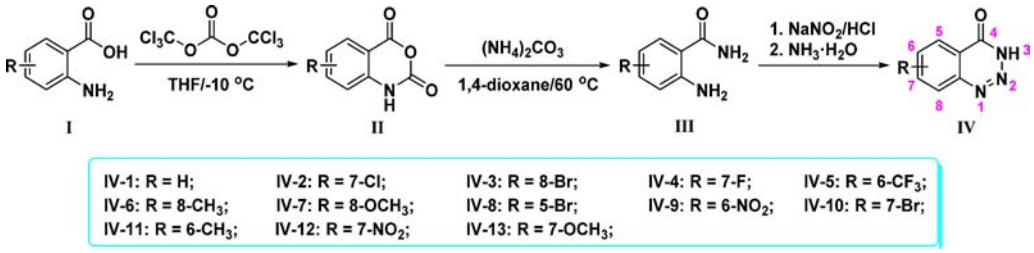

Figure 4. Synthetic route of 1,2,3-benzotriazin-4-ones (**IV-1**−**IV-13**).

187.8 °C. ^{1}H NMR (400 MHz, DMSO-d_6) δ: 8.86 (d, J = 2.4 Hz, 1H), 8.78 (dd, J_1 = 8.8 Hz, J_2 = 2.0 Hz, 1H), 8.47 (d, J = 9.2 Hz, 1H), 4.45 (t, J = 6.8 Hz, 2H), 4.30 (s, 2H), 3.76 (t, J = 6.8 Hz, 2H), 2.27−2.12 (m, 2H). ^{13}C NMR (100 MHz, DMSO-d_6) δ: 179.7, 173.0, 154.6, 149.2, 146.4, 130.8, 129.8, 121.0, 120.6, 114.1, 47.7, 40.8, 36.1, 26.0. HRMS (ES−) calcd for $C_{14}H_{10}N_7O_4S$ (M − H)$^-$, 372.0515; found, 372.0519.

N-(3-(3-(7-Bromo-4-oxobenzo[d][1,2,3]triazin-3(4H)-yl)propyl)-4-oxothiazolidin-2-ylidene)cyanamide (***VI-10***). Yield: 41%. Mp: 180.9−181.0 °C. ^{1}H NMR (400 MHz, DMSO-d_6) δ: 8.49 (s, 1H), 8.17 (d, J = 8.4 Hz, 1H), 8.10 (dd, J_1 = 8.4 Hz, J_2 = 1.6 Hz, 1H), 4.40 (t, J = 7.2 Hz, 2H), 4.29 (s, 2H), 3.73 (t, J = 7.2 Hz, 2H), 2.20−2.08 (m, 2H). ^{13}C NMR (100 MHz, DMSO-d_6) δ: 179.6, 173.0, 154.9, 144.9, 136.3, 130.7, 129.2, 127.3, 118.9, 114.1, 47.3, 40.8, 36.1, 26.0. HRMS (ES−) calcd for $C_{14}H_{10}N_6O_2S^{79}Br$ (M − H)$^-$, 404.9769; found, 404.9780. HRMS (ES−) calcd for $C_{14}H_{10}N_6O_2S^{81}Br$ (M − H)$^-$, 406.9749; found, 406.9760.

Assay of Nematicidal Activity. The second-stage juveniles (J2) of *M. incognita* used in all tests were cultured by Huzhou Modern Agricultural Biotechnology Innovation Center, Chinese Academy of Sciences, China.

In Vivo. All compounds (**VI-1**−**VI-23**) were dissolved with DMF and diluted with distilled water to obtain series concentrations of 40.0, 25.0, 10.0, 5.0, and 1.0 mg L^{-1} for bioassays. The final concentration of DMF in each treatment never exceeded 1% (v/v). The 1-week-aged cucumber seedlings were replanted in sterilized sand in test tubes (one seedling per test tube; tube size, 20 × 250 mm), and the roots of each seedling were treated with 3 mL of test solution. Then, approximately 2000 living J2 nematodes were inoculated into the rhizosphere sand of each host plant. Fenamiphos and avermectin (B1) at concentrations of 5.0 and 1.0 mg L^{-1} served as a positive control, and the negative control group was prepared in the same way but lacked the tested compound. Distilled water without nematodes served as the blank control. Each treatment was replicated 4 times, and the experiment was repeated 3 times. All of the above test tubes were incubated at 20−25 °C for 20 days, with 10 h in the daylight and 14 h in the dark per day. The number of root knots in each test tube was counted and recorded as a score. The inhibition rate on J2 of *M. incognita* was calculated by comparison to the negative control group.

$$\text{inhibition rate (\%)} = [(\text{score of negative control} - \text{score of treatment})/(\text{score of negative control})] \times 100$$

Scoring criteria: 0, 0−5 knots; 5, 6−10 knots; 10, 11−20 knots; and 20, more than 20 knots.

In Vitro. Pure compounds (**VI-1**−**VI-23**) were dissolved in DMF and diluted with distilled water to obtain stock solutions of double the treatment concentration. Then, 2 mL of J2 aqueous suspension containing approximately 200 living nematodes was added to a 6 cm diameter Petri dish and treated with 2 mL of the above solution, meanwhile providing series concentrations of 50.0, 25.0, 10.0, 5.0, and 1.0 mg L^{-1}. The final concentration of DMF in each treatment never exceeded 1% (v/v). Avermectin (B1) at the above same treatment concentrations served as a positive control, and the negative control group was prepared in the same way but lacked the tested compound. Distilled water served as a blank control. All of the above test dishes were covered with the laboratory parafilm to avoid the possible evaporation or pollution. Each treatment was incubated at 25 °C for 24 h and had three repetitions. Nematodes in each test dish were collected after washing in sterile water through a 500-mesh sieve, and finally, the activities of tested compounds were monitored under a microscope by recording the death rates of tested nematodes. Nematodes that did not move when prodded with a needle were considered to be dead. The LC_{50} values of tested compounds were calculated using the probit method.

RESULTS AND DISCUSSION

Synthesis. Starting from anthranilic acids (**I-1**−**I-13**), the desired isatoic anhydrides (**II-1**−**II-13**) were readily prepared via the annulation reaction with BTC.[32] As shown in Figure 4, various substituents at nearly every position of the benzene ring were well-tolerated, except 5-NO_2 and 8-NO_2. 5-NO_2 or 8-NO_2 isatoic anhydride could not be obtained from the corresponding anthranilic acid because of the possible formation of an intramolecular hydrogen bond between NO_2 and adjacent carboxyl or amino. Subsequently, **II-1**−**II-13** reacted with ammonium to afford anthranilamides[33] (**III-1**−**III-13**). Notably, ammonium carbonate was used here as an ammonium source, which made synthetic manipulation relatively easier. 1,2,3-Benzotriazin-4-ones (**IV-1**−**IV-13**) were synthesized from compounds **III-1**−**III-13** through the combination of diazotization, nucleophilic addition, and cyclization in one pot.[34]

The synthesis of 3-bromoalkyl-1,2,3-benzotriazin-4-ones (**V-1**−**V-13**) was carried out through *N*-alkylation of compounds **IV-1**−**IV-13** at the 3 position, using dibromoalkane as an alkylation agent[36] (Figure 6). To minimize the "bis-" product, 5 equiv of dibromoalkane was necessary, owing to the existing two reaction sites of dibromoalkane. Potassium salt of 2-cyanoimino-4-oxothiazolidine was prepared following the procedure reported in the literature[35] (Figure 5). The

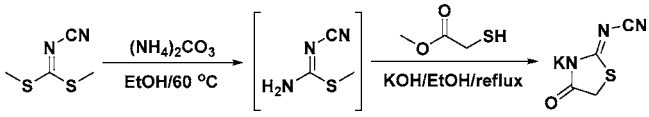

Figure 5. Synthetic route of potassium salt of 2-cyanoimino-4-oxothiazolidine.

potassium salt of 2-cyanoimino-4-oxothiazolidine has higher nucleophilic activity than 2-cyanoimino-4-oxothiazolidine, which promoted the nucleophilic substitution. Then, the title compounds (**VI-1**−**VI-23**) were synthesized by the reaction of 3-bromoalkyl-1,2,3-benzotriazin-4-ones with potassium salt of 2-cyanoimino-4-oxothiazolidine in the presence of potassium iodide (Figure 6). The structures of the title compounds were well-characterized by ^{1}H NMR, ^{13}C NMR, and HRMS (ESI).

Nematicidal Activity. As shown in Table 1, the *in vivo* nematicidal activities of title compounds (**VI-1**−**VI-23**) against

DOI: 10.1021/acs.jafc.5b01762
J. Agric. Food Chem. 2015, 63, 6883−6889

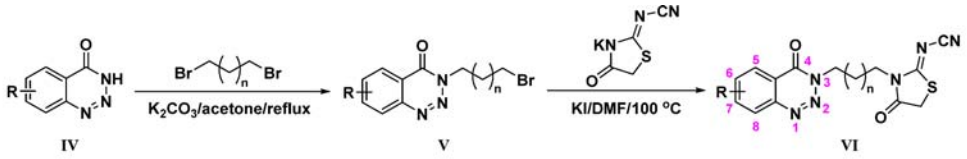

VI-1: R = H, n = 1; VI-2: R = 7-Cl, n= 1; VI-3: R = 8-Br, n = 1; VI-4: R = 7-F, n = 1; VI-5: R = 6-CF_3, n = 1;
VI-6: R = 8-CH_3, n = 1; VI-7: R = 8-OCH_3, n = 1; VI-8: R = 5-Br, n = 1; VI-9: R = 6-NO_2, n = 1; VI-10: R = 7-Br, n = 1;
VI-11: R = 6-CH_3, n = 1; VI-12: R = 7-NO_2, n = 1; VI-13: R = 7-OCH_3, n = 1; VI-14: R = 7-Cl, n= 0; VI-15: R = 7-Cl, n= 2;
VI-16: R = 7-Cl, n= 3; VI-17: R = 7-Cl, n= 4; VI-18: R = 7-NO_2, n = 2; VI-19: R = 7-NO_2, n = 3; VI-20: R = 7-NO_2, n = 4;
VI-21: R = 7-OCH_3, n = 2; VI-22: R = 7-OCH_3, n = 3; VI-23: R = 7-OCH_3, n = 4

Figure 6. Synthetic route of title compounds (**VI-1**–**VI-23**).

Table 1. Control Efficacy of Compounds VI-1–VI-23 against the Cucumber RKN Disease Caused by *M. incognita* in Test Tubes

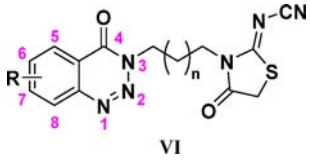

VI

			J2 of *M. incognita* inhibition rate (%)				
compound	R	*n*	40.0 mg L^{-1}	25.0 mg L^{-1}	10.0 mg L^{-1}	5.0 mg L^{-1}	1.0 mg L^{-1}
VI-1	H	1	100	76.5	58.3		
VI-2	7-Cl	1	pt[a]	100	100	38.7	27.2
VI-3	8-Br	1	100	78.0	63.5		
VI-4	7-F	1	pt	pt	74.5		
VI-5	6-CF_3	1	pt	100	90.8	31.5	19.4
VI-6	8-CH_3	1	100	88.7	67.3		
VI-7	8-OCH_3	1	100	88.1	66.7		
VI-8	5-Br	1	pt	100	91.8	34.0	20.3
VI-9	6-NO_2	1	pt	pt	100	37.2	23.9
VI-10	7-Br	1	pt	91.5	70.6		
VI-11	6-CH_3	1	pt	62.7	41.1		
VI-12	7-NO_2	1	pt	pt	64.3		
VI-13	7-OCH_3	1	pt	pt	54.0		
VI-14	7-Cl	0	pt	100	100	36.4	20.0
VI-15	7-Cl	2	pt	pt	53.6		
VI-16	7-Cl	3	pt	pt	26.1		
VI-17	7-Cl	4	pt	pt	63.4		
VI-18	7-NO_2	2	pt	pt	71.4		
VI-19	7-NO_2	3	pt	pt	90.1	30.1	17.6
VI-20	7-NO_2	4	pt	100	100	37.2	22.2
VI-21	7-OCH_3	2	pt	pt	38.9		
VI-22	7-OCH_3	3	pt	pt	83.3		
VI-23	7-OCH_3	4	pt	100	100	40.5	30.6
FM[b]						100	100
AVM[c]						100	100

[a]pt = phytotoxic. [b]FM = fenamiphos. [c]AVM = avermectin.

M. incognita were initially evaluated at the concentration of 40.0 mg L^{-1}. Some compounds, such as **VI-1**, **VI-3**, **VI-6**, and **VI-7**, showed high nematicidal activities with inhibition rates of 100%, whereas others were severely toxic to plants with a symptom of root rot. To minimize the phytotoxicity of test compounds, a lower treatment concentration was tried. When treated at the concentration of 25.0 mg L^{-1}, the phytotoxicity was significantly improved and quite a few compounds exhibited moderate to high nematicidal activities. Among them, compounds **VI-2**, **VI-5**, **VI-8**, **VI-14**, **VI-20**, and **VI-23** were 100% inhibitory against *M. incognita*. When the treatment concentration was reduced further to 10.0 mg L^{-1}, all compounds were nematicidal without phytotoxicity and compounds **VI-2**, **VI-9**, **VI-14**, **VI-20**, and **VI-23** still keep 100% inhibitory activities.

On the basis of the *in vivo* data at 10.0 mg L^{-1} in Table 1, it was found that compounds **VI-2** (7-Cl; $n = 1$), **VI-9** (6-NO_2; $n = 1$), **VI-14** (7-Cl; $n = 0$), **VI-20** (7-NO_2; $n = 4$), and **VI-23** (7-OCH_3; $n = 4$) still exhibited 100% inhibitory rate. However, we did not observe the obvious trend with electron-withdrawing or -donating substituents. When Cl, NO_2, and OCH_3 were located at the 7 position (**VI-2**, **VI-14**, **VI-19**, **VI-20**, and **VI-23**), CF_3 and NO_2 were located at the 6 position (**VI-5** and **VI-9**), or Br was located at the 5 position (**VI-8**) on the 1,2,3-benzotriazin-

DOI: 10.1021/acs.jafc.5b01762
J. Agric. Food Chem. 2015, 63, 6883–6889

4-one ring, compounds with proper linkers displayed >90% inhibitory activity. It indicated that high inhibitory activity seemed not to depend upon the type of substituents on the 1,2,3-benzotriazin-4-one ring. When the linker was fixed as a three-carbon chain, the activity of compound **VI-2** (7-Cl) was the highest among the compounds (**VI-1**−**VI-13**), considering that compound **VI-9** (6-NO_2) had phytotoxicity at 25.0 mg L^{-1}. Moreover, for other compounds with a three-carbon chain, it showed that compound **VI-8** (5-Br) had higher activity than compounds **VI-3** (8-Br) and **VI-10** (7-Br), and compounds **VI-6** (8-CH_3), **VI-7** (8-OCH_3), and **VI-9** (6-NO_2) were more active than compounds **VI-11** (6-CH_3), **VI-13** (7-OCH_3), and **VI-12** (7-NO_2), respectively. Thus, it seemed that the inhibitory activity was affected by the co-effect of substituent type and substituted position on the premise that the length of the flexible linker was fixed.

Furthermore, when the NO_2 or OCH_3 group was fixed at the 7 position, the effect of linker length on inhibitory activity was investigated. It was observed that the activities of compounds increased with the increasing linker length, except compound **VI-13**. However, for Cl at the same substituted position, the activities did not present a certain regularity with the increasing linker length. Thus, it also suggested that inhibitory activities did not always have positive correlation with linker length. From the results above, it can be concluded preliminarily that the inhibitory activity of our synthesized compounds was influenced by the combination of substituent type, substituted position, and linker length, not relying on only one factor. It is different from the results reported by Che et al. and Li et al.[37,38] Che et al. reported that a shorter chain length of R^3 and electron deficiency of the indolyl ring were favorable to nematicidal activity,[37] while Li et al. reported that electron richness of the benzyl ring was favorable to nematicidal activity.[38]

To determine the strength of activity of title compounds, the nematicidal evaluation of the compounds with >90% inhibitory activities at 10.0 mg L^{-1}, such as **VI-2**, **VI-5**, **VI-8**, **VI-9**, **VI-14**, **VI-19**, **VI-20**, and **VI-23**, was continued at lower concentrations of 5.0 and 1.0 mg L^{-1}; however, it was found that the inhibitory activities decreased very quickly with the decreasing of the treatment concentration. All of the inhibitory rates were less than 41% at these two concentrations. The reason why the inhibitory rates decreased so quickly still needs to be investigated further.

In addition, the *in vitro* nematicidal evaluation of compounds **VI-1**−**VI-23** against *M. incognita* was conducted. As a positive control, avermectin had the LC_{50} of 1.0 ± 0.1 mg L^{-1}. Unexpectedly, all synthesized compounds showed only <5% corrected mortalities at 50.0 mg L^{-1} (not listed here), which indicated that these compounds had no direct inhibition against *M. incognita*. The significant difference between *in vivo* and *in vitro* data attracted our attention. One possible reason is that these compounds could not kill the nematodes directly, like some nervous toxicants, such as avermectin, but affect the movement and host finding of nematodes,[39,40] or they could change the rhizosphere microbiology of the plant, strengthening antagonism against nematodes,[41] somewhat like the DiTera nematicide. Further research is still needed to verify the possible mechanism.

In conclusion, a series of novel 1,2,3-benzotriazin-4-one derivatives bearing 2-cyanothiazolidin-4-one were synthesized, and both *in vivo* and *in vitro* nematicidal activities against *M. incognita* were evaluated. Despite no direct inhibition *in vitro*, some of them exhibited good *in vivo* inhibitory activities at 10.0 mg L^{-1}, which implied that 1,2,3-benzotriazin-4-one is a potential active structure worth studying further.

■ ASSOCIATED CONTENT

Ⓢ Supporting Information

Data of compounds **VI-11**−**VI-23** (PDF). The Supporting Information is available free of charge on the ACS Publications website at DOI: 10.1021/acs.jafc.5b01762.

■ AUTHOR INFORMATION

Corresponding Author

*Telephone: +86-21-64252945. Fax: +86-21-64252603. E-mail: xyxu@ecust.edu.cn.

Funding

This work was financial supported by the National Natural Science Foundation of China (21272071) and the National High Technology Research and Development Program of China (863 Program, 2011AA10A207 and 2013AA065202). This work was also partly supported by the Special Fund for Agro-scientific Research in the Public Interest (201103007) and the Fundamental Research Funds for the Central Universities.

Notes

The authors declare no competing financial interest.

■ ACKNOWLEDGMENTS

We are very thankful to Dr. Bingli Gao and his co-workers in Huzhou Modern Agricultural Biotechnology Innovation Center, Chinese Academy of Sciences, China, for the discussion of nematicidal evaluation.

■ REFERENCES

(1) Abad, P.; Gouzy, J.; Aury, J. M.; Castagnone-Sereno, P.; Danchin, E. G.; Deleury, E.; Perfus-Barbeoch, L.; Anthouard, V.; Artiguenave, F.; Blok, V. C. Genome sequence of the metazoan plant-parasitic nematode *Meloidogyne incognita*. *Nat. Biotechnol.* **2008**, *26*, 909−915.

(2) Abad, P.; Favery, B.; Rosso, M. N.; Castagnone-Sereno, P. Root-knot nematode parasitism and host response: molecular basis of a sophisticated interaction. *Mol. Plant Pathol.* **2003**, *4*, 217−224.

(3) Djian-Caporalino, C.; Fazari, A.; Arguel, M. J.; Vernie, T.; VandeCasteele, C.; Faure, I.; Brunoud, G.; Pijarowski, L.; Palloix, A.; Lefebvre, V.; Abad, P. Root-knot nematode (*Meloidogyne* spp.) *Me* resistance genes in pepper (*Capsicum annuum* L.) are clustered on the P9 chromosome. *Theor. Appl. Genet.* **2007**, *114*, 473−486.

(4) Sasser, J. N.; Eisenback, J. D.; Carter, C. C.; Triantaphyllou, A. C. The international *Meloidogyne* project—its goals and accomplishments. *Annu. Rev. Phytopathol.* **1983**, *21*, 271−288.

(5) Hu, Y.; Zhang, W.; Zhang, P.; Ruan, W.; Zhu, X. Nematicidal activity of chaetoglobosin A produced by *Chaetomium globosum* NK102 against *Meloidogyne incognita*. *J. Agric. Food Chem.* **2013**, *61*, 41−46.

(6) Jang, J. Y.; Le Dang, Q.; Choi, Y. H.; Choi, G. J.; Jang, K. S.; Cha, B.; Luu, N. H.; Kim, J. C. Nematicidal activities of 4-quinolone alkaloids isolated from the aerial part of *Triumfetta grandidens* against *Meloidogyne incognita*. *J. Agric. Food Chem.* **2015**, *63*, 68−74.

(7) Haydock, P. P. J.; Woods, S. R.; Grove, I. G.; Hare, M. C. Chemical control of nematodes. In *Plant Nematology*; Perry, R. N., Moens, M., Eds.; CABI: Wallingford, U.K., 2006; pp 392−408.

(8) Tian, B.; Yang, J.; Zhang, K. Q. Bacteria used in the biological control of plant-parasitic nematodes: populations, mechanisms of action, and future prospects. *FEMS Microbiol. Ecol.* **2007**, *61*, 197−213.

(9) Whorton, M. D.; Foliart, D. E. Mutagenicity, carcinogenicity and reproductive effects of dibromochloropropane (DBCP). *Mutat. Res., Rev. Genet. Toxicol.* **1983**, *123*, 13−30.

DOI: 10.1021/acs.jafc.5b01762
J. Agric. Food Chem. 2015, 63, 6883−6889

(10) Kearn, J.; Ludlow, E.; Dillon, J.; O'Connor, V.; Holden-Dye, L. Fluensulfone is a nematicide with a mode of action distinct from anticholinesterases and macrocyclic lactones. *Pestic. Biochem. Physiol.* **2014**, *109*, 44−57.
(11) Rich, J. R.; Dunn, R. A.; Noling, J. W. Nematicides: Past and present uses. In *Nematology*; Chen, Z. X., Chen, S. Y., Dickson, D. W., Eds.; CABI: Wallingford, U.K., 2004; Vol. 2, pp 1179−1200.
(12) Meher, H. C.; Gajbhiye, V. T.; Chawla, G.; Singh, G. Virulence development and genetic polymorphism in *Meloidogyne incognita* (Kofoid & White) Chitwood after prolonged exposure to sublethal concentrations of nematicides and continuous growing of resistant tomato cultivars. *Pest Manag. Sci.* **2009**, *65*, 1201−1207.
(13) Putter, I.; MacConnell, J. G.; Preiser, F. A.; Haidri, A. A.; Ristich, S. S.; Dybas, R. A. Avermectins: Novel insecticides, acaricides and nematicides from a soil microorganism. *Experientia* **1981**, *37*, 963−964.
(14) Reddy, P. P. Avermectins. In *Recent Advances in Crop Protection*; Springer India: Bangalore, India, 2013; pp 13−24.
(15) Oka, Y.; Shuker, S.; Tkachi, N. Nematicidal efficacy of MCW-2, a new nematicide of the fluoroalkenyl group, against the root-knot nematode *Meloidogyne javanica*. *Pest Manag. Sci.* **2009**, *65*, 1082−1089.
(16) Oka, Y.; Shuker, S.; Tkachi, N. Systemic nematicidal activity of fluensulfone against the root-knot nematode *Meloidogyne incognita* on pepper. *Pest Manag. Sci.* **2012**, *68*, 268−275.
(17) Caboni, P.; Tronci, L.; Liori, B.; Tocco, G.; Sasanelli, N.; Diana, A. Tulipaline A: structure-activity aspects as a nematicide and V-ATPase inhibitor. *Pestic. Biochem. Physiol.* **2014**, *112*, 33−39.
(18) Slomczynska, U.; Dimmic, M. W.; Wideman, A.; Haakenson, W. P. Compositions and methods for controlling nematodes. U.S. Patent 20130217570, 2013.
(19) Jeschke, P.; Beck, M.; Krämer, W.; Wollweber, D.; Turberg, A.; Hansen, O.; Martin, H. D.; Sauer, P.; Erdelen, C. Azoles having an insecticidal action. U.S. Patent 7,417,150, 2008.
(20) Xu, X.; Li, Z.; Wang, G.; Li, C.; Song, G.; Shao, X.; Xu, Z. Compound containing N, S heterocycle and having nematocidal activity, preparation method and use thereof. WO Patent 2014117677, 2014.
(21) Lahm, G. P.; Lett, R. M.; Smith, B. T.; Smith, B. K.; Daly, C. A. Nematocidal sulfonamides. U.S. Patent 20120114624, 2012.
(22) Sluder, A.; Shah, S.; Cassayre, J.; Clover, R.; Maienfisch, P.; Molleyres, L. P.; Hirst, E. A.; Flemming, A. J.; Shi, M.; Cutler, P. Spiroindolines identify the vesicular acetylcholine transporter as a novel target for insecticide action. *PLoS One* **2012**, *7*, e34712.
(23) Che, Z.; Zhang, S.; Shao, Y.; Fan, L.; Xu, H.; Yu, X.; Zhi, X.; Yao, X.; Zhang, R. Synthesis and quantitative structure-activity relationship (QSAR) study of novel *N*-arylsulfonyl-3-acylindole arylcarbonyl hydrazone derivatives as nematicidal agents. *J. Agric. Food Chem.* **2013**, *61*, 5696−5705.
(24) Wen, Y.; Meyer, S. L. F.; Masler, E. P.; Zhang, F.; Liao, J.; Wei, X.; Chitwood, D. J. Nematotoxicity of drupacine and a *Cephalotaxus* alkaloid preparation against the plant-parasitic nematodes *Meloidogyne incognita* and *Bursaphelenchus xylophilus*. *Pest Manag. Sci.* **2013**, *69*, 1026−1033.
(25) Ntalli, N. G.; Caboni, P. Botanical nematicides: a review. *J. Agric. Food Chem.* **2012**, *60*, 9929−9940.
(26) Sajid, M.; Azim, M. K. Characterization of the nematicidal activity of natural honey. *J. Agric. Food Chem.* **2012**, *60*, 7428−7434.
(27) Draber, W.; Fedtke, C. Herbicide interaction with plant biochemical systems. In *Advances in Pesticide Science, Part 3*; Geissbühler, H., Ed.; Pergamon Press: Oxford, U.K., 1979; pp 475−486.
(28) Kranz, E.; Santel, H. J.; Lürssen, K.; Schmidt, R. R.; Krauskopf, B. New 6-cyclo-butyl-1,2,4-triazinone derivatives—useful as herbicides and plant growth regulators. DE Patent 3,917,043, 1990.
(29) Rigterink, R. H. Insecticidal use of *S*-((4-oxo-1,2,3-benzotriazin-3(4*H*)-yl)-methyl)phosphorothioates and phosphorodithioates. U.S. Patent 3,551,562, 1970.
(30) Hosler, J. F.; Hardy, W. B. *N*-Trichloromethylthio-1,2,3-benzotriazine-4-one as a novel nematocide. U.S. Patent 2,935,445, 1960.
(31) Nishiwaki, K.; Okamoto, A.; Matsuo, K.; Hayase, Y.; Masaki, S.; Hasegawa, R.; Ohba, K. Tetrahydrobenzotriazines as a new class of nematocide. *Bioorg. Med. Chem.* **2007**, *15*, 1341−1345.
(32) Kalusa, A.; Chessum, N.; Jones, K. An efficient synthesis of 2,3-diaryl(3*H*)-quinazolin-4-ones via imidoyl chlorides. *Tetrahedron Lett.* **2008**, *49*, 5840−5842.
(33) Staiger, R. P.; Wagner, E. C. Isatoic anhydride. II. Reactions of isatoic anhydride with ammonia. *J. Org. Chem.* **1948**, *13*, 347−352.
(34) Clark, A. S.; Deans, B.; Stevens, M. F. G.; Tisdale, M. J.; Wheelhouse, R. T.; Denny, B. J.; Hartley, J. A. Antitumor imidazotetrazines. 32. Synthesis of novel imidazotetrazinones and related bicyclic heterocycles to probe the mode of action of the antitumor drug Temozolomide. *J. Med. Chem.* **1995**, *38*, 1493−1504.
(35) Yoneda, F.; Watabe, M.; Sakae, M.; Katsurada, M.; Sabado, T. Preparation of 2-(*N*-cyanoimino)thiazolidin-4-one derivatives. JP Patent 09110845, 1997.
(36) Sarma, P. K. S.; Sharma, S.; Dharmarajan, S.; Shelke, S. Y.; Pal, A.; Kondaskar, A.; Gupta, P.; Chugh, A.; Tiwari, A.; Nanda, K. Adrenergic receptor antagonists. WO Patent 2006117760, 2006.
(37) Che, Z.; Zhang, S.; Shao, Y.; Fan, L.; Xu, H.; Yu, X.; Zhi, X.; Yao, X.; Zhang, R. Synthesis and quantitative structure-activity relationship (QSAR) study of novel *N*-arylsulfonyl-3-acylindole arylcarbonyl hydrazone derivatives as nematicidal agents. *J. Agric. Food Chem.* **2013**, *61*, 5696−5705.
(38) Li, J.; Zhang, Z.; Xu, X.; Shao, S.; Li, Z. Nematicidal activities of diamides with diphenylacetylene scaffold against *Meloidogyne incognita*. *Aust. J. Chem.* **2015**, DOI: 10.1071/CH15065.
(39) Twomey, U.; Rolfe, R. N.; Warrior, P.; Perry, R. N. Effects of the biological nematicide, DiTera®, on movement and sensory responses of second stage juveniles of *Globodera rostochiensis*, and stylet activity of *G. rostochiensis* and fourth stage juveniles of *Ditylenchus dipsaci*. *Nematology* **2002**, *4*, 909−915.
(40) Spence, K. O.; Lewis, E. E. Biopesticides with complex modes of action: Direct and indirect effects of DiTera® on *Meloidogyne incognita*. *Nematology* **2010**, *12*, 835−846.
(41) Fernández, C.; Rodríguez-Kábana, R.; Warrior, P.; Kloepper, J. W. Induced soil suppressiveness to a root-knot nematode species by a nematicide. *Biol. Control* **2001**, *22*, 103−114.

DOI: 10.1021/acs.jafc.5b01762
J. Agric. Food Chem. 2015, 63, 6883−6889

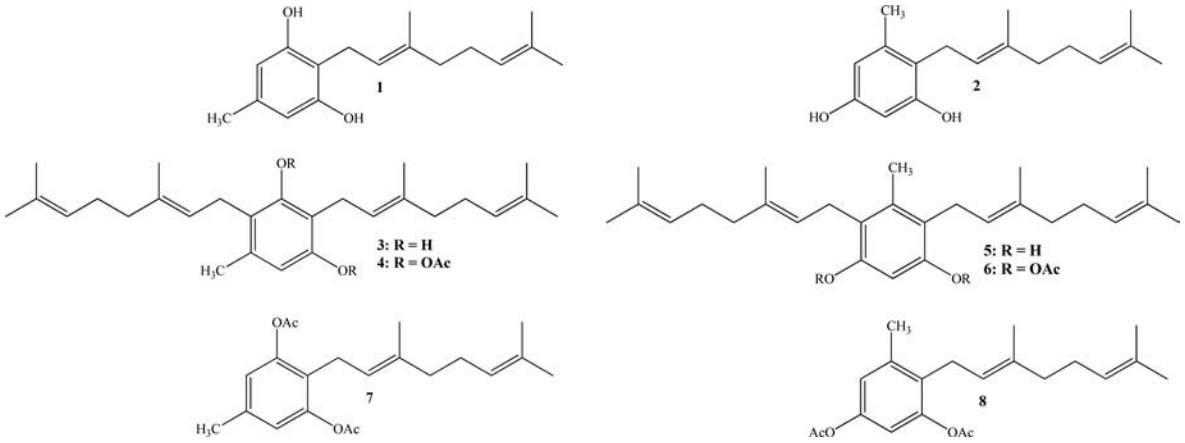

Figure 1. Structure of geranylphenols/diacetates synthesized in this work and tested against *B. cinerea*.

PPO), were used. The latter is a commercial polymer known as Pluronic F-127. In this work, we report the enhancement of antifungal activity of geranylphenols when they are solubilized in polymer micelles. In addition, the synthesis and structural determination of the studied compounds are discussed.

MATERIALS AND METHODS

Chemicals. Unless otherwise stated, all chemical reagents purchased (Merck, Darmstadt, Germany, or Aldrich, St. Louis, MO) were of the highest commercially available purity and were used without previous purification. Silica gel (200−300 mesh, Merck) was used for column chromatography (CC) and silica gel plates HF_{254} for thin-layer chromatography (TLC). TLC spots were detected by heating after spraying with 25% H_2SO_4 in H_2O.

Spectroscopies. Infrared (IR) spectra (32 scans per sample) were recorded as thin films in a Fourier transform infrared (FTIR) Nicolet 6700 spectrometer (Thermo Scientific, San Jose, CA), and wavelengths are reported in cm^{-1}. Low-resolution mass spectra were recorded on an Agilent 5973 spectrometer (Agilent Technologies, Santa Clara, CA) at 70 eV ionizing voltage in a DB-5 m, 30 m × 0.25 mm × 0.25 μm column, and data are given as m/z (percent relative intensity). High-resolution mass spectra were recorded on a LTQ Orbitrap XL spectrometer (Thermo Scientific, San Jose, CA) by applying a voltage of 1.8 kV in the positive ionization mode and 1.9 kV in the negative ionization mode. The spectra were recorded using full-scan mode, covering a mass range from m/z 100 to 1300. The resolution was set to 50 000, and maximum loading time for the ion cyclotron resonance (ICR) cell was set to 250 ms. Nuclear magnetic resonance (NMR) experiments were performed on a Bruker Avance 400 digital NMR spectrometer (Bruker, Rheinstetten, Germany), operating at 400.1 MHz for ^1H and 100.6 MHz for ^{13}C. ^1H, ^{13}C, ^{13}C distortionless enhancement by polarization transfer (DEPT-135), selective gradient-selected one-dimensional (1D) ^1H nuclear Overhauser effect spectrometry (NOESY), gradient-selected two-dimensional (2D) heteronuclear single-quantum coherence (HSQC), and gradient-selected 2D heteronuclear multiple-bond correlation (HMBC) spectra were recorded in $CDCl_3$ solutions and are referenced to the residual peaks of $CHCl_3$ at δ = 7.26 and 77.0 ppm for ^1H and ^{13}C, respectively. Chemical shifts are reported in δ parts per million (ppm), and coupling constants (J) are given in hertz.

Dynamic Light Scattering (DLS). Aqueous solutions of PEO−PCL and Pluronic F-127 (1 mM) in the absence and presence of geranyl derivatives (100 mM) were thermostated at 25 °C, and DLS measurements were performed using a Zetasizer Nano ZS (Malvern Instruments, Malvern, U.K.) equipped with a He−Ne laser (633 nm, 4 mW).

Fluorescence Probing. Steady-state fluorescence spectra of pyrene were recorded using a Horiba Jobin Yvon Fluoromax 4 fluorometer by exciting at 337 nm. All emission spectra were corrected for detector response using a correction curve supplied by the instrument manufacturer. The ratio I_1/I_3 corresponds to the ratio of intensities of peak one (λ = 372 nm) to peak three (λ = 384 nm), whereas the ratio I_M/I_E corresponds to the ratio of intensities of the monomer band to the excimer band (λ = 450 nm).

Synthesis of Geranyl Derivatives. *(E)-2-(3,7-Dimethylocta-2,6-dienyl)-5-methylbenzene-1,3-diol (**1**), (E)-4-(3,7-Dimethylocta-2,6-dienyl)-5-methylbenzene-1,3-diol (**2**), 2,4-Bis((E)-3,7-dimethylocta-2,6-dienyl)-5-methylbenzene-1,3-diol (**3**), and 4,6-Bis((E)-3,7-dimethylocta-2,6-dienyl)-5-methylbenzene-1,3-diol (**5**).* $BF_3{\cdot}OEt_2$ (0.46 g, 3.2 mmol) was slowly added dropwise, at room temperature and under a N_2 atmosphere, to a stirred solution of orcinol (6.1 g, 49 mmol) and geraniol (7.55 g, 49 mmol) in acetonitrile (2 mL) saturated with $AgNO_3$. After the addition was completed, the stirring was continued for 48 h. The end of the reaction was verified by TLC, and then the mixture was poured onto crushed ice (approximately 30 g) and salt (NaCl) vacuum filtration and extracted with EtOAc (3 × 20 mL). The organic layer was washed with $NaHCO_3$ (15 mL, 5%) and water (2 × 15 mL), dried over Na_2SO_4, and filtered. The solvent was evaporated under reduced pressure. The crude was redissolved in CH_2Cl_2 (5 mL) and chromatographed on silica gel with petroleum ether/EtOAc mixtures of increasing polarity (0:20 → 6:14). Five fractions were obtained: fraction I, 1554.8 mg of dark yellow viscous oil (9.9% yield, compound **3**); fraction II, 1281.8 mg of yellow viscous oil (12.5% yield, compound **1**); fraction III, 955.3 mg of dark yellow viscous oil (6.1% yield, compound **5**); fraction IV, 415.4 mg of dark yellow viscous oil (mixture of compounds **2** and **5**); and fraction V, 2816.2 mg of yellow viscous oil (27.6% yield, compound **2**). Unreacted orcinol (3.38 g) was recovered. Spectroscopic data of compounds **1** and **2** were consistent with those reported in the literature.[29−31] Spectroscopic data are given in the Supporting Information.

Acetylation of Geranylated Phenols. Geranylated phenols were acetylated by standard acetylation using Ac_2O and 4-dimethylaminophenol (DMAP) in CH_2Cl_2. In a typical reaction, Ac_2O (1.08 g, 10.6 mmol) is added to a solution of a geranylated phenol (0.284 mmol), DMAP (3.0 mg), and pyridine (1.0 mL) in dichloromethane (10−20 mL). The end of the reaction is verified by TLC (1.5 h), and then the mixture is extracted with EtOAc (2 × 20 mL). The organic layer is washed with 5% $KHSO_4$ (2 × 10 mL) and water (2 × 10 mL), dried over Na_2SO_4, and filtered. The solvent is evaporated under reduced pressure. The crude is redissolved in CH_2Cl_2 (5 mL) and chromatographed on silica gel with petroleum ether/EtOAc mixtures of increasing polarity (19.8:0.2 → 18.4:1.6).

*2,4-Bis((E)-3,7-dimethylocta-2,6-dienyl)-5-methyl-1,3-phenylene Diacetate (**4**).* Compound **4** was obtained by standard acetylation of compound **3** (170 mg, 0.429 mmol) with Ac_2O (1.0 mL), DMAP (3.0 mg), and pyridine (1.0 mL) in dichloromethane (15 mL). Compound **4** was obtained as dark yellow viscous oil (185 mg, 90.5% yield). Spectroscopic data are given in the Supporting Information.

*4,6-Bis((E)-3,7-dimethylocta-2,6-dien-1-yl)-5-methyl-1,3-phenylene Diacetate (**6**).* Compound **6** was obtained by standard acetylation

DOI: 10.1021/acs.jafc.5b01920
J. Agric. Food Chem. 2015, 63, 6890−6896

of compound **5** (245 mg, 0.618 mmol) with Ac_2O (1.0 mL), DMAP (3.0 mg), and pyridine (1.0 mL) in dichloromethane (20 mL). Compound **6** was obtained as dark yellow viscous oil (267.5 mg, 89.8% yield). Spectroscopic data are given in the Supporting Information.

*(E)-2-(3,7-Dimethylocta-2,6-dienyl)-5-methyl-1,3-phenylene Diacetate (**7**).* Compound **7** was obtained by standard acetylation of compound **1** (74 mg, 0.284 mmol) with Ac_2O (1.0 mL), DMAP (2.0 mg), and pyridine (1.0 mL) in dichloromethane (10 mL). Compound **7** was obtained as dark yellow viscous oil (93.3 mg, 96.4% yield). Spectroscopic data are given in the Supporting Information.

*(E)-4-(3,7-Dimethylocta-2,6-dienyl)-5-methyl-1,3-phenylene Diacetate (**8**).* Compound **8** was obtained by standard acetylation of compound **2** (362 mg, 1.39 mmol) with Ac_2O (1.0 mL), DMAP (3.0 mg), and pyridine (1.0 mL) in dichloromethane (20 mL). Compound **8** was obtained as dark yellow viscous oil (444.6 mg, 92.8% yield). Spectroscopic data are given in the Supporting Information.

Structure Determination. Spectroscopic evidence of double substitution on the aromatic nucleus by geranyl chains in compound **3** was established from the ^{1}H NMR spectrum by the following observations: a unique Ar−H signal at 6.30 ppm (s, 1H, H-6), four olefinic protons at 5.32 ppm (t, J = 6.9 Hz, 1H, H-2′), 5.19 ppm (t, J = 6.6 Hz, 1H, H-2″), 5.11 ppm (t, J = 6.6 Hz, 2H, H-6′ and H-6″), and two doublet signals at 3.46 ppm (J = 6.9 Hz, 2H, H-1′) and 3.35 ppm (J = 6.6 Hz, 2H, H-1″). Finally, the complete determination of the asymmetrical structure was established by 2D HMBC and selective 1D NOESY experiments. The major 2D HMBC correlations confirming the structure of compound **3** are $^2J_{H-C}$ coupling between H-1′ and C-2 (δ_C = 111.5 ppm), $^3J_{H-C}$ coupling of H-1′ with C-3 and C-1 (δ_C = 153.4 and 152.2 ppm), respectively, $^2J_{H-C}$ coupling of H-1″ with C-4 (δ_C = 118.1 ppm), and $^3J_{H-C}$ coupling of H-1″ with C-5 (δ_C = 135.1 ppm) and C-3 (δ_C = 153.4 ppm) (Figure S1 of the Supporting Information). From selective 1D NOESY experiments, the *E* geometry in the C-2′−C-3′ and C-2″−C3″ double-bond position of the geranyl chain was established. In this case, the most important correlations are between H-1′ with the methyl group in the C-3′ position (δ_H = 1.86 ppm) and with both OH groups (δ_H = 5.50 and 5.44 ppm), whereas H-1″ correlates with CH_3−Ar (δ_H = 2.25 ppm), CH_3−C3″ (δ_H = 1.84 ppm), and OH group (δ_H = 5.50 ppm) (Figure S2 of the Supporting Information).

A similar spectroscopic analysis was performed to determine the structure of compound **5**. Spectroscopic evidence of double substitution on the aromatic nucleus by geranyl chains in compound **5** was obtained from the ^{1}H NMR spectrum through the following observations: a unique Ar−H signal at 6.25 ppm (s, 1H, H-6), four olefinic protons at 5.11 ppm (t, J = 6,4 Hz, 2H, H-2′), 5.05 ppm (t, J = 6.6 Hz, 2H, H-6′), and a unique doublet signal at 3.33 ppm (d, J = 6.6 Hz, 4H, H-1′). Finally, the complete determination of the symmetrical structure was established by 2D HMBC and selective 1D NOESY experiments. The main 2D HMBC correlations used to confirm the structure of compound **5** were a $^2J_{H-C}$ coupling of H-1′ (δ_H = 3.33 ppm) with C-4 and C-6 (δ_C = 118.5 ppm) and $^3J_{H-C}$ with C-1 and C-3 (δ_C = 152.9 ppm). The *E* geometry in the C-2′−C-3′ double-bond position of the geranyl chain was established by selective 1D NOESY experiments. The most important spatial correlations were observed between H-1′ with CH_3−Ar (δ_H = 2.07 ppm) and with the CH_3−C-3′ position (δ_H = 1.79 ppm). The main 2D HMBC and 1D NOESY correlations are shown in Figure 2.

The presence of diacetylated derivatives **4** and **6**, obtained by standard acetylation of compounds **3** and **5**, respectively, was confirmed by NMR spectroscopy. The ^{1}H NMR spectrum of compound **4** shows two singlet signals at δ_H = 2.28 ppm (s, 3H, CH_3CO) and 2.26 ppm (s, 6H, CH_3CO and CH_3−Ar), whereas ^{1}H NMR of compound **6** show a singlet signal at δ_H = 2.28 ppm (s, 6H, 2× CH_3CO). Additionally, in the ^{13}C NMR spectrum of compound **6**, two singlet signals at δ_C = 169.2 ppm (2× C═O) and 20.7 ppm (2× CH_3CO) were observed as a result of the symmetry of the molecule.

Finally, the ^{1}H NMR spectrum of symmetric diacetylated derivative **7** shows a singlet signal at δ_H = 2.27 ppm (6H, 2× CH_3CO), whereas in the ^{13}C NMR spectrum, the signal at δ_C = 169.2 ppm (2× C═O) confirms the presence of the diacetylated derivative. On the other hand, the ^{1}H NMR spectrum of diacetylated derivative **8** shows a singlet signal at δ_H = 2.28 ppm (6H, 2× CH_3CO), whereas in the ^{13}C NMR spectrum, two singlet signals are observed at δ_C = 169.3 ppm (C═O) and 169.2 ppm (C═O) as a result of the asymmetry of the molecule, confirming the presence of the diacetylated derivative.

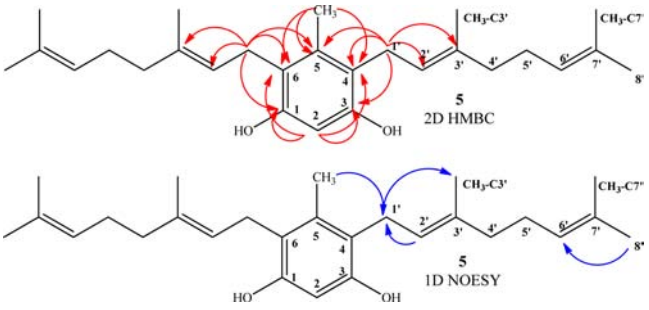

Figure 2. Most important 2D ^{1}H−^{13}C HMBC and selective 1D NOESY correlations for compound **5**.

Poly(ethylene oxide)-*b*-Poly(caprolactone) (PEO−PCL). PEO−PCL was synthesized in bulk by ring-opening polymerization using stannous octanoate (SnOct) as a catalyst. Briefly, freshly distilled ε-caprolactone was added under a nitrogen atmosphere to poly(ethylene oxide) monomethyl ether (Aldrich, M_n = 2000 g/mol). After complete dissolution of PEO, 0.01% of SnOct was added and the flask was heated at 135 °C with constant stirring. After 24 h, the resulting viscous liquid was cooled to room temperature, dissolved in 5 mL of tetrahydrofuran (THF), precipitated into a large excess of cold *n*-hexane, filtered, redissolved in THF, and precipitated in *n*-hexane. The white precipitate was collected by filtration and vacuum-dried at 35 °C for 2 days. Yield = 94%. Absolute molecular weight was measured using matrix-assisted laser desorption/ionization−time-of-flight (MALDI−TOF) (MW = 3409 g/mol). The data indicate that the degree of polymerization of ε-caprolactone is 14, and therefore, the resulting block copolymer composition is PEO_{43}-*b*-PCL_{14}.

Preparation and Characterization of Polymer Micelles. Polymer micelles were prepared by direct dissolution of block copolymers in water at a concentration well above the critical micelle concentration (cmc) (1 mM). The cmc was determined by a photophysical technique that consists of measuring the ratio I_M/I_E of pyrene fluorescence as a function of the polymer concentration. The size distributions of polymeric micelles were determined by DLS.

Fungal Isolate and Culture Condition. In this study, a strain of *B. cinerea* isolated from a naturally infected grape (*Vitis vinifera*) was used in all experiments. This strain was maintained on potato dextrose agar (PDA) medium (Difco, Detroit, MI) at 4 °C. The inoculum of the pathogen was grown on PDA in a photoperiod of 16 h light/8 h dark at 23 °C for 5 days.

Antifungal Activity. To determine the antifungal activity of geranyl derivatives, two different stock solutions were prepared for each compound. Homogeneous stock solutions were formulated by dissolving 20−40 mg of each compound in 500 μL of ethanol and then diluting in water (5 mL) to obtain a 5000 ppm concentration. On the other hand, micro-heterogeneous solutions were obtained using the emulsion method. Briefly, aliquots (100 μL) of each compound dissolved in dichloromethane were added to 10 mL of an aqueous polymer solution (1 mM). After an emulsion has been formed, the organic solvent is eliminated by heating and sonication. In this process, compounds **1**−**8** are incorporated into the hydrophobic micelle core, reaching a concentration of 0.1 M. Before their application to Petri plates, these solutions are diluted to 650−1250 ppm but keeping the polymer concentration constant (1 mM).

The radial growth rate assay on PDA medium was used to determine the antifungal activity of test compounds.[32,33] Test compounds, in ethanol/water solution or aqueous polymer solution, were added to Petri plates containing PDA medium at 50 °C to give 50, 150, and 250 ppm. When the medium was almost solidified, 4 mm

DOI: 10.1021/acs.jafc.5b01920
J. Agric. Food Chem. 2015, 63, 6890−6896

Scheme 1. Synthesis of Compounds 1−3 and 5

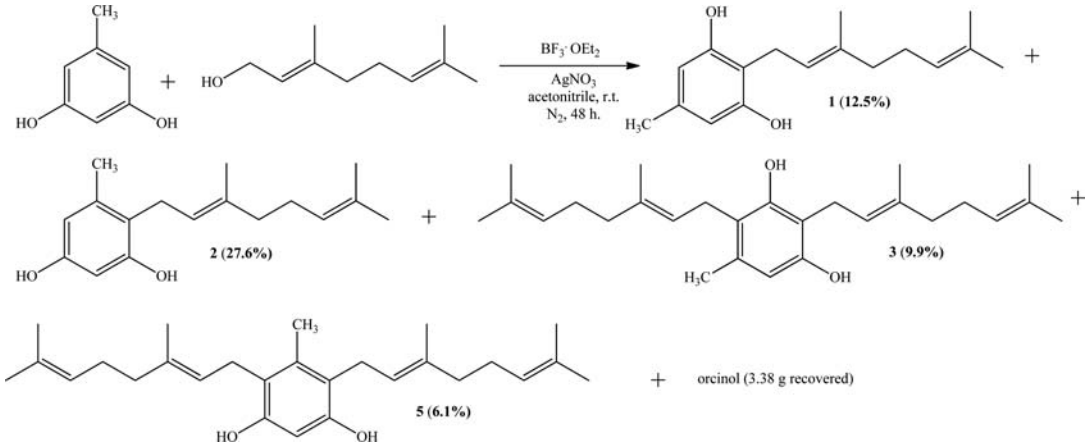

diameter disks of fungus cut were placed in the center of the plate. Negative controls (C−) are used in the corresponding stock solution with pure solvent (1% ethanol) or polymer solution (1 mM PEO−PCL or Pluronic F-127). Captan, a commercial fungicide, is used as the positive control (C+) at the same concentrations and conditions of test compounds. After incubation by 48 h (ethanol) and 72 h (polymer) at 23 °C under a photoperiod of 16 h light/8 h dark, diameters of colonies were measured with a ruler and the inhibition percentage was calculated as the average of three replicas compared to the negative control.

RESULTS AND DISCUSSION

The direct geranylation of orcinol using the acetonitrile/BF_3·Et_2O/$AgNO_3$ system leads to compounds **1** and **2** with 12.5 and 27.6% yields, respectively, which are almost identical to those reported for the standard conditions, i.e., the dioxane/BF_3·Et_2O system.[29] However, with the modified method, two additional digeranyl derivatives **3** and **5** were identified and isolated from the reaction products with 9.9 and 6.1% yields, respectively.

The synthesis of compounds **1**−**3** and **5** is described in Scheme 1.

It should be mentioned that incorporation of two geranyl chains to the aromatic ring has been previously described in the geranylation of methoxyphenols using ether as the solvent.[13] However, the reaction of 2,4,5-trimethoxyphenol with geraniol in dioxane follows a completely different reaction pathway, and no digeranylated phenols were obtained.[17] On the other hand, diprenyl phenols have also been obtained in the reaction between dihydroxybenzenes and 1,3,5-trihydroxybenzene with 3-methyl-2-buten-1-ol, using a mixture of ethyl ether/dichloromethane as the solvent.[18] Finally, digeranyl phenols have also been obtained in the geranylation of 1,3,5-trihydroxybenzene using the modified electrophilic aromatic substitution (EAS) reaction.[7] These results emphasize the important role played by solvent in this kind of reaction. Diacetylated derivatives **4** and **6** were obtained by standard acetylation of compounds **3** and **5** with 93.3 and 92.8% yields, respectively. Finally, derivatives **7** and **8** were obtained by standard acetylation of compounds **1** and **3** with 90.5 and 89.8% yields, respectively.

The physical and spectroscopic properties of compounds **1** and **2** were consistent with those previously reported.[11,29,31] The structural determination of new compounds **3**−**6** is described in detail in the Materials and Methods.

Formation of Polymer Micelles. In aqueous solution and at concentrations above the cmc, amphiphilic block copolymers self-aggregate forming spherical micelles. The values of cmc, determined by measuring the ratio I_M/I_E of pyrene fluorescence as a function of the polymer concentration, are 2.7×10^{-6} and 5.5×10^{-5} M for Pluronic F-127 and PEO−PCL, respectively. Thus, to ensure the presence of micelles, a polymer concentration of 1 mM was used in all experiments. The formation of micelles has also been evidenced by DLS measurements, which give the size and size distribution of the formed aggregates. The results shown in Figures 3 and 4

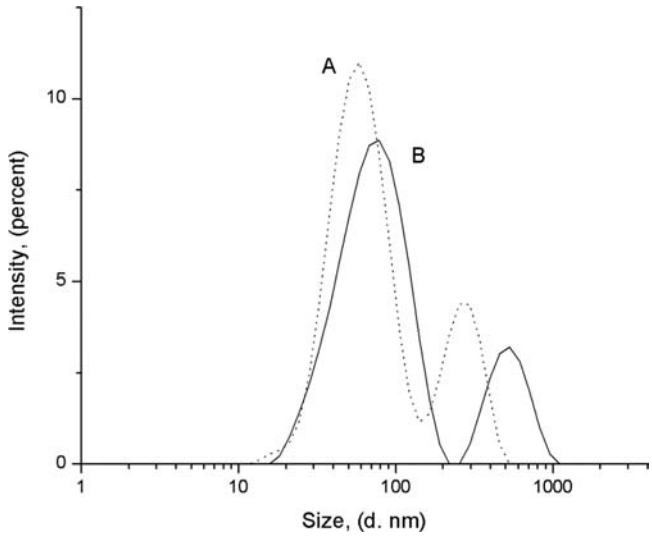

Figure 3. Distribution sizes of aggregates formed by PEO−PCL (1 mM) in the (A) absence and (B) presence of compound **1** (10 mM). DLS measurements were made at 25 °C.

indicate that small micelles and larger aggregates are formed at this polymer concentration. This agrees with previous studies, made with transmission electronic microscopy (TEM), where it has been shown that PEO−PCL forms spherical and elongated aggregates, and the sizes obtained from TEM were consistent with those obtained by DLS.[34,35] Additionally, the inclusion of geranylphenols into the micelles brings about a change in the size distribution. In both cases, the solute induces the formation of stable aggregates with a larger average diameter. This behavior is similar to that reported for solubilization of a family of alkylphenols in Pluronic F-127.[36]

DOI: 10.1021/acs.jafc.5b01920
J. Agric. Food Chem. 2015, 63, 6890−6896

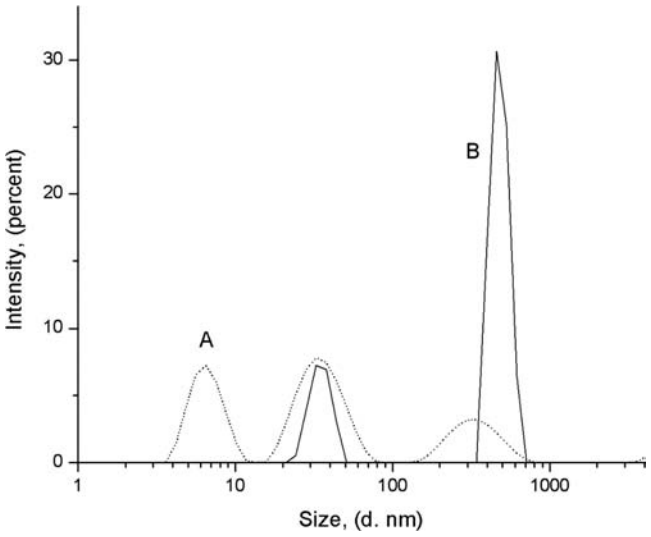

Figure 4. Distribution sizes of aggregates formed by Pluronic F-127 (1 mM) in the (A) absence and (B) presence of compound **1** (10 mM). DLS measurements were made at 25 °C.

The micropolarity of the hydrophobic micelle core was assessed by measuring the ratio I_1/I_3 in the pyrene fluorescence spectrum. It has been shown that this ratio strongly depends upon the polarity of the medium where pyrene is located,[37] and a Py polarity scale has been proposed.[38] The results indicate that the micelle formed by PEO−PCL (I_1/I_3 = 1.13) is much more hydrophobic than that formed by Pluronic F-127 (I_1/I_3 = 1.56). Consequently, nonpolar substrates should be more easily incorporated into the core of PEO−PCL micelles.

Antifungal Activity against *B. cinerea*. The effect of geranylphenols on the mycelial growth of plant pathogen *B. cinerea* was evaluated *in vitro* after 72 h of incubation using the radial growth rate assay with PDA as the medium. The test compounds were added to the incubation media in either homogeneous solution (using 1% ethanol in water as the solvent) or dissolved in an aqueous solution of polymer micelles (1 mM). The inhibitory effect is evaluated as a percentage of inhibition, which is calculated as the ratio of the area of *B. cinerea* in the presence and absence of geranylphenols. The means of three independent assays are summarized in Tables 1 and 2. For comparison, the values of the percentage of inhibition obtained with Captan, a molecule that is widely used to control the growth of *B. cinerea*, are included (measured at the same concentration used to determine the activity of geranylphenols).

Analysis of the results given in Table 1 shows that the inhibitory effect increases with increasing the compound concentration and that the antifungal activity depends upon the chemical structure of geranylphenol derivatives. Thus, monogeranyl phenols **1** and **2** exhibit inhibitory activity similar or slightly lower than that observed for diacetylated compounds (**7** and **8**) at 250 ppm. These results are in line with those reported previously for other series of geranylphenol derivatives[7] and, all together, suggest that the activity is mainly determined by the presence of the geranyl chain. On the other hand, the addition of a second geranyl chain brings about an increase on antifungal activity for all studied compounds (Table 1 compares compounds **3** and **1**, compounds **5** and **2**, compounds **4** and **7**, and compounds **6** and **8**). Compound **4** exhibits the highest inhibitory effect, i.e., 69 and 97% at 150 and 250 ppm, respectively. However, in previous work, it has been found that digeranyl derivatives exhibit lower activities than the corresponding monogeranyl compounds and that their activity strongly depends upon the presence of hydroxyl groups.[7] This structure effect on activity may be attributed to the higher solubility of digeranyl phenols, which would increase the biodisponibility of these compounds. To verify this hypothesis, a study of solubilization into polymer micelles was carried out.

Table 1. Effect of Geranylphenols on Mycelial Growth of *B. cinerea* Measured as a Percentage of Inhibition[a]

	percentage of inhibition on mycelial growth of *B. cinerea* *in vitro*[b]		
compound	50 mg/L	150 mg/L	250 mg/L
1	37	65	82
2	0	25	63
3	25	61	93
4	5	69	97
5	12	56	83
6	11	54	85
7	8	51	82
8	24	55	78
C−[c]	0	0	0
C+[c]	88	94	94

[a]Geranyl phenols were added to the incubation media from a stock solution using ethanol/water (1%) as the solvent. [b]The percentage of inhibition of mycelial growth is based on colony diameter measurements after 48 h of incubation. Each point represents the mean of at least three independent experiments. [c]C− refers to the negative control and corresponds to stock solution with pure solvent (1% ethanol), and C+ refers to the positive control (Captan).

The results given in Table 2 indicate that the inhibitory activity of all test compounds against mycelial growth of *B. cinerea* changes in the presence of micelle-forming polymers. In the case of PEO−PCL, the effect on mycelial growth depends upon the structure of geranyl compounds, i.e., at all studied concentrations, an increase is observed for compounds **2**, and **5**, whereas a decrease in activity was found for the other studied compounds. However, in the presence of Pluronic F-127, the increase in activity is very dramatic, changing from no effect to 80% of inhibition at a low concentration (compare data of compound **2** at 50 mg/L in Tables 1 and 2). This activity is independent of the geranylphenol structure and is almost the same obtained with Captan, the positive control. These results suggest that encapsulation into micelles formed by Pluronic F-127 might improve some properties of the molecules (stability or availability) or might provide new environmental conditions (homogeneous distribution), allowing for an inhibitory activity of test compounds on the growth of *B. cinerea*, even at a lower concentration, such as 50 mg/L.

The structure of the polymer micelle seems to be a determinant factor in the magnitude of the inhibitory effect exhibited by each compound. This effect could be attributed to differences in micellar sizes and polarity of the micellar core. Polymer micelles formed by Pluronic F-127 are smaller and the core is more polar than in micelles formed by PEO−PCL. These physical parameters might affect the distribution coefficients of these compounds between the aqueous phase and the pseudo-micellar phase provided by the block copolymers; i.e., these coefficients should be larger in the presence of micelles formed by PEO−PCL. On the other hand, the release rates of compounds solubilized in these micelles

DOI: 10.1021/acs.jafc.5b01920
J. Agric. Food Chem. 2015, 63, 6890−6896

Table 2. Percentage of Inhibition of Geranylphenols on Mycelial Growth of *B. cinerea* Measured in the Presence of Polymer Micelles

	percentage of inhibition on mycelial growth of *B. cinerea in vitro*[a]					
	PEO-*b*-PCL			Pluronic F-127		
compound	50 mg/L	150 mg/L	250 mg/L	50 mg/L	150 mg/L	250 mg/L
1	9	32	42	82	96	96
2	37	61	73	76	90	88
3	16	36	37	85	91	96
4	10	31	50	93	99	99
5	93	94	97	82	92	96
6	0	36	36	93	99	99
7	32	35	59	77	88	94
8	17	39	80	81	88	93
C−[b]	0	0	0	0	0	0
C+[b]	93	99	99	98	99	99

[a]The percentage of inhibition of mycelial growth is based on colony diameter measurements after 72 h of incubation. Each point represents the mean of at least three independent experiments. [b]C− refers to the negative control and corresponds to aqueous polymer solution (1 mM PEO−PCL or Pluronic F-127), and C+ refers to the positive control (Captan).

should also be lower than in micelles of Pluronic F-127. The direct consequence of these two effects is that nonpolar compounds incorporated into PEO−PCL micelles are less available during the development of mycelial growth halo. A study where these physicochemical parameters are evaluated as a function of the substrate structure is currently being carried out. Additionally, the possibility that polymer micelles penetrate the fungus membrane and releasing of entrapped compounds occurs inside of a fungus cell should also be considered. The proposal of this alternative mechanism of action is based on results that have demonstrated that both polymer micelles can be internalized into cells by endocytosis.[34,39]

The results in Table 2 also show that the activity of all encapsulated test compounds is quite similar to that measured for Captan, a fungicide widely used to protect crops. In addition, an aqueous solution of polymer micelles can be easily applied *in vivo* by simple spraying. These interesting properties turn polymer micelles into very promising systems for control of *B. cinerea* in the field. Obviously, these results should be validated evaluating *in vivo* the biological effect of encapsulated test compounds on plant tissues infected by this fungus. Finally, it is worth mentioning that these polymers are biocompatible and Pluronic F-127 copolymers are listed in U.S. and British Pharmacopoeia as pharmaceutical excipients.

■ ASSOCIATED CONTENT

Supporting Information

The Supporting Information is available free of charge on the ACS Publications website at DOI: 10.1021/acs.jafc.5b01920.

Spectroscopic information of compounds **1**−**8**, 2D $^{1}H-^{13}C$ HMBC spectrum of compound **3** (Figure S1), and main selective 1D NOESY correlations observed for compound **3** (Figure S2) (PDF)

■ AUTHOR INFORMATION

Corresponding Authors

*E-mail: andres.olea@uautonoma.cl.
*E-mail: luis.espinozac@usm.cl.

Funding

The authors thank FONDECYT (Grant 1120996) and the Dirección General de Investigación y Postgrado (DGIP-USM Grant 131305) of Universidad Técnica Federico Santa María.

Notes

The authors declare no competing financial interest.

■ REFERENCES

(1) Lee, H. J.; Choi, G. J.; Cho, K. Y. Correlation of lipid peroxidation in *Botrytis cinerea* caused by dicarboximide fungicides with their fungicidal activity. *J. Agric. Food Chem.* **1998**, *46*, 737−741.

(2) Latorre, B. A.; Flores, V.; Sara, A. M.; Roco, A. Dicarboximide-Resistant Isolates of *Botrytis cinerea* from Table Grape in Chile: Survey and Characterization. *Plant Dis.* **1994**, *78*, 990−994.

(3) Latorre, B. A.; Spadaro, I.; Rioja, M. E. Occurrence of resistant strains of *Botrytis cinerea* to anilinopyrimidine fungicides in table grapes in Chile. *Crop Prot.* **2002**, *21*, 957−961.

(4) Cotoras, M.; Folch, C.; Mendoza, L. Characterization of the antifungal activity on *Botrytis cinerea* of the natural diterpenoids kaurenoic acid and 3 beta-hydroxy-kaurenoic acid. *J. Agric. Food Chem.* **2004**, *52*, 2821−2826.

(5) Mendoza, L.; Espinoza, P.; Urzua, A.; Vivanco, M.; Cotoras, M. *In Vitro* Antifungal Activity of the Diterpenoid 7α-Hydroxy-8(17)-labden-15-oic Acid and Its Derivatives against *Botrytis cinerea*. *Molecules* **2009**, *14*, 1966−1979.

(6) Mendoza, L.; Araya-Maturana, R.; Cardona, W.; Delgado-Castro, T.; Garcia, C.; Lagos, C.; Cotoras, M. In vitro sensitivity of *Botrytis cinerea* to anthraquinone and anthrahydroquinone derivatives. *J. Agric. Food Chem.* **2005**, *53*, 10080−10084.

(7) Espinoza, L.; Taborga, L.; Diaz, K.; Olea, A. F.; Peña-Cortes, H. Synthesis of Linear Geranylphenols and their effect on mycelial growth of plant pathogen *Botrytis cinerea*. *Molecules* **2014**, *19*, 1512−1526.

(8) De Rosa, S.; De Giulio, A.; Iodice, C. Biological Effects of Prenylated Hydroquinones—Structure−Activity Relationship Studies in Antimicrobial, Brine Shrimp, and Fish Lethality Assays. *J. Nat. Prod.* **1994**, *57*, 1711−1716.

(9) Danelutte, A. P.; Lago, J. H. G.; Young, M. C. M.; Kato, M. J. Antifungal flavanones and prenylated hydroquinones from Piper crassinervium Kunth. *Phytochemistry* **2003**, *64*, 555−559.

(10) Malami, I. Prenylated benzoic acid derivates from Piper species as source of anti-infective agents. *Int. J. Pharm. Sci. Res.* **2012**, *3*, 1554−1559.

(11) Manners, G. D.; Jurd, L. The hydroquinone terpenoids of *Cordia alliodora*. *J. Chem. Soc., Perkin Trans. 1* **1977**, *1977*, 405−410.

(12) Tziveleka, L.-A.; Kourounakis, A. P.; Kourounakis, P. N.; Roussis, V.; Vagias, V. Antioxidant Potential of Natural and

DOI: 10.1021/acs.jafc.5b01920
J. Agric. Food Chem. 2015, 63, 6890−6896

Synthesised Polyprenylated Hydroquinones. *Bioorg. Med. Chem.* **2002**, *10*, 935−939.
(13) Fedorov, S. N.; Radchenko, O. S.; Shubina, L. K.; Balaneva, N. N.; Bode, A. M.; Stonik, V. A.; Dong, Z. G. Evaluation of cancer-preventive activity and structure-activity relationships of 3-demethylubiquinone Q2, isolated from the ascidian Aplidium glabrum, and its synthetic analogs. *Pharm. Res.* **2006**, *23*, 70−81.
(14) Yamaguchi, L. F.; Lago, J. H. G.; Tanizaki, T. M.; Di Mascio, P.; Kato, M. J. Antioxidant activity of prenylated hydroquinone and benzoic acid derivatives from Piper crassinervium Kunth. *Phytochemistry* **2006**, *67*, 1838−1843.
(15) Espinoza, L. E.; Baeza, E.; Catalan, K.; Osorio, M.; Carrasco, H.; Cuellar, M.; Villena, J. Synthesis and Antitumor Activity of Diterpenylhydroquinone Derivatives of Natural Ent-Labdanes. *Molecules* **2010**, *15*, 6502−6511.
(16) Baeza, E.; Catalan, K.; Pena-Cortes, H.; Espinoza, L.; Villena, J.; Carrasco, H. Synthesis of Geranylhydroquinone Derivatives with Potential Cytotoxic Activity. *Quim. Nova* **2012**, *35*, 523−526.
(17) Baeza, E.; Catalan, K.; Villena, J.; Carrasco, H.; Cuellar, M.; Espinoza, L. Synthesis and cytotoxic activity of geranylmethoxyhydroquinone derivatives. *J. Chil. Chem. Soc.* **2012**, *57*, 1219−1223.
(18) Osorio, M.; Aravena, J.; Vergara, A.; Taborga, L.; Baeza, E.; Catalan, K.; Gonzalez, C.; Carvajal, M.; Carrasco, H.; Espinoza, L. Synthesis and DPPH Radical Scavenging Activity of Prenylated Phenol Derivatives. *Molecules* **2012**, *17*, 556−570.
(19) *Amphiphilic Block Copolymers. Self-Assembly and Applications*; Alexandridis, P., Lindman, B., Eds.; Elsevier Science: Amsterdam, Netherlands, 2000.
(20) Allen, C.; Maysinger, D.; Eisenberg, A. Nano-engineering block copolymer aggregates for drug delivery. *Colloids Surf., B* **1999**, *16*, 3−27.
(21) Kabanov, A. V.; Alakhov, V. Y. Micelles of amphiphilic block copolymers as vehicles for drug delivery. In *Amphiphilic Block Copolymers. Self-Assembly and Applications*; Alexandridis, P., Lindman, B., Eds.; Elsevier: Amsterdam, Netherlands, 2000; pp 347−376.
(22) Gao, Z. S.; Eisenberg, A. A model of micellization for block-copolymers in solutions. *Macromolecules* **1993**, *26*, 7353−7360.
(23) Olea, A. F. Hydrophobic polyelectrolytes. In *Ionic Interactions in Natural and Synthetic Macromolecules*; Ciferri, A., Perico, A., Eds.; John Wiley & Sons: Hoboken, NJ, 2012.
(24) Bromberg, L.; Temchenko, M. Solubilization of hydrophobic compounds by micellar solutions of hydrophobically modified polyelectrolytes. *Langmuir* **1999**, *15*, 8627−8632.
(25) Olea, A. F.; Barraza, R. G.; Fuentes, I.; Acevedo, B.; Martinez, F. Solubilization of phenols by intramolecular micelles formed by copolymers of maleic acid and olefins. *Macromolecules* **2002**, *35*, 1049−1053.
(26) Olea, A. F.; Gamboa, C. Solubilization of phenols in surfactant/polyelectrolyte systems. *J. Colloid Interface Sci.* **2003**, *268*, 63−67.
(27) Peteu, S. F.; Oancea, F.; Sicuia, O. A.; Constantinescu, F.; Dinu, S. Responsive Polymers for Crop Protection. *Polymers* **2010**, *2*, 229−251.
(28) Nair, R.; Varghese, S. H.; Nair, B. G.; Maekawa, T.; Yoshida, Y.; Kumar, D. Nanoparticulate material delivery to plants. *Plant Sci.* **2010**, *179*, 154−163.
(29) Taborga, L.; Vergara, A.; Osorio, M.; Carvajal, M.; Madrid, A.; Marilaf, F.; Carrasco, H.; Espinoza, L. Synthesis and NMR structure determination of new linear geranylphenols by direct geranylation of activated phenols. *J. Chil. Chem. Soc.* **2013**, *58*, 1790−1796.
(30) Manners, G.; Jurd, L.; Stevens, K. Biogenetic-type syntheses of isoprenoid and diisoprenoid derivatives of orcinol. *Tetrahedron* **1972**, *28*, 2949−2959.
(31) Eisohly, H. N.; Turner, C. E.; Clark, A. M.; Eisohly, M. A. Synthesis and antimicrobial activities of certain cannabichromene and cannabigerol related compounds. *J. Pharm. Sci.* **1982**, *71*, 1319−1323.
(32) Hadacek, F.; Greger, H. Testing of antifungal natural products: Methodologies, comparability of results and assay choice. *Phytochem. Anal.* **2000**, *11*, 137−147.
(33) Hou, Z.; Yang, R.; Zhang, C.; Zhu, L.; Miao, F.; Yang, X.; Zhou, L. 2-(Substituted phenyl)-3,4-dihydroisoquinolin-2-iums as Novel Antifungal Lead Compounds: Biological Evaluation and Structure-Activity Relationships. *Molecules* **2013**, *18*, 10413−10424.
(34) Luo, L.; Tam, J.; Maysinger, D.; Eisenberg, A. Cellular internalization of poly(ethylene oxide)-*b*-poly(ε-caprolactone) diblock copolymer micelles. *Bioconjugate Chem.* **2002**, *13*, 1259−1265.
(35) Letchford, K.; Zastre, J.; Liggins, R.; Burt, H. Synthesis and micellar characterization of short block length methoxy poly(ethylene glycol)-block-poly(caprolactone) diblock copolymers. *Colloids Surf., B* **2004**, *35*, 81−91.
(36) Olea, A. F.; Carrasco, H.; Espinoza, L.; Acevedo, B. Solubilization of p-alkylphenols in Pluronics F-68 and F-127 micelles: Partition coefficients and effect of solute on the aggregate structure. *J. Chil. Chem. Soc.* **2014**, *29*, 2451−2454.
(37) Kalyanasundaram, K.; Thomas, J. K. Environmental effects on vibronic band intensities in pyrene monomer fluorescence and their application in studies of micellar systems. *J. Am. Chem. Soc.* **1977**, *99*, 2039−2044.
(38) Dong, D. C.; Winnik, M. A. The Py scale of solvent polarities. Solvent effects on the vibronic fine structure of pyrene fluorescence and empirical correlations with ET and Y values. *Photochem. Photobiol.* **1982**, *35*, 17−21.
(39) Miller, D. W.; Batrakova, E. V.; Waltner, T. O.; Alakhov, V. Y.; Kabanov, A. V. Interactions of pluronic block copolymers with brain microvessel endothelial cells: Evidence of two potential pathways for drug absorption. *Bioconjugate Chem.* **1997**, *8*, 649−657.

DOI: 10.1021/acs.jafc.5b01920
J. Agric. Food Chem. 2015, 63, 6890−6896

principal entry path of veterinary antibiotics is the application of manure on agricultural fields for fertilization.[9] In addition, the transport of veterinary antibiotics via dust in stables of medicated animals has already been reported.[10]

For FQs used in livestock husbandry, the recommended treatment dose ranges from 2.5 to 10 mg per kg of body weight and day[6,7] and consequently, manure was found to contain considerable amounts of these substances. Up to 61.3 mg kg^{-1} enrofloxacin and 18.8 mg kg^{-1} of its metabolite ciprofloxacin could be detected in feces of chicken.[11] Studies on composting processes of manure revealed that, in contrast to sulfadiazine and chlortetracycline, the FQ ciprofloxacin could not be removed completely from the composting mass.[12] Thus, using manure as fertilizer can lead to an administration of remarkable residues of antibiotics to the soil. An uptake of veterinary antimicrobials by plants used for human consumption has been shown.[7,13] For example, up to 2.8 μg kg^{-1} enrofloxacin could be detected in carrot roots.[7] Furthermore, the occurrence of FQ antibiotic residues in the environment may provide suitable conditions for the selective pressure toward resistant bacteria. Although found in trace levels, the reduction of antibiotics in the environment is required to prevent further selection of (multi)resistances among bacterial pathogens.

Numerous fungal and bacterial species have been shown to be useful in biotransformations of FQ antibiotics.[14−16] Among the degradation pathways used by fungi, esterification, oxidation due to introduction of hydroxyl groups, decarboxylation, addition of formyl or acetyl groups, defluorination, partial loss or complete replacement of the piperazine moiety by an amino group, and formation of conjugates at the piperazine ring or replacing the carboxyl group at C3 have been described.[17−19] Even the mineralization of FQs to CO_2 has been reported for various fungi.[18] Biotransformations of DFX by *Candida lipolytica* and *Penicillium* spp. led to a removal of the substituted piperazine ring.[15] The fungus *Rhizopus arrhizus* metabolized DFX to the *N*-desmethyl metabolite and to danofloxacin *N*-oxide (DFX-O) as presumed by the authors.[15]

In past decades, the formation of *N*-oxides by microorganisms, especially fungi, has been frequently described in metabolism studies not only of enrofloxacin but also of alkaloids, several xenobiotics, and other organic compounds.[18,20−25] For instance, bacterial methane monooxygenase from *Methylococcus capsulatus* and fungal peroxygenase from *Agrocybe aegerita* were reported to catalyze the oxidation of pyridine to pyridine *N*-oxide.[26,27] However, most of these studies did not perform state of the art analysis to confirm the molecular structures of the metabolites and to quantitate their formation during the degradation process.

Thus, the purpose of this study was three-fold: first, to evaluate the potential of the ascomycetous fungus *Xylaria longipes* to transform DFX in liquid media; second, to elucidate the structures of the biotransformation products; and, third, to determine their residual antibacterial activity. With this approach, we demonstrate for the first time that *X. longipes* quantitatively transforms DFX into DFX-O having a very low residual antibacterial activity.

MATERIALS AND METHODS

Microorganism. The ascomycetous fungus *X. longipes* was isolated from a wood trunk in the Schloss Rauischholzhausen Park located near Giessen (Ebsdorfergrund, Germany). The identification of the fungus was performed based on internal transcribed spacer similarity searches using the National Center for Biotechnology Information Blast search program within the GenBank database (http://www.ncbi.nlm.nih.gov/blast/). The fungus is deposited in the fungal culture collection of the Institute of Food Chemistry and Food Biotechnology (Justus Liebig University Giessen, Germany). Stock cultures of *X. longipes* were maintained on 2% malt extract agar (MEA) plates (20 g L^{-1} malt extract, 15 g L^{-1} agar−agar) at 4 °C in a refrigerator.

Chemicals. DFX (CAS Registry No. 112398-08-0, purity ≥ 98.0%) was obtained from Santa Cruz Biotechnology, Inc. (Dallas, TX, USA). For media preparation, malt extract was obtained from Fluka Analytical (St. Gallen, Switzerland); NH_4NO_3 was acquired from Acros Organics (Geel, Belgium); and agar−agar, glucose, KH_2PO_4, and $MgSO_4{\cdot}H_2O$ were purchased from Carl Roth (Karlsruhe, Germany). HPLC grade methanol was obtained from VWR (Darmstadt, Germany), and formic acid and ammonium acetate were acquired from Bernd Kraft (Duisburg, Germany) and Merck (Darmstadt, Germany), respectively. All chemicals were of the highest purity available. High-purity water was prepared in-house with a laboratory water system (Sartorius, Goettingen, Germany) resulting in a specific resistivity of >18 MΩ.

Experimental Procedures. *Biodegradation Experiment.* Inoculation material for submerged cultures was grown on MEA plates at 24 °C for 3 weeks. For preparation of precultures, agar pieces (1 cm diameter) from the leading mycelium edge of the fungus were transferred into 250 mL Erlenmeyer flasks containing 100 mL of malt extract medium (20 g L^{-1} malt extract) previously sterilized at 121 °C for 20 min. For homogenization, an Ultra-Turrax disperser (IKA, Staufen, Germany) was used for 30 s at 9800 rpm. Precultures were incubated in the dark at 24 °C for 7 days on an Orbitron orbital table shaker (150 rpm, Infors HT, Bottmingen, Switzerland). Afterward, the precultures were homogenized (30 s, 9800 rpm) and an aliquot of 4 mL was centrifuged (4000 *g*, 10 min, 4 °C) using sterile 15 mL centrifuge tubes (Greiner Bio-One, Frickenhausen, Germany). The sedimented mycelium was resuspended in 4 mL of sterile water and rinsed three times following the protocol described above. The washed mycelium was resuspended in 4 mL of sterile water and used as inoculum (10% of medium volume) for main cultures. These cultures were grown in 100 mL Erlenmeyer flasks with a final volume of 40 mL using a chemically defined medium (composition per liter: 8.0 g of glucose, 1.5 g of KH_2PO_4, 0.5 g of $MgSO_4{\cdot}H_2O$, 0.1 g of NH_4NO_3, and 1 mL trace element solution according to the method of Fraatz et al.[28] The pH of the medium was adjusted to 6.0 with 1 M NaOH prior to sterilization. DFX was dissolved in water, sterilized (0.22 μm sterile syringe filter, Carl Roth, Karlsruhe, Germany), and added to the main culture to give a final concentration of approximately 20 mg L^{-1}. The main cultures were incubated in the dark at 24 °C for 10 days as described above. During the time course experiments, 1 mL samples were withdrawn at the beginning of the trial (day 0) and after 2, 4, 6, 8, and 10 days. Samples were stored at −20 °C before analyses. Pure medium containing DFX and fungal cultures without DFX were employed as abiotic and biotic controls, respectively. All experiments were conducted in duplicate.

DFX-O Production. For metabolite isolation and characterization, the biodegradation experiment was repeated on a larger scale. Ten 250 mL Erlenmeyer flasks, each containing 100 mL of the chemically defined medium, were inoculated as described above and dosed with sterilized DFX solution to obtain a desired concentration of approximately 50 mg L^{-1}. Cultures were incubated as long as in periodically withdrawn samples analyzed by high-performance liquid chromatography with diode array detection (HPLC-DAD) the maximum peak area of the metabolite could be detected. After separation of the mycelia by filtration and centrifugation, combined supernatants were lyophilized, resuspended in 25 mL of water, and fractionated using a preparative HPLC system (see below).

Analytical Procedures. *HPLC-DAD Analysis of DFX.* The residual concentrations of DFX in main cultures were determined by HPLC-DAD. HPLC was performed using a LaChrom L-7100 low-pressure pump, an autosampler L-7200, and an L-7455 diode array detector combined with D-7000 HSM software (version 4.1, Merck-Hitachi, Darmstadt, Germany). A Hypersil GOLD PFP column (150 × 4.6 mm, 5 μm) (Thermo Scientific, Dreieich, Germany) was employed, and analytes were eluted with a binary gradient of methanol (A) and 1 mM

DOI: 10.1021/acs.jafc.5b02343
J. Agric. Food Chem. 2015, 63, 6897−6904

ammonium acetate in 0.5% formic acid (B) as follows: 0−1 min, 1% A; 1−6 min, ramp to 50% A; 6−13 min, ramp to 99% A; 13−15 min, hold at 99% A; 15−16 min, ramp to 1% A; 16−19 min, hold at 1% A. The flow rate was 1 mL min^{-1}. The detection wavelength was 284 nm, and the DAD recorded ultraviolet (UV) spectra were from 200 to 370 nm with a spectral interval of 1.6 s and a wave step of 4 nm. Blank analyses were included regularly to check for memory effects. For quantitation, a calibration curve for DFX was obtained by linear regression corresponding to the correlation between the peak area and the analyte concentration in the range from 0.02 to 30 mg L^{-1}. Linearity was evaluated with 11 different concentrations (n = 8) using standard solutions diluted in medium (0.02, 0.04, 0.06, 0.08, 0.1, 1.0, 2.5, 5.0, 10.0, 20.0, and 30.0 mg L^{-1}). Limit of detection (LOD) and limit of quantitation (LOQ) were calculated by the signal/noise ratio (S/N) employing the peak-to-peak method. S/N of 3:1 and 10:1 were used for estimating the LOD and LOQ, respectively. LOD was confirmed when the average of all measurements of the lowest standard concentration showed an S/N > 3.

Preparative Isolation of DFX-O. Preparative HPLC was performed using a Young Lin quaternary pump (YL 91105), an ultraviolet detector (YL 91205) set at 284 nm, and a CHF 122SC fraction collector (Advantec, Dublin, CA, USA) combined with YL-Clarity software (version 3.0.4.444, Young Lin Instruments, Anyang, Korea). In general, 0.7 mL of the resuspended lyophilisate extract was resolved on a Nucleosil C18 column (250 × 16 mm, 7 μm) (Macherey-Nagel, Düren, Germany) preceded by a 10 × 16 mm guard column of the same stationary phase. Methanol and 1 mM ammonium acetate in 0.5% formic acid (45:55, v/v) were used as solvent system for isocratic separation (run time = 14 min) with a flow rate of 10 mL min^{-1}. After isolation metabolite fractions were combined and lyophilized.

Mass Spectrometry. High-resolution mass spectra (HRMS) were acquired on an Orbital trapping mass spectrometer (Q Exactive, Thermo Fisher Scientific, Bremen, Germany) using a nanospray ionization source in positive mode (NSI^+) (capillary temperature = 250 °C, spray voltage = 1.5 kV) and nanoelectrospray needles for online measurements (Silica Tips, 5 μm, New Objective, Woburn, MA, USA). MS^2 experiments were performed with higher energy collision dissociation (HCD). Data acquisition was performed with Tune 2.4, and spectra were analyzed with Xcalibur 2.2.SP1.48 (Thermo Fisher Scientific). The mass spectrometer was operated in positive ion mode at a mass resolution of 140000 at m/z 200 (scan range m/z 50−400). Mass accuracy was better than 2 ppm. DFX and DFX-O were dissolved in methanol/water (1:3, v/v) with addition of 0.03% TFA (concentration of each substance = 47 μg mL^{-1}).

MS^3 was carried out using the 3200 QTRAP System (AB Sciex, Darmstadt, Germany) that allows fragmentation experiments based on hybrid triple-quadrupole/linear ion trap technology. An electrospray ionization source in positive mode (ESI^+) at a capillary voltage of 5.5 kV was used. Further mass spectrometry (MS) detection settings were as follows: source temperature = 40 °C, nebulizer gas = 14 psi, curtain gas = 10 psi, declustering potential = 40 V, and entrance potential = 10 V. Data acquisition was performed with Analyst 1.6.2 (AB Sciex).

NMR Spectroscopy. Nuclear magnetic resonance (NMR) spectroscopy data were acquired in D_2O (Euriso-top, Gif-Sur-Yvette, France) on a Bruker Avance III 600 MHz NMR spectrometer (Bruker BioSpin, Rheinstetten, Germany) equipped with 5 mm broad band BBO Z-gradient probe, operating at 600 MHz (for ^1H) and 150 MHz (for ^{13}C). For structural elucidation, 1D NMR experiments such as ^1H, ^{13}C, and distortionless enhancement by polarization transfer experiments using a 135° decoupler pulse (DEPT-135) as well as 2D NMR experiments such as ^1H, ^1H correlation (^1H, ^1H-COSY), heteronuclear single-quantum correlation (^1H, ^{13}C-HSQC), and heteronuclear multiple-bond correlation (^1H, ^{13}C-HMBC) were performed. The spectra were recorded at room temperature. The data were collected and processed by TopSpin software (Bruker). The NMR experiments were performed using Bruker standard pulse sequences and parameters. Chemical shifts are reported in parts per million (δ scale). ^1H chemical shifts were referenced to the residual solvent peak. The ^{13}C spectra were referenced to external 3-(trimethylsilyl)propionic-2,2,3,3-d_4 acid (TSP) in D_2O.

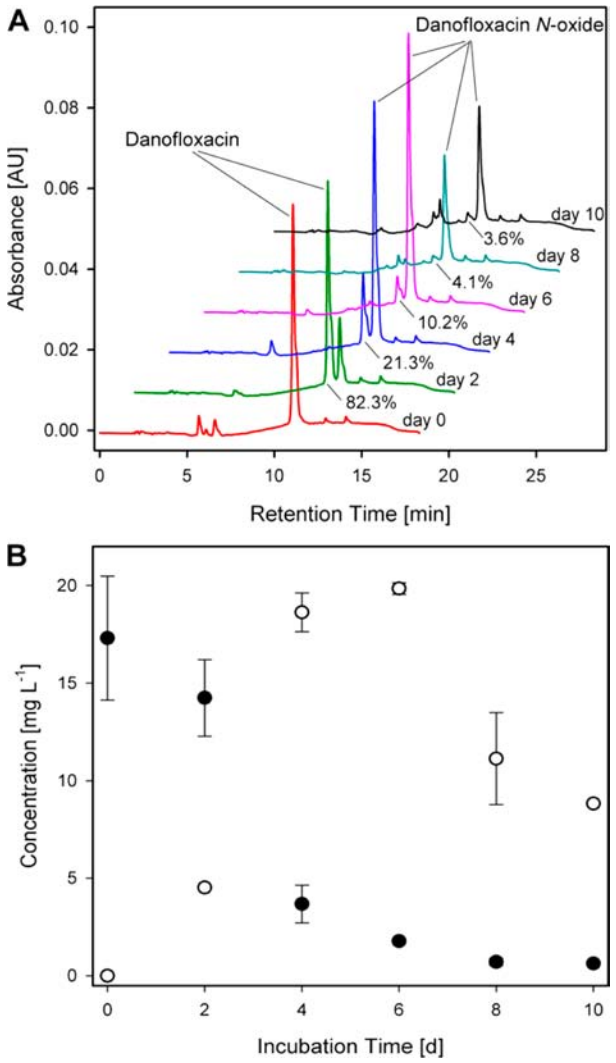

Figure 2. Degradation of danofloxacin (DFX) and formation of the main metabolite danofloxacin *N*-oxide (DFX-O) produced by *X. longipes*: (A) HPLC-DAD chromatograms (284 nm); (B) detected concentrations of DFX (solid circles) and DFX-O (open circles) in fungal culture supernatants. Values plotted are expressed as the mean of duplicates ± mean range.

Photometric Analyses. For determination of UV absorption spectra and molar extinction coefficients ε, a Specord 50 ultraviolet−visible spectrophotometer utilizing the wavelength range from 190 to 450 nm combined with WinAspect software (version 2.2.1.0, Analytik Jena, Jena, Germany) was used. The spectra were recorded using Suprasil quartz cuvettes (path length = 10 mm; Hellma, Müllheim, Germany).

Residual Antibacterial Activity. Residual antibacterial activity of the biotransformation product DFX-O was determined in comparison to DFX using the brilliant black reduction (BRT) maximum residue level (MRL) screening test (AiM, Munich, Germany). Adapted from the agar diffusion test, this microbiological test is based on the reduction of the agar−agar added synthetic black diazo dye brilliant black by the test bacterium *Geobacillus stearothermophilus* var. *calidolactis* C953. It was developed for semiquantitative determination of antibiotic residues in milk according to Commission Regulation (EU) 37/2010.[29] This test is characterized by high sensitivity against β-lactam antibiotics. Thus, penicillins are detected at MRL level, but other antibiotics can also be determined. During the incubation, brilliant black is completely reduced by the growing test organism due to reductive cleavage of the azo bonds, resulting in yellow and colorless compounds. Hence, the color of the test medium changes from blue to yellow. The presence of antibiotic residues in a sample inhibits the

DOI: 10.1021/acs.jafc.5b02343
J. Agric. Food Chem. 2015, 63, 6897−6904

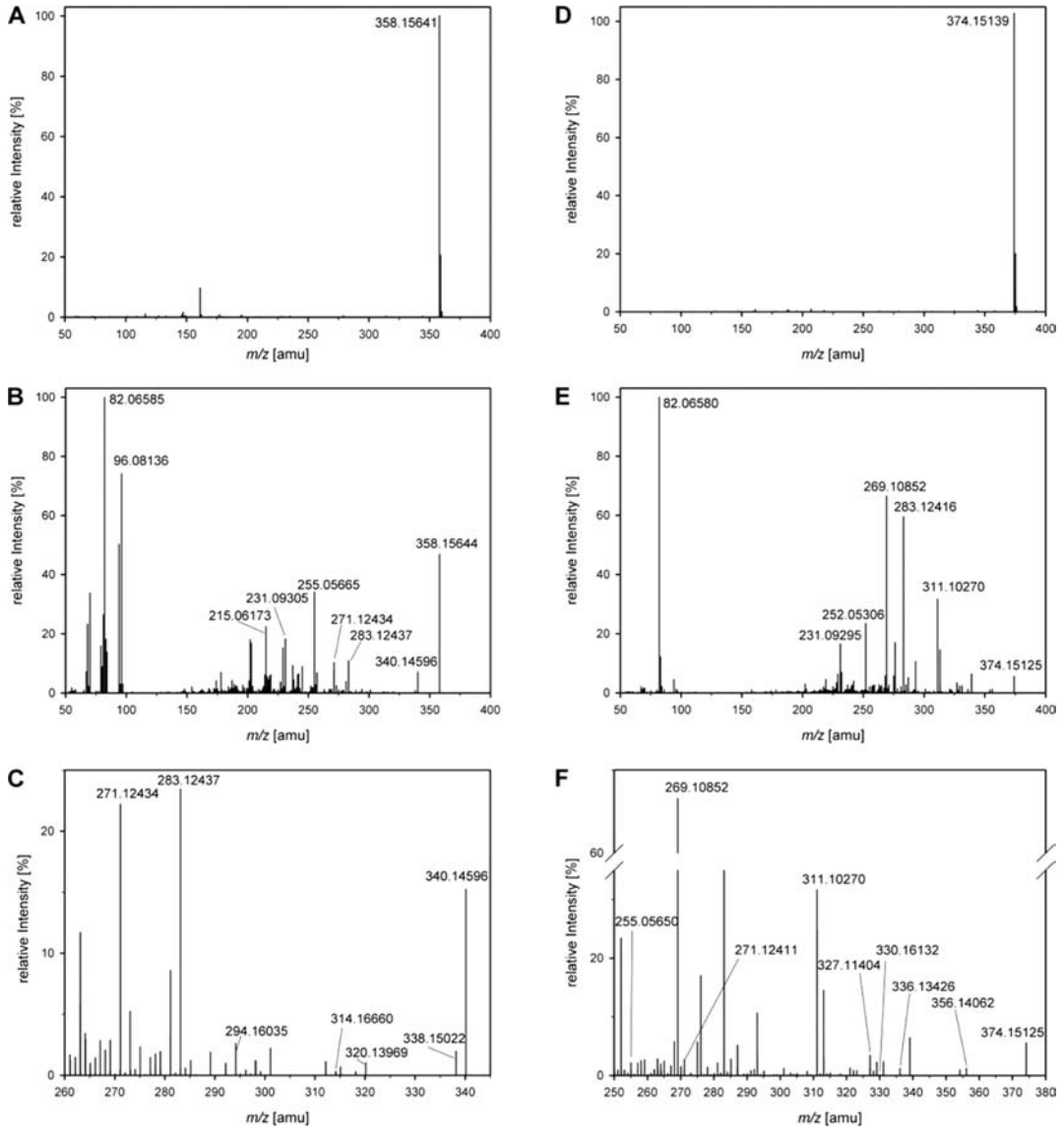

Figure 3. Accurate high-resolution MS and MS^2 spectra of danofloxacin (DFX) and danofloxacin *N*-oxide (DFX-O): (A) NSI^+-FTMS (full scan) spectrum of DFX; (B) NSI^+-$FTMS^2$ product ion spectrum of DFX with higher energy collision dissociation (HCD) at normalized collision energy of 60%; (C) zoomed range of (B); (D) NSI^+-FTMS (full scan) spectrum of DFX-O; (E) NSI^+-$FTMS^2$ product ion spectrum of DFX-O with a HCD at normalized collision energy of 45%; (F) zoomed range of (E).

growth of the test organism. Therefore, the test medium does not change the color and remains blue. Because the test was developed for detection of inhibitors in milk, stock solutions of both compounds were diluted with inhibitor-free milk (commercially available milk, 3.5% fat content) to obtain concentrations of 0.1−200 mg L^{-1}. Into each cavity of the 96-well plate were pipetted 0.1 mL of the sample solution and the positive control (penicillin G standard, 4 μg L^{-1}) or the negative control (inhibitor-free milk). The procedure for the determination of antibacterial activity in culture supernatants slightly deviated from the instructions given by the manufacturer. Penicillin G (99.4%; Sigma-Aldrich, Seelze, Germany) dissolved in medium in a concentration of 4 μg L^{-1} and medium only served as positive and negative controls, respectively. The sample volume was 0.1 mL for controls and culture supernatants. The cavities were sealed with adhesive film and incubated in a heating block at 65 °C until the cavity with the negative control turned yellow (about 2.25 h ± 15 min). After removal of the milk, each cavity was simultaneously analyzed using an Eon microplate spectrophotometer (BioTek Instruments, Bad Friedrichshall, Germany) at measurement and reference wavelengths set at 450 and 620 nm, respectively. All analyses were performed in triplicate.

RESULTS AND DISCUSSION

Degradation of DFX. HPLC-DAD analysis of a DFX standard solution showed that the retention time of DFX was 11.0 min, the LOD was found to be 8 μg L^{-1} (S/N values ranged from 2.8 to 3.4), and the LOQ was determined at 20 μg L^{-1} with a precision of 9% (n = 8).

DFX was efficiently transformed by *X. longipes* within 10 days using an initial concentration of approximately 20 mg L^{-1}. The HPLC-DAD analyses of the culture supernatants showed one apparent metabolite eluting at 11.6 min as well as residual DFX (Figure 2A). Other peaks (e.g., at 9.1 or 9.5 min) were also found in the biotic controls after the same incubation period. Thus, these signals were not considered as potential DFX metabolites.

After 6 days of incubation, about 90% of DFX had been transformed to the product according to the peak areas at 284 nm. The metabolite showed the same UV spectrum as DFX with λ_{max} (H_2O) = 280 nm (ε_{280} (H_2O, 20 °C) = 34724 L mol^{-1} cm^{-1}; for DFX, ε_{280} (H_2O, 20 °C) = 38740 L mol^{-1} cm^{-1}). Thereafter, only

DOI: 10.1021/acs.jafc.5b02343
J. Agric. Food Chem. 2015, 63, 6897−6904

Table 1. High-Resolution MS Data of Danofloxacin (DFX) and Danofloxacin *N*-Oxide (DFX-O)[a]

	$[M + H]^+$ $[m/z]$ (exptl)	elemental composition $[M + H]^+$	$[M + H]^+$ $[m/z]$ (theor)	mass deviation (mDa)	mass deviation (ppm)
DFX	358.15641	$C_{19}H_{21}FN_3O_3^+$	358.156146	0.264	0.737
MS^2 DFX fragments	340.14596	$C_{19}H_{19}FN_3O_2^+$	340.145581	0.379	1.114
	338.15022	$C_{19}H_{20}N_3O_3^+$	338.149918	0.302	0.893
	320.13969	$C_{19}H_{18}N_3O_2^+$	320.139353	0.337	1.053
	314.16660	$C_{18}H_{21}FN_3O^+$	314.166317	0.283	0.901
	294.16035	$C_{18}H_{20}N_3O^+$	294.160089	0.261	0.887
	283.12437	$C_{17}H_{16}FN_2O^+$	283.124118	0.252	0.890
	271.12434	$C_{16}H_{16}FN_2O^+$	271.124118	0.222	0.819
	255.05665	$C_{14}H_8FN_2O_2^+$	255.056432	0.218	0.855
	231.09305	$C_{13}H_{12}FN_2O^+$	231.092818	0.232	1.004
DFX-O	374.15139	$C_{19}H_{21}FN_3O_4^+$	374.151061	0.329	0.879
MS^2 DFX-O fragments	356.14062	$C_{19}H_{19}FN_3O_3^+$	356.140496	0.124	0.348
	336.13436	$C_{19}H_{18}N_3O_3^+$	336.134268	0.092	0.274
	330.16132	$C_{18}H_{21}FN_3O_2^+$	330.161232	0.088	0.267
	327.11404	$C_{18}H_{16}FN_2O_3^+$	327.113947	0.093	0.284
	283.12416	$C_{17}H_{16}FN_2O^+$	283.124118	0.042	0.148
	271.12411	$C_{16}H_{16}FN_2O^+$	271.124118	−0.008	−0.030
	255.05650	$C_{14}H_8FN_2O_2^+$	255.056432	0.068	0.267
	231.09295	$C_{13}H_{12}FN_2O^+$	231.092818	0.132	0.571

[a]Measured accurate masses, predicted elemental compositions, theoretical masses, and mass deviations of DFX and DFX-O and their MS^2 fragments.

a minor decrease of the residual DFX concentration was observed to 3.6% after 10 days. The decline of the DFX concentration was accompanied by an increase of the metabolite concentration during the first 6 days (19.85 mg L^{-1} at day 6) (Figure 2B). However, the peak area of the metabolite decreased within the next 4 days giving a final concentration of 8.82 mg L^{-1} beyond very low amounts of DFX (0.63 mg L^{-1}). The HPLC elution profiles indicated only one main metabolite reaching maximum concentrations after 4 and 6 days. Hence, an incubation time of 4 days was chosen to produce a sufficient quantity of the metabolite for structure elucidation by NMR and MS.

In the larger scale biodegradation experiment fungal cultivation was stopped after 73 h. After preparative isolation, the yield of the metabolite was 10 mg with a purity of 94%.

Structure Elucidation of DFX and DFX-O. NSI^+-HRMS measurements of DFX and the isolated compound revealed the exact masses of $[M + H]^+$ = 358.15641 and $[M + H]^+$ = 374.15139, respectively (Figure 3A,D), suggesting that the metabolite had been formed by the addition of one oxygen atom to DFX ($\Delta m/z$ = 15.99498, theoretical mass of oxygen is 15.99492 Da). Product ion analyses of the protonated molecular ions at m/z 358 and at m/z 374 revealed common fragment ions at m/z 283, 271, 255, and 231 (DFX, 283.12437, 271.12434, 255.05665, 231.09305; DFX-O, 283.12416, 271.12411, 255.05650, 231.09295) for both compounds (Figure 3 and Table 1). The mass deviations for these fragments ranged from 0.82 to 1.11 ppm and from −0.03 to 0.57 ppm for DFX and the metabolite, respectively, indicating a very good accuracy. In the product ion spectrum of the protonated DFX molecule several fragments were observed, that is, at m/z 314.16660 generated by the elimination of CO_2, at m/z 340.14596 due to the loss of water, and at m/z 255.05665 due to the loss of water and the loss of *N*-methylpyrrolidine ($C_5H_{11}N$) from the substituted piperazine moiety (Figure 3B,C). Accordingly, the product ion spectrum of the protonated metabolite molecule included a fragment ion caused by the elimination of a CO_2 group (m/z 330.16132) and an ion corresponding to the loss of water (m/z 356.14062) as well as an ion at m/z 255.05650 that results from m/z 356.14062 due to the loss $C_5H_{11}NO$ group from the substituted piperazine moiety (Figure 3E,F). The presence of a common product ion at m/z 283 indicated that the fluoroquinolone core of both compounds was intact, suggesting that the addition of an oxygen atom could be found only on the substituted piperazine moiety.

ESI^+-MS^3 fragmentation experiments were carried out to further confirm the assumed structure of the metabolite (data not shown). Fragmentation of a precursor ion at m/z 327 generated by the neutral loss of CH_5NO moiety revealed one intense fragment ion at m/z 283 corresponding to the elimination of CO_2 also detected in fragmentation experiments of DFX. The presence of the fragment ion at m/z 327, which was not observed in MS spectra of DFX, indicated the addition of an oxygen atom to the methylated nitrogen at the substituted piperazine moiety of DFX. Given the fact that the oxidized substituted piperazine moiety was present in the first-appearing product ions after the loss of water (m/z 356) and CO_2 (m/z 330), respectively, whereas the loss of the oxidized substituted piperazine moiety is observed in all following product ions, these data confirmed the assumed structure, which would be supported by previously published fragmentation patterns reported by Liu and co-workers.[30]

For further structure confirmation, a combination of 1D and 2D NMR techniques including ^1H and ^{13}C NMR, DEPT-135, $^1H,^1H$-COSY, $^1H,^{13}C$-HSQC, and $^1H,^{13}C$-HMBC was performed. The experimentally established ^1H NMR and ^{13}C NMR spectral data for DFX and DFX-O are given in Table 2. Numbering of the atoms is shown in Figure 1. To the best of our knowledge, this is the first detailed report of ^{13}C NMR data of DFX and ^1H NMR and ^{13}C NMR data of DFX-O. The protons H5 and H8 appeared as doublets due to the coupling

DOI: 10.1021/acs.jafc.5b02343
J. Agric. Food Chem. 2015, 63, 6897−6904

Table 2. ^{1}H and ^{13}C NMR Spectral Data[a] of Danofloxacin (DFX) and Danofloxacin *N*-Oxide (DFX-O)

	DFX				DFX-O			
^{1}H	δ		M	J (Hz)	δ		M	J (Hz)
H2	8.27	CH	s		8.13	CH	s	
H5	7.17	CH	d	$^{2}J(^{1}H,^{19}F)$ = 13.5	6.91	CH	d	$^{2}J(^{1}H,^{19}F)$ = 11.8
H8	6.81	CH	d	$^{3}J(^{1}H,^{19}F)$ = 7	6.69	CH	s	
H2′	4.93	CH	s		4.81	CH	s	
H5′	4.45	CH	br s		4.65	CH	br s	
$H_{a,b}3'$	4.00−3.27	CH_2	d	^{2}J = 11.5	4.01−3.87	CH_2	br s	
$H_{a,b}6'$	3.90−3.63	CH_2	d	^{2}J = 11	4.21−3.76	CH_2	br s	
H1a	3.49	CH	s		3.46	CH	s	
H8′	2.98	N−CH_3	s		3.53	N−CH_3	s	
$H_{a,b}7'$	2.44−2.35	CH_2	d	^{2}J = 11.7	2.52	CH_2	br s	
H1*b*/1c	1.29−1.05	CH_2	m		1.25−0.97	CH_2	m	
^{13}C	δ			J (Hz)	δ			J (Hz)
C4	179.3	C-q (C═O)			178.9	C-q (C═O)		
C3a	173.5	C-q (COOH)			173.2	C-q (COOH)		
C6	154.8	C-q		$^{1}J(^{13}C,^{19}F)$ = 248	154.6	C-q		$^{1}J(^{13}C,^{19}F)$ = 248
C2	152.0	CH			151.7	CH		
C7	144.7	C-q			144.5	C-q		$^{2}J(^{13}C,^{19}F)$ = 11.5
C10	143.9	C-q			143.8	C-q		
C9	119.2	C-q			118.8	C-q		$^{3}J(^{13}C,^{19}F)$ = 7.6
C5	114.9	CH		$^{2}J(^{13}C,^{19}F)$ = 23.5	114.5	CH		$^{2}J(^{13}C,^{19}F)$ = 23.3
C3	109.5	C-q			109.4	C-q		
C8	105.3	CH			104.7	CH		
C5′	70.8	CH			82.1	CH		
C3′	67.0	CH_2			81.2	CH_2		
C2′	63.4	CH			63.4	CH		
C6′	58.4	CH_2			54.1	CH_2		
C8′	47.0	N−CH_3			62.1	N−CH_3		
C1a	40.5	CH			40.4	CH		
C7′	37.8	CH_2			40.4	CH_2		
C1*b*/1c	11.9	CH_2			11.83	CH_2		
C1*b*/1c	11.8	CH_2			11.79	CH_2		

[a]Multiplicity (M) abbreviations: s, singlet; d, doublet; m multiplet; br s, broad signal. δ, chemical shift; J, coupling constant; C-q, quaternary carbon.

to the ^{19}F atom. The coupling constant between carbons and fluorine was found to be helpful for the assignment of aromatic ^{13}C signals. The ^{1}H NMR data given here for DFX agree with those found in the literature.[2] The ^{13}C NMR data (Table 2) obtained for the fluoroquinolone core of DFX were very similar to those from the same part of ciprofloxacin, which differs structurally from DFX only in the substitution of the piperazine moiety.[31]

DFX-O proton and carbon assignments were made in analogy to those of DFX. First, the ^{1}H spectrum showed an intensive singlet at 8.29 ppm, which coupled to a carbon atom at 169.4 ppm. However, there was no correlation with the NMR signals of DFX-O. After the addition of some microliters of deuterated ammonia solution ($ND_3 \cdot D_2O$), both signals disappeared, indicating that these signals might be caused by formic acid added to the eluent for preparative isolation by HPLC. The ^{1}H and ^{13}C NMR chemical shift values agree with those in the literature for formic acid.[32] The ^{1}H NMR data of DFX-O revealed a remarkable shift of the protons of the methyl group (H8′) from 2.98 ppm (DFX) to 3.53 ppm (Table 2). Other ^{1}H NMR chemical shifts of the metabolite remained similar to those of DFX. For DFX-O, carbons at position C3′, C5′, and C8′ suffered a low-field shift of 11.3−15.1 ppm compared to the analogous signals of DFX. Corresponding to ^{1}H NMR data, the chemical shifts of the remaining carbon atoms were similar to the data obtained for DFX. Therefore, the NMR data confirmed the results of the MS analyses, indicating an unchanged fluoroquinolone core with the addition of an oxygen atom on the substituted piperazine moiety. HSQC and HMBC spectra, showing direct and long-range couplings of protons with carbons, fortified the assumption of the metabolite. Hence, the isolated metabolite was identified as danofloxacin *N*-oxide (1-cyclopropyl-6-fluoro-7-[1*S*,4*S*]-5-methyl-5-oxido-2,5-diazabicyclo[2.2.1]hept-2-yl]-4-oxo-1,4-dihydro-3-quinolinecarboxylic acid, DFX-O) with the oxygen atom attached to the terminal nitrogen of the substituted piperazine ring (Figure 1B).

On the basis of metabolism studies of alkaloids, *Xylaria* sp. is known to form selectively *N*-oxides.[24,25] Among FQs, the formation of *N*-oxides was observed in transformation studies using enrofloxacin and *U. ramanniana* (syn. *M. ramannianus*), *G. striatum*, and other fungi.[18] DFX was metabolized by *R. arrhizus* to the corresponding *N*-desmethyl and *N*-oxide metabolites, whereas the formation of DFX-O was assumed due to detection of the expected mass of DFX-O ($[M + H]^+$ m/z 374) in fungal cultures. Further structural elucidation of the *N*-oxide metabolite was not performed.[15] However, such a fast, quantitative, and regioselective conversion of FQs as described here has not been reported yet.

Residual Antibacterial Activity. The antibacterial activities of DFX and DFX-O were calculated on the basis of the

DOI: 10.1021/acs.jafc.5b02343
J. Agric. Food Chem. 2015, 63, 6897−6904

positive control penicillin G, which was considered as 100% in the BRT MRL screening test. As assumed, the test was much less sensitive to FQs in comparison to penicillin G. For DFX and DFX-O, concentrations <2 mg L^{-1} caused no inhibition, whereas concentrations >30 mg L^{-1} led to an inhibition corresponding to that of the positive control (data not shown). However, a DFX concentration of 4 mg L^{-1} as well as a DFX-O concentration of 20 mg L^{-1} led to an inhibition of >60% (Figure 4). Thus, the residual antibacterial activity of DFX-O corresponded approximately to 20% of the DFX activity.

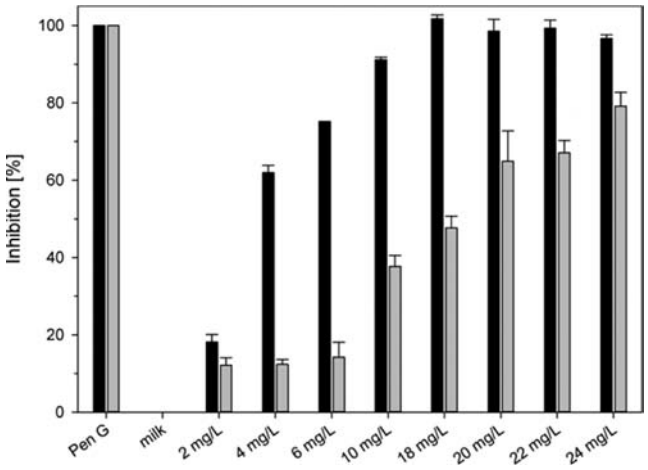

Figure 4. Antibacterial activity of DFX (black bars) and DFX-O (gray bars) in comparison to penicillin G (Pen G, 4 μg L^{-1}) as positive control and inhibitor free milk as negative control using BRT MRL screening test. Values plotted are expressed as the mean of triplicates ± standard deviation.

Fungal culture supernatants from the degradation experiment were tested as well (data not shown). Briefly, the antibacterial activity of culture supernatants of days 0 and 2 corresponded to that of the positive control, whereas in samples of day 4 an inhibition of 30% was detected. No antibacterial activity was observed in culture supernatants from day 6 until the end of the study, demonstrating a strong inactivation of DFX.

Oxidation of the nitrogen of the substituted piperazine moiety of FQs is known to cause a strong reduction of the antibacterial activity. For instance, ofloxacin *N*-oxide possesses a weaker antibacterial activity against various bacterial strains such as *Bacillus pumilus* (minimum inhibitory concentration (MIC) > 20 mg L^{-1}).[33] Compared to the parent compound (MIC = 0.675 mg L^{-1}), the MIC for ofloxacin *N*-oxide is > 29-fold higher, and thus the metabolite is quite inactive.[33] Similar results have been reported for amifloxacin and its *N*-oxide.[34] All of these findings are in good agreement with our results.

Some white rot fungi have been found to metabolize the FQs flumequine, norfloxacin, ofloxacin, and ciprofloxacin.[17,35] For flumequine, the antibacterial activity corresponded to the residual concentration of the compound remaining in the *Panus tigrinus* and *Pleurotus ostreatus* cultures. In contrast, for ciprofloxacin, although the compound was completely degraded by *Irpex lacteus*, a high residual activity was determined.[17,35] However, a decrease of the antibacterial activity in the degradation mixtures was achieved as well as generation of potentially antibacterial active metabolites, indicating that fungal biotransformation of FQ antibiotics does not necessarily lead to their inactivation. These diverse findings demonstrate that the outcome of fungal biotransformations of FQ antibiotics strongly depends on the microorganisms and individual compounds utilized, even though their structures are closely related.

In microbial biotransformation processes of antibiotics it is important to investigate the structure of the transformation products as well as their residual antibacterial activity. Even though the reduction of antibacterial activity is desirable, attention should be paid to degradation products that may promote the development of resistance in bacterial populations.[36] The evidence of potential metabolism of antibiotics is of interest because their occurrence in the environment raises serious concerns about possible risks for microorganisms, animals, and humans. Thus, fungal biotransformations of antibiotics accompanied by a remarkable reduction of their residual antibacterial activity may have an important ecological impact and are useful in biotechnological processes. In future investigations, the enzyme(s) responsible for this highly selective transformation should be identified and may be used in bioreactors to inactivate danofloxacin and potentially other FQs.

■ ASSOCIATED CONTENT

Supporting Information

Chromatographic information, detailed procedure for determination of residual antibacterial activity, UV absorption spectra, proposed fragmentation pathways, NMR spectra of parent compound and metabolite, and results of BRT MRL screening test. The Supporting Information is available free of charge on the ACS Publications website at DOI: 10.1021/acs.jafc.5b02343.

■ AUTHOR INFORMATION

Corresponding Author

*(G.H.) Phone: +49 641 99-34950. Fax: +49 641 99-34959. E-mail: Gerd.Hamscher@lcb.chemie.uni-giessen.de.

Funding

The study was financially supported by the excellence initiative of the Hessian Ministry of Science and Art, which encompasses a generous grant for the LOEWE focus "Integrative Fungal Research". Financial support by the Deutsche Forschungsgemeinschaft (DFG Sp314/13-1) is gratefully acknowledged.

Notes

The authors declare no competing financial interest.

■ ACKNOWLEDGMENTS

We thank the AiM GmbH (Munich, Germany) for kindly providing BRT MRL screening tests for determination of antibacterial activity.

■ ABBREVIATIONS USED

FQ, fluoroquinolone; DFX, danofloxacin; DFX-O, danofloxacin *N*-oxide; MEA, malt extract agar; ESI, electrospray ionization; NSI, nanospray ionization; NMR, nuclear magnetic resonance; D_2O, deuterium oxide; 1D, one-dimensional; 2D, two-dimensional; ^{1}H, proton; ^{13}C, carbon-13; ^{19}F, fluorine-19; DEPT, distortionless enhancement by polarization transfer; COSY, correlation spectroscopy; HSQC, heteronuclear single-quantum correlation; HMBC, heteronuclear multiple bond correlation; M, multiplicity; s, singlet; d, doublet; m, multiplet; C-q, quaternary carbon; br s, broad signal; δ, chemical shift; *J*, coupling constant; BRT, brilliant black reduction; MRL, maximum residue level

DOI: 10.1021/acs.jafc.5b02343
J. Agric. Food Chem. 2015, 63, 6897−6904

REFERENCES

(1) Hooper, D. C. Mode of action of fluoroquinolones. *Drugs* **1999**, *58*, 6−10.

(2) McGuirk, P. R.; Jefson, M. R.; Mann, D. D.; Elliott, N. C.; Chang, P.; Cisek, E. P.; Cornell, C. P.; Gootz, T. D.; Haskell, S. L.; Hindahl, M. S.; LaFleur, L. J.; Rosenfeld, M. J.; Shryock, T. R.; Silvia, A. M.; Weber, F. H. Synthesis and structure-activity relationships of 7-diazabicycloalkylquinolones, including danofloxacin, a new quinolone antibacterial agent for veterinary medicine. *J. Med. Chem.* **1992**, *35*, 611−620.

(3) Federal Office for Consumer Protection and Food Safety. Dritte Datenerhebung zur Antibiotikaabgabe in der Tiermedizin;http://www.bvl.bund.de/DE/08_PresseInfothek/01_FuerJournalisten/01_Presse_und_Hintergrundinformationen/05_Tierarzneimittel/2014/2014_08_01_pi_Abgabemengen_korrigiert_29_08_2014.html;jsessionid=CA13CE12470E7E50A9FD2FEB86C112C9.2_cid322 (accessed May 2015).

(4) World Health Organization. Critically important antimicrobials for human medicine; http://www.who.int/foodsafety/publications/antimicrobials-third/en/ (accessed May 2015).

(5) Carlucci, G. Analysis of fluoroquinolones in biological fluids by high-performance liquid chromatography. *J. Chromatogr. A* **1998**, *812*, 343−367.

(6) Martinez, M.; McDermott, P.; Walker, R. Pharmacology of the fluoroquinolones: a perspective for the use in domestic animals. *Vet. J.* **2006**, *172*, 10−28.

(7) Boxall, A. B. A.; Johnson, P.; Smith, E. J.; Sinclair, C. J.; Stutt, E.; Levy, L. S. Uptake of veterinary medicines from soils into plants. *J. Agric. Food Chem.* **2006**, *54*, 2288−2297.

(8) Golet, E. M.; Alder, A. C.; Giger, W. Environmental exposure and risk assessment of fluoroquinolone antibacterial agents in wastewater and river water of the Glatt Valley Watershed, Switzerland. *Environ. Sci. Technol.* **2002**, *36*, 3645−3651.

(9) Hamscher, G.; Mohring, S. A. I. Veterinary drugs in soil and in the aquatic environment. *Chem. Ing. Technol.* **2012**, *84*, 1052−1061.

(10) Hamscher, G.; Pawelzick, H. T.; Sczesny, S.; Nau, H.; Hartung, J. Antibiotics in dust originating from a pig-fattening farm: a new source of health hazard for farmers? *Environ. Health Perspect.* **2003**, *111*, 1590−1594.

(11) Janusch, F.; Scherz, G.; Mohring, S. A. I.; Hamscher, G. Determination of fluoroquinolones in chicken feces - A new liquid-liquid extraction method combined with LC-MS/MS. *Environ. Toxicol. Pharmacol.* **2014**, *38*, 792−799.

(12) Selvam, A.; Zhao, Z.; Wong, J. W. C. Composting of swine manure spiked with sulfadiazine, chlortetracycline and ciprofloxacin. *Bioresour. Technol.* **2012**, *126*, 412−417.

(13) Grote, M.; Schwake-Anduschus, C.; Michel, R.; Stevens, H.; Heyser, W.; Langenkämper, G.; Betsche, T.; Freitag, M. Incorporation of veterinary antibiotics into crops from manured soil. *Landbauforsch. Voelkenrode* **2007**, *57*, 25−32.

(14) Amorim, C. L.; Moreira, I. S.; Maia, A. S.; Tiritan, M. E.; Castro, P. M. L. Biodegradation of ofloxacin, norfloxacin, and ciprofloxacin as single and mixed substrates by *Labrys portucalensis* F11. *Appl. Microbiol. Biotechnol.* **2014**, *98*, 3181−3190.

(15) Chen, Y.; Rosazza, J. P. N.; Reese, C. P.; Chang, H. Y.; Nowakowski, M. A.; Kiplinger, J. P. Microbial models of soil metabolism: biotransformations of danofloxacin. *J. Ind. Microbiol. Biotechnol.* **1997**, *19*, 378−384.

(16) Liu, Z.; Sun, P.; Pavlostathis, S. G.; Zhou, X.; Zhang, Y. Adsorption, inhibition, and biotransformation of ciprofloxacin under aerobic conditions. *Bioresour. Technol.* **2013**, *144*, 644−651.

(17) Čvančarová, M.; Moeder, M.; Filipová, A.; Reemtsma, T.; Cajthaml, T. Biotransformation of the antibiotic agent flumequine by ligninolytic fungi and residual antibacterial activity of the transformation mixtures. *Environ. Sci. Technol.* **2013**, *47*, 14128−14136.

(18) Parshikov, I. A.; Sutherland, J. B. Microbial transformations of antimicrobial quinolones and related drugs. *J. Ind. Microbiol. Biotechnol.* **2012**, *39*, 1731−1740.

(19) Prieto, A.; Möder, M.; Rodil, R.; Adrian, L.; Marco-Urrea, E. Degradation of the antibiotics norfloxacin and ciprofloxacin by a white-rot fungus and identification of degradation products. *Bioresour. Technol.* **2011**, *102*, 10987−10995.

(20) Gröger, D.; Schmauder, H. P. Microbial conversion of thebaine. *Experientia* **1969**, *25*, 95−96.

(21) Hofrichter, M.; Ullrich, R. Oxidations catalyzed by fungal peroxygenases. *Curr. Opin. Chem. Biol.* **2014**, *19*, 116−125.

(22) Hufford, C. D.; Capiton, G. A.; Clark, A. M.; Baker, J. K. Metabolism of imipramine by microorganisms. *J. Pharm. Sci.* **1981**, *70*, 151−155.

(23) Mitsukura, K.; Hayashi, M.; Yoshida, T.; Nagasawa, T. Oxidation of aromatic *N*-heterocyclic compounds to *N*-oxides by *Verticillium* sp. GF39 cells. *J. Biosci. Bioeng.* **2013**, *115*, 651−653.

(24) Shibuya, H.; Kitamura, C.; Maehara, S.; Nagahata, M.; Winarno, H.; Simanjuntak, P.; Kim, H. S.; Wataya, Y.; Ohashi, K. Transformation of cinchona alkaloids into 1-*N*-oxide derivatives by endophytic *Xylaria* sp. isolated from *Cinchona pubescens*. *Chem. Pharm. Bull.* **2003**, *51*, 71−74.

(25) Siebers-Wolff, S.; Arfmann, H. A.; Abraham, W. R.; Kieslich, K. Microbiological hydroxylation and *N*-oxidation of cinchona alkaloids. *Biocatal. Biotransform.* **1993**, *8*, 47−58.

(26) Colby, J.; Stirling, D. I.; Dalton, H. The soluble methane monooxygenase of *Methylococcus capsulatus* (Bath). *Biochem. J.* **1977**, *165*, 395−402.

(27) Ullrich, R.; Dolge, C.; Kluge, M.; Hofrichter, M. Pyridine as novel substrate for regioselective oxygenation with aromatic peroxygenase from *Agrocybe aegerita*. *FEBS Lett.* **2008**, *582*, 4100−4106.

(28) Fraatz, M. A.; Naeve, S.; Hausherr, V.; Zorn, H.; Blank, L. M. A minimal growth medium for the basidiomycete *Pleurotus sapidus* for metabolic flux analysis. *Fungal Biol. Biotechnol.* **2014**, *1*, 10.1186/s40694-014-0009-4.

(29) European Commission. Commission Regulation (EU) No. 37/2010 on pharmacologically active substances and their classification regarding maximum residue limits in foodstuffs of animal origin; ec.europa.eu/health/files/eudralex/vol-5/reg_2010_37/reg_2010_37_en.pdf (accessed May 2015).

(30) Liu, Z. Y.; Zhou, X. N.; Zhang, H. H.; Wan, L.; Sun, Z. L. An integrated method for degradation products detection and characterization using hybrid ion trap/time-of-flight mass spectrometry and data processing techniques: Application to study of the degradation products of danofloxacin under stressed conditions. *Anal. Bioanal. Chem.* **2011**, *399*, 2475−2486.

(31) Chattah, A. K.; Linck, Y. G.; Monti, G. A.; Levstein, P. R.; Breda, S. A.; Manzo, R. H.; Olivera, M. E. NMR and IR characterization of the aluminium complexes of norfloxacin and ciprofloxacin fluoroquinolones. *Magn. Reson. Chem.* **2007**, *45*, 850−859.

(32) Jones, I. C.; Sharman, G. J.; Pidgeon, J. ^{1}H and ^{13}C NMR data to aid the identification and quantitation of residual solvents by NMR spectroscopy. *Magn. Reson. Chem.* **2005**, *43*, 497−509.

(33) White, L. O.; MacGowan, A. P.; Lovering, A. M.; Reeves, D. S.; Mackay, I. G. A preliminary report on the pharmacokinetics of ofloxacin, desmethyl ofloxacin and ofloxacin *N*-oxide in patients with chronic renal failure. *Drugs* **1987**, *34*, 56−61.

(34) Venezia, R. A.; Prymas, L. A.; Shayegani, A.; Yocum, D. M. In vitro activities of amifloxacin and two of its metabolites. *Antimicrob. Agents Chemother.* **1989**, *33*, 762−766.

(35) Čvančarová, M.; Moeder, M.; Filipová, A.; Cajthaml, T. Biotransformation of fluoroquinolone antibiotics by ligninolytic fungi − metabolites, enzymes and residual antibacterial activity. *Chemosphere* **2015**, *136*, 311−320.

(36) Palmer, A. C.; Angelino, E.; Kishony, R. Chemical decay of an antibiotic inverts selection for resistance. *Nat. Chem. Biol.* **2010**, *6*, 105−107.

DOI: 10.1021/acs.jafc.5b02343
J. Agric. Food Chem. 2015, 63, 6897−6904

Many attempts have been done to improve or modify the volatiles of tea leaves either by treating leaves during growth of the plants (raw materials) or by postharvest treatment of leaves during the tea manufacturing process.[1] Biotic stress (insect attack) and abiotic stress (light) have been utilized for the improvement of volatiles in raw tea leaves. As a typical example of biotic factors, the famous Taiwan oolong tea (Oriental Beauty) has a unique aroma reminiscent of ripe fruit and honey that is induced by the attack of tea green leafhoppers.[16] As an example of abiotic factors, Gyokuro and Tencha, known as the finest teas in Japan, are produced from tea leaves under shading treatment. It was found that tea leaves kept in darkness significantly increased levels of volatiles, especially volatile phenylpropanoids/benzenoids.[17] Besides the modification of raw materials, the manufacturing processes have significant influences on the compositions of volatiles in final tea products. In general, fermented teas including oolong tea and black tea have more volatiles and aroma properties than nonfermented green tea. This was generally thought to be due to the involvement of hydrolysis of GBVs in the manufacturing process.[18] The GBVs are present within vacuoles, while β-primeverosidase, one major glycosidase involved in the hydrolysis of GBVs, was presumed to be localized in cell walls.[18] This compartmentation of substrates and enzymes in plant cells implies that interactions between the enzyme and the substrate do not happen in intact tea leaves.[19] However, during the manufacturing process, tea leaf tissues and cells are disrupted, which results in the possibility of interactions between the glycosidase and the GBVs and liberation of the free volatiles. During the manufacturing process of black tea, the levels of primeverosides of the volatiles decreased greatly, and the glycosidase activities showed a peak during withering but were drastically reduced after rolling, suggesting that enzymatic hydrolysis of GBVs mainly occurred during the stage of rolling.[20] Therefore, enzymatic hydrolysis of GBVs is proposed as an important process during the manufacturing of black tea. In contrast, most GBVs showed no reductions in their contents during the manufacturing process of oolong tea. The contents of GBVs increased after the solar-withering stage, and reached their highest levels in the final stages of oolong tea production.[21] This result led us ask whether enzymatic hydrolysis of GBVs really contributes to the formation of volatiles during the oolong tea manufacturing process. To answer this question, we monitored changes in contents of free volatiles and GBVs, glycosidase enzyme activities, and *β-glycosidase* gene expression level during the manufacturing process of oolong tea. We attempted to give direct evidence of subcellular localization of β-primeverosidase, and also investigated the effect of the manufacturing process on the leaf cell structure. Finally relatively potent odorants occurring in oolong tea product were evaluated by gas chromatography−mass spectrometer/olfactometry (GC−MS/O). The results help us find out the truth of formation of volatiles in oolong tea, and advance our understanding of differences of formation of volatiles between oolong tea and black tea.

MATERIALS AND METHODS

Chemicals. Benzaldehyde, benzyl alcohol, β-damascenone, δ-decalactone, ethyl decanoate, Furaneol, 2-hexen-1-ol, 3-hexenyl acetate, indole, β-ionone, jasmine lactone, 3-methylnonane-2,4-dione, methyl salicylate, 2-phenylethanol, and vanillin were purchased from Wako Pure Chemical Industries Ltd., Japan. α-Farnesene, (*Z*)-3-hexen-1-ol, linalool, linalool oxides, methyl jasmonate, *trans*-nerolidol, geraniol, polyvinylpolypyrrolidone (PVPP), XAD-2, and β-glucosidase were purchased from Sigma-Aldrich Company Ltd., USA. β-Primeverosidase and *p*-nitrophenyl-β-primeveroside were purchased from Amano Enzyme Inc., Japan. *p*-Nitrophenyl-β-D-glucopyranoside was purchased from Aladdin Industrial Co. Shanghai, China. [^{15}N]Anthranilic acid (^{15}N% = 98%) was purchased from Cambridge Isotope Laboratories Inc., Cambridge, MA. Porapak Q cartridge was purchased from Waters Corporation, USA. Coomassie Blue R250, 30% acrylamide/Bis solution, *N*,*N*,*N*′, *N*′-tetramethylethylenediamine (TMEMD), sodium dodecyl sulfate (SDS), and 2× SYBR Green Universal PCR Mastermix were purchased from Bio-Rad Laboratories, USA. Quick RNA isolation Kit was purchased from Huayueyang Biotechnology Co., Ltd., China.

Plant Materials and Manufacturing Process of Oolong Tea. One bud and two or three leaves of *Camellia sinensis* var. Jinxuan were plucked at the Tea Experiment Station in the South China Agricultural University (Guangzhou, China) in October, 2014. The manufacture of oolong tea was carried out according to the general method,[21] as shown in Figure S1 (Supporting Information). The freshly plucked tea leaves (P) were exposed to sunlight (43 °C and 93,500 Lux) for 70 min as solar withering (SW). Afterward, the tea leaves were indoor-withered (IW) for 2 h at temperature of 27 °C and a relative humidity of 70%, and subsequently turned over by 5 times (T1−T5) every 1.5 h. Then the tea leaves were parched in a tea-firing roller machine at 250 °C for 2−3 min to inactivate the enzymatic activity and fix the sample (F). Finally, the tea leaves were rolled at room temperature for 15 min and dried at 105 °C for 1.5 h. The samples from P, SW, IW, and T1−T5 were immediately frozen by liquid nitrogen for enzyme activity and gene expression profiling. Three replicates were processed according to the oolong tea manufacturing.

Extraction and Analysis of Volatiles in Tea Samples. One gram of samples (finely powdered) was extracted by 2.5 mL of dichloromethane containing 5 nmol of ethyl decanoate as an internal standard in a shaker at room temperature overnight. The extraction solution was dried over anhydrous sodium sulfate and concentrated to 400 μL using nitrogen stream (MIULAB NDK200-1, MIU Instruments CO., Ltd., Hangzhou, China). One microliter of the concentrate was subjected to GC−MS QP2010 SE (Shimadzu Corporation, Japan) equipped with a SUPELCOWAXTM 10 column (30 m × 0.25 mm × 0.25 μm, Supelco Inc., Bellefonte, PA, USA). The injector temperature was 240 °C. The splitless mode was used with a splitless time of 1 min, and helium was the carrier gas with a velocity 1.0 mL/min. The GC oven temperature was 60 °C for 3 min, ramp of 4 °C/min to 240 °C, and then 240 °C for 20 min. The mass spectrometry was operated with full scan mode (mass range *m*/*z* 40−200).

Extraction and Analysis of GBVs in Tea Samples. Analysis of GBVs used the enzymatic hydrolysis combined with the GC−MS analysis method, which was the same as described previously.[15,22] Five hundred milligrams (fresh weight) of sample (finely powdered) was extracted with 2 mL of cold methanol by vortexing for 2 min followed by ultrasonic extraction in ice-cold water for 10 min. The extracts were mixed with 2 mL of cold chloroform and 0.8 mL of cold water for phase separation. The resulting upper layer was dried and dissolved in 1 mL of water. The resulting solution was mixed with 30 mg of PVPP, stood for 90 min, and was centrifuged (16400*g*, 4 °C, 10 min), and repeated with the supernatant. The final supernatant was loaded to an Amberlite XAD-2 column (1 mL) and eluted with 5 mL of water, 5 mL of pentane:dichloromethane (2:1), and 5 mL of methanol. The methanol eluent was dried using nitrogen stream, and redissolved in 400 μL of 50 mM citric acid buffer (pH 6.0) containing β-primeverosidase and β-glucosidase, and reacted at 37 °C for 14 h. Afterward, 144 mg of sodium chloride was added to the reaction solution, and stood for 15 min followed by addition of 5 nmol of ethyl decanoate as an internal standard. The solution was extracted with 400 μL of dichloromethane and centrifuged, and the dichloromethane fraction was dried over anhydrous sodium sulfate, followed by GC−MS analysis. The GC−MS conditions were the same as described above.

Determination of Enzyme Activities of β-Glucosidase and β-Primeverosidase. The enzyme assay method referred to the previous

DOI: 10.1021/acs.jafc.5b02741
J. Agric. Food Chem. 2015, 63, 6905−6914

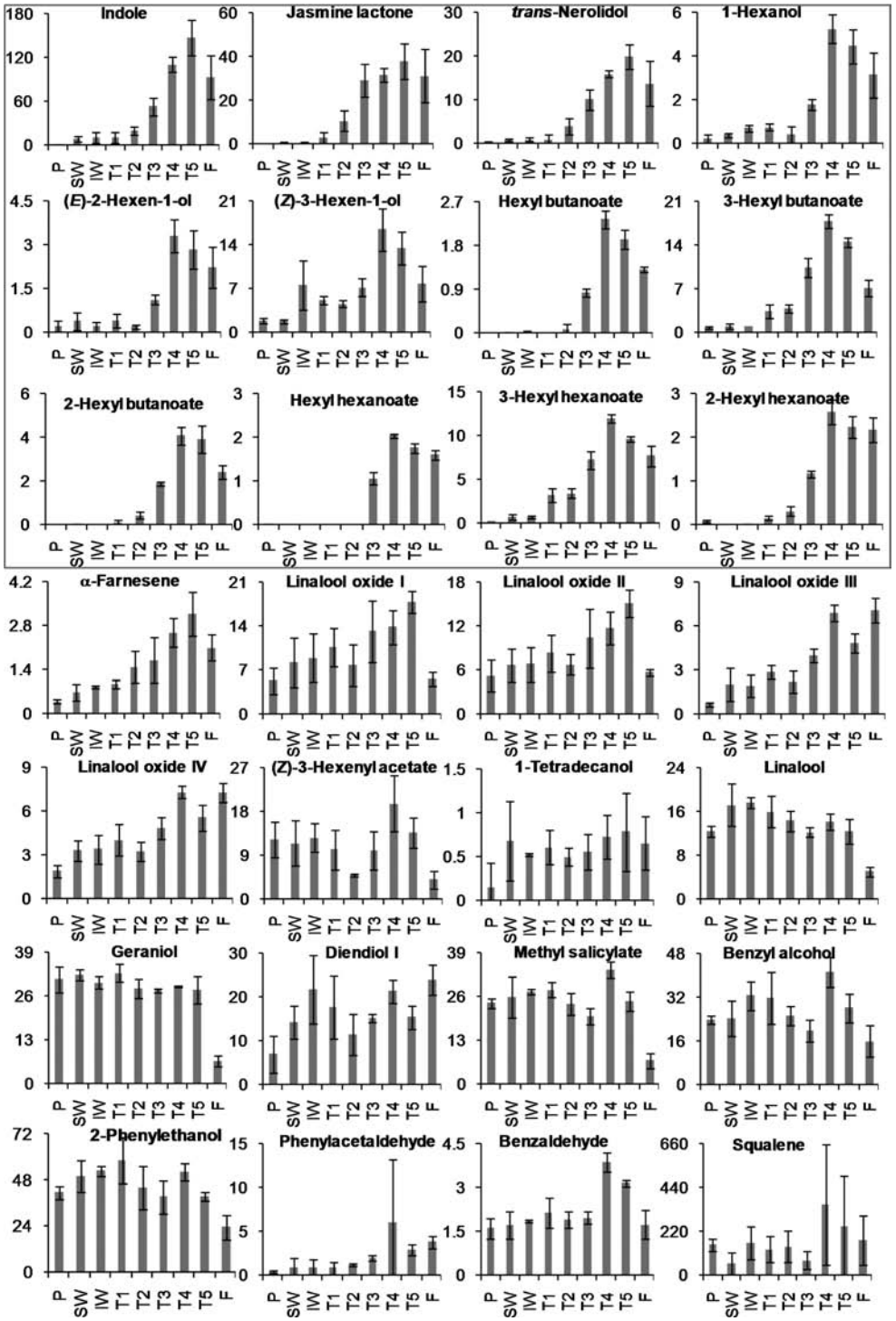

Figure 1. Changes in free volatiles during the manufacturing process of oolong tea. P, freshly plucked tea leaves; SW, solar withering; IW, indoor withering; T1−T5, turn over by 5 times; F, fixing. Data represent the mean value ± standard deviation of three in independent experiments performed in triplicate. The *y*-axis unit is peak area ratio of analyte to internal standard per g dry weight tea leaves. The volatiles in the pane showed significant increase during the manufacturing process of oolong tea.

reports.[20,23] One gram of finely powdered tea leaves was ground in ice-cold acetone and filtered using a suction pump (T-50.2L, Tianjin Jinteng Experiment Equipment Co., Ltd., Tianjin, China). The acetone-insoluble powder on the filter paper was washed with ice-cold acetone several times until clean and colorless acetone filtrate was obtained. The acetone-insoluble powder was dried by nitrogen stream to remove residual acetone and stored at −80 °C. For each 0.25 g of acetone-insoluble powder, 6.25 mL of ice-cold 50 mM sodium citrate buffer (pH 6.0) was added to dissolve the powder, accompanied by 0.125 g of PVPP. After vortexing twice for 30 s at 0 °C and centrifuging at 10000*g* (4 °C, 20 min), the supernatant was used as the crude enzyme solution. The substrate, either *p*-nitrophenyl-*β*-D-glucopyranoside or *p*-nitrophenyl-*β*- primeveroside, was dissolved in 90 μL of 50 mM sodium citrate buffer (pH 6.0) and incubated at 37 °C for 5 min. Ten microliters of crude enzyme solution was added, and then the whole reaction mixture was incubated at 37 °C for 60 min. The reaction was stopped by adding 140 μL of 0.2 M sodium carbonate, resulting in yellow color of the mixture, which was

DOI: 10.1021/acs.jafc.5b02741
J. Agric. Food Chem. 2015, 63, 6905−6914

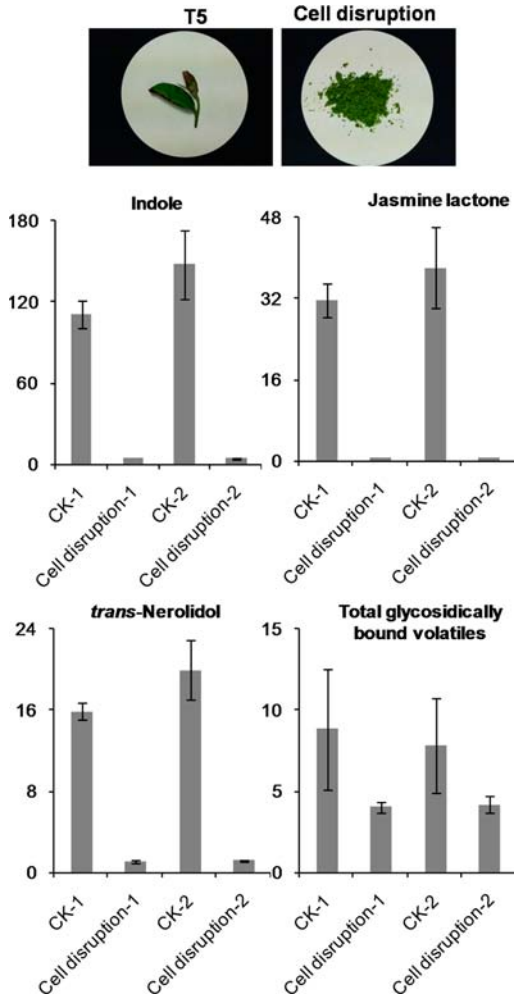

Figure 2. Effect of disruption of tea leaf cell on amounts of free volatiles and total GBVs. CK-1, The 4th turn over, at which stage tea leaf cell is not disrupted; CK-2, the 5th turn over, at which stage tea leaf cell is not disrupted; cell disruption-1, after turn over 1 (T1), parts of tea leaves were completely crushed to cause disruption of leaf cell, and indoor-withered at room temperature for 4.5 h; cell disruption-2, after turn over 1 (T1), parts of tea leaves were completely crushed to cause disruption of leaf cell, and indoor-withered at room temperature for 6.0 h. Data represent the mean value ± standard deviation of three independent experiments performed in triplicate. The *y*-axis unit is peak area ratio of analyte to internal standard per g dry weight tea leaves.

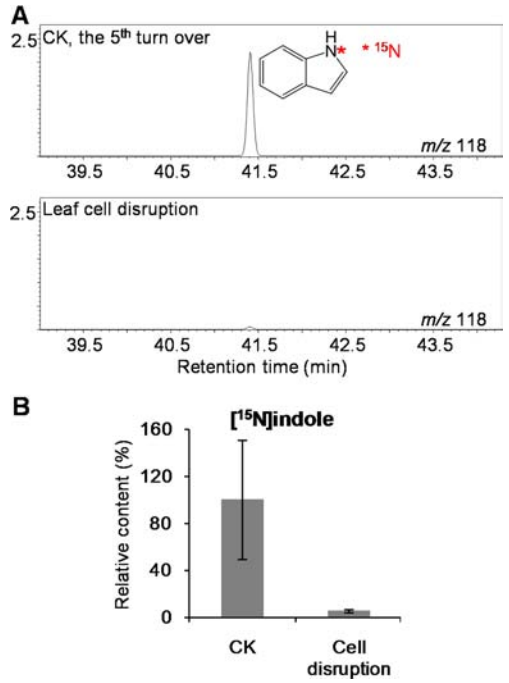

Figure 3. Effect of disruption of tea leaf cell on the transformation from [^{15}N]anthranilic acid to [^{15}N]indole. (A) GC−MS chromatography (m/z 118) of [^{15}N] indole from CK and leaf cell disruption. The [^{15}N]anthranilic acid feeding experiment started from the turn over 1 (T1). CK, the 5th turn over, at which stage tea leaf cell is not disrupted; leaf cell disruption, after T1, parts of tea leaves were completely crushed to cause disruption of leaf cell, and indoor-withered at room temperature for 6.0 h. (B) Data represent the mean value ± standard deviation of three independent experiments performed in triplicate. The relative content was calculated based on peak area of m/z 118 of [^{15}N] indole.

measured at 400 nm by a spectrophotometer (Infinite M200 PRO, TECAN, Switzerland). The amount of *p*-nitrophenol was determined according to a calibration curve.

Transcript Expression Analysis of *β-Primeverosidase*, *9/13-Lipoxygenase (LOX)*, and *Terpene Synthases* (*TPS*). Total RNA was isolated immediately after dissection. The reactions were performed using Power SYBR Green PCR Master Mix in a 20 μL volume containing 10 μL of Power SYBR Green PCR Master Mix (2×), 0.2 μM each specific forward and reverse primer. Two microliters of 10-fold diluted template was used for a 20 μL PCR reaction. The encoding elongation factors (EFs) were used as internal reference gene.[24] The *EFs*, *β-primeverosidase*,[15] *LOX*,[25] and *TPS*[26] specific primers of qRT-PCR are shown in Table S1 (Supporting Information). The qRT-PCR was carried out on Roche LightCycle 480 (Roche Applied Science, Mannheim, Germany) under the condition of one cycle of 95 °C for 10 min, 40 cycles of 95 °C for 15 s, and 60 °C for 1 min. A melt curve was performed at the end of each reaction to verify PCR product specificity. The $2^{-\Delta\Delta ct}$ method was used to calculate the relative expression level.[27] Changes in mRNA levels of the target genes were normalized to that of EFs.

Observation of Tea Leaf Cell Structure. The tea leaf samples of P, T1, T2, and T5 stages were cut into approximately 1 mm × 2 mm pieces and fixed in 0.1 M phosphate buffer (pH 7.2) containing 2% glutaraldehyde and 2.5% paraformaldehyde. After 6 times washing with 0.1 M phosphate buffer, the leaf samples were postfixed in 1% osmium tetroxide for 4 h and washed with 0.1 M phosphate buffer. Then the fixed leaf samples were dehydrated and embedded in flat molds using EPON812 resin. Ultrathin sections (80 nm) were cut by ultramicrotome (Leica UC7, Leica Microsysteme GmbH, Wetzlar, Germany), which then were stained by 4% uranyl acetate and 2% lead citrate. Ultrathin sections were observed by a transmission electron microscope (JEOL JEM-1010, Tokyo, Japan) operating at 100 kV.

Subcellular Localization of *β*-Primeverosidase in Tobacco. To construct vectors for expression of GFP-fusion protein, the stop codon of *β*-primeverosidase coding sequence was replaced by *Xma*I restriction site, with the following primers: 5′-GTCGACATGATGGCAGCGAAAGGG-3′ (forward), 5′-CCCGGGGCTTGAGGAGGAATTTCTT-3′ (reverse). The PCR product of *β*-primeverosidase cDNA fragment, in which the stop codon was eliminated, was cut with *Sal*I/*Xma*I and then cloned into the *Sal*I/*Xma*I sites of the pCAMBIA3300-GFP vector. The reorganization vector was transformed into *Agrobacterium* GV3101 by freeze−thaw. The overnight *Agrobacterium* cultures were sedimented at 5000*g* for 1 min. The pellet was resuspended in a solution containing 10 mM $MgCl_2$, 10 mM morpholineethanesulfonic acid (pH 5.6), and 100 μM acetosyringone to OD_{600} = 0.4.[28,29] Leaves of *Nicotiana benthamiana* were infiltrated by using a syringe without a needle, and then the tobacco was grown on a 16 h light/8 h dark under 25 °C regime for 4−5 days. Protoplasts were prepared as follows: tobacco leaves were cut into 2−3 cm^2 pieces

DOI: 10.1021/acs.jafc.5b02741
J. Agric. Food Chem. 2015, 63, 6905−6914

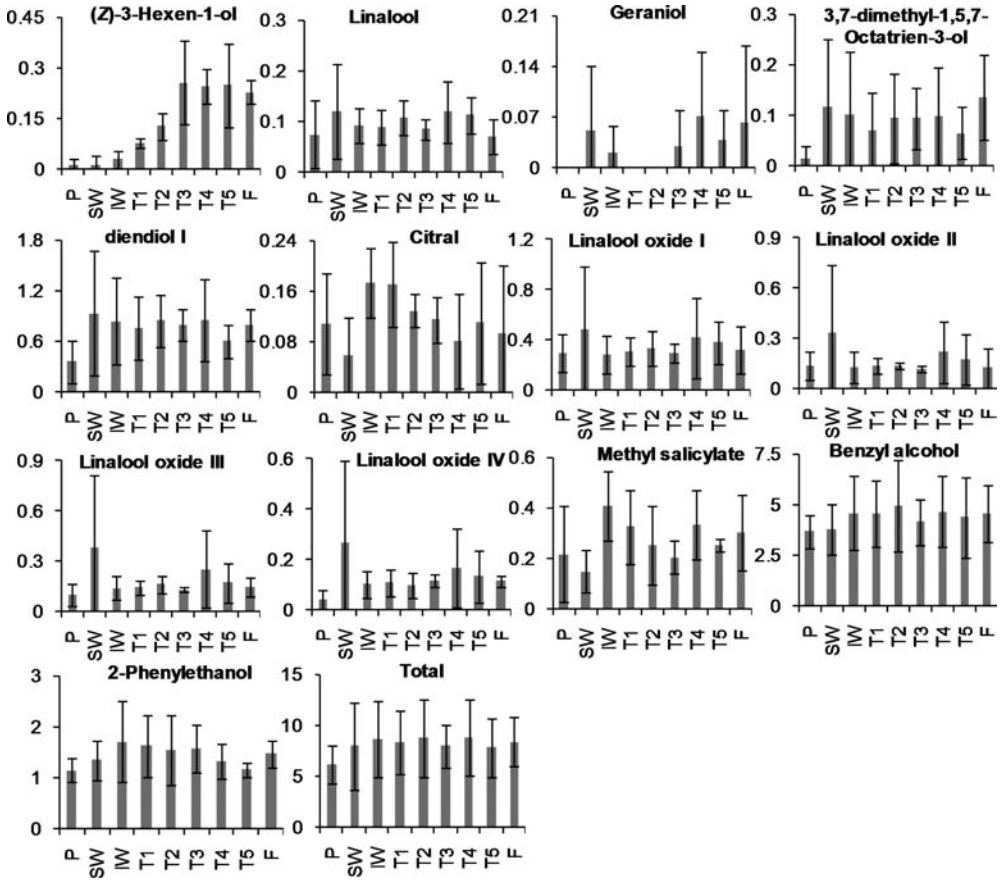

Figure 4. Changes in GBVs during the manufacturing process of oolong tea. P, freshly plucked tea leaves; SW, solar withering; IW, indoor withering; T1−T5, turn over by 5 times; F, fixing. Data represent the mean value ± standard deviation of three independent experiments performed in triplicate. The *y*-axis unit is peak area ratio of analyte (free volatiles from enzymatic hydrolysis of GBVs) to internal standard per g dry weight tea leaves.

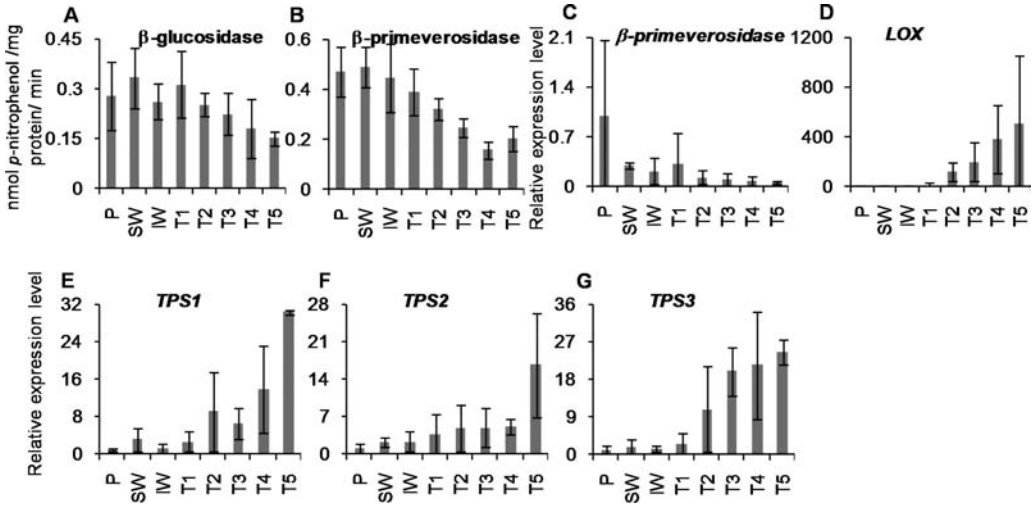

Figure 5. Changes in *β*-glycosidase enzyme activity, *β-Primeverosidase*, *LOX*, and *TPS* expression levels during the manufacturing process of oolong tea. P, freshly plucked tea leaves; SW, solar withering; IW, indoor withering; T1−T5, turn over by 5 times. Data represent the mean value ± standard deviation of three independent experiments performed in triplicate. (A, B) One unit was defined as the formed amount of *p*-nitrophenyl by the action of per mg protein per minute. (C, D, E, F, G) Transcript abundance was calculated based on the difference in cycle threshold (Ct) values between target gene and internal reference gene transcripts by the normalized relative quantification $2^{-\Delta\Delta Ct}$ method. The expression level of gene from P sample was defined as 1.

with a sterile scalpel blade. Two grams of leaf pieces was transferred to 50 mL tubes containing 10 mL of buffer solution (50 mM 2-(*N*-morpholino)ethanesulfonic acid, 0.6 M mannitol, and 10 mM calcium chloride), containing 1% cellulose and 0.05% macerozyme. The tubes were incubated at 25 °C on a reciprocating shaker (50 rpm) for 4 h. Protoplasts were washed and held in buffer solution. Confocal

DOI: 10.1021/acs.jafc.5b02741
J. Agric. Food Chem. 2015, 63, 6905−6914

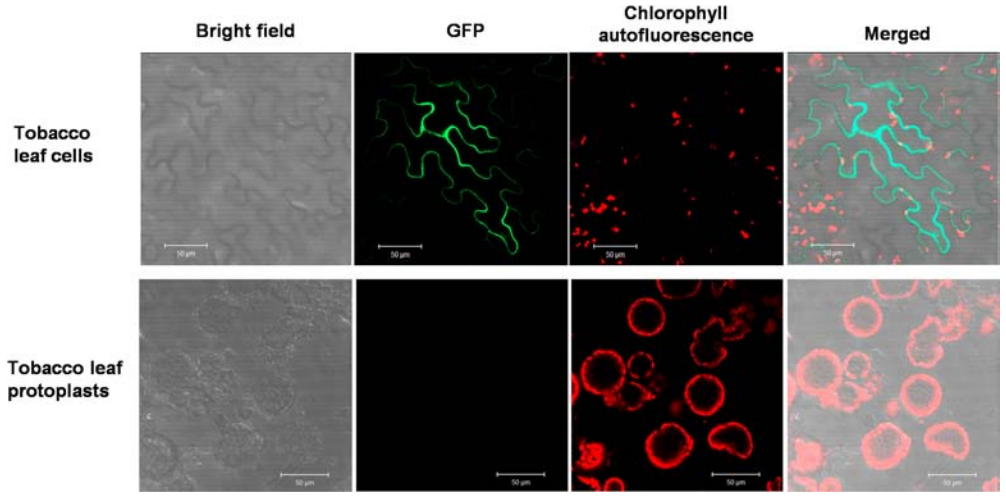

Figure 6. Subcellular localization analysis of GFP-β-primeverosidase. Upper photos: GFP-β-primeverosidase is visible in cell wall structures at the tobacco leaf cell. Lower photos: Green fluorescence was not shown in the protoplast cell prepared from the tobacco leaves (the upper photos), which proved that the GFP-β-primeverosidase protein is localized in the cell wall.

microscope images were taken using a Zeiss LSM 510 META confocal laser microscope (Cal Zeiss, Jena, Germany) with a 100× oil objective under 488 nm excitation wavelength for GFP detection.

Effect of Disruption of Tea Leaf Cell on Amounts of Free Volatiles and GBVs. After turn over 1 (T1), parts of tea leaves were completely crushed to cause disruption of leaf cell, and indoor-withered at room temperature for 4.5 and 6.0 h, respectively. Afterward, 1 g of treated sample was used for analyses of free volatiles and GBVs, which methods are described as above. The amounts of free volatiles and GBVs of the treated samples were compared with those of T4 and T5, respectively.

Administration of [^{15}N]Anthranilic Acid into Tea Leaves and Analysis of [^{15}N]Indole. Fifty microliters of solution of [^{15}N]-anthranilic acid (20 mM) was injected into each tea leaf at the T1 stage. One part of the tea leaves with [^{15}N]anthranilic acid was completely crushed to cause disruption of leaf cell and indoor-withered at room temperature for 6.0 h, while the other part of the tea leaves with [^{15}N]anthranilic acid followed the oolong tea manufacturing and was processed to the T5 stage. The amount of [^{15}N]indole was analyzed by GC−MS as described above. The characteristic ion of [^{15}N]indole is m/z 118.

Identification of Relatively Potent Odorants of Oolong Tea. The relatively potent odorants were evaluated using GC−MS/O and aroma extraction and dilution analysis (AEDA), as described previously.[30−33] The oolong tea product powders (2 g) were incubated in hot distilled water (40 mL, 80−90 °C) for 5 min and centrifuged for 10 min at 3000g. The resultant supernatant (30 mL) was loaded on a Porapak Q cartridge (2 mL volume, 50−80 mesh), eluted with 3 mL of water, and 3 mL of pentane:diethyl ether (1:1, v/v) as aroma extract. Afterward, the aroma extract was added with ethyl decanoate (20 μg/20 μL) as an internal standard, dried over anhydrous sodium sulfate, and concentrated to 100 μL in a stream of nitrogen to give an original odor concentrate sample.

The original odor concentrate of the sample infusion was stepwise diluted with pentane:diethyl ether (1:1, v/v) 1:4 = 4^1, 1:16 = 4^2, 1:64 = 4^3, 1:256 = 4^4, 1:1024 = 4^5, 1:4096 = 4^6, and 1:16384 = 4^7. The aliquots (2 μL) of each sample were analyzed by GC−MS/O. The flavor dilution (FD) factors of the odorants were determined by AEDA.

The GC/MSD (5975C, Agilent Technologies Inc., USA) equipped with a DB-WAX capillary column (60 m × 0.25 mm i.d., 0.25 μm film thickness, Agilent Technologies Inc., USA) was used for mass spectrometric identification. The splitless mode was used with a splitless time of 1 min. The split ratio at the time of the split vent liberation was 20:1. Helium was used as a carrier gas with a flow rate of 2 mL/min. The injector temperature was 240 °C. The GC oven was maintained at 40 °C for 2 min, increased by 5 °C/min to 240 °C, and was kept at this temperature for 25 min. The mass spectrometer was operated in full scan mode with a mass range of m/z 20−280. For GC−MS/O, the effluent was split into the olfactory detection port (Gerstel K.K., Japan) and MS using two deactivated, uncoated fused silica capillaries (106 cm × 0.15 mm i.d., 139 cm × 0.1 mm i.d.) at the end of the capillary. Volatile compounds were identified by direct comparison with the Kovats GC retention indices (RI), mass spectra, and those of the authentic specimens.

RESULTS AND DISCUSSION

Indole, Jasmine Lactone, and *trans*-Nerolidol Were Significantly Increased at the Turn Over Stage. To find out which volatiles, especially those also occurring in glycosidically bound form, have big changes during the manufacturing process, we monitored changes of free volatiles from the plucking process to fixing process (enzymatic reaction termination) of oolong tea. Among the manufacturing processes, the turn over process (T1−T5) had a significant influence on the contents of volatiles (Figure 1). In the present study, not all the free volatiles had big changes during the manufacturing process of oolong tea. The three volatiles including indole, jasmine lactone, and *trans*-nerolidol had significantly big increase at the turn over process (Figure 1). In addition, most fatty acid-derived volatiles such as 1-hexanol, (*E*)-2-hexen-1-ol, (*Z*)-hexen-1-ol, etc., linalool oxides, and α-farnesene increased at T1−T5, whereas some free volatiles such as linalool, geraniol, diendiol I, benzyl alcohol, 2-phenylethanol, and methyl salicylate, which also occur in glycosidically bound form, did not show significant changes during the process (Figure 1). Wang et al. first reported that the contents of free alcoholic aroma compounds remained almost unchanged or slightly decreased, but jasmine lactone and indole significantly increased in the final oolong tea products compared to dried fresh tea leaves.[21] In addition, increase of indole during the oolong manufacturing process was also demonstrated by a direct analysis in real time mass spectrometry.[34] Our previous study on comparison of volatiles of green teas, oolong teas, and black teas from different cultivars and regions also proposed that jasmine lactone and indole were characteristic volatiles in oolong tea products.[35] Furthermore, the present study indicated that these volatiles mostly accumulated at the turn over

DOI: 10.1021/acs.jafc.5b02741
J. Agric. Food Chem. 2015, 63, 6905−6914

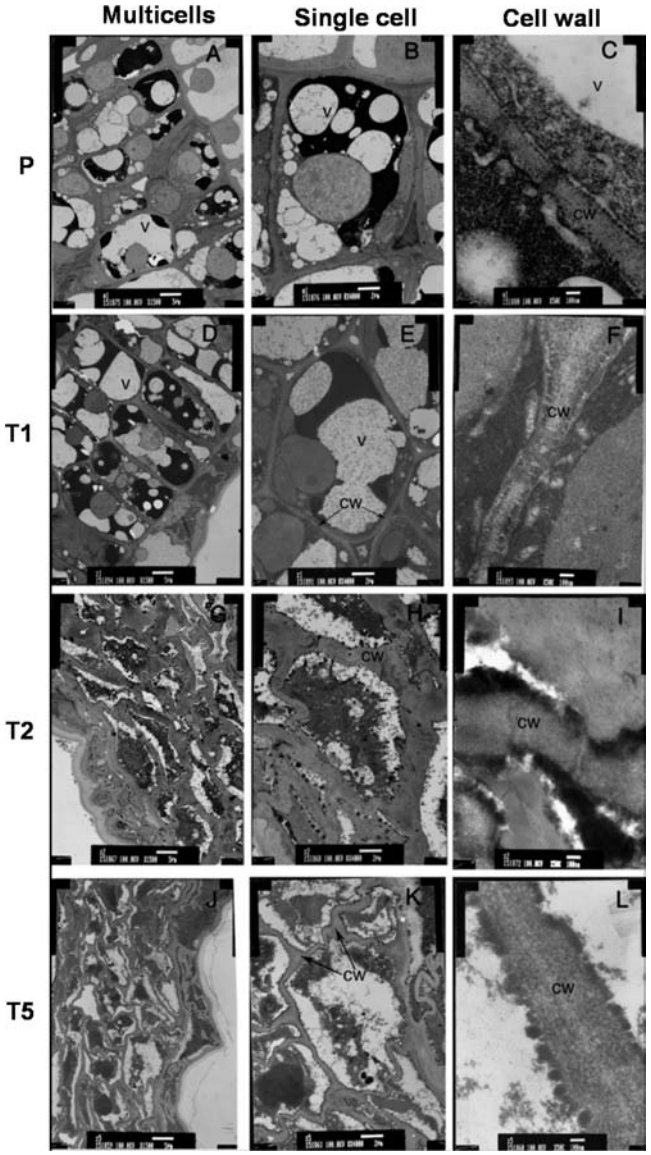

Figure 7. Transmission electron micrograph of the tea leaf cells during the oolong tea manufacturing process. P, plucking; T1, turn over 1; T2, turn over 2; T5, turn over 5; V, vacuole; CW, cell wall. (A, D, G, J) Multicells on the edge of sample tea leaves in P, T1, T2, and T5 respectively. Bar, 5 μm. (B, E, H, K) Single cell on the edge of sample tea leaves in P, T1, T2, and T5 respectively. Bar, 2 μm. (C, F, I, L) Cell wall of the cell on the edge of sample tea leaves in P, T1, T2, and T5 respectively. Bar, 0.1 μm.

process.[36,37] During the oolong tea manufacturing process, tea leaves are exposed to various stresses, such as plucking (wounding), solar withering (drought, heat, and UV/light radiation), indoor withering (drought), and turn over (wounding).[16] Therefore, the aroma formation in tea leaves during the manufacturing process of oolong tea is proposed to be the stress-responsive biochemical reactions of juvenile leaves of tea plants. Indole is a very representative stress-responsive volatile compound in the manufacturing process of oolong tea. Indole occurs with very trace amount in intact tea leaves. However, indole level increases rapidly after plucking.[38] Also indole increased during the withering process of green tea leaves even at a relatively low temperature (15 °C, for 16 h).[33] In the present study, the turn over led to more accumulations of indole (Figure 1). This evidence suggests that wounding stress from the turn over process is a key factor

Table 1. Identification of Potent Odorants (FD Factor $\geq 4^4$) in Oolong Tea

RI	identified compound	odorant quality	FD factor (4^n)
1538	linalool	fresh floral	5
1716	3-methylnonane-2,4-dione	fresh floral	5
1821	β-damascenone	honey	5
1840	unidentified[a]	minty	5
1883	unidentified[a]	fresh floral	4
1945	β-ionone	floral	4
2017	Furaneol[a]	sweet	7
2200	δ-decalactone	floral, sweet	6
2266	jasmine lactone	floral, sweet	6
2431	indole	animal-like, floral	4
2546	vanillin	sweet	5

[a]The MS spectrum is provided as Figure S2.

regulating formation of indole. Interestingly, black teas contain much less indole,[35] although wound stress is also involved in the manufacturing process of black tea. Tea leaves are still relatively intact and alive from the plucking to the turn over process of oolong tea, whereas the structure of the leaf cells is disrupted during the rolling process and the contents of the cells are completely mixed during the rolling process of black tea.[20,21] Amounts of indole, jasmine lactone, and *trans*-nerolidol reduced after tea leaf cell disruption (Figure 2), suggesting that mechanical damage with tea leaf cell disruption, which is similar to the manufacturing process of black tea, does not induce the accumulation of indole, jasmine lactone, and *trans*-nerolidol. As anthranilic acid is one of precursors of indole,[33] we investigated the formation of indole by feeding of stable isotope-labeled compound [^{15}N]anthranilic acid to the tea leaves. It was found that the amount of [^{15}N] indole in tea leaf with cell disruption was much lower than that in tea leaf without disruption (Figure 3). This suggests that indole may be oxidized by P450 enzymes after the leaf cell disruption.[39] Therefore, the pathway leading from anthranilic acid to indole may be a key step of formation of indole during the oolong tea process. As the genes involved in the pathway leading from anthranilic acid to indole are still unknown in plants, we are attempting to identify the involved genes and will investigate their responses to the stresses from the manufacturing process of oolong tea. In addition, it would be very interesting to investigate whether disruption of leaf cell and complete mixture of contents of cell may lead to the pathway competition between indole, jasmine lactone, and *trans*-nerolidol and other metabolites.

Most GBVs Did Not Show Reduction during the Manufacturing Process. To confirm whether enzymatic hydrolysis of GBVs occurs during the manufacturing process of oolong tea, we monitored changes of GBVs from the plucking process to fixing process (enzymatic reaction termination) of oolong tea. No GBVs were reduced in their contents during the enzyme-active process (Figure 4), which is consistent with the previous report.[21] This suggests that enzymatic hydrolysis of GBVs may not happen during the manufacturing process of oolong tea. The GBVs occur in vacuoles, whereas hydrolases such as β-primeverosidase were presumed to be localized in cell walls.[18] This compartmentation of substrates and enzymes in plant cells leads to little possibility of hydrolysis of GBVs in nondisrupted tea leaf cells. After additional treatment was done to disrupt tea leaf cell, GBVs were reduced (Figure 2), further demonstrating that lack of disruption of tea leaf cell during the oolong tea process resulted in unavailability of interaction of

DOI: 10.1021/acs.jafc.5b02741
J. Agric. Food Chem. 2015, 63, 6905−6914

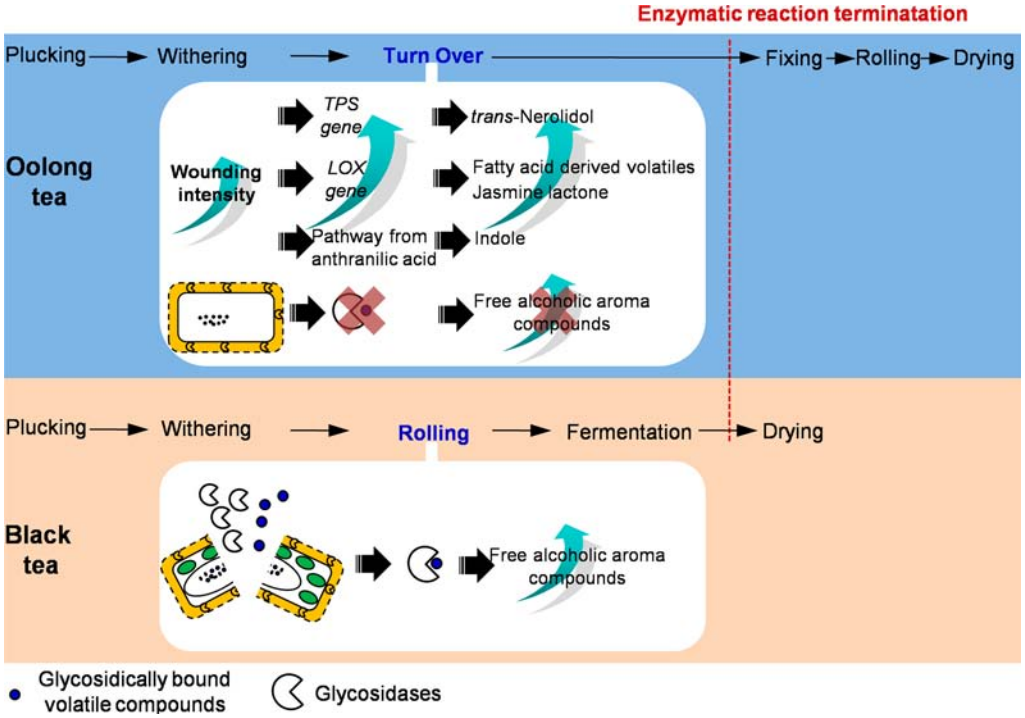

Figure 8. Hypothetical model of different formations of volatiles between the oolong tea process and the black tea process.

substrates and enzymes and no hydrolysis of GBVs. Interestingly, the previous report[21] and the present study found that the amounts of some GBVs increased (Figure 4). Currently, most studies on GBVs have concentrated on glycosidases, whereas little information on glycosyl transferases is available.[1] Recently glycosyl transferases in tea leaves have been functionally characterized;[40] it will be helpful for our understanding of the accumulation of GBVs during the oolong tea manufacturing process.

β-Glycosidases Were Not Activated during The Manufacturing Process, and Interaction of β-Glycosidases and GBVs Were Unavailable. To investigate whether β-glycosidases were activated during the manufacturing process, we monitored enzyme activities and gene expression levels of β-glycosidases from the plucking process to the fifth turn over process of oolong tea. The enzyme activities of β-glucosidase and β-primeverosidase did not show increase during the manufacturing process (Figures 5A and 5B). Moreover, expression level of *β-primeverosidase* showed reduction trend at the turn over process (Figure 5C). Although many stresses including drought, heat, wounding, and UV/light radiation are involved in the oolong tea manufacturing process, our study indicates that β-glycosidases were not activated under these stresses. This also reveals that contact of substrate (GBVs) and enzyme (β-glycosidases) is a key point determining whether enzymatic hydrolysis of GBVs happens in the tea manufacturing process.

Previously, Mizutani et al. found that β-primeverosidase is *N*-glycosylated, and has an *N*-terminal signal sequence, thus presumed that β-primeverosidase may locate in the cell wall.[18] However, a direct evidence of subcellular localization of β-primeverosidase in tea leaves is still unavailable. In the present study, subcellular localization of β-primeverosidase provided more evidence that β-primeverosidase is located in the leaf cell wall (Figure 6). Moreover, we investigated the cell structures of tea leaves from the manufacturing process of oolong tea. From the P to T1 process, the leaf cells showed complete and unwounded. The content was divided into several parts and showed the clear boundary (Figure 7A–F). From the T2 to T5 process, the cells shrank and distorted intensely, while the cell walls remained well and unwounded (Figures 7G–L). These results strongly support that lack of disruption of tea leaf cell during the oolong tea process resulted in unavailability of interaction of GBVs (substrates located in vacuole) and β-glycosidases (enzymes).

Besides *β-primeverosidase*, we also investigated the expression levels of *LOX* that is a key gene that involved in formation of fatty acid-derived volatiles and jasmine lactone,[1,25] and *TPS* that are possibly involved in formation of *trans*-nerolidol in tea leaves.[26] *LOX* is proposed as a wounding stress-response gene.[25] *LOX* gene expression level significantly increased at the turn over process (Figure 5D), which may be one of the reasons that most free fatty acid-derived volatiles and jasmine lactone increased at that process (Figure 1). Similarly, *TPS*1, 2, and 3 gene expression levels also significantly increased at the turn over process (Figures 5E,F,G). The present study provides important hints that the wounding stress at the turn over process may activate some key genes involved in formation of volatiles.

Furaneol, Jasmine Lactone, δ-Decalactone, Linalool, Vanillin, β-Ionone, β-Damascenone, 3-Methylnonane-2,4-dione, and Indole Were Identified as Relatively Potent Odorants in Oolong Tea. The above evidence shows that enzymatic hydrolysis of GBVs did not significantly contribute to the formation of volatiles of oolong tea. To further find out which volatiles contribute to flavor of oolong tea, GC–MS/O and AEDA were employed to determine the contribution of each volatile to the quality of the tea's aroma and flavor. The results revealed 49 odor-active peaks with FD factors between 4^1 and 4^7 in the final oolong tea product. Among them, the 11 compounds showed as relatively potent odorants with the higher FD factor ($\geq 4^4$) (Table 1). AEDA is most frequently used for identifying ordor-active compounds in

DOI: 10.1021/acs.jafc.5b02741
J. Agric. Food Chem. 2015, 63, 6905–6914

tea, and evaluating the flavor changes that occur during the manufacturing of tea beverages.[33,41−45] Based on this technique, many volatile compounds were identified as the most important components in Japanese and Chinese green teas and black tea beverages. However, little information on potent odorants in oolong tea is available. In the present study, Furaneol, jasmine lactone, δ-decalactone, linalool, vanillin, β-ionone, 3-methylnonane-2,4-dione, β-damascenone, indole, and two other compounds were identified as relatively potent odorants in oolong tea (Table 1). Although linalool was one of the potent odorants, its formation was not from enzymatic hydrolysis of glycosides of linalool (Figures 1 and 4). Jasmine lactone and indole were identified as relatively potent odorants, further suggesting that they were characteristic compounds derived from the manufacturing process of oolong tea (Figures 1 and 2) and partly contributed to the aroma of oolong tea. Other compounds showed high FD factors, suggesting that some compounds with low concentrations may have a comparatively low olfactory threshold detected by human and contribute to the characteristic aroma of oolong tea.

Formation of Volatiles Is Different between Oolong Tea and Black Tea. Oolong tea and black tea are fermented teas and have more aroma characters than green tea. Therefore, analysis and identification of volatile compounds during the manufacturing process of oolong tea and black tea have been well done. Based on the previous reports and the present study, we propose a hypothetical model of different formations of volatiles between the oolong tea process and the black tea process (Figure 8). (1) For oolong tea, turn over is a key process to produce tea aroma and increase of wounding intensity could lead to accumulations of indole, jasmine lactone, and *trans*-nerolidol, which may be characteristic aromas of oolong tea. However, such wounding is not sufficient for disruption of tea leaf cell, which is essential for interaction of substrates and enzymes. (2) For black tea, rolling is a key process to produce tea aroma. At this process, complete disruption of tea leaf cell leads to interaction of substrates and enzymes and many GBVs are hydrolyzed to release free alcoholic aroma compounds. The results help us find out the direct evidence of formation of volatiles in oolong tea, and advance our understanding of differences of formation of volatiles between oolong tea and black tea.

■ ASSOCIATED CONTENT

Supporting Information

The Supporting Information is available free of charge on the ACS Publications website at DOI: 10.1021/acs.jafc.5b02741.

Table of studied primers of qRT-PCR, flow chart of oolong tea manufacturing process, and mass spectra (PDF)

■ AUTHOR INFORMATION

Corresponding Author

*Tel: +86-20-38072989. E-mail: zyyang@scbg.ac.cn.

Author Contributions

§J.G. and X.F. equally contributed to this work.

Funding

This study was supported by "100 Talents Programme of the Chinese Academy of Sciences" (Y321011001 and 201209), and the Foundation of Science and Technology Program of Guangzhou (2014J4100219).

Notes

The authors declare no competing financial interest.

■ ABBREVIATIONS USED

AEDA, aroma extraction and dilution analysis; EFs, elongation factors; FD, flavor dilution; GBVs, glycosidically bound volatiles; GC−MS/O, gas chromatography−mass spectrometer/olfactometry; IW, indoor-withered; LOX, 9/13-lipoxygenase; P, freshly plucking tea leaves; PVPP, polyvinylpolypyrrolidone; RI, retention indices; SW, solar withering; T1−T5, turned over by 5 times; TMEMD, *N*, *N*,*N*′,*N*′-tetramethylethylenediamine; TPS, terpene synthases

■ REFERENCES

(1) Yang, Z. Y.; Baldermann, S.; Watanabe, N. Recent studies of the volatile compounds in tea. *Food Res. Int.* **2013**, *53*, 585−599.

(2) Nagegowda, D. A. Plant volatile terpenoid metabolism: biosynthetic genes, transcriptional regulation and subcellular compartmentation. *FEBS Lett.* **2010**, *584*, 2965−2973.

(3) Wang, X.; Wang, D.; Li, J.; Ye, C.; Kubota, K. Aroma characteristics of cocoa tea (*Camellia ptilophylla Chang*). *Biosci., Biotechnol., Biochem.* **2010**, *74*, 946−953.

(4) Schwab, W.; Davidovich-Rikanati, R.; Lewinsohn, E. Biosynthesis of plant-derived flavor compounds. *Plant J.* **2008**, *54*, 712−732.

(5) Auldridge, M. E.; McCarty, D. R.; Klee, H. J. Plant carotenoid cleavage oxygenases and their apocarotenoid products. *Curr. Opin. Plant Biol.* **2006**, *9*, 315−321.

(6) Winterhalter, P.; Skouroumounis, G. K. Glycoconjugated aroma compounds: Occurrence, role and biotechnological transformation. In *Biotechnology of Aroma Compounds*; Berger, R. G., Ed.; Advances in Biochemical Engineering/Biotechnology, Vol. *55*; Springer: Berlin, Heidelberg, 1997; pp 73−105.

(7) Nishikitani, M.; Kubota, K.; Kobayashi, A.; Sugawara, F. Geranyl 6-O-α-L-arabinopyranosyl-β-D-glucopyranoside isolated as an aroma precursor from leaves of a green tea cultivar. *Biosci., Biotechnol., Biochem.* **1996**, *60*, 929−931.

(8) Nishikitani, M.; Wang, D.; Kubota, K.; Kobayashi, A.; Sugawara, F. *Z*)-3-Hexenyl and *trans*-linalool 3, 7-oxide β-primeverosides isolated as aroma precursors from leaves of a green tea cultivar. *Biosci., Biotechnol., Biochem.* **1999**, *63*, 1631−1633.

(9) Guo, W.; Hosoi, R.; Sakata, K.; Watanabe, N.; Yagi, A.; Ina, K.; Luo, S. *S*)-Linalyl, 2-phenylethyl, and benzyl disaccharide glycosides isolated as aroma precursors from oolong tea leaves. *Biosci., Biotechnol., Biochem.* **1994**, *58*, 1532−1534.

(10) Guo, W.; Sakata, K.; Watanabe, N.; Nakajima, R.; Yagi, A.; Ina, K.; Luo, S. Geranyl 6-*O*-β-D-xylopyranosyl-β-D-glucopyranoside isolated as an aroma precursor from tea leaves for oolong tea. *Phytochemistry* **1993**, *33*, 1373−1375.

(11) Wang, D. M.; Yoshimura, T.; Kubota, K.; Kobayashi, A. Analysis of glycosidically bound aroma precursors in tea leaves. 1. Qualitative and quantitative analyses of glycosides with aglycons as aroma compounds. *J. Agric. Food Chem.* **2000**, *48*, 5411−5418.

(12) Guo, W.; Sasaki, N.; Fukuda, M.; Yagi, A.; Watanabe, N.; Sakata, K. Isolation of an aroma precursor of benzaldehyde from tea leaves (*Camellia sinensis* var. sinensis cv. Yabukita). *Biosci., Biotechnol., Biochem.* **1998**, *62*, 2052−2054.

(13) Yang, Z. Y.; Kinoshita, T.; Tanida, A.; Sayama, H.; Morita, A.; Watanabe, N. Analysis of coumarin and its glycosidically bound precursor in Japanese green tea having sweet-herbaceous odour. *Food Chem.* **2009**, *114*, 289−294.

(14) Kinoshita, T.; Hirata, S.; Yang, Z. Y.; Baldermann, S.; Kitayama, E.; Matsumoto, S.; Suzuki, M.; Fleischmann, P.; Winterhalter, P.; Watanabe, N. Formation of damascenone derived from glycosidically bound precursors in green tea infusions. *Food Chem.* **2010**, *123*, 601−606.

(15) Zhou, Y.; Dong, F.; Kunimasa, A.; Zhang, Y.; Cheng, S.; Lu, J.; Zhang, L.; Murata, A.; Mayer, F.; Fleischmann, P.; Watanabe, N.;

DOI: 10.1021/acs.jafc.5b02741
J. Agric. Food Chem. 2015, 63, 6905−6914

Yang, Z. Y. Occurrence of glycosidically conjugated 1-phenylethanol and its hydrolase β-primeverosidase in tea (*Camellia sinensis*) flowers. *J. Agric. Food Chem.* **2014**, *62*, 8042−8050.
(16) Cho, J. Y.; Mizutani, M.; Shimizu, B.; Kinoshita, T.; Ogura, M.; Tokoro, K.; Lin, M. L.; Sakata, K. Chemical profiling and gene expression profiling during the manufacturing process of Taiwan oolong tea "Oriental Beauty. *Biosci., Biotechnol., Biochem.* **2007**, *71*, 1476−1486.
(17) Yang, Z. Y.; Kobayashi, E.; Katsuno, T.; Asanuma, T.; Fujimori, T.; Ishikawa, T.; Tomomura, M.; Mochizuki, K.; Watase, T.; Nakamura, Y.; Watanabe, N. Characterization of volatile and non-volatile metabolites in etiolated leaves of tea (*Camellia sinensis*) plants in the dark. *Food Chem.* **2012**, *135*, 2268−2276.
(18) Mizutani, M.; Nakanishi, H.; Ema, J. I.; Ma, S. J.; Noguchi, E.; Inohara-Ochiai, M.; Fukuchi-Mizutani, M.; Nakao, M.; Sakata, K. Cloning of β-primeverosidase from tea leaves, a key enzyme in tea aroma formation. *Plant Physiol.* **2002**, *130*, 2164−2176.
(19) Sarry, J. E.; Günata, Z. Plant and microbial glycoside hydrolases: Volatile release from glycosidic aroma precursors. *Food Chem.* **2004**, *87*, 509−521.
(20) Wang, D. M.; Kurasawa, E.; Yamaguchi, Y.; Kubota, K.; Kobayashi, A. Analysis of glycosidically bound aroma precursors in tea leaves. 2. Changes in glycoside contents and glycosidase activities in tea leaves during the black tea manufacturing process. *J. Agric. Food Chem.* **2001**, *49*, 1900−1903.
(21) Wang, D. M.; Kubota, K.; Kobayashi, A.; Juan, I. M. Analysis of glycosidically bound aroma precursors in tea leaves. 3. Changes in glycoside contents during the oolong tea manufacturing process. *J. Agric. Food Chem.* **2001**, *49*, 5391−5396.
(22) Dong, F.; Yang, Z. Y.; Baldermann, S.; Kajitani, Y.; Ota, S.; Kasuga, H.; Imazeki, Y.; Ohnishi, T.; Watanabe, N. Characterization of L-phenylalanine metabolism to acetophenone and 1-phenylethanol in the flowers of *Camellia sinensis* using stable isotope labeling. *J. Plant Physiol.* **2012**, *169*, 217−225.
(23) Yano, M.; Okada, K.; Kubota, K.; Kobayashi, A. Studies on the precursors of monoterpene alcohols in tea leaves. *Agric. Biol. Chem.* **1990**, *54*, 1023−1028.
(24) Hao, X.; Horvath, D. P.; Chao, W. S.; Yang, Y.; Wang, X.; Xiao, B. Identification and evaluation of reliable reference genes for quantitative real-time PCR analysis in tea plant (*Camellia sinensis* (L.) O. Kuntze). *Int. J. Mol. Sci.* **2014**, *15*, 22155−22172.
(25) Liu, S.; Han, B. Differential expression pattern of an acidic 9/13-lipoxygenase in flower opening and senescence and in leaf response to phloem feeders in the tea plant. *BMC Plant Biol.* **2010**, *10*, 228.
(26) Liu, J.; Wang, F.; Liu, G.; He, Z.; Yang, H.; Wei, C.; Wan, X.; Wei, S. Correlation between spatiotemporal profiles of volatile terpenoids and relevant terpenoid synthase gene expression in *Camellia sinensis* (*in Chinese*). *Acta Hortic. Sin.* **2014**, *41*, 2094−2106.
(27) Livak, K. J.; Schmittgen, T. D. Analysis of relative gene expression data using real time quantitative PCR and $2^{-\Delta\Delta ct}$ method. *Methods* **2001**, *25*, 402−408.
(28) Liu, Z. Z.; Wang, J. L.; Huang, X.; Xu, W. H.; Liu, Z. M.; Fang, R. X. The promoter of a rice glycine-rich protein gene, Osgrp-2, confers vascular-specific expression in transgenic plants. *Planta* **2003**, *216*, 824−833.
(29) Zhou, Y.; Zhang, L.; Gui, J. D.; Dong, F.; Cheng, S.; Mei, X.; Zhang, L. Y.; Li, Y. Q.; Su, X. G.; Baldermann, S.; Watanabe, N.; Yang, Z. Y. Molecular cloning and characterization of a short chain dehydrogenase showing activity with volatile compounds isolated from *Camellia sinensis*. *Plant Mol. Biol. Rep.* **2015**, *33*, 253−263.
(30) Schmid, W.; Grosch, W. Identifizierung flüchtiger Aromastoffe mit hohen Aromawerten in Sauerkirschen (*Prunus cerasus L.*). *Z. Lebensm.-Unters. Forsch.* **1986**, *182*, 407−412.
(31) Ullrich, F.; Grosch, W. Identification of the most intense volatile flavour compounds formed during autoxidation of linoleic acid. *Z. Lebensm.-Unters. Forsch.* **1987**, *184*, 277−282.
(32) Schieberle, P.; Grosch, W. Evaluation of the flavor of wheat and rye bread crusts by aroma extract dilution analysis. *Z. Lebensm.-Unters. Forsch.* **1987**, *185*, 111−113.
(33) Katsuno, T.; Kasuga, H.; Kusano, Y.; Yaguchi, Y.; Tomomura, M.; Cui, J. L.; Yang, Z. Y.; Baldermann, S.; Nakamura, Y.; Ohnishi, T.; Mase, N.; Watanabe, N. Characterisation of odorant compounds and their biochemical formation in green tea with a low temperature storage process. *Food Chem.* **2014**, *148*, 388−395.
(34) Fraser, K.; Lane, G. A.; Otter, D. E.; Harrison, S. J.; Quek, S. Y.; Hemar, Y.; Rasmussen, S. Monitoring tea fermentation/manufacturing by direct analysis in real time (DART) mass spectrometry. *Food Chem.* **2013**, *141*, 2060−2065.
(35) Baldermann, S.; Yang, Z. Y.; Katsuno, T.; Tu, V. A.; Mase, N.; Nakamura, Y.; Watanabe, N. Discrimiantion of green, oolong, and black teas by GC-MS analysis of characeristic volatile flavor compounds. *Am. J. Anal. Chem.* **2014**, *5*, 620−632.
(36) Yamanishi, T. Tea (in Japanese). *Koryo* **1989**, *161*, 57−72.
(37) Huang, F. P.; Chen, R. B.; Liang, Y. R.; Chen, W.; Lu, J. L.; Chen, C. S.; You, X. M. Changes of aroma constituents during zouqing procedure and its relation to oolong tea quality (*in Chinese*). *J. Tea Sci.* **2003**, *23*, 31−37.
(38) Yang, Z. Y.; Mochizuki, K.; Watase, T.; Kobayashi, E.; Katsuno, T.; Asanuma, T.; Tomita, K.; Morita, A.; Suzuki, T.; Nakamura, Y.; Watanabe, N. Influences of light emitting diodes irradiations and shade treatments on volatile profiles and related metabolites of leaves of tea (*Camellia sinensis*) plants and postharvest tea leaves. In *Advances and Challenges in Flavor Chemistry & Biology*; Hofmann, T., Meyerhof, W., Schieberle, P., Eds.; Deutsche Forschungsanstalt für Lebensmittelchemie: Germany, 2010; pp 207−213.
(39) Gillam, E. M. J.; Notley, L. M.; Cai, H.; De Voss, J. J.; Guengerich, F. P. Oxidation of indole by cytochrome P450 enzymes. *Biochemistry* **2000**, *39*, 13817−13824.
(40) Ohgami, S.; Ono, E.; Horikawa, M.; Murata, J.; Totsuka, K.; Toyonaga, H.; Ohba, Y.; Dohra, H.; Asai, T.; Matsui, K.; Mizutani, M.; Watanabe, N.; Ohnishi, T. Volatile glycosylation in tea plants: Sequential glycosylations for the biosynthesis of aroma β-primeverosides are catalyzed by two *Camellia sinensis* glycosyltransferases. *Plant Physiol.* **2015**, *168*, 464.
(41) Kumazawa, K.; Masuda, H. Identification of potent odorants in Japanese green tea (Sen-cha). *J. Agric. Food Chem.* **1999**, *47*, 5169−5172.
(42) Kumazawa, K.; Masuda, H. Change in the flavor of black tea drink during heat processing. *J. Agric. Food Chem.* **2001**, *49*, 3304−3309.
(43) Kumazawa, K.; Masuda, H. Identification of potent odorants in different green tea varieties using flavor dilution technique. *J. Agric. Food Chem.* **2002**, *50*, 5660−5663.
(44) Baba, R.; Kumazawa, K. Characterization of the potent odorants contributing to the characteristic aroma of Chinese green tea infusions by aroma extract dilution analysis. *J. Agric. Food Chem.* **2014**, *62*, 8308−8313.
(45) Schuh, C.; Schieberle, P. Characterization of the key aroma compounds in beverage prepared from Darjeeling black tea: Quantitative differences between tea leaves and infusion. *J. Agric. Food Chem.* **2006**, *54*, 916−924.

DOI: 10.1021/acs.jafc.5b02741
J. Agric. Food Chem. 2015, 63, 6905−6914

Fermentation of Wort by *T. versicolor*. Wort (Kölsch type, 13 °Plato) was provided by the University of Applied Sciences (Giessen, Germany).[7] Erlenmeyer flasks containing standard nutrition solution (100 mL/250 mL, medium volume/flask volume) were inoculated with fungal mycelia as reported previously.[6] The precultures were incubated on a rotary shaker (24 °C, 150 rpm, 25 mm shaking diameter) for 5 days in the dark. The mycelium of 10 mL of preculture broth was precipitated by centrifugation (2150*g*, 10 min, 20 °C) and washed three times with sterile water. The fungal pellets were resuspended in 10 mL of sterile wort. The suspension was added into an Erlenmeyer flask (250 mL) containing 100 mL of wort, and fermentation was carried out at 24 °C for 38 h under aerobic conditions on a rotary shaker (150 rpm). Subsequently, the mycelium was removed by centrifugation (2150*g*, 10 min, 4 °C), and the fermented beverage was used for the determination of nutritionally relevant parameters, for flavor analysis, and for safety assessment.

Determination of Nutritionally Relevant Parameters. The glucose content was determined with a D-glucose kit from R-Biopharm AG (Darmstadt, Germany). The total amount of reducing sugars was analyzed according to the method of Luff-Schoorl, and crude protein was quantified by Kjeldahl analysis. Oxalic acid was determined by ion exclusion chromatography with direct conductivity detection (883 basic IEC system, Metrohm AG, Filderstadt, Germany) as described by Marten.[13] Quantitation of ethanol was carried out by gas chromatography combined with headspace solid phase microextraction (HS-SPME) using standard addition.[14]

Liquid–Liquid Extraction (LLE) and Headspace Solid Phase Microextraction. For LLE, 90 mL of wort or fermented beverage was used as described previously.[7]

For HS-SPME, a CAR/PDMS fiber (75 μm carboxen/polydimethylsiloxane, fiber length = 1 cm) (Supelco, Steinheim, Germany) in combination with an MPS 2 XL multipurpose sampler (GERSTEL, Mülheim an der Ruhr, Germany) was used according to the method of Zhang et al.[8]

Aroma (Extract) Dilution Analysis. For LLE, the flavor dilution (FD) factors were determined by aroma extract dilution analysis (AEDA).[15] The organic extracts were diluted with pentane/diethyl ether (1:1.12, v/v) in a series of 1:1 dilutions. For HS-SPME, aroma dilution analysis (ADA) was performed by increasing the GC inlet split ratios.[7] After extraction, the volatiles of the beverage were diluted stepwise by controlling the split ratio as follows: splitless (splitless time = 2 min), 2:1, 4:1, 8:1, 16:1, 32:1, 64:1, 128:1, and 256:1. After dilution, each sample was sniffed twice until no odorants were perceived at the ODP 3 olfactory detection port (GERSTEL) of the GC-MS/MS-O system.

GC-MS/MS-O Analysis. GC-MS/MS-O analysis was based on the method described by Zhang et al.[7,8]

Multidimensional Gas Chromatography–Mass Spectrometry (MDGC-MS). Chiral separations were performed on an MDGC-MS system (Shimadzu Europa GmbH, Duisburg, Germany), which consists of two Shimadzu GC-2010 Plus gas chromatographs (GC 1 and GC 2), equipped with a multi Dean's switch (MDS), a Shimadzu QP2010 Ultra mass spectrometer, and a Shimadzu AOC-20i autoinjector.

GC 1. Helium (5.0) was used as carrier gas. A polar Agilent J&W VF-WAXms column (30 m × 0.25 mm i.d. × 0.25 μm film thickness) (Agilent Technologies, Waldbronn, Germany) was used for initial separation. The operational conditions were as follows: constant inlet pressure, 208.1 kPa; inlet temperature, 250 °C; splitless, 2 min; initial linear velocity, 25 cm/s; temperature program, 40 °C (3 min), raised at 10 °C/min to 200 °C (6 min). The FID (250 °C; H_2 flow, 40 mL/min; air flow, 400 mL/min; makeup gas N_2 (5.0), 30 mL/min) was connected via a stainless steel retention gap to the MDS.

GC 2. A Hydrodex β-TBDAc column (heptakis-(2,3-di-*O*-acetyl-6-*O*-*tert*-butyldimethylsilyl)-β-cyclodextrin; 25 m × 0.25 mm i.d.; Macherey-Nagel, Düren, Germany) was applied for the analysis of linalool. The oven temperature program was held at 40 °C for 1 min, ramped at 10 °C/min to 80 °C, held for 50 min, increased at 20 °C/min to 200 °C, and finally held for 4 min. An Astec Chiraldex B-DM column ((2,3-di-*O*-methyl-6-*O*-*tert*-butyldimethylsilyl)-β-cyclodextrin; 30 m × 0.25 mm i.d. × 0.12 μm film thickness; Sigma-Aldrich, Taufkirchen, Germany) was applied for the analysis of 2-methylbutanoic acid. The oven temperature program for the analysis of 2-methylbutanoic acid was held at 40 °C for 1 min, ramped at 10 °C/min to 65 °C, held for 45 min, increased at 20 °C/min to 200 °C, and finally held for 4 min. Further conditions were as follows: transfer line temperature between GC 1 and GC 2, 200 °C; initial linear velocity, 47.2 cm/s; switching pressure, 129.1 kPa; MS modes, selected ion monitoring (*m*/*z* 57, 74, 87) for 2-methylbutanoic acid and scan mode (*m*/*z* 33–300) for linalool; electron ionization energy, 70 eV; source temperature, 200 °C; quadrupole temperature, 150 °C; MS transfer line temperature, 200 °C. All data were collected using Shimadzu MDGC solution software 1.01.

Compound Identification. The aroma compounds were identified by comparison of their respective odor impressions, their retention indices (RI) on two columns of different polarity (VF-WAXms and DB-5MS), and their mass spectra with those of authentic standards and published data.

Quantitative Analysis and Calculation of Odor Activity Values (OAVs). The concentrations of aroma compounds extracted by LLE were estimated via internal standard (IS) method (100 μL of IS; 888 mg thymol/L pentane/diethyl ether). The corresponding response factors (Rf) were calculated for each analyte according to eq 1

$$\mathrm{Rf} = \frac{A_{\mathrm{IS}} m_{\mathrm{a}}}{m_{\mathrm{IS}} A_{\mathrm{a}}} \quad (1)$$

where *A* = peak area, *m* = mass (μg), IS = internal standard, and a = analyte.

The aroma compounds extracted by HS-SPME were quantitated by standard addition.[8] A standard solution mixture was prepared containing the target compounds in their respective concentrations.

The quantifier and qualifier ions of each compound are listed in Table 1.

Table 1. *m*/*z* Fragments (Quantifier and Qualifier Ions) Used for Quantitative Analysis

compound	MS mode[a]	quantifier ion (*m*/*z*)	qualifier ion (*m*/*z*)
ethyl 2-methylpropanoate[b]	SIM	71	116
2,3-butanedione[b]	SIM	86	53
ethyl 2-methylbutanoate[b]	SIM	102	57
2,5-dimethylpyrazine[b]	SIM	108	42
methional[b]	SIM	104	76
benzaldehyde[b]	SIM	106	51
linalool[b]	SIM	71	93
2-phenylacetaldehyde[b]	SIM	120	91
2-acetylthiazole[b]	SIM	99	43
β-damascenone[b]	SIM	69	190
thymol[b]	SIM	135	150
2-methylbutanoic acid[c]	scan (EIC)	74	
3-methylbutanoic acid[c]	scan (EIC)	60	
2-methylpropanoic acid[c]	scan (TIC)	33–300	
2-phenylacetic acid[c]	scan (TIC)	33–300	
2-phenylethanol[c]	scan (TIC)	33–300	
thymol[c]	scan (EIC/TIC)	135/33–300	150/–

[a]EIC, extracted ion chromatogram; SIM, single ion monitoring; TIC, total ion current. [b]Aroma compounds extracted by HS-SPME were quantified by means of standard addition. [c]Aroma compounds extracted by LLE were quantified by means of an internal standard.

DOI: 10.1021/acs.jafc.5b02167
J. Agric. Food Chem. 2015, 63, 6915–6921

Table 2. Nutritionally Relevant Parameters of the Beverage Fermented by *T. versicolor* in Comparison to Nonfermented Wort

	total reducing sugars (g/L)	glucose (g/L)	crude protein (g/L)	oxalic acid (mg/L)	ethanol (%, v/v)	pH
nonfermented wort	57.2 ± 0.19	10.5 ± 0.12	5.5 ± 0.07	28 ± 2	–[a]	5.39 ± 0.03
fermented wort	45.3 ± 0.74	6.0 ± 0.05	5.2 ± 0.14	23 ± 2	0.385 ± 0.005	5.33 ± 0.05

[a]No distinct MS signal.

Table 3. Aroma Compounds Identified in the Beverage by Means of GC-MS/MS-O after LLE and HS-SPME

	RI[a]					FD factor[b]	
no.	VF-WAXms	DB-5MS	compound	odor impression	identification	LLE	HS-SPME
1	929	<800	3-methylbutanal	green	MS, RI, odor	–[c]	1
2	977	<800	ethyl 2-methylpropanoate	fruity	MS, RI, odor	–	8
3	994	<800	2,3-butanedione	buttery	MS, RI, odor	–	16
4	1024	<800	methyl 2-methylbutanoate	fruity	MS, RI, odor	–	2
5	1052	800	ethyl butanoate	fruity	MS, RI, odor	–	1
6	1064	853	ethyl 2-methylbutanoate	fruity	MS, RI, odor	–	32
7	1085	<800	hexanal	green	MS, RI, odor	–	1
8	1121	<800	2-pentanol	green	MS, RI, odor	1	–
9[d]	1240	<800	2-methylbutanol	fresh, sourish	MS, RI, odor	–	1
		<800	3-methylbutanol				
10[e]	1271	nd[f]	unknown	rubber		–	2
11[e,g]	1299	nd	1-octen-3-one	mushroom	RI, odor	–	8
12	1348	914	2,5-dimethylpyrazine	baked, nutty	MS, RI, odor	–	64
13[e]	1426	nd	unknown	caramel		1	–
14	1456	<800	acetic acid	sourish, vinegar	MS, RI, odor	4	–
15	1478	908	methional	boiled potato	MS, RI, odor	–	128
16[e]	1499	nd	unknown	green		32	1
17	1534	965	benzaldehyde	almond, cereal	MS, RI, odor	–	32
18	1562	1099	linalool	floral	MS, RI, odor	–	64
19	1569	<800	2-methylpropanoic acid	stinky, sourish	MS, RI, odor	16	–
20[e]	1645	nd	unknown	caramel		1	–
21	1652	1048	2-phenylacetaldehyde	floral	MS, RI, odor	–	16
22	1655	1066	2-acetylthiazole	toasted, sweetish	MS, RI, odor	–	16
23[d]	1678	861	2-methylbutanoic acid	cheesy, stinky, sourish	MS, RI, odor	128	4
		857	3-methylbutanoic acid				
24[e]	1733	nd	unknown	burnt		32	4
25	1823	1379	*β*-damascenone	fruity, like pear	MS, RI, odor	4	128
26	1920	1113	2-phenylethanol	rose	MS, RI, odor	128	4
27[e]	1933	nd	unknown	burnt		2	–
28	1960	1109	maltol	caramel	MS, RI, odor	4	–
29	1990	1019	2-acetylpyrrole	burnt, sweetish	MS, RI, odor	–	4
30[h]	2048	1363	*γ*-nonalactone	caramel	MS, RI, odor	4	4
31[e]	2189	nd	unknown	sweetish		1	-
32	2242	1301	*o*-aminoacetophenone	grape	MS, RI, odor	4	4
33[e]	2308	nd	unknown	sweetish		8	–
34	2557	1254	2-phenylacetic acid	toasted, pungent, sweetish	MS, RI, odor	128	–

[a]Mean of RI values from LLE and SPME. [b]Flavor dilution (FD) factor of the corresponding compound. [c]–, odor was not perceived. [d]Odor corresponded to two coeluting compounds. [e]Retention indices (RI) were calculated on the basis of the retention time of the odor impression perceived at the ODP. [f]nd, no distinct MS spectrum on the DB-5MS column. [g]The peak area was below the limit of detection; the compound was tentatively identified on the basis of RI, odor impression, and literature data.[25] [h]MS spectrum was obtained from wort.

The OAVs of the key aroma compounds were calculated as the ratios of the concentrations in the beverage to their respective odor thresholds in water.

Concentrations of Key Aroma Compounds during the Fermentation Process. The concentrations of the key aroma compounds were quantitated after 0 (before fermentation) and 38 h (after fermentation) by means of LLE and HS-SPME and GC-MS/MS-O analysis. Quantitative changes were expressed by the relative peak areas of each target compound. Each sample was analyzed in duplicate.

Cytotoxicity in Rat Hepatocytes in Primary Culture. Cytotoxicity of the beverage and of the nonfermented wort was determined in rat hepatocytes in primary culture by means of the resazurin reduction assay and the lactate dehydrogenase leakage assay. Before use, the pH of the beverage was adjusted to neutral.

Rat livers were perfused according to the two-step method of Seglen to isolate primary rat hepatocytes.[16] The viability of cell preparations always exceeded 90%. The procedure of hepatocyte preparation was authorized by the Ethical Committee of the State of Rhineland-Palatinate. Hepatocytes were treated with the beverage or wort at concentrations of 0.1, 1, and 10% (v/v) in culture medium and incubated at 37 °C and 5% CO_2. Addition of 0.1% (w/v) saponine (added as aqueous solution) served as a positive control, culture medium as a negative control.

DOI: 10.1021/acs.jafc.5b02167
J. Agric. Food Chem. 2015, 63, 6915−6921

For the resazurin reduction assay,[17] cells were seeded in collagenated 24-well plates at a density of 100,000 cells/cm^2. After 48 h of treatment, cells were incubated with medium containing resazurin for 90 min. The fluorescent metabolite resorufin was measured in a fluorescence plate reader.

For the lactate dehydrogenase (LDH) leakage assay,[18] cells were seeded in collagenated 60 mm dishes at a density of 100,000 cells/cm^2. After 6 h of treatment, the integrity of cell membranes was determined by measuring the activity of the cytosolic enzyme LDH leaked out of cells into the culture medium in comparison to the total amount of LDH activity (medium + cell pellet). LDH activity was measured by the fluorescence of metabolized NADH.

Mutagenicity Testing in Ames Fluctuation Assay. The mutagenicity of the beverage was tested according to the method of Maron and Ames in *Salmonella typhimurium* in a variation of the Ames fluctuation test (ISO 11350, 2012).[19,20] Strain TA98 was used to detect frameshift mutations and strain TA100 to detect base pair substitutions. The tests were performed with and without metabolic activation by rat hepatic S9 mix.

Hepatic S9 mix was prepared from the livers of rats treated with Aroclor 1254 according to the method of Maron and Ames.[19] The procedure of S9 preparation was authorized by the Ethical Committee of the State of Rhineland-Palatinate.

Bacteria suspensions were treated with the beverage at concentrations of 0.1, 1, and 10% (v/v) in histidine-deficient medium and incubated at 37 °C. 4-Nitro-*o*-phenylenediamine (for strain TA 98 without S9), nitrofurantoin (for strain TA 100 without S9), and 2-aminoanthracene (for both strains with S9) served as positive controls and medium, water, and DMSO as negative controls.

The growth of revertants in histidine-deficient medium was measured in 384-well plates by means of the pH indicator dye bromocresol purple, and the percentage of positive wells was calculated accordingly.

Statistical Analysis of Cytotoxicity and Mutagenicity Results. Statistical values (means and standard deviations) and data used in charts (bar graphs) were calculated by use of the software package Origin 9.1 (OriginLab, Northampton, MA, USA). Statistical significance was determined by ANOVA and Dunnett post test with the software InStat 3.0 (GraphPad, La Jolla, CA, USA). All experiments were performed in triplicate.

RESULTS AND DISCUSSION

Nutritionally Relevant Parameters. Due to the steadily declining consumption of beer and to satisfy market needs for non- or low-alcoholic alternatives, new fermentation systems have been developed. In the past, predominantly yeasts and lactic acid bacteria have been utilized to ferment wort.[21,22] In our study, wort was fermented by the basidiomycete *T. versicolor* for the first time.

During the fermentation, the concentrations of total reducing sugars and glucose decreased significantly by 21 and 43%, respectively (Table 2). The protein concentration decreased by about 5%, and the concentration of oxalic acid, which is typically present in wort, was reduced from 28 to 23 mg/L. Oxalic acid might be converted to formic acid and carbon dioxide by oxalate decarboxylase produced by *T. versicolor*.[23] Oxalic acid may cause haze-forming and gushing of beer. In the fermented beverage the concentration of ethanol was determined to be 0.39% (v/v), whereas no ethanol was detected in wort. An alcohol dehydrogenase of *T. versicolor* has been described previously by Kudahettige et al.[24] In most of the European Union countries and the United States, an upper limit of 0.5% alcohol by volume has been defined for alcohol-free beer.[21] Therefore, the novel beverage may still be considered a nonalcoholic refreshment.

Flavor Analysis of the Novel Fermented Beverage. The odor of the fermented beverage was perceived as fruity, fresh, sweetish, and slightly floral. It was strikingly different from the typical odor of wort and most cereal beverages fermented by lactic acid bacteria, yeasts, or lower fungi. To understand the formation of the unique aroma, the flavor of the beverage was analyzed.

Extraction and Identification of Key Aroma Compounds. Two different extraction methods were used together with GC-MS/MS-O analysis to comprehensively analyze the beverage's aroma. Previous studies have shown that fibers containing porous carbon in their stationary phase were highly effective in extracting various types of volatile compounds.[7] Therefore, a CAR/PDMS fiber was chosen for extracting the volatile compounds.

By GC-MS/MS-O analysis, 17 and 24 odor-active regions from the fermented beverage were detected at the ODP after LLE and HS-SPME, respectively (Table 3). Only seven of them were detected by both methods. Thus, in total 34 different odor impressions were perceived. Twenty-seven aroma compounds including inter alia acids, alcohols, aldehydes, ketones, and esters/lactones were identified. Most odor-active regions were attributed to a single compound. Only two odor impressions (no. 9 and 23) originated from coeluting compounds (Table 3). The mixture of 2-methylbutanol and 3-methylbutanol imparted a fresh and sourish odor (no. 9). A cheesy, stinky, and sourish odor was perceived from 2-methylbutanoic acid accompanied by 3-methylbutanoic acid (no. 23).

By performing an A(E)DA for each extraction method (Table 3), the key aroma compounds of the beverage were identified (FD factors from 8 to 128 for at least one of the two extraction techniques). A compound assigned to a high FD factor after LLE might exhibit a low FD factor after HS-SPME and vice versa (cf. 2-/3-methylbutanoic acid, 2-phenylethanol, 2-phenylacetic acid, methional, linalool, 2,3-butanedione, and ethyl 2-methylbutanoate). Compared to HS-SPME, LLE performed better in trapping organic acids and higher molecular weight alcohols and showed lower sensitivities for highly volatile compounds as well as for some trace compounds. By combining the two different extraction techniques, the aroma compounds of the beverage were trapped in a wide range.

Several of the main odor-active compounds of the beverage, such as 2-methylbutanoic acid (FD 128) and linalool (FD 64), are chiral. The enantiomeric purities of both odorants were determined by means of an MDGC-MS system. Both components showed high enantiomeric excess (ee) values of 91.5% for (*R*)-linalool and >95% for (*S*)-2-methylbutanoic acid. The aroma of (*R*)-linalool is described as floral, whereas the (*S*)-enantiomer imparts an intense green note.[34] The chiral analysis supported the perceived "floral" odor impression (Table 3). The aroma of (*S*)-2-methylbutanoic acid is perceived as sweetish and fruity.[35] However, 2-methylbutanoic acid coeluted with 3-methylbutanoic acid, which imparts a sourish and sweaty odor. Therefore, it seems reasonable that the corresponding odor impression (no. 23) was perceived as cheesy, stinky, and sourish (Table 3). As methyl 2-methylbutanoate (FD 2), 2-methylbutanol (FD 1), and γ-nonalactone (FD 4) showed only low flavor dilution factors, their ee values were not determined. No authentic enantiopure standard of ethyl 2-methylbutanoate (FD 32) was commercially available, and the absolute configuration of this compound could thus not be assigned.

Quantification and Calculation of the OAVs of Key Aroma Compounds. To evaluate the contribution of a single

DOI: 10.1021/acs.jafc.5b02167
J. Agric. Food Chem. 2015, 63, 6915−6921

compound to the overall aroma, OAVs of the key aroma compounds of the beverage were calculated. Therefore, the concentrations of 15 odorants with FD factors of 8−128 were quantified. 2-Methylbutanoic acid, 3-methylbutanoic acid, 2-methylpropanoic acid, 2-phenylacetic acid, and 2-phenylethanol were quantified in the organic extract according to the internal standard thymol. The other compounds were quantified by HS-SPME using standard addition.

2-Phenylacetaldehyde, ethyl 2-methylpropanoate, linalool, 2,3-butanedione, and methional showed high OAVs (≥10) (Table 4). Additionally, 3-methylbutanoic acid, β-damascenone, 2-methylpropanoic acid, 2-methylbutanoic acid, and ethyl 2-methylbutanoate presumably contributed to the overall aroma.

Table 4. Quantitative Data, Odor Thresholds, and Odor Activity Values (OAVs)

compound	concentration in the beverage (μg/L)	odor threshold (μg/L)	OAV
ethyl 2-methylpropanoate	0.6 ± 0.16	0.02[26]	31
2,3-butanedione	30 ± 7.4	3[27]	10
ethyl 2-methylbutanoate	0.18 ± 0.039	0.15[27]	1.2
2,5-dimethylpyrazine	2.68 ± 0.034	1700[28]	<0.1
methional	14 ± 1.1	1.4[29]	10
benzaldehyde	4.8 ± 0.66	25[26]	0.2
linalool	2.30 ± 0.011	0.14[30]	16
2-phenylacetaldehyde	162 ± 28	4[28]	40
2-acetylthiazole	2.68 ± 0.22	10[31]	0.3
β-damascenone	0.13 ± 0.013	0.056[29]	2.3
2-methylbutanoic acid	205 ± 12	100[32]	2.0
3-methylbutanoic acid	154 ± 20	22[26]	7.0
2-methylpropanoic acid	432 ± 15	190[33]	2.3
2-phenylacetic acid	84.2 ± 0.77	360[26]	0.2
2-phenylethanol	31 ± 2.0	390[29]	0.1

Changes of Key Aroma Compounds during the Fermentation Process. To control the quality of the beverage in a future industrial process, relative changes in the concentrations of the key aroma compounds were investigated before and after the fermentation process (Figure 1). Whereas

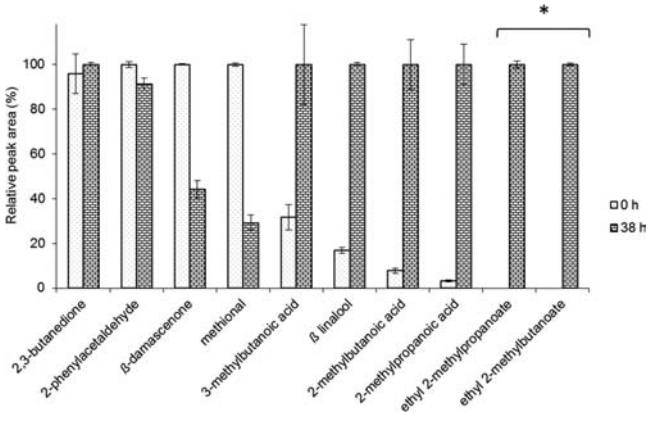

Figure 1. Relative changes of the concentrations of the key aroma compounds in the beverage during the fermentation (0 vs 38 h) (*, compounds detected only in the fermented beverage).

most of the odorants were already present in the substrate wort (0 h), the fruity aroma compounds ethyl 2-methylpropanoate and ethyl 2-methylbutanoate were synthesized de novo by *T. versicolor*. The concentrations of β-damascenone and methional were reduced, whereas those of linalool, 2-methylbutanoic acid, 3-methylbutanoic acid, and 2-methylpropanoic acid increased during the fermentation. The degradation of β-damascenone and methional and/or adsorption to the cell wall have been reported for yeasts.[36,37] Linalool with its floral odor is a known constituent of the aroma of fruiting bodies of *T. versicolor* as well as of many other fungi (e.g., *Clitocybe odora*, *Hydnum repandum*, *Lactarius salmonicolor*, *Lepista nuda*, *Mycena rosea*, and *Tricholoma sulfureum*).[38,39] Although basidiomycetes have a huge potential for producing terpenoids, relatively few biosynthetic pathways of fungal terpenoids have been described.[40] The formation of 2-methylbutanoic acid, 3-methylbutanoic acid, and 2-methylpropanoic acid might be related to the transformation of L-isoleucine, L-leucine, or L-valine present in wort.[41] The biotransformation of branched-chain amino acids by shiitake to volatiles has been described recently by Zhang et al.[9]

The odor qualities of ethyl 2-methylpropanoate and ethyl 2-methylbutanoate have been described as "fruity, strawberry"- and "fruity, green apple"-like. To our knowledge, this is the first time that these two ethyl esters have been detected in cultures of *T. versicolor*. Ethyl 2-methylpropanoate has been reported as a flavor compound formed by *Tuber melanosporum*, *Tuber indicum*, *Ceratocystis fimbriata*, yeasts, and fruits.[42−45] Ethyl 2-methylbutanoate was identified in the pine-mushroom (*Tricholoma matsutake* Sing.).[46] Comprehensive information on the pathways and control mechanisms of the biogenesis and accumulation of these two ethyl esters in basidiomycetes is not available yet. However, it is well-known that branched-chain amino acids, branched-chain fatty acids, and branched-chain alcohols serve as precursors of fruity esters in yeasts and fruits (e.g., apple, banana, and melon).[47−50] The relative concentrations of 2-methylpropanoic acid and 2-methylbutanoic acid increased significantly during fermentation.

Cytotoxicity and Mutagenicity of the Beverage and Nonfermented Wort. *Cytotoxicity in Rat Hepatocytes in Primary Culture.* Compared to the negative control, neither in the resazurin reduction assay nor in the LDH leakage assay was a statistically significant decrease in metabolic activity and membrane integrity, respectively, observed after treatment of the cells with the beverage or nonfermented wort. The functionality of both assays was validated by negative and positive controls.

Mutagenicity in the Ames Fluctuation Test. Neither in *Salmonella typhimurium* strain TA 98 used for screening for frameshift mutations nor in strain TA 100 employed for base pair substitutions were statistically significant mutagenic events detected compared to the negative control after treatment of bacteria suspensions with the beverage or nonfermented wort with or without metabolic activation by S9 mix. The functionality of the assay was validated by negative and positive controls.

In conclusion, a novel fermented beverage was developed by incubation of wort with *T. versicolor*. Due to the fermentation, changes in the concentrations of carbohydrates, proteins, and oxalic acid were observed. Its aroma was perceived as fruity, fresh, sweetish, and floral, which was significantly different from the sourish odor of traditional nonalcoholic fermented cereal beverages. Ten key aroma compounds significantly contributed

DOI: 10.1021/acs.jafc.5b02167
J. Agric. Food Chem. 2015, 63, 6915−6921

to the overall aroma of the beverage. Most of them originated from wort, but their concentrations changed during the fermentation process. The fruity odorants ethyl 2-methylbutanoate and ethyl 2-methylpropanoate were detectable only in the fermented beverage and thus synthesized by *T. versicolor*. Comprehensive toxicological studies indicated no cytotoxicity and mutagenicity activity.

Taken together, a beverage fermented by *T. versicolor* may present an interesting option for novel cereal-based products. Prior to the final product development, that is, up-scaling and control of the product quality, reconstitution and omission experiments should be performed in further studies.

■ ASSOCIATED CONTENT

Supporting Information

Table S1, preparation of standard mixture solutions; Table S2, parameters of calibration curves for the quantitation of key aroma compounds; Figure S1, cytotoxicity (resazurin assay) in rat hepatocytes in primary culture; and Figure S2, mutagenicity in the Ames fluctuation assay. The Supporting Information is available free of charge on the ACS Publications website at DOI: 10.1021/acs.jafc.5b02167.

■ AUTHOR INFORMATION

Corresponding Author

*(H.Z.) Phone: +49 641 99-34900. Fax: +49 641 99-34909. E-mail: holger.zorn@uni-giessen.de.

Funding

Y.Z. is grateful to the China Scholarship Council (CSC) for financial support. We thank the DFG and the State of Hesse for funding the major instrumentation (INST 162/381-1 FUGG). This project (HA Project 305/11-50) has been funded within the framework of Hessen ModellProjekte − Landes-Offensive zur Entwicklung Wissenschaftlich-ökonomischer Exzellenz, Förderlinie 3: KMU-Verbundvorhaben (State Offensive for the Development of Scientific and Economic Excellence).

Notes

The authors declare no competing financial interest.

■ REFERENCES

(1) Chavan, J. K.; Kadam, S. S. Nutritional improvement of cereals by fermentation. *Crit. Rev. Food Sci. Nutr.* **1989**, *28*, 349−400.
(2) Simango, C. Potential use of traditional fermented foods for weaning in Zimbabwe. *Soc. Sci. Med.* **1997**, *44*, 1065−1068.
(3) Gotcheva, V.; Pandiella, S. S.; Angelov, A.; Roshkova, Z. G.; Webb, C. Microflora identification of the Bulgarian cereal-based fermented beverage boza. *Process Biochem.* **2000**, *36*, 127−130.
(4) Díaz-Ruiz, G.; Guyot, J. P.; Ruiz-Teran, F.; Morlon-Guyot, J.; Wacher, C. Microbial and physiological characterization of weakly amylolytic but fast-growing lactic acid bacteria: a functional role in supporting microbial diversity in pozol, a Mexican fermented maize beverage. *Appl. Environ. Microbiol.* **2003**, *69*, 4367−4374.
(5) Gassem, M. A. A. A microbiological study of Sobia: a fermented beverage in the Western province of Saudi Arabia. *World J. Microbiol. Biotechnol.* **2002**, *18*, 173−177.
(6) Fraatz, M. A.; Riemer, S. J. L.; Stöber, R.; Kaspera, R.; Nimtz, M.; Berger, R. G.; Zorn, H. A novel oxygenase from *Pleurotus sapidus* transforms valencene to nootkatone. *J. Mol. Catal. B: Enzym.* **2009**, *61*, 202−207.
(7) Zhang, Y.; Fraatz, M. A.; Horlamus, F.; Quitman, H.; Zorn, H. Identification of potent odorants in a novel nonalcoholic beverage produced by fermentation of wort with shiitake (*Lentinula edodes*). *J. Agric. Food Chem.* **2014**, *62*, 4195−4203.
(8) Zhang, Y.; Hartung, N. M.; Fraatz, M. A.; Zorn, H. Quantification of key odor-active compounds of a novel nonalcoholic beverage produced by fermentation of wort by shiitake (*Lentinula edodes*) and aroma genesis studies. *Food Res. Int.* **2015**, *70*, 23−30.
(9) Giavasis, I. Bioactive fungal polysaccharides as potential functional ingredients in food and nutraceuticals. *Curr. Opin. Biotechnol.* **2014**, *26*, 162−173.
(10) Sullivan, R.; Smith, J. E.; Rowan, N. J. Medicinal mushrooms and cancer therapy: translating a traditional practice into Western medicine. *Perspect. Biol. Med.* **2006**, *49*, 159−170.
(11) Chang, S. T.; Buswell, J. A. Mushroom nutriceuticals. *World J. Microbiol. Biotechnol.* **1996**, *12*, 473−476.
(12) Lakhanpal, T. N.; Rana, M. Medicinal and nutraceutical genetic resources of mushrooms. *Plant Genet. Resour.* **2005**, *2*, 288−303.
(13) Marten, S. Ion chromatography determination of oxalic acid in beer; available at http://images.alfresco.advanstar.com/alfresco_images/pharma/2014/08/22/f83c6d87-5037-4c3f-bedd-7e312954c411/article-53697.pdf (2003).
(14) Mateus, D.; Ferreira, I. M. P. L. V. O.; Pinho, O. Headspace SPME−GC/MS evaluation of ethanol retention in cooked meals containing alcoholic drinks. *Food Chem.* **2011**, *126*, 1387−1392.
(15) Grosch, W. Detection of potent odorants in foods by aroma extract dilution analysis. *Trends Food Sci. Technol.* **1993**, *4*, 68−73.
(16) Seglen, P. O. Preparation of isolated rat liver cells. *Methods Cell Biol.* **1976**, *13*, 29−83.
(17) O'Brien, J.; Wilson, I.; Orton, T.; Pognan, F. Investigation of the Alamar Blue (resazurin) fluorescent dye for the assessment of mammalian cell cytotoxicity. *Eur. J. Biochem.* **2000**, *267*, 5421−5426.
(18) Moran, J. H.; Schnellmann, R. G. A rapid β-NADH-linked fluorescence assay for lactate dehydrogenase in cellular death. *J. Pharmacol. Toxicol. Methods* **1996**, *36*, 41−44.
(19) Maron, D. M.; Ames, B. N. Revised methods for the *Salmonella* mutagenicity test. *Mutat. Res.* **1983**, *113*, 173−215.
(20) ISO 11350:2012. Water quality − determination of the genotoxicity of water and waste water − Salmonella/microsome fluctuation test (Ames fluctuation test).
(21) Brányik, T.; Silva, D. P.; Baszczyňski, M.; Lehnert, R.; Almeida e Silva, J. B. A review of methods of low alcohol and alcohol-free beer production. *J. Food Eng.* **2012**, *108*, 493−506.
(22) Zannini, E.; Mauch, A.; Galle, S.; Gänzle, M.; Coffey, A.; Arendt, E. K.; Taylor, J. P.; Waters, D. M. Barley malt wort fermentation by exopolysaccharide-forming *Weissella cibaria* MG1 for the production of a novel beverage. *J. Appl. Microbiol.* **2013**, *115*, 1379−1387.
(23) Dutton, M. V.; Kathiara, M.; Gallagher, I. M.; Evans, C. S. Purification and characterization of oxalate decarboxylase from *Coriolus versicolor*. *FEMS Microbiol. Lett.* **1994**, *116*, 321−326.
(24) Kudahettige, R. L.; Holmgren, M.; Imerzeel, P.; Sellstedt, A. Characterization of bioethanol production from hexoses and xylose by the white rot fungus *Trametes versicolor*. *BioEnergy Res.* **2012**, *5*, 277−285.
(25) Fickert, B.; Schieberle, P. Identification of the key odorants in barley malt (caramalt) using GC/MS techniques and odour dilution analyses. *Nahrung* **1998**, *42*, 371−375.
(26) Rychlik, M.; Schieberle, P.; Grosch, W. *Compilation of Odor Thresholds, Odor Qualities and Retention Indices of Key Food Odorants*; Dt. Forschungsanst. für Lebensmittelchemie: Garching, Germany, 1998.
(27) Schieberle, P.; Hofmann, T. Evaluation of the character impact odorants in fresh strawberry juice by quantitative measurements and sensory studies on model mixtures. *J. Agric. Food Chem.* **1997**, *45*, 227−232.
(28) Buttery, R. G.; Turnbaugh, J. G.; Ling, L. C. Contribution of volatiles to rice aroma. *J. Agric. Food Chem.* **1988**, *36*, 1006−1009.
(29) Czerny, M.; Christlbauer, M.; Christlbauer, M.; Fischer, A.; Granvogl, M.; Hammer, M.; Hartl, C.; Hernandez, N. M.; Schieberle, P. Re-investigation on odour thresholds of key food aroma compounds and development of an aroma language based on odour qualities of defined aqueous odorant solutions. *Eur. Food Res. Technol.* **2008**, *228*, 265−273.

DOI: 10.1021/acs.jafc.5b02167
J. Agric. Food Chem. 2015, 63, 6915−6921

(30) Fritsch, H. T.; Schieberle, P. Identification based on quantitative measurements and aroma recombination of the character impact odorants in a Bavarian Pilsner-type beer. *J. Agric. Food Chem.* **2005**, *53*, 7544−7551.
(31) Susan, F. Sensory properties of volatile Maillard reaction products and related compounds. In *The Maillard Reaction in Foods and Nutrition*; Waller, G. R., Feather, M. S., Eds.; American Chemical Society: Washington, DC, USA, 1983; Vol. 215, pp 185−286.
(32) Park, H. J.; Lee, S. M.; Song, S. H.; Kim, Y. S. Characterization of volatile components in *makgeolli*, a traditional Korean rice wine, with or without pasteurization, during storage. *Molecules* **2013**, *18*, 5317−5325.
(33) Frauendorfer, F.; Schieberle, P. Changes in key aroma compounds of *Criollo cocoa* beans during roasting. *J. Agric. Food Chem.* **2008**, *56*, 10244−10251.
(34) Tamogami, S.; Awano, K.; Amaike, M.; Takagi, Y.; Kitahara, T. Anaylsis of enantiomeric ratios of aroma components in several flowers using a Chiramix column. *Flavour Fragrance J.* **2004**, *19*, 1−5.
(35) Siebert, T. E.; Smyth, H. E.; Capone, D. L.; Neuwöhner, C.; Pardon, K. H.; Skouroumounis, G. K.; Herderich, M. J.; Sefton, M. A.; Pollnitz, A. P. Stable isotope dilution analysis of wine fermentation products by HS-SPME-GC-MS. *Anal. Bioanal. Chem.* **2005**, *381*, 937−947.
(36) Chevance, F.; Guyot-Declerck, C.; Dupont, J.; Collin, S. Investigation of the β-damascenone level in fresh and aged commercial beers. *J. Agric. Food Chem.* **2002**, *50*, 3818−3821.
(37) Perpète, P.; Collin, S. Contribution of 3-methylthiopropional-dehyde to the worty flavor of alcohol-free beers. *J. Agric. Food Chem.* **1999**, *47*, 2374−2378.
(38) Breheret, S.; Talou, T.; Rapior, S.; Bessière, J. Monoterpenes in the aromas of fresh wild mushrooms (Basidiomycetes). *J. Agric. Food Chem.* **1997**, *45*, 831−836.
(39) Drilling, K.; Dettner, K. Electrophysiological responses of four fungivorous coleoptera to volatiles of *Trametes versicolor*: implications for host selection. *Chemoecology* **2009**, *19*, 109−115.
(40) Wawrzyn, G. T.; Bloch, S. E.; Schmidt-Dannert, C. Discovery and characterization of terpenoid biosynthetic pathways of fungi. *Methods Enzymol.* **2012**, *515*, 83−105.
(41) Kennedy, A. I.; Taidi, B.; Dolan, J. L.; Hodgson, J. A. Optimisation of a fully defined medium for yeast fermentation studies. *Food Technol. Biotechnol.* **1997**, *35*, 261−265.
(42) Culleré, L.; Ferreira, V.; Venturini, M. E.; Marco, P.; Blanco, D. Potential aromatic compounds as markers to differentiate between *Tuber melanosporum* and *Tuber indicum truffles*. *Food Chem.* **2013**, *141*, 105−110.
(43) Soares, M.; Christen, P.; Pandey, A.; Soccol, C. R. Fruity flavour production by *Ceratocystis fimbriata* grown on coffee husk in solid-state fermentation. *Process Biochem.* **2000**, *35*, 857−861.
(44) Swiegers, J. H.; Kievit, R. L.; Siebert, T.; Lattey, K. A.; Bramley, B. R.; Francis, I. L.; King, E. S.; Pretorius, I. S. The influence of yeast on the aroma of Sauvignon Blanc wine. *Food Microbiol.* **2009**, *26*, 204−211.
(45) Dharmawan, J.; Kasapis, S.; Curran, P.; Johnson, J. R. Characterization of volatile compounds in selected citrus fruits from Asia. Part I: Freshly-squeezed juice. *Flavour Fragrance J.* **2007**, *22*, 228−232.
(46) Cho, I. H.; Namgung, H. J.; Choi, H. K.; Kim, Y. S. Volatiles and key odorants in the pileus and stipe of pine-mushroom (*Tricholoma matsutake* Sing.). *Food Chem.* **2008**, *106*, 71−76.
(47) Verstrepen, K. J.; Derdelinckx, G.; Dufour, J. P.; Winderickx, J.; Thevelein, J. M.; Pretorius, I. S.; Delvaux, F. R. Flavor-active esters: adding fruitiness to beer. *J. Biosci. Bioeng.* **2003**, *96*, 110−118.
(48) Matich, A.; Rowan, D. Pathway analysis of branched-chain ester biosynthesis in apple using deuterium labeling and enantioselective gas chromatography-mass spectrometry. *J. Agric. Food Chem.* **2007**, *55*, 2727−2735.
(49) Wyllie, S. G.; Fellman, J. K. Formation of volatile branched chain esters in bananas (*Musa sapientum* L.). *J. Agric. Food Chem.* **2000**, *48*, 3493−3496.
(50) Gonda, I.; Bar, E.; Portnoy, V.; Lev, S.; Burger, J.; Schaffer, A. A.; Tadmor, Y.; Gepstein, S.; Giovannoni, J. J.; Katzir, N.; Lewinsohn, E. Branched-chain and aromatic amino acid catabolism into aroma volatiles in *Cucumis melo* L. fruit. *J. Exp. Bot.* **2010**, *61*, 1111−1123.

DOI: 10.1021/acs.jafc.5b02167
J. Agric. Food Chem. 2015, 63, 6915−6921

the QUENCHER approach.[12−15] Up to now, these assays have been successfully applied to some foods for which the antioxidant activity is largely dependent on the insoluble part, such as cereals and bakery products, seeds, nuts, pulses, and dietary fibers.[12−19] It must also be noted that a mixture of ethanol/water (50:50, v/v) has been suggested as the most appropriate reaction medium to carry out QUENCHER assays, and "neutral" powdered materials such as cellulose have been proposed as suitable diluting agents when products under study are very rich in antioxidants.[11,12]

Despite the advantages and previous applications of the QUENCHER methods, these assays are not yet extensively used, probably due to a lack of validation studies of these methodologies. In addition, to the best of our knowledge, the QUENCHER concept has still not been adapted to the methodologies that target biologically relevant radicals (SRSC, HRSC, and LPSC), and a statistical validation and correlations between the different Q-TAC and Q-FRSC assays have not yet been performed. These verifications are important to encourage the applicability of QUENCHER protocols as valuable tools for the in vitro antioxidant capacity assessment of different products such as foods, food ingredients, and others.

Therefore, to increase the use of the QUENCHER approach, the first aim of the present study was to develop new QUENCHER protocols to evaluate the scavenger capacity of some of the most biologically relevant radicals (superoxide, hydroxyl, and lipid peroxyl); the second aim was to optimize and, for the first time, validate different QUENCHER assays (Q-FC, Q-FRAP, Q-ABTS, Q-DPPH, Q-ORAC, Q-SRSC, Q-HRSC, and Q-LPSC) using three model products of different chemical properties. Secondarily, the best combination of QUENCHER assays for routine analysis was identified, and several factors that might influence the Q-TAC results, such as the presence of ethanol in the reaction medium and the use of cellulose as a diluting agent, were assessed. The study was carried out with three powdered model products, all of them rich in antioxidant compounds, but each containing antioxidants of different polarity. Powdered products were made in our pilot plant from wine pomace so that we could work with familiar products for which characteristics and composition were well-known.

MATERIALS AND METHODS

Chemicals. ABTS, cellulose, DPPH, deoxyribose (2-deoxy-D-ribose), 2,2′-diazobis(2-aminodinopropane) dihydrochloride (AAPH), gallic acid (GA), 6-hydroxyl-2,5,7,8-tetramethyl-2-carboxylic acid (Trolox), 4-nitroblue tetrazolium chloride (NBT), phenazin methosulfate (PMS), 2,4,6-tris(2-pyridyl)-*S*-triazine (TPTZ), and 2-thiobarbituric acid (TBA) were obtained from Sigma-Aldrich Co (St. Louis, MO, USA). Ethylenediaminetetraacetic acid (EDTA), iron(III) chloride acid ($FeCl_3$), iron(II) sulfate ($FeSO_4$), FC reagent, hydrogen peroxide (H_2O_2), L-ascorbic acid ($C_6H_8O_6$), potassium persulfate ($K_2O_8S_2$), sodium acetate ($NaC_2H_3O_2$), sodium carbonate (Na_2CO_3), sodium pyrophosphate anhydrous ($Na_4P_2O_7$), and trichloroacetic acid (TCA) were purchased from Panreac (Barcelona, Spain).

Samples. Red wine pomace was kindly supplied by different wineries located at Burgos (Spain). All red wine pomace was mixed and dehydrated until reaching a final water content of <10%. Dried materials were separated, ground, and sieved, thus obtaining three different powdered products,[20] which were used as model matrices. One of them was derived from grape seeds (Sd) separated from the wine pomace; this model product represented foods with a significant content of fat and rich mainly in hydrophobic antioxidants. Another product was obtained from the wine pomace free of seeds, which was mainly constituted by grape skins (Sk); this model product represented food matrices rich in hydrophilic antioxidant and without or with very low levels of fat. The third powdered product was obtained from whole (W) wine pomace; this model product represented food materials with some fat and rich in both hydrophilic and hydrophobic antioxidants. The particle size of these model products was <0.250 mm in the cases of Sk and W and <0.355 mm for Sd.[21]

QUENCHER Antioxidant Capacity Methods. The adapted Q-TAC and Q-FRSC methodologies were fixed end-point procedures with the exception of the Q-ORAC method, which was a kinetic assay. Results are given as mean values ± standard deviation of three independent samples.

Q-FC Assay. This method was adapted from the FC assay developed by Singleton and Rossi.[22] Briefly, 1 ± 0.005 mg of the tested products was weighed in a microbalance (MicroPro11, Sartorius) and mixed with 0.2 mL of Milli-Q (MQ) water and 0.2 mL of FC reagent. After 5 min of reaction, 4 mL of a 0.7 M Na_2CO_3 solution was added, and the final volume was made up to 10 mL with MQ water. After 1 h of incubation in an orbital shaker, the absorbance at 750 nm was measured using an UV−vis spectrophotometer (U-2000 Hitachi). The FC index was expressed as micromoles of gallic acid equivalents per gram of product (μmol GAE/g) by means of a dose−response curve for different quantities of the standard.

Q-FRAP Assay. The Q-FRAP procedure was adapted from the method described by Benzie et al.[23] The reactive mixture was freshly prepared by mixing 10 mM TPTZ and 20 mM $FeCl_3$ in 300 mM $NaC_2H_3O_2$ buffer (pH 3.6) at a ratio of 1:1:10 (v/v/v) and diluted 10:1 (v/v) in MQ water. Ten milliliters of the FRAP solution was added to 1 ± 0.005 mg of the samples and incubated at 37 °C for 30 min with continuous stirring. The absorbance at 593 nm was measured. The results were expressed as micromoles of iron(II) equivalents per gram of product (μmol Fe(II)E/g) using linear calibration obtained with different amounts of $FeSO_4$.

Q-ABTS Assay. The method was adapted from the assay developed by Re et al.[24] and modified by Rivero-Pérez et al.[25] The stock solution of $ABTS^{\bullet+}$ was diluted with MQ water to an absorbance of 0.70 ± 0.02 at 734 nm; 1 ± 0.005 mg of the assessed products was weighed, and the reaction was started by adding 10 mL of $ABTS^{\bullet+}$ working solution. After 30 min of incubation in darkness with continuous stirring, the absorbance of the samples at 734 nm was measured and subtracted from the absorbance of the $ABTS^{\bullet+}$ working solution. The results are expressed as micromoles of Trolox equivalents per gram of product (μmol TE/g), using the dose−response curve described by different amounts of this standard.

Q-DPPH Assay. This method is based on the scavenging of the radical $DPPH^{\bullet}$.[26] A 0.1 mM $DPPH^{\bullet}$ working solution in pure methanol was prepared and diluted until an absorbance at 517 nm of 0.70 ± 0.02.[25] Then, 1 ± 0.005 mg of the powdered products was transferred into a test tube and mixed with 10 mL of $DPPH^{\bullet}$ working solution. The absorbance at 517 nm was measured after 30 min of continuous stirring at room temperature in the samples and subtracted from the absorbance of the $DPPH^{\bullet}$ working solution. Trolox was used as standard to perform a calibration curve, and the results were expressed as micromoles of TE per gram of product (μmol TE/g).

Q-ORAC Assay. This assay was adapted from the method described by Ou et al.[27] The analysis was conducted in a four-cell fluorometer (Cary-Eclipse, Varian) with continuous stirring in the cuvette and at 37 °C. Briefly, 0.2 ± 0.005 mg of the assessed products was weighed and resuspended in 0.8 mL of 75 mM phosphate buffer (pH 7.0, warmed to 37 °C) just before use. A Trolox quality control (T10, equivalent to 10 μg of Trolox) and a 300 mM AAPH solution in phosphate buffer were also freshly prepared. At least one T10 and one blank were analyzed with every set of samples (same AAPH solution). In a glass cuvette, 0.4 mL of the samples (the resuspended products, the T10 control or just phosphate buffer for the blank) was mixed with 2 mL of a freshly prepared 87.5 nM fluorescein solution in phosphate buffer. The fluorescence reading (λ_{exc} = 493 nm and λ_{em} = 511 nm) was started, and 0.1 mL of the AAPH solution was added after 2.5 min. The fluorescence decay curve was monitored for 100 min. The net area under the curve (net AUC) was calculated for each sample by

DOI: 10.1021/acs.jafc.5b01644
J. Agric. Food Chem. 2015, 63, 6922−6931

subtracting the blank AUC from the sample AUC. Regression equations between net AUC and different quantities of Trolox were obtained and used for the expression of the Q-ORAC values as micromoles of TE per gram of product (μmol TE/g).

Q-SRSC Assay. The Q-SRSC procedure was adapted from the method described by Liu et al.[28] and Rivero-Pérez et al.[25] Briefly, 1.5 ± 0.005 mg of the products was added to the test tube and mixed with a 1.5 mL final volume of 78 μM NADH, 50 μM NBT, and 10 μM PMS in 16 mM buffer Tris-HCl (pH 8.0). After the mixture had been shaken for 10 s, the absorbance (A) of the samples (S) at 560 nm was measured. "Oxidized controls" (OC; without products) and "sample controls" (SC; products and buffer) were also prepared. The results are expressed as oxidation inhibition percentages by the equation

$$\text{oxidation inhibition } \% = (A_{OC} - (A_S - A_{SC}))/A_{OC} \times 100 \quad (1)$$

Q-HRSC Assay. The Q-HRSC assay was adapted from the method developed by Halliwell et al.[29] and modified by Rivero-Pérez et al.[25] Briefly, 1 ± 0.005 mg of the powdered products was weighed and transferred into a screw-top test tube. A 1 mL final reaction volume contained a mixture of 1 mM deoxyribose, 0.1 mM $C_6H_8O_6$, 1 mM H_2O_2, 0.1 mM $FeCl_3$, and 0.1 mM EDTA in 5 mM phosphate buffer (pH 7.4). OC and SC were also prepared. The tubes were incubated for 60 min at 37 °C with continuous stirring. Then, 1.5 mL of TCA (28% w/v) and 1 mL of TBA (1% w/v) were added, and the capped tubes were shaken and heated at 100 °C for 15 min. The absorbance was recorded at 532 nm, and the results were expressed as oxidation inhibition percent following eq 1.

Q-LPSC Assay. This assay was adapted from the method described by Rivero-Pérez et al.[25] The experiments were carried out in rat liver microsomal preparations,[30] and lipid peroxidation was induced using AAPH as oxidant. The total microsomal protein content was determined using the Bradford method.[31] A microsomal solution containing 10 mg/mL protein in 0.1 M $Na_4P_2O_7$ buffer (pH 7.4) was prepared and stored at −80 °C until the day of analysis; 0.2 ± 0.005 mg of the tested products was placed into a screw-top tube, and 400 μL of 50 mM Tris-HCl buffer (pH 7.0), 50 μL of the microsomal solution, and 50 μL of 100 mM AAPH solution in the Tris-HCl buffer were added. OC and SC (replacing the AAPH solution by Tris-HCl buffer) were also prepared. The tubes were incubated at 37 °C for 90 min under continuous stirring. Then, 750 μL of TCA (2.8% w/v) and 500 μL of TBA (1% w/v) were added, and the capped tubes were shaken and heated at 100 °C for 15 min. Finally, 750 μL of the reaction mixture was transferred to another tube, and the TBA reactive substances were extracted with the same volume of butanol. The absorbance at 532 nm of the butanol extract was measured, and the results were expressed as oxidation inhibition percent with respect to the OC sample following eq 1.

Statistical Analysis. The statistical validation of the methods was performed using Statgraphics Centurion XVI version 16.2.04 software (Statpoint Technologies, Inc., Warranton, VA, USA). The statistical analysis of the Q-TAC data was carried out using one-way analysis of variance (ANOVA). Fisher's least significant difference (LSD) test was applied to determine the statistical significance of differences among various groups. A minimum significance level of $p < 0.05$ was considered. Pearson's correlation coefficients were determined to study linear correlations between pairs of the Q-TAC methodologies.

RESULTS AND DISCUSSION

Adaptation and Optimization of the Q-TAC and Q-FRSC Methods. This study shows some modifications with respect to Q-TAC protocols (Q-ABTS,[12] Q-DPPH,[12] Q-FRAP,[14] Q-ORAC,[13] and Q-FC[15]) previously published. Moreover, three new QUENCHER methodologies were developed (Q-SRSC, Q-HRSC, and Q-LPSC), which were adapted from validated classical FRSC methods.[25]

The main modification from other Q-TAC assays was the selection of aqueous reaction mediums whenever the methodologies allowed for the use of both organic and aqueous solvents. Aqueous medium might better represent the real environment surrounding any food matrix or biological system. Therefore, MQ water or aqueous buffer was initially used in all protocols except in the Q-DPPH assay, which required an organic solvent to dissolve the radical.

The particle size of the powdered products is a factor that might influence the results of the Q-TAC and Q-FRSC measurements, and this aspect should be taken into account for comparisons among powders of different particle size. Nevertheless, Serpen et al.[17] did not find a remarkable effect of this factor, and Gökmen et al.[11] suggested the use of powdered samples of particle size ranging from 0.3 to 0.1 mm in QUENCHER assays.

All protocols in this study were optimized for the direct measurement of small quantities of powdered products, considering the final reaction volume and amount of sample weighed.

The Q-FC, Q-FRAP, Q-ABTS, and Q-DPPH methods are rather inexpensive and simple methodologies, which allow for the adjustment of the assay volumes (maintaining the proportionality among the reagents) without a relevant increase in the cost of the analysis. Preliminary studies were conducted to establish 1 mg as an advisable amount of product, although satisfactory results can also be obtained with smaller or larger quantities (0.2−5 mg), depending on the TAC of the products and the sensitivity of the assay.

In the case of the Q-ORAC method, the reaction volume is restricted by the maximum volume of the cuvette because the fluorescence decay needs to be continuously monitored (kinetic assay). Amigo-Benavent et al.[13] proposed that the Q-ORAC assay be carried out in alternating stages of incubation at 37 °C in a test tube with centrifugation, transfer to a cuvette, and fluorescence reading. The Q-ORAC method proposed in the present study avoids several centrifugation/transfer steps, is more similar to classical protocols, and reproduces more effectively the advantages of the ORAC assay with respect to other TAC methods.[2,4,8] However, a fluorometer with a temperature control chamber and constant stirring in the cuvette is required, and the assay might not be suitable for products of very high Q-TAC.

With regard to the Q-SRSC, QHRSC, and Q-LPSC methods, the final reaction volume and amount of sample weighed must be adjusted to give results in the range of 0−100% oxidation inhibition. The Q-SRSC assay is a rather simple and quick methodology that can be directly performed in the cuvette or in a test tube. However, the Q-HRSC and the Q-LPSC assays involve more tedious protocols. It is suggested that the amount of sample used be adjusted rather than increasing the final volume, although it must be remarked that the precision of the QUENCHER methods might be compromised when <0.2 mg of the samples is weighed.

QUENCHER fixed end-point procedures allow for transferring an aliquot of the reaction medium to a microplate for the absorbance reading step. This alternative increases the repeatability and reduces the time between different measurements, so it is especially appropriate for the simultaneous analyses of multiple samples. On the other hand, QUENCHER kinetic assays cannot be carried out directly in a microplate due to the interference of solid products on the absorbance measurement. Furthermore, the extremely small quantity of solid sample required, proportional to the small volume of wells, could put at risk the validity of this procedure.

DOI: 10.1021/acs.jafc.5b01644
J. Agric. Food Chem. 2015, 63, 6922−6931

Table 1. Calibration Models of the QUENCHER Total Antioxidant Capacity (Q-TAC) Methods

method	standard[a]	range (μmol)	calibration model[b]	R^2[c]
Q-FC	GA	0.059−0.588	$A_{750\ nm}$ = (1.79 ± 0.009) μmol of GA + (0.005 ± 0.004)	0.999
Q-FRAP	Fe(II)	0.036−0.285	$A_{593\ nm}$ = (2.76 ± 0.046) μmol of Fe(II) − (0.009 ± 0.008)	0.996
Q-ABTS	T	0.083−0.499	$(A_{WS} - A_S)_{734\ nm}$ = (1.20 ± 0.015) μmol of T + (0.007 ± 0.005)	0.998
Q-DPPH	T	0.040−0.200	$(A_{WS} - A_S)_{517\ nm}$ = (3.20 ± 0.033) μmol of T + (0.007 ± 0.004)	0.999
Q-ORAC	T	0.010−0.050	net AUC = (3361 ± 70.3) μmol of T + (4.78 ± 2.25)	0.996

[a]GA, gallic acid; Fe(II), iron(II); T, Trolox. [b]A_{WS}, absorbance of the radical working solution; A_S, absorbance of the sample; net AUC, net area under the curve. [c]R^2, coefficient of determination.

Table 2. Linearity Test, Proportionality Test, and Detection Limits of the QUENCHER Total Antioxidant Capacity (Q-TAC) Methods

	linearity test[a]				proportionality test[b]				detection limits[c]	
			ANOVA							
method	CV(Fr) (%)	CV(b) (%)	F_{exp}	F_{tab}	$a \pm t_{tab}S(a)$	$t_{cal}(a)$	$t_{cal}(b)$	t_{tab}	y_d[d]	x_d[e]
Q-FC	2.99	0.48	42730	4.38	0.005 ± 0.006	1.45	207	1.73	0.016	12.0 nmol of GAE
Q-FRAP	4.79	1.68	3537	4.67	−0.009 ± 0.015	1.12	59.5	1.77	0.012	15.3 nmol of Fe(II)E
Q-ABTS	3.27	1.25	6328	4.49	0.007 ± 0.009	1.49	80.2	1.75	0.020	20.4 nmol of TE
Q-DPPH	2.57	1.03	9384	4.67	0.007 ± 0.008	1.53	96.1	1.77	0.017	6.68 nmol of TE
Q-ORAC	4.86	2.10	2271	4.97	4.78 ± 4.09*	2.12*	47.7	1.81	10.1	3.08 nmol of TE

[a]CV(Fr), coefficient of variation of the response factor; CV(b), coefficient of variation of the slope; ANOVA by means of the F test (F_{exp}, experimental F; F_{tab}, tabulated F (1, n − 2, 0.05)). Linearity test acceptance criteria: CV(Fr) < 5%; CV(b) < 2%; ANOVA $F_{exp} > F_{tab}$. [b]$a \pm t_{tab}S(a)$, confidence interval of the ordinate at origin; t_{cal}, calculated Student's t; t_{tab}, tabulated Student's t (n − 2, 0.05). Proportionality acceptance criteria: interval should include 0; $t_{cal}(a) < t_{tab}$; $t_{cal}(b) > t_{tab}$. *, results do not meet the acceptance criteria. [c]y_d, detection signal; x_d, capability of detection. Detection limits calculated for α and β = 0.05. [d]y_d units, absorbance units (Q-FC, Q-FRAP, Q-ABTS, Q-DPPH); net area under the curve (net AUC) (Q-ORAC). [e]GAE, gallic acid equivalents; Fe(II)E, iron(II) equivalents; TE, Trolox equivalents.

Table 3. Precision of the QUENCHER Total Antioxidant Capacity (Q-TAC) and QUENCHER Free Radical Scavenging Capacity (Q-FRSC) Methods

		repeatability			intermediate precision	
method	units of S_r and S_R[a]	CV[b] (%)	$S_{r\ (Rp)}$[c]	$S_{r\ (IP)}$[d]	CV[e] (%)	S_R[f]
Q-FC	μmol GAE/g product	2.06	1.23	1.17	2.37	1.49
Q-FRAP	μmol Fe(II)E/g product	4.98	10.8	10.7	6.48	16.0
Q-ABTS	μmol TE/g product	2.13	2.24	2.73	3.05	3.26
Q-DPPH	μmol TE/g product	3.12	1.24	1.26	3.85	1.59
Q-ORAC	μmol TE/g product	5.45*	2.94	2.79	5.48	3.01
Q-SRSC	oxidation inhibition %	3.27	1.05	1.46	6.35	1.62
Q-HRSC	oxidation inhibition %	5.31*	2.79	3.09	6.32	3.28
Q-LPSC	oxidation inhibition %	5.26*	4.01	4.44	6.35	4.87

[a]GAE, gallic acid equivalents; Fe(II)E, iron(II) equivalents; TE, Trolox equivalents. [b]Repeatability acceptance criteria: CV < 5%. *, results do not meet the acceptance criteria. [c]Estimate of repeatability (S_r) determined by one-variable analysis of seven replicates on one day (Rp, repeatability experiment). [d]Estimate of repeatability (S_r) determined by one-way ANOVA of three replicates on three different days (IP, intermediate precision experiment). [e]Intermediate precision acceptance criteria: CV < 10%. [f]Estimate of intermediate precision (S_R) determined by one-way ANOVA of three replicates on three different days (IP, intermediate precision experiment).

Validation of the Q-TAC and Q-FRSC Methods. The validation study was done by the examination of the following parameters: linearity, proportionality, detection limits, and precision (repeatability and intermediate precision).[32] In the case of Q-FRSC assays (Q-SRSC, Q-HRSC, and Q-LPSC), only the precision was evaluated because in these methods a calibration curve is not needed. In the Q-TAC methodologies (Q-FC, Q-FRAP, Q-ABTS, Q-DPPH, and Q-ORAC), a dose−response curve was obtained by testing different amounts of the standard used in each method. The calibration was performed using linear models and the least-squares (LS) method. All of the models presented coefficient of determination (R^2) values >0.995 (Table 1).

Once the parameters were estimated, the models were validated by verifying the assumptions related to the residuals and the functions.[33] The studentized residuals were normally distributed (Kolmogorov−Smirnov, chi-square, and Shapiro−Wilk tests), independent (Durbin−Watson test), and homoscedastic (Cochran and Bartlett tests) in all cases. The functional part of each linear model was first validated in a linearity test. According to the results (Table 2), all of the models were suitable for describing the linear relationship between the standard concentration and the response of each assay. The Q-FC method obtained the best values for all of the parameters tested, whereas the Q-ORAC assay linearity response was the least satisfactory, although within the acceptance criteria. In addition, a proportionality test to determine whether the mathematical model could be used for predictive purposes was performed (Table 2). The conditions of proportionality were corroborated for all methods except Q-

DOI: 10.1021/acs.jafc.5b01644
J. Agric. Food Chem. 2015, 63, 6922−6931

Table 4. QUENCHER Total Antioxidant Capacity (Q-TAC) and QUENCHER Free Radical Scavenging Capacity (Q-FRSC) of the Model Products Obtained from Skins (Sk), Seeds (Sd), and Whole (W) Wine Pomace[a]

		Sk		W		Sd	
method	units[b]	value	CV (%)	value	CV (%)	value	CV (%)
Q-FC	μmol GAE/g product	74.4 ± 1.07 b	1.43	78.3 ± 2.37 b	3.02	52.6 ± 2.53 a	4.80
Q-FRAP	μmol Fe(II)E/g product	275 ± 4.18 c	1.52	224 ± 13.6 b	6.05	140 ± 4.92 a	3.52
Q-ABTS	μmol TE/g product	120 ± 5.21 a	4.33	150 ± 2.66 b	1.78	120 ± 0.83 a	0.69
Q-DPPH	μmol TE/g product	51.9 ± 1.10 a	2.11	110 ± 3.60 b	3.27	174 ± 4.16 c	2.39
Q-ORAC	μmol TE/g product	236 ± 9.92 b	4.19	243 ± 4.17 b	1.72	181 ± 7.96 a	4.39
Q-SRSC	oxidation inhibition %	31.7 ± 1.19 a	3.76	50.5 ± 1.88 b	3.72	30.1 ± 1.20 a	3.98
Q-HRSC	oxidation inhibition %	50.1 ± 2.59 a	5.17	59.0 ± 0.64 c	1.08	53.8 ± 1.08 b	2.01
Q-LPSC	oxidation inhibition %	52.2 ± 2.57 b	4.92	62.5 ± 3.38 c	5.41	33.7 ± 2.02 a	7.27

[a]Q-TAC and Q-FRSC values are the mean ± standard deviation (n = 3). Roman letters indicate significant differences among the model products (Sk, W, Sd) within each QUENCHER methodology. [b]GAE, gallic acid equivalents; Fe(II)E, iron(II) equivalents; TE, Trolox equivalents.

ORAC, where the ordinate at origin did not meet any of the criteria. In this assay the Q-TAC is assessed by the net AUC determination and a lag time is observed during oxidation of the fluorescein in the presence of an antioxidant.[1,27] The unsatisfactory result of the ordinate at origin is explained by the lack of proportionality of this lag time at very small amounts of Trolox. However, a linear response was observed at higher quantities of the standard, as previously observed by Ou et al.[27] in the classical approach of this assay.

Having studied the acceptability of the linear models, the detection limits y_d (detection signal) and x_d (capability of detection) of the assessed methodologies were determined as described by Ortiz et al.[33] In general, low limits of detection were observed (Table 2), which confirmed the acceptability of all methodologies to determine the TAC of very small quantities of antioxidants. Among the assays using Trolox as standard, the lowest x_d value corresponded to the Q-ORAC assay, which was corroborated as a highly sensitive methodology, and the highest limits of detection were obtained by the Q-ABTS method. A similar observation was previously reported for a comparison of classical TAC methodologies.[25]

Finally, two different terms of the precision were evaluated, the repeatability (Rp) and the intermediate precision (IP), determining their estimates (S_r and S_R, respectively) and coefficients of variance (CV).[32] The IP refers to the precision under reproducibility conditions when only some of the factors are varied. In this study a single factor (different days) was investigated. The results of the Rp and IP experiments for each methodology are shown in Table 3. It can be seen that similar S_r values were obtained in both Rp and IP experiences for all of the methods. The CV of the assays was the criteria selected to evaluate their acceptability. The Rp of the longest protocols (Q-ORAC, Q-HRSC, and Q-LPSC) exceeded the CV < 5% cutoff value, whereas those assays with just one or two steps (Q-FC, Q-ABTS, and Q-DPPH) showed a high Rp between measurements. By comparison with the Rp obtained in classical protocols validated using different wines as samples,[25] slightly higher CV were observed in the Q-TAC, and especially in the Q-FRSC methods, as all classical assays obtained CV < 5%. The only exception was the Q-ABTS assay, which showed better Rp than the classical approach. In terms of IP (Table 3), all of the methodologies presented satisfactory results, with the lowest CV (%) obtained again by two of the simplest methods (Q-FC and Q-ABTS). Therefore, the differences in the Rp and IP among the methodologies were mainly attributed to the complexity of the protocols. The sensitivity of the assays could also affect the precision observed, as might be the case for the Q-ORAC method mentioned above.

Q-TAC and Q-FRSC of the Model Products. To provide comprehensive information on the actual TAC of food, it is recommended that at least two TAC assays be used.[6,8] Similarly, in this study, a broad overview of the antioxidant capacity of the three model products (Sk, W, and Sd) was achieved with the different QUENCHER methodologies under study.

As shown in Table 4, model product W (rich in both hydrophobic and hydrophilic antioxidant compounds) showed the highest Q-TAC and Q-FRSC values in most of the methods, with the exception of the Q-FRAP assay, where Sk (model product especially rich in hydrophilic antioxidant) presented the most elevated antioxidant capacity and the Q-DPPH assay, where Sd (model product especially rich in hydrophobic antioxidant) exhibited the highest Q-TAC values. The difference between the antioxidant capacity of Sk and W was not significant in the Q-FC and Q-ORAC protocols. No significant differences were found between Sk and Sd in the Q-ABTS and Q-SRSC assays. From a comparison of the responses obtained by the three methodologies where Trolox was used as standard, Q-ORAC obtained the highest TAC values, but it must be noted that the sensitivity of this method to Trolox was also more elevated than in the Q-DPPH and Q-ABTS assays.

The obtained results were contrasted with those obtained by classical determinations, and considerable differences were found, except with the Q-DPPH method. Several studies comparing extracts from wine pomace reported a higher antioxidant capacity exhibited by seeds than skins, obtaining the same tendency using different assays (FC,[34−37] FRAP,[34,36,37] ABTS,[36] DPPH,[34−37] ORAC,[36] SRSC,[35] and HRSC[34]). This fact may be explained because classical protocols involve extraction with solvents, which are capable of extracting both hydrophobic and hydrophilic antioxidants. Therefore, the extracts obtained might not be representative of the antioxidant capacity that solid foods could actually exert, whereas QUENCHER assays may provide more reliable information.[11]

Correlation Study between the QUENCHER Methodologies. Pearson's correlation coefficients (r) between pairs of the assays were determined using the Q-TAC and Q-FRSC values obtained for Sk, W, and Sd by the different QUENCHER methodologies.

In the literature, due to the wide spectrum of analytical techniques and reaction conditions available, it is difficult to find an agreement on the correlations among different TAC methodologies.[2,8,38] To the extent of our knowledge, the

DOI: 10.1021/acs.jafc.5b01644
J. Agric. Food Chem. 2015, 63, 6922−6931

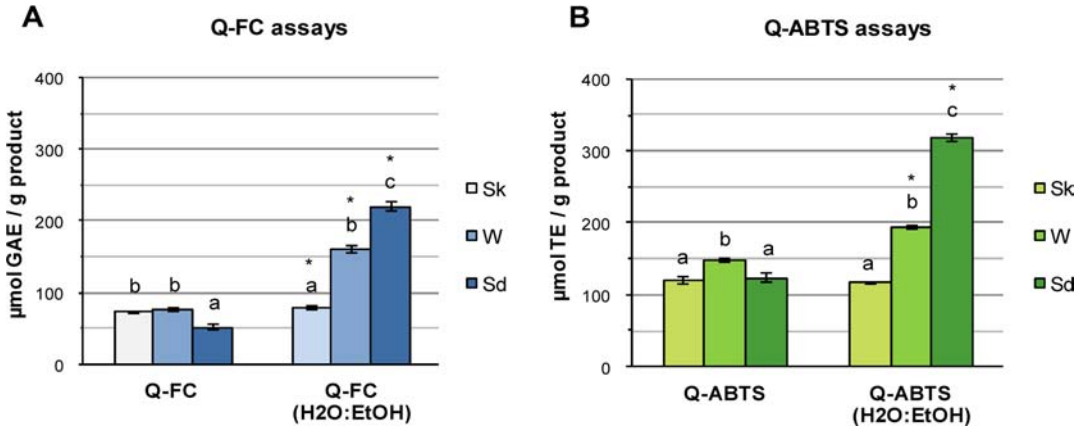

Figure 1. QUENCHER total antioxidant capacity (Q-TAC) of the model products (Sk, skins; W, whole; Sd, seeds): (A) Q-FC assays; (B) Q-ABTS assays. GAE, gallic acid equivalents; TE, Trolox equivalents. Data are expressed as mean values ± standard deviation (n = 3). Roman letters indicate significant differences among the model products (Sk, W, Sd) within each assay. The asterisk (∗) refers to significant differences between the Q-TAC and Q-TAC (H_2O:EtOH) approaches for each wine pomace product.

correlation between different QUENCHER methodologies has not been described yet. In this study, an interesting correspondence among the assays was observed, especially for the Q-FC and Q-ABTS assays with the rest of methods. A highly significant ($p < 0.01$) positive correlation was detected between Q-FC and Q-FRAP (r = 0.847), between Q-FC and Q-ORAC (r = 0.974), and between Q-FC and Q-LPSC (r = 0.926). The correspondence between Q-FC and Q-FRAP is due to the fact that both methods measure the reducing capacity of the sample,[38] also detected between the classical approaches.[36,37] Furthermore, the significant correlation between Q-ORAC and Q-LPSC (r = 0.914) may be explained because peroxyl radicals are involved in both assays.[39] The positive correlation of the Q-FC with the Q-ORAC and Q-LPSC assays is very convenient as they are more biologically relevant methods, but these assays are also more complicated, and their validation study showed some unsatisfactory results. However, the obtained results contrast with the weaker correlation (R^2 = 0.409) found between the classical approaches of the FC and the ORAC assays by Ky et al.[36] using also wine pomace as samples. In the present study, interesting high positive correlations ($p < 0.01$) between Q-ABTS and Q-SRSC (r = 0.935) and between Q-ABTS and Q-HRSC (r = 0.903) were also observed. According to Rivero-Pérez et al.,[25] such strong correlations were not detected in the classical approaches of these assays using wines as samples. On the other hand, negative correlations ($p < 0.05$) between Q-DPPH and Q-FC (r = −0.781), between Q-DPPH and Q-FRAP (r = −0.986), and between Q-DPPH and Q-ORAC (r = −0.808) were found in the present study, and the Q-DPPH method was not significantly correlated with any of the biologically relevant Q-FRSC assays. In classical methodologies, the DPPH and HRSC assays were not found to be correlated either,[34] but high positive correlations were usually detected between the DPPH and other TAC methods (FC,[35−37] FRAP,[34,37] and ABTS[25]). It must be noted that the Q-DPPH is the only QUENCHER methodology that was performed in an organic reaction medium, and its lack of positive correlation with the rest of the protocols indicates the elevated influence of the solvent used in these assays.

The different contents of hydrophilic and lipophilic compounds[40,41] of the three model products used in this study allow for assessing the response of each method toward matrices with compounds of high or low water solubility. Anyway, it would be advisable to confirm the correlations found in the current study by evaluating a wider range of products.

With the results of both the validation and correlation studies taken into account, the combination of both Q-FC and Q-ABTS assays is suggested as a good selection for a general Q-TAC analysis of powdered foods. The Q-SRSC, Q-HRSC, and Q-LPSC methods, first adapted to the QUENCHER approach in this study, might give a more biologically relevant overview of the antioxidant capacity of the samples. However, the Q-HRSC and Q-LPSC assays are complicated protocols for routine analysis, and it has been shown that the combination of the Q-FC and Q-ABTS methods covers the correspondence with the results obtained by the three biologically relevant Q-FRSC assays.

Effects of the Reaction Medium in the Q-FC and Q-ABTS Assays. In the QUENCHER methods there is no extraction step, but the reaction medium is a key factor that determines the solubility of the compounds present in the solid powdered product, as well as the interactions between the antioxidants and the radicals used as probes in the assays.

Serpen et al.[42] proposed a water/ethanol (H_2O:EtOH) 50:50 (v/v) ratio as a suitable working solution, providing accurate Q-TAC results for most of the food matrices studied. Therefore, the effect of using water or a mixture H_2O:EtOH 1:1 (v/v) as reaction medium was assessed in the current study using the two previously selected Q-TAC methods (Q-FC and Q-ABTS).

The Q-FC (H_2O:EtOH) and Q-ABTS (H_2O:EtOH) assays were validated as previously described for the rest of the methodologies and presented satisfactory results for all parameters evaluated (Supporting Information 1). Slight formation of white solids was observed in the Q-FC (H_2O:EtOH) method, probably due to the precipitation of Na_2CO_3 in the presence of ethanol. Nevertheless, these solids did not interfere in the measurement. The responses of the Q-FC and Q-FC (H_2O:EtOH) assays to different standard concentrations were not significantly different (similar slopes in the calibration models), whereas a 2.54 times lower response to Trolox in the Q-ABTS than in the Q-ABTS (H_2O:EtOH) method was detected. In contrast, Serpen et al.[42] found similar slopes of the dose−response lines obtained in the Q-ABTS assays using different solvent ratios H_2O:EtOH (0:100, 25:75, 50:50, 75:25, 100:0). A possible explanation might be that the

DOI: 10.1021/acs.jafc.5b01644
J. Agric. Food Chem. 2015, 63, 6922−6931

Table 5. Influence of the Amount of Sample Weighed and the Use of Cellulose (C) as a Diluting Agent in the Q-ABTS Assays Evaluated in Model Products Obtained from Skins (Sk) or Seeds (Sd) Separated from Red Wine Pomace[a]

method	Q-TAC values (μmol TE/g product)				
Q-ABTS	Sk 3 mg	Sk 2 mg	Sk 1 mg	Sk:C (2:1) 3 mg	Sk:C (1:2) 3 mg
	116 ± 3.97	119 ± 3.41	122 ± 3.77	121 ± 1.88	118 ± 8.32
	Sd 3 mg	Sd 2 mg	Sd 1 mg	Sd:C (2:1) 3 mg	Sd:C (1:2) 3 mg
	126 ± 5.47 a	139 ± 5.83 b	148 ± 3.30 c	153 ± 3.44 c	167 ± 5.11 d
Q-ABTS (H_2O:EtOH)	Sk 1.5 mg	Sk 1 mg	Sk 0.5 mg	Sk:C (2:1) 1.5 mg	Sk:C (1:2) 1.5 mg
	124 ± 4.10 cb	131 ± 4.56 c	116 ± 8.89 b	117 ± 4.13 b	93.4 ± 4.75 a
	Sd 0.75 mg	Sd 0.5 mg	Sd 0.25 mg	Sd:C (2:1) 0.75 mg	Sd:C (1:2) 0.75 mg
	314 ± 5.45	320 ± 9.30	318 ± 18.1	323 ± 10.1	320 ± 17.4

[a]Q-TAC values are the mean ± standard deviation (n = 3). TE, Trolox equivalents. Roman letters indicate significant differences among the different amounts of sample and the dilutions with cellulose tested within each method (Q-ABTS or Q-ABTS (H_2O:EtOH)) for each product (Sk or Sd).

calibration curves of Q-TAC methodologies carried out in this study were performed by weighing directly the standards, without their previous dilution in any solvent. Thus, the lower solubility of Trolox in water than in organic solvents played a critical role in the response observed in each method, as previously described by other authors.[9] This fact may lead to lower Q-TAC values in the Q-ABTS than in the Q-ABTS (H_2O:EtOH) assay due intrinsically to the methods used rather than the samples analyzed. Therefore, as the numeric Q-TAC values obtained by the Q-ABTS assays may not be directly comparable, the tendency observed among the samples (higher or lower Q-TAC values) was the main interest of these analyses.

The Q-TAC of Sk, W, and Sd obtained using the Q-FC and Q-ABTS assays can be seen in Figure 1. As previously described for classical methods,[1,39] the reaction medium greatly influenced the Q-TAC results, with both soluble compounds and insoluble antioxidants attached to the powdered products being affected by the solvent used in the Q-TAC assays. A similar tendency was observed in both Q-FC and Q-ABTS assays when water was replaced by a mixture of H_2O:EtOH (1:1, v/v) as reaction medium. A significant increase in the Q-TAC values of Sd was observed, reaching higher antioxidant capacity than W, for which Q-TAC was also enhanced, but to a lesser extent. The Sk product showed the lowest Q-TAC in both Q-FC (H_2O:EtOH) and Q-ABTS (H_2O:EtOH) assays. Similar results were obtained in previous studies[21] carried out using conventional methodologies including extraction steps with organic solvents. Indeed, a good correlation between general results obtained using Q-TAC (H_2O:EtOH) and classical methods was observed. In contrast, this fact was only found between Q-TAC (carried out in water) and classical methods when the matrices under study were rich in hydrophilic antioxidants (Supporting Information 2).

Differences among results obtained for the three model products using the different Q-TAC methods can be partly explained by their chemical composition, the solubility of their antioxidant compounds in the reaction medium, and their redox reactions with the radical probes or reagents used in each assay. With regard to the chemical composition of the model products tested, it is important to have in mind that skins of grapes are a rich source of anthocyanins and hydroxycinnamic acids, although they also contain some flavanols and flavonol glycosides, whereas gallic acid, flavanols, and proanthocyanidins are mainly present in the seeds of grapes.[35,37,43] According to these facts, the Sk model product was rich mainly in anthocyanins and hydroxycinnamic acids, whereas Sd was rich in flavanols from monomers to polymers (proanthocyanins and tannins). A description of the solubility of food antioxidants, including main phenolic classes, can be found in Gökmen et al.[11] In general, the water solubility of polyphenols increases with the number of glycosylated hydroxyl groups and with the amount of sugars constituting the carbohydrate moiety. On the other hand, in the case of polymerized polyphenols (such as proanthocyanidins or tannins), the water solubility considerably drops with an increased number of units and with the formation of intramolecular bonds.[44] Thus, the higher polarity of the polyphenols found in the grape skins allows that they are well solubilized when water is used as reaction medium,[44] whereas the presence of ethanol seems to favor the extraction of hydrophobic antioxidants present in the grape seeds. It must be pointed out that lower H_2O:EtOH ratios are not advised because it may cause the shrinking of the major constituents of the food matrices, such as cellulose and proteins.[17,42] This could hamper the release of the compounds or the diffusion of the radicals into the solid matrices where they can react with inner bound insoluble antioxidants, leading to lower Q-TAC values.[11]

The reaction medium also affects the interactions between the antioxidants and reagents involved in the methods by enhancing or decreasing the equilibrium constant of their redox reactions. In the QUENCHER approaches, when the redox equilibrium constant of an antioxidant compound in a determinate medium is higher than its solubility constant, the extraction of this antioxidant from the insoluble matrix and its solubilization in the reaction medium can be thermodynamically enhanced.[42]

The study of the correlations between the Q-TAC assays carried out in the same reaction medium showed a strong correspondence ($p < 0.01$) between Q-FC (H_2O:EtOH) and Q-ABTS (H_2O:EtOH) (r = 0.971), whereas there was no significant correlation between Q-FC and Q-ABTS (r = 0.496). This finding shows that, in the Q-TAC (H_2O:EtOH) methods, the factors related to the assay reaction medium (solubilization of the antioxidant compounds) play a more critical role than those related to the method used (reaction with the probes or reagents). Therefore, the mixture H_2O:EtOH 50:50 (v/v) proposed by Serpen et al.[42] might be adequate to evaluate the global TAC of food materials, but the Q-TAC of hydrophobic

DOI: 10.1021/acs.jafc.5b01644
J. Agric. Food Chem. 2015, 63, 6922−6931

antioxidants could be overestimated under certain conditions and, then, their real antioxidant role in food matrices.

Moreover, the correlations between the biologically relevant Q-FRSC assays and both Q-TAC (H_2O:EtOH) methods were not significant in the case for the Q-SRSC and Q-HRSC methods, and even a significant ($p < 0.01$) negative correlation between Q-LPSC and Q-ABTS (H_2O:EtOH) ($r = -0.716$) was found. These results further support the selection of the Q-FC and Q-ABTS assays in water as preferred protocols to assess a potentially more biologically relevant Q-TAC of food products and dietary supplements.

Effects of Using Cellulose as a Diluting Agent in the Q-ABTS Assays. Cellulose has been suggested as a diluting agent in previous Q-TAC protocols.[11,12] However, the affinity of polyphenols to cellulose is well-known,[45] so it is possible that interactions between the cellulose and these antioxidant compounds interfere in the quantification.

The possible influence of cellulose on the Q-TAC measurements was evaluated with the Q-ABTS assays (the most widely used Q-TAC assay up to now), and it was compared with the effects of weighing different amounts of sample. The two model products that presented more differences between them (Sk and Sd) were chosen to carry out this study. Two dilutions or product/cellulose ratios (2:1 and 1:2) were used. The quantities of product weighed were adapted to those required by each method to give results within their detection range. As can be seen in Table 5, no influence of the amount of sample or the presence of cellulose on the Q-TAC values was observed for Sk in the Q-ABTS assay and for Sd in the Q-ABTS (H_2O:EtOH) method. However, Q-ABTS results of Sd showed significantly higher Q-TAC values when lower amounts of sample were used, and this effect was more marked when the product was diluted with cellulose. In contrast, the opposite tendency was found for Sk in the Q-ABTS (H_2O:EtOH) assay. In this case, inferior Q-TAC values were obtained when a lower amount of Sk was used, which were only significant in Sk/cellulose (1:2) with respect to the nondiluted Sk sample.

The observed effect of weighing different amounts of Sd in the Q-ABTS assay could be due to a better water extraction of its slightly soluble hydrophobic polyphenols[11,36] when they are at a lesser concentration. Moreover, possible hydrophobic interactions between the antioxidant compounds (favored in the aqueous medium)[46] could be more relevant when a higher amount of sample is present, thus decreasing their ability to scavenge the soluble $ABTS^{\bullet+}$ radicals present in the reaction medium.

With regard to the influence of cellulose in the measurements, absorbance values similar to those of the $ABTS^{\bullet+}$ working solution were obtained in both methods (Q-ABTS and Q-ABTS (H_2O:EtOH)) when only cellulose was used as sample (data not shown), corroborating that cellulose alone is inert toward the $ABTS^{\bullet+}$ reagent, as has been previously described.[12] Therefore, the results obtained in this study could be due to the effects of cellulose in the solubility of the hydrophilic or lipophilic compounds present in the products and their capacity to interact with the $ABTS^{\bullet+}$ radicals, both factors influenced by the reaction medium. Hydrogen-bonding and hydrophobic interactions between cellulose and polyphenols have been described,[45] which are also dependent on the solvent systems used. Hydrophobic interactions are favored in hydrophilic solvents, whereas hydrogen bonding is favored in the more hydrophobic ones. Thus, the affinity of polyphenols (such as gallotannins and ellagitannins) to cellulose is expected to correlate with their hydrophobicity, their number of galloyl groups, and their molecular size.[44,45] This evidence explains that cellulose effects are of particular importance in the hydrophilic solvents when hydrophobic compounds are tested, as happened when Sd was assessed by the Q-ABTS assay. The monomeric and oligomeric proanthocyanidins of the grape seeds might remain insoluble in aqueous reaction mediums.[40,41] However, their interaction with cellulose through their hydrophobic moieties might raise their water solubility and leave the hydroxyl groups available to interact with the $ABTS^{\bullet+}$ radicals, leading to the increased Q-TAC values observed when the product/cellulose ratio was decreased. On the other hand, in the case of Sk in the Q-ABTS (H_2O:EtOH) assay, the contrary effect may take place. Hydrogen bonding between cellulose and the hydrophilic phenolics present in wine pomace skins could be favored in the presence of organic solvents. Thus, the number of hydroxyl groups available in the molecules to scavenge the radical probes of the assay is reduced.

On the basis of the cited results, the use of cellulose as a diluting agent is discouraged in the Q-TAC methodologies, especially if the antioxidant products tested are a source of polyphenols. The main motive is the possible interaction of cellulose with the phenolic compounds involved in the assays, leading to an under- or overestimation of the Q-TAC of the products.

In summary, a wide range of QUENCHER analytical techniques to provide a comprehensive initial assessment in vitro of the TAC and FRSC of food materials have been adapted and validated (Q-FC, Q-ABTS, Q-DPPH, Q-FRAP, Q-ORAC, Q-SRSC, Q-HRSC, and Q-LPSC). The Q-TAC and Q-FRSC assays skip the extraction step of the classical antioxidant capacity protocols and are simple, quick, inexpensive, and precise methodological approaches. The QUENCHER methodologies validated in this paper working with powdered model products are suitable for application to other foods and food ingredients, both rich in fat (as seeds) and not, as skins, which are rich in fiber and minerals among others. The combination of the Q-FC and Q-ABTS assays using water as reaction medium is proposed as the best choice to analyze a large number of samples. They provide more biologically relevant information than the classical TAC methods using extracts or other Q-TAC approaches using nonaqueous solvents. It is suggested that the same amount of sample be weighed, especially when products rich in hydrophobic antioxidants are assessed. The use of cellulose as a diluting agent is not recommended in the Q-TAC methods. Finally, it must be pointed out that, despite the advantages of the proposed QUENCHER assays over other in vitro methodologies, the Q-TAC or Q-FRSC of food materials and dietary supplements cannot be directly translated into healthful effects provided in vivo.

■ ASSOCIATED CONTENT

Supporting Information

Validation of Q-FC (H_2O:EtOH) and Q-ABTS (H_2O:EtOH) methods; 2) Correlations between classical TAC, Q-TAC (H_2O:EtOH) and Q-TAC methods. The Supporting Information is available free of charge on the ACS Publications website at DOI: 10.1021/acs.jafc.5b01644.

DOI: 10.1021/acs.jafc.5b01644
J. Agric. Food Chem. 2015, 63, 6922−6931

AUTHOR INFORMATION

Corresponding Author

*(P.M.) E-mail: pmuniz@ubu.es. Phone: +34-947258800, ext. 8210. Fax: +34-947258831.

Funding

This research was supported by the autonomous government of Castilla y León (Project BU268A11-2). The Ph.D. grants to R. Del Pino-García and J. García-Lomillo (FPU grants) are funded by the Ministerio de Educación, Cultura y Deporte of the Spanish government.

Notes

The authors declare no competing financial interest.

ABBREVIATIONS USED

ABTS, 2,2′-azinobis(3-ethylbenzothiazoline-6-sulfonic acid); AUC, area under the curve; DPPH, 2,2-diphenyl-1-picrylhydrazyl; FC, Folin−Ciocalteu; FRAP, ferric reducing/antioxidant power; FRSC, free radical scavenging capacity; GA, gallic acid; HRSC, hydroxyl radical scavenging capacity; LPSC, lipid peroxyl scavenging capacity; Q-, QUENCHER; OC, oxidized controls; ORAC, oxygen radical absorbance capacity; SC, sample controls; Sd, product from wine pomace seeds; Sk, product from wine pomace skins; SRSC, superoxide radical scavenging capacity; T, Trolox; TAC, total antioxidant capacity; W, product from whole wine pomace

REFERENCES

(1) Prior, R. L.; Wu, X.; Schaich, K. Standardized methods for the determination of antioxidant capacity and phenolics in foods and dietary supplements. *J. Agric. Food Chem.* **2005**, *53*, 4290−4302.

(2) Niki, E. Assessment of antioxidant capacity in vitro and in vivo. *Free Radical Biol. Med.* **2010**, *49*, 503−515.

(3) López-Alarcón, C.; Denicola, A. Evaluating the antioxidant capacity of natural products: a review on chemical and cellular-based assays. *Anal. Chim. Acta* **2013**, *763*, 1−10.

(4) Fraga, C. G.; Oteiza, P. I.; Galleano, M. In vitro measurements and interpretation of total antioxidant capacity. *Biochim. Biophys. Acta, Gen. Subj.* **2014**, *1840*, 931−934.

(5) Sanchez-Moreno, C. Review: Methods used to evaluate the free radical scavenging activity in foods and biological systems. *Food Sci. Technol. Int.* **2002**, *8*, 121−137.

(6) Pérez-Jiménez, J.; Arranz, S.; Tabernero, M.; Díaz- Rubio, M. E.; Serrano, J.; Goñi, I.; Saura-Calixto, F. Updated methodology to determine antioxidant capacity in plant foods, oils and beverages: extraction, measurement and expression of results. *Food Res. Int.* **2008**, *41*, 274−285.

(7) Frankel, E. N.; Meyer, A. S. The problems of using one-dimensional methods to evaluate multifunctional food and biological antioxidants. *J. Sci. Food Agric.* **2000**, *80*, 1925−1941.

(8) Karadag, A.; Ozcelik, B.; Saner, S. Review of methods to determine antioxidant capacities. *Food Anal. Methods* **2009**, *2*, 41−60.

(9) Pérez-Jiménez, J.; Saura-Calixto, F. Effect of solvent and certain food constituents on different antioxidant capacity assays. *Food Res. Int.* **2006**, *39*, 791−800.

(10) Serrano, J.; Goñi, I.; Saura-Calixto, F. Food antioxidant capacity determined by chemical methods may underestimate the physiological antioxidant capacity. *Food Res. Int.* **2007**, *40*, 15−21.

(11) Gökmen, V.; Serpen, A.; Fogliano, V. Direct measurement of the total antioxidant capacity of foods: the "QUENCHER" approach. *Trends Food Sci. Technol.* **2009**, *20*, 278−288.

(12) Serpen, A.; Capuano, E.; Fogliano, V.; Gökmen, V. A new procedure to measure the antioxidant activity of insoluble food components. *J. Agric. Food Chem.* **2007**, *55*, 7676−7681.

(13) Amigo-Benavent, M.; del Castillo, M. D.; Fogliano, V. Are the major antioxidants derived from soy protein and fructo-oligosaccharides model systems colored aqueous soluble or insoluble compounds? *Eur. Food Res. Technol.* **2010**, *231*, 545−553.

(14) Serpen, A.; Gökmen, V.; Fogliano, V. Total antioxidant capacities of raw and cooked meats. *Meat Sci.* **2012**, *90*, 60−65.

(15) Kraujalis, P.; Venskutonis, P. R.; Kraujalienė, V.; Pukalskas, A. Antioxidant properties and preliminary evaluation of phytochemical composition of different anatomical parts of amaranth. *Plant Foods Hum. Nutr.* **2013**, *68*, 322−328.

(16) Açar, Ö. Ç.; Gökmen, V.; Pellegrini, N.; Fogliano, V. Direct evaluation of the total antioxidant capacity of raw and roasted pulses, nuts and seeds. *Eur. Food Res. Technol.* **2009**, *229*, 961−969.

(17) Serpen, A.; Gökmen, V.; Pellegrini, N.; Fogliano, V. Direct measurement of the total antioxidant capacity of cereal products. *J. Cereal Sci.* **2008**, *48*, 816−820.

(18) Çelik, E. E.; Gökmen, V.; Fogliano, V. Soluble antioxidant compounds regenerate the antioxidants bound to insoluble parts of foods. *J. Agric. Food Chem.* **2013**, *61*, 10329−10334.

(19) Delgado-Andrade, C.; Conde-Aguilera, J. A.; Haro, A.; Pastoriza de la Cueva, S.; Rufián-Henares, J. Á. A combined procedure to evaluate the global antioxidant response of bread. *J. Cereal Sci.* **2010**, *52*, 239−246.

(20) González-Sanjosé, M. L.; García-Lomillo, J.; Del Pino-García, R.; Muñiz-Rodríguez, P.; Rivero-Pérez, M. D. Universidad de Burgos. ES Patent 2524870A1, 2013.

(21) García-Lomillo, J.; González-Sanjosé, M. L.; Del Pino-García, R.; Rivero-Perez, M. D.; Muñiz, P. Antioxidant and antimicrobial properties of wine by-products and their potential uses in the food industry. *J. Agric. Food Chem.* **2014**, *62*, 12595−12602.

(22) Singleton, V. L.; Rossi, J. A. Colorimetry of total phenolics with phosphomolybdic-phosphotungstic acid reagents. *Am. J. Enol. Vitic.* **1965**, *16*, 144−158.

(23) Benzie, I. F.; Strain, J. J. The ferric reducing ability of plasma (FRAP) as a measure of "antioxidant power": the FRAP assay. *Anal. Biochem.* **1996**, *239*, 70−76.

(24) Re, R.; Pellegrini, N.; Proteggente, A.; Pannala, A.; Yang, M.; Rice-Evans, C. Antioxidant activity applying an improved ABTS radical cation decolorization assay. *Free Radical Biol. Med.* **1999**, *26*, 1231−1237.

(25) Rivero-Pérez, M. D.; Muñiz, P.; Gonzalez-SanJosé, M. L. Antioxidant profile of red wines evaluated by total antioxidant capacity, scavenger activity, and biomarkers of oxidative stress methodologies. *J. Agric. Food Chem.* **2007**, *55*, 5476−5483.

(26) Brand-Williams, W.; Cuvelier, M. E.; Berset, C. Use of a free radical method to evaluate antioxidant activity. *LWT−Food Sci. Technol.* **1995**, *28*, 25−30.

(27) Ou, B.; Hampsch-Woodill, M.; Prior, R. L. Development and validation of an improved oxygen radical absorbance capacity assay using fluorescein as the fluorescent probe. *J. Agric. Food Chem.* **2001**, *49*, 4619−4626.

(28) Liu, F.; Ooi, V. E. C.; Chang, S. T. Free radical scavenging activities of mushroom polysaccharide extracts. *Life Sci.* **1997**, *60*, 763−771.

(29) Halliwell, B.; Gutteridge, J. M.; Aruoma, O. I. The deoxyribose method: a simple "test-tube" assay for determination of rate constants for reactions of hydroxyl radicals. *Anal. Biochem.* **1987**, *165*, 215−219.

(30) Kessler, M.; Ubeaud, G.; Jung, L. Anti- and pro-oxidant activity of rutin and quercetin derivatives. *J. Pharm. Pharmacol.* **2003**, *55*, 131−142.

(31) Bradford, M. M. A rapid and sensitive method for the quantitation of microgram quantities of protein utilizing the principle of protein-dye binding. *Anal. Biochem.* **1976**, *72*, 248−254.

(32) García, I.; Ortiz, M. C.; Sarabia, L.; Vilches, C.; Gredilla, E. Advances in methodology for the validation of methods according to the International Organization for Standardization. Application to the determination of benzoic and sorbic acids in soft drinks by high-performance liquid chromatography. *J. Chromatogr. A* **2003**, *992*, 11−27.

(33) Ortiz, M. C.; Sánchez, M. S.; Sarabia, L. A. Quality of analytical measurements: univariate regression. In *Comprehensive Chemometrics.*

DOI: 10.1021/acs.jafc.5b01644
J. Agric. Food Chem. 2015, 63, 6922−6931

Chemical and Biochemical Data Analysis; Brown, S. D., Tauler, R., Walczak, B., Eds.; Elsevier: Amsterdam, The Netherlands, 2009; pp 127−169.
(34) Makris, D. P.; Boskou, G.; Andrikopoulos, N. K. Polyphenolic content and in vitro antioxidant characteristics of wine industry and other agri-food solid waste extracts. *J. Food Compos. Anal.* **2007**, *20*, 125−132.
(35) Cheng, V. J.; Bekhit, A. E.-D. A.; McConnell, M.; Mros, S.; Zhao, J. Effect of extraction solvent, waste fraction and grape variety on the antimicrobial and antioxidant activities of extracts from wine residue from cool climate. *Food Chem.* **2012**, *134*, 474−482.
(36) Ky, I.; Lorrain, B.; Kolbas, N.; Crozier, A.; Teissedre, P. L. Wine by-products: phenolic characterization and antioxidant activity evaluation of grapes and grape pomaces from six different french grape varieties. *Molecules* **2014**, *19*, 482−506.
(37) Rockenbach, I. I.; Gonzaga, L. V.; Rizelio, V. M.; De Sauza Schmidt Gonçalves, A. E.; Genovese, M. I.; Fett, R. Phenolic compounds and antioxidant activity of seed and skin extracts of red grape (*Vitis vinifera* and *Vitis labrusca*) pomace from Brazilian winemaking. *Food Res. Int.* **2011**, *44*, 897−901.
(38) Huang, D.; Ou, B.; Prior, R. L. The chemistry behind antioxidant capacity assays. *J. Agric. Food Chem.* **2005**, *53*, 1841−1856.
(39) Becker, E. M.; Nissen, L. R.; Skibsted, L. H. Antioxidant evaluation protocols: food quality or health effects. *Eur. Food Res. Technol.* **2004**, *219*, 561−571.
(40) Yu, J.; Ahmedna, M. Functional components of grape pomace: their composition, biological properties and potential applications. *Int. J. Food Sci. Technol.* **2013**, *48*, 221−237.
(41) Arranz, S.; Silván, J. M.; Saura-Calixto, F. Nonextractable polyphenols, usually ignored, are the major part of dietary polyphenols: a study on the Spanish diet. *Mol. Nutr. Food Res.* **2010**, *54*, 1646−1658.
(42) Serpen, A.; Gökmen, V.; Fogliano, V. Solvent effects on total antioxidant capacity of foods measured by direct QUENCHER procedure. *J. Food Compos. Anal.* **2012**, *26*, 52−57.
(43) Kammerer, D.; Claus, A.; Carle, R.; Schieber, A. Polyphenol screening of pomace from red and white grape varieties (*Vitis vinifera* L.) by HPLC-DAD-MS/MS. *J. Agric. Food Chem.* **2004**, *52*, 4360−4367.
(44) Hemingway, R. W. Structural variations in proanthocyanidins and their derivatives. In *Chemistry and Significance of Condensed Tannins*; Hemingway, R. W., Karchesy, J. J., Branham, S. J., Eds.; Plenum Press: New York, 1989; pp 83−107.
(45) Tang, H. R.; Covington, A. D.; Hancock, R. A. Structure-activity relationships in the hydrophobic interactions of polyphenols with cellulose and collagen. *Biopolymers* **2003**, *70*, 403−413.
(46) Oh, H. I.; Hoff, J. E.; Armstrong, G. S.; Haff, L. A. Hydrophobic interaction in tannin-protein complexes. *J. Agric. Food Chem.* **1980**, *28*, 394−398.

DOI: 10.1021/acs.jafc.5b01644
J. Agric. Food Chem. 2015, 63, 6922−6931

method relies on using Prodan, 6-propionyl-2-(dimethylamino)naphthalene), a fluorescent probe frequently used in probing the polarity of chemical and biological systems due to its high sensitivity to the medium (Scheme 1).[16−20] Indeed, Prodan's maximum emission varies from around 390 nm in alkanes to 530 nm in water.[20−22]

Scheme 1. Structure of Prodan, log K_{ow} = 3.48[a]

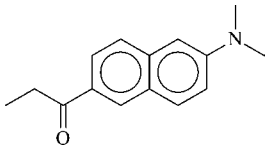

[a]Calculated using the software available http://www.molinspiration.com/cgi-bin/properties.

Although considerable research has been focused in recent years on using fluorescent probes for characterizing membrane polarity and transport through lipid membranes in biological media,[23−27] no study has reported the application of Prodan for probing the composition of leaf cuticle. Prodan is sensitive to both polarity and hydrogen bond donor ability of the solvent.[28,29] Prodan−solvent interactions were investigated using the Kamlet−Taft solvatochromic comparison method,[30] and it was shown that the emission band frequency can be correlated to the polarity/polarizability of the solvent π^*, to its hydrogen bond donor ability α, and to its hydrogen bond acceptor or electron pair donor ability to form a coordinated bond.[31] However, these data are available only for common solvents[32] and not for long-chain components of cuticles. On the basis of these correlations, we propose a simple model that relates the emission band frequency of Prodan to the chain-length constituents.

We report herein for the first time a new experimental protocol to study the polarity of plant cuticles by using Prodan and fluorescence spectroscopy. The limitations and advantages of the method are discussed, and perspectives for future applications are summarized.

EXPERIMENTAL PROCEDURES

Chemicals. Prodan (2-dimethylamino-6-propionylnaphthalene, >98%) was purchased from Sigma and used as received. Polyethylene PE-LD was obtained from SODIPRO, and wax paraffin (melting point = 53−57 °C, analysis given in the Supporting Information, Figure S1 and Table S1) and docosanol (>98%) were from Aldrich. The other chemicals and solvents were of the highest grade available.

Preparation of Solutions and Model Films Containing Prodan. Films of wax paraffin, mixtures of wax paraffin and *n*-docosanol, and mixtures of wax paraffin and were prepared as follows. Powder or pellets of the long-chain alkanes were mixed in the chosen proportions and heated until melting. Prodan was added to the melted mixture. Then the mixture was poured on aluminum foil to obtain a thin film after cooling.

Isolation of Cuticles. Leaves of *Zamioculcas zamiifolia* were refrigerated at −18 °C for several hours until frozen. Then, cuticles could be detached from the breakable leaves. Cuticles were first cleaned by gentle scraping of remaining flesh with a scalpel. Green peppers were refrigerated at −18 °C for several hours until frozen. Then, cuticles were detached with a scalpel and sonicated for 10 min to eliminate most of the epidermal remnants. Peels of white grapes were cleaned by gentle scraping of remaining flesh with a scalpel. Then cuticles were sonicated for 10 min to eliminate the epidermal remnants. All of the cuticles were finally washed with Milli-Q water.

Impregnating Films and Cuticles with Prodan. Two methods were used to impregnate polyethylene films and cuticles with Prodan: filtration and free diffusion. In the case of filtration, 5 mL of a solution of Prodan at 10^{-3} M in a mixture water/ethanol (50:50, v/v) was poured on the films or cuticles mounted on the sintered glass filter of a filter flask. Prodan solution was forced to diffuse through the films or cuticles using a vacuum. A light vacuum was maintained for 15 h, enabling the liquid to slowly diffuse. In the case of free diffusion, drops of the Prodan solution were deposited on the films or cuticles. The system was left to evolve freely for 24−48 h. Generally, the solvent was fully evaporated after 2 h. The film thickness was measured using a micrometer MI20.

Spectroscopic Analyses. UV−vis absorption spectra were recorded on an Agilent Technology Cary 300 UV−vis spectrophotometer equipped with an integration sphere model DRA-CA-301 Labsphere and the fluorescence spectra on a PerkinElmer LS55 fluorescence spectrophotometer. Prodan was excited at 340 nm. The emission spectra were corrected from the instrumental response using the files given by the manufacturer. Cuticles and polyethylene films were attached on a sample holder during the analysis. In all cases, the cuticles and polyethylene films were carefully washed with Milli-Q water prior to analysis to remove any Prodan crystals remaining at the surfaces. Rehydration of cuticles through this simple washing also greatly improved fluorescence detection by making them smooth. Fluorescence microscopy was performed on an Olympus CellR apparatus equipped with a xenon lamp using objective UPLANSApo 20x/0.75 and objective UPLANSApo 40x/1.3. The filter was 403 DAPI. In some figures, wavelengths of emission are expressed in wavenumbers (ν) according to ν (cm^{-1}) = $10^7/\lambda$ (nm).

Statistical Analyses. All of the spectra were recorded in duplicate. In the case of solid samples, at least three different positions in the sample holder were tested for each sample. Differences in the emission intensities might be observed as samples are not rigorously homogeneous, but emission maxima were very close. Uncertainty of measurement is ±1.5 nm due to the relatively flat maximum of Prodan.

RESULTS

Emission Characteristics of Prodan in Solution and Solids. Prodan shows an absorption band above 300 nm with a maximum located between 340 and 370 nm depending on the solvent.[20] Figure 1A presents the normalized emission spectra of Prodan in a variety of solvents and in films of several long-chain alkanes, wax paraffin, and docosanol, representative of long-chain alkanes contained in plant waxes. In *n*-heptane, the most hydrophobic solvent, the emission maximum is located at 390 nm. In water, the most hydrophilic solvent, two emission bands are found, one corresponding to dissolved Prodan (522 nm) and the other to solid particles of Prodan in suspension (433 nm). The other solvents exhibit emission maxima in the middle: acetonitrile gives an emission maximum at 452 nm and alcohols, 2-propanol and methanol, give maxima at 475 and 502 nm, respectively. Figure 1B also shows the influence of Prodan concentration on the emission in *n*-heptane. At 2×10^{-6} M, the emission maximum is located at 390 nm. Interestingly a shift is observed when the Prodan concentration is increased. A 2 nm shift is detectable at 5×10^{-5} M. It reaches 12 nm at 10^{-3} M. Although Prodan is freely soluble in this solvent, some interactions between Prodan molecules occur at high concentration, shifting the emission to the red. This is different from real molecules' aggregation observed in water or for crystals, giving an emission maximum around 430 nm.[33]

Interestingly, Prodan embedded into wax paraffin or in *n*-heptane solution shows the same emission maximum. The only difference between the two emission spectra is a small increase of the full width at half-maximum of 2 nm (6%). This finding shows that (1) Prodan is fully impregnated in the paraffin and

DOI: 10.1021/acs.jafc.5b02779
J. Agric. Food Chem. 2015, 63, 6932−6938

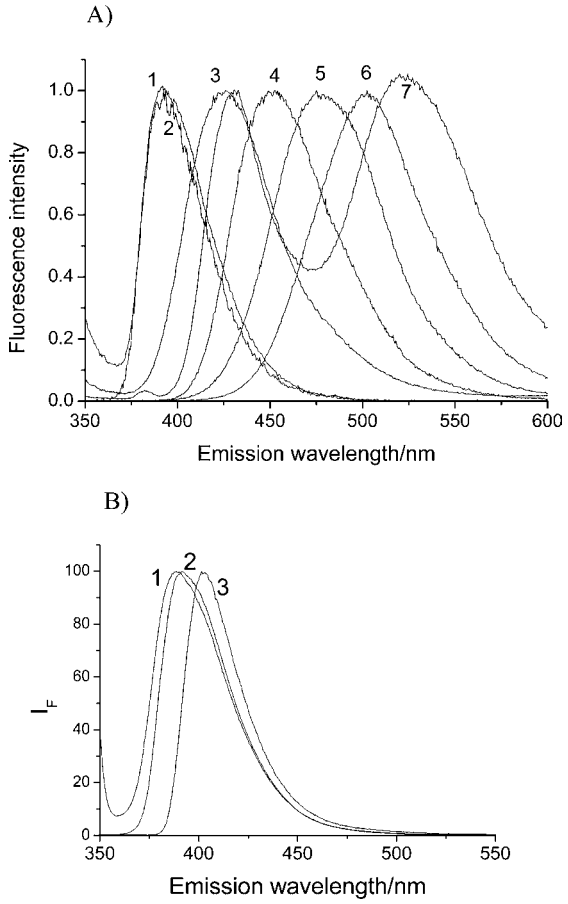

Figure 1. (A) Normalized emission spectra of Prodan in wax paraffin and in different solvents: 1, wax paraffin; 2, *n*-heptane; 3, docosanol; 4, acetonitrile; 5, 2-propanol; 6, methanol; 7, suspension in water. (B) Fluorescence of Prodan in heptane: 1, 2×10^{-6} M; 2, 5×10^{-5} M; 3, 10^{-3} M.

does not form aggregates that should give an emission around 430 nm, (2) the emission of Prodan is not influenced by the physical state of the medium, but by its chemical nature, and (3) a small band broadening occurs in solid state, which is attributed to interactions of Prodan with the solid environment.[10]

Relationship between the Emission Characteristics of Prodan and Properties of the Medium. To explain the experimental shift of emission maximum of Prodan embedded in different solid media, we attempted to establish a correlation between emission frequency and the properties of the heterogeneous media (docosanol and wax paraffin). One of the useful approaches for elucidating and quantifying different solute–solvent interactions is the Kamlet–Taft solvatochromic comparison method (KTSCM). According to the KTSCM, emission band frequency can be correlated with three parameters (Table 1), polarity–polarizability (π^*), hydrogen bond donor ability (α), and hydrogen bond acceptor ability (β), using eq 1:

$$\nu = \nu_0 + s\pi^* + a\alpha + b\beta \quad (1)$$

The *s*, *a*, and *b* coefficients measure the relative sensitivity of ν to the indicated solvent property. In recent work, the values of these coefficients have been determined by Moyano et al.,[31] on the basis of comparison with experimental data of Prodan absorption and emission in various common solvents.[32]

Table 1. KTSCM Parameters for Four Alcohol Solvents and for Docosanol[a]

solvent	π^*	α	β	$\nu/10^3$ (cm^{-1})
methanol	0.6	0.98	0.66	19.92
ethanol	0.54	0.86	0.75	20.35
n-butanol	0.47	0.84	0.84	20.73
n-octanol	0.4	0.77	0.81	21.19
docosanol	0.035	0.374	0.81	23.47 (23.62)

[a] π^* is polarity–polarizability, α represents the hydrogen bond donor ability, and β represents the hydrogen bond acceptor ability.

$$\nu^{em}_{obsvd}/10^{-3} = 25.2 \pm 0 - (2.6 \pm 0.2)\pi^* - (2.5 \pm 0.2)\alpha - (1.0 \pm 0.1)\beta$$

These results showed that the excited state of Prodan experiences a bathochromic shift with the π^*, α, and β parameters. Thus, the emission frequency shift of Prodan can be explained by the change in polarity and hydrogen-bonding interaction with the environment. To confirm if this equation applies also in our experimental conditions, we compared the measured values of ν for three alcohols (methanol, ethanol, octanol) with those reported by Moyano et al.[31] The results were almost identical, indicating that the model presented in eq 1 is valid. After validation of the model, we explored the applicability of the same model for solid media such as paraffin and docosanol. However, because the values of π^*, α, and β are not reported for these molecules, an estimation was made by plotting the variation of π^* and α as a function of the number of carbon atoms (n_C) for four primary alcohols (methanol, ethanol, butanol, octanol). As shown in Figure 2A, a linear relationship is found between π^* and n_C, which, if extrapolated to C_{22}, allows the estimation of the parameter π^* for docosanol. Similarly, we applied the same method in the case of α, which resulted in values of π^* and α of 0.035 and 0.374, respectively. On the basis of data reported by Moyano et al.,[31] it was found that β variation with the length of the carbon chain in a primary alcohol is very small and rangse between 0.81 and 0.84.[32] Therefore, we chose a value of 0.82 for docosanol.

Using these three KTSCM parameters, we estimated the predicted average value of ν for docosanol to be 23.37×10^3 cm^{-1} (minimum, 23.00×10^3; maximum, 23.73×10^3). Interestingly, this value is very close to that measured when Prodan is embedded in 100% docosanol ($\nu_{obs} = 23.47 \times 10^3$ cm^{-1}). This finding suggests that the KTSCM can be extrapolated to explain the shift in emission frequency of Prodan in heterogeneous solid media, as corroborated by the excellent linear correlation between n_C and the ν (Figure 2B). In addition, given that the emission frequency for wax paraffin was identical to that of heptane, we assumed that the KTSCM parameters of paraffin are identical to those of heptane, especially knowing that α and β are negligible and are thus not involved in the equation. Hence, we calculated the values of ν for various compositions of heptane/docosanol taking into account the relative contribution of each chemical, assuming that the overall value of ν of Prodan in the mixture is the sum of specific ν of each chemical ($\nu_{heptane}$, $\nu_{docosanol}$) multiplied by their relative mass fraction. Table 2 presents the calculated values of ν and compares them with those measured experimentally for various compositions heptane/docosanol (paraffin/docosanol). As shown in Figure 3, the predicted values of emission maximum of Prodan (ν_{calcd}) are in very good agreement with those measured (ν_{obsd}) when the percentage of

DOI: 10.1021/acs.jafc.5b02779
J. Agric. Food Chem. 2015, 63, 6932–6938

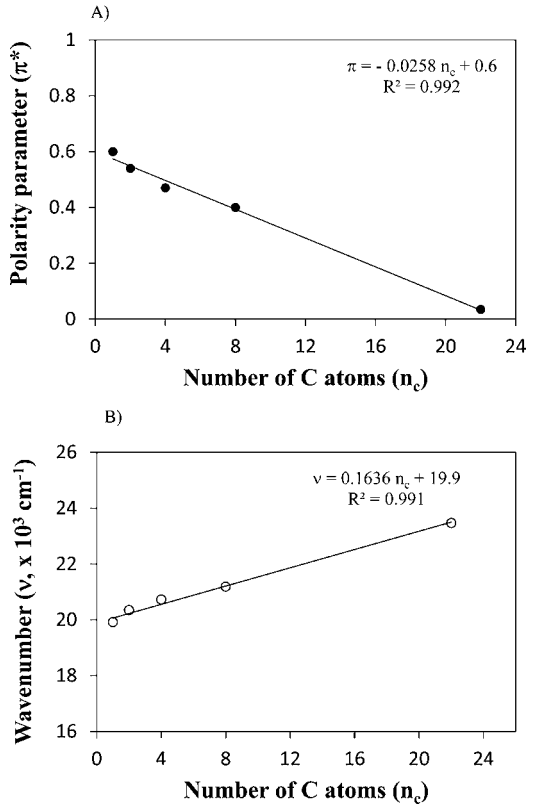

Figure 2. Correlations of the number of carbon atoms in an alcohol with the polarity factor, π^* (A), and with the emission wavenumber of Prodan (B).

Table 2. Estimates of KTSCM Parameters for Various Compositions of Paraffin/Docosanol and Comparison of Observed and Calculated Maximum Emission Wavelength of Prodan

solid medium	π^*	α	β	$\nu/10^3$ (cm^{-1})	λ_{calcd} (nm)	λ_{obsd} (nm)
paraffin (heptane)	−0.08	0	0	25.57	NA	391
90:10 paraffin/ docosanol	−0.069	0.037	0.081	25.20	397	401
80:20 paraffin/ docosanol	−0.057	0.075	0.162	25.00	400	406
70:30 paraffin/ docosanol	−0.046	0.112	0.243	24.80	403	406
50:50 parafin/ docosanol	−0.023	0.187	0.405	24.39	410	410
25:75 paraffin/ docosanol	0.006	0.280	0.608	23.88	419	419
100 docosanol	0.035	0.374	0.81	23.37	428	426

docosanol in the mixture is significant (>30%). On the other hand, for low docosanol percentage, the measured values of emission maximum are higher than those predicted by the KTCSM model, suggesting that the docosanol is not evenly distributed in the wax paraffin but forms microdomains attributed to its self-association. The formation of microdomains in the mixture of long-chain alkanes was already demonstrated by a thermodynamic analysis.[34] Despite this, these findings indicate clearly the feasibility of using the KTSCM commonly used for solvents to characterize the solvatochromic properties of heterogeneous solid media such as those reported in this work. Moreover, it appears that Prodan is sensitive enough to detect such a medium heterogeneity.

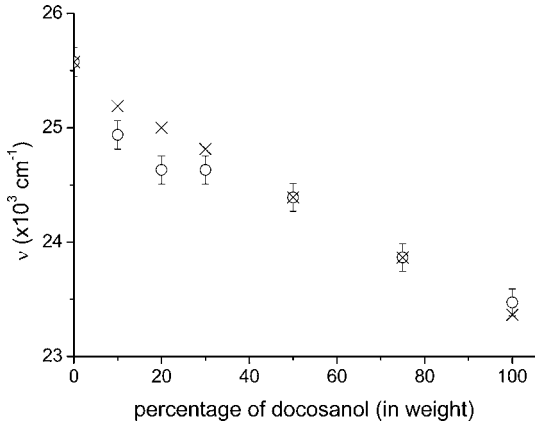

Figure 3. Shift of the maximum emission frequency of Prodan with the percentage in weight of docosanol in mixture with wax paraffin: (○) docosanol, experimental values (ν_{obsd}); (×) docosanol, calculated data (ν_{calcd}) (see text).

Impregnating Films with Prodan. In a second approach, we tested the possibility of impregnating films with Prodan. In the previous section, Prodan was introduced in films by hot mixing. This technique is not applicable in the case of real samples, especially when the objective is to work on untouched cuticles. Therefore, two methods of infiltration were tested: filtration of a Prodan solution in a water/ethanol, 50:50, mixture; and free diffusion of Prodan applied as 10 drops of 5 μL or as a single 200 μL drop. These experiments were carried out using a film of polyethylene that has the great advantage of being transparent. The two methods of infiltration give the same emission maximum at 405 ± 4 nm, indicating that in both cases the solvent has been fully eliminated and does not interfere in the result (Figure 4A). The intensity of fluorescence is, however, larger in the case of the single drop or infiltration under vacuum than in the case of small drops. To confirm that the method allows embedding Prodan in the polymer, we recorded the emission spectrum of Prodan deposited on a quartz plate in crystallized form. In this case, the emission maximum occurs at 427 nm (Figure 4A). Thus, the emission of Prodan in the polyethylene films is governed by the interaction of the single molecules with polymer chains and informs on the polarity of the medium. The maximum occurs at a wavelength slightly higher than in wax paraffin or *n*-heptane. This shift may be due to the presence of some polar additives in the polymer. Alternatively, it could be explained by a concentration effect. Indeed, the averaged concentration of Prodan is 2×10^{-3} M (see below), and in this case the maximum of emission is expected to be a little above 404 nm as experimentally observed. To clear up this question, it would be necessary to work on a polymer free of additives.

Emission of Prodan in Cuticles. Three samples were chosen to validate the analytical method: the leaf of *Zamioculcas zamiifolia*, a succulent plant, and the skins of white grape berries and green pepper. In all cases, the extracted cuticles were transparent enough for enabling Prodan to absorb light and thus generate measurable fluorescence. Figure 4A depicts emission spectra obtained for model supports to illustrate the broad range of emission wavelength. Films of wax paraffin and polyethylene show thin bands centered around 400 nm indicating that the medium is homogeneous and that there is likely one type of interaction. Emission of Prodan deposited on a thin layer plate of chromatography made of C_{18} was also

DOI: 10.1021/acs.jafc.5b02779
J. Agric. Food Chem. 2015, 63, 6932−6938

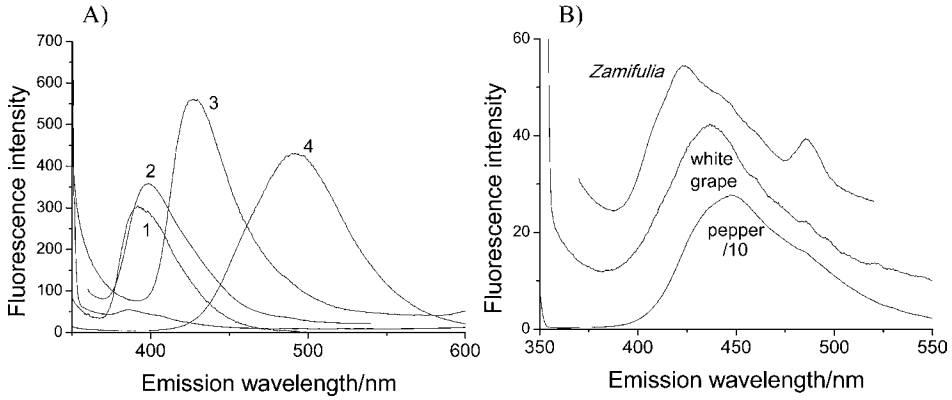

Figure 4. (A) Emission spectra of Prodan in model support: (1) film of wax paraffin; (2) film of polyethylene impregnated with a solution of Prodan 10^{-3} M in water/ethanol, 50:50 v/v added as a drop of 200 μL; (3) Prodan deposited on a quartz plate; (4) plate of thin layer chromatography C_{18} on which Prodan was deposited in heptane. (B) Emission spectra of Prodan in cuticles: *Zamioculcas zamiifolia*; white grape; green pepper.

measured. The emission maximum is at 491 nm, indicating that Prodan is located in the vicinity of free silanol groups. The emission spectra measured in the cuticles are shown in Figure 4B. The following characteristics appear:

- The main emission maximum varies from 423 nm for *Z. zamiifolia* to 436 nm for the white grape and to 448 nm for the green pepper.
- The results of the preliminary experiments strongly support that Prodan is embedded in the cuticles, and therefore these emissions are related to the chemical characteristics of the different cuticles.
- The emission intensities vary with the cuticle in the order green pepper > white grape ≫ *Z. zamiifolia*. They are expected to depend on several parameters, in particular the capacity of Prodan to enter the cuticle and the cuticle transparency between 340 and 400 nm, the wavelength range where Prodan absorbs. Transparency of cuticles depends on the cuticle constituents and especially on the presence of absorbing secondary metabolites (polyphenols or carotenoids for instance) and can vary drastically from one species to another.[35]
- Emission bands are broad compared to those measured in the model supports, and detailed examination of the spectra reveals the presence of shoulders and broad long-wavelength emissions on both sides of the maximum. For *Z. zamiifolia*, shoulders are observed at 408, 444, and around 460 nm. For white grape, there is a small shoulder at 426 nm and a broad emission extending up to 525 nm. For green pepper, one can see a clear shoulder at 433 nm and the same broad emission at long wavelength as for white grape. These fingerprints indicate that Prodan is located in zones of different polarity. In a first approach, these data can be analyzed using the relationship established between the emission characteristics of Prodan and the number of carbon atoms in primary alcohols constituting the solid medium of Figure 3B. For *Z. zamiifolia*, the maximum at 423 nm (23640 cm^{-1}) would correspond to primary alcohols in C_{23}; for the white grape, the maximum at 436 nm would correspond to primary alcohols in C_{19}; and for the green pepper, the maximum at 448 nm would correspond to primary alcohols in C_{15}.

In a second approach, we examined whether these data match the chemical composition of cuticules (wax and cutin) as reported in the literature. In the case of grape berries cuticle, alcohols (n-C_{20}−n-C_{34}) are reported to account for 40−67% of the soft wax fraction with predominating C_{26}.[34] Embedded in such a medium, Prodan should emit around 414 nm. Even though such an emission seems present in the blue part of the spectrum of Figure 4B, the maximum is significantly red-shifted, indicating that Prodan is mainly located in a more polar zone, probably the cutin. Pepper fruit waxes contain many components, among which long-chain alkanes C_{29} and C_{31} and fatty acids C_{24} and C_{26} are the most abundant, representing around 35 and 25%, respectively, of the constituents on average.[35] The former would give a maximum of emission around 390 nm and the latter around 420−425 nm if we refer to methyl tetracosanoate data (see Figure S2). Both are far from the observed maximum, indicating that Prodan is not located in the pepper fruit waxes unless polar minor constituents shift significantly the emission maximum. The other compartment in which Prodan can be inserted is the cutin. The pepper cutin is a mixture of C_{16} and C_{18} monomers and their oxygenated derivatives, dominated by 10,16-dihydroxyhexadecanoic acid that represents >50% of the total monomers.[35] These constituents are expected to give a polarity higher than corresponding primary C_{16} and C_{18} alcohols. This is not far from what we found.

This analysis points out two conclusions. First, it appears difficult to rationalize the data of Figure 4B using the reported cuticle composition because of the presence of a great variety of constituents in the cuticles, the possible great effect of some minor compounds on polarity, and the possible partitioning of constituents creating specific zones. The emission spectra of Prodan in these complex media bring, however, important information on the average polarities, and Prodan can be considered as a polarity indicator. Second, Prodan is probably mainly embedded in the cutin. The presence of Prodan in the cutin seems logical, first, because this inner compartment is larger than the outer one consisting of waxes[36] and, second, because the solubility of organic compounds can be 10-fold higher in cutin than in cuticular waxes.[36]

Experimental Proofs of the Diffusion of Prodan into the Cuticles. The amount of Prodan included in the polyethylene film was directly obtained by measuring the film transmittance at 340 nm by taking into account that the thickness is 50 μm and the extinction coefficient of Prodan is equal to 2.3×10^4 L mol^{-1} cm^{-1} in n-heptane at 340 nm. Accordingly, a film measuring an area of 6 cm^2 contained 7.1

DOI: 10.1021/acs.jafc.5b02779
J. Agric. Food Chem. 2015, 63, 6932−6938

μg. Prodan was extracted from the film by sonication for 30 min in 1 mL of ethanol. Using fluorescence, we could estimate that 7.5 μg of Prodan had been extracted, in full agreement with the result obtained by UV absorption measurements.

For the cuticles that are much less transparent, the amount of Prodan was evaluated by extraction through sonication in ethanol. In the case of *Z. zamiifolia* cuticle, we found that the film of 6 cm^2 and 19 μm thickness contained 2.4 μg. In the case of green pepper, we found 40.2 μg for a thickness of 59 μm. Results for polyethylene film and *Z. zamiifolia* cuticle are thus similar if we take into account that the polyethylene film is 2.6-fold thicker than the *Z. zamiifolia* cuticle. They both absorbed 16.3% of the deposited Prodan (45.4 μg). Green pepper took much more, 88% of the deposited Prodan being embedded in the green pepper.

To gain insights into the surface distribution of Prodan in cuticles and polyethylene films, images of Prodan fluorescence were recorded using a fluorescence microscopy. As shown in Figure 5, Prodan is clearly embedded into the polyethylene film, whereas small microcrystals remain on the surface, which might explain the unexpected emission maximum for Prodan in a nonpolar medium such as polyethylene film. When applied on green pepper cuticle, it appears that Prodan quickly diffused into cuticle and reached the residual epidermal cells, confirming that the emission spectrum of Prodan is a result of interactions within the inner cuticle. It remains, however, difficult to identify the exact type of interactions and the chemical nature of the environment that influences the fluorescence emission of Prodan.

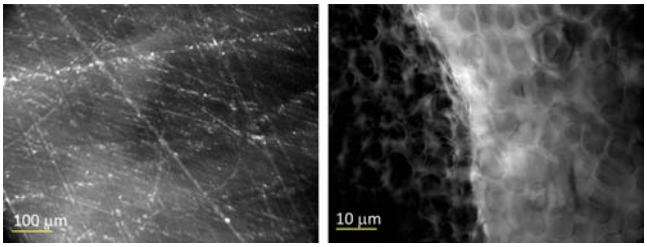

Figure 5. Fluorescence images of Prodan impregnated into polyethylene film (left panel) and into green pepper cuticle (right panel). Prodan is mainly dissolved in polyethylene, even though small microcrystals are observed at the surface. In green pepper cuticle, Prodan diffuses until it reaches the residual epidermal cells, so that emission is a result of interactions within the inner cuticle.

This case study shows that it is possible to impregnate Prodan into polymer (polyethylene) and extracted cuticles in sufficient amount to detect its fluorescence. The emission spectra obtained with the three cuticles are significantly different, confirming that Prodan is sensitive enough in these conditions and can be used as an indicator of the cuticles' polarity. The proposed method has the great advantage of being straightforward because the fluorescent probe needs to be simply deposited on the cuticle and the analysis is performed directly on the cuticle without further manipulations. One of the limits of the method is related to the optical properties of cuticles. The use of other possible fluorescent probes absorbing above 400 nm could help to overcome this issue. The method proposed could be extended to investigate changes in the chemical environment of surfaces due to reactions and/or aging. Future work will explore the potential application of Prodan and other alternative fluorescent probes to monitor the diffusion and reactivity of polar pesticides through cuticles.

■ ASSOCIATED CONTENT

Supporting Information

The Supporting Information is available free of charge on the ACS Publications website at DOI: 10.1021/acs.jafc.5b02779.

GC analysis of the paraffinic wax and shift of the maximum emission frequency of Prodan with the percentage of methyl tetracosanoate (in weight) in mixture with wax paraffin (PDF)

■ AUTHOR INFORMATION

Corresponding Author

*(C.R.) E-mail: claire.richard@univ-bpclermont.fr. Phone: +33 (0)4 73 40 71 42.

Notes

The authors declare no competing financial interest.

■ ACKNOWLEDGMENTS

We acknowledge the Confocal Microscopy Facility ICCF (Imagerie Confocale Clermont-Ferrand) at Clermont University (France).

■ REFERENCES

(1) Klymchenko, A. S.; Mely, Y.; Demchenko, A. P.; Duportail, G. Simultaneous probing of hydration and polarity of lipid bilayers with 3-hydroxyflavone fluorescent dyes. *Biochim. Biophys. Acta, Biomembr.* **2004**, *1665*, 6−19.

(2) Vendra, V. K.; Wu, L.; Krishnan, S. Polymer thin films for biomedical applications. In *Nanomaterials for the Life Sciences. Vol. 5: Nanostructured Thin Films and Surfaces*; Wiley: Weinheim, Germany, 2010.

(3) Knoche, M.; Bukovac, M. J. Finite dose diffusion studies: III. Effects of temperature, humidity and deposit manipulation on NAA penetration through isolated tomato fruit cuticles. *Pest Manage. Sci.* **2001**, *57*, 737−742.

(4) Fujisawa, T.; Ichise, K.; Fukushima, M.; Katagi, T.; Takimoto, Y. Improved uptake models of nonionized pesticides to foliage and seed of crops. *J. Agric. Food Chem.* **2002**, *50*, 532−537.

(5) Muller, C.; Riederer, M. Plant surface properties in chemical ecology. *J. Chem. Ecol.* **2005**, *31*, 2621−2651.

(6) Biology of the plant cuticle. In *Annual Plant Reviews. Vol. 23: Biology of the Plant Cuticle*; Riederer, M., Ed.; Wiley: Weinheim, Germany, 2006.

(7) Baur, P.; Marzouk, H.; Schonherr, J.; Grayson, B. T. Partition coefficients of active ingredients between plant cuticle and adjuvants as related to rates of foliar uptake. *J. Agric. Food Chem.* **1997**, *45*, 3659−3665.

(8) Petracek, P. D.; Fader, R. G.; Knoche, M.; Bukovac, M. J. Surfactant-enhanced penetration of benzyladenine through isolated tomato fruit cuticular membranes. *J. Agric. Food Chem.* **1998**, *46*, 2346−2352.

(9) Trivella, A. S.; Monadjemi, S.; Worrall, D. R.; Kirkpatrick, I.; Arzoumanian, E.; Richard, C. Perinaphthenone phototransformation in a model of leaf epicuticular waxes. *J. Photochem. Photobiol., B* **2014**, *130*, 93−101.

(10) Rung, B.; Schwack, W. Aminoparathion: a highly reactive metabolite of parathion. 1. Reactions with polyphenols and polyphenol oxidase. *J. Agric. Food Chem.* **2005**, *53*, 9140−9145.

(11) Li, Y. G.; Chen, B. L.; Chen, Z. M.; Zhu, L. Z. Surfactant effects on the affinity of plant cuticles with organic pollutants. *J. Agric. Food Chem.* **2009**, *57*, 3681−3688.

DOI: 10.1021/acs.jafc.5b02779
J. Agric. Food Chem. 2015, 63, 6932−6938

(12) Li, Y. G.; Chen, B. L. Phenanthrene sorption by fruit cuticles and potato periderm with different compositional characteristics. *J. Agric. Food Chem.* **2009**, *57*, 637−644.
(13) Liu, Z. Confocal laser scanning microscopy − an attractive tool for studying the uptake of xenobiotics into plant foliage. *J. Microsc.* **2004**, *213*, 87−93.
(14) Heini, J.; Ayala, V. R.; Walker, F.; Mainx, H. G.; Gerhards, R. Uptake studies on a fluorescein-labelled seed oil adjuvant in *Abutilon theophrasti*, *Sinapis arvensis* and *Beta vulgaris*. *Gesunde Pflanz.* **2012**, *64*, 167−174.
(15) Buda, G. J.; Isaacson, T.; Matas, A. J.; Paolillo, D. J.; Rose, J. K. C. Three-dimensional imaging of plant cuticle architecture using confocal scanning laser microscopy. *Plant J.* **2009**, *60*, 378−385.
(16) Cwiklik, L.; Aquino, A. J.; Vazdar, M.; Jurkiewicz, P.; Pittner, J.; Hof, M.; Lischka, H. Absorption and fluorescence of PRODAN in phospholipid bilayers: a combined quantum mechanics and classical molecular dynamics study. *J. Phys. Chem. A* **2011**, *115*, 11428−11437.
(17) Krasnowska, E. K.; Gratton, E.; Parasassi, T. Prodan as a membrane surface fluorescence probe: partitioning between water and phospholipid phases. *Biophys. J.* **1998**, *74*, 1984−1993.
(18) Parasassi, T.; Krasnowska, E.; Bagatolli, L.; Gratton, E. Laurdan and Prodan as polarity-sensitive fluorescent membrane probes. *J. Fluoresc.* **1998**, *8*, 365−373.
(19) Samanta, A.; Fessenden, R. W. Excited state dipole moment of PRODAN as determined from transient dielectric loss measurements. *J. Phys. Chem. A* **2000**, *104*, 8972−8975.
(20) Vequi-Suplicy, C. C.; Coutinho, K.; Teresa Lamy, M. Optical characterization of Prodan aggregates in water medium. *Phys. Chem. Chem. Phys.* **2013**, *15*, 11800−11807.
(21) Yoon, A. H.; Whitworth, L. C.; Wagner, J. D.; Abelt, C. J. 2,5-PRODAN derivatives as highly sensitive sensors of low solvent acidity. *Molecules* **2014**, *19*, 6415−6427.
(22) Mennucci, B.; Caricato, M.; Ingrosso, F.; Cappelli, C.; Cammi, R.; Tomasi, J.; Scalmani, G.; Frisch, M. J. How the environment controls absorption and fluorescence spectra of PRODAN: a quantum-mechanical study in homogeneous and heterogeneous media. *J. Phys. Chem. B* **2008**, *112*, 414−423.
(23) Flora, K. K.; Brennan, J. D. Characterization of the microenvironments of PRODAN entrapped in tetraethyl orthosilicate derived glasses. *J. Phys. Chem. B* **2001**, *105*, 12003−12010.
(24) Goto, M.; Matsui, T.; Tamai, N.; Matsuki, H.; Kaneshina, S. Prodan fluorescence detects the bilayer packing of asymmetric phospholipids. *Colloids Surf., B* **2011**, *84*, 55−62.
(25) Moyano, F.; Biasutti, M. A.; Silber, J. J.; Correa, N. M. New insights on the behavior of PRODAN in homogeneous media and in large unilamellar vesicles. *J. Phys. Chem. B* **2006**, *110*, 11838−11846.
(26) Nitschke, W. K.; Vequi-Suplicy, C. C.; Coutinho, K.; Stassen, H. Molecular dynamics investigations of PRODAN in a DLPC bilayer. *J. Phys. Chem. B* **2012**, *116*, 2713−2721.
(27) Sachl, R.; Stepanek, M.; Prochazka, K.; Humpolickova, J.; Hof, M. Fluorescence study of the solvation of fluorescent probes prodan and laurdan in poly(ε-caprolactone)-*block*-poly(ethylene oxide) vesicles in aqueous solutions with tetrahydrofurane. *Langmuir* **2008**, *24*, 288−295.
(28) Cerezo, F. M.; Rocafort, S. C.; Sierra, P. S.; Garcia-Blanco, F.; Oliva, C. D.; Sierra, J. C. Photophysical study of the probes acrylodan (1-[6-(dimethylamino)naphthaten-2-yl]prop-2-en-1-one), ANS (8-anilinonaphthalene-1-sulfonate) and prodan (1-[6-(dimethylamino)-naphthalen-2-yl]propan-1-one) in aqueous mixtures of various alcohols. *Helv. Chim. Acta* **2001**, *84*, 3306−3312.
(29) Balter, A.; Nowak, W.; Pawelkiewicz, W.; Kowalczyk, A. Some remarks on the interpretation of the spectral properties of Prodan. *Chem. Phys. Lett.* **1988**, *143*, 565−570.
(30) Kamlet, M. J.; Abboud, J. L. M.; Abraham, M. H.; Taft, R. W. Linear solvation energy relationships. 23. A comprehensive collection of the solvatochromic parameters, pi-star, alpha and beta, and some methods for simplifying the generalized solvatochromic equation. *J. Org. Chem.* **1983**, *48*, 2877−2887.
(31) Moyano, F.; Biasutti, M. A.; Silber, J. J.; Correa, N. M. New insights on the behavior of PRODAN in homogeneous media and in large unilamellar vesicles. *J. Phys. Chem. B* **2006**, *110*, 11838−11846.
(32) Marcus, Y. The properties of organic liquids that are relevant to their use as solvating solvents. *Chem. Soc. Rev.* **1993**, *22*, 409−416.
(33) Flora, K. K.; Brennan, J. D. Characterization of the microenvironments of PRODAN entrapped in tetraethyl orthosilicate derived glasses. *J. Phys. Chem. B* **2001**, *105*, 12003−12010.
(34) Casado, C. G.; Heredia, A. Self-association of plant wax components: a thermodynamic analysis. *Biomacromolecules* **2001**, *2*, 407−409.
(35) Solovchenko, A.; Merzlyak, M. Optical properties and contribution of cuticle to UV protection in plants: experiments with apple fruit. *Photochem. Photobiol. Sci.* **2003**, *2*, 861−866.
(36) Riederer, M.; Friedmann, A. Transport of lipophilic non-electrolytes across the cuticle. In *Annual Plant Reviews. Vol. 23: Biology of the Plant Cuticle*; Blackwell Publishing: Oxford, UK, 2007; pp 250−279.

DOI: 10.1021/acs.jafc.5b02779
J. Agric. Food Chem. 2015, 63, 6932−6938

Table 1. ^{1}H NMR and ^{13}C NMR Spectroscopic Data for 3−6

	3			4			5			6		
	δ ^{13}C	δ ^{1}H	J (Hz)	δ ^{13}C	δ ^{1}H	J (Hz)	δ ^{13}C	δ ^{1}H	J (Hz)	δ ^{13}C	δ ^{1}H	J (Hz)
quinic acid moiety												
1	73.2			73.6			73.1			NM[a]		
2_a	35.4	1.95 dd	13.8, 3.9	37.3	2.06 bd	13, 3	36.0	2.02 dd	13.5, 4	35.6	1.96 dd	13.5, 3.5
2_b		2.05 dd	13.8, 3.6		2.25 m*[b]			2.37 dd	13.5, 3.9		2.39 dd	13.5, 3
3	71.5	5.27 dt	6.7, 3.9, 3.6	68.2	5.49 m		69.2	5.58 ddd	4, 3.9, 3.5	68.6	5.54 ddd	3.5, 3, 3
4	72.1	3.55 dd	7.5, 3.6	73.9	5.07 dd	7.8, 2.6	72.0	5.32 dd	9, 3.5	70.5	5.28 dd	8, 3
5	66.9	3.92 td	7.5, 7.5, 4	66.4	4.26 m		68.3	5.72 td	9, 9, 3.5	68.9	5.72 ddd	8, 8, 3
6_{ax}	39.9	1.81 dd	13.5, 7.5	37.6	1.91 dd	13.5, 7	38.0	2.02−2.17 m		37.3	2.15 dd	12.5, 8
6_{eq}		1.92 dd	13.5, 4		2.22 m*			2.02−2.17 m			2.32 dd	12.5, 3
7 (COOH)	176.3			174.7			176.2			175.2		
galloyl moieties												
1′	120.6			119.1			119.8			120.0		
2′	105.3	7.12 d	1.5	104.8	6.97 d	1.7	109.1	7.02 s		110.8	7.20 bs	
3′	147.7			147.8			145.5			147.6		
4′	139.1			139.5			138.6			139.4		
5′	145.1			145.2			145.5			145.3		
6′	110.1	7.15 d	1.5	105.0	7.03 d	1.7	109.1	7.02 s		105.4	7.01 d	1.8
7′(OCH_3)	56.0	3.79 s		55.8	3.77 s					55.6	3.7 s	
COO−′	165.4			164.8			165.6			165.3		
1″				119.3			119.0			118.8		
2″				110.6	7.04 d	1.7	104.8	6.85 d	1.8	108.6	6.8 bs	
3″				147.7			145.3			145.5		
4″				139.5			139.7			138.8		
5″				145.2			147.7			145.5		
6″				110.8	7.13 d	1.7	110.7	6.97 d	1.8	108.6	6.8 bs	
7″ (OCH_3)				55.8	3.75 s		55.8	3.77 s				
COO−″				165.3			165.0			165.2		
1‴							119.2			119.0		
2‴							108.8	6.88 s		110.4	7.20 bs	
3‴							145.6			147.7		
4‴							138.8			139.6		
5‴							108.8	6.88 s		145.3		
6‴							145.6	6.88 s		104.9	6.97 d	1.8
7‴ (OCH_3)										55.8	3.78 s	
COO−‴							165.2			164.9		

[a]NM, not measured. [b]An asterisk (*) indicates overlapped signals.

and **5** on a Bruker-Avance DRX800 spectrometer operating at frequency of 200 MHz (^{13}C NMR). Samples were prepared in Aldrich deuterated dimethyl sulfoxide (DMSO-d_6). The mass spectrometry analyses were conducted in two different spectrometers, both equipped with electrospray ionization source (ESI) in negative mode over a mass range of m/z 50−1500. Mass spectra obtained for compound **3** were recorded on a Bruker Daltonics time-of-flight mass spectrometer (a) and those for compounds **4**, **5**, and **6** on a Thermo Scientific LTQ-FT-Ultra mass spectrometer (b). The following instrument settings were used: (a) nebulizer gas nitrogen (0.4 bar), dry gas nitrogen (4 L/min), 220 °C, capillary voltage of 4500 V, end plate offset −500 V, sample (0.5 g mL^{-1}) dissolved in MeOH/H_2O 1:1 and introduced in the electrospray source with a direct infusion pump operating at a flow of 5 μL/min; (b) nebulizer gas nitrogen (0.4 bar), dry gas nitrogen (9 L/min), 270 °C, capillary voltage of 47.96 V, source voltage of 40 V, samples dissolved in MeOH/H_2O 8:2 and introduced in the electrospray source with a direct infusion pump operating at a flow of 5 μL/min. Melting points were performed using Fisatom device (model 431, Brazil, series 1237344).

Plant Material. Leaves of *C. langsdorffii* were collected in the Campus of the University of São Paulo, Ribeirão Preto, Brazil. The plant material was identified by Dr. Milton Gropo from the herbarium of the Faculdade de Filosofia, Ciências e Letras, Ribeirão Preto, Brazil, where a voucher specimen (SPFR 10120) was deposited.

Extraction and Isolation. Dried leaves of *C. langsdorffii* (200 g) were ground and exhaustively extracted with ethanol/H_2O (7:3) (1.2 L, three times) by maceration at room temperature. The lyophilized extract (50 g) was suspended in MeOH/H_2O (9:1, 300 mL) and partitioned first with hexanes (300 mL, three times). The MeOH/H_2O phase was evaporated until elimination of the methanol. The remaining fraction was added of water and successively partitioned with dichloromethane (CH_2Cl_2, 300 mL, three times) and ethyl acetate (EtOAc, 300 mL, three times). After evaporation of the solvents, the hexanes-soluble fraction (9.7 g), CH_2Cl_2-solube fraction (2.6 g), EtOAc-soluble fraction (13.8 g), and the H_2O-soluble fraction (21 g) were obtained. The EtOAc-soluble fraction (3 g) was subjected to HSCCC using interconnected 2 mm diameter columns C (102 mL) and D (105 mL). Solvent system was optimized on the basis of the partition coefficients K_d of compounds **1** and **2** after dissolution of the EtOAc-soluble fraction in the upper and lower phases. Values of (K_d) were assessed by the relation of their peak areas from the analytical chromatograms of both upper and lower solutions. The final solvent system consisted of hexanes/*n*-BuOH (1:1) (upper phase) and MeOH/H_2O (0.4:1) (lower phase), which exhibited a settling time of 25 s, and optimized K_d values for **1** (K_d = 0.6) and **2** (K_d = 0.95). The coil was filled with the stationary phase (lower phase) in a tail-to-head mode, and after a starting rotation program, the mobile phase was pumped into the coil until equilibrium, that is, when only mobile

DOI: 10.1021/acs.jafc.5b01588
J. Agric. Food Chem. 2015, 63, 6939−6945

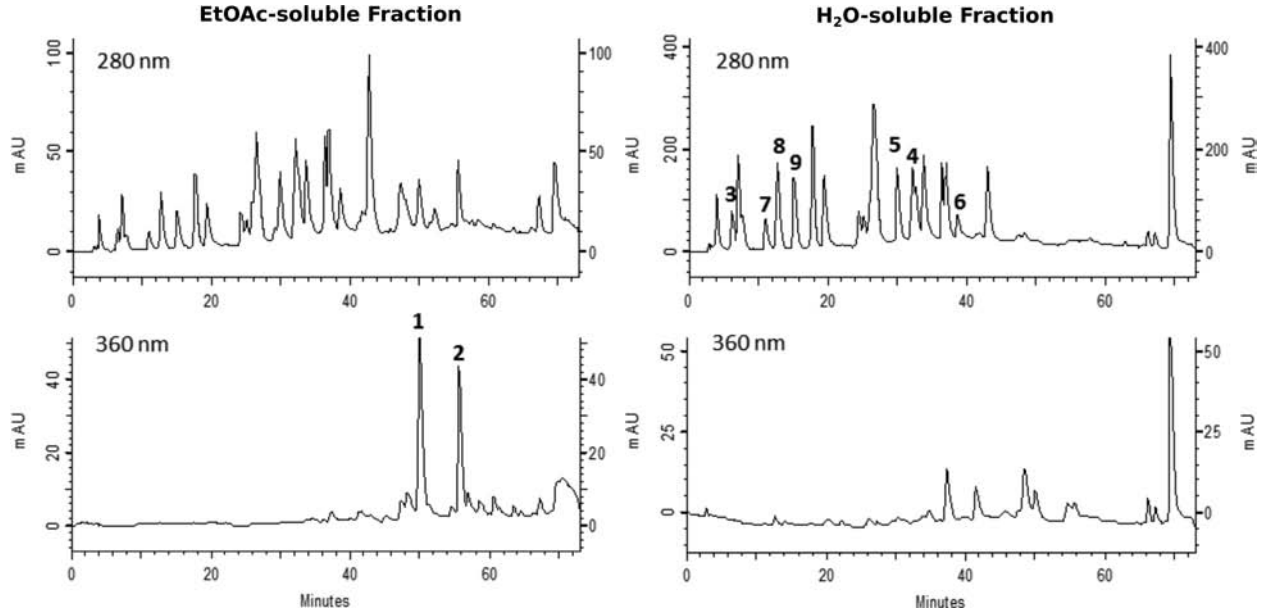

Figure 1. Chromatographic profile of the EtOAc- and H_2O-soluble fractions of the leaf hydroalcoholic extract of *C. langsdorffii* acquired by HPLC-DAD detected at the typical relative absorption maxima of flavonols (360 nm) and galloyquinic acids (280 nm). Peaks: 1, quercetrin; 2, afzelin; 3–9, methoxy-galloylquinic acid derivatives.

phase came out from the coil. Nearly 85% retention of the stationary phase inside the coils was obtained before sample injection. Fractions were combined after TLC analysis furnishing F8–14 (320 mg), F15–23 (215 mg), F24–26 (65 mg), F27–33 (93 mg), F34–41 (267 mg), and F42–51 (570 mg). Fractions F15–23 (90% of **1**) and F34–41 (90% of **2**) were subjected to preparative HPLC, performed with an elution program of 35–80% MeOH/H_2O in 20 min to yield **1** (108 mg) and **2** (94 mg). The H_2O-soluble fraction (3.5 g) was subjected to counter-current chromatography with an optimized solvent system consisting of *n*-BuOH/EtOAc/H_2O (0.1% formic acid) (1:1:1) and a settling time of 15 s, suitable for the distribution of four compounds in both upper and lower phases. The K_d values obtained for those compounds were 0.37, 0.46, 0.60, and 1.05. The coil was filled with the stationary phase (lower phase) in a tail-to-head mode. Retention of the stationary phase before sample injection of 84% was obtained. Fractionation furnished the subfractions F15–18 (134 mg), F21–25 (132 mg), F26–29 (75 mg), and F30–38, which were later purified by preparative HPLC to yield compounds **3**, **7**, **8**, and **9**. After purification and storage, three of them underwent chemical degradation. Therefore, only compound **3** (31 mg), obtained from F15–18, was fully elucidated. The H_2O-soluble fraction (3.5 g) was subjected to chromatography on a Sephadex LH-20 column, eluted with MeOH to afford several subfractions. Those subfractions were purified in preparative HPLC to yield **4** (28 mg), **5** (33 mg), and **6** (25 mg). The mobile phase optimized for the PREP-HPLC consisted of water (A) (0.01% TFA) and MeOH (B) in gradient condition as follows: 5–15% of B (20 min), 15–34% of B (20–40 min), and 34–80% of B (40–85 min); flow rate = 9 mL/min. Compounds **4**–**6** had their chemical structures elucidated.

Data for 3-*O*-(3-*O*-Methyl-galloyl)quinic Acid (3). (1*S*,3*R*,4*S*,5*R*)-1,4,5-Hydroxy-3-((3-methoxy-4,5-dihydroxybenzoyl)-oxy)cyclohexane carboxylic acid *rel*: white amorphous solid; $[\alpha]^{22}_{D}$ −36.5 (*c* 0.1, methanol); melting point 115–120 °C; ESI-qTOF-MS *m*/*z* 357.0904 [M − H]$^-$, calculated for $C_{15}H_{18}O_{10}$ 358.0900, 191 [M − 166(MeG) − H]$^-$; UV λ_{max} 220 and 275 nm (MeOH/H_2O 0.01% TFA); ^{1}H NMR (DMSO-d_6, 500 MHz) and ^{13}C NMR (DMSO-d_6, 200 MHz), see Table 1.

Data for 3,4-Di-*O*-(3-*O*-methyl-galloyl)quinic Acid (4). (1*S*,3*R*,4*S*,5*R*)-1,5-Hydroxy-3,4-bis((3-methoxy-4,5-dihydroxybenzoyl)oxy)cyclohexane carboxylic acid *rel*: light brown amorphous solid; $[\alpha]^{22}_{D}$ −38.7 (*c* 0.02, methanol); melting point 83–84 °C; ESI-LQT-FTMS *m*/*z* 523.1093 [M − H]$^-$, calculated for $C_{23}H_{24}O_{14}$ 524.1166; 357 [M − 166(MeG) − H]$^-$, 339 [M − 184(MeG acid) − H]$^-$; UV λ_{max} 219 and 278 nm (MeOH/H_2O 0.01% TFA); ^{1}H NMR (DMSO-d_6, 500 MHz) and ^{13}C NMR (DMSO-d_6, 125 MHz), see Table 1.

Data for 3,5-Di-*O*-(galloyl)- 4-*O*-(3-*O*-methyl-galloyl)quinic Acid (5). (1*S*,3*R*,4*S*,5*R*)-1-Hydroxy-4-(3-methoxy-4,5-dihydroxybenzoyl)oxy)-3,5-bis((3,4,5-trihydroxybenzoyl)oxy)-cyclohexane carboxylic acid *rel*: dark yellow amorphous solid; $[\alpha]^{24}_{D}$ −136.6 (*c* 0.08, methanol); melting point 90–94 °C; ESI-LQT-FTMS *m*/*z* 661.1046 [M − H]$^-$, calculated for $C_{29}H_{26}O_{18}$ 662.1119, 509 [M − 152(G) − H]$^-$, 491 [M − 170(G acid) − H]$^-$, 357 [M − 152(G) − 152(G) − H]$^-$; UV λ_{max} 220 and 275 nm (MeOH/H_2O 0.01% TFA); ^{1}H NMR (DMSO-d_6, 500 MHz) and ^{13}C NMR (DMSO-d_6, 200 MHz), see Table 1.

Data for 3,5-Di-*O*-(3-*O*-methyl-galloyl)-4-*O*-(galloyl)quinic Acid (6). (1*S*,3*R*,4*S*,5*R*)-1-Hydroxy-4-(3,4,5-trihydroxybenzoyl)oxy)-3,5-bis((3-methoxy-4,5-dihydroxybenzoyl)oxy)cyclohexane carboxylic acid *rel*: dark yellow amorphous solid; $[\alpha]^{23}_{D}$ −202.7 (*c* 0.12, methanol); melting point 100–107 °C; ESI-LQT-FTMS MS *m*/*z* 675.1205 [M − H]$^-$, calculated for $C_{30}H_{28}O_{18}$ 676.1275; 523 [M − 152(G) − H]$^-$, 509 [M − 166(MeG) − H]$^-$, 491 [M − 184(MeG acid) − H]$^-$, 339 [M − 152 − 184 − H]$^-$/[M − 166 − 170 − H]$^-$; UV λ_{max} 217 and 275 nm (MeOH/H_2O 0.01% TFA); ^{1}H NMR (DMSO-d_6, 500 MHz) and ^{13}C NMR (DMSO-d_6, 125 MHz), see Table 1.

RESULTS AND DISCUSSION

C. langsdorffii leaf hydroalcoholic extract was dissolved in MeOH/H_2O and partitioned with hexanes, dichloromethane, and ethyl acetate (EtOAc) to furnish fractions soluble in these solvents and a water-soluble fraction. A high content of phenolic compounds was found in the EtOAc- and H_2O-soluble fractions (Figure 1), including the known flavonoids quercetin-3-*O*-α-L-rhamnopyranoside (quercetrin, **1**) and kaempferol-3-*O*-α-L-rhamnopyranoside (afzelin, **2**), which were previously reported as validated markers for flavonoid quantification in *C. langsdorffii* leaf extracts.[14] As the reported pharmacological potential of the extract was primarily suggested to be due to its phenolics content, phytochemical investigations were oriented toward the EtOAc- and H_2O-soluble fractions.

DOI: 10.1021/acs.jafc.5b01588
J. Agric. Food Chem. 2015, 63, 6939–6945

The method developed in HSCCC was selective for separation of **1** and **2** from the EtOAc-soluble fraction to yield subfractions containing >90% of these compounds. They were identified by comparison of their UV and ^{1}H NMR spectra (Supporting Information) with the literature.[13,17] The separation of those compounds by liquid−liquid chromatography brought several advantages compared to separations previously performed in silica gel or Sephadex column chromatography, as follows: (a) no content loss due to adsorption and suitability for polar fractions; (b) higher purity for compounds of similar molecular size as the separation is based on their K_d; (c) reproducibility; and (d) lower solvent consumption for preparative separations. Column chromatography performed on Sephadex LH-20 and HSCCC, followed by preparative HPLC purification, led to the isolation of three galloylquinic acid derivatives (**4**−**6**) from the H_2O-soluble fraction, which accounts for roughly 45% (w/w) of *C. langsforffii* leaf extract (Figure 1). Method of separation in HSCCC was also performed for the H_2O-soluble fraction. Four semipurified subfractions yielded compounds **3**, **7**, **8**, and **9** after purification in preparative HPLC. Compounds **7**−**9** underwent chemical degradation most probably by hydrolysis of ester bonds due to remaining acid from the mobile phase on the fractions. The UV absorption (typical λ_{max} at 220 and 275 nm, Figure 1), along with ^{1}H NMR spectra of the isolated compounds (Supporting Information) indicated that the fraction is composed of a series of galloylquinic acid derivatives. The isolated compounds peculiarly bear a methyl group in at least one of their galloyl moieties. Leaf extraction with aqueous ethanol, followed by direct HPLC analysis, was undertaken, confirming that these methylated compounds are truly present in the plant biomass (data not shown).

The methoxy-galloylquinic acids (**3**−**6**) (Figure 2) are, to the best of our knowledge, first reported. Their structural elucidation is discussed in detail in this work. Numeration of the quinic acid is rather controversial in the literature for galloylquinic acids.[18−22] Therefore, to avoid misinterpretation when accessing some references cited throughout this work, the assignments to C-2, C-3, C-5, and C-6 positions might be inverted to C-6, C-5, C-3, and C-2, respectively. The numbering form we adopted has been also described in recent papers related to quinic acid derivatives.[23−27]

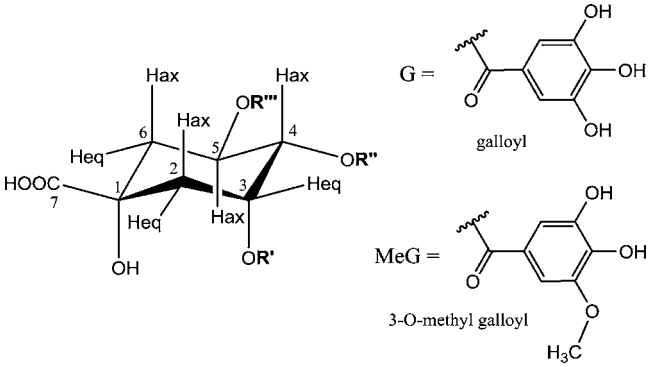

	R'	R''	R'''
3	MeG	H	H
4	MeG	MeG	H
5	G	MeG	G
6	MeG	G	MeG

Figure 2. Chemical structures of compounds **3**−**6**.

Correlations between the quinic acid protons were established via HMBC spectra, along with ^{1}H−^{1}H COSY cross-peaks H-2/H-6, H-2/H-3, H-3/H-4, H-4/H-5, and H-5/H-6 (Figure 3). Inference of the quinic acid chair conformation and assignment of its proton signals was reasoned primarily on the large vicinal coupling constants between the signals of H-4 and H-5 and between H-5 and H-6_{ax}.

The presence of one galloyl moiety bearing a methoxyl group (MeG) in compound **3** was indicated by loss of 166 units in the negative ESI-MS spectrum. This was confirmed by the signals of two aromatic protons meta coupled at δ 7.12 and 7.15 in the ^{1}H NMR spectrum, one methoxyl group (δ H, 3.79; and δ C, 56.0), and the signal of the aromatic hydroxyl carbon C-3′ (δ 147.7) shifted downfield in comparison to C-6′ (Table 1). The long-range correlation in the HMBC spectrum between C-3′ and the methylic protons (δ 3.79) confirmed the substitution at position C-3′ (Figure 3). The quinic acid unit was indicated by the ^{1}H NMR chemical shifts of four sp^3 methylene protons at δ 1.81, 1.92, 1.95, and 2.05, along with three oxymethine protons at δ 3.55, 3.92, and 5.27. Those resonances were in agreement with two sp^3 methylene and three oxymethine carbons in the ^{13}C NMR spectrum (Table 1). The ^{1}H−^{13}C long-range correlation between the proton H-3 (δ 5.27) and the carbonyl carbon signal at δ 165.4 (COO−′) indicated that the MeG moiety was linked to the quinic acid by an ester bond at C-3.

In the ^{1}H NMR spectrum, the signal of a dd (J = 7.5 and 3.2 Hz) was assigned to the proton H-4, indicating the axial position of H-4 vicinal to an equatorial proton at δ 5.27 (H-3) and an axial proton at δ 3.92 (H-5). The signal for H-4 in quinic acid derivatives is usually well-defined, even in ^{1}H NMR spectra from low-field instruments,[28] by its $^3J_{H,H}$ magnitudes (Table 1) and the ^{1}H−^{1}H COSY cross-correlation with both protons H-3 and H-5 (Figure 3).

The proton H-6_{ax} (δ 1.81, dd) was distinguished from another three methylene protons by the greater $J_{H,H}$ magnitudes ($^2J_{6ax,6eq}$ = 13.5 Hz and $^3J_{6ax,5ax}$ = 7.5 Hz). The signal at δ 1.92 (m) was associated with C-6 in the HSQC spectrum and, therefore, it was assigned to 6-H_{eq}. As the equatorial−equatorial and axial−equatorial coupling constants between the protons at C-2 and the proton H-3 assumed similar magnitudes, roughly 4 Hz, the relative position of the pair of methylene protons at C-2 (δ 1.95 and 2.05) was not defined. Therefore, they were rather assigned as H-2_a and H-2_b. The assignment of H-2_{ax} and H-2_{eq} has been previously described by using the signal multiplicity pattern, dd for H-2_{ax} and ddd for H-2_{eq}, in the ^{1}H NMR spectra in the analysis of dicaffeoylquinic and divanilloylquinc acids.[29,30] Particularly for H-2_{eq} and H-6_{eq} a pattern of ddd has been observed in these derivatives, to which the smallest coupling constant value (nearly 1.5 Hz) is attributed an $^4J_{2eq,6eq}$ W-coupling.[23,30,31]

Negative ESI-MS data for compound **4** suggested the presence of two MeG moieties. They were confirmed by signals of two sets of aromatic protons meta coupled in the ^{1}H NMR spectrum (Table 1) and two methoxyl signals (δ H, 3.77/δ C, 55.8; and δ H, 3.75/δ C, 55.8). The substitution position was suggested by the aromatic hydroxyl carbons C-3′ (δ 147.8) and C-3″(δ 147.7) shifted downfield in comparison to the carbons at δ 145.25 (C-5′ and C-5″) and confirmed by the long-range correlations in the HMBC spectrum (Figure 3).

The signal of the oxygenated methine proton at δ 5.07 (dd, J = 7.8 and 2.6 Hz) was assigned to proton H-4. Among four methylene proton signals, that at δ 1.91 was assigned to H-6_{ax} due to a greater axial−axial coupling constant (^3J = 7 Hz). The

DOI: 10.1021/acs.jafc.5b01588
J. Agric. Food Chem. 2015, 63, 6939−6945

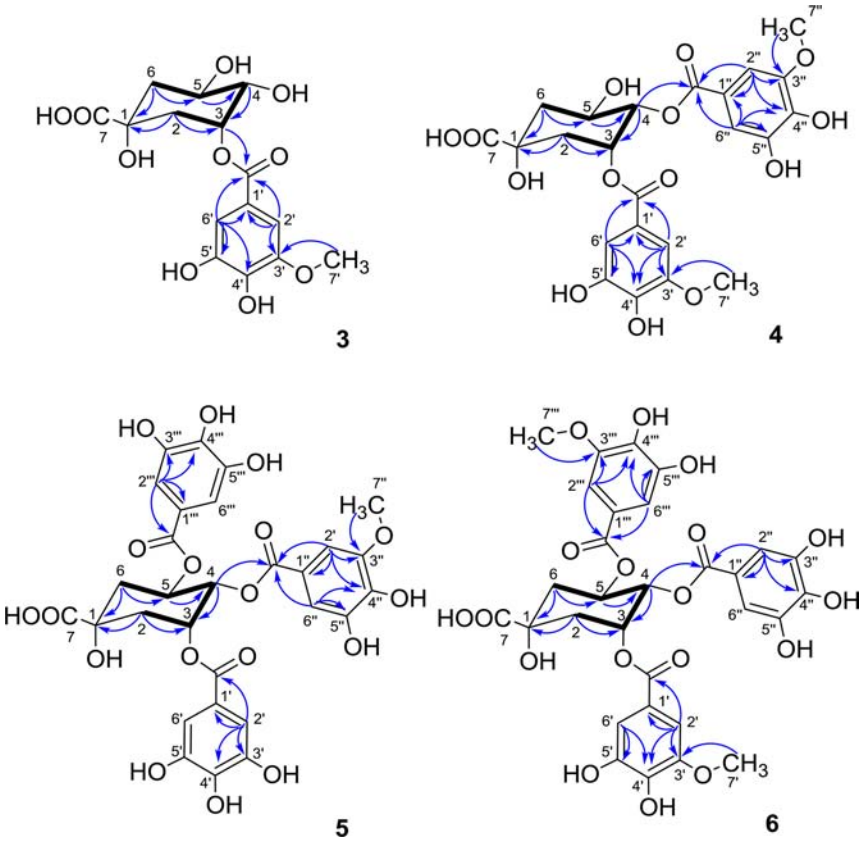

Figure 3. $^{1}H-^{1}H$ COSY (bold) and key HMBC correlations of compounds **3**–**6**.

signal at δ 4.26, which was cross-correlated in the $^{1}H-^{1}H$ COSY (Figure 3) with the signal of H-6_{ax} and H-4 (δ 5.07), was assigned to proton H-5. The lasting oxygenated methine signal at δ 5.49 was assigned to H-3.

The $^{1}H-^{13}C$ long-range correlation of the H-4 proton at δ 5.07 with the carbonyl carbon at δ 164.8 (COO−″) indicated one MeG moiety was linked to the quinic acid at the C-4 position. Due to a lack of correlation between quinic acid protons and the carbonyl carbon at δ 165.3 in the HMBC spectrum, the linkage position of the second MeG group was solved by the chemical shift of the proton signals. Acylation of an hydroxyl group produces a paramagnetic shift from 1.3 to 1.8 Hz on the oxymethine proton.[23,28,29,31] Therefore, the MeG moiety should be attached to the hydroxyl group at C-3, as the signal of H-3 (δ 5.49) was shifted downfield in comparison to H-5 (δ 4.26).

As protons H-3 and H-5 appeared as broad singlets or coalesced signals in the ^{1}H NMR spectrum (Figure 9 in the Supporting Information), they could not be unambiguously assigned by differences in $^{3}J_{H,H}$ magnitudes. Nevertheless, they should be alternatively differentiated by their signal half-width values ($J_{hw/2}$). Assuming the vicinal proton−proton angular dependence of the coupling constants, as the protons H-3, H-4, and H-5 are in equatorial, axial, and axial positions, respectively, a smaller half-width is expected for H-3, which couples with protons H-2 and H-4 at smaller values. For H-5, which couples at greater values with H-6_{ax} and H-4, a larger half-width is expected. However, their values in compound **4** were similar ($J_{hw/2}$ = 8 and 10.5) and lower than usually described in the literature ($J_{hw/2}$ = 8−10 Hz, H-3; $J_{hw/2}$ = 20−28 Hz, H-5).[22] This may be explained by the presence of two main relative conformers of the quinic acid in a ratio of nearly 1:1 (H-5_{eq}:H-5_{ax}) at 20 °C, as shown in a molecular model performed in molecular operations environment (MOE; 2010.09) (Figure 28 in the Supporting Information). It is noteworthy that in case H-6_{ax} is not assigned, unambiguous assignment of H-3 and H-5 in compounds alike may be possible only by optimizing the NMR experiments to favor the equilibrium toward one or the other conformer, that is, by performing analysis in different temperatures. Detailed experimental proof of the quantitative conformation equilibrium in quinic acid derivatives has been described by Pauli and et al.[31]

In compound **5**, the presence of two G moieties was confirmed by the ^{1}H NMR signals of two pairs of symmetric aromatic protons at δ 7.02 (H-2′/H-6′) and δ 6.88 (H-2‴/H-6‴). The MeG unity was confirmed by the signals of asymmetric aromatic protons at δ 6.85 (H-2″) and δ 6.97 (H-6″). Methylation on the hydroxyl at C-3″ position was confirmed by the long-range correlation between C-3″ and the methylic protons (δ 3.53) (Figure 3).

Cross-correlation of the proton H-5 (δ 5.72) with two methylene protons at δ 2.11−2.22 in the $^{1}H-^{1}H$ COSY spectrum indicated their position at C-6. Thus, the second pair of methylene protons (δ 2.02 and 2.37) should be attached at the C-2 position, which was confirmed by their cross-correlation with H-3 (δ 5.58) in the $^{1}H-^{1}H$ COSY spectrum. $^{1}H-^{13}C$ long-range correlation between the proton H-4 (δ 5.32) and the carbonyl carbon at δ 165.0 (COO−″) indicated the linkage of the MeG moiety at the C-4 position. No $^{1}H-^{13}C$ long-range correlations were observed between the oxymethine protons H-3 and H-5 with the carbonyl carbons at δ 165.2 and 165.6 in the HMBC spectrum. However, the paramagnetic shifts of those proton signals in the ^{1}H NMR spectrum

DOI: 10.1021/acs.jafc.5b01588
J. Agric. Food Chem. 2015, 63, 6939−6945

suggested that the two G moieties should be linked to quinic acid at the C-3 and C-5 positions.

In the ^{1}H NMR spectrum of compound **6**, signals of two pairs of asymmetric aromatic protons at δ 7.20 (H-2′)/δ 7.01 (H-6′) and δ 7.20 (H-2‴)/δ 6.97 (H-6‴) and two aromatic protons meta coupled at δ 6.8 (H-2″/H6″) (Table 1) confirmed the presence of two MeG and one G, respectively. The methylated position was confirmed by the long-range correlations in the HMBC spectrum between C-3′ and the methylic protons at δ 3.7 and between C-3‴ and the methylic protons at δ 3.78 (Figure 3).

The signal at δ 2.15 was assigned to H-6$_{ax}$ ($^2J_{6ax,6eq}$ = 12.5 Hz, $^3J_{6ax,5}$ = 8 Hz). Proton H-3 (δ 5.54) was easily assigned by its signal multiplicity (ddd) and coupling constant magnitudes ($^3J_{3,4}$ = 3.5 Hz, $^3J_{2ax,3}$ = 3 Hz, $^3J_{2eq,3}$ = 3 Hz). In the ^{1}H−^{1}H COSY spectrum, the signal of H-3 was cross-correlated with protons at δ 1.96 and 2.39, which were assigned to the pair of methylene protons at the C-2 position. The presence of a ^{1}H−^{13}C long-range correlation between H-4 (δ 5.28) and the carbonyl carbon at δ 165.2 and between H-3 (δ 5.54) and the carbonyl carbon at δ 165.3 indicated the linkage of G and MeG at the C-4 and C-3 positions, respectively. MeG, with the carbonyl carbon at δ 164.9, was linked therefore into the C-5 position.

This study will proceed to further pharmacological investigation of the isolated compounds.

■ ASSOCIATED CONTENT

Supporting Information

The Supporting Information is available free of charge on the ACS Publications website at DOI: 10.1021/acs.jafc.5b01588.

HPLC-UV-DAD chromatograms, 1D/2D NMR, MS, and UV spectra, and calculated dihedral angles (H−C−C−H) for the quinic acid in all conformers of compound **4** (PDF)

■ AUTHOR INFORMATION

Corresponding Author

*(J.K.B.) Phone: +55 16 3315-4162. Fax: +55 16 3315-4879. E-mail: jkbastos@fcfrp.usp.br.

Funding

We thank the State of São Paulo Research Foundation (FAPESP) for financial support, Grants 2009/10975-3 and 2011/13630-7.

Notes

The authors declare no competing financial interest.

■ ACKNOWLEDGMENTS

We acknowledge Dr. Thomas J. Schmidt for the use of MOE. We are also thankful to Prof. Milton Groppo for identifying the plant material and to Dr. Antonio Gilberto for helping with optimized NMR measurements.

■ ABBREVIATIONS USED

HSCCC, high-speed counter-current chromatography; MOE, molecular operations environment; K_d, Partitioning coefficient; MeG, 3-*O*-methyl-galloyl; G, galloyl

■ REFERENCES

(1) Paiva, L. A. F.; Rao, V. S. N.; Gramosa, N. V.; Silveira, E. R. Gastroprotective effect of *Copaifera langsdorffii* oleo-resin on experimental gastric ulcer models in rats. *J. Ethnopharmacol.* **1998**, *62*, 73−78.

(2) Paiva, L. A. F.; de Alencar Cunha, K. M.; Santos, F. A.; Gramosa, N. V.; Silveira, E. R.; Rao, V. S. N. Investigation on the wound healing activity of oleoresin from *Copaifera langsdorffii* in rats. *Phytother. Res.* **2002**, *16*, 737−739.

(3) Paiva, L. A. F.; Gurgel, L. A.; De Sousa, E. T.; Silveira, E. R.; Silva, R. M.; Santos, F. A.; Rao, V. S. N. Protective effect of *Copaifera langsdorffii* oleo-resin against acetic acid-induced colitis in rats. *J. Ethnopharmacol.* **2004**, *93*, 51−56.

(4) Paiva, L. A. F.; Gurgel, L. A.; Campos, A. R.; Silveira, E. R.; Rao, V. S. N. Attenuation of ischemia/reperfusion-induced intestinal injury by oleo-resin from *Copaifera langsdorffii* in rats. *Life Sci.* **2004**, *75*, 1979−1987.

(5) Gomes, N. M.; Rezende, C. M.; Fontes, S. P.; Matheus, M. E.; Fernandes, P. D. Antinociceptive activity of Amazonian copaiba oils. *J. Ethnopharmacol.* **2007**, *109*, 486−492.

(6) Souza, A. B.; Moreira, M. R.; Borges, C. H. G.; Simão, M. R.; Bastos, J. K.; de Sousa, J. P. B.; Ambrosio, S. R.; Veneziani, R. C. S. Development and validation of a rapid RP-HPLC method for analysis of (−)-copalic acid in copaíba oleoresin. *Biomed. Chromatogr.* **2013**, *27*, 280−283.

(7) Braga, W. F.; Rezende, C. M.; Antunes, O.; Pinto, A. C. Terpenoids from *Copaiba cearensis*. *Phytochemistry* **1998**, *49*, 263−264.

(8) Gelmini, F.; Beretta, G.; Anselmi, C.; Centini, M.; Magni, P.; Ruscica, M.; Cavalchini, A.; Maffei Facino, R. GC-MS profiling of the phytochemical constituents of the oleoresin from *Copaifera langsdorffii* Desf. and a preliminary *in vivo* evaluation of its antipsoriatic effect. *Int. J. Pharm.* **2013**, *440*, 170−178.

(9) Sousa, J. P. B.; Brancalion, A. P. S.; Souza, A. B.; Turatti, I. C. C.; Ambrósio, S. R.; Furtado, N. A. J. C.; Lopes, N. P.; Bastos, J. K. Validation of a gas chromatographic method to quantify sesquiterpenes in copaiba oils. *J. Pharm. Biomed. Anal.* **2011**, *54*, 653−659.

(10) Stupp, T.; de Freitas, R. A.; Sierakowski, M. R.; Deschamps, F. C.; Wisniewski, A.; Biavatti, M. W. Characterization and potential uses of *Copaifera langsdorfii* seeds and seed oil. *Bioresour. Technol.* **2008**, *99*, 2659−2663.

(11) Brancalion, A. P. S.; Oliveira, R. B.; Sousa, J. P. B.; Groppo, M.; Berretta, A. A.; Barros, M. E.; Boim, M. A.; Bastos, J. K. Effect of hydroalcoholic extract from *Copaifera langsdorffii* leaves on urolithiasis induced in rats. *Urol. Res.* **2012**, *40*, 475−81.

(12) De Oliveira, R. B.; Coelho, E. B.; Rodrigues, M. R.; Costa-Machado, A. R. D. M.; de Sousa, J. P. B.; Berretta, A. A.; Bastos, J. K. Effect of the *Copaifera langsdorffii* Desf. leaf extract on the ethylene glycol-induced nephrolithiasis in rats. *J. Evidence-Based Complement. Altern. Med.* **2013**, *2013*, 1−10.

(13) Sousa, J. P. B.; Nanayakkara, D.; Silva, A. A. B.; Bastos, J. K. Leishmanicidal and antimalarial activities of crude extracts from aerial parts of *Copaifera langsdorffii* and isolation of secondary metabolites. *J. Pharm. Res.* **2012**, *5*, 4103−4107.

(14) Sousa, J. P.; Brancalion, A. P.; Júnior, M. G.; Bastos, J. K. A validated chromatographic method for the determination of flavonoids in *Copaifera langsdorffii* by HPLC. *Nat. Prod. Commun.* **2012**, *7*, 25−28.

(15) Senedese, J. M.; Alves, J. M.; Lima, I. M. D. S.; de Andrade, E. A. P.; Furtado, R. A.; Bastos, J. K.; Tavares, D. C. Chemopreventive effect of *Copaifera langsdorffii* leaves hydroalcoholic extract on 1,2-dimethylhydrazine-induced DNA damage and preneoplastic lesions in rat colon. *BMC Complementary Altern. Med.* **2013**, *13*, 1−8.

(16) Alves, J. M.; Munari, C. C.; de Azevedo Bentes Monteiro Neto, M.; Furtado, R. A.; Senedese, J. M.; Bastos, J. K.; Tavares, D. C. *In vivo* protective effect of *Copaifera langsdorffii* hydroalcoholic extract on micronuclei induction by doxorubicin. *J. Appl. Toxicol.* **2013**, *33*, 854−860.

(17) Nugroho, A.; Choi, J.-K.; Park, J.-H.; Lee, K.-T.; Cha, B. C.; Park, H.-J. Two new flavonol glycosides from *Lamium amplexicaule* L. and their *in vitro* free radical scavenging and tyrosinase inhibitory activities. *Planta Med.* **2009**, *75*, 364−366.

DOI: 10.1021/acs.jafc.5b01588
J. Agric. Food Chem. 2015, 63, 6939−6945

(18) Clifford, M.; Stoupi, S.; Kuhnert, N. Profiling and characterization by LC-MS of the galloylquinic acids of green tea, tara tannin, and tannic acid. *J. Agric. Food Chem.* **2007**, *55*, 2797−2807.
(19) Bouchet, N.; Levesque, J.; Bodo, B.; Pousset, J. 3,4,5-Tri-*O*-galloylquinic acid ethyl ester from *Guiera senegalensis*. *Pharm. Biol.* **1998**, *36*, 63−65.
(20) Bouchet, N.; Levesque, J.; Blond, A.; Bodo, B.; Pousset, J. 1,3-Di-*O*-galloylquinic acid from *Guiera senegalensis*. *Phytochemistry* **1996**, *42*, 189−190.
(21) Ishimaru, K.; Nonaka, G.; Nishioka, I. Gallic acid esters of proto-quercitol, quinic acid and (−)-shikimic acid from *Quercus mongolica* and *Q. myrsin aefolia*. *Phytochemistry* **1987**, *26*, 1501−1504.
(22) Nishimura, H.; Nonaka, G.; Nishioka, I. Seven quinic acid gallates from *Quercus stenophylla*. *Phytochemistry* **1984**, *23*, 2621−2623.
(23) Huang, Y.-L.; Tsujita, T.; Tanaka, T.; Matsuo, Y.; Kouno, I.; Li, D.-P.; Nonaka, G.-i. Triterpene hexahydroxydiphenoyl esters and a quinic acid purpurogallin carbonyl ester from the leaves of *Castanopsis fissa*. *Phytochemistry* **2011**, *72*, 2006−2014.
(24) Wu, S.-B.; Meyer, R. S.; Whitaker, B. D.; Litt, A.; Kennelly, E. J. Antioxidant glucosylated caffeoylquinic acid derivatives in the invasive tropical soda apple, *Solanum viarum*. *J. Nat. Prod.* **2012**, *75*, 2246−2250.
(25) Lee, S. Y.; Moon, E.; Kim, S. Y.; Lee, K. R. Quinic acid derivatives from *Pimpinella brachycarpa* exert anti-neuroinflammatory activity in lipopolysaccharide-induced microglia. *Bioorg. Med. Chem. Lett.* **2013**, *23*, 2140−2144.
(26) Zhang, M.; Liu, W.-X.; Zheng, M.-F.; Xu, Q.-L.; Wan, F.-H.; Wang, J.; Lei, T.; Zhou, Z.-Y.; Tan, J.-W. Bioactive quinic acid derivatives from *Ageratina adenophora*. *Molecules* **2013**, *18*, 14096−14104.
(27) Nakamura, S.; Fujimoto, K.; Matsumoto, T.; Nakashima, S.; Ohta, T.; Ogawa, K.; Matsuda, H.; Yoshikawa, M. Acylated sucroses and acylated quinic acids analogs from the flower buds of *Prunus mume* and their inhibitory effect on melanogenesis. *Phytochemistry* **2013**, *92*, 128−36.
(28) Corse, J.; Lundin, R.; Sondheimer, E. Conformation analyses of D-(−)-quinic acid and some of its derivatives by nuclear magnetic resonance. *Phytochemistry* **1966**, *562*, 767−776.
(29) Tolonen, A.; Joutsamo, T. Identification of isomeric dicaffeoylquinic acids from *Eleutherococcus senticosus* using HPLC-ESI/TOF/MS and ^{1}H NMR methods. *Phytochem. Anal.* **2002**, *13*, 316−328.
(30) Ouattara, B.; Angenot, L.; Guissou, P.; Fondu, P.; Dubois, J.; Frédérich, M.; Jansen, O.; van Heugen, J.-C.; Wauters, J.-N.; Tits, M. LC/MS/NMR analysis of isomeric divanilloylquinic acids from the root bark of *Fagara zanthoxyloides* Lam. *Phytochemistry* **2004**, *65*, 1145−1151.
(31) Pauli, G.; Poetsch, F.; Nahrstedt, A. Structure assignment of natural quinic acid derivatives using proton nuclear magnetic resonance techniques. *Phytochem. Anal.* **1998**, *9*, 177−185.

DOI: 10.1021/acs.jafc.5b01588
J. Agric. Food Chem. 2015, 63, 6939−6945

glucuronides,[9] and a small fraction is sulfated or left unconjugated.[1] Although it is generally believed that aglycones are the most active biological compounds in humans, conjugates have also been postulated as displaying biological activities,[10] and some of them, such as sulfates, have been reported to have higher activities than the corresponding aglycones.[11]

Whereas daidzein and genistein are present in soy foods, equol is a metabolite of daidzein, the production of which depends upon the individual gut microflora;[12] only 30−50% of the adult Caucasian population is able to produce it.[1] Unlike daidzein or genistein, equol presents a stereogenic center at C-3, and therefore different enantiomeric forms exist. In humans, (*S*)-equol is the only enantiomer that is produced by intestinal bacterial flora.[13] This fact is of clinical relevance because both enantiomers have different activities; (*S*)-equol, but no (*R*)-equol, displays high affinity for the estrogen receptor beta (ERβ), and its activity is even higher than that of estradiol.[13]

Because of the beneficial health effects that soy isoflavones may provide to humans, several brands of isoflavone extracts have been commercialized over the past decades. However, there is little information concerning these preparations with respect to their specific isoflavone profile and quantity. Differences in bioavailability and pharmacokinetics may have an impact on isoflavone biological and pharmacological activities.

A number of analytical methods have been developed to detect and quantify isoflavone concentrations in biological fluids (plasma, serum, and urine). The most commonly used include gas chromatography coupled to mass spectrometry (GC-MS),[14] high-performance liquid chromatography (HPLC) with electrochemical detection,[15] HPLC with UV detection,[16] and liquid chromatography coupled to mass spectrometry (LC-MS).[4,17] At present, LC-MS/MS is the most commonly employed analytical technique due to its high sensitivity and selectivity.

The aim of the present study was to develop and validate an LC-MS/MS method for bioavailability studies of commercial isoflavone preparations that would be subsequently used in clinical research. A randomized, crossover, bioavailability study of two different, commercially available soy isoflavone extracts (Super-Absorbable Soy Isoflavones (Life Extension, USA) and Fitoladius (Merck, Spain)) was performed.

MATERIALS AND METHODS

Chemicals and Reagents. Daidzein, orthophosphoric acid (85%), β-glucuronidase from *Helix pomatia* (H-2 and H-1), β-glucuronidase from *Escherichia coli*, citric acid monohydrate, and sodium citrate dihydrate were purchased from Sigma-Aldrich Corp. (St. Louis, MO, USA). Equol and genistin were purchased from LC Laboratories (Woburn, MA, USA). Genistein was purchased from Extrasynthèse (Lyon, France). Daidzein-4-sulfate disodium salt, daidzein-7-β-D-glucuronide potassium salt, daidzein-7-β-D-glucuronide-4-sulfate disodium salt, and equol-4-sulfate were custom synthesized by Toronto Research Chemicals Inc. (Toronto, ON, Canada). Daidzein-d_6 and equol-d_4 were purchased from Medical Isotopes Inc. (Pelham, NH, USA). Methanol, acetonitrile (HPLC gradient grade), ammonium hydroxide, and acetic acid were purchased from Merck (Darmstadt, Germany). Ultrapure water was obtained using a Milli-Q purification system (Millipore Ibérica, Barcelona, Spain). Drug-free plasma was obtained from the Hospital del Mar blood bank (Barcelona, Spain).

Working Standards. Standard stock solutions of all analytes and their corresponding internal standards (IS), with the exceptions of daidzein-7-β-D-glucuronide and daidzein-7-β-D-glucuronide-4-sulfate, where water was used, were prepared by dissolving 10 mg of each substance in 10 mL of methanol. Working solutions were prepared by further diluting the starting solutions and were kept in dark flasks at −20 °C.

Instrumentation: LC-MS/MS Conditions. Identification and quantification analysis was performed using an Agilent 1200 series HPLC system (Agilent Technologies) coupled to a triple-quadrupole (6410 Triple Quad LC-MS; Agilent) mass spectrometer with an electrospray interface. Nitrogen was employed as a drying and nebulizing gas. A capillary voltage of 4 kV in negative ionization mode was used, and the source temperature was set to 325 °C.

The liquid chromatographic separation of daidzein, equol, and genistein was performed at 40 °C on an Acquity UPLC BEH C_{18} column (100 mm × 3.0 mm i.d., 1.7 μm particle size) (Waters Corp.). The mobile phase was an isocratic solvent system consisting of 0.01% ammonium acetate at pH 5 and methanol (40:60, v/v) at a flow rate of 0.3 mL/min. The injection volume was 10 μL. The total run time was 5 min per sample. All compounds were monitored in negative ionization using the multiple reaction mode. Daidzein and genistein were quantified by comparing their peak area ratios with that of daidzein-d_6 (IS1), whereas equol was quantified using equol-d_4 as internal standard (IS2). Due to the chemical structure similarities between daidzein and genistein, daidzein-d_6 was used as the internal standard of genistein.

Sample Preparation. First, a 1 mL aliquot of plasma sample was transferred into a glass tube and spiked with 30 μL of IS1 solution (containing daidzein-d_6 10 μg/mL) and 10 μL of IS2 (containing 10 μg/mL of equol-d_4). Approximately 3000 units of β-glucuronidase H1 (2 mg/mL, in 0.1 M sodium citrate buffer, pH 5) was added, and the sample was incubated at 37 °C for 16 h in a shaking water bath. Hydrolysis time could be reduced to 1 h if the temperature of the water bath was increased to 55 °C.

After the sample had cooled to room temperature, 1 mL of 4% H_3PO_4 was added, and all of the tubes were centrifuged at 3500 rpm for 5 min. They were then submitted to a solid-phase extraction (SPE) procedure using Oasis MAX cartridges (3 cm^3, 60 mg; Waters Corp., Dublin, Ireland). Cartridges were conditioned with 2 mL of methanol and equilibrated with 2 mL of water. After sample loading, interferences were washed away with 2 mL of 5% NH_4OH and 2 mL of 2% HCOOH containing 10% methanol. The compounds of interest were then eluted with 2 mL of a solution of methanol containing 2% HCOOH. After the evaporation of the solvent (<29 °C, <10 psi), analytes were reconstituted in 100 μL of CH_3COONH_4 0.01%, pH 5/MeOH (50:50). Finally, samples were centrifuged at 12000 rpm for 10 min at 4 °C and supernatants analyzed by HPLC-MS/MS.

Method Validation. *Calibration Curves and Linearity.* Calibration standards of daidzein, equol, and genistein were prepared each analysis day and consisted of two replicates at six different concentrations (5, 50, 200, 500, 750, and 1000 ng/mL). Calibration curves were prepared by adding the appropriate volume of working solutions, evaporating the solvent under N_2 (25 °C, 10 psi), and adding 1 mL of isoflavone-free plasma. Calibration curves with their corresponding slope (s), intercept, and correlation coefficient (r) were calculated by weighting ($1/x$) the least-squares linear regression of the peak area ratio (analyte/IS) versus the concentration of the standards. The method was considered linear if the coefficient of determination was >0.99.

Intra-assay Accuracy and Precision. To evaluate the precision and accuracy of the method, quality control (QC) samples were prepared by spiking known amounts of the analytes to isoflavone-free human plasma to achieve final concentrations of 5 ng/mL (lower limit of quantification; LLOQ), 10 ng/mL (low QC), 100 ng/mL (medium QC), and 800 ng/mL (high QC) of daidzein, equol, and genistein. Five replicates of each QC were analyzed against the calibration curve, and the obtained concentrations were compared to their nominal value.

Intra-assay accuracy was expressed as the percent relative error of the estimated concentrations. It was evaluated by five replicates of the QC samples that were analyzed in 1 day, at each concentration level. Accuracy was acceptable if the mean concentration was within 15% of

DOI: 10.1021/acs.jafc.5b02891
J. Agric. Food Chem. 2015, 63, 6946−6953

the nominal values with the exception of the LLOQ, which was acceptable if it was within 20% of the nominal value.

Intra-assay precision of the method was calculated as the relative standard deviation (RSD, %) of the estimated concentrations obtained for five replicates of the QC samples that were analyzed in 1 day, at each concentration level. Precision was acceptable if the RSD was within 15% of the nominal values with the exception of the LLOQ, which was acceptable if it was within 20% of the nominal value.

Interassay Accuracy and Precision. Interassay accuracy and interassay precision were calculated as described for intra-assay accuracy and precision with data obtained during three validation assays that took place during three different days.

Limit of Detection (LOD). The LOD was calculated using the standard deviations (SD) of the obtained concentrations from five replicates of the LLOQ (5 ng/mL) and the slope (s) of the calibration curve, according to the following formula: LOD = 3.3 × (SD/s). Additionally, at the estimated LOD of the surrogated analytes, it was confirmed that the LOD was at least 3 times the signal-to-noise ratio of a blank plasma sample.

Lower Limit of Quantification (LLOQ). The LLOQ was the lowest concentration calibrator experimentally tested that presented acceptable accuracy (80−120%) and precision (±20%).

Extraction Recovery. The extraction process recovery was evaluated by comparing the responses of a mixture of standards with and without extraction. For this purpose, six different sources of isoflavone-free plasma were spiked at a low (5 ng/mL) and high (800 ng/mL) level of concentration. The extraction recovery was calculated as the quotient of response of standard solutions spiked into plasma before extraction (with standard) and the response of standard solutions spiked into plasma after extraction. Results are expressed as a percentage.

Matrix Effect. In a similar way, the matrix effect was analyzed using six different batches of isoflavone-free plasma at two concentrations (5 and 800 ng/mL). It was evaluated according to the following formula: % matrix effect = 100 × [(response of the post extracted spiked sample/response of the nonextracted neat solvent with analytes) − 1]. A negative percent value indicated ion suppression, whereas a positive percent value indicated ion enhancement.

Stability. Stability of working solutions of daidzein, daidzein-d_6, equol, equol-d_4, and genistein in methanol was evaluated to ensure that neither sample preparation nor stored conditions could affect the concentration of the analytes. For this purpose, freeze and thaw stability, short-term stability at room temperature, and long-term stability in the freezer were evaluated.

Application to Real Samples: Quantification of Daidzein, Equol, and Genistein in Human Blood Samples. *Study Design.* A randomized, crossover, bioavailability study with a washout period of 3 days was performed. The study was conducted in accordance with the Helsinki Declaration, approved by the local Ethical Committee (CEIC-Parc de Salut Mar), and took place in the Clinical Research Unit of Hospital del Mar Medical Research Institute (IMIM, Barcelona, Spain). Written informed consent was obtained from all of the participants prior to any study-related procedure. Participants were financially compensated for any inconvenience caused.

Subjects. A total of 12 healthy, nonsmoker volunteers (4 females and 8 males), aged between 20 and 37 years (average 26.1 ± 5.5 years), were selected through a volunteer database. Their mean weight and height were 67.8 ± 10.3 kg and 172.5 ± 12.4 cm, respectively. The body mass index of each subject was within 19.6 and 25.4 kg/m^2 (22.7 ± 1.9 kg/m^2). The women had regular menstrual cycles (26−32 days). Subjects underwent a general physical examination, complete chemistry and hematology blood test, urinalysis, and 12-lead ECG. Moreover, during the 3 days prior to the intervention, they were asked to follow a diet free from daidzin, genistin, daidzein, and genistein (including soybeans and soy-derived foods). A list of isoflavone-rich food was provided. Alcoholic beverages were not permitted 72 h prior to each intervention.

Commercial Isoflavone Preparations. The soy isoflavone preparations used in this study were two commercially available brands: Super-Absorbable Soy Isoflavones (Life Extension, USA; hard gelatin capsules) and Fitoladius (Merck, Spain; soft gelatin capsules). As provided by the manufacturer, each capsule of Super-Absorbable Soy Isoflavones contains 123 mg of soy extract, with 54 mg of isoflavones (44%), 22 mg of which are daidzin and daidzein; 28 mg, genistin and genistein; and 6 mg, glycitin and glycitein. Each capsule of Fitoladius contains 60 mg of soybean seed extract (*Glycine max*), with 24 mg (40%) of total isoflavone content; the specific amounts of each isoflavone are not, however, described in the information leaflet.

Drug Administration and Sample Collection. The treatment with Super Absorbable Soy Isoflavones consisted of a single oral intake of 2 capsules (total dose = 108 mg of isoflavones), whereas that of Fitoladius was 4 capsules (total dose = 96 mg of isoflavones). The objective of this approach was to compensate the previously mentioned differences in isoflavone content of the extracts, as provided by the manufacturers (54 vs 24 mg in each capsule). On the intervention days, each volunteer received an oral dose of a soy isoflavone extract. To avoid batch-to-batch differences in isoflavone composition, all of the capsules of each treatment were from the same batch number. Moreover, as explained below, the composition of five different capsules corresponding to that batch was analyzed.

Subjects arrived at the clinical trial unit on the intervention day at 7:45 a.m. after an overnight fast. Spot urine samples were collected for drug testing (opiates, cocaine, amphetamines, and cannabis) by a rapid test device (Instant-View, Alpha Scientific Designs, Inc., Poway, CA, USA). In addition, a breath ethanol test was also conducted. A positive screen test was considered an exclusion criterion. Intervention days were separated by at least a 3-day washout period. An in-dwelling intravenous catheter was inserted into a subcutaneous vein in the forearm of the nondominant arm, and blood samples were collected at baseline and 1, 3, 5, 6, 7, 8, 9, 12, and 24 h after treatment administration. Blood was collected into 10 mL tubes containing EDTA and centrifuged (3000 rpm, 10 min, 4 °C). The plasma samples were then separated and frozen at −20 °C until analysis.

Quantification of Isoflavones in Soy Extract Capsules. Although the treatment dosages (based on the information provided by the manufacturers) were designed to contain similar doses of isoflavones, it was expected that there would be differences in the plasmatic concentrations of specific isoflavones (e.g., genistein and daidzein) as in the Fitoladius preparation their composition was not declared. Consequently, it was necessary to measure the exact content of isoflavones of the capsules. The isoflavone content of the preparations [aglycones (daidzein and genistein) and β-glycoside conjugates (daidzin and genistin)] was determined by LC-MS/MS as follows: a sample stock solution (1 mg/mL) from each was prepared by dissolving 10.0 mg of capsule content in 10 mL of methanol and sonicating it for 5 min to achieve complete dissolution. Analysis solutions of 100 and 10 μg/mL were prepared by further diluting the stock solution. One milliliter of the analysis solution, spiked with 30 μL of a solution containing 10 μg/mL daidzein-d_6, was subjected to the previously described solid phase extraction procedure. Ten microliters of the solution was injected in the LC-MS/MS system. Each determination was performed by analyzing five different capsules corresponding to the same batch used for the study. The separation of the compounds was carried out using the same conditions described earlier. The aglycones were quantified directly, whereas the glycosides were quantified indirectly after hydrolysis. Calculations were based on the response factor of the ratio of the analyte versus internal standard.

Pharmacokinetic Analysis. The maximum plasma concentration (C_{max}) and the time to reach C_{max} (t_{max}) were determined from the curves constructed by plotting the plasma concentrations over time. The terminal slope (k_e) of the concentration−time curve was determined by log−linear regression using at least the last three points. The elimination half-life ($t_{1/2}$) of the terminal log−linear phase was calculated following the equation ln 2/k_e. The area under the curve (AUC_{0-24h}) was calculated by the trapezoidal method during the 24 h following the ingestion of the corresponding soy isoflavone extract. All of the plasma samples collected from each subject were analyzed in the same batch of analysis. To compare the pharmacokinetics of genistein and daidzein in both preparations, the AUC_{0-24h} and C_{max} were adjusted for the dose administered (AUC_{0-24h}/dose and C_{max}/dose). Taking into account that the

DOI: 10.1021/acs.jafc.5b02891
J. Agric. Food Chem. 2015, 63, 6946−6953

Table 1. MS/MS Condition Settings

compound	retention time (min)	collision energy (eV)	precursor ion (m/z^-)	product ion (m/z^-)	dwell (s)	fragmentor (V)
daidzein	2.53	30	253	223, 208, 195	0.03	120
daidzein-d_6	5.53	35	259	229, 214, 137	0.03	140
equol	2.87	10	241	146, 121, 93	0.03	80
equol-d_4	2.87	10	245	150, 138, 123	0.03	100
genistein	3.09	30	269	159, 133, 107	0.03	120

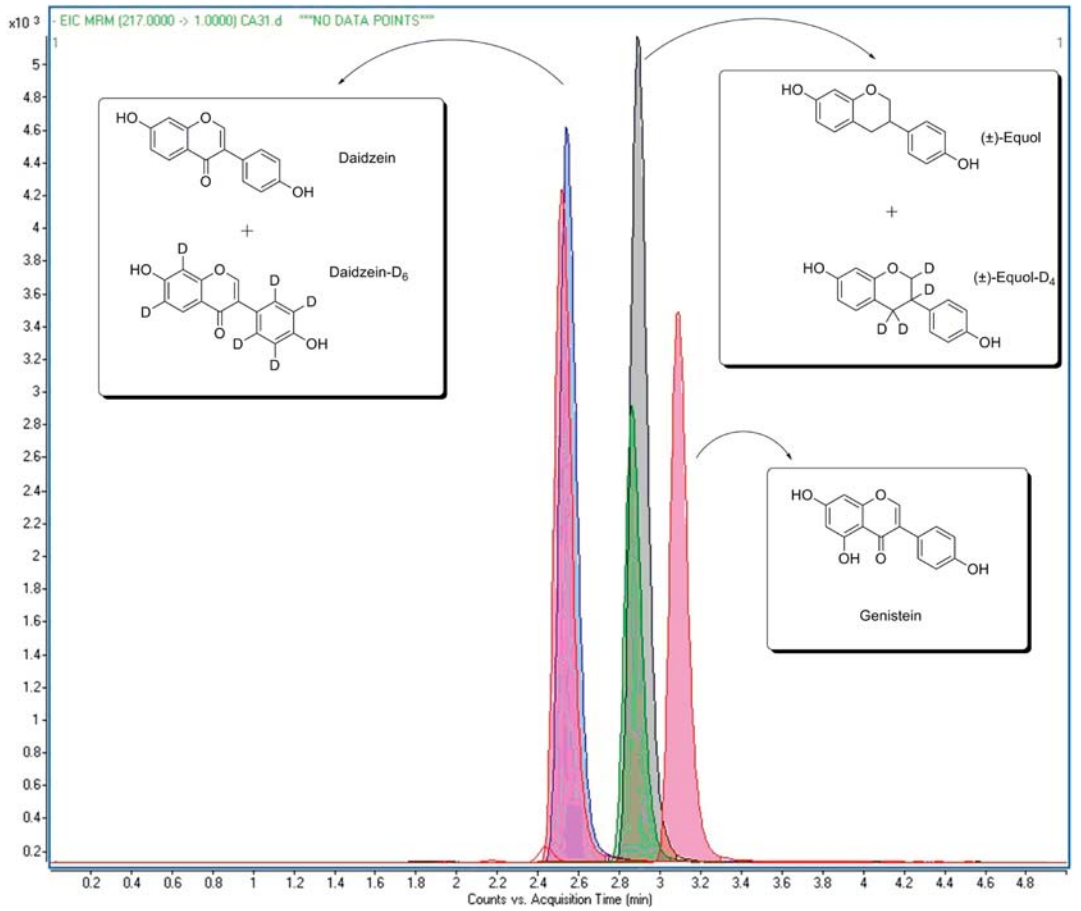

Figure 2. Chromatogram of an extracted plasma sample. A blank plasma was spiked with daidzein, equol, and genistein (500 ng/mL) and their corresponding internal standards (300 and 100 ng/mL). Following extraction and using an isocratic gradient, analytes were separated within 5 min.

isoflavone extracts contained a mixture of glycosides and aglycones, the dose administered was calculated as the sum of the amount of glycoside and aglycone, expressed in milligrams of aglycone.

Statistical Analysis. A Student's t test for paired samples was used for the statistical comparison of AUC_{0-24h}, C_{max}, $t_{1/2}$, k_e, AUC_{0-24h}/dose, and C_{max}/dose. A nonparametric method was used (Wilcoxon signed-rank test) for t_{max}. Analyses were performed using SPSS Statistics for Windows (version 18.0; SPSS Inc., Chicago, IL, USA). Significance was defined as $p < 0.05$.

RESULTS AND DISCUSSION

Method Development and Optimization. *Optimization of MS/MS Conditions.* To evaluate ionization sources and multiple reaction monitoring (MRM) transitions, the three most intense fragments of each compound (daidzein, daidzein-d_6, equol, equol-d_4, and genistein) were selected using pure standards at 10 μg/mL in negative ion mode. To further improve MRM conditions, the effect of gas temperature and collision and fragmentor energies were investigated over the ranges of 300−350 °C, 0−45 eV, and 60−140 V, respectively. The optimal gas temperature was determined at 325 °C, and the optimized values for fragmentor and collision energy of each metabolite, as well as the selected MRM transitions, are detailed in Table 1.

Optimization of LC Conditions. Different chromatographic columns were tested to study their effect on peak shapes and separation efficiency. Depending on the polarity of the stationary phase, these included cyanopropylsilyl (CN; Acquity UPLC HSS cyano 1.8 μm, 2.1 × 50 mm), n-octylsilyl (C_8; Zorbax SB-C_8 RRHT 1.8 μm, 2.1 × 100 mm), phenylhexylsilyl (Acquity UPLC BEH Phenyl 1.7 μm 2.1 × 100 mm), and n-octadecylsilyl (C_{18}; Acquity UPLC BEH C_{18} 1.7 μm, 3.0 × 100 mm) moieties on silica. After having compared the four chromatographic columns, the latter was chosen to continue with the optimization of the methodology because it provided the best separation with good resolution for equol, daidzein, and genistein.

Chromatographic separation of the analytes was optimized by evaluating four mobile phases (0.1% HCOOH, 0.01% NH_4CH_3COO, acetonitrile, and methanol). A rapid separation

DOI: 10.1021/acs.jafc.5b02891
J. Agric. Food Chem. 2015, 63, 6946−6953

Table 2. Linearity, Limit of Detection, Matrix Effect, and Extraction Recovery for the Studied Analytes

			matrix effect (%)		extraction recovery (%)	
compound	determination coefficient (r^2)	limit of detection (ng/mL)	5 ng/mL	800 ng/mL	5 ng/mL	800 ng/mL
daidzein	0.999	0.6	17.8	2.1	86.2	85.9
daidzein-d_6			−7.1	−11.6	79.2	77.5
equol	0.999	0.9	−7.6	−4.8	79.0	84.5
equol-d_4			−12.3	−17.2	76.7	80.2
genistein	0.996	1.0	−1.8	−9.4	79.1	80.5

(<5 min) of the three compounds of interest was achieved using an isocratic solvent system consisting of 0.01% ammonium acetate at pH 5 and methanol (40:60, v/v) (Figure 2).

Optimization of the Solid Phase Extraction Procedure. To optimize the extraction of the analytes of interest from plasma, several solid-phase extraction procedures were evaluated by spiking known amounts of the analytes and calculating the corresponding recoveries and matrix effect. Five different cartridges were evaluated. These included Oasis MCX, WAX, MAX, WCX, and HLB (Waters Corp.). The highest recovery of the analytes was achieved when MAX cartridges were used, although a marked matrix effect was present. To avoid the coeluting matrix components affecting the ionization efficiency of the analytes, different washes were evaluated. Neither basic washes with 5% NH_4OH nor additional washing steps using methanol improved the matrix effect. However, when acidic washes were studied using mixtures of methanol and 2% formic acid, the matrix effect was enhanced. The best results were obtained when 2% HCOOH and methanol (90:10; v/v) were employed.

Optimization of the Hydrolysis. The efficacy of different enzymes to hydrolyze the sulfate and glucuronic acid moieties present in the phase II conjugates of equol, genistein, and daidzein was evaluated. Different enzyme preparations (β-glucuronidases from *H. pomatia* H-2, purified H-2, H-1, and β-glucuronidase from *Escherichia coli*), glucuronidase and sulfatase units, incubation times, and temperatures were studied. Several custom synthesized products containing sulfate and/or glucuronide moieties (daidzein-4-sulfate, equol-4-sulfate, daidzein-7-β-D-glucuronide, daidzein-7-β-D-glucuronide-4-sulfate) were used as substrates, and the percentage of hydrolysis achieved in each case was evaluated.

The best results were obtained when the samples were treated with 3000 units of β-glucuronidase H-1 from *H. pomatia* at pH 5 after an incubation at 37 °C for 16 h. Interestingly, similar results were achieved when the hydrolysis time was reduced to 1 h and the temperature of the water was increased to 55 °C. This glucuronidase has been previously used in the analysis of soy isoflavones.[18−21]

Under the conditions described above, the percentage of hydrolysis of daidzein-4-sulfate, daidzein-7-β-D-glucuronide, and daidzein-7-β-D-glucuronide-4-sulfate was >95%. With greater amounts of β-glucuronidase (5000 units), the percentage of hydrolysis was constant, although the matrix effect increased. Whereas the hydrolysis of most of the metabolites was successful, none of the studied conditions was able to hydrolyze equol-4-sulfate, the yield being below 5%. Studies regarding equol metabolism in humans, monkeys, and rats have reported that sulfation is a minor metabolic pathway of this compound.[22] As described below, despite having detected equol in plasma samples from three volunteers, the pharmacokinetics of this metabolite has not been evaluated in this study.

It is worth noting that a total quantification of isoflavones was chosen due to the large number of isoflavone glucuronide and sulfate metabolites conjugates that have been described to date in humans[16] and animals.[9] Although some of these conjugates are commercially available, the lack of an appropriate commercially available IS for all of them for their proper quantification was a major limitation for their inclusion in the bioavailability study. For this reason, a total quantification of the isoflavones was performed following sample hydrolysis. To do so, four different representative metabolites presenting glucuronides and/or sulfate moieties were custom synthesized. The hydrolysis procedure was optimized to ensure that the conditions used were able to release the aglycones. Finally, the quantification of total isoflavones was performed in real plasma samples using the optimized hydrolysis procedure.

Method Validation. Validation of the analytical method was performed following the European Medicines Agency guidelines on bioanalytical method validation (http://www.ema.europa.eu/docs/en_GB/document_library/Scientific_guideline/2011/08/WC500109686.pdf, accessed April 30, 2014).

The linearity of the calibration curve was evaluated from three different prepared batches as described above. Satisfactory determination coefficients (r^2 > 0.99) were obtained for all of the analytes in the selected range of 5−1000 ng/mL.

Intra- and interday accuracies presented acceptable percent relative error for the three compounds, and the intra- and interday precisions were constantly below 15% RSD (Supplementary Table 1).

The LODs for daidzein, equol, and genistein were 0.6, 0.9, and 1.0 ng/mL, respectively. The LLOQ for these three isoflavones was 5 ng/mL.

The percent matrix effects for daidzein, equol, genistein, and their corresponding IS assessed at 5 and 800 ng/mL indicate that ion suppression was lower than 17.2% and ion enhancement was not higher than 17.8%. The extraction recoveries were between 77.5 and 86% (Table 2).

No significant degradation of daidzein, equol, and genistein in human plasma took place after long-term storage at −20 °C during the analysis period. The low and high QC samples presented acceptable values (±15% the nominal values) during at least 8 months after their preparation.

Quantification of Isoflavones in Soy Preparations. Supplementary Table 2 shows the quantification of daidzein, genistein, daidzin, and genistin present in one capsule of the commercially available soy preparations studied. Both commercial sources presented predominantly β-glycoside conjugates (98%), the free forms representing only a small percentage of the isoflavone content (approximately 2%). In Fitoladius, daidzin was found to account for 37.4% of the total isoflavone

DOI: 10.1021/acs.jafc.5b02891
J. Agric. Food Chem. 2015, 63, 6946−6953

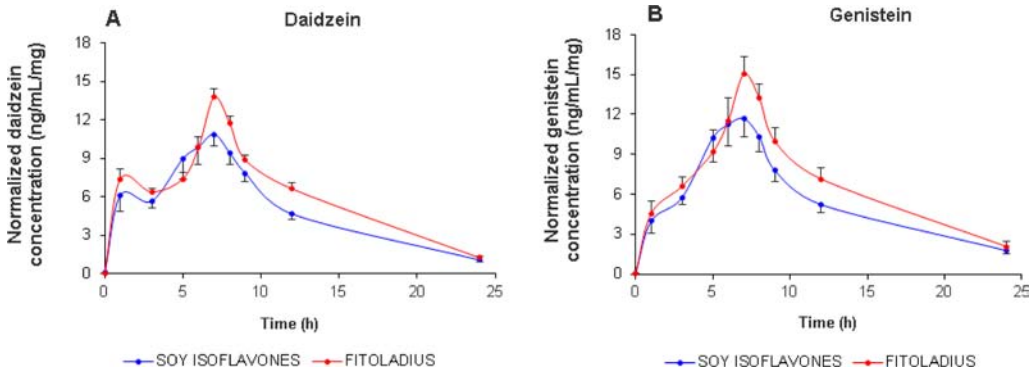

Figure 3. Time course plasma concentrations of genistein and daidzein after a single oral administration of two different isoflavone extracts to human subjects (n = 12): (A) daidzein time course plasmatic concentrations after Super Absorbable Soy Isoflavones and Fitoladius treatment; (B) genistein time course plasmatic concentrations after treatments. For comparison purposes, the concentration values were normalized by the dose administered. Data are expressed as mean ± standard error of the mean.

Table 3. Plasma Pharmacokinetic Parameters of Daidzein and Genistein after a Single Oral Administration of Fitoladius (4 Capsules) and Super Absorbable Soy Isoflavones (2 Capsules)[a]

	daidzein		genistein	
	Soy Isoflavones	Fitoladius	Soy Isoflavones	Fitoladius
AUC_{0-24h} (ng·h/mL)	5408 ± 928**	3376 ± 839**	5723 ± 1587	5838 ± 1275
AUC_{0-24h}/dose (ng·h/mL·mg)	120.8 ± 20.7*	144.8 ± 36.0*	131.5 ± 36.5**	159.7 ± 34.9**
C_{max} (ng/mL)	618.6 ± 116.8**	350.3 ± 90.8**	630.8 ± 206.3	620.5 ± 196.9
C_{max}/dose (ng/mL·mg)	13.8 ± 2.6	15.0 ± 3.9	14.5 ± 4.7*	17.0 ± 5.4*
t_{max} (h)	6.3 ± 2.0	6.8 ± 0.8	6.3 ± 2.1	6.9 ± 1.0
$t_{1/2}$ (h)	4.5 ± 1.6	5.4 ± 3.3	5.9 ± 2.1	5.8 ± 2.6
k_e (h^{-1})	0.18 ± 0.07	0.16 ± 0.07	0.13 ± 0.05	0.14 ± 0.07

[a]Data are expressed as the mean ± standard deviation: *, $p < 0.05$; **, $p < 0.005$. Abbreviations: AUC_{0-24h}, area under the curve from 0 to 24 h; C_{max}, peak plasma concentration; t_{max}, time at peak plasma concentration; $t_{1/2}$, elimination half-life; k_e, elimination rate constant.

weight, whereas genistin was the most abundant isoflavone, representing 60.3%. On the other hand, Super Absorbable Soy Isoflavones had almost the same amount of daidzin as genistin (50.0 and 48.1%, respectively). The aglycones were present only in very low amounts, daidzein being at a higher proportion (1.1−1.7%) than genistein (0.6−0.7%). The total isoflavone content of Fitoladius was found to exactly match the content provided in the information pamphlet (23.8 vs 24 mg). In the case of Super-Absorbable Soy Isoflavones, the content of genistin and genistein was 1.2-fold that described by the manufacturer (35.5 vs 28 mg). As for daidzein and daidzin concerns, the amount quantified (34.5 mg) was 1.6-fold that given in the specifications (22 mg). This fact is of relevance because the dosages administered to the volunteers were based on the information provided by the manufacturer. To compensate for these differences, the pharmacokinetic parameters were normalized by the dose administered. To do so, each plasmatic concentration value (derived from the calibration curve) was divided by the amount administered of the corresponding isoflavone.

The other constituents present in the soy preparations were excipients. In the case of Fitoladius, and according to the manufacturer, these are primrose oil, glyceryl monostearate, glycerol, cuprosodic chlorophyll, gelatin, titanium dioxide, and purified water. In the case of Super-Absorbable Soy Isoflavones, these are ascorbyl palmitate and vegetable cellulose. The analysis of these excipients is beyond the scope of this paper.

Quantification of Isoflavones in Human Plasma Samples. *Equol.* Only 3 of the 12 volunteers were found to be equol producers. In these volunteers, equol concentrations started to increase between 5 and 6 h after the treatment administration and could still be detected at 24 h. Therefore, the pharmacokinetics of this metabolite is not evaluated in this study.

Daidzein and Genistein Pharmacokinetics. Time course plasma concentrations of total genistein and daidzein are shown in Figure 3. Some studies have described that daidzein presents higher bioavailability than genistein,[23] whereas others have reported the contrary.[24] In our study, no differences in bioavailability were observed between daidzein and genistein after the treatment with Super Absorbable Soy Isoflavones or Fitoladius. The double peak found in the time course plasma concentrations suggests an enterohepatic circulation, which is characteristic of these compounds (Figure 3).[6,25] To a lesser extent, the small percentages of aglycones present in the soy extracts could also contribute to this pharmacokinetic profile, as the free forms are absorbed more quickly than the glycosides.[26]

The pharmacokinetic parameters studied (AUC_{0-24h}, C_{max}, AUC_{0-24h}/dose, C_{max}/dose, t_{max}, $t_{1/2}$, k_e) are reported in Table 3. As shown using the AUC_{0-24h}/dose ratio, the bioavailability of daidzein and genistein was higher after the intake of Fitoladius ($p < 0.05$ and $p < 0.001$, respectively), compared to Super Absorbable Soy Isoflavones (Figure 3).

C_{max}/dose values of genistein also differed significantly between treatments ($p < 0.001$). After the intake of Fitoladius, these values were higher than the other studied preparation. No differences were observed in t_{max}, $t_{1/2}$, and k_e.

Several factors can influence the metabolism and bioavailability of isoflavones in humans. These include age, ethnic background, dietary habits, food matrix, intestinal microflora,

DOI: 10.1021/acs.jafc.5b02891
J. Agric. Food Chem. 2015, 63, 6946−6953

intestinal transit time, previous exposure to isoflavones, and glycosidase production.[27,28] In our case, the differences in bioavailability suggest that the excipients/matrix in which these products are present may play an important role in the absorption process, which could have a direct impact on the bioavailability of soy isoflavones. This fact would explain the different pharmacokinetic profile observed between treatments when the same 12 volunteers received two different soy extracts.

Our study has strengths and limitations. One of the strengths is the crossover design, which allowed the same participants to be included in the different treatments, thus minimizing interferences with other confounder variables. Another strength lies in the fact of including both genders among the participants, thus providing a better representation of the overall population. One limitation of our study is that, due to the available commercial sources of the soy extracts, the isoflavone composition of the two tested products differed significantly. Consequently, the participants did not receive exactly the same doses in the two soy isoflavone extracts. To minimize these differences, the exact amount of each isoflavone was first analyzed, and normalization by the dose administered was performed prior to pharmacokinetic analyses.

In conclusion, in the present study we developed a LC-MS/MS method based on an enzymatic hydrolysis with β-glucuronidase H1 followed by a SPE procedure using Oasis MAX cartridges. The analytical method was successfully validated following the European Medicines Agency guidelines on Bioanalytical Method Validation. This methodology presents a good recovery of the analytes, very low matrix effects, a rapid chromatographic separation, and high sensitivity. The limits of detection for daidzein, equol, and genistein in 1 mL of plasma sample were 0.6, 0.9, and 1.0 ng/mL, respectively. Once the method was validated, a crossover, randomized, bioavailability study was performed. The method was then applied to the plasma samples of the 12 volunteers. The pharmacokinetic profiles of daidzein and genistein were studied.

After having been normalized, Fitoladius presented higher bioavailability and achieved higher C_{max} values than Super Absorbable Soy Isoflavones for daidzein and genistein. As the other pharmacokinetic parameters were similar between both treatments, we suggest that these differences in bioavailability come from the matrix/excipients present in the capsules of the isoflavone extracts.

The preparations studied are over-the-counter dietetic preparations, they do not require medical prescription, and some of them can be purchased on the Internet. Thus, the regulation of these products probably is not as strict as that applied to prescription drugs. Consequently, a detailed and accurate description of the specific isoflavone content present in the capsules is lacking. Indeed, describing the content of the capsules as "*X* mg of isoflavones" or "*Y* mg of genistin and genistein" does not provide clear and accurate information about composition. This is an important fact because there are a number of different isoflavones, which vary in molecular weight, pharmacokinetic profile, and biological activities.[29] As a consequence, the exact content of each isoflavone should be provided by the manufacturers in order to have better knowledge of the content of the capsules and their corresponding beneficial health effects.

The purpose of this study was the selection of one isoflavone extract preparation for its use in a clinical trial with the aim of treating drug addiction. In this context we performed the bioavailability study. Results from this study show that isoflavone extracts vary not only in their composition (not unexpected) but also in the amounts reported by manufacturers in each preparation. In a clinical pharmacology context and looking at therapeutic indications with methodologically robust designs, the results from this study are quite disturbing.

■ ASSOCIATED CONTENT

Ⓢ Supporting Information

Supplementary Table 1, intra- and interday precision and accuracy of quality control samples of daidzein, equol, and genistein in human plasma; supplementary Table 2, isoflavone content of one capsule of Fitoladius and Super Absorbable Soy Isoflavones. The Supporting Information is available free of charge on the ACS Publications website at DOI: 10.1021/acs.jafc.5b02891.

■ AUTHOR INFORMATION

Corresponding Author

*(R.T.) Phone: +34 933160484. Fax: +34 933160467. E-mail: rtorre@imim.es.

Present Address

[¶]Clinical Pharmacology Unit. Hospital Universitari Germans Trias i Pujol-IGTP, Badalona 08916, Spain.

Author Contributions

[‖]Authorship credit should be equally distributed between authors J.R.-M. and M.F. independent of the order.

Funding

Funded by grants from the Ministerio de Sanidad (Investigación Clínica Independiente, EC-10-166), Fondo de Investigación Sanitaria-ISCIII-FEDER RTA (RD12/0028/0009), CIBEROBN (CB06/03/0028), Generalitat de Catalunya (AGAUR 2014SGR680, predoctoral fellowship FI-DGR 2013 for J.R.-M.), and PN I+D+I 2008-2011 and ISCIII CA11/00215 for N.P. C.P.-M. and E.P. are Rio Hortega fellows (ISCIII, CM12/00085 and CM13/00016). The author's work was independent of the sources of funding.

Notes

The authors declare no competing financial interest.

■ REFERENCES

(1) Yuan, J. P.; Wang, J. H.; Liu, X. Metabolism of dietary soy isoflavones to equol by human intestinal microflora − implications for health. *Mol. Nutr. Food Res.* **2007**, *51*, 765−781.

(2) Milenkovic, D.; Jude, B.; Morand, C. miRNA as molecular target of polyphenols underlying their biological effects. *Free Radical Biol. Med.* **2013**, *64*, 40−51.

(3) Day, A. J.; DuPont, M. S.; Ridley, S.; Rhodes, M.; Rhodes, M. J.; Morgan, M. R.; Williamson, G. Deglycosylation of flavonoid and isoflavonoid glycosides by human small intestine and liver beta-glucosidase activity. *FEBS Lett.* **1998**, *436*, 71−75.

(4) Setchell, K. D.; Brown, N. M.; Zimmer-Nechemias, L.; Brashear, W. T.; Wolfe, B. E.; Kirschner, A. S.; Heubi, J. E. Evidence for lack of absorption of soy isoflavone glycosides in humans, supporting the crucial role of intestinal metabolism for bioavailability. *Am. J. Clin. Nutr.* **2002**, *76*, 447−453.

(5) Kurzer, M. S.; Xu, X. Dietary phytoestrogens. *Annu. Rev. Nutr.* **1997**, *17*, 353−381.

(6) Barnes, S. The biochemistry, chemistry and physiology of the isoflavones in soybeans and their food products. *Lymphatic Res. Biol.* **2010**, *8*, 89−98.

(7) Ronis, M. J.; Little, J. M.; Barone, G. W.; Chen, G.; Radominska-Pandya, A.; Badger, T. M. Sulfation of the isoflavones genistein and

DOI: 10.1021/acs.jafc.5b02891
J. Agric. Food Chem. 2015, 63, 6946−6953

daidzein in human and rat liver and gastrointestinal tract. *J. Med. Food* **2006**, *9*, 348−355.
(8) Nakano, H.; Ogura, K.; Takahashi, E.; Harada, T.; Nishiyama, T.; Muro, K.; Hiratsuka, A.; Kadota, S.; Watabe, T. Regioselective monosulfation and disulfation of the phytoestrogens daidzein and genistein by human liver sulfotransferases. *Drug Metab. Pharmacokinet.* **2004**, *19*, 216−226.
(9) Fang, N.; Yu, S.; Badger, T. M. Characterization of isoflavones and their conjugates in female rat urine using LC/MS/MS. *J. Agric. Food Chem.* **2002**, *50*, 2700−2707.
(10) Yuan, B.; Zhen, H.; Jin, Y.; Xu, L.; Jiang, X.; Sun, S.; Li, C.; Xu, H. Absorption and plasma disposition of genistin differ from those of genistein in healthy women. *J. Agric. Food Chem.* **2012**, *60*, 1428−1436.
(11) Pugazhendhi, D.; Watson, K. A.; Mills, S.; Botting, N.; Pope, G. S.; Darbre, P. D. Effect of sulphation on the oestrogen agonist activity of the phytoestrogens genistein and daidzein in MCF-7 human breast cancer cells. *J. Endocrinol.* **2008**, *197*, 503−515.
(12) Xu, X.; Harris, K. S.; Wang, H. J.; Murphy, P. A.; Hendrich, S. Bioavailability of soybean isoflavones depends upon gut microflora in women. *J. Nutr.* **1995**, *125*, 2307−2315.
(13) Setchell, K. D.; Clerici, C.; Lephart, E. D.; Cole, S. J.; Heenan, C.; Castellani, D.; Wolfe, B. E.; Nechemias-Zimmer, L.; Brown, N. M.; Lund, T. D.; Handa, R. J.; Heubi, J. E. S-equol, a potent ligand for estrogen receptor beta, is the exclusive enantiomeric form of the soy isoflavone metabolite produced by human intestinal bacterial flora. *Am. J. Clin. Nutr.* **2005**, *81*, 1072−1079.
(14) Setchell, K. D.; Brown, N. M.; Desai, P.; Zimmer-Nechemias, L.; Wolfe, B. E.; Brashear, W. T.; Kirschner, A. S.; Cassidy, A.; Heubi, J. E. Bioavailability of pure isoflavones in healthy humans and analysis of commercial soy isoflavone supplements. *J. Nutr.* **2001**, *131*, 1362S−1375S.
(15) King, R. A.; Bursill, D. B. Plasma and urinary kinetics of the isoflavones daidzein and genistein after a single soy meal in humans. *Am. J. Clin. Nutr.* **1998**, *67*, 867−872.
(16) Hosoda, K.; Furuta, T.; Ishii, K. Simultaneous determination of glucuronic acid and sulfuric acid conjugated metabolites of daidzein and genistein in human plasma by high-performance liquid chromatography. *J. Chromatogr. B: Anal. Technol. Biomed. Life Sci.* **2010**, *878*, 628−636.
(17) Twaddle, N. C.; Churchwell, M. I.; Doerge, D. R. High-throughput quantification of soy isoflavones in human and rodent blood using liquid chromatography with electrospray mass spectrometry and tandem mass spectrometry detection. *J. Chromatogr. B: Anal. Technol. Biomed. Life Sci.* **2002**, *777*, 139−145.
(18) Wyns, C.; Bolca, S.; De Keukeleire, D.; Heyerick, A. Development of a high-throughput LC/APCI-MS method for the determination of thirteen phytoestrogens including gut microbial metabolites in human urine and serum. *J. Chromatogr. B: Anal. Technol. Biomed. Life Sci.* **2010**, *878*, 949−956.
(19) Kuklenyik, Z.; Ye, X.; Reich, J. A.; Needham, L. L.; Calafat, A. M. Automated online and off-line solid-phase extraction methods for measuring isoflavones and lignans in urine. *J. Chromatogr. Sci.* **2004**, *42*, 495−500.
(20) Parker, D. L.; Rybak, M. E.; Pfeiffer, C. M. Phytoestrogen biomonitoring: an extractionless LC-MS/MS method for measuring urinary isoflavones and lignans by use of atmospheric pressure photoionization (APPI). *Anal. Bioanal. Chem.* **2012**, *402*, 1123−1136.
(21) Rybak, M. E.; Parker, D. L.; Pfeiffer, C. M. Determination of urinary phytoestrogens by HPLC−MS/MS: a comparison of atmospheric pressure chemical ionization (APCI) and electrospray ionization (ESI). *J. Chromatogr. B: Anal. Technol. Biomed. Life Sci.* **2008**, *861*, 145−150.
(22) Schwen, R. J.; Nguyen, L.; Jackson, R. L. Elucidation of the metabolic pathway of S-equol in rat, monkey and man. *Food Chem. Toxicol.* **2012**, *50*, 2074−2083.
(23) Xu, X.; Wang, H.-J.; Murphy, P. A.; Cook, L.; Hendrich, S. Daidzein is a more bioavailable soymilk isoflavone than is genistein in adult women. *J. Nutr.* **1994**, *124*, 825−832.
(24) Setchell, K. D.; Faughnan, M. S.; Avades, T.; Zimmer-Nechemias, L.; Brown, N. M.; Wolfe, B. E.; Brashear, W. T.; Desai, P.; Oldfield, M. F.; Botting, N. P.; Cassidy, A. Comparing the pharmacokinetics of daidzein and genistein with the use of ^{13}C-labeled tracers in premenopausal women. *Am. J. Clin. Nutr.* **2003**, *77*, 411−419.
(25) Sfakianos, J.; Coward, L.; Kirk, M.; Barnes, S. Intestinal uptake and biliary excretion of the isoflavone genistein in rats. *J. Nutr.* **1997**, *127*, 1260−1268.
(26) Izumi, T.; Piskula, M. K.; Osawa, S.; Obata, A.; Tobe, K.; Saito, M.; Kataoka, S.; Kubota, Y.; Kikuchi, M. Soy isoflavone aglycones are absorbed faster and in higher amounts than their glucosides in humans. *J. Nutr.* **2000**, *130*, 1695−1699.
(27) Zubik, L.; Meydani, M. Bioavailability of soybean isoflavones from aglycone and glucoside forms in American women. *Am. J. Clin. Nutr.* **2003**, *77*, 1459−1465.
(28) Setchell, K. D. Phytoestrogens: the biochemistry, physiology, and implications for human health of soy isoflavones. *Am. J. Clin. Nutr.* **1998**, *68*, 1333S−1346S.
(29) López-Gutiérrez, N.; Romero-González, R.; Garrido Frenich, A.; Martínez Vidal, J. L. Identification and quantification of the main isoflavones and other phytochemicals in soy based nutraceutical products by liquid chromatography−orbitrap high resolution mass spectrometry. *J. Chromatogr. A* **2014**, *1348*, 125−136.

DOI: 10.1021/acs.jafc.5b02891
J. Agric. Food Chem. 2015, 63, 6946−6953

Table 1. Target Illegal Adulterants with Corresponding Molecular Formula, Retention Time, Polarity, Diagnostic Precursor Ions, Sequential Multistage Fragment Ions (MS^2 and MS^3),[a] and Accurate Mass Data

compound name	element composition	CAS Registry No.	quasi-molecular ion			RT (min)	MS^2 product ion		MS^3 product ion	
			formula	exact m/z (Da)	error (ppm)		measured m/z (Da)	error (mDa)	measured m/z (Da)	error (mDa)
Weight-Loss Drugs										
bisacodyl (14)[b]	$C_{22}H_{19}NO_4$	603-50-9	$[M + H]^+$	362.1387	−4.1	31.12	226.0851	−1.2	184.0751	−0.6
fenfluramine (3)	$C_{12}H_{16}NF_3$	458-24-2	$[M + H]^+$	232.1308	−5.5	17.6	187.0735	0.6	159.0418	0.2
sibutramine (5)	$C_{17}H_{26}NCl$	106650-56-0	$[M + H]^+$	280.1827	−3.9	26.07	139.0311	0.2	103.0546	0.4
ephedrine (2)	$C_{10}H_{15}NO$	299-42-3	$[M + H]^+$	166.1226	−4.7	7.96	148.1117	−0.4	117.0699	−0.6
norephedrine (1)	$C_9H_{13}NO$	154-41-6	$[M + H]^+$	152.1070	−2.6	6.82	134.0954	−1.0	117.0678	−2.1
pseudoephedrine (2)	$C_{10}H_{15}NO$	90-82-4	$[M + H]^+$	166.1226	−6.1	7.96	148.1122	0.1	117.0690	−0.9
bendroflumethiazide	$C_{15}H_{14}N_3O_4F_3S_2$	73-48-3	$[M - H]^-$	420.0305	3.3	27.17	289.0450	−1.0	205.0810	3.9
bumetanide	$C_{17}H_{20}N_2O_5S$	28395-03-1	$[M - H]^-$	363.1020	0.67	29.39	319.1129	−0.9	262.0413	−1.0
chlorothiazide	$C_7H_6N_3O_4S_2Cl$	58-94-6	$[M - H]^-$	293.9415	1.7	8.91	213.9637	2.8	178.9961	4.0
chlorthalidone	$C_{14}H_{11}N_2O_4SCl$	77-36-1	$[M - H]^-$	337.0055	−1.8	16.10	318.9953	0.3	283.0206	2.3
furosemide	$C_{12}H_{11}N_2O_5SCl$	54-31-9	$[M - H]^-$	329.0004	−0.91	22.23	285.0120	1.4	204.9879	3.5
hydrochlorothiazide (6)	$C_7H_8N_3O_4S_2Cl$	58-93-5	$[M - H]^-$	295.9572	0.0	9.79	268.9486	2.3	204.9882	3.8
indapamide	$C_{16}H_{16}N_3O_3SCl$	26807-65-8	$[M + H]^+$	366.0674	−0.55	24.55	132.0808	0.0	117.0581	0.8
methyclothiazide (12)	$C_9H_{11}N_3O_4S_2Cl_2$	135-07-9	$[M - H]^-$	357.9495	1.9	20.55	321.9731	0.3	258.0121	1.2
doxepin (5)[c]	$C_{19}H_{21}NO$	1668-19-5	$[M + H]^+$	280.1696	–	–	235.1117	–	107.0491	–
fluoxetine (9)	$C_{17}H_{18}NOF_3$	54910-89-3	$[M + H]^+$	310.1413	−0.32	24.68	148.1127	0.6	–	–
sertraline (8)	$C_{17}H_{17}NCl_2$	79559-97-0	$[M + H]^+$	306.0811	−2.3	25.43	275.0406	1.3	158.9779	1.6
Antihypertension Drugs										
benazepril (16)	$C_{24}H_{28}N_2O_5$	86541-75-5	$[M + H]^+$	425.2071	3.8	25.13	351.1698	0.8	190.0872	−1.1
enalapril	$C_{20}H_{28}N_2O_5$	76095-16-4	$[M + H]^+$	377.2071	0.80	18.33	234.1473	−1.6	130.0860	−0.3
imidapril	$C_{20}H_{27}N_3O_6$	89371-37-9	$[M + H]^+$	406.1973	−4.2	17.74	234.1482	−0.7	130.0872	0.9
perindopril	$C_{19}H_{32}N_2O_5$	82834-16-0	$[M + H]^+$	369.2384	−4.9	19.43	172.1332	0.7	98.0977	0.8
losartan	$C_{22}H_{23}ClN_6O$	114798-26-4	$[M - H]^-$	421.1549	−1.2	26.36	335.1331	1.0	179.0885	1.9
clonidine	$C_9H_9N_3Cl_2$	4205-91-8	$[M + H]^+$	230.0246	−4.7	8.52	212.9997	1.6	151.0200	1.7
reserpine	$C_{33}H_{40}N_2O_9$	50-55-5	$[M + H]^+$	609.2807	4.1	25.64	448.1988	2.2	195.0656	0.4
prazosin (15)	$C_{19}H_{21}N_5O_4$	19216-56-9	$[M + H]^+$	384.1666	2.3	14.15	316.1411	0.7	247.1182	−0.8
atenolol	$C_{14}H_{22}N_2O_3$	29122-68-7	$[M + H]^+$	267.1703	−4.8	6.36	225.1230	−0.4	208.0958	−1.0
metoprolol	$C_{15}H_{25}NO_3$	37350-58-6	$[M + H]^+$	268.1907	−4.5	13.38	191.1054	−1.3	159.0806	0.2
amlodipine	$C_{20}H_{25}N_2O_5Cl$	88150-42-9	$[M + H]^+$	409.1525	2.4	22.55	238.0627	−0.2	206.0375	0.8
felodipine[c]	$C_{18}H_{19}NO_4Cl_2$	86189-69-7	$[M - H]^-$	382.0618	–	–	236.0928	–	164.0717	–
nifedipine	$C_{17}H_{18}N_2O_6$	21829-25-4	$[M - H]^-$	345.1092	1.2	29.45	222.0798	2.6	164.0753	3.6
nitrendipine (13)	$C_{18}H_{20}N_2O_6$	39562-70-4	$[M - H]^-$	359.1249	−1.1	32.20	236.0942	1.4	164.0767	5.0
nimodipine	$C_{21}H_{26}N_2O_7$	66085-59-4	$[M - H]^-$	417.1667	−1.2	32.85	294.1349	0.68	236.0950	2.2
nisoldipine	$C_{20}H_{24}N_2O_6$	63675-72-9	$[M - H]^-$	387.1562	−3.9	33.31	264.1253	1.2	164.0766	4.9
Sedative-Hypnotics										
alprazolam	$C_{17}H_{13}N_4Cl$	28981-97-7	$[M + H]^+$	309.0902	−4.2	25.28	274.1215	0.2	219.1051	0.8
clonazepam (10)	$C_{15}H_{10}N_3O_3Cl$	1622-61-3	$[M + H]^+$	316.0483	4.4	25.36	270.0536	−1.8	241.0518	−0.9
chlordiazepoxide (7)	$C_{16}H_{14}N_3OCl$	58-25-3	$[M + H]^+$	300.0898	−3.7	19.05	283.0878	0.7	227.0489	−0.7
diazepam	$C_{16}H_{13}N_2OCl$	439-14-5	$[M + H]^+$	285.0789	0.01	30.76	257.0843	0.3	228.0577	0.2
estazolam (6)	$C_{16}H_{11}N_4Cl$	29975-16-4	$[M + H]^+$	295.0745	−3.4	24.23	267.0567	0.9	205.0755	−0.5
lorazepam	$C_{15}H_{10}N_2O_2Cl_2$	846-49-1	$[M + H]^+$	321.0192	−3.4	24.88	303.0099	1.3	275.0126	−1.1
midazolam	$C_{18}H_{13}N_3FCl$	59467-64-0	$[M + H]^+$	326.0855	0.02	19.87	291.1168	0.2	223.0801	0.9
nitrazepam	$C_{15}H_{11}N_3O_3$	146-22-5	$[M + H]^+$	282.0873	−2.5	24.46	236.0944	0.0	207.0910	−0.7
oxazepam	$C_{15}H_{11}N_2O_2Cl$	604-75-1	$[M + H]^+$	287.0582	−3.1	24.10	269.0474	0.2	241.0535	0.8
triazolam	$C_{17}H_{12}N_4Cl_2$	28911-01-5	$[M + H]^+$	343.0512	0.0	25.76	308.0834	1.1	253.0647	−0.6
phenobarbital	$C_{12}H_{12}N_2O_3$	50-06-6	$[M - H]^-$	231.0775	5.6	18.39	188.0741	−4.8	–	–
secobarbital (4)	$C_{12}H_{18}N_2O_3$	76-73-3	$[M - H]^-$	237.1245	2.9	24.94	194.1200	1.3	–	–
amisulpride	$C_{17}H_{27}N_3O_4S$	71675-85-9	$[M + H]^+$	370.1795	0.54	11.00	242.0478	−0.4	196.0071	0.8
aripiprazole	$C_{23}H_{27}N_3O_2Cl_2$	129722-12-9	$[M + H]^+$	448.1553	0.22	23.55	285.0904	−1.6	98.0979	1.5
chlorphenamine	$C_{16}H_{19}N_2Cl$	132-22-9	$[M + H]^+$	275.1310	−0.73	17.43	230.0734	0.3	167.0752	2.2
chlorpromazine	$C_{17}H_{19}N_2SCl$	50-53-3	$[M + H]^+$	319.1030	2.5	24.26	274.0441	−1.1	246.0105	−3.4
haloperidol	$C_{21}H_{23}NO_2FCl$	52-86-8	$[M + H]^+$	376.1474	0.27	22.07	358.1391	2.3	165.0742	1.4
olanzapine	$C_{17}H_{20}N_4S$	132539-06-1	$[M + H]^+$	313.1481	−2.2	12.07	256.0898	−0.5	222.1034	0.8
quetiapine (15)	$C_{21}H_{25}N_3O_2S$	111974-69-7	$[M + H]^+$	384.1740	0.01	19.66	253.0788	−0.6	221.1077	0.4
risperidone	$C_{23}H_{27}N_4O_2F$	106266-06-2	$[M + H]^+$	411.2191	−2.9	17.29	191.1174	−0.5	110.0599	−0.1
sulpiride	$C_{15}H_{23}N_3O_4S$	15676-16-1	$[M + H]^+$	342.1482	−2.9	7.11	214.0170	0.1	156.0134	2.0
zaleplon (8)	$C_{17}H_{15}N_5O$	151319-34-5	$[M + H]^+$	306.1349	−1.6	22.91	264.1234	−1.0	236.0927	−0.4

DOI: 10.1021/acs.jafc.5b02222
J. Agric. Food Chem. 2015, 63, 6954−6967

Table 1. continued

compound name	element composition	CAS Registry No.	quasi-molecular ion			RT (min)	MS^2 product ion		MS^3 product ion	
			formula	exact m/z (Da)	error (ppm)		measured m/z (Da)	error (mDa)	measured m/z (Da)	error (mDa)
Sedative-Hypnotics										
ziprasidone	$C_{21}H_{21}N_4OSCl$	146939-27-7	$[M + H]^+$	413.1197	−1.2	19.12	194.0371	0.4	159.0685	0.6
Impotence Drugs										
acetildenafil	$C_{25}H_{34}N_6O_3$	831217-01-7	$[M + H]^+$	467.2765	2.6	18.18	353.1637	−1.1	325.1326	−0.9
aminotadalafil	$C_{21}H_{18}N_4O_4$	385769-84-6	$[M - H]^-$	389.1255	2.6	23.15	262.0896	2.2	234.0943	1.9
avanafil	$C_{23}H_{26}N_7O_3Cl$	330784-47-9	$[M + H]^+$	484.1858	−1.9	20.15	375.1231	1.3	233.1030	−0.3
carbodenafil (17)	$C_{24}H_{32}N_6O_3$	–	$[M + H]^+$	453.2609	3.9	16.57	339.1456	0.4	311.1150	1.1
chloropretadalafil (16)	$C_{22}H_{19}N_2O_5Cl$	171489-59-1	$[M - H]^-$	425.0910	−0.24	32.18	262.0892	1.8	234.0958	3.4
dimethylsildenafil (19)	$C_{23}H_{32}N_6O_4S$	1416130-63-6	$[M + H]^+$	489.2279	−4.9	19.19	377.1284	0.6	331.0862	0.3
gendenafil (11)	$C_{19}H_{22}N_4O_3$	147676-66-2	$[M + H]^+$	355.1765	−1.7	30.91	327.1453	0.1	285.1356	1.0
homosildenafil (19)	$C_{23}H_{32}N_6O_4S$	371959-09-0	$[M + H]^+$	489.2279	−3.2	18.81	461.1988	2.2	313.1658	−0.1
hydroxyacetildenafil	$C_{25}H_{34}N_6O_4$	147676-56-0	$[M + H]^+$	483.2714	−3.3	17.09	465.2615	0.6	339.1561	−0.3
hydroxyhomosildenafil (21)	$C_{23}H_{32}N_6O_5S$	139755-85-4	$[M + H]^+$	505.2228	−3.9	18.45	487.2119	−0.3	377.1316	3.8
hydroxythiohomosildenafil	$C_{23}H_{32}N_6O_4S_2$	479073-82-0	$[M + H]^+$	521.1999	4.0	26.57	503.1909	1.5	354.1516	−0.6
hydroxyvardenafil (21)	$C_{23}H_{32}N_6O_5S$	224785-98-2	$[M + H]^+$	505.2228	3.2	19.39	377.1284	0.6	312.1581	0.1
mirodenafil	$C_{26}H_{37}N_5O_5S$	862189-95-5	$[M + H]^+$	532.2588	2.6	24.82	404.1658	1.9	326.1176	0.7
N-desethylvardenafil	$C_{21}H_{28}N_6O_4S$	448184-46-1	$[M + H]^+$	461.1966	2.6	17.91	299.1144	−2.8	230.0552	−4.2
nor-acetildenafil (17)	$C_{24}H_{32}N_6O_3$	949091-38-7	$[M + H]^+$	453.2609	−2.0	17.54	353.1611	0.3	325.1302	0.7
norneosildenafil (18)	$C_{22}H_{29}N_5O_4S$	371959-09-0	$[M + H]^+$	460.2013	1.3	33.71	311.1499	−0.4	283.1194	0.4
piperiacetildenafil	$C_{24}H_{31}N_5O_3$	147676-50-4	$[M + H]^+$	438.2500	2.3	19.28	353.1613	0.5	325.1305	1.0
pseudovardenafil (18)	$C_{22}H_{29}N_5O_4S$	224788-34-5	$[M + H]^+$	460.2013	0.01	31.85	299.1141	−3.1	230.0559	−3.5
sildenafil	$C_{22}H_{30}N_6O_4S$	139755-83-2	$[M + H]^+$	475.2122	−3.2	19.71	311.1498	−0.5	283.1197	0.7
sildenafil analogue I[c]	$C_{24}H_{34}N_6O_4S_2$	479073-90-0	$[M + H]^+$	535.2156	–	–	517.2050	–	341.1067	–
tadalafil	$C_{22}H_{19}N_3O_4$	171596-29-5	$[M + H]^+$	390.1448	−0.51	25.85	268.1091	−1.0	240.1145	1.4
thiodimethyl sildenafil (21)	$C_{23}H_{32}N_6O_3S_2$	–	$[M + H]^+$	505.2050	0.79	26.14	393.1074	−2.4	347.0663	3.2
thiohomosildenafil (21)	$C_{23}H_{32}N_6O_3S_2$	479073-80-8	$[M + H]^+$	505.2050	0.40	26.46	355.1591	0.4	327.1277	0.3
thiosildenafil (20)	$C_{22}H_{30}N_6O_3S_2$	479073-79-5	$[M + H]^+$	491.1894	2.6	27.39	341.1445	1.4	313.1123	0.5
udenafil	$C_{25}H_{36}N_6O_4S$	268203-93-6	$[M + H]^+$	517.2592	−3.1	20.75	474.2220	5.0	283.1197	0.7
vardenafil (19)	$C_{23}H_{32}N_6O_4S$	224785-90-4	$[M + H]^+$	489.2279	−2.0	17.32	299.1164	−0.8	230.0555	−3.9
xanthoanthrafil	$C_{19}H_{23}N_3O_6$	1020251-53-9	$[M - H]^-$	388.1514	3.1	26.59	358.1426	1.8	298.0614	−0.8
yohimbine (11)	$C_{21}H_{26}N_2O_3$	146-48-5	$[M + H]^+$	355.2016	0.84	14.65	212.1287	0.6	180.1026	0.7
Hypolipidemics										
bezafibrate (14)	$C_{19}H_{20}ClNO_4$	41859-67-0	$[M + H]^+$	362.1154	4.7	29.07	316.1105	0.5	161.0973	−1.1
fenofibrate (13)[c]	$C_{20}H_{21}ClO_4$	49562-28-9	$[M - H]^-$	359.1056	–	–	231.0206	–	–	–
atorvastatin	$C_{33}H_{35}FN_2O_5$	134523-00-5	$[M - H]^-$	557.2457	−1.1	31.87	453.1976	−2.1	397.1720	1.3
fluvastatin	$C_{24}H_{26}FNO_4$	93957-54-1	$[M - H]^-$	410.1773	2.4	31.81	348.1712	0.6	210.0739	−0.9
lovastatin	$C_{24}H_{36}O_5$	75330-75-5	$[M + H]^+$	405.2636	4.9	34.76	285.1885	−0.8	267.1728	1.2
simvastatin	$C_{25}H_{38}O_5$	79902-63-9	$[M + H]^+$	419.2792	1.7	35.59	285.1859	3.1	267.1754	−3.3
gemfibrozil	$C_{15}H_{22}O_3$	25812-30-0	$[M - H]^-$	249.1496	−7.2	33.94	121.0683	−2.0	–	–
Antidiabetics										
buformin[c]	$C_6H_{15}N_5$	1190-53-0	$[M + H]^+$	158.1400	–	–	141.1135	–	85.0509	–
metformin	$C_4H_{11}N_5$	657-24-9	$[M + H]^+$	130.1087	1.3	2.73	113.0818	−0.4	71.0561	−4.3
phenformin	$C_{10}H_{15}N_5$	834-28-6	$[M + H]^+$	206.1400	−2.9	10.42	189.1151	1.6	105.0696	−0.3
gliclazide	$C_{15}H_{21}N_3O_3S$	21187-98-4	$[M + H]^+$	324.1376	0.62	30.69	127.1226	−0.4	110.0964	−1.9
glimepiride (20)	$C_{24}H_{34}N_4O_5S$	93479-97-1	$[M + H]^+$	491.2323	0.61	32.66	352.1335	0.9	126.0914	0.1
glipizide	$C_{21}H_{27}N_5O_4S$	29094-61-9	$[M + H]^+$	446.1857	1.3	26.79	321.1026	1.0	286.0649	1.4
gliquidone	$C_{27}H_{33}N_3O_6S$	33342-05-1	$[M + H]^+$	528.2163	2.7	33.75	403.1344	2.2	386.1073	1.6
glybenzcyclamide	$C_{23}H_{28}N_3O_5SCl$	10238-21-8	$[M + H]^+$	494.1511	−0.20	32.17	369.0665	−0.5	169.0042	−0.9
nateglinide (10)	$C_{19}H_{27}NO_3$	105816-04-4	$[M - H]^-$	316.1918	2.5	32.57	164.0721	−0.7	147.0456	0.7
pioglitazone (12)	$C_{19}H_{20}N_2O_3S$	112529-15-4	$[M + H]^+$	357.1267	−4.2	20.97	134.0958	−0.6	119.0726	−0.4
repaglinide (17)	$C_{27}H_{36}N_2O_4$	135062-02-1	$[M + H]^+$	453.2748	1.1	34.0	230.1895	0.8	174.1284	0.7
rosiglitazone	$C_{18}H_{19}N_3O_3S$	122320-73-4	$[M + H]^+$	358.1220	3.07	15.19	135.0910	−0.7	107.0606	0.2
tolbutamide	$C_{12}H_{18}N_2O_3S$	64-77-7	$[M + H]^+$	271.1111	−2.6	27.49	172.0428	0.1	155.0165	0.4
Anti-inflammatory Analgesics										
4-acetamidophenol (1)[c]	$C_8H_9NO_2$	103-90-2	$[M + H]^+$	152.0706	–	–	110.0600	–	–	–
atropine	$C_{17}H_{23}NO_3$	51-55-8	$[M + H]^+$	290.1751	−2.8	11.32	124.1141	2.0	93.0697	−0.2
carbamazepine (4)	$C_{15}H_{12}N_2O$	298-46-4	$[M + H]^+$	237.1022	−1.3	22.74	194.0975	1.1	179.0749	1.9
codeine (7)	$C_{18}H_{21}NO_3$	76-57-3	$[M + H]^+$	300.1594	0.33	8.06	215.1072	0.5	183.0816	1.2

DOI: 10.1021/acs.jafc.5b02222
J. Agric. Food Chem. 2015, 63, 6954−6967

Table 1. continued

compound name	element composition	CAS Registry No.	quasi-molecular ion formula	exact m/z (Da)	error (ppm)	RT (min)	MS^2 product ion measured m/z (Da)	error (mDa)	MS^3 product ion measured m/z (Da)	error (mDa)
Anti-inflammatory Analgesics										
4-dimethylaminoantipyrine (3)	$C_{13}H_{17}N_3O$	58-15-1	$[M + H]^+$	232.1444	1.7	9.27	113.1098	2.5	84.0851	4.3
lidocaine	$C_{14}H_{22}N_2O$	137-58-6	$[M + H]^+$	235.1805	−2.5	12.34	86.0959	−0.5	–	–
methadone (9)	$C_{21}H_{27}NO$	76-99-3	$[M + H]^+$	310.2165	−1.9	24.07	265.1586	−0.1	105.0328	−0.7
tramadol	$C_{16}H_{25}NO_2$	22204-88-2	$[M + H]^+$	264.1958	−1.1	13.47	246.1836	−1.6	–	–

[a]Fragment ions in the MS^2 and MS^3 spectra are generated from the quasi-molecular ion and its dominant MS^2 product ion, respectively. [b]Each pair of isobaric coeluting species is marked with same number (including 21 groups). [c]No analytical standard available, exact mass data shown. −, not available.

ization or semiquantitation of certain classes of adulterants,[5,6,16] advances in modern LC-MS technology have greatly improved its analytical capability to meet the new requirements. To speed the targeted screening procedure, some LC-free MS techniques based on ion mobility, flow injection, or ambient ionization have been explored to detect illicit additives in dietary supplements.[5,7,17,18] To expand the coverage of the classical LC-MS method, we have recently reported a homologue-targeted approach by using unique QqQ-based scan or data-dependent hybrid linear ion trap (IT) toward nontarget screening, quantitation, and confirmation of multianalyte analogues in food matrices.[12,19−21] To meet the new challenge in detecting emerging food fraud adulterants and unknown illegal derivatives, the current use of high-resolution MS (HRMS) analyzers with time-of-flight (TOF) or Orbitrap has gained increasing popularity in nontargeted screening of general unknowns. Owing to the increased mass-resolving power (≥10000 fwhm) and inherent sensitive full-spectrum scanning with mass measurement errors <10 ppm, HRMS can unbiasedly detect and unambiguously identify a theoretically unlimited number of analytes via retrospective post-targeted data interrogation without either prior analyte-specific information or use of authentic standards.[2,4−7,11,13,22] However, a single-stage HRMS with an ultrahigh resolution (>50000 fwhm),[23] or its use in conjunction with high-resolution LC separation,[24] is generally required for reliable mass assignment in complex matrices. In some cases even multiplexed tandem HRMS (such as Q-TOF, IT-Orbitrap, and Q-Orbitrap) is needed to improve confirmation accuracy by means of fragment ions and isotopic patterns.[25−27] IT-TOF is a hybrid instrument that serves as an alternative technique to combine the multistage fragmentation (MS^n) capability of IT with the high resolving power of a TOF for structural elucidation.[28] By taking advantages of rapid polarity-switching and data-dependent acquisition of accurate MS^n spectra "on-the-fly" in a single run, LC-IT/TOF has been reported for the global identification of herbal components, discovery of drug metabolites, and metabolomics.[29−31] However, this method has not been previously used for multiclass screening and identification of undesirable substances in food matrices.

In this work, we explore the potential of the hybrid LC-IT(MS^n)/TOF technique for wide-scope screening and library searching for over 100 illegal adulterants in various types of dietary supplements. To the best of our knowledge, this is the first report on developing a generic workflow for adulteration screening of functional foodstuffs. In addition, a new straightforward sample preparation procedure based on single-tube extraction[19−21,32,33] is adapted to expand the screening spectrum.

MATERIALS AND METHODS

Chemicals. The analytical standards of adulterant listed in Table 1 were of high purity (>92%) and purchased from TLC PharmaChem (Vaughan, Canada), Sigma-Aldrich (Shanghai, China), or the National Institute for the Control of Pharmaceutical and Biological Products (Beijing, China). Individual stock standard solutions (ca. 1.0 mg/mL) were prepared in pure methanol, acetonitrile, or water. An intermediate standard mixture of the reference compounds was prepared by appropriate dilution of the individual stock solutions in methanol/water (50:50, v/v). The selected 106 adulterants were divided in 10 mixtures with around 10 analytes each at a concentration of 50 μg/mL. Mixed standard working solutions (0.1−50 μg/mL) used to spike control samples were prepared by diluting the multianalyte intermediate standard mixture with methanol/water (25:75, v/v). All of the stock and working solutions were stored at −20 °C in the dark when not in use. HPLC-grade methanol and acetonitrile were obtained from Merck (Darmstadt, Germany). Analytical-grade sorbents of primary−secondary amine (PSA, 40 μm) and octadecylsilane (ODS, C_{18}, 40 μm) were purchased from Varian, Inc. (Palo Alto, CA, USA). Unless otherwise specified, all other reagents were of analytical grade. Ultrapure water prepared by a Milli-Q-Plus system (Millipore, Bedford, MA, USA) was used throughout the study.

Dietary Supplement Samples. Dietary supplements, which claimed functions of supporting healthy blood pressure (15), blood sugar management (16), antiobesity effect (17), hypolipidemic effect (12), antiinflammatory analgesic effect (13), sedative−hypnotic effect (18), or enhancement of sexual performance (22), were purchased from Internet vendors and local markets in China, in five different oral forms including 25 liquids, 25 capsules, 23 tablets, 22 softgels, and 18 pills.

To provide the negative controls ("blank" samples), the collected materials were preliminarily confirmed to be free from contamination of the test adulterats by LC-MS screening after sample handling with the procedure described below. Fortified samples serving as matrix-matched standards for method development and validation were prepared by spiking with the respective working standard solutions into an accurately weighed aliquot (approximate 2.0 g) of the individual analyte-free "blank" matrices. All of the collected specimens, subsamples, and control samples for both blanks (negative controls) and spikes (positive controls) were stored at −20 °C (in the dark) until analysis.

Sample Preparation Procedure. After collection, the tablets and pills (pellets) were crushed into fine powder; the capsules and softgels were cut open and the contents mixed and then thoroughly homogenized. For oral liquids, three samples were evenly mixed and divided into fractions. Then a representative portion of 2 g of the resulting powder or liquid sample was accurately weighed (precision = 0.1 mg) and transferred to a 50 mL screw-cap (Teflon-lined) centrifuge tubes. All of the test sample aliquots were processed with the subsequent procedures prior to LC-IT/TOF analysis.

Single-Tube Multifunction Adsorption Cleanup (stMAC). The protocol was carried out by using a single-tube extraction procedure based on one-pot extraction/partitioning−multifunction adsorption

DOI: 10.1021/acs.jafc.5b02222
J. Agric. Food Chem. 2015, 63, 6954−6967

sample cleanup introduced earlier with minor modifications.[20] In brief, an aliquot of the test sample was first blended with 20 mL of methanol for 5 min, and then the mixture was extracted with 20 mL of acetonitrile containing 1% formic acid by vortex for 1 min and sonication for 15 min, followed by centrifugation at 5000*g* for 3 min. Afterward, a dispersive adsorbent mixture consisting of 0.2 g of PSA and 0.4 g of ODS was added to the supernatant (crude extract) within the same tube for multifunction cleanup.[21,33] The tube was shaken vigorously for 2 min and centrifuged again for 2 min at 9000*g*. The resulting clarified supernatant was transferred for next filtration/dilution pretreatment.

In-Vial Filtration–Dilution–Injection (ivFDI). After the above centrifugation, a 0.5 mL aliquot of the final *st*-MAC extract (upper phase) was immediately withdrawn and filtered through a 0.22 μm pore PTFE syringe filter (Phenomenex, Torrence, CA, USA) into an autosampler vial containing 1.0 mL of methanol/water (1:1, v/v) for "dilute-and-shoot" LC-MS analysis.

LC-IT/TOF MS Instrumentation. LC-IT/TOF analyses were carried out on a hybrid LCMS-IT-TOF instrument (Shimadzu, Kyoto, Japan) equipped with an electrospray ionization (ESI) source interfaced to a Prominence LC system consisting of an LC-10AD binary pump, a DGU-14A degasser, an SIL-20AC autosampler, and a CTO-20AC column oven. Instrument control, data acquisition, and analysis were performed using Shimadzu LCMSsolution software (version 3.6).

Chromatographic separation was achieved on a reversed-phase Agilent ZORBAX Eclipse AAA column (150 mm × 4.5 mm i.d., 5 μm), with a binary mobile phase composed of 0.1% (v/v) acetic acid in water (eluent A) and 0.1% (v/v) acetic acid in acetonitrile (eluent B) pumped at a flow rate of 0.50 mL/min.The column temperature was maintained at 40 °C. The elution gradient started with 5% B and was changed linearly as follows: 8 min, 20% B; 26 min, 50% B; 33–40 min, 100% B; 40.1–45 min, 5% B. The total run time was 45 min, and the injection volume was 10 μL.

High-resolution mass spectrometric data were acquired with the hybrid IT/TOF mass analyzer in both the positive and negative ESI modes using an automatic polarity-switching system in full scan and multiple stage fragmentation (MS^n) modes. The optimized MS parameters were set as follows: interface voltages, 4.5 kV (for ESI+) and −3.5 kV (for ESI−); detector voltage, 1.7 kV; nebulizing gas (N_2) flow, 1.5 L/min; drying gas (N_2) pressure, 0.1 MPa; curved desolvation line (CDL) temperature, 200 °C; heat block temperature, 200 °C. The MS^n spectra were generated by collision-induced dissociation (CID) of the target precursor ions with argon (Ar) as the cooling gas and collision gas, and the relative collision energy was set at 50%. All ions were first accumulated in the IT for automatic MS^n analyses over m/z scan ranges of 100–800 for MS^1, 100–600 for MS^2, and 50–400 for MS^3, and then the selected ions were subsequently introduced into the TOF instrument for accurate mass measurements. The ion trap pressure was 1.7×10^{-2} Pa and ion accumulation time was 100 ms; the isolation width of precursor ions was 3.0 amu. A solution of sodium trifluoroacetate clusters was used as reference for calibrating the mass axis across the range of m/z 50–2000 with error below 5 ppm.

Automatic Screening by LC-IT(MS^n)/TOF MS. *Accurate Mass Database Construction.* The compound name, CAS Registry No., elemental composition, molecular weight, and theoretical exact mass of each food adulterant were collected in an Excel spreadsheet. The retention time, quasi-molecuar ion (or dominant adduct ion), MS^2 spectrum of each target parent ion, MS^n spectrum of the most intense fragment ion in the MS^{n-1} spectrum ($n \leq 4$), and characteristic fragments from the CID mass spectra acquired in the format of the instrument's raw file were also included in the database. The resulting raw data files were transformed to JCAMP format (*.jdx files), and the Excel table built was automatically converted to Access format using the Shimadzu LCMSsolution data analysis software. As such, the user-created accurate mass database was generated in which different information can be used as searching parameters, including chemical name, retention time, accurate mass, molecular formula, and characteristic fragments. When a sample is processed with the searching database, the monitoring program consists of initial rapid diagnostic test for screening out suspected noncompliant samples and further reliable confirmation of the positive samples.

Automated Library Searching. In targeted screening of the adulterants with reference standards, the LCMS-IT-TOF was operated in a multiple precursor ion scan, followed by a data-dependent MS/MS fragmentation triggered dynamically by these selected molecular ions. In the nontarget screening procedure to identify expected or unexpected analytes, the hybrid system was operated in both ionization modes for full scanning with m/z 100–800 (ESI±), followed by a two-step protocol including component extraction and database searching.[34] For nontarget compounds without analytical standards but anticipated to be present in the database, the whole total ion chromatogram (TIC) was examined and automatically searched against the custom database by in-laboratory software (MetID Solution) to pick out the peaks, acquire the CID spectrum, and determine the presence of the expected adulterants in the sample, with a user-defined search criterion of 10 mDa accurate mass tolerance. For unexpected compounds without any a priori knowledge, only intense peaks with high signal intensities above 500,000 counts (component filter) were considered for further ion extraction (XIC) and subsequent full-scan MS^n acquisition to create a list of the detected peaks.

Multiparameter Confirmation/Identification. Finally, the target analytes can be fully confirmed (or absolutely quantitated) with the standards. For expected compounds, a part of the searching parameters was entered into an in-house ACD/MS Manager program, and an Excel spreadsheet was constructed to include, per analyte, the measured accurate mass data, the molecular formula, structural fragment ions, and retention time. The matching filter for final confirmation by comparing experimental data to the database was set to be below 5 ppm mass-accuracy window, along with a threshold limit value of ±0.3 min for retention errors. For the automatic nontarget screening of every suspected peak found, the molecular mass (m/z) data corresponding to particular elemental composition was calculated and thus the proposed empirical formula was generated by using Shimadzu's Formula Predictor. Further tentative structure elucidation of unexpected molecules can be achieved by multiparameter matching algorithm to minimize the number of possible formulas, based on evaluation and interpretation of the isotopic profile, multistage accurate mass, and characteristic MS^n fragmentation pattern.

Validation Protocol. Validation of the qualitative screening method was conducted on the basis of European analytical guidelines described in Directive 2002/657/EC, its supplement CRLs 20/1/2010, and new Document SANCO 12495/2011.[35−37] The performance characteristics of the developed LC-IT/TOF approach include specificity, matrix effect (ME), extraction recovery (ER), decision limit (CCα), decision capability (CCβ), screening detection limit (SDL), and limit of confirmation (LOC) for method validation.

The specificity was checked by testing 20 unspiked blank samples for each matrix and monitoring the presence of false detects and possible overlapping peaks appearing to interfere with the target analytes. The latent matrix effect on ESI-MS detection and analyte extraction recovery were calculated as described elsewhere.[21] As established for screening methods, SDL or CCβ (beta error probability 5%), which was defined as the validation analyte concentration at which the method can detect truly contaiminated samples with a statistical certainty of 95% (i.e., a false-negative rate of 5% is accepted), was calculated from CCα, which was determined as the lowest amount of the analyte at which the response signal was 3 times the average noise level age noise level (S/N = 3) of 20 replicates of blank samples per matrix. For reliable confirmation, LOC was established to estimate the threshold concentration for unequivocal identification.[20]

RESULTS AND DISCUSSION

Accurate MS^n Acquisition by Dual-Polarity LC-IT/TOF MS. In this work, 106 prescription drugs used as potential adulterants in dietary supplements including weight-loss drugs, impotence drugs (PDE-5 inhibitors), antihypertension drugs,

DOI: 10.1021/acs.jafc.5b02222
J. Agric. Food Chem. 2015, 63, 6954−6967

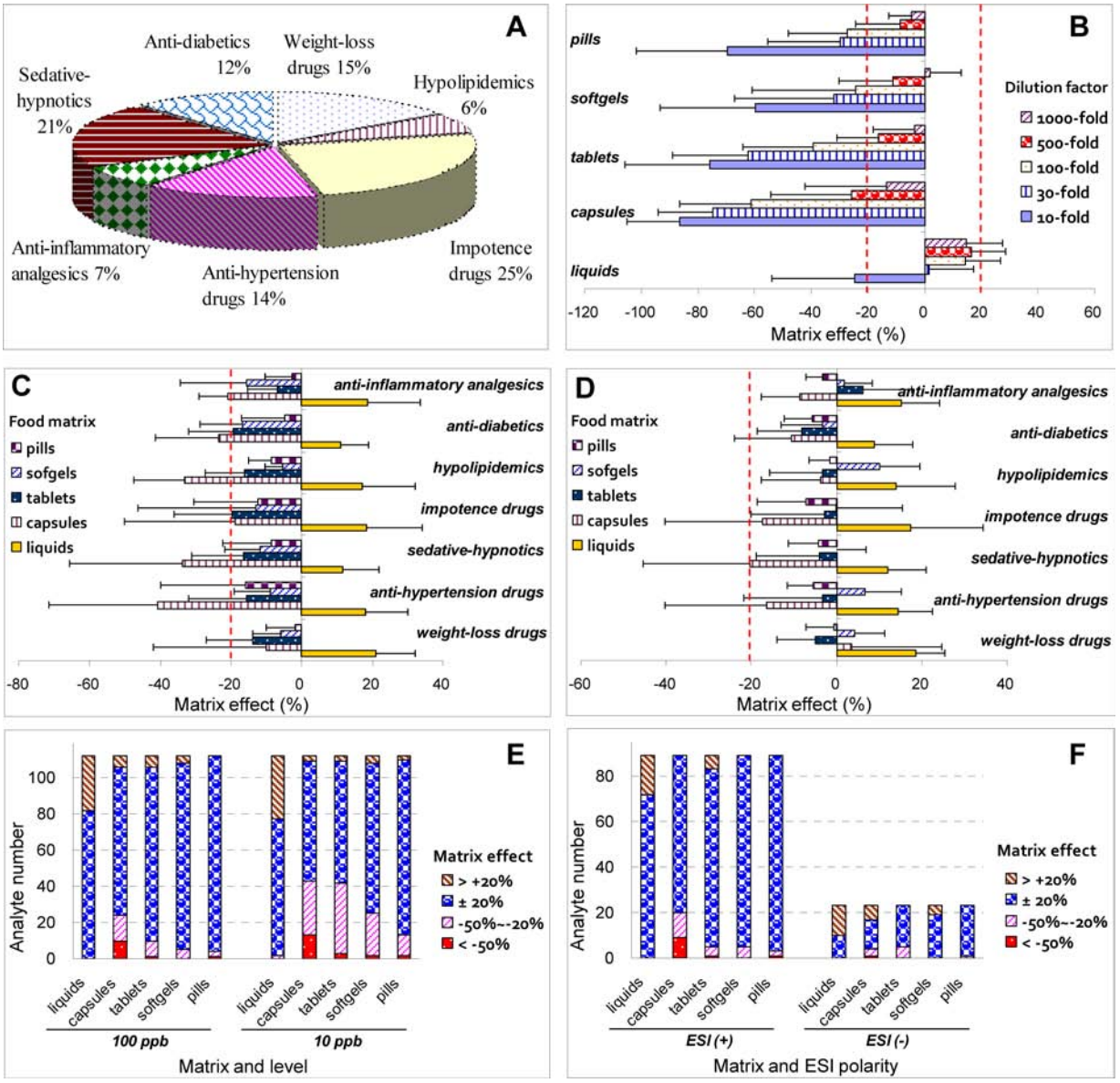

Figure 1. Optimization and validation of the *st*MAC/*iv*FDI procedure for extraction/cleanup of seven classes of adulterants in five types of food matrices: (A) pie chart of the compound proportion sorted by medical usage; matrix-induced effects obtained by (B) direct dilution-and-shoot; (C) *st*MAC protocol; (D) *st*MAC/*iv*FDI procedure, and *st*MAC/*iv*FDI procedure under (E) different analyte levels or (F) different ESI polarities.

antidiabetics, sedative−hypnotics, hypolipidemics, and anti-inflammatory analgesics (Table 1) were selected for method development for which reference standards were available in our laboratory.

Because the analytes cover a wide spectrum of polarities including very polar compounds such as biguanide antidiabetics and nonpolar molecules such as statins, the LC conditions applied were optimized to obtain the broadest distribution of all the target compounds across the whole chromatographic space. We used a long-gradient elution program with a total run time of 45 min and the retention time (RT) ranging from 2.7 min (metformin) to 35.6 min (simvastatin), which provides significantly better separation of isomers or coeluting components. Different solvent compositions were investigated for the mobile phase consisting of methanol or acetonitrile as organic phase and water with formic acid, acetic acid, ammonium formate, ammonium acetate, or ammonium hydroxide as modifier. Satisfactory results were obtained using 0.1% (v/v) acetic acid in both water (eluent A) and acetonitrile (eluent B), giving better peak shapes and higher sensitivity for the major analytes.

Although most of the analytes can be detected under positive ESI conditions, 23 compounds gave higher ionization efficiencies (sensitivity) or signal-to-noise ratios (specificity) in negative ESI mode, highlighting the necessity of using both ionization polarities to extend the screening scope. However, most TOF-based instruments cannot acquire simultaneously in both polarity modes, and thus two separate injections[38] or two temporal time segments[39] are required for this purpose. Like the new Orbitrap technique, the hybrid IT/TOF analyzer is capable of acquiring high-resolution spectra for both polarities in a single run.[40−42] Considering a fast polarity-switching (0.1−0.4 s) and data-dependent acquisition of accurate MS^n spectra (10−1000 scans/s,[28] 10 Hz[40]), an overall cycle time for acquiring MS^{1-3} scanning functions (ca. 0.8 s) was estimated to be ∼2.5 s. Under the optimized LC conditions, a peak width of

DOI: 10.1021/acs.jafc.5b02222
J. Agric. Food Chem. 2015, 63, 6954−6967

ca. 20 s obtained for each analyte accommodates well the acquisition time for these scan events, allowing for at least 8 scans/peak to ensure reliable identification.

Matching of both dual-polarity detection and high mass resolution can further increase the detection selectivity to reduce risks of false results due to coeluting isobaric interferences.[42] In general, however, an increase in mass resolution (thereby selectivity) will decrease sensitivity and scanning speed.[2,42] The IT/TOF mass spectrometer provides a resolving power of over 10000 fwhm (at m/z 1000), with a typical error lower than 5 ppm,[43] at the range of m/z 200−2000 after mass calibration with the reference standard.[28] Table 1 shows that, with few exceptions, the measured masses for all precusor ions were in accordance with the theoretical values with a sufficiently high level of confidence. Furthermore, another advantage of this hybrid IT/TOF analyzer is the ability to acquire multistage MS^n spectra ($n \leq 10$) with accurate mass (error <10 ppm) in both MS and MS^n modes in a single run, as exemplified below for confirmation and elucidation purposes.

Sample Pretreatment Optimization. There is a clear trend toward using fast generic pretreatment methods such as QuEChERS for multianalyte, multimatrix extraction in a single procedure.[38,44−46] Currently, we have shown that the combination of liquid extraction and dispersive solid-phase extraction (dSPE) cleanup in a single tube can provide more flexible alternatives to QuEChERS to cover a broad array of analyte−matrix combinations,[20,21,32,33] based on one-pot spontaneous extraction/in situ multifunction cleanup for direct LC-MS injection. In this work, a straightforward nonselective extraction/"dilute-and-shoot" procedure, which involves *st*MAC and *iv*FDI, is proposed to permit simultaneous extraction/purification of seven classes of adulterants in five types of sample matrices (Figure 1).

The *st*MAC/*iv*FDI procedure was optimized for minimizing matrix-induced effects without sacrificing extraction recovery. Matrix effects are a major concern in LC-MS bioanalysis as they can adversely affect quantitative reliability as well as mass measurement accuracy.[43,46] Direct dilution of samples is an easy approach to reduce matrix interference in popular dilute-and-shoot ESI-MS methods.[17,44−47] To examine the occurrence of matrix effect in the dilute-and-shoot analysis, we compared the response of analyte standards spiked to each control extract after extraction by acetonitrile/methanol/formic acid (70:29.5:0.5, v/v/v) under different dilution factors (10, 30, 100, 500, and 1000) with that in the extracting solvent. Of the five matrices studied, liquid was the one with the least matrix-induced effects, whereas capsules exhibited the strongest signal suppression. As shown in Figure 1B, considerable matrix effects (<−20% or >+20%) were observed for most of the resulting 530 combinations (106 analytes × 5 matrices) when the extract was directly injected after a dilution up to 500-fold. In the case of capsule samples, higher dilution factors were required for further removing the extensive matrix effects. Despite the low matrix equivalent in the dilute-and-shoot extract, strong matrix interferences were still observed, indicating additional cleanup treatment was necessary.

In the *st*MAC protocol, such severe matrix suppression was significantly improved (Figure 1C), by multifunction dSPE with a lower dilution factor of about 20 (i.e., an absolute amount of 2 g sample extracted to a final volume of 40 mL). To further diminish the matrix effects, the *st*MAC extract was processed with an *iv*FDI protocol, by which a clarified filtrate and another 3-fold dilution of the final extract was obtained for direct injection. Therefore, the combination of *st*MAC and *iv*FDI yields a moderate dilution of extracts by a factor of 60, corresponding to 16.7 mg/mL (i.e., 1/3 × 2 g/40 mL) of matrix equivalent in the final extract, which resulted in acceptable sensitivity and consistent low matrix effects (within ±20%) for all of the analyte/matrix pairs (Figure 1D), even at relatively low parts per billion levels (Figure 1E), regardless of the matrix complexity (capsules and tablets) or the ESI polarity mode (Figure 1F). Overall, the newly developed *st*MAC/*iv*FDI procedure can minimize most of the matrix effects by coextracted or coeluting residual components on nontargeted LC-IT/TOF screening of samples.

Qualitative Validation with Target Analytes. For wide-scope screening methods, the objective of a qualitative validation is typically focused on detectability, that is, to ensure the sensitive detection and reliable confirmation of the presence and identity of an analyte in a fortified sample at a certain level of concentration. To examine the feasibility of the *st*MAC/*iv*FDI-based LC-IT/TOF approach, the method was validated for the "easiest" matrix (liquids) and two of the most problematic matrices (capsules and tablets). The performance characteristics in terms of CCα, CCβ (SDL), LOC, and ER, for which the analytical criteria of sensitivity, specificit,y and reliability were met, are evaluated and summarized in Table 2.

The detection limits of the 106 analytes reached a sensitivity at low picogram level (i.e., a 10 μL injection of 0.2−5 ng/mL extract). In all of the tested matrices, almost 70% of the adulterants have CCα values ≤30 μg/kg, and only 6% have

Table 2. Validation Parameters of Qualitative Screening by Using *st*MAC/*iv*FDI-Based LC-IT/TOF MS

drug class	CCα (μg/kg)	SDL[a] (μg/kg)	LOC (μg/kg)	ER (%)
In Liquids				
weight-loss	10−20	13−25	20−50	71−94
antihypertension	15−30	26−38	50−100	73−87
sedative−hypnotics	10−40	12−45	20−50	80−90
impotence	10−30	15−41	20−50	81−96
hypolipidemics	15−30	21−40	50−100	72−95
antidiabetics	20−40	30−47	50−100	69−92
anti-inflammatory	20−30	26−40	50−100	74−88
In Capsules				
weight-loss	20−100	25−117	50−200	57−86
antihypertension	30−40	39−50	100−200	71−90
sedative−hypnotics	20−40	28−48	50−100	75−91
impotence	10−100	12−132	20−200	63−91
hypolipidemics	20−200	26−211	50−300	62−85
antidiabetics	30−300	36−363	100−500	61−87
anti-inflammatory	30−100	37−115	100−200	59−82
In Tablets				
weight-loss	10−30	16−35	20−50	62−90
antihypertension	20−40	23−43	50−100	73−91
sedative−hypnotics	15−40	17−46	50−100	77−89
impotence	15−40	21−50	50−100	70−92
hypolipidemics	20−40	28−49	50−100	66−83
antidiabetics	30−40	37−50	100−200	62−85
anti-inflammatory	20−40	25−47	50−100	67−89

[a]SDL = CCα + 1.64 × SD; SD is the standard deviation obtained from the 20 representative blank samples spiked at the CCα level.

DOI: 10.1021/acs.jafc.5b02222
J. Agric. Food Chem. 2015, 63, 6954−6967

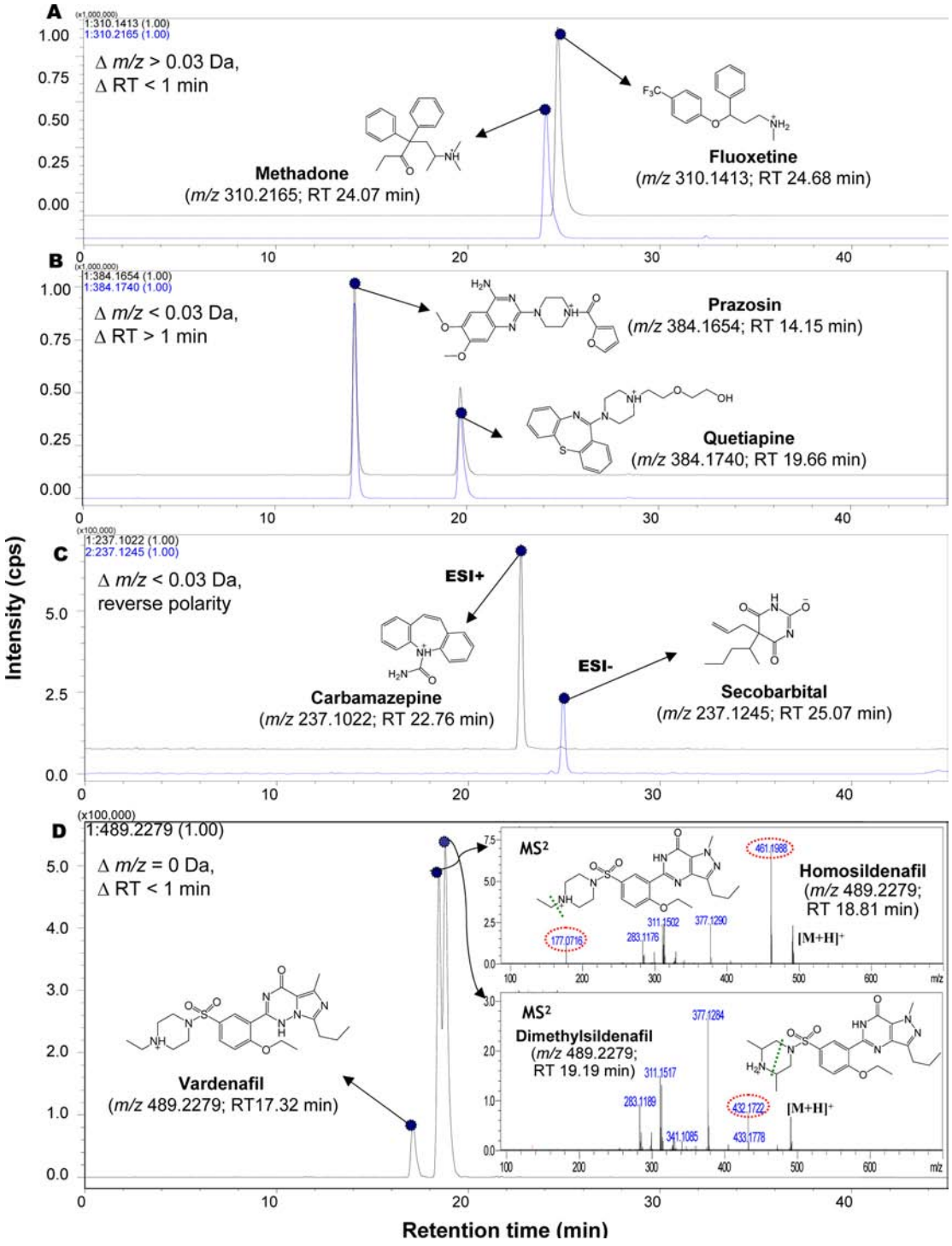

Figure 2. LC-IT/TOF-based targeted screening, discrimination, and confirmation of isobaric or isomeric species coexisting in a representative tablet sample extract spiked at 20 μg/kg, by (A) accurate mass and narrow XICs of coeluting isobars (Δ m/z > 0.03 Da, Δ RT < 1 min), (B) chromatographic separation of isobars with small mass defects (Δ m/z < 0.03 Da, Δ RT > 1 min), (C) dual-polarity detection channels, and (D) chromatographic separation of isomers (Δ m/z = 0, Δ RT > 1 min) or MS/MS fragmentation spectra of coeluting isomers (Δ m/z = 0, Δ RT < 0.5 min).

detection limits >50 μg/kg, indicating the sensitivity of this screening method is sufficient for most of the analyte/matrix combinations for adulterated dietary supplements. The statistical limit of CCβ is considered as SDL to evaluate the critical levels above which the screening method is valid with 95% confidence (i.e., 19 of 20 samples). All of these analytes were satisfactorily validated in all samples at 0.05 mg/kg spike level except for capsules, for which a SDL of 0.4 mg/kg was finally established (Table 2). The LOCs of the target compounds, which were achieved at 0.1 and 0.4 mg/kg for 73 and 97% of the detected adulterants, respectively, are sufficient to verify compliance of the majority of the test adulterated samples.

DOI: 10.1021/acs.jafc.5b02222
J. Agric. Food Chem. 2015, 63, 6954−6967

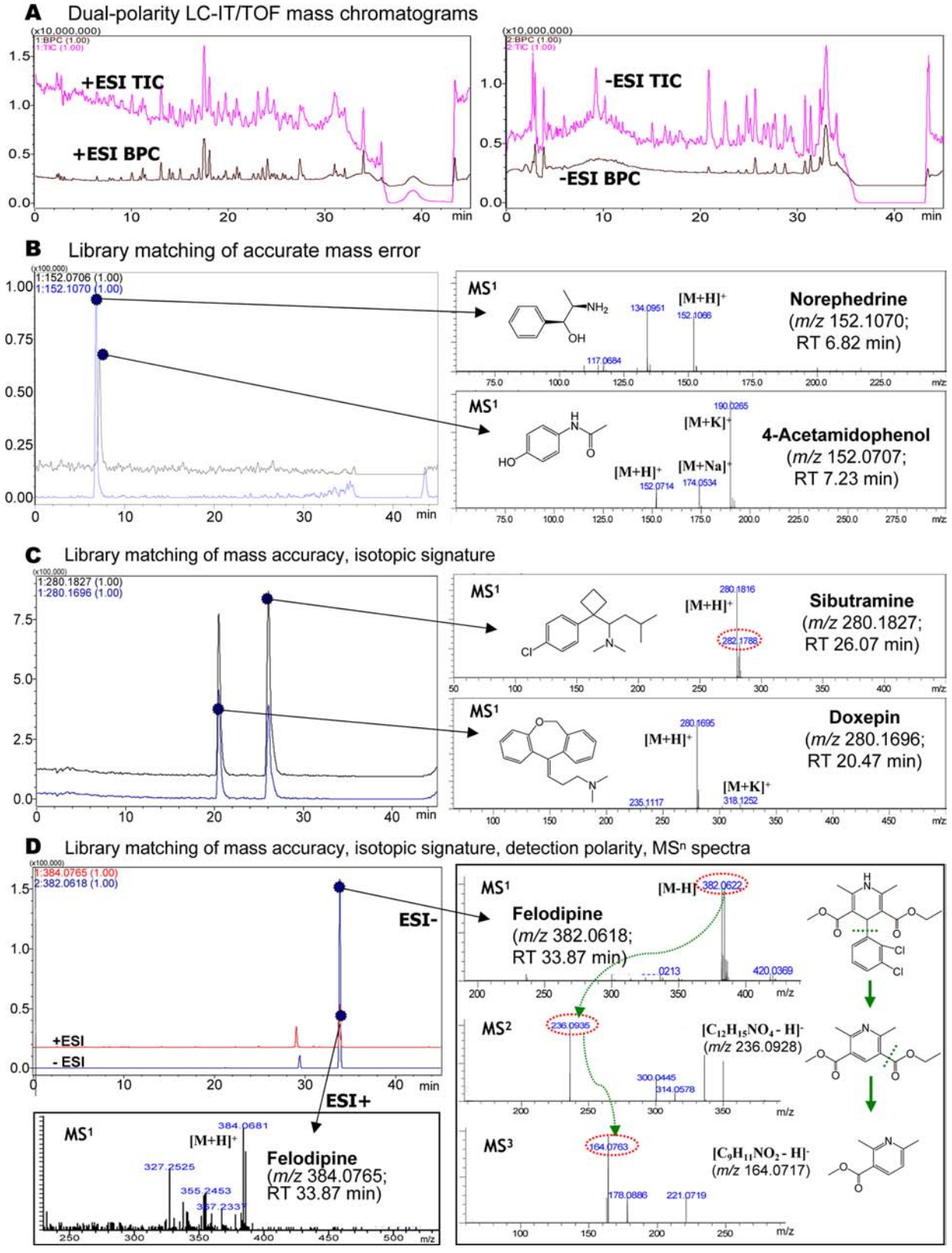

Figure 3. LC-IT(MS^n)/TOF-based nontargeted screening and identification of three expected library compounds along with their isomers or coeluting isobars in a mixture of 20 capsule samples: (A) overlaid TIC and BPC mass chromatograms obtained from the capsule extract mixture in both ESI polarity modes; (B) identification of 4-acetamidophenol and its coeluting isobar norephedrine by library matching of accurate mass error; (C) identification of doxepin and its isobar sibutramine by library matching of mass accuracy and isotopic signature; (D) identification of felodipine and the interfering ion from bezafibrate by library matching of detection polarity, mass accuracy, isotopic signature, and MS^n CID spectra. Overlaid XICs at different m/z values, and their corresponding structures and MS^n spectra are included as insets. 1, ESI+; 2, ESI−.

DOI: 10.1021/acs.jafc.5b02222
J. Agric. Food Chem. 2015, 63, 6954−6967

Table 3. Adulterant-Positive Results of Commercial Dietary Supplements by Applying the *st*MAC/*iv*FDI-Based LC-IT(MS^n)/TOF Nontargeted Screening Method to Real Samples

sample	dosage form	label claim	occurring adulterant	analyte type	content[a] (mg/mL or mg/g)
L007	liquid	weight loss	sibutramine	targeted	~20
L012	liquid	antifatigue	tadalafil	targeted	>20
			sildenafil analogue I	expected	>50 (sildenafil)[b]
L013	liquid	hypolipid	hydrochlorothiazide	targeted	>5
L019	liquid	enhancement of sexual performance	dimethylsildenafil	targeted	~20
			thiodimethylsildenafil	targeted	>15
			N-ethylated dimethylsildenafil	unexpected	~15 (dimethylsildenafil)[b]
L021	liquid	weight loss	sibutramine	targeted	>10
L025	liquid	hypotension	nitrendipine	targeted	~5
C002	capsule	weight loss	doxepin	expected	>10 (diazepam)[b]
			norephedrine	targeted	~5
C005	capsule	hypotension	felodipine	expected	~4 (nifedipine)[b]
C011	capsule	hypolipid	metformin	targeted	~20
			bezafibrate	targeted	>5
C012	capsule	antiphlogosis	4-acetamidophenol	expected	~4 (phenacetin)[b]
C016	capsule	blood sugar management	glimepiride	targeted	~5
			metformin	targeted	>40
C017	capsule	weight loss	sibutramine	targeted	>20
C020	capsule	support of healthy blood pressure	felodipine	expected	~0.8 (nifedipine)[b]
			sibutramine	targeted	~10
C023	capsule	antifatigue	tadalafil	targeted	~100
T015	tablet	weight loss	sibutramine	targeted	~15
T021	tablet	nerves-soothing	estazolam	targeted	>0.2
S003	softgel	enhancement of sexual performance	sildenafil	targeted	~30
			sildenafil analogue I	expected	>50 (sildenafil)[b]
S007	softgel	weight loss	sibutramine	targeted	>30
S012	softgel	support of healthy blood pressure	reserpine	targeted	~1
			hydrochlorothiazide	targeted	>5
S019	softgel	hypoglycemic effect	phenformin	targeted	~20
P011	pill	weight loss	doxepin	expected	~2.5 (diazepam)[b]

[a]Adulteration level is calculated by multiplying the LOC data by the sample dilution factor. [b]For nontarget compound, the LOC data are estimated to be identical to those of its structural analogue (given in parentheses).

The detection specificity is also a key feature to assess the viability of the LC-IT/TOF screening procedure. As exemplified by elucidating isobaric or isomeric species[24] occurring in the database (46 species in 21 groups found in Table 1), a highly reliable identification could be achieved with the multimode selectivity provided by the LC-IT(MS^n)/TOF procedure from accurate mass measurement, chromatographic retention, and multistage fragmentation data.

The TOF-based analysis allows isobars to be readily discriminated from differences in mass defect (Δ m/z > 0.03 Da) without sufficient prior LC separation of the coeluting compounds (Figure 2A). With respect to isobars with small mass defects (Δ m/z < 0.03) or isomeric compounds (Δ m/z = 0), efficient chromatography is a common tool to discriminate these species (Figure 2B,D). In Table 1, most (14 pairs) of the isobars or isomers were resolved by significant retention differences (Δ RT > 1 min), demonstrating the importance of chromatographic separation for simultaneous screening purpose. Also, detection polarity may increase the discrimination selectivity, as exemplified in Figure 2C for complete separation of carbamazepine and secobarbital by their reverse ESI polarity without any difference in mass defect or retention index. As for some more closely related isobaric coeluting species (Δ m/z < 0.03 Da, Δ RT < 0.5 min), neither exact mass nor retention time could itself be enough for reliably distinguishing the overlapped peaks. In this case, complementary information on molecular fragmentation and additional isotopic profiles if available must be explored for isomeric differentiation and unambiguous structural confirmation. As observed in Figure 2D, there were considerable differences in the MS^2 spectrum between the coeluting isomers homosildenafil (m/z 461, 177) and dimethylsildenafil (m/z 432),[6] highlighting the need and advantages of using the hybrid LC-IT/TOF instrument to generate high-resolution multistage fragmentation spectra, but for stereoisomers ephedrine and pseudoephedrine, the present method could not distinguish between them successfully, and a further chiral separation would be required for stereoselective detection of the epimer mixtures.

Library-Based Postrun Nontarget Screening. To evaluate the feasibility of LC-IT(MS^n)/TOF for qualitative screening in dietary supplements of nontarget or expected adulterants without analytical standards but that were present in the database, a mixture of sample extracts from 20 capsule products intended for weight loss, hypotension, hypolipid, or antiphlogosis was processed using the library-based postrun screening algorithm. Figure 3A shows the base peak chromatograms (BPCs) in both polarity modes for the capsule mixture, in which only the most intense peak in the spectrum at every point was monitored and thus the BPC is cleaner and more informative than the TIC mass chromatogram. The acquired spectra were automatically searched for in the database, and some adulterants including three nontarget compounds (4-

DOI: 10.1021/acs.jafc.5b02222
J. Agric. Food Chem. 2015, 63, 6954−6967

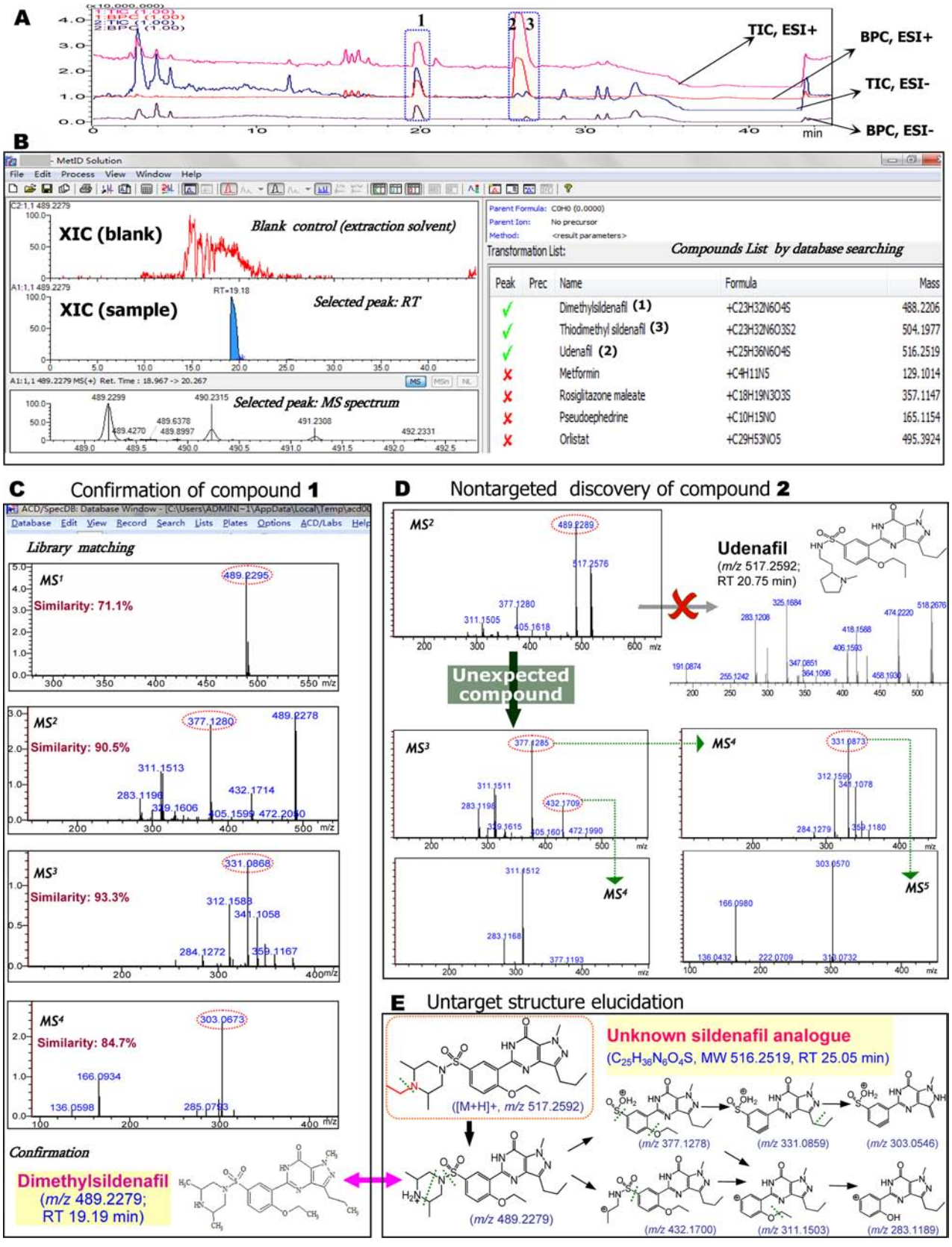

Figure 4. Example of the LC-IT(MS^n)/TOF-based automated library searching procedure applied to nontarget screening of a suspected positive real sample (healthcare wine product) involving (A) acquiring dual-polarity full-scan accurate mass chromatograms; (B) peak assignment (1, 2, 3) by database searching with MetID Solution; (C) target confirmation of 1 (dimethylsildenafil) via library matching by using ACD/MS Manager based on retention precision and MS^n spectrum similarity; (D) nontargeted discovery of unexpected compound **2** (udenafil isomer); and (E) structure elucidation of **2** as a novel sildenafil analogue (*N*-ethylated dimethylsildenafil).

DOI: 10.1021/acs.jafc.5b02222
J. Agric. Food Chem. 2015, 63, 6954−6967

acetamidophenol, doxepin, and felodipine) were tested positive in the samples. For nontarget compounds, because no reference standards were available and thus the retention data were not included in the database, their identification was made only through comparison of spectra based on the precursor ion (mass error) and its characteristic MS^n fragments (similarity).

Figure 3B shows the narrow-window XICs and the corresponding mass spectra of two nearly coeluting compounds, norephedrine (m/z 152.1066, −2.6 ppm error) and 4-acetamidophenol (m/z 152.0714, 4.6 ppm error). The exact mass difference (about 36 mDa) could be enough to differentiate both compounds with the instrument resolution. In addition, 4-acetamidophenol also exists as adducts of $[M + Na]^+$ (m/z 174.0534) and $[M + K]^+$ (m/z 190.0265) with errors of 4.7 and 0 ppm, respectively. In Figure 3C, there are two m/z 280 isobars that cannot be differentiated by the exact mass difference (Δ m/z < 20 mDa). However, they can be well separated with the LC retention (Δ RT > 5 min). Moreover, the isotopic abundance ratio[24,41] at M + 2 (1:3) indicates one chlorine atom is present in the ion at m/z 280.1816 (3.9 ppm error) corresponding to sibutramine (Table 1). As shown in Figure 3D, matching dual polarity detection[42] and high-abundant M + 2 isotopic signatures in both synchronous ESI− and ESI+ chromatographic windows around 33.9 min allows reducing the possibilities of false identification of felodipine, which contains two chlorine atoms in the molecule. Besides, the MS^2 and MS^3 product ions matched well with the expected fragmentation data in the MS library, further confirming the presence of felodipine. A second small peak observed at 29.2 min in the ESI+ XIC of m/z 384 seemed to correspond to the sodium adduct ion of bezafibrate by matching retention time and mass spectrum against the authentic standard, which shows the base peak $[M + H]^+$ at m/z 362 along with its ^{37}Cl-isotope profile in the mass spectrum (data not shown).

It should be noted that the mass accuracies of the protonated felodipine, sodiated bezafibrate, and MS^3 ions of felodipine might be worse than 5 ppm error (Figure 3D), mainly due to matrix complexity, low abundance of these ion species, or kinetic energy differences between fragment ions in MS^n mode.[43] In fact, there is a general consensus that at lest two physicochemical parameters (i.e., retention time, accurate mass, isotope profile, and fragment ion[26]) are required to confirm an analyte identity. In the present case, unique MS^n fragment ions and dual polarity spectra may be useful alternatives to distinguish between isomers and identify unexpected compounds.

Application to Qualitative Screening of Real Samples. To check the applicability of the new LC-IT(MS^n)/TOF method for real-world sample analysis, the presence of illegal adulterants was assessed in dietary supplements of different origin labeled for antihypertension, antidiabetes, antihyperlipidemia, anti-inflammation, sedation−hypnotization, antiobesity, or anti-impotence. These samples were processed automatically using the generic workflow. The proposed screening strategy allowed the detection and further identification of target, nontarget, or unexpected adulterants in the suspected positive samples (Table 3).

As an example, Figure 4 illustrates the screening process of discovery, confirmation, and identification of dimethylsildenafil (aildenafil) and its unknown analogue in a representative positive sample (L019), which is used as a health wine product for aphrodisia. The mass chromatograms in Figure 4A indicate that at least three main peaks (1, 2, and 3) appeared around 19−26 min. The chromatograms were automatically screened from the database with MetID Solution by mass accuracy (±5 ppm), and the searching result is shown in Figure 4B. According to the XIC peaks table, the peaks 1, 2, and 3 were initially assigned to dimethylsildenafil ($C_{23}H_{32}N_6O_4S$, 19.2 min), udenafil ($C_{25}H_{36}N_6O_4S$, 25.1 min), and thiodimethylsildenafil ($C_{23}H_{32}N_6O_3S_2$, 26.0 min), respectively. In the next step, their retention times and fragment ions were subsequently searched against the user-created database by ACD/MS Manager. Compound **1** was further confirmed to be dimethylsildenafil on the basis of the high degree of retention precision and spectrum similarity. As can be seen from the MS/MS patterns in Figure 4C, the product ions and their relative intensities agree well with the MS^n library (similarity = 71−93%), demonstrating a high level of confidence for correct identification of the target analyte. Also, the combined MS^n spectra of the third peak at 26 min (compound **3**) revealed diagnostic ions at m/z 393, 327, and 299 (in MS^2) and at m/z 347 and 328 (in MS^3) with acceptable deviations (−3.6 to 5.1 ppm), proving the presence of thiodimethylsildenafil (target compound) in the sample.

For compound **2** (m/z 517.2613, RT 25 min), despite the closest match by accurate mass (4.1 ppm error) with udenafil (m/z 517.2592, RT 21 min), the resulting unique empirical formula ($C_{25}H_{36}N_6O_4S$) produced a false-positive identification with any library compounds, because its retention time and MS/MS spectra contrast unfavorably with the standard library data (Figure 4D). In the MS^3 spectrum of its major product ion at m/z 489.2289, the presence of m/z 377.1285, 311.1511, and 283.1198 confirms that it belongs to the sildenafil family.[13−15] More interestingly, its accurate multistage fragmentation spectra of MS^{3-5} (in Figure 4D) were in perfect accordance with the CID MS^{2-4} spectra of dimethylsildenafil (in Figure 4C), respectively. These good matches indicate compound **2**, as an udenafil isomer, is a precursor of dimethylsildenafil, which may be generated by loss of C_2H_4 from an unknown molecule. Because the structural modifications of sildenafil are commonly carried out on the piperazine ring,[4] it is a good indication of the insertion of one ethyl group attached to the nitrogen in the piperazine ring of dimethylsildenafil, in which the 2,6-dimethylpiperazine moiety is replaced with *N*-ethyl-2,6-dimethylpiperazine. As expected, the loss of C_2H_4 in MS/MS fragmentation probably corresponds to the piperazine N-deethylation. The chemical structures and the proposed fragmentation pathways for its main fragment ions are outlined in Figure 4E, which matches the findings reported by other authors,[4,13−15] further confirming the unexpected compound as N-ethylated dimethylsildenafil.

In conclusion, the nontarget screening of illegal adulterants in dietary supplements is a difficult crucial task, due to the increasing and concealed adulteration with undeclared chemical ingredients for which no analytical standards or structural information is available. A generic and efficient hybrid LC-IT/TOF workflow for wide-scope screening, library searching, and confirmation of over 100 illegal adulterants was first developed and validated in various types of dietary supplements. By combining the advantages of rapid polarity-switching and accurate multistage mass measurements in a single LC-MS run, the hybrid LC-IT/TOF system offers the potential to expand coverage of analyte species. Particularly, the use of the consecutive MS^n spectra enables a more comprehensive and precise structural assignment and confident identity confirma-

DOI: 10.1021/acs.jafc.5b02222
J. Agric. Food Chem. 2015, 63, 6954−6967

tion of unexpected compounds. On the whole, the integration of the rapid "*st*MAC/*iv*FDI" procedure, the unique LC-IT(MS^n)/TOF acquisition with accurate database searching, may serve as an alternative nontargeted discovery strategy for large-scale qualitative screening and confirmatory analysis of complex real-life samples.

■ ASSOCIATED CONTENT

Supporting Information

More details on the LC-IT(MS^n)/TOF screening workflow (Figure S1); automated database searching by MetID Solution software (Figure S2); and library matching by ACD/MS Manager (Figure S3). The Supporting Information is available free of charge on the ACS Publications website at DOI: 10.1021/acs.jafc.5b02222.

■ AUTHOR INFORMATION

Corresponding Authors

*(Z.H.) Phone: +86 731 85627801. Fax: +86 731 85627818. E-mail: huangzqq@126.com.

*(B.G.) E-mail: binguo@hunnu.edu.cn

Funding

This work was financially supported by the National Science and Technology Support Program (2012BAK08B01,2012-BAK08B02), the National Natural Science Foundation of China (Grants 81274178, 21005027), the Innovative Research Team in Higher Educational Institutions of Hunan Province (2010TT1001, 05K009), and the Foundation for University Young Key Teacher by the Education Department of Hunan Province.

Notes

The authors declare no competing financial interest.

■ ABBREVIATIONS USED

QqQ-MS/MS, triple-quadrupole tandem mass analyzer; MS^n, multistage mass fragmentation; IT, ion trap; TOF, time-of-flight; IT/TOF, hybrid ion trap/time-of-flight mass analyzer; IT(MS^n)/TOF, multistage ion trap/time-of-flight mass analyzer; HRMS, high-resolution mass spectrometry; fwhm, full width at half-maximum; PDE-5, phosphodiesterase type-5; PSA, primary−secondary amine; ODS, octadecylsilane; *iv*FDI, in-vial filtration−dilution−injection; *st*MAC, single-tube multifunction adsorption cleanup; ESI, electrospray ionization; CDL, curved desolvation line; CID, collision-induced dissociation; XIC, extracted ion chromatogram; BPC, base peak chromatogram; ME, matrix effect; ER, extraction recovery; CCα, decision limit; CCβ, decision capability; SDL, screening detection limit; LOC, limit of confirmation; dSPE, dispersive solid-phase extraction

■ REFERENCES

(1) Song, F.; El-Demerdash, A.; Lee, S. J. Screening for multiple phosphodiesterase type 5 inhibitor drugs in dietary supplement materials by flow injection mass spectrometry and their quantification by liquid chromatography tandem mass spectrometry. *J. Pharm. Biomed. Anal.* **2012**, *70*, 40−46.

(2) Shi, F.; Guo, C.; Gong, L.; Li, J.; Dong, P.; Zhang, J.; Cui, P.; Jiang, S.; Zhao, Y.; Zeng, S. Application of a high resolution benchtop quadrupole-Orbitrap mass spectrometry for the rapid screening, confirmation and quantification of illegal adulterated phosphodiesterase-5 inhibitors in herbal medicines and dietary supplements. *J. Chromatogr., A* **2014**, *1344*, 91−98.

(3) Ediage, E. N.; Di Mavungu, J. D.; Scippo, M. L.; Schneider, Y. J.; Larondelle, Y.; Callebaut, A.; Robbens, J.; Van Peteghem, C.; De Saeger, S. Screening, identification and quantification of glucosinolates in black radish (*Raphanus sativus* L. *niger*) based dietary supplements using liquid chromatography coupled with a photodiode array and liquid chromatography-mass spectrometry. *J. Chromatogr., A* **2011**, *1218*, 4395−4405.

(4) Kee, C. L.; Koh, H. L.; Bloodworth, B. C.; Zeng, Y.; Kiang, K. H.; Low, M. Y.; Ge, X. Structural elucidation of propoxyphenyl isobutyl aildenafil, adulterant in a health supplement using high-resolution Orbitrap mass spectrometry. *J. Pharm. Biomed. Anal.* **2014**, *98*, 153−159.

(5) Patel, D. N.; Li, L.; Kee, C. L.; Ge, X.; Low, M. Y.; Koh, H. L. Screening of synthetic PDE-5 inhibitors and their analogues as adulterants: analytical techniques and challenges. *J. Pharm. Biomed. Anal.* **2014**, *87*, 176−790.

(6) Singh, S.; Prasad, B.; Savaliya, A. A.; Shah, R. P.; Gohil, V. M.; Kaur, A. Strategies for characterizing sildenafil, vardenafil, tadalafil and their analogues in herbal dietary supplements, and detecting counterfeit products containing these drugs. *TrAC, Trends Anal. Chem.* **2009**, *28*, 13−28.

(7) Vaclavik, L.; Krynitsky, A. J.; Rader, J. I. Targeted analysis of multiple pharmaceuticals, plant toxins and other secondary metabolites in herbal dietary supplements by ultra-high performance liquid chromatography-quadrupole-orbital ion trap mass spectrometry. *Anal. Chim. Acta* **2014**, *810*, 45−60.

(8) Aqai, P.; Cevik, E.; Gerssen, A.; Haasnoot, W.; Nielen, M. W. High-throughput bioaffinity mass spectrometry for screening and identification of designer anabolic steroids in dietary supplements. *Anal. Chem.* **2013**, *85*, 3255−3262.

(9) Lee, H. M.; Lee, B. J. A novel approach to simultaneous screening and confirmation of regulated pharmaceutical compounds in dietary supplements by LC/MS/MS with an information-dependent acquisition method. *Food Addit. Contam., Part A* **2011**, *28*, 396−407.

(10) Lebel, P.; Gagnon, J.; Furtos, A.; Waldron, K. C. A rapid, quantitative liquid chromatography-mass spectrometry screening method for 71 active and 11 dysfunction natural erectile ingredients present in potentially adulterated or counterfeit products. *J. Chromatogr., A* **2014**, *1343*, 143−151.

(11) Hird, S. J.; Lau, B. P. Y.; Schuhmacher, R.; Krska, R. Liquid chromatography-mass spectrometry for the determination of chemical contaminants in food. *TrAC, Trends Anal. Chem.* **2014**, *59*, 59−72.

(12) Guo, B.; Chen, B.; Liu, A.; Zhu, W.; Yao, S. Liquid chromatography-mass spectrometric multiple reaction monitoring-based strategies for expanding targeted profiling towards quantitative metabolomics. *Curr. Drug Metab.* **2012**, *13*, 1226−1243.

(13) Gratz, S. R.; Gamble, B. M.; Flurer, R. A. Accurate mass measurement using Fourier transform ion cyclotron resonance mass spectrometry for structure elucidation of designer drug analogs of tadalafil, vardenafil and sildenafil in herbal and pharmaceutical matrices. *Rapid Commun. Mass Spectrom.* **2006**, *20*, 2317−2327.

(14) Lee, S. K.; Kim, D. H.; Yoo, H. H. Comparative metabolism of sildenafil in liver microsomes of different species by using LC/MS-based multivariate analysis. *J. Chromatogr. B: Anal. Technol. Biomed. Life Sci.* **2011**, *879*, 3005−3011.

(15) Venhuis, B. J.; de Kaste, D. Towards a decade of detecting new analogues of sildenafil, tadalafil and vardenafil in food supplements: a history, analytical aspects and health risks. *J. Pharm. Biomed. Anal.* **2012**, *69*, 196−208.

(16) Lanzarotta, A.; Crowe, J. B.; Witkowski, M.; Gamble, B. M. A multidisciplinary approach for the analysis of an adulterated dietary supplement where the active pharmaceutical ingredient was embedded in the capsule shell. *J. Pharm. Biomed. Anal.* **2012**, *67−68*, 22−27.

(17) Song, F.; Monroe, D.; El-Demerdash, A.; Palmer, C. Screening for multiple weight loss and related drugs in dietary supplement materials by flow injection tandem mass spectrometry and their confirmation by liquid chromatography tandem massspectrometry. *J. Pharm. Biomed. Anal.* **2014**, *88*, 136−143.

DOI: 10.1021/acs.jafc.5b02222
J. Agric. Food Chem. 2015, 63, 6954−6967

(18) Wang, H.; Wu, Y.; Zhao, Y.; Sun, W.; Ding, L.; Guo, B.; Chen, B. Rapid screening of illicit additives in weight loss dietary supplements with desorption corona beam ionisation (DCBI) mass spectrometry. *Food Addit. Contam., Part A* **2012**, *29*, 1194−1201.
(19) Wang, M.; Guo, B.; Huang, Z.; Duan, J.; Chen, Z.; Chen, B.; Yao, S. Improved compatibility of liquid chromatography with electrospray tandem mass spectrometry for tracing occurrence of barbital homologous residues in animal tissues. *J. Chromatogr., A* **2010**, *1217*, 2821−2831.
(20) Guo, B.; Huang, Z.; Wang, M.; Wang, X.; Zhang, Y.; Chen, B.; Li, Y.; Yan, H.; Yao, S. Simultaneous direct analysis of benzimidazole fungicides and relevant metabolites in agricultural products based on multifunction dispersive solid-phase extraction and liquid chromatography-mass spectrometry. *J. Chromatogr., A* **2010**, *1217*, 4796−4807.
(21) Huang, C.; Guo, B.; Wang, X.; Li, J.; Zhu, W.; Chen, B.; Ouyang, S.; Yao, S. A generic approach for expanding homolog-targeted residue screening of sulfonamides using a fast matrix separation and class-specific fragmentation- dependent acquisition with a hybrid quadrupole-linear ion trap mass spectrometer. *Anal. Chim. Acta* **2012**, *737*, 83−98.
(22) Peters, R. J. B.; Stolker, A. A. M.; Mol, J. G. J.; Lommen, A.; Lyris, E.; Angelis, Y.; Vonaparti, A.; Stamou, M.; Georgakopoulos, C.; Nielen, M. W. F. Screening in veterinary drug analysis and sports doping control based on full-scan, accurate-mass spectrometry. *TrAC, Trends Anal. Chem.* **2010**, *29*, 1250−1268.
(23) Kellmann, M.; Muenster, H.; Zomer, P.; Mol, H. Full scan MS in comprehensive qualitative and quantitative residue analysis in food and feed matrices: how much resolving power is required? *J. Am. Soc. Mass Spectrom.* **2009**, *20*, 1464−1476.
(24) Thurman, E. M.; Ferrer, I.; Zavitsanos, P.; Zweigenbaum, J. A. Analysis of isobaric pesticides in pepper with high-resolution liquid chromatography and mass spectrometry: complementary or redundant? *J. Agric. Food Chem.* **2013**, *61*, 2340−2347.
(25) Nácher-Mestre, J.; Ibáñez, M.; Serrano, R.; Pérez-Sánchez, J.; Hernández, F. Qualitative screening of undesirable compounds from feeds to fish by liquid chromatography coupled to mass spectrometry. *J. Agric. Food Chem.* **2013**, *61*, 2077−2087.
(26) Turnipseed, S. B.; Lohne, J. J.; Storey, J. M.; Andersen, W. C.; Young, S. L.; Carr, J. R.; Madson, M. R. Challenges in implementing a screening method for veterinary drugs in milk using liquid chromatography quadrupole time-of-flight mass spectrometry. *J. Agric. Food Chem.* **2014**, *62*, 3660−3674.
(27) Martínez Bueno, M. J.; Ulaszewska, M. M.; Gomez, M. J.; Hernando, M. D.; Fernández-Alba, A. R. Simultaneous measurement in mass and mass/mass mode for accurate qualitative and quantitative screening analysis of pharmaceuticals in river water. *J. Chromatogr., A* **2012**, *1256*, 80−88.
(28) Liu, Z. Y. An introduction to hybrid ion trap/time-of-flight mass spectrometry coupled with liquid chromatography applied to drug metabolism studies. *J. Mass Spectrom.* **2012**, *47*, 1627−1642.
(29) Hao, H.; Cui, N.; Wang, G.; Xiang, B.; Liang, Y.; Xu, X.; Zhang, H.; Yang, J.; Zheng, C.; Wu, L.; Gong, P.; Wang, W. Global detection and identification of nontarget components from herbal preparations by liquid chromatography hybrid ion trap time-of-flight mass spectrometry and a strategy. *Anal. Chem.* **2008**, *80*, 8187−8194.
(30) Xu, J.; Duan, J.; Xue, C.; Feng, T.; Dong, P.; Sugawara, T.; Hirata, T. Analysis and comparison of glucocerebroside species from three edible sea cucumbers using liquid chromatography-ion trap-time-of-flight mass spectrometry. *J. Agric. Food Chem.* **2011**, *59*, 12246−12253.
(31) Zhang, F.; Jia, Z.; Gao, P.; Kong, H.; Li, X.; Lu, X.; Wu, Y.; Xu, G. Metabonomics study of urine and plasma in depression and excess fatigue rats by ultra fast liquid chromatography coupled with ion trap-time of flight mass spectrometry. *Mol. BioSyst.* **2010**, *6*, 852−861.
(32) Tang, L.; Wang, X.; Guo, B.; Ma, M.; Chen, B.; Zhan, S.; Yao, S. Salt-triggered liquid phase separation and facile nanoprecipitation of aqueous colloidal gold dispersion in miscible biofluids for direct chromatographic measurement. *RSC Adv.* **2013**, *3*, 15875−15886.
(33) Zeng, L.; Wang, M.; Yuan, Y.; Guo, B.; Zhou, J.; Tan, Z.; Ye, M.; Ding, L.; Chen, B. Simultaneous multi-component quantitation of Chinese herbal injection Yin-zhi-huang in rat plasma by using a single-tube extraction procedure for mass spectrometry-based pharmacokinetic measurement. *J. Chromatogr. B: Anal. Technol. Biomed. Life Sci.* **2014**, *967*, 245−254.
(34) Malato, O.; Lozano, A.; Mezcua, M.; Agüera, A.; Fernandez-Alba, A. R. Benefits and pitfalls of the application of screening methods for the analysis of pesticide residues in fruits and vegetables. *J. Chromatogr., A* **2011**, *1218*, 7615−7626.
(35) European Commission Decision of 12 August 2002 implementing Council Directive 96/23/EC concerning the performance of analytical methods and the interpretation of results (2002/657/EC). *Off. J. Eur. Communities* **2002**, *L221*, 8−36.
(36) Community Reference Laboratories Residues (CRLs). Guidelines for the validation of screening methods for residues of veterinary medicines (initial validation and transfer); 20/1/2010, http://ec.europa.eu/food/food/chemicalsafety/residues/Guideline_Validation_Screening_en.pdf.
(37) Document No. SANCO 12495/2011. Method validation and quality control procedures for pesticide residues analysis in food and feed.
(38) Aguilera-Luiz, M. M.; Romero-González, R.; Plaza-Bolaños, P.; Martínez Vidal, J. L.; Garrido Frenich, A. Wide-scope analysis of veterinary drug and pesticide residues in animal feed by liquid chromatography coupled to quadrupole-time-of-flight mass spectrometry. *Anal. Bioanal. Chem.* **2013**, *405*, 6543−6553.
(39) González-Mariño, I.; Quintana, J. B.; Rodríguez, I.; González-Díez, M.; Cela, R. Screening and selective quantification of illicit drugs in wastewater by mixed-mode solid-phase extraction and quadrupole-time-of-flight liquid chromatography-mass spectrometry. *Anal. Chem.* **2012**, *84*, 1708−1717.
(40) Holčapek, M.; Jirásko, R.; Lísa, M. Recent developments in liquid chromatography-mass spectrometry and related techniques. *J. Chromatogr., A* **2012**, *1259*, 3−15.
(41) Gómez-Pérez, M. L.; Plaza-Bolaños, P.; Romero-González, R.; Martínez-Vidal, J. L.; Garrido-Frenich, A. Comprehensive qualitative and quantitative determination of pesticides and veterinary drugs in honey using liquid chromatography-Orbitrap high resolution mass spectrometry. *J. Chromatogr., A* **2012**, *1248*, 130−138.
(42) Musenga, A.; Cowan, D. A. Use of ultra-high pressure liquid chromatography coupled to high resolution mass spectrometry for fast screening in high throughput doping control. *J. Chromatogr., A* **2013**, *1288*, 82−95.
(43) Gómez-Ramos, M. M.; Ferrer, C.; Malato, O.; Agüera, A.; Fernández-Alba, A. R. Liquid chromatography- high-resolution mass spectrometry for pesticide residue analysis in fruit and vegetables: screening and quantitative studies. *J. Chromatogr., A* **2013**, *1287*, 24−37.
(44) Stahnke, H.; Kittlaus, S.; Kempe, G.; Alder, L. Reduction of matrix effects in liquid chromatography-electrospray ionization-mass spectrometry by dilution of the sample extracts: how much dilution is needed? *Anal. Chem.* **2012**, *84*, 1474−1482.
(45) Yang, P.; Chang, J. S.; Wong, J. W.; Zhang, K.; Krynitsky, A. J.; Bromirski, M.; Wang, J. Effect of sample dilution on matrix effects in pesticide analysis of several matrices by liquid chromatography-high-resolution mass spectrometry. *J. Agric. Food Chem.* **2015**, *63*, 5169−5177.
(46) Ferrer, C.; Lozano, A.; Agüera, A.; Girón, A. J.; Fernández-Alba, A. R. Overcoming matrix effects using the dilution approach in multiresidue methods for fruits and vegetables. *J. Chromatogr., A* **2011**, *1218*, 7634−7639.
(47) Nanita, S. C. Quantitative mass spectrometry independence from matrix effects and detector saturation achieved by flow injection analysis with real-time infinite dilution. *Anal. Chem.* **2013**, *85*, 11866−11875.

DOI: 10.1021/acs.jafc.5b02222
J. Agric. Food Chem. 2015, 63, 6954−6967

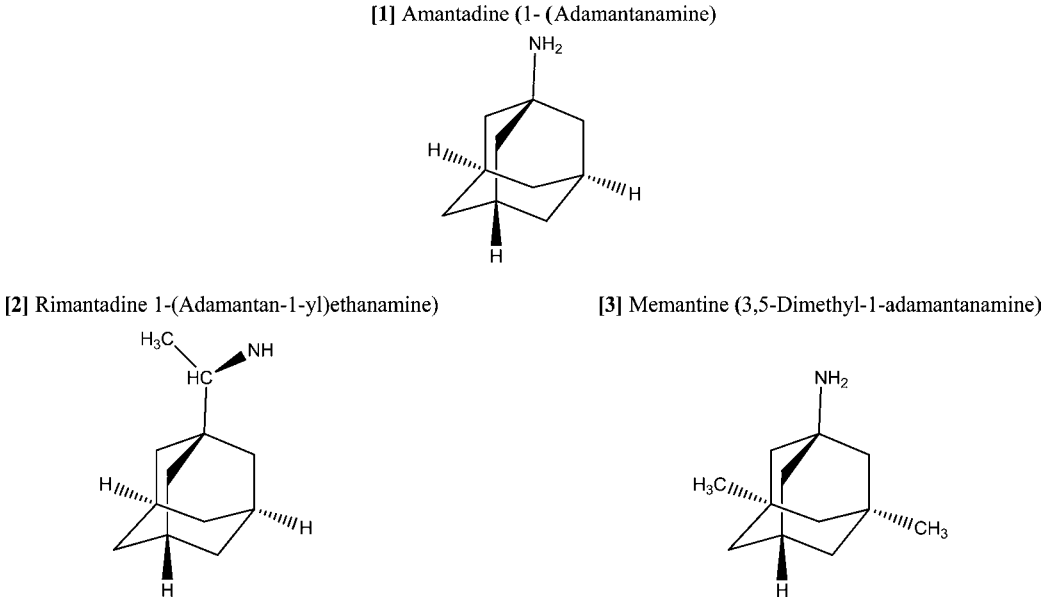

Figure 1. Structures of amantadine and its analogues.

solution and a QuEChERS (Quick, Easy, Cheap, Effective, Rugged, Safe) cleanup. Reversed-phase UPLC separation was coupled to high resolution MS (Orbitrap) detection. Similarly, Zhao et al.[7] utilized a QuEChERS approach for the analysis of amantadine and rimantadine and the antihistamine chlorphenir-amine in a variety of tissues including chicken. In this case, a primary−secondary amine dispersive sorbent was used for sample cleanup, and analysis was performed on a triple quadrupole LC-MS/MS instrument. Wu et al.[8] modified QuEChERS methodology to include multiwalled carbon nanotubes as a reversed-dispersive SPE material for the extraction of amantadine, rimantadine, and memantine in chicken muscle also using LC-MS/MS detection. Although none of these methods are specific to the analysis of antiviral residues in jerky prepared from chicken muscle, they served as a useful starting point for the analysis of amantadine and its analogues in chicken-based pet treats. One published method was developed specifically for chicken jerky pet treats for the analysis of antibiotic residues (sulfaquinoxaline, sulfaclozine, sulfamethoxazole, trimethoprim, tilmicosin, and enrofloxacin).[9] With this method, the jerky samples were prepared by grinding to a fine powder (Retch mill with 0.75 mm screen) followed by extraction with a water/acetonitrile mixture and analysis by UPLC triple quadrupole MS without any extensive cleanup procedures. Chicken jerky treat sample preparation techniques from this procedure were also incorporated into our method development.

To quantitate and confirm the presence of amantadine in imported chicken jerky treats, as well as investigate possible contamination with other adamantane residues, analytical methodology for routine laboratory monitoring was needed. Methods utilizing two complementary LC-MS technologies for detection of the antiviral residues after extraction from the pet jerky treats with a QuEChERS procedure were developed and validated.

MATERIALS AND METHODS

Instrumentation. Two different types of LC-MS instruments were used for this method in both the CAHFS laboratory and FDA laboratories. The first was an ion trap instrument. This was either a Thermo (San Jose, CA) Velos Pro LC-MS^n with a Thermo/Dionex Ultimate 3000 HPLC system (CAHFS laboratory) or a Thermo Velos Pro LC-MS^n coupled to a Thermo Accela 1250 LC pump and CTC autosampler (FDA). An ESI (FDA) or heated ESI (CAHFS) ion source was used in positive ion mode along with XCaliber (V2.1) data acquisition and analysis software. The second LC-MS system for both laboratories was a Thermo single-stage Orbitrap (Exactive) high-resolution MS equipped with an Agilent (Santa Clara, CA) 1100 Rapid Resolution HPLC system (CAHFS) or a Thermo Accela 1250 LC pump and CTC autosampler (FDA). A heated ESI ion source was used in positive ion mode along with XCaliber (V2.1) data acquisition and analysis software.

Reagents and Standards. Standards of amantadine, rimantadine, and memantine were purchased from Sigma Aldrich (St. Louis, MO). The internal standard, amantadine-d_{15} was purchased from Toronto Research Chemicals (North York, ON, Canada). Stock solutions were prepared as individual 100−200 μg/mL solutions for amantadine, amantadine-d_{15}, rimantadine, and memantine in methanol. Corrections were made for salt (HCl salts) and purity. For the FDA method, magnesium sulfate and sodium chloride were obtained from Thermo Fisher (Houston, TX) and EMD Millipore (Billerica, MA), respectively. Alternative sources, including a QuEChERS packet containing a preweighed amount of salts, could be used (Thermo Fisher or equivalent). The C18 (Bondesil 40 μm) sorbent material used was obtained from Agilent or tubes containing preweighed amount of C18 (DSC-18) sorbent could be purchased from Sigma Aldrich. Preweighed tubes containing 6 g of magnesium sulfate and 1.5 g of sodium acetate (UCT, Bristol, PA.) were used for the QuEChERS extraction at the CAHFS lab. Reagents used for sample extraction including acetonitrile, methanol, and acetic acid were chromatographic and spectrophotometric grade from EMD Millipore or equivalent. Syringe filters were Acrodisc 13 mm syringe filter with 0.2 μm nylon membrane (Sigma Aldrich) or 0.22 μm polyethersulfone membrane from Thermo Fisher or Millipore Corp.

Initial Screening and Confirmatory Method at the CAHFS Laboratory. Amantadine was first found and confirmed in chicken- and duck-based pet treats by the CAHFS laboratory. The CAHFS general screening method was as follows:

Sample Preparation. A Stein mill with carbide-tipped blades (Steinlite Corp., Atchison, KS) was used to grind pet treat samples until the contents were uniform and had the consistency of a fine powder.

Sample Extraction. The ground material was weighed (1 ± 0.05 g) into a 50 mL plastic centrifuge tube, and 5 mL of 0.1% formic acid in

DOI: 10.1021/acs.jafc.5b02416
J. Agric. Food Chem. 2015, 63, 6968−6978

water was added. The samples were further processed by adding two ball bearings and placing the tubes into a GenoGrinder (SPEX SamplePrep, Metuchen, NJ) for 5 min at 900 strokes/min. The ball bearings were removed, and 15 mL of 0.1% formic acid in acetonitrile were added. The sample was then extracted by shaking the tubes with the GenoGrinder without any ball bearings for another 5 min. The extracts were then centrifuged (1300*g* for 10 min), and the supernatant was decanted into a 50 mL tube containing 6 g of magnesium sulfate and 1.5 g of sodium acetate. The tubes were capped tightly and shaken well immediately. Following centrifugation (1300*g* for 10 min), the acetonitrile layer was transferred into a 15 mL glass tube. The acetonitrile was evaporated to dryness under nitrogen and reconstituted in 200 μL of 20% methanol in 0.1% aqueous formic acid. The final extract was filtered using a 0.20 μm polyethersulfone syringe filter into an autosampler vial.

LC-MS Conditions. Amantadine was initially tested at the CAFHS laboratory by analysis of a standard solution using an LC-MS screening method with the single stage Orbitrap platform that has been described earlier, with some minor modifications.[10] Briefly a heated electrospray ion source (HESI) was used and the MS was scanned from m/z 80−1000. The resolution was set to 50000, automatic gain control at 1×10^6, and the maximum inject time was 50 ms. An Agilent Eclipse Plus C18 LC column (100 mm × 2.1 mm i.d., 1.8 μm) was used with an LC gradient that consisted of 0.1% formic acid in water (solvent A) and acetonitrile (solvent B). The gradient was programmed from 99% A to 5% A over 5 min at a flow rate of 0.35 mL/min. The injection volume was 20 μL, and the column was maintained at 30 °C. For some analyses, a second scan function utilizing high collision dissociation (HCD) fragmentation at 35 V was included. Using these conditions, the expected accurate mass ion of the protonated molecule of amantadine at m/z 152.1434 was found at a retention time of 3.9 min. Furthermore, a single fragment ion produced by amantadine under HCD fragmentation conditions corresponding to loss of NH_3 (m/z 135.1168) was also present in these samples.

The initial findings of amantadine in these pet jerky samples were confirmed at the CAHFS laboratory with an ion trap LC-MS^n method. Again, electrospray ionization was used in positive mode. The instrument was tuned with an amantadine solution and the conditions were: sheath gas (N_2, 50 arbitrary units). auxiliary gas (N_2, 5 arbitrary units), and sweep gas (N_2, 0 arbitrary units). S-lens RF level 52.5%, capillary temperature 350 °C, spray voltage 4.5 kV. The ion trap parameters were: isolation width (IW) 1.5 Da for all transitions, and the collision energies were 25 V for both MS^2 and MS^3 transitions. The $[M + H]^+$ ion for amantadine at m/z 152 was fragmented to an ion at m/z 135, which was then fragmented to produce a full scan spectrum with three prominent ions at m/z 79, 93, and 107. The LC column was a 50 mm × 2.1 mm, 1.8 μm Zorbax SB-C18 (Agilent, Wilmington, DE). The LC mobile phase consisted of 0.1% aqueous formic acid (solvent A) and 0.1% formic acid in acetonitrile (solvent B). Flow rate was 0.30 mL/min, and the column was kept at 35 °C. In this case, the gradient initially started at 95% A (held for 1 min) and was then ramped to 30% A in 2 min and held at 30% A for an additional minute.

Although the methods used at CAHFS were not validated for quantitation, estimates of amantadine levels were determined. Calibration curves consisting of jerky treats spiked at 1, 5, 20, 50, and 100 μg/kg were extracted and analyzed as above on both the high resolution and linear ion trap LC-MS systems.

Antiviral Residue Method: Optimization and Validation at the FDA Laboratory. A second method specific to the antiviral residues (amantadine, rimantadine, and memantine) in pet treats prepared from chicken muscle was optimized and validated in the FDA laboratory.[11] The initial level of interest for all three compounds was 5 μg/kg.

Sample Sources. Several sources of chicken-based pet treats were purchased at the local market for method development and validation. These included chicken tenders, dried chicken breasts, chicken jerky, chicken meatballs, and soft chicken bites. If the samples were found to be free of amantadine, they were used as matrix controls for method validation.

Sample Preparation. Samples were blended with dry ice in a blender/homogenizer (RobotCoupe USA, Inc., Ridgeland, MS) with pulsed action until the contents were uniform and had the consistency of a fine powder. The homogenate was placed in a Whirl-Pak bag, loosely sealed, and stored in the freezer (−25 °C) overnight to allow the carbon dioxide to dissipate, and then sealed until the time of analysis. A Stein mill with carbide-tipped blades was used to grind smaller (<50 g) samples. Then 3 grams (±0.05 g) of sample were weighed into a 50 mL centrifuge tube and stored frozen (−25 °C) until use.

For each sample batch, a matrix blank and at least two matrix spikes were analyzed. A mixed intermediate standard containing 200 ng/mL of amantadine, memantine, and rimantadine in methanol was used to prepare matrix spikes. An internal standard fortification solution (600 ng/mL) was also prepared in methanol. As an example, to prepare a matrix spike with 5 μg/kg of amantadine, rimantadine, and memantine and 10 μg/kg of internal standard (amantadine-d_{15}), 75 μL of the mixed intermediate standard and 50 μL of the amantadine-d_{15} fortification solution would be added to 3 g of sample. The internal standard solution (50 μL, 600 ng/mL amantadine-d_{15}) was added to all samples prior to extraction.

Sample Extraction. Water (6 mL) was added to 3 (±0.05) g of ground sample in a 50 mL centrifuge tube. The sample was vortex mixed for 5 min and then sonicated for 5 min. The residues were extracted by adding 10 mL of 1% acetic acid in acetonitrile and vortex mixing for another 5 min. A combination of 4 g of $MgSO_4$ and 1 g of NaCl was then added to the tubes and mixed by vortex mixing for 5 min. The samples were then centrifuged at 17000*g* for 10 min at 4 °C. Then 6 mL of the supernatant were combined with 150 mg of C18 sorbent in a 15 mL centrifuge tube and vortex mixed for 1 min. These tubes were centrifuged at 17000*g* for 5 min at 4 °C. Then 5 mL of the supernatant was transferred to a glass test tube and evaporated to dryness using a Turbovap with N_2 at 45−50 °C. The extracts were reconstituted in 0.5 mL of 80:20 0.1% formic acid:methanol. The samples were filtered with a 0.2 μm nylon syringe filter into 2 mL of polypropylene LC vial with conical insert. The sample extraction procedure resulted in a 3× concentration of the residues.

LC-MS Conditions. The primary LC-MS method was an ion trap procedure similar to the one described above in the CAHFS laboratory method for amantadine that has been modified to include amantadine-d_{15}, rimantadine, and memantine. An Agilent Zorbax SB-C18 (100 mm × 2.1 mm i.d., 3.5 μm) LC column was used with a gradient of 0.1% aqueous formic acid in channel A and 0.1% formic acid in acetonitrile in channel B. The flow rate was 0.30 mL/min, and the column was kept at room temperature. Injection volume was 10 μL. The mobile phase gradient consisted of 90% A for 1 min, ramping to 30% A in 7 min, then holding at 30% A for an additional 2 min. Positive ions were generated using ESI (not heated), and MS^3 scans were used to detect the residues. Amantadine tuning solution (10 ug/mL) introduced through a T-junction into the LC mobile phase (0.3 mL/min 30:70 A:B) was used to optimize the source voltages and gases: sheath gas (N_2, 40 arbitrary units), auxiliary and sweep gas (N_2, 0 arbitrary units), S-lens RF level 58%, capillary temperature 275 °C; spray voltage 5 kV. The ion trap parameters were: isolation width (IW) 2 Da for all transitions, Q = 0.25, and activation time = 10 ms. Tuning solutions for all of the compounds were infused separately to optimize for their collision energy (CE) values. The following ion trap MS parameters were used: amantadine (1−4 min, MS^2 m/z 152 → m/z 135, CE 27; MS^3 m/z 135 → m/z 65−140, CE 30 monitoring MS^3 ions at m/z 79, 93, 107), amantadine-d_{15} (1−4 min, MS^2 m/z 167 → m/z 150, CE 27; MS^3 m/z 150 → m/z 65−155, CE 30 monitoring MS^3 ions at m/z 86, 102, 118), rimantadine and memantine (4−7 min, MS^2 m/z 180 → m/z 163, CE 30; MS^3 m/z 163 → m/z 65−140, CE 30 monitoring MS^3 ions at m/z 81, 107, 121, 135).

A complimentary HRMS method was also used at FDA using a Thermo single stage Orbitrap LC-MS instrument and a heated electrospray ion source (HESI). The Orbitrap was tuned similarly to the ion trap using amantadine solution combined with LC flow (0.5

DOI: 10.1021/acs.jafc.5b02416
J. Agric. Food Chem. 2015, 63, 6968−6978

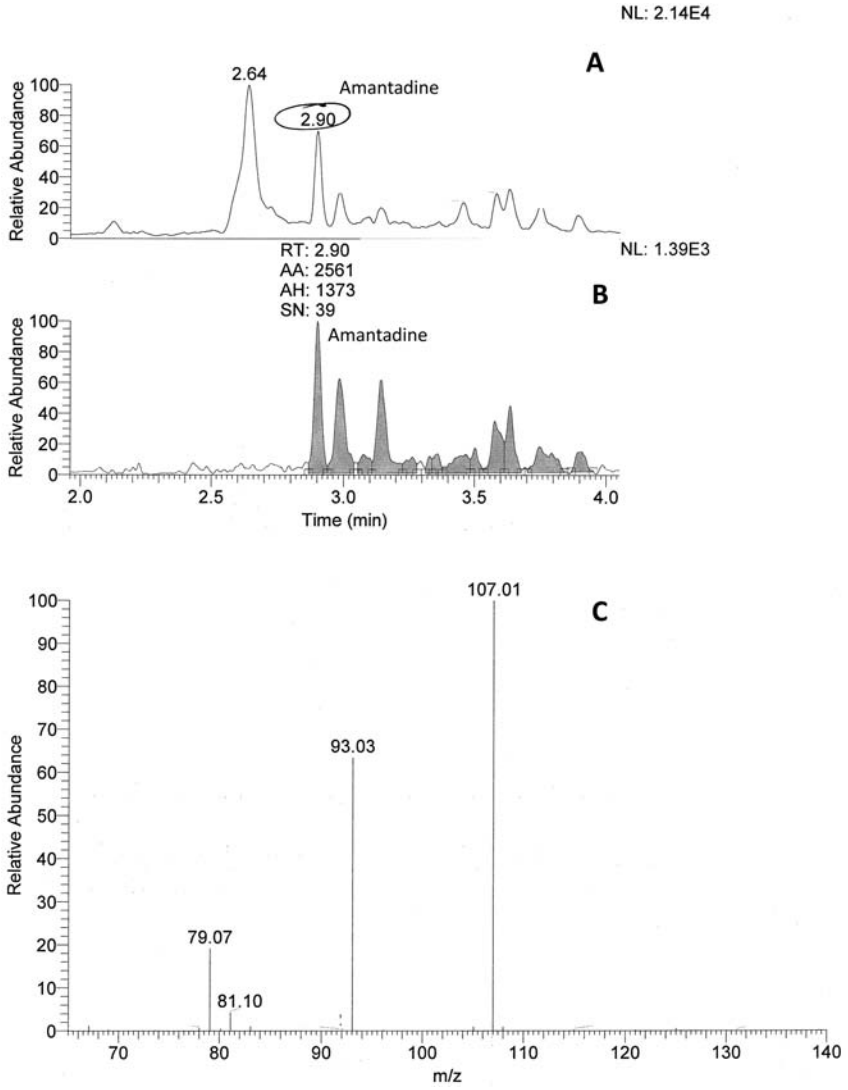

Figure 2. Ion trap LC-MS^3 analysis of matrix fortified with 1 μg/kg amantadine (CAHFS method). (A) Total ion chromatogram (TIC) of m/z 152 → m/z 135. (B) TIC of m/z 152 → m/z 135 → m/z 79. (C) Amantadine MS^3 product ion spectrum.

mL/min 50:50 A:B). Optimized MS conditions include: HESI Positive (350 °C), spray voltage 3.5 kV, capillary temperature 380 °C, capillary voltage 55 V, skimmer 18 V, sheath gas N_2 (50 arbitrary units), auxiliary gas N_2 (10 arbitrary units), sweep gas N_2 (0 arbitrary units), tube lens 75 V. The MS was scanned from m/z 70−400. Data from a second scan event using in-source collision-induced dissociation (CID) at 20 V were also collected (m/z 70−350) to detect the $[MH - NH_3]^+$ ions. No additional fragment ions were observed using either in-source CID or the high collision dissociation (HCD) cell on the single stage Orbitrap. For both scan events, resolution was set to 50000, automatic gain control at 1× 10^6, and the maximum inject time was 50 ms. For this procedure, a gradient of 0.1% aqueous formic acid (A) and acetonitrile (B) was used with an Ascentis Express C18 (75 mm × 2.1 mm i.d., 2.7 μm) from Supelco (St. Louis, MO) column, and the flow rate was 0.50 mL/min. The column was kept at room temperature; injection volume was 10 μL. The mobile phase gradient was held at 97% A for 1.5 min, ramped to 50% A in 7 min, and quickly ramped to 1% A in 0.5 min.

Data Analysis and Quantification of Amantadine. Solvent-based calibration curves using amantadine-d_{15} as an internal standard were used to quantify residues of amantadine. Solvent standards with amantadine, rimantadine, and memantine at 7.5, 15, 30, 60, 150, and 300 ng/mL (corresponding to 2.5, 5, 10, 20, 50, and 100 μg/kg in samples) and amantadine-d_{15} at 30 ng/mL (corresponding to 10 μg/kg in samples) were prepared in 0.1% formic acid. If any of the three residues were detected in samples analyzed by the ion trap LC-MS^n with a calculated value ≥50% of the lowest calibration standard (2.5 μg/kg), then the MS^3 ion ratios were examined to determine if the identity is confirmed according to FDA Center for Veterinary Medicine (CVM) Guidance no. 118.[12] A complementary high resolution HRMS LC-MS method was also used to obtain additional quantitative and confirmatory data by measuring the exact mass of relevant ions. Samples found to have levels of amantadine below the level of quantification (2.5 μg/kg) that also met criteria for confirmation of identity would be reported as "amantadine identified at levels below LOQ". Samples with levels of amantadine well above the highest calibration solution (100 μg/kg) were reanalyzed by mixing 0.5 (±0.02) g with 2.5 g of matrix control and re-extracting the sample.

RESULTS AND DISCUSSION

CAHFS: Initial Screening and Confirmatory Method. The FDA has been receiving reports of illnesses in pets associated with jerky treat consumption since 2007.[2] These illnesses involve GI tract disturbances, renal injury, and Fanconi syndrome, a rare tubular dysfunction that can be induced by some toxicants. In 2012, as part of a larger investigation into a potential cause for these illnesses, CAHFS began analyzing

DOI: 10.1021/acs.jafc.5b02416
J. Agric. Food Chem. 2015, 63, 6968−6978

various jerky samples made from chicken and duck muscle, as well as sweet potato-based treats, for a wide variety of toxic chemicals. One of the analyses used was the broad range LC-MS screen on the Orbitrap platform. In late 2013, FDA toxicologists indicated that a number of antiviral compounds, including amantadine, should be included in the jerky treat investigation. Amantadine, in particular, had been reported to have been widely used in the Chinese poultry industry.

Amantadine was initially tested by analysis of a standard solution using the Exactive platform under the chromatographic conditions used for the HRMS LC-MS screen,[10] giving the expected accurate mass ion at m/z 152.1434 and a retention time of 3.9 min (data not shown). Several samples of jerky treats were then spiked and analyzed in order to demonstrate that amantadine is recoverable from jerky using the QuEChERS method. Retention time and accurate mass data were then used to retrospectively review data from previously analyzed jerky treats in order to determine whether this compound was potentially present in the samples. A number of these samples showed a peak with the correct accurate mass and retention time for amantadine. Furthermore, the single fragment ion produced by amantadine under HCD fragmentation conditions (m/z 135.1168) was also present in these samples. All of the samples that tested positive for amantadine residues contained chicken or duck muscle; amantadine was not detected in pet treats made primarily from sweet potatoes.

A confirmatory method using an ion trap LC-MS was developed and tested by spiking five aliquots of ground chicken jerky with amantadine at levels of 1.0, 5.0, 10, 50, and 100 μg/kg. Quantitation was performed using the peak at m/z 79 (the lowest-intensity ion in the MS^3 spectrum). The 1 μg/kg spike gave signal-to-noise measurements greater than 10 for m/z 79 (Figure 2). The response for amantadine was linear (r^2 >0.995) when analyzed by either the ion trap LC-MS or the Orbitrap LC-MS instrument.

Extracted standard curves were analyzed on the ion trap LC-MS along with fresh extracts from samples that had tested positive for amantadine using the Orbitrap LC-MS screening method to estimate the amount of residue present. The batch of samples was extracted and analyzed with two control jerky samples spiked at 5.0 μg/kg. Spike recoveries for these samples as measured against the curve were 66% and 80%. A second calibration curve using the same spiking levels was then extracted and analyzed for confirmation of samples from another second group of pet treats. Two spiked controls were extracted with the batch of samples at 1 μg/kg and a third at 5 μg/kg. Recoveries for these three samples were 93%, 112%, and 124%.

FDA Antiviral Residue Method: Optimization. The ion trap LC-MS^n method was adapted from the procedure used at CAHFS laboratory. Some modifications were made to separate rimantadine and memantine, which are isomers and share the same product ions. The HRMS chromatographic conditions were also optimized to separate the two analogues. The only product ion observed with the HRMS method was the loss of NH_3. It was found that the abundance of this ion was greater when formed using in-source collision induced dissociation (skimmer offset) as opposed to using the high collision dissociation (HCD) in the mass analyzer.

Several extraction methods for amantadine in chicken muscle were tested including one that uses a cation exchange solid phase extraction (SPE) to isolate amantadine from the matrix[6] and a QuEChERS type extraction with a C18 dispersive cleanup step.[4] Another method[5] for amantadine and rimantadine in chicken tissue described in the literature that also included a cation exchange SPE was more complicated because it was a multiresidue method that included a wider scope of antiviral compounds. Several variations of a procedure using the cation exchange SPE were tested for amantadine in chicken jerky, but they did not provide adequate cleanup of the extracts. The jerky matrices had a large amount of oily, yellow residue and seemed to saturate the cation SPE; this oily residue became positively charged with the addition of acid and did not rinse off the SPE column with organic solvents but would elute off the SPE under basic conditions. Recoveries as compared to solvent standards were quite low (10−20% for amantadine, less than 5% for rimantadine and memantine). The procedure described by Yan et al.[4] provided much better results for the recovery and detection of these compounds from chicken pet treats. This method is similar to that used at CAHFS laboratory but includes additional cleanup with C18 sorbent. Variations of the method were also attempted using two different Z-Sep matrix cleanup products, but these did not improve recoveries as compared to using a C18 sorbent. Uncorrected recoveries calculated using a standard curve were ∼40−50% for amantadine and ∼30−50% for the other compounds depending on the matrix and the fortification level. A deuterated internal standard (amantadine-d_{15}) was added to the method for more robust quantification, and these results are described below.

FDA Antiviral Residue Method: Qualitative Validation. The antiviral-specific method was validated according to the agency's guidelines for chemical methods for the FDA foods program[11−13] and focused on chicken-based pet treats. Initially, a small set of controls and fortified samples (at 2.5, 5, and 10 μg/kg in duplicate) were analyzed using five different sources of chicken-based pet treats including several jerkys, meatballs, and soft chicken bites. Additional validation data were collected using a larger number of spike replicates, and these results were also analyzed for confirmation of amantadine, rimantadine, and memantine.

With the ion trap LC-MS^n method, CVM Guidance for Industry no. 118[12] for MS^n partial scan data was used to determine confirmation of identity along with retention time matching. The ratio of ions m/z 107, 93, and 79 in the MS^3 spectra for amantadine in spiked samples were compared to that found in standards. The relative abundances from the spectrometric tabulations in samples compared to standards were required to be within 20%; typical ion ratios found were m/z 107 (100%), m/z 93 (∼60%), and m/z 79 (∼20%). Similar data analysis was performed for m/z 135, m/z 121, m/z 107, and m/z 81 in the MS^3 spectra for rimantadine and memantine. Official confirmation of identity guidelines have not yet been published by the U.S. FDA for high resolution MS data, but the presence (using extracted ion chromatograms of ± 5 ppm) of both m/z 152.1434 (MH^+) and 135.1168 ($[MH - NH_3]^+$) in the HRMS data for amantadine (m/z 180.1747 and 163.1481 for the analogues) was used as additional information to confirm identity of these residues.

All three residues were confirmed in all fortified samples (n = 64) using both ion trap and HRMS instruments; there were no instances of false negatives. The use of MS^3 on the ion trap provided excellent selectivity; in general, residues were not detected in the solvent blanks, reagent blanks, or matrix blanks. However, higher background signal was observed with some matrices, and adequate chromatography was required to resolve the residues of interest. With the Orbitrap HRMS, detection of

DOI: 10.1021/acs.jafc.5b02416
J. Agric. Food Chem. 2015, 63, 6968−6978

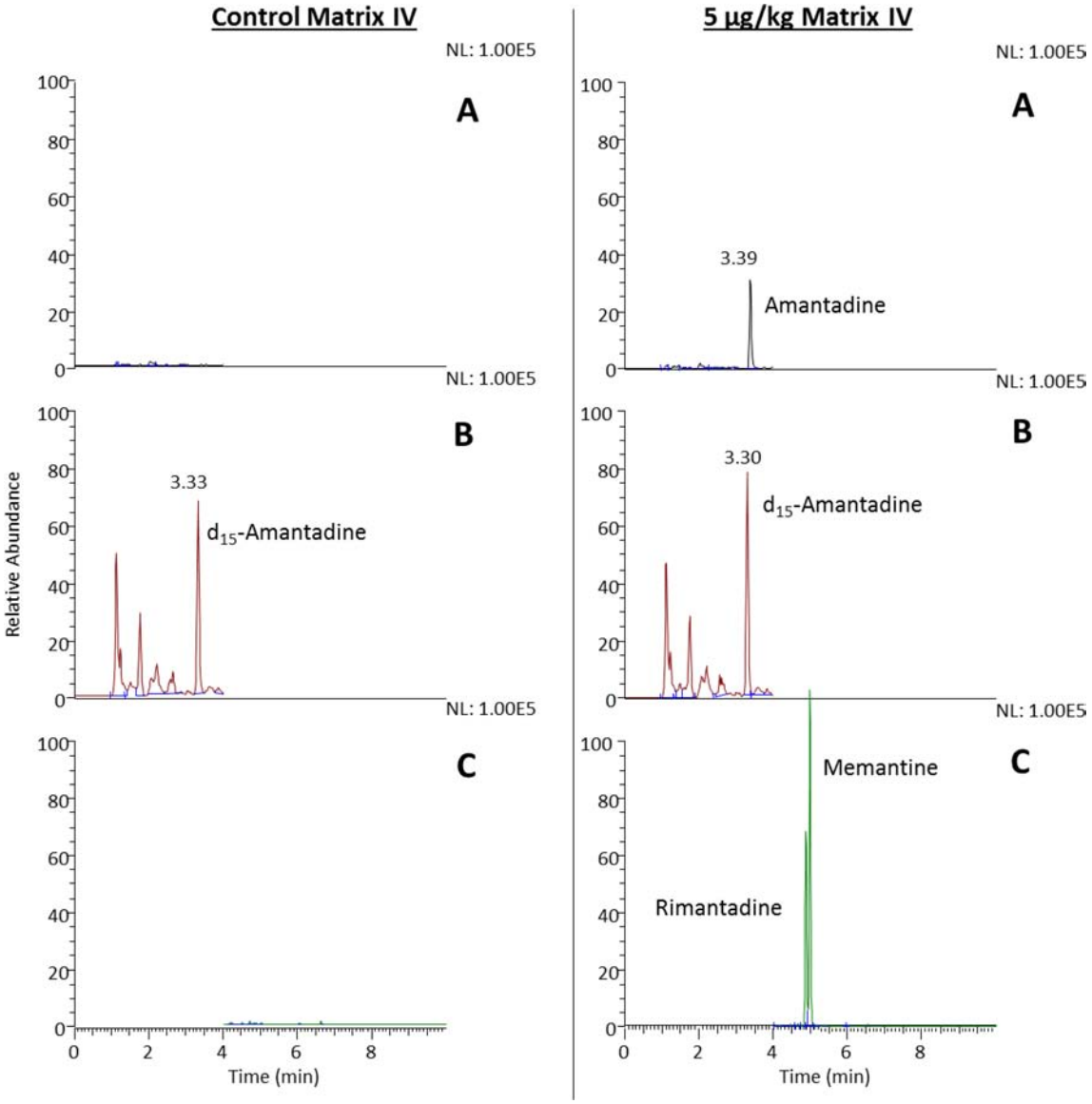

Figure 3. Ion trap LC-MS^3 analysis of control matrix and matrix fortified at 5 μg/kg with amantadine, rimantadine, and memantine. Amantadine-d_{15} (10 μg/kg) was added to both matrix blank and fortified matrix (FDA method). (A) Amantadine: total ion chromatogram (TIC) of m/z 152 → m/z 135→ m/z 65−140. (B) Amantadine-d_{15}: TIC of m/z 167 → m/z 150→ m/z 65−155. (C) Rimantadine/memantine: TIC of m/z 180 → m/z 163→ m/z 65−140.

both MH^+ and $[MH - NH_3]^+$ was required to confirm the presence of residues. In samples of chicken jerky purchased locally, amantadine was confirmed by both instrument methods in one product (at levels of <2.5 μg/kg). Amantadine was also detected, but did not meet confirmation of identity criteria, in another related product. Low levels of amantadine (2−3 μg/kg) were also found in similar products by the CAHFS laboratory, so these purchased samples were not considered to be false positives. Occasionally a peak corresponding to the retention time of memantine was detected in blanks (solvent, reagent, and matrix blanks) with approximately the correct ion ratios. However the signal-to-noise for these peaks was very low and the absolute signal was < 10% compared to what was found in the 2.5 μg/kg fortified samples; therefore, confirmation criteria were not met. Figures 3 and 4 show examples of data for control matrix and matrix fortified with antiviral compounds at 5 μg/kg for the ion trap LC-MS^n and HRMS, respectively.

FDA Antiviral Residue Method: Quantitative Validation. The quantitative validation focused on amantadine. A deuterated internal standard (amantadine-d_{15}) was purchased and added to samples prior to extraction at a level of 10 μg/kg. Additional sets of fortified samples (at 2.5 μg/kg, n = 5; 5 μg/kg, n = 5; 10 μg/kg, n = 5; 50 μg/kg, n = 1) were prepared and analyzed along with duplicate matrix blanks and a reagent blank for four different sources of chicken containing pet treats. Solvent-based calibration curves were used with standards prepared at levels corresponding to 2.5, 5, 10, 20, 50 and 100 μg/kg in tissue (7.5, 15, 30, 60,150 and 300 ng/mL). Calibration curves were linear with $R^2 \geq 0.995$. The sum of ions m/z 107, 93, and 79 for amantadine and m/z 118, 102, and 86 for amantadine-d_{15} from the MS^3 spectra were used for quantification with the ion trap. Quantitative results from the HRMS data were also calculated and compared to that from the Velos ion trap data. The ion at m/z 135.1168 $[MH - NH_3]^+$ was used to quantify amantadine because of significant

DOI: 10.1021/acs.jafc.5b02416
J. Agric. Food Chem. 2015, 63, 6968−6978

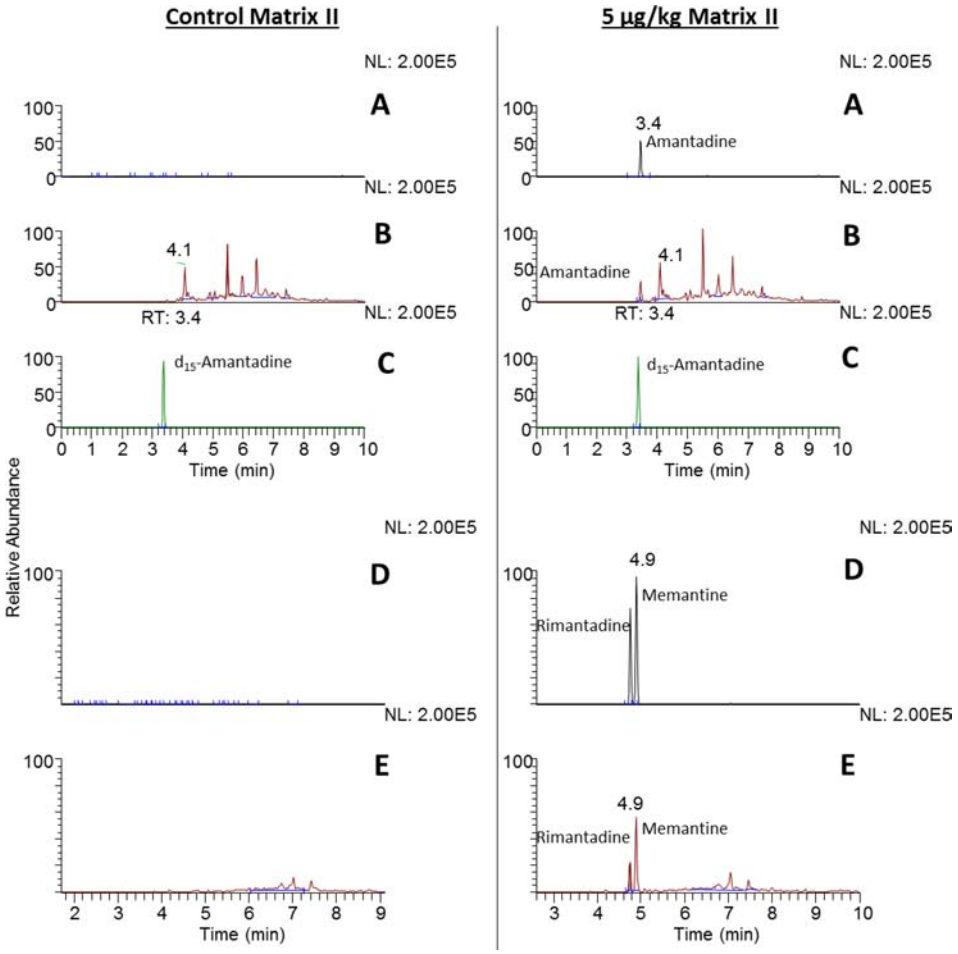

Figure 4. Orbitrap LC-MS analysis of control matrix and matrix fortified at 5 μg/kg with amantadine, rimantadine, and memantine. Amantadine-d_{15} (10 μg/kg) was added to both matrix blank and fortified matrix. Extracted ion chromatogram windows = 5 ppm (FDA method). (A) Amantadine MH^+ m/z 152.1434. (B) Amantadine $[MH - NH_3]^+$ m/z 135.1168. (C) Amantadine-d_{15} MH^+ m/z 167.2375. (D) Rimantadine/memantine MH^+ m/z 180.1747. (E) Rimantadine/memantine $[MH - NH_3]^+$ m/z 163.1481.

Table 1. Recoveries and Relative Standard Deviations for Amantadine in Fortified Pet Treats

matrix	10 μg/kg[a] % recovery (RSD) ion trap MS^3/ Orbitrap HRMS (m/z 135.1168)	5 μg/kg[a] % recovery (RSD) ion trap MS^3/ Orbitrap HRMS (m/z 135.1168)	2.5 μg/kg[a] % recovery (RSD) ion trap MS^3/ Orbitrap HRMS (m/z 135.1168)	50 μg/kg[b] % recovery (RSD) ion trap MS^3/ Orbitrap HRMS (m/z 135.1168)
matrix I chicken jerky	110 (4.3)	95.7 (12)	76.0 (6.6)	123
	100.8 (9.9)	*90.7 (15.8)*	*80.6 (8.7)*	*116*
matrix II chicken meatballs	104 (3.2)	105 (3.4)	101 (4.5)	101
	110 (16.5)	*92.4 (11.0)*	*84.8 (11.0)*	*110*
matrix III chicken jerky	111 (7.5)	100 (5.5)	82.0 (6.5)	117
	73.6 (5)	*59.2 (10.8)*	*25.5(6.8)*	*80*
matrix IV chicken bites	103 (6.1)	91.8 (2.8)	82.2 (3.2)	120
	101.4 (8.9)	*95.9 (9.1)*	*80.1 (9.8)*	*105*

[a] n = 5 for each matrix, [b] n = 1 for each matrix

background that appeared at m/z 152.1434 for at least one matrix. The MH^+ ion for amantadine-d_{15} (m/z 167.2375) was used. These results are shown in Table 1. The lowest level of quantitation (LOQ) was 2.5 μg/kg based on signal-to-noise ≥10 and consistency in meeting identification criteria. A statistical method detection limit (MDL) was calculated with the data from samples fortified at 2.5 μg/kg by multiplying the standard deviation times the Student's t value (n = 20) and was found to be 0.68 μg/kg for the ion trap method and 1.68 μg/kg for the HRMS.

In addition, postfortified matrix-matched standards were prepared and curves were generated using this type of calibration. In general, with the use of an internal standard, the solvent-based curves provided similar recoveries as

DOI: 10.1021/acs.jafc.5b02416
J. Agric. Food Chem. 2015, 63, 6968−6978

Table 2. Analysis of Amantadine Residues in Chicken Jerky Test Samples

sample	amount (μg/kg) determined by ion trap LC-MS^n	amount (μg/kg) determined by Orbitrap HRMS (m/z 135.1168)	amount (μg/kg) found in similar products by UC Davis
sample A-1[a]	**66.1**	**79.0**	550, 180, 95, 7, 1.7, ND, ND
	(n = 3[b], RSD = 2%)	(n = 3[c], RSD = 1%)	
sample A-2	**8.54**	**9.0**	5.7[d]
	(n = 3, RSD = 0.6%)	(n = 3, RSD = 11%)	
sample A-3	**60.8**	**69.2**	95
	(n = 3, RSD = 0.7%)	(n = 3, RSD = 5%)	
sample A-4	**223**	**229**	180
	(n = 3, RSD = 10%)	(n = 3, RSD = 10%)	
	214[e]	***194***[e]	
	(n = 3, RSD = 3%)	(n = 3, RSD = 7%)	
sample A-5	**547**	**604**	550
	(n = 3, RSD = 5.6%)	(n = 3, RSD = 5.0%)	
	605[e]	***603***[e]	
	(n = 3, RSD = 1%)	(n = 3, RSD = 11%)	
sample B-1	**164**	**173**	110, 82
	(n = 3, RSD = 5%)	(n = 3, RSD = 7%)	
sample B-2	**633**	**631**	110[d]
	(n = 3, RSD = 6.5%)	(n = 3, RSD = 7%)	
	590[e]	***577***[e]	
	(n = 3, RSD = 5%)	(n = 3, RSD = 3%)	
sample B-3	**111**	**125**	82[d]
	(n = 3, RSD = 2%)	(n = 3, RSD = 7%)	
sample B-4	**187**	**201**	100
	(n = 3, RSD = 2%)	(n = 3, RSD = 6%)	
	176[e]	***166***[e]	
	(n = 3, RSD = 3%)	(n = 3, RSD = 5%)	
sample C-1	**13.9**	**13.4**	77, 44, 43
	(n = 1)	(n = 1)	
sample C-2	**86.9**	**105**	44
	(n = 1)	(n = 1)	
sample D-1	**16.3**	**17.8**	33
	(n = 3, RSD = 4%)	(n = 3, RSD = 8%)	
sample D-2	**80.1**	**86.2**	33[d]
	(n = 3, RSD = 4%)	(n = 3, RSD = 6%)	
sample E-1	**<2.5** (n = 3[f])	**<2.5** (n = 3)	+/ND
sample F-1	**<2.5** (n = 3)	**<2.5** (n = 3)	3.1
sample F-2	**15.3**	**14.3**	3.1[d]
	(n = 3, RSD = 3%)	(n = 3, RSD = 9%)	

[a]A-1 = brand "A", sample "1". [b]All replicates met confirmation of identity criteria[12] unless otherwise specified. [c]All replicates detected ions at m/z 152.1434 and m/z 135.1168. [d]Same pieces of sample tested. [e]Smaller sample size (0.5 g) was diluted with 2.5 g of matrix control, re-extracted, and reanalyzed. [f]Only 2 of 3 replicates met confirmation of identity criteria.

compared to the matrix-matched curves. Loss of signal (ion suppression) from matrix effects, as measured by the difference in slope for uncorrected solvent-based curves and matrix-matched curves, was typically 20−25%, but as much as 70% signal loss was observed for one matrix. Because it is expected that many different types of pet treats will be analyzed and providing a matrix-matched curve for each sample is not reasonable, solvent standards are preferred for routine analysis.

An evaluation of quantitative data for the other two compounds, rimantadine and memantine, was also performed. Data were acceptable for some matrices at higher fortification levels (10 μg/kg), especially using matrix-matched curves, but often the calculated recoveries were unacceptably low or high. This may indicate that the use of a deuterated amantadine as the internal standard does not always provide acceptable corrections for the calculation of rimantadine and memantine due to differences in matrix effects and/or extraction recovery. Deuterated standards of the rimantadine and memantine were not obtained as the focus of this method was amantadine; the method was not modified to optimize for the determination of these other residues. The method was able to detect the presence (confirm identity) of these compounds at levels greater than 2.5 μg/kg.

For ruggedness testing, experimental variables that were evaluated included use of different matrices, different sources of extraction salts and C18 sorbents, and several different analysts. For samples fortified at 5 μg/kg including validation data in Table 1, plus additional ruggedness testing and positive controls analyzed with test sample batches, the average recovery using the ion trap LC-MS^n method was 102% with RSD of 10.4% (n = 37). These data were collected over 9 days with four analysts performing different parts of the procedure. Most of these samples (n = 27) were also analyzed on the HRMS instrument with average recovery of 84% and RSD of 19%. The stock solutions, intermediate mixed standards, and LC-MS standard solutions were found to be stable when stored

DOI: 10.1021/acs.jafc.5b02416
J. Agric. Food Chem. 2015, 63, 6968−6978

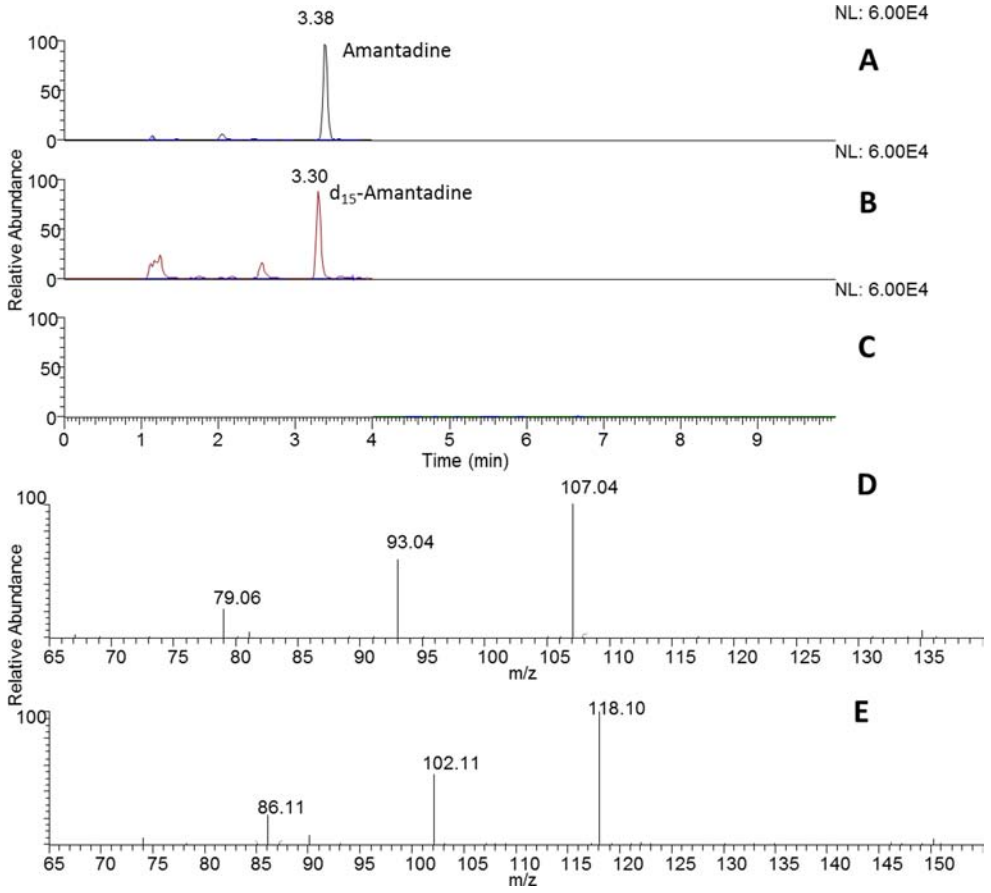

Figure 5. Ion trap LC-MS^3 analysis of sample no. C-1. Amantadine-d_{15} (10 μg/kg) was also added to sample (FDA method). (A) Amantadine: total ion chromatogram (TIC) of m/z 152 → m/z 135→ m/z 65−140. (B) Amantadine-d_{15}: TIC of m/z 167 → m/z 150→ m/z 65−155. (C) Rimantadine/memantine: TIC of m/z 180 → m/z 163→ m/z 65−140. (D) Amantadine MS^3 product ion spectrum. (E) Amantadine-d_{15} MS^3 product ion spectrum.

in the refrigerator (4 °C) for at least one month. Extracts were stable for at least a few days. Long-term stability testing has not been performed.

Analysis of Test Samples. Test samples of chicken-based pet treats, including some collected from consumer reported cases, were obtained by the CVM Veterinary Laboratory Investigation and Response Network and analyzed by both the CAHFS laboratory and FDA laboratories. In some cases, the same pieces of sample were analyzed by the two laboratories; in other instances, the samples analyzed by FDA were similar (same brand/product but different bag) to those that had been analyzed previously by CAHFS laboratory. The levels of amantadine found in these samples varied from below the limit of quantitation (2.5 μg/kg) to above 600 μg/kg. Results were similar regardless of which instrument method was used and are listed in Table 2. Additional samples made from duck muscle were also analyzed at CAHFS (but not FDA), and amantadine was found in some of these samples at levels ranging from 2 to 23 μg/kg (data not shown).

The amount of amantadine found by FDA generally corresponded to levels of the residue found in similar samples previously analyzed by CAHFS laboratory. In general, the amount of amantadine found by FDA was higher (usually 2−3 times higher) than what was reported previously. This may be due to different approaches in obtaining quantitative data. For example, the FDA method used an internal standard (amantadine-d_{15}) to correct for recovery and matrix effects, while the CAHFS laboratory method utilized an extracted calibration curve with a similar matrix for all samples. Rimantadine and memantine were not detected in any of these test samples. Data from the analysis of test samples are shown in Figure 5 (ion trap LC-MS^n) and Figure 6 (Orbitrap HRMS).

In summary, amantadine residues were initially found in chicken and duck jerky using a wide-scope HRMS screening method. These results were verified with a method that was developed specifically to analyze and quantify amantadine in chicken-based pet food treats; the method was also suitable for the qualitative detection and identification of rimantadine and memantine. Analysis of these compounds in chicken jerky treats can be performed either by using ion trap LC-MS^n or a single stage Orbitrap LC-MS high resolution instrument. The use of these two complementary LC-MS analyses has unequivocally confirmed the presence of amantadine in test samples analyzed at both the CAFHS and FDA laboratories.

The relationship between residues of amantadine and toxicity in dogs is not known. In addition to being used as antiviral medicine, amantadine can be prescribed to dogs for pain management,[14] although caution is advised as some toxic effects have been observed in humans with compromised renal function.[15] The dosage that would cause toxicity is, however, much higher than what would be consumed in jerky treats. Nevertheless, residues of amantadine should not be present in chicken-based dog treats, and monitoring this compound, as

DOI: 10.1021/acs.jafc.5b02416
J. Agric. Food Chem. 2015, 63, 6968−6978

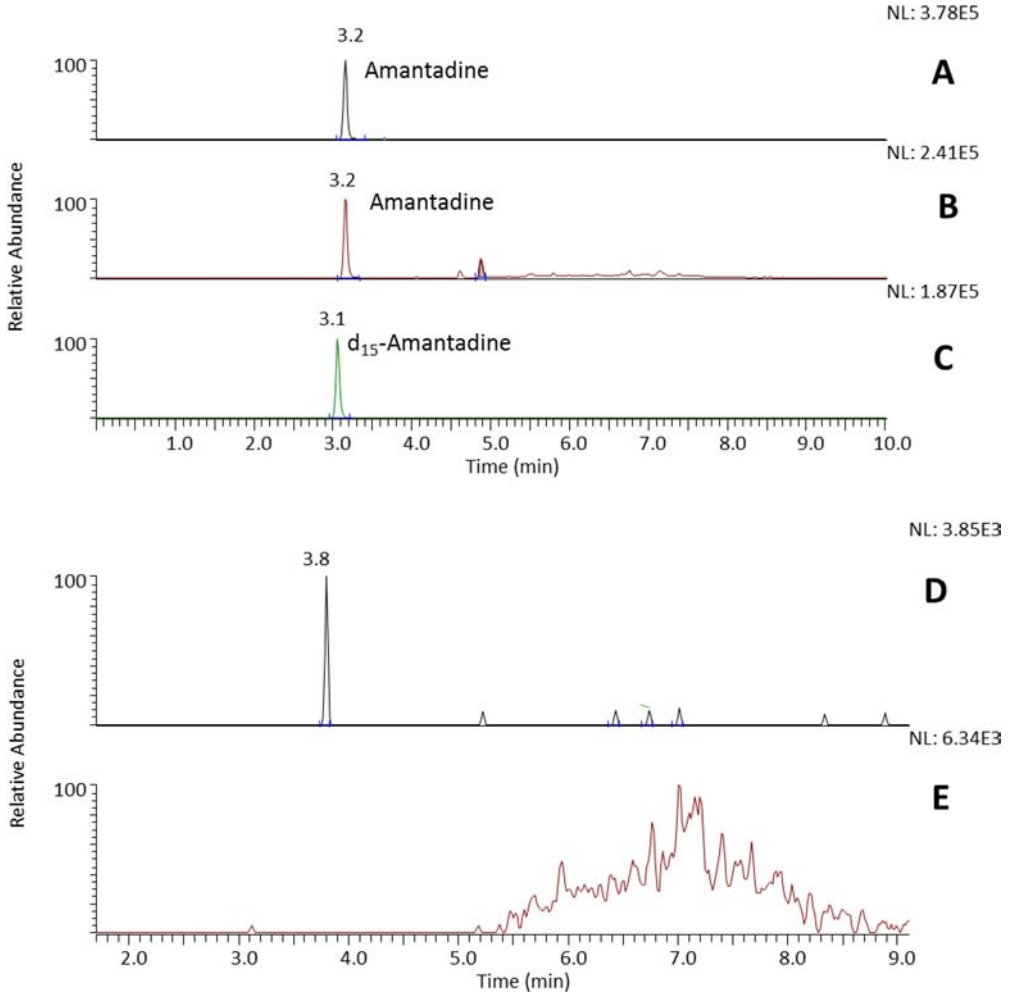

Figure 6. Orbitrap LC-MS analysis of sample no. D-1. Amantadine-d_{15} (10 μg/kg) was also added to sample. Extracted ion chromatogram windows = 5 ppm (FDA method). (A) Amantadine MH^+ m/z 152.1434. (B) Amantadine $[MH - NH_3]^+$ m/z 135.1168. (C) Amantadine-d_{15} MH^+ m/z 167.2375. (D) Rimantadine/memantine MH^+ m/z 180.1747. (E) Rimantadine/memantine $[MH - NH_3]^+$ m/z 163.1481.

well as additional drug residues and other chemical and biological contaminants, is recommended.

AUTHOR INFORMATION

Corresponding Author

*Phone: 303-236-3072. Fax: 303-236-3100. E-mail: sherri.turnipseed@fda.hhs.gov.

Notes

The authors declare no competing financial interest.

ACKNOWLEDGMENTS

The authors would like to acknowledge helpful discussions with scientists at FDA/ORA Office of Regulatory Science and FDA/CVM Office of Research. The views expressed in this paper are those of the author(s) and may not reflect the official policy of the Department of Health and Human Services, the U.S. Food and Drug Administration, or the U.S. Government.

REFERENCES

(1) Why are jerky treats making pets sick?*FDA Consumer Health Information*; U.S. Food and Drug Administration: Silver Spring, MD, 2013

(2) *FDA Provides Latest Information on Jerky Pet Treat Investigation*; U.S. Food and Drug Administration Center for Veterinary Medicine: Rockville, MD. 2014; http://www.fda.gov/animalveterinary/newsevents/cvmupdates/ucm397713.htm (accessed June 30, 2015).

(3) He, G.; Qiao, J.; Dong, C.; He, C.; Zhao, L.; Tian, Y. Amantadine-resistance among H5N1 avian influenza viruses isolated in Northern China. *Antiviral Res.* **2008**, *77*, 72−79.

(4) Yan, H.; Liu, X.; Cui, F.; Yun, H.; Li, J.; Ding, S.; Yang, Dajin; Zhang, Z. Determination of amantadine and rimantadine in chicken muscle by QuEChERS pretreatment method and UHPLC coupled with LTQ Orbitrap mass spectrometry. *J. Chromatogr. B: Anal. Technol. Biomed. Life Sci.* **2013**, *938*, 8−13.

(5) Berendsen, B. J. A.; Wegh, R. S.; Essers, M. L.; Stolker, A. A. M.; Weigel, S. Quantitative trace analysis of broad range of antiviral drugs in poultry muscle using column-switching liquid chromatography coupled to tandem mass spectrometry. *Anal. Bioanal. Chem.* **2012**, *402*, 1611−1623.

(6) Chan, D.; Tarbin, J.; Sharman, M.; Carson, M.; Smith, M.; Smith, S. Screening method for the analysis of antiviral drugs in poultry tissues using zwitterionic hydrophilic interaction liquid chromatography mass spectrometry. *Anal. Chim. Acta* **2011**, *700*, 194−200.

(7) Zhao, S.; Li, D.; Qiu, J.; Wang, M.; Yang, S.; Chen, D. Simultaneous determination of amantadine, rimantadine, and chlorpheniramine in animal-derived food by liquid chromatography-tandem mass spectrometry after fast sample preparation. *Anal. Methods* **2014**, *6*, 7062−7067.

(8) Wu, Y.-L.; Chen, R.-X.; Xue, Y.; Yang, T.; Zhao, J.; Zhu, Y. Simultaneous determination of amantadine, rimantadine and memantine in chicken muscle using multi-walled carbon nanotubes as a

DOI: 10.1021/acs.jafc.5b02416
J. Agric. Food Chem. 2015, 63, 6968−6978

reversed-dispersive solid phase extraction sorbent. *J. Chromatogr. B: Anal. Technol. Biomed. Life Sci.* **2014**, *965*, 197−205.
(9) Sheridan, R.; Mirabile, J.; Hafler, K. Determination of six illegal antibiotics in chicken jerky dog treats. *J. Agric. Food Chem.* **2014**, *62*, 3690−3696.
(10) Filigenzi, M. S.; Ehrke, N.; Aston, L. S.; Poppenga, R. H. Evaluation of a rapid screening method for chemical contaminants of concern in four food-related matrices using QuEChERS extraction, UHPLC and high resolution mass spectrometry. *Food Addit. Contam., Part A* **2011**, *28*, 1324−1339.
(11) Turnipseed, S.; Storey, J. M.; Andersen, W. C.; Heise, A.; Lohne, J. J.; Madson, M. R. Determination and confirmation of the antiviral drug amantadine and its analogs in chicken jerky pet treats. *U.S. Food and Drug Administration Laboratory Information Bulletin*; U.S. Food and Drug Administration: Silver Spring, MD, 2014; no. 4563.
(12) *Mass Spectrometry for Confirmation of the Identity of Animal Drug Residues*; Guidance for Industry no. 118; U.S. Food and Drug Administration Center for Veterinary Medicine: Rockville, MD, 2003.
(13) *Guidelines for the Validation of Chemical Methods for the FDA Foods Program*; U.S. Food and Drug Administration: Silver Spring, MD, 2012.
(14) Lacelles, B. D. X.; Gaynor, G. S.; Smith, E. S.; Roe, S. C.; Marcellin-Little, D. J.; Davidson, G.; Boland, E.; Carr, J. Amantadine in a multimodal analgesic regimen for alleviation of refractory osteoarthritis pain in dogs. *J. Vet. Intern. Med.* **2008**, *22*, 53−59.
(15) Miller, K. S.; Miller, J. M. Toxic effects of amantadine in patients with renal failure. *Chest* **1994**, *105*, 1630.

DOI: 10.1021/acs.jafc.5b02416
J. Agric. Food Chem. 2015, 63, 6968−6978

Chinese medicinal herb *Lycoris radiata*, is currently licensed for use in Europe as an acetylcholinesterase inhibitor for AD treatment.[19] Recent research has also reported anticancer[20] and anti-inflammatory[21] effects of plant extracts or active compounds isolated from *Lycoris* species. However, there has been no report on whether *Lycoris* directly affects AD pathological pathways, such as the formation of Aβ. More specifically, no biological effects have been reported for *Lycoris chejuensis* K. Tae et S. Ko (CJ), which originates from Jeju Island in Korea.[22,23] Because of their rich starch contents, *Lycoris* species plants, including CJ, have been traditionally used for hunger crops.[24,25]

In this study, we found that the CJ extract potently lowered Aβ levels in vitro and in vivo. CJ was also observed to decrease several byproducts of secretase activity. We assumed that the action of the CJ extract was related to decreased level of both immature and mature APPs, which is one of the novel mechanisms in APP processing. Furthermore, we were able to elucidate active components of the CJ extract that play a causal role in its effects. Taken together, we have revealed that CJ extract can reduce Aβ levels via the attenuation of APP while minimally altering the activity of β-, γ-, and α-secretases. Furthermore, we suggest that the effect of CJ extract is mediated by its active components, narciclasine, 7-deoxynarciclasine, and 7-deoxy-*trans*-dihydronarciclasine.

MATERIALS AND METHODS

Chemicals. Plant extraction and partition used an extra pure grade solvent (DUKSAN, Gyeonggi-do, Republic of Korea). All HPLC analyses used HPLC grade CHROMASOLV solvents (Sigma-Aldrich, MO, USA). Methanol-d_4 (99.8%, Cambridge Isotope Laboratories, MA, USA) and dimethyl sulfoxide (DMSO)-d_6 (99.9%, Cambridge Isotope Laboratories, MA, USA) were used for nuclear magnetic resonance (NMR) measurements. Diaion HP-20 (SUPELCO, MO, USA) was used as an adsorbent for flash column chromatography. Deionized (DI) water (18 MΩ-cm) was generated using a Barnstead Water Purification Systems (Thermo Fisher Scientific, MA, USA).

Plant Materials. CJ plants were obtained by collecting samples at the Hantaek Botanical Garden in Yongin, Gyunggi-do, Republic of Korea, from April to June 2010. The plant was identified by Jung Hwa Kang from Hantaek Botanical Garden. A voucher specimen was deposited in the herbarium of the Korea Institute of Science and Technology (Gangneung, Gangwon-do, Republic of Korea) under the number KNB00065. Samples were immediately stored at −20 °C until they were analyzed.

Spectroscopic Analyses. NMR spectra were recorded on a Varian VNMRS 500 MHz NMR spectrometer (Agilent, CA, USA) or a Bruker AVANCE III 400 MHz NMR spectrometer (Bruker, MA, USA). Low-resolution electrospray ionization mass spectrometry data were acquired by an Agilent 1200 series HPLC system/6120 quadrupole MSD (Agilent, CA, USA). A Waters 1525 binary pump/2996 photodiode array detector (Waters, MA, USA) with a Phenomenex Luna column (Phenomenex, CA, USA) [C18, 5 μm, 150 mm × 4.6 mm] was used for HPLC analysis. Preparative HPLC were performed with a Gilson 321 HPLC system with a Phenomenex Luna column [C18, 10 μm, 250 mm × 21.20 mm].

Preparation of CJ Extract. Air-dried bulbs (590 g) of CJ were extracted with 3 L of EtOH (50% v/v) by reflux for 3 h. The extract was then cooled at room temperature and filtrated. Finally, the filtrate was evaporated under reduced pressure at 40 °C to result in 200 g of CJ EtOH extract (yield 34%).

Isolation and Analysis of Active Compounds. First, 200 g of CJ EtOH extract was suspended in 1 L of water and then subjected to successive liquid partition chromatography. Using the same amount of *n*-hexane, CH_2Cl_2 and *n*-BuOH solvent gave 1, 1, and 5.5 g of organic soluble fractions, respectively. Then the *n*-BuOH soluble fraction (CJ-3) was refractionated by a Diaion-HP20 flash column chromatography with a stepwise elution of aqueous MeCN that was further divided to eight fractions (CJ-3-F1-8). For isolation of active compounds, preparative HPLC was conducted. To isolate 7-deoxynarciclasin and 7-deoxy-*trans*-dihydroxynarciclasine, fraction CJ-3-F4 (500 mg, 40% MeCN in water eluate) was subjected to reversed phase chromatography [C18, 250 mm × 21.20 mm, flow rate 10 mL/min, gradient elution of 10−20% aqueous MeCN containing 0.02% trifluoroacetic acid for 40 min]. Narciclasine was isolated from the CJ-3-F6 fraction (400 mg, 60% MeCN in water eluate) by reversed-phase chromatography [C_{18}, 250 mm × 21.20 mm, flow rate 10 mL/min, gradient elution of 10−50% aqueous MeCN containing 0.02% trifluoroacetic acid for 40 min]. The EtOH extract of CJ (20 mg) was dissolved in 1 mL of water, and 10 μL of the resulting sample solution was injected for HPLC analysis. The mobile phase used for analysis started at 10% MeCN in water (v/v) and was then changed to 20% MeCN in water (v/v) for 30 min. The flow rate was 1 mL/min. Narciclasine and 7-deoxynarciclasine were detected at 254 nm wavelength, and wavelength of 223 nm was used for 7-deoxy-*trans*-dihydronarciclasine detection.

Cell Culture. HeLa cells stably transfected with APP751 carrying the Swedish mutation (APPsw) were cultured at 37 °C with 5% CO_2. The culture media was Dulbecco's Modified Eagle Medium (DMEM) supplemented with 10% heat-inactivated fetal bovine serum containing 100 units/mL penicillin, 100 μg/mL streptomycin, 260 μg/mL Zeocin, and 400 μg/mL G418.

sAPPα, sAPPβ, and Aβ Peptide Assay. Cells at 80% confluence in a 35 mm dish were cultured for the times indicated in DMEM culture medium without serum but with CJ extract or active compounds solubilized in DMSO. Control cells were treated similarly and incubated with serum-free DMEM solution containing DMSO. For Aβ detection, the conditioned media were analyzed by a sandwich enzyme-linked immune-sorbent assay (ELISA; Invitrogen, CA, USA) according to the supplier's instructions. Similarly, sAPPα, sAPPβ-WT, and sAPPβ-sw were analyzed by ELISA (IBL, Hamburg, Germany).

Western Blotting. Cells were incubated at 37 °C with CJ extract for the times indicated. Cells were washed twice with ice-cold phosphate-buffered saline (PBS) and homogenized with lysis buffer (10 mM Tris·HCl, pH 7.4, 150 mM NaCl, 1% Triton X-100, 0.25% Nonidet P-40, 2 mM EDTA) using a cell scraper. Cell lysates were complemented with a protease inhibitor mixture (Calbiochem, MA, USA). The lysed cells were centrifuged at 12000*g* for 10 min at 4 °C, and the amount of protein in the supernatant was determined by Bradford assay (Biorad, CA, USA). A total of 40 μg of protein from each sample was subjected to SDS-PAGE using 4−20% gradient Tris/glycine gels (Invitrogen, CA, USA). Next, the proteins were transferred to a nitrocellulose membrane and blocked with 5% skim milk powder in Tris-buffered saline/Tween 20 for 1 h at room temperature. Membranes were then incubated with primary antibodies and rabbit anti β-tubulin (Sigma, MO, USA) overnight at 4 °C. After washing, membranes were incubated for 1 h at room temperature with horseradish peroxidase-conjugated goat antirabbit IgG antibody (1:2000 dilution; Invitrogen, USA) and washed. Peroxidase activity was visualized with enhanced chemiluminescence. Blots were quantified with Multi Gauge software using a LAS-3000 system (Fujifilm, Tokyo, Japan). The following antibodies were used: Anti-APP, C-terminal (Sigma-Aldrich, MO, USA), anti-Aβ, 6E10 (Covance, NJ, USA), anti-β-site APP cleaving enzyme, BACE1 (Chemicon, MA, USA), anti-ADAM9 (Cell Signaling, MA, USA), anti-ADAM10 (Calbiochem, MA, USA), and anti-TACE, ADAM17 (Chemicon, MA, USA).

Secretase Activity Assay. The activities of α- and β-secretases were measured using the InnoZyme TACE activity kit (Calbiochem, MA, USA) and the β-secretase activity assay kit (BioVision, CA, USA). Each of the α- and β-secretase activity assays were conducted according to the manufacturer's protocol. Subsequently, lysates, which were lysed with protein extraction reagent (Novagen, MA, USA), plated onto precoated plates, and the activities of bound secretases measured using the fluorescence of the substrates.

Animals and Drug Administration. Male APP/Presenilin-1 (PS1) double transgenic (TG) mice (Strain name, B6C3-Tg(APPswe/

DOI: 10.1021/acs.jafc.5b00889
J. Agric. Food Chem. 2015, 63, 6979−6988

PSEN 1dE9)85Dbo/J; stock number no. 004462) used in this study were obtained from Jackson Laboratory (ME, USA) at the age of 4 months. Mice expressed a chimeric mouse/human APP containing the K595N/M596L Swedish mutations as well as a mutant human PS1 carrying the exon 9-deleted variant under the control of mouse prion promoter elements. These promotor elements predominantly directed transgene expression to central nervous system neurons. All animals were housed in solid bottom cages with pellet food and water available ad libitum. The mice were also maintained on a 12/12 h light−dark cycle in a temperature and humidity-controlled room (23 °C, 50%). Starting at the age of 5 months, the TG mice were randomly distributed into groups of seven mice. One group of mice was administered CJ extract in doses of 50 or 150 mg/kg/10 mL daily per os until the end of all experiments. The other groups of mice served as controls and were administered saline during the drug administration period. The animal protocols used in this study were in accordance with and granted (grant no. AP-2010KB001) by the Korea Institute of Science and Technology Animal Care and Ethics Committee.

Morris Water Maze Test. At the age of 8 months, the mice were subjected to the Morris water maze (MWM) test. The MWM consists of a circular pool (120 cm in diameter and 60 cm in depth) filled with 24−26 °C water to a depth of 40 cm. The water was made opaque (white in color) with water-soluble nontoxic paint. A nonvisible escape platform, 8 cm in diameter, was submerged approximately 1 cm below the water surface in the center of the designated target quadrant of the pool. The two phases of the MWM tests, acquisition and retention, were conducted for six consecutive days. During the first five days, the acquisition phase was conducted by placing each mouse in the MWM to swim for a total of four trials per day, with a 1 h intertrial interval. During each trial, mice were given a maximum of 90 s to find the platform and had to remain on the platform for at least 5 s. If the mouse was unable to find the platform within the 90 s time frame, it was placed directly on the platform for 5 s and then returned to its cage. For each trial, the mouse was randomly placed under one of the four visual cues. During the acquisition phase, the amount of time it took for a mouse to find the hidden platform (escape latency) was measured. For those mice that did not find the hidden platform in the allotted time, a score of 90 s was given. The retention phase of the MWM occurred on the day immediately following the last day of the acquisition phase. During the retention phase, the platform was removed and mice were given 120 s to freely explore the pool. The total duration of time spent in the target quadrant, which had contained the escape platform during the acquisition phase, was measured. After the test, mice were removed from the pool and returned to their cages.

Novel Object Recognition Test. After the MWM test, mice were left to rest in their home cages for 1 week. After this period, a novel object recognition test (NORT) was conducted to test the spontaneous tendency of mice to explore a novel object more often than a familiar one.[26] A plastic chamber (50 cm × 50 cm × 50 cm) with 10 cm spaced grids at the bottom was used. The NORT procedure consisted of three different phases: three days of habituation, one day of acquisition, and one day of retention. During the habituation phase, each day mice were individually subjected to a single 10 min habituation session during which they were introduced to an empty arena. On the fourth day (acquisition phase), mice were subjected to a single 10 min exploring session, during which two floor-fixed objects (A and B) were placed in a symmetric position from the center of the arena with enough space between each other and from the walls. Both plastic objects were the same in color, smell, shape, and size. Mice were allowed to explore the objects freely in the arena. On the fifth day (retention phase), mice were subjected to a single 5 min exploration session. In this session, mice were placed in the arena, which contained two objects, A and C. Object C was a novel object with a different color, smell, and shape than object B. The memory index for each mouse was expressed as the ratio of the amount of time spent exploring the novel object C $(T_C \times 100)/(T_A + T_C)$, where T_A and T_C were the time spent exploring objects A and C during the 5 min, respectively.

In Vivo Soluble Aβ42 Detection. For in vivo detection of brain soluble Aβ42 peptides, after undergoing behavior tests, mice were anesthetized and decapitated at the age of 9 months. The cerebral cortex was dissected from the exposed brains, and the tissue samples were stored at −80 °C until use. The cerebral cortex samples (100 mg) were homogenized in Tris-buffered saline solution (20 mM Tris; 137 mM NaCl; pH 7.4) containing a complete protease inhibitors tablet (Sigma, MO, USA). The extraction ratio (brain tissue:Tris-buffered saline) was 1:5 or 1:10 (w/v). Tissue homogenates were centrifuged at 100000*g* for 1 h at 4 °C. Aβ42 levels in the resulting supernatants, but not in the pellet, were determined using the same sandwich ELISA kit used for in vitro detection.

Immunohistochemistry. At biopsy, three randomly selected mice from each group were killed and whole brains were removed. These brains were immersion-fixed in 10% neutral buffered formalin and processed in paraffin wax. Brains in paraffin blocks were sagitally sectioned (50 μm) across the hippocampus and were immunostained using 4G8, which recognizes the 17−24 amino acid segment within Aβ as the primary antibody. After washing, a goat antimouse secondary antibody was incubated for an additional 30 min at room temperature, and sections were visualized with avidin−biotin−horse radish peroxidase complex according to the manufacturer's instruction. The number of dark-stained plaques was counted and the groups were compared.

Statistical Analysis. All results are presented as the mean ± SEM. The overall significance of experimental results was examined by Levene's test for variance homogeneity. A One-Way analysis of variance (ANOVA) was then conducted along with a two-tailed Dunnett *t*-test. The threshold for statistical significance was $p < 0.05$ with the appropriate Bonferroni correction for multiple comparisons.

RESULTS AND DISCUSSION

CJ Extract Decreased Levels of Aβ40 and Aβ42 Secreted from Cells. We tested whether CJ extract can alter Aβ40 and Aβ42 production in HeLa cells stably transfected with APPsw. Transfected HeLa cells showed very reproducible results with Aβ production. Cells were incubated with 1, 5, 10, and 25 μg/mL of CJ extract for 8 h, and Aβ40 and Aβ42 levels from the conditioned media were measured using specific ELISA kits (Figure 1). Aβ40 and Aβ42 levels were

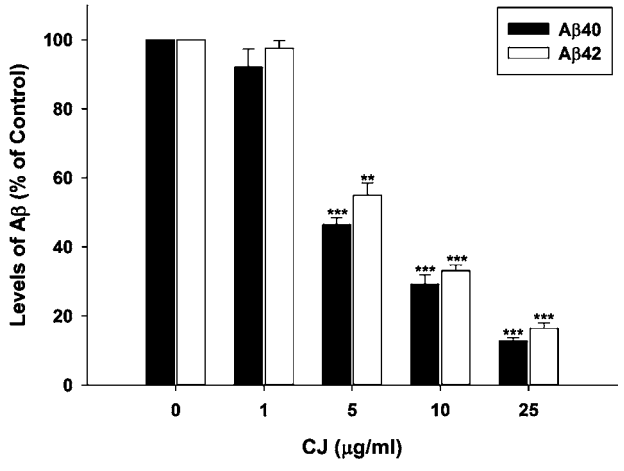

Figure 1. Effect of CJ extract on Aβ40 and Aβ42 secretion in cells. HeLa−APPsw cells were incubated with the indicated concentration of CJ extract for 8 h. The culture media were collected and analyzed for Aβ levels by using sandwich ELISA. Both forms of Aβ levels were significantly decreased by CJ extract treatment at 5, 10, and 25 μg/mL ($n = 6$). The results were quantified and expressed as mean ± SEM. (**,***) Significantly different ($p < 0.01$, $p < 0.001$) from the control group.

DOI: 10.1021/acs.jafc.5b00889
J. Agric. Food Chem. 2015, 63, 6979−6988

decreased in cells cultured with CJ extract in a dose-dependent manner. At 5 μg/mL, CJ extract significantly decreased the levels of Aβ40 and Aβ42 by 53.5 ± 2.1% and 45 ± 3.6%, respectively. Furthermore, incubating cells with CJ extract even at a concentration of 25 μg/mL for 8 h had no effect on cell viability according to the MTT-based assay (data not shown). These results suggest that the CJ extract significantly decreases levels of both Aβ40 and Aβ42 without inducing cell toxicity.

CJ Extract Decreased sAPPα, sAPPβ, and C-Terminal Fragments (CTFs) Levels. Aβ is produced through the sequential proteolysis of APP by β- and γ-secretases. Alternatively, the cleavage of APP can be mediated by α- and γ-secretases, precluding the production of Aβ. Thus, Aβ levels are determined by which secretase processes APP. If the effect of CJ extract on Aβ production occurs via modulation of β- or α-secretase, the levels of APP proteolytic products would have been altered accordingly. Therefore, we examined the effects of CJ extract on the levels of the APP proteolytic products sAPPα, sAPPβ, CTFα, and CTFβ.

First, the levels of sAPPα were measured from the conditioned media after cells were incubated with 1, 5, 10, and 25 μg/mL CJ extract for 8 h. CJ extract at 5 μg/mL significantly reduced the levels of sAPPα by 39.8 ± 2.0% (Figure 2A). Therefore, the CJ extract was able to reduce levels of the α-secretase product. We next measured levels of sAPPβ-wt (the product resulting from cleavage of the endogenous APP) and sAPPβ-sw (the product from the transfected APPsw) using specific ELISA kits. Both sAPPβ-wt and sAPPβ-sw levels were significantly decreased by CJ extract in a dose-dependent manner (Figure 2A). After culture with 5 μg/mL CJ extract, the levels of sAPPβ-wt and sAPPβ-sw were decreased by 25.6 ± 2.0% and 28.6 ± 2.6%, respectively. These results indicated that β-secretase products were also reduced by the CJ extract. We also examined the levels of C-terminal stubs of APP, CTFβ, and CTFα. CTFβ and CTFα are produced from APP by β- and α-secretases, respectively. Figure 2B shows a typical Western blot derived from cell lysates in which the band densities are expressed relative to β-tubulin density. At the 5, 10, and 25 μg/mL of CJ extract, the levels of CTFβ were decreased in a dose-dependent manner by 37, 70, and 87%, respectively. The CJ extract concentrations of 10 and 25 μg/mL were also effective in decreasing CTFα levels by 29 and 32%, respectively. These results demonstrate that CJ extract was effective in decreasing the products of APP cleavage from both pathways. Therefore, we can hypothesize that the inhibitory effect of CJ extract on Aβ production is unlikely to be mediated via the modulation of β- or α-secretase activities.

CJ Extract Decreased Levels of both ADAM10 and ADAM17. To confirm our hypothesis, we examined the effects of CJ extract on the expression of BACE1 and ADAMs in HeLa cells. BACE1 has been identified as the major β-secretase and is the rate-limiting factor in Aβ production.[24] The ADAM family, more specifically ADAM9, ADAM10, and ADAM17, are known to function as α-secretases that catalyze the shedding of the APP ectodomain. Among them, ADAM10 is accountable for the constitutive activity as it is the major ADAM family member, while ADAM9 and ADAM17 are responsible for the regulation of cleavage.[27,28]

In the current study, we treated cells with 1, 5, 10, and 25 μg/mL of CJ extract for 8 h. We then measured the expression of BACE1, ADAM9, ADAM10, and ADAM17 from cell lysates using Western blot analysis. Figure 3A shows typical results obtained from four different experiments. The CJ extract did not affect the expression of BACE1, and densitometry analysis of the bands corresponding to BACE1 clearly supports this conclusion (Figure 3B). ADAM9 exists as pro-ADAM9 and is converted to mature ADAM9. CJ extract did not change the level of pro-ADAM9, but it did show a trend toward increasing the level of mature ADAM9 as shown in Figure 3A,C. ADAM10 is present in the Golgi apparatus as a pro-enzyme at steady state, but its mature form is found in the plasma

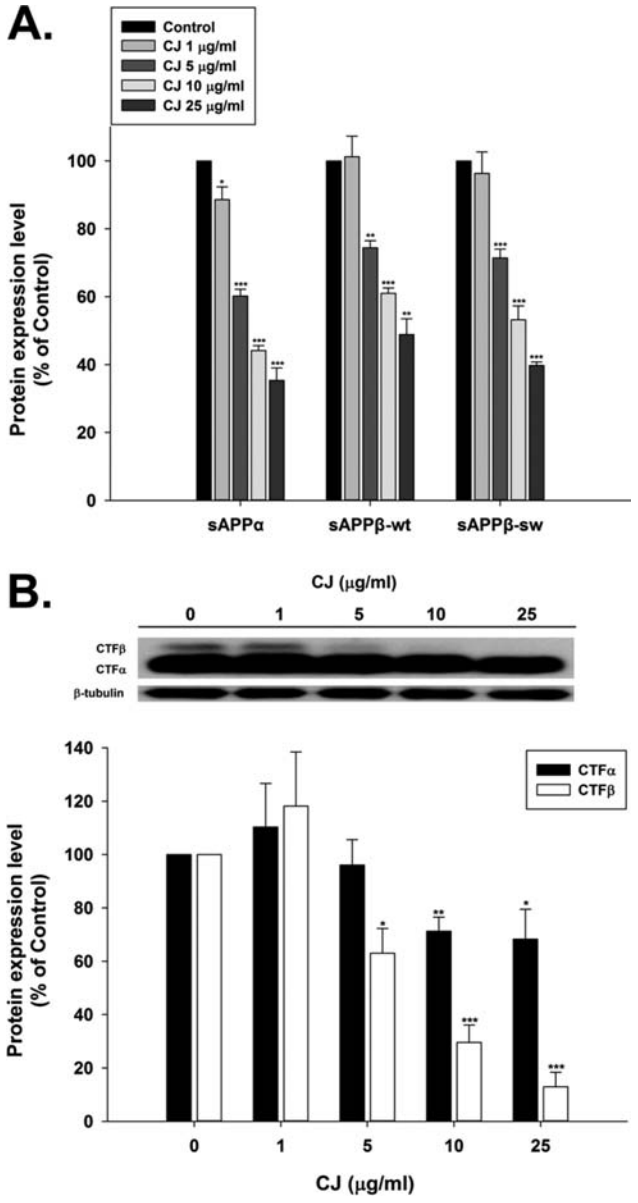

Figure 2. Effect of CJ extract on sAPPα, sAPPβ and CTFα, CTFβ formation. HeLa−APPsw cells were incubated for 8 h with 1, 5, 10, and 25 μg/mL CJ extract. (A) sAPPα, sAPPβ-wt, and sAPPβ-sw levels were quantified using sandwich ELISA. CJ extract significantly reduced the levels of sAPPα (n = 5), sAPPβ-wt (n = 4), and sAPPβ-sw (n = 5). (B) Representative Western blot result showed that the levels of CTFα and CTFβ decreased by CJ extract treatment. Proteins in the cell lysate were analyzed by the immunoblotting and immunoblotting results were quantified from 5 different experiments. The levels of CTFα and CTFβ were significantly decreased by CJ extract treatment. All of the results were quantified and expressed as mean ± SEM (*,**,***) Significantly different (p < 0.05, p < 0.01, p < 0.001) from the control group.

DOI: 10.1021/acs.jafc.5b00889
J. Agric. Food Chem. 2015, 63, 6979−6988

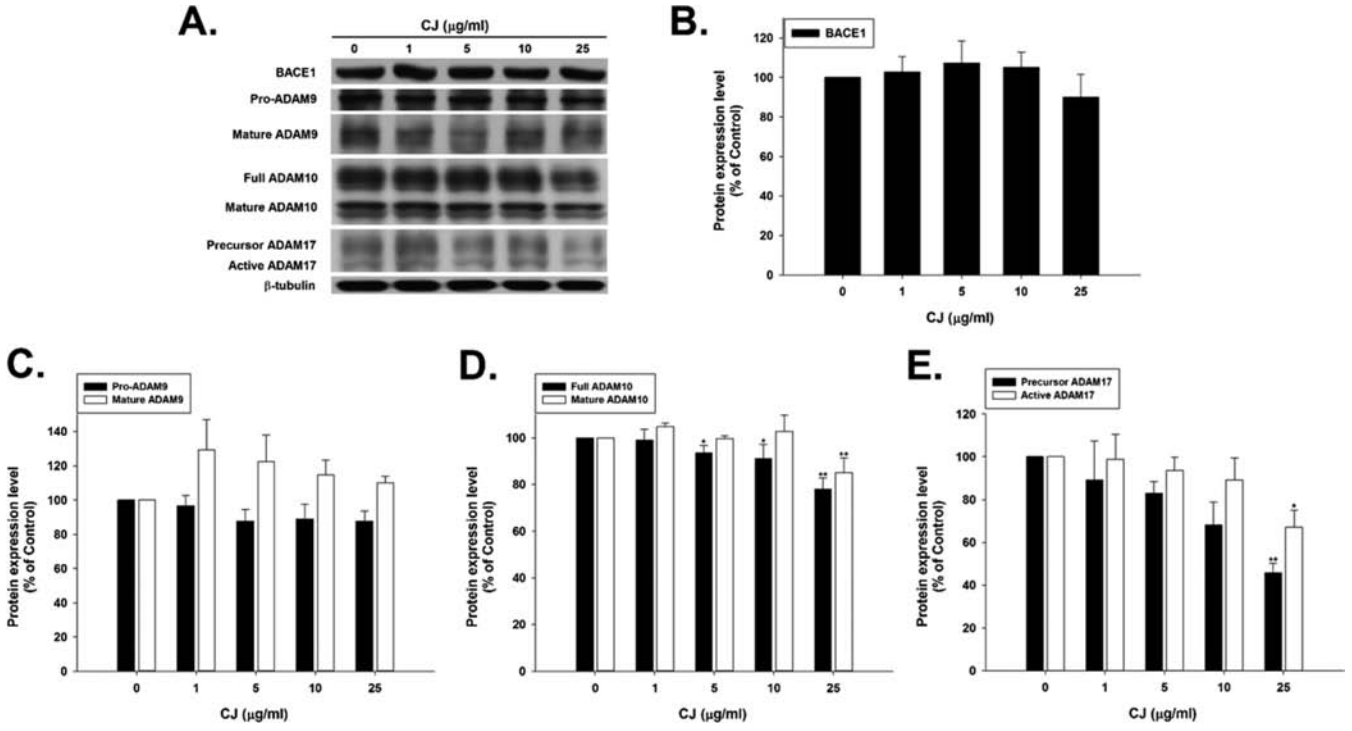

Figure 3. Effect of CJ extract on protein expressions of α-secretases and β-secretase. HeLa−APPsw cells were incubated for 8 h with 1, 5, 10, and 25 μg/mL CJ extract. Representative Western blot result showed that the expression levels of BACE1 (n = 5; (A,B) and ADAM9 (n = 4; (A,C)) were not significantly changed by CJ extract treatment. However, CJ extract reduced the expression of ADAM10 (n = 4; (A,D)) and ADAM17 (n = 4; (A,E)). The results were quantified and expressed as mean ± SEM. (∗,∗∗) Significantly different ($p < 0.05$, $p < 0.01$) from the control group.

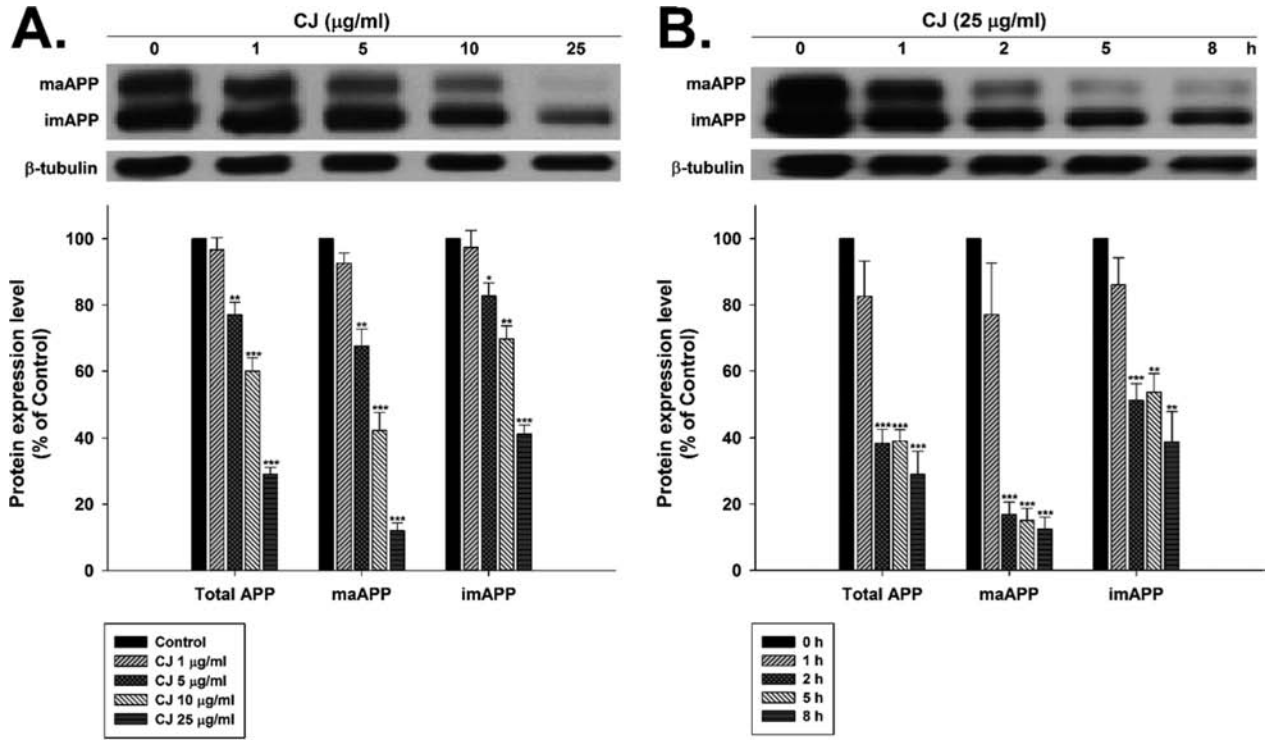

Figure 4. Effect of CJ extract on levels of mature and immature APP. (A) HeLa−APPsw cells were incubated for 8 h with 1, 5, 10, and 25 μg/mL CJ extract. A representative Western blot result showed that both maAPP and imAPP levels were significantly reduced by the CJ extract in a dose-dependent manner. (B) HeLa−APPsw cells were incubated with 25 μg/mL CJ extract for 1, 2, 5, and 8 h, respectively. A representative Western blot result showed that both maAPP and imAPP levels were significantly decreased in a time-dependent manner. The results were quantified and expressed as mean ± SEM (n = 5). (∗,∗∗,∗∗∗) Significantly different ($p < 0.05$, $p < 0.01$, $p < 0.001$) from the control group.

DOI: 10.1021/acs.jafc.5b00889
J. Agric. Food Chem. 2015, 63, 6979−6988

membrane.[8] We found that the level of the mature form of ADAM10 was slightly decreased by 15% with 25 μg/mL of CJ extract treatment (Figure 3A,D). Moreover, both precursor and active forms of ADAM17 were significantly decreased as shown in Figure 3A,E. Quantitative analysis showed that CJ extract at 25 μg/mL decreased precursor and active forms of ADAM17 by 54% and 33%, respectively. These data suggest that CJ extract did not affect the levels of BACE1 and ADAM9. Furthermore, CJ extract decreased ADAM10, which may underlie the constitutive α-secretase activity. However, the effect of CJ extract on ADAM10 is not large enough to fully account for the inhibitory effect of the extract on Aβ production.

CJ Extract Did Not Affect α- and β-Secretase Activities. Compared to the minimal effects of CJ extract on ADAM 9 and ADAM10, ADAM17 was significantly decreased by treatment with CJ extract (Figure 3E). To confirm if this reduction corresponded with changes in ADAM17 activity, we further investigated whether CJ extract would influence secretase activities. As a way to test the effect of CJ extract on α-secretase activity by ADAM17 in cell lysates, we utilized an ADAM17 activity assay kit. Briefly, an ADAM17-specific fluorogenic substrate was incubated in the presence of 1, 5, 10, and 25 μg/mL CJ extract, and then the quenched fluorescence substrate was measured. Using this approach, we found that CJ extract did not show any effect on ADAM17 activity (Supporting Information Figure S1). We also tested the effect of CJ extract on BACE1 activity in cell lysates using a BACE1 assay kit and found that CJ extract also did not show any effects on the BACE1-specific substrate (Supporting Information Figure S1). Both results are included as Figure S1 of the Supporting Information. These results show that CJ extract did not affect β- and α-secretase activity even though the extract slightly decreased ADAM10 and ADAM17 protein levels.

CJ Extract Decreased Levels of Both Mature and Immature APP. We observed that CJ extract decreased the levels of products generated by both β- and α-secretases while failing to change their activities. Therefore, we examined whether CJ extract affected the level of their common substrate, APP. APP undergoes N-glycosylation in the endoplasmic reticulum, where it is referred to as imAPP. This form of APP then transits to the Golgi apparatus, where it undergoes O-glycosylation to become maAPP. We measured the time-dependent effects of CJ extract on APP levels by incubating cells with 25 μg/mL of CJ extract for 1, 2, 5, and 8 h. A typical Western blot result shows that the levels of APP were decreased by CJ extract in a time-dependent manner. Quantitative analysis showed that after 2 h of treatment, CJ extract reduced the totalAPP, maAPP, and imAPP by 62%, 83%, and 49%, respectively (Figure 4A). We then measured the level of these APPs from cell lysates using Western blot analysis after cells were treated with 1, 5, 10, and 25 μg/mL of CJ extract for 8 h. By using this technique, we found that CJ extract decreased both maAPP and imAPP in a dose-dependent manner (Figure 4B). Moreover, the amount of maAPP was decreased by 32%, 58%, and 88% with 5, 10, and 25 μg/mL of CJ extract, respectively. However, imAPP levels were less sensitive to CJ extract when compared to those of maAPP. These results demonstrate that CJ extract may attenuate Aβ production via decreasing levels of both maAPP and imAPP.

CJ Extract Improved Performance in the Morris Water Maze Test. To confirm that the effect of CJ extract on Aβ reduction resulted in improvements in cognitive performance, we assessed the spatial memory of mice in the MWM. As shown in Figure 5A, the non-TG background mouse group

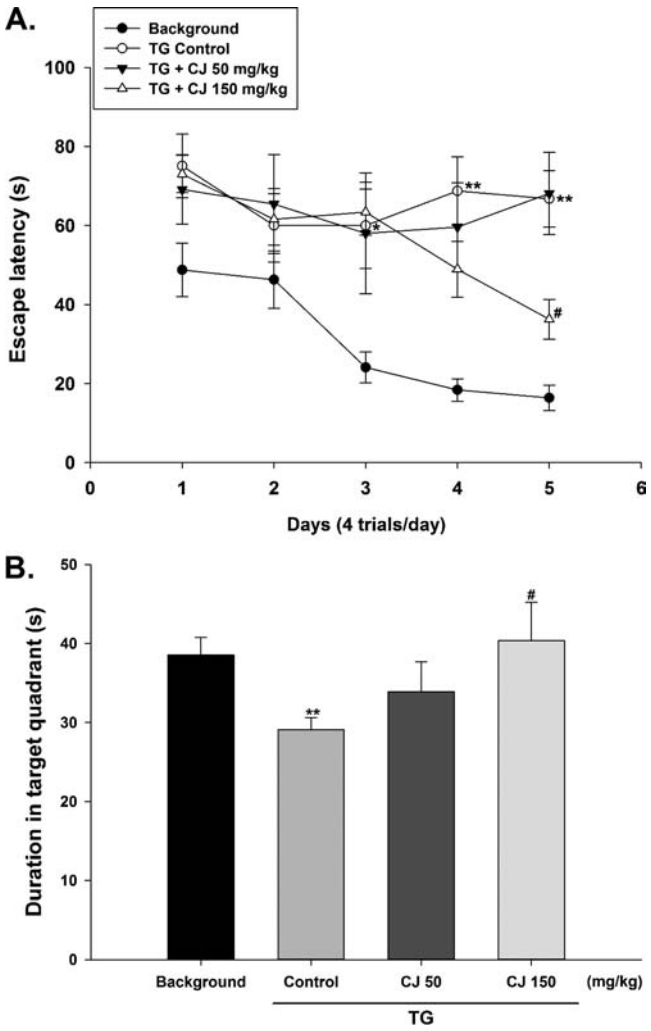

Figure 5. Effect of CJ extract on mouse performance in the Morris water maze test. CJ extract (50 or 150 mg/kg/day) or saline was administered orally to 5-month-old transgenic (TG) mice for 3 months and 1 h before the first trial of each acquisition day. The acquisition phase (A) consisted of five consecutive days in which each TG mouse underwent a total of four trials with a 1 h intertrial interval. During the acquisition phase, the amount of time taken for the mouse to find the hidden platform (escape latency) was measured. The retention phase (B) occurred the day immediately following the last day of the acquisition phase. During the retention phase, the platform was removed and the mice were allowed 120 s to explore the pool. The time spent in the target quadrant, which had contained the escape platform during the acquisition phase, was recorded. The data are shown as mean ± SEM (n = 7/group). (∗,∗∗) Significantly different ($p < 0.05$, $p < 0.01$) from the background group. (#) Significantly different ($p < 0.05$) from the TG control group.

showed a significant decrease in the escape latency from the first day (48.8 ± 6.8 s) to the fifth day (16.4 ± 3.2 s) of acquisition. In contrast, TG mice showed no progress in finding the escape platform from the first day (75.1 ± 8.0 s) to the fifth day (66.8 ± 7.2 s). Treating TG mice with the CJ extract (150 mg/kg) induced a significant improvement in learning, with the escape latency starting at 73.0 ± 4.7 s on the first day and progressing to 36.3 ± 5.0 s on the fifth day. Following the acquisition phase, we tested the retention of spatial memory on

DOI: 10.1021/acs.jafc.5b00889
J. Agric. Food Chem. 2015, 63, 6979−6988

the sixth day. As shown in Figure 5B, the time spent in the target quadrant, which had contained the escape platform, was significantly lower in the TG mouse group (29.1 ± 1.5 s) than the non-TG mouse group (38.5 ± 2.2 s). However, 150 mg/kg of CJ extract lead to a significant increase in the time mice spent in the target quadrant, increasing it to 40.4 ± 4.8 s. TG mice treated with 50 mg/kg of CJ extract also showed a trend toward spending more time in the target quadrant relative to the untreated TG mouse group.

CJ Extract Improved Object Memory Function in the Novel Object Recognition Test. In the NORT, non-TG mice spent over 80% of the total exploration time interacting with a novel object, whereas TG mice only spent 60% of their time with the same object. Both 50 and 150 mg/kg of CJ extract significantly increased the ratio of the time spent with the novel object, up to 79.2 ± 3.8 and 82.0 ± 4.5%, respectively (Figure 6). Taken together with the MWM test results, this

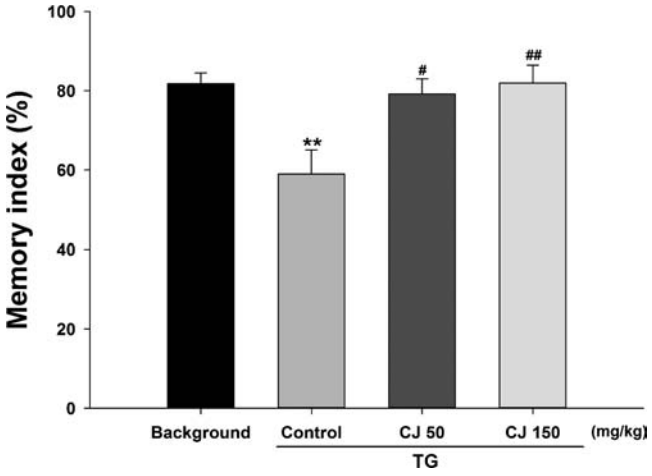

Figure 6. Effect of CJ extract on novel object recognition test. CJ extract (50 or 150 mg/kg/day) or saline was administered orally to 5-month-old transgenic (TG) mice for 3 months and 1 h before the acquisition phase test. During the acquisition phase test, mice were placed in a square-shaped arena and allowed to habituate to two identical objects for 10 min. On the following day, mice were placed in the same arena and and familiar object and one novel object were placed in the arena while the mice explored freely for 5 min. The total time spent exploring each object was measured and the memory index was calculated according to the following equation: Memory index (%) = (exploring time on novel object/total exploring time for both objects) × 100. The data represent the mean ± SEM (n = 7/group). (**) Significantly different (p < 0.01) from the background group. (#,##) Significantly different (p < 0.05, p < 0.01) from the TG control group.

suggests that the CJ extract significantly improved the cognitive performance of TG mice, which are a model for the major symptoms of AD in mice and humans.

CJ Extract Decreased Aβ42 Level in TG Mouse Brains. Aβ42 usually stays at undetectable levels in non-TG background mice. However, it is dramatically increased (up to 106.9 ± 9.7 pg/mL) in the cerebral cortex of TG mice. 150 mg/kg of CJ extract significantly reduced Aβ42, down to 81.0 ± 2.9 pg/mL. On the other hand, 50 mg/kg of CJ extract showed no change relative to the TG mouse group (Figure 7).

CJ Extract Reduced Aβ Plaques Detected by Immunohistochemistry. The extracellular accumulation of Aβ in the form of plaques is a pathological hallmark of AD. The

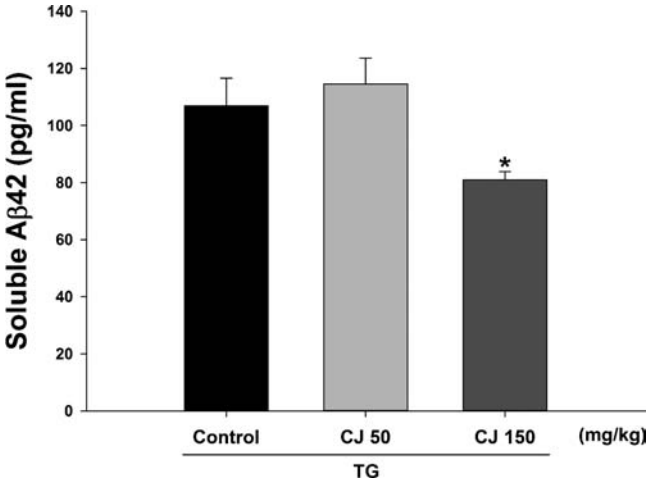

Figure 7. Effect of CJ extract on the level of soluble Aβ42 protein in mouse cerebral cortex. Transgenic (TG) mouse brain tissue was collected after behavioral tests at 9 months of age. The cerebral cortex samples (100 mg) were homogenized in Tris-buffered saline solution (20 mM Tris; 137 mM NaCl; pH 7.4) containing complete protease inhibitors tablets. The extraction ratio (brain tissue:Tris-buffered saline) was 1:5 or 1:10 (w/v). The tissue homogenates were centrifuged at 100000g for 1 h at 4 °C. The soluble Aβ42 level in the resulting supernatants was measured using the sandwich ELISA kit according to the manufacturer's protocol. The data represent the mean ± SEM (n = 4). * Significantly different (p < 0.05) from the TG control group.

amount of the plaque depends on the rates of its production, secretion, aggregation, and clearance.[29] We performed an immunohistochemical examination of TG and non-TG mouse brain sections and found that although non-TG mice did not exhibit significant Aβ plaques, TG mice showed significant accumulation of Aβ plaques in the cerebral cortex and hippocampal regions. Importantly, treatment with both 50 and 150 mg/kg of CJ extract for four months significantly reduced the amount of plaque in the cerebral cortex to 50.9 ± 4.5% and 44.9 ± 1.9%, and in the hippocampus to 64.8 ± 13.9% and 42.5 ± 9.2%, respectively (Figure 8). Taken together with the obvious enhancement of cognitive function, the decreased levels of Aβ42 and the changes in the amount of plaque in mouse brains clearly demonstrates that CJ extract has beneficial effects on the pathology and symptoms of these mouse models of AD.

Isolation and Analysis of Active Compounds. With its profound effect on both in vitro and in vivo AD models, we decided to determine which active components account for the effects of the CJ extract. To accomplish this, hydroethanolic extracts of CJ bulbs were further partitioned with n-hexane, CH_2Cl_2, and n-BuOH successively, then each organic soluble fraction was obtained as 1, 1, and 5.5 g, respectively. Flash column chromatography of the n-BuOH soluble fraction resulted in eight subfractions [CJ-3-F1−8]. 7-Deoxynarciclasine (40 mg) and 7-deoxy-*trans*-dihydronarciclasine (10 mg) were yielded from fraction CJ-3-F4. Narciclasine (80 mg) was isolated from another fraction, CJ-3-F6, by reversed-phase chromatography. The structures of the isolated compounds were confirmed by comparing previously reported spectral data.[30,31] To confirm the composition of the three active components in the CJ extract, a 50% EtOH extract of CJ (20 mg) was analyzed using HPLC. The results of this analysis are included as Figure S2 of the Supporting Information.

DOI: 10.1021/acs.jafc.5b00889
J. Agric. Food Chem. 2015, 63, 6979−6988

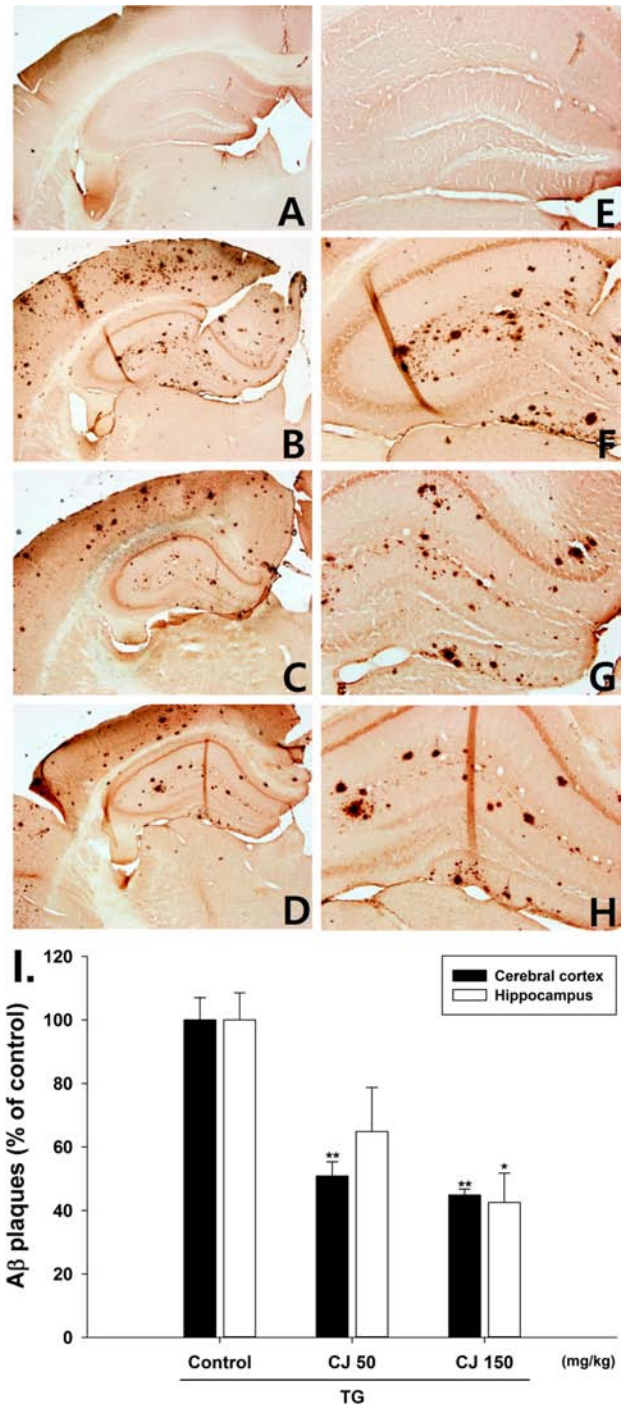

Figure 8. Effect of CJ extract on plaque deposition in the brains of transgenic mice. Mouse brain tissue was collected after behavioral tests at 9 months of age. Representative photomicrographs show the results of anti-Aβ antibody (4G8) staining in the cerebral cortex (A–D) and hippocampus (E–H) of mice from background group (A,E), transgenic (TG) control group (B,F), and TG mice treated with the CJ extract at 50 (C,G) and 150 (D,H) mg/kg. The numbers of Aβ plaques in each slice were counted and compared with the TG control group (I). The data represent the mean ± SEM (n = 3). (*,**) Significantly different (p < 0.05, p < 0.01) from the TG control group.

Active Compounds from CJ Extract Also Decreased Levels of Aβ40 and Aβ42 in Cells. Isolated narciclasine, 7-deoxynarciclasine, and 7-deoxy-*trans*-dihydronarciclasine were used to treat APPsw-transfected HeLa cells at various concentrations for 8 h. The levels of Aβ40 and Aβ42 in the conditioned media were determined using specific ELISA kits (Figure 9). Levels of both Aβ40 and Aβ42 were significantly decreased by all three active compounds in a dose-dependent manner without any cytotoxicity. Among them, 7-deoxynarci-

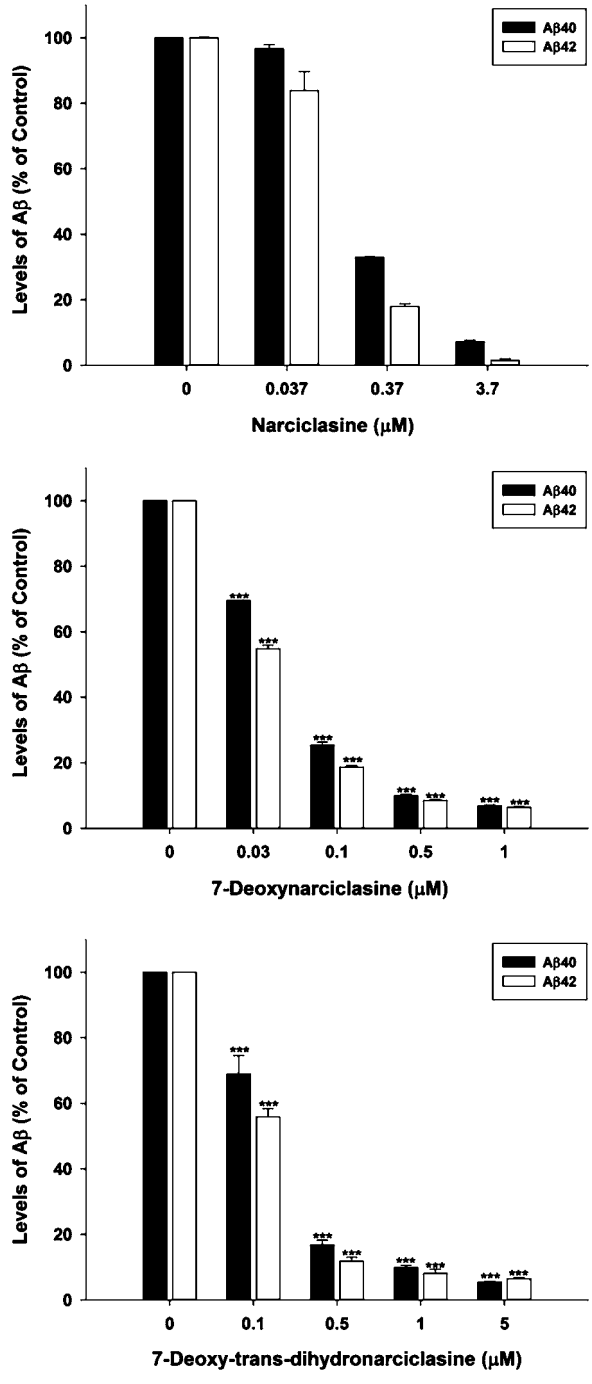

Figure 9. Effect of the three active compounds from CJ on Aβ40 and Aβ42 secretions in cells. HeLa–APPsw cells were incubated with the indicated concentrations of narciclasine, 7-deoxynarciclasine, and 7-deoxy-*trans*-narciclasine, the three active compounds from CJ, for 8 h. The culture media were collected and analyzed for Aβ levels by using sandwich ELISA. Both forms of Aβ levels were significantly decreased by three of the active components from CJ (n = 6). The results were quantified and expressed as mean ± SEM. *** Significantly different (p < 0.001) from the control group.

DOI: 10.1021/acs.jafc.5b00889
J. Agric. Food Chem. 2015, 63, 6979–6988

clasine and 7-deoxy-*trans*-dihydronarciclasine showed stronger Aβ reduction at lower concentrations. As such, the inhibitory effect of CJ extract on Aβ production is most likely due to these three compounds.

The effect of CJ on the reduction of APP levels is very interesting. This extract preferentially decreased maAPP over imAPP, which in turn induced a reduction of Aβ levels. We propose that CJ may delay the exit of imAPP from the ER and thereby decrease transport to the Golgi apparatus. This would lead to attenuation of maAPP formation. This reduction of APP maturation could impair APP trafficking to the plasma membrane and disrupt its cleavage by α-secretase.[5,6] Our data showed that CJ significantly reduced both sAPPα and CTFα levels. Once mature APP reaches the plasma membrane, it can undergo clathrin-dependent endocytosis. APP can also be cleaved by β-secretase in the early endosome.[32−35] Therefore, CJ may also affect the endocytosis of APP from the plasma membrane, which can explain the decreased levels of sAPPβ and CTFβ and subsequently the levels of Aβ40 and Aβ42. CJ extract also decreased the production of Aβ42 as well as the number of Aβ plaques in the brains of TG mice. Treatment with CJ extract recovered cognitive dysfunction observed in the MWM and NORT, consistent with decreases in Aβ42 and the number of plaques in the cerebral cortex and hippocampus. Such modulatory functions have not been previously reported in natural products. As such, this extract could prove beneficial as a treatment for AD. Moreover, CJ would not produce the various side effects that come from interfering with secretase activities.

In conclusion, we found a novel function of CJ that decreases Aβ levels via the attenuation of APP. This showed beneficial effects on cognitive function and plaque formation in animal models of AD. We also revealed that the active components of CJ extract were narciclasine, 7-deoxynarciclasine, and 7-deoxy-*trans*-dihydronarciclasine. Further study on these three active components should be conducted in vivo to elucidate the specific action of their mechanisms toward the goal of treating patients with AD, and additional research using human islet amyloid polypeptides may contribute to better understanding in interactions with Aβ proteins.[36]

■ ASSOCIATED CONTENT

Supporting Information

The effect of CJ extract on the activities of ADAM17 and BACE1. HPLC analysis of CJ extract. The Supporting Information is available free of charge on the ACS Publications website at DOI: 10.1021/acs.jafc.5b00889.

■ AUTHOR INFORMATION

Corresponding Authors

*For H.O.Y.: phone, +82 33 650 3501; fax, +82 33 650 3529; E-mail, hoyang@kist.re.kr.

*For S.C.: phone, +82 31 299 6103; fax, +82 31 299 6129; E-mail, schung@skku.edu.

Author Contributions

⊥J.K. and Y.P. contributed equally to this work.

Funding

This work was funded and supported by the institutional programs of the Korea Institute of Science and Technology (grant no. 2Z04381) and the Bio-Synergy Research Project (NRF-2012M3A9C4048793) of the Ministry of Science, ICT and Future Planning through the National Research Foundation, Republic of Korea to H.O.Y. This work was also supported by the Basic Science Research Program through the National Research Foundation of Korea (NRF) funded by the Ministry of Education, Science and Technology (2013R1A1A2006475) to S.C.

Notes

The authors declare no competing financial interest.

■ ABBREVIATIONS USED

Aβ, β-amyloid; AD, Alzheimer's disease; ADAM, A disintegrin and metalloproteinase; APP, Amyloid β precursor protein; BACE1, β secretase 1; CJ, *Lycoris chejuensis* K. Tae et S. Ko; imAPP, immature amyloid beta precursor protein; maAPP, mature amyloid beta precursor protein; MWM, Morris water maze; NORT, novel object recognition test; PS1, presenilin-1; TG, transgenic

■ REFERENCES

(1) Selkoe, D. J. Alzheimer's disease: genes, proteins, and therapy. *Physiol. Rev.* **2001**, *81*, 741−66.

(2) Tanzi, R. E.; Bertram, L. Twenty years of the Alzheimer's disease amyloid hypothesis: a genetic perspective. *Cell* **2005**, *120*, 545−55.

(3) Yoon, S.-S.; Ahn Jo, S. M. Mechanisms of amyloid-β peptide clearance: Potential therapeutic targets for Alzheimer's disease. *Biomol. Ther.* **2012**, *20*, 245−255.

(4) Bertram, L.; Tanzi, R. E. Thirty years of Alzheimer's disease genetics: the implications of systematic meta-analyses. *Nat. Rev. Neurosci.* **2008**, *9*, 768−78.

(5) Xia, W.; Zhang, J.; Kholodenko, D.; Citron, M.; Podlisny, M. B.; Teplow, D. B.; Haass, C.; Seubert, P.; Koo, E. H.; Selkoe, D. J. Enhanced production and oligomerization of the 42-residue amyloid beta-protein by Chinese hamster ovary cells stably expressing mutant presenilins. *J. Biol. Chem.* **1997**, *272*, 7977−82.

(6) Small, S. A.; Gandy, S. Sorting through the cell biology of Alzheimer's disease: intracellular pathways to pathogenesis. *Neuron* **2006**, *52*, 15−31.

(7) Gandy, S. The role of cerebral amyloid beta accumulation in common forms of Alzheimer disease. *J. Clin. Invest.* **2005**, *115*, 1121−9.

(8) Lammich, S.; Kojro, E.; Postina, R.; Gilbert, S.; Pfeiffer, R.; Jasionowski, M.; Haass, C.; Fahrenholz, F. Constitutive and regulated alpha-secretase cleavage of Alzheimer's amyloid precursor protein by a disintegrin metalloprotease. *Proc. Natl. Acad. Sci. U. S. A.* **1999**, *96*, 3922−7.

(9) Buxbaum, J. D.; Liu, K. N.; Luo, Y.; Slack, J. L.; Stocking, K. L.; Peschon, J. J.; Johnson, R. S.; Castner, B. J.; Cerretti, D. P.; Black, R. A. Evidence that tumor necrosis factor alpha converting enzyme is involved in regulated alpha-secretase cleavage of the Alzheimer amyloid protein precursor. *J. Biol. Chem.* **1998**, *273*, 27765−7.

(10) Wolfe, M. S. Inhibition and modulation of gamma-secretase for Alzheimer's disease. *Neurotherapeutics* **2008**, *5*, 391−8.

(11) Ghosh, A. K.; Bilcer, G.; Hong, L.; Koelsch, G.; Tang, J. Memapsin 2 (beta-secretase) inhibitor drug, between fantasy and reality. *Curr. Alzheimer Res.* **2007**, *4*, 418−422.

(12) Ghosh, A. K.; Brindisi, M.; Tang, J. Developing beta-secretase inhibitors for treatment of Alzheimer's disease. *J. Neurochem.* **2012**, *120* (Suppl 1), 71−83.

(13) Rezai-Zadeh, K.; Shytle, D.; Sun, N.; Mori, T.; Hou, H.; Jeanniton, D.; Ehrhart, J.; Townsend, K.; Zeng, J.; Morgan, D.; Hardy, J.; Town, T.; Tan, J. Green tea epigallocatechin-3-gallate (EGCG) modulates amyloid precursor protein cleavage and reduces cerebral amyloidosis in Alzheimer transgenic mice. *J. Neurosci.* **2005**, *25*, 8807−8814.

(14) Yang, P.; Baker, K. A.; Hagg, T. The ADAMs family: coordinators of nervous system development, plasticity and repair. *Prog. Neurobiol.* **2006**, *79*, 73−94.

DOI: 10.1021/acs.jafc.5b00889
J. Agric. Food Chem. 2015, 63, 6979−6988

(15) da Rocha, M. D.; dias Viegas, F. P.; Campos, H. C.; Nicastro, P. C.; Fossaluzza, P. C.; Fraga, C. A. M.; Barreiro, E. J.; Viegas, C., Jr. The role of natural products in the discovery of new drug candidates for the treatment of neurodegenerative disorders ii: Alzheimer's disease. *CNS Neurol. Disord: Drug Targets* **2011**, *10*, 251−270.
(16) Kim, J. Y.; Lee, W. S.; Kim, Y. S.; Curtis-Long, M. J.; Lee, B. W.; Ryu, Y. B.; Park, K. H. Isolation of cholinesterase-inhibiting flavonoids from *Morus Ihou*. *J. Agric. Food Chem.* **2011**, *59*, 4589−96.
(17) Qiao, A.; Wang, Y.; Zhang, W.; He, X. Neuroprotection of brain-targeted bioactive dietary artoindonesianin O (AIO) from mulberry on rat neurons as a novel intervention for Alzheimer's disease. *J. Agric. Food Chem.* **2015**, *63*, 3687−93.
(18) Papandreou, M. A.; Kanakis, C. D.; Polissiou, M. G.; Efthimiopoulos, S.; Cordopatis, P.; Margarity, M.; Lamari, F. N. Inhibitory activity on amyloid-beta aggregation and antioxidant properties of Crocus sativus stigmas extract and its crocin constituents. *J. Agric. Food Chem.* **2006**, *54*, 8762−8.
(19) Howes, M. J.; Houghton, P. J. Plants used in Chinese and Indian traditional medicine for improvement of memory and cognitive function. *Pharmacol., Biochem. Behav.* **2003**, *75*, 513−27.
(20) Liao, N.; Ao, M.; Zhang, P.; Yu, L. Extracts of Lycoris aurea induce apoptosis in murine sarcoma S180 cells. *Molecules* **2012**, *17*, 3723−35.
(21) Yamazaki, Y.; Kawano, Y. Inhibitory effects of herbal alkaloids on the tumor necrosis factor-α and nitric oxide production in lipopolysaccharide-stimulated RAW264 macrophages. *Chem. Pharm. Bull.* **2011**, *59*, 388−391.
(22) Tae, K. H.; Ko, S. C. New taxa of the genus Lycoris. *Korean J. Plant Taxonomy* **1993**, *23*, 233−241.
(23) Tae, K. H.; Ko, S. C. Cytological evolution in the genus Lycoris (Amaryllidaceae). *Korean J. Bot.* **1996**, *39*, 209−214.
(24) Kurita, S. *Natural History of Higanbana (Lycoris adiata)*. Tokyo Kensei-shya Press: Tokyo, 1998; p 177−188.
(25) Oh, M.-J.; Park, J.-M.; Tae, K.-H.; Liu, J.-R.; Kim, S.-W. Plant regeneration from leaf and root cultures of Lycoris chejuensis via bulblet formation. *J Plant Biotechnol.* **2007**, *34*, 223−227.
(26) Ennaceur, A.; Delacour, J. A new one-trial test for neurobiological studies of memory in rats. 1: Behavioral data. *Behav. Brain Res.* **1988**, *31*, 47−59.
(27) Vassar, R.; Kovacs, D. M.; Yan, R.; Wong, P. C. The beta-secretase enzyme BACE in health and Alzheimer's disease: regulation, cell biology, function, and therapeutic potential. *J. Neurosci.* **2009**, *29*, 12787−94.
(28) Kuhn, P. H.; Wang, H.; Dislich, B.; Colombo, A.; Zeitschel, U.; Ellwart, J. W.; Kremmer, E.; Rossner, S.; Lichtenthaler, S. F. ADAM10 is the physiologically relevant, constitutive alpha-secretase of the amyloid precursor protein in primary neurons. *EMBO J.* **2010**, *29*, 3020−32.
(29) Greco, S. J.; Bryan, K. J.; Sarkar, S.; Zhu, X.; Smith, M. A.; Ashford, J. W.; Johnston, J. M.; Tezapsidis, N.; Casadesus, G. Leptin reduces pathology and improves memory in a transgenic mouse model of Alzheimer's disease. *J. Alzheimer's Dis.* **2010**, *19*, 1155−1167.
(30) Ingrassia, L.; Lefranc, F.; Dewelle, J.; Pottier, L.; Mathieu, V.; Spiegl-Kreinecker, S.; Sauvage, S.; El Yazidi, M.; Dehoux, M.; Berger, W.; Van Quaquebeke, E.; Kiss, R. Structure-activity relationship analysis of novel derivatives of narciclasine (an Amaryllidaceae isocarbostyril derivative) as potential anticancer agents. *J. Med. Chem.* **2009**, *52*, 1100−14.
(31) Pettit, G. R.; Melody, N. Antineoplastic agents. 527. Synthesis of 7-deoxynarcistatin, 7-deoxy-trans-dihydronarcistatin, and trans-dihydronarcistatin 1(1). *J. Nat. Prod.* **2005**, *68*, 207−11.
(32) Huse, J. T.; Pijak, D. S.; Leslie, G. J.; Lee, V. M.; Doms, R. W. Maturation and endosomal targeting of beta-site amyloid precursor protein-cleaving enzyme. The Alzheimer's disease beta-secretase. *J. Biol. Chem.* **2000**, *275*, 33729−37.
(33) Kinoshita, A.; Fukumoto, H.; Shah, T.; Whelan, C. M.; Irizarry, M. C.; Hyman, B. T. Demonstration by FRET of BACE interaction with the amyloid precursor protein at the cell surface and in early endosomes. *J. Cell Sci.* **2003**, *116*, 3339−3346.
(34) De Toma, A. S.; Salamekh, S.; Ramamoorthy, A.; Lim, M. H. Misfolded proteins in Alzheimer's disease and type II diabetes. *Chem. Soc. Rev.* **2012**, *41*, 608−21.
(35) Kotler, S. A.; Walsh, P.; Brender, J. R.; Ramamoorthy, A. Differences between amyloid-beta aggregation in solution and on the membrane: insights into elucidation of the mechanistic details of Alzheimer's disease. *Chem. Soc. Rev.* **2014**, *43*, 6692−700.
(36) Nanga, R. P. R.; Brender, J. R.; Vivekanandan, S.; Ramamoorthy, A. Structure and membrane orientation of IAPP in its natively amidated form at physiological pH in a membrane environment. *Biochim. Biophys. Acta, Biomembr.* **2011**, *1808*, 2337−2342.

DOI: 10.1021/acs.jafc.5b00889
J. Agric. Food Chem. 2015, 63, 6979−6988

scavenging free radicals, antioxidation, and antilipid peroxidation.[15] In vivo and in vitro studies have demonstrated that intestinal lipid absorption, chylomicron secretion by the intestine, and very low-density lipoprotein secretion by the liver are the processes that are most repressed by procyanidins, thus inducing hypolipidemia.[16] Furthermore, Zou reported that high molecular weight persimmon tannin was a pivotal constituent of persimmon fruit accounting for prevention of liver steatosis and its progression to NASH by activation of the AMP-activated protein kinase (AMPK) and regulation of its downstream targets, suppressing NF-κB activation, and inhibiting lipid and bile acid absorption.[17] However, there is no literature about the effect of procyanidins on NAFLD from an AGEs/RAGE perspective. In our previous studies, we have shown that LSOPC could inhibit AGE formation effectively in a simulated physiological environment and the underlying mechanism is to scavenge reactive carbonyls by forming adducts with them.[18] Therefore, we presumed that AGEs/RAGE might also be a central target for the antihyperlipidemic effect of LSOPC.

Therefore, the purpose of this study is to evaluate the protective potential of LSOPC against the development of NAFLD in a rat model of long-term HFD-induced obesity. We further identify the underlying molecular mechanisms involved in AGEs/RAGE expression and MAPK or NF-κB signaling pathways. This study provides possibilities for new applications of LSOPC as functional food ingredients.

MATERIALS AND METHODS

Chemicals. Mature lotus seedpods of *N. nucifera* Gaertn. (cv.: Number 2 Wuhan plant) were harvested from Honghu District (113°7′−114°5′ E, 29°39′−30°2′ N) in Hubei province, China, in late July 2012, and arrived in the laboratory within 24 h postharvest; they were kept at −20 °C prior to extraction. Lotus seedpod was identified by Prof. Xueming Ni from the Department of Botany, Wuhan Plant Institute of the Chinese Academy of Science.

Rabbit polyclonal antibodies against p38 MAPK (catalog no. 8690) and phospho-p38 MAPK (catalog no. 4631) were purchased from Cell Signaling Technology (Beverly, MA, USA). Rabbit polyclonal antibodies against p65 NF-κB (catalog no. ab72555) were purchased from Abcam Inc. (Hongkong, China). Commercial kits for determination of the total antioxidant capacity (T-AOC), nitrogen monoxide (NO), superoxide dismutase (SOD), malonaldehyde (MDA), glutathione reductase (GRAC), glutathione (GSH), cholesterol (TC), high-density lipoprotein cholesterol (HDL-C), triglyceride (TG), aspartate aminotransferase (AST), alanine aminotransferase (ALT), and alkaline phosphatase (ALP) were purchased from Nianjing Jiancheng Bioengineering Institute (Nanjing, China). The enzyme-linked immunosorbent assay (ELISA) kits for measuring reactive oxygen species (ROS), free fatty acids (FFA), AGEs, and N^{ϵ}-(carboxymethyl)lysine (CML) were purchased from Cloud-Clone Corp. (Houston, TX, USA). All solvents and reagents were obtained from Sinopharm Chemical Reagent Co., Ltd. (Shanghai, China) and were of analytical grade.

Preparation of LSOPC. Fresh lotus seedpod fragments were extracted using 70% ethanol at 60 °C for 1.5 h. The crude procyanidin aqueous solution was loaded onto an AB-8 resin (weak polarity macroporous resin, 0.3−1.25 mm particle size, Nankai Hecheng Science & Technology Co., Tianjin, China) column (15 × 3.5 cm, i.d.), and the fraction eluted by 70% ethanol was collected. The eluent was evaporated, and the procyanidin extract of lotus seedpod was obtained. Subsequently, they were extracted by ethyl acetate to get LSOPC.

Ethics Statement. All experimental procedures involving animals followed the Guiding Principles in the Care and Use of Animals and were approved by the ethics committee of Reference Laboratory for the test of Veterinary Drug Residues of Huazhong Agricultural University (SYXK 2007-0044), Hubei Province, China. We made all efforts to minimize suffering, and the animals were killed by cervical dislocation under anesthesia.

Experimental Animals and Diets. Sprague−Dawley (SD) male rats (n = 40) were obtained at 6 weeks of age from the Animal Committee of Wuhan University (Wuhan, China). For adaptation, the rats were kept in a controlled environment at 23 °C and 55% relative humidity under a 12 h dark−light cycle, with free access to a pelleted diet (Tongji Medical College, Wuhan, China) and deionized water for 1 week. The experiment was performed in accordance with the *Guide for the Care and Use of Laboratory Animals*, prepared by the U.S. National Institute of Health (1996).

The SD rats weighing 180 ± 15 g were randomly divided into four groups (n = 10) and given different dietary supplements. Group 1 (C group) rats were fed the basic diet (20.34% protein, 4.14% fat, 50.75% carbohydrates; 12% calories from fat); group 2 (H group) rats were fed a high-fat diet (HFD) (16.60% protein, 17.50% fat (mainly from lard, cholesterol, and egg yolk powder), 47.45% carbohydrates; 38% calories from fat); group 3 (HD group) rats were fed the HFD plus 0.5% of LSOPC; group 4 (LD group) rats were fed the HFD plus 0.2% of LSOPC. Doses of LSOPC was referred to previous studies.[17,19,20] Rats were given free access to food and water during the experimental period. Food consumption and body weight were recorded daily and weekly. The experiment was terminated after 12 weeks. Before death, all animals were fasted for 14 h, blood samples were collected from the hepatic portal vein, and integral liver, epididymal, and retroperitoneal white adipose tissues were collected and weighed when dissected.

Histological Examination of the Liver. Small portions of the liver were immediately fixed with 10% formalin in water at the time of killing, dehydrated gradually in a graded series of ethanol, and then clarified in xylene and embedded in paraffin wax. The morphology of the liver was observed with the method of hematoxylin and eosin staining by using a Nikon Eclipse 80i advanced research microscope (Tokyo, Japan).

Blood Analysis. The serum levels of AST, ALT, TC, TG, and HDL-C were determined by enzymatic colorimetric methods using commercial kits ((Jiancheng, Nanjing, China). LDL was calculated by using the formula of Friedewald et al.[21] The serum free fatty acid (FFA) was measured using an ELISA kit (Houston, TX, USA).

Determination of Antioxidant Profiles and Lipid Peroxidation in Serum and Liver. The liver tissues were homogenized in cold saline (1 g of tissue in 9 mL of normal saline) and then centrifuged at 8000g for 10 min, and the supernatants were collected and stored at −20 °C before analysis. Protein concentrations were determined by Coomassie blue protein binding method using bovine serum albumin (BSA) as a standard.[22] All parameters were determined using the respective kits according to the manufacturer's specifications.

Western Blot Analysis. Each liver (500 mg) was homogenized in a lysis buffer (5 mL, 20 mM Tris-HCl, pH 7.4, 150 mM NaCl, 1% Triton X-100, 0.1% SDS, 1 mM EDTA, 1 mM EGTA, 2.5 mM sodium pyrophosphate, 1 mM sodium orthovanadate, 1 mM β-glycerolphosphate, 2 μg/mL leupeptin, 2 μg/mL aprotinin, 2 μg/mL pepstatin, and 1 mM PMSF) and kept for 30 min on ice. After centrifugation at 12000g for 15 min at 4 °C, the supernatants were used for Western blotting. Nuclear extracts from liver were isolated using a separate nuclear extraction kit (Beyotime, Shanghai, China), and the extracts were used for determining p65NFκB, p38MAPK, and p-p38MAPK levels by Western blotting. Protein concentrations were determined by BCA protein assay kit (Jiancheng, Nanjing, China). For Western blotting, 40 mg of protein was separated by 7.5% (FAS, the marker molecular weight from 10 to 250 kDa) or 10% (the marker molecular weight from 14 to 120 kDa) SDS−polyacrylamide gel electrophoresis (SDS-PAGE) in 25 mM Tris buffer, containing 250 mM glycine and 0.1% SDS and then electrotransferred to polyvinylidene difluoride (PVDF) membranes (Millipore, Bedford, MA, USA) in 25 mM Tris buffer, containing 192 mM glycine and 20% methanol. The membranes were blocked with 5% nonfat dry milk in TBST (50 mM Tris-HCl, pH 7.4, 150 mM NaCl, and 0.1% Tween 20) for 1 h at room temperature and incubated overnight at 4 °C with primary

DOI: 10.1021/acs.jafc.5b01082
J. Agric. Food Chem. 2015, 63, 6989−6998

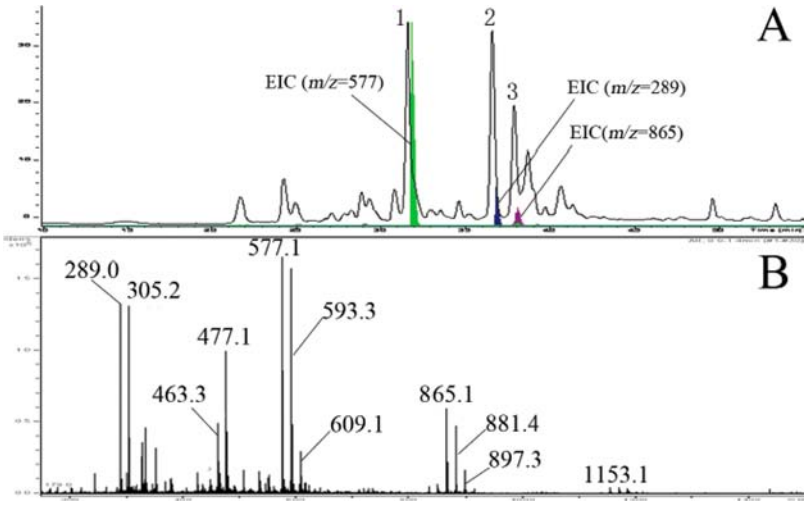

Figure 1. HPLC chromatogram, EICs, and mass spectrum of LSOPC using LC-ESI-MS. Reprinted from ref 24.

Table 1. Effect of LSOPC on Body Weight, Liver Coefficient, and Food Intake in Rats Fed a HFD[a]

	C	H	HD	LD
initial body wt (g)	176 ± 5.03	172 ± 6.51	175 ± 6.51	177 ± 8.50
final body wt (g)	468 ± 25.5	459 ± 20.5	452 ± 36.5	455 ± 30.0
body wt gain (g)	292 ± 25.5	288 ± 20.5	278 ± 36.5	278 ± 31.0
food intake (g/day)	30.6 ± 3.50	28.0 ± 1.03*	30.3 ± 2.52#	31.0 ± 2.96#
liver coefficient	0.032 ± 0.001	0.062 ± 0.002*	0.056 ± 0.005*#	0.053 ± 0.002*#

[a]Results are means ± SD from 10 rats per group. C, normal control group; H, HFD group; HD, HFD plus 0.5% (w/w) LSOPC group; LD, HFD plus 0.2% (w/w) LSOPC group. Liver coefficient = liver weight/body weight × 100. (*) $p < 0.05$ versus C group; (#) $p < 0.05$ versus H group.

antibodies in TBST (p65NFκB, 1:800; p38MAPK, 1:800; p-p38MAPK, 1:800; β-actin, 1:800), followed by incubation with horseradish peroxidase-conjugated secondary antibodies (1:3000) for 45 min at room temperature. Immunoreactive bands were visualized by the enhanced chemiluminescent reagents (Beyotime). The intensity of bands was quantified using Image Lab software (Bio-Rad). The band density were normalized to β-actin.

Quantitative Real-Time PCR. Total RNA was isolated from liver using Trizol reagent (Invitrogen, Carlsbad, CA, USA). Reverse transcription was performed with a first-strand cDNA synthesis kit (Toyobo, Osaka, 21 Japan). After cDNA synthesis, quantitative real-time PCR was performed on a SLAN PCR system (Hongshi, Shanghai, China) using SYBR Green PCR Master Mix (Toyobo) according to the manufacturer's instructions. The reverse transcription consisted of an initial denaturation at 94 °C for 4 min, followed by 30 cycles of amplification by denaturation at 94 °C for 30 s, annealing at 56 °C for 30 s, and extension at 72 °C for 25 s. Primers were designed according to the GenBank database using Primer Express software (Table 4). Expression of mRNA values was calculated using the threshold cycle (C_T) value. For each sample, the $\Delta C_{T,sample}$ value was determined by calculating the difference between the C_T value of the target gene and the C_T value of the β-actin reference gene. The expression levels relative to control were estimated by calculating $\Delta\Delta C_T$($\Delta C_{T,sample} - \Delta C_{T,control}$) and subsequently using the $2^{-\Delta\Delta CT}$method.[23]

Measurement of AGE, CML, and RAGE Levels. Liver AGEs and CML were determined using the ELISA kits (Cloud-Clone Corp.) according to the manufacturer's instructions. The expression level of RAGE was measured using quantitative RT-PCR according to the method above.

Statistical Analyses. All statistical analyses were performed using Origin software 8.0. All data were presented as means ± standard deviation (SD) and calculated using one-way ANOVA of SPSS 17.0 followed by the Tukey's multiple-range test. The statistical significance was defined as $p < 0.05$ or $p < 0.01$.

RESULTS

Analysis of LSOPC. Using the butanol–HCl assay, we found that LSOPC was rich in procyanidins. The procyanidin content of LSOPC was 106.22 ± 0.46% compared with grape seed procyanidins, which was used as a standard product with purity >95%. Our laboratory has identified the structural information about procyanidins in the lotus seedpod previously.[24] The mean degree of polymerization of LSOPC was 3.2. The terminal units in LSOPC contained 74% catechin units and 26% epicatechin units. The extension units in LSOPC contained 26% catechin units, 43% epicatechin units, and 31% epigallocatechin. Figure 1A is the HPLC chromatogram of LSOPC. Peaks 1, 2, and 3 exhibited maximum absorption at 279 nm and corresponded to extracted ion current chromatogram (EIC) peaks of m/z 577, 289, and 865, suggesting that peaks 1, 2, and 3 were probably procyanidin dimer, monomer (i.e., catechin or epicatechin), and trimer, respectively. By coelution with procyanidins B1, B2, and B3, peak 1 was confirmed as procyanidin B3. From its ESI-MS spectrum (Figure 1B) injected by a syringe pump, the compounds in LSOPC could be tentatively identified according to their m/z ratios as follows: catechin or epicatechin (m/z 289), gallocatechin or epigallocatechin (m/z 305), quercetin glycoside (m/z 463), quercetin glucuronide (m/z 477), procyanidin dimers (m/z 577.1), proanthocyanidin dimer gallate (m/z 593.3), prodelphinidin dimers (m/z 609.1), procyanidin trimers (m/z 865.1), proanthocyanidin trimers with one gallocatechin or epigallocatechin unit and two catechin units (m/z 881.4), proanthocyanidin trimers with two gallocatechin or epigallocatechin units and one catechin or epicatechin unit (m/z 897.3), and procyanidin tetramers (m/z 1153.1). Thus, LSOPC

DOI: 10.1021/acs.jafc.5b01082
J. Agric. Food Chem. 2015, 63, 6989–6998

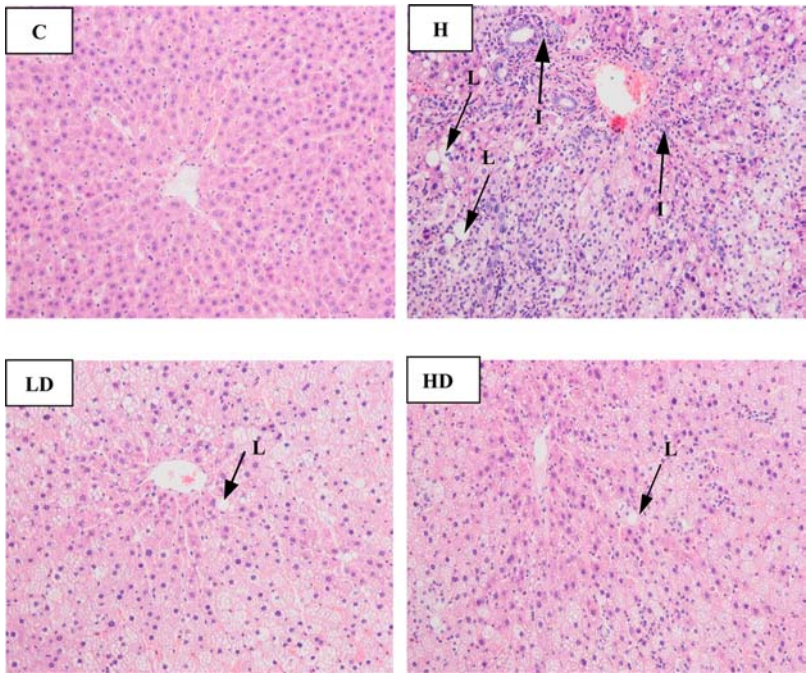

Figure 2. HE staining of rat liver tissue. C, normal control group; H, HFD group; HD, HFD plus 0.5% (w/w) LSOPC group; LD, HFD plus 0.2% (w/w) LSOPC group. "I" indicates inflammatory cell infiltration, and "L" indicates lipid droplet.

Table 2. Effect of LSOPC on Serum Lipids and Enzyme Activities in Rats Fed a HFD[a]

	C	H	LD	HD
triglyceride (mmol/L)	0.77 ± 0.11	1.40 ± 0.21**	0.69 ± 0.08##	0.81 ± 0.10##
total cholesterol (mmol/L)	1.66 ± 0.18	3.92 ± 0.28**	2.81 ± 0.20**##	3.27 ± 0.27**##
LDL-C (mmol/L)	0.15 ± 0.01	2.42 ± 0.21**	1.24 ± 0.14**##	1.69 ± 0.13**##
HDL-C (mmol/L)	1.16 ± 0.09	0.86 ± 0.10**	1.25 ± 0.09##	1.21 ± 0.07##
free fatty acids (μmol/L)	409 ± 11.7	446 ± 14.4**	343 ± 12.97**##	359 ± 13.0**##
AST (U/L)	179 ± 8.50	286 ± 10.1**	254 ± 9.91**##	220 ± 8.91**##
ALT (U/L)	93.9 ± 3.95	174 ± 4.12**	137 ± 4.45**##	138 ± 3.89**##
ALP (U/L)	90.8 ± 3.21	165 ± 2.89**	131 ± 2.78**##	154 ± 3.50**##

[a]Results are means ± SD from 10 rats per group. C, normal control group; H, HFD group; HD, HFD plus 0.5% (w/w) LSOPC group; LD, HFD plus 0.2% (w/w) LSOPC group. (**) $p < 0.01$ versus C group; (##) $p < 0.01$ versus H group.

Table 3. Effect of LSOPC on Serum and Hepatic Antioxidant Defenses in Rats Fed a HFD[a]

	C	H	LD	HD
Serum				
T-AOC (U/mL)	4.00 ± 0.56	2.83 ± 0.35**	3.76 ± 0.17##	4.69 ± 0.12**##
SOD (U/mL)	297 ± 14.6	261 ± 19.2**	293 ± 31.6#	326 ± 32.8*##
GRAC	5.02 ± 2.45	7.76 ± 1.80*	3.25 ± 0.21*##	2.98 ± 1.67*##
GSH-PX (U)	1882 ± 148	1603 ± 162**	1799 ± 143#	1832 ± 186##
MDA (nmol/mL)	3.77 ± 0.26	4.33 ± 0.25**	3.80 ± 0.15##	4.04 ± 0.28*#
NO (μmol/L)	42.6 ± 4.07	47.6 ± 3.63**	40.7 ± 4.53##	34.5 ± 2.14##
Liver				
T-AOC (U/mL)	1.10 ± 0.14	1.97 ± 0.88**	2.15 ± 0.96**	3.25 ± 0.25**##
SOD (U/mL)	273 ± 14.5	280 ± 19.8	333 ± 22.3**##	300 ± 13.5**#
GRAC	4.69 ± 1.30	16.5 ± 4.05**	9.01 ± 3.88**##	8.18 ± 0.95**##
GSH-PX (U)	232 ± 15.2	173 ± 27.2**	303 ± 37.5**##	246 ± 23.2##
MDA (nmol/mL) (nmol/mg prot)	1.47 ± 0.16	1.96 ± 0.19**	1.58 ± 0.19##	1.54 ± 0.19##
NO (μmol/L)	1.11 ± 0.39	1.46 ± 0.44	1.27 ± 0.31	0.68 ± 0.12##
ROS (ng/mL)	55.2 ± 8.02	132 ± 10.2**	71.7 ± 4.65**##	92.2 ± 8.75**##

[a]Results are means ± SD from ten rats per group. C, normal control group; H, HFD group; HD, HFD plus 0.5% (w/w) LSOPC group; LD, HFD plus 0.2% (w/w) LSOPC group. (**) $p < 0.01$ versus C group; (##) $p < 0.01$ versus H group; (*) $p < 0.05$ versus C group; (#) $p < 0.05$ versus H group.

DOI: 10.1021/acs.jafc.5b01082
J. Agric. Food Chem. 2015, 63, 6989−6998

consisted of proanthocyanidin monomers, dimers, trimers, and tetramers.

Establishment of NAFLD Model Rats. After 12 weeks of HFD, the body weight and liver coefficient of NAFLD model rats (including groups H, HD, and LD) were significantly increased (Table 1), which proved that the establishment of the obesity rat model was successful according to the assessment of the study.[25] Furthermore, tissues from rats were also subjected to histopathologic examination, which proved that an excess of high-fat intake induced a significantly high degree of steatosis and inflammatory cell infiltration, accompanied by an apparent accumulation of fat in comparison with normal rats, matching the symptom of NAFLD (Figure 2). Taken together, this indicated that the establishment of the NAFLD model was successful. Meanwhile, fat deposition appeared to be inhibited in the livers of LSOPC groups, although some fat vacuoles were evident. Inflammatory cell infiltration was also alleviated in the livers from rats fed LSOPC compared with the animals in the H group (Figure 2). These results indicated that LSOPC may be an effective compound to inhibit hepatic steatosis.

Effect of LSOPC on Serum Lipid Profiles and Serum AST, ALT, and ALP Activities. The serum lipids and enzyme activities of AST, ALT and ALP are shown in Table 2. It was indicated that a HFD induced a significant increase in serum TC, TG, and FFA levels, accompanied by a notable decrease in the HDL-C level in comparison with normal rats ($p < 0.01$). Administration of 0.2 or 0.5% (w/w) LSOPC reduced serum level of TG in HFD-fed rats by 50.71 and 42.14%, respectively, compared to the animals in the H group. In addition, treatment with LSOPC also significantly decreased ($p < 0.01$) the serum TC and FFA contents and markedly elevated ($p < 0.01$) the level of serum HDL-C by 45.35 and 40.70%, separately, compared to the H group.

Moreover, after 12 weeks of HFD, the serum levels of AST, ALT, and ALP significantly increased by 1.6-, 1.9-, and 1.8-fold, respectively. As compared to the H group, supplementation of 0.2 or 0.5% (w/w) LSOPC resulted in the reduction of AST, ALT, and ALP notably ($p < 0.01$) by 11.23% (22.87%), 21.22% (20.38%), and 20.94% (6.59%), respectively.

Effect of LSOPC on Serum and Hepatic Oxidative Stress. Malondialdehyde (MDA) is a reactive aldehyde formed during lipid peroxidation. As shown in Table 3, the serum MDA levels in rats fed a normal diet and HFD were 3.77 and 4.33 nmol/mg protein, respectively. The serum MDA levels in rats fed HFD containing 0.2 or 0.5% (w/w) LSOPC were 3.80 and 4.04 nmol/mg protein, respectively, indicating that lipid peroxidation was attenuated by LSOPC treatment. The serum GRAC level in HFD-treated rats was increased by 54.58% compared to that of the control group, whereas treatment with 0.2 or 0.5% (w/w) LSOPC resulted in decreases in serum GRAC level by 35.26 and 40.64%, respectively. Similarly, LSOPC supplementation decreased the serum NO level significantly compared to the H group. In addition, 12 weeks of HFD feeding was accompanied by 12.12−29.25% inhibition of serum T-AOC, SOD, and GSH-PX activities compared to rats in the control group. The effect of HFD on the activities of these antioxidant enzymes was dose-dependently reversed by administration of LSOPC. Additionally, LSOPC significantly reversed HFD-induced hepatic ROS level after 12 weeks of treatment. Meanwhile, a quantitative real-time RT-PCR analysis showed the expression of NADPH and COX significantly decreased by treatment with LSOPC (Figure 5). Other hepatic parameters of oxidative stress were similar to those observed in serum.

Table 4. Primer Sequences for Real-Time PCR

isoform	sequence	length (bp)
β-actin	F: 5′-CACGATGGAGGGGCCGGACTCATC-3′ R: 5′-TAAAGACCTCTATGCCAACACAGT-3′	240
NADPH Nox3	F: 5′-GTGGAGACGGCAACTAGACAAA-3′ R: 5′-TATACAAGGTGCGGACCGGATT-3′	215
COX	F: 5′-GGCTTCGGGAGCACAACAGAGT-3′ R: 5′-AGCAGCGGATGCCAGTGATAGA-3′	259
TNF-α	F: 5′-TGCCTCAGCCTCTTCTCATT-3′ R: 5′-GGGCTTGTCACTCGAGTTTT-3′ R: 5′-ACTGAAGCGAAAGCCCTGTA-3′	180
IL-1	F: 5′-CTGTGACTCGTGGGATGATG-3′ R: 5′-AGGGATTTTGTCGTTGCTTG-3′	211
IL-6	F: 5′-AGTTGCCTTCTTGGGACTGA-3′ R: 5′-ACAGTGCATCATCGCTGTTC-3′	218
IL-8	F: 5′-ATGACTTCCAACCTGGCCGTG-3′ R: 5′-TTCTCAGCCCTCTTCAAAAAC-3′	385
ICAM-1	F: 5′-TGTCAAACGGGAGATGAATGGT-3′ R: 5′-CTGGCGGTAATAGGTGTAAATGG-3′	187
VCAM-1	F: 5′-ACAAAACGCTCGCTCAGATT-3′ R: 5′-GTCCATGGTCAGAACGGACT-3′	152
MCP-1	F: 5′-GATGCAGTTAATGCCCCACT-3′ R: 5′-TTCCTTATTGGGGTCAGCAC-3′	168
E-selectin	F: 5′-TGCCAAGAACAGGAATACCC-3′ R: 5′-CTCCCAGGATTTGAGGAACA-3′	248
RAGE	F: 5′-ACAGAAACCGGTGATGAAGG-3′ R: 5′-ATTCAGCTCTGCACGTTCCT-3′	207

Effect of LSOPC on Hepatic AGEs Production and RAGE Expression. AGEs are known to accumulate in diabetic subjects and may be important mediators of untoward effects of NAFLD.[26] CML is reportedly a major component of AGEs.[27] Therefore, we investigated the expression of AGEs and CML by ELISA. The results showed that AGEs and CML were significantly elevated in HFD-fed rats compared with the normal control rats. Treatment of rats with 0.2 or 5% (w/w) LSOPC in the diet for 12 weeks resulted in lowering of these elevated levels (Figure 3A,B).

Given that AGEs exert inflammatory and oxidative stress inducing NAFLD mainly through the receptor RAGE,[28] we examined the mRNA expression of RAGE in the livers by RT-PCR. The mRNA level of RAGE was markedly elevated by 4.5-fold in HFD-fed rats compared with the animals in the normal control group (Figure 3C). However, 0.5% (w/w) LSOPC treatment remarkably ($p < 0.01$) reversed the increasing tendency to normal level.

Effect of LSOPC on Hepatic p38MAPK, p-p38MAPK, and p65NF-κB Expression. We further examined the effects

DOI: 10.1021/acs.jafc.5b01082
J. Agric. Food Chem. 2015, 63, 6989−6998

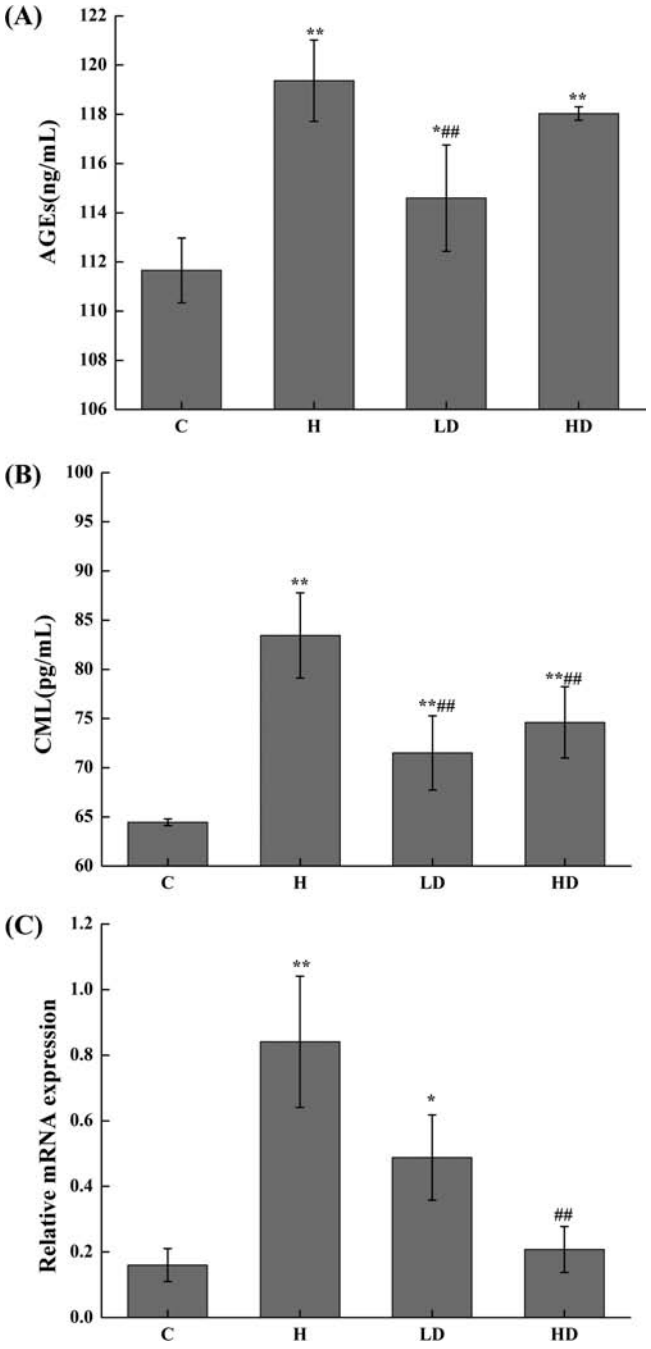

Figure 3. LSOPC prevented accumulation of AGEs and CML and led to a decreased RAGE level in liver: (A) detection of the liver AGEs level by ELISA; (B) detection of the liver CML level by ELISA (both AGEs and CML levels were normalized to total protein concentration in the tissue sample, $n = 5$ rats per group); (C) expression of RAGE by RT-PCR in liver. Results are means ± SD. C, normal control group; H, HFD group; HD, HFD plus 0.5% (w/w) LSOPC group; LD, HFD plus 0.2% (w/w) LSOPC group. (*) $p < 0.05$; (**) $p < 0.01$ versus C group; (#)$p < 0.05$; (##) $p < 0.01$ versus H group.

of LSOPC administration on several representative hepatic protein expressions related to lipid metabolism and oxidative stress modulation by Western blotting. As shown in Figure 4, expression levels of p38MAPK, p-p38MAPK, and p65NF-κB in HFD-fed rats were 4.7-, 6.7-, and 1.9-fold higher than that in the control group, respectively. When compared to those of the rats in the HFD-fed group, the levels of p38MAPK, p-p38MAPK, and p65NF-κB were significantly down-regulated by LSOPC treatments in a dose-related manner. The relative density values of the bands were normalized with that of β-actin and are presented in panels A and B of Figure 4, respectively.

Effects of LSOPC on Hepatic Injury and Inflammation. Both pro-inflammatory cytokines and adhesion molecules play an important role in the pathogenesis of NAFLD.[29] We finally measured the effects of LSOPC administration on several representative genes involved in hepatic inflammation in the livers of the rats. As a result of HFD, the liver levels of tumor necrosis factor-α (TNF-α), interleukin 1 (IL-1), IL-6, IL-8, intercellular adhesion molecule-1 (ICAM-1), vascular cell adhesion molecule-1 (VCAM-1), monocyte chemoattractant protein-1 (MCP-1), and E-selectin were significantly elevated, indicating a considerable level of inflammation compared with the normal control rats. Administration of 0.2 or 5% (w/w) LSOPC in the diet for 12 weeks resulted in a notably and dose-dependent reduction of these elevated levels. This reduction is shown in Figure 5.

DISCUSSION

NAFLD is emerging as one of the most common causes of chronic liver disease, and obesity is intimately related to chronic metabolic disorders. Rodent animal models of NAFLD induced by HFD, which shows the characteristics of metabolic disorders such as hyperlipidemia, obesity, inflammation, and oxidative stress, have been widely used due to its similar pathogenesis in humans.[30] In the present study, we fed male SD rats a HFD for 12 weeks and found that serum levels of TC, TG, LDL-C, AST, ALT, and ALP and liver weight significantly increased. In addition, moderate levels of oxidative stress and inflammation were induced. These results suggested that long-term consumption of a HFD by rat caused typical NAFLD, with clinical characteristics similar to those observed in NAFLD patients. This model could help elucidate the alterations seen in target organs and the molecular mechanisms underlying the development of NAFLD.

Traditional medicine and medicinal plants in most developing countries used as normative basis for the maintenance of good health have been widely studied.[31] In recent years, dietary plants with antioxidative property have been the center of focus. It is believed that these plants could prevent or protect tissues against the damage of free radicals.[32] Moreover, a number of plant-derived products have been shown to possess good capacities to adjust sugar and lipid metabolism.[33] LSOPC, which comprises natural plant polyphenols, was reported to have a broad spectrum of pharmacological and therapeutic properties against oxidative stress.[34,35] Therefore, we hypothesized that LSOPC was responsible for the protecting effect against NAFLD.

There has been major interest in the pathogenic effects of AGEs in a range of diseases, including, most importantly, diabetes, but also atherosclerosis and chronic renal disease. In addition to increasing during normal aging, AGEs are known to be elevated in the serum and accumulated in various tissues at an accelerated rate in NAFLD patients. Furthermore, accumulating evidence suggests that the binding of AGEs with their receptor (RAGE) results in generation of ROS from activated NADPH oxidase.[36] This culminates in the activation of p38MAPK and translocation of the NF-κB p65 submit into the nucleus, leading to the transcription of growth factors, inflammatory cytokines, chemokines, and adhesion molecules.[37,38] The promoter region of the RAGE gene contains

DOI: 10.1021/acs.jafc.5b01082
J. Agric. Food Chem. 2015, 63, 6989−6998

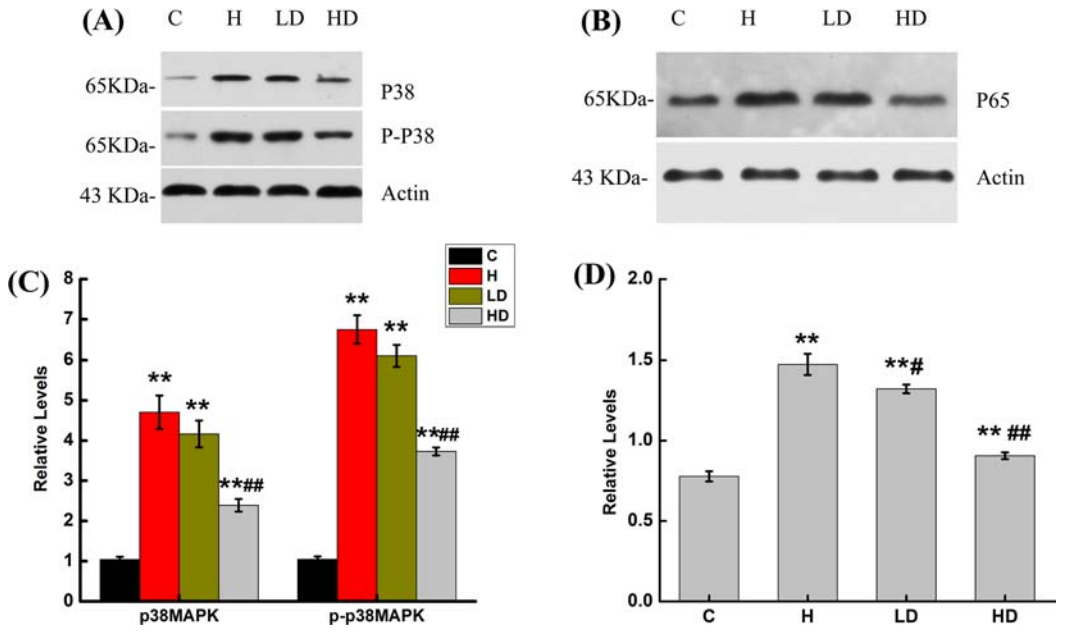

Figure 4. Protein level of NFκB, p38MAPK, and p-p38MAPK in liver of rats fed a HFD with/without high dose of LSOPC or low dose of LSOPC. The total protein extracts of 10 rats in the same group were combined. Equal amounts of liver protein extracts of each group (40 μg) were separated by 10% SDS-PAGE. Results are means ± SD. A representative blot from three independent experiments is shown. C, normal control group; H, HFD group; HD, HFD plus 0.5% (w/w) LSOPC group; LD, HFD plus 0.2% (w/w) LSOPC group. (**) $p < 0.01$ versus C group; (##)$p < 0.01$ versus H group.

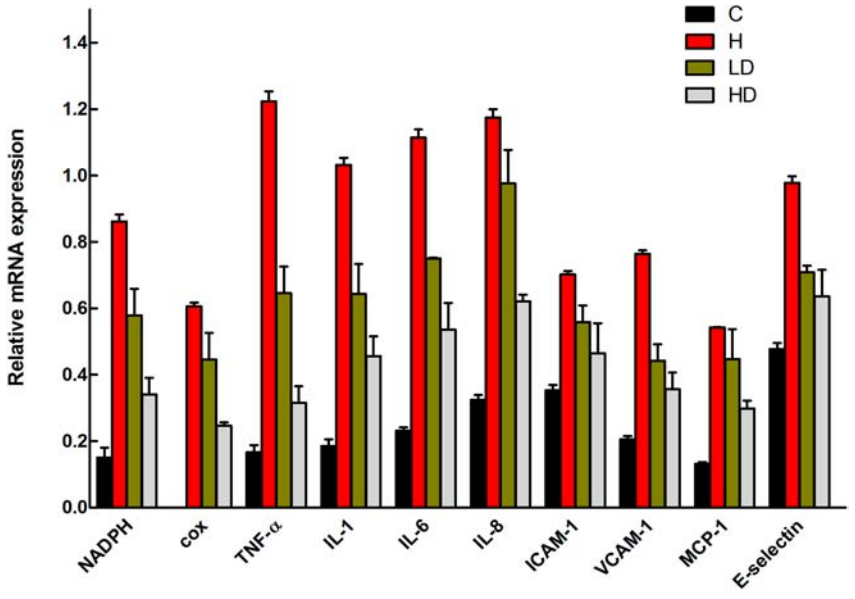

Figure 5. Gene expressions of lipid metabolism in liver of rats fed a HFD with/without LSOPC. Results are means ± SD. C, normal control group; H, HFD diet group; HD, HFD plus 0.5% (w/w) LSOPC group; LD, HFD plus 0.2% (w/w) LSOPC group. All $p < 0.01$ versus C group; all $p < 0.01$ versus H group.

an NF-κB binding site and, therefore, one of the important consequences of NF-κB activation and translocation is up-regulation of RAGE itself. This sets up a positive feedback loop and ensures maintenance of RAGE signaling. On the other hand, the generation of ROS via NADPH oxidase triggered by RAGE activation causes increased AGE formation and contributes to a vicious cycle of AGE formation, generation of oxidative stress, and further RAGE activation.[39,40] Our results demonstrate that administration of LSOPC reduced the hepatic ROS, NADPH overproduction and associated AGEs, and CML expression, which were in accordance with our previous studies in vitro.[18] Additionally, 0.5% (w/w) LSOPC treatment remarkably reversed the increasing tendency of RAGE to a normal level. Moreover, the protein expressions of hepatic p38MAPK and p65 NF-κB were significantly decreased dose-dependently by LSOPC treatment in HFD-fed rats. Thus, it was suggested that part of the beneficial effects of LSOPC included the disruption of the detrimental RAGE−MAPK−NF-κB pathways.

The two-hit hypothesis of NASH pathogenesis suggests that a second injury or cofactor is required for progression from simple benign steatosis to harmful steatohepatitis, which can

DOI: 10.1021/acs.jafc.5b01082
J. Agric. Food Chem. 2015, 63, 6989−6998

subsequently lead to fibrosis, cirrhosis, and hepatocellular carcinoma. There has been considerable interest in factors that could serve as this "second hit". Oxidative stress and the inflammatory response have emerged as important mechanisms involved in the development and progression of NAFLD.[41] Superoxide dismutase (SOD) is an important antioxidant enzyme and the primary means of free radical scavenging in organisms.[42] MDA is the advanced lipoxidation end product of the peroxidation reaction, which results from the action of free radicals on lipids.[43] The amount of hepatic MDA can indirectly reflect the degree of cell damage. The combination of SOD and MDA is usually used to evaluate the oxidative stress level in liver. Our results showed that administration of LSOPC remarkably decreased the serum and hepatic MDA and increased SOD compared to the H group in long-term HFD-fed rats.

Disorders of lipid metabolism also played a central role in the initiation and progression of NAFLD. When NAFLD occurs, excess FFA in the liver cells lead to the development of lipid peroxidation and the generation of a large number of ROS, which are the major indicators of oxidative stress.[40] Consequently, ROS prompted the generation of pro-inflammatory cytokines and adhesion molecules. Sustained inflammatory infiltrate upon chronic hepatocellular damage further induces the development of NASH.[44] In this study, LSOPC supplementation dose-dependently decreased the levels of pro-inflammatory cytokines (TNF-α, IL-1, IL-6, IL-8) and adhesion molecules (ICAM-1, VCAM-1, MCP-1, E-selectin) in the liver in long-term HFD-induced NAFLD. Although our results could not exclude the possibility that LSOPC directly suppress the activation of NF-κB and the expression of pro-inflammatory factors via its antioxidative effects, LSOPC inhibited the progression of NAFLD in HFD rats, at least partly, by suppressing the activation RAGE axis and subsequently decreasing adhesion molecule-induced monocyte/macrophage infiltration in the damaged endothelial cells; the proposed inhibition pathway is shown in Figure 6.

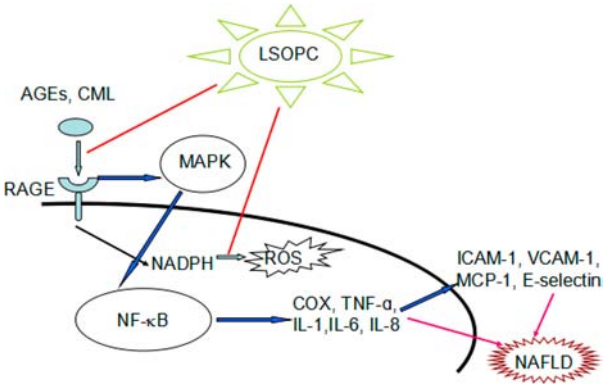

Figure 6. Proposed effect of LSOPC against NAFLD induced by HFD.

In summary, the present study clearly demonstrated LSOPC have potent protective effects against long-term HFD-induced NAFLD. Moreover, the protective effects on regulation of hepatic lipid metabolism, antioxidant defense system, and inflammatory response were mainly mediated through RAGE–MAPK–NF-κB signaling during NAFLD development. Thus, LSOPC could be considered as potent dietary supplements for preventing NAFLD-related metabolic diseases. Further research in vitro will be needed to explore the exact molecular mechanism by which LSOPC generate their protective effect against NAFLD injury.

AUTHOR INFORMATION

Corresponding Author

*(Z.S.) Phone: +86-27-87283201. Fax: +86-27-87282966. E-mail: sunzhida@mail.hzau.edu.cn, qianwill2007@163.com.

Funding

We are thankful for the help from the National Natural Science Foundation of China (NSFC No. 31071633) and Excellent Doctoral Dissertation Funding Scheme of HZAU (No. 2013YB07).

Notes

The authors declare no competing financial interest.

ACKNOWLEDGMENTS

We are grateful for the help from the Reference Laboratory for the test of Veterinary Drug Residues of Huazhong Agricultural University (HZAU).

ABBREVIATIONS USED

LSOPC lotus seedpod oligomeric procyanidins
SD Sprague–Dawley
HFD high-fat diet
AGEs advanced glycation endproducts
TG triglyceride
TC cholesterol
FFA free fatty acids
LDL-C low-density lipoprotein cholesterol
HDL-C high-density lipoprotein cholesterol
AST aspartate aminotransferase
ALT alanine aminotransferase
ALP alkaline phosphatase
ROS reactive oxygen species
NADPH nicotinamide adenine dinucleotide phosphate
COX cyclooxygenase
NO nitrogen monoxide
MDA malondialdehyde
GRAC glutathione reductase
T-AOC total antioxidant capacity
SOD superoxide dismutase
GSH glutathione
CML N^{ϵ}-(carboxymethyl) lysine
RAGE receptor of advanced glycation endproduct
NF-κB nuclear factor-kappa B
MAPK mitogen-activated protein kinases
NAFLD nonalcoholic fatty liver disease
TNF-α tumor necrosis factor-α
IL-1 interleukin 1
IL-6 interleukin 6
IL-8 interleukin 8
ICAM-1 intercellular adhesion molecule-1
VCAM-1 vascular cell adhesion molecule-1
MCP-1 monocyte chemoattractant protein-1

REFERENCES

(1) Kim, S.; Lee, D.; Kim, J. K.; Kim, J. H.; Park, J. H.; Lee, J. W.; Kwon, J. Viscothionin isolated from Korean mistletoe improves nonalcoholic fatty liver disease via the activation of adenosine monophosphate-activated protein kinase. *J. Agric. Food Chem.* **2014**, *62*, 11876–11883.

DOI: 10.1021/acs.jafc.5b01082
J. Agric. Food Chem. 2015, 63, 6989–6998

(2) Lai, Y. S.; Chen, W. C.; Ho, C. T.; Lu, K. H.; Lin, S. H.; Tseng, H. C.; Lin, S. Y.; Sheen, L. Y. Garlic essential oil protects against obesity-triggered nonalcoholic fatty liver disease through modulation of lipid metabolism and oxidative stress. *J. Agric. Food Chem.* **2014**, *62*, 5897−5906.
(3) Masterjohn, C.; Bruno, R. S. Therapeutic potential of green tea in nonalcoholic fatty liver disease. *Nutr. Rev.* **2012**, *70*, 41−56.
(4) Park, H. J.; Lee, J. Y.; Chung, M. Y.; Park, Y. K.; Bower, A. M.; Koo, S. I.; Giardina, C.; Bruno, R. S. Green tea extract suppresses NF κB activation and inflammatory responses in diet-induced obese rats with nonalcoholic steatohepatitis. *J. Nutr.* **2012**, *142*, 57−63.
(5) Li, X.; Zheng, T.; Sang, S.; Lv, L. Quercetin inhibits advanced glycation end product formation by trapping methylglyoxal and glyoxal. *J. Agric. Food Chem.* **2014**, *62*, 12152−12158.
(6) Goldberg, T.; Cai, W.; Peppa, M.; Dardaine, V.; Baliga, B. S.; Uribarri, J. Advanced glycoxidation end products in commonly consumed foods. *J. Am. Diet. Assoc.* **2004**, *104*, 1287−1291.
(7) Hsu, W. H.; Lee, B. H.; Hsu, Y. W.; Pan, T. M. Peroxisome proliferator-activated receptor-gamma activators monascin and rosiglitazone attenuate carboxymethyllysine-induced fibrosis in hepatic stellate cells through regulating the oxidative stress pathway but independent of the receptor for advanced glycation end products signaling. *J. Agric. Food Chem.* **2013**, *61*, 6873−6879.
(8) Patel, R.; Baker, S. S.; Liu, W.; Desai, S.; Alkhi, R.; Kozielski, R.; Mastrandrea, L.; Sarfraz, A.; Cai, W. J.; Vlassara, H. E. Effect of dietary advanced glycation end products on mouse liver. *PLoS One* **2012**, *7*, e35143.
(9) Ekong, U.; Zeng, S.; Dun, H.; Feirt, N.; Guo, J.; Ippagunta, N.; Guarrera, J. V.; Lu, Y.; Weinberg, A.; Qu, W.; Ramasamy, R.; Schmidt, A. M.; Emond, J. C. Blockade of the receptor for advanced glycation end products attenuates acetaminopheninduced hepatotoxicity in mice. *J. Gastroenterol. Hepatol.* **2006**, *21*, 682−688.
(10) Zeng, S.; Feirt, N.; Goldstein, M.; Guarrera, J.; Ippagunta, N.; Ekong, U.; Dun, H.; Lu, Y.; Qu, W.; Schmidt, A. M.; Emond, J. C. Blockade of receptor for advanced glycation end product (RAGE) attenuates ischemia and reperfusion injury to the liver in mice. *Hepatology* **2004**, *39*, 422−432.
(11) Goodwin, M.; Herath, C.; Jia, Z.; Leung, C.; Coughlan, M. T.; Forbes, J.; Angus, P. Advanced glycation end products augment experimental hepatic fibrosis. *J. Gastroenterol. Hepatol.* **2013**, *28*, 369−376.
(12) Hoefen, R. J.; Berk, B. C. The role of MAP kinases in endothelial activation. *Vasc. Pharmacol.* **2002**, *38*, 271−273.
(13) Harja, E.; Bu, D. X.; Hudson, B. I.; Chang, J. S.; Shen, X.; Hallsmk, K.; Kalea, A. Z.; Lu, Y.; Rosario, R. H.; Oruganti, S.; Nikolla, Z.; Belov, D.; Lalla, E.; Ramasamy, R.; Yan, S. F.; Schmidt, A. M. Vascular and inflammatory stresses mediate atherosclerosis via RAGE and its ligands in apoE$^{-/-}$ mice. *J. Clin. Invest.* **2008**, *118*, 183−194.
(14) Goldin, A.; Beckman, J. A.; Schmidt, A. M.; Creager, M. A. Advanced glycation end products: sparking the development of diabetic vascular injury. *Circulation* **2006**, *114*, 597−605.
(15) Xu, J. Q.; Rong, S.; Xie, B. J.; Sun, Z. D.; Zhang, L.; Wu, H. L.; Yao, P.; Zhang, Y. J.; Liu, L. G. Procyanidins extracted from the lotus seedpod ameliorate scopolamine-induced memory impairment in mice. *Phytother. Res.* **2009**, *12*, 1742−1747.
(16) Blade, C.; Arola, L.; Salvado, M. J. Hypolipidemic effects of proanthocyanidins and their underlying biochemical and molecular mechanisms. *Mol. Nutr. Food Res.* **2010**, *54*, 37−59.
(17) Zou, B.; Ge, Z. Z.; Zhang, Y.; Du, J.; Xua, Z.; Li, C. M. Persimmon tannin accounts for hypolipidemic effects of persimmon through activating of AMPK and suppressing NF-κB activation and inflammatory responses in high-fat diet rats. *Food Funct.* **2014**, *5*, 1536−1546.
(18) Wu, Q.; Chen, H. Y.; Lv, Z. J.; Li, S. Y.; Hu, B.; Guan, Y. F.; Xie, B. J.; Sun, Z. D. Oligomeric procyanidins of lotus seedpod inhibits the formation of advanced glycation end-products by scavenging reactive carbonyls. *Food Chem.* **2013**, *138*, 1493−1502.
(19) Lee, M. K.; Kim, C. T.; Kim, Y. Green tea (−)-epigallocatechin-3-gallate reduces body weight with regulation of multiple genes expression in adipose tissue of diet-induced obese mice. *Ann. Nutr. Metab.* **2009**, *54*, 151−157.
(20) Ribas-Latre, A.; BDel as, J. M.; Escudero, L. B.; Casanova, E.; Arola-Arnal, A.; Salvado, M. J.; Arola, L.; Blade, C. Dietary proanthocyanidins modulate melatonin levels in plasma and the expression pattern of clock genes in the hypothalamus of rats. *Mol. Nutr. Food Res.* **2015**, *59*, 865−878.
(21) Friedewald, W. T.; Levy, R. I.; Fredrickson, D. S. Estimation of the concentration of low-density lipoprotein cholesterol in plasma, without use of the preparative ultracentrifuge. *Clin. Chem.* **1972**, *18*, 499−502.
(22) Bradford, M. M. A rapid and sensitive method for the quantitation of microgram quantities of protein utilizing the principle of protein-dye binding. *Anal. Biochem.* **1976**, *72*, 248−254.
(23) Livak, K. J.; Schmittgen, T. D. Analysis of relative gene expression data using real-time quantitative PCR and the 2(−ΔΔC-(T)) method. *Methods* **2001**, *25*, 402−408.
(24) Xiao, J. S.; Xie, B. J.; Gao, Y. P.; Wu, H.; Sun, Z. D.; Xiao, D. Characterization of oligomeric procyanidins and identification of quercetin glucuronide from lotus (*Nelumbo nucifera* Gaertn.) seedpod. *J. Agric. Food Chem.* **2012**, *60*, 2825−2829.
(25) Liu, R.; Sun, C. H.; Li, Y.; Yu, X. F.; Wang, S. R. Comparation of blood hormore level between DIO-R and DIO rats. *J. Hyg. Res.* **2003**, *32*, 212−214.
(26) Leuner, B.; Max, M.; Thamm, K.; Kausler, C.; Yakobus, Y.; Bierhaus, A.; Sel, S.; Hofmann, B.; Silber, R. E.; Simm, A.; Nass, N. RAGE influences obesity in mice: effects of the presence of RAGE on weight gain, AGE accumulation, and insulin levels in mice on a high fat diet. *Z. Gerontol. Geriatrie* **2012**, *45*, 102−108.
(27) Fu, M. X.; Requena, J. R.; Jenkins, A. J.; Lyons, T. J.; Baynes, J. W.; Thorpe, S. R. The advanced glycation end product, *N*-(carboxymethyl) lysine, is a product of both lipid peroxidation and glycoxidation reactions. *J. Biol. Chem.* **1996**, *271*, 9982−9986.
(28) Flyvbjerg, A.; Denner, L.; Schrijvers, B. F.; Tilton, R. G.; Mogensen, T. H.; Paludan, S. R.; Rasch, R. Long-term renal effects of a neutralizing RAGE antibody in obese type 2 diabetic mice. *Diabetes* **2004**, *53*, 166−172.
(29) Goel, R.; Boylan, B.; Gruman, L.; Newman, P. J.; North, P. E.; Newman, D. K. The proinflammatory phenotype of PECAM-1-deficient mice results in atherogenic diet-induced steatohepatitis. *Am. J. Physiol. Gastrointest. Liver Physiol.* **2007**, *293*, G1205−G1214.
(30) Takahashi, Y.; Soejima, Y.; Fukusato, T. Animal models of nonalcoholic fatty liver disease/nonalcoholic steatohepatitis. *World J. Gastroenterol* **2012**, *18*, 2300−2308.
(31) Furusho, T.; Kataota, E.; Yasuhara, T.; Wada, M.; Innami, S. Administration of β-carotene suppresses lipidperoxidation in tissues and improves the glucose tolerance ability of streptozotocin-induced diabetic rats. *Int. J. Vitam. Nutr. Res.* **2002**, *72*, 71−76.
(32) Osawa, T.; Kato, Y. Protective role of antioxidative food factors in oxidative stress caused by hyperglycemia. *Ann. N. Y. Acad. Sci.* **2005**, *1043*, 440−451.
(33) Vasu, V. T.; Modi, H.; Thaikoottathil, J. V.; Gupta, S. Hypolipidaemic and antioxidant effect of *Enicostemma littorale* Blume aqueous extract in cholesterol fed rats. *J. Ethnopharmacol.* **2005**, *101*, 277−282.
(34) Xiao, J.; Sui, Y.; Li, S. Y.; Wu, Q.; Yang, T.; Xie, B. J.; Sun, Z. D. Combination of proanthocyanidins extracted from lotus seedpod and L-cysteine ameliorates memory impairment induced by alcohol and scopolamine in mice. *Eur. Food Res. Technol.* **2013**, *236*, 671−679.
(35) Xiao, J.; Li, S. Y.; Sui, Y.; Wu, Q.; Li, X. P.; Xie, B. J.; Zhang, M. W.; Sun, Z. D. *Lactobacillus casei*-01 facilitates the ameliorative effects of proanthocyanidins extracted from lotus seedpod on learning and memory impairment in scopolamine-induced amnesia mice. *PLoS One* **2014**, *9*, e112773.
(36) Li, J.; Schmidt, A. M. Characterization and functional analysis of the promoter of RAGE, the receptor for advanced glycation end products. *J. Biol. Chem.* **1997**, *272*, 16498−16506.
(37) Yan, S. D.; Schmidt, A. M.; Anderson, G. M.; Zhang, J.; Brett, J.; Zou, Y. S.; Pinsky, D.; Stern, D. Enhanced cellular oxidant stress by the

DOI: 10.1021/acs.jafc.5b01082
J. Agric. Food Chem. 2015, 63, 6989−6998

interaction of advanced glycation end products with their receptors/binding proteins. *J. Biol. Chem.* **1994**, *269*, 9889−9897.
(38) Haslbeck, K. M.; Schleicher, E.; Bierhaus, A.; Nawroth, P.; Haslbeck, M.; Neundoerfer, B.; Heuss, D. The AGE/RAGE/NF-κB pathway may contribute to the pathogenesis of polyneuropathy in impaired glucose tolerance (IGT). *Exp. Clin. Endocrinol. Diabetes* **2005**, *113*, 288−291.
(39) Gou, Z. J.; Niu, H. X.; Hou, F. F.; Zhang, L.; Fu, N.; Nagai, R.; Lu, X.; Chen, B. H.; Shan, Y. X.; Tian, J. W.; Nagaraj, R. H.; Xie, D.; Zhang, X. Advanced oxidation protein products activate vascular endothelial cells via a RAGE-mediated signaling pathway. *Antioxid. Redox Signal.* **2008**, *10*, 1699−1712.
(40) Yao, D.; Brownlee, M. Hyperglycemia-induced reactive oxygen species increase expression of the receptor for advanced glycation end products (RAGE) and RAGE ligands. *Diabetes* **2010**, *59*, 249−255.
(41) Malaguarnera, M.; Di Rosa, M.; Nicoletti, F.; Malaguarnera, L. Molecular mechanisms involved in NAFLD progression. *J. Mol. Med. (Heidelberg, Germany)* **2009**, *87*, 679−695.
(42) Zelko, I. N.; Mariani, T. J.; Folz, R. J. Superoxide dismutase multigene family: a comparison of the CuZn-SOD (SOD1), Mn-SOD (SOD2), and EC-SOD (SOD3) gene structures, evolution, and expression. *Free Radical Biol. Med.* **2002**, *33*, 337−349.
(43) Niki, E.; Yoshida, Y.; Saito, Y.; Noguchi, N. Lipid peroxidation: mechanisms, inhibition, and biological effects. *Biochem. Biophys. Res. Commun.* **2005**, *338*, 668−676.
(44) Fromenty, B.; Robin, M. A.; Igoudjil, A.; Mansouri, A.; Pessayre, D. The ins and outs of mitochondrial dysfunction in NASH. *Diabetes Metab.* **2004**, *30*, 121−138.

DOI: 10.1021/acs.jafc.5b01082
J. Agric. Food Chem. 2015, 63, 6989−6998

contribute to the reported beneficial health effects in humans. Studies have shown that blueberry fruits have a positive effect on brain aging, diabetes, cancers, and vascular diseases.[23−25] To the best of our knowledge, no one has investigated the potential beneficial effects of blueberry polyphenols on periodontal disease. In the present study, we investigated the effect of a polyphenol-rich lowbush blueberry (*Vaccinium angustifolium* Ait.) extract on the growth and biofilm formation of *F. nucleatum*. We also assessed the inhibitory effect of the blueberry extract on the NF-κB signaling pathway and cytokine/MMP secretion in monocytes and macrophages.

MATERIALS AND METHODS

Plant Material. A blueberry extract (BlueCan NV Pure) prepared from the fruit of *V. angustifolium* Ait. was kindly provided by Nutra Canada (Champlain, QC, Canada). BlueCan NV Pure is a 70% ethanolic extract of whole blueberry from which sugar has been removed by passing the supernatant on an XAD-7 chromatographic column. According to the company data sheet, the total phenolic content of the extract is 40%, as determined by the Folin−Ciocalteu method.

Chemicals. The phenolic standards gallic acid, chlorogenic acid, protocatechuic acid, *p*-hydroxybenzoic acid, *p*-coumaric acid, *m*-coumaric acid, caffeic acid, ferulic acid, quercetin, quercetin 3-glucoside, kaempferol, myricetin, isorhamnetin, catechin, and epicatechin were purchased from Sigma-Aldrich Canada Co. (Oakville, ON, Canada). Delphinidin 3-glucoside was from Extrasynthèse (Lyon, France). Liquid chromatography grade solvents acetone, methanol, and acetonitrile were from EMD Millipore Canada (Mississauga, ON, Canada), and formic acid was from VWR International (Mississauga, ON, Canada). Ultrapure water was obtained using a Millipore Milli-Q water purification system (EMD Millipore Canada).

Phenolic Characterization of the Blueberry Extract. *Characterization of Anthocyanins and Procyanidins by HPLC.* Anthocyanins and procyanidins were characterized as described previously.[26] Briefly, anthocyanins were separated and analyzed by reverse-phase analytical HPLC with an Agilent 1100 series system (Agilent Technologies Canada Inc., Mississauga, ON, Canada) using the following gradient of 5% formic acid in ultrapure water (solvent A) and methanol (solvent B): 0−2 min, 5% B; 2−10 min, 5−20% B; 10−15 min, 20% B; 15−30 min, 20−25% B; 30−35 min, 25% B; 35−50 min, 25−33% B; 50−55 min, 33% B; 55−65 min, 33−36% B; 65−70 min, 36−45% B; 70−75 min, 45−53% B; 75−80 min, 53−55% B; 80−84 min, 55−70% B; 84−88 min, 70−5% B; 88−90 min, 5% B. Chromatographic data were acquired at 520 nm. Anthocyanins were quantified using an external calibration curve of delphinidin 3-glucoside standard, for which the LOD and LOQ were respectively 0.03 and 0.08 ppm. Procyanidins were separated and analyzed by normal-phase analytical HPLC using an Agilent 1260/1290 infinity system equipped with a fluorescence detector. The elution was performed using the following linear gradient of acetonitrile/acetic acid 98:2 (v/v) (solvent A) and methanol/ultrapure water/acetic acid 95:3:2 (v/v/v) (solvent B): from 0 to 40% B over 35 min, from 40 to 100% B over 5 min, 100% isocratic B for 5 min, and from 100 to 0% B over 5 min. Fluorescence was monitored at the excitation and emission wavelengths of 230 and 321 nm. Procyanidins, which eluted on the basis of their degree of polymerization, were quantified using epicatechin monomer as a standard.

Characterization of Phenolic Acids and Flavonoids by UHPLC-MS/MS. Phenolic acids and flavonoids were characterized as previously described[26] using an Acquity UHPLC-MS/MS coupled to a TQD mass spectrometer equipped with a Z-spray electrospray interface (Waters Ltd., Mississauga, ON, Canada). The phenolic acids and flavonoids were eluted using the following gradient of 0.1% formic acid in ultrapure water (solvent A) and acetonitrile (solvent B): 0−4.5 min, 5−20% B; 4.5−6.45 min, 20% B; 6.45−13.5 min, 20−45% B; 13.5−16.5 min, 45−100% B; 16.5−19.5 min, 100% B; 19.5−19.52 min, 100−5% B; 19.52−22.5 min, 5% B. The MS/MS analyses were performed in negative mode using the following electrospray source parameters: electrospray capillary voltage, 2.5 kV; source temperature, 140 °C; desolvation temperature, 350 °C; and cone and desolvation gas flows, 80 and 900 L/h, respectively. Data were acquired through multiple reaction monitoring using Waters Masslynx V4.1 software. Phenolic standards were analyzed using the same parameters and were used for the quantification.

Bacterial Strain and Growth Conditions. *F. nucleatum* ATCC 25586 was grown anaerobically (80% N_2, 10% CO_2, 10% H_2) for 24 h at 37 °C in Todd−Hewitt broth (THB; BD-Canada, Mississauga, ON, Canada) supplemented with 0.001% hemin and 0.0001% vitamin K.

Determination of Minimal Inhibitory and Minimal Bactericidal Concentrations. A microplate dilution assay was used to determine the minimal inhibitory concentration (MIC) and minimal bactericidal concentration (MBC) values of the blueberry extract against *F. nucleatum*. To determine the MIC, a 24 h culture of *F. nucleatum* was diluted in fresh culture medium to obtain an optical density of 0.2 at 660 nm (OD_{660}). Equal volumes (100 μL) of bacterial suspension and serial dilutions of the blueberry extract (from 1000 to 15.63 μg/mL) in culture medium were added to the wells of 96-well plates. Wells with no *F. nucleatum* or no blueberry extract were used as controls, whereas tetracycline was used as a reference antibiotic. After a 48 h incubation at 37 °C under anaerobic conditions, bacterial growth was monitored by recording the OD_{660} using a Synergy 2 microplate reader (BioTek Instruments, Winooski, VT, USA). The MIC value was the lowest concentration of the blueberry extract that completely inhibited the growth of *F. nucleatum*. To determine the MBC, 5 μL aliquots from the wells with no visible growth were spread on sheep blood-supplemented THB agar plates, which were incubated for 3 days at 37 °C. The MBC value was the lowest concentration at which no colony formation occurred. All assays were performed in triplicate to ensure reproducibility.

Determination of Siderophore Activity. The universal siderophore assay of Schwyn and Neils[27] was used to measure the iron-chelating activity of the blueberry extract. Ferrichrome (Sigma-Aldrich Canada Ltd.), a siderophore produced by *Ustilago sphaerogena*, was used as the positive control.[28]

Effect of the Blueberry Extract on Biofilm Formation. *Microplate Assay. F. nucleatum* was grown for 48 h under anaerobic conditions in the absence or presence of the blueberry extract (from 1000 to 15.63 μg/mL) as described above. The medium containing free-floating bacteria was removed by aspiration using a 26G needle. Then, the wells were washed three times with distilled water, and the biofilms were stained with 100 μL of 0.05% crystal violet. After a 15 min incubation, the wells were washed three times with distilled water and were dried for 2 h at 37 °C. Ethanol [100 μL, 95% (v/v)] was added to each well, and the plate was shaken for 10 min to release the dye from the biofilms. The absorbance at 550 nm (A_{550}) was recorded.

Scanning Electron Microscopy. The effect of the blueberry extract on *F. nucleatum* biofilm formation was also examined by scanning electron microscopy. One milliliter of *F. nucleatum* suspended to an OD_{660} of 0.2 in culture medium, with (62.5, 125, 250, or 500 μg/mL) or without the blueberry extract, was added to the wells of a 12-well plate containing a 13 mm diameter plastic coverslip. After a 48 h incubation under anaerobiosis, the medium and free-floating bacteria were removed by aspiration, and the plastic coverslips were washed twice with 0.1 M cacodylate buffer (pH 7.2). The biofilm-coated coverslips were incubated for 3 h in fixation buffer [2.5% (w/v) glutaraldehyde (grade I) and 1 mM $CaCl_2$ in 0.1 M cacodylate buffer, pH 7.2], washed three times (20 min each time) with 0.1 M cacodylate buffer (pH 7.2), and postfixed for 90 min at room temperature in 1% (w/v) osmic acid containing 2 mM potassium ferrocyanide and 6% (w/v) sucrose in cacodylate buffer. Samples were dehydrated using a graded series of ethanol (50, 70, 95, 100%), critical point-dried, gold-sputtered, and examined using a JEOL JSM6360LV scanning electron microscope operating at 30 kV.

Determination of Quorum Sensing Inhibitory Activity. The bioluminescence assay using the reporter strain *Vibrio harveyi* BB170 (ATCC BAA-1117) was performed as previously described.[29] *V. harveyi* BB120 (ATCC BAA-1116) was grown overnight in auto-

DOI: 10.1021/acs.jafc.5b01525
J. Agric. Food Chem. 2015, 63, 6999−7008

inducer bioassay (AB) medium at 30 °C with agitation and was then diluted 1:100 in fresh culture medium containing the blueberry extract at concentrations (31.25, 62.5, 125, 250 μg/mL) that did not interfere with the bacterial growth (data not shown). After a 16 h incubation at 30 °C, the supernatant was recovered by centrifugation at 10000*g* for 10 min, filter-sterilized (0.22 μm), and stored at −80 °C. The presence of autoinducer-2 (AI-2) was then assayed by adding 20 μL of cell-free supernatant from each test sample to the wells of a 96-well, clear bottom, black wall microplate. An overnight culture of *V. harveyi* BB170 diluted 1:5000 (180 μL) was added to each well containing a supernatant sample. The positive control consisted of 20 μL of cell-free supernatant from *V. harveyi* BB120 grown in the absence of blueberry extract, whereas the negative control consisted of AB medium. The plate was incubated for 15 h in a Synergy 2 microplate reader at 30 °C with agitation (200 rpm). The bioluminescence and OD_{660} were measured every 15 min during the incubation.

Effect of the Blueberry Extract on the Activation of the NF-κB Transcription Factor. The human monoblastic leukemia cell line U937 3xκB-LUC, a subclone of the U937 cell line stably transfected with a luciferase gene coupled to a promoter of three NF-κB-binding sites, was kindly provided by Dr. Rune Blomhoff (University of Oslo, Norway).[30] Cells were routinely cultivated in Roswell Park Memorial Institute 1640 medium (RPMI-1640; Life Technologies Inc., Burlington, ON, Canada) supplemented with 10% heat-inactivated fetal bovine serum (FBS), 100 μg/mL penicillin G/streptomycin, and 75 μg/mL hygromycin B at 37 °C in a 5% CO_2 atmosphere. First, the effect of the blueberry extract at concentrations ≤500 μg/mL on U937 3xκB-LUC viability was determined using a 3-(4,5-diethylthiazol-2-yl)-2,5-diphenyltetrazolim bromide (MTT) assay, according to the manufacturer's instructions (Roche Diagnostics, Laval, QC, Canada). Briefly, U937 3xκB-LUC cells were treated with the blueberry extract for 6.5 h prior to monitoring viability. To induce activation of the NF-κB transcription factor, the U937 3xκB-LUC cells (10^6 cells/well) were placed in the wells of a 96-well black bottom microplate (Greiner Bio-One North America Inc., Monroe, NC, USA) and were stimulated for 6 h (optimal activation based on preliminary assays) with *F. nucleatum* cells at a multiplicity of infection (MOI) of 2, 10, 50, or 100. To assess the effect of the blueberry extract on the pro-inflammatory potential of *F. nucleatum*, an overnight culture was pre-incubated with various concentrations of the blueberry extract (31.25−250 μg/mL) for 30 min with shaking. The *F. nucleatum* cells were then harvested by centrifugation (10000*g* for 10 min), washed three times, and suspended in RPMI supplemented with 1% FBS. They were then added to wells containing U937 3xκB-LUC cells at an MOI of 100. Finally, to investigate the effect of the blueberry extract on *F. nucleatum*-induced NF-κB activation, U937 3xκB-LUC cells were pre-incubated with the extract (15.6−500 μg/mL; in RPMI containing 1% FBS) for 30 min and were then stimulated for 6 h with bacteria at an MOI of 100. Wells with no *F. nucleatum* or no blueberry extract were used as controls to measure basal NF-κB activity. Assays using a commercial inhibitor (BAY-11-7082; 25 μM; EMD Millipore Canada) were used as negative control of the NF-κB signaling pathway. NF-κB activation was determined by measuring luciferase activity following the addition of Bright-Glo reagent (Promega Corp., Madison, WI, USA) in accordance with the manufacturer's protocol. Luminescence was monitored using a Synergy 2 microplate reader.

Effect of the Blueberry Extract on Cytokine and MMP Secretion by Macrophages. U937 human monocytes (ATCC CRL-1593.2) from the American Type Culture Collection (Manassas, VA, USA) were cultivated in RPMI-1640 supplemented with 10% FBS and 100 μg/mL penicillin G/streptomycin at 37 °C in a 5% CO_2 atmosphere. The monocytes (2.5×10^5 cells/mL) were then incubated in RPMI−10% FBS containing 100 ng/mL phorbol-12-myristate-13-acetate (PMA; Sigma-Aldrich Canada Ltd.) for 48 h to induce differentiation into adherent macrophage-like cells.[31] Adherent macrophage-like cells were harvested by scraping and were centrifuged at 1200*g* for 5 min. The cells were washed, suspended in RPMI−1% FBS at a concentration of 1×10^6 cells/mL, seeded into the wells of a 12-well microplate (1×10^6 cells/well), and incubated overnight at 37 °C in a 5% CO_2 atmosphere. The macrophage-like cells were treated with the blueberry extract (62.5−500 μg/mL) for 2 h. They were then stimulated with *F. nucleatum* at an MOI of 100. After a 24 h incubation at 37 °C in a 5% CO_2 atmosphere, the culture medium supernatants were collected and stored at −20 °C until used. Cells incubated in culture medium with or without the blueberry extract and stimulated or not with bacteria were used as controls. Enzyme-linked immunosorbent assay (ELISA) kits (eBioscience Inc., San Diego, CA, USA) were used to quantify IL-1β, IL-6, CXCL8, TNF-α, MMP-8, and MMP-9 concentrations according to the manufacturer's protocols. To exclude the possibility that cell toxicity due to the blueberry extract might have been responsible for a decrease in cytokine and MMP levels, the viability of the blueberry extract-treated macrophages was assessed using an MTT test and by Trypan blue exclusion.

Effect of the Blueberry Extract on MMP-9 Activity. Human recombinant MMP-9 (active form) purchased from AnaSpec (Fremont, CA, USA) was diluted in reaction buffer (300 mM NaCl, 50 mM Tris-HCl, 5 mM $CaCl_2$, 20 μM $ZnCl_2$, pH 7.5) to a final concentration of 50 ng/mL and was incubated for 4 h in the absence or presence of the blueberry extract (7.9−500 μg/mL) and the fluorogenic substrate Gelatin DQ (Molecular Probes, Eugene, OR, USA) at a concentration of 100 μg/mL. The fluorogenic substrate alone or with blueberry extract was used as control. An assay using a specific inhibitor of MMP (1 μM, GM6001; Calbiochem, San Diego, CA, USA) was also performed. The assay mixtures were incubated in the dark for 2 h at 37 °C. The fluorescence was measured using a fluorometer with excitation and emission wavelengths set at 495 and 525 nm, respectively. Two independent assays performed in triplicate were performed.

Statistical Analysis. Unless indicated otherwise, all experiments were performed in triplicate. The data are expressed as means ± standard deviations (SD). Statistical analyses were performed using a one-way analysis of variance with a post hoc Bonferroni multiple-comparison test (GraphPad Software Inc., La Jolla, CA, USA). All results were considered statistically significant at $p < 0.001$ or $p < 0.05$.

RESULTS

Phenolic Composition of the Blueberry Extract. The phenolic composition of the blueberry extract is presented in detail in Table S1. Phenolic acids, flavonoids (flavonols, anthocyanins, flavan-3-ols), and procyanidins made up 16.6, 12.9, and 2.7% of the blueberry extract, respectively. Chlorogenic acid (67%) was the most abundant phenolic acid, whereas flavonols and anthocyanins accounted for 99% of the total flavonoids, and quercetin and its sugar-conjugated derivatives accounted for 98% of the flavonols. The procyanidin content was mostly monomers, dimers, and polymers with a degree of polymerization >10.

Antibacterial and Antibiofilm Properties of the Blueberry Extract. The ability of the blueberry extract to interfere with the growth of *F. nucleatum* was assessed first. The MIC of the blueberry extract against *F. nucleatum* was 1 mg/mL (Figure 1). This concentration also corresponded to the MBC. The blueberry extract at a concentration of 500 μg/mL reduced the growth of *F. nucleatum* by 29.9 ± 12.3%, whereas it had no growth inhibitory effect at concentrations ≤250 μg/mL. Tetracycline used as a reference antibiotic showed a MIC of 0.39 μg/mL and a MBC of 1.56 μg/mL (data not shown). To identify the mechanism by which the blueberry extract exerted its antimicrobial activity against *F. nucleatum*, we investigated its ability to chelate iron. The blueberry extract dose-dependently chelated iron in a universal siderophore assay (Figure 2). This activity was comparable to that of ferrichrome, the positive control, a siderophore produced by *U. sphaerogena*.

We then tested the effect of the blueberry extract on biofilm formation by *F. nucleatum* (Figure 1). Blueberry extract

DOI: 10.1021/acs.jafc.5b01525
J. Agric. Food Chem. 2015, 63, 6999−7008

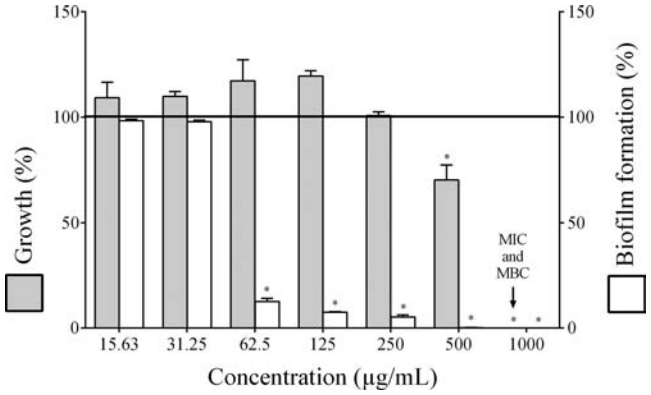

Figure 1. Effect of the blueberry extract on *F. nucleatum* growth and biofilm formation. A value of 100% was assigned to growth and biofilm formation in the absence of the blueberry extract. Results are expressed as the means ± SD of triplicate assays from two independent experiments. (∗) Significantly different from the control ($p < 0.001$).

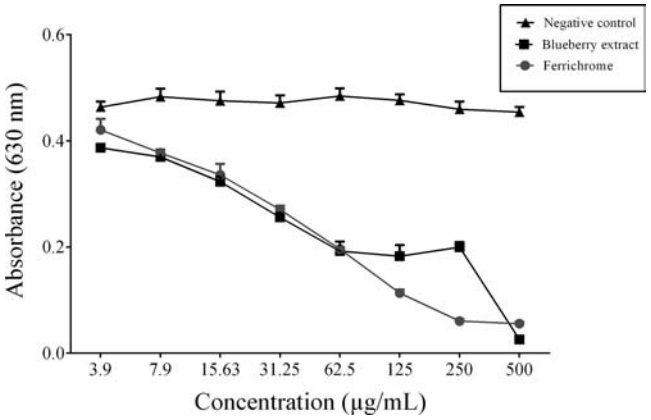

Figure 2. Iron-chelating activity of the blueberry extract determined using a chrome azurol sulfate colorimetric assay. A reduction in A_{630} values occurs when a strong chelator removes the iron from the chrome azurol dye. Ferrichrome, a siderophore produced by *U. sphaerogena*, was used as positive control. Results are expressed as the means ± SD of triplicate assays from two independent experiments. (∗) Significantly different from the control ($p < 0.05$).

concentrations ranging from 500 to 62.5 μg/mL had a significant effect on biofilm formation. More specifically, 62.5 μg/mL of the blueberry extract, which did not reduce the growth of *F. nucleatum*, inhibited biofilm formation by 87.5 ± 2.3%. The effect of the blueberry extract on biofilm formation by *F. nucleatum* was visualized by scanning electron microscopy. Electron micrographs clearly showed that there was a marked reduction in mature biofilm and that the architecture was disrupted when *F. nucleatum* was grown in the presence of the blueberry extract (Figure 3).

Given that the blueberry extract reduced biofilm formation by *F. nucleatum*, we then investigated the quorum sensing inhibitory activity of the blueberry extract. *V. harveyi* BB120 was grown in the presence of various concentrations of blueberry extract, and the supernatants were then collected. The levels of secreted AI-2 were determined by monitoring bioluminescence using the reporter strain *V. harveyi* BB170. The blueberry extract dose-dependently inhibited AI-2-mediated bioluminescence (Figure 4). Quorum sensing activity was inhibited at concentrations that had no effect on the growth of *V. harveyi* BB120 (data not shown).

Effect of the Blueberry Extract on NF-κB Activation in Monocytes. We first showed that *F. nucleatum* dose-dependently activates the NF-κB transcription factor, as indicated by the increase in luciferase activity (Figure S1). The strongest activity was obtained with an MOI of 100. A 30 min pre-incubation of bacterial cells (MOI = 100) with the blueberry extract reduced the ability of *F. nucleatum* to activate the NF-κB pathway (Figure 5). More specifically, 250 and 125 μg/mL of the blueberry extract decreased NF-κB activation by 33.19 ± 7.48 and 17.46 ± 0.32%, respectively.

We then determined whether the presence of blueberry extract prevented *F. nucleatum*-induced NF-κB activation in U937-3xκB cells. The blueberry extract dose-dependently inhibited the activation of NF-κB induced by *F. nucleatum* at an MOI of 100 (Figure 6). More specifically, 250, 125, 62.5, and 31.25 μg/mL of the blueberry extract reduced NF-κB activity by 97 ± 0.56, 88.6 ± 0.9, 68.8 ± 5.7, and 48.5 ± 2%, respectively. As expected, the commercial inhibitor BAY-11-7082 (25 μM) completely prevented NF-κB activation. The blueberry extract alone (in the absence of *F. nucleatum*) was not cytotoxic and had no effect on NF-κB activity (data not shown).

Effect of the Blueberry Extract on Cytokine and MMP Secretion by Macrophages. We used a macrophage-like model (PMA-treated U937 cells) stimulated with *F. nucleatum* to determine whether the ability of the blueberry extract to attenuate NF-κB activation in U937-3xκB cells also reduced inflammatory mediator secretion. Adherent macrophage-like cells were pretreated for 2 h with the blueberry extract and were then stimulated for 48 h with *F. nucleatum* (MOI = 100). We then measured the secretion of cytokines (IL-6, IL-1β, TNF-α, CXCL8) and MMPs (MMP-8, MMP-9) by the adherent macrophage-like cells. Using an MTT test and by Trypan blue exclusion, the blueberry extract displayed no cytotoxicity and had no effect on cell viability, which was ≥98 ± 6.8% for all concentrations tested compared to the untreated controls (data not shown). Therefore, a decrease in cytokine and MMP levels cannot result from loss of cell viability. *F. nucleatum* significantly increased the secretion of IL-6 (234.6 fold), IL-1β (5.2-fold), TNF-α (215-fold), CXCL8 (6.2-fold), MMP-8 (1.8-fold), and MMP-9 (1.3-fold) by macrophages (Figures 7 and 8). The secretion of pro-inflammatory cytokines (IL-1β, IL-6, TNF-α) by macrophages stimulated with *F. nucleatum* was significantly and dose-dependently attenuated by the blueberry extract compared to control cells. At a concentration of 62.5 μg/mL, the blueberry extract reduced the secretion of IL-1β by 87.3 ± 1.3% (Figure 7A), that of TNF-α by 80.7 ± 5.6% (Figure 7B), and that of IL-6 by 28.2 ± 9.3% (Figure 7C). Whereas the secretion of the chemokine CXCL8 was not affected by 62.5 μg/mL of the blueberry extract, 500, 250, or 125 μg/mL of the blueberry extract decreased CXCL8 secretion by 79 ± 6.3, 57.9 ± 0.2, and 11.2 ± 0.3%, respectively (Figure 7D). Treating the cells with the highest concentration of the blueberry extract (500 μg/mL) decreased IL-1β, TNF-α IL-6, and CXCL8 secretions to the same degree as the commercial inhibitor (Figure 7). The blueberry extract in the absence of *F. nucleatum* had no effect on the basal levels of secreted cytokine (data not shown). Finally, MMP-8 and MMP-9 secretion by *F. nucleatum*-stimulated macrophages was also attenuated by the blueberry extract, in some cases below basal levels. More specifically, 500, 250, and 125 μg/mL of the blueberry extract reduced the secretion of MMP-8 by 67.7 ± 0.4, 66.9 ± 0.4, and 60.2 ±

DOI: 10.1021/acs.jafc.5b01525
J. Agric. Food Chem. 2015, 63, 6999−7008

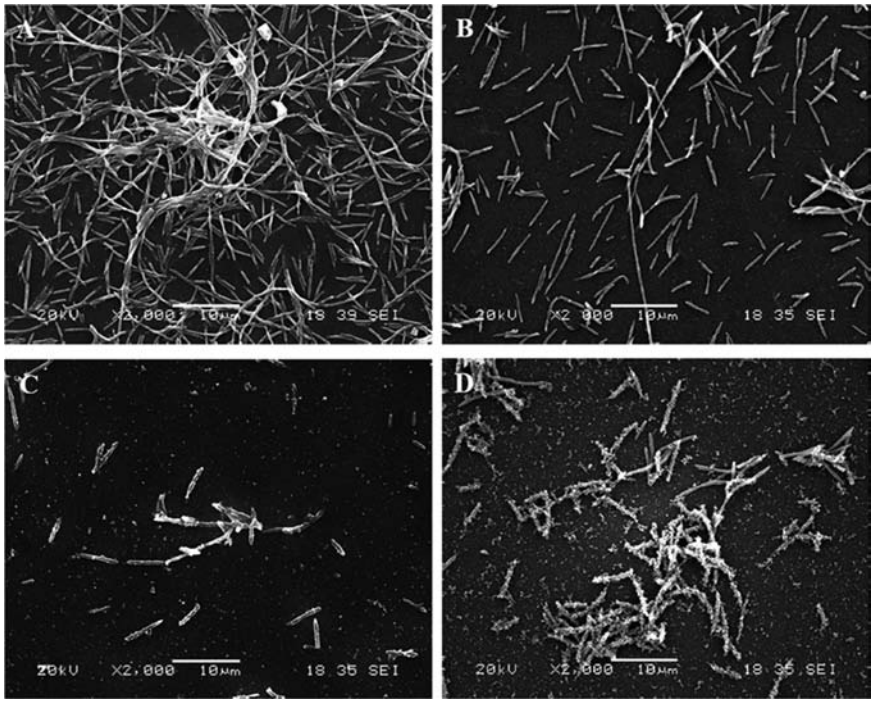

Figure 3. Scanning electron micrographs of *F. nucleatum* biofilms: (A) control biofilm (no blueberry extract); biofilm formed in the presence of (B) 62.5 μg/mL, (C) 250 μg/mL, and (D) 500 μg/mL of the blueberry extract.

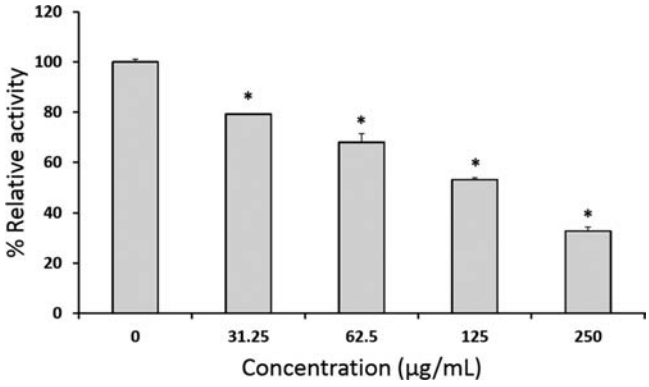

Figure 4. Effect of the blueberry extract on the production of AI-2 by *V. harveyi* BB120 as determined using the reporter strain *V. harveyi* BB170. (∗) Significantly different from the control ($p < 0.001$).

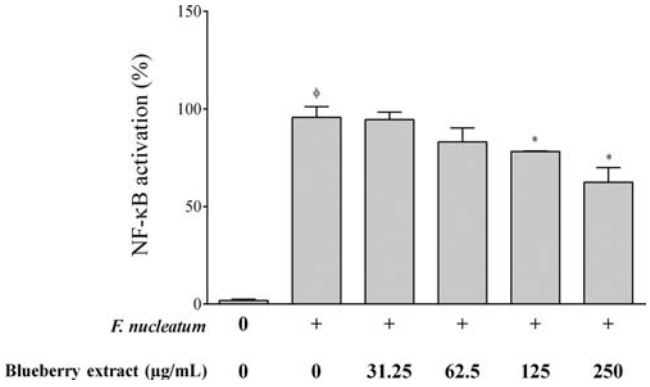

Figure 5. Effect of pre-incubating *F. nucleatum* with the blueberry extract on NF-κB activation using the U937-3xκB cell model. A value of 100% was assigned to the activation obtained after a 6 h incubation in the absence of the blueberry extract. Results are expressed as the means ± SD of triplicate assays from three independent experiments. (ϕ) Significant increase ($p < 0.001$) compared to nonstimulated control cells. (∗) Significant decrease ($p < 0.001$) compared to *F. nucleatum*-stimulated cells not treated with the blueberry extract.

0.2%, respectively, and the secretion of MMP-9 by 93.0 ± 2.24, 62.7 ± 1.7, and 26.7 ± 7.8%, respectively (Figure 8).

Effect of the Blueberry Extract on MMP-9 Activity. After demonstrating that the blueberry extract can decrease MMP-9 secretion in a macrophage model, we evaluated its effect on the gelatinase activity of MMP-9. As reported in Table 1, the blueberry extract at 500, 250, and 125 μg/mL reduced MMP-9 activity by 99.7 ± 1.8, 82.6 ± 2.4, and 56.7 ± 5.5%, respectively.

DISCUSSION

Conventional periodontal treatments rely primarily on removing the subgingival dental biofilm that modulates the host inflammatory response associated with periodontal tissue destruction. Whereas physical removal of the biofilm by scaling and root planing is usually sufficient to reverse the progression of the disease, adjunctive treatments, such as antibiotics, are occasionally required. Over the past two decades, natural compounds exhibiting both antibacterial and anti-inflammatory properties have received considerable attention as potential new therapeutic agents for the prevention and treatment of periodontal infections.[32] Blueberries are mainly native to North America and are recognized for their health benefits.[23,24] There are two main commercial species of blueberries: highbush (*Vaccinium corymbosum* L.) and lowbush (*V. angustifolium* Ait.). Lowbush blueberries, also known as wild blueberries, are often harvested from wild patches and are endemic to the boreal forests. They are smaller in size than *V. corymbosum* L. and have a distinct intense flavor and aroma. Lowbush blueberries are also grown commercially, especially in Maine, Atlantic Canada, and Quebec. Many studies have reported that blueberries

DOI: 10.1021/acs.jafc.5b01525
J. Agric. Food Chem. 2015, 63, 6999−7008

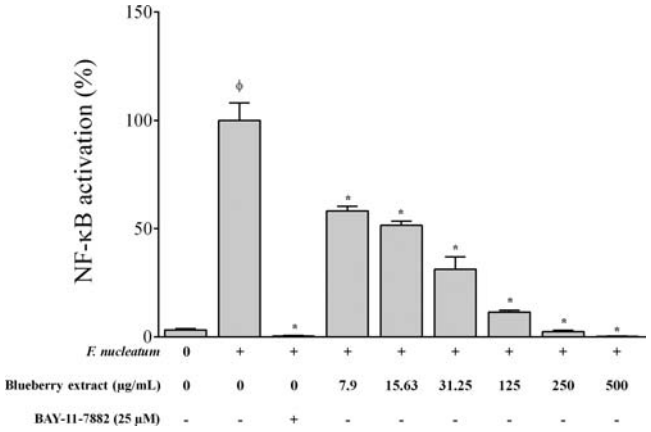

Figure 6. Effect of the blueberry extract on *F. nucleatum*-mediated activation of the NF-κB signaling pathway using the U937-3xκB cell model. A value of 100% was assigned to the activation obtained with *F. nucleatum* (MOI = 100 for 6 h) in the absence of the blueberry extract. The commercial inhibitor BAY-11-7082 (25 μM) was used as a positive inhibitory control. Results are expressed as the means ± SD of triplicate assays from three independent experiments. (ϕ) Significant increase ($p < 0.001$) compared to nonstimulated control cells. (∗) Significant decrease ($p < 0.001$) compared to *F. nucleatum*-stimulated cells not treated with the blueberry extract.

contain health-promoting compounds, including phenolic acids and flavonoids such as chlorogenic acid, ellagic acid, quercetin, anthocyanins, and procyanidins, which account for their pronounced antioxidant, anti-inflammatory, and immunomodulatory properties.[33,34] The blueberry extract used in our study was particularly rich in a variety of polyphenols and more specifically chlorogenic acid and flavonols, as well as monomers, dimers, and polymers of procyanidins. Given that blueberry polyphenols are potential candidates for the prevention and treatment of periodontal diseases, the present study was aimed at investigating the effects of a lowbush blueberry extract (*V. angustifolium* Ait.) on various aspects of the etiopathogenesis of periodontitis.

On the basis of our previous studies showing that cranberry proanthocyanidins interfere with the pathogenic properties of periodontopathogens,[35] we hypothesized that blueberry polyphenols may have a beneficial effect on periodontal diseases by attenuating the growth and pathogenic properties of *F. nucleatum*, a bacterial species that has been associated with various forms of the disease. The blueberry extract displayed potent antibacterial activity against *F. nucleatum*, with MIC and MBC values of 1 mg/mL. This finding was consistent with previous studies by Lacombe et al., who reported that North American lowbush blueberry polyphenols exhibit marked antibacterial effects against Gram-negative bacteria, including *E. coli* 157:H7, and foodborne pathogens.[36] Blueberry

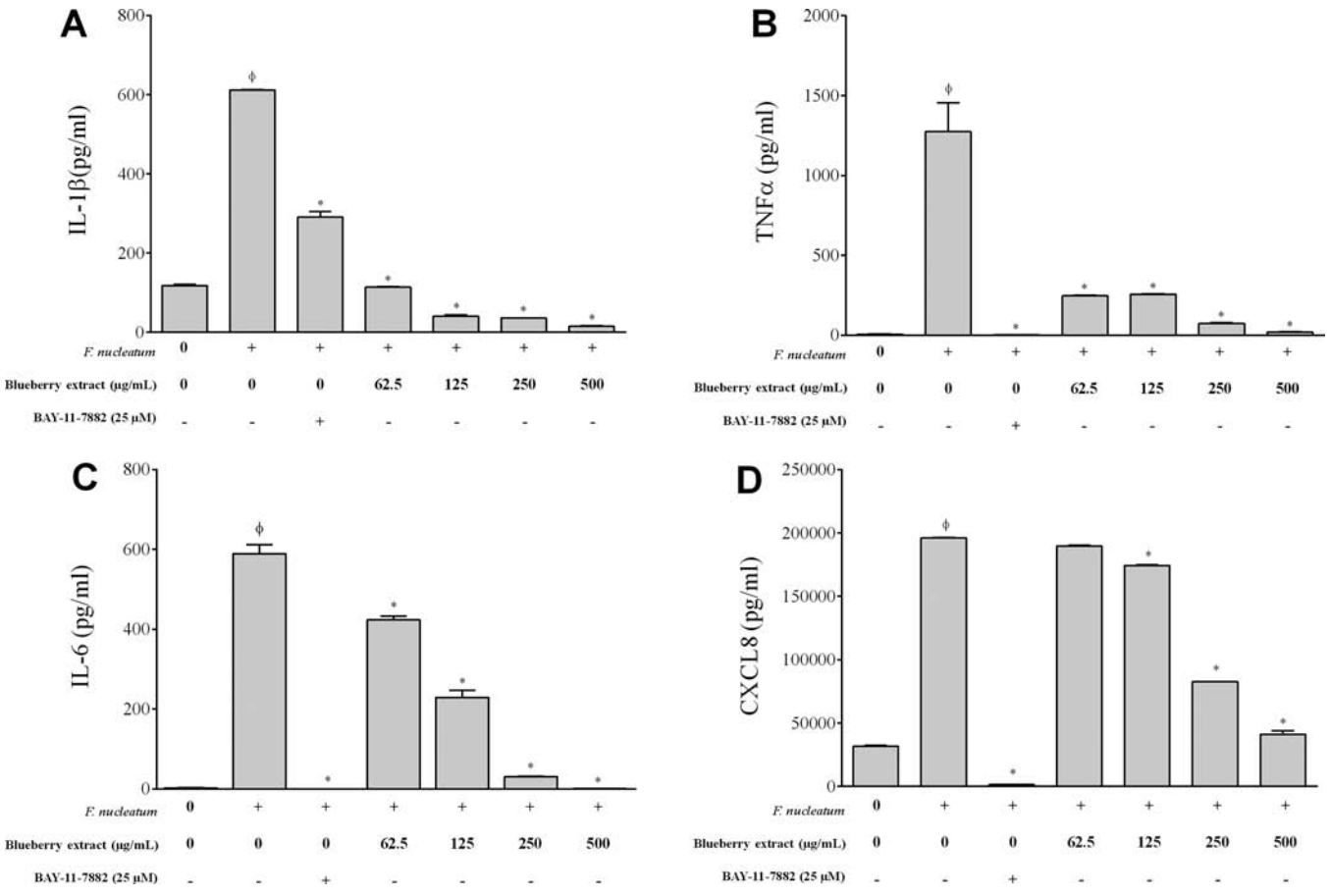

Figure 7. Effect of the blueberry extract on the secretion of (A) IL-1β, (B) TNF-α, (C) IL-6, and (D) CXCL8 by macrophages stimulated with *F. nucleatum* (MOI = 100 for 24 h). The commercial inhibitor BAY-11-7082 (25 μM) was used as a positive inhibitory control. Results are expressed as the means ± SD of triplicate assays from three independent experiments. (ϕ) Significant increase ($p < 0.001$) compared to nonstimulated control cells. (∗) Significant decrease ($p < 0.001$) compared to *F. nucleatum*-stimulated cells not treated with the blueberry extract.

DOI: 10.1021/acs.jafc.5b01525
J. Agric. Food Chem. 2015, 63, 6999−7008

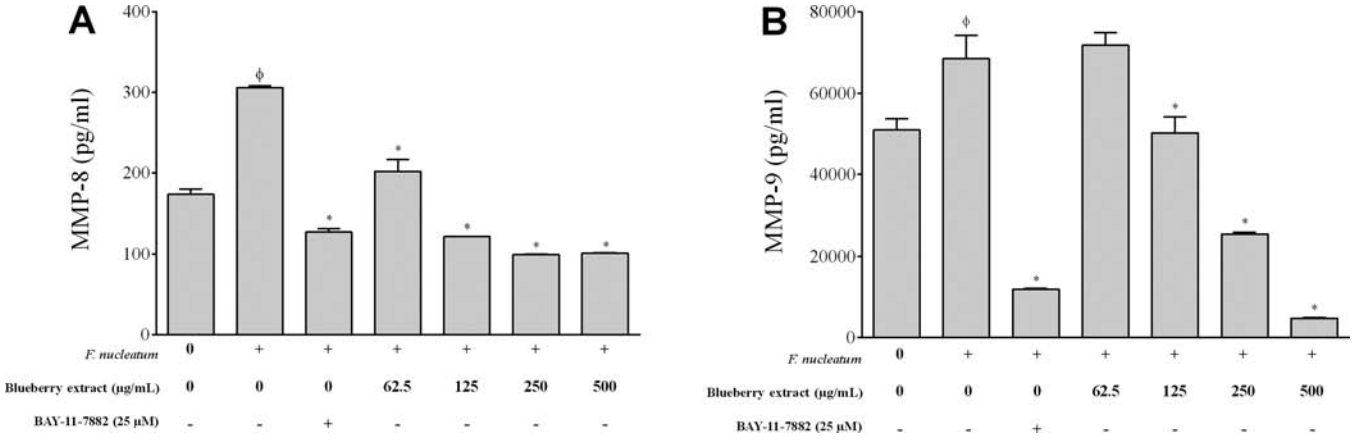

Figure 8. Effect of the blueberry extract on the secretion of (A) MMP-8 and (B) MMP-9 by macrophage-like cells stimulated with *F. nucleatum* (MOI = 100). The commercial inhibitor BAY-11-7082 was used as a positive inhibitory control. Results are expressed as the means ± SD of triplicate assays from three independent experiments. (ϕ) Significant increase ($p < 0.001$) compared to nonstimulated control cells. (*) Significant decrease ($p < 0.001$) compared to *F. nucleatum*-stimulated cells not treated with the blueberry extract.

Table 1. Effect of Blueberry Extract on the Activity of MMP-9

compound	MMP-9 (% activity)
none	100 ± 8.9
commercial inhibitor[a]	20.9 ± 9.4
blueberry extract (μg/mL)	
500	0.3 ± 1.8
250	17.4 ± 2.4
125	43.3 ± 5.5
62.5	49.1 ± 7.3
31.25	56.3 ± 11.8
15.62	59.8 ± 3.9
7.9	66.0 ± 4.9

[a]GM6001 (1 μM).

polyphenols may alter the bacterial membrane by destabilizing the LPS and increasing the efflux of ATP from the cytoplasm.[37] Moreover, anthocyanins, phenolic acids (caffeic acid, chlorogenic acid, protocatechuic acid), and quercetin, which were present in our blueberry extract, have been associated with antibacterial and membrane permeabilizing activities.[38] In the present study, we showed that blueberry polyphenols possess marked iron-chelating activity, which may be another antimicrobial mechanism. Indeed, by chelating iron, which is an essential cofactor for bacterial growth, blueberry polyphenols may compete with bacteria for iron, creating an iron-deficient, bacteriostatic environment. Interestingly, Dastmalchi et al. investigated the antioxidative properties of a variety of edible neotropical blueberries and identified iron-chelating activity in some varieties of blueberry, although they did not test the lowbush blueberry.[39] Because the ferrous form of iron is responsible for the formation of reactive oxygen species (ROS), this iron-scavenging property may contribute to the antioxidative activity of blueberry polyphenols.[40] Moreover, given that ROS are known to activate MMPs, the iron-chelating property of blueberry polyphenols may also contribute to decreasing proteolytic activity in diseased periodontal sites.

Because *F. nucleatum* plays a critical role in subgingival biofilm formation by bridging early and late colonizers, we investigated the antibiofilm activity of the blueberry extract using concentrations that did not inhibit bacterial growth. On the basis of the results of a colorimetric microplate assay, the blueberry extract almost completely prevented *F. nucleatum* biofilm formation at concentrations as low as 62.5 μg/mL. The antibiofilm activity of the blueberry extract was confirmed by scanning electron microscopy. The above observations suggest that the blueberry extract may inhibit the attachment and maturation of periodontal biofilms through dynamic and sequential processes. This may help prevent or slow periodontal disease initiation and progression because biofilms, which are structured microbial communities attached to oral surfaces, enable bacteria to evade immune defenses, resist mechanical removal, and avoid chemotherapeutic agents. In addition, the blueberry extract disrupted biofilm formation, a major virulence property of *F. nucleatum*, at concentrations that were not antibacterial, indicating that bacteria may not develop resistance to bioactive molecules in blueberry extracts. Zimmer et al. studied hydroethanolic extracts of blueberries from various *Vaccinium virgatum* cultivars and reported that the caffeic and chlorogenic acids in the extracts were likely responsible for the inhibition of biofilm formation by *Staphylococcus epidermidis* and *Pseudomonas aeruginosa*, two major human bacterial pathogens.[41] These two compounds were also present in our blueberry extract.

Given the fact that blueberry polyphenols interfere with biofilm formation by *F. nucleatum*, we hypothesized that the blueberry extract might also possess antiquorum sensing activity. Quorum sensing refers to the coordinated regulation of virulence gene expression modulated by cell density. Using the *V. harveyi* quorum sensing model, we showed that the blueberry extract attenuated AI-2-mediated cell−cell signaling. Such an attenuation of bacterial virulence by the inhibition of quorum sensing has been suggested be a promising strategy for reducing antibiotic use.[42]

Although the colonization of subgingival sites and subsequent biofilm formation by periodontopathogens such as *F. nucleatum* is the initial step in the pathogenesis of periodontitis,[2] the host immune response, which results in the overproduction of a large variety of inflammatory mediators involved in tissue and bone destruction, is critical.[8−11] Given that polyphenols have anti-inflammatory properties that contribute to the human health benefits of berries,[43] we thus investigated the effect of the blueberry extract on the inflammatory response of host cells. Macrophages are major immune cells involved in the continuous and excessive host

DOI: 10.1021/acs.jafc.5b01525
J. Agric. Food Chem. 2015, 63, 6999−7008

responses that result in the secretion of large amounts of pro-inflammatory cytokines, chemokines, and MMPs, which in turn are involved in tissue and bone destructive processes.[7] In the present study, we showed that lowbush blueberry polyphenols significantly reduce the secretion of IL-1β, TNF-α, IL-6, and CXCL8 by *F. nucleatum*-stimulated macrophages. These results are in agreement with those of Kang et al.,[20] who showed that two phenolic acid extracts prepared from lowbush blueberries and highbush blueberries reduced the production of IL-6 and TNF-α by LPS-stimulated macrophages and that the anti-inflammatory activity of the lowbush extract was greater than that of the highbush extract. They also provided evidence that the decreased production of IL-6 and TNF-α was associated with the inhibition of the NF-κB signaling pathway and that chlorogenic acid (67% of all phenolic acids in our blueberry extract) was likely the main contributor to the anti-inflammatory property of blueberries.[20] Ruifeng et al.[44] reported that chlorogenic acid inhibits the TLR4-mediated and LPS-induced NF-κB signaling pathway and reduces the secretion of the pro-inflammatory cytokines TNF-α, IL-1β, and IL-6 involved in mastitis. Cheng et al. provided proof that blueberry anthocyanins (petunidin, peonidin, malvidin, and cyanidin) inhibit the expression of IL-1β, IL-6, and IL-12 genes in LPS-stimulated RAW264 macrophages, a further indication that blueberry extracts possess anti-inflammatory activity.[45]

Inhibitors of the NF-κB transcription factor hold great promise for the prevention and treatment of chronic inflammatory disorders.[46] Plant polyphenols act on host cells by activating or inhibiting various cell signaling pathways by, for example, modulating kinase activity and activating the NF-κB transcription factor.[43] The mechanism by which the blueberry extract used in the present study reduced inflammatory mediator secretion may be related to its capacity to block NF-κB activation because this signaling pathway is central to the inflammatory response.[43] Using the U937-3xκB cell model, we showed that the blueberry extract inhibited NF-κB activation induced by *F. nucleatum*, most likely its cell surface LPS. Whereas the exact bioactive molecule in our blueberry extract has not been identified, anthocyanins, which made up 23% of the total polyphenolic content of the extract, may be involved. Indeed, Taverniti et al.[34] previously reported that an anthocyanin-rich lowbush blueberry extract reduced IL-1β-induced NF-κB activation in Caco-2 epithelial cells. In addition, cranberry proanthocyanidins reduce the LPS-induced inflammatory response in oral epithelial cells via the NF-κB pathway.[47]

MMP-9 and MMP-8 have been strongly associated with the progression of periodontitis.[48] Interestingly, we showed that our blueberry extract reduced MMP-8 and MMP-9 secretion by *F. nucleatum*-stimulated macrophages. This result was in agreement with those of a previous study by Matchett et al.,[49] who reported that lowbush blueberry anthocyanins and proanthocyanidins down-regulate MMP-2 and MMP-9 activities in the DU-145 prostate tumor model and increase the expression of tissue inhibitors of metalloproteinases 1 (TIMP-1). Matchett et al. suggested that this effect was mainly due to proanthocyanidins and that it involved the protein kinase C (PKC) and mitogen-activated protein kinase pathways.[49] In addition to attenuating MMP-8 and MMP-9 secretion by macrophages, we also showed that the blueberry extract inhibits the catalytic activity of MMP-9 (gelatinase-2). Because MMPs are associated with periodontal tissue destruction, our results suggested that blueberry polyphenols may contribute to reducing host cell damage, including bone resorption. Interestingly, Zhang et al.[50] reported that feeding rats a blueberry diet inhibits bone resorption through suppression of receptor activator of nuclear factor-κB ligand (RANKL).

In conclusion, we showed that polyphenols in a lowbush blueberry extract are active against the two main etiologic components of periodontitis. On the one hand, the blueberry extract inhibited the growth and biofilm formation of the periodontopathogenic bacterium *F. nucleatum*. On the other, it reduced the secretion of cytokines and MMPs by macrophages by blocking the activation of the NF-κB signaling pathway. This dual action of lowbush blueberry polyphenols suggests that they may be promising candidates for novel therapeutic agents.

■ ASSOCIATED CONTENT

Supporting Information

The Supporting Information is available free of charge on the ACS Publications website at DOI: 10.1021/acs.jafc.5b01525.

Detailed phenolic composition of the blueberry extract (PDF)

Effect of *F. nucleatum* on NF-κB activation using the U937-3xκB cell model (PDF)

■ AUTHOR INFORMATION

Corresponding Author

*(D.G.) Mail: Oral Ecology Research Group, Faculty of Dentistry, Université Laval, 2420 rue de la Terrasse, Quebec City, QC, Canada G1V 0A6. Phone: (418) 656-7341. Fax: (418) 656-2861. E-mail: Daniel.Grenier@greb.ulaval.ca.

Funding

This study was supported by the Laboratoire de Contrôle Microbiologique de l'Université Laval.

Notes

The authors declare no competing financial interest.

■ ACKNOWLEDGMENTS

We are grateful to Nutra Canada (Champlain, QC, Canada) for providing the blueberry extract and to R. Blomhoff and H. Carlsen (University of Oslo, Norway) for providing the U937-3xκB-LUC cell line. We thank G. LeBel for technical assistance.

■ REFERENCES

(1) Eke, P. I.; Dye, B. A.; Wei, L.; Thornton-Evans, G. O.; Genco, R. J. CDC Periodontal Disease Surveillance workgroup: Prevalence of periodontitis in adults in the United States: 2009 and 2010. *J. Dent. Res.* **2012**, *91*, 914−920.

(2) Haffajee, A. D.; Socransky, S. S. Microbial etiological agents of destructive periodontal diseases. *Periodontology 2000* **1994**, *5*, 78−111.

(3) Moore, W. E.; Moore, L. V. The bacteria of periodontal diseases. *Periodontology 2000* **1994**, *5*, 66−77.

(4) Kolenbrander, P. E. Oral microbial communities: biofilms, interactions, and genetic systems. *Annu. Rev. Microbiol.* **2000**, *54*, 413−437.

(5) Han, Y. W. *Fusobacterium nucleatum*: a commensal-turned pathogen. *Curr. Opin. Microbiol.* **2015**, *23C*, 141−147.

(6) Ebersole, J. L.; Dawson, D. R., 3rd; Morford, L. A.; Peyyala, R.; Miller, C. S.; Gonzalez, O. A. Periodontal disease immunology: 'double indemnity' in protecting the host. *Periodontol. 2000* **2013**, *62*, 163−202.

(7) Hasturk, H.; Kantarci, A.; Van Dyke, T. E. Oral inflammatory diseases and systemic inflammation: role of the macrophage. *Front. Immunol.* **2012**, *3*, 118.

DOI: 10.1021/acs.jafc.5b01525
J. Agric. Food Chem. 2015, 63, 6999−7008

(8) Park, S. R.; Kim, D. J.; Han, S. H.; Kang, M. J.; Lee, J. Y.; Jeong, Y. J.; Lee, S. J.; Kim, T. H.; Ahn, S. G.; Yoon, J. H.; Park, J. H. Diverse Toll-like receptors mediate cytokine production by *Fusobacterium nucleatum* and *Aggregatibacter actinomycetemcomitans* in macrophages. *Infect. Immun.* **2014**, *82*, 1914−1920.
(9) Bodet, C.; Chandad, F.; Grenier, D. Anti-inflammatory activity of a high-molecular-weight cranberry fraction on macrophages stimulated by lipopolysaccharides from periodontopathogens. *J. Dent. Res.* **2006**, *85*, 235−239.
(10) Hannas, A. R.; Pereira, J. C.; Granjeiro, J. M.; Tjaderhane, L. The role of matrix metalloproteinases in the oral environment. *Acta Odontol. Scand.* **2007**, *65*, 1−13.
(11) Liu, Y. C.; Lerner, U. H.; Teng, Y. T. Cytokine responses against periodontal infection: protective and destructive roles. *Periodontology 2000* **2010**, *52*, 163−206.
(12) Tak, P. P.; Firestein, G. S. NF-κB: a key role in inflammatory diseases. *J. Clin. Invest.* **2001**, *107*, 7−11.
(13) Neish, A. S.; Naumann, M. Microbial-induced immunomodulation by targeting the NF-κB system. *Trends Microbiol.* **2011**, *19*, 596−605.
(14) Rahman, M. M.; McFadden, G. Modulation of NF-κB signalling by microbial pathogens. *Nat. Rev. Microbiol.* **2011**, *9*, 291−306.
(15) Kumar, A.; Takada, Y.; Boriek, A. M.; Aggarwal, B. B. Nuclear factor-κB: its role in health and disease. *J. Mol. Med. (Heidelberg, Ger.)* **2004**, *82*, 434−448.
(16) Abu-Amer, Y. NF-κB signaling and bone resorption. *Osteoporosis Int.* **2013**, *24*, 2377−2386.
(17) Gupta, S. C.; Sundaram, C.; Reuter, S.; Aggarwal, B. B. Inhibiting NF-κB activation by small molecules as a therapeutic strategy. *Biochim. Biophys. Acta, Gene Regul. Mech.* **2010**, *1799*, 775−787.
(18) Kirkwood, K. L.; Cirelli, J. A.; Rogers, J. E.; Giannobile, W. V. Novel host response therapeutic approaches to treat periodontal diseases. *Periodontology 2000* **2007**, *43*, 294−315.
(19) Kaye, E. K. Nutrition, dietary guidelines and optimal periodontal health. *Periodontology 2000* **2012**, *58*, 93−111.
(20) Kang, J.; Thakali, K. M.; Jensen, G. S.; Wu, X. Phenolic acids of the two major blueberry species in the US market and their antioxidant and anti-inflammatory activities. *Plant Foods Hum. Nutr.* **2015**, *70*, 56−62.
(21) Wu, X.; Beecher, G. R.; Holden, J. M.; Haytowitz, D. B.; Gebhardt, S. E.; Prior, R. L. Concentrations of anthocyanins in common foods in the United States and estimation of normal consumption. *J. Agric. Food Chem.* **2006**, *54*, 4069−4075.
(22) Harnly, J. M.; Doherty, R. F.; Beecher, G. R.; Holden, J. M.; Haytowitz, D. B.; Bhagwat, S.; Gebhardt, S. Flavonoid content of U.S. fruits, vegetables, and nuts. *J. Agric. Food Chem.* **2006**, *54*, 9966−9977.
(23) Papandreou, M. A.; Dimakopoulou, A.; Linardaki, Z. I.; Cordopatis, P.; Klimis-Zacas, D.; Margarity, M.; Lamari, F. N. Effect of a polyphenol-rich wild blueberry extract on cognitive performance of mice, brain antioxidant markers and acetylcholinesterase activity. *Behav. Brain Res.* **2009**, *198*, 352−358.
(24) Neto, C. C. Cranberry and blueberry: evidence for protective effects against cancer and vascular diseases. *Mol. Nutr. Food Res.* **2007**, *51*, 652−664.
(25) Martineau, L. C.; Couture, A.; Spoor, D.; Benhaddou-Andaloussi, A.; Harris, C.; Meddah, B.; Leduc, C.; Burt, A.; Vuong, T.; Mai Le, P.; Prentki, M.; Bennett, S. A.; Arnason, J. T.; Haddad, P. S. Anti-diabetic properties of the Canadian lowbush blueberry. *Phytomedicine* **2006**, *13*, 612−623.
(26) Dudonne, S.; Dube, P.; Pilon, G.; Marette, A.; Jacques, H.; Weisnagel, J.; Desjardins, Y. Modulation of strawberry/cranberry phenolic compounds glucuronidation by co-supplementation with onion: characterization of phenolic metabolites in rat plasma using an optimized muSPE-UHPLC-MS/MS method. *J. Agric. Food Chem.* **2014**, *62*, 3244−3256.
(27) Schwyn, B.; Neilands, J. B. Universal chemical assay for the detection and determination of siderophores. *Anal. Biochem.* **1987**, *160*, 47−56.
(28) Emery, T. Role of ferrichrome as a ferric ionophore in *Ustilago sphaerogena*. *Biochemistry* **1971**, *10*, 1483−1488.
(29) Zhang, H.; Zhou, W.; Zhang, W.; Yang, A.; Liu, Y.; Jiang, Y.; Huang, S.; Su, J. Inhibitory effects of citral, cinnamaldehyde, and tea polyphenols on mixed biofilm formation by foodborne *Staphylococcus aureus* and *Salmonella enteritidis*. *J. Food Prot.* **2014**, *77*, 927−933.
(30) Carlsen, H.; Moskaug, J. O.; Fromm, S. H.; Blomhoff, R. In vivo imaging of NF-κB activity. *J. Immunol.* **2002**, *168*, 1441−1446.
(31) Rovera, G.; Santoli, D.; Damsky, C. Human promyelocytic leukemia cells in culture differentiate into macrophage-like cells when treated with a phorbol diester. *Proc. Natl. Acad. Sci. U. S. A.* **1979**, *76*, 2779−2783.
(32) Palaska, I.; Papathanasiou, E.; Theoharides, T. C. Use of polyphenols in periodontal inflammation. *Eur. J. Pharmacol.* **2013**, *720*, 77−83.
(33) Johnson, M. H.; Lucius, A.; Meyer, T.; de Mejia, E. G. Cultivar evaluation and effect of fermentation on antioxidant capacity and in vitro inhibition of α-amylase and α-glucosidase by highbush blueberry (*Vaccinium corombosum*). *J. Agric. Food Chem.* **2011**, *59*, 8923−8930.
(34) Taverniti, V.; Fracassetti, D.; Del Bo, C.; Lanti, C.; Minuzzo, M.; Klimis-Zacas, D.; Riso, P.; Guglielmetti, S. Immunomodulatory effect of a wild blueberry anthocyanin-rich extract in human Caco-2 intestinal cells. *J. Agric. Food Chem.* **2014**, *62*, 8346−8351.
(35) Feghali, K.; Feldman, M.; La, V. D.; Santos, J.; Grenier, D. Cranberry proanthocyanidins: natural weapons against periodontal diseases. *J. Agric. Food Chem.* **2012**, *60*, 5728−5735.
(36) Lacombe, A.; Wu, V. C.; White, J.; Tadepalli, S.; Andre, E. E. The antimicrobial properties of the lowbush blueberry (*Vaccinium angustifolium*) fractional components against foodborne pathogens and the conservation of probiotic *Lactobacillus rhamnosus*. *Food Microbiol.* **2012**, *30*, 124−131.
(37) Lacombe, A.; Tadepalli, S.; Hwang, C. A.; Wu, V. C. Phytochemicals in lowbush wild blueberry inactivate *Escherichia coli* O157:H7 by damaging its cell membrane. *Foodborne Pathog. Dis.* **2013**, *10*, 944−950.
(38) Shen, X.; Sun, X.; Xie, Q.; Liu, H.; Zhao, Y.; Pan, Y.; Hwang, C.-A.; Wu, V. C. H. Antimicrobial effect of blueberry (*Vaccinium corymbosum* L.) extracts against the growth of *Listeria monocytogenes* and *Salmonella Enteritidis*. *Food Control* **2014**, *35*, 159−165.
(39) Dastmalchi, K.; Flores, G.; Petrova, V.; Pedraza-Penalosa, P.; Kennelly, E. J. Edible neotropical blueberries: antioxidant and compositional fingerprint analysis. *J. Agric. Food Chem.* **2011**, *59*, 3020−3026.
(40) Chvátalová, K.; Slaninová, I.; Březinová, L.; Slanina, J. Influence of dietary phenolic acids on redox status of iron: ferrous iron autoxidation and ferric iron reduction. *Food Chem.* **2008**, *106*, 650−660.
(41) Zimmer, K. R.; Blum-Silva, C. H.; Souza, A. L.; Wulffschuch, M.; Reginatto, F. H.; Pereira, C. M.; Macedo, A. J.; Lencina, C. L. The antibiofilm effect of blueberry fruit cultivars against *Staphylococcus epidermidis* and *Pseudomonas aeruginosa*. *J. Med. Food* **2014**, *17*, 324−331.
(42) Kalia, V. C.; Purohit, H. J. Quenching the quorum sensing system: potential antibacterial drug targets. *Crit. Rev. Microbiol.* **2011**, *37*, 121−140.
(43) Joseph, S. V.; Edirisinghe, I.; Burton-Freeman, B. M. Berries: anti-inflammatory effects in humans. *J. Agric. Food Chem.* **2014**, *62*, 3886−3903.
(44) Ruifeng, G.; Yunhe, F.; Zhengkai, W.; Ershun, Z.; Yimeng, L.; Minjun, Y.; Xiaojing, S.; Zhengtao, Y.; Naisheng, Z. Chlorogenic acid attenuates lipopolysaccharide-induced mice mastitis by suppressing TLR4-mediated NF-κB signaling pathway. *Eur. J. Pharmacol.* **2014**, *729*, 54−58.
(45) Cheng, A.; Yan, H.; Han, C.; Wang, W.; Tian, Y.; Chen, X. Polyphenols from blueberries modulate inflammation cytokines in LPS-induced RAW264.7 macrophages. *Int. J. Biol. Macromol.* **2014**, *69*, 382−387.

DOI: 10.1021/acs.jafc.5b01525
J. Agric. Food Chem. 2015, 63, 6999−7008

(46) Souza, J. A.; Junior, C. R.; Garlet, G. P.; Nogueira, A. V.; Cirelli, J. A. Modulation of host cell signaling pathways as a therapeutic approach in periodontal disease. *J. Appl. Oral Sci.* **2012**, *20*, 128−138.
(47) La, V. D.; Howell, A. B.; Grenier, D. Anti-*Porphyromonas gingivalis* and anti-inflammatory activities of A-type cranberry proanthocyanidins. *Antimicrob. Agents Chemother.* **2010**, *54*, 1778−1784.
(48) Sorsa, T.; Tjaderhane, L.; Konttinen, Y. T.; Lauhio, A.; Salo, T.; Lee, H. M.; Golub, L. M.; Brown, D. L.; Mantyla, P. Matrix metalloproteinases: contribution to pathogenesis, diagnosis and treatment of periodontal inflammation. *Ann. Med.* **2006**, *38*, 306−321.
(49) Matchett, M. D.; MacKinnon, S. L.; Sweeney, M. I.; Gottschall-Pass, K. T.; Hurta, R. A. Inhibition of matrix metalloproteinase activity in DU145 human prostate cancer cells by flavonoids from lowbush blueberry (*Vaccinium angustifolium*): possible roles for protein kinase C and mitogen-activated protein-kinase-mediated events. *J. Nutr. Biochem.* **2006**, *17*, 117−125.
(50) Zhang, J.; Lazarenko, O. P.; Kang, J.; Blackburn, M. L.; Ronis, M. J.; Badger, T. M.; Chen, J. R. Feeding blueberry diets to young rats dose-dependently inhibits bone resorption through suppression of RANKL in stromal cells. *PLoS One* **2013**, *8*, e70438.

DOI: 10.1021/acs.jafc.5b01525
J. Agric. Food Chem. 2015, 63, 6999−7008

phenol-sulfuric acid method using glucose as a standard. Samples were tested for the absence of free sugars by thin layer chromatography on silica gel G type 60 plates (MERCK, Tokyo, Japan) using chloroform−methanol−water (3:3:1 v/v/v) as the mobile phase. The ethanol-precipitated and dried EPS was then finely milled and moderately sonicated to dissolve in distilled water (for the in vivo experiment) or saline (for the in vitro cell assay).

Characterization of NTM048 EPS. To determine the monosaccharide composition of purified NTM048 EPS, 3 mg of EPS was hydrolyzed by addition of 750 μL of perchloric acid (1.75 M) and incubated at 80 °C for 16 h. After incubation, 250 μL of KOH (5 M) was added to precipitate the potassium perchlorate. The solution was centrifuged, and then the supernatant was filtered through a 0.45 μm pore size filter and the monosaccharide composition was analyzed by high performance anion exchange chromatography and pulsed amperometric detection (HPAEC-PAD) using a 4 × 250 mm Dionex CarboPac PA1 column. A gradient of sodium acetate from 0 to 500 mM in 100 mM sodium hydroxide was used for elution over 40 min at 1 mL/min. Detection was performed using a Dionex ICS-3000 module. D-Glucose and D-fructose (Nacalai Tesque, Tokyo, Japan) were used as standards.

The average molecular mass of NTM048 EPS was determined by size exclusion chromatography using Sepharose CL6B (Sigma-Aldrich, Missouri, USA). Two types of commercially purchased dextrans (Sigma-Aldrich, average MW 36,000−45,000 and 9,000−11,000) were used as standards.

In Vitro Analysis of IgA-Inducing Activity of EPS on Peyer's Patch Cells. To evaluate the IgA-inducing activity of NTM048 EPS, mouse Peyer's patch (PP) cells were prepared according to our previous study[10] and resuspended at 2.5 × 10^6 cells/mL in RPMI 10 medium [RPMI 1640 (Gibco BRL, CA, USA) containing 100 U/mL penicillin, 100 μg/mL streptomycin, 55 μmol/L 2-mercaptoethanol, and 10% fetal bovine serum (FBS; Gibco BRL)]. Various concentrations of size-exclusion chromatography-purified NTM048 EPS were added to PP cells (1.25 × 10^6 cells/mL final concentration) and incubated in 96-well T-cell activation plates (Becton Dickinson, Franklin Lakes, NJ) at 37 °C in a humidified atmosphere of 5% CO_2 in air. After 5 days, the IgA levels in the supernatants were measured by ELISA using a mouse IgA ELISA kit (Bethyl Laboratories, Montgomery, TX).

Assay for Specific IgA-Inducing Activity of EPS. The specific IgA-inducing ability of NTM048 EPS to the H1N1 antigen was measured according to the method of Yasui et al.[11] with some modifications. Mouse PP cells (4 × 10^6 cells/mL) in Eagle's minimum essential medium (Nissui, Tokyo, Japan) were cultured with size exclusion chromatography-purified NTM048 EPS (250 μg/mL) and influenza A (H1N1) virus antigen (0.34 μg/mL) on 96-well T-cell activation plates (Becton Dickinson) at 37 °C in a humidified atmosphere of 5% CO_2 in air to which a 10% v/v aliquot of a nutrient mixture was added daily.[12] After 2 days of incubation, the medium containing H1N1 antigen was removed by centrifugation, and then the PP cells were further incubated with NTM048 EPS (250 μg/mL) for an additional 6 days. Specific IgA levels against H1N1 antigen in the cultured medium were measured by ELISA as follows. H1N1 antigens (3 μg/mL) were coated on the wells of a 96-well ELISA plate (Thermo Scientific, MA, USA), and the culture supernatant was added to each well. Horseradish peroxidase-labeled mouse IgA detection antibody (Bethyl Laboratories) was added to the wells, and then an aliquot of 3,3′,5,5′-tetramethylbenzidine substrate solution was added to each well. After 15 min, the reaction was stopped by addition of 1 M HCl, and the absorbance of the contents of the wells was measured at 450 nm.

In Vitro Analysis of Immune Responses on Splenocytes. To evaluate the response of NTM048 EPS stimulation on splenocytes, mice were euthanized by CO_2 gas, and their spleens were harvested. Their spleens were gently teased and dispersed through a 70-μm cell strainer to obtain single-cell suspensions. After centrifugation (100 × *g*, 8 min), red blood cell lysis buffer (NH_4Cl 0.83%, $KHCO_3$ 0.1%, EDTA-2Na 0.00372%) was added to the pellet and incubated for 5 min. After washing with RPMI 10 medium twice, the cells were used as splenocytes. The prepared splenocytes were cultured (5 × 10^5 cells/well) on 96-well T-cell activation plates (Becton Dickinson) with size-exclusion chromatography-purified NTM048 EPS (20 μg/mL) for 66 h, followed by fluorescence-augmented cell sorter (FACS) analysis to examine the frequency of T cells (CD4+ and CD8+). Aliquots of 1 × 10^6 splenocytes were incubated with 10 μg/mL of Purified Rat Anti-Mouse CD16/32 (BD Biosciences, San Diego, CA) for 15 min on ice and washed twice in stain buffer (PBS with 2% FBS). Cells were then stained with PE-Cy7 conjugated antimouse CD3e (clone 145-2C11), PE conjugated antimouse CD4 (clone RM4-5), and APC conjugated antimouse CD8a (clone 53-6.7) using Mouse T Lymphocyte Subset Antibody Cocktail (BD Biosciences) for 30 min at 4 °C. Flow cytometry was performed on 20,000 cells by using FACSAria and FACSDiVa4.1 software (Becton Dickinson).

The frequency of CD4+ cells producing IFN-γ, IL-4, and IL-17 in splenocytes cultured with NTM048 EPS was examined by intracellular cytokine staining (ICCS) using the BD Cytofix/Cytoperm Plus Fixation/Permeabilization Kit (BD Biosciences) according to the manufacturer's instructions. In brief, the NTM048 EPS-stimulated splenocytes were resuspended in 1 mL of stimulation medium [RPMI 1640 medium containing 10 ng/mL of phorbol 12-myristate 13 acetate (Sigma-Aldrich), 1 ng/mL of ionomycin calcium salt (Sigma-Aldrich), 0.6 μL/ml of BD Golgistop] and incubated at 37 °C in 5% CO_2 for 5 h. Cells were washed twice with staining buffer and incubated with fixation/permeabilization solution for 20 min in the dark. Cells were washed twice again and stained by CD4 PERCP-Cy5.5, IL-17 PE, IFN-γ FITC, and IL-4 APC antibodies using a Mouse Th1/Th2/Th17 Phenotyping Kit (BD Biosciences) for 30 min on ice in the dark. Cells were washed twice and resuspended in staining buffer. Staining was assessed by FACSAria (BD Biosciences) and analyzed using BD FACSDiVa 4.1 software (BD Biosciences). A total of 30,000 events/sample were analyzed.

In Vivo Analysis of Immune Responses for NTM048 EPS. After 2 weeks of acclimation, 20 mice were assigned to 5 groups of four each based on body weights and fecal IgA levels. Each group was administered ad labium the NTM048 EPS-containing experimental water at a concentration of 0, 0.05, 0.1, 0.5 or 1% w/v. The mice were individually housed and administered experimental water for up to 42 days. Feces were collected every 7 days, and the IgA content in the feces was analyzed according to our previous study.[10] On day 42, the mice were euthanized with excessive somnopentyl, and Peyer's patch cells, spleen, and blood were harvested.

Plasma aspartate aminotransferase (AST) and alanine aminotransferase (ALT) were analyzed using the Transaminase CII kits (Wako Pure Chemical Industries, Osaka, Japan) to detect liver damage. Plasma creatinine (CRE) content was analyzed by the LabAssay Creatinine kit (Wako Pure Chemical Industries) to detect kidney disease. Measurements of plasma IgA and IgG levels were performed using a mouse IgA ELISA kit (Bethyl Laboratories) and a mouse IgG ELISA kit (Bethyl Laboratories), respectively.

Gene Expression Analysis of Peyer's Patch cells. Peyer's patch cells collected from the small intestine of mice were used for gene expression analysis. Total RNA samples were isolated using a QuickPrep total RNA extraction kit (GE Healthcare, Piscataway, NJ, USA). For preparation of cDNA, 1 μg of each total RNA sample was reverse-transcribed using Super Script III reverse transcriptase (Invitrogen, Carlsbad, CA, USA) and oligo (dT) primers (Invitrogen), and the obtained cDNA was then purified using a PCR Purification kit (Qiagen, Cambridge, MA, USA). Quantitative real-time RT-PCR was performed in a 7300 Fast Real-Time PCR system (Life Technologies Japan, Tokyo, Japan), using a Power SYBR Green Master Mix (Life Technologies) according to the manufacturer's instructions. A housekeeping transcript, glyceraldehyde 3-phosphate dehydrogenase (GAPDH), was used as an internal control to standardize the efficiency of each reaction. The sequences of the primers used were as follows: GAPDH (*Gapdh*), 5′-ctacactgaggaccaggttgtct-3′ and 5′-attgtcataccaggaaatgagctt-3′; IL-5 (*Il5*), 5′-tgaggcttcctgtccctactcataa-3′ and 5′-ttggaatagcatttccacagtaccc-3′; IL-6 (*Il6*), 5′-aatagtccttcctacccc-aatttc-3′ and 5′-atttcaagatgaattggatggtct-3′; IL-21 (*Il21*),[13] 5′-gcagcac-aggctaagagcttgta-3′ and 5′-tggctagtggagaagccttca-3′; BCL6 (*Bcl6*),[13]

DOI: 10.1021/acs.jafc.5b01960
J. Agric. Food Chem. 2015, 63, 7009−7015

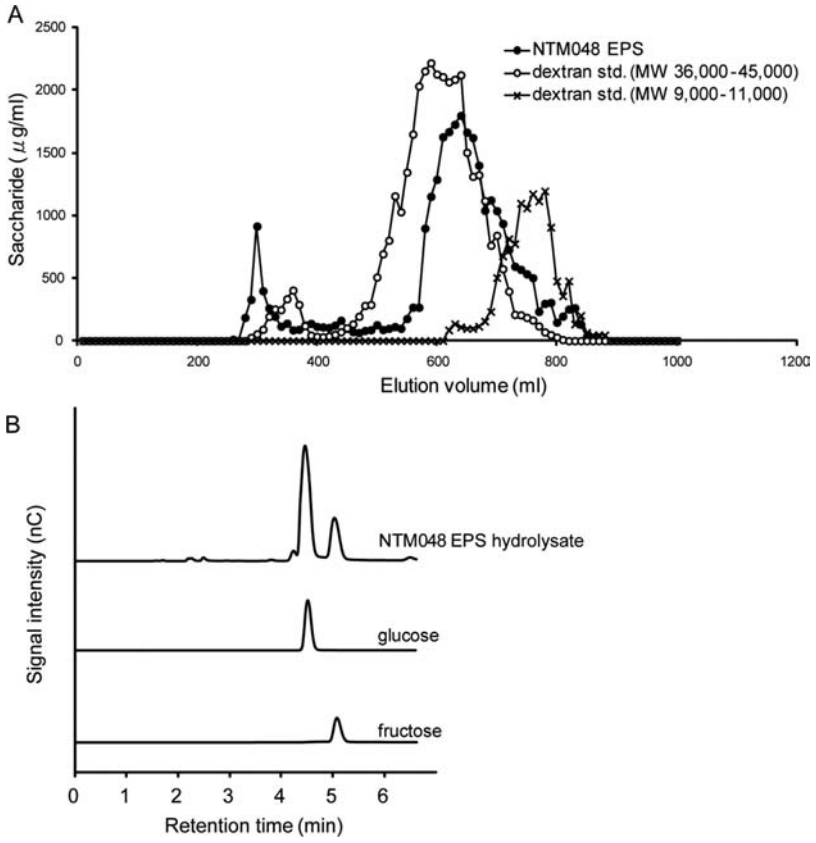

Figure 1. Characterization of NTM048 EPS. A: Molecular mass distribution of NTM048 EPS by size exclusion chromatography. Two kinds of industrial dextrans (average MW 36,000−45,000 and 9,000−11,000) were used as standards. B: HPAEC-PAD analysis of the monosaccharide composition of NTM048 EPS hydrolysate. Glucose and fructose were used as standards.

5′-gcactgggcaaacacaacat-3′ and 5′-agcgtgccgggtaaactg-3′; BAFF (*Tnfsf13b*),[14] 5′-tgctatgggtcatgtcatcca-3′ and 5′-ggcagtgttttgggcatattc-3′; APRIL (*Tnfsf13*),[14] 5′-tcacaatgggtcaggtggtatc-3′ and 5′-tgtaaatg-aaagacacctgcactgt-3′; RALDH1 (*Aldh1al*),[15] 5′-atggtttagcagcaggac-tcttc-3′ and 5′-ccagacatcttgaatccaccgaa-3′; CD40L (*Cd40l*), 5′-tttatc-cttgctgaactgtgagga-3′ and 5′-gatcctcatcacctctttgcattt-3′; TGF-β1 (*Tgfb1*),[15] 5′-tggagcaacatgtggaactc-3′ and 5′-tgccgtacaactccagtgac-3′; TGF-βR2 (*Tgfbr2*),[16] 5′-cctactctgtctgtggatga-3′ and 5′-gctcgtaatcct-tcacttctc-3′; and AID (*Aicda*),[17] 5′-aaattctgtccggctaacca-3′ and 5′-cattccaggaggttgctttc-3′. To confirm whether or not PCR correctly amplified the aimed genes, the PCR products were sequenced and identified by means of BLAST search (DNA Data Bank of Japan), and we analyzed their melting curves (data not shown). All experiments were performed in triplicate.

Flow Cytometric Analysis of Splenocytes. Single-cell suspensions of splenocytes were prepared, and the frequencies of T cells (CD4+ and CD8+) were examined as described above using a FACSAria (BD Biosciences) and analyzed by BD FACSDiVa4.1 software (BD Biosciences). A total of 20,000 events/sample were analyzed.

Statistical Analysis. Each result is expressed as the mean ± standard error (SE). Dunnett's test or two-way repeated-measures ANOVA with a posthoc analysis followed by Dunnett's test was used to compare multiple groups. Statistical analyses were conducted using Ekuseru-Toukei software version 2010 (SSRI, Tokyo, Japan). *P* values less than 0.05 were considered statistically significant.

RESULTS

Characterization of NTM048 EPS. We obtained 1.46 g of NTM048 EPS from a 50-mL culture in the EPS-production medium. To estimate the molecular mass of the NTM048 EPS, size exclusion chromatography was performed. The majority of NTM048 EPS was eluted between the two dextran standards whose sizes ranged from 36,000−45 000 Da and 9,000−11 000 Da, respectively, indicating the NTM048 EPS molecular mass range is approximately 10−40 kDa (Figure 1A). Next, we attempted to determine the monosaccharide composition of NTM048 EPS. HPAEC-PAD analysis was used to monitor the partial hydrolysis of the EPS to its monosaccharides. The chromatogram showed two monosaccharide peaks, which corresponded to the retention time of D-glucose and D-fructose, respectively (Figure 1B). This result suggests that NTM048 EPS contains glucose and fructose.

Effect of NTM048 EPS on Immune Cells in Vitro. Isolated PP cells and splenocytes were used to examine the effect of NTM048 EPS on immune cells. As shown in Figure 2A, total IgA production of PP cells was dose-dependently stimulated by NTM048 EPS (1.5-fold and 1.7-fold increases compared with that of the saline control in the presence of 25 and 250 μg/mL EPS, respectively). Moreover, costimulation of NTM048 EPS with H1N1 antigen significantly induced anti-H1N1 IgA production by 1.5-fold (Figure 2B). These results indicate that NTM048 EPS can stimulate PP cells to produce total and antigen-specific IgA (see Discussion). FACS analysis on the NTM048 EPS-stimulated splenocytes was also carried out. The isolated splenocytes were treated 20 μg/mL of NTM048 EPS. The number of CD3+ cells and the ratio of CD4+ T cells to CD8+ T cells from the NTM048 EPS-stimulated splenocytes were significantly higher ($P < 0.05$) than those of nonstimulated splenocytes (Figure 3A and B). Additionally, NTM048 EPS stimulation significantly expanded the CD4+ T cell population ($P < 0.01$) (Figure 3C upper

DOI: 10.1021/acs.jafc.5b01960
J. Agric. Food Chem. 2015, 63, 7009−7015

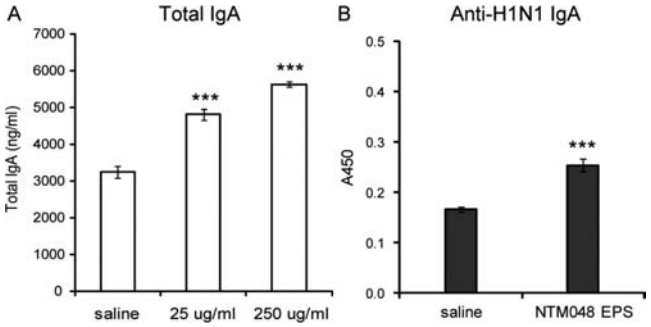

Figure 2. In vitro response of Peyer's patch cells stimulated by NTM048 EPS. A: IgA-inducing ability of NTM048 EPS. Each value is presented as the mean ± SE (n = 5; ***P < 0.001). B: Augmentation of anti-influenza virus H1N1 IgA antibody production by NTM048 EPS. Each value is presented as the mean ± SE (n = 8; ***P < 0.001).

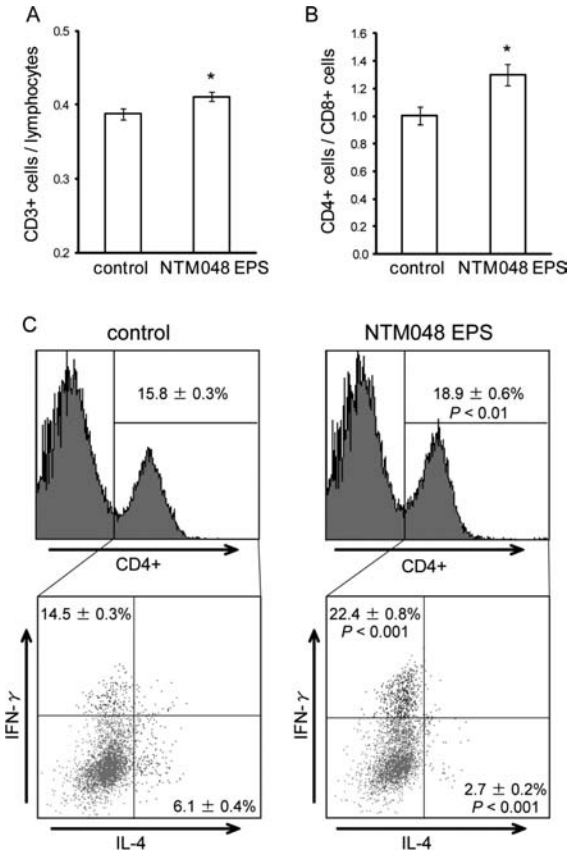

Figure 3. Flow cytometric analysis of splenocytes in vitro. Splenocytes were cultured with 20 μg/mL of NTM048 EPS or saline (control). Each value is presented as the mean ± SE (n = 5). A: Ratio of CD3+ cells/lymphocytes. B: Ratio of CD4+ cells/CD8+ cells (*P < 0.05). C: Ratio of CD4+ cells/lymphocytes, IFN-γ+ cells/CD4+ cells, and IL-4+ cells/CD4+ cells. Statistical results are shown in the panels.

panel). The ratio of a subset of CD4+ T cells producing IFN-γ was significantly increased by NTM048 EPS stimulation (14.5% vs 22.4%, P < 0.001) with a concomitant decrease in the ratio of a subset of CD4+ T cells producing IL-4 (6.1% vs 2.7%, P < 0.001) (Figure 3C lower panel). We also examined the effects of 100 μg/mL of EPS treatment on splenocytes, which results were almost the same as those of 20 μg/mL of EPS treatment (data not shown). This indicates that the immune stimulation of splenocytes by NTM048 EPS was induced enough at the concentration of 20 μg/mL. No change was observed in the frequency of CD4+ T cells producing IL-17 (nontreated, 1.7 ± 0.1%; NTM048 EPS treated, 1.7 ± 0.1% [data not shown]). These results suggest that EPS stimulation affects the Th1 and Th2 cell-mediated response in splenocytes.

Effect of NTM048 EPS on the Mouse Intestinal Immune System. Having established the in vitro effect of NTM048 on mucosal and systemic immune responses as described above, we next performed in vivo experiments using BALB/cA mice. Drinking water supplemented with NTM048 EPS at 0, 0.05, 0.1, 0.5, or 1.0% (w/v) was given to mice ad libitum for 42 days. All animals were in good health throughout the experimental period, and no side effects, such as diarrhea, occurred. There were no significant differences in food and water intake, body weight gain, and plasma AST, ALT, and CRE levels among the groups (Table 1).

In agreement with the in vitro study, oral administration of NTM048 EPS increased the fecal IgA concentration (Figure 4). While the fecal IgA content of the 0 and 0.05% groups were minimally changed through the experimental period, those of the 0.1, 0.5, and 1% groups were significantly increased after 35 days compared with their initial IgA content.

Peyer's patches are the main inductive sites for intestinal IgA responses.[18,19] To determine the mechanism responsible for the mucosal IgA production upon administration of NTM048 EPS, we analyzed the expression levels of genes involved in intestinal immunostimulation in isolated PP cells (Figure 5). The gene expression of the TGF-β receptor 2 (TGF-βR2) found on B cells was significantly increased in the 0.5 and 1% groups (P < 0.05), suggesting the occurrence of TGF-β1 signaling.[5] The gene expression of retinal dehydrogenase (RALDH), which is required for retinoic acid (RA) production from dendritic cells (DCs), was also increased in the 1% group (P < 0.05). The gene expression of B cell lymphoma 6 (BCL6), which is abundantly expressed by follicular helper T (T_{FH}) cells, tended to increase in the 0.5 and 1% groups (P = 0.14 and P = 0.17, respectively). On the other hand, the expression of IL-5, IL-6, IL-21, B cell-activating factor (BAFF), a proliferation-inducing ligand (APRIL), CD40 ligand (CD40L), TGF-β1, and activation-induced cytidine deaminase (AID) genes remained unchanged.

Effect of NTM048 EPS on the Systemic Immune System in Mice. To investigate the effect of NTM048 EPS administration on the systemic immune system, we examined the plasma IgA and IgG levels and carried out flow cytometric analysis on the isolated splenocytes of NTM048 administrated-mice. Oral administration of NTM048 EPS did not affect plasma IgA and IgG levels (Table 1), but a significant effect on T cell population in the spleen was observed. The CD3 positive T-cell population in total lymphocytes of the 0.5% and 1% groups were significantly higher than that of the control group (Figure 6A) (P < 0.05). Additionally, the CD4+ T cells/CD8+ T cells of the 1% group were significantly higher than that of the control group (Figure 6B) (P < 0.01), which was consistent with the in vitro result (Figure 3A and B).

DISCUSSION

One of the immunomodulating properties induced by LAB is the promotion of host mucosal IgA secretion to strengthen the first lines of defense, such as the mucosal barrier.[20−22] It has been reported that several types of LAB are effective against pathogenic infection via their IgA-inducing ability. *Lactobacillus pentosus* strain b240[23] and *Lactobacillus plantarum* strain AYA[24]

DOI: 10.1021/acs.jafc.5b01960
J. Agric. Food Chem. 2015, 63, 7009−7015

Table 1. Physiological Parameters of Mice Administered NTM048 EPS at Doses of 0, 0.05, 0.1, 0.5, and 1%[a]

	0% group	0.05% group	0.1% group	0.5% group	1% group
water intake (g/d)	3.8 ± 0.1	4.4 ± 0.3	3.9 ± 0.1	4.3 ± 0.4	4.2 ± 0.2
initial body weight (g)	30.4 ± 0.9	30.8 ± 1.4	30.9 ± 0.8	31.1 ± 0.4	30.0 ± 1.3
final body weight (g)	37.1 ± 1.5	37.1 ± 2.0	37.3 ± 1.7	36.1 ± 1.3	35.9 ± 2.0
body weight gain (g)	6.7 ± 0.7	6.3 ± 1.4	6.4 ± 1.0	5.1 ± 1.3	5.9 ± 0.9
blood chemistry					
AST (Karmen unit)	32.9 ± 6.3	25.9 ± 3.4	24.1 ± 3.8	21.5 ± 1.3	22.2 ± 3.1
ALT (Karmen unit)	28.1 ± 5.5	19.4 ± 1.6	18.8 ± 3.0	14.4 ± 1.3	14.8 ± 3.0
CRE (μg/mL)	3.1 ± 0.2	4.4 ± 0.4	4.3 ± 0.3	4.9 ± 0.5	4.4 ± 0.3
IgA (μg/mL)	227.7 ± 9.9	220.9 ± 16.9	235.8 ± 14.1	259.7 ± 42.5	266.3 ± 10.0
IgG (μg/mL)	87.8 ± 4.8	92.5 ± 4.5	94.3 ± 6.3	93.5 ± 13.3	82.0 ± 4.3

[a]Results are shown as the mean ± SE (n = 4).

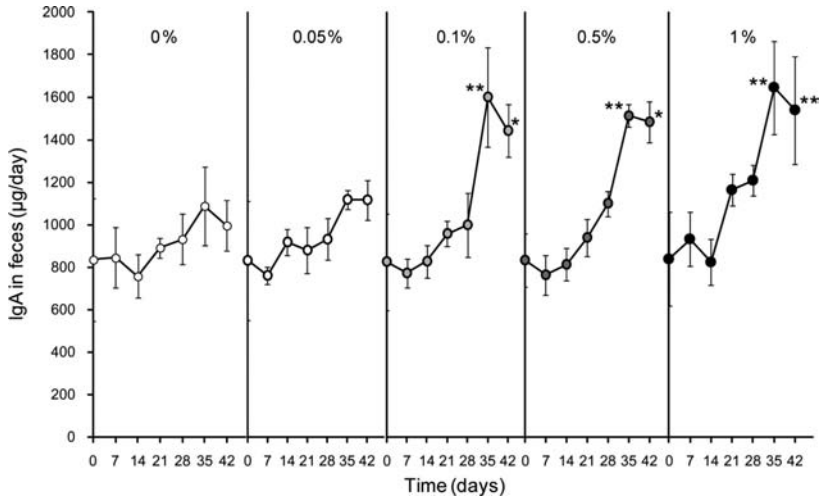

Figure 4. Fecal IgA content induced by NTM048 EPS intake. Mice were administered 0, 0.05, 0.1, 0.5, and 1% of EPS-containing water and the IgA content in feces were compared. Differences were assessed by a two-way repeated-measure ANOVA with a *post hoc* analysis by Dunnett's test. Each value is presented as the mean ± SE (n = 4). *P < 0.05, **P < 0.01 vs each initial IgA content (day 0).

were selected for their IgA-inducing potency on mouse PP cells, and oral administration of the cells could facilitate protection against influenza virus in mice. However, the IgA-inducible components of these LABs remain unclear.

In our previous study, we identified *Leuc. mesenteroides* strain NTM048 having IgA-inducing potency from among 173 LABs.[10] NTM048 cells were tolerant to gastric and intestinal digestion in vitro, and oral administration of this strain induced intestinal IgA secretion in mice. Moreover, the NTM048 EPS dose-dependently induced IgA secretion from PP cells, suggesting that NTM048 EPS plays a pivotal role as an immunostimulant of strain NTM048. To confirm that NTM048 EPS is an immunostimulant, we investigated the effect of NTM048 EPS on the intestinal and systemic immune system in the present study.

In agreement with the results from our previous study, NTM048 EPS dose-dependently enhanced total IgA secretion by isolated PP cells. Furthermore, we revealed that NTM048 EPS could induce specific IgA secretion by isolated PP cells. To effectively prevent mucosal infection, the ability to induce a specific IgA response is also important.[25] In particular, a successful influenza virus vaccine containing an adjuvant which stimulates mucosal antigen-specific IgA production is attractive because of the insufficient efficacy of the systemic IgG response. Therefore, NTM048 EPS might be useful as an effective adjuvant of mucosal vaccination.

The spleen contains various immune cells including T and B cells, DCs, and macrophages and regulates the systemic immune system to protect the body against blood-borne bacterial, viral, and fungal infections.[26] NTM048 EPS influenced the T cell population of splenocytes in vitro and in vivo. In both experiments, NTM048 EPS increased the T cell (CD3+ cell) population and the ratio of CD4+ cells/CD8+ cells. Given the results of its IgA-inducing ability, intake of NTM048 EPS influenced not only the mucosal immune system but also the systemic immune system. Medrano et al. reported that oral treatment of EPS produced by microorganisms present in kefier grains modulated the balance of immune cells in intestinal mucosa including the increase in IgA+ cells but did not affect the cells in the spleen.[27] Therefore, immunomodulation ability on the systemic immune system is considered as a marked characteristic of NTM048 EPS. Additionally, NTM048 EPS treatment of isolated splenocytes increased IFN-γ-producing CD4+ cells and decreased IL-4-producing CD4+ cells. IFN-γ is a cytokine associated with the Th1 immune response rather than the allergic Th2 response, and IL-4 is a cytokine required for Th2 cell differentiation and Th1 development suppression.[28] Hence, NTM048 EPS might influence the Th1 and Th2 cell-mediated response of systemic immune system.

IgA induction through a T cell-dependent pathway leads to the production of high-affinity IgA because of the occurrence of somatic hypermutation (SHM), which is responsible for affinity

DOI: 10.1021/acs.jafc.5b01960
J. Agric. Food Chem. 2015, 63, 7009−7015

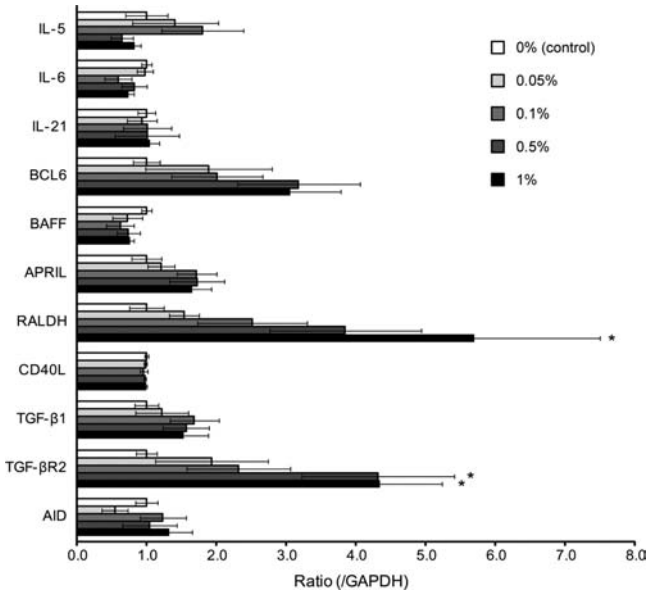

Figure 5. Gene expression analysis of Peyer's patch cells from mice treated with 0, 0.05, 0.1, 0.5, and 1% of NTM048 EPS. Gene expression was analyzed by SYBR Green-Based Real-Time RT-PCR. GAPDH was used as a control to standardize the efficiency of each reaction. Each value is presented as the mean ± SE (n = 4). Statistical analysis was performed with Dunnett's multiple comparison test. *P < 0.05 vs the control group.

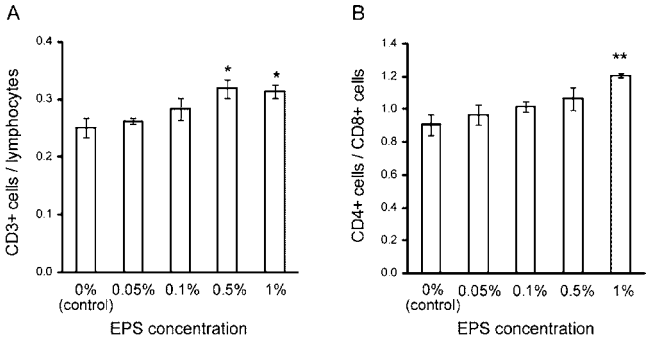

Figure 6. T cell stimulation in the spleen of mice fed water containing 0, 0.05, 0.1, 0.5 and 1% of NTM048 EPS. A: Ratio of CD3+ cells/lymphocytes. B: Ratio of CD4+ cells/CD8+ cells. Each values is presented as the mean ± SE (n = 4). *P < 0.05, **P < 0.01 vs the control group.

maturation.[22] On this pathway, T_{FH} cells, which highly express BCL6, are differentiated from Foxp3+ regulatory T cells and promote B cell responses toward intestinal antigens.[29] T_{FH} cell-signaling promotes B cells to undergo SHM with the help of TGF-β1, IL-21, and RA.[30] In this study, the gene expression levels of BCL6, TGF-βR2, and RALDH were upregulated or tended to be upregulated by NTM048 EPS intake. Given the in vitro observation of specific IgA-induction, NTM048 EPS may be inducing the production of high-affinity IgA through a T cell-dependent pathway.

Dextran is an extracellular bacterial polymer of D-glucopyranose containing predominantly α-(1,6) linkages in the main chain and a variable amount of α-(1,2), α-(1,3), α-(1,4) branched linkages and is produced primarily by *Leuconostoc* strains. Chemically modified dextrans, such as sulfated dextran,[31] diethylaminoethyl dextran,[32] and acetylated dextran,[33] were reported to act as adjuvants to enhance immunogenicity. Natural NTM048 EPS stimulated immune responses in mice without prominent side effects, suggesting its potency as a nontoxic mucosal adjuvant.[34] Some strains of *Leuc. mesenteroides* produce fructose-containing dextrans,[35] but their immunomodulating activity has not been reported yet. The precise determination of the NTM048 EPS structure is currently underway in our laboratory.

In summary, we showed that *Leuc. mesenteroides* NTM048-secreted EPS was a specific IgA-inducible immunostimulant and influenced systemic immunity in mice. These properties of NTM048 EPS indicate that it may be an effective immunostimulant useful for protection from mucosal pathogens.

AUTHOR INFORMATION

Corresponding Author

*Phone: 81-76-227-7513. Fax: 81-76-227-7557. E-mail: chiaki@ishikawa-pu.ac.jp.

Notes

The authors declare no competing financial interest.

ACKNOWLEDGMENTS

We thank Tetsuro Kitao, Kohei Kitao, and Dr. Yasunori Yonejima, Nitto Pharmaceutical Industries, Ltd., for helpful discussion and comments. We also thank Dr. Seiya Makino, Meiji Co., Ltd., for technical advice.

REFERENCES

(1) Ruas-Madiedo, P.; Hugenholtz, J.; Zoon, P. An overview of the functionality of exopolysaccharides produced by lactic acid bacteria. *Int. Dairy J.* **2002**, *12*, 163−171.

(2) Chabot, S.; Yu, H. L.; De Leseleuc, L.; Cloutier, D.; Van Calsteren, M. R.; Lessard, M.; Roy, D.; Lacroix, M.; Oth, D. Exopolysaccharides from *Lactobacillus rhamnosus* RW-9595M stimulate TNF, IL-6 and IL-12 in human and mouse cultured immunocompetent cells, and IFN-gamma mouse splenocytes. *Lait* **2001**, *81*, 683−697.

(3) Lycke, N.; Erlandsson, L.; Ekman, L.; Schön, K.; Leanderson, T. Lack of J chain inhibits the transport of gut IgA and abrogates the development of intestinal antitoxic protection. *J. Immunol.* **1999**, *163*, 913−919.

(4) Forbes, S. J.; Eschmann, M.; Mantis, N. Inhibition of *Salmonella enterica* serovar typhimurium motility and entry into epithelial cells by a protective antilipopolysaccharide monoclonal immunoglobulin A antibody. *Infect. Immun.* **2008**, *76*, 4137−4144.

(5) Cerutti, A. The regulation of IgA class switching. *Nat. Rev. Immunol.* **2008**, *8*, 421−434.

(6) Corthésy, B. Multi-faceted functions of secretory IgA at mucosal surfaces. *Front. Immunol.* **2013**, *4*, 185.

(7) van Riet, E.; Ainai, A.; Suzuki, T.; Hasegawa, H. Mucosal IgA responses in influenza virus infections; thoughts for vaccine design. *Vaccine* **2012**, *30*, 5893−5900.

(8) Makino, S.; Ikegami, S.; Kano, H.; Sashihara, T.; Sugano, H.; Horiuchi, H.; Saito, T.; Oda, M. Immunomodulatory effects of polysaccharides produced by *Lactobacillus delbrueckii* ssp. *bulgaricus* OLL1073R-1. *J. Dairy Sci.* **2006**, *89*, 2873−2881.

(9) Vinderola, G.; Perdigon, G.; Duarte, J.; Farnworth, E.; Matar, C. Effects of the oral administration of the exopolysaccharide produced by *Lactobacillus kefiranofaciens* on the gut mucosal immunity. *Cytokine* **2006**, *36*, 254−260.

(10) Matsuzaki, C.; Kamishima, K.; Matsumoto, K.; Koga, H.; Katayama, T.; Yamamoto, K.; Hisa, K. Immunomodulating activity of exopolysaccharide-producing *Leuconostoc mesenteroides* strain NTM048 from green peas. *J. Appl. Microbiol.* **2014**, *116*, 980−989.

(11) Yasui, H.; Nagaoka, N.; Hayakawa, K. Augmentation of anti-influenza virus hemagglutinin antibody production by Peyer's patch

DOI: 10.1021/acs.jafc.5b01960
J. Agric. Food Chem. 2015, 63, 7009−7015

cells with *Bifidobacterium breve* YIT4064. *Clin. Diagn. Lab. Immunol.* **1994**, *1*, 244−246.
(12) Yasui, H.; Mike, A.; Ohwaki, M. Immunogenicity of *Bifidobacterium breve* and change in antibody production in Peyer's patches after oral administration. *J. Dairy Sci.* **1989**, *72*, 30−35.
(13) Mondal, A.; Sawant, D.; Dent, A. L. Transcriptional repressor BCL6 controls Th17 responses by controlling gene expression in both T cells and macrophages. *J. Immunol.* **2010**, *184*, 4123−4132.
(14) Tezuka, H.; Abe, Y.; Asano, J.; Sato, T.; Liu, J.; Iwata, M.; Ohteki, T. Prominent Role for Plasmacytoid Dendritic Cells in Mucosal T Cell-Independent IgA Induction. *Immunity* **2011**, *34*, 247−257.
(15) Massacand, J. C.; Kaiser, P.; Ernst, B.; Tardivel, A.; Bürki, K.; Schneider, P.; Harris, N. L. Intestinal bacteria condition dendritic cells to promote IgA production. *PLoS One* **2008**, *3*, e2588.
(16) Tezuka, H.; Abe, Y.; Iwata, M.; Takeuchi, H.; Ishikawa, H.; Matsushita, M.; Shiohara, T.; Akira, S.; Ohteki, T. Regulation of IgA production by naturally occurring TNF/iNOS-producing dendritic cells. *Nature* **2007**, *448*, 929−933.
(17) Yanagibashi, T.; Hosono, A.; Oyama, A.; Tsuda, M.; Hachimura, S.; Takahashi, Y.; Kaminogawa, S. *Bacteroides* induce higher IgA production than *Lactobacillus* by increasing activation-induced cytidine deaminase expression in B cells in murine Peyer's patches. *Biosci., Biotechnol., Biochem.* **2009**, *73*, 372−377.
(18) Lycke, N.; Bemark, M. The role of Peyer's patches in synchronizing gut IgA responses. *Front. Immunol.* **2012**, *3*, 329.
(19) Kawamoto, S.; Maruya, M.; Kato, L. M.; Suda, W.; Atarashi, K.; Doi, Y.; Tsutsui, Y.; Qin, H.; Honda, K.; Okada, T.; Hattori, M.; Fagarasan, S. Foxp3(+) T cells regulate immunoglobulin a selection and facilitate diversification of bacterial species responsible for immune homeostasis. *Immunity* **2014**, *41*, 152−65.
(20) Fagarasan, S.; Honjo, T. Intestinal IgA synthesis: regulation of front-line body defences. *Nat. Rev. Immunol.* **2003**, *3*, 63−72.
(21) Pabst, O. New concepts in the generation and functions of IgA. *Nat. Rev. Immunol.* **2012**, *12*, 821−832.
(22) Tsai, Y. T.; Cheng, P. C.; Pan, T. M. The immunomodulatory effects of lactic acid bacteria for improving immune functions and benefits. *Appl. Microbiol. Biotechnol.* **2012**, *96*, 853−862.
(23) Kobayashi, N.; Saito, T.; Uematsu, T.; Kishi, K.; Toba, M.; Kohda, N.; Suzuki, T. Oral administration of heat-killed *Lactobacillus pentosus* strain b240 augments protection against influenza virus infection in mice. *Int. Immunopharmacol.* **2011**, *11*, 199−203.
(24) Kikuchi, Y.; Kunitoh-Asari, A.; Hayakawa, K.; Imai, S.; Kasuya, K.; Abe, K.; Adachi, Y.; Fukudome, S.; Takahashi, Y.; Hachimura, S. Oral administration of *Lactobacillus plantarum* strain AYA enhances IgA secretion and provides survival protection against influenza virus infection in mice. *PLoS One* **2014**, *9*, e86416.
(25) Kim, S. H.; Lee, K. Y.; Jang, Y. S. Mucosal immune system and M cell-targeting strategies for oral mucosal vaccination. *Immune. Netw.* **2012**, *12*, 165−175.
(26) Bronte, V.; Pittet, M. J. The spleen in local and systemic regulation of immunity. *Immunity* **2013**, *39*, 806−818.
(27) Medrano, M.; Racedo, S. M.; Rolny, I. S.; Abraham, A. G.; Pérez, P. F. Oral administration of kefiran induces changes in the balance of immune cells in a murine model. *J. Agric. Food Chem.* **2011**, *59*, 5299−5304.
(28) Hansbro, P. M.; Kaiko, G. E.; Foster, P. S. Cytokine/anti-cytokine therapy − novel treatments for asthma? *Br. J. Pharmacol.* **2011**, *163*, 81−95.
(29) Tsuji, M.; Komatsu, N.; Kawamoto, S.; Suzuki, K.; Kanagawa, O.; Honjo, T.; Hori, S.; Fagarasan, S. Preferential generation of follicular B helper T cells from Foxp3+ T cells in gut Peyer's patches. *Science* **2009**, *323*, 1488−1492.
(30) Fagarasan, S.; Kawamoto, S.; Kanagawa, O.; Suzuki, K. Adaptive immune regulation in the gut: T cell-dependent and T cell-independent IgA synthesis. *Annu. Rev. Immunol.* **2010**, *28*, 243−273.
(31) Bauer, C.; Duewell, P.; Mayer, C.; Lehr, H. A.; Fitzgerald, K. A.; Dauer, M.; Tschopp, J.; Endres, S.; Latz, E.; Schnurr, M. Colitis induced in mice with dextran sulfate sodium (DSS) is mediated by the NLRP3 inflammasome. *Gut* **2010**, *59*, 1192−1199.
(32) Houston, W. E.; Crabbs, C. L.; Kremer, R. J.; Springer, J. W. Adjuvant effects of diethylaminoethyl-dextran. *Infect. Immun.* **1976**, *13*, 1559−1562.
(33) Sato, T.; Nishimura-Uemura, J.; Shimosato, T.; Kawai, Y.; Kitazawa, H.; Saito, T. Dextran from *Leuconostoc mesenteroides* augments immunostimularory effects by the introduction of phosphate groups. *J. Food Prot.* **2004**, *67*, 1719−1724.
(34) Otczyk, D. C.; Cripps, A. W. Mucosal immunization: a realistic alternative. *Hum. Vaccines* **2010**, *6*, 978−1006.
(35) Bounaix, M. S.; Gabriel, V.; Morel, S.; Robert, H.; Rabier, P.; Remaud-Siméon, M.; Gabriel, B.; Fontagné-Faucher, C. Biodiversity of exopolysaccharides produced from sucrose by sourdough lactic acid bacteria. *J. Agric. Food Chem.* **2009**, *57*, 10889−10897.

DOI: 10.1021/acs.jafc.5b01960
J. Agric. Food Chem. 2015, 63, 7009−7015

Table 1. Fatty Acid Composition of Oils[a]

fatty acid			ROO (%)	EVOO (%)	tuna (%)	Alsepa (%)
myristic acid	C14:0		nd	nd	2.24	nd
palmitic acid	C16:0		10.09	12.64	19.77	0.35
palmitoleic acid	C16:1	*cis*-9	0.59	0.71	4.25	0.30
margaric acid	C17:0		nd	nd	1.4	nd
heptadecenoic acid	C17:1	*cis*-10	nd	nd	0.96	nd
stearic acid	C18:0		3.25	8.63	8.98	1.25
oleic acid	C18:1	*cis*-9	71.54	70.03	18.68	3.32
vaccenic acid	C18:1	*trans*-11	2.17	1.94	3.05	nd
linoleic acid	C18:2	*cis*-9,12	7.81	4.05	1.25	0.29
α-linolenic acid	C18:3	*cis*-9,12,15	0.49	0.6	0.58	1.09
stearidonic acid	C18:4	*cis*-6,9,12,15	nd	nd	nd	1.47
arachidic acid	C20:0		0.58	0.55	0.63	0.46
gondoic acid	C20:1	*cis*-11	0.38	0.24	1.85	1.09
eicosadienoic acid	C20:2	*cis*-11,14	nd	nd	0.38	0.28
dihomo-γ-linolenic acid	C20:3	*cis*-8,11,14	nd	nd	0.24	0.17
eicosatrienoic acid	C20:3	*cis*-11,14,17	nd	nd	0.51	0.33
arachidonic acid	C20:4	*cis*-5,8,11,14	nd	nd	1.59	0.73
eicosapentaenoic acid (EPA)	C20:5	*cis*-5,8,11,14,17	nd	nd	3.32	41.13
heneicosylic acid	C21:0		nd	nd	nd	0.10
behenic acid	C22:0		0.2	0.13	0.37	0.26
erucic acid	C22:1	*cis*-13	nd	nd	0.55	0.54
docosadienoic acid	C22:2	*cis*-13,16	nd	nd	nd	1.59
docosatrienoic acid	C22:3	*cis*-13,16,19	nd	nd	nd	1.03
adrenic acid	C22:4	*cis*-7,10,13,16	nd	nd	nd	2.21
docosapentaenoic acid (DPA)	C22:5	*cis*-7,10,13,16,19	nd	nd	nd	5.53
osbond acid	C22:5	*cis*-4,7,10,13,16	nd	nd	nd	1.30
docosahexaenoic acid (DHA)	C22:6	*cis*-4,7,10,13,16,19	nd	nd	20.66	31.75
tricosylic acid	C23:0		nd	nd	nd	1.57
lignoceric acid	C24:0		0.12	0.08	0.36	0.19
nervonic acid	C24:1	*cis*-15	nd	nd	1.47	0.43

[a]Standard deviation <5%. nd = LOQ < 0.01%.

MATERIALS AND METHODS

Chemicals. Fresh turkey muscle, frozen tuna, olive oils, both refined (ROO) and extra virgin (EVOO) (BORGES, Spain; expiration October 2015), and ω-3 supplement fish oil "Alsepa MAX" (Ocean-Nutrition, Canada; expiration June 2015) were obtained from a local store. Gallic acid, D-α-tocopherol, myoglobin, Folin−Ciocalteu reagent, 2-thiobarbituric acid (TBA), pepsin from porcine stomach mucosa, triphenylphosphin (TPP), hydrochloric acid (HCl), butylated hydroxytoluene (BHT), xylenol orange, and ammonium iron(II) sulfate were obtained from Sigma Chemical Co., St. Louis, MO, USA. Hydrochloric acid, sodium chloride, trichloroacetic acid, and sodium carbonate were obtained from Merck (Darmstadt, Germany). High-performance liquid chromatography (HPLC) grade methanol and pure water were obtained from J. T. Baker, Phillipsburg, NJ, USA. Petroleum ether was obtained from Bio-Lab Ltd., Jerusalem, Israel. Simulated gastric fluid (SGF) was freshly prepared according to the United States Pharmacopeia (Rockville, MD; 2000). The SGF contained NaCl (200 mg), pepsin (320 mg), and HCl (700 μL of 36%) was added to DDW (100 mL).

Muscle Tissue Lipid Peroxidation in Stomach Medium. Fresh turkey red muscle was divided in three portions; each portion was cut into small cubes of ∼1 cm^3 and heated for 1 min in a microwave (Dow, S-Korea, at 800 W), chilled, and kept at −80 °C until needed for the second stage of experiments. The oils were added to the muscle tissue (25g), repeated three times with each portion of muscle, and then ground with simulated gastric fluid adjusted to pH 3.0 (75 mL) for 60 s in a laboratory blender (Warring, New Hartford, CT, USA). The meat−liquid mixture in each treatment was divided among several open Erlenmeyer flasks and incubated in a shaking bath at 37 °C for 180 min or more, in the dark. At four time points (0, 30, 90, 180 min), lipid peroxidation was determined by measuring TBA levels. After incubation, each sample was mixed immediately with 15% TCA at 1:1 ratio and centrifuged for 10 min at 7000 rpm This treatment terminated lipid peroxidation and extracted the carbonyls into the supernatant. The intermediate supernatant was then treated with TBA (2.8 mg/mL) at a 1:1 ratio. The samples were heated in a boiling water bath for 20 min and then read at 532 nm (Synergy HT, Bio-Tek). Malondialdehyde was determined, as described by Bidlack et al.,[36] and calculated according to 1 μmol/L = 0.156 absorbance. D-α-Tocopherol (solubilized in ethanol) was added to red meat (control) before grinding or directly into oils.

Determination of Lipid Hydroperoxides. Lipid peroxides were determined according to the FOX-2 assay.[37] Red meat was treated as described for malondialdehyde. After incubation, 1 mL of the homogenate was mixed with 9 mL of methanol containing BHT (4.4 mM) for peroxide extraction and then centrifuged at 14500 rpm for 3.5 min. The supernatant (100 μL) was added (triplicates) to tubes containing 10 μL of methanol (or methanol + TPP) and incubated at 25 °C for 30 min. After incubation, FOX-2 reagent (890 μL), which contains BHT (4.4 mM), was added and incubated for an additional 30 min. The samples were measured by a spectrophotometer at 560 nm. Lipid hydroperoxides were calculated by taking into account reduction of the results of methanol alone from samples of methanol + TPP. A standard curve was performed using hydrogen peroxide of pure high grade.[23] Determination of H_2O_2 in oils was done with FOX2 reagent with and without catalase for determining the presence of H_2O_2 (1000 μM hydroperoxides is the same as 1 mmol equiv peroxides/kg oil).

Determination of Total Polyphenols in Olive Oil. The polyphenol content of the different olive oils was determined using Folin−Ciocalteu reagent. The polar fraction was extracted from 2.5 g of olive oil dissolved in 5 mL of hexane using an equal volume of methanol/water (60:40 v/v). After mixing for 2 min, the samples were centrifuged for 10 min at 3500 rpm. The isolated polar fraction (100 μL) was then subjected to 500 μL of Folin−Ciocalteu reagent (diluted at 1:10 with

DOI: 10.1021/acs.jafc.5b02149
J. Agric. Food Chem. 2015, 63, 7016−7023

DDW) and 400 μL of 7.5% w/w sodium bicarbonate. The solution was incubated for 30 min and measured at 765 nm by a spectrophotometer (Synergy HT, Bio-Tek). The working reagent was calibrated against gallic acid of known concentration.[38]

Fatty Acid Profile. Samples were analyzed using a gas chromatograph (Agilent 7890A) equipped with a flame ionization detector. Fatty acid methyl esters (FAMEs) were separated on a capillary column (DB-23, 60 m × 0.25 mm, 0.25 um, Agilent) using hydrogen as a carrier gas. Specific FAMEs were identified by superposition of retention times with standards of known FAMEs (Food FAMEs mix and Marine oil FAMEs mix, Restek). Oil samples were methylated by a transesterification reaction using 2 N KOH solution in methanol. Briefly, oil (100 μL) was mixed with 3 mL of derivatization solution, left for 15 min at room temperature, and extracted with 2 mL of hexane. Hexane phase (1 μL) was taken for GC-FID analysis similarly to the method described by Kristinova et al.[39]

Statistical Analysis. Results (means ± SD) were expressed on a molar basis. The results are the means of triplicates; each point was determined three times. In the figures, each error bar denotes the standard deviation. Data were analyzed by analysis of variance with one-way ANOVA post hoc Tukey–Kramer HSD test, using JMP Pro 10.0.0 (SAS Institute Inc.) software. Differences were considered significant at probability levels of $p < 0.05$ and indicated by different letters.

RESULTS

Fatty Acid Composition, Hydroperoxides, and Hydrogen Peroxide in Oils. The olive oils were found to be rich sources of oleic acid with levels of 70–71%, whereas tuna oil and Alsepa MAX ω-3 supplement contained only 19 and 3.3%, oleic acid, respectively. Linoleic (18:2) and linolenic (18:3) acids were at levels of 7.8 and 4.0% in ROO and EVOO, respectively, and also relatively low in fish oils. In contrast, long-chain highly unsaturated ω-3 fatty acids were abundant in fish oils, ∼24% in tuna and 82% in Alsepa MAX oils (Table 1). The hydroperoxides in the olive oils were almost the same but somewhat lower in Alsepa MAX oil but higher in tuna oil. The highest amount of H_2O_2 in oils was found in tuna oil, ∼680 μM (Table 2).

Table 2. Oil Hydroperoxide Concentration[a]

oil type	hydroperoxides (μM)	H_2O_2 (μM)
refined olive oil (ROO)	2253 ± 64bc	145 ± 42a
extra virgin olive oil (EVOO)	2187 ± 69c	225 ± 46ab
fish oil (Alsepa MAX)	1080 ± 61a	299 ± 42b
fish oil (tuna oil)	2353 ± 20b	679 ± 12c

[a]Differences were considered significant at probability levels of $p < 0.05$, indicated by different letters.

Red-Meat Lipid Peroxidation As Affected by Refined Olive Oil. Lipid peroxidation of heated turkey muscles in simulated gastric fluid was significantly affected by the addition of olive oil. ROO at concentrations of 10 and 15% (w/w) inhibited red-meat lipid peroxidation as determined by the accumulation of MDA by 40 and 60%, respectively (Figure 1A). However, the inhibition recorded by the determination of hydroperoxide accumulation was 75, 80, and 82% for ROO additions of 5, 10, and 15%, respectively (Figure 1B).

Red-Meat Lipid Peroxidation As Affected by Refined and Extra Virgin Olive Oils. To identify the possible effects of the polyphenols present in olive oil on inhibition of lipid peroxidation in red meat, two kinds of olive oils produced by the same producer, refined and extra virgin olive oils, were tested in the same system. The amount of polyphenols found in ROO was 16.0 mg/L and in EVOO, 159.6 mg/L (gallic acid equivalents). The results presented in Figure 2 demonstrate that the inhibitions of meat lipid peroxidation by both oils (added at 10%) were almost identical, as determined by MDA and hydroperoxide accumulation. These results demonstrate that the inhibition of lipid peroxidation is not due to the polyphenol content of the oil.

Red-Meat Lipid Peroxidation As Affected by the Trioleate Glyceride. To demonstrate a possible net effect by olive oil triglycerides, we replaced them with pure trioleate glyceride. The addition of 5, 10, and 15% of trioleate to red meat inhibited lipid peroxidation as determined by accumulation of MDA by 40, 85, and 90%, respectively. The inhibition of red-meat lipid peroxidation was more pronounced when the process was determined by the accumulation of hydroperoxides; at the same concentrations of trioleate inhibition was shown to be 86, 90, and 100%, respectively (Figure 3).

Red-Meat Lipid Peroxidation As Affected by Fish Oil. It has been shown that ω-3 fatty acids oxidize ∼200–400 times more rapidly than ω-9 fatty acids.[21] We evaluated the effects of addition of fish oil to red-meat lipid peroxidation determined by the two methods. The results obtained show that addition of 10% tuna oil increased meat lipid peroxidation as determined by MDA by almost 5-fold and hydroperoxides by almost 2.5-fold. These results led us to test the possible effects of taking ω-3 fatty acid pills together with a meal containing red meat. The addition of 10% fish oil (Alsepa MAX) was found to increase red-meat lipid peroxidation as determined by MDA by ∼2.5-fold and hydroperoxides by 2.0-fold (Figure 4).

Lipid Peroxidation in Stomach Medium, Correlation between MDA/ROOH. Results from all of the treatments obtained in this study calculated as MDA and its parallel LOOH were integrated to receive the correlation coefficient between the two methods: $r^2 = 0.88$ and $p < 0.0001$ (see Figure 5).

Red-Meat Lipid Peroxidation in the Presence of Olive Oil or Fish Oil As Affected by α-Tocopherol. The possible inhibition by α-tocopherol of red-meat lipid peroxidation affected by the addition of 5% ROO or fish oil (Alsepa MAX) was evaluated and is presented in Figure 6 (control, red-meat lipid peroxidation without oil addition was inhibited by ∼25% by the same concentration of α-tocopherol). The results show that the addition of α-tocopherol (18 μM, a concentration possible to attain by the amount present in olive oil) to ROO decreased meat lipid peroxidation at 180 min from 100 to 25 μM of MDA, a decrease of 75%. In contrast, the addition of α-tocopherol (18 μM) to fish oil increased red-meat lipid peroxidation from 100 to 300 μM of MDA ∼3.0-fold, acting as a pro-oxidant. This effect was achieved because α-tocopherol as a reducing compound could affect two active factors simultaneously, lipid free radicals and the Fe ions' oxidation state (Figure 6).

Lipid Peroxidation Affected by 10% Added Oils and Correlation between Results In-vitro and In-vivo (previous clinical studies). Figure 7, left panel, represents the results of MDA accumulation from all of the treatments containing the same amount of added oil (10%) to red meat after incubation in simulated gastric fluid for 180 min, at 37 °C. All of the results differ significantly, $p < 0.05$. The panel on the right represents the correlation of the results accumulating from our three clinical studies[3,4,7] with $R^2 = 0.9139$ between in vitro and in vivo results and incorporation/prediction to possible in vivo effects of supplementation of the fish and olive oil with red meat.

DOI: 10.1021/acs.jafc.5b02149
J. Agric. Food Chem. 2015, 63, 7016–7023

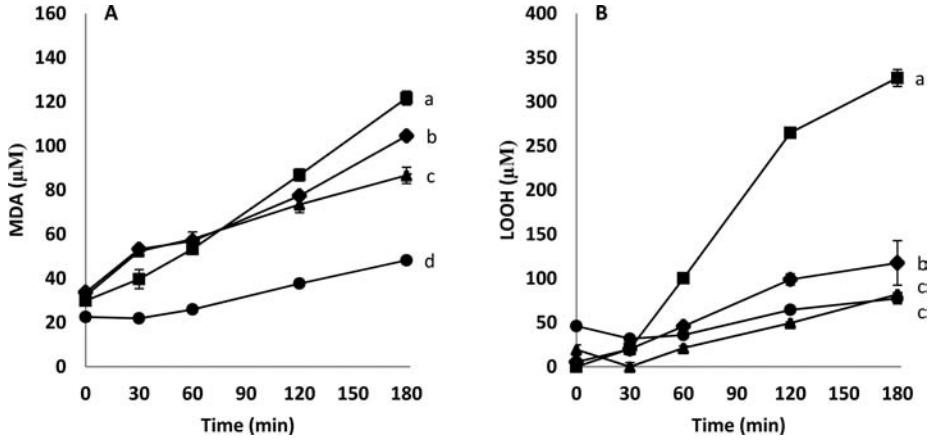

Figure 1. Red-meat lipid peroxidation as affected by refined olive oil: MDA accumulation (A); hydroperoxide accumulation (B). Control, meat only (■); meat + 5% (w/w) olive oil (◆); meat + 10% (w/w) olive oil (▲); meat + 15% (w/w) olive oil (●). Standard deviation bars are smaller than data points in some instances.

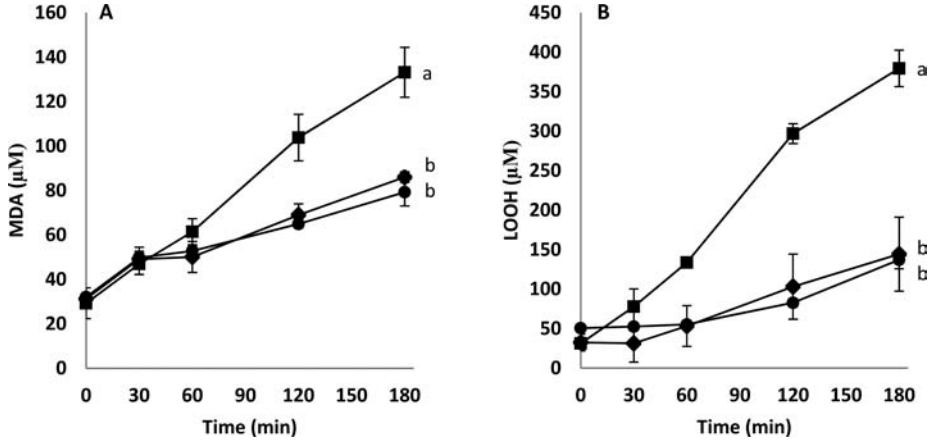

Figure 2. Red-meat lipid peroxidation as affected by refined and extra virgin olive oils: MDA accumulation (A); hydroperoxide accumulation (B). Control, meat only (■); meat + 10% refined olive oil (◆); meat + 10% extra virgin olive oil (●). Standard deviation bars are smaller than data points in some instances.

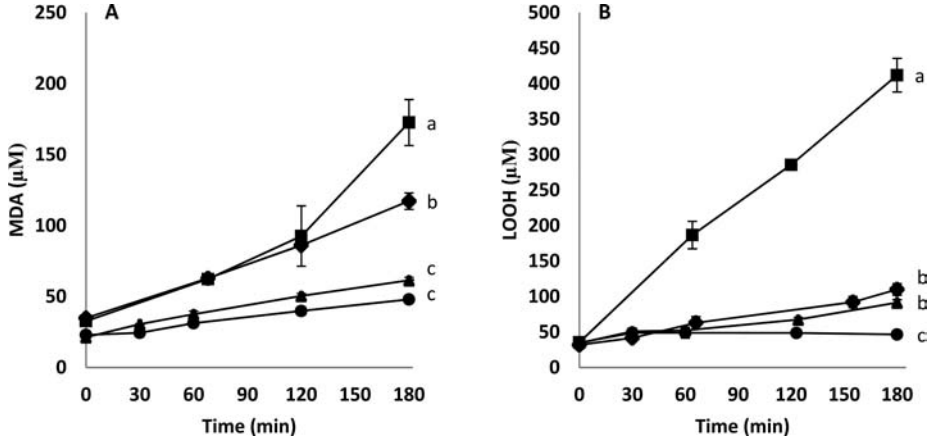

Figure 3. Red-meat lipid peroxidation as affected by the trioleate glyceride: MDA accumulation (A); hydroperoxide accumulation (B). Control, meat only (■); meat + 5% trioleate glyceride (◆); meat + 10% trioleate glyceride (▲); meat + 15% trioleate glyceride (●). Standard deviation bars are smaller than data points in some instances.

DISCUSSION

Our study demonstrated potentially hazardous health effects of consuming red meat combined with additional oil or other foods sensitive to oxidation. However, consuming red meat together with salads containing olive oil, vegetables, fruits, or beverages such as red wine, coffee, or tea containing antioxidants, is very common in the Mediterranean diet. Lipid peroxidation by meat proceeded rapidly because it contains high concentrations of iron catalyzers (~8.5 μg/g iron-heme and 2.5 μg/g free-iron ions) and

DOI: 10.1021/acs.jafc.5b02149
J. Agric. Food Chem. 2015, 63, 7016−7023

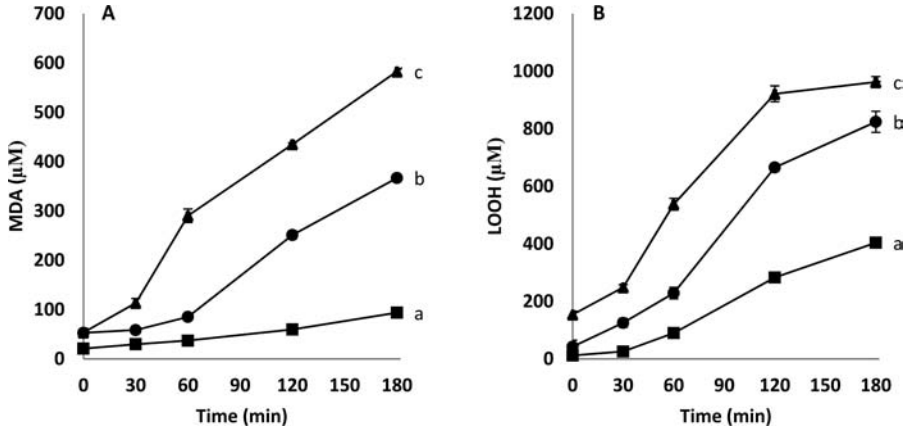

Figure 4. Red-meat lipid peroxidation as affected by fish oil: MDA accumulation (A); hydroperoxide accumulation (B). Control, meat only (■); meat + 10% tuna oil; (▲); meat + 10% Alsepa MAX (●). Standard deviation bars are smaller than data points in some instances.

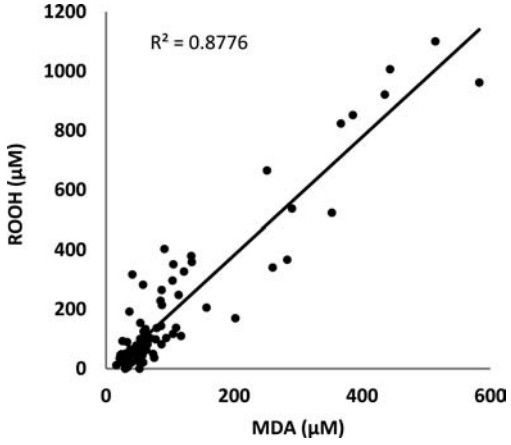

Figure 5. Correlation between two independent methods to determine lipid peroxidation, TBARS, as MDA/ROOH (hydroperoxides), r^2 = 0.88, $p < 0.0001$.

polyunsaturated fatty acids (PUFA) such as linoleic, linolenic, arachidonic, and docosahexaenoic acids.[40] In addition, lipid peroxidation proceeds rapidly when the raw meat structure is disrupted. This occurs after heating, during cooking, frying, roasting, or grilling, which disturbs cellular biochemical integrity and shifts the balance between pro- and antioxidants in favor of pro-oxidant activity.[40] In the stomach, red-meat lipid peroxidation is further enhanced because of the low pH and the presence of oxygen.[1,23] Meals supplemented with oils containing different fatty acids may readily affect lipid peroxidation, as found in our present research. The relatively low rate of autoxidation of oleic acid (18:1) could, in part, explain the lower levels of red-meat lipid peroxidation in the simulated stomach medium in the presence of added olive oil rich in this fatty acid. The decrease in lipid peroxidation by the olive oil could be explained by a sparing and dilution effect generated by oleic acid and saturated fatty acids. Decreasing lipid peroxidation by a pure oleic triglyceride was demonstrated in our study by using trioleate, which showed a high inhibition of lipid peroxidation as determined by both methods of measurement. The effect of oleic acid seems to act not only via an enthalpy effect, decreasing the energy required to attract a hydrogen atom, but also due to the possible chelation of transition metals by oleic acid. Such an effect has been reported previously for nonesterified fatty acids.[41] We believe that triglycerides act in a similar fashion, an effect produced by the nonbonding electrons of oxygen atoms around the ester bond and the carbonyl group, moving the iron catalyzers and the oxidation from the red-meat fatty acids to oleic acid triglycerides.

Our observation of the protective effects of oleic acid on red-meat lipid peroxidation in stomach medium presented here

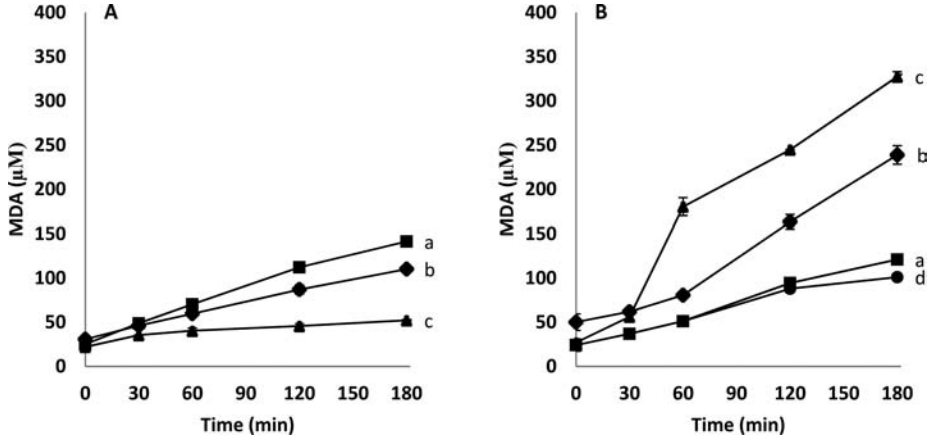

Figure 6. α-Tocopherol effect on red-meat lipid peroxidation in the presence of refined olive oil (A) and fish oil (Alsepa MAX) (B). MDA accumulation: control, meat only (■); meat + 5% oil (◆); meat + 5% oil + vitamin E (18 μM) (▲); meat + vitamin E (18 μM) (●). Standard deviation bars are smaller than data points in some instances.

DOI: 10.1021/acs.jafc.5b02149
J. Agric. Food Chem. 2015, 63, 7016−7023

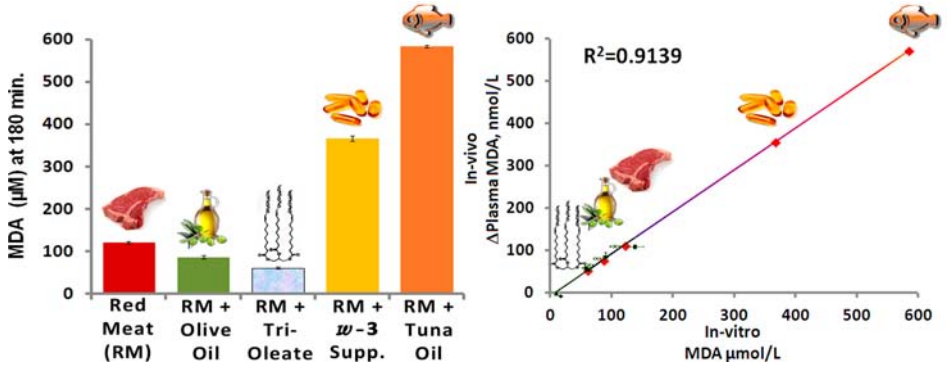

Figure 7. (Left) Results of MDA accumulation from all treatments (10% oils) and (right) correlation betweenr in-vitro and in-vivo (previous clinical studies).

indicated that the protective effect of olive oil is independent of its polyphenol content and is related to the high content of oleic acid. This conclusion fits well the results published recently by Khymenets et al.,[42] who suggested that the antioxidant activities of hydroxytyrasol, the main polyphenol in olive oil, do not contribute to the beneficial health effects after olive oil ingestion in humans. The effects of olive oil components were studied on LDL and biomarkers of oxidative stress, and it was found that only F_2-isoprostanes were inversely related with the oleic acid ratios in LDL, independent of the type of olive oil polyphenol consumed.[43] Hollman et al.,[44] in a recent review, concluded that the biological relevance of direct antioxidant effects of polyphenols in human cardiovascular health has yet to be established, including the effects of those from olive oils. In general, olive oil decreased red-meat lipid peroxidation in the stomach medium, whereas lipid peroxidation was greatly enhanced by fish oils such as tuna and Alsepa MAX, which contain high amounts of ω-3 fatty acids. These fatty acids not only oxidized more rapidly but produced relatively more MDA, other reactive carbonyls, and in general ALEs.[30,34,39,45]

A significant inhibition of lipid peroxidation of red meat in the presence of olive oil (added at 5%) was obtained in simulated stomach medium by the addition of vitamin E. Vitamin E, at the same concentration that inhibited red-meat lipid peroxidation in the presence of olive oil, paradoxically accelerated lipid peroxidation in the presence of fish oil. The inversion of catalysis from antioxidation to pro-oxidation most likely occurred because vitamin E can reduce ferric to ferrous ions along with the presence of hydroperoxides and the high oxidation rate of the unsaturated fatty acids present in fish oil (400-fold higher than oleic acid), which form new free radicals and hydroperoxides (reactions 1−3). Vitamin E, as a reducing compound, could both reduce free iron ions to ferrous state, acting as a pro-oxidant, and at the same time operate as a scavenger of lipid free radicals, acting as an antioxidant in a similar manner to polyphenols,[4] by the following reactions:

$$\text{T-OH} + \text{Fe}^{+3} \rightarrow \text{T-O}^{\bullet} + \text{Fe}^{2+} \quad (1)$$

$$\text{Fe}^{2+} + \text{LOOH} \rightarrow \text{Fe}^{3+} + \text{LO}^{\bullet} + {}^{-}\text{OH} \quad (2)$$

$$\text{LO}^{\bullet} + \text{LH} \rightarrow \text{LOH} + \text{L}^{\bullet}$$

$$\text{L}^{\bullet} + \text{O}_2 \rightarrow \text{LOO}^{\bullet} \quad (3)$$

$$\text{LOO}^{\bullet} + \text{LH} \rightarrow \text{LOOH} + \text{L}^{\bullet}$$

$$\text{T-OH} + \text{LO}^{\bullet}/\text{LOO}^{\bullet} \rightarrow \text{T-O}^{\bullet} + \text{LOH/LOOH} \quad (4)$$

$$\text{T-O}^{\bullet} + \text{LO}^{\bullet}/\text{LOO}^{\bullet} \rightarrow \text{T-OLO/T-OLOO} \quad (5)$$

Fe^{3+}/ Fe^{2+} = ferric/ferrous ions; T-OH = α-tocopherol; $\text{T-O}^{\bullet}$ = tocopheryl radical; $\text{L}^{\bullet}$ = allyl radical; $\text{LOO}^{\bullet}$ = peroxyl radical; $\text{LO}^{\bullet}$ = alkoxyl radical; LOOH = hydroperoxide; LH = unsaturated fatty acid; LOH = alcohol; T-OLO/T-OLOO = adducts of tocopherol with unsaturared fatty acids.

In our food system the balance between the reactions of lipid pro-oxidation and antioxidation is very much dependent on the type and concentration of the fatty acids, fatty acid hydroperoxides/H_2O_2, iron catalyzers. and type and amounts of antioxidants.[1,4,22,23]

The ALEs, mostly reactive carbonyls that are generated during lipid peroxidation in the stomach, can be absorbed into the blood system and potentially interact with functional proteins. This includes receptors or blood particles such as LDL, leading to production of modified-LDL, a well known atherogenic particle.[1,46] The RCs are absorbed from the gut into the blood system in proportion to the amount present in consumed foods[47] and/or generated in the stomach.[1−3] Absorption of these compounds is thought to be deleterious to human health.[1,47−50]

We hypothesize that there are meaningful differences in the health impact of the Western and Mediterranean diets due to the amount of ALEs generated in the stomach during the meal and subsequently absorbed into the bloodstream. Because lipid peroxidation in the stomach is propagated by free radicals, the timing of consuming foods or beverages containing antioxidants should be either prior to or during consumption of red meat. The Western diet contains higher amounts of red meat and unsaturated fatty acids oxidized by frying or other cooking processes and fewer reducing agents (plant food antioxidants), which can act pro-oxidatively. The Mediterranean diet, in contrast, contains lower amounts of red meat due to a higher consumption of vegetables, fruits, and other plant-derived foods and more monounsaturated fatty acids and plant food antioxidants. Overall, this Mediterranean pattern of diet appears to inhibit lipid peroxidation and ALEs formation, thus decreasing the risk of diet-related diseases.

AUTHOR INFORMATION

Corresponding Author

*(J.K.) E-mail: jokanner@gmail.com. Phone: 972-50-6220761. Fax: 972-8-9363208.

Notes

The authors declare no competing financial interest.

DOI: 10.1021/acs.jafc.5b02149
J. Agric. Food Chem. 2015, 63, 7016−7023

■ ACKNOWLEDGMENTS

We thank Dr. Aliza Stark for English editing.

■ REFERENCES

(1) Kanner, J.; Gorelik, S.; Roman, S.; Kohen, R. Protection by polyphenols of postprandial human plasma and low-density lipoprotein modification: the stomach as a bioreactor. *J. Agric. Food Chem.* **2012**, *60*, 8790−8796.

(2) Gorelik, S.; Ligumsky, M.; Kohen, R.; Kanner, J. The stomach as a "bioreactor": when red meat meets red wine. *J. Agric. Food Chem.* **2008**, *56*, 5002−5007.

(3) Gorelik, S.; Ligumsky, M.; Kohen, R.; Kanner, J. A novel function of red wine polyphenols in humans: prevention of absorption of cytotoxic lipid peroxidation products. *FASEB J.* **2008**, *22*, 41−46.

(4) Sirota, R.; Gorelik, S.; Harris, R.; Kohen, R.; Kanner, J. Coffee polyphenols protect human plasma from postprandial carbonyl modifications. *Mol. Nutr. Food Res.* **2013**, *57*, 916−919.

(5) Ahotupa, M.; Suomela, J. P.; Vuorimaa, T.; Vasankari, T. Lipoprotein-specific transport of circulating lipid peroxides. *Ann. Med.* **2010**, *42*, 521−529.

(6) Li, Z. P.; Henning, S. M.; Zhang, Y. J.; Zerlin, A.; Li, L. Y.; Gao, K.; Lee, R. P.; Karp, H.; Thames, G.; Bowerman, S.; Heber, D. Antioxidant-rich spice added to hamburger meat during cooking results in reduced meat, plasma, and urine malondialdehyde concentrations. Reply. *Am. J. Clin. Nutr.* **2010**, *92*, 997−997.

(7) Gorelik, S.; Kanner, J.; Schurr, D.; Kohen, R. A rational approach to prevent postprandial modification of LDL by dietary polyphenols. *J. Funct. Foods* **2013**, *5*, 163−169.

(8) Micha, R.; Wallace, S. K.; Mozaffarian, D. Red and processed meat consumption and risk of incident coronary heart disease, stroke, and diabetes mellitus: a systematic review and meta-analysis. *Circulation* **2010**, *121*, 2271−2283.

(9) Cohn, J. S. Oxidized fat in the diet, postprandial lipaemia and cardiovascular disease. *Curr. Opin. Lipidol.* **2002**, *13*, 19−24.

(10) Koeth, R. A.; Wang, Z.; Levison, B. S.; Buffa, J. A.; Org, E.; Sheehy, B. T.; Britt, E. B.; Fu, X.; Wu, Y.; Li, L.; Smith, J. D.; DiDonato, J. A.; Chen, J.; Li, H.; Wu, G. D.; Lewis, J. D.; Warrier, M.; Brown, J. M.; Krauss, R. M.; Tang, W. H.; Bushman, F. D.; Lusis, A. J.; Hazen, S. L. Intestinal microbiota metabolism of L-carnitine, a nutrient in red meat, promotes atherosclerosis. *Nat. Med.* **2013**, *19*, 576−585.

(11) Fretts, A. M.; Howard, B. V.; McKnight, B.; Duncan, G. E.; Beresford, S. A.; Mete, M.; Eilat-Adar, S.; Zhang, Y.; Siscovick, D. S. Associations of processed meat and unprocessed red meat intake with incident diabetes: the Strong Heart Family Study. *Am. J. Clin. Nutr.* **2012**, *95*, 752−758.

(12) Pan, A.; Sun, Q.; Bernstein, A. M.; Manson, J. E.; Willett, W. C.; Hu, F. B. Changes in red meat consumption and subsequent risk of type 2 diabetes mellitus: three cohorts of US men and women. *JAMA Int. Med.* **2013**, *173*, 1328−1335.

(13) Pillon, N. J.; Croze, M. L.; Vella, R. E.; Soulere, L.; Lagarde, M.; Soulage, C. O. The lipid peroxidation by-product 4-hydroxy-2-nonenal (4-HNE) induces insulin resistance in skeletal muscle through both carbonyl and oxidative stress. *Endocrinology* **2012**, *153*, 2099−2111.

(14) White, D. L.; Collinson, A. Red meat, dietary heme iron, and risk of type 2 diabetes: the involvement of advanced lipoxidation endproducts. *Adv. Nutr.* **2013**, *4*, 403−411.

(15) Joshi, A. D.; Corral, R.; Catsburg, C.; Lewinger, J. P.; Koo, J.; John, E. M.; Ingles, S. A.; Stern, M. C. Red meat and poultry, cooking practices, genetic susceptibility and risk of prostate cancer: results from a multiethnic case-control study. *Carcinogenesis* **2012**, *33*, 2108−2118.

(16) Farvid, M. S.; Cho, E.; Chen, W. Y.; Eliassen, A. H.; Willett, W. C. Adolescent meat intake and breast cancer risk. *Int. J. Cancer* **2014**, *136*, 1909−1920.

(17) Alexander, D. D.; Cushing, C. A. Red meat and colorectal cancer: a critical summary of prospective epidemiologic studies. *Obes. Rev.* **2011**, *12*, e472−493.

(18) Demeyer, D.; Honikel, K.; De Smet, S. The World Cancer Research Fund report 2007: A challenge for the meat processing industry. *Meat Sci.* **2008**, *80*, 953−959.

(19) Magalhaes, B.; Peleteiro, B.; Lunet, N. Dietary patterns and colorectal cancer: systematic review and meta-analysis. *Eur. J. Cancer Prev.* **2012**, *21*, 15−23.

(20) Pan, A.; Sun, Q.; Bernstein, A. M.; Schulze, M. B.; Manson, J. E.; Stampfer, M. J.; Willett, W. C.; Hu, F. B. Red meat consumption and mortality: results from 2 prospective cohort studies. *Arch. Int. Med.* **2012**, *172*, 555−563.

(21) Holman, R. T.; Ellmer, O. C. The rates of oxidation of unsaturated fatty acids and esters. *J. Am. Oil Chem. Soc.* **1947**, *24*, 127−129.

(22) Kanner, J.; German, J. B.; Kinsella, J. E. Initiation of lipid peroxidation in biological systems. *Crit. Rev. Food Sci. Nutr.* **1987**, *25*, 317−364.

(23) Kanner, J.; Lapidot, T. The stomach as a bioreactor: dietary lipid peroxidation in the gastric fluid and the effects of plant-derived antioxidants. *Free Radical Biol. Med.* **2001**, *31*, 1388−1395.

(24) Mente, A.; de Koning, L.; Shannon, H. S.; Anand, S. S. A systematic review of the evidence supporting a causal link between dietary factors and coronary heart disease. *Arch. Intern. Med.* **2009**, *169*, 659−669.

(25) Estruch, R.; Ros, E.; Salas-Salvado, J.; Covas, M. I.; Corella, D.; Aros, F.; Gomez-Gracia, E.; Ruiz-Gutierrez, V.; Fiol, M.; Lapetra, J.; Lamuela-Raventos, R. M.; Serra-Majem, L.; Pinto, X.; Basora, J.; Munoz, M. A.; Sorli, J. V.; Martinez, J. A.; Martinez-Gonzalez, M. A. Primary prevention of cardiovascular disease with a Mediterranean diet. *N. Engl. J. Med.* **2013**, *368*, 1279−1290.

(26) Covas, M. I.; Nyyssonen, K.; Poulsen, H. E.; Kaikkonen, J.; Zunft, H. J.; Kiesewetter, H.; Gaddi, A.; de la Torre, R.; Mursu, J.; Baumler, H.; Nascetti, S.; Salonen, J. T.; Fito, M.; Virtanen, J.; Marrugat, J. The effect of polyphenols in olive oil on heart disease risk factors: a randomized trial. *Ann. Int. Med.* **2006**, *145*, 333−341.

(27) Lavie, C. J.; Milani, R. V.; Mehra, M. R.; Ventura, H. O. Omega-3 polyunsaturated fatty acids and cardiovascular diseases. *J. Am. Coll. Cardiol.* **2009**, *54*, 585−594.

(28) Mata Lopez, P.; Ortega, R. M. Omega-3 fatty acids in the prevention and control of cardiovascular disease. *Eur. J. Clin. Nutr.* **2003**, *57* (Suppl. 1), S22−S25.

(29) Dyall, S. C.; Michael, G. J.; Michael-Titus, A. T. Omega-3 fatty acids reverse age-related decreases in nuclear receptors and increase neurogenesis in old rats. *J. Neurosci. Res.* **2010**, *88*, 2091−2102.

(30) Awada, M.; Soulage, C. O.; Meynier, A.; Debard, C.; Plaisancie, P.; Benoit, B.; Picard, G.; Loizon, E.; Chauvin, M. A.; Estienne, M.; Peretti, N.; Guichardant, M.; Lagarde, M.; Genot, C.; Michalski, M. C. Dietary oxidized n-3 PUFA induce oxidative stress and inflammation: role of intestinal absorption of 4-HHE and reactivity in intestinal cells. *J. Lipid Res.* **2012**, *53*, 2069−2080.

(31) Kenmogne-Domguia, H. B.; Moisan, S.; Viau, M.; Genot, C.; Meynier, A. The initial characteristics of marine oil emulsions and the composition of the media inflect lipid oxidation during in vitro gastrointestinal digestion. *Food Chem.* **2014**, *152*, 146−154.

(32) Cahill, L. E.; Pan, A.; Chiuve, S. E.; Sun, Q.; Willett, W. C.; Hu, F. B.; Rimm, E. B. Fried-food consumption and risk of type 2 diabetes and coronary artery disease: a prospective study in 2 cohorts of US women and men. *Am. J. Clin. Nutr.* **2014**, *100*, 667−675.

(33) Visioli, F. Rusting the pipes: ingestion of oxidized lipids and vascular disease. *Vasc. Pharmacol.* **2014**, *62*, 47−48.

(34) Goicoechea, E.; Brandon, E. F.; Blokland, M. H.; Guillen, M. D. Fate in digestion in vitro of several food components, including some toxic compounds coming from omega-3 and omega-6 lipids. *Food Chem. Toxicol.* **2011**, *49*, 115−124.

(35) Halvorsen, B. L.; Blomhoff, R. Determination of lipid oxidation products in vegetable oils and marine omega-3 supplements. *Food Nutr. Res.* **2011**, *55*, 10.3402/fnr.v55i0.5792

(36) Bidlack, R. W.; Okita, R. T.; Hochstein, P. The role of NADPH-Cytochrome b_5 reductase in microsomal lipid peroxidation. *Biochem. Biophys. Res. Commun.* **1973**, *53*, 459−465.

DOI: 10.1021/acs.jafc.5b02149
J. Agric. Food Chem. 2015, 63, 7016−7023

(37) Nourooz-Zadeh, J. Ferrous ion oxidation in presence of xylenol orange for detection of lipid hydroperoxides in plasma. *Methods Enzymol.* **1999**, *300*, 58−62.
(38) Mastralexi, A.; Nenadis, N.; Tsimidou, M. Z. Addressing analytical requirements to support health claims on "Olive Oil Polyphenols" (EC Regulation 432/2012). *J. Agric. Food Chem.* **2014**, *62*, 2459−2461.
(39) Kristinova, V.; Storro, I.; Rustad, T. Influence of human gastric juice on oxidation of marine lipids - in vitro study. *Food Chem.* **2013**, *141*, 3859−3871.
(40) Kanner, J. Oxidative processes in meat and meat-products − quality implications. *Meat Sci.* **1994**, *36*, 169−189.
(41) Balasubramanian, K. A.; Nalini, S.; Manohar, M. Nonesterified fatty acids and lipid peroxidation. *Mol. Cell. Biochem.* **1992**, *111*, 131−135.
(42) Khymenets, O.; Fito, M.; Tourino, S.; Munoz-Aguayo, D.; Pujadas, M.; Torres, J. L.; Joglar, J.; Farre, M.; Covas, M. I.; de la Torre, R. Antioxidant activities of hydroxytyrosol main metabolites do not contribute to beneficial health effects after olive oil ingestion. *Drug Metab. Dispos.* **2010**, *38*, 1417−1421.
(43) Cicero, A. F.; Nascetti, S.; Lopez-Sabater, M. C.; Elosua, R.; Salonen, J. T.; Nyyssonen, K.; Poulsen, H. E.; Zunft, H. J.; Kiesewetter, H.; de la Torre, K.; Covas, M. I.; Kaikkonen, J.; Mursu, J.; Koenbick, C.; Baumler, H.; Gaddi, A. V. Changes in LDL fatty acid composition as a response to olive oil treatment are inversely related to lipid oxidative damage: the EUROLIVE study. *J. Am. Coll. Nutr.* **2008**, *27*, 314−320.
(44) Hollman, P. C.; Cassidy, A.; Comte, B.; Heinonen, M.; Richelle, M.; Richling, E.; Serafini, M.; Scalbert, A.; Sies, H.; Vidry, S. The biological relevance of direct antioxidant effects of polyphenols for cardiovascular health in humans is not established. *J. Nutr.* **2011**, *141*, 989S−1009S.
(45) Larsson, K.; Cavonius, L.; Alminger, M.; Undeland, I. Oxidation of cod liver oil during gastrointestinal in vitro digestion. *J. Agric. Food Chem.* **2012**, *60*, 7556−7564.
(46) Steinberg, D.; Parthasarathy, S.; Carew, T. E.; Khoo, J. C.; Witztum, J. L. Beyond cholesterol. Modifications of low-density lipoprotein that increase its atherogenicity. *N. Engl. J. Med.* **1989**, *320*, 915−924.
(47) Uribarri, J.; Cai, W.; Sandu, O.; Peppa, M.; Goldberg, T.; Vlassara, H. Diet-derived advanced glycation end products are major contributors to the body's AGE pool and induce inflammation in healthy subjects. *Ann. N. Y. Acad. Sci.* **2005**, *1043*, 461−466.
(48) Cai, W.; Gao, Q. D.; Zhu, L.; Peppa, M.; He, C.; Vlassara, H. Oxidative stress-inducing carbonyl compounds from common foods: novel mediators of cellular dysfunction. *Mol. Med.* **2002**, *8*, 337−346.
(49) Kanner, J. Dietary advanced lipid oxidation endproducts are risk factors to human health. *Mol. Nutr. Food Res.* **2007**, *51*, 1094−1101.
(50) Negre-Salvayre, A.; Coatrieux, C.; Ingueneau, C.; Salvayre, R. Advanced lipid peroxidation end products in oxidative damage to proteins. Potential role in diseases and therapeutic prospects for the inhibitors. *Br. J. Pharmacol.* **2008**, *153*, 6−20.

DOI: 10.1021/acs.jafc.5b02149
J. Agric. Food Chem. 2015, 63, 7016−7023

MATERIALS AND METHODS

Chemicals. TNBS and RPMI 1640 were purchased from Sigma-Aldrich (St. Louis, MO, USA). Antibodies for inducible NO synthase (iNOS), cyclooxygenase (COX)-2, and β-actin were purchased from Santa Cruz Biotechnology (Santa Cruz, CA, USA). Antibodies for transforming growth factor beta-activated kinase 1 (TAK1), p-TAK1, interleukin-1 receptor-associated kinase 1 (IRAK1), p-IRAK1, inhibitor of nuclear factor kappa-B kinase subunit beta (IKKβ), p-IKKβ, IκB kinase alpha (IκBα), p-IκBα, p65, p-p65, p38, p-p38, extracellular signal-regulated kinases (ERK), p-ERK, c-jun N-terminal kinases (JNK), and p-JNK were purchased from Cell Signaling Technology (Beverly, MA, USA). Enzyme-linked immunosorbent assay (ELISA) kits for cytokines were purchased from R&D Systems (Minneapolis, MN, USA). Heat-inactivated fetal calf serum (FCS) and fetal bovine serum (FBS) were purchased from Invitrogen (Carlsbad, CA, USA). Pan T Cell Isolation Kit II, anti-IL-17A, anti-FoxP3, anti-CD3, anti-CD28, recombinant IL-6, and recombinant tumor growth factor beta (TGFβ, 1 ng/mL were purchased from Miltenyi Biotec (Bergisch Gladbach, Germany). MR2 (purity, > 95%), pseudoginsenoside RT4 (PRT4; purity, > 95%), and ocotillol (purity, > 95%) were isolated according to the previously published method of Nguyen et al.[16,17]

Table 1. Primers Used for Real-Time PCR

	forward	reverse
IFN-γ	TCA AGT GGC ATA GAT GTG GAA GAA	TGG CTC TGC AGG ATT TTC ATG
TGFβ	CAC CGG AGA GCC CTG GAT A	TGT ACA GCT GCC GCA CAC A
IL-5	AAA GAG AAG TGT GGC GAG GAG AGA C	CCT TCC ATT GCC CAC TCT GTA CTC ATC
IL-10	ATG CTG CCT GCT CTT ACT GAC TG	CCC AAG TAA CCC TTA AAG TCC TGC
IL-12 (p35)	AGC CTC CTC CTT GTG GCT A	GCT GGG AGT ACC CTG ACA C
IL-17	TTT AAC TCC CTT GGC GCA AAA	CTT TCC CTC CGC ATT GAC AC
IL-23 (p19)	TGT GCC CCG TAT CCA GTG T	CGG ATC CTT TGC AAG CAG AA
T-bet	CCT CTT CTA TCC AAC CAG TAT C	CTC CGC TTC ATA ACT GTG T
GATA3	GAA GGC ATC CAG ACC CGA AAC	ACC CAT GGC GGT GAC CAT GC
RORγt	ACA GCC ACT GCA TTC CCA GTT T	TCT CGG AAG GAC TTG CAG ACA T
Foxp3	CCC ATC CCC AGG AGT CTT	ACC ATG ACT AGG GGC ACT GTA
β-actin	CCG TGA AAA GAT GAC CCA GAT C′	CAC AGC CTG GAT GGC TAC GT

Isolation of MR2, an Inhibitor of Th 17 Cell Differentiation. Vietnamese ginseng was collected in Mt. Ngoc Linh, Quang Nam province, Vietnam, and identified by one of the authors (M.D.N.). A voucher specimen was deposited in the herbarium of College of Pharmacy, Seoul National University (SNUP-2012-A-01). Vietnamese ginseng (150 g) was refluxed with MeOH to yield the MeOH extract (64 g), which was partitioned between EtOAc and H_2O. The water layer was evaporated to give ∼50 g of dried extract and suspended in distilled water, which was partitioned between water and *n*-BuOH to yield 25 g of *n*-BuOH fraction. The *n*-BuOH fraction (10 g) was applied to a silica gel column with a stepwise gradient of a $CHCl_3$–MeOH mixture (9:1 → 7:1 → 5:1) to yield 11 subfractions. Subfraction 6 (1000 mg) was further separated on C18 column chromatography eluting with MeOH-H_2O (1:1 → 2:1 → 1:0) to obtain MR2 (320 mg), which was the most potent inhibition against Th17 cell differentiation, as needles in EtOAc–MeOH mixture. The isolated compound was identified by the direct comparison of spectroscopic and chromatographic data to those of authentic samples.[17,18] MR2: white amorphous powder; purity, >95%; FAB-MS *m*/*z*, 785 $[M - H]^-$.

Analysis of MR2 Metabolites by Mouse Gut Microbiota. First, we orally administered MR2 (50 mg/kg) to five mice, killed 12 h after the oral administration, collected the colon fluid, and extracted with 1 mL of MeOH. The metabolite(s) in the supernatant was analyzed by HPLC.[18] HPLC was performed using a PerkinElmer series 200 HPLC (Waltham, MA, USA) system equipped with evaporative light scattering detector (Alltech ELSD 2000, Alltech, Deerfield, IL, USA) and Sunfire C18 column (250 mm × 4.6 mm i.d., 5 μm; Waters Corp, MA, USA). Mobile phase, water (A) and acetonitrile (B): 0–1 min (18% B), 1–5 min (18 → 25% B), 5–25 min (25 → 32% B), 25–29 min (32% B), 29–40 min (32 → 38% B), 40–45 min (38 → 49.5% B), 45–59 min (49.5 → 100% B), 59–69 min (100% B). The flow rate was 1 mL/min, and the injection volume was 10 μL. ELSD was set to a probe temperature of 80 °C, and the nebulizer gas (N_2) was adjusted to 1.5 L/min. Retention times of MR2, PRT4, and ocotillol were 15.9, 16.3, and 41.8 min, respectively.

Assay of Majonoside R2-Metabolizing Activity of Mouse Microbiota. To analyze the metabolic pathway of MR2, the reaction mixture (5 mL) containing 0.5 mL of the mouse colon fluid suspension (fecal bacterial suspension), 0.5 mL of 1 mM MR2, and 4 mL of diluted general anaerobic medium was anaerobically incubated at 37 °C for 24 h. The supernatant (0.5 mL) was periodically removed, and then 2 mL of MeOH was added to stop the reaction. The reaction mixture was centrifuged at 3000*g* for 10 min and the levels of MR2 and their metabolites PRT4 and ocotillol were analyzed by HPLC and TLC. TLC was developed with CH_3Cl:MeOH:H_2O (=75:25:10 lower layer), stained with 10% sulfuric acid in MeOH, and quantified by densitometry.

Animals. Male ICR mice (20–23 g, 4.5 weeks old) were supplied from Orient Animal Breeding Center (Sungnam, Korea). All animals were fed standard laboratory chow, housed in wire cages at 20–22 °C and 50 ± 10% humidity, and allowed water ad libitum. All experiments were performed in accordance with the NIH and Kyung Hee University guides for Laboratory Animals Care and Use and approved by the Committee for the Care and Use of Laboratory Animals in the College of Pharmacy, Kyung Hee University (IRB No. KHUASP(SE)-14-055).

Preparation of Splenocytes. Spleens were aseptically removed from mice, crushed into a single cell suspension, and washed with tris-buffered ammonium chloride.[19] The cell suspension was prepared in RPMI 1640 medium containing 10% fetal calf serum. T cells were isolated from splenocytes by Pan T Cell Isolation Kit II (Miltenyi Biotec 130-095-130) and plated. Cells were stimulated with anti-CD3 (1 μg/mL) and anti-CD28 (1 μg/mL) in the presence of recombinant IL-6 (20 ng/mL), recombinant TGFβ (1 ng/mL) with or without ginsenosides for 4 days, and analyzed by a flow cytometer (C6 Flow Cytometer System).

Preparation of Experimental Colitis in Mice. To measure the anticolitic effect of ocotillol in mice, mice were divided into five groups: normal and TNBS-induced colitic groups treated with or without ocotillol (10 and 20 mg/kg) or sulfasalazine (20 mg/kg). Each group consisted of 6 mice. Colitis was induced by the intrarectal injection of 2.5% (w/v) TNBS solution (100 μL) in 50% ethanol into the colon of lightly anesthetized mice via a round-tip needle equipped with a syringe.[20] Normal mouse group was treated with vehicle alone. TNBS solution quickly excreted mice were excluded: >95% of the mice caused TNBS enema. Test agents were orally administered once a day for 3 days from the first day after TNBS treatment. Mice were killed 20 h after the final administration of test agents. Colon was quickly removed, opened longitudinally, and gently washed with ice-cold phosphate-buffered saline. Macroscopic assessment of the colitis severity was scored according to a previously reported scoring method,[20] and the colon tissue was then stored at −80 °C until the experiment.

For the histological exam, colons were fixed in 10%-buffered formalin solution, cut into 10-μm sections, stained with hematoxylin–eosin, toluidine blue, or safranin O, and observed under a light microscope.

DOI: 10.1021/acs.jafc.5b02183
J. Agric. Food Chem. 2015, 63, 7024–7031

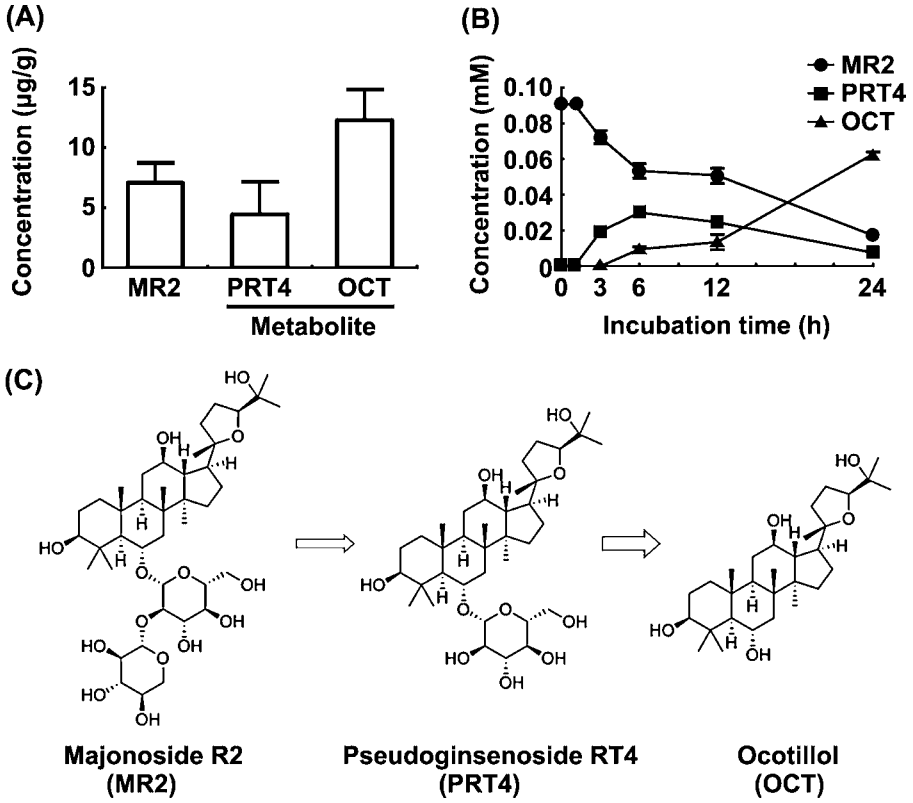

Figure 1. Metabolism of orally administered MR2 by the gut microbiota of mice. (A) Metabolism of orally administered MR2 in mice. MR2 was orally administered to mice and measured in the colon fluid of mice 12 h after the administration of MR2. (B) Metabolism of MR2 by the mouse fecal suspension. The fecal suspensions were incubated with MR2 (0.1 mM), and periodically extracted with ethyl acetate. The amounts of MR2 and its metabolites PRT4 and ocotillol (OCT) were analyzed using thin layer chromatography (solvent: CH_3Cl:MeOH:H_2O = 75:25:10 lower layer) and quantified by densitometry. (C) Proposed metabolic pathway of MR2 by gut microbiota.

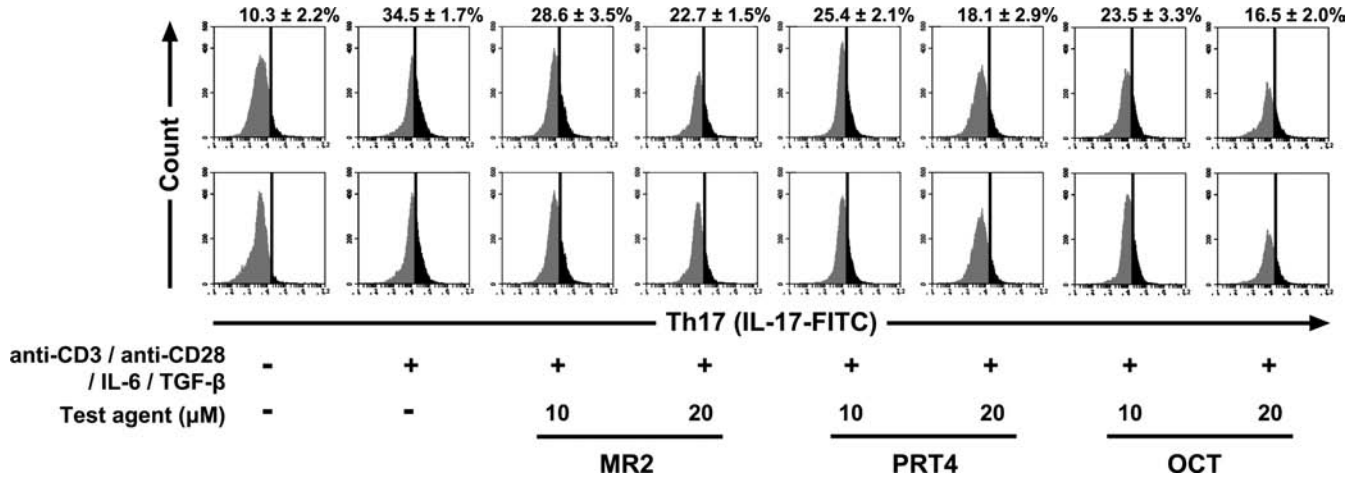

Figure 2. Effect of MR2 and its metabolites PRT4 and ocotillol (OCT) on Th17 cell differentiation. (A) Effect on Th17 cell differentiation. Splenocytes were stimulated with anti-CD3 (1 μg/mL) and anti-CD28 (1 μg/mL) with or without IL-6 (20 ng/mL) plus TGF-β (1 ng/mL) in the presence of MR2 and its metabolites (10 and 20 μM) for 4 days. Staining of cell surface CD4 antigen and intracellular IL-17 was performed and analyzed using flow cytometry. (B) Effect on cytotoxicity. For the cytotoxicity assay, cells were incubated for 4 days and survival was determined by the trypan blue method. All data indicate mean ± SD (n = 3). $^{\#}p < 0.05$ indicated a significant difference vs normal control. $^{*}p < 0.05$ indicated a significant difference vs cells stimulated with anti-CD3/anti-CD28 and IL-6/TGF-β.

Assay of Myeloperoxidase Activity. Colons were homogenized in 10 mM potassium phosphate buffer (pH 7.0) containing 0.5% hexadecyl trimethylammonium bromide, and centrifuged at 4 °C (20000g, 20 min). An aliquot (50 μL) of the supernatant was added to a reaction mixture containing 0.1 mM H_2O_2 and 1.6 mM tetramethylbenzidine and then incubated at 37 °C. The absorbance was measured at 650 nm over time.[21] Myeloperoxidase activity was defined as the quantity degrading 1 μmol/mL of peroxide and expressed in unit per mg protein. The protein amount was assayed using the Bradford protein assay reagent.

Real-Time Polymerase Chain Reaction (PCR). Reverse transcription was performed with 2 μg of total RNA isolated from the colon. Real-time PCR for IL-5, IL-10, IL-12/p35, IL-17, IL-23, TGFβ, IFN-γ, T-bet, GATA3, RORγt, Foxp3, and β-actin (Table 1) was

DOI: 10.1021/acs.jafc.5b02183
J. Agric. Food Chem. 2015, 63, 7024−7031

performed as described previously,[22] utilizing a Takara thermal cycler, which used SYBER premix agents, as per the instructions from Takara Bio Inc. Thermal cycling conditions were as follows: activation of DNA polymerase at 95 °C for 5 min, followed by 38 cycles of amplification at 95 °C for 10 s and at 60 °C for 30 s. The normalized expression of the assayed genes, with respect to β-actin, was computed for all samples by using the Microsoft Excel data spreadsheet.

ELISA and Immunoblotting. For the ELISA assay, colons were homogenized in 1 mL of ice-cold RIPA lysis buffer containing 1% phosphatase inhibitor cocktail and 1% protease inhibitor cocktail. The lysate was centrifuged (15000*g*, 4 °C) for 10 min, and the supernatant was transferred to 96-well ELISA plates.[20]

For the immunoblotting, colons were carefully homogenized in 1 mL of RIPA lysis buffer containing 1% phosphatase inhibitor cocktail and 1% protease inhibitor cocktail and centrifuged for 10 min, and the supernatant was subjected to 8−10% sodium dodecyl sulfate polyacrylamide gel electrophoresis and then transferred to nitrocellulose membrane.[20] Immunodetection was performed using an enhanced chemiluminescence detection kit.

Flow Cytometry of Th17 and Treg Cells in the Colonic Lamina Propria. To assay Th17 and Treg cells, the colons of mice were cut into small pieces, incubated with 2.5 mM EDTA at 37 °C with agitation for 20 min to remove cells, minced, and digested for 20 min with 1 mg/mL collagenase type VIII (Sigma) at 37 °C.[23] Colonic lamina propria cells were then filtered, and T cells were isolated using a Pan T cell Isolation Kit II. T cells isolated from colons were fixed and stained with anti-FoxP3 or anti-IL-17A antibodies and then analyzed by flow cytometry.

Statistical Analysis. The data are presented as the means ± standard deviation. The data of animal experiments were analyzed by one-way analysis of variance (ANOVA) followed by the Student−Newman−Keuls test for multiple comparisons. *P* values of 0.05 or less were considered statistically significant.

RESULTS

Metabolism of MR2 by Gut Microbiota. To understand the anti-inflammatory effect and absorbable metabolite(s) of MR2 in vivo, we administered MR2 orally and analyzed its metabolites in the feces after 12 h (Figure 1). The dominant metabolite was ocotillol, followed by PRT4. Next, we incubated MR2 with mouse fecal microbiota and investigated its hydrophobic metabolites absorbable from the intestine into the blood. MR2 concentration was gradually decreased, but that of ocotillol increased, followed by PRT4.

Effect of MR2 and Its Metabolites PRT4 and Ocotillol on Th17 Cell Differentiation. To understand the anti-inflammatory effects of MR2 and its metabolites, we measured their inhibitory effects against the differentiation of splenic T cells to Th17 cells, stimulated with IL-6 and TGF-β in the presence of anti-CD3 and anti-CD28 (Figure 2). Treatment with IL-6 and TGFβ significantly induced Th17 cell differentiation (34.5%). However, treatment with MR2, PRT4, or ocotillol significantly suppressed the Th17 cell population compared with nontreated cells, with the highest inhibition exhibited by ocotillol. Moreover, these ginsenosides inhibited IL-17 and RORγt expression, suggesting that MR2 and its metabolites may suppress IL-17 expression by regulating the expression of the transcription factor RORγt, resulting in the inhibition of Th17 cell differentiation.

Anticolitic Effect of Ocotillol. We investigated the anti-inflammatory effects of ocotillol in mice with TNBS-induced colitis (Figure 3). Treatment with TNBS significantly shortened the colon length and reduced body weight, similar to previous reports.[24] TNBS treatment also increased myeloperoxidase activity and showed severe disruption of mucosa and epithelial cell layers caused by ulcerations.

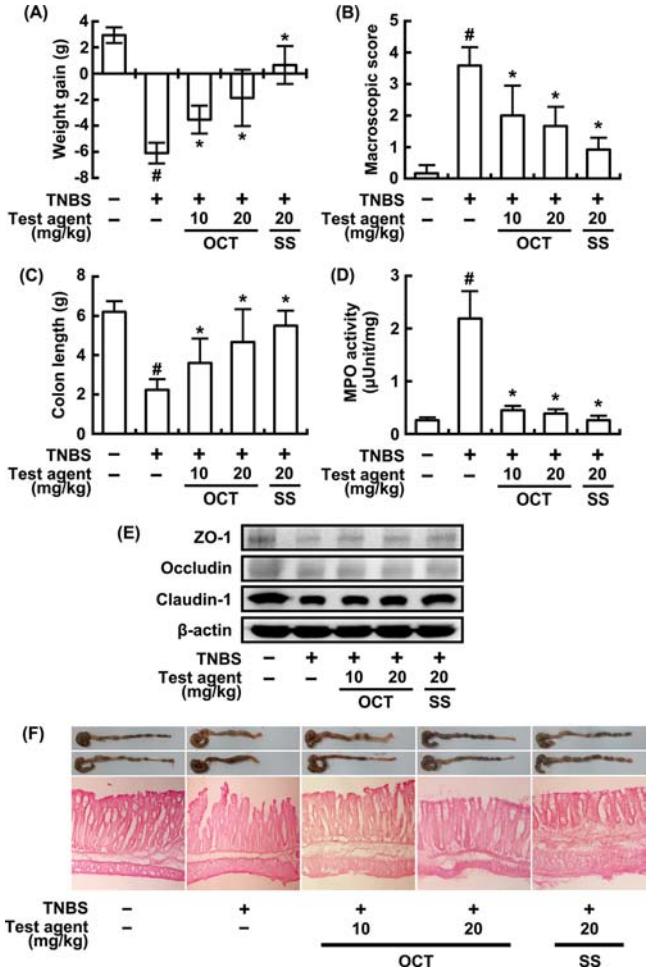

Figure 3. Effects of ocotillol on body weight (A), macroscopic disease (B), colon length (C), tight junction proteins (D), colonic myeloperoxidase (MPO) activity (E), and histological exam (F) in mice with TNBS-induced colitis. TNBS, except in the control group, was intrarectally administered to mice treated with saline, ocotillol (OCT), or sulfasalazine (SS). Test agent or saline was orally administered for 3 days after TNBS treatment. The mice were sacrificed 18 h after the final administration of test agents. All data are mean ± SD (n = 6). $^{\#}p < 0.05$ indicated a significant difference vs control group. $^{*}p < 0.05$ indicated a significant difference vs the TNBS group.

Moreover, TNBS suppressed the expression of tight junction proteins claudin, occludin-1, and ZO-1 in the colon. However, treatment with ocotillol suppressed TNBS-induced colon shortening, increased expression of the colonic tight junction proteins, and inhibited TNBS-induced myeloperoxidase activity.

Next we measured the effect of ocotillol on the expression of proinflammatory cytokines TNF-α, IL-1β, IL-6, and IL-17 and the anti-inflammatory cytokine IL-10 (Figure 4A). Ocotillol treatment suppressed TNBS-induced expression of TNF-α, IL-1β, IL-6, and IL-17. Additionally, ocotillol treatment increased TNBS-induced suppression of IL-10 expression. Ocotillol showed the greatest inhibition of TNBS-induced expression of proinflammatory cytokines and increased IL-10 expression. Next, we measured the effect of ocotillol on the expression of the inflammatory markers COX-2 and iNOS and the activation of their transcription factors NF-κB and MAPKs (Figure 4B). Treatment with ocotillol inhibited both TNBS-induced

DOI: 10.1021/acs.jafc.5b02183
J. Agric. Food Chem. 2015, 63, 7024−7031

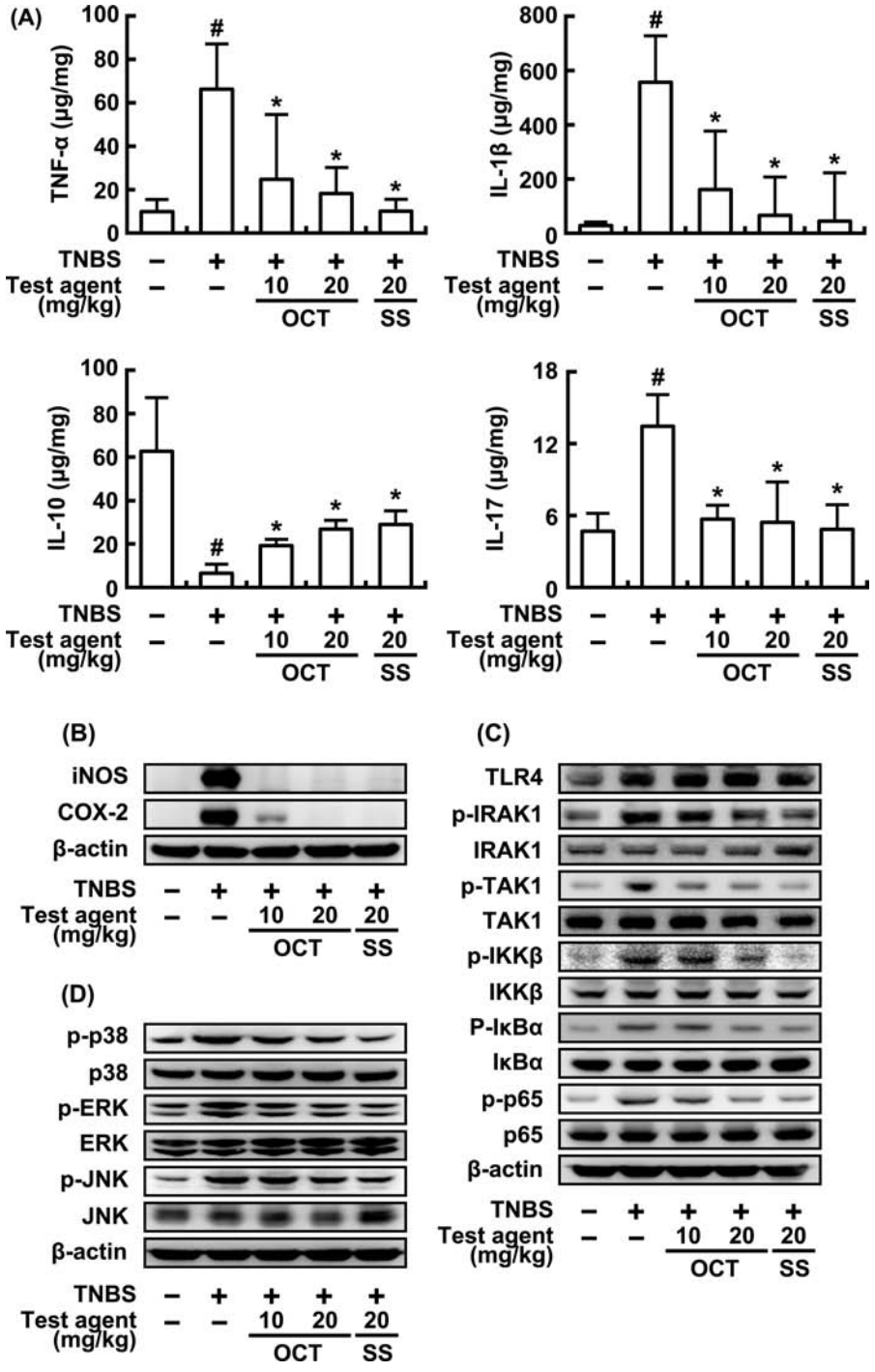

Figure 4. Effects of ocotillol on the expression of inflammatory cytokines (A), iNOS and COX-2 (B), and the activation of TLR4-NF-κB (C) and MAPKs (D) in mice with TNBS-induced colitis. TNBS, except in the control group, was intrarectally administered to mice treated with saline, ocotillol (OCT), or sulfasalazine (SS). Test agents or saline was orally administered for 3 days after TNBS treatment. The mice were sacrificed 18 h after the final administration of test agents. TNF-α, IL-1β, IL-10, and IL-17 were determined by ELISA. iNOS, COX-2, and NF-κB signaling molecules were determined by immunoblotting. All values are mean ± SD ($n = 6$). $^{\#}p < 0.05$ indicated a significant difference vs control group. $^{*}p < 0.05$ indicated a significant difference vs the TNBS group.

expression of COX-2 and iNOS and activation of NF-κB and MAPKs.

Furthermore, we investigated the effect of ocotillol on T cell differentiation in the luminal propria of the colon (Figure 5). Treatment with TNBS significantly increased Th17 cell differentiation and inhibited Treg cell differentiation. However, treatment with ocotillol inhibited TNBS-induced Th17 cell differentiation and increased Treg cell differentiation. We also measured T cell differentiation markers in the luminal propria of the colon using qRT-PCR (Figure 6). Treatment with TNBS significantly induced T-bet, RORγt, T-bet, interferon-γ, IL-5, IL-12, IL-17, and IL-23 expression and suppressed Foxp3 and IL-10 expression. Treatment with TNBS weakly, but not significantly, increased GATA3 and IL-5 expression. Ocotillol treatment, on the other hand, resulted in significant inhibition of TNBS-induced IL-12, IL-17, IL-23, and RORTγt expression,

DOI: 10.1021/acs.jafc.5b02183
J. Agric. Food Chem. 2015, 63, 7024−7031

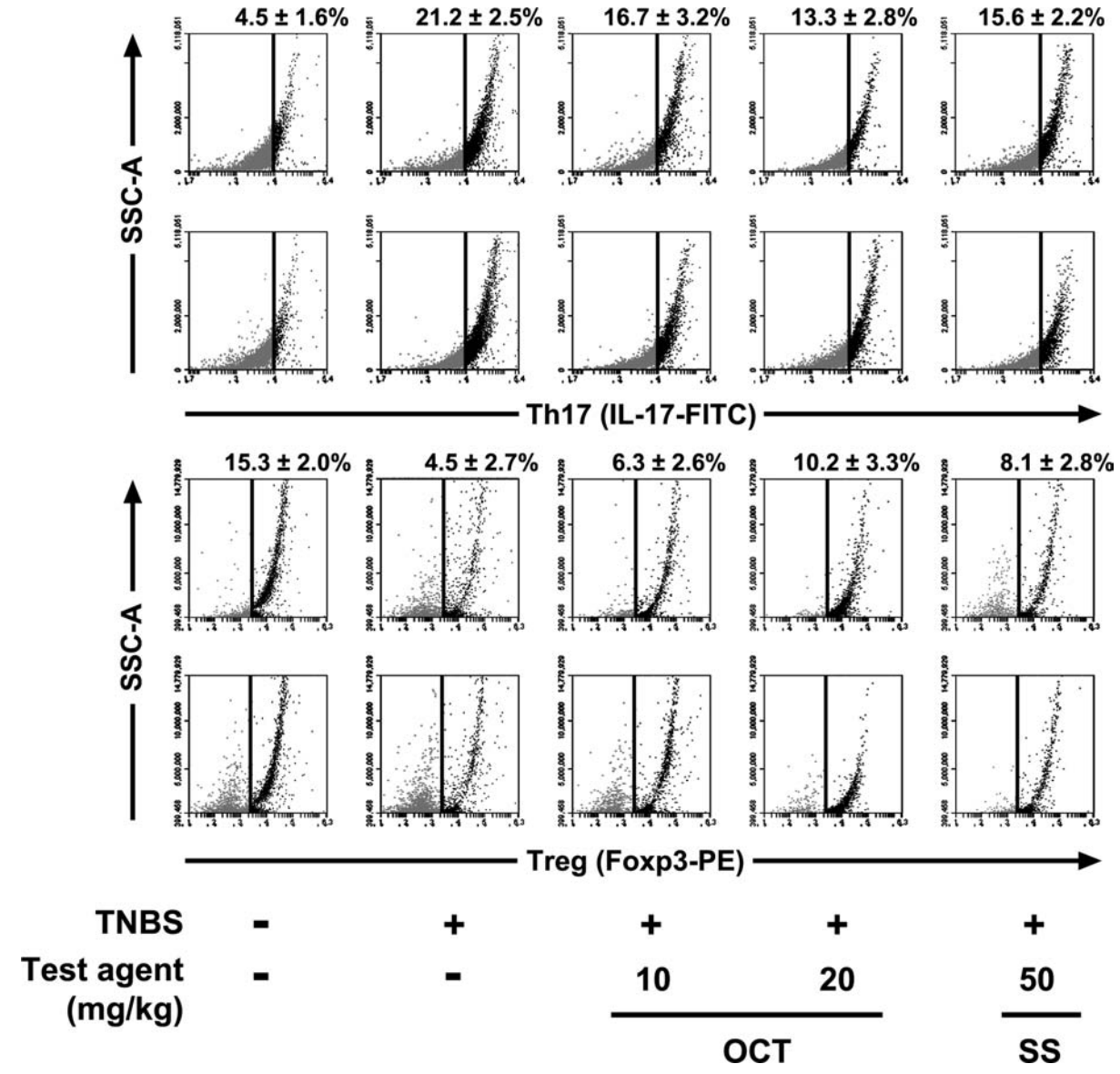

Figure 5. Effects of ocotillol on the differentiation to Th17 and Treg cells in mice with TNBS-induced colitis. TNBS, except in the control group, was intrarectally administered to mice treated with saline, ocotillol (OCT), or sulfasalazine (SS). Test agent (TO10, 10 mg/kg ocotillol; TO20, 20 mg/kg ocotillol; or SS50, 50 mg/kg SS) or saline was orally administered for 3 days after TNBS treatment. The mice were sacrificed 18 h after the final administration of test agents. The T cells were isolated from the lamina propria of the colon, and Th17 and Treg cells were then analyzed by flow cytometry. All values are mean ± SD (n = 6). $^{\#}p < 0.05$ indicated a significant difference vs control group. $^{*}p < 0.05$ indicated a significant difference vs the TNBS group.

whereas Foxp3 and IL-10 expression increased. Treatment with ocotillol, however, did not significantly influence GATA3 and IL-5 expression.

DISCUSSION

Mucosal dendritic cells and macrophages present pathogens as antigens to the adaptive immune system in the colon and direct the differentiation of naive CD4+ T cells to various effector T-helper (Th1, Th2, and Th17) and Treg cells.[25] Thus, dendritic cells and macrophages promote Th17 differentiation by secreting IL-23, thereby sustaining and reinforcing the Th17 phenotype. Moreover, IL-23 induces proinflammatory cytokines such as TNF-α, IFN-γ, and IL-6 in the colon and inhibits Foxp3+ Treg cells, resulting in chronic colitis. Foxp3+ Treg cells regulate immune responses by suppressing Th effector cells.[26] However, in IBD patients, the number of Foxp3+ Treg cells, which produce an anti-inflammatory cytokine IL-10, is reduced in the peripheral blood and intestinal mucosa. Additionally, Th17 cell differentiation is induced in inflamed colons of mice and patients with IBD,[27] which subsequently increases the production of IL-17A and IL-17F by regulation of transcription factor RORγt expression.[28] IL-17 simulates the inflammatory response, and therefore, excessive Th17 and deficient Treg responses contribute to IBD. The effects of several natural products such as icariin, apigenin, baicalin, and resveratrol have been studied for their roles in the activation of Foxp3+ Treg cell differentiation or/and the inhibition of Th17 differentiation in order to correct Th17/Treg imbalance in autoimmune diseases.[29−32]

Ginsenosides, which are representative constituents of *Panax ginseng*, *Panax quinquefolius*, and *Panax vietnamensis*,[33] are structurally classified into protopanaxadiol, protopanaxatriol,

DOI: 10.1021/acs.jafc.5b02183
J. Agric. Food Chem. 2015, 63, 7024−7031

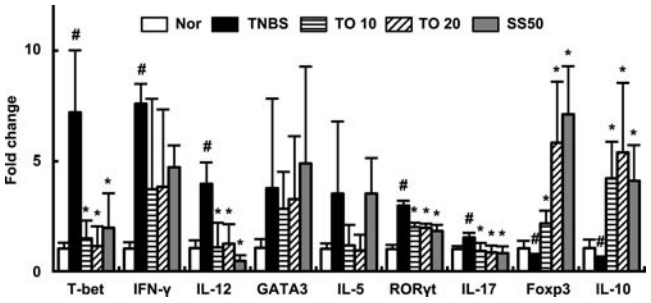

Figure 6. Effects of ocotillol on the expression of T cell cytokines, IL-23, and T cell transcription factors in mice with TNBS-induced colitis. TNBS, except in the control group, was intrarectally administered to mice treated with saline, ocotillol, or sulfasalazine (SS). Test agent (TO10, 10 mg/kg ocotillol; TO20, 20 mg/kg ocotillol; or SS50, 50 mg/kg SS) or saline was orally administered for 3 days after TNBS treatment. The mice were sacrificed 18 h after the final administration of test agents. IL-5, IL-10, IL-12, IL-17, IL-23, interferon (IFN)-γ, T-bet, GATA3, RORγt, and Foxp3 in colon were by real-time PCR. All values are mean ± SD (n = 6). $^{\#}p < 0.05$ indicated a significant difference vs control group. $^{*}p < 0.05$ indicated a significant difference vs the TNBS group.

ocotillol, and oleanane types depending on their aglycons. Many ginsenosides suppress inflammation.[24,34,35] Ginsenoside Rb1 and its metabolite compound K, which is a protopanaxadiol-type ginsenoside, ameliorate dextran sulfate sodium- or TNBS-induced colitis by inhibiting IRAK-1 activation in the NF-κB signaling pathway.[24,37] Ginsenoside Rd ameliorates TNBS-induced colitis in rats by inhibiting the signaling pathway of MAPKs (p38 and JNK).[36] Ginsenoside Rh2, which is a protopanaxadiol-type ginsenoside, improves dextran sulfate sodium-induced colitis by activating the TGFβ signaling pathway.[38] These results suggest that orally administered protopanaxadiol-type ginsenosides may be metabolized to compound K or ginsenoside Rh2 by gut microbiota and, in turn, these metabolites may ameliorate inflammation by inhibiting the NF-κB and MAPK signaling pathways as well as alleviating TGFβ signaling pathway. Protopanaxatriol-type ginsenoside Re also ameliorates TNBS-induced colitis in mice, by inhibiting the NF-κB signaling pathway.[39] However, the effects of ginsenosides in Th17 and Treg differentiation have not been studied thoroughly.

In the present study, when MR2 was orally administered to mice, MR2 was metabolized to ocotillol via PRT4. Therefore, we investigated anti-inflammatory effects of MR2 and its metabolites in vitro and in mice with TNBS-induced acute colitis, which is frequently used for understanding the anticolitic effects (efficacy and mechanism) of drugs and phytochemicals.[24,36] Ocotillol strongly ameliorated TNBS-induced iNOS and COX-2 expression, as well as activation of their transcription factors NF-κB and MAPKs in mice. Ocotillol was found to ameliorate TNBS-induced colitis in mice by reversing TNBS-induced shortening, myeloperoxidase activity, and attenuation of tight junction protein expression in the colon. Additionally, ocotillol inhibited the expression of proinflammatory cytokines TNF-α, IL-1β, IL-6, IL-17, IL-23, and IFN-γ, while increasing IL-10 expression. Moreover, ocotillol treatment inhibited Th17 cell differentiation in vitro and in vivo. These results suggest that ocotillol may regulate inflammation by regulating T cell differentiation. This was confirmed by the finding that ocotillol significantly inhibited TNBS-induced Th17 cell differentiation and increased Treg cell differentiation suppressed by TNBS in mice. Moreover, ocotillol suppressed TNBS-induced expression of Th1-producing cytokines IL-12 and interferon-γ, as well as their transcription factor T-bet in mice. Additionally, ocotillol inhibited TNBS-induced expression of Th17 cell-derived cytokine IL-17 and its transcription factor RORγt, while also increasing Treg cell-derived cytokine IL-10 and its transcription factor Foxp3, in mice with TNBS-induced colitis. However, ocotillol did not influence the expression of Th2 cell-derived cytokine IL-5 and its transcription factor GATA3. Moreover, ocotillol inhibited differentiation to Th17 cells in vitro. These results suggest that ocotillol may restore TNBS-induced imbalance of Th17/Treg cells. Additionally, the long-term administration of majonoside R2 may be quickly transformed to ocotillol, which may strongly show anticolitic effect. These findings suggest that orally administered MR2 may be metabolized to ocotillol via PRT4, which may ameliorate colitis by restoring Th17/Treg balance via the regulation of their cytokine expression.

AUTHOR INFORMATION

Corresponding Author

*Department of Life and Nanopharmaceutical Sciences, College of Pharmacy, Kyung-Hee University, 1, Hoegi, Dongdaemun-gu, Seoul 130-701, Korea. Phone: +82-2-961-0357. Fax: +82-2-957-5030. E-mail: dhkim@khu.ac.kr.

Funding

This study was supported by BK21 Plus Program from through the National Research Foundation funded by the Ministry of Education of Korea.

Notes

The authors declare no competing financial interest.

ABBREVIATIONS USED

COX, cyclooxygenase; ELISA, enzyme-linked immunosorbent assay; FBS, fetal bovine serum; IBD, intestinal bowel disease; IKKβ, inhibitor of nuclear factor kappa-B kinase subunit beta; IL, interleukin; iNOS, inducible NO synthetase; IRAK1, interleukin 1 receptor-associated kinase 1; LPS, lipopolysaccharide; MPO, myeloperoxidase; MR2, majonoside R2; NF-κB, nuclear factor kappa-light-chain-enhancer of activated B cells; PRT4, pseudoginsenoside RT4; TAK1, transforming growth factor beta-activated kinase 1; TGFβ, tumor growth factor beta; TNBS, 2,4,6-trinitrobenzenesulfonic acid; TNF, tumor necrosis factor

REFERENCES

(1) Maloy, K. J.; Powrie, F. Intestinal homeostasis and its breakdown in inflammatory bowel disease. *Nature* **2011**, *474*, 298−306.

(2) Binder, V. Epidemiology of IBD during the twentieth century: An integrated view. *Best Pract. Res. Clin. Gastroenterol.* **2004**, *18*, 463−479.

(3) Chandran, P.; Satthaporn, S.; Robins, A.; Eremin, O. Inflammatory bowel disease: Dysfunction of GALT and gut bacterial flora (II). *Surgeon* **2003**, *1*, 125−136.

(4) McLean, M. H.; Dieguez, D., Jr; Miller, L. M.; Young, H. A. Does the microbiota play a role in the pathogenesis of autoimmune diseases? *Gut* **2015**, *64*, 332−341.

(5) Mayne, C. G.; Williams, C. B. Induced and natural regulatory T cells in the development of inflammatory bowel disease. *Inflammatory Bowel Dis.* **2013**, *19*, 1772−1788.

(6) Eastaff-Leung, N.; Mabarrack, N.; Barbour, A.; Cummins, A.; Barry, S. Foxp3+ regulatory T cells, Th17 effector cells, and cytokine environment in inflammatory bowel disease. *J. Clin. Immunol.* **2010**, *30*, 80−89.

DOI: 10.1021/acs.jafc.5b02183
J. Agric. Food Chem. 2015, 63, 7024−7031

(7) Leppkes, M.; Becker, C.; Ivanov, I. I.; Hirth, S.; Wirtz, S.; Neufert, C.; Pouly, S.; Murphy, A. J.; Valenzuela, D. M.; Yancopoulos, G. D.; Becher, B.; Littman, D. R.; Neurath, M. F. RORgamma-expressing Th17 cells induce murine chronic intestinal inflammation via redundant effects of IL-17A and IL-17F. *Gastroenterology* **2009**, *136*, 257−267.
(8) Kanai, T.; Mikami, Y.; Sujino, T.; Hisamatsu, T.; Hibi, T. RORγt-dependent IL-17A-producing cells in the pathogenesis of intestinal inflammation. *Mucosal Immunol.* **2012**, *5*, 240−224.
(9) Sarra, M.; Pallone, F.; Macdonald, T. T.; Monteleone, G. IL-23/IL-17 axis in IBD. *Inflamm. Bowel Dis.* **2010**, *16*, 1808−1818.
(10) Yang, J.; Sundrud, M. S.; Skepner, J.; Yamagata, T. Targeting Th17 cells in autoimmune diseases. *Trends Pharmacol. Sci.* **2014**, *35*, 493−500.
(11) Monteleone, I.; Sarra, M.; Pallone, F.; Monteleone, G. Th17-related cytokines in inflammatory bowel diseases: friends or foes? *Curr. Mol. Med.* **2012**, *12*, 592−597.
(12) Granet, C.; Miossec, P. Combination of the pro-inflammatory cytokines IL-1, TNF-alpha and IL-17 leads to enhanced expression and additional recruitment of AP-1 family members, Egr-1 and NF-kappaB in osteoblast-like cells. *Cytokine* **2004**, *26*, 169−177.
(13) Gizinski, A. M.; Fox, D. A.; Sarkar, S. Pharmacotherapy: concepts of pathogenesis and emerging treatments. Co-stimulation and T cells as therapeutic targets. *Best Pract. Res. Clin. Rheumatol.* **2010**, *24*, 463−477.
(14) Banskota, A. H.; Tezuka, Y.; Tran, Q. L.; Kadota, S. Chemical constituents and biological activities of Vietnamese medicinal plants. *Curr. Top. Med. Chem.* **2003**, *3*, 227−248.
(15) Huong, N. T. T.; Matsumoto, K.; Yamasaki, K.; Watanabe, H. Majonoside-R2 reverses social isolation stress-induced decrease in pentobarbital sleep in mice: possible involvement of neuroactive steroids. *Life Sci.* **1997**, *61*, 395−402.
(16) Huong, N. T. T.; Matsumoto, K.; Yamasaki, K.; Duc, N. M.; Nham, N. T.; Watanabe, H. Crude saponin extracted from Vietnamese ginseng and its major constituent majonoside-R2 attenuate the psychological stress- and foot-shock stress-induced antinociception in mice. *Pharmacol., Biochem. Behav.* **1995**, *52*, 427−432.
(17) Minh Duc, N.; Thoi Nham, N.; Kasai, R.; Ito, A.; Yamasaki, K.; Tanaka, O. Saponins from Vietnamese ginseng, Panax vietnamensis Ha et Grushv. Collected in central Vietnam. I. *Chem. Pharm. Bull.* **1993**, *41*, 2010−2014.
(18) Le, T. H.; Lee, S. Y.; Kim, T. R.; Kim, J. Y.; Kwon, S. W.; Nguyen, N. K.; Park, J. H.; Nguyen, M. D. Processed Vietnamese ginseng: Preliminary results in chemistry and biological activity. *J. Ginseng Res.* **2014**, *38*, 154−9.
(19) Okamoto, Y.; Tanaka, M.; Fukui, T.; Masuzawa, T. Brazilian propolis inhibits the differentiation of Th17 cells by inhibition of interleukin-6-induced phosphorylation of signal transducer and activator of transcription 3. *Immunopharmacol. Immunotoxicol.* **2012**, *34*, 803−809.
(20) Jang, S. E.; Hyam, S. R.; Jeong, J. J.; Han, M. J.; Kim, D. H. Penta-O-galloyl-β-D-glucose ameliorates inflammation by inhibiting MyD88/NF-κB and MyD88/MAPK signalling pathways. *Br. J. Pharmacol.* **2013**, *170*, 1078−1091.
(21) Jang, S. E.; Jeong, J. J.; Hyam, S. R.; Han, M. J.; Kim, D. H. Ursolic acid isolated from the seed of Cornus officinalis ameliorates colitis in mice by inhibiting the binding of lipopolysaccharide to Toll-like receptor 4 on macrophages. *J. Agric. Food Chem.* **2014**, *62*, 9711−9721.
(22) Gu, W.; Kim, K. A.; Kim, D. H. Ginsenoside Rh1 ameliorates high fat diet-induced obesity in mice by inhibiting adipocyte differentiation. *Biol. Pharm. Bull.* **2013**, *36*, 102−107.
(23) Eastaff-Leung, N.; Mabarrack, N.; Barbour, A.; Cummins, A.; Barry, S. Foxp3+ regulatory T cells, Th17 effector cells, and cytokine environment in inflammatory bowel disease. *J. Clin. Immunol.* **2010**, *30*, 80−89.
(24) Joh, E. H.; Lee, I. A.; Jung, I. H.; Kim, D. H. Ginsenoside Rb1 and its metabolite compound K inhibit IRAK-1 activation–the key step of inflammation. *Biochem. Pharmacol.* **2011**, *82*, 278−286.
(25) Zhu, J.; Paul, W. E. CD4 T cells: fates, functions, and faults. *Blood* **2008**, *112*, 1557−1569.
(26) Nguyen, T. L.; Sullivan, N. L.; Ebel, M.; Teague, R. M.; DiPaolo, R. J. Antigen-specific TGF-β-induced regulatory T cells secrete chemokines, regulate T cell trafficking, and suppress ongoing autoimmunity. *J. Immunol.* **2011**, *187*, 1745−1753.
(27) Ogino, T.; Nishimura, J.; Barman, S.; Kayama, H.; Uematsu, S.; Okuzaki, D.; Osawa, H.; Haraguchi, N.; Uemura, M.; Hata, T.; Takemasa, I.; Mizushima, T.; Yamamoto, H.; Takeda, K.; Doki, Y.; Mori, M. Increased Th17-inducing activity of CD14+ CD163 low myeloid cells in intestinal lamina propria of patients with Crohn's disease. *Gastroenterology* **2013**, *145*, 1380−1391.
(28) Rauen, T.; Juang, Y. T.; Hedrich, C. M.; Kis-Toth, K.; Tsokos, G. C. A novel isoform of the orphan receptor RORγt suppresses IL-17 production in human T cells. *Genes Immun.* **2012**, *13*, 346−350.
(29) Tao, F.; Qian, C.; Guo, W.; Luo, Q.; Xu, Q.; Sun, Y. Inhibition of Th1/Th17 responses via suppression of STAT1 and STAT3 activation contributes to the amelioration of murine experimental colitis by a natural flavonoid glucoside icariin. *Biochem. Pharmacol.* **2013**, *85*, 798−807.
(30) Kang, H. K.; Ecklund, D.; Liu, M.; Datta, S. K. Apigenin, a non-mutagenic dietary flavonoid, suppresses lupus by inhibiting auto-antigen presentation for expansion of autoreactive Th1 and Th17 cells. *Arthritis Res. Ther.* **2009**, *11*, R59.
(31) Yang, J.; Yang, X.; Chu, Y.; Li, M. Identification of Baicalin as an immunoregulatory compound by controlling T(H)17 cell differentiation. *PLoS One* **2011**, *6*, e17164.
(32) Petro, T. M. Regulatory role of resveratrol on Th17 in autoimmune disease. *Int. Immunopharmacol.* **2011**, *11*, 310−318.
(33) Kim, D. H. Chemical Diversity of Panax ginseng, Panax quinquifolium, and Panax notoginseng. *J. Ginseng Res.* **2012**, *36*, 1−15.
(34) Zhang, J.; Ding, L.; Wang, B.; Ren, G.; Sun, A.; Deng, C.; Wei, X.; Mani, S.; Wang, Z.; Dou, W. Notoginsenoside R1 attenuates experimental inflammatory bowel disease via pregnane X receptor activation. *J. Pharmacol. Exp. Ther.* **2015**, *352*, 315−324.
(35) Jin, Y.; Hofseth, A. B.; Cui, X.; Windust, A. J.; Poudyal, D.; Chumanevich, A. A.; Matesic, L. E.; Singh, N. P.; Nagarkatti, M.; Nagarkatti, P. S.; Hofseth, L. J. American ginseng suppresses colitis through p53-mediated apoptosis of inflammatory cells. *Cancer Prev. Res.* **2010**, *3*, 339−347.
(36) Yang, X. L.; Guo, T. K.; Wang, Y. H.; Huang, Y. H.; Liu, X.; Wang, X. X.; Li, W.; Zhao, X.; Wang, L. P.; Yan, S.; Wu, D.; Wu, Y. J. Ginsenoside Rd attenuates the inflammatory response via modulating p38 and JNK signaling pathways in rats with TNBS-induced relapsing colitis. *Int. Immunopharmacol.* **2012**, *12*, 408−414.
(37) Li, J.; Zhong, W.; Wang, W.; Hu, S.; Yuan, J.; Zhang, B.; Hu, T.; Song, G. Ginsenoside metabolite compound K promotes recovery of dextran sulfate sodium-induced colitis and inhibits inflammatory responses by suppressing NF-κB activation. *PLoS One* **2014**, *9*, e87810.
(38) Ye, H.; Wu, Q.; Zhu, Y.; Guo, C.; Zheng, X. Ginsenoside Rh2 alleviates dextran sulfate sodium-induced colitis via augmenting TGFβ signaling. *Mol. Biol. Rep.* **2014**, *41*, 5485−5490.
(39) Lee, I. A.; Hyam, S. R.; Jang, S. E.; Han, M. J.; Kim, D. H. Ginsenoside Re ameliorates inflammation by inhibiting the binding of lipopolysaccharide to TLR4 on macrophages. *J. Agric. Food Chem.* **2012**, *60*, 9595−9602.

DOI: 10.1021/acs.jafc.5b02183
J. Agric. Food Chem. 2015, 63, 7024−7031

alternative substrate and producing an *o*-quinone other than *o*-dopaquinone, rather than inhibiting the enzyme. Owing to the nonadjacent meta disposition of the two hydroxyl groups in HR, the diphenolase activity of tyrosinase is not possible on this compound but it can be hydroxylated in the ortho position due to the monophenolase activity of the enzyme. For the enzyme to act on monophenols, the presence of the enzymatic form, E_{ox}, is necessary. In the case of L-tyrosine, this can be achieved through the formation of *o*-diphenol from *o*-dopaquinone in the reaction medium.[32] Many monophenolic compounds have been described as tyrosinase inhibitors, although they are really alternative substrates, because, after their testing with the enzyme, it shows no activity. This is because the monophenol gives rise to an *o*-quinone that evolves chemically without originating *o*-diphenol in the medium, so there is no turnover on the part of the enzyme (and the E_{ox} form is not generated).

Our previous studies on the action mechanism of tyrosinase[33,34] revealed that the enzymatic form E_{ox} and, therefore, the monophenolase activity of the enzyme can be observed by adding one of the following to the reaction medium: (a) a reductant (ascorbic acid, AH_2) capable of transforming E_m to E_d, which, with oxygen, generates E_{ox}, b) hydrogen peroxide, which transforms E_m to E_{ox} or c) catalytic concentrations of *o*-diphenol (to transform E_m to E_d, which, with oxygen, becomes E_{ox}) and a reductant (AH_2 or NADH) to keep the quantity of *o*-diphenol in the medium constant, so that E_{ox} continues to be generated.[35−39]

The aim of this study is to demonstrate that HR is not an inhibitor but an alternative substrate of tyrosinase. We propose a kinetic mechanism to explain the action of the enzyme on this compound, the kinetic analysis of which leads us to obtain the analytic expression of the *o*-quinone formation rate. From the expression obtained, an experimental design that permits the kinetic characterization of the HR is established. This aspect should be taken into consideration by the food, cosmetics, and pharmaceutical industries when using HR as an antibrowning and depigmenting agent.

MATERIALS AND METHODS

Enzyme Source. Mushroom tyrosinase (3130 U/mg) was purchased from Sigma (Madrid, Spain) and purified as previously described.[40] Bradford's method was used to determine the protein content using bovine serum albumin as standard.[41]

Reagents. The substrate, L-dopa, 4-hexylresorcinol (HR, Figure 1), *tert*-butylcatechol (TBC), reduced β-nicotinamide adenine dinucleotide (NADH), hydrogen peroxide (H_2O_2) and ascorbic acid (AH_2) were obtained from Sigma. To prevent autoxidation, stock solutions of L-dopa, TBC, and HR were prepared in 0.15 mM phosphoric acid. Milli-Q system (Millipore Corp.) ultrapure water was used throughout.

Spectrophotometric Assays. These assays were carried out with a PerkinElmer Lambda-35 spectrophotometer, online interfaced with a compatible PC 486DX microcomputer controlled by UV-Winlab software, where the kinetic data were recorded, stored, and later analyzed.

The activity of tyrosinase on L-dopa[42,43] was measured at 475 nm, the maximum absorption wavelength of dopachrome. The activity of tyrosinase on HR as a substrate was measured in the presence of (a) hydrogen peroxide, (b) ascorbic acid, and (c) catalytic concentrations of TBC and NADH as reductant to maintain the *o*-diphenol in the medium constant and to ensure the constant generation of the enzymatic form E_{ox}.[35−37] Recordings were made at 490 nm, the maximum absorption wavelength of the *p*-quinone generated.

All of the assays were carried out at 25 °C, using 30 mM phosphate buffer, pH 7.0, and beginning the reaction by adding the enzyme to the reaction medium. Three repetitions of every experiment were made.

Kinetic Analysis Data. Initial rate values ($V_0^{p\text{-}Q}$) were calculated at different substrate concentrations. The assays were carried out in saturating conditions of H_2O_2 and oxygen.[44−46] In these conditions, the equation rate obtained (eq A1) using the REFERASS computer program[47,49] was simplified to eq 1 (equivalent to eq A12) (see the Appendix). $V_0^{p\text{-}Q}$ versus $[HR]_0$ data were represented and fitted to the Michaelis−Menten equation using the Sigma Plot 9.0 program for Windows,[50] obtaining the maximum rate ($V_{max}^{p\text{-}Q}$) and the Michaelis constant (K_M^{HR}).

Nuclear Magnetic Resonance. ^{13}C NMR spectra of HR and the rest of the monophenols were obtained in a Varian Unity spectrometer of 300 MHz at the optimum pH for mushroom tyrosinase (6.8) and using D_2O as solvent for the substrates. The δ values were measured relative to those for tetramethylsilane (δ = 0). The maximum line width accepted in the NMR spectra was 0.06 Hz. Therefore, the maximum accepted error for each peak was ±0.03 ppm.[51,52]

RESULTS AND DISCUSSION

4-Hexylresorcinol as an Apparent Inhibitor of Tyrosinase. HR was assayed as a possible inhibitor of the diphenolase activity of tyrosinase. Recording the enzyme's activity on L-dopa in the absence and presence of various concentrations of HR, a strong inhibitory effect was evident from the decrease in the dopachrome formation rate at very low concentrations of HR (Figure 2), as described in the bibliography.[5,6,9,11,13−31] The recordings enabled the degrees of inhibition to be calculated and, by nonlinear regression, the IC_{50} value: IC_{50} = 0.33 ± 0.02 μM (Figure 2, inset).

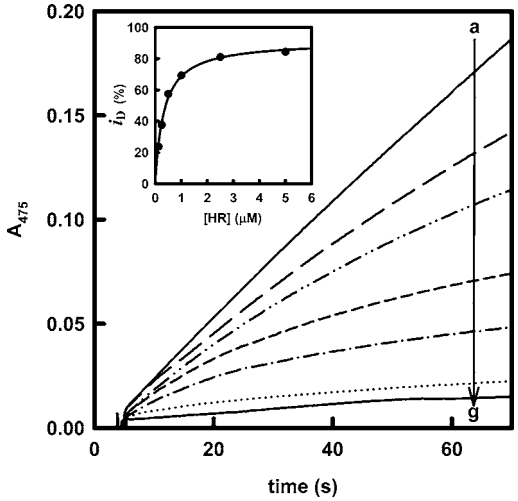

Figure 2. Diphenolase activity of tyrosinase on L-dopa in the absence (a) and presence of different concentrations of HR (μM): (b) 0.13; (c) 0.25; (d) 0.50; (e) 1.00; (f) 2.50; (g) 5.00. The rest of the experimental conditions were $[D]_0$ = 0.5 mM and $[E]_0$ = 8 nM. (Inset) Degree of inhibition of the diphenolase activity in the presence of HR obtained from the experimental assays.

Because HR has a structure analogous to that of monophenolic substrates of tyrosinase and bearing in mind studies that demonstrate that established inhibitors with structures similar to classic substrates of the enzyme act as alternative substrates of tyrosinase,[35−37,53,54] we decided to assess the activity of this enzyme on HR.

4-Hexylresorcinol as Substrate of Tyrosinase. After assaying the action of tyrosinase on HR, we observed zero

DOI: 10.1021/acs.jafc.5b02523
J. Agric. Food Chem. 2015, 63, 7032−7040

activity (data not shown). Given the structure of the compound, it can be deduced that even if it is a substrate of the enzyme, this result will always be negative, because the molecule is a *m*-diphenol and, among the three possible forms of the enzyme (E_m, E_d, and E_{ox}), only E_{ox} can act on it by hydroxylation (monophenolase activity). The E_m form cannot oxidize it because the molecule does not have hydroxyls in ortho position. Between 2 and 30% of the native enzyme may be in the form E_{ox},[55] which is the enzymatic form that initiates the action on monophenols. The E_{ox} form hydroxylates HR and is transformed into E_m, which has to regenerate E_{ox} for the catalysis to continue.

The regeneration of this enzymatic form (E_{ox}) in the assay medium can be attained in the presence of hydrogen peroxide, ascorbic acid, or catalytic concentrations of *o*-diphenol and a reductant such as ascorbic acid or NADH, which reduces the *o*-quinone generated from the *o*-diphenol, maintaining it constant in the reaction medium.[35−37] In this way, the activity of tyrosinase on HR was measured.

Enzymatic Activity in the Presence of Hydrogen Peroxide. To assay the action of tyrosinase on HR in the presence of H_2O_2, recordings were made of the changes in absorbance with time at different wavelengths (Figure 3). As

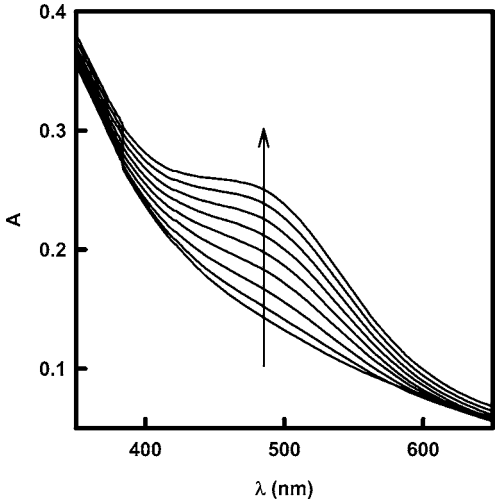

Figure 3. Scan spectra of the action of tyrosinase on HR in the presence of hydrogen peroxide. The experimental conditions were $[HR]_0$ = 100 μM, $[H_2O_2]_0$ = 30 mM, and $[E]_0$ = 345 nM. Recordings were made every 1 min.

can be seen, absorbance varied between 350 and 650 nm, with a maximum at 490 nm, indicating the formation of a new product during the reaction. To confirm that this product proceeded from the enzymatic reaction and not from the attack of HR by H_2O_2, we recorded the absorbance of the HR at 490 nm in the presence of H_2O_2 and in the absence of enzyme (Figure 4, recording a). Note that the absorbance signal did not change, meaning that the HR was not attacked by the H_2O_2 during the time that measurements were made, so that the compound generated was a product of the enzymatic reaction. Moreover, when the activity on HR was measured in the presence of different concentrations of tyrosinase, the initial rate increased with the concentration of enzyme (Figure 4).

To explain the activity of tyrosinase on HR in the presence of H_2O_2, we propose a structural mechanism (Figure 5). As can be seen in the figure, tyrosinase hydroxylates HR in position 6 and

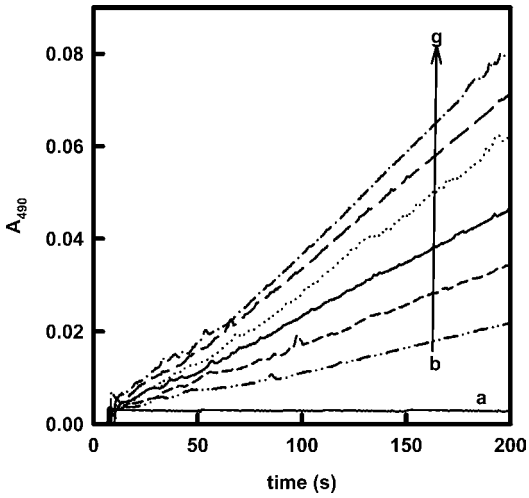

Figure 4. Spectrophotometric recordings at 490 nm of the action of tyrosinase on HR in the presence of different concentrations of tyrosinase (nM): (a) 0; (b) 140; (c) 210; (d) 275; (e) 345; (f) 415; (g) 485. The rest of the experimental conditions were $[HR]_0$ = 0.5 mM and $[H_2O_2]_0$ = 30 mM.

subsequently oxidizes it to *o*-quinone, which rapidly isomerizes to *p*-quinone.[56−59]

Enzymatic Activity in the Presence of Ascorbic Acid. Similarly to the above, the activity of tyrosinase on HR was assayed by adding ascorbic acid to the reaction medium, thus transforming E_m to E_d, which, with oxygen, gives rise to E_{ox}. Recordings were made of the absorbance with time at different wavelengths (Figure 6). As in the presence of H_2O_2, the presence of ascorbic acid led to an increase in absorbance between 350 and 650 nm, with a maximum once again at 490 nm. Figure 7 displays a kinetic mechanism to explain the action of tyrosinase on HR in the presence of ascorbic acid.

Kinetic Characterization of 4-Hexylresorcinol as Tyrosinase Substrate. After confirmation that HR is an alternative substrate of tyrosinase, a kinetic characterization of the same was made, for which it was necessary to calculate the molar absorptivity coefficient of the *p*-quinone generated at the working pH and wavelength. The action of the enzyme on HR was measured at 490 nm, in the presence of catalytic concentrations of TBC and NADH as reductant. Low concentrations of HR were used, and the substrate was exhausted in relatively short times (Figure 8). TBC and NADH as reductant could be used in these assays due to the capacity of NADH to reduce the *o*-*tert*-butylquinone produced by the oxidation of TBC and its inability to reduce the *p*-quinone generated from the HR, at these concentrations. This made it possible to measure the absorbance of the *p*-quinone alone and to regenerate the catalytic *o*-diphenol necessary to generate the enzymatic form E_{ox} in the medium, which continued acting on HR until its exhaustion. Figure 9 proposes a kinetic scheme for this mechanism.

To use this methodology to calculate the molar absorptivity coefficient of the *p*-quinone generated, it is essential that the reductant (NADH) in the system does not become exhausted because, in this case, the product would cease to be generated before the substrate is exhausted. To confirm that the NADH added to the reaction medium was sufficient to keep the system working until the exhaustion of HR, the disappearance of the NADH was measured at 380 nm (Figure 10, inset). It can be seen how at 550 s (maximum recorded time) NADH was still

DOI: 10.1021/acs.jafc.5b02523
J. Agric. Food Chem. 2015, 63, 7032−7040

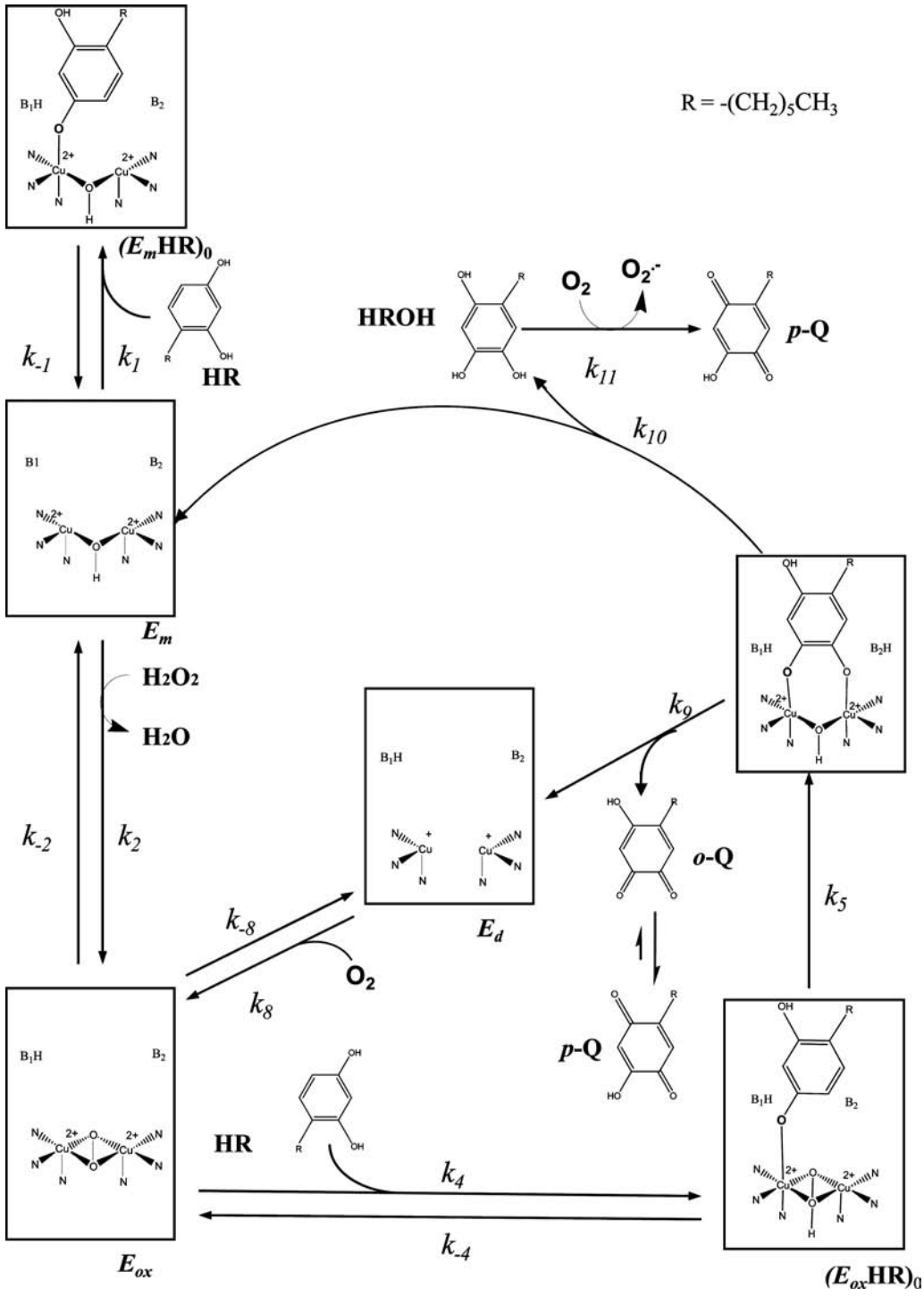

Figure 5. Structural mechanism of the action of tyrosinase on HR in the presence of hydrogen peroxide. E_m = met-tyrosinase, E_d = deoxy- tyrosinase, E_{ox} = oxy-tyrosinase, HR = 4-hexylresorcinol, E_mHR = met-tyrosinase/4-hexylresorcinol complex, E_{ox}HR = oxy-tyrosinase/4-hexylresorcinol complex, HROH = 5-hexylbenzene-1,2,4-triol, *o*-Q = *o*-quinone from 4-hexylresorcinol, and *p*-Q = *p*-quinone from 4-hexylresorcinol.

available in the medium, confirming that the HR was exhausted in these assays.

The experiment was repeated at several concentrations of HR (Figure 8), and the final absorbance values obtained were represented versus the concentration of substrate (Figure 10). The molar absorptivity coefficient was calculated by linear regression using the Sigma Plot 9.0 program for Windows.[50] The final value obtained was 2081 ± 37 M^{-1} cm^{-1}.

The next step was the kinetic characterization of HR by measuring the initial rate values ($V_0^{p\text{-}Q}$) at different substrate concentrations (Figure 11, inset). Hydrogen peroxide was chosen as cosubstrate to simplify the rate equation to eq 1 (equivalent to eq A12), working at saturating conditions of both H_2O_2 and oxygen (see the Appendix).[44−46] In this way, the action rate was expressed as a function of HR concentration (by measuring the formation of *p*-quinone).

DOI: 10.1021/acs.jafc.5b02523
J. Agric. Food Chem. 2015, 63, 7032−7040

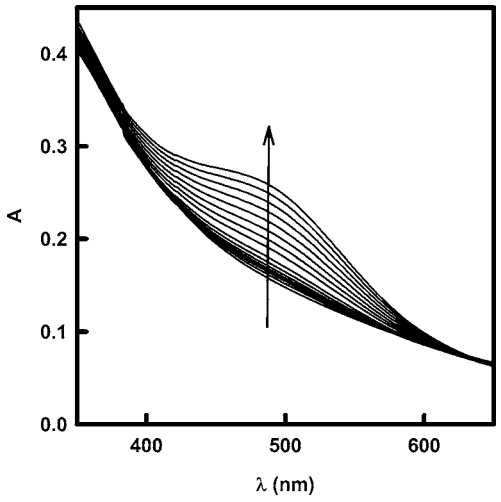

Figure 6. Scan spectra of the action of tyrosinase on HR in the presence of ascorbic acid. The experimental conditions were $[HR]_0$ = 100 μM, $[AH_2]_0$ = 200 μM, and $[E]_0$ = 415 nM. Recordings were made every 2 min.

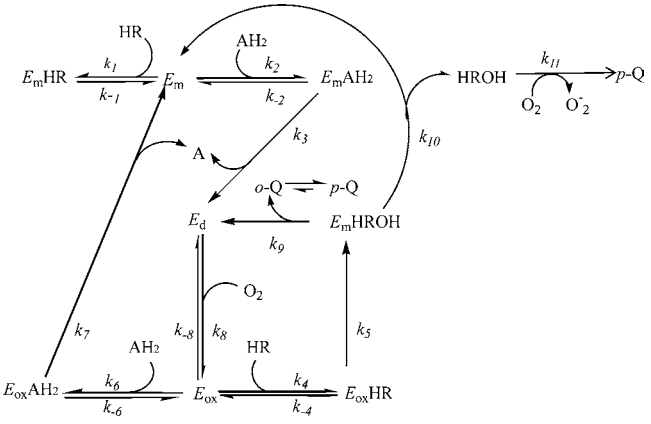

Figure 7. Kinetic mechanism of the action of tyrosinase on HR in the presence of ascorbic acid. E_m = met-tyrosinase, E_d = deoxy-tyrosinase, E_{ox} = oxy-tyrosinase, HR = 4-hexylresorcinol, HROH = 5-hexylbenzene-1,2,4-triol, *o*-Q = *o*-quinone from 4-hexylresorcinol, *p*-Q = *p*-quinone from 4-hexylresorcinol, AH_2 = ascorbic acid, and A = dehydroascorbic acid.

$$V_0^{p\text{-}Q} = \frac{V_{max}^{p\text{-}Q}[HR]_0}{K_M^{HR} + [HR]_0} \quad (1)$$

In these experimental conditions and in the measurement times used for determining the initial rate, the enzymatic activity was not affected. The values of $V_0^{p\text{-}Q}$ were represented versus $[HR]_0$ and fitted by nonlinear regression to eq 1 (equivalent to eq A12) using the Sigma Plot 9.0 program for Windows (Figure 11),[50] providing the values of K_M^{HR} and $V_{max}^{p\text{-}Q}$.

In view of the obtained results, it can be said that HR acts as a substrate of tyrosinase, alternative to L-dopa and L-tyrosine, with a low Michaelis constant and therefore high affinity (K_M^{HR} = 60.31 ± 6.73 μM) and a low catalytic constant (k_{cat}^{HR} = 0.85 ± 0.04 s^{-1}). Tyrosinase hydroxylates the HR and then oxidizes it to an *o*-quinone, which finally isomerizes to *p*-quinone (Figures 5, 7, and 9).[56−59]

Comparison of the Kinetic Constants Obtained for 4-Hexylresorcinol and Those Described for Classic Tyrosinase Substrates. When the catalytic (k_{cat}) and

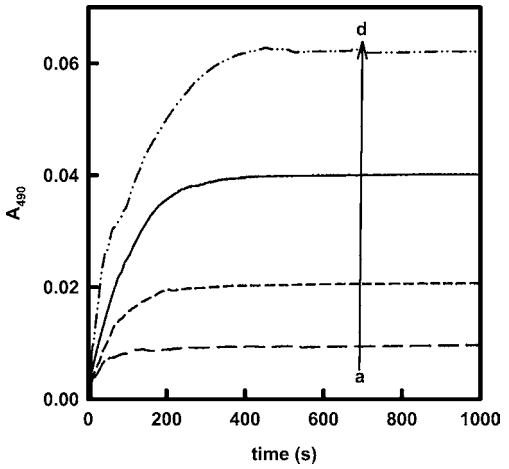

Figure 8. Spectrophotometric recordings of the action of tyrosinase on different concentrations of HR until its consumption. The experimental conditions were $[HR]_0$ (μM), (a) 5, (b) 10, (c) 20, and (d) 30; $[TBC]_0$ (μM), (a) 1, (b) 2, (c) 4, and (d) 6; $[NADH]_0$ = 200 μM; and $[E]_0$ = 345 nM.

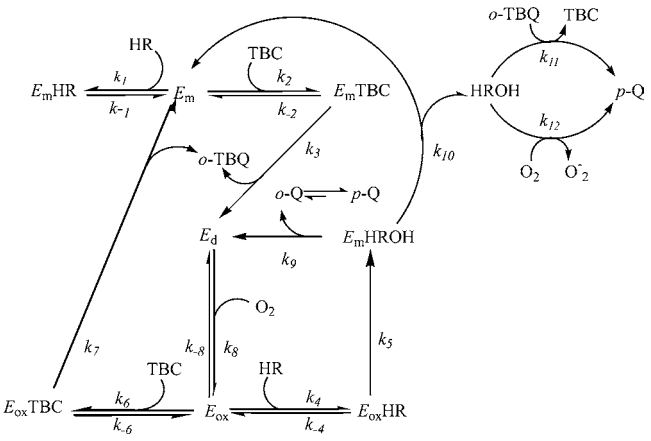

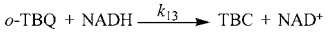

Figure 9. Kinetic mechanism of the action of tyrosinase on HR in the presence of TBC and NADH. E_m = met-tyrosinase, E_d = deoxy-tyrosinase, E_{ox} = oxy-tyrosinase, HR = 4-hexylresorcinol, HROH = 5-hexylbenzene-1,2,4-triol, *o*-Q = *o*-quinone from 4-hexylresorcinol, *p*-Q = *p*-quinone from 4-hexylresorcinol, TBC = 4-*tert*-butylcatechol, *o*-TBC = *o*-*tert*-butylquinone, NADH = reduced β-nicotinamide adenine dinucleotide, and NAD^+ = oxidized β-nicotinamide adenine dinucleotide.

Michaelis (K_M) constants obtained for HR are compared with those of monophenols, their low value is particularly notable (see Table 1).[51]

The dependence of chemical shift values (δ) in ^{13}C for a carbon atom on its electron density has been described.[60,61] The electron-donating capacity of the oxygen atom from phenolic compounds (nucleophilic power) is correlated with experimental δ values in ^{13}C for the carbon atom that supports the hydroxyl group.[51] With regard to k_{cat}, according to the chemical shift values shown in Table 2, the nucleophilic attack of the oxygen in the hydroxyl group in C-1 (Figure 1) on the copper atom in E_{ox} would be favored in the case of HR by the presence of an electron donor group (hexyl group) in the C-4 position (intermediate position in Table 2). Moreover, with

DOI: 10.1021/acs.jafc.5b02523
J. Agric. Food Chem. 2015, 63, 7032−7040

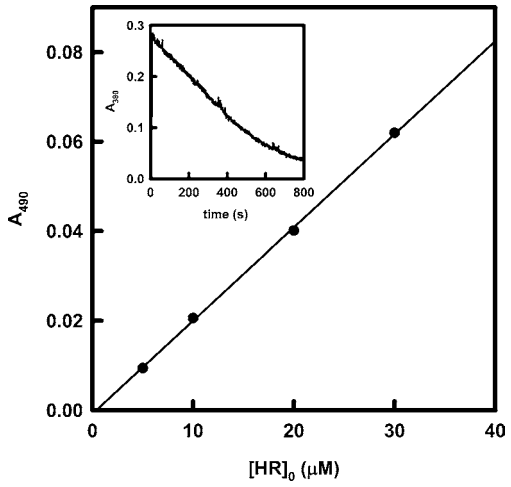

Figure 10. Final absorbance values at 490 nm reached after HR consumption in the assays described in Figure 8 versus $[HR]_0$. (Inset) Recording at 380 nm of NADH disappearance in the experiments of HR consumption (Figure 8). The experimental conditions were $[HR]_0$ = 30 μM, $[TBC]_0$ = 6 μM, $[NADH]_0$ = 200 μM, and $[E]_0$ = 345 nM.

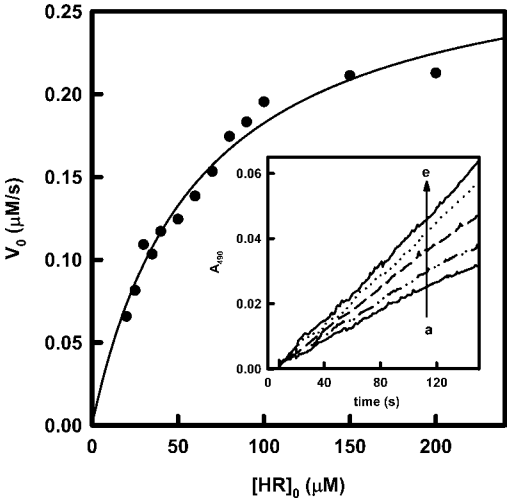

Figure 11. Representation of initial rate values obtained from the action of tyrosinase on HR in the presence of saturating concentrations of hydrogen peroxide and oxygen versus $[HR]_0$. The experimental conditions were $[HR]_0$ (μM), 20, 25, 30, 35, 40, 50, 60, 70, 80, 90, 100, 150, and 200; $[H_2O_2]_0$ = 120 mM; and $[E]_0$ = 345 nM. (Inset) Spectrophotometric recordings of the action of tyrosinase on different concentrations of HR in the presence of saturating concentrations of hydrogen peroxide and oxygen. The experimental conditions were $[HR]_0$ (μM), (a) 35, (b) 50, (c) 70, (d) 100, and (e) 200; $[H_2O_2]_0$ = 120 mM; and $[E]_0$ = 345 nM.

Table 2. δ_1 and δ_2 Values for C-1 and C-2, Respectively, of the Benzene Ring of Monophenols and 4-Hexylresorcinol

compound	δ_1	δ_2	ref
4-hydroxyanisole	152.29	118.90	51, 52
4-ethoxyphenol	152.39	119.01	51
PHPPA	156.13	118.02	51
PHPAA	156.49	118.05	51
4-hexylresorcinol	157.05	110.02[a]	this paper
tyramine	157.28	118.49	51
phenol	158.15	118.13	51
L-tyrosine	158.86	118.08	51
L-α-methyltyrosine	159.10	118.11	51

[a]This value corresponds to the ^{13}C NMR chemical shift of the carbon atom in position 6, the equivalent position 2 in monophenols.

regard to the electrophilic attack, it must be noted that HR displays low values of δ_2 and δ_6 compared with those of the monophenols from Tables 1 and 2 and, therefore, we expected that this compound should behave as a moderate substrate, but it is really a weak substrate. This is due to the fact that the monophenols could be attacked in the C-2 and C-6 positions (double possibility of attack), whereas HR could be attacked only in the C-6 position because of the steric interference of the hydroxyl group in the C-3 position. Furthermore, the intermediate generated during the action of E_{ox} on HR, E_mHROH, has axial and equatorial bonds between the *o*-diphenol and copper atoms of the active site. Because the orbitals are not coplanar, the concerted oxidation−reduction reaction cannot occur. Instead, a bond, probably that of C-1, is broken to achieve coplanarity, producing a more labile intermediate that will then release the *o*-diphenol to the medium or reunite it diaxially, involving oxidation to *o*-quinone.[32] We suggest that this step also suffers certain steric hindrance due to the effective size of the substituent determined by the C−C bond rotation of the hexyl group, indirectly affecting the catalysis.

With regard to the K_M values, it should be emphasized that the presence of a large hydrophobic group, such as hexyl, contributes to the value being the lowest of those described in Table 1. This agrees with the increased inhibition provoked by a homologous series of alkylbenzaldehyde inhibitors, in which the substituent hydrophobic radical group varies.[62]

From these values of k_{cat} and K_M it is deduced that the catalytic efficiency of tyrosinase acting on HR is low but of the same order of magnitude as those of other physiological substrates of the enzyme (Table 1).[51]

In conclusion, HR has been characterized as a substrate of tyrosinase. The long hydrophobic chain in the C-4 position increases the affinity of the enzyme (small K_M). In turn, this

Table 1. Kinetic Constants for the Monophenolase Activity of Mushroom Tyrosinase

compound	k_{cat} (s^{-1})	K_M (μM)	k_{cat}/K_M (mM^{-1} s^{-1})	ref
4-hydroxyanisole	184.20 ± 6.10	80.00 ± 3.00	2300.00 ± 162.00	51
4-ethoxyphenol	132.00 ± 4.40	170.00 ± 5.00	776.47 ± 48.00	51
PHPPA	66.70 ± 2.70	440.00 ± 10.00	151.59 ± 10.00	51
tyramine	25.90 ± 1.10	510.00 ± 20.00	50.78 ± 4.00	51
L-tyrosine	7.90 ± 0.30	210.00 ± 10.00	37.62 ± 3.00	51
PHPAA	44.30 ± 1.50	1910.00 ± 80.00	23.19 ± 2.00	51
phenol	12.70 ± 0.60	700.00 ± 40.00	18.14 ± 2.00	51
4-hexylresorcinol	0.85 ± 0.04	60.31 ± 6.73	14.09 ± 1.70	this paper
L-α-methyltyrosine	0.60 ± 0.03	1200.00 ± 80.00	0.50 ± 0.06	51

DOI: 10.1021/acs.jafc.5b02523
J. Agric. Food Chem. 2015, 63, 7032−7040

long chain and the fact that its rotation around C-4 produces unfavorable interactions in the enzymatic pocket would be a reasonable cause of the obtained low catalytic constant. Whatever the case, the most important thing is that this compound, which is used as an antibrowning and depigmenting agent, may produce *p*-quinones, which may react with nucleophilic reagents such as cysteine and glutathione, diminishing the antioxidant capacity of the cell in which tyrosinase acts.[63−65]

APPENDIX

Applying the steady-state approximation to the mechanism shown in Figure 5 provides the following expression for the *p*-quinone (*p*-Q) formation rate:[47−49]

$$V_0^{p\text{-Q}} = (\alpha_1[H_2O_2]_0[O_2]_0[HR]_0[E]_0) / (\beta_1[O_2]_0 + \beta_2[H_2O_2]_0 + \beta_3[O_2]_0[HR]_0 + \beta_4[H_2O_2]_0[HR]_0 + \beta_5[H_2O_2]_0[O_2]_0 + \beta_6[O_2]_0[HR]_0^2 + \beta_7[H_2O_2]_0[O_2]_0[HR]_0) \quad (A1)$$

Expressions of α_1 and $\beta_1-\beta_7$ are given by eqs A2−A9:

$$\alpha_1 = K_1k_2k_4k_5k_8(k_9 + k_{10}) \quad (A2)$$

$$\beta_1 = K_1k_{-2}k_8(k_{-4} + k_5)(k_9 + k_{10}) \quad (A3)$$

$$\beta_2 = K_1k_2k_{-8}(k_{-4} + k_5)(k_9 + k_{10}) \quad (A4)$$

$$\beta_3 = k_{-2}k_8(k_9 + k_{10})(k_{-4} + k_5) + K_1k_4k_5k_{10}k_8 \quad (A5)$$

$$\beta_4 = K_1k_2k_4k_5k_9k_8 \quad (A6)$$

$$\beta_5 = K_1k_2k_8(k_9 + k_{10})(k_{-4} + k_5) \quad (A7)$$

$$\beta_6 = k_4k_5k_{10}k_8 \quad (A8)$$

$$\beta_7 = K_1k_2k_4k_8(k_5 + k_9 + k_{10}) \quad (A9)$$

The oxygen concentration is saturating,[44,45] and so from eq A1 we obtain

$$V_0^{p\text{-Q}} = (\alpha_1[H_2O_2]_0[HR]_0[E]_0) / (\beta_1 + \beta_3[HR]_0 + \beta_5[H_2O_2]_0 + \beta_6[HR]_0^2 + \beta_7[H_2O_2]_0[HR]_0) \quad (A10)$$

With $[H_2O_2]_0 \to \infty$,[46] eq A10 gives

$$V_0^{p\text{-Q}} = \frac{\alpha_1[HR]_0[E]_0}{\beta_5 + \beta_7[HR]_0} \quad (A11)$$

Considering that the hydroxylation step is limiting, $k_5 \ll k_9, k_{10}$, we obtain

$$V_0^{p\text{-Q}} = \frac{k_5[HR]_0[E]_0}{\frac{k_5}{k_4} + [HR]_0} = \frac{k_{cat}^{HR}[HR]_0[E]_0}{K_M^{HR} + [HR]_0} = \frac{V_{max}^{p\text{-Q}}[HR]_0}{K_M^{HR} + [HR]_0} \quad (A12)$$

where

$$k_{cat}^{HR} = k_5 \quad (A13)$$

and

$$K_M^{HR} = \frac{k_5}{k_4} \quad (A14)$$

From the analysis of $V_0^{p\text{-Q}}$ versus $[HR]_0$ by nonlineal regression, we obtain the catalytic constant eq A13) and the Michaelis constant (eq A14).

AUTHOR INFORMATION

Corresponding Author

*(F.G.-C.) Phone: +34 868 884764. Fax: +34 868 883963. E-mail: canovasf@um.es.

Funding

This work was partially supported by grants from several Spanish organizations: Projects SAF2013-48375-C2-1-R (MINECO, Madrid) and UMU15452 and UMU17766 (University of Murcia, Murcia), C.V.O.R. has a MEC-FPU fellowship (AP2010-4300).

Notes

The authors declare no competing financial interest.

ABBREVIATIONS USED

E_m	met-tyrosinase
E_d	deoxy-tyrosinase
E_{ox}	oxy-tyrosinase
D	L-dopa
$[D]_0$	initial concentration of L-dopa
HR	4-hexylresrocinol
$[HR]_0$	initial concentration of 4-hexylresorcinol
E_mHR	met-tyrosinase/4-hexylresorcinol complex
$E_{ox}HR$	oxy-tyrosinase/4-hexylresorcinol complex
HROH	5-hexylbenzene-1,2,4-triol
E_mHROH	met-tyrosinase/5-hexylbenzene-1,2,4-triol complex
o-Q	*o*-quinone from 4-hexylresorcinol
p-Q	*p*-quinone from 4-hexylresorcinol
H_2O_2	hydrogen peroxide
$[H_2O_2]_0$	initial concentration of hydrogen peroxide
AH_2	ascorbic acid
$[AH_2]_0$	initial concentration of ascorbic acid
A	dehydroascorbic acid
E_mAH_2	met-tyrosinase/ascorbic acid complex
$E_{ox}AH_2$	oxy-tyrosinase/ascorbic acid complex
TBC	4-*tert*-butylcatechol
$[TBC]_0$	initial concentration of 4-*tert*-butylcatechol
o-TBQ	*o*-*tert*-butylquinone
E_mTBC	met-tyrosinase/4-*tert*-butylcatechol complex
$E_{ox}TBC$	oxy-tyrosinase/4-*tert*-butylcatechol complex
$[NADH]_0$	initial concentration of reduced β-nicotinamide adenine dinucleotide
$[E]_0$	initial concentration of tyrosinase
K_M^{HR}	Michaelis constant of tyrosinase for 4-hexylresorcinol
k_{cat}^{HR}	catalytic constant of tyrosinase for 4-hexylresorcinol
PHPAA	*p*-hydroxyphenylacetic acid
PHPPA	*p*-hydroxyphenylpropionic acid
δ_1	^{13}C NMR chemical shift value of the 1 carbon
δ_2	^{13}C NMR chemical shift value of the 2 carbon
δ_6	^{13}C NMR chemical shift value of the 6 carbon
$V_0^{p\text{-Q}}$	initial *p*-quinone formation rate

DOI: 10.1021/acs.jafc.5b02523
J. Agric. Food Chem. 2015, 63, 7032−7040

$V_{max}^{p\text{-}Q}$ maximum action rate of tyrosinase on 4-hexylresorcinol

REFERENCES

(1) Sánchez-Ferrer, A.; Rodríguez-López, J. N.; García-Cánovas, J.; García-Carmona, F. Tyrosinase: a comprehensive review of its mechanism. *Biochim. Biophys. Acta, Protein Struct. Mol. Enzymol.* **1995**, *1247*, 1−11.

(2) Solomon, E. I.; Sundaram, U. M.; Machonkin, T. E. Multicopper oxidases and oxygenases. *Chem. Rev.* **1996**, *96*, 2563−2605.

(3) Vámos-Vigyázó, L. Polyphenol oxidase and peroxidase in fruits and vegetables. *Crit. Rev. Food Sci. Nutr.* **1981**, *15*, 49−127.

(4) Mcevily, A. J.; Iyengar, R.; Otwell, W. S. Inhibition of enzymatic browning in foods and beverages. *Crit. Rev. Food Sci. Nutr.* **1992**, *32*, 253−273.

(5) Weemaes, C. A.; Ludikhuyze, L. R.; Van den Broeck, I.; Hendrickx, M. E. Influence of pH, benzoic acid, glutathione, EDTA, 4-hexylresorcinol, and sodium chloride on the pressure inactivation kinetics of mushroom polyphenol oxidase. *J. Agric. Food Chem.* **1999**, *47*, 3526−3530.

(6) Montero, P.; Martínez-Álvarez, O.; Zamorano, J. P.; Alique, R.; Gómez-Guillén, M. C. Melanosis inhibition and 4-hexylresorcinol residual levels in deepwater pink shrimp (*Parapenaeus longirostris*) following various treatments. *Eur. Food Res. Technol.* **2006**, *223*, 16−21.

(7) Ito, S.; Wakamatsu, K. Chemistry of melanins. In *The Pigmentary System. Physiology and Pathophysiology*, 2nd ed.; Nordlund, J. J., Boissy, R. E., Hearing, V. J., King, R. A., Oetting, W. S., Ortonne, J. P., Eds.; Blackwell Publishing: Oxford, UK, 2006; pp 282−310.

(8) Urabe, K.; Nakayam, J.; Hori, Y. Mixed epidermal and dermal hypermelanoses. In *The Pigmentary System. Physiology and Pathophysiology*; Nordlund, J. J., Boissy, R. E., Hearing, V. J., King, R. A., Ortonne, J. P., Eds.; Oxford University Press: New York, 1998; pp 909−911.

(9) Won, Y. K.; Loy, C. J.; Randhawa, M.; Southall, M. D. Clinical efficacy and safety of 4-hexyl-1,3-phenylenediol for improving skin hyperpigmentation. *Arch. Dermatol. Res.* **2014**, *306*, 455−465.

(10) Mendes, E.; Perry, M.; de, J.; Francisco, A. P. Design and discovery of mushroom tyrosinase inhibitors and their therapeutic applications. *Expert Opin. Drug Discovery* **2014**, *9*, 533−554.

(11) Pillaiyar, T.; Manickam, M.; Jung, S. H. Inhibitors of melanogenesis: a patent review (2009−2014). *Expert Opin. Ther. Pat.* **2015**, *25*, 775−788.

(12) Lee, S. Y.; Baek, N.; Nam, T. G. Natural, semisynthetic and synthetic tyrosinase inhibitors. *J. Enzyme Inhib. Med. Chem.* **2015**, 1.

(13) Frankos, V. H.; Schmitt, D. F.; Haws, L. C.; McEvily, A. J.; Iyengar, R.; Miller, S. A.; Munro, I. C.; Clydesdale, F. M.; Forbes, A. L.; Sauer, R. M. Generally recognized as safe (GRAS) evaluation of 4-hexylresorcinol for use as a processing aid for prevention of melanosis in shrimp. *Regul. Toxicol. Pharmacol.* **1991**, *14*, 202−212.

(14) Torihara, M.; Tamai, Y.; Shiono, M.; Tasaka, K. Alkylresorcinol skin depigmental agents. Eur. Pat. Appl. EP 341664, Nov 15, 1989; *Chem. Abstr.* **1990**, *113*, 178024.

(15) McEvily, A. J.; Iyengar, R.; Gross, A. Browning inhibitors for foods and beverages. PCT Int. Appl. WO 9222213, Dec 23, 1992; *Chem. Abstr.* **1993**, *118*, 146573.

(16) Huber, S.; Mujica-Fernaud, T. Use of hydroxyphenylester-type tyrosinase inhibitors for skin lightening cosmetics. PCT Int. Appl. WO 2009021590, Feb 19, 2009; *Chem. Abstr.* **2009**, *150*, 244611.

(17) Chaudhuri, R. K. Skin lightening cosmetic compositions. U.S. Pat. Appl. Publ. US 20080305059, Dec 11, 2008; *Chem. Abstr.* **2008**, *150*, 40863.

(18) Dawley, R. M.; Flurkey, W. H. 4-Hexylresorcinol, a potent inhibitor of mushroom tyrosinase. *J. Food Sci.* **1993**, *58*, 609.

(19) Jiménez, M.; García-Carmona, F. 4-Substituted resorcinols (sulfite alternatives) as slow-binding inhibitors of tyrosinase catecholase activity. *J. Agric. Food Chem.* **1997**, *45*, 2061−2065.

(20) Pilizota, V.; Subaric, D. Control of enzymatic browning of foods. *Food Technol. Biotechnol.* **1998**, *36*, 219−227.

(21) Buta, J. G.; Moline, H. E.; Spaulding, D. W.; Wang, C. Y. Extending storage life of fresh-cut apples using natural products and their derivatives. *J. Agric. Food Chem.* **1999**, *47*, 1−6.

(22) Shimizu, K.; Kondo, R.; Sakai, K. Inhibition of tyrosinase by flavonoids, stilbenes and related 4-substituted resorcinols: structure-activity investigations. *Planta Med.* **2000**, *66*, 11−15.

(23) Kaur, C.; Kapoor, H. C. Inhibition of enzymatic browning in apples, potatoes and mushrooms. *J. Sci. Ind. Res.* **2000**, *59*, 389−394.

(24) Iyidogan, N. F.; Bayindirli, A. Effect of L-cysteine, kojic acid and 4-hexylresorcinol combination on inhibition of enzymatic browning in Amasya apple juice. *J. Food Eng.* **2004**, *62*, 299−304.

(25) Chen, Q. X.; Ke, L. N.; Song, K. K.; Huang, H.; Liu, X. D. Inhibitory effects of hexylresorcinol and dodecylresorcinol on mushroom (*Agaricus bisporus*) tyrosinase. *Protein J.* **2004**, *23*, 135−141.

(26) Alvarez-Parrilla, E.; de la Rosa, L. A.; Rodrigo-García, J.; Escobedo-González, R.; Mercado-Mercado, G.; Moyers-Montoya, E.; Vázquez-Flores, A.; González-Aguilar, G. A. Dual effect of β-cyclodextrin (β-CD) on the inhibition of apple polyphenol oxidase by 4-hexylresorcinol (HR) and methyl jasmonate (MJ). *Food Chem.* **2007**, *101*, 1346−1356.

(27) Arias, E.; Gonzalez, J.; Oria, R.; Lopez-Buesa, P. Ascorbic acid and 4-hexylresorcinol effects on pear PPO and PPO catalyzed browning reaction. *J. Food Sci.* **2007**, *72*, C422−C429.

(28) Arias, E.; González, J.; Peiró, M.; Oria, R.; Lopez-Buesa, P. Browning prevention by ascorbic acid and 4-hexylresorcinol: different mechanisms of action on polyphenol oxidase in the presence and in the absence of substrates. *J. Food Sci.* **2007**, *72*, C464−C470.

(29) Thepnuan, R.; Benjakul, S.; Visessanguan, W. Effect of pyrophosphate and 4-hexylresorcinol pretreatment on quality of refrigerated white shrimp (*Litopenaeus vannamei*) kept under modified atmosphere packaging. *J. Food Sci.* **2008**, *73*, S124−S133.

(30) Martínez-Alvarez, O.; Gómez-Guillén, C.; Montero, P. Effect of different chemical compounds as coadjutants of 4-hexylresorcinol on the appearance of deepwater pink shrimp (*Parapenaeus longirostris*) during chilled storage. *Int. J. Food Sci. Technol.* **2008**, *43*, 2010−2018.

(31) Kolbe, L.; Mann, T.; Gerwat, W.; Batzer, J.; Ahlheit, S.; Scherner, C.; Wench, H.; Stäb, F. 4-n-butylresorcinol, a highly effective tyrosinase inhibitor for the topical treatment of hyperpigmentation. *J. Eur. Acad. Dermatol. Venereol.* **2013**, *27*, 19−23.

(32) Fenoll, L. G.; Rodríguez-López, J. N.; García-Sevilla, F.; García-Ruiz, P. A.; Varón, R.; García-Cánovas, F.; Tudela, J. Analysis and interpretation of the action mechanism of mushroom tyrosinase on monophenols and diphenols generating highly unstable *o*-quinones. *Biochim. Biophys. Acta, Protein Struct. Mol. Enzymol.* **2001**, *1548*, 1−22.

(33) Rodriguez-Lopez, J. N.; Tudela, J.; Varon, R.; Garcia-Carmona, F.; Garcia-Canovas, F. Analysis of a kinetic model for melanin biosynthesis pathway. *J. Biol. Chem.* **1992**, *267*, 3801−3810.

(34) Rodriguez-Lopez, J. N.; Fenoll, L. G.; Peñalver, M. J.; Garcia-Ruiz, P. A.; Varon, R.; Martinez-Ortiz, F.; Garcia-Canovas, F.; Tudela, J. Tyrosinase action on monophenols: evidence for direct enzymatic release of *o*-diphenol. *Biochim. Biophys. Acta, Protein Struct. Mol. Enzymol.* **2001**, *1548*, 238−256.

(35) Garcia-Molina, M.; Muñoz-Muñoz, J. L.; Berna, J.; Rodriguez-Lopez, J. N.; Varon, R.; Garcia-Canovas, F. Hydrogen peroxide hepls in the identification of monophenols as possible substrates of tyrosinase. *Biosci., Biotechnol., Biochem.* **2013**, *77*, 2383−2388.

(36) Garcia-Molina, M. M.; Muñoz Muñoz, J. L.; Martinez-Ortiz, F.; Rodriguez Martinez, J.; Garcia-Ruiz, P. A.; Rodriguez-Lopez, J. N.; Garcia-Canovas, F. Tyrosinase-catalyzed hydroxylation of hydroquinone, a depigmenting agent, to hydroxyhydroquinone: a kinetic study. *Bioorg. Med. Chem.* **2014**, *22*, 3360−3369.

(37) Garcia-Molina, M. M.; Berna, J.; Muñoz-Muñoz, J. L.; Garcia-Ruiz, P. A.; Garcia Moreno, M.; Rodriguez Martinez, J.; Garcia-Canovas, F. Action of tyrosinase on hydroquinone in the presence of catalytic amounts of *o*-diphenol. A kinetic study. *React. Kinet., Mech. Catal.* **2014**, *112*, 305−320.

(38) Garcia-Molina, M. M.; Munoz-Munoz, J. L.; Garcia-Molina, F.; Garcia-Ruiz, P. A.; Garcia-Canovas, F. Action of tyrosinase on ortho-

DOI: 10.1021/acs.jafc.5b02523
J. Agric. Food Chem. 2015, 63, 7032−7040

substituted phenols: possible influence on browning and melanogenesis. *J. Agric. Food Chem.* **2012**, *60*, 6447−6453.
(39) Jimenez, M.; Garcia-Carmona, F. Hydrogen peroxide-dependent 4-t-butylphenol hydroxylation by tyrosinase − a new catalytic activity. *Biochim. Biophys. Acta, Protein Struct. Mol. Enzymol.* **1996**, *1297*, 33−39.
(40) Rodriguez-Lopez, J. N.; Fenoll, L. G.; Garcia-Ruiz, P. A.; Varon, R.; Tudela, J.; Thorneley, R. N.; Garcia-Canovas, F. Stopped-flow and steady-state study of the diphenolase activity of mushroom tyrosinase. *Biochemistry* **2000**, *39*, 10497−10506.
(41) Bradford, M. M. A rapid and sensitive method for the quantitation of microgram quantities of protein utilizing the principle of protein-dye binding. *Anal. Biochem.* **1976**, *72*, 248−254.
(42) Garcia-Molina, F.; Munoz, J. L.; Varon, R.; Rodriguez-Lopez, J. N.; Garcia-Canovas, F.; Tudela, J. A review on spectrophotometric methods for measuring the monophenolase and diphenolase activities of tyrosinase. *J. Agric. Food Chem.* **2007**, *55*, 9739−9749.
(43) Muñoz, J. L.; Garcia-Molina, F.; Varon, R.; Rodriguez-Lopez, J. N.; Garcia-Canovas, F.; Tudela, J. Calculating molar absorptivities for quinones: application to the measurement of tyrosinase activity. *Anal. Biochem.* **2006**, *351*, 128−138.
(44) Rodriguez-Lopez, J. N.; Ros, J. R.; Varon, R.; Garcia-Canovas, F. Oxygen Michaelis constants for tyrosinase. *Biochem. J.* **1993**, *293*, 859−866.
(45) Fenoll, L. G.; Rodriguez-Lopez, J. N.; Garcia-Molina, F.; Garcia-Canovas, F.; Tudela, J. Michaelis constants of mushroom tyrosinase with respect to oxygen in the presence of monophenols and diphenols. *Int. J. Biochem. Cell Biol.* **2002**, *34*, 332−336.
(46) Garcia-Molina, F.; Hiner, A. N.; Fenoll, L. G.; Rodriguez-Lopez, J. N.; Garcia-Ruiz, P. A.; Garcia-Canovas, F.; Tudela, J. Mushroom tyrosinase: catalase activity, inhibition, and suicide inactivation. *J. Agric. Food Chem.* **2005**, *53*, 3702−3709.
(47) Varon, R.; Garcia-Sevilla, F.; Garcia-Moreno, M.; Garcia-Canovas, F.; Peyro, R.; Duggleby, R. G. Computer program for the equations describing the steady state of enzyme reactions. *Bioinformatics* **1997**, *13*, 159−167.
(48) Varón-Castellanos, R.; García-Moreno, M.; García-Sevilla, F.; Ruiz-Galea, M. M.; García-Canovas, F. In *Computerized Derivation of the Steady-State Equations of Enzyme Reactions*; Editorial A5: Albacete, Spain, 1995.
(49) García-Sevilla, F.; Garrido-del Solo, C.; Duggleby, R. G.; García-Cánovas, F.; Peyró, R.; Varón, R. Use of a windows program for simulation of the progress curves of reactants and intermediates involved in enzyme-catalyzed reactions. *BioSystems* **2000**, *54*, 151−164.
(50) Jandel Scientific, Sigma Plot 9.0 for Windows, Core Madera, Spain, 2006.
(51) Espín, J. C.; Varón, R.; Fenoll, L. G.; Gilabert, M. A.; García-Ruiz, P. A.; Tudela, J.; García-Cánovas, F. Kinetic characterization of the substrate specificity and mechanism of mushroom tyrosinase. *Eur. J. Biochem.* **2000**, *267*, 1270−1279.
(52) Espin, J. C.; Tudela, J.; Garcia-Canovas, F. 4-Hydroxyanisole: the most suitable monophenolic substrate for determining spectrophotometrically the monophenolase activity of polyphenol oxidase from fruits and vegetables. *Anal. Biochem.* **1998**, *259*, 118−126.
(53) Ortiz-Ruiz, C. V.; Garcia-Molina, M.; del, M.; Serrano, J. T.; Tomas-Martinez, V.; Garcia-Canovas, F. Discrimination between alternative substrates and inhibitors of tyrosinase. *J. Agric. Food Chem.* **2015**, *63*, 2162−2171.
(54) Ortiz-Ruiz, C. V.; Berna, J.; Garcia-Molina, M. D.; Tudela, J.; Tomas, V.; Garcia-Canovas, F. Identification of *p*-hydroxybenzyl alcohol, tyrosol, phloretin and its derívate phloridzin as tyrosinase substrates. *Bioorg. Med. Chem.* **2015**, *23*, 3738.
(55) Lerch, K. In *Metal Ions in Biological Systems*; Siegel, H., Ed.; Dekker: New York, 1981; Vol. 13, pp 143−186.
(56) Kutyrev, A. A.; Moskva, V. V. Nucleophilic reactions of quinones. *Russ. Chem. Rev.* **1991**, *60*, 134−168.
(57) Grundmann, C. In *Methoden der Organischen Chemie (Houben-Weyl)*; Georg Thieme: Stuttgart, Germany, 1977; Vol. VII/3A, pp 768.
(58) Patai, S.; Rappoport, Z. In *The Chemistry of the Quinonoid Compounds*; Wiley: New York, 1988; Vol. 2, p 1.
(59) Smith, M. B. *March's Advanced Organic Chemistry: Reactions, Mechanisms, and Structure*, 7th ed.; Wiley: Hoboken, NJ, USA, 2013; pp 581.
(60) Günter, H. Nuclear magnetic resonance of fluorine-19 and carbon-13. In *NMR Spectroscopy*; Wiley: New York, 1980; pp364−374.
(61) Farnum, D. G. Charge density-NMR chemical shift correlations in organic ions. In *Advances in Physical Organic Chemistry*; Gold, V., Bethell, D., Eds.; Elsevier: Amsterdam, The Netherlands, 1975; Vol. 11, pp 123−173 DOI: 10.1016/S0065-3160(08)60341-X.
(62) Chen, Q. X.; Song, K. K.; Wang, Q.; Huang, H. Inhibitory effects on mushroom tyrosinase by some alkylbenzaldehydes. *J. Enzyme Inhib. Med. Chem.* **2003**, *18*, 491−496.
(63) Galván, I.; Moller, A. P. Brain size and the expression of pheomelanin-based colour in birds. *J. Evol. Biol.* **2011**, *24*, 999−1006.
(64) Galván, I.; Alonso-Alvarez, C.; Negro, J. J. Relationships between hair melanization, glutathione levels, and senescence in wild boars. *Physiol. Biochem. Zool.* **2012**, *85*, 332−347.
(65) Morgan, A. M.; Lo, J.; Fisher, D. E. How does pheomelanin synthesis contribute to melanomagenesis: Two distinct mechanisms could explain the carcinogenicity of pheomelanin synthesis. *BioEssays* **2013**, *35*, 672−676.

DOI: 10.1021/acs.jafc.5b02523
J. Agric. Food Chem. 2015, 63, 7032−7040

authors found that Stev content was not affected by the presence or absence of nitrogen fertilizer,[17] and no effect of P and K on this SG was shown.[18] Similarly, rebaudioside A was not affected by supply of different concentrations of N, P, and K.[19,20] Thus, according to the importance of phytochemicals and antioxidant power for functional aspect of Stevia, the aim of this study was to evaluate the effects of N supply on SG content and total phenol and flavonoid compositions, as well as on total antioxidant capacity in Stevia leaves. At the same time, the effects of harvest time, as well as of N supply × harvest time interaction, were also investigated, with the aim to define the best conditions to maximize the levels of beneficial bioactive compounds in Stevia leaves.

MATERIALS AND METHODS

Chemicals. Ethanol, methanol, and ferrous sulfate were purchased from Carlo Erba SpA (Milan, Italy). Water and acetonitrile were obtained from J. T. Baker (Phillipsburg, NJ, USA). Pure Stev (99.9% purity) and pure RebA (97.4% purity) were purchased from Extrasynthese (Genay, France). 2,2-Diphenyl-1-picrylhydrazyl (DPPH), gallic acid monohydrate (3,4,5-trihydroxybenzoic acid), 2,4,6-tri(2-pyridyl)-s-triazine (TPTZ), Trizma acetate, Folin−Ciocalteu reagent, sodium carbonate, and ferric chloride were obtained from Sigma-Aldrich Chemical Co. (Milan, Italy). The standards luteolin-7-*O*-glucoside, rutin, myricetin, apigenin-7-*O*-glucoside, quercitrin, and kaempferol were purchased from Extrasynthèse (Genay, France). All reagents and solvents used were of analytical or high-performance liquid chromatography (HPLC) grade. All solvents and water were accurately degassed before being used in the analyses.

Plant Material and Experimental Conditions. A pot trial was carried out at the Experimental Centre of the Department of Agriculture, Food and Environment (DAFE) of the University of Pisa, located in San Piero a Grado, Pisa, Italy (43°40′ N; 10°19′ E, 5 m above sea level), during the 2010 growing season. A selected clone (RG) of *S. rebaudiana*, belonging to the DAFE germplasm collection, was used. The plants were obtained by stem cuttings taken from 3-year-old parental plants grown in the open field at the DAFE experimental center. The stem cuttings, 4−5 cm long, were placed into 20 L pots to allow the maximum development of the roots, which were then filled with sandy-loam and low-fertility soil (68.5% sand; 25.9% silt; 5.6% clay; pH 7.74; organic matter = 0.83%; total N = 0.32 g kg^{-1}; available P = 11.49 mg kg^{-1}; exchangeable K = 44.84 g kg^{-1}; 1.65 g cm^{-3} bulk density). The trial was conducted in open air from May to September. The area has a Mediterranean climate, with rainfall mainly concentrated in the autumn and spring (mean = 948 mm $year^{-1}$). Mean maximum and minimum temperatures in the growing season were 26.9 and 13.1 °C, respectively.

Stevia plants were grown under different rates of nitrogen: N0 (without N fertilization); N50 (50 kg N ha^{-1} equal to 0.4 g N per pot as ammonium nitrate); N150 (150 kg N ha^{-1}, equal to 1.2 g N per pot as ammonium nitrate), N300 (300 kg N ha^{-1}, equal to 2.4 g N per pot as ammonium nitrate), and Norg (150 kg N ha^{-1}, equal to 1.2 g N per pot as organic nitrogen from Nutex N7 based on wool wastes, poultry manure, blood, and pomace with 7% organic N and 35% organic carbon).

The pots were arranged in a randomized block design with five replications (one pot per replicate) for each treatment. Starting from the middle part of May, during the vegetative growth, the nitrogen was split in four applications every 30 days. In addition, a mix of macro (Mg) and microelements (Bo, Cu, Fe, Mn, Mo, Zn) was supplied, at the dose of 0.1 g L^{-1} per pot. A constant source of phosphorus and potassium was distributed to all treatments at the rate of 100 kg ha^{-1} of P and K, respectively (equal to 0.80 g P per pot as triple superphosphate and 0.80 g K per pot as potassium sulfate), before the plants were transplanted. Water (20 m^3 ha^{-1}) was supplied to all pots to facilitate transplanting recovery. During the trial, the plants were maintained under optimal water supply through a drip irrigation system to maintain soil moisture to 75−80% of field capacity. No pests and diseases were observed during the trial.

Crop Sampling. Three different samplings of the leaves were carried out to evaluate the dynamics of accumulation of bioactive compounds in Stevia leaves. Leaf samplings were accomplished at the beginning and end of July, during vegetative growth (H1 = July 9, H2 = July 21) and at the beginning of September, when the plants started flowering (H3 = September 10). After each sampling, the leaves were air-dried in a ventilated oven at 40 °C until constant weight (8% residual water content) and ground to a fine powder using a laboratory mill. Samples were used to determine SG content, total phenols, flavonoid composition, and antioxidant capacity.

Preparation of Extracts. Samples (0.5 g of powder) were randomly chosen from each plant treatment and placed in 250 mL Erlenmeyer flasks. Extracts were sonicated for 30 min at 60 °C with 50 mL of 70% (v/v) ethanol. Before analysis, extracts were passed through a 0.45 μm nylon filter attached to a syringe to remove any suspended material.

Steviol Glycoside Content. The procedure was performed following the method described by Hearn and Subedi[21] and Kolb et al.[22] Briefly, 20 μL of filtered extract was injected into a HPLC system (Jasco PU980) coupled with a UV−visible wavelength detector. A LiChrospher NH2 column, 5 μm, 250 mm × 4.6 mm (Alltech Italia), in conjunction with a LiChrospher Amino All-Guard and All-Guard Cartridge Holder (Alltech Italia) was used. The following HPLC operating conditions were used: an isocratic mobile phase, acetonitrile/water (80:20), pH 5 adjusted with acetic acid, a flow rate of 1.0 mL/min, and a run time of 20 min. Detection was at 210 nm at ambient temperature. Chromatograms were acquired online, and data were collected via a Jasco interface (Hercules 2000 interface chromatography). The identity of SG was confirmed by chromatography on HPLC with authentic standards, and quantification was performed using a standard curve in the range of 0.25−1 g/L of standard mixtures containing Stev and RebA.

Total Phenolic Content. Determination of total phenolic compounds was performed on ethanolic extracts by the Folin−Ciocalteu method according to the procedure of Dewanto et al.[23] This procedure involves the reduction of Folin−Ciocalteu reagent by phenolic compounds, with concomitant formation of a blue complex determined at 765 nm by UV−visible spectrophotometer (Varian Cary 1E, Palo Alto, CA, USA). Calculations were performed using a calibration curve prepared with gallic acid as standard, and results were expressed as milligrams of gallic acid equivalents (GAE) per gram of dry weight (DW).

Ferric-Reducing Antioxidant Power (FRAP) Assay. The FRAP method, based on the reduction of the ferric tripyridyltriazine complex (Fe^{3+}−TPTZ) by antioxidants, was carried out according to Benzie and Strain[24] with slight modifications. Briefly, 2 mL of freshly prepared FRAP reagent, containing 300 mM acetate buffer (pH 3.6), 10 mM TPTZ solution (in 40 mM HCl), and 20 mM ferric chloride in a 10:1:1 (v/v/v) ratio, was added to a known aliquot of Stevia leaf ethanolic extract. After incubation at 37 °C for 10 min, absorbance at 593 nm was recorded. Ferrous sulfate was used as a standard (0−1500 μM). Total antioxidant capacity was expressed as micromoles of Fe^{2+} per gram of DW.

DPPH Radical-Scavenging Assay. The free radical-scavenging activity of Stevia leaf extracts was evaluated by the DPPH free radical method according to Tadhani et al.[25] Briefly, 200 μL of ethanolic extract was placed in a test tube, and the volume was made up to 1 mL with methanol. Then 3 mL of freshly prepared DPPH solution (200 μmol L^{-1} in methanol) was added, and the tube contents were mixed vigorously. The tube was subsequently kept in a water bath at 37 °C for 20 min, after which the absorbance of the sample was measured at 517 nm using a UV−visible spectrophotometer (Varian Cary 1E). The decrease in absorbance at 517 nm was measured against a blank of pure methanol to estimate the radical-scavenging capacity of the samples. Radical-scavenging activity was calculated as the inhibition of the free radical by the sample using the formula

$$\%\ \text{inhibition}\ (\%\text{I}) = [(A_0 - A_t)/A_0] \times 100$$

where A_0 is the absorbance of the control DPPH solution at 0 min and A_t is the absorbance in the presence of the extract after t = 20 min. The extract concentration providing 50% of radical-scavenging activity

DOI: 10.1021/acs.jafc.5b02147
J. Agric. Food Chem. 2015, 63, 7041−7050

Table 1. Effect of Nitrogen Fertilization[a] and Harvest Time[b] on Stevioside and Rebaudioside A Contents and Rebaudioside A/Stevioside Ratios in Leaves of *Stevia rebaudiana*[c]

	N0	N50	N150	N300	Norg	mean harvest
			Stevioside (g 100 g^{-1} DW)			
H1	6.47 ± 0.73 ab	3.08 ± 0.01 fg	5.60 ± 0.03 cd	4.93 ± 0.29 d	7.08 ± 0.52 a	5.43 A
H2	6.32 ± 0.96 bc	5.08 ± 0.25 d	3.63 ± 0.18 efg	4.18 ± 0.53 e	3.98 ± 0.83 e	4.64 B
H3	4.97 ± 0.07 d	3.18 ± 0.06 fg	3.78 ± 0.11 ef	2.97 ± 0.01 g	3.77 ± 0.01 ef	3.73 C
mean N	5.92 A	3.78 D	4.34 C	4.03 CD	4.94 B	
source of variation: N = ***; H = ***; N × H = ***						
			Rebaudioside A (g 100 g^{-1} DW)			
H1	1.79 ± 0.05 h	1.69 ± 0.06 h	3.46 ± 0.62 bcde	3.69 ± 0.18 abcd	3.19 ± 0.06 de	2.75 C
H2	3.96 ± 0.35 ab	4.10 ± 0.10 a	3.88 ± 0.64 ab	3.75 ± 0.62 abc	2.35 ± 0.11 g	3.61 A
H3	3.19 ± 0.02 de	3.08 ± 0.08 ef	3.27 ± 0.01 cde	3.17 ± 0.06 e	2.64 ± 0.09 fg	3.07 B
mean N	2.98 B	2.94 B	3.54 A	3.54 A	2.73 B	
source of variation: N = ***; H = ***; N × H = ***						
			Rebaudioside A/Stevioside			
H1	0.28 ± 0.03 j	0.55 ± 0.01 hi	0.62 ± 0.08 gh	0.75 ± 0.06 def	0.45 ± 0.02 i	0.53 B
H2	0.63 ± 0.11 fgh	0.81 ± 0.01 cde	1.07 ± 0.16 a	0.92 ± 0.15 bc	0.60 ± 0.09 gh	0.81 A
H3	0.64 ± 0.01 fgh	0.97 ± 0.01 ab	0.86 ± 0.02 bcd	1.07 ± 0.01 a	0.70 ± 0.02 efg	0.85 A
mean N	0.52 C	0.78 B	0.85 AB	0.91 A	0.58 C	
source of variation: N = ***; H = ***; N × H = ***						

[a]N0, without N fertilization; N50, 50 kg N ha^{-1}; N150, 150 kg N ha^{-1}; N300, 300 kg N ha^{-1}; Norg, 150 kg N ha^{-1} as organic nitrogen. [b]H1, July 9; H2, July 21; H3, September 10. [c]Results are the means ± SD of five replicates that were each analyzed in triplicate. A two-way ANOVA was used to evaluate the effect of nitrogen fertilization (N), harvest time (H), and the interaction between nitrogen and harvest time (N × H). Significance was as follows: ***, significant at $P < 0.001$ level. Upper-case letters indicate effect of nitrogen rate (N) and harvest time (H); lower case letters indicate N × H interaction.

(IC_{50}) was calculated from the graph of inhibition percentage against extract concentration. The results were also expressed as ascorbic acid equivalent.

Flavonoid Determination. Qualitative and quantitative analyses were performed by RP-HPLC. Twenty microliters of extract was injected into a Waters model 515 HPLC system (Waters, Milford, MA, USA) fitted with a 4.6 mm × 250 mm Prodigy ODS column (Phenomenex, Bologna, Italy). Detection was carried out at 360 nm, using a Waters 2487 dual λ UV−visible detector. Mobile phase A contained water acidified with formic acid (pH 2.7), and mobile phase B contained methanol. A linear gradient of 10−90% mobile phase B was run for 26 min at 1 mL/min. The identity of the free flavonoids was confirmed by cochromatography with authentic standards. Quantification was performed using standard curves in the range of 10−500 ng of a standard mixture containing luteolin-7-*O*-glucoside, rutin, myricetin, apigenin-7-*O*-glucoside, quercitrin, quercetin, luteolin, and kaempferol. Chromatogram analysis was performed by the software Millennium 32 (Waters).

Statistical Analysis. All data were subjected to analysis of variance (ANOVA) using CoStat version 6.2 (CoHort Software, Monterey, CA, USA). Two-way completely randomized ANOVA was carried out to estimate the variance components of N supply (N), harvest time (H), and their interaction (N × H). Means were separated on the basis of least significant difference (LSD) only when the ANOVA *F* test showed significance at the 0.05 or 0.01 probability level. Finally, linear regression analyses using GraphPad PRISM version 4.0 (GraphPad Software, Inc., La Jolla, CA, USA) were performed to evaluate the relationships between antioxidant capacity, total phenols, total flavonoids, and SG. For inhibition percentage data, obtained by the DPPH assay, an arcsine transformation was applied before statistical analysis was performed.

RESULTS

Nitrogen fertilization (N), harvest time (H), and their mutual interaction (N × H) significantly affected the Stev and RebA contents, although the individual compounds showed different behaviors (Table 1). The results indicated that the Stev content in the leaf changed with the stage of plant development. Results showed that the Stev content was higher in the vegetative stage (H1) and decreased until the beginning of flowering time (H3). In fact, the maximum Stev content was reached in the leaves collected at the beginning of July (H1) during maximum vegetative development, and it decreased thereafter (Table 1). With regard to N, the maximum Stev content was observed in plants grown without N (N0), followed by Norg. Taking into consideration the N × H effect, the highest Stev contents were recorded in plants grown at N0 and Norg and harvested in H1.

In contrast to Stev, the RebA content increased significantly from the beginning to the end of July, reaching its highest value in the second harvest (Table 1). Considering mean values, the N rate also significantly affected RebA content, with the maximum values in leaves of Stevia plants grown with 150 and 300 kg N ha^{-1}. In contrast, considering the N × H interaction, at H2 the Norg-treated plants showed the lowest level of this compound, whereas no significant differences were observed among the mineral N doses (Table 1).

Due to the changes in the two main SG, the RebA/Stev ratio significantly varied depending on N rates, harvest time, and N × H interaction. The maximum ratio was recorded in plants harvested at H2 and H3 and in plants grown with 150 and 300 kg N ha^{-1}. In particular, the leaves of plants grown with 150 kg N ha^{-1} and harvested in H2 showed the highest ratio, whereas the lowest ratio was found in plants grown without N and harvested at H1.

Similarly to SG, total phenols and total flavonoids were significantly affected by N rate, harvest time, and N × H interaction (Figure 1). With regard to total phenols, the highest values were recovered at H1 in leaves of plants grown with 50 and 150 kg N ha^{-1} (105.50 and 110.41 mg g^{-1} DW, respectively). At the same harvest time, the N150-treated plants showed the highest level of total flavonoids (104.03 mg g^{-1} DW). As a general trend, by averaging over N treatments, both phenols and flavonoids were significantly higher in H1 (83.4 and 68.9 mg g^{-1} DW for phenols and flavonoids, respectively) than in H2 (60.8

DOI: 10.1021/acs.jafc.5b02147
J. Agric. Food Chem. 2015, 63, 7041−7050

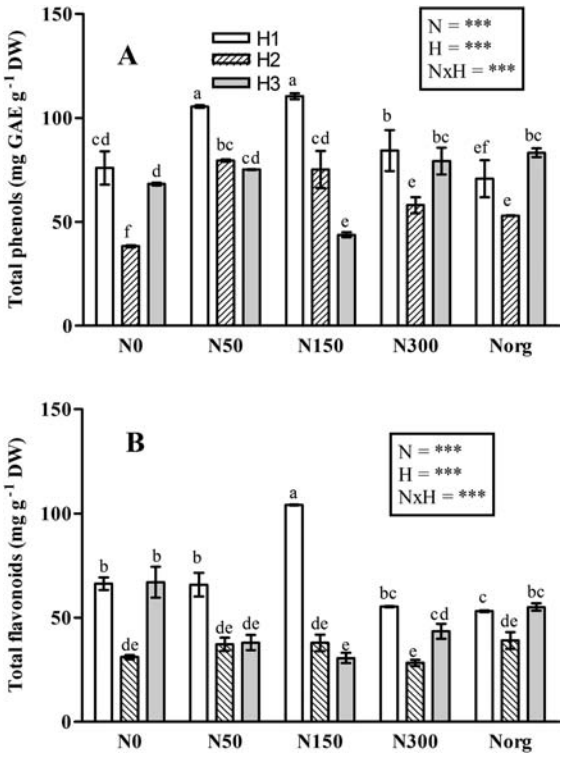

Figure 1. Effect of nitrogen rate and harvest time on total phenolic content (A) and total flavonoids (B) in leaves of *Stevia rebaudiana* plants. Data are means of five replicates ± SDs; bars represent standard deviation. Means with the same letters are not significantly different for $P = 0.05$ following two-way ANOVA test with nitrogen rate and harvest time as variability factors. Asterisks indicate significant differences according to two-way ANOVA test (***, significant at $P < 0.001$ probability level).

and 34.7 mg g^{-1} DW for phenols and flavonoids, respectively) and H3 (69.9 and 46.9 mg g^{-1} DW for phenols and flavonoids, respectively). With regard to the N effect, as an average over harvest times, the N50-treated plants showed the highest phenolic content (86.7 mg g^{-1} DW), followed by N150 and N300 treatments (76.5 and 73.9 mg g^{-1} DW, respectively). Otherwise, the N150-treated plants were characterized by the highest flavonoids (58.0 mg g^{-1} DW), followed by the N0-treated plants (54.5 mg g^{-1} DW).

Among the flavonoids, rutin, myricetin, apigenin-7-*O*-glucoside, quercitrin, kaempferol, and luteolin-7-*O*-glucoside have been identified (Table 2). All of the flavonoids were significantly affected by the N rate, harvest time, and N × H interaction with the exception of myricetin, for which H was not significant. Luteolin-7-*O*-glucoside was the main flavonoid in Stevia leaf extracts, ranging from 43 to 74% of the total flavonoids (Table 2), depending on nitrogen rate and harvest time. In particular, it was recovered at higher amounts in H1 compared to the other harvests, reaching the highest content in plants grown with 150 kg N ha^{-1} (74%). In contrast, in H2, luteolin-7-*O*-glucoside content was 2−4 times lower than the one recorded in H1. In H3, the amount of this compound increased in each N treatment in comparison with H2, with the exception of the N150 treatment, whereas under N0 and Norg treatments, it approached again values recorded in H1 (Table 2).

Among the identified flavonoids, kaempferol appeared to be present in minor amount, representing 0.1−2% of the total flavonoid pool (Table 2). Myricetin and quercitrin showed values around 2−3 mg g^{-1} DW, representing 3−9% of the total flavonoid amount. Rutin and apigenin-7-*O*-glucoside values were about 4−5 and 7−10 mg g^{-1} DW, respectively. Apigenin-7-*O*-glucoside showed a value 2-fold higher than rutin, representing 14% of the total flavonoid pool (Table 2). As observed for luteolin-7-*O*-glucoside, both rutin and apigenin-7-*O*-glucoside showed the highest value at H1 under N150 treatment, contributing to determine also the highest value of total flavonoid in these conditions (Figure 1; Table 2). In contrast to what was observed for luteolin-7-*O*-glucoside and apigenin-7-*O*-glucoside, rutin and quercitrin showed no increase from H2 to H3, and the lowest values were recorded in the last harvest.

To evaluate the total antioxidant capacity, both FRAP and DPPH assays have been performed (Figure 2). N, H, and the N × H interaction significantly affected also the antioxidant activity, measured with both FRAP and DPPH assays. According both methods, the higher antioxidant capacities, and consequently the higher presence of bioactive molecules, have been observed in H1 (589 mmol $FeSO_4$ g^{-1} DW and 83 mmol ASA g^{-1} DW, for FRAP and DPPH, respectively) and H3 (475 mmol $FeSO_4$ g^{-1} DW and 80 mmol ASA g^{-1} DW for FRAP and DPPH, respectively) in comparison with H2 (354 mmol $FeSO_4$ g^{-1} DW and 78 mmol ASA g^{-1} DW for FRAP and DPPH, respectively). The only exception to this trend was observed for Norg treatment, where the values recorded in H1 did not differ significantly from those obtained in H2, whereas at H3 they reached the highest values (Figure 2). With regard to the effect of N rate, the on-average highest values, measured by FRAP method, were recorded under N50 and Norg treatments (545 and 536 mmol $FeSO_4$ g^{-1} DW, respectively), whereas considering the N× H interaction, the highest FRAP values were recorded for N50- and N150-treated plants when harvested at H1 (Figure 2A).

DPPH radical scavenging has been used widely to test the antioxidant activities of plant extracts and foods. Figure 3 shows the IC_{50} value (the antioxidant concentration necessary to decrease the initial concentration of DPPH by 50%) calculated, for each N dose, by pooling data from the three harvest times, and for ascorbic acid, luteolin, and BHT, used as positive controls (Figure 3). In the DPPH assay, the lower is the IC_{50} value, the higher is its ability to scavenge radicals, particularly peroxy radicals, which are the propagators of the autoxidation of lipid molecules and thereby break the free radical chain reaction.[26] Our results showed that the Stevia leaf extracts were potent radical scavengers. In fact, notwithstanding their IC_{50} values were higher than those of ascorbic acid and luteolin, they were lower than that of BHT (Figure 3).

Significant high correlations between secondary metabolites of Stevia leaves and antioxidant capacities were found by both antioxidant measuring methods (Table 3). In particular, positive correlations were found among antioxidant activity and total phenols and flavonoids for N50, N150, and N300 treatments (Table 3). In addition, it was demonstrated that the antioxidant activity, measured by both assays, was negatively correlated with the amount of RebA for N0 treatment and positively correlated with the Stev content under N150 treatment. In the plants grown under Norg treatment, total flavonoid, Stev, and RebA contents did not correlate with the antioxidant activities. In addition, interesting positive statistic correlations have been found in N150-treated plants between Stev and total flavonoids, rutin, myricetin, apigenin-7-*O*-glucoside, quercitrin, and luteolin-7-*O*-glucoside (Table 4). In contrast, no significant correlation was observed in N150-treated plants either between RebA and total

DOI: 10.1021/acs.jafc.5b02147
J. Agric. Food Chem. 2015, 63, 7041−7050

Table 2. Effect of Nitrogen Fertilization[a] and Harvest Time[b] on the Main Flavonoids in Leaves of *Stevia rebaudiana*[c]

	N0	N50	N150	N300	Norg	mean harvest
			Rutin (mg g^{-1} DW)			
H1	5.58 ± 0.38 bcd	6.45 ± 0.48 ab	7.03 ± 0.40 a	4.12 ± 0.20 fg	5.28 ± 0.02 cde	5.69 A
H2	5.32 ± 0.11 cde	6.63 ± 0.72 ab	4.82 ± 1.46 def	4.80 ± 0.33 def	6.22 ± 1.03 abc	5.55 A
H3	5.01 ± 0.65 def	4.36 ± 0.41 efg	3.32 ± 0.25 g	4.54 ± 0.88 def	6.41 ± 0.53 ab	4.73 B
mean N	5.30 BC	5.81 AB	5.06 CD	4.49 D	5.97 A	
source of variation: N = ***; H = ***; N × H = ***						
			Myricetin (mg g^{-1} DW)			
H1	2.19 ± 0.13 def	2.59 ± 0.21 bcde	2.84 ± 0.14 ab	2.15 ± 0.16 ef	2.27 ± 0.01 def	2.41 A
H2	2.53 ± 0.00 bcdef	2.65 ± 0.64 bcd	2.22 ± 0.56 def	2.50 ± 0.18 bcdef	2.77 ± 0.36 abc	2.53 A
H3	2.60 ± 0.27 bcde	2.50 ± 0.50 bcdef	2.06 ± 0.07 f	2.31 ± 0.13 cdef	3.24 ± 0.09 a	2.54 A
mean N	2.44 B	2.58 AB	2.37 B	2.32 B	2.76 A	
source of variation: N = *; H = ns; N × H = **						
			Apigenin-7-*O*-glucoside (mg g^{-1} DW)			
H1	9.60 ± 0.63 bc	8.91 ± 0.02 bcde	14.68 ± 0.98a	10.04 ± 0.54 b	7.25 ± 0.23 efg	10.10 A
H2	3.97 ± 0.10 h	7.91 ± 0.08 cdefg	9.11 ± 2.90 bcde	6.37 ± 0.58 g	8.13 ± 1.53 bcdefg	7.10 C
H3	9.31 ± 1.80 bcd	7.37 ± 0.52 defg	6.42 ± 1.36 fg	8.34 ± 0.95 bcdef	13.09 ± 0.62 a	8.91 B
mean N	7.63 B	8.06 B	10.07 A	8.25 B	9.49 A	
source of variation: N = ***; H = ***; N × H = ***						
			Quercitrin (mg g^{-1} DW)			
H1	3.06 ± 0.07 a	2.49 ± 0.02 d	2.84 ± 0.16 bc	2.48 ± 0.08 d	3.03 ± 0.19 ab	2.78 A
H2	2.68 ± 0.05 cd	2.09 ± 0.07 e	1.77 ± 0.36 f	2.15 ± 0.01 e	2.64 ± 0.07 cd	2.27 B
H3	2.79 ± 0.22 c	1.23 ± 0.03 h	1.51 ± 0.00 g	1.65 ± 0.08 fg	2.09 ± 0.08 e	1.85 C
mean N	2.84 A	1.94 D	2.04 CD	2.09 C	2.59 B	
source of variation: N = ***; H = ***; N × H = ***						
			Kaempferol (mg g^{-1} DW)			
H1	0.16 ± 0.02 f	0.11 ± 0.03 fgh	0.12 ± 0.04 fg	0.03 ± 0.00 h	0.04 ± 0.00 gh	0.09 C
H2	0.47 ± 0.07 ab	0.05 ± 0.01 gh	0.09 ± 0.01 fgh	0.35 ± 0.05 cd	0.10 ± 0.00 fgh	0.21 B
H3	0.43 ± 0.14 bc	0.34 ± 0.02 de	0.52 ± 0.08 a	0.49 ± 0.04 ab	0.26 ± 0.06 e	0.41 A
mean N	0.35 A	0.17 C	0.24 B	0.29 B	0.13 C	
source of variation: N = ***; H = ***; N × H = ***						
			Luteolin-7-*O*-glucoside (mg g^{-1} DW)			
H1	45.67 ± 3.96 b	45.28 ± 2.50 b	76.51 ± 0.76 a	36.46 ± 0.80 c	35.20 ± 0.39 c	47.82 A
H2	16.04 ± 1.38 fg	17.85 ± 1.20 fg	19.93 ± 1.44 ef	12.15 ± 1.52 g	19.16 ± 3.96 efg	17.03 C
H3	47.30 ± 9.76 b	22.18 ± 0.98 ef	16.83 ± 5.80 fg	26.08 ± 4.01 de	30.00 ± 1.80 cd	28.48B
mean N	36.34 A	28.44 B	37.76 A	24.90 B	28.12 B	
source of variation: N = ***; H = ***; N × H = ***						

[a]N0, without N fertilization; N50, 50 kg N ha^{-1}; N150, 150 kg N ha^{-1}; N300, 300 kg N ha^{-1}; Norg, 150 kg N ha^{-1} as organic nitrogen. [b]H1 = July 9; H2 = July 21; H3 = September 10. [c]Results are the means ± SD of five replicates that were each analyzed in triplicate. A two-way ANOVA was used to evaluate the effect of nitrogen fertilization (N), harvest time (H), and the interaction between nitrogen and harvest time (N × H). Significance was as follows: ***, significant at $P < 0.001$ level; **, significant at $P < 0.01$ level; *, significant at $P < 0.05$ level; ns, not significant. Upper case letters indicate effect of nitrogen rate (N) and harvest time (H); lower case letters indicate N × H interaction.

flavonoids or between RebA and individual flavonoids (Table 4). Moreover, RebA was negatively correlated at N0 and N50 with total flavonoid contents, apigenin-7-*O*-glucoside, and luteolin-7-*O*-glucoside (Table 4). Notably, the two latter N doses did not in general correlate with either total or individual flavonoids.

DISCUSSION

The achieved results showed that most of the phytochemical contents, as well as the antioxidant capacity, were significantly affected by N rate, harvest time, and the N × H interaction, emphasizing the importance of these preharvest factors in the biosynthesis of Stevia secondary metabolites and, consequently, in determining the Stevia leaf extract quality. Considering the mean N values, our findings point out that 150 kg N ha^{-1} appeared to be the optimal dose giving an improvement of the quality, because, for this N rate, the highest contents of RebA, RebA/Stev ratio, total phenol and flavonoid, apigenin-7-*O*-glucoside, luteolin-7-*O*-glucoside, and antioxidant activity have been recorded.

Our study demonstrates that, using an adequate N rate and choosing an appropriate harvest time, it is possible to increase significantly the content of RebA and, consequently the ratio between RebA/Stev, considered to be a good qualitative measure of sweetness.[27] The maximum Stev content was recorded in N deficiency conditions (N0), whereas, in the presence of higher N supply, Stev decreased and RebA significantly increased (N150 and N300). Because Stev is the substrate for the synthesis of RebA,[28] our findings indicated that N supply could modulate the composition of SG, promoting the transformation of Stev in RebA. At the same time, the harvest time was found to be an extremely important factor in affecting the SG content and, consequently, RebA/Stev ratio, that increased in the Stevia leaves from July to September.

These findings are extremely important because RebA represents the preferred SG for sweetening purposes. Due to

DOI: 10.1021/acs.jafc.5b02147
J. Agric. Food Chem. 2015, 63, 7041−7050

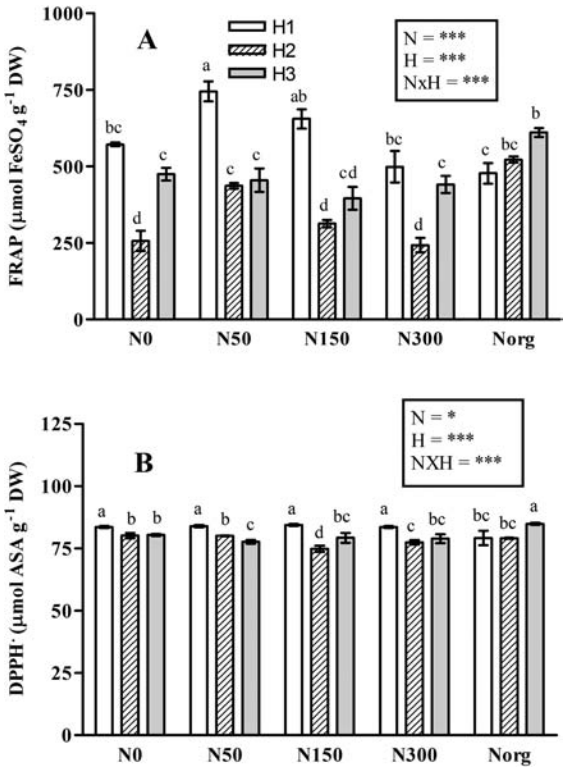

Figure 2. Effect of nitrogen rate and harvest time on total antioxidant capacity (A) and radical-scavenging activity (B) in leaves of *Stevia rebaudiana* plants. Data are means of five replicates ± SDs; bars represent standard deviation. Means with the same letters are not significantly different for $P = 0.05$ following two-way ANOVA test with nitrogen rate and harvest time as variability factors. Asterisks indicate significant differences according to two-way ANOVA test (***, significant at $P < 0.001$ probability level).

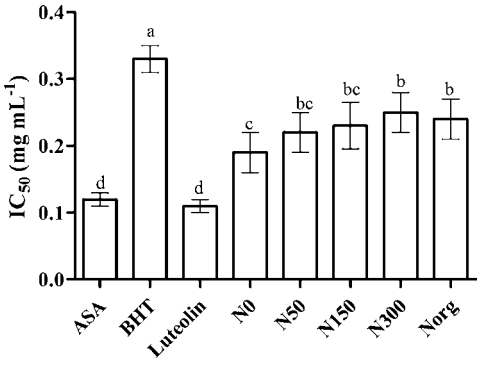

Figure 3. DPPH radical-scavenging activity (half-inhibitory concentration, IC_{50}) of different scavengers and *Stevia rebaudiana* leaf extracts. Data are means of three replicates ± SDs; bars represent standard deviation. Means with the same letters are not significantly different for $P = 0.05$ following one-way ANOVA test, with scavenger/leaf extract as variability factor.

the commercialization of RebA, intensive selection and cultivation practices have yielded cultivars with markedly altered SG compositions in their leaves.[29,30] One parameter to evaluate cultivars/genotypes for the commercial extraction of RebA is the ratio of its concentration against that of Stev within the leaves.[31] Some studies have been carried out to investigate this ratio as a function of different parameters, but no evidence is reported about the effect of N status on the RebA/Stev ratio. For example, it was reported that, within the same cultivar, this ratio appeared to be relatively stable during vegetative growth, but a 35% increase occurred in the lower leaves during reproductive development.[31] Similarly to the individual SG pools, this pattern was also influenced by photoperiod and genotype.[32,33] Consequently, our study gives new information for better understanding the complex interactions underlying the accumulation of SG within the Stevia leaves. The SG accumulation has emerged as a dynamic process, strongly influenced not only by the genetic variability[31] but also by the nutrient conditions and their temporal availability.

Similarly to that observed for SG, total phenols and flavonoids, as well as the antioxidant activity and flavonoid composition, changed markedly in response to different N rates. Such variability may be due to the regulation of individual enzymes involved in the biosynthesis of these compounds, such as phenylalanine ammonia-lyase (PAL, EC 4.3.1.5).[34,35] Our findings showed an increase in total phenols and flavonoids from N0 to N150 treatments. At high supply rates, N may inhibit the synthesis of phenols and flavonoids via enhancing the channeling of L-phenylalanine toward proteins.[36] Because polyphenols contribute mostly to the antioxidant activity of plant extract,[37] also the antioxidant activity of Stevia may be reduced at high N supply.

There are conflicting reports regarding the effects of N fertilization on the plant antioxidant concentrations and capacities[16] and, generally, it was found that high nitrogen supply has a negative effect on the biosynthesis of soluble phenolics, condensed tannins, and flavonoids in plant tissues.[38,39] The lack of plant nutrients may cause alterations in phenolic content and composition for several crops, although most studies conclude that its effect is difficult to prove.[40] Besides the effects of other potential covariables (e.g., weather conditions, UV radiation, pest incidence), the variable effect of nutrient shortage on phenolic content might also be due to the complexity of plant response to nutrient availability. According to the growth/differentiation balance theory, plants always optimize the resources available by exploiting them in growth or differentiation processes (primary or secondary metabolism), even taking into account the particular needs of each crop stage.

In the case of Stevia, our findings demonstrate that the bioactive compounds and their related antioxidant activity increased by optimizing the N supply and decreased with increasing or decreasing N rates compared to the optimal N dose (150 kg N ha^{-1}). The lower values recorded in Norg, compared with N150, could be related to the slow N release pattern of organic N sources, attributable to the dependence of organic manure on microbial decomposition and subsequent mineralization of N, a process largely affected by climate as well as by manure quality, such as the C:N ratio and polyphenolic content.[41−43]

With regard to flavonoid composition, the flavonoids detected in Stevia leaves, under the different N rates, belong to the subgroups of flavonols and flavones, as already observed in previous studies.[9,11,44] All flavonoids, except myricetin, have already been described.[9,11,44,45] Myricetin has a unique chemical structure and, recently, the health benefits of this flavonoid have been demonstrated; in particular, its therapeutic potential in diabetes mellitus has been investigated.[46] This finding adds to the Stevia extract's particular importance, confirming the beneficial role of Stevia and its metabolites on health-promoting properties. Particular attention should be paid to its insulinotropic activity, which could make Stevia's role most promising.[47]

DOI: 10.1021/acs.jafc.5b02147
J. Agric. Food Chem. 2015, 63, 7041−7050

Table 3. Correlation Coefficients (r^2) among Total Antioxidant Capacity (FRAP) and DPPH and Total Phenols, Total Flavonoids, Stevioside, and Rebaudioside A in Leaves of *Stevia rebaudiana* Plants Grown under Different Nitrogen Rates[a]

antioxidant assay	sample	phenols (mg GAE g^{-1} DW)	flavonoids (mg g^{-1} DW)	stevioside (g 100 g^{-1} DW)	rebaudioside A (g 100 g^{-1} DW)
FRAP (μmol $FeSO_4$ g^{-1} DW)	N0	0.727 **	0.807 **	6.8×10^{-4} ns	0.609 **
		$y = 0.089x + 21.80$	$y = 0.101x + 10.59$		$y = -0.005x + 4.98$
	N50	0.641 **	0.604 **	0.071 ns	0.403 ns
		$y = 0.098x + 29.45$	$y = 0.096x - 8.98$		
	N150	0.583 *	0.913 ***	0.956 ***	0.048 ns
		$y = 0.138x + 15.29$	$y = 0.206x - 33.89$	$y = 0.006x + 1.80$	
	N300	0.885 ***	0.946 ***	0.104 ns	0.008 ns
		$y = 0.059x + 46.60$	$y = 0.055x + 16.91$		
	Norg	0.725 **	0.136 ns	0.092 ns	0.187 ns
		$y = -0.100x + 25.40$			
DPPH (μmol ASA g^{-1} DW)	N0	0.433 ns	0.243 ns	0.357 ns	0.823 **
					$y = -0.495x + 43.21$
	N50	0.923 ***	0.829 ***	0.031 ns	0.523 *
		$y = 4.905x - 308.3$	$y = 4.696x - 33.1$		$y = -0.261x + 23.93$
	N150	0.500 *	0.867 ***	0.792 **	0.223 ns
		$y = 4.528x - 278.3$	$y = 7.369x - 527.7$	$y = 0.197x - 11.35$	
	N300	0.661 **	0.862 ***	0.318 ns	0.025 ns
		$y = 3.643x - 217.4$	$y = 3.744x - 257.0$		
	Norg	0.668 *	0.293 ns	0.176 ns	0.024 ns
		$y = 3.429x - 208.9$			

[a]Significance was as follows: ***, significant at $P < 0.001$ level; **, significant at $P < 0.01$ level; *, significant at $P < 0.05$ level; ns, not significant. N0, without N fertilization; N50, 50 kg N ha^{-1}; N150, 150 kg N ha^{-1}; N300, 300 kg N ha^{-1}; Norg, 150 kg N ha^{-1} as organic nitrogen.

The most abundant flavonoid appears to be luteolin-7-*O*-glucoside, which was strongly affected by the harvest time, with a 2-fold higher value in the first sampling than in the other two harvests. Furthermore, the choice of the optimal harvest time can contribute to enhance the phytochemical quality of Stevia leaf extracts. The great differences in the bioactive compounds and antioxidant activity of Stevia leaves harvested at different times may be a consequence of some physiological changes. Samples collected at H1 (beginning of July) generally showed higher phenolic and flavonoid contents, antioxidant activity and Stev levels, compared to samples collected in H2 and, with the exception of a few cases, in H3. Environmental factors such as photoperiod, water availability, temperature, and pest and disease incidence, as well as physiological status of the plant, have a direct impact on biochemical pathways, thus affecting the metabolism of secondary products.[48] Our results point out that time of harvest, being related with the physiological stage of the plant, is an important factor in influencing the secondary metabolites of Stevia leaf extracts. Stevia is an obligate short-day plant with a critical day length of about 12−13 h.[32,33] Under long-day condition, the vegetative growth phase of short-day plants is retained for a long time by prohibiting precocious flowering. It was reported that the long-day conditions significantly increased leaf biomass and Stev content in Stevia leaves.[49] Similarly, it was reported that, in leaves of sweet potato plants, photoperiod regimes influenced the accumulation of phenolic acids, anthocyanins, and other flavonoids by increasing the total contents of these compounds under long-day conditions, suggesting a role for these compounds in protection against enhanced light exposure.[48]

Antioxidant capacity depends on the type of antioxidant that prevails in the extract and, thus, on the type of plant extract, which can be essentially distinguished on the basis of its hydrophobic/hydrophilic nature. At present, none of the antioxidant capacity assays truly reflect the "total antioxidant capacity", because this measure needs to reflect both lipophilic and hydrophilic capacity and to differentiate between hydrogen atom transfer (radical quenching) and electron transfer (radical reduction). Consequently, to comprehensively evaluate a sample's ROS scavenging capacity, more than one assay measuring individual ROS scavenging capacity is needed. For this reason, both FRAP and DPPH assays have been performed. The difference found here by applying the two assays on Stevia extracts (Figure 2) lies in the chemistry of the reaction involved, namely, the biomolecule acting as reductant (type and number of functional groups involved) as well as the detection radical and the solvent used.[50] However, with both FRAP and DPPH assays, the high correlations found between secondary metabolites of Stevia leaves and antioxidant capacities confirm that the high antioxidant capacity characterizing Stevia leaves is mainly attributable to the presence of both phenolic compounds, such as flavonoids, and SG. In particular, the high and positive correlations found between Stev and FRAP and between Stev and DPPH in the N150-treated plants (Table 3) confirm that SG are potent ROS scavengers and that Stev is a stronger scavenger than RebA for superoxide radicals, as reported by Geuns et al.[51]

Interestingly, in leaves of plants grown under N150 treatment, Stev positively correlated with both the content of total and individual flavonoids, with the exception of kaempferol (Table 4). In contrast, for the N150 dose, RebA did not significantly correlate with either total or individual flavonoids, whereas significant and negative correlations have been found between this compound and total flavonoid content and luteolin-7-*O*-glucoside and apigenin-7-*O*-glucoside, in N0- and N50-treated plants (Table 4).

Further investigations are needed to elucidate a possible interrelationship of flavonoids with the metabolic pathway of Stev synthesis. In fact, key functions of flavonoids as developmental regulators—signaling molecules in plants and humans have been reported.[52] This could shed light on a possible

DOI: 10.1021/acs.jafc.5b02147
J. Agric. Food Chem. 2015, 63, 7041−7050

Table 4. Correlation Coefficients (r^2) among Steviol Glycosides (Stevioside and Rebaudioside A) and Total Flavonoids and Each Single Flavonoid (Rutin, Myricetin, Apigenin-7-*O*-glucoside, Quercitrin, Kaempferol, Luteolin-7-*O*-glucoside) in Leaves of *Stevia rebaudiana* Plants Grown under Different Nitrogen Rates[a]

steviol glycoside (g 100 g^{-1} DW)	sample	flavonoids (mg g^{-1} DW)	rutin (mg g^{-1} DW)	myricetin (mg g^{-1} DW)	apigenin-7-*O*-glucoside (mg g^{-1} DW)	quercitrin (mg g^{-1} DW)	kaempferol (mg g^{-1} DW)	luteolin-7-*O*-glucoside (mg g^{-1} DW)
stevioside	N0	0.078 ns	0.431 ns	0.357 ns	0.050 ns	0.690 **	0.155 ns	0.052 ns
						$y = 2.060x + 0.47$		
	N50	0.310 ns	0.271 ns	0.582 *	0.044 ns	0.023 ns	0.378 ns	0.426 ns
				$y = 11.05x - 24.76$				
	N150	0.945 ***	0.658 **	0.648 **	0.728 **	0.814 ***	0.139 ns	0.979 ***
		$y = 0.027x + 2.81$	$y = 0.445x + 2.10$	$y = 1.863x - 0.09$	$y = 0.212x + 2.20$	$y = 1.345x + 1.59$		$y = 0.032x + 3.11$
	N300	0.100 ns	0.060 ns	0.059 ns	0.110 ns	0.907 ***	0.781 **	0.090 ns
						$y = 2.302x - 0.80$	$y = -3.725x + 5.13$	
	Norg	0.138 ns	0.742 **	0.795 **	0.441 ns	0.588 *	0.526 *	0.556 *
			$y = -2.127x + 17.65$	$y = -3.352x + 14.19$		$y = 2.812x - 2.26$	$y = -11.79x + 6.53$	$y = 0.212x - 1.28$
RebA	N0	0.531 *	0.169 ns	0.570 *	0.598 *	0.355 ns	0.705 **	0.614 **
		$y = -0.038x + 5.06$		$y = 3.360x - 5.23$	$y = -0.263x + 4.99$		$y = 4.974x + 1.23$	$y = -0.051x + 4.79$
	N50	0.838 ***	2.8×10^{-4} ns	0.089 ns	0.494 *	0.161 ns	0.009 ns	0.916 ***
		$y = -0.068x + 6.15$			$y = -1.086x + 11.71$			$y = -0.079x + 5.19$
	N150	0.001 ns	0.065 ns	0.101 ns	0.029 ns	0.036 ns	0.217 ns	0.008 ns
	N300	0.018 ns	0.055 ns	0.051 ns	0.023 ns	0.159 ns	0.128 ns	0.014 ns
	Norg	0.362 ns	0.362 ns	0.613 *	0.078 ns	0.279 ns	0.204 ns	0.854 ***
				$y = -0.614x + 4.49$				$y = 0.048x + 1.38$

[a]Significance was as follows: ***, significant at $P < 0.001$ level; **, significant at $P < 0.01$ level; *, significant at $P < 0.05$ level; n.s., not significant. N0, without N fertilization; N50, 50 kg N ha^{-1}; N150, 150 kg N ha^{-1}; N300, 300 kg N ha^{-1}; Norg, 150 kg N ha^{-1} as organic nitrogen.

DOI: 10.1021/acs.jafc.5b02147
J. Agric. Food Chem. 2015, 63, 7041−7050

additional role of flavonoids, besides those well-known of being potent antioxidants.

All together, the results obtained in this study provide useful information on Stevia response to different N regimes and harvest date, emphasizing the possibility to increase, from a phytochemical point of view, Stevia quality. Moreover, this work succeeded in improving the knowledge about the changing SG, flavonoid composition, and antioxidant capacity of Stevia in response to different N rates and harvest dates. In fact, our results indicate that the manipulation of N fertilization might be an effective tool to increase the accumulation of bioactive compounds in Stevia. In fact, higher RebA/Stev ratio, total phenolic content, total flavonoids, luteolin-7-*O*-glucoside levels, and antioxidant capacity were observed in Stevia when nitrogen supply was equal to 150 kg ha^{-1}. Moreover, at the highest nitrogen treatment level, Stevia exhibited significantly lower bioactive compounds and antioxidant activity than under N150 treatment. The lower phytochemical content and antioxidant capacity observed in Norg-treated plants in comparison with N150-treated plants may be attributable to a distinct temporal N availability that characterized organic and inorganic N sources. In addition to nitrogen fertilization, harvest time or more precise plant developmental stage was also found to have a significant influence on bioactive compounds and antioxidant activity in Stevia.

AUTHOR INFORMATION

Corresponding Author

*(L.G.A.) Mail: Department of Agriculture, Food and Environment, University of Pisa, Via del Borghetto 80, 56124 Pisa, Italy. Phone: +39-050-2218901. Fax: +39-050-2218970. E-mail: luciana.angelini@unipi.it.

Notes

The authors declare no competing financial interest.

ACKNOWLEDGMENTS

We thank to Dr. Matteo Ghilardi and Valentina Sgambati for their helpful and skillful technical assistance during the laboratory analysis.

ABBREVIATIONS USED

DPPH, 1,1-diphenyl-2-picrylhydrazyl; GAE, gallic acid equivalents; H1, harvest at July 9; H2, harvest at July 21; H3, harvest at September 10; N0, no nitrogen; N150, 150 kg N ha^{-1} as mineral nitrogen; N300, 300 kg N ha^{-1} as mineral nitrogen; N50, 50 kg N ha^{-1} as mineral nitrogen; NNS, non-nutritive sweeteners; Norg, 150 kg N ha^{-1} as organic nitrogen; RebA, rebaudioside A; ROS, reactive oxygen species; SG, steviol glycosides; Stev, stevioside

REFERENCES

(1) Lobo, V.; Patil, A.; Phatak, A.; Chandra, N. Free radicals, antioxidants and functional foods: impact on human health. *Pharmacogn. Rev.* **2010**, *4*, 118−126.

(2) Pawar, R. S.; Krynitsky, A. J.; Rader, J. I. Sweeteners from plants − with emphasis on *Stevia rebaudiana* (Bertoni) and *Siraitia grosvenorii* (Swingle). *Anal. Bioanal. Chem.* **2013**, *405*, 4397−4407.

(3) Risso, D.; Morini, G.; Pagani, L.; Quagliariello, A.; Giuliani, C.; De Fanti, S.; Sazzini, M.; Luiselli, D.; Tofanelli, S. Genetic signature of differential sensitivity to stevioside in the Italian population. *Genes Nutr.* **2014**, *9*, 401.

(4) Chatsudthipong, V.; Muanprasat, C. Stevioside and related compounds: therapeutic benefits beyond sweetness. *Pharmacol. Ther.* **2009**, *121*, 41−54.

(5) Gardana, C.; Scaglianti, M.; Simonetti, P. Evaluation of steviol and its glycosides in *Stevia rebaudiana* leaves and commercial sweetener by ultrahigh performance liquid chromatography−mass spectrometry. *J. Chromatogr. A* **2010**, *1217*, 1463−1470.

(6) Kinghorn, A. D.; Soejarto, D. D. Stevioside. In *Economic and Medicinal Plant Research*; Wagner, H., Norman, R. F., Eds.; Academic Press: New York, 1991; Vol. 7, pp 157−171.

(7) Jeppesen, P. B.; Gregersen, S.; Poulsen, C. R.; Hermansen, K. Stevioside acts directly on pancreatic β cells to secrete insulin: actions independent of cyclic adenosine monophosphate and adenosine triphosphate-sensitive K^+-channel activity. *Metab. Clin. Exp.* **2000**, *49*, 208−214.

(8) Geuns, J. M. Stevioside. *Phytochemistry* **2003**, *64*, 913−921.

(9) Wolwer-Rieck, U. The leaves of *Stevia rebaudiana* (Bertoni), their constituents and the analyses thereof: a review. *J. Agric. Food Chem.* **2012**, *60*, 886−895.

(10) Lemus-Mondaca, R.; Vega-Gálvez, A.; Zura-Bravo, L.; Ah-Hen, K. *Stevia rebaudiana* Bertoni, source of a high-potency natural sweetener: a comprehensive review on the biochemical, nutritional and functional aspects. *Food Chem.* **2012**, *132*, 1121−1132.

(11) Ghanta, S.; Banerjee, A.; Poddar, A.; Chattopadhyay, S. Oxidative DNA damage preventive activity and antioxidant potential of *Stevia rebaudiana* Bertoni, a natural sweetener. *J. Agric. Food Chem.* **2007**, *55*, 10962−10967.

(12) Karaköse, H.; Jaiswal, R.; Kuhnert, N. Characterization and quantification of hydroxycinnamate derivatives in *Stevia rebaudiana* leaves by LC-MS^n. *J. Agric. Food Chem.* **2011**, *59*, 10143−10150.

(13) Shukla, S.; Mehta, A.; Mehta, P.; Bajpai, V. K. Antioxidant ability and total phenolic content of aqueous leaf extracts of *Stevia rebaudiana* Bert. *Exp. Toxicol. Pathol.* **2012**, *64*, 807−811.

(14) Tavarini, S.; Angelini, L. G. *Stevia rebaudiana* Bertoni as a source of bioactive compounds: the effect of harvest time, experimental site and crop age on steviol glycoside content and antioxidant properties. *J. Sci. Food Agric.* **2013**, *93*, 2121−2129.

(15) Sugiharto, B.; Sugiyama, T. Effects of nitrate and ammonium on gene expression of phosphoenolpyruvate carboxylase and nitrogen metabolism in maize leaf tissue during recovery from nitrogen stress. *Plant Physiol.* **1992**, *98*, 1403−1408.

(16) Åkerström, A.; Forsum, A.; Rumpunen, K.; Jäderlund, A.; Bång, U. Effects of sampling time and nitrogen fertilization on anthocyanidin levels in *Vaccinium myrtillus* fruits. *J. Agric. Food Chem.* **2009**, *57*, 3340−3345.

(17) Kawatani, T.; Kaneki, Y.; Tanabe, T.; Takahashi, T. On the cultivation of Kaa He-e (*Stevia rebaudiana* Bertoni). III. Response of Kaa He-e to fertilizer application amount and to nitrogen fertilization rates. *Jpn. J. Trop. Agric.* **1978**, *21*, 165−172.

(18) Kawatani, T.; Kaneki, Y.; Tanabe, T.; Sakamoto, I.; Murakami, K.; Tanaka, O. On the cultivation of Kaa He-e (*Stevia rebaudiana* Bertoni). IV. Response of Kaa He-e to nitrogen fertilization rates and to the three major elements of fertilizer. *Jpn. J. Trop. Agric.* **1978**, *21*, 173−178.

(19) Kawatani, T.; Kaneki, Y.; Tanabe, T.; Takahashi, T. On the cultivation of Kaa He-e (*Stevia rebaudiana* Bertoni). V. Response of Kaa He-e to phosphorus fertilization rates and to the three major elements of fertilizer. *Jpn. J. Trop. Agric.* **1980**, *24*, 54−61.

(20) Kawatani, T.; Kaneki, Y.; Tanabe, T.; Takahashi, T. On the cultivation of Kaa He-e (*Stevia rebaudiana* Bertoni). VI. Response of Kaa He-e to potassium fertilization rates and to the three major elements of fertilizer. *Jpn. J. Trop. Agric.* **1980**, *24*, 105−112.

(21) Hearn, L. K.; Subedi, P. P. Determining levels of steviol glycosides in the leaves of *Stevia rebaudiana* by near infrared reflectance spectroscopy. *J. Food Compos. Anal.* **2009**, *22*, 165−168.

(22) Kolb, N.; Herrera, J. L.; Ferreyra, D. J.; Uliana, R. F. Analysis of sweet diterpene glycosides from *Stevia rebaudiana*: improved HPLC method. *J. Agric. Food Chem.* **2001**, *49*, 4538−4541.

(23) Dewanto, V.; Wu, X.; Adom, K. K.; Liu, R. H. Thermal processing enhances the nutritional value of tomatoes by increasing total antioxidant activity. *J. Agric. Food Chem.* **2002**, *50*, 3010−3014.

(24) Benzie, I. F. F.; Strain, J. J. Ferric reducing/antioxidant power assay: direct measure of total antioxidant activity of biological fluids and

DOI: 10.1021/acs.jafc.5b02147
J. Agric. Food Chem. 2015, 63, 7041−7050

modified version for simultaneous measurement of total antioxidant power and ascorbic acid concentration. *Methods Enzymol.* **1996**, *299*, 15−27.
(25) Tadhani, M. B.; Patel, V. H.; Subhash, R. In vitro antioxidant activities of *Stevia rebaudiana* leaves and callus. *J. Food Compos. Anal.* **2007**, *20*, 323−329.
(26) Frankel, E. N. Recent advances in lipid oxidation. *J. Sci. Food Agric.* **1991**, *54*, 495−511.
(27) Yadav, A. K.; Singh, S.; Dhyani, D.; Ahuja, P. S. A review on the improvement of stevia [*Stevia rebaudiana* (Bertoni)]. *Can. J. Plant Sci.* **2011**, *91*, 1−27.
(28) Shibata, H.; Sonoke, S.; Ochiai, H.; Nishihashi, H. Glycosylation of steviol and steviol-glucosides in extracts from *Stevia rebaudiana* Bertoni. *Plant Physiol.* **1991**, *95*, 152−156.
(29) Ohta, M.; Sasa, S.; Inoue, A.; Tamai, T.; Fujita, I.; Morita, K.; Matsuura, F. Characterization of novel steviol glycosides from leaves of *Stevia rebaudiana* Morita. *J. Appl. Glycosci.* **2010**, *57*, 199−209.
(30) Lankes, C.; Zabala, U. M. In *Stevia: Break-through in Europe*, Proceedings of the 5th EUSTAS Stevia Symposium; Geuns, J. M. C., Ed.; Euprint: Heverlee, Belgium, 2011; pp 75−87.
(31) Ceunen, S.; Geuns, J. M. C. Steviol glycosides: chemical diversity, metabolism, and function. *J. Nat. Prod.* **2013**, *76*, 1201−1228.
(32) Ceunen, S.; Geuns, J. M. C. Influence of photoperiodism on the spatio-temporal accumulation of steviol glycosides in *Stevia rebaudiana* (Bertoni). *Plant Sci.* **2013**, *198*, 72−82.
(33) Ceunen, S.; Geuns, J. M. C. Spatio-temporal variation of the diterpene steviol in *Stevia rebaudiana* grown under different photoperiods. *Phytochemistry* **2013**, *89*, 32−38.
(34) Bongue-Bartelsman, M.; Phillips, D. A. Nitrogen stress regulates gene expression of enzymes in the flavonoid biosynthetic pathway of tomato. *Plant Physiol. Biochem.* **1995**, *33*, 539−549.
(35) Strissel, T.; Halbwirth, H.; Hoyer, U.; Zistler, C.; Stich, K.; Treutter, D. Growth-promoting nitrogen nutrition affects flavonoid biosynthesis in young apple (*Malus domestica* Borkh.) leaves. *Plant Biol.* **2005**, *7*, 677−685.
(36) Margna, U.; Margna, E.; Vainjarv, T. Influence of nitrogen on the utilization of L-phenylalanine for building flavonoids in buck wheat seedling tissues. *J. Plant Physiol.* **1989**, *134*, 697−702.
(37) Pérez-López, U.; Pinzino, C.; Quartacci, M. F.; Ranieri, A.; Sgherri, C. Phenolic composition and related antioxidant properties in differently colored lettuces: a study by electron paramagnetic resonance (EPR) kinetics. *J. Agric. Food Chem.* **2014**, *62*, 12001−12007.
(38) Lavola, A.; Julkunen-Tiitto, R. The effect of elevated carbon dioxide and fertilization on primary and secondary metabolites in birch, *Betula pendula* (Roth). *Oecologia* **1994**, *99*, 315−32.
(39) Lindroth, R. L.; Osier, T. L.; Barnhill, H. R. H.; Wood, S. A. Effects of genotype and nutrient availability on phytochemistry of trembling aspen (*Populus tremuloides* Michx.) during leaf senescence. *Biochem. Syst. Ecol.* **2002**, *30*, 297−307.
(40) Gasztonyi, M. N.; Farkas, R. T.; Berki, M.; Petróczi, I. M.; Daood, H. G. Content of phenols in wheat as affected by varietal and agricultural factors. *J. Food Compos. Anal.* **2011**, *24*, 785−789.
(41) Ladd, J. N.; Amato, M. The fate of nitrogen from legume and fertilizer sources in soils successively cropped with wheat under field conditions. *Soil Biol. Biochem.* **1986**, *18*, 417−425.
(42) Palm, C. A.; Sanchez, P. A. Decomposition and nutrient release patterns of the leaves of three tropical legumes. *Biotropica* **1990**, *22*, 330−338.
(43) Sisworo, W. H.; Mitrosuhardjo, M. M.; Rasjid, H.; Myers, R. J. K. The relative roles of N fixation, fertilizer, crop residues and soil in supplying N in multiple cropping systems in a humid, tropical upland cropping system. *Plant Soil* **1990**, *121*, 73−82.
(44) Cacciola, F.; Delmonte, P.; Jaworska, K.; Dugo, P. Employing ultra high pressure liquid chromatography as the second dimension in a comprehensive two-dimensional system for analysis of *Stevia rebaudiana* extracts. *J. Chromatog., A* **2011**, *1218*, 2012−2018.
(45) Li, J.; Jiang, H.; Shi, R. A new acetylated quercetin glycoside from the leaves of *Stevia rebaudiana*. Bertoni. *Nat. Prod. Res.* **2009**, *23*, 1378−1383.
(46) Li, Y.; Ding, Y. Minireview: Therapeutic potential of myricetin in diabetes mellitus. *Food Sci. Human Wellness* **2012**, *1*, 19−25.
(47) Yadav, S.; Guleria, P. Steviol glycosides from *Stevia*: biosynthesis pathway review and their application in foods and medicine. *Crit. Rev. Food Sci. Nutr.* **2012**, *52*, 988−998.
(48) Carvalho, I. S.; Cavaco, T.; Carvalho, L. M.; Duque, P. Effect of photoperiod on flavonoid pathway activity in sweet potato (*Ipomoea batatas* (L.) Lam.) leaves. *Food Chem.* **2010**, *118*, 384−390.
(49) Ceunen, S.; Werbrouck, S.; Geuns, J. M. C. Stimulation of steviol glycoside accumulation in *Stevia rebaudiana* by red LED light. *J. Plant Physiol.* **2012**, *169*, 749−752.
(50) Sgherri, C.;Pérez-López, U.; Pinzino, C. Antioxidant properties of food products containing lycopene are increased by the presence of chlorophyll. In *Lycopene: Food Sources, Potential Role in Human Health and Antioxidant Effects*; Bailey, J. R., Ed.; Nova Publishers: New York, 2015; pp 39−89, ISBN 978-1-63117-927-3.
(51) Geuns, J. M. C.; Hajihashemi, S.; Claes, A. Radical scavenging activity of steviol glycosides, steviol glucuronide and crude *Stevia* extracts. In *Stevia: Six Months beyond Authorisation*, Proceedings of the 6th EUSTAS Stevia Symposium; Geuns, J. M. C., Ed.; Euprint: Heverlee, Belgium, 2012; pp 157−180.
(52) Brunetti, C.; Di Ferdinando, M.; Fini, A.; Pollastri, S.; Tattini, M. Flavonoids as antioxidants and developmental regulators: relative significance in plants and humans. *Int. J. Mol. Sci.* **2013**, *14*, 3540−3555.

DOI: 10.1021/acs.jafc.5b02147
J. Agric. Food Chem. 2015, 63, 7041−7050

mashing and brewing quality.[35,36] In finger millet [*Eleucine coracana* (L.) Gaertn.], Siwela et al. (2010)[37] found that phenolics are positively correlated with diastatic power and amylase, whereas Chethan et al. (2008)[38] reported an opposing result that phenolic compounds are detrimental to malt quality due to their inhibitory effect on malt amylase. However, there has been no report on the relationships between phenolics and these parameters in barley malt.

The genetic control of polyphenol has been intensively investigated in pear,[39] cider apple,[40] tomato,[41] sorghum,[42] rice,[43] and barley.[44] Most studies were limited to determining the total polyphenol content and did not consider individual phenolic compounds. Phenolic acids represent only a small portion of total polyphenols. Thus, any identified quantitative trait loci (QTLs) associated with total polyphenol could not be linked to an individual phenolic acid, which may potentially be the key ingredient for the brewing industry and functional foods. Modification of the biosynthesis pathway and breeding barley for high accumulation of economically important phenolic acids will only be possible after the identification of QTLs or genes for individual phenolic acids and by understanding the links between phenolic acids and malt quality.

Accordingly, the aims of this study were (1) to determine the relationship between barley grain and corresponding malt in their content of individual phenolic acids in 68 barley genotypes, (2) to investigate the potential relationship between individual phenolic acids and malt quality, and (3) to identify QTLs associated with content of the key phenolic acids in barley grain and malt.

MATERIALS AND METHODS

Plant Materials. Sixty-eight barley genotypes (Supplementary Table 1, Supporting Information) were planted in the field of the experimental farm at Zhejiang University, Huajiachi campus, Hangzhou, China (Hangzhou, 120.2°E, 30.5°N). All of these genotypes are hulled barley with only one genotype, Xindengmenggumai, being a hulless barley. Each genotype was sown in a 2 m row with 0.25 m between rows with three replications. Field management, including fertilization, weed, and disease control, were the same as that applied locally. At maturity, barley grains were harvested and stored in a cool room at 4 °C.[45,46]

Grain samples (150 g) were micromalted in a Phoenix System Micromalting Apparatus (John & White, Adelaide, Australia) according to the method described by Dai et al. (2007)[45] and Dvořáková et al. (2008b)[28] with some modifications. The procedure for the malting process was as follows: (1, steeping stage) 5 h of wet stage at 17 °C, 8 h of air-rest stage at 17 °C, 8 h of wet stage at 16 °C, 12 h of air-rest stage at 16 °C, 4 h of wet stage at 15 °C, 5 h of air-rest stage at 15 °C, and 2 h of wet stage at 15 °C; (2, germination stage) 48 h of germination at 16 °C and 48 h of germination at 15 °C; (3, Kilning stage) 2 h at 50 °C, 4 h at 55 °C, 6 h at 60 °C, 4 h at 65 °C, 1 h at 70 °C, 1 h at 75 °C, 1 h at 80 °C, and 2 h at 82 °C. The malt was stored at 4 °C for further analysis. The barley grains and malt were finely ground and fitted with a 0.5 mm screen.

Extraction of Phenolic Acids. The procedure for extraction of phenolic acids was based on that described by Zhao et al. (2006)[47] with some modification. Two hundred milligrams of ground sample was sonicated (40 kHz, 120 W) for 40 min with 4 mL of 80% methanol (v/v) at 70 °C. After centrifugation (5,000 *g* for 15 min), the supernatant was collected and freeze-dried in a vacuum freezing dryer. The residue was redissolved in 250 μL of 70% methanol (v/v) and filtered through a 0.45 μm membrane. The filtrate was transferred to 2 mL autosampler vials (Agilent, Santa Clara, USA) equipped with 200 μL glass inserts.

Determination of Phenolic Acids by High-Performance Liquid Chromatography. Measurement of phenolic acid content was carried out by high-performance liquid chromatography (HPLC) analysis with an Agilent 1260 Liquid Chromatograph (Agilent, Santa Clara, USA). Separation was performed with a Diamonsil 5u C18 (250 × 4.6 mm) column (Dikma, China) at 40 °C. Elution was performed using a gradient procedure with a mobile phase containing Solvent A (0.1% formic acid in water) and Solvent B (methanol) through the following steps: 0 min, 30% B; 10 min, 45% B; 20 min, 50% B; 25 min, 80% B; 32 min, 30% B; 37 min, 30% B. The total run time was 37 min at a solvent flow rate of 0.8 mL min^{-1} and with a 15 μL injection volume. The content of the individual phenolic compound in the extracts was calculated using a standard curve.

Association Mapping of Individual Phenolic Acids. Association analysis between 758 DArT markers and phenolic acids was performed using TASSEL v3.0 (http://www.maizegenetics.net). Three different models were employed in the association analysis according to a previous study with some modifications.[48−50] The structure matrix and kinship were included as a covariate to correct the population structure in the model $y = X\beta + Q\nu + Z\mu + e$, where X is the DArT marker matrix, Q is the structure matrix, Z is the kinship matrix, β and ν are coefficient vectors for DArT marker and population structure, respectively, μ is a vector of random genetic effects [$\mu \sim N(0, 2K)$], and e is the random error vector. Other models including only the structure matrix or kinship were also applied in the association analysis. These models are as follows: $y = X\beta + Z\mu + e$, and $y = X\beta + Q\nu + e$. For the fitness and efficiency of different models to be evaluated, the quantile-quantile (Q-Q) plot was displayed using TASSEL v3.0. The Benjamini−Hochberg false discovery rate (BHFDR) of $P < 0.01$ was applied in association with a significance test.

Statistical Analysis. Person correlation index among grain and malt phenolic acids and between malt phenolic acids and malt quality parameters were calculated using SPSS 19.0 (SPSS Inc., Chicago, USA). One-way ANOVA with the Tukey method was employed in a significance test using SPSS 19.0.

RESULTS

Genotypic Diversity of Phenolic Acid Content in the Grain and Malt of Barley. Two types of phenolic acids, FA and *p*-CA, were identified in all of the genotypes (Supplementary Table 1, Supporting Information), except for *p*-CA in Xindengmenggumai, a hulless barley. The mean content of FA and *p*-CA in the grains were 2.15 μg g^{-1} (ranging from 1.13 to 4.04 μg g^{-1}) and 1.10 μg g^{-1} (ranging from 0.19 to 3.53 μg g^{-1}), respectively (Table 1, Figure 1). The mean content of *p*-CA in malt was 1.44 μg g^{-1}, ranging from 0.65 to 3.56 μg g^{-1}, which was similar to those in grains (Table 1, Figure 1). However, the average content of FA at 4.07 μg g^{-1} in malt was nearly double that in the grains, including the highest FA content at 11.27 μg g^{-1} found in the malt of genotype, Belae (Table 1, Figure 1). The coefficient of variation (CV) for FA and *p*-CA content was 0.48 and 0.33, respectively (Table 1).

Table 1. Descriptive Statistics of Phenolic Acids in Grain and Malt[a]

	p-CA in grain	FA in grain	*p*-CA in malt	FA in malt
min	0.19	1.13	0.65	1.64
median	0.97	1.94	1.36	3.99
max	3.53	4.04	3.56	11.27
mean	1.10	2.15	1.44	4.07
CV	0.48	0.33	0.40	0.40

[a] *p*-CA: *p*-coumaric acid. FA: ferulic acid. CV: coefficient of variation. The units for the phenolic acids are μg g^{-1}.

DOI: 10.1021/acs.jafc.5b02960
J. Agric. Food Chem. 2015, 63, 7051−7057

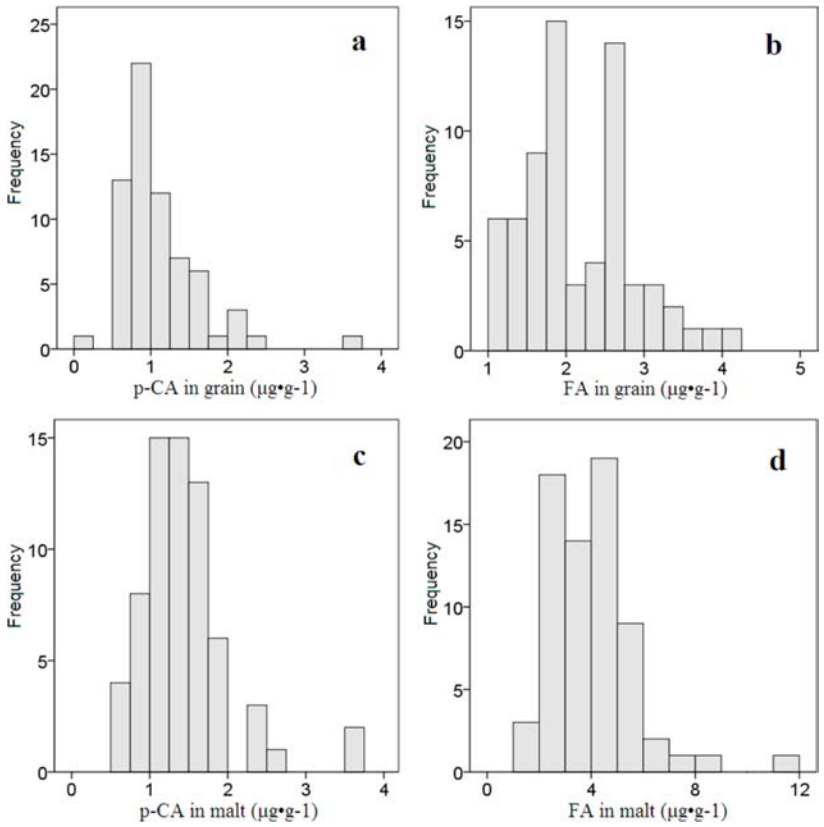

Figure 1. Distribution of phenolic acids in grain and malt among 68 genotypes for (a) *p*-CA in grain, (b) FA in grain, (c) *p*-CA in malt, and (d) FA in malt.

Correlation of FA and *p*-CA Content in Barley Grain and Malt. There were significant and positive correlations between FA and *p*-CA in grains (r = 0.758, P < 0.01, n = 67) and in malt (r = 0.745, P < 0.01, n = 68) (Table 2). However, no significant correlation of FA or *p*-CA was found between grain and malt of barley. For determining the effect of malting on phenolic acid content, the difference of phenolic acid content between grains and malt was evaluated by one way ANOVA analysis. After malting, *p*-CA increased significantly in 37 genotypes and was reduced in 14 genotypes (Figure 2; Supplementary Table 1, Supporting Information). Fifty-five genotypes exhibited a remarkable increase in FA content after malting, whereas the FA content of two genotypes was reduced (Figure 2; Supplementary Table 1, Supporting Information). The ratios of grains to malt ranged from 0.39 to 8.65 for *p*-CA among all genotypes and from 0.68 to 6.28 for FA (Figure 2; Supplementary Table 1, Supporting Information), indicating that the effect of malting on phenolic acid is highly genotype independent.

Table 2. Correlation Analysis of Phenolic Acids in Barley Grains and Malt

	p-CA in grain	FA in grain	*p*-CA in malt
FA in grain	0.758[a]		
p-CA in malt	0.092	−0.002	
FA in malt	0.044	0.043	0.745[a]

[a]Significant correlation at the P < 0.01 level.

Phenolic Acids Are Associated with Malt Quality. Correlation analysis was conducted between phenolic acids in malt and six malt quality parameters, including diastatic power, malt extract, Kolbach index, viscosity, and soluble and total N content.[51] The two phenolic acids were positively correlated with Kolbach index (r = 0.496 and r = 0.393 for *p*-CA and FA, respectively) and soluble N (r = 0.539 and r = 0.307, respectively). Negative correlations between *p*-CA and FA with malt extract (r = −0.283 and r = −0.271, respectively) and viscosity (r = −0.299 and r = −0.408, respectively) were also observed (Table 3).

Association Analysis of DArT Markers and Phenolic Acids in Grains and Malt. The content of phenolic acids in grains and malt and 758 DArT markers were used to perform association mapping. Q-Q plots showed that the k model has the best fit to the association analysis (Supplementary Figure 1, Supporting Information). A total of 13 markers were identified to be significantly associated with phenolic acids (Table 4). Twelve molecular markers were found in grain, but only one was identified in malt. Eight markers on Chromosomes 1H, 2H, 4H, and 7H were associated with *p*-CA in grain, and 4 markers on Chromosomes 3H and 7H were associated with FA in grain. Marker bpb-3484 on Chromosome 7H was found to be associated with both FA and *p*-CA in grain. Additionally, a marker on Chromosome 3H was associated with FA in malt. Each of these markers could account for 15.7−22.7% of the phenotypic variation. Moreover, the marker associated with FA in malt, bpb-9583, was located at 6.0 cM of 3H, independent of any locus linked to FA in grains (Table 4), suggesting a large impact of malting on the content of phenolic acids.

DOI: 10.1021/acs.jafc.5b02960
J. Agric. Food Chem. 2015, 63, 7051−7057

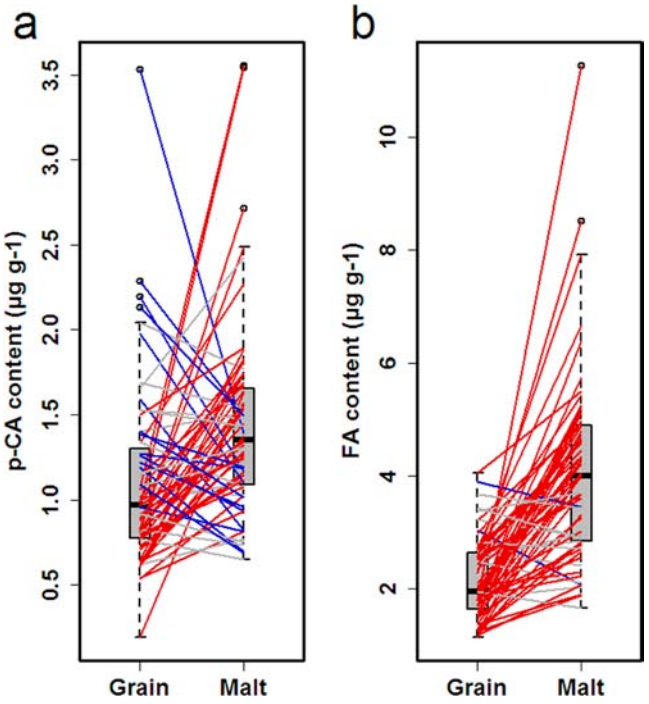

Figure 2. Changes of phenolic acids in grain and their corresponding malt for each genotype for (a) *p*-CA and (b) FA. The left and right point of each line (between two boxplots) represents the content of phenolic acid in grain and the corresponding malt, respectively. Red and blue lines represent a significant increase and decrease in the phenolic acid after the malting process, respectively. Gray lines represent no significant difference between the content of phenolic acid in grain and that in malt.

Table 3. Correlation Analysis of Malt Phenolic Acids and Malt Quality Parameters

	p-CA	FA
diastatic power	0.236	0.060
Kolbach index	0.496[b]	0.393[b]
malt extract	−0.283[a]	−0.271[a]
viscosity	−0.299[a]	−0.408[b]
soluble N	0.539[b]	0.307[a]
total N	0.230	0.097

[a]Significant correlation at $P < 0.05$ level. [b]Significant correlation at $P < 0.01$ level.

DISCUSSION

Barley and malt contain a large number of antioxidant compounds, such as phenolics, ascorbic acid, phytic acid, and melanoidins, which can impact beer stability.[52] Of these, polyphenol and melanoidins are the main sources of natural antioxidants, which originate from either raw barley or malting processes.[53] Malting processes, including steeping, germination, and kilning, have a huge effect on the fate of endogenous phenolic compounds.[25] It was found that malt always has a higher total polyphenol content as well as higher antioxidant activity than corresponding barley grains, suggesting that the malting process results in an increase in the antioxidant activity and total polyphenols.[24,25] However, controversial results were documented regarding the changes of individual phenolic compounds during the malting process.[26−28]

In this study, we determined the contents of two main phenolic acids, FA and *p*-CA, in 68 barley genotypes and corresponding malts to investigate the genotypic difference of the effect of the malting process on individual phenolic acids. Most of the genotypes exhibited a notable increase in the contents of FA and *p*-CA after malting. The increase may be attributed to the effect of the Maillard reaction during the early stage of the kilning process, which leads to enzymatic release of extractable bound phenolics in the matrix.[52,54−56] For example, ferulic acid esterase is released during the germination and early kilning steps of the malting process, thus facilitating the release of bound FA associated with lignin and arabinoxylans.[57,58] Similar results have been reported on the effect of the germination process on phenolic acid in rice.[59,60] Shibuya (1984)[59] reported that free phenolics increased in germinated brown rice due to dismantling of the cell wall. Tian et al. (2004)[60] found that bound phenolic compounds were released during the germination of rice due to carbohydrase enzymes hydrolyzing the endosperm.

However, a decrease in the content of malt phenolic acid was observed in a few genotypes (2 and 14 genotypes for FA and *p*-CA, respectively) in this study, as well as in some previous reports.[27,28] The reason for this decrease could be due to leaching of phenolic compounds into the steeping water[61] or due to formation of insoluble complexes with proteins.[62] High kilning temperature in the late stage of the kilning process may also lead to degradation of phenolic compounds.[56]

Phenolic acids exhibited a complex change during the malting process.[25] However, it remains unknown whether these compounds have an impact on barley malt qualities, such as diastatic power, malt extract, viscosity, Kolbach index, and soluble and total N. To our knowledge, this study is the first attempt to investigate the causal relationships between individual phenolic acids and these malt quality indicators. The current experiment employed 68 genotypes (Supplementary Table 1, Supporting Information) to ensure the representativeness and reliability of the results. The phenolic acids showed significant and positive correlations with soluble N and Kolbach index (Table 3). Obviously, the malt extract with high soluble N is rich in hydrolytic enzymes (i.e., esterase),

Table 4. DArT Markers with a Significant Marker-Trait Association[a]

trait	marker	chromosome	genetic position (cM)	*P* value	R^2 (marker)
p-CA in grain	bPb-4909	1H	72.9	0.0086	0.157
	bPb-0631	1H	128.5	0.0071	0.165
	bPb-1959	1H	133.1	0.0056	0.175
	bPb-6822	2H	114.4	0.0018	0.227
	bPb-8949	2H	122.3	0.0034	0.204
	bPb-1469	4H	14.6	0.0039	0.198
	bPb-0027	7H	111.7	0.0056	0.176
	bPb-3484	7H	133.4	0.0026	0.210
FA in grain	bPb-9746	3H	54.8	0.0074	0.163
	bPb-6347	3H	55.6	0.0053	0.197
	bPb-7156	7H	27.2	0.0083	0.158
	bPb-3484	7H	133.4	0.0061	0.172
FA in malt	bPb-9583	3H	6.0	0.0054	0.178

[a]These markers were identified using the *k* model. The significance test for association analysis is $P < 0.01$. R^2 (marker) denotes the contribution of the marker for phenotypic variation.

DOI: 10.1021/acs.jafc.5b02960
J. Agric. Food Chem. 2015, 63, 7051−7057

facilitating the release of phenolic acids.[57,58] These hydrolytic enzymes can modify the endosperm to liberate some of the bound phenolic compounds during germination.[63] Conversely, the phenolic acids were significantly and negatively correlated with malt extract and viscosity. It is well-known that phenolic acids are mainly located in the husk and aleurone layer.[13,14] Thus, we proposed that the genotypes with more husk and/or aleurone (in another words, fewer endosperm) might contain a higher content of phenolic acids, and fewer endosperm will obviously lead to a lower malt extract. An extreme example is that the *p*-CA content of a hulless genotype, Xindengmenggumai, was below the detection limit of HPLC analysis. This result was in agreement with the observation that hulled barley has a higher content of phenolic acid than dehulled barley.[17]

Identifying QTLs and genes controlling phenolic acids in barley grain and malt could improve the understanding of the molecular genetic basis of phenolic acid metabolism. The results of association mapping indicated that phenolic acids in barley grain are polygenic traits. Although QTLs associated with total polyphenol content have been identified in barley,[44] none of them are colocated with the QTLs detected in the present study. This could be due to the fact that QTLs of total polyphenol content are not likely to be responsible for the genetic variation in the individual phenolic acids. As phenolic acids only represent a small portion of total polyphenols, which also include flavonoids, tannins, and anthocyanins. Interestingly, *p*-CA associated marker bpb-8949 (122.3 cM, 2H) colocalized with the major QTL (119−125 cM, 2H) controlling polyphenol oxidase (PPO) activity.[44,64,65] PPO enzyme functions to catalyze the oxidation of phenolic substrates to quinines; therefore, its activity could influence the content of the phenolic compound.[66,67] This may explain the colocalization of QTLs for *p*-CA and PPO.

The barley genomic information facilitates the identification of probable candidate genes based on QTL results.[68] The sequences of DArT markers were obtained from the Web site of Diversity Array Technology Pty Ltd. (http://www.diversityarrays.com). These sequences were used to search the corresponding contigs in the IPK barley genome database, some of which contain genes with annotations (http://webblast.ipk-gatersleben.de/barley). Interestingly, the sequence of marker bpb-0027 was found to match contig_137941, which contains the cytochrome P450 (CYP73 encoding cinnamate 4-hydroxylase) gene. It has been well-established that cytochrome P450 catalyzes cinnamic acid to *p*-CA in the phenylpropanoid pathway, leading to the biosynthesis of lignin and numerous other phenolic compounds in plants.[69,70] Another search for the sequence of marker bpb-7156 was found to match contig_51262, which contains the oxidoreductase gene. Oxidoreductases, such as PPO and peroxidase (PDX), play vital roles in the regulation of the phenolic content of virgin olive oil.[71] These identified genes may participate in phenolic acid metabolism; however, the functions of these genes need to be studied thoroughly using transgenic approach in the future.

It is worth noting that marker bpb-3484 is associated with both FA and *p*-CA, indicating that the two phenolic acids could be tightly linked or even likely be controlled by the same group of genes. This hypothesis was partially supported by the highly positive correlations between the contents of the two phenolic acids. Conversely, the results provide some insights into understanding of the molecular mechanisms controlling the two traits. The lack of any common marker between grain and malt phenolic acids is consistent with the finding that there is no correlation between grain and malt for this trait. Moreover, our results may provide some preliminary genetic evidence for the significant effect of the malting process on phenolic acid metabolism.

■ ASSOCIATED CONTENT

Supporting Information

FA and *p*-CA concentrations and malt/grain ratios in 68 barley genotypes and quantile-quantile plots of estimated and expected $\log_{10}(P)$ values. The Supporting Information is available free of charge on the ACS Publications website at DOI: 10.1021/acs.jafc.5b02960.

■ AUTHOR INFORMATION

Corresponding Author

*E-mail: fdai@zju.edu.cn, Phone: +86 571 88982115, Fax: +86 571 88982117.

Author Contributions

†S. C. and Z. H. contributed equally to this work.

Funding

This study was supported by the Natural Science Foundation of China (31201166, 31471480, and 31401369) and the Fundamental Research Funds for the Central Universities.

Notes

The authors declare no competing financial interest.

■ ACKNOWLEDGMENTS

We thank Ms. Jingqun Yuan and Mei Li, technicians of the 985-Institute of Agrobiology and Environmental Sciences of Zhejiang University, for assistance in HPLC analysis and Ms Michelle Mak (University of Western Sydney, Australia) for English language editing.

■ REFERENCES

(1) Acosta-Estrada, B. A.; Gutiérrez-Uribe, J. A.; Serna-Saldívar, S. O. Bound phenolics in foods, a review. *Food Chem.* **2014**, *152*, 46−55.

(2) Zhao, Z.; Moghadasian, M. H. Chemistry, natural sources, dietary intake and pharmacokinetic properties of ferulic acid: A review. *Food Chem.* **2008**, *109*, 691−702.

(3) Ghimire, B. K.; Seong, E. S.; Goh, E. J.; Kang, E. Y.; Ahn, J. K.; Yu, C. Y.; Chung, I. M. Improving antioxidant activity in transgenic *Codonopsis lanceolata* plants via overexpression of the γ-tocopherol methyltransferase (*γ-tmt*) gene. *Plant Growth Regul.* **2011**, *63*, 1−6.

(4) Bizjak, J.; Weber, N.; Mikulic-Petkovsek, M.; Alam, Z.; Thill, J.; Stich, K.; Halbwirth, H.; Veberic, R. Polyphenol gene expression and changes in anthocyanins and polyphenols in the skin of 'Braeburn' apples after the autumn application of prohexadione-calcium. *Plant Growth Regul.* **2013**, *71*, 225−233.

(5) Liu, Q.; Yao, H. Y. Antioxidant activities of barley seeds extracts. *Food Chem.* **2007**, *102*, 732−737.

(6) Karabín, M.; Dostálek, P.; Hofta, P. Review of methods for estimation of antioxidant activity in brewing industry. *Chem. Listy* **2006**, *100*, 184−189.

(7) Goupy, P.; Hugues, M.; Boivin, P.; Amoit, M. J. Antioxidant composition and activity of barley (*Hordeum vulgare* L.) and malt extracts and of isolated phenolic compounds. *J. Sci. Food Agric.* **1999**, *79*, 1625−1634.

(8) Madhujith, T.; Shahidi, F. Antioxidative and antiproliferative properties of selected barley (*Hordeum vulgare* L.) cultivars and their potential for inhibition of low-density lipoprotein (LDL) cholesterol oxidation. *J. Agric. Food Chem.* **2007**, *55*, 5018−5024.

(9) Etoh, H.; Murakami, K.; Yogoh, T.; Ishikawa, H.; Fukuyama, Y.; Tanaka, H. Anti-oxidative compounds in barley tea. *Biosci., Biotechnol., Biochem.* **2004**, *68*, 2616−2618.

DOI: 10.1021/acs.jafc.5b02960
J. Agric. Food Chem. 2015, 63, 7051−7057

(10) Quinde-Axtell, Z.; Baik, B. K. Phenolic compounds of barley grain and their implication in food product discoloration. *J. Agric. Food Chem.* **2006**, *54*, 9978−9984.
(11) McCarthy, A. L.; O'Callaghan, Y. C.; Neugart, S.; Piggott, C. O.; Connolly, A.; Jansen, M. A.; Krumbein, A.; Schreiner, M.; FitzGerald, R. J.; O'Brien, N. M. The hydroxycinnamic acid content of barley and brewers' spent grain (BSG) and the potential to incorporate phenolic extracts of BSG as antioxidants into fruit beverages. *Food Chem.* **2013**, *141*, 2567−2574.
(12) Soong, Y. Y.; Tan, S. P.; Leong, L. P.; Henry, J. K. Total antioxidant capacity and starch digestibility of muffins baked with rice, wheat, oat, corn and barley flour. *Food Chem.* **2014**, *164*, 462−469.
(13) Nordkvist, E.; Salomonssen, A.; Åman, P. Distribution of insoluble bound phenolic acids in barley grain. *J. Sci. Food Agric.* **1984**, *35*, 657−661.
(14) Ahluwalia, B.; Fry, S. C. Barley endosperm cell walls contain a feruloylated arabinoxylan and a non-feruloylated β-glucan. *J. Cereal Sci.* **1986**, *4*, 287−295.
(15) Zupfer, J. M.; Churchill, K. E.; Rasmusson, D. C. Variation in ferulic acid concentration among diverse barley cultivars measured by HPLC and microspectrophotometry. *J. Agric. Food Chem.* **1998**, *46*, 1350−1354.
(16) Hernanz, D.; Nunez, V.; Sancho, A. I.; Faulds, C. B.; Williamson, G.; Bartolome, B.; Gomez-Cordoves, C. Hydroxycinnamic acids and ferulic acid dehydrodimers in barley and processed barley. *J. Agric. Food Chem.* **2001**, *49*, 4884−4888.
(17) Holtekjølen, A. K.; Kinitz, C.; Knutsen, S. H. Flavanol and bound phenolic acid contents in different barley varieties. *J. Agric. Food Chem.* **2006**, *54*, 2253−2260.
(18) Eticha, F.; Grausgruber, H.; Berghoffer, E. Multivariate analysis of agronomic and quality traits of hull-less spring barley (*Hordeum vulgare* L.). *J. Plant Breed. Crop Sci.* **2010**, *2*, 81−95.
(19) Naczk, M.; Shahidi, F. The effect of methanol-ammonia-water treatment on the content of phenolic acids of canola. *Food Chem.* **1989**, *31*, 159−164.
(20) Chandrasekara, A.; Shahidi, F. Content of insoluble bound phenolics in millets and their contribution to antioxidant capacity. *J. Agric. Food Chem.* **2010**, *58*, 6706−6714.
(21) Leitao, C.; Marchioni, E.; Bergaentzlé, M.; Zhao, M.; Didierjean, L.; Taidi, B.; Ennahar, S. Effects of processing steps on the phenolic content and antioxidant activity of beer. *J. Agric. Food Chem.* **2011**, *59*, 1249−1255.
(22) Friedrich, W.; Galensa, R. Identification of a new flavanol glucoside from barley (*Hordeum vulgare* L.) and malt. *Eur. Food Res. Technol.* **2002**, *214*, 388−393.
(23) Samaras, T. S.; Camburn, P. A.; Chandra, S. X.; Gordon, M. H.; Ames, J. M. Antioxidant properties of kilned and roasted malts. *J. Agric. Food Chem.* **2005**, *53*, 8068−8074.
(24) Qingming, Y.; Xianhui, P.; Weibao, K.; Hong, Y.; Yidan, S.; Li, Z.; Yanan, Z.; Yuling, Y.; Lan, D.; Guoan, L. Antioxidant activities of malt extract from barley (*Hordeum vulgare* L.) toward various oxidative stress in vitro and in vivo. *Food Chem.* **2010**, *118*, 84−89.
(25) Lu, J.; Zhao, H.; Chen, J.; Fan, W.; Dong, J.; Kong, W.; Sun, J.; Cao, Y.; Cai, G. Evolution of phenolic compounds and antioxidant activity during malting. *J. Agric. Food Chem.* **2007**, *55*, 10994−11001.
(26) Leitao, C.; Marchioni, E.; Bergaentzlé, M.; Zhao, M.; Didierjean, L.; Miesch, L.; Holder, E.; Miesch, M.; Ennahar, S. Fate of polyphenols and antioxidant activity of barley throughout malting and brewing. *J. Cereal Sci.* **2012**, *55*, 318−322.
(27) Dvořáková, M.; Douanier, M.; Jurková, M.; Kellner, V.; Dostálek, P. Comparison of antioxidant activity of barley (*Hordeum vulgare* L.) and malt extracts with the content of free phenolic compounds measured by high performance liquid chromatography coupled with CoulArray detector. *J. Inst. Brew.* **2008**, *114*, 150−159.
(28) Dvořáková, M.; Guido, L. F.; Dostálek, P.; Skulilová, Z.; Moreira, M. M.; Barros, A. A. Antioxidant properties of free, soluble ester and insoluble-bound phenolic compounds in different barley varieties and corresponding malts. *J. Inst. Brew.* **2008**, *114*, 27−33.
(29) Iyuke, S. E.; Madigoe, E. M.; Maponya, R. The effect of hydroxycinnamic acids and volatile phenols on beer quality. *J. Inst. Brew.* **2008**, *114*, 300−305.
(30) Bierman, U. Composition of wort. *Fermentation* **1991**, *4*, 229−231.
(31) Uchida, M.; Ono, M. Improvement of oxidative flavor stability of beer-role of OH-radical in beer oxidation. *J. Am. Soc. Brew. Chem.* **1996**, *54*, 198−204.
(32) Bvochora, J. M.; Danner, H.; Miyafuji, H.; Braun, R.; Zvauya, R. Variation of phenolic compounds during the preparation of opaque beer. *Process Biochem.* **2005**, *40*, 1207−1213.
(33) Guido, L. F.; Curto, A. F.; Boivin, P.; Benismail, N.; Gonçalves, C. R.; Barros, A. A. Correlation of malt quality parameters and beer flavor stability: multivariate analysis. *J. Agric. Food Chem.* **2007**, *55*, 728−733.
(34) Vanbeneden, N.; Gils, F.; Delvaux, F.; Delvaux, F. R. Formation of 4-vinyl and 4-ethyl derivatives from hydroxycinnamic acids: Occurrence of volatile phenolic flavour compounds in beer and distribution of Pad1-activity among brewing yeasts. *Food Chem.* **2008**, *107*, 221−230.
(35) Bamforth, C. W.; Barclay, A. H. P. Malting technology and the uses of malt. In *Barley: Chemistry and Technology*; Macgregor, A. W., Bhatty, R. S., Eds.; American Association of Cereal Chemistry: St. Paul, MN, 1993; pp 297−354.
(36) Ullrich, S. E.; Han, F.; Jones, B. L. Genetic complexity of the malt extract trait in barley suggested by QTL analysis. *J. Am. Soc. Brew. Chem.* **1997**, *55*, 1−4.
(37) Siwela, M.; Taylor, J.; Milliano, W.; Duodu, K. Influence of phenolics in finger millet on grain and malt fungal load, and malt quality. *Food Chem.* **2010**, *121*, 443−449.
(38) Chethan, S.; Sreerama, Y. N.; Malleshi, N. G. Mode of inhibition of finger millet malt amylases by the millet phenolics. *Food Chem.* **2008**, *111*, 187−191.
(39) Saeed, M.; Brewer, L.; Johnston, J.; McGhie, T. K.; Gardiner, S. E.; Heyes, J. A.; Chagné, D. Genetic, metabolite and developmental determinism of fruit friction discolouration in pear. *BMC Plant Biol.* **2014**, *14*, 241.
(40) Verdu, C. F.; Guyot, S.; Childebrand, N.; Bahut, M.; Celton, J. M.; Gaillard, S.; Lasserre-Zuber, P.; Troggio, M.; Guilet, D.; Laurens, F. QTL analysis and candidate gene mapping for the polyphenol content in cider apple. *PLoS One* **2014**, *9*, e107103.
(41) Rigano, M. M.; Raiola, A.; Tenore, G. C.; Monti, D. M.; Giudice, R. D.; Frusciante, L.; Barone, A. Quantitative trait loci pyramiding can improve the nutritional potential of tomato (*Solanum lycopersicum*) fruits. *J. Agric. Food Chem.* **2014**, *62*, 11519−11527.
(42) Rhodes, D. H.; Hoffmann, L., Jr.; Rooney, W. L.; Ramu, P.; Morris, G. P.; Kresovich, S. Genome-wide association study of grain polyphenol concentrations in global sorghum [*Sorghum bicolor* (L.) Moench] germplasm. *J. Agric. Food Chem.* **2014**, *62*, 10916−10927.
(43) Shao, Y.; Jin, L.; Zhang, G.; Lu, Y.; Shen, Y.; Bao, J. Association mapping of grain color, phenolic content, flavonoid content and antioxidant capacity in dehulled rice. *Theor. Appl. Genet.* **2011**, *122*, 1005−1016.
(44) Mohammadi, M.; Endelman, J. B.; Nair, S.; Chao, S.; Jones, S. S.; Muehlbauer, G. J.; Ullrich, S. E.; Baik, B.; Wise, M. L.; Smith, K. P. Association mapping of grain hardness, polyphenol oxidase, total phenolics, amylose content, and β-glucan in US barley breeding germplasm. *Mol. Breed.* **2014**, *34*, 1229−1243.
(45) Dai, F.; Wang, J. M.; Zhang, S. H.; Xu, Z. Z.; Zhang, G. P. Genotypic and environmental variation in phytic acid content and its relation to protein content and malt quality in barley. *Food Chem.* **2007**, *105*, 606−611.
(46) Dai, F.; Qiu, L.; Xu, Y.; Cai, S. G.; Qiu, B. Y.; Zhang, G. P. Differences in phytase activity and phytic acid content between cultivated and Tibetan annual wild barley. *J. Agric. Food Chem.* **2010**, *58*, 11821−11824.
(47) Zhao, H.; Dong, J.; Lu, J.; Chen, J.; Li, Y.; Shan, L.; Lin, Y.; Fan, W.; Gu, G. Effects of extraction solvent mixtures on antioxidant activity evaluation and their extraction capacity and selectivity for free

DOI: 10.1021/acs.jafc.5b02960
J. Agric. Food Chem. 2015, 63, 7051−7057

phenolic compounds in barley (*Hordeum vulgare* L.). *J. Agric. Food Chem.* **2006**, *54*, 7277−7286.
(48) Yu, J. M.; Pressoir, G.; Briggs, W. H.; Vroh Bi, I.; Yamasaki, M.; Doebley, J. F.; McMullen, M. D.; Gaut, B. S.; Nielsen, D. M.; Holland, J. B.; Kresovich, S.; Buckler, E. S. A unifiedmixed-model method for association mapping that accounts for multiple levels ofrelatedness. *Nat. Genet.* **2006**, *38*, 203−208.
(49) Cai, S.; Wu, D.; Jabeen, Z.; Huang, Y. Q.; Huang, Y. C.; Zhang, G. Genome-wide association analysis of aluminum tolerance in cultivated and Tibetan wild barley. *PLoS One* **2013**, *8*, e69776.
(50) Huang, Y. Q.; Cai, S. G.; Ye, L. Z.; Han, Y.; Wu, D. Z.; Dai, F.; Li, C. D.; Zhang, G. P. Genetic Architecture of Limit Dextrinase Inhibitor (LDI) Activity in Tibetan Wild Barley. *BMC Plant Biol.* **2014**, *14*, 117.
(51) Jin, X. L.; Cai, S. G.; Han, Y.; Wang, J.; Wei, K.; Zhang, G. P. Genetic variants of HvGlb1 in Tibetan annual wild barley and cultivated barley and their correlation with malt quality. *J. Cereal Sci.* **2011**, *53*, 59−64.
(52) Boivin, P. Pro- and anti-oxidant enzymatic activities in malt. *Cerevisia* **2001**, *26*, 109−115.
(53) Chandra, C. S.; Buggey, L. A.; Peters, S.; Cann, C.; Liegeois, C. Factors affecting the development of antioxidant properties of malt during the malting and roasting process. *Home Grown Cereals Association*, Project No. 242.; HGCA Publications: London, 2001.
(54) Maillard, M. N.; Berset, C. Evolution of antioxidant activity during kilning: role of insoluble bound phenolic acids of barley and malt. *J. Agric. Food Chem.* **1995**, *43*, 1789−1793.
(55) Maillard, M. N.; Soum, M. H.; Boivin, P.; Berset, C. Antioxidant activity of barley and malt, relationship with phenolic content. *Lebensm. Wiss. Technol.* **1996**, *29*, 238−244.
(56) Inns, E. L.; Buggey, L. A.; Booer, C.; Nursten, H. E.; Ames, J. M. Effect of modification of the kilning regimen on levels of free ferulic acid and antioxidant activity in malt. *J. Agric. Food Chem.* **2011**, *59*, 9335−9343.
(57) Sancho, A. I.; Faulds, C. B.; Bartolome, B.; Williamson, G. Characterisation of feruloyl esterase activity in barley. *J. Sci. Food Agric.* **1999**, *79*, 447−449.
(58) Humberstone, F. J.; Briggs, D. E. Extraction and assay of ferulic acid esterase from malted barley. *J. Inst. Brew.* **2000**, *106*, 21−29.
(59) Shibuya, N. Phenolic acids and their carbohydrate esters in rice endosperm cell wall. *Phytochemistry* **1984**, *23*, 2233−2237.
(60) Tian, S.; Nakamura, K.; Kayahara, H. Analysis of phenolic compounds in white rice, brown rice, and germinated brown rice. *J. Agric. Food Chem.* **2004**, *52*, 4808−4813.
(61) Dicko, M. H.; Gruppen, H.; Traore, A. S.; Van-Berkel, W. J. H.; Voragen, A. G. J. Evaluation of the effect of germination on phenolic compounds and antioxidant Activities in sorghum varieties. *J. Agric. Food Chem.* **2005**, *53*, 2581−2588.
(62) Beta, T.; Rooney, L. W.; Marovatsanga, L. T.; Taylor, J. R. N. Phenolic compounds and kernel characteristics of Zimbabwean sorghums. *J. Sci. Food Agric.* **1999**, *79*, 1003−1010.
(63) Doblado, R.; Frias, J.; Valverde, C. V. Changes in vitamin C content and antioxidant capacity of raw and germinated (*Vigna sinensis* var. carilla) seeds induced by high pressure treatment. *Food Chem.* **2007**, *101*, 918−923.
(64) Taketa, S.; Matsuki, K.; Amano, S.; Saisho, D.; Himi, E.; Shitsukawa, N.; Yuo, T.; Noda, K.; Takeda, K. Duplicate polyphenol oxidase genes on barley chromosome 2H and their functional differentiation in the phenol reaction of spikes and grains. *J. Exp. Bot.* **2010**, *61*, 3983−3993.
(65) Berger, G. L.; Liu, S.; Hall, M. D.; Brooks, W. S.; Chao, S.; Muehlbauer, G. J.; Baik, B. K.; Steffenson, B.; Griffey, C. A. Marker-trait associations in Virginia Tech winter barley identified using genome-wide mapping. *Theor. Appl. Genet.* **2013**, *126*, 693−710.
(66) Yoruk, R.; Marshall, M. R. Physiochemical properties and function of plant polyphenol oxidase: a review. *J. Food Biochem.* **2003**, *27*, 361−422.
(67) Mayer, A. M. Polyphenol oxidases in plants and fungi: going places? A review. *Phytochemistry* **2006**, *67*, 2318−2331.
(68) International Barley Genome Sequencing Consortium. A physical, genetic and functional sequence assembly of the barley genome. *Nature* **2012**, *491*, 711−716.
(69) Batard, Y.; Hehn, A.; Nedelkina, S.; Schalk, M.; Pallett, K.; Schaller, H.; Werck-Reichhart, D. Increasing expression of P450 and P450-reductase proteins from monocots in heterologous systems. *Arch. Biochem. Biophys.* **2000**, *379*, 161−169.
(70) Ehlting, J.; Hamberger, B.; Million-Rousseau, R.; Werck-Reichhart, D. Cytochromes P450 in phenolic metabolism. *Phytochem. Rev.* **2006**, *5*, 239−270.
(71) García-Rodríguez, R.; Romero-Segura, C.; Sanz, C.; Pérez, A. G. Modulating oxidoreductase activity modifies the phenolic content of virgin olive oil. *Food Chem.* **2015**, *171*, 364−369.

DOI: 10.1021/acs.jafc.5b02960
J. Agric. Food Chem. 2015, 63, 7051−7057

creating affinity sites for divalent cations to "lock" the junctions. It is hypothesized that in this way the ability to dissipate energy will be affected. For that purpose gelatins are chemically modified on the available lysine residues using succinic anhydride with various degrees of substitution, converting positive charges into negative ones. Using calcium ions, the strands, bearing now a higher negative charge density, could become stabilized at their interstrand junction zones. The materials are chemically and physically characterized and tested for helix propensity and thermal behavior, and the impact of the modification on the mechanical behavior is studied using small and large deformation rheology.

MATERIALS AND METHODS

Gelatin Modification by Succinylation. Gelatin type A (PGS from pork skin, Bloom 150, and an average molecular weight of ∼124 kDa) was kindly provided from Rousselot (Gent, Belgium). The material was succinylated according to a protocol described elsewhere.[8] To this end, 1% w/v gelatin was dispersed in 0.02 M phosphate buffer (pH 8), stirred for 1 h at 60 °C, and cooled to 40 °C to dissolve all material. Succinic anhydride (239690-250G, Sigma-Aldrich) was gradually added in small aliquots (∼10 mg portions) to the gelatin solutions under continuous stirring at 40 °C up to fixed amounts between 5 and 35 mg/g of gelatin (see Table 1), to obtain batches with different degrees of modification. The pH was continuously adjusted to 8.0 using a pH-stat by titration with 1 M NaOH. After addition of the succinic anhydride, the solutions were stirred for another 30 min. The solutions were extensively dialyzed (Thermo Scientific 10 kDa cutoff, 22 mm diameter) against deionized water (at room temperature; pH 6.8) in four repetitions with equilibration times of 6 h each and subsequently lyophilized. A reference sample was subjected to the same procedure without addition of succinic anhydride.

Table 1. Characterization of Gelatin Materials Subjected to Different Degrees of Succinylation (DS), As Determined from the Chromogenic OPA Assay, and the Apparent Isoelectric Point, As Established from Zetasizer Measurements As Described under Materials and Methods[a]

material (code)	mg of succinic anhydride added per g of gelatin	DS (%)	apparent IEP
reference	0	0	7.5
A	5	12	4.9
B	10	26	4.7
C	20	43	4.5
D	30	65	4.5
E	35	82	4.4

[a]Estimated error in determination of DS as determined by the OPA assay is ±3%.

Chromogenic OPA Assay. To quantify the degree of succinylation (DS), the availability of lysine residues was determined using the specific reaction between *o*-phthaldialdehyde (OPA) and free primary amino groups in the proteins in the presence of 2-(dimethylamino)ethanethiol hydrochloride (DMA) as described previously.[9] The measured absorbance was corrected with that of a sample containing nonreacted reagent. A calibration curve was obtained by diluting the OPA reagent with a series of L-leucine (1 mM stock). All assays were done in triplicate. The DS is expressed as 100% minus the percentage of nonreacted primary amines relative to the reference material.

Apparent Isoelectric Point. To determine the apparent isoelectric point, freeze-dried gelatin (reference and modified) was dissolved in Milli-Q water at a concentration of 0.5% (w/v). Zeta potential (ζ) values were determined as a function of pH at 20 °C using a Zetasizer Nano ZS (Malvern Instruments, UK). Automatic titration was performed with 0.1 M HNO_3 and 0.1 M NaOH solutions under continuous stirring. The isoelectric point was evaluated as the pH at which the detected zeta potential value of the material (mV) was zero. For each sample five runs were performed. All experiments were performed at least in duplicate.

Calcium-Binding Measurements. A 0.1 M $CaCl_2$ stock solution was prepared by dissolving calcium chloride dihydrate (Sigma-Aldrich, Germany) in the appropriate acetate buffer (pH 6.5). The concentration of free Ca^{2+} ions was measured using a calcium ion selective electrode device (Ca ISE, connected to an Orion Star A214 ISE meter). The potentiometric readings (mV) of the electrode were calibrated using standard $CaCl_2$ solutions (0.5−30 mM) with the addition of ISA solution to match the ionic strength in all solutions. Gelatin samples (0.9% w/v; pH 6.5) were titrated with $CaCl_2$, and the corresponding amount of moles of calcium bound per mole of protein (assuming an average molecular weight of 124 kDa) was established using a Scatchard analysis (see elsewhere for details[10]). This higher protein concentration was chosen to increase the sensitivity in the experiment by providing a higher absolute number of calcium-binding sites, but to refrain from too viscous solutions. The contribution of the potassium acetate buffer with gelatin was neglected in the determination of calcium activity, and all samples were adjusted to a similar ionic strength as described previously.[11] All experiments were performed in triplicate at 20 °C.

Calorimetric Analysis. The enthalpic transition of succinylated solution samples 3% (w/v) in 20 mM acetate buffer (pH 6.5) in the absence or presence of calcium (0−20 mM) during heating−cooling ramps (60−5 °C and vice versa) was measured by differential scanning calorimetry (TA Instrument Q1000 Tzero DSC) under ambient conditions. Gelatin solutions (20 μL) were placed in aluminum pans and sealed followed by heating−cooling ramps The heat flow was recorded at 2 °C/min speed rate in duplicate for each modified and reference sample relative to a protein-free sample. Temperature and enthalpy transition values were obtained by integration of melting and cooling thermograms using Universal Analysis V1.7F software (TA Instruments).

Optical Rotation Measurements. The triple-helix propensity in gelatin in the absence or presence of calcium was monitored by optical rotation at 436 nm using a PerkinElmer 341 polarimeter equipped with a thermostated water bath (HAAKE Phoexix II C25P model). Solutions were prepared by pre-equilibration at 60 °C for 1 h and subsequent cooling from 50 to 5 °C at 0.5 °C/min. Samples (0.5% w/v; 20 mM acetate buffer, pH 6.5) were incubated in a cell with a path length of 10 mm. The specific rotation, $(\alpha)\lambda = \alpha/cl$, where α is the optical rotation angle in degrees at λ = 436 nm, c is gelatin concentration (g/mL), and l is the length of optical path (dm), was continuously measured. The helix content (h) at a given concentration is determined by means of eq 1.

$$h = ((\alpha)\lambda - (\alpha_{coil})\lambda)/((\alpha_{collagen})\lambda - (\alpha_{coil})\lambda) \quad (1)$$

Representative values for $(\alpha_{coil})\lambda$ and $(\alpha_{collagen})\lambda$ at 436 nm of −256° and −800° are used, respectively.[12]

Mechanical Deformation. The evolution of the storage and viscous moduli (G' and G'', respectively) is monitored during temperature ramps for (modified) gelatin solutions in 20 mM acetate buffer (pH 6.5) (3% w/v) in the presence of 0−20 mM calcium. Strain-controlled dynamic oscillatory measurements were carried out in an Anton Paar MCR 502 rheometer (Anton Paar, Graz, Austria) using a concentric cylinder geometry. A scan rate of 0.5 °C/min was used during cooling and heating ramps from 5 to 50 °C and vice versa.

For large deformation studies, preformed 3% w/v gelatin gels were used, prepared as described above, cooled to room temperature (20 ± 1 °C), and equilibrated for 24 h. Uniaxial compression to fracture experiments were performed using an Instron universal testing machine (model 5543, Instron International LDT, Edegem, Belgium) equipped with plate−plate geometry. A uniaxial (de)compression speed of 1 mm/s was used. Cylindrical gelatin gels were prepared in 50 mL (diameter = 21.7 mm) syringes prelubricated with paraffin oil and cut with a wire in self-supported specimens of 20 mm height. To

DOI: 10.1021/acs.jafc.5b01962
J. Agric. Food Chem. 2015, 63, 7058−7065

determine the fracture properties, the gels were compressed for 90% of the original height and the stress response was monitored as a function of applied strain.

Determination of the recoverable energy (RE) was established by applying a compression−decompression cycle to a strain of 20% at a deformation speed of 1 mm/s. The work necessary to compress the samples to this strain (W_c) was calculated from the area below the stress−strain curve. After reaching the maximal strain, the samples were decompressed immediately at the same speed and the work (W_s) released by the gel specimen was determined accordingly. The results were expressed as RE (%) = 100% × W_s/W_c. All gels were analyzed at least in triplicate.

In a similar setup as described above stress relaxation was evaluated for specimens prepared in the same way. The gels were compressed up to a set strain of 20% at a compression speed of 1 mm/s and held at the maximal loading strain for 5 min. During this time interval the stress was recorded with a step resolution of 60 ms. Every sample was analyzed at least in duplicate. Analysis of the time intervals was performed using a two-exponential decay nonlinear regression curve-fitting procedure (normalized stress = $A_1 \times \exp(-\tau_1/t) + A_2 \times \exp(-\tau_2/t) + A_0$), as described in detail elsewhere.[13] This provided two relaxation times, τ_1 and τ_2, with corresponding proportions A_1 and A_2. A_0 reflects in this analysis the stress contribution that does not dissipate in the experimental time regime of 5 min. Typically, in all cases R^2 values >0.995 were obtained. A higher order of exponents did not give fits with higher R^2 values. For this study, with an experimental time scale for the RE measurements of ∼8 s, only the fast-relaxing contribution is reported.

RESULTS AND DISCUSSION

Characterization of the Material. The conceptual idea behind this study is to enable a fortification of the strand−strand interaction points by affinity binding with calcium. For that purpose different degrees of succinylation of the protein were performed. Table 1 presents the different materials obtained when gelatin is subjected to different degrees of succinylation (DS) as described under Materials and Methods. The DS shows a linear relationship with the amount of succinic anhydride added, indicating that the number of lysine groups available for chemical modification is not limiting and/or hampered by steric or electrostatic constraints. It can also be observed that, where the reference material has an isoelectric point (IEP) of around 7.5, the lowest DS already yields an apparent IEP just below 5. The IEP gradually decreases further with increasing DS to 4.4 when ∼82% of all lysine residues are modified with negative succinate groups. From its amino acid composition this gelatin contains about 27 lysines per 1000 residues with an average molecular weight of 124 kDa, which implies that for the highest DS about 26 succinate groups have been introduced per molecule. All experiments described in this work have been carried out at a pH of 6.5, above the isoelectric point of all succinylated variants but below that of the reference material.

Figure 1 shows the triple-helix content as obtained from optical rotation measurements during a cooling ramp to 5 °C for aqueous solutions of reference and succinylated gelatins with different DS. It can be observed that even a high DS does not affect the onset temperature for helix formation. Moreover, a DS of 43% does not impair the extent of helix induction, whereas this is marginally affected at a DS of 65%. Only for a DS of 82% is a significant reduction of the helix content found of about 20−25%. Recent work showed that the ability of gelatin to form helices decreased when the availability of lysine decreased.[14] Prolonged incubation at low temperature did not

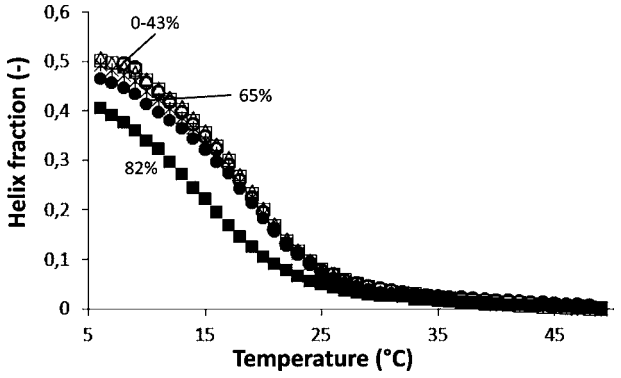

Figure 1. Helicity as established from optical rotation measurements as described in the text for aqueous solutions of reference and succinylated gelatin with different DS. The materials with a DS of 82 (solid squares) and 65% (solid circles) are indicated separately from the other DS and reference (open crosses, triangles, squares, and circles).

increase the helicity of this latter sample, illustrating that the observed reduction is not the result of a slower kinetic process.

Overall, it can be concluded that a series of succinylated gelatins can be prepared that, when studied above their isoelectric point, all exhibit the ability to adopt a triple-helical configuration essential for developing a spatial network.

Gelling Behavior in the Absence of Calcium. The gelling properties of the various materials have been studied using small deformation rheology at concentrations well above the critical gel concentration (3% w/v). The subsequent cooling and heating traces are shown in Figure 2. It can be

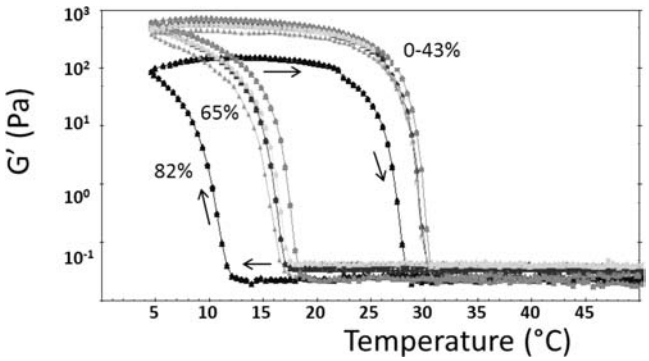

Figure 2. Storage modulus (G') as a function of cooling/heating temperatures at 0.5 °C/min scan rate for reference and gelatin solutions with different DS (3% w/v). Only the traces with a DS of 82 and 65% are indicated separately. The small arrows in the figure illustrate the applied temperature ramp of cooling and subsequent heating of the sample.

observed that up to a DS of 65% the introduced succinate groups have only very limited impact on both gelling/melting temperatures as well as on the gel strength developed. Only at a DS of 82% was a significant loss in gel strength (factor of 5−6) observed, and the gelling temperature shifted from 17 to 11 °C. Also, the helix melting temperature was lowered. Lowering the cooling rate from 0.5 to 0.2 °C/min had a marginal effect on the transition temperature and no significant impact on G' (results not shown).

The gelling temperatures observed with small deformation rheology are confirmed by those obtained from thermal calorimetric analysis (Table 2). The corresponding transition

DOI: 10.1021/acs.jafc.5b01962
J. Agric. Food Chem. 2015, 63, 7058−7065

Table 2. Calorimetric Analysis of Reference and Succinylated Gelatin

material (% DS)	transition temperature gelling (°C)	transition enthalpy gelling (J/g)	transition enthalpy melting (J/g)
reference	20.3 ± 0.9	15.0 ± 1.8	40.2 ± 1.6
12	17.8 ± 0.8	13.2 ± 0.9	39.2 ± 1.4
26	18.2 ± 0.7	9.2 ± 0.8	37.4 ± 1.6
43	17.9 ± 0.7	7.2 ± 0.5	35.9 ± 2.1
65	17.3 ± 0.6	6.3 ± 1.1	34.4 ± 1.2
82	11.8 ± 0.9	0.8 ± 0.4	28.5 ± 0.9

enthalpy (related to cooperative thermal processes) decreases with increasing DS and shows a strong reduction for the highest DS of 82%. A lower transition enthalpy was suggested to result from a less cooperative assembly of the triple helices as found by Dardelle and co-workers[15] using different cross-linkers that distorted the gelatin strand formation locally. Alternatively, the energy content related to the melting process (Table 2, last column) shows much higher values compared to those found for the gelling and a smaller dependence on the DS. This suggests that during the gel assembly the kinetics of strand−strand interactions is strongly hindered by the electrostatic repulsions, making the process of network formation less cooperative.

Calcium Binding. Figure 3 shows the calcium-binding curves for reference and succinylated gelatin at concentrations

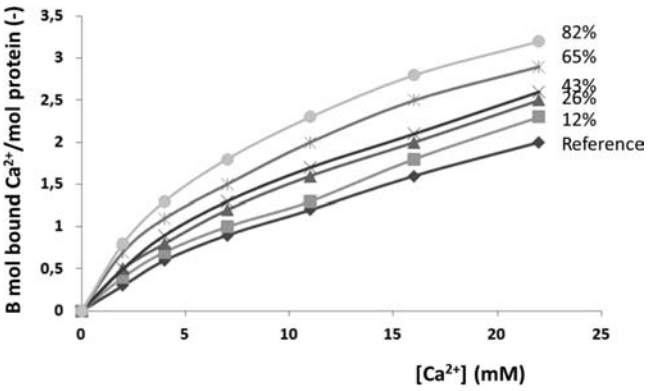

Figure 3. Calcium binding curves for 0.5% w/v solutions of reference succinylated gelatin with different DS as indicated in the graph. An ensemble-averaged molecular weight of 124 kDa is used to calculate *B*.

below the critical gel concentration (0.5% w/v). It can be observed that reference gelatin (net negatively charged under the conditions) shows a moderate calcium binding, and with increasing succinate content (all positively charged) the number of calcium ions that are bound to the protein steadily increases. The fact that no plateau value is reached for any of the samples indicates that the binding affinity to molecular gelatin is relatively weak and there is a continuous equilibrium between bound and nonbound calcium that is shifted toward the bound state by increasing the bulk calcium concentration.

The macroscopic impact of the presence of calcium on gel formation is evaluated by assessment of the physical state of protein solutions (pre-equilibrated at 60 °C), after cooling to 20 °C, qualitatively in terms of whether the sample appears liquid (free flow), viscous (a lumpy cohesive flow), or gelled (immobilized) at room temperature. In all cases visually transparent samples (liquids/gels) were obtained. It can be observed in Figure 4A that in the absence of calcium for reference gelatin a concentration >0.8% (w/v) is needed to

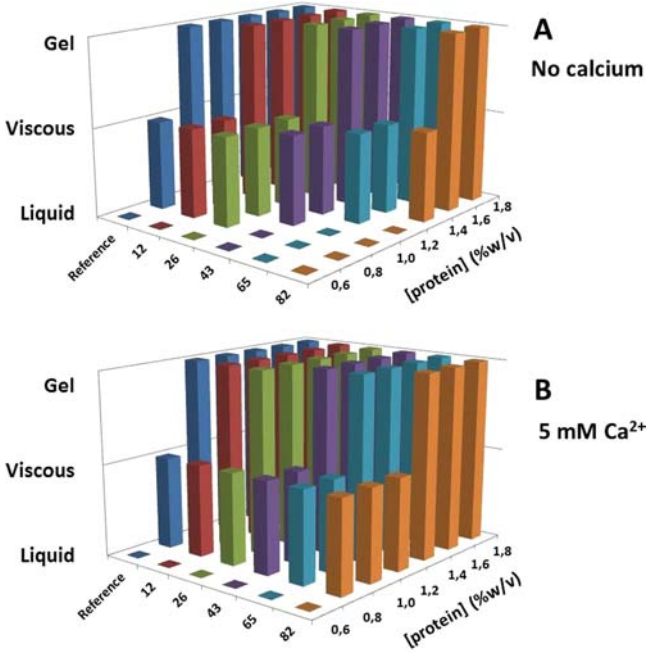

Figure 4. Qualitative assessment of gelatin solutions (reference and with various DS) at different protein concentrations in terms of liquid, viscous, or gel (definitions see text) in the (A) absence or (B) presence of 5 mM calcium. Protein solutions are preheated for 30 min at 60 °C, subsequently cooled to 20 °C, and assessed after 1 h of equilibration at this temperature.

obtain a viscous solution and >1.0% to obtain a gel. In the absence of added calcium it can also be observed that with increasing DS the protein concentration required to obtain a viscous or a gel state shifts to higher protein concentrations. This can be explained by the increased intermolecular electrostatic repulsions with increasing DS. Figure 4B shows the same samples in the same concentration range but cooled to room temperature in the presence of 5 mM calcium. Whereas for reference gelatin no effect of added calcium is present, for all succinylated samples a fortification of the protein network can be observed and most effectively at higher DS. For example, gelatin with a DS of 26% behaves in the presence of 5 mM calcium physically like reference gelatin. A 1.2% (w/v) gelatin with a DS of 82% behaves like a liquid in the absence of calcium, but is gelled in the presence of 5 mM calcium.

To elaborate on this effect, the impact of calcium on the gel properties has been studied for all materials. To illustrate this, the gel properties of reference gelatin and that with a DS of 82% are presented in more detail below.

Calcium Sensitivity in Gel Formation. Figure 5 shows the small deformation rheology of 3% (w/v) gelatin solutions (reference and DS 82%) when a cooling ramp is applied to pre-equilibrated samples from 50 to 4 °C and subsequently a heating ramp to 50 °C in the presence of different calcium concentrations. For reference gelatin (Figure 5A) there is no detectable impact of the presence of added calcium up to a concentration of 20 mM, nor in gelling or melting temperature, nor in the maximal gel strength developed. For the succinylated gelatin it was already shown in Figure 2 that in the absence of

DOI: 10.1021/acs.jafc.5b01962
J. Agric. Food Chem. 2015, 63, 7058−7065

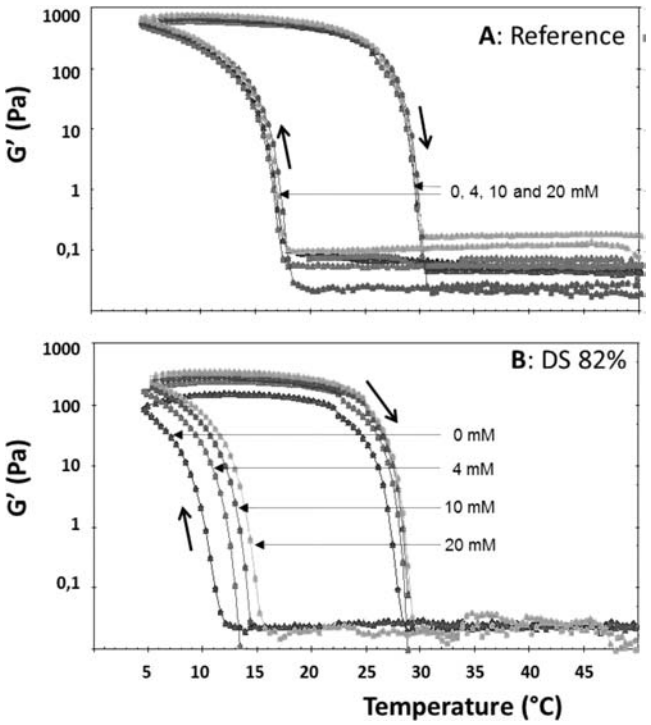

Figure 5. Small deformation rheology on 3% (w/v) (A) reference and (B) succinylated (DS = 82%) gelatin during a cooling and subsequent heating ramp between 50 and 5 °C in the presence of different calcium concentrations (0−20 mM) as indicated in the graphs. The arrows indicate the cooling−heating cycle.

calcium both the gelling temperature and the gel strength were significantly reduced. Figure 5B shows that addition of calcium "restores" both the gelling temperature and gel strength to those observed for reference gelatin. For DS 65% it has been found that whereas in the absence of calcium (see Figure 2) a slightly reduced G' was observed at 5 °C, in the presence of 4 mM calcium no differences with the reference gelatin were observed any longer (results not shown).

This behavior was confirmed when these systems were analyzed calorimetrically, as illustrated in Figure 6. Whereas for reference gelatin no impact is observed of the presence of calcium either on the gelling temperature or on the concomitant enthalpy change, for the 82% succinylated sample the gelling temperature steadily increases from 11 to 17 °C. Moreover, the concomitant enthalpy change increases from almost negligible in the absence of calcium to about 10 J/g in the presence of 10 mM calcium. This is still considerably lower (∼30−40%) compared to that observed for reference gelatin. For the 65% DS sample the transition temperature and enthalpy were fully restored by the addition of 10 mM calcium.

To evaluate whether the calcium acts at the level of strand−strand interactions or at the level of helix assembly, the optical rotation of these samples is followed. Figure 7 shows the optical rotation as monitored during cooling for reference (panel A) and 82% succinylated gelatins (panel B) at concentrations below the critical gelling concentration in the presence of different calcium concentrations. In line with the above results calcium does not have an impact on the helix formation of reference gelatin. As was already shown in Figure 1, in the absence of calcium highly succinylated gelatin has a lower helix propensity. This can, as shown in Figure 7B, be partly (for about half of the loss of helicity in the absence of calcium) restored by the presence of 20 mM calcium. The increased helicity as induced by the presence of calcium does not, however, fully explain the enhancement of the gel mechanical properties as shown in Figure 5, suggesting that the effect of calcium is not limited to the ability to adopt a triple helix only.

To study this in more detail, the effects of 20 mM calcium on the helix content and maximal gel strength are determined and presented in Table 3 for the different succinylated materials. It can be observed that the helicity steadily declines with increasing DS in the presence of 20 mM calcium. The storage modulus, on the other hand, shows a maximum at a DS of 43%,

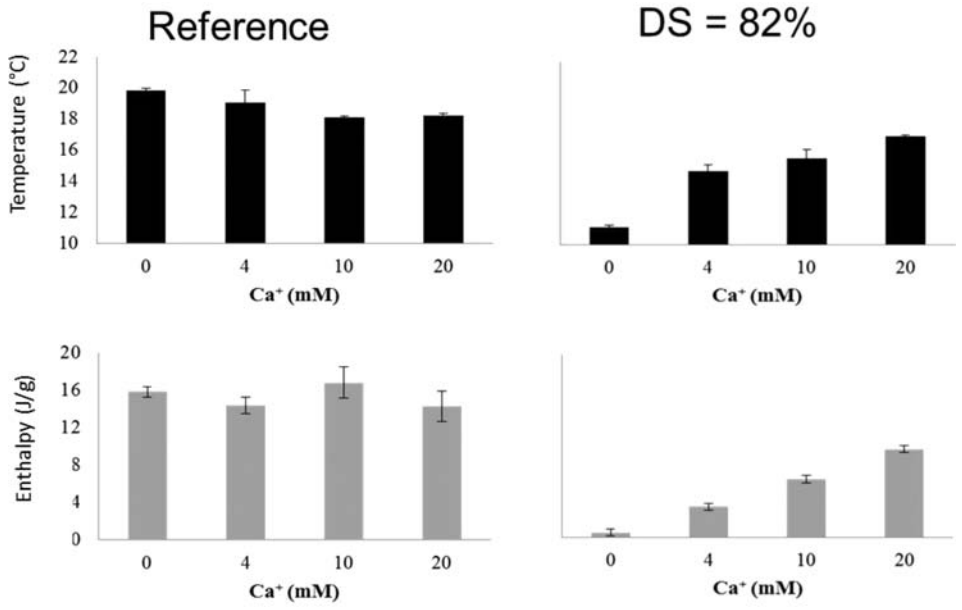

Figure 6. Calorimetric analysis of the cooling ramp from 50 to 5 °C of a 3% w/v reference (left panels) and an 82% succinylated (right panels) gelatin in the presence of different concentrations of calcium. The upper panels present the onset of the gelling temperature, and the lower panels show the concomitant change in enthalpy.

DOI: 10.1021/acs.jafc.5b01962
J. Agric. Food Chem. 2015, 63, 7058−7065

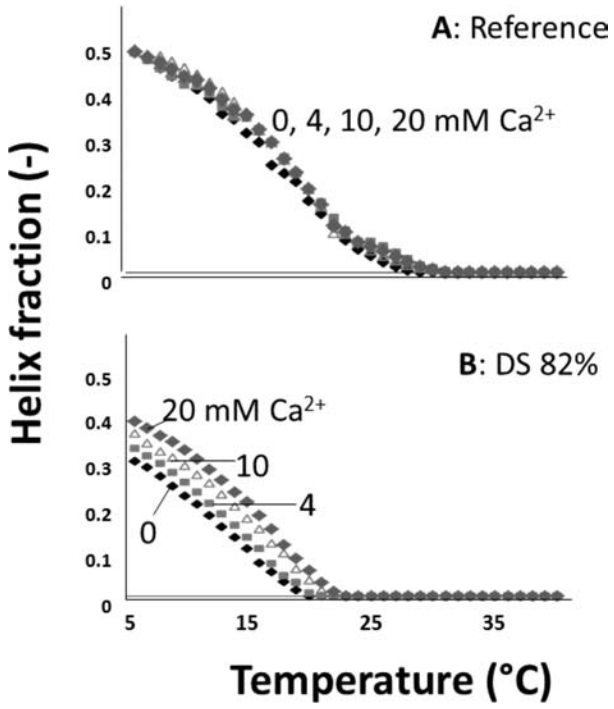

Figure 7. Helix fraction as established from optical rotation measurements for reference (top panel) and 82% succinylated (lower panel) gelatin in the presence of various calcium concentrations (0−20 mM) as indicated in the panels during cooling from 50 to 5 °C.

Table 3. Helix Propensity (Optical Rotation) and Maximal Gel Strength (Small Deformation Rheology of Reference and Various Succinylated Gelatins in the Presence of 20 mM Calcium)

material (% DS)	helicity (fraction) at 5 °C	maximal G' (Pa)
reference	0.45 ± 0.02	760 ± 20
12	0.44 ± 0.03	780 ± 30
26	0.42 ± 0.02	830 ± 40
43	0.40 ± 0.02	930 ± 50
65	0.37 ± 0.03	550 ± 40
82	0.34 ± 0.03	280 ± 30

where an enhancement of the gel strength of ∼20% is found, and the helicity is reduced compared to the reference. At higher DS G' decreases again rather drastically, despite the fact that under these conditions the helicity is not concomitantly reduced.

Responses to Large Mechanical Deformation. The above-presented results show that extensive succinylation of gelatin does not prohibit gel formation. At high DS helix formation is hampered, but still profound, and the gel strength is reduced only slightly. The presence of calcium restores the material properties to those of unmodified gelatin to some extent. There are two opposing aspects introduced by succinylation of the protein. Increasing DS gradually reduces the helix propensity (Figure 1), the cooperativity in network assembly (Table 2), and the storage modulus of the gel (Figure 2) due to increased electrostatic repulsions. Alternatively, succinylation also increases calcium binding with moderate affinity (Figure 3), which leads to at a DS of 43% even to a significant fortification of the gel elasticity (Table 3). Obviously, calcium binding not only affects the molecular interactions but also acts as a fortifier of strand−strand interactions.

For technological impact it is most relevant to study the gel responses to large deformation from a product storage, handling, and oral processing perspective. In the evaluation of the strain required to create sufficient stress in the gel to result in fracture events (Table 4), it can be observed that for reference gelatin the addition of calcium has no effect but that the stress evoked by the applied strain leading to fracture diminishes 10−15% with increasing calcium concentration. This situation is different for the gelatin with a DS of 82% (Table 4), where in the absence of calcium almost half the strain is sufficient to initiate fracture compared to the reference material. Calcium restores this property and even to strains beyond that observed for the reference material. Interestingly the fracture stress remains, independent of the calcium concentration, approximately 30% lower than that of the reference material.

The picture that emerges is that increased electrostatics increases the structural heterogeneity in the gel, thereby lowering the fracture strain. The addition of calcium "glues" the strands together, smooths the heterogeneities, and thereby reduces the brittleness of the material. As the fracture stress is the result of unzipping of the triple helices and dissociation of the strands, this is less affected by electrostatics or the presence of calcium.

Table 4. Responses to Large Deformation of 3% w/v Reference and 82% Succinylated Gelatin Gels for Various Calcium Concentrations[a]

					stress relaxation	
	[calcium] (mM)	fracture stress (kPa)	fracture strain (−)	RE (%)	time[b] (s)	fraction[c] (−)
reference	0	27.5 ± 1.6	0.76 ± 0.08	94.6 ± 0.10	8.6	0.06
	4	25.2 ± 1.4	0.77 ± 0.12	94.5 ± 0.11	8.4	0.05
	10	25.7 ± 1.5	0.79 ± 0.11	94.9 ± 0.03	8.5	0.06
	20	24.2 ± 1.6	0.81 ± 0.09	94.9 ± 0.06	8.5	0.06
82% DS	0	16.2 ± 1.8	0.42 ± 0.11	93.3 ± 0.07	7.4	0.10
	4	18.3 ± 1.2	0.77 ± 0.08	93.9 ± 0.11	7.7	0.11
	10	20.3 ± 1.5	0.86 ± 0.10	94.2 ± 0.06	8.2	0.10
	20	19.7 ± 1.4	0.94 ± 0.04	94.4 ± 0.07	8.2	0.07

[a]The compression speed is 1 mm/s and the experiments were performed at room temperature. The RE data are obtained from a compression−decompression cycle (up to a 20% strain), and the stress relaxation data are obtained from a compression and strain-hold experiment. [b]Estimated error ±0.3. [c]Estimated error ±0.02.

DOI: 10.1021/acs.jafc.5b01962
J. Agric. Food Chem. 2015, 63, 7058−7065

Gelatins are renowned for their high recoverable energy and elastic nature.[13] As these rheological properties have been related to texture perception of food products,[16,17] it is essential to evaluate how these varied electrostatics in the network assembly and calcium-induced network stabilization affect these mechanical responses. Table 4 presents the recoverable energies (from a compression−decompression cycle up to a 20% compressive strain, so below the observed fracture strains) for reference gelatin and for a gelatin with a DS of 82% as the two extreme cases. It can be observed that rheological response is not affected at all by increased electrostatic repulsions between the individual network strands. Moreover, also the addition of calcium has no impact. For the gelatins with the other DS values comparable RE values between 93 and 95% were obtained, and none of the samples showed a sensitivity toward calcium (results not shown). These results emphasize that the RE is not related to the elastic modulus or gel stiffness or a network characteristic, but set by the energy dissipation modes as suggested in the literature.[13]

As gelatin networks have a fine coarseness with typical mesh sizes on the order 30−100 nm,[18] their water-holding capacity is consequently close to 100%.[19] This indicates that the enclosed liquid phase in the gel deforms along with the protein network, not giving rise to significant energy dissipation by friction caused by serum flow through the protein network.[13] Also, the occurrence of (micro)fractures during deformation is not likely as the fracture stress is only marginally affected by succinylation or by the addition of calcium. As stress relaxation, related to spontaneous rearrangements of the microstructure upon deformation of the material, was shown to be a dominant energy dissipation mode for these gels,[13] the relevant stress relaxation times and their corresponding fraction of the total applied stress have been determined. The results are presented in the last two columns of Table 4. It can be observed that both the relaxation times and the corresponding fractions are not affected by either succinylation or the addition of calcium. A relaxation time around 8 s for 6% of the total stress (the average numbers from Table 4) implies that this dissipation mode, acting from the very start of the deformation applied (total cycle for compression−decompression takes 8 s), accounts for about 2% of the energy loss during the RE measurement. Apparently, stress relaxation is set by the inherent molecule and maybe to a limited extent by the ability to adopt triple helices, rather than strand−strand interactions, of the network. This explains why the RE is not affected by the succinylation or the restored storage modulus by the addition of calcium.

In summary, in this work it is shown that extensive succinylation of gelatin does not prohibit gel formation. Properties such as helix propensity, gelling/melting temperatures, and concomitant transition enthalpy changes and gel strength are shown to become calcium sensitive by high degrees of succinylation. The presence of relatively low concentrations of calcium restores these material properties mostly to those of nonmodified gelatin. However, although succinylation has a major impact on the brittleness of the gels formed and the addition of calcium makes the material even less brittle compared to the nonmodified gelatin, the modification has no impact on the energy balance in the gel, where all of the energy applied is stored in the material. This insight allows food industries to tailor gelatins for texture attributes.

AUTHOR INFORMATION

Corresponding Author

*(H.H.J.J.) Mail: TI Food and Nutrition, P.O. Box 557, 6700 AN, Wageningen, The Netherlands. Phone: +31 317 486160. E-mail: dejongh@tifn.nl.

Funding

We gratefully acknowledge CONACYT for providing funding for D.B.A.

Notes

The authors declare no competing financial interest.

ACKNOWLEDGMENTS

We thank Eefjan Timmerman for technical and Peng Cho for experimental support. We acknowledge Inge Gazi for performing initial mechanical deformation experiments.

REFERENCES

(1) Tzaphlidou, M.; Chapman, J. A.; Meek, K. M. A study of positive staining for electron microscopy using collagen as a model system. I. Staining by phosphotungstate and tungstate ions. *Micron* **1982**, *13*, 119−131.

(2) Johnston-Banks, F. A. In *Food Gels*; Harris, P., Ed.; Elsevier: New York, 1990; pp 233−289.

(3) Schreiber, R.; Gareis, H. In *Gelatin Handbook—Theory and Industrial Practice*; Schreiber, R., Gareis, H., Eds.; Wiley-VCH: Weinheim, Germany, 2007; pp 63−71.

(4) van Vliet, T. On the relation between texture perception and fundamental mechanical parameters for liquids and time dependent solids. *Food Qual. Pref.* **2002**, *13*, 227−236.

(5) van Vliet, T.; Walstra, P. In *Food Colloids and Polymer, Stability and Mechanical Properties*; Royal Society of Chemistry: Cambridge, UK, 1993; pp 175−190.

(6) Gornall, J. L.; Terentjev, E. M. Helix-coil transition of gelatin: helical morphology and stability. *Soft Matter* **2008**, *4*, 544−549.

(7) Baigts Allende, D.; de Jongh, H. H. J. Ligation of pork skin gelatin with glucose moieties affects the junction zones in gelled networks. *Food Hydrocolloids* **2015**, *49*, 82−88.

(8) Kosters, H. A.; Broersen, K.; de Groot, J.; Simons, J. W. F. A.; Wierenga, P. A.; de Jongh, H. H. J. Chemical processing as a tool to generate ovalbumin variants with controlled stability. *Biotechnol. Bioeng.* **2003**, *84*, 61−70.

(9) Church, F. C.; Swaisgood, H. E.; Porter, D. H.; Catignani, G. L. Spectrophotometric assay using *o*-phthaldialdehyde for determination of proteolysis in milk and isolated milk proteins. *J. Dairy Sci.* **1983**, *66*, 1219−1227.

(10) Simons, J. W. F. A.; Kosters, H. A.; Visschers, R. W.; de Jongh, H. H. J. Role of calcium as trigger in thermal *β*-lactoglobulin aggregation. *Arch. Biochem. Biophys.* **2002**, *406*, 143−152.

(11) Mekmene, O.; Gaucheron, F. Determination of calcium-binding constants of caseins, phosphoserine, ctrate and pyrophosphate: a modelling approach using free calcium measurement. *Food Chem.* **2011**, *127*, 676−682.

(12) Djabourov, M.; Leblond, J.; Papon, P. Gelation of aqueous gelatin solutions: I. Structural investigation. *J. Phys. (Paris)* **1988**, *49*, 319−332.

(13) de Jong, S.; van Vliet, T.; de Jongh, H. H. J. The contribution of time-dependent stress relaxation in protein gels to the recoverable energy that is used as tool to describe food texture. *Mech. Time-Dependent Mater.* **2015**, in press.

(14) Rbii, K.; Violleau, F.; Brambati, N.; Buchert, A.; Surel, O. Decrease of available lysine in thermally treated gelatin followed by LC−UV: influence on molar mass and ability to helixes' formation. *Food Hydrocolloids* **2011**, *25*, 1409−1412.

(15) Dardelle, G.; Subramaniam, A.; Normand, V. Determination of covalent cross-linker efficacy of gelatin strands using calorimetric analyses of the gel state. *Soft Matter* **2011**, *7*, 3315−3322.

DOI: 10.1021/acs.jafc.5b01962
J. Agric. Food Chem. 2015, 63, 7058−7065

(16) Peleg, M. Considerations of a general rheological model for the mechanical behavior of viscoelastic solid food materials. *J. Texture Stud.* **1976**, *7*, 243−255.
(17) van den Berg, L.; Carolas, A. L.; van Vliet, T.; van der Linden, E.; van Boekel, M. A. J. S.; van de Velde, F. Energy storage controls crumbly perception in whey proteins/polysaccharide mixed gels. *Food Hydrocolloids* **2008**, *22*, 1404−1417.
(18) Okuyama, K.; Xu, X.; Iguchi, M.; Noguchi, K. Revision of collagen molecular structure. *Biopolymers* **2006**, *84*, 181−191.
(19) Urbonaite, V.; de Jongh, H. H. J.; van der Linden, E.; Pouvreau, L. Origin of Water Loss from Soy Protein Gels. *J. Agric. Food Chem.* **2014**, *62*, 7550−7558.

DOI: 10.1021/acs.jafc.5b01962
J. Agric. Food Chem. 2015, 63, 7058−7065

Table 1. Molecular Structures of the Cyanidin Compounds That Comprise the Black Carrot Anthocyanin Mixture and Proton-Numbering Schemes Used in the Assignment of NMR Spectra

Name	Anthocyanin Structure	Sugar Structure	Retention Time (min)	m/z [M^+]
1 Cyanidin-3-xy-glc-galactoside	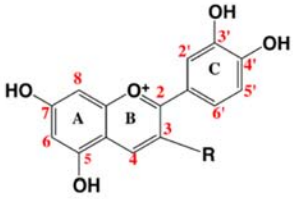	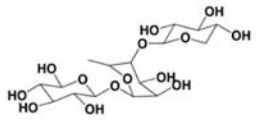	15.4	743.2
2 Cy-3-xy-galactoside		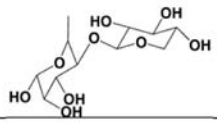	16.3	581.2
3 Cy-3-sin-xy-glc-galactoside		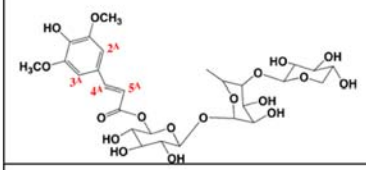	17.1	949.2
4 Cy-3-fer-xy-glc-galactoside		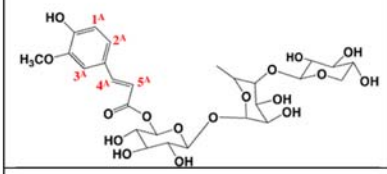	17.6	919.2
5 Cy-3-coum-xy-glc-galactoside		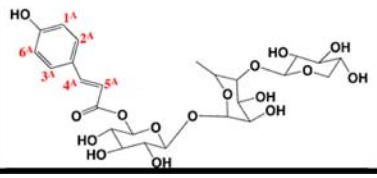	18.2	889.2

also suggested that coumarin 3,5-diglycosides are common degradation products for anthocyanin 3,5-diglycosides.[4,17]

During heat exposure, the stability of anthocyanins depends upon the composition and the characteristics of the medium, with pH playing an important role. Anthocyanins adopt different chemical structures, which exist in pH-dependent equilibrium.[18−20]

Some studies indicate that acylated anthocyanins, mainly those with planar aromatic substituents, exhibit greater stability, especially when kept in aqueous solutions, and play an important role in increasing the thermal stability of the dye compared to the non-acylated counterparts. It is believed that the aromatic residues of the acyl groups stack with the pyrylium ring of the flavylium cation, which reduces the likelihood of the hydration reaction in the vulnerable C-2 and C-4 positions.[21−25]

Black carrot consists of a high ratio of monoacylated anthocyanins.[10−13] The question that arises is are black carrot acylated anthocyanins more stable compared to the non-acylated anthocyanins? In other words, does the structure of anthocyanins affect the stability?

Previous studies of black carrot have typically used HPLC and ultraviolet/visible (UV/vis) analysis for quantification of the compounds, but there are some weaknesses to these techniques. For HPLC, there are concerns about pH-dependent variation in the wavelengths of absorption maxima and the values of absorption coefficients, leading to unreliable quantification. Using UV/vis spectroscopy alone, it is impossible to resolve and quantify the separate compounds; only the total anthocyanin concentration can be approximated.

In the present study, proton nuclear magnetic resonance (^{1}H NMR) spectroscopy and signal integration was used to investigate the thermal degradation of the individual anthocyanin compounds of a commercial black carrot concentrate and the effect of pH on this degradation. Complementary UV/vis spectroscopy and CIE color space measurements[26] were used to follow color degradation. Separation of the mixture into individual compounds and assignment of each compound followed by integration of ^{1}H NMR signals in spectra of the mixtures were the steps used. The resulting understanding of the relative stabilities of the different compounds, in particular, the role of structure (acylation) on the stability, should be valuable in developing future strategies to enhance the stability of this commercially available natural colorant.

MATERIALS AND METHODS

Plant Materials. Commercial concentrate of black carrot (*Daucus carota* L.) was supplied by Naturex, Ltd. (manufacturer's code, COPG4167; sample code, G00017). The concentrate was stored at −18 °C.

Solvents and Reagents. Deuterated NMR solvents were purchased as follows: methanol-d_4 from Sigma-Aldrich (St. Louis,

DOI: 10.1021/acs.jafc.5b02543
J. Agric. Food Chem. 2015, 63, 7066−7073

MO), trifluoroacetic acid-*d* from Sigma-Aldrich (St. Louis, MO) or Cambridge Isotope Laboratories (CIL) (Tewksbury, MA). Hydrochloric acid with specific gravity (SG) of 1.18 (≈37%), sodium hydroxide (97%), and sodium dihydrogen orthophosphate dihydrate were purchased from Fisher Scientific (U.K.). Disodium hydrogen phosphate dihydrate and citric acid monohydrate were obtained from Sigma-Aldrich (St. Louis, MO). Acetonitrile and water for HPLC were purchased from VWR International. All of the HPLC solvents were of analytical grade. C-18 cartridges with a vacuum of 35 cm^3 (10 g) (WAT043345) were purchased from Waters (Ireland).

Sample Preparation. A two-step extraction process was applied to the black carrot sample to remove non-anthocyanin compounds. A total of 100 g of black carrot concentrate was mixed with 150 mL of chloroform in a separating funnel and left overnight. The aqueous phase was collected and further purified by solid-phase extraction,[27] using mini columns [C-18 cartridges with a vacuum of 35 cm^3 (10 g) (WAT043345)] purchased from Waters (Ireland). The eluent of the extraction (methanolic mobile phase) was concentrated in a rotary evaporator (IKA RV 10 basic) at 25 °C and further dried under vacuum, using liquid nitrogen, yielding 5 g of powder.

HPLC. A total of 100 mg of the extracted black carrot powder (see the Sample Preparation) was dissolved in 1 mL of distilled water. Semi-preparative reverse-phase (RP)-HPLC was performed on a HP1100 system equipped with a semi-preparative C_{18} Agilent column Eclipse XDB-C18 (9.4 × 250 mm inner diameter, 5 μm) at a constant temperature of 20 °C and a flow rate of 2 mL/min. A mobile-phase gradient was used for elution; eluent A consisted of water with 0.1 mL of formic acid, and eluent B consisted of acetonitrile (ACN) and water with 0.1% formic acid (1:1). The elution profile was 10% B at 0 min, 35% B at 10 min, 50% B at 35 min, 80% B at 40 min, and 10% B at 45 min. The injection volume was 20 μL, and the detector was set at 520 nm. The fractions were transferred into vials, and mass spectrometric analysis was performed on an Agilent Series 1100 HPLC system fitted with an electrospray ionization (ESI) source. Repeated injections were performed, and the isolated fractions were combined until a mass of 2−5 mg per fraction was obtained. The purified fractions were frozen using dry ice and acetone and then dried under vacuum on a freeze drier.

Heating Experiments. A domestic oven (Dēlonghi E012001W) was used to heat treat aqueous solutions with pH values of 3.6, 6.8, and 8.0. Citric acid/phosphate and phosphate buffers were used to adjust the pH. Hydrochloric acid and sodium hydroxide were also used where necessary for adjusting the pH, to avoid salts that interfere with the HPLC column. The samples were heated in an oven at around 180 °C, to maintain the aqueous sample temperature at 100 °C, for periods up to 100 min. A 60 min heat treatment was also applied to samples for which the pH ranged between 3.4 and 8.2.

Powder samples of black carrot were prepared by dissolving black carrot in aqueous solutions, adjusting the pH to 3.6 and 6.8, followed by freeze drying. The powders were then exposed to heat in a high-performance furnace [Carbolite (U.K.) at 180 °C].

NMR Spectroscopy. A mixed solvent consisting of 10 g of MeOH-d_4/0.5 mL of trifluoacetic acid-*d* (TFA-*d*) was used for all NMR measurements. The structures of the compounds isolated by RP-HPLC were determined using one-dimensional (1D) ^{1}H NMR analysis on a Bruker 500 MHz spectrometer (10 mg in 0.8 mL of MeOH/TFA) in combination with two-dimensional (2D) correlation spectroscopy (COSY) NMR to assign aromatic peaks. High-resolution ^{1}H NMR spectra of the purified (unseparated) black carrot (10 mg in 0.8 mL of MeOH/TFA) were acquired on a Bruker 800 MHz spectrometer. In addition, ^{1}H NMR spectra (800 MHz) used for integration of the samples exposed to heat were also acquired (10 mg in 0.8 mL of MeOH/TFA).

UV/vis Spectroscopy. Absorption spectra in the visible region (300−800 nm) were recorded using a Jasco V-670 series spectrophotometer. Solutions (40 μL of sample solution in 3 mL of citric acid/phosphate buffer) were contained in a quartz cell (d = 1 cm), and the data were collected using Spectra Manager II software.

Color Measurements. The Spectra Manager II software was used to calculate the CIE lab coordinates using the Jasco V-670 series spectrophotometer (Tokyo, Japan). Chroma value C^* [$C^* = (a^{*2} + b^{*2})^{1/2}$] and hue angle $h°$ [$h° = \arctan(b^*/a^*)$] were calculated from parameters a^* (from green to red) and b^* (from blue to yellow) values. The hue angles were expressed on a 360° color wheel, in which 0° and 360° represent red, 90° represents yellow, 180° represents green, and 270° represents blue. The illuminant was D65, and the observer angle was 10°. The change in color produced by heat treatment was calculated using the $\Delta E^* = [(\Delta L^*)^2 + (\Delta a^*)^2 + (\Delta b^*)^2]^{1/2}$ equation at pH 3.6, 6.8, and 8 for several time intervals.[26]

RESULTS AND DISCUSSION

Isolation and Structure Characterization: NMR Studies. As shown in Figure 1, even after purification by solid-phase extraction, the NMR spectrum of the black carrot mixture contains many overlapping peaks, preventing the assignment of individual compounds. The extraction process has simplified the aromatic region (6.2−9 ppm), as shown by comparison to Figures S1 and S2 of the Supporting Information, but further information on the individual compounds is needed to enable assignment of the aromatic protons.

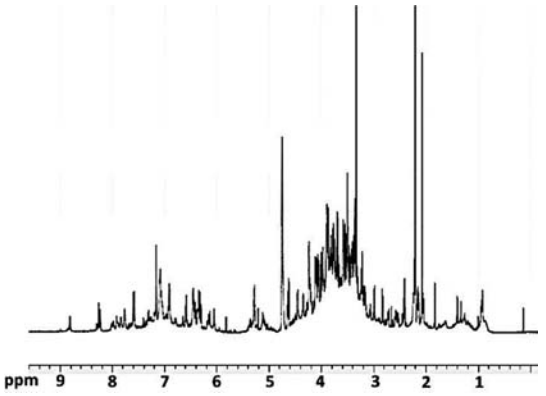

Figure 1. ^{1}H NMR spectrum (800 MHz) of black carrot mixture following purification by solid-phase extraction.

Montilla et al. describe that, for different black carrot species, the composition of anthocyanins can vary.[11] Using RP-HPLC, five major anthocyanin compounds of black carrot were isolated, as shown in the chromatogram in Figure 2. Mass spectrometric analysis indicated that each fraction corresponds to a particular anthocyanin molecule (identifiable as the molecular ion), as summarized in Table 1 (see Figures S3−S7 of the Supporting Information). These results are consistent with previous studies of the composition of black carrot.[10−13]

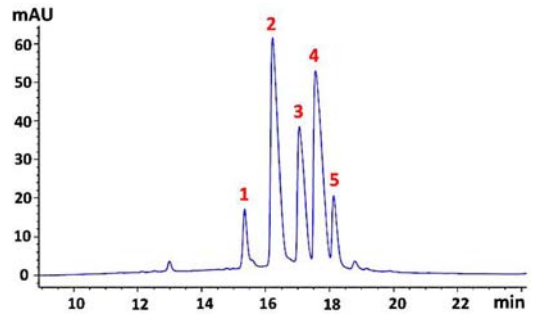

Figure 2. HPLC profile of anthocyanin compounds of the specific black carrot species: (**1**) Cy-3-xy-glc-galactoside, (**2**) Cy-3-xy-galactoside, (**3**) Cy-3-sin-xy-glc-galactoside, (**4**) Cy-3-fer-xy-glc-galactoside, and (**5**) Cy-3-coum-xy-glc-galactoside.

DOI: 10.1021/acs.jafc.5b02543
J. Agric. Food Chem. 2015, 63, 7066−7073

1D ^{1}H NMR and 2D COSY NMR analyses (see Figures S3–S7 of the Supporting Information) enabled assignment of each aromatic proton of each compound (Tables 1 and 2). The

Table 2. ^{1}H NMR Chemical Shifts of Aromatic Protons for the Anthocyanin Fractions in MeOH-d_4/TFA-d[a]

flavilium aglycone						
compound	H-4	H-6	H-8	H-2′	H-5′	H-6′
1	9.016	6.929	6.696	8.126	7.052	8.302
2	9.010	6.918	6.672	8.101	7.046	8.307
3	8.522	6.652	6.530	7.980	7.054	8.153
4	8.540	6.656	6.535	7.976	7.077	8.097
5	8.557	6.646	6.596	7.982	7.084	8.086
acylated aromatic region						
compound	H-1^A	H-2^A	H-3^A	H-4^A	H-5^A	H-6^A
1						
2						
3		6.227	6.227	6.198	7.338	
4	6.376	6.603	6.508	6.163	7.350	
5	6.393	6.977	6.799	6.153	7.390	7.064

[a]See Table 1 for the proton-numbering scheme.

chemical shifts are consistent with the chemical shifts assigned for the anthocyanins from cell suspension culture of *D. carota* L. in the study by Gläßgen et al.[28] The NMR results from the present study (Table 2) show that compounds **1** and **2** are the non-acylated compounds and compounds **3**–**5** are the acylated anthocyanin compounds, confirming results from previous studies. It can also be seen that the presence of sinapic, ferulic, and coumaric acids on the glucose moiety has an effect on the chemical shift of the cyanidin protons. For example, the chemical shifts of H-4 in the non-acylated compounds are in the range of δ = 9.016–9.010, while those for the acylated compounds appear at δ close to 8.540. The same effect is seen on the chemical shifts of the H-6 and H-8 protons. In the study by Gläßgen et al., a low-frequency shift of H-4 protons of black carrot anthocyanins acylated with sinapic, ferulic, and coumaric acids compared to the non-acylated counterparts was also noted.[28] Also, Dougall et al. described a marked effect of cinnamic or benzoic acids on the chemical shifts of the cyanidin H-4, H-6, and H-8 protons in the acylated compounds, providing evidence for NMR shifting caused by acylation.[29]

The aromatic region of the black carrot mixture could be assigned completely with reference to the NMR spectra of the five separated compounds. Each signal in the spectrum of the mixture can be identified with a single signal or with overlapping signals from the spectra of the five compounds, as illustrated in Figure 3. In the region between δ = 6.0 and 7.5 ppm, there is considerable overlap between peaks of the individual compounds in the spectrum of the mixture. On the other hand, in the region between δ = 7.8 and 9 ppm, the individual compound peaks are generally well-resolved. The small intensity doublets in the region δ = 7.55, highlighted in red, and δ = 6.25 (overlapped), are attributed to minor impurities and also appeared in the spectrum for compound **5**.

Thermal Degradation Studies. The clear assignment of the NMR peaks in the black carrot mixture enables the fractional concentration of compounds **1**–**5** to be unambiguously determined and to be followed during thermal degradation. The well-resolved region between δ = 8.4 and 9 ppm was used for integration to determine the composition of the mixture and to quantify the degradation of each compound. Specifically, the integrals were determined for the combined H-4 proton signals of compounds **1** and **2** at δ = 9 ppm and the individual H-4 proton signals of the other three compounds in the region around 8.5 ppm. Overall, the expected general trend was noticed; the longer the exposure to heat, the more the integrated NMR signals of the compounds were reduced. However, it was also apparent that the integrals of the individual compounds were decreasing at different rates, resulting in variation in the composition of the mixture during thermal degradation.

Before examining the NMR results in detail, we first describe the general degradation behavior observed in the UV/vis spectra of the anthocyanin mixture in solution and as a solid powder.

UV/vis Spectroscopy and Color Measurements: Black Carrot in Solution. Exposure to heat at pH 3.6 for 100 min resulted in an increase in lightness, L^*, by 7.99 units, insignificant change in the hue angle h°, and a decrease in the chroma, C^*, by 16.13 units (see Table S1 of the Supporting Information). This indicated that the color of the anthocyanins was fading with a slight change of the hue. The UV/vis spectra (Figure 4a) showed a decrease in absorbance, but λ_{max} was not notably shifted. Heat treatment at pH 6.8 for 100 min also resulted in an increase in lightness (8.65 units) and a decrease in chroma (22.26 units), but there was also an increase in the hue angle by 18.12 units (see Table S1 of the Supporting Information). Therefore, in neutral conditions, the color not only faded but the hue also changed from red to a more orange

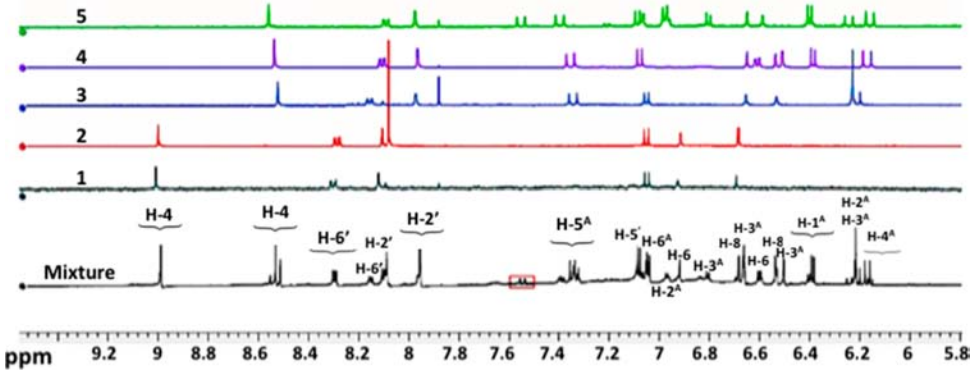

Figure 3. NMR spectra of black carrot mixture (bottom, black) and the HPLC compounds **1**–**5**. The singlet at δ = 8.08 ppm of compound **2** and δ = 7.9 ppm of compounds **3**–**5** are solvent residual signals.

DOI: 10.1021/acs.jafc.5b02543
J. Agric. Food Chem. 2015, 63, 7066–7073

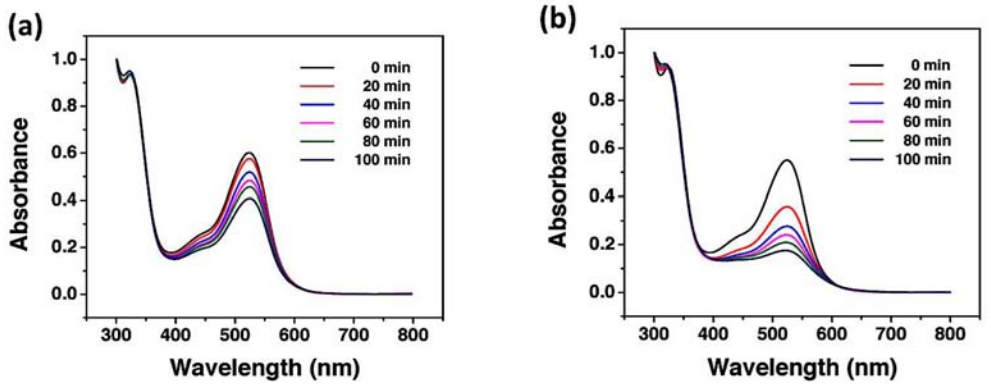

Figure 4. UV/vis spectra as a function of time for heat treatment of black carrot solution at (a) pH 3.6 and (b) pH 6.8.

shade. The UV/vis spectra (Figure 4b) showed both a decrease in absorbance and a slight bathochromic shift in λ_{max}. To explore the pH dependence of these effects, the UV/vis spectra of the black carrot heat treated for 60 min at a range of pH values, from 3.4 to 8.2, were recorded. As shown in Figure 5,

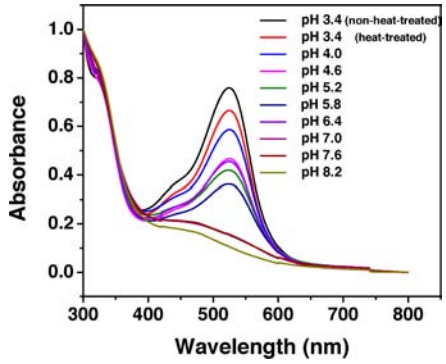

Figure 5. UV/vis spectra as a function of pH for heat treatment of black carrot solution for 60 min.

with increasing pH, λ_{max} shifted bathochromically and the absorbance maximum was noticeably decreased. Observing the CIE lab parameters, the lightness gradually enhanced by 25.89 units, h° increased dramatically to 70.43 units, and the color of neutral and more basic solutions decolorized and gradually turned brown. The color saturation decreased 40.52 units (see Table S2 of the Supporting Information). It is clear from the UV/vis spectra that there is more rapid degradation of the anthocyanins at higher pH values. This can be related to the different forms of the anthocyanins present as a function of pH; in the case of the acidic solution, more of the stable flavilium cationic form of anthocyanin is present, whereas in neutral conditions, the percentage of less stable chalcone, carbinol, and quinonoidal forms will be increased.

Black Carrot Powders. To assess the effect of pH on solid-state samples, the pH was adjusted to 3.6 and 6.8 before freeze drying. After 60 min of heat treatment, the colors showed a slight increase in lightness (L^*) by 2.73 and 5.03 units, respectively. The hue value change was negligible for both cases, and the chroma (C^*) value decreased by 7.92 and 12.47 units, respectively (see Table S1 of the Supporting Information). The difference in the absolute absorbance between the two samples is also negligible in λ_{max} of the UV−vis spectra (panels a and b of Figure 6). The UV/vis spectra show that, at pH 3.6, the thermal stabilities of the solution and powder samples are similar; however, at pH 6.8, the powder shows much higher stability than the solution. In comparison of the two powder samples, it is evident that the pH prior to freeze drying has little effect on the stability.

NMR Spectroscopy. Integration of the H-4 proton peaks in the aromatic region of NMR spectrum (δ = 8.4−9), as indicated in Figure 3, enabled the percentage of each compound in the anthocyanin mixture to be quantified as a function of the heating time, over a range of pH. The results are presented in Figures 7−11. As shown in the insets of the figures, the overall degradation of the total anthocyanin content determined from the NMR integrals follows a similar trend to

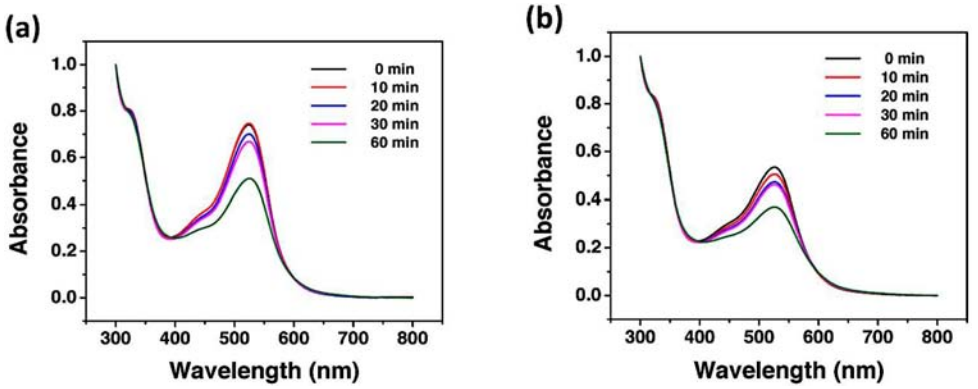

Figure 6. UV/vis spectra as a function of time for heat treatment of black carrot powder prepared by freeze drying of solution at (a) pH 3.6 and (b) pH 6.8.

DOI: 10.1021/acs.jafc.5b02543
J. Agric. Food Chem. 2015, 63, 7066−7073

that derived from the UV/vis absorbance. Notably, however, the absorbance measurements imply a lesser extent of degradation than that quantified by the NMR data. This can be attributed to residual absorbance, in this spectral region, by the decomposition products, which persist after degradation of the primary anthocyanin compounds. Thus, the NMR data are able to give a better quantitative measurement of degradation than the commonly used UV/vis data.

Black Carrot in Solution. As shown in Figure 7, at pH 3.6, all compounds showed substantial degradation after heating for

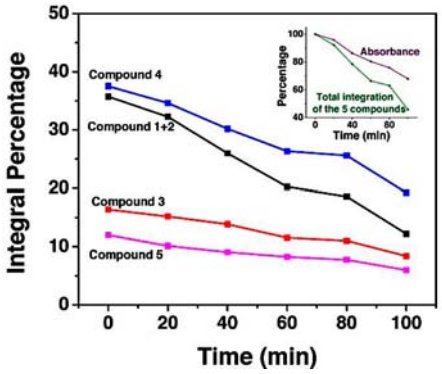

Figure 7. Percentage of each compound (determined from NMR integrals) in black carrot solution as a function of the heating time, at pH 3.6. The inset compares the heating time dependence of the total anthocyanin content derived from NMR data (green) to that derived from UV/vis data (purple). The lines are a guide to the eye.

100 min but there was not complete destruction; the total anthocyanin concentration was decreased by about 60%. In contrast, at pH 6.8, there was almost complete thermal degradation after 100 min, with only about 10% of the total anthocyanin content remaining. These observations are consistent with the expectation that the anthocyanins are more stable in acidic conditions.[18] In basic conditions (pH 8), we found complete degradation of black carrot solution after 48 h of storage at room temperature in the dark (see Figure S10 of the Supporting Information).

The rate of degradation of the anthocyanin compounds can be assessed by considering the percentage decrease in the concentration after 60 min of heating. At pH 3.6, the non-acylated compounds, **1** + **2**, showed the greatest rate of decomposition, resulting in a 43% decrease in the concentration in 60 min, compared to a decrease of about 30% for each of the acylated compounds (Figure 7). At pH 6.8, the rate of decomposition of all of the compounds was accelerated. However, the non-acylated compounds (**1** + **2**) decomposed more slowly than the acylated compounds; the former showed a 66% drop in concentration after 60 min compared to a 75% drop for the latter (Figure 8).

The effect of pH on the composition of the thermally degraded anthocyanin mixture after heating for 1 h is illustrated in Figure 9. It is evident that the stability of all compounds decreases significantly with increasing pH in the range of pH 3.4−5.8. There is little pH dependence between pH 5.8 and 6.4 (a slight increase in stability is seen). An abrupt drop-off in stability occurs as neutral pH is approached, with complete decomposition at pH 7 and above.

To summarize, the thermal stability of all of the anthocyanin compounds is greater under acidic conditions, but the relative stability of acylated and non-acylated compounds is pH-

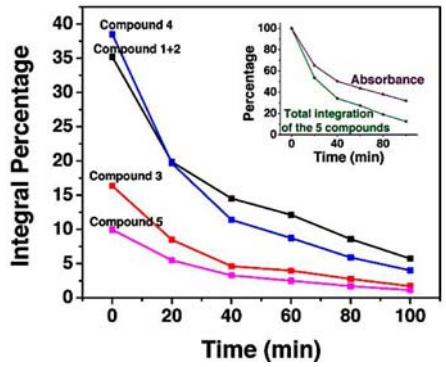

Figure 8. Percentage of each compound (determined from NMR integrals) in black carrot solution as a function of heating time, at pH 6.8. The inset compares the heating time dependence of the total anthocyanin content derived from NMR data (green) to that derived from UV/vis data (purple). The lines are a guide to the eye.

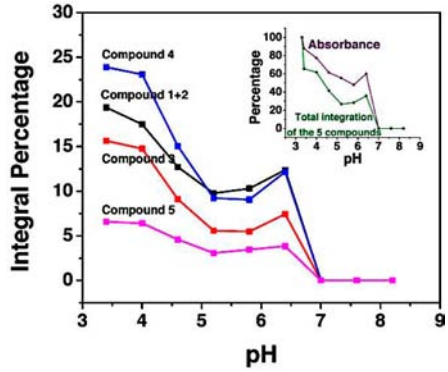

Figure 9. Percentage of each compound (determined from NMR integrals) in black carrot solution heated for 60 min, as a function of pH. The inset compares the pH dependence of the total anthocyanin content derived from NMR data (green) to that derived from UV/vis data (purple). The lines are a guide to the eye.

dependent. At low pH, the acylated compounds are more stable than the non-acylated compounds but become less stable at higher pH. This is contrary to the general consensus in the literature that acylation enhances the stability of anthocyanins at higher pH by protecting the flavilium cation from nucleophilic attack by water molecules at C-2 and C-3 positions.[21−24,30] However, previous studies have been based on the comparison of the color stabilities of anthocyanin pigments with different degrees of acylation rather than direct quantitation of individual acylated and non-acylated compounds.[21−24,30]

Black Carrot Powders. To investigate the thermal degradation of black carrot in the solid state, powder samples were prepared by freeze drying solution samples of pH 3.6 and 6.8. After heating, the solid samples were dissolved and NMR spectra were recorded.

The thermal degradation of powder and solution samples, after 1 h of heating, is compared in Figures 10 and 11 (note that the solids were effectively heated at a higher temperature because no evaporation was occurring). For the samples at pH 3.6 (Figure 10), the degradation properties of the powder are similar to those of the solution. At pH 6.8, there is only a small overall increase in degradation in the powder compared to pH 3.6. In solution at pH 6.8, however, the powder is significantly more stable than in solution. With regard to the individual

DOI: 10.1021/acs.jafc.5b02543
J. Agric. Food Chem. 2015, 63, 7066−7073

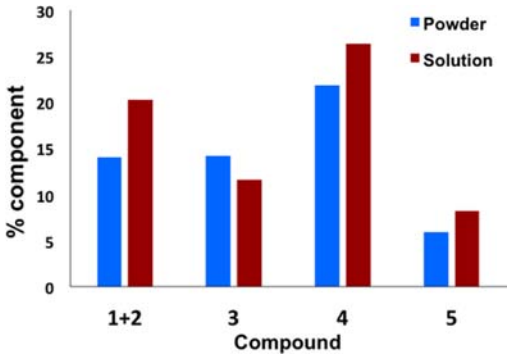

Figure 10. Comparison of the effect of heating on a solution sample (red) at pH 3.6 and a powder sample (blue) freeze dried at pH 3.6. The percentage of each compound (determined from NMR integrals) in each sample after 1 h of heating is shown (the solution sample was heated in a domestic oven at around 180 °C, and the solid sample was accurately heated in a furnace at 180 °C).

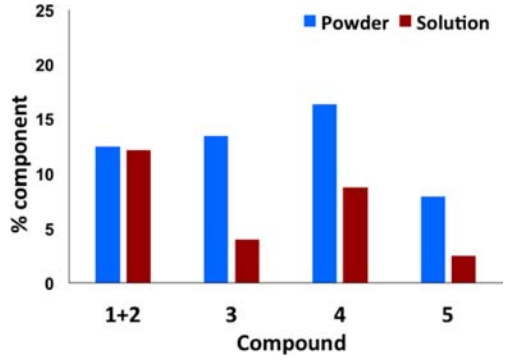

Figure 11. Comparison of the effect of heating on a solution sample (red) at pH 6.8 and a powder sample (blue) freeze dried at pH 6.8. The percentage of each compound (determined from NMR integrals) in each sample after 1 h of heating is shown (the solution sample was heated in a domestic oven at around 180 °C, and the solid sample was accurately heated in a furnace at 180 °C).

anthocyanins, it appears that changing the pH from acidic to neutral prior to freeze drying has little effect on the relative stability of the acylated and non-acylated compounds in the resulting solid sample. This is consistent with the UV/vis results (*vide supra*). It is also notable that, at pH 6.8, the stability of the acylated compounds is markedly higher in the powder than in the solution. These observations imply differences in the degradation mechanism between solid and aqueous conditions.

To conclude, the anthocyanin compounds in a black carrot concentrate were successfully isolated using HPLC, and their chemical shifts were fully assigned using 1D ^{1}H NMR and 2D COSY NMR. The UV/vis and the CIE lab color measurements showed an increased degradation with increasing the pH and heating time. NMR measurements confirmed these general trends. The summed NMR integrals of the five anthocyanin compounds followed a similar trend to the UV/vis absorbance. However, the UV/vis data underestimate the extent of degradation, as a result of the residual absorbance of decomposition species, making the NMR method more accurate. Furthermore, integration of the H-4 proton peaks between the region δ = 8.4 and 9 enabled percentage degradation of the individual compounds of the mixture to be quantified.

The NMR results show that, in acidic aqueous solution, there is enhanced stability of the monoacylated compounds, whereas in neutral conditions, their stability is lower compared to the non-acylated compounds. The thermal stability of powder samples, produced by freeze drying solutions at pH 3.6 and 6.8, was similar, and the heat stability of the powders at pH 6.8 was superior to that of the solutions.

It is important to emphasize the benefits of NMR for studying individual anthocyanin compounds, avoiding factors such as the pH dependence of the absorption, interfering absorbing compounds, and only approximate knowledge of molar absorption coefficients at different pH values, which are severe disadvantages using the common methods of HPLC and UV/vis. Although there are some limitations, such as overlapping chemical shifts for the compounds **1** and **2**, reliable information can be gleaned on the relative stability of the different anthocyanins. The observation of an unexpected effect of pH on the relative stability of monoacylated and non-acylated anthocyanins emphasizes the utility of NMR in providing insight into the degradation of multi-compound natural colorants, such as black carrot.

■ ASSOCIATED CONTENT

Ⓢ Supporting Information

^{1}H NMR spectra of the unpurified and partly purified black carrot mixture, 1D and 2D COSY ^{1}H NMR and MS of the separated compounds, tables of the CIE lab color measurements, description of the integral quantification, ^{1}H NMR spectra used for integration, and HPLC data (PDF). The Supporting Information is available free of charge on the ACS Publications website at DOI: 10.1021/acs.jafc.5b02543.

■ AUTHOR INFORMATION

Corresponding Author

*Telephone: +44-131-6504755. E-mail: neil.robertson@ed.ac.uk.

Funding

The authors thank the Engineering and Physical Sciences Research Council for a Scottish Enterprise/EPRSE Industrial Case Award (11330371).

Notes

The authors declare no competing financial interest.

■ ACKNOWLEDGMENTS

Open data: http://dx.doi.org/10.7488/ds/279.

■ REFERENCES

(1) Chapman, S. *Guidelines on Approaches to the Replacement of Tartazine, Allura Red, Ponceau 4R, Quinoline Yellow, Sunset Yellow and Carmoisine in Food and Beverages*; Campden BRI: Chipping Campden, U.K., 2011; http://www.food.gov.uk/sites/default/files/multimedia/pdfs/publication/guidelinessotonsixcolours.pdf.

(2) Jackman, R.; Smith, J. Anthocyanins and betalains. In *Natural Food Colorants*; Hendry, G. A. F., Houghton, J. D., Eds.; Springer: New York, 1996; pp 244−309.

(3) Sadilova, E.; Carle, R.; Stintzing, C. F. Thermal degradation of anthocyanins and its impact on colour and in vitro antioxidant capacity. *Mol. Nutr. Food Res.* **2007**, *51*, 1461−1471.

(4) Patras, A.; Brunton, N. P.; O' Donnell, C.; Tiwari, B. K. Effect of thermal processing on anthocyanin stability in foods; mechanisms and kinetics of degradation. *Trends Food Sci. Technol.* **2010**, *21*, 3−11.

(5) Mullen, W.; Edwards, C. A.; Serafini, M.; Crozier, A. Bioavailability of pelargonidin-3-O-glucoside and its metabolites in

DOI: 10.1021/acs.jafc.5b02543
J. Agric. Food Chem. 2015, 63, 7066−7073

human following the ingestion of strawberries with and without cream. *J. Agric. Food Chem.* **2008**, *56*, 713−719.
(6) Qin, C. G.; Li, Y.; Niu, W.; Shang, X.; Xu, C. Composition analysis and structural identification of anthocyanins in fruit of waxberry. *Czech J. Food Sci.* **2011**, *29*, 171−180.
(7) Türker, N.; Erdoğdu, F. Effects of pH and temperature of extraction medium on effective diffusion coefficient of anthocyanidin pigments of black carrot (*Daucus carota* var. L.). *J. Food Eng.* **2006**, *76*, 579−583.
(8) Guisti, M. M.; Wrolstad, R. E. Acylated anthocyanins from edible sources and their applications in food systems. *Biochem. Eng. J.* **2003**, *14*, 217−225.
(9) Zozio, S.; Pallet, D.; Dornier, M. Evaluation of anthocyanin stability during storage of a coloured drink made from extracts of the andean blackberry (*Rubus glaucus* Benth.), acai (*Euterpe oleracea* Mart.) and black carrot (*Daucus Carota* L.). *Fruits* **2011**, *66*, 203−215.
(10) Elham, G.; Reza, H.; Jabbar, K.; Parisa, S.; Rashid, J. Isolation and structure characterization of anthocyanin pigments in black carrot (*Daucus carota* L.). *Pak. J. Biol. Sci.* **2006**, *9*, 2905−2908.
(11) Montilla, C. E.; Arzaba, R. M.; Hillebrand, S.; Winterhalter, P. Anthocyanin composition of black carrot (*Daucus carota* ssp. *Sativus* var. *atrorubens* Alef.). Cultivars antonina, beta sweet, deep purple, and purple haze. *J. Agric. Food Chem.* **2011**, *59*, 3385−3390.
(12) Turker, N.; Aksay, S.; Istanbullu, O.; Artuvan, E. A study on the relation between anthocyanin content and product quality: salgam as a model beverage. *J. Food Qual.* **2007**, *30*, 953−969.
(13) Schwarz, M.; Wray, V.; Winterhalter, P. Isolation and identification of novel pyranoanthocyanins from black carrot (Dausus carota L.) juice. *J. Agric. Food Chem.* **2004**, *52*, 5095−5101.
(14) Hrazdina, G. Reactions of the anthocyanidin-3,5-diglucosides. Formation of 3,5-di-(O-*β*-D-glucosyl)-7-hydroxy coumarin. *Phytochemistry* **1971**, *10*, 1125−1130.
(15) Markaris, P.; Livingston, G. E.; Fellers, C. R. Quantitative aspects of strawberry pigment degradation. *J. Food Sci.* **1957**, *22*, 117−130.
(16) Adams, J. B. Thermal degradation of anthocyanins with particular reference to the 3- glycosides of cyanidin. I. In acidified aqueous solution at 100 °C. *J. Sci. Food Agric.* **1973**, *24*, 747−762.
(17) Von Elbe, J. H.; Schwartz, S. J. Colorants. In *Food Chemistry*, 3rd ed.; Fennema, O. R., Ed.; Markel Dekker, Inc.: New York, 1996; pp 651−722.
(18) Mazza, G.; Brouillard, R. Colour stability and structural transformations of cyanidin-3,5-diglucoside and four 3-deoxyanthocyanins in aqueous solutions. *J. Agric. Food Chem.* **1987**, *35*, 422−426.
(19) Lapidot, T.; Harel, S.; Akiri, B.; Granit, R.; Kanner, J. pH-dependent forms of red wine anthocyanins as antioxidants. *J. Agric. Food Chem.* **1999**, *47*, 67−70.
(20) Março, H. P.; Scarminio, S. I. Q-mode curve resolution of UV-vis spectra for structural transformation studies of anthocyanins in acidic solutions. *Anal. Chim. Acta* **2007**, *583*, 138−146.
(21) Brouillard, R. Origin of the exceptional colour stability of the *zebrina* anthocyanin. *Phytochemistry* **1981**, *20*, 143−145.
(22) Brouillard, R. The *in vivo* expression of anthocyanin colour plants. *Phytochemistry* **1983**, *22*, 1311−1323.
(23) Dangles, O.; Saito, N.; Brouillard, R. Anthocyanin intramolecular copigment effect. *Phytochemistry* **1993**, *34*, 119−124.
(24) Francis, F. J.; Markakis, C. P. Food colourants: anthocyanins. *Crit. Rev. Food Sci. Nutr.* **1989**, *28*, 273−314.
(25) Goto, T.; Kondo, T.; Tamura, H.; Imagawa, H. Structure of gentiondelphin. An acylated anthocyanin isolated from *gentiana makinoi*, that is stable in dilute aqueous solutions. *Tetrahedron Lett.* **1982**, *23*, 3695−3698.
(26) International Organisation of Vine and Wine (OIV). *Determination of Chromatic Characteristics According to CIElab*; OIV: Paris, France, 2006; Method OIV-MA-AS2-11, http://www.oiv.int/oiv/files/6%20-%20Domaines%20scientifiques/6%20-%204%20Methodes%20d%20analyses/6-4-1/EN/OIV-MA-AS2-11.pdf (accessed Jan 2006).
(27) Rodriguez-Saona, E. L.; Wrolstad, E. R. Extraction, isolation, and purification of anthocyanins. *Current Protocols in Food Analytical Chemistry*; Wiley: Hoboken, NJ, 2001; DOI: 10.1002/0471142913.faf0101s00.
(28) Gläßgen, E. W.; Wray, V.; Strack, D.; Metzger, W. J.; Seitz, U. H. Anthocyanins from cell suspension cultures of *Daucus carota* L. *Phytochemistry* **1992**, *31*, 1593−1601.
(29) Dougall, K. D.; Baker, C. D.; Gakh, G. E.; Redus, A. M.; Whittemore, A. N. Anthocyanins from wild carrot suspension cultures acylated with supplied carboxylic acids. *Carbohydr. Res.* **1998**, *310*, 177−189.
(30) Bąkowska-Barczak, A. Acylated anthocyanins as stable, natural food colourants—A review. *Pol. J. Food Nutr. Sci.* **2005**, *14/55*, 107−116.

DOI: 10.1021/acs.jafc.5b02543
J. Agric. Food Chem. 2015, 63, 7066−7073

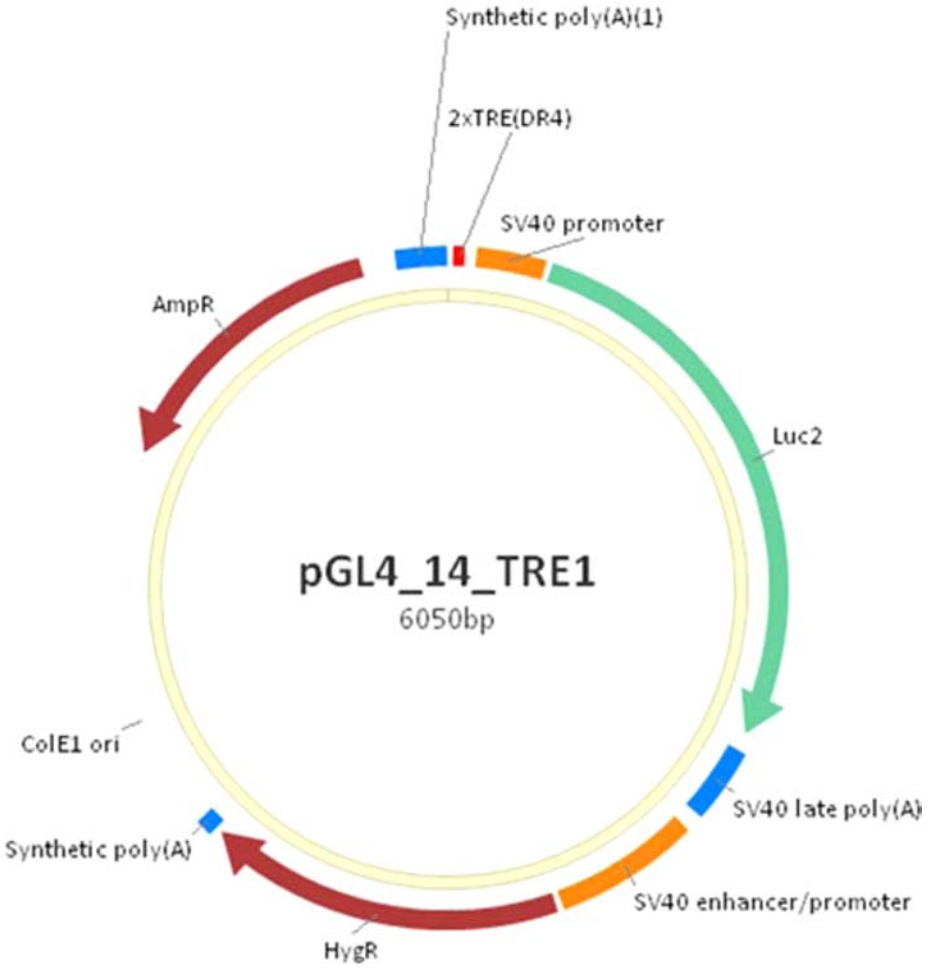

Figure 1. Map of the pGL4.14-TRE luciferase reporter plasmid.

sone, aldosterone, progesterone, testosterone, estradiol, diethylstilbestrol, tributyltin chloride (TBTC), tributyltin bromide (TBTB), tributyltin iodide (TBTI), tributyltin hydroxide (TBTOH), triphenyltin chloride (TPTC), triphenyltin hydride (TPTH), and triphenyltin hydroxide (TPTOH) were purchased from Sigma-Aldrich (Prague, Czech Republic). All other chemicals were of the highest commercially available quality.

Human Cell Lines. The A-172 (ECACC no. 88062428), A549 (ECACC no. 86012804), HEK293T (ECACC no. 85120602), HeLa (ECACC no. 93021013), HepG2 (ECACC no. 85011430), HOS (ECACC no. 87070202), MCF-7 (ECACC no. 86012803), MIA-Pa-Ca-2 (ECACC no. 85062806), OACP4C (ECACC no. 11012005), SK-HEP-1 (ECACC no. 91091816), and U2OS (ECACC no. 92022711) cell lines were cultivated in Dulbecco's modified Eagle's medium (DMEM) supplemented with 10% fetal bovine serum, 100 U/mL penicillin, 100 μg/mL streptomycin, 4 mM L-glutamine, 1% nonessential amino acids, and 1 mM sodium pyruvate. The A2780 (ECACC no. 93112519) and LNCaP (ECACC no. 89110211) cell lines were cultivated in RPMI-1640 medium supplemented with 10% fetal bovine serum, 100 U/mL penicillin, 100 μg/mL streptomycin, and 4 mM L-glutamine. The G-361(ECACC no. 88030401) cell line was cultivated in McCoy's 5A medium supplemented with 10% fetal bovine serum, 100 U/mL penicillin, 100 μg/mL streptomycin, 4 mM L-glutamine, and 1 mM HEPES. The FTC-133 (ECACC no. 94060901) cell line was cultivated in DMEM/F-12 nutrient mixture (DMEM/F-12) supplemented with 10% fetal bovine serum, 100 U/mL penicillin, 100 μg/mL streptomycin, 4 mM L-glutamine, and 1% nonessential amino acids. All cells were cultivated at 37 °C and 5% CO_2 in a humidified incubator.

Electrophoretic Separation of Proteins and Western Blot Analyses. The total protein extracts were prepared as previously described.[12] The proteins were separated on an 8% SDS-PAGE gel using the Mini-PROTEAN Tetra System (Bio-Rad, Hercules, CA, USA) according to the manufacturer's instructions, followed by transfer onto a PVDF membrane. The blots were probed with primary antibodies against TRα1/α2, TRα1/β1, and RXRα. As a positive control, human recombinant TR-α1, TR-β1, and in vitro translated RXRα proteins were used. Chemiluminescent detection was performed using horseradish peroxidase-conjugated secondary antibodies against mouse and rabbit IgG and the Western blotting luminol reagent kit.

Quantitative Reverse Transcriptase PCR (qRT-PCR). The total RNA was isolated using TRI reagent, and, after treatment with DNase I, the cDNA was synthesized using M-MuLV reverse transcriptase, according to the manufacturer's instructions. qRT-PCR was performed in a LightCycler 480 II instrument (Roche Diagnostic Corp., Prague, Czech Republic), and the levels of Spot14 and GAPDH mRNAs were determined. The gene expression levels of *Spot14* were normalized to the housekeeping gene *glyceraldehyde-3-phosphate dehydrogenase* (*GAPDH*). The measurements were performed in triplicate, and the data were processed using the delta−delta method.

Reporter Plasmid. The luciferase reporter plasmid that is responsive to transcriptionally active TR pGL4.14-TRE was prepared by cloning the synthesized fragment containing two copies of tandem TREs oriented as direct repeats separated by four nucleotides (DR4) with the sequence TA**AGGTCA**TTTA**AGGTCA**TTTA**AGGTCA**-TTTA**AGGTCA**A into the multiple cloning region of the promoterless pGL4.14[*luc2*/Hygro] vector (catalog no. E6691) from Promega. As a control for luciferase gene expression, the basic SV40 promoter

DOI: 10.1021/acs.jafc.5b01519
J. Agric. Food Chem. 2015, 63, 7074−7083

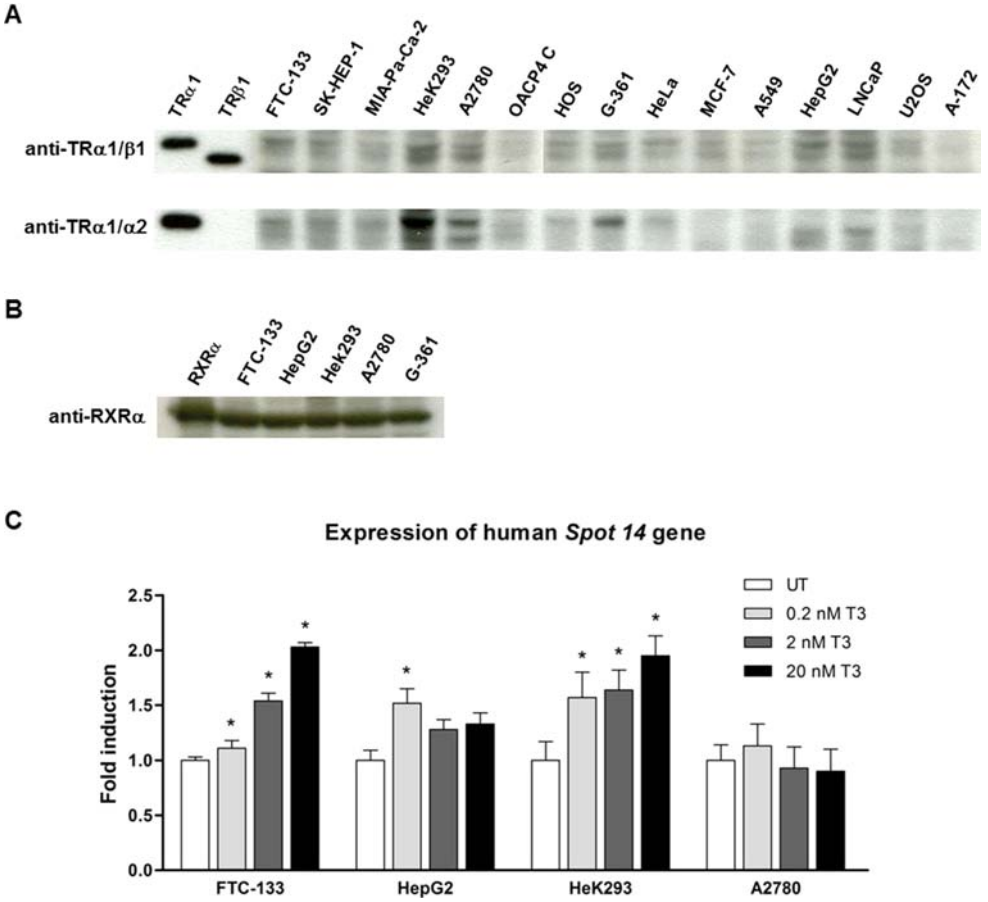

Figure 2. Characterization of the human cell lines suitable for stable transfection with the pGL4.14-TRE luciferase reporter plasmid. (A) Western blot of endogenous TRα and TRβ in protein lysates from 15 different human cell lines. As positive controls, commercial recombinant TRα1 and TRβ1 were used. (B) Western blot of the five selected cell lines for the detection of endogenous RXRα using in vitro translated RXRα as a positive control. (C) Quantitative real-time PCR analysis of the human *Spot 14* mRNA following T3 treatment in four selected cell lines. The analyses were performed after treatment of the cells with vehicle (UT; 0.1% DMSO v/v), 0.2, 2, or 20 nM T3 for 24 h, and the data were normalized to the GAPDH mRNA levels. The data are the means ± SD of triplicate measurements from three independent experiments and are expressed as the fold induction over the DMSO-treated cells. (∗) Values are significantly different from the vehicle-treated cells ($p < 0.05$) as determined by Student's *t* test.

with a deleted 5′ enhancer region was attached upstream of the TREs, and the entire insert was cloned between the *Kpn*I and *Hin*dIII restriction sites (Figure 1).

Stable Transfection of HepG2 Cells and the Selection Process. Human hepatocarcinoma HepG2 cells were seeded into 60 mm cell culture dishes at a density of 1.5×10^6 cells in 5 mL of DMEM culture medium. After 16 h of stabilization, the cells were transfected with 2 μg of the pGL4.14-TRE reporter plasmid using the FuGENE HD transfection reagent according to the manufacturer's standard protocol. After 48 h, the culture medium was replaced by selection medium supplemented with hygromycin B (500 μg/mL). The medium was changed every 4−5 days for a period of 8 weeks, until a polyclonal population of transfected cells was selected. The cells were subsequently transferred into 10 mm cell culture dishes at a density of 100−500 cells in 10 mL of selection medium supplemented with hygromycin B (500 μg/mL) and were cultivated for an additional 5 weeks, until small colonies appeared. Thereafter, 21 colonies were isolated and transferred into 24-well tissue culture plates to obtain monoclonal populations of cells (PZ-TR cells). The stably transfected, hygromycin B-resistant clones were tested for their responsiveness to T3. The use of GMO at the Faculty of Science, Palacky University Olomouc, was approved by the Ministry of the Environment of the Czech Republic (Ref. 91997/ENV/10).

Luciferase Gene Reporter Assay. The PZ-TR cells were seeded into 24-well tissue culture plates at a density of 0.15×10^6 cells in 0.5 mL of DMEM culture medium supplemented with 10% charcoal-stripped fetal bovine serum instead of normal fetal bovine serum. After 16 h of stabilization, the cells were treated with the compounds under investigation or vehicle (0.1% DMSO or ethanol v/v) as described in the figure captions for the indicated period of time. After the treatments, the cells were lysed in reporter lysis buffer and the luciferase activity was measured using a Tecan Infinite M200 reader (Tecan, Männedorf, Switzerland).

Data and Statistical Analyses. The results represent two or three independent experiments (indicated in the figure captions). The data correspond to the means ± standard deviation (SD) of triplicate measurements. Standard error of the mean (SEM) was used in the analysis of variance. Statistical significance was tested by Student's *t* test or one-way analysis of variance (ANOVA) followed by Tukey's test. Differences were considered significant at $p < 0.05$. The dose−response curve fits and EC_{50} values were determined using GraphPad Prism 5 software (GraphPad Software, San Diego, CA, USA).

RESULTS

Selection of Human Cell Lines. Fifteen human cell lines were examined for the presence of endogenously expressed TRs. The Trα1 and TRβ1 isoforms were detected in the total protein extracts by Western blot analyses using primary antibodies against TRα1/α2 and TRα1/β1 and a secondary polyclonal goat anti-mouse IgG−HRP antibody. We preselected A2780, FTC-133, G-361, HEK293, and HepG2 cells,

DOI: 10.1021/acs.jafc.5b01519
J. Agric. Food Chem. 2015, 63, 7074−7083

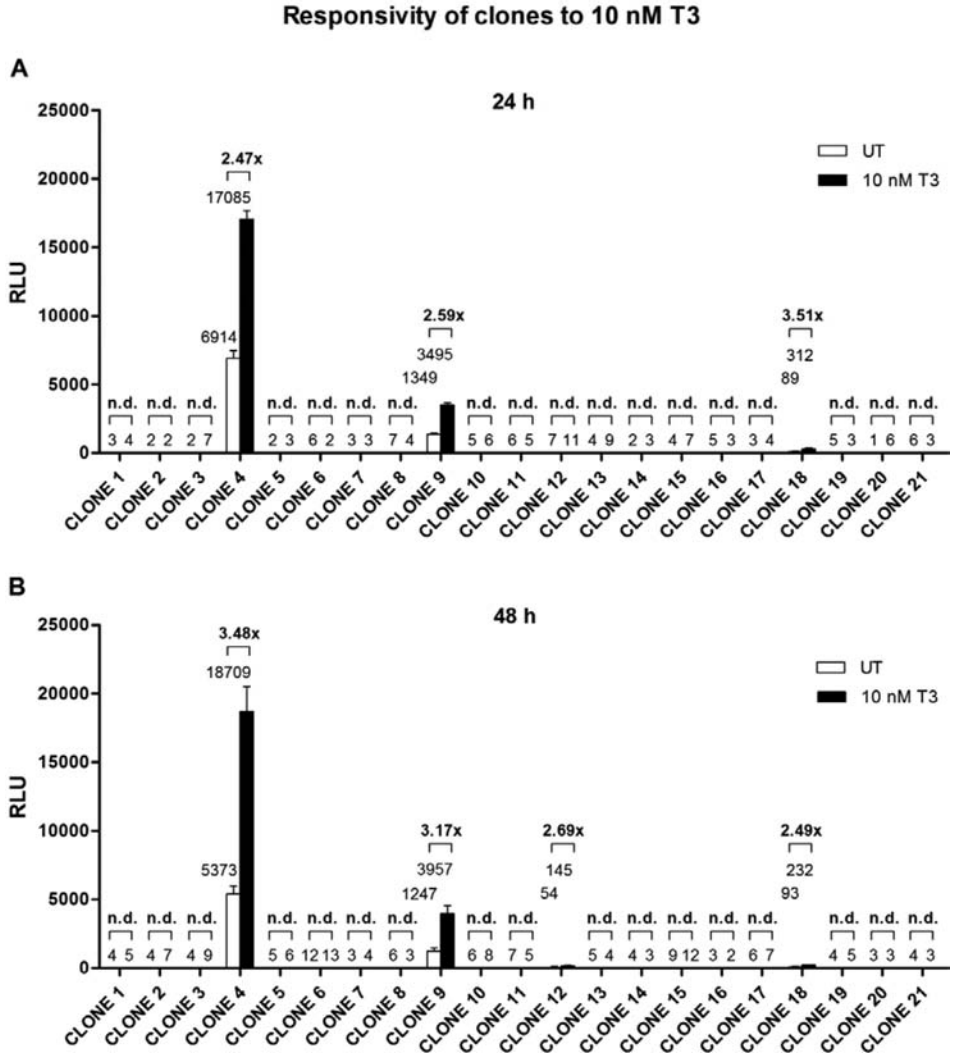

Figure 3. Response of stably transfected clones to T3. Cells seeded into 24-well plates were stabilized for 16 h and treated with vehicle (UT; 0.1% DMSO v/v) or 10 nM T3. After 24 h (A) and 48 h (B), the cells were lysed and the luciferase activity was measured. The data correspond to the means ± SD of triplicate measurements from two independent experiments and are expressed as the relative luciferase units (RLU). The fold induction for T3 over the DMSO-treated cells is indicated above the UT-T3 pair in the bar graph.

which were identified as the cell lines with the highest levels of endogenously expressed TRs (Figure 2A). Consequently, we confirmed the presence of the main TR heterodimer partner RXRα in all five lines using a primary antibody against RXRα and a goat anti-rabbit IgG−HRP antibody (Figure 2B). Because the presence of TRs in cells does not solely provide the functionality of the mechanism responsible for TR-dependent regulation of gene expression, qRT-PCR studies were performed in preselected cell lines. The changes in levels of the human *Spot 14* mRNA were measured after treatment of the cells with 0.2, 2, and 20 nM T3. We found that among the five preselected lines, the most prominent induction of *Spot 14* mRNA expression was in the FTC-133 and HEK293 cells, and the level of expression was T3 dose-dependent (Figure 2C). T3-induced *Spot 14* mRNA expression was observed also in HepG2 cells, but its intensity was lower (Figure 2C). According to these results, we designated the FTC-133, HEK293, and HepG2 cell lines to be suitable candidates that met the criteria for successful transfection with prepared reporter plasmid.

Transfection and Selection of Clones. Before stable transfection, the susceptibility of the selected cell lines to transfection with the pGL4.14-TRE reporter plasmid was tested. The results of the luciferase reporter assays from the transient transfections showed that luciferase activity was induced only in the transiently transfected HepG2 cells following the 10 nM T3 treatment, but not in the FTC-133 or HEK293 cells (data not shown). Therefore, the HepG2 human hepatocellular carcinoma cells were used to construct the stably transfected reporter cell line for the assessment of thyroid receptor transcriptional activity. After transfecting the HepG2 cells with the pGL4.14-TRE reporter plasmid and cultivating them under the selection pressure of hygromycin B, we obtained 21 hygromycin B-resistant, stably transfected clones. All isolated clones were tested for their responsivity to T3. We found that after 24 and 48 h of treatment with 10 nM T3, luciferase activity was significantly induced in only three clones, ranging from 2.5- to 3.5-fold induction (Figure 3). However, the relative luciferase units (RLU) in clones 9 and 18 were too low for their practical use in the experiments; thus, clone 4 (termed PZ-TR) was selected as the most reliable candidate and was further characterized.

DOI: 10.1021/acs.jafc.5b01519
J. Agric. Food Chem. 2015, 63, 7074−7083

Characterization of PZ-TR Cell Line. In the first step, we characterized the dose-dependent response of the PZ-TR cell line to T3. PZ-TR cells were treated with increasing concentrations of T3 (0.1−1000 nM), which yielded typical sigmoid logarithmic dose−response curves (Figure 4).

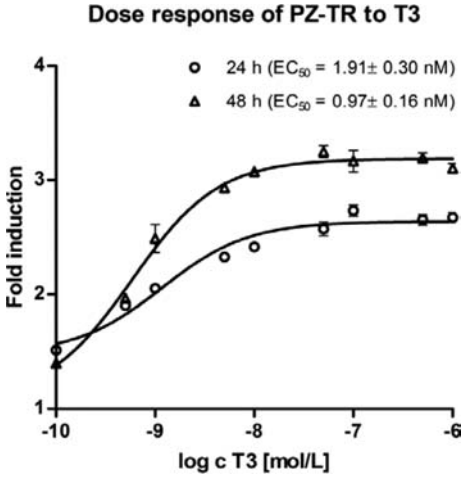

Figure 4. Dose−response of the PZ-TR cell line to T3. Cells seeded into 24-well plates were stabilized for 16 h and treated with vehicle (0.1% DMSO v/v) or T3 (0.1−1000 nM) for 24 and 48 h. After the treatments, the cells were lysed and the luciferase activity was measured. The data represent the means ± SD of triplicate measurements from three independent experiments and are expressed as the fold induction of T3 over the DMSO-treated cells.

Prolonged exposure of the cells to T3 (48 h) resulted in a higher maximum induction of luciferase activity (3.25-fold) compared to cells treated for 24 h (2.73-fold). The T3-induced luciferase activity started to reach its maximum at concentrations of 10−50 nM, and the calculated EC_{50} values corresponded to 1.91 ± 0.30 nM for the 24 h treatment and 0.97 ± 0.16 nM for the 48 h treatment.

As a second parameter, the PZ-TR cell line was cryopreserved to test the effects of this treatment of cellular functionality. The cells were frozen in fetal bovine serum and the cryoprotectant DMSO using a standard procedure and were stored for 1 week in liquid nitrogen. The thawed cells were treated with 10 nM T3 for 24 h, and the luciferase activity was measured. We found that after the freeze−thaw cycle, the RLU values in the cryopreserved cells decreased slightly, but the luciferase activity was induced to the same level as in the fresh cells (Figure 5).

The maintenance of luciferase inducibility is another important feature of the newly prepared reporter cell line that is required for its practical use. Therefore, we studied the ability of PZ-TR cell line to respond to T3 over a long period. The cells were treated with 10 nM T3 for 24 h every third passage, and the luciferase activity was measured. The induction of luciferase activity was stable for 54 days (corresponding to 12 passages), and there was no substantial decrease in the T3-induced luciferase activity in both the absolute RLU values and the fold induction (Table 1).

Finally, we compared the morphology of the stably transfected PZ-TR cells and parental HepG2 cells. We did not observe any significant differences in the morphology of the PZ-TR and HepG2 cells, even after maintaining the cells in culture for 10 passages (Figure 6).

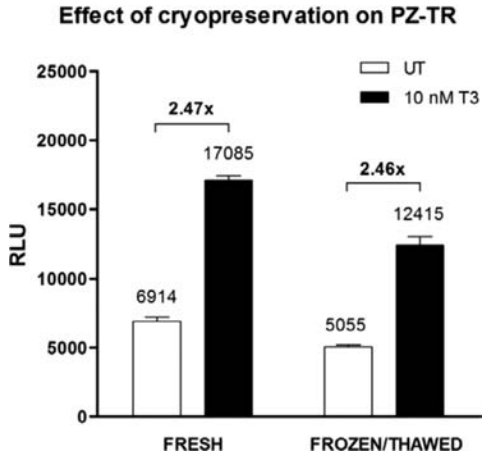

Figure 5. Effect of cryopreservation on functionality of the PZ-TR cell line. Fresh cells and frozen−thawed cells were grown on 24-well plates, stabilized for 16 h, and treated with vehicle (UT; 0.1% DMSO v/v) or 10 nM T3. After the treatments, the cells were lysed and the luciferase activity was measured. The data correspond to the means ± SD of triplicate measurements from two independent experiments and are expressed as relative luciferase units (RLU). The fold induction for T3 over the DMSO-treated cells was calculated, and the value is indicated above the UT-T3 pair in the bar graph.

Table 1. Maintenance of Luciferase Inducibility by 10 nM T3

passage no.	days in culture	RLU ± SD	fold
0	4	12415 ± 1109	2.46
3	16	9205 ± 68	2.57
6	29	11344 ± 954	2.73
9	41	8944 ± 520	2.42
12	54	8954 ± 276	2.45

Responsiveness of the PZ-TR Cell Line to Diverse Hormonal Treatments. Thyroid receptors belong to the subfamily of nuclear receptors, and their activity is regulated by thyroid hormone ligand binding. Therefore, it was necessary to demonstrate the ability of PZ-TR cells to be specifically induced by TH and exclude the possibility of luciferase activity induction by other hormones. The PZ-TR cells were treated with steroid hormones and ligands for nuclear receptors in concentrations ranging from 0.1 to 10 μM for 24 h. We did not observe any substantial changes in the luciferase activity after the application of corticosteroids (corticosterone, cortisol, betamethasone, and aldosterone), sex steroid hormones (progesterone, testosterone, estradiol, and diethylstilbestrol), and VDR ligands (25-hydroxyvitamin D3 and vitamin D3) (Figure 7). The application of 9-*cis*-retinoic acid (cisRA) induced a significant increase of luciferase activity in the PZ-TR cells. The luciferase activity was dose-dependently induced and ranged from 1.61-fold at 1 μM to 2.27-fold at 10 μM (Figure 7). These values corresponded to 56% (1 μM) and 83% (10 μM) of the level of induction obtained after treatment with 10 nM T3. These findings were in accord with our expectation that cisRA, a ligand of RXR (the main heterodimer partner of TR), might partially induce luciferase activity in the PZ-TR cells. Surprisingly, increased luciferase activity was detected also after treatment with all-*trans*-retinoic acid (transRA). The luciferase activity was again dose-dependently induced, but the intensity was lower than that of cisRA, ranging from 1.26-fold at 1 μM to 1.82-fold at 10 μM (Figure 7). These values corresponded to

DOI: 10.1021/acs.jafc.5b01519
J. Agric. Food Chem. 2015, 63, 7074−7083

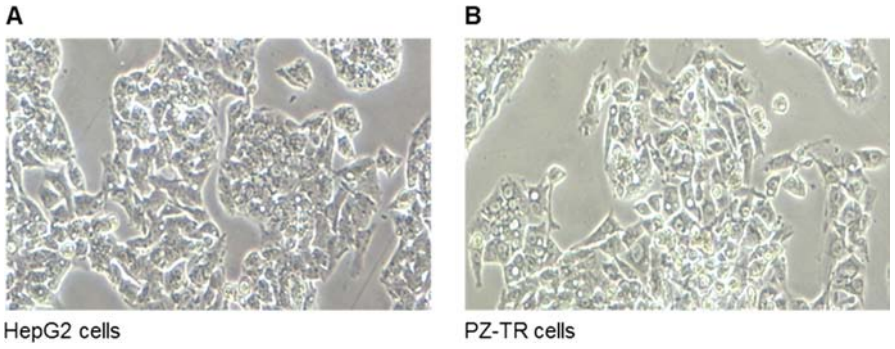

Figure 6. Morphology of the HepG2 and PZ-TR cell lines. Phase contrast micrographs of the parental HepG2 cells at the eighth passage (A) and the PZ-TR reporter cells at the 10th passage (B).

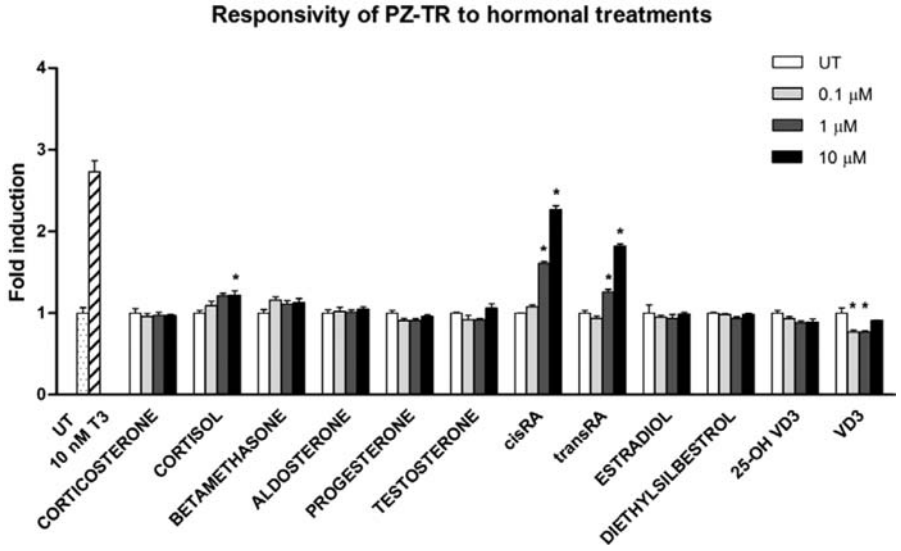

Figure 7. Response of the PZ-TR cell line to hormones. Cells seeded into 24-well plates were stabilized for 16 h and treated with vehicle (UT; 0.1% DMSO v/v) or the different hormones for 24 h. After the treatments, the cells were lysed and the luciferase activity was measured. The data represent the means ± SEM of triplicate measurements from three independent experiments and are expressed as the fold induction of the hormone-treated cells over the DMSO-treated cells. (∗) Values are significantly different from the vehicle-treated cells ($p < 0.05$) as determined by ANOVA followed by Tukey's test.

46% (1 μM) and 67% (10 μM) of the levels of induction obtained after treatment with 10 nM T3.

Responsivity of the PZ-TR Cell Line to Retinoic Acids. To explain the luciferase activity that was induced in the PZ-TR cell line after RA application, we studied the effect of RAs in more detail. PZ-TR cells were treated with cisRA and transRA in concentrations of 0.1, 1, and 10 μM, alone and in combination with 10 nM T3. After 24 h of treatment, both cisRA and transRA induced a significant increase in luciferase activity in the PZ-TR cells at 1 and 10 μM (Figure 8), similar to previous experiments (see Responsiveness of the PZ-TR Cell Line to Diverse Hormonal Treatments.). The luciferase activity was dose-dependently induced, with the highest intensities of 2.27-fold at 10 μM cisRA and 2.03-fold at 10 μM transRA. These values corresponded to 93% (10 μM cisRA) and 83% (10 μM transRA) of the level of induction obtained after treatment with 10 nM T3. The luciferase activity was induced 2.45-fold in the PZ-TR control cells treated with 10 nM T3 (Figure 8).

In cells treated for 24 h with combinations of RAs and 10 nM T3, we observed a slight inhibition of luciferase activity by 0.1 μM cisRA and 0.1 μM transRA compared to the control cells treated with 10 nM T3 (Figure 8). However, the differences were statistically significant only in the case of cisRA. The 2.11-fold (0.1 μM cisRA + 10 nM T3) and 2.35-fold inductions (0.1 μM transRA + 10 nM T3) corresponded to 86 and 96% of the level of induction obtained after treatment with 10 nM T3, respectively. In contrast, 10 μM cisRA and 10 μM transRA enhanced the effect of 10 nM T3, with 3.15-fold (10 μM cisRA + 10 nM T3) and 2.79-fold (10 μM transRA + 10 nM T3) inductions, representing 129 and 114% of the level of induction of the control cells treated with 10 nM T3, respectively (Figure 8). Application of 1 μM cisRA and 1 μM transRA in combination with 10 nM T3 did not significantly affect the induction of luciferase activity compared to the 10 nM T3-treated PZ-TR cells (Figure 8).

To determine whether RAs are able to trigger the expression of TR-inducible genes or if this phenomenon is specific only for the induction of luciferase activity in the novel PZ-TR cell line, qRT-PCR studies were performed to monitor the changes in the expression of human *Spot 14* gene. The levels of the *Spot 14* mRNA were measured 24 h after treatment of the cells with 0.1, 1, and 10 μM T3. We found that both cisRA and transRA induced the expression of the *Spot 14* gene in the PZ-TR cells (Figure 9). Whereas significant increases of the mRNA levels were observed only in the cisRA-treated cells at the 1 and 10

DOI: 10.1021/acs.jafc.5b01519
J. Agric. Food Chem. 2015, 63, 7074−7083

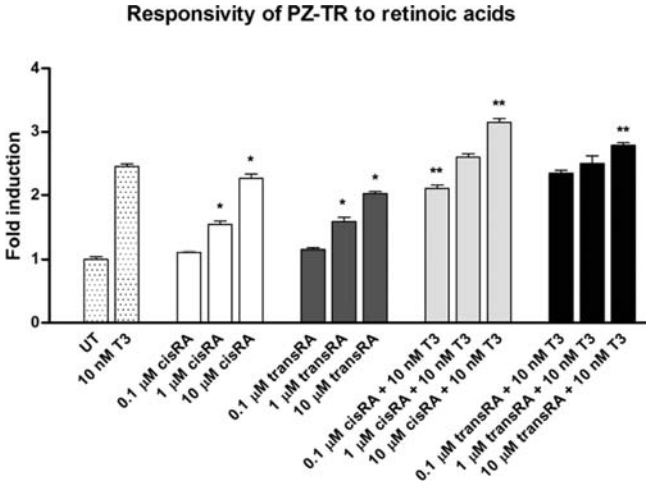

Figure 8. Response of the PZ-TR cell line to retinoic acids. Cells seeded into 24-well plates were stabilized for 16 h and treated for 24 h with vehicle (UT; 0.1% DMSO v/v), 9-*cis*-retinoic acid, or all-*trans*-retinoic acid, alone and in combination with 10 nM T3. The cells were lysed, and the luciferase activity was measured. The data represent the means ± SEM of triplicate measurements from three independent experiments and are expressed as the fold induction over the DMSO-treated cells. (∗) Values are significantly different from the vehicle-treated cells ($p < 0.05$) as determined by ANOVA followed by Tukey's test. (∗∗) Values are significantly different from the 10 nM T3-treated cells ($p < 0.05$) as determined by ANOVA followed by Tukey's test.

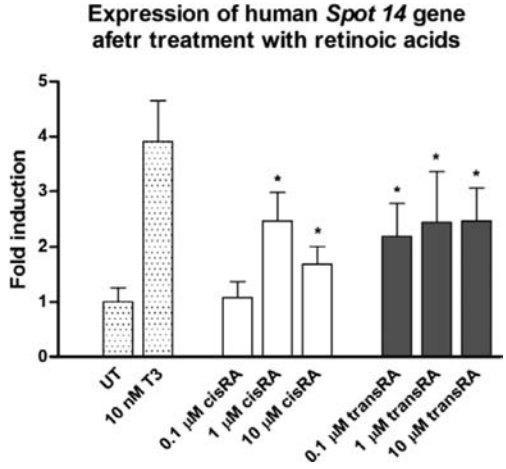

Figure 9. Quantitative real-time PCR analysis of the human *Spot 14* mRNA levels following retinoic acid treatment in the PZ-TR cell line. Cells were treated with vehicle (UT; 0.1% DMSO v/v), 9-*cis*-retinoic acid, or all-*trans*-retinoic acid for 24 h. The measurements were normalized to the GAPDH mRNA levels. The data are the means ± SD of triplicate measurements from three independent experiments and are expressed as the fold induction over the DMSO-treated cells. (∗) Values are significantly different from the vehicle-treated cells ($p < 0.05$) as determined by Student's t test.

μM concentrations (2.46- and 1.69-fold, respectively), transRA induced a significant increase of the mRNA levels at all tested concentrations. The transRA-induced expression of the *Spot 14* mRNA was dose-dependent, with 2.18-fold (0.1 mM), 2.44-fold (1 mM), and 2.46-fold (10 mM) inductions. Although the increased mRNA levels reached a maximum of 62−63% (1 μM cisRA, 1 μM transRA, and 10 μM transRA) of the mRNA level detected after treatment of the PZ-TR cells with 10 nM T3, we provide clear evidence that the expression of human *Spot 14* (TH-regulated gene) can be activated by both cisRA and transRA.

Effect of Organic Tin Compounds on the Transcriptional Activity of TR. We studied the effect of two groups of organic tin compounds on the transcriptional activity of TR using the novel PZ-TR reporter cell line. The first group was represented by the tributyltin derivatives TBTC, TBTB, TBTI, and TBTOH. PZ-TR cells were treated with the studied compounds at concentrations of 1, 10, and 100 nM (higher concentrations had a strong cytotoxic effect, data not shown) for 24 h. After application of all four tested tributyltin derivatives, we observed a significant increase of luciferase activity at the 10 and 100 nM concentrations (Figure 10A). The luciferase activity was dose-dependently induced and ranged from 1.60- to 1.90-fold for TBTC, from 1.29- to 1.30-fold for TBTB, from 1.33- to 1.48-fold for TBTI, and from 1.37- to 1.53-fold for TBTOH. These values corresponded to 36−54% (TBTC), 17−18% (TBTB), 20−29% (TBTI), and 22−32% (TBTOH) of the level of induction attained after treatment with 10 nM T3.

In parallel experiments, we studied the possible effects of the tributyltin derivatives on the transcriptional activity of TR in the presence of T3, the natural ligand of TR. PZ-TR cells were treated with the examined compounds at concentrations of 1, 10, and 100 nM in combination with 10 nM T3 for 24 h. After the treatments, we observed only slight and statistically insignificant changes in luciferase activity compared to the control cells treated with 10 nM T3, in which the luciferase activity was induced by approximately 2.68-fold (Figure 10B). The luciferase activity was induced from 2.58- to 2.84-fold for TBTC, from 2.82- to 2.91-fold for TBTB, from 2.87- to 2.91-fold for TBTI, and from 2.98- to 3.07-fold for TBTOH, and these inductions corresponded to 94−110% (TBTC), 108−114% (TBTB), 111−114% (TBTI), and 118−123% (TBTOH) of the level of induction attained after treatment with 10 nM T3 alone.

The second group of examined compounds contained three triphenyltin derivatives, TPTC, TPTH, and TPTOH. The PZ-TR cells were similarly treated with the studied compounds in concentrations of 1, 10, and 100 nM (higher concentrations had a strong cytotoxic effect, data not shown) for 24 h. We observed an increase in luciferase activity after application of all three tested compounds (Figure 10C). The luciferase activity was dose-dependently induced and reached highest statistically significant values at the 100 nM concentration. The luciferase activity was induced 1.57-fold for TPTC, 1.68-fold for TPTH, and 1.70-fold for TPTOH. These values corresponded to 33% (TPTC), 39% (TPTH), and 40% (TPTOH) of the level of induction attained after treatment with 10 nM T3.

In parallel experiments, the PZ-TR cells were treated with the tested compounds in concentrations of 1, 10, and 100 nM in combination with 10 nM T3 for 24 h. After the treatments, we observed an increase of luciferase activity compared to the control cells treated with 10 nM T3, in which the luciferase activity was induced by approximately 2.74-fold (Figure 10D). The differences were more prominent than in the cells treated with the tributyltin derivatives. The luciferase activity was significantly induced by 3.26−3.36-fold for TPTC, 3.29−3.54-fold for TPTH, and 3.40−3.47-fold for TPTOH, and these values corresponded to 130−136% (TPTC), 132−146% (TPTH), and 138−142% (TPTOH) of the level of induction attained after treatment with 10 nM T3 only.

DOI: 10.1021/acs.jafc.5b01519
J. Agric. Food Chem. 2015, 63, 7074−7083

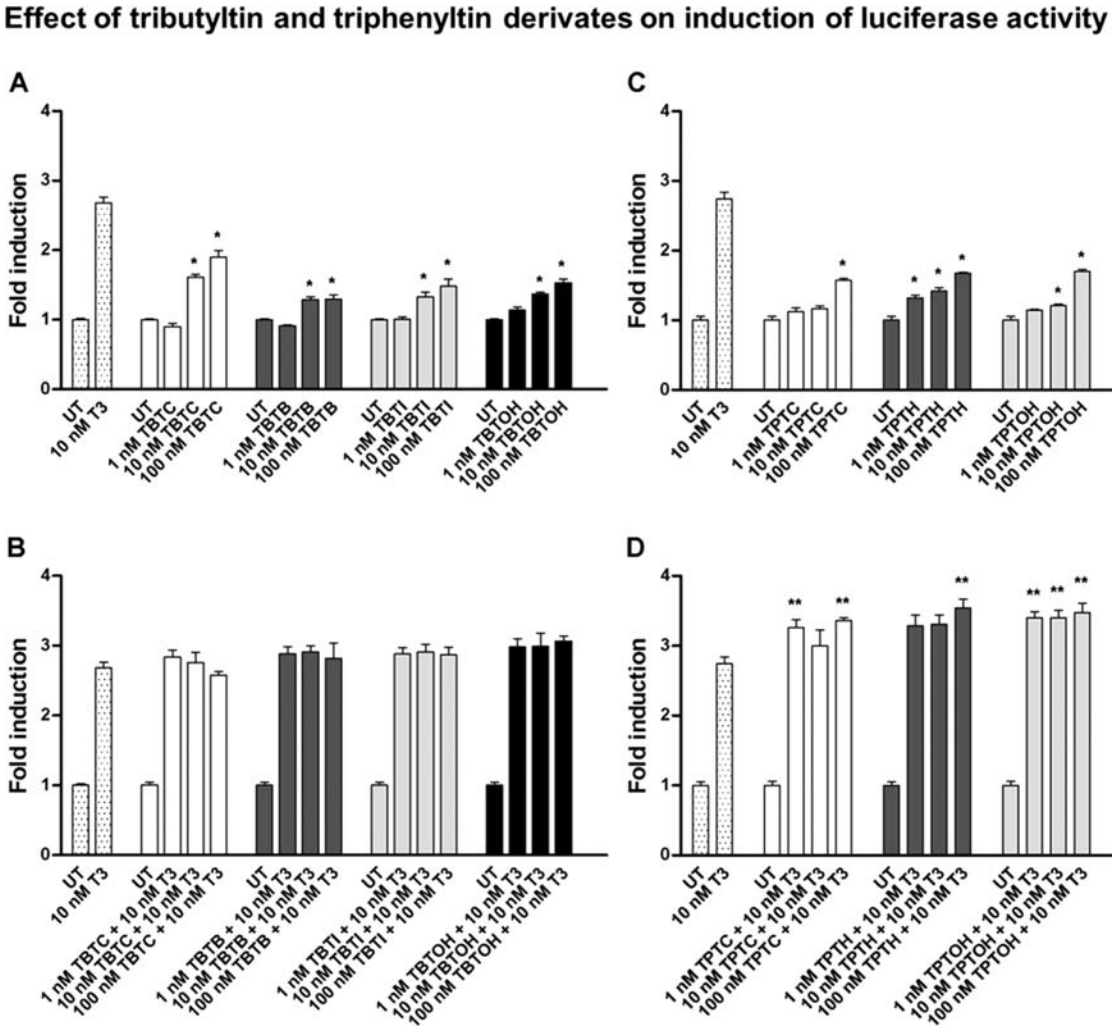

Figure 10. Effects of organic tin compounds on the transcriptional activity of TR in the PZ-TR reporter cell line. Cells seeded into 24-well plates were stabilized for 16 h and treated with vehicle (UT; 0.1% DMSO or ethanol v/v), tributyltin derivatives (TBTC, TBTB, TBTI, TBTOH) (A), or triphenyltin derivatives (TPTC, TPTH, TPTOH) (C), alone and in combination with 10 nM T3 (B, D). After 24 h, the cells were lysed and the luciferase activity was measured. The data represent the means ± SEM of triplicate measurements from three independent experiments and are expressed as the fold induction over the vehicle-treated cells. (∗) Values are significantly different from the vehicle-treated cells ($p < 0.05$) as determined by ANOVA followed by Tukey's test. (∗∗) Values are significantly different from the 10 nM T3-treated cells ($p < 0.05$) as determined by ANOVA followed by Tukey's test.

DISCUSSION

It is known that a large group of natural and synthetic compounds, generally termed endocrine disruptors, can interfere with the endocrine system and disrupt the homeostasis of the processes that regulate hormones in humans. Several in vitro models have been developed to screen for substances that may potentially disrupt the hormone system.[13] Among them, reporter gene-based assays have been widely used as reliable tools to detect various biologically active compounds in many environmental and biological applications. The construction of reporter gene systems is based on transient or stable transfection of cells with a reporter plasmid that contains a domain that binds a hormonal receptor (response element) and a reporter gene located downstream. Different genes, such as those coding for proteins such as luciferase,[14] galactosidase,[15] chloramphenicol acetyl transferase,[16] and green fluorescent protein,[17] are usually used as reporter genes because their activities can easily be measured. There is also a large diversity in the selection of cells or cell lines used for transfection. There are many paper describing the development of gene reporter systems derived from yeast,[15,18,19] amphibian,[6] mammalian,[7−10,20,21] or human[14,21−23] cell lines for screening endocrine disruptors. Because gene reporter systems play such a crucial role, the presence of a functional receptor and the high variability and natural characteristics of the parental cell lines used for construction of such systems often result in the necessity of additional cotransfections. In particular, the introduction of an expression plasmid encoding the receptor of interest is required in yeast-derived reporter systems.[15,17,19] However, cotransfection with the appropriate receptor construct is also essential in animal[9,20,21] and human[16,22,23] cell line-derived gene reporter systems when the parental cells lack adequate endogenous expression of the receptor. These manipulations may lead to changes in the stoichiometric ratio between the introduced receptor protein, which is usually overexpressed, and other transcriptional regulators, and does not reflect the natural situation.

Although the construction of a stable gene reporter cell line is time- and material-consuming process, the prospective long-

DOI: 10.1021/acs.jafc.5b01519
J. Agric. Food Chem. 2015, 63, 7074−7083

term advantages of this type of system are indisputable. Stable gene reporter systems are characterized by highly sensitive assays, good reproducibility of the results, homogeneity of the data, and no need for additional normalization, which permits high-throughput and low-cost experimentation. Large-scale stable reporter cell lines have been constructed for the detection of potential hormonal disruptors using mainly corticosteroids and sex steroid hormones. In an effort to expand the field of research of endocrine disruptors to the thyroid axis, several stable luciferase reporter systems have been developed over the past decade. The thyroid hormone-responsive gene reporter cell line XL58-TRE-Luc was constructed by introducing LV-TRE-Luc, a self-inactivating lentivirus vector containing the luciferase reporter gene downstream of the *Xenopus laevis* TRE, into *Xenopus laevis* XL58 cells.[6] XL58-TRE-Luc was used by the authors to study the effects of chlorinated derivatives of bisphenol A on the TR transcriptional activity, revealing their possible influence on TR-regulated gene expression. Soon after, Jugan and co-workers developed a new stable reporter cell line, PC-DR-LUC, which allowed them to measure the effects of putative thyroid-disrupting chemicals on the modulation of TRα1 transcriptional activity.[7] The reporter cell line was derived from rat PC12 cells expressing TRα1 of avian origin by transfecting the cells with a pGL3-DR4 reporter plasmid carrying four TRE half-sites separated by four nucleotides located upstream of the luciferase gene. Using the PC-DR-LUC cell line, the authors determined the influence of several halogenated phenolic and phenol compounds on the transcriptional activity of TRα1. Later, the PC-DR-LUC cell line was successfully used to evaluate the thyroid-disrupting potential of water from wastewater treatment plants, rivers, and drinking water supplies.[24] Recently, a novel reporter cell line, GH3-TRE.Luc, has been developed to detect TR disruptors.[8] The rat GH3 cell line constitutively expressing both isoforms of TR was stably transfected with the pGL4CP-SV40-2xtaDR4 construct containing two TREs upstream of the firefly luciferase gene. The authors used the GH3-TRE reporter cell line to test hydroxylated polybrominated diphenyl ethers, hydroxylated polychlorinated biphenyls, and halogenated derivatives of bisphenol A as chemicals with potential thyroid-disrupting effects.

Because TH-mediated signaling in amphibian and rodent cells can be substantially different from signaling in human cells,[25] it is of great interest to establish a reporter cell line to assess the thyroid receptor transcriptional activity based on the human system. We developed and described a new stably transfected gene reporter cell line, PZ-TR. The PZ-TR cell line presented here is an exclusively human system derived from HepG2 human hepatocellular carcinoma cells, which endogenously expresses both isoforms of TR (Figure 2). The stable transfection with a reporter gene driven by TRE from the human gene needs no additional cotransfections with a TR expression vector, guarantees the preservation of the stoichiometric ratio between the TR receptor and other transcriptional regulators, and reflects natural situations. These characteristics demonstrate significant advancements for the PZ-TR cell line compared to as yet developed cell lines.

AUTHOR INFORMATION

Corresponding Author

*(Z.D.) E-mail: moulin@email.cz.

Funding

This work was supported by the European Social Fund and the Ministry of Education, Youth and Sports of the Czech Republic, Project CZ.1.07/2.3.00/30.0004 (POST-UP), CEMAN grants, a grant from the Slovak Research and Development Agency, APVV-0160-11, and a grant from the Czech Scientific Agency, GACR 303/12/G163.

Notes

The authors declare no competing financial interest.

ABBREVIATIONS USED

25-OH VD3, 25-hydroxyvitamin D3; cisRA, 9-*cis*-retinoic acid; DR4, direct repeat separated by four nucleotides; RA, retinoic acid; RXR, retinoic X receptor; T3, 3,3′,5-triiodo-L-thyronine; T4, L-thyroxine; TBTB, tributyltin bromide; TBTC, tributyltin chloride; TBTI, tributyltin iodide; TBTOH, tributyltin hydroxide; TH, thyroid hormone; TPTC, triphenyltin chloride; TPTH, triphenyltin hydride; TPTOH, triphenyltin hydroxide; TR, thyroid receptor; transRA, all-*trans*-retinoic acid; TRE, thyroid hormone response element; VD3, vitamin D3; VDR, vitamin D3 receptor

REFERENCES

(1) Zoeller, R. T. Environmental chemicals as thyroid hormone analogues: new studies indicate that thyroid hormone receptors are targets of industrial chemicals? *Mol. Cell. Endocrinol.* **2005**, *242*, 10−15.

(2) Boas, M.; Feldt-Rasmussen, U.; Skakkebaek, N. E.; Main, K. M. Environmental chemicals and thyroid function. *Eur. J. Endocrinol.* **2006**, *154*, 599−611.

(3) Murk, A. J.; Rijntjes, E.; Blaauboer, B. J.; Clewell, R.; Crofton, K. M.; Dingemans, M. M. L.; Furlow, J. D.; Kavlock, R.; Köhrle, J.; Opitz, R.; Traas, T.; Visser, T. J.; Xia, M.; Gutleb, A. C. Mechanism-based testing strategy using in vitro approaches for identification of thyroid hormone disrupting chemicals. *Toxicol. In Vitro* **2013**, *27*, 1320−1346.

(4) Wauters, J.; Vanden Bussche, J.; Bizec, B. L.; Kiebooms, J. A.; Dervilly-Pinel, G.; Prevost, S.; Wozniak, B.; Sterk, S. S.; Grønningen, D.; Kennedy, D. G.; Russell, S.; Delahaut, P.; Vanhaecke, L. Toward a new European threshold to discriminate illegally administered from naturally occurring thiouracil in livestock. *J. Agric. Food Chem.* **2015**, *63*, 1339−1346.

(5) Wang, C. H.; Lin, J. H.; Lu, T. J.; Chiang, A. N.; Chiou, S. T.; Chen, Y. A.; Pan, M. H.; Hsieh, S. C. Establishment of reporter platforms capable of detecting NF-κB mediated immuno-modulatory activity. *J. Agric. Food Chem.* **2013**, *61*, 12582−12587.

(6) Sugiyama, S.; Miyoshi, H.; Yamauchi, K. Characteristics of a thyroid hormone responsive reporter gene transduced into a *Xenopus laevis* cell line using lentivirus vector. *Gen. Comp. Endocrinol.* **2005**, *144*, 270−279.

(7) Jugan, M. L.; Lévy-Bimbot, M.; Pomérance, M.; Tamisier-Karolak, S.; Blondeau, J. P.; Lévi, Y. A new bioluminescent cellular assay to measure the transcriptional effects of chemicals that modulate the α-1 thyroid hormone receptor. *Toxicol. In Vitro* **2007**, *21*, 1197−1205.

(8) Freitas, J.; Cano, P.; Craig-Veit, C.; Goodson, M. L.; Furlow, J. D.; Murk, A. J. Detection of thyroid hormone receptor disruptors by a novel stable in vitro reporter gene assay. *Toxicol. In Vitro* **2011**, *25*, 257−266.

(9) Schriks, M.; Roessig, J. M.; Murka, A. J.; Furlow, J. D. Thyroid hormone receptor isoform selectivity of thyroid hormone disrupting compounds quantified with an *in vitro* reporter gene assay. *Environ. Toxicol. Pharmacol.* **2007**, *23*, 302−307.

(10) Sun, H.; Shen, O.-X.; Wang, X.-R.; Zhou, L.; Zhen, S.-Q; Chen, X.-D. Anti-thyroid hormone activity of bisphenol A, tetrabromobisphenol A and tetrachlorobisphenol A in an improved reporter gene assay. *Toxicol. In Vitro* **2009**, *23*, 950−954.

DOI: 10.1021/acs.jafc.5b01519
J. Agric. Food Chem. 2015, 63, 7074−7083

(11) Ferreira, M.; Blanco, L.; Garrido, A.; Vieites, J. M.; Cabado, A. G. In vitro approaches to evaluate toxicity induced by organotin compounds tributyltin (TBT), dibutyltin (DBT), and monobutyltin (MBT) in neuroblastoma cells. *J. Agric. Food Chem.* **2013**, *61*, 4195−4203.
(12) Novotna, A.; Srovnalova, A.; Svecarova, M.; Korhonova, M.; Bartonkova, I.; Dvorak, Z. Differential effects of omeprazole and lansoprazole enantiomers on aryl hydrocarbon receptor in human hepatocytes and cell lines. *PLoS One* **2014**, *9*, e98711.
(13) Charles, G. D. In vitro models in endocrine disruptor screening. *ILAR J.* **2004**, *45*, 494−501.
(14) Novotna, A.; Pavek, P.; Dvorak, Z. Construction and characterization of a reporter gene cell line for assessment of human glucocorticoid receptor activation. *Eur. J. Pharm. Sci.* **2012**, *47*, 842−847.
(15) Gaido, K. W.; Leonard, L. S.; Lovell, S.; Gould, J. C.; Babaï, D.; Portier, C. J.; McDonnell, D. P. Evaluation of chemicals with endocrine modulating aktivity in a yeast-based steroid hormone receptor gene transcription assay. *Toxicol. Appl. Pharmacol.* **1997**, *143*, 205−212.
(16) Tully, D. B.; Cox, V. T.; Mumtaz, M. M.; Davis, V. L.; Chapin, R. E. Six high-priority organochlorine pesticides, either singly or in combination, are nonestrogenic in transfected HeLa cells. *Reprod. Toxicol.* **2000**, *14*, 95−102.
(17) Bovee, T. F. H.; Helsdingen, R. J. R.; Koks, P. D.; Kuiper, H. A.; Hoogenboom, R. L. A. P.; Keijer, J. Development of a rapid yeast estrogen bioassay, based on the expression of green fluorescent protein. *Gene* **2004**, *325*, 187−200.
(18) O'Connor, J. C.; Davis, L. G.; Frame, S. R.; Cook, J. C. Evaluation of a tier I screening battery for detecting endocrine-active compounds (EACs) using the positive controls testosterone, coumestrol, progesterone, and RU486. *Toxicol. Sci.* **2000**, *54*, 338−354.
(19) Sugawara, T.; Nakajima, A.; Nomura, E. Development of a simple screening system for endocrine disruptors. *Med. Sci. Monit.* **2002**, *8*, BR431−438.
(20) Vinggaard, A. M.; Joergensen, E. C.; Larsen, A. C. Rapid and sensitive reporter gene assays for detection of antiandrogenic and estrogenic effects of environmental chemicals. *Toxicol. Appl. Pharmacol.* **1999**, *155*, 150−160.
(21) Hartig, P. C.; Bobseine, K. L.; Britt, B. H.; Cardon, M. C.; Lambright, C. R.; Wilson, V. S.; Gray, L. E., Jr. Development of two androgen receptor assays using adenoviral transduction of MMTV-luc reporter and/or hAR for endocrine screening. *Toxicol. Sci.* **2002**, *66*, 82−90.
(22) Charles, G. D.; Bartels, M. J.; Freshour, N. L.; Zacharewski, T. R.; Gollapudi, B. B.; Carney, E. W. Activity of benzo[a]pyrene and its hydroxylated metabolites in an ER-α reporter gene assay. *Toxicol. Sci.* **2000**, *55*, 320−326.
(23) Térouanne, B.; Tahiri, B.; Georget, V.; Belon, C.; Poujol, N.; Avances, C.; Orio, F., Jr.; Balaguer, P.; Sultan, C. A stable prostatic bioluminescent cell line to investigate androgen and antiandrogen effects. *Mol. Cell. Endocrinol.* **2000**, *160*, 39−49.
(24) Jugan, M. L.; Oziol, L.; Bimbot, M.; Huteau, V.; Tamisier-Karolak, S.; Blondeau, J. P.; Lévi, Y. In vitro assessment of thyroid and estrogenic endocrine disruptors in wastewater treatment plants, rivers and drinking water supplies in the greater Paris area (France). *Sci. Total Environ.* **2009**, *407*, 3579−3587.
(25) Darras, V. M.; Houbrechts, A. M.; Van Herck, S. L. J. Intracellular thyroid hormone metabolism as a local regulator of nuclear thyroid hormone receptor-mediated impact on vertebrate development. *Biochim. Biophys. Acta, Gene Regul. Mech.* **2015**, *1849*, 130−141.

DOI: 10.1021/acs.jafc.5b01519
J. Agric. Food Chem. 2015, 63, 7074−7083

and Leydig cells in the male offspring, leading to disorganization in seminiferous tubules and reductions in daily sperm production, sperm motility, and Sertoli cell number in mice,[37] and male mice exposed to TiO_2 NPs by intraperitoneal injection showed significant decreases in sperm numbers and motility, and elevated abnormal sperm and germ cell apoptosis in the testes.[38] Gao et al. reported that TiO_2 NPs can be translocated to the ovary and testis, leading to injuries of both organs, lower fertility, sperm concentration, and sperm motility, higher malformation rates of sperm, and alter gene expression profile in the damaged mouse ovary and testes.[39,40] The reproductive system of male mammals mainly consists of the testis, epididymis, and ductus deferens. The testis produces spermatozoa, and the epididymis stores the spermatozoa and completes sperm maturation. While spermatogenesis is a complex process of multi phase, activities of testicular marked enzymes, including lactate dehydrogenase (LDH), sorbitol dehydrogenase (SODH), succinate dehydrogenase (SDH), glucose-6-phosphate dehydrogenase (G-6PD), acid phosphatase (ACP), alkaline phosphatase (AKP), nitric oxide synthase (NOS), are related to this process in the testes.[41−46] In addition, the ion channels are suggested to associate with various sperm functions such as spermatogenesis, sperm activation, and sperm−egg interaction. As important enzymes to keep energy utilization of spermatogenesis, ATPases (including Ca^{2+}-ATPase, Ca^{2+}/Mg^{2+}-ATPase, and Na^+/K^+-ATPase) are key ion pumps on the plasma membrane to maintain cell membrane structure and keep physiological and biochemical activities in the testes.[47] We hypothesize that the lowered sperm numbers and sperm motility and the increased percentage of abnormal sperm caused by exposure to TiO_2 NPs may be associated with testicular biochemical dysfunctions. To date, no studies have examined whether TiO_2 NPs induce testicular biochemical dysfunction by assessing the activities of LDH, SODH, SDH, G-6PD, ACP, AKP, NOS, Ca^{2+}-ATPase, Ca^{2+}/Mg^{2+}-ATPase, and Na^+/K^+-ATPase in the damaged testes in male mice. In addition, many conditions or events associated with male infertility can induce oxidative stress and germ cell apoptosis. Given that spermatozoa are rich in polyunsaturated fatty acids, they are very susceptible to attack by reactive oxygen species (ROS).[48,49] Thus, the aims of the current study were to test the hypothesis that TiO_2 NPs induce biochemical dysfunction and oxidative stress in the damaged testes of mice by causing alterations in the enzymatic activities and ROS production. In addition, the mechanisms of TiO_2 NP-inhibited spermatogenesis in mouse testes were evaluated.

MATERIALS AND METHODS

Chemicals. The preparation of TiO_2 NPs was described and fully characterized in Yang's study[50] and our previous studies, suggesting anatase for phase, 5−6 nm for particle size, 174.8 m^2/g for surface area, mainly 294 nm for mean hydrodynamic diameter, and 9.28 mV for zeta potential, respectively.[50,51]

Animals and Treatment. 160 ICR (Imprinting Control Region) male mice, aged 5 weeks with a mean body mass of 22 ± 2 g, were purchased from the Animal Center of Soochow University (Jiangsu, China). All procedures performed on the animals were approved by the Institutional Animal Care and Use Committee of Soochow University, and thus within the guidelines for human care of laboratory animals for scientific purposes. Both water and food were provided ad lib.

Hydroxypropylmethylcellulose (HPMC) K4M (Sigma-Aldrich, St. Louis, MO, USA) of concentration 0.5% was used as a suspending agent. TiO_2 NP powder was dispersed onto the surface of 0.5% w/v HPMC solution, and then the suspending solutions containing TiO_2 NPs were treated ultrasonically for 30 min and mechanically vibrated for 5 min. During the experiment, the mice were randomly divided into four groups (n = 40 each), including a control group (treated with 0.5% w/v HPMC) and three experimental groups (2.5, 5, or 10 mg/kg BW of TiO_2 NPs). For dose selection, we consulted a report of the World Health Organization from 1969. According to the report, the LD 50 of TiO_2 for rats is >12 g/kg body weight after oral administration. In addition, the quantity of TiO_2 NPs does not exceed 1% by weight of the food according to U.S. federal regulations. In the present study, we selected 2.5, 5, and 10 mg/kg TiO_2 NPs, which were given to mice by intragastric administration every day. They were equal to about 0.15−0.7 g of TiO_2 NPs for humans with 60−70 kg body weight with such exposure, which are relatively safe doses. All mice were weighed, and the TiO_2 NP suspensions of different doses were administered to mice by intragastric feeding every day for 60 days. Food and water intake were carefully recorded at the last week in the second month. Food and water intake were calculated according to the Drozdz method.[52]

Testicular and Epididymis Collection. After the 60-day study period, all mice were weighed and lightly anesthetized with ether, and the testes and epididymis were quickly removed and placed on ice. After the body and testes were weighed, the relative testicular weight was calculated as the ratio of testis (wet weight, mg) to body weight (g). Fresh testes and epididymis from 5 mice in each group were quickly soaked in 10% formaldehyde solution for histopathological examination. The remaining fresh testes were quickly stored in liquid nitrogen and subsequently assayed for enzymatic activity and oxidative stress.

Semen Evaluation. Each left cauda epididymis was dissected and incised using a pin in 1.5 mL of Dulbecco's modified Eagle's medium with 10 mg/mL bovine serum albumin and then incubated for several minutes to release the sperm. Measurements of total sperm concentrations, sperm motility, and percentage of abnormal sperm were described in Gao's study.[40]

Histopathological Evaluation. After fixation in 10% neutral formalin and being embedded in paraffin, testes and epididymis from 5 mice in each group were sliced at a thickness of 5 μm, and placed on separate glass slides. After hematoxylin and eosin staining, the testis and epididymis simples were routinely evaluated by a histopathologist unaware of the treatments for light microscopy (U-III Multipoint Sensor System; Nikon, Tokyo, Japan).

Assay of Enzyme Activities. For enzymatic activity determinations, the testes were homogenized in 10 volumes of 0.15 M NaCl with a certain quantity of the homogenate. The activities of LDH, SODH, SDH, G-6PD, ACP, AKP, total nitric oxide synthase (TNOS), Ca^{2+}-ATPase, Ca^{2+}/Mg^{2+}-ATPase, and Na^+/K^+-ATPase in the testes were spectrophotometrically measured with a commercially available apparatus (Nanjing Jiancheng Bioengineering Institute, Jiangsu, China).

Oxidative Stress Assay. Reactive oxygen species (ROS) ($O_2^{\bullet-}$ and H_2O_2) production and levels of malondialdehyde (MDA), protein carbonyl (PC), and 8-hydroxydeoxyguanosine (8-OHdG) in the testicular tissues (n = 5 in each group) were assayed using commercial enzyme-linked immunosorbent assay kits (Nanjing Jiancheng Bioengineering Institute, Jiangsu, China) according to the manufacturer's instructions.

Statistical Analysis. All data are expressed as the mean ± standard deviation (SD). Statistical analysis was performed using SPSS 19 software (SPSS, Inc., Chicago, IL, USA), and statistical comparisons were analyzed using one way ANOVA followed by Tukey's HSD post hoc test. Differences with P values of less than 0.05 were considered significant.

RESULTS

Daily Food and Water Intake. The daily food and water intake of male mice after intragastric feeding with TiO_2 NPs at the last week in the second month is exhibited in Figure 1, suggesting that the daily food intake and water intake due to

DOI: 10.1021/acs.jafc.5b02652
J. Agric. Food Chem. 2015, 63, 7084−7092

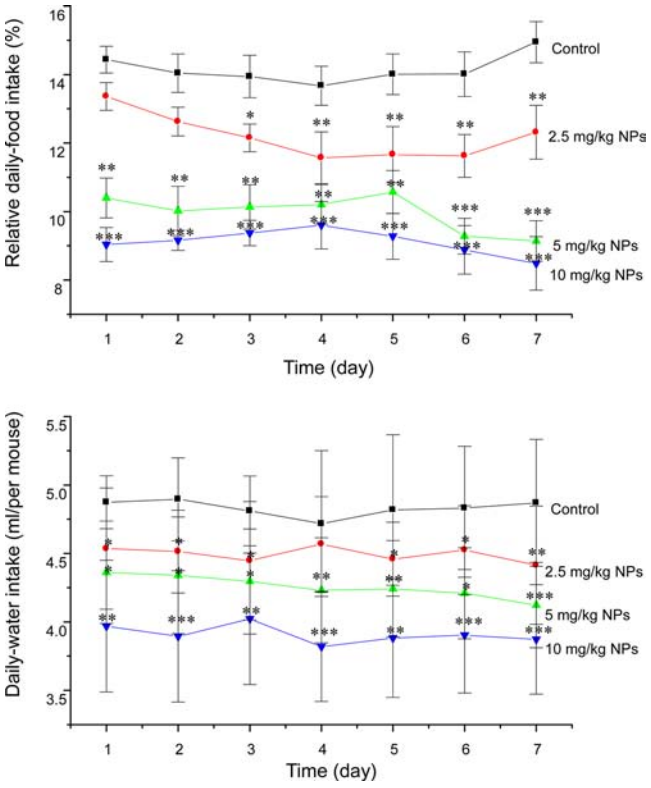

Figure 1. Daily food intake and water intake of male mice after intragastric feeding with TiO_2 NPs at the last week in the second month. *, $P < 0.05$, ** $P < 0.01$, and *** $P < 0.001$. Values represent means ± SD ($n = 10$).

TiO_2 NP exposure (2.5, 5, or 10 mg/kgbw) were decreased by 7.44% to 43.24% for daily food intake ($P < 0.05$), and by 3.82% to 16.41% for daily water intake ($P < 0.05$), respectively.

Body Weight and Testis Indices. The mice were weighed and sacrificed, and testis was also collected and weighed following the 60-day treatment with TiO_2 NPs. As shown in Table 1, with increasing TiO_2 NP dose, significant reductions in final body weight, testicular weight, and relative testicular weight were observed, e.g., final body weight, testicular weight, and relative testicular weight were reduced by 5.92%, 15.29%, and 19.6%, by 12.9%, 32.26%, and 41.94%, and by 7.41%, 20.0%, and 27.81% ($P < 0.05$), respectively. It suggested that decreases of testicular weight and relative testicular weight caused by TiO_2 NPs were higher than that of final body weight.

Semen Assay. Sperms from the cauda epididymis were collected, and the total sperm concentrations, sperm motility, and percentage of abnormal sperm were evaluated. With increasing TiO_2 NP dose (2.5, 5, or 10 mg/kgbw), sperm numbers and sperm motility were remarkably reduced by 29.73%, 40.54%, and 48.65% and by 7.45%, 27.65%, and 41.49%, respectively; whereas abnormal sperm was significantly elevated by 3.78-, 5.59-, and 11.64-fold in the TiO_2 NP-exposed groups (Figure 2, $P < 0.05$), respectively. In addition, we

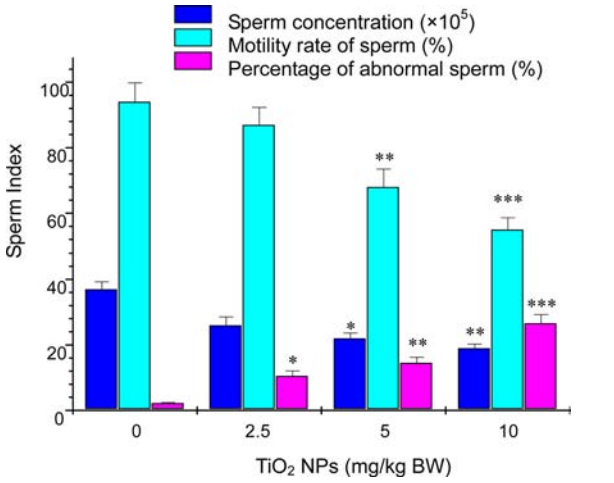

Figure 2. Total sperm concentration, sperm motility, and percentage of abnormal sperm following exposure to TiO_2 NPs for 60 consecutive days. * $P < 0.05$, ** $P < 0.01$, and *** $P < 0.001$. Values represent means ± SD ($n = 5$).

observed that TiO_2 NP exposure impaired sperm morphology, such as smears of treated mice with detached heads, an acute bend at the cephalocaudal junction from which fibrils projected out, in Figure 3.

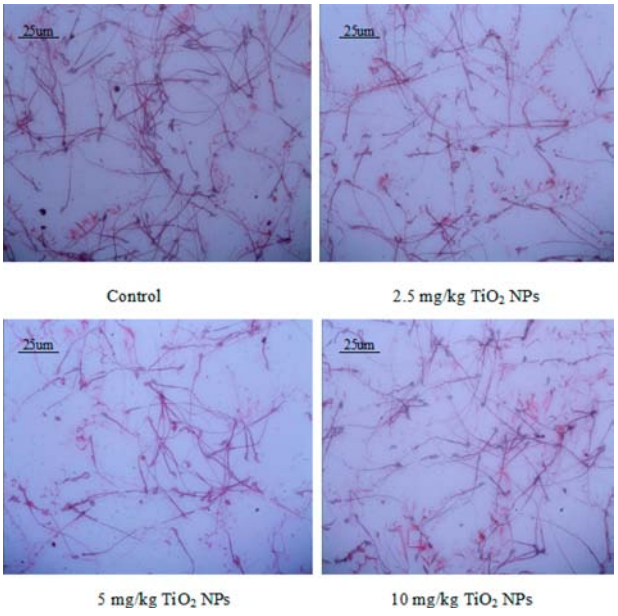

Figure 3. Morphological changes in sperm from male mice following intragastric administration of TiO_2 NPs for 60 consecutive days.

Table 1. Body Weight, Testicular Weight, and Relative Testicular Weight of Mice Following Exposure to TiO_2 NPs for 60 Consecutive Days[a]

index	0[b]	2.5[b]	5[b]	10[b]
final body wt (g)	38.32 ± 2.31	36.05 ± 2.46	32.46 ± 1.96*	30.81 ± 2.28**
testicular wt (g)	0.31 ± 0.06	0.27 ± 0.03	0.21 ± 0.04**	0.18 ± 0.02**
rel testicular wt (mg/g)	8.09 ± 0.81	7.49 ± 0.53	6.47 ± 0.55*	5.84 ± 0.49*

[a]* $P < 0.05$ and ** $P < 0.01$. Values represent means ± SD ($n = 10$). [b]Dose of TiO_2 NPs (mg/kg BW).

DOI: 10.1021/acs.jafc.5b02652
J. Agric. Food Chem. 2015, 63, 7084−7092

Histopathological Evaluation. Testis and epididymis histopathological images are shown in Figures 4 and 5.

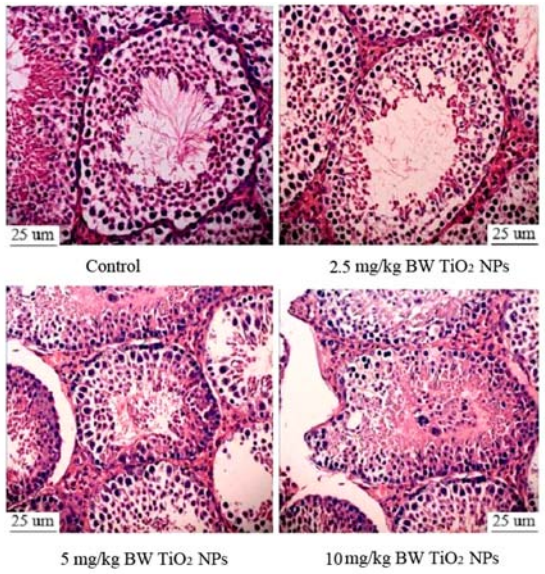

Figure 4. Histopathological observation of testis of male mice following exposure to TiO_2 NPs for 60 consecutive days. 2.5 mg/kg BW TiO_2 NPs: fragmentary seminiferous tubule and immature sperm. 5 mg/kg BW TiO_2 NPs: decreased seminiferous tubule epithelium layer and degeneration, sperm breakages, and spano-sperm within the lumen. 10 mg/kg BW TiO_2 NPs: decreased seminiferous tubule epithelium layer and degeneration, androgone fusion and pycnosis, and spano-sperm within the lumen.

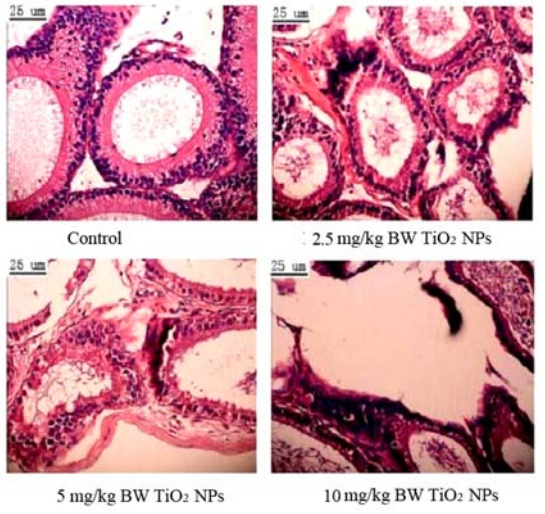

Figure 5. Histopathological observation of epididymis of male mice following exposure to TiO_2 NPs for 60 consecutive days. 5 mg/kg BW TiO_2 NPs: cell pycnosis, necrosis and abscission, spano-sperm within the lumen. 5 mg/kg BW TiO_2 NPs: cell pycnosis, necrosis and abscission, and spano-sperm within the lumen. 10 mg/kg BW TiO_2 NPs: severe destruction of tissue structure, and spano-sperm within the lumen.

Unexposed testis and epididymis samples presented intact architecture and regularly arranged cells, while those from the mice exposed to increasing concentrations of TiO_2 NPs exhibited severe pathological changes, including lowered seminiferous tubule epithelium layer and degeneration, reductions of Leydig cells and mature sperm within the lumen, immature sperm, sperm breakages, androgone fusion and/or pycnosis, and spermatolysis (Figure 4), cell pycnosis, necrosis and abscission, severe disorganization of tissue, and spano-sperm within the lumen (Figure 5).

Activity Testicular Marked Enzyme. The activities of testicular marked enzymes in mouse testis after intragastric administration with TiO_2 NPs for 60 consecutive days are presented in Table 2 and Figure 6. As suggested, with

Table 2. Changes of Testicular Marked Enzyme Activities of in Mouse Testis Following Exposure to TiO_2 NPs for 60 Consecutive Days[a]

	enzyme act. (U/g prot·min)			
	0[b]	2.5[b]	5[b]	10[b]
LDH	906 ± 60	801 ± 43	684 ± 41*	545 ± 50**
SODH	69.6 ± 6.2	53.2 ± 4.9	40.8 ± 4.0*	29.7 ± 2.3**
SDH	13.5 ± 1.3	9.9 ± 1.1*	7.9 ± 0.8**	5.7 ± 0.5***
G-6PD	15.9 ± 1.4	11.4 ± 1.5*	8.9 ± 1.1**	6.9 ± 0.8**
ACP	105 ± 10	116 ± 12	130 ± 14*	147 ± 13**
AKP	70.7 ± 6.8	85.3 ± 7.3*	97.2 ± 7.0*	116 ± 8.6**
NOS	15.8 ± 1.1	26.5 ± 2.0*	37.8 ± 2.5**	52.1 ± 4.2***

[a]* $P < 0.05$, ** $P < 0.01$, and *** $P < 0.001$. Values represent means ± SD ($n = 5$). [b]Dose of TiO_2 NPs (mg/kg BW).

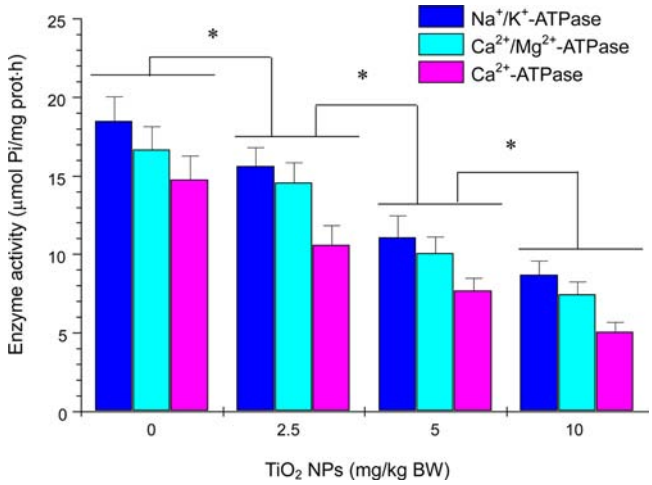

Figure 6. Changes of enzyme activities of testis in mice following exposure to TiO_2 NPs for 60 consecutive days. * $P < 0.05$. Values represent means ± SD ($n = 5$).

increasing TiO_2 NP dose (2.5, 5, or 10 mg/kgbw), the activities of LDH, SODH, SDH, G6PD, Na^+/K^+-ATPase, Ca^{2+}-ATPase, and Ca^{2+}/Mg^{2+}-ATPase were significantly decreased, with reductions of 11.59%, 24.5%, and 39.85% for LDH, 23.56%, 41.38%, and 57.33% for SODH, 27.03%, 41.33%, and 57.85% for SDH, 28.3%, 44.34%, and 56.42% for G6PD, 15.59%, 40.01%, and 53.11% for Na^+/K^+-ATPase, 12.44%, 39. %, and 55.41% for Ca^{2+}-ATPase, and 28.25%, 48.04%, and 65.72% for Ca^{2+}/Mg^{2+}-ATPase ($P < 0.05$), respectively, whereas the activities of ACP, AKP, and NOS were markedly elevated, with increases of 10.48%, 23.81%, and 40.0% for ACP, 20.65%, 37.48%, and 64.07% for AKP, and 67.72%, 139.24%, and 229.75% for NOS in the testis ($P < 0.05$), respectively.

Oxidative Damage of Testis. To confirm oxidative damage caused by exposure to TiO_2 NPs in the testis, oxidative indices including $O_2^{\bullet-}$, H_2O_2, MDA, and PC as well as 8-

DOI: 10.1021/acs.jafc.5b02652
J. Agric. Food Chem. 2015, 63, 7084−7092

Table 3. Oxidative Stress in Testis of Male Mice Caused by Intragastric Administration with TiO_2 NPs for 60 Consecutive Days[a]

index	oxidative stress			
	0[b]	2.5[b]	5[b]	10[b]
$O_2^{\bullet-}$ (nmol/mg prot·min)	45.2 ± 3.9	52.5 ± 4.0	88.6 ± 7.3**	95.2 ± 9.2**
H_2O_2 (nmol/mg prot·min)	58.3 ± 4.5	79.2 ± 7.2*	85.7 ± 13.6*	119 ± 10.1**
MDA (nmol/mg prot)	498 ± 42	692 ± 54*	918 ± 88**	1086 ± 102**
PC (nmol/mg prot)	753 ± 47	911 ± 78*	1105 ± 96**	1567 ± 146***
8-OHdG (ng/mL)	1.08 ± 0.17	2.05 ± 0.22**	2.25 ± 0.32**	3.06 ± 0.35***

[a]$P < 0.05$, ** $P < 0.01$, and *** $P < 0.001$. Values represent means ± SD ($n = 5$). [b]Dose of TiO_2 NPs (mg/kg BW).

OHdG levels were examined. As shown in Table 3, $O_2^{\bullet-}$, H_2O_2, MDA, and PC levels were significantly elevated, with increases of 16.15%, 96.02%, and 110.52% for $O_2^{\bullet-}$, 35.87%, 47.0%, and 104.11% for H_2O_2, 38.96%, 84.34%, and 118.07% for MDA, and 20.98%, 46.74%, and 108.1% for PC ($P < 0.05$) with increasing TiO_2 NPs dose, respectively. A marked increase in testicular 8-OHdG level was observed, with increases of 89.81%, 108.33%, and 183.33%, in the TiO_2 NP-treated groups ($P < 0.05$), respectively, indicating that excessive ROS production led to DNA damage in the testis due to TiO_2 NP-induced toxicity.

DISCUSSION

As an integral part of the nanotoxicology, the reproductive and developmental toxicity due to exposure to TiO_2 NPs has been demonstrated.[32,39,40,53−56] As suggested, testis is highly sensitive to toxic and hazardous nanomaterials; even when extremely low amounts of the substances are in the testis, they will still cause severe damage.[55] In testicular injuries, suppression of spermatogenesis and/or decreased sperm production have been suggested to be a significant state[56] and nanoparticles could affect spermatogenesis.[32,40,53] Our findings indicated that exposure to TiO_2 NPs for 60 consecutive days decreased daily food and water intake (Figure 1), final body weight testicular weight, relative testicular weight (Table 1), sperm concentrations and motility, increased the percentage of abnormal sperm (Figure 2), and caused sperm lesions in the cauda epididymis (Figure 3), impaired testis and epididymis architecture, and presented severe histopathological changes (Figures 4, 5); this is consistent with our previous reports.[40,53] Importantly, the present study observed that reductions of final body weight were lower than those of testicular weight, and relative testicular weight under TiO_2 NPs, indicating that exposure to TiO_2 NPs resulted in testicular toxicity, thus suppressed spermatogenesis in male mice. Decreased body weight may be related to appetite loss. Reduced food intake is closely involved in excessive ROS,[57] and TiO_2 NP exposure could result in the overproduction of ROS in mouse testis.[53] In our study, alterations of spermatogenesis-related factors of testicular marked enzymes and oxidative stress in the testis are examined, suggesting that exposure to TiO_2 NPs significantly inhibited the activities of LDH, SDH, SODH, G-6PD, Na^+/K^+-ATPase, Ca^{2+}-ATPase, and Ca^{2+}/Mg^{2+}-ATPase (Table 2, Figure 6) and increased the activities of ACP, AKP, and NOS (Table 2), promoted production of ROS, lipid and protein peroxidation and DNA injury (Table 3), which may be associated with reductions of both sperm concentrations and motility, and sperm lesions. The main results are discussed below.

As suggested, male fertility is associated with the successful perpetuation of spermatogenesis, the multistep process of male germ cell expansion and development in the seminiferous tubules of the testes.[58] In this process, a spermatogonium that yields a primary spermatocyte by mitosis divides into two secondary spermatocytes, then completes meiosis as it divides into two spermatids, which finally develop into mature sperm cells. However, hazardous substances could produce toxic effects (such as ROS overproduction) on the growth and development of male germ cells, leading to spermatogenesis disorder.[59] Importantly, spermatogenesis is considered to be a high-energy-demanding process, and the activities of energy metabolism-related enzymes, including LDH, SDH, and SODH, play key roles for the growth and development of testicular cells, while the energy metabolism disequilibrium in the spermatogenesis process may damage testicular cells.[41−43] As an important glycolytic enzyme, LDH catalyzes the conversion of pyruvate to lactate and is related to the maturation of the germinal epithelial layer of seminiferous tubule.[60] Due to spermatogenic cells locating behind the tight junction of Sertoli cells in the convoluted tubules of the testis, it is difficult for them to obtain nutrition from the testicular interstitium, and glycolysis is the pathway of dominating energy metabolism in the testis.[42] SDH is part of both the citric acid cycle and respiratory electron transfer chain and is a vital enzyme for aerobic respiration that is mainly located in spermatogenic cells and on sperm mitochondrial membrane,[61] and it could be a marker of maturity and perfect form of sperm function.[62] Because spermatozoa contain only a small amount of cytosol, the energy obtained is dependent upon SDH that is quicker than glucose in energy production.[41] SODH is considered to provide energy to sperm cells by converting sorbitol to fructose, and its activity elevates during the maturation of germ cells and reduces during the depletion of germ cells.[63,64] In our study, the decreased daily food intake (Figure 1) and activities of LDH, SODH, and SDH caused by TiO_2 NP exposure in the testis (Table 1) may be associated with disturbance to energy metabolism in germ cells, deterioration of germinal epithelium, and spermatogenic cell damage, further resulting in attenuation of both spermatogenesis and motility, and sperm lesions.

It has been demonstrated that testicular G-6PD is associated with androgen biogenesis.[43,65] The reduced testosterone (T) production from cholesterol is mainly ascribed to the lower supply of decreased NADPH that may be related to the reduced activity of G-6PD.[66] While G-6PD largely presents in the Leydig cells of seminiferous tubules, it is an important source of NADPH and a signal of Leydig cell function whether it promotes spermatogenesis or maintains sperm function.[67] It implies that reduction of G-6PD activity caused by TiO_2 NPs could influence the function of Leydig cells, thereby affecting

DOI: 10.1021/acs.jafc.5b02652
J. Agric. Food Chem. 2015, 63, 7084−7092

androgen secretion and spermatogenesis. Our previous study has suggested that TiO_2 NP exposure could lower T, follicle stimulating hormone (FSH), and luteinizing hormone (LH) levels in male mice,[40] showing that the growth and development of germ cells and Leydig cells in male mice treated by TiO_2 NPs could be inhibited, thus leading to spermatogenesis suppression, which is confirmed by the histopathological evaluation of testis (Figure 4).

To further determine whether testicular function is normal or not, activities of other testis-marker enzymes related with Sertoli (ACP) and germinal epithelium (AKP) were measured (Table 2). ACP is largely located in the cytoplasm of Sertoli cells, and its activity is directly associated with the degeneration of the seminiferous epithelium. The AKP activity in the testis is related to the division activity of testicular germ cell and the transport from glucose to spermatogenic cells.[45] Therefore, activities of ACP and AKP could be used as markers whether spermatogenesis was impaired. The increased activities of ACP and AKP due to TiO_2 NP exposure in mouse testis may reflect testicular degeneration, which may likely be a consequence of suppressed T and indicative of lytic activity,[68] and increase permeability of the cell membrane or cell degeneration and necrosis,[69] which is consistent with the histopathological evaluation of testis (Figure 4).

As suggested, NO signaling is involved in fertilization and in development in vertebrates, NOS is an important enzyme in the production of NO, and NO produced by NOS can decrease oxidative stress in reproductive system. A study found that the NOS expression of Sertoli cells depends on the presence of sperm cells, and is closely associated with the degree of development of sperm cells in the testis of infertile male.[46] Furthermore, the NO concentration in the testis also influences spermatogenesis, and reasonable NO concentration can maintain sperm motility, whereas excessive NO would damage the spermatogenesis and inhibit the sperm motility.[62] Due to significant elevations in NOS activity may be the most important determinant of increasing NO levels, and over NO production can quickly react with ROS resulting in the formation of the peroxynitrite anion ($ONOO^-$),[70] which can cause the testicular damage, as found in the pathological observations (Figure 4). Therefore, over higher NOS activity in mouse testis (Table 2) is related to impairment of sperm cell development and spermatogenesis under TiO_2 NP exposure. In addition, the changes of three important membrane ATP enzymes including Na^+/K^+-ATPase, Ca^{2+}/Mg^{2+}-ATPase, and Ca^{2+}-ATPase following exposure to TiO_2 NPs in the testis were examined. Na^+/K^+-ATPase and Ca^{2+}/Mg^{2+}-ATPase are demonstrated to keep intracellular gradients of ions that are essential for signal transduction. Na^+/K^+-ATPase plays the most important role in regulating of ion transport and generating of membrane potential in the male reproductive system.[71] Vignini et al. indicated that the decreased sperm motility and the lower sperm concentration are due to reductions of Na^+/K^+-ATPase and Ca^{2+}-ATPase activities.[72] In an in vitro study about testis Sertoli cells, the activities of Ca^{2+}-ATPase, Ca^{2+}/Mg^{2+}-ATPase, and Na^+/K^+-ATPase were increased shortly to help the outward transport of positive ions and finally reduced due to the disturbance of the membrane structure.[73] It is well-known that, in the front of sperm DNA, there is a top body containing calcium, and progesterone (P4) could greatly induce stimulation of Ca^{2+} channel on the sperm flagella.[74] According to the serum level of P_4, P_4-mediated intracellular Ca^{2+} could be evaluated, to judge the viability of sperm in male.[75] Ca^{2+} in cells is an essential element for cellular activities that are closely related with mitotic activity and development of cells. Its homeostasis in germ cells is dependent upon the function of Ca^{2+}-ATPase that transport cytosolic free Ca^{2+} into intracellular storage compartments.[76] It is also reported that Ca^{2+}-ATPase plays a key role in regulating spermatogenesis processes,[77] for instance, in the transition of spermatogenic cell to sperm cell, Ca^{2+} gradients across the plasma membrane and establish Ca^{2+} homeostasis and signaling are both maintained in part by plasma membrane Ca^{2+}-ATPase activity.[78] Our previous findings suggested that, with increased P_4 level following TiO_2 NP exposure, the intracellular calcium may be disordered, and resulted in spermatogenesis suppression.[40] In the present study, the significant reductions of Na^+/K^+-ATPase, Ca^{2+}/Mg^{2+}-ATPase, and Ca^{2+}-ATPase activities (Figure 6) were observed following TiO_2 NP induced toxicity in the testis, which may be associated with spermatogenesis disorder in male mice (Figures 2−5). These results give rise to a hypothesis: the lowered enzyme levels in the testis raise the possibility of imbalance in intracellular ion concentrations as a promoter of spermatogenesis dysfunction.

Oxidative damage can affect many classes of molecules including lipids, proteins, nucleic acids, and sugars. Thus, the cell nucleus, mitochondrial membranes, structural and cytoplasmic proteins, complex carbohydrates, RNA, and DNA may all potentially be affected by oxidative stress.[79] In the testis with high rates of metabolism and cell replication, oxidative stress can be especially produced. To further confirm oxidative damage in the testis, reactive oxygen specifics (such as $O_2^{\bullet-}$, H_2O_2), lipid peroxidative product (such as MDA), protein oxidative product (such as PC), and DNA damaged marker (such as 8-OHdG) levels were detected. Our data showed that increased MDA was concurrent with significant oxidative damage to testicular protein ((increased carbonyl level) and DNA (increased 8-OHdG level), which resulted from the overproduction of ROS due to TiO_2 NPs during the spermatogenesis process (Table 3), which is consistent with our previous reports.[53] Rajesh Kumar et al. showed that oxidative stress associated DNA damage in mouse testis could induce abnormal sperm and adverse effect on fertility.[80] When the oxidative stress in the male germ line is high level, normal fertilization could not occur successfully with peroxidation of unsaturated fatty acids in the sperm plasma membrane.[81] This excessive ROS production has been suggested to be closely connected with the imbalance of oxidative/antioxidative system in the testis.[82] The results indicated that testis underwent severe oxidative stress by exposure to TiO_2 NPs, leading to testicular dysfunctions and sperm lesions.

In conclusion, the current study indicated that dose-dependent exposure to TiO_2 NPs caused testicular toxicity, reduced sperm production, and induced sperm lesions in mouse testes, which were closely related to reductions of daily food and water intake, biochemical dysfunctions, and oxidative stress. Especially, LDH, SODH, SDH, G-6PD, AKP, ACP, NOS, and ATPases may be the biomarkers of spermatogenesis suppression caused by TiO_2 NP exposure. Therefore, in the application of TiO_2 NPs in different kinds of areas, more attention should be paid to the workers and consumers. Especially, potential epidemiological connections between nano TiO_2 consumption and reproductive health for male consumers or exposed male workers in nano workshop should be investigated in the future.

DOI: 10.1021/acs.jafc.5b02652
J. Agric. Food Chem. 2015, 63, 7084−7092

AUTHOR INFORMATION

Corresponding Authors

*E-mail: hfshui666@126.com. Tel: 86-13915553751.
*E-mail: nau_zjh@njau.edu.cn.

Author Contributions

‖F.H., W.S., and X.Z. contributed equally to this work.

Funding

This work was supported by National Natural Science Foundation of China (Grant No. 81473007, 81273036, 30901218).

Notes

The authors declare no competing financial interest.

REFERENCES

(1) Smolkova, B.; El Yamani, N.; Collins, A. R.; Gutleb, A. C.; Dusinska, M. Nanoparticles in food. Epigenetic changes induced by nanomaterials and possible impact on health. *Food Chem. Toxicol.* **2015**, *77*, 64−73.

(2) Bradley, E. L.; Castle, L.; Chaudhry, Q. Application of nanomaterials in food packaging with a consideration of opportunities for developing countries. *Trends Food Sci. Technol.* **2011**, *22*, 604−610.

(3) Skocaj, M.; Filipic, M.; Petkovic, J.; Novak, S. Titanium dioxide in our everyday life; is it safe? *Radiol. Oncol.* **2011**, *45*, 227−247.

(4) Mohammed Fayaz, A.; Balaji, K.; Girilal, M.; Kalaichelvan, P. T.; Venkatesan, R. Mycobased synthesis of silver nanoparticles and their incorporation into sodium alginate films for vegetable and fruit preservation. *J. Agric. Food Chem.* **2009**, *57*, 6246−6252.

(5) Lopez-Moreno, M. L.; de la Rosa, G.; Hernandez-Viezcas, J. A.; Peralta-Videa, J. R.; Gardea-Torresdey, J. L. X-ray absorption spectroscopy (XAS) corroboration of the uptake and storage of CeO_2 nanoparticles and assessment of their differential toxicity in four hdible plant species. *J. Agric. Food Chem.* **2010**, *58*, 3689−3693.

(6) Weir, A.; Westerhoff, P.; Fabricius, L.; Hristovski, K.; von Goetz, N. Titanium dioxide nanoparticles in food and personal care products. *Environ. Sci. Technol.* **2012**, *46*, 2242−2250.

(7) Chaudhry, Q.; Scotter, M.; Blackburn, J.; Ross, B.; Boxall, A.; Castle, L.; Aitken, R.; Watkins, R. Applications and implications of nanotechnologies for the food sector. *Food Addit. Contam., Part A* **2008**, *25*, 241−258.

(8) Baan, R.; Straif, K.; Grosse, Y.; Secretan, B.; El Ghissassi, F.; Cogliano, V. Carcinogenicity of carbon black, titanium dioxide, and talc. *Lancet Oncol.* **2006**, *7*, 295−296.

(9) Chen, X. X.; Cheng, B.; Yang, Y. X.; Cao, A.; Liu, J. H.; Du, L. J.; Liu, Y.; Zhao, Y.; Wang, H. Characterization and preliminary toxicity assay of nano-titanium dioxide additive in sugar-coated chewing gum. *Small* **2013**, *9*, 1765−1774.

(10) Oberdörster, G.; Stone, V.; Donaldson, K. Toxicology of nanoparticles: a historical perspective. *Nanotoxicology* **2007**, *1*, 2−25.

(11) Ma, L. L.; Zhao, J. F.; Wang, J.; Liu, J.; Duan, Y. M.; Liu, H. T.; Li, N.; Yan, J. Y.; Ruan, J.; Wang, H.; Hong, F. S. The acute liver injury in mice caused by nano-anatase TiO_2. *Nanoscale Res. Lett.* **2009**, *4*, 1275−1285.

(12) Duan, Y. M.; Liu, J.; Ma, L. L.; Li, N.; Liu, H. T.; Wang, J.; Zheng, L.; Liu, C.; Wang, X. F.; Zhao, X. Y.; Yan, J. Y.; Wang, S. S.; Wang, H.; Zhang, X. G.; Hong, F. S. Toxicological characteristics of nanoparticulate anatase titanium dioxide in mice. *Biomaterials* **2010**, *31*, 894−899.

(13) Cui, Y. L.; Liu, H. T.; Zhou, M.; Duan, Y. M.; Li, N.; Gong, X. L.; Hu, R. P.; Hong, M. M.; Hong, F. S. Signaling pathway of inflammatory responses in the mouse liver caused by TiO_2 nanoparticles. *J. Biomed. Mater. Res., Part A* **2011**, *96A*, 221−229.

(14) Cui, Y. L.; Liu, H. T.; Ze, Y. G.; Zengli, Z. L.; Hu, Y.; Cheng, Z.; Cheng, J.; Hu, R. P.; Gao, G. D.; Wang, L.; Tang, M.; Hong, F. S. Gene expression in liver injury caused by long-term exposure to titanium dioxide nanoparticles in mice. *Toxicol. Sci.* **2012**, *128* (1), 171−185.

(15) Hong, J.; Wang, L.; Zhao, X. Y.; Yu, X. H.; Sheng, L.; Xu, B. Q.; Liu, D.; Zhu, Y. T.; Long, Y.; Hong, F. S. Th2 Factors may be involved in TiO_2 NP-induced hepatic inflammation. *J. Agric. Food Chem.* **2014**, *62*, 6871−6878.

(16) Liu, X.; Li, N.; Sang, X.; Sun, Q.; Gao, G.; Cheng, Z.; Cheng, J.; Wang, L.; Tang, M.; Hong, F. S. The molecular mechanism of kidney injury of mice caused by exposure to titanium dioxide nanoparticles. *J. Hazard. Mater.* **2011**, *195*, 365−370.

(17) Gui, S. X.; Sang, X. Z.; Zheng, L.; Ze, Y. G.; Zhao, X. Y.; Sheng, L.; Sun, Q. Q.; Cheng, Z.; Cheng, J.; Hu, R. P.; Wang, L.; Hong, F. S.; Tang, M. Intragastric exposure to titanium dioxide nanoparticles induced nephrotoxicity in mice, assessed by physiological and gene expression modifications. *Part. Fibre Toxicol.* **2013**, *10*, 4.

(18) Gui, S. X.; Li, B. Y.; Zhao, X. Y.; Sheng, L.; Hong, J.; Yu, X. H.; Sang, X. Z.; Sun, Q. Q.; Ze, Y. G.; Wang, L.; Hong, F. S. Renal injury and Nrf2 modulation in mouse kidney following exposure to titanium dioxide nanoparticles. *J. Agric. Food Chem.* **2013**, *61*, 8959−8968.

(19) Hong, F. S.; Hong, J.; Wang, L.; Zhou, Y. J.; Liu, D.; Xu, B. Q.; Yu, X. H.; Sheng, L. Chronic exposure to nanoparticulate TiO_2 causes renal fibrosis involving activation of the Wnt pathway in mouse kidney. *J. Agric. Food Chem.* **2015**, *63* (5), 1639−1647.

(20) Sang, X. Z.; Zheng, L.; Sun, Q. Q.; Li, N.; Cui, Y. L.; Hu, R. P.; Gao, G. D.; Cheng, Z.; Cheng, J.; Gui, S. X.; Liu, H. T.; Zhang, Z. L.; Hong, F. S. The chronic spleen injury of mice following long-term exposure to titanium dioxide nanoparticles. *J. Biomed. Mater. Res., Part A* **2012**, *100A* (4), 894−902.

(21) Sang, X. Z.; Li, B.; Ze, Y. G.; Hong, J.; Ze, X.; Gui, S. X.; Sun, Q. Q.; Liu, H. T.; Zhao, X. Y.; Sheng, L.; Liu, D.; Yu, X. H.; Wang, L.; Hong, F. S. Toxicological Mechanisms of Nanosized Titanium Dioxide-Induced Spleen Injury in Mice after Repeated Peroral Application. *J. Agric. Food Chem.* **2013**, *61* (23), 5590−5599.

(22) Sang, X. Z.; Fei, M.; Sheng, L.; Zhao, X. Y.; Yu, X. H.; Hong, J.; Ze, Y. G.; Gui, S. X.; Sun, Q. Q.; Ze, X.; Wang, L.; Hong, F. S. Immunomodulatory effects in the spleen-injured mice following exposure to titanium dioxide nanoparticles. *J. Biomed. Mater. Res., Part A* **2014**, *102A*, 3562−3572.

(23) Sheng, L.; Wang, L.; Sang, X. Z.; Zhao, X. Y.; Hong, J.; Cheng, S.; Yu, X. H.; Liu, D.; Xu, B. Q.; Hu, R. P.; Sun, Q. Q.; Cheng, J.; Cheng, Z.; Gui, S. X.; Hong, F. S. Nano-sized titanium dioxide-induced splenic toxicity: A biological pathway explored using microarray technology. *J. Hazard. Mater.* **2014**, *278*, 180−188.

(24) Sun, Q. Q.; Tan, D.; Ze, Y. G.; Sang, X. Z.; Liu, X.; Gui, S. X.; Cheng, Z.; Cheng, J.; Hu, R. P.; Gao, G. D.; Liu, G.; Zhu, M.; Zhao, X. Y.; Sheng, L.; Wang, L.; Tang, M.; Hong, F. S. Pulmotoxicological effects caused by long-term titanium dioxide nanoparticles exposure in mice. *J. Hazard. Mater.* **2012**, *235*−*236*, 47−53.

(25) Sun, Q. Q.; Tan, D. L.; Zhou, Q. P.; Liu, X. R.; Cheng, Z.; Liu, G.; Zhu, M.; Sang, X. Z.; Gui, S. X.; Cheng, J.; Hu, R. P.; Tang, M.; Hong, F. S. Oxidative damage of lung and its protective mechanism in mice caused by long-term exposure to titanium dioxide nanoparticles. *J. Biomed. Mater. Res., Part A* **2012**, *100A* (10), 2554−2562.

(26) Li, B.; Ze, Y. G.; Sun, Q. Q.; Zhang, T.; Sang, X. Z.; Cui, Y. L.; Wang, X. C.; Gui, S. X.; Tan, D. L.; Zhu, M.; Zhao, X. Y.; Sheng, L.; Wang, L.; Hong, F. S.; Tang, M. Molecular mechanisms of nanosized titanium dioxide-induced pulmonary injury in mice. *PLoS One* **2013**, *8* (2), e55563.

(27) Ma, L. L.; Liu, J.; Li, N.; Wang, J.; Duan, Y. M.; Yan, J. Y.; Liu, H. T.; Wang, H.; Hong, F. S. Oxidative stress in the brain of mice caused by translocated nanoparticulate TiO_2 delivered to the abdominal cavity. *Biomaterials* **2010**, *31*, 99−105.

(28) Hu, R. P.; Gong, X. L.; Duan, Y. M.; Li, N.; Che, Y.; Cui, Y. L.; Zhou, M.; Liu, C.; Wang, H.; Hong, F. S. Neurotoxicological effects and the impairment of spatial recognition memory in mice caused by exposure to TiO2nanoparticles. *Biomaterials* **2010**, *31*, 8043−8050.

(29) Ze, Y. G.; Hu, R. P.; Wang, X. C.; Sang, X. Z.; Ze, X.; Li, B.; Su, J. J.; Wang, Y.; Guan, N.; Zhao, X. Y.; Gui, S. X.; Zhu, L. Y.; Cheng, Z.; Cheng, J.; Sheng, L.; Sun, O. O.; Wang, L.; Hong, F. S. Neurotoxicity and gene-expressed profile in brain-injured mice caused by exposure to

DOI: 10.1021/acs.jafc.5b02652
J. Agric. Food Chem. 2015, 63, 7084−7092

titanium dioxide nanoparticles. *J. Biomed. Mater. Res., Part A* **2014**, *102A*, 470−478.
(30) Ze, Y. G.; Sheng, L.; Zhao, X. Y.; Ze, X.; Wang, X. C.; Zhou, Q. P.; Liu, J. L.; Yuan, Y. F.; Gui, S. X.; Sang, X. Z.; Sun, Q. Q.; Hong, J.; Yu, X. H.; Wang, L.; Li, B. Y.; Hong, F. S. Neurotoxic characteristics of spatial recognition damage of the hippocampus in mice following subchronic peroral exposure to TiO_2 nanoparticles. *J. Hazard. Mater.* **2014**, *264*, 219−229.
(31) Su, M. Y.; Ze, Y. G.; Zhao, X. Y.; Wang, L.; Yu, X. H.; Hong, J.; Xu, B. Q.; Liu, D.; Hong, F. S. Involvement of neurotrophins and related signaling genes in TiO_2 nanoparticle − induced inflammation in the hippocampus of mice . *Toxicol. Res.* **2015**, *4*, 344−350.
(32) Lan, Z.; Yang, W.-X. Nanoparticles and spermatogenesis: how do nanoparticles affect spermatogenesis and penetrate the blood−testis barrier. *Nanomedicine* **2012**, *7* (4), 579−596.
(33) Komatsu, T.; Tabata, M.; Kubo-Irie, M.; Shimizu, T.; Suzuki, K. I.; Nihei, Y.; Takeda, K. The effects of nanoparticles on mouse testis Leydig cells *in vitro*. *Toxicol. In Vitro* **2008**, *22*, 1825−1831.
(34) Hou, J.; Wan, X.-y.; Wang, F.; Xu, G.-f.; Liu, Z.; Zhang, T.-b. Effects of titanium dioxide nanoparticles on development and maturation of rat preantral follicle *in vitro*. *Acad. J. Second Mil. Med. Univ.* **2009**, *30* (8), 869−873 (abstract in English).
(35) Suzuki, H.; Toyooka, T.; Ibuki, Y. Simple and easy method to evaluate uptake potential of nanoparticles in mammalian cells using a Flow Cytometric Light Scatter Analysis. *Environ. Sci. Technol.* **2007**, *41* (8), 3018−3024.
(36) Ema, M.; Kobayashi, N.; Naya, M.; Hanai, S.; Nakanishi, J. Reproductive and developmental toxicity studies of manufactured nanomaterials. *Reprod. Toxicol.* **2010**, *30* (3), 343−352.
(37) Takeda, K.; Suzuki, K.; Ishihara, A.; Kubo-Irie, M.; Fujimoto, R.; Tabata, M.; Oshio, S.; Nihei, Y.; Ihara, T.; Sugamata, M. Nanoparticles transferred from pregnant mice to their offspring can damage the genital and cranial nerve systems. *J. Health Sci.* **2009**, *55*, 95−102.
(38) Guo, L. L.; Liu, X. H.; Qin, D. X.; Gao, L.; Zhang, H. M.; Liu, J. Y.; Cui, Y. G. Effects of nanosized titanium dioxide on the reproductive system of male mice. *Zhonghua Nankexue* **2009**, *15*, 517−522 (abstract in English).
(39) Gao, G.; Ze, Y.; Li, B.; Zhao, X.; Zhang, T.; Sheng, L.; Hu, R.; Gui, S.; Sang, X.; Sun, Q.; Cheng, J.; Cheng, Z.; Wang, L.; Tang, M.; Hong, F. Ovarian dysfunction and gene-expressed characteristics of female mice caused by long-term exposure to titanium dioxide nanoparticles. *J. Hazard. Mater.* **2012**, *243*, 19−27.
(40) Gao, G.; Ze, Y.; Zhao, X.; Sang, X.; Zheng, L.; Ze, X.; Gui, S.; Sheng, L.; Sun, Q.; Hong, J.; Yu, X.; Wang, L.; Hong, F.; Zhang, X. Titanium dioxide nanoparticle-induced testicular damage, spermatogenesis suppression, and gene expression alterations in male mice. *J. Hazard. Mater.* **2013**, *258*−*259*, 133−143.
(41) Abdul-Ghani, A.-S.; Dabdoub, N.; Muhammad, R.; Abdul-Ghani, R.; Qazzaz, M. Effect of Palestinian honey on spermatogenesis in rats. *J. Med. Food* **2008**, *11*, 799−802.
(42) Yan, L.; Yue, D.; Luo, H.; Jin, X.; Xu, X. Effect of vitamin E supplementation on the enzymatic activity of selected markers in Aohan fine-wool sheep testis. *Anim. Reprod. Sci.* **2010**, *122*, 264−269.
(43) Lv, Y.; Liu, Z.; Tian, Y.; Chen, H. Effect on morphology, oxidative stress and energy metabolism enzymes in the testes of mice after a 13-week oral administration of melamine and cyanuric acid combination. *Regul. Toxicol. Pharmacol.* **2013**, *65* (2), 183−8.
(44) Pankajakshy, A.; Madambath, I. Spermatotoxic effects of Cananga odorata (Lam): a comparison with gossypol. *Fertil. Steril.* **2009**, *91* (5), 2243−2246.
(45) Khan, I. A.; Reddy, B. V.; Mahboob, M.; Rahman, M. F.; Jamil, K. Acute and sub-acute effects of 2-butenoic acid-3-(diethoxy phosphinothioyl) methyl ester (RPR-II) on testis of albino rat. *Indian J. Exp. Biol.* **2002**, *40* (2), 162−168.
(46) Fujisawa, M.; Yamanaka, K.; Tanaka, H.; Tanaka, H.; Okada, H.; Arakawa, S.; Kamidono, S. Expression of endothelial nitric oxide synthase in the Sertoli cells of men with infertility of various causes. *BJU Int.* **2001**, *87* (1), 85−88.
(47) Chan, H. C.; Wu, W. L.; Sun, Y. P.; Leung, P. S.; Wong, T. P.; Chung, Y. W.; So, S. C.; Zhou, T. S.; Yan, Y. C. Expression of sperm Ca^{2+}-activated K^+ channels in Xenopus oocytes and their modulation by extracellular ATP. *FEBS Lett.* **1998**, *438* (3), 177−182.
(48) Sikka, S. C. Relative impact of oxidative stress on male reproductive function. *Curr. Med. Chem.* **2001**, *8*, 851−862.
(49) Murugesan, P.; Muthusamy, T.; Balasubramanian, K.; Arunakaran, J. Studies on the protective role of vitamin C and E against polychlorinated biphenyl (Aroclor 1254)-induced oxidative damage in Leydig cells. *Free Radical Res.* **2005**, *39*, 1259−1272.
(50) Yang, P.; Lu, C.; Hua, N.; Du, Y. Titanium dioxide nanoparticles co-doped with Fe^{3+} and Eu^{3+} ions for photocatalysis. *Mater. Lett.* **2002**, *57*, 794−801.
(51) Hu, R.; Zheng, L.; Zhang, T.; Gao, G.; Cui, Y.; Cheng, Z.; Cheng, J.; Hong, M.; Tang, M.; Hong, F. Molecular mechanism of hippocampal apoptosis of mice following exposure to titanium dioxide nanoparticles. *J. Hazard. Mater.* **2011**, *191*, 32−40.
(52) Drozdz, A. Food habits and food assimilation in mammals. In *Methods for ecological bioenergetics*; Grodzinki, W., Klekowski, R. Z., Duncan, A., Eds.; Oxford Blackwell: 1975; pp 333−337.
(53) Zhao, X. Y.; Sheng, L.; Wang, L.; Hong, J.; Yu, X. H.; Sang, X. Z.; Sun, Q. Q.; Ze, Y. g.; Hong, F. S. Mechanisms of nanosized titanium dioxide-induced testicular oxidative stress and apoptosis in male mice. *Part. Fibre Toxicol.* **2014**, *11*, 47.
(54) Ema, M.; Kobayashi, N.; Naya, M.; Hanai, S.; Nakanishi, J. Reproductive and developmental toxicity studies of manufactured nanomaterials. *Reprod. Toxicol.* **2010**, *30* (3), 343−352.
(55) Moline, J. M.; Golden, A. L.; Bar-Chama, N.; Smith, E.; Rauch, M. E.; Chapin, R. E.; Perreault, S. D.; Schrader, S. M.; Suk, W. A.; Landrigan, P. J. Exposure to hazardous substances and male reproductive health: a research framework. *Environ. Health Perspect* **2000**, *108*, 803−813.
(56) Kyjovska, Z. O.; Boisen, A. M.; Jackson, P.; Wallin, H.; Vogel, U.; Hougaard, K. S. Daily sperm production: Application in studies of prenatal exposure to nanoparticles in mice. *Reprod. Toxicol.* **2013**, *36*, 88−97.
(57) Benani, A.; Troy, S.; Carmona, M. C.; Fioramonti, X.; Lorsignol, A.; Leloup, C.; Casteilla, L.; Pé nicaud, L. Role for mitochondrial reactive oxygen species in brain lipid sensing: Redox regulation of food intake. *Diabetes* **2007**, *56*, 152−160.
(58) Smith, L. B.; Walker, W. H. The regulation of spermatogenesis by androgens. *Semin. Cell Dev. Biol.* **2014**, *30*, 2−13.
(59) Adedara, I. A.; Lawal, T. A.; Adesina, A. A.; Oyebiyi, O. O.; Ebokaiwe, A. P.; Farombi, E. O. Sperm functional parameters and erythrocytes oxidant-antioxidant imbalance during municipal landfill leachate treatment withdrawal in rats. *Environ. Toxicol. Pharmacol.* **2014**, *37* (1), 460−467.
(60) Pant, N.; Murthy, R. C.; Srivastava, S. P. Male reproductive toxicity of sodium arsenite in mice. *Hum. Exp. Toxicol.* **2004**, *23*, 399−403.
(61) Rutter, J.; Winge, D. R.; Schiffman, J. D. Succinate dehydrogenase − Assembly, regulation and role in human disease. *Mitochondrion* **2010**, *10* (4), 393−401.
(62) Mylchreest, E.; Cattley, R. C.; Foster, P. M. Male reproductive tract malformations in rats following gestational and lactational exposure to di(n-butyl)phthalate an antiandrogenic mechanism. *Toxicol. Sci.* **1998**, *43* (1), 47−60.
(63) Srivastava, S.; Sing, G. B.; Srivastava, S. P.; Seth, P. K. Testicular toxicity of di-n-butyl phthalate in adult rats: effect on marker enzymes of spermatogenesis. *Indian J. Exp. Biol.* **1990**, *28*, 67−70.
(64) Samadder, A.; Das, J.; Das, S.; Khuda-Bukhsh, A. R. Dihydroxy-isosteviol- methyl-ester, an active biological component of Pulsatilla nigricans, reduces arsenic induced cellular dysfunction in testis of male mice. *Environ. Toxicol. Pharmacol.* **2012**, *34* (3), 743−752.
(65) Anuja, M. N.; Nithya, R. N.; Rajamanickam, C.; Madambath, I. Spermatotoxicity of a protein isolated from the root of Achyranthes aspera: a comparative with gossypol. *Contraception* **2010**, *82* (4), 385−390.

DOI: 10.1021/acs.jafc.5b02652
J. Agric. Food Chem. 2015, 63, 7084−7092

(66) Gupta, R. S.; Sharma, A. Antifertility effects of Tinospora cordifolia stem extracts in male rats. *Indian J. Exp. Biol.* **2003**, *41*, 885−889.
(67) Dhanapal, R.; Ratna, J. V.; Sarathchandran, I.; Gupta, M. Reversible antispermatogenic and antisteroidogenic activities of Feronia limonia fruit pulp in adult male rats. *Asian Pac. J. Trop. Biomed.* **2012**, *2* (9), 684−690.
(68) Kaur, R.; Dhanuju, C. K.; Kaur, K. Effect of dietary selenium on biochemical composition in rat testis. *Indian J. Exp. Biol.* **1999**, *37*, 509−511.
(69) Yousef, M. I. Aluminium-induced changes in hemato-biochemical parameters, lipid peroxidation and enzyme activities of male rabbits: protective role of ascorbic acid. *Toxicology* **2004**, *199* (1), 47−57.
(70) Lipton, S. A.; Choi, Y.-B.; Pan, Z.-H.; Lei, S. Z.; Chen, H.-S. V.; Sucher, N. J.; Loscalzo, J.; Singel, D. J.; Stamler, J. S. A redox-based mechanism for the neuroprotective effects of nitric oxide and related nitroso-compounds. *Nature* **1993**, *364*, 626−632.
(71) Florman, H. M.; Babcock, D. F. *Elements of Mammalian Fertilization: Basic Concepts*; Wassarman, P. M., Ed.; CRC Press: Boca Raton, FL, 1991; pp 105−132.
(72) Hickey, K. D.; Buhr, M. M. Characterization of Na^+K^+-ATPase in bovine sperm. *Theriogenology* **2012**, *77* (7), 1369−1380.
(73) Vignini, A.; Buldreghini, E.; Nanetti, L.; Amoroso, S.; Boscaro, M.; Ricciardo-Lamonica, G.; Mazzanti, L.; Balercia, G. Free thiols in human spermatozoa: are Na^+K^+-ATPase, Ca^{2+}-ATPase activities involved in sperm motility through peroxynitrite formation? *Reprod. BioMed. Online* **2009**, *18* (1), 132−140.
(74) Strünker, T.; Goodwin, N.; Brenker, C.; Kashikar, N. D.; Weyand, I.; Seifert, R.; Kaupp, U. B. The CatSper channel mediates progesterone-induced Ca^{2+} influx in human sperm. *Nature* **2011**, *471* (7338), 382−386.
(75) Ren, D.; Navarro, B.; Perez, G.; Jackson, A. C.; Hsu, S.; Shi, Q.; Tilly, J. L.; Clapham, D. E. A sperm ion channel required for sperm motility and male fertility. *Nature* **2001**, *413* (6856), 603−609.
(76) Gong, Y.; Pan, X. P.; Huang, Y. F.; Gao, Z. S.; Yu, H. X.; Han, X. D. NP-induced biophysical and biochemical alterations of rat testicular Sertoli cell membranes related to disturbed intracellular Ca^{2+} homeostasis. *Toxicol. Lett.* **2008**, *183*, 10−20.
(77) Sengupta, T.; Ghoshal, S.; Dungdung, S. R.; Majumder, G. C.; Sen, P. C. Structural and functional characterization and physiological significance of a stimulator protein of Mg^{2+}-independent Ca^{2+}-ATPase isolated from goat spermatozoa. *Mol. Cell. Biochem.* **2008**, *311* (1−2), 93−103.
(78) Kumosani, T. A.; Elshal, M. F.; Al-Jonaid, A. A.; Abduljabar, H. S. The influence of smoking on semen quality, seminal microelements and Ca^{2+}-ATPase activity among infertile and fertile men. *Clin. Biochem.* **2008**, *41* (14−15), 1199−1203.
(79) Pryor, W. A.; Houk, K. N.; Foote, C. S.; Fukuto, J. M.; Ignarro, L. J.; Squadrito, G. L.; Davies, K. J. A. Free radical biology and medicine: it's a gas, man! *Am. J. Physiol.: Regul., Integr. Comp. Physiol.* **2006**, *291*, R491−R511.
(80) Rajesh Kumar, T.; Doreswamy, K.; Shrilatha, B.; Muralidhara. Oxidative stress associated DNA damage in testis of mice: induction of abnormal sperms and effects on fertility. *Mutat. Res., Genet. Toxicol. Environ. Mutagen.* **2002**, *513* (1−2), 103−111.
(81) Aitken, R. J.; Baker, M. A. Oxidative stress, sperm survival and fertility control. *Mol. Cell. Endocrinol.* **2006**, *250* (1−2), 66−69.
(82) Liu, Y.; Long, J.; Zhang, L. W.; Zhang, H.; Liu, B.; Zhao, W. P.; Wu, Z. H. Low-dose carbon ion irradiation effects on DNA damage and oxidative stress in the mouse testis. *Adv. Space Res.* **2011**, *47* (1), 55−59.

DOI: 10.1021/acs.jafc.5b02652
J. Agric. Food Chem. 2015, 63, 7084−7092

JOURNAL OF AGRICULTURAL AND FOOD CHEMISTRY

Addition/Correction

pubs.acs.org/JAFC

Correction to MALDI-TOF-MS Platform for Integrated Proteomic and Peptidomic Profiling of Milk Samples Allows Rapid Detection of Food Adulterations

Mauro Sassi, Simona Arena, and Andrea Scaloni*

J. Agric. Food Chem. **2015**, *63* (27), 6157−6171. DOI: 10.1021/acs.jafc.5b02384

Table 3 was missing two subheadings in the original publication.
The corrected table appears below.

Table 3. Marker Species Recognized during MALDI-TOF-MS Protein Profiling for Milk Speciation[a]

DAve	description	exptl MH^+	theor MH^+ (UniProt Code)
	Bovine Milk		
36.26	α-lactalbumin	14181	14179 (P00711)
29.46	γ2-casein/β-casein f(106−209)	11827	11825 (P02666)
17.55	γ3-casein/β-casein f(108−209)	11560	11560 (P02666)
15.97	unknown	12006	
10.29	proteoso peptone p.p.8.I/β-casein f(29−105)	8640	8638 (P02666)
	Buffalo Milk		
33.66	β-casein f(69−209)	15749	15750 (Q9TSI0)
30.90	unknown	11991	
30.39	γ3-casein/β-casein f(108−209)	11521	11520 (Q9TSI0)
27.62	β-casein f(1−68)P_5	8251	8252 (Q9TSI0)
20.56	γ2-casein/β-casein f(106−209)	11786	11785 (Q9TSI0)
16.63	α-lactalbumin variant B	14236	14236
	Goat Milk		
36.26	α-lactalbumin variant A	14186	14187 (P00712)
29.02	unknown	11882	
21.33	γ3-casein/β-casein f(108−207)	11288	11287 (Q95L76)
16.48	unknown	11922	
15.17	unknown	5891	
14.06	γ2-casein/β-casein f(106−207)	11554	11553 (Q95L76)
9.48	β-casein f(98−207)	12466	12466 (Q95L76)
8.66	β-lactoglobulin	18185	18187 (P02756)
	Ovine Milk		
36.25	γ2-casein/β-casein f(106−207)	11536	11535 (P11839)
31.26	γ3-casein/β-casein f(108−207)	11271	11270 (P11839)
22.59	unknown	8573	
14.40	β-casein f(98−207)	12449	12448 (P11839)
9.48	unknown	9712	

[a]MS experiments were performed in linear mode as reported under Experimental Procedures. Difference value between the maximal and the minimal average peak/area intensity of all classes (DAve) (see ClinProt Tools software for details), protein/polypeptide name, and experimental/theoretical MH^+ (average) value are reported. Theoretical MH^+ values were calculated according to the amino acid sequence entries present in the UniProt Knowledge Database and the corresponding post-translational modifications. P, phosphate; f, fragment. α-Lactalbumin variant B mass value was calculated according to dedicated studies.[35]

Published: July 29, 2015

ACS Publications © 2015 American Chemical Society

DOI: 10.1021/acs.jafc.5b03524
J. Agric. Food Chem. 2015, 63, 7093−7093

JOURNAL OF AGRICULTURAL AND FOOD CHEMISTRY

Editorial

pubs.acs.org/JAFC

Vanishing Boundaries between Chemistry and Biology: Reflections on Our Journal

Six months after taking over the position of the Editor-in-Chief of the *Journal of Agricultural and Food Chemistry* (JAFC), it is time to draw a first summary. First of all, I would like to thank the authors for consistently submitting the best of their scientific work to our journal during this transition time, our international team of Associate Editors for their unbroken passion to further increase the quality of papers published, and Matt Hotze for his continuous efforts as the Managing Editor of JAFC. My transition into the role of EIC would never have been successful without Matt being highly committed to pursuing the everyday tasks of dealing with papers and reviewers, growing experiences that are pivotal for us. As you might have noticed that the journal has been changing within the past months, I would like to take this opportunity to share changes in personnel with you, define the scope of the journal, and clarify our current thinking on the standard for papers we wish to publish.

Since March 2015, the team of 12 Associate Editors has been expanded by a new member: Holger Zorn, Director of the Institute of Food Chemistry and Food Biotechnology, Justus Liebig University Giessen, Germany. Holger is a trained food chemist focusing on the enzymology of basidiomycetous fungi and insects. He is building a bridge from the discovery of biochemical phenomena to novel biocatalysts tailored to industrial applications (e.g., flavor biotechnology and enzymatic utilization of renewable resources including the final downstream processing). Besides knowledge on enzymology and protein chemistry, he brings new expertise on molecular biotechnology and modern bioanalytics to the team. Holger, cordial welcome to our team!

The changes in the Editorial Team have mirrored adjustments to the scope of JAFC. Founded in 1953, the journal has been the home of significant advances in agricultural and food chemistry, while reflecting the broad interest of those who practice it. The journal's scope had grown organically over the decades to include the related fields of bioactive molecules, molecular nutrition, and chemosensory research, to name a few. This has resulted in our citations increasing to over 82000 in 2014. In the future, the journal will continue to publish original and high-quality chemical research advancing the molecular understanding of renewable resources, product attributes, processes, and technologies, as well as health aspects encompassing the agriculture–food–nutrition continuum. However, the boundaries between chemistry and biology are vanishing. With this in mind we will now also consider manuscripts that have a fundamental component of biochemistry and/or molecular biology. This can be combined with novel aspects of process engineering and food technology, authenticity and origin aspects of food, or the biological evaluation of agricultural and/or food systems. The latter may include microbial, nutritional, physiological, sensory, or toxicological properties; however, data must accompany sufficient discussion to demonstrate their relevance to food and nutrition. Concurrent with these changes to our scope, we have also reconsidered the sections the journal is divided into. Current specific categories within the scope of the journal include the following:

(i) *Agricultural and Environmental Chemistry*: to advance molecular knowledge (e.g., crop protection chemistry, nanotechnology, natural toxins, fate and biotransformation of residues) and understanding of mechanisms of action of agrochemicals and to promote innovative solutions for increased agricultural productivity, a sustainable supply of food and fiber, and protection of public health and the environment including water quality/treatment, agricultural waste, and energy-related issues.

(ii) *Bioactive Constituents, Metabolites, and Functions*: to increase knowledge of chemical structures of bioactive constituents, phytonutrients, and nutraceuticals in foods, their human metabolism, and their mechanisms of biological function to affect human health status, including various aspects of molecular nutrition such as nutritional biochemistry, nutrigenomics, and metabolomics.

(iii) *Biofuels and Biobased Materials*: to advance knowledge of the chemistry, biology, and processing of biobased products and biofuels including all of the related areas of biodiesel, bioethanol, biogas, biotransformations, and bioprocesses (plants, algae, etc.), waste utilization, biorefinery and bioresource technologies associated with the conversion or production of biobased materials, and sustainability and environmental emissions and effects associated with these processes.

(iv) *Biotechnology and Biological Transformations*: to foster technological advances in plant/agricultural biotechnology (e.g., crop improvement, nutraceuticals, bioenergy, transgenic plants, phytoremediation), microbial and insect biotechnology (metabolic engineering and synthetic/systems biology of bacteria, fungi, insects, yeasts, and algae in the context of fermentation/bioproduction, biocatalysis, bioremediation, biodegradation), food and flavor biotechnology (biotransformations and metabolic aspects of food/beverage systems), and protein and enzyme technology (recombinant proteins/enzymes, cell-free protein expression systems, and biocatalysis using immobilized enzymes).

(v) *Chemistry and Biology of Odor and Taste*: to advance molecular knowledge of the instrumental analysis (e.g., bioelectronics sensors), chemical structures, formation pathways of aroma and taste molecules of plant- and animal-derived foods and beverages, chemosensory receptors mediating flavor object recognition (in vitro cell assays etc.), human in vivo psychophysics (including multisensory integration), and neurological processing of flavor stimuli (imaging technologies etc.).

(vi) *Food and Beverage Chemistry/Biochemistry*: to deepen the fundamental understanding of chemical structures, structural modifications, interactions, and (bio)chemical

Published: August 19, 2015

ACS Publications © 2015 American Chemical Society

DOI: 10.1021/acs.jafc.5b03450
J. Agric. Food Chem. 2015, 63, 7095−7096

transformations of major and minor components in foods and beverages, potentially in combination with novel aspects of process engineering, food technology, nanotechnology, packaging and storing, authenticity and origin aspects of food, or the biological evaluation of food and beverage systems.

(vii) *Food Safety and Toxicology*: to advance our knowledge of detrimental health effects and the mechanisms of adverse physiological or pathological changes induced by natural or synthetic chemicals occurring in the human environment with particular emphasis on foods, crop protection chemicals, contaminants, and related chemicals (e.g., nanomaterials, biotechologically derived products), including agricultural safety and consumer product safety, and the design and action of chemically related processes that enhance food safety.

(viii) *Functional Structure/Activity Relationships*: to increase the knowledge of the relationship between chemical structure and biological (microorganisms, insects, animals, human) or technofunctional activity (e.g., emulsifying, foaming, gelation) of agricultural and food components; the category comprises (a) organic synthetic studies and structural biological studies (X-ray, NMR, etc.) of relevant ligands and targets with the aim of investigating molecular recognition processes in the action of biologically active compounds, (b) molecular biological studies (e.g., site-directed mutagenesis) of macromolecular targets that lead to an improved understanding of molecular recognition, and (c) computational studies that analyze the SAR of compound series of general interest and lead to experimental studies or analysis of other available chemical and/or biological data that substantially advance the knowledge in agricultural and food chemistry.

(ix) *New Analytical Methods*: to expand the repertoire of analytical methods in agricultural and food research by new analytical method development using chemical, physical, and biological principles.

(x) *Omics Technologies Applied to Agriculture and Food*: to promote a more integrative understanding of complex systems in agriculture, food, and nutrition by the application of metabolomics, proteomics, and transcriptomics/genomics technologies combined with but not limited to bioinformatics and computational biology.

This scope makes JAFC a broad and large journal; we currently publish about 120 articles per month. In a sense, JAFC could be considered many journals in one. We embrace participation by scientists across traditionally defined fields and international boundaries. JAFC is the place to publish when you want the attention of scientists not just in your specialty area, and it is the place to publish when you want those same scientists to know your manuscript cleared a high standard for publication. Today the pressure to publish may be surpassing the pace of major scientific progress. In this atmosphere, I believe that JAFC has a responsibility to the scientific community to maintain a large signal-to-noise ratio. Therefore, JAFC's publication criteria require papers to present significant new and important molecular knowledge on key topics encompassing the agriculture–food–nutrition nexus. Correctness of data alone is not sufficient for publication in JAFC, and premature publication of the latest increment of what could be further developed to become a more comprehensive and stronger paper does not serve the scientific community. For example, manuscripts presenting omics data should go beyond a sheer holistic fingerprinting of samples; that is, metabolic changes need to be identified on a molecular level and validated by means of targeted analysis of the key metabolites. Similarly, incremental extensions of existing compound series without a better understanding of the structure–activity relationships or without any novel chemical/biological approaches only consume reviewer and editor time better spent on other studies. In particular in an era when biological evaluations of extracts and fractions, as well as the mechanistic understanding of biological activities of compounds, are en vogue, it is mandatory that manuscripts reporting biological properties of crude extracts include detailed information on the chemical composition of the extracts responsible for the described properties. Moreover, discussion of data on nutritional or physiological relevance and conclusions drawn about human health benefits should be formulated carefully considering the experimental design used (appropriate cell-based or other in vitro assays, animal models, clinical human trials, significance of test/trail, relevant dose levels, etc.) and the robustness of the data obtained. Although new findings on food product health benefits attract media attention, it is our responsibility as scientists to treat our data with care; we should not allow ourselves to overestimate findings and present specific solutions to cure life-threatening diseases without a solid scientific basis. "Overselling of certainty" will undermine the credibility of science and will lead to more confusion than progress.

Although these criteria are not new and to a certain extent subjective, authors should expect a stricter application. I wish to emphasize that for a manuscript to be suitable for JAFC, it should conform to the highest standards of chemical/biological research, be comprehensive in content, make a significant contribution to one of the journal's categories (i–x above), and also present interesting science for our broad group of international readers. We look forward to your participation in our endeavor to continue improving JAFC so it can best serve the needs of our community.

Thomas F. Hofmann, Editor in Chief

AUTHOR INFORMATION

Notes

Views expressed in this editorial are those of the author and not necessarily the views of the ACS.

DOI: 10.1021/acs.jafc.5b03450
J. Agric. Food Chem. 2015, 63, 7095–7096

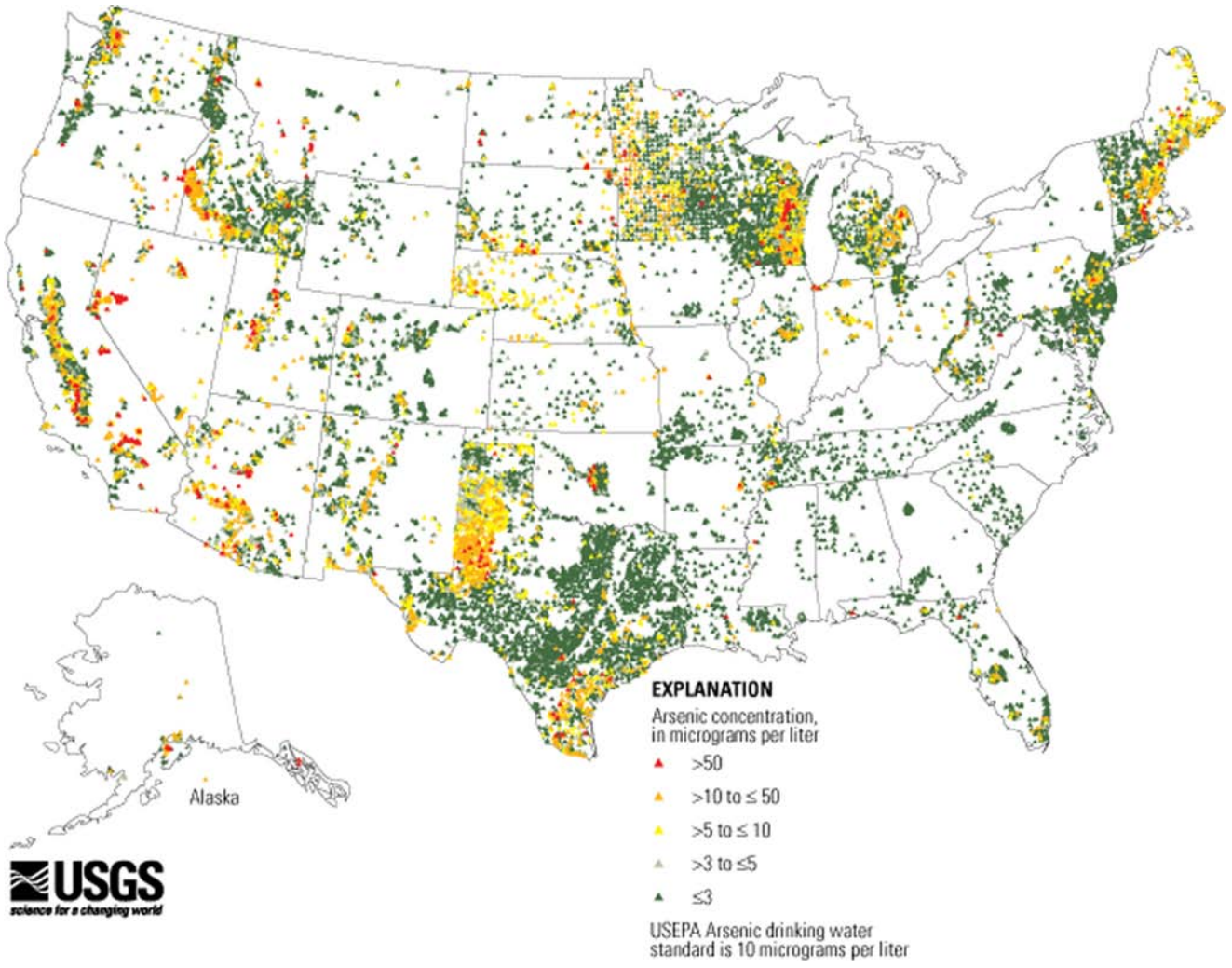

Figure 1. Arsenic levels in groundwater in the United States (data found by U.S. Geological Survey; chart source http://water.usgs.gov/nawqa/trace/arsenic/).

H_3AsO_3) are even more toxic.[4,14] Distinguishing between species is important due to the differences in properties and mechanisms of toxicity.[15] An example of a property that influences arsenic stability differently for separate species is pH. One study employed the agricultural residue rice polish to sorb inorganic arsenic. Rice polish is a byproduct of the milling process composed of a starchy material and inner coating of the rice hull, and this study found that the maximum sorption for AsO_4^{3-}/H_3AsO_4 on rice polish occurs at neutral pH, whereas AsO_3^{3-}/H_3AsO_3 has maximum sorption at a pH of 4.[2,16] The relatively higher stability of AsO_4^{3-}/H_3AsO_4 at neutral pH makes it more readily removed than AsO_3^{3-}/H_3AsO_3.

A third factor to consider in toxicity is the route of exposure. According to the WHO, most human diseases can be attributed to water pollution.[17] Uptake through drinking water is the most important source of arsenic in humans.[18] Inhalation is another relevant mode of exposure and is known to contribute to respiratory system problems including lung cancer.[10] Another route known for causing deleterious effects in humans is dermal exposure. The susceptibility of the skin to arsenic can lead to lesions and aggressive, non-melanoma skin cancers.[19] Another less direct route that has come to public attention in recent years is the uptake of arsenic via contaminated fruits and vegetables.

Arsenic Interaction in Plants and Soil. Clearly, arsenic contamination is not limited to water sources. The contamination of soil has emerged as a serious environmental hazard, especially in agricultural areas of the world.[20] The health of the soil can be compromised by chemical contaminants including arsenic.[21] Arsenic can cause problems with microbial activities in the soil, which in turn affects the microbes' interaction with other life.[22] Soil can act as a sink for arsenic and other hazardous metals with the capacity to transfer these pollutants to plant roots.[23] High concentrations of arsenic can cause deleterious effects to the plant including cell necrosis, chlorosis, inhibition of growth, and even death.[24] Human consumption of arsenic-contaminated food products may also provide a hazardous amount of the element. Food chain transport of arsenic and trace metals is thus a threat to human health.[23] Because research has yielded inconclusive evidence on the health effects of consuming contaminated crops,[5] more studies are needed in this area. It is worth noting that different species of plants have unique methods of reaction to arsenic exposure.[25] For example, data suggest that tomatoes do not efficiently accumulate arsenic,[9] yet rice is so efficient an accumulator that millions of tons of grain are rendered unsafe for consumption on a yearly basis.[26] The behavior of each plant in response to chemical contamination is important both in

DOI: 10.1021/acs.jafc.5b02487
J. Agric. Food Chem. 2015, 63, 7097−7107

terms of consumption and for the plant's ability to take up and tolerate contaminants.

With regard to the health risks of consuming contaminated plants, it is helpful to consider the capacity of plants for remediation. Phytoremediation is the process of plants extracting arsenic and other contaminants from soil via their roots.[27] Although there is ongoing experimental research concerning direct remediation of water,[28] phytoremediation has emerged as the most promising potential technique for reducing arsenic and heavy metals from contaminated areas due to its eco-friendly methods. However, the process has a few important drawbacks. One problem is that phytoremediation tends to be time-consuming. Another is that if the remediating crops are not properly disposed of or treated, these contaminants can still enter the food chain through fodder or other means of animal consumption.[18] A recent study has investigated the possibility of effluxing arsenic from plants,[29] but the efficiency of these experimental technologies needs further study. Although phytoremediation is not yet an ideal solution to the problem of arsenic contamination, it is a promising technology that could evolve over time into the most effective method of arsenic cleanup. An improved understanding of this technique will pave the way for greater insight into the worldwide problem of contaminated crops.

Purpose of Review. The purpose of this review is to consider the chemical and physical properties of arsenic in the broad context of human toxicity and phytoremediation. The behavior of arsenic is key to its interaction with plants and humans. Therefore, attention will be brought to the results of recent studies concerning arsenic and its mechanisms of toxicity and transport. The connection of arsenic to human health will be evaluated in relation to its toxicological properties. Although some ailments such as cancer have been attributed to arsenic exposure for many years, new studies are being conducted to determine other deleterious effects for which arsenic may be responsible. Effects of exposure proposed by recent experimentation will also be evaluated and compared.

Another area of interest to be addressed will be the interaction of plants with arsenic and other contaminants such as heavy metals. This review will cover mechanisms and interactions commonly seen between plants and metals including arsenic. Details of specific plants that are well-suited for remediation will be noted, as will a few species that are resistant to the process. This process will be covered in depth with an emphasis on arsenic cleanup. Finally, the commonly employed methods of arsenic determination, alongside a few newly proposed techniques, will be described. It is important to understand the potential health risks posed by arsenic and heavy-metal accumulation as well as the possible environmental utility of phytoremediation. Compiling this research will create a greater understanding of arsenic toxicity and provide insight on where further research may be needed.

PHYSICOCHEMICAL AND MECHANISTIC PROPERTIES OF ARSENIC AND IMPLICATIONS ON HUMAN HEALTH

Origin and Behavior. Arsenic is an important element because it is ubiquitous in the environment.[30] It is a naturally occurring element in rock formations containing copper and lead. The metalloid is known to persist in soil, water, and air as well as their rock structures of origin.[31] Arsenic in groundwater ranges from 0.5 to 5000 μg/L in more than 70 countries worldwide.[32] It makes up only 0.0001% of the Earth's crust and is far from the earth's most abundant element.[33] Water and soil near arsenic-enriched formations tend to have high concentrations of the element.[1] Areas with soils of high organic carbon content are generally more susceptible to accumulating arsenic than sandy soils.[34] Arsenic is a member of group 15 on the periodic table of elements and is classified as a heavy metalloid.[35] It has been compared to other elements including phosphorus, antimony, chromium, and selenium[22,36,37] to help assess its physicochemical properties and toxicity. These comparisons are particularly helpful when arsenic accumulation in plants is evaluated.

The inorganic arsenic-containing compounds are considered a much more important threat to environmental health than the organic forms. AsO_4^{3-}/H_3AsO_4 and AsO_3^{3-}/H_3AsO_3 are often separated and speciated because they have different mechanistic properties and interact differently with biological systems.[38] In aerobic environments of moderate, near-neutral pH, most AsO_4^{3-}/H_3AsO_4 is present as anions $H_2AsO_4^-$ and $HAsO_4^{-2}$. In anoxic settings, AsO_3^{3-}/H_3AsO_3 occurs as H_3AsO_3.[33] Studies of the different species of arsenic show trivalent species are generally more toxic than pentavalent ones,[3] although one review suggests that the species' potencies are ultimately dependent on the biological system in question.[18] Research has determined that different species may target different parts of biological systems. One study suggests that AsO_3^{3-}/H_3AsO_3 targets human prostate stem cells and gives them an aggressive, malignant phenotype, whereas other research has revealed that AsO_4^{3-}/H_3AsO_4 is an analogue for inorganic phosphate that can potentially replace the phosphate nutrient in essential reactions and disrupt normal processes.[18,39] The subtle differences in the species of arsenic are key to defining the mechanisms of remediation.

Common Effects on Human Health. The effects of arsenic on human health are well-known, and both chronic and acute toxicities have been connected with exposure to the metalloid. Symptoms widely attributed to the element such as skin lesions, liver fibrosis, and cancer have been reported in more than 30 countries worldwide.[40] Cases of "black-foot" disease have been reported in areas of extreme contamination such as Bangladesh.[1] Black-foot is a peripheral vascular disease that can result in severe pain in the extremities and eventually the mummification and falling off of affected areas.[41] More common lesions caused by arsenic on the skin are less debilitating, but are unique from other dermal damage such as that caused by UV light because they can affect multiple sites.[19] Damage to skin by the toxicant can result in hyperpigmentation and hyperkeratosis, which can act as a precursor to cancer.[42] Chronic exposure to arsenic is connected to non-cirrhotic portal fibrosis (NCPF).[43] This disease can manifest even at an early age. One study found a statistical correlation between arsenic-affected areas and NCPF in children in Kolkata, India.[44]

The skin, lungs, and bladder are considered to be the main target areas of arsenic carcinogenesis.[42] Arsenic-related skin lesions can progress to malignancies including squamous cell carcinoma, Bowen's disease, and basal-cell carcinoma. This process may be potentiated by other carcinogens such as those in tobacco products.[1] There is a higher risk of developing lung cancer as a result of arsenic exposure. Studies show that the element is both cytotoxic and genotoxic to human lung cells.[45] Although it is primarily connected to contaminated drinking water,[1] there is research speculating that arsenic inhalation also plays a significant role in inducing lung cancer.[46] In the bladder, cytokines can be inflamed by the metalloid, leading to potential

DOI: 10.1021/acs.jafc.5b02487
J. Agric. Food Chem. 2015, 63, 7097−7107

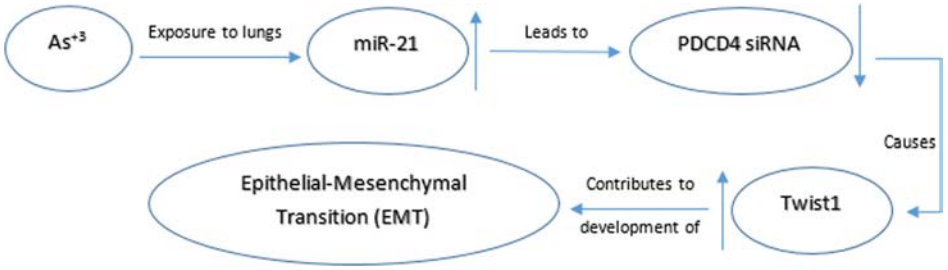

Figure 2. Flowchart of the development mechanism of EMT as a result of arsenite toxicity. Mechanism proposed in ref 62.

malignancies.[47] Bladder cancer follows mechanisms of carcinogenesis similar to those of lung cancer.[48] Evidence suggests a synergistic relationship of the toxicant with tobacco.[1] This may promote cancer development in both organs for smokers.[49] The study of these common forms of cancer resulting from arsenic exposure will be instrumental in determining future cancer treatment options as well as understanding the nature of the element and its role in carcinogenesis.

Other Target Organs and Cancer. Although arsenic is most commonly associated with malignancies in the skin, bladder, and lungs, there is evidence that strongly suggests that the toxicant may contribute to cancer development in other organs as well. Organs that have been experimentally associated with arsenic carcinogenesis include the kidneys, liver, and prostate.[42] Although these may not be as prevalent as cancers of the skin and lungs, there has been research to strongly suggest the connection. One study in Bangladesh reported that the statistical relationship between arsenic concentration and renal cancer cells indicates that it is a causal factor even in nonsmokers.[50] Because the liver is the body's primary organ for detoxification, it is expected that the liver would be a target of this toxic element. A previous thorough review of the literature found that chronic exposure from drinking water increases liver cancer mortality.[51] Another study suggests that the metalloid causes androgen independence of the prostate, promoting cancer progression.[52] Even though it is not yet widely connected to the toxicant, one study suggests a tie between arsenic methylation and breast cancer.[14] The broad spectrum of target sites for arsenic carcinogenesis illustrates the versatility of the metalloid and its threat to human health.

Cancer has historically been the focus of worldwide study of chronic arsenic exposure. However, new studies have reported that the metalloid may be responsible for other deleterious effects as well.[13] An interesting characteristic of arsenic is its ability to adversely affect entire multiorgan body systems via chronic toxicity called arsenicosis.[40] This effect has been linked to the element's mutagenic and carcinogenic potential.[53] Arsenicosis is pronounced during periods of development, where the toxicant can potentially leave the patient immunocompromised and at higher risk for other diseases.[12] Thus, the toxicant can affect almost the entire body in some way. Experimental studies have revealed potential links to a variety of problems. Patients experiencing arsenicosis have shown cognitive impairment and other neuropathic issues.[40] Some evidence suggests that children are especially vulnerable to these cognitive effects due to their continuing development.[54] One study determined a connection between arsenic exposure and the dilation of the pulmonary artery in response to chronic lung disease.[55] Another study reported low levels of chronic arsenic exposure might contribute to the development of diabetes.[56] Cardiovascular diseases such as ischemic heart disease have also been found to be related to inorganic arsenic exposure.[40] Toxicant accumulation of heavy metals and arsenic is largely individualized and can be influenced by genetics and environmental surroundings.[57] This list of potential effects is therefore not complete or universally applicable. Nevertheless, it is clear that the scope of arsenic toxicity is broad, and research will almost certainly discover new disease connections in the future.

Possible Mechanisms of Action. The scientific understanding of the arsenic mechanism of action in biological systems is far from complete. Unlike some xenobiotics, arsenic can affect several biological mechanisms and result in a wide range of effects.[12] It has the potential for both genetic and epigenetic changes, meaning it can have mutagenic effects at the DNA sequence level.[58] Short-term exposure is connected to the increased production of reactive oxygen species (ROS),[59] which are apoptosis-inducing agents that are capable of disrupting a number of key processes.[59] One human mechanism ROS may interrupt is mRNA deadenylation. In this case, AsO_3^{3-}/H_3AsO_3 selectively induces proteolytic degradation of two enzymes, Tob and Pan3, which results in disruptive oxidative stress.[60] Oxidative stress has also been connected with cancer as well as other benign diseases.[61]

Research suggests that one of the most sensitive sites for arsenic exposure is the lungs.[55] The methylation of arsenic species to organic acids is considered to be connected to cancer in the lungs and the bladder.[48] This sensitivity may also be in part because of the miRNA-21 molecules in the lungs. One study has indicated that AsO_3^{3-}/H_3AsO_3 up-regulates miR-21, which in turn represses the expression of the PDCD4 siRNA. The up-regulation of the oncogene Twist1 caused by a decrease in the neoplastic transformation inhibitor programmed cell death 4 (PDCD4) small interfering RNA (siRNA) contributes to epithelial−mesenchymal transition (EMT).[62] This effect is more clearly illustrated in the flowchart in Figure 2.

Human prostate epithelial cells are another target of arsenic and ROS. One study showed that the expression of DNA repair genes ERCC6, XPC, and OGG1 are influenced by arsenic.[63] The study concluded that chronic exposure causes DNA damage while increasing cell survivability, promoting the possibility of neoplastic transformation. The sensitivity of the skin to the toxicant may be partially due to the inhibition of SIRT1 activity.[19] The number of potential targets for arsenic is daunting, but it means that there are many proteins that can be used to detect the effects of arsenic exposure. A study on urinary tract epithelial cells identified one example where three cytokines were found that can potentially be monitored as arsenic biomarkers.[47] Establishing these biomarkers and analyzing the related mechanisms are among the most promising leads available in controlling and eliminating arsenic-related ailments as a worldwide threat.

DOI: 10.1021/acs.jafc.5b02487
J. Agric. Food Chem. 2015, 63, 7097−7107

Therapeutic Applications. Whereas arsenic has long been associated with cancer and other health problems, it has also been shown to have therapeutic effects in blood and solid cancers.[64] Arsenic trioxide is a chemotherapeutic that has been adopted for the treatment of leukemia.[65] Studies demonstrate that it can be an effective countermeasure for cancers such as mesothelioma, breast cancer, and cervical cancer.[64,66,67] This is possible because of arsenic's capacity to induce apoptosis. Arsenic trioxide is specifically used due to its ability to cause autophagic cell death.[68] It induces the mitochondrial pathway via oxidative stress, DNA damage, change of mitochondrial membrane potential, and translocation/up-regulation of apoptotic protein.[65] Experiments with arsenic sulfide have shown promise that it could be an effective anticancer drug.[69] This new compound has not yet been as widely adapted as arsenic trioxide. Despite its success in combating cancer, the use of arsenic and autophagy is still somewhat controversial.[68] This is due to the bidirectional nature of the element and its capacity to harm as well as help.[61]

Worldwide Exposure and Study. Arsenic contamination worldwide is a problem of epidemic proportions. This is particularly true in terms of polluted water sources. Surveys from organizations such as the EPA and the British Geological Survey predict that millions of people have been exposed to arsenic via contaminated drinking water.[70] Recent research has investigated the role of accumulation in edible plants as a potential source of heavy metals and arsenic. Studies in places such as (Sargohda) Pakistan, (Delhi) India, Bangladesh, and the Xinjiang province in China are all in agreement that metal and arsenic contamination in produce poses a threat to human health.[5,20,71,72] There is research in (San Luis Potosi) Mexico, (Gejiu) China, and the Bengal Delta Plain[5,24,26,73] that has focused on the effects of arsenic contamination on the plants themselves as well as in soil biota. All of these studies have contributed to a better understanding of the interaction of plants with arsenic and heavy metals.

INTERACTIONS OF PLANTS WITH ARSENIC AND HEAVY METALS

Plants and Arsenic Uptake. There are several key factors to consider in the interaction of plants with arsenic and other pollutants. A very thorough review of arsenic's interaction and metabolism in plants was conducted in Meharg and Hartley-Whitaker's paper.[74] Due to the broader scope of the present review, these processes will be only summarized and expanded for subsequent experimental evidence. The most important thing to note is the nature of the mechanisms activated within plants in response to the contamination. Plants grown in areas of high arsenic contamination have been shown to exhibit slightly reduced biomass,[25] but the problem of contamination is broader than just the size of the plant. Most of the arsenic and heavy metals present in plants come from the cultivation soil,[9] which in most cases is initially contaminated via irrigation water and tainted fertilizers.[73]

Hazards and Risks of Accumulation. The safety of consuming produce irrigated by arsenic- or metal-contaminated water is a worldwide health concern. Even plants that contain only trace levels of a contaminant can still contribute to the total risk of exposure.[71] Some research states that vegetables with higher water retention accumulate more arsenic.[20] This has led to studies of plants such as lettuce, which showed a high concentration of arsenic in the roots.[7] Produce that has shown potential for dangerous arsenic accumulation include maize, tobacco, lotus roots, spinach, bitter gourd, Chinese jujubes, arum, radish, and most grains.[3,13,19,21,70−73] One grain of particular interest in the research community is rice. This plant is an inherently efficient accumulator of arsenic and constitutes a major exposure route for arsenic's inorganic species.[75] The high sensitivity of rice to contamination is attributed to its nodulin 26-like intrinsic aquaporin channels, which allow arsenic to interfere with amino acid mechanisms and compromise the nutritional value of the grain.[76] This makes growing rice problematic worldwide. It becomes especially difficult in flooded paddy fields, which facilitates the mobilization of AsO_3^{3-}/H_3AsO_3 and enhances its bioavailability in the soil.[73] Although research states that brown rice tends to accumulate more arsenic than white rice,[75] all types of rice are potentially significant sources of contamination. Rice is so efficient an accumulator that one study even incorporated rice in experimental phytoremediation techniques.[25]

Whereas many studies have been conducted on phytoremediation of polluted areas, other research has sought to identify plants naturally resistant to contamination. One such plant that has shown promise is the tomato. Analysis of tomato roots grown in contaminated soil showed a high concentration of arsenic uptake,[20] but another study found very little accumulation of arsenic or any metals in the fruit portion of the plant.[9] This means that tomato roots serve as an effective protection mechanism and might make it an effective crop for areas where contamination is a concern. Extreme arsenic concentrations have still been found to decrease root length and fruit size in tomatoes.[31] The prevalent emphasis of research is therefore still on phytoremediation of the soil.

Environmental Effects and Interactions. Arsenic and heavy metals in soil can present problems for soil biota as well as plants and animals. Research suggests that polluted soil, particularly sites that suffer repeated contamination, suffers a decrease in enzyme activity, bacterial life, and fungal growth.[77] Because of the major role the biota play in soil function, the resulting environmental stress can have far-reaching effects.[22] Xenobiotics enter the plants alongside other nutrients in the rhizosphere through the roots and enter the shoots. These parts have a unique relationship of translocation, which varies from plant to plant.[78] Generally, metal accumulation is higher in the roots than in the shoots, forming a natural barrier to protect the sensitive fruits from potential toxicity.[20] There are several plants that are exceptions to this general rule, however, and accumulate metals in their shoots.[79] Studies suggest that this protective mechanism has various degrees of success depending on the contaminant.[6] For example, one study reported that arsenic is more bioaccessible for edible parts of plants than the similar group 15 element antimony.[36] Vegetables are also capable of absorbing metals out of the air in their exposed parts,[5] although this is not the most efficient mechanism.

Effects of Arsenic Speciation on Plant. Another important factor in the interaction between plants and arsenic is speciation. Research has determined that the species of arsenic present makes a noticeable impact on uptake and translocation.[30] AsO_4^{3-}/H_3AsO_4 is generally more easily absorbed through roots than other inorganic species.[76] This property, along with the affinity of AsO_4^{3-}/H_3AsO_4 to replace phosphate in reactions, has translated into the use of phosphate fertilizers to prevent arsenic accumulation in crops such as tobacco.[80] Once it is inside the plant it has been determined that AsO_4^{3-}/H_3AsO_4 is readily reduced to AsO_3^{3-}/H_3AsO_3.[18] The concentrations of AsO_4^{3-}/H_3AsO_4 and AsO_3^{3-}/H_3AsO_3

DOI: 10.1021/acs.jafc.5b02487
J. Agric. Food Chem. 2015, 63, 7097−7107

tend to fluctuate in plant systems but maintain a stable ratio over time.[15]

Areas of Potential Further Study. The unique interactions of arsenic with each plant system make it an area in need of further research. A more complete understanding of these relationships will be vital in the effort to better control human exposure. It may also provide new insight into the safe removal of arsenic from contaminated areas. The natural accumulation of nutrients and contaminants by plants has already given rise to phytoremediation and similar bioremediation methods as highly promising mechanisms of cost-effective environmental cleanup.[35] These methods have already been the topic of thorough research, and studies are ongoing to improve worldwide practices of remediation.

TECHNIQUES FOR THE REMEDIATION OF ARSENIC AND OTHER METALS FROM WATER AND SOIL

Commonly Accepted Methods of Remediation. Remediation techniques are broad in scale and scope. They are often large-scale undertakings that are both laborious and costly.[34] Remediation can be used to remove metals such as arsenic and organic contaminants such as pesticides from water and soil, both of which employ unique methods. Water remediation methods have been the topic of particularly intense study. Two well-established methods include oxidation and forward osmosis.[32] Experimental methods also continue to be developed for the removal of arsenic from water. One such method is electrocoagulation, which aims to remove the toxicant using iron electrolysis with locally available materials.[81] Titanium dioxide-based technology is another method that uses granular columns to adsorb AsO_3^{3-}/H_3AsO_3 and cadmium from highly concentrated areas such as smelting wastewater.[82] There are also hybrid technologies that combine different methods to create a potentiating effect.[28] Improved water remediation could have widespread effects on biological systems. Improving soil conditions is equally important for plant life. There are fewer techniques used to remediate contaminants in soil. Two that are commonly used include thermal treatment to volatize molecules or simple soil washing to try to pull away soluble ions.[83] These methods are useful for removing arsenic, but can also be used effectively for mercury.

Experimental Methods and Appropriate Application. Experimental work in remediation has yielded potential techniques such as nanoscale iron particles, which react with particles in soil or water when injected.[84] Another study investigated biosurfactants that use anionic agents to mobilize contaminants including arsenic.[85] A third process focused on phosphate fixation, which transforms many contaminants including arsenic into insoluble or barely soluble species and can be used in extremely cold environments.[86] Chemical coagulation is a particularly effective method for removing arsenic from water but can potentially leave undesired anions behind and is therefore not very environmentally efficient.[81]

Remediation techniques vary based on conditions, and the most efficient application method for remediation is highly situational based on chemical circumstances.[87] Therefore, the most experimentally proven bioremediation techniques such as phytoremediation are widely used due to their environmental consciousness and versatility.[34] Bioremediation is the use of microorganisms and plants for the purpose of remediating soil.[88] These methods are unique from older methods of environmental cleanup in that they exploit natural biological processes to help certain microorganisms better remediate soil and groundwater.[32] They are particularly effective when it comes to the treatment of heavy metals. Two examples of this are the use of bacteria such as hay bacillus (*Bacillus subtilis*), which employs chemical reduction of Cr(VI) to the less toxic Cr(III), and the organic material biochar, which is charcoal used to improve soil productability, to raise soil pH to make hazardous metals less bioavailable for plant uptake.[88] In terms of arsenic, both AsO_3^{3-}/H_3AsO_3 and AsO_4^{3-}/H_3AsO_4 can be treated with bacteria for remediation, although AsO_3^{3-}/H_3AsO_3 can also be aerobically oxidized via arsenite oxidase enzymes.[33] One microbial agent that is particularly adept at detoxifying AsO_4^{3-}/H_3AsO_4 is *Chrysiogenes arsenatis*, which uses nitrate and nitrite as electron acceptors.[33]

Some research has attempted to develop new, advanced techniques to improve remediation efforts. Biosorbents such as iron oxide-coated biomass (IOCB) have increased in popularity due to their eco-friendly nature. The capacity of IOCB to remove aqueous arsenic makes it an effective alternative to more conventional treatments.[2] A recent study developed an in situ method involving the injection of iron-containing reagents into an aquifer, causing the arsenic to participate in the iron oxidation process and be trapped in crystalline structures. A simulation of this technique involving added arsenic yielded promising results, with all of the aqueous arsenic being removed.[89] Another approach to establishing new techniques is to combine bioremediation techniques with phytoremediation to reduce the level of a target contaminant. Called phytobial remediation, these hybrid methods are designed to utilize both types of technique in a way that they complement each other's limitations.[35] Although they are not yet widely adopted over more traditional approaches such as phytoremediation, these advanced methods could represent the future of environmental arsenic cleanup.

Phytoremediation and Environmental Fate. Phytoremediation of contaminants such as arsenic can occur through at least five mechanisms, including phytoextraction, phytostabilization, phytovolatization, phytofiltration, and phytostimulation.[35] The downside to this technique is that regardless of the mechanism, contaminants can potentially interfere with growth and essential metabolic processes.[18] Some evidence suggests that contaminants accumulate more readily in the roots of plants than in their shoots. This may be a mechanism to protect the plant's other more susceptible parts.[7] This effect is dependent on the plant. For arsenic, speciation is key to how the contaminant interacts with plant uptake and translocation.[30] For example, AsO_4^{3-}/H_3AsO_4 is reportedly more prone to being absorbed by roots than AsO_3^{3-}/H_3AsO_3.[76] Once inside the plant, however, AsO_4^{3-}/H_3AsO_4 is readily reduced to AsO_3^{3-}/H_3AsO_3.[18] AsO_3^{3-}/H_3AsO_3 is considered in most cases to have more deleterious effects on plants, such as shorter root systems and decreased fruit size, than AsO_4^{3-}/H_3AsO_4. This may be because it inhibits enzymes that need free sulfhydryl groups to function properly or because AsO_3^{3-}/H_3AsO_3 is the more soluble of the two inorganic species.[31]

Although speciation of contaminants is important, bioaccumulation, bioavailability, and bioaccessibility are the most important properties of phytoremediation and environmental fate.[87] Whether one is considering metal uptake in edible plants or environmental restoration, the capacity of each metal's bioaccumulation, bioavailability, and bioaccessibility must not be overlooked. These properties are closely related, but each serves a different purpose in the phytoremediation process. Studies in toxicology and human health are particularly

DOI: 10.1021/acs.jafc.5b02487
J. Agric. Food Chem. 2015, 63, 7097−7107

Instrumentation	Detection Limit	Strengths	Weaknesses
GFAAS Thermo Elemental AAS, GFAAS, ICP or ICP-MS? Which technique should I use? 2001	Sub-ppb range	• Small sample size • Compact • Few spectral interferences	• Slower • Chemical interferences • 1 – 6 elements / determination • No screening ability • Limited range
ICP-OES Thermo Elemental AAS, GFAAS, ICP or ICP-MS? Which technique should I use? 2001	1 – 10 ppb range	• Multi-element (73) • High productivity • Few chemical interferences • Robust • Excellent screening abilities • High total dissolved solids • Solid or organic samples	• Moderate to low detection limits • Spectral interferences • Some element limitations
ICP-MS Thermo Elemental AAS, GFAAS, ICP or ICP-MS? Which technique should I use? 2001	ppt range	• Multi-element (82) • High productivity • Wide dynamic range • Isotopic measurements • Fast semi-quant screening • Hybrid techniques (LA, LC) • Easily interpreted data	• Method development skill required • Higher initial capital cost • Some spectral interferences (well defined) • <0.2% dissolved solids
XRF http://serc.carleton.edu/research_education/geochemsheets/techniques/XRF.html	Ppm range	• Well-suited for bulk analysis in rock/sediment • Field applications (FPXRF)	• Not as precise or accurate with elements Z<11 • Cannot distinguish isotopes • Large sample sizes
Mercury CVAA http://www.labcompare.com/10-Featured-Articles/133134-Mercury-Analyzers-in-the-Laboratory/	ppt range	• Short analysis time (1-3 min)	• Only analyzes for mercury

Figure 3. Strengths and weaknesses of several common techniques of analysis. Inductively coupled plasma optical emission spectrometry (ICP-OES) is also called inductively coupled plasma atomic emission spectroscopy (ICP-AES). Graphite furnace atomic absorption spectrometry (GFAAS), inductively coupled plasma mass spectrometry (ICP-MS), and ICP-OES are all useful for determining arsenic concentration. Sources: Labcompare, Thermo Scientific, and Science Education Resource Center at Carleton College.

interested in bioaccumulation. Bioaccumulation is the process of contaminants moving up the food chain, and it is important to take into account intake, biotransformation, and elimination of each species on the food chain, which all affect the ultimate human toxicity of the contaminant.[90]

The difference in bioaccessibility and bioavailability is that the former refers to the total amount of a contaminant in an environment, whereas the latter is only the amount that can enter living beings.[87] Bioaccessibility can be affected by environmental conditions. Thiols can cause an increase of bioaccessible arsenic in the form of methylarsenicals including monomethyl monothio arsenic acid ($MMMTA^{5+}$) and dimethyl monothio arsenic acid ($DMMTA^{5+}$).[91] Bioavailability has been reported to be the most vital of the three when it comes to remediation.[87] One environmental assessment states that this is due to the fact that bioavailability is closely tied to risk characterization.[92] Determining the phytoremediation abilities of individual plants provides more information not only about how to clean up environmental contaminants but also which consumable crops pose a risk to human health.

Hyperaccumulators. Phytoremediation is based on a group of plants called hyperaccumulators. In these plants arsenic is naturally stored in the shoots instead of in the roots, as is the case in most plants.[34] In hyperaccumulators, organic acids serve as chelating agents, which allow the plant to store more metals and arsenic than other plants without suffering deleterious effects to their growth and metabolism.[93] This removal of contaminants from the soil system can help make the system safer for future crops. One study recommends multiple phytoremediation cycles to further optimize the soil.[27]

The first plant established as a hyperaccumulator was the Chinese brake fern (*Pteris vitatta*), and today the species is used for its tolerance of up to 1500 ppm of arsenic in soil.[94] The fern can increase arsenic bioavailability by exuding dissolved organic carbon to change rhizospheric pH.[30] Other plants considered to be hyperaccumulators of arsenic include barnyard grass, curly endives, and most other ferns.[25,31,73] It is important to note that different plant species hyperaccumulate different contaminants. For example, fire phoenix (*Festuca arundinacea*) and alfalfa (*Medicago sativa*) are highly efficient in extracting polycyclic aromatic hydrocarbons (PAHs),[95] whereas Alpine penny-cress (*Noccaea caerulescens*) can tolerate large amounts of zinc and cadmium.[93] Choosing the proper phytoremediation technique and hyperaccumulating species is essential to effective environmental remediation. Understanding the properties of individual plants has important implications for human consumption and health.

Controlling the Contamination Problem. Although phytoremediation and other techniques have helped improve conditions in arsenic-contaminated areas, the effects of arsenic toxicity are still spread throughout the world, although the removal of environmental arsenic is extremely important, understanding the nature of its toxicity is key to minimizing its influence on society. This is especially true in places where exposure has reached epidemic proportions such as Bangladesh and India.[20,23] Determining all possible targets of arsenic toxicity will greatly support future efforts to fight the symptoms

DOI: 10.1021/acs.jafc.5b02487
J. Agric. Food Chem. 2015, 63, 7097−7107

and even identify methods of early detection. To further aid in the understanding of arsenic, research is constantly being conducted on better ways to analyze contaminants. One such experiment combined traditional methods to help better track its inorganic species in water.[38] The continued study of these new methods will lead to better phytoremediation in the future.

METHODS OF ARSENIC AND METAL QUANTIFICATION

Commonly Accepted Methods of Metal Determination. There are several accepted methods used to determine metal concentrations. Figure 3 contains brief descriptions of a few commonly used techniques. The appropriate technique is dependent on factors such as sample size and necessary detection limit. One method that is commonly employed due to its capacity to test for multiple metal concentrations is inductively coupled plasma mass spectroscopy (ICP-MS).[57] Some experiments have conducted arsenic speciation using high-performance liquid chromatography (HPLC).[30] One method uses HPLC to separate different species of arsenic in blood plasma and then find the concentration of each using ICP-MS with a detection limit of 2.5 ppb.[10] When a study is primarily interested in the total concentration, atomic absorption spectrometry can assess a digested solution via graphite furnace (GFAAS).[27] This technique can employ digestion of soft tissue samples from a plant to determine the total arsenic present with a detection limit of 200 ppb.[10] It is useful for assessing accumulation and has been used experimentally to evaluate vegetable uptake.[72] Other analytical methods that are proficient for finding even low arsenic concentrations include hydride generation atomic fluorescence spectrometry (HG-AFS), which has arsenic detection limits as low as 100 ppb, and inductively coupled plasma optical emission spectroscopy (ICP-OES), which can detect as little as 8 ppb in an acid solution.[7,10,38,96]

Emerging and Experimental Methods. Several emerging studies propose that developing hybrid techniques, such as coupling HPLC and HG-AFS, may result in simple, reliable methods for routine laboratory procedures.[97] One study aims to find a viable method of direct water determination by combining dispersive liquid−liquid microextraction with solid-phase extraction to prepare samples for the graphite furnace.[38] Another method sometimes used for its uniquely non-destructive testing is magnetic resonance imaging (MRI) alongside high-resolution magic angle spinning nuclear magnetic resonance (HR-MAS NMR) to observe changes in metabolites of polluted samples.[98] All established and experimental methods should be considered in future studies and could serve a role in solving the problem of arsenic worldwide.

DISCUSSION

On the basis of this assessment of the literature, arsenic toxicity is clearly a topic of widespread importance. Even with the foundation of knowledge established by years of research, the scientific understanding of the metalloid is continuously evolving. Arsenic has unique physical and chemical properties that facilitate dozens of interactions with biological systems, and each year more mechanisms in various plants and animals are proposed through new studies. Some of these involve human health, and the effects of the element on different organs and systems in the body can be dangerous and even fatal. Continuing to study the interactions between arsenic and human systems is important, as it will help guide not only options of toxicity treatment but also methods of safe cleanup and exposure prevention all the way down to the trophic level of plants.

Accumulation of the toxicant in plants has ramifications across the entire food chain. Several methods of remediation have been investigated for the cleanup of this contaminant. However, the most important problem at present is the tainting of food crops for millions of people in over a dozen countries. Although there is some ongoing research into human arsenic uptake via consumable plants, more is needed to assess the risk of eating specific products. More studies would yield new information concerning which plants are resistant to arsenic accumulation, which ones to avoid planting in contaminated areas, and which are contributing a significant amount of arsenic to the human diet. This research would be instrumental in controlling arsenic exposure and make major progress in permanently solving the problem on a worldwide scale.

AUTHOR INFORMATION

Corresponding Author

*(D.M.K.) E-mail: david.klein@ttu.edu. Phone: (806) 834-6044. Fax: (806) 885-4577.

Notes

The authors declare no competing financial interest.

ABBREVIATIONS USED

WHO: World Health Organization
IARC: International Agency of Research on Cancer
ATSDR: Agency for Toxic Substances and Disease Registry
MRL: minimum risk level
EPA: U.S. Environmental Protection Agency
MMA: monomethylarsonic acid
DMA: dimethylarsinic acid
AsO_4^{3-}/H_3AsO_4: arsenate
AsO_3^{3-}/H_3AsO_3: arsenite
As-GAC: granular activated carbon-based, iron-containing adsorbents
NCPF: noncirrhotic portal fibrosis
ROS: reactive oxygen species
PDCD4: programmed cell death 4
EMT: epithelial−mesenchymal transition
$MMMTA^{5+}$: monomethyl monothio arsenic acid
$DMMTA^{5+}$: dimethyl monothio arsenic acid
IOCB: iron oxide-coated biomass
PAH: polycyclic aromatic hydrocarbons
ICP-MS: inductively coupled plasma mass spectroscopy
HPLC: high-performance liquid chromatography
GFAAS: graphite furnace atomic absorption spectrometry
MRI: magnetic resonance imaging
HR-MAS NMR: high-resolution magic angle spinning nuclear magnetic resonance
HG-AFS: hydride generation atomic fluorescence spectrometry
ICP-OES: inductively coupled plasma atomic emission spectroscopy

REFERENCES

(1) Martinez, V. D.; Vucic, E. A.; Becker-Santos, D. D.; Gil, L.; Lam, W. L. Arsenic exposure and the induction of human cancers. *J. Toxicol.* **2011**, *2011*, 1−13.

DOI: 10.1021/acs.jafc.5b02487
J. Agric. Food Chem. 2015, 63, 7097−7107

(2) Basu, A.; Saha, D.; Saha, R.; Ghosh, T.; Saha, B. A review on sources, toxicity and remediation technologies for removing arsenic from drinking water. *Res. Chem. Intermed.* **2014**, *40* (2), 447−485.
(3) Bhattacharyya, R.; Chatterjee, D.; Nath, B.; Jana, J.; Jacks, G.; Vahter, M. High arsenic groundwater: Mobilization, metabolism and mitigation − an overview in the Bengal Delta Plain. *Mol. Cell. Biochem.* **2003**, *253* (1−2), 347−355.
(4) Jedynak, Ł.; Kowalska, J.; Leporowska, A. Arsenic uptake and phytochelatin synthesis by plants from two arsenic-contaminated sites in Poland. *Polish J. Environ. Stud.* **2012**, *21* (6), 1629−1633.
(5) Bibi, Z.; Khan, Z. I.; Ahmad, K.; Ashraf, M.; Hussain, A.; Akram, N. A. Vegetables as a potential source of metals and metalloids for human nutrition: a case study of *Momordica charantia* grown in soil irrigated with domestic sewage water in Sargodha, Pakistan. *Pakistan J. Zool.* **2014**, *46* (3), 633−641.
(6) Randjelovic, S. S.; Kostic, D. A.; Stojanovic, G. S.; Mitic, S. S.; Mitic, M. N.; Arsic, B. B.; Pavlovic, A. N. Metals content of soil, leaves and wild fruit from Serbia. *Cent. Eur. J. Chem.* **2014**, *12* (11), 1144−1151.
(7) Hüvely, A.; Petö, J.; Hoyk, E. The arsenic accumulating capacity of lettuce growing in aggregate hydroponics under the influence of arsenic polluted nutrient solution. *Acta Tech. Corvininesis − Bull. Eng.* **2014**, *7* (2), 89−92.
(8) Soltani, N.; Keshavarzi, B.; Moore, F.; Tavakol, T.; Lahijanzadeh, A. R.; Jaafarzadeh, N.; Kermani, M. Ecological and human health hazards of heavy metals and polycyclic aromatic hydrocarbons (PAHs) in road dust of Isfahan metropolis, Iran. *Sci. Total Environ.* **2015**, *505* (0), 712−723.
(9) Rodriguez-Iruretagoiena, A.; Trebolazabala, J.; Martinez-Arkarazo, I.; De Diego, A.; Madariaga, J. M. Metals and metalloids in fruits of tomatoes (*Solanum lycopersicum*) and their cultivation soils in the Basque Country: concentrations and accumulation trends. *Food Chem.* **2015**, *173*, 1083−1089.
(10) *Toxicological Profile for Arsenic*; U.S. Department of Health and Human Services, Public Health Service: Atlanta, GA, USA, 2007.
(11) Jaishankar, M.; Tseten, T.; Anbalagan, N.; Mathew, B. B.; Beeregowda, K. N. Toxicity, mechanism and health effects of some heavy metals. *Interdiscip. Toxicol.* **2014**, *7* (2), 60−72.
(12) Dangleben, N. L.; Skibola, C. F.; Smith, M. T. Arsenic immunotoxicity: a review. *Environ. Health* **2013**, *12* (1), 73.
(13) Schmidt, C. W. Low-dose arsenic. *Environ. Health Perspect.* **2014**, *122* (5), A130−A134.
(14) Lopez-Carrillo, L.; Hernandez-Ramirez, R. U.; Gandolfi, A. J.; Ornelas-Aguirre, J. M.; Torres-Sanchez, L.; Cebrian, M. E. Arsenic methylation capacity is associated with breast cancer in northern Mexico. *Toxicol. Appl. Pharmacol.* **2014**, *280* (1), 53−59.
(15) Amaral, C. D. B.; Nobrega, J. A.; Nogueira, A. R. A. Investigation of arsenic species stability by HPLC-ICP-MS in plants stored under different conditions for 12 months. *Microchem. J.* **2014**, *117*, 122−126.
(16) Kik, M. C. Nutrients in rice bran and rice polish and improvement of protein quality with amino acids. *J. Agric. Food Chem.* **1956**, *4* (2), 170−172.
(17) Hu, Y. H.; Wang, X. M.; Dong, Z. B.; Liu, G. J. Determination of heavy metals in the groundwater of the Huaibei Plain, China, to characterize potential effects on human health. *Anal. Lett.* **2015**, *48* (2), 349−359.
(18) Finnegan, P. M.; Chen, W. Arsenic toxicity: the effects on plant metabolism. *Front. Physiol.* **2012**, *3*, 1−18.
(19) Herbert, K. J.; Holloway, A.; Cook, A. L.; Chin, S. P.; Snow, E. T. Arsenic exposure disrupts epigenetic regulation of SIRT1 in human keratinocytes. *Toxicol. Appl. Pharmacol.* **2014**, *281* (1), 136−145.
(20) Mishra, B. K.; Dubey, C. S.; Shukla, D. P.; Bhattacharya, P.; Usham, A. L. Concentration of arsenic by selected vegetables cultivated in the Yamuna flood plains (YFP) of Delhi, India. *Environ. Earth Sci.* **2014**, *72* (9), 3281−3291.
(21) Pena-Fernandez, A.; Gonzalez-Munoz, M. J.; Lobo-Bedmar, M. C. Establishing the importance of human health risk assessment for metals and metalloids in urban environments. *Environ. Int.* **2014**, *72*, 176−185.
(22) Mandal, A.; Purakayastha, T. J.; Patra, A. K. Phytoextraction of arsenic contaminated soil by Chinese brake fern (*Pteris vittata*): effect on soil microbiological activities. *Biol. Fertil. Soils* **2014**, *50* (8), 1247−1252.
(23) Islam, M. S.; Ahmed, M. K.; Habibullah-Al-Mamun, M.; Masunaga, S. Trace metals in soil and vegetables and associated health risk assessment. *Environ. Monit. Assess.* **2014**, *186* (12), 8727−8739.
(24) Rosas-Castor, J. M.; Guzman-Mar, J. L.; Alfaro-Barbosa, J. M.; Hernandez-Ramirez, A.; Perez-Maldonado, I. N.; Caballero-Quintero, A.; Hinojosa-Reyes, L. Evaluation of the transfer of soil arsenic to maize crops in suburban areas of San Luis Potosi, Mexico. *Sci. Total Environ.* **2014**, *497*, 153−162.
(25) Sultana, R.; Kobayashi, K.; Kim, K. H. Comparison of arsenic uptake ability of barnyard grass and rice species for arsenic phytoremediation. *Environ. Monit. Assess.* **2015**, *187* (1), 4101−4101.
(26) Li, Y. Y.; Wang, H. B.; Wang, H. J.; Yin, F.; Yang, X. Y.; Hu, Y. J. Heavy metal pollution in vegetables grown in the vicinity of a multi-metal mining area in Gejiu, China: total concentrations, speciation analysis, and health risk. *Environ. Sci. Pollut. Res.* **2014**, *21* (21), 12569−12582.
(27) Mandal, A.; Purakayastha, T. J.; Patra, A. K.; Sanyal, S. K. Phytoremediation of arsenic contaminated soil by *Pteris vittata* L. II. Effect on arsenic uptake and rice yield. *Int. J. Phytorem.* **2012**, *14* (6), 621−628.
(28) Mondal, P.; Bhowmick, S.; Chatterjee, D.; Figoli, A.; Van der Bruggen, B. Remediation of inorganic arsenic in groundwater for safe water supply: a critical assessment of technological solutions. *Chemosphere* **2013**, *92* (2), 157−170.
(29) Lundh, D. A. N.; Larsson, D.; Nahar, N.; Mandal, A. Arsenic accumulation in plants − outlining strategies for developing improved variety of crops for avoiding arsenic toxicity in foods. *J. Biol. Syst.* **2010**, *18* (1), 223−241.
(30) Xu, J. Y.; Li, H. B.; Liang, S.; Luo, J.; Ma, L. N. Q. Arsenic enhanced plant growth and altered rhizosphere. Characteristics of hyperacaimulator *Pteris vittata*. *Environ. Pollut.* **2014**, *194*, 105−111.
(31) Calvo, C.; Bolado, S.; Alvarez-Benedí, J.; Andrade, M. A. Arsenic uptake and accumulation in curly endives (*Cichorium endivia* L.) irrigated with contaminated water. *J. Environ. Sci. Health, Part B* **2006**, *41* (4), 459−470.
(32) Singh, R.; Singh, S.; Parihar, P.; Singh, V. P.; Prasad, S. M. Arsenic contamination, consequences and remediation techniques: a review. *Ecotoxicol. Environ. Saf.* **2015**, *112* (0), 247−270.
(33) Yamamura, S.; Amachi, S. Microbiology of inorganic arsenic: from metabolism to bioremediation. *J. Biosci. Bioeng.* **2014**, *118* (1), 1−9.
(34) Ampiah-Bonney, R. J.; Tyson, J. F.; Lanza, G. R. Phytoextraction of arsenic from soil by *Leersia oryzoides*. *Int. J. Phytorem.* **2007**, *9* (1), 31−40.
(35) Roy, M.; Giri, A. K.; Dutta, S.; Mukherjee, P. Integrated phytobial remediation for sustainable management of arsenic in soil and water. *Environ. Int.* **2015**, *75* (0), 180−198.
(36) Wilson, S. C.; Tighe, M.; Paterson, E.; Ashley, P. M. Food crop accumulation and bioavailability assessment for antimony (Sb) compared with arsenic (As) in contaminated soils. *Environ. Sci. Pollut. Res.* **2014**, *21* (20), 11671−11681.
(37) Sun, H.-J.; Rathinasabapathi, B.; Wu, B.; Luo, J.; Pu, L.-P.; Ma, L. Q. Arsenic and selenium toxicity and their interactive effects in humans. *Environ. Int.* **2014**, *69* (0), 148−158.
(38) Shamsipur, M.; Fattahi, N.; Assadi, Y.; Sadeghi, M.; Sharafi, K. Speciation of As(III) and As(V) in water samples by graphite furnace atomic absorption spectrometry after solid phase extraction combined with dispersive liquid-liquid microextraction based on the solidification of floating organic drop. *Talanta* **2014**, *130*, 26−32.
(39) Tokar, E. J.; Diwan, B. A.; Waalkes, M. P. Arsenic exposure transforms human epithelial stem/progenitor cells into a cancer stem-like phenotype. *Environ. Health Perspect.* **2010**, *118* (1), 108−115.

DOI: 10.1021/acs.jafc.5b02487
J. Agric. Food Chem. 2015, 63, 7097−7107

(40) Mazumder, G. Chronic arsenic toxicity & human health. *Indian J. Med. Res.* **2008**, *128* (4), 436−447.
(41) Lamm, S. H.; Robbins, S.; Chen, R.; Lu, J.; Goodrich, B.; Feinleib, M. Discontinuity in the cancer slope factor as it passes from high to low exposure levels − arsenic in the BFD-endemic area. *Toxicology* **2014**, *326* (0), 25−35.
(42) Martinez, V. D.; Becker-Santos, D. D.; Vucic, E. A.; Lam, S.; Lam, W. L. Induction of human squamous cell-type carcinomas by arsenic. *J. Skin Cancer* **2011**, *2011*, 1−9.
(43) Ghatak, S.; Biswas, A.; Dhali, G. K.; Chowdhury, A.; Boyer, J. L.; Santra, A. Oxidative stress and hepatic stellate cell activation are key events in arsenic induced liver fibrosis in mice. *Toxicol. Appl. Pharmacol.* **2011**, *251* (1), 59−69.
(44) Sinha, A.; Samanta, T.; Mallik, S.; Pal, D.; Ganguly, S. Non-cirrhotic portal fibrosis among children admitted in a tertiary care hospital of Kolkata: a search for possible aetiologies. *J. Indian Med. Assoc.* **2012**, *109* (12), 889−891, http://www.researchgate.net/publication/235883959_Non-cirrhotic_portal_fibrosis_among_children_admitted_in_a_tertiary_care_hospital_of_Kolkata_a_search_for_possible_aetiologies.
(45) Xie, H.; Huang, S.; Martin, S.; Wise, J. P. Arsenic is cytotoxic and genotoxic to primary human lung cells. *Mutat. Res., Genet. Toxicol. Environ. Mutagen.* **2014**, *760*, 33−41.
(46) Lewis, A. S.; Beyer, L. A.; Zu, K. Considerations in deriving quantitative cancer criteria for inorganic arsenic exposure via inhalation. *Environ. Int.* **2015**, *74* (0), 258−273.
(47) Liu, S.; Sun, Q.; Wang, F.; Zhang, L.; Song, Y.; Xi, S.; Sun, G. Arsenic induced overexpression of inflammatory cytokines based on the human urothelial cell model in vitro and urinary secretion of individuals chronically exposed to arsenic. *Chem. Res. Toxicol.* **2014**, *27* (11), 1934−1942.
(48) Melak, D.; Ferreccio, C.; Kalman, D.; Parra, R.; Acevedo, J.; Pérez, L.; Cortés, S.; Smith, A. H.; Yuan, Y.; Liaw, J.; Steinmaus, C. Arsenic methylation and lung and bladder cancer in a case-control study in northern Chile. *Toxicol. Appl. Pharmacol.* **2014**, *274* (2), 225−231.
(49) Tsuji, J. S.; Alexander, D. D.; Perez, V.; Mink, P. J. Arsenic exposure and bladder cancer: quantitative assessment of studies in human populations to detect risks at low doses. *Toxicology* **2014**, *317* (0), 17−30.
(50) Mostafa, M. G.; Cherry, N. Arsenic in drinking water and renal cancers in rural Bangladesh. *Occup. Environ. Med.* **2013**, *70* (11), 768−773.
(51) Wang, W.; Cheng, S.; Zhang, D. Association of inorganic arsenic exposure with liver cancer mortality: a meta-analysis. *Environ. Res.* **2014**, *135* (0), 120−125.
(52) Benbrahim-Tallaa, L.; Waalkes, M. P. Inorganic arsenic and human prostate cancer. *Environ. Health Perspect.* **2008**, *116* (2), 158−164.
(53) Kaur, H.; Kumar, R.; Babu, J. N.; Mittal, S. Advances in arsenic biosensor development − a comprehensive review. *Biosens. Bioelectron.* **2015**, *63* (0), 533−545.
(54) do Nascimento, S. N.; Barth, A.; Göethel, G.; Baierle, M.; Charão, M. F.; Brucker, N.; Moro, A. M.; Bubols, G. B.; Sobreira, J. S.; Sauer, E.; Rocha, R.; Gioda, A.; Dias, A. C.; Salles, J. F.; Garcia, S. C. Cognitive deficits and ALA-D-inhibition in children exposed to multiple metals. *Environ. Res.* **2015**, *136*, 387−395.
(55) Bhattacharyya, P.; Sen, P.; Ghosh, A.; Saha, C.; Bhattacharya, P. P.; Das, A.; Majumdar, K.; Mazumder, D. G. Chronic lung disease and detection of pulmonary artery dilatation in high resolution computerized tomography of chest in chronic arsenic exposure. *J. Environ. Sci. Health, Part A: Toxic/Hazard. Subst. Environ. Eng.* **2014**, *49* (13), 1453−1461.
(56) Brauner, E. V.; Nordsborg, R. B.; Andersen, Z. J.; Tjonneland, A.; Loft, S.; Raaschou-Nielsen, O. Long-term exposure to low-level arsenic in drinking water and diabetes incidence: a prospective study of the Diet, Cancer and Health Cohort. *Environ. Health Perspect.* **2014**, *122* (10), 1059−1065.
(57) Whitfield, J. B.; Dy, V.; McQuilty, R.; Gu, Z.; Heath, A. C.; Montgomery, G. W.; Martin, N. G. Genetic effects on toxic and essential elements in humans: arsenic, cadmium, copper, lead, mercury, selenium, and zinc in erythrocytes. *Environ. Health Perspect.* **2010**, *118* (6), 776−782.
(58) Singh, K. P.; DuMond, J. W., Jr. Genetic and epigenetic changes induced by chronic low dose exposure to arsenic of mouse testicular Leydig cells. *Int. J. Oncol.* **2007**, *30* (1), 253−260.
(59) Zhang, Z.; Pratheeshkumar, P.; Budhraja, A.; Son, Y.-O.; Kim, D.; Shi, X. Role of reactive oxygen species in arsenic-induced transformation of human lung bronchial epithelial (BEAS-2B) cells. *Biochem. Biophys. Res. Commun.* **2015**, *456* (2), 643−648.
(60) Yamagishi, R.; Hosoda, N.; Hoshino, S.-i. Arsenite inhibits mRNA deadenylation through proteolytic degradation of Tob and Pan3. *Biochem. Biophys. Res. Commun.* **2014**, *455* (3−4), 323−331.
(61) Thang, N. D.; Yajima, I.; Kumasaka, M. Y.; Kato, M. Bidirectional functions of arsenic as a carcinogen and an anti-cancer agent in human squamous cell carcinoma. *PLoS One* **2014**, *9* (5), 1−7.
(62) Luo, F.; Ji, J.; Liu, Y.; Xu, Y.; Zheng, G.; Jing, J.; Wang, B.; Xu, W.; Shi, L.; Lu, X.; Liu, Q. MicroRNA-21, up-regulated by arsenite, directs the epithelial−mesenchymal transition and enhances the invasive potential of transformed human bronchial epithelial cells by targeting PDCD4. *Toxicol. Lett.* **2015**, *232* (1), 301−309.
(63) Singh, K. P.; Kumari, R.; Treas, J.; DuMond, J. W. Chronic exposure to arsenic causes increased cell survival, DNA damage, and increased expression of mitochondrial transcription factor A (mtTFA) in human prostate epithelial cells. *Chem. Res. Toxicol.* **2011**, *24* (3), 340−349.
(64) Wang, H.; Gao, P.; Zheng, J. Arsenic trioxide inhibits cell proliferation and human papillomavirus oncogene expression in cervical cancer cells. *Biochem. Biophys. Res. Commun.* **2014**, *451*, 556−561.
(65) Kumar, S.; Yedjou, C. G.; Tchounwou, P. B. Arsenic trioxide induces oxidative stress, DNA damage, and mitochondrial pathway of apoptosis in human leukemia (HL-60) cells. *J. Exp. Clin. Cancer Res.* **2014**, *33* (1), 1−20.
(66) Lam, S. K.; Li, Y. Y.; Zheng, C. Y.; Ho, J. C. M. Downregulation of thymidylate synthase and E2F1 by arsenic trioxide in mesothelioma. *Int. J. Oncol.* **2015**, *46* (1), 113−122.
(67) Jun, X.; Youjian, L.; Qingling, Y.; Chuanzhong, M.; Zhiwen, C.; Bao, B.; Ahmad, A.; Miele, L.; Sarkar, F. H.; Zhiwei, W. Arsenic trioxide inhibits cell growth and induces apoptosis through inactivation of notch signaling pathway in breast cancer. *Int. J. Mol. Sci.* **2012**, *13* (8), 9627−9641.
(68) Chiu, H.-W.; Tseng, Y.-C.; Hsu, Y.-H.; Lin, Y.-F.; Foo, N.-P.; Guo, H.-R.; Wang, Y.-J. Arsenic trioxide induces programmed cell death through stimulation of ER stress and inhibition of the ubiquitin-proteasome system in human sarcoma cells. *Cancer Lett.* **2015**, *356* (2 Part B), 762−772.
(69) Ding, W.; Zhang, L.; Kim, S.; Tian, W.; Tong, Y.; Liu, J.; Ma, Y.; Chen, S. Arsenic sulfide as a potential anti-cancer drug. *Mol. Med. Rep.* **2015**, *11* (2), 968−974.
(70) Chen, Y.; Wu, F.; Liu, M.; Parvez, F.; Slavkovich, V.; Eunus, M.; Ahmed, A.; Argos, M.; Islam, T.; Rakibuz-Zaman, M.; Hasan, R.; Sarwar, G.; Levy, D.; Graziano, J.; Ahsan, H. A prospective study of arsenic exposure, arsenic methylation capacity, and risk of cardiovascular disease in Bangladesh. *Environ. Health Perspect.* **2013**, *121* (7), 832−838.
(71) Zhu, F. K.; Yang, S. K.; Fan, W. X.; Wang, A. R.; Hao, H. L.; Yao, S. W. Heavy metals in jujubes and their potential health risks to the adult consumers in Xinjiang province, China. *Environ. Monit. Assess.* **2014**, *186* (10), 6039−6046.
(72) Islam, M. N.; Das, B. K.; Huque, M. E. Arsenic accumulation in common vegetables from irrigation. *J. Sci. Res.* **2012**, *4* (3), 675−688.
(73) Chakraborty, S.; Alam, M. O.; Bhattacharya, T.; Singh, Y. N. Arsenic accumulation in food crops: a potential threat in Bengal Delta Plain. *Water Qual., Exposure Health* **2014**, *6* (4), 233−246.

DOI: 10.1021/acs.jafc.5b02487
J. Agric. Food Chem. 2015, 63, 7097−7107

(74) Meharg, A. A.; Hartley-Whitaker, J. Arsenic uptake and metabolism in arsenic resistant and nonresistant plant species. *New Phytol.* **2002**, *154* (1), 29−43.
(75) Ma, R.; Shen, J. L.; Wu, J. S.; Tang, Z.; Shen, Q. R.; Zhao, F. J. Impact of agronomic practices on arsenic accumulation and speciation in rice grain. *Environ. Pollut.* **2014**, *194*, 217−223.
(76) Kumar, A.; Dwivedi, S.; Singh, R. P.; Chakrabarty, D.; Mallick, S.; Trivedi, P. K.; Adhikari, B.; Tripathi, R. D. Evaluation of amino acid profile in contrasting arsenic accumulating rice genotypes under arsenic stress. *Biol. Plant.* **2014**, *58* (4), 733−742.
(77) Burges, A.; Epelde, L.; Garbisu, C. Impact of repeated single-metal and multi-metal pollution events on soil quality. *Chemosphere* **2015**, *120* (0), 8−15.
(78) Bergqvist, C.; Herbert, R.; Persson, I.; Greger, M. Plants influence on arsenic availability and speciation in the rhizosphere, roots and shoots of three different vegetables. *Environ. Pollut.* **2014**, *184*, 540−546.
(79) Dinh, N. T.; Vu, D. T.; Mulligan, D.; Nguyen, A. V. Accumulation and distribution of zinc in the leaves and roots of the hyperaccumulator *Noccaea caerulescens*. *Environ. Exp. Bot.* **2015**, *110* (0), 85−95.
(80) Zvobgo, G.; Hu, H.; Shang, S.; Shamsi, I. H.; Zhang, G. The effects of phosphate on arsenic uptake and toxicity alleviation in tobacco genotypes with differing arsenic tolerances. *Environ. Toxicol. Chem.* **2015**, *34* (1), 45−52.
(81) Li, L.; Li, J.; Shao, C.; Zhang, K.; Yu, S.; Gao, N.; Deng, Y.; Yin, D. Arsenic removal in synthetic ground water using iron electrolysis. *Sep. Purif. Technol.* **2014**, *122* (0), 225−230.
(82) Yan, L.; Huang, Y.; Cui, J.; Jing, C. Simultaneous As(III) and Cd removal from copper smelting wastewater using granular TiO_2 columns. *Water Res.* **2015**, *68* (0), 572−579.
(83) Xu, J.; Bravo, A. G.; Lagerkvist, A.; Bertilsson, S.; Sjöblom, R.; Kumpiene, J. Sources and remediation techniques for mercury contaminated soil. *Environ. Int.* **2015**, *74* (0), 42−53.
(84) Zhang, W.-x. Nanoscale iron particles for environmental remediation: an overview. *J. Nanopart. Res.* **2003**, *5* (3−4), 323−332.
(85) Gusiatin, Z. M. Tannic acid and saponin for removing arsenic from brownfield soils: mobilization, distribution and speciation. *J. Environ. Sci.* **2014**, *26* (4), 855−864.
(86) Hafsteinsdóttir, E. G.; Fryirs, K. A.; Stark, S. C.; Gore, D. B. Remediation of metal-contaminated soil in polar environments: phosphate fixation at Casey Station, East Antarctica. *Appl. Geochem.* **2014**, *51* (0), 33−43.
(87) Wyke, S.; Peña-Fernández, A.; Brooke, N.; Duarte-Davidson, R. The importance of evaluating the physicochemical and toxicological properties of a contaminant for remediating environments affected by chemical incidents. *Environ. Int.* **2014**, *72* (0), 109−118.
(88) Chibuike, G. U.; Obiora, S. C. Heavy metal polluted soils: effect on plants and bioremediation methods. *Appl. Environ. Soil Sci.* **2014**, *2014*, 1−12.
(89) Xie, X.; Wang, Y.; Pi, K.; Liu, C.; Li, J.; Liu, Y.; Wang, Z.; Duan, M. In situ treatment of arsenic contaminated groundwater by aquifer iron coating: experimental study. *Sci. Total Environ.* **2015**, *527−528*, 38−46.
(90) Ashauer, R.; Hintermeister, A.; O'Connor, I.; Elumelu, M.; Hollender, J.; Escher, B. I. Erratum: Significance of xenobiotic metabolism for bioaccumulation kinetics of organic chemicals in *Gammarus pulex*. *Environ. Sci. Technol.* **2012**, *46* (8), 4682.
(91) Alava, P.; Du Laing, G.; Tack, F.; De Ryck, T.; Van De Wiele, T. Westernized diets lower arsenic gastrointestinal bioaccessibility but increase microbial arsenic speciation changes in the colon. *Chemosphere* **2015**, *119* (0), 757−762.
(92) Pacini, N. Environmental background assessment: basic principles and practice. *Ann. Ist. Sup. Sanita* **2008**, *44* (3), 258−267.
(93) Lu, L.; Liao, X.; Labavitch, J.; Yang, X.; Nelson, E.; Du, Y.; Brown, P. H.; Tian, S. Speciation and localization of Zn in the hyperaccumulator *Sedum alfredii* by extended X-ray absorption fine structure and micro-X-ray fluorescence. *Plant Physiol. Biochem.* **2014**, *84* (0), 224−232.
(94) Shen, H.; He, Z.; Yan, H.; Xing, Z.; Chen, Y.; Xu, W.; Wenzhong, X.; Ma, M. The fronds tonoplast quantitative proteomic analysis in arsenic hyperaccumulator *Pteris vittata* L. *J. Proteomics* **2014**, *105*, 46−57.
(95) Xiao, N.; Liu, R.; Jin, C.; Dai, Y. Efficiency of five ornamental plant species in the phytoremediation of polycyclic aromatic hydrocarbon (PAH)-contaminated soil. *Ecol. Eng.* **2015**, *75* (0), 384−391.
(96) Sánchez-Rodas, D.; Corns, W. T.; Chen, B.; Stockwell, P. B. Atomic fluorescence spectrometry: a suitable detection technique in speciation studies for arsenic, selenium, antimony and mercury. *J. Anal. At. Spectrom.* **2010**, *25* (7), 933−946.
(97) Farías, S. S.; Londonio, A.; Quintero, C.; Befani, R.; Soro, M.; Smichowski, P. On-line speciation and quantification of four arsenical species in rice samples collected in Argentina using a HPLC−HG−AFS coupling. *Microchem. J.* **2015**, *120* (0), 34−39.
(98) Sturchio, E.; Boccia, P.; Meconi, C.; Zanellato, M.; Marconi, S.; Beni, C.; Aromolo, R.; Ciampa, A.; Diana, G.; Valentini, M. Effects of arsenic on soil-plant systems. *Chem. Ecol.* **2011**, *27*, 67−78.

DOI: 10.1021/acs.jafc.5b02487
J. Agric. Food Chem. 2015, 63, 7097−7107

subclade is mainly composed of representatives from East Asia. Because new *Hericium* species continue to be discovered,[13] it would be of interest to compare the compositions and bioactivities of taxonomically and phylogenetically related and different *Hericium* species to those of *H. erinaceus*, the subject of the present study.

COMPOSITION

H. erinaceus fruit bodies and mycelia contain an exceptionally large amount of structurally different bioactive and potentially bioactive components. Figure 1 shows a photograph of an *H. erinaceus* mushroom with its mane-like surface. Figures 2–6 depict structures arbitrarily subdivided into five classes of organic compounds (erinacines, aromatic compounds, steroids, alkaloids, and lactones) isolated from the fruit bodies and mycelia. It seems to be a unique event in nature for a single mushroom species to biosynthesize about 70 different secondary metabolites. Here, the chemical nature of some of the compounds that might be responsible for the observed health-promoting properties is described below. The reader is referred to the cited references for details about structural and stereochemical characterization and nomenclature.

Figure 1. Photograph of Lion's Mane mushroom (from Congaree National Park, South Carolina, USA, courtesy of the National Park Service).

Hericerins. Hericerins—aromatic compounds with medicinal properties—have been isolated and identified from *H. erinaceus*. In a recent publication, Li et al. describe the isolation and structural characterization of two new aromatic compounds (hericerin A and isohericenone J) along with five known compounds (isoericerin, hericerin, *N*-dephenylethyl isohericerin, hericenone J, and 4-(3′,7′-dimethyl-2′,6′-octadienyl)-2-formyl-3-hydroxy-5-methoxybenzylalcohol) from a chloroform extract of the *H. erinaceus* fruiting bodies.[14] In related studies, Li et al.[15] describe the isolation of a new aromatic compound, erinacene D, from *H. erinaceus*. Miyazawa et al.[16] reported on the isolation of two new aromatic compounds, including a new D-arabinol ester, and two known compounds from *H. erinaceus*, and Zhang et al.[17] identified a new diterpene from *H. erinaceus* mycelia. The anticancer properties of some of these compounds are mentioned below.

Kobayashi et al.[18] achieved the total synthesis of bioactive resorcinols, erinacerins, and hericenols, isolated from the fruiting bodies of *H. erinaceus*. The structure of hericenone B was revised as the carbonyl regioisomer at the lactam moiety.

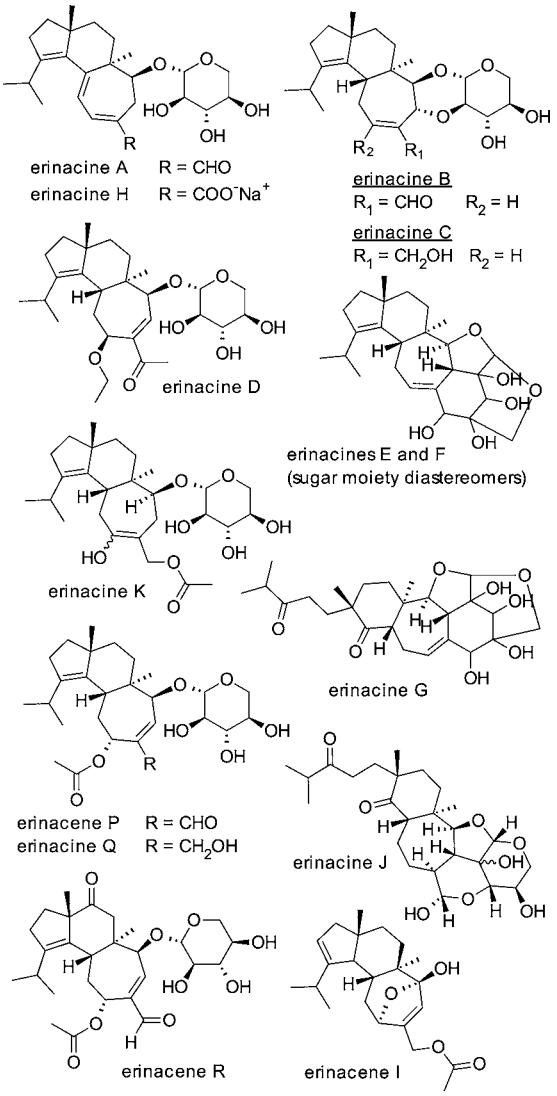

Figure 2. Structures of erinacines isolated from *Hericium erinaceus* fruit bodies and mycelia. Researchers at Shizuoka University first identified erinacines A–I;[80,103,132–134] Kenmoku et al.[135,136] characterized erinacines P and Q; and Ma et al.[137] characterized erinacine R.

Erinacines. The erinacines are a group of cyathane-type diterpenoids, including 20 members of 24 diterpenoids in *H. erinaceus* described by Tang et al.,[19] that have potential neuroprotective properties. Lee et al.[20] isolated erinacine A from an ethanol extract *H. erinaceus* mycelia. The compound contains the usual seven-member ring with two conjugated double bonds, which enables analysis by HPLC with UV detection at 340 nm.

Erinacerins—Isoindolin-1-ones. The isoindoline-1-ones are another group of secondary metabolites produced by *H. erinaceus*. Wang et al.[21] isolated 10 new isoindoline-1-ones, named erinacerins C–L, from a solid *H. erinaceus* culture. The structures of the compounds were established using spectroscopic methods, and the absolute configurations of some of these were assigned by comparing the specific rotations with those of related phthalimidines. The authors suggest that the described solid-state fermentation technique seems to be a useful method to stimulate the biosynthesis of secondary metabolites in edible and medicinal mushrooms and offer a hypothetical biogenesis pathway for the formation of the

DOI: 10.1021/acs.jafc.5b02914
J. Agric. Food Chem. 2015, 63, 7108–7123

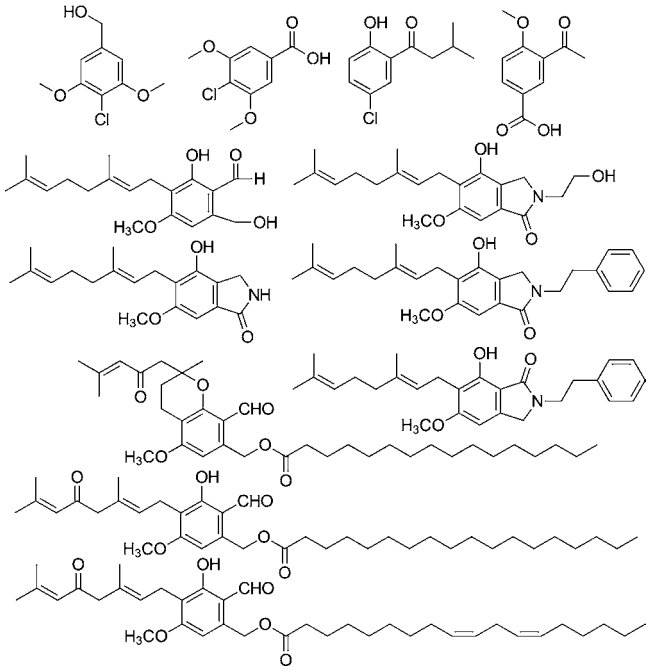

Figure 3. Structures of aromatic compounds isolated from *Hericium erinaceus* fruit bodies and mycelia. Adapted from Li et al.,[14] Noh et al.,[109] Zhang et al.,[17] and Miyazawa et al.[16]

erinacerins. Some of the compounds inhibited the growth of cancer cells, as described below.

Erinaceolactones. A recent study describes the isolation and characterization by spectroscopic methods of three novel erinaceolactones from the culture broth of *H. erinaceus*.[22] The absolute configuration of one of the compounds was determined by X-ray crystallography. A bioassay of plant-growth regulatory activity revealed that the new and structurally related *Hericium* compounds inhibited hypocotyl and root growth of lettuce at nanomolar concentrations.

Glycoprotein. Cui et al. isolated a novel glycoprotein (HEG-5) from cultures of *H. erinaceus* mycelia. The compound has a molecular weight of 14.4 kDa and has been shown to have hemagglutinating activity.[23] The protein/polysaccharide ratio of HEG-5 is 10:1 (%/%), and it contains D-glucose, L-rhamnose, D-galactose, and D-mannose in a molar ratio of 1.00:1.09:2.45:7.14 in the polysaccharide fraction. Analysis using FT-IR and NMR showed that HEG-5 contains the protein and carbohydrate parts with (1→4)-linked β-galactose and β-glucose residues, and circular dichroism showed that the HEG-5 is a predominantly β-sheet glycoprotein. The complete three-dimensional structure was obtained by protein sequencing and modeling using matrix-assisted laser desorption/ionization time-of-flight mass spectrometry (MALDI-TOF-MS), NCBI blast search, and online SWISS-MODEL Workplace service. The glycoprotein inhibited the growth of human gastric carcinoma cells in the MTT cell viability assay and exhibited hemagglutinating, but not hemolytic, activity in rat erythrocytes, as described below.

Polysaccharides. Polysaccharides from *H. erinaceus* have been of particular interest because of the bioactivities that have been attributed to them. There are therefore a number of studies on their isolation and analysis. For example, a Russian study[24] describes the isolation of two polysaccharides from *H. erinaceus* mycelia that differ in solubility in aqueous ethanol. Both products contained the following sugars in different ratios: fucose, galactose, glucose, rhamnose, and xylose.

Wu et al. used colorimetry with iodine and KI, high-performance size exclusion chromatography coupled with multiangle laser light scattering and refractive index detection (HPSEC-MALLS-rid analysis), gas chromatography−mass spectrometry (GC-MS) analysis, and saccharide mapping based on carbohydrate gel electrophoresis (PACE) analysis to identify polysaccharides isolated from *H. erinaceus* fruiting

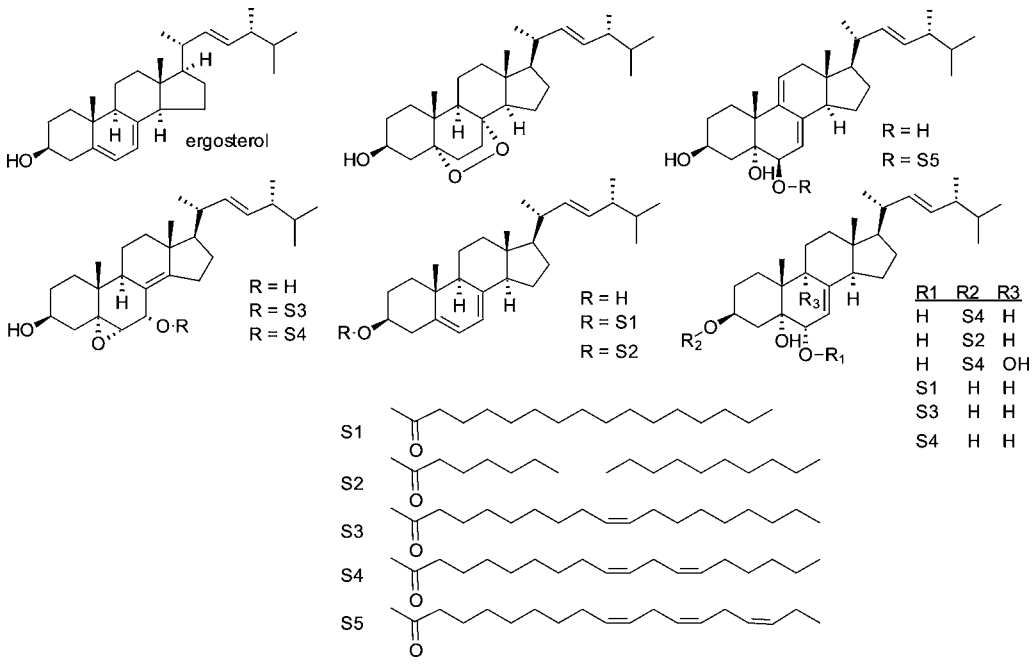

Figure 4. Structures of steroid compounds isolated from *Hericium erinaceus* fruit bodies and mycelia. Adapted from Avtonomova et al.,[24] Zan et al.,[32] and Li et al.[44]

DOI: 10.1021/acs.jafc.5b02914
J. Agric. Food Chem. 2015, 63, 7108−7123

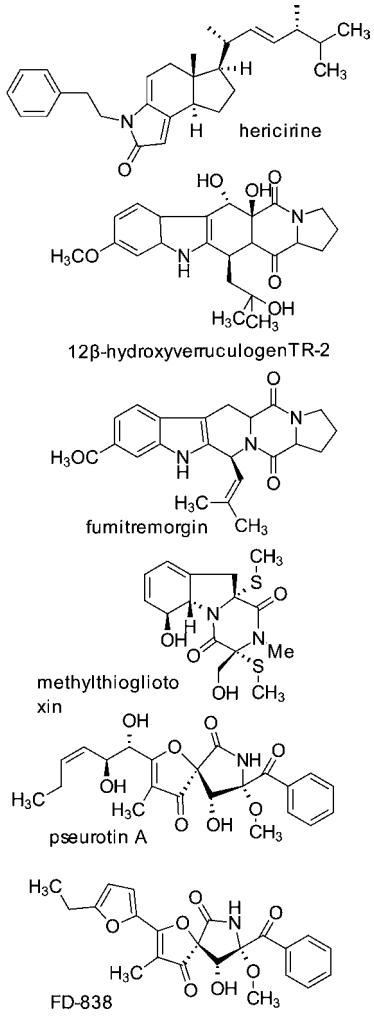

Figure 5. Structures of alkaloids isolated from *Hericium erinaceus* fruit bodies and mycelia. Adapted from Li et al.[138] and Lu et al.[139]

bodies collected from different parts of China.[25] The results show similarity in their profiles, including molecular weights, the composition of monosaccharides, and the glycosidic linkages in the polysaccharides, suggesting that the described experimental approach could be used for quality control of polysaccharides in edible and medicinal mushrooms as well as in commercial mushroom products. In addition, Hou et al.[26] isolated a water-soluble oligosaccharide from *H. erinaceus* with antioxidative properties. Other studies on the identification and characterization of *H. erinaceus* polysaccharides (*β*-D-glucans) are also reported by Kim et al.,[7] Bhandari et al.,[27] Li et al.,[28] Malinowska et al.,[29] Semedo et al.,[30] Shang et al.,[31] Wu et al.,[25] Zan et al.,[32] Zhang et al.,[33,34] and Zhu et al.,[35] some of which we elaborate here.

Using HPSEC to establish the degree of homogeneity and molecular weights, Malinowska et al.[29] evaluated several factors that govern the mycelial growth in a submerged culture of *H. erinaceus* and production of intracellular polysaccharides (IPS) and exopolysaccharides (EPS). They found that the kinetics of EPS biosynthesis in a bioreactor proceeded until depletion of the carbon source in the medium on day 14 of cultivation, suggesting the value of the method for large-scale production of bioactive polysaccharides from *H. erinaceus*.

An enzyme mixture (cellulase, pectinase, and tryptinase) facilitated extraction of polysaccharides from the fruits of *H.*

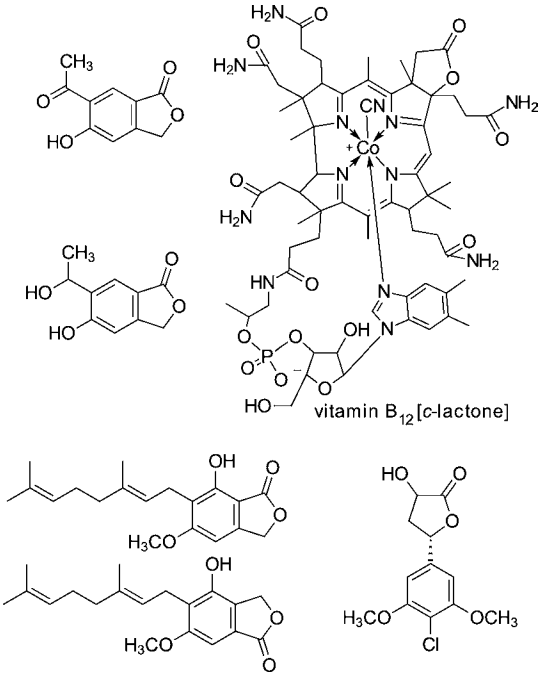

Figure 6. Structures of lactones isolated from *Hericium erinaceus* fruit bodies and mycelia. Adapted from Wu et al.[22] and Teng et al.[47]

erinaceus mushrooms using response surface methodology and the Box−Behnken design based on single-factor and orthogonal experiments to optimize the extraction conditions (pH 5.7, 52.0 °C, and 33.8 min).[35] The optimal extraction produces a high yield (13.5%) corresponding to an increase of 67.7% compared to hot water extraction. The functional groups of the two extracted polysaccharides seemed to be identical but differed in conformations. The authors suggest that the method might be useful for extracting polysaccharides from other mushroom species. Related studies describe the isolation and structural characterization of a rhamnoglucoagalactan[36] and a *β*-D-glucan[37] from *H. erinaceus* fruiting bodies.

H. erinaceus and other mushroom varieties are reported to be a useful source of lignocellulose-degrading (ligninolytic) carboxymethyl cellulase and laccase enzymes, suggesting that mushrooms can provide enzymes for use in the development of bioenergy.[38] Mushroom spent straw, an important lignocellulosic biomass, might serve as a potential substrate for an ethanol-based biorefinery.[39]

Sterols. The identification of various sterols from *H. erinaceus* has also been reported. For example, Avtonomova et al.[24] detected the presence of ergosterol in the *H. erinaceus* mycelia biomass. Because exposure of ergosterol to UV(B) light transforms ergosterol in mushrooms to vitamin D,[40,41] a process used to commercially market vitamin D-containing mushrooms, it would be of interest to find out whether such exposure would also induce an analogous transformation of *H. erinaceus* fruiting bodies and mycelia, thus further enhancing the health-promoting potential of this mushroom.

Because the amounts of such bioactive sterols, including ergosterol, are fairly low in *H. erinaceus*, Dai et al. evaluated the biomass and ergosterol content of *H. erinaceus* mycelium following supplementation of the liquid culture with the plant-derived compounds salicylic acid and methyl jasmonate.[42] The highest ergosterol content of 2.33 mg/g was obtained following 6 days of cultivation with 100 *μ*mol/L salicylic acid. With 50

DOI: 10.1021/acs.jafc.5b02914
J. Agric. Food Chem. 2015, 63, 7108−7123

μm/L methyl jasmonate, the highest ergosterol content was 2.0 mg/g. Both values were significantly higher than ergosterol production without the additives. Because methyl jasmonate induced significant increases in both mycelium biomass and ergosterol content during the logarithmic growth phase, whereas salicylic acid enhanced only the production of ergosterol but not biomass, the authors conclude that the use of added jasmonate might be preferable over methyl salicylate.

In other examples of sterol identification, Li et al.[43] compared the nature of sterols present in *H. erinaceus* in ethanol and water extracts, finding them mainly in the ethanol extract and identifying new sterols. Related studies describe the isolation and structural characterization of 6 new (erinarols A−F) and 5 known ergostane-type sterol fatty acid esters and 10 known ergostane-type sterols and erinarols G−J from methanol extracts of the dried fruiting bodies of *H. erinaceum* as well as anti-inflammatory and antiproliferative properties of some of these compounds in cell assays.[32,44]

Vitamin B_{12} Lactone. Some mushrooms, not including *H. erinaceus*, are reported to contain vitamin B_{12},[45] which is of particular interest to vegetarians,[46] because animal-derived foods are the usual dietary sources of vitamin B_{12}. *H. erinaceus* is, however, reported to contain the biologically inactive vitamin B_{12}[c-lactone],[47] and it may be possible to generate the active vitamin from this compound by chemically opening the lactone ring.

Volatile Compounds. Analysis of dried fruiting bodies of *H. erinaceus* by GC and GC-MS identified 77 components, representing 87.6% of the total volatile oil.[48] The main components of the oil were hexadecanoic acid (26.0%), linoleic acid (13.1%), phenylacetaldehyde (8.9%), and benzaldehyde (2.5%). Aroma evaluation of the oil using GC-MS−olfactometry and aroma extract dilution analysis showed that 2-methyl-3-furanthiol, 2-ethylpyrazine, and 2,6-diethylpyrazine seem to be the major contributors to the mushroom aroma. Because plant essential oils and aromatic aldehydes inactivate pathogenic bacteria,[49,50] will the mushroom oil and components also be active against pathogenic microorganisms? (See also Antibiotic Properties.)

NUTRIENTS, NUTRITION, AND FOOD USE

Here, we will first mention some general aspects associated with mushroom production, composition, and nutrition followed by a discussion of the limited studies on the nutrition of *H. erinaceus*.

Nutritional Composition. In describing culinary aspects of mushrooms, McGee notes that mushrooms are fungi that have no chlorophyll and thus they cannot harvest energy from the sun.[51] Instead, they live off plants and plant remains. They are therefore distinct from biologically derived foods such as cereals, fruits, and vegetables, and meat and dairy products.[1] The distinctive flavor of mushrooms is associated with a high content of free amino acids, especially glutamic acid, and numerous volatile compounds. Many mushrooms contain enzymes such as polyphenol oxidase that catalyze rapid enzymatic browning reactions[52] and, therefore, darken rapidly when cut or crushed.

A comprehensive review by Sawant et al.[53] provides information on mushroom cultivation and production methods including solid state and submerged culture; diseases caused by pathogenic fungi, bacteria, viruses, and pests; harvesting, grading, and packaging; storage; and processing (canning, dehydration, freezing and freeze-drying, and pickling). The reader is referred to the above-mentioned chapter by Savant for specific details on growing, harvesting, and processing of mushrooms.

An earlier review by Kurtzman,[54] reports that (a) the proximate composition of five mushroom species (not including *Hericium*) ranged as follows: water, from 73 to 91%; crude protein (N × 4.38), from 10.5 to 28.5%; fat, from 1.6 to 8.0%; carbohydrate, from 57.4 to 81.8 g/100 g dry wt; fiber, from 7.5 to 17.4 g/100 g dry wt; ash, from 6.1 to 12.0 g/100 g dry wt; and energy, from 271 to 387 kcal/100 g dry weight; and (b) the total essential amino acid composition ranged from 38.4 to 50.1 g amino acid/100 g of crude protein compared to 51.3 g amino acid/100 g for high-quality egg protein, suggesting that the nutritional quality of these mushrooms is quite high and that the content of essential amino acids approaches that of egg protein.

Ulziijargal and Mau summarize the results of proximate composition studies of 38 fruiting bodies and 19 mycelia of 32 species of culinary−medicinal mushrooms, including *Hericium*.[55] Most fruiting bodies and mycelia are low in fat and rich in protein and dietary fiber; some are rich in polysaccharides and others in crude fiber, suggesting that proximate composition and energy for fruiting bodies and mycelia should be taken into account for proposed uses as culinary and health food and as food additives.

In another study, Rodrigues et al. determined the composition and nutritive values of five mushroom species, including *H. erinaceus*.[56] Protein, sugar, and fat contents were in the ranges of 16.22−26.6, 52.7−64.9, and 2.3−3.5 g/100 g dry mushrooms, respectively. These mushroom are also good sources of phenolic compounds and contain more monounsaturated and polyunsaturated fatty acids than saturated fatty acids, with a high concentration of linoleic acid (>30 g/100 g fat), and they are good sources of magnesium, phosphorus, and especially potassium (2.6−3.7 g/kg dry mushroom). The mushrooms also contain significant amounts of copper, iron, and zinc, suggesting their dietary nutritional potential as a source of multiple macro- and micronutrients.

A comprehensive quantitative study by Cohen at al. of the composition of 15 Basidiomycetes medicinal mushroom strains belonging to 12 species, including *H. erinaceus* fruiting body (FB) and mycelia biomass (MB), found that almost all investigated mushrooms are a good source of proteins and carbohydrates, the levels of which are 8.6−42.5 and 42.9−83.6%, respectively, and that different species exhibited distinct free amino acid profiles.[2] The following information is limited to their reported findings with *H. erinaceus*. The analyses were performed on mushrooms dried at 50 °C and then ground into a powder. The dried powder of *H. erinaceus* FB contained 20.8% protein, 61.1% total carbohydrate, 5.1% fat, 6.8% ash, 6.2% water, and 374 kcal/100 g energy, whereas the MB contained 42.5% protein, 42.9% total carbohydrate 6.3% fat, 4.4% ash, 3.9% water, and 398 kcal/100 energy. The corresponding values for the total free amino acid content are 14.3 and 30.6 mg/g dry weight basis for the FB and MB, respectively. The total fatty acid content consisted of 11 individual unsaturated and saturated forms for FB and 7 for MB. Both FB and MB also contained various amounts of nutritional macro- and microelements (calcium, chromium, cobalt, copper, iron, magnesium, manganese, molybdenum, phosphorus, selenium, sodium, sulfur, and zinc) as well as low amounts potentially toxic elements (aluminum, arsenic, barium, boron, cadmium, nickel, silver, strontium, tin, titanium, and

DOI: 10.1021/acs.jafc.5b02914
J. Agric. Food Chem. 2015, 63, 7108−7123

vanadium). The content of amino-acid-derived bioactive compounds (in μg/g dry weight) in FB and MB, respectively, was as follows: γ-aminobutyric acid (GABA), 42.9 and 56.0; ergothioneine, 630.0 and 149.2; and lovostatin, 14.4 (FB). A levostatin value for MB was not reported.

It seems that both FB and MB contained useful nutrients and bioactive compounds and can as well serve as a resource for their use in food and pharmaceuticals (neutraceuticals); because of differences in composition among the MB and FB of the same species and among different species, combination of different species could be used to optimize their nutritional and health-promoting potential.

Because the use of mushrooms in main entrées in plant-based diets is growing, Feeney et al.[1,3] suggest that the nutritional and health benefits of mushrooms in terms of their nutrient, culinary, and health-promoting characteristics should be re-evaluated in the context of three separate food kingdoms: plants/botany, animals/zoology, and fungi/mycology. Because of the increasing availability of complete compositional data for different mushroom species, Feeney et al.[1,3] suggest the need for mathematical modeling designed to optimize the nutritional and health potential of combinations of different fruiting bodies and mycelia followed by animal and human feeding studies to confirm the predicted benefits. It may be possible to help meet this need by applying a mathematical modeling method to the relationship of composition to nutritional and health properties of mushrooms developed by Finotti et al.[57,58] for other food categories as well as principal component analysis of the bioactive *H. erinaceus* compounds as described for other mushroom species.[59,60] Moreover, the composition of the mushrooms also seems to depend on whether they are cultivated or grown in the wild.[61]

There is also a need to confirm the calculated nutritional values (scores) of mushrooms based on the content of essential amino acids,[62] by nutritional evaluation using feeding studies with mice, rats, and humans (as described elsewhere for free amino acids and other food proteins).[63−66] Unlike the in vitro results, the in vivo results are influenced by the digestibility of the proteins, absorption of the digested amino acids into the circulation, and their utilization for the synthesis of essential proteins.

Food Uses. The following three studies suggest the potential of *H. erinaceus* as a source of bioactive compounds and antioxidants in bread and in fermented mushroom wine, vinegar, and nonalcoholic beverages. Possible ways to inhibit enzymatic browning in mushrooms are also mentioned.

Bread Additive. Bread baked with 5% of *H. erinaceus* and other mushroom mycelia contained significant amounts of γ-aminobutyric acid (0.23−86 and 0.79−2.1 mg/g dry matter, respectively), reported to affect brain function,[67] and ergothioneine, reported to impact heart function,[68,69] suggesting that adding mushroom mycelia to bread might provide health benefits.[70]

Mushroom Wine and Vinegar. Another food application might be the reported use of *H. erinaceus* as a fermentation substrate for the production of wine and vinegar.[71] After 9 days of fermentation of 5% *H. erinaceus* powder, the alcohol content of the resulting mushroom wine reached 16%. A sensory evaluation by a human panel expressed overall acceptance of the organoleptic properties of the new wine. The wine was then treated with *Acidophilus aceti* bacteria to produce vinegar with an acidity of 4.09% due to presence of acetic, malic, and succinic acids. The new vinegar showed antioxidant activity possibly associated with its phenolic content comparable to those of known vinegars, suggesting the possibility that the *H. erinaceus* vinegar might represent a new food product with antioxidant capacity.

Fermented Mushroom Beverages. Because non-alcoholic fermented plant beverages are produced by fermentation of plant sources with different lactic acid bacteria, Woraharn et al.[72] evaluated the production of L-glutamic and γ-aminobutyric acid in a fermented *H. erinaceus* beverage by two *Lactobacilli* starter cultures. Glutamic acid production was significantly influenced by K_2HPO_4, pH, and temperature, whereas γ-aminobutyric acid production was significantly influenced by pH and temperature, suggesting that the mushrooms can be used to prepare high-quality fermented beverages at low cost.

Inhibition of Browning. Because heat used in cooking and baking is reported to adversely and beneficially affect the composition of mushrooms,[73,74] it would be of interest to find out to what extent food processing (canning, cooking, baking, frying, grilling, microwaving, sautéing) might affect the composition of *H. erinaceus* fruit bodies and mycelia. For example, the enzymatic browning reaction (formation of brown spots) that occurs on storage and heat drying of mushrooms, catalyzed by the enzyme tyrosinase, is a problem that has been addressed by Li et al.[75] for the culinary mushroom *Lentinus edodes* (Shiitake). They pretreated the mushrooms with the amino acid L-cysteine and other inhibitors of the enzyme tyrosinase to inhibit the browning process. L-Cysteine is reported to also inhibit enzymatic browning in potatoes[76] and nonenzymatic (Maillard) browning that can produce the potentially toxic acrylamide.[77,78]

MEDICINAL PROPERTIES

As mentioned, *H. erinaceus* has long been used for its beneficial health properties, which are reported to be wide ranging, as outlined in the sections below. Many of the activities reported for *H. erinaceus* can have crossover (overlapping) effects on different medical conditions as indicated in some of the sections below.

ANTIBIOTIC PROPERTIES

The following observations indicate that *H. erinaceus* extracts and bioactive erinacines and polysaccharides have been shown to have antimicrobial activities against both antibiotic-resistant and nonresistant (susceptible) pathogenic bacteria.

Methicillin-Resistant *Staphylococcus aureus* (MRSA). The prevalence of antibiotic-resistant pathogenic bacteria, especially MRSA, is a major unsolved problem in microbial food safety and human health, as reviewed by Friedman.[79] The identification of new compounds to treat antibiotic-resistant bacteria is therefore welcome. To contribute to this aim, using a Petri dish agar and microplate assays, Kawagishi et al. found that several erinacines isolated from cultured *H. erinaceus* mycelia showed potent anti-MRSA activity, with minimum inhibitory concentrations (MIC) values ranging from 62.5 to 500 μM.[80] An examination of the structure−antimicrobial activity relationship showed that the ring skeleton of the aglycone in the active compounds was indispensable to the anti-MSRA activity. It would be of interest to confirm this useful finding against MRSA-containing food and MRSA-infected animals and humans.[81]

***Salmonella* Typhimurium.** *Salmonella* Typhimurium is a pathogen that contaminates numerous foods, including leafy

DOI: 10.1021/acs.jafc.5b02914
J. Agric. Food Chem. 2015, 63, 7108−7123

greens, meat, and poultry. Kim et al.[82] discovered that although *H. erinaceus* extracts were inactive against this pathogen in vitro, they protected mice against lethal infection through the activation of innate macrophage immune cells. Two of the four extracts evaluated stimulated the activity of macrophage cells in vitro and protected infected mice against mortality and liver damage. Because systemic salmonellosis induces liver necrosis, liver injury was used as a biomarker for the incidence for in vivo salmonellosis in the mice. It seems that the protection of the liver by the mushroom extracts might be the result of stimulation of the innate immune cells, which then kill the *Salmonella* bacteria that induced the liver injury, analogous to that observed with the cultured macrophage cells. This first report on the inhibition of adverse effects of *Salmonella* in mice via stimulation of the immune system by mushroom extracts suggests that *H. erinaceus* mushrooms or extracts could be used to improve microbial food safety and infectious diseases. It would be of interest to find out whether the *H. erinaceus* extracts and/or pure compounds would also protect mice and humans against adverse effects caused by other foodborne pathogenic bacteria, including *Bacillus cereus*, *Escherichia coli*, *Listeria monocytogenes*, and *Vibrio cholerae*.

In a related study Kim et al.[83] also reported that a polysaccharide isolated from the liquid culture of *L. edodes* mushroom mycelia containing black rice bran protected mice against salmonellosis-induced liver injury and mortality through stimulation of the immune system. The same polysaccharide–black rice bran formulation also protected mice against *Salmonella* lipopolysaccharide-induced endotoxemia.[84] It would be interesting to investigate whether a similar *H. erinaceus* formulation might also protect mice against *Salmonella*-induced lethal infections and often fatal endotoxemia.

Helicobacter pylori. *H. pylori* is a human gastrointestinal pathogen that may contribute to the cause of adverse effects, possibly including ulcers. Shang et al.[85] determined the minimum inhibitory concentration (MIC) values of extracts prepared from the fruiting bodies of 14 mushroom species including *H. erinaceus* against *H. pylori* clinical strains using a microplate agar diffusion assay. MIC values of ethyl acetate fractions of *H. erinaceus* against nine clinical isolates of *H. pylori* ranged between 62.5 and 250 μg/mL. Ethanol extracts were less effective. The extracts of *H. erinaceus* also inhibited *Staphylococcus aureus* (MIC = 10 mg/mL) but had no effect on the growth of two *Escherichia coli* test strains (MIC > 10 mg/mL). The in vitro inhibitory effect of *H. erinaceus* extracts against *H. pylori* suggests antimicrobial mechanisms that do not seem to involve the immunomodulating effects observed with polysaccharides.[82]

Anti-*H. pylori* activities in vitro were evaluated using an agar dilution assay of two novel polysaccharides isolated from *H. erinaceus* with molecular weights of 197 and 20 kDa.[86] Although the polysaccharides alone inhibited the bacteria, complexes with bismuth exhibited stronger inhibition effects (MIC = 20 μg/mL), suggesting the need to evaluate these novel *H. erinaceus*-derived compounds against *H. pylori* infections in humans. It would be of interest to determine whether *H. erinaceus* and bioactive compounds would also inhibit the biological activity of microbial and plant toxins.[87]

Multiple Pathogens. A study by Wong et al.[88] using the well diffusion method that measures inhibition zones on Petri plates found that various *H. erinaceus* extracts inhibited the growth of multiple Gram-positive and Gram-negative pathogenic bacteria. The inhibition depended on the type of extract tested. Oven-dried fruit body extract was inactive.

■ ANTICARCINOGENIC PROPERTIES

Carcinogenesis is a sequential multistage cellular process consisting of tumor initiation, tumor promotion, and tumor progression. Plant compounds in some foods are a potential source of bioactive safe compounds for cancer chemoprevention and suppression of tumor initiation, promotion, and metastasis.[89] Dietary components can protect against cell proliferation and induce cell death (apoptosis) by a variety of mechanisms, including destruction of reactive oxygen species (ROS) that damage DNA and essential proteins, suppression of signaling pathways, and expression of proteins involved in carcinogenesis, inhibition of angiogenesis (blood flow to cancer cells), cancer cell metastasis (migration of cells from the origin to other organs), and stimulation of the immune system that helps eliminate carcinogens.[82,83,90,91] Here, we will briefly mention selected reported studies on the antioxidative, antimutagenic, antitumor-promoting, and anticarcinogenic activities of *H. erinaceus* and bioactive components in mammalian cells and rodents (mice, rats).

Inhibition of Cancer Cells. The recently isolated newly discovered diterpene mentioned under Nutritional Composition above both exhibited anti-*H. pylori* activity and inhibited the growth of human leukemia (K562) and human prostate cancer (LANCAP) cells.[17] The isolated hericerin A and hericerin also significantly reduced the proliferation of leukemia cells with IC_{50} values of 3.06 and 5.47 μM.[14]

A study by Lee and Hong[92] on the mechanism of *H. erinaceus* inhibition of human liver (HepG2) cancer cells showed that (a) hot-water *H. erinaceus* extract enhances the apoptosis induced by the clinical cancer drug doxorubicin and (b) the *H. erinaceus* extract acts as an enhancer to sensitize doxorubicin-mediated apoptotic signaling by reducing C-FLIP expression via JNK activation and enhancing intracellular doxorubicin accumulation via inhibition of NF-κB activity. The mushroom extract seems to have the potential to provide therapeutic effects against drug-resistant human liver carcinoma.

Li et al. isolated a lectin (agglutinin) from dried fruiting bodies of *H. erinaceus* with a molecular mass estimated at 51 kDa, a hemagglutinating activity of 12.5 mM by the inulin assay, and high heat and pH stability.[93] The lectin showed antiproliferative activity toward hepatoma (HepG2) and breast cancer (MCF7) cells with IC_{50} values of 56.1 and 76.5 μM, respectively, HIV-1 reverse transcriptase inhibitory activity with an IC_{50} of 31.7 μM, and mitogen activity toward mouse splenocytes. Because lectins are non-immunglobulin proteins that can agglutinate cells through sugar-specific binding sites, their mechanism of anticancer and antimicrobial action differs from that of other mushroom components, reviewed by Hassan et al.[94]

Kim et al.[8] also evaluated hot water (HWE), microwaved 50% ethanol (MWE), acidic (ACE), and alkaline (AKE) extracts of the fruit body (sporocarp) of *H. erinaceus* for their ability to induce apoptosis (programmed cell death) in U937 human monocytic leukemia cells. Cell culture, cell viability, cytotoxicity, flow cytometry, chromosomal DNA integrity, mitochondrial membrane potential, expression of pro- and anti-apoptotic proteins, and activation and inhibition of caspase assays were carried out to help define the mechanism of observed apoptosis. The aqueous and aqueous/ethanol extracts were active in all assays, whereas the acidic and alkaline extracts

DOI: 10.1021/acs.jafc.5b02914
J. Agric. Food Chem. 2015, 63, 7108−7123

with similar proximate compositions were both inactive. The results of the bioassays with the active extracts are consistent with an apoptosis mechanism governing suppression of the cell proliferation pathway that involves activation of mitochondria-mediated caspase-3 and caspase-9 but not caspase-8. Proximate analysis of the freeze-dried mushroom powder showed that it contains high amounts of proteins, carbohydrates, and minerals. The described observations indicate that aqueous and aqueous/ethanol extracts of *H. erinaceus* that induced NO production in macrophage cells strongly suppressed the proliferation of U937 leukemia but not normal cells, by induction of apoptosis, suggesting that *H. erinaceus* may have therapeutic potential against human leukemia.

The novel HEG-5 polysaccharide-protein isolated from fermented *H. erinaceus* mycelia inhibited human gastric SGC-7901 cancer cells by promoting apoptosis and cell cycle arrest at the S-phase.[32] RT-PCR and Western blot analysis showed that HEG-5 decreased the expressions of Bcl2, PI3K, and AKT1 proteins and increased the expressions of caspase-3, caspase-8, p53, CDK4, Bax, and Bad, suggesting that caspase- and p53-dependent mitochondrial-mediated signaling pathways participate in the molecular events of apoptosis. The results imply that the novel polysaccharide might be a candidate for treating gastric cancer. The use of HEG-5 against human gastric cancer is expected to be successful in light of the fact that *H. erinaceus* mushrooms are reported to prevent gastric ulcers, chronic gastritis, and other digestive tract-related diseases.[95,96]

Chen et al.[97] isolated polysaccharides from eight mushroom species by water extraction and alcohol precipitation. The *H. erinaceus* polysaccharide exhibited the highest antioxidant capacity and strongly inhibited MCF-7 breast cancer cells.

Inhibition of Tumor Growth. Kim et al.[7] investigated antitumor effects of the four extracts of freeze-dried *H. erinaceus* in Balb/c mice intracutaneously transplanted on their backs with CT-26 colon cancer cells; HWE and MWE, with a higher content of β-glucans than ACE and MKE and determined using an assay kit, were active in all bioassays. GC-MS analyses showed the presence of 40, 27, 16, and 13 compounds, respectively, in the four extracts. Daily intraperitoneal (ip) injections of HWE and MWE for 2 weeks significantly reduced tumor weights by 38 and 41%. Tumor regressions were associated with changes in the following cancer biomarkers as compared to phosphate buffer (PBS)-treated control mice: 2.7- and 2.4-fold increases in cytolytic activity of splenic natural killer (NK) cells; restored nitric oxide production and phagocytosis (engulfing and destruction of cancer cells by phagocyte cells) in peritoneal macrophages to 95−98% of normal levels; 2-fold increase in released pro-inflammatory cytokines tumor necrosis factor-α, interleukin-1β, and interleukin-6 from macrophages; and 56 and 60% reductions in the number of blood vessels inside the tumor. The pro-angiogenic factors vascular endothelial growth factor (VEGF), cyclooxygenase 2 (COX-2), and 5-lipoxygenase (5-LOX) were also significantly reduced in mRNA and protein expression by tumor genes. Enzyme-linked immunosorbent assay of tumor cells confirmed reduced expression of COX-2 and 5-LOX (32 and 31%). Reduced COX-2 and 5-LOX expression down-regulated VEGF expression, resulting in the inhibition of neo-angiogenesis inside the tumors. It seems that induction of NK activity, activation of macrophages, and inhibition of angiogenesis all contribute to the mechanism of reducing tumor size.

Another study by Kim et al. investigated the antimetastatic activity of four *H. erinaceus* mushroom extracts using CT-26 murine colon carcinoma cells as an indicator of inhibition of cell migration to the lung.[6] The HWE and MWE extracts strongly elicited cancer cell death through apoptosis and inhibited metastasis of cancer cells to the lungs by 66 and 69%, respectively. The same extracts reduced the expression of matrix metalloproteinases MMP-2 and MMP-9 in cells and their activities in culture media. Urokinase-type plasminogen activator (u-PA), another extracellular matrix (ECM)-degrading proteinase, also showed decreased protein expression. In CT-26 cells, HWE and MWE down-regulated extracellular signal-regulated kinase (ERK), c-Jun N-terminal kinase (JNK), and p38 mitogen-activated protein kinase (MAPK) phosphorylations. The reduced phosphorylations seem to cause reduction of activity of the MMPs, thereby blocking migration and invasion of cells. Dietary administration of HWE and MWE reduced the formation of tumor nodules in the lung by about 50 and 55%, respectively, and prevented increases in lung weight caused by cancer cell metastasis.

It seems that HWE and MWE behaved as antimetastatic agents, targeting their upstream signaling molecules for mediating the expression of the ECM-degrading proteinases. Acidic and alkaline extracts were not bioactive. This study elucidated the mechanism of the observed inhibition of metastasis of cancer cells from one organ to another in terms of biomarkers known to be associated with prevention of metastasis, suggesting that inhibition of metastasis seems to be related to the composition of *H. erinaceus*.

Daily oral administration of three amounts (50, 100, and 200 mg/kg/day for 10 days) of *H. erinaceus* polysaccharides to 50 mice with S180 solid tumors reduced the increase in tumor weight from 100% for the control group to 68.5, 32.1, and 43.2% in treated groups, respectively, as compared to 18.5% for treatment with the cancer drug cyclophosphamide.[98] The reduced tumor weight gains were accompanied by increased serum levels of antigen-specific-γ (IFN-γ) and interleukin-2 (IL-2), suggesting that the antitumor effect might be associated with immunostimulation. A related study on the antitumor and immunoenhancing effects of polysaccharides is mentioned under Stimulation of the Immune System.

The cited studies suggest that *H. erinaceus* polysaccharides merit further study to determine if their anticarcinogenic activities in mice also occur in humans.

An interesting finding was that the replacement of aspartic acid/glutamic acid with asparagine/glutamine residues in ribonuclease from *H. erinaceus* resulted in a modified enzyme that inhibited the proliferation of a human leukemia cell line.[99] The authors suggest that the modified ribonuclease, which was expressed by recombinant methods in *E. coli* bacteria, might be of general importance for the production of anticancer biologics that are based on ribonuclease activity.

NEUROPROTECTION AGAINST NEURODEGENERATION

Cell and Mice Studies. A review by Wong et al. on the treatment of peripheral nerve injury by *H. erinaceus* concludes that the neuroprotective effects of *H. erinaceus* and other mushrooms in rodents need to be confirmed in human studies.[100] Here, we will be briefly examine selected studies on the neuroprotective effects of *H. erinaceus* in cells and animals and their potential impact on cognitive abilities in humans, which suggest that such mushrooms may help improve brain and nerve diseases in humans.[20,101,102]

DOI: 10.1021/acs.jafc.5b02914
J. Agric. Food Chem. 2015, 63, 7108−7123

A systematic screening of 19 commercial *Hericium* strains revealed that the administration of fruiting bodies of *H. erinaceus* could attenuate (protect against) Aβ25-35-triggered damage in rat pheochromocytoma (PC12) cells, which are widely used to study neuritogenesis in vitro.[11] The observed effects were an increase in cell viability and a decrease in the release of lactate dehydrogenase; the described method could therefore be used to screen for the neuroprotective effects of mushrooms.

Nerve growth factor (NGF) is involved maintaining and organizing the function of cholinergic neurons of the basal forebrain complex (BFC) of the central nervous system, the neurons of which degenerate during the progression of Alzheimer's disease (dementia). Kawagishi et al. discovered and named the bioactive diterpenoids erinacine A, B, and C from *H. erinaceus* mycelia that stimulated NGF synthesis.[103] Phan et al.[104] cultured *H. erinaceus* mycelia and screened pure compounds isolated from the basidiocarps for neurite outgrowth activity using PC12 cells.

The use of HPLC, LC-MS, and ^{1}NMR facilitated the elucidation of the structures of six compounds from the basidiocarps: hericenones B−E, erinacerin A, and isohericerin. Hericenone E stimulated NGF secretion to a level that was 2 times higher than that of the positive control, by potentiating outgrowth in the PC12 cells, possibly mediated by ERK1/2 (extracellular signal-regulating kinases) and P12Akt (protein kinase) signaling pathways to induce neuronal differentiation and neuritogenesis.

A related study by Mori et al. examined the effect of four edible mushroom fruiting bodies including *H. erinaceus* on NGF gene expression in 1321N1 human astrocytoma cells (astrocytes).[105] The results show that *H. erinaceus* fruiting bodies, but not the isolated hericenones C, D, and E, promoted NGF mRNA expression in a concentration-dependent manner and enhanced the secretion of the NGF protein from the cells. Additional studies showed that the extract also enhanced the neurite outgrowth of PC12 cells in vitro and increased NGF mRNA expression in the hippocampus, but not in the cortex, of mice fed a 5% dry *H. erinaceus* powder for 7 days and that the stimulation of NGF production occurs via activation of the JNK pathway.

Another study by Mori et al. examined the effect of oral administration of *H. erinaceus* powder added to the mouse diet over a 23 day experimental period on the amyloid β(25−35) peptide-induced learning and memory deficits (cognitive dysfunctions) in mice.[106] Evaluation of the learning function of the mice by behavioral pharmacological methods (Y-maze and novel-object recognition tests) indicates that the mushroom powder improves the cognitive deficits induced by the amyloid peptide, suggesting that the powder might be a promising treatment for cognitive dysfunction. Additional HPLC studies showed that the powder contained the following three hericenones: C, 4.12 mg/g; D, 0.21 mg/g; and E, 0.49 mg/g.

The cited cell and mice feeding studies imply that because NGF levels decrease in the basal forebrain of Alzheimer's patients and in the frontal cortices of people with senile plaques, the results of the cell and mice feeding studies showing increased secretion of NGF indicated that hericenone E and the *H. erinaceus* powder merit further studies for their potential to prevent progress of dementia and senile plaques in humans.

Antifatigue Effects. A study by Li et al. examined the antifatigue activity of a polysaccharide extracted from *H. erinaceus* in a mouse model using the following criteria.[107] A control group and three test groups of mice were treated with the polysaccharide (50, 100, and 200 mg/kg for 28 days). The results of a force swimming test, a measure of fatigue, decreased blood lactic acid (BLA), serum urea nitrogen (SUN), and malondialdehyde (MDA) content, and increased tissue glycogen content and antioxidant enzyme activity suggest that an *H. erinaceus* component induced significant antifatigue activity and might, therefore, be of value in the field of sport nutrition.

Acceleration of Wound Healing in Rats. A Malaysian study found that the topical application of an *H. erinaceus* aqueous extract (0.2 mL of 20, 30, and 40 mg/mL) accelerated the rate of wound healing in rats.[108] The healed wounds contain fewer macrophages and more collagen, suggesting that the healing effect might be associated with the up-regulation of collagen formation and an increase in the tensile strength of the wounds. Because the livers and kidneys of the rats were not affected by the treatment, hematology and clinical biochemistry were within the range of control animals tested, and the highest dose of the extract (5 g/kg body weight) did not cause any toxicity, it seems that the mushroom extract is relatively nontoxic. The authors suggest the need to identify the bioactive component in the extract that has possible immunostimulatory potential.

Inhibition of Cell Senescence. Noh et al. evaluated the inhibitory effects of six compounds isolated from *H. erinaceus* on adriamycin-induced cellular senescence in human dermal fibroblasts (HDFs) and human umbilical vein endothelial cells (HUVECs).[109] One of the compounds—ergosterol peroxide—reduced senescence-associated β-galactosidase (SA-β-gal) activity that is increased in HUVECs treated with adriamycin, suggesting that one or more of the pure compounds might have the potential to treat/prevent age-related diseases in humans.

HUMAN STUDIES

Beneficial Effects on Depression and Anxiety. Nagano et al. investigated the effect of *H. erinaceus* on depression, menopause, and sleep quality using epidemiological-based questionaires.[110] In a randomized, double-blind, placebo-control trial conducted over 4 weeks, 30 females aged 41.3 ± 5.6 years were randomly assigned to either *H. erinaceus* or placebo groups and fed *H. erinaceus* cookies containing 0.5 g of the powdered fruiting body 4 times a day for 4 weeks or placebo cookies for the same regimen. The mean standard scores at the end of the test were lower for the *H. erinaceus* than for the placebo group, suggesting that orally consumed *H. erinaceus* has the potential to reduce depression and anxiety in women but this is by a different, and as yet unknown, mechanism from the NGF-enhancing effect by the mushroom extracts and hericenones mentioned above.

Improvement in Cognitive Impairment. Mori et al. examined the efficacy of oral administration of 250 mg tablets containing *H. erinaceus* mushrooms (prepared by air-drying harvested fruiting bodies at 60 °C overnight and powdering) to patients diagnosed with mild cognitive impairments.[111] A double-blind, parallel-group, placebo-controlled trial was used on two 15-person groups of 50−80-year-old Japanese men and women for 4 weeks. At weeks 8, 12, and 16 of the trial, the mushroom group significantly increased scores on the cognitive function scale compared with the placebo group. Following treatment, a comparison of 21 medical laboratory tests of the two groups showed no significant differences, suggesting that

DOI: 10.1021/acs.jafc.5b02914
J. Agric. Food Chem. 2015, 63, 7108−7123

the mushroom tablets were safe and that their consumption improved mild cognitive impairment without serious adverse effects.

ANTIOXIDANT AND ANTIDIABETIC PROPERTIES

The antioxidant activity of *H. erinaceus* has been associated with the proposed treatment of several conditions. For example, the reduction of alloxan-induced diabetic neuropathic pain in rats following oral administration of an ethanol *H. erinaceus* extract was associated with a significant increase in the total in vivo antioxidant status (TAOS) in *Hericium*-treated groups, suggesting that the mushrooms might relieve diabetic neuropathic pain in humans.[112] The results of a related study on the antidiabetic and in vitro antioxidant activities of eight medicinal mushroom species seem to support the apparent relationship between antioxidant and antidiabetic effects.[113]

Indeed, it has also been shown that the ip administration of an aqueous extract of *H. erinaceus* (100 and 200 mg/kg body weight) to diabetic rats for 28 days resulted in a significant decrease in the serum glucose level and a significant increase in the insulin level and attenuated serum lipid profiles (disorders) as compared to control rats.[114] These findings were accompanied by increased activities in the antioxidative enzymes catalase (CAT), superoxide dismutase (SOD), and glutathione peroxidase (GSH-Px) and increased GSH (glutathione) and reduced malondialdehyde (MDA) levels in the liver, suggesting that the mechanism of the health-promoting effects seems to be the result of inhibition of ROS (oxidative stress parameters) known to damage the liver function. The specific compounds in the extract that may be responsible for the described effects are not known.

BENEFICIAL EFFECTS ON ISCHEMIA

Because ischemia (deficient supply of blood to organs) followed by reperfusion is a frequent clinical problem in cardiovascular surgery, Han et al. evaluated the effect of the preadministration of an *H. erinaceus* polysaccharide to mice by gavage at a dose of 300 mg/kg for 15 days on induced ischemia.[115] The results show that the treated mice had a significant decline in levels of blood urea nitrogen and serum creatinine and an increase in creatinine clearance levels compared to a renal ischemia−reperfusion control group. Additional studies with associated biomarkers (glutathione, malondialdehyde, antioxidative enzymes) showed that the polysaccharide pretreatment significantly decreased the lipid peroxidation level and increased antioxidant enzyme activities compared to the renal ischemia reperfusion group, suggesting that the polysaccharide prevented oxidative injury in the kidneys of the experimental animals and that it might help prevent acute kidney failure in humans.

ANTIOXIDATIVE AND HEPATOPROTECTIVE EFFECTS

As mentioned briefly above, *H. erinaceus* has been reported to have hepatoprotective effects, and these can be linked to its antioxidative activity. For example, a study by Zhang et al. of antioxidant and hepatoprotective effects of endo(intracellular)-polysaccharides from three fractions of *H. erinaceus* grown on the soybean processed product tofu whey found that the polysaccharide isolated from one of the fractions had strong in vitro antioxidant activity and protected mice against liver damage (assessed by observed changes in liver enzyme levels) induced by carbon tetrachloride (300 mg/kg body weight).[116] The beneficial effect on the liver is presumably the result of the potent antioxidant capacity of the polysaccharide, as determined by several different methods. The polysaccharides from the other two fractions were less effective. The most active polysaccharide could be used as a dietary supplement to prevent hepatic disease.

ANTIOXIDATIVE, ANTIHYPOLIPIDEMIC, AND ANTIHYPERTENSIVE EFFECTS

Feeding rats an exobiopolymer (molecular mass ∼ 40 kDa; protein and sugar contents of 8.8 and 91.2%, respectively) isolated from a submerged mycelia culture of *H. erinaceus* at a dose of 200 mg/kg body weight significantly reduced in a concentration-depended manner plasma total cholesterol (32.9%), bad low-density lipoprotein (LDL) cholesterol (45.4%), triglyceride level (34.3%), and the atherogenic index (58.7%) and increased good plasma high-density lipoprotein (HDL) cholesterol level (31.1%) as compared to the control diet.[117] The authors suggest the need to define the mechanism of the striking hypolipidemic effect.

Because oxidation of LDL might be a key factor in the pathogenesis of atherosclerosis, Rahman et al. investigated the in vitro inhibitory effect of *H. erinaceus* fractions extracted with different solvents on LDL oxidation and the activity of the cholesterol biosynthetic enzyme 3-hydroxy-3-methylglutaryl coenzyme A (HMG Co-A) reductase.[118] Of the solvent extractions, the hexane fraction showed the highest inhibition of oxidation and strongly inhibited the activity of the enzyme by up to 59.9% at 10 mg/mL. GC-MS analysis revealed that this fraction contained ergosterol and linoleic (9,12-octadecadienoic) and octadecanoic acids, suggesting that these components and possibly also a polysaccharide (not evaluated) might be responsible for the observed antioxidative properties of the mushroom extract and that the hexane extract might help to prevent oxidative stress-induced pathogenesis of atherosclerosis.

Because platelet aggregation in blood vessels causes vascular disease such as arterial thrombosis (formation of a blood clot) that may be accompanied by the formation of atherosclerotic lesions associated with myocardial infraction and stroke, Mori et al. evaluated the compound hericenone B isolated from *H. erinaceus* on collagen-induced platelet activity in rabbit and human platelets.[119] The results show that hericenone B exhibited strong antiplatelet aggregation activity by a mechanism that blocks collagen-induced platelet aggregation through the inhibition of arachidonic acid release in integrin $\alpha 2/\beta 1$ signaling, suggesting that it has potential to be used in antiplatelet therapy to prevent cardiovascular disease and stroke.

An in vitro study was conducted by Abdullah et al. on the inhibition of lipid peroxidation of buffered egg yolk and angiotensin converting enzyme inhibitory effects, an indicator of in vivo hypertensive activity, by water extracts of 10 culinary−medicinal mushrooms, including *H. erinaceus*. They found that *Ganoderma lucidum* mushrooms, with the highest phenolic content (63.5 GAE/g extract), exhibited the highest angiotensin converting enzyme inhibitory activity (IC_{50} = 0.05 mg/mL),[120] whereas the corresponding values for *H. erinaceus* were much lower: 10.2 GAE/g and IC_{50} = 0.58 mg/mL. There seems to be a good correlation between total phenolic content of the 10 mushroom varieties and their antioxidant capacities as determined by different methods. To determine whether

DOI: 10.1021/acs.jafc.5b02914
J. Agric. Food Chem. 2015, 63, 7108−7123

mushroom extracts can serve as protective agents against hypertension, however, the in vitro results need to be reproduced in vivo, in particular in humans, as is the case for many of these studies.

STIMULATION OF THE IMMUNE SYSTEM

Here, we will briefly describe reported studies on the stimulation of the immunes system in various animals and also the effect on dendritic cells by *H. erinaceus* mushrooms and associated polysaccharides.

Wang et al. compared the antitumor and immunoenhancing effects of polysaccharides with molecular weight > 1×10^5 kDa isolated from *H. erinaceus* and *H. laciniatum* mushrooms cultivated in a shaker at 25 °C for 25 days.[121] The results showed that both polysaccharides had significant antiartificial pulmonary metastatic tumor effects in mice, with the polysaccharide from *H. erinaceus* being more effective than that from *H. laciniatum* and that both enhanced the increase of T cells in the mouse model at the same rate, indicated by higher numbers of $CD4^+$ cells and macrophages in the test than in the control group. The results suggest that the antitumor effects might be associated with the immunoenhancing activities of the polysaccharides.

Supplementation of the diet of the olive flounder fish (*Paralichthys olivaceus*) with 0.1 and 1.0% *H. erinaceus* mushroom protected the fish that were infected with the parasite *Philasterides dicentrarchi* against mortality via enhancement of the innate immune response, as indicated by cumulative mortalities during the 4 weeks of 45 and 30%, respectively, compared to 90% in the control group, suggesting that the mushrooms modulated the nonspecific defense mechanisms against the pathogen.[122] The protection was associated with an increase in scuticocidal activity, enhanced respiratory burst activity of phagocyte cells, phagocytosis, and lysozyme activities in plasma. The authors suggest that, because of their biodegradability, mushroom diets merit further study for their beneficial effects in aquaculture.

A related study evaluated the effect of particle size (100−150, 74−100, and <74 μm) of dried *H. erinaceus* powder on the immune response and disease resistance against the pathogen *Vibrio alginolyticus* in white shrimp (*Litopenaeus vannamei*).[123] The results show that shrimp mortality was particle size dependent, with particles of <74 μm inducing a significantly greater effect on the disease resistance than those >74 μm, as indicated by a significantly lower mortality of the shrimp during the 28 day test period with a diet containing the mushroom powder at a concentration of 0.2 μg/g shrimp. The protective effect was accompanied by an increase in phenol oxidase activity, respiratory bursts, superoxide dismutase activity, and glutathione peroxidase activity, parameters usually associated with destruction of ROS. It seems that the smaller particle size improves the bioavailability of the dietary mushroom powder.

Dendritic cells are antigen-presenting cells that act as mediators of peripheral immune tolerance and help maintain immune homeostasis.[124,125] An evaluation of several biomarkers associated with the immunostimulatory effects of polysaccharides isolated from *H. erinaceus* mushrooms on murine dendritic cells showed that treatment with 50 μg/L of a 20% β-glucan-containing polysaccharide extract induced activation and promoted morphological changes, reduced endocytosis (incorporation of the polysaccharide into the cells by phagocytosis), increased the expression of surface molecules that are important for antigen presentation, and stimulated the secretion of cytokines that promote immune responses,[126] suggesting the potential value of the polysaccharides as an immunostimulatory food additive and adjuvant to enhance the immunogenicity of vaccines.

OUTLOOK

This overview covers an area of food medical science of current importance to mushroom growers, consumers, and food and biomedical scientists. Although the described results of the extensive, worldwide studies on multifunctional health properties of *H. erinaceus* in cells and in rodents, and to some extent in humans, need to be further confirmed in human nutritional, clinical, and epidemiological studies, a number of suggested research needs on the chemistry and numerous health-promoting aspects have been mentioned in the text. Because *H. erinaceus* species seems to lack toxicity in rodents and humans, nutritionists, pharmacists, and physicians should consider recommending these mushrooms to their clients and patients. The apparent exceptional beneficial properties will, hopefully, induce mushroom growers in the United States and elsewhere to produce *H. erinaceus* mushrooms for sale in stores. Because a large number of other *Hericium* species exist in nature, it would also be of interest to compare the described results on the composition, nutrition, and health benefits of *H. erinaceus* to phylogenetically related species. The suggested studies might lead to the discovery of new, highly bioactive *Hericium* species with high health-promoting potential. We anticipate that these efforts will contribute to the improvement of human nutrition and health.

It is also relevant to note that a meal consisting of *H. erinaceus* and other foods such as tomatoes that contain bioactive lycopene and tomatine[90] or pigmented rice that contains bioactive γ-oryzanol[127] will contribute multiple types of health-promoting properties to the diet that might induce additive or synergistic beneficial effects after consumption. This aspect also merits study. Finally, we expect readers to also benefit from our earlier related reviews on the health benefits of other food categories and their bioactive compounds that complement the present review.[77,79,87,91,127−131]

AUTHOR INFORMATION

Corresponding Author

*Phone: (510) 559-5615. E-mail: mendel.friedman@ars.usda.gov.

Notes

The author declares no competing financial interest.

ACKNOWLEDGMENTS

I am grateful to Carol E. Levin for assistance with the preparation of the manuscript.

ABBREVIATIONS USED

ACE, AKE, HWE, MWE: acid, alkaline, hot water, and microwave *H. erinaceus* extracts
CD-4: helper T cells that promote adhesion to antigen-presenting cells in response to infection
Bad, Bax: pro-apoptotic proteins
Bcl2,: apoptotic protein
BFC: basal forebrain complex
BUN: blood urea nitrogen
COX-2: cyclooxygenase-2
BLA: blood lactic acid

DOI: 10.1021/acs.jafc.5b02914
J. Agric. Food Chem. 2015, 63, 7108−7123

ECM: extracellular matrix
DC: dendritic cells
EPS: exopolysaccharides
ERK: extracellular signal-regulating kinase
FB: fruit body
FT-IR: Fourier transform infrared spectroscopy
GABA: γ-aminobutyric acid
GAE: gallic acid equivalents
HDFs: human dermal fibroblasts
HEG-5: *H erinaceus* glycoprotein
HUVECs: human umbilical vein endothelial cells
HPSEC-MALLS-RID: high-performance size exclusion chromatography with multiangle laser light scattering and refractive index detection
IC_{50}: concentration of test compound that inhibits 50% of cancer cells
IFN-γ: antigen-specific-γ
IL: interleukin-2
IPS: intracellular polysaccharides
ITS: rDNA internal transcribed tracer
JNK: c-Jun N-terminal kinase
5-LOX: 5-lipoxygenase
MAPK: mitogen-activated protein kinase
MIC: minimum inhibitory concentration
MDA: malondialdehyde
MMP: metalloproteinase
MRSA: methicillin-resistant *Staphylococcus aureus*
MTT: methyl tetrazolium cell viability assay
NF-κB: nuclear factor kappa-light-chain-enhancer of activated B cells
NK: killer cells
NGF: nerve growth factor
P12Aκt: protein kinase
RT-PCR: reverse transcription polymerase chain reaction
ROS: reactive oxygen species
TAOS: total in vivo antioxidant status
u-PA: urokinase-type plasminogen activator
VGEF: endothelial growth factor

REFERENCES

(1) Feeney, M. J.; Miller, A. M.; Roupas, P. Mushrooms − biologically distinct and nutritionally unique: exploring a "third food kingdom". *Nutr. Today* **2014**, *49*, 301−307.
(2) Cohen, N.; Cohen, J.; Asatiani, M. D.; Varshney, V. K.; Yu, H. T.; Yang, Y. C.; Li, Y. H.; Mau, J. L.; Wasser, S. P. Chemical composition and nutritional and medicinal value of fruit bodies and submerged cultured mycelia of culinary-medicinal higher Basidiomycetes mushrooms. *Int. J. Med. Mushrooms* **2014**, *16*, 273−291.
(3) Feeney, M. J.; Dwyer, J.; Hasler-Lewis, C. M.; Milner, J. A.; Noakes, M.; Rowe, S.; Wach, M.; Beelman, R. B.; Caldwell, J.; Cantorna, M. T.; Castlebury, L. A.; Chang, S.-T.; Cheskin, L. J.; Clemens, R.; Drescher, G.; Fulgoni, V. L.; Haytowitz, D. B.; Hubbard, V. S.; Law, D.; Myrdal Miller, A.; Minor, B.; Percival, S. S.; Riscuta, G.; Schneeman, B.; Thornsbury, S.; Toner, C. D.; Woteki, C. E.; Wu, D. Mushrooms and Health Summit Proceedings. *J. Nutr.* **2014**, *144*, 1128S−1136S.
(4) Sabaratnam, V.; Kah-Hui, W.; Naidu, M.; Rosie David, P. Neuronal health − can culinary and medicinal mushrooms help? *J. Tradit. Complement. Med.* **2013**, *3*, 62−68.
(5) Jiang, S.; Wang, S.; Sun, Y.; Zhang, Q. Medicinal properties of *Hericium erinaceus* and its potential to formulate novel mushroom-based pharmaceuticals. *Appl. Microbiol. Biotechnol.* **2014**, *98*, 7661−7670.
(6) Kim, S. P.; Nam, S. H.; Friedman, M. *Hericium erinaceus* (Lion's Mane) mushroom extracts inhibit metastasis of cancer cells to the lung in CT-26 colon cancer-transplanted mice. *J. Agric. Food Chem.* **2013**, *61*, 4898−4904.
(7) Kim, S. P.; Kang, M. Y.; Kim, J. H.; Nam, S. H.; Friedman, M. Composition and mechanism of antitumor effects of *Hericium erinaceus* mushroom extracts in tumor-bearing mice. *J. Agric. Food Chem.* **2011**, *59*, 9861−9869.
(8) Kim, S. P.; Kang, M. Y.; Choi, Y. H.; Kim, J. H.; Nam, S. H.; Friedman, M. Mechanism of *Hericium erinaceus* (Yamabushitake) mushroom-induced apoptosis of U937 human monocytic leukemia cells. *Food Funct.* **2011**, *2*, 348−356.
(9) Khan, M. A.; Tania, M.; Liu, R.; Rahman, M. M. *Hericium erinaceus*: an edible mushroom with medicinal values. *J. Complementary Integr. Med.* **2013**, *10*, 253−258.
(10) Lu, L.; Li, J.; Cang, Y. PCR-based sensitive detection of medicinal fungi *Hericium* species from ribosomal internal transcribed spacer (ITS) sequences. *Biol. Pharm. Bull.* **2002**, *25*, 975−980.
(11) Liu, Z.; Wang, Q.; Cui, J.; Wang, L.; Xiong, L.; Wang, W.; Li, D.; Liu, N.; Wu, Y.; Mao, C. Systemic screening of strains of the Lion's Mane medicinal mushroom *Hericium erinaceus* (higher Basidiomycetes) and its protective effects on Aβ-triggered neurotoxicity in PC12 cells. *Int. J. Med. Mushrooms* **2015**, *17*, 219−229.
(12) Hallenberg, N.; Nilsson, R. H.; Robledo, G. Species complexes in *Hericium* (Russulales, Agaricomycota) and a new species − *Hericium rajchenbergii* − from southern South America. *Mycol. Prog.* **2013**, *12*, 413−420.
(13) Das, K.; Stalpers, J. A.; Stielow, J. B. Two new species of hydnoid-fungi from India. *IMA Fungus* **2013**, *4*, 359−369.
(14) Li, W.; Zhou, W.; Kim, E. J.; Shim, S. H.; Kang, H. K.; Kim, Y. H. Isolation and identification of aromatic compounds in Lion's Mane mushroom and their anticancer activities. *Food Chem.* **2015**, *170*, 336−342.
(15) Li, W.; Sun, Y. N.; Zhou, W.; Shim, S. H.; Kim, Y. H. Erinacene D, a new aromatic compound from *Hericium erinaceum*. *J. Antibiot.* **2014**, *67*, 727−729.
(16) Miyazawa, M.; Takahashi, T.; Horibe, I.; Ishikawa, R. Two new aromatic compounds and a new D-arabinitol ester from the mushroom *Hericium erinaceum*. *Tetrahedron* **2012**, *68*, 2007−2010.
(17) Zhang, Z.; Liu, R. N.; Tang, Q. J.; Zhang, J. S.; Yang, Y.; Shang, X. D. A new diterpene from the fungal mycelia of *Hericium erinaceus*. *Phytochem. Lett.* **2015**, *11*, 151−156.
(18) Kobayashi, S.; Tamanoi, H.; Hasegawa, Y.; Segawa, Y.; Masuyama, A. Divergent synthesis of bioactive resorcinols isolated from the fruiting bodies of *Hericium erinaceum*: total syntheses of hericenones A, B, and I, hericenols B−D, and erinacerins A and B. *J. Org. Chem.* **2014**, *79*, 5227−5238.
(19) Tang, H. Y.; Yin, X.; Zhang, C. C.; Jia, Q.; Gao, J. M. Structure diversity, synthesis, and biological activity of cyathane diterpenoids in higher fungi. *Curr. Med. Chem.* **2015**, *22*, 2375−2391.
(20) Lee, K. F.; Chen, J. H.; Teng, C. C.; Shen, C. H.; Hsieh, M. C.; Lu, C. C.; Lee, K. C.; Lee, L. Y.; Chen, W. P.; Chen, C. C.; Huang, W. S.; Kuo, H. C. Protective effects of *Hericium erinaceus* mycelium and its isolated erinacine A against ischemia-injury-induced neuronal cell death via the inhibition of iNOS/p38 MAPK and nitrotyrosine. *Int. J. Mol. Sci.* **2014**, *15*, 15073−15089.
(21) Wang, K.; Bao, L.; Qi, Q.; Zhao, F.; Ma, K.; Pei, Y.; Liu, H. Erinacerins C−L, isoindolin-1-ones with α-glucosidase inhibitory activity from cultures of the medicinal mushroom *Hericium erinaceus*. *J. Nat. Prod.* **2015**, *78*, 146−154.
(22) Wu, J.; Tokunaga, T.; Kondo, M.; Ishigami, K.; Tokuyama, S.; Suzuki, T.; Choi, J.-H.; Hirai, H.; Kawagishi, H. Erinaceolactones A to C, from the culture broth of *Hericium erinaceus*. *J. Nat. Prod.* **2015**, *78*, 155−158.
(23) Cui, F. J.; Li, Y. H.; Zan, X. Y.; Yang, Y.; Sun, W. J.; Qian, J. Y.; Zhou, Q.; Yu, S. L. Purification and partial characterization of a novel hemagglutinating glycoprotein from the cultured mycelia of *Hericium erinaceus*. *Process Biochem.* **2014**, *49*, 1362−1369.
(24) Avtonomova, A. V.; Bakanov, A. V.; Shuktueva, M. I.; Vinokurov, V. A.; Popova, O. V.; Usov, A. I.; Krasnopol'skaia, L. M.

DOI: 10.1021/acs.jafc.5b02914
J. Agric. Food Chem. 2015, 63, 7108−7123

[Submerged cultivation and chemical composition of *Hericium erinaceus* mycelium]. *Antibiot. Khimioter.* **2012**, *57*, 7−11.
(25) Wu, D. T.; Li, W. Z.; Chen, J.; Zhong, Q. X.; Ju, Y. J.; Zhao, J.; Bzhelyansky, A.; Li, S. P. An evaluation system for characterization of polysaccharides from the fruiting body of *Hericium erinaceus* and identification of its commercial product. *Carbohydr. Polym.* **2015**, *124*, 201−207.
(26) Hou, Y.; Ding, X.; Hou, W. Composition and antioxidant activity of water-soluble oligosaccharides from *Hericium erinaceus*. *Mol. Med. Rep.* **2015**, *11*, 3794−3799.
(27) Bhandari, D. R.; Shen, T.; Rompp, A.; Zorn, H.; Spengler, B. Analysis of cyathane-type diterpenoids from *Cyathus striatus* and *Hericium erinaceus* by high-resolution MALDI MS imaging. *Anal. Bioanal. Chem.* **2014**, *406*, 695−704.
(28) Li, Q. Z.; Wu, D.; Chen, X.; Zhou, S.; Liu, Y.; Yang, Y.; Cui, F. Chemical compositions and macrophage activation of polysaccharides from Lion's Mane culinary-medicinal mushroom *Hericium erinaceus* (higher Basidiomycetes) in different maturation stages. *Int. J. Med. Mushrooms* **2015**, *17*, 443−452.
(29) Malinowska, E.; Krzyczkowski, W.; Łapienis, G.; Herold, F. Improved simultaneous production of mycelial biomass and polysaccharides by submerged culture of *Hericium erinaceum*: optimization using a central composite rotatable design (CCRD). *J. Ind. Microbiol. Biotechnol.* **2009**, *36*, 1513−1527.
(30) Semedo, M. C.; Karmali, A.; Fonseca, L. A high throughput colorimetric assay of *β*-1,3-D-glucans by Congo red dye. *J. Microbiol. Methods* **2015**, *109*, 140−148.
(31) Shang, H. M.; Song, H.; Shen, S. J.; Yao, X.; Wu, B.; Wang, L. N.; Jiang, Y. Y.; Ding, G. D. Effects of dietary polysaccharides from the submerged fermentation concentrate of *Hericium caput-medusae* (Bull.:Fr.) Pers. on fat deposition in broilers. *J. Sci. Food Agric.* **2015**, *95*, 267−274.
(32) Zan, X.; Cui, F.; Li, Y.; Yang, Y.; Wu, D.; Sun, W.; Ping, L. *Hericium erinaceus* polysaccharide-protein HEG-5 inhibits SGC-7901 cell growth via cell cycle arrest and apoptosis. *Int. J. Biol. Macromol.* **2015**, *76*, 242−253.
(33) Zhang, A.-Q.; Zhang, J.-S.; Tang, Q.-J.; Jia, W.; Yang, Y.; Liu, Y.-F.; Fan, J.-M.; Pan, Y.-J. Structural elucidation of a novel fucogalactan that contains 3-O-methyl rhamnose isolated from the fruiting bodies of the fungus. *Carbohydr. Res.* **2006**, *341*, 645−649.
(34) Zhang, A. Q.; Sun, P. L.; Zhang, J. S.; Tang, C. H.; Fan, J. M.; Shi, X. M.; Pan, Y. J. Structural investigation of a novel fucoglucogalactan isolated from the fruiting bodies of the fungus *Hericium erinaceus*. *Food Chem.* **2007**, *104*, 451−456.
(35) Zhu, Y.; Li, Q.; Mao, G.; Zou, Y.; Feng, W.; Zheng, D.; Wang, W.; Zhou, L.; Zhang, T.; Yang, J.; Yang, L.; Wu, X. Optimization of enzyme-assisted extraction and characterization of polysaccharides from *Hericium erinaceus*. *Carbohydr. Polym.* **2014**, *101*, 606−613.
(36) Jia, L. M.; Liu, L.; Dong, Q.; Fang, J. N. Structural investigation of a novel rhamnoglucogalactan isolated from the fruiting bodies of the fungus *Hericium erinaceus*. *Carbohydr. Res.* **2004**, *339*, 2667−2671.
(37) Dong, Q.; Jia, L. M.; Fang, J. N. A *β*-D-glucan isolated from the fruiting bodies of *Hericium erinaceus* and its aqueous conformation. *Carbohydr. Res.* **2006**, *341*, 791−795.
(38) Fen, L.; Xuwei, Z.; Nanyi, L.; Puyu, Z.; Shuang, Z.; Xue, Z.; Pengju, L.; Qichao, Z.; Haiping, L. Screening of lignocellulose-degrading superior mushroom strains and determination of their CMCase and laccase activity. *Sci. World J.* **2014**, *2014*, 763108.
(39) Balan, V.; da Costa Sousa, L.; Chundawat, S. S.; Vismeh, R.; Jones, A. D.; Dale, B. Mushroom spent straw: a potential substrate for an ethanol-based biorefinery. *J. Ind. Microbiol. Biotechnol.* **2008**, *35*, 293−301.
(40) Chen, S. Y.; Yu, H. T.; Kao, J. P.; Yang, C. C.; Chiang, S. S.; Mishchuk, D. O.; Mau, J. L.; Slupsky, C. M. Consumption of vitamin D_2 enhanced mushrooms is associated with improved bone health. *J. Nutr. Biochem.* **2015**, *26*, 696−703.
(41) Roberts, J. S.; Teichert, A.; McHugh, T. H. Vitamin D_2 formation from post-harvest UV-B treatment of mushrooms (*Agaricus bisporus*) and retention during storage. *J. Agric. Food Chem.* **2008**, *56*, 4541−4544.
(42) Dai, X.; Zhan, Y.; Zhang, J.; Zhang, P.; Han, Z.; Ma, Q.; Kong, X.; Liu, J.; Ma, Y. Regulatory effect of salicylic acid and methyl jasmonate supplementation on ergosterol production in *Hericium erinaceus* mycelia. *J. For. Res.* **2015**, *26*, 71−77.
(43) Li, J. L.; Lu, L.; Dai, C. C.; Chen, K.; Qiu, J. Y. [A comparative study on sterols of ethanol extract and water extract from *Hericium erinaceus*]. *Zhongguo Zhong Yao Za Zhi* **2001**, *26*, 831−834.
(44) Li, W.; Zhou, W.; Song, S. B.; Shim, S. H.; Kim, Y. H. Sterol fatty acid esters from the mushroom *Hericium erinaceum* and their PPAR transactivational effects. *J. Nat. Prod.* **2014**, *77*, 2611−2618.
(45) Watanabe, F.; Yabuta, Y.; Bito, T.; Teng, F. Vitamin B_{12}-containing plant food sources for vegetarians. *Nutrients* **2014**, *6*, 1861−1873.
(46) Schwarz, J.; Dschietzig, T.; Schwarz, J.; Dura, A.; Nelle, E.; Watanabe, F.; Wintgens, K. F.; Reich, M.; Armbruster, F. P. The influence of a whole food vegan diet with Nori algae and wild mushrooms on selected blood parameters. *Clin. Lab.* **2014**, *60*, 2039−2050.
(47) Teng, F.; Bito, T.; Takenaka, S.; Yabuta, Y.; Watanabe, F. Vitamin B_{12}[*c*-lactone], a biologically inactive corrinoid compound, occurs in cultured and dried lion's mane mushroom (*Hericium erinaceus*) fruiting bodies. *J. Agric. Food Chem.* **2014**, *62*, 1726−1732.
(48) Miyazawa, M.; Matsuda, N.; Tamura, N.; Ishikawa, R. Characteristic flavor of volatile oil from dried fruiting bodies of *Hericium erinaceus* (Bull.: Fr.) Pers. *J. Essent. Oil Res.* **2008**, *20*, 420−423.
(49) Friedman, M.; Henika, P. R.; Mandrell, R. E. Bactericidal activities of plant essential oils and some of their isolated constituents against *Campylobacter jejuni*, *Escherichia coli*, *Listeria monocytogenes*, and *Salmonella enterica*. *J. Food Prot.* **2002**, *65*, 1545−1560.
(50) Friedman, M.; Henika, P. R.; Mandrell, R. E. Antibacterial activities of phenolic benzaldehydes and benzoic acids against *Campylobacter jejuni*, *Escherichia coli*, *Listeria monocytogenes*, and *Salmonella enterica*. *J. Food Prot.* **2003**, *66*, 1811−1821.
(51) McGee, H. *On Food and Cooking − The Science and Lore of the Kitchen*; Scribner: New York, 2004; p 884.
(52) Friedman, M. Food browning and its prevention: an overview. *J. Agric. Food Chem.* **1996**, *44*, 631−653.
(53) Sawant, D. M.; Kate, K. M.; Dhamane, V. M., Mushrooms. In *Handbook of Vegetable Science and Technology: Production, Composition, Storage and Processing*; Salunke, D. K., Kadam, S. S., Eds.; Dekker: New York, 1998; pp 647−682.
(54) Kurtzman, R. Mushrooms as a source of food protein. In *Protein Nutritional Quality of Foods and Feeds. Part II. Quality Factors - Plant Breeding, Composition, Processing, and Antinutrients*; Friedman, M., Ed.; Dekker: New York, 1975; pp 305−318.
(55) Ulziijargal, E.; Mau, J. L. Nutrient compositions of culinary-medicinal mushroom fruiting bodies and mycelia. *Int. J. Med. Mushrooms* **2011**, *13*, 343−349.
(56) Rodrigues, D. M. F.; Freitas, A. C.; Rocha-Santos, T. A. P.; Vasconcelos, M. W.; Roriz, M.; Rodríguez-Alcalá, L. M.; Gomes, A. M. P.; Duarte, A. C. Chemical composition and nutritive value of *Pleurotus citrinopileatus* var cornucopiae, *P. eryngii*, *P. salmoneo stramineus*, *Pholiota nameko* and *Hericium erinaceus*. *J. Food Sci. Technol.* **2015**, DOI: 10.1007/s13197-015-1826-z.
(57) Finotti, E.; Bersani, E.; Del Prete, E.; Friedman, M. Application of a functional mathematical index (FMI) for predicting effects of the composition of jujube fruit on nutritional quality and health. *J. Food Compos. Anal.* **2015**, *42*, 164−170.
(58) Finotti, E.; Bersani, E.; Friedman, M. Application of a functional mathematical index for antibacterial and anticarcinogenic effects of tea catechins. *J. Agric. Food Chem.* **2011**, *59*, 864−869.
(59) Carvalho, L. M.; Carvalho, F.; de Lourdes Bastos, M.; Baptista, P.; Moreira, N.; Monforte, A. R.; da Silva Ferreira, A. C.; de Pinho, P. G. Non-targeted and targeted analysis of wild toxic and edible mushrooms using gas chromatography-ion trap mass spectrometry. *Talanta* **2014**, *118*, 292−303.

DOI: 10.1021/acs.jafc.5b02914
J. Agric. Food Chem. 2015, 63, 7108−7123

(60) Mishra, K. K.; Pal, R. S.; Arunkumar, R. Antioxidant activities and bioactive compound determination from caps and stipes of specialty medicinal mushrooms *Calocybe indica* and *Pleurotus sajor-caju* (higher Basidiomycetes) from India. *Int. J. Med. Mushrooms* **2014**, *16*, 555−567.
(61) Kalač, P. A review of chemical composition and nutritional value of wild-growing and cultivated mushrooms. *J. Sci. Food Agric.* **2013**, *93*, 209−218.
(62) Mercer, L. P.; Dodds, S. J.; Smith, D. I. Dispensable, indispensable, and conditionally indispensable amino acid ratios in the diet. In *Absorption and Utilization of Amino Acids*; Friedman, M., Ed.; CRC Press: Boca Raton, FL, USA, 1989; Vol. 1, pp 1−13.
(63) Friedman, M.; Gumbmann, M. R. Nutritional value and safety of methionine derivatives, isomeric dipeptides and hydroxy analogs in mice. *J. Nutr.* **1988**, *118*, 388−397.
(64) Friedman, M.; Finot, P. A. Nutritional improvement of bread with lysine and γ-glutamyllysine. *J. Agric. Food Chem.* **1990**, *38*, 2011−2020.
(65) Friedman, M. Nutritional value of proteins from different food sources. A review. *J. Agric. Food Chem.* **1996**, *44*, 6−29.
(66) Millward, D. J. Identifying recommended dietary allowances for protein and amino acids: a critique of the 2007 WHO/FAO/UNU report. *Br. J. Nutr.* **2012**, *108*, S3−S21.
(67) Meyerhoff, D. J.; Mon, A.; Metzler, T.; Neylan, T. C. Cortical gamma-aminobutyric acid and glutamate in posttraumatic stress disorder and their relationships to self-reported sleep quality. *Sleep* **2014**, *37*, 893−900.
(68) Sotgia, S.; Zinellu, A.; Mangoni, A. A.; Pintus, G.; Attia, J.; Carru, C.; McEvoy, M. Clinical and biochemical correlates of serum L-ergothioneine concentrations in community-dwelling middle-aged and older adults. *PLoS One* **2014**, *9*, e84918.
(69) Saing, L.; Wei, Y. C.; Tseng, C. J. Ergothioneine represses inflammation and dysfunction in human endothelial cells exposed to oxidized low-density lipoprotein. *Clin. Exp. Pharmacol. Physiol.* **2015**, DOI: 10.1111/1440-1681.12374.
(70) Ulziijargal, E.; Yang, J. H.; Lin, L. Y.; Chen, C. P.; Mau, J. L. Quality of bread supplemented with mushroom mycelia. *Food Chem.* **2013**, *138*, 70−76.
(71) Li, T.; Lo, Y. M.; Moon, B. Feasibility of using *Hericium erinaceus* as the substrate for vinegar fermentation. *LWT−Food Sci. Technol.* **2014**, *55*, 323−328.
(72) Woraharn, S.; Lailerd, N.; Sivamaruthi, B. S.; Wangcharoen, W.; Sirisattha, S.; Peerajan, S.; Chaiyasut, C. Evaluation of factors that influence the L-glutamic and γ-aminobutyric acid production during *Hericium erinaceus* fermentation by lactic acid bacteria. *CyTA−J. Food* **2015**, 1.
(73) Lam, Y. S.; Okello, E. J. Determination of lovastatin, β-glucan, total polyphenols, and antioxidant activity in raw and processed oyster culinary-medicinal mushroom, *Pleurotus ostreatus* (higher Basidiomycetes). *Int. J. Med. Mushrooms* **2015**, *17*, 117−128.
(74) Tan, Y. S.; Baskaran, A.; Nallathamby, N.; Chua, K. H.; Kuppusamy, U. R.; Sabaratnam, V. Influence of customized cooking methods on the phenolic contents and antioxidant activities of selected species of oyster mushrooms (*Pleurotus* spp.). *J. Food Sci. Technol.* **2015**, *52*, 3058−3064.
(75) Li, G.; Wang, Q.; Sun, P.; Chen, F.; Chen, X.; Wang, C.; Zhao, X. Effect of L-cysteine pretreatment on the control of formaldehyde and browning of the culinary-medicinal Shiitake mushroom, *Lentinus edodes* (higher Basidiomycetes) during drying and canning processes. *Int. J. Med. Mushrooms* **2015**, *17*, 385−395.
(76) Friedman, M.; Bautista, F. F. Inhibition of polyphenol oxidase by thiols in the absence and presence of potato tissue suspensions. *J. Agric. Food Chem.* **1995**, *43*, 69−76.
(77) Friedman, M. Acrylamide: inhibition of formation in processed food and mitigation of toxicity in cells, animals, and humans. *Food Funct.* **2015**, *6*, 1752−1772.
(78) Williams, J. R.; Rayburn, J. R.; Cline, G. R.; Sauterer, R.; Friedman, M. The potential protective effect of L-cysteine against the toxicity of acrylamide and furan in exposed *Xenopus laevis* embryos: an interaction study. *J. Agric. Food Chem.* **2014**, *62*, 7927−7938.
(79) Friedman, M. Antibiotic-resistant bacteria: prevalence in food and inactivation by food-compatible compounds and plant extracts. *J. Agric. Food Chem.* **2015**, *63*, 3805−3822.
(80) Kawagishi, H.; Masui, A.; Tokuyama, S.; Nakamura, T. Erinacines J and K from the mycelia of *Hericium erinaceum*. *Tetrahedron* **2006**, *62*, 8463−8466.
(81) Peacock, S. J.; Paterson, G. K. Mechanisms of methicillin resistance in *Staphylococcus aureus*. *Annu. Rev. Biochem.* **2015**, *84*, 577−601.
(82) Kim, S. P.; Moon, E.; Nam, S. H.; Friedman, M. *Hericium erinaceus* mushroom extracts protect infected mice against *Salmonella* Typhimurium-induced liver damage and mortality by stimulation of innate immune cells. *J. Agric. Food Chem.* **2012**, *60*, 5590−5596.
(83) Kim, S. P.; Park, S. O.; Lee, S. J.; Nam, S. H.; Friedman, M. A polysaccharide isolated from the liquid culture of *Lentinus edodes* (Shiitake) mushroom mycelia containing black rice bran protects mice against salmonellosis through up-regulation of the Th1 immune reaction. *J. Agric. Food Chem.* **2014**, *62*, 2384−2391.
(84) Kim, S. P.; Park, S. O.; Lee, S. J.; Nam, S. H.; Friedman, M. A polysaccharide isolated from the liquid culture of *Lentinus edodes* (Shiitake) mushroom mycelia containing black rice bran protects mice against a *Salmonella* lipopolysaccharide-induced endotoxemia. *J. Agric. Food Chem.* **2013**, *61*, 10987−10994.
(85) Shang, X.; Tan, Q.; Liu, R.; Yu, K.; Li, P.; Zhao, G. P. In vitro anti-*Helicobacter pylori* effects of medicinal mushroom extracts, with special emphasis on the Lion's Mane mushroom, *Hericium erinaceus* (higher Basidiomycetes). *Int. J. Med. Mushrooms* **2013**, *15*, 165−174.
(86) Zhu, Y.; Chen, Y.; Li, Q.; Zhao, T.; Zhang, M.; Feng, W.; Takase, M.; Wu, X.; Zhou, Z.; Yang, L.; Wu, X. Preparation, characterization, and anti-*Helicobacter pylori* activity of Bi^{3+}-*Hericium erinaceus* polysaccharide complex. *Carbohydr. Polym.* **2014**, *110*, 231−237.
(87) Friedman, M.; Rasooly, R. Review of the inhibition of biological activities of food-related selected toxins by natural compounds. *Toxins* **2013**, *5*, 743−775.
(88) Wong, K. H.; Sabaratnam, V.; Abdullah, N.; Kuppusamy, U. R.; Naidu, M. Effects of cultivation techniques and processing on antimicrobial and antioxidant activities of *Hericium erinaceus* (Bull.:Fr.) Pers. extracts. *Food Technol. Biotechnol.* **2009**, *47*, 47−55.
(89) Nam, S. H.; Choi, S. P.; Kang, M. Y.; Kozukue, N.; Friedman, M. Antioxidative, antimutagenic, and anticarcinogenic activities of rice bran extracts in chemical and cell assays. *J. Agric. Food Chem.* **2005**, *53*, 816−822.
(90) Friedman, M. Anticarcinogenic, cardioprotective, and other health benefits of tomato compounds lycopene, α-tomatine, and tomatidine in pure form and in fresh and processed tomatoes. *J. Agric. Food Chem.* **2013**, *61*, 9534−9550.
(91) Friedman, M. Chemistry and anticarcinogenic mechanisms of glycoalkaloids produced by eggplants, potatoes, and tomatoes. *J. Agric. Food Chem.* **2015**, *63*, 3323−3337.
(92) Lee, J. S.; Hong, E. K. *Hericium erinaceus* enhances doxorubicin-induced apoptosis in human hepatocellular carcinoma cells. *Cancer Lett.* **2010**, *297*, 144−154.
(93) Li, Y.; Zhang, G.; Ng, T. B.; Wang, H. A novel lectin with antiproliferative and HIV-1 reverse transcriptase inhibitory activities from dried fruiting bodies of the monkey head mushroom *Hericium erinaceum*. *J. Biomed. Biotechnol.* **2010**, *2010*, 716515.
(94) Hassan, M.; Rouf, R.; Tiralongo, E.; May, T.; Tiralongo, J. Mushroom lectins: specificity, structure and bioactivity relevant to human disease. *Int. J. Mol. Sci.* **2015**, *16*, 7802−7838.
(95) Caprioli, G.; Logrippo, S.; Cahill, M. G.; James, K. J. High-performance liquid chromatography LTQ-Orbitrap mass spectrometry method for tomatidine and non-target metabolites quantification in organic and normal tomatoes. *Int. J. Food Sci. Nutr.* **2014**, *65*, 942−947.
(96) Wong, J. Y.; Abdulla, M. A.; Raman, J.; Phan, C. W.; Kuppusamy, U. R.; Golbabapour, S.; Sabaratnam, V. Gastroprotective

effects of Lion's Mane mushroom *Hericium erinaceus* (Bull.:Fr.) Pers. (Aphyllophoromycetideae) extract against ethanol-induced ulcer in rats. *Evidence-Based Complement. Altern. Med.* **2013**, *2013*, 492976.
(97) Chen, P.; Yong, Y.; Gu, Y.; Wang, Z.; Zhang, S.; Lu, L. Comparison of antioxidant and antiproliferation activities of polysaccharides from eight species of medicinal mushrooms. *Int. J. Med. Mushrooms* **2015**, *17*, 287−295.
(98) Xia, S. Antineoplastic effect and influence on serum cytokine of *Hericium erinaceus* polysaccharides on S180 tumor-bearing mice. *Pract. Pharm. Clin. Rem.* **2014**, *17*, 5−7.
(99) Kobayashi, H.; Motoyoshi, N.; Itagaki, T.; Suzuki, M.; Inokuchi, N. Effect of the replacement of aspartic acid/glutamic acid residues with asparagine/glutamine residues in RNase He1 from *Hericium erinaceus* on inhibition of human leukemia cell line proliferation. *Biosci., Biotechnol., Biochem.* **2015**, *79*, 211−217.
(100) Wong, K. H.; Naidu, M.; David, R. P.; Bakar, R.; Sabaratnam, V. Neuroregenerative potential of Lion's Mane mushroom, *Hericium erinaceus* (Bull.: Fr.) Pers. (higher Basidiomycetes), in the treatment of peripheral nerve injury (review). *Int. J. Med. Mushrooms* **2012**, *14*, 427−446.
(101) Lai, P. L.; Naidu, M.; Sabaratnam, V.; Wong, K. H.; David, R. P.; Kuppusamy, U. R.; Abdullah, N.; Malek, S. N. Neurotrophic properties of the Lion's Mane medicinal mushroom, *Hericium erinaceus* (higher Basidiomycetes) from Malaysia. *Int. J. Med. Mushrooms* **2013**, *15*, 539−554.
(102) Kim, M. K.; Choi, W. Y.; Lee, H. Y. Enhancement of the neuroprotective activity of *Hericium erinaceus* mycelium co-cultivated with *Allium sativum* extract. *Arch. Physiol. Biochem.* **2015**, *121*, 19−25.
(103) Kawagishi, H.; Shimada, A.; Shirai, R.; Okamoto, K.; Ojima, F.; Sakamoto, H.; Ishiguro, Y.; Furukawa, S. Erinacines A, B and C, strong stimulators of nerve growth factor (NGF)-synthesis, from the mycelia of *Hericium erinaceum*. *Tetrahedron Lett.* **1994**, *35*, 1569−1572.
(104) Phan, C. W.; Lee, G. S.; Hong, S. L.; Wong, Y. T.; Brkljaca, R.; Urban, S.; Abd Malek, S. N.; Sabaratnam, V. *Hericium erinaceus* (Bull.: Fr) Pers. cultivated under tropical conditions: isolation of hericenones and demonstration of NGF-mediated neurite outgrowth in PC12 cells via MEK/ERK and PI3K-Akt signaling pathways. *Food Funct.* **2014**, *5*, 3160−3169.
(105) Mori, K.; Obara, Y.; Hirota, M.; Azumi, Y.; Kinugasa, S.; Inatomi, S.; Nakahata, N. Nerve growth factor-inducing activity of *Hericium erinaceus* in 1321N1 human astrocytoma cells. *Biol. Pharm. Bull.* **2008**, *31*, 1727−1732.
(106) Mori, K.; Obara, Y.; Moriya, T.; Inatomi, S.; Nakahata, N. Effects of *Hericium erinaceus* on amyloid β(25−35) peptide-induced learning and memory deficits in mice. *Biomed. Res.* **2011**, *32*, 67−72.
(107) Liu, J.; Du, C.; Wang, Y.; Yu, Z. Anti-fatigue activities of polysaccharides extracted from *Hericium erinaceus*. *Exp. Ther. Med.* **2015**, *9*, 483−487.
(108) Abdulla, M. A.; Fard, A. A.; Sabaratnam, V.; Wong, K. H.; Kuppusamy, U. R.; Abdullah, N.; Ismail, S. Potential activity of aqueous extract of culinary-medicinal Lion's Mane mushroom, *Hericium erinaceus* (Bull.: Fr.) Pers. (Aphyllophoromycetideae) in accelerating wound healing in rats. *Int. J. Med. Mushrooms* **2011**, *13*, 33−39.
(109) Noh, H. J.; Yang, H. H.; Kim, G. S.; Lee, S. E.; Lee, D. Y.; Choi, J. H.; Kim, S. Y.; Lee, E. S.; Ji, S. H.; Kang, K. S.; Park, H. J.; Kim, J. R.; Kim, K. H. Chemical constituents of *Hericium erinaceum* associated with the inhibitory activity against cellular senescence in human umbilical vascular endothelial cells. *J. Enzyme Inhib. Med. Chem.* **2015**, 1.
(110) Nagano, M.; Shimizu, K.; Kondo, R.; Hayashi, C.; Sato, D.; Kitagawa, K.; Ohnuki, K. Reduction of depression and anxiety by 4 weeks *Hericium erinaceus* intake. *Biomed. Res.* **2010**, *31*, 231−237.
(111) Mori, K.; Inatomi, S.; Ouchi, K.; Azumi, Y.; Tuchida, T. Improving effects of the mushroom Yamabushitake (*Hericium erinaceus*) on mild cognitive impairment: a double-blind placebo-controlled clinical trial. *Phytother. Res.* **2009**, *23*, 367−372.
(112) Yi, Z.; Shao-Long, Y.; Ai-Hong, W.; Zhi-Chun, S.; Ya-Fen, Z.; Ye-Ting, X.; Yu-Ling, H. Protective effect of ethanol extracts of *Hericium erinaceus* on alloxan-induced diabetic neuropathic pain in rats. *Evidence-Based Complement. Altern. Med.* **2015**, *2015*, 595480.
(113) Wu, T.; Xu, B. Antidiabetic and antioxidant activities of eight medicinal mushroom species from China. *Int. J. Med. Mushrooms* **2015**, *17*, 129−140.
(114) Liang, B.; Guo, Z.; Xie, F.; Zhao, A. Antihyperglycemic and antihyperlipidemic activities of aqueous extract of *Hericium erinaceus* in experimental diabetic rats. *BMC Complement. Altern. Med.* **2013**, *13*, 253.
(115) Han, Z. H.; Ye, J. M.; Wang, G. F. Evaluation of in vivo antioxidant activity of *Hericium erinaceus* polysaccharides. *Int. J. Biol. Macromol.* **2013**, *52*, 66−71.
(116) Zhang, Z.; Lv, G.; Pan, H.; Pandey, A.; He, W.; Fan, L. Antioxidant and hepatoprotective potential of endo-polysaccharides from *Hericium erinaceus* grown on tofu whey. *Int. J. Biol. Macromol.* **2012**, *51*, 1140−1146.
(117) Yang, B. K.; Park, J. B.; Song, C. H. Hypolipidemic effect of an exo-biopolymer produced from a submerged mycelial culture of *Hericium erinaceus*. *Biosci., Biotechnol., Biochem.* **2003**, *67*, 1292−1298.
(118) Rahman, M. A.; Abdullah, N.; Aminudin, N. Inhibitory effect on *in vitro* LDL oxidation and HMG Co-A reductase activity of the liquid-liquid partitioned fractions of *Hericium erinaceus* (Bull.) Persoon (Lion's Mane mushroom). *BioMed Res. Int.* **2014**, *2014*, 828149.
(119) Mori, K.; Kikuchi, H.; Obara, Y.; Iwashita, M.; Azumi, Y.; Kinugasa, S.; Inatomi, S.; Oshima, Y.; Nakahata, N. Inhibitory effect of hericenone B from *Hericium erinaceus* on collagen-induced platelet aggregation. *Phytomedicine* **2010**, *17*, 1082−1085.
(120) Abdullah, N.; Ismail, S. M.; Aminudin, N.; Shuib, A. S.; Lau, B. F. Evaluation of selected culinary-medicinal mushrooms for antioxidant and ACE inhibitory activities. *Evidence-Based Complement. Altern. Med.* **2012**, *2012*, 464238.
(121) Wang, J. C.; Hu, S. H.; Su, C. H.; Lee, T. M. Antitumor and immunoenhancing activities of polysaccharide from culture broth of *Hericium* spp. *Kaohsiung J. Med. Sci.* **2001**, *17*, 461−467.
(122) Harikrishnan, R.; Kim, J. S.; Kim, M. C.; Balasundaram, C.; Heo, M. S. *Hericium erinaceum* enriched diets enhance the immune response in *Paralichthys olivaceus* and protect from *Philasterides dicentrarchi* infection. *Aquaculture* **2011**, *318*, 48−53.
(123) Yeh, S.-P.; Hsia, L.-F.; Chiu, C.-S.; Chiu, S.-T.; Liu, C.-H. A smaller particle size improved the oral bioavailability of monkey head mushroom, *Hericium erinaceum*, powder resulting in enhancement of the immune response and disease resistance of white shrimp, *Litopenaeus vannamei*. *Fish Shellfish Immunol.* **2011**, *30*, 1323−1330.
(124) Kim, S. K.; Son, C. G.; Yun, C. H.; Han, S. H. *Hericium erinaceum* induces maturation of dendritic cells derived from human peripheral blood monocytes. *Phytother. Res.* **2010**, *24*, 14−19.
(125) Wallet, M. A.; Sen, P.; Tisch, R. Immunoregulation of dendritic cells. *Clin. Med. Res.* **2005**, *3*, 166−175.
(126) Sheu, S. C.; Lyu, Y.; Lee, M. S.; Cheng, J. H. Immunomodulatory effects of polysaccharides isolated from *Hericium erinaceus* on dendritic cells. *Process Biochem.* **2013**, *48*, 1402−1408.
(127) Friedman, M. Rice brans, rice bran oils, and rice hulls: composition, food and industrial uses, and bioactivities in humans, animals, and cells. *J. Agric. Food Chem.* **2013**, *61*, 10626−10641.
(128) Friedman, M. Overview of antibacterial, antitoxin, antiviral, and antifungal activities of tea flavonoids and teas. *Mol. Nutr. Food Res.* **2007**, *51*, 116−134.
(129) Friedman, M.; Juneja, V. K. Review of antimicrobial and antioxidative activities of chitosans in food. *J. Food Prot.* **2010**, *73*, 1737−1761.
(130) Friedman, M. Antibacterial, antiviral, and antifungal properties of wines and winery byproducts in relation to their flavonoid content. *J. Agric. Food Chem.* **2014**, *62*, 6025−6042.
(131) Friedman, M. Chemistry and multi-beneficial bioactivities of carvacrol (4-isopropyl-2-methylphenol), a component of essential oils produced by aromatic plants and spices. *J. Agric. Food Chem.* **2014**, *62*, 7652−7670.
(132) Kawagishi, H.; Shimada, A.; Hosokawa, S.; Mori, H.; Sakamoto, H.; Ishiguro, Y.; Sakemi, S.; Bordner, J.; Kojima, N.;

DOI: 10.1021/acs.jafc.5b02914
J. Agric. Food Chem. 2015, 63, 7108−7123

Furukawa, S. Erinacines E, F, and G, stimulators of nerve growth factor (NGF)-synthesis, from the mycelia of *Hericium erinaceum*. *Tetrahedron Lett.* **1996**, *37*, 7399−7402.
(133) Kawagishi, H.; Simada, A.; Shizuki, K.; Mori, H.; Okamoto, K.; Sakamoto, H.; Furukawa, S. Erinacine D, a stimulator of NGF-synthesis, from the mycelia of *Hericium erinaceum*. *Heterocycl. Commun.* **1996**, *2*, 51−54.
(134) Lee, E. W.; Shizuki, K.; Hosokawa, S.; Suzuki, M.; Suganuma, H.; Inakuma, T.; Li, J.; Ohnishi-Kameyama, M.; Nagata, T.; Furukawa, S.; Kawagishi, H. Two novel diterpenoids, erinacines H and I from the mycelia of *Hericium erinaceum*. *Biosci., Biotechnol., Biochem.* **2000**, *64*, 2402−2405.
(135) Kenmoku, H.; Sassa, T.; Kato, N. Isolation of erinacine P, a new parental metabolite of cyathane-xylosides, from *Hericium erinaceum* and its biomimetic conversion into erinacines A and B. *Tetrahedron Lett.* **2000**, *41*, 4389−4393.
(136) Kenmoku, H.; Shimai, T.; Toyomasu, T.; Kato, N.; Sassa, T. Erinacine Q, a new erinacine from *Hericium erinaceum*, and its biosynthetic route to erinacine C in the basidiomycete. *Biosci., Biotechnol., Biochem.* **2002**, *66*, 571−575.
(137) Ma, B. J.; Zhou, Y.; Li, L. Z.; Li, H. M.; Gao, Z. M.; Ruan, Y. A new cyathane-xyloside from the mycelia of *Hericium erinaceum*. *Z. Naturforsch., B: J. Chem. Sci.* **2008**, *63*, 1241−1242.
(138) Li, W.; Zhou, W.; Lee, D. S.; Shim, S. H.; Kim, Y. C.; Kim, Y. H. Hericirine, a novel anti-inflammatory alkaloid from *Hericium erinaceum*. *Tetrahedron Lett.* **2014**, *55*, 4086−4090.
(139) Lu, Q. Q.; Tian, J. M.; Wei, J.; Gao, J. M. Bioactive metabolites from the mycelia of the basidiomycete *Hericium erinaceum*. *Nat. Prod. Res.* **2014**, *28*, 1288−1292.

DOI: 10.1021/acs.jafc.5b02914
J. Agric. Food Chem. 2015, 63, 7108−7123

there is very limited information available on the inhibitors of SA signaling.

Recently, we screened a chemical library for inhibitors of SA signaling and found that 4-phenyl-2-{[3-(trifluoromethyl)-aniline]methylidene}cyclohexane-1,3-dione (PAMD, **1**) suppresses the expression of SA-related genes in *Arabidopsis* and increases its susceptibility to pathogens.[22] In addition to the suppressive effects of PAMD on the expression of *PR* genes, PAMD also inhibits the growth of *Arabidopsis*, including its root growth, seedling establishment, and fresh weight. These side effects limit the utility of PAMD in studies of the SA signaling pathway. Structure−activity relationship studies of PAMD derivatives predicted that a 2-substituted enamine moiety conjugated with 1,3-cyclohexadione is essential for the inhibition of the SA signal. On the basis of this structure−activity relationship analysis, a number of derivatives of PAMD were synthesized in the present study to develop better candidate SA signaling inhibitors. We ultimately selected a compound that strongly suppresses the expression of the *PR* genes with fewer adverse effects on the growth of *Arabidopsis* than PAMD. We also found that the retardation effect of these new compounds on plant growth partly depends on the stabilization of the DELLA proteins, negative regulators of GA signaling, which are also involved in the pathogen defense responses.

MATERIALS AND METHODS

Plant Materials and Growth Conditions. Most of the experiments were carried out with *Arabidopsis thaliana* Col-0. Landsberg *erecta* (L*er*) was used as the genetic background of 5Δ*della*, a mutant with loss-of-function mutations in all five DELLA proteins. *RGA*:*GFP-RGA*, a line that expresses GFP-RGA driven by the *RGA* promoter, was used to detect GA-induced DELLA degradation. The seeds were surface-sterilized with 70% ethanol for 20 min, rinsed with 99% ethanol, dried on sterilized filter paper, and then placed onto culture medium containing half-strength Murashige and Skoog ($^1/_2$ MS) Plant Salt Mixture (Wako, Osaka, Japan), 1% sucrose, 0.8% agar, vitamin mixture, and 0.01% myo-inositol (Wako). After stratification under dark conditions at 4 °C for 2 days, the seeds were germinated under constant light (18.2−46.5 μmol/m^2/s) at 22.5 °C. For the dark treatment in the hypocotyl experiment, the seeds were light-pulsed (18.2−46.5 μmol/m^2/s) for 6 h before they were kept under constant dark at 22.5 °C.

SA Treatment. Seedlings grown on plates with or without the test compound, as indicated, were foliar sprayed with a 2 mM SA aqueous solution (0.5% DMSO), cultured for a further 3 days under the same conditions, and then frozen in liquid nitrogen.

RT-PCR Analyses. Total RNA was extracted from seedlings treated with or without SA, purified with the Total RNA Extraction Mini Kit (RBC Bioscience, Taipei, Taiwan), and then converted to cDNA with the PrimeScript RT Reagent Kit (Takara Bio, Shiga, Japan) according to the manufacturers' protocols. Quantitative PCR was carried out with Thermal Cycler Dice Real Time System TP800 (Takara Bio) and the SYBR Premix Ex Taq (Takara Bio). The transcript levels of *PR* genes were normalized against those of *Actin7* (encoding actin 7), using primers specific for *PR1* (5′-CGTCTTTGTAGCTCTTGT-AGGTGC-3′ and 5′-TGCCTGGTTGTGAACCCTTAG-3′), *PR2* (5′-CGTCTTTGTAGCTCTTGTAGGTGC-3′ and 5′-TGCCTG-GTTGTGAACCCTTAG-3′), *PR5* (5′-CGTCTTTGTAGC-TCTTGTAGGTGC-3′ and 5′-TGCCTGGTTGTGAACCCTTAG-3′), and *Actin7* (5′-GATATTCAGCCACTTGTCTGTGAC-3′ and 5′-CATGTTCGATTGGATACTTCAGAG-3′).

Phenotypic Observations. *Germination Rate.* After sterilization (as described in the Plant Materials and Growth Conditions section), more than 30 seeds for each treatment were placed on $^1/_2$ MS medium with or without the test compound. Germination was defined as the emergence of the radicle.

Hypocotyl Growth. To determine hypocotyl growth during the constant dark treatment, the seeds were germinated on $^1/_2$ MS medium with or without the test compound. After stratification at 4 °C for 2 days, the seeds were light-pulsed for 6 h to improve their germination and then kept in the dark for 5 days at 22.5 °C. The 5 day old seedlings were raised in the dark, and the lengths of the hypocotyls were measured with ImageJ software (National Institutes of Health, Bethesda, MD). For hypocotyl growth under constant light, seedlings of L*er* and the 5Δ*della* mutants were grown on $^1/_2$ MS medium under constant light (18.2−46.5 μmol/m^2/s) at 22.5 °C, transferred 3 days after germination (3 DAG) to $^1/_2$ MS medium containing GA_4 (10 μM), PAMD (25 μM), **4** (25 μM), or combinations of them, and monitored during culture for 9 days under constant light at 22.5 °C. The lengths of the hypocotyls were measured with ImageJ software.

Fresh Weight. The seeds were germinated on $^1/_2$ MS medium with or without the test compound under constant light at 22.5 °C. The seedlings were sampled at 10 DAG or 12 DAG and their weights measured.

Colletotrichum higginsianum Infection Assay. Seedlings (5 DAG) germinated and grown on $^1/_2$ MS medium at constant light were transferred to treatment medium $^1/_2$ MS (no sucrose) and further cultivated for 8 days. Seedlings (8 day-after-treatment (DAT)) were sprayed with *Colletotrichum higginsianum* (*C. higginsianum*) and further cultivated for 4 days. The leaves of 4 day-after-infection (DAI) seedlings were sampled by liquid nitrogen. The RNA samples were extracted and converted to the cDNA as described above. The *actin* mRNA of *C. higginsianum* (*Ch-Actin*) was quantified by qRT-PCR using primers specific for *Ch-Actin* (5′- CCGCAGACCGCAATCTT-3′ and 5′- AATGGAGGCTGAGAGCTGGTT-3′). The transcript levels of *Ch-ACT* were normalized against those of *Arabidopsis Actin7*.

Quantification of Endogenous SA and ABA. *Chemicals.* Deuterium-labeled SA (SA-d_4) and deuterium-labeled ABA (ABA-$^{13}C_2$) were purchased from Wako Pure Chemical Industries, Ltd. (Japan).

Growth Condition. Seedlings (5 DAG) grown on $^1/_2$ MS medium under constant light at 22.5 °C were transferred to $^1/_2$ MS medium with or without the 25 μM compounds (PAMD or **4**) for further cultivation for 8 days under constant light at 22.5 °C. The plants were frozen by liquid nitrogen.

Extraction and Purification. The frozen plant tissues were homogenized and purified by using solid-phase extraction (SPE) as described by Miyazaki et al.,[23] with the exception that SA or ABA was eluted with 0.2 M formic acid (FA) in acetonitrile (AcCN) in this paper.

LC-MS/MS Analysis. LC-MS/MS was equipped as described Miyazaki et al.[23] The dried samples were reconstituted in 50 μL of 10 mM FA in 10% (v/v) methanol (MeOH), and 10 μL of each sample was then injected onto a reversed-phase UPLC column (Acquity UPLC BEH C18, 2.1 mm × 50 mm, 1.7 μm, Waters) with a guard column (Acquity UPLC BEH C18 VanGuardTM Precolumn, 1.7 μm, 2.1 mm × 5 mm, Waters) coupled to the ESI-MS/MS system. SA and ABA were analyzed in the negative ion mode as $[M - H]^-$. MS/MS analysis conditions for SA were as follows: cone energy, 24 eV; collision energy, 17 V; and MRM, 137.0 > 93.0 for unlabeled SA and 141.0 > 97.0 for labeled SA. The cone energy and collision energy for ABA and ABA-$^{13}C_2$ were 22 and 24 eV, and 14 and 12 eV, respectively, and those of MRM were 263.2 > 153.0 and 165.2 > 153.0, respectively. SA and ABA were analyzed by a linear gradient of 1% (v/v) FA in water (A) and 1% FA in MeOH (B) at a flow rate of 0.20 mL/min, from 80:20 A/B (v/v) (0 min), 55:45 A/B (v/v) (1 min), 25:75 A/B (v/v) (8 min), and 0:100 A/B (v/v) (9 min), maintaining this composition until 1 min and equilibrated to initial conditions.

Chemicals. PAMD (**1**, ID: KM05261) was purchased from MayBridge (Cornwall, UK), as described previously.[22] The PAMD derivatives were synthesized as follows.

2, *2-((3-(Trifluoromethyl)phenylamino)methylene)cyclohexane-1,3-dione.* 1,3-Cyclohexanedione (10 mmol), orthoacetic acid triethyl ester (13 mmol), and 10 mmol trifluoromethylaniline were combined and stirred for 5 min at 130 °C. Ethanol (3 mL) was added, and the mixture was stirred for 3 min at 130 °C. The mixture was then cooled

DOI: 10.1021/acs.jafc.5b01521
J. Agric. Food Chem. 2015, 63, 7124−7133

to room temperature, and 10 mL of distilled water was added to quench the reaction. Suction filtration was carried out with distilled water, then twice with 60% ethanol, and once with hexane. The compound was purified by recrystallization with ethyl acetate and hexane. The crystal was collected by suction filtration. ^{1}H NMR (500 MHz, $CDCl_3$): δ 2.03 (2 H, quin, J = 6.9), 2.55 (2 H, t, J = 6.3), 2.60 (2 H, t, J = 6.9), 7.43 (1 H, d, J = 7.4), 7.48−7.50 (2 H, m), 7.53 (1 H, d, J = 8.6), 8.61 (1 H, d, J = 13.2).

***3**, 2-((Phenylamino)methylene)cyclohexane-1,3-dione.* 1,3-Cyclohexanedione (10 mmol), orthoacetic acid triethyl ester (13 mmol), and aniline (10 mmol) were combined and stirred for 5 min at 130 °C. Ethanol (3 mL) was added, and the mixture stirred for 3 min at 130 °C. The mixture was then cooled to room temperature, and 10 mL of distilled water was added to quench the reaction. Suction filtration was carried out with distilled water, then twice with 60% ethanol and once with hexane. The compound was purified by recrystallization with ethyl acetate and hexane. The crystal was collected by suction filtration. ^{1}H NMR (500 MHz, $CDCl_3$): δ 2.02 (2 H, quin, J = 6.9), 2.54 (2 H, t, J = 6.9), 2.58 (2 H, t, J = 6.9), 7.20−7.25 (3 H, m), 7.40 (2 H, t, J = 8.0), 8.60 (1 H, d, J = 13.7).

***4**, 5,5-Dimethyl-2-((phenylamino)methylene)cyclohexane-1,3-dione.* 5,5-Dimethyl-1,3-cyclohexanedione (10 mmol), orthoacetic acid triethyl ester (13 mmol), and aniline (10 mmol) were combined and stirred for 5 min at 130 °C. Ethanol (3 mL) was added, and the mixture stirred for 3 min at 130 °C. The mixture was then cooled to room temperature, and 10 mL of distilled water was added to quench the reaction. Suction filtration was carried out with distilled water, then twice with 60% ethanol and once with hexane. The compound was purified by recrystallization with ethyl acetate and hexane. The crystal was collected by suction filtration. ^{1}H NMR (500 MHz, $CDCl_3$): δ 1.08 (6 H, s), 2.41 (2 H, s), 2.45 (2 H, s), 7.22−7.26 (3 H, m), 7.40 (2 H, t, J = 8.6), 8.60 (1 H, d, J = 13.7).

***5**, 2-((2,4-Dichlorophenylamino)methylene)-5,5-dimethylcyclohexane-1,3-dione.* 5,5-Dimethyl-1,3-cyclohexanedione (10 mmol), orthoacetic acid triethyl ester (13 mmol), and 2,4-dichloroaniline (10 mmol) were combined and stirred for 5 min at 130 °C. Ethanol (3 mL) was added, and the mixture was stirred for 3 min at 130 °C. The mixture was then cooled to room temperature, and 10 mL of distilled water was added to quench the reaction. Suction filtration was carried out with distilled water, then twice with 60% ethanol and hexane. The compound was purified by recrystallization with ethyl acetate and once with hexane. The crystal was collected by suction filtration. ^{1}H NMR (500 MHz, $CDCl_3$): δ 1.09 (6 H, s), 2.43 (2 H, s), 2.49 (2 H, s), 7.32 (1 H, d, J = 11.5), 7.40 (1 H, d, J = 8.6), 7.47 (1 H, s), 8.54 (1 H, d, J = 13.2).

***6**, 2-((3-Chlorophenylamino)methylene)-5,5-dimethylcyclohexane-1,3-dione.* 5,5-Dimethyl-1,3-cyclohexanedione (10 mmol), orthoacetic acid triethyl ester (13 mmol), and 3-chloroaniline (10 mmol) were combined and stirred for 5 min at 130 °C. Ethanol (3 mL) was added, and the mixture was stirred for 3 min at 130 °C. The mixture was then cooled to room temperature, and 10 mL of distilled water was added to quench the reaction. Suction filtration was carried out with distilled water, then twice with 60% ethanol and once with hexane. The compound was purified by recrystallization with ethyl acetate and hexane. The crystal was collected by suction filtration. ^{1}H NMR (500 MHz, $CDCl_3$): δ 1.08 (6 H, s), 2.41 (2 H, s), 2.46 (2 H, s), 7.14 (1 H, d, J = 18.9), 7.21−7.27 (2 H, m), 7.31−7.34 (1 H, m), 8.53 (1 H, d, J = 13.2).

***7**, 2-((3-Chloro-2-methylphenylamino)methylene)-5,5-dimethylcyclohexane-1,3-dione.* 5,5-Dimethyl-1,3-cyclohexanedione (10 mmol), orthoacetic acid triethyl ester (13 mmol), and 3-chrolo-2-methylaniline (10 mmol) were combined and stirred for 5 min at 130 °C. Ethanol (3 mL) was added, and the mixture was stirred for 3 min at 130 °C. The mixture was then cooled to room temperature, and 10 mL of distilled water was added to quench the reaction. Suction filtration was carried out with distilled water, then twice with 60% ethanol and once with hexane. The compound was purified by recrystallization with ethyl acetate and hexane. The crystal was collected by suction filtration. ^{1}H NMR (500 MHz, $CDCl_3$): δ 1.09 (6 H, s), 2.37 (3 H, s), 2.42 (2 H, s), 2.47 (2 H, s), 7.09−7.11 (1 H, m), 7.15−7.17 (1 H, m), 7.37 (1 H, d, J = 1.7), 8.56 (1H, d, J = 13.2).

***8**, 2-((4-Hydroxyphenylamino)methylene)-5,5-dimethylcyclohexane-1,3-dione.* 5,5-Dimethyl-1,3-cyclohexanedione (10 mmol), orthoacetic acid triethyl ester (13 mmol), and 4-hydroxyaniline (10 mmol) were combined and stirred for 5 min at 130 °C. Ethanol (3 mL) was added, and the mixture was stirred for 3 min at 130 °C. The mixture was then cooled to room temperature, and 10 mL of distilled water was added to quench the reaction. Suction filtration was carried out with distilled water, then twice with 60% ethanol and once with hexane. The compound was purified by recrystallization with ethyl acetate and hexane. The crystal was collected by suction filtration. ^{1}H NMR (500 MHz, $CDCl_3$): δ 1.08 (6 H, s), 2.42 (2 H, s), 2.45 (2 H, s), 6.91 (2 H, d, J = 9.2), 7.12 (1 H, d, J = 8.6), 8.50 (1 H, d, J = 13.7).

***9**, 5,5-Dimethyl-2-((3-(trifluoromethyl)phenylamino)methylene)-cyclohexane-1,3-dione.* 5,5-Dimethyl-1,3-cyclohexanedione (10 mmol), orthoacetic acid triethyl ester (13 mmol), and trifluoromethylaniline (10 mmol) were combined and stirred for 5 min at 130 °C. Ethanol (3 mL) was added, and the mixture was stirred for 3 min at 130 °C. The mixture was then cooled to room temperature, and 10 mL of distilled water was added to quench the reaction. Suction filtration was carried out with distilled water, then twice with 60% ethanol and once with hexane. The compound was purified by recrystallization with ethyl acetate and hexane. The crystal was collected by suction filtration. ^{1}H NMR (500 MHz, $CDCl_3$): δ 1.07 (6 H, s), 2.41 (2 H, s), 2.45 (2 H, s), 7.42 (1 H, s), 7.47−7.52 (3 H, m), 8.55−8.58 (1 H, m).

***10**, 2-((2-Chlorophenylamino)methylene)-5,5-dimethylcyclohexane-1,3-dione.* 5,5-Dimethyl-1,3-cyclohexanedione (10 mmol), orthoacetic acid triethyl ester (13 mmol), and 2-chloroaniline (10 mmol) were combined and stirred for 5 min at 130 °C. Ethanol (3 mL) was added, and the mixture was stirred for 3 min at 130 °C. The mixture was then cooled to room temperature, and 10 mL of distilled water was added to quench the reaction. Suction filtration was carried out with distilled water, then twice with 60% ethanol and once with hexane. The compound was purified by recrystallization with ethyl acetate and hexane. The crystal was collected by suction filtration. ^{1}H NMR (500 MHz, $CDCl_3$): δ 1.08 (6 H, s), 2.42 (2 H, s), 2.48 (2 H, s), 7.15 (1 H, t, J = 8.0), 7.33 (1 H, t, J = 8.0), 7.44 (1 H, d, J = 8.0), 7.46 (1 H, t, J = 8.6), 8.60 (1 H, d, J = 13.2).

***11**, 2-((2,4-Dimethylphenylamino)methylene)-5,5-dimethylcyclohexane-1,3-dione.* 5,5-Dimethyl-1,3-cyclohexanedione (10 mmol), orthoacetic acid triethyl ester (13 mmol), and 2,4-dimethylaniline (10 mmol) were combined and stirred for 5 min at 130 °C. Ethanol (3 mL) was added, and the mixture was stirred for 3 min at 130 °C. The mixture was then cooled to room temperature, and 10 mL of distilled water was added to quench the reaction. Suction filtration was carried out with distilled water, then twice with 60% ethanol and once with hexane. The compound was purified by recrystallization with ethyl acetate and hexane. The crystal was collected by suction filtration. ^{1}H NMR (500 MHz, $CDCl_3$): δ 1.08 (6 H, s), 2.30 (3 H, s), 2.35 (3 H, s), 2.39 (2 H, s), 2.45 (2 H, s), 7.03 (1 H, s), 7.06 (1 H, d, J = 8.0), 7.24 (1 H, d, J = 9.0), 8.56 (1H, d, J = 13.5).

***12**, 5,5-Dimethyl-2-((2-nitrophenylamino)methylene)-cyclohexane-1,3-dione.* 5,5-Dimethyl-1,3-cyclohexanedione (10 mmol), orthoacetic acid triethyl ester (13 mmol), and 2-nitroaniline (10 mmol) were combined and stirred for 5 min at 130 °C. Ethanol (3 mL) was added, and the mixture was stirred for 3 min at 130 °C. The mixture was the cooled to room temperature, and 10 mL of distilled water was added to quench the reaction. Suction filtration was carried out with distilled water, then twice with 60% ethanol and once with hexane. The compound was purified by recrystallization with ethyl acetate and hexane. The crystal was collected by suction filtration. ^{1}H NMR (500 MHz, $CDCl_3$): δ 1.09 (6 H, s), 2.45 (2 H, s), 2.52 (2 H, s), 7.33 (1 H, t, J = 8.6), 7.65 (1 H, d, J = 8.0), 7.71 (1 H, t, J = 8.6), 8.27 (1 H, d, J = 9.7), 8.61 (1 H, d, J = 13.2).

Quantitative Analysis of Anthocyanin. The frozen plant tissues treated with or without compounds were homogenized, pretreated, and then applied to cation-exchange SPE (Oasis MCX) using the same procedure as described by Miyazaki et al.[23] The SPE column was

DOI: 10.1021/acs.jafc.5b01521
J. Agric. Food Chem. 2015, 63, 7124−7133

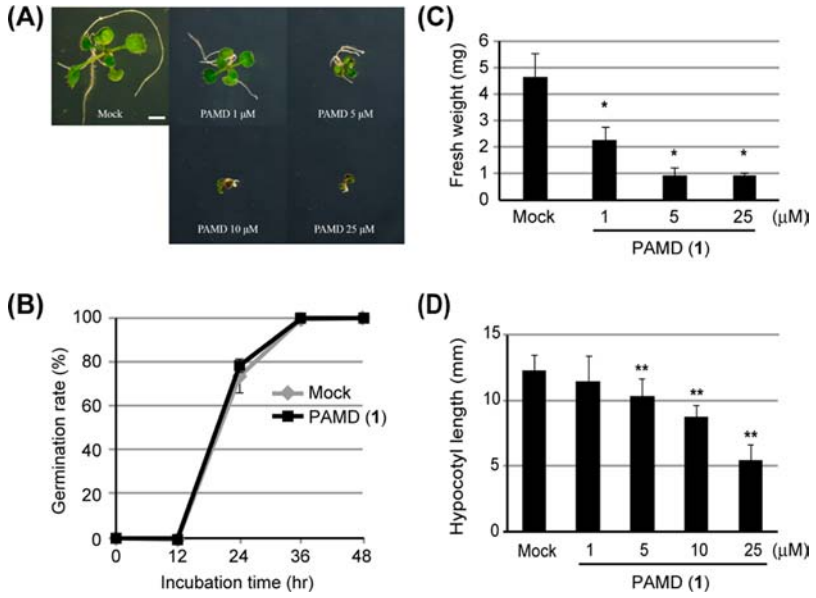

Figure 1. Effects of PAMD on *Arabidopsis* growth. (A) At 12 days after germination (12 DAG), *Arabidopsis thaliana* Col-0 was grown on $^1/_2$ MS medium with or without PAMD (as indicated) under constant light at 22.5 °C. Scale = 5 mm. (B) Seeds were germinated on $^1/_2$ MS medium with or without PAMD and grown under constant light at 22.5 °C. Error bars indicate the means ± SE of three independent replicates, $n > 30$. (C) Fresh weights of 10 DAG Col-0 plants grown on $^1/_2$ MS medium with or without PAMD under constant light at 22.5 °C. Error bars indicate means ± SE of three independent replicates, $n > 10$. Student's t test was used to determine the significance of differences relative to the mock treatment; *, $P < 0.05$. (D) After stratification for 2 days at 4 °C, Col-0 seeds were light-pulsed for 6 h and were germinated and grown on $^1/_2$ MS medium with or without the test compound under constant dark at 22.5 °C. Hypocotyl length was measured at 5 DAG. Error bars indicate the means ± SE of three independent replicates, $n = 10$. Student's t test was used to determine the significance of differences relative to the mock treatment; **, $P < 0.01$.

washed with 5 mM FA and MeOH successively. Anthocyanins were eluted with MeOH (1% NH_4OH) and water/MeOH (40:60 in volume ration, 1% NH_4OH) successively. The two successive elutions were combined together and quantified by reading the absorbance at 530 nm (A_{530}) and 657 nm (A_{657}) using GeneQuant (GE Healthcare Life Science). The relative level of anthocyanin was calculated as $(A_{530} - 0.25 \times A_{657})$ g^{-1} FW.

GA-induced DELLA Degradation. The *RGA:GFP-RGA* line of *Arabidopsis* was used to observe the GA-induced degradation of DELLA. After stratification for 2 days at 4 °C in the dark, the *RGA:GFP-RGA* line was germinated on $^1/_2$ MS medium under constant light at 22.5 °C. The primary roots of the seedlings (2 DAG) were placed on a microscope slide with a drop of liquid-phase $^1/_2$ MS containing GA_4 (10 μM) or GA_4 combined with PAMD (25 μM) or **4** (25 μM). The green fluorescence of green fluorescent protein (GFP) was observed under a confocal-laser scanning microscope (LSM700, Zeiss, Oberkochen, Germany), and the degradation of GFP-RGA was recorded with time-lapse photography.

RESULTS

PAMD Inhibits the Growth of *A. thaliana*. PAMD was isolated from a chemical library of 9600 randomly synthesized compounds using SA-induced β-glucuronidase (GUS)-expressing plants (*PR1::GUS* line) and was determined to be an effective inhibitor of SA signaling.[22] However, the *Arabidopsis* seedlings treated with PAMD were smaller than the untreated seedlings, indicating that PAMD suppresses plant growth (Figure 1A). Further studies showed that PAMD had no obvious suppressive effect on the seed germination time or germination rate (Figure 1B). We then investigated the dose-dependence of the phenotype of the seedlings treated with PAMD and found a positive correlation between the PAMD concentration and *Arabidopsis* growth suppression, including rosette size, fresh weight, and hypocotyl growth (Figure 1A,C,D). However, it was unclear whether the plant-growth-suppressing effects of PAMD were relevant to its inhibitory effect on SA signaling.

Synthesis of PAMD Derivatives. To investigate the relationship between the chemical structure and SA-signal-inhibiting activity of PAMD (**1**) and to reduce its inhibitory effects on plant growth without affecting its SA-signal-inhibiting activity, several PAMD derivatives with deletions or changes to various groups were synthesized (Figure 2). The PAMD derivatives were synthesized with one-step reactions, which are much simpler than the reaction used to synthesize PAMD (Figure 2A).

SA-Signal-Inhibiting Activities of PAMD Derivatives. The effects of the derivatives described above on the suppression of *PR1* expression were determined with real-time PCR (Figure 3). Compound **2**, in which the 2-phenyl group is deleted, and compound **3**, in which both the 2-phenyl group and the trifluoromethyl group on the phenyl group attached to the N atom are deleted, did not suppress *PR1* expression, suggesting that the phenyl group on the cyclohexadione group contributes to this activity. The substitution of **3** with a dimethyl group at the 5-position of the cyclohexadione group generated compound **4**, which recovered its capacity to suppress *PR1* expression, although this activity was weaker than that of PAMD. This suggests that in addition to the phenyl group the dimethyl group on the cyclohexane ring also contributes to the suppression of *PR1* expression, perhaps as an electron-donating group. On the basis of the structure of **4**, various derivatives with several substituents on the N-attached phenyl group of **4** were synthesized, and their activities were determined. Compound **5**, with 2,4-dichloro groups on the N-attached phenyl group, showed more potent activity in suppressing *PR1* expression than did **4**. Compound **6**, with a 3-chloro group, compound **7**, with 3-chloro and 2-methyl groups, and compound **8**, with a 4-hydroxyl group, each

DOI: 10.1021/acs.jafc.5b01521
J. Agric. Food Chem. 2015, 63, 7124−7133

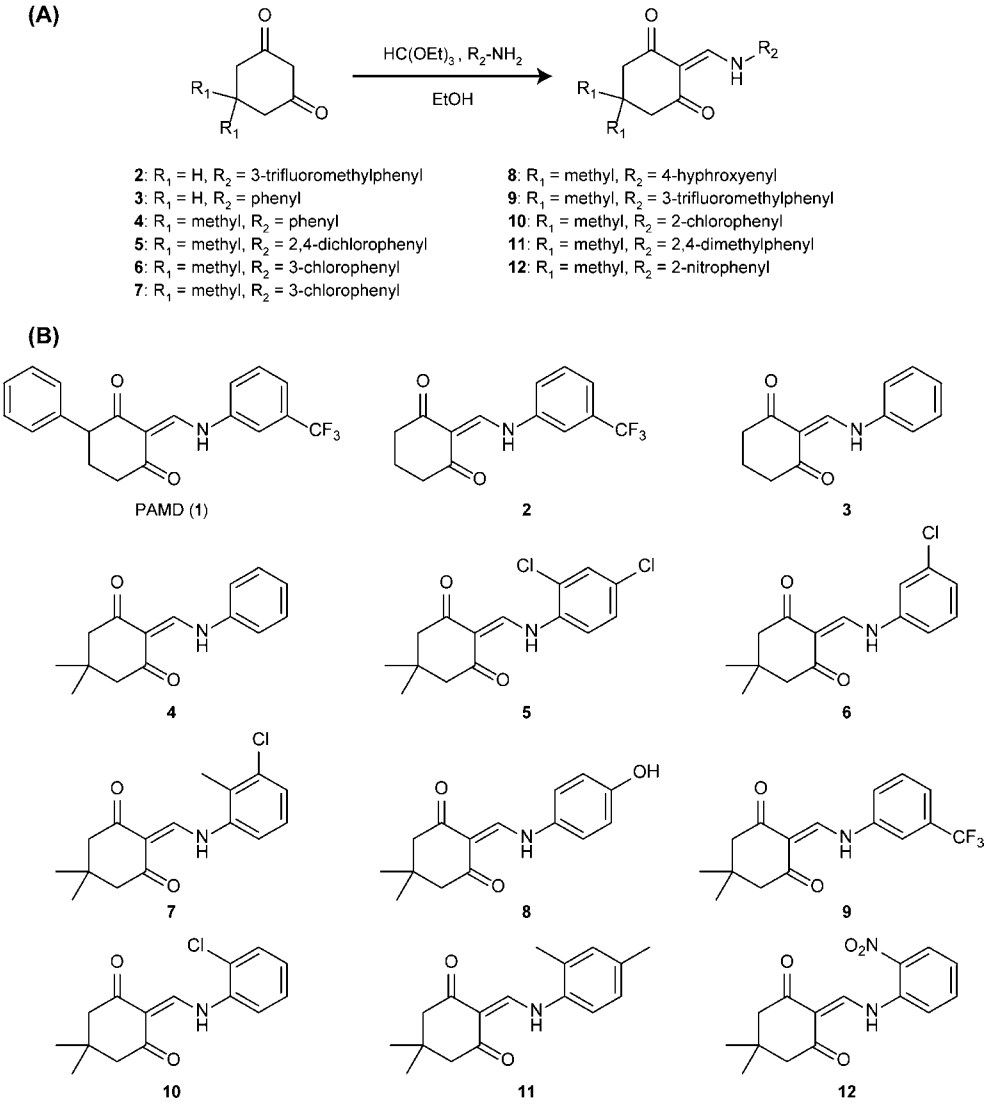

Figure 2. Synthesis of PAMD derivatives. (A) Scheme of the synthesis of derivatives with one-step methods. (B) Chemical structure of PAMD (**1**) and its derivatives newly synthesized in this paper.

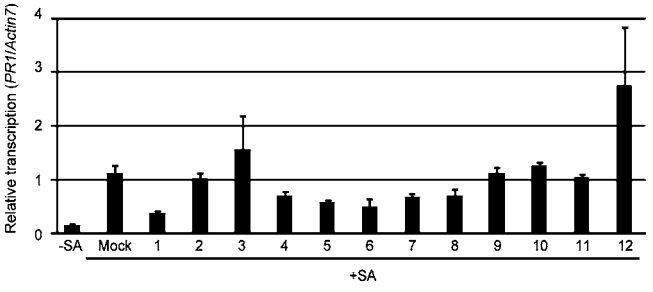

Figure 3. Determination of SA signal inhibition by PAMD derivatives. Seedlings grown for 5 DAG on $^1/_2$ MS medium under constant light at 22.5 °C were transferred to $^1/_2$ MS medium containing the indicated compounds (25 μM) for further cultivation for 8 days under constant light at 22.5 °C, followed by foliar-sprayed SA treatment. *PR1* expression was determined relative to *Actin7*. Error bars indicate the means ± SD of three replicates.

showed activity almost equal to that of **4**. However, some other derivatives, such as compound **9**, with a 3-trifluoromethyl group, compound **10**, with a 2-chloro group, and compound **11**, with 2,4-dimethyl groups on the N-attached phenyl group, lost the capacity to suppress *PR1* gene expression. Unexpectedly, compounds **3** and **12** increased *PR1* gene expression. It is noteworthy that although substituted with the same atom(s) the activities of compounds **5** and **6** differed significantly from that of compound **10** in suppressing *PR1* gene expression suggesting the importance of the positions and the combinations of the substituents on the N-attached phenyl group. Various groups on the N-attached phenyl group also played important roles in suppressing *PR1* expression and further study of the structure−activity relationships of the substituents on the N-attached phenyl group should reveal important factors that increase or reduce *PR1* expression.

Effects of Treatment with PAMD Derivatives on Plant Growth. The side effects of the PAMD derivatives on *Arabidopsis* growth were investigated (Figure 4). At a concentration of 10 μM, **2** reduced the fresh weight of *Arabidopsis* less than did PAMD, which indicates that the inhibitory effect may be partly induced by the 2-phenyl group. Compound **3** did not differ significantly from PAMD in reducing the fresh weight of *Arabidopsis*. However, **4** showed clearly less inhibitory effect on growth than did PAMD. These results indicate that the growth-inhibitory effect may result

DOI: 10.1021/acs.jafc.5b01521
J. Agric. Food Chem. 2015, 63, 7124−7133

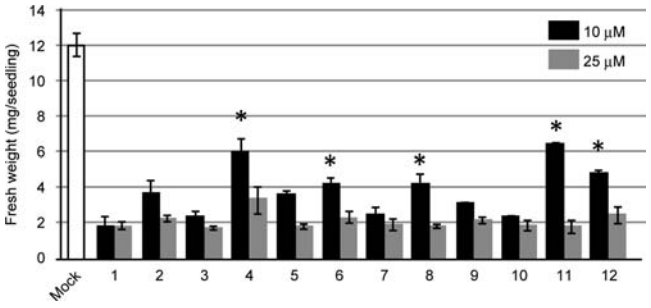

Figure 4. Estimation of the inhibitory effects of PAMD and its derivatives. Seedlings (5 DAG) grown on $^1/_2$ MS medium under constant light at 22.5 °C were transferred to $^1/_2$ MS medium with or without the test compound and further cultivated for 11 days under constant light at 22.5 °C. Fresh weight was determined as an estimate of growth. Error bars indicate the means ± SE of three independent replicate measurements of the average weights of 10 seedlings. Student's *t* test was used to determine the significance of differences relative to the PAMD (**1**) treatment; *, $P < 0.05$.

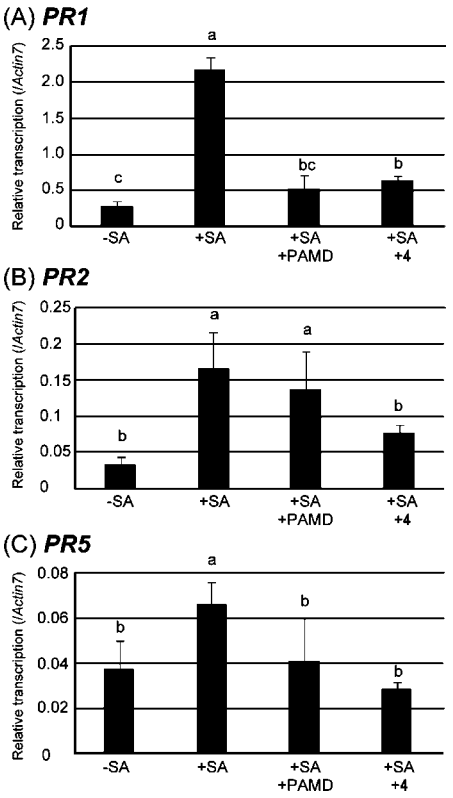

Figure 5. Suppressive effect of PAMD (**1**) and **4** on the expression of *PR2* and *PR5*. Seedlings (5 DAG) grown on $^1/_2$ MS medium under constant light at 22.5 °C were transferred to $^1/_2$ MS medium containing 25 μM of the test compound, as indicated, for further cultivation for 8 days under constant light at 22.5 °C, followed by foliar-sprayed SA treatment. *PR1* expression was determined relative to *Actin7*. Error bars indicate the means ± SD of three replicates. Statistical differences between the groups were calculated with ANOVA analysis (Posthoc: Duncan). Bars with different letters are significantly different, with $P < 0.01$.

from the basic structure of **3** and that the 5,5-dimethyl groups reduce the inhibitory effect on growth. The result for **9** showed that the trifluoro group has a negative effect on plant growth when it exists in combination with the 3,3-dimethyl groups. Except for **11**, which showed similar levels of growth inhibition as **4**, all the derivatives based on the structure of **4**, including **5**−**8**, **10**, and **12**, inhibited growth more strongly than **4**, but most of them, including **5**, **8**, **10**, and **12**, inhibited growth less strongly than PAMD.

However, at a concentration of 25 μM, all the PAMD derivatives suppressed the growth of *Arabidopsis* (Figure 4). The growth-inhibitory effect of **4** was smallest of all the PAMD derivatives tested, even though it did not differ significantly from that of PAMD (Figure 4). Compound **4** also suppressed the expression of the *PR2* and *PR5* genes even more strongly than PAMD (Figure 5), indicating that **4** is not a specific inhibitor of *PR1* expression. The *Collectotrichum higginsianum* (*C. higginsianum*) infection assay indicated that **4** likely increased the susceptibility of *Arabidopsis* to *C. higginsianum* (Figure 6). Because some of the PAMD derivatives showed less growth-inhibitory activity than PAMD when applied at 10 μM, we tested whether a lower concentration of **4** suppressed the induction of *PR1* gene expression by SA and found that **4** inhibited SA-induced *PR1* expression in a concentration-dependent manner (Figure 7A). This result clearly shows that **4** suppresses SA-induced *PR1* expression as strongly as PAMD (**1**) at 10 μM (Figure 7B) at which concentration **4** affects plant growth less than it does at 25 μM (Figure 4).

Compound **4** showed less adverse effects on plant growth than PAMD, including on seed germination, fresh weight, seedling establishment, and root growth under constant light (Figure 8A−E). Remarkably, hypocotyl growth in the dark was only slightly inhibited by **4**, even when 25 μM of **4** was applied (Figure 8F). On the basis of these results, **4** could be considered a better inhibitor of SA signaling than PAMD because it suppresses *PR* gene expression to a similar or greater extent than PAMD but with a less adverse effect on growth.

Quantification of Endogenous Salicylic Acid and Abscisic Acid in *Arabidopsis* using LC-MS/MS. Although the inhibitory effects of PAMD and its derivatives on *PR1* expression were determined under exogenous SA treatment, it is still an open question whether PAMD and its derivatives impact SA biosynthesis, which may also contribute to the final effects of the compound. To answer this question, the endogenous level of SA in the *Arabidopsis* treated by PAMD or **4** was quantified. The results showed that treatment by PAMD or **4** increased the SA level compared to mock treatment (Figure 9A). Meanwhile, we also quantified the endogenous level of ABA, which is well-known for its accumulation in plants under stresses and its negative roles in regulating plant growth. The plant treated with PAMD or **4** accumulated a higher level of ABA compared to the mock treatment (Figure 9B). In accordance with the increasing level of ABA, the anthocyanin level was also higher in the plants treated by PAMD (Supporting Information Figure 1). The increasing levels of ABA and anthocyanin by PAMD treatment are considered to be the side effects of the compounds, which caused stresses to the plant. Treatment by **4** induced a moderate increase in the ABA level and no change in anthocyanin level compared to that effected by the treatment with PAMD (Figure 9B, Supporting Information Figure 1). These results further indicate that **4** is a better candidate than PAMD with less adverse effects on plants.

Inhibitory Effects of PAMD and Its Derivatives Depend Partly on DELLA. Although **4** is a better SA signal inhibitor than PAMD, it still inhibits plant growth to some extent (Figure 8). The positive regulatory roles of GA in plant growth are well-known, and the binding of GA to its receptor

DOI: 10.1021/acs.jafc.5b01521
J. Agric. Food Chem. 2015, 63, 7124−7133

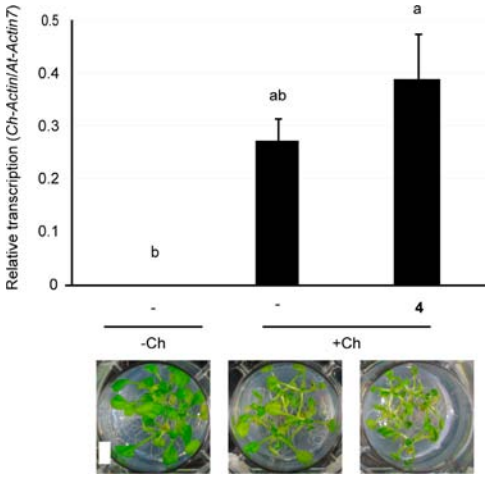

Figure 6. *Collectotrichum higginsianum* (*C. higginsianum*) infection assay. Seedlings (5 DAG) were transferred to treatment medium containing compounds as indicated or not and further cultivated for 8 days. The 8 day-after-treatment (DAT) seedlings were sprayed by 1×10^7 spores/ml of *C. higginsianum* and followed by 4 days' cultivation. *Ch-Actin* expression was determined relative to *Arabidopsis Actin7* (*At-Actin7*). Error bars indicate the means ± SD of three replicates. Statistical differences between the groups were calculated with ANOVA analysis (Posthoc: Duncan). Bars with different letters are significantly different, with $P < 0.01$. Scale = 5 mm.

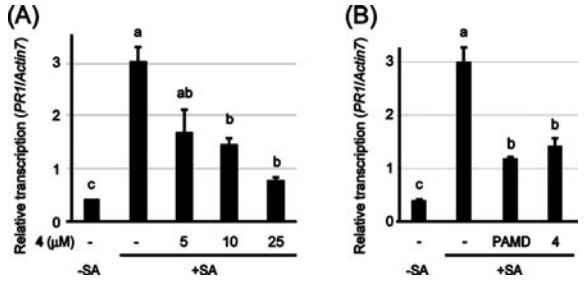

Figure 7. Suppressive effects of PAMD or **4** on the expression of the *PR1* gene. (A) Dose-dependent inhibition of SA-induced *PR1* expression by **4**. (B) Suppressive effect of PAMD (**1**) or **4** at the concentration of 10 μM. Seedlings (5 DAG) grown on $^1/_2$ MS medium under constant light at 22.5 °C were transferred to $^1/_2$ MS medium containing a serial concentration of test compound, as indicated, for further cultivation for 8 days under constant light at 22.5 °C, followed by foliar-sprayed SA treatment. After treatment with SA for 3 days, the seedlings were frozen in liquid nitrogen. *PR1* expression was determined relative to *Actin7*. Error bars indicate the means ± SD of three replicates. Statistical differences between the groups were calculated with ANOVA analysis (Posthoc: Duncan). Bars with different letters are significantly different with $P < 0.01$.

GID1 triggers the degradation of the DELLA proteins, negative regulators of GA signaling, by 26S proteasomes.[24] The defective GA biosynthesis in the *ga1-3* mutant or the loss of DELLA degradation in the *gai-1* and *rga-Δ17* mutants, in which the DELLA domain is deleted, cause a severe dwarf phenotype in *Arabidopsis*.[25,26] Therefore, suspecting that PAMD and **4** might inhibit plant growth by compromising GA signaling, we tested whether the growth suppression effects of **1** and **4** were restored by treatment with GA (Figure 10A). Both PAMD and **4** suppressed hypocotyl growth under constant light, and GA treatment partly restored this growth-suppression effect in wild-type plants (L*er*). To further investigate whether this restorative effect of GA on hypocotyl growth is related to the DELLA proteins, we applied GA_4 with PAMD or **4** to the *5Δdella* mutant line of *Arabidopsis*, which is insensitive to GA biosynthesis inhibitors or GA antagonists because it carries loss-of-function mutations in all five DELLA proteins.[27] The results showed that the hypocotyl growth of the *5Δdella* line was less inhibited by PAMD or **4** than was the wild-type line (L*er*), although there was still a significant difference between the effects of the mock treatment and test compound treatments in the *5Δdella* line (Figure 10A). The restorative effect of GA on the hypocotyl growth suppressed by PAMD or **4** was observed in L*er* plants but not in *5Δdella* plants (Figure 10A). We then analyzed the effects of treatment with PAMD or **4** on the accumulation of the DELLA proteins using the *RGA:GFP-RGA* line. Treatment with either of the two compounds delayed the GA-mediated degradation of the GFP-RGA fusion protein (Figure 10B). These results indicate that PAMD and its derivative **4** alleviate the DELLA degradation induced by GA treatment and GA signaling. Therefore, their effects on plant growth partly depend on the function of the DELLA proteins.

DISCUSSION

Not only plant hormone mimics, but also chemical inhibitors such as paclobutrazole, an inhibitor of GA biosynthesis, brassinazole, an inhibitor of brassinosteroids biosynthesis,[28] and naphthylphthalamic acid, an inhibitor of auxin transport,[29] are useful in studies on plant hormone signaling. Until recently, there has been limited information about inhibitors of SA signaling. In a previous paper, we reported that PAMD (**1**) inhibits SA signaling in *Arabidopsis* and increases the susceptibility of the plants to pathogens,[22] suggesting that PAMD is an inhibitor of SA signaling and may be a useful tool for determining the SAR mechanism. However, besides its effects on SA signaling, PAMD adversely affected plant growth. In the present study, we prepared several derivatives of PAMD and found that one of them compound **4** suppressed the expression of the SA-response-marker *PR* genes with a smaller adverse effect on growth than PAMD. Therefore, we selected **4** as a better SA-signaling inhibitor than PAMD. LC-MS/MS analysis confirmed that PAMD and **4** increased the endogenous level of SA, which should have induced the expression of *PR* gene. This inconsistency between the increasing SA level and the decreasing *PR* gene expression level in the *Arabidopsis* treated by PAMD or **4** indicated that these compounds affect the SA signaling pathway and resistance to *C. higginsianum* by impairing the *PR* gene expression but not through an impact on the biosynthesis of SA. The induction of SA level could be considered negative feedback resulting from the inhibitory effects of PAMD and **4** on the SA signaling pathway. Our study of the structure−activity relationships of the PAMD derivatives demonstrated that the suppression of *PR1* expression by the PAMD derivatives is not directly related to their inhibition of plant growth and that structural modification of the PAMD derivatives dramatically altered their effects on *PR1* expression. These results suggest that further chemical modification of the PAMD derivatives may identify more specific inhibitors of SA signaling.

The side effects of PAMD on growth have also been investigated here. PAMD severely impacted seedling establishment and root growth and induced an accumulation of a higher level of ABA and anthocyanin compared to mock treatment. These limitations were overcome to some extent by structure−activity relationship modification, and compound **4** was

DOI: 10.1021/acs.jafc.5b01521
J. Agric. Food Chem. 2015, 63, 7124−7133

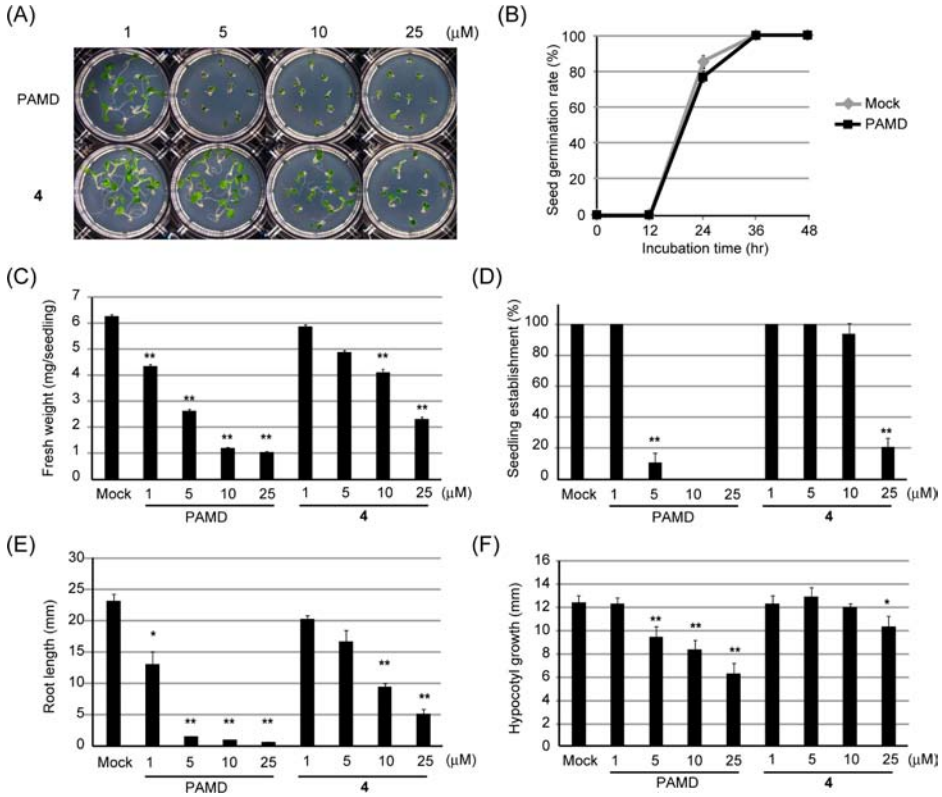

Figure 8. Inhibitory effects of PAMD and **4** on *Arabidopsis* growth. (A) Seedlings (5 DAG) of *Arabidopsis* grown on $^1/_2$ MS medium containing PAMD or **4** under constant light at 22.5 °C. (B) Seeds were germinated on $^1/_2$ MS medium with or without **4** under constant light at 22.5 °C. Error bars indicate the means ± SE of three independent replicates, $n > 30$. (C) Fresh weight of seedlings (12 DAG) grown on $^1/_2$ MS medium with or without the test compound under constant light at 22.5 °C. Error bars indicate the means ± SE of three independent replicates, $n > 30$. Student's t test was used to determine the significance of difference relative to the mock treatment; **, $P < 0.01$. (D) Seeds were germinated on $^1/_2$ MS medium with or without the test compound under constant light at 22.5 °C. Seedling establishment was determined as the appearance of the first pair of true leaves at 5 DAG. Error bars indicate the means ± SE of three independent replicates, $n = 10$. (E) Primary root lengths of seedlings (6 DAG) that were germinated on $^1/_2$ MS medium with or without the test compound under constant light at 22.5 °C. Error bars indicate the means ± SE of three independent replicates, $n = 10$. Student's t test was used to determine the significance of differences relative to the mock treatment: *, $P < 0.05$; **, $P < 0.01$. (F) After stratification at 4 °C for 2 days, seeds were light-pulsed for 6 h and germinated and grown on $^1/_2$ MS medium with or without the test compound under constant dark at 22.5 °C. Hypocotyl length was measured at 5 DAG. Error bars indicate the means ± SE of three independent replicates, $n = 10$. Student's t test was used to determine the significance of differences relative to the mock treatment: *, $P < 0.05$; **, $P < 0.01$.

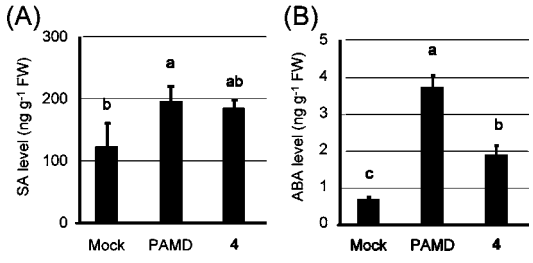

Figure 9. Quantification of salicylic acid and abscisic acid in *Arabidopsis*. Seedlings (5 DAG) were transferred to $^1/_2$ MS medium containing 25 μM of the test compound, as indicated, for further cultivation for 8 days, followed by being sampled and analyzed by LC-MS/MS. Error bars indicate the means ± SD of three replicates. Statistical differences between the groups were calculated with ANOVA analysis (Posthoc: Duncan). Bars with different letters are significantly different: $P < 0.05$ (SA) or $P < 0.01$ (ABA).

selected as a better candidate for SAR studies. However, at present, no derivative has yet been found that suppresses *PR* gene expression but does not inhibit plant growth. The new PAMD derivatives, such as **4**, are more selective inhibitors of SA signaling but still inhibit *Arabidopsis* growth. Here, we have demonstrated that the inhibitory effects of PAMD and its derivative **4** are partly dependent on their effects on GA signaling by interrupting GA-induced DELLA degradation (Figure 10).

Recently, many studies of plant immunity to pathogens have indicated a cross talk between SA and other plant hormones.[30] Tan et al. showed that the effector protein of the pathogenic bacterium *Xanthomonas campestris*, $XopD_{Xcc8004}$, initiates the disease defense mechanisms of plants by interacting with RGA and delaying its degradation.[31] This confirms that the stabilization of the DELLA proteins affects the plant's disease responses. It has been shown that DELLA increases the plant's resistance to necrotrophs but reduces its resistance to biotrophs, thus demonstrating that the DELLA proteins control plant immune responses by modulating the balance between SA and JA signaling.[13] This supports our results that PAMD and **4** suppress the expression of SA-responsive genes and also stabilize the DELLA proteins. We suggest that the activity of PAMD and its derivatives in repressing *PR* gene expression is partly dependent on the DELLA proteins, although further study is required to confirm this.

It is noteworthy that the growth of the 5Δ*della* mutant line was still suppressed by both PAMD and compound **4** (Figure 10A), indicating that DELLA and DELLA-induced signaling are

DOI: 10.1021/acs.jafc.5b01521
J. Agric. Food Chem. 2015, 63, 7124−7133

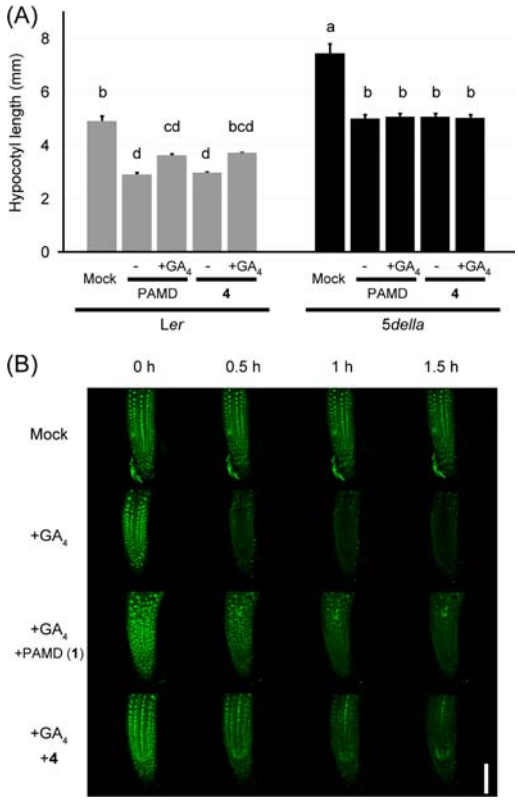

Figure 10. Effects of PAMD and **4** on GA signaling. (A) Seedlings (3 DAG) of L*er* and 5Δ*della* grown on $^1/_2$ MS medium under constant light at 22.5 °C were transferred to $^1/_2$ MS medium containing GA_4 (10 μM), PAMD (25 μM), **4** (25 μM), or combinations of them as indicated, followed by several days' cultivation under constant light at 22.5 °C. Hypocotyl length was measured 9 days after treatment. Error bars indicate the means ± SE of three independent replicates (n = 6). Statistical differences between the groups were calculated with ANOVA analysis (Posthoc: Duncan). Bars with different letters are significantly different with $P < 0.01$. (B) The primary roots of 2 DAG *RGA:GFP-RGA* seedlings grown on $^1/_2$ MS medium under constant light at 22.5 °C were placed onto slides and immersed in $^1/_2$ MS medium with or without GA_4 (10 μM) combined with PAMD (25 μM) or **4** (25 μM), as indicated. Green fluorescence was observed with a confocal-laser scanning microscope and time-lapse photography. Scale = 100 μm.

not the only points at which these compounds function. Although the exact target(s) of PAMD and its derivatives is (are) still unclear, investigation of these targets and their modes of function will extend our understanding of SA signaling and/or its cross talk with other plant hormones.

■ ASSOCIATED CONTENT

Supporting Information

The Supporting Information is available free of charge on the ACS Publications website at DOI: 10.1021/acs.jafc.5b01521.

Anthocyanin level of *Arabidopsis* treated with PAMD or **4**. (PDF)

■ AUTHOR INFORMATION

Corresponding Author

*Phone: 81-3-5841-5157. E-mail: asami@pgr1.ch.a.u-tokyo.ac.jp.

Funding

This work was supported, in part, by a grant from the Core Research for Evolutional Science and Technology (CREST) Program of the Japan Science and Technology Agency (JST) and a JSPS Grant-in-Aid for Scientific Research (C; grant number 26440132).

Notes

The authors declare no competing financial interest.

■ ACKNOWLEDGMENTS

We thank Miguel A. Blázquez (Instituto de Biología Molecular Celular de Plantas, Spain) for kindly providing the 5Δ*della* mutant.

■ REFERENCES

(1) Savary, S.; Ficke, A.; Aubertot, J. N.; Hollier, C. Crop losses due to diseases and their implications for global food production losses and food security. *Food Secur.* **2012**, *4*, 519−537.
(2) Reina-Pinto, J. J.; Yephremov, A. Surface lipids and plant defenses. *Plant Physiol. Biochem.* **2009**, *47*, 540−549.
(3) Fu, Z. Q.; Dong, X. Systemic acquired resistance: turning local infection into global defense. *Annu. Rev. Plant Biol.* **2013**, *64*, 839−863.
(4) Henry, E.; Yadeta, K. A.; Coaker, G. Recognition of bacterial plant pathogens: local, systemic and transgenerational immunity. *New Phytol.* **2013**, *199*, 908−915.
(5) Durrant, W. E.; Dong, X. Systemic acquired resistance. *Annu. Rev. Phytopathol.* **2004**, *42*, 185−209.
(6) Kaltdorf, M.; Naseem, M. How many salicylic acid receptors does a plant cell need? *Sci. Signaling* **2013**, *6*, jc3.
(7) Yan, S.; Dong, X. Perception of the plant immune signal salicylic acid. *Curr. Opin. Plant Biol.* **2014**, *20*, 64−68.
(8) Fu, Z. Q.; Yan, S.; Saleh, A.; Wang, W.; Ruble, J.; Oka, N.; Mohan, R.; Spoel, S. H.; Tada, Y.; Zheng, N.; Dong, X. NPR3 and NPR4 are receptors for the immune signal salicylic acid in plants. *Nature* **2012**, *486*, 228−232.
(9) Wu, Y.; Zhang, D.; Chu, J. Y.; Boyle, P.; Wang, Y.; Brindle, I. D.; De Luca, V.; Despres, C. The *Arabidopsis* NPR1 protein is a receptor for the plant defense hormone salicylic acid. *Cell Rep.* **2012**, *1*, 639−647.
(10) Bari, R.; Jones, J. G. Role of plant hormones in plant defence responses. *Plant Mol. Biol.* **2009**, *69*, 473−488.
(11) Robert-Seilaniantz, A.; Grant, M.; Jones, J. D. G. Hormone crosstalk in plant disease and defense: more than just JASMONATE-SALICYLATE antagonism. *Annu. Rev. Phytopathol.* **2011**, *49*, 317−343.
(12) Hou, X.; Lee, L. Y. C.; Xia, K.; Yan, Y.; Yu, H. DELLAs modulate jasmonate signaling via competitive binding to JAZs. *Dev. Cell* **2010**, *19*, 884−894.
(13) Navarro, L.; Bari, R.; Achard, P.; Lisón, P.; Nemri, A.; Harberd, N. P.; Jones, J. D. G. DELLAs control plant immune responses by modulating the balance of jasmonic acid and salicylic acid signaling. *Curr. Biol.* **2008**, *18*, 650−655.
(14) Hicks, G. R.; Raikhel, N. V. Opportunities and challenges in plant chemical biology. *Nat. Chem. Biol.* **2009**, *5*, 268−272.
(15) Nakashita, H.; Yoshioka, K.; Yasuda, M.; Nitta, T.; Arai, Y.; Yoshida, S.; Yamaguchi, I. Probenazole induces systemic acquired resistance in tobacco through salicylic acid accumulation. *Physiol. Mol. Plant Pathol.* **2002**, *61*, 197−203.
(16) Yoshioka, K.; Nakashita, H.; Klessig, D. F.; Yamaguchi, I. Probenazole induces systemic acquired resistance in *Arabidopsis* with a novel type of action. *Plant J.* **2001**, *25*, 149−157.
(17) Friedrich, L.; Lawton, K.; Ruess, W.; Masner, P.; Specker, N.; Rella, M. G.; Meier, B.; Dincher, S.; Staub, T.; Uknes, S.; Métraux, J.-P.; Kessmann, H.; Ryals, J. A benzothiadiazole derivative induces systemic acquired resistance in tobacco. *Plant J.* **1996**, *10*, 61−70.
(18) Görlach, J.; Volrath, S.; Knauf-Beiter, G.; Hengy, G.; Beckhove, U.; Kogel, K. H.; Oostendorp, M.; Staub, T.; Ward, E.; Kessmann, H.;

DOI: 10.1021/acs.jafc.5b01521
J. Agric. Food Chem. 2015, 63, 7124−7133

Ryals, J. Benzothiadiazole, a novel class of inducers of systemic acquired resistance, activates gene expression and disease resistance in wheat. *Plant Cell* **1996**, *8*, 629−643.
(19) Lawton, K. A.; Friedrich, L.; Hunt, M.; Weymann, K.; Delaney, T.; Kessmann, H.; Staub, T.; Ryals, J. Benzothiadiazole induces disease resistance in *Arabidopsis* by activation of the systemic acquired resistance signal transduction pathway. *Plant J.* **1996**, *10*, 71−82.
(20) Métraux, J. P.; Signer, H.; Ryals, J.; Ward, E.; Wyss-Benz, M.; Gaudin, J.; Raschdorf, K.; Schmid, E.; Blum, W.; Inverardi, B. Increase in salicylic acid at the onset of systemic acquired resistance in cucumber. *Science* **1990**, *250*, 1004−1006.
(21) Uknes, S.; Mauch-Mani, B.; Moyer, M.; Potter, S.; Williams, S.; Dincher, S.; Chandler, D.; Slusarenko, A.; Ward, E.; Ryals, J. Acquired resistance in Arabidopsis. *Plant Cell* **1992**, *4*, 645−656.
(22) Seo, E. K.; Nakamura, H.; Mori, M.; Asami, T. Screening and characterization of a chemical regulator for plant disease resistance. *Bioorg. Med. Chem. Lett.* **2012**, *22*, 1761−1765.
(23) Miyazaki, S.; Kimura, H.; Natsume, M.; Asami, T.; Hayashi, K.; Kawaide, H.; Nakajima, M. Analysis of *ent*-kaurenoic acid by ultra performance liquid chromatography-tandem mass spectrometry. *Biochem. Biophys. Reports* **2015**, *2*, 103−107.
(24) Sun, T. The Molecular Mechanism and Evolution of the GA−GID1−DELLA Signaling Module in Plants. *Curr. Biol.* **2011**, *21*, R338−R345.
(25) Sun, T.; Goodman, H. M.; Ausubel, F. M. Cloning the Arabidopsis GA1 locus by genomic subtraction. *Plant Cell* **1992**, *4*, 119−128.
(26) Dill, A.; Jung, H.-S.; Sun, T.-p. The DELLA motif is essential for gibberellin-induced degradation of RGA. *Proc. Natl. Acad. Sci. U. S. A.* **2001**, *98*, 14162−14167.
(27) Feng, S.; Martinez, C.; Gusmaroli, G.; Wang, Y.; Zhou, J.; Wang, F.; Chen, L.; Yu, L.; Iglesias-Pedraz, J. M.; Kircher, S.; Schafer, E.; Fu, X.; Fan, L. M.; Deng, X. W. Coordinated regulation of *Arabidopsis thaliana* development by light and gibberellins. *Nature* **2008**, *451*, 475−479.
(28) Asami, T.; Yoshida, S. Brassinosteroid biosynthesis inhibitors. *Trends Plant Sci.* **1999**, *4*, 348−353.
(29) Ma, Q.; Robert, S. Auxin biology revealed by small molecules. *Physiol. Plant.* **2014**, *151*, 25−42.
(30) Kazan, K.; Lyons, R. Intervention of phytohormone pathways by pathogen effectors. *Plant Cell* **2014**, *26*, 2285−2309.
(31) Tan, L.; Rong, W.; Luo, H.; Chen, Y.; He, C. The Xanthomonas campestris effector protein XopDXcc8004 triggers plant disease tolerance by targeting DELLA proteins. *New Phytol.* **2014**, *204*, 595−608.

DOI: 10.1021/acs.jafc.5b01521
J. Agric. Food Chem. 2015, 63, 7124−7133

identification of different variants or 2DGEs (2DGE protein spots produced either from a single gene or from paralogous genes as per the classification given previously)[11] of β-conglycinin and glycinin proteins.[12] In addition to their high abundance in seed, recent proteomic studies revealed their presence in soybean seed coat.[13,14] Methods have been developed to deplete these major soybean SSPs using isopropanol,[15] calcium,[16] and protamine sulfate (PS).[17] However, these methods have not been fully utilized for the comparative soybean proteome analysis to get a better insight into the nutritional values of the seeds.

Because soybean seeds are rich source of proteins and oils, one of the major goals of plant breeders worldwide is to enhance the nutritional properties of soybean seeds by increasing either their oil content or their protein content. However, for successful breeding programs, it is highly essential to understand the biochemical pathways underlying the accumulation of proteins and oils in soybean seeds. In this direction, we have carried out a comparative biochemical and proteomic profiling of protein- versus oil-rich-seed cultivars of *G. max* and *G. soja*. In this study, a combination of the PS and 2DGE methods was used to establish the proteomes of two cultivars each of *G. max* (Daewon and Saedanbaek) and *G. soja* (WS15 and WS22), differing in protein and oil reserve contents in order to get a better understanding of why soybean seeds differ in their protein and oil content.

2. MATERIALS AND METHODS

Plant Materials. Seeds of *G. max* (Daewon and Saedanbaek) and *G. soja* (WS22 and WS15) cultivars were grown in silt loam soil in the experimental fields of the National Institute of Crop Science, Rural Development Administration (RDA) at Miryang, South Korea, in the month of June. The soil was supplemented with a standard RDA N−P−K fertilizer (N−P−K = 3−3−3.3 kg/10 acre). Seeds were harvested in October (average temperature = 23.5 ± 3.5 °C, average day length = 12 h 17 min).[13]

Analysis of Total Protein and Amino Acid Contents. Total protein content in the soybean seeds was measured using a protein analyzer (rapid N cube, Hanau, Germany). Using a high-speed vibrating sample mill (CMT T1−100, CMT Company Ltd., Tokyo, Japan), seeds were powdered, and 50 mg of each sample was then wrapped in nitrogen-free paper and pressed to pellets. All the parameters were set to default. Glutamic acid (9.52% N) was used as test standard, and a protein factor of 6.25 was used. Each sample was analyzed in duplicate.

Amino acids were analyzed using an amino acid analyzer (Biochrom 30, Biochrom Ltd., Cambridge, UK). Briefly, the samples were hydrolyzed with 6 N HCl in sealed glass tubes filled with nitrogen at 110 °C for 24 h. The HCl was removed from the hydrolyzed sample on a rotary evaporator and brought to 10 mL with 0.2 M sodium citrated buffer, pH 2.2. Amino acids were analyzed by Biochrom 30 amino acid analyzer using nihydrin as color reactant on a cation-exchange resin column. Obtained data were analyzed using Ezchrom E software, and the quantity of amino acids was calculated by comparison with a known concentration of amino acid standard.[14]

Fatty Acid Composition Analysis. Fatty acid (FA) analysis was carried out as described previously.[18] Fatty acid methyl esters (FAMEs) were prepared by Soxhlet extraction, saponification, acid-catalyzed transesterification, and finally extraction of FAMEs in hexane. FAMEs were subsequently analyzed by capillary gas chromatography (column: 30 m × 0.25 μm I.D., 0.5 μm; flame ionization detected temperature, 210 °C; carrier gas, N_2 at 1.0 mL/min; injector temperature, 210 °C; and oven temperature, programmed from 180 to 210 °C) using an Agilent 1100 capillary gas chromatograph. Quantitative data were calculated using the peak area ratio (% total FAs).

Protein Extraction and Enrichment of Low-Abundance Proteins. Total seed proteins were extracted as described previously.[17] Briefly, soybean seeds (cv. Daewon, Saedanbaek, WS22, and WS15) were powdered in liquid nitrogen using pestle and mortar. Powdered samples (1 g) were homogenized in 10 mL of Mg/NP-40 protein extraction buffer (0.5 M Tris-HCl (pH 8.3), 2% (v/v) NP-40, 20 mM $MgCl_2$), followed by centrifugation at 12 000 g for 10 min at 4 °C. Supernatant thus obtained was incubated with 0.1% PS in ice for 30 min after which the extract was again centrifuged at 12 000 g for 10 min at 4 °C to separate the PS supernatant (PSS) and PS pellet (PSP) fractions, as described earlier.[17] PSP fraction was dissolved in an equal volume of Mg/NP40 buffer, and then proteins were extracted from the PSS and PSP fractions using a TCA/acetone precipitation method. At the final step, proteins were stored in 80% acetone until analysis.

2D Gel Electrophoresis. 2DGE was carried out as described previously.[17] Briefly, proteins from the 80% acetone solution were precipitated by centrifugation at 12 000 g for 5 min, and the pellet obtained was dissolved in the rehydration buffer containing 7 M urea, 2 M thiourea, 4% v/v CHAPS, 2 M DTT, and 0.5% v/v IPG buffer, pH 4−7 (GE Healthcare, Waukesha, WI, USA). Protein concentrations in each fraction were determined by 2D-Quant kit (GE Healthcare). Proteins (600 μg) of each sample were loaded on 24 cm IPG strips (pH 4−7) by rehydration loading overnight at 20 °C, and isoelectric focusing was carried out using following protocol: 50 V for 4 h, 100 V for 1 h, 500 V for 1 h, 1000 V for 1 h, 2000 V for 1 h, 4000 V for 2 h, 8000 V for 5 h, 8000 V for 9 h, and 50 V for 6 h on the IPGphor II platform (GE Healthcare). The second-dimensional separation was carried out on 12% SDS-PAGE, after sequential equilibration of the strips in in equilibration buffer (6 M urea, 30% v/v glycerol, 2% v/v SDS, 50 mM Tris-HCl (pH 6.8), and 0.1 mg/mL bromophenol blue) containing 100 mM DTT and 55 mM iodoacetamide. Gels were stained with colloidal Coomassie Brilliant Blue (CBB). A total of three biological replicates were carried out for each data set.

Image Acquisition and Data Analysis. Images of all the CBB-stained gels were acquired using a transmissive scanner (PowerLook 1129, UMAX) at 32 bit pixel depth and 300 dpi resolution and saved as a TIFF file. The gel spots were detected using ImageMaster2DPlatinum software 6.0 (GE Healthcare). For analyzing the differential expression of proteins, spot volumes were normalized in the percentage volume mode, and spots showing a ≥1.5-fold change in spot volume were considered as differentially expressed spots. Student's *t* test ($p < 0.05$) was carried out to check the significance of differential expression.

Mass Spectrometry. Differentially expressed spots were excised from the gel, destained, and subjected to in-gel digestion.[19] In brief, first, spots were subjected to in-gel reduction using 10 mM DTT in 100 mM ammonium bicarbonate at 56 °C for 30 min and then alkylated using 50 mM iodoacetamide in 100 mM ammonium bicarbonate for 30 min in the dark. Gel pieces were washed with 1:1 ammonium bicarbonate/acetonitrile (ACN) solution and dehydrated using 100% ACN for 5 min. Gel pieces were digested with 5 μL of trypsin solution (20 ng/μL, gold mass-spectroscopy-grade, Promega, Madison, USA) in 50 mM ammonium bicarbonate, pH 7.8, for 16 h at 37 °C. Trypsin-digested peptides were extracted twice with 0.1% trifluoroacetic acid (TFA). Each sample was mixed with same volume of matrix (10 mg/mL α-cynohydroxycinnamic acid, 0.1% TFA, 50% ACN), loaded on a MALDI target plate and allowed to dry at 25 °C. Prepared samples of trypsin-digested peptides were subjected to MALDI-TOF/TOF MS analysis using ABI 4800 Plus TOF-TOF Mass Spectrometer (Applied Biosystems, Framingham, MA, USA).[14] Spectra were calibrated with the peptide calibration standard (Mass Standard Kit for the 4700 Proteomics Analyzer, Calibration Mixture 1) prepared in the same way. The 10 most and least intense ions per MALDI spot with signal/noise ratios >25 were selected for subsequent MS/MS analysis in 1 kV mode using 800−1000 consecutive laser shots.[13,17] MS/MS spectra were searched against the Uniprot/Swiss-Prot database (14 926 175 sequences, 5 299 740 401 residues) and soybean peptide database obtained from the soybean genome database (Phytozome ver. 8.0, http://www.phytozome.net/soybean) by Protein

DOI: 10.1021/acs.jafc.5b03196
J. Agric. Food Chem. 2015, 63, 7134−7142

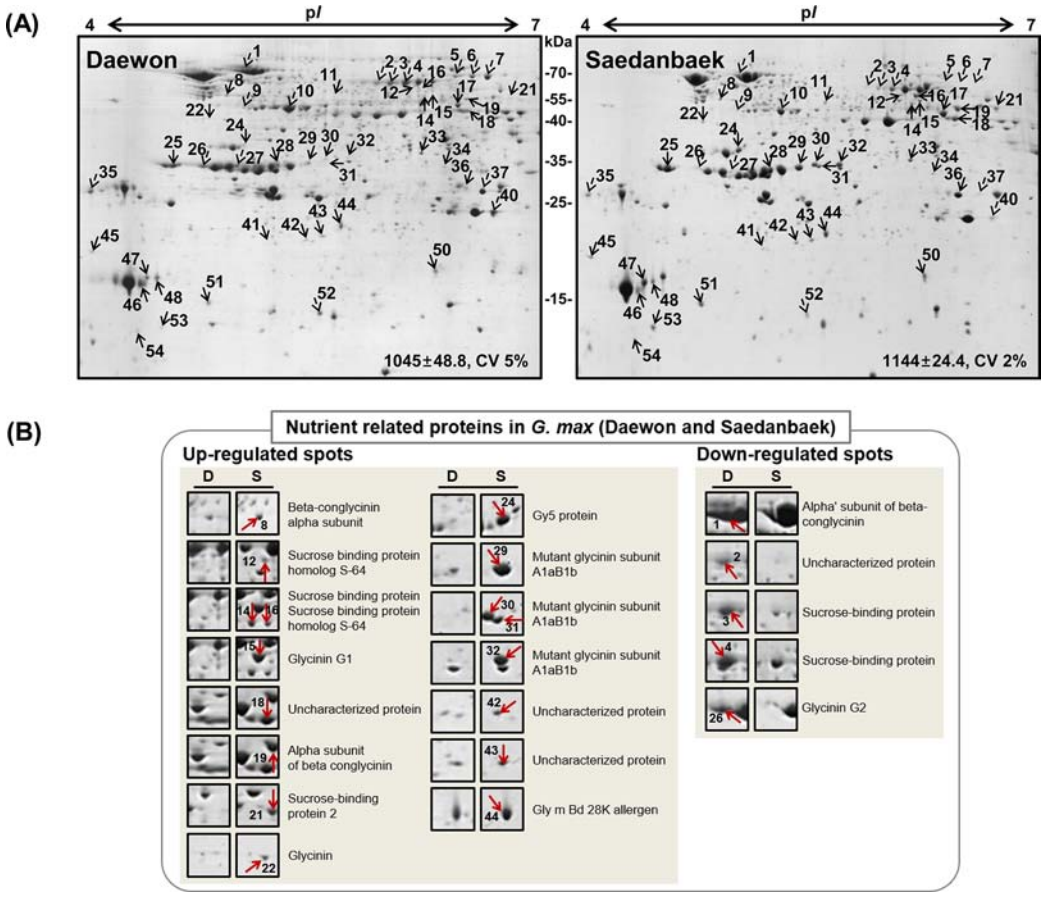

Figure 1. (A) Representative 2D gels of PSS fractions of Daewon and Saedanbaek cultivars of *G. max*. First-dimension separation was carried out on 24 cm IPG strips, pH 4−7, and second-dimension separation was carried out on 12% SDS-PAGE. Gels were stained with colloidal CBB stain. Differentially expressed spots in supernatant fractions are marked by arrows. (B) Enlarged view of 2D gel areas showing differentially expressed protein spots in PSS fractions of Daewon and Saedanbaek.

Pilot v.3.0 software (AB Sciex, Framingham, MA, USA) using MASCOT as search engine (ver. 2.3.0, Matrix Science, London, UK). The search parameters used for the protein identification were as follows: fixed modifications, carbamidomethylation of cysteine; variable modification, methionine oxidation; peptide and fragment-ion mass tolerances, 50 ppm; maximum trypsin missed cleavage, 1; and instrument type, MALDI-TOF/TOF. Only high-confidence identifications with statistically significant search scores (greater than 95% confidence, $p < 0.05$) were used for further analyses.

Data Processing and Statistical Analysis. Functional categories and statistical analyses were carried out on differential protein spots. Gene ontology (GO) terms analysis was carried out using an UFO web server (http://ufo.gobics.de/). Spot volumes of all the differentially expressed proteins were subsequently $\log_2$-transformed to equalize the scale of expression. The $\log_2$-transformed values of each spot were then used for hierarchical clustering analysis (HCL) using MultiExperimental viewer (MeV) software to generate the heat map. Principal component analysis (PCA) of the differentially expressed protein spots was carried out using the statistical tool of the Microsoft Excel program (XLSTAT).

Tofu Production. For production of tofu, a previously published protocol based on $MgSO_4$ precipitation was used.[20,21] In brief, seeds were soaked in water and incubated at 4 °C for 24 h. After incubation, soaked seeds were ground with water for 5 min at high speed in a blender (Koco-4800, Koco Silver Co., Incheon, Korea). Soybean slurry thus obtained was filtered using a cheese cloth and squeezed manually to obtain the filtrate. The residue was mixed with water and the slurry was filtered again to obtain the soymilk. After adding 3% $MgSO_4$, the soymilk was boiled in a tofu maker. The bean curd thus obtained was pressed smoothly. After pressing, the tofu was stored at 4 °C until analysis.

Antibody Generation and Western Blot Analysis. For production of antibodies, spots corresponding to the different subunits of SSPs were excised from the 2D gels, and the proteins were identified by MS/MS. Protein sequences thus obtained were used for designing the primers, and the genes for respective proteins were cloned in a pQE30 expression vector. Recombinant proteins were purified according to the manufacturer's protocol (Qiagen, Valencia, CA, USA) and used for generation of polyclonal antibodies by immunizing rabbits. Antibodies were then purified from rabbit's blood as described previously.[22] For immunoblotting experiments, the total, PSS, PSP, tofu, and whey protein samples (25 μg) were resolved on SDS-PAGE and transferred to a PVDF membrane.[17] Transfer of proteins to the membrane was confirmed by Ponceau-S staining. Membrane was incubated in blocking solution for 2 h in 5% nonfat dry milk in TTBS (50 mM Tris-HCl, pH 8.2, 0.1% (v/v) Tween-20, and 150 mM NaCl), after which the membrane was incubated overnight with antibodies against the SSPs (β-conglycinin α subunit, α' subunit, β subunit, glycinin acidic chain; 1:10 000). After three washings of the membrane in TTBS for 15 min, it was incubated with secondary anti-rabbit-IgG antibody (1:6500) conjugated with horseradish peroxidase. Finally, the immunoblot signals were detected using SuperSignal West pico Chemiluminescent Substrate Kit (Thermo Scientific, Waltham, MA, USA).

3. RESULTS

Protein, Oil, and Fatty Acid Analysis. The protein content in seeds of Daewon, Saedanbaek, WS22 and WS15, was

DOI: 10.1021/acs.jafc.5b03196
J. Agric. Food Chem. 2015, 63, 7134−7142

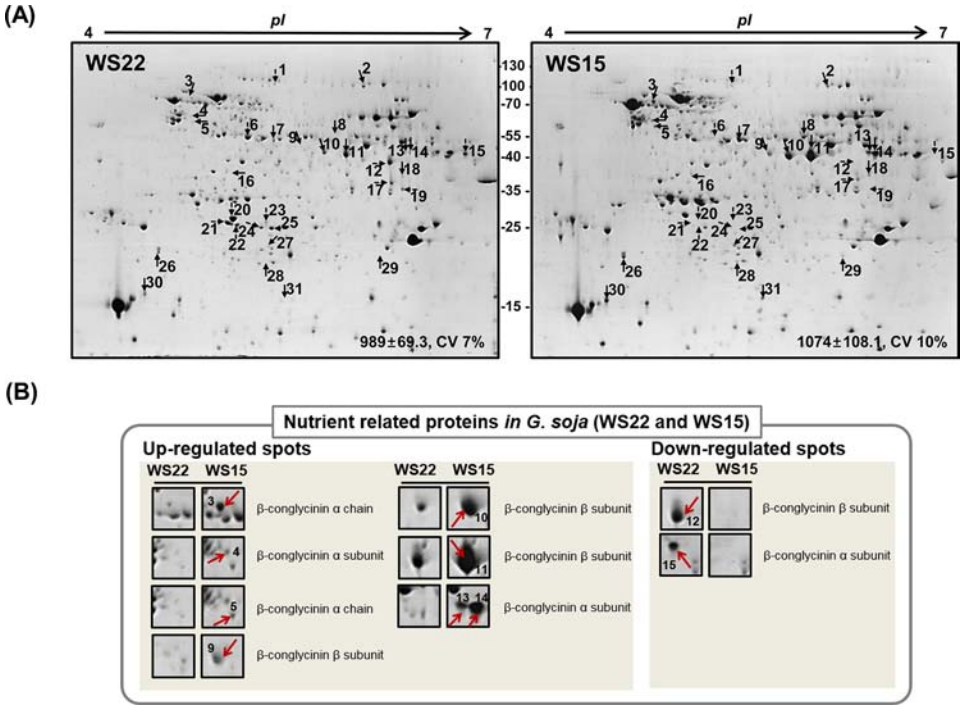

Figure 2. (A) Representative 2D gels of PSS fractions of WS22 and WS15. (B) Enlarged view of the differentially expressed protein spots.

39.2, 47.9, 46.9, and 56.5%, respectively, whereas the oil content was 19.7, 16.3, 10.9, and 6.9%, respectively (Figure S1A). Out of the total 17 amino acids analyzed, only glutamate and arginine showed significant differences between Daewon and Saedanbaek (Table S1).

A total of five FA content levels were analyzed in seed cultivars of *G. max* and *G. soja* including palmitic acid (C16:0), stearic acid (C18:0), oleic acid (C18:1), linoleic acid (C18:2), and linolenic acid (C18:3). The content of linoleic acid was highest among all FAs analyzed, constituting 50.3, 57.9, 56.7, and 56.6% in Saedanbaek, Daewon, WS22, and WS15, respectively (Figure S1B). Contents of palmitic acid and stearic acid were almost similar in *G. max* and *G. soja*. In the case of the *G. max* seeds, significant differences in the contents of oleic acid and linolenic acid were observed, whereas *G. soja* seeds contained an almost similar concentration of these two FAs. The contents of oleic acid and linolenic acid were 24.6 and 10.6% in Saedanbaek, respectively, whereas they were 18.7 and 9.3% in Daewon. In case of *G. soja* cultivars, these were 10.5 and 10.4% in WS22 and 18.1 and 18.5% in WS15, respectively (Figure S1B).

SDS-PAGE Analysis of Daewon and Saedanbaek Seed Proteins. Following the observation that there are significant differences in the protein and oil contents, total seed proteins were isolated from Daewon and Saedanbaek and resolved on SDS-PAGE. In each cultivar, approximately 30 bands were observed, ranging from 12−130 kDa, of which two polypeptides of ∼19 and 35 kDa were the most abundant, representing the major SSPs in soybean. Addition of 0.1% PS precipitated major SSPs in the pellet fractions, thus allowing the enrichment of rare or low-abundance proteins (LAPs) in the PSS fraction (lanes 3 and 6, Figure S2A).[17]

Comparative 2DGE Proteome Analysis of Two *G. max* Cultivars. Using ImageMaster2DPlatinum software, a total of 1045 ± 48.8 (coefficient of variation, CV = 5%) and 1144 ± 24.4 (CV = 2%) spots were detected in the 2D gels of Daewon and Saedanbaek, respectively (Figures 1A and S3). Of these spots, a total of 71 differential spots were identified, wherein 39 and 32 spots showed increased and decreased abundance, respectively, in Saedanbaek compared to Daewon (Figure 1A). MALDI-TOF/TOF MS analysis of the 71 differential spots resulted in confident assignment of 48 spots (Tables S2 and S3). Gene ontology (GO) analysis of the differentially expressed protein spots showed that up-regulated proteins in protein-rich Saedanbaek were associated with nutrient reservoir activity and majorly included SSPs (53%; spots 8, 12, 14−16, 18, 19, 21, 22, 24, 29−32, and 42−44), seed maturation proteins (spots 33, 36, 45, and 51), and trypsin inhibitors (spots 41, 47, and 48). Out of the total 53% nutrient-related proteins, nine were identified as different 2DGEs of glycinin and three as β-conglycinin. Except for the α' subunit of β-conglycinin (spot 1) and glycinin G2 (spot 26), the rest of the 2DGEs of β-conglycinin and glycinin were increased in abundance in Saedanbaek. GO functional annotation of the identified proteins showed two major categories: nutrient-related (42.6%) and metabolism-related (14.8%) proteins in Saedanbaek. In contrast, the up-regulated proteins in oil-rich Daewon were mainly associated with the proteasome core complex and ubiquitin-dependent protein catabolic processes such as proteasome subunit alpha type (spot 27) and UDP-glucose pyrophosphorylase 2 (spot 9) (Figure 1B and Table S3).

Validation of the Results in Two *G. soja* Cultivars. To validate the above findings in *G. max* cultivars, the same approach was applied to *G. soja* cultivars: WS22 and WS15. SDS-PAGE of WS22 and WS15 proteins showed significant depletion of SSPs in the pellet fractions (lanes 4 and 7, Figure S2B). 2DGE analysis of the PSS fractions of WS22 and WS15 revealed a total of 989 ± 69.3 (CV = 7%) and 1074 ± 108.1 (CV = 10%) protein spots, respectively (Figures 2A and S3). A comparison of the 2D gels of WS22 and WS15 proteins identified a total of 53 differentially expressed spots, wherein 38

DOI: 10.1021/acs.jafc.5b03196
J. Agric. Food Chem. 2015, 63, 7134−7142

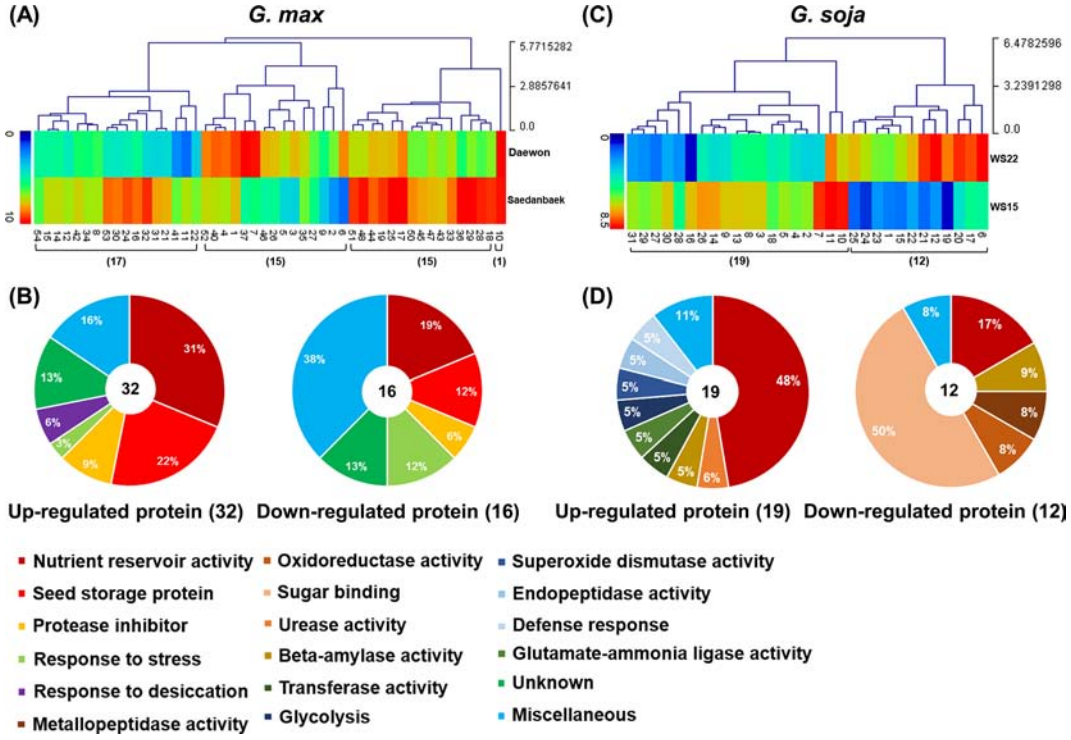

Figure 3. (A) Hierarchical clustering (HCL) analysis of the differentially expressed proteins of *G. max* (Daewon and Saedanbaek) and *G. soja* (WS15 and WS22). For HCL, percentage spot volumes for each spot were calculated using ImageMaster 2D Platinum software and subsequently log-transformed to base 2. Clustering was carried out using MultiExperiment Viewer (MeV) software. (B) GO enrichment analysis of the identified differentially expressed proteins.

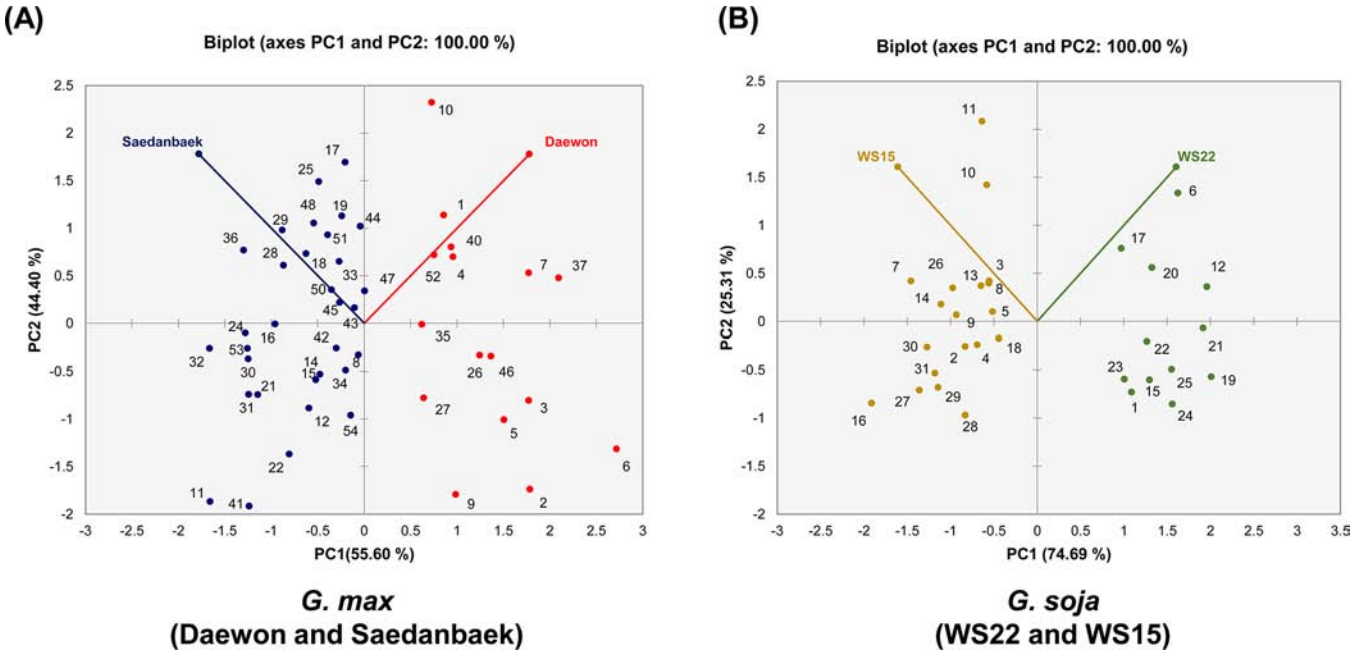

Figure 4. Principal component analysis of the differentially expressed proteins of (A) Daewon and Saedanbaek and (B) WS22 and WS15. Two principal components formed accounted for 100% cumulative variance in both the data sets.

and 15 had increased and decreased abundance, respectively, in WS15 compared to WS22 (Figure 2A). Protein assignment by MALDI-TOF/TOF MS and their GO annotation revealed a similar trend as observed in the *G. max* cultivars (Tables S4 and S5). Protein spots showing increased abundance in protein-rich WS15 cultivar were mainly SSPs with nutrient reservoir activity (spots 3−5, 9−14, and 26), beta-amylase activity (spot 7), and urease activity (spot 2), whereas in oil-rich WS22 cultivar, proteins having increased abundance were mainly involved in the sugar binding activity (spots 20−25, Figure 2B and Table S5).

Hierarchical Clustering and PCA Analysis. To analyze the expression pattern of differential protein spots in protein- versus oil-rich cultivars of *G. max* and *G. soja*, normalized spot

DOI: 10.1021/acs.jafc.5b03196
J. Agric. Food Chem. 2015, 63, 7134−7142

volumes of identified differentially expressed spots were calculated using the ImageMaster software. The obtained values for each spot were subsequently transformed to its base 2 logarithm and finally the obtained $\log_2$ values of spots were used for hierarchical clustering using MeV software (ver. 4.9.0). A total of four and two clusters were formed on the basis of the similar expression pattern in *G. max* and *G. soja*, respectively (Figures 3A and 3C). Functional groups, associated with the up- and down-regulated proteins in *G. max* and *G. soja* are depicted Figure 3B,D, respectively. To identify the protein groups responsible for correlated variations, the differential data set was subjected to PCA. Two principal components, PC1 and PC2, contained 55.6 and 44.4% cumulative variance in *G. max* (Figure 4A) and 74.69 and 25.31% in *G. soja*, respectively (Figure 4B). The distribution of spots in two PCs was highly pronounced, suggesting significant differences in the spot volumes of the differential protein spots between protein- versus oil-rich soybean seed cultivars.

Western Blots Confirmed Differential Regulation of SSPs in Protein- versus Oil-Rich Seed Cultivars. Western blotting was carried out to confirm the differential modulation of SSPs in Daewon and Saedanbaek seeds using antibodies against β-conglycinin α subunit, β-conglycinin α' subunit, β-conglycinin β subunit, and glycinin acidic chain. As expected, very strong signals of β-conglycinin α subunit, β-conglycinin α' subunit, and glycinin acidic chain were seen in the total and PSP fractions, and no differences could be observed, which might be due to the saturation of the signal even though only 25 μg of proteins were loaded into each lane (Figure S4). Even in the PSS fraction, no significant modulation of SSPs was observed in Daewon and Saedanbaek (Figure 5A). At first, use of a high concentration of primary antibody might be expected to be one of the possible causes of these strong signals observed in the Western blots. Therefore, to check the effect of primary antibodies, different dilutions of primary antibodies ranging from 1:10 000−1:80 000 were tried; however, even at the lowest concentration used (1:80 000), no differential expression of these SSPs were observed in the Western blots of total, PSS, and PSP fractions (Figure S5). Therefore, to further detect the differential expression, soybean proteins were fractionated as tofu and whey fractions. Surprisingly, even in the tofu fraction, no differences in the expression pattern of the glycinin and β-conglycinin were observed (Figure 5B). However, when the whey fractions of Daewon and Saedanbaek seeds were analyzed, differences in all the subunits of β-conglycinin were observed (Figure 5C). All the subunits of β-conglycinin including α subunit, α' subunit, and β subunit showed higher expression in the Saedanbaek in comparison with Daewon (Figure 5C). The fold change of expression between Daewon and Saedanbaek was highest for the α' subunit of β-conglycinin and lowest for the β subunit of β-conglycinin (Figure 5C). In the case of glycinin acidic chain, no differences were observed even in the whey fraction, suggesting that it does not contribute to the increased protein content in soybean cultivars.

4. DISCUSSION

The commercial importance of soybean seeds is primarily due to their high protein and oil content. Therefore, our first study objective was to investigate the total protein and oil content in the seed cultivars of *G. max* (cv. Daewon and Saedanbaek) and *G. soja* (cv. WS22 and WS15). Our results showed that of *G. max* cultivars, Saedanbaek is rich in protein, whereas Daewon is rich in oil content. In the case of *G. soja*, WS15 contained more

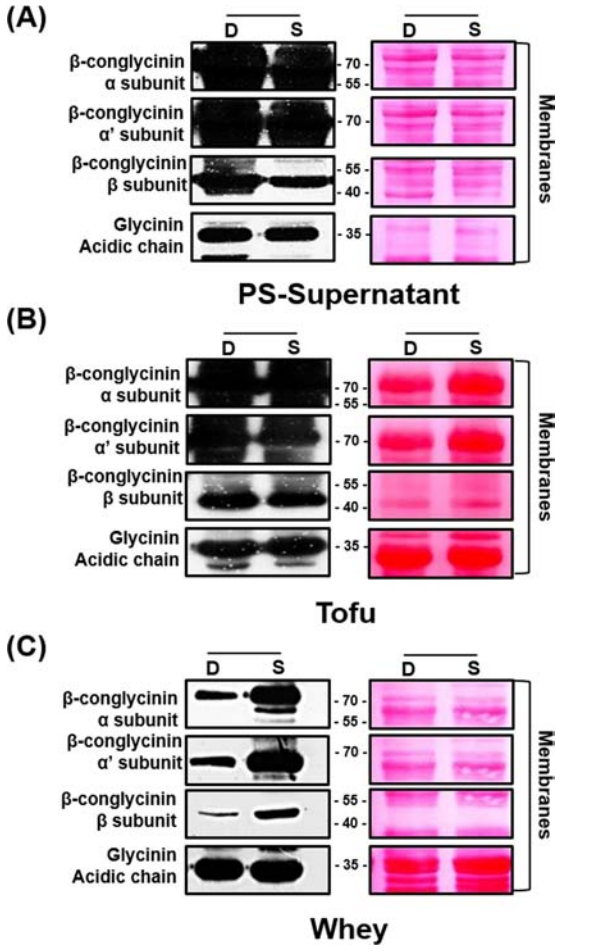

Figure 5. Immunoblotting of the Daewon and Saedanbaek proteins in different protein fractions using β-conglycinin and glycinin antibodies. A total of 25 μg of protein was loaded in each lane of 14% SDS-PAGE, and then the proteins were transferred to a PVDF membrane. After blocking in 5% skim milk, membrane was incubated first with 1:10 000 dilutions of primary antibody and second with 1:10 000 dilutions of secondary antibody. Blot was developed using Super signal Westpico chemiluminescent substrate kit (Thermo Scientific).

protein than did WS22. These results suggested that the selected cultivars of *G. max* and *G. soja* differ in the total protein and oil content significantly and hence can be used for analyzing their proteome as high-protein and high-oil cultivars. FAs are important constituents of the oil, determining the quality of the oil for human consumption. The commercial application of the soybean oil is due to its unique FAs composition. Linoleic acid and linolenic acids are polyunsaturated FAs (PUFA), and both are essential FAs because human beings are not able to synthesize these FAs.

PS Precipitation Leads to Enrichment of LAPs in the PSS Fraction. Soybean seeds are rich in SSPs including different subunits of glycinin and β-conglycinin.[1] These SSPs are major HAPs of the seeds that inhibit the detection and identification of LAPs. It has been shown that without incorporation of any depletion method identification of SSPs can reach up to 80% resulting in loss of time, efforts, and resources. Because LAPs are crucial components of the signaling and regulation machinery in cells, their identification might provide a better picture of the seed physiology. In the past few years, several methods have been developed to reduce or completely deplete these HAPs from the total seed proteins

DOI: 10.1021/acs.jafc.5b03196
J. Agric. Food Chem. 2015, 63, 7134−7142

with an aim to enhance the detection and identification of LAPs.[15−17] These methods are based on the specific depletion of SSPs using 40% isopropanol,[15] 10 mM calcium,[16] or 0.1% PS.[17] Here, we used the PS method for the depletion of SSPs and concurrently enrichment of the LAPs. After PS treatment, proteins were resolved by high-resolution 2DGE to enhance the detection of LAPs. Percent CV for different replicates of 2DGE of each sample were calculated as 5 and 2%, respectively, for Daewon and Saedanbaek, representing high reproducibility of the used PS method. 2DGE followed by MS identification of PSS fractions of *G. max* and *G. soja* showed that out of the total 79 identified proteins (48 from *G. max* and 31 from *G. soja*), only 30% (24 spots) were identified as SSPs (i.e., different 2DGEs/subunits of glycinin and β-conglycinin), validating the efficacy of PS precipitation method in the enrichment of LAPs. Enrichment of LAPs by isopropanol or calcium-based depletion methods has also been shown previously. Using 10 mM calcium, 541 LAPs were detected, of which 197 showed more than 2.5-fold enrichment after isopropanol treatment.[15] In this study, identified LAPs in *G. max* and *G. soja* included different 2DGEs of sucrose-binding proteins, trypsin inhibitors, seed maturation proteins, seed biotin-containing proteins, seed-biotinylated proteins, urease, beta-amylase, glutamine synthetase, phosphoglycerate kinase, superoxide dismutase, proteasome subunit beta type, stress-induced protein SAM22, and lectins (Tables S3 and S5). In addition to these proteins, 15 spots were identified as uncharacterized proteins. As the annotation suggest, these proteins are not yet characterized most probably because of their masking by HAPs that hinders their identification and characterization. Moreover, a few novel proteins including Ran-binding protein 1 homologue a (spot 25, *G. max*), and tau-class glutathione S-transferase (spot 29, *G. soja*) were also identified, and these have not been reported previously in the matured-seed proteome. A more comprehensive identification of PSS proteins in a future study is likely to identify many more novel proteins, which can increase our understanding of the seed physiology.

Up-Regulated Proteins in High Protein Cultivars Were Mainly SSPs. 2DGE analysis followed by MS identification of the differentially expressed proteins showed a similar trend on accumulation of SSPs in the high-protein cultivars of *G. max* and *G. soja*. Although a similar trend of SSPs accumulation was observed in the high-protein cultivars, a contrasting pattern of accumulation of SSPs was observed in WS15 and Saedanbaek. In *G. soja*, only different subunits of β-conglycinin were identified with no identification of glycinin subunits, whereas in the case of *G. max*, the total number of glycinin subunits was three times higher than that of β-conglycinin. It has been shown that the ratio of glycinin and β-conglycinin is important for the texture of the tofu.[23] Similar results were also observed in a comparative study of *G. max* and *G. soja* seed where less 2DGEs of glycinin were observed in *G. soja*.[11] In *G. max*, 32 2DGEs of glycinin were observed, whereas in *G. soja*, only 23 2DGEs could be detected. These results suggest that the protein-rich Saedanbaek cultivar accumulates a higher amount of SSPs than do oil-rich Daewon seeds. This finding is in line with a previous observation that the amount of either β-conglycinin or/and glycinin is associated with protein-rich seeds.[24]

Recently, Xu and co-workers compared the protein profiles of four soybean cultivars.[8] A comparison of the results of this study with their study showed 15 common proteins identified in both studies, with 25 and 39 unique proteins in the previous and current study, respectively (Figure S6). Common proteins were divergent in nature and included glycinin A1aBx subunit, dehydrin, sucrose-binding protein-like, glycinin G4 allergen Gly m Bd 28 K, and beta-conglycinin alpha subunit. Unique proteins identified in this study were mainly stress related, whereas the unique proteins identified in the previous study were associated with sugar metabolism. These differences might be cultivar specific and were probably due to the use of different cultivars in this and the previous study. In this study, we used Saedanbaek and Daewon cultivars whereas Jiyu-73 and Zhonghuang-13 cultivars were used in the previous study.[8]

Western Blotting Confirmed the Association of SSPs with the Enhanced Protein Amount. Our findings showed significant changes in the abundance of glycinin and β-conglycinin between high- and low-protein cultivars of *G. max* and *G. soja*. A previous proteomic study also found higher accumulation of SSPs in the protein-rich cultivars. However, because there is high variability in MS results, it is always advisible to have some confirmatory experiments. Therefore, here we used Western blotting to confirm the association of SSPs with enhanced protein amount. Although PS precipitation led to significant depletion of the SSPs from the PSS fraction, we could not visualize any differential expression of these SSPs in the PSS fraction of Daewon and Saedanbaek using Western blotting approach (Figure 5A). Therefore, to further analyze the differential modulation of the SSPs, a novel approach was employed. Soybean seeds are being largely used for the production of tofu. The precipitated proteins are used for tofu production, whereas rest of the proteins is washed away as whey. Therefore, we used both Daewon and Saedanbaek seeds for the production of tofu, and both tofu and whey protein samples were analyzed by Western blotting. Even though the total protein and SSP amount were higher in the Saedanbaek as compared with those in Daewon, no differences in the amount of SSPs in the tofu fractions were observed. One of the possible explanations of this could lie in the tofu-making procedure. Tofu production involves precipitation of proteins using $MgSO_4$, and because the same amount of $MgSO_4$ (3%, unsaturated concentrations) was used for precipitation of seed proteins, it is expected that an equal amount of seed proteins are precipitated from both Daewon and Saedanbaek seeds. Thus, the rest of the proteins come out in the whey fraction. Using this methodology, we found the differential expression of the SSPs, suggesting the efficacy of the used approach. Taken together, our results confirm that the high protein content in some of soybean cultivars is due to the accumulation of SSPs.

Established Differential Protein Profiles Provide a Possible Explanation for Soybean Cultivars Differing in Protein- versus Oil-Rich Seeds. Urease enzymes are involved in the degradation of urea to form ammonia and carbon dioxide.[25,26] The ammonia thus formed is converted into glutamine by the action of glutamine synthetase.[25] Surprisingly, both urease and glutamine synthetase proteins showed increased abundance in seeds of the protein-rich cultivars Saedanbaek and WS15 (Tables S3 and S5), including one urease-activating protein, namely, Ni-binding urease accessory protein UreG found in Saedanbaek. Urease accessory proteins are involved in the activation of urease by incorporating nickel ions to the active site of urease, which is critical for urease activity.[26] Up-regulation of glutamine synthetase in a high-protein cultivar of soybean was also observed previously.[8] Taken together, increased accumulation

DOI: 10.1021/acs.jafc.5b03196
J. Agric. Food Chem. 2015, 63, 7134−7142

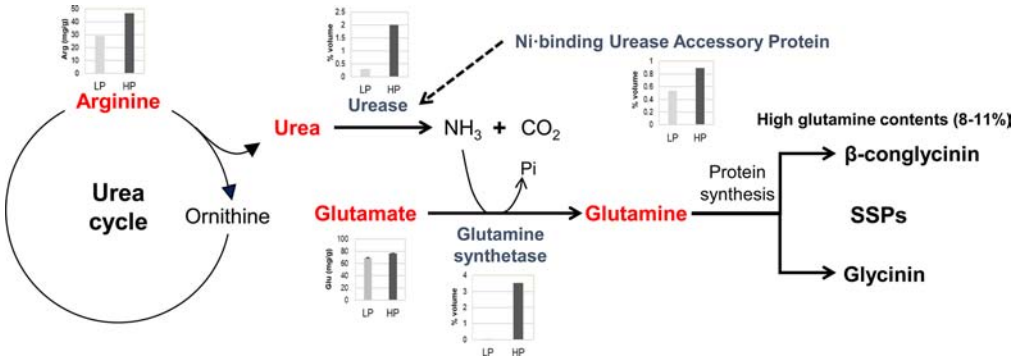

Figure 6. A hypothetical model explaining why some soybean seeds are rich in proteins. Up-regulation of urease, Ni-binding urease accessory protein, and glutamine synthetase suggest higher production of urea and thus glutamine in the high-protein cultivar. This was further confirmed by the amino acid analysis, which showed the higher concentration of glutamate and arginine, precursors of urea and glutamine, in high-protein cultivars. Glutamine thus formed is used for the synthesis of SSPs that are rich in glutamine (8−11%). On the basis of these results, it can be concluded that glutamine concentration can be the determining factor of total protein contents in soybean seeds.

of these proteins indicates the production of a higher amount of glutamine in the protein-rich cultivars (Saedanbaek and WS15) in comparison with that in the Daewon and WS22. Interestingly, soybean SSPs, which govern the total protein content of soybean seeds, are rich (8−11%) in the amino acid glutamine, whereas the glutamine content of other proteins is less than 2−5%. On the basis of these results, it could be proposed that glutamine content is likely to be one of the factors involved in determining the total amount of SSPs accumulation in soybean seeds. Because the amount of SSPs is directly associated with the increased protein amount, restriction of the glutamine concentration could be one of the limiting factors determining the amount of protein accumulation in seeds. Moreover, analysis of amino acid contents in the Daewon and Saedanbaek seeds also revealed higher concentrations of glutamate and arginine in Saedanbaek. Because both of these amino acids are the precursors of urea and glutamine, their higher concentrations in Saedanbaek further suggest the increased production of urea and thus glutamine in high-protein cultivar Saedanbaek (Figure 6). Overall, it can be speculated the high protein content in the protein-rich cultivars is potentially due to a higher amount of glutamine, which is the result of the higher activities of urease, its accessory proteins, and glutamine synthetase.

In the case of the high-oil cultivar Daewon, increased accumulation of many biotinylated proteins (spots 5−7) including seed biotin-containing protein SBP65 and seed biotinylated protein 68 kDa isoform was observed. The exact role/functions of these SBPs remain largely unclear in plants; however, the majority of the biotinylated enzymes of plants like acetyl-CoA carboxylase, 3-methylcrotonoyl-CoA carboxylase, propionyl CoA carboxylase, and pyruvate carboxylase are involved in the FA biosynthesis, suggesting similar functions of SBPs in plants.[27,28] Observed increased abundance of these biotinylated proteins in the oil-rich cultivars may partially explain the high accumulation of oil in Daewon and WS22 seeds in comparison with that in Saedanbaek and WS15.

Taken together, our results confirmed that the protein-rich cultivars Saedanbaek and WS15 accumulate higher amounts of SSPs including various subunits of glycinin and β-conglycinin. Moreover, our results also indicate that the levels of glutamine might be one of the potential factors for SSPs synthesis, which determines the total protein content in soybean seeds.

■ ASSOCIATED CONTENT

Supporting Information

The Supporting Information is available free of charge on the ACS Publications website at DOI: 10.1021/acs.jafc.5b03196.

Comparative analysis of protein, oil, and fatty acids in *G. max* and *G. soja* seeds; SDS-PAGE analysis of *G. max* and *G. soja* seed proteins; biological replicates of 2-D gels of PSS fraction proteins of *G. max* and *G. soja* seeds; immunoblotting of the total and PSP fractions using SSPs antibodies and of the β-conglycinin α subunit with different dilutions of antibodies; Venn diagram of the identified proteins in this study with the previous published study (Xu et al.);[8] amino acid profiling of Daewon and Saedanbaek seeds; percentage volumes of differentially expressed spots from the three biological replicates of Daewon and Saedanbaek seeds; identification of differentially expressed *G. max* proteins by MALDI-TOF/TOF and MS/MS; percentage volumes of differentially expressed spots from the three biological replicates of WS22 and WS15; and identification of differentially expressed *G. soja* proteins by MALDI-TOF/TOF and MS/MS. (PDF)

■ AUTHOR INFORMATION

Corresponding Author

*E-mail: stkim71@pusan.ac.kr. Fax: +82-55-350-5509.

Funding

This work was supported by a grant from the Next-Generation Bio Green 21 Program (no. PJ011070032015) and National Agenda Programs for Agricultural R&D of Rural Development Administration (PJ01002002), Republic of Korea.

Notes

The authors declare no competing financial interest.

■ ABBREVIATIONS USED

2D GE, 2D gel electrophoresis; FA, fatty acid; HAP, high-abundance protein; LAP, low-abundance protein; PS, protamine sulfate; PSP, protamine sulfate pellet; PSS, protamine sulfate supernatant; SSP, seed-storage protein

■ REFERENCES

(1) Natarajan, S. S. Analysis of soybean seed proteins using proteomics. *J. Data Min. Genomics Proteomics* **2014**, *5*, 1.

DOI: 10.1021/acs.jafc.5b03196
J. Agric. Food Chem. 2015, 63, 7134−7142

(2) Xiao, C. W. Health effects of soy protein and isoflavones in humans. *J. Nutr.* **2008**, *138*, 1244S−1249S.
(3) Koo, S. C.; Bae, D. W.; Seo, J. S.; Park, K. M.; Choi, M. S.; Kim, S. H.; Kim, K. M.; Chung, J. I.; Kim, M. C. Proteomic analysis of seed storage proteins in low allergenic soybean accession. *Han'guk Eungyong Sangmyong Hwahakhoeji* **2011**, *54*, 332−339.
(4) Rajjou, L.; Duval, M.; Gallardo, K.; Catusse, J.; Bally, J.; Job, C.; Job, D. Seed germination and vigor. *Annu. Rev. Plant Biol.* **2012**, *63*, 507−533.
(5) Miernyk, J. A.; Hajduch, M. Seed proteomics. *J. Proteomics* **2011**, *74*, 389−400.
(6) Hajduch, M.; Ganapathy, A.; Stein, J. W.; Thelen, J. J. A Systematic Proteomic Study of Seed Filling in Soybean. Establishment of high-resolution two-dimensional reference maps, expression profiles, and an interactive proteome database. *Plant Physiol.* **2005**, *137*, 1397−1419.
(7) Agrawal, G. K.; Hajduch, M.; Graham, K.; Thelen, J. J. In-depth investigation of the soybean seed-filling proteome and comparison with a parallel study of rapeseed. *Plant Physiol.* **2008**, *148*, 504−518.
(8) Xu, X. P.; Liu, T.; Dong, X. B.; Shen, S. H.; Qu, L. Q. Integrated and comparative proteomics of high-oil and high protein soybean seeds. *Food Chem.* **2015**, *172*, 105−116.
(9) Gomes, L. S.; Senna, R.; Sandim, V.; Sliva-Neto, M. A. C.; Perales, J. E. A.; Zingali, R. B.; Soares, M. R.; Fialho, E. Four conventional soybean [Glycine max (L.) Merrill] seeds exhibit different protein profiles as revealed by proteomic analysis. *J. Agric. Food Chem.* **2014**, *62*, 1283−1293.
(10) Wilson, K. A.; Rightmire, B. R.; Chen, J. C.; Tan-Wilson, A. L. Differential proteolysis of glycinin and β-conglycinin polypeptide during soybean germination and seedling growth. *Plant Physiol.* **1986**, *82*, 71−76.
(11) Agrawal, G. K.; Jwa, N. S.; Lebrun, M. H.; Job, D.; Rakwal, R. Plant secretome: unlocking secreted proteins. *Proteomics* **2010**, *10*, 799−827.
(12) Natarajan, S. S.; Xu, C.; Bae, H.; Caperna, T. J.; Garrett, W. M. Characterization of storage proteins in wild (*Glycine soja*) and cultivated (*Glycine max*) soybean seeds using proteomic analysis. *J. Agric. Food Chem.* **2006**, *54*, 3114−3120.
(13) Kim, Y. J.; Lee, S. J.; Lee, H. M.; Lee, B. W.; Ha, T. J.; Bae, D. W.; Son, B. Y.; Kim, Y. H.; Baek, S. B.; Kim, Y. C.; Kim, S. G.; Kim, S. T. Comparative proteomics analysis of seed coat from two black colored soybean cultivars during seed development. *Plant Omics* **2013**, *6*, 456−463.
(14) Gupta, R.; Min, C. W.; Kim, S. W.; Wang, Y.; Agrawal, G. K.; Rakwal, R.; Kim, S. G.; Lee, B. W.; Ko, J. M.; Baek, I. Y.; Bae, D. W.; Kim, S. T. Comparative investigation of seed coats of brown-versus yellow-colored soybean seeds using an integrated proteomics and metabolomics approach. *Proteomics* **2015**, *15*, 1706−1716.
(15) Natarajan, S. S.; Krishnan, H. B.; Lakshman, S.; Garrett, W. M. An efficient extraction method to enhance analysis of low abundant proteins from soybean seed. *Anal. Biochem.* **2009**, *394*, 259−68.
(16) Krishnan, H. B.; Oehrle, N. W.; Natarajan, S. S. A rapid and simple procedure for the depletion of abundant storage proteins from legume seeds to advance proteome analysis: A case study using Glycine max. *Proteomics* **2009**, *9*, 3174−3188.
(17) Kim, Y. J.; Wang, Y.; Gupta, R.; Kim, S. W.; Min, C. W.; Kim, Y. C.; Park, K. H.; Agrawal, G. K.; Rakwal, R.; Choung, M. G.; Kang, K. Y.; Kim, S. T. Protamine sulfate precipitation method depletes abundant plant seed-storage proteins: A case study on legume plants. *Proteomics* **2015**, *15*, 1760−1764.
(18) Christie, W. W. Preparation of ester derivatives of fatty acids for chromatographic analysis. In *Advances in Lipid Methodology-Two*; Christie, W. W., Ed.; Oily Press: Dundee, Scotland, 1993; pp 69−111.
(19) Kim, S. G.; Wang, Y.; Lee, C. H.; Mun, B. G.; Kim, P. J.; Lee, S. Y.; Kim, Y. C.; Kang, K. Y.; Rakwal, R.; Agrawal, G. K.; Kim, S. T. A comparative proteomics survey of proteins responsive to phosphorous starvation in roots of hydroponically-grown rive seedlings. *Han'guk Eungyong Sangmyong Hwahakhoeji* **2011**, *54*, 667−677.
(20) Cai, T. D.; Chang, K. C.; Shih, M. C.; Hou, H. J.; Ji, M. Comparison of bench and production scale methods for making soymilk and tofu from 13 soybean varieties. *Food Res. Int.* **1997**, *30*, 659−668.
(21) Mullin, W. J.; Fregeau-Reid, J. A.; Butler, M.; Poysa, V.; Woodrow, L.; Jessop, D. B.; Raymond, D. An interlaboratory test of a procedure to assess soybean quality for soymilk and tofu production. *Food Res. Int.* **2001**, *34*, 669−677.
(22) Kim, S. T.; Cho, K. S.; Yu, S.; Kim, S. G.; Hong, J. C.; Han, C. D.; Bae, D. W.; Nam, M. H.; Kang, K. Y. Proteomic analysis of differentially expressed proteins induced by rice blast fungus and elicitor in suspension-cultured rice cells. *Proteomics* **2003**, *3*, 2368−2378.
(23) Saio, K.; Kamiya, M.; Watanabe, T. Food processing characteristics of soybean 11S and 7S proteins. *Agric. Biol. Chem.* **1969**, *33*, 1301−1308.
(24) Krishnan, H. B.; Natarajan, S. S.; Mahmoud, A. A.; Nelson, R. L. Identification of glycinin and β-conglycinin subunits that contribute to increased protein content of high-protein soybean lines. *J. Agric. Food Chem.* **2007**, *55*, 1839−1845.
(25) Sirko, A.; Brodzik, R. Plant ureases: Roles and regulation. *Acta. Biochim. Polym.* **2000**, *47*, 1189−1195.
(26) Witte, C. P. Urea metabolism in plants. *Plant Sci.* **2011**, *180*, 431−438.
(27) Natarajan, S. S.; Krishnan, H. B.; Khan, F.; Chen, X.; Garrett, W. M.; Lakshman, D. Analysis of soybean embryonic axis proteins by two-dimensional gel electrophoresis and mass spectrometry. *J. Basic Appl. Sci.* **2013**, *9*, 309−332.
(28) Charles, D. J.; Cherry, J. H. Purification and characterization of acetyl-coa carboxylase from developing soybean seeds. *Phytochemistry* **1986**, *25*, 1067−1071.

DOI: 10.1021/acs.jafc.5b03196
J. Agric. Food Chem. 2015, 63, 7134−7142

Table 1. Data Related to the Concentration of PAHs Solubilized, Mobilized, and/or Biodegraded from Sewage Sludge at the End of Treatment (27 Days)

sample	naphthalene	anthracene	pyrene
initial concn of PAHs in sludge (mg/kg)	408.34 ± 28.58	368.83 ± 22.13	561.30 ± 44.90
concn of PAHs that can be achieved in the washing solution (solid/liquid ratio 1:10 v/v) (mg/L)	40.83 ± 2.86	36.88 ± 2.21	56.13 ± 4.49
concn of PAHs in washing solution after treatment (mg/L)			
AcN	17.78 ± 1.24	36.90 ± 2.21	56.20 ± 4.50
BS	nd[a]	7.26 ± 0.44	12.73 ± 1.02
PAHs in the washing solution after treatment (%)			
AcN	43.55 ± 3.05	100.05 ± 6.00	100.13 ± 8.01
BS	nd	19.68 ± 1.18	22.68 ± 1.81
amount of PAHs that remain in sewage sludge after treatment (mg/kg)			
AcN	230.52 ± 16.14	nd	nd
BS	6.92 ± 0.48	190.81 ± 11.45	389.32 ± 31.15
PAHs that remain in sewage sludge after treatment (%)			
AcN	56.45 ± 3.95	nd	nd
BS	1.69 ± 0.12	51.73 ± 3.10	69.36 ± 5.55
amount of PAHs mobilized (mg/kg)			
AcN	177.81 ± 12.45	368.83 ± 22.13	561.30 ± 44.90
BS	401.42 ± 28.10	178.02 ± 10.68	171.98 ± 13.76
amount of PAHs mobilized (%)			
AcN	43.55 ± 3.05	100.00 ± 6.00	100.00 ± 8.00
BS	98.31 ± 6.88	48.27 ± 2.90	30.64 ± 2.45
amount of PAHs biodegraded (mg/kg)			
AcN	nd	nd	nd
BS	401.42 ± 28.10	105.45 ± 6.33	44.68 ± 3.57
PAHs biodegraded (%)			
AcN	nd	nd	nd
BS	98.31 ± 6.88	28.59 ± 1.72	7.96 ± 0.64

[a]nd, not detected.

their biodegradation. Biosurfactants possess different chemical structures consisting of glycopeptides, lipopeptides, glycolipids, neutral lipids, and fatty acids and in comparison with chemical surfactants they are less toxic, more biodegradable, and effective at extreme operational conditions.[10]

Some biosurfactants also are able to stabilize emulsions between hydrophilic and hydrophobic solutions. For instance, biosurfactants produced by *Lactobacillus pentosus* exhibited a strong emulsion capacity when added to kerosene/water emulsions,[11] gasoline/water emulsions,[12] octane/water emulsions,[13] rosemary oil/water emulsions,[14] and fluorene/water emulsions.[15]

In the literature have been reported several works about the utilization of chemical surfactants for the bioremediation of contaminated soils[16,17] because these are cheaper and more available to the consumer than biosurfactants produced biotechnologically. Therefore, few works deal with the utilization of biosurfactants for the biocorrection of contaminated soils or sludge.[18] Shin et al.[19] have used a rhamnolipid biosurfactant produced by the genus *Pseudomonas* to remediate phenanthrene-contaminated soil by the combination of solubilization and biodegradation processes, whereas Das and Mukherjee[20] studied the utilization of pyrene as the sole source of carbon by *Bacillus subtilis* and *Pseudomonas aeruginosa* strains as well as the role of biosurfactants in enhancing the bioavailability of this organic contaminant, although most works focus on studying the solubilization of PAHs in aqueous solutions in the presence of biosurfactants.[21,22]

This work aims to study the bioremediation of sewage sludge provided by a municipal wastewater treatment plant and contaminated with high doses of PAHs. The bioremediation processes will be performed using a low-cost biosurfactant extracted form corn steep liquor, and the biodegradation of the persistent organic pollutants will be studied by applying different kinetic models.

MATERIALS AND METHODS

Reagents. Anthracene (99%) and pyrene (98%) were purchased from Acros Organics (Morris Plains, NJ, USA).

Naphthalene, acetonitrile (supergradient HPLC grade), and acetone (synthesis grade for contamination of sewage sludge) were supplied by Scharlau (Barcelona, Spain).

Chloroform (stabilized with 50 ppm of amylene as preservative, 99.8%) was purchased from Panreac (Barcelona, Spain).

Corn steep liquor, hexane (Chromasolv, HPLC, ≥97.0%), and acetone (puriss. p.a., ACS reagent, reag. ISO, reag. Ph. Eur., ≥99.5% for ASE extraction) were purchased from Sigma-Aldrich (St. Louis, MO, USA).

Nitrogen (Extrapure 3× (high purity, >99.998%)) was supplied by Praxair (Spain).

Characteristics of the Sewage Sludge. *Composition of Sewage Sludge.* For the determination of inorganic carbon (IC) 0.5 g of sewage sludge was introduced in a muffle at 400 °C during 3 h to eliminate the organic matter contained in the sewage sludge samples, whereas for the determination of organic carbon (OC) and total nitrogen (TN) samples did not undergo this process. An Elemental Analyzer (LECO, CN-2000) was used for carbon and nitrogen determination using infrared (IR) detection and thermal conductivity detection (TCD), respectively.

Scanning Electron Microscope (SEM) Images of Sewage Sludge. Samples were dried, covered with gold, and then observed using a scanning electron microscope (JEOL JSM-6700F FEG), operating at an acceleration voltage of 5.0 kV for secondary-electron imaging (SEI).

Optical Images of Sewage Sludge. The macroviews of sewage sludge samples treated with water, acetonitrile, or biosurfactant

DOI: 10.1021/acs.jafc.5b02346
J. Agric. Food Chem. 2015, 63, 7143−7150

solution were obtained with a regular digital camera (Sony optical SteadyShot) using an Optical Zoom 4× with 26 mm wide-angle lens and 14.1 megapixels.

Contamination of Sewage Sludge. Sewage sludge used in this work was obtained after a secondary wastewater treatment in a local water treatment plant in Galicia (Spain), which was contaminated with a mixture of naphthalene, anthracene, and pyrene. Hence, 250 g of sewage sludge was contacted with different PAHs solubilized in acetone and stirred vigorously for 30 min to promote the homogeneous distribution of persistent organic pollutants. Before mobilization and biodegradation of PAHs was begun, the sewage sludge samples were left to rest for 48 h at 28 °C, to eliminate all of the acetone, in a shaker at 150 rpm. Table 1 includes the initial concentration of PAHs achieved in the sewage sludge after the acetone evaporation.

Characteristics of the Biosurfactant Solution. The biosurfactant used in this work was obtained from a liquid stream of the corn milling industry usually called corn steep liquor (CSL). Prior to the preparation of washing solution, biosurfactant was extracted from CSL, with chloroform, using the methodology proposed by Vecino et al.[23] The efficiency of a biosurfactant is determined by its critical micelle concentration (CMC), which is the point at which micelles start to form; hence, biosurfactant washing solution was formulated with concentration over 2.5 times the CMC (998.5 mg/L).

Mobilization and Biodegradation of PAHs Contained in Sewage Sludge. Sewage sludge (10 g) samples contaminated with PAHs were placed in 250 mL Erlenmeyer flasks together with 100 mL of an aqueous solution containing the lipopeptide biosurfactant. The experiments were conducted in a shaker at 150 rpm, for 27 days at 30 °C. Moreover, acetonitrile (AcN) was used as solvent control extractant under the same conditions.

Analysis of PAHs in the Sewage Sludge by Accelerated Solvent Extraction Process. Sewage sludge samples (around 5 g) were submitted to an extraction process using an accelerated solvent extraction system (Dionex-ASE 200). The empty spaces of extraction tubes were filled with diatomaceous earth. The cell contents (11 mL extraction cell) were extracted during four cycles of 5 min, at 100 °C and 1500 psi, with a hexane/acetone 1:1 (v/v) flush volume of 6 mL (60% of ASE cell capacity) and purged with nitrogen (60 s). The extracts were evaporated to dryness under a gentle stream of nitrogen gas in a TurboVap station (at 35 °C and 12 psi). Subsequently, samples were transferred by adding acetonitrile to reach a final volume of 5 mL, filtered through a 0.45 μm syringe filter, and injected into the HPLC-DAD-FLD system.

Quantification of PAHs in the Liquid Phase by HPLC-DAD-FLD. To analyze the PAHs mobilized to the liquid phase, sewage sludge samples were removed from the washing solution consisting of acetonitrile or biosurfactant, by filtration (PTFE syringe filter). Subsequently, PAHs solubilized in the liquid phase were identified and quantified by high-performance liquid chromatography (HPLC) with diode array detection (DAD) and fluorescence detection (FLD) (Agilent Technologies 1200 series, Germany) using an Envirosep PP column (125 × 4.60 mm) (Phenomenex, Torrance, CA, USA) with the column oven kept at 35 °C. The mobile phase consisted of Milli-Q water/acetonitrile (1:1), the injection volume was 20 μL, and the flow rate was 2 mL/min.

RESULTS AND DISCUSSION

Physicochemical Characterization of Treated Sewage Sludge. In this work, sewage sludge was submitted to a bioremediation process in the presence of lipopeptide biosurfactant, extracted from corn steep liquor, for the removal of naphthalene, anthracene, and pyrene. Table 2 shows the elemental analysis of sewage sludge under different conditions. It was observed that contaminated samples treated with acetonitrile gave the highest percentages of organic and inorganic carbon, whereas the contaminated sewage sludge samples treated with biosurfactant reduced the concentration of organic and inorganic carbon at levels lower than those achieved in the untreated sewage sludge. The same behavior was observed regarding the nitrogen percentage.

Table 2. Elemental Analysis of Sewage Sludge at the Beginning of the Bioremediation Process and after Treatment with Acetonitrile (AcN) or Biosurfactant (BS)

sample	total N (%)	inorganic C (%)	organic C (%)
sewage sludge contaminated	5.39 ± 0.38	3.15 ± 0.22	29.75 ± 2.08
sewage sludge treated with AcN	5.90 ± 0.47	3.19 ± 0.26	32.02 ± 2.56
sewage sludge treated with BS	4.51 ± 0.27	1.80 ± 0.11	28.39 ± 1.70

Figure 1 shows the FTIR spectra of sewage sludge before and after treatment with acetonitrile or biosurfactant, showing a decrease in the main bands for treated samples in comparison with untreated sewage sludge. In addition Figure 2 shows SEM images of untreated and treated sewage sludge; samples containing biosurfactant gave a more homogeneous aspect, with less roughness in comparison with untreated sewage sludge or samples treated with acetonitrile.

On the other hand, Figure 3 shows the macroview aspect of sewage sludge when it was introduced in water, acetonitrile, or biosurfactant solution. It was observed that biosurfactant allowed the homogenization of sewage sludge in water and stabilized the emulsion of the aqueous phase with the sewage sludge. This aspect is consistent with the pictures shown in Figure 2. Otherwise, when the sewage sludge was dissolved in acetonitrile, a clear separation between solid samples and the organic phase was observed (Figure 3b); similar behavior was detected when sewage sludge was dissolved in water in the absence of biosurfactant (Figure 3a).

Bioremediation of Sewage Sludge Contaminated with PAHs. A bioremediation experiment for the decontamination of sewage sludge containing PAHs was developed during 27 days in the presence of a lipopeptide biosurfactant extracted from CSL. During the experiments, solid (sewage sludge) and liquid samples were obtained at several intervals of time to follow the solubilization and the kinetic biodegradation of PAHs. A control consisting of contaminated sewage sludge treated with acetonitrile was included in the study to compare the efficiency of treatment, using biosurfactant, with classical and less ecofriendly washing methodologies.

Table 1 includes data about the amount of PAHs solubilized and biodegraded from sewage sludge as well as the amount of PAHs that remain in the sewage sludge at the end of the treatment (27 days), in comparison with the initial concentration of PAHs contained in the sewage sludge. The amount of PAHs mobilized from sewage sludge was calculated as the difference between the amount of PAHs contained in the sewage sludge at the beginning of the experiment and the amount of PAHs at specific interval of times that remained in the sewage sludge. In Table 1 are included the maximum amounts of PAHs mobilized after 27 days of treatment with acetonitrile and biosurfactant.

Furthermore, Table 1 shows the maximum concentrations of PAHs that could be achieved in the washing solution. These values were calculated by taking into account the amount of PAHs in the sewage sludge before the bioremediation experiments and the liquid−solid ratio used during the bioremediation experiments.

DOI: 10.1021/acs.jafc.5b02346
J. Agric. Food Chem. 2015, 63, 7143−7150

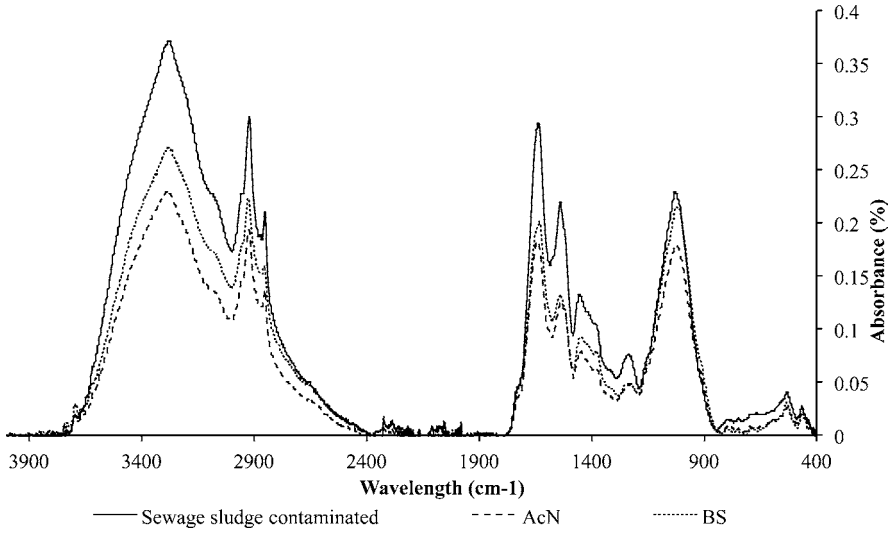

Figure 1. Comparison of the FTIR spectra of sewage sludge (—) without treatment, (- - -) treated with acetonitrile, and (···) treated with biosurfactant.

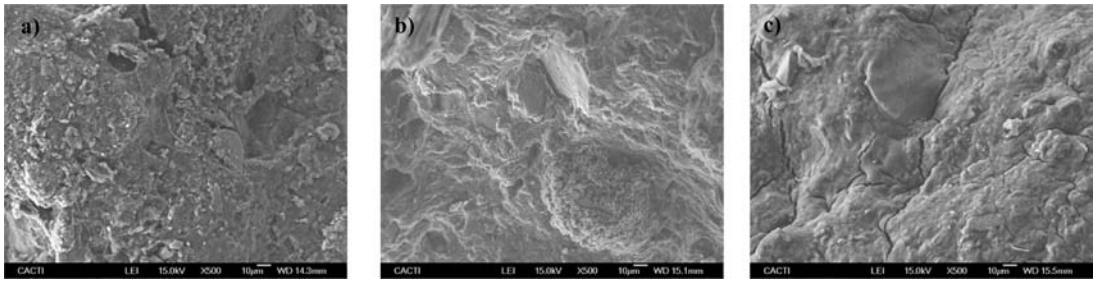

Figure 2. SEM images of the sewage sludge, at ×500 magnification, (a) without treatment, (b) treated with acetonitrile, and (c) treated with biosurfactant.

Figure 3. Optical images of sewage sludge (a) in water, (b) in acetonitrile, or (c) in biosurfactant solution.

In addition, Figures 4 and 5 show the variation in PAH percentages contained in the sewage sludge or in the washing solution, as well as the biodegraded PAH percentages in experiments carried out with acetonitrile or biosurfactant, respectively, at different intervals of time. At the end of the bioremediation experiments the concentration of PAHs in the sewage sludge, in the presence of biosurfactant, was reduced about 98.3, 48.3, and 30.6% for naphthalene, anthracene, and pyrene, respectively, after 27 days of treatment. Probably PAHs were removed from sewage sludge by combining desorption mechanisms induced by the ambiphilic nature of the biosurfactant and the biodegradative processes carried out by the microbial biomass contained in the sewage sludge. Biosurfactants reduce the surface tension between the aqueous phase of sewage sludge and the hydrophobic contaminants through the formation of micelles favoring the sequential solubilization and biodegradation of PAHs contained in the sewage sludge. Thus, the biosurfactant, extracted from CSL, not only promoted the solubilization of PAHs from sewage sludge but also induced the biodegradation of these organic contaminants. For instance, from the 48.3% of anthracene removed from sewage sludge, 19.7% remained in the aqueous phase and 28.6% was biodegraded, whereas 100% of the solubilized naphthalene was biodegraded.

In the current work, it was observed that acetonitrile was able to remove all anthracene and pyrene from sewage sludge, although they remained undigested in the aqueous phase, whereas acetonitrile was able to extract only 43.5% of naphthalene, probably due to the stronger adsorption ability of sewage sludge for naphthalene rather than anthracene and pyrene. Oluseyi et al.[24] also observed that methanol and acetonitrile gave lower extraction yields for naphthalene in comparison with anthracene and pyrene.

DOI: 10.1021/acs.jafc.5b02346
J. Agric. Food Chem. 2015, 63, 7143−7150

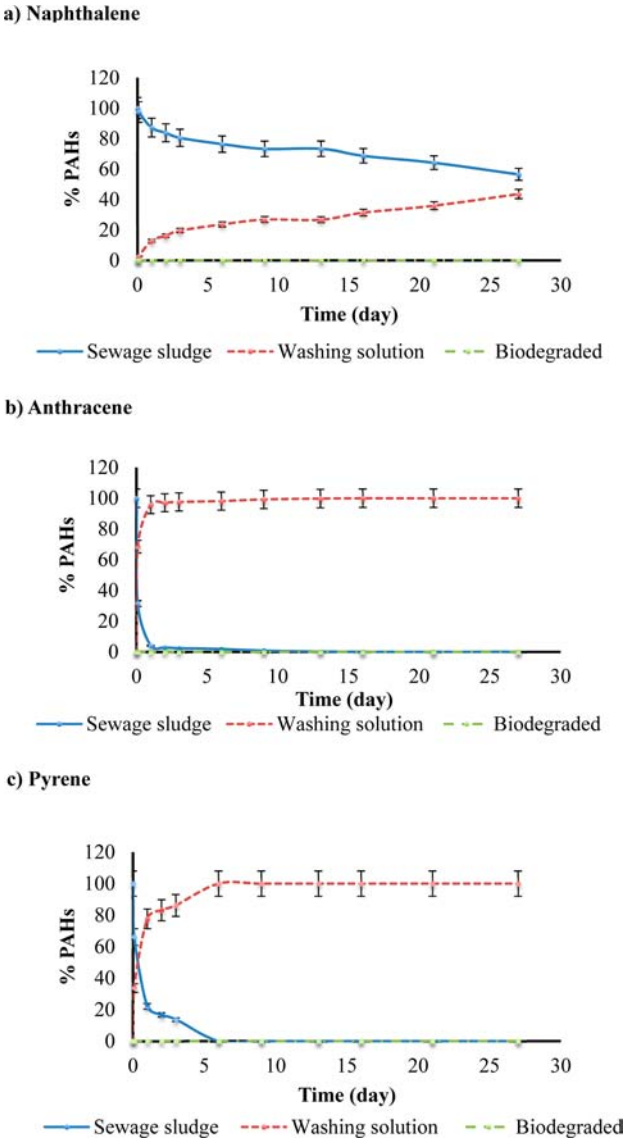

Figure 4. Variation of PAH percentages in sewage sludge and in the washing solution as well as the biodegradation percentages of PAHs in samples treated with acetonitrile.

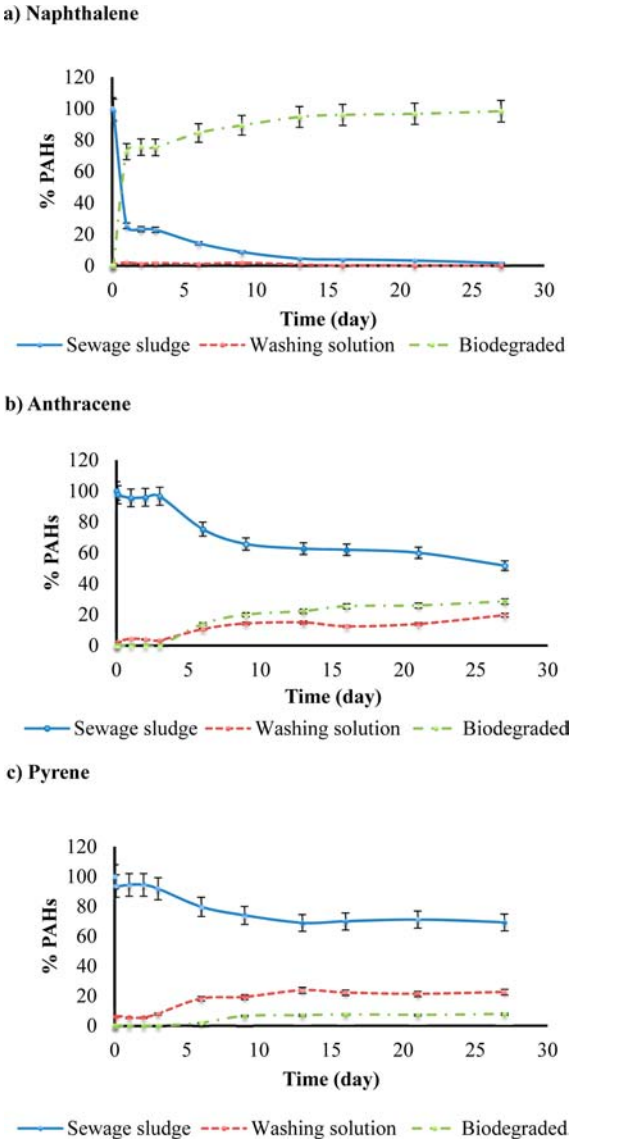

Figure 5. Variation of PAH percentages in sewage sludge and in the washing solution as well as the biodegradation percentages of PAHs in samples treated with biosurfactant.

Remediation methods relying on the immobilization of contamination or its removal may be carried out in place of its formation (in situ) or out of the place of its original location (ex situ).[18] Organic solvents were the first agents used for extracting PAHs from soil, both in laboratory-scale studies and in field scale remediation projects.[25] Some authors have proposed the utilization of physical−chemical methods to remove polycyclic aromatic hydrocarbons from sewage sludge,[26] but in comparison with the utilization of biosurfactants[13] or fermentation process,[27,28] these methods are less ecofriendly. Bacteria able to form biosurfactants are of increasing interest as biosurfactants, have low toxicity, and are easily biodegraded.[18] Moreover, it has been reported that some species, such as white rot fungi (e.g., *Pleurotus ostreatus*), allow high efficiency in the cleanup of soil contaminated with PAHs.[29]

There are few works in the literature dealing with the direct biodegradation of PAHs in soil or sewage sludge; thus, to discuss the results obtained in the current work, references related with the biodegradation of PAHs in aqueous streams will be introduced. Once the PAHs contained in sewage sludge achieve the aqueous phase, the biodegradation of these pollutants could follow a behavior similar to that observed in aqueous streams, obviously with lower biodegradation kinetic rates. Thus, Lima et al.[30] performed consecutive washings of soil contaminated with 200 mg/kg of phenanthrene using different lipopeptide biosurfactants, observing that 80−88% of phenanthrene from soil can be removed using lipopeptide biosurfactant as washing solution.

The results obtained in the current study also are consistent with those achieved by other authors.[31,32] Thus, Jacques et al.[31] reported biodegradation values for pyrene between 24.8 and 36.8%, for phenanthrene between 31.4 and 48.2%, and for anthracene between 24.4 and 71.1% in the presence of *Pseudomoma* species isolated from a petrochemical sludge land farming site, which produced biosurfactants. Additionally, Obayori et al.[32] found that pyrene degradation rates were increased when media were supplemented with CSL, probably not only because the presence of nutrients in CSL can induce the growth rate of *Pseudomona* but also due to the presence in

DOI: 10.1021/acs.jafc.5b02346
J. Agric. Food Chem. 2015, 63, 7143−7150

CSL of biosurfactants that increased the solubilization and biodegradation of pyrene, achieving pyrene biodegradation percentages about 55.5% after 21 days of treatment.

Biodegradation of PAHs: Kinetic Study. Microbial degradation of organic compounds can be defined following kinetic models, typically used to describe the consumption of reagents during a chemical reaction.[33−36]

Usually, microbial degradation of different carbon sources tends to be hyperbolic saturation functions and can be expressed by eq 1:

$$r_p = r_{pmax}\frac{C}{K} + C \quad (1)$$

where r_p is the biodegradation rate, r_{pmax} is the maximum specific biodegradation rate, C is the pollutant concentration, and K is the half-saturation coefficient.

Assuming that the pollutant concentration is much lower than the half-saturation coefficient ($C \ll K$), eq 1 can be converted to eq 2:

$$r_p = r_{pmax}\frac{C}{K} \quad (2)$$

Furthermore, if $K_1 = r_p/K$, a linearized first-order kinetic reaction can be shown, eq 3:

$$\ln C = C_0 + K_1 t \quad (3)$$

Hence, following the first-order kinetic reaction, the biodegradation half-life can be calculated according to eq 4:

$$t_{1/2} = \frac{\ln 2}{K_1} \quad (4)$$

On the other hand, taking into consideration eq 1, if it is assumed that the amount of PAHs contained in the sewage sludge is much higher than the half-saturation constants ($C \gg K$), the biodegradation of PAHs could be described following eq 5, where the biodegradation rate is independent of the concentration of PAHs ($r_p = r_{pmax}$). Thus, increasing the concentration of PAHs will not increase the biodegradation rate of these pollutants; hence, the amount of PAHs biodegraded will be proportional to the time. If the biodegradation rate is constant, $K_0 = r_p$ approaching a zero-order kinetic model is described by eq 5:

$$C = C_0 + K_0 t \quad (5)$$

where C_0 is the initial concentration of PAHs and K_0 is the zero-order kinetic constant. For a zero-order reaction the half-life is given by eq 6:

$$t_{1/2} = \frac{C_0}{2K_0} \quad (6)$$

Figure 6 shows the description of naphthalene, anthracene, and pyrene biodegradation by first-order kinetic model, observing a good agreement between the experimental data and the theoretical results predicted by the model with relative high correlation coefficient values. Moreover, Table 3 includes the kinetic parameters (C_0, K_0, K_1, and $t_{1/2}$) predicted by the equation as well as the relative coefficients (R^2). Otherwise, when the biodegradation of PAHs was adjusted to a zero-order kinetic model, a good concordance was not observed between experimental and theoretical data as can be deduced by the correlation coefficients included in Table 3. Thus, the biodegradation of PAHs in sewage sludge will be directly

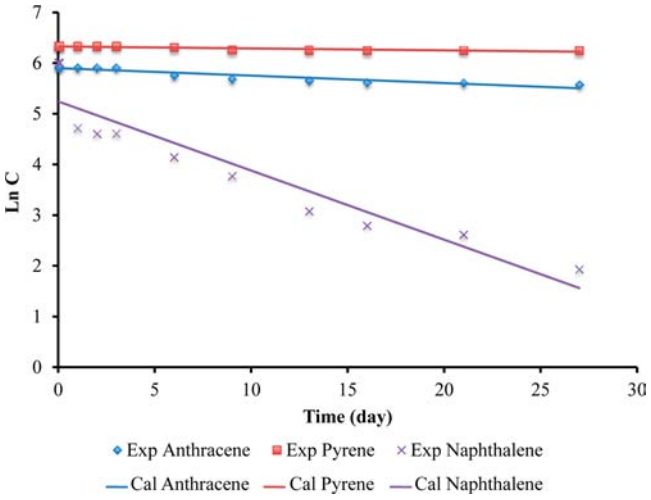

Figure 6. Kinetic plots achieved for the biodegradation of different PAHs, contained in sewage sludge, in the presence of biosurfactant extracted from corn steep liquor.

related with the initial concentration of PAHs in the solid matrix. It was observed that naphthalene gave the lowest half-life value (around 5 days), whereas the half-life for biodegrading anthracene and pyrene was 47 and 182 days, respectively. Half-life values obtained in this work are higher than those achieved by other authors who studied the biodegradation of phenanthrene and pyrene contained in aqueous solutions in the presence of surfactants such as Tween 80 or Tween 20.[36] However, it is necessary to take into consideration that in the current work the biodegradation occurs from a solid substrate (sewage sludge); thus, PAHs have to be first mobilized from sewage, solubilized, and then biodegraded and, therefore, it is obvious that the biodegradation of PAHs adsorbed in a solid matrix has to be slower than the biodegradation of any carbon source contained in an aqueous stream. Jianlong et al.[33] also described the microbial biodegradation of phthalic acid esters, contained in mixed anaerobic digested sludge collected from a local wastewater treatment plant, by a first-order kinetic model. They observed that the biodegradation rate and biodegradability of three phthalates under anaerobic conditions appeared to be related to the length of the alkyl side chains. Thus, >90% of dimethyl and di-*n*-butyl phthalate were biodegraded, whereas the biodegradation of dinoctyl phtalate was limited, with a half-life value of 21 days.

Some authors have reported that the half-life of hydrocarbons in biotic conditions was 17−126 days, whereas in abiotic conditions this ranged increased to 32−2048 days.[3]

In other work, Jianlong et al.[37] studied the biodegradation of four phthalic acid esters (dimethyl phthalate, diethyl phthalate, di-*n*-butyl phthalate, and di-*n*-octyl phthalate) in soil supplemented with acclimated sludge, observing that those phthalic acid esters with a shorter alkyl chain were biodegraded more quickly than phthalic acid esters with higher alkyl chains. These results are consistent with the data achieved in the current work during the biodegradation of PAHs contained in sewage sludge, in the presence of biosurfactant, observing that those more complex PAHs were biodegraded more slowly. In the present work it was also observed that PAHs with a lower carbon chain length (naphthalene) gave higher biodegradation rates than anthracene and pyrene.

Jianlong et al.[37] also observed that the biodegradation of phthalic acid esters followed a first-order reaction kinetic

DOI: 10.1021/acs.jafc.5b02346
J. Agric. Food Chem. 2015, 63, 7143−7150

Table 3. Kinetic Parameters for Zero- and First-Order Kinetic Models

	zero-order kinetic model				first-order kinetic model			
PAH	C_0 (mg/L)	K_0 (day^{-1})	$t_{1/2}$ (days)	R^2	C_0 (mg/L)	K_1 (day^{-1})	$t_{1/2}$ (days)	R^2
naphthalene	213.14	−10.70	9.96	0.44	5.24	−0.136	5.08	0.88
anthracene	364.15	−4.61	39.52	0.86	5.90	−0.015	47.51	0.88
pyrene	559.81	−2.05	136.62	0.82	6.33	−0.004	182.43	0.82

equation with a biodegradation half-life that decreased significantly with increasing carbon number of the alcohol moiety and correlated with the alkyl chain length and their octanol−water partition coefficients.

Other authors[36] proposed these models to explain the biodegradation of phenanthrene and pyrene in the presence of nonionic surfactants produced by chemical synthesis. These authors observed low correlation coefficient values when trying to describe the biodegradation of phenanthrene and pyrene in the presence of Tween 20 and Tween 80 at different concentrations applying zero-order kinetic model; however, they found relatively high correlation coefficient values when applying the first-order kinetic model to describe the biodegradation of both PAHs, and the same behavior was observed in the current work.

Furthermore, related with the kinetic description of PAH biodegradation, Lu et al.[35] found that the biodegradation of two- and three-ring PAHs can be described by a first-order kinetic model, whereas the biodegradation of four-ring PAHs followed a zero-order kinetic model.

Biosurfactants have the ability to increase apparent aqueous solubility and bioavailability of PAHs, and they can be used to stimulate the biodegradation of these persistent contaminants contained in sewage sludge. The utilization of biosurfactants as washing agent not only has the advantage of allowing the solubilization of hydrophobic contaminants but also can promote their simultaneous biodegradation. Therefore, the elimination of PAHs from sewage sludge using biosurfactants could allow the safe use of this sewage sludge as fertilizer or as organic soil improver in agriculture.

AUTHOR INFORMATION

Corresponding Author

*(A.B.M.) Phone: (34) 986812022. Fax: (34) 986812201. E-mail: amoldes@uvigo.es.

Funding

We thank the Spanish Ministry of Economy and Competitiveness (this work was funded by FEDER funds under Project CTM2012-31873).

Notes

The authors declare no competing financial interest.

REFERENCES

(1) Navalón, P.; Valor, I. El uso agrícola de los lodos de EDAR y los COPs. In *Ingeniería Química*; 2008; No. 458, pp 188−196.

(2) Smith, S. R. Organic contaminants in sewage sludge (biosolids) and their significance for agricultural recycling. *Philos. Trans. R. Soc., A* **2009**, *367*, 4005−4041.

(3) Włodarczyk-Makuła, M. Half-life of carcinogenic polycyclic aromatic hydrocarbons in stored sewage sludge. *Arch. Environ. Prot.* **2012**, *38*, 33−44.

(4) Cai, Q. Y.; Mo, C. H.; Wu, Q. T.; Zeng, Q. Y. Polycyclic aromatic hydrocarbons and phthalic acid esters in the soil−radish (*Raphanus sativus*) system with sewage sludge and compost application. *Bioresour. Technol.* **2008**, *99*, 1830−1836.

(5) Nam, J. J.; Gareth, O. T.; Foday, M. J.; Steinnes, E.; Gustafsson, O.; Jones, K. C. PAHs in background soils from Western Europe: influence of atmospheric deposition and soil organic matter. *Chemosphere* **2008**, *70*, 1596−1602.

(6) U.S. Environmental Protection Agency (EPA). Appendix A to 4 CFR Part 423, November 2010; available from http://www.epa.gov/waterscience/methods/pollutants.htm.

(7) Regulation (EC) No. 850/2004 of the European parliament and of the council on persistent organic pollutants and amending Directive 79/117/EEC.

(8) EU Directive (2000). Council of the European Community, 27 April, Working document on Sludge, 3rd draft, Brussels, Belgium.

(9) Suciu, N. A.; Lamastra, L.; Trevisan, M. PAHs content of sewage sludge in Europe and its use as soil fertilizer. *Waste Manage.* **2015**, *41*, 119−127.

(10) Desai, J. D.; Banat, I. M. Microbial production of surfactants and their commercial potential. *Microbiol. Mol. Biol. Rev.* **1997**, *61*, 47−64.

(11) Portilla-Rivera, O.; Torrado, A.; Domínguez, J. M.; Moldes, A. B. Stability and emulsifying capacity of biosurfactants obtained from lignocellulosic sources using *Lactobacillus pentosus*. *J. Agric. Food Chem.* **2008**, *56*, 8074−8080.

(12) Vecino Bello, X.; Devesa-Rey, R.; Cruz, J. M.; Moldes, A. B. Study of the synergistic effects of salinity, pH, and temperature on the surface-active properties of biosurfactants produced by *Lactobacillus pentosus*. *J. Agric. Food Chem.* **2012**, *60*, 1258−1265.

(13) Moldes, A. B.; Paradelo, R.; Vecino, X.; Cruz, J. M.; Gudiña, E.; Rodrigues, L.; Teixeira, J. A.; Domínguez, J. M.; Barral, M. T. Partial characterization of biosurfactant from lactobacillus pentosus and comparison with sodium dodecyl sulphate for the bioremediation of hydrocarbon contaminated soil. *BioMed Res. Int.* **2013**, No. 961842.

(14) Vecino, X.; Barbosa-Pereira, L.; Devesa-Rey, R.; Cruz, J. M.; Moldes, A. B. Optimization of extraction conditions and fatty acid characterization of *Lactobacillus pentosus* cell-bound biosurfactant/bioemulsifier. *J. Sci. Food Agric.* **2015**, *95*, 313−320.

(15) Vecino, X.; Bustos, G.; Devesa-Rey, R.; Cruz, J. M.; Moldes, A. B. Salt-free aqueous extraction of a cell-bound biosurfactant: a kinetic study. *J. Surfactants Deterg.* **2015**, *18*, 267−274.

(16) Collina, E.; Lasagni, M.; Pitea, D.; Franzetti, A.; Di Gennaro, P.; Bestetti, G. Bioremediation of diesel fuel contaminated soil: effect of non ionic surfactants and selected bacteria addition. *Ann. Chim.* **2007**, *97*, 799−805.

(17) Zhou, W.; Zhu, L. Enhanced desorption of phenanthrene from contaminated soil using anionic/nonionic mixed surfactant. *Environ. Pollut.* **2007**, *147*, 350−357.

(18) Popenda, A.; Włodarczyk-Makuła, M. The application of biosurfactants into removal of selected micropollutants from soils and sediments. *Desalin. Water Treat.* **2015**, 1, DOI: 10.1080/19443994.2014.996007.

(19) Shin, K. H.; Kim, K. W.; Ahn, Y. Use of biosurfactant to remediate phenanthrene-contaminated soil by the combined solubilization-biodegradation process. *J. Hazard. Mater.* **2006**, *137*, 1831−1837.

(20) Das, K.; Mukherjee, A. K. Differential utilization of pyrene as the sole source of carbon by *Bacillus subtilis* and *Pseudomonas aeruginosa* strains: role of biosurfactants in enhancing bioavailability. *J. Appl. Microbiol.* **2007**, *102*, 195−203.

(21) Dasari, S.; Venkata Subbaiah, K. C.; Wudayagiri, R.; Valluru, L. Biosurfactant-mediated biodegradation of polycyclic aromatic hydrocarbons-naphthalene. *Biorem. J.* **2014**, *18*, 258−265.

DOI: 10.1021/acs.jafc.5b02346
J. Agric. Food Chem. 2015, 63, 7143−7150

(22) Yu, H.; Huang, G.; Wei, J.; An, C. Solubilization of mixed polycyclic aromatic hydrocarbons through a rhamnolipid biosurfactant. *J. Environ. Qual.* **2011**, *40*, 477−483.
(23) Vecino, X.; Barbosa-Pereira, L.; Devesa-Rey, R.; Cruz, J. M.; Moldes, A. B. Optimization of liquid-liquid extraction of biosurfactants from corn steep liquor. *Bioprocess. Biosyst. Eng.* **2015**, DOI: 10.1007/s00449-015-1404-9.
(24) Oluseyi, T.; Olayinka, K.; Alo, B.; Smith, R. M. Improved analytical extraction and clean-up techniques for the determination of PAHs in contaminated soil samples. *Int. J. Environ. Res.* **2011**, *5*, 681−690.
(25) Von Lau, E.; Gan, S.; Ng, H. K.; Poh, P. E. Extraction agents for the removal of polycyclic aromatic hydrocarbons (PAHs) from soil in soil washing technologies. *Environ. Pollut.* **2014**, *184*, 640−649.
(26) Janosz-Rajczyk, M.; Wiśniowska, E.; Włodarczyk-Makula, M.; Mann, J. Preliminary studies of separation method effect on PAH recovery from digested sewage sludge. *Chem. Anal.* **2001**, *46*, 633−645.
(27) Włodarczyk-Makuła, M. PAHs balance in solid and liquid phase of sewage sludge during fermentation process. *J. Environ. Sci. Health, Part A: Toxic/Hazard. Subst. Environ. Eng.* **2008**, *43*, 1602−1609.
(28) Macherzyński, B.; Włodarczyk-Makuła, M.; Skowron-Grabowska, B.; Starostka-Patyk, M. Degradation of PCBs in sewage sludge during methane fermentation process concerning environmental management. *Desalin. Water Treat.* **2014**, 1, DOI: 10.1080/19443994.2014.988407.
(29) Gąsecka, M.; Włodarczyk-Makuła, M.; Popenda, A.; Drzewiecka, K. Phytoremediation of PAH-contaminated areas. In *Phytoremediation*; Ansari, A. A., Gill, S. S., Gill, R., Lanza, G. R., Newman, L., Eds.; 2015, Vol. 1, Part 4, pp 295−308.10.1007/978-3-319-10395-2_21
(30) Lima, T. M. S.; Procópio, L. C.; Brandao, F. D.; Carvalho, A. M. X.; Tótola, M. R.; Borges, A. C. Simultaneous phenanthrene and cadmium removal from contaminated soil by a ligand/biosurfactant solution. *Biodegradation* **2011**, *22*, 1007−1015.
(31) Jacques, R. J. S.; Santos, E. C.; Bento, F. M.; Peralba, M. C. R.; Selbach, P. A.; Sá, E. L. S.; Camargo, F. A. O. Anthracene biodegradation by *Pseudomonas* sp. isolated from a petrochemical sludge landfarming site. *Int. Biodeterior. Biodegrad.* **2005**, *56*, 143−150.
(32) Obayori, O. S.; Adebusoye, S. A.; Ilori, M. O.; Oyetibo, G. O.; Omotayo, A. E.; Amund, O. O. Effects of corn steep liquor on growth rate and pyrene degradation by *Pseudomonas* strains. *Curr. Microbiol.* **2010**, *60*, 407−411.
(33) Jianlong, W.; Lujun, C.; Hanchang, S.; Yi, Q. Microbial degradation of phthalic acid esters under anaerobic digestion of sludge. *Chemosphere* **2000**, *41*, 1245−1248.
(34) Jianlong, W.; Xiangchun, Q.; Liping, H.; Qian, Yi; Hegemann, W. Microbial degradation of quinoline by immobilized cells of *Burkholderia pickettii*. *Water Res.* **2002**, *36*, 2288−2296.
(35) Lu, L.; Zhu, L. Effect of soil components on the surfactant-enhanced soil sorption of PAHs. *J. Soils Sediments* **2012**, *12*, 161−168.
(36) Aryal, M.; Liakopoulou-Kyriakides, M. Biodegradation and kinetics of phenanthrene and pyrene in the presence of nonionic surfactants by *Arthrobacter* strain Sphe3. *Water, Air, Soil Pollut.* **2013**, *224*, 1−10.
(37) Jianlong, W.; Xuan, Z.; Weizhong, W. Biodegradation of phthalic acid esters (PAEs) in soil bioaugmented with acclimated activated sludge. *Process Biochem.* **2004**, *39*, 1837−1841.

DOI: 10.1021/acs.jafc.5b02346
J. Agric. Food Chem. 2015, 63, 7143−7150

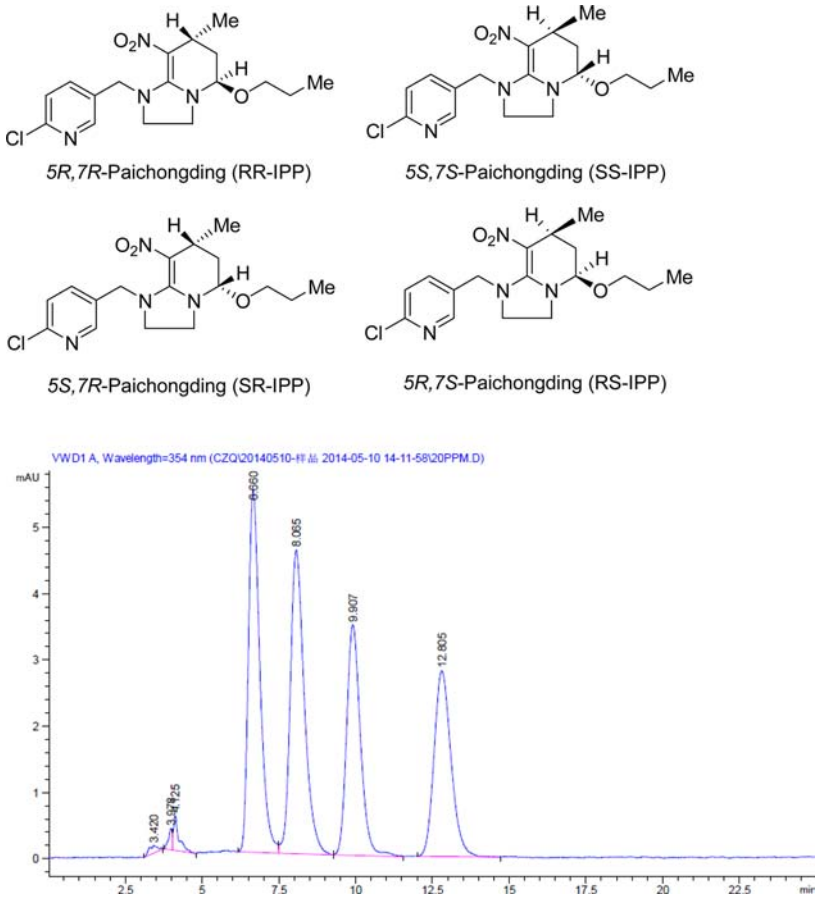

Figure 1. Stereostructures of four isomers of Paichongding (IPP) and HPLC chromatograms of IPP. Peaks 1, 2, 3, and 4 represent stereoisomers RR-IPP, SS-IPP, SR-IPP, and RS-IPP, respectively.

Table 1. Physicochemical Characteristics of the Experimental Soils

characteristic	yellow loam soil (F)	Huangshi soil (J)	paddy field on desalting muddy polder (C)	yellow paddy soil (H)
location	Longquan, Fujian province	Changzhou, Jiangsu province	Cixi, Zhejiang province	Jingzhou, Hubei province
pH (H_2O)	6.63	5.95	8.25	6.70
OM[a] (%)	2.67	1.52	2.48	1.98
CEC[b] (cmol kg^{-1})	14.09	7.11	16.1	13.9
clay (%)	38.7	33.5	24.3	33.0
silt (%)	50.4	49.8	71.1	51.2
sand (%)	10.9	16.7	4.6	15.8
texture (%)				
<0.01 mm	67.4	60.7	64.7	67.4
0.01−0.09 mm	28.3	32.6	34.5	28.3
>0.09 mm	4.3	6.7	0.8	4.3
total N (%)	0.24	0.08	1.03	0.12
P (mg kg^{-1})	21.25	7.65	15.37	10.25
K (g kg^{-1})	13.47	10.7	22.9	5.22

[a]Organic matter. [b]Cation exchange capacity.

province), and yellow paddy soil (H, GB/T-A2111511, Jingzhou, Hubei province), respectively. The soil samples were taken from the surface zone (0−15 cm depth) in rice fields in Fujian, Jiangsu, Zhejiang, and Hubei provinces, China. Their basic physicochemical characteristics were determined according to methods previously reported by Gee et al. and are listed in Table 1.[20]

Degradation Experiments in Soils. To study the behavior and degradation of IPP in anaerobic soils, IPP was sprayed into the test soils to give a final concentration of 20 mg kg^{-1} of soil and thoroughly mixed. The soil moisture content was adjusted to about 60% of the maximum water-holding capacity by adding Milli-Q (MQ) water. The incubation temperature was controlled at 25 ± 1 °C in an anaerobic incubator. Ten grams of soil was sampled from the flask at different time intervals (0, 5, 10, 20, 30, 45, 60, 75, and 100 days after treatment, DAT) for determining the concentration of IPP and its metabolites. All experiments were carried out in triplicate.

IPP Extraction. IPP in soils was extracted according to the reported methods.[21,22] The extraction procedure was employed with each subsequent solvent being less polar. The extraction system was performed as follows in three steps: 0.01 M $CaCl_2$, dichloromethane, and acetonitrile/water (9:1, v/v). Fifty milliliters of each successive solvent was added and shaken for 1 h. After the first step, the $CaCl_2$ extract was

DOI: 10.1021/acs.jafc.5b02645
J. Agric. Food Chem. 2015, 63, 7151−7160

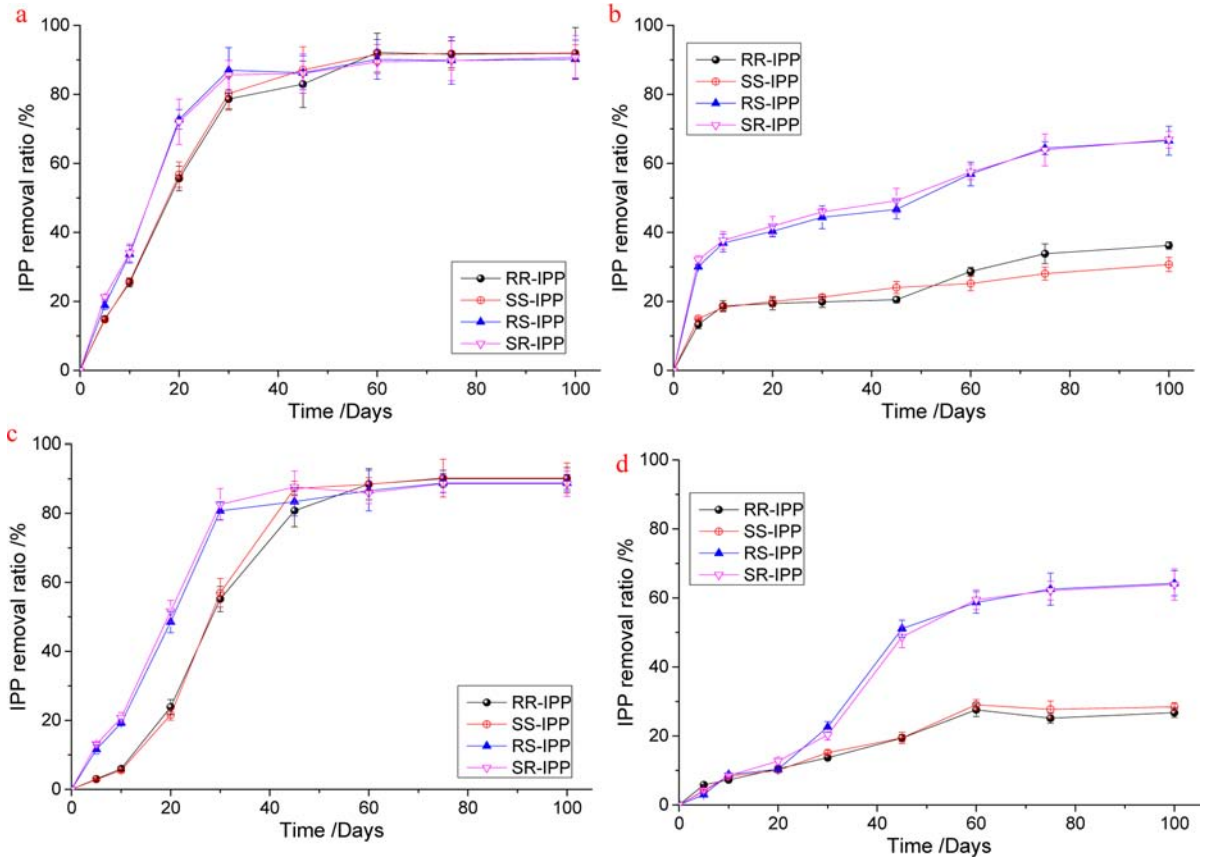

Figure 2. Degradation of RR-IPP, SS-IPP, SR-IPP, and RS-IPP in anaerobic soil: (a) yellow loam soil (F); (b) Huangshi soil (J); (c) paddy field on desalting muddy polder (C); (d) yellow paddy soil (H).

adjusted to pH 3.0 and then extracted with dichloromethane (1:1, v/v) three times. The dichloromethane extract was combined with the other two extracts obtained from the last three extraction steps and concentrated on a vacuum rotary evaporator at 40 °C until dry, and the residue was dissolved in 1 mL of methanol. The overall average recovery of IPP in soils varied from approximately 89.32 to 96.15% in the final extract solution. The relative standard deviations (RSDs) for IPP extraction within each run of soil samples ranged from 2 to 5%, which indicated that the variation between the soil samples was relatively small and within control. These results showed that the method used for IPP extraction and analysis in this study was reproducible and reliable.

Statistical Analysis and Calculation. The aerobic degradation of IPP in soils followed a first-order exponential decay model. The rate constant from the first-order model was used to determine the DT_{50} (half-life value). DT_{50} was calculated by

$$-\ln \frac{c_t}{c_0} = kt \text{ or } c_t = c_0\, e^{-kt} \quad (1)$$

where C_0 is the initial concentration of IPP (mg kg^{-1} soil), C_t is the concentration of insecticide at time t, t is the incubation time (days), and k is the degradation rate constant of the insecticide (day^{-1}). DT_{50} and DT_{90} were calculated as ln 2/k and ln 10/k, respectively.

Analytical Procedures. IPP was determined with high-performance liquid chromatography (HPLC, Agilent 1260, Agilent Technologies, USA); the photodiode array (PDA) detector was operated at 354 nm, with a Daicel Chiralpak IC (5 μm, 4.6 × 250 mm), and the column temperature was 30 °C. The mobile phase was ethanol and pure water (90:10, v/v), and the flow rate was 1.0 mL min^{-1}.

IPP biodegradation intermediates were monitored and analyzed with HPLC (Agilent 1260), 268 nm, C_{18} column (3.5 μm, 4.6 × 250 mm) and 30 °C according to the methods reported by Fu et al.[5−7] Acetonitrile with 0.1% (v/v) acetic acid (HPLC grade) and a mixture of 0.1% (v/v) acetic acid in water (HPLC grade) was at a linear gradient program (minutes/% acetonitrile: 0/15; 7/15; 20/35; 40/100; 45/100; 50/15; 60/15). The flow rate was 1.0 mL min^{-1}.

LC-MS/MS analysis was conducted using a Dionex U3000 HPLC system coupled with a Bruker maXis 4G ion trap mass spectrometer with electrospray ionization source (ESI). LC separation conditions were accordance with those used for HPLC analysis. The ion source

Table 2. Degradation of IPP in Different Anaerobic Soils

soil	IPP	equation	k (day^{-1})	R^2	DT_{50} (days)	DT_{90} (days)
F	RR-IPP	$c_t = 100\, e^{-0.0286t}$	0.0286	0.8744	24	81
	SS-IPP	$c_t = 100\, e^{-0.0288t}$	0.0288	0.9573	24	80
	RS-IPP	$c_t = 100\, e^{-0.0244t}$	0.0244	0.9043	28	94
	SR-IPP	$c_t = 100\, e^{-0.0246t}$	0.0246	0.9801	28	94
J	RR-IPP	$c_t = 100\, e^{-0.0037t}$	0.0037	0.8660	187	622
	SS-IPP	$c_t = 100\, e^{-0.0034t}$	0.0034	0.9493	204	677
	RS-IPP	$c_t = 100\, e^{-0.0094t}$	0.0094	0.8863	74	245
	SR-IPP	$c_t = 100\, e^{-0.0092t}$	0.0092	0.8760	75	250
H	RR-IPP	$c_t = 100\, e^{-0.0033t}$	0.0033	0.8860	210	698
	SS-IPP	$c_t = 100\, e^{-0.0036t}$	0.0036	0.8953	193	640
	RS-IPP	$c_t = 100\, e^{-0.0122t}$	0.0122	0.9202	57	189
	SR-IPP	$c_t = 100\, e^{-0.0121t}$	0.0121	0.9218	57	190
C	RR-IPP	$c_t = 100\, e^{-0.0286t}$	0.0286	0.9055	24	81
	SS-IPP	$c_t = 100\, e^{-0.0291t}$	0.0291	0.9634	24	79
	RS-IPP	$c_t = 100\, e^{-0.0245t}$	0.0245	0.9302	28	94
	SR-IPP	$c_t = 100\, e^{-0.0241t}$	0.0241	0.8962	29	96

DOI: 10.1021/acs.jafc.5b02645
J. Agric. Food Chem. 2015, 63, 7151−7160

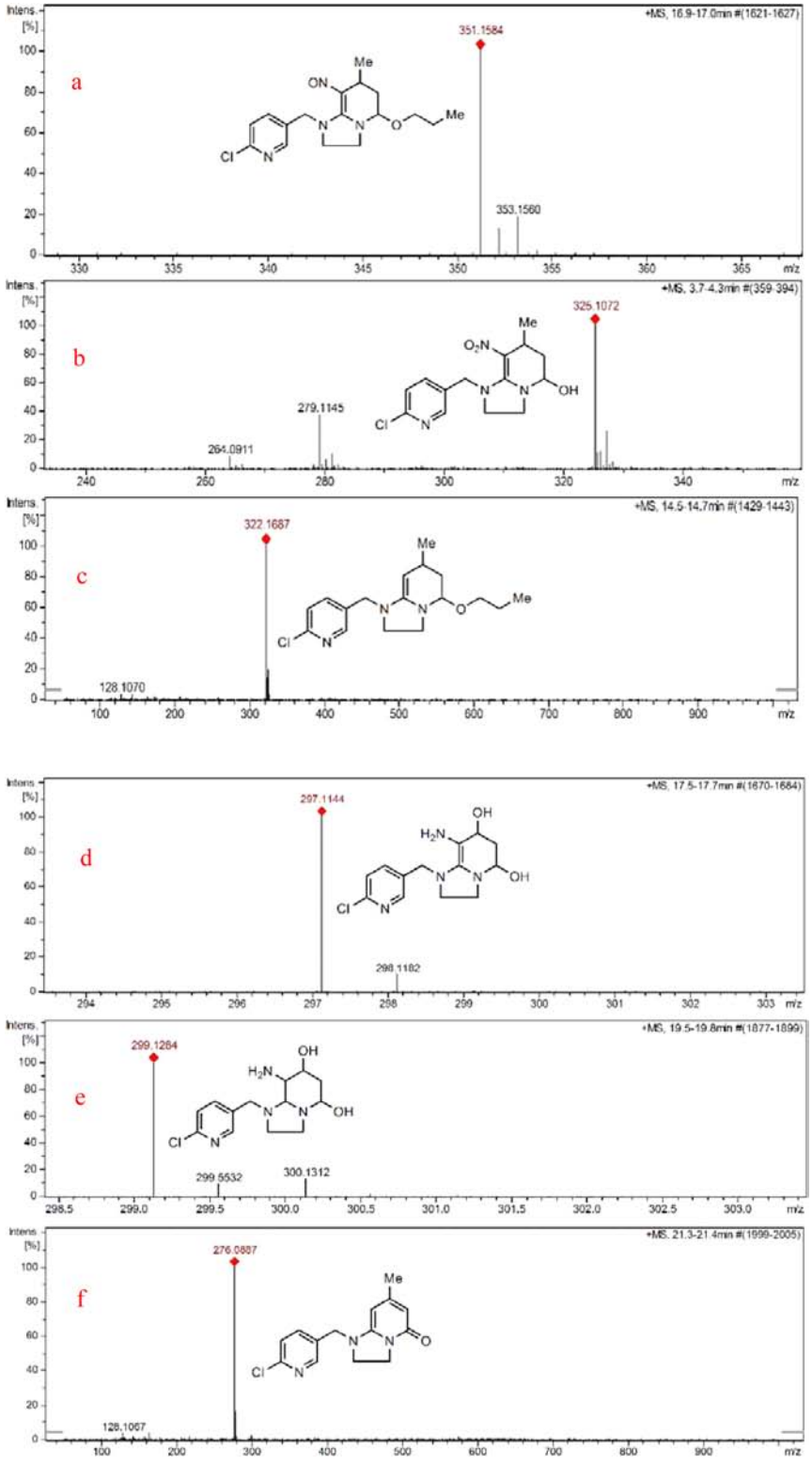

Figure 3. Mass spectra of metabolites (M1, M2, M3, M4, M5, and M6) formed during IPP anaerobic degradation in soils: (a) M1, 1-(6-chloropyridin-3-ylmethyl)-7-methyl-8-nitroso-5-propoxy-1,2,3,5,6,7-hexahydroimidazo [1,2-α]pyridine; (b) M2, 1-((6-chloropyridin-3-yl) methyl)-7-methyl-8-nitro-5-hydroxy-1,2,3,5,6,7-hexahydroimidazo[1,2-α-]pyridine; (c) M3, 1-(6-chloropyridin-3-ylmethyl)-7-methyl-5-propoxy-1,2,3,5,6,7-hexahydroimidazo[1,2-α]pyridine; (d) M4, 1-((6-chloropyridin-3-yl)methyl)-5,7-diol-8-amino-1,2,3,5,6,7-hexahydroimidazo[1,2-α]pyridine; (e) M5, 1-((6-chloropyridin-3-yl)methyl)-5,7-diol-8-amino-octahydroimidazo[1,2-α]pyridine; (f) M6, 1-((6-chloropyridin-3-yl)methyl)-2,3-dihydro-5-one-7-methylimidazo[1,2-α]pyridine.

temperature was controlled at 250 °C, and the capillary voltage was −4.5 kV. The analysis mode of ionization was electrospray ionization (ESI, positive). The operation conditions were as follows: collision energy, 10.0 eV; ISCID energy and ion energy, 5.0 eV; dry gas, 6 L min^{-1}; dry temperature, 180 °C; gas pressure, 1.5 bar. The continuous full scanning from m/z 50 to 500 Da was performed in positive ion mode.

PCR Amplification of 16S rRNA and Pyrosequencing. The primers 515F (5′-GTGCCAGCMGCCGCGG-3′) and 907R

DOI: 10.1021/acs.jafc.5b02645
J. Agric. Food Chem. 2015, 63, 7151−7160

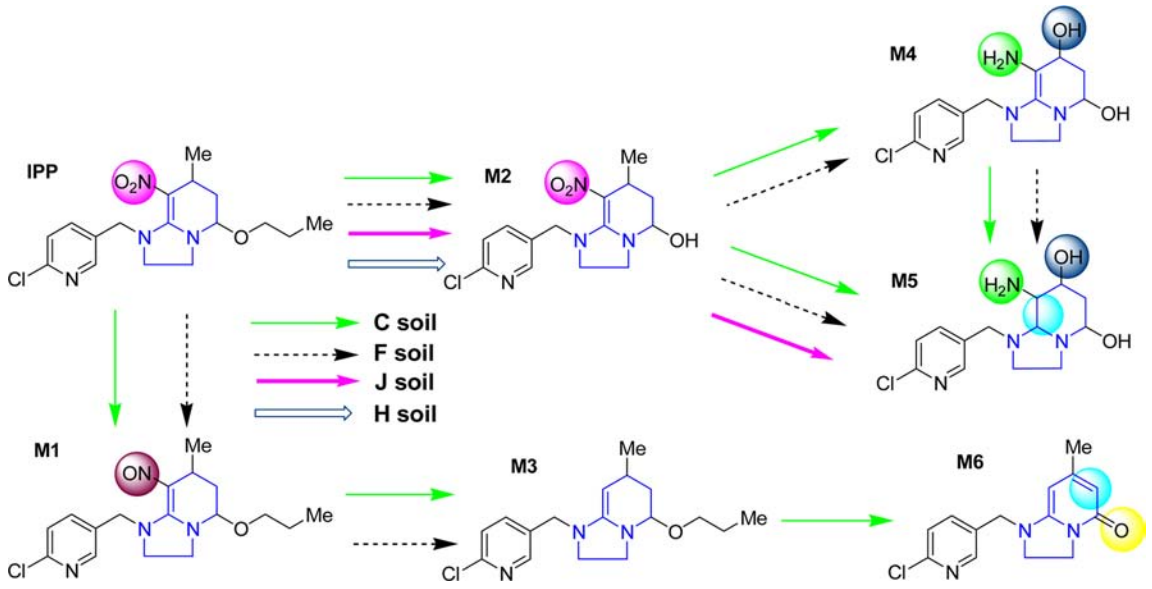

Figure 4. Proposed pathways of IPP degradation in anaerobic soils.

(5′-CCGTCAATTCMTTTRAGTTT-3′) were used for amplifying the fragment of the 16S rRNA gene. The PCR reaction program was as follows: 0.2 μM of each primer and 0.2 mM dNTP, 1.5 mM $MgCl_2$, and 0.2 unit of Taq polymerase. The cycling conditions were 98 °C for 30 s, followed by 30 cycles of 98 °C for 10 s, 55 °C for 20 s, and 72 °C for 30 s, with a final extension step at 72 °C for 5 min (GeneAmp 9700, ABI, USA). PCR products were purified with the DNA gel recovery kit (Axygen BioScience) and were sent for sequencing service using Miseq sequencing technique (Majorbio Co., Shanghai, China).

Bioinformatic and Statistical Analysis. Totally 240,414 16S rRNA sequence reads were filtered; Trimmomatic was used for denoising and processing. Trimmomatic is a fast, multithreaded command line tool that can be used to trim and crop Illumina (FASTQ) data as well as to remove adapters. The resulting sequences after quality control were analyzed through QIIME. The reads were clustered into operational taxonomic units (OTUs) at 97% sequence similarity using Usearch (version 7.1, http://drive5.com/uparse/). OTU representative sequences were aligned against the Greengenes (release 13.5, http://greengenes.secondgenome.com/), and chimeric sequences were identified using Mothur (version 1.26). OTU sequences were classified by RDP classifier and QIIME by BLASTING, and the obtained data were used in the subsequent analyses. Community richness was assessed with Chao 1 estimator (http://www.mothur.org/wiki/Chao) and ACE estimator (http://www.mothur.org/wiki/Ace). Community diversity was estimated with the Shannon index (http://www.mothur.org/wiki/Shannon) and the Simpson index (http://www.mothur.org/wiki/Simpson).

Statistical analysis was performed in R 2.15.2, using vegan (redundancy analysis (RDA) with significance testing by permutation—ANOVA) and Hmisc packages.

RESULTS AND DISCUSSION

Degradation of IPP in Anaerobic Soils. The results of IPP anaerobic degradation in soils is shown in Figure 2. The removal ratio of all IPP stereoisomers (RR-IPP, SS-IPP, RS-IPP, and SR-IPP) reached >90% at 60 DAT in F and C soils, whereas the RR-IPP and SS-IPP only were <30% in J and H soils. In J and H soils, the removal of RS-IPP and SR-IPP was greater than that of RR-IPP and SS-IPP, and RR-IPP and SS-IPP were hard to degrade in these two soils. The results showed that IPP enantiomer degradation rate differed in different soilsand that the IPP degradation rate was higher in F and C soils. IPP, especially RR-IPP and SS-IPP, were relatively hard to degrade in J and H soils. Degradation of IPP in anaerobic soils followed a first-order exponential decay model. The first-order exponential equation, k, DT_{50}, and DT_{90} are listed in Table 2. The IPP degradation rate was the same in F and C soils, and a similar degradation rate was observed in J and H soils. DT_{50} values of RR-IPP, SS-IPP, RS-IPP, and SR-IPP in F soil were 24, 24, 28, and 28 days, respectively.

It has been reported that greater total carbon (TC) contributes to a larger organic chemical biodegradation rate because the increased carbon content can enhance microorganisms that are responsible for degrading organic pollutants.[23] In this study, the TC content in F and C soils was higher than that in J and H soils. Moreover, the pH value of soil also affects the soil microbial and enzyme activity, which acted as the key important role during IPP degradation process. The IPP degradation rate in F and C soils was higher than that in J and H soils, the reason being that the pH value in F and C soil was appropriate for microbial growth and activity. The lower pH value in J and H soils lead to the slower degradation rate. These results illustrate that the soils with rich OM and neutral pH lead to a greater IPP degradation rate, because these provide suitable conditions for IPP-degrading bacterial growth and biodegradation.

Identification of Metabolites of IPP. During the degradation of IPP in anaerobic soils, six degradation metabolites were detected by HPLC analysis with retention times of 16.9 min (M1), 4.1 min (M2), 14.6 min (M3), 17.6 min (M4), 19.7 min (M5), and 21.3 min (M6). These intermediates occurred with the decrease of IPP. All six intermediates were determined in C soil, and M1, M2, M3, M4, and M5 appeared during IPP anaerobic degradation in F soil. M2 and M5 were determined in J soil, whereas M2 was found in H soil. Six degradation intermediates of IPP were analyzed and identified by high-performance chromatography-time-of flight mass spectrometry (LC-MS) and LC-MS/MS.

The ion fragments of IPP were at m/z 367.1500 ($C_{17}H_{23}ClN_4O_3$) $[M + H]^+$ and m/z 321.1578, and the ion fragment of m/z 367.1500 includes daughter ions of 306.1368 (100), 308.4442 (15), and 137.1069 (62), which were in accordance with the structure of standard IPP.[5−7,14]

DOI: 10.1021/acs.jafc.5b02645
J. Agric. Food Chem. 2015, 63, 7151−7160

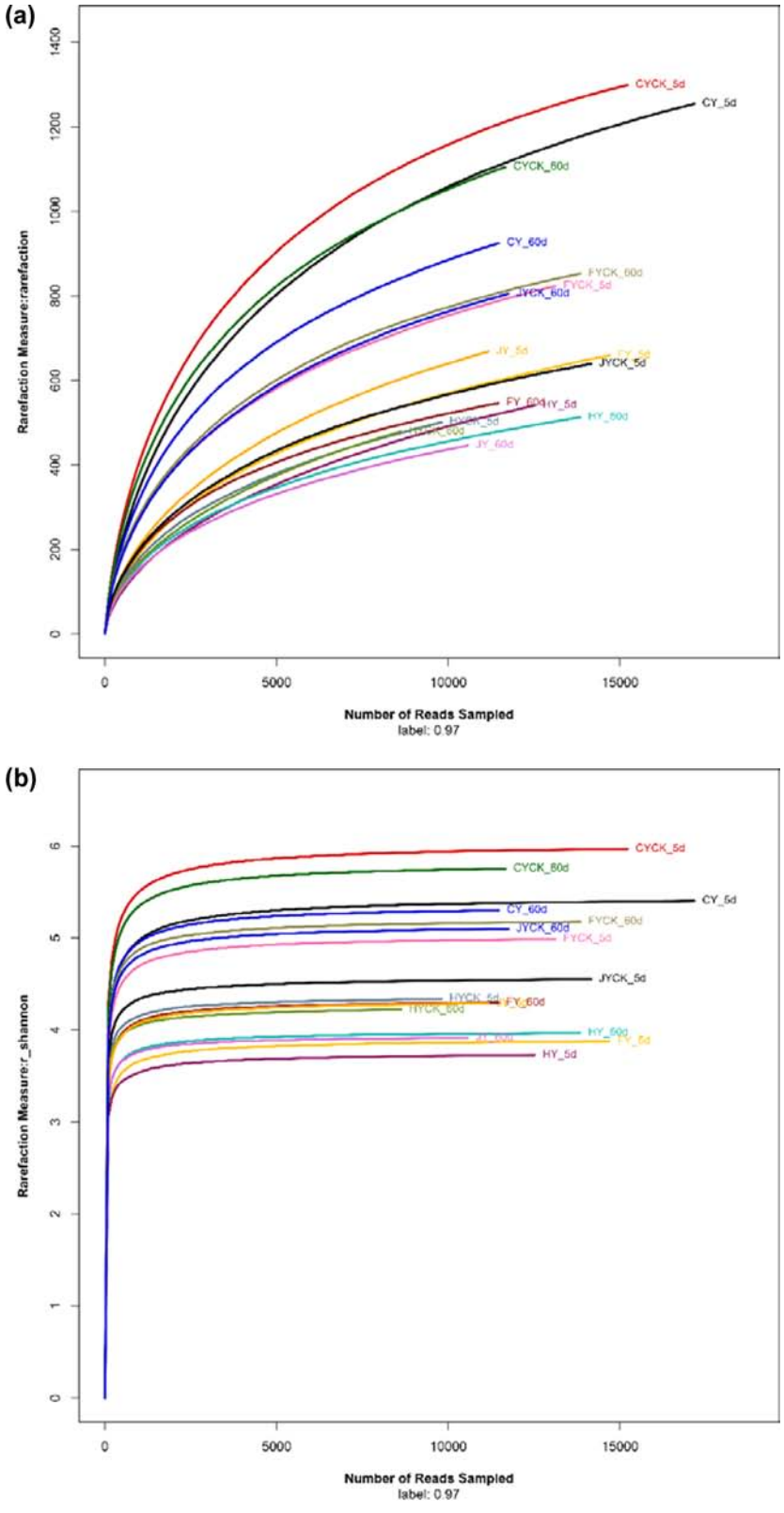

Figure 5. Bacterial diversity comparison with rarefaction curves (a) and Shannon−Wiener curves (b) in different soils at 5 and 60 DA: (CK_5d and CK_60d) control experiment without IPP spray at 5 and 60 DAT; (CY_5d and CY_60d) C soil with IPP spray at 5 and 60 DAT; (JY_5d and JY_60d) J soil with IPP spray at 5 and 60 DAT; (HY_5d and HY_60d) H soil with IPP spray at 5 and 60 DAT; (JY_5d and JY_60d) J soil with IPP spray at 5 and 60 DAT.

M1 showed m/z 351.1583, and the daughter ion showed m/z 278.1039; the daughter ion should be formed by the loss of a propoxyl group from the parent compound IPP. M1 was attributed to loss of oxygen from the nitro group and was identified as 1-(6-chloropyridin-3-ylmethyl)-7-methyl-8-nitroso-5-propoxy-1,2,3,5,6,7-hexahydroimidazo[1,2-α]pyridine

DOI: 10.1021/acs.jafc.5b02645
J. Agric. Food Chem. 2015, 63, 7151−7160

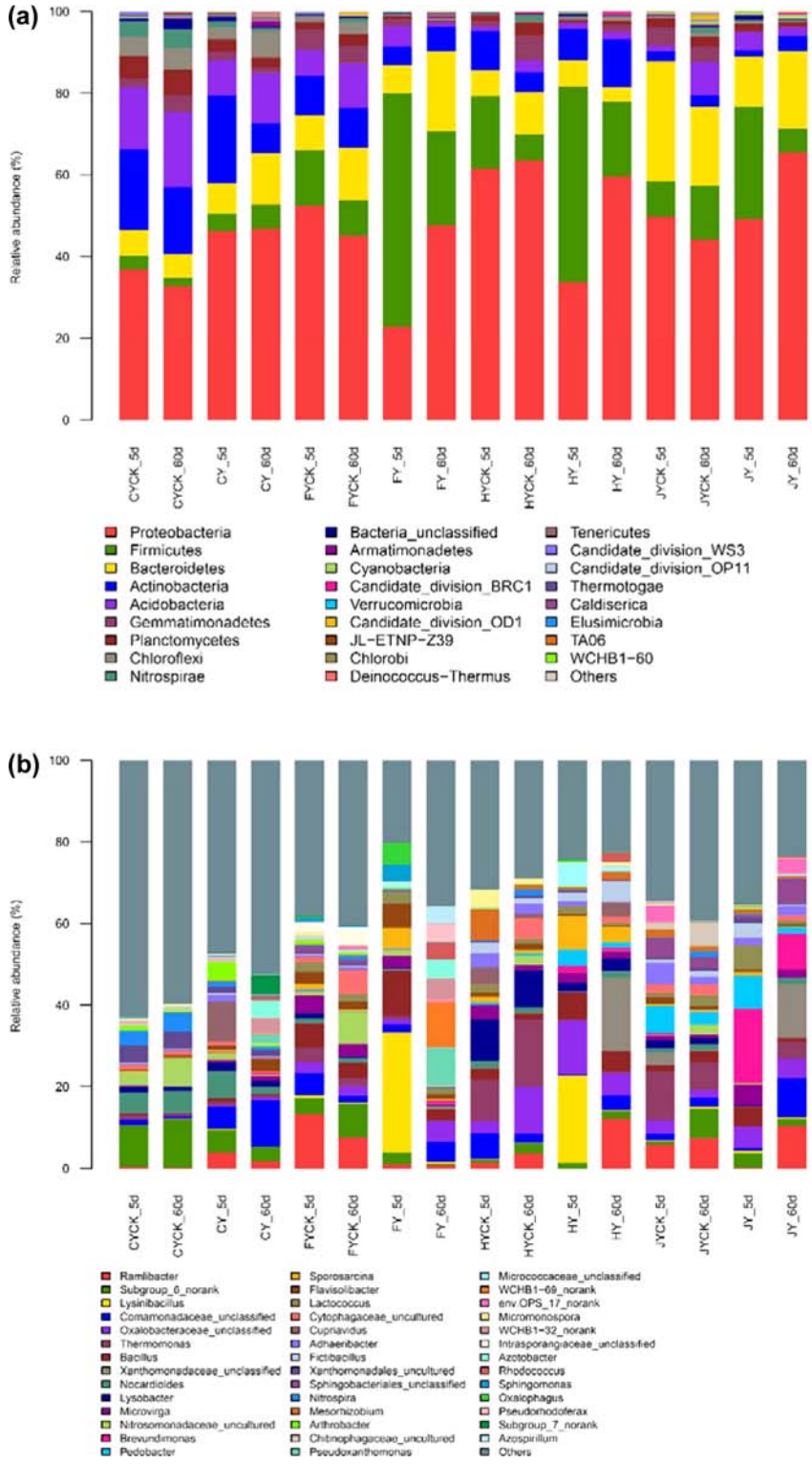

Figure 6. Bacterial composition of the different communities in anaerobic soils: (a) % of relative read abundance of bacterial phyla within each community; (b) % of relative read abundance of bacterial genus within each community.

(Figure 3a). Metabolite M2 was identified as 1-((6-chloropyridin-3-yl)methyl)-7-methyl-8-nitro-5-hydroxy-1,2,3,5,6,7-hexahydroimidazo[1,2-α-]pyridine according to its LC-MS/MS and MS^2 spectra (Figure 3b). The ion fragment of M2 was at m/z 325.1072 $[M + H]^+$, which indicated that M2 was generated through hydrolysis of the propoxyl group of IPP.

The intermediate M3 was at m/z 322.1687 ($C_{17}H_{24}ClN_3O$) $[M + H]^+$, and its daughter ions were m/z 322.1687 and 324.1672. M3 likely corresponded to the loss of the group of 8-nitroso on M1 and was identified as 1-(6-chloropyridin-3-ylmethyl)-7-methyl-5-propoxy-1,2,3,5,6,7-hexahydroimidazo-[1,2-α]pyridine, which was in accordance with previous reports (Figure 3c).[7,14] Figure 3d shows that the m/z of metabolite M4

DOI: 10.1021/acs.jafc.5b02645
J. Agric. Food Chem. 2015, 63, 7151−7160

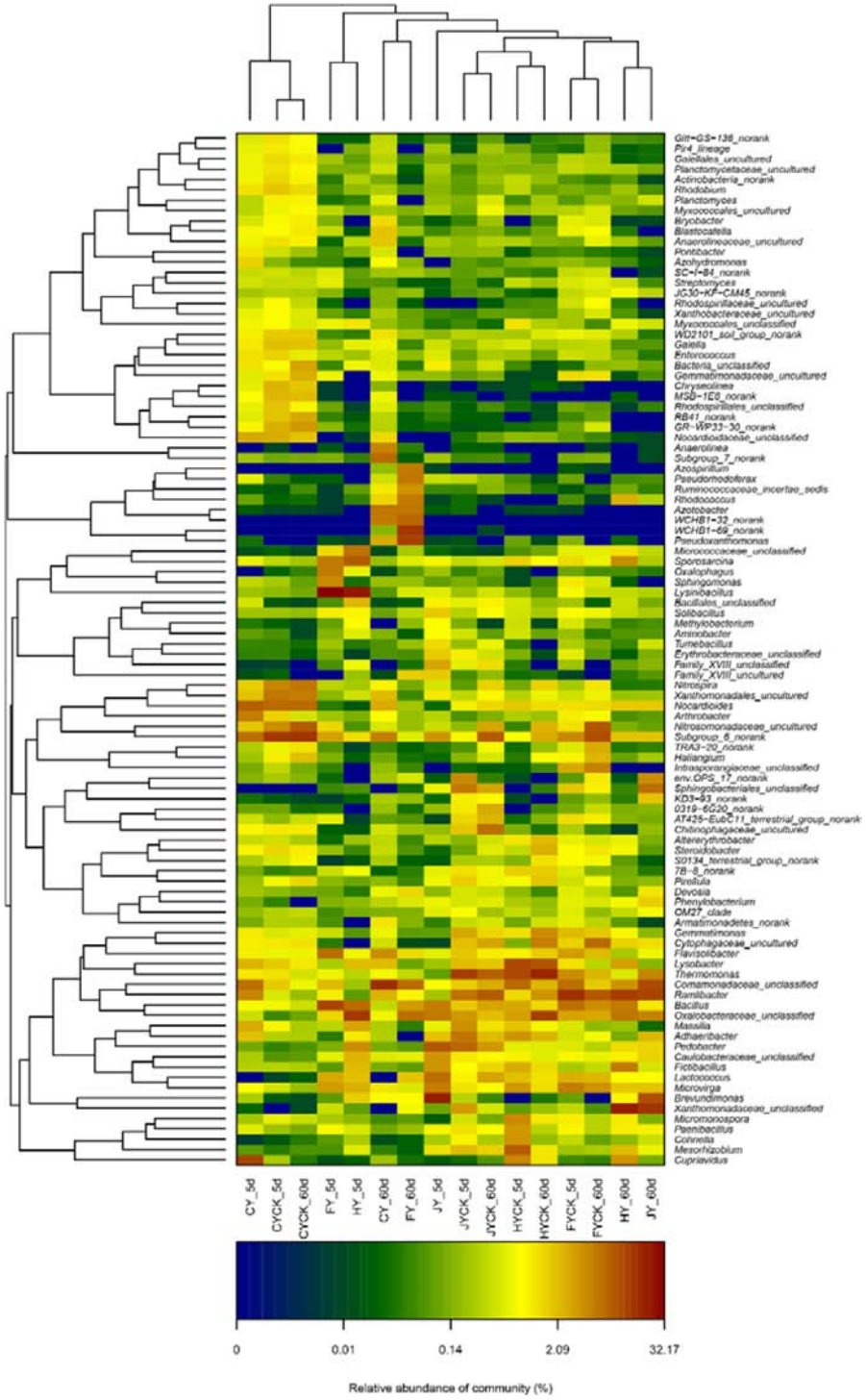

Figure 7. Distribution heatmap of microbial genus arranged by hierarchical clustering of S1 and S2 soils with different treatments.

was 297.1144, which should be the transformation of the group of 8-nitroso on M2 to the 8-amino group, and the nitroso group on M1 transformed to hydroxyl. On the basis of these characteristics, M4 was preliminarily identified as 1-((6-chloropyridin-3-yl)methyl)-5,7-diol-8-amino-1,2,3,5,6,7-hexahydroimidazo[1,2-α]pyridine.

The intermediate M5, with m/z 299.1284 (M + H, Figure 3e), was determined as a derivative of M4 on the basis of the elemental formula fit, adding a mass unit of 2 corresponding to hydrogenation of the C═C double bond. The M5 ions matched the formula $C_{13}H_{18}ClN_3O_3$, Thus, M5 was identified as 1-((6-chloropyridin-3-yl)methyl)-5,7-diol-8-amino-octahydroimidazo[1,2-α]pyridine. M6 appeared after M3 and its m/z was 276.0887 (M + H, Figure 3f); the M6 ions matched the formula $C_{14}H_{14}ClN_3O$, and M6 was identified as 1-((6-chloropyridin-3-yl)methyl)-2,3-dihydro-5-one-7-methylimidazo[1,2-α]pyridine.

IPP Anaerobic Degradation Pathway in Soils. In J soil, only two metabolites, M2 and M5, were determined, M2 appearing first and then M5 forming from M2; in H soil, only M2 appeared. Therefore, an anaerobic degradation pathway in J and H soils was proposed (Figure 4). The propyl group of IPP was de-esterified and hydrolyzed to form M2, which was in

DOI: 10.1021/acs.jafc.5b02645
J. Agric. Food Chem. 2015, 63, 7151−7160

accordance with the previous study.[5−7] The nitro group of M2 could be aminated to form amino, and methyl was hydrolyzed to a hydroxyl group. Thus, M5 was generated through these biocatalyzed reactions.

Therefore, the biodegradation pattern can be described as follows: M1 and M2 are first produced and then increased, and this was then followed by M3, M4, and M5, which appeared at almost the same time. M6 was generated in C soil, and M6 was formed from M3 by the loss of a propyl group on M3. On the basis of the identified metabolites during degradation and their patterns of appearance, the proposed degradation pathway of IPP in soils is as follows (Figure 4): In anaerobic F soil, the nitro group of IPP was reduced to a nitroso group and then formed M1. The nitroso group was eliminated during IPP biodegradation, resulting in the denitration product M3. M2 was determined and generated by the loss of a propyl group from the IPP parent. Subsequently, the nitro group on M2 was aminated to form an amino group, and 7-methyl was transformed to a hydroxyl group; thus, M4 was generated. Both M2 and M4 could be transformed to M5. M6 was generated from M3 only in C soil. On the basis of the identified metabolites during degradation and their patterns of appearance, the proposed degradation pathway of IPP in soils is shown in Figure 4. The metabolites M1, M2, and M3 were in accordance with previous reports.[5−7] M4 and M5 were first observed and identified during IPP anaerobic degradation in soils. In anaerobic soils, a hydroxyl group appeared during M2 transformation to M4, and the reaction should be catalyzed by methyltransferase from microorganism.

Bacterial Diversity and Community Structure in Anaerobic Soils. The community species diversity is shown in Figure 5a. It can be concluded that the bacterial communities in the CK soils (soils without IPP application) were more diverse than in soils with IPP-spraying, which indicated that IPP can affect soil microbial species diversity and IPP could inhibit some bacteria growth and their activity in soils. Under the same conditions, bacteria in the C and F soils were more diverse than in the J and H soils. The sequence of high-to-low order of organic matter (OM) content was C and F > H and J. OM content affects bacterial growth and activity; this was in accordance with the community diversity. The results of rarefaction analysis (Figure 5a) were also similar to the comparison of Shannon's H′ (Figure 5b). Evenness in all samples was close to 0.97 for the 0.03 clustering level, and the highest values were observed in C soil. All of the reads in the microbial community were assigned to bacteria. Proteobacteria was the most abundant phylum in all samples (20.5−62.4%, Figure 6a), Firmicutes was the most abundant in F and H soils with IPP-spraying after 5 DAT (56.2 and 48.3%, respectively). Other major phyla were Bacteroidetes, Actinobacteria, Acidobacteria, Gemmatimonadetes, Planctomycetes, Chloroflexi, and Nitrospirae. The most abundant genera were *Ramlibacter*, *Lysinibacillus*, *Comamonadaceae*, *Oxalobacteraceae*, *Thermomonas*, *Bacillus*, *Nitrosomonadaceae*, and *Sporasarcina* (Figure 6b). The community composition was affected by IPP in anaerobic soils. The relative abundance of *Ramlibacter*, *Thermomonas*, *Nitrosomonadaceae*, and *Nocardioides* was higher in C soil with IPP spraying than in CK soil, whereas in F soil, the genera *Lysinibacillus*, *Thermomonas*, *Cytophagaceae*, *Sporosarcina*, and *Nitrospira* were stimulated to increase after IPP application. RS-IPP and SR-IPP were quickly degraded in the first 10 days in J soil, whereas in H soil, the two insecticides were quickly degraded between 20 and 40 days (Figure 2b,d). Figure 6 shows that phylum relative abundance of Acidobacteria, Planctomycetes, Cyanobacteria, and Chlorobi in J soil was higher than in H soil, and *Deinococcus-Thermus* was determined only in J soil. Several studies showed that despite similar microbial composition at the initial stage, microbial response to insecticide application was remarkably different.[24−27] Insecticide-degrading bacteria rapidly increased in the soils after insecticide application. Itoh et al. reported that *O*,*O*-dimethyl *O*-(3-methyl-*p*-nitrophenyl) phosphorothioate (MEP) degrading microbes increased rapidly after MEP application. Microbial response to MEP application was different, and MEP-degrading *Burkholderia* bacteria are predominant in soils.[24] Formesafen and its residues also affect soil microbial activity and soil microbial communities.[27] The clustered heatmap analysis based on the bacterial community profiles at the genus level disclosed that the bacterial communities in anaerobic soils after spray IPP shared higher similarity (Figure 7). The bacterial profile in anaerobic soils was distant from that of anaerobic soils after IPP-spraying.

Conclusions. The results in this study show that IPP anaerobic degradation rate is different in four different kinds of soil. Soils' physical−chemical characteristics strongly influenced IPP degradation rate. The metabolites of IPP degradation in soils were identified, and anaerobic degradation pathways were proposed, which presents novel biodegradation pathway of IPP in soils. The determination of new metabolites is very important for better understanding of the mechanism and pathway of IPP biodegradation in anaerobic soils. The bacterial communities in the CK soils were more diverse than in soils with IPP-spraying. Both the rarefaction curves and Shannon−Wiener diversity index in anaerobic soils showed significant difference after IPP application, and the community composition also differed at both phyla and genus levels. The results suggest that application of IPP may change the soil microbial community; IPP-degrading bacteria increased quickly after IPP application in soils.

AUTHOR INFORMATION

Corresponding Authors

*(Z.C.) Phone: 86-519-86330165. Fax: 86-519-86330165. E-mail: zhqcai@cczu.edu.cn.

*(G.Y.) Phone: 86-519-86330194. Fax: 86-519-86330194. E-mail: yguanghua@cczu.edu.cn.

Funding

The research was financially funded by grants from the National Natural Science Foundation of China (NSFC) (Project 11275033) and the Talent Introduction Foundation of Changzhou University (No. ZMF13020003).

Notes

The authors declare no competing financial interest.

REFERENCES

(1) Liu, W.; Gan, J.; Schlenk, D.; Jury, W. A. Enantioselectivity in environmental safety of current chiral insecticides. *Proc. Natl. Acad. Sci. U. S. A.* **2005**, *102* (3), 701−706.

(2) Liu, W. P.; Gan, J. Y.; Lee, S.; Werner, I. Isomer selectivity in aquatic toxicity and biodegradation of bifenthrin and permethrin. *Environ. Toxicol. Chem.* **2005**, *24*, 1861−1866.

(3) Liu, W. P.; Lin, K. D.; Gan, J. Y. Separation and aquatic toxicity of enantiomers of the organophosphorus insecticide trichloronate. *Chirality* **2006**, *18*, 713−716.

(4) Li, J.; Zhang, J.; Li, C.; Wang, W.; Yang, Z.; Wang, H.; Gan, J.; Ye, Q.; Xu, X.; Li, Z. Stereoisomeric isolation and stereoselective fate of insecticide Paichongding in flooded paddy soils. *Environ. Sci. Technol.* **2013**, *47*, 12768−12774.

(5) Fu, Q.; Wang, Y.; Zhang, J.; Zhang, H.; Bai, C.; Li, J.; Wang, W.; Wang, H.; Ye, Q.; Li, Z. Soil microbial effects on the stereoselective mineralization, extractable residue, bound residue and metabolism of a

DOI: 10.1021/acs.jafc.5b02645
J. Agric. Food Chem. 2015, 63, 7151−7160

novel chiral cis neonicotinoid, paichongding. *J. Agric. Food Chem.* **2013**, *61*, 7689−7695.
(6) Fu, Q.; Zhang, J.; Xu, X.; Wang, H.; Wang, W.; Ye, Q.; Li, Z. Diastereoselective metabolism of a novel *cis*-nitromethylene neonicotinoid paichongding in aerobic soils. *Environ. Sci. Technol.* **2013**, *47*, 10389−10396.
(7) Cai, Z.; Zhang, W.; Li, S.; Ma, J.; Wang, J.; Zhao, X. Microbial degradation mechanism and pathway of the novel insecticide Paichongding by a newly isolated *Sphingobacterium* sp. P1-3 from soil. *J. Agric. Food Chem.* **2015**, *63*, 3823−3829.
(8) Wang, H.; Yang, Z.; Liu, R.; Fu, Q.; Zhang, S.; Cai, Z.; Li, J.; Zhao, X.; Ye, Q.; Wang, W.; Li, Z. Stereoselective uptake and distribution of the chiral neonicotinoidinsecticide, Paichongding, in Chinese pak choi (*Brassica campestris* ssp. *chinenesis*). *J. Hazard. Mater.* **2013**, *262*, 862−869.
(9) Kalyani, S. S.; Sharma, J.; Dureja, P.; Singh, S.; Lata. Influence of endosulfan on microbial biomass and soil enzymatic activities of a tropical Alfisol. *Bull. Environ. Contam. Toxicol.* **2010**, *84*, 351−356.
(10) Defo, M. A.; Njine, T.; Nola, M.; Beboua, F. S. Microcosm study of the long term effect of endosulfan on enzyme and microbial activities on two agricultural soils of Yaounde-Cameroon. *Afr. J. Agric. Res.* **2011**, *6*, 2039−2050.
(11) Cycon, M.; Markowicz, A.; Borymski, S.; Wojcik, M.; Piotrowska-Seget, Z. Imidacloprid induces changes in the structure, genetic diversity and catabolic activity of soil microbial communities. *J. Environ. Manage.* **2013**, *131*, 55−65.
(12) Nasreen, C.; Jaffer Mohiddin, G.; Srinivasulu, M.; Rekha Padmini, A.; Ramanamma, P.; Rangaswamy, V. Interaction effects of insecticides on enzyme activities in black clay soil from groundnut (*Arachis hypogaea* L.) fields. *Environ. Res. Eng. Manage.* **2012**, *2* (60), 21−28.
(13) Gundi, V.; Viswanath, B.; Chandra, M. S.; Kumar, V. N.; Reddy, B. R. Activities of cellulase and amylase in soils as influenced by insecticide interactions. *Ecotoxicol. Environ. Saf.* **2007**, *68*, 278−285.
(14) Zhao, X.; Shao, X.; Zou, Z.; Xu, X. Photodegradation of novel nitromethylene neonicotinoids with tetrahydropyridine-fixed cis configuration in aqueous solution. *J. Agric. Food Chem.* **2010**, *58*, 2746−2754.
(15) Shao, X.; Zhang, W.; Peng, Y.; Li, Z.; Tian, Z.; Qian, X. *cis*-Nitromethylene neonicotinoids as new nicotinic family: synthesis, structural diversity, and insecticidal evaluation of hexahydroimidazo-[1,2-α]pyridine. *Bioorg. Med. Chem. Lett.* **2008**, *18*, 6513−6516.
(16) Tian, Z.; Shao, X.; Li, Z.; Qian, X.; Huang, Q. Synthesis, insecticidal activity, and QSAR of novel nitromethylene neonicotinoids with tetrahydropyridine fixed cis configuration and exo-ring ether modification. *J. Agric. Food Chem.* **2007**, *55*, 2288−2292.
(17) Fu, Q.; Wang, W.; Wang, H.; Zhang, J.; Shen, J.; Li, Z.; Ye, Q. Stereoselective fate kinetics of chiral neonicotinoid insecticide paichongding in aerobic soils. *Chemosphere* **2015**, *138*, 170−175.
(18) Shao, X.; Fu, H.; Xu, X.; Liu, Z.; Li, Z.; Qian, X. Divalent and oxabridged neonicotinoids constructed by dialdehydes and nitromethylene analogues of imidacloprid: design, synthesis, crystal structure, and insecticidal activities. *J. Agric. Food Chem.* **2010**, *58*, 2696−2702.
(19) Shao, X.; Lee, P. W.; Liu, Z.; Xu, X.; Li, Z.; Qian, X. *cis*-Configuration: a new tactic/rationale for neonicotinoid molecular design. *J. Agric. Food Chem.* **2011**, *59*, 2943−2949.
(20) Gee, G. W.; Bauder, J. W. Particle-size analysis. In *Methods of Soil Analysis, Part 1, Physical and Mineralogical Methods*; Klute, A., Ed.; Soil Science Society of America: Madison, WI, USA, 1986; pp 383−412.
(21) Cai, Z.; Wang, H.; Shi, S.; Wang, W.; Chen, Q.; Zhao, X.; Ye, Q. Aerobic biodegradation kinetics and pathway of the novel herbicide ZJ0273 in soils. *Eur. J. Soil Sci.* **2013**, *64*, 37−46.
(22) Mordaunt, C. J.; Gevao, B.; Jones, K. C.; Semple, K. T. Formation of non-extractable pesticide residues,observations on compound defferences, measurement and regulatory issues. *Environ. Pollut.* **2005**, *133* (1), 25−34.
(23) Hirano, T.; Ishida, T.; Kokyo, O.; Sudo, R. Biodegradation of chlordane and hexachlorobenzenes in river sediment. *Chemosphere* **2007**, *67* (3), 428−434.
(24) Itoh, H.; Navarro, R.; Takeshita, K.; Tago, K.; Hayatsu, M.; Hori, T.; Kikuchi, Y. Bacterial population succession and adaptation affected by insecticide application and soil spraying history. *Front. Microbiol.* **2014**, *5*, 457.
(25) Fang, H.; Cai, L.; Yang, Y.; Ju, F.; Li, X.; Yu, Y. Metagenomic analysis reveals potential biodegradation pathways of persistent pesticides in fresh water and marine sediments. *Sci. Total Environ.* **2014**, *470-471*, 983−992.
(26) Jacobsen, C. S.; Hjelmsø, M. H. Agriculturalsoils, pesticides and microbial diversity. *Curr. Opin. Biotechnol.* **2014**, *27*, 15−20.
(27) Wu, X.; Xu, J.; Dong, F.; Liu, X.; Zheng, Y. Responses of soil microbial community to different concentration of fomesafen. *J. Hazard. Mater.* **2014**, *273*, 155−164.

DOI: 10.1021/acs.jafc.5b02645
J. Agric. Food Chem. 2015, 63, 7151−7160

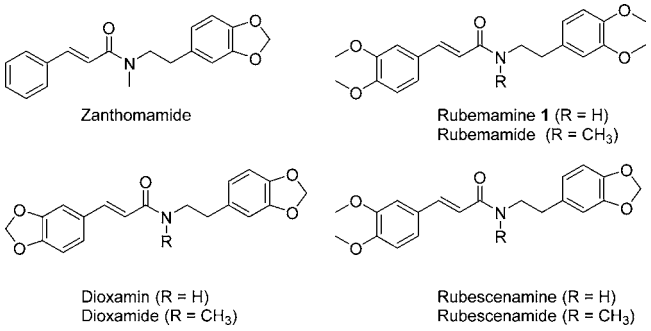

Figure 2. Amides from *Zanthoxylum rubescens*.[13]

The subject of this work includes the synthesis of many cinnamic acid related amides, their sensory evaluation for umami taste, the necessary structural features for umami taste,[19] and the subsequent analysis of *Zanthoxylum piperitum* to show the natural occurrence of these umami amides.

MATERIALS AND METHODS

General. Unless otherwise specified, commercially available reagents and solvents were purchased from Fluka-Sigma-Aldrich, Buchs, Switzerland; Acros Organics, Geel, Belgium; and Carlo-Erba, Val de Reuil, France.

NMR Spectra. ^{1}H and ^{13}C NMR spectra were recorded in $CDCl_3$ on a DPX 400 spectrometer (Bruker, Rheinstetten, Germany) at 25 °C operated at 400 MHz (^{1}H) or 100 MHz (^{13}C), with tetramethylsilane as the internal standard. The ^{13}C signal assignments were obtained from standard gradient-selected correlated spectroscopy, heteronuclear single-quantum coherence, and heteronuclear multiple bond correlation experiments performed on a Bruker Avance 500 spectrometer. NMR spectra were processed with Bruker TopSpin 2.0 software (s, singlet; d, doublet; t, triplet; m, multiplet).

UPLC-MS Method. Analyses of samples were performed on a Acquity I-Class UPLC system (Waters, Milford, USA) coupled with a Q-Exactive Plus mass spectrometer (Thermo, San Jose, CA, USA). The column was an Acquity HSS-T3, 100 mm × 2.1 mm i.d. (Waters) operated at 30 °C. Solvent A was UPLC/MS-grade water (BioSolve, Valkenswaard, The Netherlands) containing 0.1% MS-grade formic acid (Sigma-Aldrich, Steinheim, Germany). Solvent B was acetonitrile (Biosolve) containing 0.1% formic acid at 0.3 mL/mL. The gradient elution was as follows: 40% B, 1 min; 40−80% B for 9 min; 80% B, 1 min; and re-equilibration at 40% B for 1 min.

The mass spectrometer was equipped with an H-ESI II electrospray source operated in the positive mode: spray 3500 V, probe heater 400 °C, heated capillary 300 °C, sheath gas 50 arb units, auxiliary gas 10. The mass calibration was performed each week. The full scan/ddMS^2 mode combined with the targeted MS^2 (tMS^2) acquisition mode were used. The full scan/ddMS^2 triggered the recording of the MS^2 spectra for the three most intense ions. The tMS^2 mode recorded the MS^2 spectra of 15 amides (Results and Discussion) on the basis of an inclusion list containing their molecular formulas. The full-scan spectra were acquired with a resolution of 70 000 from 100 to 1000 Da, and the MS^2 spectra were acquired with a resolution of 17 500 and a higher energy collisional dissociation cell energy of 30 V. Automated gain control was targeted to 3×10^6 and 1×10^5 ions with a maximum injection time of 100 ms for full scan and 50 ms for ddMS^2.

Synthesis of Amides with Ethyl Chloroformate, General Procedure. The acid component (typically 33 mmol) and diisopropyl ethyl amine (2 equiv) were diluted in 200 mL of EtOAc and 50 mL of dichloromethane. The solution was cooled to 15 °C, and ethyl chloroformate (1 molar equiv) was added dropwise. The reaction was stirred for 1 h before the primary amine component (1 molar equiv, diluted 2−3× in EtOAc) was added. The reaction was stirred overnight at room temperature. It was washed with aqueous 5% $KHSO_4$, brine, aqueous 5% $NaHCO_3$, and brine and then dried over Na_2SO_4 and evaporated under high vacuum for 3 h. The crude product was purified by flash chromatography (silica gel; cyclohexane/EtOAc, e.g., 2:8). Yields were between 50 and 80% of the purified product. MS and UV data only are given below. The description of ^{1}H and ^{13}C NMR spectra can be found in the Supporting Information.

*Amide **1**, Rubemamine, (E)-N-(3,4-Dimethoxyphenethyl)-3-(3,4-dimethoxyphenyl)acrylamide.* ESI (+): 372.1798 ($C_{21}H_{26}O_5N$, −2.1 ppm). UV max (nm): 316, 287, 222.

*Amide **2**, (E)-N-(3,4-Dimethoxyphenethyl)-3-(4-methoxyphenyl)-acrylamide.* ESI (+): 342.1690 ($C_{20}H_{24}O_4N$, −2.8 ppm). UV max (nm): 310, 288, 224.

*Amide **3**, (E)-3-(Benzo[d][1,3]dioxol-5-yl)-N-(3,4-dimethoxyphenethyl)acrylamide.* ESI (+): 356.1483 ($C_{20}H_{22}O_5N$, −4.2 ppm). UV max (nm): 322, 286, 228, 219.

*Amide **4**, (E)-3-(3,4-Dimethoxyphenyl)-N-(4-methoxyphenethyl)-acrylamide.* ESI (+): 342.1693 ($C_{20}H_{24}O_4N$, −2.0 ppm). UV max (nm): 316, 291, 223.

*Amide **5**, (Z)-3-(3,4-Dimethoxyphenyl)-N-(4-methoxyphenethyl)-acrylamide.* Amide **4** (500 mg) in 50 mL of ethanol was irradiated for 16 h by using a water-cooled 125 W Hg lamp. UPLC analysis showed that the crude product contained 50% of the (*Z*) isomer. The product was chromatographed over a Puriflash 50 C18 cartridge (Interchim Montluçon, France) eluted with a water/ethanol mixture (60:40). A mixture of amides **5** and **4** (90:10) was obtained (96 mg). ESI (+): 342.1693 ($C_{20}H_{24}O_4N$, −2.1 ppm). UV max (nm): 310, 276, 224.

*Amide **6**, 3-(3,4-Dimethoxyphenyl)-N-(4-methoxyphenethyl)-propanamide.* ESI (+): 344.1849 ($C_{20}H_{26}O_4N$, −2.0 ppm). UV max (nm): 277, 225.

*Amide **7**, N-(4-Methoxyphenethyl)cinnamamide.* ESI (+): 282.1481 ($C_{18}H_{20}O_2N$, −2.8 ppm). UV max (nm): 275, 222.

*Amide **8**, N-(3-Methoxyphenethyl)cinnamamide.* ESI (+): 282.1491 ($C_{18}H_{20}O_2N$, −2.6 ppm). UV max (nm): 274, 223.

*Amide **9**, (E)-N-(4-Methoxyphenethyl)-3-(4-methoxyphenyl)-acrylamide.* ESI (+): 312.1585 ($C_{19}H_{22}O_3N$, −2.9 ppm). UV max (nm): 310, 290, 224.

*Amide **10**, (E)-N-(4-Methoxyphenethyl)-3-(2-methoxyphenyl)-acrylamide.* ESI (+): 312.1586 ($C_{19}H_{22}O_3N$, −2.7 ppm). UV max (nm): 317, 274, 225.

*Amide **11**, (E)-N-(4-Methoxyphenethyl)-3-(3-methoxyphenyl)-acrylamide.* ESI (+): 312.1587 ($C_{19}H_{22}O_3N$, −2.4 ppm). UV max (nm): 310, 277, 224.

*Amide **12**, (E)-3-(2,5-Dimethoxyphenyl)-N-(4-methoxyphenethyl)acrylamide.* ESI (+): 342.1690 ($C_{20}H_{24}O_4N$, −2.8 ppm). UV max (nm): 342, 276, 223.

*Amide **13**, (E)-N-(4-Methoxyphenethyl)-3-(3,4,5-trimethoxyphenyl)acrylamide.* ESI (+): 372.1797 ($C_{21}H_{26}O_5N$, −2.4 ppm). UV max (nm): 299, 228.

*Amide **14**, (E)-2-Methoxy-4-(3-((4-methoxyphenethyl)amino)-3-oxoprop-1-en-1-yl)phenyl Acetate.* ESI (+): 370.1639 ($C_{21}H_{24}O_5N$, −2.6 ppm). UV max (nm): 310, 277, 224.

*Amide **15**, (E)-3-(4-Hydroxy-3-methoxyphenyl)-N-(4-methoxyphenethyl)acrylamide.* Amide **14** was deprotected in MeOH/Na_2CO_3. The reaction was acidified and extracted from EtOAc. The product was recrystallized from EtOAc (yield 75%). ESI (+): 328.1535 ($C_{19}H_{22}O_4N$, −2.5 ppm). UV max (nm): 317, 293, 222.

*Amide **16**, (E)-3-(Benzo[d][1,3]dioxol-5-yl)-N-(4-methoxyphenethyl)acrylamide.* ESI (+): 326.1379 ($C_{19}H_{20}O_4N$, −2.4 ppm). UV max (nm): 322, 284, 219.

*Amide **17**, (E)-3-(3,4-Dimethylphenyl)-N-(4-methoxyphenethyl)-acrylamide.* ESI (+): 310.1794 ($C_{20}H_{24}O_2N$, −2.6 ppm). UV max (nm): 285, 224.

*Amide **18**, (E)-3-(3,4-Dimethoxyphenyl)-N-phenethylacrylamide.* ESI (+): 312.1588 ($C_{19}H_{22}O_3N$, −2.0 ppm). UV max (nm): 317, 291, 235, 211.

*Amide **19**, (E)-3-(3,4-Dimethoxyphenyl)-N-(3-methoxyphenethyl)acrylamide.* ESI (+): 342.1693 ($C_{20}H_{24}O_4N$, −2.1 ppm). UV max (nm): 317, 291, 218.

*Amide **20**, (E)-3-(3,4-Dimethoxyphenyl)-N-(2-methoxyphenethyl)acrylamide.* ESI (+): 342.1691 ($C_{20}H_{24}O_4N$, −2.7 ppm). UV max (nm): 317, 291, 220.

*Amide **21**, (E)-N-(3,5-Dimethoxyphenethyl)-3-(3,4-dimethoxyphenyl)acrylamide.* ESI (+): 372.1797 ($C_{21}H_{26}O_5N$, −2.4 ppm). UV max (nm): 317, 292, 219.

DOI: 10.1021/acs.jafc.5b02359
J. Agric. Food Chem. 2015, 63, 7161−7168

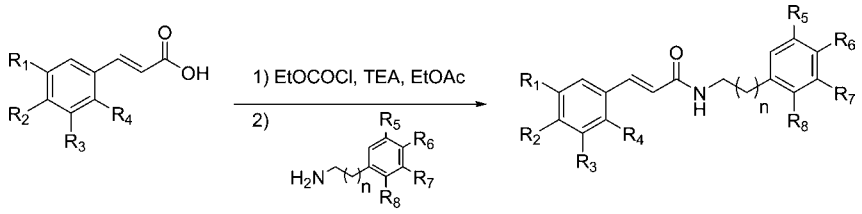

N°	R_1	R_2	R_3	R_4	R_5	R_6	R_7	R_8	n	double bond
1	OMe	OMe	H	H	H	OMe	OMe	H		
2	H	OMe	H	H	H	OMe	OMe	H		
3	a	a	H	H	H	OMe	OMe	H		
4	OMe	OMe	H	H	H	OMe	H	H		
5	OMe	OMe	H	H	H	OMe	H	H		(*Z*)
6	OMe	OMe	H	H	H	OMe	H	H		single bond
7	H	H	H	H	H	OMe	H	H		
8	H	H	H	H	H	H	OMe	H		
9	H	OMe	H	H	H	OMe	H	H		
10	H	H	H	OMe	H	OMe	H	H		
11	OMe	H	H	H	H	OMe	H	H		
12	OMe	H	H	OMe	H	OMe	H	H		
13	OMe	OMe	OMe	H	H	OMe	H	H		
14	OMe	OAc	H	H	H	OMe	H	H		
15	OMe	OH	H	H	H	OMe	H	H		
16	a	a	H	H	H	OMe	H	H		
17	Me	Me	H	H	H	OMe	H	H		
18	OMe	OMe	H	H	H	H	H	H		
19	OMe	OMe	H	H	H	H	OMe	H		
20	OMe	OMe	H	H	H	H	H	OMe		
21	OMe	OMe	H	H	OMe	H	OMe	H		
22	OMe	OMe	H	H	H	H	OEt	H		
23	OMe	OMe	H	H	H	H	O*n*Pr	H		
24	OMe	OMe	H	H	H	O*i*Pr	H	H		
25	OMe	OMe	H	H	H	Et	H	H		
26	OMe	OMe	H	H	H	*i*Pr	H	H		
27	OMe	OMe	H	H	H	Me	Me	H		
28	OMe	OMe	H	H	H	OMe	H	H	0	
29	OMe	OMe	H	H	H	a	a	H	0	

Figure 3. Structure of cinnamic acid derived amides synthesized for umami taste evaluation. Double bond is of (*E*) configuration except when otherwise designated. a, R_1−R_2 or R_6−R_7 = O−CH_2−O (methylenedioxy). *n* = 1 (phenethylamine series) except when designated as 0 (benzylamine series).

Amide ***22****, (E)-3-(3,4-Dimethoxyphenyl)-N-(3-ethoxyphenethyl)-acrylamide.* ESI (+): 356.1848 ($C_{21}H_{26}O_4N$, −2.4 ppm). UV max (nm): 316, 292, 219.

Amide ***23****, (E)-3-(3,4-Dimethoxyphenyl)-N-(3-propoxyphenethyl)-acrylamide.* ESI (+): 370.2005 ($C_{22}H_{28}O_4N$, −2.2 ppm). UV max (nm): 316, 290, 226.

Amide ***24****, (E)-3-(3,4-Dimethoxyphenyl)-N-(4-isopropoxy-phenethyl)acrylamide.* ESI (+): 370.2005 ($C_{21}H_{28}O_4N$, −2.1 ppm). UV max (nm): 316, 290, 226.

Amide ***25****, (E)-3-(3,4-Dimethoxyphenyl)-N-(4-ethylphenethyl)-acrylamide.* ESI (+): 340.1899 ($C_{21}H_{26}O_3N$, −2.3 ppm). UV max (nm): 316, 292, 220.

Amide ***26****, (E)-3-(3,4-Dimethoxyphenyl)-N-(4-isopropylphenethyl)acrylamide.* ESI (+): 354.2055 ($C_{22}H_{28}O_3N$, −2.4 ppm). UV max (nm): 316, 292, 219.

Amide ***27****, (E)-3-(3,4-Dimethoxyphenyl)-N-(3,4-dimethylphenethyl)acrylamide.* ESI (+): 340.1899 ($C_{21}H_{26}O_3N$, −2.6 ppm). UV max (nm): 316, 292, 218.

Amide ***28****, (E)-3-(3,4-Dimethoxyphenyl)-N-(4-methoxybenzyl)-acrylamide.* ESI (+): 328.1537 ($C_{19}H_{22}O_4N$, −2.6 ppm). UV max (nm): 317, 292, 223.

Amide ***29****, (E)-N-(Benzo[d][1,3]dioxol-5-ylmethyl)-3-(3,4-dimethoxyphenyl)acrylamide.* ESI (+): 342.1327 ($C_{19}H_{20}O_5N$, −2.7 ppm). UV max (nm): 317, 292, 235, 218.

Amide ***30****, Beecheyamide, (E)-3-(3,4-Dimethoxyphenyl)-N-(4-methoxyphenethyl)-N-methylacrylamide.* A solution of amide **4** (478 mg, 1.4 mmol) in 14 mL of tetrahydrofuran (THF) was added to a suspension of sodium hydride (120 mg, 5.0 mmol) in 9 mL of THF at 0 °C under argon atmosphere. The reaction was stirred for 30 min at 0 °C before 240 mg of methyl iodide was added. The reaction was stirred at room temperature overnight, the mixture poured into 50 mL of cold water, and the pH adjusted to 7 with 5% $KHSO_4$. Extraction from EtOAc, followed by flash chromatography (pure EtOAc), gave 402 mg of **20** (yield 81%). The product was fully in agreement with the NMR data (showing two rotamers of the amide bond) described by Cheng et al.[20] ESI (+): 356.1847 ($C_{21}H_{26}O_4N$, −2.6 ppm). UV max (nm): 320, 285, 224.

Amide ***31****, Podocarpamide, (E)-N-(2-(Benzo[d][1,3]dioxol-5-yl)-ethyl)-3-(3,4-dimethoxyphenyl)-N-methylacrylamide.* Amide **16** (1.70 g, 5.2 mmol) in 50 mL of THF was added dropwise to a suspension of sodium hydride (150 mg, 1.2 equiv) in 34 mL of THF at 0 °C under argon atmosphere. The reaction was stirred for 30 min at 0

DOI: 10.1021/acs.jafc.5b02359
J. Agric. Food Chem. 2015, 63, 7161−7168

Table 1. Cinnamic Acid Derived Amides and Their Umami Taste Score

product no.	natural occurrence	no. of panelists	rel. umami score	product no.	natural occurrence	no. of panelists	rel. umami score
1	*Z. rubescens*[13]	4	3.3	**17**		3	2.6
2		5	3.9	**18**	*Chloranthus serratus*[24]	7	3.8
3	*Z. rubescens*[14]	*b*		**19**		9	10.2
4	*Z. piperitum*[a]	6	5.6	**20**		7	3.2
5		4	1.3	**21**		7	3.7
6		5	0.9	**22**		6	9.8
7	*Pisonia aculeata*[22]	4	1.6	**23**		7	9.9
8		4	1.5	**24**		5	6.5
9		6	2.4	**25**		5	11.5
10		5	1.0	**26**		5	5.9
11		4	2.2	**27**		4	13.3
12		9	1.8	**28**		6	1.4
13		4	0.3	**29**		6	0.8
14		6	2.2	**30**	*Z. beecheyanum*[20]	*b*	
15	*Z. piperitum*[a]	4	1.1	**31**	*Z. piperitum*[a]	*b*	
16	*Z. armatum*[23]	9	2.1	**32**	*Z. piperitum*[a]	*c*	

[a]This work. [b]Evaluated in large panel only (Table 2). [c]Not evaluated.

°C. Iodomethane (390 μL, 1.2 equiv) was added, and the reaction was stirred overnight at room temperature. After workup and flash chromatography (cyclohexane/EtOAc, 60:40), 1.37 g was obtained (77% yield). NMR data (showing two rotamers of the amide bond) were compliant with those reported by Delle Monache et al.[21] ESI (+): 340.1535 ($C_{20}H_{22}O_4N$, −2.4 ppm). UV max (nm): 321, 285, 232.

Amide ***32****, (E)-3-(4-Hydroxy-3-methoxyphenyl)-N-(4-methoxyphenethyl)-N-methylacrylamide.* 4-Acetoxy-3-methoxycinnamic acid (360 mg, 1.5 mmol, Alfa Aesar) was condensed on [2-(4-methoxyphenyl)-ethyl]methylamine (1 equiv, Aldrich) as described above. The product was purified by flash chromatography (cyclohexane/EtOAc, 50:50) and subsequently deprotected (MeOH/1 M KOH, 1/1 v:v). The reaction was neutralized by addition of 5% $KHSO_4$, and the product was extracted 3 times with EtOAc, then with CH_2Cl_2. After drying over Na_2SO_4 and evaporation, 132 mg of pale-yellow oil was obtained (26%). NMR showed the presence of two rotamers (as described for amide **30**)[20] in a 55:45 ratio. ESI (+): 342.1691 ($C_{20}H_{24}O_4N$, −2.6 ppm). UV max (nm): 321, 285, 232.

Preparation of the Extracts from *Z. piperitum* (L.) DC. The stems and roots were separately cut from the fresh plants, and 207.15 g of stems and 110.44 g of roots were obtained. The stems were ground into a fine powder, poured into 4 L of dichloromethane, stirred for 6 h, and left standing over the weekend. The suspension was filtered, and the solvent was evaporated to yield 1.06 g of brownish oil (0.51% w/w). Similarly, the roots gave 1.6 g of extract (1.45% w/w). The botanical identification of the species was confirmed by a professional botanist (Y.-M. Yuan). Voucher specimens were prepared and kept in the herbarium of the company.

Sensory Evaluation. All of the compounds were assessed by a toxicologist, and many of them were classified as Cramer class III. Therefore, a daily intake of 90 μg/day was allowed. Only one compound of the cinnamic amides family was tasted per session using the "sip and spit" method for 20 mL of solution at 20 ppm, therefore minimizing the amount of ingested product. All panelists had signed a consent form informing them about the risk associated with such tasting of new compounds.

Umami Score (Small Panel). Most of the amides were evaluated by a panel of 4−9 trained people. Each amide was evaluated at 20 ppm in Henniez water against 0.05% monosodium glutamate (MSG) in a blind pair test. The panelists were asked to score the umami taste on a scale of 0−10 for the sample in each cup. The relative umami score was calculated as follows: relative umami score = (amide score/MSG score) × 10

Umami Score (Large Panel). To assess the sensory performance of the selected amides with a larger panel, we asked 15 panelists to evaluate them at 20 or 100 ppm in water (Henniez mineral water) alone and in a 0.05% MSG solution. They were asked to taste the sample while using nose clips in order to focus on taste and trigeminal sensations in the mouth and then without nose clips in order to describe the olfactive notes. The panelists evaluated the samples (20 mL served in a black cup) blind by sipping and spitting the sample out after 5 s before answering the questions. For the pure water system, the panelists had to select the most appropriate attributes from lists of attributes (see below) when they were and were not using nose clips. The attributes were ranked by decreasing order as a function of attribute number cited by the panelists. In the MSG model system, all solutions tasted contained 0.05% MSG and the panelists had to evaluate the perceived umami intensity in the reference solution and in the samples by using a linear scale score ranging from 0 (not intense) to 10 (very intense). The potential umami-enhancing effect of the amide was then evaluated by comparing the perceived intensity of the samples "amide in MSG" versus "MSG alone" (i.e., Δ score corresponding to the intensities of "amide in MSG" minus "MSG alone"). Student's test (paired test, one-tailed) was performed to evaluate the significance of the observed umami difference. The following is the list of attributes: with nose clips: astringent, bitter, cooling, fatty, hot, licorice taste, metallic, mouthfeel, pungent, salivating, salty, sour, sweet, tingling, and umami; without nose clips: earthy, fruity, green, herbal, mushroom, nutty, tea, and woody.

RESULTS AND DISCUSSION

Structure Taste Relationship Study of Nature-Inspired Amides. Most of the amides occurring in *Z. rubescens* consist of amides of substituted cinnamic acid and phenethylamine.[13] Throughout this study, 29 such amides (**1**−**29**) bearing different substituents were synthesized (Figure 3 and Table 1). A few amides shown in Table 1 were already identified in plants[13,22,23] or microorganisms.[24] We limited the study to amides formed from acids and amines whose structural scaffolds were close to those already known to occur in nature. We thought it might increase the chances of showing the natural occurrence of these amides afterward by targeted analysis. Thus, for example, 4-methoxyphenethylamine clearly derives from the amino acid tyrosine, but 3-methoxyphenethylamine could also form from the uncommon but naturally occurring *meta*-tyrosine.[25] The amide bond was formed from the mixed carbonic anhydride generated by reaction of the acid with ethyl chloroformate, followed by addition of the amine. The synthetic amides were subsequently evaluated for their umami taste by a panel of 4−9 trained people. A relative umami score was calculated as follows: (amide score/MSG score) ×

DOI: 10.1021/acs.jafc.5b02359
J. Agric. Food Chem. 2015, 63, 7161−7168

Table 2. Sensory Evaluation of Selected Amides by a Large Panel[a]

compound no.	conc. (ppm)[b]	Δ with NC[c]	Δ without NC[c]	*t*test with NC[d]	*t* test without NC[d]	comments for amides in water evaluated with NC[e]	comments for amides in water evaluated w/o NC[e]
1	20	0.9	0.8	***	**	umami (4), astringent (3)	no
4	20	1.1	1.3	***	***	umami (9), mouthfeel (6), salty (5), astringent (4)	no
19	20	1.7	1.7	**	**	umami (10), mouthfeel (4), salty (4), sour (3)	green (3), herbal (3)
23	20	1.3	1.3	**	**	umami (11), astringent (3), salty (3)	no
24	20	1	1.2	**	**	umami (4), sweet (3)	no
25	20	0.9	0.9	**	**	umami (12)	no
26	20	1	1.1	**	**	umami (7), salty (4), sweet (4), metallic (3)	no
27	20	0.8	1.0	NS	NS	umami (11)	green (3), herbal (3)
30	20	0.7	0.6	NS	*	no	no
31	100	0.1	0.0	NS	NS	bitter (10), astringent (4)	no

[a]Abbreviations: NC, nose clip; NS, not significant; no, no comments or comments given by less than 20% of the panel (fewer than three panelists). [b]The amides were diluted to 10% in ethanol. The quantity of ethanol added to the solution was therefore 0.02% for the compounds tasted at 20 ppm and 0.1% for compound **31** tasted at 100 ppm. [c]Difference in perceived intensity between the amide+MSG vs MSG alone. [d]*, **, and ***: levels of confidence at 95, 99, and 99.9%, respectively. NS, not significant [e]The numbers in parentheses indicate the number of panelists among the 15 who made this comment.

Table 3. Identification of Selected Amides in *Z. piperitum* Root Extract

no.	RT (min)	accurate mass	MS/MS fragment 1	MS/MS fragment 2	MS/MS fragment 3	quantity (mg/kg of extract)
1	2.94	372.1805	191.0702	163.0753		41
		$C_{21}H_{26}NO_5$ (−0.2)	$C_{11}H_{11}O_3$ (−0.2)	$C_{10}H_{11}O_2$ (−0.2)		
4	3.82	342.1699	191.0702	135.0846		29
		$C_{20}H_{24}NO_4$ (−0.2)	$C_{11}H_{11}O_3$ (−0.5)	$C_9H_{11}O$, (+0.1)		
5	3.62	n.d.	n.d.	n.d.		
15	2.85	n.d.	177.0546	145.0284	135.0805	6
			$C_{10}H_9O_3$ (−0.1)	$C_9H_5O_2$ (+0.0)	$C_9H_{11}O$ (+0.4)	
16	4.47	326.1387	175.0389	145.0284	135.0847	527
		$C_{19}H_{20}NO_4$ (−0.0)	$C_{10}H_7O_3$ (−0.2)	$C_9H_5O_2$ (−0.2)	$C_9H_{11}O$ (+0.2)	
19	3.92	n.d.	n.d.	n.d.		
22	4.79	n.d.	n.d.	n.d.		
23	5.92	n.d.	n.d.	n.d.		
24	5.44	n.d.	n.d.	n.d.		
25	5.80	n.d.	n.d.	n.d.		
26	6.63	n.d.	n.d.	n.d.		
27	5.64	n.d.	n.d.	n.d.		
30	4.26	356.1854	191.0703	135.0805		5784[a]
		$C_{21}H_{26}NO_4$ (−0.6)	$C_{11}H_{11}O_3$ (−0.1)	$C_9H_{11}O$ (+0.5)		
31	5.01	340.1541	175.0389	145.0284	135.0805	18723[a]
		$C_{20}H_{22}NO_4$ (−0.6)	$C_{10}H_7O_3$ (+0.0)	$C_9H_5O_2$ (+0.0)	$C_9H_{11}O$ (+0.5)	
32	3.18	342.1700	175.0390	145.0284	135.0805	845
		$C_{20}H_{24}NO_4$ (+0.2)	$C_{10}H_9O_3$ (−0.2)	$C_9H_5O_2$ (−0.2)	$C_9H_{11}O$ (+0.1)	

[a]Above the highest point of calibration.

10. For a umami score of 10, the umami taste intensity of the amide at 20 ppm was perceived as being equal to that of 0.05% MSG. Thus, rubemamine (**1**), which was perceived as umami with a score of 3.3, was used as a lead compound in this study. The structural optimization was performed step by step by varying the substituents independently.

The comparison of the relative umami score for the amides shown in Table 1 led to the following conclusions. The double bond of (*E*) configuration in the acid part was needed because compound **5** with the (*Z*) configuration and the saturated compound **6** did not have a umami taste. Two methoxy groups were the most favorable (**4** vs **7**, **9**−**11**, and **13**), and they should be in the meta and para positions (i.e., **4** was better than **12**). With substituents other than methoxy groups (**14**−**17**), the umami taste intensity decreased significantly. Thus, it appeared that 3,4-dimethoxycinnamic acid was needed as the acid part of the amide. The phenethylamine part (n = 1) tolerated much more variation on the aromatic ring. Thus, compounds **18** and **19** and **20**−**27**, bearing different R_5 and R_6 groups, were perceived as umami-tasting, either moderately (**18**, **21**, and **22**) or strongly (**19** and **22**−**27**). In particular, compounds having one alkoxy or one alkyl group in meta position were all very strong (**19** > **4** > **20**). Benzylamides (n = 0) **29** and **30** were only very weakly umami-tasting.

In the large panel study, all but two of the evaluated amides significantly enhanced the umami taste (Table 2). The delta scores represent the average difference between the perceived umami intensity of the model solution (MSG) and that with the amide added. A positive value denotes an increase of umami taste intensity when the amide was present. Student's test

DOI: 10.1021/acs.jafc.5b02359
J. Agric. Food Chem. 2015, 63, 7161−7168

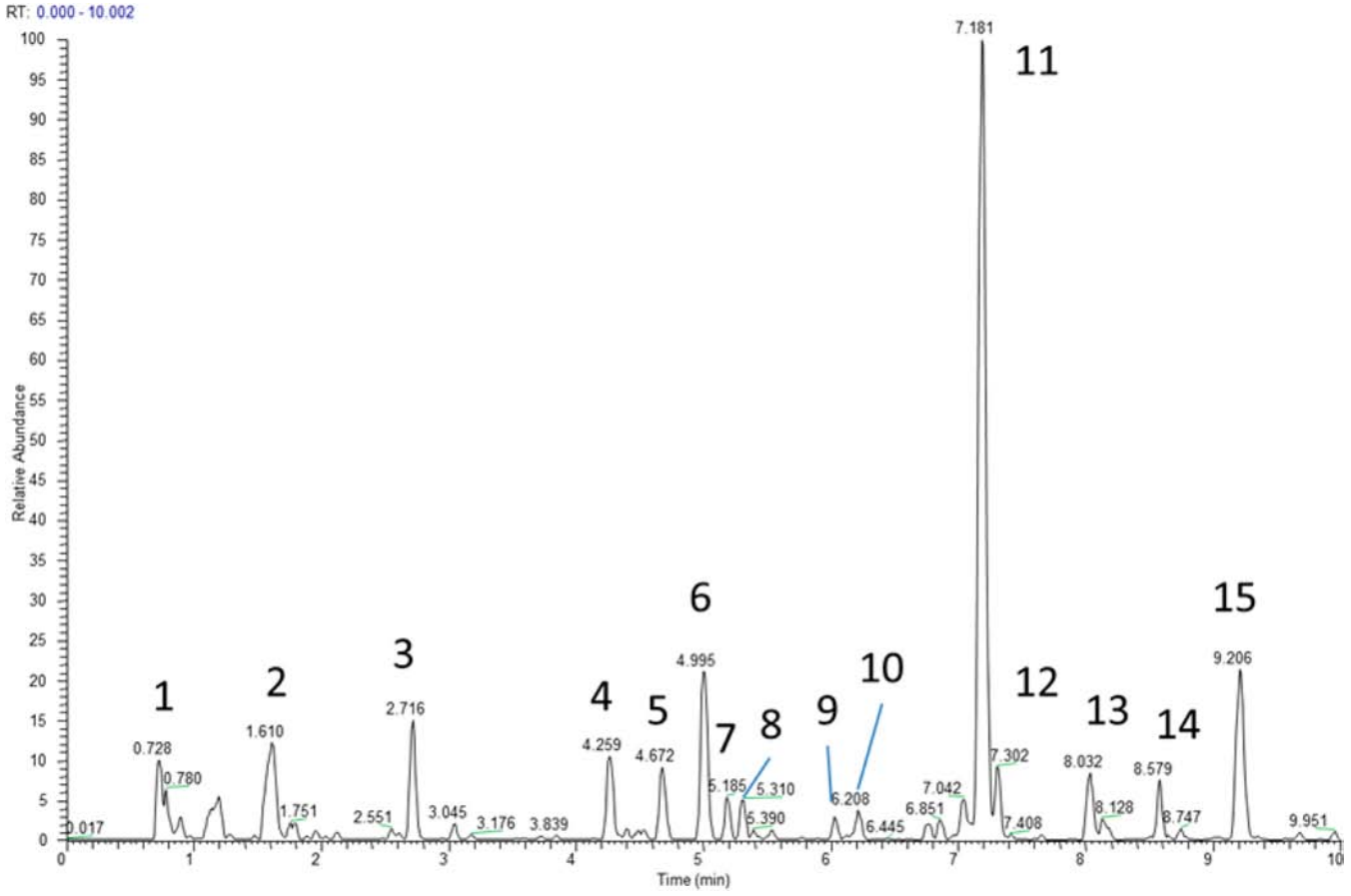

Figure 4. UPLC/MS chromatogram (Full scan mode) of *Z. piperitum* root extract.

(paired test, one-tailed) indicates whether this difference is significant at different levels of confidence between these two samples (*, **, and ***, at 95, 99, and 99.9%, respectively). The best performing amides were **1**, **4**, **19**, and **23**−**27**. One of the most interesting compounds was **4**, which increased the perceived intensity of umami by 1.3, with a significance level of 99.9% with and without the nose clip. Furthermore, the comments regarding the water system with the nose clips were quite positive, except for the astringency; there was no olfactive off-note (no comment without the nose clips).

Targeted UPLC/MS/MS Analysis and Occurrence of Amides 1, 4, 15, 16, and 30−**32 in *Z. piperitum*.** There are more than 500 species in the genus *Zanthoxylum* (Rutaceae),[15] which often used as medicinal plants, as ornamentals, or in culinary applications. Cheng et al. analyzed *Z. beecheyanum* K. Koch, which K. Koch purchased in Taiwan, and it contained many aromatic amides.[20] The description of this plant as an evergreen shrub originating from Japan introduced as an ornamental plant in Taiwan is very similar to that of *Z. piperitum*. The latter plant is used as ornamental plant in China and as bonsai in Japan, whereas the pericarp of the species is commonly used as a spice in Japan.[15] We decided to focus our study on this plant. Dichloromethane was selected as the solvent for the extraction because the synthetic amides described earlier were all very soluble in it. The stems and the roots were extracted separately and analyzed by UPLC/MS operated in positive electrospray ionization mode. For this study, we used a high-resolution hybrid quadrupole-Orbitrap mass spectrometer in full scan/data-dependent MS^2 experiment mode followed by a targeted MS^2 experiment (t-MS^2) within the same run. The t-MS^2 mode used an inclusion list comprising the molecular formulas of the 15 selected amides (Table 3) to record the corresponding product ion spectra. Figure 4 shows the UPLC/MS profile of the root extract of *Z. piperitum*. It was not the aim of this study to fully characterize the extract, but some major products already known to occur in *Zanthoxylum* species could be tentatively identified on the basis of their accurate masses. The major products identified in Figure 4 were amides such as α-sanshool (peak 11), beecheyamide (**30**, peak 4), podocarpamide (**31**, peak 6), alkaloids such as skimmianine (peak 3) and zanthoxyline (peak 2), and probably lignan-related products (peaks 9−10). Amides **30**−**32** (Figure 5) were synthesized to be used in the study.

According to the International Organization of the Flavor Industry guidelines for the positive identification of chemicals

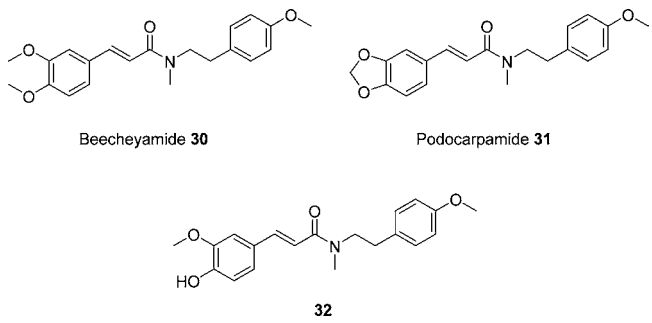

Figure 5. Amides **30**−**32** synthesized for targeted UPLC/MS analysis of *Z. piperitum*.

DOI: 10.1021/acs.jafc.5b02359
J. Agric. Food Chem. 2015, 63, 7161−7168

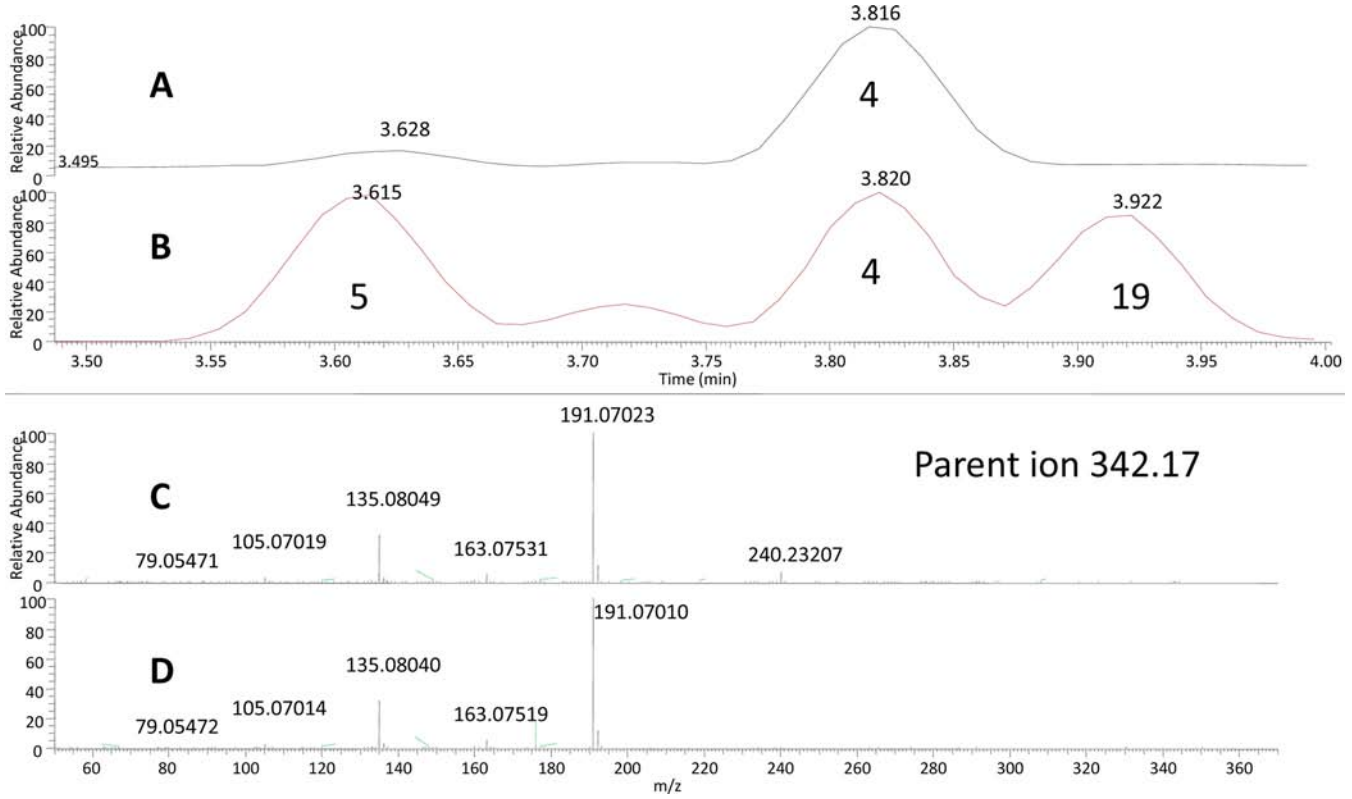

Figure 6. UPLC/MS trace in targeted-MS^2 mode (Materials and Methods) of ion 342.17 in (A) *Z. piperitum* root extract and (B) a mixture of synthetic products. MS/MS spectra of (C) peak at 3.827 min in *Z. piperitum* and (D) peak at 3.820 min in the synthetic mixture, showing the natural occurrence of amide **4**.

by high-resolution LC/MS/MS,[26] an undisputed identification of new compounds in plants requires six points of identification when comparing the reference synthetic material with the analyte in the plant: 1 precursor in low resolution + 2 product ions in high resolution + 1 ratio → 6 identification points (IPs). A mixture of 15 amides (Table 3) was injected at concentrations ranging from 0.1 to 1000 ppb. The t-MS^2 data were then compared with those obtained from the injection of the extract at 1000 ppm after blank runs were performed. The comparison of the chromatographic and mass spectral data (Table 3 and the Supporting Information) between the synthetic compounds and the natural extract showed the unambiguous occurrence of amides **1**, **4**, **15**, **16**, and **30**−**32** in *Z. piperitum* root extract. Quantitative results presented below should be considered with care because we did not check for ion suppression effects. Also, the most abundant amides were present at concentrations higher than the highest concentration of the calibration curves.

Amides **1** (rubemamine), **16**, **20** (beecheyamide), and **31** (podocarpamide) were already reported to occur in *Zanthoxylum* species (Table 1). Amides **30** and **31** were abundant compounds in our extract, accounting for 0.57 and 1.87% w/w, respectively. Figure 6 shows the t-MS^2 trace of ion 342.17. The peak at 3.816 min in the plant extract (Figure 6A) and the synthetic amide **4** eluting at 3.820 min in the reference mixture (Figure 6B) injected separately showed identical MS/MS spectra (Figure 6C,D; same fragments, same ratio). Because amide **4** was well-separated from its isomers **5** and **19**, its occurrence is thus unambiguously supported. The comparisons between the UPLC/MS/MS data of the synthetic products and the natural products for the other amides are available in the Supporting Information.

This work illustrates how compounds already known to occur in plants served as a starting point for umami taste relationship studies to find more intense ingredients. Targeted UPLC/MS/MS analyses then unambiguously supported the natural occurrence of a few of these molecules in a plant extract. The combination of plant knowledge, chemical synthesis, and modern LC/MS techniques thus provided an efficient way to discover new taste-active and naturally occurring ingredients. A similar approach was used by Süss et al., who synthesized a series of kitchenlike amides by reaction of lactones and amines, evaluated them for their umami taste and finally showed the natural occurrence of one of them in blue cheese.[27]

■ ASSOCIATED CONTENT

Supporting Information

The Supporting Information is available free of charge on the ACS Publications website at DOI: 10.1021/acs.jafc.5b02359.

^{1}H and ^{13}C NMR descriptions of products **1**−**32** and chromatograms and mass spectra comparison of synthetic amides versus natural amides in *Z. piperitum*. (PDF)

■ AUTHOR INFORMATION

Corresponding Author

*Tel.: +41 22 780 35 66. Fax: +41 22 780 33 34. E-mail eric.frerot@firmenich.com.

DOI: 10.1021/acs.jafc.5b02359
J. Agric. Food Chem. 2015, 63, 7161−7168

Present Address

N.N.: Schwarzkopf Professional, 161 rue de Silly, 92 642 Boulogne, Billancourt, France.

Notes

The authors declare no competing financial interest.

■ ACKNOWLEDGMENTS

We thank Mr. Alain Bagnoud for his help in chemical synthesis, Mrs. Esmeralda Cicchetti for preliminary LC/MS analyses, Mrs. Aurore Planchais and Christine Saint-Léger for the organization of the large panel evaluations, Dr. Sylvain Etter for toxicology assessment, and Mrs. Kasia Aeberhardt for stimulating discussions. The reviewers for their constructive suggestions to improve the manuscript are also acknowledged.

■ ABBREVIATIONS USED

MSG, monosodium glutamate; THF, tetrahydrofuran; UPLC/MS, ultraperformance liquid chromatography mass spectrometry; ESI, electrospray ionization

■ REFERENCES

(1) Strunz, G. M. Unsaturated amide in *Piper* species (*Piperaceae*). In *Studies in Natural Products Chemistry*; Elsevier Science B.V.: Amsterdam, The Netherlands, 2000; pp 683−738.

(2) Galopin, C. C.; Furrer, S. M.; Goeke, A. Pungent and tingling compounds in Asian cuisine. In *Challenges in Taste Chemistry and Biology*; Hofmann, T., Ho, C.-T., Pickenhagen, W., Eds.; ACS Symposium Series *867*; American Chemical Society: Washington, D.C., 2004; pp 139−152. DOI: 10.1021/bk-2003-0867.ch009

(3) Dawid, C.; Henze, A.; Frank, O.; Glabasnia, A.; Rupp, M.; Büning, K.; Orlikowski, D.; Bader, M.; Hofmann, T. Structural and sensory characterization of key pungent and tingling compounds from black pepper (*Piper nigrum* L.). *J. Agric. Food Chem.* **2012**, *60*, 2884−2895.

(4) Yang, X. Aroma constituents and alkylamides of red and green huajiao (*Zanthoxylum bungeanum* and *Zanthoxylum schinifolium*). *J. Agric. Food Chem.* **2008**, *56*, 1689−1696.

(5) Nagashima, M.; Nakatani, N. LC-MS analysis and structure determination of pungent alkamides from *Spilanthes acmella* L. flowers. *Lebensm.-Wiss. Technol. (1968-2004)* **1992**, *25*, 417−421.

(6) Gulland, J. M.; Hopton, G..U. Pellitorine, the pungent principle of *Anacyclus pyrethrum*. *J. Chem. Soc.* **1930**, 6−11.

(7) Winkel, C.; de Klerk, A.; Visser, J.; de Rijke, E.; Bakker, J.; Koenig, T.; Renes, H. New developments in umami (enhancing) molecules. *Chem. Biodiversity* **2008**, *5*, 1195−1203.

(8) Tachdjian, C.; Patron, A. P.; Qi, M.; Adamski-Werner, S. L.; Tang, X.-Q.; Chen, Q.; Darmohusodo, V.; Lebl-Rinnova, M.; Priest, C. Aromatic amides and ureas and their uses as sweet and/or umami flavor modifiers, tastants and taste enhancers. U.S. Patent 20060045953 A1 20060302, March 2, 2006.

(9) Shigemura, R.; Chen, Q.; Darmohusodo, V.; Dean, A. R. Comestible compositions comprising high potency savory flavorants, and processes for producing them. PCT International Application WO 2007124152 A2, April 19, 2007.

(10) Dewis, M. L.; Conklin, G.; Pei, T. Saturated and unsaturated N-alkamides exhibiting taste and flavor enhancement effect in flavored compositions. U.S. Patent 20080317922, December 25, 2008.

(11) Bombuwala, K.; Janczuk, A. J.; John, T. V.; Kraut, K.; Liu, Z.; Mannava, N.; Wu, H.; Yang, Y. Production and application of flavor-enhancing amide compounds. Eur. Pat. Appl. EP 2386212 A2 20111116, 2011. Applied for by International Flavors & Fragrances.

(12) Backes, M.; Paetz, S.; Vössing, T.; Ley, J. P. Synthesis and Sensory Studies of Umami-Active Scaffolds. *Chem. Biodiversity* **2014**, *11*, 1782−1797.

(13) Adesina, S. K.; Reisch, J. Amides from *Zanthoxylum rubescens*. *Phytochemistry* **1989**, *28*, 839−842.

(14) Adesina, S. K. Three new amides from *Zanthoxylum rubescens*. *Planta Med.* **1989**, *55*, 324−326.

(15) Patiño, L. O. J.; Prieto, R. J. A.; Cuca, S. L. E. *Zanthoxylum* genus as potential source of bioactive compounds. In *Bioactive Compounds in Phytomedicine*; Rasooli, I., Ed.; InTech: Rijeka, Croatia, 2012; pp 185−218.

(16) Adesina, S. K. The Nigerian *Zanthoxylum*; chemical and biological values. *Afr. J. Tradit., Complementary Altern. Med.*. **2005**, *2*, 282−301.

(17) Ley, J. P.; Krammer, G.; Muche, S.; Kindel, G.; Reiss, I. Use of ferulic acid amides as flavor compounds. U.S. Patent 20030152682, 2003. To Symrise.

(18) Ley, J. P.; Reichelt, K.; Paetz, S.; Backes, M.; Obst, K. Cinnamamides as savory flavorings. U.S. Pat. Appl. Publ. 20120308703, 2012. To Symrise.

(19) Frerot, E.; Aeberhardt, K. Taste modifying product to improve or modify the kokumi or umami taste of a flavored food. PCT Int. Appl. WO 2013000673 A1 20130103, 2013. To Firmenich.

(20) Cheng, M. J.; Wu, C. C.; Tsai, I. L.; Chen, I. S. Chemical and antiplatelet constituents from the stem of *Zanthoxylum beecheyanum*. *J. Chin. Chem. Soc.* **2004**, *51*, 1065−1072.

(21) Delle Monache, F.; Di Benedetto, R.; De Moraes E Souza, M. A.; Sandor, P. *Esenbeckia leiocarpa*: II. Further components. *Gazzetta Chim. Ital.* **1990**, *120*, 387−389.

(22) Wu, M.-C.; Peng, C.-F.; Chen, I.-S.; Tsai, I.-L. Antitubercular Chromones and Flavonoids from *Pisonia aculeata*. *J. Nat. Prod.* **2011**, *74*, 976−982.

(23) Kalia, N. K.; Singh, B.; Sood, R. P. A New Amide from *Zanthoxylum armatum*. *J. Nat. Prod.* **1999**, *62*, 311−312.

(24) Takemoto, T.; Uchida, M.; Koike, K.; Hoshina, Y.; Kusano, G. Constituents of Chloranthus species. I. Structures of two new amides from *Chloranthus serratus* and the isolation of isofraxidin from *C. japonicas*. *Chem. Pharm. Bull.* **1975**, *23*, 1161−1163.

(25) Huang, T.; Rehak, L.; Jander, G. *Meta*-tyrosine in *Festuca rubra* ssp. *commutata* (Chewings fescue) is synthesized by hydroxylation of phenylalanine. *Phytochemistry* **2012**, *75*, 60−66.

(26) IOFI Working Group on Methods of Analysis. Guidelines for LC-MS identifications of flavouring substances in nature, made by the Working Group on Methods of Analysis of the International Organization of the Flavor Industry (IOFI). Guidelines for LC-MS identifications of flavouring substances in nature, made by the Working Group on Methods of Analysis of the International Organization of the Flavor Industry (IOFI). *Flavour Fragrance J.* **2010**, *25*, 2−3.

(27) Suess, B.; Brockhoff, A.; Meyerhof, W.; Hofmann, T. Structures, orosensory activity, and T1R1/T1R3 receptor activation of amides generated by lactone aminolysis using food-related processing conditions. *Eur. Food Res. Technol.* **2013**, *237*, 57−70.

DOI: 10.1021/acs.jafc.5b02359
J. Agric. Food Chem. 2015, 63, 7161−7168

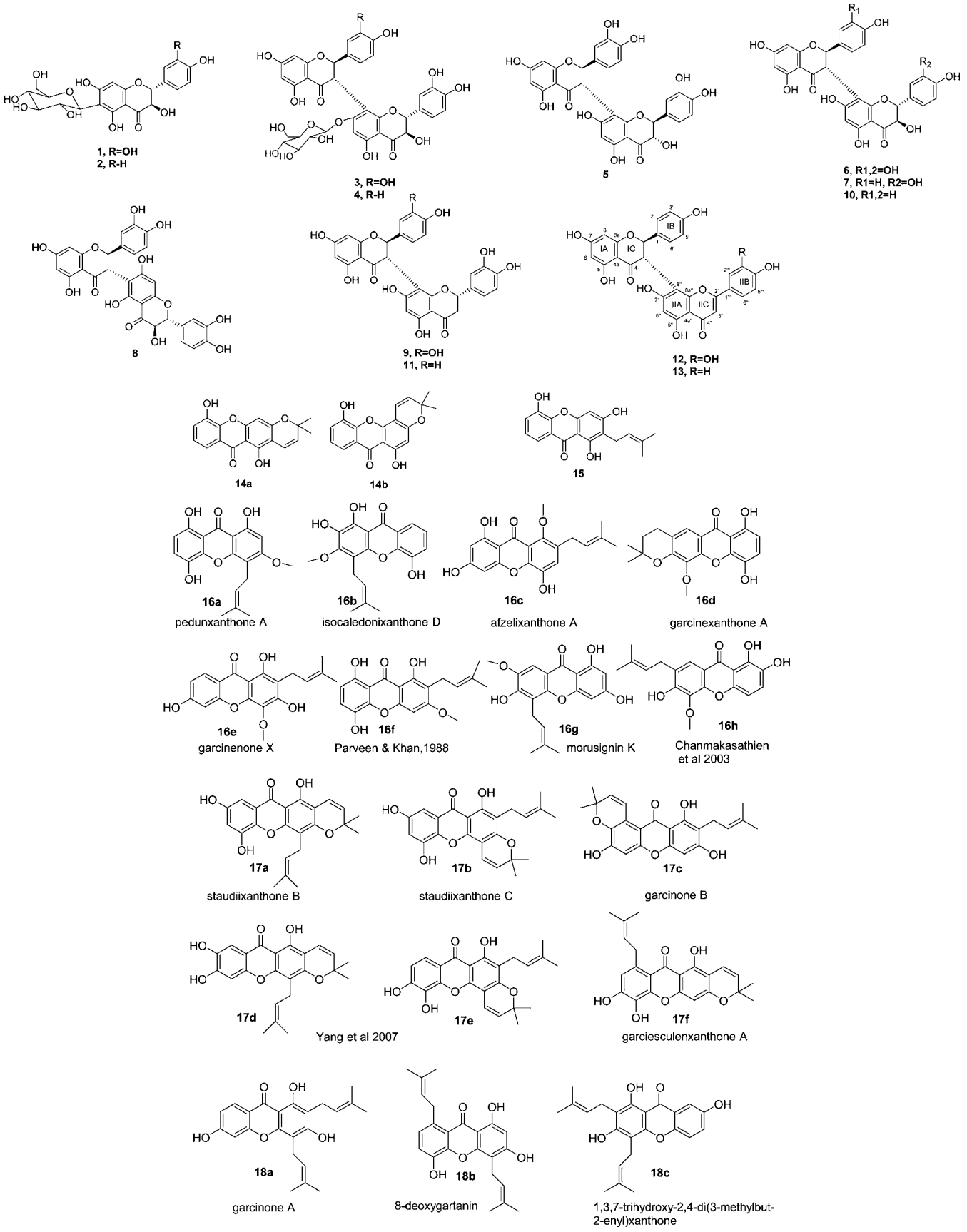

Figure 1. continued

DOI: 10.1021/acs.jafc.5b02544
J. Agric. Food Chem. 2015, 63, 7169−7179

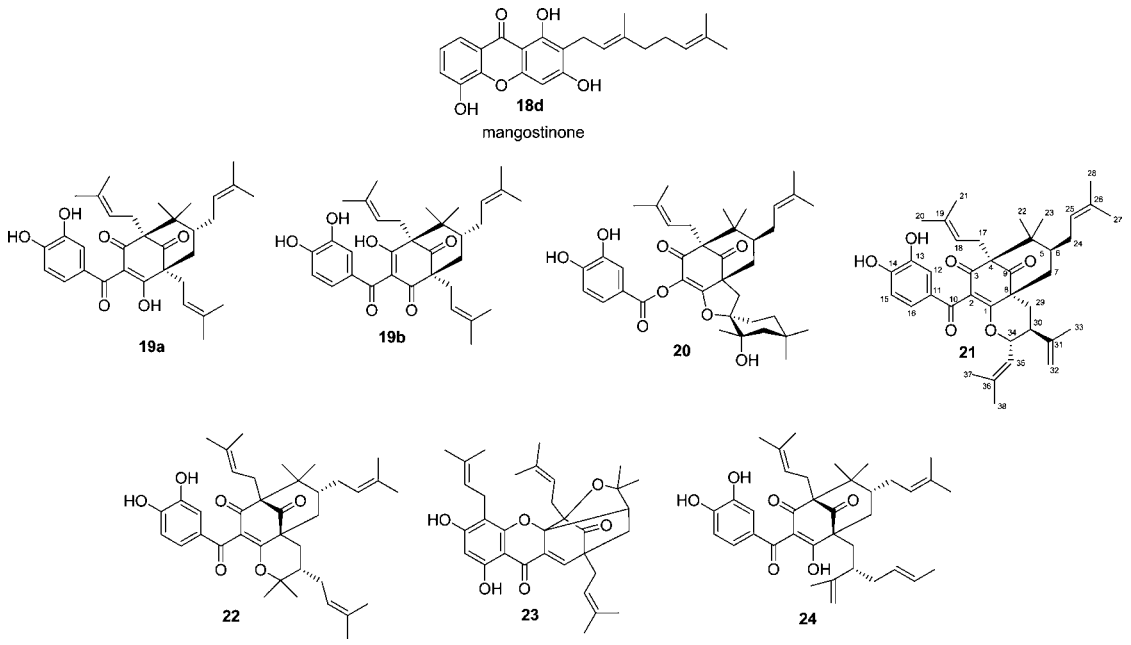

Figure 1. Chemical structures of compounds **1**−**24**.

compounds. Thus, tree marker compounds were isolated and characterized via MS, 1D- and 2D-NMR, and CD spectroscopy and evaluated for their antioxidative properties via H_2O_2 scavenging, hydrophilic and lipophilic oxygen radical absorbance capacity (H-/L-ORAC), and Trolox equivalent antioxidant capacity (H-/L-TEAC) assays.

MATERIALS AND METHODS

Chemicals. The following reagents were obtained commercially: H_2O_2 (Merck, Hohenbrunn, Germany); 2,2′-azinobis(3-ethylbenzothiazoline-6-sulfonic acid) diammonium salt (ABTS), peroxidase from horseradish (HRP), *rac*-6-hydroxy-2,5,7,8-tetramethylchromane-2-carboxylic acid (Trolox), fluorescein sodium salt (FL), 2,2′-azobis(2-methylpropinamidine) (AAPH), quercetin, and ascorbic acid (Sigma-Aldrich, Steinheim, Germany). H_2O for chromatographic separations was purified with a Milli-Q Gradient A10 system (Millipore, Schwalbach, Germany), and solvents used were of HPLC grade (Merck, Darmstadt, Germany). Deuterated solvents were obtained from Euriso-Top (Saarbrücken, Germany).

General Experimental Procedure. 1D- and 2D-NMR spectroscopy ^{1}H, ^{1}H−^{1}H COSY, HSQC, HMBC, and ^{13}C were performed on an Avance III 500 MHz spectrometer with a CTCI probe (Bruker, Rheinstetten, Germany). Mass spectra of the compounds were measured on a Waters Synapt G2-S HDMS mass spectrometer (Waters, Manchester, UK) coupled to an Acquity UPLC core system (Waters, Milford, MA, USA). For ECD spectroscopy, methanolic solutions of the samples were analyzed by means of a Jasco J-810 spectropolarimeter (Hachioji, Japan). HPLC separations were performed using a preparative HPLC system (PrepStar, Varian, Darmstadt, Germany). Medium-pressure liquid chromatography (MPLC) separations were performed on a Büchi Sepacore (Flawil, Switzerland) system using a YMC (YMC Europe, Dinslaken, Germany) DispoPackAT ODS-25 flash cartridge (120 g, i.d. = 40 mm, l = 150 mm).

Plant Material. Leaves, stem bark, and roots from *G. buchananii* were collected from trees in their natural habitats in Karagwe, Tanzania, dried, and ground to powder.[2] A voucher specimen of the powders was deposited at the University of Idaho Stillinger herbarium (voucher 159918).

Extraction and Isolation. Extraction of *G. buchananii* leaf powder and MPLC separation were performed as described for root and bark powder.[9,10,12,27] Ten fractions were collected, concentrated under reduced pressure, and freeze-dried. (2*R*,3*S*)-Morelloflavone (**12**, Figure 1) was obtained from MPLC fraction 8: yellow amorphous powder (yield, 9% from extract); UV (MeOH) λ_{max} (log ε) 227 (4.85), 288 (4.58), 339 (4.32) nm; ECD (c 4.2 × 10^{-4} M, MeOH) λ_{max} nm ($\Delta\varepsilon$) 348 (+4.6), 316 (+1.4), 286 (+10.4), 250 (−1.9), 224 (−13.1); ^{1}H and ^{13}C NMR (DMSO-d_6, 22 °C, 500, 125 MHz) data (Supporting Information, Tables S1 and S2); HRESIMS m/z 555.0921 $[M - H]^-$ (calcd for $C_{30}H_{19}O_{11}$, 555.0927).

HPLC Isolation of (2*R*,3*S*)-Volkensiflavone (13) from Leaf Extract. Chromatography of MPLC fraction 9 was performed using a RP column (10 × 250 mm, phenylhexyl, 5 μm; Phenomenex, Aschaffenburg, Germany) as the stationary phase. The effluent (4.2 mL/min) was monitored at 300 nm. The separation started with a mixture (65:35, v/v) of aqueous HCO_2H (0.1% in H_2O) and MeCN, and the MeCN content was linearly increased to 45% within 20 min. Collected fractions were concentrated under reduced pressure and freeze-dried twice, affording (2*R*,3*S*)-volkensiflavone (**13**, Figure 1): slight yellow amorphous powder (yield, 1% from extract); UV (MeOH) λ_{max} (log ε) 227 (4.94), 289 (4.67), 339 (4.40) nm; ECD (c 2.9 × 10^{-4} M, MeOH) λ_{max} nm ($\Delta\varepsilon$) 347 (+4.9), 316 (−0.2), 287 (+10.7), 250 (−1.8), 223 (−12.5); ^{1}H and ^{13}C NMR (DMSO-d_6, 22 °C, 500, 125 MHz) data (Supporting Information, Tables S3 and S4); HRESIMS m/z 539.0978 $[M - H]^-$ (calcd for $C_{30}H_{19}O_{10}$, 539.0978).

HPLC Isolation of Garcicowin C (21) from Bark Extract. Preparative HPLC separation of MPLC fraction 8 was performed as described.[10] Collected fractions were concentrated under reduced pressure and freeze-dried twice, affording 18 fractions, M8-1−M8-19. Garcicowin C was obtained from M8-14 by semipreparative HPLC (4.2 mL/min, 278 nm) using ThermoHypersil ODS (10 × 250 mm, 5 μm; Kleinostheim, Germany) as the stationary phase and a mixture (28:72, v/v) of aqueous HCO_2H (0.1% in H_2O) and MeCN. Collected fractions were concentrated under reduced pressure and freeze-dried twice, affording garcicowin C (**21**, Figure 1): slight yellow amorphous powder (yield, 0.3% from extract); UV (MeOH) λ_{max} (log ε) 231 (4.37), 273 (4.24), 319 (3.94) nm; ECD (c 8.3 × 10^{-4} M, MeOH) λ_{max} nm ($\Delta\varepsilon$) 313 (+2.3), 267 (−9.6), 220 (+5.5); ^{1}H and ^{13}C NMR (MeOD-d_3, 27 °C, 500, 125 MHz) data (Supporting Information, Tables S5 and S6); HRESIMS m/z 599.3380 $[M - H]^-$ (calcd for $C_{38}H_{47}O_6$, 599.3373).

Antioxidant Assays. *H_2O_2 Scavenging Assay.* The H_2O_2 scavenging assay was performed in accordance with the method of Ichikawa et al.[21] Sample solutions at appropriate concentration were prepared using phosphate buffer (100 mM, pH 6.0). Sample solution

DOI: 10.1021/acs.jafc.5b02544
J. Agric. Food Chem. 2015, 63, 7169−7179

Table 1. Antioxidant Activities of Stem Bark, Leaf, and Root Extracts as well as Compounds 12, 13, and 21

extract	H-TEAC[a,b] (mmol/TE/g)	L-TEAC[a,b] (mmol/TE/g)	H-ORAC[a,b] (mmol/TE/g)	L-ORAC[a,b] (mmol/TE/g)	H_2O_2[c,d] (EC_{50}, mg/L)
leaf	2.48 ± 0.24	5.95 ± 0.14	10.14 ± 0.50	21.92 ± 1.32	6.06 (5.39−6.85)
stem bark	4.89 ± 0.58	7.02 ± 0.15	12.34 ± 0.89	26.72 ± 0.78	6.00 (5.54−7.46)
root	4.07 ± 0.20	7.61 ± 0.20	11.49 ± 0.58	30.66 ± 2.04	8.62 (7.53−10.1)

compound	H-TEAC[a,b] (mmol/TE/mmol)	L-TEAC[a,b] (mmol/TE/mmol)	H-ORAC[a,b] (mmol/TE/mmol)	L-ORAC[a,b] (mmol/TE/mmol)	H_2O_2[c,d] (EC_{50}, μM)	lit.
12	0.79 ± 0.01	1.34 ± 0.11	5.35 ± 0.07	13.64 ± 0.83	12.41 (10.90−14.26)	nr
13	0.47 ± 0.03	2.22 ± 0.25	7.00 ± 0.06	14.75 ± 0.52	34.86 (32.93−36.61)	nr
21	0.99 ± 0.02	1.75 ± 0.11	0.59 ± 0.04	2.63 ± 0.06	83.43 (74.59−93.34)	nr
ascorbic acid	1.14 ± 0.09[e]	1.13 ± 0.03[e]	0.57 ± 0.02[e]	0.88 ± 0.06[e]	31.14[e] (28.36−35.25)	1.05[f]
quercetin	5.54 ± 0.33[e]	5.56 ± 0.46[e]	8.92 ± 0.21[e]	9.95 ± 1.48[e]	8.31[e] (7.50−9.34)	3.10[f]/10.4−13.5[g]

[a]Each sample was analyzed by means of ORAC and ABTS assays by quadruplicate studies. [b]Values represents the mean ± SD. [c]Each sample was analyzed by means of H_2O_2 assay by triplicate studies. [d]Range in parentheses represents 95% confidence interval. [e]Values comparable to those of Stark et al.[9,10,12] [f]L-TEAC values from Re et al.[55] [g]L-ORAC values from Mercader-Ros et al.[56]

(100 μL), phosphate buffer (30 μL, 100 mM, pH 6.0), and H_2O_2 solution (10 μL, 500 μM) were mixed in a transparent 96-well microplate (VWR, Ismaning, Germany). Then peroxidase (40 μL, 150 U/mL) and ABTS (40 μL, 0.1%) were added. The microplate was incubated at 37 °C for 15 min. The absorbance (A) of each well was measured at 414 nm with FLUOstar OPTIMA (BMG LABTECH, Offenburg, Germany). The scavenging effect (E) was calculated as shown using the formula below (blank stands for solution without hydrogen peroxide, and control did not include a test compound), and EC_{50} was calculated by the probit analysis.

$$E = [(A - A_{blank})_{control} - (A - A_{blank})_{test}]/(A - A_{blank})_{control} \times 100$$

Hydrophilic Oxygen Radical Absorbance Capacity (H-ORAC) Assay. The ORAC assay was carried out according to the method of Ou et al.[22] with some modifications. Trolox and FL were used as standard and fluorescent probe, respectively. Free radicals were produced by AAPH to oxidize FL. Different dilutions of Trolox (200, 100, 50, 25, and 12.5 μM) and appropriate dilutions of tested sample were prepared with phosphate buffer (10 mM, pH 7.4). Trolox dilution (25 μL) or sample solution was pipetted into a black 96-well microplate (VWR), and then FL (150 μL, 10 nM) was added. The reaction mixture was incubated at 37 °C for 30 min. Afterward, fluorescence was measured every 90 s at the excitation of 485 nm and the emission of 520 nm using FLUOstar OPTIMA. After three cycles, AAPH (25 μL, 240 mM) was added quickly, and then the measurement was resumed and continued up to 90 min (60 cycles in total). The background signal was determined using the first three cycles. The ORAC values were calculated according to the method of Cao et al.[23] and expressed as Trolox equivalent (μmol TE/μmol).

Lipophilic Oxygen Radical Absorbance Capacity (L-ORAC) Assay. The lipophilic ORAC assay was adapted from the Madrona procedure with some modifications.[24] Trolox standards (200, 100, 50, 25, and 12.5 μM) as well as dilutions of each sample solution were prepared using 7% (w/v) randomly methylated methyl-β-cyclodextrin (RMCD) in acetone/H_2O (1:1 v/v). FL and AAPH solutions were prepared in the same way as the H-ORAC method using phosphate buffer (10 mM, pH 7.4). After FL solution (150 μL) was added in a black 96-well microplate, Trolox standards, the diluted samples, and the 7% RMCD solution as blank, 25 μL each, were applied with mixing. Incubation of the microplate was done as described for the H-ORAC assay, and an AAPH solution (25 μL) was immediately added to all wells. All conditions of the measurement as well as data handling and export were the same as for the H-ORAC assay.

Hydrophilic Trolox Equivalent Antioxidant Capacity (H-TEAC) Assay with ABTS. The ABTS radical scavenging activity was measured employing ABTS assay as previously described by Floegel et al.[25] with some modifications. Briefly, ABTS (2.5 mM) solution was prepared with phosphate-buffered saline (PBS, 10 mM, pH 7.4), and AAPH (1 mM) was added in the solution. The mixture was heated in a water bath at 68 °C for 40 min. The blue-green ABTS radical solution was cooled to room temperature, filtered through a syringe membrane (0.45 μm), and diluted with PBS buffer until an absorbance of 0.325 ± 0.01 at 730 nm. Then Trolox standards (1000, 500, 250, 125, and 62.5 μM, 4 μL each) or samples were mixed with the diluted ABTS radical solution (196 μL) in a transparent 96-well microplate. The microplate was incubated at 37 °C for 10 min. The absorbance of each well was measured at 730 nm with FLUOstar OPTIMA. ABTS radical scavenging activity was calculated employing standard curves and expressed as Trolox equivalent (mmol TE/mmol).

Lypophilic Trolox Equivalent Antioxidant Capacity Assay with ABTS (L-TEAC). To measure TEAC of lypophilic compounds, the H-TEAC method was modified.[26] In brief, Trolox was dissolved in aqueous DMSO (50%, v/v) for standard solutions (1000, 500, 250, 125, and 62.5 μM), and the dilution of sample solutions was also performed with aqueous DMSO (50%, v/v). Neat DMSO (20 μL) was added in a transparent 96-well microplate, and subsequently all of the wells (final DMSO concentration, 10%) were processed in the same way as described for the H-TEAC method. Finally, all conditions of the measurement as well as data handling and export were the same as for the H-TEAC assay.

Ultraperformance Liquid Chromatography−Electrospray Ionization−Time-of-Flight Mass Spectrometry (UPLC-ESI-TOF MS). Aliquots (3 μL) of the extracts (10 mg/10 mL, 50% MeCN, each) were analyzed in five replicates by means of UPLC-ESI-TOF MS on a Waters Synapt G2-S HDMS mass spectrometer (Waters, Manchester, UK) coupled to an Acquity UPLC core system (Waters, Milford, MA, USA) equipped with a 2 × 150 mm, 1.7 μm, BEH C18 column (Waters, Manchester, UK) consisting of a binary solvent manager, sample manager, and column oven. Operated with a flow rate of 0.4 mL/min at 50 °C, the following gradient was used for chromatography: starting with a mixture (1:99, v/v) of aqueous HCO_2H (0.1% in H_2O) and MeCN (0.1% HCO_2H), the MeCN content was increased to 50% within 6 min, to 98% within 1 min, kept constant for 1 min, decreased to 1% within 0.2 min, and finally kept constant for 0.8 min at 1%. Scan time for the MS^e method (centroid) was set to 0.1 s. Analyses were performed with negative ESI in high-resolution mode using the following ion source parameters: capillary voltage, −2.0 kV; sampling cone, 50 V; source offset, 30 V; source temperature, 120 °C; desolvation temperature, 450 °C; cone gas flow, 2 L/h; nebulizer, 6.5 bar; and desolvation gas, 800 L/h. Data processing was performed by using MassLynx 4.1 SCN 9.16 (Waters, Manchester, UK) and the elemental composition tool for determining the accurate mass. All data were lock mass corrected on the pentapeptide leucine enkephaline (Tyr-Gly-Gly-Phe-Leu, m/z 554.2615, $[M - H]^-$) in a solution (1 ng/μL) of MeCN/0.1% HCO_2H (1:1, v/v). Scan time for the lock mass was set to 0.3 s, at intervals of 15 and 3 scans to average with a mass window of ±0.3 Da. Calibration of the Synapt G2-S in the range from m/z 50 to 1200 was performed using a solution of HCO_2Na (5 mmol/L) in 2-propanol/H_2O (9:1, v/v). The UPLC and Synapt G2-S systems were operated with MassLynx software (Waters). The collision energy ramp for MS^e was set from 20 to 40 eV.

DOI: 10.1021/acs.jafc.5b02544
J. Agric. Food Chem. 2015, 63, 7169−7179

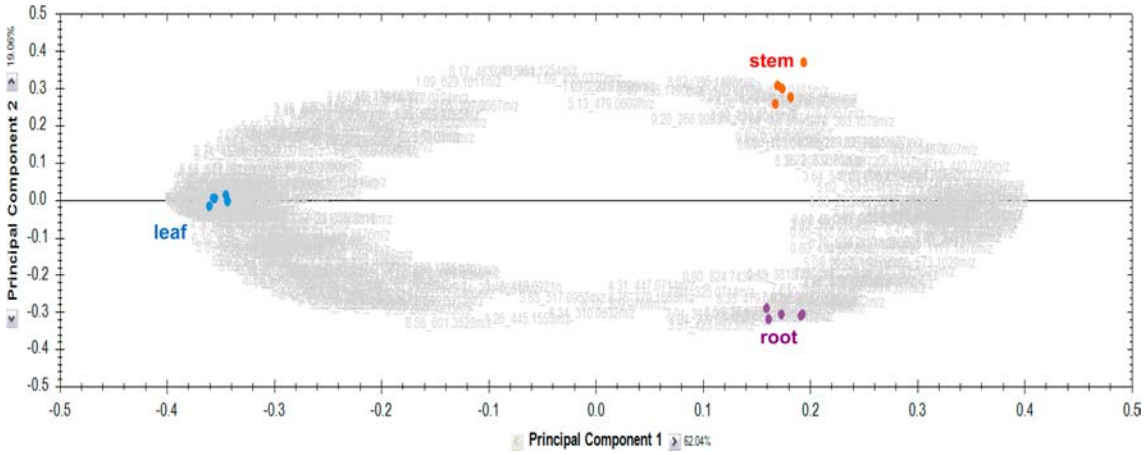

Figure 2. Score plot (comp 1 vs comp 2]) of UPLC-ESI-TOF MS full scan analysis (50−1200 Da, ESI^-, high-resolution mode) of *G. buchananii* tree (five replicates per sample).

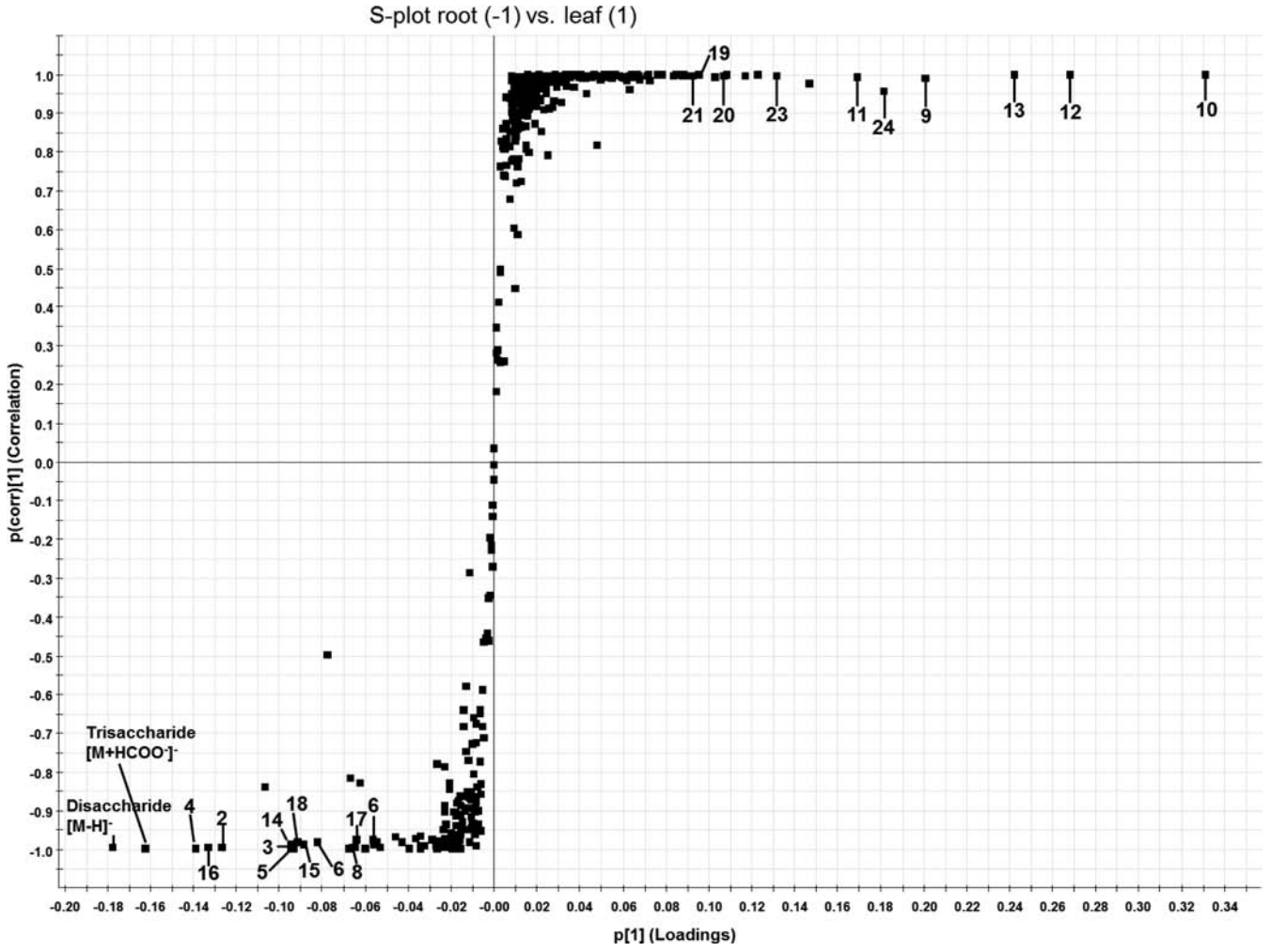

Figure 3. S-plot of root versus leaf extract.

The raw data of all organs and replicates obtained from UPLC-ESI-TOF MS analysis were processed with Progensis QI using the following peak picking conditions: all runs, limits automatic, sensitivity 3, and retention time limits 0.5−9.25 min. Compounds used for principal component analysis (PCA) were filtered by means of ANOVA p value ≤0.05 and a fold change of ≥2. The processed data were exported to EZinfo, where the matrix was analyzed by PCA with pareto scaling. Group differences were calculated using orthogonal partial least-squares discriminant analysis (OPLS-DA) highlighted as S-plots.

RESULTS AND DISCUSSION

As the aqueous ethanolic stem bark extract of *G. buchananii* showed high antioxidative activity comparable to that of grape seed extract,[9,22] the question arose as to whether other organs

DOI: 10.1021/acs.jafc.5b02544
J. Agric. Food Chem. 2015, 63, 7169−7179

Table 2. Identified Compounds (Markers) in the Dataset

compound[a]	retention time	observed mass	exact mass	empirical formula	m/z diff (ppm)	diagnostic fragments[b]
1	3.51	465.1034	465.1033	$C_{21}H_{22}O_{12}$	+0.2	125.0238, 167.0344, 345.0610, 375.0714
2	3.64	449.1078	449.1084	$C_{21}H_{22}O_{11}$	−1.3	125.0234, 167.0341, 301.0705, 329.0655, 359.0761
3	4.15	751.1505	751.1510	$C_{36}H_{31}O_{18}$	−0.7	151.0031, 285.0392, 435.0708, 437.0866, 445.0556, 463.0660
4	4.32	735.1564	735.1561	$C_{36}H_{31}O_{17}$	+0.4	125.0237, 269.0448, 403.0818, 429.0609, 447.0717
5	4.86	589.0975	589.0982	$C_{30}H_{22}O_{13}$	−1.2	125.0237, 269.0448, 403.0818, 429.0609, 447.0717
6	5.06	589.0972	589.0982	$C_{30}H_{22}O_{13}$	−1.7	125.0237, 151.0028, 285.0393, 435.0713, 463.0660
7	5.37	573.1043	573.1033	$C_{30}H_{22}O_{12}$	+1.7	125.0237, 296.0313, 419.0761,447.0711
8	5.51	589.0981	589.0982	$C_{30}H_{22}O_{13}$	−0.2	125.0237, 151.0028, 285.0393, 463.0660, 435.0713
9	5.65	573.1024	573.1033	$C_{30}H_{22}O_{12}$	−1.6	125.0234, 151.0027, 285.0392, 311.0186, 421.0912, 447.0708
10	5.69	557.1084	557.1084	$C_{30}H_{22}O_{11}$	± 0.0	125.2038, 269.0443, 296.0317, 403.0813, 431.0764
11	5.95	557.1073	557.1084	$C_{30}H_{22}O_{11}$	−2.0	125.0235, 135.0443, 269.0444, 295.0237, 431.0759, 453.0574
12	5.97	555.0930	555.0927	$C_{30}H_{20}O_{11}$	+0.5	125.0239, 295.0243, 401.0660, 403.0817, 429.0613, 451.0429
13	6.39	539.0982	539.0978	$C_{30}H_{20}O_{10}$	+0.7	125.0238, 151.0032, 295.0243, 385.0711, 387.0871, 413.0661, 435.0481
14[c] **a,b**	7.87	309.0766	309.0763	$C_{18}H_{14}O_5$	+0.1	91.0180, 293.0448
15[c]	7.87	311.0921	311.0919	$C_{18}H_{16}O_5$	+0.6	91.0180, 242.0212, 293.0448
16[c] **a−h**	7.91	341.1028	341.1025	$C_{19}H_{18}O_6$	+0.9	91.0186, 135.0085, 271.0241, 325.0712
17[c] **a−f**	8.25	393.1338	393.1338	$C_{23}H_{22}O_6$	± 0.0	337.0710
18[c] **a−d**	8.35	379.1546	379.1545	$C_{23}H_{24}O_5$	+0.8	256.0367, 309.0762
19[c] **a,b**	8.36	533.2907	533.2903	$C_{33}H_{42}O_6$	+0.8	109.0293
20[c]	8.42	633.3429	633.3427	$C_{38}H_{50}O_8$	+0.3	109.0292
21	8.45	599.3379	599.3373	$C_{38}H_{48}O_6$	+1.0	109.0291, 273.1489, 329.2117, 409.1653
22	8.58	601.3528	601.3529	$C_{38}H_{50}O_6$	−0.2	109.0290, 273.1488, 335.1282, 409.1651, 465.3370
23[c]	8.64	531.2751	531.2747	$C_{33}H_{40}O_6$	+0.8	462.2048
24	9.15	601.3527	601.3529	$C_{38}H_{50}O_6$	−0.3	109.0288, 177.0191, 273.1490, 387.1577, 409.1644, 431.1476, 465.3376

[a]Compound numbering relates to the retention time. [b]The sum formula of all fragments is given in the Supporting Information. [c]Identified via accurate mass, fragments, and database searching focused on *Garcinia* species.

of this tree might be an alternative source for antioxidative extracts or for strong antioxidative and bioactive purified compounds. Also, the idea of a faster or more efficient isolation procedure from other parts of this tree for already known lead compounds from stem bark arose. Comparative antioxidative analysis of aqueous ethanolic leaf, root, and stem bark extract revealed high capacities for all three tree organs; however, the antioxidative activity of leaf extract was slightly lower in four of five assays (Table 1).

To investigate the metabolite composition of the different parts of *G. buchananii*, we conducted an untargeted metabolomics approach using UPLC-ESI-TOF MS with simultaneous acquisition of low- and high-collision energy mass spectra (MS^e). Using the Progensis QI workflow consisting of import data, review alignment, experiment design setup, peak picking, review deconvolution, review compounds, and compound statistics, unsupervised statistics were performed to evaluate if any differences in the metabolomes of the organs were detectable. Compounds used for PCA were filtered by means of ANOVA p value ≤ 0.05 and fold change of ≥ 2, resulting in a reduction from 1008 to 450 compounds and the PCA displayed in Figure 2. Analysis of each organ in five replicates showed a rather good clustering of each replicate in close proximity, thus confirming the reproducibility of the UPLC-ESI-TOF MS profiling method. Inspection of the PCA output illustrated that the largest differences were observed between leaf and stem bark as well as root extracts along PC1, whereas root and stem bark extracts could be clearly separated along PC2 (Figure 2).

As the root extract showed higher antioxidative activity than leaf extract, at first, these two organs were compared by means of OPLS-DA. To visualize similarities and differences between root and leaf extracts, S-plots of data pairs of accurate mass and retention time of each metabolite were calculated (Figure 3).

As the y-axis of the S-plot denotes confidence of a metabolite's contribution to the group difference and the x-axis denotes the contribution of a particular metabolite to the group difference, the S-plot indicates the ion m/z 557.1083 (**10**) showing by far the highest difference for both organs (Figure 3; Supporting Information). In addition, the ions m/z 555.0924 (**12**), 539.0979 (**13**), 573.1030 (**9**), 601.3527 (**24**), and 557.1079 (**11**) for leaf and m/z 341.1082, 549.1665, 735.1560 (**4**), 341.1027 (**16**), and 449.1082 (**2**) for root were found to clearly contribute to the differences between both tree tissue extracts. On the basis of the accurate mass data, the sum formulas of **2**, **4**, **9**−**13**, **16**, **24** were determined (Table 2), and the ions m/z 341.1082 and 549.1665 were calculated to be $C_{12}H_{21}O_{11}$ and $C_{19}H_{33}O_{18}$, respectively. The ion m/z 341.1082 could be proposed as a disaccharide such as sucrose, cellobiose, or maltose and ion m/z 549.1665 as the formic acid adduct of a trisaccharide such as raffinose, maltotriose, or cellotriose. Chromatography of authentic samples as well as cochromatography with the pooled sample of all *G. buchananii* tree organs confirmed the compounds (2*R*,3*R*)-aromadendrin-6-*C*-*β*-D-glucopyranoside (**2**), (2*R*,3*S*,2″*R*,3″*R*)-GB-2 7″-*O*-*β*-D-glucopyranoside (**4**), (2*R*,3*S*,2″*S*)-buchananiflavanone (**9**), (2*R*,3*S*,2″*R*,3″*R*)-GB-1 (**10**), (2*R*,3*S*,2″*S*)-GB-2a (**11**), and garcinol (**24**).[9,10,12,27,28] The marker compounds m/z 555.0924 (**12**) and 539.0979 (**13**) were isolated from leaf extract by means of MPLC and HPLC and unequivocally identified via MS analysis, 1D- and 2D-NMR, and CD spectroscopy (Supporting Information) as (2*R*,3*S*)-morello-

DOI: 10.1021/acs.jafc.5b02544
J. Agric. Food Chem. 2015, 63, 7169−7179

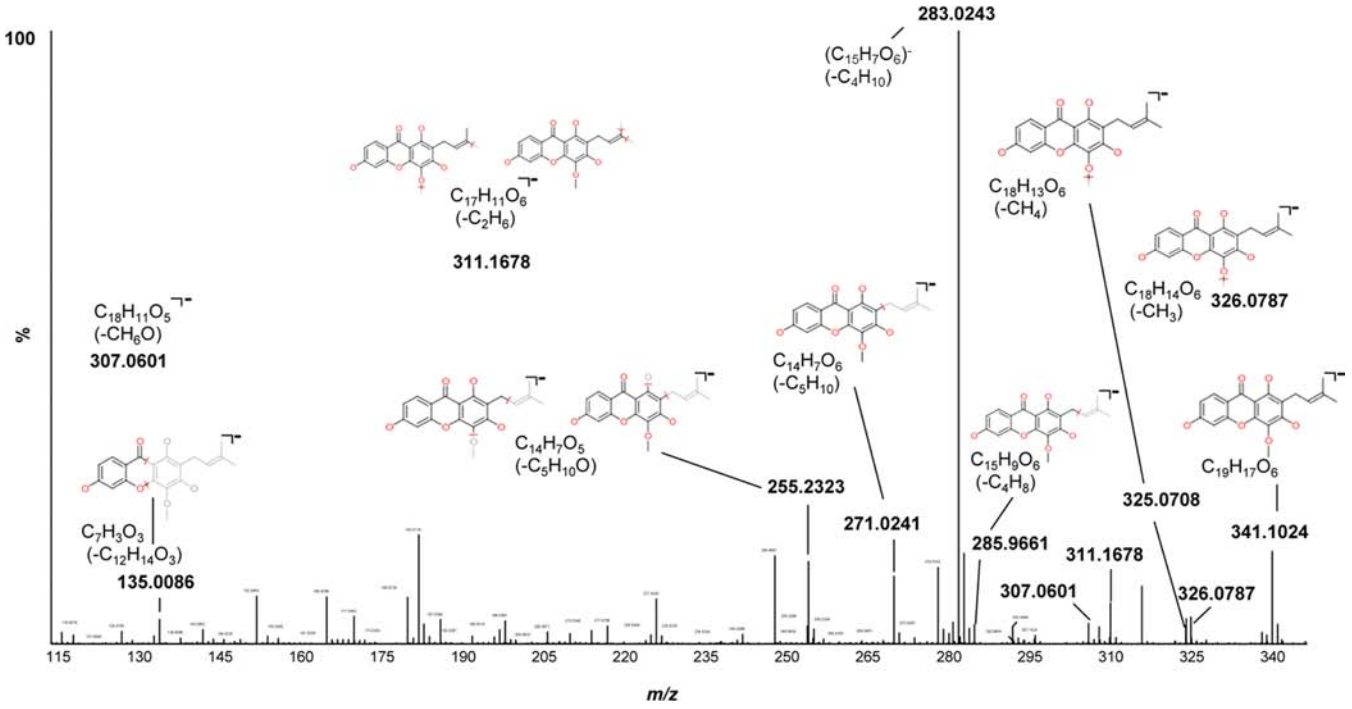

Figure 4. High-collision energy (MS^e) mass spectrum of **16** exemplified with **16e**.

flavone (**12**) and (2*R*,3*S*)-volkensiflavone (**13**) and are in very good agreement with the literature.[29−32] Additional compounds identified in the S-plot by means of chromatography of authentic samples as well as cochromatography are (2*R*,3*S*,2″*R*,3″*R*)-manniflavanone-7″-*O*-*β*-D-glucopyranoside (**3**), (2*R*,3*S*,2″*S*,3″*S*)-manniflavanone (**5**), (2*R*,3*S*,2″*R*,3″*R*)-manniflavanone (**6**), and (2*R*,3*S*,2″*S*,3″*S*)-isomanniflavanone (**8**).[9,10,12,27,28] Compound *m*/*z* 599.3364 (**21**) was isolated from stem bark and identified via MS, NMR, and CD spectroscopy as garcicowin C (**21**).[33] For the ions *m*/*z* 309.0765 (**14**), 311.0919 (**15**), 341.1030 (**16**), 393.1342 (**17**), 379.1544 (**18**), 533.2899 (**19**), 633.3423 (**20**), and 531.2744 (**23**), the corresponding sum formulas were calculated (Table 2), and compounds annotated by database searching focused on compounds that have only been isolated from *Garcinia* species. 6-Deoxyjacareubin or 6-deoxyisojacareubin and 1,3,5-trihydroxy-2-prenylxanthone could be proposed for **14** and **15**,[34−38] which were further strengthened by their fragments in the high-collision energy mass spectra (Table 2; Supporting Information). The calculated elemental composition of $C_{19}H_{18}O_6$ for **16** revealed eight possible structures (**16a**−**16h**) identified in *Garcinia* species so far (Figure 1).[35,39−45] Several fragment ions such as *m*/*z* 255.2323, 271.0241, 285.9661, and 325.0712 supported their identification in *G. buchananii* (Figure 4). The fingerprint fragments of *m*/*z* 91.0186 ($C_6H_3O^-$) and 135.0085 ($C_7H_3O_3^-$) as well as the absence of *m*/*z* 108.0186 ($C_6H_4O_2^-$) indicated isocaledonixanthone D (**16b**) or garcinenone X (**16e**) with a higher probability (Figure 4). Staudiixanthones B (**17a**) and C (**17b**),[46] or garcinone B (**17c**),[47] or 1,6,7-trihydroxy-6′,6′-dimethyl-2*H*-pyrano(2′,3′:3,2)-4-(3-methylbut-2-enyl)-xanthone (**17d**) and 1,5,6-trihydroxy-6′,6′-dimethyl-2*H*-pyrano(2′,3′:3,4)-2-(3-methylbut-2-enyl)xanthone (**17e**),[36] or garciesculenxanthone A (**17f**)[36] could be putatively identified as compound **17** by means of the elemental composition of $C_{23}H_{22}O_6$ and accurate mass fragment. From the determined sum formula for compound **18** of $C_{23}H_{24}O_6$ and fragments, four compounds could be proposed: garcinone A (**18a**),[47] or 8-deoxygartanin (**18b**),[34,37] or 1,3,7-trihydroxy-2,4-di(3-methylbut-2-enyl)xanthone (**18c**),[48] or mangostinone (**18d**).[49] The fact that we detected the diagnostic fragment of *m*/*z* 91.0186 ($C_6H_3O^-$) for compound **16** but not for **18** displayed a more reliable identification of 8-deoxygartanin (**18b**). Aristophenone A or B (**19a**,**b**) could be proposed as compound **19**,[50−52] which additionally showed the corresponding key fragment of *m*/*z* 109.0293 ($C_6H_5O_2$) (Table 2; Supporting Information). Paucinone C and hanburin could be tentatively identified as compounds **20** and **23**, respectively[53,54]

Comparing leaf and stem bark extract by means of OPLS-DA yielded an S-plot (Figure S2 in the Supporting Information) highlighting similar marker compound distribution as described above for leaf versus root extract. Compounds **10**, **12**, **13**, **24**, **11**, **9**, **23**, **19**, **20**, and **22** for leaf extract and disaccharide(s) as well as trisaccharide(s) for stem bark extract were the most important *m*/*z* for the differentiation. This is not surprising as leaf could be separated from stem bark as well as root extracts along PC1 (Figure 2).

S-plotting root versus stem bark extract revealed (2*R*,3*S*,2″*S*)-buchananiflavanone (**9**) as the decisive marker compound for stem bark, whereas (2*R*,3*S*,2″*R*,3″*R*)-GB-1 (**10**), garcinol (**24**), **16**, isogarcinol (**22**), (2*R*,3*S*,2″*R*,3″*R*)-GB-2 7″-*O*-*β*-D-glucopyranoside (**4**), (2*R*,3*R*)-aromadendrin-6-*C*-*β*-D-glucopyranoside (**2**), **14**, **18**, **15**, and (2*R*,3*S*,2″*R*,3″*R*)-manniflavanone 7″-*O*-*β*-D-glucopyranoside (**3**) could be identified as markers for root extract (Figure S3 in the Supporting Information).

In summary, (2*R*,3*S*,2″*R*,3″*R*)-GB-1 (**10**), (2*R*,3*S*)-morelloflavone (**12**), and (2*R*,3*S*)-volkensiflavone (**13**) were identified as the most decisive marker compounds discriminating leaf from root and stem extract. The normalized abundance (ArcSinh) of all five replicates, the mean, and SD as well as trend plots of all three organs are summarized in Figure 5 and

DOI: 10.1021/acs.jafc.5b02544
J. Agric. Food Chem. 2015, 63, 7169−7179

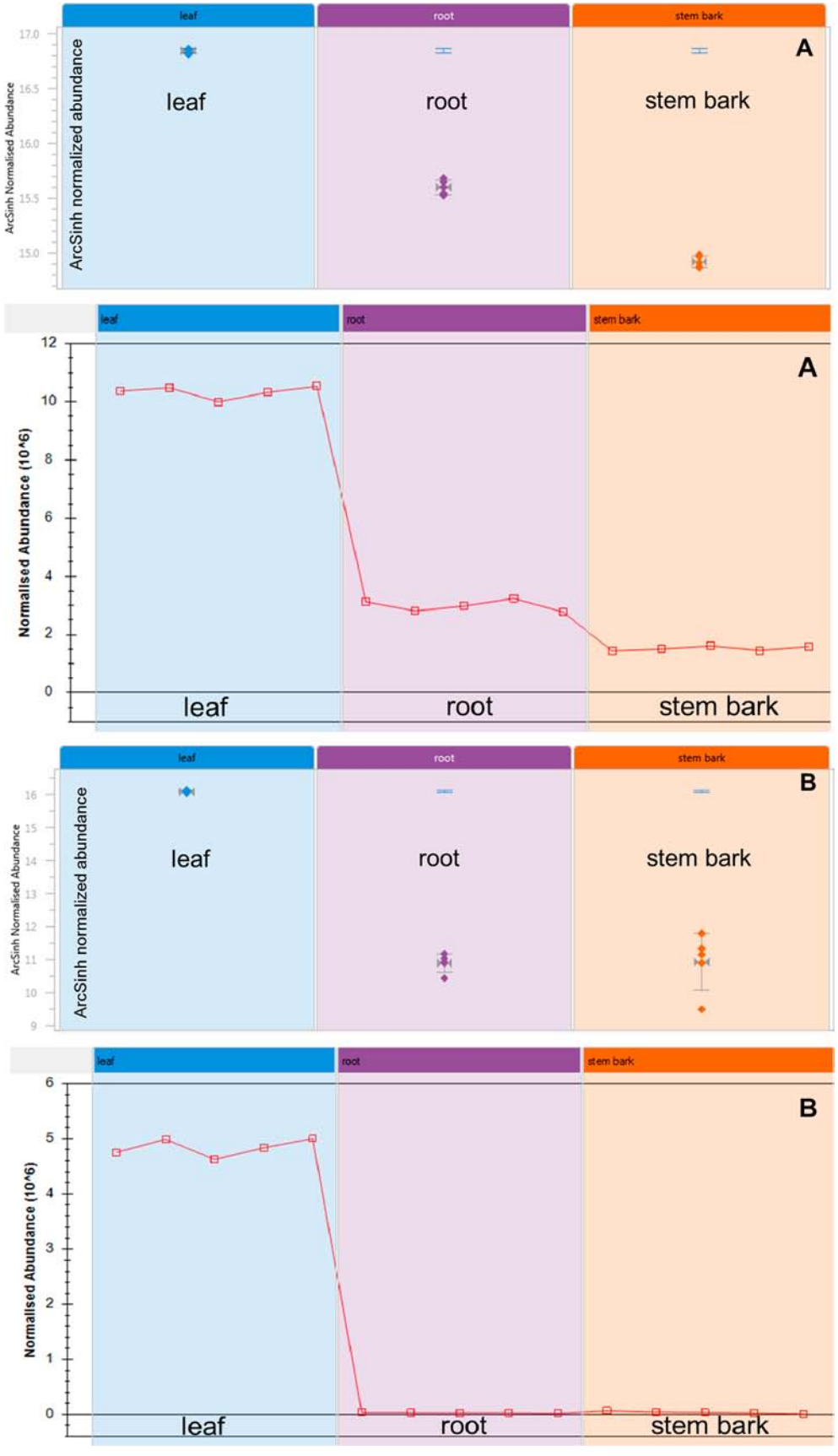

Figure 5. continued

DOI: 10.1021/acs.jafc.5b02544
J. Agric. Food Chem. 2015, 63, 7169−7179

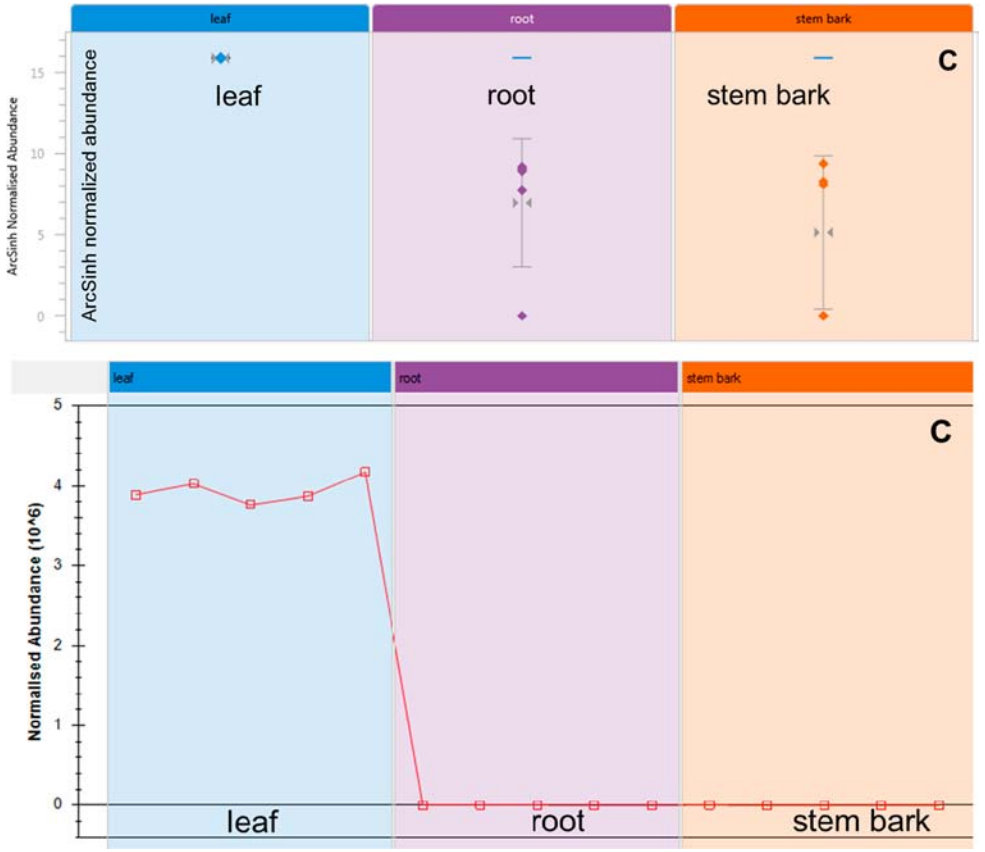

Figure 5. ArcSinh normalized compound abundance and chemometric trend plot illustrating normalized abundance (area) of (A) (2*R*,3*S*,2″*R*,3″*R*)-GB-1 (**10**), (B) (2*R*,3*S*)-morelloflavone (**12**), and (C) (2*R*,3*S*)-volkensiflavone (**13**).

in the Supporting Information for all other compounds (Figures S4−S25). On the basis of the relative abundance of the compounds, leaves represent the best organ to isolate **10**, **12**, and **13**. In fact, **12** and **13** were not detectable in root and stem bark extract (Figure 5). In contrast, the glycosides **2**, **3**, and **4** as well as isomanniflavanone (**8**) were isolated in higher yields from root extract, whereas the biflavanone-7″-*O*-glucosides **3** and **4** and **8** were not observed in leaves (Supporting Information). In general, root extract was the best organ of *G. buchananii* to isolate the described xanthones (**14**−**18**), which are hardly or not detectable in the other two organs (Supporting Information). Stem bark extract was the best source to isolate (2*R*,3*S*,2″*R*,3″*R*)-manniflavanone (**6**), and the identified or annotated polyisoprenylated benzophenones (**19**−**22** and **24**) are characteristic compounds for the leaf organ, which were hardly or not detectable in root and stem bark extracts (Supporting Information). The putatively identified polyisoprenylated xanthone hanburin (**23**), described earlier in *G. hanburyi*,[54] represents an exception compared to xanthones **14**−**18**, as the highest abundance was observable in leaves and was not detectable in the other two organs (Supporting Information).

Compounds **12**, **13**, and **21** were evaluated for their in vitro antioxidative activities using H_2O_2 scavenging, H/L-TEAC, and the H/L-ORAC assays, respectively. When compared to reference compounds ascorbic acid and quercetin, compounds **12** and **13** exhibited especially strong antioxidative capacity in both ORAC assays (Table 1). The activities of **12** and **13** in both TEAC assays (0.47/2.22 and 0.79/1.34 mmol TE/mmol) were in the range of those of ascorbic acid. (2*R*,3*S*)-Morelloflavone (**12**) showed a strong and comparable activity to quercetin in the H_2O_2 scavenging assay (12.4 μM, EC_{50}), whereas (2*R*,3*S*)-volkensiflavone (**13**) displayed almost 3-fold lower activity. The antioxidative capacity of the flavanone−flavone biflavanoids **12** and **13** is clearly lower than those of the biflavanone marker compounds **9** and **10**,[9,12] indicating a strong structure−activity relationship. Garcicowin C (**21**) revealed moderate activities comparable to those of isogarcinol (**22**) and garcinol (**24**) in all assays.[10]

■ ASSOCIATED CONTENT

Supporting Information

The Supporting Information is available free of charge on the ACS Publications website at DOI: 10.1021/acs.jafc.5b02544.

UPLC-UV-ESI-TOF MS, MS^e, CD, and 1D- and 2D-NMR spectra of compounds **12**, **13**, and **21**, tables summarizing all COSY, HSQC, and HMBC couplings, S-plot of root versus leaf, S-plot of root versus stem bark, compound abundance, and normalized abundance as well as MS and MS^e of **1**−**9** and **11**−**24** (PDF)

■ AUTHOR INFORMATION

Corresponding Author

*(T.D.S.) Phone: +49-8161-71-2911. Fax: +49-8161-71-2949. E-mail: timo.stark@tum.de.

Notes

The authors declare no competing financial interest.

DOI: 10.1021/acs.jafc.5b02544
J. Agric. Food Chem. 2015, 63, 7169−7179

REFERENCES

(1) Balemba, O. B.; Bhattarai, Y.; Stenkamp-Strahm, C.; Lesakit, M. S. B.; Mawe, G. M. The traditional anti-diarrheal remedy, *Garcinia buchananii* stem bark extract, inhibits propulsive motility and fast synaptic potentials in the guinea pig distal colon. *Neurogastroenterol. Motil.* **2010**, *22*, 1332−1339.

(2) Boakye, P. A.; Brierley, S. M.; Pasilis, S. P.; Balemba, O. B. *Garcinia buchananii* bark extract is an effective anti-diarrheal remedy for lactose-induced diarrhea. *J. Ethnopharmacol.* **2012**, *142*, 539−547.

(3) Castro, J.; Balemba, O. B.; Blackshaw, L. A.; Brierley, S. M. *Garcinia buchananii* bark extract inhibits nociceptors, with greater efficacy during inflammation. *Gastroenterology* **2011**, *140* (Suppl. 1), S866.

(4) Boakye, P. A.; Stenkamp-Strahm, C.; Bhattarai, Y.; Hechman, M. D.; Brierley, S. M.; Pasilis, S. P.; Balemba, O. B. 5-HT_3 and 5-HT_4 receptors contribute to the anti-motility effects of *Garcinia buchananii* bark extract in the guinea-pig distal colon. *Neurogastroenterol. Motil.* **2012**, *24*, e27−e40.

(5) Kisangau, D. P.; Lyaruu, H. V.; Hosea, K. M.; Joseph, C. C. Use of traditional medicines in the management of HIV/AIDS opportunistic infections in Tanzania: a case in the Bukoba rural district. *J. Ethnobiol. Ethnomed.* **2007**, *3*, 29−37.

(6) Chinsembu, K. C.; Hedimbi, M. An ethnobotanical survey of plants used to manage HIV/AIDS opportunistic infections in Katima Mulilo, Caprivi region, Namibia. *J. Ethnobiol. Ethnomed.* **2010**, *6*, 25.

(7) De Wet, H.; Nkwanyana, M. N.; van Vuuren, S. F. Medicinal plants used for the treatment of diarrhoea in northern Maputaland, KwaZulu-Natal Province, South Africa. *J. Ethnopharmacol.* **2010**, *130*, 284−289.

(8) Okullo, J. B. L.; Omujal, F.; Bigirimana, C.; Isubikalu, P.; Malinga, M.; Bizuru, E.; Namutebi, A.; Obaa, B. B.; Agea J. G. Ethno-medicinal uses of selected indigenous fruit trees from the Lake Victoria basin districts in Uganda. *J. Med. Plants Stud.* **2014**, *2*, 78−88.

(9) Stark, T. D.; Matsutomo, T.; Lösch, S.; Boakye, P. A.; Balemba, O. B.; Pasilis, S. P.; Hofmann, T. Isolation and structure elucidation of highly antioxidative 3,8″-linked biflavanones and flavanone-*C*-glycosides from *Garcinia buchananii* bark. *J. Agric. Food Chem.* **2012**, *60*, 2053−2062.

(10) Stark, T. D.; Salger, M.; Frank, O.; Balemba, O. B.; Wakamatsu, J.; Hofmann, T. Antioxidative compounds from *Garcinia buchananii* stem bark. *J. Nat. Prod.* **2015**, *78*, 234−240.

(11) Jackson, B.; Locksley, H. D.; Moore, I.; Scheinmann, F. Extractives from Guttiferae. Part IX. The isolation of buchanaxanthone and two related xanthones from *Garcinia buchananii* Baker. *J. Chem. Soc. C* **1968**, *20*, 2579−2583.

(12) Stark, T. D.; Germann, D.; Balemba, O. B.; Wakamatsu, J.; Hofmann, T. New highly in vitro antioxidative 3,8″-linked biflav(an)-ones and flavanone-*C*-glycosides from *Garcinia buchananii* stem bark. *J. Agric. Food Chem.* **2013**, *61*, 12572−12581.

(13) Jackson, B.; Locksley, H. D.; Scheinmann, F.; Wolstenholme, W. A. The isolation of a new series of biflavanones from the heartwood of *Garcinia buchananii*. *Tetrahedron Lett.* **1967**, *9*, 787−792.

(14) Jackson, B.; Locksley, H. D.; Scheinmann, F. The structure of the "GB" biflavanones from *Garcinia buchananii* Baker and *G. eugeniifolia* Wall. *Chem. Commun.* **1968**, *18*, 1125−1127.

(15) Jackson, B.; Locksley, H. D.; Scheinmann, F.; Wolstenholme, W. A. Extractives from Guttiferae. Part XXII. The isolation and structure of four novel biflavanones from the heartwoods of *Garcinia buchananii* Baker and *G. eugeniifolia* Wall. *J. Chem. Soc. C* **1971**, *22*, 3791−3804.

(16) Balemba, O. B.; Stark, T. D.; Lösch, S.; Patterson, S.; McMillan, J. S.; Mawe, G. M.; Hofmann, T. (2*R*,3*S*,2″*R*,3″*R*)-Manniflavanone, a new gastrointestinal smooth muscle L-type calcium channel inhibitor, which underlies the spasmolytic properties of *Garcinia buchananii* stem bark extract. *J. Smooth Muscle Res.* **2014**, *50*, 48−65.

(17) Lang, R.; Wahl, A.; Stark, T.; Hofmann, T. Urinary *N*-methylpyridinium and trigonelline as candidate dietary biomarkers of coffee consumption. *Mol. Nutr. Food Res.* **2011**, *55*, 1613−1623.

(18) Stark, T.; Marxen, S.; Rütschle, A.; Lücking, G.; Scherer, S.; Ehling-Schulz, M.; Hofmann, T. Mass spectrometric profiling of *Bacillus cereus* strains and quantitation of the emetic toxin cereulide by means of stable isotope dilution analysis and HEp-2 bioassay. *Anal. Bioanal. Chem.* **2013**, *405*, 191−201.

(19) Stark, T.; Wollmann, N.; Lösch, S.; Hofmann, T. Quantitation of resveratrol in red wines by means of stable isotope dilution analysis-ultra-performance liquid chromatography-quan-time-of-flight mass spectrometry and cross validation. *Anal. Chem.* **2011**, *83*, 3398−3405.

(20) Stark, T. D.; Angelov, A.; Hofmann, M.; Liebl, W.; Hofmann, T. Comparative direct infusion ion mobility mass spectrometry profiling of *Thermus thermophilus* wild-type and mutant ΔcruC carotenoid extracts. *Anal. Bioanal. Chem.* **2013**, *405*, 9843−9848.

(21) Ichikawa, M.; Ryu, K.; Yoshida, J.; Ide, N.; Yoshida, S.; Sasaoka, T.; Sumi, S. Antioxidant effects of tetrahydro-*β*-carboline derivatives identified in aged garlic extract. *BioFactors* **2002**, *16*, 57−72.

(22) Ou, B.; Hampsch-Woodill, M.; Prior, R. L. Development and validation of an improved oxygen radical absorbance capacity assay using fluorescein as the fluorescent probe. *J. Agric. Food Chem.* **2001**, *49*, 4619−4926.

(23) Cao, G.; Alessio, H. M.; Cutler, R. G. Oxygen-radical absorbance capacity assay for antioxidants. *Free Radical Biol. Med.* **1993**, *14*, 303−311.

(24) Madrona, A.; Pereira-Caro, G.; Bravo, L.; Mateos, R.; Espartero, J. L. Preparation and antioxidant activity of tyrosyl and homovanillyl ethers. *Food Chem.* **2011**, *129*, 1169−1178.

(25) Floegel, A.; Kim, D.-O.; Chung, S.-J.; Koo, S. I.; Chun, O. K. Comparison of ABTS/DPPH assays to measure antioxidant capacity in popular antioxidant-rich US foods. *J. Food Compos. Anal.* **2011**, *24* (7), 1043−1048.

(26) Van den Berg, R.; Haenen, G. R. M. M.; van den Berg, H.; Bast, A. Applicability of an improved Trolox equivalent antioxidant capacity (TEAC) assay for evaluation of antioxidant capacity measurements of mixtures. *Food Chem.* **1999**, *66*, 511−517.

(27) Stark, T. D.; Lösch, S.; Salger, M.; Balemba, O. B.; Wakamatsu, J.; Frank, O.; Hofmann, T. A strategy to counteract heat-induced damage in NMR experiments to characterize biflavanones and two new biflavanone-7″-*O*-*β*-D-glucopyranosides from *Garcinia buchananii* root. *Magn. Reson. Chem.* **2015**, DOI: 10.1002/mrc.4269.

(28) Stark, T. D.; Lösch, S.; Frank, O.; Balemba, O. B.; Hofmann, T. Purification procedure for (2*R*,3*S*,2″*R*,3″*R*)-manniflavanone and its minor (2*R*,3*S*,2″*S*,3″*S*)-isomer from *Garcinia buchananii* stem bark extract. *Eur. Food Res. Technol.* **2015**, *240*, 1075−1080.

(29) Herbin, G. A.; Jackson, B.; Locksley, H. D.; Scheinmann, F.; Wolstenholme, W. A. The biflavonoids of *Garcinia volkensii* (Guttiferae). *Phytochemistry* **1970**, *9*, 221−226.

(30) Chari, V. M.; Ilyas, M.; Wagner, H.; Neszmelyi, A.; Chen, F.-C.; Chen, L.-K.; Lin, Y.-C.; Lin, Y.-M. ^{13}C-NMR spectroscopy of biflavanoids. *Phytochemistry* **1977**, *16*, 1273−1278.

(31) Waterman, P. G.; Crichton, E. G. Xanthones and biflavonoids from *Garcinia densivenia* stem bark. *Phytochemistry* **1980**, *19*, 2723−2726.

(32) Li, X.-C.; Joshi, A. S.; Tan, B.; ElSohly, H. N.; Walker, L. A.; Zjawiony, J. K.; Ferreira, D. Absolute configuration, conformation and chiral properties of flavanone-(3−8″)-flavone biflavonoids from *Rheedia acuminate*. *Tetrahedron* **2002**, *58* (43), 8709−8717.

(33) Xu, G.; Kan, W. L.; Zhou, Y.; Song, J. Z.; Han, Q. B.; Qiao, C. F.; Cho, C. H.; Rudd, J. A.; Lin, G.; Xu, H. X. Cytotoxic acylphloroglucinol derivatives from the twigs of *Garcinia cowa*. *J. Nat. Prod.* **2010**, *73*, 104−108.

(34) Rukachaisirikul, V.; Tadpetch, K.; Watthanaphanit, A.; Saengsanae, N.; Phongpaichit, S. Benzopyran, biphenyl, and tetraoxygenated xanthone derivatives from the twigs of *Garcinia nigrolineata*. *J. Nat. Prod.* **2005**, *68*, 1218−1221.

(35) Chen, Y.; Zhong, F. F.; He, H. W.; Hu, Y.; Zhu, D.; Yang, G. Z. Structure elucidation and NMR spectral assignment of five new xanthones from the bark of *Garcinia xanthochymus*. *Magn. Reson. Chem.* **2008**, *46*, 1180−1184.

(36) Yang, N. Y.; Han, Q. B.; Cao, X. W.; Qiao, C. F.; Song, J. Z.; Chen, S. L.; Yang, D. J.; Yiu, H.; Xu, H. X. Two new xanthones

DOI: 10.1021/acs.jafc.5b02544
J. Agric. Food Chem. 2015, 63, 7169−7179

isolated from the stem bark of *Garcinia lancilimba*. *Chem. Pharm. Bull.* **2007**, *55*, 950−952.
(37) Nguyen, L. H. D.; Vo, H. T.; Pham, H. D.; Connolly, J. D.; Harrison, L. J. Xanthones from the bark of *Garcinia merguensis*. *Phytochemistry* **2003**, *63*, 467−470.
(38) Ito, C.; Miyamoto, Y.; Nakayama, M.; Kawai, Y.; Rao, K. S.; Furukawa, H. A novel depsidone and some new xanthones from *Garcinia* species. *Chem. Pharm. Bull.* **1997**, *45*, 1403−1413.
(39) Vo, H. T.; Nguyen, N. T. T.; Maas, G.; Werz, U. R.; Pham, H. D.; Nguyen, L. H. D. Xanthones from the bark of *Garcinia pedunculata*. *Phytochem. Lett.* **2012**, *5*, 766−769.
(40) Khalid, R. M.; Jabit, M. L.; Abas, F.; Stanslas, J.; Shaari, K.; Lajis, N. H. Cytotoxic xanthones from the leaves of *Garcinia urophylla*. *Nat. Prod. Commun.* **2007**, *2*, 271−276.
(41) Ji, F.; Li, Z. L.; Liu, G. F.; Niu, S. L.; Zhao, N.; Liu, X. Q.; Hua, H. M. Xanthones with antiproliferative effects on prostate cancer cells from the stem bark of *Garcinia xanthochymus*. *Nat. Prod. Commun.* **2012**, *7*, 53−56.
(42) Waffo, A. F. K.; Mulholland, D.; Wansi, J. D.; Mbaze, L. M.; Powo, R.; Mpondo, T. N.; Fomum, Z. T.; Konig, W.; Nkengfack, A. E. Afzeliixanthones A and B, two new prenylated xanthones from *Garcinia afzelii* ENGL. (Guttiferae). *Chem. Pharm. Bull.* **2006**, *54*, 448−451.
(43) Chanmahasathien, W.; Li, Y. S.; Satake, M.; Oshima, Y.; Ruangrungsi, N.; Ohizumi, Y. Prenylated xanthones with NGF-potentiating activity from *Garcinia xanthochymus*. *Phytochemistry* **2003**, *64*, 981−986.
(44) Siridechakorn, I.; Maneerat, W.; Sripisut, T.; Ritthiwigrom, T.; Cheenpracha, S.; Laphookhieo, S. Biphenyl and xanthone derivatives from the twigs of a *Garcinia* sp. (Clusiaceae). *Phytochem. Lett.* **2014**, *8*, 77−80.
(45) Parveen, M.; Khan, N. U. D. 2 Xanthones from *Garcinia mangostana*. *Phytochemistry* **1988**, *27*, 3694−3696.
(46) Ngoupayo, J.; Tabopda, T. K.; Ali, M. S. Antimicrobial and immunomodulatory properties of prenylated xanthones from twigs of *Garcinia staudtii*. *Bioorg. Med. Chem.* **2009**, *17*, 5688−5695.
(47) Sen, A. K.; Sarkar, K. K.; Mazumder, P. C.; Banerji, N.; Uusvuori, R.; Hase, T. A. The structures of garcinones A, B and C: 3 new xanthones from *Garcinia mangostana*. *Phytochemistry* **1982**, *21*, 1747−1750.
(48) Iinuma, M.; Tosa, H.; Tanaka, T.; Riswan, S. Three new xanthones from the bark of *Garcinia dioica*. *Chem. Pharm. Bull.* **1996**, *44*, 232−234.
(49) Asai, F.; Tosa, H.; Tanaka, T.; Iinuma, M. A xanthone from pericarps of *Garcinia mangostana*. *Phytochemistry* **1995**, *39*, 943−944.
(50) Liu, X.; Yu, T.; Gao, X. M.; Zhou, Y.; Qiao, C. F.; Peng, Y.; Chen, S. L.; Luo, K. Q.; Xu, H. X. Apoptotic effects of polyprenylated benzoylphloroglucinol derivatives from the twigs of *Garcinia multiflora*. *J. Nat. Prod.* **2010**, *73*, 1355−1359.
(51) Baggett, S.; Protiva, P.; Mazzola, E. P.; Yang, H.; Ressler, E. T.; Basile, M. J.; Weinstein, I. B.; Kennelly, E. J. Bioactive benzophenones from *Garcinia xanthochymus* fruits. *J. Nat. Prod.* **2005**, *68*, 354−360.
(52) Cuesta-Rubio, O.; Padron, A.; Castro, H. V.; Pizza, C.; Rastrelli, L.; Aristophenones, A. Aristophenones A and B. A new tautomeric pair of polyisoprenylated benzophenones from *Garcinia aristata*. *J. Nat. Prod.* **2001**, *64*, 973−975.
(53) Gao, X. M.; Yu, T.; Lai, F. S. F.; Pu, J. X.; Qiao, C. F.; Zhou, Y.; Liu, X.; Song, J. Z.; Luo, K. Q.; Xu, H. X. Novel polyisoprenylated benzophenone derivatives from *Garcinia paucinervis*. *Tetrahedron Lett.* **2010**, *51*, 2442−2446.
(54) Asano, J.; Chiba, K.; Tada, M.; Yoshii, T. Cytotoxic xanthones from *Garcinia hanburyi*. *Phytochemistry* **1996**, *41*, 815−820.
(55) Re, R.; Pellegrini, N.; Proteggente, A.; Pannala, A.; Yang, M.; Rice-Evans, C. Antioxidant activity applying an improved ABTS radical cation decolorization. *Free Radical Biol. Med.* **1999**, *26*, 1231−1237.
(56) Mercader-Ros, M. T.; Lucas-Abellán, C.; Fortea, M. I.; Gabaldón, J. A.; Núñez-Delicado, E. Effect of HP-β-cyclodextrins complexation on the antioxidant activity of flavonols. *Food Chem.* **2010**, *118*, 769−773.

DOI: 10.1021/acs.jafc.5b02544
J. Agric. Food Chem. 2015, 63, 7169−7179

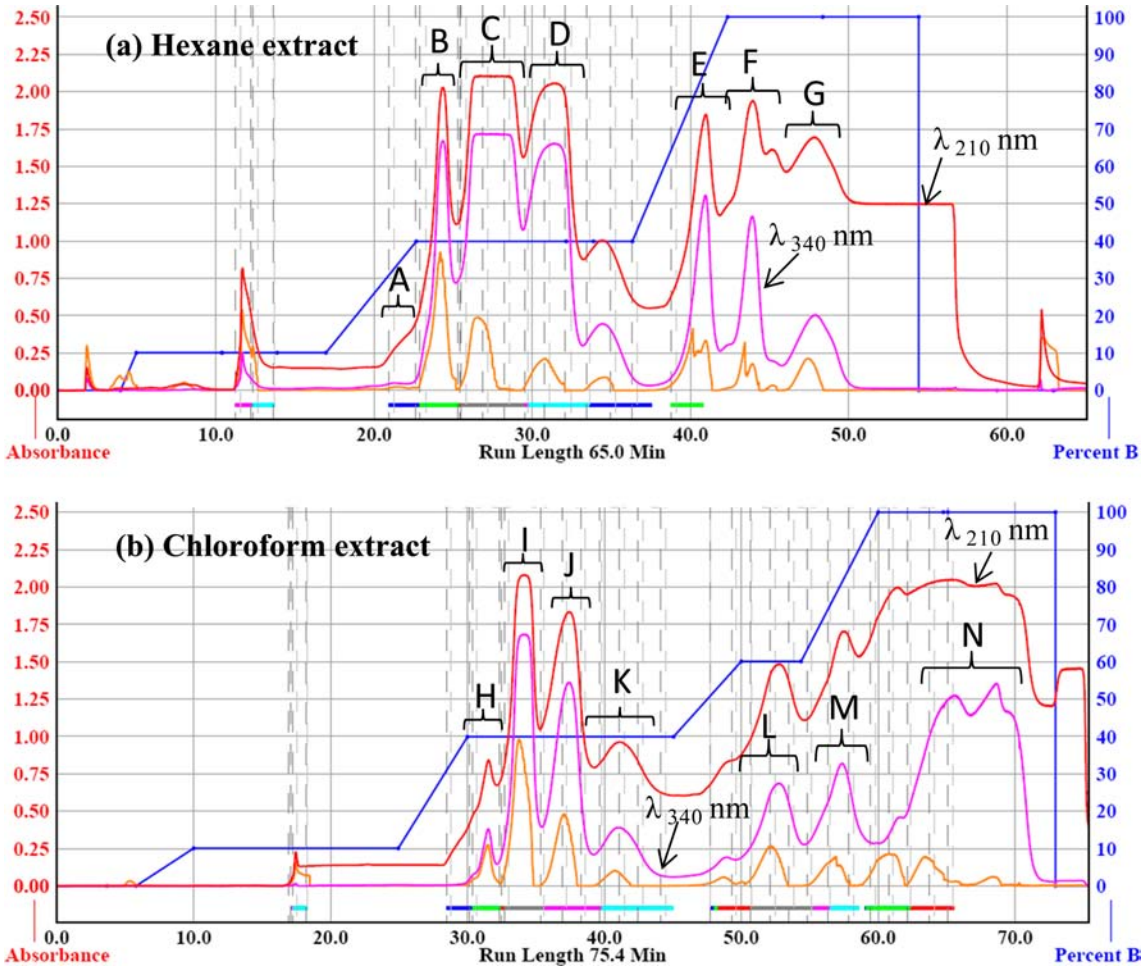

Figure 1. Flash chromatograms obtained by the separation of extracts of Miaray mandarin peel using silica gel columns. The individual peaks A–G yielded compounds **1**–**7**, and H–N yielded compounds **1**, **3**, **4**, and **7**–**10**.

including large sample volumes, a wide range of solvents, automated detection, and inline ultraviolet–visible spectral scanning (UV–vis). This improved technique enables medium-pressure liquid chromatographic separations as well as real-time monitoring of the compounds by their unique UV–vis spectral characteristics. Flash chromatography has been successfully applied for the separation and isolation of several bioactive compounds such as curcuminoids, flavonoids, and coumarins from a wide range of plant extracts and industrial by-products.[17,23,24]

The antimicrobial activity of citrus peel extracts has been intensively investigated,[25,26] but only a few studies have evaluated the effect of pure polymethoxyflavones, primarily due to commercial unavailability. Furthermore, polymethoxyflavones do not demonstrate potent bactericidal or bacteriostatic effects. For example, a recent study showed that polymethoxyflavones nobiletin and tangeretin exhibit low antimicrobial activities against six strains of microorganisms, including *Escherichia coli*, *Staphylococcus* sp., and *Salmonella typhi*.[26] An alternative mechanism to attenuate bacterial pathogenicity is interference with bacterial cell–cell communication pathways. We have previously demonstrated that several citrus limonoids and flavonoids interfere with bacterial signaling cascades, leading to attenuation of various virulence mechanisms including biofilm formation.[27−29] Our prior study showed that 3′,4′,5,6,7-pentamethoxyflavone (sinensitin) exerts biofilm inhibitory activity in a dose-dependent manner. Citrus has approximately 28 structurally distinct reported polymethoxyflavones, with variation in the number and position of the methoxyls attached to the flavone backbone.[30] These structural variants may potentially demonstrate a wide range of inhibitory activities on bacterial biofilms and help in the identification of novel antimicrobial agents.

In the present study, nine polymethoxyflavones and one limonoid were isolated for the first time from Miaray mandarins using rapid flash chromatography along with 3,5,7,3′,4′-pentamethoxyflavone (pentamethylquercetin). These compounds were characterized by spectral analysis using high-performance liquid chromatography (HPLC), matrix-assisted laser desorption/ionization-time-of-flight-mass spectrometry (MALDI-TOF), and 1D and 2D nuclear magnetic spectroscopy (NMR). All identified compounds were evaluated for their biofilm inhibitory activity using *Vibrio harveyi*.

MATERIALS AND METHODS

Plant Material. Mature *Citrus miaray* mandarin fruits (Figure S1) were harvested in December 2010 from the Texas A&M University–Kingsville Citrus Center orchard (Weslaco, TX, USA). A voucher specimen (249960) has been submitted to the S. M. Tracy Herbarium, Texas A&M University (College Station, TX, USA). The peels were separated and dried to ≤5% moisture. The peels were blended to obtain 40–60 mesh size powder in a Vita-prep blender (Vita-Mix Corp., Cleveland, OH, USA) and used for extraction.

DOI: 10.1021/acs.jafc.5b02445
J. Agric. Food Chem. 2015, 63, 7180−7189

Reagents and Instrumentation. Solvents used for analysis were of HPLC grade and obtained from Fisher Scientific (Pittsburgh, PA, USA). Nanopure water (NANOpure, Barnstead/Thermolyne, Dubuque, IA, USA) was used for HPLC analysis. The solvents used for flash chromatography were of analytical grade and purchased from Fisher Scientific. The separation of polymethoxyflavones was carried out on a flash chromatography system (Combiflash Rf, Teledyne ISCO, Lincoln, NE, USA). Silica gel (particle size 35−60 μm) columns (220 g) were purchased from ISCO Inc. (RediSep Rf ISCO Inc.).

Soxhlet Extraction of Peels. Eight hundred grams of dried peel powder was loaded into a Soxhlet-type apparatus and extracted with hexane and chloroform sequentially for 16 h each. The extracts were concentrated to obtain 31 and 23 g of hexane and chloroform extracts, respectively.

Sample Preparation and Chromatographic Separation. The hexane extract (31 g) was dissolved in 50 mL of hexane, impregnated with 20 g of silica gel, and dried at room temperature in a hood. A similar procedure was followed for the chloroform extract and used for purification. The chromatography system Teledyne ISCO CombiFlash Rf 4x system equipped with a fiber optic spectrometer, a UV−vis ($\lambda_{200\ nm}$−$\lambda_{700\ nm}$) detector, and a 220 g silica gel flash column was used for the separation. This detector can detect and monitor UV spectra of the eluent after separation from the flash column using PeakTrak 2.0.0 software.

Hexane Extract. The silica gel impregnated hexane extract of Miaray mandarin was subjected to flash chromatography on a silica gel column. The column was equilibrated with hexane for 3 column volumes prior to separations. Polymethoxyflavones were separated with a 65 min gradient program of solvent A (hexane) and solvent B (chloroform): 100% A held for 4 min, linearly increased to 10% B over 1 min, held for 12 min, linearly increased to 40% B over 6 min, held for 14 min, linearly increased to 100% B over 6 min, held for 12 min, and then finally returned to the initial conditions and held for 10 min. The flow rate was maintained at 150 mL/min, and individual fractions were collected by monitoring the eluting analytes at $\lambda_{210\ nm}$ and $\lambda_{340\ nm}$. The eluent from the column was also monitored using an inline UV−vis detector for monitoring the absorption spectra of the separating compounds. Individual peaks were tentatively identified on the basis of the distinct absorption spectrum of each fraction. Seven major peaks (A−G) were observed and collected in individual fractions (Figure 1A). The retention times of the separated peaks were as follows: peak A, 22.5−25 min; peak B, 25−29.5 min; peak C, 29.5−34 min; peak D, 34−37.5 min; peak E, 39−42 min; peak F, 42−45 min; peak G, 45−50 min. The individual peak fractions were further analyzed by HPLC and pooled on the basis of their similarity in retention time and matching UV spectral data. Evaporation of the solvent from the pooled fractions of peaks A−G yielded crystallization of compounds **1**−**5**, **8**, and **9**, respectively.

Chloroform Extract. The silica gel impregnated chloroform extract was subjected to flash chromatography on a silica gel column (220 g). The column was equilibrated with hexane for 3 column volumes prior to separations. Polymethoxyflavones were separated with a 75 min gradient program of solvent A and solvent B: 100% A held for 6 min, linearly increased to 10% B over 4 min, held for 15 min, linearly increased to 40% B over 5 min, held for 15.5 min, linearly increased to 60% B over 5 min, held for 4.5 min, linearly increased to 100% B over 6 min, held for 12 min, and then finally returned to the initial conditions and held for 2 min. The flow rate was maintained at 150 mL/min, and individual fractions were collected by monitoring the eluting analytes at $\lambda_{210\ nm}$ and $\lambda_{340\ nm}$. The eluent from the column was also monitored using an inline UV−vis detector for monitoring the absorption spectra of the separating compounds. Individual peaks were tentatively identified on the basis of the distinct absorption spectrum of each fraction. Seven major peaks (H−N) were observed and collected (Figure 1B). The retention times of the separated peaks were as follows: peak H, 30−32.5 min; peak I, 32.5−35 min; peak J, 35−39 min; peak K, 39−44 min; peak L, 51−55 min; peak M, 55−59 min; peak N, 62−70 min. Twenty microliters of each fraction was diluted with 500 μL of acetone and analyzed by HPLC for detection of polymethoxyflavones and further pooling of fractions with similar compounds. Evaporation of the solvent from the pooled fractions of peaks H−N yielded crystallized compounds **1**, **3** **4**, **5**, **6**, **7**, and **10**.

Liquid Chromatography. The HPLC system consisted of a Waters 1525 HPLC series (Milford, MA, USA) connected to a photodiode array detector. A Gemini C_{18} column (3 μm, 250 × 4.6 mm) (Phenomenex, Torrance, CA, USA) was used for the separations. A gradient mobile phase of 3 mM phosphoric acid (A) and acetonitrile (B) was used for the separations at a flow rate of 1 mL/min. Initially, elution was started with a gradient of 5% B followed by a linear increase to 50% in 20 min and then returned to 5% in 5 min. The injection volume was set at 10 μL, and the polymethoxyflavones were detected at $\lambda_{280\ nm}$ and $\lambda_{340\ nm}$. Chromatographic data were collected and processed using Empower2 software (Waters).

Matrix-Assisted Laser Desorption/Ionization-Time of Flight-Mass Spectrometry (MALDI-TOF-MS) Analysis. The samples for MS analysis were prepared by dissolving the isolated compounds (**1**−**10**) in acetonitrile and mixed with 2′,4′,6′-trihydroxyacetophenone (THAP) matrix. Half a microliter of the matrix mixture was spotted on a MALDI sample plate and air-dried. MALDI-TOF mass spectra were acquired using a Voyager DE-Pro (Applied Biosystems, Carlsbad, CA, USA) mass spectrometer in positive reflector ion mode. After time-delayed extraction of 275 ns, the ions were accelerated to 20 kV for TOF mass spectrometric analysis. A total of 100 laser shots were acquired with the signal averaged per mass spectrum.

NMR Analysis. ^{1}H and ^{13}C NMR attached proton test (APT) spectra were recorded at 400 and 100 MHz, respectively, by FT NMR (JEOL USA, Inc., Peabody, MA, USA). The isolated compounds were dissolved in chloroform ($CDCl_3$) except compound **8**, which was dissolved in deuterated dimethyl sufoxide (DMSO-d_6). Compounds **1**, **5**, **6**, **8**, and **10**) were identified by using 1D and 2D NMR data including heteronuclear single-quantum correlation spectroscopy (HSQC); heteronuclear multiple-bond correlation spectroscopy (HMBC), double quantum filter correlation spectroscopy (DQF-COSY), and nuclear Overhauser effect spectroscopy (NOSEY).

Bacterial Strains and Media. *V. harveyi* strains BB170 (luxN::Tn5), BB886 (luxPQ::Tn5), BB120 (wild-type), JAF483 (luxO D47A), and BNL258 (hfq::Tn5lacZ) were kindly provided by B. L. Bassler (Princeton University, Princeton, NJ, USA).[31−34] *E. coli* 5, an environmental isolate, was used as a positive control for autoinducer-2 (AI-2) activity.[35] Autoinducer bioassay (AB) or Luria Marine (LM) media were used to culture the *V. harveyi* strains.[36]

Growth Assay. Overnight cultures of *V. harveyi* BB120 were diluted 100-fold in AB media and treated with polymethoxyflavones (50 μM) or an equivalent volume of DMSO. The cultures were grown for 16 h, and OD_{570} was measured every 15 min by using a Synergy HT multimode microplate reader (BioTek Instruments, Winooski, VT, USA). The instrument was set to maintain a temperature of 30 °C, and plates were constantly shaken at medium speed between readings. The data are presented as the mean of three biological replicates.

Bioluminescence Assay. The bioluminescence was measured using the method described previously from our laboratory.[27] In brief, *E. coli* 5 and *V. harveyi* BB120 were cultured overnight in Luria−Bertani (LB) and LM media, respectively, to obtain high concentrations of autoinducer activity. The overnight cultures were centrifuged at 10000 rpm for 10 min in a microcentrifuge and filtered using a 0.2 μm cellulose acetate membrane filter to obtain clear cell-free supernatant (CFS). The CFSs were stored at −20 °C until use. Inhibition of autoinducer [harveyi autoinducer (HAI) and AI-2]-mediated bioluminescence was measured in a 96-well plate assay.[27] The final concentrations of polymethoxyflavones tested were 12.5, 25, and 50 μM. Diluted (2500-fold) overnight cultures (900 μL) of reporter strains BB886 (for HAI) and BB170 (for AI-2) were incubated with 5 μL of CFS, 0.5 μL of polymethoxyflavones or DMSO, and 4.5 μL of sterile Autoinducer Bioassay (AB) medium at 30 °C with shaking at 100 rpm. Light production was measured by a Victor2 1420 multilabel counter (Beckman Coulter) in luminescence mode. The values were recorded as relative light units and used for calculations. The relative activity was calculated as the ratio of luminescence of the test sample to the control (DMSO) sample.[36]

DOI: 10.1021/acs.jafc.5b02445
J. Agric. Food Chem. 2015, 63, 7180−7189

Biofilm Assay. The biofilm assay was conducted using the method described previously from our laboratory.[29] Briefly, an overnight culture of *V. harveyi* BB120 was diluted 1:50 in LM medium, and 190 μL of this fresh culture was incubated with 7 μL of sterile medium and 0.5 μL of DMSO or polymethoxyflavones (12.5, 25, 50 μM) dissolved in DMSO. The biofilm mass was quantified by washing with phosphate buffer (0.1 M, pH 7.4), followed by staining with 0.3% Crystal Violet (Fisher) for 20 min. The dye associated with biofilm was dissolved with 200 μL of 33% acetic acid, and A_{570} was measured. The mean ± standard deviation of three biological replicates is presented.

RESULTS AND DISCUSSION

Extraction. Successive extractions of mandarin peels using nonpolar hexane and medium-polar chloroform in a Soxhlet type apparatus yielded 3.9 and 2.9% of concentrated crude extract, respectively. HPLC analysis of the extracts (Figure S2) suggested that the extracts contain high levels of polymethoxyflavones. Additionally, the chromatograms suggested that the successive extractions with hexane and chloroform enabled fractionation of low-polar and medium-polar molecules, respectively. The individual polymethoxyflavones were purified by flash chromatography.

Purification of Polymethoxyflavones. *Hexane Extract.* The step gradient elution using hexane and acetone enabled clear separation of individual polymethoxyflavones (Figure 1a). The eluent from the column was monitored using an inline UV−vis detector to show the absorption spectra of the compounds, which were subsequently collected in fractions. The initial isocratic elution using 10% acetone separated the oil from the crude extract. After separation of the oils, the linear change in gradient elution to 60:40 hexane/acetone resulted in good separation of the low-polarity polymethoxyflavones, whereas medium-polar polymethoxyflavones were separated by the gradual increase in the solvent polarity to 100% acetone. On the basis of HPLC analysis, fractions showing similar peak profiles were pooled and concentrated under vacuum. The concentrated peak (A−G) fractions yielded crystallized compounds, which were collected, their purity was analyzed by HPLC, and they were identified by spectroscopic data.

Chloroform Extract. The impregnated chloroform extract was subjected to flash chromatographic separation using a step gradient of hexane and acetone solvents with a total run time of 75 min. To enable good separation of medium- and low-polar polymethoxyflavones, an additional step gradient of 40:60 hexane/acetone was used, followed by a linear increase to 100% acetone (Figure 1b). The step gradient elution resulted in separation of peaks H−N. Similar to the chromatographic separation of the hexane extract, the eluent from the column was monitored using an inline UV−vis detector. Individual peaks with distinct absorption spectra were collected in individual fractions. The fractions collected for individual peaks were analyzed by HPLC and concentrated to obtain crystallized compounds. These were further subjected to spectral analysis using MS and NMR to identify the compounds.

Altogether, 10 purified compounds were isolated from hexane and chloroform extracts. The yields of the isolated compounds were as follows: **1**, 18 mg; **2**, 76 mg; **3**, 8628 mg; **4**, 2012 mg; **5**, 210 mg; **6**, 121 mg; **7**, 1077 mg; **8**, 79 mg; **9**, 810 mg; and **10**, 820 mg.

Identification. The identification and structural elucidation of the isolated compounds from Miaray mandarin were conducted using spectral analysis by HPLC, MS, and NMR. The chromatograms of the HPLC analysis of the isolated compounds are presented in Figure 2. The absence of other peaks demonstrates the purity of the isolated compounds. The purity of the isolated compounds ranged between ≥95 and ≤98%. The absorption spectra of the compounds were obtained using a photodiode array detector. All of the isolated

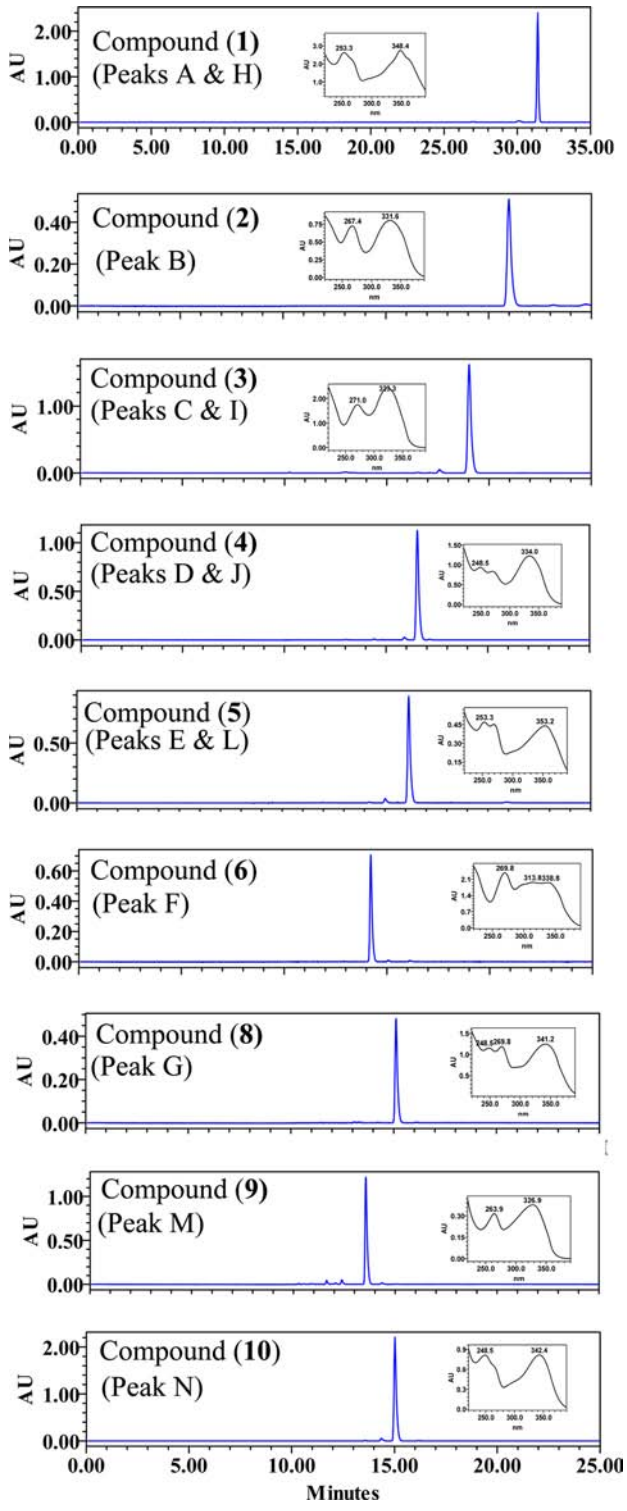

Figure 2. HPLC chromatograms of isolated compounds (**1**−**10**) along with their UV spectra. The separation was conducted on a Gemini C_{18} column using gradient mobile phase.

DOI: 10.1021/acs.jafc.5b02445
J. Agric. Food Chem. 2015, 63, 7180−7189

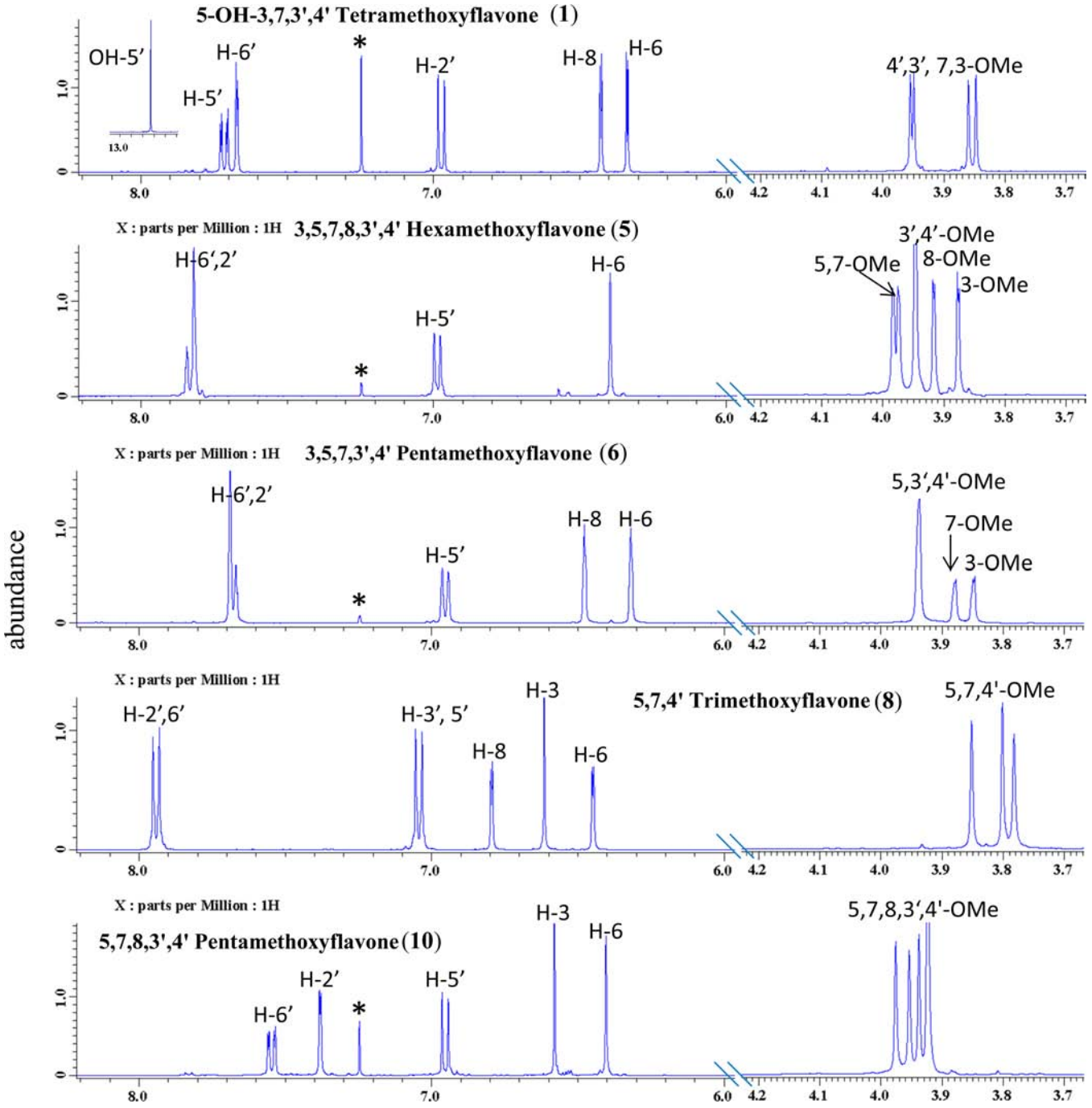

Figure 3. [1] H NMR spectra of purified compounds (**1**, **5**, **6**, **8**, and **10**) recorded on a JEOL ECS NMR spectrometer at 400 MHz. All compounds were dissolved in $CDCl_3$ except **8**, which was dissolved in DMSO-d_6. The solvent peak is denoted by an asterisk (*).

compounds had distinct UV maxima in the range of $\lambda_{325\ nm}$–$\lambda_{353\ nm}$, which is characteristic of polymethoxyflavones. The results are consistent with earlier studies.[16,37,38] The MALDI-TOF mass spectral data for compounds **2**, **3**, **4**, **7**, and **9** were found to be 373.04, 433.16, 403.31, 470.21, and 343.26, respectively (Figure S3). The NMR chemical shifts (not shown) of these compounds were matched to reported values.[16,39] Using these data, the structures of compounds **2**, **3**, **4**, **7**, and **9** were confirmed and identified as 5,6,7,8,4′-pentamethoxyflavone (tangeretin), 3,5,6,7,8,3′,4′-heptamethoxyflavone, 5,6,7,8,3′,4′-hexamethoxyflavone (nobiletin), limonin, and 5,7,8,4′-tetramethoxyflavone, respectively. The structure of tangeretin was also confirmed by 2D NMR spectral assignments (Figure S4). These data were helpful when assigning the chemical shifts of another three pentamethoxyflavones of compounds **6** and **10**.

Compounds **4** and **5** are hexamethoxyflavones, whereas compound **2**, **6**, and **10** are pentamethoxyflavones with $[M + 1]^+$ of 403 and 373, respectively. The structural confirmation is not very accurate using only mass spectral data. Therefore, we have used 1D and 2D NMR spectral data to validate the findings (Figures 3 and 4 and Figures S4–S9). ^{1}H NMR signals (Figure 3) of compounds **1**, **5**, **6**, **8**, and **10** showed at δ 3.5–4.0 and 6.3–8.0, indicating that all compounds had structures typical of polymethoxyflavones. Their characteristics and assignments were made using ^{13}C APT NMR (Figure 4) and

DOI: 10.1021/acs.jafc.5b02445
J. Agric. Food Chem. 2015, 63, 7180–7189

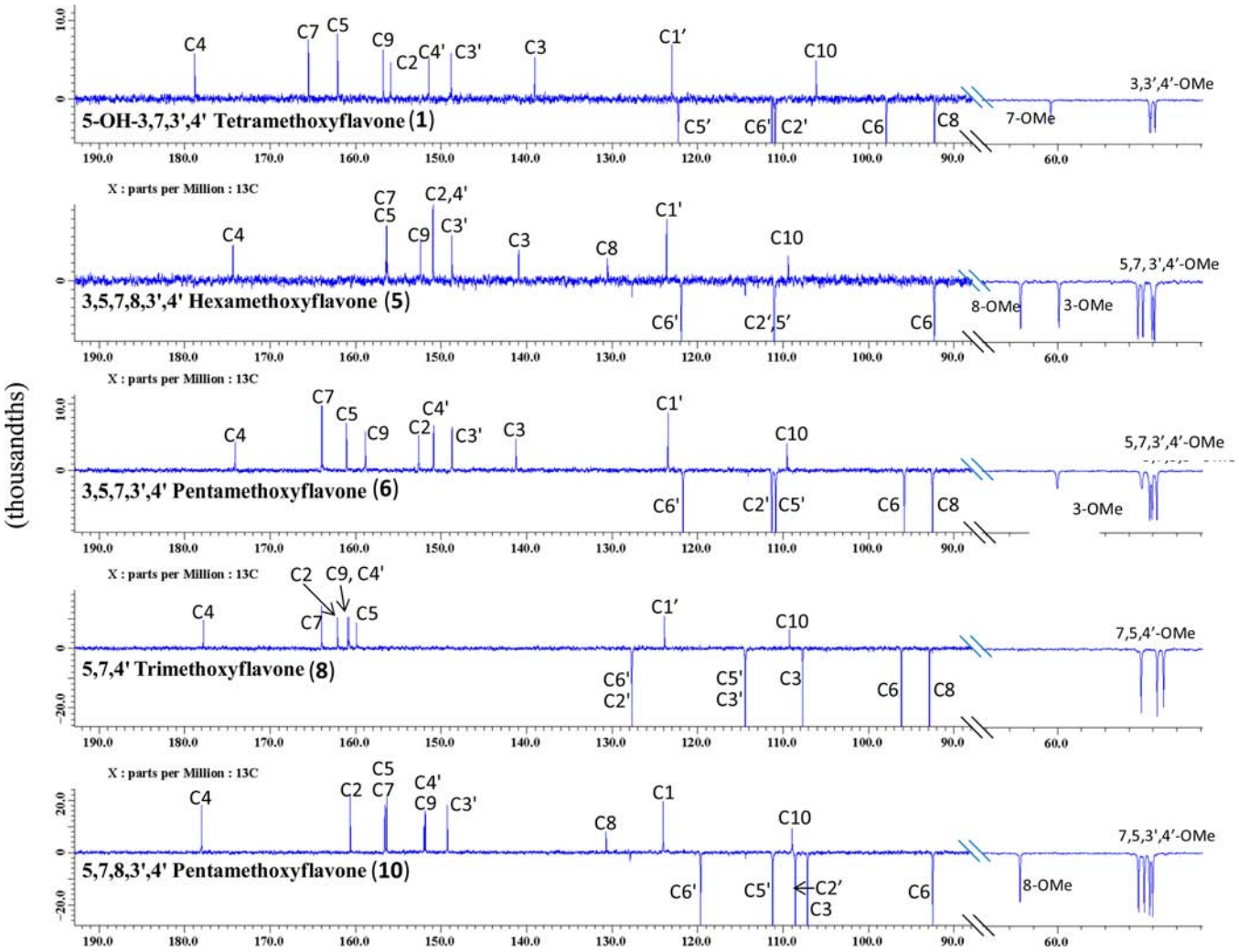

Figure 4. ^{13}C NMR attached proton test (APT) spectra of the isolated compounds (**1**, **5**, **6**, **8**, and **10**) recorded on a JEOL ECS spectrometer at 100 MHz. All compounds were dissolved in $CDCl_3$ except **8**, which was dissolved in DMSO-d_6.

2D experiments including HMBC, HMQC, DQFCOSY, and NOSEY.

Compound **1**: The presence of a downfield proton resonance at 12.5 ppm on ^{1}H NMR is a characteristic indicator of a chelated hydroxyl group at the fifth position of the flavone skeleton. Due to the presence of the hydroxyl group at C-5, the carbonyl signal at the fourth position in ^{13}C NMR showed at δ 178.5. Moreover, the lack of a resonance at δ 6.6 for the olefinic proton in ^{1}H NMR indicated that there is a substituent at the 3-position. The ^{1}H NMR spectrum showed the ABX-type aromatic proton signals indicating the existence of 1′,3′,4′-trisubstituted flavones. ^{13}C NMR showed the presence of three methyl groups at around δ 56 and one distinct signal at δ 60.2 for the 7-methoxyl group. The MALDI-TOF-MS spectrum showed the $[M + 1]^+$ at m/z 359.3011. Using these spectral data identified compound **1** as 5-hydroxyl-3,7,3′,4′-tetramethoxyflavone. The chemical shifts show good agreement with the earlier papers by Li et al.[40]

Compound **5**: The ^{1}H NMR spectrum showed the presence of six methoxyl groups at δ 3.88−3.98, and those were tentatively assigned to the 3-, 5-, 7-, 8-, 3′-, and 4′-positions. These assignments were further confirmed from ^{13}C NMR APT chemical shifts with two signals observed at low field (δ 59.9 and 61.5) for two typical methoxyl groups at 3- and 8-substitution. A sharp singlet at δ 6.4 was assigned to the sixth position, which was evidenced from the δ 92.32 signal. The B-ring proton signals showed a pattern similar to ABX coupling for three protons at H-2′, H-5′, and H-6′ (Figure S5). However, the H-2′ displayed a broad singlet due to NOE effect caused by methoxyl substitution at the C-3 position. Using these spectral data and MALDI-TOF-MS (m/z at 403.3491), compound **5** was identified as 3,5,7,8,3′,4′-hexamethoxyflavone and signals were matched to reported values.[45]

Compound **6**: The ^{1}H NMR spectrum showed the presence of five methoxyl groups, and those were shown from the ^{13}CNMR APT spectrum to be similar to compound **5**, with substitutions at 3-, 5-, 7-, 3′-, and 4′-positions. These data suggested that compound **6** is a pentamethoxylated flavonoid. In ^{1}H NMR two aromatic broad singlets at δ 6.34 and 6.48 well correlated in DQFCOSY to two different neighboring methoxy groups at δ 3.88 and 3.93, which indicates meta substitution in the A-ring (Figure S6). On the other hand, in the proton NMR spectrum, the δ 6.34 proton had a meta coupling to δ 6.48 (J = 1.8 Hz), which was assigned to H-6 and H-8. Spectra in the B-ring had ABX type aromatic proton signals, which confirms the presence of three protons, and it was confirmed by integrated area of three protons. The size of the coupling constant (J = 1.1 and 8.4 Hz) is characteristic of meta and ortho coupling as found in

DOI: 10.1021/acs.jafc.5b02445
J. Agric. Food Chem. 2015, 63, 7180−7189

3′,4′-methoxylated flavonoids, whereas such correction were not found in tangeretin due to the absence of ABX coupling (Figure S7). Moreover, proton signals for H-2′ displayed downfield at δ 7.9 as compared to PMF (**10**) due to the presence of methoxyl substitution at the C-3-position, which will cause NOE effect. A similar trend was observed for hexamethoxyflavone (**5**). Using this NMR and mass spectral data ($[M + 1]^+ - 373.3003$), we confirmed compound **6** as 3,5,7,3′,4′-pentamethoxyflavone (pentamethylquercetin). These chemical shifts were identical to those from the scientific literature.[42] This compound was previously identified in the bark extract of *Melicope subunifoliolata*.[43]

Compound **8**: The TOF-MS spectrum showed a molecular ion peak at m/z 313.2550. The ^{1}H NMR (DMSO-d_6) spectral analysis showed the presence of three methoxyl signals at δ 3.78, 3.8, and 3.86, which were confirmed in the ^{13}C NMR APT spectrum at δ 55.5, 55.9, and 56.5. Two broad singlets for one proton in the aromatic region showed the presence of two meta-coupled doublets at δ 6.38 (J = 2 Hz) and δ 6.55 (J = 2 Hz) in the A-ring for H-6 and H-8 protons. Another two ortho-coupled doublets at δ 7.05 (J = 9 Hz, 2H) and δ 7.92 (J = 9 Hz, 2H) were assigned to the B-ring (H-3′, H-5′, H-2′, H-6′) (Figure 3). This compound had one proton singlet at δ 6.61, which was assigned to the olefinic proton at H-3.[44] Thus, compound **8** was determined to be 5,7,4′-trimethoxyflavone, and the spectral data were consistent with data from the literature.[30,41]

Compound **10** had a TOF-MS m/z 373.2725 $[M + 1]^+$, which indicates the compound is a pentamethoxyflavone. The ^{1}H NMR spectrum showed the presence of five methoxyls at δ 3.91−3.99 and two proton singlets at δ 6.4 and 6.6 (Figure 3). In the APT spectrum (Figure 4), the A-ring carbon signals coincided well with those of compound **9** (tetramethoxyflavone).[17] The ^{1}H NMR spectrum revealed the presence of an ABX system for the three aromatic protons in the B-ring at H-2′, H-5′, and H-6′ as demonstrated by coupling constant signals at δ 7.39 (d, 1H, J = 1.8 Hz), δ 6.95 (d, 1H, J = 8.2 Hz), and δ 7.6 (d, 1H, J = 8.2 Hz), respectively (Figure 3 and Figure S8). These results indicate the presence of methoxyls at the 3′- and 4′-positions in the B-ring. The singlets at δ 6.58 and 6.4 were assigned to the H-3 and H-6 protons, respectively, using DQFCOSY data in Figure S8. ^{1}HNMR spectra of four pentamethoxyflavones for understanding the chemical shifts and structural assignments of all signals are presented in Figure S9. Although sinensetin is not isolated from Miaray mandarins, the spectrum was given for comparison purposes from our earlier study. Using these spectral data, compound **10** was determined to be 5,7,8,3′,4′-pentamethoxyflavone, and the chemical shifts were compared to reported data.[33,45]

In summary, results from the spectral analysis of the isolated compounds confirm the identity of the isolated compounds as 5-hydroxy-3,7,3′,4′-tetramethoxyflavone (**1**), 5,6,7,8,4′-pentamethoxyflavone (tangeretin) (**2**), 3,5,6,7,8,3′,4′-heptamethoxyflavone (**3**), 5,6,7,8,3′,4′-hexamethoxyflavone (nobiletin) (**4**), 3,5,7,8,3′,4′-hexamethoxyflavone (**5**), 3,5,7,3′,4′-pentamethoxyflavone (pentamethylquercetin) (**6**), limonin (**7**), 5,7,4′-trimethoxyflavone (**8**), 5,7,8,4′-tetramethoxyflavone (**9**), and 5,7,8,3′,4′-pentamethoxyflavone (**10**), respectively (Figure 5). The results are consistent with the reported values.[38,45,46] To the best of our knowledge, this is the first report of the isolation of 3,5,7,3′,4′-pentamethylquercetin from the genus *Citrus*. It is worth noting that this compound was previously reported in a review describing the various compounds present in citrus species by Manthey et al.[47]

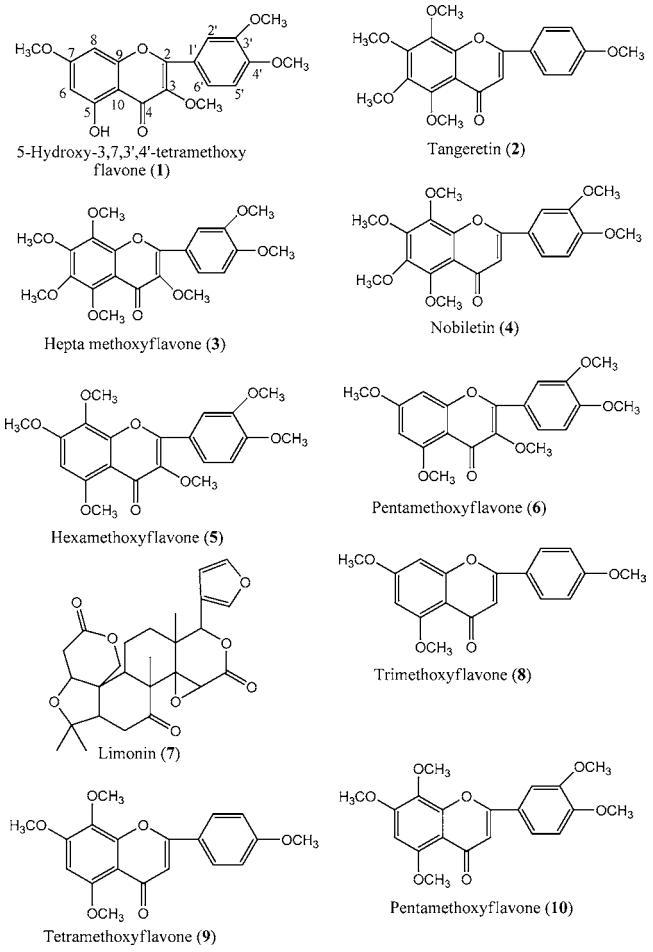

Figure 5. Structures of isolated compounds (**1**−**10**) from Miaray mandarins. Compounds **1**, **5**, **6**, **8**, and **10** were identified by NMR and mass spectral analysis as 5-hydroxy-3,7,3′,4′-tetramethoxyflavone, 3,5,7,8,3′,4′-hexamethoxyflavone, 3,5,7,3′,4′-pentamethoxyflavone (pentamethylquercetin), 5,7,4′-trimethoxyflavone, and 5,7,8,3′,4′-pentamethoxyflavone, respectively. Compounds **2**, **3**, **4**, **7**, and **9** were identified by mass spectral analysis as tangeretin, heptamethoxyflavone, nobiletin, limonin, and tetramethoxyflavone, respectively.

Antimicrobial Activity of Polymethoxyflavones. We next examined whether these compounds affect bacterial growth by treating *V. harveyi* with polymethoxyflavones. The kinetic growth curve was calculated by recording the OD_{570} for 16 h of growth at optimal temperature. Figure 6 illustrates the growth kinetics of *V. harveyi* BB120 after treatment with 50 μM of the eight polymethoxyflavones. The sigmoid bacterial growth curve observed indicates the polymethoxyflavones do not inhibit the bacterial growth at 50 μM concentration. Similar results were also observed in other studies evaluating the antimicrobial activity of polymethoxyflavones (nobiletin and tangeretin), which had minimum inhibitory concentration (MIC) of ≥1600 μg/mL,[26] suggesting that these compounds are not bactericidal.

Inhibition of Biofilm Formation and Bioluminescence. Biofilms are surface adherent colonies of bacteria that form an extracellular polymeric matrix to protect themselves. Control of biofilm formation remains a concern among medical personnel, primarily related to medical devices and implants. The bacterial biofilms in medical devices and implants are difficult to control

DOI: 10.1021/acs.jafc.5b02445
J. Agric. Food Chem. 2015, 63, 7180−7189

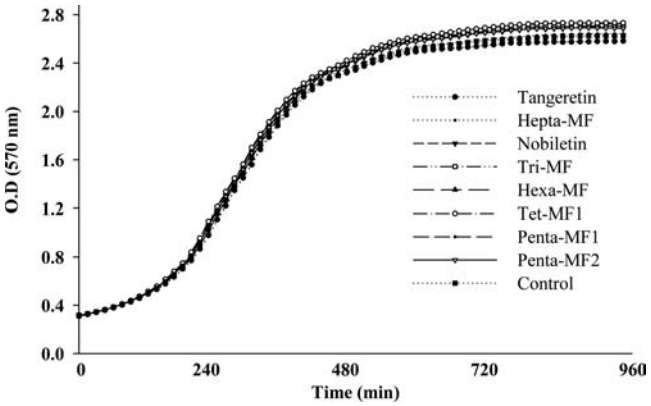

Figure 6. Growth curve of *V. harveyi* BB120 in the presence of polymethoxyflavones. The evaluated polymethoxyflavones were tangeretin, 3,5,6,7,8,3′,4′-heptamethoxyflavone (Hepta-MF), nobiletin, 5,7,4′-trimethoxyflavone (Tri-MF), 3,5,7,8,3′,4′-hexamethoxyflavone (Hexa-MF), 5,7,8,4′-tetramethoxyflavone (Tet-MF), 3,5,7,3′,4′-pentamethoxyflavone (Penta-MF1), and 5,7,8,3′,4′-pentamethoxyflavone (Penta-MF2).

due to increased antimicrobial resistance of biofilms.[48] As biofilm formation is regulated by several factors including quorum sensing, interference with the quorum sensing pathway is currently thought to be a viable strategy to control biofilms.

Quorum sensing is a population-dependent phenomenon that is mediated through the concentration of autoinducers, signaling molecules synthesized by bacteria.[49] Quorum sensing regulated bioluminescence production in *V. harveyi* and its signal transduction pathway has been well studied. The autoinducers are detected by three coincidence detectors, LuxN, LuxPQ, and CqsS, that phosphorylate LuxU, a phosphorelay protein. LuxU then phosphorylates the response regulator LuxO that in turn regulates the expression of downstream genes including bioluminescence genes.[31−34] Furthermore, interference with *V. harveyi* bioluminescence has been widely used as a model to study and identify quorum sensing inhibitors.[27−29] Panels A and B of Figure 7 illustrate the results obtained from the analysis of bioluminescence in BB886 and BB170 strains of *V. harveyi*, respectively. Among the evaluated polymethoxyflavones, only 3,5,6,7,8,3′,4′-heptamethoxyflavone and 3,5,7,8,3′,4′-hexamethoxyflavone seem to interfere with AI-2-mediated bioluminescence in BB170. The treatment of BB886 strain with polymethoxyflavones demonstrated <40% inhibition over control (DMSO).

The inhibition of bioluminescence suggests that certain polymethoxyflavones may interfere with biofilm formation. Consistent with the bioluminescence interference results, only 3,5,6,7,8,3′,4′-heptamethoxyflavone and 3,5,7,8,3′,4′-hexamethoxyflavone inhibited biofilm formation in a dose-dependent manner (Figure 8). Approximately 61% (with respect to control−DMSO treatment) of biofilm formation was inhibited by 3,5,7,8,3′,4′-hexamethoxyflavone at a concentration of 50 μM. The IC_{50} value of 3,5,7,8,3′,4′-hexamethoxyflavone was calculated to be 37.38 μM. Although 3,5,6,7,8,3′,4′-heptamethoxyflavone inhibited biofilm, the percent inhibition was approximately 35% at the maximum evaluated concentration of 50 μM. Other polymethoxyflavones did not have >35% inhibition of biofilm with respect to control.

Analyzing the bioluminescence in specific mutant strains after treatment with polymethoxyflavones may enable us to understand the possible pathway through which these

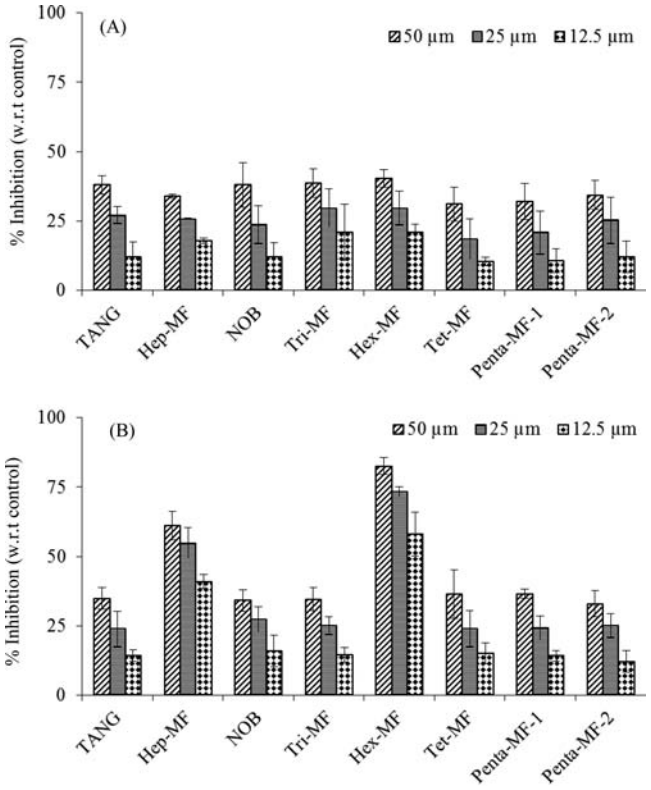

Figure 7. HAI-1 and AI-2 induced bioluminescence inhibition in *V. harveyi* BB886 (A) and BB170 in the presence of polymethoxyflavones (B). The evaluated polymethoxyflavones were tangeretin (TANG), 3,5,6,7,8,3′,4′-heptamethoxyflavone (Hep-MF), nobiletin (NOB), 5,7,4′-trimethoxyflavone (Tri-MF), 3,5,7,8,3′,4′-hexamethoxyflavone (Hex-MF), 5,7,8,4′-tetramethoxyflavone (Tet-MF), 3,5,7,3′,4′-pentamethoxyflavone (Penta-MF-1), and 5,7,8,3′,4′-pentamethoxyflavone (Penta-MF-2).

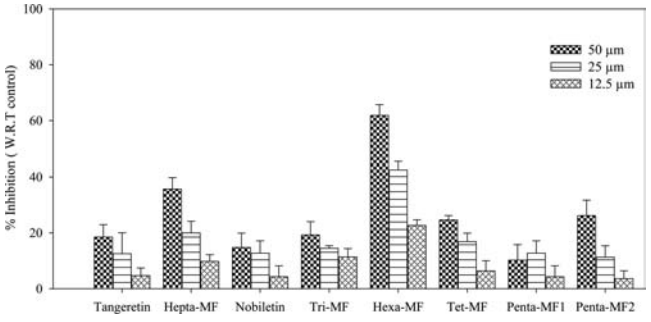

Figure 8. Inhibition of *V. harveyi* BB120 biofilm after treatment with polymethoxyflavones. The evaluated polymethoxyflavones were tangeretin, 3,5,6,7,8,3′,4′-heptamethoxyflavone (Hepta-MF), nobiletin, 5,7,4′-trimethoxyflavone (Tri-MF), 3,5,7,8,3′,4′-hexamethoxyflavone (Hexa-MF), 5,7,8,4′-tetramethoxyflavone (Tet-MF), 3,5,7,3′,4′-pentamethoxyflavone (Penta-MF1), and 5,7,8,3′,4′-pentamethoxyflavone (Penta-MF2).

compounds might inhibit biofilm formation. Therefore, constitutively luminescent *V. harveyi* mutants were investigated after treatment with 50 μM 3,5,7,8,3′,4′-hexamethoxyflavone (Figure 9). The results demonstrated an increase in bioluminescence in the *luxO* mutant strain (JAF483), but showed no change in the *hfq* mutant (BNL258), suggesting an effect on LuxO. However, further studies are needed to validate the effect on LuxO. The results indicate that 3,5,7,8,3′,4′-hexamethoxy-

DOI: 10.1021/acs.jafc.5b02445
J. Agric. Food Chem. 2015, 63, 7180−7189

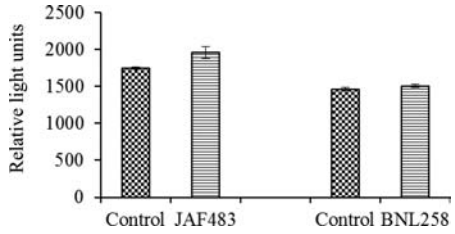

Figure 9. Bioluminescence inhibition in *V. harveyi* mutants JAF483 (*luxO*) and BNL258 (*hfq*) by 3,5,7,8,3′,4′-hexamethoxyflavone (50 μm).

flavone is a potent inhibitor of *V. harveyi* quorum sensing and appears to have larger effect on the AI-2 system. The effect on *luxO* mutants seems to suggest that 3,5,7,8,3′,4′-hexamethoxyflavone may be a nonspecific inhibitor. Further studies are required to evaluate the ability of polymethoxyflavones to interfere with quorum sensing-mediated biofilm formation in human pathogens.

In summary, 10 bioactive compounds were successfully isolated from Miaray mandarin using flash chromatography, and their structural identification was confirmed by spectral analysis using MALDI-TOF and NMR. Among the isolated compounds, 3,5,7,3′,4′-pentamethoxyflavone is reported here for the first time from *Citrus spp.*. Among the evaluated polymethoxyflavones, 3,5,7,8,3′,4′-hexamethoxyflavone demonstrated inhibitory activity on autoinducer-mediated cell−cell signaling and biofilm formation in *V. harveyi*. Further research is required to understand the role of polymethoxyflavones in the inhibition of biofilm in pathogenic bacteria. Results from this study could enable the development of strategies using polymethoxyflavones for preventing bacterial pathogenicity. Moreover, identification of potent antimicrobials from citrus species will provide added economic benefits to both producers and the citrus-processing industry.

■ ASSOCIATED CONTENT

Supporting Information

Additional figures as cited in the text. The Supporting Information is available free of charge on the ACS Publications website at DOI: 10.1021/acs.jafc.5b02445.

■ AUTHOR INFORMATION

Corresponding Authors

*(B.S.P.) Phone: (979) 862-4521. Fax: (979) 862-4522. E-mail: b-patil@tamu.edu.

*(G.K.J.) E-mail: gkjp@tamu.edu.

Funding

This project is based upon work supported by the USDA-NIFA 2010-34402-20875, "Designing Foods for Health", through the Vegetable & Fruit Improvement Center.

Notes

The authors declare no competing financial interest.

■ ACKNOWLEDGMENTS

We acknowledge Chandra Mohan, Shiva Rani, and Kalpana for assisting in harvesting and peeling the fruits.

■ REFERENCES

(1) Uckoo, R. M.; Jayaprakasha, G. K.; Balasubramaniam, V. M.; Patil, B. S. Grapefruit (*Citrus paradisi* Macfad) phytochemicals composition is modulated by household processing techniques. *J. Food Sci.* **2012**, *77* (9), C921−C926.

(2) Uckoo, R. M.; Jayaprakasha, G. K.; Somerville, J. A.; Balasubramaniam, V. M.; Pinarte, M.; Patil, B. S. High pressure processing controls microbial growth and minimally alters the levels of health promoting compounds in grapefruit (*Citrus paradisi* Macfad) juice. *Innovative Food Sci. Emerging Technol.* **2013**, *18*, 7−14.

(3) Kim, J.; Jayaprakasha, G. K.; Uckoo, R. M.; Patil, B. S. Evaluation of chemopreventive and cytotoxic effect of lemon seed extracts on human breast cancer (MCF-7) cells. *Food Chem. Toxicol.* **2012**, *50* (2), 423−430.

(4) Uckoo, R. M.; Jayaprakasha, G. K.; Patil, B. S. Phytochemical analysis of organic and conventionally cultivated Meyer lemons (*Citrus meyeri* Tan.) during refrigerated storage. *J. Food Compos. Anal.* **2015**, *42*, 63−70.

(5) Androula, G. Evaluation of rootstocks for 'Clementine' mandarin in Cyprus. *Sci. Hortic.* **2002**, *93* (1), 29−38.

(6) Gmitter, F.; Hu, X. The possible role of Yunnan, China, in the origin of contemporary citrus species (rutaceae). *Econ. Bot.* **1990**, *44* (2), 267−277.

(7) USDA. *Citrus: World Markets and Trade*; U.S. Department of Agriculture, Foreign Agricultural Service, Government Printing Office: Washington, DC, USA, 2011.

(8) Wu, G. A.; Prochnik, S.; Jenkins, J.; Salse, J.; Hellsten, U.; Murat, F.; Perrier, X.; Ruiz, M.; Scalabrin, S.; Terol, J. Sequencing of diverse mandarin, pummelo and orange genomes reveals complex history of admixture during citrus domestication. *Nat. Biotechnol.* **2014**, *32* (7), 656−662.

(9) Luro, F.; Gatto, J.; Costantino, G.; Pailly, O. Analysis of genetic diversity in *Citrus*. *Plant Genet. Resour.* **2011**, *9* (2), 218−221.

(10) Coletta Filho, H. D.; Machado, M. A.; Targon, M. L. P. N.; Moreira, M. C. P. Q. D. G.; Pompeu, J. Analysis of the genetic diversity among mandarins (*Citrus* spp.) using RAPD markers. *Euphytica* **1998**, *102* (1), 133−139.

(11) Hutchison, D. J.; Hearne, C. J.; Bistline, F. W. The performance of 'Valencia' orange trees on 21 rootstocks in the Florida flatwoods. *Proc. Fla. State Hortic. Soc.* **1992**, *105*, 60−63.

(12) Kurowska, E.; Manthey, J.; Casaschi, A.; Theriault, A. Modulation of hepG2 cell net apolipoprotein B secretion by the citrus polymethoxyflavone, tangeretin. *Lipids* **2004**, *39* (2), 143−151.

(13) Li, S.; Pan, M.-H.; Lai, C.-S.; Lo, C.-Y.; Dushenkov, S.; Ho, C.-T. Isolation and syntheses of polymethoxyflavones and hydroxylated polymethoxyflavones as inhibitors of HL-60 cell lines. *Bioorg. Med. Chem.* **2007**, *15* (10), 3381−3389.

(14) Sergeev, I. N.; Li, S.; Ho, C.-T.; Rawson, N. E.; Dushenkov, S. Polymethoxyflavones cctivate Ca^{2+}-dependent apoptotic targets in adipocytes. *J. Agric. Food Chem.* **2009**, *57* (13), 5771−5776.

(15) Nakajima, A.; Ohizumi, Y.; Yamada, K. Anti-dementia activity of nobiletin, a citrus flavonoid: a review of animal studies. *Clin. Psychopharmacol. Neurosci.* **2014**, *12* (2), 75−82.

(16) Uckoo, R. M.; Jayaprakasha, G. K.; Patil, B. S. Rapid separation method of polymethoxyflavones from citrus using flash chromatography. *Sep. Purif. Technol.* **2011**, *81* (2), 151−158.

(17) Uckoo, R. M.; Jayaprakasha, G. K.; Patil, B. S. Hyphenated flash chromatographic separation and isolation of coumarins and polymethoxyflavones from byproduct of citrus juice processing industry. *Sep. Sci. Technol.* **2013**, *48* (10), 1467−1472.

(18) Yamamoto, K.; Yahada, A.; Sasaki, K.; Ogawa, K.; Koga, N.; Ohta, H. Chemical markers of shiikuwasha juice adulterated with calamondin juice. *J. Agric. Food Chem.* **2012**, *60* (44), 11182−11187.

(19) Lou, S.-N.; Hsu, Y.-S.; Ho, C.-T. Flavonoid compositions and antioxidant activity of calamondin extracts prepared using different solvents. *J. Food Drug Anal.* **2014**, *22* (3), 290−295.

(20) Wilson, I. D.; Brinkman, U. A. T. Hyphenation and hypernation: the practice and prospects of multiple hyphenation. *J. Chromatogr., A* **2003**, *1000* (1−2), 325−356.

(21) Griffiths, P. R.; Pentoney, S. L.; Giorgetti, A.; Shafer, K. H. The hyphenation of chromatography and FT-IR. *Anal. Chem.* **1986**, *58* (13), 1349A−1366A.

(22) Marston, A.; Hostettmann, K. Natural product analysis over the last decades. *Planta Med.* **2009**, *75*, 672−682.
(23) Uckoo, R. M.; Jayaprakasha, G. K.; Patil, B. S. Rapid separation method of polymethoxyflavones from citrus using flash chromatography. *Sep. Purif. Technol.* **2011**, *81* (2), 151−158.
(24) Jayaprakasha, G. K.; Negi, P. S.; Sikder, S.; Mohanrao, L. J.; Sakariah, K. K. Antibacterial activity of *Citrus reticulata* peel extracts. *Z. Naturforsch., C: J. Biosci.* **2000**, *55*, 1030.
(25) Nannapaneni, R.; Muthaiyan, A.; Crandall, P. G.; Johnson, M. G.; O'Bryan, C. A.; Chalova, V. I.; Callaway, T. R.; Carroll, J. A.; Arthington, J. D.; Nisbet, D. J.; Ricke, S. C. Antimicrobial activity of commercial citrus-based natural extracts against *Escherichia coli* O157:H7 isolates and mutant strains. *Foodborne Pathog. Dis.* **2008**, *5* (5), 695−699.
(26) Yi, Z.; Yu, Y.; Liang, Y.; Zeng, B. In vitro antioxidant and antimicrobial activities of the extract of *Pericarpium Citri Reticulatae* of a new *Citrus* cultivar and its main flavonoids. *LWT−Food Sci. Technol.* **2008**, *41* (4), 597−603.
(27) Vikram, A.; Jesudhasan, P. R.; Jayaprakasha, G. K.; Pillai, S. D.; Patil, B. S. Citrus limonoids interfere with *Vibrio harveyi* cell−cell signalling and biofilm formation by modulating the response regulator LuxO. *Microbiology* **2011**, *157* (1), 99−110.
(28) Vikram, A.; Jesudhasan, P. R.; Jayaprakasha, G. K.; Pillai, S. D.; Jayaraman, A.; Patil, B. S. Citrus flavonoid represses *Salmonella* pathogenicity island 1 and motility in *S.* Typhimurium LT2. *Int. J. Food Microbiol.* **2011**, *145* (1), 28−36.
(29) Vikram, A.; Jayaprakasha, G. K.; Jesudhasan, P. R.; Pillai, S. D.; Patil, B. S. Suppression of bacterial cell−cell signalling, biofilm formation and type III secretion system by citrus flavonoids. *J. Appl. Microbiol.* **2010**, *109* (2), 515−527.
(30) Uckoo, R. M.; Jayaprakasha, G. K.; Patil, B. S. Chromatographic techniques for the separation of polymethoxyflavones from citrus. In *Emerging Trends in Dietary Components for Preventing and Combating Disease*; Patil, B. S., Jayaprakasha, G. K., Murthy, K. N. C., Seeram, N., Eds.; ACS Symposium Series 1093; American Chemical Society: Washington, DC, USA, 2012.
(31) Surette, M. G.; Bassler, B. L. Quorum sensing in *Escherichia coli* and *Salmonella typhimurium*. *Proc. Natl. Acad. Sci. U. S. A.* **1998**, *95* (12), 7046−7050.
(32) Freeman, J. A.; Bassler, B. L. A genetic analysis of the function of LuxO, a two-component response regulator involved in quorum sensing in *Vibrio harveyi*. *Mol. Microbiol.* **1999**, *31* (2), 665−677.
(33) Freeman, J. A.; Bassler, B. L. Sequence and function of LuxU: a two-component phosphorelay protein that regulates quorum sensing in *Vibrio harveyi*. *J. Bacteriol.* **1999**, *181*, 899−906.
(34) Lenz, D. H.; Mok, K. C.; Lilley, B. N.; Kulkarni, R. V.; Wingreen, N. S.; Bassler, B. L. The small RNA chaperone Hfq and multiple small RNAs control quorum sensing in *Vibrio harveyi* and *Vibrio cholerae*. *Cell* **2004**, *118* (1), 69−82.
(35) Qin, Y.; Luo, Z.-Q.; Farrand, S. K. Domains formed within the N-terminal region of the quorumsensing activator TraR are required for transcriptional activation and direct interaction with RpoA from *Agrobacterium*. *J. Biol. Chem.* **2004**, *279* (39), 40844−40851.
(36) Lu, L.; Hume, M. E.; Pillai, S. D. Autoinducer-2-like activity associated with foods and its interaction with food additives. *J. Food Prot.* **2004**, *67* (7), 1457−1462.
(37) Yao, X.; Xu, X.; Fan, G.; Qiao, Y.; Cao, S.; Pan, S. Determination of synergistic effects of polymethoxylated flavone extracts of Jinchen orange peels (*Citrus sinensis* Osberk) with amino acids and organic acids using chemiluminescence. *Eur. Food Res. Technol.* **2009**, *229* (5), 743−750.
(38) Wang, D.; Wang, J.; Huang, X.; Tu, Y.; Ni, K. Identification of polymethoxylated flavones from green tangerine peel (*Pericarpium Citri Reticulatae Viride*) by chromatographic and spectroscopic techniques. *J. Pharm. Biomed. Anal.* **2007**, *44* (1), 63−69.
(39) Perez, J. L.; Jayaprakasha, G. K.; Valdivia, V.; Munoz, D.; Dandekar, D. V.; Ahmad, H.; Patil, B. S. Limonin methoxylation influences the induction of glutathione S-transferase and quinone reductase. *J. Agric. Food Chem.* **2009**, *57* (12), 5279−5286.
(40) Li, S.; Yu, H.; Ho, C.-T. Nobiletin: efficient and large quantity isolation from orange peel extract. *Biomed. Chromatogr.* **2006**, *20* (1), 133−138.
(41) Machida, K.; Osawa, K. On the flavonoid constituents from the peels of Citrus hassaku Hort. ex Tanaka. *Chem. Pharm. Bull.* **2012**, *37* (4), 1092−1094.
(42) Silva, T.; Carvalho, M.; Braz-Filho, R. Estudo espectroscópico em elucidação estrutural de flavonóides de *Solanum jabrense* Agra & Nee e *S. paludosum* Moric. *Quim. Nova* **2009**, *32*, 1119−1128.
(43) Chung, L. Y.; Yap, K. F.; Goh, S. H.; Mustafa, M. R.; Imiyabir, Z. Muscarinic receptor binding activity of polyoxygenated flavones from *Melicope subunifoliolata*. *Phytochemistry* **2008**, *69* (7), 1548−1554.
(44) Sugiyama, S.; Umehara, K.; Kuroyanagi, M.; Ueno, A.; Taki, T. Studies on the differentiation inducers of myeloid leukemic cells from *Citrus* species. *Chem. Pharm. Bull.* **1993**, *41* (4), 714−719.
(45) Koichi, M.; Keisuke, O. On the flavonoid constituents from the peels of *Citrus hassaku* Hort. ex Tanaka. *Chem. Pharm. Bull.* **1989**, *37* (4), 1092−1094.
(46) Raman, G.; Cho, M.; Brodbelt, J. S.; Patil, B. S. Isolation and purification of closely related *Citrus* limonoid glucosides by flash chromatography. *Phytochem. Anal.* **2005**, *16* (3), 155−160.
(47) Manthey, J. A.; Guthrie, N.; Grohmann, K. Biological properties of citrus flavonoids pertaining to cancer and inflammation. *Curr. Med. Chem.* **2001**, *8* (2), 135−153.
(48) Djeribi, R.; Bouchloukh, W.; Jouenne, T.; Menaa, B. Characterization of bacterial biofilms formed on urinary catheters. *Am. J. Infect. Control* **2012**, *40* (9), 854−859.
(49) Reading, N. C.; Sperandio, V. Quorum sensing: the many languages of bacteria. *FEMS Microbiol. Lett.* **2006**, *254* (1), 1−11.

DOI: 10.1021/acs.jafc.5b02445
J. Agric. Food Chem. 2015, 63, 7180−7189

analyze the key pathways and subcategories of the proteins that were shown to have differential expression. Our results provide fundamental information regarding the mechanism of action of the antimicrobial peptide F1.

MATERIALS AND METHODS

Bacterial Strain and Antimicrobial Peptide. The pathogenic *E. coli* ATCC 25922 was stored at the microbial culture laboratory in the College of Food Science, South China Agricultural University (Guangzhou, China). The antimicrobial peptide F1 was isolated as previously described.[24] The minimal inhibition concentration (MIC) against *E. coli* ATCC 25922 was 62.5 μg/mL.[24]

Examination of Morphological Changes of *E. coli* Caused by Antimicrobial Peptide F1. Antimicrobial peptide F1 was incubated with *E. coli* ATCC 25922 (10^8 CFU/mL) during the exponential growth phase at a final concentration of 5 MIC in Luria−Bertani (LB) broth for 2 h at 37 °C. Cells were harvested and pelleted at different time points during the incubation, including 0, 0.5, 1, and 2 h, using centrifugation at 3000*g* for 10 min. The cells were then processed as previously described, and a transmission electron microscope (Hitachi H-7000, Japan) at a magnification of 11000× was used to examine the ultrastructural changes of *E. coli* cells.[25]

Determination of Growth Rate of *E. coli*. Cultures of *E. coli* were incubated in LB broth at 37 °C on an orbital shaker set at 150 rpm. Overnight cultures were diluted to an optical density of 0.075 in LB broth and allowed to grow to an optical density of 0.25 at 600 nm, as determined using an ultraviolet spectrophotometer (Shimadzu UV-1201). The bacterial cultures, at an optical density of 0.25 at 600 nm, were then incubated either with or without antimicrobial peptide F1 at 0.8 MIC. The growth rate was determined by measuring the optical density at 600 nm every 5 min.

Extraction, Quantification and Digestion of Cellular Proteins. Cultures of *E. coli*, at an optical density of 0.25 at 600 nm, were incubated either with or without peptide F1 at 0.8 MIC for 30 min and then harvested using centrifugation at 5000*g* for 10 min at 4 °C. Total cellular protein was extracted as previously described.[26] The protein concentration was quantified using the Bradford method.[27] One hundred micrograms of total cellular protein from each treatment group was digested with Trypsin Gold (Promega, Madison, WI, USA) at a 30:1 weight ratio of trypsin to extract protein and was incubated at 37 °C for 16 h. Following the digestion with trypsin, vacuum centrifugation was done to dry the peptides.

iTRAQ Labeling and SCX Fractionation. The iTRAQ labeling method was performed as previously reported with slight modifications.[28] The dried peptide samples were dissolved in 0.5 M triethylammonium bicarbonate (TEAB). iTRAQ reagents 114 and 116 were used to label the peptide samples from the treated and control bacterial cultures, respectively. The labeled peptides were incubated at room temperature for 2 h and then pooled and dried using vacuum centrifugation. The iTRAQ-labeled peptide mixture was dissolved in 4 mL of buffer A (25 mM NaH_2PO_4 in 25% ACN, pH 2.7) and separated using an LC-20AB HPLC pump system (Shimadzu, Kyoto, Japan) with an Ultremex SCX column (4.6 × 250 mm, 5 μm, Phenomenex, Torrance, CA, USA). Elution was carried out using a linear gradient of buffer A for 10 min, 50−60% buffer B (25 mM NaH_2PO_4 and 1 M KCl in 25% ACN, pH 2.7) for 27 min, and 60−100% buffer B for 1 min. The flow rate was set at 1 mL/min, and the absorbance wavelength was 214 nm. The eluted peptides were collected every minute, pooled into 20 fractions, desalted using a Strata X C18 column (Phenomenex), and dried using vacuum centrifugation.

LC-ESI-MS/MS Analysis Based on Triple TOF 5600. The analytical separation was performed using an LC-20AD nanoHPLC (Shimadzu) coupled to a triple TOF 5600 system (AB SCIEX, Concord, ON, Canada) fitted with a Nanospray III source (AB SCIEX) and a pulled quartz tip as the emitter (New Objectives, Woburn, MA, USA). The system was equipped with a C18 trap column (5 μm, 180 μm × 20 mm) for online trapping and desalting, and a C18 column (1.7 μm, 100 μm × 100 mm) for analytical separation. During experimentation, a 10 μL (0.5 μg/μL) sample was loaded along with mobile phase A (5% acetonitrile in double-distilled water with 0.1% formic acid). Separation was achieved using a gradient of 2% mobile phase B (95% acetonitrile in double-distilled water with 0.1% formic acid) at a flow rate of 300 μL/min for 1 min, followed by a 2−35% gradient of mobile phase B for 40 min, a 35−60% gradient of mobile phase B for 5 min, a 60−80% gradient of mobile phase B for 2 min, 80% mobile phase B for 4 min, and finally 5% mobile phase B for 1 min. Data were acquired using an ion spray voltage of 2.5 kV, curtain gas of 30 psi, nebulizer gas of 15 psi, and an interface heater temperature of 150 °C.

Data Analysis. MS/MS data were matched using the Mascot search engine (Matrix Science, London, UK; version 2.3.02) against the *Ecol* 3493 (5108 sequences) database to both identify and quantify the proteins. The search parameters were set as follows: enzyme specificity was set to trypsin with one missed cleavage; potential variable modifications were Gln- > pyro-Glu (N-term Q), oxidation (M), and deamidated (NQ); fixed modifications were carbamidomethyl (C), iTRAQ8plex (N-term), and iTRAQ8plex (K); peptide mass tolerance was set to ±0.05 Da; fragment mass tolerance was set to ±0.1 Da; charge states of peptides were set to +2 and +3; and monoisotopic mass was used.

Protein identification was based on Mascot probability analysis. Peptides with significant scores ≥20 and a 99% confidence interval, indicative that matches were greater than "homology", were counted as identified.[21] Each successful protein identification involved at least one unique peptide. Only proteins that had at least two unique peptides were used for protein quantification. The quantitative protein ratios were weighted and normalized using the median ratio in Mascot. Results were considered statistically significant only if there was a 1.2-fold increase or decrease in protein expression levels ($P < 0.05$).

The Blast2GO program against the nonredundant protein database (NR; NCBI) was used in the functional annotation of the proteins. Gene Ontology (GO) annotation (http://www.geneontology.org/) and the Kyoto Encyclopedia of Genes and Genomes (KEGG) pathway (http://www.genome.jp/kegg/) enrichment analysis were both used to determine the functional subcategories and the metabolic pathways for the differentially expressed proteins.[29,30]

Real-Time PCR. RNA was prepared from both the *E. coli* cell cultures that had been treated with peptide F1 at 0.8 MIC for 30 min and the control *E. coli* cell cultures that had been used for iTRAQ analysis. Total RNA was extracted using the E.Z.N.A. Total RNA kit II (Omega, USA) and was subsequently analyzed for both purity and total RNA content. Total RNA was reverse-transcribed into cDNA using the ReverTra Ace qPCR RT Kit (TOYOBO, Japan). The forward (F) and reverse (R) primer sequences were designed (see Supporting Information file 3 for more information), and the efficiency was confirmed using the standard curve method. Real-time PCR reactions were carried out using a Bio-Rad CFX96 Real-Time System in a total volume of 20 mL volume with 10 μL of SYBR qPCR Mix (TOYOBO), 1.0 μL of template cDNA, 1 μL (final concentration of 0.2 mM) of each primer, and PCR grade water to a final volume of 20 μL. The following procedure was used: initial denaturation at 95 °C for 1 min; followed by 40 cycles of amplification (95 °C for 15 s and 60 °C for 30 s). The fold change of selected genes was normalized to the fold change of the reference gene (16S rRNA gene). The formula $2^{-\Delta\Delta Ct}$ was used to determine the relative expression.[31] Three technical replicates and two biological replicates were done for all PCR experiments. Significant differences in the data were determined using one-way ANOVA ($P < 0.05$).

RESULTS AND DISCUSSION

Peptide F1, with a molecular weight of 2113.8 Da, was identified in our previous study as a potent bacteriocin produced by a lactic acid bacterium that was isolated from Tibetan kefir.[24] Peptide F1 was shown to potently inhibit not only Gram-negative bacteria (*E. coli*, *S. enterica*, and *S. dysenteriae*) but also Gram-positive bacteria (*S. aureus* and *B. thuringiensis*) and fungi (*A. flavus*, *A. niger*, *R. nigricans*, and *P. glaucum*), which is rarely seen among bacteriocins produced by lactic acid bacteria.[24]

DOI: 10.1021/acs.jafc.5b00678
J. Agric. Food Chem. 2015, 63, 7190−7197

Additionally, the antimicrobial activities of peptide F1 were over a wide range of stressful conditions, including a pH range between 3 and 9 for 2 h, 121 °C for 20 min, and treatments with proteases (e.g., pepsin and trypsin). To gain mechanistic insights on peptide F1 modes of action, we investigated the alterations in the morphology and global protein expression of *E. coli* induced by peptide F1.

Alteration in the Morphology of *E. coli* Induced by Antimicrobial Peptide F1. The effects of peptide F1 on the morphology of the bacterial cells were determined after treatment of the bacteria with peptide F1 at 5 MIC (MIC was previously determined[24]). Morphological alterations induced by peptide F1 treatment were visualized using transmission electron microscopy (Figure 1). The morphology of the untreated

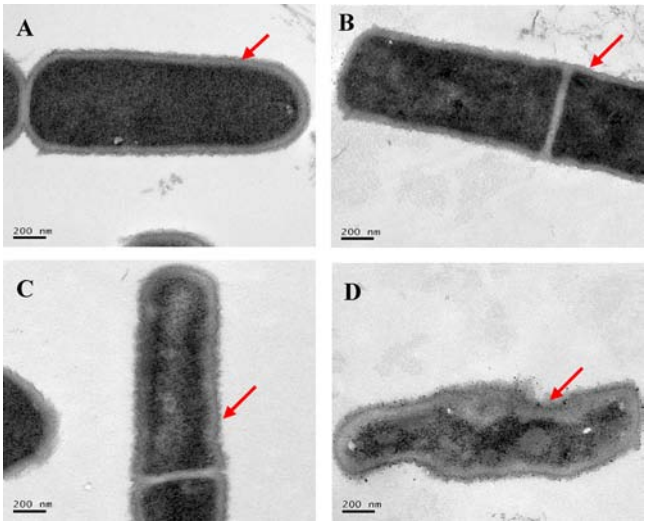

Figure 1. Transmission electron microscopic analysis of *Escherichia coli* treated with 5 MIC of peptide F1 for 0 h (A), 0.5 h (B), 1 h (C), and 2 h (D), respectively. Twenty pictures were taken for each treatment, and representative pictures are shown here.

bacteria (Figure 1A) appeared smooth with a uniform cytoplasmic region and a well-defined cell membrane. Following peptide F1 treatment for 0.5 h (Figure 1B) and 1 h (Figure 1C), the well-defined outline of the cell membrane was lost, especially at the 1 h post-treatment time point. The bacteria also became gradually smaller in size during the course of the treatment. These results were indicative of a potential cytoplasmic leakage through the damaged cell membrane, resulting in the shrinkage of the bacterial cells. Two hours of peptide F1 treatment resulted in severely deformed and partially lysed bacterial cells, with an unidentifiable cellular morphology (Figure 1D). The effects of peptide F1 on the morphology of *E. coli* were different from those previously reported for other antimicrobial peptides. For example, lactoferrin was shown to cause membrane blistering and clumping of cytoplasmic elements.[32] Peptide HLP2 resulted in a marked accumulation of electron-dense material in the periplasmic space and the outer membranes of *E. coli* cells.[7] Additionally, the HLP 2-treated *E. coli* cells showed a separation of the outer membranes at the ends of the cells or at the junction of dividing cells and blisters on the outer membrane.[33] The specific mechanism underlying the different effects of these antimicrobial peptides on *E. coli* cells warrants further investigations.

Inhibition on the Growth of *E. coli* by Antimicrobial Peptide F1. The inhibitory effects of peptide F1 on *E. coli* were investigated to determine the appropriate conditions to induce alterations in the global expression of cellular proteins. The bacteria were incubated with peptide F1 at 0.8 MIC (50 μg/mL). This lower level of the MIC, which is 62.5 μg/mL, was used to minimize bacterial cell death caused by the peptide to observe meaningful protein expression level information. As shown in Figure 2, peptide F1 caused static effects on the

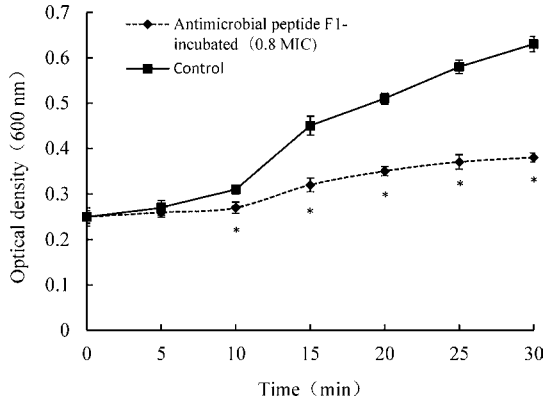

Figure 2. Growth rate of *E. coli* in the absence (control) or presence of antimicrobial peptide F1 at 0.8 MIC. (*) Statistical significance ($p < 0.01$, $n = 8$).

bacteria. After only 5 min of being treated with peptide F1, the optical density of the treated bacteria was lower in comparison to the control bacteria. After about 30 min, the optical density of treated bacteria became relatively stable. At this time point, examination of cell morphology by transmission electron microscopy revealed that there was no difference in the cellular morphology between treated and control cells. Thus, bacterial cells used to isolate cellular proteins for proteomic analysis were treated with peptide F1 at 0.8 MIC for 30 min.

Identification and GO Analysis of Proteins with Altered Expression Induced by Peptide F1. The isolated proteins were processed as described under Materials and Methods and subjected to MS/MS analysis. The MS/MS spectra of the total proteins in *E. coli* cells were processed using the Mascot software and resulted in the identification of 280 proteins (Supporting Information file 1). The expression levels of 31 proteins were shown to be significantly different (>1.2-fold change, $p < 0.05$) between treated and untreated cells. Among these proteins, 21 were up-regulated and 10 were down-regulated in the treated cells as compared to the untreated cells (Table 1). GO enrichment analysis was done to classify the cellular components, molecular functions, and biological processes that these proteins are involved in, and the results of this analysis are presented in Figure 3 (see Supporting Information file 2 for more information). The cellular component analysis revealed that most of the proteins with altered expression belong to the nitrate reductase complex, the macromolecular complex, the protein complex, the ribosomal subunit, the cytoplasmic and organelle parts, the cytosol, or the ribosome. Among the 31 differentially expressed proteins, 29 proteins have distinct molecular functions, mainly involving the binding of different factors (such as cofactors, molybdenum, and pyridoxal phosphate), enzymatic activity (such as 3′−5′ exonuclease, transaminase, nitrate reductase, oxidoreductase, transferase, and peptidase activities), catalytic activity, and act on nitrogenous compounds as donors or transfer nitrogenous groups. The biological process analysis indicated that 28 of the 31 proteins play a role in 132

DOI: 10.1021/acs.jafc.5b00678
J. Agric. Food Chem. 2015, 63, 7190−7197

Table 1. *Escherichia coli* Cellular Proteins with Altered Expression Induced by Peptide F1

accession	description	score	fold change
gi|407055679|gb|AFS75730.1|	ATP-dependent protease ATP-binding subunit ClpX	698	1.486
gi|407055280|gb|AFS75331.1|	DNA starvation/stationary phase protection protein Dps	573	2.054
gi|407053148|gb|AFS73199.1|	protein disaggregation chaperone	523	2.255
gi|407052369|gb|AFS72420.1|	50S ribosomal protein L24	456	2.711
gi|407055970|gb|AFS76021.1|	glutamate-1-semialdehyde aminotransferase	321	1.203
gi|407053351|gb|AFS73402.1|	aminotransferase	256	1.317
gi|407052368|gb|AFS72419.1|	50S ribosomal protein L14	143	8.222
gi|407056180|gb|AFS76231.1|	hypothetical protein O3K_21850	116	1.409
gi|407052548|gb|AFS72599.1|	DNA-binding transcriptional activator TdcA	100	1.556
gi|407054218|gb|AFS74269.1|	hypothetical protein O3K_11895	94	3.307
gi|407053705|gb|AFS73756.1|	6-phosphogluconate dehydrogenase	60	1.811
gi|407054803|gb|AFS74854.1|	isocitrate dehydrogenase	56	5.116
gi|407056709|gb|AFS76760.1|	putative acyltransferase	46	1.572
gi|407053138|gb|AFS73189.1|	putative inner membrane diguanylate cyclase	42	1.28
gi|407053659|gb|AFS73710.1|	signal transduction histidine-protein kinase BaeS	40	2.502
gi|407052686|gb|AFS72737.1|	hypothetical protein O3K_04040	34	7.636
gi|407054553|gb|AFS74604.1|	universal stress protein F	32	1.417
gi|407057033|gb|AFS77082.1|	AatP permease	26	1.641
gi|407052427|gb|AFS72478.1|	protease TldD	25	1.294
gi|407054232|gb|AFS74283.1|	putative ATP-dependent helicase Lhr	23	1.448
gi|407051886|gb|AFS71937.1|	DNA polymerase III subunit β	20	1.995
gi|407052361|gb|AFS72412.1|	chain N, structure of the 50S subunit of *E. coli* ribosome in pre-accommodation state	80	0.739
gi|407054468|gb|AFS74519.1|	nitrate reductase 2 (NRZ), β subunit	332	0.477
gi|407056635|gb|AFS76686.1|	ATP-dependent protease ATP-binding subunit HslU	349	0.705
gi|407052948|gb|AFS72999.1|	*N*-acetylglutamate synthase	56	0.53
gi|407056449|gb|AFS76500.1|	fumarate hydratase FumB	51	0.791
gi|407055221|gb|AFS75272.1|	L-threonine aldolase	43	0.277
gi|407056823|gb|AFS76874.1|	ATP synthase F0F1 subunit α	41	0.816
gi|407056301|gb|AFS76352.1|	putative sugar transporter subunit: membrane component of ABC superfamily protein	27	0.239
gi|407054467|gb|AFS74518.1|	nitrate reductase 2, α subunit	23	0.117
gi|407053267|gb|AFS73318.1|	phosphoribosylaminoimidazolesuccinocarboxamide synthase	18	0.471

different biological processes, with a high concentration of them acting in a variety of metabolic and proteolytic processes.

KEGG Pathway Analysis of the Differentially Expressed Cellular Proteins. KEGG pathway analysis was done to determine the biological pathways that the 31 differentially expressed proteins are involved in, and the results of the analysis are shown in Table 2. The results indicate that the 31 differentially expressed proteins are mainly involved in metabolic pathways, degradative pathways, and biosynthesis pathways. Additionally, these proteins were also found to be related to the two-component system, cell cycle—caulobacter, tricarboxylic acid cycle, carbon fixation, oxidative phosphorylation, homologous recombination, bacterial chemotaxis, DNA replication, ribosomes, pentose phosphate pathway, and mismatch repair. The following sections will focus on the involvement of these proteins in the four major pathways, including the tricarboxylic acid cycle, oxidative phosphorylation, glycerophospholipid metabolism, and cell cycle—caulobacter.

Roles of the Down-regulated Proteins. Among the 10 proteins that were shown to be down-regulated upon peptide F1 treatment, several of them are involved in the energy and metabolism pathways, including fumarate hydratase FumB (gi|407056449|gb|AFS76500.1|), ATP synthase F0F1 subunit α (gi|407056823|gb|AFS76874.1|), *N*-acetylglutamate synthase (gi|407052948|gb|AFS72999.1|), L-threonine aldolase (gi|407055221|gb|AFS75272.1|), nitrate reductase 2 (NRZ), β subunit (gi|407054468|gb|AFS74519.1|), and nitrate reductase 2 α subunit (gi|407054467|gb|AFS74518.1|).

Fumarate hydratase FumB is an important enzyme in *E. coli*, playing important roles in multiple metabolic pathways. One of the most important metabolic pathways related to fumarate hydratase FumB is the tricarboxylic acid cycle, which is the major cellular process involved in the generation of energy and is a common metabolic pathway in the complete oxidation of proteins, carbohydrates, and lipids (pathway ID ko00020) (Table 2). Fumarate hydratase FumB catalyzes the reaction that converts fumarate into malic acid in the seventh step of tricarboxylic acid cycle. Down-regulation of fumarate hydratase FumB inhibits the tricarboxylic acid cycle and negatively affects cellular functions. Treatment of *E. coli* with peptide F1 resulted in the down-regulation of fumarate hydratase FumB, which partly explains the inhibited cell growth observed above (Figure 2).

The ATP synthase F0F1 subunit α is an ATP synthase that has many functions, including catalytic activity, ATPase activity, hydrolase activity, pyrophosphatase activity, and transporter activity (see Supporting Information file 2 for more information). This enzyme plays an important role in the oxidative phosphorylation pathway (pathway ID ko00190). Oxidative phosphorylation serves as the main source of ATP production in the cells, during which ATP synthesis is completed by ATP synthase. ATP synthase is composed of two units, the F_O unit and F_1 unit. The spherical F1 unit is composed of five different polypeptides (α, β, γ, δ, and ε) and is an ATP multienzyme complex. The ATP synthase FOF1 subunit α is one of the ATP synthases in the multienzyme complex (α, β, γ, δ, and ε).

DOI: 10.1021/acs.jafc.5b00678
J. Agric. Food Chem. 2015, 63, 7190−7197

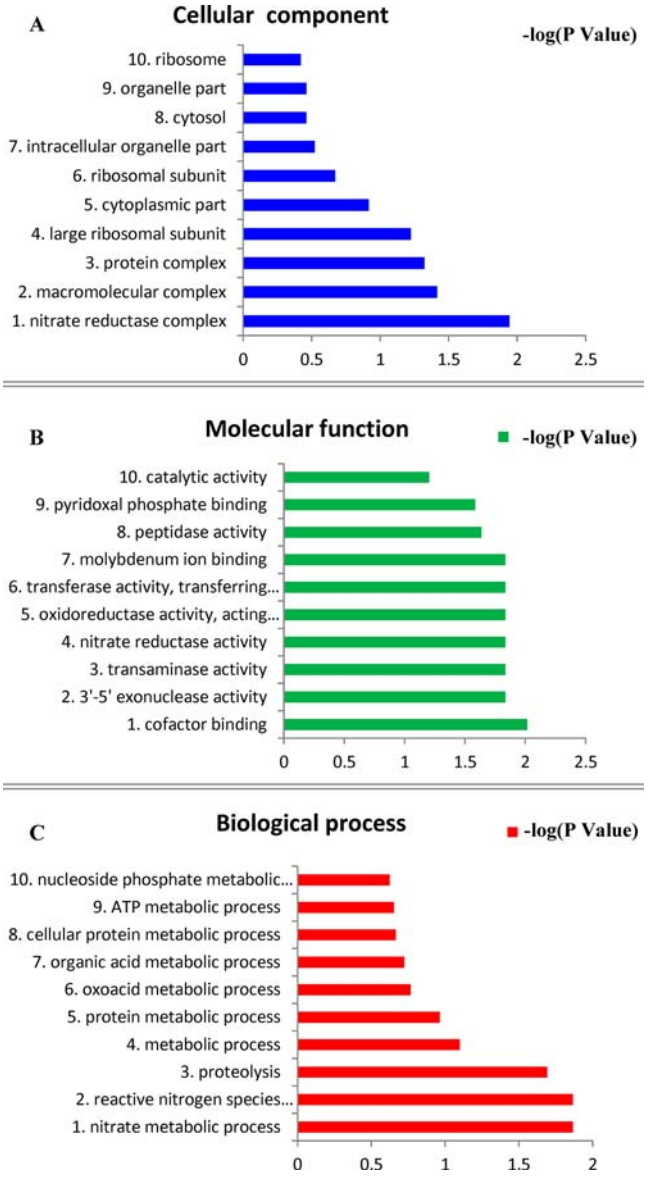

Figure 3. GO enrichment analysis of the differentially expressed proteins. The top 10 components for cellular component (A), molecular function (B), and biological process (C) of the differentially expressed proteins are presented along with their enrichment score represented as a *P* value.

Treatment with peptide F1 resulted in the down-regulation of the ATP synthase FOF1 subunit α, suggesting that treatment of peptide F1 may negatively affect oxidative phosphorylation and decrease ATP production.

Roles of Up-regulated Proteins. Among the 21 differentially expressed proteins shown to be up-regulated, several, including the putative inner membrane diguanylate cyclase (gil 407053138|gb|AFS73189.1|), DNA polymerase III subunit β (gil407051886|gb|AFS71937.1|), putative acyltransferase (gil 407056709|gb|AFS76760.1|), and ATP-dependent protease ATP-binding subunit ClpX (gil407055679|gb|AFS75730.1|), have been shown to have macromolecular degradation activity or hydrolase activity. The putative inner membrane diguanylate cyclase protein is present in both the cell membrane and the cytoplasm. This protein has been observed to have catalytic activity, signal transducer activity, molecular transducer activity, and lyase activity (see Supporting Information file 2 for more information). The primary pathways in which this protein is involved include the two-component system, cell cycle, and bacterial chemotaxis (Table 2). DNA polymerase III subunit β is a protein complex with 3′−5′ exonuclease activity, catalytic activity, nuclease activity, transferase activity, and hydrolase activity (Supporting Information file 2). The pathways this protein is primarily involved in include microbial metabolism in diverse environments; glycine, serine, and threonine metabolism; lysine biosynthesis; selenocompound metabolism; cysteine and methionine metabolism; biosynthesis of secondary metabolites; homologous recombination; DNA replication; purine metabolism; mismatch repair; metabolic pathways; and pyrimidine metabolism.

The putative acyltransferase possesses catalytic activity, transferase activity, and hydrolase activity and is capable of transferring acyl groups. Additionally, it has also been shown to be involved in pathways relating to microbial metabolism in diverse environments, benzoate degradation, ethylbenzene degradation, glycerolipid metabolism, aminobenzoate degradation, limonene and pinene degradation, glycerophospholipid metabolism, tyrosine metabolism, and metabolic pathways (Table 2). Among these pathways, the putative acyltransferase is primarily involved in the glycerophospholipid metabolism (pathway ID ko00564). Up-regulation of putative acyltransferase accelerates the catalytic conversion process of lyso-phosphatidic acid (1-acyl-*sn*-glycerol 3-phosphate) to phosphatidic acid (1,2-diacyl-*sn*-glycerol 3-phosphate) using acyl-CoA as the acyl donor. Acyl-CoA is an important enzyme that catalyzes the synthesis of cholesteryl esters from free cholesterol and long-chain fatty acids, which is closely associated with the microstructure and function of the cell membrane. Phosphatidic acid is a component of the cell membrane, as well as a predecessor of phosphatidylcholine, phosphatidylethanolamine, and other macromolecules. Phosphatidic acid or one of its metabolites may recruit or activate downstream effectors, directly inducing membrane bending and/or destabilization.[34] Up-regulation of putative acyltransferase leads to a disruption in the normal glycerophospholipid metabolic pathway, which results in changes in the lipid composition of the membrane and microstructures, affecting the normal biophysical properties of the cellular membrane. This is consistent with our finding that treatment of peptide F1 results in extensive morphological changes in *E. coli* as described above (Figure 1).

The ATP-dependent protease ATP-binding subunit ClpX, which is a heat shock protein, is also a protein disaggregation chaperone.[35,36] It has been shown to have peptidase activity, catalytic activity, and hydrolase activity. On the basis of the KEGG pathway analysis, ClpX appears to be involved only in the cell cycle-caulobacter pathway (pathway ID ko04112) (Table 2). In *E. coli*, there are two types of Clp proteases, including the ClpP proteolytic subunit and the ClpQ (or HslV) proteolytic subunit. Among them, the ClpP proteolytic subunit, along with ClpP that serves as the proteolytic core, is capable of interacting with either ClpX or ClpA.[35,37,38] In the cell cycle−caulobacter pathway, the ClpP proteolytic subunit associates with ClpX, referred to as the ClpP−ClpX protease system, which is an autolyzed system that governs normal cell division and proliferation. Up-regulation of CLpX leads to an increased ability to depredate proteins, and it also enhances the effectiveness of the ClpP proteolytic core. An autolysis system in bacterial cells has been reported that, under normal circumstances, is involved in the regulation of cell division and the elimination of unwanted cell wall components and governs the

DOI: 10.1021/acs.jafc.5b00678
J. Agric. Food Chem. 2015, 63, 7190−7197

Table 2. Distribution of Differentially Expressed Proteins in *Escherichia coli* Pathways

pathway	pathway ID	no. of proteins	proteins
glutathione metabolism	ko00480	2	gi|407053705|gb|AFS73756.1|, gi|407054803|gb|AFS74854.1|
microbial metabolism in diverse environments	ko01120	9	gi|407056180|gb|AFS76231.1|, gi|407055221|gb|AFS75272.1|, gi|407056709|gb|AFS76760.1|, gi|407053705|gb|AFS73756.1|, gi|407056449|gb|AFS76500.1|, gi|407051886|gb|AFS71937.1|, gi|407054467|gb|AFS74518.1|, gi|407054803|gb|AFS74854.1|, gi|407054468|gb|AFS74519.1|
two-component system	ko02020	5	gi|407055221|gb|AFS75272.1|, gi|407053659|gb|AFS73710.1|, gi|407053267|gb|AFS73318.1|, gi|407053138|gb|AFS73189.1|, gi|407054803|gb|AFS74854.1|
benzoate degradation	ko00362	2	gi|407056180|gb|AFS76231.1|, gi|407056709|gb|AFS76760.1|
cell cycle−caulobacter	ko04112	2	gi|407055679|gb|AFS75730.1|, gi|407053138|gb|AFS73189.1|
ethylbenzene degradation	ko00642	1	gi|407056709|gb|AFS76760.1|
tricarboxylic acid cycle (TCA cycle)	ko00020	2	gi|407056449|gb|AFS76500.1|, gi|407054803|gb|AFS74854.1|
carbon fixation pathways in prokaryotes	ko00720	2	gi|407056449|gb|AFS76500.1|, gi|407054803|gb|AFS74854.1|
glycine, serine and threonine metabolism	ko00260	2	gi|407055221|gb|AFS75272.1|, gi|407051886|gb|AFS71937.1|
lysine biosynthesis	ko00300	1	gi|407051886|gb|AFS71937.1|
nitrogen metabolism	ko00910	2	gi|407054467|gb|AFS74518.1|, gi|407054468|gb|AFS74519.1|
oxidative phosphorylation	ko00190	2	gi|407052686|gb|AFS72737.1|, gi|407056823|gb|AFS76874.1|
glycerolipid metabolism	ko00561	1	gi|407056709|gb|AFS76760.1|
porphyrin and chlorophyll metabolism	ko00860	1	gi|407055970|gb|AFS76021.1|
selenocompound metabolism	ko00450	1	gi|407051886|gb|AFS71937.1|
photosynthesis	ko00195	1	gi|407056823|gb|AFS76874.1|
cysteine and methionine metabolism	ko00270	1	gi|407051886|gb|AFS71937.1|
biosynthesis of secondary metabolites	ko01110	8	gi|407055221|gb|AFS75272.1|, gi|407053705|gb|AFS73756.1|, gi|407056449|gb|AFS76500.1|, gi|407052948|gb|AFS72999.1|, gi|407053267|gb|AFS73318.1|, gi|407051886|gb|AFS71937.1|, gi|407055970|gb|AFS76021.1|, gi|407054803|gb|AFS74854.1|
homologous recombination	ko03440	1	gi|407051886|gb|AFS71937.1|
aminobenzoate degradation	ko00627	1	gi|407056709|gb|AFS76760.1|
bacterial chemotaxis	ko02030	1	gi|407053138|gb|AFS73189.1|
limonene and pinene degradation	ko00903	1	gi|407056709|gb|AFS76760.1|
glycerophospholipid metabolism	ko00564	1	gi|407056709|gb|AFS76760.1|
DNA replication	ko03030	1	gi|407051886|gb|AFS71937.1|
ribosome	ko03010	3	gi|407052361|gb|AFS72412.1|, gi|407052369|gb|AFS72420.1|, gi|407052368|gb|AFS72419.1|
pentose phosphate pathway	ko00030	1	gi|407053705|gb|AFS73756.1|
arginine and proline metabolism	ko00330	1	gi|407052948|gb|AFS72999.1|
purine metabolism	ko00230	2	gi|407053267|gb|AFS73318.1|, gi|407051886|gb|AFS71937.1|
mismatch repair	ko03430	1	gi|407051886|gb|AFS71937.1|
tyrosine metabolism	ko00350	1	gi|407056709|gb|AFS76760.1|
metabolic pathways	ko01100	11	gi|407056180|gb|AFS76231.1|, gi|407055221|gb|AFS75272.1|, gi|407056709|gb|AFS76760.1|, gi|407053705|gb|AFS73756.1|, gi|407056449|gb|AFS76500.1|, gi|407052948|gb|AFS72999.1|, gi|407053267|gb|AFS73318.1|, gi|407051886|gb|AFS71937.1|, gi|407055970|gb|AFS76021.1|, gi|407054803|gb|AFS74854.1|, gi|407056823|gb|AFS76874.1|
pyrimidine metabolism	ko00240	1	gi|407051886|gb|AFS71937.1|

DOI:10.1021/acs.jafc.5b00678
J. Agric. Food Chem. 2015, 63, 7190−7197

regeneration process after damage occurs from external factors. The autolysis system consists of enzymes with muramidase activity, *N*-acetylglucosaminidase activity, amidase activity, and peptidase activity.[39] Under normal conditions, these autolytic enzymes are inhibited by the endogenous lipids, such as phospholipids and lipoteichoic acid. When an external stimuli disrupts the balance between these autolytic enzymes and the inhibitory lipids, the autolytic enzymes are activated, resulting in autolysis of the cell.[40] Our results suggested that the ClpP−ClpX protease system, acting within the cell cycle−caulobacter pathway, was activated by antimicrobial peptide F1, which subsequently resulted in the autolysis and death of *E. coli* cells. The morphological changes observed for the *E. coli* cells that had been treated by peptide F1 confirmed the process of autolysis and cell death (Figure 1).

Real-Time PCR Analysis of the Differentially Expressed Proteins. To validate the iTRAQ results, real-time PCR was used to analyze the transcripts of the proteins found to be differentially expressed (Figure 4). The mRNA transcription

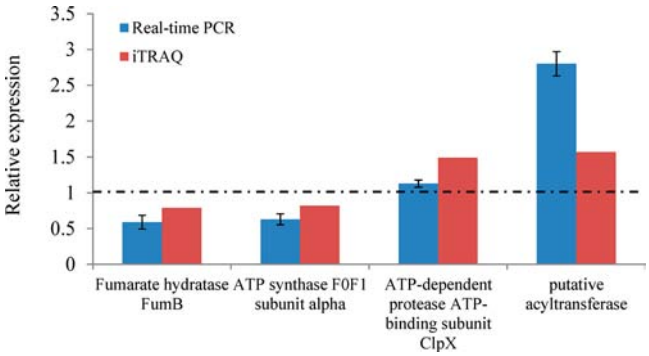

Figure 4. Comparative analysis of RNA and protein levels of specific differentially expressed proteins revealed by real-time PCR and iTRAQ.

levels were measured for four of the differentially expressed proteins, including the genes encoding for two proteins that were found to be up-regulated (ATP-dependent protease ATP-binding subunit ClpX and putative acyltransferase) and the genes encoding for two proteins that were found to be down-regulated (fumarate hydratase FumB and ATP synthase F0F1 subunit α), which include the important proteins functioning in the cell cycle−caulobacter pathway (pathway ID ko04112), glycerophospholipid metabolism (pathway ID ko00564), tricarboxylic acid cycle (pathway ID ko00020), and oxidative phosphorylation pathway (pathway ID ko00190). The expression levels of the transcripts for the two proteins found to be down-regulated were in agreement with the iTRAQ data, which indicated that the two genes displayed both similar protein and mRNA expression patterns and similar overall quantitative values. The mRNA level for the gene of the ATP-dependent protease ATP-binding subunit ClpX, in which the protein level had been found to be increased, was also increased by 1.13-fold, which is similar to the 1.486-fold increase in the protein expression level as determined from the iTRAQ analysis. The mRNA level of the putative acyltransferase was significantly increased by 2.81-fold, which is higher than the 1.572-fold increase in the protein expression level as determined from the iTRAQ analysis. The real-time PCR results demonstrated that these genes displayed similar protein and mRNA expression patterns with similar or slightly divergent overall quantitative values.

In conclusion, our findings revealed that upon treatment of *E. coli* with the antimicrobial peptide F1, there is a comprehensive global protein response characterized by the down-regulation of major catalytic enzymes involved in energy metabolism and the up-regulation of proteins with peptidase activity, catalytic activity, and hydrolase activity. The inhibitions of the tricarboxylic acid cycle pathway and the oxidative phosphorylation pathway were potentially associated with the observed decrease in cell growth and cell death. The promotion of the glycerophospholipid metabolic pathway and the cell cycle−caulobacter pathway potentially increased the permeability of the cellular membrane, resulting in the autolysis of the cellular structures, which may result in cell death. Overall, our study provides novel insights into the mechanisms underlying the mode of action of the antimicrobial peptide F1.

■ ASSOCIATED CONTENT

Supporting Information

The Supporting Information is available free of charge on the ACS Publications website at DOI: 10.1021/acs.jafc.5b00678.

Identification of proteins (XLSX)
GO enrichment analysis (XLSX)
Primers used for real-time PCR (PDF)

■ AUTHOR INFORMATION

Corresponding Authors

*(H.X.) Phone: (413) 545-2281. Fax: (413) 545-1262. E-mail: hangxiao@foodsci.umass.edu.
*(Y.C.) Phone: +86 020 85286234. Fax: +86 020 85286234. E-mail: caoyong2181@scau.edu.cn.

Funding

We express our gratitude to the National Natural Science Foundation of China (No. 31171768) for financial support.

Notes

The authors declare no competing financial interest.

■ REFERENCES

(1) Siegel, R. E. Emerging Gram-negative antibiotic resistance: daunting challenges, declining sensitivities, and dire consequences. *Resp. Care* **2008**, *53*, 471−479.
(2) Rice, L. B. Challenges in identifying new antimicrobial agents effective for treating infections with *Acinetobacter baumannii* and *Pseudomonas aeruginosa*. *Clin. Infect. Dis.* **2006**, *43*, S100−S105.
(3) Weinstein, R. A.; Gaynes, R.; Edwards, J. R. Overview of nosocomial infections caused by Gram-negative bacilli. *Clin. Infect. Dis.* **2005**, *41*, 848−854.
(4) Kamysz, W. Are antimicrobial peptides an alternative for conventional antibiotics. *Nucl. Med. Rev. Cent. East Eur.* **2005**, *8*, 78−86.
(5) Shai, Y. Mode of action of membrane active antimicrobial peptides. *Biopolymers* **2002**, *66*, 236−248.
(6) Hancock, R. E.; Chapple, D. S. Peptide antibiotics. *Antimicrob. Agents Chemother.* **1999**, *43*, 1317−1323.
(7) Lehrer, R.; Barton, A.; Daher, K.; Harwig, S.; Ganz, T.; Selsted, M. Interaction of human defensins with *Escherichia coli*: mechanism of bactericidal activity. *J. Clin. Invest.* **1989**, *84*, 553−561.
(8) Zhang, L.; Dhillon, P.; Yan, H.; Farmer, S.; Hancock, R. E. Interactions of bacterial cationic peptide antibiotics with outer and cytoplasmic membranes of *Pseudomonas aeruginosa*. *Antimicrob. Agents Chemother.* **2000**, *44*, 3317−3321.
(9) Chitnis, S.; Prasad, K. Seminalplasmin, an antimicrobial protein from bovine seminal plasma, inhibits peptidoglycan synthesis in *Escherichia coli*. *FEMS Microbiol. Lett.* **1990**, *72*, 281−284.

DOI: 10.1021/acs.jafc.5b00678
J. Agric. Food Chem. 2015, 63, 7190−7197

(10) del Castillo, F. J.; del Castillo, I.; Moreno, F. Construction and characterization of mutations at codon 751 of the *Escherichia coli* gyrB gene that confer resistance to the antimicrobial peptide microcin B17 and alter the activity of DNA gyrase. *J. Bacteriol.* **2001**, *183*, 2137−2140.
(11) Kim, D. H.; Lee, D. G.; Kim, K. L.; Lee, Y. Internalization of tenecin 3 by a fungal cellular process is essential for its fungicidal effect on *Candida albicans*. *Eur. J. Biochem.* **2001**, *268*, 4449−4458.
(12) Kragol, G.; Lovas, S.; Varadi, G.; Condie, B. A.; Hoffmann, R.; Otvos, L. The antibacterial peptide pyrrhocoricin inhibits the ATPase actions of DnaK and prevents chaperone-assisted protein folding. *Biochemistry* **2001**, *40*, 3016−3026.
(13) Xiong, Y. Q.; Bayer, A. S.; Yeaman, M. R. Inhibition of intracellular macromolecular synthesis in *Staphylococcus aureus* by thrombin-induced platelet microbicidal proteins. *J. Infect. Dis.* **2002**, *185*, 348−356.
(14) Zhou, Y.; Chen, W. N. iTRAQ-coupled 2-D LC-MS/MS analysis of membrane protein profile in *Escherichia coli* incubated with apidaecin IB. *PLoS One* **2011**, *6*, e20442.
(15) Gygi, S. P.; Rist, B.; Gerber, S. A.; Turecek, F.; Gelb, M. H.; Aebersold, R. Quantitative analysis of complex protein mixtures using isotope-coded affinity tags. *Nat. Biotechnol.* **1999**, *17*, 994−999.
(16) Ong, S. E.; Blagoev, B.; Kratchmarova, I.; Kristensen, D. B.; Steen, H.; Pandey, A.; Mann, M. Stable isotope labeling by amino acids in cell culture, SILAC, as a simple and accurate approach to expression proteomics. *Mol. Cell. Proteomics* **2002**, *1*, 376−386.
(17) Ross, P. L.; Huang, Y. N.; Marchese, J. N.; Williamson, B.; Parker, K.; Hattan, S.; Khainovski, N.; Pillai, S.; Dey, S.; Daniels, S. Multiplexed protein quantitation in *Saccharomyces cerevisiae* using amine-reactive isobaric tagging reagents. *Mol. Cell. Proteomics* **2004**, *3*, 1154−1169.
(18) Wu, W. W.; Wang, G.; Baek, S. J.; Shen, R. F. Comparative study of three proteomic quantitative methods, DIGE, cICAT, and iTRAQ, using 2D gel-or LC-MALDI TOF/TOF. *J. Proteome Res.* **2006**, *5*, 651−658.
(19) Kambiranda, D.; Katam, R.; Basha, S. M.; Siebert, S. iTRAQ-based quantitative proteomics of developing and ripening muscadine grape berry. *J. Proteome Res.* **2014**, *13*, 555−569.
(20) Lü, A.; Hu, X.; Wang, Y.; Shen, X.; Li, X.; Zhu, A.; Tian, J.; Ming, Q.; Feng, Z. iTRAQ analysis of gill proteins from the zebrafish (*Danio rerio*) infected with *Aeromonas hydrophila*. *Fish Shellfish Immunol.* **2014**, *36*, 229−239.
(21) Meng, Q.; Hou, L.; Zhao, Y.; Huang, X.; Huang, Y.; Xia, S.; Gu, W.; Wang, W. iTRAQ-based proteomic study of the effects of *Spiroplasma eriocheiris* on Chinese mitten crab *Eriocheir sinensis* hemocytes. *Fish Shellfish Immunol.* **2014**, *40*, 182−189.
(22) Shen, X. L.; Zhang, Y.; Xu, W.; Liang, R.; Zheng, J.; Luo, Y.; Wang, Y.; Huang, K. An iTRAQ-based mitoproteomics approach for profiling the nephrotoxicity mechanisms of ochratoxin A in HEK 293 cells. *J. Proteomics* **2013**, *78*, 398−415.
(23) Yu, Y.; Pan, X.; Ding, Y.; Liu, X.; Tang, H.; Shen, C.; Shen, H.; Yang, P. An iTRAQ based quantitative proteomic strategy to explore novel secreted proteins in metastatic hepatocellular carcinoma cell lines. *Analyst* **2013**, *138*, 4505−4511.
(24) Miao, J.; Guo, H.; Ou, Y.; Liu, G.; Fang, X.; Liao, Z.; Ke, C.; Chen, Y.; Zhao, L.; Cao, Y. Purification and characterization of bacteriocin F1, a novel bacteriocin produced by *Lactobacillus paracasei* subsp. *tolerans* FX-6 from Tibetan kefir, a traditional fermented milk from Tibet, China. *Food Control* **2014**, *42*, 48−53.
(25) Duan, H.; Jin, S.; Zhang, Y.; Li, F.; Xiang, J. Granulocytes of the red claw crayfish *Cherax quadricarinatus* can endocytose beads, *E. coli* and WSSV, but in different ways. *Dev. Comp. Immunol.* **2014**, *46*, 186−193.
(26) Guo, H.; Chen, C.; Lee, D. J.; Wang, A.; Gao, D.; Ren, N. Coupled carbon, sulfur and nitrogen cycles of mixotrophic growth of *Pseudomonas* sp. C27 under denitrifying sulfide removal conditions. *Bioresour. Technol.* **2014**, *171*, 120−126.
(27) Bradford, M. M. A rapid and sensitive method for the quantitation of microgram quantities of protein utilizing the principle of protein-dye binding. *Anal. Biochem.* **1976**, *72*, 248−254.
(28) Martin, B.; Brenneman, R.; Becker, K. G.; Gucek, M.; Cole, R. N.; Maudsley, S. ITRAQ analysis of complex proteome alterations in 3xTgAD alzheimer's mice: understanding the interface between physiology and disease. *PLoS One* **2008**, *3*, e2750.
(29) Conesa, A.; Götz, S.; García-Gómez, J. M.; Terol, J.; Talón, M.; Robles, M. Blast2GO: a universal tool for annotation, visualization and analysis in functional genomics research. *Bioinformatics* **2005**, *21*, 3674−3676.
(30) Ogata, H.; Goto, S.; Sato, K.; Fujibuchi, W.; Bono, H.; Kanehisa, M. KEGG: Kyoto Encyclopedia of Genes and Genomes. *Nucleic Acids Res.* **1999**, *27*, 29−34.
(31) Bustin, S. A. Absolute quantification of mRNA using real-time reverse transcription polymerase chain reaction assays. *J. Mol. Endocrinol.* **2000**, *25*, 169−193.
(32) Yamauchi, K.; Tomita, M.; Giehl, T. J.; Ellison, R. T. Antibacterial activity of lactoferrin and a pepsin-derived lactoferrin peptide fragment. *Infect. Immun.* **1993**, *61*, 719−728.
(33) Chapple, D. S.; Mason, D. J.; Joannou, C. L.; Odell, E. W.; Gant, V.; Evans, R. W. Structure-function relationship of antibacterial synthetic peptides homologous to a helical surface region on human lactoferrin against *Escherichia coli* serotype O111. *Infect. Immun.* **1998**, *66*, 2434−2440.
(34) Kooijman, E. E.; Chupin, V.; de Kruijff, B.; Burger, K. N. Modulation of membrane curvature by phosphatidic acid and lysophosphatidic acid. *Traffic* **2003**, *4*, 162−174.
(35) Gottesman, S.; Clark, W. P.; de Crecy-Lagard, V.; Maurizi, M. R. ClpX, an alternative subunit for the ATP-dependent Clp protease of *Escherichia coli*. Sequence and in vivo activities. *J. Biol. Chem.* **1993**, *268*, 22618−22626.
(36) Wawrzynow, A.; Wojtkowiak, D.; Marszalek, J.; Banecki, B.; Jonsen, M.; Graves, B.; Georgopoulos, C.; Zylicz, M. The ClpX heat-shock protein of *Escherichia coli*, the ATP-dependent substrate specificity component of the ClpP-ClpX protease, is a novel molecular chaperone. *EMBO J.* **1995**, *14*, 1867−1877.
(37) Katayama, Y.; Gottesman, S.; Pumphrey, J.; Rudikoff, S.; Clark, W. P.; Maurizi, M. The two-component, ATP-dependent Clp protease of *Escherichia coli*. Purification, cloning, and mutational analysis of the ATP-binding component. *J. Biol. Chem.* **1988**, *263*, 15226−15236.
(38) Porankiewicz, J.; Wang, J.; Clarke, A. K. New insights into the ATP-dependent Clp protease: *Escherichia coli* and beyond. *Mol. Microbiol.* **1999**, *32*, 449−458.
(39) Wecke, J.; Lahav, M.; Ginsburg, I.; Giesbrecht, P. Cell wall degradation of *Staphylococcus aureus* by lysozyme. *Arch. Microbiol.* **1982**, *131*, 116−123.
(40) Bierbaum, G.; Sahl, H. G. Induction of autolysis of *staphylococci* by the basic peptide antibiotics pep 5 and nisin and their influence on the activity of autolytic enzymes. *Arch. Microbiol.* **1985**, *141*, 249−254.

DOI: 10.1021/acs.jafc.5b00678
J. Agric. Food Chem. 2015, 63, 7190−7197

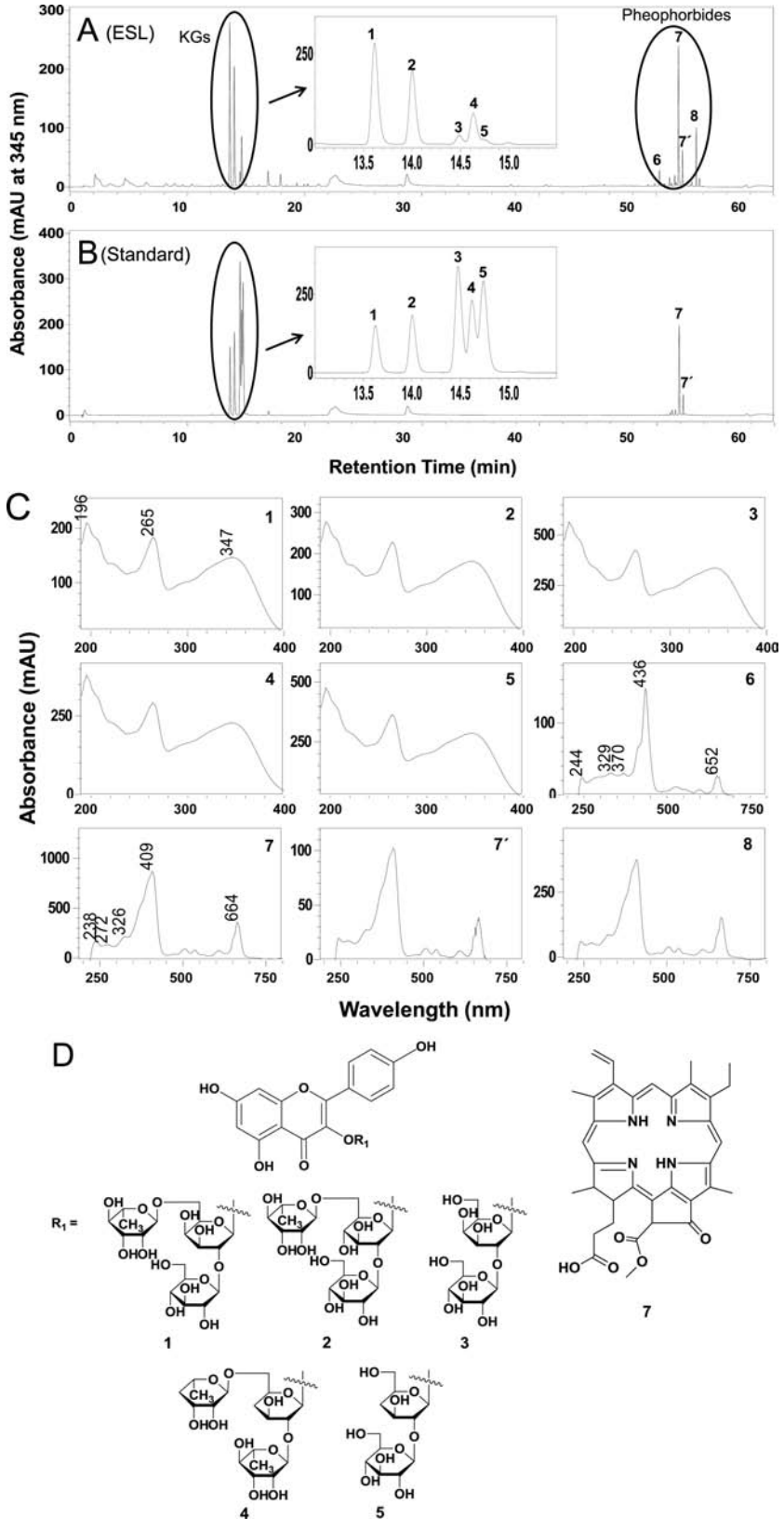

Figure 1. HPLC profile of ESL and the chemical structures of the main components. HPLC chromatograms of (A) ESL (20 mg/mL) and (B) standard compounds, KGs and PA (0.4 mg/mL each), were detected at 345 nm. (C) UV−vis spectra of KGs **1**−**5** and pheophorbides **6**−**8**. (D) Chemical structures of KGs **1**−**5** and PA (**7**) isolated from ESL. KGs, kaempferol glycosides; PA, pheophorbide *a*.

Soybean, *Glycine max*, is a source of dietary protein and oil and contains various phenolic compounds with biological activity. Although soybeans are used as a food source, soy leaves are also consumed in some parts of Asia. In the Gyungsang-do province of Korea, soy leaves are used to prepare traditional dishes, including *jangachi* and *kimchi*. Many studies have reported the

DOI: 10.1021/acs.jafc.5b01639
J. Agric. Food Chem. 2015, 63, 7198−7210

health benefits of soybeans; however, evidence of health benefits from soy leaves is limited, although they can exert effects on serum lipid profile,[8,9] carotid arteries,[10] in vitro α-glucosidase activity,[11,12] and diabetes.[13−16] Soy leaves contain isoflavonols (kaempferol and its glycosides), isoflavones (daidzin, genistin, and malonyl-genistin),[10] pterocarpans (glyceofurans, coumestrol, isotrifoliol, and phaseol),[11,12] and pheophorbides, products of chlorophyll breakdown. We previously demonstrated that pterocarpan-enriched soy leaf extract improved glucose homeostasis by enhancing insulin sensitivity and pancreatic β-cell proliferation in high-fat diet (HFD)-induced type 2 diabetic mice.[16] A kaempferol glycoside (KG)-rich fraction from unripe soy leaves decreased fasting blood glucose and glycated hemoglobin (HbA1c) levels and regulated lipid metabolism in KK-A^y and HFD-fed mice.[14,15] A recent study reported that soy leaf extracts have beneficial effects on fasting blood glucose, HbA1c, and homeostasis model assessment of insulin resistance (HOMA-IR) levels, as well as adiposity and dyslipidemia, in prediabetic patients.[13] However, these studies did not fully investigate the mechanisms or active components. In this study, we used obese diabetic *db*/*db* mice to verify the antidiabetic effect of ethanol extract of soy leaves (ESL) containing KGs and pheophorbides and to study the mechanisms focusing on these effects in enhancing IRS-mediated β-cell insulin signaling and suppressing hepatic lipid accumulation. Furthermore, we investigated the active components of ESL and their mechanisms in MIN6 pancreatic β-cells.

MATERIALS AND METHODS

Chemicals and Reagents. Glucose, kaempferol, and pheophorbide *a* (PA) were obtained from Sigma-Aldrich (St. Louis, MO, USA). Anti-fatty acid synthase (FAS), anti-phospho-Akt, anti-Akt, anti-phospho-FoxO1, and anti-FoxO1 antibodies were purchased from Cell Signaling Technology (Danvers, MA, USA), and anti-insulin, anti-sterol regulatory element-binding protein (SREBP)-1, anti-phospho-protein kinase A (PKA), anti-PKA, and anti-β-actin antibodies were purchased from Santa Cruz Biotechnology (Santa Cruz, CA, USA).

Diaion HP-20 resin (250−850 μm Mitsubishi Chemical Corp., Tokyo, Japan), flash octadecyl SiO_2 (ODS) (Biotage SNAP Cartridge KP-C18-HS, 9.5 × 15 cm; Biotage, Charlottesville, VA, USA), RP-18 silica gel (ODS-A, 12 nm, S-150 μm; Merck, Darmstadt, Germany), and Sephadex LH-20 (25−100 μm; GE Healthcare Biosciences, Uppsala, Sweden), Sep-Pak C18 (Waters, MA, USA), and ODS prep-HPLC columns (Cosmosil 5C18-MS-II column, 10 × 150 mm or 10 × 250 mm, 5 μm; Nacalai Tesque, Inc., Kyoto, Japan) were used for column chromatography. All solvents used for extraction and isolation were of analytical grade. All purifications were monitored on commercially available glass-backed Merck precoated TLC plates and visualized under UV at 254 and 365 nm or stained with *p*-anisaldehyde solution.

Preparation and HPLC Analysis of ESL. Soybeans, *G. max* (L.) Merr., were cultured in JeungPyeong county (Chungcheongbuk-do, Korea) for 80 days. The air-dried leaves (500 g) were chopped and extracted twice with 70% ethanol (5 L) at room temperature for 48 h. The extract was filtered and evaporated to dryness under reduced pressure at a temperature below 40 °C to afford ESL (112 g).

The main components present in ESL were analyzed and confirmed using a Shimadzu HPLC system equipped with a binary pump delivery system, a diode array detector (DAD), and an autosampler (Shimadzu Corp., Tokyo, Japan) and a Brownlee SPP C18 column (4.6 × 100 mm, 2.7 μm; PerkinElmer, Inc., Waltham, MA, USA). The injection volume was 5 μL, and the mobile phase was 0.1% acetic acid in water (solvent A) and acetonitrile (solvent B). The linear gradient elution program was as follows: 5−40% B for 0−40 min, 40−100% B for 40−50 min, 100% B for 50−55 min, and 5% B for 55−60 min. The flow rate was 1.4 mL/min, and the absorbance was 345 nm. KGs **1**−**5**, which were isolated from ESL, and PA, which was obtained from Sigma-Aldrich, were used as external standards for the HPLC analysis.

Isolation and Identification of KGs and Phoephorbides. The 70% EtOH extract of air-dried leaves (500 g) was concentrated under reduced pressure, and the ESL, as an aqueous suspension, was subjected to Diaion HP-20 absorption column chromatography (CC) (9.5 × 20 cm). The column was washed with H_2O to remove unabsorbed materials and subsequently eluted with 30, 50, 70, and 100% aqueous MeOH (v/v) to yield four fractions (A−D). Fractions that were rich in KGs (A and B), as evidenced by HPLC DAD monitoring, were combined (23.2 g) and separated using ODS flash CC (Biotage SNAP cartridge KP-C18-HS, 9.5 × 15 cm) by eluting with aqueous MeOH (10, 20, 30, 40, 50, and 70% MeOH, v/v). Six fractions (AB-1−AB-6) were produced. The KG-rich fractions AB-1 and AB-2 were combined (9.0 g) and further purified using Sephadex LH-20 CC (5.0 × 90 cm) and eluted with 50% MeOH to yield five subfractions (S-1−S-5). Subfraction S-3 was subjected to CC on Sep-Pak C18 and eluted with 20% MeOH, followed by separation by reversed-phase (RP) preparative HPLC (Cosmosil 5C18-MS-II column, 10 × 150 mm, 5 μm; 254 nm; 11% aqueous acetonitrile; 4 mL/min) to afford compounds **1** (17.5 mg) and **2** (19.2 mg). Subfraction S-4 was also separated by RP preparative HPLC and eluted with 12% aqueous acetonitrile to afford compound **3** (14.9 mg). Subfraction S-5 was subjected to CC on Sep-Pak C18, eluted with 20−25% aqueous MeOH, and then separated by RP preparative HPLC and eluted with 11% aqueous acetonitrile to afford compounds **4** (15.6 mg) and **5** (8.0 mg). Isolated KGs were identified using the UV spectra gathered during HPLC DAD monitoring (Figure 1A−C), ^{1}H and ^{13}C NMR data (Supporting Information, Tables S1 and S2), and ESI-MS data and were consistent with previously reported data.[14,17,18] For chemical structure elucidation of KGs **1**−**5**, see the Supporting Information.

Pheophorbide-rich fraction D (10.6 g) was identified using HPLC DAD monitoring and applied to RP-18 silica gel (5.0 × 29 cm); it was eluted with 80 and 100% MeOH and $CHCl_3$/MeOH (1:9, v/v) to produce 15 fractions (D-1−D-13). Subfraction D-5 (1.35 g) was eluted with 100% MeOH and was further separated using RP preparative HPLC (Cosmosil 5C18-MS-II column, 10 × 250 mm, 5 μm; 410 nm; mobile phase A, 0.1% acetic acid in water; mobile phase B, acetonitrile) to afford compounds **7** (T_R = 37.3 min, 20.9 mg) and **7′** (T_R = 39.1 min, 6.1 mg). The linear gradient elution program was as follows: 5−80% B for 0−15 min, 80−95% B for 15−30 min, 95−100% B for 30−40 min, 100% B for 40−50 min, and 100−5% B for 50−60 min; the flow rate was 3 mL/min. PA was identified on the basis of the spectroscopic data (Supporting Information, Figure S1), which were consistent with those previously reported.[19−21] For chemical structure elucidation of PA, see the Supporting Information.

Animals and Diets. Five-week-old male C57BLKS/J lar-Lepr^{db}/Lepr^{db} (*db*/*db*) and C57BLKS/J lar-m$^+$/Lepr^{db} (*db*/+) mice purchased from Japan SLC (Shizuoka, Japan) were kept at a constant temperature (25 ± 2 °C), humidity (50 ± 5%), and lighting (12 h light/dark cycle) at the Korean Research Institute of Bioscience and Biotechnology (KRIBB, Daejeon, Korea). After 2 weeks of acclimation, the *db*/*db* mice were randomly divided into two groups (n = 8 per group). The *db*/+ and *db*/*db* control groups were fed a standard diet (AIN-76A diet, Research Diets, Inc., New Brunswick, NJ, USA) with no supplement, and the *db*/*db*-ESL group was fed a standard diet with 1% (wt/wt diet) ESL for 8 weeks. Animal study protocols were approved by the Animal Care Committee of KRIBB (KRIBB-AEC-11101).

Oral Glucose Tolerance Test (OGTT). The OGTT was performed 7 weeks after initiation of the animal experiments. Mice were fasted for 6 h and then orally administered glucose (1 g/kg body weight).[22] The blood glucose level was measured in tail vein blood at 0, 15, 30, 60, and 90 min postglucose injection using a glucometer (Accu-Check Active; Roche, Mannheim, Germany).

Measurement of Metabolic Parameters. For analyses of all metabolic parameters, see previous papers.[16,23] Hepatic TG contents were determined using the methods described by Folch et al.[24] Plasma tumor necrosis factor α (TNFα) levels were measured by mouse ELISA kits (Enzo Life Sciences, Inc., Farmingdale, NY, USA).

Histological Analysis of the Pancreas and Liver. Freshly isolated pancreas and liver tissues were fixed for histopathological

DOI: 10.1021/acs.jafc.5b01639
J. Agric. Food Chem. 2015, 63, 7198−7210

Table 1. Sequences of Primer Used for Real-Time qRT-PCR

gene name	forward primer	reverse primer
GAPDH	ACATCATCCCTGCATCCACT	AGATCCACGACGGACACATT
Pax4	CCCAGTGTGTCCTCTATCAATCG	GGGAAGAACTGGAGCCAACA
Ngn3	CACTCAGCAAACAGCGAAGAAG	GTCAGTGCCCAGATGTAGTTGTG
Ins1	TTTCTCACCTGGAAGACAGC	TGATGCTCTTCACCTTCCTG
Ins2	CCCCACCCAGGCTTTTGT	GCGGGACATGGGTGTGTAG
IRS1	GAGAAGAGACTGGCTCGGAAGA	GCCTATTCTGCCCAACTCAACT
IRS2	GGCCCGAACCTCAATAACAA	CCGCGCAACACGAAAAAG
FoxO1	TGGGCCCTAATTCGGTCAT	TTGGGTCAGGCGGTTCATAC
SREBP-1	GAGCGAGCGTTGAACTGTAT	ATGCTGGAGCTGACAGAGAA
ACC1	AGTTTCCCAGCCAGCAGATT	ATCCATCACCACAGCCTTCA
FAS	TGTGAGTGGTTCAGAGGCAT	TTCTGTAGTGCCAGCAAGCT
FATP4	CTTTCTGCGTATCGTCTGCA	GTGCGAAGGTCCAGCATATA
PDX1	CGGAACCCGAGGAAAACAA	TCTCTCGGTCAAGTTCAACATCA
PKA	GGTTTTGCCAAGCGTGTGA	CAGCCTTGTTGTAGCCTTTGC
IL-1β	ATGGCAACTGTTCCTGAACTCAACT	ATATTCTGTCCATTGAGGTGGAGAGCT
IL-6	GCTACCTGGAGTACATGAAG	CTGTGACTCCAGCTTATCTG
TNFα	CTCAGATCATCTTCTCAAAATTCGAGTGACA	CTTCACAGAGCAATGACTCCAAAGT

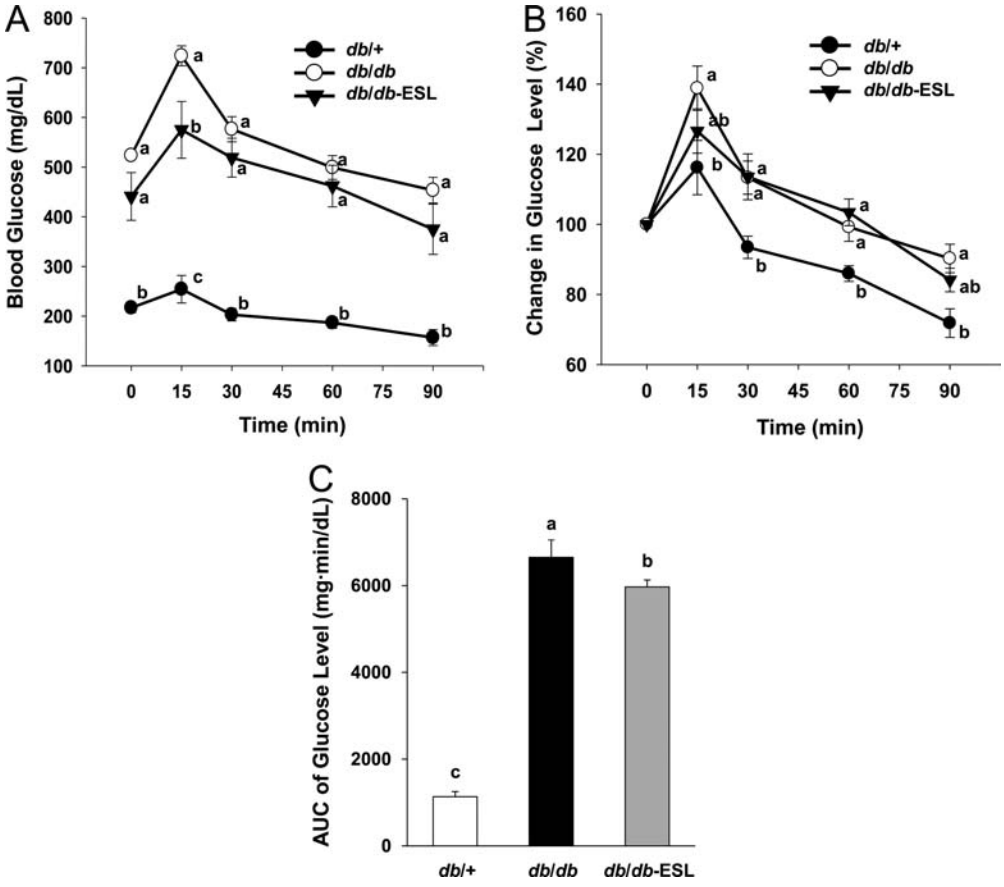

Figure 2. Effect of ESL supplementation on OGTT in *db*/*db* mice. The OGTT was performed in the seventh week after the start of the animal experiments. (A) Changes in glucose levels after glucose (1 g/kg body weight) administration. Blood glucose level was measured in tail vein blood at 0, 15, 30, 60, and 90 min. (B) Percentage of changed glucose levels during the OGTT. The glucose levels were expressed in percentage change in glucose level at 0 min. (C) Area under the curve (AUC) of plasma glucose during OGTT. Values are presented as the mean ± SE. Different letters (a−c) within a variable are significantly different at $p < 0.05$.

analysis.[16,23] Stained section images per each sample were obtained using an Olympus BX61 with an Olympus DP71 digital camera (Tokyo, Japan) and Metamorph imaging software (Molecular Devices, Sunnyvale, CA, USA).

Pancreatic Insulin Content. Pancreases were cut in half and weighed; insulin was then extracted using 70% EtOH solution containing 1.5% HCl.[16] Insulin content was determined by ELISA kit (Alpco Diagnostics, Salem, NH, USA) and calculated by tissue weight.

Real-Time Quantitative RT-PCR (qRT-PCR). For detection of gene expression, see previous papers.[16,23] Results were normalized using glyceraldehyde-3-phosphate dehydrogenase (*GAPDH*) as a reference gene. The primer sequences used in the experiments are shown in Table 1.

DOI: 10.1021/acs.jafc.5b01639
J. Agric. Food Chem. 2015, 63, 7198−7210

Western Blot Analysis. For detection of protein expression, see previous papers.[23] Mouse pancreas, liver, and total cell extracts were subjected to immunoblot analysis with antibodies against phospho-FoxO1, FoxO1, FAS, SREBP-1, phospho-Akt, Akt, phospho-PKA, and PKA.

MIN6 Cell Culture and Insulin Secretion Test. MIN6 pancreatic β-cells were cultured in Dulbecco's modified Eagle's medium (DMEM), containing 25 mM glucose, 15% fetal bovine serum, 100 U/mL penicillin, and 100 U/mL streptomycin at 37 °C in a 5% CO_2 atmosphere. To measure glucose-stimulated insulin secretion, MIN6 cells were seeded into a 24-well plate and grown for 48 h. Medium was removed from the cells, and the cells were washed twice and pre-incubated for 1 h. Cells were then treated with medium containing low (3 mM) and high (30 mM) glucose levels, with or without compounds, and incubated for 1 h. After incubation, the medium was stored at −20 °C until insulin measurement.

Statistical Analyses. Data from tissue and plasma are presented as the mean ± SE. Significant differences among the groups were assessed by one-way ANOVA with Tukey's post hoc test by using JMP software (SAS Institute Inc., Cary, NC, USA). Data from MIN6 cell experiments are expressed as the mean ± SD and analyzed by using Student's *t* test. A p value <0.05 was considered significant.

RESULTS AND DISCUSSION

HPLC Analysis of KGs and Pheophorbides in ESL. ESL and standard compounds were analyzed using HPLC DAD at 345 nm (Figure 1A,B). ESL primarily contained KGs and pheophorbides; the total peak area percentages of KGs **1**−**5** and pheophorbides **6**−**8** were 50.4 ± 2.8 and 23.2 ± 1.2%, respectively. The five KGs were identified as kaempferol 3-*O*-β-D-glucopyranosyl(1→2)-*O*-[α-L-rhamnopyranosyl(1→6)]-β-D-galactopyranoside (**1**), kaempferol 3-*O*-β-D-glucopyranosyl-(1→2)-*O*-[α-L-rhamnopyranosyl(1 → 6)]-β-D-glucopyranoside (**2**), kaempferol 3-*O*-(2-*O*-β-D-glucopyranosyl)-β-D-galactopyranoside (**3**), 3-*O*-(2,6-di-*O*-α-L-rhamnopyranosyl]-β-D-glucopyranoside (**4**), and kaempferol 3-*O*-β-D-glucopyranosyl-(1→2)-β-D-glucopyranoside (**5**). The chlorophyll derivatives were identified as pheophorbide *a* (PA, **7**), pheophorbide *a*′ (**7**′) and other pheophorbides (**6**, **8**). Figure 1 shows that compounds **1** and **2** were most abundant KGs in ESL on the basis of the peak area of standard compounds (Figure 1A,B). The contents of KGs **1** and **2** and PA in ESL were measured using HPLC DAD with their own standard curves. The contents of KG1, KG2, and PA were 30.60 ± 1.26, 16.41 ± 0.03, and 14.54 ± 0.57 μg/mg ESL, respectively (Supporting Information, Table S3 and Figure S2).

ESL Improved Glucose Tolerance. The OGTT was used to evaluate pancreatic β-cell insulin secretion and tissue insulin sensitivity. The *db*/*db* group showed impaired glucose tolerance, as compared to age-matched *db*/+ group (Figure 2). In human and rodent physiology, insulin secretion reaches a peak in the first phase (approximately 5−10 min), followed by a sustained second phase of release, during which insulin pulses are secreted over 3−8 min.[25] The 6 h fasting glucose levels at week 7 were lower in the *db*/*db*-ESL group (15.8%) than in the *db*/*db* group (Figure 2A). In the OGTT, the glucose levels of all groups reached individual peaks at 15 min and then declined gradually. ESL supplementation markedly reduced early-phase blood glucose levels. The glucose levels at 15 min were significantly lower in the *db*/*db*-ESL group (20.6%) than in the *db*/*db* group (Figure 2A), and the change in glucose level at 15 min, as compared to 0 min, was also decreased in the *db*/*db*-ESL group (15.8%, Figure 2B). Finally, the area under the curve (AUC) of the blood glucose levels revealed that ESL significantly improved glucose tolerance (Figure 2C).

ESL Improved Plasma Profiles. At the end of the experiment, *db*/*db* mice showed hallmark characteristics of T2DM models. The body weight, food intake, organ weight (liver, pancreas, muscle, abdominal adipose, and inguinal adipose), and all plasma levels (glucose, HbA1c, insulin, FFA, TC, TG, GOT, and GPT) were significantly higher in the *db*/*db* group, as compared to the *db*/+ group. ESL had no effect on body weight gain, food intake, and the organ weights of the liver, muscle, and WAT (abdominal and inguinal adipose tissues). However, ESL supplementation increased pancreatic tissue weight 25% versus the *db*/*db* group, although this change was not significant (Table 2). The plasma glucose and HbA1c levels were significantly lower in the *db*/*db*-ESL group (23.1 and 21.2%, respectively) than in the *db*/*db* group (Table 3). These results indicate that ESL improved glucose tolerance. Fasting plasma insulin concentrations in *db*/*db* mice are significantly increased, indicating insulin resistance.[26] Plasma insulin levels in ESL-treated mice were slightly decreased. The HOMA-IR index of the *db*/*db* group was dramatically higher than that of the *db*/+ group. ESL supplementation also significantly decreased the HOMA-IR index, although the value was still high. Therefore, the *db*/*db*-ESL group still exhibited hyperinsulinemia to compensate for the sustained severe hyperglycemia. Additionally, plasma TG levels

Table 2. Effects of ESL Supplementation on Body and Organ Weights in *db*/*db* Mice[a]

	db/+	*db*/*db*	*db*/*db*-ESL
initial (g)	26.9 ± 0.6	34.1 ± 0.6	33.3 ± 0.8
final (g)	37.0 ± 1.1	43.9 ± 0.9	45.3 ± 1.6
wt gain (g)	10.1 ± 0.7a	9.9 ± 0.6a	11.9 ± 1.1a
food intake (g/day)	3.2 ± 0.1b	3.8 ± 0.2a	3.9 ± 0.1a
liver (g)	1.25 ± 0.07b	3.72 ± 0.18a	3.52 ± 0.26a
pancreas (g)	0.16 ± 0.01a	0.12 ± 0.01a	0.15 ± 0.01a
muscle (g)	0.26 ± 0.01a	0.17 ± 0.02b	0.16 ± 0.01b
fat tissues			
abdominal (g)	0.63 ± 0.07b	0.94 ± 0.07a	1.10 ± 0.05a
inguinal (g)	1.17 ± 0.16b	2.65 ± 0.58a	2.76 ± 0.19a

[a]Values are presented as the mean ± SE, n = 8. Means not sharing a common letter (a, b) are significantly different between groups (p < 0.05). ESL, ethanol extracts of soy leaves.

Table 3. Effects of ESL Supplementation on Plasma Profiles in *db*/*db* Mice[a]

	db/+	*db*/*db*	*db*/*db*-ESL
glucose (mg/dL)	232 ± 7c	502 ± 51a	386 ± 49b
HbA1c (%)	4.7 ± 0.1c	9.9 ± 0.7a	7.8 ± 0.3b
insulin (ng/mL)	3.37 ± 0.54b	8.00 ± 1.01a	7.65 ± 1.04a
HOMA-IR index	41.1 ± 4.7c	220.6 ± 19.8a	169.1 ± 20.5b
TG (mg/dL)	106 ± 5b	157 ± 12a	104 ± 6b
TC (mg/dL)	121 ± 6a	287 ± 16a	268 ± 25a
FFA (mequiv/L)	0.88 ± 0.04b	1.82 ± 0.16a	1.50 ± 0.15a
GOT (IU/L)	67 ± 2c	188 ± 7a	154 ± 13b
GPT (IU/L)	30 ± 1b	174 ± 11a	155 ± 19a

[a]Values are presented as the mean ± SE, n = 8. Means not sharing a common letter (a−c) are significantly different between groups (p < 0.05). ESL, ethanol extracts of soy leaves; HbA1c, glycated hemoglobin; FFA, free fatty acid; TC, total cholesterol; TG, triglyceride; GOT, glutamate oxaloacetate transaminase; GPT, glutamate pyruvate transaminase.

DOI: 10.1021/acs.jafc.5b01639
J. Agric. Food Chem. 2015, 63, 7198−7210

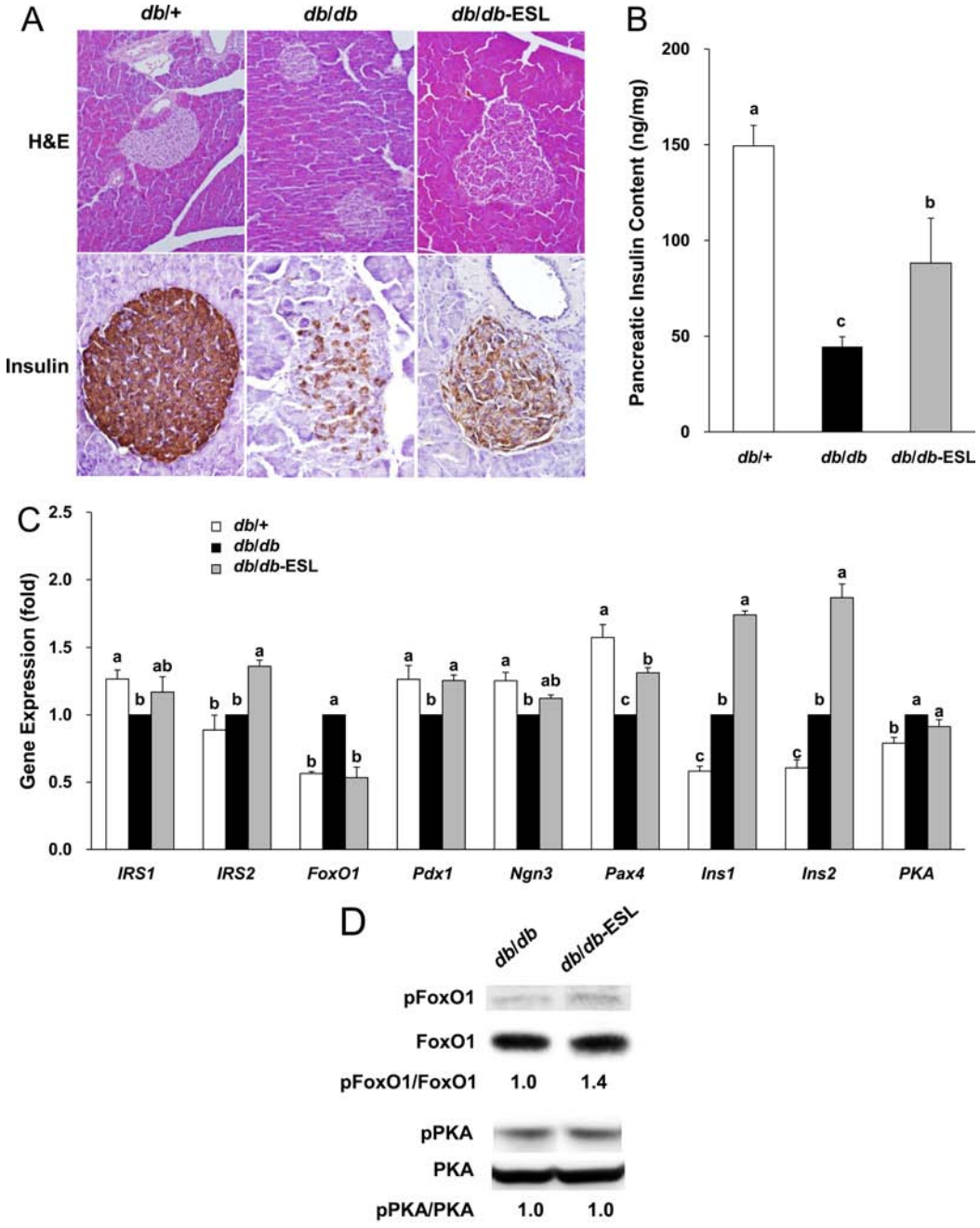

Figure 3. Effects of ESL supplementation on pancreatic dysfunction and insulin content in *db*/*db* mice. (A) Sections from pancreas stained with H&E and insulin IHC. (B) Insulin content in the pancreas. (C) mRNA levels measured by real-time qRT-PCR in pancreas and normalized using *GAPDH* as a reference gene. Values are presented as the mean ± SE. Different letters (a−c) within a variable are significantly different at $p < 0.05$. (D) Protein levels measured in the pancreas. Protein expressions of FoxO1, PKA, and their phosphorylated forms were analyzed by Western blot.

were markedly decreased in the *db*/*db*-ESL group (33.8%, $p < 0.05$). ESL showed a tendency to decrease TC and FFA levels, although this change was not significant. The liver function parameters, GOT and GPT, were decreased in the *db*/*db*-ESL group (18.1 and 10.9%, respectively), with GOT showing a significant difference versus the *db*/*db* group (Table 3).

Our results indicate that ESL effectively regulates hyperglycemia in diabetic mice. Recent studies also agree with our results, as KGs regulate glucose homeostasis and lipid profiles in KK-Ay and high-fat diet-fed mice.[14,15] In KK-Ay mice, KGs significantly decreased blood HbA1c level and slightly lowered fasting glucose and glucose tolerance, although these changes were not significant.[14] In high-fat diet-fed mice, KGs decreased fasting blood glucose, HbA1c, and insulin levels, as well as the AUC on the OGTT. In this study, ESL significantly decreased glucose and HbA1c levels and the HOMA-IR index. Furthermore, it improved glucose tolerance in *db*/*db* mice with severe hyperglycemia. Both KK-Ay and *db*/*db* mice are T2DM models, displaying hyperglycemia, hyperinsulinemia, and obesity. These characteristics revert to normal in KK-Ay mice older than 40 weeks of age; in contrast, hyperglycemia in *db*/*db* mice is sustained over the entire life span.[26] In the pancreas, KK-Ay mice display pancreatic β-cell hypertrophy, whereas *db*/*db* mice showed pancreatic β-cell necrosis and islet atrophy. Next, we investigated whether ESL affected β-cell dysfunction in pancreatic islets.

DOI: 10.1021/acs.jafc.5b01639
J. Agric. Food Chem. 2015, 63, 7198−7210

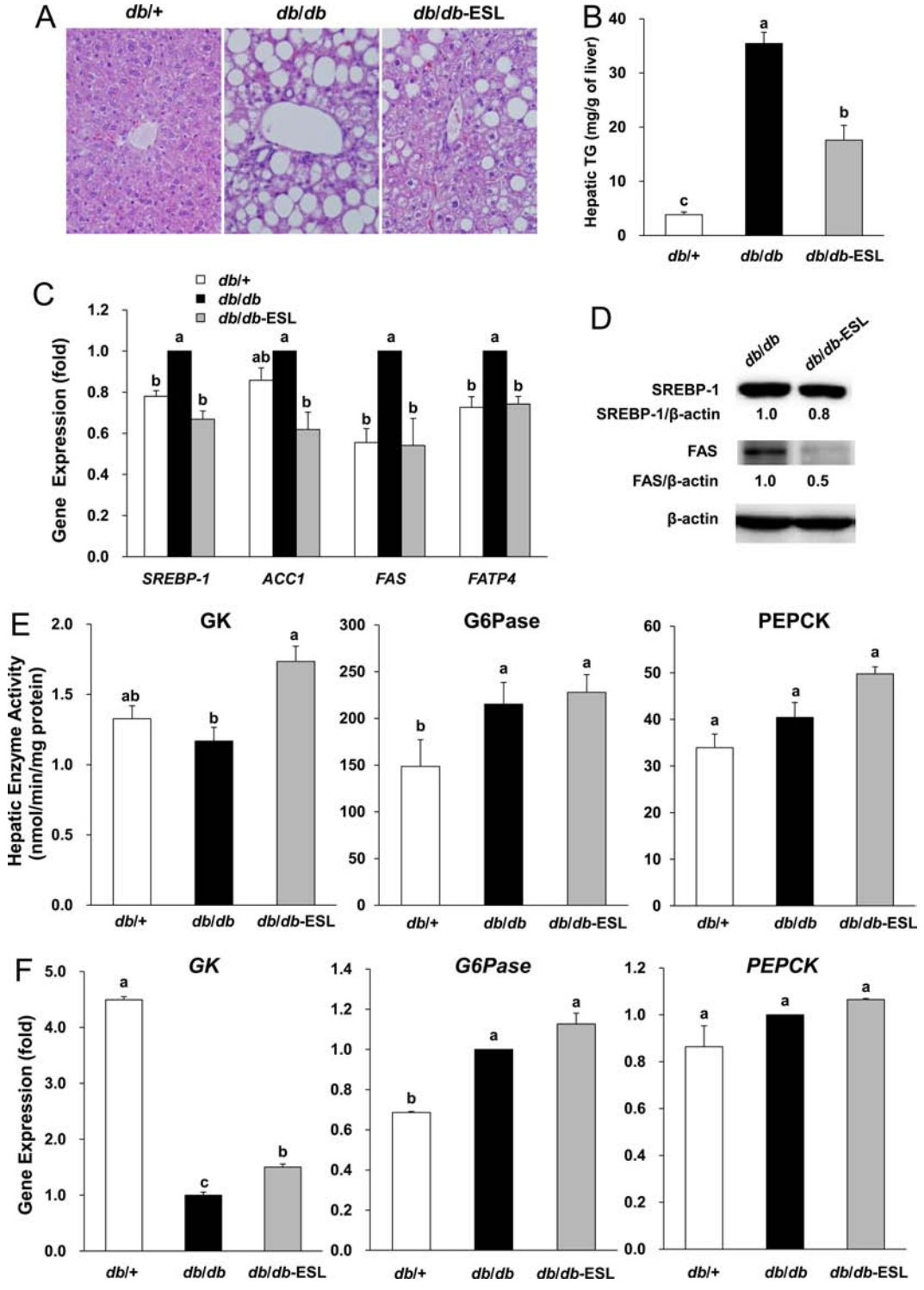

Figure 4. Effects of ESL supplementation on the regulation of hepatic lipid accumulation in *db*/*db* mice. (A) Histology of the livers stained with H&E. (B) Hepatic TG contents. (C) Relative mRNA expression levels in the liver. The mRNA levels were measured by real-time qRT-PCR and normalized using *GAPDH* as a reference gene. (D) Western blot of hepatic SREBP-1 and FAS detected with specific antibodies. (E) Hepatic enzyme activities and (F) relative mRNA expression levels in the liver. Values are presented as the mean ± SE. Different letters (a−c) within a variable are significantly different at $p < 0.05$.

ESL Improved Impared Pancreatic Function. ESL improved glucose tolerance, as indicated by plasma glucose, HbA1c, and insulin levels. This may occur by improving pancreatic or liver function. In T2DM, β-cell numbers and function are decreased, underlying much of the disease pathology.[27] Therefore, identifying ways to preserve or expand pancreatic β-cell number and function may be an effective therapeutic approach for T2DM. We investigated the histology of the pancreas. H&E staining revealed that the size of the pancreatic islet was markedly decreased in *db*/*db* mice, as compared to *db*/+ mice; however, ESL treatment recovered the islet size (Figure 3A). Furthermore, the pancreatic insulin

DOI: 10.1021/acs.jafc.5b01639
J. Agric. Food Chem. 2015, 63, 7198−7210

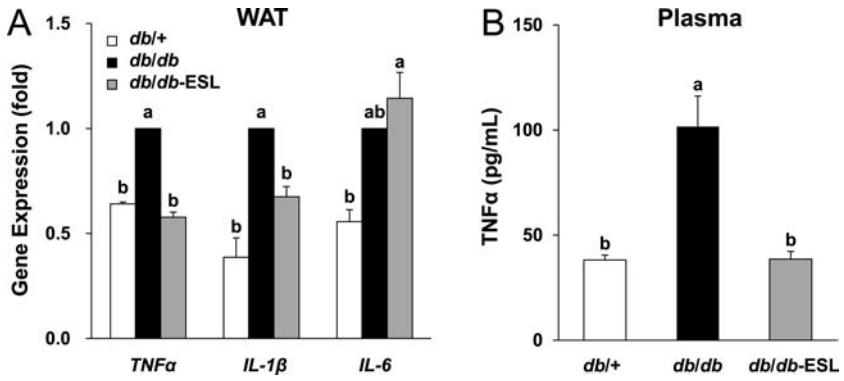

Figure 5. Effects of ESL supplementation on relative mRNA levels of WAT genes and plasma TNFα levels in *db*/*db* mice. (A) Relative mRNA expression levels in the WAT. The mRNA levels were measured by real-time qRT-PCR and normalized using *GAPDH* as a reference gene. (B) Plasma TNFα levels measured by ELISA. Values are presented as the mean ± SE. Different letters (a, b) within a variable are significantly different at $p < 0.05$.

content was significantly increased in the *db*/*db*-ESL group, as compared to the *db*/*db* group (Figure 3A,B).

β-Cells can be generated from pancreatic α-cells, ductal cells, and exocrine cells in mice by overexpressing the transcription factors *MafA*, *Ngn3*, and *Pax4* and pancreatic and duodenal homeobox 1 (*Pdx1*).[28−30] These transcription factors are closely regulated during β-cell reprogramming and differentiation. *Pdx1* drives *Ngn3* expression, and *Pax4* is directly downstream of *Ngn3*.[31] In pancreatic β-cells, the IRS plays an important role in β-cell survival, proliferation, and insulin secretion via PI3K/Akt signaling.[5] Activated Akt inhibits FoxO1 and its transcriptional activity. Phosphorylation of FoxO1 sequesters this protein in the cytoplasm, leading to ubiquitin−proteasome degradation. Nuclear import of FoxO1 directly contributes to the suppression of *Ins2* and *Pdx1*, but not *Ins1*, gene expression in pancreatic β-cells.[32] FoxO1 also inhibits β-cell differentiation by repressing *Ngn3* gene expression.[33] In contrast, activation of the PI3K/Akt pathway leads to increased expression of *MafA*, *Ngn3*, *Pax4*, and *Pdx1*, thereby enhancing insulin gene expression in insulin-producing cells.[34,35] Therefore, we investigated ESL-induced changes in the expression of pancreatic genes associated with reprogramming and differentiation of β-cell using real-time qRT-PCR analyses.

The mRNA levels of *IRS1* and transcription factors, including *Pdx1*, *Ngn3*, and *Pax4*, were down-regulated in the *db*/*db* group, as compared to the *db*/+ group (Figure 3C). Additionally, *FoxO1* gene expression was up-regulated in the *db*/*db* group. ESL supplementation increased the gene expression of *IRS1*, *IRS2*, *Pdx1*, *Ngn3*, and *Pax4* and decreased that of *FoxO1* (Figure 3C). Interestingly, insulin I (*Ins1*) and insulin II (*Ins2*) gene expression were higher in the *db*/*db* group than in the *db*/+ group. This discrepancy in insulin gene expression could be due to a compensatory response for enhanced insulin demands in diabetics or other factors that also regulate insulin gene expression. Nevertheless, the mRNA levels of *Ins1* and *Ins2* in the *db*/*db*-ESL group were higher than those of the *db*/*db* group (Figure 3C). Additionally, phosphorylation of FoxO1 was increased by ESL supplementation, although there were no changes in PKA mRNA or protein expression (Figure 3C,D). These results indicate that ESL treatment improved pancreatic function though regulation of *IRS1*, *IRS2*, and their downstream effectors, *FoxO1*, *Pdx1*, *Ngn3*, and *Pax4*.

ESL Suppressed Hepatic Lipogenesis. The liver plays a key role in glucose and lipid metabolism. The liver stores excess energy through glycogen synthesis and lipogenesis. Hepatic lipogenesis is induced by excess carbohydrate ingestion, leading to TG formation for long-time energy storage. During feeding or overnutrition, the liver enhances lipogenesis, converting the surplus nutrients to TGs, stored in lipid droplets. In this study, hepatic lipid accumulation in the *db*/*db* group was markedly enhanced, as compared to the *db*/+ group. Although there were no differences in liver weight between the *db*/*db* and *db*/*db*-ESL groups (Table 2), the *db*/*db*-ESL group accumulated many fewer hepatic lipid droplets than the *db*/*db* group (Figure 4A). To clarify the histology of livers, the hepatic TG contents were measured: the hepatic TG contents in the *db*/*db*-ESL group were significantly reduced, compared to the contents in the *db*/*db* group (Figure 4B).

SREBP-1 is a master regulator of the lipogenic pathway. SREBP-1 also plays a critical role in potentiating the effects of hyperinsulinemia by regulating insulin sensitivity during hepatic lipid accumulation.[36] Insulin drastically increases *SREBP-1c* mRNA levels in diabetic livers, and overexpression of *SREBP-1c* in the mouse liver markedly enhances the expression of lipogenic genes and causes massive hepatosteatosis.[37] Fatty liver and insulin sensitivity can be markedly improved by decreasing SREBP-1c activation and lipogenesis while inhibiting endoplasmic reticulum stress in obese rodents.[38] Additionally, hepatic activation of SREBP-1 suppresses IRS2 expression via negative feedback.[39] Fatty acid transport protein 4 (FATP4) mediates fatty acid influx from plasma in hepatocyte membranes, and the recruitment of fatty acids can contribute to the development of fatty liver. Our data revealed that the expression levels of *SREBP-1*, *FAS*, acetyl-CoA carboxylase (*ACC1*), and *FATP4* were significantly decreased in ESL-treated mice, as compared to *db*/*db* control mice (Figure 4C). Furthermore, SREBP-1 and FAS protein expression were markedly decreased by ESL supplementation (Figure 4D). Therefore, ESL improved insulin sensitivity in the liver by suppressing SREBP-1 expression and lipogenesis.

Zang et al. reported that KGs decrease liver lipid levels, including TC, TG, nonesterified fatty acids (NEFA), and phospholipids, by decreasing *peroxisome proliferator-activated receptor gamma* (PPARγ) and *SREBP-1c* in HFD-fed obese mice.[15] In our recent study, ESL containing primarily KGs suppressed body weight gain and reduced WAT weight and plasma TG via down-regulation of adipogenesis-related genes including PPARγ, c/EBPα, SREBP-1, aP2, and FAS, and up-regulation of fat oxidation-related genes including HSL, CPT-1, and UCP2 in the WAT of HFD-induced obese mice.[23] Kwon et al. suggest that luteolin, a natural flavone, improves IRS2-mediated insulin resistance by suppressing SREBP-1 through the

DOI: 10.1021/acs.jafc.5b01639
J. Agric. Food Chem. 2015, 63, 7198−7210

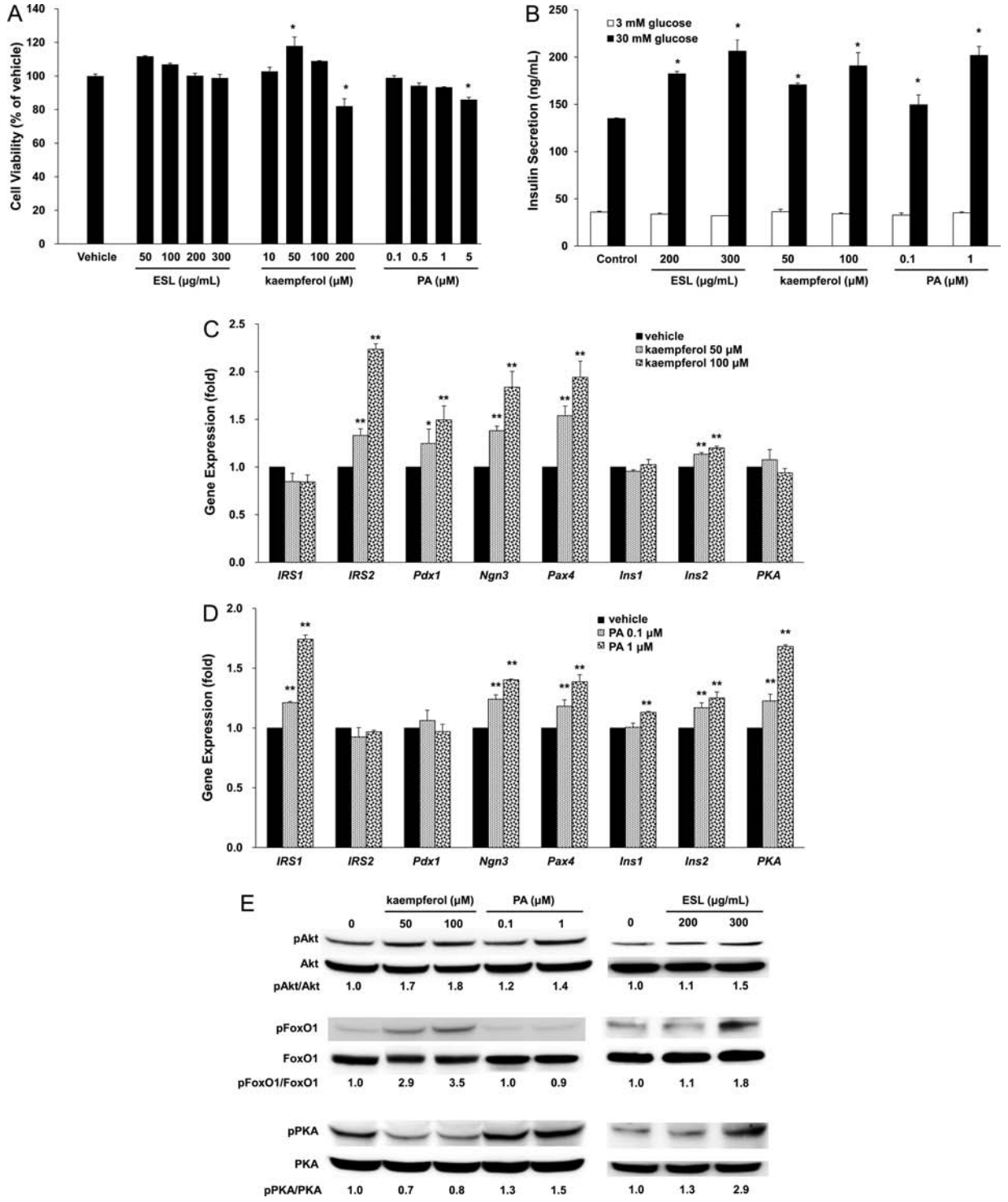

Figure 6. Effects of kaempferol and PA in pancreatic MIN6 cells. (A) Cytotoxicity of ESL, kaempferol, and PA in MIN6 cells. (∗) $p < 0.05$ versus the media alone treated group. Kaempferol 100 μM = 28.6 μg/mL; PA 5 μM = 2.97 μg/mL. (B) Effects of ESL, kaempferol, and PA on glucose-induced insulin secretion in MIN6 cells. (∗) $p < 0.05$ versus the glucose alone treated group. (C, D) Effects of kaempferol and PA on relative mRNA levels of insulin secretion-related genes in MIN6 cells. MIN6 cells were incubated with or without compounds for 48 h. The mRNA levels were measured by real-time qRT-PCR and normalized using *GAPDH* as a reference gene. Data from MIN6 cells are expressed as mean ± SD values of three independent experiments performed in duplicate. (∗) $p < 0.05$ and (∗∗) $p < 0.01$ versus vehicle. (E) Effects of kaempferol, PA, and ESL on protein expression of Akt, FoxO1, PKA, and their phosphorylated forms in MIN6 cells. PA, pheophorbide *a*.

interplay between the liver and adipose tissue in HFD-induced obese mice.[40] From these results, we found that the action mechanism of ESL in the liver and adipose tissue is similar to that of luteolin. In the same vein, we speculate that the improvement of glucose homeostasis by KGs in ESL-treated *db*/*db* mice may be associated with IRS-mediated insulin signaling and lipid accumulation in liver via inhibition of adipogenesis and stimulation of fat oxidation in WAT.

Next, we investigated the activity and gene expression of hepatic glucose-regulating enzymes, glucokinase (GK),

DOI: 10.1021/acs.jafc.5b01639
J. Agric. Food Chem. 2015, 63, 7198−7210

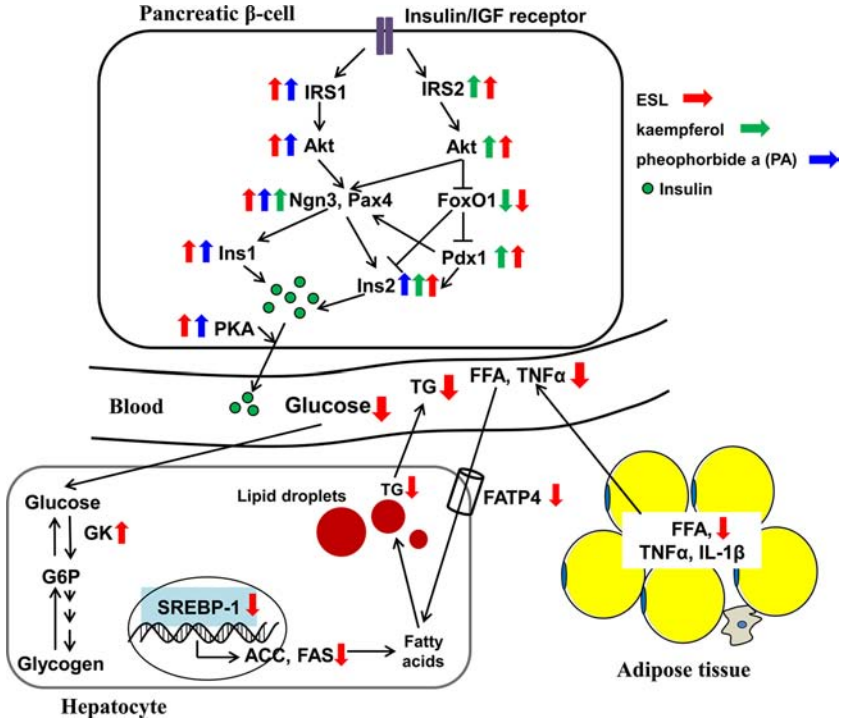

Figure 7. Possible molecular mechanisms of antidiabetic effect by ESL, kaempferol, and pheophorbide *a* (PA). ESL improved glucose homeostasis in diabetic *db*/*db* mice by enhancing *β*-cell survival and insulin secretion via IRS-mediated insulin signaling, suppressing SREBP-1-mediated lipogenesis in the liver, and decreasing inflammatory cytokines and FFA to improve insulin sensitivity.

glucose-6-phosphatase (G6Pase), and phosphoenolpyruvate carboxykinase (PEPCK). The hepatic enzyme activity and mRNA level of GK decreased in the *db*/*db* group, compared to the *db*/+ group (Figure 4E,F). The decreased enzyme activity and mRNA level of GK were significantly restored by ESL treatment (Figure 4E,F); however, ESL did not alter G6Pase and PEPCK activity and gene expression levels (Figure 4E,F). Hepatic GK plays a major role in controlling glucose utilization.[41] Low hepatic GK activity in diabetic mice leads to impaired insulin secretion in response to glucose.[42] Thus, the activation of glucose via increased hepatic GK activity is associated with improved hepatic insulin sensitivity in ESL-treated *db*/*db* mice.

ESL Inhibited Inflammation in WAT. Inflammation contributes to the pathogenesis of T2DM and its associated complications. Chronic inflammation is associated with visceral obesity and insulin resistance, which is characterized by the production of adipocytokines, including tumor necrosis factor *α* (TNF*α*), interleukin (IL)-1, IL-6, leptin, and adiponectin.[43] TNF*α* is overexpressed and mediates insulin resistance in obese animal models.[43] Secretion of inflammatory cytokines, such as IL-1*β* and TNF*α*, by adipose tissue macrophages impairs insulin secretion[44] and inhibits insulin action in adipocytes.[45] In this study, the gene expressions of *TNFα*, *IL-1β*, and *IL-6* in WAT of the *db*/*db* group were markedly higher than those of the *db*/+ group; however, the mRNA levels of *TNFα* and *IL-1β* but not *IL-6* were significantly decreased in the *db*/*db*-ESL group (Figure 5A). Plasma TNF*α* levels were also decreased by ESL supplementation (Figure 5B). This anti-inflammatory action of ESL in WAT may improve insulin secretion and sensitivity.

Kaempferol and PA Improved Insulin Secretion in MIN6 Cells. ESL primarily contained KGs and pheophorbides (Figure 1A). Kaempferol (3,4′,5,7-tetrahydroxyflavone) is an aglycone of KGs, and PA is a main component among pheophorbides, which are the products of chlorophyll. Deglycosylation of flavone glycosides increases absorption of the dietary flavone, aglycone, in vivo. The anti-inflammatory activity of dietary flavones is higher than that of their glycosides in vitro.[46] To clarify the mechanisms of ESL-induced improvement in insulin sensitivity and suppression of lipid accumulation in *db*/*db* mice, we investigated the antidiabetic effects of the major components, kaempferol and PA, and their mechanisms in MIN6 pancreatic *β*-cells.

ESL and kaempferol did not exert cytotoxicity up to 300 *μ*g/mL and 100 *μ*M (28.6 *μ*g/mL), respectively, in MIN6 cells; however, PA was cytotoxic at the relatively low concentration of 5 *μ*M (2.97 *μ*g/mL) (Figure 6A). Treatment with 200 and 300 *μ*g/mL of ESL significantly increased high glucose (30 mM)-induced insulin secretion in MIN6 cells (Figure 6B). Treatment with kaempferol (50 and 100 *μ*M) and PA (0.1 and 1 *μ*M) did not exert cytotoxicity and also increased insulin secretion in a dose-dependent manner (Figure 6B).

Next, we investigated whether kaempferol and PA influenced the expression of genes associated with pancreatic function in MIN6 cells. Treatment with 50 or 100 *μ*M kaempferol enhanced the mRNA levels of *IRS2*, but not *IRS1* (Figure 6C). Disruption of IRS2 impairs both peripheral insulin signaling and pancreatic *β*-cell function and causes T2DM.[47] IRS2 mediates PI3K/Akt signaling, and Akt-mediated FoxO1 phosphorylation promotes *β*-cell survival via the expression of Ngn3, Pax4, and Pdx1. Kaempferol was previously reported to improve pancreatic *β*-cell viability and insulin secretion through the modulation of Pdx1 protein expression.[48] Additionally, FoxO1-silenced MIN6 cells displayed increased basal *Ins2* gene expression.[33] This study demonstrated that the effects of kaempferol are initiated by IRS2 induction. Kaempferol also increased Akt and FoxO1 phosphorylation (Figure 6E). Kaempferol treatment induced the gene expression of *Pdx1*, *Ngn3*, *Pax4*, and *Ins2*, but not *Ins1* (Figure 6C). This may be related to the degradation of phosphorylated FoxO1.

DOI: 10.1021/acs.jafc.5b01639
J. Agric. Food Chem. 2015, 63, 7198−7210

Thus, kaempferol improved β-cell survival and proliferation through IRS2-related signaling via FoxO1.

PA, a product of chlorophyll breakdown, has anticancer, antioxidant, and virucidal activities.[20,29] In contrast to the effect of *IRS1* and *IRS2* gene expression by kaempferol, treatment with 0.1 or 1 μM PA induced *IRS1* expression, but not that of *IRS2* (Figure 6D). PA also increased *Ngn3*, *Pax4*, *Ins1*, *Ins2*, and *PKA* gene expression (Figure 6D) and induced Akt and PKA but not FoxO1 phosphorylation (Figure 6E). PKA, a mediator of the second-messenger cAMP, plays an important role in β-cell function. These results suggest that PKA is involved in the up-regulation of pro-insulin processing by PA in MIN6 cells. Therefore, PA increased the β-cell survival-related gene expression, including *Ngn3* and *Pax4*, via enhancing Akt phosphorylation. To conclude, PA improved both β-cell proliferation and insulin secretion through IRS1-mediated signaling. Above all, this is the first report describing the antidiabetic effects of PA in pancreatic β-cells.

Taken together, kaempferol and PA were induced insulin secretion via different pathways; kaempferol improved β-cell survival and proliferation through IRS2-related PI3K/Akt signaling via FoxO1, whereas PA improved both β-cell proliferation and insulin secretion through up-regulation of the IRS1-mediated PI3K/Akt pathway with PKA. Furthermore, ESL containing KGs and pheophorbides also enhanced phosphorylation of Akt, FoxO1, and PKA (Figure 7). Thus, both kaempferol and PA could contribute to the antidiabetic effects of ESL.

In summary, this study established the mechanisms of the antidiabetic effects and active components of soy leaf ethanol extracts. ESL improved diabetes-associated phenotypes, including glucose tolerance, glucose, HbA1c, and HOMA-IR. These effects may be induced by improved β-cell function in the pancreas and reduced lipid accumulation in the liver. ESL increased pancreatic *IRS1*, *IRS2*, *Pdx1*, *Ngn3*, and *Pax4* gene expression. Additionally, ESL decreased *FoxO1* gene expression and increased FoxO1 phosphorylation. Finally, ESL increased *Ins1* and *Ins2* gene expression. Importantly, KGs and PA were identified as the active components of ESL. Kaempferol improved β-cell survival and proliferation via IRS2 signaling through FoxO1, whereas PA increased insulin secretion through IRS1-related signaling and PKA in MIN6 cells. ESL decreased lipogenesis-related gene expression in the liver, including *SREBP-1*, *ACC1*, *FAS*, and *FATP4*. Furthermore, SREBP-1 and FAS protein expression was also decreased by ESL supplementation. Additionally, inflammatory cytokine gene expression, including *TNFα* and *IL-1β*, was suppressed following ESL treatment. Plasma TNFα levels were also decreased by ESL. The suppression of lipogenesis and cytokines by ESL supplementation could contribute to improved insulin sensitivity. Taken together, soy leaves may be a good component for the development of antidiabetic health foods.

■ ASSOCIATED CONTENT

Supporting Information

The Supporting Information is available free of charge on the ACS Publications website at DOI: 10.1021/acs.jafc.5b01639.

Chemical structure elucidation of kamepferol glycosides (KGs) **1**−**5** and pheophorbide *a* (PA) (Tables S1 and S2; Figure S1); and quantitative analysis of compounds **1**, **2**, and **7** (Table S3) (PDF)

■ AUTHOR INFORMATION

Corresponding Author

*(T.-S.J.) Mail: Industrial Biomaterials Research Center, Korea Research Institute of Bioscience and Biotechnology (KRIBB), 125 Gwahak-ro, Yuseong, Daejeon 305-806, Republic of Korea. Phone: +82-42-860-4558. Fax: +82-42-861-2675. E-mail: tsjeong@kribb.re.kr.

Funding

This research was supported by the Agricultural Biotechnology Development Program (No. 111064-3) and High Value-added Food Technology Development Program (No. 313044-3) funded by the Ministry of Agriculture, Food and Rural Affairs, Republic of Korea.

Notes

The authors declare no competing financial interest.

■ ABBREVIATIONS USED

ACC1: acetyl-CoA carboxylase
CREB: cAMP-response element-binding protein
ESL: ethanol extract of soy leaves
FAS: fatty acid synthase
FATP4: fatty acid transport protein 4
FFA: free fatty acid
FoxO1: forkhead box protein O1
GK: glucokinase
G6Pase: glucose-6-phosphatase
GOT: glutamate oxaloacetate transaminase
GPT: glutamate pyruvate transaminase
H&E: hematoxylin and eosin
HbA1c: glycated hemoglobin
IHC: immunohistochemistry
IL: interleukin
Ins1: insulin I
Ins2: insulin II
IRS: insulin receptor substrate
KGs: kaempferol glycosides
MafA: V-maf musculoaponeurotic fibrosarcoma oncogene homologue A
Ngn3: neurogenin 3
OGTT: oral glucose tolerance test
PA: pheophorbide a
Pax4: paired box 4
Pdx1: pancreatic and duodenal homeobox 1
PEPCK: phosphoenolpyruvate carboxykinase
PI3K: phosphatidyl inositol-3 kinase
PKA: protein kinase A
SREBP-1: sterol regulatory element-biding transcription factor 1
TC: total cholesterol
TG: triglyceride
TNFα: tumor necrosis factor α
WAT: white adipose tissue

■ REFERENCES

(1) Min, H. K. Clinical characteristics of diabetes in Korea. *Diabetes Metab. J.* **1992**, *16*, 163−174 (in Korean).

(2) Kim, D. J.; Song, K. E.; Park, J. W.; Cho, H. K.; Lee, K. W.; Huh, K. B. Clinical characteristics of Korean type 2 diabetic patients in 2005. *Diabetes Res. Clin. Pract.* **2007**, *77*, S252−257.

(3) Kim, C. H.; Kim, H. K.; Kim, E. H.; Bae, S. J.; Park, J. Y. Relative contributions of insulin resistance and β-cell dysfunction to the development of Type 2 diabetes in Koreans. *Diabetes Med.* **2013**, *30*, 1075−1079.

DOI: 10.1021/acs.jafc.5b01639
J. Agric. Food Chem. 2015, 63, 7198−7210

(4) Donath, M. Y. Targeting inflammation in the treatment of type 2 diabetes: time to start. *Nat. Rev. Drug Discovery* **2014**, *13*, 465−476.
(5) Nandi, A.; Kitamura, Y.; Kahn, C. R.; Accili, D. Mouse models of insulin resistance. *Physiol. Rev.* **2004**, *84*, 623−647.
(6) Burks, D. J.; White, M. F. IRS proteins and beta-cell function. *Diabetes* **2001**, *50*, S140−145.
(7) Buteau, J.; Accili, D. Regulation of pancreatic beta-cell function by the forkhead protein FoxO1. *Diabetes, Obes. Metab.* **2007**, *9* (Suppl. 2), 140−146.
(8) Ho, H. M.; Leung, L. K.; Chan, F. L.; Huang, Y.; Chen, Z. Y. Soy leaf lowers the ratio of non-HDL to HDL cholesterol in hamsters. *J. Agric. Food Chem.* **2003**, *51*, 4554−4558.
(9) Kim, J. E.; Jeon, S. M.; Park, K. H.; Lee, W. S.; Jeong, T. S.; McGregor, R. A.; Choi, M. S. Does *Glycine max* leaves or *Garcinia cambogia* promote weight-loss or lower plasma cholesterol in overweight individuals: a randomized control trial. *Nutr. J.* **2011**, *10*, 94.
(10) Ho, H. M.; Chen, R.; Huang, Y.; Chen, Z. Y. Vascular effects of a soy leaves (*Glycine max*) extract and kaempferol glycosides in isolated rat carotid arteries. *Planta Med.* **2002**, *68*, 487−491.
(11) Yuk, H. J.; Lee, J. H.; Curtis-Long, M. J.; Lee, J. W.; Kim, Y. S.; Ryu, H. W.; Park, C. G.; Jeong, T. S.; Park, K. H. The most abundant polyphenol of soy leaves, coumestrol, displays potent α-glucosidase inhibitory activity. *Food Chem.* **2011**, *126*, 1057−1063.
(12) Yuk, H. J.; Curtis-Long, M. J.; Ryu, H. W.; Jang, K. C.; Seo, W. D.; Kim, J. Y.; Kang, K. Y.; Park, K. H. Pterocarpan profiles for soybean leaves at different growth stages and investigation of their glycosidase inhibitions. *J. Agric. Food Chem.* **2011**, *59*, 12683−12690.
(13) Choi, M. S.; Ryu, R.; Seo, Y. R.; Jeong, T. S.; Shin, D. H.; Park, Y. B.; Kim, S. R.; Jung, U. J. The beneficial effect of soybean (*Glycine max* (L.) Merr.) leaf extracts in adults with prediabetes: a randomized placebo controlled trial. *Food Funct.* **2014**, *5*, 1621−1630.
(14) Zang, Y.; Sato, H.; Igarashi, K. Anti-diabetic effects of a kaempferol glycoside-rich fraction from unripe soybean (Edamame, *Glycine max* L. Merrill. 'Jindai') leaves on KK-A^{y} mice. *Biosci., Biotechnol., Biochem.* **2011**, *75*, 1677−1684.
(15) Zang, Y.; Zhang, L.; Igarashi, K.; Yu, C. The anti-obesity and anti-diabetic effects of kaempferol glycosides from unripe soybean leaves in high-fat-diet mice. *Food Funct.* **2015**, *6*, 834−841.
(16) Kim, U. H.; Yoon, J. H.; Li, H.; Kang, J. H.; Ji, H. S.; Park, K. H.; Shin, D. H.; Park, H. Y.; Jeong, T. S. Pterocarpan-enriched soy leaf extract ameliorates insulin sensitivity and pancreatic β-cell proliferation in type 2 diabetic mice. *Molecules* **2014**, *19*, 18493−18510.
(17) Ho, H. M.; Chen, R. Y.; Leung, L. K.; Chan, F. L.; Huang, Y.; Chen, Z. Y. Difference in flavonoid and isoflavone profile between soybean and soy leaf. *Biomed. Pharmacother.* **2002**, *56*, 289−295.
(18) Murai, Y.; Takahashi, R.; Rodas, F. R.; Kitajima, J.; Iwashina, T. New flavonol triglycosides from the leaves of soybean cultivars. *Nat. Prod Commun.* **2013**, *8*, 453−456.
(19) Cho, K. L.; Lee, H. S.; Kang, I. J.; Won, M. H.; You, S. G. Antioxidant properties of extract and fractions from *Enteromorpha prolifera*, a type of green seaweed. *Food Chem.* **2011**, *127*, 999−1006.
(20) Lai, C. S.; Mas, R. H. M. H.; Nair, J. K.; Mansor, S. M.; Navaratnam, V. Chemical constituents and in vitro anticancer activity of *Typhonium flagelliforme* (Araceae). *J. Ethnopharmacol.* **2010**, *127*, 486−494.
(21) Hynninen, P. A.; Wasielewski, M. R.; Katz, J. J. Chlorophylls. VI. Epimerization and enolization of chlorophyll a and its magnesium-free derivatives. *Acta Chem. Scand.* **1979**, *33*, 637−648.
(22) Saha, P. K.; Reddy, V. T.; Konopleva, M.; Andreeff, M.; Chan, L. The triterpenoid 2-cyano-3,12-dioxooleana-1,9-dien-28-oic-acid methyl ester has potent anti-diabetic effects in diet-induced diabetic mice and lepr$^{db/db}$ mice. *J. Biol. Chem.* **2010**, *285*, 40581−40592.
(23) Li, H.; Kang, J. H.; Han, J. M.; Cho, M. H.; Chung, Y. J.; Park, K. H.; Shin, D. H.; Park, H. Y.; Choi, M. S.; Jeong, T. S. Anti-obesity effects of soy leaf via regulation of adipogenic transcription factor and fat oxidation in diet-induced obese mice and 3T3-L1 adopocytes. *J. Med. Food* **2015**, *18*, 899−908.
(24) Folch, J.; Lees, M.; Sloane Stanley, G. H. A simple method for the isolation and purification of total lipides from animal tissues. *J. Biol. Chem.* **1957**, *39*, 101−108.
(25) Benninger, R. K.; Piston, D. W. Cellular communication and heterogeneity in pancreatic islet insulin secretion dynamics. *Trends Endocrinol. Metab.* **2014**, *25*, 399−406.
(26) Katsuda, Y.; Ohta, T.; Shinohara, M.; Bin, T.; Yamada, T. Diabetic mouse models. *Open J. Anim. Sci.* **2013**, *3*, 334−342.
(27) Ferrannini, E. The stunned beta cell: a brief history. *Cell Metab.* **2010**, *11*, 349−352.
(28) Al-Hasani, K.; Pfeifer, A.; Courtney, M.; Ben-Othman, N.; Gjernes, E.; Vieira, A.; Druelle, N.; Avolio, F.; Ravassard, P.; Leuckx, G.; Lacas-Gervais, S.; Ambrosetti, D.; Benizri, E.; Hecksher-Sorensen, J.; Gounon, P.; Ferrer, J.; Gradwohl, G.; Heimberg, H.; Mansouri, A.; Collombat, P. Adult duct-lining cells can reprogram into β-like cells able to counter repeated cycles of toxin-induced diabetes. *Dev. Cell* **2013**, *26*, 86−100.
(29) Swales, N.; Martens, G. A.; Bonné, S.; Heremans, Y.; Borup, R.; Van de Casteele, M.; Ling, Z.; Pipeleers, D.; Ravassard, P.; Nielsen, F.; Ferrer, J.; Heimberg, H. Plasticity of adult human pancreatic duct cells by neurogenin3-mediated reprogramming. *PLoS One* **2012**, *7*, e37055.
(30) Zhou, Q.; Brown, J.; Kanarek, A.; Rajagopal, J.; Melton, D. A. *In vivo* reprogramming of adult pancreatic exocrine cells to beta-cells. *Nature* **2008**, *455*, 627−632.
(31) Courtney, M.; Pfeifer, A.; Al-Hasani, K.; Gjernes, E.; Vieira, A.; Ben-Othman, N.; Collombat, P. In vivo conversion of adult α-cells into β-like cells: a new research avenue in the context of type 1 diabetes. *Diabetes, Obes. Metab.* **2011**, *13*, 47−52.
(32) Meur, G.; Qian, Q.; da Silva Xavier, G.; Pullen, T. J.; Tsuboi, T.; McKinnon, C.; Fletcher, L.; Tavaré, J. M.; Hughes, S.; Johnson, P.; Rutter, G. A. Nucleo-cytosolic shuttling of FoxO1 directly regulates mouse Ins2 but not Ins1 gene expression in pancreatic beta cells (MIN6). *J. Biol. Chem.* **2011**, *286*, 13647−13656.
(33) Kitamura, T. The role of FOXO1 in β-cell failure and type 2 diabetes mellitus. *Nat. Rev. Endocrinol.* **2013**, *9*, 615−623.
(34) Furuya, F.; Shimura, H.; Asami, K.; Ichijo, S.; Takahashi, K.; Kaneshige, M.; Oikawa, Y.; Aida, K.; Endo, T.; Kobayashi, T. Ligand-bound thyroid hormone receptor contributes to reprogramming of pancreatic acinar cells into insulin-producing cells. *J. Biol. Chem.* **2013**, *288*, 16155−16166.
(35) Brun, T.; Hu He, K. H.; Lupi, R.; Boehm, B.; Wojtusciszyn, A.; Sauter, N.; Donath, M.; Marchetti, P.; Maedler, K.; Gauthier, B. R. The diabetes-linked transcription factor Pax4 is expressed in human pancreatic islets and is activated by mitogens and GLP-1. *Hum. Mol. Genet.* **2008**, *17*, 478−489.
(36) Brown, M. S.; Goldstein, J. L. The SREBP pathway: regulation of cholesterol metabolism by proteolysis of a membrane-bound transcription factor. *Cell* **1997**, *89*, 331−340.
(37) Bécard, D.; Hainault, I.; Azzout-Marniche, D.; Bertry-Coussot, L.; Hisatake, K.; Kako, K.; Mukai, H.; Kasuya, Y.; Fukamizu, A. Adenovirus-mediated overexpression of sterol regulatory element binding protein-1c mimics insulin effects on hepatic gene expression and glucose homeostasis in diabetic mice. *Diabetes* **2001**, *50*, 2425−2430.
(38) Ferré, P.; Foufelle, F. Hepatic steatosis: a role for de novo lipogenesis and the transcription factor SREBP-1c. *Diabetes, Obes. Metab.* **2010**, *12* (Suppl.2), 83−92.
(39) Ide, T.; Shimano, H.; Yahagi, N.; Matsuzaka, T.; Nakakuki, M.; Yamamoto, T.; Nakagawa, Y.; Takahashi, A.; Suzuki, H.; Sone, H.; Toyoshima, H.; Fukamizu, A.; Yamada, N. SREBPs suppress IRS-2-mediated insulin signalling in the liver. *Nat. Cell Biol.* **2004**, *6*, 351−357.
(40) Kwon, E. Y.; Jung, U. J.; Park, T.; Yun, J. W.; Choi, M. S. Luteolin attenuates hepatic steatosis and insulin resistance through the interplay between the liver and adipose tissue in mice with diet-induced obesity. *Diabetes* **2015**, *64*, 1658−1669.
(41) Postic, C.; Shiota, M.; Niswender, K. D.; Jetton, T. L.; Chen, Y.; Moates, J. M.; Shelton, K. D.; Lindner, J.; Cherrington, A. D.; Magnuson, M. A. Dual roles for glucokinase in glucose homeostasis as determined by liver and pancreatic β-cell-specific gene knock-outs using Cre recombinase. *J. Biol. Chem.* **1999**, *274*, 305−315.

DOI: 10.1021/acs.jafc.5b01639
J. Agric. Food Chem. 2015, 63, 7198−7210

(42) Iynedjian, P. B.; Gjinovci, A.; Renold, A. E. Stimulation by insulin of glucokinase gene transcription in liver of diabetic rats. *J. Biol. Chem.* **1988**, *263*, 740−744.
(43) Xu, H.; Barnes, G. T.; Yang, Q.; Tan, G.; Yang, D.; Chou, C. J.; Sole, J.; Nichols, A.; Ross, J. S.; Tartaglia, L. A.; Chen, H. Chronic inflammation in fat plays a crucial role in the development of obesity-related insulin resistance. *J. Clin. Invest.* **2003**, *112*, 1821−1830.
(44) Dandona, P.; Aljada, A.; Chaudhuri, A.; Mohanty, P.; Garg, R. Metabolic syndrome: a comprehensive perspective based on interactions between obesity, diabetes, and inflammation. *Circulation* **2005**, *111*, 1448−1454.
(45) Odegaard, J. I.; Chawla, A. Connecting type 1 and type 2 diabetes through innate immunity. *Cold Spring Harbor Perspect. Med.* **2012**, *2*, a007724.
(46) Hostetler, G.; Riedl, K.; Cardenas, H.; Diosa-Toro, M.; Arango, D.; Schwartz, S.; Doseff, A. I. Flavone deglycosylation increases their anti-inflammatory activity and absorption. *Mol. Nutr. Food Res.* **2012**, *56*, 558−569.
(47) Withers, D. J.; Gutierrez, J. S.; Towery, H.; Burks, D. J.; Ren, J. M.; Previs, S.; Zhang, Y.; Bernal, D.; Pons, S.; Shulman, G. I.; Bonner-Weir, S.; White, M. F. Disruption of IRS-2 causes type 2 diabetes in mice. *Nature* **1998**, *391*, 900−904.
(48) Zhang, Y.; Zhen, W.; Maechler, P.; Liu, D. Small molecule kaempferol modulates PDX-1 protein expression and subsequently promotes pancreatic β-cell survival and function via CREB. *J. Nutr. Biochem.* **2013**, *24*, 638−646.

DOI: 10.1021/acs.jafc.5b01639
J. Agric. Food Chem. 2015, 63, 7198−7210

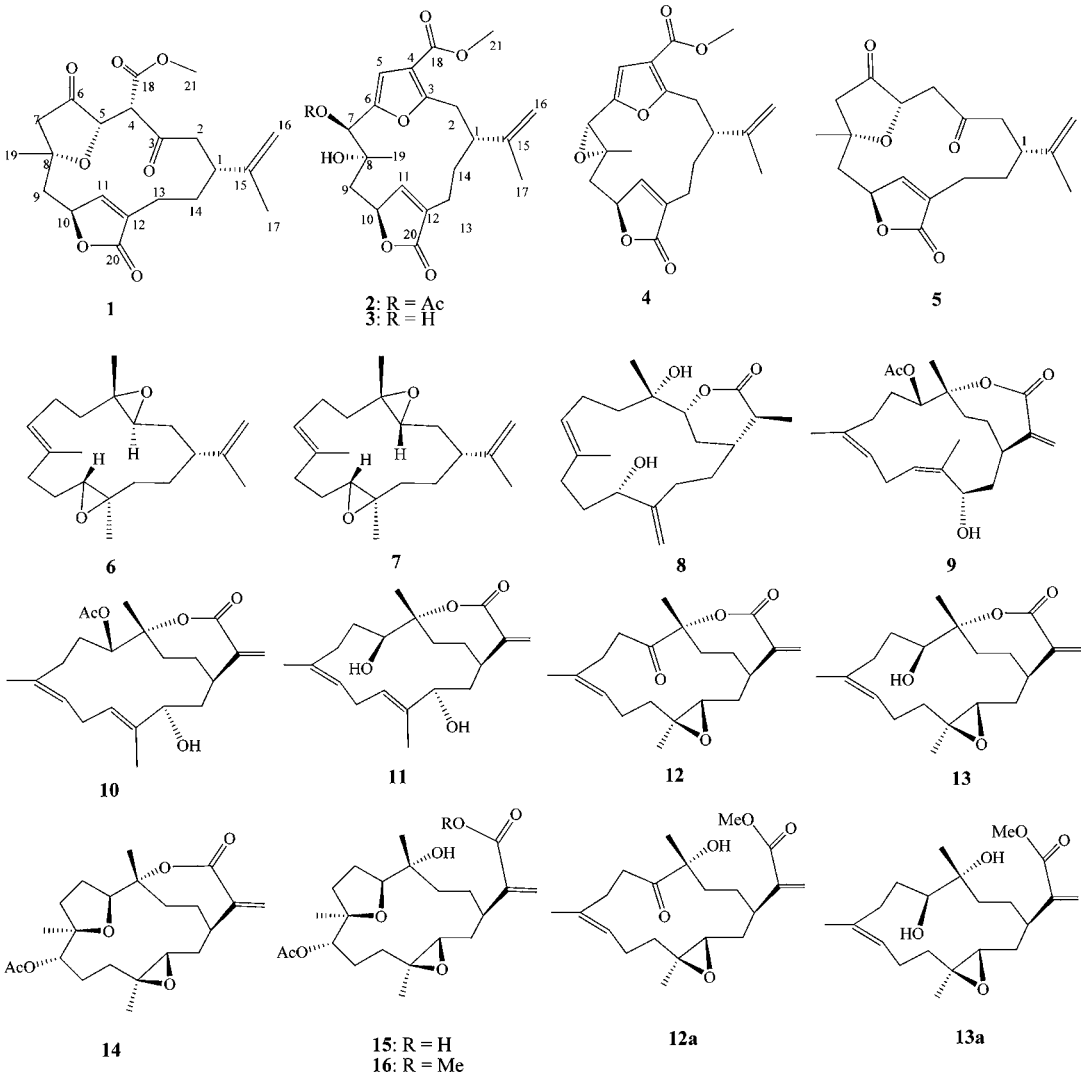

Figure 1. Structures of metabolites **1**−**16**, **12a**, and **13a**.

(Figure 1) were tested for anti-inflammatory activity to inhibit the protein expressions of inducible nitric oxide synthetase (iNOS) and cyclooxygenase-2 (COX-2). The structural determination and anti-inflammatory activities, in addition to the structure−activity relationships, of the isolates are reported herein.

MATERIALS AND METHODS

General Method. Infrared (IR) spectra were obtained on a Fourier-transform IR spectrophotometer (Varian Digilab FTS 1000). ^{1}H and ^{13}C NMR spectra were recorded on a Varian Unity INOVA 500 FT-NMR instrument at 500 and 125 MHz, respectively. Optical rotations were determined by a digital polarimeter (Jasco P-1010). Electrospray ionization mass spectrometry (ESIMS) analyses were performed on an APEX II Instrument (Bruker). Single-crystal X-ray analyses were performed on a Bruker APEX DUO diffractometer. Gravity column chromatography was performed with 230−400 mesh silica gel (Merck). TLC analyses were conducted on 0.2 mm thick precoated Kieselgel 60 F254 plates (Merck), and visualization of TLC spots was conducted by spraying the plate with a 10% aqueous H_2SO_4 solution followed by heating. High-performance liquid chromatography (HPLC) was performed using a system consisting of a Hitachi L-7100 pump and a Rheodyne 7725 injection port. A preparative normal phase column (φ 21.2 mm × 25 cm, silica gel 60, 5 μm) and a Supelco C_{18} column (φ 21.2 mm × 25 cm, 5 μm) were used for HPLC.

Animal Material. The two light yellow cultured soft corals *S. sandensis* and *S. flexibilis* were initially collected from the wild and subsequently grown for 8 years in an 80 ton cultivation tank located in the National Museum of Marine Biology & Aquarium. The tank was a flow-through seawater system, and deliberate feeding was not required. This was the first successful system that has been reported for the farming of *S. sandensis*. The specimens were collected by hand in January 2013, frozen immediately, and kept frozen until extraction. Two soft corals were identified by one of the authors (C.-F.D.). Voucher specimens were deposited in the National Museum of Marine Biology & Aquarium (Specimens 2013CSC-1 and 2013CSC-2).

Extraction and Isolation. The frozen *S. sandensis* material (2.8 kg, wet weight) was freeze-dried, and the resulting material (320 g) was then minced and extracted exhaustively with EtOAc (6 × 1.5 L). The EtOAc extract was evaporated under reduced pressure to afford a residue (20.5 g), and the residue was subjected to column chromatography on silica gel, using *n*-hexane, an *n*-hexane/EtOAc mixture of increasing polarity, and finally pure acetone to yield 12 fractions: Fr-1 (eluted with *n*-hexane/EtOAc, 100:1), Fr-2 (eluted with *n*-hexane/EtOAc, 50:1), Fr-3 (eluted with *n*-hexane/EtOAc, 30:1), Fr-4 (eluted with *n*-hexane/EtOAc, 20:1), Fr-5 (eluted with *n*-hexane/EtOAc, 10:1), Fr-6 (eluted with *n*-hexane/EtOAc, 8:1), Fr-7 (eluted with *n*-hexane/EtOAc, 5:1), Fr-8 (eluted with *n*-hexane/EtOAc, 3:1), Fr-9 (eluted with *n*-hexane/EtOAc, 1:1), Fr-10 (eluted with *n*-hexane/

DOI: 10.1021/acs.jafc.5b01931
J. Agric. Food Chem. 2015, 63, 7211−7218

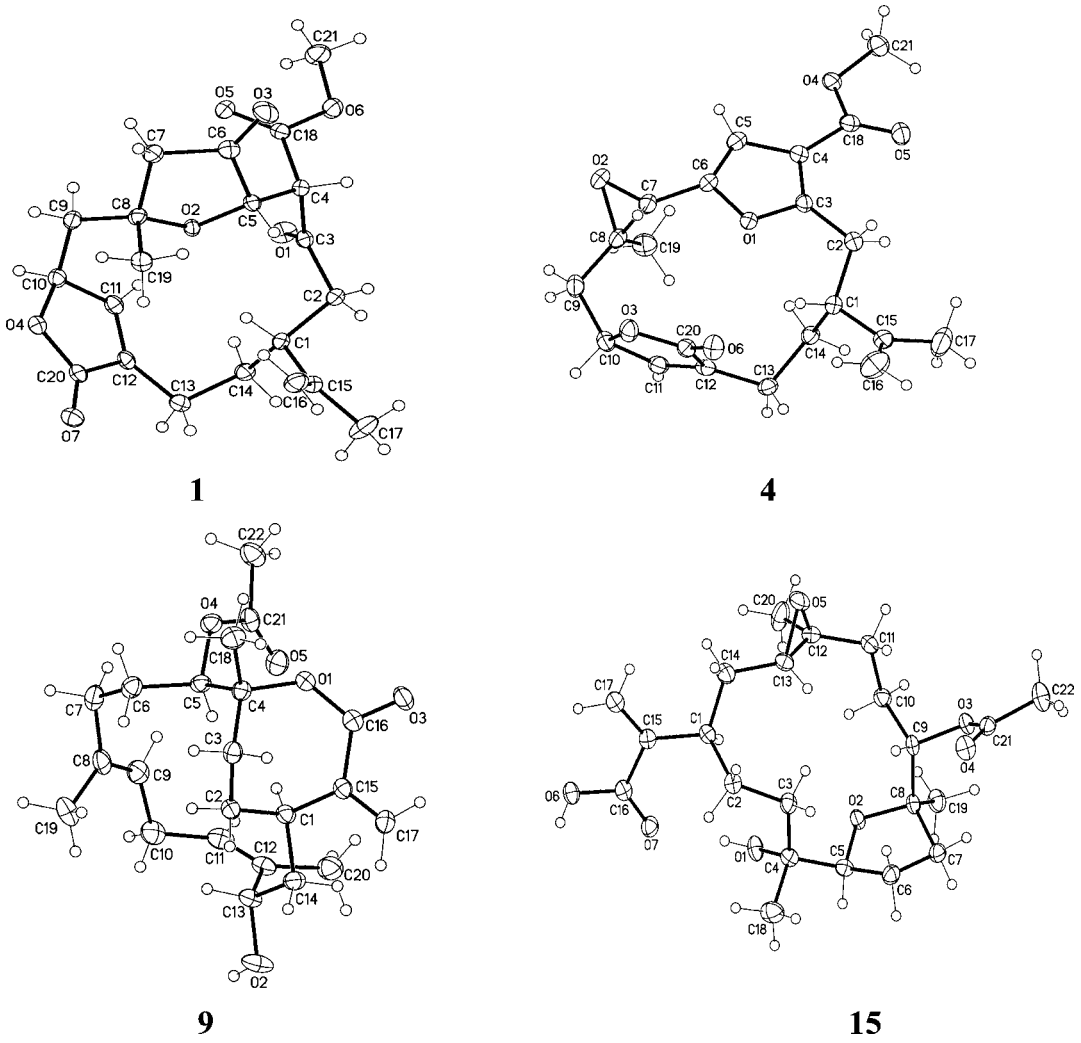

Figure 2. Molecular plots of **1**, **4**, **9**, and **15** with confirmed absolute configurations.

EtOAc, 1:2), Fr-11 (eluted with EtOAc), and Fr-12 (eluted with acetone). Fr-9 was further purified with silica gel (*n*-hexane/acetone, 3:1 to 2:1) to afford 10 subfractions (9A–9J). Subfraction 9E was then separated by normal-phase HPLC (*n*-hexane/acetone, 3:1) to obtain **4** (560 mg). Subfraction 9G was separated by normal-phase HPLC (*n*-hexane/EtOAc, 1:1) to afford **5** (1.2 mg) and **1** (10.2 mg). Fraction 10 was separated by normal-phase HPLC with gradient elution (*n*-hexane/acetone, 3:1 to 2:1) to yield five subfractions (10A–10E). Subfraction 10C was separated by reverse-phase HPLC (CH_3CN/H_2O, 7:3) to afford **2** (4.5 mg). Compound **3** (9.4 mg) was obtained from subfraction 10E using normal-phase HPLC (*n*-hexane/acetone, 1:1).

The frozen *S. flexibilis* (4.2 kg, wet weight) was freeze-dried, and the resulting material (450 g) was minced and extracted exhaustively with EtOAc (6 × 2 L). The EtOAc extract was evaporated under reduced pressure to afford a residue (30.5 g), and the residue was subjected to column chromatography on silica gel using *n*-hexane (H), an *n*-hexane/EtOAc (E) mixture of increasing polarity, and finally pure acetone to yield 13 fractions: Fr-1 (eluted with H/E, 100:1), Fr-2 (eluted with H/E, 50:1), Fr-3 (eluted with H/E, 30:1), Fr-4 (eluted with H/E, 20:1), Fr-5 (eluted with H/E, 10:1), Fr-6 (eluted with H/E, 8:1), Fr-7 (eluted with H/E, 5:1), Fr-8 (eluted with H/E, 3:1), Fr-9 (eluted with H/E, 2:1), Fr-10 (eluted with H/E, 1:1), Fr-11 (eluted with H/E, 1:2), Fr-12 (eluted with EtOAc), and Fr-13 (eluted with acetone). By using acetone as the mobile phase, Fr-7 was purified by passage over a Sephadex LH-20 column to afford five subfractions (7A–7E). Subfraction 7C was separated by normal-phase HPLC (CH_2Cl_2/*n*-hexane/EtOAc, 2:2:0.5) to obtain **6** (3.0 mg) and **7** (10.2 mg). Fr-9 was separated by normal-phase HPLC (*n*-hexane/EtOAc, 2:3) to yield **12** (71.5 mg) and **14** (55.2 mg). Fr-10 was separated by normal-phase HPLC (*n*-hexane/acetone, 4:1) to afford **8** (3.2 mg), **13** (2150 mg), and **16** (105.3 mg). Fr-11 was separated by normal-phase HPLC with gradient elution (*n*-hexane/EtOAc, 1:2 to 1:3) to yield four subfractions (11A–11D). Subfraction 11A was separated by normal-phase HPLC (*n*-hexane/EtOAc, 2:3) to afford **9** (4.5 mg) and **10** (4.1 mg). Compound **11** (25.6 mg) was obtained from subfraction 11C using normal-phase HPLC (*n*-hexane/EtOAc, 1:1). Compound **15** (19.9 mg) was obtained from subfraction 11D using normal-phase HPLC (*n*-hexane/acetone, 2:1).

*4-Carbomethoxyl-10-epigyrosanoldie E (**1**).* Colorless needles: UV (MeOH) λ_{max} (log ε) 213 (3.87) nm; $[\alpha]^{25}_D$ −28.0 (*c* 0.5, $CHCl_3$); IR (neat) ν_{max} 2935, 1755, 1715, 1642, 1443, 1383, 1280 cm^{-1}; ^{13}C and ^1H NMR data in Table 1; ESIMS *m*/*z* 413 $[M + Na]^+$; HRESIMS *m*/*z* 413.1571 $[M + Na]^+$ (calcd for $C_{21}H_{26}O_7Na$, *m*/*z* 413.1570).

*7-Acetylsinumaximol B (**2**).* White powder: UV (MeOH) λ_{max} (log ε) 235 (3.30), 260 (3.42), 290 (3.38) nm; $[\alpha]^{25}_D$ −56.0 (*c* 0.6, $CHCl_3$); IR (neat) ν_{max} 3480, 2948, 1749, 1715, 1645, 1610, 1569, 1441, 1228 cm^{-1}; ^{13}C and ^1H NMR data in Table 1; ESIMS *m*/*z* 455 $[M + Na]^+$; HRESIMS *m*/*z* 455.1675 $[M + Na]^+$ (calcd for $C_{23}H_{28}O_8Na$, *m*/*z* 455.1676).

*Diepoxycembrene B (**6**).* Colorless oil: $[\alpha]^{25}_D$ +28.0 (*c* 0.5, $CHCl_3$); IR (neat) ν_{max} 2964, 2927, 2864, 1644, 1453, 1382 cm^{-1}; ^{13}C and ^1H NMR data in Table 2; ESIMS *m*/*z* 327 $[M + Na]^+$; HRESIMS *m*/*z* 327.2295 $[M + Na]^+$ (calcd for $C_{20}H_{32}O_2Na$, *m*/*z* 327.2294).

DOI: 10.1021/acs.jafc.5b01931
J. Agric. Food Chem. 2015, 63, 7211–7218

Table 1. ^{1}H and ^{13}C NMR Data for 1 and 2

	1		2	
position	δ_H (J in hertz)[a]	δ_C (mult.)[b]	δ_H (J in hertz)[a]	δ_C (mult.)[b]
1	2.66 m	42.0 (CH)	2.18 m	44.0 (CH)
2	2.55 m; 2.45 m	45.1 (CH_2)	3.41 dd (14.5, 12.5); 2.73 dd (14.5, 2.0)	31.9 (CH_2)
3		202.5 (C)		161.1 (C)
4	3.97 d (3.5)	61.5 (CH)		116.2 (C)
5	4.26 d (3.5)	75.0 (CH)	6.66 s	109.5 (CH)
6		212.3 (C)		149.4 (C)
7	2.66 m; 2.39 m	50.0 (CH_2)	5.59 s	75.9 (CH)
8		79.9 (C)		72.6 (C)
9	2.58 m; 2.38 m	42.3 (CH_2)	2.60 dd (15.0, 4.0); 1.95 dd (14.5, 11.5)	43.1 (CH_2)
10	5.19 s	79.0 (CH)	4.94 d (11.0)	78.3 (CH)
11	7.16 s	151.9 (CH)	5.81 s	148.2 (CH)
12		130.4 (C)		133.7 (C)
13	2.38 m; 2.20 m	20.8 (CH_2)	2.33 m; 2.10 m	21.6 (CH_2)
14	2.04 m; 1.78 m	27.3 (CH_2)	1.84 m; 1.52 m	28.1 (CH_2)
15		145.8 (C)		146.0 (C)
16	4.79 s; 4.61 s	113.0 (CH_2)	4.84 s; 4.80 s	112.6 (CH_2)
17	1.67 s	18.0 (CH_3)	1.77 s	19.0 (CH_3)
18		167.8 (C)		163.7 (C)
19	1.31 s	24.9 (CH_3)	1.48 s	21.0 (CH_3)
20		174.4 (C)		173.2 (C)
21	3.74 s	52.4 (CH_3)	3.85 s	51.7 (CH_3)
Ac				169.4 (C)
			2.16 s	21.0 (CH_3)

[a]At 500 MHz in $CDCl_3$. [b]At 125 MHz in $CDCl_3$.

*Dihydromanaarenolide I (**8**).* White powder: $[\alpha]^{25}_D$ −20.5 (*c* 0.6, $CHCl_3$); IR (neat) ν_{max} 3436, 2930, 2862, 1710, 1455, 1374 cm^{-1}; ^{13}C and ^{1}H NMR data in Table 2; ESIMS *m*/*z* 359 $[M + Na]^+$; HRESIMS *m*/*z* 359.2200 $[M + Na]^+$ (calcd for $C_{20}H_{32}O_4Na$, *m*/*z* 359.2198).

*Isosinulaflexiolide K (**9**).* Colorless needles" $[\alpha]^{25}_D$ −73.6 (*c* 0.1, $CHCl_3$); IR (neat) ν_{max} 3462, 2976, 2943, 2858, 1742, 1698, 1645, 1451, 1373, 1235 cm^{-1}; ^{13}C and ^{1}H NMR data in Table 2; ESIMS *m*/*z* 399 $[M + Na]^+$; HRESIMS *m*/*z* 399.2139 $[M + Na]^+$ (calcd for $C_{22}H_{32}O_5Na$, *m*/*z* 399.2142).

*Single-Crystal X-ray Analysis of **1**.*[11] The ethyl acetate solution was allowed to slowly evaporate to generate a suitable colorless crystal. Diffraction intensity data were obtained on a Bruker APEX DUO X-ray diffractometer using graphite-monochromated Cu Kα radiation (λ = 1.54178 Å). Crystal data for this compound: $C_{21}H_{26}O_7$ (formula weight 390.42), approximate crystal size of 0.40 mm × 0.40 mm × 0.40 mm, monoclinic, space group $P2_1$ (No. 4), T = 100(2) K, a = 9.1141(2) Å, b = 8.9035(2) Å, c = 12.2954(3) Å, V = 962.98(4) Å,^{3} Z = 2, D_{calcd} = 1.346 mg/m^3, F(000) = 416, and $\mu_{(MoK\alpha)}$ = 0.838 mm^{-1}. A total of 6772 reflections were collected in the θ range of 5.420–66.673°, with 2603 independent reflections [R(int) = 0.0210], and completeness to θ_{max} was 96.2%; semiempirical from equivalents of absorption correction was applied. The refinement method was full-matrix least-squares on F^2; the data, restraints, and parameters were 2603, 1, and 256, respectively. The goodness of fit on F^2 = 1.080. Final R indices [$I > 2\sigma(I)$] R_1 = 0.0266 and wR_2 = 0.0707. R indices (all data) R_1 = 0.0267 and wR_2 = 0.0707. The largest difference peak and hole were 0.185 and −0.190 e/Å^3, respectively; the absolute structure parameter was 0.04(5).

*Single-Crystal X-ray Analysis of **4**.*[11] The ethyl acetate solution was allowed to slowly evaporate to generate a suitable colorless crystal. Diffraction intensity data were obtained on a Bruker APEX DUO X-ray diffractometer using graphite-monochromated Cu Kα radiation (λ = 1.54178 Å). Crystal data for this compound: $C_{21}H_{24}O_6$ (formula weight of 372.40), approximate crystal size of 0.30 mm × 0.20 mm × 0.15 mm, monoclinic, space group $P2_1$ (No. 4), T = 100(2) K, a = 8.862(3) Å, b = 12.539(4) Å, c = 16.776(5) Å, V = 1864.1(10) Å,^{3} Z = 4, D_{calcd} = 1.327 mg/m^3, F(000) = 792, and $\mu_{(MoK\alpha)}$ = 0.800 mm^{-1}. A total of 6658 reflections were collected in the θ range of 5.646–66.464°, with 3026 independent reflections [R(int) = 0.0225], and completeness to θ_{max} was 94.7%; semiempirical from equivalents of absorption correction was applied. The refinement method was full-matrix least squares on F^2; the data, restraints, and parameters were 3026, 0, and 247, respectively. The goodness of fit on F^2 = 1.175. Final R indices [$I > 2\sigma(I)$] R_1 = 0.0330 and wR_2 = 0.0960. R indices (all data) R_1 = 0.0332 and wR_2 = 0.0963. The largest difference peak and hole were 0.347 and −0.261 e/Å^3, respectively; the absolute structure parameter was 0.12(5).

*Single-Crystal X-ray Analysis of **9**.*[11] The ethyl acetate solution was allowed to slowly evaporate to generate a suitable colorless crystal. Diffraction intensity data were obtained on a Bruker APEX DUO X-ray diffractometer using graphite-monochromated Cu Kα radiation (λ = 1.54178 Å). Crystal data for this compound: $C_{22}H_{32}O_5$ (formula weight of 376.47), approximate crystal size of 0.60 mm × 0.35 mm × 0.30 mm, monoclinic, space group $P2_1$ (No. 4), T = 100(2) K, a = 8.0404(2) Å, b = 14.3426(4) Å, c = 17.9352(6) Å, V = 2068.29(10) Å,^{3} Z = 4, D_{calcd} = 1.209 mg/m^3, F(000) = 816, and $\mu_{(MoK\alpha)}$ = 0.681 mm^{-1}. A total of 14442 reflections were collected in the θ range of 3.946–66.656°, with 3651 independent reflections [R(int) = 0.0225], and completeness to θ_{max} was 97.7%. Semiempirical from equivalents of absorption correction was applied. The refinement method was full-matrix least squares on F^2; the data, restraints, and parameters were 3651, 0, and 249, respectively. The goodness of fit on F^2 = 1.046. Final R indices [$I > 2\sigma(I)$] R_1 = 0.0263 and wR_2 = 0.0677. R indices (all data) R_1 = 0.0264 and wR_2 = 0.0678. The largest difference peak and hole were 0.164 and −0.128 e/Å^3, respectively; the absolute structure parameter was 0.09(3).

*Single-Crystal X-ray Analysis of **15**.*[11] The ethyl acetate solution was allowed to slowly evaporate to generate a suitable colorless crystal. Diffraction intensity data were obtained on a Bruker APEX DUO X-ray diffractometer using graphite-monochromated Cu Kα radiation (λ = 1.54178 Å). Crystal data for this compound: $C_{44}H_{68}O_{14}$ (formula weight of 820.98), approximate crystal size of 0.40 mm × 0.30 mm × 0.30 mm, monoclinic, space group $P2_1$ (No. 4), T = 100(2) K, a = 9.7079(6) Å, b = 23.0869(14) Å, c = 9.72692(6) Å, V = 2172.1(2) Å,^{3} Z = 2, D_{calcd} = 1.255 mg/m^3, F(000) = 888, and $\mu_{(MoK\alpha)}$ = 0.760 mm^{-1}. A total of 3825 reflections were collected in the θ range of 3.829–66.665°, with 3825 independent reflections [R(int) = 0.0334], and completeness to θ_{max} was 95.7%. Semiempirical from equivalents of absorption correction was applied. The refinement method was full-matrix least squares on F^2; the data, restraints, and parameters were 3825, 1, and 536, respectively. The goodness of fit on F^2 = 1.032. Final R indices [$I > 2\sigma(I)$] R_1 = 0.0289 and wR_2 = 0.0751. R indices (all data) R_1 = 0.0291 and wR_2 = 0.0752. The largest difference peak and hole were 0.180 and −0.227 e/Å^3, respectively; the absolute structure parameter was 0.14(8).

*Acetylation of **3**.* Ac_2O (0.1 mL) was added to a solution of **3** (4.0 mg) in pyridine (0.2 mL), and the mixture was stirred at room temperature. After 24 h, pyridine and excess Ac_2O were evaporated by adding EtOAc, and the residue was subjected to column chromatography over Si gel (*n*-hexane/EtOAc, 1:1) to yield acetyl derivative **2** (3.9 mg, 8%). The specific rotation [$[\alpha]^{25}_D$ −50.0 (*c* 0.05, $CHCl_3$)] and ^{1}H NMR spectrum were in full agreement with those of natural product **2**.

*Hydrolysis of **12**.* A solution of **12** (16.0 mg) was dissolved in a 5% methanolic NaOH solution (1.0 mL). After being stirred at room temperature for 12 h, the mixture was neutralized with diluted HCl (0.1 M) and evaporated. The resulting residue was extracted with $CHCl_3$. The $CHCl_3$ soluble layers were dried over anhydrous $NaSO_4$

DOI: 10.1021/acs.jafc.5b01931
J. Agric. Food Chem. 2015, 63, 7211−7218

Table 2. ^{1}H and ^{13}C NMR Data for 6, 8, and 9

	6		8		9	
position	δ_H (J in hertz)[a]	δ_c (mult.)[b]	δ_H (J in hertz)[a]	δ_c (mult.)[b]	δ_H (J in hertz)[a]	δ_c (mult.)[b]
1	2.07 m	44.9 (CH)	1.61 m	35.3 (CH)	2.43 m	31.8 (CH)
2	1.96 m; 1.42 m	33.0 (CH_2)	1.94 m; 1.34 m	27.6 (CH_2)	1.86 m; 1.17 m	29.3 (CH_2)
3	2.94 dd (8.5, 4.5)	61.2 (CH)	3.96 dd (11.5, 2.0)	84.6 (CH)	1.96 m; 1.80 m	33.0 (CH_2)
4		60.3 (C)		74.3 (C)		86.1 (C)
5	2.10 m; 1.36 m	38.1 (CH_2)	1.78 m; 1.62 m	38.4 (CH_2)	5.46 d (10.0)	71.4 (CH)
6	2.18 m	23.1 (CH_2)	2.30 m; 1.92 m	22.6 (CH_2)	1.55 m; 1.38 m	27.5 (CH_2)
7	5.18 t (5.5)	126.1 (CH)	5.06 t (8.0)	124.0 (CH)	2.04 m; 1.85 m	34.6 (CH_2)
8		134.5 (C)		135.8 (C)		129.6 (C)
9	2.28 m; 2.08 m	36.6 (CH_2)	2.11 m; 1.96 m	32.3 (CH_2)	5.22 d (10.0)	127.9 (CH)
10	2.07 m; 1.33 m	24.5 (CH_2)	1.98 m; 1.78 m	30.2 (CH_2)	3.18 m; 2.51 m	26.8 (CH_2)
11	2.61 dd (10.5, 3.5)	62.3 (CH)	4.12 t (4.0)	73.0 (CH)	5.74 dd (11.5, 6.5)	129.5 (CH)
12		61.7 (C)		148.1 (C)		134.6 (C)
13	1.90 m; 0.85 m	37.6 (CH_2)	2.20 m; 2.10 m	28.2 (CH_2)	4.69 dd (11.5, 3.0)	66.2 (CH_2)
14	1.55 m	28.1 (CH_2)	2.08 m; 1.28 m	30.8 (CH_2)	2.06 m; 1.70 m	39.1 (CH_2)
15		146.8 (C)	2.10 m	42.5 (C)		145.0 (C)
16	4.78 s; 4.70 s	111.4 (CH_2)		174.7 (C)		169.0 (C)
17	1.67 s	19.1 (CH_3)	1.39 d (7.0)	15.9 (CH_3)	6.20 s; 5.51 s	124.4 (CH_2)
18	1.26 s	16.9 (CH_3)	1.41 s	25.1 (CH_3)	1.32 s	23.7 (CH_3)
19	1.66 s	15.0 (CH_3)	1.63 s	16.1 (CH_3)	1.66 s	16.0 (CH_3)
20	1.27 s	16.2 (CH_3)	5.25 s; 4.98 s	108.7 (CH_2)	1.69 s	16.7 (CH_3)
OAc						170.7 (C)
					2.11 s	21.1 (CH_3)

[a]At 500 MHz in $CDCl_3$. [b]At 25 MHz in $CDCl_3$.

and evaporated. The dried residue was purified by silica gel column chromatography (*n*-hexane/acetone, 6:1) to yield **12a** (8.2 mg, 46.9%).

Hydrolysis of ***13***. Using the same preparation method that was used for **12**, the reaction of **13** (10.0 mg) with 1 mL of a 5% methanolic NaOH solution yielded a crude product, which was further separated by normal-phase HPLC (*n*-hexane/EtOAc, 1:2) to afford **13a** (3.8 mg, 34.4%).

***In Vitro* Anti-Inflammatory Assay.** A macrophage-like mouse cell line, RAW 264.7, was purchased from ATCC. Using Western blot analysis,[12,13] the *in vitro* anti-inflammatory activities of compounds **1**–**4** and **6**–**16**, and two derivatives **12a** and **13a**, were assessed by measuring their suppression effects on lipopolysaccharide (LPS)-stimulated iNOS and COX-2 protein overexpression in RAW 264.7 cells.

RESULTS AND DISCUSSION

4-Carbomethoxyl-10-epigyrosanoldie E (**1**) was isolated as colorless needles. Its infrared (IR) absorptions showed the presence of both lactone (1755 cm^{-1}) and ketone (1715 cm^{-1}) functionalities. The molecular formula of **1** was determined to be $C_{21}H_{26}O_7$ by HRESIMS (m/z 413.1571 $[M + Na]^+$) and ^{13}C NMR data (Table 1), requiring nine degrees of unsaturation. Resonances due to two ketones (δ 212.3 and 202.5), two ester carbonyl carbons (δ 174.4 and 167.8), and two olefinic carbons (δ 151.9, CH; 145.8, C; 130.4, C; 113.0, CH_2) in the ^{13}C NMR and DEPT spectral data accounted for six double-bond equivalents, which indicated that **1** was a tricyclic compound. The ^{1}H NMR spectrum of **1** (Table 1) revealed the presence of resonances of one olefinic methine proton (δ 7.16, s), two olefinic methylene protons (δ 4.79 and 4.61, each s), two oxygenated methines (δ 5.19, s, and δ 4.26, d, J = 3.5 Hz), and one oxymethyl group (δ 3.74, s). By comparison of the NMR data of **1** with those of **5**,[14−16] it was found that **1** differed from **5** only in the presence of a carbomethoxyl group instead of a proton at C-4. Moreover, single-crystal X-ray crystallographic analysis using Cu Kα irradiation at 100 K (Figure 2) confirmed the stereostructures of **1**. The Flack parameter [0.04(5)] (CCDC 1028007) allowed the assignment of the absolute configuration of **1** as (1*R*,4*S*,5*S*,8*S*,10*S*)-5(8)-epoxy-4-carbomethoxyl-1-isopropenyl-8-methyl-3,6-dioxocyclotetradec-11(12)-en-10,12-carbolactone.

The HRESIMS spectrum of 7-acetylsinumaximol B (**2**) exhibited an ion peak at m/z 455.1675 $[M + Na]^+$, which matched the formula $C_{23}H_{28}O_8$. The ^{1}H and ^{13}C NMR spectral data (Table 1) of **2** were similar to those of **3**,[17] the difference being that the hydroxy group attached at C-7 in **3** was replaced with an acetoxy group in **2**. Acetylation of **3** gave an acetyl derivative, whose ^{1}H and ^{13}C NMR spectral data were identical to those of the 7-acetyl derivative (**2**) derived from **3**. Hence, **2** was the 7-acetyl derivative of **3**. Therefore, **2** was established as (1*R*,7*R*,8*R*,10*S*,11*Z*)-3(6)-epoxy-7-acetoxy-4-carbomethoxyl-8-hydroxy-1-isopropenyl-8-methyl-3(4),5(6),11(12)-trien-10,12-carbolactone

Diepoxycembrene B (**6**) had the same molecular formula ($C_{20}H_{32}O_2$) as **7**, as indicated by HRESIMS and NMR spectra (Table 2). The gross structure of **6** was established by interpretation of two-dimensional (2D) NMR data, especially by analysis of $^{1}H-^{1}H$ COSY and HMBC correlations (Figure 3). The $^{1}H-^{1}H$ COSY spectral data assigned three isolated consecutive proton spin systems. The aforementioned results indicated that **6** had the same molecular framework as known compounds diepoxycembrene A (**7**) [(1*R**,3*R**,4*S**,11*R**,12*R**)-3,4,11,12-diepoxycembra-7,15-diene][18] and diepoxycembrane A [(1*R**,3*S**,4*S**,11*S**,12*S**-3,4,11,12-diepoxycembra-7,15-diene],[19] which were isolated previously from soft corals *Sinularia* sp. and *S. flexibilis*, respectively. NOE correlations observed in the NOESY spectrum were used to determine the relative configuration of **6** (Figure 4). The NOE correlations observed between H_2-6 and H_3-19 reflected the *E* configuration of the double bond

DOI: 10.1021/acs.jafc.5b01931
J. Agric. Food Chem. 2015, 63, 7211−7218

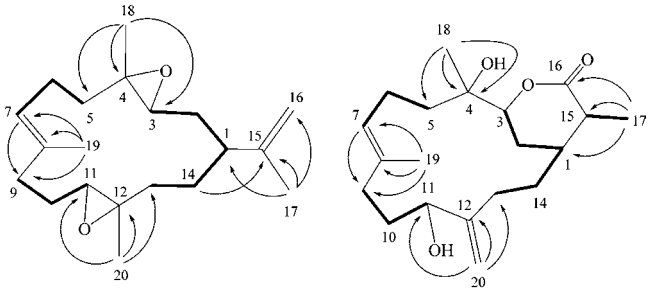

6 8

Figure 3. Selected ^{1}H−^{1}H COSY (—) and HMBC (→) correlations of **6** and **8**.

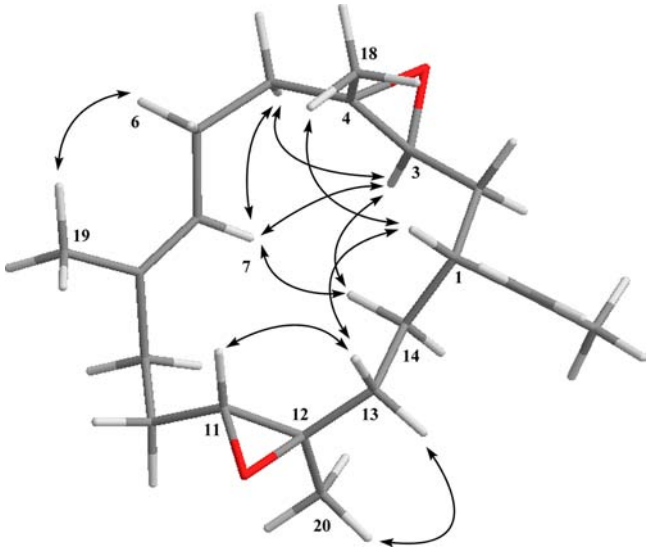

Figure 4. Selected NOE correlations of **6**.

between C-7 and C-8. In addition, it was found that H-1 showed NOE interactions with one proton of the C-13 methylene (δ 0.85) and H_3-18. Thus, assuming a β-orientation of H-1, H_3-18 should be positioned on the β face. Moreover, H-13β was found to exhibit correlations with H-11 (δ 2.61, dd, J = 10.3, 3.5 Hz), indicating that H-11 was situated on the β face; H-11 was assigned as a β proton, as the C-20 methyl was α-oriented at C-12, which was verified by a correlation between H_3-20 and H-13α (δ 1.90 m). This result shows that the epoxide at C-11/C-12 was of a *trans* geometry of the trisubstituted epoxide. Furthermore, the epoxide at C-3/C-4 was also of a *trans* geometry of the trisubstituted epoxide from the NOE correlations displayed by H-3 with the one proton of the C-5 methylene (δ 1.36), but not with H_3-18. In light of these results and other detailed analyses of NOE correlations, **6** was unambiguously identified as (1*R**,3*S**,4*S**,11*R**,12*R**)-3,4,11,12-diepoxycembra-7,15-diene.

Dihydromanaarenolide I (**8**) was isolated as a colorless amorphous powder. The HRESIMS (m/z 359.2200, [M + Na]$^+$) and NMR data of **8** indicated the molecular formula $C_{20}H_{32}O_4$. Both the ^{1}H and ^{13}C NMR signals of **8** (Table 2) were found to be very closely related to those of known compound manaarenolide I, which was isolated previously from the soft coral *Sinularia manaarensis*.[20] NMR comparison of **8** with manaarenolide I demonstrated that the two exomethylene proton signals in manaarenolide I were replaced by a methyl proton signal (δ_H 1.39, d, J = 7.0 Hz) in **8**. Additionally, 2D NMR data (^{1}H−^{1}H COSY and HMBC) further revealed that **8** possesses one methyl group at C-15 (Figure 3). The relative configurations of all stereocenters except C-15 of **8** were determined to be the same as those of manaarenolide I by comparisons of the coupling constants and proton shifts. Because of the NOE correlation between H_3-17 and H-1, the methyl at C-15 was assigned a β-configuration primarily. Moreover, by comparison of the NMR data of **8** with those of similar known compounds, it was confirmed that all compounds have the same relative stereochemical configuration at C-15.[20] According to the aforementioned results, the structure of **8** was established as (1*R**,3*R**,4*S**,11*S**,15*S**,7*E*)-4,11-dihydroxy-cembr-7(8),12-(20)-dien-16,3-olide.

Isosinulaflexiolide K (**9**) was found to have the [M + Na]$^+$ ion at m/z 399 in its ESIMS spectrum. The molecular formula was deduced to be $C_{22}H_{32}O_5$ from HRESIMS and NMR data (Table 2). The structure and absolute stereochemistry of **9** were also confirmed by single-crystal X-ray diffraction (Figure 2) with Cu Kα irradiation [Flack parameter of 0.09(3)] (CCDC 1044093). On the basis of the results presented above, compound **9** was established as (1*R*,4*R*,5*R*,13*S*,8*E*,11*Z*)-5-acetoxy-13-hydroxy-cembr-8(9),11(12),15(17)-trien-16,4-olide

In addition, the 11 known compounds obtained were identified as sinumaximol B (**3**),[17] pukalide (**4**),[21] 10-epigyrosanoldie E (**5**),[14,15] diepoxycembrene A (**7**),[17] sinulaflexiolide K (**10**),[22] (−)-sandensolide (**11**),[23] 11-dehydrosinulariolide (**12**),[24] sinulariolide (**13**),[25] 3,4:8,11-bisepoxy-7-acetoxycembra-15(17)-en-1,12-olide (**14**),[26] dendronpholide F (**15**),[27] and dendronpholide G (**16**)[24] by comparison of spectroscopic data with published values. The absolute configurations of **4** and **15** were confirmed by single-crystal X-ray diffraction analysis with Cu Kα radiation [Flack parameters of 0.12(5) and 0.14(8), respectively] for the first time (Figure 2). In the previous report, compound **4** was obtained from Gorgonacean coral *Leptogorgia rigida*, and the absolute configuration of **4** was fully determined by CD spectroscopic data analysis.[21] One hypothesis suggested that all cembranes of the known absolute configuration of an isopropyl group at C-1 obtained from Alcyonacean soft corals belong to the α series, whereas analogues isolated from Gorgonacean corals belong to the β series.[28,29] However, compounds **9** and **15** isolated from an Alcyonacean soft coral have a β conformation, with the isopropyl group pointing upward at position C1, and **4** was obtained from Gorgonacean and Alcyonacean corals. Thus, this result showed that this hypothesis is not applicable for a small number of cembranoids.

Using Western blotting, the effects of **1**−**4** and **6**−**16** on the inhibition of the accumulation of pro-inflammatory iNOS and COX-2 in LPS-stimulated RAW 264.7 cells were studied. The results presented in Figure 5 show that compounds **9**−**14** were found to significantly reduce the levels of iNOS to 30.9 ± 4.1, 37.4 ± 5.9, 61 ± 3.4, 31.9 ± 5.1, 47.7 ± 6.3, and 25.7 ± 5.2%, respectively, and the levels of COX-2 to 47.1 ± 3.8, 51.4 ± 5.6, 51.9 ± 7.2, 49 ± 5.6, 52.2 ± 5.1, and 55.3 ± 8.2%, respectively. Preliminary structure−activity relationships in diterpenes of the cembrane type may be deduced from anti-inflammatory bioassays. In the bioassays, the presence of one seven-membered lactone functional group is critical for the anti-inflammatory action of this class of compounds. Moreover, to confirm the active moiety, base-catalyzed hydrolysis of both **12** and **13** was performed, and the reactions were found to afford **12a** and **13a**. The two derivatives were inactive against the

DOI: 10.1021/acs.jafc.5b01931
J. Agric. Food Chem. 2015, 63, 7211−7218

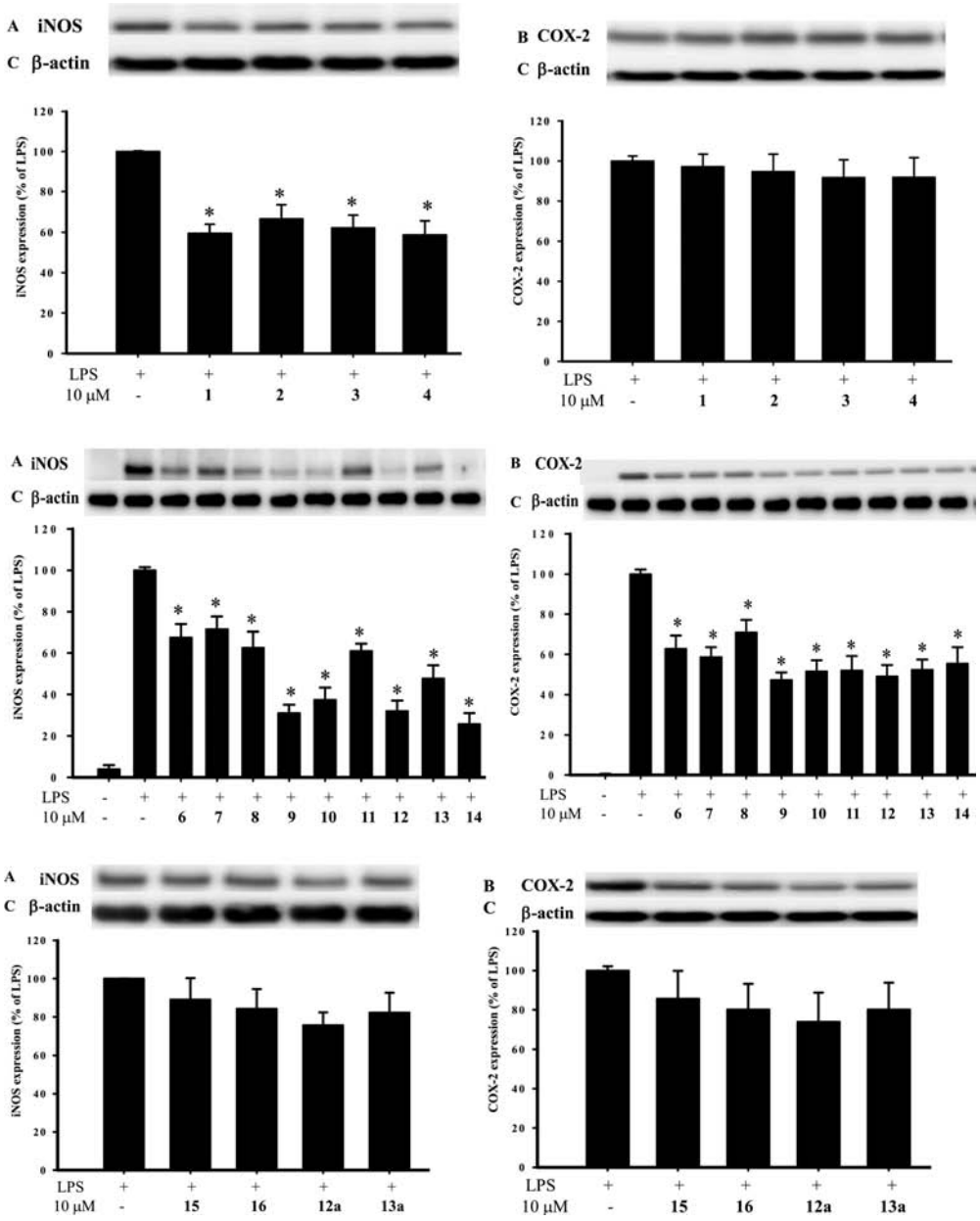

Figure 5. Effects of compounds **1**−**4**, **6**−**16**, **12a**, and **13a** at 10 μM on pro-inflammatory iNOS and COX-2 protein expression in LPS-induced RAW 264.7 macrophage cells by Western blot analysis: (A) quantification of iNOS expression, (B) quantification of COX-2 expression, and (C) quantification of β-actin expression. Band intensities were quantified by densitometry and normalized to that of the group treated with LPS only (set to 100%). At a concentration of 10 μM, positive control, dexamethasone was found to significantly reduce the levels of iNOS to 30.8 ± 9.6 and 6.9 ± 3.4%, respectively, relative to that of the control cells stimulated with LPS only in this study. This experiment was repeated three times. *$p < 0.05$ as compared with the LPS-stimulated group.

expressions of both iNOS and COX-2 proteins (Figure 5). These results showed that the anti-inflammatory activity depended on the seven-membered lactone functional group at position C1.

■ ASSOCIATED CONTENT

Supporting Information

The Supporting Information is available free of charge on the ACS Publications website at DOI: 10.1021/acs.jafc.5b01931.

Cif file for **1** (CIF)
Cif file for **4** (CIF)
Cif file for **9** (CIF)
NMR spectra of compounds **1**, **2**, **6**, **8**, and **9** (PDF)
Cif file for **15** (CIF)

■ AUTHOR INFORMATION

Corresponding Author

*Telephone: +886-8-8822370. Fax: +886-8-8825087. E-mail: x2219@nmmba.gov.tw.

Funding

This research was supported by grants from the National Museum of Marine Biology & Aquarium and the Ministry of Science and Technology (MOST 103-2320-B-291-001-MY3), Taiwan, awarded to J.-H. Su.

Notes

The authors declare no competing financial interest.

DOI: 10.1021/acs.jafc.5b01931
J. Agric. Food Chem. 2015, 63, 7211−7218

REFERENCES

(1) Blunt, J. W.; Copp, B. R.; Keyzers, R. A.; Munro, M. H. G.; Prinsep, M. R. Marine natural products. *Nat. Prod. Rep.* **2015**, *32*, 116−211 and previous reports in this series.

(2) Yang, B.; Zhou, X.-F.; Lin, X.-P.; Liu, J.; Peng, Y.; Yang, X.-W.; Liu, Y. Cembrane diterpenes chemistry and biological properties. *Curr. Org. Chem.* **2012**, *16*, 1512−1539.

(3) Lin, Y.-Y.; Jean, Y.-H.; Lee, H.-P.; Chen, W.-F.; Sun, Y.-M.; Su, J.-H.; Lu, Y.; Huang, S.-Y.; Hung, H.-C.; Sung, P.-J.; Sheu, J.-H.; Wen, Z.-H. A soft coral-derived compound, 11-*epi*-sinulariolide acetate suppresses inflammatory response and bone destruction in adjuvant-induced arthritis. *PLoS One* **2013**, *8*, e62926.

(4) Huang, S.-Y.; Chen, N.-F.; Chen, W.-F.; Hung, H.-C.; Lee, H.-P.; Lin, Y.-Y.; Wang, H.-M.; Sung, P.-J.; Sheu, J.-H.; Wen, Z.-H. Sinularin from indigenous soft coral attenuates nociceptive responses and spinal neuroinflammation in carrageenan-induced inflammatory Rat Model. *Mar. Drugs* **2012**, *10*, 1899−1919.

(5) Chen, N.-F.; Huang, S.-Y.; Lu, C.-H.; Chen, C.-L.; Feng, C.-W.; Chen, C.-H.; Hung, H.-C.; Lin, Y.-Y.; Sung, P.-J.; Sung, C.-S.; Yang, S.-N.; Wang, H.-M. D.; Chang, Y.-C.; Sheu, J.-H.; Chen, W.-F.; Wen, Z.-H. Flexibilide obtained from cultured soft coral has anti-neuroinflammatory and analgesic effects through the upregulation of spinal transforming growth factor-β1 in neuropathic rats. *Mar. Drugs* **2014**, *12*, 3792−3817.

(6) Su, J.-H.; Lin, Y.-F.; Lu, Y.; Yeh, H.-C.; Wang, W.-H.; Fan, T.-Y.; Sheu, J.-H. Oxygenated cembranoids from the cultured and wild-type soft corals *Sinularia flexibilis*. *Chem. Pharm. Bull.* **2009**, *57*, 1189−1192.

(7) Lin, H.-F.; Su, H.-J.; Lee, N.-L.; Su, J.-H. Cembranoids from the cultured soft coral *Sinularia gibberosa*. *Nat. Prod. Commun.* **2013**, *8*, 1363−1364.

(8) Chen, W.-F.; Yin, C.-T.; Cheng, C.-H.; Lu, M.-C.; Fang, L.-S.; Wang, W.-H.; Wen, Z.-H.; Chen, J.-J.; Wu, Y.-C.; Sung, P.-J. Norcembranoidal diterpenes from the cultured-type octocoral *Sinularia numerosa*. *Int. J. Mol. Sci.* **2015**, *16*, 3298−3306.

(9) Su, J.-H.; Lu, Y.; Lin, W.-Y.; Wang, W.-H.; Sung, P.-J.; Sheu, J.-H. A cembranoid, trocheliophorol, from the cultured soft coral *Sarcophyton trocheliophorum*. *Chem. Lett.* **2010**, *39*, 172−173.

(10) Lee, N.-L.; Su, J.-H. Tetrahydrofuran cembranoids from the cultured soft coral *Lobophytum crassum*. *Mar. Drugs* **2011**, *9*, 2526−2536.

(11) Crystallographic data for compounds **1**, **4**, **9**, and **15** have been deposited with the Cambridge Crystallographic Data Centre (CCDC 1028007, 1004365, 1044093, and 1056407, respectively). Copies of the data can be obtained, free of charge, on application to the Director, CCDC, 12 Union Road, Cambridge CB21EZ, UK (fax: +44-1223-336033 or e-mail: deposit@ccdc.cam.ac.uk).

(12) Ho, F.-M.; Lai, C.-C.; Huang, L.-J.; Kuo, T.-C.; Chao, C.-M.; Lin, W.-W. The anti-inflammatory carbazole, LCY-2-CHO, inhibits lipopolysaccharide-induced inflammatory mediator expression through inhibition of the p38 mitogen-activated protein kinase signaling pathway in macrophages. *Br. J. Pharmacol.* **2004**, *141*, 1037−1047.

(13) Park, E.-K.; Shin, Y.-W.; Lee, H.-U.; Kim, S.-S.; Lee, Y.-C.; Lee, B.-Y.; Kim, D.-H. Inhibitory effect of ginsenoside Rb1 and compound K on NO and prostaglandin E2 biosyntheses of RAW264.7 cells induced by lipopolysaccharide. *Biol. Pharm. Bull.* **2005**, *28*, 652−656.

(14) Cheng, C.-T.; Chuang, C.-T.; Wen, Z.-H.; Wang, S.-K.; Chiou, S.-F.; Hsu, C.-H.; Dai, C.-F.; Duh, C.-Y. Bioactive norditerpenoids from the soft coral *Sinularia gyrosa*. *Bioorg. Med. Chem.* **2010**, *18*, 3379−3386.

(15) Kwon, M. S.; Sim, S. H.; Chung, Y. K.; Lee, E. Synthetic studies on soft coral norcembranolides: total synthesis of (+)-10-epigyrosanolide E. *Tetrahedron* **2011**, *67*, 10179−10185.

(16) Qin, M.; Li, X.; Wang, B. Cembranoid, steroid, and sesquiterpenoid derivatives from the South China Sea soft coral *Sinularia numerosa*. *Chin. J. Chem.* **2012**, *30*, 1278−1282.

(17) Thao, N. P.; Nam, N. H.; Cuong, N. X.; Quang, T. H.; Tung, P. T.; Tai, B. H.; Luyen, B. T. T.; Chae, D.; Kim, S.; Koh, Y.-S.; Kiem, P. V.; Minh, C. V.; Kim, Y. H. Diterpenoids from the soft coral *Sinularia maxima* and their inhibitory effects on lipopolysaccharide-stimulated production of pro-inflammatory cytokines in bone marrow-derived dendritic cells. *Chem. Pharm. Bull.* **2012**, *60*, 1581−1589.

(18) Qin, S.; Huang, H.; Guo, Y.-W. A new cembranoid from the Hainan soft coral *Sinularia* sp. *J. Asian Nat. Prod. Res.* **2008**, *10*, 1075−1079.

(19) Hérin, M.; Colin, M.; Tursch, B. Chemical studies of marine invertebrates. XXV. Flexibilene, an unprecedented fifteen-membered ring diterpene hydrocarbon from the soft coral *Sinularia flexibilis* (Coelenterata, Octocorallia, Alcyonacea). *Bull. Soc. Chim. Belg.* **1976**, *85*, 801−803.

(20) Su, J.-H.; Ahmed, A. F.; Sung, P.-J.; Chao, C.-H.; Kuo, Y.-H.; Sheu, J.-H. Manaarenolides A−I, new diterpenoids from the soft coral *Sinularia manaarensis*. *J. Nat. Prod.* **2006**, *69*, 1134−1139.

(21) Gutiérrez, M.; Capson, T. L.; Guzmán, H. M.; González, J.; Ortega-Barría, E.; Quiñoá, E.; Riguera, R. Leptolide, a new furanocembranolide diterpene from *Leptogorgia alba*. *J. Nat. Prod.* **2005**, *68*, 614−616.

(22) Wen, T.; Ding, Y.; Deng, Z.; van Ofwegen, L.; Proksch, P.; Lin, W. Sinulaflexiolides A-K, cembrane-type diterpenoids from the Chinese soft coral *Sinularia flexibilis*. *J. Nat. Prod.* **2008**, *71*, 1133−1140.

(23) Hu, L.-C.; Su, J.-H.; Chiang, M.Y.-N.; Lu, M.-C.; Hwang, T.-L.; Chen, Y.-H.; Hu, W.-P.; Lin, N.-C.; Wang, W.-H.; Fang, L.-S.; Kuo, Y.-H.; Sung, P.-J. Flexibilins A−C, new cembrane-type diterpenoids from the Formosan soft coral. *Mar. Drugs* **2013**, *11*, 1999−2012.

(24) Hsieh, P.-W.; Chang, F.-R.; Mcphail, A. T.; Lee, K.-H.; Wu, Y.-C. New cembranolide analogues from the Formosan soft coral *Sinularia flexibilis* and their cytotoxicity. *Nat. Prod. Res.* **2003**, *17*, 409−418.

(25) Tursch, B.; Braekman, J. C.; Daloze, D.; Herin, M.; Karlsson, R.; Losman, D. Chemical studies of marine invertebrates−XI. Sinulariolide, a new cembranolide diterpene from the soft coral. *Tetrahedron* **1975**, *31*, 129−133.

(26) Su, J.; Yang, J. S. R.; Kuang, Y.; Zeng, L. A new cembranoids from the soft coral *Sinularia capillpsa*. *J. Nat. Prod.* **2000**, *63*, 1543−1545.

(27) Ma, A.; Deng, Z.; van Ofwegen, L.; Bayer, M.; Proksch, P.; Lin, W. Dendronpholides A−R, cembranoid diterpenes from the chinese soft coral *Dendronephthya* sp. *J. Nat. Prod.* **2008**, *71*, 1152−1160.

(28) Rodriguez, A. D.; Li, Y.; Dhasmana, H.; Barnes, C. New marine cembrane diterpenoids isolated from the Caribbean gorgonian *Eunicea mammosa*. *J. Nat. Prod.* **1993**, *56*, 1101−1113.

(29) Pham, N. B.; Butler, M. S.; Quinn, R. J. Naturally occurring cembranes from an Australian *Sarcophyton* species. *J. Nat. Prod.* **2002**, *65*, 1147−1150.

DOI: 10.1021/acs.jafc.5b01931
J. Agric. Food Chem. 2015, 63, 7211−7218

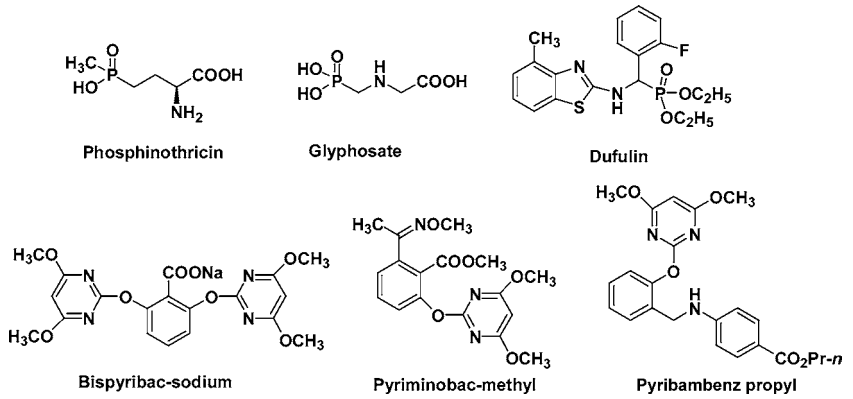

Figure 1. Structures of commercial α-amino phosphonic acid and pyrimidine pesticides.

four series of novel α-amino alkyl phosphonate derivatives containing a pyrimidinyl moiety via a Lewis acid (magnesium perchlorate) catalyzed Mannich-type reaction of aldehydes, amines, and phosphites (Schemes 1 and 2). The target compounds were evaluated for herbicidal activities in vitro and in vivo, and their preliminary herbicidal mode of action and structure−activity relationship were also studied.

Scheme 1. Molecular Design of Title Compounds I−IV

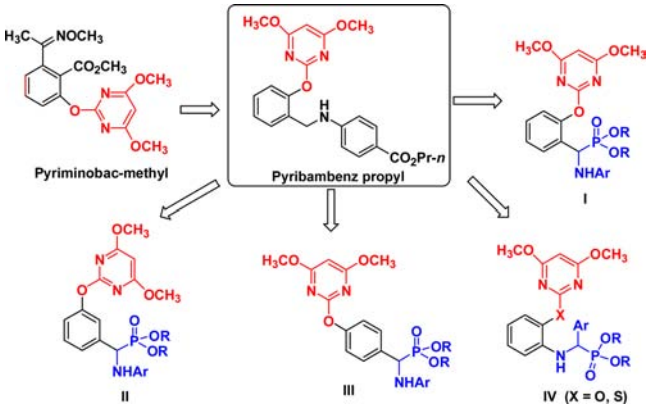

MATERIALS AND METHODS

Instruments. ^{1}H and ^{31}P NMR spectra were performed on a Varian Mercury-PLUS400 (400 MHz) or Varian Mercury Plus-600 (600 MHz) spectrometer at room temperature in $CDCl_3$ with TMS and 85% H_3PO_4 as the internal and external standards, respectively; chemical shift values (δ) are given in parts per million. Elemental analyses were taken on a Vario EL III elemental analysis instrument. Mass spectra were measured on a Finnigan TraceMS 2000 spectrometer at 70 eV using EI method or an Applied Biosystems API 2000 LC/MS/MS (ESI-MS) spectrometer. The IR spectra were recorded on a Nicolet NEXUS470 spectrometer as KBr pellets with absorption given in cm^{-1}. The melting points were determined on an X-4 binocular microscope melting point apparatus (Beijing Tech Instruments Co., Beijing, China) and were uncorrected. Analytical TLC was performed on silica gel GF254. Column chromatographic purification was carried out using silica gel. Yields were not optimized. Unless otherwise noted, all materials were commercially available and were used directly without further purification. All solvents were dried and redistilled before use.

General Procedure for the Preparation of *O,O*′-Dialkyl (Diphenyl) N-Substituted Phenyl-1-amino-[2 or 3 or 4-(4,6-dimethoxypyrimidin-2-yloxy)phenyl]methyl Phosphonates I−III. The mixture of aldehyde **1a−1c** (3 mmol), dialkyl phosphite, or diphenyl phosphite (3 mmol), substituted aniline (3.3 mmol), and anhydrous $Mg(ClO_4)_2$ (0.033 g, 0.15 mmol) in anhydrous acetonitrile (5 mL) was stirred at 50−60 °C until the reaction finished (monitored by TLC). The solid was filtered off, the solvent was removed under reduced pressure, and the crude product was purified by column chromatography on silica gel using a mixture of petroleum ether and acetone (v/v, 2:1) as eluent to give the target compounds **I**, **II**, and **III** as a white solid or light yellow oil. The detailed procedures and spectral data for intermediates **1a−1c** and **2a−2b** and the target compounds **I−IV** are available in the Supporting Information. **Ia−Ir** are known compounds, and their spectra data can also be found in the literature.[32]

Data for compound **Is** (R = Et, Ar = 4-FC_6H_4): white solid; yield, 71%; mp, 125.3−126.5 °C; IR (KBr) ν 3316 (NH), 2981 (Ar—H), 1600, 1572, 1502, 1468 (Ar), 1362 (P═O), 1216, 1193 (P—O—C), 1066, 1025 (C—O—C) cm^{-1}; ^{1}H NMR ($CDCl_3$, 600 MHz) δ 1.06 (t, J = 7.8 Hz, 3H, CH_3), 1.30 (t, J = 7.2 Hz, 3H, CH_3), 3.70−3.74 (m, 1H, CH_2), 3.79 (s, 6H, $2CH_3O$), 3.88−3.94 (m, 1H, CH_2), 4.17−4.22 (m, 2H, CH_2), 4.65 (t, J = 8.4 Hz, 1H, NH), 5.15 (dd, J = 8.4 Hz, J = 24.0 Hz, 1H, PCH), 5.79 (s, 1H, pyrimidine-H), 6.49−6.51 (m, 2H, ArH), 6.71 (t, J = 8.4 Hz, 2H, ArH), 7.20 (d, J = 7.2 Hz, 2H, ArH), 7.28 (t, J = 7.8 Hz, 1H, ArH), 7.63 (d, J = 7.2 Hz, 1H, ArH); ^{31}P NMR ($CDCl_3$, 162 MHz) δ 21.90; EI-MS (70 eV) m/z (%) 491.4 (M^+, 2.7), 355 (23.7), 354 (100), 214 (12.8). Anal. Calcd for $C_{23}H_{27}FN_3O_6P$: C, 56.21; H, 5.54; N, 8.55. Found: C, 56.07; H, 5.39; N, 8.31.

Data for compound **It** (R = Me, Ar = 4-FC_6H_4): white solid; yield, 66%; mp, 159.4−160.7 °C; IR (KBr) ν 3319 (NH), 2983 (Ar—H), 1605, 1571, 1507, 1470 (Ar), 1358 (P═O), 1219, 1187 (P—O—C), 1065, 1022 (C—O—C) cm^{-1}; ^{1}H NMR ($CDCl_3$, 600 MHz) δ 3.46 (d, J = 10.8 Hz, 3H, OCH_3), 3.80 (s, 6H, $2CH_3O$), 3.88 (d, J = 10.8 Hz, 3H, OCH_3), 4.64 (br s, 1H, NH), 5.19 (dd, J = 7.8 Hz, J = 24.0 Hz, 1H, PCH), 5.79 (s, 1H, pyrimidine-H), 6.50−6.53 (m, 2H, ArH), 6.72 (t, J = 7.8 Hz, 2H, ArH), 7.22 (t, J = 7.8 Hz, 2H, ArH), 7.31 (t, J = 7.8 Hz, 1H, ArH), 7.62 (d, J = 7.8 Hz, 1H, ArH); ^{31}P NMR ($CDCl_3$, 162 MHz) δ 24.20; EI-MS (70 eV) m/z (%) 463.4 (M^+, 2.9), 355 (22.0), 354 (100), 322 (5.1), 214 (14.4). Anal. Calcd for $C_{21}H_{23}FN_3O_6P$: C, 54.43; H, 5.00; N, 9.07. Found: C, 54.62; H, 5.15; N, 9.26.

Data for compound **Iu** (R = Ph, Ar = 4-FC_6H_4): white solid; yield, 75%; mp, 173.4−174.3 °C; IR (KBr) ν 3311 (NH), 2980 (Ar—H), 1608, 1577, 1502, 1475 (Ar), 1361 (P═O), 1216, 1182 (P—O—C), 1062, 1028 (C—O—C) cm^{-1}; ^{1}H NMR ($CDCl_3$, 600 MHz) δ 3.71 (s, 6H, $2CH_3O$), 4.74 (br s, 1H, NH), 5.62 (dd, J = 9.0 Hz, J = 24.6 Hz, 1H, PCH), 5.72 (s, 1H, pyrimidine-H), 6.56−6.58 (m, 2H, ArH), 6.73−6.78 (m, 4H, ArH), 7.06−7.09 (m, 3H, ArH), 7.12−7.18 (m, 3H, ArH), 7.21−7.25 (m, 4H, ArH), 7.33 (t, J = 7.8 Hz, 1H, ArH), 7.70 (d, J = 8.4 Hz, 1H, ArH); ^{31}P NMR ($CDCl_3$, 162 MHz) δ 14.60; EI-MS (70 eV) m/z (%) 587.5 (M^+, 1.7), 355 (21.0), 354 (100), 353 (39.3), 338 (5.9), 258 (6.8). 234 (18.0), 214 (47.5). Anal. Calcd for $C_{31}H_{27}FN_3O_6P$: C, 63.37; H, 4.63; N, 7.15. Found: C, 63.16; H, 4.58; N, 7.22.

DOI: 10.1021/acs.jafc.5b02335
J. Agric. Food Chem. 2015, 63, 7219−7229

Scheme 2. Synthetic Route of Title Compounds I−III

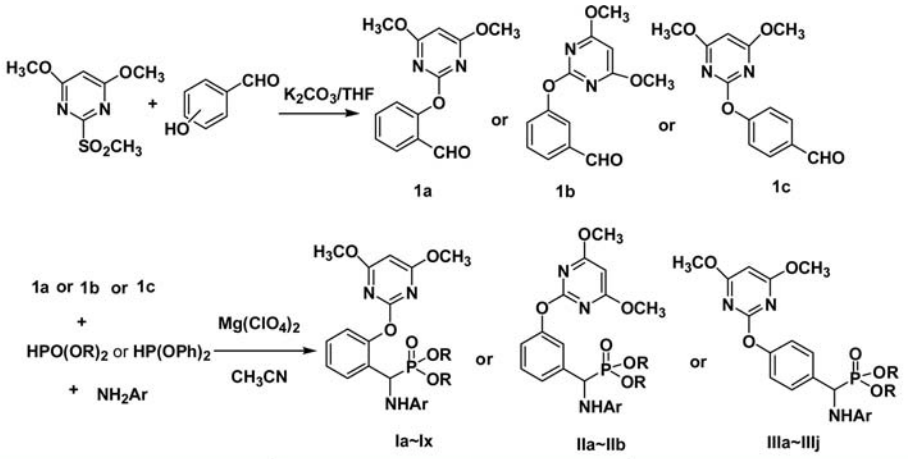

Compd.	R	Ar	Compd.	R	Ar	Compd.	R	Ar
Ia	Me	C_6H_5	**Ib**	Et	C_6H_5	**Ic**	Et	4-NO_2-C_6H_4
Id	Me	4-NO_2-C_6H_4	**Ie**	Me	4-Br-C_6H_4	**If**	Et	4-Br-C_6H_4
Ig	Me	4-CH_3O-C_6H_4	**Ih**	Et	4-CH_3O-C_6H_4	**Ii**	Me	2-Cl-C_6H_4
Ij	Et	2-Cl-C_6H_4	**Ik**	Me	3-Br-C_6H_4	**Il**	Et	3-Br-C_6H_4
Im	Me	4-Cl-C_6H_4	**In**	Et	4-Cl-C_6H_4	**Io**	Me	4-CF_3-C_6H_4
Ip	Et	4-CF_3-C_6H_4	**Iq**	Ph	4-CF_3-C_6H_4	**Ir**	*n*-Bu	4-CF_3-C_6H_4
Is	Et	4-F-C_6H_4	**It**	Me	4-F-C_6H_4	**Iu**	Ph	4-F-C_6H_4
Iv	Et	2-Br-C_6H_4	**Iw**	Et	4-CN-C_6H_4	**Ix**	Et	4-EtOCO-C_6H_4
IIa	Et	4-F-C_6H_4	**IIb**	Et	2-Br-C_6H_4	**IIIa**	Et	4-F-C_6H_4
IIIb	Et	2-Br-C_6H_4	**IIIc**	Et	4-Cl-C_6H_4	**IIId**	Et	4-CH_3-C_6H_4
IIIe	Et	4-NO_2-C_6H_4	**IIIf**	Et	4-Br-C_6H_4	**IIIg**	Et	C_6H_5
IIIh	Et	2,4-Cl_2-C_6H_3	**IIIi**	Me	4-Cl-C_6H_4	**IIIj**	Et	2-F-C_6H_4

Data for compound **Iv** (R = Et, Ar = 2-BrC_6H_4): white solid; yield, 64%; mp, 113.2−114.6 °C; IR (KBr) ν 3309 (NH), 2976 (Ar—H), 1598, 1563, 1500, 1472 (Ar), 1359 (P═O), 1218, 1194 (P—O—C), 1062, 1028 (C—O—C) cm^{-1}; ^1H NMR ($CDCl_3$, 600 MHz) δ 1.11 (t, J = 7.2 Hz, 3H, CH_3), 1.29 (t, J = 7.2 Hz, 3H, CH_3), 3.65−3.68 (m, 1H, CH_2), 3.81 (s, 6H, $2CH_3O$), 3.96−3.99 (m, 1H, CH_2), 4.18−4.20 (m, 2H, CH_2), 5.24 (d, J = 24.0 Hz, 1H, PCH), 5.41 (br s, 1H, NH), 5.77 (s, 1H, pyrimidine-H), 6.48−6.51 (m, 2H, ArH), 6.89−6.90 (m, 1H, ArH), 7.21−7.23 (m, 2H, ArH), 7.28 (t, J = 8.4 Hz, 1H, ArH), 7.35 (d, J = 7.2 Hz, 1H, ArH), 7.61−7.63 (m, 1H, ArH); ^{31}P NMR ($CDCl_3$, 162 MHz) δ 21.15; EI-MS (70 eV) m/z (%) 553.4 (5.1), 551.4 (M^+, 3.5), 417 (21.5), 416 (94.3), 415 (23.8), 414 (100), 334 (8.3), 229 (6.3), 196 (5.8). Anal. Calcd for $C_{23}H_{27}BrN_3O_6P$: C, 50.01; H, 4.93; N, 7.61. Found: C, 50.15; H, 4.97; N, 7.43.

Data for compound **Iw** (R = Et, Ar = 4-CNC_6H_4): white solid; yield, 59%; mp, 142.3−143.6 °C; IR (KBr) ν 3315 (NH), 2982 (Ar—H), 2245 (CN), 1563, 1556, 1485, 1461 (Ar), 1365 (P═O), 1215, 1185 (P—O—C), 1060, 1024 (C—O—C) cm^{-1}; ^1H NMR ($CDCl_3$, 600 MHz) δ 1.06 (t, J = 7.2 Hz, 3H, CH_3), 1.28 (t, J = 7.2 Hz, 3H, CH_3), 3.68−3.72 (m, 1H, CH_2), 3.81 (s, 6H, $2CH_3O$), 3.90−3.94 (m, 1H, CH_2), 4.15−4.20 (m, 2H, CH_2), 5.20 (d, J = 7.8 Hz, J = 24.0 Hz, 1H, PCH), 5.33 (br s, 1H, NH), 5.80 (s, 1H, pyrimidine-H), 6.57(d, J = 9.0 Hz, 2H, ArH), 7.20−7.24 (m, 2H, ArH), 7.27−7.29 (m, 2H, ArH), 7.33 (t, J = 7.8 Hz, 1H, ArH), 7.59 (d, J = 7.8 Hz, 1H, ArH); ^{31}P NMR ($CDCl_3$, 162 MHz) δ 20.96; EI-MS (70 eV) m/z (%) 498.4 (M^+, 5.8), 362 (24.4), 361 (100), 329 (2.2), 246 (2.4), 244 (3.1), 229 (4.2). Anal. Calcd for $C_{24}H_{27}N_4O_6P$: C, 57.83; H, 5.46; N, 11.24. Found: C, 57.70; H, 5.33; N, 11.31.

Data for compound **Ix** (R = Et, Ar = 4-EtOCOC_6H_4): white solid; yield, 66%; mp, 160.2−161.3 °C; IR (KBr) ν 3316 (NH), 2975 (Ar—H), 1738 (C═O), 1561, 1554, 1481, 1459 (Ar), 1362 (P═O), 1218, 1183 (P—O—C), 1057, 1028 (C—O—C) cm^{-1}; ^1H NMR ($CDCl_3$, 600 MHz) δ 1.07 (t, J = 7.2 Hz, 3H, CH_3), 1.28 (t, J = 7.2 Hz, 3H, CH_3), 1.33 (t, J = 7.8 Hz, 3H, CH_3), 3.71−3.74 (m, 1H, CH_2), 3.80 (s, 6H, $2CH_3O$), 3.92−3.95 (m, 1H, CH_2), 4.20 (q, J = 7.2 Hz, 2H, CH_2), 4.28 (q, J = 7.2 Hz, 2H, CH_2), 5.21 (br s, 1H, NH), 5.28 (d, J = 7.8 Hz, J = 24.0 Hz, 1H, PCH), 5.78 (s, 1H, pyrimidine-H), 6.54 (t, J = 6.0 Hz, 2H, ArH), 7.20−7.23 (m, 2H, ArH), 7.28−7.31 (m, 1H, ArH), 7.62 (d, J = 6.6 Hz, 1H, ArH), 7.71 (t, J = 6.0 Hz, 2H, ArH); ^{31}P NMR ($CDCl_3$, 162 MHz) δ 21.31; EI-MS (70 eV) m/z (%) 545.5 (M^+, 2.5), 410 (4.0), 409 (26.9), 408 (100), 362 (3.6). Anal. Calcd for $C_{26}H_{32}N_3O_8P$: C, 57.24; H, 5.91; N, 7.70. Found: C, 57.06; H, 5.97; N, 7.63.

Data for compound **IIa** (R = Et, Ar = 4-FC_6H_4): white solid; yield, 65%; mp, 135.2−136.3 °C; IR (KBr) ν 3310 (NH), 2985 (Ar—H), 1561, 1548, 1482, 1459 (Ar), 1358 (P═O), 1219, 1176 (P—O—C), 1057, 1025 (C—O—C) cm^{-1}; ^1H NMR ($CDCl_3$, 600 MHz) δ 1.12 (t, J = 7.8 Hz, 3H, CH_3), 1.29 (t, J = 7.8 Hz, 3H, CH_3), 3.70 (s, 6H, $2CH_3O$), 3.71−3.74 (m, 1H, CH_2), 3.93−3.97 (m, 1H, CH_2), 4.10−4.14 (m, 2H, CH_2), 4.67 (dd, J = 7.2 Hz, J = 24.0 Hz, 1H, PCH), 4.73 (br s, 1H, NH), 5.76 (s, 1H, pyrimidine-H), 6.50−6.52(m, 2H, ArH), 6.78−6.80 (m, 2H, ArH), 7.14 (t, J = 6.6 Hz, 1H, ArH), 7.32 (d, J = 7.2 Hz, 2H, ArH), 7.37 (t, J = 7.8 Hz, 1H, ArH); ^{31}P NMR ($CDCl_3$, 162 MHz) δ 21.43; EI-MS (70 eV) m/z (%) 491.5 (M^+, 6.0), 355 (19.2), 354 (100), 353 (7.1), 198 (2.6), 122 (2.9). Anal. Calcd for $C_{23}H_{27}FN_3O_6P$: C, 56.21; H, 5.54; N, 8.55. Found: C, 56.03; H, 5.77; N, 8.39.

Data for compound **IIb** (R = Et, Ar = 2-BrC_6H_4): white solid; yield, 72%; mp, 108.2−109.8 °C; IR (KBr) ν 3302 (NH), 2988 (Ar—H), 1567, 1542, 1479, 1452 (Ar), 1367 (P═O), 1211, 1170 (P—O—C),

DOI: 10.1021/acs.jafc.5b02335
J. Agric. Food Chem. 2015, 63, 7219−7229

1068, 1024 (C—O—C) cm^{-1}; ^1H NMR ($CDCl_3$, 600 MHz) δ 1.19 (t, J = 7.8 Hz, 3H, CH_3), 1.28 (t, J = 7.2 Hz, 3H, CH_3), 3.73 (s, 6H, $2CH_3O$), 3.82−3.86 (m, 1H, CH_2), 4.00−4.14 (m, 3H, CH_2), 4.76 (dd, J = 6.6 Hz, J = 24.6 Hz, 1H, PCH), 5.45 (br s, 1H, NH), 5.76 (s, 1H, pyrimidine-H), 6.43 (d, J = 7.8 Hz, 1H, ArH), 6.59 (d, J = 6.0 Hz, 1H, ArH), 6.99 (t, J = 7.2 Hz, 1H, ArH), 7.14 (d, J = 7.8 Hz, 1H, ArH), 7.35−7.39 (m, 3H, ArH), 7.42 (d, J = 7.8 Hz, 1H, ArH); ^{31}P NMR ($CDCl_3$, 162 MHz) δ 20.55; EI-MS (70 eV) m/z (%) 553.4 (4.1), 551 (M^+, 4.6), 417 (22.6), 416 (99.7), 415 (24.3), 414 (100), 208 (5.3). Anal. Calcd for $C_{23}H_{27}BrN_3O_6P$: C, 50.01; H, 4.93; N, 7.61. Found: C, 49.93; H, 4.74; N, 7.82.

Data for compound **IIIa** (R = Et, Ar = 4-FC_6H_4): white solid; yield, 75%; mp, 138.5−139.6 °C; IR (KBr) ν 3319 (NH), 2983 (Ar—H), 1604, 1569, 1506 (Ar), 1364 (P═O), 1217, 1196 (P—O—C), 1065, 1024 (C—O—C) cm^{-1}; ^1H NMR ($CDCl_3$, 600 MHz) δ 1.13 (t, J = 7.8 Hz, 3H, CH_3), 1.30 (t, J = 7.2 Hz, 3H, CH_3), 3.69−3.74 (m, 1H, CH_2), 3.77 (s, 6H, $2CH_3O$), 3.94−3.98 (m, 1H, CH_2), 4.10−4.16 (m, 2H, CH_2), 4.70 (dd, J = 7.8 Hz, J = 26.4 Hz, 1H, PCH), 4.73 (br s, 1H, NH), 5.77 (s, 1H, pyrimidine-H), 6.53 (dd, J = 4.2 Hz, J = 7.8 Hz, 2H, ArH), 6.80 (t, J = 8.4 Hz, 2H, ArH), 7.19 (d, J = 8.4 Hz, 2H, ArH), 7.47 (dd, J = 1.8 Hz, J = 8.4 Hz, 2H, ArH); ^{31}P NMR ($CDCl_3$, 162 MHz) δ 21.74; EI-MS (70 eV) m/z (%) 491.4 (M^+, 2.2), 355 (17.8), 354 (100), 353 (8.7), 197 (2.8), 111 (2.4). Anal. Calcd for $C_{23}H_{27}FN_3O_6P$: C, 56.21; H, 5.54; N, 8.55. Found: C, 56.43; H, 5.37; N, 8.62.

Data for compound **IIIb** (R = Et, Ar = 2-BrC_6H_4): white solid; yield, 70%; mp, 100.4−101.3 °C; IR (KBr) ν 3395 (NH), 2982 (Ar—H), 1592, 1573, 1505 (Ar), 1367 (P═O), 1224 (P—O—C), 1164, 1020 (C—O—C) cm^{-1}; ^1H NMR ($CDCl_3$, 600 MHz) δ 1.19 (t, J = 7.2 Hz, 3H, CH_3), 1.28 (t, J = 7.8 Hz, 3H, CH_3), 3.76 (s, 6H, $2CH_3O$), 3.81−3.85 (m, 1H, CH_2), 4.00−4.16 (m, 3H, CH_2), 4.80 (dd, J = 7.2 Hz, J = 24.6 Hz, 1H, PCH), 5.45 (t, J = 7.8 Hz, 1H, NH), 5.77 (s, 1H, pyrimidine-H), 6.44 (d, J = 7.8 Hz, 1H, ArH), 6.58 (t, J = 7.2 Hz, 1H, ArH), 7.01 (t, J = 7.8 Hz, 1H, ArH), 7.19 (d, J = 8.4 Hz, 2H, ArH), 7.43 (d, J = 8.4 Hz, 1H, ArH), 7.48 (d, J = 8.4 Hz, 2H, ArH); ^{31}P NMR ($CDCl_3$, 162 MHz) δ 20.85; EI-MS (70 eV) m/z (%) 553.4 (M^+, 1.5), 417 (19.0), 416 (100), 415 (23.6), 414 (94.8), 259 (3.3). Anal. Calcd for $C_{23}H_{27}BrN_3O_6P$: C, 50.01; H, 4.93; N, 7.61. Found: C, 49.85; H, 4.80; N, 7.44.

Data for compound **IIIc** (R = Et, Ar = 4-ClC_6H_4): white solid; yield, 78%; mp, 142.3−143.9 °C; IR (KBr) ν 3367 (NH), 2987 (Ar—H), 1582, 1574, 1501 (Ar), 1364 (P═O), 1228 (P—O—C), 1161, 1026 (C—O—C) cm^{-1}; ^1H NMR ($CDCl_3$, 600 MHz) δ 1.12 (t, J = 7.2 Hz, 3H, CH_3), 1.30 (t, J = 7.2 Hz, 3H, CH_3), 3.65−3.72 (m, 1H, CH_2), 3.78 (s, 6H, $2CH_3O$), 3.93−3.97 (m, 1H, CH_2), 4.10−4.15 (m, 2H, CH_2), 4.72 (d, J = 24.0 Hz, 1H, PCH), 5.77 (s, 1H, pyrimidine-H), 6.52 (d, J = 7.8 Hz, 2H, ArH), 7.03 (d, J = 8.4 Hz, 2H, ArH), 7.18 (d, J = 8.4 Hz, 2H, ArH), 7.45 (d, J = 8.4 Hz, 2H, ArH); ^{31}P NMR ($CDCl_3$, 243 MHz) δ, 21.80. Anal. Calcd for $C_{23}H_{27}ClN_3O_6P$: C, 54.39; H, 5.36; N, 8.27. Found: C, 54.53; H, 5.22; N, 8.39.

Data for compound **IIId** (R = Et, Ar = 4-$CH_3C_6H_4$): white solid; yield, 72%; mp, 133.3−134.5 °C; IR (KBr) ν 3351 (NH), 2990 (Ar—H), 1575, 1568, 1506 (Ar), 1360 (P═O), 1232 (P—O—C), 1159, 1027 (C—O—C) cm^{-1}; ^1H NMR ($CDCl_3$, 600 MHz) δ 1.13 (t, J = 7.2 Hz, 3H, CH_3), 1.29 (t, J = 7.2 Hz, 3H, CH_3), 2.19 (s, 3H, CH_3), 3.71−3.74 (m, 1H, CH_2), 3.78 (s, 6H, $2CH_3O$), 3.93−3.99 (m, 1H, CH_2), 4.06−4.17 (m, 2H, CH_2), 4.75 (dd, J = 6.0 Hz, J = 24.0 Hz, 1H, PCH), 5.77 (s, 1H, pyrimidine-H), 6.52 (d, J = 7.8 Hz, 2H, ArH), 6.91 (d, J = 7.8 Hz, 2H, ArH), 7.17 (d, J = 7.8 Hz, 2H, ArH), 7.48 (d, J = 7.2 Hz, 2H, ArH); ^{31}P NMR ($CDCl_3$, 243 MHz) δ 21.58. Anal. Calcd for $C_{24}H_{30}N_3O_6P$: C, 59.13; H, 6.20; N, 8.62. Found: C, 59.01; H, 6.08; N, 8.51.

Data for compound **IIIe** (R = Et, Ar = 4-$NO_2C_6H_4$): white solid; yield, 79%; mp, 195.3−196.3 °C; IR (KBr) ν 3334 (NH), 2993 (Ar—H), 1579, 1562, 1507 (Ar), 1354 (P═O), 1229 (P—O—C), 1164, 1033 (C—O—C) cm^{-1}; ^1H NMR ($CDCl_3$, 600 MHz) δ 1.13 (t, J = 7.2 Hz, 3H, CH_3), 1.31 (t, J = 7.2 Hz, 3H, CH_3), 3.65−3.71 (m, 1H, CH_2), 3.79 (s, 6H, $2CH_3O$), 3.93−3.98 (m, 1H, CH_2), 4.11−4.18 (m, 2H, CH_2), 4.85 (dd, J = 7.8 Hz, J = 24.0 Hz, 1H, PCH), 5.78 (s, 1H, pyrimidine-H), 5.91 (t, J = 8.4 Hz, 1H, NH), 6.61 (d, J = 9.0 Hz, 2H, ArH), 7.22 (d, J = 8.4 Hz, 2H, ArH), 7.48 (d, J = 8.4 Hz, 2H, ArH), 8.02 (d, J = 9.0 Hz, 2H, ArH); ^{31}P NMR ($CDCl_3$, 243 MHz) δ 20.49. Anal. Calcd for $C_{23}H_{27}N_4O_8P$: C, 53.28; H, 5.25; N, 10.81. Found: C, 53.12; H, 5.40; N, 10.87.

Data for compound **IIIf** (R = Et, Ar = 4-BrC_6H_4): white solid; yield, 81%; mp, 136.5−137.3 °C; IR (KBr) ν 3361 (NH), 2985 (Ar—H), 1579, 1572, 1499 (Ar), 1360 (P═O), 1226 (P—O—C), 1158, 1025 (C—O—C) cm^{-1}; ^1H NMR ($CDCl_3$, 600 MHz) δ 1.12 (t, J = 7.2 Hz, 3H, CH_3), 1.29 (t, J = 7.2 Hz, 3H, CH_3), 3.65−3.72 (m, 1H, CH_2), 3.77 (s, 6H, $2CH_3O$), 3.92−3.98 (m, 1H, CH_2), 4.08−4.16 (m, 2H, CH_2), 4.72 (dd, J = 6.0 Hz, J = 24.0 Hz, 1H, PCH), 4.93 (br s, 1H, NH), 5.76 (s, 1H, pyrimidine-H), 6.47 (d, J = 9.0 Hz, 2H, ArH), 7.16 (d, J = 8.4 Hz, 2H, ArH), 7.18 (d, J = 8.4 Hz, 2H, ArH), 7.46 (d, J = 8.4 Hz, 2H, ArH); ^{31}P NMR ($CDCl_3$, 243 MHz) δ 21.47. Anal. Calcd for $C_{23}H_{27}BrN_3O_6P$: C, 50.01; H, 4.93; N, 7.61. Found: C, 49.87; H, 4.74; N, 7.80.

Data for compound **IIIg** (R = Et, Ar = C_6H_5): white solid; yield, 74%; mp, 131.7−133.1 °C; IR (KBr) ν 3345 (NH), 2980 (Ar—H), 1582, 1570, 1486 (Ar), 1359 (P═O), 1223 (P—O—C), 1153, 1027 (C—O—C) cm^{-1}; ^1H NMR ($CDCl_3$, 600 MHz) δ 1.13 (t, J = 10.8 Hz, 3H, CH_3), 1.29 (t, J = 10.8 Hz, 3H, CH_3), 3.66−3.74 (m, 1H, CH_2), 3.78 (s, 6H, $2CH_3O$), 3.93−3.99 (m, 1H, CH_2), 4.08−4.17 (m, 2H, CH_2), 4.78 (d, J = 24.0 Hz, 1H, PCH), 4.82 (br s, 1H, NH), 5.76 (s, 1H, pyrimidine-H), 6.60 (d, J = 12 Hz, 2H, ArH), 6.70 (t, J = 10.8 Hz, 1H, ArH), 7.10 (t, J = 12.0 Hz, 2H, ArH), 7.18 (d, J = 12.0 Hz, 2H, ArH), 7.49 (d, J = 12.0 Hz, 2H, ArH); ^{31}P NMR ($CDCl_3$, 243 MHz) δ 21.76. Anal. Calcd for $C_{23}H_{28}N_3O_6P$: C, 58.35; H, 5.96; N, 8.88. Found: C, 58.51; H, 6.03; N, 8.74.

Data for compound **IIIh** (R = Et, Ar = 2,4-$Cl_2C_6H_3$): white solid; yield, 73%; mp, 147.5−148.7 °C; IR (KBr) ν 3364 (NH), 2982 (Ar—H), 1577, 1570, 1500 (Ar), 1360 (P═O), 1223 (P—O—C), 1159, 1022 (C—O—C) cm^{-1}; ^1H NMR ($CDCl_3$, 600 MHz) δ 1.18 (t, J = 10.8 Hz, 3H, CH_3), 1.28 (t, J = 10.8 Hz, 3H, CH_3), 3.79 (s, 6H, $2CH_3O$), 3.80−3.83 (m, 1H, CH_2), 3.98−4.17 (m, 3H, CH_2), 4.74 (dd, J = 10.8 Hz, J = 36.0 Hz, 1H, PCH), 5.39 (dd, J = 10.8 Hz, J = 15.6 Hz, 1H, NH), 5.77 (s, 1H, pyrimidine-H), 6.38 (d, J = 13.2 Hz, 1H, ArH), 6.93 (d, J = 13.2 Hz, 1H, ArH), 7.20 (d, J = 12.6 Hz, 2H, ArH), 7.27 (s, 1H, ArH), 7.44 (dd, J = 3.6 Hz, J = 13.2 Hz, 2H, ArH); ^{31}P NMR ($CDCl_3$, 243 MHz) δ 19.98. Anal. Calcd for $C_{23}H_{26}Cl_2N_3O_6P$: C, 50.94; H, 4.83; N, 7.75. Found: C, 50.81; H, 4.88; N, 7.91.

Data for compound **IIIi** (R = Me, Ar = 4-ClC_6H_4): white solid; yield, 87%; mp, 145.0−146.4 °C; IR (KBr) ν 3351 (NH), 2980 (Ar—H), 1577, 1571, 1496 (Ar), 1353 (P═O), 1231 (P—O—C), 1159, 1022 (C—O—C) cm^{-1}; ^1H NMR ($CDCl_3$, 400 MHz) δ 3.48 (d, J = 10.4 Hz, 3H, OCH_3), 3.77 (s, 6H, $2CH_3O$), 3.79 (d, J = 10.4 Hz, 3H, OCH_3), 4.76 (d, J = 25.6 Hz, 1H, PCH), 4.87 (br s, 1H, NH), 5.77 (s, 1H, pyrimidine-H), 6.52 (d, J = 8.8 Hz, 2H, ArH), 7.04 (d, J = 8.8 Hz, 2H, ArH), 7.20 (d, J = 8.4 Hz, 2H, ArH), 7.47 (dd, J = 2.4 Hz, J = 8.8 Hz, 2H, ArH); ^{31}P NMR ($CDCl_3$, 162 MHz) δ 23.49. Anal. Calcd for $C_{21}H_{23}ClN_3O_6P$: C, 52.56; H, 4.83; N, 8.76. Found: C, 54.72; H, 4.97; N, 8.94.

Data for compound **IIIj** (R = Et, Ar = 2-FC_6H_4): white solid; yield, 73%; mp, 133.6−135.1 °C; IR (KBr) ν 3318 (NH), 2991 (Ar—H), 1559, 1561, 1477, 1463 (Ar), 1366 (P═O), 1227, 1170 (P—O—C), 1052, 1028 (C—O—C) cm^{-1}; ^1H NMR ($CDCl_3$, 400 MHz) δ 1.16 (t, J = 7.2 Hz, 3H, CH_3), 1.28 (t, J = 7.2 Hz, 3H, CH_3), 3.77 (s, 6H, $2CH_3O$), 3.80−3.84 (m, 1H, CH_2), 3.95−4.03 (m, 1H, CH_2), 4.05−4.16 (m, 2H, CH_2), 4.77 (d, J = 22.8 Hz, 1H, PCH), 4.98 (br s, 1H, NH), 5.77 (s, 1H, pyrimidine-H), 6.51(t, J = 8.4 Hz, 1H, ArH), 6.63(q, J = 7.6 Hz, 1H, ArH), 6.83 (t, J = 7.6 Hz, 1H, ArH), 6.97 (t, J = 9.6 Hz, 1H, ArH), 7.19 (d, J = 8.4 Hz, 2H, ArH), 7.48 (dd, J = 2.4 Hz, J = 8.8 Hz, 2H, ArH); ^{31}P NMR ($CDCl_3$, 162 MHz) δ 20.73. Anal. Calcd for $C_{23}H_{27}FN_3O_6P$: C, 56.21; H, 5.54; N, 8.55. Found: C, 56.31; H, 5.39; N, 8.42.

General Procedure for the Preparation of *O,O*′-Dialkyl (Diphenyl) *N*-[2-(4,6-Dimethoxypyrimidin-2-yloxy or thio phenyl]-1-amino (Substituted Phenyl) Methyl Phosphonates IV. The mixture of amine **2** (3 mmol), dialkyl phosphite or diphenyl phosphite (3 mmol), substituted benzaldehyde (3.3 mmol), and

DOI: 10.1021/acs.jafc.5b02335
J. Agric. Food Chem. 2015, 63, 7219−7229

Scheme 3. Synthetic Route of Title Compounds IV

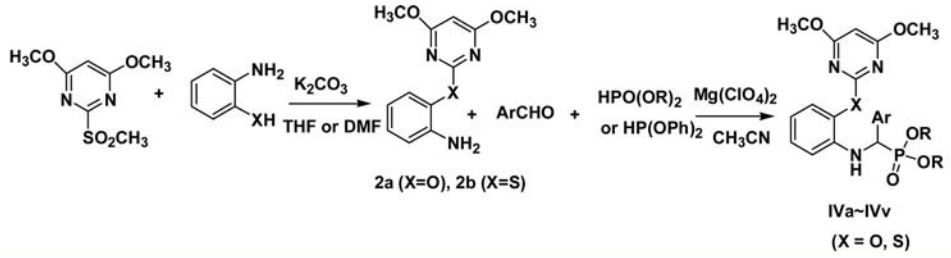

Compd.	R	X	Ar	Compd.	R	X	Ar
IVa	Et	S	C_6H_5	**IVb**	Et	S	4-CH_3-C_6H_4
IVc	Et	S	4-CH_3O-C_6H_4	**IVd**	Et	S	4-F-C_6H_4
IVe	Et	S	2-F-C_6H_4	**IVf**	Et	S	2-Cl-C_6H_4
IVg	Et	S	4-Cl-C_6H_4	**IVh**	Me	S	4-Cl-C_6H_4
IVi	Ph	S	4-Cl-C_6H_4	**IVj**	Et	S	4-Br-C_6H_4
IVk	Et	S	3-NO_2-C_6H_4	**IVl**	Et	S	4-NO_2-C_6H_4
IVm	Et	S	2,4-$(CH_3O)_2$-C_6H_3	**IVn**	Et	S	2,4-Cl_2-C_6H_3
IVo	Et	S	4-HO-C_6H_4	**IVp**	Et	O	C_6H_5
IVq	Et	O	2-Cl-C_6H_4	**IVr**	Et	O	2-F-C_6H_4
IVs	Et	O	4-F-C_6H_4	**IVt**	Et	O	4-Cl-C_6H_4
IVu	Et	O	4-CH_3-C_6H_4	**IVv**	Et	O	4-NO_2-C_6H_4

anhydrous $Mg(ClO_4)_2$ (0.033 g, 0.15 mmol) in anhydrous acetonitrile (5 mL) was stirred at 50−60 °C until the reaction completed (monitored by TLC). The solid was filtered off, the solvent was removed under reduced pressure, and the crude product was purified by column chromatography on silica gel using a mixture of petroleum ether and acetone (v/v, 2:1) as eluent to yield the target compound **IV** (Scheme 3) as white solid or light yellow oil.

Data for compound **IVa** (R = Et, X = S, Ar = C_6H_5): white solid; yield, 68%; mp, 120.3−122.2 °C; IR (KBr) ν 3345 (NH), 2985 (Ar—H), 1586, 1552, 1504 (Ar), 1370 (P═O), 1278, 1190 (P—O—C), 1042, 1015 (C—O—C) cm^{-1}; ^1H NMR ($CDCl_3$, 600 MHz) δ 1.10 (t, J = 7.2 Hz, 3H, CH_3), 1.18 (t, J = 7.2 Hz, 3H, CH_3), 3.64 (s, 6H, $2CH_3O$), 3.70−3.74 (m, 1H, CH_2), 3.89−3.95 (m, 2H, CH_2), 3.99−4.02 (m, 1H, CH_2), 4.78 (dd, J = 7.8 Hz, J = 24.0 Hz, 1H, PCH), 5.72 (s, 1H, pyrimidine-H), 5.91 (t, J = 8.4 Hz, 1H, NH), 6.48 (d, J = 8.4 Hz, 1H, ArH), 6.68 (t, J = 7.2 Hz, 1H, ArH), 7.15 (t, J = 7.8 Hz, 1H, ArH), 7.23−7.28 (m, 3H, ArH), 7.35 (d, J = 7.8 Hz, 2H, ArH), 7.46 (d, J = 7.2 Hz, 1H, ArH); ^{31}P NMR ($CDCl_3$, 162 MHz) δ 20.96; EI-MS (70 eV) m/z (%) 489.4 (M^+, 5.0), 354 (7.0), 353 (22.9), 352 (100), 212 (14.8), 180 (6.1), 136 (3.5), 109 (4.9). Anal. Cacld for $C_{23}H_{28}N_3O_5PS$: C, 56.43; H, 5.77; N, 8.58. Found: C, 56.65; H, 5.58; N, 8.70.

Data for compound **IVb** (R = Et, X = S, Ar = 4-$CH_3C_6H_4$): white solid; yield, 72%; mp, 109.1−110.3 °C; IR (KBr) ν 3347 (NH), 2988 (Ar—H), 1581, 1558, 1501 (Ar), 1366 (P═O), 1275, 1182 (P—O—C), 1041, 1021 (C—O—C) cm^{-1}; ^1H NMR ($CDCl_3$, 600 MHz) δ 1.12 (t, J = 7.2 Hz, 3H, CH_3), 1.19 (t, J = 7.2 Hz, 3H, CH_3), 2.30 (s, 3H, CH_3), 3.64 (s, 6H, $2CH_3O$), 3.72−3.76 (m, 1H, CH_2), 3.90−3.95 (m, 2H, CH_2), 3.99−4.03 (m, 1H, CH_2), 4.74 (dd, J = 7.8 Hz, J = 24.6 Hz, 1H, PCH), 5.72 (s, 1H, pyrimidine-H), 5.86 (t, J = 9.0 Hz, 1H, NH), 6.50 (d, J = 8.4 Hz, 1H, ArH), 6.68 (t, J = 7.2 Hz, 1H, ArH), 7.06 (d, J = 7.8 Hz, 2H, ArH), 7.15 (t, J = 7.2 Hz, 1H, ArH), 7.22 (d, J = 7.8 Hz, 2H, ArH), 7.45 (d, J = 7.8 Hz, 1H, ArH); ^{31}P NMR ($CDCl_3$, 162 MHz) δ 21.16; EI-MS (70 eV) m/z (%) 503.3 (M^+, 4.7), 368 (7.5), 367 (23.7), 366 (100), 274 (7.0), 226 (18.2), 194 (6.8). Anal. Calcd for $C_{24}H_{30}N_3O_5PS$: C, 57.24; H, 6.00; N, 8.34. Found: C, 57.11; H, 6.13; N, 8.24.

Data for compound **IVc** (R = Et, X = S, Ar = 4-$CH_3OC_6H_4$): white solid; yield, 66%; mp, 169.7−170.9 °C; IR (KBr) ν 3342 (NH), 2984 (Ar—H), 1583, 1549, 1508 (Ar), 1371 (P═O), 1260, 1193 (P—O—C), 1054, 1014 (C—O—C) cm^{-1}; ^1H NMR ($CDCl_3$, 600 MHz) δ 1.12 (t, J = 7.2 Hz, 3H, CH_3), 1.18 (t, J = 7.2 Hz, 3H, CH_3), 3.64 (s, 6H, $2CH_3O$), 3.71−3.75 (m, 1H, CH_2), 3.77 (s, 3H, OCH_3), 3.88−3.95 (m, 2H, CH_2), 3.97−4.03 (m, 1H, CH_2), 4.73 (dd, J = 6.0 Hz, J = 24.0 Hz, 1H, PCH), 5.72 (s, 1H, pyrimidine-H), 5.84 (t, J = 7.8 Hz, 1H, NH), 6.50 (d, J = 8.4 Hz, 1H, ArH), 6.68 (t, J = 7.8 Hz, 1H, ArH), 6.80 (d, J = 8.4 Hz, 2H, ArH), 7.16 (t, J = 8.4 Hz, 1H, ArH), 7.25 (d, J = 7.8 Hz, 2H, ArH), 7.45 (d, J = 7.8 Hz, 1H, ArH); ^{31}P NMR ($CDCl_3$, 162 MHz) δ 21.23; EI-MS (70 eV) m/z (%) 519.3 (M^+, 3.9), 384 (7.8), 383 (23.7), 382 (100), 274 (11.8), 247 (3.4), 243 (3.6), 242 (21.9), 210 (4.5). Anal. Calcd for $C_{24}H_{30}N_3O_6PS$: C, 55.48; H, 5.82; N, 8.09. Found: C, 57.63; H, 5.73; N, 7.97.

Data for compound **IVd** (R = Et, X = S, Ar = 4-FC_6H_4): white solid; yield, 69%; mp, 164.6−165.9 °C; IR (KBr) ν 3348 (NH), 2984 (Ar—H), 1586, 1550, 1503 (Ar), 1372 (P═O), 1293, 1194 (P—O—C), 1045, 1014 (C—O—C) cm^{-1}; ^1H NMR ($CDCl_3$, 600 MHz) δ 1.13 (t, J = 7.2 Hz, 3H, CH_3), 1.18 (t, J = 7.2 Hz, 3H, CH_3), 3.65 (s, 6H, $2CH_3O$), 3.76−3.79 (m, 1H, CH_2), 3.91−3.96 (m, 2H, CH_2), 4.00−4.02 (m, 1H, CH_2), 4.76 (dd, J = 5.4 Hz, J = 24.6 Hz, 1H, PCH), 5.73 (s, 1H, pyrimidine-H), 5.86 (br s, 1H, NH), 6.44 (d, J = 7.8 Hz, 1H, ArH), 6.70 (t, J = 7.8 Hz, 1H, ArH), 6.97 (t, J = 9.0 Hz, 2H, ArH), 7.16 (t, J = 7.8 Hz, 1H, ArH), 7.33 (t, J = 6.0 Hz, 2H, ArH), 7.47 (d, J = 7.8 Hz, 1H, ArH); ^{31}P NMR ($CDCl_3$, 162 MHz) δ 20.40; EI-MS (70 eV) m/z (%) 507.3 (M^+, 5.2), 372 (6.3), 371 (21.8), 370 (100), 274 (5.0), 230 (16.5), 198 (7.6), 136 (4.4), 109 (9.6). Anal. Calcd for $C_{23}H_{27}FN_3O_5PS$: C, 54.43; H, 5.36; N, 8.28. Found: C, 54.55; H, 5.51; N, 8.40.

Data for compound **IVe** (R = Et, X = S, Ar = 2-FC_6H_4): white solid; yield, 72%; mp, 138.6−139.5 °C; IR (KBr) ν 3345 (NH), 2987 (Ar—H), 1582, 1551 (Ar), 1370 (P═O), 1289, 1191 (P—O—C), 1048, 1016 (C—O—C) cm^{-1}; ^1H NMR ($CDCl_3$, 600 MHz) δ 1.10 (t, J = 6.6 Hz, 3H, CH_3), 1.23 (t, J = 7.2 Hz, 3H, CH_3), 3.60 (s, 6H, $2CH_3O$), 3.78−3.81 (m, 1H, CH_2), 3.93−3.97 (m, 1H, CH_2), 4.05−4.12 (m, 2H, CH_2), 5.22 (dd, J = 8.4 Hz, J = 24.6 Hz, 1H, PCH), 5.70 (s, 1H, pyrimidine-H), 5.90 (t, J = 6.0 Hz, 1H, NH), 6.59 (d, J = 8.4 Hz, 1H,

DOI: 10.1021/acs.jafc.5b02335
J. Agric. Food Chem. 2015, 63, 7219−7229

ArH), 6.70 (t, J = 7.2 Hz, 1H, ArH), 6.99 (t, J = 7.8 Hz, 1H, ArH), 7.04 (t, J = 9.0 Hz, 1H, ArH), 7.18−7.24 (m, 2H, ArH), 7.27 (t, J = 7.2 Hz, 1H, ArH), 7.45 (dd, J = 1.2 Hz, J = 8.4 Hz, 1H, ArH); ^{31}P NMR ($CDCl_3$, 162 MHz) δ 20.33; EI-MS (70 eV) m/z (%) 507.3 (M^+, 6.0), 372 (6.6), 371 (22.0), 370 (100), 274 (3.9), 247 (2.8), 230 (16.2), 198 (5.6), 139 (4.2), 136 (4.2), 109 (6.5). Anal. Calcd for $C_{23}H_{27}FN_3O_5PS$: C, 54.43; H, 5.36; N, 8.28. Found: C, 54.37; H, 5.17; N, 8.33.

Data for compound **IVf** (R = Et, X = S, Ar = 2-ClC_6H_4): white solid; yield, 75%; mp, 140.7−141.4 °C; IR (KBr) ν 3356 (NH), 2982 (Ar—H), 1587, 1550 (Ar), 1373 (P═O), 1289, 1191 (P—O—C), 1050, 1027 (C—O—C) cm^{-1}; ^{1}H NMR ($CDCl_3$, 600 MHz) δ 1.07 (t, J = 7.2 Hz, 3H, CH_3), 1.24 (t, J = 7.2 Hz, 3H, CH_3), 3.60 (s, 6H, $2CH_3O$), 3.66−3.73 (m, 1H, CH_2), 3.87−3.94 (m, 1H, CH_2), 4.04−4.13 (m, 2H, CH_2), 5.40 (dd, J = 8.4 Hz, J = 24.6 Hz, 1H, PCH), 5.71 (s, 1H, pyrimidine-H), 6.03 (t, J = 9.0 Hz, 1H, NH), 6.52 (d, J = 8.4 Hz, 1H, ArH), 6.69 (t, J = 7.2 Hz, 1H, ArH), 7.10 (t, J = 7.8 Hz, 1H, ArH), 7.18 (d, J = 7.8 Hz, 2H, ArH), 7.31 (d, J = 7.8 Hz, 1H, ArH), 7.36 (d, J = 7.8 Hz, 1H, ArH), 7.44 (d, J = 7.2 Hz, 1H, ArH); ^{31}P NMR ($CDCl_3$, 162 MHz) δ 20.52; EI-MS (70 eV) m/z (%) 523.3 (M^+, 0.39), 489 (4.6), 488 (18.4), 389 (8.4), 388 (42.9), 387 (20.5), 386 (100). Anal. Calcd for $C_{23}H_{27}ClN_3O_5PS$: C, 52.72; H, 5.19; N, 8.02. Found: C, 52.51; H, 5.07; N, 8.14.

Data for compound **IVg** (R = Et, X = S, Ar = 4-ClC_6H_4): white solid; yield, 78%; mp, 143.2−144.4 °C; IR (KBr) ν 3359 (NH), 2980 (Ar—H), 1584, 1553 (Ar), 1370 (P═O), 1285, 1193 (P—O—C), 1049, 1024 (C—O—C) cm^{-1}; ^{1}H NMR ($CDCl_3$, 600 MHz) δ 1.14 (t, J = 7.2 Hz, 3H, CH_3), 1.18 (t, J = 7.2 Hz, 3H, CH_3), 3.66 (s, 6H, $2CH_3O$), 3.78−3.84 (m, 1H, CH_2), 3.91−3.98 (m, 2H, CH_2), 4.00−4.04 (m, 1H, CH_2), 4.75 (dd, J = 7.2 Hz, J = 24.6 Hz, 1H, PCH), 5.74 (s, 1H, pyrimidine-H), 5.86 (t, J = 7.8 Hz, 1H, NH), 6.42 (d, J = 8.4 Hz, 1H, ArH), 6.71 (t, J = 7.2 Hz, 1H, ArH), 7.16 (t, J = 7.8 Hz, 1H, ArH), 7.25 (d, J = 8.4 Hz, 2H, ArH), 7.30 (d, J = 6.6 Hz, 2H, ArH), 7.47 (d, J = 7.2 Hz, 1H, ArH); ^{31}P NMR ($CDCl_3$, 162 MHz) δ 20.62; EI-MS (70 eV) m/z (%) 523.3 (M^+, 5.6), 389 (6.6), 388 (34.0), 387 (22.5), 386 (100), 248 (8.2), 247 (7.4), 246 (18.8), 214 (5.2), 140 (4.8), 139 (6.8), 136 (5.7), 109 (9.7). Anal. Calcd for $C_{23}H_{27}ClN_3O_5PS$: C, 52.72; H, 5.19; N, 8.02. Found: C, 52.83; H, 5.35; N, 8.09.

Data for compound **IVh** (R = Me, X = S, Ar = 4-ClC_6H_4): white solid; yield, 69%; mp, 157.8−158.4 °C; IR (KBr) ν 3368 (NH), 2985 (Ar—H), 1577, 1550 (Ar), 1377 (P═O), 1281, 1196 (P—O—C), 1054, 1027 (C—O—C) cm^{-1}; ^{1}H NMR ($CDCl_3$, 600 MHz) δ 3.52 (d, J = 10.2 Hz, 3H, OCH_3), 3.64 (d, J = 10.8 Hz, 3H, OCH_3), 3.66 (s, 6H, $2CH_3O$), 4.78 (dd, J = 7.2 Hz, J = 24.0 Hz, 1H, PCH), 5.73 (s, 1H, pyrimidine-H), 5.81 (t, J = 7.2 Hz, 1H, NH), 6.45 (d, J = 8.4 Hz, 1H, ArH), 6.72 (t, J = 7.8 Hz, 1H, ArH), 7.17 (t, J = 7.8 Hz, 1H, ArH), 7.25 (d, J = 7.8 Hz, 2H, ArH), 7.32 (d, J = 7.2 Hz, 2H, ArH), 7.47 (d, J = 7.2 Hz, 1H, ArH); ^{31}P NMR ($CDCl_3$, 162 MHz) δ 22.83; EI-MS (70 eV) m/z (%) 495.2 (10.7), 493.8 (M^+, 100), 213 (10.2), 212 (95.2), 202 (27.0), 81 (6.6). Anal. Calcd for $C_{21}H_{23}ClN_3O_5PS$: C, 50.86; H, 4.67; N, 8.47. Found: C, 50.66; H, 4.80; N, 8.29.

Data for compound **IVi** (R = Ph, X = S, Ar = 4-ClC_6H_4): white solid; yield, 67%; mp, 129.6−130.8 °C; IR (KBr) ν 3372 (NH), 2987 (Ar—H), 1571, 1553 (Ar), 1374 (P═O), 1275, 1190 (P—O—C), 1057, 1025 (C—O—C) cm^{-1}; ^{1}H NMR ($CDCl_3$, 600 MHz) δ 3.63 (s, 6H, $2CH_3O$), 5.11 (dd, J = 7.8 Hz, J = 25.2 Hz, 1H, PCH), 5.68 (s, 1H, pyrimidine-H), 6.09 (t, J = 7.8 Hz, 1H, NH), 6.50 (d, J = 8.4 Hz, 1H, ArH), 6.76 (t, J = 7.2 Hz, 1H, ArH), 6.91 (d, J = 8.4 Hz, 2H, ArH), 6.94 (d, J = 8.4 Hz, 2H, ArH), 7.11 (t, J = 7.8 Hz, 2H, ArH), 7.18−7.25 (m, 7H, ArH), 7.37 (d, J = 9.0 Hz, 2H, ArH), 7.51 (d, J = 7.8 Hz, 1H, ArH); ^{31}P NMR ($CDCl_3$, 162 MHz) δ 12.99; EI-MS (70 eV) m/z (%) 619.4 (9.3), 618.7 (M^+, 16.2), 617 (15.1), 608 (22.3), 607 (16.9), 556 (13.8), 504 (11.9), 415 (11.0), 254 (57.8), 253 (73.2), 200 (100). Anal. Calcd for $C_{31}H_{27}ClN_3O_5PS$: C, 60.05; H, 4.39; N, 6.78. Found: C, 59.87; H, 4.44; N, 6.97.

Data for compound **IVj** (R = Et, X = S, Ar = 4-BrC_6H_4): white solid; yield, 64%; mp, 135.6−136.5 °C; IR (KBr) ν 3363 (NH), 2982 (Ar—H), 1580, 1557 (Ar), 1366 (P═O), 1289, 1190 (P—O—C), 1057, 1028 (C—O—C) cm^{-1}; ^{1}H NMR ($CDCl_3$, 600 MHz) δ 1.14 (t, J = 7.2 Hz, 3H, CH_3), 1.18 (t, J = 7.2 Hz, 3H, CH_3), 3.66 (s, 6H, $2CH_3O$), 3.78−3.85 (m, 1H, CH_2), 3.91−4.04 (m, 3H, CH_2), 4.73 (dd, J = 7.2 Hz, J = 24.6 Hz, 1H, PCH), 5.74 (s, 1H, pyrimidine-H), 5.85 (t, J = 9.0 Hz, 1H, NH), 6.42 (d, J = 8.4 Hz, 1H, ArH), 6.71 (t, J = 7.2 Hz, 1H, ArH), 7.16 (t, J = 7.2 Hz, 1H, ArH), 7.24 (d, J = 8.4 Hz, 2H, ArH), 7.40 (d, J = 8.4 Hz, 2H, ArH), 7.47 (d, J = 7.2 Hz, 1H, ArH); ^{31}P NMR ($CDCl_3$, 162 MHz) δ 20.85; EI-MS (70 eV) m/z (%) 569.2 (6.0), 567.2 (M^+, 6.4), 433 (20.1), 432 (100), 431 (21.6), 430 (95.5), 292 (15.9), 290 (13.5), 247 (5.6), 211 (6.8), 140 (7.2), 139 (7.4), 136 (9.7), 109 (8.8). Anal. Calcd for $C_{23}H_{27}BrN_3O_5PS$: C, 48.60; H, 4.79; N, 7.39. Found: C, 48.71; H, 4.55; N, 7.17.

Data for compound **IVk** (R = Et, X = S, Ar = 3-$NO_2C_6H_4$): light yellow solid; yield, 69%; mp, 173.2−174.3 °C; IR (KBr) ν 3352 (NH), 2979 (Ar—H), 1587, 1551 (Ar), 1362 (P═O), 1292, 1186 (P—O—C), 1053, 1025 (C—O—C) cm^{-1}; ^{1}H NMR ($CDCl_3$, 600 MHz) δ 1.16 (t, J = 7.2 Hz, 3H, CH_3), 1.20 (t, J = 7.2 Hz, 3H, CH_3), 3.66 (s, 6H, $2CH_3O$), 3.86−3.93 (m, 1H, CH_2), 3.95−4.09 (m, 2H, CH_2), 4.13−4.20 (m, 1H, CH_2), 4.88 (dd, J = 7.2 Hz, J = 25.2 Hz, 1H, PCH), 5.75 (s, 1H, pyrimidine-H), 5.95 (t, J = 8.4 Hz, 1H, NH), 6.41 (d, J = 8.4 Hz, 1H, ArH), 6.75 (t, J = 7.2 Hz, 1H, ArH), 7.17 (t, J = 7.8 Hz, 1H, ArH), 7.47 (t, J = 7.8 Hz, 1H, ArH), 7.50 (d, J = 7.2 Hz, 1H, ArH), 7.73 (d, J = 7.8 Hz, 1H, ArH), 8.13 (d, J = 7.8 Hz, 1H, ArH), 8.25 (s, 1H, ArH); ^{31}P NMR ($CDCl_3$, 162 MHz) δ 19.35; EI-MS (70 eV) m/z (%) 534.3 (M^+, 5.5), 399 (7.9), 398 (23.4), 397 (100), 212 (4.3), 140 (5.4), 136 (8.4). Anal. Calcd for $C_{23}H_{27}N_4O_7PS$: C, 51.68; H, 5.09; N, 10.48. Found: C, 51.87; H, 5.23; N, 10.61.

Data for compound **IVl** (R = Et, X = S, Ar = 4-$NO_2C_6H_4$): light yellow solid; yield, 74%; mp, 180.2−181.5 °C; IR (KBr) ν 3340 (NH), 2959 (Ar—H), 1574, 1544 (Ar), 1359 (P═O), 1285, 1180 (P—O—C), 1049, 1027 (C—O—C) cm^{-1}; ^{1}H NMR ($CDCl_3$, 600 MHz) δ 1.17 (t, J = 7.2 Hz, 3H, CH_3), 1.19 (t, J = 7.2 Hz, 3H, CH_3), 3.69 (s, 6H, $2CH_3O$), 3.86−3.92 (m, 1H, CH_2), 3.93−3.97 (m, 1H, CH_2), 3.99−4.07 (m, 2H, CH_2), 4.89 (dd, J = 6.0 Hz, J = 25.2 Hz, 1H, PCH), 5.76 (s, 1H, pyrimidine-H), 5.92 (t, J = 7.2 Hz, 1H, NH), 6.35 (d, J = 7.8 Hz, 1H, ArH), 6.74 (t, J = 7.2 Hz, 1H, ArH), 7.16 (t, J = 7.8 Hz, 1H, ArH), 7.50 (d, J = 7.2 Hz, 1H, ArH), 7.58 (d, J = 7.2 Hz, 2H, ArH), 8.15 (d, J = 8.4 Hz, 2H, ArH); ^{31}P NMR ($CDCl_3$, 162 MHz) δ 19.14; EI-MS (70 eV) m/z (%) 534.3 (M^+, 6.7), 399 (7.1), 398 (21.0), 397 (100), 211 (4.0), 140 (5.3), 136 (6.7). Anal. Calcd for $C_{23}H_{27}N_4O_7PS$: C, 51.68; H, 5.09; N, 10.48. Found: C, 51.52; H, 5.05; N, 10.39.

Data for compound **IVm** (R = Et, X = S, Ar = 2,4-$(MeO)_2C_6H_3$): white solid; yield, 69%; mp, 110.9−112.1 °C; IR (KBr) ν 3345 (NH), 2951 (Ar—H), 1578, 1541 (Ar), 1350 (P═O), 1283, 1184 (P—O—C), 1055, 1028 (C—O—C) cm^{-1}; ^{1}H NMR ($CDCl_3$, 600 MHz) δ 1.08 (t, J = 7.2 Hz, 3H, CH_3), 1.22 (t, J = 7.2 Hz, 3H, CH_3), 3.59 (s, 6H, $2CH_3O$), 3.69−3.73 (m, 1H, CH_2), 3.75 (s, 3H, CH_3O), 3.88 (s, 3H, CH_3O), 3.89−3.92 (m, 1H, CH_2), 4.00−4.10 (m, 2H, CH_2), 5.30 (dd, J = 9.0 Hz, J = 24.6 Hz, 1H, PCH), 5.69 (s, 1H, pyrimidine-H), 5.87 (t, J = 9.0 Hz, 1H, NH), 6.32 (d, J = 8.4 Hz, 1H, ArH), 6.42 (s, 1H, ArH), 6.59 (d, J = 8.4 Hz, 1H, ArH), 6.65 (t, J = 7.2 Hz, 1H, ArH), 7.09 (dd, J = 2.4 Hz, J = 8.4 Hz, 1H, ArH), 7.17 (t, J = 7.2 Hz, 1H, ArH), 7.41 (d, J = 7.8 Hz, 1H, ArH); ^{31}P NMR ($CDCl_3$, 162 MHz) δ 22.09; EI-MS (70 eV) m/z (%) 549.3 (M^+, 0.7), 414 (6.9), 413 (24.6), 412 (100), 274 (9.1), 273 (6.8), 272 (38.2). Anal. Calcd for $C_{25}H_{32}N_3O_7PS$: C, 54.64; H, 5.87; N, 7.65. Found: C, 54.70; H, 5.93; N, 7.47.

Data for compound **IVn** (R = Et, X = S, Ar = 2,4-$Cl_2C_6H_3$): white solid; yield, 74%; mp, 190.2−191.3 °C; IR (KBr) ν 3348 (NH), 2955 (Ar—H), 1584, 1546 (Ar), 1352 (P═O), 1287, 1178 (P—O—C), 1051, 1033 (C—O—C) cm^{-1}; ^{1}H NMR ($CDCl_3$, 600 MHz) δ 1.12 (t, J = 7.2 Hz, 3H, CH_3), 1.24 (t, J = 7.2 Hz, 3H, CH_3), 3.63 (s, 6H, $2CH_3O$), 3.76−3.82 (m, 1H, CH_2), 3.91−3.97 (m, 1H, CH_2), 4.04−4.13 (m, 2H, CH_2), 5.33 (dd, J = 8.4 Hz, J = 24.6 Hz, 1H, PCH), 5.73 (s, 1H, pyrimidine-H), 5.97 (t, J = 9.0 Hz, 1H, NH), 6.47 (d, J = 7.8 Hz, 1H, ArH), 6.72 (t, J = 7.2 Hz, 1H, ArH), 7.09 (d, J = 8.4 Hz, 1H, ArH), 7.20 (t, J = 8.4 Hz, 1H, ArH), 7.25 (dd, J = 2.4 Hz, J = 8.4 Hz, 1H, ArH), 7.39 (s, 1H, ArH), 7.45 (d, J = 9.0 Hz, 1H, ArH); ^{31}P NMR ($CDCl_3$, 162 MHz) δ 21.69; EI-MS (70 eV) m/z (%) 557.3 (M^+, 0.5), 524 (6.1), 523 (5.4), 522 (14.8), 424 (14.2), 423 (14.6),

DOI: 10.1021/acs.jafc.5b02335
J. Agric. Food Chem. 2015, 63, 7219−7229

Table 1. Herbicide Activity of Some Compounds I–III (in Vitro, Plate Method, Inhibition Percent)[a]

compd	*Arabidopsis thaliana* (10 mg/L)			*Poa annua* (32 mg/L)			compd	*Arabidopsis thaliana* (10 mg/L)			*Poa annua* (32 mg/L)		
Is	99	99	99	99	99	99	**IIIb**	99	99	99	0	0	0
It	99	99	99	99	99	99	**IIIc**	99	99	99	0	0	0
Iu	0	0	0	99	99	99	**IIId**	99	99	99	0	0	0
Iv	99	99	99	99	99	99	**IIIe**	99	99	99	0	0	0
Iw	99	99	99	99	99	99	**IIIf**	99	99	99	0	0	0
Ix	99	99	99	99	99	99	**IIIg**	99	99	99	0	0	0
IIa	99	99	99	99	0	49	**IIIh**	99	99	99	0	0	0
IIb	0	0	0	0	0	0	**IIIi**	99	99	99	0	0	0
IIIa	99	99	99	0	0	0	**IIIj**	99	99	99	0	0	0

[a]Each sample was tested against each plant three times.

Table 2. Herbicide Activity of Some Compounds I–IV (in Vivo, Glass House Screen, GH1)[a,b]

		postemergence				pre-emergence					
compd	dopse (g/ha)	*Amaranthus retroflexus*	*Lolium perenne*	*Stellaria media*	*Digitaria sanguinalis*	*Amaranthus retroflexus*	*Lolium perenne*	*Stellaria media*	*Digitaria sanguinalis*	symptomology	
Ib	1000	100	80	80	80	80	80	60	70	ST	NC
Ic	1000	100	80	80	70	70	70	80	60	NC	ST
If	1000	70	60	40	40	30	20	0	0	NC	ST
Ig	1000	100	80	80	60	80	90	50	70	ST	NC
Ii	1000	100	70	70	60	70	50	10	20	NC	ST
Ik	1000	90	60	60	60	70	40	40	30	NC	CL
In	1000	90	70	60	70	70	70	60	20	NC	CL
Ip	1000	70	30	40	20	70	0	0	0	ST	MR
Iq	1000	0	0	0	0	0	0	0	0		
Is	1000	100	100	70	80	80	80	40	50	NC	BL
It	1000	90	100	80	80	70	80	70	90	NC	ST
Iu	1000	90	60	40	50	70	60	30	30	ST	CL
Iv	1000	100	20	50	0	70	20	40	0	NC	ST
Iw	1000	70	20	20	0	20	0	0	0	CL	NC
Ix	1000	70	20	20	40	60	60	40	60	BL	ST
IIIa	1000	30	0	0	0	0	0	0	0	MR	DG
acetochlor	750	40	70	90	70	100	100	90	100	GI	ST
atrazine	1000	100	100	90	80	100	100	100	50	NC	GI
glyphosate	1000	100	100	90	100	40	100	90	10	NC	ST
mesotrione	250	100	80	100	100	100	70	100	100	BL	NC

[a]Scores are given as percent phytotoxicity score. The higher the score (% phytotoxicity), the greater the efficacy of the compound. Herbicide symptomologies are given as a phytotoxicity type: NC, necrosis; ST, stunting; GI, germination inhibition; CL, chlorosis; DG, darker green; BL, bleaching. [b]Compounds **II–IV** displayed no herbicidal activity in the GH1 bioassay screening.

422 (70.4), 421 (21.6), 420 (100), 384 (5.8). Anal. Calcd for $C_{23}H_{26}Cl_2N_3O_5PS$: C, 49.47; H, 4.69; N, 7.52. Found: C, 49.33; H, 4.40; N, 7.73.

Data for compound **IVo** (R = Et, X = S, Ar = 4-HOC_6H_4): white solid; yield, 75%; mp, 201.3–202.5 °C; IR (KBr) ν 3365 (NH), 2987 (Ar—H), 1573, 1559 (Ar), 1361 (P═O), 1284, 1183 (P—O—C), 1056, 1034 (C—O—C) cm^{-1}; ^1H NMR ($CDCl_3$, 600 MHz) δ 1.15 (t, J = 7.2 Hz, 3H, CH_3), 1.18 (t, J = 7.2 Hz, 3H, CH_3), 3.63 (s, 6H, $2CH_3O$), 3.71–3.74 (m, 1H, CH_2), 3.78–3.83 (m, 1H, CH_2), 3.89–4.03 (m, 2H, CH_2), 4.71 (dd, J = 7.8 Hz, J = 24.0 Hz, 1H, PCH), 5.70 (s, 1H, pyrimidine-H), 5.78 (t, J = 8.4 Hz, 1H, NH), 6.50 (d, J = 8.4 Hz, 1H, ArH), 6.56 (d, J = 8.4 Hz, 2H, ArH), 6.69 (t, J = 7.2 Hz, 1H, ArH), 7.07 (d, J = 8.4 Hz, 2H, ArH), 7.16 (t, J = 7.8 Hz, 1H, ArH), 7.45 (d, J = 7.8 Hz, 1H, ArH), 7.96 (br s, 1H, OH); ^{31}P NMR ($CDCl_3$, 162 MHz) δ 22.79; EI-MS (70 eV) m/z (%) 505.3 (M^+, 5.0), 370 (9.1), 369 (22.5), 368 (100), 274 (10.9), 263 (6.1), 230 (15.3), 228 (23.4), 196 (5.7). Anal. Calcd for $C_{23}H_{28}N_3O_6PS$: C, 54.65; H, 5.58; N, 8.31. Found: C, 54.50; H, 5.74; N, 8.57.

Data for compound **IVp** (R = Et, X = O, Ar = C_6H_5): light yellow oil; yield, 68%; IR (KBr) ν 3371 (NH), 2984 (Ar—H), 1570, 1552 (Ar), 1357 (P═O), 1280, 1175 (P—O—C), 1046, 1023 (C—O—C) cm^{-1}; ^1H NMR ($CDCl_3$, 400 MHz) δ 1.09 (t, J = 7.2 Hz, 3H, CH_3), 1.18 (t, J = 7.2 Hz, 3H, CH_3), 3.66–3.74 (m, 1H, CH_2), 3.80 (s, 6H, $2CH_3O$), 3.88–4.06 (m, 3H, CH_2), 4.77 (d, J = 24.0 Hz, 1H, PCH), 5.04 (br s, 1H, NH), 5.79 (s, 1H, pyrimidine-H), 6.54 (d, J = 8.0 Hz, 1H, ArH), 6.69 (t, J = 7.6 Hz, 1H, ArH), 6.95 (t, J = 7.6 Hz, 1H, ArH), 7.05 (d, J = 8.0 Hz, 1H, ArH), 7.24–7.30 (m, 3H, ArH), 7.40 (d, J = 7.6 Hz, 2H, ArH); ^{31}P NMR ($CDCl_3$, 162 MHz) δ 21.03. Anal. Calcd for $C_{23}H_{28}N_3O_6P$: C, 58.35; H, 5.96; N, 8.88. Found: C, 58.51; H, 6.07; N, 9.00.

Data for compound **IVq** (R = Et, X = O, Ar = 2-ClC_6H_4): white solid; yield, 85%; mp, 90.5–91.3 °C; IR (KBr) ν 3353 (NH), 2981 (Ar—H), 1563, 1547 (Ar), 1351 (P═O), 1277, 1169 (P—O—C), 1042, 1021 (C—O—C) cm^{-1}; ^1H NMR ($CDCl_3$, 600 MHz) δ 1.06 (t, J = 7.2 Hz, 3H, CH_3), 1.24 (t, J = 7.2 Hz, 3H, CH_3), 3.64–3.71 (m, 1H, CH_2), 3.79 (s, 6H, $2CH_3O$), 3.86–3.92 (m, 1H, CH_2), 4.05–4.14 (m, 2H, CH_2), 5.19 (t, J = 9.0 Hz, 1H, NH), 5.39 (dd, J = 9.0 Hz, J = 24.6 Hz, 1H, PCH), 5.79 (s, 1H, pyrimidine-H), 6.56 (d, J = 8.4 Hz, 1H, ArH), 6.69 (t, J = 7.8 Hz, 1H, ArH), 6.98 (t, J = 7.8 Hz, 1H, ArH), 7.04 (d, J = 7.8 Hz, 1H, ArH), 7.17 (q, J = 7.2 Hz, 2H, ArH), 7.36 (d, J = 7.2 Hz, 1H, ArH), 7.45 (d, J = 7.2 Hz, 1H, ArH); ^{31}P NMR ($CDCl_3$, 162 MHz) δ 20.78; EI-MS (70 eV) m/z (%) 507.5 (M^+, 4.8), 370.5 (100), 336 (4.0), 232 (5.9), 136 (6.7). Anal. Calcd for

DOI: 10.1021/acs.jafc.5b02335
J. Agric. Food Chem. 2015, 63, 7219–7229

Table 3. Herbicide Activity of Some Compounds I (in Vivo, Glass House Screen, GH2)[a]

		postemergence								symptomology		pre-emergence								symptomology	
compd	dose (g/ha)	*Abutilon theophrasti*	*Bidens pilosa*	*Chenopodium album*	*Kochia scoparia*	*Echinochloa crus galli*	*Setaria Faberi*	*Eleusine indica*	*Sorghum halepense*	1	2	*Abutilon theophrasti*	*Bidens pilosa*	*Chenopodium album*	*Kochia scoparia*	*Echinochloa crus galli*	*Setaria Faberi*	*Eleusine indica*	*Sorghum halepense*	1	2
Ib	1000	70	10	90	90	70	70	70	60	ST	NC	50	10	80	80	70	70	60	70	ST	CL
Ic	1000	70	0	80	80	60	70	60	60	ST	NC	40	0	70	80	60	60	70	NC	ST	CL
Ig	1000	50	30	100	80	60	60	60	60	ST	NC	70	50	80	80	70	70	70	70	ST	CL
Ii	1000	20	0	70	90	60	70	60	20	ST	NC	0	0	70	70	50	50	40	0	ST	CL
Ik	1000	0	0	100	80	60	40	10	40	NC	ST	0	0	70	70	40	60	60	50	ST	BL
In	1000	30	0	70	70	60	60	50	20	ST	NC	50	0	70	70	40	60	40	0	ST	
mesotrione	62.5	80	40	70	70	70	60	70	60	BL	NC	80	80	90	70	80	50	90	50	BL	NC
atrazine	300	70	20	70	50	100	100	90	60	NC	ST	40	20	NC	30	90	100	100	80	GI	ST
glyphosate	1000	80	90	100	100	60	80	60	50	NC	ST										
acetochlor	250											0	0	60	0	90	90	100	90	ST	NC

[a]Results from testing on the GH2 screen, with positive controls. Scores are given as percent phytotoxicity score. Herbicide symptomologies are given as a phytotoxicity type: NC, necrosis; ST, stunting; GI, germination inhibition; CL, chlorosis; BL, bleaching.

$C_{23}H_{27}ClN_3O_6P$: C, 54.39; H, 5.36; N, 8.27. Found: C, 54.41; H, 5.50; N, 8.08.

Data for compound **IVr** (R = Et, X = O, Ar = 2-FC_6H_4): light yellow oil; yield, 73%; IR (KBr) ν 3364 (NH), 2988 (Ar—H), 1560, 1542 (Ar), 1357 (P═O), 1270, 1173 (P—O—C), 1048, 1026 (C—O—C) cm^{-1}; ^1H NMR ($CDCl_3$, 400 MHz) δ 1.09 (t, J = 6.8 Hz, 3H, CH_3), 1.23 (t, J = 6.8 Hz, 3H, CH_3), 3.65−3.72 (m, 1H, CH_2), 3.78 (s, 6H, $2CH_3O$), 3.87−3.97 (m, 1H, CH_2), 4.04−4.13 (m, 2H, CH_2), 5.07 (t, J = 6.8 Hz, 1H, NH), 5.20 (dd, J = 8.0 Hz, J = 24.4 Hz, 1H, PCH), 5.78 (s, 1H, pyrimidine-H), 6.63 (d, J = 8.0 Hz, 1H, ArH), 6.71 (t, J = 7.6 Hz, 1H, ArH), 6.80 (d, J = 7.6 Hz, 1H, ArH), 6.91 (d, J = 7.6 Hz, 1H, ArH), 7.04 (q, J = 7.2 Hz, 2H, ArH), 7.22 (d, J = 7.2 Hz, 1H, ArH), 7.40 (t, J = 7.2 Hz, 1H, ArH); ^{31}P NMR ($CDCl_3$, 162 MHz) δ 20.34. Anal. Calcd for $C_{23}H_{27}FN_3O_6P$: C, 56.21; H, 5.54; N, 8.55. Found: C, 56.37; H, 5.34; N, 8.31.

Data for compound **IVs** (R = Et, X = O, Ar = 4-FC_6H_4): light yellow oil; yield, 75%; IR (KBr) ν 3353 (NH), 2972 (Ar—H), 1553, 1547 (Ar), 1351 (P═O), 1267, 1169 (P—O—C), 1052, 1029 (C—O—C) cm^{-1}; ^1H NMR ($CDCl_3$, 400 MHz) δ 1.12 (t, J = 6.8 Hz, 3H, CH_3), 1.18 (t, J = 6.8 Hz, 3H, CH_3), 3.80 (s, 6H, $2CH_3O$), 3.91−4.06 (m, 4H, CH_2), 4.77 (dd, J = 6.4 Hz, J = 24.0 Hz, 1H, PCH), 5.02 (t, J = 8.0 Hz, 1H, NH), 5.80 (s, 1H, pyrimidine-H), 6.51 (d, J = 8.0 Hz, 1H, ArH), 6.71 (t, J = 7.6 Hz, 1H, ArH), 6.94−7.01 (m, 3H, ArH), 7.07 (d, J = 7.6 Hz, 1H, ArH), 7.39 (t, J = 7.6 Hz, 2H, ArH); ^{31}P NMR ($CDCl_3$, 162 MHz) δ 20.18. Anal. Calcd for $C_{23}H_{27}FN_3O_6P$: C, 56.21; H, 5.54; N, 8.55. Found: C, 56.04; H, 5.48; N, 8.63.

Data for compound **IVt** (R = Et, X = O, Ar = 4-ClC_6H_4): light yellow oil; yield, 79%; IR (KBr) ν 3356 (NH), 2979 (Ar—H), 1567, 1543 (Ar), 1359 (P═O), 1272, 1161 (P—O—C), 1045, 1028 (C—O—C) cm^{-1}; ^1H NMR ($CDCl_3$, 400 MHz) δ 1.13 (t, J = 7.2 Hz, 3H, CH_3), 1.19 (t, J = 6.8 Hz, 3H, CH_3), 3.81 (s, 6H, $2CH_3O$), 3.90−4.06 (m, 4H, CH_2), 4.75 (d, J = 24.4 Hz, 1H, PCH), 4.98 (br s, 1H, NH), 5.80 (s, 1H, pyrimidine-H), 6.49 (d, J = 8.0 Hz, 1H, ArH), 6.71 (t, J = 7.6 Hz, 1H, ArH), 6.95 (t, J = 7.6 Hz, 1H, ArH), 7.07 (d, J = 7.6 Hz, 1H, ArH), 7.25 (d, J = 8.0 Hz, 2H, ArH), 7.35 (d, J = 6.4 Hz, 2H, ArH); ^{31}P NMR ($CDCl_3$, 162 MHz) δ 20.92. Anal. Calcd for $C_{23}H_{27}ClN_3O_6P$: C, 54.39; H, 5.36; N, 8.27. Found: C, 54.13; H, 5.31; N, 8.33.

Data for compound **IVu** (R = Et, X = O, Ar = 4-$CH_3C_6H_4$): light yellow oil; yield, 66%; IR (KBr) ν 3341 (NH), 2994 (Ar—H), 1573, 1560, 1497 (Ar), 1362 (P═O), 1271, 1177 (P—O—C), 1047, 1026 (C—O—C) cm^{-1}; ^1H NMR ($CDCl_3$, 600 MHz) δ 1.10 (t, J = 6.6 Hz, 3H, CH_3), 1.17 (t, J = 6.6 Hz, 3H, CH_3), 2.28 (s, 3H, CH_3), 3.65−3.73 (m, 1H, CH_2), 3.78 (s, 6H, $2CH_3O$), 3.87−3.95 (m, 2H, CH_2), 3.98−4.03 (m, 1H, CH_2), 4.75 (d, J = 24.0 Hz, 1H, PCH), 5.68 (br s, 1H, NH), 5.78 (s, 1H, pyrimidine-H), 6.55 (d, J = 7.8 Hz, 1H, ArH), 6.67 (t, J = 7.2 Hz, 1H, ArH), 6.93 (t, J = 7.8 Hz, 1H, ArH), 7.04 (d, J = 7.8 Hz, 1H, ArH), 7.07 (d, J = 7.2 Hz, 2H, ArH), 7.27 (d, J = 7.2 Hz, 2H, ArH); ^{31}P NMR ($CDCl_3$, 162 MHz) δ 21.25; EI-MS (70 eV) m/z (%) 487.3 (M^+, 4.8), 351 (24.2), 350 (100), 258 (4.2), 210 (15.8). Anal. Calcd for $C_{24}H_{30}N_3O_6P$: C, 59.13; H, 6.20; N, 8.62. Found: C, 59.31; H, 6.28; N, 8.50.

Data for compound **IVv** (R = Et, X = O, Ar = 4-$NO_2C_6H_4$): white solid; yield, 64%; mp, 115.4−117.3 °C; IR (KBr) ν 3362 (NH), 2999 (Ar—H), 1570, 1564, 1492 (Ar), 1357 (P═O), 1266, 1171 (P—O—C), 1046, 1028 (C—O—C) cm^{-1}; ^1H NMR ($CDCl_3$, 600 MHz) δ 1.16 (t, J = 7.2 Hz, 3H, CH_3), 1.20 (t, J = 7.2 Hz, 3H, CH_3), 3.80 (s, 6H, $2CH_3O$), 3.83−3.88 (m, 1H, CH_2), 3.98−4.04 (m, 3H, CH_2), 4.88 (dd, J = 6.6 Hz, J = 25.2 Hz, 1H, PCH), 5.08 (t, J = 7.8 Hz, 1H, NH), 5.82 (s, 1H, pyrimidine-H), 6.40 (d, J = 7.8 Hz, 1H, ArH), 6.75 (t, J = 7.8 Hz, 1H, ArH), 6.95 (t, J = 7.8 Hz, 1H, ArH), 7.10 (d, J = 7.8 Hz, 1H, ArH), 7.61 (d, J = 7.2 Hz, 2H, ArH), 7.16 (d, J = 7.2 Hz, 2H, ArH); ^{31}P NMR ($CDCl_3$, 162 MHz) δ 21.03. Anal. Calcd for $C_{24}H_{27}N_4O_8P$: C, 53.28; H, 5.25; N, 10.81. Found: C, 53.17; H, 5.35; N, 10.98.

Herbicidal Activity Assays. All of the herbicidal activity assays (in vitro and in vivo) were performed in the bioactive activity evaluation platform at Syngenta Jealott's Hill International Research Centre.

Herbicidal Plate Assays (in Vitro). The compounds were tested for herbicidal activity against *Arabidopsis thaliana* at 10 mg/L and

DOI: 10.1021/acs.jafc.5b02335
J. Agric. Food Chem. 2015, 63, 7219−7229

Table 4. Insecticidal Activity of Compounds IVs, IVt, and IVl

	Aphis species (mixed-population mortality, 1000 mg/L)				*Plutella xylostella* (larval mortality, 500 mg/L)				*Diabrotica balteata* (larval mortality, 500 mg/L)			
compd	Rep1	Rep2	Rep3	av	Rep1	Rep2	Rep3	av	Rep1	Rep2	Re p 3	av
IVs	0	99	99	66	0	0	0	0	0	0	0	0
IVt	99	99	99	99	0	0	0	0	0	99	0	33
IVl	0	0	0	0	99	99	99	99	0	0	0	0
thiamethoxam	99	99	99	99	0	0	0	0	99	99	99	99
indoxacarb	0	0	0	0	99	99	99	99	99	99	99	99

against *Poa annua* at 32 mg/L. Test plates were stored for 7 days in a controlled environment cabinet. They were scored as 0 or 99, where 99 means significant herbicidal effect and 0 means no effect. The herbicidal activity is summarized in Table 1.

Herbicide Glasshouse Screening (in Vivo, GH1). The substances were dissolved in dimethyl sulfoxide (DMSO) for storage. Subsamples to be tested were dried down and formulated into spray solution for application. The compounds were tested for pre- and postemergence activity against four weed species, with the compounds applied at 1000 g/ha. The plants were then stored in the glasshouse for 12 days. The weeds tested were *Amaranthus retroflexus*, *Stellaria media*, *Lolium perenne*, and *Digitaria sanguinalis*. Assessments were made of pecent phytotoxicity and converted to a banded score between 0 and 100, where complete control of the target is 100 and 0 is no control. Acetochlor, atrazine, mesotrione, and glyphosate were used as positive controls for the test. The herbicidal activity is summarized in Table 2.

Herbicide Glasshouse Screening (in Vivo, GH2). The substances were dissolved in DMSO for storage. Subsamples to be tested were dried down and formulated into spray solution for application. The compounds were tested for pre- and postemergence activity against a range of weed species (dicotolydon plant weeds *Chenopodium album*, *Abutalon theophrasti*, *Koschia scoparia*, and *Bidens pilosa*; monocotolydon plant weeds *Echinochloa crus-galli*, *Setaria fabari*, *Eleusine indica*, and *Sorghum halapense*), with the compounds applied at 1000 g/ha. The plants were then stored in the glasshouse for 12 days. Assessments were made of percent phytotoxicity and converted to a banded score between 0 and 100, where complete control of the target is 100 and 0 is no control. Acetochlor, atrazine, mesotrione, and glyphosate were used as positive controls for the test. The herbicidal activity is summarized in Table 3.

Insecticide Assays. All of the insecticidal assays were carried out in the bioactive activity evaluation platform at Syngenta Jealott's Hill International Research Centre. The compounds were tested for activity against an aphid species at 1000 mg/L on a leaf-piece-based assay and against *Plutella xylostella* and *Diabrotica balteata* at 500 mg/L in artificial diet assays. Chemicals were applied to feeding aphids or prior to infestation with *P. xylostella* and *D. balteata* larvae. Mortality was assessed relative to control wells using a two-band system (0 or 99 where 99 = significant mortality and 0 = no effect), 3−6 days after the treatments depending on the assay. In addition to the test compounds, thiamethoxam and indoxacarb as the positive control compounds were included in each insecticide assays. For all screens, data were recorded for replicates and averaged. The insecticidal activity is summarized in Table 4.

Mode of Action Investigation. *Methodology.* The mode of action screen (MOA1) comprises a series of biochemical, cell-based, and whole plant assays that enable scientists at Syngenta to determine if test compounds have any of the major herbicide modes of action. Compounds are tested only once in MOA1 (i.e., there is no duplicate or replicate), so the IC_{50} values are just an approximation.

Compounds **Ib**, **Ic**, **Ig**, and **Ii** did not give any specific MOA in MOA1 as it was inactive in all of the assays; for example, compounds **Ib** and **Ig** did not give any specific MOA in MOA1 as it was inactive in all of the assays apart from some activity on tobacco cells (EC_{50} = 1 mg/L, 0.4 mg/L, respectively) and some weak injury on *Arabidospsis* seedlings (EC_{50} = 36 mg/L, 1 mg/L respectively) and tobacco seedlings (EC_{50} = 36 mg/L, 18 mg/L, respectively), so it suggested that these compounds perhaps have novel herbicidal modes of action. Further herbicidal mode of action determination is underway at Syngenta Jealott's Hill International Research Centre.

RESULTS AND DISCUSSION

Synthesis. Series of novel α-amino phosphonate derivatives containing a pyrimidinyl moiety, **I**, **II**, **III**, and **IV**, were designed and synthesized by Lewis acid (magnesium perchlorate) catalyzed Mannich-type reaction of benzoaldehyde containing a pyrimidinyl group, substituted benzylamine, and phosphites. It was found that Lewis acid (magnesium perchlorate) has a large effect on the rate of the reaction and yields of products; without the use of the catalyst, the rates of the reaction were remarkably slowed and the yields were very low, too (about 20%). The structures of target compounds **I**−**IV** were determined by their spectral data (IR, ^{1}H NMR, ^{31}P NMR, EI-MS, or ESI-MS) and elemental analyses.

Herbicidal Activities and Structure−Activity Relationships. The results of herbicidal activities, in vitro and in vivo (GH1, GH2), of these compounds are listed in Tables 1, 2, and 3, respectively. To our delight, most compounds **I** exhibited good herbicidal activities in vivo (Tables 2 and 3). However, their meta-position and para-position pyrimidin-2-oxy-substituted structural isomers **II** and **III** and their analogues **IV** did not display any herbicidal activities in vivo (GH1; data not listed), although some of them displayed good selectivity inhibitory activity against *Arabidopsis thaliana* at a concentration of 10 mg/L in vitro (Table 1).

For the in vivo (GH1) herbicidal activity, it was found that compounds **Ib**, **Ic**, **Ig**, **Ii**, **Is**, and **Iv** displayed 100% inhibition against *Amaranthus retroflexus* at the dose of 1000 g/ha in postemergence treatment. Moreover, both compounds **Is** and **It** showed 100% inhibition against *Lolium perenne* at the dose of 1000 g/ha in postemergence treatment. Furthermore, all compounds **I** exhibited better inhibition against the four plants tested in postemergence treatment than in pre-emergence one. Finally, compounds **Ib**, **Ic**, **Ig**, **Is**, and **It** displayed good broad-spectrum herbicidal activities against the four plants in both post- and pre-emergence treatments. As for the preliminary structure−activity relationships, it was shown that the different phosphonic acid esters affected the herbicidal activity significantly; phosphonic acid methyl and ethyl esters were universally advantageous for the herbicidal activities compared with the butyl and phenyl esters. However, the electronic effects of substituent on the benzene ring have no remarkable effect on the herbicidal activity. Both electron-donating (**Ig**, 4-methoxy-substituted) and electron-withdrawing compounds (**Ic**, 4-nitro-substituted; **Is** and **It**, 4-fluoro-substituted) displayed as good herbicidal activity; even nonsubstituted compound **Ib** also exhibited good herbicidal activity.

As for the in vivo (GH2) herbicidal activity of **I**, as shown in Table 3, all of the tested compounds (**Ib**, **Ic**, **Ig**, **Ii**, **Ik**, and **In**)

DOI: 10.1021/acs.jafc.5b02335
J. Agric. Food Chem. 2015, 63, 7219−7229

showed better inhibition activity against *Chenopodium album* and *Kochia scoparia* than against the other six plants (*Abutilon theophrasti*, *Bidens pilosa*, *Echinochloa crus galli*, *Setaria faberi*, *Eleusine indica*, and *Sorghum halepense*) at the dose of 1000 g/ha in both post- and pre-emergence treatments; for instance, both compounds **Ig** and **Ik** displayed 100% inhibition against *Chenopodium album* in the postemergence treatment. However, these test compounds exhibited weak herbicidal activity against *Bidens pilosa* relative to the other seven plants in both post- and pre-emergence treatments, except for compound **Ig**, which displayed 50% inhibition in the pre-emergence treatment. Further herbicidal activity evaluation in a lower dose and mode of action investigation are underway at Syngenta Jealott's Hill International Research Centre.

Insecticidal Activities. It is worth noting that some of the analogues **IV** showed selective insecticidal activities (Table 4), although compounds **IV** did not display any herbicidal activities in vivo. For example, compounds **IVs** and **IVt** exhibited insecticidal activity against *Aphis* species to some extent at the concentration of 1000 mg/L. Moreover, the sulfur analogue **IVl** showed insecticidal activity against *Plutella xylostella* at the concentration of 500 mg/L. Further insecticidal activity study will be performed and will be reported in due course.

In summary, α-amino phosphonic acids and their ester derivatives, as bioisosteres of natural amino acids, exhibited versatile biological activities. To find novel high-activity and low-toxicity herbicide lead compounds with novel herbicidal modes of action, four series of novel α-amino phosphonate derivatives containing a pyrimidinyl moiety **I**, **II**, **III**, and **IV** were designed and synthesized by Lewis acid (magnesium perchlorate) catalyzed Mannich-type reaction of aldehydes, amines, and phosphites. The bioassay (in vivo, GH1 and GH2) showed that most compounds **I** exhibited good selective herbicidal activities. However, their structural isomers **II** and **III** and analogues **IV** did not display any herbicidal activities in vivo, although some of them displayed selectivity inhibitory activity against *Arabidopsis thaliana* in vitro. Interestingly, compounds **IVs**, **IVt**, and **IVl** possessed selective insecticidal activities against *Aphis* species or *Plutella xylostella*, respectively. Their preliminary herbicidal mode of action and structure–activity relationships were also investigated.

■ ASSOCIATED CONTENT

Supporting Information

The Supporting Information is available free of charge on the ACS Publications website at DOI: 10.1021/acs.jafc.5b02335.

Synthetic procedures for the intermediates and the target compounds methods, data of intermediates **1a–1c**, **2a–2b**, and title compounds **I–IV**, and ^{1}H NMR spectra of **I–IV** (PDF)

■ AUTHOR INFORMATION

Corresponding Author

*(D. Q. SHI) Phone: +86-27-67687958. Fax: +86-27-67862041. E-mail: chshidq@mail.ccnu.edu.cn.

Funding

We are grateful to the National Natural Science Foundation of China (No. 21342004), self-determined research funds of CCNU from the colleges' basic research and operation of MOE (No. CCNU14A02007), and the Syngenta Ph.D. (postgraduate) program for support of this work.

Notes

The authors declare no competing financial interest.

■ REFERENCES

(1) Palacios, F.; Alonso, C.; de los Santos, J. M. Synthesis of α-aminophosphonates and -phosphinates. *Chem. Rev.* **2005**, *105*, 899–931.

(2) Kuhkar, V. P., Hudson, H. R., Eds. *Synthesis of α-Aminoalkanephosphonic and α-Aminophosphinic Acids [M]*; Wiley: Chichester, UK, 2000.

(3) Montchamp, J.-L. Phosphinate chemistry in the 21st Century: a viable alternative to the use of phosphorus trichloride in organophosphorus synthesis. *Acc. Chem. Res.* **2014**, *47*, 77–87.

(4) Crépy, K. V. L; Imamoto, T. New P-chirogenic phosphine ligands and their use in catalytic asymmetric reactions, new aspects in phosphorus chemistry III. *Curr. Chem.* **2003**, *223*, 1–40.

(5) Tang, W.; Zhang, X. New chiral phosphorus ligands for enantioselective hydrogenation. *Chem. Rev.* **2003**, *103*, 3029–3070.

(6) Cupta, H. C. L. *Insecticides: Toxicology and Uses [M]*; Agrotech Publishing Academy Press: Udaipur, India, 1999; 51211.

(7) Matsumara, F. *Tocicology of Insecticides [M]*, 2nd ed.; Plenum Press: New York, 1985; pp 62–90.

(8) Priestman, M. A.; Healy, M. L.; Becker, A.; Alberg, D. G.; Bartlett, P. A.; Lushington, G. H.; Schonbrunn, E. Interaction of phosphonate analogues of the tetrahedral reaction intermediate with 5-enolpyruvylshikimate-3-phosphate synthase in atomic detail. *Biochemistry* **2005**, *44*, 3241–3248.

(9) Kafarski, P.; Lejczak, B.; Forlani, G. Herbicidally active aminomethylenebisphosphonic acids. *Heteroat. Chem.* **2000**, *11*, 449–453.

(10) Chen, M. H.; Chen, Z.; Song, B. A.; Bhadury, P. S.; Yang, S.; Cai, X. J.; Hu, D. Y.; Xue, W.; Zeng, S. Synthesis and antiviral activities of chiral thiourea derivatives containing α-aminophosphonate moiety. *J. Agric. Food Chem.* **2009**, *57*, 1383–1388.

(11) Hu, D. Y.; Wan, Q. Q.; Yang, S.; Song, B. A.; Bhadury, P. S.; Jin, L. H.; Yan, K.; Liu, F.; Chen, Z.; Xue, W. Synthesis and antiviral activities of amide derivatives containing α-aminophosphonate moiety. *J. Agric. Food Chem.* **2008**, *56*, 998–1001.

(12) Long, N.; Cai, X. J.; Song, B. A.; Yang, S.; Chen, Z.; Bhadury, P. S.; Hu, D. Y.; Jin, L. H.; Xue, W. Synthesis and antiviral activities of cyanoacrylate derivatives containing an α-aminophosphonate moiety. *J. Agric. Food Chem.* **2008**, *56*, 5242–5246.

(13) Liu, J. Z.; Song, B. A.; Fan, H. T.; Bhadury, P. S.; Wan, W. T.; Yang, S.; Xu, W. M.; Wu, J.; Jin, L. H.; Xue, W.; Hu, D. Y.; Zeng, S. Synthesis and in vitro study of pseudo-peptide thioureas containing α-aminophosphonate moiety as potential antitumor agents. *Eur. J. Med. Chem.* **2010**, *45*, 5108–5112.

(14) Zhang, Y. P.; Bai, S.; Song, B. A.; Bhadury, P. S.; Hu, D. Y.; Yang, S.; Zhang, X. Y.; Fan, H. T.; Lu, P. Enantioseparation and plant virucidal bioactivity of new quinazoline derivatives with α-aminophosphonate moiety. *J. Chromatogr. B: Anal. Technol. Biomed. Life Sci.* **2010**, *878*, 1285–1289.

(15) Yang, X.; Song, B. A.; Jin, L. H.; Wei, X.; Bhadury, S. P.; Li, X. Y.; Yang, S.; Hu, D. Y. Synthesis and antiviral bioactivities of novel chiral bis-thiourea-type derivatives containing α-aminophosphonate moiety. *Sci. China: Chem.* **2011**, *54*, 103–109.

(16) Hoerlein, G. Glufosinate (phosphinothricin), a natural amino acid with unexpected herbicidal properties. *Rev. Environ. Contam. Toxicol.* **1994**, *138*, 73–145.

(17) Baylis, A. D. Why glyphosate is a global herbicide: strengths, weaknesses and prospects. *Pest Manage. Sci.* **2000**, *56*, 299–308.

(18) Forlani, G.; Giberti, S.; Berlicji, Ł.; Petrollino, D.; Kafarski, P. Analogues of phosphinothricin as inhibitors of plant glutamine synthetases. *J. Agric. Food Chem.* **2006**, *54*, 796–802.

(19) Song, B. A.; Zhang, G. P.; Hu, D. Y.; Pang, L. L.; Yang, S.; Liu, G.; Wang, H. Preparation of dialkyl 1-(substituted benzothiazol-2-yl)amino-1-(substituted phenyl)methyl phosphonate derivatives and their antiviral and antitumor activities. CN Patent 1687088, 2005; *Chem. Abstr. 145*, 145879.

DOI: 10.1021/acs.jafc.5b02335
J. Agric. Food Chem. 2015, 63, 7219–7229

(20) Song, B.; Jin, L.; Yang, S.; Bhadury, P. S. *Environment-Friendly Antiviral Agents for Plant [M]*; Chemical Industry Press, Beijing, and Springer-Verlag: Berlin, Germany, 2010.
(21) Forlani, G.; Giberti, S.; Berlicki, L.; Petrollino, D.; Kafarski, P. Plant P5C reductase as a new target for aminomethylenebisphosphonates. *J. Agric. Food Chem.* **2007**, *55*, 4340−4347.
(22) Forlani, G.; Occhipinti, A.; Berlicki, Ł.; Dziedziola, G.; Wieczorek, A.; Kafarski, P. Tailoring the structure of aminobisphosphonates to target plant P5C reductase. *J. Agric. Food Chem.* **2008**, *56*, 3193−3199.
(23) Hirai, K.; Uchida, A.; Ohno, R. Major synthetic routes for modern herbicide class and agrochemical characteristics [A]. In *Herbicide Classes in Development, Mode of Action, Targets, Genetic Engineering, Chemistry [M]*; Springer-Verlag: Berlin, Germany, 2002; pp 179−278.
(24) Shimizu, T. Action mechanism of pyrimidinyl carboxy herbicides. *J. Pestic. Sci.* **1997**, *22* (3), 245−256.
(25) Tamaru, M.; Inoue, J.; Hanai, R. Studies of the new herbicide KIH-6127.4. Crystal structure of KIH-6127 and quantitative structure-activity relationship of the iminoxy moiety of KIH-6127 derivatives. *J. Agric. Food Chem.* **1997**, *45*, 2777−2783.
(26) Tamaru, M.; Takehi, T.; Masuyama, N. Studies of the new herbicide KIH-6127. Part II. Synthesis and herbicidal activity of 6-acyl pyrimin-2-yl salicylates and analogues against barnyard grass. *Pestic. Sci.* **1996**, *47*, 327−335.
(27) Tomlin, C. D. S. *The Pesticide Manual, A World Compendium [M]*, 14th ed.; British Crop Production Council: Surrey, UK, 2006; p 911.
(28) Lu, L.; Chen, J.; Wu, J.; Ling, W.; Mao, L. S.; Li, M. Z.; Cai, X.; Peng, W. L.; Wu, Y.; Wu, S. G.; Wang, H. J.; Wang, G. C.; Cui, H.; Han, S. D.; Qiu, W. L.; Wang, Y. H. Preparation processes and herbicidal uses of 2-pyrimidinyloxy-*N*-aryl-benzylamine derivatives. WO Patent 2002034724, 2002; *Chem. Abstr. 136*, 355244.
(29) Lu, L.; Chen, J.; Cai, X.; Li, M. Z.; Wu, Y.; Wang, Y. H. Herbicidal 2-pyrimidyloxy-*N*-amidophenylbenzyl amine, its preparation and application. CN Patent 1323788, 2001; *Chem. Abstr. 137*, 74803.
(30) Wu, J.; Cheng, J.; Lu, L. *N*-(2-Bromophenyl)-2-(4,6-dimethoxypyrimidin-2-yloxy)benzylamine, a new selective postemergent herbicide for weed control in winter oilseed rape. *J. Agric. Food Chem.* **2006**, *54*, 5954−5957.
(31) Lima, L. M. A.; Barreiro, E. J. Bioisosterism: a useful strategy for molecular modification and drug design. *Curr. Med. Chem.* **2005**, *12*, 23−49.
(32) Tang, W.; Yu, Z. H.; Shi, D. Q. Synthesis, crystal structure, and herbicidal activity of pyrimidinyl benzylamine analogues containing a phosphonyl group. *Heteroat. Chem.* **2010**, *21*, 148−155.

DOI: 10.1021/acs.jafc.5b02335
J. Agric. Food Chem. 2015, 63, 7219−7229

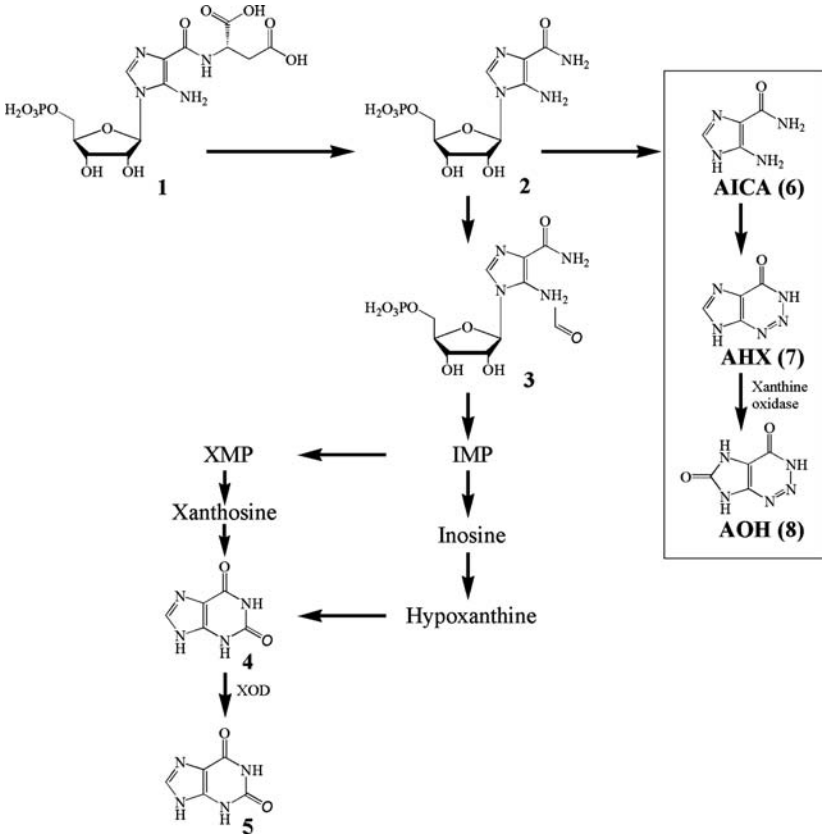

Figure 1. Purine metabolic pathway in animals, plants, and microorganisms, including the novel route. (1) succino-AICAR, (2) AICA ribotide, (3) 5-formyl AICAR, (4) xanthine, (5) uric acid, (6) 5-aminoimidazole-4-carboxamide (AICA), (7) 2-azahypoxanthine (AHX), (8) 2-aza-8-oxohypoxanthine (AOH).

some progress has been made in elucidating growth-promoting effects of AHX and AOH in plants, the effects of AHX and AOH on the accumulation of carotenoids are completely unknown. In the present study, to elucidate the roles of AHX and AOH in carotenoid metabolism in plants, the effects of AHX and AOH on carotenoid content and composition and the expression of carotenoid metabolic genes were investigated using the culture system. These results presented herein will contribute to a better understanding of the roles of AHX and AOH in plants and provide insights into elucidating the mechanism of AHX and AOH regulation of plant growth.

MATERIALS AND METHODS

Plant Materials. Satsuma mandarin (*Citrus unshiu* Marc.) harvested in October at the Fujieda Farm of Shizuoka University was used as materials.

***In Vitro* Culture System and Treatments.** The fruits were surface-sterilized by a 10 min soak in 70% ethanol and a 30 min soak in 1% (w/v) NaOCl and rinsed in sterile water. Juice sacs excised from the equatorial region of the fruit were placed on 10 mL of agar medium in culture tubes (22 × 120 mm^2) and incubated in the dark at 25 °C. The explants were placed with the endocarp side up, so that the juice sacs were not in contact with the Murashige and Skoog (MS) medium supplemented with 10% (w/v) sucrose and 1% (w/v) agar. The pH of the MS medium was adjusted to 5.7 and autoclaved.[19] AHX and AOH were added into the MS medium, and the final concentration was 100 μM. The juice sacs were treated with AHX or AOH for 4 weeks. Juice sacs cultured on the MS medium without AHX and AOH were used as the control. At each sampling point, 50 juice sacs from 5 fruits were used for each treatment. After each treatment, the juice sacs were immediately frozen in liquid nitrogen, ground into granules, and kept at −80 °C until used.

Extraction and Determination of Carotenoids. The identification, extraction, and quantification of carotenoids in citrus fruits have been described previously.[15] The contents of β-carotene, β-cryptoxanthin, all-*trans*-violaxanthin, 9-*cis*-violaxanthin, and lutein in the juice sacs were examined every 2 weeks during the experiment periods. The content of carotenoid was expressed as $\mu g\ g^{-1}$ fresh weight. Carotenoid quantification was performed in three replicates.

Total RNA Extraction and Real-Time Quantitative RT-PCR. Total RNA was extracted from the juice sacs of Satsuma mandarin according to a previously reported method.[15] The total RNA was cleaned up with the RNeasy Mini Kit (Qiagen, Hilden, Germany) with on-column DNase digestion. The reactions of reverse transcription (RT) were performed with 2 μg of purified RNA and a random hexamer at 37 °C for 60 min using TaqMan reverse transcription reagents (Applied Biosystems).

TaqMan MGB probes and sets of primers for *CitPSY*, *CitPDS*, *CitZDS*, *CitLCYb1*, *CitLCYb2*, *CitLCYe*, *CitHYb*, *CitZEP*, *CitNCED2*, and *CitNCED3* were designed according to Ma et al.[20] For endogenous control, the TaqMan Ribosomal RNA Control Reagents VIC Probe (Applied Biosystems) was used. TaqMan real-time PCR was carried out with the TaqMan Universal PCR Master Mix (Applied Biosystems) using StepOnePlus Real-Time PCR system (Applied Biosystems) according to the manufacturer's instructions. Each reaction mixture contained 900 nM primers, a 250 nM TaqMan MGB Probe, and template cDNA. The thermal cycling conditions were 95 °C for 10 min followed by 40 cycles of 95 °C for 15 s and 60 °C for 60 s. The levels of gene expression were analyzed with StepOnePlus Real-Time PCR system software (Applied Biosystems) and normalized with the results of 18S rRNA. Real-time quantitative RT-PCR was performed in three replicates for each sample.

Statistical Analysis. All values are shown as the mean ± SE for three replicates. The data were analyzed, and Tukey's HSD test (at $P < 0.05$) was used to compare the treatment means.

DOI: 10.1021/acs.jafc.5b02455
J. Agric. Food Chem. 2015, 63, 7230−7235

RESULTS

Effect of AHX and AOH on Carotenoid Content and Composition. In the present study, the juice sacs of Satsuma mandarin were treated with AHX or AOH for 4 weeks, and the changes in carotenoid contents were examined every 2 weeks. Under treatment with AHX, the contents of β-carotene, β-cryptoxanthin, and total carotenoid were increased in the second week. In the fourth week, the content of β-carotene was slightly decreased, while the contents of β-cryptoxanthin, all-*trans*-violaxanthin, 9-*cis*-violaxanthin, lutein, and total carotenoid were not significantly affected by the AHX treatment. Under treatment with AOH, the contents of all the carotenoids examined in the present study were similar to those of the control in the second week. In the fourth week, however, the accumulation of carotenoid was clearly induced by AOH. Under treatment with AOH, the contents of β-cryptoxanthin, all-*trans*-violaxanthin, 9-*cis*-violaxanthin, lutein, and total carotenoid were significantly increased in the fourth week (Figure 2).

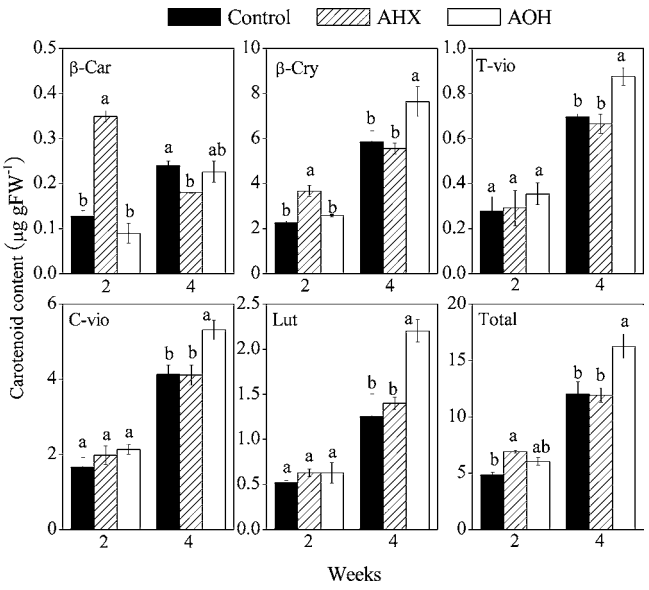

Figure 2. Effect of AHX and AOH on the carotenoid content in citrus juice sacs *in vitro*. β-Car, β-carotene; β-Cry, β-cryptoxanthin; T-vio, all-*trans*-violaxanthin; C-vio, 9-*cis*-violaxanthin; Lut, lutein; Total, total carotenoids. The value for total carotenoids was the sum of identified carotenoids. Columns and bars represent the means and SE (n = 3), respectively. Different letters indicate significant differences at the 5% level by Tukey's HSD test.

Effect of AHX and AOH on the Expression of Genes Related to Carotenoid Metabolism. In citrus fruits, transcriptional regulation of carotenoid metabolic genes is a major mechanism by which carotenoid accumulation is regulated during the ripening process.[15,16,18−20,22] As shown in Figure 3, gene expression of *CitPDS*, *CitZDS*, and *CitLCYb2* was up-regulated, while gene expression of *CitLCYb1*, *CitHYb*, and *CitZEP* was down-regulated by AHX treatment in the second week. In the fourth week, the expression of genes related to β,β-xanthophyll biosynthesis (*CitPSY*, *CitPDS*, *CitZDS*, *CitLCYb1*, *CitHYb*, and *CitZEP*) and genes related to carotenoid catabolism (*CitNCED2* and *CitNCED3*) was simultaneously up-regulated by the AHX treatment. With AOH treatment, the expression of genes investigated in the present study was not significantly affected in the second week, except for *CitHYb* and *CitZEP*. In the fourth week, gene expression of *CitPSY*, *CitPDS*, *CitZDS*, *CitLCYb1*, *CitLCYb2*, *CitHYb*, and *CitZEP* was up-regulated by the treatment with AOH, while the gene expression of *CitNCED2* and *CitNCED3* was not significantly affected. The up-regulation of the expression of β,β-xanthophyll biosynthetic genes was in parallel with the increase in carotenoid contents in AOH treatment in the fourth week.

DISCUSSION

AHX and AOH are novel plant-growth promoting compounds isolated from one fairy forming fungus, *Lepista sordida*. Recently, the presence of endogenous AHX and AOH has been confirmed in various plants, such as rice, tomato, potato, and *Arabidopsis*. In bentgrass seedings, the shoots and roots were elongated by different concentrations of AHX (from 0.05 to 1 mM).[2] Choi et al. reported that treatments with AHX and AOH stimulated the growth of all the plants tested regardless of their families, and the growth-promoting effect of AHX was independent of cytokinin (6-benzylaminopurine) and auxin (naphthalene acetic acid).[2,4] To date, the molecular mechanisms by which AHX and AOH regulate plant growth have not been completely elucidated, and their effects on carotenoid metabolism in plants are still unknown. Citrus fruits are useful materials for studying carotenoid metabolism in plants, due to their high carotenoid contents and complex carotenoid compositions. In recent years, extensive efforts have been made to elucidate the mechanisms of carotenoid accumulation in different citrus varieties, and some key factors that affected carotenoid metabolism have been identified.[15−22,24−26] Rodrigo et al. found that high temperature (37 °C) dramatically decreased the contents of carotenoids, especially β-citraurin, while low temperature (12 °C) increased carotenoid contents in citrus fruits.[21,27] In addition, carotenoid accumulation in citrus fruits was induced by ethylene and abscission agents, while it was suppressed by ABA and GA.[19,20,28] In the present study, the results showed that the carotenoid accumulation was temporally induced by AHX. The total carotenoid content was increased by AHX in the second week, while not significantly affected in the fourth week (Figure 2). In the second week, the contents of β-carotene and β-cryptoxanthin in AHX treatment were 2.7 times and 1.6 times of those in the control, respectively. Gene expression results showed that the up-regulation of the gene expression of *CitPDS*, *CitZDS*, and *CitLCYb2* was consistent with the accumulation of β-carotene and β-cryptoxanthin in the AHX treatment in the second week (Figure 3). In the fourth week, the expression of carotenoid biosynthetic and catabolic genes was simultaneously increased, and as a result, the total carotenoid content was not significantly affected by the treatment with AHX (Figure 3). With AOH treatment, the induction of carotenoid accumulation and the expression of carotenoid biosynthetic genes occurred in the fourth week, which was later than that in the AHX treatment, indicating that the juice sacs might be less sensitive to AOH compared with AHX (Figures 2 and 3). In the fourth week, the up-regulation of the expression of β,β-xanthophyll biosynthetic genes was in parallel with the increase in the contents of β-cryptoxanthin, all-*trans*-violaxanthin, and 9-*cis*-violaxanthin in the treatment of AOH. The results from this study suggest that the two "fairy chemicals", AHX and AOH, regulate carotenoid metabolism in citrus juice sacs. Because carotenoid metabolism is closely related to the biosynthesis of

DOI: 10.1021/acs.jafc.5b02455
J. Agric. Food Chem. 2015, 63, 7230−7235

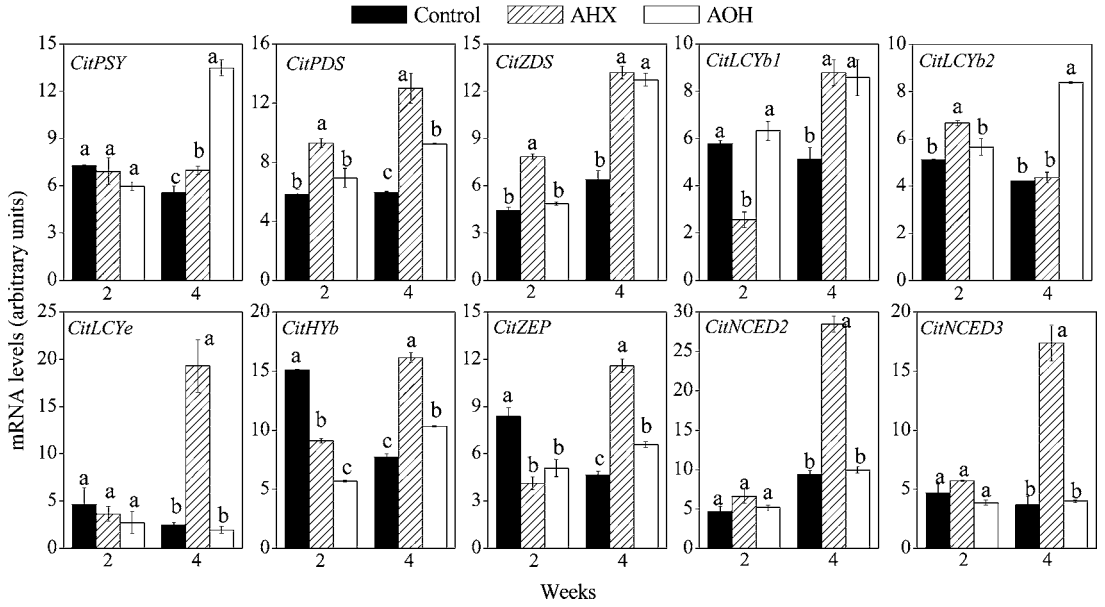

Figure 3. Effect of AHX and AOH on the expression of carotenoid metabolism related genes in citrus juice sacs *in vitro*. The mRNA levels were analyzed by TaqMan real-time quantitative RT-PCR. Real-time RT-PCR amplification of 18S rRNA was used to normalize the expression of the genes under identical conditions. Columns and bars represent the means and SE ($n = 3$), respectively. Different letters indicate significant differences at the 5% level by Tukey's HSD test.

the plant hormones, GA, ABA and strigolactone, we deduced that treatment with AHX and AOH might affect the levels of GA, ABA, and strigolactone through regulating carotenoid metabolism in plants. Moreover, the regulation of GA, ABA, and strigolactone biosynthesis might be a mechanism by which AHX and AOH stimulate plant growth. Further research is needed to confirm this.

β-Cryptoxanthin, the major carotenoid in Satsuma mandarin, is a precursor of vitamin A and beneficial to human health. Some epidemiological studies have shown that serum *β*-cryptoxanthin inversely associated with the risks for cancers, diabetes, rheumatism atherosclerosis, liver dysfunction, metabolic syndrome, and low bone mineral density, as well as oxidative stress.[29−34] In recent years, several efforts have been devoted to enhancing the content of *β*-cryptoxanthin in Satsuma mandarin.[19,35] Rodrigo et al. reported that postharvest storage of citrus fruit at 12 °C promoted the accumulation of *β*-cryptoxanthin in both pulp and juice.[27] Previously, we found that the accumulation of *β*-cryptoxanthin in juice sacs was induced significantly by blue LED light irradiation.[19] In the present study, the results showed that the content of *β*-cryptoxanthin was increased by 60% and 30% by AHX treatment in the second week and AOH treatment in the fourth week, respectively. This suggested that the application of AHX and AOH might be a new strategy for improving nutritional value of Satsuma mandarin.

Previously, it has been found that plants developed tolerance to environmental stress by increasing gene expression of glutathione-*S*-transferases and Bowman-Birk-type proteinase inhibitor after AHX treatment.[2] In rice and wheat, the increase of the yields was due to AHX-induced tolerance to environmental stress.[5] NCEDs, the rate-limiting enzymes for ABA biosynthesis, are also tolerance-related in plants. In *Arabidopsis*, overexpression of *AtNCED3* led to an improvement in drought tolerance.[36] In the present study, the results showed that the expression of *CitNCED2* and *CitNCED3* was simultaneously up-regulated by the AHX treatment in the fourth week. The up-regulation of NCED contributed to enhancing tolerance of juice sacs treated with AHX. Additionally, these results suggested that the regulation of ABA level might be a mechanism by which AHX treatment induced tolerance in plants.

In conclusion, the effects of two "fairy chemicals", AHX and AOH, on carotenoid metabolism of citrus juices sacs were investigated in the present study. The results showed AHX and AOH treatments were effective for enhancing carotenoid content in juice sacs *in vitro*. Meanwhile, the modification of carotenoid accumulation by AHX and AOH treatments was highly regulated at the transcriptional level. This study provides new information on the functions of AHX and AOH in plants, which will contribute to elucidating the mechanisms by which AHX and AOH stimulate plant growth.

■ ASSOCIATED CONTENT

Supporting Information

The Supporting Information is available free of charge on the ACS Publications website at DOI: 10.1021/acs.jafc.5b02455.

Carotenoid metabolic pathway in citrus (PDF)

■ AUTHOR INFORMATION

Corresponding Author

*Masaya Kato. Telephone: 81-54-238-4830. Fax: 81-54-238-4830. E-mail: amkato@ipc.shizuoka.ac.jp.

Notes

The authors declare no competing financial interest.

■ ABBREVIATIONS USED

ABA, abscisic acid; AICA, 5-aminoimidazole-4-carboxamide; AICAR, 5-aminoimidazole-4-carboxamide ribonucleotide; AHX, 2-azahypoxanthine; AOH, 2-aza-8-oxohypoxanthine; C-vio, 9-*cis*-violaxanthin; GA, gibberellin; GGPP, geranylgeranyl diphosphate; HYb, *β*-ring hydroxylase; LCYb, lycopene *β*-cyclase; LCYe, lycopene *ε*-cyclase; Lut, lutein; NCED, 9-*cis*-

DOI: 10.1021/acs.jafc.5b02455
J. Agric. Food Chem. 2015, 63, 7230−7235

epoxycarotenoid dioxygenase; PDS, phytoene desaturase; PSY, phytoene synthase; T-vio, all-*trans*-violaxanthin; ZDS, ζ-carotene desaturase; ZEP, zeaxanthin epoxidase; α-Car, α-carotene; β-Car, β-carotene; β-Cry, β-cryptoxanthin

REFERENCES

(1) Evershed, H. Fairy rings. *Nature* **1884**, *29*, 384−385.

(2) Choi, J.-H.; Fushimi, K.; Abe, N.; Tanaka, H.; Maeda, S.; Morita, A.; Hara, M.; Motohashi, R.; Matsunaga, J.; Eguchi, Y.; Ishigaki, N.; Hashizume, D.; Koshino, H.; Kawagishi, H. Disclosure of the "fairy" of fairy-ring forming fungus *Lepista sordida*. *ChemBioChem* **2010**, *11*, 1373−1377.

(3) Mitchinson, A. Fairy chemicals. *Nature* **2014**, *505*, 298.

(4) Choi, J.-H.; Ohnishi, T.; Yamakawa, Y.; Takeda, S.; Sekiguchi, S.; Maruyama, W.; Yamashita, K.; Suzuki, T.; Morita, A.; Ikka, T.; Motohashi, R.; Kiriiwa, Y.; Tobina, H.; Asai, T.; Tokuyama, S.; Hirai, H.; Yasuda, N.; Noguchi, K.; Asakawa, T.; Sugiyama, S.; Kan, T.; Kawagishi, H. The source of "fairy rings": 2-azahypoxanthine and its metabolite found in a novel purine metabolic pathway in plants. *Angew. Chem., Int. Ed.* **2014**, *53*, 1552−1555.

(5) Tobina, H.; Choi, J.-H.; Asai, T.; Kiriiwa, Y.; Asakawa, T.; Kan, T.; Morita, A.; Kawagishi, H. 2-Azahypoxanthine and Imidazole-4-carboxamide produced by the fairy-ring-forming fungus increase yields of wheat. *Field Crop Res.* **2014**, *162*, 6−11.

(6) Asai, T.; Choi, J.-H.; Ikka, T.; Fushimi, K.; Abe, N.; Tanaka, H.; Yamakawa, Y.; Kobori, H.; Kiriiwa, Y.; Motohashi, R.; Deo, V. P.; Asakawa, T.; Kan, T.; Morita, A.; Kawagishi, H. Effect of 2-azahypoxanthine (AHX) produced by the fairy-ring-forming fungus on the growth and the grain yield of rice. *JARQ* **2015**, *49*, 45−49.

(7) Havaux, M. Carotenoids as membrane stabilizers in chloroplasts. *Trends Plant Sci.* **1998**, *3*, 147−151.

(8) Ledford, H. K.; Niyogi, K. K. Singlet oxygen and photo-oxidative stress management in plants and algae. *Plant, Cell Environ.* **2005**, *28*, 1037−1045.

(9) Cazzonelli, C. I. Carotenoids in nature: insights from plants and beyond. *Funct. Plant Biol.* **2011**, *38*, 833−847.

(10) Nisar, N.; Li, L.; Lu, S.; Khin, N. C.; Pogson, B. Carotenoid Metabolism in Plants. *Mol. Plant* **2015**, *8*, 68−82.

(11) Schwartz, S. H.; Tan, B. C.; Gage, D. A.; Zeevaart, J. A.; McCarty, D. R. Specific oxidative cleavage of carotenoids by VP14 of maize. *Science* **1997**, *276*, 1872−1874.

(12) Cunningham, F. X.; Gantt, E. Genes and enzymes of carotenoid biosynthesis in plants. *Annu. Rev. Plant Physiol. Plant Mol. Biol.* **1998**, *49*, 557−583.

(13) Alder, A.; Jamil, M.; Marzorati, M.; Bruno, M.; Vermathen, M.; Bigler, P.; Ghisla, S.; Bouwmeester, H.; Beyer, P.; Al-Babili, S. The path from β-carotene to carlactone, a strigolactone-like plant hormone. *Science* **2012**, *335*, 1348−1351.

(14) Seto, Y.; Sado, A.; Asami, K.; Hanada, A.; Umehara, M.; Akiyama, K.; Yamaguchi, S. Carlactone is an endogenous biosynthetic precursor for strigolactones. *Proc. Natl. Acad. Sci. U. S. A.* **2014**, *111*, 1640−1645.

(15) Kato, M.; Ikom, Y.; Matsumot, H.; Sugiura, M.; Hyodo, H.; Yano, M. Accumulation of carotenoids and expression of carotenoid biosynthetic genes during maturation in citrus fruit. *Plant Physiol.* **2004**, *134*, 824−837.

(16) Kato, M.; Matsumoto, H.; Ikoma, Y.; Okuda, H.; Yano, M. The role of carotenoid cleavage dioxygenases in the regulation of carotenoid profiles during maturation in citrus fruit. *J. Exp. Bot.* **2006**, *57*, 2153−2164.

(17) Kita, M.; Kato, M.; Ban, Y.; Honda, C.; Yaegaki, H.; Ikoma, Y.; Moriguchi, T. Carotenoid accumulation in Japanese Apricot (Prunus mume Siebold and Zucc.): molecular analysis of carotenogenic gene expression and ethylene regulation. *J. Agric. Food Chem.* **2007**, *55*, 3414−3420.

(18) Alquézar, B.; Zacarías, L.; Rodrigo, M. J. Molecular and functional characterization of a novel chromoplast-specific lycopene β-cyclase from Citrus and its relation to lycopene accumulation. *J. Exp. Bot.* **2009**, *60*, 1783−1797.

(19) Zhang, L.; Ma, G.; Kato, M.; Yamawaki, K.; Takagi, T.; Kiriiwa, Y.; Ikoma, Y.; Matsumoto, H.; Yoshioka, T.; Nesumi, H. Regulation of carotenoid accumulation and the expression of carotenoid metabolic genes in citrus juice sacs in vitro. *J. Exp. Bot.* **2012**, *63*, 871−886.

(20) Ma, G.; Zhang, L.; Matsuta, A.; Matsutani, K.; Yamawaki, K.; Yahata, M.; Wahyudi, A.; Motohashi, R.; Kato, M. Enzymatic formation of β-citraurin from β-cryptoxanthin and zeaxanthin by carotenoid cleavage dioxygenase4 in the flavedo of citrus fruit. *Plant Physiol.* **2013**, *163*, 682−695.

(21) Rodrigo, M. J.; Alquézar, B.; Alós, E.; Medina, V.; Carmona, L.; Bruno, M.; Al-Babili, S.; Zacarías, L. A novel carotenoid cleavage activity involved in the biosynthesis of citrus fruit-specific apocarotenoid pigments. *J. Exp. Bot.* **2013**, *64*, 4461−4478.

(22) Wei, X.; Chen, C.; Yu, Q.; Gady, A.; Yu, Y.; Liang, G.; Gmitter, F. G., Jr. Comparison of carotenoid accumulation and biosynthetic gene expression between Valencia and Rohde Red Valencia sweet oranges. *Plant Sci.* **2014**, *227*, 28−36.

(23) Zhang, L.; Ma, G.; Yamawaki, K.; Ikoma, Y.; Matsumoto, H.; Yoshioka, T.; Ohta, S.; Kato, M. Regulation of ascorbic acid metabolism by blue LED light irradiation in citrus juice sacs. *Plant Sci.* **2015**, *233*, 134−142.

(24) Pons, E.; Alquézar, B.; Rodríguez, A.; Martorell, P.; Genovés, S.; Ramón, D.; Rodrigo, M. J.; Zacarías, L.; Peña, L. Metabolic engineering of β-carotene in orange fruit increases its in vivo antioxidant properties. *Plant Biotechnol. J.* **2014**, *12*, 17−27.

(25) Lado, J.; Cronje, P.; Alquézar, B.; Page, A.; Manzi, M.; Gómez-Cadenas, A.; Stead, A. D.; Zacarías, L.; Rodrigo, M. J. Fruit shading enhances peel color, carotenes accumulation and chromoplast differentiation in red grapefruit. *Physiol. Plant.* **2015**, *154*, 469.

(26) Guo, F.; Yu, H.; Xu, Q.; Deng, X. Transcriptomic analysis of differentially expressed genes in an orange-pericarp mutant and wild type in pummelo (Citrus grandis). *BMC Plant Biol.* **2015**, *15*, 44.

(27) Rodrigo, M. J.; Cilla, A.; Barberá, R.; Zacarías, L. Carotenoid bioaccessibility in pulp and fresh juice from carotenoid-rich sweet oranges and mandarins. *Food Funct.* **2015**, *6*, 1950−1959.

(28) Alferez, F.; Pozo, L. V.; Rouseff, R. R.; Burns, J. K. Modification of carotenoid levels by abscission agents and expression of carotenoid biosynthetic genes in 'valencia' sweet orange. *J. Agric. Food Chem.* **2013**, *61*, 3082−3089.

(29) Cerhan, J. R.; Saag, K. G.; Merlino, L. A.; Mikuls, T. R.; Criswell, L. A. Antioxidant micronutrients and risk of rheumatoid arthritis in a cohort of older women. *Am. J. Epidemiol.* **2003**, *157*, 345−354.

(30) Yamaguchi, M.; Hamamoto, R.; Uchiyama, S.; Ishiyama, K.; Hashimoto, K. Anabolic effects of Bee Pollen Cistus ladaniferus extract on bone components in the Femoral-Diaphyseal and -Metaphyseal Tissues of rats *in vitro* and *in vivo*. *J. Health Sci.* **2006**, *52*, 43−49.

(31) Sugiura, M.; Nakamura, M.; Ogawa, K.; Ikoma, Y.; Ando, F.; Shimokata, H.; Yano, M. Dietary patterns of antioxidant vitamin and carotenoid intake associated with bone mineral density: findings from post-menopausal Japanese female subjects. *Osteoporosis Int.* **2011**, *22*, 143−152.

(32) Takayanagi, K.; Morimoto, S.; Shirakura, Y.; Mukai, K.; Sugiyama, T.; Tokuji, Y.; Ohnishi, M. Mechanism of visceral fat reduction in Tsumura Suzuki obese, diabetes (TSOD) mice orally administered β-cryptoxanthin from Satsuma mandarin oranges (Citrus unshiu Marc). *J. Agric. Food Chem.* **2011**, *59*, 12342−12351.

(33) Yamaguchi, M. Role of carotenoid β-cryptoxanthin in bone homeostasis. *J. Biomed. Sci.* **2012**, *19*, 36.

(34) Iskandar, A. R.; Liu, C.; Smith, D. E.; Hu, K. Q.; Choi, S. W.; Ausman, L. M.; Wang, X. D. β-Cryptoxanthin restores nicotine-reduced lung SIRT1 to normal levels and inhibits nicotine-promoted lung tumorigenesis and emphysema in A/J mice. *Cancer Prev. Res.* **2013**, *6*, 309−320.

(35) Ma, G.; Zhang, L. C.; Kato, M.; Yamawaki, K.; Kiriiwa, Y.; Yahata, M.; Ikoma, Y.; Matsumoto, H. Effect of blue and red LED light irradiation on β-cryptoxanthin accumulation in the flavedo of citrus fruits. *J. Agric. Food Chem.* **2012**, *60*, 197−201.

DOI: 10.1021/acs.jafc.5b02455
J. Agric. Food Chem. 2015, 63, 7230−7235

(36) Iuchi, S.; Kobayashi, M.; Taji, T.; Naramoto, M.; Seki, M.; Kato, T.; Tabata, S.; Kakubari, Y.; Yamaguchi-Shinozaki, K.; Shinozaki, K. Regulation of drought tolerance by gene manipulation of 9-cis-epoxycarotenoid dioxygenase, a key enzyme in abscisic acid biosynthesis in Arabidopsis. *Plant J.* **2001**, *27*, 325−333.

DOI: 10.1021/acs.jafc.5b02455
J. Agric. Food Chem. 2015, 63, 7230−7235

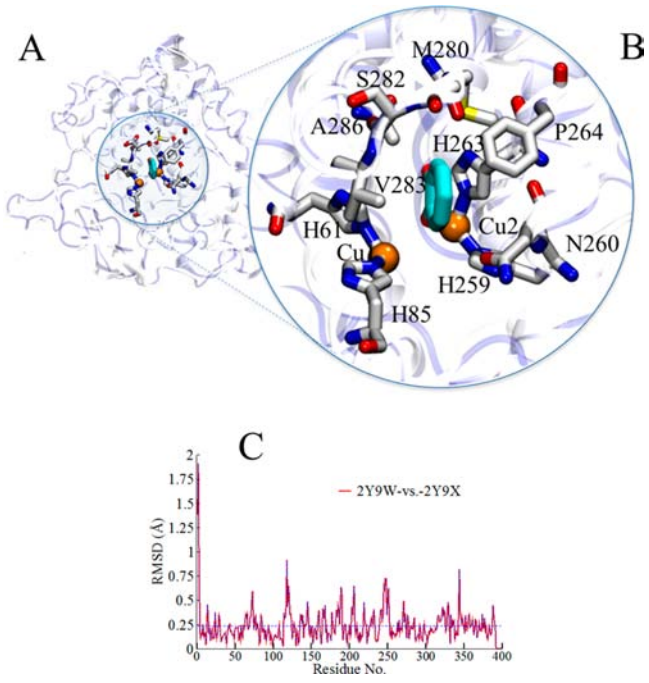

Figure 1. Structural comparison between 2Y9W and 2Y9X: (A) superimposition of 2Y9W (blue) and 2Y9X (white) (binding site residues are rendered in licorice and in an atom-wise type: C, white; O, red; N, blue; S, yellow; whereas tropolone is shown in licorice and in a cyan color); (B) inset view of tropolone binding site; (C) RMSD per residue of the two structures under study.

Scheme 1. Chemical Structure of the Hydroxy-Substituted Coumarins

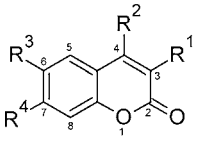

3-Hydroxycoumarin	R^1 = -OH	R^2 = -H
	R^3 = -H	R^4 = -H
4-Hydroxycoumarin	R^1 = -H	R^2 = -OH
	R^3 = -H	R^4 = -H
6-Hydroxycoumarin	R^1 = -H	R^2 = -H
	R^3 = -OH	R^4 = -H
7-Hydroxycoumarin	R^1 = -H	R^2 = -H
	R^3 = -H	R^4 = -OH

lead compounds for the synthesis of new potent PPO inhibitors that are suitable for biotechnological applications.[13−15]

MATERIALS AND METHODS

Mushroom Tyrosinase and Enzymatic Assay. MT (5771 U/mg) was purchased from Sigma-Aldrich (Milan, Italy). A stock solution of the enzyme contained 1 mg/mL. Before use, the enzyme solution was accurately inspected by means of syringaldazine, a typical and sensitive laccase substrate, which allowed us to exclude any laccase contamination. This was necessary because some lots of commercial tyrosinase contain laccase activity.[16,17] This could lead to measurements with ambiguous results as contaminant laccases could share the same substrates with tyrosinase (i.e., *o*-diphenols). A tyrosinase unit was defined according to the manufacturer's definition and calculated such that 1 unit will cause an increase in A_{280} of 0.001 per minute at pH 6.5 and 25 °C in a 3 mL reaction mix containing L-tyrosine. All experiments were performed in 100 mM potassium phosphate buffer, pH 6.5, at 25 °C.

The monophenolase activity using L-tyrosine as its substrate was measured at 468 nm by following the formation of dopachrome with an Ultrospec 2100 Pro UV−vis (Amersham Biosciences) spectrophotometer in the presence of various putative substrates or inhibitors. A control reaction was also conducted. Diphenolase activity was monitored spectrophotometrically by tracking the adduct formation between 4-*tert*-butyl-1,2-benzoquinone and 4-amino-*N*,*N*-diethylaniline at 625 nm (ε_{625} = 11120 M^{-1} cm^{-1}).[18,19] The percentage of inhibition (I %) of the enzyme activity was also calculated according to the equation $I\% = (\Delta A - \Delta B)/\Delta A \times 100$, where ΔA is the difference in the absorbance of the control sample between two incubation times when the absorbance increased linearly and ΔB is the difference in the absorbance of the test sample calculated in the same range of time.[20] The results were the average of at least three readings. Other details are given in the text and in the figure captions.

HPLC Analysis and Sample Preparation. Identification of the products was performed by HPLC analysis using a Beckman System Gold apparatus that was equipped with an UV−vis detector module. An RPC18 column (Phenomenex, Luna, 250 mm × 3 mm i.d., 5 μm), purchased from Chemtek Analytica (Bologna, Italy), was equilibrated with 0.085% phosphoric acid and 5% methanol in water, v/v (solvent A). Solvent B was 0.085% phosphoric acid and 95% methanol in water, v/v. After an initial isocratic elution (10% B for 10 min), a gradient phase of 10−90%, using solvent B, was applied for 10 min (1 mL/min flow rate).

Before the HPLC run was performed, aliquots of the samples were withdrawn at a fixed time, deproteinized by adding phosphoric acid up to 0.085% v/v, and centrifuged at 8000*g* for 10 min. The supernatants were then filtered using a 0.22 μm pore size membrane.

Molecular Docking. *Protein Modeling.* The X-ray crystal structures of MT (PDB entries 2Y9X and 2Y9W)[3] were used as templates for molecular docking studies of the enzyme in complex with our compounds. Note that the crystal structure denoted with the PDB entry 2Y9X contained tropolone, a well-known inhibitor that binds to the active site of the enzyme.

The protein structures were prepared using the Amber tool Xleap,[21] which included all hydrogen atoms. The orientation of polar hydrogen atoms was optimized, the protein protonation state was adjusted, and each structure was minimized with harmonic restraints on the heavy atoms. Successively, all hetero groups and water molecules were deleted. The structures of the enzyme were compared through root-mean-square distance (RMSD) analysis by superimposing the 2Y9W and 2Y9X structures. The RMSD for Cα is low (~0.3 Å), which indicates that the structures are similar (Figure 1C). Because no significant difference was observed in the protein structures, particularly in the binding site, the prepared cocrystal structure (after removal of tropolone) was used for docking studies.

Ligand Modeling. The lead molecules were first drawn with ACD Chem Sketch 11.0 (http://www.acdlabs.com/resources/freeware/chemsketch/). The resulting molecular geometry was then optimized at the B3 LYP/6-31G (d, p) level until a convergence, in energy, of 10^{-5} au using the Gaussian 03 package.[22]

Docking Protocol. Because no explicit information concerning the interaction between MT and the compounds under investigation has been reported previously, we searched for putative binding sites on the enzyme using two different protocols. These protocols were modified from our previous works.[23,24] First, we exploited the available empirical data from the guided docking runs concerning the binding of tropolone to the enzyme.[3] To assess the validity of our results, we performed blind docking calculations. More details about the docking steps and binding site detection programs are provided in the next sections.

From the ligand clusters that were obtained from blind docking on the protein surface, the top five clusters were chosen for further analysis. We then compared these poses with those obtained from guided docking. Once consensus sites were identified, we performed focused docking ("redocking") calculations that centered the docking grid on the center of mass of our compounds in the top pose. All docking runs were performed with AutoDock version 4.2.[25] This program uses a semiempirical, free energy force field to evaluate

DOI: 10.1021/acs.jafc.5b02636
J. Agric. Food Chem. 2015, 63, 7236−7244

conformations during docking simulations. More details about the formulation of the scoring function and its testing can be found in the manual for the program (http://autodock.scripps.edu/faqs-help/manual/autodock-4-2-user-guide/AutoDock4.2_UserGuide.pdf, pp 8−11). The binding site is composed of two copper ions that are coordinated by three histidine residues (for CuA, H61, H85, and H94; and for CuB, H259, H263, and H296). The other residues involved in the stability of compound bonding are as follows: C83, F90, E256, N260, H263, M280, G281, S282, and F292 (see Figure 1B). Therefore, in all docking runs, we modeled the flexibility of these residues.

In an additional protocol for defining the binding sites, we defined the center of the binding site as the center of mass of the residues surrounding the tropolone (Figure 1B), that is, H61, H85, H259, N260, H263, P264, M280, S282, V283, and A286.

Guided Docking. Guided docking is a biased docking procedure, for which we used previously acquired information about the binding of the substrate on the target protein (MT). The availability of the cocrystal structure of MT with tropolone allows us to perform this guided docking. Thus, to check the reproducibility of our docking protocol, we first performed the docking with the tropolone molecule [the complexed structure (PDB-ID 2Y9X)]. In step 1, the tropolone molecule was removed and then redocked. In step 2, the modeled and optimized structure of tropolone (drawn by Chemsketch and optimized through the Gaussian 03 package) was used to perform the docking. The binding pocket of the tropolone was chosen as the grid center in both steps.

Grids with dimensions of 68 × 80 × 80 and a spacing of 0.375 Å were used. The Lamarckian genetic algorithm was used for conformational sampling of the compound. For each docking simulation, 200 runs were carried out with 300 random individuals in the first population and 2.5×10^6 energy evaluations. For a local search, the so-called pseudo-Solis and Wets algorithms[25] were applied using the default parameter. The low RMSD difference (0.6 Å) between the complex docked-pose of tropolone obtained from the above-described steps 1 and 2 (data not shown) confirmed the reliability of the docking protocol. Furthermore, the optimized structures of our compounds were docked in the same binding site by using the same input parameters. The binding poses of compounds were ranked and clustered on the basis of their energy scores and populations.

Blind Docking. This docking protocol is an unbiased docking approach, whereby a grid covers the whole surface of the protein to locate the most likely binding site of lead molecules. AutoGrid 4.0 was employed to build a 126 × 126 × 126 grid map covering the whole RdRp, with grid spacing of 0.586 Å and a center on the center of mass of the whole MT. The Lamarckian genetic algorithm was used for conformational sampling of the compounds. For each docking simulation, 200 runs were carried out with 300 random individuals in the first population, 2.5×10^7 energy evaluations, and 2.7×10^7 generation numbers. For each run, the lowest energy conformation of the compounds was chosen for clustering according to an RMSD cutoff of 2 Å. Clusters were then ranked and clustered on the basis of the AutoDock energy scores and populations. The goal of conducting blind docking was to validate the guided docking outcome: whether the lead substrate candidate sat only in the tropolone-binding site or in some other binding location. Indeed, the top cluster representatives obtained from the blind docking (i.e., the clusters having the lowest docking energy and maximum number of confirmations/population) confirmed that each lead occupied the same binding site.

RESULTS AND DISCUSSION

In this study, we explored the effects of four hydroxycoumarins (3-, 4-, 6- and 7 isomers, see Scheme 1) on the activity of MT under different conditions. This will ultimately provide us with mechanistic insights from kinetic data.

Hydroxycoumarins with a Hydroxy Substituent on the Aromatic Ring. Two of the four hydroxy-substituted coumarins studied in this work (6- and 7-isomers) are hydroxylated on the aromatic ring. Of these, only one has a reported interaction with PPOs.[26−28] In particular, the inhibitory action of 7-hydroxycoumarin (7-HC, also known as umbelliferone) toward L-tyrosine hydroxylation was noted.[27] The MT-catalyzed transformation of L-tyrosine was monitored through the detection of dopachrome formation. As shown in Figure 2, dopachrome is strongly inhibited by 7-HC in a

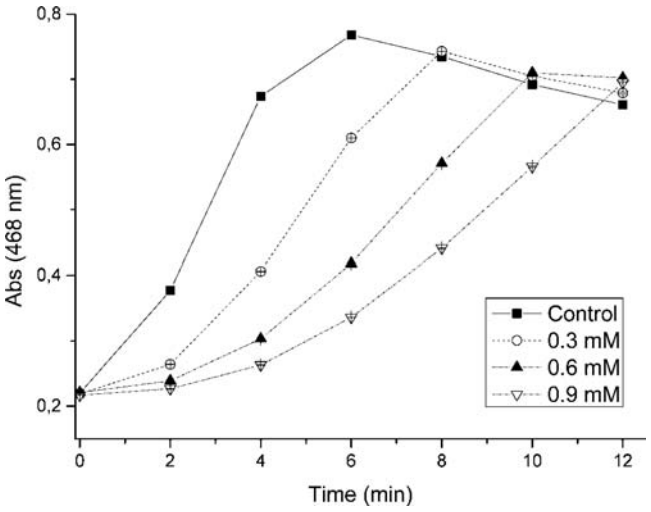

Figure 2. Tyrosinase-catalyzed oxidation of L-tyrosine in the presence of 7-hydroxycoumarin (7-HC). The reaction mixture contained 3 mM L-tyrosine, 95 enzyme units, and 7-HC substrate at a concentration that ranged from 0.3 to 0.9 mM. Other experimental conditions were 100 mM potassium phosphate buffer, pH 6.5, in a 1 mL final volume and 25 °C temperature.

concentration range of 0.3−0.9 mM. At the maximum 7-HC concentration, the inhibition reached 88%. This phenomenon is due to the specific inhibition of L-tyrosine conversion, which is confirmed by HPLC analysis of the reaction products (see the Supporting Information, Figure SM1) and not due to any interference by a putative quinone arising from 7-HC hydroxylation and oxidation, as previously suggested.[26] A further confirmation of the reduced conversion of L-tyrosine can be observed in the decreased appearance of L-3,4-dihyroxyphenylalanine (DOPA), which is the product of the reaction (see the Supporting Information, Figure SM2).

Moreover, the hydroxylation of 7-HC by MT, which yielded 6,7-dihydroxycoumarin (also known as esculetin), has been observed; however, this occurred only under particular experimental conditions and with a very low k_{cat}.[26] Although these observations appear contradictory, they are not surprising. A substantial reduction of the conversion speed of a certain substrate is normally observed in the presence of another substrate, the affinity of which is much higher and having a k_{cat} much smaller than those observed for the first substrate. The second substrate then behaves as a "competitive substrate", as its enzymatic transformation is too slow to be observed during the planned reaction time for the first enzymatic reaction. However, if the favorable substrate is absent from the reaction mixture, then even the less favorable substrate can be converted by the enzyme. Recently, a method to discriminate between alternative substrates and inhibitors of tyrosinase has been proposed.[29]

Unlike 7-HC, 6-hydroxycoumarin (6-HC) is rare in nature and has been found in only a few plants[30] and as a secondary

DOI: 10.1021/acs.jafc.5b02636
J. Agric. Food Chem. 2015, 63, 7236−7244

metabolite of an unsubstituted coumarin in certain animals. Yet, like 7-HC, it bears its hydroxyl substituent on the aromatic ring; for this reason, it could be considered a true monophenol derivative. Therefore, given the monophenolase/hydroxylase activity of the enzyme, this compound could behave as a substrate. This was confirmed by the experimental results, with the consumption of 6-HC in the presence of the enzyme. Therefore, 6-HC was found to be a substrate for MT (Figure 3A, line a). 6-HC behaved as a monophenol substrate and was

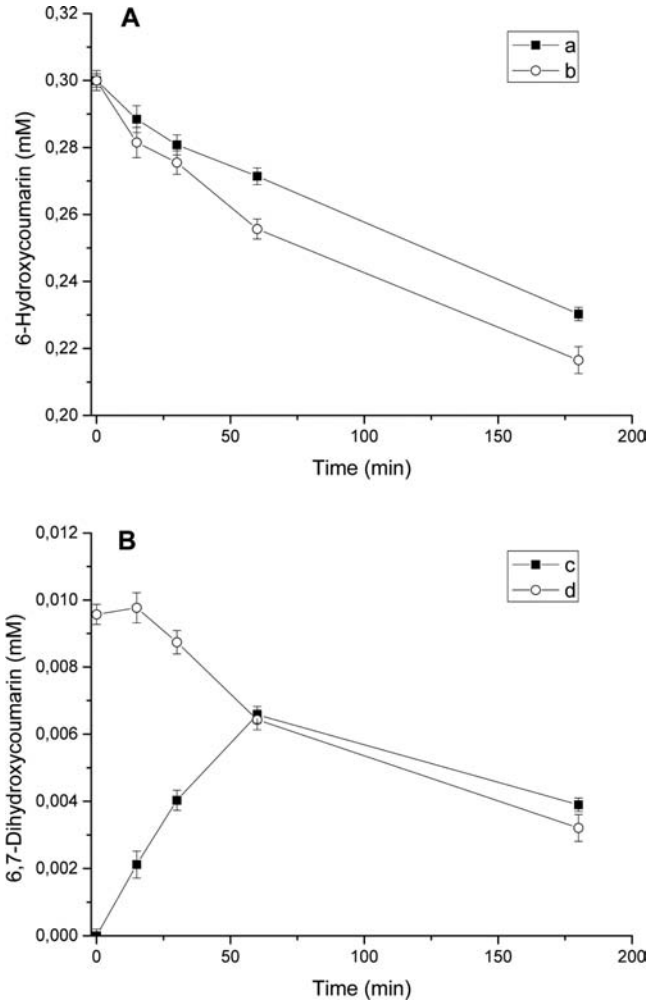

Figure 3. Tyrosinase-catalyzed oxidation of 6-hydroxycoumarin (6-HC) and 6,7-dihydroxycoumarin (esculetin). HPLC measurement was performed in a time course of 6-HC (A) and esculetin (B) concentration in a reaction mixture containing mushroom tyrosinase (95 enzyme units), 0.3 M 6-HC (lines a, c), and 0.3 mM 6-HC plus 10 μM esculetin (lines b, d) as the initial concentrations. Other experimental conditions were 100 mM potassium phosphate buffer, pH 6.5, in a 1 mL final volume and 25 °C temperature.

therefore *o*-hydroxylated to yield the corresponding *o*-diphenol. Two different compounds could be the products of 6-HC *o*-hydroxylation: esculetin and 5,6-dihydroxycoumarin. From our experiments, this latter unnatural compound was not detected at all, indicating that 6-HC exclusively was converted into esculetin, (Figure 3B, line c), which is a substrate for the enzyme.[27] Indeed, after 60 min, the esculetin concentration decreased as it was enzymatically converted to the corresponding *o*-quinone. It is already known that low concentrations of diphenols can operate by activating the monophenolase activity of tyrosinase.[31] Indeed, when the reaction was conducted in the presence of sufficient concentrations of esculetin (Figure 3B, line b), the disappearance of 6-HC and the formation/disappearance of esculetin (Figure 3B, line d) accelerated. This confirmed the ability of this compound to play the dual role of both a substrate and an activator of tyrosinase.

Hydroxycoumarins with an Unsubstituted Aromatic Ring. 3-Hydroxycoumarin (3-HC) is also rare in nature, but is sometimes found in plants.[32] Interestingly, 3-HC was recently demonstrated to protect sea urchin reproductive cells against ultraviolet B damage.[33] It has been chosen for the present study because MT should not hydroxylate it. This is because the hydroxyl-bearing ring is not aromatic and the aromatic ring of the compound is unsubstituted. MT is only able to ortho-hydroxylate phenols and aromatic amines.[31,34,35] Furthermore, the close proximity of the carbonyl moiety in 3-HC renders the putative hydroxylation site, the 4-position, relatively electrophilic and therefore not suitable for hydroxylation by MT,[36] which performs ortho-hydroxylation through an electrophilic mechanism that requires relatively high electron density on the target carbon atom.[37] The HPLC analysis of the products of the reaction of tyrosinase with 3-HC as a possible substrate shows that there was no consumption of 3-HC (see the Supporting Information, Figure SM3). Finally, 3-HC shows the same structural motif (i.e., an enol−ketone) that is typical of some well-known PPO inhibitors, such as tropolone, kojic acid, and mimosine.[38] On the basis of these considerations, we tested 3-HC as a possible inhibitor of MT and compared its effectiveness with that of tropolone.

Figure 4 shows the trend of catalytic consumption of L-tyrosine by MT in the presence of 3-HC or tropolone in comparison to a control. Figure 4A shows that the consumption of L-tyrosine is negligible when the reaction is carried out in the presence of tropolone, whereas in the presence of 3-HC, only approximately 3% of the substrate is consumed after 30 min of incubation. This behavior of the two inhibitors was confirmed by the concentration of L-DOPA in the same samples (Figure 4B), which is below the limit of measurement in the presence of 3-HC and tropolone.

This sharp inhibitory behavior of 3-HC on MT follows from the general trend of the structure−activity relationship between MT and phenolics (and phenolic analogs).

In contrast, nonsubstituted coumarin (1,2-benzopyrone) was reported to inhibit apple PPO.[39] Docking studies performed with this enzyme revealed that the compound is able to enter the enzyme active site, where it is anchored to a specific L-tyrosine residue by a hydrogen bond.[39] The alleged complexing ability of coumarin toward Cu^{2+} is not presently well evidenced and, therefore, should not be considered as a driving force for the observed PPO and coumarin interaction(s). However, we could not find any interaction between the MT and the unsubstituted coumarin. This observation highlights the importance of the hydroxy substituent(s) for a specific interaction with the enzyme active site to occur.

We can conclude that the chelating ability of tropolone toward the cupric ions of the dicopper cluster is not important to explain its inhibitory properties: the molecule lays too far from the metal center and is most likely connected to one cupric ion by means of a hydrogen-bond-engaged water molecule. The kinetics of the inhibition of MT by tropolone has been already studied,[40] and a specific interaction with the oxy form of the enzyme was proposed to explain the particular behavior of the inhibitor. To establish the true mechanism of

DOI: 10.1021/acs.jafc.5b02636
J. Agric. Food Chem. 2015, 63, 7236−7244

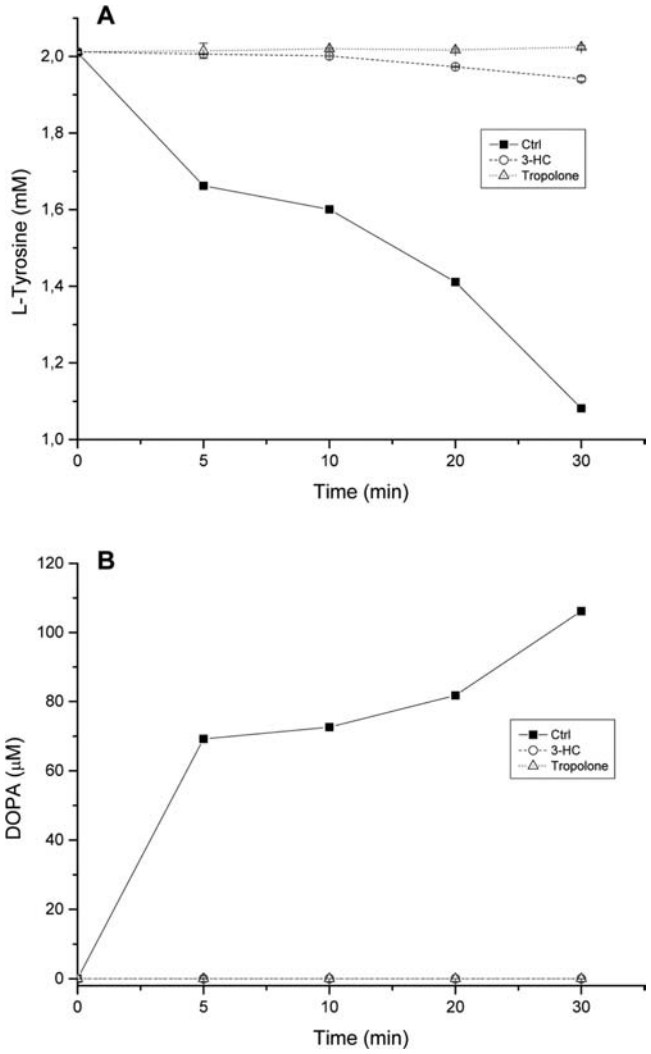

Figure 4. Tyrosinase-catalyzed oxidation of L-tyrosine in the presence of 3-hydroxycoumarin (3-HC) and tropolone. HPLC measurements of L-tyrosine (A) and L-DOPA (B) concentrations were performed over time in the presence of 0.5 mM 3-HC and 0.5 mM tropolone and in their absence (Ctrl). Other experimental conditions were 2 mM L-tyrosine, 100 mM potassium phosphate buffer, pH 6.5, in a 1 mL final volume and 25 °C temperature.

MT inhibition by 3-HC, we conducted spectrophotometric experiments to compare the kinetics of tropolone and 3-HC as inhibitors of MT under identical experimental conditions. Whereas tropolone behaved as a slow-binding inhibitor, which confirmed the findings of Espin and Wichers,[40] 3-HC behaved as a "normal" inhibitor (data not shown). This finding suggests that the two molecules are accommodated differently within the enzyme active site. More specifically, 3-HC most likely interacts with the most abundant form of MT, namely, the met form.[1] Remarkably, even the addition of 0.2 mM $CuSO_4$ was not able to remove the inhibition.[40]

Due to the bonding pattern described above, 4-hydroxycoumarin (4-HC) also should not behave as a substrate for MT. HPLC analysis confirmed that 4-HC did not behave as a substrate for MT (see the Supporting Information, Figure SM4).

In Figure 5, the reaction of MT with L-tyrosine in the presence of increasing concentrations of 4-HC is reported. Note that in the first minutes, the formation of dopachrome is

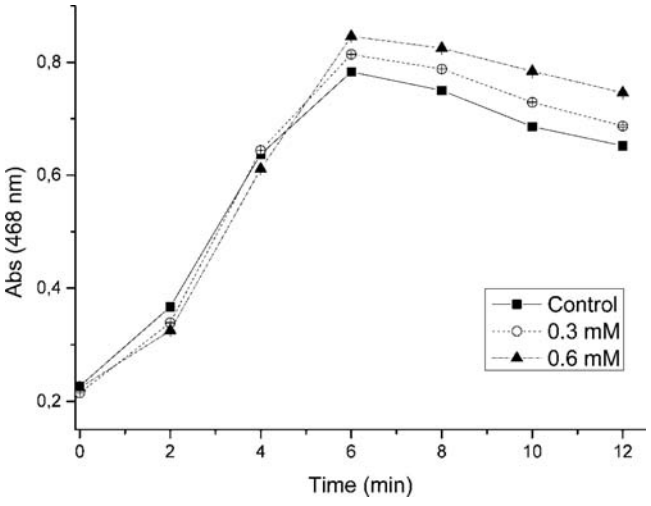

Figure 5. Tyrosinase-catalyzed oxidation of L-tyrosine in the presence of 4-hydroxycoumarin (4-HC). The reaction mixture contained 3 mM L-tyrosine and 95 enzyme units. The 4-HC concentration ranged from 0.3 to 0.6 mM. Other experimental conditions were 100 mM potassium phosphate buffer, pH 6.5, in a 1 mL final volume and 25 °C temperature.

not substantially affected by the presence of 4-HC. In its presence, the formation of dopachrome appears to be slightly increased between the fourth and sixth minutes and then persists for a longer period before it decreases because of nonenzymatic reactions that lead to the formation of melanin. The origin of this behavior is still unknown, but we can assume that, at concentrations much higher than the amount of dopachrome, 4-HC can create an effect of crowding at the catalytic site of the enzyme, thereby slowing the release of the product of the reaction. Yet, a reaction between 4-HC and nonenzymatic transformation products of dopachrome is also possible.

A comparison of the overall effect of the examined hydroxycoumarins can be observed in Figure 6. The four compounds, 3-, 4-, 6-, and 7-hydroxycoumarin, were incubated in the presence of MT. We then used L-tyrosine as a substrate and measured the formation of melanin over time. Both 4-HC and 6-HC had no inhibitory effect on enzymatic activity, as the formation of melanin did not decrease. The presence of 7-HC, however, slowed the formation of dopachrome in the early stages of the reaction but failed to prevent melanin formation after an adequate period of time. In contrast, only 3-HC persisted in its inhibitory activity, as the formation of melanin was not observed in the 2 h following the start of the experiment. Moreover, the inhibitory activity of 3-HC is strictly dose-dependent (see the Supporting Information, Figure SM5).

Molecular Docking Study. Prompted by these findings, we searched for the putative positions of three compounds within the active site of the enzyme (3-HC, 6-HC, and 7-HC) via in silico molecular docking (4-HC was not considered in the molecular docking investigation, being neither a substrate nor an inhibitor). The results of the docking runs are summarized in Table 1.

Concerning the comparatively bulky 3-HC, the molecular modeling investigation resulted in two clusters, of which the representative Ori1 and Ori2 clusters are shown in Figures 7A,B. The two clusters have very different populations (46% of the configurations are in Ori1, whereas 14% of the configurations are in Ori2; see Table 1), and Ori1 has a

DOI: 10.1021/acs.jafc.5b02636
J. Agric. Food Chem. 2015, 63, 7236−7244

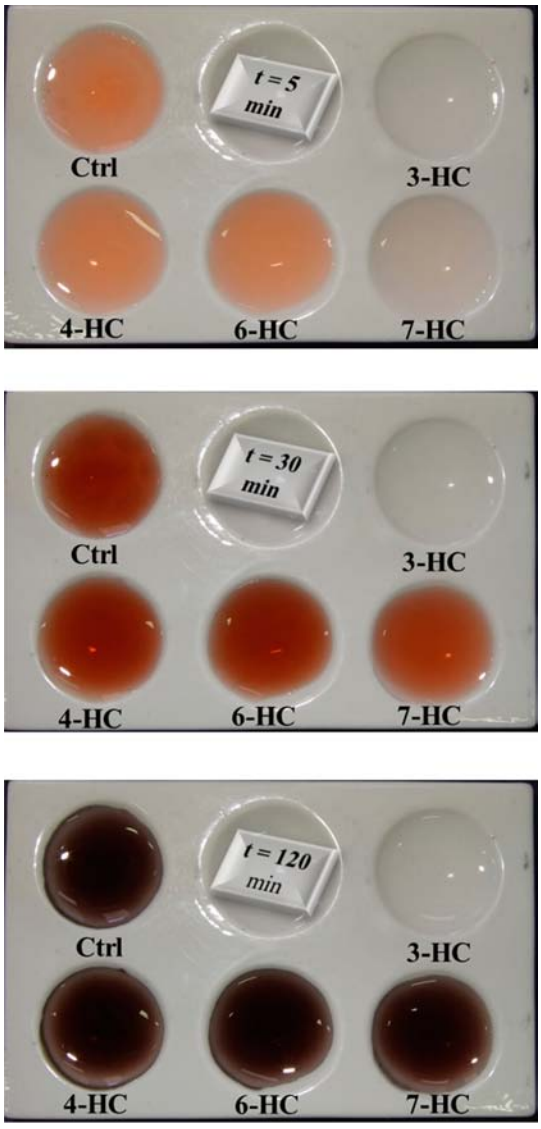

Figure 6. Effect of the four studied hydroxycoumarins on the formation of melanin via mushroom tyrosinase in the presence of L-tyrosine as the substrate. The following enzymatic reactions have been performed on a porcelain spot plate: Ctrl, incubation of tyrosinase (46 EU) and L-tyrosine (2 mM) as the control; 3-HC, 4-HC, 6-HC, and 7HC, incubation of tyrosinase (46 EU) and L-tyrosine (2 mM) in the presence of 0.6 mM of each hydroxycoumarin. The enzymatic reaction was buffered with 0.1 M potassium phosphate, pH 6.5. Pictures were taken over the reported time.

Table 1. Results of Molecular Docking[a]

compound	orientation	scoring function (kcal/mol)	population (%)
3-HC	Ori1	−7.88	46.0
	Ori2	−7.36	14.0
6-HC	Ori1	−8.29	29.5
	Ori2	−8.15	38.0
7-HC	Ori1	−6.52	17.5
	Ori2	−6.28	21.5

[a]The population is given over the total population of the run associated with each compound.

slightly better scoring function. The two configurations are rotated with respect to one another by an angle of approximately 180° around the major axis of the molecule (flip orientation). In Figure 7C, the two orientations are superimposed upon one another. The H atoms of the hydroxyl groups of the two conformations are directed in an opposing manner, whereas, in both conformations, the oxygen atom of the OH group occupies a position along the location of the oxygen atom of a crystallographic water molecule. Therefore, 3-HC accommodates within the MT active site in a manner quite similar to that proposed for mimosine[41] and kojic acid.[42] With these inhibitors, which are transition state analogues, the oxygen of the hydroxyl group acted as a bridge between the two cupric ions, thus displacing the pre-existing water (or hydroxide) already present in the met form. As a consequence, a stable adduct between the dicupric cluster and the inhibitor molecule is formed, preventing the approach of the substrate to the catalytic site. In principle, both Ori1 and Ori2 poses fit well with such an inhibitory mechanism.

However, the distances of the O atom of the OH group from the Cu ions differ in the two poses. The O atom of Ori1 is roughly at the same distance from both Cu ions (2.4 vs 2.6 Å), whereas the O atom of Ori2 is located 2.0 and 3.0 Å away from CuA and CuB, respectively. Ori1 is characterized by the position of the O atom of the OH group, which is more symmetric with respect to the two Cu ions when compared with Ori2. The different population of the two clusters associated with Ori1 and Ori2 suggests that the hydroxyl group interacts with the two Cu ions, thus confirming the bridging role of the oxygen atom of the hydroxyl group as depicted above. Both kinetic and docking data confirm the strict analogy between the inhibitory behavior of mimosine and kojic acid and that of 3-HC. However, despite the structural analogy, tropolone behaves differently, due to its peculiar positioning within the active MT site that follows from the water molecule bridging the inhibitor to the oxy form of the enzyme.[40] The Ori2 pose is less symmetrical than the Ori1 and could be less effective as an inhibitor; however, due to the above-described structural and mechanistic reasons, the potential substrate role for this pose is not possible.

For the 6-HC substrate, two clusters have been identified that have the lowest docking scoring functions. Interestingly, the highest affinity site obtained from the blind docking protocol is similar to the site obtained from the guided docking protocol (i.e., Ori1 and Ori2 are representatives of the two clusters that are reported in Figure 7D,E, respectively, with Figure 7F displaying both poses). The difference in the scoring function of the two orientations was small, and also the populations of the two clusters did not differ remarkably (29.5 and 38.0% over the total population, respectively, as reported in Table 1). The two poses are characterized by the opposite orientation of the hydroxyl group. In Ori1, the pose that belonged to the cluster with a better scoring function but a slightly lower population, the hydroxyl group is close to the two Cu ions with the OH group at distances of 1.9 and 2.8 Å from CuA and CuB, respectively. The asymmetrical positioning of the hydroxyl group in Ori1 is in agreement with the substrate nature of 6-HC, which can be ortho-hydroxylated to esculetin by the oxy-MT. The hydroxyl group of Ori2 points toward the opening of the active site, and the distances between the CuA and CuB and the closest oxygen atom of Ori2 are 2.1 and 2.9 Å, respectively. It is readily apparent that this pose is unproductive as a MT substrate; however, it could act, in principle, as a slight inhibitor by obstructing the active site. Interestingly, the stability of the poses of this compound appears to be unaffected

DOI: 10.1021/acs.jafc.5b02636
J. Agric. Food Chem. 2015, 63, 7236−7244

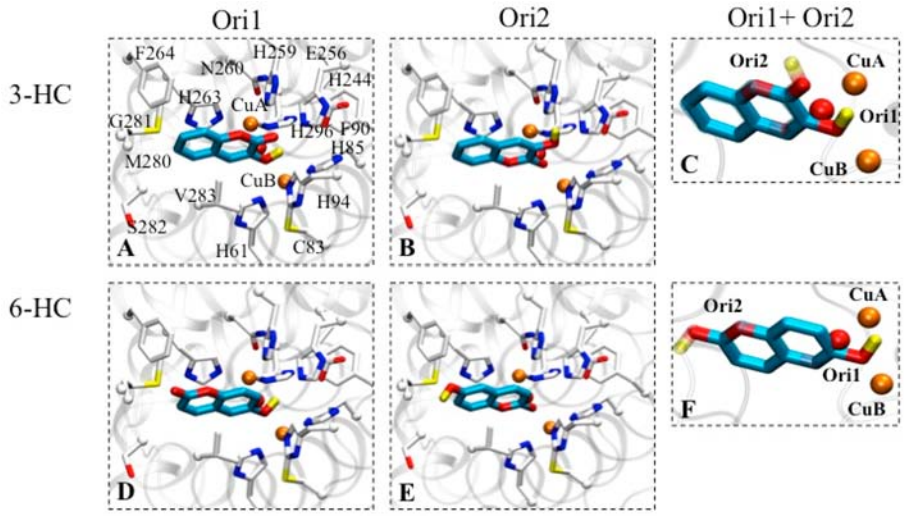

Figure 7. Characterization of the binding site and of representatives of the most populated clusters of the lead molecules (3-HC, upper panels; 6-HC, lower panels). Panels A and B show the two representatives (Ori1 and Ori2) of 3-HC (in thick licorice), and panel C shows the combination of the two poses (in solid Ori1, in transparence Ori2). In panel A, the residues of the binding site are shown in licorice and are labeled. In all panels, the Cu ions are colored dark orange and the residues of the binding site are rendered in an atom type manner, such that C is white, O is red, N is blue, and S is yellow. Panels D and E contain the two representatives of the most populated clusters of 6-HC, and panel F collects both poses. The binding site residue's name and their positions are the same in all of the panels as well as the color and rendering codes.

by the position of the hydroxyl group relative to the active site groups.

The docking runs for the 7-HC substrate also yielded two main clusters with populations that were not dissimilar (17.5 and 21.5% for Ori1 and Ori2, respectively, over the total population; Table 1). The two clusters were characterized by the worst scoring functions among the three compounds. This might suggest a poor affinity of the compound for the enzyme. Yet, the 7-HC substrate behaves as an effective "competitive substrate" during MT-catalyzed L-tyrosine conversion to melanin, even though its affinity for the MT active site appears from the docking calculations to be comparatively low in comparison with that of 6-HC. Additionally, the 6-HC substrate is a distinctly more effective MT substrate than the 7-HC substrate (see the Supporting Information, Figure SM6). Moreover, it is unable to reduce the L-tyrosine conversion into melanin (Figure 6). The answer could be that the two top poses found for the 7-HC substrate account for <40% of the whole population, whereas the remaining 60% of the population is distributed over several configurations that are poorly populated.

However, the ranking of the poses might be affected by the intrinsic limitations of the docking procedure, such as the absence of the solvent or the limited description of the flexibility of the enzyme and compounds. The apparent contradiction between kinetic and docking data indicates that a variety of factors affect the complicated MT and substrate interactions. Thus, a more complete picture requires a molecular dynamics study in which the solvent, temperature, and dynamical effects are considered. This might be a future direction of investigation.

In conclusion, our study, which was based on the structure–activity relationship of four hydroxycoumarins and MT, allowed us to identify anti-tyrosinase properties for use in developing molecules that are derived from coumarin. In particular, the positioning of the hydroxyl group of the hydroxycoumarin on the aromatic ring determines the substrates' behavior. For example, the hydroxyl group at positions 6 or 7 results in the molecule behaving as a weak substrate for the enzyme. This follows from the direct interaction of the hydroxyl group with the two Cu ions of the enzyme active site. However, if the hydroxyl group is located on the pyrone ring of coumarin, the interaction with the enzyme is only possible if the molecule enters the active site with a rotation of 180°. Because the pyrone ring cannot be hydroxylated by tyrosinase, the presence of a pre-existing hydroxyl group makes this molecule unreactive with the enzyme (e.g., the 4-HC substrate) or a potent inhibitor (e.g., the 3-HC substrate).

The results obtained from both the kinetics experiments and molecular docking approach studies demonstrate that the structure of 3-hydroxycoumarin may represent a lead compound for the development of a new class of inhibitors.

■ ASSOCIATED CONTENT

Supporting Information

The Supporting Information is available free of charge on the ACS Publications website at DOI: 10.1021/acs.jafc.5b02636.

MT-catalyzed oxidation of L-tyrosine and formation of L-DOPA in the presence of 7-HC; HPLC analysis of products of MT activity acting on 3-HC and 4-HC; effect of 3-HC on the formation of MT-catalyzed melanin; comparison between MT actions on 6-HC and 7-HC (PDF)

■ AUTHOR INFORMATION

Corresponding Author

*(A.R.) E-mail: rescigno@unica.it.

Author Contributions

‖S.A. and P.Z. contributed equally to this work.

Notes

The authors declare no competing financial interest.

DOI: 10.1021/acs.jafc.5b02636
J. Agric. Food Chem. 2015, 63, 7236–7244

ABBREVIATIONS USED

MT, mushroom tyrosinase; PPO, polyphenol oxidase; 3-HC, 3-hydroxycoumarin; 4-HC, 4-hydroxycoumarin; 6-HC, 6-hydroxycoumarin; 7-HC, 7-hydroxycoumarin

REFERENCES

(1) Sanchez-Ferrer, A.; Rodriguez-Lopez, J. N.; Garcia-Canovas, F.; Garcia-Carmona, F. Tyrosinase: a comprehensive review of its mechanism. *Biochim. Biophys. Acta, Protein Struct. Mol. Enzymol.* **1995**, *1247*, 1−11.

(2) Ismaya, W. T.; Rozeboom, H. J.; Schurink, M.; Boeriu, C. G.; Wichers, H.; Dijkstra, B. W. Crystallization and preliminary X-ray crystallographic analysis of tyrosinase from the mushroom *Agaricus bisporus*. *Acta Crystallogr., Sect. F: Struct. Biol. Cryst. Commun.* **2011**, *67*, 575−578.

(3) Ismaya, W. T.; Rozeboom, H. J.; Weijn, A.; Mes, J. J.; Fusetti, F.; Wichers, H. J.; Dijkstra, B. W. Crystal structure of *Agaricus bisporus* mushroom tyrosinase: identity of the tetramer subunits and interaction with tropolone. *Biochemistry* **2011**, *50*, 5477−5486.

(4) de Faria, R. O.; Moure, V. R.; Amazonas, M.; Krieger, N.; Mitchell, D. A. The biotechnological potential of mushroom tyrosinases. *Food Technol. Biotechnol.* **2007**, *45*, 287−294.

(5) Solano, F.; Briganti, S.; Picardo, M.; Ghanem, G. Hypopigmenting agents: an updated review on biological, chemical and clinical aspects. *Pigm. Cell Res.* **2006**, *19*, 550−571.

(6) Rescigno, A.; Casañola-Martin, G. M.; Sanjust, E.; Zucca, P.; Marrero-Ponce, Y. Vanilloid derivatives as tyrosinase inhibitors driven by virtual screening-based QSAR models. *Drug Test. Anal.* **2011**, *3*, 176−181.

(7) Cui, Y.; Liang, G.; Hu, Y. H.; Shi, Y.; Cai, Y. X.; Gao, H. J.; Chen, Q. X.; Wang, Q. Alpha-substituted derivatives of cinnamaldehyde as tyrosinase inhibitors: inhibitory mechanism and molecular analysis. *J. Agric. Food Chem.* **2015**, *63*, 716−722.

(8) Kostova, I. Synthetic and natural coumarins as cytotoxic agents. *Curr. Med. Chem.: Anti-Cancer Agents* **2005**, *5*, 29−46.

(9) Kostova, I.; Bhatia, S.; Grigorov, P.; Balkansky, S.; Parmar, V. S.; Prasad, A. K.; Saso, L. Coumarins as antioxidants. *Curr. Med. Chem.* **2011**, *18*, 3929−3951.

(10) de Araújo, R. S. A.; Guerra, F. Q. S.; Lima, E. O.; de Simone, C. A.; Tavares, J. F.; Scotti, L.; Scotti, M. T.; de Aquino, T. M.; de Moura, R. O.; Mendonça, F. J. B., Jr; Barbosa-Filho, J. M. Synthesis, structure-activity relationships (SAR) and in silico studies of coumarin derivatives with antifungal activity. *Int. J. Mol. Sci.* **2013**, *14*, 1293−1309.

(11) Bourgaud, F.; Hehn, A.; Larbat, R.; Doerper, S.; Gontier, E.; Kellner, S.; Matern, U. Biosynthesis of coumarins in plants: a major pathway still to be unravelled for cytochrome P450 enzymes. *Phytochem. Rev.* **2006**, *5*, 293−308.

(12) Murray, R. D. Coumarins. *Nat. Prod. Rep.* **1995**, *12*, 477−505.

(13) Casañola-Martin, G. M.; Le-Thi-Thu, H.; Marrero-Ponce, Y.; Castillo-Garit, J. A.; Torrens, F.; Rescigno, A.; Abad, C.; Khan, M. T. H. Tyrosinase enzyme: 1. An overview on a pharmacological target. *Curr. Top. Med. Chem.* **2014**, *14*, 1494−1501.

(14) Le-Thi-Thu, H.; Casañola-Martín, G. M.; Marrero-Ponce, Y.; Rescigno, A.; Abad, C.; Khan, M. T. H. A rational workflow for sequential virtual screening of chemical libraries on searching for new tyrosinase inhibitors. *Curr. Top. Med. Chem.* **2014**, *14*, 1473−1485.

(15) Le-Thi-Thu, H.; Casañola-Martín, G. M.; Marrero-Ponce, Y.; Rescigno, A.; Saso, L.; Parmar, V. S.; Torrens, F.; Abad, C. Novel coumarin-based tyrosinase inhibitors discovered by OECD principles-validated QSAR approach from an enlarged, balanced database. *Mol. Diversity* **2011**, *15*, 507−520.

(16) Flurkey, A.; Cooksey, J.; Reddy, A.; Spoonmore, K.; Rescigno, A.; Inlow, J.; Flurkey, W. H. Enzyme, protein, carbohydrate, and phenolic contaminants in commercial tyrosinase preparations: potential problems affecting tyrosinase activity and inhibition studies. *J. Agric. Food Chem.* **2008**, *56*, 4760−4768.

(17) Rescigno, A.; Zucca, P.; Flurkey, A.; Inlow, J.; Flurkey, W. H. Identification and discrimination between some contaminant enzyme activities in commercial preparations of mushroom tyrosinase. *Enzyme Microb. Technol.* **2007**, *41*, 620−627.

(18) Rescigno, A.; Sanjust, E.; Pedulli, G. F.; Valgimigli, L. Spectrophotometric method for the determination of polyphenol oxidase activity by coupling of 4-*tert*-butyl-*o*-benzoquinone and 4-amino-*N*,*N*-diethylaniline. *Anal. Lett.* **1999**, *32*, 2007−2017.

(19) Valgimigli, L.; Pedulli, G. F.; Cabiddu, S.; Sanjust, E.; Rescigno, A. Formation of a blue adduct between 4-*tert*-butyl-1,2-benzoquinone and 4-amino-*N*,*N*-diethylaniline. *Tetrahedron* **2000**, *56*, 659−662.

(20) Marongiu, B.; Piras, A.; Porcedda, S.; Tuveri, E.; Sanjust, E.; Meli, M.; Sollai, F.; Zucca, P.; Rescigno, A. Supercritical CO_2 extract of *Cinnamomum zeylanicum*: chemical characterization and antityrosinase activity. *J. Agric. Food Chem.* **2007**, *55*, 10022−10027.

(21) Case, D. A.; Babin, V.; Berryman, J. T.; Betz, R. M.; Cai, Q.; Cerutti, D. S.; Cheatham, T. E.; Darden, T. A.; Duke, R. E.; Gohlke, H.; Goetz, A. W.; Gusarov, S.; Homeyer, N.; Janowski, P.; Kaus, Y.; Kolossváry, I.; Kovalenko, A.; Lee, T. S.; LeGrand, S.; Luchko, T.; Luo, R.; Madej, B.; Merz, K. M.; Paesani, F.; Roe, D. R.; Roitberg, A.; Sagui, C.; Salomon-Ferrer, R.; Seabra, G.; Simmerling, C. L.; Smith, W.; Swails, J.; Walker, R. C.; Wang, J.; Wolf, R. M.; Wu, X.; Kollman, P. A. *AMBER 14*; University of California: San Francisco, CA, USA, 2014.

(22) Frisch, M. J.; Trucks, G. W.; Schlegel, H. B.; Scuseria, G. E.; Robb, M. A.; Cheeseman, J. R.; Montgomery, Jr., J. A.; Vreven, T.; Kudin, K. N.; Burant, J. C.; Millam, J. M.; Iyengar, S. S.; Tomasi, J.; Barone, V.; Mennucci, B.; Cossi, M.; Scalmani, G.; Rega, N.; Petersson, G. A.; Nakatsuji, H.; Hada, M.; Ehara, M.; Toyota, K.; Fukuda, R.; Hasegawa, J.; Ishida, M.; Nakajima, T.; Honda, Y.; Kitao, O.; Nakai, H.; Klene, M.; Li, X.; Knox, J. E.; Hratchian, H. P.; Cross, J. B.; Bakken, V.; Adamo, C.; Jaramillo, J.; Gomperts, R.; Stratmann, R. E.; Yazyev, O.; Austin, A. J.; Cammi, R.; Pomelli, C.; Ochterski, J. W.; Ayala, P. Y.; Morokuma, K.; Voth, G. A.; Salvador, P.; Dannenberg, J. J.; Zakrzewski, V. G.; Dapprich, S.; Daniels, A. D.; Strain, M. C.; Farkas, O.; Malick, D. K.; Rabuck, A. D.; Raghavachari, K.; Foresman, J. B.; Ortiz, J. V.; Cui, Q.; Baboul, A. G.; Clifford, S.; Cioslowski, J.; Stefanov, B. B.; Liu, G.; Liashenko, A.; Piskorz, P.; Komaromi, I.; Martin, R. L.; Fox, D. J.; Keith, T.; Al-Laham, M. A.; Peng, C. Y.; Nanayakkara, A.; Challacombe, M.; Gill, P. M. W.; Johnson, B.; Chen, W.; Wong, M. W.; Gonzalez, C.; Pople, J. A. *Gaussian 03*, revision C.02; Gaussian Inc.: Wallingford, CT, USA, 2004.

(23) Asthana, S.; Shukla, S.; Ruggerone, P.; Vargiu, A. V. Molecular mechanism of viral resistance to a potent non-nucleoside inhibitor unveiled by molecular simulations. *Biochemistry* **2014**, *53*, 6941−6953.

(24) Asthana, S.; Shukla, S.; Vargiu, A. V.; Ceccarelli, M.; Ruggerone, P.; Paglietti, G.; Marongiu, M. E.; Blois, S.; Giliberti, G.; La Colla, P. Different molecular mechanisms of inhibition of bovine viral diarrhea virus and hepatitis C virus RNA-dependent RNA polymerases by a novel benzimidazole. *Biochemistry* **2013**, *52*, 3752−3764.

(25) Morris, G. M.; Huey, R.; Lindstrom, W.; Sanner, M. F.; Belew, R. K.; Goodsell, D. S.; Olson, A. J. AutoDock4 and AutoDockTools4: automated docking with selective receptor flexibility. *J. Comput. Chem.* **2009**, *30*, 2785−2791.

(26) Garcia-Molina, S.; Munoz-Munoz, J. L.; Garcia-Molina, F.; Rodriguez-Lopez, J. N.; Garcia-Canovas, F. Study of umbelliferone hydroxylation to esculetin catalyzed by polyphenol oxidase. *Biol. Pharm. Bull.* **2013**, *36*, 1140−1145.

(27) Sollai, F.; Zucca, P.; Sanjust, E.; Steri, D.; Rescigno, A. Umbelliferone and esculetin: inhibitors or substrates for polyphenol oxidases? *Biol. Pharm. Bull.* **2008**, *31*, 2187−2193.

(28) Zucca, P.; Sanjust, E.; Loi, M.; Sollai, F.; Ballero, M.; Pintus, M.; Rescigno, A. Isolation and characterization of polyphenol oxidase from Sardinian poisonous and non-poisonous chemotypes of *Ferula communis* (L.). *Phytochemistry* **2013**, *90*, 16−24.

(29) Ortiz-Ruiz, C. V.; Garcia-Molina, M. D. M.; Serrano, J. T.; Tomas-Martinez, V.; Garcia-Canovas, F. Discrimination between alternative substrates and inhibitors of tyrosinase. *J. Agric. Food Chem.* **2015**, *63*, 2162−2171.

DOI: 10.1021/acs.jafc.5b02636
J. Agric. Food Chem. 2015, 63, 7236−7244

(30) Rattanapan, J.; Sichaem, J.; Tip-pyang, S. Chemical constituents and antioxidant activity from the stems of *Alyxia reinwardtii*. *Rec. Nat. Prod.* **2012**, *6*, 288−291.
(31) Rescigno, A.; Sanjust, E.; Soddu, G.; Rinaldi, A. C.; Sollai, F.; Curreli, N.; Rinaldi, A. Effect of 3-hydroxyanthranilic acid on mushroom tyrosinase activity. *Biochim. Biophys. Acta, Protein Struct. Mol. Enzymol.* **1998**, *1384*, 268−276.
(32) Sribuhom, T.; Sriphana, U.; Thongsri, Y.; Yenjai, C. Chemical constituents from the stems of *Alyxia schlechteri*. *Phytochem. Lett.* **2015**, *11*, 80−84.
(33) De Araujo Leite, J. C.; De Castro, T. M. X.; Barbosa-Filho, J. M.; De Siqueira-Junior, J. P.; Marques-Santos, L. F. Photoprotective effect of coumarin and 3-hydroxycoumarin in sea urchin gametes and embryonic cells. *J. Photochem. Photobiol., B* **2015**, *146*, 44−51.
(34) Rescigno, A.; Bruyneel, F.; Padiglia, A.; Sollai, F.; Salis, A.; Marchand-Brynaert, J.; Sanjust, E. Structure-activity relationships of various amino-hydroxy-benzenesulfonic acids and sulfonamides as tyrosinase substrates. *Biochim. Biophys. Acta, Gen. Subj.* **2011**, *1810*, 799−807.
(35) Soddu, G.; Sanjust, E.; Murgia, S.; Rescigno, A. Interference of some tryptophan metabolites in the formation of melanin in vitro. *Pigm. Cell Res.* **2004**, *17*, 135−141.
(36) Mead, J. A.; Smith, J. N.; Williams, R. T. Studies in detoxication. 72. The metabolism of coumarin and of *o*-coumaric acid. *Biochem. J.* **1958**, *68*, 67−74.
(37) Conrad, J. S.; Dawso, S. R.; Hubbard, E. R.; Meyers, T. E.; Strothkamp, K. G. Inhibitor binding to the binuclear active site of tyrosinase: temperature, pH, and solvent deuterium isotope effects. *Biochemistry* **1994**, *33*, 5739−5744.
(38) Rescigno, A.; Sollai, F.; Pisu, B.; Rinaldi, A.; Sanjust, E. Tyrosinase inhibition: general and applied aspects. *J. Enz. Inhib. Med. Chem.* **2002**, *17*, 207−218.
(39) Thada, R.; Chockalingam, S.; Dhandapani, R. K.; Panchamoorthy, R. Extraction and quantitation of coumarin from cinnamon and its effect on enzymatic browning in fresh apple juice: a bioinformatics approach to illuminate its antibrowning activity. *J. Agric. Food Chem.* **2013**, *61*, 5385−5390.
(40) Espin, J. C.; Wichers, H. J. Slow-binding inhibition of mushroom (*Agaricus bisporus*) tyrosinase isoforms by tropolone. *J. Agric. Food Chem.* **1999**, *47*, 2638−2644.
(41) Woolery, G. L.; Powers, L.; Winkler, M.; Solomon, E. I.; Lerch, K.; Spiro, T. G. Extended X-ray absorption fine structure study of the coupled binuclear copper active site of tyrosinase from *Neurospora crassa*. *Biochim. Biophys. Acta, Protein Struct. Mol. Enzymol.* **1984**, *788*, 155−161.
(42) Bubacco, L.; Spinazze, R.; della Longa, S.; Benfatto, M. X-ray absorption analysis of the active site of *Streptomyces antibioticus* tyrosinase upon binding of transition state analogue inhibitors. *Arch. Biochem. Biophys.* **2007**, *465*, 320−327.

DOI: 10.1021/acs.jafc.5b02636
J. Agric. Food Chem. 2015, 63, 7236−7244

Table 1. Main Ingredients Relative to Protein and Fat Fractions of Infant Formulas (IFs) Analyzed, Fat Content Determined, and Reconstitution Factors (RF)[a]

IFs	country	ingredients	fat (% w/w)	RF (% w/v)
1	Spain	milk lipids, skimmed milk, vegetable oils (rapeseed, sunflower, oleic sunflower), whey protein, fish oil (DHA), *Mortierella alpina* oil (ARA), emulsifier (soya lecithin)	22.0 ± 2.1	13.5
2		demineralized whey protein, skimmed milk, vegetable oils (palm, rapeseed, coconut, sunflower), mortierella alpine oil (ARA), fish oil, soya lecithin, milk proteins	25.5 ± 1.0	12.9
3		skimmed milk, vegetable oils (palm, palm kernel, rapeseed, sunflower, sunflower high oleic, arachidonic acid), whey protein enriched with α-lactoalbumin, emulsifier (soya lecithin), fish oil (source of DHA)	23.7 ± 0.3	13.5
4		vegetable oils (palm, coconut, rapeseed, high oleic sunflower, sunflower), skimmed milk, whey protein concentrate, fungi and seedweed oils	25.3 ± 0.8	12.9
5		skimmed milk, milk fat, whey enriched in MFGM, whey enriched in α-lactoalbumin, soya lecithin, fish oil, vegetable oils (sunflower, rapeseed, palm, coconut, single cell oil)	27.2 ± 0.6	13.0
6		vegetable oils (sunflower, rapeseed, palm, coconut, single cell oil), skimmed milk, milk fat, whey protein rich in MFGM, whey protein rich in α-lactoalbumin, milk protein, fish oil, emulsifier (soya lecithin)	34.8 ± 0.7	11.4
7	Sweden	whey powder, vegetable oil (palm, canola, coconut, sunflower), skimmed milk powder, fish oil, oil from *Mortierella alpina*, emulsifier (soy lecithin)	25.8 ± 0.1	12.9
8		organic skimmed milk, organic demineralized whey powder, organic vegetable oils (palm, rapeseed, sunflower), polyunsaturated oils (fish, vegetable)	23.2 ± 0.6	13.0
9		skimmed milk, milk fat, whey enriched in MFGM, whey enriched in α-lactoalbumin, soya lecithin, fish oil, vegetable oils (sunflower, rapeseed, palm, coconut, single cell oil)	27.7 ± 2.2	13.0
10	Czech Republic	demineralized whey powder, vegetable oils, whole milk powder, skimmed milk powder, emulsifier (lecithin)	22.4 ± 2.0	12.9
11		demineralized whey, skimmed milk powder, vegetable oils (palm, rapeseed, sunflower, coconut, microbiologic (ARA)), soya lecithin, fish oil	22.3 ± 2.6	13.5
12		demineralized whey (from milk), vegetable oil, dried skimmed milk, whey protein concentrate (from milk), fish oil, soya lecithin	24.3 ± 0.4	13.5
13		demineralized whey, vegetable oils (palm, rape, coconut, sunflower, oils from microbial resource (ARA)), dried skim milk, concentrated whey milk, soya lecithin	21.4 ± 0.5	13.8

[a]DHA: docosahexaenoic acid. ARA: arachidonic acid. MFGM: milk fat globule membrane.

MATERIALS AND METHODS

Reagents. *Standards.* For sterol determination, the standards used were 5β-cholestan-3α-ol (epicoprostanol) (purity ≥95%) as internal standard (IS), 5-cholesten-3β-ol (cholesterol) (purity 99%), 5,24-cholestadien-3β-ol, (desmosterol) (purity 84%), stigmasta-5,22-dien-3β-ol (stigmasterol) (purity 95%), stigmast-5-en-3-ol (β-sitosterol) (purity 98%), and 24α-ethyl-5α-cholestan-3β-ol (stigmastanol) (purity 97.4%) from Sigma Chemical Co. (St. Louis, MO, USA) and 5,22-cholestadien-24β-methyl-3β-ol (brassicasterol) (purity 98.6%) and 5-cholesten-24α-methyl-3β-ol (campesterol) (purity 98.6%) purchased from Steraloids (Newport, RI, USA).

Reagents. Chloroform, diethyl ether, ethanol, methanol, potassium chloride, sodium chloride, anhydrous sodium sulfate, acetone, and 2-propanol were purchased from Merck & Co., Inc. (Whitehouse Station, NJ, USA). Potassium hydroxide, butylated hydroxytoluene (BHT), and *N*,*O*-bis(trimethylsilyl)trifluoroacetamide with 1% trimethylchlorosilane (silylating reagent) were purchased from Sigma Chemical Co. (St. Louis, MO, USA). Anhydrous pyridine (silylating reagent) was from Fluka (Buchs, Switzerland), and *n*-hexane (purity 96%, HPLC grade) was from Scharlau Chemie, S.A. (Sentmenat, Barcelona, Spain). All reagents were of analytical grade. Ultrapure water was obtained by means of a Millipore Q water purification system (Milford, MA, USA).

Preparation of Solutions. Internal standard (IS) solution of epicoprostanol in ethanol was prepared at a concentration of 1 mg/mL. Standard solutions of sterols were prepared by dissolving the standards in an *n*-hexane:2-propanol (3:2, v/v) mixture at the following concentrations: 1 mg/mL (β-sitosterol), 100 μg/mL (brassicasterol), 1 mg/mL (campesterol), 1 mg/mL (cholesterol), 100 μg/mL (desmosterol), 2.5 μg/mL and 100 μg/mL (stigmastanol), and 100 μg/mL (stigmasterol). All solutions were aliquoted (1 mL) and stored at −20 °C under a nitrogen atmosphere (purity >99%, nitrogen generator Zefiro 40 F-DBS, Courtaboeuf-Cedex, France). To prevent falsely elevated values of IS and standard solutions, immediately prior to analysis the solvents of the stock solutions were completely evaporated with a stream of nitrogen and dissolved with 1 mL of solvent.

A mixture of pyridine:*N*,*O*-bis(trimethylsilyl)trifluoroacetamide (with 1% trimethylchlorosilane) (3:10, v/v) was prepared weekly and stored at 4 °C in an amber glass flask for derivatization. Glass material used for this preparation was rinsed with acetone immediately before use to remove moisture.

Samples. Thirteen powdered IFs marketed in three European countries (Sweden, the Czech Republic, and Spain), for infants between 0 and 6 months of age, were selected for sterol analysis. The label-stated compositions referring to compounds of the protein and fat fractions as a source of sterols are summarized in Table 1. It should be mentioned that, in addition to vegetable oils and fish oils commonly added to these products, some formulas (1, 5, and 9) contain milk fat and whey enriched with MFGM.

Determination of Plant Sterols. Samples were reconstituted as indicated on the labeling (reconstitution factor between 11.4 and 13.8% w/v), and a volume of sample (2 mL) providing approximately 70 mg of fat. Three independent assays of the same batch were analyzed. Lipids were extracted applying the method described by Alemany-Costa et al.,[15] though filtration was made with Whatman no. 2V, 125 mm, (Buckinghamshire, U.K.), and 20 mL of 1 M KCl solution was added to the filtrate instead of 10 mL. The lipid fraction obtained (approximately 70 mg) was processed using the method described by González-Larena et al.,[16] with minor modifications. Briefly, IS (20 μg of epicoprostanol) was added to the lipid fraction, and hot saponification (2.5 mL of 2 N KOH in 90% ethanol at 65 °C during 1 h) was performed. The unsaponifiable material was then extracted with diethyl ether and subjected to derivatization with BSTFA-1%TMCS:pyridine (10:3). The trimethylsilyl ether (TMSE) derivatives obtained were dissolved in *n*-hexane, filtered (syringe-driven Millex-FH filter unit, 1 mL, 0.45 μm Millipore, Milford, MA, USA), and evaporated with nitrogen. The TMSE derivatives were dissolved in 100 μL of *n*-hexane, and 1 μL was injected into a gas chromatograph with flame ionization detector (GC-FID) (AutoSystem XL, PerkinElmer, Norwalk, CT, USA) equipped with a CP-Sil 8 low bleed/MS (50 m × 0.25 mm × 0.25 μm film thickness) capillary column (Chromopack-Varian, Middelburg, The Netherlands), with application of the chromatographic conditions previously proposed for serum sterol determination,[11] with a split ratio of 1:10.

DOI: 10.1021/acs.jafc.5b02647
J. Agric. Food Chem. 2015, 63, 7245−7251

Table 2. Animal Sterol Contents (mg/100 mL)[a]

IFs	cholesterol	desmosterol	desmosterol (% total animal sterol)	total animal sterol
1	2.63 ± 0.04 a	0.308 ± 0.003 a,b	10.50 ± 0.10	2.93 ± 0.04 a
2	1.93 ± 0.04 b,c,d	0.286 ± 0.003 a,c,d	12.91 ± 0.14	2.22 ± 0.04 b,c
3	1.71 ± 0.05 c,d,e	0.428 ± 0.015 e	20.03 ± 0.70	2.14 ± 0.06 b,c,d
4	1.46 ± 0.06 e	0.251 ± 0.009 d,f	14.64 ± 0.53	1.71 ± 0.06 d
5	5.10 ± 0.22 f	0.364 ± 0.010 g	6.66 ± 0.18	5.46 ± 0.23 e
6	4.73 ± 0.13 f	0.425 ± 0.013 e	8.24 ± 0.25	5.16 ± 0.14 e
7	1.72 ± 0.02 c,d,e	0.27 ± 0.004 c,d,f	13.37 ± 0.28	1.98 ± 0.01 c,d
8	1.64 ± 0.03 c,d,e	0.371 ± 0.011 g	18.44 ± 0.55	2.01 ± 0.04 c,d
9	3.95 ± 0.30 g	0.311 ± 0.014 a,b	7.30 ± 0.33	4.26 ± 0.31 f
10	2.03 ± 0.03 b,c	nd[b]	nd	2.03 ± 0.03 c,d
11	1.56 ± 0.07 d,e	0.293 ± 0.002 a,c	15.82 ± 0.11	1.85 ± 0.07 c,d
12	1.59 ± 0.04 d,e	0.248 ± 0.005 f	13.53 ± 0.27	1.83 ± 0.043 c,d
13	2.22 ± 0.09 a,b	0.340 ± 0.012 b,g	13.28 ± 0.47	2.56 ± 0.10 a,b
p[c]	*[d]	*[d]		*[d]

[a]Values are expressed as mean ± standard deviation of three replicates. Different letters in the same column indicate significant differences between infant formulas (IFs). Tukey's HSD test. [b]Not detectable. [c]ANOVA results for each sterol and total animal sterols among IFs. [d]*$p < 0.001$.

All glassware (tubes and vials) was scrupulously cleaned, rinsed with distilled water, and introduced in a Heraeus Thermicon K1253A oven at 450 °C during 8 h to remove contamination according to García-Llatas et al.[17] The Pyrex glass tubes with a conical bottom, employed for derivatization, were previously silanized with derivatization solution in order to avoid the adsorption of TMSE derivatives.[18]

Sterols were identified by comparing standards derivatized by the same procedure as the samples. For quantification, sterol calibration curves of brassicasterol (1−6 μg), β-sitosterol (25−78 μg), campesterol (10−39 μg), cholesterol (20−317 μg), desmosterol (1.7−227 μg), stigmasterol (2−15 μg), and sitostanol (stigmastanol) (0.24−6 μg) containing 20 μg of IS (epicoprostanol) were performed. The correlation coefficients (r) obtained for the different sterols were >0.99.

Estimation of Intake. To calculate intake during the first months of life, the average intake (mL/day) obtained from the literature and corresponding to a total of 1113 healthy infants born at term was used.[19−26] The mean volumes of the IFs (mL/day) ingested by these newborn infants were evaluated at 7 concrete moments of lactation: 0.5 months, 607 ± 31 (n = 307); 1 month, 754 ± 112 (n = 1093); 2 months, 877 ± 158 (n = 937); 3 months, 895 ± 160 (n = 937); 4 months, 933 ± 157 (n = 875); 5 months, 990 ± 31 (n = 645); and 6 moths 873 ± 125 (n = 665).

Statistical Analysis. Analysis of variance (ANOVA) and Tukey's HSD test ($p < 0.001$) were applied to total sterols and individual sterol contents to evaluate possible differences according to the type of sample involved.

In estimating intake, two-tailed (sample and lactation stage) ANOVA was applied to the mean values, followed by Tukey's HSD test. A significance level of $p < 0.001$ was adopted for all comparisons.

The Statgraphics Plus version 5.1 statistical package (Rockville, MD, USA) was used throughout.

RESULTS AND DISCUSSION

Animal Sterols. The total and individual contents of the main animal sterols (cholesterol and desmosterol) are summarized in Table 2. Total animal sterols ranged from 1.71 to 5.46 mg/100 mL sample, cholesterol being the main animal sterol (1.46−5.1 mg/100 mL). The cholesterol concentrations found in our study were comparable to those reported by other authors (Table 3). It has been shown that the amount of cholesterol in IFs is lower than the levels found in HM (4.3−29.2 mg/100 mL) (Table 3).

In our study, IFs 5 and 6 (marketed in Spain) and 9 (marketed in Sweden) showed the highest cholesterol contents (≥4.0 mg/100 mL). It should be underscored that whey protein enriched with MFGM and milk fat is included in these formulations, and MFGM is a good source of cholesterol.[30] The small differences in cholesterol content between IFs 5 and 9 (involving the same formula manufactured in different countries) could be due to different origins of the milk fat used, and even to the different technological treatments applied during the cream separation process.[31]

Table 3. Cholesterol and Desmosterol Content in Infant Formulas (IFs) and Human Milk Indicated in Bibliography

cholesterol (mg/100 mL)		desmosterol (mg/100 mL)	
IFs	human milk	human milk	ref
	9.7−11.0	0.6−1.3	Clark et al.[27]
	15.6−18.9	1.2−1.5	Kallio et al.[28]
	10.0−20.0		Jensen[29]
1.16−4.64	12.0−16.6		Huisman et al.[12]
0.3−25.8	6.5−18.4		Scopesi et al.[13]
	9.0−15.0		Koletzko et al.[7]
7.5−12.8	9.5−29.2	0.5−3.1	Ramalho et al.[14]
0.93−5.45	4.3−21.8[a]		Kamelska et al.[9]

[a]Determined by ATR-FTIR (attenuated total reflectance Fourier transform infrared) spectroscopy.

Infant formula 1 (marketed in Spain) presented an intermediate cholesterol content (2.6 mg/100 mL) that may be related to the use of milk fat. The lowest IF cholesterol content ranged from 1.46 to 2.22 mg/100 mL. All these formulas contain vegetable oils as the main source of fat.

From a compositional point of view, the amount of cholesterol in IFs seems to be positively related to the dairy ingredient used in the formulation (whole milk/milk fat and MFGM). This observation is also supported by the study published by Scopesi et al.,[13] in which the cholesterol content was also related to the source of fat: lower cholesterol contents corresponding to formulas in which the fat source was vegetable oil, intermediate contents corresponding to formulas containing milk fat with the addition of vegetable oil, and the highest contents (approximately 22−26 mg/100 mL) corresponding to samples containing animal fat and eggs, in addition to vegetable oils.[13]

On the other hand, Maduko and Park[10] determined cholesterol in 5 formulations based on skimmed goat milk with different blends of coconut, safflower, and soybean oils.

DOI: 10.1021/acs.jafc.5b02647
J. Agric. Food Chem. 2015, 63, 7245−7251

Table 4. Phytosterol and Phytostanol Contents (mg/100 mL)[a]

IFs	brassicasterol	campesterol	stigmasterol	β-sitosterol	sitostanol	total plant sterol
1	0.21 ± 0.02 a,b,c (6.01 ± 5.68)	0.96 ± 0.02 a,b,c (25.73 ± 0.76)	0.36 ± 0.04 a,b,c (9.57 ± 0.95)	2.17 ± 0.07 a,b (57.73 ± 0.72)	0.05 ± 0.004 a (1.28 ± 0.11)	3.75 ± 0.07 a,b
2	0.25 ± 0.01 c,d (5.62 ± 0.03)	1.13 ± 0.05 c,d (25.41 ± 0.08)	0.43 ± 0.02 a,b,c (9.65 ± 0.09)	2.61 ± 0.11 a,b,c (58,55 ± 0.12)	0.03 ± 0.003 a (1.09 ± 0.04)	4.46 ± 0.19 b,c
3	0.14 ± 0.01 e (4.65 ± 0.11)	0.72 ± 0.04 e (23.29 ± 0.23)	0.39 ± 0.05 a,b,c (12.43 ± 0.75)	1.82 ± 0.12 a (58.55 ± 0.42)	0.03 ± 0.002 a (1.09 ± 0.04)	3.11 ± 0.22 a
4	0.16 ± 0.01 e,f (4.53 ± 0.12)	0.81 ± 0.05 a,e (23.12 ± 0.16)	0.39 ± 0.02 a,b,c (11.16 ± 0.06)	2.09 ± 0.11 a,b (59.88 ± 0.14)	0.05 ± 0.001 a (1.31 ± 0.09)	3.49 ± 0.19 a,b
5	0.25 ± 0.01 c,d (4.98 ± 0.32)	1.15 ± 0.07 d (22.97 ± 0.51)	0.50 ± 0.04 b,c (10.08 ± 0.14)	3.01 ± 0.12 c (60.17 ± 0.73)	0.90 ± 0.06 a,b (1.80 ± 0.20)	5.0 ± 0.29 c
6	0.19 ± 0.01 a,b,f (4.60 ± 0.09)	0.83 ± 0.03 a,e (19.84 ± 0.67)	0.53 ± 0.05 c (12.56 ± 0.42)	2.61 ± 0.16 a,b,c (62.03 ± 0.13)	0.04 ± 0.01 a (0.98 ± 0.21)	4.21 ± 0.25 a,b,c
7	0.20 ± 0.01 a,b (5.52 ± 0.20)	0.90 ± 0.01 a,b,e (24.70 ± 1.21)	0.38 ± 0.04 a,b,c (10.50 ± 0.51)	2.14 ± 0.16 a,b (58.42 ± 1.08)	0.03 ± 0.02 a (0.86 ± 0.45)	3.66 ± 0.21 a,b
8	0.17 ± 0.01 a,e,f (4.32 ± 0.35)	0.96 ± 0.06 a,b,c (23.73 ± 1.08)	0.40 ± 0.04 a,b,c (9.95 ± 0.95)	2.45 ± 0.28 a,b,c (60.34 ± 1.60)	0.07 ± 0.04 a,b (1.66 ± 0.77)	4.05 ± 0.38 a,b,c
9	0.21 ± 0.01 a,b (5.73 ± 0.09)	0.82 ± 0.04 a,e (22.50 ± 0.53)	0.35 ± 0.01 a,b,c (9.64 ± 0.09)	2.12 ± 0.09 a,b (58.23 ± 0.23)	0.14 ± 0.03 b (3,89 ± 0.71)	3.65 ± 0.14 a,b
10	0.18 ± 0.01 a,e,f (5.49 ± 0.28)	0.78 ± 0.01 a,e (24.48 ± 0.73)	0.27 ± 0.01 a (8.43 ± 0.50)	1.89 ± 0.05 a,b (59.24 ± 0.79)	0.08 ± 0.06 a,b (2.36 ± 1.73)	3.20 ± 0.08 a
11	0.22 ± 0.01 b,c (5.41 ± 0.60)	1.02 ± 0.02 b,c,d (24.89 ± 2.41)	0.35 ± 0.11 a,b (8.31 ± 1.74)	2.48 ± 0.31 a,b,c (60.18 ± 1.54)	0.05 ± 0.02 a (1.21 ± 0.53)	4.12 ± 0.41 a,b,c
12	0.23 ± 0.01 b,c (5.84 ± 0.37)	1.06 ± 0.07 b,c,d (26.85 ± 1.48)	0.29 ± 0.01 a (7.41 ± 0.74)	2.34 ± 0.33 a,b,c (58.67 ± 1.72)	0.05 ± 0.04 a,b (1.24 ± 0.85)	3.98 ± 0.45 a,b,c
13	0.28 ± 0.02 d (6.32 ± 0.64)	1.08 ± 0.09 b,c,d (23.64 ± 1.82)	0.35 ± 0.08 a,b (7.87 ± 0.98)	2.65 ± 0.40 b,c (60.29 ± 1.44)	0.04 ± 0.01 a (0.89 ± 0.04)	4.39 ± 0.57 b,c
p[b]	*[c]	*[c]	*[c]	*[c]	*[c]	*[c]

[a]Values are expressed as mean ± standard deviation of three replicates. Relative percentage to total plant sterols content is indicated in parentheses. Different letters in the same column indicate significant differences between infant formulas (IFs). Tukey's HSD test. [b]ANOVA results for each sterol and total plant sterols among IFs. [c]*$p < 0.001$.

Cholesterol contents of these caprine IFs ranged from 9.7 to 9.9 mg/100 g of formula and were higher than in the formulas analyzed in our study (1.41−4.81 mg/100 g of reconstituted formula or 1.46−5.10 mg/100 mL). This may be due to the greater quantity of whole goat milk added to infant milk formulas analyzed by Maduko and Park.[10]

The cholesterol contents in our study are in line with those reported by Wong et al.[11] (2.2 ± 1.1 mg/100 g of reconstituted formula). Only our formulas with dairy fats showed higher cholesterol contents than those indicated by these authors.

The cholesterol concentrations in IF analyzed by Huisman et al.[12] were 3−35 times lower compared with the levels in HM. In our study, the cholesterol concentration in IFs was 2.7−10 times lower compared with the mean HM data described by Huisman[12] (14 mg/100 mL). Interestingly, only the formulas with dairy lipid ingredients (IFs 5, 6, and 9) showed a concentration between 2.7 and 3.5 times lower versus HM. The dairy lipid enriched formulas come closer to the lowest cholesterol contents found in HM in previous studies (6.5 mg/100 mL described by Scopesi et al.[13]).

Albeit to a lesser degree, desmosterol was quantified in all the formulas (0.25−0.43 mg/100 mL) except IF 10 (showing only detectable traces) (Table 2). This is the first time that desmosterol is quantified in IFs. In the study conducted by Ramalho et al.,[14] desmosterol was not detected in IF. Desmosterol is a precursor of cholesterol that is present both in human milk fat globule and in cow's milk.[3]

In IFs, desmosterol expressed as a percentage of total animal sterols is higher than in HM. A significant correlation ($y = 0.0152x + 0.053$; $R^2 = 0.8449$) was observed between desmosterol content and the label stated values of docosahexaenoic acid (DHA) and arachidonic acid (AA). Fish, fungi, and algae oils are frequently used as DHA and AA sources (see Table 1), which could explain these results.

Lathosterol was not detected in the IFs analyzed in our study, and has not been detected in IFs in other studies to date. However, in human milk, Kallio et al.[28] found lathosterol values ranging from 2.7 to 4.9 μg/mg cholesterol. Benoit et al.[3] in turn found lathosterol in HM to range from nondetectable levels to 4.40 μg/mg cholesterol (with a mean value of 0.44 μg/mg cholesterol).

Cholesterol/Desmosterol Ratio: Infant Formulas vs Human Milk. In general, cholesterol and desmosterol contents in the analyzed IFs were lower than the HM values indicated by other authors (Table 3). Although a significant correlation to total cholesterol in HM has not always been observed, most authors report desmosterol contents below or close to 10% of the cholesterol content. The desmosterol content in the analyzed IFs was less variable than the cholesterol content, and represented ≤10% of the total sterols in the formulas with the highest cholesterol content (IFs 1, 5, 6, and 9). The IFs with the highest desmosterol percentages (>10%) with respect to the animal sterol contents contained algae and/or fungi and/or fish oils (see ingredients, Table 1). It is now well-known that cholesterol and desmosterol (two C_{27} sterols) are the major sterols in crabs, mussels, and crustaceans in general. In snow crab hepatopancreas, desmosterol was found to be the second most predominant sterol (>15%), after cholesterol (67−76%).

DOI: 10.1021/acs.jafc.5b02647
J. Agric. Food Chem. 2015, 63, 7245−7251

Furthermore, desmosterol is abundant in many red algae,[32] and may be absorbed in large quantities from the crab diet, though it may also have an endogenous origin.[33]

Some Zygomycetes synthesize primarily C28 sterols (ergosterol), while others synthesize primarily C27 sterol. These fungi include members of the family Mortierellaceae, in which desmosterol (approximately 86% of total sterol) has been reported as the most abundant sterol.[34] *Mortierella alpina* is an oleaginous fungus which can produce lipids accounting for up to 50% of its dry weight in the form of triacylglycerols. It is commercially used for the production of arachidonic acid employed in the formulation of IFs. This fungus produces only two major sterol lipids, desmosterol and 24(28)-methylenecholesterol.[35]

Plant Sterols. In the IFs studied we identified plant sterols such as brassicasterol, campesterol, stigmasterol, β-sitosterol, and sitostanol. Total plant sterol contents ranged from 3.1 to 5.0 mg/100 mL sample, and β-sitosterol (ranging from 1.82 to 3.01 mg/100 mL) was found to be the most abundant phytosterol, followed by campesterol (0.72−1.15 mg/100 mL), stigmasterol (0.27−0.53 mg/100 mL), and brassicasterol (0.14−0.28 mg/100 mL) (Table 4). Sitostanol was detected in amounts (0.031−0.142 mg/100 mL) always lower than those of the respective plant sterols (Table 4).

Few studies have evaluated the plant sterol contents in IFs. Huisman et al.[12] analyzed the sterols in 10 types of cow's milk-based IFs, and reported total plant sterol contents ranging from 5.345 to 11.936 mg/100 mL. These total plant sterols and individual plant sterol (β-sitosterol, campesterol, stigmasterol, and fucosterol) contents were higher than those determined in our study, and β-sitosterol showed the highest content in both studies.

Maduko and Park[10] found higher plant sterol levels (7.2−13.5 mg/100 g) in ready to drink milk blends (goat milk and vegetal oils) than in our study (2.98−4.72 mg/100 g of reconstituted formula or 3.11−5.0 mg/100 mL). Regarding the content of plant sterols, the 13 IFs had quantities markedly higher (Table 4) than human milk, as reported Laitinen et al.[36] (0.108 mg/100 mL) and Benoit et al.[3] (0.16 μg/mg cholesterol). This could be because the IFs were formulated with a combination of vegetable oils (coconut, soy, canola, high oleic safflower, high oleic sunflower, and palm oleic oils), in order to more closely simulate the fatty acid profile of HM.[37]

The total plant sterol contents in the analyzed IFs were higher than in HM. From a functional point of view, no data are available in the literature describing a possible beneficial role of plant sterols in infants. In this sense, in hypercholesterolemic children and adolescents, an emulsified combination of plant sterols, fish oil (with EPA + DHA), and B vitamins decreased LDL-cholesterol, and thus exerts beneficial effects upon cardiovascular risk factors.[38]

Total Sterol Content and Sterol Ratio. As far as we know, the total sterol contents obtained in our study (5.20−10.47 mg/100 mL or 5.01−9.87 mg/100 g of reconstituted IF) can only be compared with those reported by Huisman et al.[12] (7.69−13.37 mg/100 mL) and Maduko and Park[10] (21.3−27.00 mg/100 g of reconstituted IF). These latter data are very surprising, because the authors indicated that the IFs were prepared using skimmed goat milk (0.17 g residual fat/100 g) with very high cholesterol contents.

Except in the formulas with dairy lipids (IFs 5, 6, and 9), the total vegetable sterol levels were higher than those of the animal sterols (see Figure 1a). Although the physiological meaning of this has not been studied, the higher proportion of plant sterols in IFs is one more difference to add to the list when IFs and HM are compared.

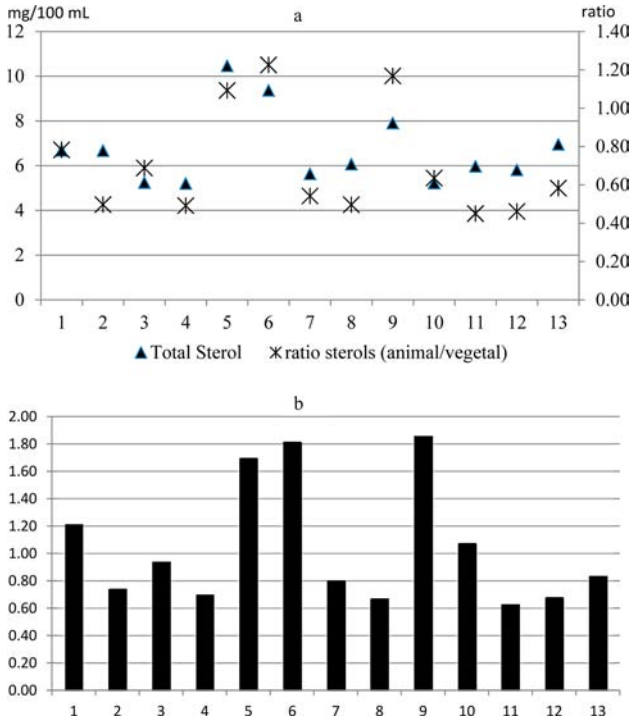

Figure 1. Sterol contents: (a) total sterol contents and ratio of animal and vegetal sterols; (b) ratio cholesterol and β-sitosterol.

The same tendency can be observed in relation to the cholesterol/β-sitosterol ratio (see Figure 1b). The four formulas that included dairy lipids (IFs 1, 5, 6, and 9) were the only ones with significantly higher levels of cholesterol than β-sitosterol. Surprisingly, only Maduko and Park[10] found plant sterol and total sterol contents closely simulating those of HM, despite their use of skimmed caprine milk and vegetable oils (coconut, sunflower, and soybean).

Estimation of Intake. Cholesterol intake (mg/day) ranged from a minimum of 9 mg/day (0.5 month old infant IF 4) to 51 mg/day (5 month old infant IF 5). Cholesterol is the sterol contributing most to animal sterol intake. Variability in cholesterol in animal sterol intake was attributable to the high cholesterol variability seen in the IFs (Figure 1a,b). Independently of the IF for the calculation, the average cholesterol and total animal sterol intake ranged from 15 to 25 mg/day and from 17 to 28 mg/day, respectively, at 0.5 and 6 months (Figure 2a,b). Wong et al.[11] determined cholesterol intakes at 5 months (24.14 mg/day) for formula-fed infants, and the values were in line with our own results. Daily cholesterol intake in breastfed infants has been estimated to range from 75 to 150 mg/day[39] or 131 ± 38 mg/day[40] or 116 mg/day.[11] These values are twice the intake in formula-fed infants. Therefore, the cholesterol intakes in formula-fed infants are still too far from the cholesterol intakes corresponding to HM. Although there is still controversy about the effects of early cholesterol intake upon long-term cardiovascular health,[7] the addition of dairy lipids, and therefore an increase in the cholesterol content, may be a good approach to close the gap in intake between breastfed and formula-fed infants.

Plant sterol intake (mg/day) ranged from a minimum of 19 mg/day (0.5 month old infant IF 3) to 50 mg/day (5 months

DOI: 10.1021/acs.jafc.5b02647
J. Agric. Food Chem. 2015, 63, 7245−7251

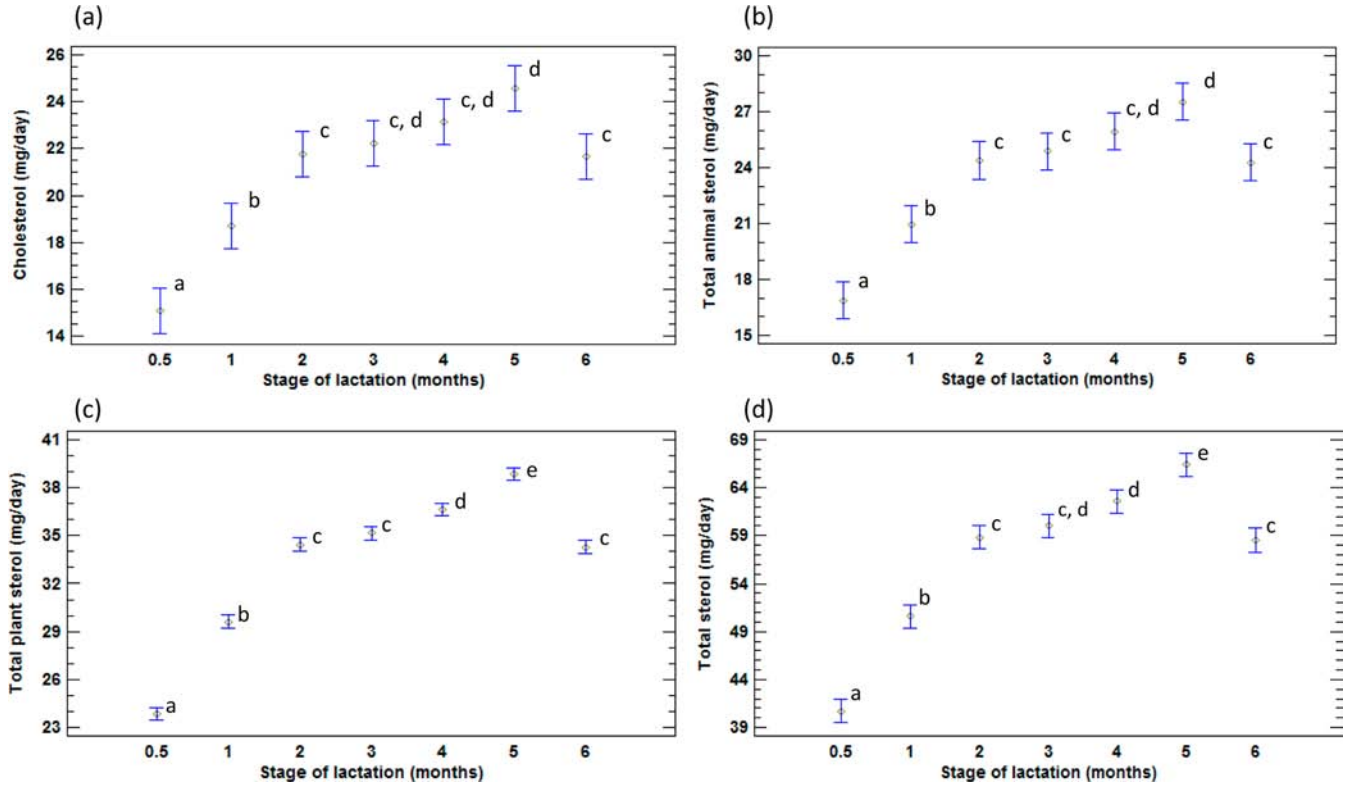

Figure 2. Average intakes of cholesterol (a), animal sterol (b), plant sterol (c) and total sterol (d). Different superscript letters denote significant differences ($p < 0.001$) between lactation stages. Tukey's HSD test.

old infant IF 5) contributing significantly to total sterol intake (see Figure 2d). Independently of the IF, average plant sterol intake ranged from 24 to 39 mg/day at 0.5 and 6 months (see Figure 2c). To the best of our knowledge, no data on plant sterol intake in infant have been published to date.

In summary, mean total sterol intake estimated was 41−66 mg/day (see Figure 2d). Taking into account the formula milk volume intake from the literature, sterol intake increased during first 5 months (see Figure 2), when the values were highest ($p < 0.001$). The introduction of complementary food, and therefore less infant formula, in the sixth month could explain the significant decrease ($p < 0.001$) in animal sterol intake in this month.

The sterol profile of IFs is highly dependent upon the type and quantity of oils and fats used in their formulation. The use of bovine milk fat and whey protein rich in MFGM in the IF formulations can approximate the profile of animal sterols to those found in HM, though cholesterol intakes in breastfed infants are still higher than in formula-fed infants. Furthermore, in order for the sterol composition of IFs to resemble that of HM, it would be necessary to decrease the desmosterol content to less than 10% and reduce plant sterols in order to obtain an animal/plant sterol ratio closer to that of HM. Further research is needed to characterize the sterol contents of ingredients to improve the formulations of IFs, that allow mimicking the composition and functionality of HM. Such requires technological advances in different areas such as analytical research, food and ingredient technology, and nutritional and clinical science. The main starting point for innovation in IFs is research on the nutritional and functional properties of HM and to assess whether the differences in sterol contents between IFs and human milk are related to health outcomes.

AUTHOR INFORMATION

Corresponding Author

*Tel: +34-963544909. Fax: +34-963544954. E-mail: m.j.lagarda@uv.es.

Funding

This work belongs to a CDTI (Centro para el Desarrollo Tecnológico Industrial) project granted to Hero Spain S.A., and L. Claumarchirant is holder of a fellowship from this company.

Notes

The authors declare no competing financial interest.

ABBREVIATIONS USED

IFs, infant formulas; AA, arachidonic acid; DHA, docosahexaenoic acid; EPA, icosapentaenoic acid; HM, human milk; IS, internal standard; MFGM, milk fat globule membrane; TMSE, trimethylsilyl ether

REFERENCES

(1) Lönnerdal, B. Infant formula and infant nutrition: bioactive proteins of human milk and implications for composition of infant formulas. *Am. J. Clin. Nutr.* **2014**, *99*, 712S−717S.

(2) Stam, J.; Sauer, P. J.; Boehm, G. Can we define an infant's need from the composition of human milk? *Am. J. Clin. Nutr.* **2013**, *98*, 521S−528S.

(3) Benoit, B.; Fauquant, C.; Daira, P.; Peretti, N.; Guichardant, M.; Michalski, M. C. Phospholipid species and minor sterols in French human milks. *Food Chem.* **2010**, *120*, 684−691.

(4) Cortes, V. A.; Busso, D.; Mardones, P.; Maiz, A.; Arteaga, A.; Nervi, F.; Rigotti, A. Advances in the physiological and pathological implications of cholesterol. *Biol. Rev.* **2013**, *88*, 825−843.

(5) Owen, C. G.; Whincup, P. H.; Kaye, S. J.; Martin, R. M.; Smith, G. D.; Cook, D. G.; Bergstrom, E.; Black, S.; Wadsworth, M. E.; Fall, C. H.; Freudenheim, J. L.; Nie, J.; Huxley, R. R.; Kolacek, S.; Leeson,

DOI: 10.1021/acs.jafc.5b02647
J. Agric. Food Chem. 2015, 63, 7245−7251

C. P.; Pearce, M. S.; Raitakari, O. T.; Lisinen, I.; Viikari, J. S.; Ravelli, A. C.; Rudnicka, A. R.; Strachan, D. P.; Williams, S.M. Does initial breastfeeding lead to lower blood cholesterol in adult life? A quantitative review of the evidence. *Am. J. Clin. Nutr.* **2008**, *88*, 305−14.

(6) Harit, D.; Faridi, M. M. A.; Aggarwal, A.; Sharma, S. B. Lipid profile of term infants on exclusive breastfeeding and mixed feeding: a comparative study. *Eur. J. Clin. Nutr.* **2008**, *62*, 203−209.

(7) Koletzko, B.; Agostoni, C.; Bergmann, R.; Ritzenthaler, K.; Shamir, R. Physiological aspects of human milk lipids and implications for infant feeding: a workshop report. *Acta Paediatr.* **2011**, *100*, 1405−1415.

(8) Ostlund, R. E. Phytosterols, cholesterol absorption and healthy diets. *Lipids* **2007**, *42*, 41−45.

(9) Kamelska, A. M.; Pietrzak-Fiecko, R.; Bryl, K. Determination of cholesterol concentration in human milk samples using attenuated total reflectance Fourier transform infrared spectroscopy. *J. Appl. Spectrosc.* **2013**, *80*, 148−152.

(10) Maduko, C. O.; Park, Y. W. Modication of fatty acid and sterol composition of caprine milk for use as infant formula. *Int. Dairy J.* **2007**, *17*, 1434−1440.

(11) Wong, W. W.; Hachey, D. L.; Insull, W.; Opekun, A. R.; Klein, P. D. Effect of dietary cholesterol on cholesterol synthesis in breast-fed and formula-fed infants. *J. Lipid Res.* **1993**, *34*, 1403−1411.

(12) Huisman, M.; van Beusekom, C. M.; Lanting, C. I.; Nijeboer, H. J.; Muskiet, F. A. J.; Boersma, E. R. Triglycerides, fatty acids, sterols, mono- and disaccharides and sugar alchols in human milk and current types of infant formula milk. *Eur. J. Clin. Nutr.* **1996**, *50*, 255−260.

(13) Scopesi, F.; Zunin, P.; Mazzella, M.; Testa, M.; Boggia, R.; Evangelisti, F.; Serra, G. 7-Ketocholesterol in human and adapted milk formulas. *Clin. Nutr.* **2002**, *21*, 379−384.

(14) Ramalho, H. M. M.; Casal, S.; Oliveira, M. B. P. P. Total Cholesterol and Desmosterol Contents in Raw, UHT, IF Powder and Human Milks Determined by a New Fast Micro-HPLC Method. *Food Anal. Meth.* **2011**, *4*, 424−430.

(15) Alemany-Costa, L.; González-Larena, M.; García-Llatas, G.; Alegría, A.; Barberá, R.; Sánchez-Siles, L. M.; Lagarda, M. J. Sterol stability in functional fruit beverages enriched with different plant sterol sources. *Food Res. Int.* **2012**, *48*, 265−270.

(16) González-Larena, M.; Cilla, A.; García-Llatas, G.; Barberá, R.; Lagarda, M. J. Plant sterols and antioxidant parameters in enriched beverages: storage stability. *J. Agric. Food Chem.* **2012**, *60*, 4725−4734.

(17) García-Llatas, G.; Vidal, C.; Cilla, A.; Barberá, R.; Lagarda, M. J. Simultaneous quantication of serum phytosterols and cholesterol precursors using a simple gas chromatographic method. *Eur. J. Lipid Sci. Technol.* **2012**, *114*, 520−526.

(18) Guardiola, F.; Codony, R.; Rafecas, M.; Boatella, J. Adsorption of oxysterols on dferent microtube materials during silanyzation prior to gas-chromatographic determination. *J. Chromatogr. A* **1995**, *705*, 396−399.

(19) Ben, X. M.; Li, J.; Feng, Z. T.; Shi, S. Y.; Lu, Y. D.; Chen, R.; Zhou, X. Y. Low level of galacto-oligosaccharide in IF stimulates growth of intestinal Bidobacteria and Lactobacilli. *World J. Gastroenterol.* **2008**, *14*, 6564−6568.

(20) Chouraqui, J. P.; Grathwohl, D.; Labaune, J. M.; Hascoet, J. M.; de Montgolfier, I.; Leclaire, M.; Giarre, M.; Steenhout, P. Assessment of the safety, tolerance, and protective effect against diarrhea of IFs containing mixtures of probiotics or probiotics and prebiotics in a randomized controlled trial. *Am. J. Clin. Nutr.* **2008**, *87*, 1365−1367.

(21) Lasekan, J. B.; Jacobs, J.; Reisinger, K. S.; Montalto, M. B.; Frantz, M. P.; Blatter, M. M. Lactose-free milk protein−based IF: impact on growth and gastrointestinal tolerance in infants. *Clin. Pediatr.* **2011**, *50*, 330−337.

(22) Luque, V. Nutrición temprana: efecto de la ingesta de protein durante los primeros meses de vida sobre el tamaño y función renales. Thesis. 2010. Universitat Rovira i Virgili. Reus, Spain.

(23) Mennella, J. A.; Ventura, A. K.; Beauchamp, G. K. Differential growth patterns among healthy infants fed protein hydrolysate or cow-milk formulas. *Pediatrics* **2011**, *127*, 110−118.

(24) Salvini, F.; Riva, E.; Salvatici, E.; Boehm, G.; Jelinek, J.; Banderali, G.; Giovannini, M. A specific prebiotic mixture added to starting IF has long-lasting bifidogenic effects. *J. Nutr.* **2011**, *141*, 1335−1339.

(25) Sandstrom, O.; Lönnerdal, B.; Graverholt, G.; Hernell, O. Effects of α-lactalbumin− enriched formula containing different concentrations of glycomacropeptide on infant nutrition. *Am. J. Clin. Nutr.* **2008**, *87*, 921−928.

(26) Weizman, Z.; Alsheikh, A. Safety and tolerance of a probiotic formula in early infancy comparing two probiotic agents: a pilot study. *J. Am. Coll. Nutr.* **2006**, *25*, 415−419.

(27) Clark, R. M.; Fey, M. B.; Jensen, R. G.; Hill, D. W. Desmosterol in human milk. *Lipids* **1983**, *18*, 264−266.

(28) Kallio, M. J. T.; Siimes, M. A.; Perheentupa, J.; Salmenpera, L.; Miettinen, T. A. Cholesterol and its precursors in human milk during prolonged exclusive breast-feeding. *Am. J. Clin. Nutr.* **1989**, *50*, 782−785.

(29) Jensen, R. G. The lipids in human milk. *Prog. Lipid Res.* **1996**, *35*, 53−92.

(30) Fauquant, C.; Briard-Bion, V.; Leconte, N.; Guichardant, M.; Michalski, M. C. Membrane phospholipids and sterols in microfiltered milk fat globules. *Eur. J. Lipid Sci. Technol.* **2007**, *109*, 1167−1173.

(31) Morin, P.; Jiménez-Flores, R.; Pouliot, Y. Effect of processing on the composition and microstructure of buttermilk and its milk fat globule membranes. *Int. Dairy J.* **2007**, *17*, 1179−1187.

(32) Lopes, G.; Sousa, C.; Bernardo, J.; Andrade, P. B.; Valentao, P.; Ferreres, F.; Mouga, T. Sterol profiles in 18 macroalgae of the portuguese coast. *J. Phycol.* **2011**, *47*, 1210−1218.

(33) Souchet, N.; Laplante, S. Seasonal and geographical variations of sterol composition in snow crab hepatopáncreas and pelagic fish viscera from Eastern Quebec. *Comp. Biochem. Physiol., Part B: Biochem. Mol. Biol.* **2007**, *147*, 378−386.

(34) Nes, W. D.; Nichols, S. D. Phytosterol biosynthesis pathway in *Mortierella alpine*. *Phytochemistry* **2006**, *67*, 1716−1721.

(35) Wang, L.; Chen, W.; Feng, Y.; Ren, Y.; Gu, Z.; Chen, H.; Wang, H.; Thomas, M. J.; Zhang, B.; Berquin, I. M.; Li, Y.; Wu, J.; Zhang, H.; Song, Y.; Liu, X.; Norris, J. S.; Wang, S.; Du, P.; Shen, J.; Wang, N.; Yang, Y.; Wang, W.; Feng, L.; Ratledge, C.; Zhang, H.; Chen, Y. Q. Genome characterization of the oleaginous Fungus Mortierella alpina. *PLoS One* **2011**, *6*, e28319.

(36) Laitinen, K.; Isolauri, E.; Kaipiainen, L.; Gylling, H.; Miettinen, T. A. Plant stanol ester spreads as components of a balanced diet for pregnant and breast-feeding women: evaluation of clinical safety. *Br. J. Nutr.* **2009**, *101*, 1797−1804.

(37) Long, A. C.; Kaiser, J. L.; Katz, G. E. Lipids in infant formulas: Current and future innovations. *Lipid Technol.* **2013**, *25*, 127−129.

(38) Garaiova, I.; Muchová, J.; Najyová, Z.; Mislanová, C.; Oravec, S.; Dukát, A.; Wang, D.; Plummer, S. F.; Duracková, Z. Effect of a plant sterol, fish oil and B vitamin combination on cardiovascular risk factors in hypercholesterolemic children and adolescents: a pilot study. *Nutr. J.* **2013**, *12*, 7.

(39) Jensen, R. G.; Lammi-Keefe, C. J.; Ferris, A. M.; Jackson, M. B.; Couch, S. C.; Capacchione, C. M.; Ahn, H. S.; Murtaugh, M. Human milk total lipid cholesterol are dependent on interval of sampling during 24 h. *J. Pediatr. Gastroenterol. Nutr.* **1995**, *20*, 91−94.

(40) Kallio, M. J. T.; Salmenpera, L.; Siimes, M. A.; Perheentupa, J.; Miettinen, T. A. Exclusive breast-feeding and weaning: effect on serum cholesterol and lipoprotein concentrations in infants during the first year of life. *Pediatrics* **1992**, *89*, 663−666.

DOI: 10.1021/acs.jafc.5b02647
J. Agric. Food Chem. 2015, 63, 7245−7251

Table 1. ^{1}H NMR Data for Compounds 1−8 (600 MHz)[a]

H	1[b]	2[b]	3[b]	4[b]	5[b]	6[b]	7[b]	8[c]
2	6.89 (d, 1.6)	6.91 (br s)	6.95 (d, 1.8)	6.96 (d, 1.8)	6.79 (br s)	6.79 (d, 1.6)	6.91 (br s)	6.69 (s)
5	6.75 (d, 8.1)	6.78 (br s)	6.78 (d, 8.2)	6.78 (d, 8.1)	6.66 (br s)	6.65 (d, 8.1)	6.76 (br s)	
6	6.77 (dd, 8.1, 1.6)	6.78 (br s)	6.83 (dd, 8.2, 1.8)	6.83 (dd, 8.1, 1.7)	6.66 (br s)	6.67 (dd, 8.1, 1.6)	6.76 (br s)	6.69 (s)
7	5.49 (d, 5.5)	5.48 (d, 6.0)	5.53 (d, 5.8)	5.53 (d, 6.3)	5.36 (d, 6.1)	5.38 (d, 5.5)	5.47 (d, 6.6)	5.56 (d, 6.2)
8	3.40 (m)	3.41 (m)	3.46 (m)	3.47 (m)	3.32 (m)	3.31 (m)	3.44 (m)	3.52 (m)
9	3.67 (dd, 11.0, 5.1)	3.79 (m)	3.67 (dd, 11.5, 7.7)	3.69 (dd, 10.7, 7.7)	3.68 (dd, 9.2, 3.3)	3.56 (dd, 10.9, 5.2)	3.62 (m)	3.88 (m)
	3.48 (dd, 11.0, 8.3)	3.70 (m)	3.76 (dd, 11.5, 6.4)	3.85 (dd, 10.7, 2.9)	3.58 (m)	3.44 (dd, 10.9, 8.3)	3.70 (m)	3.79 (m)
2′	6.51 (br s)	6.51 (br s)	6.50 (br s)	6.49 (br s)	6.41 (br s)	6.43 (br s)	6.97 (br s)	6.97 (br s)
6′	6.54 (br s)	6.63 (br s)	6.61 (br s)	6.68 (br s)	6.52 (br s)	6.44 (br s)	6.97 (br s)	6.92 (br s)
7′	4.32 (d, 8.6)	4.35 (d, 8.3)	4.55 (d, 5.2)	4.53 (d, 5.5)	4.33 (d, 8.4)	4.31 (d, 8.6)	6.52 (d, 15.9)	4.59 (d, 6.0)
8′	2.96 (m)	3.03 (m)	286 (m)	2.89 (m)	2.90 (m)	2.85 (m)	6.18 (dt, 15.9, 6.0)	3.71 (m)
9′	3.92 (dd, 10.9, 7.1)	3.92 (dd, 11.0, 6.8)	3.92 (dd, 10.7, 7.2)	3.89 (dd, 10.7, 6.8)	3.99 (dd, 10.9, 5.8)	4.00 (dd, 10.9, 5.2)	4.00 (d, 6.0)	3.52 (m),
	4.07 (dd, 10.9, 5.0)	4.07 (dd, 11.0, 5.3)	3.76 (m)	3.76 (dd, 10.7, 4.3)	3.81 (dd, 10.9, 7.2)	3.82 (dd, 10.9, 8.3)		3.41 (m)
2″	6.43 (d, 1.8)	6.49 (br s)	6.60 (d, 1.7)	6.63 (d, 1.6)	6.39 (d, 1.1)	6.35 (d, 1.8)		
5″	6.61 (d, 8.1)	6.63 (d, 7.3)	6.69 (d, 8.0)	6.69 (d, 8.2)	6.51 (d, 8.2)	6.52 (d, 8.1)		
6″	6.50 (dd, 8.1, 1.8)	6.52 (d, 7.3)	6.58 (d, 8.1, 1.7)	6.60 (d, 8.2, 1.6)	6.42 (d, 8.0, 1.1)	6.41 (d, 8.1, 1.8)		
3-OCH_3	3.79 (3H, s)	3.81 (3H, s)	3.83 (3H, s)	3.83 (3H, s)	3.69 (3H, s)	3.68 (3H, s)	3.80 (3H, s)	3.83 (3H, s)
5-OCH_3								3.83 (3H, s)
3′-OCH_3	3.72 (3H, s)	3.72 (3H, s)	3.73 (3H, s)	3.76 (3H, s)	3.60 (3H, s)	3.62 (3H, s)	3.74 (3H, s)	3.91 (3H, s)
3″-OCH_3	3.64 (3H, s)	3.70 (3H, s)	3.72 (3H, s)	3.71 (3H, s)	3.59 (3H, s)	3.55 (3H, s)		
7′-OCH_3	3.24 (3H, s)	3.24 (3H, s)	3.20 (3H, s)	3.20 (3H, s)				
9′-OCH_3							3.26 (3H, s)	
7′-OCH_2CH_3					3.30 (2H, m)	3.30 (2H, m)		
					1.08 (3H, t, 7.0)	1.07 (3H, t, 7.0)		

[a]Coupling constants (J) in hertz are given in parentheses; chemical shift values are expressed in ppm. [b]Measured in CD_3OD. [c]Measured in DMSO-d_6.

DOI: 10.1021/acs.jafc.5b02835
J. Agric. Food Chem. 2015, 63, 7252−7260

Table 2. ^{13}C NMR Data (150 MHz) of Compounds 1−8

no.	1[a]	2[a]	3[a]	4[a]	5[a]	6[a]	7[a]	8[b]
1	134.8	134.6	134.8	134.7	134.6	134.8	132.2	136.4
2	110.4	110.6	110.5	110.6	110.6	110.4	110.5	104.2
3	149.0	149.1	149.1	149.1	149.1	149.0	147.4	149.4
4	147.4	147.5	147.5	147.5	147.5	147.4	146.4	133.9
5	116.1	116.2	116.1	116.2	116.2	116.1	115.3	149.4
6	119.5	119.7	119.5	119.7	119.7	119.4	118.5	104.2
7	89.2	89.3	89.2	89.2	89.3	89.2	87.4	89.3
8	55.3	55.1	55.3	55.3	55.1	55.3	52.9	55.5
9	65.4	65.1	65.3	65.0	65.1	65.3	62.9	64.9
1′	134.9	134.8	135.4	135.3	135.5	135.6	130.0	137.0
2′	113.3	113.3	112.8	112.8	113.2	113.1	110.3	116.6
3′	144.9	144.9	145.1	145.1	144.9	144.9	143.7	145.3
4′	148.5	148.6	148.6	148.7	148.5	148.4	147.5	148.9
5′	129.2	129.4	129.3	129.5	129.4	129.1	129.5	129.7
6′	117.5	117.5	117.1	117.2	117.3	117.3	115.2	112.7
7′	87.5	87.5	84.8	85.0	85.9	85.9	131.9	75.4
8′	56.7	56.6	56.5	56.5	56.2	56.3	123.6	77.5
9′	64.9	64.9	64.3	64.3	65.0	65.0	72.3	64.3
1″	132.6	132.6	132.1	132.2	132.7	132.7		
2″	114.4	114.4	114.7	114.8	114.4	114.4		
3″	148.3	148.3	148.3	148.3	148.8	148.4		
4″	146.0	146.1	146.1	146.2	146.1	146.0		
5″	115.7	115.7	115.5	115.6	115.7	115.7		
6″	122.5	122.6	123.3	123.2	122.5	122.5		
3-OCH_3	56.3	56.4	56.5	56.5	56.6	56.7	55.6	56.8
5-OCH_3								56.8
3′-OCH_3	56.3	56.4	56.4	56.4	56.4	56.4	55.6	56.8
3″-OCH_3	56.3	56.1	56.4	56.4	56.4	56.3		
7′-OCH_3	57.0	56.9	57.2	57.2				
9′-OCH_3							57.1	
7′-OCH_2CH_3					65.2 15.7	65.5 15.7		

[a]Measured in CD_3OD. [b]Measured in DMSO-d_6.

seeds and help in the use of this byproduct generated in food processing to improve human health.

MATERIALS AND METHODS

Chemicals and Reagents. Minocycline, silybin, 2,2-diphenyl-1-picrylhydrazyl (DPPH), 2,2′-azinobis(3-ethylbenzothiazoline-6-sulfonic acid) (ABTS), 6-hydroxy-2,5,7,8-tetramethylchromane-2-carboxylic acid (trolox), lipopolysaccharide (LPS), and 3-(4,5-dimethylthiazol-2-yl)-2,5-diphenyltetrazolium bromide (MTT) were purchased from Sigma-Aldrich. Cell culture medium [Dulbecco's modified Eagle's medium (DMEM)], fetal bovine serum (FBS), penicillin, streptomycin, and all other materials required for culturing cells were purchased from Gibco BRL, Life Technologies.

Apparatus. Optical rotations were determined using a JASCO P-1020 polarimeter. The UV spectra were recorded on a Shimadzu UV-1700 spectrometer, and the CD spectra were obtained using an MOS 450 detector from BioLogic. The FT-IR spectra were measured using a Bruker IFS-55 spectrometer. NMR spectra were performed on a Bruker AV-600 spectrometer. HRESIMS experiments were measured using an Agilent G6520 Q-TOF spectrometer. Preparative and semipreparative RP-HPLC isolation was achieved with Agilent 1100 and 1200 instruments using an Acchrom XAqua C18 column (5 μm, 250 mm × 20 mm) and a YMC C18 column (5 μm, 250 mm × 10 mm). Peaks were identified using a refractive index detector (RID). The absorbances in bioassays were measured using a varioskan flash multimode reader (Thermo Scientific). Column chromatography (CC) was performed using silica gel (200−300 mesh; Qingdao Marine Chemical Inc.), macroporous adsorption resin D101 (Cangzhou Bon Adsorber Technology Co., Ltd.), and ODS (50 μm, YMC Co. Ltd.). TLC was conducted on precoated glass plates (SiO_2 GF254; Qingdao Marine Chemical Inc.).

Plant Material. The seeds of *C. pinnatifida* were collected in Hebei province, China, in June 2011 and were identified by Professor Jin-Cai Lu (School of Traditional Chinese Materia Medica, Shenyang Pharmaceutical University). A voucher specimen (no. 20110701) has been deposited in the Herbarium of Shenyang Pharmaceutical University, Liaoning, China.

Extraction and Isolation. The air-dried seeds of *C. pinnatifida* (30 kg) were crushed and refluxed with 70% EtOH (3 × 30 L) for 4 h. The solvent was filtered, concentrated under vacuum and, then, the extract (1500 g) was suspended in H_2O and partitioned sequentially with ethyl acetate and *n*-BuOH. The ethyl acetate and *n*-butyl alcohol fractions were tested in antioxidant (scavenging activities for DPPH and $ABTS^{\bullet+}$) and anti-inflammatory assays, and the ethyl acetate extract was found to exhibit stronger activities. The ethyl acetate extract (420 g) was suspended in H_2O and then chromatographed on a D101 macroporous resin column using H_2O/EtOH (from 100:0 to 5:95) as eluents, yielding four fractions (fractions A−D). The four fractions were also tested in antioxidant and anti-inflammatory assays, and fraction B (H_2O:EtOH = 70:30; 128.0 g) was found to exhibit more potent activities.

Fraction B was subjected to silica gel CC and eluted with CH_2Cl_2/CH_3OH to yield eight fractions (B_1−B_8). Among them, B_3 (20.2 g) was further purified by ODS CC using H_2O/MeOH as a mobile phase gradient (from 95:5 to 50:50) to afford five fractions ($B_{3\text{-}1}$−$B_{3\text{-}5}$) on the basis of HPLC analysis. $B_{3\text{-}3}$ (3.4 g) was subjected to further silica gel column chromatography and eluted with CH_2Cl_2/CH_3OH (from 95:5 to 80:20) to yield eight fractions ($B_{3\text{-}3\text{-}1}$−$B_{3\text{-}3\text{-}8}$) on the basis of silica gel TLC analysis. $B_{3\text{-}3\text{-}5}$ was subjected to preparative HPLC and

DOI: 10.1021/acs.jafc.5b02835
J. Agric. Food Chem. 2015, 63, 7252−7260

eluted with CH_3OH/H_2O (40:60) to yield two fractions ($B_{3\text{-}3\text{-}5\text{-}1}$ and $B_{3\text{-}3\text{-}5\text{-}2}$). $B_{3\text{-}3\text{-}5\text{-}1}$ was subjected to semipreparative HPLC and eluted with CH_3CN/H_2O (23:77) to yield **1** (18 mg, t_R 31 min, 4 mL/min) and **3** (8 mg, t_R 36 min, 4 mL/min). $B_{3\text{-}3\text{-}5\text{-}2}$ was subjected to semipreparative HPLC and with CH_3CN/H_2O (23:77) as eluents to afford **2** (8 mg, t_R 29 min, 4 mL/min) and **4** (6 mg, t_R 39 min, 4 mL/min). $B_{3\text{-}4}$ was also subjected to silica gel column chromatography and eluted with CH_2Cl_2/CH_3OH (from 95:5 to 80:20) to afford nine fractions ($B_{3\text{-}4\text{-}1}$–$B_{3\text{-}4\text{-}9}$) on the basis of silica gel TLC analysis. $B_{3\text{-}4\text{-}4}$ was subjected to semipreparative HPLC and eluted with CH_3CN/H_2O (30:70) to yield **5** (4 mg, t_R 27 min, 4 mL/min) and **6** (15 mg, t_R 28 min, 4 mL/min). $B_{3\text{-}2}$ was separated by silica gel column and eluted with CH_2Cl_2/CH_3OH to afford seven fractions ($B_{3\text{-}2\text{-}1}$–$B_{3\text{-}2\text{-}7}$). $B_{3\text{-}2\text{-}3}$ was subjected to semipreparative HPLC and with CH_3CN/H_2O (22:78) as eluent to give **13** (16 mg, t_R 40 min, 4 mL/min), **14** (20 mg, t_R 29 min, 4 mL/min), **15** (11 mg, t_R 21 min, 4 mL/min), and **7** (8 mg, t_R 33 min, 4 mL/min). $B_{3\text{-}2\text{-}5}$ was subjected to semipreparative HPLC with CH_3OH/H_2O (19:81) as eluent to yield **8** (4 mg, t_R 52 min, 4 mL/min). $B_{3\text{-}2\text{-}5}$ was subjected to semipreparative HPLC and eluted with CH_3CN/H_2O (9:91) to give **9** (42 mg, t_R 18 min, 4 mL/min), **10** (40 mg, t_R 19 min, 4 mL/min), **11** (66 mg, t_R 23 min, 4 mL/min), and **12** (68 mg, t_R 24 min, 4 mL/min).

Hawthornnin A (**1**): yellow oil; $[\alpha]_D^{20}$ −7.0 (*c* 0.10, MeOH); UV (MeOH) λ_{max} (log ε) 233 (0.63), 283 (0.31); CD [*c* 0.20 mg/mL, MeOH, nm (ε)] 234 nm (9.02), 256 nm (−7.72), 283 nm (−9.97); IR (KBr) ν_{max} 3384, 2938, 1605, 1516, 1463, 1141, 1032, 822, and 760 cm^{-1}; HRESIMS *m*/*z* 535.1902 $[M + Na]^+$ (calcd for $C_{28}H_{32}O_9Na$, 535.1939). For ^1H and ^{13}C NMR, see Tables 1 and 2.

Hawthornnin B (**2**): yellow oil; $[\alpha]_D^{20}$ +3.5 (*c* 0.13, MeOH); UV (MeOH) λ_{max} (log ε) 227 (0.66), 281 (0.32); CD [*c* 0.20 mg/mL, MeOH, nm (ε)] 226 nm (3.52), 233 nm (0.86), 284 nm (1.52); IR (KBr) ν_{max} 3407, 2928, 1610, 1510, 1453, 1243, 1112, 821, and 753 cm^{-1}; HRESIMS *m*/*z* 535.1937 $[M + Na]^+$ (calcd for $C_{28}H_{32}O_9Na$, 535.1939). For ^1H and ^{13}C NMR, see Tables 1 and 2.

Hawthornnin C (**3**): yellow oil; $[\alpha]_D^{20}$ −4.5 (*c* 0.12, MeOH); UV (MeOH) λ_{max} (log ε) 227 (0.73), 281 (0.33); CD [*c* 0.15 mg/mL, MeOH, nm ($\Delta\varepsilon$)] 237 nm (3.45), 267 nm (−10.26), 279 nm (−11.02), 286 nm (−7.01); IR (KBr) ν_{max} 3357, 2938, 1604, 1517, 1464, 1276, 1217, 822, and 765 cm^{-1}; HRESIMS *m*/*z* 535.1941 $[M + Na]^+$ (calcd for $C_{28}H_{32}O_9Na$, 535.1939). For ^1H and ^{13}C NMR, see Tables 1 and 2.

Hawthornnin D (**4**): yellow oil; $[\alpha]_D^{20}$ +7.2 (*c* 0.10, MeOH); UV (MeOH) λ_{max} (log ε) 228 (0.53), 282 (0.37); CD [c 0.15 mg/mL, MeOH, nm (ε)] 231 nm (4.46), 245 nm (2.02), 278 nm (3.44); IR (KBr) ν_{max} 3406, 2936, 1605, 1498, 1452, 1274, 1029, 822, and 765 cm^{-1}; HRESIMS *m*/*z* 535.1944 $[M + Na]^+$ (calcd for $C_{28}H_{32}O_9Na$, 535.1939). For ^1H and ^{13}C NMR, see Tables 1 and 2.

Hawthornnin E (**5**): yellow oil; $[\alpha]_D^{20}$ +4.2 (*c* 0.16, MeOH); UV (MeOH) λ_{max} (log ε) 228 (0.63), 285 (0.32); CD [*c* 0.10 mg/mL, MeOH, nm (ε)] 219 nm (3.86), 242 nm (2.58), 281 nm (1.26); IR (KBr) ν_{max} 3382, 2940, 1603, 1518, 1432, 1274, 1030, 819, and 769 cm^{-1}; HRESIMS *m*/*z* 549.2064 $[M + Na]^+$ (calcd for $C_{29}H_{34}O_9Na$, 549.2095). For ^1H and ^{13}C NMR, see Tables 1 and 2.

Hawthornnin F (**6**): yellow oil; $[\alpha]_D^{20}$ −8.7 (*c* 0.13, MeOH); UV (MeOH) λ_{max} (log ε) 226 (0.73), 281 (0.38); CD [*c* 0.15 mg/mL, MeOH, nm (ε)] 234 nm (−7.52), 283 nm (−4.87); IR (KBr) ν_{max} 3405, 2969, 1603, 1518, 1274, 1124, 1031, 819, and 769 cm^{-1}; HRESIMS *m*/*z* 549.2057 $[M + Na]^+$ (calcd for $C_{29}H_{34}O_9Na$, 549.2095). For ^1H and ^{13}C NMR, see Tables 1 and 2.

Hawthornnin G (**7**): yellow oil; $[\alpha]_D^{20}$ −5.8 (*c* 0.11, MeOH); UV (MeOH) λ_{max} (log ε) 230 (0.72), 280 (0.41); CD [*c* 0.10 mg/mL, MeOH, nm (ε)] 222 nm (5.26), 261 nm (3.78), 282 nm (−0.91); IR (KBr) ν_{max} 3357, 2940, 1667, 1599, 1512, 1133, 1031, 819, and 594 cm^{-1}; HRESIMS *m*/*z* 395.1469 $[M + Na]^+$ (calcd for $C_{21}H_{24}O_6Na$, 395.1465). For ^1H and ^{13}C NMR, see Tables 1 and 2.

Hawthornnin H (**8**): yellow oil; $[\alpha]_D^{20}$ −6.5 (*c* 0.10, MeOH); UV (MeOH) λ_{max} (log ε) 230 (0.63), 280 (0.28); CD [*c* 0.10 mg/mL, MeOH, nm (ε)] 236 nm (−5.72), 281 nm (−0.84); IR (KBr) ν_{max} 3381, 2904, 1604, 1514, 1422, 1267, 1135, 1030, 817, and 751 cm^{-1}; HRESIMS *m*/*z* 445.1458 $[M + Na]^+$ (calcd for $C_{21}H_{26}O_9Na$, 445.1469). For ^1H and ^{13}C NMR, see Tables 1 and 2.

Assay for DPPH Radical-Scavenging Activity. The DPPH scavenging activity assay was adopted from a previous paper.[20] The 0.1 mM solution of DPPH in ethanol was prepared first, and then 100 μL of this solution was mixed with 100 μL of sample solution in a 96-well microplate. After 30 min of incubation in the dark at 37 °C, the absorbance was measured using a varioskan flash multimode reader at 517 nm. The percentage of scavenged DPPH was calculated using the following equation: DPPH scavenging activity (%) = $[1 - (S - S_b)/(C - C_b)] \times 100\%$, where S, S_b, C, and C_b are the absorbances of the sample, blank sample, control, and blank control, respectively. All experiments were performed in triplicate, and trolox was used as a positive control.

Assay for ABTS Radical-Scavenging Activity. The ABTS radical-scavenging activity of isolates was determined as in a previous study with some modifications.[20] ABTS radical cations ($ABTS^{\bullet+}$) were produced by reacting a 7 mM stock solution of ABTS with 2.45 mM potassium persulfate and allowing the mixture to stand in the dark at room temperature for 12 h before use. The $ABTS^{\bullet+}$ solution was then diluted with ethanol to the absorbance of 0.7 ± 0.05 at 734 nm. Different concentrations of test samples (100 μL) and $ABTS^{\bullet+}$ solution (150 μL) were added to each well of the 96-well plates. After 30 min of incubation at 37 °C, the absorbance at 734 nm was recorded, and the percentage of ABTS free radical scavenging activity was calculated using the same formula as for the DPPH assay.

Cell Culture and Cell Viability Assay. Mouse macrophage RAW264.7 cells were cultured in DMEM, 100 mg/mL streptomycin, and 100 U/mL penicillin. Cells were plated at a density of 5×10^5/mL and then cultured in a 96-well plate containing DMEM, which was supplemented with 10% FBS for 24 h until almost confluent. Cell viability was evaluated by MTT assay. Cells were treated with test samples (100 μM) for 1 h and stimulated with LPS (100 ng/mL) for 24 h, and then the cells were incubated with MTT (0.25 mg/mL) followed by incubation for 4 h at 5% CO_2 and 37 °C. The formation of formazan was recorded at 540 nm using a varioskan flash instrument.[21,22]

NO Assay in RAW264.7 Cells. NO produced by the cells was determined by assaying the levels of NO^{2-} using the Griess reagent.[22] RAW264.7 cells were plated at a density of 5×10^5/mL in a 96-well plate and pretreated with test samples at concentrations of 100, 50, 10, and 1 μM, respectively. After the cells were incubated with samples and stimulated with LPS (100 ng/mL) for 24 h, the cell culture media were collected to determinate NO. Briefly, a 100 μL aliquot of each sample was added to an equal volume of Griess reagent (1% sulfanilamide in 5% H_3PO_4 and 0.1% *N*-naphthylethylenediamine dihydrochloride) in a 96-well plate and then incubated at 37 °C for 10 min. After incubation, the absorbance was recorded at 540 nm on a varioskan flash instrument. The amount of NO in the sample was calculated using $NaNO_2$ standard curve, and minocycline was used as a positive control.

TNF-α Assay in RAW264.7 Cells. The levels of TNF-α were determined using an ELISA kit (R&D Co.) according to the manufacturer's instructions. TNF-α was determined from a standard curve, and silybin was used as positive control.[23]

Statistical Analysis. Results were expressed as the mean ± standard error of means (SEM) of three determinations. The IC_{50} values were calculated using Microsoft Excel software. One-way analysis of variance (ANOVA) followed by Dunnett's test was used for statistical analysis.

RESULTS AND DISCUSSION

The HRESIMS of **1** revealed the molecular formula of $C_{28}H_{32}O_9$ from the pseudomolecular ion at *m*/*z* 535.1902 $[M + Na]^+$. The UV spectrum showed the absorbances at λ_{max} 233 and 283 nm, and the IR spectral data indicated the presence of OH (3384 cm^{-1}) and an aromatic ring (1605, 1516, and 1463 cm^{-1}). Eight aryl proton signals [δ_H 6.89 (d, J = 1.6 Hz, H-2), 6.75 (d, J = 8.1 Hz, H-5), 6.77 (dd, J = 8.1, 1.6 Hz, H-6), 6.51

DOI: 10.1021/acs.jafc.5b02835
J. Agric. Food Chem. 2015, 63, 7252−7260

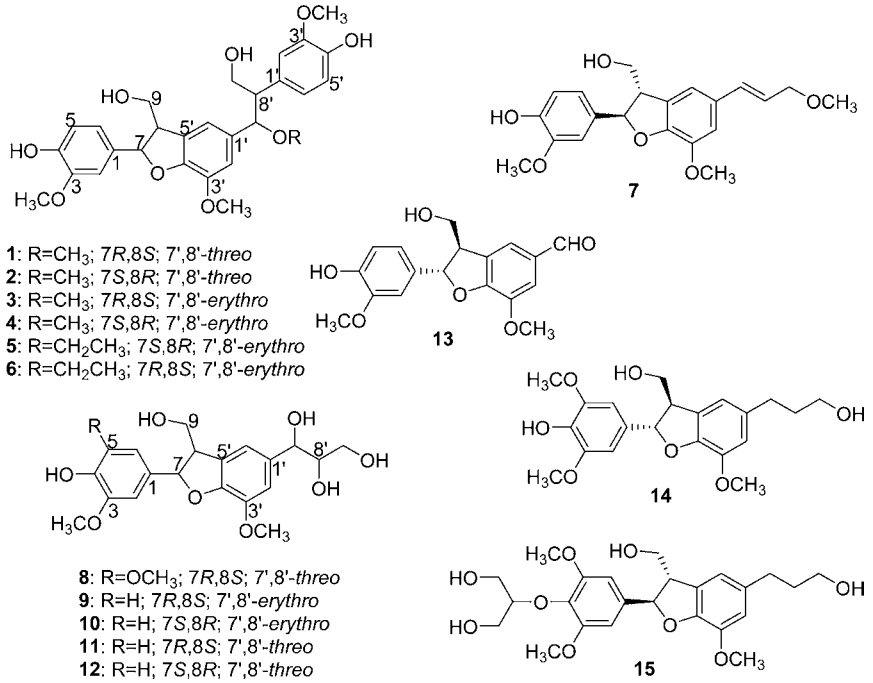

Figure 1. Structures of compounds **1**−**15**.

(br s, H-2′), 6.54 (br s, H-6′), 6.43 (d, J = 1.8 Hz, H-2″), 6.61 (d, J = 8.1 Hz, H-5″), 6.50 (d, J = 8.1, 1.8 Hz, H-6″)] found in the ^{1}H NMR spectrum of **1** (Table 1) were attributed to two 1,3,4-trisubstituted (ABX system) moieties and one 1,3,4,5-tetrasubstituted (AX system) phenyl moiety. In addition, signals for four aliphatic methine protons [δ_H 5.49 (d, J = 5.5 Hz, H-7), 3.40 (m, H-8), 4.32 (d, J = 8.6 Hz, H-7′), 2.96 (m, H-8′)], four methoxy protons [δ_H 3.79 (3H, s, OCH_3-3), 3.72 (3H, s, OCH_3-3′), 3.64 (3H, s, OCH_3-3″), 3.24 (3H, s, OCH_3-7′)], and two sets of oxygenated methylene protons [δ_H 3.67 (dd, J = 11.0, 5.1 Hz, H-9a), 3.48 (dd, J = 11.0, 8.3 Hz, H-9b), 4.07 (dd, J = 10.9, 5.0 Hz, H-9′a), 3.92 (dd, J = 10.9, 7.1 Hz, H-9′b)] were observed. The ^{13}C NMR spectrum (Table 2) showed 28 signals, characteristic of 4 methoxy carbons, 18 phenyl carbons, and 6 aliphatic carbons. In addition to the above spectroscopic findings, the HMBC spectrum of **1** showed cross-peaks between H-7/C-1, C-2, C-6, C-9, C-4′, C-5′ and H-7′/C-1′, C-2′, C-6′, C-9′, C-1″. Moreover, other long-range correlations, including H-8/C-4′, C-5′ and H-8′/C-1″, C-2″, C-6″, were also found (Figure 2). Thus, the postulated structure of **1** contains two phenylpropanoid moieties and one benzene moiety. Subtracting 9 double bonds from the 13 degrees of unsaturation suggested that 4 rings remained in **1**. Together with the above findings, **1** was proposed to have a dihydrobenzo[*b*]furan neolignan skeleton, which is similar to that of the dehydrodiconiferyl alcohol. Furthermore, long-range correlations between H-7′/C-1″, H-9′/C-1″, and H-8′/C-2″, 6″, as well as the other correlated cross-peaks found in the HMBC spectrum, supported the presence of a C−C linkage between the dehydrodiconiferyl moiety and a 3-methoxy-4-hydroxybenzene moiety (Figure 2).[24] In addition, the coupling constant between H-7 and H-8 was 5.5 Hz (in CD_3OD) in the ^{1}H NMR spectrum and cross-peaks of H-7/H-9, H-8/H-2, and H-8/H-6 were observed in the NOESY spectrum in **1**, suggested the relative conformation of H-7 and H-8 as *trans*. The CD spectrum showed a negative Cotton effect (ε_{283} −9.97), so it was found that **1** had the 7*R*,8*S*-configuration.[25,26]

The *threo* relative configuration at the C-7′/C-8′ in **1** was suggested by comparing the ^{13}C NMR spectra with those of *threo* and *erythro* isomers.[27,28] Thus, the structure of **1** was established, and it was named hawthornnin A.

Compound **2** was assigned as $C_{28}H_{32}O_9$ from its HRESIMS data, and its UV, IR, ^{1}H NMR, and ^{13}C NMR spectroscopic data were identical with those of compound **1**, which suggested the planar structure of **2** was the same as for **1**. The *trans* relative configuration at C-7 and C-8 was confirmed by the $J_{7,8}$ value of 6.0 Hz in the ^{1}H NMR spectrum and the existence of cross-peaks (H-7/H-9, H-8/H-2, and H-8/H-6) in the NOESY spectrum. Furthermore, the CD cotton curve (ε_{284} 1.52) of **2** was opposite to that of **1**, indicating the configuration of the dihydrofuran ring was 7*S*,8*R*.[25,26] In addition, the chemical shifts of C-7′ and C-8′ indicated compound **2** also had a 7′,8′-*threo*-configuration.[27,28] Thus, compound **2** was identified as an optical isomer of **1** and given the trivial name hawthornnin B.

Compound **3** was also identified as $C_{28}H_{32}O_9$ by HRESIMS at m/z 535.1941 $[M + Na]^+$. Its ^{13}C NMR data were very similar to those of **1** except for a small difference in the chemical shift of C-7′ ($\Delta\delta$ 2.7), and a small coupling constant of H-7′ (J = 5.2 Hz) was observed in the ^{1}H NMR spectrum, which was different from that of **1** and indicated that **3** had a 7′,8′-*erythro*-configuration.[27,28] In addition, the 7,8-*trans* configuration of **3** was obtained from the $J_{7,8}$ value (5.8 Hz) and the NOESY spectrum. The positive Cotton effect at 278 nm in the CD spectrum supported the 7*S*,8*R*-configuration.[25,26] Therefore, the structure of **3** was identified as shown in Figure 1 and accorded the trivial name hawthornnin C.

The UV, IR, and NMR spectra of **4** were identical to those of **3**, suggesting that the planar structure of **4** was the same as that of **3**. The chemical shifts of C-7′ and C-8′ suggested a 7′,8′-*erythro* relative configuration.[27,28] In addition, the relative configuration of C-7/C-8 was suggested to be relative-*trans* according to the $J_{7,8}$ value of 6.3 Hz. This was also verified by NOE correlations of H-7/H_2-9 and H-8/H-6 and H-8/H-2 in the NOESY spectrum. The positive CD effect at 278 nm of **4**

DOI: 10.1021/acs.jafc.5b02835
J. Agric. Food Chem. 2015, 63, 7252−7260

supported the 7*R*,8*S*-configuration,[25,26] and compound **4** was named hawthornnin D.

Compound **5** was obtained as a yellow oil, with $C_{29}H_{34}O_9$ as its molecular formula, as indicated by HRESIMS at *m*/*z* 549.2064 $[M + Na]^+$. The IR spectrum displayed absorption bands for OH (3382 cm^{-1}) and an aromatic ring (1603 and 1518 cm^{-1}) groups. The ^1H and ^{13}C NMR spectra of **5** showed similarities to those of **1**, except for the presence of the OCH_3-7′ (δ_H 3.24; δ_C 57.0), which was replaced by an ethoxy group (δ_H 3.30, 1.08; δ_C 65.2, 15.7) in compound **5**. These minor structural changes were further supported by HMQC and HMBC correlations (Figure 2). The *erythro* configuration

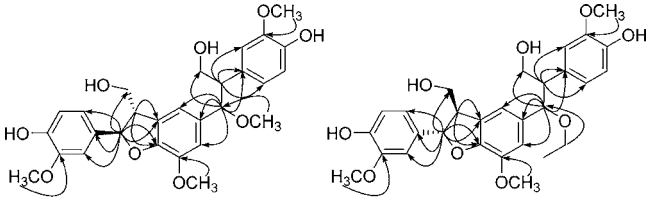

Figure 2. Key HMBC correlations of **1** and **5**.

between the two chiral centers at C-7′ and C-8′ was determined by comparing the NMR spectra with those of the *erythro* and *threo* isomers.[27,28] The *trans* relationship between H-7 and H-8 was inferred from their coupling constant ($J_{7,8}$ = 6.1 Hz), which was also further verified by the NOE correlations between H-7 and H_2-9 and between H-8 and H-2, 6. The positive CD effect at 281 nm of **5** supported the 7*S*,8*R*-configuration,[25,26] and it was named hawthornnin E.

The molecular formula of **6** was determined as $C_{29}H_{34}O_9$ by the $[M + Na]^+$ ion peak at *m*/*z* 549.2057 in the HRESIMS. Its IR and NMR spectroscopic data were in good agreement with those of **5** (Tables 1 and 2), suggesting that the planar structure and relative configuration of **6** were the same as those of compound **5**. The CD spectrum showed a negative Cotton effect (ε_{283} −4.87), which indicated that the absolute configuration of the dihydrofuran ring was 7*R*,8*S*.[25,26] Consequently, the structure of **6** was fully identified, and it was named hawthornnin F.

Compound **7** gave a positive HRESIMS *m*/*z* 395.1469 $[M + Na]^+$ (calcd for $C_{21}H_{24}O_6Na$, 395.1465), consistent with the molecular formula $C_{21}H_{24}O_6$. The IR spectrum of **7** showed absorption for hydroxyl (3357 cm^{-1}) and aromatic (1599 and 1512 cm^{-1}) functions. The NMR data of **7** (Tables 1 and 2) were in good agreement with those of 2-(4-hydroxy-3-methoxyphenyl)-3-hydroxymethyl-5-(3-methoxyallyl)-7-methoxycoumaran.[29] The relative configuration of compound **7** was suggested to be relative-*trans* according to the $J_{7,8}$ value of 6.6 Hz. In addition, the CD spectrum of **7** showed a negative Cotton effect at 282 nm, indicating that the absolute configuration of **7** was (7*R*,8*S*).[25,26] Therefore, the structure of **7** was assigned as 7*R*,8*S*-2-(4-hydroxy-3-methoxyphenyl)-3-hydroxymethyl-5-(3-methoxyallyl)-7-methoxycoumaran, and it was named hawthornnin G.

In its HRESIMS, compound **8** exhibited a pseudomolecular ion peak at *m*/*z* 445.1458 $[M + Na]^+$ (calcd for $C_{21}H_{26}O_9Na$, 445.1469), which is compatible with the molecular formula $C_{21}H_{26}O_9$. The UV spectrum showed absorbances at λ_{max} 230 and 280 nm, and the IR spectrum of **8** showed the presence of an aromatic moiety (1604 and 1514 cm^{-1}). Inspection of the NMR data (Tables 1 and 2) of **8** showed signals for two substituted aromatic rings, a characteristic doublet at δ_H 5.56 (1H, d, *J* = 6.2 Hz, H-7) for a dihydrobenzofuran-type lignan, and three OMe groups. A detailed NMR data analysis revealed the similarity between **8** and the known compound bennettin, previously isolated from *Flacourtia ramontch*,[30] suggesting that they shared the same structural skeleton. The *trans*-relative configuration of C-7 and C-8 was determined by comparison of the coupling constant of H-7 and H-8 (6.2 Hz) with that in the literature.[25] The absolute configurations at C-7 and C-8 of **8** were assigned to be *R* and *S* on the basis of the negative CD Cotton effects at 281 nm.[25,26] Furthermore, according to the literature,[31] the chemical shifts of C-8′ and C-7′ and the value of $\Delta\delta_{C8'-C7'}$ were different due to the *threo* and *erythro* isomers. The relative configuration of C-7′ and C-8′ was determined to be *threo* by its ^{13}C NMR data at δ_C 75.4 (C-7′) and 77.5 (C-8′) and the value of $\Delta\delta_{C8'-C7'}$ > 1.0 ppm. Consequently, the full structure of **8** was deduced, and it was named hawthornnin H.

The known compounds from the seeds of *C. pinnatifida* were identified by comparing their physical and spectroscopic data with values reported in the literature. They are 7*R*,8*S*-*erythro*-dihydroxydehydrodiconiferyl alcohol (**9**),[32] 7*S*,8*R*-*erythro*-dihydroxydehydrodiconiferyl alcohol (**10**),[31] 7*R*,8*S*-*threo*-dihydroxydehydrodiconiferyl alcohol (**11**),[32] 7*S*,8*R*-*threo*-dihydroxydehydrodiconiferyl alcohol (**12**),[31] 7*S*,8*R*-ficusal (**13**),[33] 7*S*,8*R*-5-methoxydihydrodehydroconiferyl alcohol (**14**),[34] and 7*R*,8*S*-sakuraresinol (**15**).[35]

Various lignans are distributed in significant concentrations in edible plants, especially in flax seed, sesame seed, and other oil seeds.[36−38] Most lignans possess a phenolic hydroxyl group in their structures and, therefore, they should exhibit high antioxidant ability.

The DPPH and $ABTS^{\bullet+}$ radical-scavenging assays are usually used to evaluate the antioxidant abilities of extracts or pure compounds.[39] The radical-scavenging activities of all isolates are summarized in Table 3. In the DPPH assay, compounds **1**−**6** and **8** showed more potent activity in the DPPH assay, although they are slightly weaker than trolox, and the other compounds exhibited only weak antioxidant activity. In the ABTS assay, most of the isolated compounds exhibited

Table 3. Antioxidant Activities of Compounds 1−15

compound	DPPH (IC_{50},[a] μM)	ABTS (IC_{50},[a] μM)
1	82.1 ± 1.8	11.7 ± 0.7
2	79.2 ± 1.8	10.6 ± 1.1
3	75.1 ± 1.2	12.6 ± 0.6
4	72.0 ± 0.9	12.0 ± 1.2
5	89.0 ± 1.0	13.6 ± 0.9
6	89.5 ± 2.6	14.3 ± 1.2
7	323.1 ± 1.4	35.51 ± 2.1
8	71.1 ± 2.5	30.7 ± 1.8
9	279.7 ± 5.1	23.4 ± 0.9
10	298.5 ± 3.3	24.5 ± 0.8
11	309.9 ± 2.5	29.6 ± 0.9
12	299.5 ± 3.00	31.3 ± 1.3
13	202.2 ± 1.3	49.8 ± 1.4
14	252.9 ± 2.4	18.7 ± 0.9
15	242.0 ± 2.1	24.8 ± 1.1
Trolox	31.4 ± 0.2	23.7 ± 0.3

[a]IC_{50} values represent the means ± SEM of three parallel measurements.

DOI: 10.1021/acs.jafc.5b02835
J. Agric. Food Chem. 2015, 63, 7252−7260

Table 4. Effects of Compounds 1−15 on Nitric Oxide (NO) Production in LPS-Stimulated RAW 264.7 Cells[a]

	inhibition (%)					
compound	0 μM	1 μM	10 μM	50 μM	100 μM	IC_{50} (μM)
1	0.0 ± 4.7	10.4 ± 3.2*	13.3 ± 4.7*	57.1 ± 2.1**	82.0 ± 1.5**	30.5
2	0.0 ± 4.2	8.3 ± 4.6*	21.2 ± 2.0**	49.8 ± 2.4**	85.1 ± 1.1**	27.3
3	0.0 ± 6.8	13.6 ± 2.2*	12.1 ± 3.1*	37.8 ± 1.6**	87.1 ± 3.9**	35.3
4	0.0 ± 6.2	8.2 ± 1.7	12.9 ± 1.2*	65.6 ± 1.8**	80.2 ± 2.5**	29.1
5	0.0 ± 3.9	3.1 ± 4.4	14.8 ± 2.0**	51.1 ± 2.7**	92.6 ± 3.5**	26.0
6	0.0 ± 3.2	2.6 ± 3.1	11.3 ± 2.4**	61.7 ± 2.6**	87.9 ± 1.4**	29.4
7	0.0 ± 4.4	6.7 ± 3.3	64.8 ± 2.2**	67.1 ± 3.5**	82.0 ± 2.4**	14.1
8	0.0 ± 5.7	3.7 ± 3.5	10.2 ± 2.9*	38.0 ± 2.1*	59.8 ± 1.3**	86.8
9	0.0 ± 5.9	6.9 ± 2.8	20.8 ± 3.6**	39.4 ± 1.2**	47.2 ± 2.1**	>100
10	0.0 ± 4.6	9.5 ± 3.8*	16.4 ± 1.3**	29.8 ± 3.3*	42.1 ± 2.2**	>100
11	0.0 ± 4.0	10.1 ± 4.9*	10.9 ± 3.1*	31.6 ± 3.7**	44.9 ± 1.0**	>100
12	0.0 ± 5.7	4.5 ± 3.2	19.1 ± 3.6**	22.1 ± 2.4**	40.6 ± 2.5**	>100
13	0.0 ± 4.4	13.1 ± 5.7*	49.2 ± 2.**5	77.2 ± 3.3**	82.5 ± 3.2**	11.3
14	0.0 ± 6.4	21.8 ± 2.1**	48.3 ± 1.9**	75.5 ± 1.5**	82.1 ± 1.2**	8.8
15	0.0 ± 2.0	9.3 ± 1.2**	16.5 ± 2.2**	24.2 ± 3.1**	34.2 ± 1.4**	>100
mino	0.0 ± 3.2	15.6 ± 1.6**	22.7 ± 2.1**	51.8 ± 2.8**	59.7 ± 1.9**	55.1

[a]Each value represents the means ± SEM of three parallel measurements. Significantly different from the control: *, $p < 0.05$; **, $p < 0.01$.

Table 5. Effects of Compounds 1−15 on Tumor Necrosis Factor α (TNF-α) Production in LPS-Stimulated RAW 264.7 Cells[a]

	inhibition (%)					
compound	0 μM	1 μM	10 μM	50 μM	100 μM	IC_{50} (μM)
1	0.0 ± 3.7	7.1 ± 2.6*	23.5 ± 1.0**	46.5 ± 1.4**	55.3 ± 3.4**	67.4
2	0.0 ± 4.3	10.5 ± 2.0*	30.2 ± 2.3**	49.1 ± 3.1**	59.5 ± 2.1**	50.2
3	0.0 ± 3.5	4.1 ± 2.5	32.1 ± 2.7**	44.7 ± 1.8**	52.4 ± 1.0**	63.1
4	0.0 ± 3.2	6.9 ± 3.0*	33.5 ± 1.5**	43.6 ± 3.3**	61.5 ± 2.7**	50.8
5	0.0 ± 5.2	5.3 ± 2.2	23.1 ± 1.8**	41.2 ± 1.3**	51.1 ± 2.5**	85.0
6	0.0 ± 3.2	15.0 ± 2.3**	21.5 ± 2.9**	48.0 ± 1.7**	57.0 ± 1.9**	71.8
7	0.0 ± 5.7	11.3 ± 3.0*	31.0 ± 3.2**	55.3 ± 2.2**	69.5 ± 2.0**	31.4
8	0.0 ± 4.0	3.2 ± 2.0	19.2 ± 2.6**	29.5 ± 3.9**	35.1 ± 3.7**	>100
9	0.0 ± 5.0	2.4 ± 3.5	11.9 ± 3.4*	24.3 ± 1.8**	28.6 ± 3.2**	>100
10	0.0 ± 4.2	5.2 ± 4.7	17.2 ± 2.2**	21.8 ± 2.3**	23.1 ± 3.4**	>100
11	0.0 ± 2.4	7.2 ± 4.3*	19.1 ± 3.5**	25.6 ± 2.0**	31.2 ± 2.8**	>100
12	0.0 ± 5.7	3.1 ± 4.2	14.2 ± 2.6*	27.2 ± 3.5**	34.0 ± 1.3**	>100
13	0.0 ± 2.8	21.0 ± 2.4**	49.2 ± 3.7**	62.1 ± 3.2**	69.8 ± 1.6**	15.2
14	0.0 ± 3.7	14.6 ± 3.2**	29.3 ± 2.5**	51.2 ± 1.4**	63.8 ± 2.7**	41.4
15	0.0 ± 4.5	7.5 ± 4.2	16.5 ± 1.6**	27.3 ± 1.9**	42.1 ± 2.2**	>100
silybin	0.0 ± 3.4	10.3 ± 2.5**	27.0 ± 3.8**	47.0 ± 3.1**	53.8 ± 3.7**	69.2

[a]Each value represents the means ± SEM of three parallel measurements. Significantly different from the control: *, $p < 0.05$; **, $p < 0.01$.

significant antioxidant activity, with compounds **1**−**6** being the most potent (IC_{50} = 10.6−14.3 μM), whereas compounds **7**−**15** exhibited moderate ABTS radical-scavenging activities (IC_{50} = 18.7−49.8 μM), comparable with that of the standard compound trolox, with an IC_{50} value of 23.7 μM. A comparison of the structures of **1**−**6** with those of **7**−**15** indicated that the additional 3-methoxy-4-hydroxybenzene moiety groups at C-8′ appeared to increase the antioxidant activity of the dihydrobenzofuran neolignans. This fact indicated that the free phenolic hydroxyl was crucial for the antioxidant activity, which was consistent with previous observations.[40]

Pro-inflammatory cytokines (such as TNF-α, IL-1β, IL-6, IFN-γ) and NO are the key mediators for the pathogenesis of osteoarthritis, inflammatory bowel diseases, psoriasis, ulcerative colitis, and rheumatoid arthritis. Hence, the inhibition of pro-inflammatory cytokines and NO will be an important strategy for the treatment of these inflammatory conditions.[23,41,42] In this investigation, we further evaluated the anti-inflammatory activities of the isolated compounds **1**−**15** using exposure to LPS-induced NO and TNF-α production in the mouse macrophage RAW264.7 cell line. At a concentration of 100 μM, the MTT assay results showed that **1**−**15** did not affect cell viability (data not shown). Thus, the effects of compounds **1**−**15** on LPS-induced production of the inflammatory mediators NO and TNF-α in RAW 264.7 cells were evaluated at concentrations lower than 100 μM.

As shown in Tables 4 and 5, compounds **1**−**7**, **13**, and **14** showed potent inhibition of NO and TNF-α production. In particular, the activities of **7**, **13**, and **14** were more potent than that of the positive control. The observed NO and TNF-α inhibitory activities appear to be correlated with their structures. For example, with regard to the results for **14** and **15**, it appeared that the 4-OH might be important for higher activities. In addition, comparing the structures and inhibitory activities of **7** and **14** with those of **8**−**12**, it appeared that the two hydroxyl groups at C-7′, 8′ may cause a reduction in the inhibition of NO and TNF-α production. Interestingly, consideration of the structures of **1**−**6** versus **8**−**12** suggested

DOI: 10.1021/acs.jafc.5b02835
J. Agric. Food Chem. 2015, 63, 7252−7260

that 8′-OH was replaced by a 3-methoxy-4-hydroxybenzoic group, resulting in an increase in the NO and TNF-α inhibitory activities of those dihydrobenzofuran neolignans that have the 7, 8-OH moiety in their side chain. A structure−activity relationship study of the related diverse derivatives might be needed to identify the key moiety in dihydrobenzofuran neolignans responsible for inhibiting NO and TNF-α production.

In conclusion, 15 dihydrobenzofuran neolignans were isolated from the active fraction of *C. pinnatifida* seeds and evaluated for inhibition of NO and TNF-α along with antioxidant activities. The results of the present investigations indicate the importance of these neolignans as potential anti-inflammatory and antioxidant agents. From the activity results of the tested compounds, **1**−**6** showed promising activity against NO and TNF-α with less cytotoxicity and considerable antioxidant activity. The results of **7**, **13**, and **14** as inhibitors of NO and TNF-α are certainly encouraging, but the antioxidant activity of these compounds possibly limits their therapeutic applications. The structure−activity relationship of isolated lignans was also discussed. It is notable that the additional 3-methoxy-4-hydroxybenzene moiety at position C-8′ appeared to increase the antioxidant and anti-inflammatory activities of the dihydrobenzofuran neolignans. The results obtained in our study provide a potential justification for the use of the seeds from *C. pinnatifida* industrial byproducts as a valuable source of raw material for new antioxidant and anti-inflammatory agents.

■ ASSOCIATED CONTENT

Supporting Information

The Supporting Information is available free of charge on the ACS Publications website at DOI: 10.1021/acs.jafc.5b02835.

UV, CD, IR, NMR, and HRESIMS data for compounds **1**−**8** (PDF)

■ AUTHOR INFORMATION

Corresponding Author

*(S.-J.S.) Mail: School of Traditional Chinese Materia Medica, Shenyang Pharmaceutical University, 103 Wenhua Road, Shenyang Liaoning 110016, China. Phone: +86-24-23986088. E-mail: songsj99@163.com.

Funding

The financial support from the Program for the National Natural Science Foundation of China (81302661) and the Scientific Research Starting Foundation (20121106) for Doctors of Liaoning province of People's Republic of China is gratefully acknowledged.

Notes

The authors declare no competing financial interest.

■ ABBREVIATIONS USED

NMR, nuclear magnetic resonance spectrometry; HPLC, high-performance liquid chromatography; HSQC, heteronuclear single-quantum coherence; HMBC, heteronuclear multiple-bond correlation; NOESY, nuclear Overhaser effect spectroscopy; ESI-MS, electrospray ionization mass spectrometry; UV, ultraviolet spectrometry; CD, electronic circular dichroism; IR, infared absorption spectrum

■ REFERENCES

(1) Deng, J.; Cheng, W.; Yang, G. A novel antioxidant activity index (AAU) for natural products using the DPPH assay. *Food Chem.* **2011**, *125*, 1430−1435.

(2) Scherer, R.; Godoy, H. T. Antioxidant activity index (AAI) by the 2,2-diphenyl-1-picrylhydrazyl method. *Food Chem.* **2009**, *112*, 654−658.

(3) Nathan, C. Points of control in inflammation. *Nature* **2002**, *420*, 846−852.

(4) Hensley, K.; Robinson, K. A.; Gabbita, S. P.; Salsman, S.; Floyd, R. A. Reactive oxygen species, cell signaling, and cell injury. *Free Radical Biol. Med.* **2000**, *28*, 1456−1462.

(5) Li, F.; Nitteranon, V.; Tang, X.; Liang, J.; Zhang, G.; Parkin, K. L.; Hu, Q. *In vitro* antioxidant and anti-inflammatory activities of 1-dehydro-[6]-gingerdione, 6-shogaol, 6-dehydroshogaol and hexahydrocurcumin. *Food Chem.* **2012**, *135*, 332−337.

(6) Su, C. R.; Shen, Y. C.; Kuo, P. C.; Leu, Y. L.; Damu, A. G.; Wang, Y. H.; Wu, T. S. Total synthesis and biological evaluation of viscolin, a 1,3-diphenylpropane as a novel potent anti-inflammatory agent. *Bioorg. Med. Chem. Lett.* **2006**, *16*, 6155−6160.

(7) Vagiri, M.; Conner, S.; Stewart, D.; Andersson, S. C.; Verrall, S.; Johansson, E.; Rumpunen, K. Phenolic compounds in blackcurrant (*Ribes nigrum* L.) leaves relative to leaf position and harvest date. *Food Chem.* **2015**, *172*, 135−142.

(8) Pan, M. H.; Ghai, G.; Ho, C. T. Food bioactives, apoptosis, and cancer. *Mol. Nutr. Food Res.* **2008**, *52*, 43−52.

(9) Cuevas-Rodríguez, E. O.; Dia, V. P.; Yousef, G. G.; García-Saucedo, P. A.; López-Medina, J.; Paredes-López, O.; Mejia, E. G. D.; Lila, M. A. Inhibition of pro-inflammatory responses and antioxidant capacity of mexican blackberry (*Rubus* spp.) extracts. *J. Agric. Food Chem.* **2010**, *58*, 9542−9548.

(10) Rice-Evans, C. A.; Miller, N. J.; Bolwell, P. G.; Bramley, P. M.; Pridham, J. B. The relative antioxidant activities of plant-derived polyphenolic flavonoids. *Free Radical Res.* **1995**, *22*, 375−383.

(11) Mitjans, M.; del Campo, J.; Abajo, C.; Martínez, V.; Selga, A.; Lozano, C.; Torres, J. L.; Vinardell, M. P. Immunomodulatory activity of a new family of antioxidants obtained from grape polyphenols. *J. Agric. Food Chem.* **2004**, *52*, 7297−7299.

(12) Dong, W.; Ni, Y.; Kokot, S. A near-infrared reflectance spectroscopy method for direct analysis of several chemical components and properties of fruit, for example, Chinese hawthorn. *J. Agric. Food Chem.* **2013**, *61*, 540−546.

(13) Li, T.; Zhu, J.; Guo, L.; Shi, X.; Liu, Y.; Yang, X. Differential effects of polyphenols-enriched extracts from hawthorn fruit peels and fleshes on cell cycle and apoptosis in human MCF-7 breast carcinoma cells. *Food Chem.* **2013**, *141*, 1008−1018.

(14) Cui, T.; Li, J. Z.; Kayahara, H.; Ma, L.; Wu, L. X.; Nakamura, K. Quantification of the polyphenols and triterpene acids in Chinese hawthorn fruit by high-performance liquid chromatography. *J. Agric. Food Chem.* **2006**, *54*, 4574−4581.

(15) Edwards, J. E.; Brown, P. N.; Talent, N.; Dickinson, T. A.; Shipley, P. R. A review of the chemistry of the genus. *Phytochemistry* **2012**, *79*, 5−26.

(16) Liu, P.; Yang, B.; Kallio, H. Characterization of phenolic compounds in Chinese hawthorn (*Crataegus pinnatifida* Bge. var. *major*) fruit by high performance liquid chromatography-electrospray ionization mass spectrometry. *Food Chem.* **2010**, *121*, 1188−1197.

(17) Liu, P.; Kallio, H.; Yang, B. Phenolic compounds in hawthorn (*Crataegus grayana*) fruits and leaves and changes during fruit ripening. *J. Agric. Food Chem.* **2011**, *59*, 11141−11149.

(18) Chu, C. Y.; Lee, M. J.; Liao, C. L.; Lin, W. L.; Yin, Y. F.; Tseng, T. H. Inhibitory effect of hot-water extract from dried fruit of *Crataegus pinnatifida* on low-density lipoprotein (LDL) oxidation in cell and cell-free systems. *J. Agric. Food Chem.* **2003**, *51*, 7583−7588.

(19) Kao, E. S.; Wang, C. J.; Lin, W. L.; Yin, Y. F.; Wang, C. P.; Tseng, T. H. Anti-inflammatory potential of flavonoid contents from dried fruit of *Crataegus pinnatifida* in vitro and in vivo. *J. Agric. Food Chem.* **2005**, *53*, 430−436.

DOI: 10.1021/acs.jafc.5b02835
J. Agric. Food Chem. 2015, 63, 7252−7260

(20) Wu, S. B.; Dastmalchi, K.; Long, C.; Kennelly, E. J. Metabolite profiling of jaboticaba (*Myrciaria cauliflora*) and other dark-colored fruit juices. *J. Agric. Food Chem.* **2012**, *60*, 7513−7525.
(21) Chien, S. C.; Chen, M. L.; Kuo, H. T.; Tsai, Y. C.; Lin, B. F.; Kuo, Y. H. Anti-inflammatory activities of new succinic and maleic derivatives from the fruiting body of *Antrodia camphorata*. *J. Agric. Food Chem.* **2008**, *56*, 7017−7022.
(22) Huang, G. J.; Deng, J. S.; Liao, J. C.; Hou, W. C.; Wang, S. Y.; Sung, P. J.; Kuo, Y. H. Inducible nitric oxide synthase and cyclooxygenase-2 participate in anti-inflammatory activity of imperatorin from *Glehnia littoralis*. *J. Agric. Food Chem.* **2012**, *60*, 1673−1681.
(23) Wang, J.; Mazza, G. Effects of anthocyanins and other phenolic compounds on the production of tumor necrosis factor α in LPS/IFN-γ-activated RAW 264.7 macrophages. *J. Agric. Food Chem.* **2002**, *50*, 4183−4189.
(24) Gan, M.; Zhang, Y.; Lin, S.; Liu, M.; Song, W.; Zi, J.; Yang, Y.; Fan, X.; Shi, J.; Hu, J.; Sun, J.; Chen, N. Glycosides from the root of *Iodes cirrhosa*. *J. Nat. Prod.* **2008**, *71*, 647−654.
(25) Xiong, L.; Zhu, C.; Li, Y.; Tian, Y.; Lin, S.; Yuan, S.; Hu, J.; Hou, Q.; Chen, N.; Yang, Y.; Shi, J. G. Lignans and neolignans from *Sinocalamus affinis* and their absolute configurations. *J. Nat. Prod.* **2011**, *74*, 1188−1200.
(26) Antus, S.; Kurtán, T.; Juhász, L.; Kiss, L.; Hollósi, M.; Májer, Z. S. Chiroptical properties of 2,3-dihydrobenzo[*b*]furan and chromane chromophores in naturally occurring *O*-heterocycles. *Chirality* **2001**, *13*, 493−506.
(27) Hsiao, J. J.; Chiang, H. C. Lignans from the wood of *Aralia bipinnata*. *Phytochemistry* **1995**, *39*, 899−902.
(28) Rayanil, K. O.; Nimnoun, C.; Tuntiwachwuttikul, P. New phenolics from the wood of *Casearia grewiifolia*. *Phytochem. Lett.* **2012**, *5*, 59−62.
(29) Ohta, M.; Higuchi, T.; Iwahara, S. Microbial degradation of dehydrodiconiferyl alcohol, a lignin substructure model. *Arch. Microbiol.* **1979**, *121*, 23−28.
(30) Chai, X. Y.; Ren, H. Y.; Xu, Z. R.; Bai, C. C.; Zhou, F. R.; Ling, S. K.; Pu, X. P.; Li, F. F.; Tu, P. F. Investigation of two flacourtiaceae plants: *Bennettiodendron leprosipes* and *Flacourtia ramontchi*. *Planta Med.* **2009**, *75*, 1246−1252.
(31) Wang, L.; Li, F.; Yang, C. Y.; Khan, A. A.; Liu, X.; Wang, M. K. Neolignans, lignans and glycoside from the fruits of *Melia toosendan*. *Fitoterapia* **2014**, *99*, 92−98.
(32) Deyama, T.; Ikawa, T.; Kitagawa, S.; Nishibe, S. The constituents of *Eucommia ulmoides* Oliv. V. Isolation of dihydroxydehydrodiconiferyl alcohol isomers and phenolic compounds. *Chem. Pharm. Bull.* **1987**, *35*, 1785−1789.
(33) Li, Y. C.; Kuo, Y. H. Four new compounds, ficusal, ficusesquilignan A, B and ficusolide diacetate from the heartwood of *Ficus microcarpa*. *Chem. Pharm. Bull.* **2000**, *48*, 1862−1865.
(34) Chin, Y. W.; Chai, H. B.; Keller, W. J.; Kinghorn, A. D. Lignans and other constituents of the fruits of *Euterpe oleracea* (Açai) with antioxidant and cytoprotective activities. *J. Agric. Food Chem.* **2008**, *56*, 7759−7764.
(35) Kouno, I.; Yanagida, Y.; Shimono, S.; Shintomi, M.; Ito, Y.; Yang, C. S. Neolignans and a phenylpropanoid glucoside from *Illicium difengpi*. *Phytochemistry* **1993**, *32*, 1573−1577.
(36) Wen, L.; He, J.; Wu, D.; Jiang, Y.; Prasad, K. N.; Zhao, M.; Lin, S.; Jiang, G.; Luo, W.; Yang, B. Identification of sesquilignans in litchi (*Litchi chinensis* Sonn.) leaf and their anticancer activities. *J. Funct. Foods* **2014**, *8*, 26−34.
(37) Masuda, T.; Akiyama, J.; Fujimoto, A.; Yamauchi, S.; Maekawa, T.; Sone, Y. Antioxidation reaction mechanism studies of phenolic lignans, identification of antioxidation products of secoisolariciresinol from lipid oxidation. *Food Chem.* **2010**, *123*, 442−450.
(38) Peñalvo, J. L.; Adlercreutz, H.; Uehara, M.; Ristimaki, A.; Watanabe, S. Lignan content of selected foods from Japan. *J. Agric. Food Chem.* **2008**, *56*, 401−409.
(39) Chung, Y. M.; Wang, H. C.; El-Shazly, M.; Leu, Y. L.; Cheng, M. C.; Lee, C. L.; Chang, F. R.; Wu, Y. C. Antioxidant and tyrosinase inhibitory constituents from a desugared sugar cane extract, a byproduct of sugar production. *J. Agric. Food Chem.* **2011**, *59*, 9219−9225.
(40) Hamerski, L.; Bomm, M. D.; Silva, D. H. S.; Young, M. C. M.; Furlan, M.; Eberlin, M. N.; Castro-Gamboa, I.; Cavalheiro, A. J.; Bolzani, V. D. S. Phenylpropanoid glucosides from leaves of *Coussarea hydrangeifolia* (Rubiaceae). *Phytochemistry* **2005**, *66*, 1927−1932.
(41) Pu, W.; Lin, Y.; Zhang, J.; Wang, F.; Wang, C.; Zhang, G. 3-Arylcoumarins: synthesis and potent anti-inflammatory activity. *Bioorg. Med. Chem. Lett.* **2014**, *24*, 5432−5434.
(42) Patel, N. K.; Bairwa, K.; Gangwal, R.; Jaiswal, G.; Jachak, S. M.; Sangamwar, A. T.; Bhutani, K. K. 2′-Hydroxy flavanone derivatives as an inhibitors of pro-inflammatory mediators: experimental and molecular docking studies. *Bioorg. Med. Chem. Lett.* **2015**, *25*, 1952−1955.

DOI: 10.1021/acs.jafc.5b02835
J. Agric. Food Chem. 2015, 63, 7252−7260

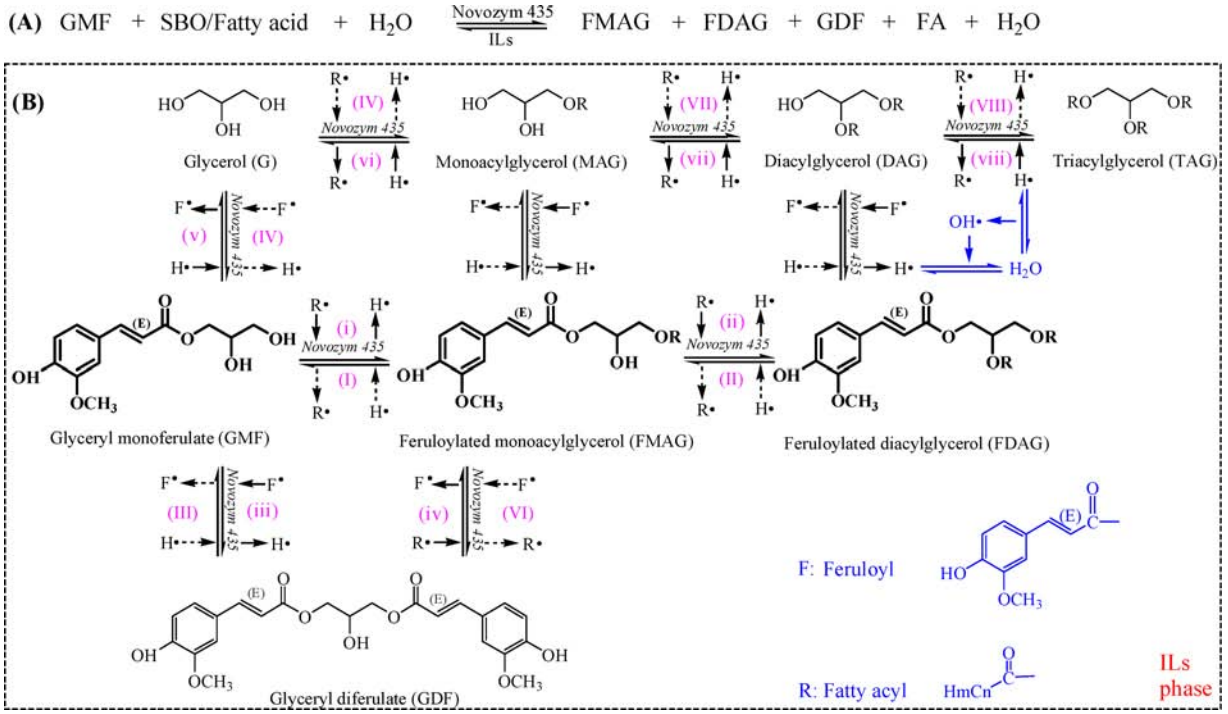

Figure 1. (A) Reaction scheme of enzymatic transesterification of glyceryl monoferulate (GMF) with soybean oil (SBO) and the mixed fatty acid (MFA). (B) Reaction mechanism for enzymatic synthesis of feruloylated monoacylglycerols (FMAG) + feruloylated diacylglycerols (FDAG) in ILs.

Sigma (Shanghai, China). Linoleic acid ($C_{18:2}$, purity >95%) was purchased from Anqing Zhong Chuang Bioengineering Co., Ltd. (Anqing, China). The mixed fatty acids (MFA, in which lauric acid ($C_{12:0}$) 2.1%, palmitic acid ($C_{16:0}$) 3.5%, stearic acid ($C_{18:0}$) 2.5%, oleic acid ($C_{18:1}$) 78.6%, and linoleic acid ($C_{18:2}$) 12.5% were contained) was purchased from Aladdin (Shanghai, China).

Ionic liquids, 1-ethyl-3-methylimidazolium hexafluorophosphate ([Emim][PF_6]), 1-butyl-3-methylimidazolium hexafluorophosphate ([Bmim][PF_6]), 1-octyl-3-methylimidazolium hexafluorophosphate ([Omim][PF_6]), 1-decyl-3-methylimidazolium hexafluorophosphate ([C_{10}mim][PF_6]), 1-dodecyl-3-methylimidazolium hexafluorophosphate ([C_{12}mim][PF_6]), 1-tetradecyl-3-methylimidazolium hexafluorophosphate ([C_{14}mim][PF_6]), 1-octadecyl-3-methylimidazolium hexafluorophosphate ([C_{18}mim][PF_6]), 1,3-dimethylimidazolium bis[(trifluoromethyl)-sulfonyl]imide ([Mmim][TF_2N]), 1-ethyl-3-methylimidazolium bis-[(trifluoromethyl)sulfonyl]imide ([Emim][TF_2N]), 1-butyl-3-methyl-imidazolium bis[(trifluoromethyl)sulfonyl]imide ([Bmim][TF_2N]), 1-ethyl-3-methylimidazolium tetrafluoroborate ([Emim][BF_4]), 1-butyl-3-methylimidazolium tetrafluoroborate ([Bmim][BF_4]), and 1-hexyl-3-methylimidazolium tetrafluoroborate ([Hmim][BF_4]), were purchased from Shanghai Cheng Jie Chemical Co., Ltd. (Shanghai, China). Methanol (HPLC grade) and glacial acetic acid (HPLC grade) were purchased from Sinopharm Chemical Reagent Co., Ltd. (Shanghai, China). All other reagents were of analytical grade.

Methods. *GMF Preparation by the Enzymatic Transesterification of EF with Glycerol in Room Temperature Ionic Liquid (RTIL).* RTILs are salts that are composed entirely of ions with melting points below room temperature, for example, [Emim]TF_2N (mp 15 °C). GMF was prepared in 100 mL round-bottom flasks with a vacuum evaporator. EF was mixed with glycerol (molar ratio, 1:1.4), which was catalyzed by Novozym 435 (60 mg/mL) at 80 °C in [Emim]TF_2N. The reaction mixture was stirred with a magnetic stirrer at 300 rpm for 5.0 h under 90 kPa. Then, the RTIL solutions of the transesterification mixture were obtained by filtration to remove the immobilized Novozym 435. Then, GMF was separated and purified according to previous report.[38]

Enzymatic Transesterification of GMF with SBO or the Esterification of GMF with Fatty Acids. The reactions of GMF (1.50 mmol/mL) with SBO (or fatty acids) (molar ratio of GMF and SBO (or fatty acids), 1:2) were carried out in 25 mL round-bottom flasks. ILs (1 mL) were used as reaction media. The reaction mixtures (reactants and ILs) were incubated at various temperatures using an oil bath with a magnetic stirrer at 200 rpm under 90 kPa, and then Novozym 435 (45 mg/mL) was added to the reaction mixtures. Meanwhile, control experiments without lipase or IL were carried out. Samples (5 μL) were withdrawn at specified time intervals.

Experimental Design for RSM. A three-level-four-factor Box–Behnken design was employed to investigate the effect of reaction variables on the transesterification of GMF with SBO or the esterification of GMF with fatty acids, respectively. The factors and levels selected were as follows: reaction time (2, 8, 14 h for SBO and 0.5, 6, 11.5 h for fatty acids), reaction temperature (60, 90, 120 °C for SBO and 60, 80, 100 °C for fatty acids), molar ratio (1.0, 3.0, 5.0 for SBO/GMF and 1.0, 2.5, 4 for fatty acids/GMF), enzyme load (10, 35, 60 mg/mL for SBO and 10, 30, 50 mg/mL for fatty acids).

Analytical Techniques. Reactants and products were analyzed and identified as in previous reports.[23] HPLC and internal standard method (ISTD) were used to determine the purity of GMF in the product.

Reaction selectivity for FAGs formation can be defined as follows:

$$\text{FAG selectivity} = \frac{\text{FAG yield (\%)}}{\text{GMF conversion (\%)}}$$

Statistical Analysis. The experiments were carried out for analysis using a three-level-four-factor Box–Behnken design. The mathematical relationship relating the variables to the responses can be calculated by the quadratic polynomial equation (from Box–Behnken design):

$$Y = \beta_0 + \sum_{4}^{i=1} \beta_i X_i + \sum_{4}^{i=1} \beta_{ii} X_i^2 + \sum_{3}^{i=1} \sum_{4}^{j=i+1} \beta_{ij} X_i X_j$$

where Y is one of the responses (GMF conversion or FAG yields); X_i and X_j represent the represent the independent variables; and β_0, β_i, β_{ii}, and β_{ij} are the constant coefficients.

All experiments were performed at least in triplicate. Results were expressed as average ± SEM. A two-way analysis of variance (ANOVA) was used. Statistical significance was considered at $p < 0.05$.

DOI: 10.1021/acs.jafc.5b03479
J. Agric. Food Chem. 2015, 63, 7261–7269

Table 1. Effect of Different Fatty Acyl Donors on the GMF Conversion and Product Yield[a,b]

	1 h					12 h				
fatty acids	GMF convn[c] (%)	FAG selectivity	FMAG (%)	FDAG (%)	GDF (%)	GMF convn[c] (%)	FAG selectivity	FMAG (%)	FDAG (%)	GDF (%)
10:0	88.7 ± 0.4 bc	0.9541 b	71.1 ± 0.9 b	13.6 ± 0.8 c	3.5 ± 0.3 bc	96.9 ± 0.3 b	0.8624 d	35.0 ± 0.9 b	48.6 ± 0.5 c	12.6 ± 1.1 bc
14:0	88.9 ± 0.3 b	0.9546 b	64.9 ± 0.3 d	19.9 ± 0.6 b	3.5 ± 0.1 bc	97.9 ± 0.5 ab	0.8909 b	31.5 ± 1.3 c	55.7 ± 0.9 b	9.9 ± 1.2 c
18:0	82.3 ± 0.3 d	0.9346 c	77.0 ± 0.5 a	0 d	4.4 ± 0.3 ab	96.5 ± 0.1 b	0.7412 f	71.5 ± 0.3 a	0 d	23.2 ± 0.2 a
18:1	81.9 ± 0.7 d	0.9366 c	64.8 ± 0.3 d	11.9 ± 0.5 c	4.6 ± 0.8 ab	98.7 ± 0.4 a	0.8764 c	30.1 ± 1.5 c	56.5 ± 0.9 b	11.2 ± 1.3 bc
18:2	87.3 ± 0.4 c	0.9235 d	68.6 ± 0.3 c	12.0 ± 0.3 c	5.7 ± 0.2 a	98.7 ± 0.5 a	0.8433 e	32.7 ± 0.9 bc	50.5 ± 0.4 c	14.4 ± 0.9 b
MFA	95.7 ± 0.2 a	0.9629 a	65.2 ± 0.3 d	26.9 ± 0.4 a	2.2 ± 0.1 c	99.2 ± 0.5 a	0.9213 a	21.8 ± 0.1 d	69.6 ± 0.6 a	6.0 ± 0.3 d

[a]Reaction conditions: GMF:fatty acid = 1:2 (mol/mol), Novozym 435 concentration 40 mg/mL, GMF 1.50 mmol/mL, $[C_{10}mim]PF_6$ 1 mL, 80 °C, 90 kPa. [b]The results are expressed as average ± SEM with three replications. Values within a column followed by the same letter are not significantly different ($p < 0.05$). [c]The yield of byproduct FA <2% not shown.

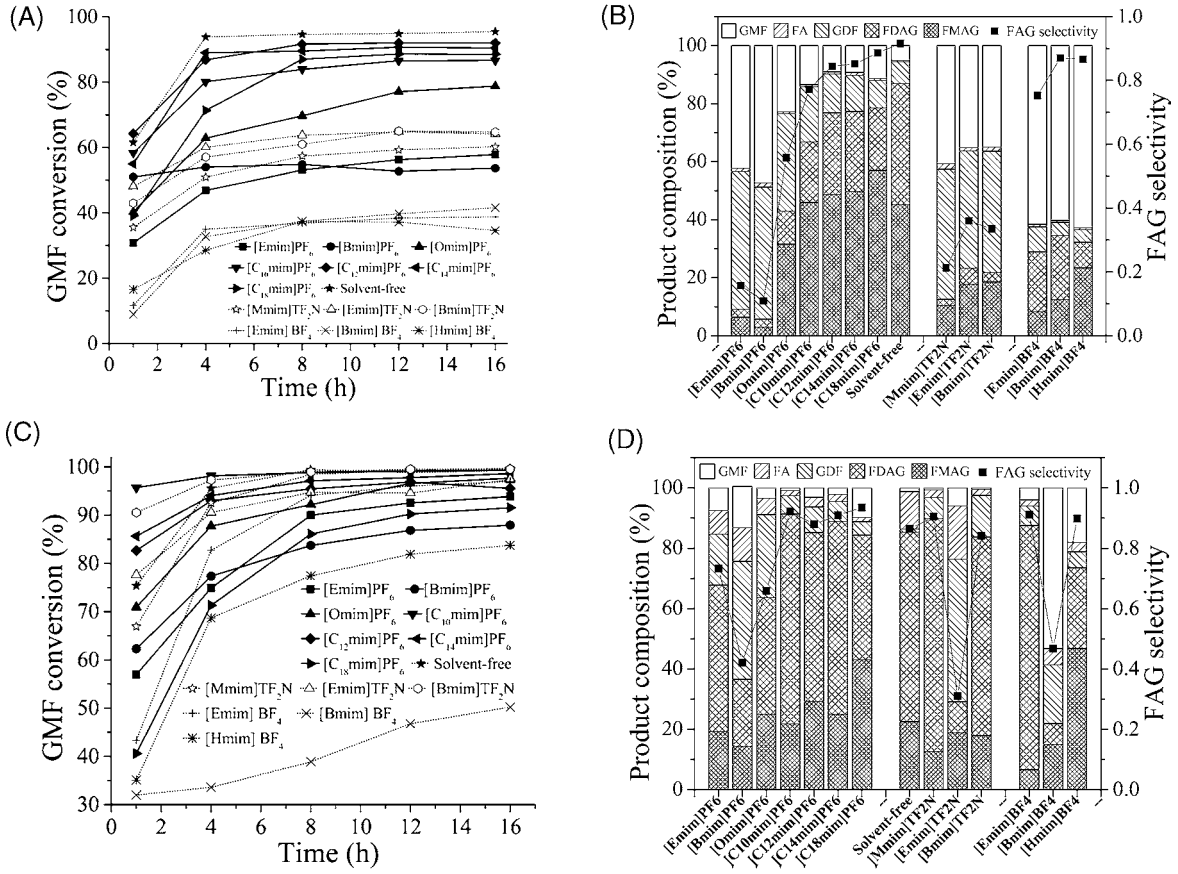

Figure 2. (A) Effect of different ionic liquids on the reaction of GMF with SBO. (B) Effect of different ionic liquids on the reaction of GMF with MFA. (C) Product composition and FAG selectivity when SBO were used in different ILs (12 h). (D) Product composition and FAG selectivity when MFA was used in different ILs (12 h). Reaction conditions: GMF/SBO (or MFA) = 1:2 (mol/mol), Novozym 435 concentration 45 mg/mL, GMF 1.50 mmol/mL, ILs 1 mL, 80 °C, 90 kPa.

RESULTS AND DISCUSSION

Effect of Different Fatty Acids as Acyl Donors. Different fatty acids as GMF acceptors showed a clear effect on FAG selectivity (Table 1). However, the effect of different fatty acids on GMF conversions was not significant. GMF conversions rapidly increased up to >80% (1 h), and then maintained at high levels (>95.7 ± 1.5%) after 4 h, which indicated that GMF was completely bonded with fatty acyl (or another feruloyl) donors. Using $C_{18:0}$ as acyl donor, feruloylated diacylglycerols (FDAG) were not found in the products, and the byproduct glyceryl diferulate (GDF) yield was up to 23.2 ± 0.2% after 12 h (Table 1), which was higher than those of other fatty acids (<15.0%). Low FAG selectivity (0.74) was found using $C_{18:0}$ as acyl donor. These results can be explained by the fact that the primary product feruloylated monoacylglycerols (FMAG) (contain feruloyl and stearoyl in 1,3-position) were difficult to bind with another stearoyl in sn-2 of glycerol to form FDAG, and excess water formed by the esterification of GMF with fatty acids can favor GDF formation (Figure 1B). However, maximum FDAG yield (69.6 ± 0.6%) and minimum byproduct GDF yield (6.0 ± 0.3%) were obtained using mixed fatty acids (MFA) as acyl donor, and the maximum GMF conversion (99.2 ± 0.5%) and FAG selectivity (0.92) were achieved. Therefore, the MFA was used as GMF acceptors in the subsequent work.

Effect of Soybean Oil (SBO) and MFA as Acyl Donors in ILs. Figure 2A shows the effect of different ILs on the

DOI: 10.1021/acs.jafc.5b03479
J. Agric. Food Chem. 2015, 63, 7261−7269

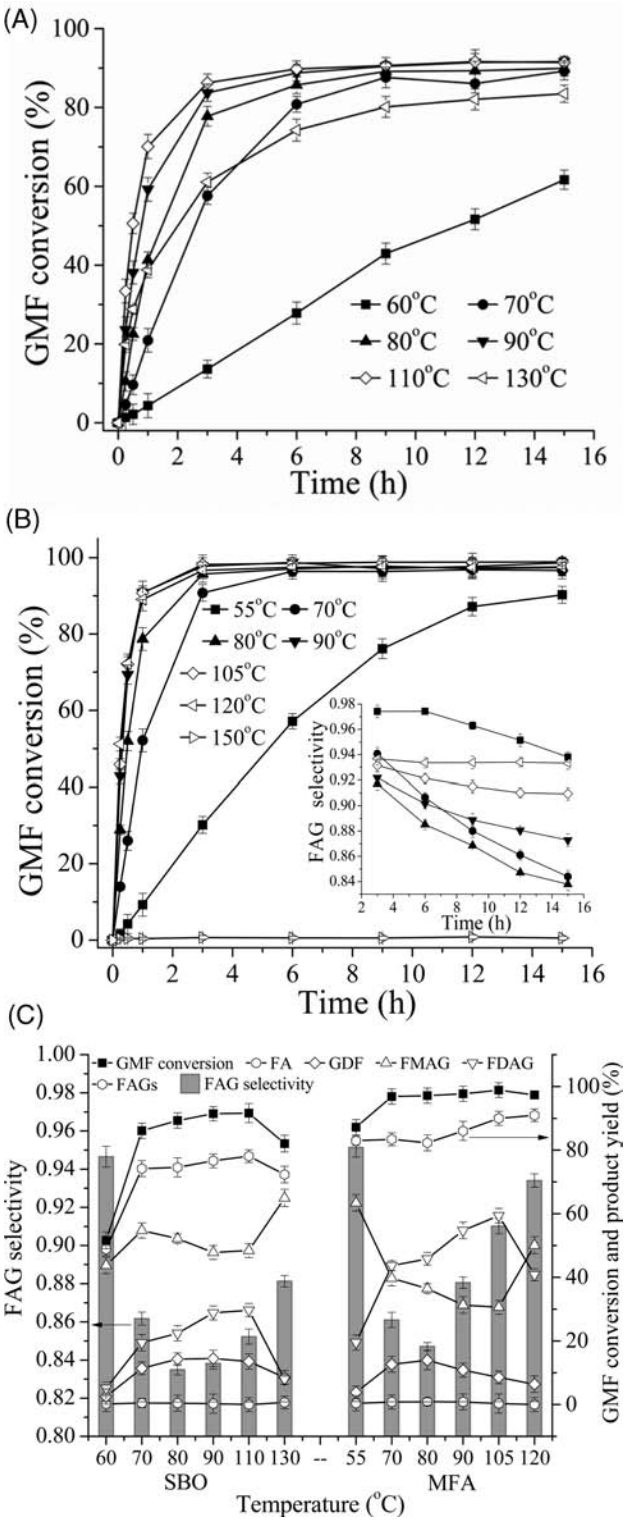

Figure 3. (A) Effect of temperature on the reaction of GMF with SBO in $[C_{12}mim]PF_6$. (B) Effect of temperature on the reaction of GMF with MFA in $[C_{10}mim]PF_6$. (C) Product yields (curve) and FAG selectivity (column) when SBO or MFA were used in ILs at different temperature (12 h). Reaction conditions: GMF/SBO (or MFA) = 1:2 (mol/mol), Novozym 435 concentration 45 mg/mL, GMF 1.50 mmol/mL, ILs 1 mL, 90 kPa.

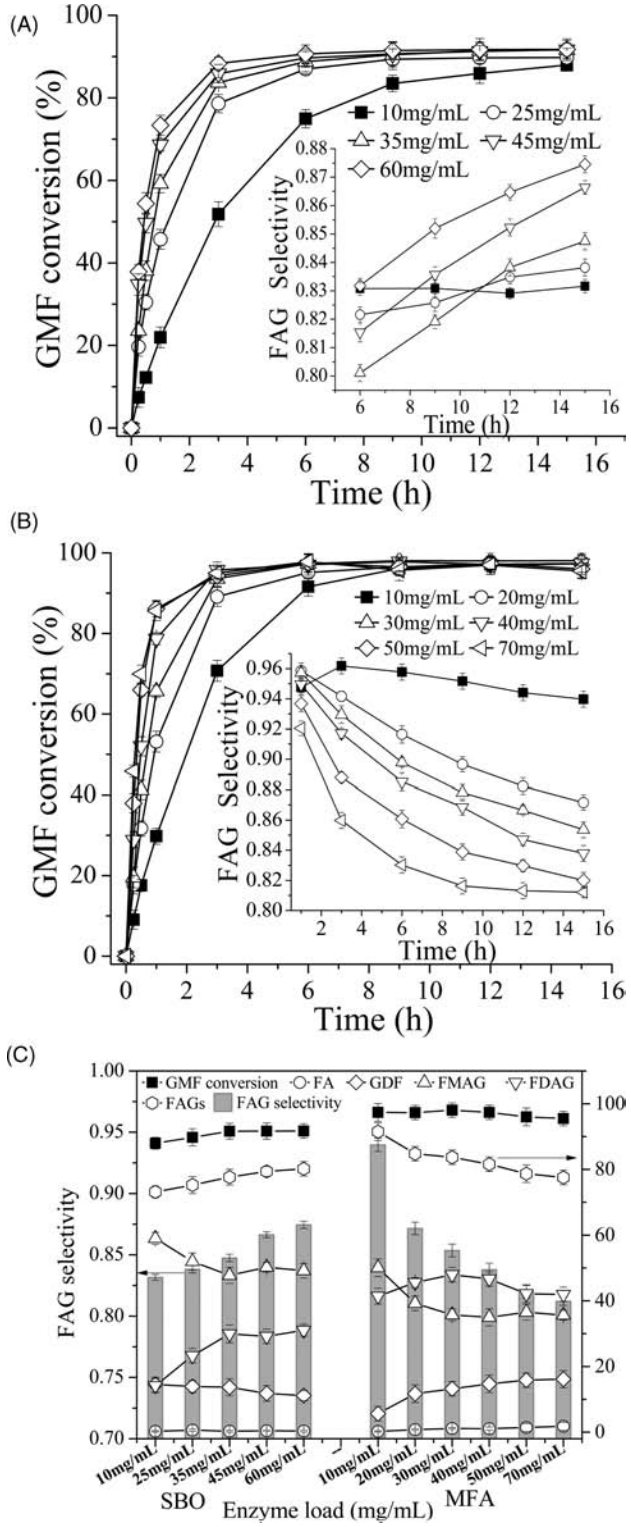

Figure 4. (A) Effect of enzyme concentration on the reaction of GMF with SBO in $[C_{12}mim]PF_6$. (B) Effect of enzyme concentration on the reaction of GMF with MFA in $[C_{10}mim]PF_6$. (C) Product yields (curve) and FAG selectivity (column) when SBO or MFA were used in ILs at different enzyme concentration (15 h). Reaction conditions: GMF/SBO (or MFA) = 1:2 (mol/mol), 80 °C, GMF 1.50 mmol/mL, ILs 1 mL, 90 kPa.

enzymatic transesterification of GMF with SBO. Using $[Emim]BF_4$, $[Bmim]BF_4$, and $[Hmim]BF_4$ as reaction media, GMF conversions were all <40% after 16 h; and using $[Mmim]TF_2N$, $[Emim]TF_2N$, and $[Bmim]TF_2N$ as reaction media, GMF conversions were ~60% at 16 h. These low reaction rates were attributed to shorter alkyl chains of $[Emim]BF_4$,

DOI: 10.1021/acs.jafc.5b03479
J. Agric. Food Chem. 2015, 63, 7261−7269

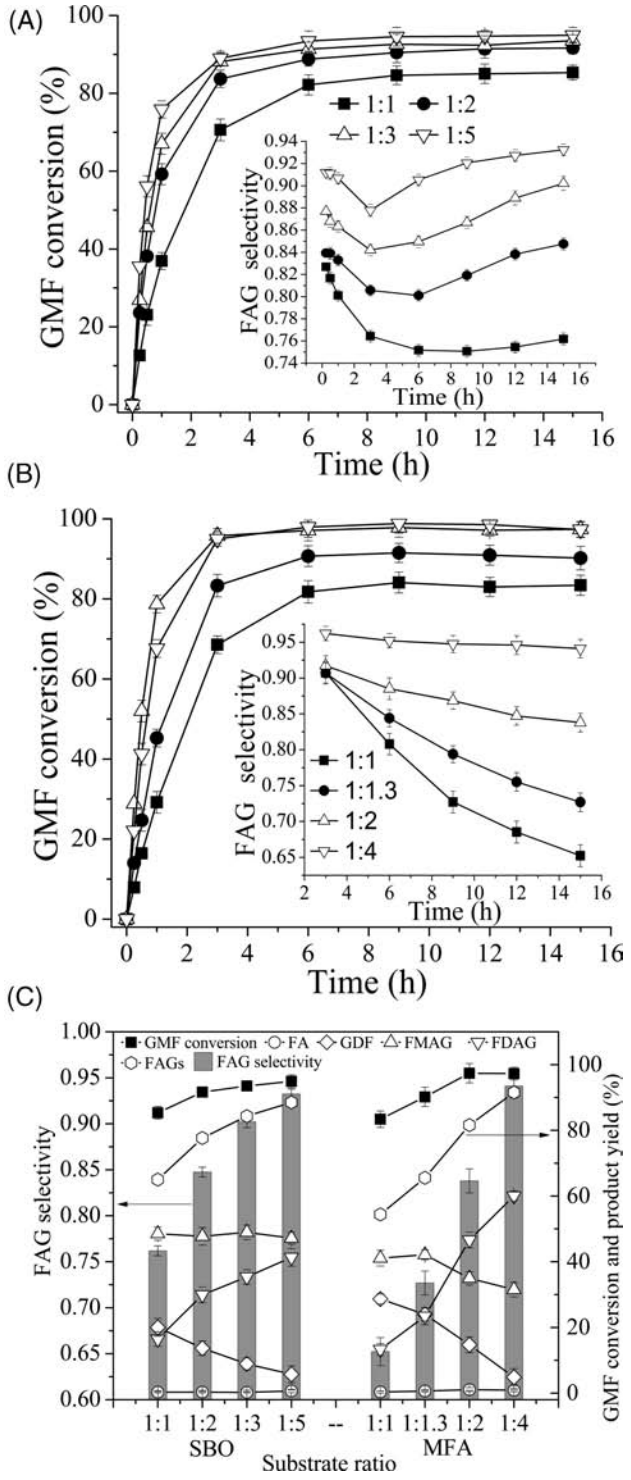

Figure 5. (A) Effect of substrate ratio (GMF/SBO, mol/mol) on the reaction of GMF with SBO in $[C_{12}mim]PF_6$. (B) Effect of substrate ratio (GMF/MFA, mol/mol) on the reaction of GMF with MFA in $[C_{10}mim]PF_6$. (C) Product yields (curve) and FAG selectivity (column) when SBO or MFA was used in ILs at different substrate ratio (15 h). Reaction conditions: Novozym 435 concentration 45 mg/mL, 80 °C, GMF 1.50 mmol/mL, ILs 1 mL, 90 kPa.

$[Bmim]BF_4$, $[Hmim]BF_4$, $[Mmim]TF_2N$, $[Emim]TF_2N$, and $[Bmim]TF_2N$ than that of $[C_{10}$-$C_{18}mim]PF_6$, which resulted in the loss of bound water of the enzyme in these hydrophilic ILs. Similar results that hydrophilic ILs decreased enzyme activity were also found in previous reports.[39,40] However, when the

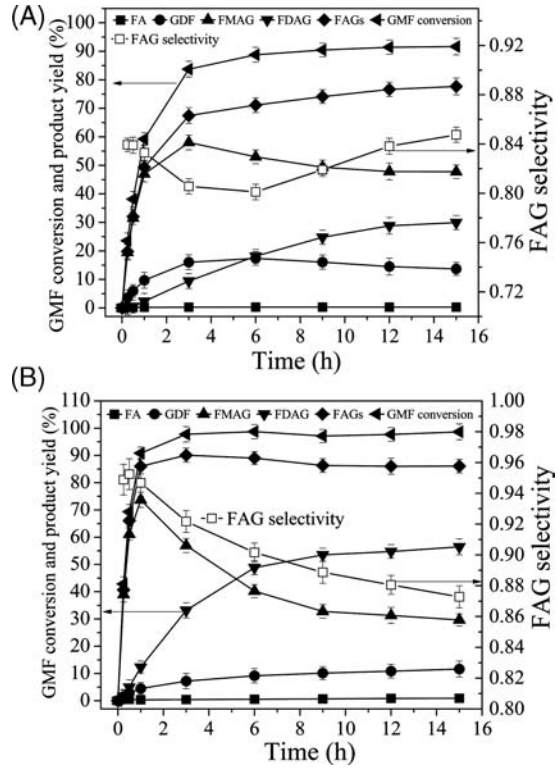

Figure 6. (A) Effect of reaction time on the transesterification of GMF with SBO in $[C_{12}mim]PF_6$. (B) Effect of reaction time on the esterification of GMF with MFA in $[C_{10}mim]PF_6$. Reaction conditions: GMF/SBO (or MFA) = 1:2 (mol/mol), Novozym 435 concentration 45 mg/mL, 80 °C, GMF 1.50 mmol/mL, ILs 1 mL, 90 kPa.

MFA was used as GMF acceptor in $[Emim]BF_4$, $[Bmim]BF_4$, $[Hmim]BF_4$, $[Mmim]TF_2N$, $[Emim]TF_2N$, and $[Bmim]TF_2N$ (Figure 2B), higher GMF conversions (97.0 ± 0.8%, 50.2 ± 2.2%, 83.8 ± 1.3%, 99.7 ± 0.2%, 97.4 ± 1.6%, and 99.5 ± 0.3%) were achieved at 16 h. These results can be explained by the fact that MFA has good compatibility with ILs and low steric hindrance of MFA can enhance the transfer rate of MFA to the glycerol of GMF (or FMAG) to form FMAG and FDAG.

Using PF_6^- based ILs as reaction media for the transesterification of GMF with SBO, GMF conversions increased with the increase of carbon chain number of ILs (Figure 2A). These results can be explained by the fact that, for those ILs with PF_6^-, with the increase of carbon chain number of ILs, the hydrophobicity of ILs increased, which resulted in better compatibility of SBO with ILs. However, when the carbon chain number of ILs increased up to >14, great mass transfer limitations between ILs and SBO were found, which may be ascribed to the great viscosity and high melting point of ILs. Similar results were also found in the reaction using the MFA as GMF acceptor, and the maximum GMF conversions (99.3 ± 0.5% after 16 h) were found in the esterification of GMF with MFA using $[C_{10}mim]PF_6$ as reaction medium. FAG selectivity showed similar change with GMF conversion using SBO (Figure 2C) and MFA (Figure 2D) as acyl donors. Compared with solvent-free system about FAG preparation, ILs can accelerate reaction rates, favor the FAG formation in the esterification of GMF with MFA, and show protective effect on the inactivation of enzyme at high temperature. ILs as reaction media instead of soybean oil[22] can make the transformation of the substrate molecule more economical and efficient. The control experiments, without lipase or IL, showed that GMF

DOI: 10.1021/acs.jafc.5b03479
J. Agric. Food Chem. 2015, 63, 7261−7269

Table 2. Response Surface Design and Results of Transesterification of GMF with SBO/MFA

treatment no.[a]	X_1, temp (°C)	X_2, enzyme load (mg/mL)	X_3, substrate ratio (mol/mol)	X_4, time (h)	GMF_{SBO} convn (%)	FAG_{-SBO} yield (%)	GMF_{MFA} convn (%)	FAG_{-MFA} yield (%)
1	0	0	1	−1	89.7 ± 2.0	76.1 ± 1.2	47.0 ± 0.8	45.7 ± 0.5
2	0	0	0	0	90.0 ± 2.1	78.7 ± 1.3	98.9 ± 0.4	92.9 ± 1.6
3	0	1	−1	0	81.0 ± 1.7	59.6 ± 0.9	83.4 ± 1.6	51.4 ± 2.1
4	0	−1	0	−1	60.0 ± 1.5	47.6 ± 1.0	19.5 ± 0.5	16.4 ± 1.0
5	1	−1	0	0	89.0 ± 2.0	75.9 ± 0.5	93.3 ± 1.3	91.1 ± 1.4
6	0	−1	0	1	89.0 ± 1.8	72.5 ± 1.4	95.8 ± 1.9	91.7 ± 1.7
7	1	0	0	−1	88.6 ± 1.3	72.0 ± 0.7	62.1 ± 1.5	58.4 ± 0.9
8	0	1	0	1	90.2 ± 2.1	80.0 ± 0.5	98.6 ± 1.1	89.9 ± 0.8
9	0	1	1	0	93.2 ± 2.3	83.8 ± 1.8	98.2 ± 1.0	94.6 ± 1.6
10	0	0	−1	1	84.6 ± 1.6	63.6 ± 1.0	84.0 ± 2.2	51.4 ± 1.0
11	−1	1	0	0	83.8 ± 1.4	75.0 ± 1.4	94.0 ± 1.8	89.9 ± 2.0
12	1	0	0	1	92.2 ± 2.2	83.2 ± 1.3	99.9 ± 0.1	94.4 ± 2.2
13	1	0	−1	0	85.8 ± 2.1	71.0 ± 0.8	97.1 ± 0.5	90.0 ± 1.8
14	0	0	0	0	95.1 ± 1.3	82.0 ± 2.1	93.3 ± 3.2	91.1 ± 1.7
15	1	1	0	0	93.3 ± 1.9	83.5 ± 1.6	97.9 ± 1.2	90.2 ± 2.3
16	−1	0	0	1	81.7 ± 1.3	74.5 ± 1.5	90.5 ± 1.5	86.0 ± 1.6
17	1	0	1	0	92.1 ± 1.8	83.2 ± 2.0	99.3 ± 0.3	96.4 ± 1.2
18	0	−1	−1	0	55.2 ± 0.9	43.9 ± 1.0	65.9 ± 2.3	61.7 ± 1.5
19	0	0	−1	−1	66.9 ± 1.4	47.2 ± 1.2	23.7 ± 2.2	22.6 ± 0.6
20	−1	−1	0	0	38.7 ± 1.2	35.7 ± 0.9	32.0 ± 1.9	31.3 ± 0.4
21	−1	0	−1	0	26.6 ± 0.8	24.8 ± 0.7	35.1 ± 1.7	34.1 ± 0.7
22	−1	0	1	0	70.8 ± 1.9	67.8 ± 1.9	90.5 ± 1.5	88.3 ± 1.9
23	0	0	0	0	95.3 ± 1.1	80.0 ± 1.8	94.1 ± 3.5	88.0 ± 1.2
24	−1	0	0	−1	21.1 ± 1.2	19.8 ± 0.5	7.2 ± 0.3	7.0 ± 0.2
25	0	1	0	−1	87.6 ± 2.1	71.0 ± 0.6	68.1 ± 2.5	65.3 ± 1.0
26	0	−1	1	0	90.6 ± 1.7	82.6 ± 1.3	93.3 ± 1.3	87.0 ± 1.4
27	0	0	0	0	90.5 ± 1.5	88.3 ± 1.7	98.7 ± 1.0	96.0 ± 1.1
28	0	0	0	0	89.1 ± 2.2	76.8 ± 1.2	99.0 ± 0.4	96.6 ± 1.0
29	0	0	1	1	94.4 ± 2.4	86.6 ± 2.1	98.7 ± 0.7	92.5 ± 0.8

[a]Numbers were run randomly.

conversions were all lower than 2%, which were mainly ascribed to the thermal decomposition of GMF.

Effect of Reaction Temperature. Figure 3A shows the effect of temperature (60−130 °C) on the transesterification of GMF with SBO in $[C_{12}mim]PF_6$. Reaction temperatures in the range of 70−110 °C resulted in high GMF conversion (91.7 ± 1.1% after 15 h, 90 °C), which could be attributed to high enzyme activity and low viscosity of reaction system. Similar effect of temperature on the viscosity of ILs can also be found in some previous reports.[32,41] However, when reaction temperature increased up to 130 °C, GMF conversion decreased to 83.5 ± 2.2% after 15 h, which may be ascribed to the inactivation of Novozym 435 at higher temperatures (≥110 °C). It is an interesting fact that immobilized Novozym 435 has activity at higher temperatures (90−130 °C), which may be attributed to the remarkably protective effect of ILs on the inactivation of enzyme at high temperature. Similar protective effect of ILs on the enzyme activity at high temperature can also be found in other previous reports.[42,43] When the MFA was used as acyl donor, the time to reach equilibrium was shortened to 3 h (≥80 °C), and high GMF conversions (98.7 ± 1.5% at 90 °C, 98.9 ± 1.0% at 105 °C after 15 h) were obtained (Figure 3B) in $[C_{10}mim]PF_6$, respectively, which could be attributed to the lower steric hindrance of MFA than that of SBO.

Figure 3C shows the effect of reaction temperature on GMF conversion, product yields (curve), and FAG selectivity (column) of the transesterification of GMF with SBO in $[C_{12}mim]PF_6$ or MFA in $[C_{10}mim]PF_6$. When SBO was used, the main product FMAG yield initially decreased to 47.8 ± 2.2% at 110 °C, and then increased to 65.0 ± 2.7% at 130 °C. However, FDAG yield initially increased to 29.7 ± 2.1% at 110 °C, and then decreased sharply to 7.9 ± 1.5% at 130 °C. These results indicated that high temperatures (<110 °C) can favor the FDAG formation (Figure 1B-ii).

When MFA was used as acyl donor, the FMAG yields initially decreased to 30.6 ± 2.2% at 105 °C, and then increased to 50.1 ± 2.7% at 120 °C. However, FDAG yields initially increased to 59.4 ± 2.3% at 105 °C, and then sharply decreased to 40.8 ± 1.9% at 120 °C (Figure 3C). FDAG yields using MFA as acyl donor were significantly higher than those of SBO, which could be ascribed to the lower steric hindrance of MFA than that of SBO.

To obtain good reaction rates and equilibrium yields without thermally deactivating the lipase in reuses, the temperature of the transesterification (or esterification) of GMF with SBO (or MFA) should be kept around 90 °C.

Effect of Enzyme Load. Figure 4A,B shows the effect of enzyme concentration on the transesterification of GMF with SBO in $[C_{12}mim]PF_6$ or MFA in $[C_{10}mim]PF_6$. The increase of the enzyme concentration can enhance reaction rate and shorten the time to reach equilibrium. However, GMF conversions almost maintained the same levels (~90% for SBO and ~98% for MFA) after 15 h among all tested enzyme concentrations. These results can be explained by the fact that the increase of enzyme concentration provides more active site of enzyme, however, excessive immobilized enzyme can result

DOI: 10.1021/acs.jafc.5b03479
J. Agric. Food Chem. 2015, 63, 7261−7269

in the aggregation of enzyme, which can lead to the low catalytic efficiency of enzyme. The maximum GMF conversion (91.7 ± 2.2%), using SBO as acyl donor, was obtained at 35 mg/mL, and using MFA as acyl donor, the maximum GMF conversion (98.1 ± 1.2%) was achieved at 30 mg/mL.

Figure 4C shows the effect of enzyme concentration on product yields (curve) and FAG selectivity (column) of the transesterification of GMF with SBO in $[C_{12}mim]PF_6$ and the esterification of GMF with MFA in $[C_{10}mim]PF_6$. When SBO was used as acyl donor, with the increase of enzyme concentration from 10 mg/mL to 60 mg/mL, FMAG yield decreased to ~50%; however, FDAG yield increased to ~30%. At different enzyme concentrations, when MFA was used as acyl donor, FDAG yields were almost higher than those of FMAG, and FAG selectivity decreased linearly with the increase of enzyme concentration, which were different from that of SBO as acyl donor (Figure 4C).

Effect of Substrate Ratio and Reaction Time. Figure 5A,B shows the effect of substrate ratio (GMF/SBO (or MFA), mol/mol) on the transesterification of GMF with SBO (or MFA) in $[C_{12}mim]PF_6$ (or $[C_{10}mim]PF_6$). The increase of acyl donor (SBO or MFA) concentration can enhance reaction rates and GMF conversions and shorten the time to reach equilibrium (Figure 5A,B). With the increase of acyl donor concentration, main product FAG yields and FAG selectivity all increased significantly (Figure 5C).

When SBO was used as acyl donor, FMAG yield initially increased and then decreased with the reaction progress; however, FDAG yield increased during the reaction (Figure 6A). These results indicated that FMAG as intermediate product were initially formed and then more acyl donors reacted with FMAG to form FDAG. Therefore, the transesterification mechanism of SBO with GMF can be explained as follows (Figure 1): GMF is initially bonded with a fatty acyl from SBO to form FMAG (Figure 1B-i); and then FMAG as an intermediate reacts with another fatty acyl to form FDAG (Figure 1B-ii). Meanwhile, feruloyl from GMF and FMAG can react with another GMF to form GDF (Figure 1B-iii); and then GDF reacts with fatty acyl to form FMAG (Figure 1B-iv). Figure 6B shows the esterification process of GMF with MFA. Similar reaction mechanism of the esterification of GMF with MFA can also be explained in Figure 1. Similar other reaction mechanisms can also be found in previous reports.[16,23]

Model Fitting. Models of factors and responses were performed by RSM to predict the highest possible GMF conversion and FAG yields. The results obtained for the models are listed in Table 2. The data were analyzed employing a multiple regression technique to evaluate the true relationship between the factors and responses. The analysis of variance (ANOVA) indicated that the quadratic regression models were all extremely significant ($P < 0.0001$) (Table 3), which suggested that these models were prominent and adequate to explain the actual relationship between the response and the significant variables, with satisfactory coefficients of determination ($R_1^2 = 0.9500$, $R_2^2 = 0.9482$, $R_3^2 = 0.9802$, $R_4^2 = 0.9461$). The values of *R*-squared indicated that these models are suitable to represent the relationships among the selected factors. As a result, the models for GMF conversions and FAG yields were successfully established. The following second-order models satisfactorily explained GMF conversion and FAG yields, and X_1, X_2, X_3, and X_4 are the coded variables as described in Table 2. Four quadratic regression models are given as follows:

Table 3. Analysis of Variance (ANOVA) for Quadratic Model for the GMF Conversions and FAG Yields

source	sum of squares	degrees of freedom	mean square	*F* value	*P* > *F*
		(1) GMF_{SBO} Conversion (%)			
model	10987.51	14	784.82	19.01	<0.0001
residual	578.1	14	41.29		
lack of fit	541.61	10	54.16	5.94	0.0504
pure error	36.48	4	9.12		
cor total	11565.6	28			
R^2 = 0.9500					
		(2) FAG_{-SBO} Yield (%)			
model	8892.17	14	635.16	18.31	<0.0001
residual	485.48	14	34.68		
lack of fit	449.6	10	44.96	5.01	0.0671
pure error	35.88	4	8.97		
cor total	9377.65	28			
R^2 = 0.9482					
		(3) GMF_{MFA} Conversion (%)			
model	22521.13	14	1608.65	49.47	<0.0001
residual	455.22	14	32.52		
lack of fit	422.10	10	42.21	5.1	0.0652
pure error	33.12	4	8.28		
cor total	22976.35	28			
R^2 = 0.9802					
		(4) FAG_{-MFA} Yield (%)			
model	20467.93	14	1461.99	17.54	<0.0001
residual	1166.81	14	83.34		
lack of fit	1089.22	10	108.92	5.62	0.0554
pure error	77.59	4	19.40		
cor total	21634.74	28			
R^2 = 0.9461					

$$GMF_{SBO}\ \text{conversion}\ (\%) = 91.92 + 18.18X_1 + 8.88X_2 + 10.87X_3 + 9.86X_4 - 14.92X_1^2 - 3.92X_2^2 - 6.53X_3^2 - 4.64X_4^2 - 10.2X_1X_2 - 9.46X_1X_3 - 14.26X_1X_4 - 5.82X_2X_3 - 6.58X_2X_4 - 3.24X_3X_4 \quad (1)$$

$$FAG_{-SBO}\ \text{yield}\ (\%) = 79.25 + 13.40X_1 + 7.88X_2 + 14.86X_3 + 10.84X_4 - 10.68X_1^2 - 3.83X_2^2 - 7.3X_3^2 - 5.54X_4^2 - 7.06X_1X_2 - 5.62X_1X_3 - 10.85X_1X_4 - 3.62X_2X_3 - 4.84X_2X_4 - 1.48X_3X_4 \quad (2)$$

$$GMF_{MFA}\ \text{conversion}\ (\%) = 96.81 + 16.69X_1 + 11.7X_2 + 11.5X_3 + 28.32X_4 - 9.99X_1^2 - 4.89X_2^2 - 7.86X_3^2 - 22.97X_4^2 - 14.36X_1X_2 - 13.32X_1X_3 - 11.39X_1X_4 - 3.15X_2X_3 - 11.47X_2X_4 - 2.15X_3X_4 \quad (3)$$

DOI: 10.1021/acs.jafc.5b03479
J. Agric. Food Chem. 2015, 63, 7261−7269

$$\begin{aligned} \mathrm{FAG}_{-\mathrm{MFA}}\ \text{yield}\ (\%) &= 99.14 + 15.08X_1 + 8.41X_2 + 16.43X_3 + 24.21X_4 \\ &\quad - 14.14X_1^2 - 11.95X_2^2 - 10.77X_3^2 - 3.42X_4^2 \\ &\quad - 14.14X_1X_2 - 11.95X_1X_3 - 10.77X_1X_4 + 3.42X_2X_3 \\ &\quad - 12.68X_2X_4 + 4.50X_3X_4 \end{aligned} \quad (4)$$

Optimum Conditions and Model Verification. Reaction conditions were optimized using RSM as follows: (1) for the transesterification of GMF with SBO in $[C_{12}mim]PF_6$, enzyme concentration 45 mg/mL, 90 °C, GMF/SBO 1:2.5 (mol/mol), and 11 h. Under these optimal conditions, GMF conversion and FAG yield were 94.3 ± 0.7% and 83.8 ± 1.0%, respectively; (2) for the esterification of GMF with MFA in $[C_{10}mim]PF_6$, enzyme concentration 20 mg/mL, 90 °C, GMF/MFA 1:2 (mol/mol), and 8 h. Under these optimal conditions, high GMF conversion (98.9 ± 0.9%) and FAG yield (88.9 ± 0.6%) were achieved, which are both higher than that of using SBO and the previous reports of using GMF to synthesize FAGs.[44] Furthermore, either SBO or MFA as acyl donor can remarkably improve the lipophilic FAG yields compared to previous reactions that using EF/FA/VF in shorter reaction time.[15−22]

In conclusion, FAGs, the lipophilic feruloyl structure lipids, were successfully synthesized by the enzymatic reaction of GMF with different acyl donors (SBO and MFA) in IL systems. For the esterification of GMF with MFA, higher FAG selectivity (0.90) was obtained; and for the transesterification of GMF with SBO, relative high FAG selectivity (0.89) was also obtained. The low reaction rate, using SBO as acyl donor, was attributed to the steric hindrance of SBO. Although, using MFA as acyl donor, GMF conversion (98.9 ± 0.9%) and FAG yield (88.9 ± 0.6%) were both higher than those (94.3 ± 0.7% and 83.8 ± 1.0%) of SBO, SBO is still a good choice for FAG preparation considering the price of raw materials and the more convenient use of SBO.

AUTHOR INFORMATION

Corresponding Author

*E-mail: sunshangde@hotmail.com. Tel/fax (086)371-67758022.

Notes

The authors declare no competing financial interest.

The authors gratefully acknowledge financial support from Program for Science & Technology Innovation Talents in Universities of Henan Province (15HASTIT030), and Funding Scheme for Young Teachers Cultivating Program in Henan University of Technology.

ABBREVIATIONS USED

SBO, soybean oil; MFA, mixed fatty acids; GMF, glyceryl monoferulate; GDF, glyceryl diferulate; FMAG, feruloylated monoacylglycerols; FDAG, feruloylated diacylglycerols; FAGs, feruloylated acylglycerols (FMAG + FDAG); EF, ethyl ferulate; FA, ferulic acid

REFERENCES

(1) D'Archivio, M.; Filesi, C.; Di Benedetto, R.; Gargiulo, R.; Giovannini, C.; Masella, R. Polyphenols, dietary sources and bioavailability. *Ann. Ist. Super. Sanita* **2007**, *43*, 348.

(2) Rechner, A. R.; Pannala, A. S.; Rice-Evans, C. A. Caffeic acid derivatives in artichoke extract are metabolised to phenolic acids in vivo. *Free Radical Res.* **2001**, *35*, 195−202.

(3) Ou, S.; Kwok, K. C. Ferulic acid: pharmaceutical functions, preparation and applications in foods. *J. Sci. Food Agric.* **2004**, *84*, 1261−1269.

(4) Mancuso, C.; Santangelo, R. Ferulic acid: pharmacological and toxicological aspects. *Food Chem. Toxicol.* **2014**, *65*, 185−195.

(5) Damasceno, S. S.; Santos, N. A.; Santos, I. M. G.; Souza, A. L.; Souza, A. G.; Queiroz, N. Caffeic and ferulic acids: An investigation of the effect of antioxidants on the stability of soybean biodiesel during storage. *Fuel* **2013**, *107*, 641−646.

(6) Saija, A.; Tomaino, A.; Trombetta, D.; De Pasquale, A.; Uccella, N.; Barbuzzi, T.; Paolino, D.; Bonina, F. In vitro and in vivo evaluation of caffeic and ferulic acids as topical photoprotective agents. *Int. J. Pharm.* **2000**, *199*, 39−47.

(7) Saija, A.; Tomaino, A.; Cascio, R. L.; Trombetta, D.; Proteggente, A.; De Pasquale, A.; Uccella, N.; Bonina, F. Ferulic and caffeic acids as potential protective agents against photooxidative skin damage. *J. Sci. Food Agric.* **1999**, *79*, 476−480.

(8) Chen, J. H.; Ho, C. T. Antioxidant activities of caffeic acid and its related hydroxycinnamic acid compounds. *J. Agric. Food Chem.* **1997**, *45*, 2374−2378.

(9) Son, S.; Lewis, B. A. Free radical scavenging and antioxidative activity of caffeic acid amide and ester analogues: structure-activity relationship. *J. Agric. Food Chem.* **2002**, *50*, 468−472.

(10) Cooper, R.; Gottlieb, H. E.; Lavie, D. New phenolic diglycerides from *Aegilops ovata*. *Phytochemistry* **1978**, *17*, 1673−1675.

(11) Graça, J.; Pereira, H. Suberin structure in potato periderm: glycerol, long-chain monomers, and glyceryl and feruloyl dimers. *J. Agric. Food Chem.* **2000**, *48*, 5476−5483.

(12) Compton, D. L.; Laszlo, J. A. Sunscreens from vegetable oil and plant phenols. US Patent, 6,346,236, Feb 12, 2002.

(13) Compton, D. L.; DeFilippi, L. J.; Grall, S. G.; Kinney, J. F.; Laszlo, J. A. Formulations with feruloyl glycerides and methods of preparation. US Patent, 7,744,856, Jun 29, 2010.

(14) Sun, S.; Zhu, S.; Bi, Y. Solvent-free enzymatic synthesis of feruloylated structured lipids by the transesterification of ethyl ferulate with castor oil. *Food Chem.* **2014**, *158*, 292−295.

(15) Xin, J.; Chen, L.; Zhang, Y.; Zhang, S.; Xia, C. Lipase-catalyzed transesterification of ethyl ferulate with triolein in solvent-free medium. *Food Bioprod. Process.* **2011**, *89*, 457−462.

(16) Laszlo, J. A.; Compton, D. L.; Eller, F. J.; Taylor, S. L.; Isbell, T. A. Packed-bed bioreactor synthesis of feruloylated monoacyl-and diacylglycerols: clean production of a "green" sunscreen. *Green Chem.* **2003**, *5*, 382−386.

(17) Sabally, K.; Karboune, S.; St-Louis, R.; Kermasha, S. Lipase-catalyzed transesterification of trilinolein or trilinolenin with selected phenolic acids. *J. Am. Oil Chem. Soc.* **2006**, *83*, 101−107.

(18) Yu, Y.; Zheng, Y.; Quan, J.; Wu, C.; Wang, Y.; Branford-White, C.; Zhu, L. Enzymatic synthesis of feruloylated lipids: comparison of the efficiency of vinyl ferulate and ethyl ferulate as substrates. *J. Am. Oil Chem. Soc.* **2010**, *87*, 1443−1449.

(19) Sun, S.; Zhou, W. Enhanced enzymatic preparation of lipophilic feruloylated lipids using distearin as feruloyl acceptors: optimization by response surface methodology. *J. Oleo Sci.* **2014**, *63*, 1011−1018.

(20) Laszlo, J. A.; Compton, D. L. Enzymatic glycerolysis and transesterification of vegetable oil for enhanced production of feruloylated glycerols. *J. Am. Oil Chem. Soc.* **2006**, *83*, 765−770.

(21) Sun, S.; Song, F.; Bi, Y.; Yang, G.; Liu, W. Solvent-free enzymatic transesterification of ethyl ferulate and monostearin: Optimized by response surface methodology. *J. Biotechnol.* **2013**, *164*, 340−345.

(22) Compton, D. L.; Laszlo, J. A.; Berhow, M. A. Lipase-catalyzed synthesis of ferulate esters. *J. Am. Oil Chem. Soc.* **2000**, *77*, 513−519.

(23) Sun, S.; Shan, L.; Liu, Y.; Jin, Q.; Wang, X.; Wang, Z. A novel, two consecutive enzyme synthesis of feruloylated monoacyl-and diacyl-glycerols in a solvent-free system. *Biotechnol. Lett.* **2007**, *29*, 1947−1950.

DOI: 10.1021/acs.jafc.5b03479
J. Agric. Food Chem. 2015, 63, 7261−7269

(24) Compton, D. Sunscreens based on vegetable oil. *Lipid Technol.* **2005**, *17*, 276.
(25) Compton, D. L.; Laszlo, J. A.; Evans, K. O. Antioxidant properties of feruloyl glycerol derivatives. *Ind. Crops Prod.* **2012**, *36*, 217−221.
(26) Laszlo, J. A.; Evans, K. O.; Vermillion, K. E.; Appell, M. Feruloyl dioleoylglycerol antioxidant capacity in phospholipid vesicles. *J. Agric. Food Chem.* **2010**, *58*, 5842−5850.
(27) Dobberstein, D.; Bunzel, M. Separation and detection of cell wall-bound ferulic acid dehydrodimers and dehydrotrimers in cereals and other plant materials by reversed phase high-performance liquid chromatography with ultraviolet detection. *J. Agric. Food Chem.* **2010**, *58*, 8927−8935.
(28) Sun, S.; Chen, X.; Bi, Y.; Chen, J.; Yang, G.; Liu, W. Functionalized ionic liquid-catalyzed 1-feruloyl-sn-glycerol synthesis. *J. Am. Oil Chem. Soc.* **2014**, *91*, 759−765.
(29) Sun, S.; Qin, F.; Bi, Y.; Chen, J.; Yang, G.; Liu, W. Enhanced transesterification of ethyl ferulate with glycerol for preparing glyceryl diferulate using a lipase in ionic liquids as reaction medium. *Biotechnol. Lett.* **2013**, *35*, 1449−1454.
(30) Sun, S.; Shan, L.; Jin, Q.; Liu, Y.; Wang, X. Solvent-free synthesis of glyceryl ferulate using a commercial microbial lipase. *Biotechnol. Lett.* **2007**, *29*, 945−949.
(31) Persson, M.; Bornscheuer, U. T. Increased stability of an esterase from *Bacillus stearothermophilu* in ionic liquids as compared to organic solvents. *J. Mol. Catal. B: Enzym.* **2003**, *22*, 21−27.
(32) Chiappe, C.; Pieraccini, D. Ionic liquids: solvent properties and organic reactivity. *J. Phys. Org. Chem.* **2005**, *18*, 275−297.
(33) De Diego, T.; Lozano, P.; Gmouh, S.; Vaultier, M.; Iborra, J. L. Understanding structure-stability relationships of *Candida antartica* Lipase B in ionic liquids. *Biomacromolecules* **2005**, *6*, 1457−1464.
(34) Ríos, A. P.; Hernández-Fernández, F. J.; Tomás-Alonso, F.; Gómez, D.; Víllora, G. Synthesis of esters in ionic liquids: the effect of vinyl esters and alcohols. *Process Biochem.* **2008**, *43*, 892−895.
(35) Lue, B.; Guo, Z.; Xu, X. Effect of room temperature ionic liquid structure on the enzymatic acylation of flavonoids. *Process Biochem.* **2010**, *45*, 1375−1382.
(36) Ab Rani, M. A.; Brant, A.; Crowhurst, L.; Dolan, A.; Lui, M.; Hassan, N. H.; Hallett, J. P.; Hunt, P. A.; Niedermeyer, H.; Perez-Arlandis, J. M.; Schrems, M.; Welton, T.; Wilding, R. Understanding the polarity of ionic liquids. *Phys. Chem. Chem. Phys.* **2011**, *13*, 16831−16840.
(37) Hu, Y.; Guo, Z.; Lue, B.; Xu, X. Enzymatic synthesis of esculin ester in ionic liquids buffered with organic solvents. *J. Agric. Food Chem.* **2009**, *57*, 3845−3852.
(38) Sun, S.; Chen, X.; Bi, Y.; Yang, G. Selective separation of mono glyceryl ferulate using water from an ionic liquid solution of enzymatic transesterification. *J. Am. Oil Chem. Soc.* **2014**, *91*, 1339−1345.
(39) Husum, T. L.; Jørgensen, C. T.; Christensen, M. W.; Kirk, O. Enzyme catalysed synthesis in ambient temperature ionic liquids. *Biocatal. Biotransform.* **2001**, *19*, 331−338.
(40) Bélafi-Bakó, K.; Dörmõ, N.; Ulbert, O.; Gubicza, L. Application of pervaporation for removal of water produced during enzymatic esterification in ionic liquids. *Desalination* **2002**, *149*, 267−268.
(41) Yang, Z.; Pan, W. Ionic liquids: Green solvents for nonaqueous biocatalysis. *Enzyme Microb. Technol.* **2005**, *37*, 19−28.
(42) Lozano, P.; Diego, T.; Carrié, D.; Vaultier, M.; Iborra, J. L. Lipase catalysis in ionic liquids and supercritical carbon dioxide at 150 °C. *Biotechnol. Prog.* **2003**, *19*, 380−382.
(43) Baker, S.; Mccleskey, T. M.; Pandey, S. K.; Baker, G. A. Fluorescence studies of protein thermostability in ionic liquids. *Chem. Commun.* **2004**, 940−941.
(44) Sun, S.; Shan, L.; Liu, Y.; Jin, Q.; Zhang, L.; Wang, X. Solvent-free enzymatic preparation of feruloylated monoacylglycerols optimized by response surface methodology. *J. Agric. Food Chem.* **2008**, *56*, 442−447.

DOI: 10.1021/acs.jafc.5b03479
J. Agric. Food Chem. 2015, 63, 7261−7269

verified by high-performance liquid chromatography (HPLC) analysis (Figure 1A).

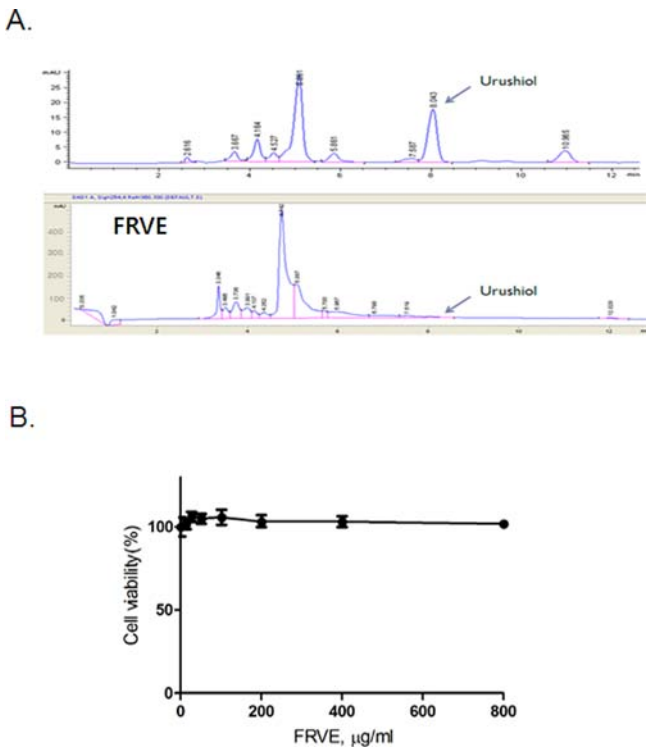

Figure 1. Determination of allergen-free FRVE by HPLC analysis. (A) Urushiol standard and FRVE. The solvent flow rate was 0.8 mL/min, and the ambient temperature was set at 30 °C. UV detection was at wavelengths of 280 nm. (B) Cytotoxicity of FRVE against HepG2 cells was determined by the MTT assay. Cells were treated with various concentrations of FRVE (0, 12.5, 25, 50, 100, 200, 400, and 800 μg/mL) for 24 h.

Cell Culture Assay. The human hepatoma cell line HepG2 was cultured in Dulbecco's modified Eagle's medium (DMEM) (Welgene, Korea) that contained 10% fetal bovine serum (FBS), 2 mM L-glutamine, and 100 units/mL penicillin and streptomycin. The cells were maintained at 37 °C in an incubator under 5% CO_2.

Cell Viability Assay. The cell viability assay was measured by a colorimetric 3-(4,5-dimethylthiazol-2-yl)-2,5-diphenyltetrazolium bromide (MTT) assay (Sigma, St, Louis, MO). Cells (1×10^4 cells/well) were exposed to various concentrations (0, 12.5, 25, 50, 100, 200, 400, and 800 μg/mL) of FRVE in 96-well sterile plastic plates (SPL Life Science, Korea). After 24 h of incubation, 50 μL of the MTT reagent (1 mg/mL) was added. After 1 h of incubation, cell counts were determined by an enzyme-linked immunosorbent assay (ELISA) reader (Tecan, Switzerland) at a wavelength of 570 nm. The final sample of cells included less than 0.1% dimethyl sulfoxide (DMSO).

HPLC Analysis (for Compounds of FRVE). To analyze the compounds of FRVE, compound standards were run on Hichrom HPLC columns (5 μm, 250 × 4.6 mm, Hichrom, Ltd.) using a high HPLC system (Agilent Technologies, Santa Clara, CA). The binary mobile phase consisted of 80% methanol/tetrahydrofuran solvent (99.8:0.2, v/v). The solvent flow rate was 0.3 mL/min, and the ambient temperature was set at 30 °C. Ultraviolet (UV) detection was at wavelengths of 254 and 280 nm (see Supplementary Figure 1 of the Supporting Information).

Oil-Red-O (ORO) Staining. Cells were cultured in 6-well plates at 1×10^5 cells/well in medium supplemented with 10% fetal bovine serum (FBS) and 1% antibiotics (penicillin and streptomycin, 100 units/mL). The cells were incubated in the absence of serum for 24 h and treated with FRVE (400 μg/mL) or fustin, fisetin, gallic acid, quercetin, and 1-hexacosanol individually (20 μM) with OA (200 μM, Sigma-Aldrich) for 24 h. The AMPK inhibitor compound C (10 μM, Sigma-Aldrich) was added to the HepG2 cell culture media.

The HepG2 cells were then washed twice with phosphate-buffered saline (PBS) buffer followed by 10 min of incubation with 0.3% ORO working solution. After the HepG2 cells were washed twice with PBS buffer, they were then dried. The plate was examined using a camera connected to an Axio observer a1 inverted microscope (Zeiss, Germany) at 200× magnification.

Western Blot Analysis. Cell lysates were prepared by adding 20 μL of RIPA lysis buffer (Cell Signaling) to the cell cultures. Proteins were separated on sodium dodecyl sulfate (SDS)−polyacrylamide gels and were electrotransferred to nitrocellulose blotting membranes (GE Healthcare Life Sciences, U.K.). The membranes were blocked in 3% nonfat dry milk and probed with primary antibodies for p-AMPK (Cell Signaling), AMPK (Cell Signaling), low-density lipoprotein receptor (LDLR, Abcam), PPARα (Cell Signaling), CPT-1 (Cell Signaling), fatty acid synthase (FAS, Cell Signaling), SREBP-1 (Santa Cruz), glycerol 3-phosphate acyltransferase (GPAT, Cell Signaling), and β-actin (Sigma). Detection of specific proteins was carried out using an enhanced chemiluminescence (ECL) assay (GE Healthcare Life Sciences, U.K.).

Reverse Transcriptase Polymerase Chain Reaction (RT-PCR). The total RNA of cells was isolated using Qiazol lysis reagent (Qiagen Sciences, Germantown, MD), according to the instructions of the manufacturer, and cDNA was synthesized from 1 μg of total RNA and subjected to PCR by the SuperScript One-Step RT-PCR kit (Invitrogen, Carlsbad, CA). The PCR conditions were 30 cycles of 95 °C for 30 s, the annealing temperature of the primer for 30 s, and 72 °C for 30 s. Primer sequences used were synthesized by Bioneer (Daejeon, Korea) with the following sequences: LDLR (forward, 5′-CAA TGT CTC ACC AAG CTC TG-3′; reverse, 5′-TCT GTC TCG AGG GGT AGC TG-3′), 3-hydroxy-3-methylglutaryl coenzyme A reductase (HMGCR) (forward, 5′-A GG TTC CAA TGG CAA CAA CAG AAG-3′; reverse, 5′-ATG CTC CTT GAA CAC CTA GCA TCT-3′), SREBP-1 (forward, 5′-GGA TTG CAC TTT CGA AGA CAT-3′; reverse, 5′-AGG ATG CTC AGT GGC ACT G-3′), GPAT (forward, 5′-GCC GCT TCT GTT TCT ACC AG-3′; reverse, 5′-ACA CCG GTT TCT GAC TTT GG-3′), and glyceraldehyde-3-phosphate dehydrogenase (GAPDH) (forward, 5′-TCA CCA TCT TCC AGG AGC GA-3′; reverse, 5′-CAC AAT GCC GAA GTG GTC GT-3′). RT-PCR products were run with loading star (DyneBio, South Korea) on a 1% agarose gel. Stained bands were visualized under UV light and photographed.

Measurement of Cellular Triglyceride (TG) and Total Cholesterol (TC). Cells were collected (less than 6×10^6 cells) and mixed with 1 mL of chloroform/methanol (2:1, v/v). The resulting mixture was shaken at room temperature (RT) for 20 min and then centrifuged (500*g*) for 10 min. The bottom layer was collected and resuspended for analysis of TG and TC. TGs were measured using an enzymatic method kit from Asan Pharm (AM157S-K, South Korea) in accordance with the instructions of the manufacturer. TC was measured using an enzymatic method kit from Asan Pharm (AM 202-K, South Korea) in accordance with the instructions of the manufacturer.

Statistical Analysis. The data were expressed as means ± standard deviation (SD) of three replications per experiment. Analysis of variance (ANOVA) was conducted to determine the significance of differences between groups. $p < 0.05$ was considered significant.

RESULTS

Confirmation for Detoxified FRVE. To confirm FRVE detoxification, HPLC analysis was performed. As shown in Figure 1A, urushiol (the standard urushiol peak was found at 5.091 min) was not detected in FRVE (Figure 1A).

FRVE Inhibits OA-Induced Cellular Lipid Accumulation in HepG2 Cells. The effect of FRVE on the viability of HepG2 cells is presented in Figure 1B. The cytotoxicity of FRVE was determined by the MTT assay. Cells were treated

DOI: 10.1021/acs.jafc.5b01954
J. Agric. Food Chem. 2015, 63, 7270−7276

with various concentrations of FRVE for 24 h. FRVE did not significantly affect HepG2 cell viability. OA reduced cell viability at concentrations of 0.5 mM and higher (data not shown). In this study, both OA (0.2 mM) and FRVE (200 and 400 μg/mL) were used at non-cytotoxic concentrations. To investigate whether FRVE could affect OA-induced cellular steatosis, ORO staining, a simple qualitative method to analyze the amount of lipid-droplet-stored TG in cells,[18] was performed in OA-induced HepG2 cells with FRVE. As shown in Figure 2A, OA increased the intracellular lipid content. The number and size of lipid droplets significantly reduced after FRVE and OA treatment in HepG2 cells compared to the OA group. Additionally, fat deposits decreased by 24.6 and 48.8% with 200 and 400 μg/mL FRVE treatments, respectively, compared to OA treatment alone (Figure 2A).

FRVE Inhibits OA-Induced Lipogenesis in HepG2 Cells. To assess the regulation of lipogenesis-related key factors by FRVE, the expression of AMPK, SREBP, FAS, GPAT, LDLR, and HMGCR in HepG2 cells was determined. The OA-treated group displayed increased protein expression levels of SREBP-1, FAS, and GPAT and increased mRNA levels of SREBP-1, GPAT, and HMGCR (panels B and C of Figure 2). In the presence of OA, FRVE treatment prevented the increased protein and mRNA expression levels of SREBP-1, FAS, GPAT, and HMGCR (panels B and C of Figure 2). LDLR and AMPK phosphorylation significantly increased after FRVE treatment in the presence of OA (panels B and C of Figure 2).

FRVE Promotes Hepatic Lipolysis in HepG2 Cells. To assess whether FRVE regulates fatty-acid-oxidation-related factors, the levels of PPARα and its target gene, CPT-1, in OA-treated HepG2 cells were determined by western blotting. As shown in Figure 2B, FRVE increased the expression of PPARα and CPT-1.

FRVE Inhibits OA-Induced Intracellular TG and TC Amounts. To evaluate the effect of OA treatment on TG accumulation in HepG2 cells, cellular TG and TC from cell lysates were measured. As shown in panels D and E of Figure 2, OA treatment in HepG2 cells increased the TG and TC contents compared to the control. The amount of TG decreased by 36.7 and 46.1% following 200 and 400 μg/mL FRVE treatment, respectively, compared to OA treatment alone (Figure 2D). The amount of TC decreased by 32.7 and 35.3% following 200 and 400 μg/mL FRVE treatment, respectively, compared to OA treatment alone (Figure 2E).

FRVE Inhibits OA-Induced Steatosis in the Liver through AMPK Activation. AMPK is a key sensor of hepatic lipid metabolism. As shown in Figure 2B, FRVE significantly increased the levels of phosphorylated AMPK as well as fatty-acid-oxidation-related factors and inhibited hepatic lipogenic factors. To assess the underlying mechanism of FRVE, the AMPK antagonist compound C was used in OA-induced HepG2 cells. AMPK activation was blocked by compound C; thus, FRVE-induced AMPK activation was suppressed by compound C (Figure 3B). In addition, compound C prevented FRVE-mediated inhibition of SREBP-1. ORO staining indicated the effect of compound C on lipid accumulation. As shown in Figure 3A, FRVE-mediated inhibition of lipid accumulation was blocked by compound C. Consistently, compound C blocked FRVE-mediated inhibition of intracellular TG and TC contents (panels C and D of Figure 3).

FRVE Contains Phenolics and Cosanols. To determine the active compounds in FRVE, the phenolic and cosanol

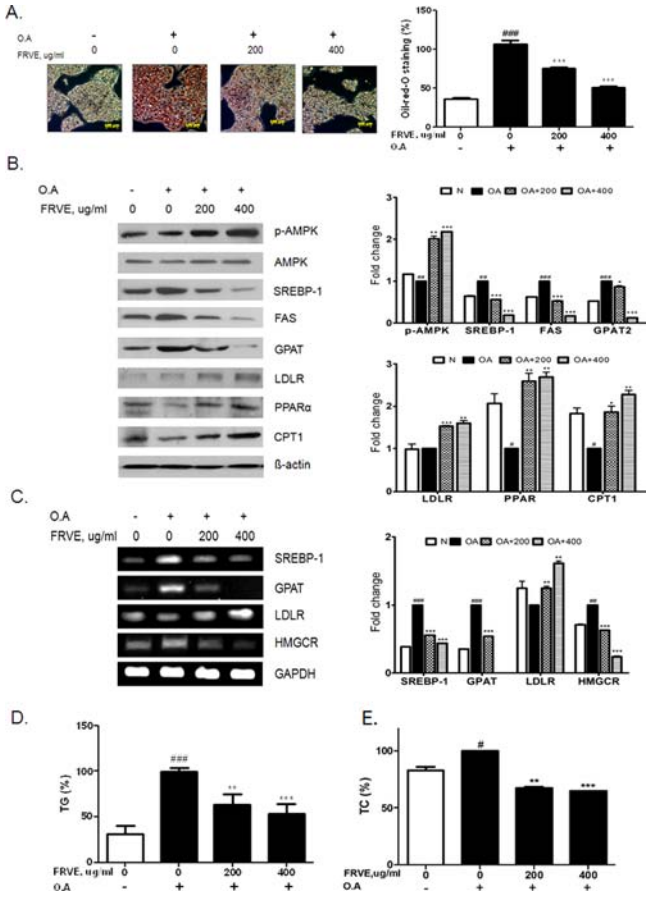

Figure 2. Effects of FRVE on cellular lipid accumulation and lipogenesis in OA-induced HepG2 cells. Cells were co-treated with OA (0.2 mM) and indicated concentrations of FRVE for 24 h. (A) Cells were stained with ORO as described in the Materials and Methods and then quantitatively analyzed. (###) $p < 0.001$ (in comparison to the non-OA-treated control). (***) $p < 0.001$ (in comparison to the OA-treated control). (B) Protein extracts were prepared and subjected to western blotting to determine the expression of AMPK, SREBP-1, FAS, GPAT, LDLR, PPARα, and CPT-1. Quantitative protein levels were shown. (#) $p < 0.05$, (##) $p < 0.01$, and (###) $p < 0.001$ (in comparison to the non-OA-treated control). (*) $p < 0.05$, (**) $p < 0.01$, and (***) $p < 0.001$ (in comparison to the OA-treated control). (C) Total RNA was isolated and subjected to RT-PCR for SREBP-1, GPAT, LDLR, and HMGCR levels. Quantitative mRNA levels are shown. (##) $p < 0.01$ and (###) $p < 0.001$ (in comparison to the non-OA-treated control). (**) $p < 0.01$ and (***) $p < 0.001$ (in comparison to the OA-treated control). (D) Total intracellular TGs were analyzed by an enzymatic colorimetric method. Data are represented as the mean ± SD for three experiments. (###) $p < 0.001$ (in comparison to the non-OA-treated control). (**) $p < 0.01$ and (***) $p < 0.001$ (in comparison to the OA-treated control). (E) Total intracellular TC was analyzed by an enzymatic colorimetric method. Data are represented as the mean ± SD for three experiments. (#) $p < 0.05$ (in comparison to the non-OA-treated control). (**) $p < 0.01$ and (***) $p < 0.001$ (in comparison to the OA-treated control).

contents were determined by HPLC. As shown in Figure 4A, FRVE comprised fustin (Fu, PubChem CID 5317435), gallic acid (G, PubChem CID 370), fisetin (Fi, PubChem CID 5281614), 1-hexacosanol (H, PubChem CID 68171), and quercetin (Q, PubChem CID 5280343). The peak showed that the retention times of fustin, gallic acid, fisetin, quercetin, and 1-hexacosanol were 8.447, 8.901, 9.254, 9.716, and 10.092 min,

DOI: 10.1021/acs.jafc.5b01954
J. Agric. Food Chem. 2015, 63, 7270−7276

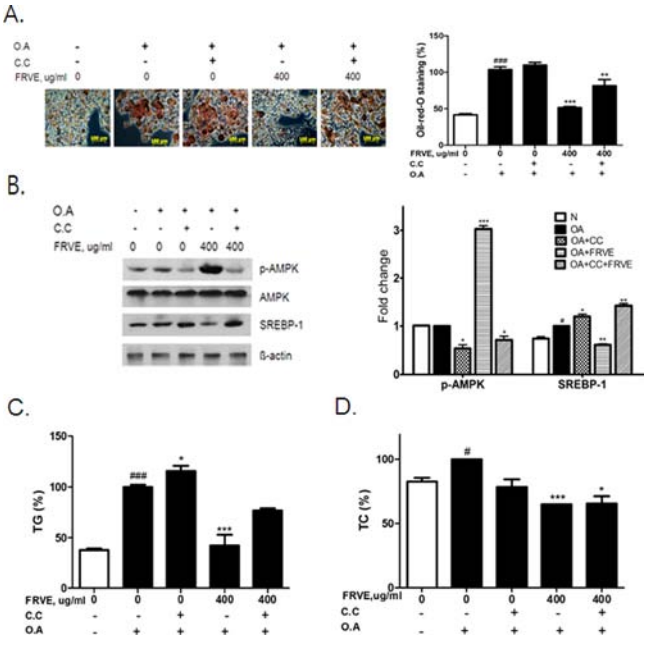

Figure 3. Inhibitory effects of FRVE on OA-induced steatosis through AMPK pathway activation. Cells were co-treated with OA and FRVE for 24 h. Cells were pretreated with compound C for 30 min before OA and FRVE treatment. (A) Cells were stained with ORO and analyzed by a spectrophotometer. Quantitative data of ORO staining are shown. (###) $p < 0.001$ (in comparison to the non-OA-treated control). (**) $p < 0.01$ and (***) $p < 0.001$ (in comparison to the OA-treated control). (B) Cell lysates were prepared and subjected to western blotting using p-AMPK, AMPK, and SREBP-1 antibodies. Quantitative western blotting data are shown. (#) $p < 0.05$ and (###) $p < 0.001$ (in comparison to the non-OA-treated control). (*) $p < 0.05$, (**) $p < 0.01$, and (***) $p < 0.001$ (in comparison to the OA-treated control). (C) Intracellular TG. (###) $p < 0.001$ (in comparison to the non-OA-treated control). (*) $p < 0.05$ and (***) $p < 0.001$ (in comparison to the OA-treated control). (D) Intracellular TC. (#) $p < 0.05$ (in comparison to the non-OA-treated control). (*) $p < 0.05$ and (***) $p < 0.001$ (in comparison to the OA-treated control).

respectively. FRVE comprised 55.0 ± 0.2 mg/g of fustin, 15.0 ± 2.8 mg/g of gallic acid, 0.33 ± 0.2 mg/g of fisetin, 5.0 ± 2.5 mg/g of 1-hexacosanol, and 1.7 ± 0.3 mg/g of quercetin (Table 1).

Table 1. Single Compounds in FRVE Organ Extracts

compound	mg/g
fustin	55.0 ± 0.2
gallic acid	15.0 ± 2.8
1-hexacosanol	5.0 ± 2.5
quercetin	1.7 ± 0.3
fisetin	0.33 ± 0.2

FRVE Components Fustin, Gallic Acid, Fisetin, Quercetin, and 1-Hexacosanol Activate AMPK. To identify the active compounds in FRVE, we tested the effects of 20 μM fustin, fisetin, gallic acid, quercetin, and 1-hexacosanol individually on p-AMPK and SREBP-1 expression, lipid accumulation, and TG content. All of these compounds (20 μM) reduced lipid accumulation in OA-induced HepG2 cells without affecting cell viability (Figure 5A). Consistently, all of these compounds also reduced the TG levels in OA-induced HepG2 cells (Figure 5C), and they increased the levels of phosphorylated AMPK and decreased SREBP-1 expression compared to the OA treatment group (Figure 5B).

DISCUSSION

In this study, we evaluated whether FRVE inhibits cellular lipid accumulation and promotes lipolysis through AMPK activation. AMPK activation induces fatty acid oxidation and inhibits lipogenesis in the liver through SREBP-1.[19] As a transcription factor, SREBP-1 directly activates the expression of more than 30 genes, such as FAS and GPAT. In addition, SREBP-1 is responsible for the synthesis and uptake of fatty acids, cholesterol, and TG.[20−22] The loss of SREBP-1 mediates fatty acid oxidation, thereby activating PPARα.[23,24] PPARα activation increases fatty acid oxidation and reduces cellular lipids.[25] Many extracts from various natural sources act as AMPK activators, including mulberry extract, which can inhibit hepatic steatosis by activating AMPK and inhibiting SREBP-

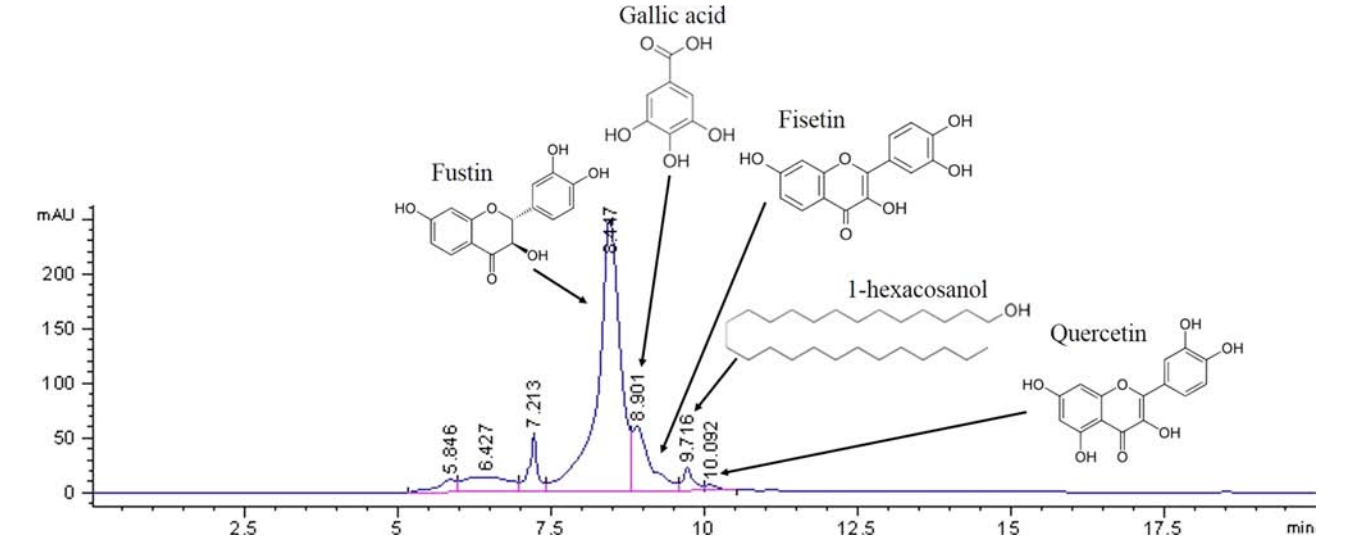

Figure 4. HPLC profile of FRVE.

DOI: 10.1021/acs.jafc.5b01954
J. Agric. Food Chem. 2015, 63, 7270−7276

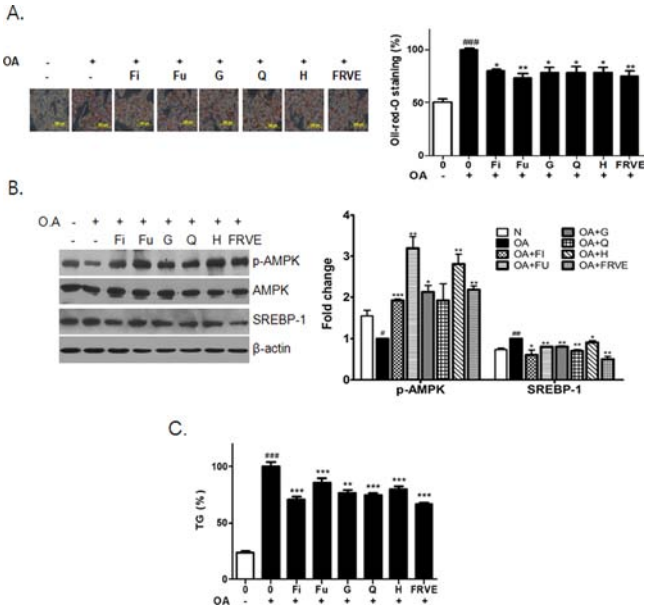

Figure 5. Effect of fustin, gallic acid, fisetin, quercetin, and 1-hexacosanol on AMPK activity. Cells were co-treated with OA and fustin, fisetin, gallic acid, quercetin, and 1-hexacosanol (each at 20 μM) for 24 h. (A) Cells were stained with ORO and analyzed using a spectrophotometer. Quantitative data of ORO staining is shown. (###) $p < 0.001$ (in comparison to the non-OA-treated control). (*) $p < 0.05$ and (**) $p < 0.01$ (in comparison to the OA-treated control). (B) Cell lysates were prepared and subjected to western blotting using p-AMPK, AMPK, and SREBP-1 antibodies. Quantitative western blotting data are shown. (#) $p < 0.05$ (in comparison to the non-OA-treated control). (*) $p < 0.05$, (**) $p < 0.01$, and (***) $p < 0.001$ (in comparison to the OA-treated control). (C) Intracellular TG. (###) $p < 0.001$ (in comparison to the non-OA-treated control). (**) $p < 0.01$ and (***) $p < 0.001$ (in comparison to the OA-treated control).

1.[26] Hepatic expression of LDLR is important for low-density lipoprotein (LDL) cholesterol homeostasis regulation, because LDLR is a membrane-spanning glycoprotein that plays a role in removing LDL from the blood.[27,28] Here, FRVE upregulated LDLR mRNA and protein levels in OA-induced HepG2 cells (panels B and C of Figure 2).

HMGCR catalyzes the rate-limiting step in cholesterol biosynthesis and modulates cholesterol levels.[29] HMGCR inhibitors reduce TG levels, and HMGCR knockdown reduces plasma LDL cholesterol levels.[30] Our results show that FRVE treatment decreases both TG (Figure 2D) and HMGCR levels (Figure 2C).

The HPLC data show that FRVE contains fustin, gallic acid, fisetin, quercetin, and 1-hexacosanol (Figure 4 and Table 1). In previous studies with *R. verniciflua* extracts, phenolic compounds, such as 2,4-dihydroxybenzoic acid, protocatechuic acid, caffeic acid, chlorogenic acid, *p*-coumaric acid, phloretin-20-*O*-glucoside, kaempferol-3-*O*-glucoside, quercetin, butein, and kaempferol, in addition to gallic acid, 2,6,30,40-tetrahydroxy-2-benzylcoumaran-3-one, fustin, fisetin, and sulfuretin have been reported.[31,32] Additionally, according to another previous report,[33] the phenolic compounds gallic acid, compound R, fustin, and fisetin were reported as the main components present in RV water extract (similar to FRVE).[33] Recently, it was reported that fisetin protects against hepatosteatosis in mice by inhibiting miR-378. However, fustin has never been reported to be associated with AMPK or NAFLD.

Gallic acid is a naturally abundant plant phenolic compound in vegetables and fruits.[34] It has been recently reported to ameliorate impaired glucose and lipid homeostasis in high-fat-diet-induced NAFLD mice.[35] Quercetin is a dietary flavonoid found in various fruits, teas, red wines, and many medicinal herbs.[36] Much is known about the role of quercetin in NAFLD. Quercetin upregulates the expression of PPARα and CPT-1, two regulators of fatty acid oxidation, and downregulates the expression of SREBP-1 in the liver.[37]

Hexacosanol is a major constituent of policosanol and occurs naturally in the epicuticular wax and plant cuticle of many plant species.[38] Policosanol is known to inhibit cholesterol synthesis through AMPK.[39] Hexacosanol from barley sprouts has recently been reported to activate AMPK in HepG2 cells.[40] From these data, we surmised that fustin, fisetin, quercetin, gallic acid, and 1-hexacosanol are the major contributors to the beneficial effects of FRVE. Therefore, these compounds were assessed for their effect on the phosphorylation of AMPK and SREBP-1 by western blotting and lipid accumulation using ORO staining. Five compounds were shown to increase AMPK phosphorylation and reduce fat accumulation in OA-induced HepG2 cells. Fustin, fisetin, gallic acid, quercetin, and 1-hexacosanol displayed decreased expression of SREBP-1. The fustin content was enriched in FRVE (5.5%), whereas quercetin (0.17%) or fisetin (0.33%) content was decreased in FRVE. A total of 400 μg of FRVE tested in this study contained 22 μg of fustin, 6 μg of gallic acid, 2 μg of 1-hexacosanol, 0.68 μg of quercetin, and 0.132 μg of fisetin. Tested 20 μM fustin (5.76 μg/mL) had a much lower content than the fustin content in FRVE, whereas tested 20 μM 1-hexacosanol (3 times higher content), quercetin (9 times higher content) and fisetin (43 times higher content) were much higher than the content of individual compounds in FRVE. Furthermore, fustin increased AMPK phosphorylation more than others. The fustin content correlated and predicted the potency of FRVE in an antihepatic lipogenic effect via AMPK upregulation.

There was no report on the antilipogenic activity of fustin in NAFLD. This study is the first to demonstrate the activity of fustin in NAFLD. Therefore, an improved study is required to further verify the antilipogenic effect of fustin in NAFLD in the near future.

■ ASSOCIATED CONTENT

Supporting Information

The Supporting Information is available free of charge on the ACS Publications website at DOI: 10.1021/acs.jafc.5b01954.

HPLC chromatogram of the standards (PDF)

■ AUTHOR INFORMATION

Corresponding Author

*Telephone: +82-02-964-2730. Fax: +82-02-964-1064. E-mail: strong79@khu.ac.kr.

Funding

This work was supported by the National Research Foundation of Korea (NRF) Grant 2007-0054931 funded by the Korean government [Ministry of Science, Information and Communications Technology (ICT) and Future Planning (MSIP)].

Notes

The authors declare no competing financial interest.

DOI: 10.1021/acs.jafc.5b01954
J. Agric. Food Chem. 2015, 63, 7270−7276

ABBREVIATIONS USED

FRVE, fermented *Rhus verniciflua* Stokes extract; SREBP-1, sterol regulatory element-binding protein-1; FAS, fatty acid synthase; GPAT, glycerol-3-phosphate acylrasferase; HMGCR, 3-hydroxy-3-methylglutaryl coenzyme A reductase; PPARα, peroxisome proliferator activated receptor α; CPT-1, carnitine palmitoyltransferase 1

REFERENCES

(1) Wong, R. J.; Ahmed, A. Obesity and non-alcoholic fatty liver disease: Disparate associations among Asian populations. *World J. Hepatol.* **2014**, *6*, 263.

(2) Iacono, A.; Raso, G. M.; Canani, R. B.; Calignano, A.; Meli, R. Probiotics as an emerging therapeutic strategy to treat NAFLD: focus on molecular and biochemical mechanisms. *J. Nutr. Biochem.* **2011**, *22*, 699−711.

(3) Farrell, G. C.; Larter, C. Z. Nonalcoholic fatty liver disease: from steatosis to cirrhosis. *Hepatology* **2006**, *43*, S99−S112.

(4) Assy, N.; Kaita, K.; Mymin, D.; Levy, C.; Rosser, B.; Minuk, G. Fatty infiltration of liver in hyperlipidemic patients. *Dig. Dis. Sci.* **2000**, *45*, 1929−1934.

(5) Assy, N.; Nasser, G.; Kamayse, I.; Nseir, W.; Beniashvili, Z.; Djibre, A.; Grosovski, M. Soft drink consumption linked with fatty liver in the absence of traditional risk factors. *Can. J. Gastroenterol.* **2008**, *22*, 811−816.

(6) Tu, Z.; Moss-Pierce, T.; Ford, P.; Jiang, A. Rosemary extract regulates glucose and lipid metabolism by activating AMPK and PPAR pathways in HepG2 cells. *FASEB J.* **2013**, *27*, 247.5.

(7) Pan, M. H.; Lai, C. S.; Tsai, M. L.; Ho, C. T. Chemoprevention of nonalcoholic fatty liver disease by dietary natural compounds. *Mol. Nutr. Food Res.* **2014**, *58*, 147−171.

(8) Horton, J. D.; Goldstein, J. L.; Brown, M. S. SREBPs: activators of the complete program of cholesterol and fatty acid synthesis in the liver. *J. Clin. Invest.* **2002**, *109*, 1125−1131.

(9) Foretz, M.; Carling, D.; Guichard, C.; Ferre, P.; Foufelle, F. AMP-activated protein kinase inhibits the glucose-activated expression of fatty acid synthase gene in rat hepatocytes. *J. Biol. Chem.* **1998**, *273*, 14767−14771.

(10) Long, Y. C.; Zierath, J. R. AMP-activated protein kinase signaling in metabolic regulation. *J. Clin. Invest.* **2006**, *116*, 1776−1783.

(11) Viollet, B.; Guigas, B.; Leclerc, J.; Hébrard, S.; Lantier, L.; Mounier, R.; Andreelli, F.; Foretz, M. AMP-activated protein kinase in the regulation of hepatic energy metabolism: from physiology to therapeutic perspectives. *Acta Physiol.* **2009**, *196*, 81−98.

(12) Lin, H. Z.; Yang, S. Q.; Chuckaree, C.; Kuhajda, F.; Ronnet, G.; Diehl, A. M. Metformin reverses fatty liver disease in obese, leptin-deficient mice. *Nat. Med.* **2000**, *6*, 998−1003.

(13) Tailleux, A.; Wouters, K.; Staels, B. Roles of PPARs in NAFLD: potential therapeutic targets. *Biochim. Biophys. Acta, Mol. Cell Biol. Lipids* **2012**, *1821*, 809−818.

(14) Svegliati-Baroni, G.; Candelaresi, C.; Saccomanno, S.; Ferretti, G.; Bachetti, T.; Marzioni, M.; De Minicis, S.; Nobili, L.; Salzano, R.; Omenetti, A. A model of insulin resistance and nonalcoholic steatohepatitis in rats: role of peroxisome proliferator-activated receptor-α and n-3 polyunsaturated fatty acid treatment on liver injury. *Am. J. Pathol.* **2006**, *169*, 846−860.

(15) Kim, J.; Kwon, Y.; Chun, W.; Kim, T.; Sun, J.; Yu, C.; Kim, M. Rhus verniciflua Stokes flavonoid extracts have anti-oxidant, anti-microbial and α-glucosidase inhibitory effect. *Food Chem.* **2010**, *120*, 539−543.

(16) Kim, K. H.; Moon, E.; Choi, S. U.; Kim, S. Y.; Lee, K. R. Polyphenols from the bark of Rhus verniciflua and their biological evaluation on antitumor and anti-inflammatory activities. *Phytochemistry* **2013**, *92*, 113−21.

(17) Kobayashi, S.; Ikeda, R.; Oyabu, H.; Tanaka, H.; Uyama, H. Artificial Urushi. Design, Synthesis, and Enzymatic Curing of New Urushiol Analogues. *Chem. Lett.* **2000**, 1214−1215.

(18) Mcvean, D. E.; Patrick, R. L.; Witchett, C. E. An Aqueous Oil Red O Fixative Stain for Histological Preparations. *Am. J. Clin. Pathol.* **1965**, *43*, 291−293.

(19) Zhou, G.; Myers, R.; Li, Y.; Chen, Y.; Shen, X.; Fenyk-Melody, J.; Wu, M.; Ventre, J.; Doebber, T.; Fujii, N.; Musi, N.; Hirshman, M. F.; Goodyear, L. J.; Moller, D. E. Role of AMP-activated protein kinase in mechanism of metformin action. *J. Clin. Invest.* **2001**, *108*, 1167−1174.

(20) Shimomura, I.; Bashmakov, Y.; Shimano, H.; Horton, J. D.; Goldstein, J. L.; Brown, M. S. Cholesterol feeding reduces nuclear forms of sterol regulatory element binding proteins in hamster liver. *Proc. Natl. Acad. Sci. U. S. A.* **1997**, *94*, 12354−12359.

(21) Edwards, P. A.; Tabor, D.; Kast, H. R.; Venkateswaran, A. Regulation of gene expression by SREBP and SCAP. *Biochim. Biophys. Acta, Mol. Cell Biol. Lipids* **2000**, *1529*, 103−113.

(22) Sakakura, Y.; Shimano, H.; Sone, H.; Takahashi, A.; Inoue, K.; Toyoshima, H.; Suzuki, S.; Yamada, N. Sterol regulatory element-binding proteins induce an entire pathway of cholesterol synthesis. *Biochem. Biophys. Res. Commun.* **2001**, *286*, 176−183.

(23) Browning, J. D.; Horton, J. D. Molecular mediators of hepatic steatosis and liver injury. *J. Clin. Invest.* **2004**, *114*, 147−152.

(24) Rosen, E. D.; Spiegelman, B. M. Molecular regulation of adipogenesis. *Annu. Rev. Cell Dev. Biol.* **2000**, *16*, 145−171.

(25) Banke, N. H.; Wende, A. R.; Leone, T. C.; O'Donnell, J. M.; Abel, E. D.; Kelly, D. P.; Lewandowski, E. D. Preferential oxidation of triacylglyceride-derived fatty acids in heart is augmented by the nuclear receptor PPARalpha. *Circ. Res.* **2010**, *107*, 233−241.

(26) Ou, T. T.; Hsu, M. J.; Chan, K. C.; Huang, C. N.; Ho, H. H.; Wang, C. J. Mulberry extract inhibits oleic acid-induced lipid accumulation via reduction of lipogenesis and promotion of hepatic lipid clearance. *J. Sci. Food Agric.* **2011**, *91*, 2740−2748.

(27) Sudhof, T. C.; Goldstein, J. L.; Brown, M. S.; Russell, D. W. The LDL receptor gene: a mosaic of exons shared with different proteins. *Science* **1985**, *228*, 815−822.

(28) Kovanen, P. T.; Bilheimer, D. W.; Goldstein, J. L.; Jaramillo, J. J.; Brown, M. S. Regulatory role for hepatic low density lipoprotein receptors in vivo in the dog. *Proc. Natl. Acad. Sci. U. S. A.* **1981**, *78*, 1194−1198.

(29) Nawrocki, J. W.; Weiss, S. R.; Davidson, M. H.; Sprecher, D. L.; Schwartz, S. L.; Lupien, P. J.; Jones, P. H.; Haber, H. E.; Black, D. M. Reduction of LDL cholesterol by 25% to 60% in patients with primary hypercholesterolemia by atorvastatin, a new HMG-CoA reductase inhibitor. *Arterioscler., Thromb., Vasc. Biol.* **1995**, *15*, 678−682.

(30) Kasim, S. E.; LeBoeuf, R. C.; Khilnani, S.; Tallapaka, L.; Dayananda, D.; Jen, K. L. Mechanisms of triglyceride-lowering effect of an HMG-CoA reductase inhibitor in a hypertriglyceridemic animal model, the Zucker obese rat. *J. Lipid Res.* **1992**, *33*, 1−7.

(31) Jung, C. H.; Jun, C.; Lee, S.; Park, C.; Cho, K.; Ko, S. Rhus verniciflua stokes extract: radical scavenging activities and protective effects on H2O2-induced cytotoxicity in macrophage RAW 264.7 cell lines. *Biol. Pharm. Bull.* **2006**, *29*, 1603−1607.

(32) Na, C. S.; Kim, H. C.; Choi, B. R.; Choo, D. W.; Choi, W. I.; Kim, J. B.; Park, Y. I.; Dong, M. S. Effect of flavonoid fractions extracted from Rhus verniciflua Stokes on the reproductive parameters in SD male rats. *J. Toxicol. Public Health* **2005**, *21*, 309−318.

(33) Kim, S.; Kim, S. H.; Kim, I. S.; Lee, D.; Dong, M.; Na, C.; Nhiem, N. X.; Yoo, H. H. Simultaneous determination of bioactive phenolic compounds in the stem extract of Rhus verniciflua stokes by high performance liquid chromatography. *Food Chem.* **2013**, *141*, 3813−3819.

(34) Robards, K. Strategies for the determination of bioactive phenols in plants, fruit and vegetables. *J. Chromatogr A* **2003**, *1000*, 657−691.

(35) Chao, J.; Huo, T.; Cheng, H.; Tsai, J.; Liao, J.; Lee, M.; Qin, X.; Hsieh, M.; Pao, L.; Peng, W. Gallic Acid Ameliorated Impaired Glucose and Lipid Homeostasis in High Fat Diet-Induced NAFLD Mice. *PLoS One* **2014**, *9*, e96969.

DOI: 10.1021/acs.jafc.5b01954
J. Agric. Food Chem. 2015, 63, 7270−7276

(36) Alrawaiq, N. S.; Abdullah, A. A Review of Flavonoid Quercetin: Metabolism, Bioactivity and Antioxidant Properties. *Int. J. PharmTech Res.* **2014**, *6*, 933−941.
(37) Poudyal, H.; Panchal, S. K.; Waanders, J.; Ward, L.; Brown, L. Lipid redistribution by α-linolenic acid-rich chia seed inhibits stearoyl-CoA desaturase-1 and induces cardiac and hepatic protection in diet-induced obese rats. *J. Nutr. Biochem.* **2012**, *23*, 153−162.
(38) BakerE.Chemistry and morphology of plant epicuticular waxes In *The Plant Cuticle*; Cutler, D. J., Alvin, K. L., Price, C. E., Eds.; Academic Press: London, U.K., 1982; pp 139−165.
(39) Singh, D. K.; Li, L.; Porter, T. D. Policosanol inhibits cholesterol synthesis in hepatoma cells by activation of AMP-kinase. *J. Pharmacol. Exp. Ther.* **2006**, *318*, 1020−1026.
(40) Seo, W. D.; Yuk, H. J.; Curtis-Long, M. J.; Jang, K. C.; Lee, J. H.; Han, S.; Kang, H. W.; Nam, M. H.; Lee, S.; Lee, J. H. Effect of the growth stage and cultivar on Policosanol profiles of barley sprouts and their adenosine 5′-monophosphate-activated protein kinase activation. *J. Agric. Food Chem.* **2013**, *61*, 1117−1123.

DOI: 10.1021/acs.jafc.5b01954
J. Agric. Food Chem. 2015, 63, 7270−7276

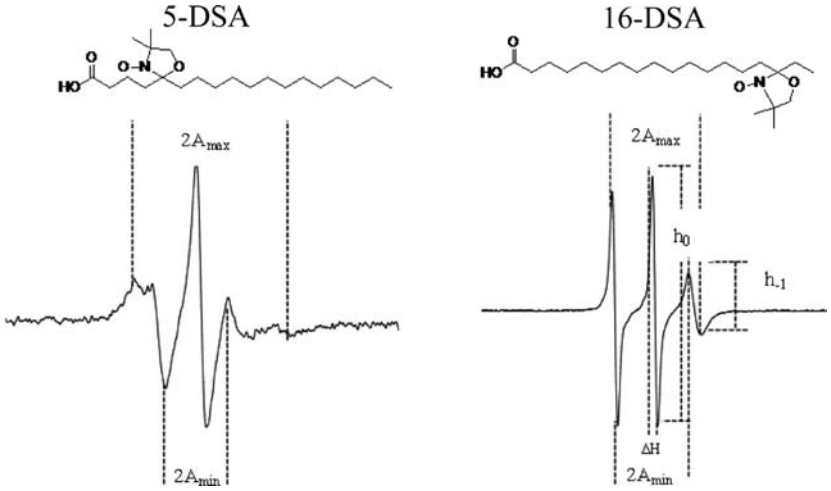

Figure 1. Molecular formula of the spin probes 5-DSA and 16-DSA and the corresponding EPR spectrum.

2.0 mg/mL) and packed coil structures (>2.0 mg/mL).[13] Such conformational change of chitosan molecules suggested that they could adopt various interaction mechanisms with liposomal membrane, besides the flat adsorption, which seemed of interest to further investigate.

On the other hand, it is important to point out that most of the suggestions aforementioned were based on a simple model membrane system composed of synthesized phospholipids. From a food industry perspective, egg yolk phosphatidylcholine (EYPC) is the commonly used lipid for the preparation of liposomes as it is a generally recognized as safe (GRAS) food ingredient. Previously, we explored a new type of liposome composed of mixed lipids including EYPC and a nonionic surfactant (Tween 80) as carriers for coenzyme Q_{10},[14,15] carotenoids,[16−19] and vitamin E.[20] The appropriate amount of Tween 80 in the formulation was demonstrated to impart high rigidity to the liposomal membrane, thus favoring the encapsulation efficiency and stability of liposomes. To the best of our knowledge, however, there is little information regarding the interaction of chitosan with mixed lipids-based liposomes.

Taken together, further detailed knowledge of such chitosan−lipid bilayer composite structure is required with special attention to the role of polymer conformation. Herein, the effect of chitosan conformation on the physical characterization of liposomes is thoroughly investigated including membrane dynamics, structure, hydrophobicity, surface morphology, and size. Several analysis techniques are introduced, including fluorescence anisotropy, electron paramagnetic resonance (EPR), transmission electron microscopy (TEM), atomic force microscopy (AFM), and dynamic light scattering (DLS). The aggregation and fusion behaviors of decorated liposomes as well as membrane permeability against surfactant are also evaluated.

MATERIALS AND METHODS

Materials. Egg yolk phospholipid (EYPC, composed of approximately 80% phosphatidylcholine, 5% lysophosphatidylcholine, and phosphatidic acid, and 15% fatty acids) was purchased from Chemical Reagent Plant of East China Normal University (Shanghai, China). Polyoxyethylene sorbitan monooleate (Tween 80) was obtained from China Medicine (Group) Shanghai Chemical Reagent Co. (Shanghai, China). Partially deacetylated chitosan (85%) with an average molecular weight of 200,000 was purchased from Ao Xing Biotechnology Co., Ltd. (Zhejiang, China). The fluorescent probe, 5(6)-carboxyfluorescein (CF), 1-[4-(trimethylammonio)phenyl]-6-phenyl-1,3,5-hexatriene (TMA-DPH, 98% purity), 8-anilino-1-naphthalenesulfonic acid (ANS, 98% purity), and the spin labels 5-doxyl-stearic acid (5-DSA) and 16-doxyl-stearic acid (16-DSA) were all purchased from Sigma Chemical Co. (St. Louis, MO, USA). All other reagents were of analytical grade.

Preparation of Chitosan-Decorated Liposomes. Bare liposomes were prepared according to our earlier method.[14] Briefly, phospholipid (6 g) and Tween 80 (4.32 g) were dissolved in 12 mL of warm ethanol at 55 °C. The ethanol solution was rapidly injected using a syringe as a pump into 120 mL of buffer solution (0.1 M acetic acid/0.01 M phosphate, 75 mM NaCl, pH 4.0) at 55 °C in a water bath under stirring at 700 rpm using an IKA RW 20 digital overhead stirrer (IKA Works Guangzhou). After agitation for 30 min, the liposomal system was transferred to a round-bottom flask attached to a rotary evaporator at 55 °C under reduced pressure to remove ethanol. The obtained liposomal suspension was then submitted to a probing sonication process in an ice bath for 10 min at 240 W with a sequence of 1 s of sonication and 1 s of rest using a sonicator (Sonics & Materials, Inc., 20 kHz). The final samples were filled into vials (the headspace of the vials was blanketed with nitrogen) and kept in a refrigerator (4 °C in the dark). The CF-entrapped liposomes were prepared in the same way expect for using 20 mM CF solution (0.1 M acetic acid/0.01 M phosphate, 75 mM NaCl, pH 4.0) instead of buffer solution. Unencapsulated CF was removed from the liposomal suspension by gel filtration through a Sephadex G-25 column.

The chitosan-decorated liposomes were prepared as follows: the chitosan was dissolved in the same buffer solution for bare liposomes and then added dropwise to bare liposomal suspension at equal volume at 1000 rpm for 30 min using an overhead stirrer at room temperature. The final concentration of chitosan was adjusted from 0.5 to 4 mg/mL. The phospholipid concentration was kept at 25 mg/mL. The final samples were filled into vials and stored at the same conditions as bare liposomes.

Liposomal Membrane Fluidity. A weighed amount of ANS probe was dissolved in ethanol solution, and the final concentration was 6×10^{-3} mol/L. The TMA-DPH stock solution was prepared by dissolving the TMA-DPH powder in tetrahydrofuran/water (1:1, v/v) and adjusting the concentration to 10^{-2} mol/L. The final TMA-DPH concentration was adjusted to 10^{-4} mol/L by PBS dilution before use. When the liposomal fluidity was determined, aliquots of probe solution were first mixed with bare liposomes in a 10 mL tube and incubated at 37 °C for 30 min. Then, different concentrations of chitosan in the same buffer were added dropwise to the incubated sample under stirring at 1000 rpm for 30 min. Note that before being mixed with liposomal samples, the ANS solution should be dried by

DOI: 10.1021/acs.jafc.5b01422
J. Agric. Food Chem. 2015, 63, 7277−7285

nitrogen to avoid the destructive effect of ethanol on liposomal membrane.

Microviscosity of liposomal membrane was measured at 25 °C using a fluorescence spectrometer (Hitachi F-7000, Japan) equipped with excitation and emission polarization filters. The excitation and emission wavelengths were, respectively, for ANS, λ_{ex} = 337 nm and λ_{em} = 480 nm and for TMA-DPH, λ_{ex} = 365 nm and λ_{em} = 430. The slit widths for both excitation and emission were 5 nm. The fluorescence intensities were measured according to our previous study.[19] The microviscosity (η) was calculated by fluorescence polarization (P) according to the equation[21]

$$\eta = 2P/(0.46 - P)$$

$$P = (I_{0,0} - GI_{0,90})/(I_{0,0} + GI_{0,90}),\ G = I_{90,0}/I_{90,90}$$

where $I_{0,0}$ and $I_{0,90}$ are the fluorescence intensities of the emitted light polarized parallel and vertical to the exciting light, respectively, and G is the grating correction coefficient.[22]

Electron Paramagnetic Resonance. The EPR technique was applied to monitor the molecular dynamics of lipids by observing the changes in the spin tropic movement of an unpaired electron. EPR measurements were performed using a Bruker EMX spectrometer (Bruker, Rheinstetten, Germany) at the X-band (9 GHz). The spectra were recorded at a microwave power of 20 mW with sweep width 120 G, center field 3511 G, and 20 s sweep time. All measurements were performed in triplicate at room temperature. In the present study, 5-DSA and 16-DSA were used as spin markers. These compounds consist of a radical group and a hydrocarbonated chain (stearic acid), which acts as a radical support (Figure 1). The radical in the 5- or 16-position of the alkyl chain will determine local motional profiles in the two main regions of the lipid bilayer, near the polar headgroup (5-DSA) or at the end of the hydrophobic chain (16-DSA). A weighed amount of 5-DSA or 16-DSA was dissolved in ethanol solution, with the final concentration adjusted to 1.0 or 0.9 mol/L, respectively. One milliliter of spin probe solution was added into a 10 mL tube followed by nitrogen dryness to remove the ethanol solution. An aliquot of 2.5 mL of bare liposomes was added into the tube and incubated at 25 °C for 30 min. Then, the chitosan solution was added dropwise to the incubated sample under stirring for 30 min.

Line widths $2A_{max}$, $2A_{min}$, and ΔH, in gauss (G), and heights of the high-field and midfield lines, h_{-1} and h_0, respectively, were obtained from the first derivative of each absorption spectrum. Spectral parameters used to study the location of spin labels in liposomal membrane are shown in Figure 1.

The order parameter (S) reflects the segmental order parameter of the segment to which the nitroxide fragment is attached.[23] It can be obtained from the conventional EPR spectra and calculated as $S = 0.5407 \times (A_{max} - A_{min})/a_0$, where $a_0 = (A_{max} + 2A_{min})/3$. The order parameter S is equal to zero for the membrane in total disorder. When it equals 1, the membrane has a crystal structure.[24]

The EPR spectrum of 16-DSA incorporated into the lipid bilayer reflects an isotropic motion of the acyl chain. In this case, rotational correlation time (τ, ns), assuming isotropic rotational diffusion of 16-DSA, can be used to measure the motion of the phospholipid acyl chains near the hydrophobic end.[25] An increase in τ indicates a decrease of membrane fluidity. It can be calculated from the following equation:

$$\tau = 6.5 \times 10^{-10} \times \Delta H \times \left(\sqrt{\frac{h_0}{h - 1}} - 1 \right)$$

Transmission Electron Microscopy. TEM micrographs were performed on a Hitachi-7650 at an accelerating voltage of 200 kV. The samples (bare liposomes and chitosan-decorated liposomes) were prepared as described above. An aqueous suspension of the samples was deposited upon a carbon-coated copper grid, followed by air-drying for 1 min. Then, the sample was instantly stained with 2 wt % phosphotungstic acid for 15 s.

Atomic Force Microscopy. AFM imaging was carried out using a commercial AFM (Dimension Icon, Bruker Co., Santa Barbara, CA, USA). The ScanAsyst mode was applied using silicon tip (TESP, Bruker, nominal frequency of 320 kHz, nominal spring constant of 42 N/m) with a scan resolution of 512 samples per line. Mica sheets were freshly cleaved to obtain a flat and uniform surface and were used as the substrate for AFM observations. Just before the analysis, the liposomal samples were diluted in water to obtain a less sticky fluid. An aliquot of 1 μL of liposome suspension was deposited on the mica surface and incubated for 30 min at room temperature. Afterward, samples were carefully washed with ultrapure water to eliminate salts and nonadsorbed vesicles and dried for 24 h at room temperature. Height mode images are acquired simultaneously at a fixed scan rate (0.997 Hz) with a resolution of 512 × 512 pixels in the dimension of 5 μm × 5 μm. Processing of images and analysis was carried out using NanoScope software (Digital Instruments, version V614r1). All height images are presented after the zero-order two-dimensional flattening.

Particle Size Distribution. Size measurements were performed at 25 ± 0.1 °C using a commercial zeta-sizer (Nano-ZS90, Malvern Instruments Ltd., Worcestershire, UK) with a He/Ne laser (λ = 633 nm) and scattering angle of 90°. To evaluate the aggregation and fusion of particles, the liposomal sample was heated at 37 °C for 5 h. After heat treatment, 2 mL of liposomal dispersion was transferred into the polystyrene cuvette for size determination, and then the particle size distribution was recorded by DLS. The measurements were repeated three times.

5(6)-Carboxyfluorescein Release Study. It is generally assumed that the fluorescence emission of CF is quenched to a high extent when the molecules are encapsulated in the interior aqueous compartments of liposomes at high concentration.[26] Upon release of CF from liposomes to the bulk aqueous phase, the fluorescence intensity would increase greatly. Therefore, the release of CF was taken as a measure of the membrane permeability after the incubation of liposomes with chitosan. Briefly, an aliquot of chitosan solution (1 mL) at different concentrations was added into 1 mL of liposomal suspension. At proper time intervals, 10 μL of sample was withdrawn and diluted with 2 mL of tris buffer (50 mM, pH 7.5). The fluorescence intensity of the samples was then measured at 25 °C with a spectrofluorimeter (Hitachi F-7000, Japan) with excitation at 488 nm and emission at 520 nm. The percentage of CF release from liposomes was calculated from the equation % release = $100 \times (F_t - F_0)/(F_\infty - F_0)$, where F_0 and F_t are the fluorescence intensities of the liposome samples before and after incubation with chitosan for the time period t and F_∞ is the total flurescence intensity after liposome lysis with 10% Triton X-100. To evaluate the stability of decorated liposomes against surfactant Triton X-100, 100 μL of 10% Triton X-100 solution was added to the liposomal sample (1 mL). The CF fluorescence was immediately monitored every second by spectrofluorimeter.

Statistical Analysis. Data are presented as a mean value with its standard deviation indicated (mean ± SD). All experiments were carried out in triplicate using freshly prepared samples.

RESULTS AND DISCUSSION

Fluidity of Liposomal Membrane. The fluidity of a liposomal membrane quantitatively characterizes the mobility and molecular rotation rate of lipid.[27] Lower membrane fluidity represents a higher structural order. It is well-known that ANS and TMA-DPH serve as markers for the molecular movement on the exterior membrane surface[28] and superficial region including the surface and glycerol side-chain region,[29] respectively. The relative microviscosity η/η_0 as a function of chitosan shows that the influence of chitosan binding was more pronounced on the fluidity in membrane surface than in the glycerol side-chain region (Figure 2). As the chitosan concentration increased from 0.25 to 1.5 mg/mL, microviscosity in membrane surface region was considerably increased, but remained virtually unchanged in the superficial region. Apparently, chitosan chains mainly adsorbed to the membrane surface and restricted the motion of the polar headgroup. Notably, restriction was stronger in the case of

DOI: 10.1021/acs.jafc.5b01422
J. Agric. Food Chem. 2015, 63, 7277−7285

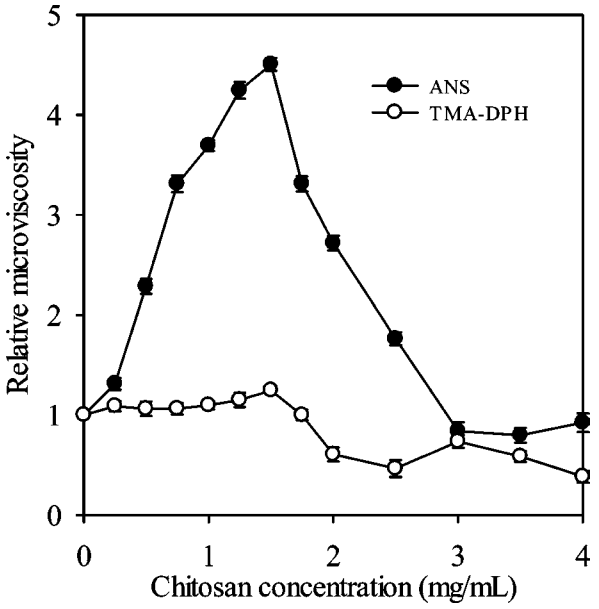

Figure 2. Relative microviscosity η/η_0 in liposomes for ANS and TMA-DPH as a function of decorated chitosan concentration. η_0 refers to the calculated microviscosity in bare liposomes, and η refers to the microviscosity in chitosan-decorated liposomes. Each point represents the mean value ± standard deviation (n = 3).

crimped chains. Considering the appearance of hydrophobic interaction accompanied by crimped chains, we speculated that besides electrostatic attraction, a weak hydrophobic force also contributed to the stabilizing effect on liposomal membrane. This hypothesis was supported by earlier research which concluded that the involvement of hydrophobic interaction could promote the physical adsorption and deposition of chitosan on membranes.[11] However, when the concentration was >1.5 mg/mL, η/η_0 values were decreased greatly surrounding ANS but only slightly surrounding TMA-DPH. This indicated that the presence of coils not only increased the fluidity of membrane surface but also somewhat disturbed the superficial region. The destabilization of chitosan coils might be correlated with the enhancement of hydrophobic interaction and, consequently, different adsorption patterns are expected instead of flat adsorption.

Motion of Alkyl Chains. EPR is a useful technique for determining the fluidity and structural changes of the lipid bilayers of liposomes. Figure 3 reveals that decoration of chitosan chains (<1.5 mg/mL) enhanced the order in the polar headgroup (at the 5-DSA position) and in the center of the bilayer (16-DSA position). This result was consistent with the Raman spectra analysis in relation to the *gauche* conformation change in the choline groups and lateral packing enhancement of the lipid chains.[19] However, the presence of chitosan coils (2.0−4.0 mg/mL) reduced the order of both regions. Combined with the high fluidizing properties, it was believed that the chitosan coils exerted a disturbing effect across the liposomal membrane. As evidenced previously, the zeta potential values were practically constant above the decorated concentration of 2 mg/mL.[13] Besides, the hydrophobic character along the chitosan chains became stronger, accompanied by the formation of chitosan coils. Therefore, it was concluded that the hydrophobic interaction prevailed in the formation of chitosan coil−liposome composites. Wydro's group[30] has also demonstrated that strong hydrophobic

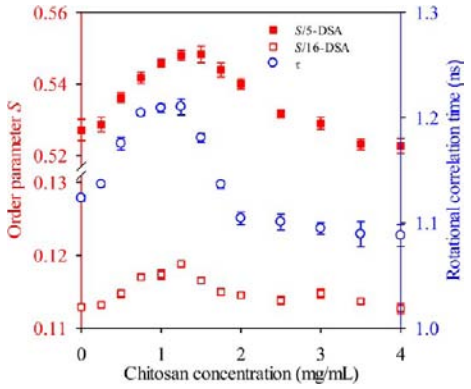

Figure 3. Order parameter S of spin probes and rotational correlation time of 16-DSA measured as a function of decorated chitosan concentration. Each point represents the mean value ± standard deviation (n = 3).

interaction between the phospholipid tails and chitosan allowed chitosan to come up to the monolayer and fill in the empty space. With these points taken into consideration, it was very likely that chitosan coils penetrated into the lipid hydrophobic core by hydrophobic interaction. On the other hand, it was noted that the disturbing effect of chitosan on the bilayer center was less pronounced than on membrane surface. This indicated that chitosan coils shallowly embedded into the one leaflet of the membrane.

Figure 3 also shows that the correlation time of 16-DSA free radical moiety increased from 0.25 to 1.5 mg/mL, whereas beyond this range, it was considerably decreased. This indicated that the segmental motion of the alkyl chains was restricted by the binding of chitosan chains, whereas chitosan coils failed to restrict the motion of the alkyl chains. The fluidizing property of chitosan deduced from correlation time was well in accordance with the results of membrane fluidity. On the basis of the analysis of membrane fluidity and structure, it was believed that besides providing a physical barrier, chitosan chains also exerted a rigidifying effect on the lipid membrane. Through modifying the membrane fluidity and ordering state, chitosan could mediate the permeation of foreign molecules into the membrane, thereby exhibiting a stabilizing role in liposome. These advantages of chitosan contribute to the development of composite phospholipid−chitosan vesicles (chitosomes) as new structures for the encapsulation of drugs and nutraceuticals.

Membrane Hydrophobicity. The isotropic hyperfine coupling constant a_0 of 5-DSA and 16-DSA was measured to determine the hydrophobicity of the polar headgroup region of the membrane and hydrophobic core, respectively. A decrease of the a value indicates an increase of hydrophobicity at the spin label position.[31] The hydrophobicity of the membrane headgroup region did not vary when the chitosan concentration was <0.5 mg/mL, whereas it was greatly increased in the range of 0.75−1.5 mg/mL (Figure 4). Apparently, the coated layer of chitosan chains can effectively increase the activation energy for polar small molecules to get across the membrane. Furthermore, the thicker the coated layer formed by the crimped chains, the higher was the physical barrier against the penetration of polar molecules. Another reason for the high hydrophobicity was that the decoration of crimped chains rigidified the organization of phospholipids at the polar headgroup and decreased the membrane permeability. These

DOI: 10.1021/acs.jafc.5b01422
J. Agric. Food Chem. 2015, 63, 7277−7285

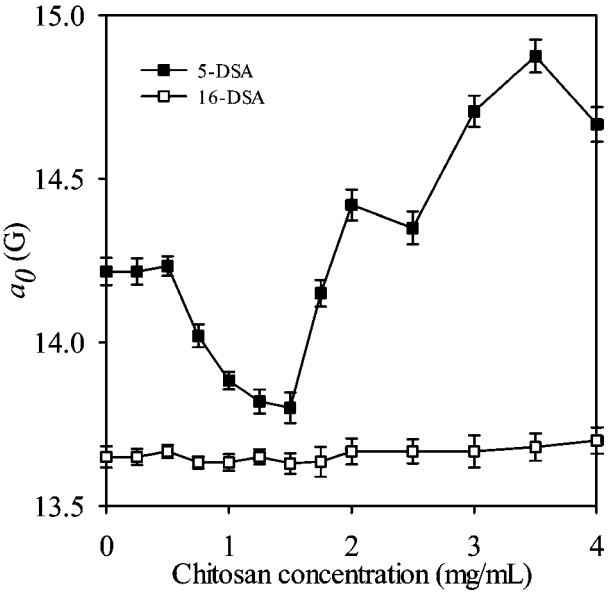

Figure 4. Isotropic hyperfine coupling constant a_0 of 5-DSA and 16-DSA in chitosan-decorated liposomes as a function of concentration. Each point represents the mean value ± standard deviation (n = 3).

mechanisms may contribute to the controlled release of encapsulated compounds in vehicles by decreasing water penetration.[32,33] However, a sudden increase in the a_0 values of 5-DSA was observed as the concentration was increased to 1.5 mg/mL. This phenomenon was understandable because the chitosan coils tended to penetrate into the liposomal membrane, rather than flat adsorption. Consequently, the polar region of the membrane was loosened, and more additional space was available for water penetration. By contrast, the effect of chitosan decoration on the hydrophobicity of membrane bilayer core was not pronounced, with a slight increase in a_0 values of 16-DSA from 1.75 mg/mL. In combination with the small influence of chitosan decoration on the fluidity of bilayer centre, this observation further confirmed the shallow insertion of chitosan coils, thus practically preserving the hydrophobic barrier of bilayer core.

Liposome Morphology. Alteration of adsorption behavior is always accompanied by a change in mechanisms of membrane deformation.[34] The morphological characterization of bare liposomes and chitosan-decorated liposomes was visualized by TEM after negative staining (Figure 5). It can be seen that bare particles were spherical. After decoration by chitosan, a different trend in morphological change was observed. At chitosan concentrations of 1.0, 1.5, and 2.0 mg/mL, the composite particles seemed to exhibit rectangular shape but maintained relatively monodispersion. The particle size was roughly in the range of 70−150 nm. The size observed from the microscopic images was somewhat greater than that determined using DLS technique.[13] This difference may have been related to the artifact effect of the analytical methods. For instance, the light-scattering instrument requires the high dilution of samples prior to analysis, which may have changed the particle size of the samples.[35] On the other hand, a very thin

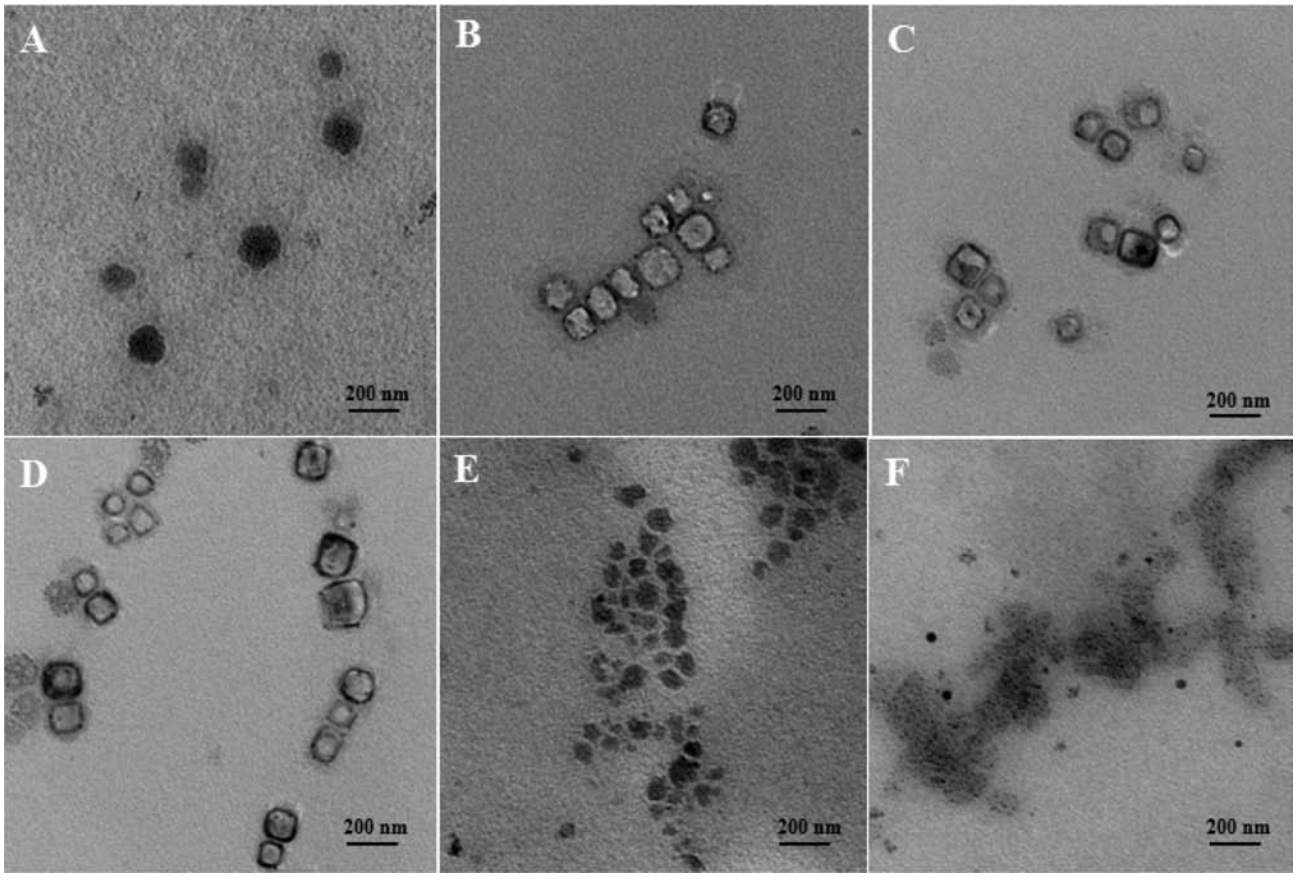

Figure 5. Transmission electron micrographs of bare liposomes (A) and liposomes decorated by chitosan at 1.0 mg/mL (B), 1.5 mg/mL (C), 2.0 mg/mL (D), 3.0 mg/mL (E), and 4.0 mg/mL (F).

DOI: 10.1021/acs.jafc.5b01422
J. Agric. Food Chem. 2015, 63, 7277−7285

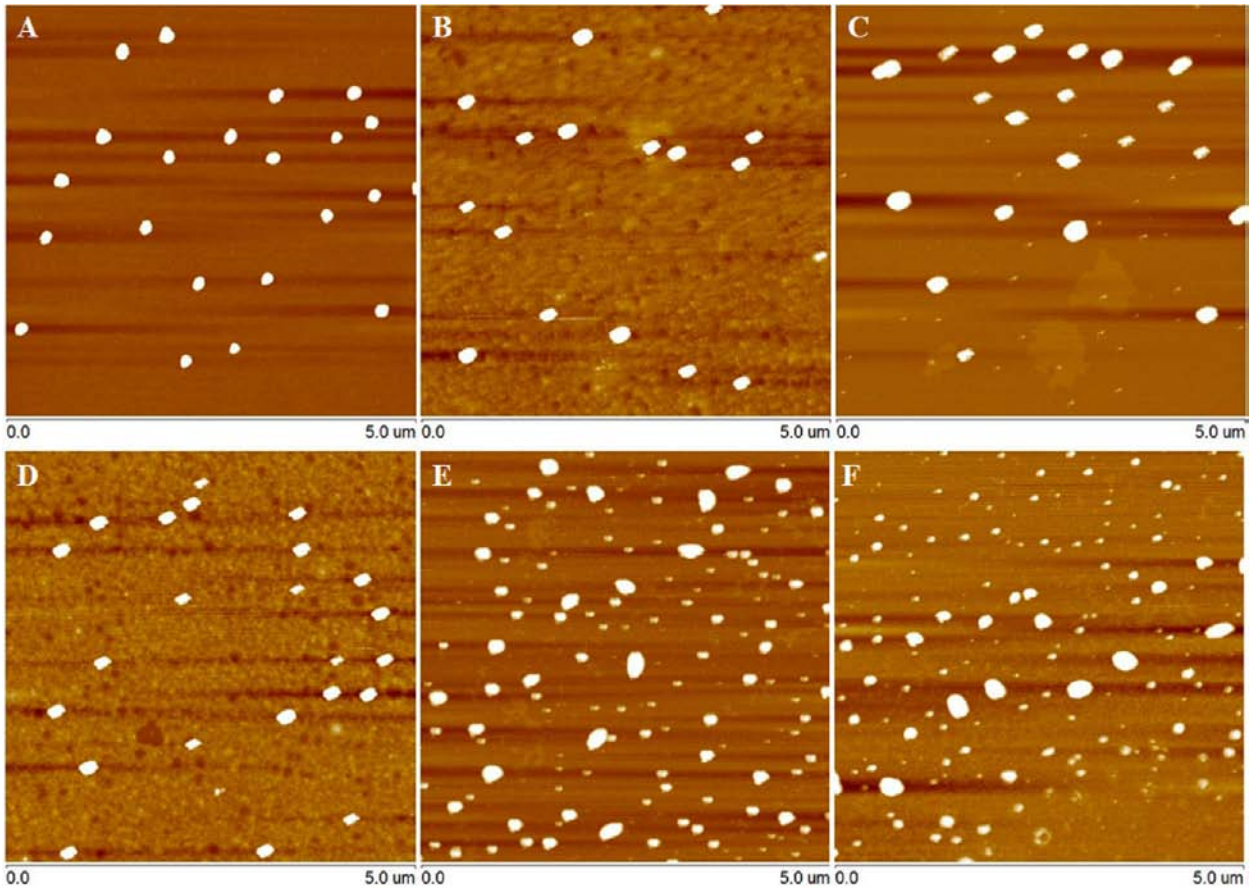

Figure 6. Scan Asyst mode AFM images of bare liposomes and liposomes decorated by chitosan at concentrations of 1.0, 1.5, 2.0, 3.0, and 4.0 mg/mL. The study was performed immediately after the preparation. Scan size = 5 μm × 5 μm.

coated layer (~10 nm) around the liposomal particles can be observed, demonstrating the interaction of chitosan with liposomes as well as the flat adsorption of chitosan chains.[13] The dimension and charged property of the system also revealed an electrostatic interaction that, after titration with chitosan to attain a concentration of 0.5 mg/mL, increased the average diameter of liposomes from 82.9 to 90 nm, with a charge inversion from −17.9 (bare liposomes) to 10.6 (decorated liposomes).[13] However, with further increase of chitosan concentration (from 3.0 to 4.0 mg/mL), the suspension became very heterogeneous and the shape of the particles was completely distorted (Figure 5E,F). Many small particles (<50 nm) were found in the field of vision. Diameter distribution analysis provided a complementary picture of a strong volume peak of liposomes located in the range of 10−50 nm in the presence of chitosan coils.[13]

AFM images of bare liposomes and chitosan-decorated liposomes are shown in Figure 6. The majority of bare liposomes maintained a spherical and well-defined shape. The presence of chitosan led to a change in the shape of liposomes, depending upon the chitosan concentration. The shape of liposomes appeared rectangular at concentrations of 1.0, 1.5, and 2.0 mg/mL, but was more irregular at 3.0 and 4.0 mg/mL. This observation supported the results obtained by TEM analysis. Deformation of particles observed from AFM images could be attributed to different factors, such as particle collapse during evaporation[36] and interactions of adsorbed polymer with supported surface.[10] In our case, it appeared that the original morphology of liposome was not significantly influenced by the spontaneous collapse, as evidenced from the fairly spherical shape of bare liposomes (Figure 6A).

In combination with TEM observation, the morphological alteration of liposomes has to be related to the modification of chitosan on the lipid headgroup. Upon binding of chitosan to the surface of small vesicles, the chitosan chain would bend to adapt to the large curvature of the sphere. This process probably, in turn, builds tension in the membrane and increases the spontaneous curvature of the bilayer. This phenomenon brought about the change in morphology. Moreover, if the binding of polyelectrolyte becomes stronger, the membrane would be subjected to a higher degree of bending.[34] Thus, the deformation of liposomes was more apparent in the presence of crimped chains (at 1.5 and 2.0 mg/mL). It was also possible that the hydrophobic residues of crimped chains incorporated into the membrane interior and occupied the position of phospholipid molecules. As a result, a portion of lipid acyl chains orientated toward higher curvature, leading particles to be elongated.[37] At higher chitosan concentrations (3.0 and 4.0 mg/mL), a number of very heterogeneous particles were visible, which may be generated probably due to the reorganization of particles subsequent to collapse. This observation can be explained by the fact that chitosan coils progressively penetrated into the lipid bilayer until disrupting it. At this stage, the hydrophobic interaction was intensified, accompanying the formation of chitosan coils. The almost unchanged zeta potential values of the system (>2 mg/mL) also confirmed the existence of hydrophobic interaction.[13] Therefore, it was believed that the main forces involved were

DOI: 10.1021/acs.jafc.5b01422
J. Agric. Food Chem. 2015, 63, 7277−7285

hydrophobic in nature, as demonstrated by the incorporation of surfactant molecules into the phospholipid bilayer.[38] If the main aim of chitosan modification was to stabilize liposome, high concentrations at which chitosan adopted coil conformation should be avoided, considering the lipid bilayer membrane disruption. On the other hand, the "polymeric surfactant" property of chitosan provided us a new perspective to elucidate that the ability of chitosan to disrupt the lipid bilayer membrane for the antimicrobial[39] and biological activity[40] partially related to its coil conformation.

Aggregation and Fusion of Liposomes. The susceptibility of liposome to aggregation or fusion during production, storage, transport, and after administration is highly challenging.[41] Here, we briefly discuss the observations on the aggregation and fusion of the composite chitosan−lipid particles after heat treatment.

Analysis on the particle size using DLS technique showed that there was only a single volume peak observed for the chitosan-decorated liposomes at 1.0, 1.5, and 2.0 mg/mL after 5 h of incubation at 37 °C (Figure 7). This indicated that the

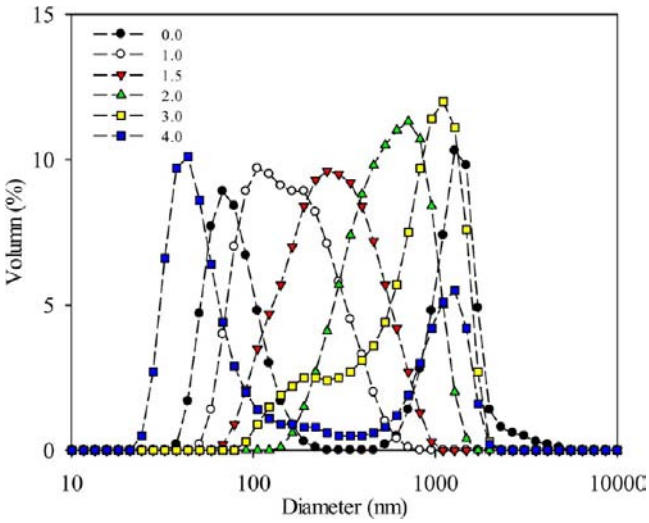

Figure 7. Diameter distribution of bare liposomes and chitosan-decorated liposome after 5 h of incubation at 37 °C.

suspensions can maintain the homogeneous distribution even though they were heated. However, bimodal distribution occurred for uncoated liposomes and liposomes decorated by chitosan of 3.0 and 4.0 mg/mL. It is very likely that the volume peak located at large diameter (around 1100 nm) was caused by the particle aggregation or fusion.

AFM measurement provided direct visualization of the aggregated and fused behavior of particles (Figure 8). In the absence of chitosan, particles adhered to each other after incubation. The diameter of fused particles ranged from 295 to 957 nm. After decoration by chitosan at 1.0 and 1.5 mg/mL, few particles aggregated together and the boundary of the unit particle was clearly observed. It was believed that the combining effect of electrostatic repulsion and steric hindrance by externally adsorbed polymers inhibited particle aggregation. However, decoration of high chitosan concentration induced the aggregation and fusion. We can observe that four or five individual particles adhered to each other, forming bigger aggregates in the whole vision field (Figure 8D). This interesting phenomenon might be associated with the bridging effect of chitosan-bound chains to neighboring vesicles.[11] The aggregated liposomes fused into a single liposome resembling the shape of a distorted rod or an elongated sphere (Figure 8E) or into large irregular clusters (Figure 8F). The lateral segregation of the anionic lipid by polyelectrolyte adsorption and consequently disordered lipid packing could be a possible reason for liposome fusion.[42] In addition, a low level of membrane fluidity was supposed to prevent particle aggregation effectively, whereas it behaved oppositely at high fluidity.[43] Thus, liposome aggregation was also readily understandable when correlated with the analysis on fluorescence anisotropy (Figure 2).

Liposomal Membrane Permeability. To understand whether the interaction of chitosan affected membrane permeability, leakage of CF from liposomes was monitored during the interaction process of chitosan and liposomes. Figure 9A shows that bare liposomes (0.0 mg/mL) spontaneously released very small amounts of encapsulated CF due to instability. After liposomes had been incubated with chitosan in the range of 0.5−1.5 mg/mL, the release profile of CF was not significantly affected. Only when incubation time exceeded 15 min were the leaked amounts of CF from decorated liposomes lower than that from bare liposomes, suggesting the gradual formation of a chitosan layer. This process also implied that although the morphology was modified by chitosan, the permeability of the membrane was not significantly altered. However, once the chitosan concentration increased (2.0−4.0 mg/mL), a progressive and higher leakage of CF appeared. This observation demonstrated that the interaction process of chitosan coils with liposomes was accompanied by the penetration of chitosan coils into the membrane.

The physicochemical barrier of the lipid bilayer against the penetration of foreign elements plays a key role in protecting the incorporated bioactive components. To evaluate the rigidity of liposomal particles, their resistance against surfactant Triton X-100 was carried out. Figure 9B shows that the release of CF from bare liposomes increased dramatically, as around 30% of encapsulated CF molecules leaked after 120 s. It was suggested that a large amount of Triton X-100 penetrated into the bilayer and initiated the solubilization process. Liposomes decorated by chitosan ranging from 0.5 to 1.5 mg/mL possessed higher durability against Triton X-100 penetration and maintained the release rate at a low level. The strong resistance could be due to the dense mesh covering the membrane surface and rigidification of chitosan. Conversely, liposome membrane decorated by a high concentration of chitosan became more permeable to surfactant, as observed from serious leakage of CF. After 120 s of incubation, around 30, 35, and 38% of CF leaked from liposomes decorated by 2.0, 3.0, and 4.0 mg/mL chitosan, respectively, confirming the destabilizing effect of chitosan coils.

Conclusion. In the present study, we have demonstrated the contrasting modulations of chitosan on the dynamics, structure, hydrophobicity, morphology, and permeability of liposomal membrane. The extended and crimped chains of chitosan not only provided a physical barrier to the liposome surface but also rigidified the lipid membrane. Although the morphology was altered by chitosan decoration, the membrane permeability was preserved or decreased. Such characteristics make these composite vesicles potential candidates for an efficient delivery system for drugs and nutraceuticals. However, chitosan coils displayed a "polymer surfactant" nature by penetrating into the interior of lipid bilayer. These destabilizing

DOI: 10.1021/acs.jafc.5b01422
J. Agric. Food Chem. 2015, 63, 7277−7285

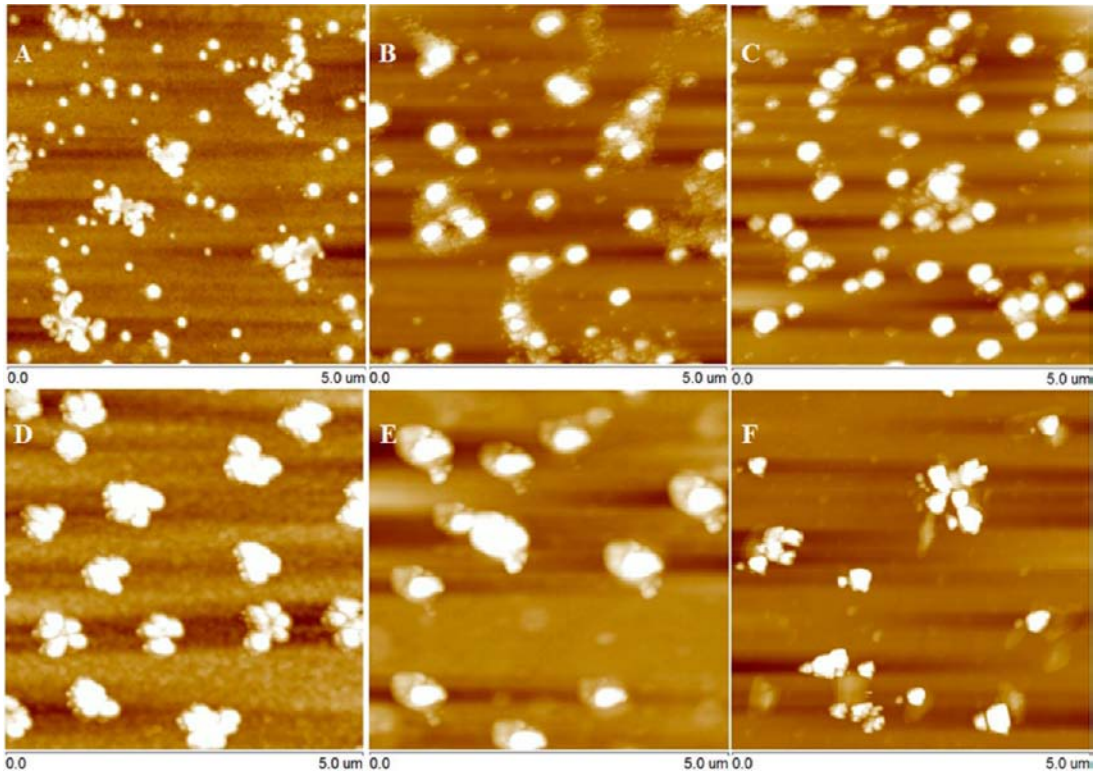

Figure 8. Scan Asyst mode AFM images of bare liposomes (A) and liposomes decorated by chitosan at concentrations of 1.0 mg/mL (B), 1.5 mg/mL (C), 2.0 mg/mL (D), 3.0 mg/mL (E), and 4.0 mg/mL (F). The study was performed after 5 h of incubation at 37 °C. Scan size = 5 μm × 5 μm.

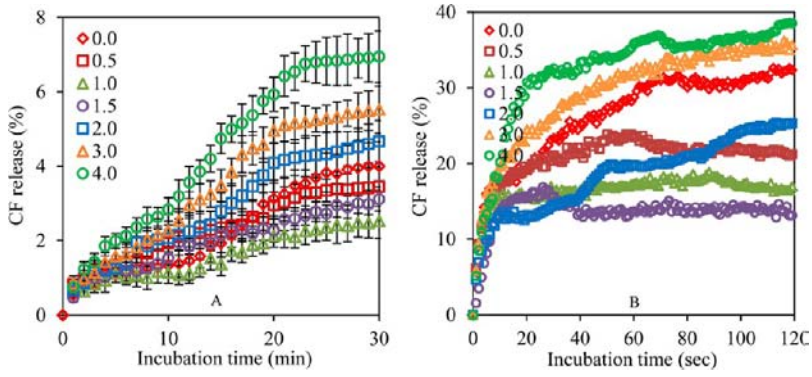

Figure 9. Time course of CF release kinetic from bare liposomes after exposure to chitosan of different concentrations (A) or from chitosan-decorated liposomes after exposure to Triton X-100 (B). When Triton X-100 was added to the suspension, the CF fluorescence was immediately monitored every second by a spectrofluorimeter.

effects of coils implied the ability of chitosan to disrupt cell membranes and the infeasibility in the design of nutraceutical delivery systems.

AUTHOR INFORMATION

Corresponding Author

*(S.X.) E-mail: sqxia2006@hotmail.com. Phone: +86-510-85884496. Fax: +86-510-85884496.

Funding

This research was financially supported by projects of the National Science Foundation of China (31471624) and the Natural Science Foundation of Jiangsu Province (BK 20141111) and by 111 Project B07029.

Notes

The authors declare no competing financial interest.

REFERENCES

(1) Elsabee, M. Z.; Morsi, R. E.; Al-Sabagh, A. M. Surface active properties of chitosan and its derivatives. *Colloids Surf., B* **2009**, *74*, 1−16.

(2) Gonçalves, M. C.; Mertins, O.; Pohlmann, A. R.; Silveira, N. P.; Guterres, S. S. Chitosan coated liposomes as an innovative nanocarrier for drugs. *J. Biomed. Nanotechnol.* **2012**, *8*, 240−250.

(3) Lee, J.-H.; Oh, H.; Baxa, U.; Raghavan, S. R.; Blumenthal, R. Biopolymer-connected liposome networks as injectable biomaterials capable of sustained local drug delivery. *Biomacromolecules* **2012**, *13*, 3388−3394.

(4) Shin, G. H.; Chung, S. K.; Kim, J. T.; Joung, H. J.; Park, H. J. Preparation of chitosan-coated nanoliposomes for improving the mucoadhesive property of curcumin using the ethanol injection method. *J. Agric. Food Chem.* **2013**, *61*, 11119−11126.

(5) Madrigal-Carballo, S.; Lim, S.; Rodriguez, G.; Vila, A. O.; Krueger, C. G.; Gunasekaran, S.; Reed, J. D. Biopolymer coating of

DOI: 10.1021/acs.jafc.5b01422
J. Agric. Food Chem. 2015, 63, 7277−7285

soybean lecithin liposomes via layer-by-layer self-assembly as novel delivery system for ellagic acid. *J. Funct. Foods* **2010**, *2*, 99−106.
(6) Panya, A.; Laguerre, M.; Lecomte, J.; Villeneuve, P.; Weiss, J.; McClements, D. J.; Decker, E. A. Effects of chitosan and rosmarinate esters on the physical and oxidative stability of liposomes. *J. Agric. Food Chem.* **2010**, *58*, 5679−5684.
(7) Helander, I.; Nurmiaho-Lassila, E.-L.; Ahvenainen, R.; Rhoades, J.; Roller, S. Chitosan disrupts the barrier properties of the outer membrane of Gram-negative bacteria. *Int. J. Food Microbiol.* **2001**, *71*, 235−244.
(8) Fang, N.; Chan, V.; Mao, H.-Q.; Leong, K. W. Interactions of phospholipid bilayer with chitosan: effect of molecular weight and pH. *Biomacromolecules* **2001**, *2*, 1161−1168.
(9) Young, D. H.; Köhle, H.; Kauss, H. Effect of chitosan on membrane permeability of suspension-cultured *Glycine max* and *Phaseolus vulgaris* cells. *Plant Physiol.* **1982**, *70*, 1449−1454.
(10) Mertins, O.; Dimova, R. Insights on the interactions of chitosan with phospholipid vesicles. Part II: Membrane stiffening and pore formation. *Langmuir* **2013**, *29*, 14552−14559.
(11) Mertins, O.; Dimova, R. Binding of chitosan to phospholipid vesicles studied with isothermal titration calorimetry. *Langmuir* **2011**, *27*, 5506−5515.
(12) Pepić, I.; Filipović-Grčić, J.; Jalšenjak, I. Interactions in a nonionic surfactant and chitosan mixtures. *Colloids Surf., A* **2008**, *327*, 95−102.
(13) Tan, C.; Xue, J.; Eric, K.; Feng, B.; Zhang, X.; Xia, S. Dual effects of chitosan decoration on the liposomal membrane physicochemical properties as affected by chitosan concentration and molecular conformation. *J. Agric. Food Chem.* **2013**, *61*, 6901−6910.
(14) Xia, S.; Xu, S.; Zhang, X.; Zhong, F. Effect of coenzyme Q10 incorporation on the characteristics of nanoliposomes. *J. Phys. Chem. B* **2007**, *111*, 2200−2207.
(15) Xia, S.; Xu, S.; Zhang, X. Optimization in the preparation of coenzyme Q10 nanoliposomes. *J. Agric. Food Chem.* **2006**, *54*, 6358−6366.
(16) Tan, C.; Zhang, Y.; Abbas, S.; Feng, B.; Zhang, X.; Xia, S. Modulation of the carotenoid bioaccessibility through liposomal encapsulation. *Colloids Surf., B* **2014**, *123*, 692−700.
(17) Tan, C.; Xue, J.; Abbas, S.; Feng, B.; Zhang, X.; Xia, S. Liposome as a delivery system for carotenoids: comparative antioxidant activity of carotenoids as measured by ferric reducing antioxidant power, DPPH assay and lipid peroxidation. *J. Agric. Food Chem.* **2014**, *62*, 6726−6735.
(18) Tan, C.; Xue, J.; Lou, X.; Abbas, S.; Guan, Y.; Feng, B.; Zhang, X.; Xia, S. Liposomes as delivery systems for carotenoids: comparative studies of loading ability, storage stability and in vitro release. *Food Funct.* **2014**, *5*, 1232−1240.
(19) Tan, C.; Xia, S.; Xue, J.; Xie, J.; Feng, B.; Zhang, X. Liposomes as vehicles for lutein: preparation, stability, liposomal membrane dynamics, and structure. *J. Agric. Food Chem.* **2013**, *61*, 8175−8184.
(20) Xia, S.; Tan, C.; Xue, J.; Lou, X.; Zhang, X.; Feng, B. Chitosan/tripolyphosphate-nanoliposomes core-shell nanocomplexes as vitamin E carriers: shelf-life and thermal properties. *Int. J. Food Sci. Technol.* **2014**, *49*, 1367−1374.
(21) Shinitzky, M.; Barenholz, Y. Fluidity parameters of lipid regions determined by fluorescence polarization. *Biochim. Biophys. Acta, Rev. Biomembr.* **1978**, *515*, 367−394.
(22) Imura, T.; Sakai, H.; Yamauchi, H.; Kaise, C.; Kozawa, K.; Yokoyama, S.; Abe, M. Preparation of liposomes containing Ceramide 3 and their membrane characteristics. *Colloids Surf., B* **2001**, *20*, 1−8.
(23) Subczynski, W. K.; Markowska, E.; Gruszecki, W. I.; Sielewiesiuk, J. Effects of polar carotenoids on dimyristoylphosphatidylcholine membranes: a spin-label study. *Biochim. Biophys. Acta, Biomembr.* **1992**, *1105*, 97−108.
(24) Gordon, L. M.; Sauerheber, R. D.; Esgate, J. A. Spin label studies on rat liver and heart plasma membranes: Effects of temperature, calcium, and lanthanum on membrane fluidity. *J. Supramol. Struct.* **1978**, *9*, 299−326.
(25) Coderch, L.; Fonollosa, J.; De Pera, M.; Estelrich, J.; De La Maza, A.; Parra, J. L. Influence of cholesterol on liposome fluidity by EPR: Relationship with percutaneous absorption. *J. Controlled Release* **2000**, *68*, 85−95.
(26) De la Maza, A.; Parra, J.; Sanchez Leal, J. Alteration of permeability of neutral and electronegatively charged liposomes by alkyl sulfate surfactants. *Langmuir* **1992**, *8*, 2422−2426.
(27) Lee, H.; Kim, H. R.; Park, J. C. Dynamics and stability of lipid bilayers modulated by thermosensitive polypeptides, cholesterols, and PEGylated lipids. *Phys. Chem. Chem. Phys.* **2014**, *16*, 3763−3770.
(28) Marczak, A. Fluorescence anisotropy of membrane fluidity probes in human erythrocytes incubated with anthracyclines and glutaraldehyde. *Bioelectrochemistry* **2009**, *74*, 236−239.
(29) Prendergast, F. G.; Haugland, R. P.; Callahan, P. J. 1-[4-(Trimethylamino)phenyl]-6-phenylhexa-1,3,5-triene: synthesis, fluorescence properties and use as a fluorescence probe of lipid bilayers. *Biochemistry* **1981**, *20*, 7333−7338.
(30) Wydro, P.; Krajewska, B.; Hąc-Wydro, K. Chitosan as a lipid binder: a langmuir monolayer study of chitosan−lipid interactions. *Biomacromolecules* **2007**, *8*, 2611−2617.
(31) Wisniewska, A.; Widomska, J.; Subczynski, W. K. Carotenoid-membrane interactions in liposomes: effect of dipolar, monopolar, and nonpolar carotenoids. *Acta Biochim. Polym.* **2006**, *53*, 475−484.
(32) Lis, M.; Wizert, A.; Przybylo, M.; Langner, M.; Swiatek, J.; Jungwirth, P.; Cwiklik, L. The effect of lipid oxidation on the water permeability of phospholipids bilayers. *Phys. Chem. Chem. Phys.* **2011**, *13*, 17555−17563.
(33) Lee, Y.-H.; Mei, F.; Bai, M.-Y.; Zhao, S.; Chen, D.-R. Release profile characteristics of biodegradable-polymer-coated drug particles fabricated by dual-capillary electrospray. *J. Controlled Release* **2010**, *145*, 58−65.
(34) McMahon, H. T.; Gallop, J. L. Membrane curvature and mechanisms of dynamic cell membrane remodelling. *Nature* **2005**, *438*, 590−596.
(35) Salvia-Trujillo, L.; Qian, C.; Martín-Belloso, O.; McClements, D. J. Influence of particle size on lipid digestion and β-carotene bioaccessibility in emulsions and nanoemulsions. *Food Chem.* **2013**, *141*, 1472−1480.
(36) Pentak, D. Physicochemical properties of liposomes as potential anticancer drugs carriers. Interaction of etoposide and cytarabine with the membrane: spectroscopic studies. *Spectrochim. Acta, Part A* **2014**, *122*, 451−460.
(37) Peter, B. J.; Kent, H. M.; Mills, I. G.; Vallis, Y.; Butler, P. J. G.; Evans, P. R.; McMahon, H. T. BAR domains as sensors of membrane curvature: the amphiphysin BAR structure. *Science* **2004**, *303*, 495−499.
(38) De la Maza, A.; Parra, J. L.; Sanchez Leal, J. Alteration of permeability of neutral and electronegatively charged liposomes by alkyl sulfate surfactants. *Langmuir* **1992**, *8*, 2422−2426.
(39) Kong, M.; Chen, X. G.; Xing, K.; Park, H. J. Antimicrobial properties of chitosan and mode of action: a state of the art review. *Int. J. Food Microbiol.* **2010**, *144*, 51−63.
(40) Pavinatto, F. J.; Pavinatto, A.; Caseli, L.; dos Santos, D. S.; Nobre, T. M.; Zaniquelli, M. E. D.; Oliveira, O. N. Interaction of chitosan with cell membrane models at the air−water interface. *Biomacromolecules* **2007**, *8*, 1633−1640.
(41) Takeuchi, H.; Kojima, H.; Yamamoto, H.; Kawashima, Y. Evaluation of circulation profiles of liposomes coated with hydrophilic polymers having different molecular weights in rats. *J. Controlled Release* **2001**, *75*, 83−91.
(42) Brender, J. R.; Hartman, K.; Gottler, L. M.; Cavitt, M. E.; Youngstrom, D. W.; Ramamoorthy, A. Helical conformation of the SEVI precursor peptide $PAP_{248-286}$, a dramatic enhancer of HIV infectivity, promotes lipid aggregation and fusion. *Biophys. J.* **2009**, *97*, 2474−2483.
(43) Heurtault, B.; Saulnier, P.; Pech, B.; Proust, J.-E.; Benoit, J.-P. Physico-chemical stability of colloidal lipid particles. *Biomaterials* **2003**, *24*, 4283−4300.

DOI: 10.1021/acs.jafc.5b01422
J. Agric. Food Chem. 2015, 63, 7277−7285

Figure 1. (A) Brittle, crystalline structure of the native Frost grape arabinogalactan polysaccharide. The piece shown is approximately 1 cm in length. (B) Viscous FGP exuding from a cut, debarked vine stem after 20 h.

DMSO, powdered NaOH), acid hydrolyzed with trifluoroacetic acid (2 M, 120 °C, 1 h), and converted to partially methylated aldononitrile acetates for GC-MS analysis of the glycosidic linkage positions.[18] The permethylation analysis was done in triplicate. Hydroxyproline was determined colorimetrically.[19]

Acetylation under Aqueous Condition. To acetylate the FGP, freeze-dried material (30 mg) was dissolved in 2 mL of 3% aqueous solution of trisodium phosphate. Vinyl acetate (400 μL) was added dropwise, and the reaction was maintained at room temperature for 18 h. Excess vinyl acetate was extracted with ethyl acetate, and the aqueous phase containing the acetated FGP was freeze-dried.

NMR Analysis. All NMR experiments were performed on an Avance spectrometer (Bruker Biospin, Billerica, MA, USA) operating at 500.11 MHz using a standard 5 mm *z*-gradient BBI probe at either 27, 60, or 80 °C. The deuterated solvents used were obtained from Cambridge Isotope Laboratories (Tewksbury, MA, USA). The diffusion-orientated NMR pulse sequence used was ledbpgp2s (standard Bruker ^{1}H DOSY sequence), and the spectra were recorded at 27 °C. The processing was done with the Bruker TOPSPIN software package (v. 1.3), and other pulse sequences used were those supplied by Bruker Biospin.

Preparation of Frost Grape Polysaccharide and Emulsification Assays. Clove oil (>85% eugenol) was obtained from Spectrum Chemical Mfg. Corp. (Gardena, CA, USA). Grapefruit essential oil (>95% terpenoids) was obtained from Eden's Garden (San Clemente, CA, USA). Both of these oils are practically insoluble in water. FGP was isolated from Frost grape (*V. riparia* Michx.) stem sections by cutting the stems into ∼15 cm sections and placing these in a plastic bag for 24 h, after which time the FGP had exuded into nearly clear, tubular crystals. After drying in an oven at 40 °C for 48 h, the crystals were ground in a coffee grinder to a fine powder. Solutions of FGP were prepared at 0.1 and 1.0% (w/v). Subsequently, 0.1 mL of clove oil and 0.1 mL of grapefruit oil were added to 100 mL of the 0.1% FGP solution, and 1.0 mL of the oils was added to the 1.0% FGP solution. The mixtures were then homogenized with a Polytron homogenizer for 30 s at 2000 rpm. Photographs were taken after 48 h with no further agitation.

Table 1. Compositional Analysis of the Frost Grape Polysaccharide

		% of total		
component	t_R (min)	native FGP	hot water	cold water
1. L-Ara	8.50	55.0	21.0	18.0
2. D-Xyl	8.70	11.0	3.0	1.5
3. D-Man	12.50	3.5	1.5	1.0
4. D-Glc	12.70	0.0	61.0	69.0
5. D-Gal	13.15	30.0	15.0	13.0
6. D-GlcA		∼2	nd[a]	nd
7. Hyp[b]		<0.02	nd	nd

[a]nd = not determined. [b]Hyp = hydroxyproline.

RESULTS

Extraction and Carbohydrate Compositional Analysis.

An arabinogalactan polysaccharide was found to be exuded from the cut stems of Frost grape and was first noticed from the vine growing around oak trees. Saw-cut stems exuded a colorless, low-viscosity sap, which dried within hours first to a gel and later to a brittle, crystalline solid (Figure 1). About 8 g of the material was recovered from cut sections of vine stem about 30 cm long × 2.5 cm diameter. This brittle solid polysaccharide was recovered by breaking it from the cut ends of the vine, and this material is referred to as the native Frost grape polysaccharide. Larger quantities of material were prepared by debarking the vine stems, cutting them into small sections about 3−5 cm in length, splitting them open lengthways, and extracting the pieces for 15 min with either cold or boiling water. These water extracts were viscous and yellowish in color.

The component monosaccharides in the FGP extracts were determined by GC-MS analysis of aldononitrile acetate (Figure 2; Table 1), as described.[15] In the first extraction, the brittle solid polysaccharide was recovered from the cut ends of the Frost grape vine, and we refer to this as the native polysaccharide. The polysaccharide is composed of approximately 2:1 L-arabinofuranose/D-galactopyranose, with minor components of D-xylose (∼11%) and D-mannose (∼3%). We also tested for hydroxyproline (Hyp) using a colorimetric assay[19] and compared it to commercial gum arabic (Table 1). We conclude that there is <0.02% Hyp in the FGP and probably none since this was below the detection limit. A bicinchoninic acid protein assay was also negative.

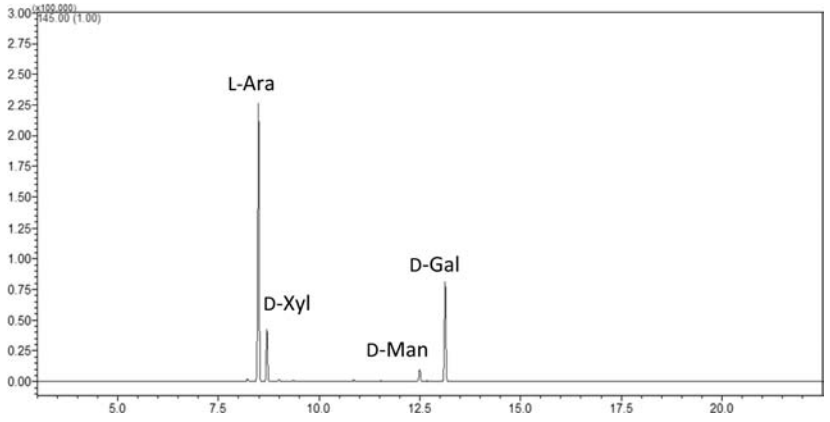

Figure 2. Monosaccharide compositional analysis of the native Frost grape polysaccharide. The FGP was acid hydrolyzed, and component sugars were determined by GC-MS as aldononitrile acetates.

DOI: 10.1021/acs.jafc.5b02316
J. Agric. Food Chem. 2015, 63, 7286−7293

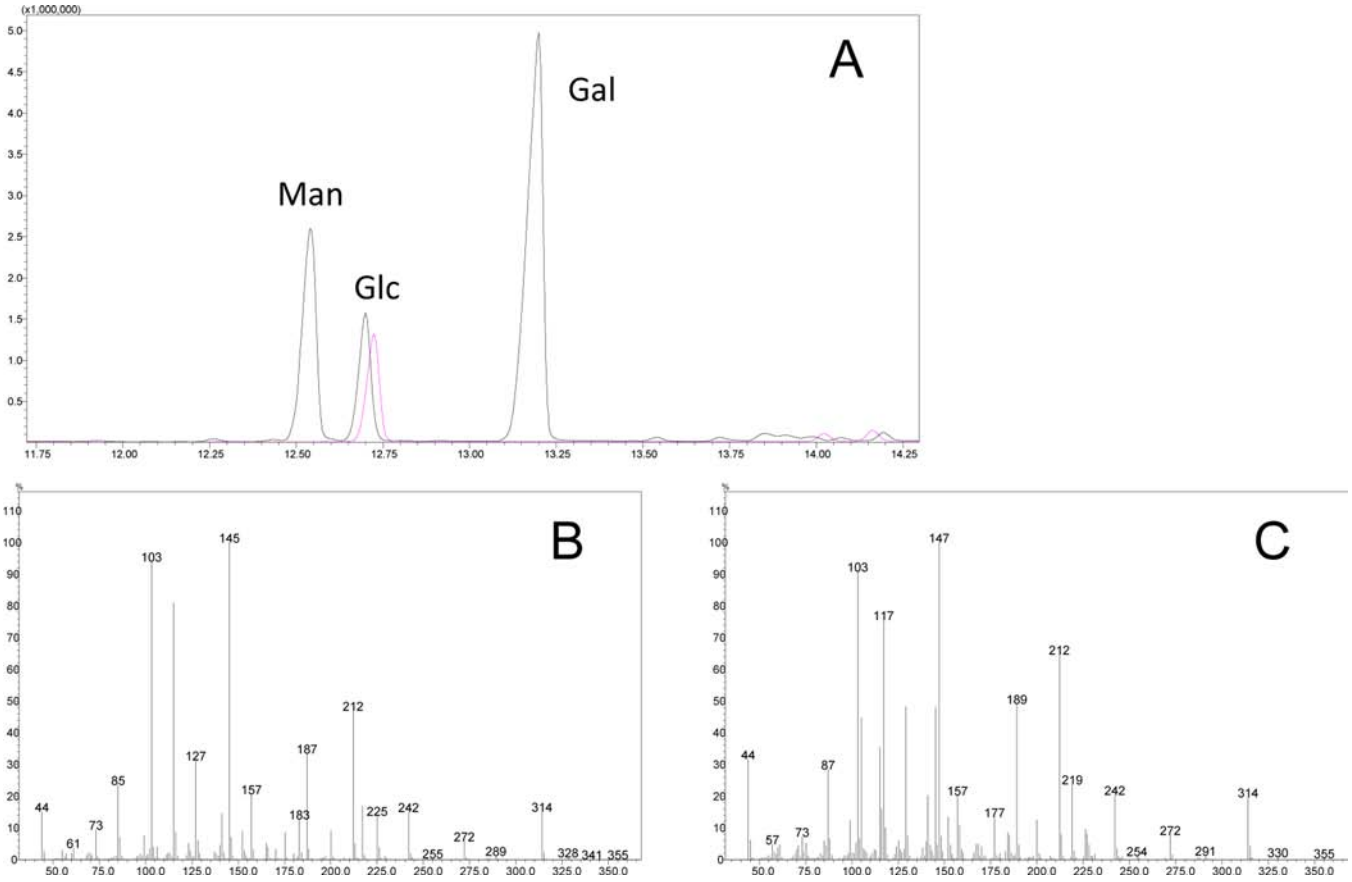

Figure 3. Uronates from FGP after $NaBD_4$ reduction, overlaid with Man, Glc, and Gal aldononitrile acetate standards: (A) composition determined by GC-MS (the deuterated Glc at 12.71 min arising from glucuronic acid (GlcA) is shown in magenta); EI-MS spectra of the GlcA residue from (B) $NaBH_4$-reduced FGP and from (C) $NaBD_4$-reduced FGP.

Frost Grape Uronic Acid Component Analysis. The acidic sugar residues present on the FGP were analyzed by the standard carbazole colorimetric assay for hexuronates,[16] which was inconclusive due to a high dark brown background color. We therefore made hexuronate methyl esters by treating the polysaccharide with methanolic HCl (+ chloroform) and reduced these with either sodium borohydride or borodeuteride. The reduced polysaccharides were acid hydrolyzed (2 M TFA), and PAANs derivatives were prepared for analysis by GC-MS.[15] After the reduction with borohydride, a new GC peak was observed for glucose at 12.7 min (Figure 3A), but only after the reduction step. The evidence that this glucose is derived from glucuronic acid comes from the observed incorporation of two deuterium atoms at carbon-6 following the reduction with borodeuteride and is evident from analysis of the electron impact mass spectrometric (EI-MS) data. Noticeably, the reduction of the glucuronate 6-methyl ester with $NaBD_4$ is evident from the 2 mass unit increase of ions m/z 87, 105, 117, 129, 147, and 189 (Figure 3B,C) and shows that the borodeuteration has occurred at the glucuronic carboxyl group. Hence this relatively small amount (peak integration indicates about 75% relative to the small mannose component) of glucuronic acid is derived from the FGP.

There is also a minor peak arising later in the GC chromatograph at 19.97 min due to a disaccharide peracetate (Supporting Information). The mass spectra arising from this peak also indicate that the disaccharide component is labeled with two deuterium ions. The +2 mass increase at m/z 407, 347, 333, 305, and 171 shows that this is a disaccharide composed of two neutral hexose sugars, one residue of which is derived from the borodeuteride-reduced glucuronic acid. The other residue is not deuterium labeled; otherwise, there would be an increase of +4 deuterium atoms. Moreover, the masses and the fragmentation ions indicate that this unlabeled second residue is a neutral hexose (i.e., probably Gal or possibly Man) rather than an arabinose residue. We conclude that the GlcA residue is attached to the polysaccharide backbone linked via galactosyl residues, but not to an arabinosyl part of the chain.

Permethylation Linkage Analysis of Native Frost Grape Polysaccharide. The GC separated seven peaks between 4 and 10 min giving EI-MS ions characteristic for partially methylated sugars (Table 2). The three fast eluting peaks before 5.5 min were assigned as methylated pentoses arising

Table 2. Assignments from the Permethylation Linkage Analysis

peak	t_R (integral)[a]	methyl PAANs	structural assignment
1	4.27 (21.1)	2,3,5-Me-Ara	terminal Ara*f*
2	4.61 (6.4)	2,3,4-Me-Xyl	terminal Xyl*p*
3	5.43 (18.3)	3-acetyl-2,5-Me-Ara	internal Ara*f*
4	6.83 (13.3)	2,3,4,6-Me-Hex	terminal Gal*p* or Man*p*
5	8.38 (13.2)	3,5-acetyl-2,4,6-Me-Gal	3-linked Gal*p*
6	9.66 (9.7)	2,3,5-acetyl-4,6-Me-Gal	3-linked, 2-substituted Gal*p*
7	10.00 (5.5)	2,3,5-acetyl-4,6-Me-Hex	3-linked, 2-substituted Man*p*

[a]Gas chromatography retention times (min) with the peak integrals in parentheses.

DOI: 10.1021/acs.jafc.5b02316
J. Agric. Food Chem. 2015, 63, 7286−7293

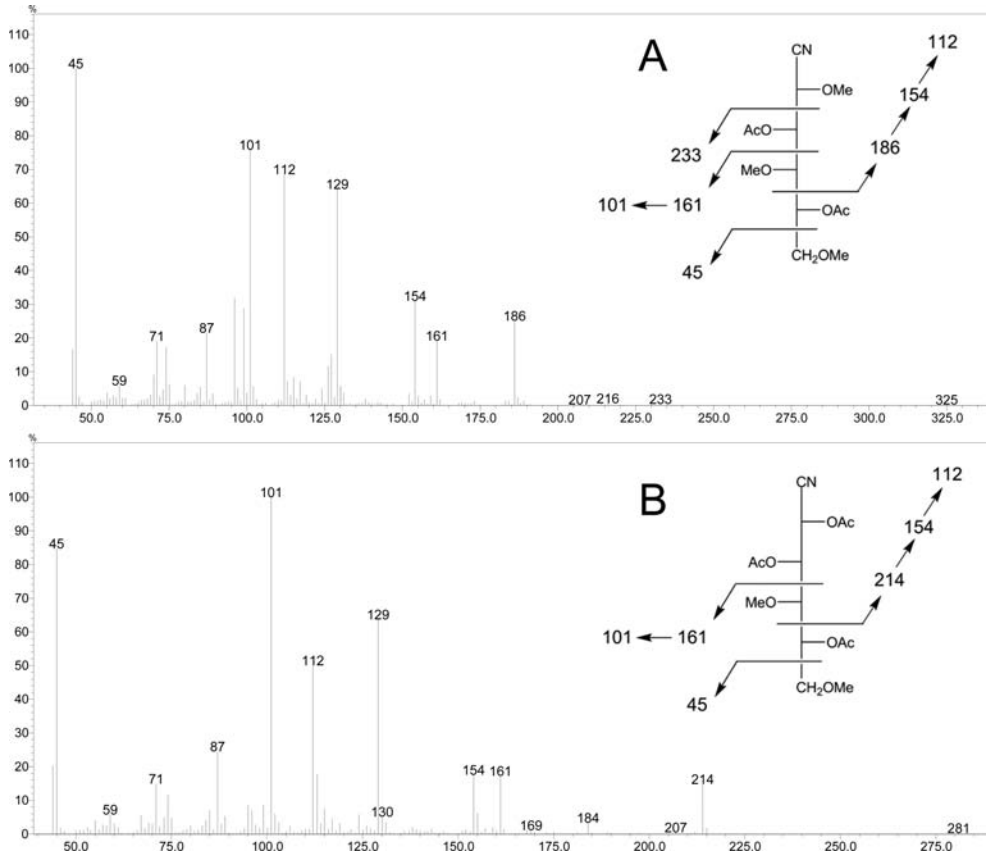

Figure 4. GC-MS permethylation linkage data: GC-MS spectra of (A) 3,5-diacetyl-2,4,6-trimethylgalactose aldononitrile acetate (t_R 8.38 min) and (B) 2,3,5-triacetyl-4,6-dimethyl-galactose aldononitrile acetate (t_R 9.66 min). The major fragmentation pathways are as shown.

from the variously linked arabinosyl and xylosyl residues. The presence of 4-acetyl-2,3,5-methylarabinose indicates that the arabinose residues are in the furanosyl form, as is confirmed by NMR. The peak at 6.38 min corresponds to 2,3,4,6-MeHex*p*, indicating a terminal hexopyranose, either Gal*p* or the small component of Man*p*. The three later peaks correspond to trimethylated (8.38 min) and dimethylated (9.66 and 10.00 min) hexopyranosyl residues and integrate approximately 3:2:1. Importantly, the GC peak at 9.66 min is readily assigned as 4,6-*O*-dimethyl-2,3,5-*O*-triacetylgalactose, arising from 2,3-linked Gal*p*. The EI-MS ion series m/z 214 → 154 → 112 indicates C4−C5 cleavage adjacent to the 4-methoxy group with retention of change at the nitrile end (Figure 4B). Similarly, m/z 161 → 101 is evidence for C3−C4 bond cleavage with charge retention in the other direction. This shows that two *O*-acetyl groups have been introduced into the galactopyranosyl residues at the 2- and 3-positions, indicating a core 1→3-linked galactosyl chain that is 1→2-substituted with Ara*f* residues. Similar analysis indicates that the GC peak at 8.38 min is due to 2,4,6-trimethyl-3,5-diacetylgalactose, arising from 3-linked Gal*p* (Figure 4A). This contains the ion sequences m/z 186 → 154 → 112 (m/z 214 is absent, hence only 3-linked) and m/z 161 → 101, plus a major ion at m/z 45 due to cleavage of a terminal C-6−CH_2OMe group. The smaller GC-MS peak at 10.0 min gave a mass spectrum identical to the 9.66 min peak and is possibly due to 2,3-linked mannosyl residues. Taken together, these data are consistent with a carbohydrate backbone of 1,3-linked Gal*p* residues with a 2-substituted Gal*p* present at a ratio of 3:2. Hence, the most probable linkage arrangement is that the 2-linked substituent is arabinofuranosyl side chains, the structure of which is determined by NMR as described below.

Analysis of the Native Frost Grape by HSQC-NMR, TOCSY-NMR, COSY-NMR, and Diffusion-Orientated (DOSY) NMR. The high viscosity made it difficult to obtain NMR data at room temperature, as is often common with polysaccharides, and this was not improved by switching the solvent to either d_6-DMSO or a 50:50 d_6-DMSO/D_2O mixed solvent. However, better HSQC, COSY, and TOCSY spectra of FGP were obtained at higher temperatures (80 and 60 °C in D_2O). The acquisition at high temperature led to a ∼0.5 ppm downfield shift of the proton signals (Figure 5), but by comparison with the HSQC data it was possible to extrapolate these assignments to room temperature (Table 3). The structural assignments were initially made by reference to published data on gum arabic and other arabinogalactans.[20−24] Three α-linked arabinofuranose anomeric signals, α-Ara-A, -A′, and -A″, were detected at 5.44, 5.38, and 5.19 ppm at room temperature and are coupled to ^{13}C NMR signals at 107.2, 108.3, and 109.4 ppm, respectively (Figure 5; Table 3). The corresponding β-Gal G1 signals are at 4.54/101.4 ppm. Unlike gum arabic there are no NMR signals for rhamnose, confirming the GC-MS compositional analysis (Table 1). Integration of the ^{1}H NMR signals showed that α-Ara-A, -A′, and -A″ are present in a ratio of 1:0.6:1. The α-Ara-A residue is structurally distinct from the other two, and the α-Ara-A H-2 is detected at 4.35 ppm and is coupled to the corresponding C-2 at 87.5 ppm. This carbon shift is ∼6 ppm downfield of the C2 carbons for the Ara-A′ and Ara-A″ residues, showing that the Ara-A is glycosidically linked at this position.

DOI: 10.1021/acs.jafc.5b02316
J. Agric. Food Chem. 2015, 63, 7286−7293

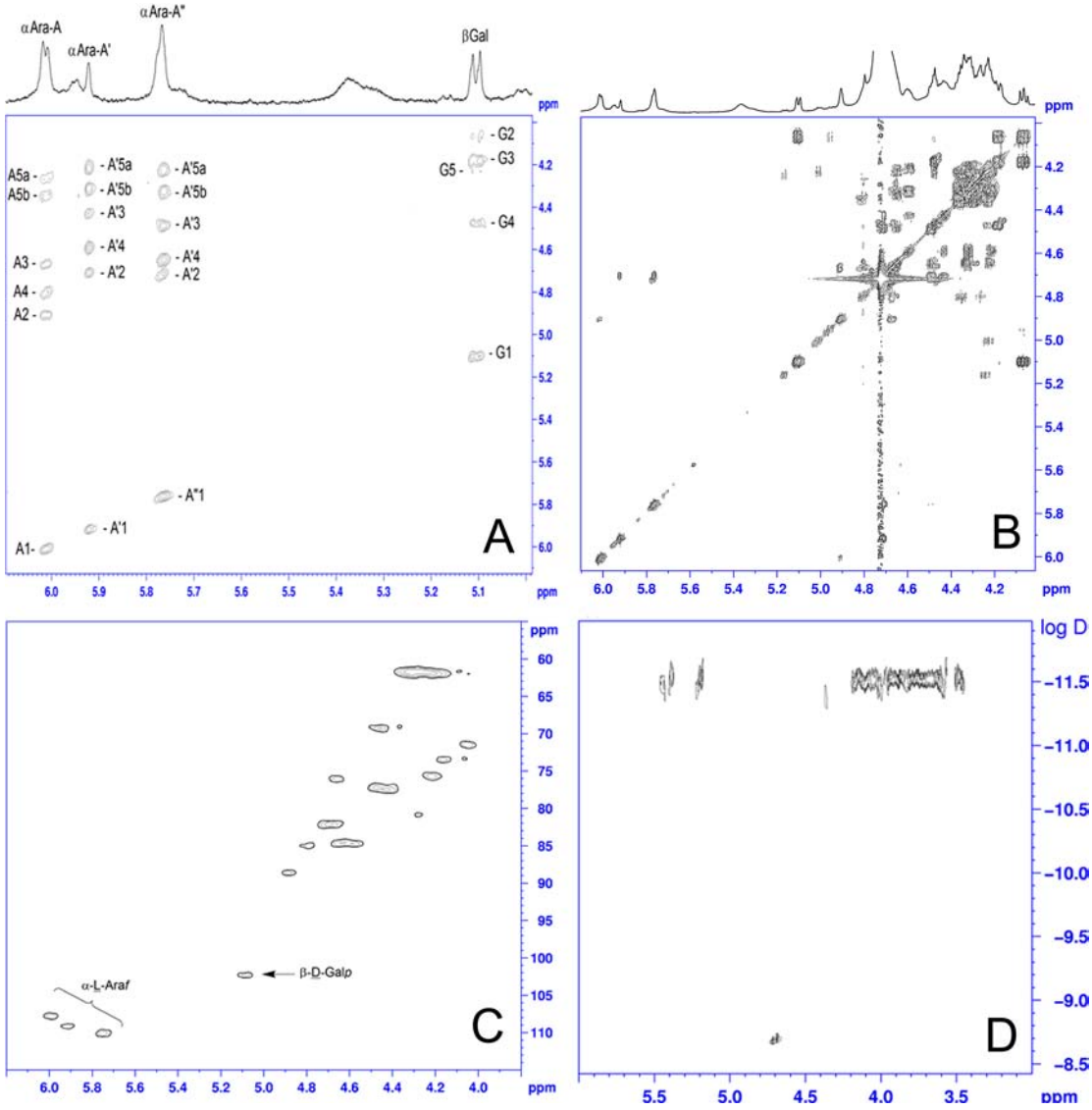

Figure 5. Total (TOCSY, A), $^{1}H-^{1}H$ (COSY, B), and $^{1}H-^{13}C$ correlation (HSQC, C) NMR spectra of D_2O-exchanged native Frost grape polysaccharide at 80 °C. Four spin systems are evident: the α-linked Ara*f* residues (A, A′, and A″) with anomeric proton shifts at 6.01, 5.92, and 5.76 ppm respectively, and a β-linked Gal*p* residue at 5.10 ppm at 80 °C. The corresponding carbohydrate ring protons are at 4.0−5.2 ppm and correlate to ^{13}C signals at 60−90 ppm in the HSQC spectrum. The full assignments are in Table 3, and the deduced FGP structure is shown in Figure 7. (D) Diffusion-ordered NMR spectra (DOSY) obtained at 27 °C in D_2O for Frost grape polysaccharide (−11.5 log D). The *x*-axis is ^{1}H NMR spectra and the *y*-axis is −log diffusion constants. The 4.7 ppm signal is due to the residual HDO signal.

Correlation (COSY) and total correlation (TOCSY) spectra were used to assign the arabinosyl A, A′, and A″ ring protons and the G1−G5 protons for the β-galactosyl residue (Figure 5A,B). Noticeably weak coupling was observed between G4 and G5 protons in the galactosyl ring and is consistent with the H4-equatorial-H5-axial dihedral angle that is characteristic for a galactopyranosyl ring configuration. Also, no coupling was observed between G5 and the geminal G6 CH_2 protons. Generally, the H4 protons of galactose have the lowest field chemical shift, although for FGP the H3 (G3 = 3.60 ppm) and H2 (G2 = 3.47 ppm) shifts are both found at lower field than this. This suggests that the Gal ring is glycosidically linked at both positions 2 and 3, by the β-1,3-Gal backbone and the 1,2-linked arabinosyl side chain, as is confirmed by the permethylation analysis (Figure 4). The corresponding ^{13}C NMR signals were fully assigned by correlations through the HSQC spectrum (Figure 5C; Table 3) and confirmed the positions and anomericity of the glycosidic linkage. The Gal G6 carbon shift is at 61.5 ppm, showing that it is not substituted at this position. If it was, the expected shift would be closer to 67 ppm.[24] The homogeneity, purity, and molecular weight of the FGP were estimated by a diffusion-ordered (DOSY) NMR experiment (Figure 5D). A single polysaccharide chain was observed at −11.5 log *D*, which by comparison with a 1.6 MDa pullulan standard indicated a probable molecular mass of about 1−10 MDa. Furthermore, unlike gum arabic or arabinogalactans from larch, there is no evidence for terpenoids or other small molecule impurities.

Further structural assignments were obtained from comparison of the HSQC data with a NOESY-NMR spectrum (Figure 6 and Supporting Information). A through-space coupling was observed from the αAra-A anomeric H1 proton to the corresponding anomeric proton of the αAra-A″ residue (Figure 6). This assigns these two protons as being close

DOI: 10.1021/acs.jafc.5b02316
J. Agric. Food Chem. 2015, 63, 7286−7293

Table 3. Frost Grape Polysaccharide NMR Assignments[a]

residue	80 °C	60 °C	27 °C
α-Ara-A			
1	6.01/107.9	5.80/107.6	5.44/107.2
2	4.90/88.7	4.70/88.2	4.35/87.5
3	4.67/76.1	4.47/75.6	4.11/74.9
4	4.80/85.0	4.60/84.7	4.27/83.9
5a	4.26/61.8	4.07/na	na/na
5b	4.34/61.8	4.17/na	na/na
α-Ara-A′			
1	5.92/109.2	5.73/108.8	5.38/108.3
2	4.71/82.2	4.50/81.8	4.15/81.2
3	4.43/77.6	4.23/77.3	3.85/76.6
4	4.59/84.7	4.38/84.5	4.01/83.8
5a	4.21/62.1	4.01/na	3.64/na
5b	4.31/62.1	4.13/na	3.78/na
α-Ara-A″			
1	5.76/110.1	5.56/109.8	5.19/109.4
2	4.71/82.2	4.51/81.8	4.15/81.2
3	4.49/77.2	4.29/76.6	3.92/75.9
4	4.65/84.9	4.45/84.3	4.07/83.9
5a	4.22/62.1	4.02/na	3.64/na
5b	4.32/62.1	4.14/na	3.78/na
β-Gal			
1	5.10/102.4	4.90/102.0	4.54/101.4
2	4.07/71.5	3.85/71.1	3.47/70.6
3	4.18/73.5	3.98/73.0	3.60/72.5
4	4.47/69.4	4.26/69.0	3.88/68.5
5	4.22/75.8	4.03/75.4	3.65/75.1
6a	4.30/61.5	na/na	na/na
6b	4.35/61.5	na/na	na/na

[a]The assignments were made from ^{1}H, COSY, TOCSY, and HSQCNMR data acquired at 80, 60, and 27 °C in D_2O. na, not assigned. The units are in ppm.

together and is confirmed by a second NOE signal from the αAra-A″ H1 to the αAra-A H2 (Supporting Information). This is consistent with the αAra-A″ ring being glycosidically linked to the 2-position of the αAra-A ring and with the 6 ppm downfield shift observed for the αAra-A C2 carbon. The smaller NOESY signal observed in the opposite direction, from αAra-A H1 to the αAra-A″ H2 (Supporting Information), is also consistent with this structure. A final NOESY through-space correlation was seen from the αAra-A′ H1 to the αAra-A″ H4 proton, which is consistent with these two residues being connected via an α-1,3-linkage. It is also apparent that the chemical shifts for the αAra-A′ arabinosyl residue are very close to those reported for synthetic α-L-Araf-(1→2)-β-D-Galp-(1→6)-β-D-Galp,[24] confirming that the αAra-A′ is indeed a terminal residue. However, it is also conceivable that the terminal Ara-A′ forms a separate branch from the galactosyl backbone, so that Ara-A′ and Ara-A″ are both terminal residues. This arrangement would explain the absence of a predicted downfield shift for the 3-linked Ara-A′ H3/C3 signals,[20] but it also contradicts the A′-to-A″4 NOESY correlation (Supporting Information) and the data from the permethylation analysis. Indeed, the NMR integral ratios for Ara-A and A″ are 1:1, whereas Ara-A′ is 0.6 of these, suggesting that there is probable structural diversity in the arabinosyl side chains.

Acetyl Modification and Emusifying Properties. The native Frost grape polysaccharide was soluble in water at concentrations <2% w/v. At higher concentrations the FGP formed gels that were difficult to dissolve even at elevated temperatures. Aqueous 1−2% w/v solutions are viscous, but the FGP material was readily pourable at concentrations up to 0.5% w/v. The point at which gels formed was about 12% w/v, whereas less concentrated solutions were viscous liquids (Figure 7A). It was also noted that the FGP was poorly soluble in dimethyl sulfoxide (DMSO) and that it remained as an insoluble gel during attempted acetylation with acetic anhydride. Indeed, attempts to peracetylate the polysaccharide in acetic anhydride catalyzed by either pyridine, DMAP, or even sodium hydroxide were entirely unsuccessful, even when reacted at elevated temperatures. A considerable amount of coloration occurred at reflux temperature in acetic anhydride, and the majority of the FGP remained as a solid mass. To circumvent these problems we acetyl-modified the native FGP in aqueous phosphate buffer using vinyl acetate as the acetyl donor as described by Adeuya and Price.[25] This acetylated FGP was compared with the native FGP and commercial gum arabic for the ability to emulsify oil/water mixtures (Table 4; Figure 7B).

DISCUSSION

In summary, we report the structure of a new arabinogalactan polysaccharide produced from the cut stems of the North American grape species *V. riparia* (Frost grape). The neutral sugars composition of the native FGP, determined by aldononitrile acetate GC-MS analysis, consists of predominantly L-arabinofuranose (L-Araf, 55.2%) and D-galactopyranose (D-Galp 30.1%), with smaller components of D-xylose (11.2%) and D-mannose (3.5%). Permethylation linkage analysis indicates a complex nonlinear structure containing terminal arabosyl and mannosyl residues and β-1,3-linked internal galactosyl residues. Analysis of the uronic acid sugars present identified a minor component of glucuronic acid (GlcA) at about 2% of the total sugars. GC-MS analysis of the borodeuteride-reduced GlcA showed that the GlcA is linked via a galactosyl residue, rather than through the arabinose groups. HSQC, COSY, TOCSY, and DOSY NMR data were obtained on the native polysaccharide by acquiring spectra at high temperature (80 °C) and from the analysis of the anomeric signals showed the presence of at least three distinct α-linked arabinosyl groups and a major β-linked galactosyl residue. Unlike gum arabic and several other arabinogalactans, the FGP did not give a positive colorimetric test for hydroxyproline or a positive Bradford assay, and we conclude that the hydroxyproline-rich protein (AGP) content is low or entirely absent. DOSY NMR indicated a single high-molecular-weight arabinogalactan (molecular mass of about 1−10 MDa) and confirmed that it contains no smaller molecules such as oligosaccharides, terpenoids, free monosaccharides, or hydroxylproline-rich glycoprotein. We therefore conclude that the structure of FGP is as presented in Figure 6.

Gum arabics typically consist of a mixture of arabinogalactan polysaccharide and a hydroxyproline-rich glycoprotein but with significant variability with source, such that the exact molecular structures are uncertain. The glycoprotein is a hydroxyproline-rich arabinogalactan (~2% protein) and is attached to oligo-α-1,3-L-arabinofurans and the galactose residues of oligo-arabinogalactans.[26−28] The polysaccharide component is a β-1,3-D-galactopyran core with 1,6-linked side chains of β-D-uronic acids, β-D-galactose, α-L-arabinose, and α-L-rhamnose and terminal sugars composed of α-L-rhamnopyranose, α-L-arabinofuranose, and β-D-uronic acids via 1,2- and 1,4-linkages.[12−14,20,29]

A related arabinogalactan is tragacanth gum (*Astragalus gummifer*, E413) which is an exudate gum consisting of a mixture of

DOI: 10.1021/acs.jafc.5b02316
J. Agric. Food Chem. 2015, 63, 7286−7293

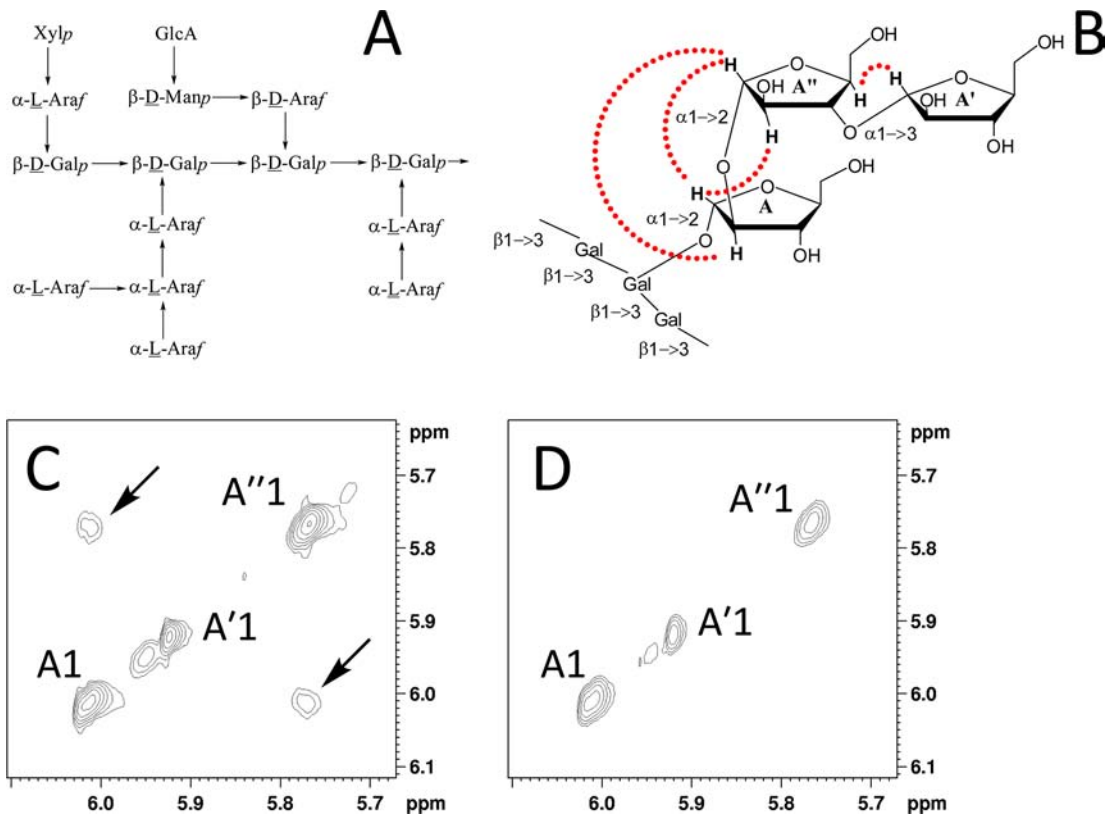

Figure 6. Structure of the Frost grape polysaccharide, a high-Ara α-1,2-substituted β-1,3-linked arabinogalactan, structurally analogous to gum arabic: (A) based on composition and linkage assignments; (B) major Ara*f*-α1,3-Ara*f*-α1,2-Ara*f*-α1,2-Gal*p* branching motif as determined by NMR (the four NOESY through-space correlations are shown in red); (C) NOESY (the Ara-A1-to-Ara-A″1 NOESY correlations are arrowed; the three other NOESY correlations are shown in the Supporting Information); (D) TOCSY assignments for the arabinosyl anomeric region.

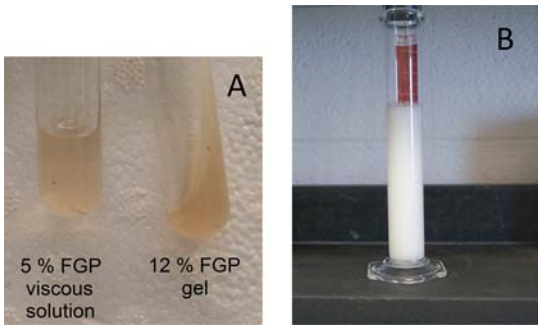

Figure 7. (A) Gelling point of Frost grape polysaccharide in aqueous solution (5 and 12% w/v); (B) stable emulsion with 0.1% w/v FGP with 1% v/v grapefruit oil after 72 h.

polysaccharides containing α-L-arabinofuranose and 1,4-linked β-D-galactopyranose, plus an acidic complex poly-1,4-linked α-D-galacturonate.[30] It is used as an acid-resistant thickener and emulsifier in sauces, salad dressings, and confectionery lozenges. Other related commercial gums are Western larch arabinogalactan[31] and mesquite gum, which is an arabinogalactan also with a β-1,3-galactopyran core and L-arabinose side chains.[32] Corn fiber gum is an alternative arabinogalactan replacement for gum arabic but requires an alkaline-peroxide pretreatment to enable its recovery.[33] The present Frost grape arabinogalactan polysaccharide is structurally analogous to gum arabic but gives a superior noncolored product that is readily extractable in large quantities. It differs from these prior mentioned gums, noticeably by rhamnosyl and AGP components, and is readily distinguished by minor unique xylosyl and mannosyl groups. With regard to the function and biosynthesis of the FGP, this is as yet unknown, although a possible role in cold tolerance or a resistance to insects (especially phylloxera aphids) remains a possibility. Because of the attributes the FGP has considerable potential as a replacement or extender for gum arabic in the food and beverage industries.

Table 4. Emulsifying Properties of Frost Grape Polysaccharide

polysaccharide	lipid[a]	emulsion stability (h)
1% native FGP	1% clove oil	++ (72)
0.1% native FGP	1% clove oil	++ (72)
1% native FGP	1% grapefruit oil	++ (72)
0.1% native FGP	1% grapefruit oil	++ (72)
native FGP	15% lemongrass oil	− (<1)
acetyl-modified FGP	15% lemongrass oil	+ (3)
20% gum arabic	15% lemongrass oil	+ (3)

[a]Controls without the emulsifier addition were immiscible.

■ ASSOCIATED CONTENT

Supporting Information

The Supporting Information is available free of charge on the ACS Publications website at DOI: 10.1021/acs.jafc.5b02316.

Additional GC-MS and NMR data in Figures S1 and S2 (PDF)

DOI: 10.1021/acs.jafc.5b02316
J. Agric. Food Chem. 2015, 63, 7286−7293

AUTHOR INFORMATION

Corresponding Author

*(N.P.J.P.) Phone: (309) 681-6246. Fax: (309) 681-6240. E-mail: Neil.Price@ars.usda.gov.

Notes

The authors declare no competing financial interest.

ACKNOWLEDGMENTS

We thank Trina Hartman (NCAUR-ARS, Peoria, IL, USA) for excellent technical assistance and Dr. Joseph Rich (NCAUR-ARS, Peoria, IL, USA) for review of the manuscript. Mention of trade names or commercial products in this paper is solely for the purpose of providing specific information and does not imply recommendation or endorsement by the U.S. Department of Agriculture.

REFERENCES

(1) Powell, K. S.; Cooper, P. D.; Forneck, A. The biology, physiology and host-plant interactions of grape phylloxera *Daktulosphaira vitifoliae*. *Adv. Insect Physiol.* **2013**, *45*, 159−218.

(2) Griesser, M.; Lawo, N. C.; Crespo-Martinez, S.; Griesser, M.; Lawo, N. C.; Crespo-Martinez, S.; Schoedl-Hummel, K.; Wieczorek, K.; Gorecka, M.; Liebner, F.; Zweckmair, T.; Stralis Pavese, N.; Kreil, D.; Forneck, A. Phylloxera (*Daktulosphaira vitifoliae* Fitch) alters the carbohydrate metabolism in root galls to allowing the compatible interaction with grapevine (*Vitis* ssp.) roots. *Plant Sci.* **2015**, *234*, 38−49.

(3) Zhang, J.; Wu, X.; Niu, R.; Liu, Y.; Liu, N.; Xu, W.; Wang, Y. Cold-resistance evaluation in 25 wild grape species. *Vitis.* **2012**, *51*, 153−160.

(4) Brillouet, J.-M.; Bosso, C.; Moutonet, M. Isolation, purification, and characterization of an arabinogalactan from a red wine. *Am. J. Enol. Vitic.* **1990**, *41*, 29−36.

(5) Doco, T.; Vuchot, P.; Cheynier, V.; Moutonet, M. Structural modification of wine arabinogalactans during aging on lees. *Am. J. Enol. Vitic.* **2003**, *54*, 150−157.

(6) Pellerin, P.; Vidal, S.; Williams, P.; Brillouet, J. M. Characterization of five type II arabinogalactan-protein fractions from red wine of increasing uronic acid content. *Carbohydr. Res.* **1995**, *277*, 135−143.

(7) Saulnier, L.; Brillouet, J.-M. An arabinogalactan-protein from the pulp of grape berries. *Carbohydr. Res.* **1989**, *188*, 137−144.

(8) Villetaz, J. C.; Amado, R.; Neukom, H. Structural investigations of an arabinan from grape juice. *Carbohydr. Polym.* **1981**, *1*, 101−105.

(9) Phillips, G. O., Williams, P. A., Wedlock, D. J., Eds. *Gums and Stabilisers for the Food Industry 7*; IRL Press: Oxford, UK, 1994.

(10) Phillips, G. O. Acacia gum: a nutritional fibre; metabolism and calorific value. *Food Addit. Contam.* **1998**, *15*, 251−264.

(11) Ray, A. K.; Bird, P. B.; Iacobucci, G. A.; Clark, B. C., Jr. Functionality of gum arabic: fractionation characterization and evaluation of gum fractions in citrus oil emulsions and model beverages. *Food Hydrocolloids* **1995**, *9*, 123−131.

(12) Churms, S. C.; Merrifield, E. H.; Stephen, A. M. Some new aspects of the molecular structure of *Acacia senegal* gum (gum arabic). *Carbohydr. Res.* **1983**, *123*, 267−279.

(13) Defaye, J.; Wong, E. Structural studies of gum arabic, the exudate polysaccharide from *Acacia senegal*. *Carbohydr. Res.* **1986**, *150*, 221−231.

(14) Osman, M. E.; Menzies, A. R.; Williams, P. A.; Phillips, G. O.; Baldwin, T. C. The molecular characterisation of the polysaccharide gum from *Acacia senegal*. *Carbohydr. Res.* **1993**, *246*, 303−318.

(15) Price, N. P. J. Acylic sugar derivatives for GC/MS analysis of ^{13}C-enrichment during carbohydrate metabolism. *Anal. Chem.* **2004**, *76*, 6566−6574.

(16) Cesaretti, M.; Luppi, E.; Maccari, F.; Volpi, N. A 96-well assay for uronic acid carbazole reaction. *Carbohydr. Polym.* **2003**, *54*, 59−61.

(17) Taylor, R. L.; Conrad, H. E. Stoichiometric depolymerization of polyuronides and glycosaminoglycuronans to monosaccharides following reduction of their carbodiimide-activated carboxyl groups. *Biochemistry* **1972**, *11*, 1383−1388.

(18) Ciucanu, I.; Kerek, F. A simple and rapid method for the permethylation of carbohydrates. *Carbohydr. Res.* **1984**, *131*, 209−217.

(19) Kivirikko, K. I.; Liesmaa, M. A. A colorimetric method for determination of hydroxyproline in tissue hydrolysates. *Scand. J. Clin. Lab. Invest.* **1959**, *11*, 128−133.

(20) Nie, S.-P.; Wang, C.; Cui, S. W.; Wang, Q.; Xie, M.-Y.; Phillips, G. O. A further amendment to the classical core structure of gum arabic (*Acacia senegal*). *Food Hydrocolloids* **2013**, *31*, 42−48.

(21) Odonmazig, P.; Ebringerová, A.; Machová, E.; Alföldi, J. Structural and molecular properties of the arabinogalactan isolated from Mongolian larchwood (*Larix dahurica* L.). *Carbohydr. Res.* **1994**, *252*, 317−324.

(22) Bou Raad, R.; Méniche, X.; de Sousa-d'Auria, C.; Chami, M.; Salmeron, C.; Tropis, M.; Labarre, C.; Daffé, M.; Houssin, C.; Bayan, N. A deficiency in arabinogalactan biosynthesis affects *Corynebacterium glutamicum* mycolate outer membrane stability. *J. Bacteriol.* **2010**, *192*, 2691−2700.

(23) Suárez, E. R.; Kralovec, J. A.; Noseda, M. D.; Ewart, H. S.; Barrow, C. J.; Lumsden, M. D.; Grindley, T. B. Isolation, characterization and structural determination of a unique type of arabinogalactan from an immunostimulatory extract of *Chlorella pyrenoidosa*. *Carbohydr. Res.* **2005**, *340*, 1489−1498.

(24) Csávás, M.; Borbás, A.; Jánossy, L.; Batta, G.; Lipták, A. Synthesis of the α-L-Ara*f*-(1→2)-β-D-Gal*p*-(1→6)-β-D-Gal*p*-(1→6)-[α-L-Ara*f*-(1→2)]-β-D-Gal*p*-(1→6)-D-Gal hexasaccharide as a possible repeating unit of the cell-cultured exudates of *Echinacea purpurea* arabinogalactan. *Carbohydr. Res.* **2001**, *336*, 107−115.

(25) Adeuya, A.; Price, N. P. J. Enumeration of hydroxyl groups of sugars and sugar alcohols by aqueous-based acetylation and matrix-assisted laser desorption/ionization time-of-flight mass spectrometry. *Rapid Commun. Mass Spectrom.* **2012**, *26*, 1372−1376.

(26) Showalter, A. M. Arabinogalactan-proteins: structure, expression and function. *Cell. Mol. Life Sci.* **2001**, *58*, 1399−1417.

(27) Seifert, G. J.; Roberts, K. The biology of arabinogalactan proteins. *Annu. Rev. Plant Biol.* **2007**, *58*, 137−161.

(28) Fincher, G. B.; Stone, B. A.; Clarke, A. E. Arabinogalactan-proteins: structure, biosynthesis, and function. *Annu. Rev. Plant Physiol.* **1983**, *34*, 47−70.

(29) Qi, W.; Fong, C.; Lamport, D. T. A. Gum arabic is a twisted hairy root. A new model based on *O*-galactosylhydroxyproline as the polysaccharide attachment side. *Plant Physiol.* **1991**, *96*, 848−855.

(30) Tischer, C. A.; Iacomini, M.; Gorin, P. A. J. Structure of the arabinogalactan from gum tragacanth (*Astralagus gummifer*). *Carbohydr. Res.* **2002**, *337*, 1647−1655.

(31) Chandrasekaran, R.; Janaswamy, S. Morphology of Western larch arabinogalactan. *Carbohydr. Res.* **2002**, *337*, 2211−2222.

(32) Vernon-Carter, E. J.; Beristain, C. I.; Pedroza-Islas, R. Mesquite gum (*Prosopis* gum). *Dev. Food Sci.* **2000**, *41*, 217−238.

(33) Yadav, M. P.; Parris, N.; Johnston, D. B.; Hicks, K. B. Fractionation, characterization, and study of the emulsifying properties of corn fiber gum. *J. Agric. Food Chem.* **2008**, *56*, 4181−4187.

DOI: 10.1021/acs.jafc.5b02316
J. Agric. Food Chem. 2015, 63, 7286−7293

Table 1. Proximate Composition and Fatty Acid Quantification[a]

sample[b]	moisture (%)	proteins (%, dw)	ashes (%, dw)	lipids (%, dw)	C16:0	C18:0	C18:1$_{\Delta 9}$	C18:1$_{\Delta 11}$	C18:2
1TGT	3.18 ± 0.01	12.1 ± 0.2	2.13 ± 0.09	62.7 ± 1.5	6.14 ± 0.04	3.40 ± 0.08	81.9 ± 0.2	1.36 ± 0.01	7.23 ± 0.15
1TGT-160	3.05 ± 0.01	13.0 ± 0.2	2.23 ± 0.09	64.2 ± 0.7	6.48 ± 0.07	3.31 ± 0.10	81.4 ± 0.2	1.46 ± 0.14	7.37 ± 0.11
1TGT-180	3.04 ± 0.01	13.2 ± 0.1	2.36 ± 0.06	64.4 ± 0.8	6.13 ± 0.10	3.41 ± 0.03	81.9 ± 0.1	1.29 ± 0.01	7.25 ± 0.05
2TGT	3.69 ± 0.09	12.9 ± 0.1	2.07 ± 0.09	63.3 ± 1.2	6.18 ± 0.10	2.88 ± 0.09	83.2 ± 0.3	1.30 ± 0.07	6.49 ± 0.15
2TGT-160	3.13 ± 0.01	13.0 ± 0.1	2.13 ± 0.06	64.4 ± 0.8	6.15 ± 0.30	3.02 ± 0.18	84.9 ± 2.7	1.31 ± 0.12	6.66 ± 0.15
2TGT-180	3.11 ± 0.01	13.2 ± 0.2	2.14 ± 0.08	64.5 ± 2.4	6.11 ± 0.02	2.79 ± 0.09	82.7 ± 0.1	1.27 ± 0.01	7.12 ± 0.15
3TGT	3.26 ± 0.06	11.8 ± 0.3	2.36 ± 0.06	63.5 ± 0.3	6.92 ± 0.01	2.98 ± 0.09	80.8 ± 0.4	1.61 ± 0.06	7.73 ± 0.26
3TGT-160	3.12 ± 0.01	12.6 ± 0.1	2.42 ± 0.07	64.4 ± 1.0	7.16 ± 0.26	3.00 ± 0.07	80.2 ± 0.4	1.65 ± 0.16	7.97 ± 0.06
3TGT-180	3.10 ± 0.03	12.6 ± 0.2	2.35 ± 0.01	63.4 ± 2.0	7.15 ± 0.09	3.35 ± 0.03	80.4 ± 0.1	1.53 ± 0.03	7.57 ± 0.02
4TG	4.28 ± 0.09	14.0 ± 0.2	2.34 ± 0.15	61.3 ± 0.8	5.55 ± 0.02	2.85 ± 0.08	80.2 ± 1.3	1.77 ± 0.04	10.90 ± 0.22
4TG-160	4.06 ± 0.03	15.2 ± 0.3	2.69 ± 0.13	64.5 ± 0.9	5.45 ± 0.06	2.96 ± 0.05	79.6 ± 0.4	1.11 ± 0.02	10.89 ± 0.16
4TG-180	4.05 ± 0.01	14.9 ± 0.2	2.75 ± 0.02	62.9 ± 0.7	5.56 ± 0.06	3.11 ± 0.06	81.1 ± 0.2	1.16 ± 0.09	9.06 ± 0.17
5T	3.69 ± 0.09	14.2 ± 0.1	2.12 ± 0.12	63.6 ± 0.4	5.55 ± 0.15	2.80 ± 0.07	80.7 ± 0.4	1.39 ± 0.12	9.61 ± 0.20
5T-160	3.67 ± 0.19	15.4 ± 0.1	2.54 ± 0.15	64.6 ± 1.4	5.54 ± 0.10	2.73 ± 0.18	82.0 ± 1.2	1.15 ± 0.05	8.49 ± 1.56
5T-180	3.50 ± 0.00	15.2 ± 0.3	2.24 ± 0.13	64.5 ± 1.4	5.57 ± 0.08	2.54 ± 0.06	80.3 ± 0.2	1.24 ± 0.08	10.33 ± 0.17
6CL	2.27 ± 0.20	15.0 ± 0.1	2.49 ± 0.16	65.5 ± 0.8	7.79 ± 0.16	4.86 ± 0.25	76.8 ± 0.6	1.33 ± 0.03	9.24 ± 0.21
7CB	3.37 ± 0.14	12.2 ± 0.3	2.33 ± 0.10	65.1 ± 1.3	7.67 ± 0.32	4.05 ± 0.06	80.5 ± 0.4	1.43 ± 0.12	6.29 ± 0.14
8CF	2.66 ± 0.12	12.7 ± 0.1	2.29 ± 0.13	67.2 ± 1.7	8.49 ± 0.92	4.92 ± 0.38	78.5 ± 2.3	1.60 ± 0.43	6.17 ± 0.24
9FR	3.30 ± 0.17	12.8 ± 0.2	2.31 ± 0.19	65.4 ± 0.6	7.77 ± 0.13	2.88 ± 0.09	77.8 ± 0.2	1.34 ± 0.11	10.05 ± 0.22
10CG	2.54 ± 0.08	13.5 ± 0.2	2.25 ± 0.10	64.4 ± 1.4	6.60 ± 0.10	3.40 ± 0.10	82.0 ± 0.2	1.34 ± 0.07	6.51 ± 0.08
11RS	2.41 ± 0.22	17.0 ± 0.2	1.30 ± 0.04	67.0 ± 1.8	6.56 ± 0.20	3.48 ± 0.08	79.4 ± 2.0	1.38 ± 0.11	8.98 ± 2.18

[a]Relative percentage of FAMEs, expressed as mean ± SD ($n \geq 3$). [b]TGT, Tonda Gentile Trilobata; TG, Tonda di Giffoni; T, Turkish.

isolated from commercial products, with the aim to discriminate their cultivar and origin. This approach allowed us not only to describe the chemical changes occurring in hazelnut after roasting but also (and this is the main object our work) to evaluate whether chemical composition permits hazelnut identification and which chemical parameters can be useful "markers" for hazelnut traceability.

MATERIALS AND METHODS

Chemicals. Methanol and acetonitrile (HPLC grade) and formic acid (50%, LC–MS grade) were purchased from Sigma–Aldrich (Milan, Italy). Water (HPLC grade) was obtained by Elga Purelab Ultra system (M-medical, Cornaredo, Milano, Italy). Polyphenol standard molecules (gallic acid, protocatechuic acid, *p*-hydroxybenzoic acid, caffeic acid, catechin, epicatechin, myricetin, quercetin, and kaempferol) were purchased also from Sigma–Aldrich (Milan, Italy). All the other chemicals and solvents were of reagent-grade level and purchased also from Sigma–Aldrich (Milan, Italy).

Samples. Three different lots of "Tonda Gentile Trilobata" hazelnuts (1TGT and 2TGT samples from Piedmont, Italy; 3TGT sample from Chile), one lot of "Tonda di Giffoni" (4TG sample, from Campania, Italy), and one lot of "Tombul" hazelnuts (5T sample, from Turkey) were kindly provided and certified by INOQ (Istituto Nord Ovest Qualità, Moretta, Cuneo, Italy). Hazelnuts were all from the same harvesting year (2007), except the 2TGT hazelnuts, which were harvested in the 2008 season. The hazelnut lots (2000 g) were divided in three subsamples (600 g). From each subsample, a portion (50 g) was analyzed as raw (shelled with perisperm). The other portions (each 200 g) were roasted in a ventilated conventional oven, following two different roasting conditions (160 °C for 25 min and 180 °C for 10 min). These two different roasting protocols were previously selected in order to obtain similar browning degree and optimal organoleptic properties (unpublished data). All the roasted hazelnuts were analyzed after removing perisperm.

Hazelnuts obtained from commercial processed food (whole roasted hazelnuts without perisperm) were also analyzed: hazelnuts in milk chocolate bars (6CL and 11RS samples), white chocolate bars (7CB sample), and gianduja chocolate bars (10CG sample), hazelnuts with a dark chocolate coating (8CF), and hazelnuts contained in pralines (9FR). 7CB and 10CG samples were labeled as Tonda Gentile Trilobata hazelnuts from Piedmont (Italy). Whole hazelnuts were separated by melting chocolate at 40 °C, and any chocolate residue was removed using filter paper. For each commercial product, at least 200 g of hazelnuts was obtained; afterward, the hazelnuts were pooled and subsampled in three portions (each 50 g) that were independently analyzed.

Proximate Composition Analysis. The proximate composition was determined as previously described.[15] Raw, roasted, and commercial hazelnuts were ground in a mortar (particle size <2 mm) and then subjected to the determination of moisture, proteins, ashes, and lipid content. Lipid fraction was extracted using a semiautomatic Soxhlet Büchi extraction system B-811 (Büchi Labortechnik AG, Flawil, Switzerland) for 6 h, employing dichloromethane as solvent. Fatty acid methyl esters (FAMEs) were obtained by transesterification of triacylglycerols and successively analyzed by GC-FID;[15] the semiquantification of individual compounds was done as relative percentage.

Extraction and Characterization of Phenolic Fraction. The extraction and characterization of phenolic fraction were performed as previously described.[15] Polyphenols were extracted from defatted hazelnut powders using methanol; each sample was extracted in triplicate and dry extracts were stored at −20 °C until use. The antioxidant activity of hazelnut extracts was evaluated using the DPPH$^{\bullet}$ scavenging assay and expressed as inhibition percentage (I %).[15] Polyphenol separations were obtained by RP-HPLC/DAD.[15] Phenolic acids and flavonoids were tentatively identified by comparison with retention times and UV spectra of individual standard molecules (gallic acid, protocatechuic acid, *p*-hydroxybenzoic acid, caffeic acid, catechin, epicatechin, myricetin, quercetin, and kaempferol); the quantification was performed on the basis of calibration curves obtained with the corresponding standards.

The total phenol content was determined using the Folin–Ciocalteu method,[16] modified as follows. One hundred microliters of Folin–Ciocalteu reagent and 350 μL of aqueous Na_2CO_3 (5% w/v) were added to 200 μL of sample (methanolic solution of phenolic extract at concentration 3 mg mL^{-1}), and then the solutions were diluted to a final volume of 2900 μL with distilled water. After 1 h, the absorbance was read at 760 nm, using a Kontron UVIKON 930 spectrophotometer (Kontron Instruments, Milan, Italy). Results were expressed as gallic acid equivalents.

DOI: 10.1021/acs.jafc.5b03201
J. Agric. Food Chem. 2015, 63, 7294–7303

Determination of Protein Fingerprint (SDS-PAGE). Proteins were extracted from hazelnut powders obtained after removing the polyphenols, using the Laemmli sample buffer, prepared by adding 2 mg of bromophenol blue to 4.2 mL of 0.5 M TRIS-HCl (pH 6.8), 0.8 mL of 80% glycerol, and 1.6 mL of sodium dodecyl sulfate (SDS) 15% (w/v).[17] Each sample (0.5 mg) was suspended in 1.5 mL of sample buffer and then mixed in a Thermomixer apparatus (Thermomixer comfort, Eppendorf, Milan, Italy) at 37 °C and 750 rpm for 2 h. The solid residue was separated by centrifugation at 20800*g* for 20 min, and supernatant (i.e., protein extract) was directy loaded on the gel. Proteins were separated by sodium dodecyl sulfate−polyacrylamide gel electrophoresis (SDS-PAGE; Mini-PROTEAN 3 Cell, Bio-Rad, Richmond, CA, USA) with 15% acrylamide resolving and 4% acrylamide stacking gel. Following electrophoresis, the gel was stained with 0.1% Coomassie blue R-250 (w/v) in 10% acetic acid (v/v) and 40% methanol (v/v) for 1 h and destained with 10% acetic acid (v/v) and 40% methanol (v/v) overnight.

Fluor-S Multimager and Quantity One software (Bio-Rad) were used for gel analysis. Gel bands were expressed as relative percentage for each sample and used as parameters for statistical analysis.

Statistical Analysis. Results were expressed as mean ± standard deviation (SD) of at least three independent experiments. All statistical analyses were performed using the free statistical software R 2.8.1 version (http://www.R-project.org).[18] Differences were estimated by analysis of variance (ANOVA) and Tukey HSD test (Laercio package). Pearson's correlation analysis was used to determine correlation coefficients and their statistical significance. The statistical significance level was set to 0.05. Multivariate statistical analysis was performed using principal component analysis (PCA) and hierarchical clustering on principal components (HCPC), both implemented on FactoMineR package for R. For details concerning the statisical analysis results, readers are referred to the Supporting Information (Tables 1S−10S; Figures 1S−7S).

RESULTS AND DISCUSSION

Proximate Composition of Hazelnut Samples. The proximate composition of hazelnut samples is reported in Table 1. The values are in agreement with the data previously reported in literature.[8,19]

As expected, moisture values significantly decrease after the roasting process (no significant differences were observed between the two different roasting conditions); thus the other parameters were expressed on a dry weight (dw) basis.

Concerning lipid content, roasting slightly increased the oil extractability, although this increment was not statistically significant. In a general way, the commercial hazelnuts showed significantly higher values (mean value 65.8%) than the other hazelnut samples (mean values of 62.9% and 64.2% for raw and roasted hazelnuts, respectively. Presumably, the impact of the industrial process was stronger than that of experimental laboratory roasting (for example, higher damage of membranes or higher protein denaturation, as suggested by Amaral and coauthors).[8] No differences were observed depending on the hazelnut origin.

In contrast, the protein content was significant for hazelnut discrimination. Tombul (5T) and Tonda di Giffoni (4TG) samples showed significantly higher values than Tonda Gentile Trilobata hazelnuts. In a previous work, we additionally observed that Italian TGT hazelnuts have a higher protein content than that of the same cultivar cultivated in Chile.[15] Also in the present work, the Chilean TGT hazelnuts showed minimal but statistically significant differences from the Italian TGT ones, which showed higher protein content in both raw and roasted samples. Furthermore, the protein content was significantly lower in raw hazelnuts than in the corresponding roasted ones. This difference could be related to detachment and successive removal of perisperm after roasting, because the protein content of hazelnut skin (perisperm) is lower than that of hazelnut kernel.[20,21]

The ash content, which is the expression of the total mineral content, was in the range 1.30−2.75%. Also in this case, for the major part of the samples, the roasting process caused a significant increase of the values. In a general way, the ash content was not so useful for geographic origin identification, excepting for Tonda di Giffoni hazelnuts, which presented significantly higher values than those of TGT hazelnuts. In a previous work, it was demonstrated that the analysis of individual trace metals, especially lanthanides, is able to identify hazelnuts coming from different areas of cultivation, having individuated a link among hazelnuts and soil through lanthanide distribution.[12]

Considering roasted hazelnuts from commercial products, a quite homogeneous composition was observed for lipids and ashes (the only exception was 11RS sample, which presented lower ash content with respect to the other samples). The protein content was more variable, ranging from 12% (7CB sample) to 17% (11RS).

Characterization of Fatty Acid Fraction (FAMEs). The hazelnut oil was characterized by GC-analysis of fatty acid methyl esters (FAMEs). The major fatty acids were identified and quantified in terms of relative percentage: palmitic acid (C16:0), stearic acid (C18:0), oleic acid ($C18:1_{\Delta 9}$) and its isomer vaccenic acid ($C18:1_{\Delta 11}$), and linoleic acid (C18:2) (Table 1).

The relative content of fatty acids in hazelnut oil is in agreement with literature data;[22,23] oleic acid was the predominant fatty acid, ranging from 76.7% to 84.9%. The roasting process did not influenced the relative composition of FAMEs (generally no significant differences were observed between raw and roasted hazelnuts); however, a significantly higher palmitic and, particularly, stearic acid content in commercial samples than in all the other hazelnuts (raw and roasted in laboratory) was observed. In this regard, it is interesting to note that stearic acid is the major fatty acid of cocoa butter (35.8%), followed by oleic (33.6%), palmitic (26.2%), and linoleic (2.68%) acids.[24] Considering that all the commercial hazelnuts were obtained from chocolate-based products, it is presumable that a phenomenon of fat migration, typical of composite confectionery products and thoroughly studied in different model systems, occurred. Fat migration is driven by the concentration gradient between the differing triacylglycerol compositions of the adjacent fat phases and depends on temperature of storage, formulation, and structure of the layers.[25] Thus, the different triacylglycerol compositions of hazelnut and cocoa could be responsible of the higher content of stearic and palmitic acids in the commercial products. Another reason for stearic acid increasing could be the partial degradation of unsaturated fatty acids during technological processing, but no information is known about the treatment of hazelnuts isolated from the commercial products, thus it is difficult to argue this hypothesis.

Fatty acid composition also varied depending on hazelnut cultivar and their geographic origin. Considering roasted hazelnuts, palmitic and vaccenic acids were higher in TGT hazelnuts, while linoleic acid was prevalent in Turkish and TG samples. TGT hazelnuts from Italy and from Chile differ for the relative percentage of oleic acid (higher in Italian TGT) and palmitic acid and vaccenic acid (higher in Chilean TGT). The same results were obtained from analysis of raw and roasted

DOI: 10.1021/acs.jafc.5b03201
J. Agric. Food Chem. 2015, 63, 7294−7303

Table 2. Total Phenols, Antioxidant Activity and Phenolic Acid Content of Hazelnut Samples[a]

	GAE (mg g^{-1}, dw)	AA (DPPH•, I%)	Gal (mg g^{-1}, dw)	Proto (mg g^{-1}, dw)	pOH (mg g^{-1}, dw)	Caff (mg g^{-1}, dw)
1TGT	11.84 ± 0.70	90.1 ± 0.3	1.99 ± 0.23	4.31 ± 0.37	1.32 ± 0.15	1.72 ± 0.13
1TGT-160	3.18 ± 0.20	19.3 ± 0.5	3.40 ± 0.33	6.69 ± 0.55	2.85 ± 0.35	2.42 ± 0.14
1TGT-180	2.35 ± 0.12	20.0 ± 0.3	7.31 ± 0.97	7.49 ± 0.14	3.06 ± 0.14	2.44 ± 0.10
2TGT	23.28 ± 1.81	86.0 ± 0.2	3.01 ± 0.33	6.32 ± 0.28	2.14 ± 0.29	2.54 ± 0.18
2TGT-160	4.62 ± 0.38	41.1 ± 1.0	10.22 ± 1.55	4.49 ± 0.81	1.87 ± 0.13	2.34 ± 0.09
2TGT-180	3.41 ± 0.08	40.0 ± 0.1	6.80 ± 0.30	5.77 ± 0.25	2.04 ± 0.22	2.47 ± 0.08
3TGT	13.67 ± 0.85	90.4 ± 0.4	2.98 ± 0.11	6.59 ± 0.76	4.01 ± 0.36	2.51 ± 0.06
3TGT-160	4.05 ± 0.44	38.2 ± 0.1	8.57 ± 0.98	5.82 ± 0.90	2.01 ± 0.11	2.46 ± 0.38
3TGT-180	4.66 ± 0.42	39.0 ± 0.3	10.83 ± 0.50	4.71 ± 0.47	2.10 ± 0.09	2.41 ± 0.13
4TG	10.21 ± 0.71	84.9 ± 0.2	1.85 ± 0.16	5.78 ± 0.33	2.73 ± 0.22	1.63 ± 0.11
4TG-160	4.09 ± 0.08	21.0 ± 0.2	12.29 ± 1.51	3.55 ± 1.02	1.87 ± 0.21	1.94 ± 0.10
4TG-180	2.25 ± 0.04	21.2 ± 0.3	6.51 ± 0.42	8.11 ± 0.93	2.34 ± 0.24	2.05 ± 0.11
5T	20.05 ± 0.04	93.60 ± 0.3	2.39 ± 0.10	5.31 ± 0.74	2.51 ± 0.18	1.99 ± 0.02
5T-160	4.27 ± 0.66	27.5 ± 1.0	12.51 ± 0.59	4.38 ± 0.29	1.64 ± 0.00	1.82 ± 0.23
5T-180	4.38 ± 0.29	26.6 ± 0.3	12.36 ± 0.83	5.26 ± 0.51	2.13 ± 0.16	2.21 ± 0.11
6CL	1.71 ± 0.09	9.1 ± 0.5	6.27 ± 0.86	5.49 ± 0.57	b	2.21 ± 0.03
7CB	2.70 ± 0.25	15.3 ± 0.5	4.73 ± 0.52	4.47 ± 1.16	1.54 ± 0.11	2.60 ± 0.35
8CF	2.13 ± 0.14	8.1 ± 0.5	5.57 ± 0.32	3.07 ± 0.09	1.42 ± 0.06	2.34 ± 0.16
9FR	3.57 ± 0.30	25.4 ± 0.5	11.26 ± 1.51	9.63 ± 1.86	1.77 ± 0.17	2.29 ± 0.17
10CG	2.17 ± 0.10	11.3 ± 0.3	17.66 ± 3.20	7.45 ± 0.75	1.86 ± 0.16	3.60 ± 0.34
11RS	1.59 ± 0.12	11.2 ± 0.3	11.20 ± 0.87	2.62 ± 0.27	1.55 ± 0.06	2.40 ± 0.16

[a]Mean ± SD, $n \geq 3$. Abbreviations: AA, antioxidant activity; GAE, gallic acid equivalent; Gal, gallic acid; Proto, protocatechuic acid; pOH, p-hydroxybenzoic acid; Caff, caffeic acid; TGT, Tonda Gentile Trilobata; TG, Tonda di Giffoni; T, Turkish. [b]Not detectable.

hazelnuts together, thus confirming that fatty acid composition is related to the hazelnut cultivar and origin.

Determination of Total Phenol Content, Antioxidant Activity and Polyphenolic Profile. The hazelnut phenolic fraction, obtained after removing lipid and using methanol as solvent, was preliminarily characterized for the total phenol content and the antiradical activity (DPPH• method); then some phenolic acids and flavonoids (free phenolic fraction extractable in methanol) were individually identified and quantified.

The total phenol content of raw hazelnuts was in the range 10.21−23.28 mg of gallic acid equivalents (GAE) per gram of hazelnut (dry weight) and was in the order 2TGT > 5T > 3TGT > 1TGT > 4TG (Table 2). After roasting, a strong decrease was observed (from 60% in 4TG-160 to 85% for 2TGT-180). These results are consistent with those reported by Pelvan and coauthors,[9] which observed a loss of total phenols after roasting (140 °C for 30 min) from 42% to 88%, but differ in the absolute values, being about 3.5-fold higher. This difference could be ascribed to the different extraction protocol (80% acetone as solvent) but also to the different cultivars analyzed, their geographical origin, and the harvest season.

The loss of polyphenols after roasting is prevalently due to removal of hazelnut skin (perisperm), which is an important source of phenolic compounds containing about 40-fold higher polyphenols than kernels.[20,26] Furthermore, the high temperatures applied during the process could cause the degradation of thermally sensitive compounds, thus negatively influencing the total phenol content.

The hazelnuts isolated from the commercial products showed values in the range or lower than that obtained for the hazelnuts experimentally roasted in laboratory (from 1.59 to 3.57 mg GAE g^{-1} for 11RS and 9FR samples, respectively). In a general way, commercial samples did not evidence significant differences with respect to the experimentally roasted hazelnuts.

In the same manner, the antioxidant activity drastically decreased as a consequence of roasting. Polyphenolic extracts were evaluated at 200 μg mL^{-1} concentration, and results were expressed as DPPH• inhibition percentage (I%) (Table 2). The major antioxidant activity was observed for 5T hazelnuts (93.6%), followed by 3TGT, 1TGT, 2TGT, and 4TG hazelnuts (90.4%, 90.1%, 86.0%, and 84.9%, respectively). After roasting, the antioxidant activity diminished in different proportions, from about 79% for 1TGT to about 53% for 2TGT hazelnuts; in general, no significant differences were evidenced between the two roasting protocols employed. The amount of loss of antioxidant activity seems to be not dependent on hazelnut variety and only partially related to the loss of polyphenolic compounds, for which a higher decrease was observed (even though the correlation between these two parameters was significant; $r = 0.8932$, $p = 5.07 \times 10^{-8}$). In fact, the overall effect of roasting depends on the balance between the loss of natural hazelnut polyphenols, through both their thermal degradation and the removal of skin from roasted kernels, and the formation of new antioxidant molecules derived from the Maillard reaction (melanoidins). A previous work demonstrated that the antioxidant activity of roasted hazelnuts tends to increase from 10 to 60 min of roasting (at the constant temperature of 150 °C).[11] In the experimental conditions adopted in the present work (180 °C for 10 min and 160 °C for 25 min), no significant differences were observed; presumably the effect of prolonged roasting time was counterbalanced by the reduction of the temperature.

Different from that observed for the total polyphenol content, the antioxidant activity of commercial hazelnuts was significantly lower than that of experimentally roasted ones. Among them, only the 9FR sample (praline) showed an antioxidant activity similar to that of experimentally roasted

DOI: 10.1021/acs.jafc.5b03201
J. Agric. Food Chem. 2015, 63, 7294−7303

Table 3. Flavonoid Content of Hazelnut Samples[a]

	Cat (mg g^{-1}, dw)	Epi (mg g^{-1}, dw)	Mir (mg g^{-1}, dw)	Quer (mg g^{-1}, dw)	Kaem (mg g^{-1}, dw)
1TGT	5.59 ± 1.20	2.20 ± 0.13	5.52 ± 0.48	5.40 ± 0.36	2.92 ± 0.34
1TGT-160	20.95 ± 1.34	2.87 ± 0.16	7.12 ± 0.38	8.10 ± 0.39	3.88 ± 0.27
1TGT-180	16.42 ± 2.26	2.81 ± 0.15	6.95 ± 0.11	7.70 ± 0.38	3.75 ± 0.06
2TGT	5.39 ± 0.51	4.49 ± 0.26	8.16 ± 0.44	7.93 ± 0.62	4.42 ± 0.33
2TGT-160	11.08 ± 1.06	2.83 ± 0.29	7.11 ± 0.40	7.44 ± 0.39	4.02 ± 0.31
2TGT-180	11.29 ± 2.03	2.89 ± 0.18	7.42 ± 0.16	7.55 ± 0.27	4.01 ± 0.09
3TGT	7.55 ± 2.10	3.58 ± 0.20	8.10 ± 0.10	7.99 ± 0.34	4.34 ± 0.41
3TGT-160	12.57 ± 2.11	3.07 ± 0.32	6.99 ± 0.68	7.40 ± 0.73	3.73 ± 0.36
3TGT-180	12.01 ± 1.56	3.25 ± 0.32	7.13 ± 0.42	7.43 ± 0.44	3.82 ± 0.16
4TG	9.55 ± 0.88	2.13 ± 0.15	5.04 ± 0.32	5.84 ± 0.44	2.65 ± 0.28
4TG-160	8.45 ± 1.11	2.96 ± 0.27	5.98 ± 0.31	6.99 ± 0.69	3.14 ± 0.22
4TG-180	14.95 ± 1.37	2.55 ± 0.18	6.31 ± 0.33	7.80 ± 0.05	3.33 ± 0.17
5T	7.32 ± 0.23	3.02 ± 0.29	7.05 ± 0.41	7.50 ± 0.03	3.58 ± 0.41
5T-160	9.53 ± 0.15	2.62 ± 0.43	6.00 ± 0.24	5.84 ± 0.69	3.03 ± 0.40
5T-180	11.61 ± 1.58	2.68 ± 0.25	6.82 ± 0.38	6.47 ± 0.09	3.50 ± 0.08
6CL	12.17 ± 0.62	2.29 ± 0.03	6.41 ± 0.11	7.61 ± 0.12	3.64 ± 0.09
7CB	15.49 ± 2.45	2.21 ± 0.15	6.61 ± 0.52	6.45 ± 0.59	3.36 ± 0.24
8CF	15.62 ± 0.59	2.30 ± 0.04	5.97 ± 0.21	5.86 ± 0.22	3.08 ± 0.21
9FR	27.23 ± 8.78	2.35 ± 0.15	6.94 ± 0.37	7.62 ± 0.97	3.52 ± 0.17
10CG	22.81 ± 2.10	2.54 ± 0.15	8.18 ± 0.60	7.78 ± 0.28	3.94 ± 0.23
11RS	25.94 ± 4.40	2.12 ± 0.07	6.77 ± 0.33	6.90 ± 0.42	3.54 ± 0.13

[a]Mean ± SD, $n \geq 3$. Abbreviations: Cat, catechin; Epi, epicatechin; Mir, miricetin; Quer, quercetin; Kaem, kaempferol; TGT, Tonda Gentile Trilobata; TG, Tonda di Giffoni; T, Turkish.

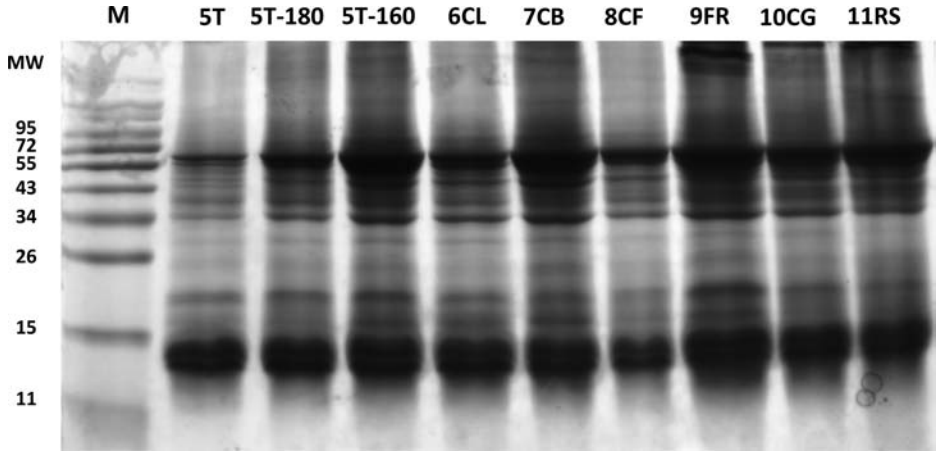

Figure 1. Electrophoretic separation (SDS−PAGE) of hazelnut proteins. MW, molecular weight (kDa); M, markers.

hazelnuts (25.4%), presumably because of its higher total phenol content (3.57 mg GAE g^{-1}).

Individual phenolic compounds were tentatively identified and quantified by RP-HPLC/DAD; results, expressed as micrograms per gram of hazelnut (dry weight), are reported in Table 2 (free phenolic acids) and Table 3 (flavonoids).

Considering raw hazelnuts, the major compound was catechin (mean value 7.08 μg g^{-1}), followed by quercetin (6.93 μg g^{-1}), and miricetin (6.78 μg g^{-1}); among phenolic acids, protocatechuic acid (5.66 μg g^{-1}) was prevalent. The highest catechin content was observed in 4TG hazelnuts, while the other compounds were generally present in higher concentration in the other cultivars.

The effect of the roasting process was different depending on both individual compounds and hazelnut cultivar. In a general way, all the phenolic compounds diminished or remained unvaried during roasting, except gallic acid and catechin, which increased. Previously, Schmitzer and coauthors observed a significant positive effect of roasting on gallic acid concentration (up to 9-fold higher in roasted than in raw hazelnuts), suggesting that this could be due to degradation of polymerized polyphenols (hydrolyzable tannins), and hydrolysis of other glycosylated flavonoids.[10] In contrast, Pelvan and coauthors reported a significant decrease of gallic acid in roasted hazelnuts, calculating an average loss of 52.7% and of 75.5% for its free and bound form, respectively.[9] Concerning catechin, this is the first time that an increase after roasting has been observed in hazelnut kernels. Schmitzer and coauthors registered a general decrease of flavan-3-ols, suggesting their thermal degradation. Nevertheless, our results are in agreement with observations in other food matrices, cocoa as an example, in which catechin content increases probably because of epicatechin epimerization.[27] In this regard, a negative significant correlation between catechin and epicatechin content in roasted hazelnuts was observed ($r = -0.5079$; $p = 0.0446$).

DOI: 10.1021/acs.jafc.5b03201
J. Agric. Food Chem. 2015, 63, 7294−7303

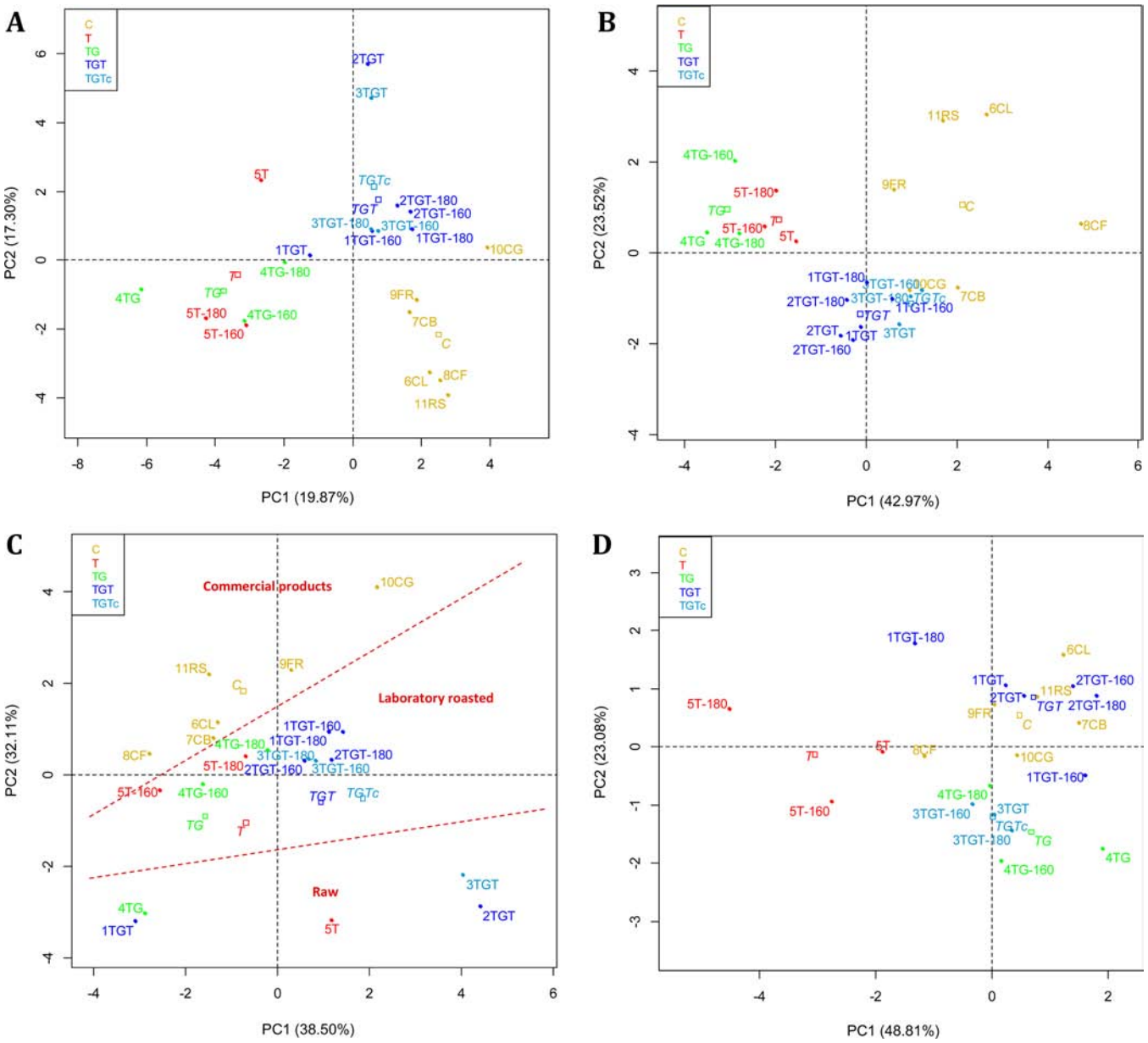

Figure 2. Two-dimensional representation of PCA (raw and roasted hazelnuts) based on complete data set (panel A), proximate composition and fatty acid profile (panel B), phenolic composition and antioxidant activity (panel C), and relative percentage of SDS-PAGE bands at molecular weight 75, 60, 43, 39, and 10 kDa (panel D). C, hazelnuts from commercial products; T, Turkish hazelnuts; TG, Tonda di Giffoni hazelnuts; TGT, Tonda Gentile Trilobata hazelnuts from Piedmont (Italy); TGTc, Tonda Gentile Trilobata hazelnuts from Chile.

Individual polyphenol content of commercial hazelnuts was in the range of experimentally roasted hazelnuts; the only exception was epicatechin, for which significantly lower values were generally observed in industrially roasted products.

Protein Fingerprint. Protein fingerprint was evaluated in nondenaturing conditions by SDS-PAGE; as an example, in Figure 1 is depicted the electrophoretic gel representing the proteins extracted from 5T hazelnuts (both raw and roasted) and commercial samples.

The protein migration profiles obtained for different hazelnut samples are comparable and similar to others previously reported in the literature.[15,28,29] Based on molecular weights and literature data (http://www.uniprot.org), some bands can be referred to well-known hazelnut allergens. Particularly, the 60 kDa band is attributable to 11S globulin (UniProt Q8W1C2), the 50 kDa band to 7S vicilin (UniProt Q8S4P9), and the 18 kDa band to Bet v 1 omologue (UniProt Q9SWR4), the 15 kDa band can contain profilin (UniProt Q9AXH5) and oleosin (UniProt Q84T21), and the 13.5 kDa band is ascribable to a protein group including lipid transfer protein (LTP, UniProt Q9ATH2).

In order to obtain quantitative data for statistical analyses, the relative percentages of individual bands were calculated; 13 common bands were determined. The major bands identified were those at 13.5, 15, and 60 kDa, with mean relative percentages of 23.4%, 18.0%, and 10.5%, respectively. In a general way, no significant variations were observed between raw and roasted samples, while significant differences were determined depending on hazelnut cultivar and origin. Turkish hazelnuts presented the highest values of the 60 kDa band (mean relative percentage 18.0%), followed in the order by Chilean TGT (10.3%), TG (10.09), TGT (10.0%) and

DOI: 10.1021/acs.jafc.5b03201
J. Agric. Food Chem. 2015, 63, 7294−7303

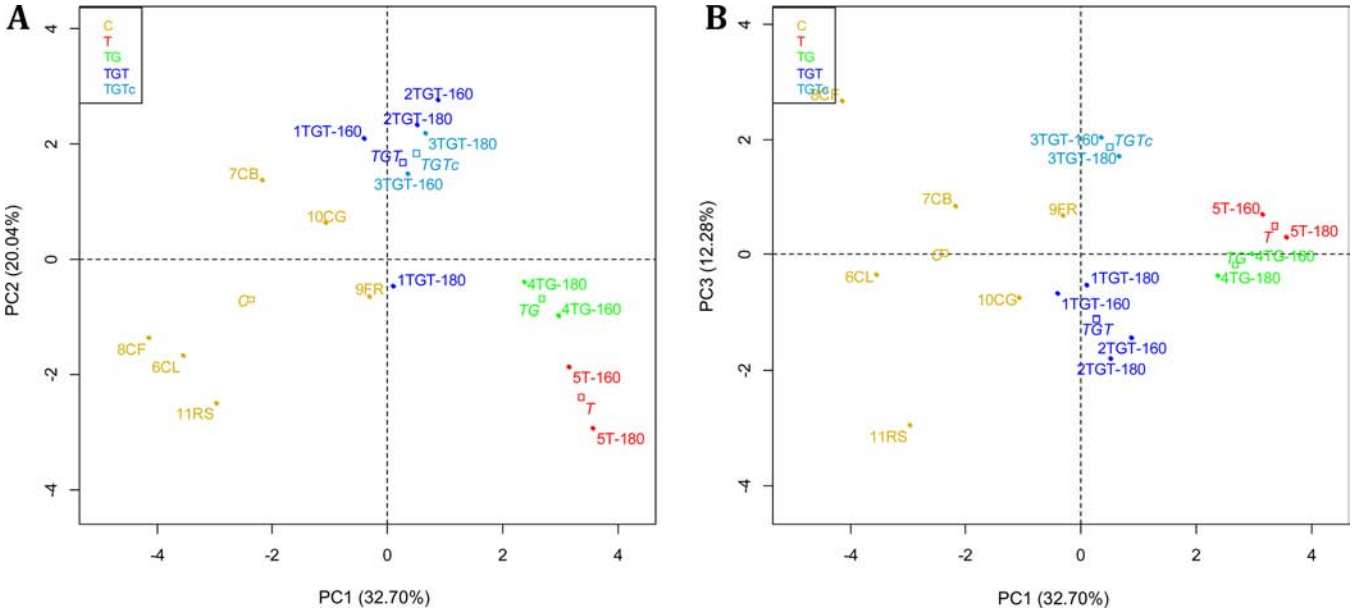

Figure 3. Two-dimensional representation of PCA (roasted hazelnuts) based on proximate composition, fatty acids, total polyphenol content, antioxidant activity, and SDS-PAGE bands at molecular weight 75, 60, 43, 39, and 10 kDa (panel A, PC1 vs PC2; panel B, PC1 vs PC3). C, hazelnuts from commercial products; T, Turkish hazelnuts; TG, Tonda di Giffoni hazelnuts; TGT, Tonda Gentile Trilobata hazelnuts from Piedmont (Italy); TGTc, Tonda Gentile Trilobata hazelnuts from Chile.

commercial (8.0%) hazelnuts. This result is in accord with our previous work on unroasted hazelnuts, in which the band at 58 kDa (presumably including 11S globulin) showed the highest values in Turkish (mean relative percentage 30%) and Chilean TGT (26%) hazelnuts.[15] In contrast, 39 kDa band showed the lowest values in Turkish hazelnuts. This band was putatively associated with 11S globulin acidic subunit, primarily because of the molecular weight but also for the strong negative correlation with the 60 kDa band ($r = -0.7545$, $p = 7.75 \times 10^{-5}$). Other unspecified bands at molecular weight 75, 43, and 10 kDa elicited significant differences among hazelnuts of different origin, while the other bands ascribable to major allergens were not significant for the origin discrimination.

Chemometric Evaluation of the Data. The chemometric characterization of hazelnuts was performed using a complex data set, in which all the chemical data were collected (33 variables). The principal component analysis led to nine principal components (PCs) explaining about 90% of total variance (cumulative variance for PC1−PC9 88.99%). The representation of the first two principal components (percentage of variance 19.87% and 17.30%, respectively) did not permit a clear discrimination of hazelnuts based on their different origin and cultivar. Even if three subgroups related to TGT (Italian and Chilean), Turkish and TG, and commercial hazelnuts can be tentatively identified, it is evident that raw hazelnuts are generally separated from their corresponding roasted samples (Figure 2A). The visualization of the third principal component (12.34% of the total variance) was not useful to improve the hazelnut separation. Among commercial hazelnuts, the 10CG sample presents high similarity with the TGT cluster (Figure 2A); this result is in accord with the fact that it contains Piedmontese TGT hazelnuts, as declared on the product label.

Afterward, chemical variables were grouped in four reduced data sets: proximate composition (moisture, proteins, ashes, lipids), fatty acids (C16:0, C18:0, C18:$1_{\Delta 9}$, C18:$1_{\Delta 11}$, and C18:2), phenolic fraction (total polyphenol content, antiradical activity, individual phenolic compounds identified by HPLC), and protein fingerprint (13 common bands identified by SDS-PAGE). Analyzing the individual reduced data sets by PCA, we observed that general composition and fatty acids included useful variables to identify hazelnut origin; thus they were successively combined and processed together. The individual plot of the first two principal components (42.97% and 23.52% of the total variance for PC1 and PC2, respectively) permitted separation of TG and T from TGT hazelnuts, while 10CG and 7CB samples, declared to contain TGT hazelnuts from Piedmont, clustered with TGT (Figure 2B). Considering also PC3 (percentage of variance 16.30%), TG were separated from Turkish hazelnuts and Chilean TGT from Italian ones; the chemical parameters significantly contributing to discriminate samples on PC3 were ashes and relative percentage of C18:$1_{\Delta 9}$ (correlation coefficient 0.8251 and −0.4498, respectively).

The PCA performed on the variables related to phenolic fraction led to a slightly different result. In fact, the graphical representation of the samples on PC1 and PC2 (total variance 70.61%) shows a less clear clustering based on hazelnut cultivar, but it is possible to note three areas in which raw, laboratory roasted, and commercial hazelnuts are prevalently located. In fact, as previously described, roasting process had a strong impact on phenolic compounds and antioxidant activity and, consequently, the hazelnut clustering was significantly influenced (Figure 2C).

Protein fingerprint did not permit the identification of different cultivar or origin, except in the case of Turkish hazelnuts, which presented lower values of PC2. The most important variables for Turkish hazelnut discrimination were the bands at molecular weight 39, 75, 43, and 28.5 kDa (which were significantly correlated to PC2 by a positive correlation) and the bands at 15 and 60 kDa (significant negative correlation).

In our previous work on raw hazelnuts, we observed that protein fingerprint is useful to differentiate the hazelnut origin.[15] This different result seems to be related to the

DOI: 10.1021/acs.jafc.5b03201
J. Agric. Food Chem. 2015, 63, 7294−7303

roasting process. In fact, even if the overall protein profile of raw and roasted hazelnuts was almost the same, the bands of roasted hazelnuts were generally less resolved and this could have negatively influenced the possibility to discriminate different hazelnuts. Moreover, in order to improve the protein extraction yield, in this work we employed a different extraction solvent (sample buffer instead of NaCl solution), and this change of the analytical protocol could be partially responsible for having obtained different results. However, considering only the bands for which hazelnut samples resulted significant differences (i.e., bands at molecular weight 75, 60, 43, 39, and 10 kDa), the first two principal components permitted separation of Chilean and Piedmontese TGT hazelnuts and Turkish from TG (Figure 2D).

Finally, we decided to omit raw hazelnuts from PCA computations, in order to focus attention on roasted samples and avoid misinterpretation of the results due to the impact of roasting on sensitive parameters. In a general way, hazelnuts can be better separated on the basis of their origin; for example, considering the total data set, Chilean TGT hazelnuts are separated from the Italian TGT. In the case of general composition and fatty acids data set, the exclusion of raw hazelnuts had an uninfluential effect on the capacity to discriminate different samples, because these parameters, expressed on a dry weight basis, are not influenced by roasting. The combination of chemical parameters that permitted us to obtain the best discrimination based on hazelnut cultivar and origin was as follows: general composition, fatty acids, total polyphenol content, antioxidant activity, and SDS-PAGE bands at molecular weight 75, 60, 43, 39, and 10 kDa (overall 16 variables). The two-dimensional representation of PCA (PC1 vs PC2, cumulative variance explained 52.74%) shows the discrimination of TGT hazelnuts from those belonging to the other cultivars; on PC2 also TG are separated from Turkish hazelnuts (Figure 3A). Considering the third principal component (12.27% of the total variance), TGT samples cultivated in Chile are clearly distinguished from Italian ones, gathering in a cluster at higher values of PC3 (Figure 3B). The chemical variable mainly responsible for this clustering is the ash content, being the unique one significantly correlated to the third principal component (r = 0.5464, p = 0.0285).

The results of PCA were further processed by an unsupervised clustering method, that is, HCPC (hierarchical clustering on principal components). HCPC is an unsupervised method, which combines principal component analysis, hierarchical clustering, and partitional clustering (specifically k-means). In HCPC, PCA is a preprocessing step that reduces the number of dimensions in parameter space. In a second step, hierarchical clustering is performed on the PCA axes using Ward's criterion. The number of clusters is chosen on the basis of the increase of inertia. Finally, the clusters obtained from the hierarchical tree cut are used to initialize the k-means algorithm, which consolidates the initial clustering. For this analysis, the minimum number of clusters was set to three, and sample partition was performed by cutting the dendrogram at the higher relative loss of inertia. As reported in Figure 4, the hazelnuts were automatically grouped in three different clusters (the clusters are identified by rectangles). The first cluster includes both TG and Turkish hazelnuts, highlighting major similarities within the same cultivar; the second cluster contains all the TGT hazelnuts and three commercial products (9FR, 7CB, and 10CG samples); in the third cluster are included the remaining commercial hazelnuts, more specifically 11RS, 8CF, and 6CL samples. Concerning the TGT cluster, two subgroups can be further identified, in which hazelnuts are separated depending on their geographic origin (Chile or Italy). Moreover, it is interesting to note that hazelnuts isolated from 7CB and 10CG commercial products, declaring to contain TGT hazelnuts from Piedmont, were correctly inserted in the TGT cluster, showing high similarity with Italian hazelnuts. Also 9FR sample was associated with TGT hazelnuts but highlighting higher homology with Chilean samples.

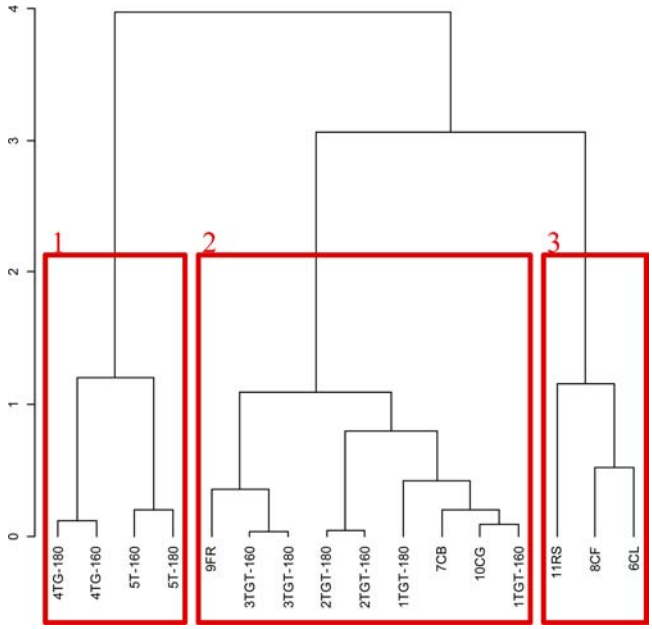

Figure 4. Hierarchical classification of roasted hazelnuts by HCPC analysis.

In conclusion, the chemometric evaluation of chemical parameters selected within proximate composition, fatty acids profile, polyphenols, antioxidant activity, and protein fingerprint, permitted us to recognize hazelnuts belonging to different cultivars and, considering TGT samples, also their different geographic origin (Chile and Italy). Among the parameters considered, phenolic compounds and antioxidant activity were the most influenced by the hazelnut roasting.

The identification of hazelnuts based on their chemical profile is important because it can permit their traceability and, consequently, ensure the quality of their derived products. This is fundamental to certify the quality of high value hazelnuts and, particularly, after the roasting process, which drastically modifies the organoleptic and chemical characteristics of raw hazelnuts, compromising their identification. In this contest, the present study, prevalently based on the identification of Tonda Gentile Trilobata hazelnuts, can be considered as preliminary for the traceability of roasted hazelnuts analyzing their chemical composition. In the future, other research will be necessary to confirm our results, more particularly considering hazelnuts from other geographic origin and cultivars and different harvesting years.

■ ASSOCIATED CONTENT

Supporting Information

The Supporting Information is available free of charge on the ACS Publications website at DOI: 10.1021/acs.jafc.5b03201.

Statistical significance for the proximate composition and the fatty acid relative percentage obtained comparing

DOI: 10.1021/acs.jafc.5b03201
J. Agric. Food Chem. 2015, 63, 7294−7303

hazelnut samples each other (Table 1S), comparing raw, lab-roasted, and commercial hazelnuts (Table 2S), and comparing laboratory-roasted hazelnuts from different origin and cultivar (Table 3S). Statistical significance for the total polyphenols, the antioxidant activity, the phenolic acid content (Table 4S), and the flavonoid content (Table 5S) obtained comparing hazelnut samples each other; for total polyphenols, antioxidant activity, phenolic acid content (Table 6S), and flavonoid content (Table 7S) obtained comparing raw, lab-roasted, and commercial hazelnuts; for total polyphenols, antioxidant activity, phenolic acid content (Table 8S) and the flavonoid content (Table 9S) obtained comparing laboratory-roasted hazelnuts from different origin and cultivar. Screeplot of the PCA performed on the complete data set (Figure 1S). Loading plots of the PCA performed on both raw and roasted hazelnuts using the complete data set (Figure 2S), the proximate composition and fatty acid profile (Figure 3S), the phenolic composition and the antioxidant activity (Figure 4S), and the relative percentage of SDS-PAGE bands at molecular weight 75, 60, 43, 39, and 10 kDa (Figure 5S). Loading plots of the PCA performed on the proximate composition, fatty acids, total polyphenol content, antioxidant activity and SDS-PAGE bands at molecular weight 75, 60, 43, 39, and 10 kDa of roasted hazelnuts (PC1 vs PC2, Figure 6S; PC1 vs PC3, Figure 7S). Contribution of the variables defining PCs obtained from the analysis of proximate composition, fatty acids, total polyphenol content, antioxidant activity and SDS-PAGE bands (molecular weight 75, 60, 43, 39, and 10 kDa) of roasted hazelnuts (Table 10S) (PDF)

AUTHOR INFORMATION

Corresponding Author

*Phone: +39 0321 375774. Fax: +39 0321 375751. E-mail: monica.locatelli@pharm.unipmn.it.

Funding

This work was funded by a grant from Regione Piemonte (Ricerca Agricola 2008).

Notes

The authors declare no competing financial interest.

ABBREVIATIONS USED

AA, antioxidant activity; GAE, gallic acid equivalent; Gal, gallic acid; Proto, protocatechuic acid; pOH, *p*-hydroxybenzoic acid; Caff, caffeic acid; Cat, catechin; Epi, epicatechin; Mir, miricetin; Quer, quercetin; Kaem, kaempferol; PCA, principal component analysis; HCPC, hierarchical clustering on principal components

REFERENCES

(1) Masthoff, L. J.; Hoff, R.; Verhoeckx, K. C. M.; van Os-Medendorp, H.; Michelsen-Huisman, A.; Baumert, J. L.; Pasmans, S. G.; Meijer, Y.; Knulst, A. C. A systematic review of the effect of thermal processing on the allergenicity of tree nuts. *Allergy* **2013**, *68*, 983−993.

(2) Arzandeh, S.; Jinap, S. Effect of initial aflatoxin concentration, heating time and roasting temperature on aflatoxin reduction in contaminated peanuts and process optimization using response surface modelling. *Int. J. Food Sci. Technol.* **2011**, *46*, 485−491.

(3) Burdack-Freitag, A.; Schieberle, P. Changes in the key odorants of Italian hazelnuts (*Corylus avellana* L. var. Tonda Romana) induced by roasting. *J. Agric. Food Chem.* **2010**, *58*, 6351−6359.

(4) Ozdemir, M.; Devres, O. Analysis of color development during roasting of hazelnuts using response surface methodology. *J. Food Eng.* **2000**, *45*, 17−24.

(5) Saklar, S.; Ungan, S.; Katnas, S. Microstructural changes in hazelnuts during roasting. *Food Res. Int.* **2003**, *36*, 19−23.

(6) Alasalvar, C.; Pelvan, E.; Amarowicz, R. Effects of roasting on taste-active compounds of Turkish hazelnut varieties (*Corylus avellana* L.). *J. Agric. Food Chem.* **2010**, *58*, 8674−8679.

(7) Alasalvar, C.; Pelvan, E.; Topal, B. Effects of roasting on oil and fatty acid composition of Turkish hazelnut varieties (*Corylus avellana* L.). *Int. J. Food Sci. Nutr.* **2010**, *61*, 630−642.

(8) Amaral, J. S.; Casal, S.; Seabra, R. M.; Oliveira, B. P. P. Effects of roasting on hazelnut lipids. *J. Agric. Food Chem.* **2006**, *54*, 1315−1321.

(9) Pelvan, E.; Alasalvar, C.; Uzman, S. Effects of roasting on the antioxidant status and phenolic profiles of commercial Turkish hazelnut varieties (*Corylus avellana* L.). *J. Agric. Food Chem.* **2012**, *60*, 1218−1223.

(10) Schmitzer, V.; Slatnar, A.; Veberic, R.; Stampar, F.; Solar, A. Roasting affects phenolic composition and antioxidative activity of hazelnuts (*Corylus avellana* L.). *J. Food Sci.* **2011**, *76*, S14−S19.

(11) Açar, Ö.Ç.; Gökmen, V.; Pellegrini, N.; Fogliano, V. Direct evaluation of the total antioxidant capacity of raw and roasted pulses, nuts and seeds. *Eur. Food Res. Technol.* **2009**, *229*, 961−969.

(12) Oddone, M.; Aceto, M.; Baldizzone, M.; Musso, D.; Osella, D. Authentication and traceability study of hazelnuts from Piedmont, Italy. *J. Agric. Food Chem.* **2009**, *57*, 3404−3408.

(13) Cordero, C.; Liberto, E.; Bicchi, C.; Rubiolo, P.; Schieberle, P.; Reichenbach, S. E.; Tao, Q. Profiling food volatiles by comprehensive two-dimensional gas chromatography coupled with mass spectrometry: advanced fingerprinting approaches for comparative analysis of the volatile fraction of roasted hazelnuts (*Corylus avellana* L.) from different origins. *J. Chromatogr. A* **2010**, *1217*, 5848−5858.

(14) Caligiani, A.; Coïsson, J. D.; Travaglia, F.; Acquotti, D.; Palla, G.; Palla, L.; Arlorio, M. Application of ^{1}H NMR for the characterisation and authentication of "Tonda Gentile Trilobata" hazelnuts from Piedmont (Italy). *Food Chem.* **2014**, *148*, 77−85.

(15) Locatelli, M.; Coïsson, J. D.; Travaglia, F.; Cereti, E.; Garino, C.; D'Andrea, M.; Martelli, A.; Arlorio, M. Chemotype and genotype chemometrical evaluation applied to authentication and traceability of "Tonda Gentile Trilobata" hazelnuts from Piedmont (Italy). *Food Chem.* **2011**, *129*, 1865−1873.

(16) Singleton, V. L.; Rossi, J. A. Colorimetry of total phenolics with phosphomolybdic - phosphotungstic acid reagents. *Am. J. Enol. Vitic.* **1965**, *16*, 144−158.

(17) Laemmli, U. K. Cleavage of structural proteins during the assembly of the head of bacteriophage T4. *Nature* **1970**, *227*, 680−685.

(18) R Development Core Team. *R: A language and environment for statistical computing*, R Foundation for Statistical Computing, Vienna, Austria, 2008.

(19) Alasalvar, C.; Shahidi, F.; Liyanapathirana, C. M.; Ohshima, T. Turkish Tombul Hazelnut (*Corylus avellana* L.). 1. Compositional characteristics. *J. Agric. Food Chem.* **2003**, *51*, 3790−3796.

(20) Locatelli, M.; Travaglia, F.; Coïsson, J. D.; Martelli, A.; Stévigny, C.; Arlorio, M. Total antioxidant activity of hazelnut skin (Nocciola Piemonte PGI): impact of different roasting conditions. *Food Chem.* **2010**, *119*, 1647−1655.

(21) Montella, R.; Coïsson, J. D.; Travaglia, F.; Locatelli, M.; Malfa, P.; Martelli, A.; Arlorio, M. Bioactive compounds from hazelnut skin (*Corylus avellana* L.): effects on *Lactobacillus plantarum* P17630 and *Lactobacillus crispatus* P17631. *J. Funct. Foods* **2013**, *5*, 306−315.

(22) Alasalvar, C.; Shahidi, F.; Ohshima, T.; Wanasundara, U.; Yurttas, H.; Liyanapathirana, C. M.; Rodrigues, F. B. Turkish Tombul hazelnut (*Corylus avellana* L.). 2. Lipid characteristics and oxidative stability. *J. Agric. Food Chem.* **2003**, *51*, 3797−3805.

DOI: 10.1021/acs.jafc.5b03201
J. Agric. Food Chem. 2015, 63, 7294−7303

(23) Moser, B. R. Preparation of fatty acid methyl esters from hazelnut, high-oleic peanut and walnut oils and evaluation as biodiesel. *Fuel* **2012**, *92*, 231−238.
(24) Lipp, M.; Simoneau, C.; Ulberth, F.; Anklam, E.; Crews, C.; Brereton, P.; de Greyt, W.; Schwack, W.; Wiedmaier, C. Composition of genuine cocoa butter and cocoa butter equivalents. *J. Food Compos. Anal.* **2001**, *14*, 399−408.
(25) Motwani, T.; Hanselmann, W.; Anantheswaran, R. C. Diffusion, counter-diffusion and lipid phase changes occurring during oil migration in model confectionery systems. *J. Food Eng.* **2011**, *104*, 186−195.
(26) Shahidi, F.; Alasalvar, C.; Liyana-Pathirana, C. M. Antioxidant phytochemicals in hazelnut kernel (*Corylus avellana* L.) and hazelnut byproducts. *J. Agric. Food Chem.* **2007**, *55*, 1212−1220.
(27) Payne, M. J.; Hurst, W. J.; Miller, K. B.; Rank, C.; Stuart, D. A. Impact of fermentation, drying, roasting, and Dutch processing on epicatechin and catechin content of cacao beans and cocoa ingredients. *J. Agric. Food Chem.* **2010**, *58*, 10518−10527.
(28) Prieto, N.; Burbano, C.; Iniesto, E.; Rodríguez, J.; Cabanillas, B.; Crespo, J. F.; Pedrosa, M. M.; Muzquiz, M.; del Pozo, J. C.; Linacero, R.; Cuadrado, C. A novel proteomic analysis of the modifications induced by high hydrostatic pressure on hazelnut water-soluble proteins. *Foods* **2014**, *3*, 279−289.
(29) Platteau, C. M. F.; Bridts, C. H.; Daeseleire, E. A.; De Loose, M. R.; Ebo, D. G.; Taverniers, I. V. Comparison and functional evaluation of the allergenicity of different hazelnut (*Corylus avellana*) protein extracts. *Food Anal. Method* **2010**, *3*, 382−388.

DOI: 10.1021/acs.jafc.5b03201
J. Agric. Food Chem. 2015, 63, 7294−7303

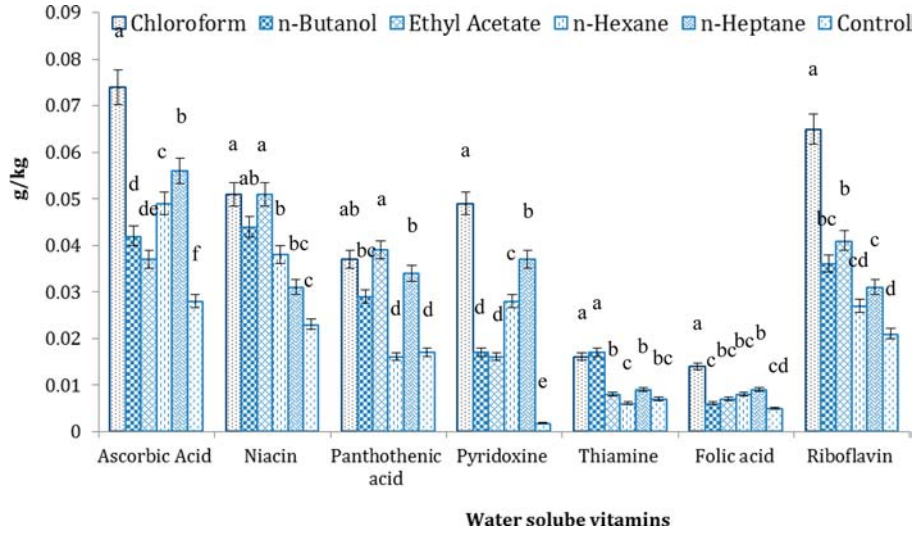

Figure 1. Quantities of vitamin contents in barley treated with organic fractions of *Acetobacter aceti* extracts. Control treatment refers to no application of bacterial extracts. Error bars show the standard error among each treatment, while different alphabetic letters show significant difference between treatments, calculated through Duncan's multiple range test (DMRT) at $p \leq 0.05$. Statistical analysis was performed through DSAASTAT (Onofri, Italy).

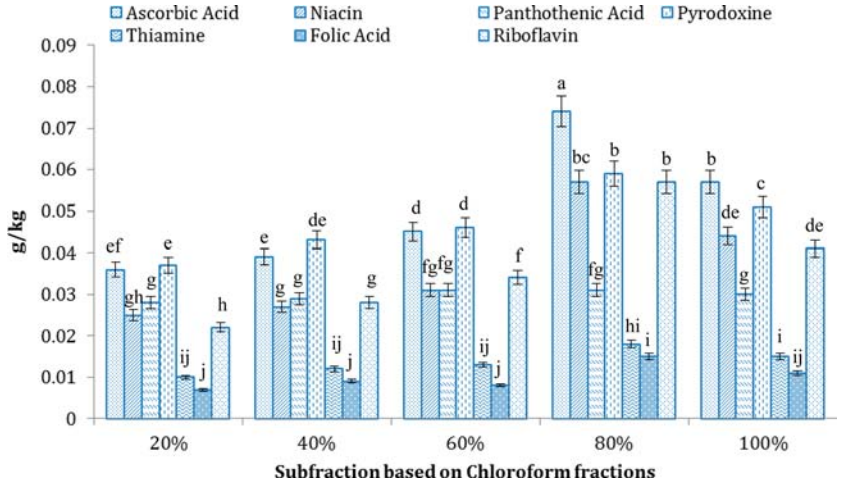

Figure 2. Quantities of water-soluble vitamins in barley obtained from treated plants. Plants had been treated with subfractions of chloroform extracts, prepared in, i.e., 20, 40, 60... 100% concentrations of chloroform in ethyl acetate (plotted on *X*-axis). The quantities of vitamins in g/kg have been presented on the *Y*-axis. Error bars have been plotted to represent the standard error among each data set, whereas changing lowercase letters represent significant difference in data. Data were statistically analyzed through Duncan's multiple range test the (DMRT) at $p \leq 0.05$ and using the MS-Excel add-in statistical package DSAASTAT (Onofri, Italy).

SF01, SF02, SF03, SF04, and SF05. The biochemical profile of each subfraction was estimated through thin layer chromatography, while bioactivity was studied by applying subfractions on barley plants.

Organic subfraction induced maximum quantities in barley were analyzed through chromatographic techniques to identify the specific compound(s) responsible for vitamin induction in the greenhouse assay. Barley plants were grown under 24 ± 2 °C in a greenhouse, and watering was carried out when needed. Vitamin contents of barley were quantified, and the best organic fraction was screened out. The organic fraction was further fractionated into 5 subfractions (i.e., FR01, FR02, FR03, FR04, and FR05) through column chromatography (CC). For this purpose, the concentrate of the previous fraction was mixed with a small quantity of silica gel of Uni-Chem (mesh 60−100) to make its slurry. A two third portion of the column (200 g) was filled with silica gel, and then a thin layer of prepared slurry was uniformly spread over the surface of the silica column. Moreover, the slurry was again overlaid by a uniform thin layer of silica gel. A stepwise elution of samples was performed with a solvent system of ethanol/chloroform, having a constant increment of 20% in concentration of chloroform. All prepared subfractions were studied for vitamin elevation potential, through the bioactivity guided assay. Therefore, all these subfractions were applied to barley plants, and plants were allowed to grow up to seed harvesting stage. These seeds were crushed and tested for water-soluble vitamin quantities (i.e., ascorbic acid, niacin, panthothenic acid, pyridoxine thiamine, folic acid, and riboflavin). These quantities were quantified by measuring peak height and peak area of gas chromatograms of vitamins along with some other contaminants. Moreover, preparative thin layer chromatography (PTLC) was performed to remove the maximum possible contaminants from the fractions. PTLC was performed through glass plates (20 × 20 cm^2) coated with silica. Bioactive compounds were isolated with the minimum possible number of contaminants before performing gas chromatography−mass spectrometery (GCMS).

Gas Chromatography−Mass Spectrometery. GCMS was performed on a gas chromatography unit of Agilent Technologies (7890A), accompanied by a mass spectrometer unit of (5975C) and column HP-5MS. Operation was started from 70 °C temperature with continuous increments of 5 °C/min up to 200 °C temperature.

DOI: 10.1021/acs.jafc.5b01817
J. Agric. Food Chem. 2015, 63, 7304−7310

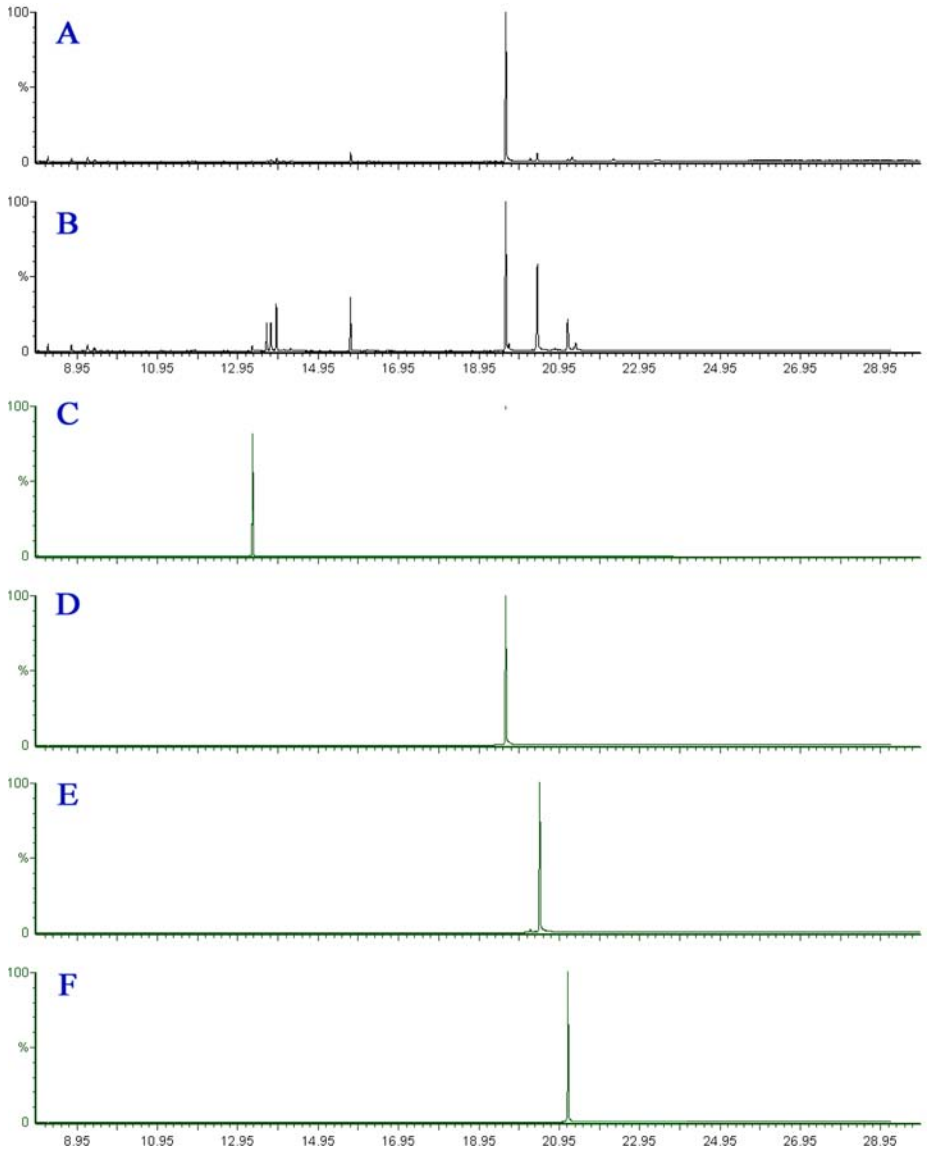

Figure 3. GCMS profiles of the two most active chloroform fractions, i.e., 80% (A) and 100% (B). Standard run of most active compounds were performed providing identical GCMS conditions on the same GCMS apparatus. Quinolinic acid (C), pyridoxic acid (D), *p*-aminobenzoate (E), and *α*-oxobutanoic acid (F). *X*-Axis has been marked with the time elapsed for chemical elution, and the *Y*-axis represents the height of peaks dependent upon chemical quantities.

Operation was further continued up to 240 °C at a continuous increment of 10 °C/min. The flow rate of carrier gas (helium) was maintained 1 mL/min during the entire operation. Mass spectra of compounds were identified using TURBOMASS (Perkinelmer, Shelton, USA) equipped with a mass spectral NIST library.

Data Analysis. Statistical analysis of data was carried out through analysis of variance (ANOVA) and Duncan's multiple range test (DMRT) at $p \leq 0.05$. Statistical operations were performed using the statistical package of MS-Excel based add-in DSAASTAT (Onofri, Italy). Principal component analysis (PCA) was performed to determine the most active bacterial metabolite, and the screened chemical was applied to barley plants to verify the results of the study.

Activity Verification of Identified Compound. Purified chemicals were purchased from Sigma-Aldrich (Lahore) and applied separately to sets of barley plants of 2 weeks of age, treating the control with distilled sterilized water. Seeds of the plants were tested for vitamin contents, and data were compared with the standard GCMS run of purified compounds to test the efficacy of treatment. The whole experiment was independently repeated thrice to ensure the authenticity of the results.

RESULTS

Chloroform fraction provided the maximum levels of most of the tested vitamins. Significantly higher quantities of ascorbic acid, pyridoxine, folic acid and riboflavin were recorded in barley. Niacin and pantothenic acid were recorded in equal quantities in both treatments of chloroform and ethyl acetate, whereas *n*-butanol exhibited nonsignificantly more amounts of thiamine contents than chloroform treatment. *n*-Hexane was recorded with nonsignificantly lower quantities of panthothenic acid and thiamine contents than the respective values of control treatment (Figure 1).

Eighty percent chloroform treatment induced the highest quantities of vitamins in barley. It was most efficient for inducing ascorbic acid content in barley seeds. Moreover, the quantity of riboflavin was also elevated by 80% chloroform in the most efficient way. Pyrodixine was recorded to be significantly elevated after getting 80% chloroform treatment. Similarly, the quantity of niacin was found to be significantly

DOI: 10.1021/acs.jafc.5b01817
J. Agric. Food Chem. 2015, 63, 7304−7310

Table 1. Chemical Compounds in Chloroform Fractions (with Concentrations of 80% and 100%) Were Identified through GCMS Analysis[a]

serial no.	chemical	retention time (min)	total peak area (E)
1	thymol	8.03	4.7
2	eugenol	8.88	4.9
3	globulol	9.17	5.1
4	mevalonic lactone	9.29	4.3
5	quinolinic acid	12.33	4.7
6	*E*-8-octadecacen-1-ol acetate (ODCA)	13.68	5.6
7	pentadenoic acid	13.85	5.8
8	phthalic ester (methyl octyl ester)	14.08	5.9
9	octadecatrienoic acid (ODTA)	15.75	6.1
10	pyridoxic acid	19.67	7.4
11	*p*-aminobenzoate	20.41	6.5
12	α-oxobutanoic acid	21.18	5.3
13	glycine	21.28	4.2

[a]MZmine (Pluskal, Okinawa, Japan) was used to analyze chromatograms and mass spectra. Properties of each compound were recorded and mentioned against it. Retention time is the time taken by chemicals for their individual elution and has been calculated in minutes (min), whereas total peak area has been calculated through MZmine unit of relativity (E).

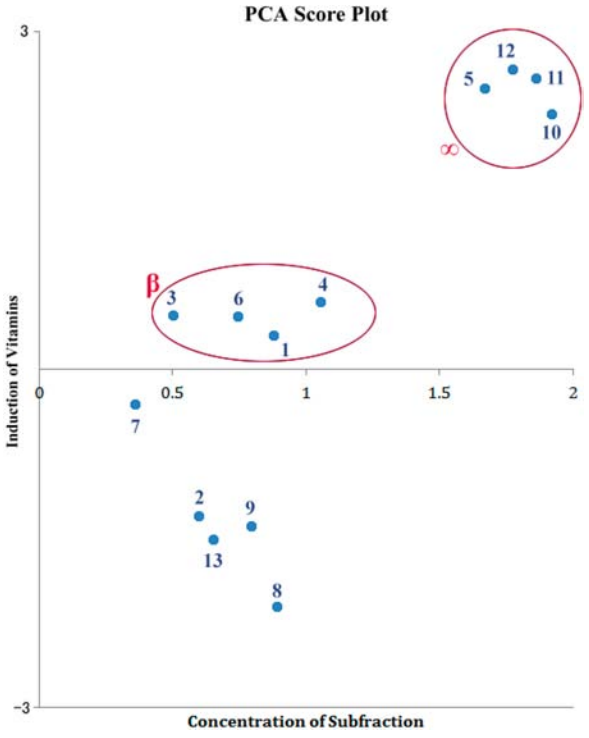

Figure 4. Principal component analysis (PCA) of all detected compounds through GCMS analysis of chloroform subfractions of *A. aceti* extracts. Thirteen chemical componds detected in GCMS analysis were 1, thymol; 2, eugenol; 3, globulol; 4, mevalonic lactone; 5, quinolinic acid; 6, *E*-8-octadecacen-1-ol acetate (ODCA); 7, pentadenoic acid; 8, phthalic ester; 9, octadecatrienoic acid (ODTA); 10, pyridoxic acid; 11, *p*-aminobenzoate; 12, α-oxobutanoic acid; and 13, glycine. Association of all compounds was calculated with the concentration of chloroform in extraction solvent and induction of vitamins. The statistical package DSAASTAT (Onofri, Italy) was used to perform PCA analysis.

higher in 80% chloroform than in all other treatments. The second most efficient treatment in terms of vitamins induction was 100% chloroform. It induced ascorbic acid at significantly higher concentrations than 20, 40, and 60% chloroform treatments. Induction in the quantity of pyrodoxine was also significantly higher in 100% chloroform treatment than 20, 40, and 60%. A similar trend was found in the case of riboflavin, which was detected in significantly higher amounts in 100 chloroform treatments than 20%, 40%, and 60% treatments. Thiamine was the only vitamin, which did not show any significant variation in its quantities among all treatments; however, the quantity folic acid was recorded to be significantly greater in the 80% treatment in comparison to the respective quantities in 20, 40, and 60% treatment (Figure 2). Two fractions (i.e., 80% and 100%) possessed the most efficient vitamin induction activities and were thus analyzed by GCMS to figure out active compounds.

Thirteen chemical compounds were detected in the most active (80%) chloroform fraction. These chemicals were identified as thymol, eugenol, globulol, mevalonic lactone, quinolinic acid, *E*-8-octadecacen-1-ol acetate (ODCA), pentadenoic acid, phthalic ester, octadecatrienoic acid (ODTA), pyridoxic acid, *p*-aminobenzoate, α-oxobutanoic acid, and glycine. The second most active (100%) chloroform fraction was missing in quinolinic acid and ODCA. However, the concentration of most of the compounds (i.e., quinolinic acid, ODCA, pentadenoic acid, phthalic ester, ODTA, *p*-aminobenzoate, and α-oxobutanoic acid) was lower in the 100% chloroform fraction than in the 80% fraction (Figure 3).

Chemical properties of all detected compounds were recorded in order to evaluate the principal compound. All 13 compounds had peaks sufficiently apart with good resolution. Thymol was the first compound detected at 8.03 min of the chromatographic run with a peak area of 4.7E. Eugenol was eluted at 8.88 min and recorded a peak area of 4.9E. Mass spectra of globulol (peak area: 5.1E) and mevalonic lactone (peak area: 4.3E) were recorded after chromatographic runs of 9.17 and 9.29 min, respectively. Quinolinic acid with a peak area of 4.7E was detected at 12.33 min. Pyridoxic acid (19.67 min) exhibited the highest peak area 7.4E. The second highest peak area (6.5E) was recorded in the case of *p*-aminobenzoate, which had the retention time of 20.41 min. α-Oxobutanoic acid and glycine (peak area: 5.3E and 4.2E, respectively) were the last eluting compounds with retention times of 21.18 and 21.28 min, respectively (Table 1).

Pyridoxic acid was a compound having maximum affinity with the concentration of chloroform in the extraction solvent. *p*-Aminobenzoate had a lower affinity with chloroform concentration than pyridoxic acid. However, it exhibited stronger association with vitamin induction than pyridoxic acid. Similarly, α-oxobutanoic acid had the third strongest association with chloroform concentration, but it recorded the strongest correlation with vitamins induction. Quinolinic acid recorded the third strongest relationship with vitamin induction, just after *p*-aminobenzoate; but it was fourth according to its interrelationship with chloroform concentration. All these four compounds (i.e., quinolinic acid, *p*-aminobenzoate, pyridoxic acid, and α-oxobutanoic acid) collectively construct a group (∞) and are closely placed over a PCA plot. Similarly, thymol, globulol, mevalonic lactone, and ODCA were members of a second group (β), and this group had more variable association with chloroform concentration than with vitamin induction. Mevalonic lactone

DOI: 10.1021/acs.jafc.5b01817
J. Agric. Food Chem. 2015, 63, 7304−7310

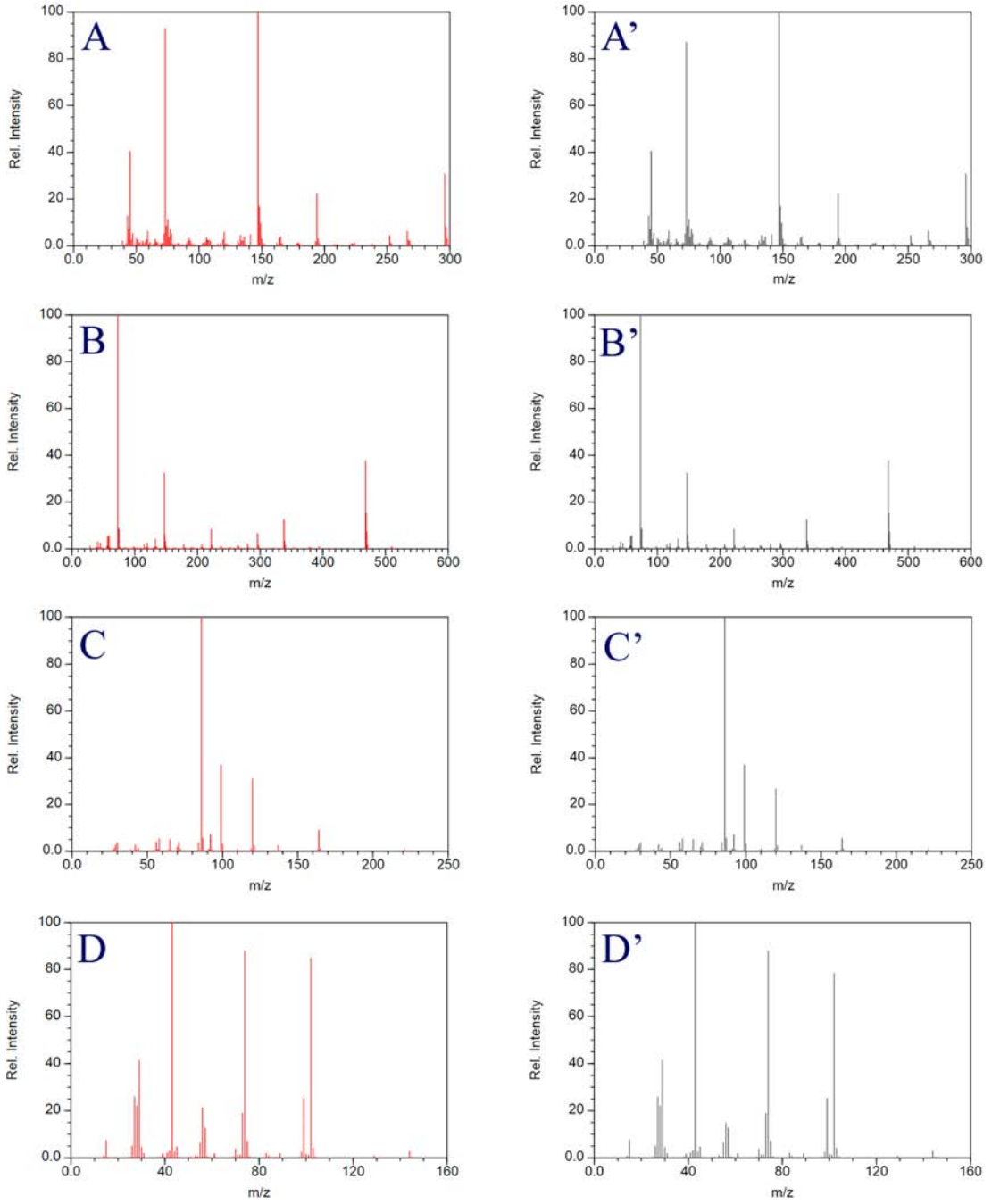

Figure 5. Standard mass spectra of active compounds taken from the NIST library, i.e., quinolinic acid (A), pyridoxic acid (B), *p*-aminobenzoate (C), α-oxobutanoic acid (D). Mass spectrum recorded during an experimental run of *A. aceti* fractions has been tagged with the English alphabet followed by symbol -'-. Compoounds were identified using TURBOMASS (Perkinelmer, Shelton, USA) equipped with the NIST library.

had the strongest association with chloroform concentration as well as vitamin induction among all the members of group β. Thymol was the least associated member of group β with vitamin induction. Eugenol, pentadenoic acid, phthalic ester, ODTA, and glycine were found in inverse relationship with vitamins induction; however, they were positively associated with concentration of chloroform in extraction solvent (Figure 4). All compounds which occupied distinct positions in the correlation matrix plot were purified up to >99% to test their effectiveness for the induction of vitamin contents.

Mass spectra of bioactive compounds were recorded through TURBOMASS (Perkinelmer, Shelton, USA) and their respective compounds in the NIST library compared. More than 800 similarity scores were calculated in the case of all identified compounds (Figure 5).

Activity Verification of Identified Compounds. Maximum quantities of vitamins were induced after the application of *p*-aminobenzoate. It recorded significantly higher quantities of six vitamins, i.e., ascorbic acid, niacin, pathothenic acid, pyridoxine, and thiamine and folic acid (Figure 6). However, the highest quantities of riboflavin were recorded in the case of quinolinic acid and *p*-aminobenzoate. Quinolinic acid was the second best inducer of vitamins in barley seeds. However, pyridoxic acid and α-oxobutanoic acid had a variable behavior

DOI: 10.1021/acs.jafc.5b01817
J. Agric. Food Chem. 2015, 63, 7304−7310

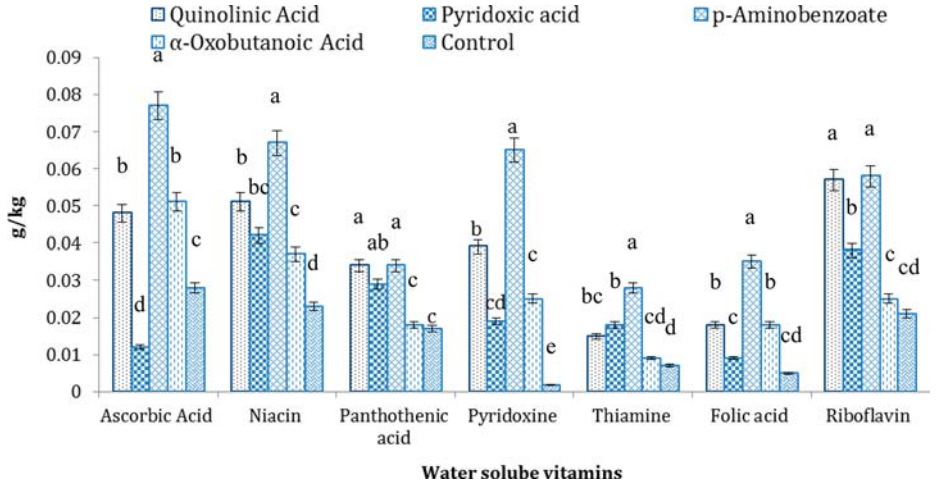

Figure 6. Vitamin contents in barley seeds treated with different biochemicals (i.e., quinolinic acid, pyridoxic acid, *p*-aminobenzoate, and *α*-oxobutanoic acid). Control treatment refers to no chemical application. Data were statistically analyzed through analysis of variance (ANOVA) using DSAASTAT (Onofri, Italy), and error bars show standard error of the data, and each change in lowercase letters represents the significant difference among treatments calculated through Duncan's multiple range test (DMRT) at $p \leq 0.05$.

with respect to each individual vitamin. They could not induce significant quantities of most of the vitamins with respect to the control treatment. However, pyridoxic acid inhibited the production of ascorbic acid in barley seeds (Figure 6).

DISCUSSION

The current investigation describes an array of microbial metabolites which affect plant biochemicals. This study has highlighted the metabolites which more specifically enhanced nutritional quality related biochemicals in barley seeds. Barley is a staple food crop which can be routinely consumed by humans and animals. Therefore, the current investigation is an advancement in the improvement of food quality of large populations. It recommends the microbial application for getting augmented agricultural yields in terms of nutritional contents.

The solubility of different compounds is extremely variable in a single organic solvent.[13] Similarly, different organic solvents dissolve highly variable amounts of a single compound.[14] Thus, the optimization of solvent is necessarily required to isolate a desired compound with minimum number of contaminants; and this optimization is imperative when an active compound is needed to be isolated from a mixture containing thousands of bacterial metabolites.[15] This study suggests a solvent system of 80% chloroform and 20% ethanol to isolate active compounds with a minimum number of impurities from bacterial metabolites. The individual purity index of these metabolites is >99.9%. However, their concentrations in subfractions were recorded as quinolinic acid (1.09%), pyridoxic acid (50.54%), *p*-aminobenzoate (36.26%), and *α*-oxobutanoic acid (12.11%).

Plants respond to external applications of chemicals, while metabolites of *A. aceti* contain a number of chemicals which had unknown effects on plants. Hence, the purification of active compounds becomes very important in order to reduce the number of undesired compounds. Furthermore, the composition solvent system affects the quantity and quality of compounds being extracted.[16,17] The current study approves the two step extraction of *A. aceti* metabolites: first, the extraction with 100% chloroform and subsequent extraction with an 80% chloroform solvent system in ethanol (chloroform/ethanol (4:1) solvent system). Thus, the resulting extracts have more amounts of active compounds and are more specific in action.

GCMS analysis of biologically active fractions identified the compounds present in them; however, PCA analysis determined the activity of each identified biochemical and arranged them in a hierarchal manner on the basis of their ability to induce vitamins. Four compounds were found to be strongly associated with the induction of vitamins; however, the interactions among these chemicals have not been studied. It might be possible that they have a cumulative effect on vitamin biosynthesis or that they have synergistic effects on vitamin metabolism.[18,19]

All the biochemicals identified in this research are either precursors of vitamin biosynthesis pathways (e.g., quinolinic acid and pyridoxic acid)[20,21]or they are facilitators of these pathways (e.g., *p*-aminobenzoate and *α*-oxobutanoic).[22,23] Thus, the increased production of vitamins in barley can be supported with the logic that "providing precursors of vitamins would facilitate plants in their production process."[24,25]

PCA analysis categorized the compounds on the basis of their affinity with induced vitamin quantities and concentration of chloroform in extraction solvent. This revealed mevalonic acid as the most active compound among group *β* of the identified compounds. Mevalonic acid was the compound with the highest concentration in extracted fraction, as compared to the other compounds of group *β*. Moreover, this compound plays a key role in the isoprenoid pathway for the biosynthesis of squalene,[26] which is responsible for the ultimate production of sterols.[27]

GCMS analysis also revealed the presence of glycine in tested fractions. Glycine takes part in the process of folate biosynthesis for the production of glutamic acid. It is a three step former biochemical reaction just equivalent to the production of 5,10-methenyltetrahydrofolate polyglutamate. Logically, glycine would be in positive relationship with vitamin induction; however, it was inversely related with vitamin quantities. These findings indicate some complexities in folate metabolism, which still need to be resolved. Pyridoxic acid treatment on plants results in the decreased sensitivity of plant photosystem II and protects plants against photooxidative stress.[28] However, the decreased sensitivity of the photosystem II reaction center

DOI: 10.1021/acs.jafc.5b01817
J. Agric. Food Chem. 2015, 63, 7304−7310

hampers light acclimation and reduced ascorbate content.[29] Moreover, the quenching of O_2 starts proteolytic degradation of ascorbate and lowers its contents in plant tissues.[30] All these studies support the decreased ascorbic acid contents recorded after treating barley plants with pyridoxic acid.

The study concludes that two biochemicals, i.e., *p*-aminobenzoate and quinolinic acid can induce vitamin contents in barley seeds. However, *p*-aminobezoate is recommended as the best vitamin inducer. All of these two biochemicals can be isolated from the metabolites of *A. aceti* using an organic solvent system (chloroform/ethanol 4:1). This study would be a step toward the cultivation of food crops with improved nutritional values.

AUTHOR INFORMATION

Corresponding Author

*Tel: +92 322 414 7507. E-mail: anamyousaf@outlook.com.

Notes

The authors declare no competing financial interest.

REFERENCES

(1) Dong, H.; Cohen, Y. Extract of killed *Penicillium chrysogenum* induce resistance against Fusarium wilt of melon. *Phytoparasitica* **2001**, *29* (5), 421−430.

(2) Ragab, M. M. M.; Saber, M. M.; El-Morsy, S. A.; Abd El-Aziz, A. R. M. Induction of systemic resistance against root rot of basil using some chemical inducers. *Egypt. J. Phytopathol.* **2009**, *37* (1), 59−70.

(3) Ahmad, A.; Shafique, S.; Shafique, S. Intracellular interactions involved in induced systemic resistance in tomato. *Sci. Hortic.* **2014**, *176* (11), 127−133.

(4) Guijarro, B.; Melgarejo, P.; De Cal, A. Effect of stabilizers on the shelf-life of Penicillium frequentans conidia and their efficacy as a biological agent against peach brown rot. *Int. J. Food Microbiol.* **2007**, *113* (2), 117−124.

(5) Vazquez, G.; Melgarejo, P.; De Cal, A.; Larena, I. Persistence, survival, vertical dispersion, and horizontal spread of the biocontrol agent, *Penicillium oxalicum* strain 212, in different soil types. *Applied Soil Ecology* **2013**, *67*, 27−36.

(6) Ahmad, A.; Shafique, S.; Shafique, S.; Akram, W. *Penicillium oxalicum* directed systemic resistance in tomato against *Alternaria alternata*. *Acta Physiol. Plant.* **2014**, *36* (5), 1231−1240.

(7) Benhamou, N.; Bélanger, R. R. Benzothiadiazole-Mediated Induced Resistance to *Fusarium oxysporum* f. sp. *radicis-lycopersici* in Tomato. *Plant Physiology* **1998**, *118* (4), 1203−1212.

(8) Colson-Hanks, E. S.; Deverall, B. J. Effect of 2, 6-dichloroisonicotinic acid, its formulation materials and benzothiadiazole on systemic resistance to alternaria leaf spot in cotton. *Plant Pathol.* **2000**, *49*, 171−178.

(9) Langston, R.; Leopold, A. C. The dark fixation of carbon dioxide as a factor in photoperiodism. *Plant Physiol.* **1954**, *29* (5), 436−440.

(10) Rice, D. A.; McMurray, C. H. Use of sodium hydroxide treated selenium deficient barley to induce vitamin E and selenium deficiency in yearling cattle. *Vet. Rec.* **1986**, *118* (7), 173−176.

(11) Lichtenthaler, H. K.; Becker, K. Inhibition of the light-induced vitamin K1 and pigment synthesis by abscisic acid. *Phytochemistry* **1970**, *9*, 2109−2113.

(12) Buddenhagen, I. W.; Dull, G. G. Pink disease of pineapple fruit caused by strains of acetic acid bacteria. *Phytopathology* **1967**, *57*, 806.

(13) Granberg, R. A.; Rasmuso, A. C. Solubility of paracetamol in pure solvents. *J. Chem. Eng. Data* **1999**, *44*, 1391−1395.

(14) Miller-Chou, B. A.; Koenig, J. L. A review of polymer dissolution. *Prog. Polym. Sci.* **2003**, *28*, 1223−1270.

(15) Heryanto, R.; Hasan, M.; Abdullah, E. C.; Kumoro, A. C. Solubility of stearic acid in various organic solventsand its prediction using non-ideal solution models. *ScienceAsia* **2007**, *33*, 469−472.

(16) Kaufmann, B.; Christen, P. Recent extraction techniques for natural products: microwave-assisted extraction and pressurised solvent extraction. *Phytochem. Anal.* **2002**, *13*, 105−113.

(17) Sultana, B.; Anwar, F.; Ashraf, M. Effect of extraction solvent/technique on the antioxidant activity of selected medicinal plant extracts. *Molecules* **2009**, *14*, 2167−2180.

(18) Baider, A.; Cohen, Y. Synergistic interaction between BABA and mancozeb in controlling *Phytophthora infestans* in potato and tomato and *Pseudoperonospora cubensis* in cucumber. *Phytoparasitica* **2003**, *31* (4), 399−409.

(19) Brent, K. J.; Hollomon, D. W. *Fungicide Resistance in Crop Pathogens: How Can It Be Managed?* Fungicide Resistance Action Committee; Crop life International: Belgium, 2007.

(20) Sauve, A. A. NAD^+ and vitamin B3: from metabolism to therapies. *J. Pharmacol. Exp. Ther.* **2008**, *324* (3), 883−893.

(21) Gropper, S.; Smith, J. Water Soluble Vitamins. *Advanced Nutrition and Human Metabolism. Section III: The Regulatory Nutrition*; Wadsworth: Belmont, CA, 2012; pp 307−370, Chapter 9.

(22) Robins, D. J.; Yee, R. B.; Bentley, R. Biosynthetic precursors of vitamin K as growth promoters for Bacteroides melaninogenicus. *J. Bacteriol.* **1973**, *116* (2), 965−971.

(23) Velíšek, J.; Cejpek, K. Biosynthesis of food constituents: Vitamins. 2. Water-Soluble Vitamins: Part 1 − a Review. *Czech Journal of Food Science* **2007**, *25* (2), 49−64.

(24) Pourcel, L.; Moulin, M.; Fitzpatrick, T. B. Examining strategies to facilitate vitamin B1 biofortification of plants by genetic engineering. *Front. Plant Sci.* **2013**, *4*, 160.

(25) Mohammed, Y.; Lee, B.; Kang, Z.; Du, G. Development of a two-step cultivation strategy for the production of vitamin B12 by *Bacillus megaterium*. *Microb. Cell Fact.* **2014**, *13*, 102.

(26) Closa, M.; Vranová, E.; Bortolotti, C.; Bigler, L.; Arró, M.; Ferrer, A.; Gruissem, W. The *Arabidopsis thaliana* FPP synthase isozymes have overlapping and specific functions in isoprenoid biosynthesis, and complete loss of FPP synthase activity causes early developmental arrest. *Plant J.* **2010**, *63*, 512−525.

(27) Masferrer, A.; ArroÂ, M.; Manzano, D.; Schaller, H.; FernaÂndez-Busquets, X.; MoncaleaÂn, P.; FernaÂndez, B.; Cunillera, N. R.; Boronat, A.; Ferrer, A. Overexpression of Arabidopsis thaliana farnesyl diphosphate synthase (FPS1S) in transgenic Arabidopsis induces a cell death/senescence-like response and reduced cytokinin levels. *Plant J.* **2002**, *30* (2), 123−132.

(28) Titiz, O.; Tambasco-Studart, M.; Warzych, E.; Apel, K.; Amrhein, N.; Laloi, C.; Fitzpatrick, T. B. PDX1 is essential for vitamin B6 biosynthesis, development and stress tolerance in Arabidopsis. *Plant J.* **2006**, *48*, 933−946.

(29) Havaux, M.; Ksas, B.; Szewczyk, A.; Rumeau, D.; Fabrice Franck, F.; Caffarri, S.; Christian Triantaphylidès, C. Vitamin B6 deficient plants display increased sensitivity to high light and photo-oxidative stress. *BMC Plant Biol.* **2009**, *9*, 130.

(30) Ehrenshaft, M.; Bilski, P.; Li, M. Y.; Chignell, C. F.; Daub, M. E. A highly conserved sequence is a novel gene involved in de novo vitamin B6 biosynthesis. *Proc. Natl. Acad. Sci. U. S. A.* **1999**, *96*, 9374−9378.

DOI: 10.1021/acs.jafc.5b01817
J. Agric. Food Chem. 2015, 63, 7304−7310

Table 1. Comparison of the Amount of the Various Classes of Immunoglobulins in Serum and Mammary Secretions for Humans and Cows

		concentration (g/L)			% of total Ig[a]		
species	Ig	serum	colostrum	milk	serum	colostrum	milk
human[b]	IgG	12.10	0.43	0.04	78.0	2.0	3.0
	IgA	2.50	17.35	1.00	16.0	90.0	87.0
	IgM	0.93	1.59	0.10	6.0	8.0	10.0
cow[c]	IgG_1	11.20	46.40	0.58	47.0	75.5	71.6
	IgG_2	9.20	2.87	0.06	38.6	4.7	7.4
	IgA	0.37	5.36	0.08	1.6	8.8	9.9
	IgM	3.05	6.77	0.09	12.8	11.0	11.1

[a]Ig, immunoglobulin. [b]Butler, 1974. [c]Butler, 1983.

0.5−2 g/L in human milk.[17,18] These Ig ratios reflect the different events occurring in utero: infants are born with circulating maternal IgG transferred via the placenta,[19,20] whereas calves are born agammaglobulinemic. For this reason, bovine colostrum has very high levels of IgG, derived mainly from serum during the last few weeks of pregnancy. Calves are singularly dependent on ingesting maternal IgG in colostrum to provide them with protection against environmental pathogens until their own immune system matures.[21] After this time, the major function of milk Igs in ruminants is a protective, developmental role in the intestinal lumen, as in humans.[22]

GLYCOSYLATION OF sIgA

The glycans (carbohydrates groups), attached to both the Fc and Fab regions of sIgA, play a key role in its protein structure and stability and ultimately its function.[23−25] In humans (and higher primates) IgA has two isoforms, IgA_1 and IgA_2, which are produced in approximately equal amounts in human milk.[26,27] Most other species, including ruminants, have only one isoform, which is similar to human IgA_2.[28,29] There are differences in the glycosylation of the two isoforms. The hinge region of IgA_1 is longer than that of IgA_2 and has O- and N-glycosylation sites, whereas IgA_2 contains only N-glycosylation sites.[30] Along the Fc portion of IgA_2, there are a greater number of *N*-glycans compared with IgA_1.[30] SC is also heavily glycosylated, constituting between 15 and 24% of its whole molecular mass,[31] with seven N-linked sites. In human milk, the presence and patterns of glycans on Igs vary with stage of lactation, with maternal genotype controlling expression of the glycosyl transferases.[32]

Glycosylation is important in the functional activities of sIgA and FSC. The diverse array of glycan epitopes are targets for lectins and bacterial adhesins.[30] SC glycans can help anchor sIgA to the mucosal lining of the epithelium,[33] where bacteria can be sequestered, thus increasing the bacterial binding capability of IgA.[34] In addition, SC glycans nonspecifically bind to Gram-positive commensal bacteria[24] as well as reduce virulence of *Vibrio cholera* (Gram-negative), thereby preventing pathogenic biofilm formation.[35] FSC derived from milk has been shown to act as a nonspecific microbial scavenger reducing the effects of *Clostridium difficile* toxins[36] and inflammatory cytokine IL-8[37] and preventing adhesion of bacteria[38,39] via interactions with its glycans.[31] A recent study comparing the *N*-glycome of human and bovine milk observed species-specific variations in the glycan repertoire;[40] however, the significance of these differences with regard to function has yet to be determined.

sIgA AND IMMUNE EXCLUSION

Termed immune exclusion, the binding of IgA to microbes and microbial metabolic products and toxins promotes bacterial aggregation, entrapment in mucus, and clearance from the gastrointestinal tract.[41] sIgA purified from human milk has been shown to have a nonspecific "exclusion" function similar to that of intestinal-derived sIgA. In a study using human buccal epithelial cells, sIgA from human colostrum inhibited adhesion of *Escherichia coli*, a major agent of sepsis and meningitis in newborns.[42] Adhesion of *E. coli* is often mediated by bacterial fimbriae, which recognize specific receptors on the epithelial cells. The mechanism of inhibition in this instance was shown to involve specific interactions between sialyloligosaccharides on sIgA and the bacterial adhesins.[43] Similarly, bacterial toxins, such as the plant-derived shiga-like toxin, ricin, have been shown to interact with human colostral sIgA.[44]

Human milk sIgA also protects infants from specific pathogens (reviewed by Liu et al.[45]) via Fab epitopes. The Fab region of sIgA (Figure 1) interacts specifically with enteric

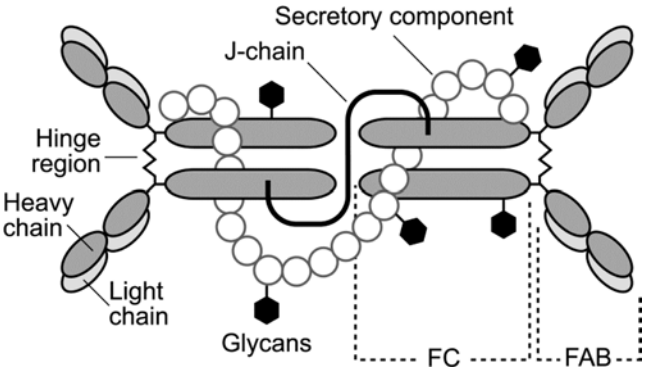

Figure 1. Schematic representation of the structure of sIgA showing the heavy and light chains, the antigen binding sites (Fab), effector (Fc) regions, the hinge region, and glycosylation sites (glycans). Secretory component binds the dimerized IgA molecule, composed of two monomeric IgA molecules, that are joined by the J chain. Diagram adapted from Woof and Russell.[78]

toxins and pathogens that in turn impede the processes of early infection. Protection of infants against infections, including *Vibrio cholera*,[46] *Campylobacter jejuni*,[47] *Shigella* species,[48] *enterotoxigenic E. coli (ETEC)*,[49] and *Giardia lamblia*,[50] relates to the specific sIgA content in human milk. In addition, human and animal studies have demonstrated that delivery of specific sIgA antibodies directly to mucosal surfaces can prevent,

DOI: 10.1021/acs.jafc.5b01836
J. Agric. Food Chem. 2015, 63, 7311−7316

diminish, or cure bacterial infections including *Campylobacter jejuni*[51] and *Clostridium difficile*[52] (reviewed by Corthesy[53]).

sIgA may also have a direct impact on the ability of microbial pathogens to secrete virulence factors required for invasion of intestinal epithelial cells. For example, *Shigella flexneri* usually enters intestinal epithelial cells via a type 3 secretion (T3S) system; however, when sIgA antibodies specific to the *O*-antigen of *Shigella flexneri* are present, entry is prevented.[54] These data suggest milk-derived sIgA may have potential as an antidiarrheal agent for at-risk populations. People with low IgA levels have been shown to have increased risk of inflammatory disorders of the gut.[55] It is possible dietary supplementation with milk-derived sIgA could reduce these inflammatory processes.

BIOFILMS AND sIgA

Bacteria do not always exist singularly, but form complex structures called biofilms. A biofilm is defined as an aggregate of microorganisms that self-produce a matrix of extracellular polymeric substance (EPS), containing polysaccharides, proteins, and DNA.[56] There are two types of biofilms described in the literature: those where the biofilm matrix is produced by the bacteria themselves and those where the colonizing bacteria depend to a lesser or greater extent on the host organism to provide the extracellular matrix. Host-supported biofilms can be utilized by the resident microbes for support and nutrition.[57−59] In turn, the biofilm and its residents provide a barrier against other invading pathogens and provide metabolites, which are of use to the host.[57−59] This is of benefit if the colonizing bacteria are commensals; however, 60−80% of human microbial infections are caused by pathogenic bacteria growing in biofilms. These "protected" bacterial colonies are exceptionally resistant to environmental stresses, especially antibiotics,[60] and this poses a major public health problem.[61] In a recent study, specific IgA antibodies, produced in response to an anti-caries vaccine against *Streptococcus mutans*, were shown to inhibit the formation of pathogenic bacterial biofilm formation in the mouth, by preventing the initial adherence, the first stage of biofilm formation.[62,63] This suggests another application for sIgA-based functional food products.

sIgA AND IMMUNE INCLUSION

Seemingly at odds with the previous section, human sIgA can also facilitate biofilm formation.[64] The hydrophilic glycosylated regions of sIgA allow the molecule to associate with both adhesins and lectin-like receptors expressed by the bacteria as well as the mucus lining on the mucosal surface.[65] Microorganisms bound by sIgA are thereby more readily entrapped by the mucus,[33] and this has been demonstrated in in vitro studies.[66,67] Furthermore, the glycans of sIgA facilitate adhesion of bacteria to both the gut epithelium and mucins.[66,68]

Whereas the length of the human gastrointestinal tract is populated with bacteria, the principal areas of permanent bacterial colonization are in the terminal ileum and the large intestine. This is primarily because of the passing of gastric acid and rapid food transit through the stomach and small intestine.[69] Transit slows in the large bowel, enabling ecosystems to develop,[70] and bacteria can live freely, in microcolonies (biofilms) or on surfaces of particulate matter (food).[71] Milk-derived sIgA could also play a role in promoting commensal biofilm formation. Studies have shown that sIgA from human milk can transit intact through the infant gut and be recovered from infant feces with retained activity.[10] The presence of SC protects sIgA against proteolytic degradation.[7,8] Thus, there is potential for milk-derived sIgA to act in a prebiotic manner, aiding colonization of probiotic bacteria in the gut.

IgA VERSUS IgG

There are a plethora of immune products that are based on the functionality and content of IgG from mammalian milk. IgG antibodies act by fixing complement, opsonizing and agglutinating bacteria, and neutralizing toxins and viruses. All of these functions include inflammatory processes. In contrast, IgA antibodies are less inflammatory acting by agglutinating antigens, neutralizing bacterial toxins and viruses, and preventing the adhesion of enteropathogenic bacteria to mucosal epithelial cells.[72] Compared to IgG, sIgA has several advantageous capabilities. For example, it has greatly increased nonspecific bacterial binding capacity via its glycosylated regions.[34] It has greater stability against proteolytic degradation,[7−9] helping sIgA retain its activity for prolonged periods in hostile environments, such as the gut lumen.[10] The anti-inflammatory profile of sIgA makes it attractive for development as a functional food product that may benefit sufferers of intestinal inflammatory disorders. However, the amount of IgA required to give a health benefit is an important question that has not been adequately answered to date. Data on naturally occurring mucosal IgA titer range are also lacking. These questions will need to be addressed to evaluate the feasibility of IgA-enriched foods.

EFFECTS OF FOOD PROCESSING ON Igs

Milk is processed at industrial scale into a wide range of consumer products, including liquid milks, yogurts, cheeses, ice creams, milk powders. As with all manufactured food products, consumer safety is of paramount importance. For milk products this is assured primarily through the use of heat treatments, with various temperature and time combinations prescribed to inactivate the spoilage and pathogenic bacteria in raw milk.[73] Milk is also subjected to heating during other processing operations, for example, separation, thermal evaporation, and spray-drying, depending on the product being manufactured.

However, immunoglobulins are among the more thermolabile milk proteins. Exposure to processing operations involving heat, pressure, or pH change can affect the conformation of these proteins and ultimately their antibody activity (reviewed in Hurley et al.[74]). Indeed, the exclusion of colostrum from dairy-processing plants as part of regular milk supply is, in part, based on the high proportion of Igs and their different physicochemical properties such as lower stability to heat compared with the major milk proteins. Denaturation of these heat-sensitive proteins during thermal processes can result in aggregation, precipitation, and consequent fouling of equipment, particularly of heat exchangers, limiting processing run times and increasing cleaning frequencies.[75] Using lower temperatures and longer retention times is an effective way of improving the quality of human heat-treated milk,[75] whereas high-pressure processing has been used for human breast milk with apparent minimal effect on IgA.[76] Methods aiming to identify markers of heat damage to milk products have been investigated.[77] Other alternative methods, which retain the bioactivity of milk while meeting product safety requirements,

DOI: 10.1021/acs.jafc.5b01836
J. Agric. Food Chem. 2015, 63, 7311−7316

are being developed. This will create an opportunity for the manufacture of bovine bioactive sIgA-enriched milk.

In summary, the role of IgA in mucosal homeostasis could be exploited using bovine milk-derived sIgA. Glycobiology, an emerging area of immunology, may reveal new opportunities for heavily glycated proteins such as sIgA, for application in novel functional food products. Recent developments in extraction and processing techniques, to retain functionality, will help realize the opportunity for the untapped resource of sIgA in bovine milk. A key question to address is the amount of IgA required to observe functional health benefit. This is not known and needs to be better defined to evaluate the feasibility of sIgA in functional products. Potential applications for sIgA have been illustrated throughout this paper, but understanding how exogenous bovine sIgA could benefit the gastrointestinal environment to provide health benefits to the consumer is an area waiting to be further explored.

AUTHOR INFORMATION

Corresponding Author

*(J.A.C.) Mail: Food and Biobased Products, Ruakura Research Centre, 10 Bisley Street, Private Bag 3123, Hamilton 3240, New Zealand. Phone: +64(0)7 838 5317. Fax: +64(0)7 838 5628. E-mail: Julie.Cakebread@agresearch.co.nz.

Notes

The authors declare no competing financial interest.

ACKNOWLEDGMENTS

We thank Dr. Tom Wheeler for his useful comments.

REFERENCES

(1) Evershed, R. P.; Payne, S.; Sherratt, A. G.; Copley, M. S.; Coolidge, J.; Urem-Kotsu, D.; Kotsakis, K.; Ozdogan, M.; Ozdogan, A. E.; Nieuwenhuyse, O.; Akkermans, P. M.; Bailey, D.; Andeescu, R. R.; Campbell, S.; Farid, S.; Hodder, I.; Yalman, N.; Ozbasaran, M.; Bicakci, E.; Garfinkel, Y.; Levy, T.; Burton, M. M. Earliest date for milk use in the Near East and southeastern Europe linked to cattle herding. *Nature* **2008**, *455*, 528−531.

(2) Butler, J. E.; Seawright, G. L.; McGivern, P. L.; Gilsdorf, M. Preliminary evidence for a diagnostic immunoglobulin G1 antibody response among culture-positive cows vaccinated with *Brucella abortus* strain 19 and challenge exposed with strain 2308. *Am. J. Vet. Res.* **1986**, *47*, 1258−1264.

(3) Chung, H.; Pamp, S. J.; Hill, J. A.; Surana, N. K.; Edelman, S. M.; Troy, E. B.; Reading, N. C.; Villablanca, E. J.; Wang, S.; Mora, J. R.; Umesaki, Y.; Mathis, D.; Benoist, C.; Relman, D. A.; Kasper, D. L. Gut immune maturation depends on colonization with a host-specific microbiota. *Cell* **2012**, *149*, 1578−15.

(4) Della Corte, E.; Parkhouse, R. M. Biosynthesis of immunoglobulin A (IgA) and immunoglobulin M (IgM). Requirement for J chain and a disulphide-exchanging enzyme for polymerization. *Biochem. J.* **1973**, *136*, 597−606.

(5) Koshland, M. E. Structure and function of the J chain. *Adv. Immunol.* **1975**, *20*, 41−69.

(6) Kaetzel, C. S. The polymeric immunoglobulin receptor: bridging innate and adaptive immune responses at mucosal surfaces. *Immunol. Rev.* **2005**, *206*, 83−99.

(7) Crottet, P.; Corthesy, B. Secretory component delays the conversion of secretory IgA into antigen-binding competent F(ab′)2: a possible implication for mucosal defense. *J. Immunol* **1998**, *161*, 5445−5453.

(8) Lindh, E. Increased resistance of immunoglobulin A dimers to proteolytic degradation after binding of secretory component. *J. Immunol* **1975**, *114*, 284−286.

(9) Berdoz, J.; Blanc, C. T.; Reinhardt, M.; Kraehenbuhl, J. P.; Corthesy, B. In vitro comparison of the antigen-binding and stability properties of the various molecular forms of IgA antibodies assembled and produced in CHO cells. *Proc. Natl. Acad. Sci. U. S. A.* **1999**, *96*, 3029−3034.

(10) Haneberg, B. Immunoglobulins in feces from infants fed human or bovine milk. *Scand. J. Immunol.* **1974**, *3*, 191−197.

(11) Groves, M. L.; Gordon, W. G. Isolation of a new glycoprotein-a and a gamma-G-globulin from individual cow milks. *Biochemistry* **1967**, *6*, 2388−2394.

(12) Labib, R. S.; Calvanico, N. J.; Tomasi, T. B. Bovine secretory component. Isolation, molecular size and shape, composition, and NH_2-terminal amino acid sequence. *J. Biol. Chem.* **1976**, *251*, 1969−1974.

(13) Lamm, M. E.; Weisz-Carrington, P.; Roux, M. E.; McWilliams, M.; Phillips-Quagliata, J. M. Development of the IgA system in the mammary gland. *Adv. Exp. Med. Biol.* **1978**, *107*, 35−42.

(14) Newburg, D. S. Bioactive components of human milk: evolution, efficiency, and protection. *Adv. Exp. Med. Biol.* **2001**, *501*, 3−10.

(15) Hanson, L. A.; Korotkova, M. The role of breastfeeding in prevention of neonatal infection. *Semin. Neonatol.* **2002**, *7*, 275−281.

(16) Rogier, E. W.; Frantz, A. L.; Bruno, M. E.; Wedlund, L.; Cohen, D. A.; Stromberg, A. J.; Kaetzel, C. S. Secretory antibodies in breast milk promote long-term intestinal homeostasis by regulating the gut microbiota and host gene expression. *Proc. Natl. Acad. Sci. U. S. A.* **2014**, *111*, 3074−3079.

(17) Farrell, H. M., Jr.; Jimenez-Flores, R.; Bleck, G. T.; Brown, E. M.; Butler, J. E.; Creamer, L. K.; Hicks, C. L.; Hollar, C. M.; Ng-Kwai-Hang, K. F.; Swaisgood, H. E. Nomenclature of the proteins of cows' milk − sixth revision. *J. Dairy Sci.* **2004**, *87*, 1641−1674.

(18) Goldman, A. S. The immune system of human milk: antimicrobial, antiinflammatory and immunomodulating properties. *Pediatr. Infect. Dis. J.* **1993**, *12*, 664−671.

(19) Brambell, F. W. R. The transfer of passive immunity from mother to young. In *Frontiers of Biology*; Tatum, A. N. a. E. L., Ed.; North-Holland Publishing: Amsterdam, The Netherlands, 1970.

(20) Hanson, L. A.; Johansson, B. G. *Milk Proteins: Chemistry and Molecular Biology*; Academic Press: New York, 1970; Vol. 1.

(21) Kruse, V. Absorption of immunoglobulin from colostrum in newborn calves. *Anim. Prod.* **1970**, *12*, 627−638.

(22) Butler. A concept of humoral immunity among ruminants and an approach to its investigation. *Adv. Exp. Med. Biol.* **1981**, *137*, 3−55.

(23) Imperiali, B.; O'Connor, S. E. Effect of N-linked glycosylation on glycopeptide and glycoprotein structure. *Curr. Opin. Chem. Biol.* **1999**, *3*, 643−649.

(24) Mathias, A.; Corthesy, B. *N*-Glycans on secretory component: mediators of the interaction between secretory IgA and Gram-positive commensals sustaining intestinal homeostasis. *Gut Microbes* **2011**, *2*, 287−293.

(25) Froehlich, J. W.; Dodds, E. D.; Barboza, M.; McJimpsey, E. L.; Seipert, R. R.; Francis, J.; An, H. J.; Freeman, S.; German, J. B.; Lebrilla, C. B. Glycoprotein expression in human milk during lactation. *J. Agric. Food Chem.* **2010**, *58*, 6440−6448.

(26) Gregory, R. L.; Filler, S. J. Protective secretory immunoglobulin A antibodies in humans following oral immunization with *Streptococcus mutans*. *Infect. Immun.* **1987**, *55*, 2409−2415.

(27) Tregoat, V.; Montagne, P.; Bene, M. C.; Faure, G. Increases of IgA milk concentrations correlate with IgA2 increment. *J. Clin. Lab. Anal.* **2001**, *15*, 55−58.

(28) Almogren, A.; Senior, B. W.; Kerr, M. A. A comparison of the binding of secretory component to immunoglobulin A (IgA) in human colostral S-IgA1 and S-IgA2. *Immunology* **2007**, *120*, 273−280.

(29) Brown, W. R.; Rabbani, H.; Butler, J. E.; Hammarstrom, L. Characterization of the bovine C alpha gene. *Immunology* **1997**, *91*, 1−6.

(30) Royle, L.; Roos, A.; Harvey, D. J.; Wormald, M. R.; van Gijlswijk-Janssen, D.; Redwan el, R. M.; Wilson, I. A.; Daha, M. R.; Dwek, R. A.; Rudd, P. M. Secretory IgA *N*- and *O*-glycans provide a

DOI: 10.1021/acs.jafc.5b01836
J. Agric. Food Chem. 2015, 63, 7311−7316

link between the innate and adaptive immune systems. *J. Biol. Chem.* **2003**, *278*, 20140−20153.
(31) Perrier, C.; Sprenger, N.; Corthesy, B. Glycans on secretory component participate in innate protection against mucosal pathogens. *J. Biol. Chem.* **2006**, *281*, 14280−14287.
(32) Newburg, D. S. Glycobiology of human milk. *Biochemistry* **2013**, *78*, 771−785.
(33) Phalipon, A.; Cardona, A.; Kraehenbuhl, J. P.; Edelman, L.; Sansonetti, P. J.; Corthesy, B. Secretory component: a new role in secretory IgA-mediated immune exclusion in vivo. *Immunity* **2002**, *17*, 107−115.
(34) Mestecky, J.; Russell, M. W. Specific antibody activity, glycan heterogeneity and polyreactivity contribute to the protective activity of S-IgA at mucosal surfaces. *Immunol. Lett.* **2009**, *124*, 57−62.
(35) Murthy, A. K.; Chaganty, B. K.; Troutman, T.; Guentzel, M. N.; Yu, J. J.; Ali, S. K.; Lauriano, C. M.; Chambers, J. P.; Klose, K. E.; Arulanandam, B. P. Mannose-containing oligosaccharides of non-specific human secretory immunoglobulin A mediate inhibition of *Vibrio cholerae* biofilm formation. *PLoS One* **2011**, *6*, e16847.
(36) Dallas, S. D.; Rolfe, R. D. Binding of *Clostridium difficile* toxin A to human milk secretory component. *J. Med. Microbiol.* **1998**, *47*, 879−888.
(37) Marshall, L. J.; Perks, B.; Ferkol, T.; Shute, J. K. IL-8 released constitutively by primary bronchial epithelial cells in culture forms an inactive complex with secretory component. *J. Immunol.* **2001**, *167*, 2816−2823.
(38) de Araujo, A. N.; Giugliano, L. G. Lactoferrin and free secretory component of human milk inhibit the adhesion of enteropathogenic *Escherichia coli* to HeLa cells. *BMC Microbiol.* **2001**, *1*, 25.
(39) de Oliveira, I. R.; de Araujo, A. N.; Bao, S. N.; Giugliano, L. G. Binding of lactoferrin and free secretory component to enterotoxigenic *Escherichia coli*. *FEMS Microbiol. Lett.* **2001**, *203*, 29−33.
(40) Nwosu, C. C.; Aldredge, D. L.; Lee, H.; Lerno, L. A.; Zivkovic, A. M.; German, J. B.; Lebrilla, C. B. Comparison of the human and bovine milk *N*-glycome via high-performance microfluidic chip liquid chromatography and tandem mass spectrometry. *J. Proteome Res.* **2012**, *11*, 2912−2924.
(41) Lamm, M. E. Interaction of antigens and antibodies at mucosal surfaces. *Annu. Rev. Microbiol.* **1997**, *51*, 311−340.
(42) Korhonen, T. K.; Valtonen, M. V.; Parkkinen, J.; Vaisanen-Rhen, V.; Finne, J.; Orskov, F.; Orskov, I.; Svenson, S. B.; Makela, P. H. Serotypes, hemolysin production, and receptor recognition of *Escherichia coli* strains associated with neonatal sepsis and meningitis. *Infect. Immun.* **1985**, *48*, 486−491.
(43) Schroten, H.; Stapper, C.; Plogmann, R.; Kohler, H.; Hacker, J.; Hanisch, F. G. Fab-independent antiadhesion effects of secretory immunoglobulin A on S-fimbriated *Escherichia coli* are mediated by sialyloligosaccharides. *Infect. Immun.* **1998**, *66*, 3971−3973.
(44) Mantis, N. J.; Farrant, S. A.; Mehta, S. Oligosaccharide side chains on human secretory IgA serve as receptors for ricin. *J. Immunol.* **2004**, *172*, 6838−6845.
(45) Liu, B.; Newburg, D. S. Human milk glycoproteins protect infants against human pathogens. *Breastfeeding Med.* **2013**, *8*, 354−362.
(46) Glass, R. I.; Svennerholm, A. M.; Stoll, B. J.; Khan, M. R.; Hossain, K. M.; Huq, M. I.; Holmgren, J. Protection against cholera in breast-fed children by antibodies in breast milk. *N. Engl. J. Med.* **1983**, *308*, 1389−1392.
(47) Ruiz-Palacios, G. M.; Calva, J. J.; Pickering, L. K.; Lopez-Vidal, Y.; Volkow, P.; Pezzarossi, H.; West, M. S. Protection of breast-fed infants against *Campylobacter* diarrhea by antibodies in human milk. *J. Pediatr.* **1990**, *116*, 707−713.
(48) Hayani, K. C.; Guerrero, M. L.; Morrow, A. L.; Gomez, H. F.; Winsor, D. K.; Ruiz-Palacios, G. M.; Cleary, T. G. Concentration of milk secretory immunoglobulin A against *Shigella* virulence plasmid-associated antigens as a predictor of symptom status in *Shigella*-infected breast-fed infants. *J. Pediatr.* **1992**, *121*, 852−856.
(49) Cruz, J. R.; Gil, L.; Cano, F.; Caceres, P.; Pareja, G. Breast milk anti-*Escherichia coli* heat-labile toxin IgA antibodies protect against toxin-induced infantile diarrhea. *Acta Paediatr.* **1988**, *77*, 658−662.
(50) Walterspiel, J. N.; Morrow, A. L.; Guerrero, M. L.; Ruiz-Palacios, G. M.; Pickering, L. K. Secretory anti-Giardia lamblia antibodies in human milk: protective effect against diarrhea. *Pediatrics* **1994**, *93*, 28−31.
(51) Hammarstrom, V.; Smith, C. I. E.; Hammarstrom, L.; Heaton, P. Oral immunoglobulin treatment in *Campylobacter jejuni* enteritis. *Lancet* **1993**, *341*, 1036.
(52) Tjellström, B.; Stenammar, L.; Eriksson, S.; Magnusson, K.-E. Oral immunoglobulin A supplement in treatment of *Clostridium difficile* enteritis. *Lancet* **1993**, *341*, 701−702.
(53) Corthesy, B. Recombinant secretory immunoglobulin A in passive immunotherapy: linking immunology and biotechnology. *Curr. Pharm. Biotechnol.* **2003**, *4*, 51−67.
(54) Forbes, S. J.; Bumpus, T.; McCarthy, E. A.; Corthesy, B.; Mantis, N. J. Transient suppression of *Shigella flexneri* type 3 secretion by a protective O-antigen-specific monoclonal IgA. *mBio* **2011**, *2*, e00042−11.
(55) Cunningham-Rundles, C. Physiology of IgA and IgA deficiency. *J. Clin. Immunol.* **2001**, *21*, 303−309.
(56) Pamp, S. J.; Tolker-Nielsen, T. Multiple roles of biosurfactants in structural biofilm development by *Pseudomonas aeruginosa*. *J. Bacteriol.* **2007**, *189*, 2531−2539.
(57) Everett, M. Immune exclusion and immune inclusion: a new model of host-bacterial interactions in the gut. *Clin. Appl. Immunol. Rev.* **2004**, *4*, 321−332.
(58) Sonnenburg, J. L.; Angenent, L. T.; Gordon, J. I. Getting a grip on things: how do communities of bacterial symbionts become established in our intestine? *Nat. Immunol.* **2004**, *5*, 569−573.
(59) Thomas, A. D.; Parker, W. Cultivation of epithelial-associated microbiota by the immune system. *Future Microbiol.* **2010**, *5*, 1483−1492.
(60) Hoiby, N.; Bjarnsholt, T.; Givskov, M.; Molin, S.; Ciofu, O. Antibiotic resistance of bacterial biofilms. *Int. J. Antimicrob. Agents* **2010**, *35*, 322−332.
(61) Costerton, J. W.; Stewart, P. S.; Greenberg, E. P. Bacterial biofilms: a common cause of persistent infections. *Science* **1999**, *284*, 1318−1322.
(62) Huang, L.; Xu, Q. A.; Liu, C.; Fan, M. W.; Li, Y. H. Anti-caries DNA vaccine-induced secretory immunoglobulin A antibodies inhibit formation of Streptococcus mutans biofilms in vitro. *Acta Pharmacol. Sin.* **2013**, *34*, 239−246.
(63) Landini, P.; Antoniani, D.; Burgess, J. G.; Nijland, R. Molecular mechanisms of compounds affecting bacterial biofilm formation and dispersal. *Appl. Microbiol. Biotechnol.* **2010**, *86*, 813−823.
(64) Friman, V.; Adlerberth, I.; Connell, H.; Svanborg, C.; Hanson, L. A.; Wold, A. E. Decreased expression of mannose-specific adhesins by *Escherichia coli* in the colonic microflora of immunoglobulin A-deficient individuals. *Infect. Immun.* **1996**, *64*, 2794−2798.
(65) Sharon, N.; Ofek, I. Safe as mother's milk: carbohydrates as future anti-adhesion drugs for bacterial diseases. *Glycoconjugate J.* **2000**, *17*, 659−664.
(66) Bollinger, R. R.; Everett, M. L.; Palestrant, D.; Love, S. D.; Lin, S. S.; Parker, W. Human secretory immunoglobulin A may contribute to biofilm formation in the gut. *Immunology* **2003**, *109*, 580−587.
(67) Mathias, A.; Duc, M.; Favre, L.; Benyacoub, J.; Blum, S.; Corthesy, B. Potentiation of polarized intestinal Caco-2 cell responsiveness to probiotics complexed with secretory IgA. *J. Biol. Chem.* **2010**, *285*, 33906−33913.
(68) Allen, A.; Pearson, J. P. The gastrointestinal adherent mucous gel barrier. *Methods Mol. Biol.* **2000**, *125*, 57−64.
(69) Gorbach, S. L. Population control in the small bowel. *Gut* **1967**, *8*, 530−532.
(70) Cummings, J. H.; Bingham, S. A.; Heaton, K. W.; Eastwood, M. A. Fecal weight, colon cancer risk and dietary intake of non starch polysaccharides (dietary fibre). *Gastroenterology* **1993**, *103*, 1783−1789.
(71) Englyst, H.; Hay, S.; Macfarlane, G. Polysaccharide breakdown by mixed populations of human fecal bacteria. *FEMS Microbiol. Lett.* **1987**, *95*, 163−171.

DOI: 10.1021/acs.jafc.5b01836
J. Agric. Food Chem. 2015, 63, 7311−7316

(72) Marnila, P.; Korhonen, H. *Immunoglobulins*; Academic Press: London, UK, 2002.
(73) Giffel, M. C. t.; Wells-Bennik, M. H. J. Good hygienic practice in milk production and processing. In *Improving the Safety and Quality of Milk*; Woodhead Publishing Series in Food Science, Technology and Nutrition 188; Griffiths, M. W., Ed.; Woodhead Publishing: Cambridge, UK, 2010; pp 179−193.
(74) Hurley, W. L.; Theil, P. K. Perspectives on immunoglobulins in colostrum and milk. *Nutrients* **2011**, *3*, 442−474.
(75) Czank, C.; Prime, D. K.; Hartmann, B.; Simmer, K.; Hartmann, P. E. Retention of the immunological proteins of pasteurized human milk in relation to pasteurizer design and practice. *Pediatr. Res.* **2009**, *66*, 374−379.
(76) Permanyer, M.; Castellote, C.; Ramirez-Santana, C.; Audi, C.; Perez-Cano, F. J.; Castell, M.; Lopez-Sabater, M. C.; Franch, A. Maintenance of breast milk Immunoglobulin A after high-pressure processing. *J. Dairy Sci.* **2010**, *93*, 877−883.
(77) Meltretter, J.; Schmidt, A.; Humeny, A.; Becker, C. M.; Pischetsrieder, M. Analysis of the peptide profile of milk and its changes during thermal treatment and storage. *J. Agric. Food Chem.* **2008**, *56*, 2899−2906.
(78) Woof, J. M.; Russell, M. W. Structure and function relationships in IgA. *Mucosal Immunol.* **2011**, *4*, 590−597.

DOI: 10.1021/acs.jafc.5b01836
J. Agric. Food Chem. 2015, 63, 7311−7316

protects liver function.[22] Anticancer activities have been observed in various mammalian cancer cell lines.[23−25] Sesamin retards the growth of HepG2 cells and induces apoptosis by inhibiting STAT3 signaling and upregulating p53 and p21, leading to cell cycle arrest in G_2/M.[26] A combination of γ-tocotrienol and sesamin treatment has a synergistic antiproliferative effect on +SA, MCF-7, and MDA-MB-231 mammary cancer cells and induced G_1 cell cycle arrest by decreasing the levels of cyclin D1, CDK2, CDK4, CDK6, and p-Rb, and increasing $p27^{KIP1}$ and $p16^{INK4a}$ expression, in +SA cells.[27] However, the effects of sesamin on VSMCs remain poorly understood. Thus, we explored the inhibitory effects of sesamin on PDGF-induced VSMC proliferation and growth, and the molecular mechanisms of sesamin action.

MATERIALS AND METHODS

Chemicals. Dulbecco's modified Eagle's medium (DMEM), fetal bovine serum (FBS), phosphate-buffered saline (PBS), penicillin/streptomycin, and trypsin−EDTA were from Gibco BRL (Grand Island, NY). Anti-phospho-ERK 1/2 (Thr^{202}/Tyr^{204}), anti-ERK1/2, anti-phospho-JNK (Thr^{180}/Tyr^{182}), anti-phospho-p38 (Thr^{180}/Tyr^{182}), anti-p38, anti-phospho-PLCγ1 (Tyr^{783}), anti-PLCγ1, anti-phospho-PDGF-Rβ chain (Tyr^{751}), anti-PDGF-Rβ, anti-phospho-STAT3 (Tyr^{705}), anti-STAT3, anti-Akt, anti-cleaved poly-ADP ribose polymerase (PARP), anti-PCNA, and anti-Alexa 555 antibodies were from Cell Signaling Technology, Inc. (Beverly, MA, USA). Anti-phospho-Akt (Ser^{473}), anti-p53, and anti-$p27^{KIP1}$ antibodies were obtained from Millipore Corporation (Billerica, MA, USA). Anti-phospho-pRb (Ser^{807}), anti-CDK2, anti-CDK4, anti-cyclin D1, anti-cyclin E, and anti-β-actin were from Abfrontier (Geumcheon, Seoul, Korea). Anti-$p21^{CIP1}$ was from Calbiochem (Darmstadt, Germany). Anti-FITC was from Sigma (St. Louis, MO, USA). PDGF-BB was obtained from Upstate Biotechnology (Lake Placid, NY, USA). All other chemicals were of the highest available analytical grade.

Cell Culture. Rat aortic VSMCs were isolated via enzymatic dispersion, as previously described.[28] Cells were cultured in DMEM supplemented with 10% (v/v) heat-inactivated FBS, 100 IU/mL penicillin, and 100 μg/mL streptomycin, at 37 °C in a humidified incubator under 95% air and 5% CO_2 (both v/v). VSMC purity was confirmed by immunocytochemical visualization of β-smooth-muscle actin. VSMCs were used at passages 4−8. Sesamin was dissolved in DMSO, but the final concentration of DMSO in any experimental medium did not exceed 0.1% (v/v).

Cell Proliferation Assay. VSMC proliferation was measured using both an indirect colorimetric WST-1 assay (premix WST-1; Takara, Otsu, Japan) and direct cell counting. For the indirect assay, VSMCs were seeded into 96-well culture plates at 4×10^4 cells/mL and incubated in DMEM with 10% (v/v) FBS at 37 °C for 24 h. The medium was then replaced with serum-free DMEM, and incubation continued for 24 h prior to addition of various concentrations of sesamin, followed by a further 24 h of incubation in fresh serum-free medium. Cells were next stimulated by PDGF-BB (50 ng/mL) for another 24 h. After 22 h, WST-1 solution was added, and absorbances at 450 nm were determined 2 h later with the aid of a microplate reader (Tecan Group Ltd., Männedorf, Switzerland). All results were expressed as percentages of the control value (no PDGF stimulation). To obtain direct cell counts, VSMCs were seeded into 12-well culture plates at 1×10^5 cells/mL and treated as described above, with the exception of WST-1 addition. After PDGF-BB treatment for 24 h, cells were suspended by addition of trypsin−EDTA and microscopically counted using a hemocytometer.

Cell Viability Assay. VSMCs were seeded into 96-well culture plates at 4×10^4 cells/mL and incubated in DMEM with 10% (v/v) FBS at 37 °C for 24 h and in serum-free medium for another 24 h, and next they were exposed to 10 μM sesamin or 100 μg/mL digitonin (a cytotoxic control) for various times. WST-1 solution was added, and absorbances at 450 nm were measured 2 h later with the aid of a microplate reader.

DNA Synthesis Assay. [^{3}H]-Thymidine incorporation was measured. The assay conditions were as described above for the cell proliferation assay, to the time of PDGF-BB treatment. After cell stimulation via addition of PDGF-BB (50 ng/mL) in serum-free medium, [^{3}H]-thymidine (2 μCi/mL) was added 4 h prior to harvesting. Each reaction was terminated by aspiration of medium and sequential washing in PBS with 10% (v/v) trichloroacetic acid, and ethanol/ether (1:1, v/v). Acid-insoluble [^{3}H]-thymidine was extracted into 500 μL amounts of 0.5 M NaOH/well, and these solutions mixed with 3 mL amounts of scintillation cocktail (Ultimagold; Packard Bioscience, Waltham, MA, USA). Radioactivity was measured with the aid of a liquid scintillation counter (LS3801; Beckman, Düsseldorf, Germany).

Analysis of Cell Cycle Progression. Cell cycle progression was monitored as described previously.[8] VSMCs were seeded into six-well culture plates and treated as described above (the cell proliferation assay) until the time of PDGF-BB treatment. After stimulation with PDGF-BB (50 ng/mL) for 24 h, cells were harvested by trypsinization and centrifuged at 1,500 rpm for 10 min. The pellets were suspended in 1 mL amounts of 1× PBS, washed twice, fixed in 70% (v/v) ethanol at −20 °C for 24 h, briefly vortexed, and centrifuged at 3,000 rpm for 10 min. The ethanol was discarded and the pellets stained with 500 μL propidium iodide (PI) solution (50 μg/mL PI in sample buffer with 100 μg/mL of DNase-free RNase A). After incubation at 4 °C for 30 min, the level of PI−DNA complex in each nucleus was measured using a FACScalibur (Becton Dickinson Co., Franklin Lakes, NJ, USA). The fluorescence intensity of incorporated PI was used as a measure of nuclear DNA content. The rate of cell cycle progression from the G_0/G_1 to the S and G_2/M phases was determined using the Modfit LT software (Verity Software House, Topsham, ME, USA).

Immunoblotting. Immunoblotting was performed as described previously with slight modifications.[4,5] VSMCs were stimulated with 50 ng/mL PDGF-BB to trigger phosphorylation of JNK (3 min poststimulation [ps]); ERK 1/2 (5 min ps); p38 and PDGF-Rβ (10 min ps); PLCγ1, STAT3, and Akt (15 min ps). Cells were stimulated with 50 ng/mL PDGF-BB for 24 h prior to evaluation of cyclin D1, cyclin E, CDK2, CDK4, PCNA, $p21^{CIP}$, $p27^{KIP}$, and p53 expression levels; the extent of PARP cleavage; and the pRb phosphorylation level. Each reaction was terminated by washing the cells twice in ice-cold PBS followed by addition of Laemmli sample buffer; each lysate was next boiled for 10 min. For each blot, equal amounts of cell lysates were separated via sodium dodecyl sulfate−polyacrylamide gel electrophoresis (SDS−PAGE; 7.5−12.5% [w/v] acrylamide gels) and transferred to polyvinylidene fluoride (PVDF) membranes (Atto Corp., Tokyo, Japan) via application of 200 mA for 2 h. Blots were blocked with 5% (w/v) bovine serum albumin (BSA) in TBS-T and incubated with 1:500−1:1,000 dilutions of primary antibodies overnight at 4 °C, and then with 1:2,000 dilutions of secondary antibody. Bands were detected using ECL kits (Atto) and band intensities (normalized to those of β-actin) quantified using the Quantity One software (Bio-Rad, Hercules, CA, USA).

RNA Extraction and Reverse Transcription-Polymerase Chain Reaction (RT-PCR). Prior to RNA extraction, VSMCs were seeded into six-well culture plates and cultured in DMEM with 10% (v/v) FBS at 37 °C for 24 h. The assay conditions were as described above for the cell proliferation assay. RNA was isolated using Total RNA Extraction kits (Real-Biotech Co., Ping-Tung, Taiwan). All preparations were treated with DNaseI (RNase-free; Takara, Japan), and approximately 1 μg amounts of total RNA were reverse-transcribed to cDNA using AccuPower CycleScript RT PreMix (dN12) (Bioneer, Daejeon, Korea). RT-PCR was performed with the aid of HiPi Plus PCR Premix (ELPIS, Daejeon, Korea) and specific primer pairs, on a MyCycler (Bio-Rad). All primers were synthesized by Bioneer, and all primer pairs spanned introns (Supplementary Table 1). The PCR conditions were as follows: 1 cycle of 5 min at 95 °C; followed by 30 cycles of 10 s at 95 °C, 10 s at 58 °C (p27) or 56 °C (p21 and p53), and 10 s at 72 °C; and 1 cycle of 5 min at 72 °C. The products were subjected to 2% (w/v) agarose gel electrophoresis and visualized by ethidium bromide staining.

DOI: 10.1021/acs.jafc.5b03374
J. Agric. Food Chem. 2015, 63, 7317−7325

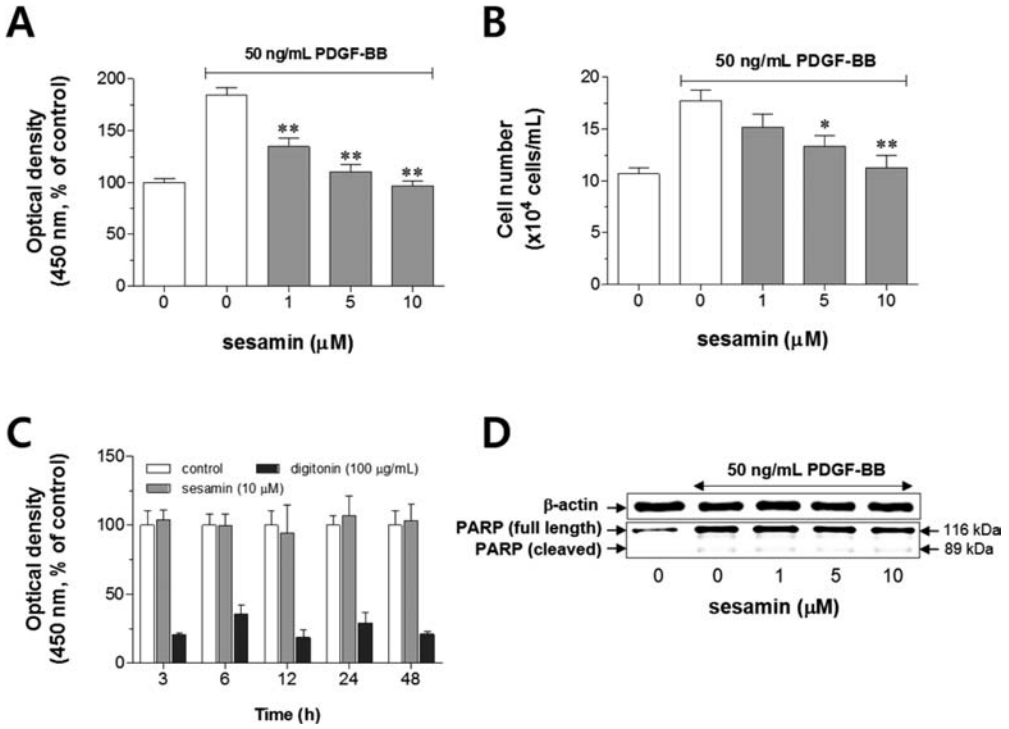

Figure 2. Effects of sesamin on proliferation of PDGF-stimulated VSMCs and cell viability. (A) Serum-deprived VSMCs were treated with sesamin (1−10 μM) for 24 h and next stimulated with 50 ng/mL PDGF-BB for a further 24 h. The WST-1 assay was performed, and the optical densities at 450 nm are shown (n = 3). (B) For direct cell counting, cells were harvested after treatment with 50 ng/mL PDGF-BB and microscopically counted using a hemocytometer (n = 4). (C) Cell viability levels were determined using the WST-1 assay. Serum-deprived VSMCs were incubated with control solution (0.1% [v/v] DMSO), or sesamin (10 μM) or digitonin (100 μg/mL), for various times (3−48 h). The values shown are means ± SEM, and significant differences from PDGF control (PDGF-stimulated, but no sesamin) values are shown by either * ($P < 0.05$) or ** ($P < 0.01$). (D) The extent of VSMC apoptosis was determined by assessment of PARP (a cell apoptosis marker) cleavage levels. The levels of full-length PARP (116 kDa) and the cleaved fragment thereof (89 kDa) were measured by immunoblotting as described in Materials and Methods. Band densities were normalized to those of β-actin. The images shown are representative of those obtained in three similar, independent experiments.

Immunofluorescence. To detect PCNA, p21, and p27 via immunofluorescence, VSMCs were seeded onto glass coverslips in 24-well culture plates. The assay conditions were the same as described above for the cell proliferation assay. After treatment of VSMCs, the cells were washed twice with ice-cold PBS, fixed in 4% (v/v) formaldehyde in PBS for 15 min, and quenched in 100 mM glycine in PBS for 10 min. The cells were next washed twice with PBS; permeabilized with 0.1% (v/v) Triton X-100 for 3 min; blocked in 5% (v/v) goat serum in PBS for 1 h; and incubated with anti-PCNA antibody solution (1:500 dilution in 3% [w/v] BSA in PBS), anti-p21 antibody solution (1:100 dilution in 3% [w/v] BSA in PBS), or anti-p27 antibody solution (1:200 dilution in 3% [w/v] BSA in PBS), for 1.5 h. After washing with PBS, the cells were incubated with secondary antibody (FITC-IgG; 1:200 dilution in 3% [w/v] BSA in PBS) for 1.5 h. Cells were washed with PBS, mounted in Mounting Medium containing DAPI (Vector Laboratories Inc., Burlingame, CA, USA), and observed under a confocal laser microscope (LSM5 live configuration Variotwo VRGB; Zeiss, Jena, Germany).

siRNA Transfection. The $p27^{KIP1}$ siRNA (accession no. NM_031762.3), $p21^{CIP1}$ siRNA (accession no. NM_080782.3), and negative control siRNA (si-con) oligonucleotides were synthesized by Bioneer Corp. (Daejeon, Korea). The target sequences of the siRNA for $p27^{KIP1}$ (si-p27) were sense 5′-AGU ACA CUU GAU CAC UGA A(dTdT)-3′ and antisense 5′-UUC AGU GAU CAA GUG UAC U(dTdT)-3′, and for $p21^{CIP1}$ (si-p21) were sense 5′-UGA CAG UGA AGC AGU CAC A(dTdT)-3′ and antisense 5′-UGU GAC UGC UUC ACU GUC A(dTdT)-3′. Transfection of siRNAs was performed using TransIT-X2 (Mirus BIO LLC, Madison, WI, USA) according to the manufacturer's protocol. Final concentrations of 50 nM si-con, si-p27, and si-p21 oligonucleotides with TransIT-X2 in OptiMEM were incubated with VSMCs for 6 h; then transfection medium was removed and cells were changed to serum free medium. The ability of the siRNA oligonucleotide to knockdown target protein expression was analyzed by immunoblotting of whole cell extracts.

Statistical Analysis. Data are expressed as means ± SEM. One-way ANOVA was used to perform multiple comparisons (GraphPad Software, San Diego, CA, USA). Dunnett's test was applied if a significant difference was evident between treatment groups. A p value less than 0.05 was considered to reflect significance.

RESULTS

Effects of Sesamin on VSMC Proliferation and Viability. To evaluate the effect of sesamin on PDGF-induced VSMC proliferation, we performed both the WST-1 and direct cell counting assays. As shown in Figure 2A, sesamin significantly inhibited PDGF-BB-stimulated VSMC proliferation in a concentration-dependent manner. The levels of inhibition at 1, 5, and 10 μM sesamin were 49.8%, 74.6%, and 87.8%, respectively. Direct cell counting showed that VSMC numbers increased significantly after treatment with 50 ng/mL PDGF-BB (to 17.7 ± 1.5 × 10^4 cells/well) compared to the nonstimulated group (10.7 ± 1.8 × 10^4 cells/well) (Figure 2B). As the sesamin concentration increased to 1, 5, and 10 μM, the cell numbers fell significantly to 15.2 ± 2.4, 13.4 ± 1.8, and 11.2 ± 2.0 × 10^4 cells/well, respectively. We used the WST-1 assay to show that the antiproliferative effect was not attributable to cytotoxicity (Figure 2C). Exposure to the highest tested sesamin concentration (10 μM) for various times was not cytotoxic to VSMCs suspended in serum-free medium. Digitonin (100 μg/mL), which permeabilizes the cell

DOI: 10.1021/acs.jafc.5b03374
J. Agric. Food Chem. 2015, 63, 7317−7325

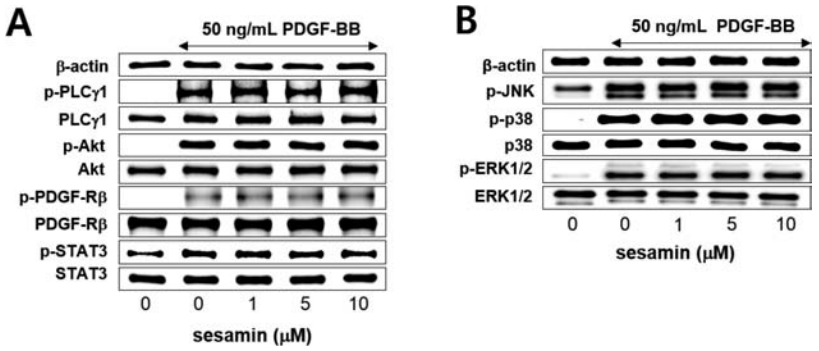

Figure 3. Effects of sesamin on PDGF-Rβ downstream signaling in PDGF-stimulated VSMCs. Serum-deprived VSMCs were treated with sesamin (1−10 μM) for 24 h and next stimulated with 50 ng/mL PDGF-BB to activate PDGF-Rβ downstream signaling. After termination of the reactions, cells were lysed and immunoblotting was performed as described in Materials and Methods (A, B). Regulation by sesamin of the PDGF-induced phosphorylation of PLCγ1, Akt, PDGF-Rβ, STAT3, JNK, p38, and ERK1/2 was assessed. The gel images are representative of those obtained in four similar, independent experiments.

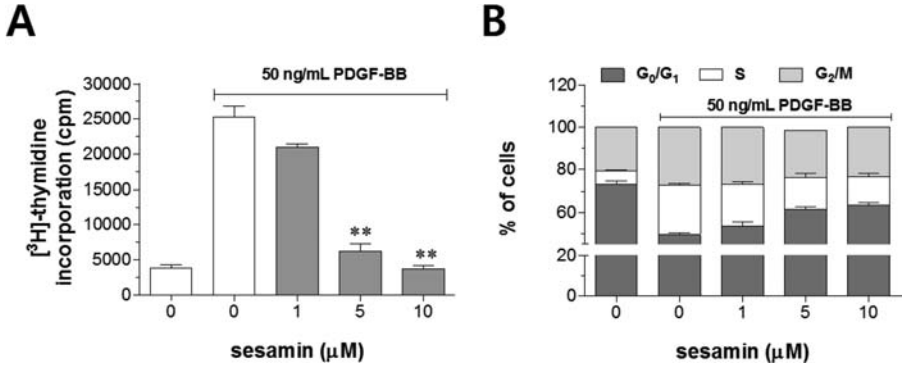

Figure 4. Effects of sesamin on DNA synthesis by and cell cycle progression of PDGF-stimulated VSMCs. (A) Serum-deprived VSMCs were treated with sesamin (1−10 μM) for 24 h and next stimulated with 50 ng/mL PDGF-BB for a further 24 h. To measure DNA synthesis, [^{3}H]-thymidine (2 μCi/mL) was added 4 h prior to harvesting. Radioactivity levels were determined using a liquid scintillation counter (n = 3). All data are expressed as means ± SEM, and significant differences compared to the PDGF control (PDGF-stimulated, but no sesamin) are shown by ** (P < 0.01). (B) Serum-deprived VSMCs were treated with sesamin (1−10 μM) for 24 h and next stimulated with 50 ng/mL PDGF-BB for 24 h. Cells were harvested via trypsinization and the DNA contents of individual nuclei analyzed by flow cytometry. Each value shown was derived by counting at least 10,000 events. The numbers of cells in the G_0/G_1, S, and G_2/M phases are expressed as percentages of total cells. The values shown are averages of data obtained in three similar, independent experiments.

membrane, was used as a positive cytotoxic control.[29] To explore whether sesamin caused apoptosis PARP cleavage, a marker of cell apoptosis, was examined via immunoblotting. As shown in Figure 2D, PARP was not obviously cleaved in the presence of 1−10 μM sesamin, and we thus concluded that sesamin did not cause apoptotic cell death.

Effects of Sesamin on PDGF-Rß Downstream Signaling in PDGF-Stimulated VSMCs. After angioplasty, or in the early stages of atherosclerosis, PDGF-R is overexpressed and PDGF-BB may bind thereto, triggering downstream phosphorylation of PDGF-R, phospholipase Cγ (PLCγ), protein kinase B (Akt/PKB), signal transducer, and activator of transcription 3 (STAT3), members of the mitogen-activated protein kinase (MAPK) family including c-Jun N-terminal kinases (JNK), p38, and extracellular signal-regulated kinase 1/2 (ERK1/2).[30] To explore the molecular basis of the antiproliferative activity of sesamin, we determined whether PDGF-R-activated downstream signaling molecules were induced when PDGF bound to its receptors. Figure 3A shows that stimulation of PLCγ1, Akt, PDGF-Rß, and STAT3 phosphorylation by PDGF-BB (50 ng/mL) was not inhibited by sesamin; also, the total amounts of these proteins were not affected by sesamin. Phosphorylation of JNK, p38, and ERK1/2 was stimulated by addition of PDGF-BB (50 ng/mL), and this was not affected by preincubation with sesamin (Figure 3B). These results indicate that the antiproliferative activity of sesamin did not involve an effect of sesamin on the PDGF-R-induced activation of downstream signaling pathways.

Effects of Sesamin on DNA Synthesis and Cell Cycle Progression in PDGF-Stimulated VSMCs. To assess the effects of sesamin on DNA synthesis, we measured [^{3}H]-thymidine incorporation by VSMCs. As shown in Figure 4A, such incorporation increased significantly after stimulation with 50 ng/mL PDGF-BB (to 25,325.0 ± 3372.5 cpm/well) compared to the nonstimulated control (3,856.2 ± 813.2 cpm/well). [^{3}H]-Thymidine incorporation into DNA of PDGF-stimulated VSMCs was significantly inhibited by sesamin, in a concentration-dependent manner. The counts after addition of 1, 5, and 10 μM sesamin were 21,628, 19,122, and 4,354 cpm/well, respectively.

Flow cytometry showed that sesamin affected cell cycle progression in PDGF-induced VSMCs. As shown in Figure 4B, about 72.8 ± 3.0% and 6.5 ± 1.0% of VSMCs were in the G_0/G_1 and S phases in the absence of PDGF, but these percentages changed to 49.5 ± 1.4% and 23.0 ± 1.6% upon stimulation with PDGF. Sesamin significantly inhibited cell cycle progression, in

DOI: 10.1021/acs.jafc.5b03374
J. Agric. Food Chem. 2015, 63, 7317−7325

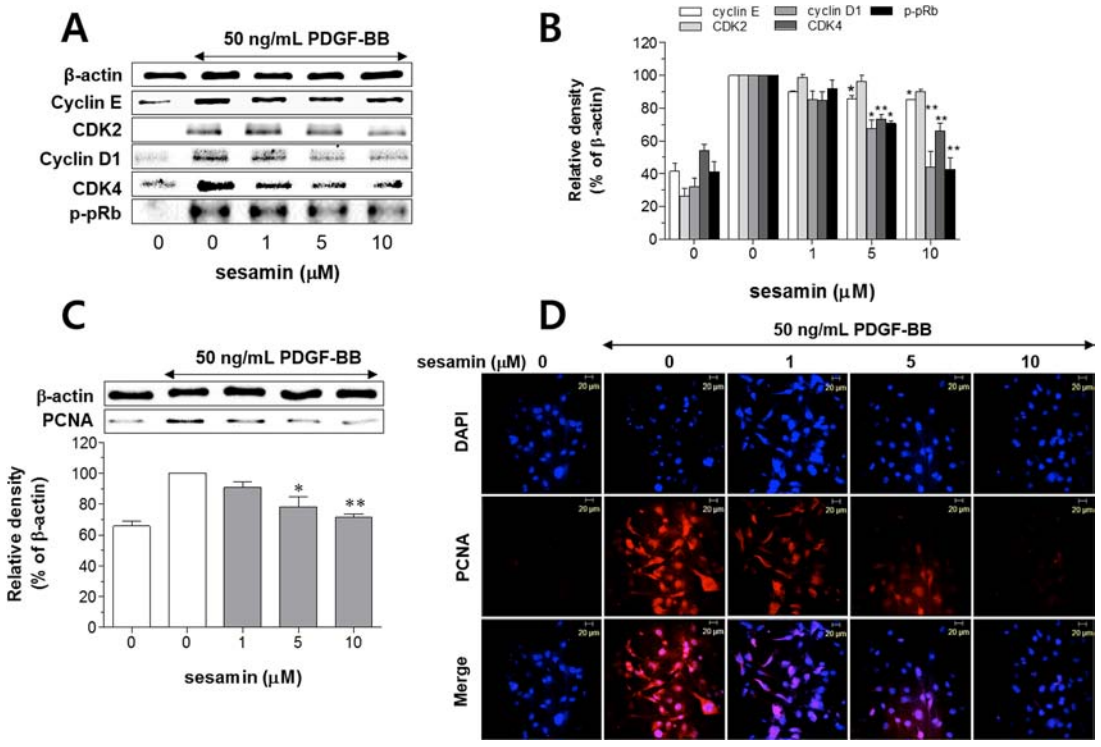

Figure 5. Effects of sesamin on cyclin E, CDK2, cyclin D1, CDK4, and PCNA expression levels, and pRb phosphorylation in PDGF-stimulated VSMCs. (A, B) Serum-deprived VSMCs were treated with sesamin (1−10 μM) for 24 h and next stimulated with 50 ng/mL PDGF-BB for 24 h. After termination of the reactions, immunoblotting was performed as described in Materials and Methods. The expression levels of CDK2, cyclin E, CDK4, and cyclin D1 and the phosphorylation status of pRb were measured via immunoblotting and normalized to the total levels of β-actin. The values shown were derived from three similar, independent experiments. Data are expressed as means ± SEM, and significant differences compared to the PDGF control (PDGF-stimulated, but no sesamin) are shown using either * ($P < 0.05$) or ** ($P < 0.01$). (C) PCNA expression levels were normalized to those of total β-actin. The values shown were derived from three similar, independent experiments. Data are expressed as means ± SEM, and significant differences compared to the PDGF control (PDGF-stimulated, but no sesamin) are shown using either * ($P < 0.05$) or ** ($P < 0.01$). (D) PCNA expression levels were measured by confocal microscopy. Serum-deprived VSMCs were treated with sesamin (1−10 μM) for 24 h and next stimulated with 50 ng/mL PDGF-BB for a further 24 h. Immunofluorescence evaluation was performed using anti-PCNA and anti-Alexa 555 antibodies. The images are representative of those obtained in two similar, independent experiments. Scale bar = 20 μm.

a concentration-dependent manner. The reductions in S-phase cell numbers were 19.3 ± 2.0% ($P < 0.01$), 14.8 ± 3.5% ($P < 0.01$), and 13.2 ± 2.1% ($P < 0.01$) at sesamin concentrations of 1, 5, and 10 μM, respectively. The percentages of cells in the G_0/G_1 phase increased by 53.6 ± 3.0% ($P < 0.01$), 61.3 ± 2.7% ($P < 0.01$), and 63.6 ± 2.1% ($P < 0.01$), at the same sesamin concentrations. These results indicated that sesamin inhibited PDGF-induced VSMC proliferation by triggering cell-cycle arrest in the G_0/G_1 phase, and that this effect was associated with a reduction in DNA synthesis.

Effect of Sesamin on Cell-Cycle-Related Protein Expression and Phosphorylation. Cell-cycle progression is controlled by CDKs and the cyclin proteins that regulate CDK activities. During the G_0/G_1-S transition, the cyclin E−cyclin dependent kinase (CDK)2 complex and the cyclin D1−CDK4 complex hyperphosphorylate pRb, inducing expression of PCNA, E2F release from pRb, and transcription of growth-associated genes.[31] To explore how sesamin induced cell cycle arrest, we measured the expression levels of cyclin E, CDK2, cyclin D1, CDK4, and PCNA and the extent of pRb hyperphosphorylation. The data of Figures 5A and 5B show that sesamin significantly suppressed PDGF-induced cyclin D1 and CDK4 expression, and slightly suppressed that of cyclin E and CDK2, in a dose-dependent manner. Also, sesamin dose-dependently inhibited pRb hyperphosphorylation. Sesamin-induced inhibition of VSMC proliferation and pRb phosphorylation was shown to reduce PCNA expression (Figure 5C), as also revealed by immunofluorescence (Figure 5D). Together, the results indicate that sesamin affects the expression of G_0/G_1 phase- and S phase-associated cell cycle components of VSMCs.

Effect of Sesamin on Expression of CDK Inhibitors. The kinase activities of CDK−cyclin complexes are regulated by CKIs. We explored whether the inhibitory effect of sesamin on VSMC proliferation was mediated by modulation of CKI expression. First, the effect of sesamin alone on the expression of CKIs was measured. The results showed that sesamin enhanced expression of $p27^{KIP1}$, $p21^{CIP1}$, and p53 in a concentration-dependent manner (Figure 6). Since sesamin alone did not cleave PARP at the concentration rage of 1−10 μM, sesamin alone did not induce apoptosis.

In PDGF-stimulated proliferative condition, the mRNA (Figure 7A) and protein (Figure 7B) levels of $p27^{KIP1}$ fell upon addition of PDGF-BB. The level of $p27^{KIP1}$ in PDGF-stimulated VSMCs was about 52.2% that of the control (no PDGF) (Figure 7C). Inhibition of $p27^{KIP1}$ expression was rescued to the extents of 10.8%, 19.6%, and 30.0% upon treatment with 1, 5, and 10 μM sesamin, respectively. The $p21^{CIP1}$ protein level increased by about 36.6% upon addition of PDGF-BB. $p21^{CIP1}$ expression was increased, in a concentration-dependent manner, by sesamin (the increases were 75.5%, 102.1%, and 193.5% upon treatment with 1, 5, and 10

DOI: 10.1021/acs.jafc.5b03374
J. Agric. Food Chem. 2015, 63, 7317−7325

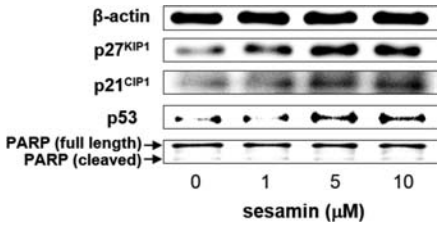

Figure 6. Effects of sesamin alone on $p21^{CIP1}$, $p27^{KIP1}$, and p53 expression levels and PARP cleavage in VSMCs. Serum-deprived VSMCs were treated with sesamin (1−10 μM) for 48 h, and the cell lysates were obtained after reactions terminated. Immunoblotting was performed as described in Materials and Methods using the specific antibodies for $p21^{CIP1}$, $p27^{KIP1}$, p53, and PARP. β-Actin was used for normalization. The images are representative of those obtained in three similar, independent experiments.

μM sesamin, respectively), compared to the no-PDGF group. As expected, the mRNA and protein levels of p53, an upstream regulator of $p21^{CIP1}$, increased in a similar manner. As the concentration of sesamin increased (from 1 to 5 and 10 μM sesamin), the p53 protein expression levels rose by 34.0%, 61.3%, and 92.8%, respectively. The images of cells shown in Figure 7D ($p27^{KIP}$) and Figure 7E ($p21^{CIP1}$) are consistent with the development of sesamin-induced alterations in mRNA and protein expression levels. Together, the results indicate that $p27^{KIP1}$ and $p21^{CIP1}$ are involved in inhibition of VSMC proliferation by sesamin.

Effects of siRNA for $p27^{KIP1}$ and $p21^{CIP1}$ on Sesamin-Induced Inhibition of DNA Synthesis. To determine whether the inhibition of VSMC proliferation by sesamin is mediated via $p27^{KIP1}$ and $p21^{CIP1}$, cells were transfected with specific siRNA for $p27^{KIP1}$ or $p21^{CIP1}$ to knock down these proteins. Since $p27^{KIP1}$ expression is higher in serum-deprived condition than PDGF-treated condition, it was examined only in serum-deprived condition, but $p21^{CIP1}$ expression is increased by PDGF-BB, and it was examined in both conditions. In Figures 8A and 8B, $p27^{KIP1}$ expression and $p21^{CIP1}$ expression were silenced about ~60% in VSMCs. The sesamin-induced inhibition of DNA synthesis was decreased in cells transfected with either siRNA (Figure 8C). Under si-con (negative control siRNA) treatment in VSMCs, 10 μM sesamin inhibited 91% of DNA synthesis. However, the inhibitory effect was alleviated to 50.6% by si-p27 ($p27^{KIP1}$ siRNA) and 25% by si-p21 ($p21^{CIP1}$ siRNA). Together, the results indicate that $p27^{KIP1}$ and $p21^{CIP1}$ may contribute to sesamin-induced inhibition of VSMC proliferation.

DISCUSSION

We present two major findings: (1) sesamin exerts an antiproliferative action on VSMCs by inhibiting cell cycle progression via arrest in G_0/G_1; and (2) sesamin enhances the

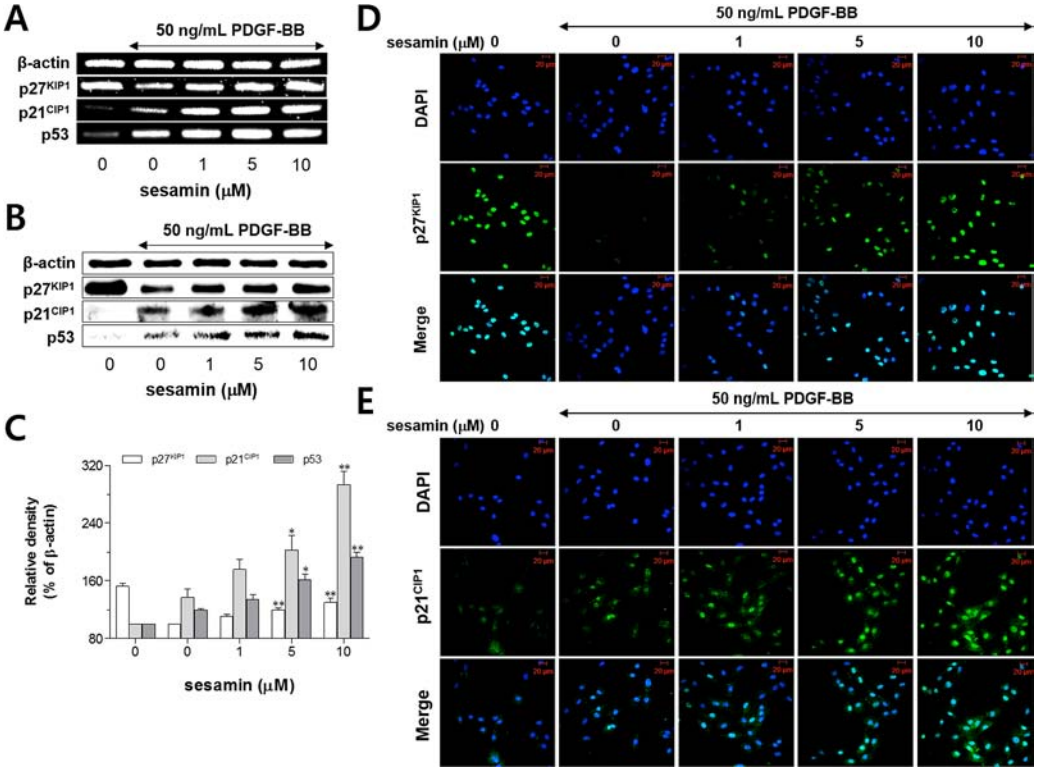

Figure 7. Sesamin upregulation of $p21^{CIP1}$, $p27^{KIP1}$, and p53 in PDGF-stimulated VSMCs. (A) Serum-deprived VSMCs were exposed to sesamin (1−10 μM) for 24 h and then stimulated with 50 ng/mL PDGF-BB for a further 24 h. Total RNA was extracted and RT-PCR analysis performed as described in Materials and Methods. Representative blots from three similar, independent experiments are shown; band intensities were normalized to those of total β-actin. (B) $p21^{CIP1}$, $p27^{KIP1}$, and p53 expression levels were quantified by immunoblotting after normalization of all band intensities to those of total β-actin (C). The values in the bar graphs (means ± SEM) were derived in three similar, independent experiments. Significant differences from the PDGF control (PDGF-stimulated, but no sesamin added) are noted as either * ($P < 0.05$) or ** ($P < 0.01$). (D, E) $p27^{KIP1}$ and $p21^{CIP1}$ were detected via confocal microscopy. Serum-deprived VSMCs were treated with sesamin (1−10 μM) for 24 h and next stimulated with 50 ng/mL PDGF-BB for a further 24 h. Immunofluorescence detection featured the use of anti-$p27^{KIP1}$, anti-$p21^{CIP1}$, and anti-FITC-conjugated IgGs. The images are representative of those obtained in two similar, independent experiments. Scale bar = 20 μm.

DOI: 10.1021/acs.jafc.5b03374
J. Agric. Food Chem. 2015, 63, 7317−7325

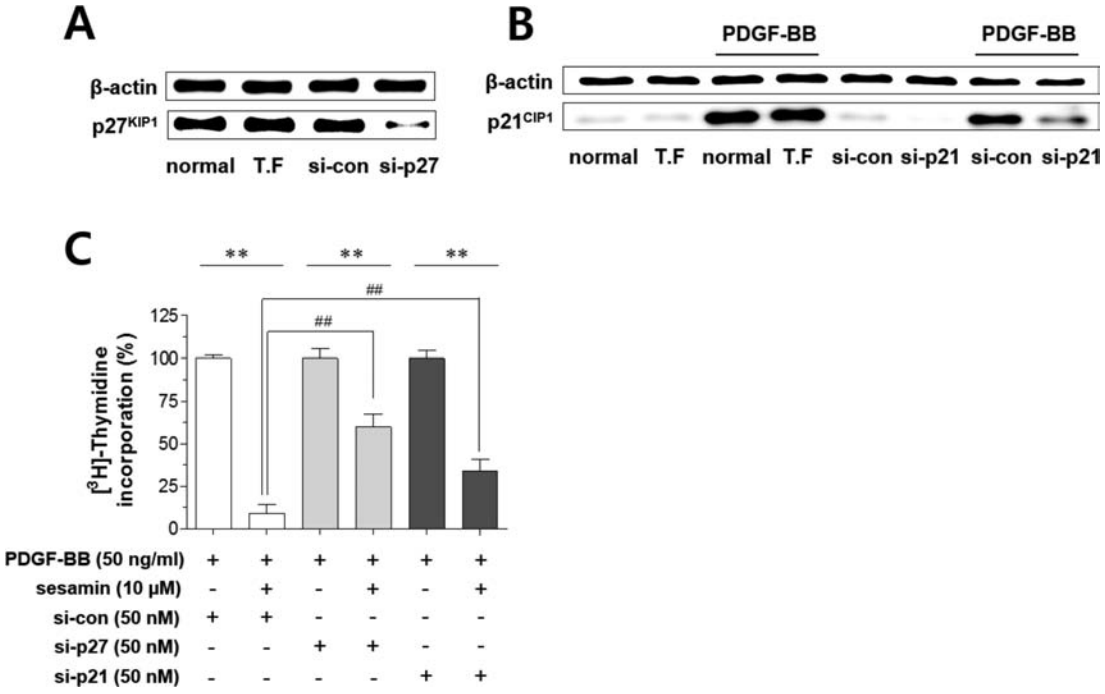

Figure 8. Effects of siRNA for $p27^{KIP1}$ or $p21^{CIP1}$ on sesamin-induced inhibition of VSMC proliferation. The siRNAs for negative control (si-con, 50 nM), $p27^{KIP1}$ (si-p27, 50 nM) or $p21^{CIP1}$ (si-p21, 50 nM) were transfected for 54 h in VSMCs. TransIT-X2 was used as transfection reagent (T.F), and normal means no treatment with T.F and siRNA. Serum-deprived VSMCs were incubated with transfection mixture for 6 h and changed to serum-free medium. After 48 h, cells were lysed, and $p27^{KIP1}$ (A) and $p21^{CIP1}$ (B) expression was detected. (C) After incubated with transfection medium for 6 h, medium was removed and cells in serum-free medium were treated with sesamin (1−10 μM) for 24 h. After 24 h, VSMCs were stimulated with 50 ng/mL PDGF-BB for a further 24 h. To measure DNA synthesis, [^{3}H]-thymidine incorporation was performed as described in Materials and Methods (n = 3). All data are expressed as means ± SEM, and significant differences compared to the PDGF control (PDGF-stimulated, but no sesamin) are shown by ** ($P < 0.01$), and compared to si-con treated group are shown by $^{\#\#}$ ($P < 0.01$).

expression of CKIs including $p27^{KIP1}$, $p21^{CIP1}$, and p53; thus suppressing the binding and activation of CDK−cyclin complexes. The data suggest that sesamin may play a role in suppressing PDGF-induced VSMC proliferation in vitro, and explain the molecular mechanisms in play.

VSMCs are the principal cells of arterial vessels; abnormal proliferation of such cells is associated with progression of atherosclerotic lesions.[32] PDGF released mainly in activated platelet stimulates the growth of VSMCs.[33] Associations between PDGF levels and the extent of VSMC proliferation have been noted in various models; inhibition of PDGF signaling prevented neointimal cellular proliferation.[34] Thus, it seemed worthwhile to screen for compounds that might limit inappropriate VSMC growth under conditions of high-level PDGF expression.

Sesamin is a major lignan constituent of sesame seed oil and has many biological activities, but no study to date has explored the effects of sesamin on signaling pathways associated with PDGF, the principal growth factor regulating VSMC proliferation after angioplasty. We found that sesamin inhibited PDGF-induced VSMC proliferation, but that this was not attributable to cytotoxicity or apoptosis (Figure 2). However, sesamin did not suppress PDGF-induced phosphorylation of PDGF-Rβ or downstream signaling molecules thereof, including PLCγ1, Akt, STAT3, and MAPK kinase family members (Figure 3). Thus, the antiproliferative action of sesamin is not mediated by PDGF-R-induced activation of early signaling pathways. We next explored whether sesamin acted at another level of the cellular machinery.

PDGF-stimulated cell cycle progression of VSMCs requires the binding and activation of CDK−cyclin complexes. Activation of cyclin D1, followed by cyclin E, CDK4, and CDK2, triggers phosphorylation of the Rb protein. Such phosphorylation plays a role in the G_1−S transition by sequestering E2F, and stimulating the expression of PCNA, which promotes DNA synthesis.[35] Sesamin suppressed PDGF-stimulated DNA synthesis and caused VSMCs to arrest in the G_0/G_1 phase (Figure 4), implying that the actions of several cell cycle regulatory proteins may be affected by sesamin. We found that sesamin significantly suppressed cyclin D1 and CDK4 expression, thus inhibiting pRb hyperphosphorylation (Figures 5A and 5B). Although the sesamin-induced inhibition of cyclin E and CDK2 expression was weak, this was nonetheless adequate to prevent pRb hyperphosphorylation, as both cyclin D1 and CDK4 were potently suppressed.[36] Moreover, sesamin inhibited PCNA expression, normally induced by hyperphosphorylated pRb in the early G_0/G_1 and S phases of the cell cycle (Figures 5C and 5D).

CKIs are classified two families. One is Cip/Kip family including $p21^{CIP1}$, $p27^{KIP1}$, and $p57^{KIP2}$, the other is INK4 family including $p15^{INK4b}$, $p16^{INK4a}$, $p18^{INK4c}$, and $p19^{INKd}$. It is known that the Cip/Kip family members bind to both cyclin and CDK subunits, cyclin D−, E−, A−, and B−CDK complexes, and regulate their activities. INK4 family members bind only to CDK4 or CDK6 not to cyclins and, thus, affect cell cycle progression.[37] Since sesamin was shown to decrease cyclin E−CDK2 and cyclin D−CDK4 in Figure 5, $p21^{CIP1}$ and $p27^{KIP1}$, Cip/Kip family members, were focused on in this study. Interestingly, expression of $p21^{CIP1}$, $p27^{KIP1}$, and p53,

DOI: 10.1021/acs.jafc.5b03374
J. Agric. Food Chem. 2015, 63, 7317−7325

upstream of $p21^{CIP1}$, is increased by sesamin alone without influence of PARP cleavage (Figure 6). p53, tumor suppressor protein, regulates $p21^{CIP1}$ activation in G_1−S transition point, thus occurred cell cycle arrest.[38] In another aspect, it is known that p53 leads to DNA damage, senescence, or apoptosis. However, p53-induced apoptotic effect may not occur in every cell line, and other cofactors or modifications are required for dead pathway.[39] Furthermore, it is reported that some substances have antiproliferative effects on VSMCs by upregulation of $p21^{CIP1}$ and p53.[40−43] Thus, these phenomena might be cytostatic, not cytotoxic or apoptotic.

The expression levels of CKIs were upregulated by sesamin in VSMCs treated with PDGF-BB (Figure 7). Upregulated CKIs bind to cyclin−CDK complexes and inhibit the catalytic activity of these complexes, and subsequently Rb phosphorylation was decreased. Sesamin-induced inhibition of DNA synthesis was restored in PDGF transfected with $p27^{KIP1}$ or $p21^{CIP1}$ siRNAs, and recovery rate in cells treated with $p27^{KIP1}$ siRNA is larger than that in $p21^{CIP1}$ siRNA (Figure 8). These results suggest that $p27^{KIP1}$ may be the major factor compared to $p21^{CIP1}$; however, further studies are needed. Thus, our results indicate that the inhibitory effect of sesamin on PDGF-stimulated VSMC proliferation is attributable to upregulation of $p27^{KIP1}$, $p21^{CIP1}$, and p53, in turn triggering G_0/G_1 cell cycle arrest.

In conclusion, we provide the first evidence that sesamin, the most abundant lignan of sesame seed oil, present also in several medicinal herbs including *A. heterotropoides*, inhibits PDGF-induced VSMC proliferation in vitro, attributable to upregulation of $p27^{KIP1}$, $p21^{CIP}$, and p53, in turn downregulating the expression levels of CDK−cyclin complexes. Therefore, sesamin may be valuable to prevent and treat vascular disorders such as restenosis developing after angioplasty, and atherosclerosis.

■ ASSOCIATED CONTENT

Supporting Information

The Supporting Information is available free of charge on the ACS Publications website at DOI: 10.1021/acs.jafc.5b03374.

Table of primers used for PCR (PDF)

■ AUTHOR INFORMATION

Corresponding Author

*Department of Pharmacology, Chungnam National University College of Pharmacy, 99 Daehak-ro, Yuseong-gu, Daejeon 305-764, Republic of Korea. Tel: +82-42-821-5923. Fax: +82-42-821-8925. E-mail: cm8r@cnu.ac.kr.

Author Contributions

‡J.-H.H. and S.-G.L. contributed equally to this work and therefore share first authorship.

Funding

This work was supported by the Priority Research Centers Program through the National Research Foundation of Korea (NRF), funded by the Ministry of Education, Science, and Technology (Grant No. 2009-0093815).

Notes

The authors declare no competing financial interest.

■ ABBREVIATIONS USED

Akt/PKB, protein kinase B; BSA, bovine serum albumin; CDK, cyclin-dependent kinase; Rb, retinoblastoma; CKI, CDK inhibitor; DMEM, Dulbecco's modified Eagle's medium; ERK1/2, extracellular signal-regulated kinase 1/2; FBS, fetal bovine serum; JNK, c-Jun N-terminal kinases; MAPK, mitogen-activated protein kinase; PBS, phosphate-buffered saline; PCNA, proliferating cell nuclear antigen; PDGF, platelet-derived growth factor; PLCγ, phospholipase Cγ; PVDF, polyvinylidene fluoride; SDS−PAGE, sodium dodecyl sulfate−polyacrylamide gel electrophoresis; STAT3, signal transducer and activator of transcription 3; VSMCs, vascular smooth muscle cells

■ REFERENCES

(1) Ross, R. Cell biology of atherosclerosis. *Annu. Rev. Physiol.* **1995**, *57*, 791−804.

(2) Ahn, H. Y.; Hadizadeh, K. R.; Seul, C.; Yun, Y. P.; Vetter, H.; Sachinidis, A. Epigallocathechin-3 gallate selectively inhibits the PDGF-BB-induced intracellular signaling transductionpathway in vascular smooth muscle cells and inhibits transformation of sis-transfected NIH 3T3 fibroblasts and human glioblastoma cells (A172). *Mol. Biol. Cell* **1999**, *10*, 1093−1104.

(3) Dzau, V. J.; Braun-Dullaeus, R. C.; Sedding, D. G. Vascular proliferation and atherosclerosis: new perspectives and therapeutic strategies. *Nat. Med.* **2002**, *8*, 1249−1256.

(4) Kim, Y.; Han, J. H.; Yun, E.; Jung, S. H.; Lee, J. J.; Song, G. Y.; Myung, C. S. Inhibitory effect of a novel naphthoquinone derivative on proliferation of vascular smooth muscle cells through suppression of platelet-derived growth factor receptor beta tyrosine kinase. *Eur. J. Pharmacol.* **2014**, *733*, 81−89.

(5) Kim, Y.; Lee, J. J.; Lee, S. G.; Jung, S. H.; Han, J. H.; Yang, S. Y.; Yun, E.; Song, G. Y.; Myung, C. S. 5,8-Dimethoxy-2-nonylamino-naphthalene-1,4-dione inhibits vascular smooth muscle cell proliferation by blocking autophosphorylation of PDGF-receptor β. *Korean J. Physiol. Pharmacol.* **2013**, *17*, 203−208.

(6) Lee, J. J.; Yi, H.; Kim, I. S.; Kim, Y.; Nhiem, N. X.; Kim, Y. H.; Myung, C. S. 2S)-Naringenin from *Typha angustata* inhibits vascular smooth muscle cell proliferation via a G_0/G_1 arrest. *J. Ethnopharmacol.* **2012**, *139*, 873−878.

(7) Lee, J. J.; Yu, J. Y.; Zhang, W. Y.; Kim, T. J.; Lim, Y.; Kwon, J. S.; Kim, D. W.; Myung, C. S.; Yun, Y. P. Inhibitory effect of fenofibrate on neointima hyperplasia via G_0/G_1 arrest of cell proliferation. *Eur. J. Pharmacol.* **2011**, *650*, 342−349.

(8) Lee, J. J.; Zhang, W. Y.; Yi, H.; Kim, Y.; Kim, I. S.; Shen, G. N.; Song, G. Y.; Myung, C. S. Anti-proliferative actions of 2-decylamino-5,8-dimethoxy-1,4-naphthoquinone in vascular smooth muscle cells. *Biochem. Biophys. Res. Commun.* **2011**, *411*, 213−218.

(9) Xiong, Y.; Hannon, G. J.; Zhang, H.; Casso, D.; Kobayashi, R.; Beach, D. p21 is a universal inhibitor of cyclin kinases. *Nature* **1993**, *366*, 701−704.

(10) Hunter, T.; Pines, J. Cyclins and cancer. II: Cyclin D and CDK inhibitors come of age. *Cell* **1994**, *79*, 573−582.

(11) Coqueret, O. New roles for p21 and p27 cell-cycle inhibitors: a function for each cell compartment? *Trends Cell Biol.* **2003**, *13*, 65−70.

(12) Besson, A.; Dowdy, S. F.; Roberts, J. M. CDK inhibitors: cell cycle regulators and beyond. *Dev. Cell* **2008**, *14*, 159−169.

(13) Jung, S. M.; Park, S. S.; Kim, W. J.; Moon, S. K. Ras/ERK1 pathway regulation of $p27^{KIP1}$-mediated G_1-phase cell-cycle arrest in cordycepin-induced inhibition of the proliferation of vascular smooth muscle cells. *Eur. J. Pharmacol.* **2012**, *681*, 15−22.

(14) Lim, Y.; Kwon, J. S.; Kim, D. W.; Lee, S. H.; Park, R. K.; Lee, J. J.; Hong, J. T.; Yoo, H. S.; Kwon, B. M.; Yun, Y. P. Obovatol from Magnolia obovata inhibits vascular smooth muscle cell proliferation and intimal hyperplasia by inducing p21Cip1. *Atherosclerosis* **2010**, *210*, 372−380.

(15) Macleod, K. F.; Sherry, N.; Hannon, G.; Beach, D.; Tokino, T.; Kinzler, K.; Vogelstein, B.; Jacks, T. p53-dependent and independent expression of p21 during cell growth, differentiation, and DNA damage. *Genes Dev.* **1995**, *9*, 935−944.

DOI: 10.1021/acs.jafc.5b03374
J. Agric. Food Chem. 2015, 63, 7317−7325

(16) Rogi, T.; Tomimori, N.; Ono, Y.; Kiso, Y. The mechanism underlying the synergetic hypocholesterolemic effect of sesamin and alpha-tocopherol in rats fed a high-cholesterol diet. *J. Pharmacol. Sci.* **2011**, *115*, 408−416.
(17) Liang, Y. T.; Chen, J.; Jiao, R.; Peng, C.; Zuo, Y.; Lei, L.; Liu, Y.; Wang, X.; Ma, K. Y.; Huang, Y.; Chen, Z. Y. Cholesterol-lowering activity of sesamin is associated with down-regulation on genes of sterol transporters involved in cholesterol absorption. *J. Agric. Food Chem.* **2015**, *63*, 2963−2969.
(18) Lee, C. C.; Chen, P. R.; Lin, S.; Tsai, S. C.; Wang, B. W.; Chen, W. W.; Tsai, C. E.; Shyu, K. G. Sesamin induces nitric oxide and decreases endothelin-1 production in HUVECs: possible implications for its antihypertensive effect. *J. Hypertens.* **2004**, *22*, 2329−2338.
(19) Nakano, D.; Kurumazuka, D.; Nagai, Y.; Nishiyama, A.; Kiso, Y.; Matsumura, Y. Dietary sesamin suppresses aortic NADPH oxidase in DOCA salt hypertensive rats. *Clin. Exp. Pharmacol. Physiol.* **2008**, *35*, 324−326.
(20) Lee, W. J.; Ou, H. C.; Wu, C. M.; Lee, I. T.; Lin, S. Y.; Lin, L. Y.; Tsai, K. L.; Lee, S. D.; Sheu, W. H. Sesamin mitigates inflammation and oxidative stress in endothelial cells exposed to oxidized low-density lipoprotein. *J. Agric. Food Chem.* **2009**, *57*, 11406−11417.
(21) Bankole, M. A.; Shittu, L. A.; Ahmed, T. A.; Bankole, M. N.; Shittu, R. K.; Kpela, T.; Ashiru, O. A. Synergistic antimicrobial activities of phytoestrogens in crude extracts of two sesame species against some common pathogenic microorganisms. *Afr. J. Tradit., Complementary Altern. Med.* **2007**, *4*, 427−433.
(22) Periasamy, S.; Hsu, D. Z.; Chang, P. C.; Liu, M. Y. Sesame oil attenuates nutritional fibrosing steatohepatitis by modulating matrix metalloproteinases-2, 9 and PPAR-γ. *J. Nutr. Biochem.* **2014**, *25*, 337−344.
(23) Hibasami, H.; Fujikawa, T.; Takeda, H.; Nishibe, S.; Satoh, T.; Fujisawa, T.; Nakashima, K. Induction of apoptosis by Acanthopanax senticosus HARMS and its component, sesamin in human stomach cancer KATO III cells. *Oncol. Rep.* **2000**, *7*, 1213−1219.
(24) Ju, Y.; Still, C. C.; Sacalis, J. N.; Li, J.; Ho, C. T. Cytotoxic coumarins and lignans from extracts of the northern prickly ash (*Zanthoxylum americanum*). *Phytother. Res.* **2001**, *15*, 441−443.
(25) Miyahara, Y.; Komiya, T.; Katsuzaki, H.; Imai, K.; Nakagawa, M.; Ishi, Y.; Hibasami, H. Sesamin and episesamin induce apoptosis in human lymphoid leukemia Molt 4B cells. *Int. J. Mol. Med.* **2000**, *6*, 43−46.
(26) Deng, P.; Wang, C.; Chen, L.; Wang, C.; Du, Y.; Yan, X.; Chen, M.; Yang, G.; He, G. Sesamin induces cell cycle arrest and apoptosis through the inhibition of signal transducer and activator of transcription 3 signalling in human hepatocellular carcinoma cell line HepG2. *Biol. Pharm. Bull.* **2013**, *36*, 1540−1548.
(27) Akl, M. R.; Ayoub, N. M.; Abuasal, B. S.; Kaddoumi, A.; Sylvester, P. W. Sesamin synergistically potentiates the anticancer effects of γ-tocotrienol in mammary cancer cell lines. *Fitoterapia* **2013**, *84*, 347−359.
(28) Chamley, J. H.; Campbell, G. R.; McConnell, J. D.; Groschel-Stewart, U. Comparison of vascular smooth muscle cells from adult human, monkey and rabbit in primary culture and in subculture. *Cell Tissue Res.* **1977**, *177*, 503−522.
(29) Eid, S. Y.; El-Readi, M. Z.; Wink, M. Digitonin synergistically enhances the cytotoxicity of plant secondary metabolites in cancer cells. *Phytomedicine* **2012**, *19*, 1307−1314.
(30) Claesson-Welsh, L. Platelet-derived growth factor receptor signals. *J. Biol. Chem.* **1994**, *269*, 32023−32026.
(31) Black, A. R.; Jensen, D.; Lin, S. Y.; Azizkhan, J. C. Growth/cell cycle regulation of Sp1 phosphorylation. *J. Biol. Chem.* **1999**, *274*, 1207−1215.
(32) Gutstein, W. H.; Teresi, J. A.; Wu, J. M.; Ramirez, M.; Salimian, F.; Cui, Y.; Paul, I.; Jabr, S. Increased serum mitogenic activity for arterial smooth muscle cells associated with relaxation and low educational level in human subjects with high but not low hostility traits: implications for atherogenesis. *J. Psychosom. Res.* **1999**, *46*, 51−61.
(33) Uchida, K.; Sasahara, M.; Morigami, N.; Hazama, F.; Kinoshita, M. Expression of platelet-derived growth factor B-chain in neointimal smooth muscle cells of balloon injured rabbit femoral arteries. *Atherosclerosis* **1996**, *124*, 9−23.
(34) Leppanen, O.; Janjic, N.; Carlsson, M. A.; Pietras, K.; Levin, M.; Vargeese, C.; Green, L. S.; Bergqvist, D.; Ostman, A.; Heldin, C. H. Intimal hyperplasia recurs after removal of PDGF-AB and -BB inhibition in the rat carotid artery injury model. *Arterioscler., Thromb., Vasc. Biol.* **2000**, *20*, E89−95.
(35) Zhu, P.; Chen, J. M.; Chen, S. Z.; Zhang, C.; Zheng, S. Y.; Long, G.; Chen, J.; Zhou, Z. L.; Fan, R. X.; Fan, X. P.; Chen, Y. F.; Zhuang, J. Matrine inhibits vascular smooth muscle cell proliferation by modulating the expression of cell cycle regulatory genes. *Acta Pharmacol. Sin.* **2010**, *31*, 1329−1335.
(36) Connell-Crowley, L.; Elledge, S. J.; Harper, J. W. G1 cyclin-dependent kinases are sufficient to initiate DNA synthesis in quiescent human fibroblasts. *Curr. Biol.* **1998**, *8*, 65−68.
(37) Sherr, C. J.; Roberts, J. M. CDK inhibitors: positive and negative regulators of G1-phase progression. *Genes Dev.* **1999**, *13*, 1501−1512.
(38) el-Deiry, W. S.; Tokino, T.; Velculescu, V. E.; Levy, D. B.; Parsons, R.; Trent, J. M.; Lin, D.; Mercer, W. E.; Kinzler, K. W.; Vogelstein, B. WAF1, a potential mediator of p53 tumor suppression. *Cell* **1993**, *75*, 817−825.
(39) Aylon, Y.; Oren, M. Living with p53, dying of p53. *Cell* **2007**, *130*, 597−600.
(40) Igata, M.; Motoshima, H.; Tsuruzoe, K.; Kojima, K.; Matsumura, T.; Kondo, T.; Taguchi, T.; Nakamaru, K.; Yano, M.; Kukidome, D.; Matsumoto, K.; Toyonaga, T.; Asano, T.; Nishikawa, T.; Araki, E. Adenosine monophosphate-activated protein kinase suppresses vascular smooth muscle cell proliferation through the inhibition of cell cycle progression. *Circ. Res.* **2005**, *97*, 837−844.
(41) Ki, S. H.; Lee, J. W.; Lim, S. C.; Hien, T. T.; Im, J. H.; Oh, W. K.; Lee, M. Y.; Ji, Y. H.; Kim, Y. G.; Kang, K. W. Protective effect of nectandrin B, a potent AMPK activator on neointima formation: inhibition of Pin1 expression through AMPK activation. *Br. J. Pharmacol.* **2013**, *168*, 932−945.
(42) Wu, W. Y.; Yan, H.; Wang, X. B.; Gui, Y. Z.; Gao, F.; Tang, X. L.; Qin, Y. L.; Su, M.; Chen, T.; Wang, Y. P. Sodium tanshinone IIA silate inhibits high glucose-induced vascular smooth muscle cell proliferation and migration through activation of AMP-activated protein kinase. *PLoS One* **2014**, *9*, e94957.
(43) Chien, M. H.; Lee, T. S.; Liang, Y. C.; Lee, W. S. β-Sitosterol inhibits cell cycle progression of rat aortic smooth muscle cells through increases of p21cip1 protein. *J. Agric. Food Chem.* **2010**, *58*, 10064−10069.

DOI: 10.1021/acs.jafc.5b03374
J. Agric. Food Chem. 2015, 63, 7317−7325

There is an urgent need for counter-measures against ionizing radiation in fields that run the gamut from medical radiation therapeutics to the nuclear industry to space travel. Apart from external physical shielding, there is little that can be done currently to protect individuals who are exposed to large doses of radiation. However, we have observed,[9] and others have confirmed,[10,11] that the presence of melanin in the intestinal lumen during extra-corporeal irradiation translates into remarkable protection against the deleterious effects of extra-corporeal ionizing radiation in mice. The presumed mechanism of action for this melanin protective effect is shielding of the gut tissue, including the associated lymphatic tissue, which in turn provides cells to replenish radiation-depleted bone marrow. More specifically, melanin involves physical shielding of the cells via Compton scattering of the incoming photons, accompanied by the scavenging of Compton electrons and free radicals by the melanin macromolecules.[9]

Melanin is an insoluble and non-digestible pigment with a complex molecular structure that is generated by polymerization of indolic and phenolic compounds.[12] Melanins are found in all biological kingdoms, but their structure and function remain poorly understood, as these heterogeneous pigments cannot be crystallized for high-resolution structural studies. There are five types of melanin commonly found in nature: eumelanin, pheomelanin, neuromelanin, pyomelanin, and allomelanin.[13] Of the five, eumelanin is the most abundant and is a brown to black pigment.[13−15] The eumelanin polymer is composed 5,6-dihydroxyindole (DHI) and 5,6-dihydroxyindole-2-carboxylic acid (DHICA) units.[9] It can be highly concentrated in the human epidermal, retinal, and auditory systems.[13,14] Structures for both oligomers for eumelanin and pheomelanin have been already proposed.[9] Melanins are readily produced by many fungi, including edible fungi, where their functions could include energy transduction.[16] Consequently, the edible fungi constitute a potential source of nutritional melanin that could find important use as a radiation countermeasure; e.g., the benefits from the *A. auricula* mushroom could be gained by ingesting the raw material. In addition to radiation protection, melanins have semiconductor properties that could be exploited in the design of edible electronic devices.[17] Hence, there is a need for identifying good sources of melanin from edible biomaterials in such diverse areas as radioprotection and electronic design. As mushroom powders are now sold as food supplements, we conducted an essential study of the melanin content and associated molecular characteristics in commercial preparations of powdered *A. auricula*.

MATERIALS AND METHODS

Melanin Sources. *Auricularia auricula* mushroom preparations were obtained from Maypro (New York, NY, http://maypro.com/). As a control for L-DOPA melanin, we isolated melanin from *Cryptococcus neoformans* as described previously.[16] Briefly, melanized cells were obtained by growing *C. neoformans* strain H99 (American Type Culture Collection, Rockville, MD) in defined minimal medium (15 mM glucose, 10 mM $MgSO_4$, 29.4 mM KH_2PO_4, 13 mM glycine, 3 μM vitamin B1 [Sigma Chemical Co., Cleveland, OH]) with 1 mM L-DOPA (Sigma) at 30 °C for 10 days with shaking at 150 rpm.

Melanin Isolation. The same protocols were used to isolate melanin from melanized *C. neoformans* and powdered mushrooms. For *C. neoformans*, melanized cells were harvested by centrifugation at 2000 rpm and washed with phosphate-buffered saline (PBS). Similarly, 20 g samples of *A. auricula* mushroom powders were dissolved in PBS. Fungal cells and powdered mushroom material were each suspended in a 1 M sorbitol/0.1 M pH 5.5 sodium citrate solution and incubated at 30 °C for 24 h with 10 mg/mL of lysing enzymes from *Trichoderma harzianum* (Sigma). The enzyme-digested materials were collected by centrifugation at 3000 rpm for 10 min and washed repeatedly with PBS until the supernatant was nearly clear. Proteinaceous materials were denatured by incubating the pellets with 4 M guanidine thiocyanate in a rocker for 12 h at room temperature. The recovered debris was collected by centrifugation, washed two or three times with ∼20 mL of PBS , and then incubated for 4 h at 65 °C in 10 mL of buffer (10 mM pH 8.0 Tris-HCl, 5 mM $CaCl_2$, 5% SDS) containing 1 mg/mL of proteinase K (Boehringer, Mannheim, Germany). The debris was recovered and washed two or three times with ∼20 mL of PBS, after which lipids were extracted three successive times by the Folch method, maintaining chloroform, methanol, and saline solution in the final mixture at 8:4:3 (v/v/v). The product was suspended in 20 mL of 6 M HCl and boiled for 1 h to hydrolyze cellular contaminants associated with the melanin. The resulting acid-resistant insoluble material was dialyzed against distilled water for 14 d with daily water changes and lyophilized. Elemental analysis (carbon, nitrogen, and hydrogen) was performed by Intertek (Whitehouse, NJ).

Scanning Electron Microscopy (SEM). Mushroom powders and melanin extracts were suspended in PBS, incubated on coverslips coated with 0.01% poly-L-lysine, and fixed with 2.5% glutaraldehyde in 0.1 M sodium phosphate buffer (pH 7.3) for 24 h at 4 °C. Mushroom and melanin extracts were post-fixed with 1% OsO_4, dehydrated progressively in 70%, 90%, 95%, and 100% ethanol, and critical-point-dried in CO_2. The material was sputter-coated with gold using an EMitech K550 sputter coater and viewed in a Zeiss Supra 40 scanning electron microscope operating at a voltage of 10 kV.

Transmission Electron Microscopy (TEM). Samples were fixed with 2% paraformaldehyde−2.5% glutaraldehyde−0.1 M sodium cacodylate buffer, followed by a post-fixation step with 1% osmium tetroxide and 1% uranyl acetate. Samples were then dehydrated by immersion in a graded series of ethanol concentrations and embedded in LX112 resin (LADD Research Industries, Burlington, VT). A Reichert Ultracut UCT instrument was used to cut ultrathin (80 nm thick) sections that were then stained with uranyl acetate followed by lead citrate. TEM was done using a JEOL 1200EX transmission electron microscope operating at 80 kV.

Electron Paramagnetic Resonance (EPR) Spectroscopy. EPR spectra were obtained at 77 K using a Varian E112 X-Band model spectrometer equipped with a TE102 resonator. Approximately 5 mg samples of melanin preparations were loaded into 4 mm quartz EPR tubes (Wilmad LabGlass, Buena, NJ), which were held in place in the resonator using a quartz finger dewar. Typical parameters used to acquire the spectra were as follows: modulation amplitude, 1.6 G; microwave frequency, 9.11 GHz; and microwave power, 0.10 mW. The quartz EPR signal generated as a result of the irradiation was subtracted from the spectra of the irradiated samples. EPR spectra were also obtained after illumination of melanin suspensions with a 150 W fiber optic lamp for 30 min at 77 K or by suspending the melanins in 0.1 M $ZnCl_2$.

Solid-State Nuclear Magnetic Resonance (NMR) spectroscopy. Solid-state ^{13}C NMR measurements were performed using a Varian (Agilent Technologies, Santa Clara, CA) DirectDrive1 (VNMRs) NMR spectrometer operating at a ^1H frequency of 600 MHz (^{13}C frequency of 150 MHz) and a temperature set to 25 °C. The ^{13}C cross-polarization (CP) experiments were conducted at a magic-angle spinning (MAS) frequency of 20 kHz (±20 Hz) using a 1.6 mm HXY fastMAS probe filled with 4−6 mg of powdered sample. Ramped-amplitude ^{13}C CPMAS (RAMP-CP)[18] measurements were conducted to identify the carbon chemical moieties, and ^{13}C multiple-CP experiments[19] were carried out to achieve high-throughput quantification of the carbon-containing pigment functional groups. Detailed experimental parameters for CPMAS measurements on fungal melanins have been reported elsewhere.[20,21] The recycle delay for the ramp CP measurements and at the beginning of the multiple-CP sequence was 3 s, and the duration of the re-polarization period in multiple-CP was 0.8 s for the pigment samples. The CP times were 1.0−1.5 ms for the RAMP-CP[22] and 1.0 ms for the multiple-CP

DOI: 10.1021/acs.jafc.5b02713
J. Agric. Food Chem. 2015, 63, 7326−7332

measurement, each with 10 recursive cycles. The SPINAL method[23] was used to apply high-power heteronuclear ^{1}H decoupling of 170–185 kHz, and 2048–7400 transients were acquired to generate each ^{13}C spectrum. 1D ^{13}C spectral data sets were processed with 100–200 Hz of line broadening; chemical shifts were referenced externally to the ethylene ($-CH_2-$) group of adamantane (Sigma) at δ_C = 38.48 ppm. Reproducibility of the spectroscopic measurements was assessed by obtaining replicate ^{13}C spectra on each sample; biological replicates of these materials and previously reported *C. neoformans* melanins[20] displayed minor variations in their ^{13}C NMR spectra due to differences in cellular media, scale of synthesis, extent of polymerization, and pigment deposition within the cellular matrix.

RESULTS

Microscopic Analysis of Commercial Mushroom Preparations. Commercial edible mushroom preparations are usually available as powders. We studied the ultra-structural features of commercial powders of *A. auricula* edible mushrooms. *A. auricula* mushroom appears as a dark powder (Figure 1A). Analysis of these "raw" preparations by SEM showed that

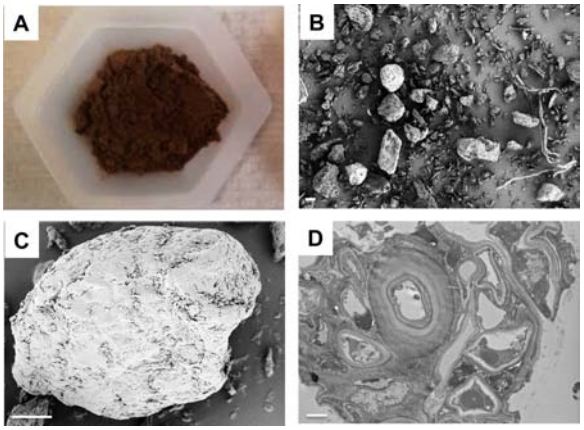

Figure 1. Electron microscopy analysis of the *A. auricula* mushroom powders (A). *A. auricula* mushroom preparations were processed for scanning electron microscopy (SEM, B and C) and transmission electron microscopy (TEM, D). Scale bars in B and D are 10 μm, and scale bar in C is 1 μm.

A. auricula powder was composed of a heterogeneous mixture of amorphous fragments with a size distribution ranging between 1 and 50 μm (Figure 1B). Higher magnifications of some of the mushroom pieces showed that the surface of these fragments appeared to have a rough morphology (Figure 1C).

Melanin is associated with the cell wall in the human pathogen *C. neoformans* and often appears as an electron-dense layer in transmission electron micrographs.[24] We performed TEM on mushroom extracts and found that both mushroom powders have very similar internal structure, including circular units with a dense cell wall made of several concentric layers embedded in a heterogeneous mass of material with different textures (Figure 1D). However, the *A. auricula* mushroom powder had more electron-dense material. The darker areas in this mushroom were associated with material randomly distributed across the section, although we could observe that the inner layers of the circular units were also highly electron dense (Figure 1D), suggesting that melanin might not have a regular distribution pattern in edible mushrooms.

Melanin Content of Commercial Mushroom Preparations. A prior analysis of *A. auricula* mushrooms obtained at a local market revealed that melanin comprises approximately 10% of the dry weight of the fungal mass.[9] To determine the melanin content of commercial mushroom preparations, we used a quantitative melanin isolation protocol adapted from the fungus *C. neoformans*. Twenty grams of powder was processed for melanin isolation, beginning with suspension in PBS (Figure 2A). Of note, we observed a remarkable expansion in

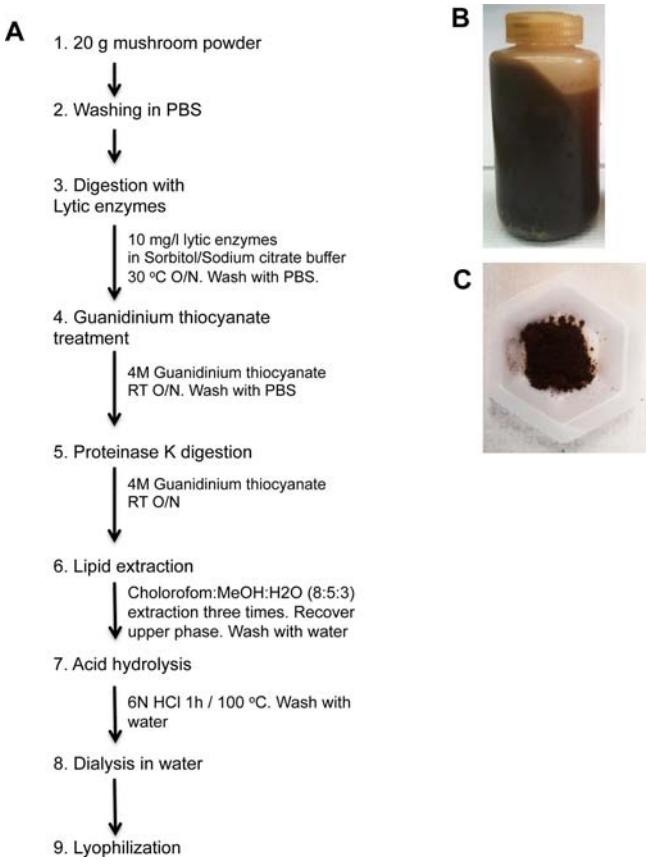

Figure 2. Melanin isolation protocol from commercial mushroom preparations. (A) The protocol was adapted from that for the fungus *C. neoformans* and involved digestion of cell walls, de-proteination, de-lipidation, and acid hydrolysis. (B) Appearance of *A. auricula* commercial mushroom powders after dissolving in PBS and centrifugation (steps 1 and 2 in the melanin isolation protocol). Note that 20 g of *A. auricula* powder expanded when dissolved in PBS. (C) Appearance of the melanin extract from *A. auricula* mushrooms.

the volume of the *A. auricula* powder upon hydration (Figure 2B). Subsequent steps in the melanin isolation from *A. auricula* involved digestion of cell-wall structural components and protein denaturation and digestion. Extraction of lipids by chloroform and methanol treatment revealed that 0.5% of the dry weight was due to lipids. Subsequent acid hydrolysis of the denatured, proteinase-digested and de-lipidated material reduced the wet weight by 50%. After hydrolysis, the product was dialyzed and lyophilized. The color of the extract was significantly darker than the original mushroom powder, which reflects enrichment in the melanin pigment (Figure 2C). Approximately 10% of the dry weight of the mushroom powder corresponded to melanin pigment that is resistant to acid hydrolysis.

Ultrastructural characterization of the final (melanin) product by SEM revealed a very different morphology relative to the original mushroom powder, namely an amorphous material with little structural resemblance to the commercial

DOI: 10.1021/acs.jafc.5b02713
J. Agric. Food Chem. 2015, 63, 7326–7332

powder (Figure 3). The removal of acid-digestible material was apparent as an increase in effective surface area. TEM analysis

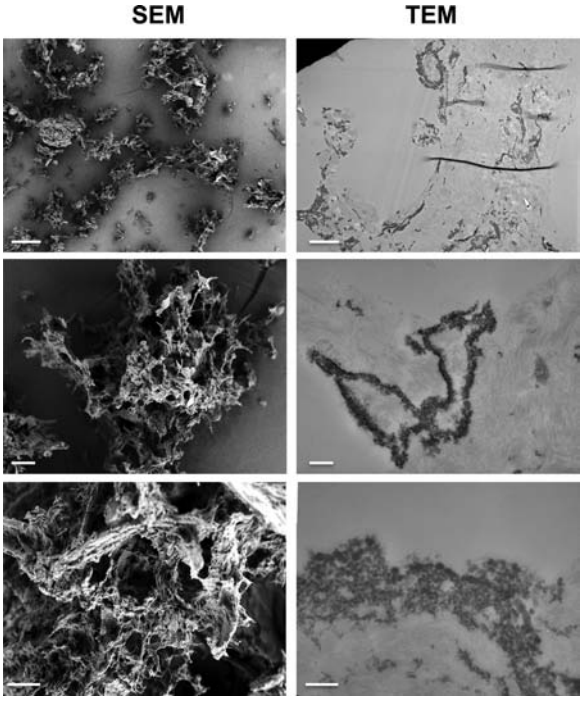

Figure 3. Electron micrographs of isolated melanin from commercial *A. auricula* mushrooms. Note the hollowness of the isolated material. Scale bars are 100 μm (top panel), 20 μm (medium panel), and 10 μm (lower panel).

of the isolated melanin showed that the units observed by SEM were hollow and consisted mainly of a melanin ring with no associated internal material. High-magnification micrographs revealed that mushroom melanin is composed of small spherical units with an estimated diameter of 20−30 nm (Figure 3).

Physicochemical Characterization of Mushroom Melanins. Melanins are complex, amorphous, and incompletely understood polymeric pigments.[12] Demonstration that a compound is melanin by chemical means is difficult, and not all dark pigments in nature are melanins. Fungal melanins include DHI and DHICA monomer units with 6−9% nitrogen or 1,8-dihydroxynaphthalene (DHN) with no nitrogen in its structure.[9] Elemental analysis of *C. neoformans* melanin showed 59% C, 7% H, and 6% N (C/N of 10.6, no S), indicating that *C. neoformans* melanin was primarily a DHI/DHICA eumelanin. In contrast, *A. auricula* melanin contained 41% C, 5% H, and 1.6% N (C/N of 24.8, no significant S), suggesting that it contained a mixture of DHICA/DHI and DHN eumelanin, as previously reported (Table 1).[9] Of note, structural formulas for DHN melanins have been already reported.[9]

Melanin pigments are remarkable in that they contain a stable population of organic free radicals, making EPR spectroscopy a particularly effective method for identifying and classifying them. A set of qualitative EPR criteria were established for melanin identification based on the increase in EPR signal upon (a) illumination with a bright white light or (b) addition of $ZnCl_2$.[9,24,25] As previously reported, irradiation of *C. neoformans* melanin with a bright light or supplementation with 0.1 M $ZnCl_2$ increased the EPR by approximately 200% and 500%, respectively (Figure 4A).[9,24] To assess whether the dark product resulting from the *A. auricula* commercial mushroom preparation was melanin, we performed EPR measurements before and after bright illumination and upon addition of $ZnCl_2$. The EPR spectra of the material isolated from mushroom powder revealed a stable free radical signal like that described for melanin (Figure 4B). Illumination of this material for 30 min with white light from a 150 W fiber optic lamp and suspension in 0.1 M $ZnCl_2$ increased the magnitude of the EPR signal by 150% and 900%, respectively (Figure 4B). Thus, the acid insolubility of the dark residue combined with the EPR results established the material derived from *A. auricula* as a melanin.

Table 1. Elemental Composition of Melanins

melanin	C	H	N	(O)[a]
C. neoformans	58.99	7.11	5.56	28.34
A. auricula	41.18	5.56	1.66	51.60

[a]Calculated from 100% − C − H − N.

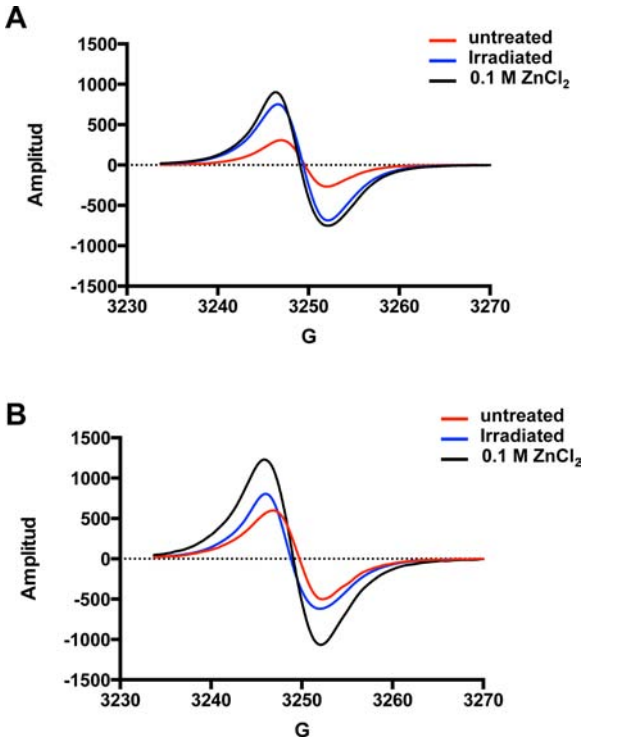

Figure 4. Electron paramagnetic resonance spectroscopy analysis of fungal melanins. (A) EPR of *C. neoformans* H99 melanin using standard conditions (red) or after exposure to either bright light stimulation (blue) or supplementation with $ZnCl_2$ (black). (B) EPR of *A. auricula* commercial mushroom melanin using the same conditions as in A.

NMR Spectroscopy of Commercial and *C. neoformans* Fungal Mushroom Preparations. The heterogeneous and amorphous character of melanin pigments combined with their insolubility in aqueous buffers requires specialized techniques such as solid-state NMR to elucidate the constituent chemical moieties present in the intact pigment. The ^{13}C CPMAS spectrum of *C. neoformans* L-DOPA melanin revealed similar resonances to prior ^{13}C NMR reports for fungal melanin ghosts, exhibiting major indole-based aromatic and/or olefinic

DOI: 10.1021/acs.jafc.5b02713
J. Agric. Food Chem. 2015, 63, 7326−7332

carbons (110−160 ppm) and additional long-chain methylene groups ($(CH_2)_n$, 20−40 ppm), oxygenated aliphatic carbons (CH_nO, 50−105 ppm), and carboxyls or amides (COO or CONH, 170−173 ppm)[20,21] (Figure 5). The resonances at 30, 24, and 15 ppm can be attributed to a typical pattern from $-(CH_2)_n-CH_2CH_3$ alkyl chains.[20] The broad aromatic spectral envelope centered at ∼128 ppm is attributable to overlap of resonances from slightly dissimilar aromatic indole-based constituents, structural heterogeneity of the disordered pigment materials, and/or the presence of paramagnetic species, as demonstrated by the EPR results.

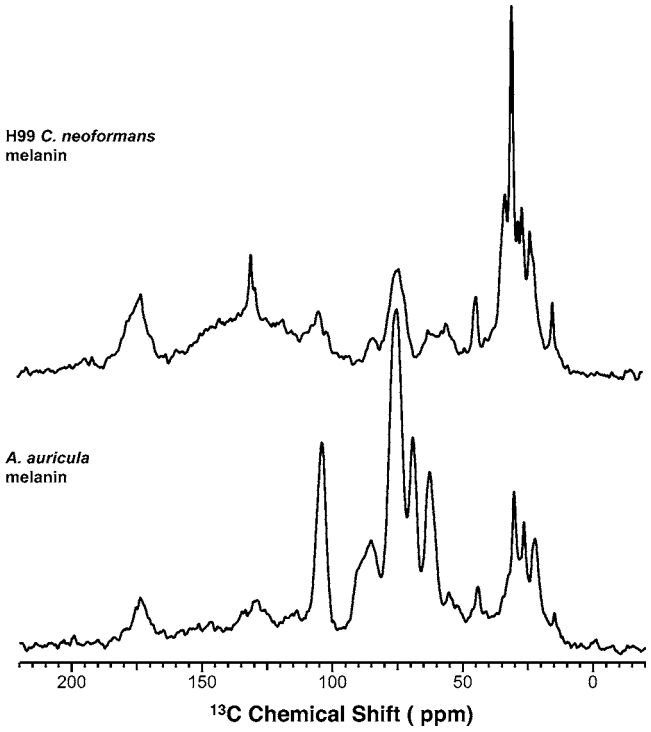

Figure 5. 150 MHz ^{13}C NMR spectra of *C. neoformans* melanin produced with natural abundance L-DOPA (top) and commercial mushroom melanin (bottom), measured at 20 kHz MAS using the quantitatively reliable multiple cross-polarization magic-angle spinning technique. Each spectrum is normalized by setting the largest peak to full scale.

The quantitatively reliable multiple-CPMAS ^{13}C spectra of the purified melanin pigment obtained from commercial *A. auricula* mushroom materials had several features comparable to those of the *C. neoformans* melanin. However, the spectra also manifested several structural differences, including modest signal intensity from aromatic moieties (110−160 ppm), diminished signals from the alkyl chains (20−40 ppm), and significantly enhanced signals from oxygenated carbons (50−105 ppm) (Figure 5). As deduced for the NMR spectra of *C. neoformans* melanin ghosts, key oxygenated aliphatic carbon moieties in the mushroom sample included signals from a range of functional groups, such as CH_3O and CH_2CH_2O (40−60 ppm), CH_2O (62 ppm), and CHO groups (69, 75, 86, and 105 ppm), that could be derived from attached cell-wall polysaccharides. A set of relatively sharper oxygenated carbon resonances for the mushroom-derived material suggests a comparatively ordered cell-wall matrix; the prominence of the oxygenated carbon NMR signals also conforms with elemental analysis results that imply a larger percentage of oxygen. Our NMR spectra supported the presence of chemically recalcitrant aliphatic frameworks associated with melanization in both pigmented samples that underwent exhaustive degradative treatments (Figure 2).

DISCUSSION

The aim of this study was to analyze the nature of the melanin pigment from *A. auricula* commercial mushroom preparations, in the context of exploring the feasibility of using those products as sources of edible protectants for ionizing radiation. SEM revealed significant ultrastructural differences in the morphology of the constituents of these preparations. The yield of the melanin obtained from the *A. auricula* commercial powder was in agreement with that reported previously from intact mushrooms.[9] Scanning electron micrographs of isolated melanin showed a very different product compared to the initial mushroom preparations: isolated melanin consisted of a heterogeneous population of fragments with high specific surface area. This final material was resistant to acid hydrolysis, a property that it shares with *C. neoformans* fungal melanin.

Isolated melanin from *C. neoformans* appears as empty melanin spheres that conserve the fungal cell's shape and were thus named melanin "ghosts". The morphology observed in the TEM images of *A. auricula* commercial mushroom preparations was more heterogeneous than fungal cells, and the dark material appeared to be associated with different areas of the respective materials. However, when the melanin recovered from the mushroom powder was analyzed by TEM, very discrete, closed, and empty dark structures were observed that retained the shape of the inner layer of cell walls. Hence, these *A. auricula* cell-wall ghosts could be viewed as comparable to the *C. neoformans* melanin ghosts that retained the shape of individual yeast cells.[24,26] Electron micrographs at higher magnification showed that the commercial mushroom melanin is composed of small spherical units with an estimated diameter of 20−100 nm, with the smallest particle size estimated as 20−30 nm. An in-depth microscopy analysis of *C. neoformans* melanin showed a similar size distribution,[28] indicating that the ultrastructural morphology of melanin is similar in both microscopic and macroscopic fungi. Similar analysis of the surfaces of isolated melanin from hair melanosomes and *Sepia officinalis* showed substructures in the size range of a few to 30 nm.[29]

To confirm that the black residue recovered from commercial mushroom powder was melanin, we conducted a standardized test based on EPR analysis, which takes advantage of the fact that melanin pigments contain a stable free radical population.[25] The dark material from commercial mushroom had a spectrum similar to that of *C. neoformans* melanin[24] and responded to either illumination with a bright lamp or addition of $ZnCl_2$ with a significant increase in the EPR signal.[24] These results establish that the pigment conforms to spectroscopic criteria assigned to melanins.

The molar C/N ratios of the *C. neoformans* and black mushroom melanin were 10.6 and 24.8, respectively, indicating differences between the melanin structures. No sulfur was found, so both materials could be classified as eumelanins. In agreement with previous studies on *A. auricula* melanin,[9] the low percentage of N revealed by elemental analysis suggested that commercial *A. auricula* mushroom melanin contains some DHN melanin. Nonetheless, oxidative high-performance liquid chromatography of *A. auricula* melanin in the cited study detected the presence of pyrrole-2,3-dicarboxylic acid, an

DOI: 10.1021/acs.jafc.5b02713
J. Agric. Food Chem. 2015, 63, 7326−7332

oxidation product of DHI. Thus, it is possible that *A. auricula* contains a mixture of DHN and DHI/DHICA melanins. Of note, both *C. neoformans* and commercial mushroom melanins showed a higher C/N ratio compared to synthetic and human hair melanins, also suggesting a divergence in structural features and/or an association with denaturant- and proteinase-resistant materials for these latter eumelanins.

Solid-state NMR analysis provided additional evidence for differences in carbon-containing structures between *C. neoformans* and commercial mushroom melanins. Analysis of the ^{13}C CPMAS spectral features associated with carbon-containing moieties showed diminished contributions at chemical shifts corresponding to aromatic and alkyl chain moieties, but significantly enhanced signals from the oxygenated carbons. The larger proportion of oxygenated carbons was also reflected in our elemental analysis results, from which percentage O values can be calculated as 51.60 for *A. auricula* and 28.34 for *C. neoformans*, respectively. Given the comparable colors, EPR intensities, and EPR line widths for *C. neoformans* and *A. auricula* mushroom samples, the weaker mushroom aromatic spectral contributions could reflect broadening associated with closer proximity to the unpaired electrons. Similar to *C. neoformans* melanin, NMR signatures associated with cell-wall polysaccharides were detected in the commercial mushroom preparation.[20,21,26,27] The sharper oxygenated carbon resonances displayed for commercial mushroom melanin suggested a more ordered cell-wall matrix as well as a different type of scaffolding on which the pigment can assemble.

A previous study demonstrated that isolated melanin from *A. auricula* mushrooms protects mice from acute ionizing radiation when administered orally.[9] Although the current study did not test the capacity of the fungal melanin isolated from mushroom powder to protect mice, the near identity of the melanins isolated from *A. auricula* whole mushrooms and commercially available powdered mushroom preparations suggests that the latter can offer a relatively cheap and plentiful source of melanin for future radioprotective studies. The location of melanin at the cell wall, according to our ultrastructural studies, suggests that cells will be protected from ionizing radiation going deeper into the cells.

Given the ongoing necessity of new oral radioprotectors suitable for treatment before acute radiotherapy or to alleviate the effects of radiation during catastrophic events, ingestion of melanin from powdered mushrooms could represent a new inexpensive and safe protective protocol.

In summary, we characterized the pigment derived from a commercial *A. auricula* mushroom as an edible source, established that it was a melanin by spectroscopic criteria, and characterized it using ultrastructural techniques and solid-state NMR as well as EPR. Melanin is insoluble and indigestible, yet it can provide medicinal effects by its presence in the gastrointestinal tract through its ability to mediate local shielding against external radiation. Melanin has the additional distinction of being an edible stable free radical, although the biological effects associated with this characteristic during its residence in the gastrointestinal tract remain to be determined. Melanins have electronic properties and metal-binding capacities that could be exploited for several purposes, making the availability of commercial non-toxic melanin sources promising for future studies to assess their clinical and technological usefulness.

AUTHOR INFORMATION

Corresponding Author

*Tel.: (718) 430-2811. Fax: (718) 430-8771. E-mail: rafael.prados-rosales@einstein.yu.edu.

Notes

The authors declare the following competing financial interest(s): Three of the authors (E.D., P.T., and A.C.) are involved in an effort to develop melanin for radiation protection through the company Goodwin & Wells (http://www.goodwinandwells.com/technology/). Furthermore, E.D. and A.C. hold patents describing the radioprotective properties of melanin. However, none of the authors have any connection with the supplier of these mushroom powders (Maypro).

ACKNOWLEDGMENTS

A.C., A.N., S.T., and R.P.-R. are supported by grants from the National Institutes of Health. S.C. and R.S. are supported by NIH grant R01-AI052733. The 600 MHz NMR facilities used in this work are operated by The City College and the CUNY Institute for Macromolecular Assemblies, with additional infrastructural support provided by grant 8G12 MD007603 from the National Institute on Minority Health and Health Disparities, National Institutes of Health.

REFERENCES

(1) Bolhassani, A.; Khavari, A.; Bathaie, S. Z. Saffron and natural carotenoids: Biochemical activities and anti-tumor effects. *Biochim. Biophys. Acta, Rev. Cancer* **2014**, *1845*, 20−30.

(2) Khavari, A.; Bolhassani, A.; Alizadeh, F.; Bathaie, S. Z.; Balaram, P.; Agi, E.; Vahabpour, R. Chemo-immunotherapy using saffron and its ingredients followed by E7-NT (gp96) DNA vaccine generates different anti-tumor effects against tumors expressing the E7 protein of human papillomavirus. *Arch. Virol.* **2015**, *160*, 499.

(3) Lei, M.; Wang, J.; Wang, Y.; Pang, L.; Wang, Y.; Xu, W.; Xue, C. Study of the radio-protective effect of cuttlefish ink on hemopoietic injury. *Asia Pac. J. Clin. Nutr.* **2007**, *16* (Suppl 1), 239−43.

(4) Chang, R. Functional properties of edible mushrooms. *Nutr. Rev.* **1996**, *54*, S91−3.

(5) Zhu, H.; He, C. C.; Chu, Q. H. Inhibition of quorum sensing in Chromobacterium violaceum by pigments extracted from *Auricularia auricula*. *Lett. Appl. Microbiol.* **2011**, *52*, 269.

(6) Zou, Y.; Hu, W.; Ma, K.; Tian, M. Physicochemical properties and antioxidant activities of melanin and fractions from Auricularia auricula fruiting bodies. *Food Sci. Biotechnol.* **2015**, *24*, 15.

(7) Zou, Y.; Yang, Y.; Zeng, B.; Gu, Z.; Han, Y. Comparison of Physicochemical Properties and Antioxidant Activities of Melanins from Fruit-Bodies and Fermentation Broths of *Auricularia auricula*. *Int. J. Food Prop.* **2013**, *16*, 803.

(8) Zou, Y.; Xie, C.; Fan, G.; Gu, Z.; Han, Y. Optimization of ultrasound-assisted extraction of melanin from Auricularia auricula fruit bodies. *Innovative Food Sci. Emerging Technol.* **2010**, *11*, 611.

(9) Revskaya, E.; Chu, P.; Howell, R. C.; Schweitzer, A. D.; Bryan, R. A.; Harris, M.; Gerfen, G.; Jiang, Z.; Jandl, T.; Kim, K.; Ting, L. M.; Sellers, R. S.; Dadachova, E.; Casadevall, A. Compton scattering by internal shields based on melanin-containing mushrooms provides protection of gastrointestinal tract from ionizing radiation. *Cancer Biother. Radiopharm.* **2012**, *27*, 570−6.

(10) Kunwar, A.; Adhikary, B.; Jayakumar, S.; Barik, A.; Chattopadhyay, S.; Raghukumar, S.; Priyadarsini, K. I. Melanin, a promising radioprotector: mechanisms of actions in a mice model. *Toxicol. Appl. Pharmacol.* **2012**, *264*, 202−11.

(11) Rageh, M. M.; El-Gebaly, R. H.; Abou-Shady, H.; Amin, D. G. Melanin Nanoparticles (MNPs) provide protection against whole-body-irradiation in mice via restoration of hematopoietic tissues. *Mol. Cell. Biochem.* **2015**, *399*, 59.

DOI: 10.1021/acs.jafc.5b02713
J. Agric. Food Chem. 2015, 63, 7326−7332

(12) Chedekel, M. R.; Ahene, A. B.; Zeise, L. Melanin standard method: empirical formula 2. *Pigm. Cell Res.* **1992**, *5*, 240−6.
(13) Solano, F. Melanins: Skin Pigments and Much More—Types, Structural Models, Biological Functions, and Formation Routes. *New J. Sci.* **2014**, *2014*, 498276.
(14) Eisenman, H. C.; Casadevall, A. Synthesis and Assembly of Fungal Melanin. *Appl. Microbiol. Biotechnol.* **2012**, *93*, 931−940.
(15) Plonka, P. M.; Grabacka, M. Melanin synthesis in microorganisms-biotechnology and medical aspects. *Acta Biochim. Pol.* **2006**, *53* (3), 429−443.
(16) Dadachova, E.; Bryan, R. A.; Huang, X.; Moadel, T.; Schweitzer, A. D.; Aisen, P.; Nosanchuk, J. D.; Casadevall, A. Ionizing radiation changes the electronic properties of melanin and enhances the growth of melanized fungi. *PLoS One* **2007**, *2*, e457.
(17) Kim, Y. J.; Wu, W.; Chun, S. E.; Whitacre, J. F.; Bettinger, C. J. Biologically derived melanin electrodes in aqueous sodium-ion energy storage devices. *Proc. Natl. Acad. Sci. U. S. A.* **2013**, *110*, 20912−7.
(18) Metz, G.; Wu, X. L.; Smith, S. O. Ramped-Amplitude Cross Polarization in Magic-Angle-Spinning NMR. *J. Magn. Reson., Ser. A* **1994**, *110*, 219−227.
(19) Johnson, R. L.; Schmidt-Rohr, K. Quantitative solid-state 13C NMR with signal enhancement by multiple cross polarization. *J. Magn. Reson.* **2014**, *239*, 44−9.
(20) Chatterjee, S.; Prados-Rosales, R.; Frases, S.; Itin, B.; Casadevall, A.; Stark, R. E. Using solid-state NMR to monitor the molecular consequences of Cryptococcus neoformans melanization with different catecholamine precursors. *Biochemistry* **2012**, *51*, 6080−8.
(21) Chatterjee, S.; Prados-Rosales, R.; Tan, S.; Itin, B.; Casadevall, A.; Stark, R. E. Demonstration of a common indole-based aromatic core in natural and synthetic eumelanins by solid-state NMR. *Org. Biomol. Chem.* **2014**, *12*, 6730−6.
(22) Morcombe, C. R.; Zilm, K. W. Chemical shift referencing in MAS solid state NMR. *J. Magn. Reson.* **2003**, *162*, 479−86.
(23) Fung, B. M.; Khitrin, A. K.; Ermolaev, K. An improved broadband decoupling sequence for liquid crystals and solids. *J. Magn. Reson.* **2000**, *142*, 97−101.
(24) Wang, Y.; Aisen, P.; Casadevall, A. Melanin, melanin "ghosts," and melanin composition in Cryptococcus neoformans. *Infect. Immunity* **1996**, *64*, 2420−2424.
(25) Enochs, W. S.; Nilges, M. J.; Swartz, H. M. A standardized test for the identification and characterization of melanins using electron paramagnetic resonance (EPR) spectroscopy. *Pigm. Cell Res.* **1993**, *6*, 91−9.
(26) Tian, S.; Garcia-Rivera, J.; Yan, B.; Casadevall, A.; Stark, R. E. Unlocking the molecular structure of fungal melanin using 13C biosynthetic labeling and solid-state NMR. *Biochemistry* **2003**, *42*, 8105−9.
(27) Zhong, J.; Frases, S.; Wang, H.; Casadevall, A.; Stark, R. E. Following fungal melanin biosynthesis with solid-state NMR: biopolymer molecular structures and possible connections to cell-wall polysaccharides. *Biochemistry* **2008**, *47*, 4701−10.
(28) Eisenman, H. C.; Nosanchuk, J. D.; Webber, J. B.; Emerson, R. J.; Camesano, T. A.; Casadevall, A. Microstructure of cell wall-associated melanin in the human pathogenic fungus Cryptococcus neoformans. *Biochemistry* **2005**, *44*, 3683−93.
(29) Liu, Y.; Simon, J. D. Isolation and biophysical studies of natural eumelanins: applications of imaging technologies and ultrafast spectroscopy. *Pigm. Cell Res.* **2003**, *16*, 606−18.

DOI: 10.1021/acs.jafc.5b02713
J. Agric. Food Chem. 2015, 63, 7326−7332

published procedure.[13] Preparative silica gel (SiO_2) chromatography was used to fractionate TWK10-fermented soy milk water extract. Sequential elution using ethyl acetate (EA)/methanol (MeOH) (9:1), EA/MeOH/H_2O (7:3:0.5), EA/MeOH/H_2O (7:3:2), EA/MeOH/H_2O (7:3:4), and isopropanol/H_2O (7:3) resulted in five fractions (F1−F5) being obtained. Fractions F2 and F4 were further separated using a RP-HPLC system (Thermo, Waltham, MA, USA) coupled to a variable UV absorbance detector (Thermo) operated at 254 nm. The chromatogram was recorded using an electronic integrator (Thermo). Chromatographic separation was performed using a C18 RP analytical HPLC column [YMC-Pack ODS-AQ (25 μm, 12 nm) 250 × 10 mm i.d.] (YMC Co., Ltd., Kyoto, Japan). The composition of the mobile phase during the gradient elution was increased linearly from 0 min (100% water and 0% acetonitrile) to 30 min (85% water and 15% acetonitrile). The flow rate was held constant at 2 mL/min. Five isolates were collected from each fraction, named F2-1−F2-5 and F4-1−F4-5, and the inhibitory effects of these subfractions on ACE activity were investigated. Moreover, F2-2 and F2-3 were further isolated using TLC [solvent EA/MeOH/H_2O (8:3:1)], and detected at a UV absorbance of 254 nm. Four subfractions were obtained from F2-2 and F2-3, which were named F2-2A, F2-2B, F2-3A, and F2-3B, respectively. The inhibitory effects of these four subfractions on ACE activity were then determined. Finally, the ACE inhibitor, F2-2A, was identified. Time-of-flight mass spectrometry TOF MS data were obtained using a Microflex MALDI-TOF MS (Bruker Daltonics, Billerica, MA, USA). NMR spectra were obtained using Varian NMR spectrometers (Varian Gemini 500 MHz; Varian Inc., Palo Alto, CA, USA) using D_2O as solvent.

Measurement of ACE Inhibition. ACE inhibition was measured according to the method described by Cushman and Cheung with some modifications.[14] Aliquots (50 μL) of buffered substrate solution (12.5 mM HHL in 100 mM borate buffer solution containing 300 mM NaCl; pH 8.3) were mixed with samples (50 μL) at each tested concentration, and then pre-incubated at 37 °C for 5 min. ACE (25 μL; 25 mU/mL) was added to the reaction, which was incubated at 37 °C for 20 min. The enzymatic reaction was stopped by adding 0.5 N HCl (1 mL). The hippuric acid that was released because of ACE activity was extracted with ethyl acetate (1 mL), which was then dried. The sediment was dissolved in deionized water (1 mL), and the absorbance at 228 nm was measured. The inhibitory activity was calculated using the following equation: ACE inhibitory activity (%) = $100 \times [(A - B) - (C - D)]/(A - B)$, where A is the absorbance of a solution containing ACE but no sample, B is the absorbance of a solution containing ACE that had been previously inactivated by the addition of HCl but no sample, C is the absorbance of a solution containing both ACE and the sample, and D is the absorbance of a solution containing HCl-inactivated ACE and the sample.

Lineweaver−Burk Plots. The kinetics parameters were evaluated by Lineweaver−Burk's method. Briefly, 160 μL of FAPGG (dissolved in 50 mM Tris-HCl buffer containing 0.3 M NaCl, pH 7.5) was mixed with 20 μL of ACE (final activity of 20 mU) and 20 μL of CUG. The rate of decrease in absorbance at 345 nm was recorded for 10 min at room temperature. Distilled water was used instead of CUG solution in the blank experiment. The kinetics of ACE inhibition was studied with 0.0625, 0.125, 0.25, and 0.5 mM FAPGG.

In Vivo Assay of Antihypertensive Effect over Short- and Long-Term Intake. A total of 42 SHRs (13 weeks old, 260−300 g) and 6 Wistar Kyoto (WKY) rats (13 weeks old, 260−300 g) were used in this experiment and were obtained from BioLASCO Taiwan Co., Ltd. (Taipei, Taiwan). The animals were maintained at a temperature of 21 ± 2 °C and a relative humidity of 55 ± 10% with 12 h light/dark cycles in the Fu Jen Laboratory Animal Center (Taipei, Taiwan). Rats were fed tap water and a standard diet (5001-Laboratory Rodent Diet; LabDiet, St. Louis, MO, USA).

Each sample was dissolved in distilled water (1 mL) and was administered orally by gastric intubation between 12 and 1 p.m. Distilled water was used as a negative control, and the known antihypertensive agents CAP (50 mg/kg) and GABA (0.76 mg/kg) were used as positive controls.[15] The dose was based on 400 mL/day/person (weight was 65 kg and height of 170 cm), and human doses were converted to animal equivalent doses using the Boyd formula.[16] The dose of TWK10-fermented soy milk water extract powder was 0.51 g/kg.

The dose of combined uracil and glycerol (CUG) was based on the content of TWK10-fermented soy milk water extracts. The 1:1, 1:2, and 1:3 ratios of uracil/glycerol (1.24/1.24 mg/kg, 1.24/2.48 mg/kg, and 1.24/3.72 mg/kg, respectively) were dissolved in distilled water and administrated orally, and their antihypertensive effects in SHRs were evaluated 8 h after treatment. Moreover, low- and high-doses of soy milk extracts (0.51 and 2.55 g/kg, respectively) and low (uracil, 1.24 mg/kg; glycerol, 3.72 mg/kg) and high (uracil, 6.20 mg/kg; glycerol, 18.60 mg/kg) doses of CUG were administered. Systolic blood pressure (SBP) and diastolic blood pressure (DBP) were recorded using the tail-cuff method before administration and at 4, 8, and 24 h postadministration using a BP-2000 Blood Pressure Analysis System (Visitech System, Inc., Apex, NC, USA). Before measurements, the rats were kept at 37 °C for 40 min to detect pulsations in the tail artery. Five readings were taken, and the mean of all measurements was calculated. To minimize stress-induced variations in BP, the same individual made all measurements in the same peaceful environment. A training period of 2 weeks was established before the actual trial time, during which time the rats became accustomed to the procedure, to guarantee the reliability of the measurements.

After the short-term tests, the SHRs continued to receive low and high doses of CUG for 8 weeks, and SBP and DBP were recorded biweekly. Twenty-four hours before sacrifice, all food was removed. Animals were anesthetized by carbon dioxide inhalation and sacrificed. Blood was collected by cardiac puncture, and serum samples were obtained by drawing the blood into a serum separated tube, allowing it to clot, and centrifuging it for 10 min at 3000g to separate serum. In addition, plasma was obtained by collecting blood in heparinized syringes containing 5% heparin and 2% sodium citrate and centrifuging at 3000g for 15 min. The aorta, liver, lung, and kidney tissues were cleaved and divided into two parts; one part was homogenized (2 g in 10 mL of PBS) using a FastPrep System (MP Biomedicals, Santa Ana, CA, USA), and the other was immediately fixed in 10% neutral buffered formalin for further histological analysis. The experiment was reviewed and approved by the Animal Care and Research Ethics Committee of the Fu Jen Catholic University (IACUC approval A10105).

Biochemical and Histological Assessment. The activity of ACE in liver, lung, and kidney tissues was determined as previously described (see Measurement of ACE Inhibition). The serum level of bradykinin in SHRs was determined using a bradykinin enzyme immunoassay kit (Uscn Life Science Inc., Houston, TX, USA). The levels of aldosterone and renin activity in plasma were evaluated using a Wallac 2470 WIZARD^2 gamma counter (PerkinElmer Life and Analytical Sciences, Waltham, MA, USA), and AngII levels were measured using an AngII EIA kit (Phoenix Pharmaceuticals, Inc., Burlingame, CA, USA). The level of nitrite (NO^{2-}) and nitrate (NO^{3-}) anions in plasma was measured using a nitric oxide EIA kit (Cayman Chemical Co., Ann Arbor, MI, USA). The level of lipid peroxide in serum was determined by measuring the thiobarbituric acid reactive substance (TBARS) concentration as an index of lipid peroxidation, according to the Yagi method.[17] In addition, the activity of SOD was measured using an SD125 kit supplied by Randox Laboratories Ltd. (Crumlin, UK).

The aorta samples from each of the rats were divided into two parts. One part was for evaluating the vascular elastin distribution and nitric oxide synthase (eNOS) protein expression. The other part was used to determine the protein expression of calmodulin (CaM). To prepare them for optical microscopy, the aorta samples were embedded in paraffin, and sections were stained with hematoxylin−eosin. Verhoff's stain was used to evaluate the expression and distribution of vascular elastin. eNOS protein expression was quantified with an immunohistochemical assay according to the method of Zhao et al. and examined using an Nikon TS-100 microscope (Tokyo, Japan). Motic Images 2000 software (Xiamen, China) was used for examination of hypertensive tissues changes. In addition, CaM protein levels were

DOI: 10.1021/acs.jafc.5b01649
J. Agric. Food Chem. 2015, 63, 7333−7342

investigated using Western blotting. The aorta samples (0.2 g) were homogenized with Nonidet P-40/SDS lysis buffer (200 μL; 1% Nonidet P-40, 0.01% SDS, 0.1 M Tris-HCl at pH 7.2, 100 mM phenylmethanesulfonyl fluoride, and 1 mg/mL of aprotinin) using a FastPrep System (MP Biomedicals). The lysate was centrifuged at 11000*g* for 20 min at 4 °C, and supernatants were collected. Each gel lane was loaded with total protein from the cell extracts (40 μg). Proteins were resolved by SDS-PAGE using a 7.5% acrylamide gel and then transferred to a nitrocellulose membrane. Blocking was performed in Tris-buffered saline containing 2% nonfat milk powder. Membranes were incubated overnight at 4 °C, in blocking solution containing anti-CaM antibody (Santa Cruz Biotechnology, Inc., Dallas, TX, USA) (1:500) and mouse anti-β-actin monoclonal antibody (Chemicon International, Inc., Temecula, CA, USA) (1:5000). Blots were then incubated in blocking buffer containing the corresponding horseradish peroxidase-conjugated secondary antibodies for 1 h at 25 °C. Protein bands were visualized using an enhanced chemiluminescence kit (Amersham Pharmacia Biotech, Arlington Heights, IL, USA), and a UVP image analysis system (UVP, Upland, CA, USA). Analysis was performed using Gel-Pro Analyzer 4 (Media Cybernetics, Inc., Rockville, MD, USA).

Statistical Analysis. All values represent means and standard deviations of three repeats. Data were then compared using Duncan's multiple-range method using SPSS statistical analysis software.

Table 1. Inhibitory Effect of the Uracil and Glycerol on ACE[a]

group	ACE inhibitory activity (%)
CAP	74.21 ± 0.73 A
uracil, 10 μg/mL	24.31 ± 8.45 B
glycerol, 30 μg/mL	ND
1:1 ratio of uracil/glycerol (10 μg/mL/10 μg/mL)	72.92 ± 3.14 A
1:2 ratio of uracil/glycerol (10 μg/mL/20 μg/mL)	72.58 ± 2.88 A
1:3 ratio of uracil/glycerol (10 μg/mL/30 μg/mL)	70.94 ± 3.83 A

[a]Data are presented as the mean ± SD (N = 3). Values with different letters in the same column are significantly different by Duncan's multiple-range test (p < 0.05). ND, not detected; CAP, captopril at a concentration of 3.4 mM.

RESULTS AND DISCUSSION

ACE-Inhibitory Ingredients in TWK10-Fermented Soy Milk Extract. The half-maximal inhibitory concentration (IC_{50}) value of water extract from TWK10-fermented soy milk for ACE inhibition was 5.61 mg/mL. After extensive fractionation of the TWK10-fermented soy milk water extract, the IC_{50} values of F2, F3, and F4 were 43.44, 100.00, and 36.91 μg/mL, respectively. Fractions F2 and F4 had the higher inhibitory effect on ACE and were further separated using a RP-HPLC system. In addition, subfractions F2-3 and F4-3, derived from F2 and F4, respectively, had the same retention time (13 min) during the separation using the RP-HPLC system. Moreover, the IC_{50} values of F2-2, F2-3, and F4-3 were 7.26, 9.19, and 9.35 μg/mL, respectively. According to our findings, F2-3 and F4-3 had similar retention times and IC_{50} values; there is an empirical basis to support the fact that these two isolates were hypothesized as the same one. Furthermore, F2-2A and F2-3B had better ACE inhibitory effect than others, and the IC_{50} values of F2-2A and F2-3B were 1.35 and 2.37 μg/mL, respectively, after extensive fractionation of F2-2 and F2-3. A component fraction, F2-2A, was isolated as a white amorphous solid and identified as one of the inhibitors having ACE inhibitory activity (68.94 ± 7.47 and 49.3 ± 4.7% at 10 and 1 μg/mL, respectively). The following spectral data allowed the fraction to be identified as a mixture of uracil and glycerol (Supplemental Figure 1): TOF MS, m/z 113.0498 $[M + H]^+$ for uracil and 115.0516 $[M + Na]^+$ for glycerol (Supplemental Figure 2); ^{1}H NMR (D_2O, 500 MHz) δ 3.54 (2H, dd, J = 6.5 and 11.5, H-7 and 9), 3.63 (2H, dd, J = 6.5 and 12.0, H-7 and 9), 3.76 (H, tt, H-8), 5.78 (H, d, J = 8.0, H-5), and 7.51 (H, d, J = 8.0, H-6) (Supplemental Figure 3); ^{13}C NMR (D_2O, 125 MHz) δ 63.46 (C-7 and 9), 79.04 (C-8), 101.38 (C-5), 144.33 (C-6), 153.99 (C-2), and 168.35 (C-4) (Supplemental Figure 4).

Sugar nucleotides act as substrates during the biosynthesis of polysaccharides in higher plants. Uridine diphosphoglucuronic acid donates D-glucuronosyl units for the synthesis of several types of structural polysaccharides. It is also the precursor of other nucleotide sugars, including uridine diphosphate galacturonic acid, uridine diphosphate xylose, uridine diphosphate L-arabinose, and uridine diphosphate D-apiose, which are incorporated into pectin and hemicelluloses in plants.[18] Previous

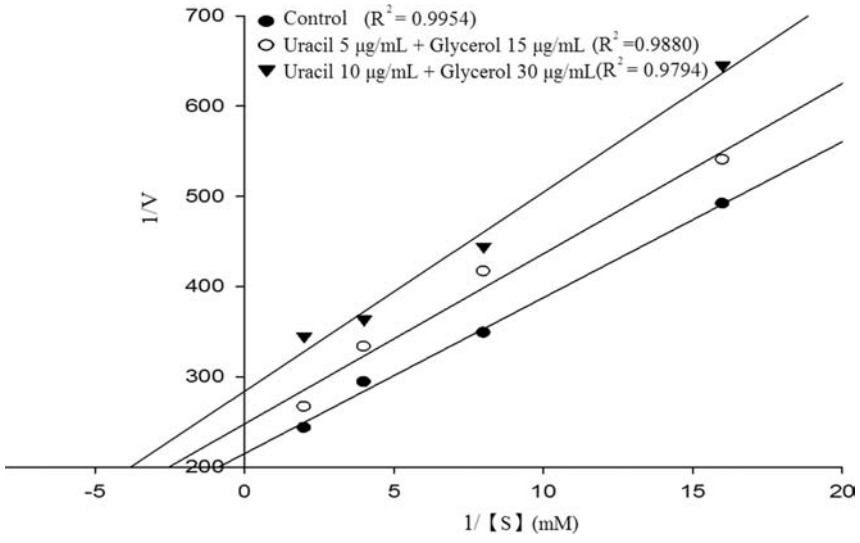

Figure 1. Lineweaver–Burk plots of ACE inhibition by different concentrations of combination of uracil and glycerol at various substrate concentrations (0.0625–0.5 mM). V = initial rate of reaction [ΔA_{345} (nm)/min].

DOI: 10.1021/acs.jafc.5b01649
J. Agric. Food Chem. 2015, 63, 7333–7342

studies suggested that uracil formation is a consequence of the enzymatic hydrolysis of uridine by microorganisms.[19] In addition, Hidalgo et al. reported that the presence of uracil in tomato products is an index of LAB contamination, suggesting that uracil is a metabolic product that correlates with the growth of LAB in the presence of uridine.[20] In the present study, lipids were present in unfermented soy milk (1.4%, w/w), and lipase activity was observed (data not shown). Taken together, these data suggest that the functional ingredients, uracil and glycerol, were present TWK10-fermented soy milk. In addition, Schanker and Tocco demonstrated that uracil is absorbed across the rat intestinal epithelium via an active transport mechanism.[21] Moreover, the principal transport mechanism for glycerol in the rat small intestine is passive (diffusive) transport via the paracellular route and an Na^+-dependent carrier-mediated transport system. Therefore, these two functional ingredients are theoretically both absorbed in the rat small intestine.

Inhibitory Effects of Uracil and Glycerol on ACE Activity in Vitro. The uracil content in TW10-fermented soy milk water extracts was analyzed using HPLC according to a method described by Deporte et al.[22] and was found to be 2.44 ± 0.07 mg/g in dried powder. In addition, the glycerol content of soy milk extract was 7.31 ± 0.58 mg/g as shown using enzymatic kits (GY105, Randox Laboratories Ltd., Crumlin, UK). The ratio of uracil and glycerol was nearly 1:3. The ACE inhibitory effects of different ratios of pure uracil and glycerol were then evaluated. As shown in Table 1, there were no significant differences between each ratio of uracil/glycerol ($p > 0.05$) and the positive control. Each substance alone had little or no effect on ACE activity.

Glycerol is a water-soluble trivalent alcohol normally present in human tissues as an integral part of both fats and triglycerides. It is readily metabolized, primarily in the liver, and systemic hyperosmolarity may be reduced and dehydration limited. MacDonald and Uden (1982)[23] indicated that intravenous glycerol and mannitol were equally effective in lowering acute elevations of intracranial pressure. Previous studies employing glycerol as a major osmotherapy agent entailed pharmacologically inert substances that increase the osmotic pressure of plasma, promoting movement of water from interstitial spaces to vascular spaces.[24] Osmotic agents include mannitol, urea, sorbitol, glycerol, and hypertonic saline, and they have primarily been applied in the treatment of cerebral infarction, experimental ischemia, traumatic intracranial hypertension, or edema.[25] In the current study, uracil and glycerol had low or no ACEI activity, respectively, and the inhibitory effect rose with an increase in the ratio of uracil/glycerol (from 1:1 to 1:3), indicating that the presence of glycerol increased the inhibitory effects of ACE by increasing the level of uracil to bind to ACE.

The mode of ACE inhibition by CUG was investigated by kinetic studies using Lineweaver–Burk plots. As shown in Figure 1, the double-reciprocal plots of ACE-catalyzed reactions in the absence and presence of a combination of uracil and glycerol indicate mostly uncompetitive inhibition of ACE activity. The result suggests that the combination of uracil and glycerol exhibited activities by binding to only the enzyme–substrate complex. The combination of uracil and glycerol as an uncompetitive inhibitor can bind to the enzyme–substrate complex to prevent catalysis. The K_m value for ACE activity in the absence of the combination of uracil and glycerol was 0.08 mM FAPGG, and V_{max} was 0.005. The presence of the

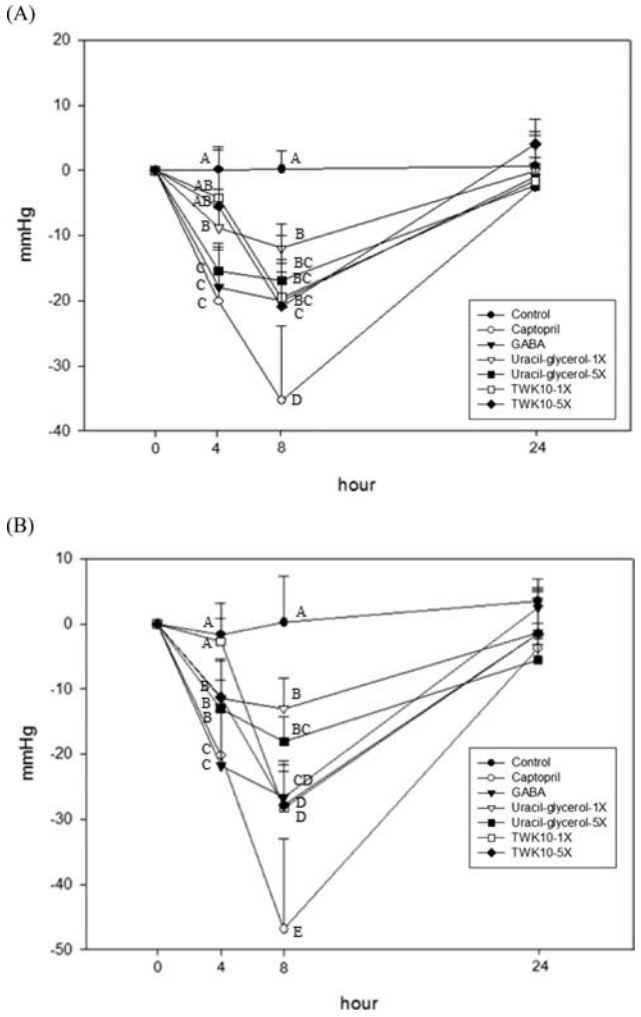

Figure 2. Effect of the single oral administration of TWK10-fermented soy milk water extract and combined uracil and glycerol treatment on (A) systolic and (B) diastolic blood pressure in spontaneously hypertensive rats. Control, administration of H_2O; captopril, administration of captopril at a dose of 50 mg/kg; GABA, administration of γ-aminobutyric acid at a dose of 0.76 mg/kg; uracil-glycerol-1×, administration of combined uracil and glycerol at doses of 1.24 and 3.72 mg/kg bw, respectively, 0.76 mg/kg bw; uracil-glycerol-5×, administration of combined uracil and glycerol at doses of 6.20 and 18.60 mg/kg bw, respectively, 0.76 mg/kg bw; TWK10-1×, administration of soy milk extracts at a dose of 0.51 g/kg bw; TWK10-5×, administration of soy milk extracts at a dose of 2.55 g/kg bw. Data are presented as means ± SD ($n = 6$). Values with different letters were significantly different according to Duncan's multiple-range test ($p < 0.05$).

combination of uracil and glycerol resulted in concentration-dependent decreases in both V_{max} and K_m values.

In the uncompetitive inhibition system, the inhibitor bound only to the enzyme–substrate complex and decreased the maximum enzyme activity, taking longer for the substrate or product to leave the active site. Most ACE inhibitory peptides obtained from the hydrolysis of pea (*Pisum sativum* var. Bajka) globulins,[26] rapeseed protein digest,[27] chickpea,[28] or wakame (*Undaria pinnatifida*)[29] belong to uncompetitive inhibitors. In addition, nonpeptide compounds such as usnic acid from lichen species *Usnea complanata* under submerged fermentation or polyphenols from tea (*Camellia sinensis*) also showed an uncompetitive type of ACE inhibition.[30,31] According to our

DOI: 10.1021/acs.jafc.5b01649
J. Agric. Food Chem. 2015, 63, 7333–7342

Table 2. Effect of Chronic Oral Administration of the Mixture of Uracil and Glycerol on Systolic Blood Pressure in SHR[a]

	SBP (mmHg)				
group	0 weeks	2 weeks	4 weeks	6 weeks	8 weeks
N	157.18 ± 4.38 a	156.05 ± 5.20 a	153.46 ± 8.33 a	150.79 ± 5.45 a	151.25 ± 8.53 a
C	185.54 ± 3.62 Aa	199.84 ± 4.05 Ab	204.03 ± 2.65 Ac	206.89 ± 2.27 Ac	207.12 ± 3.11 Ac
GABA	185.30 ± 4.21 Aa	185.73 ± 3.45 Ba	187.44 ± 4.41 Cab	189.15 ± 3.64 Cab	190.72 ± 3.12 Cb
LDG	185.47 ± 2.47 Aa	185.60 ± 4.62 Ba	192.09 ± 2.22 Bb	193.97 ± 1.38 Bbc	195.82 ± 2.01 Bc
HDG	184.93 ± 2.54 Aa	186.97 ± 4.96 Ba	187.13 ± 5.31 Ca	188.28 ± 3.95 Ca	188.67 ± 3.31 Ca

[a]Data are presented as means ± SD ($N = 6$). Values with different upper and lower case letters in columns and rows, respectively, are significantly different by Duncan's multiple-range test ($p < 0.05$). N, normal control group; C, hypertension control group; GABA, administration of γ-aminobutyric acid at a dose of 0.76 mg/kg bw; LDG, administration of combined uracil and glycerol at doses of 1.24 and 3.72 mg/kg bw, respectively; HDG, administration of combined uracil and glycerol at doses of 6.20 and 18.60 mg/kg bw, respectively.

Table 3. Effect of Chronic Oral Administration of the Mixture of Uracil and Glycerol on Diastolic Blood Pressure in SHR[a]

	DBP (mmHg)				
group	0 weeks	2 weeks	4 weeks	6 weeks	8 weeks
N	133.92 ± 9.13 a	139.67 ± 7.32 a	131.79 ± 6.15 a	133.64 ± 5.37 a	133.36 ± 5.16 a
C	165.85 ± 6.01 Aa	181.52 ± 6.10 Ab	184.06 ± 4.15 Abc	185.94 ± 3.89 Abc	189.02 ± 3.98 Ac
GABA	165.89 ± 6.79 Aa	169.13 ± 3.26 Ba	166.71 ± 8.19 Ca	167.26 ± 4.28 Ca	167.86 ± 5.99 Ca
LDG	166.25 ± 3.00 Aa	168.24 ± 6.37 Ba	173.50 ± 2.16 Bb	174.75 ± 2.60 Bb	177.45 ± 2.45 Bb
HDG	168.48 ± 5.30 Aa	168.14 ± 4.79 Ba	170.15 ± 2.12 BCa	171.06 ± 5.43 BCa	168.14 ± 5.27 Ca

[a]Data are presented as means ± SD ($N = 6$). Values with different upper and lower letters in columns and rows, respectively, are significantly different by Duncan's multiple-range test ($p < 0.05$). N, normal control group; C, hypertension control group; GABA, administration of γ-aminobutyric acid at a dose of 0.76 mg/kg bw; LDG, administration of combined uracil and glycerol at doses of 1.24 and 3.72 mg/kg bw, respectively; HDG, administration of combined uracil and glycerol at doses of 6.20 and 18.60 mg/kg bw, respectively.

findings, based on kinetic studies using Lineweaver−Burk plots, the CUG demonstrated mostly uncompetitive inhibition of ACE activity, and we can hypothesize that a conformational change in ACE occurs upon binding to the substrate, which presents a binding site for CUG. As a result, inhibition occurs because the substrate−enzyme−inhibitor complex cannot form the final product in vitro.

Antihypertensive Effects of Soy Milk Extract and CUG on SHRs in Short-Term Study. The antihypertensive effects of TWK10-fermented soy milk water extracts and CUG were investigated in SHRs. The initial SBP and DBP were measured as reference values before the oral administration of samples. As shown in Figure 2, there was no significant difference in the SBP and DBP of the control group during the 24 h after oral administration of the samples ($p > 0.05$). In the CAP group, SBP and DBP were suppressed by 20.11 ± 8.35 and 20.20 ± 7.84 mmHg, respectively, after 4 h, and by 35.31 ± 11.52 and 46.91 ± 13.92 mmHg after 8 h ($p < 0.05$). GABA was used as an additional positive control and suppressed SBP by 17.90 ± 5.75 and 19.96 ± 6.25 mmHg ($p < 0.05$) after 4 and 8 h, respectively.

The uracil content in the low dose of soy milk extract was 1.24 mg/kg, and this was used to determine the low dose of uracil in CUG. Doses of 1:1, 1:2, and 1:3 ratios of uracil/glycerol (1.24/1.24 mg/kg, 1.24/2.48 mg/kg, and 1.24/3.72 mg/kg, respectively) were administered orally to evaluate their antihypertensive effect 8 h after treatment of SHRs. The SBP and DBP of rats was suppressed most effectively by the 1:3 uracil/glycerol, which induced reductions of 12.18 ± 3.13 and 10.47 ± 3.07 mmHg, respectively ($p < 0.05$). This ratio was used in subsequent experiments.

As shown in Figure 2, there was no significant difference between the SBP and DBP in the negative control group rats and those that received the low dose of soy milk extract (0.51 g/kg) 4 h after treatment ($p > 0.05$). However, 8 h after treatment, the extract decreased SBP and DBP significantly by 19.54 ± 9.54 and 28.19 ± 7.14 mmHg, respectively ($p < 0.05$ versus negative control). A high dose of soy milk extract (2.55 g/kg) significantly suppressed DBP 4 h after treatment and SBP after 4 and 8 h, compared with the negative control group ($p < 0.05$). Moreover, the SBP of rats treated with low and high doses of CUG was decreased by 8.83 ± 4.18 and 15.42 ± 4.21 mmHg, respectively, 4 h after oral administration ($p < 0.05$), compared with the control group. It was also reduced 8 h after oral administration ($p < 0.05$), compared with the low and high doses of soy milk extract. The low and high doses CUG suppressed SBP significantly by 11.97 ± 3.71 and 16.89 ± 2.59 mmHg and DBP by 13.01 ± 4.77 and 18.03 ± 3.74 mmHg, respectively, compared with the control group. The initial DBP and SBP values were restored to the initial levels after 24 h. These data show that CUG was more effective than soy milk extract 4 h after oral administration. However, the TWK10-fermented soy milk water extract suppressed DBP more potently than CUG after 8 h, suggesting that there might be additional functional ingredients in the other fractionated extract.

Antihypertensive Effects of CUG on SHR in Long-Term Study. Tables 2 and 3 show the changes in SBP and DBP during 8 weeks of CUG administration. There was no significant difference in the SBP and DBP of the all groups before oral administration of the samples ($p > 0.05$). During the 8 week period, SBP and DBP of the control group increased. The low and high doses of CUG significantly suppressed SBP and DBP after 4 and 8 weeks of administration ($p < 0.05$) compared to control. In the low-dose CUG group, SBP and DBP both increased significantly between the baseline and after 4 weeks of administration and between 4 and 8 weeks ($p < 0.05$). However, in the high-dose CUG group neither SBP nor DBP had significant changes over the 8 weeks ($p > 0.05$). In summary, although long-term oral administration of a

DOI: 10.1021/acs.jafc.5b01649
J. Agric. Food Chem. 2015, 63, 7333−7342

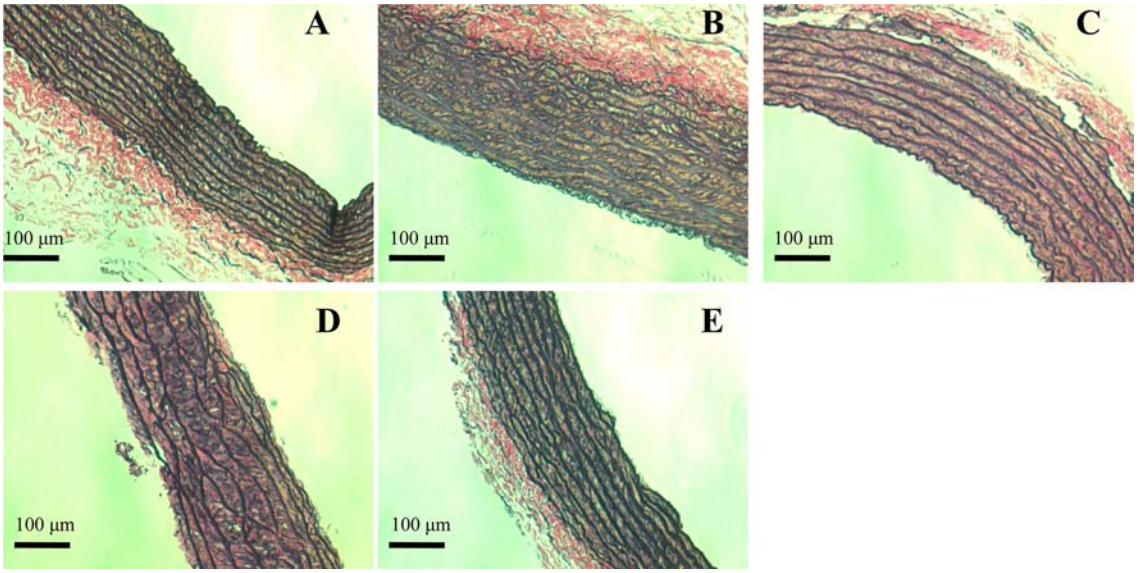

Figure 3. Effect of the combination of uracil and glycerol on microscopic examination of aorta elastin thin section in spontaneously hypertensive rats: (A) normal; (B) control; (C) GABA treated; (D) low dose; (E) high dose (×100 magnification).

Table 4. Effect of Mixture of Uracil and Glycerol on Microscopic Examination of Aorta Elastin Band Number in SHR[a]

group	aortic elastin bands (number)
N	6.50 ± 0.55 D
C	10.67 ± 1.03 A
GABA	8.00 ± 0.63 BC
LDG	8.67 ± 0.52 B
HDG	7.50 ± 0.55 C

[a]Data are presented as means ± SD (N = 6). The elastin bands were counted from three different sections/specimens. Values with different letters are significantly different by Duncan's multiple-range test (p < 0.05). N, normal control group; C, hypertension control group; GABA, administration of γ-aminobutyric acid at a dose of 0.76 mg/kg bw; LDG, administration of combined uracil and glycerol at doses of 1.24 and 3.72 mg/kg bw, respectively; HDG, administration of combined uracil and glycerol at doses of 6.20 and 18.60 mg/kg bw, respectively.

Table 5. Effect of the Mixture of Uracil and Glycerol on ACE Activity in Organs of SHRs[a]

	ACE activity (U/mL)		
group	kidney	lung	liver
N	12.01 ± 2.90 BC	24.74 ± 4.76 C	26.67 ± 4.19 AB
C	21.54 ± 4.82 A	37.00 ± 3.54 A	29.70 ± 5.99 A
GABA	18.40 ± 4.87 A	31.57 ± 3.27 B	23.60 ± 3.42 BC
LDG	14.08 ± 2.27 B	18.29 ± 2.60 D	26.86 ± 6.79 AB
HDG	7.95 ± 2.96 C	13.20 ± 2.98 E	18.28 ± 3.24 C

[a]Data are presented as means ± SD (N = 6). Values with different letters are significantly different by Duncan's multiple-range test (p < 0.05). N, normal control group; C, hypertension control group; GABA, administration of γ-aminobutyric acid at a dose of 0.76 mg/kg bw; LDG, administration of combined uracil and glycerol at doses of 1.24 and 3.72 mg/kg bw, respectively; HDG, administration of combined uracil and glycerol at doses of 6.20 and 18.60 mg/kg bw, respectively.

low-dose CUG suppresses the increase in SBP and DBP in SHRs, a high dose of CUG is required to prevent an increase in BP entirely. In addition, the difference in effectiveness between low and high doses of CUG after 8 weeks of administration reached significant levels (p < 0.05), indicating a positive correlation between the dose of CUG and its efficacy.

Effect of Long-Term CUG Treatment on Elastin Arrangement in Arcuate Arteries of SHRs. Elastin is a protein that maintains vascular elasticity and gives blood vessels the capacity to stretch and contract. Previous studies have indicated that hypertension causes excessive pressure within blood vessels, leading to an altered distribution of elastic fibers.[32] Figure 3 shows that elastin in untreated SHRs was the most disorganized. After 8 weeks of treatment with higher doses of CUG, fibers were more ordered, indicating a positive correlation between CUG dose and elastin arrangement. This result indicated that CUG can improve the elasticity and tensile strength of blood vessels. In addition, there have been reports that spontaneous hypertension increases levels of elastin and causes inelastic fibrous masses to accumulate within blood vessels.[33] In this study, elastin bands in arteries were counted (Table 4), and significantly fewer were found in the two CUG-treated groups (p < 0.05). In summary, the elastin fibers in the aorta of CUG-treated SHRs were significantly straighter than those of controls, affecting the elasticity of vessels and aiding in the improvement of hypertension.

Regulatory Effects of Long-Term Administration of CUG on the RAS in SHRs. Figure 4A shows the aldosterone levels in plasma of SHRs after 8 weeks of administration of CUG and indicates that administration of low and high doses of CUG caused significant decreases in aldosterone level, compared with the control group (p < 0.05). The results also show that AngII was significantly suppressed by both low and high doses of CUG, compared to the control group (p < 0.05) (Figure 4B). Figure 4C shows that only a high dose of CUG significantly increased the concentration of bradykinin after long-term administration. These results indicate that suppression of aldosterone levels may lead to the inactivation of the upstream catalytic enzyme. Moreover, Table 5 shows the effects of 8 weeks of CUG administration on ACE activity in the kidney, lung, and liver of SHRs. CUG was found to dose-dependently

DOI: 10.1021/acs.jafc.5b01649
J. Agric. Food Chem. 2015, 63, 7333−7342

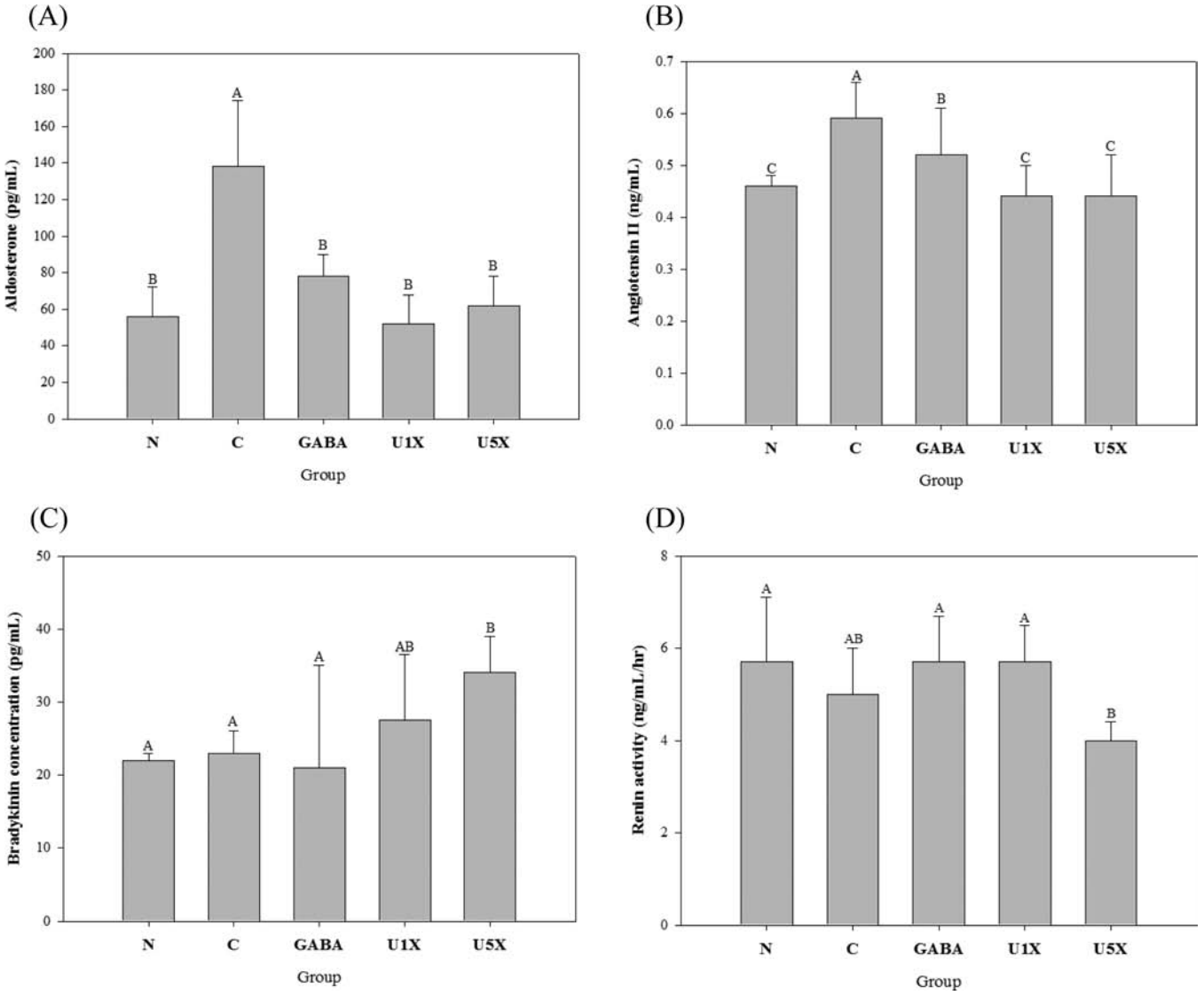

Figure 4. Effect of the combination of uracil and glycerol on (A) angiotensin II, (B) aldosterone, (C) bradykinin, and (D) rennin activity in SHR. Data are presented as means ± SD (n = 6). Bars with different letters are significantly different by Duncan's multiple-range test (p < 0.05).

Table 6. Effect of the Mixture of Uracil and Glycerol on Superoxide Dismutase and Malondialdehyde Concentration in Serum of SHR[a]

group	SOD (U/mL)	MDA (μM)
N	2.28 ± 0.32 B	10.13 ± 1.73 B
C	1.80 ± 0.12 A	17.00 ± 4.14 A
GABA	3.04 ± 0.30 C	10.38 ± 2.45 B
LDG	2.38 ± 0.22 B	10.00 ± 1.69 B
HDG	2.43 ± 0.18 B	10.75 ± 2.71 B

[a]Data are presented as means ± SD (N = 6). Values with different letters are significantly different by Duncan's multiple-range test (p < 0.05). N, normal control group; C, hypertension control group; GABA, administration of γ-aminobutyric acid at a dose of 0.76 mg/kg bw; LDG, administration of combined uracil and glycerol at doses of 1.24 and 3.72 mg/kg bw, respectively, HDG, administration of combined uracil and glycerol at doses of 6.20 and 18.60 mg/kg bw, respectively.

Table 7. Effect of the Mixture of Uracil and Glycerol on Immunohistochemical of eNOS in the Sections of Aorta and Nitric Oxide Concentration in Plasma in SHRs[a]

group	eNOS density (%)	nitrate + nitrite (μM)
N	4.50 ± 2.84 A	16.73 ± 1.12 A
C	3.87 ± 1.76 A	16.23 ± 3.09 A
GABA	3.39 ± 2.59 A	16.58 ± 4.06 A
LDG	6.75 ± 2.91 A	15.50 ± 2.39 A
HDG	18.23 ± 4.89 B	22.45 ± 5.89 B

[a]Data are presented as means ± SD (N = 6). Values with different letters are significantly different by Duncan's multiple-range test (p < 0.05). N, normal control group; C, hypertension control group; GABA, administration of γ-aminobutyric acid at a dose of 0.76 mg/kg bw; LDG, administration of combined uracil and glycerol at doses of 1.24 and 3.72 mg/kg bw, respectively; HDG, administration of combined uracil and glycerol at doses of 6.20 and 18.60 mg/kg bw, respectively.

suppress ACE activity in the liver, kidneys, and lungs, and the results were significant (p < 0.05). In addition, GABA decreased ACE activity in the lung and liver because GABA suppresses BP through inhibition of sympathetic nerve activation and reduction of binding with α_1-receptors on vascular smooth muscle cells that connect with the RAS.[34,35]

DOI: 10.1021/acs.jafc.5b01649
J. Agric. Food Chem. 2015, 63, 7333−7342

Figure 4D shows that only the high dose of CUG caused a significant decrease in renin activity in SHRs, compared to the control group ($p < 0.05$). Previous studies indicate that blockade of the RAS leads to a feedback increase in renin secretion and synthesis.[36] The inhibitory effect of CUG on renin activity was determined in vitro in this study using a Renin Inhibitor Screening Kit (K799-100, BioVision, Inc., Milpitas, CA, USA). It was found that renin activity was significantly inhibited by 52.94 ± 6.79, 29.41 ± 3.23, 20.59 ± 3.19, 17.65 ± 4.24, and 5.88 ± 1.23% at concentrations of 1000, 100, 50, 10, and 1 μg/mL, respectively. In summary, CUG can decrease BP through AngII and the hormone aldosterone, downstream products of RAS. These downstream factors were regulated by suppressing renin activity and reducing ACE activity.

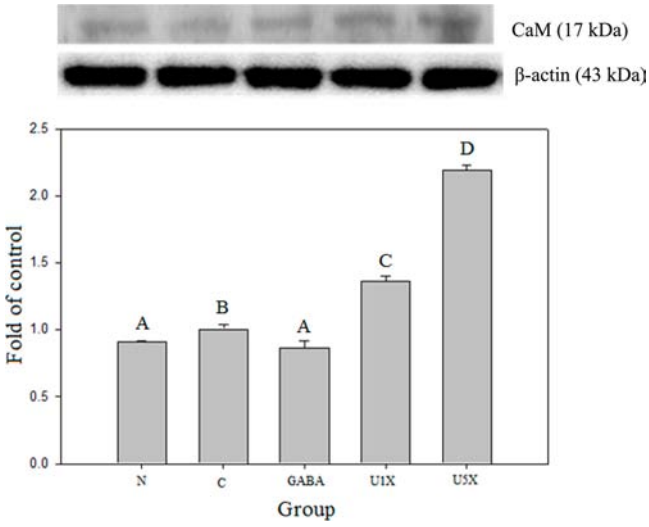

Figure 5. Expression of calmodulin by administration of combination of uracil and glycerol. Data are presented as means ± SD ($n = 3$). Bars with different letters are significantly different by Duncan's multiple-range test ($p < 0.05$).

Effects of Long-Term Administration of CUG on Antioxidant Capacity and Nitric Oxide (NO) Production in SHRs. Free radicals bind with NO, which then is then oxidized into peroxynitrate, reducing NO levels and affecting vasodialation. Additionally, the accumulation of products of lipid overoxidation—such as malondialdehyde (MDA)—in blood vessels causes atherosclerosis, resulting in an increase in BP. The effect of CUG administration on SOD activity and MDA was determined. Table 6 shows that the administration of low and high doses of CUG and GABA significantly increased SOD activity and decreased MDA levels compared to the control group ($p < 0.05$).

Table 7 shows the effect of CUG administration on plasma NO level and eNOS expression in SHRs. Plasma NO levels following a high dose of CUG increased 1.38 times, compared with the control group ($p < 0.05$); however, low-dose CUG administration made no difference ($p > 0.05$). Immunostaining showed that there was no difference in eNOS expression between low-dose CUG-treated and GABA-treated groups, compared to the control group ($p > 0.05$). However, the high-dose CUG administration significantly increased eNOS expression within arcuate arteries, 4.71 times greater than the control group ($p < 0.05$). This result corresponds with the NO level in the treated SHRs. Figure 5 shows that long-term administration of low and high doses of CUG increased CaM protein expression by 1.36 and 2.19 times, respectively, compared to the control group ($p < 0.05$). It can mediate eNOS activity by binding calcium ions to further produce NO.[37] In summary, administration of low and high doses of CUG can increase the SOD activity and decrease the MDA level to prevent NO bound with free radicals. In addition, eNOS and CaM expressions were also improved to increase the NO

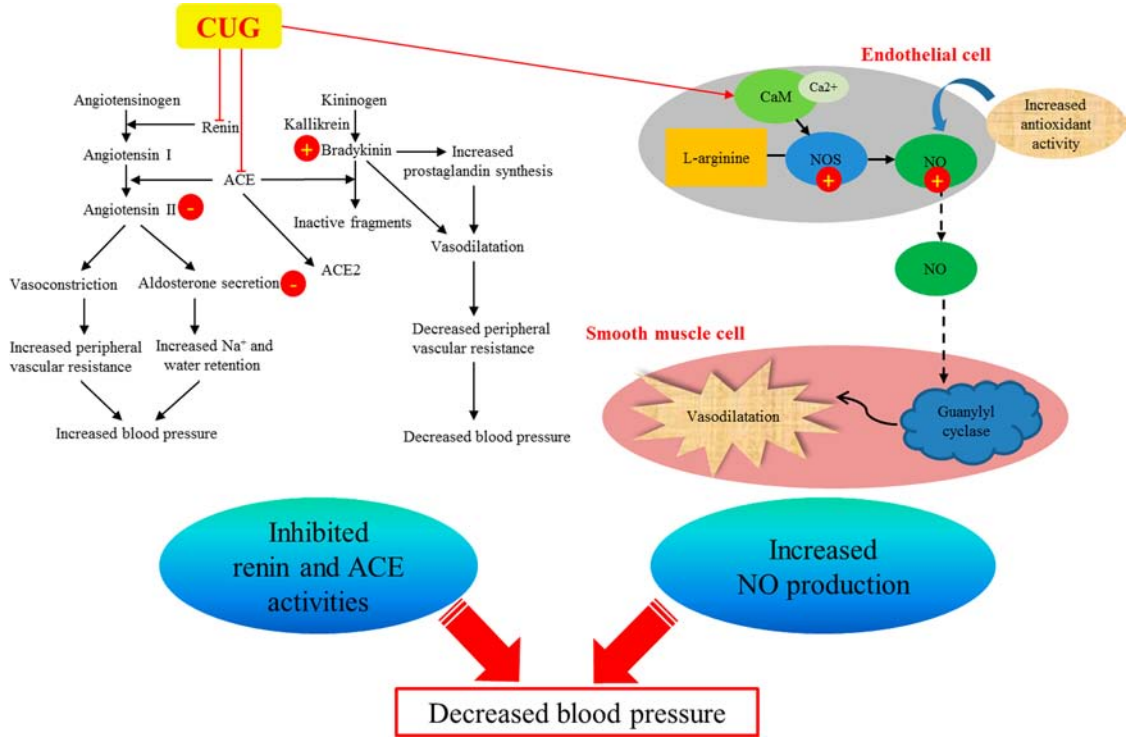

Figure 6. Mechanism of antihypertensive effect of combined uracil and glycerol treatment.

DOI: 10.1021/acs.jafc.5b01649
J. Agric. Food Chem. 2015, 63, 7333−7342

production. These factors can promote vasodilation, resulting in the improvement of hypertension (Figure 6).

BP is controlled by a number of different biochemical pathways. NO levels can be increased indirectly by enhancing the activity of endothelial eNOS. Upon entering smooth muscle cells, NO can activate guanylyl cyclase, increasing the accumulation of cyclic guanosine monophosphate and promoting smooth muscle relaxation.[38−40] Along with NO, ACE is an important factor that exerts a cardiovascular protective effect and regulates BP.[41] Oxidative stress has been implicated as a causal factor in diseases such as hypertension and atherosclerosis.[42,43] Martinez-Villaluenga reported that *Enterococcus faecium*-fermented soy milk inhibited ACE, had antioxidant activity, and had an antihypertensive effect.[10] The regulation of BP involves the RAS, which involves ACE; therefore, inhibiting ACE is a key target for regulating BP. Specifically, ACE inhibitors can lower BP by reducing the production of AngII and inhibiting the degradation of bradykinin.[44] This study indicated that SBP and DBP were suppressed following treatment with the CUG. A previous study indicated that the administration of LAB or related fermentation products suppressed SBP and DBP by 4.4−16 and 3.4−11 mmHg, respectively,[45−47] which was similar to the effect exerted by CUG in this study. In this work, we confirmed that the mechanism by which CUG reduces BP is by inhibiting ACE activity and suppressing the downstream vasoactive peptide AngII and the hormone aldosterone. Additionally, in the case of ACE inhibitors, blockade of the RAS leads to a feedback increase in renin activity,[36] and angiotensin I (AngI) can be observed; however, the renin activity of SHRs administered with CUG was suppressed. Moreover, the results revealed that renin activity was inhibited by CUG in vitro. It has been suggested that the CUG derivative derived from TWK10-fermented soy milk can be effective in lowering BP as either renin or ACE inhibitors and is an important novel finding as a functional foods.

In conclusion, we identified that a combination of uracil and glycerol was one of the ACE inhibitory functional ingredients in TWK10-fermented soy milk and have demonstrated that it works as a renin inhibitor, an ACE inhibitor, and a promotor of NO production and have shown that it is as effective as an existing drug at lowering BP in vivo for the first time. We are currently in the process of confirming another ACE inhibitor, F2-3B. Compared with peptides or other organic compounds described previously, CUG has significant BP-lowering effects, suggesting that they could be novel and potent natural ingredients in antihypertensive functional foods.[48−50]

■ ASSOCIATED CONTENT

Supporting Information

The Supporting Information is available free of charge on the ACS Publications website at DOI: 10.1021/acs.jafc.5b01649.

Supplemental figures 1−4 (PDF)

■ AUTHOR INFORMATION

Corresponding Author

*(T.-Y. Tsai) Phone: +886-2-2905-2539. E-mail: tytsai@mail.fju.edu.tw. Mail: No. 510 Zhongzheng Road, Xinzhuang District, 24205 New Taipei City, Taiwan.

Author Contributions

‖Y.-Y. Liu and S.-Y. Zeng made equal contributions to this paper.

Funding

Financial support (MOST 102-2221-E-030-006 and MOST 103-2221-E-030-013) from the Ministry of Science and Technology of Taiwan is gratefully acknowledged.

Notes

The authors declare no competing financial interest.

■ ACKNOWLEDGMENTS

We express our gratitude to James Chang, Chuan Gui Bio-Organic Co., who kindly provided soybean (*Glycine max* (L.) Merrill BB50).

■ ABBREVIATIONS USED

ACE, angiotensin-converting enzyme; AngI, angiotensin I; BP, blood pressure; CaM, calmodulin; CAP, captopril; CUG, combined uracil and glycerol; DBP, diastolic blood pressure; EA, ethyl acetate; EIA, enzyme immunoassay; eNOS, endothelial nitric oxide synthase; GABA, γ-aminobutyric acid; HHL, hippuryl-L-histidyl-L-leucine; LAB, lactic acid bacteria; MDA, malondialdehyde; MeOH, methanol; MRS, de Man, Rogosa, and Sharpe; NO, nitric oxide; RAS, renin−angiotensin system; SBP, systolic blood pressure; SHR, spontaneous hypertensive rat; TBARS, thiobarbituric acid reactive substance; WKY, Wistar Kyoto

■ REFERENCES

(1) Tsai, Y.-T.; Cheng, P.-C.; Pan, T.-M. Immunomodulating activity of *Lactobacillus paracasei* subsp. *paracasei* NTU 101 in enterohemorrhagic *Escherichia coli* O157H7-infected mice. *J. Agric. Food Chem.* **2010**, *58*, 11265−11272.

(2) Chang, C.-J.; Dai, R.-Y.; Leu, Y.-L.; Tsai, T.-Y. Effects of the melanogenic inhibitor, uracil, derived from *Lactobacillus plantarum* TWK10-fermented soy milk on anti-melanogenesis in B16F0 mouse melanoma cells. *J. Funct. Foods* **2015**, *17*, 314−327.

(3) Chen, Y.-M.; Shih, T.-W.; Chiu, C. P.; Pan, T.-M.; Tsai, T.-Y. Effects of lactic acid bacteria-fermented soy milk on melanogenesis in B16F0 melanocytes. *J. Funct. Foods* **2013**, *5*, 395−405.

(4) Chiu, C.-H.; Lu, T.-Y.; Tseng, Y.-Y.; Pan, T.-M. The effects of *Lactobacillus*-fermented milk on lipid metabolism in hamsters fed on high-cholesterol diet. *Appl. Microbiol. Biotechnol.* **2006**, *71*, 238−245.

(5) Lee, B.-H.; Lo, Y.-H.; Pan, T.-M. Anti-obesity activity of *Lactobacillus* fermented soy milk products. *J. Funct. Foods* **2013**, *5*, 905−913.

(6) Tsai, Y.-T.; Cheng, P.-C.; Pan, T.-M. The immunomodulatory effects of lactic acid bacteria for improving immune functions and benefits. *Appl. Microbiol. Biotechnol.* **2012**, *96*, 853−862.

(7) Tsai, T.-Y.; Chu, L.-H.; Lee, C.-L.; Pan, T.-M. Atherosclerosis-preventing activity of lactic acid bacteria-fermented milk-soymilk supplemented with *Momordica charantia*. *J. Agric. Food Chem.* **2009**, *57*, 2065−2071.

(8) Lavie, C. J.; Milani, R. V.; O'Keefe, J. H. Dyslipidemia intervention in metabolic syndrome: emphasis on improving lipids and clinical event reduction. *Am. J. Med. Sci.* **2011**, *341*, 388−393.

(9) Hernandez-Ledesma, B.; Amigo, L.; Ramos, M.; Recio, I. Angiotensin converting enzyme inhibitory activity in commercial fermented products. Formation of peptides under simulated gastrointestinal digestion. *J. Agric. Food Chem.* **2004**, *52*, 1504−1510.

(10) Martinez-Villaluenga, C.; Torino, M. I.; Martin, V.; Arroyo, R.; Garcia-Mora, P.; Estrella Pedrola, I.; Vidal-Valverde, C.; Rodriguez, J. M.; Frias, J. Multifunctional properties of soy milk fermented by *Enterococcus faecium* strains isolated from raw soy milk. *J. Agric. Food Chem.* **2012**, *60*, 10235−41024.

(11) Yeo, S. K.; Liong, M. T. Angiotensin I-converting enzyme inhibitory activity and bioconversion of isoflavones by probiotics in soymilk supplemented with prebiotics. *Int. J. Food Sci. Nutr.* **2010**, *61*, 161−181.

DOI: 10.1021/acs.jafc.5b01649
J. Agric. Food Chem. 2015, 63, 7333−7342

(12) Fung, W. Y.; Woo, Y. P.; Liong, M. T. Optimization of growth of *Lactobacillus acidophilus* FTCC 0291 and evaluation of growth characteristics in soy whey medium: a response surface methodology approach. *J. Agric. Food Chem.* **2008**, *56*, 7910−7918.
(13) Cheng, C.-P.; Tsai, S.-W.; Chiu, C. P.; Pan, T.-M.; Tsai, T.-Y. The effect of probiotic-fermented soy milk on enhancing the NO-mediated vascular relaxation factors. *J. Sci. Food Agric.* **2013**, *93*, 1219−1225.
(14) Cushman, D. W.; Cheung, H. S. Spectrophotometric assay and properties of the angiotensin-converting enzyme of rabbit lung. *Biochem. Pharmacol.* **1971**, *20*, 1637−1648.
(15) Diana, M.; Quílez, J.; Rafecas, M. Gamma-aminobutyric acid as a bioactive compound in foods: a review. *J. Funct. Foods* **2014**, *10*, 407−420.
(16) Boyd, E. *The Growth of the Surface Area of Human Body*; University of Minnesota Press: Minneapolis, MN, USA, 1935.
(17) Yagi, K. A simple fluorometric assay for lipoperoxide in blood plasma. *Biochem. Med.* **1976**, *15*, 212−216.
(18) Feingold, D. S.; Neufeld, E. F.; Hassid, W. Z. Enzymic synthesis of uridine diphosphate glucuronic acid and uridine diphosphate galacturonic acid with extracts from *Phaseolus aureus* seedlings. *Arch. Biochem. Biophys.* **1958**, *78*, 401−406.
(19) Sakai, T.; Tochikura, T.; Ogata, K. Metabolisms of nucleosides in bacteria. Part II. Studies on nucleoside-*N*-ribosyl group transfer reaction in bacteria. *Agric. Biol. Chem.* **1965**, *29*, 742−750.
(20) Hidalgo, A.; Pompei, C.; Galli, A.; Cazzola, S. Uracil as an index of lactic acid bacteria contamination of tomato products. *J. Agric. Food Chem.* **2005**, *53*, 349−355.
(21) Schanker, L. S.; Tocco, D. J. Active transport of some pyrimidines across the rat intestinal epithelium. *J. Pharmacol. Exp. Ther.* **1960**, *128*, 115−121.
(22) Deporte, R.; Amiand, M.; Moreau, A.; Charbonnel, C.; Campion, L. High-performance liquid chromatographic assay with UV detection for measurement of dihydrouracil/uracil ratio in plasma. *J. Chromatogr. B: Anal. Technol. Biomed. Life Sci.* **2006**, *834*, 170−177.
(23) MacDonald, J. T.; Uden, D. L. Intravenous glycerol and mannitol therapy in children with intracranial hypertension. *Neurology* **1982**, *32*, 437−440.
(24) Zornow, M. H.; Oh, Y. S.; Scheller, M. S. A comparison of the cerebral and haemodynamic effects of mannitol and hypertonic saline in an animal model of brain injury. *Acta. Neurochir. Suppl.* **1990**, *51*, 324−325.
(25) Wald, S. L.; McLaurin, R. L. Oral glycerol for the treatment of traumatic intracranial hypertension. *J. Neurosurg.* **1982**, *56*, 323−31.
(26) Jakubczyk, A.; Baraniak, B. Angiotensin I converting enzyme inhibitory peptides obtained after *in vitro* hydrolysis of pea (*Pisum sativum* var. *Bajka*) globulins. *BioMed Res. Int.* **2014**, *2014*, 438459.
(27) He, R.; Malomo, S. A.; Girgih, A. T.; Ju, X.; Aluko, R. E. Glycinyl-histidinyl-serine (GHS), a novel rapeseed protein-derived peptide has blood pressure-lowering effect in spontaneously hypertensive rats. *J. Agric. Food Chem.* **2013**, *61*, 8396−8402.
(28) Pedroche, J.; Yust, M. M.; Giron-Calle, J.; Alaiz, M.; Millan, F.; Vioque, J. Utilisation of chickpea protein isolates for production of peptides with angiotensin I-converting enzyme (ACE)-inhibitory activity. *J. Sci. Food Agric.* **2002**, *82*, 960−965.
(29) Sato, M.; Hosokawa, T.; Yamaguchi, T.; Nakano, T.; Muramoto, K.; Kahara, T.; Funayama, K.; Kobayashi, A.; Nakano, T. Angiotensin I-converting enzyme inhibitory peptides derived from wakame (*Undaria pinnatifida*) and their antihypertensive effect in spontaneously hypertensive rats. *J. Agric. Food Chem.* **2002**, *50*, 6245−6252.
(30) Behera, B. C.; Mahadik, N.; Morey, M. Antioxidative and cardiovascular-protective activities of metabolite usnic acid and psoromic acid produced by lichen species *Usnea complanata* under submerged fermentation. *Pharm. Biol.* **2012**, *50*, 968−979.
(31) Dong, J.; Xu, X.; Liang, Y.; Head, R.; Bennett, L. Inhibition of angiotensin converting enzyme (ACE) activity by polyphenols from tea (*Camellia sinensis*) and links to processing method. *Food Funct.* **2011**, *2*, 310−319.
(32) Moraes-Teixeira, J. A.; Felix, A.; Fernandes-Santos, C.; Moura, A. S.; Mandarim-de-Lacerda, C. A.; de Carvalho, J. J. Exercise training enhances elastin, fibrillin and nitric oxide in the aorta wall of spontaneously hypertensive rats. *Exp. Mol. Pathol.* **2010**, *89*, 351−357.
(33) Wolinsky, H. Long-term effects of hypertension on the rat aortic wall and their relation to concurrent aging changes. Morphological and chemical studies. *Circ. Res.* **1972**, *30*, 301−309.
(34) Coates, D. The angiotensin converting enzyme (ACE). *Int. J. Biochem. Cell Biol.* **2003**, *35*, 769−773.
(35) Cole, D. C.; Stock, J. R.; Lennox, W. J.; Bernotas, R. C.; Ellingboe, J. W.; Boikess, S.; Coupet, J.; Smith, D. L.; Leung, L.; Zhang, G. M.; Feng, X.; Kelly, M. F.; Galante, R.; Huang, P.; Dawson, L. A.; Marquis, K.; Rosenzweig-Lipson, S.; Beyer, C. E.; Schechter, L. E. Discovery of N1-(6-chloroimidazo[2,1-b][1,3]thiazole-5-sulfonyl)-tryptamine as a potent, selective, and orally active 5-HT(6) receptor agonist. *J. Med. Chem.* **2007**, *50*, 5535−5538.
(36) Nussberger, J.; Wuerzner, G.; Jensen, C.; Brunner, H. R. Angiotensin II suppression in humans by the orally active renin inhibitor Aliskiren (SPP100): comparison with enalapril. *Hypertension* **2002**, *39*, E1−E8.
(37) Vera, R.; Sanchez, M.; Galisteo, M.; Villar, I. C.; Jimenez, R.; Zarzuelo, A.; Perez-Vizcaino, F.; Duarte, J. Chronic administration of genistein improves endothelial dysfunction in spontaneously hypertensive rats: involvement of eNOS, caveolin and calmodulin expression and NADPH oxidase activity. *Clin. Sci.* **2007**, *112*, 183−191.
(38) Alonso, D.; Radomski, M. W. Nitric oxide, platelet function, myocardial infarction and reperfusion therapies. *Heart Failure Rev.* **2003**, *8*, 47−54.
(39) Kotamraju, S.; Hogg, N.; Joseph, J.; Keefer, L. K.; Kalyanaraman, B. Inhibition of oxidized low-density lipoprotein-induced apoptosis in endothelial cells by nitric oxide. Peroxyl radical scavenging as an antiapoptotic mechanism. *J. Biol. Chem.* **2001**, *276*, 17316−17323.
(40) Shin, W. S.; Hong, Y. H.; Peng, H. B.; De Caterina, R.; Libby, P.; Liao, J. K. Nitric oxide attenuates vascular smooth muscle cell activation by interferon-gamma. The role of constitutive NF-kappa B activity. *J. Biol. Chem.* **1996**, *271*, 11317−11324.
(41) Zhou, M. S.; Schulman, I. H.; Raij, L. Nitric oxide, angiotensin II, and hypertension. *Semin. Nephrol.* **2004**, *24*, 366−378.
(42) de Champlain, J.; Wu, R.; Girouard, H.; Karas, M.; El Midaoui, A.; Laplante, M. A.; Wu, L. Oxidative stress in hypertension. *Clin. Exp. Hypertens.* **2004**, *26*, 593−601.
(43) Lusis, A. J. Atherosclerosis. *Nature* **2000**, *407*, 233−241.
(44) Udenigwe, C. C.; Mohan, A. Mechanisms of food protein-derived antihypertensive peptides other than ACE inhibition. *J. Funct. Foods* **2014**, *8*, 45−52.
(45) Agerholm-Larsen, L.; Raben, A.; Haulrik, N.; Hansen, A. S.; Manders, M.; Astrup, A. Effect of 8 week intake of probiotic milk products on risk factors for cardiovascular diseases. *Eur. J. Clin. Nutr.* **2000**, *54*, 288−297.
(46) Seppo, L.; Jauhiainen, T.; Poussa, T.; Korpela, R. A fermented milk high in bioactive peptides has a blood pressure-lowering effect in hypertensive subjects. *Am. J. Clin. Nutr.* **2003**, *77*, 326−330.
(47) Tuomilehto, J.; Lindstrom, J.; Hyyrynen, J.; Korpela, R.; Karhunen, M. L.; Mikkola, L.; Jauhiainen, T.; Seppo, L.; Nissinen, A. Effect of ingesting sour milk fermented using *Lactobacillus helveticus* bacteria producing tripeptides on blood pressure in subjects with mild hypertension. *J. Hum. Hypertens.* **2004**, *18*, 795−802.
(48) Chen, J.; Liu, S.; Ye, R.; Cai, G.; Ji, B.; Wu, Y. Angiotensin-I converting enzyme (ACE) inhibitory tripeptides from rice protein hydrolysate: purification and characterization. *J. Funct. Foods* **2013**, *5*, 1684−1692.
(49) Li, F.; Ohnishi-Kameyama, M.; Takahashi, Y.; Yamaki, K. Angiotensin I-converting enzyme inhibitory activities of Chinese fermented soypaste and estimation of the inhibitory substances. *J. Funct. Foods* **2013**, *5*, 1991−1995.
(50) Ngo, D.-H.; Kang, K.-H.; Jung, W.-K.; Byun, H.-G.; Kim, S.-K. Protective effects of peptides from skate (*Okamejei kenojei*) skin gelatin against endothelial dysfunction. *J. Funct. Foods* **2014**, *10*, 243−251.

DOI: 10.1021/acs.jafc.5b01649
J. Agric. Food Chem. 2015, 63, 7333−7342

summarized that the natural compounds may be potential to improve inflammasome-related diseases, including renal injury, diabetes, infection, and liver diseases.[15] However, it remains unclear whether the phenolic compounds exert the inhibitory effects on MSU-induced inflammation. We examined and selected the potential agents in several phenolic compounds, and this study aimed to investigate the effects and underlying mechanisms of these candidate molecules on MSU-induced inflammation and inflammasome activation in vivo and in vitro.

MATERIALS AND METHODS

Chemicals. Cinnamic acid, *o*-coumaric acid, *m*-coumaric acid, ferulic acid, *p*-hydroxybenzoic acid, vanillic acid, syringic acid, protocatechuic acid, gentisic acid, gallic acid, catechin, monosodium urate (MSU), 2′,7′-dichlorofluorescin diacetate (DCFH-DA), xanthine oxidase, phorbol 12-myristate 13-acetate (PMA), 4-(2-hydroxyethyl)-1-piperazineethanesulfonic acid (HEPES), colchicine, 3-(4,5-dimethylthiazol-2-yl)-2,5-diphenyltetrazolium bromide (MTT), sulforhodamine B (SRB), β-mercaptoethanol, and nitro blue tetrazolium (NBT) were purchased from Sigma-Aldrich (St. Louis, MO, USA). The purity of the phenolic compounds was over 95%. RPMI-1640 medium and fetal bovine serum (FBS) were obtained from Gibco BRL (Grand Island, NY, USA). Penicillin−streptomycin and sodium pyruvate solution were obtained from Hyclone (Logan, UT, USA). Antibodies against caspase-1, β-actin, Bcl-2, DJ-1, and TRX were obtained from Cell Signaling Technology (Beverly, MA, USA). NLRP3 antibody was purchased from Abgent (San Diego, CA, USA). Dihydroethidium (DHE), MitoSOX red mitochondrial superoxide indicator, the TXNIP antibody, and Fluo3-AM were purchased from Life Technologies (Carlsbad, CA, USA). The JC-1 mitochondrial transmembrane potential assay kit was obtained from Cayman Chemical Co. (Ann Arbor, MI, USA).

Scavenging Free Radical Assay. The free radical scavenging assay was performed according to the methods of Orallo et al.[16] Briefly, free radical scavenging was measured as the absorbance at 570 nm using a FLUOstar Omega spectrophotometer (BMG Labtechnologies, Germany) after incubation with 200 μL of working solution (50 mM phosphate buffer, pH 7.4, 100 μM EDTA-2Na, 100 μM xanthine, and 100 μM NBT), 25 μL sample solution (5, 10, or 25 μM), and 25 μL xanthine oxidase (0.066 U) for 10 min. Allopurinol was used as a positive control.

Animal Treatment. The animal experiments were conducted in accordance with the guidelines of the National Institutes of Health and approved by the Institutional Animal Care and Use Committee (IACUC) of National Chung Hsing University (no. 101-81). Male C57BL/6 mice were purchased from the National Laboratory Animal Center (Taipei, Taiwan). The animals were provided a chow diet and water ad libitum under conditions of 22−24 °C, 40−70% relative humidity, and a 12 h light−dark cycle. Acute gout inflammation was induced by intraperitoneal injection with 3 mg of MSU in 0.5 mL of phosphate-buffered saline (PBS), and the mice were subcutaneously treated with or without phenolic compounds at 100 mg/kg body weight (BW) (n = 5). After 6 h, all mice were sacrificed using carbon dioxide (CO_2), and the mice were intraperitoneally injected with 4 mL of PBS.[17] The peritoneal fluid was then collected, and the volume of peritoneal fluid was about 2.5−3.0 mL from each mouse.

Identification of MSU Crystal-Elicited Neutrophils. The collected peritoneal exudate cells were washed and resuspended in PBS. The cells were stained with fluorescent antibodies against the specific surface markers Ly-6G (eBioscience, San Diego, CA, USA) and 7/4 (AbD Serotec, Raleigh, NC, USA) for 20 min at 37 °C in the dark, and the cell populations were sorted using a FACScan flow cytometer (Becton-Dickinson, San Jose, CA).

Cell Culture. The THP-1 cell line was purchased from the Bioresource Collection and Research Center (BCRC 60430, Food Industry Research and Development Institute, Hsinchu, Taiwan) and cultured in RPMI-1640 media with 10% (v/v) FBS, 100 μg/mL streptomycin, 100 U/mL penicillin, 10 mM HEPES, 1 mM sodium pyruvate, 1.5 g/L sodium bicarbonate, and 50 μM β-mercaptoethanol at 37 °C in a humidified atmosphere of 5% CO_2. THP-1 cells were treated with 100 nM PMA for 3 h to initiate the NF-κB pathway. The cells were subsequently treated with 75 μg/mL MSU crystals in the presence or absence of 20 μM phenolic compounds for 6 h as our previous methods.[18]

Cell Viability Assay. Cell viability was examined using MTT and sulforhodamine B (SRB) assays. For the MTT assay, the cells were cultured in 0.5 mg/mL MTT for 2 h at 37 °C, and formazan blue formation in cells was dissolved using dimethyl sulfoxide (DMSO). The optical density (OD) was detected at 570 nm using a FLUOstar Omega spectrophotometer. For the SRB assay, the cells were fixed in cold 10% trichloroacetic acid at 4 °C. A solution of SRB in 1% acetic acid was added to each well and incubated for 30 min. Cell-bound SRB was dissolved in 10 mM Tris base solution, and the absorbance was measured at 510 nm using a FLUOstar Omega spectrophotometer.

Cytokine ELISA Assay. Human IL-1β, mouse IL-1β, and mouse IL-6 cytokine secretions were measured using the ELISA kits (eBioscience, San Diego, CA, USA) according to the manufacturer's instructions.

Immunoprecipitation Assay. Immunoprecipitation was performed using the Catch and Release Reversible Immunoprecipitation System (Millipore, Billerica, MA, USA) according to the manufacturer's instructions. Treated THP-1 cells were washed with PBS and resuspended in lysis buffer containing 1× protease inhibitor cocktail (Sigma-Aldrich, St. Louis, MO, USA). Each cell lysate (500 μg) was incubated with 4 μg of anti-TXNIP antibody and 10 μL of antibody capture affinity ligand for 30 min at room temperature. The immunoprecipitated proteins were washed twice in 1× wash buffer, and the bound proteins were eluted in 70 μL of elution buffer.

Detection of Superoxide Anion and MtROS Production. The levels of superoxide anion and MtROS production were determined after treatment with 8 μM DHE and 2.5 μM MitoSOX red mitochondrial superoxide indicator, respectively, for 20 min at 37 °C using the FL-2 channel (excitation 488 nm and emission 585 nm) of a FACScan flow cytometer.

Detection of Mitochondrial Transmembrane Potential. The mitochondrial transmembrane potential was determined using the Cayman JC-1 assay kit according to the manufacturer's protocol. The mitochondrial transmembrane potential was detected using the FL-2 channel of a FACScan flow cytometer.

Detection of Intracellular Calcium Levels. Intracellular calcium levels were determined using Fluo3-AM stain. The cells were treated with 5 μM Fluo3-AM for 40 min, and the fluorescent intensity was analyzed at 485/530 nm using a FLUOstar Galaxy fluorescence plate reader (BMG Labtechnologies, Offenburg, Germany).

Western Blot. The protein lysates were boiled in 4× protein loading dye [8% SDS, 40% glycerol, 200 mM Tris-HCl (pH 6.8), 0.04% Coomassie blue R-250, and 10% 2-mercaptoethanol], and the samples were subjected to SDS-polyacrylamide gel electrophoresis. The proteins were transferred to nitrocellulose membrane (Sartorius Stedim Biotech, Aubagne Cedex, France) and incubated with specific primary antibodies at 4 °C. The membranes were washed three times with Tris-buffered saline containing 0.05% Tween-20 (TBST) and incubated with horseradish peroxide-conjugated secondary antibody before analysis using a chemiluminescence ECL detection system (Millipore, Billerica, MA, USA). The levels of protein were normalized to the β-actin or TXNIP signals and quantitated using Vision Works LS 6.3.3 (UVP, Cambridge, UK).

Statistical Analysis. All results are expressed as the means ± SD from at least three independent experiments. ANOVA was used to evaluate the differences between multiple groups. Significant differences ($p < 0.05$) between the means were determined using Duncan's multiple range test or Student's t-test. All statistical analyses were performed with SPSS 12.0 software.

RESULTS

Gallic Acid and Catechin Exhibited Potent Free Radical Scavenging. Previous studies have suggested that

DOI: 10.1021/acs.jafc.5b02605
J. Agric. Food Chem. 2015, 63, 7343−7352

redox molecules are major signals for MSU-induced inflammation.[8−10] This study investigated potential inflammation inhibitors, including cinnamic acid, *o*-coumaric acid, *m*-coumaric acid, ferulic acid, *p*-hydroxybenzoic acid, vanillic acid, syringic acid, protocatechuic acid, gentisic acid, gallic acid, and catechin. The results showed that gallic acid and catechin exhibited higher free radical scavenging activity than other phenolic compounds (Figure 1). Therefore, the effects of gallic acid and catechin on MSU-induced inflammation were further explored using MSU-challenged models in vivo and in vitro.

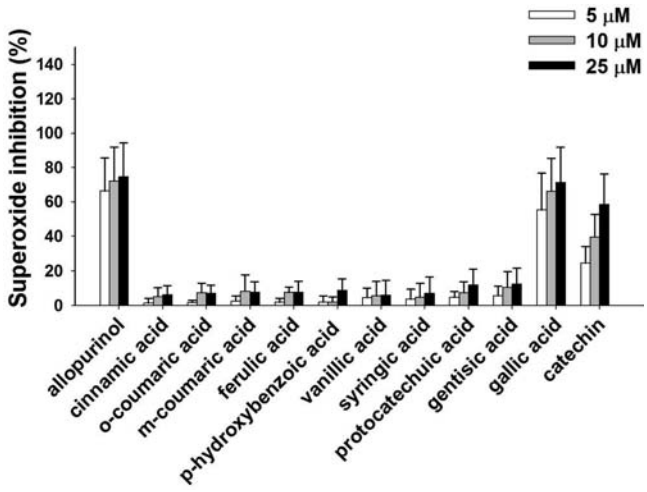

Figure 1. Effects of phenolic compounds on free radical scavenging activity. The values are presented as the means ± SD (n = 3).

Effects of Gallic Acid and Catechin on Murine Peritoneal Inflammation in C57BL/6 Mice. Intraperitoneal injection of MSU (3 mg) significantly (p < 0.05) increased IL-1β (Figure 2A) and IL-6 (Figure 2B) secretion compared with the control group in C57BL/6 mice. The subcutaneous administration of gallic acid (100 mg/kg BW) or catechin (100 mg/kg BW) significantly (p < 0.05) attenuated MSU-induced IL-1β and IL-6 secretions in the murine peritoneal fluid. The positive control colchicine (1 mg/kg BW) also showed the inhibitory effects on IL-1β and IL-6 secretions. MSU also significantly stimulated the population of Ly-6G$^+$ neutrophils (Figure 2C), ROS level (Figure 2D), and superoxide anion production (Figure 2E). However, gallic acid and catechin did not affect the levels of MSU-induced Ly-6G$^+$ neutrophils, ROS, and superoxide anion (Figure 2C−E).

Effects of Gallic Acid and Catechin on the IL-1β Activation in THP-1 Cells. The inhibitory mechanisms of gallic acid and catechin on MSU-induced IL-1β secretion were investigated in vitro. THP-1 cells were cultured in MSU (75 μg/mL) with gallic acid (20 μM) or catechin (20 μM) for 6 h, and THP-1 cells showed no cytotoxicity (cell viability >95%) according to MTT (Figure 3A) and SRB (Figure 3B) assays. Pro-inflammatory cytokine IL-1β secretion was significantly (p < 0.05) induced by MSU compared with control, but MSU-induced IL-1β secretion was significantly (p < 0.05) suppressed by catechin treatment; however, gallic acid had no significant effect on MSU-induced IL-1β secretion (p > 0.05) (Figure 3C).

IL-1β secretion was modulated through two signaling pathways. NF-κB pathway provides pro-IL-1β, and NLRP3 inflammasome promotes the release of IL-1β from pro-IL-1β.[7,8] As shown in Supporting Information Figure S1, MSU treatment showed no significant effect on NF-κB-mediated IL-1β mRNA expression compared with control group, but gallic acid and catechin significantly attenuated IL-1β mRNA expression (Figure S1A). The levels of nuclear NF-κB were down-regulated following treatment with MSU, gallic acid, and catechin (Figure S1B). The levels of inhibitor of κ Bα (IκBα) phosphorylation (Figure S1C) and extracellular signal-regulated kinases (ERK) phosphorylation (Figure S1D) were down-regulated by gallic acid and catechin.

This study further elucidated the effects of gallic acid and catechin on MSU-induced NLRP3 activation. MSU increased the conjugation of TXNIP and NLRP3 complex, but this activity was attenuated from 2.0-fold to 1.3-fold following catechin treatment (Figure 3D). However, NLRP3 and pro-caspase-1 expressions in the cell lysates were not altered following treatments with MSU, gallic acid, and catechin (Figure 3E,F), indicating that catechin inhibited NLRP3 inflammasome activation without reducing NLRP3 and pro-caspase-1 protein levels.

Effects of Gallic Acid and Catechin on the Oxidative Stress in THP-1 Cells. NLRP3 inflammasome activation is initiated through frustrated phagocytosis and lysosomal disruption.[19] The effects of gallic acid and catechin on phagocytosis and lysosomal function were studied, and the results showed that gallic acid and catechin did not decrease phagocytosis index and lysosomal disruption (Supporting Information Figure S2).

To obtain further evidence of the inhibitory mechanisms of catechin on NLRP3 inflammasome activation, we investigated the status of oxidative stress. THP-1 cells treated with MSU significantly increased superoxide anion and ROS productions. Gallic acid and catechin had no significant inhibition on MSU-induced superoxide anion (p > 0.05), but both compounds significantly (p < 0.05) suppressed MSU-triggered ROS generation (Supporting Information Figure S3). In addition, the level of MtROS was significantly (p < 0.05) increased in MSU-challenged THP-1 cells, but MSU-induced MtROS level was significantly (p < 0.05) ameliorated by catechin treatment. However, gallic acid did not affect MSU-triggered MtROS levels (Figure 4A,B).

Previous study indicates that TRX is the redox protein modulating oxidative stress and NLRP3 inflammasome activation,[9,11] and TRX is modulated by DJ-1.[20] The results showed that the expressions of TRX and its modulating protein DJ-1 were up-regulated by catechin but not gallic acid (Figure 4C,D). Glutathione (GSH) level, a kind of redox protein, was significantly decreased by MSU treatment, but MSU-induced consumption of GSH levels was not affected by gallic acid and catechin treatments (Supporting Information Figure S4).

Effects of Gallic Acid and Catechin on the Calcium Levels in THP-1 Cells. Calcium accumulation could lead to MtROS generation and NLRP3 inflammasome activation.[21,22] This study tested calcium level after THP-1 cells were treated with MSU for 1, 3, or 6 h. After treatment with MSU, the calcium levels were significantly (p < 0.05) elevated at 3 and 6 h compared with control (Figure 5A,B). Therefore, THP-1 cells were cultured in MSU with gallic acid or catechin for 3 h. MSU-induced calcium levels were significantly (p < 0.05) ameliorated by catechin compared with MSU (Figure 5C,D); however, gallic acid had no significant effect on MSU-triggered calcium levels (p > 0.05).

Effects of Gallic Acid and Catechin on Mitochondrial Damage in THP-1 Cells. Bcl-2 overexpression significantly

DOI: 10.1021/acs.jafc.5b02605
J. Agric. Food Chem. 2015, 63, 7343−7352

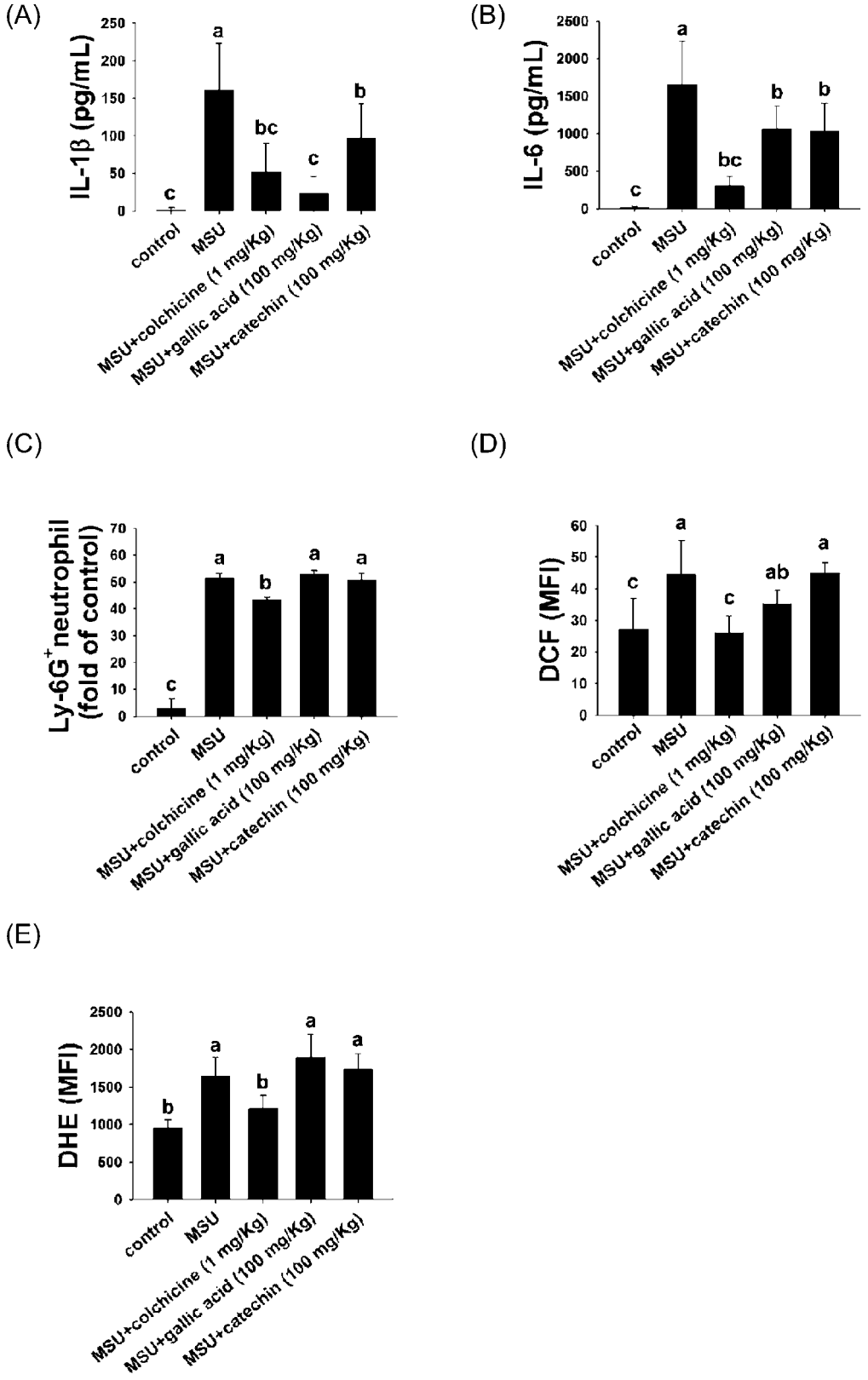

Figure 2. Effects of gallic acid and catechin on MSU-induced murine peritoneal inflammation. C57BL/6 mice were intraperitoneally injected with 3 mg of MSU, followed by subcutaneous injection of gallic acid (100 mg/kg BW) or catechin (100 mg/kg BW). The collected peritoneal fluid was assayed for (A) IL-1β secretion, (B) IL-6 secretion, (C) Ly-6G$^+$ neutrophil, (D) ROS, and (E) superoxide anion production. Values are presented as the mean ± SD (n = 5). The values denoted by the different letters show significantly at $p < 0.05$ as determined using Duncan's multiple range test. MFI, mean fluorescent intensity.

impaired calcium influx and IL-1β secretion.[10,23] The result revealed that Bcl-2 expression was significantly elevated following catechin treatment (Figure 6A). MtROS accumulation and increased calcium levels could lead to mitochondrial

DOI: 10.1021/acs.jafc.5b02605
J. Agric. Food Chem. 2015, 63, 7343−7352

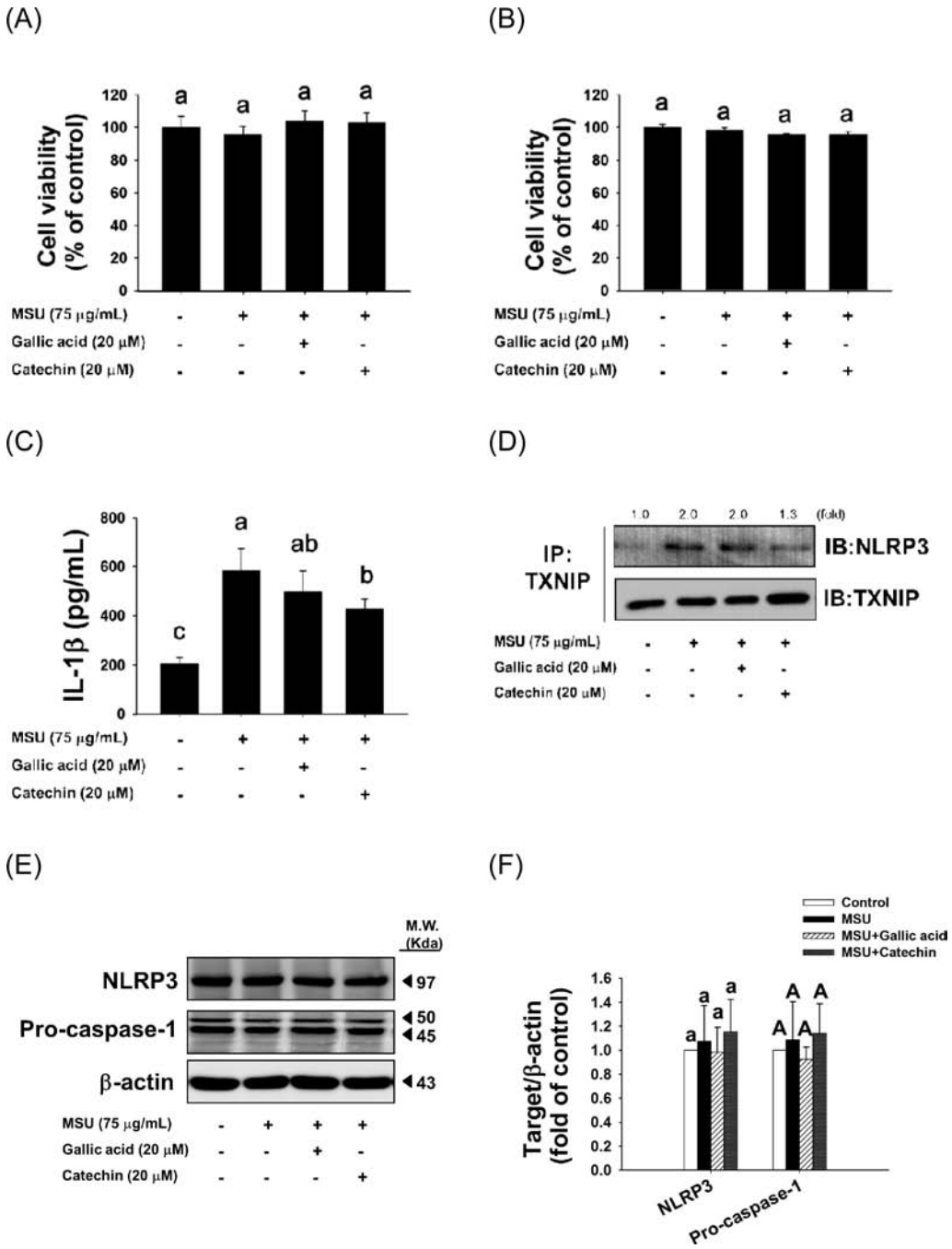

Figure 3. Effects of gallic acid and catechin on cell viability using (A) MTT and (B) SRB assay, (C) IL-1β secretion, (D) TXNIP-NLRP3 conjugation, and (E) NLRP3 and pro-caspase-1 protein expression in MSU-challenged THP-1 cells. Cells were cultured with 75 μg/mL MSU in the presence or absence of 20 μM gallic acid or catechin for 6 h. (F) The relative protein expression levels of NLRP3 and pro-caspase-1 were compared based on fold changes in the levels of each protein with respect to the levels of β-actin. The values are presented as the mean ± SD (n = 3). The values denoted by the different letters show significantly at $p < 0.05$ as determined using Duncan's multiple range test. IP, immunoprecipitation. IB, immunoblotting.

damage.[10,23] To elucidate the level of mitochondrial damage in MSU-treated cells, this study detected the mitochondrial transmembrane potential using the fluorescent probe, JC-1. The level of JC-1 was significantly ($p < 0.05$) reduced by MSU treatment (64%), and this reduction in JC-1 was significantly ($p < 0.05$) reversed through gallic acid (90%) and catechin (84%) in THP-1 cells (Figure 6B,C).

DISCUSSION

Uric acid is a purine metabolite derived from the conversion of xanthine and hypoxanthine.[1] Accumulated uric acid crystallizes into MSU and precipitates in the joint cavity.[1] MSU crystals trigger arthritic inflammation, known as gout, and neutrophil infiltration and IL-1β secretion are the primary clinical manifestations of early MSU attack.[3−5] This study selected two compounds, gallic acid and catechin, to examine their inhibitory effects on MSU-induced inflammation. Consistent

DOI: 10.1021/acs.jafc.5b02605
J. Agric. Food Chem. 2015, 63, 7343−7352

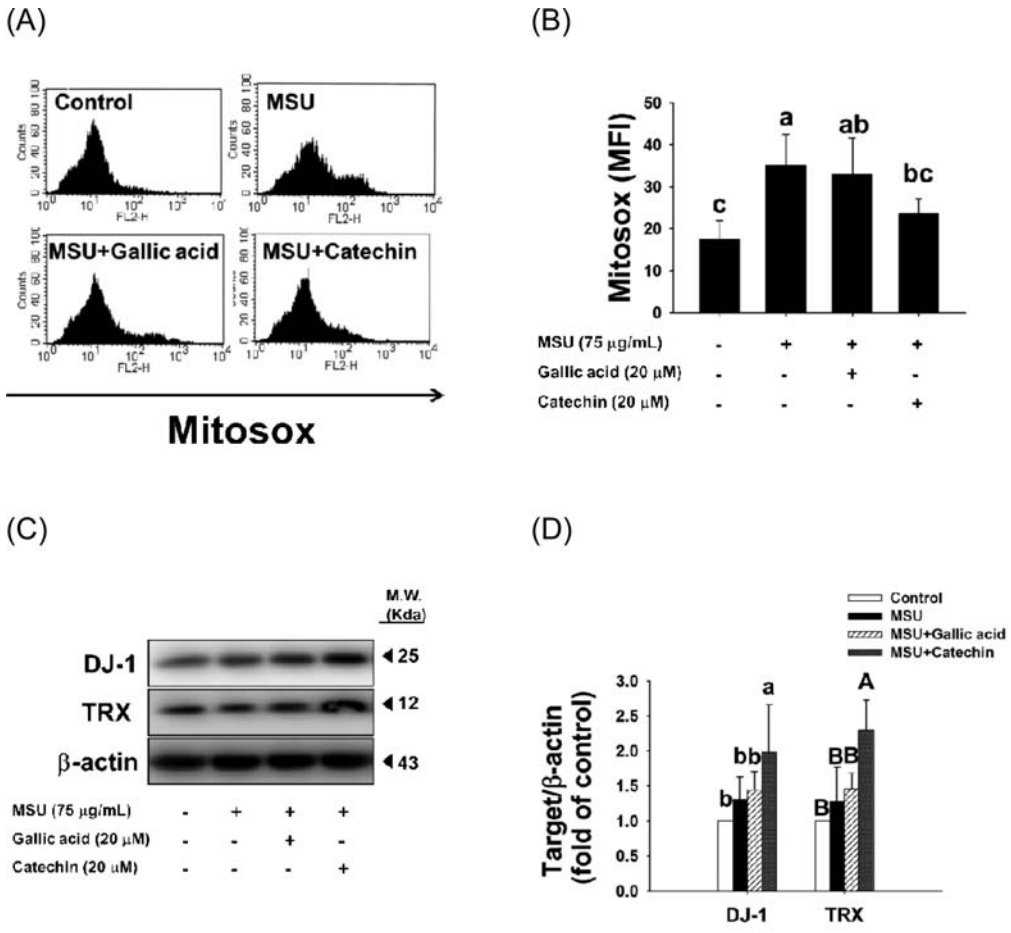

Figure 4. Effects of gallic acid and catechin on (A) MtROS production, (B) quantitative level of MtROS, and (C) DJ-1 and TRX protein level in MSU-challenged THP-1 cells. THP-1 cells were cultured with 75 μg/mL MSU in the presence or absence of 20 μM gallic acid or catechin for 6 h. (D) The relative protein expressions of DJ-1 and TRX were compared based on fold changes in the levels of each protein with respect to the levels of β-actin. The values are presented as the means ± SD (n = 3). The values denoted with the different letters show significantly at $p < 0.05$.

with the results of previous studies,[24−26] we observed that gallic acid and catechin acted as highly effective antioxidants (Figure 1). In animal study, the levels of ROS and superoxide anion were not altered by gallic acid and catechin (Figure 2D,E) because ROS and superoxide anion production were observed to accompany with neutrophil infiltration.[27] In addition, these two compounds suppressed pro-inflammatory cytokines but not neutrophil infiltration, suggesting that the inhibitory effects of gallic acid and catechin on pro-inflammatory cytokine release were not associated with neutrophil infiltration. Our findings demonstrated that catechin suppressed IL-1β release in animal (Figure 2A) and cell (Figure 3C) models; however, gallic acid suppressed the release of IL-1β secretion in vivo but not in vitro. The result of gallic acid on IL-1β secretion in the animal experiment was inconsistent with the cell model. The reason for the discrepancy is the different types of cells. Overall, the cell model was mainly monocytes, but neutrophils were the major reactive cells in the animal model.[27] On the basis of the results of IL-1β in vivo and in vitro, it suggested that gallic acid and catechin differently inhibited at least one of the inflammatory pathways to suppress IL-1β secretion.

During in vitro IL-1β secretion, NF-κB signaling provides pro-IL-1β formation, and NLRP3 inflammasome activation controls IL-1β cleavage from pro-IL-1β.[7,8] Gallic acid and catechin are known to act as inflammation suppressors in the NF-κB-mediated pathway.[12,28,29] These two compounds inhibited IL-1β mRNA, IκB phosphorylation, and ERK phosphorylation in this study. Importantly, NLRP3 inflammasome activation was specifically inhibited by catechin but not gallic acid (Figure 3D). Previous studies indicated that the inhibition of MtROS generation prevented NLRP3 inflammasome activation.[10] However, ROS scavenging by antioxidants was independent to inhibit NLRP3 inflammasome activation.[30] ROS scavengers, such as *N*-acetyl cysteine, exhibited potent anti-inflammatory effects on the specific inhibition of NF-κB pathway but not on NLRP3 inflammasome activation.[30] We observed that catechin inhibited ROS and MtROS levels, but gallic acid only suppressed ROS levels (Figure 4B and Figure S3C). Taken together, these results suggest that catechin inhibits both NF-κB signaling and NLRP3 inflammasome activation, while gallic acid only suppresses NF-κB signaling.

The protective effects of catechin on NLRP3 inflammasome activation involve three mechanisms. First, catechin reversed the mitochondrial transmembrane potential impairment and up-regulated Bcl-2 expression (Figure 6). The maintenance of mitochondrial membrane stabilization is a vital approach to prevent NLRP3 inflammasome activation because the release of mitochondrial DNA from damaged mitochondria could trigger NLRP3 inflammasome activation.[23,31] NLRP3 inflammasome activation was not affected by gallic acid although this compound reversed the mitochondrial transmembrane potential impairment. Because MAPK signaling could mediate the

DOI: 10.1021/acs.jafc.5b02605
J. Agric. Food Chem. 2015, 63, 7343−7352

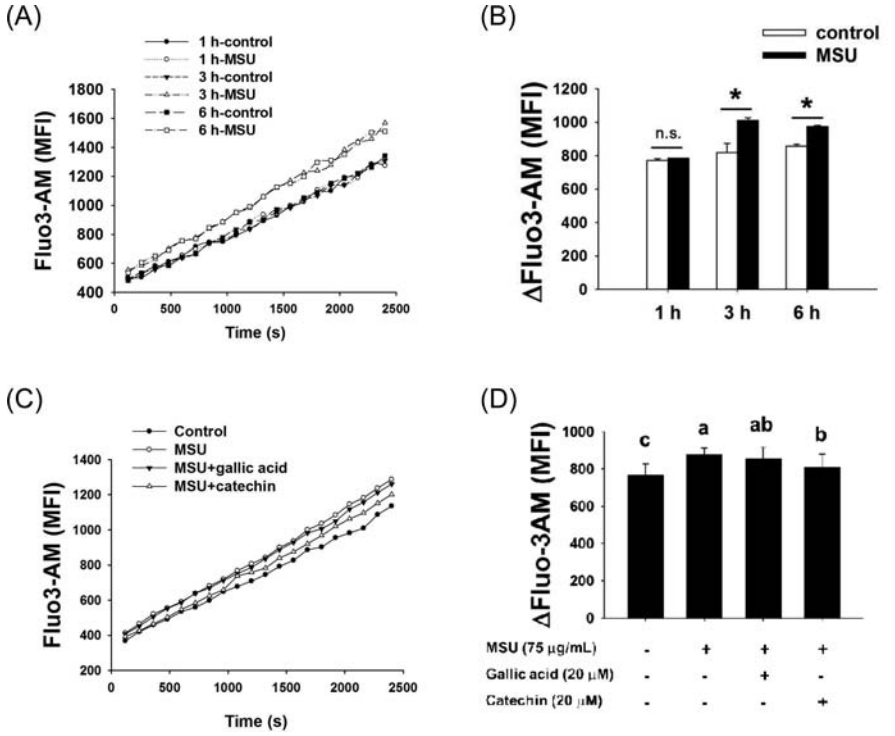

Figure 5. Effects of gallic acid and catechin on MSU-induced calcium accumulation. THP-1 cells were treated with 75 μg/mL MSU for 1, 3, or 6 h. (A) The calcium level was detected using Fluo3-AM, and (B) the fluorescent intensity levels are shown. *p < 0.05 was considered significant compared with the control using student's t-test. After THP-1 cells were treated with 75 μg/mL MSU in the presence or absence of 20 μM gallic acid or catechin for 3 h, (C) the fluorescent intensity of Fluo3-AM was detected and (D) quantified. The mean changes in the fluorescent intensity from 0 to 2400 s are shown. The values are presented as the means ± SD (n = 6). The values denoted with the different letters show significantly at p < 0.05.

mitochondrial transmembrane potential,[32] we speculated that the down-regulation of MAPK signaling by gallic acid indirectly maintained mitochondrial transmembrane potential. On the other hand, it has been suggested that the inhibition of NLRP3 inflammasome activation requires the significant up-regulation of Bcl-2 because the overexpression of Bcl-2 effectively prevents NLRP3 inflammasome activation.[10,23] Second, we observed that catechin inhibited calcium influx (Figure 5D), while calcium accumulation could induce mitochondrial damage and NLRP3 inflammasome activation.[21,22] Furthermore, the results showed that catechin inhibited MSU-stimulated calcium accumulation after 3 h treatment, and catechin reduced NLRP3 inflammasome activation after 6 h exposure, suggesting that catechin suppressed calcium overloading before mitochondrial damages and NLRP3 inflammasome activation. Moreover, catechin up-regulated the expression of redox proteins such as TRX and DJ-1 (Figure 4D). We concluded that the up-regulation of TRX by catechin inhibited the release of TXNIP and impaired IL-1β secretion. In agreement with the studies, the regulation of TRX expression contributes to IL-1β secretion.[9,11] In addition, DJ-1 is the ROS scavenger that degrades DJ-1 at cysteine 106 and prevents oxidative stress through the up-regulation of TRX.[20,33] Therefore, the preventive effect of catechin on NLRP3 inflammasome activation is to mediate the status of oxidative stress in the mitochondria and conferred protection to the mitochondria.

An association between catechin and the NLRP3 inflammasome has been suggested. It has been demonstrated that catechin attenuated *Helicobacter pylori* infection through a decrease in caspase-1 activity.[34] In addition to catechin, EGCG also prevented NLRP3-dependent lupus nephritis development in mice,[13] and EGCG suppressed melanoma growth through the inhibition of the NLRP1 inflammasome and IL-1β secretion.[35] Structurally, EGCG differs from catechin, possessing a third B-ring hydroxyl group at C5′ and a gallic acid residue esterified to the C3 hydroxyl.[36] Taken together, the inhibitory effects of flavan-3-ols (catechin and EGCG) on NLRP3 inflammasome activation reflect catechin monomers. Therefore, catechin derivatives, such as epicatechin, epigallocatechin (EGC), epicatechin gallate (ECG), and catechin-rich green tea extract, should be further determined whether these compounds inhibit NLRP3 inflammasome activation.

Catechin was given using the subcutaneous injection rather than the oral administration because of the low bioavailability of catechin and acute MSU attacks. The pharmacokinetics estimates of tea catechins with oral (5000 mg/kg) and intravenous (50 mg/kg) administration have pointed out the low bioavailability, slow C_{max} and long T_{max} in an animal model.[37] Therefore, subcutaneous injection of catechin is proposed to speed (or to increase) the concentration of catechin in serum. Colchicine was investigated to administrate using subcutaneous or intraperitoneal injection or using oral gavage for 4 h after MSU challenged C57BL/6 mice. Subcutaneous and intraperitoneal administration of colchicine significantly suppressed MSU-induced superoxide production and neutrophil infiltration,[38] but oral colchicine exhibited a delayed inhibitory effect on MSU-induced inflammation.[38] In addition, the natural compounds are commonly treated intraperitoneally to investigate their preventive effects on MSU-challenged animal models because MSU triggers acute inflammatory responses during 24 h.[39−41] On the basis of these findings, mice were treated with an intraperitoneal injection of

DOI: 10.1021/acs.jafc.5b02605
J. Agric. Food Chem. 2015, 63, 7343−7352

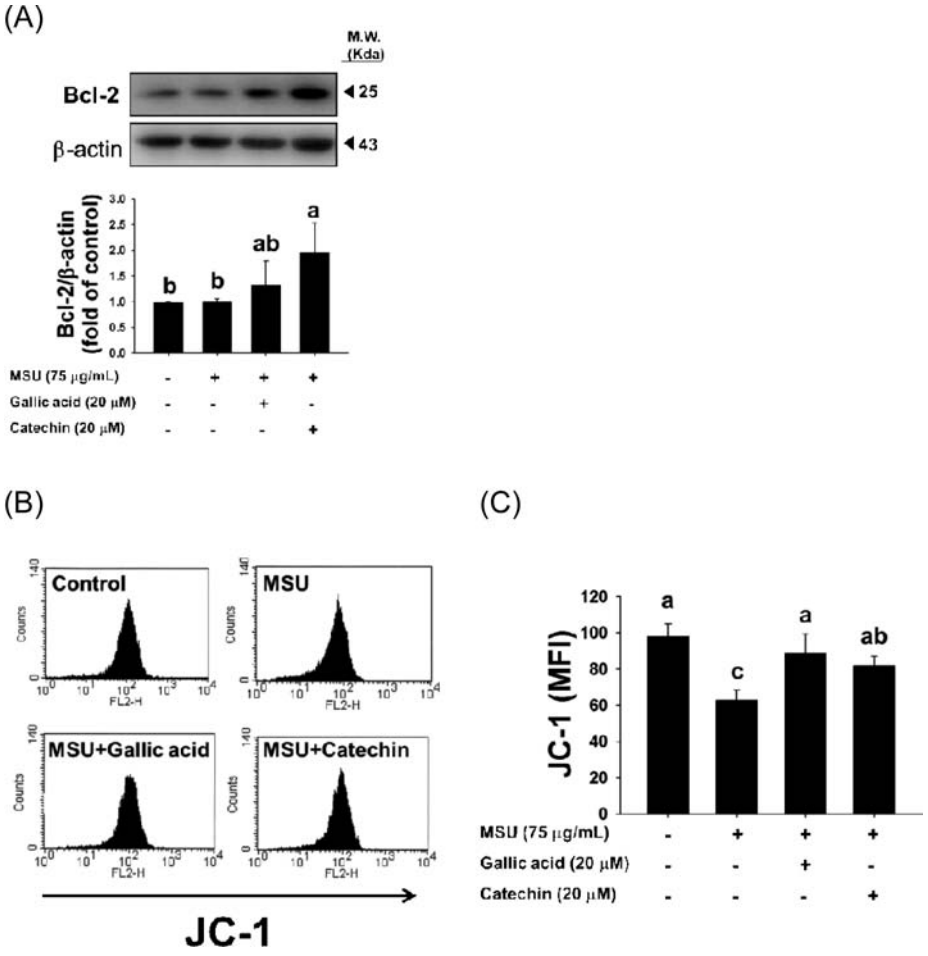

Figure 6. Effects of gallic acid and catechin on (A) Bcl-2 expression and (B) mitochondrial transmembrane potential. THP-1 cells were cultured with 75 μg/mL MSU in the presence or absence of 20 μM gallic acid or catechin for 6 h. (C) The quantitative value of JC-1 stain is shown. The values are presented as the means ± SD (n = 3). The values denoted with the different letters show significantly at $p < 0.05$.

MSU and with a subcutaneous injection of gallic acid or catechin.

It is a weakness of this study that the treatments of gallic acid and catechin are using subcutaneous injection in the animal model. Although subcutaneous injection of catechin might increase the concentration of catechin in plasma, subcutaneous injection is toward to drug system.[42] Catechin has multiple health-promoting properties when catechin is given orally for a long period,[43] but few studies report that subcutaneous injection of catechin could promote health. In addition, the metabolite of catechin is present in serum and urine predominantly as glucuronide, sulfate, or methylated conjugates.[44] Catechin exhibits the anti-inflammatory activity in MSU-challenged THP-1 cells; however, the inhibitory effect of catechin metabolites on MSU-induced inflammation remains unclear. Although the present results cannot determine the realistic dose of catechin as food to prevent MSU-induced inflammation, catechin has potential to protect gout attack by modulation of NLRP3 inflammasome activation.

In conclusion, this study demonstrates that catechin possesses potent superoxide anion scavenging activity greatly to inhibit MSU-induced IL-1β secretion and NLRP3 inflammasome activation. Catechin also regulates the status of oxidative stress in mitochondria via the up-regulation of TRX and DJ-1, and these effects prevent mitochondrial damage from MSU attack. These results suggest that catechin intake has potential to prevent acute gout attack.

■ ASSOCIATED CONTENT

Supporting Information

The Supporting Information is available free of charge on the ACS Publications website at DOI: 10.1021/acs.jafc.5b02605.

Effects of gallic acid and catechin on NF-κB signaling in THP-1 cells; effects of gallic acid and catechin on phagocytosis and lysosomal function in THP-1 cells; effects of gallic acid and catechin on superoxide anion and ROS; effects of gallic acid and catechin on glutathione (PDF)

■ AUTHOR INFORMATION

Corresponding Author

*Phone: 886-4-2287-9755. Fax: 886-4-2285-4378, E-mail: gcyen@nchu.edu.tw.

Funding

This research work was supported in part by the Minister of Science and Technology, MOST102-2313-B005-006-MY3, Taiwan, and by the Ministry of Education, Taiwan, under the ATU plan.

Notes

The authors declare no competing financial interest.

DOI: 10.1021/acs.jafc.5b02605
J. Agric. Food Chem. 2015, 63, 7343−7352

ABBREVIATIONS USED

IL-1β, interleukin-1β; MSU, monosodium urate; MtROS, mitochondrial reactive oxygen species; NLRP3, nucleotide-binding oligomerization domain-like receptor containing pyrin domain 3; TRX, thioredoxin; TXNIP, thioredoxin interaction protein

REFERENCES

(1) Choi, H. K.; Mount, D. B.; Reginato, A. M. Pathogenesis of gout. *Ann. Intern. Med.* **2005**, *143*, 499−516.

(2) Cronstein, B. N.; Terkeltaub, R. The inflammatory process of gout and its treatment. *Arthritis Res. Ther.* **2006**, *8*, S3.

(3) Terkeltaub, R. Gout. Novel therapies for treatment of gout and hyperuricemia. *Arthritis Res. Ther.* **2009**, *11*, 236.

(4) Stamp, L. K.; O'Donnell, J. L.; Chapman, P. T. Emerging therapies in the long-term management of hyperuricaemia and gout. *Intern. Med. J.* **2007**, *37*, 258−266.

(5) Burns, C. M.; Wortmann, R. L. Gout therapeutics: new drugs for an old disease. *Lancet* **2011**, *377*, 165−177.

(6) Martinon, F.; Petrilli, V.; Mayor, A.; Tardivel, A.; Tschopp, J. Gout-associated uric acid crystals activate the NALP3 inflammasome. *Nature* **2006**, *440*, 237−241.

(7) Martinon, F. Mechanisms of uric acid crystal-mediated autoinflammation. *Immunol. Rev.* **2010**, *233*, 218−232.

(8) Tschopp, J.; Schroder, K. NLRP3 inflammasome activation: The convergence of multiple signalling pathways on ROS production? *Nat. Rev. Immunol.* **2010**, *10*, 210−215.

(9) Zhou, R.; Tardivel, A.; Thorens, B.; Choi, I.; Tschopp, J. Thioredoxin-interacting protein links oxidative stress to inflammasome activation. *Nat. Immunol.* **2010**, *11*, 136−140.

(10) Zhou, R.; Yazdi, A. S.; Menu, P.; Tschopp, J. A role for mitochondria in NLRP3 inflammasome activation. *Nature* **2011**, *469*, 221−225.

(11) Dostert, C.; Petrilli, V.; Van Bruggen, R.; Steele, C.; Mossman, B. T.; Tschopp, J. Innate immune activation through Nalp3 inflammasome sensing of asbestos and silica. *Science* **2008**, *320*, 674−677.

(12) Rahman, I.; Biswas, S. K.; Kirkham, P. A. Regulation of inflammation and redox signaling by dietary polyphenols. *Biochem. Pharmacol.* **2006**, *72*, 1439−1452.

(13) Tsai, P. Y.; Ka, S. M.; Chang, J. M.; Chen, H. C.; Shui, H. A.; Li, C. Y.; Hua, K. F.; Chang, W. L.; Huang, J. J.; Yang, S. S.; Chen, A. Epigallocatechin-3-gallate prevents lupus nephritis development in mice via enhancing the Nrf2 antioxidant pathway and inhibiting NLRP3 inflammasome activation. *Free Radical Biol. Med.* **2011**, *51*, 744−754.

(14) Wang, C.; Pan, Y.; Zhang, Q. Y.; Wang, F. M.; Kong, L. D. Quercetin and allopurinol ameliorate kidney injury in STZ-treated rats with regulation of renal NLRP3 inflammasome activation and lipid accumulation. *PLoS One* **2012**, *7*, e38285.

(15) Chuang, S. Y.; Lin, C. H.; Fang, J. Y. Natural compounds and aging: between autophagy and inflammasome. *BioMed Res. Int.* **2014**, *2014*, 297293.

(16) Orallo, F.; Alvarez, E.; Camina, M.; Leiro, J. M.; Gomez, E.; Fernandez, P. The possible implication of trans-Resveratrol in the cardioprotective effects of long-term moderate wine consumption. *Mol. Pharmacol.* **2002**, *61*, 294−302.

(17) Martin, W. J.; Walton, M.; Harper, J. Resident macrophages initiating and driving inflammation in a monosodium urate monohydrate crystal-induced murine peritoneal model of acute gout. *Arthritis Rheum.* **2009**, *60*, 281−289.

(18) Jhang, J. J.; Cheng, Y. T.; Ho, C. Y.; Yen, G. C. Monosodium urate crystals trigger Nrf2- and heme oxygenase-1-dependent inflammation in THP-1 cells. *Cell. Mol. Immunol.* **2015**, *12*, 424−434.

(19) Hornung, V.; Bauernfeind, F.; Halle, A.; Samstad, E. O.; Kono, H.; Rock, K. L.; Fitzgerald, K. A.; Latz, E. Silica crystals and aluminum salts activate the NALP3 inflammasome through phagosomal destabilization. *Nat. Immunol.* **2008**, *9*, 847−856.

(20) Im, J. Y.; Lee, K. W.; Woo, J. M.; Junn, E.; Mouradian, M. M. DJ-1 induces thioredoxin 1 expression through the Nrf2 pathway. *Hum. Mol. Genet.* **2012**, *21*, 3013−3024.

(21) Murakami, T.; Ockinger, J.; Yu, J.; Byles, V.; McColl, A.; Hofer, A. M.; Horng, T. Critical role for calcium mobilization in activation of the NLRP3 inflammasome. *Proc. Natl. Acad. Sci. U. S. A.* **2012**, *109*, 11282−11287.

(22) Lee, G. S.; Subramanian, N.; Kim, A. I.; Aksentijevich, I.; Goldbach-Mansky, R.; Sacks, D. B.; Germain, R. N.; Kastner, D. L.; Chae, J. J. The calcium-sensing receptor regulates the NLRP3 inflammasome through Ca^{2+} and cAMP. *Nature* **2012**, *492*, 123−127.

(23) Shimada, K.; Crother, T. R.; Karlin, J.; Dagvadorj, J.; Chiba, N.; Chen, S.; Ramanujan, V. K.; Wolf, A. J.; Vergnes, L.; Ojcius, D. M.; Rentsendorj, A.; Vargas, M.; Guerrero, C.; Wang, Y.; Fitzgerald, K. A.; Underhill, D. M.; Town, T.; Arditi, M. Oxidized mitochondrial DNA activates the NLRP3 inflammasome during apoptosis. *Immunity* **2012**, *36*, 401−414.

(24) Masuoka, N.; Nihei, K.; Kubo, I. Xanthine oxidase inhibitory activity of alkyl gallates. *Mol. Nutr. Food Res.* **2006**, *50*, 725−731.

(25) Cos, P.; Ying, L.; Calomme, M.; Hu, J. P.; Cimanga, K.; Van Poel, B.; Pieters, L.; Vlietinck, A. J.; Vanden Berghe, D. Structure-activity relationship and classification of flavonoids as inhibitors of xanthine oxidase and superoxide scavengers. *J. Nat. Prod.* **1998**, *61*, 71−76.

(26) Yilmaz, Y.; Toledo, R. T. Major flavonoids in grape seeds and skins: antioxidant capacity of catechin, epicatechin, and gallic acid. *J. Agric. Food Chem.* **2004**, *52*, 255−260.

(27) Popa-Nita, O.; Naccache, P. H. Crystal-induced neutrophil activation. *Immunol. Cell Biol.* **2010**, *88*, 32−40.

(28) Kim, S. H.; Jun, C. D.; Suk, K.; Choi, B. J.; Lim, H.; Park, S.; Lee, S. H.; Shin, H. Y.; Kim, D. K.; Shin, T. Y. Gallic acid inhibits histamine release and pro-inflammatory cytokine production in mast cells. *Toxicol. Sci.* **2006**, *91*, 123−131.

(29) Murase, T.; Kume, N.; Hase, T.; Shibuya, Y.; Nishizawa, Y.; Tokimitsu, I.; Kita, T. Gallates inhibit cytokine-induced nuclear translocation of NF-kappaB and expression of leukocyte adhesion molecules in vascular endothelial cells. *Arterioscler., Thromb., Vasc. Biol.* **1999**, *19*, 1412−1420.

(30) Bauernfeind, F.; Bartok, E.; Rieger, A.; Franchi, L.; Nunez, G.; Hornung, V. Cutting edge: reactive oxygen species inhibitors block priming, but not activation, of the NLRP3 inflammasome. *J. Immunol.* **2011**, *187*, 613−617.

(31) Nakahira, K.; Haspel, J. A.; Rathinam, V. A.; Lee, S. J.; Dolinay, T.; Lam, H. C.; Englert, J. A.; Rabinovitch, M.; Cernadas, M.; Kim, H. P.; Fitzgerald, K. A.; Ryter, S. W.; Choi, A. M. Autophagy proteins regulate innate immune responses by inhibiting the release of mitochondrial DNA mediated by the NALP3 inflammasome. *Nat. Immunol.* **2011**, *12*, 222−230.

(32) McCubrey, J. A.; Steelman, L. S.; Chappell, W. H.; Abrams, S. L.; Wong, E. W.; Chang, F.; Lehmann, B.; Terrian, D. M.; Milella, M.; Tafuri, A.; Stivala, F.; Libra, M.; Basecke, J.; Evangelisti, C.; Martelli, A. M.; Franklin, R. A. Roles of the Raf/MEK/ERK pathway in cell growth, malignant transformation and drug resistance. *Biochim. Biophys. Acta, Mol. Cell Res.* **2007**, *1773*, 1263−1284.

(33) Canet-Aviles, R. M.; Wilson, M. A.; Miller, D. W.; Ahmad, R.; McLendon, C.; Bandyopadhyay, S.; Baptista, M. J.; Ringe, D.; Petsko, G. A.; Cookson, M. R. The Parkinson's disease protein DJ-1 is neuroprotective due to cysteine-sulfinic acid-driven mitochondrial localization. *Proc. Natl. Acad. Sci. U. S. A.* **2004**, *101*, 9103−9108.

(34) Yang, J. C.; Yang, H. C.; Shun, C. T.; Wang, T. H.; Chien, C. T.; Kao, J. Y. Catechins and Sialic Acid Attenuate Helicobacter pylori-Triggered Epithelial Caspase-1 Activity and Eradicate Helicobacter pylori Infection. *Evid. Based Complement Alternat. Med.* **2013**, *2013*, 248585.

(35) Ellis, L. Z.; Liu, W.; Luo, Y.; Okamoto, M.; Qu, D.; Dunn, J. H.; Fujita, M. Green tea polyphenol epigallocatechin-3-gallate suppresses melanoma growth by inhibiting inflammasome and IL-1beta secretion. *Biochem. Biophys. Res. Commun.* **2011**, *414*, 551−556.

DOI: 10.1021/acs.jafc.5b02605
J. Agric. Food Chem. 2015, 63, 7343−7352

(36) Neilson, A. P.; Ferruzzi, M. G. Influence of formulation and processing on absorption and metabolism of flavan-3-ols from tea and cocoa. *Annu. Rev. Food Sci. Technol.* **2011**, *2*, 125−151.
(37) Zhu, M.; Chen, Y.; Li, R. C. Oral absorption and bioavailability of tea catechins. *Planta Med.* **2000**, *66*, 444−447.
(38) Chia, E. W.; Grainger, R.; Harper, J. L. Colchicine suppresses neutrophil superoxide production in a murine model of gouty arthritis: a rationale for use of low-dose colchicine. *Br. J. Pharmacol.* **2008**, *153*, 1288−1295.
(39) Martin, W. J.; Herst, P. M.; Chia, E. W.; Harper, J. L. Sesquiterpene dialdehydes inhibit MSU crystal-induced superoxide production by infiltrating neutrophils in an in vivo model of gouty inflammation. *Free Radical Biol. Med.* **2009**, *47*, 616−621.
(40) Chen, H.; Zheng, S.; Wang, Y.; Zhu, H.; Liu, Q.; Xue, Y.; Qiu, J.; Zou, H.; Zhu, X. The effect of resveratrol on the recurrent attacks of gouty arthritis. *Clin. Rheumatol.* **2014**, DOI: 10.1007/s10067-014-2836-3.
(41) Yao, X.; Ding, Z.; Xia, Y.; Wei, Z.; Luo, Y.; Feleder, C.; Dai, Y. Inhibition of monosodium urate crystal-induced inflammation by scopoletin and underlying mechanisms. *Int. Immunopharmacol.* **2012**, *14*, 454−462.
(42) Wechalekar, M. D.; Vinik, O.; Schlesinger, N.; Buchbinder, R. Intra-articular glucocorticoids for acute gout. *Cochrane Database Syst. Rev.* **2013**, *4*, CD009920.
(43) Zaveri, N. T. Green tea and its polyphenolic catechins: medicinal uses in cancer and noncancer applications. *Life Sci.* **2006**, *78*, 2073−2080.
(44) Clifford, M. N.; van der Hooft, J. J.; Crozier, A. Human studies on the absorption, distribution, metabolism, and excretion of tea polyphenols. *Am. J. Clin. Nutr.* **2013**, *98*, 1619S−1630S.

DOI: 10.1021/acs.jafc.5b02605
J. Agric. Food Chem. 2015, 63, 7343−7352

plasma at a 7 μM peak concentration, 3 h after the ingestion of four cactus pear fruits containing 28 mg.[7] Moreover, the oral administration of a dose of pure indicaxanthin (2 μmol/kg), equivalent to a dietary amount ingested with cactus pear fruits in humans,[7] generated in rats a plasma peak concentration of 0.2 μM, which appeared to be safe and exhibited a strong anti-inflammatory effect in a carrageenan-induced acute inflammation model.[15]

While consumption of most phytochemicals has been associated with an extended life span,[16] the intake of quite a few has been reported to exert neuroprotective effects,[17] mainly due to the sealing nature of the blood brain barrier (BBB) that shields brain from the majority of xenobiotics.[18] Among all flavonoids, flavanols and anthocyanins are the only ones that have been reported to cross the BBB, accumulate within several regions of the brain, and modulate memory and learning proceses.[17−19] However, because of limited bioavailability, these molecules are poorly absorbed in the brain, especially anthocyanins.[17] On the other hand many studies claimed accumulation of phytochemicals assayed at amounts much higher than those ingested with a normal diet.[20]

Taking into account its bioavailability in rats,[15] this work first researched whether indicaxanthin crossed the BBB and accumulated in the rat brain. In addition, eventual action of the molecule on the neuronal function in the central nervous system (CNS), in particular the hippocampus, was investigated. This study was carried out exploiting recording techniques associated with microiontophoresis, a current-based approach for direct drug delivery, applied to locally investigate the neuromodulatory effects of molecular messengers on the electrophysiological properties of CNS neurons in vivo.[21] Indicaxanthin activity in the framework of glutamatergic synaptic system has been considered on the basis of inhibition studies in the presence of glutamate. The impact of indicaxanthin on the neuronal bioelectric activity in a structure involved in basic physiological processes is discussed.

MATERIALS AND METHODS

Reagents. Unless stated otherwise, all reagents were from Sigma-Aldrich (Milan, Italy) and of the highest grade commercially available.

Extraction and Purification of Indicaxanthin from Cactus Pear Fruits. Indicaxanthin was isolated from cactus pear (*Opuntia ficus-indica*) fruits (yellow cultivar). Briefly, the phytochemical was separated from a methanol extract of the pulp by liquid chromatography on Sephadex G-25 as previously reported.[1] Fractions containing the pigment were submitted to cryodesiccation, purified as described,[1] quantified by HPLC as below reported, and suspended in PBS for the experiments.

Animals and Surgery. Adult male Wistar rats (Morini, Milan, Italy) weighing 220−280 g were used in all experiments. Animals were fed and had access to water ad libitum. The light cycle was automatically controlled (on at 07:00, off at 19:00) and the room temperature was thermostatically regulated at 22° ± 1 °C. Before the experiments, rats were housed and acclimatized under these conditions for 3−4 d. In each experimental step, all efforts were made to minimize the number of animals used and their sufferance. All experiments were performed in strict accordance with the European Directive (2010/63/EU) on animal experimentation and with the National Institutes of Health Guide for the Care and Use of Laboratory Animals (1986).

As for pharmacokinetic studies, the animals were anesthetized on the day of the experiment with urethane at a dose of 1.2 g/kg (ip). One group received indicaxanthin (2 μmol/kg) by oral gavage, while control rats received saline alone. Animals were sacrificed at 1, 2.5, 3, 4, and 5 h after indicaxanthin administration, and brain samples were collected[15] and processed as described below. Each experiment was performed three times with groups of 10 rats. Data from separate experiments were pooled.

With regard to electrophysiological experiments, after having been anesthetized as above reported, rats were positioned in a stereotaxic apparatus (David Kopf Instruments, Tujunga, CA). A 3 mm burr hole was drilled in the skull, 5 mm anterior to the interaural line and 2.4 mm lateral to the midline. Physiological parameters were monitored throughout all experimental sessions.

Quantification of Indicaxanthin in Brain Samples. The amount of indicaxanthin within brain samples was evaluated at selected time intervals after a single oral administration of the pigment, as reported below. Briefly, animals were perfused with normal saline to remove any compounds still circulating in the blood. Brains (10 per time point) were then isolated, carefully washed with saline, pooled, and homogenized in PBS. Indicaxanthin was extracted from samples with chloroform:methanol, 2:1 by volume (1 g of tissue with 3 volumes of extraction mixture). The methanol phase from all samples at each time point was dried under nitrogen, resuspended in 1% acetic acid in water, analyzed on a Varian Microsorb C-18 column (4.6 × 250 mm; Varian, Palo Alto, CA), and eluted with a 20 min linear gradient elution from solvent A (1% acetic acid in water) to 20% solvent B (1% acetic acid in acetonitrile) with a flow rate of 1.5 mL/min. Spectrophotometric revelation was at 482 nm. Under these conditions, indicaxanthin eluted after 8.15 min and was quantified by reference to standard curves constructed with 5−100 ng of purified compounds and by relating its amount to the peak area.

Electrophysiological Recordings. A seven-barrel glass microelectrode was directed stereotaxically to the hippocampus for both recording and drug ejection (4.8−5.8 mm anterior to the interaural line, 1−3 mm lateral to the midline, 2.4−4 mm ventral to the cortical surface).[22] The system was set as previously reported.[23] The center recording barrel (1.1−2.0 MΩ resistance) was filled with 2 M NaCl with 1% Fast Green (Sigma), one side barrel was filled with 2 M NaCl 0.9% buffered saline solution (for automatic current balancing), and the others were filled with 12 mM, 6 mM, and 3 mM indicaxanthin (pH 7.4) and 100 mM L-glutamic acid monosodium salt (GLU, pH 8).

Retaining currents of 8−10 nA (positive for GLU and negative for the indicaxanthin solutions) were applied to drug barrels (20−70 MΩ) (Neurophore BH-2 System, Harvard Apparatus, Hamden, CT). At the beginning of each track (0.5 mm ventral to the cortical surface), maximal ejection currents were applied to each barrel for 30 min, to concentrate the drug at the pipet tip. Electrical signals were amplified, filtered, acquired, and stored on a computer together with their temporal markers (time precision 100 ms) for off-line analysis as previously described.[24] A ratemeter histogram of neuronal activity was continuously displayed and updated every 5 s on the computer screen with a counter window, to detect variations of neuronal firing rate online. All computer operations were performed using the SciWorks package, version 5.0 (Datawave Technologies, Loveland, CO). Neuronal units were not added to the database if marked changes in amplitude or configuration of the spike were observed, or if there was early death of the cell in the course of recording. Baseline activity of each neuron was recorded for 3−5 min before acute vehicle or drug administration.

Indicaxanthin Treatment. Microiontophoretic preliminary procedures were previously described.[24] Drug-test recordings were carried out at increasing ejection currents to identify both the kinetics of phytochemical action and the minimal current exerting an effect on all responsive neurons. For this purpose, 90 s pulses at 40, 60, and 80 nA ejection currents were tested, with a 90 s interpulse interval between pulses to prevent any influence of the previous pulse on the following one. After this step, all recorded neurons underwent the iontophoretic administration of indicaxanthin (in the concentration range reported above) for 5 min at the current of 60 nA in order to outline a correlation between the modifications of neuronal response and the concentration of the drug. Once the application of indicaxanthin was terminated, recording continued until the spontaneous firing rate recovered to baseline. Control tests, applying the same ejection currents used for the treatments, were performed with vehicle solutions; no changes in the neuronal firing were recorded. It is

DOI: 10.1021/acs.jafc.5b02612
J. Agric. Food Chem. 2015, 63, 7353−7360

worth highlighting that ejection times and currents in our microiontophoretic approach were set to result in an actual amount of indicaxanthin interacting with single neurons in a nanogram range compatible with the amount measured in the rat brain after the ingestion of the pigment. Indeed, indicaxanthin interacting with a single neuron was approximately 0.34 ng (for 12 mM), 0.17 ng (for 6 mM), and 0.085 ng (for 3 mM).

When required, the group of neurons that had received 0.34 ng of indicaxanthin per neuron were tested in coadministration with GLU; namely, at the recovering of baseline, GLU was ejected (40 nA ejection current)[25] before and during subsequent administration of the phytochemical, and responses were assessed. For all groups, only data from cells exhibiting recovery at the end of treatments were included in statistical analysis.

At the end of each electrophysiological experiment, the recording sites were marked with Fast Green through the electrode by using a 50 mA ejection current for 15 min. Coronal frozen sections were cut at 50 mm and stained with cresyl violet for histological verification and reconstruction of recording sites.

Preparation of Protein and Ligand. The crystal structure of amino terminal domains of the *N*-methyl-D-aspartate (NMDA) glutamate receptor dimeric GluN1/GluN2B subunit, in complex with antagonist ifenprodil (Pdb: 3QEL),[26] and dimeric GluN1/GluN2A subunit, in complex with either D-(−)-2-amino-5-phosphonopentanoic acid (D-AP5) (Pdb: 4NF5) or 1-(phenanthrene-2-carbonyl)piperazine-2,3-dicarboxylic acid (PPDA) (Pdb: 4NF6),[27] were retrieved from the RCSB Protein Data Bank. The starting coordinates of the crystal complexes were subjected to protein preparation using the protein preparation wizard of Glide software 5.9 (Schrodinger, LLC, New York, NY). The proteins were minimized by applying the OPLS-2005 force field. Water molecules and other nonligand molecules were deleted, and the structures refined by means the optimization of H-bond assignment, and the minimization until the average root-mean-square deviation of the non-hydrogen atoms reached 0.3 Å.

The structures of the ligands were then extracted from the X-ray complexes, and appropriate bond order was assigned using the LigPrep software 2.6 (Schrodinger, LLC, New York, NY). The same treatment was carried out on indicaxanthin, generating all the possible states and tautomers at pH = 7.0 ± 2.0.

Docking Experiments. The ligands were extracted and docked by the Glide XP high performance docking procedure, to evaluate if the docking algorithm fits the crystallized conformation.[28−31]

Binding Free Energy Calculation. Prime/MM-GBSA software 3.2 (Schrodinger, LLC, New York, NY) was used to calculate the free energy of binding between the receptor subunits and either the ligands or indicaxanthin, according to the default parameters for in water estimation.

Computational Mutagenesis. Alanine scanning studies were carried out using the Mutate Residue script from Maestro (Schrodinger, LLC, New York, NY). Computational mutagenesis is an approach used to find out the contribution of specific residues to the protein function by mutating the original residues to alanine[32] to recognize the structural and energetic characteristics of the hotspots. The mutated systems were not minimized, and it was assumed that no local rearrangements occur after the mutation. The interacting residues with indicaxanthin were mutated to alanine, and the binding free energy was recalculated.

Statistical Analysis. Data from electrophysiological study were analyzed using 1-factor ANOVA, followed by a Bonferroni's test. Neuronal firing rate was off-line analyzed before, during, and after drug administration for each recorded unit. Individual rate-meter histograms (5 s bin width) were analyzed by means of a nonparametric Mann−Whitney *U* test to detect any statistically significant treatment-related change in neuronal firing. To analyze the effects induced by treatments, neurons were considered responsive if changes were significant (probability level $P < 0.05$) for at least six consecutive bins for indicaxanthin and two for glutamate, the first of which was respectively labeled as the onset of a response. The intensity of the effect on neuronal firing (changes in the discharge with respect to baseline) was expressed as percentage magnitude, rather than absolute values, in order to normalize the responses of neurons with different baseline discharge frequencies. The dose−effect of indicaxanthin on the mean magnitude of discharge frequencies and on latency and duration of the effect was analyzed by a Mann−Whitney *U* test. For all statistical tests used, the null hypothesis was rejected at a *P* lower than 0.05. If not otherwise indicated, all results are expressed as mean ± SD.

RESULTS AND DISCUSSION

Indicaxanthin Crosses the BBB and Accumulates within the Rat Brain. Pharmacokinetic data from this study fall within the area of research on neuromodulatory effects of dietary phytochemicals.[17−20,33−35] Here we explored the potential for indicaxanthin to cross the BBB and accumulate within the brain. Taking into account previous studies[15] and human bioavailability,[7] rats received a single oral administration of 2 μmol/kg body weight, an amount calculated to be nutritionally relevant that can easily be provided to humans with a single serving of cactus pear fruit.[7,36]

Entry of indicaxanthin in rat brain was investigated kinetically by assessing the amount of the pigment in the whole brain (1.2 ± 0.1 g fresh weight, $n = 15$) between 60 min and 5 h after administration. The pigment was detectable after 60 min, and a peak of 20 ± 2.4 ng/g of fresh brain was reached 2.5 h after administration (Figure 2). Indicaxanthin disappeared from

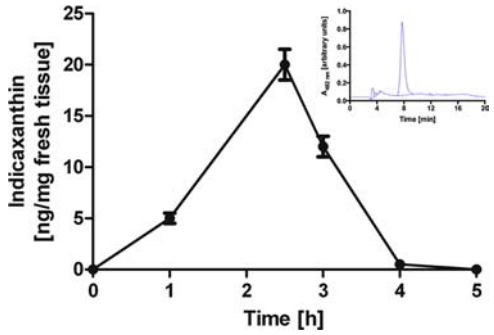

Figure 2. Kinetics of indicaxanthin accumulation in the rat brain after ingestion of 2 μmol/kg. Values are means ± SEMs, $n = 30$ (ten rats in 3 separate experiments). The inset shows a representative chromatographic profile of the indicaxanthin extracted from ten brains.

brain at 4 h, and log transformation of its amount within 2.5−4 h after ingestion indicated that the disposal followed first-order kinetics. The calculated half-life was 0.82 ± 0.07 h (Figure 2). As previously reported,[15] oral administration of 2 μmol/kg resulted in a 0.20 μM indicaxanthin plasma peak at 2.5 h, with total disappearance within 4 h with first-order kinetics. Comparing present and previous data,[15,37] and considering a mean rat blood volume of 16 mL, it can be calculated that the amount of indicaxanthin in the brain at 2.5 h (a time point reflecting an equilibrium of distribution already reached), is approximately 2% of that absorbed.

Brain is highly perfused; the distribution rate of compounds in cells is then determined primarily by permeability. While demonstrating that indicaxanthin crossed the rat BBB, our kinetic data showing parallel disposal kinetics in plasma and brain suggest simple diffusional mechanisms. Similarly, dietary indicaxanthin from cactus pear fruits has been found to distribute in human red blood cells with kinetics that paralleled plasma kinetics.[5]

Indicaxanthin Modulates Bioelectric Activity of Hippocampal Neurons. Taking into account that indicaxanthin

DOI: 10.1021/acs.jafc.5b02612
J. Agric. Food Chem. 2015, 63, 7353−7360

crossed the rat BBB, a putative influence of the molecule on neuronal cell function was explored. We examined the effect of indicaxanthin on the neuronal activity of the hippocampus applying microiontophoresis[38] to classical techniques of extracellular recording in in vivo models. By means of a multibarrel electrode, this methodology allows recording of a well-defined bioelectric activity of single neuronal units in conjunction with the local ejection of molecules of interest. Consequently, every change in the neuronal activity recorded is due to the substance administered, with negligible or null external interference.

Under the applied conditions a spontaneous discharge was evident for all recorded cells. Groups of 10 hippocampal neurons received 0.34 ng, 0.17 ng, or 0.085 ng of indicaxanthin per neuron, and the effect was evaluated as magnitude, latency, and duration of response; these parameters respectively express: (a) the percentage difference between mean values of the discharge frequency in basal condition and during the drug administration, (b) the time from the appearance of the effect, and (c) its timespan (Figure 3). With respect to baseline, treatment with 0.34 ng of indicaxanthin caused a statistically significant ($P < 0.05$) decrease of firing rate in 7 cells (70%). The effect had a mean magnitude of −73.93 ± 11.94%, a mean latency of 7.86 ± 2.67 s, and a mean duration of 260.00 ± 64.81 s. The firing rate of neurons treated with 0.17 ng of indicaxanthin decreased significantly ($P < 0.05$) in 6 cells (60%), with a mean magnitude of −49.71 ± 14.00%, a mean latency of 25.83 ± 13.93 s, and a mean duration of 241.67 ± 58.20 s. Finally, 5 of 10 neurons treated with 0.085 ng of indicaxanthin showed a significant reduction of the rate of discharge ($P < 0.05$). The effect had a mean magnitude of −29.59 ± 7.02%, a mean latency of 69.00 ± 36.64 s, and a mean duration of 65.00 ± 47.57 s.

Statistical analysis revealed that the effect of indicaxanthin was dose-dependent (Figure 3). In detail, considering the magnitude values (Figures 3, 4), the inhibitory effect of 0.34 ng/neuron was higher than the effect of both 0.17 ng ($P = 0.0152$) and 0.085 ng ($P = 0.0045$), and a significant reduction was observed comparing the effect of 0.17 ng with 0.085 ng ($P = 0.0176$). With regard to the latency of the effect (Figure 3), neurons treated with 0.34 ng showed a reduced latency when compared to 0.17 ng ($P = 0.015$) and to 0.085 ng ($P = 0.0045$). In addition, the latency for neurons treated with 0.17 ng was significantly lower than that for neurons treated with 0.085 ng

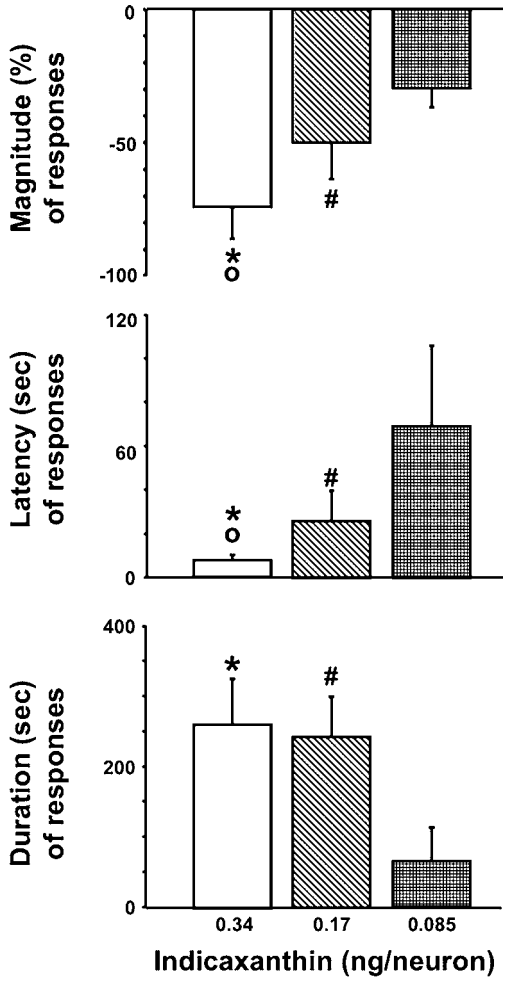

Figure 3. Bar histogram for magnitude, latency, and duration showing the effect of indicaxanthin at different amounts (0.34, 0.17, 0.085 ng/neuron) on hippocampal neuronal responses. Each bar represents mean values (±standard deviation) (○statistically significant effect of indicaxanthin 0.34 versus 0.17 ng/neuron; *statistically significant effect of indicaxanthin 0.34 versus 0.085 ng/neuron; #statistically significant effect of 0.17 versus 0.085 ng/neuron). Statistical significance for $P < 0.05$.

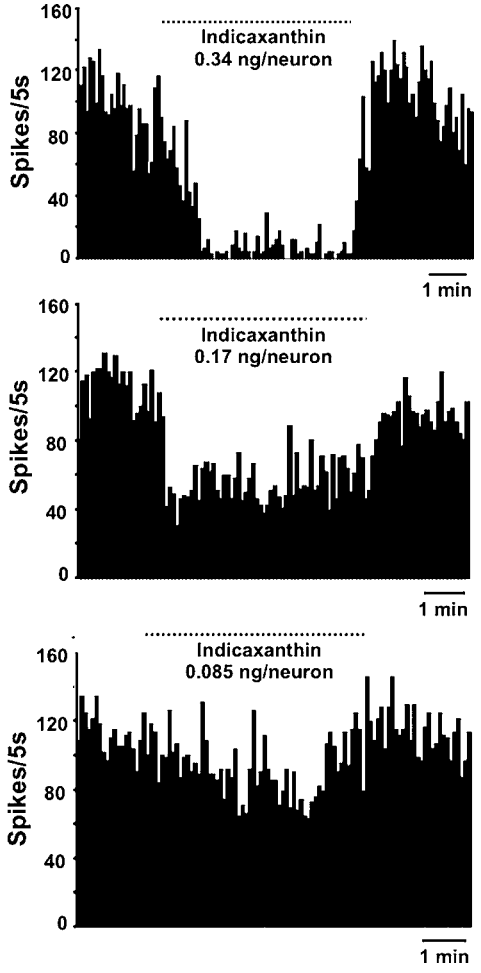

Figure 4. Representative rate-meter histogram (bin width 5 s) showing decreased magnitude of responses following indicaxanthin administration at various amounts (0.34, 0.17, 0.085 ng/neuron) for 5 min.

DOI: 10.1021/acs.jafc.5b02612
J. Agric. Food Chem. 2015, 63, 7353−7360

(P = 0.0446). As for the duration (Figure 3), in the 0.34 ng treated neurons the effect was greater than in 0.17 and 0.085 ng treated ones, though significant only for the latter (P = 0.058); also, there was a greater duration of the effect of 0.17 ng compared to 0.085 treated neurons (P = 0.0062). As a whole, our data revealed the ability of indicaxanthin to remarkably and dose-dependently inhibit the magnitude of spontaneous neuronal discharge of hippocampal cells, with a global modulation of neuronal bioelectric activity.

The hippocampus is involved in a variety of normal brain function and implicated in synaptic processes underlying memory formation, learning, modulation of emotions, regulation of the stress response, and cognition.[39] Cells of this brain region are mainly equipped with glutamatergic synapses, underpinning hippocampal activity.[40] Interestingly, reports reveal that phytochemicals can modulate excitatory glutamate-dependent hippocampal processes.[41]

Our results showing that indicaxanthin interfered with the hippocampal neuronal activity prompted us to investigate potential effects on the hippocampal glutamate-induced excitatory transmission. Therefore, the neurons that had previously reacted to 0.34 ng of indicaxanthin were subsequently submitted to coadministration of GLU and indicaxanthin (Figure 5A,B). This treatment affected the GLU-induced excitation of the neural discharge of 6 neurons (85,71%). In detail, 40 nA GLU pulses were first administered alone; this caused a mean increase in neuronal firing by +62.00 ± 21.34%. When GLU pulses were administered during ejection of indicaxanthin, the excitation was significantly reduced to +29.67 ± 8.08% (percentage difference: −52.14%; P = 0.0039). Latency and duration of GLU action were not significantly altered, due to the rapid kinetics of GLU and to the time-limited pulse ejection. Our results show that that indicaxanthin has the potential to modulate the hippocampal synaptic activity affecting glutamatergic transmission. These effects, observed with amounts of nutritional relevance, suggest the phytochemical as a natural compound with the potential of acting as a functional brake in the context of excitatory circuits, under a physiological condition.

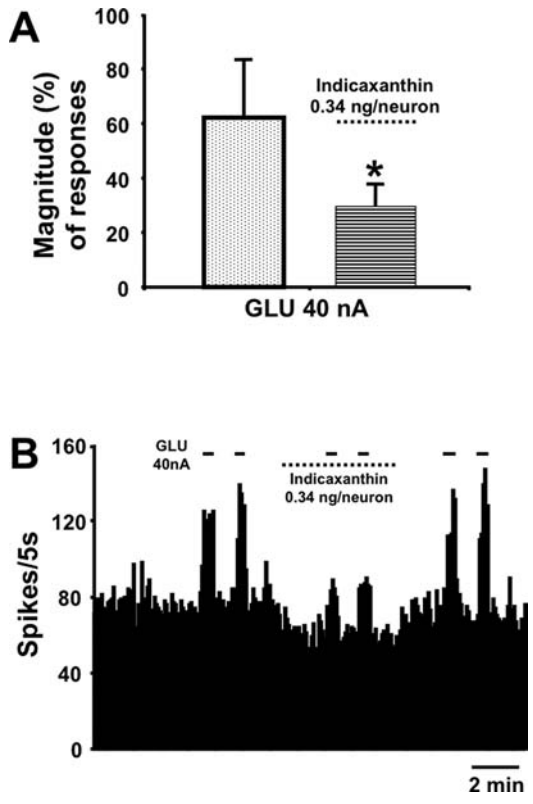

Figure 5. (A) Bar histogram for magnitude showing the effect of indicaxanthin (0.34 ng/neuron, at 60 nA) on GLU-induced responses of hippocampal neuronal. Each bar represents mean values (±standard deviation). *Statistically significant effect of coadministration of indicaxanthin (0.34 ng/neuron, at 60 nA) during GLU pulses (40 nA for 30 s) versus GLU-induced effect. Statistical significance for P < 0.05. (B) Representative rate-meter histogram (bin width 5 s) showing decreased magnitude of neuronal responses to GLU during indicaxanthin administration (0.34 ng/neuron, at 60 nA) for 5 min.

Interactions of Indicaxanthin with Glutamate Receptors. A number of receptors, including NMDAR, 2-amino-3-(3-hydroxy-5-methyl-isoxazol-4-yl)propanoic acid receptor (AMPAR), and metabotropic glutamate receptor (mGluR), are involved with the glutamatergic transmission, NMDAR being the most represented in the hippocampus, playing a central role in controlling synaptic plasticity and metaplasticity.[42,43] In this context, an in silico approach has been used to achieve a preliminary assessment of eventual interactions of indicaxanthin with these receptors.

The NMDA glutamate receptor forms a heterotetramer with two GluN1 and two GluN2 subunits, with various isoforms known to have distinct brain distribution. A number of studies showed that the GluN2A and GluN2B subunits are highly expressed in cortex and hippocampus,[42,43] which prompted us to focus our molecular modeling experiments on these subunits. Several crystallographic structures of GluN2A/B exist in the RCSB Protein Data Bank, free or in complex with natural agonists or antagonists. X-ray data of GluN1/GluN2B amino terminal domain (ATD) in complex with ifenprodil (Pdb: 3QEL), a selective antagonist of GluN2B subunit that interacts with ATD as an allosteric modulator, were selected for our aims. Ifenprodil represents the prototype of a prodil-like antagonist class of ligands.[44,45] In addition, the X-ray data of GluN1−GluN2A in complex with two selective competitive antagonists, the small D-AP5 (Pdb: 4NF5) and the larger PPDA (Pdb: 4NF6), were selected. PPDA has higher degree of GluN2A selectivity than D-AP5 because the core of glutamate binding pocket is highly conserved for these subunits; then small antagonists are generally unable to exert selectivity.[46] Therefore, selection of complexes with a small antagonist and a larger one to be compared with indicaxanthin could provide good information on the binding mode of indicaxanthin with the NMDAR. The modeling study was performed redocking the three antagonists and docking indicaxanthin into the coordinates of the three crystallographic structures of the receptor. The redocking procedure showed a root mean square deviation (RMSD) < 1 Å for ifenprodil, D-AP5, and PPDA with respect to the experimental conformation, confirming the suitability of the docking software to discriminate the correct poses. When compared with PPDA (docking score 5.72), indicaxanthin showed a better docking pose (score 9.63) on the interaction with GluN2A subunit residues. Four H-bonds were formed: oxygen of carboxyl C13 with the $-NH_2$ of Gly89; oxygen of carboxyl C15 with the $-NH_2$ of Arg176; oxygen of carboxyl C2 with Ser173 and Tyr214. In addition, the carboxyl group C2 and C15 form three salt bridges with Arg121, Arg176, and Lys87 (Figure 6). The

DOI: 10.1021/acs.jafc.5b02612
J. Agric. Food Chem. 2015, 63, 7353−7360

docking pose with the GluN2B (score 7.08) was weaker than with GluN2A, quite lower than that of ifenprodil (score 10.98).

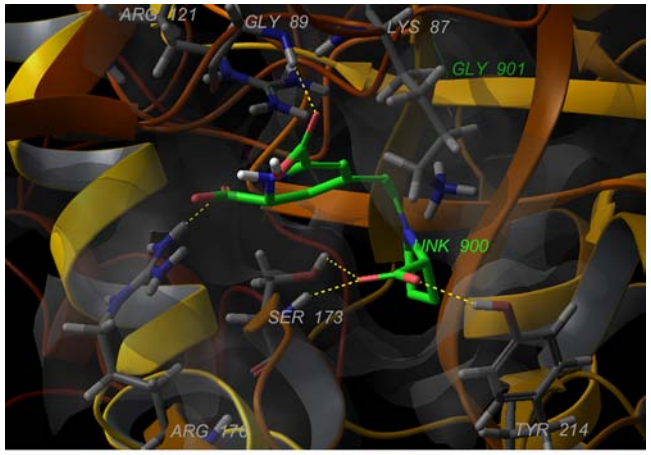

Figure 6. Binding pose of indicaxanthin in GluN2A subunit.

The free energy of binding for the GluN2B and GluN2A subunits in complex with ifenprodil, PPDA, D-AP5, and indicaxanthin was then calculated using the MM/GBSA approach. The free energy was −87.3 kcal/mol for ifenprodil/GluN2B, −92.7 kcal/mol for PPDA/GluN2A, and −57.6 kcal/mol for D-AP5/GluN2A. The binding free energy of indicaxanthin with GluN2B was −41.3 kcal/mol, indicating the ability to bind this subunit, with a quite higher ΔG binding than the selective antagonist ifenprodil. On the other hand, the free energy of binding with GluN2A was −80.7 kcal/mol, much higher than that of D-AP5 and comparable with that of PPDA.

The relevance of the residues in the ligand−GluN2A subunit interaction was explored by computational mutagenesis, replacing each of the aforementioned residues with alanine.[32] The energetic data are reported in Table 1. All mutations applied were unfavorable, with an increase of ΔG_{Bind} in a range between 20 and 40 kcal/mol, indicating that K87, R176, G89, S173, Y214, and R121 were fundamental for the indicaxanthin binding with the receptor subunit.

In conclusion, dietary phytochemicals are now acknowledged to exert positive effects on cell functions and then contribute to maintain health. Only a few of them, however, have been reported to cross the BBB and have activity at the brain level.[17,47,48] This study in rats was aimed at addressing whether indicaxanthin, a highly bioavailable dietary phytochemical from cactus pear fruits, shown to be absorbed in humans without being transformed,[7,9] has the ability to cross the BBB. In our model we clearly demonstrate that orally administered indicaxanthin accumulates within the brain and is released with kinetics consistent with its plasma kinetics. We also show that amounts of the pigment comparable with those recovered in the brain, locally applied in the rat hippocampus, can modulate dose-dependently the bioelectric activity of hippocampal cells, possibly acting at the level of glutamatergic synapses. Molecular modeling studies, carried out to have an insight into eventual interactions of indicaxanthin with Glu receptors, may suggest involvement of the NMDAR. The interaction with other Glu receptors cannot be ruled out at this time and deserves further electrophysiology and molecular modeling studies.

The hippocampal glutamatergic transmission is involved in many processes both physiological and pathological, from learning and memory to excitotoxicity, anxiety, and seizures, and is controlled by inner mechanisms of inhibition finely tuning synaptic transmission, exerting a negative feedback in glutamatergic-activated terminals.[49,50] In this context the neuromodulatory activity of dietary phytochemicals inhibiting the Glu-induced hippocampal synaptic transmission may contribute to a balanced control of neuronal activity and appears of remarkable interest.

Finally, it should be mentioned that present findings in rats have been obtained with amounts of indicaxanthin of the same order as those measured in human plasma after a dietary consumption of cactus pear fruits.[7] While molecular activity and pharmacological effects of indicaxanthin may deserve further studies in specific pathology models, effects on neural function could be expected from foods containing this molecule.

AUTHOR INFORMATION

Corresponding Author

*Phone: +39 091 23896803. E-mail: maria.livrea@unipa.it.

Funding

The present study has been supported by grants from the Ministero dell'Istruzione, Università e Ricerca (University of Palermo, Fondi di Ateneo ex 60%).

Notes

The authors declare no competing financial interest.

REFERENCES

(1) Butera, D.; Tesoriere, L.; Di Gaudio, F.; Bongiorno, A.; Allegra, M.; Pintaudi, A. M.; Kohen, R.; Livrea, M. A. Antioxidant activities of sicilian prickly pear (Opuntia ficus indica) fruit extracts and reducing

Table 1. Relative Binding Free Energies (kcal/mol) between Wild and Mutant Indicaxanthin/GluN2A Subunit Complex

	ΔG_{Bind} [a]	ΔG_{Hbond} [b]	$\Delta G_{Coulomb}$ [c]	$\Delta G_{Covalent}$ [d]	ΔG_{Lipo} [e]	ΔG_{SolvGB} [f]	ΔG_{vdW} [g]
WT[h]	−80.60	−8.35	36.62	7.37	−22.75	−58.02	−35.46
K87A	−38.94	−7.95	89.38	6.95	−18.38	−71.69	−37.24
R176A	−43.24	−7.22	85.70	7.71	−19.38	−68.87	−41.18
G89A	−46.82	−10.63	78.99	13.87	−20.75	−66.85	−41.46
S173A	−51.49	−9.84	22.05	9.13	−30.44	−4.83	−37.54
Y214A	−43.92	−9.97	21.88	8.87	−28.79	0.88	−36.79
R121A	−61.94	−4.28	75.34	9.30	−27.61	−74.66	−40.04

[a] ΔG_{Bind}, free energy of binding. [b] Contribution to the MMGBSA free energy of binding from hydrogen bonding. [c] Contribution to the MMGBSA free energy of binding from the Coulomb energy. [d] Contribution to the MMGBSA free energy of binding from covalent binding. [e] Contribution to the MMGBSA free energy of binding from lipophilic binding. [f] Contribution to the MMGBSA free energy of binding from the generalized Born electrostatic solvation energy. [g] Contribution to the MMGBSA free energy of binding from the van der Waals energy. [h] WT, wild type.

DOI: 10.1021/acs.jafc.5b02612
J. Agric. Food Chem. 2015, 63, 7353−7360

properties of its betalains: betanin and indicaxanthin. *J. Agric. Food Chem.* **2002**, *50*, 6895−901.
(2) Tesoriere, L.; Allegra, M.; Butera, D.; Gentile, C.; Livrea, M. A. Kinetics of the lipoperoxyl radical-scavenging activity of indicaxanthin in solution and unilamellar liposomes. *Free Radical Res.* **2007**, *41*, 226−33.
(3) Allegra, M.; Tesoriere, L.; Livrea, M. A. Betanin inhibits the myeloperoxidase/nitrite-induced oxidation of human low-density lipoproteins. *Free Radical Res.* **2007**, *41*, 335−41.
(4) Tesoriere, L.; Allegra, M.; Butera, D.; Gentile, C.; Livrea, M. A. Cytoprotective effects of the antioxidant phytochemical indicaxanthin in beta-thalassemia red blood cells. *Free Radical Res.* **2006**, *40*, 753−61.
(5) Tesoriere, L.; Butera, D.; Allegra, M.; Fazzari, M.; Livrea, M. A. Distribution of betalain pigments in red blood cells after consumption of cactus pear fruits and increased resistance of the cells to ex vivo induced oxidative hemolysis in humans. *J. Agric. Food Chem.* **2005**, *53*, 1266−70.
(6) Allegra, M.; Furtmuller, P. G.; Jantschko, W.; Zederbauer, M.; Tesoriere, L.; Livrea, M. A.; Obinger, C. Mechanism of interaction of betanin and indicaxanthin with human myeloperoxidase and hypochlorous acid. *Biochem. Biophys. Res. Commun.* **2005**, *332*, 837−44.
(7) Tesoriere, L.; Allegra, M.; Butera, D.; Livrea, M. A. Absorption, excretion, and distribution of dietary antioxidant betalains in LDLs: potential health effects of betalains in humans. *Am. J. Clin. Nutr.* **2004**, *80*, 941−5.
(8) Tesoriere, L.; Butera, D.; D'Arpa, D.; Di Gaudio, F.; Allegra, M.; Gentile, C.; Livrea, M. A. Increased resistance to oxidation of betalain-enriched human low density lipoproteins. *Free Radical Res.* **2003**, *37*, 689−96.
(9) Tesoriere, L.; Gentile, C.; Angileri, F.; Attanzio, A.; Tutone, M.; Allegra, M.; Livrea, M. A. Trans-epithelial transport of the betalain pigments indicaxanthin and betanin across Caco-2 cell monolayers and influence of food matrix. *Eur. J. Nutr.* **2013**, *52*, 1077−87.
(10) Turco Liveri, M. L.; Sciascia, L.; Allegra, M.; Tesoriere, L.; Livrea, M. A. Partition of indicaxanthin in membrane biomimetic systems. A kinetic and modeling approach. *J. Agric. Food Chem.* **2009**, *57*, 10959−63.
(11) Liveri, M. L.; Sciascia, L.; Lombardo, R.; Tesoriere, L.; Passante, E.; Livrea, M. A. Spectrophotometric evidence for the solubilization site of betalain pigments in membrane biomimetic systems. *J. Agric. Food Chem.* **2007**, *55*, 2836−40.
(12) Tesoriere, L.; Attanzio, A.; Allegra, M.; Gentile, C.; Livrea, M. A. Phytochemical indicaxanthin suppresses 7-ketocholesterol-induced THP-1 cell apoptosis by preventing cytosolic Ca(2+) increase and oxidative stress. *Br. J. Nutr.* **2013**, *110*, 230−40.
(13) Tesoriere, L.; Attanzio, A.; Allegra, M.; Gentile, C.; Livrea, M. A. Indicaxanthin inhibits NADPH oxidase (NOX)-1 activation and NF-kappaB-dependent release of inflammatory mediators and prevents the increase of epithelial permeability in IL-1beta-exposed Caco-2 cells. *Br. J. Nutr.* **2014**, *111*, 415−23.
(14) Gentile, C.; Tesoriere, L.; Allegra, M.; Livrea, M. A.; D'Alessio, P. Antioxidant betalains from cactus pear (Opuntia ficus-indica) inhibit endothelial ICAM-1 expression. *Ann. N. Y. Acad. Sci.* **2004**, *1028*, 481−6.
(15) Allegra, M.; Ianaro, A.; Tersigni, M.; Panza, E.; Tesoriere, L.; Livrea, M. A. Indicaxanthin from cactus pear fruit exerts anti-inflammatory effects in carrageenin-induced rat pleurisy. *J. Nutr.* **2014**, *144*, 185−92.
(16) Howitz, K. T.; Sinclair, D. A. Xenohormesis: sensing the chemical cues of other species. *Cell* **2008**, *133*, 387−91.
(17) Rendeiro, C.; Guerreiro, J. D.; Williams, C. M.; Spencer, J. P. Flavonoids as modulators of memory and learning: molecular interactions resulting in behavioural effects. *Proc. Nutr. Soc.* **2012**, *71*, 246−62.
(18) Milbury, P. E.; Kalt, W. Xenobiotic metabolism and berry flavonoid transport across the blood-brain barrier. *J. Agric. Food Chem.* **2010**, *58*, 3950−6.
(19) Papandreou, M. A.; Dimakopoulou, A.; Linardaki, Z. I.; Cordopatis, P.; Klimis-Zacas, D.; Margarity, M.; Lamari, F. N. Effect of a polyphenol-rich wild blueberry extract on cognitive performance of mice, brain antioxidant markers and acetylcholinesterase activity. *Behav. Brain Res.* **2009**, *198*, 352−8.
(20) Del Rio, D.; Borges, G.; Crozier, A. Berry flavonoids and phenolics: bioavailability and evidence of protective effects. *Br. J. Nutr.* **2010**, *104* (Suppl. S3), S67−90.
(21) Sardo, P.; Carletti, F.; D'Agostino, S.; Rizzo, V.; Ferraro, G. Effects of nitric oxide-active drugs on the discharge of subthalamic neurons: microiontophoretic evidence in the rat. *European journal of neuroscience* **2006**, *24*, 1995−2002.
(22) Paxinos, G.; Katritsis, D.; Kakouros, S.; Toutouzas, P.; Camm, A. J. Long-term effect of VVI pacing on atrial and ventricular function in patients with sick sinus syndrome. *Pacing and clinical electrophysiology: PACE* **1998**, *21*, 728−34.
(23) Carletti, F.; Ferraro, G.; Rizzo, V.; D'Agostino, S.; Lonobile, G.; Sardo, P. Nitric oxide- and cGMP-active compounds affect the discharge of substantia nigra pars reticulata neurons: in vivo evidences in the rat. *J. Neural Transm* **2009**, *116*, 539−49.
(24) Carletti, F.; Ferraro, G.; Rizzo, V.; Friscia, S.; Sardo, P. Modulation of in vivo GABA-evoked responses by nitric oxide-active compounds in the globus pallidus of rat. *J. Neural Transm* **2012**, *119*, 911−21.
(25) Sardo, P.; Carletti, F.; Rizzo, V.; Lonobile, G.; Friscia, S.; Ferraro, G. Nitric oxide-active compounds modulate the intensity of glutamate-evoked responses in the globus pallidus of the rat. *Life Sci.* **2011**, *88*, 1113−20.
(26) Karakas, E.; Simorowski, N.; Furukawa, H. Subunit arrangement and phenylethanolamine binding in GluN1/GluN2B NMDA receptors. *Nature* **2011**, *475*, 249−53.
(27) Jespersen, A.; Tajima, N.; Fernandez-Cuervo, G.; Garnier-Amblard, E. C.; Furukawa, H. Structural insights into competitive antagonism in NMDA receptors. *Neuron* **2014**, *81*, 366−78.
(28) Almerico, A. M.; Tutone, M.; Lauria, A. Receptor-guided 3D-QSAR approach for the discovery of c-kit tyrosine kinase inhibitors. *J. Mol. Model.* **2012**, *18*, 2885−95.
(29) Almerico, A. M.; Tutone, M.; Lauria, A. 3D-QSAR pharmacophore modeling and in silico screening of new Bcl-xl inhibitors. *Eur. J. Med. Chem.* **2010**, *45*, 4774−82.
(30) Almerico, A. M.; Tutone, M.; Pantano, L.; Lauria, A. A3 adenosine receptor: homology modeling and 3D-QSAR studies. *J. Mol. Graphics Modell.* **2013**, *42*, 60−72.
(31) Tutone, M.; Pantano, L.; Lauria, A.; Almerico, A. M. Molecular dynamics, dynamic site mapping, and highthroughput virtual screening on leptin and the Ob receptor as anti-obesity target. *J. Mol. Model.* **2014**, *20*, 2247.
(32) Massova, I.; Kollman, P. A. Computational alanine scanning to probe protein-protein interactions: A novel approach to evaluate binding free energies. *J. Am. Chem. Soc.* **1999**, *121*, 8133−8143.
(33) Andres-Lacueva, C.; Shukitt-Hale, B.; Galli, R. L.; Jauregui, O.; Lamuela-Raventos, R. M.; Joseph, J. A. Anthocyanins in aged blueberry-fed rats are found centrally and may enhance memory. *Nutr. Neurosci.* **2005**, *8*, 111−20.
(34) Borges, G.; Roowi, S.; Rouanet, J. M.; Duthie, G. G.; Lean, M. E.; Crozier, A. The bioavailability of raspberry anthocyanins and ellagitannins in rats. *Mol. Nutr. Food Res.* **2007**, *51*, 714−25.
(35) Letenneur, L.; Proust-Lima, C.; Le Gouge, A.; Dartigues, J. F.; Barberger-Gateau, P. Flavonoid intake and cognitive decline over a 10-year period. *Am. J. Epidemiol.* **2007**, *165*, 1364−71.
(36) Tesoriere, L.; Butera, D.; Pintaudi, A. M.; Allegra, M.; Livrea, M. A. Supplementation with cactus pear (Opuntia ficus-indica) fruit decreases oxidative stress in healthy humans: a comparative study with vitamin C. *Am. J. Clin. Nutr.* **2004**, *80*, 391−5.
(37) Lee, H. B.; Blaufox, M. D. Blood volume in the rat. *J. Nucl. Med.* **1985**, *26*, 72−6.
(38) Gerhardt, G. A.; Palmer, M. R. Characterization of the techniques of pressure ejection and microiontophoresis using in vivo electrochemistry. *J. Neurosci. Methods* **1987**, *22*, 147−59.

DOI: 10.1021/acs.jafc.5b02612
J. Agric. Food Chem. 2015, 63, 7353−7360

(39) Leuner, B.; Gould, E. Structural plasticity and hippocampal function. *Annu. Rev. Psychol.* **2010**, *61*, 111−40.
(40) Michaelis, E. K. Molecular biology of glutamate receptors in the central nervous system and their role in excitotoxicity, oxidative stress and aging. *Prog. Neurobiol.* **1998**, *54*, 369−415.
(41) Coultrap, S. J.; Bickford, P. C.; Browning, M. D. Blueberry-enriched diet ameliorates age-related declines in NMDA receptor-dependent LTP. *Age (Dordr)* **2008**, *30*, 263−72.
(42) Sanz-Clemente, A.; Nicoll, R. A.; Roche, K. W. Diversity in NMDA receptor composition: many regulators, many consequences. *Neuroscientist* **2013**, *19*, 62−75.
(43) Paoletti, P. Molecular basis of NMDA receptor functional diversity. *Eur. J. Neurosci* **2011**, *33*, 1351−65.
(44) Mony, L.; Kew, J. N.; Gunthorpe, M. J.; Paoletti, P. Allosteric modulators of NR2B-containing NMDA receptors: molecular mechanisms and therapeutic potential. *Br. J. Pharmacol.* **2009**, *157*, 1301−17.
(45) Carter, C.; Benavides, J.; Legendre, P.; Vincent, J. D.; Noel, F.; Thuret, F.; Lloyd, K. G.; Arbilla, S.; Zivkovic, B.; MacKenzie, E. T.; et al. Ifenprodil and SL 82.0715 as cerebral anti-ischemic agents. II. Evidence for N-methyl-D-aspartate receptor antagonist properties. *J. Pharmacol. Exp. Ther.* **1988**, *247*, 1222−32.
(46) Gitto, R.; De Luca, L.; De Grazia, S.; Chimirri, A. Glutamatergic neurotransmission as molecular target of new anticonvulsants. *Curr. Top. Med. Chem.* **2012**, *12*, 971−93.
(47) Spencer, J. P. The impact of flavonoids on memory: physiological and molecular considerations. *Chem. Soc. Rev.* **2009**, *38*, 1152−61.
(48) Dias, G. P.; Cavegn, N.; Nix, A.; do Nascimento Bevilaqua, M. C.; Stangl, D.; Zainuddin, M. S.; Nardi, A. E.; Gardino, P. F.; Thuret, S. The role of dietary polyphenols on adult hippocampal neurogenesis: molecular mechanisms and behavioural effects on depression and anxiety. *Oxid. Med. Cell. Longevity* **2012**, *2012*, 541971.
(49) Monory, K.; Massa, F.; Egertova, M.; Eder, M.; Blaudzun, H.; Westenbroek, R.; Kelsch, W.; Jacob, W.; Marsch, R.; Ekker, M.; Long, J.; Rubenstein, J. L.; Goebbels, S.; Nave, K. A.; During, M.; Klugmann, M.; Wolfel, B.; Dodt, H. U.; Zieglgansberger, W.; Wotjak, C. T.; Mackie, K.; Elphick, M. R.; Marsicano, G.; Lutz, B. The endocannabinoid system controls key epileptogenic circuits in the hippocampus. *Neuron* **2006**, *51*, 455−66.
(50) Fagni, L.; Bockaert, J. Effects of nitric oxide on glutamate-gated channels and other ionic channels. *J. Chem. Neuroanat.* **1996**, *10*, 231−40.

DOI: 10.1021/acs.jafc.5b02612
J. Agric. Food Chem. 2015, 63, 7353−7360

oxidized NAD^+ form.[32,33] Thus, it is of interest to study whether tNOX and the NAD^+/NADH ratio are involved in the differential effect of capsaicin. Here, we present evidence for the first time that the intracellular NAD^+/NADH ratio and SIRT1 deacetylase activity are central to the regulation of capsaicin-induced cell death.

MATERIALS AND METHODS

Cell Culture and Reagents. Capsaicin with purity >95% was purchased from Sigma-Aldrich Corp. (St. Louis, MO, USA). Anti-Bax, anti-Bak, anti-PARP, anti-Bcl-2, anti-p53, anti-acetyl-p53, anti-SIRT1, anti-mTOR, anti-phospho-mTOR, anti-phospho-AMPK, anti-phospho-JNK, and anti-acetyl-Lys antibodies were from Cell Signaling Technology, Inc. (Beverly, MA, USA). Anti-beclin-1, anti-Atg5, anti-Atg7, and anti-LC3 antibodies were from Novus Biologicals, Inc. (Littleton, CO, USA). The anti-survivin antibody was purchased from Santa Cruz Biotechnology, Inc. (Santa Cruz, CA, USA). Anti-β-actin antibody was from Millipore Corp. (Temecula, CA, USA). Antisera to tNOX were generated as described previously.[34] Other chemicals were from Sigma-Aldrich Corp.

A549 (human lung adenocarcinoma epithelial) cells were grown in DMEM, and MRC-5 (human lung tissue) cells were grown in MEM. All media were supplemented with 10% FBS, 100 U/mL penicillin, and 50 μg/mL streptomycin. Cells were maintained at 37 °C in a 5% CO_2−95% air-humidified incubator. ON-TARGETplus tNOX (ENOX2) siRNA and negative control siRNA were purchased from Thermo Scientific, Inc. (Grand Island, NY, USA), and SignalSilence Sirt1 siRNA I and control siRNA were from Cell Signaling Technology, Inc. Briefly, cells were seeded in 10 cm dishes and allowed to attach overnight. The next day, cells were transfected with tNOX/Sirt1 siRNA and control siRNA using Lipofectamin RNAiMAX reagent (Life Technologies, Grand Island, NY, USA) according to the manufacturer's instructions.[35]

Cell Impedance Measurements. Cell impedance technology was used to continuously monitor changes in cell growth. Cells (10^4 cells/well) were seeded onto E-plates. After 30 min of incubation at room temperature, E-plates were then set down onto the Real-Time Cell Analysis station (Roche, Mannheim, Germany). Cells were grown overnight before exposure to ethanol or different concentrations of capsaicin, and cell impedance was measured every hour, as previously described.[36]

WST-1 Cell Viability Assay. Cells (5×10^3) were seeded in 96-well culture plates and permitted to adhere overnight. Cells were then treated with capsaicin or ethanol for 72 h, and at the end of treatment, cell viability was determined using a WST-1 assay (Roche Applied Science, Mannheim, Germany).

Apoptosis Determination. Annexin V-FITC Apoptosis Detection Kits were used to determine apoptosis (BD Pharmingen, San Jose, CA, USA). Briefly, cells treated with ethanol or different concentrations of capsaicin were harvested by centrifugation after trypsinization. Cell pellet was washed with PBS and resuspended in 1× binding buffer. Next, cell pellet was stained with annexin V-FITC (fluorescein isothiocyanate) and also propidium iodide (PI) according to the manufacturer's protocol. The patterns of cell death (necrosis and apoptosis) were analyzed using a Beckman Coulter FC500 flow cytometer, and results were expressed as a percentage of total cells.

Autophagy Determination. Autophagosomes were visualized by staining with Acridine Orange (AO). After incubation, cells were washed with PBS and stained with 1 mg/mL AO for 15 min at 37 °C. AO-stained cells were then washed, trypsinized, and analyzed using a Beckman Coulter FC500. The results are expressed as a percentage of total cells.

Visualization of Autophagosome Formation Using EGFP-LC3. For autophagy experiments, MRC-5 cells were transiently transfected with a pEGFP-LC3 construct (a generous gift from Dr. Tamotsu Yoshimori, Osaka University, Japan) using Lipotectamine 2000 reagent according to the manufacturer's instructions (Invitrogen, Carlsbad, CA, USA).[37] MRC-5-EGFP-LC3 cells were either starved or exposed to capsaicin or ethanol, and autophagosomes formation was visualized.

Measurement of Intracellular NAD^+/NADH Ratio. Both oxidized and reduced forms of intracellular nicotinamide adenine dinucleotide were determined using an NADH/NAD Quantification Kit (BioVision Inc., Milpitas, CA, USA). Briefly, 2×10^5 cells were washed with cold PBS, pelleted, and extracted with 400 μL of NADH/NAD extraction buffer by two freeze/thaw cycles. Samples were vortexed and centrifuged at 14000 rpm for 5 min. For each sample, a 200 μL aliquot of extracted NADH/NAD supernatant was transferred to a microcentrifuge tube. Samples were first heated to 60 °C for 30 min to allow decomposition of all NAD^+, while retaining NADH intact, and then placed on ice. Samples were rapidly centrifuged and transferred to a multiwall plate. Standards and a NAD cycling mix were prepared according to the manufacturer's protocol. One hundred microliters of the reaction mix was added into each well of NADH standards and samples, and all samples were incubated at room temperature for 5 min to convert NAD^+ to NADH. NADH Developer Solution was added to each well, and plates were incubated at room temperature for 30 min. The reaction was stopped by adding 10 μL of Stop Solution, and absorbance was measured at 450 nm.

Measurement of SIRT1 Deacetylase Activity in Vitro. SIRT1 deacetylase activity was determined using a SIRT1 direct Fluorescent Screening Assay Kit (Cayman Chemical Co., Ann Arbor, MI, USA). Briefly, the substrate solution was first prepared by adding 240 μL of NAD^+ solution and 850 μL of diluted assay buffer to 15 μL of the p53 peptide Arg-His-Lys-Lys(ε-acetyl)-AMC, to yield final concentrations of 125 μM peptide (substrate) and 3 mM NAD^+. Background was determined in wells containing 30 μL of assay buffer and 5 μL of solvent. Maximal initial activity (defined as 100%) was determined in wells containing 5 μL of diluted human recombinant SIRT1, 25 μL of assay buffer, and 5 μL of solvent. For our experiments, 5 μL of capsaicin was added to wells containing 25 μL of assay buffer and 5 μL of diluted human recombinant SIRT1. Reactions were initiated by adding 15 μL of substrate solution to all of the wells. The plate was then covered and incubated on a shaker for 45 min at room temperature. Reactions were stopped by adding 50 μL of Stop/Developing Solution to each well and incubating the plate for 30 min at room temperature. Plates were read in a fluorometer using an excitation wavelength of 350−360 nm and an emission wavelength of 450−465 nm.

Western Blot Analysis. Cell extracts were prepared in lysis buffer containing 20 mM Tris-HCl, pH 7.4, 100 mM NaCl, 5 mM EDTA, 2 mM phenylmethanesulfonyl fluoride (PMSF), 10 ng/mL leupeptin, and 10 μg/mL aprotinin. Volumes of extract containing equal amounts of proteins (40 μg) were applied to SDS-PAGE gels, and resolved proteins were transferred to nitrocellulose membranes (Schleicher & Schuell, Keene, NH, USA). The membranes were blocked with nonfat milk solution for 30 min, then washed, and probed with primary antibody. Membranes were then rinsed with Tris-buffered saline containing 0.1% Tween 20 to remove unbound primary antibody and incubated with horseradish peroxidase-conjugated secondary antibody for 2 h. The membranes were rinsed again and developed using enhanced chemiluminescence (ECL) reagents (Amersham Biosciences, Piscataway, NJ, USA).

Statistics. All data are expressed as the mean ± SE of three or more independent experiments. Comparison between groups was made by one-way analysis of variance (ANOVA) followed by an appropriate post hoc test to analyze the difference. A value of $p < 0.05$ was considered to be statistically significant.

RESULTS

A549 Cells Exhibit Greater Responsiveness to Capsaicin than MRC-5 Cells. Given that transformed and noncancerous cells exhibit differential cytotoxicity to capsaicin, we decided to choose lines from lung tissue, MRC-5 (human lung tissue) and A549 (human lung adenocarcinoma), cells in this study. We continuously monitored the dynamic effects of capsaicin on cell growth, measuring cell impedance and

DOI: 10.1021/acs.jafc.5b02876
J. Agric. Food Chem. 2015, 63, 7361−7370

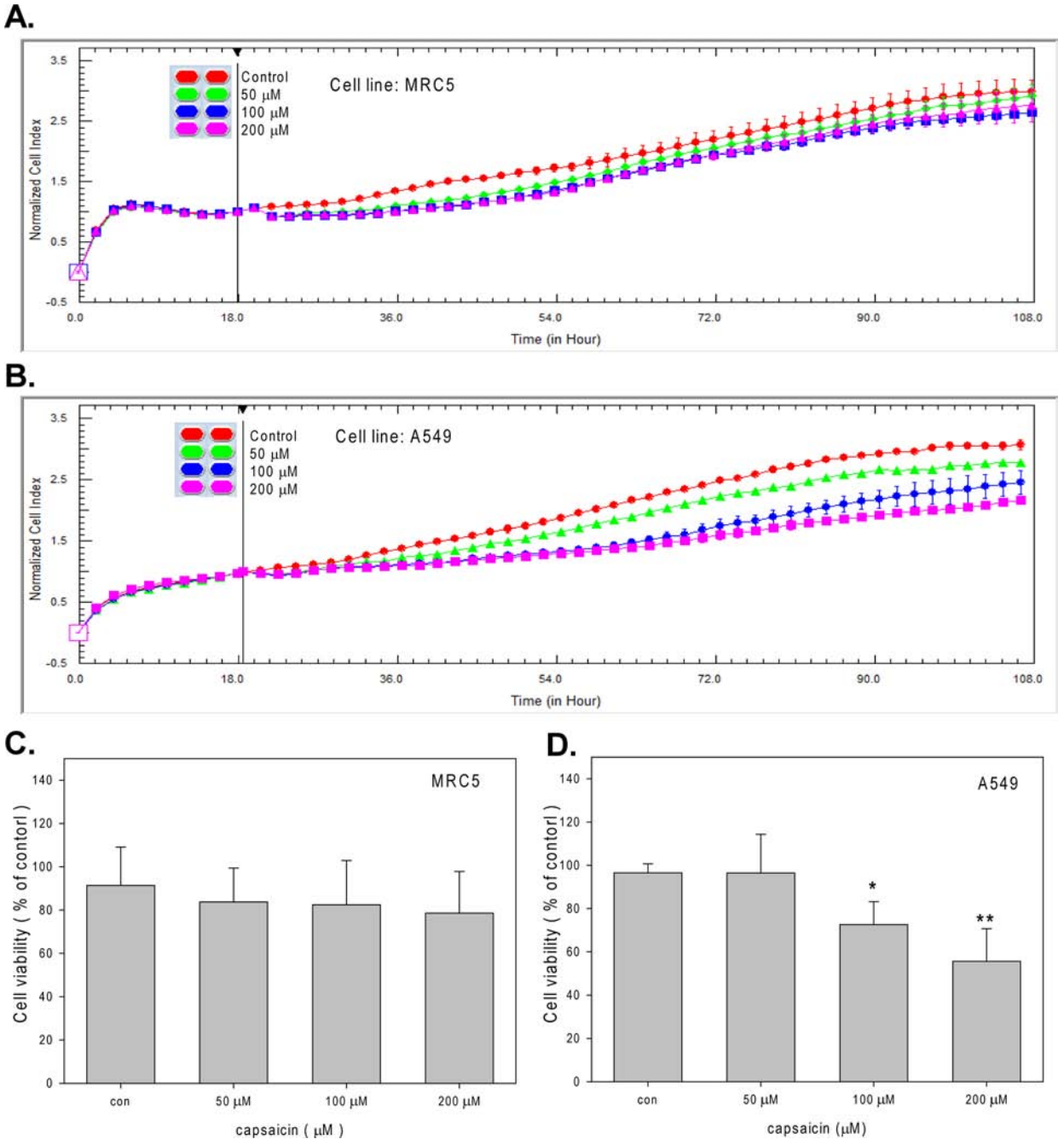

Figure 1. Capsaicin inhibits cell growth in A549 cells but not in MC-5 cells. (A, B) Cell growth with or without capsaicin was dynamically monitored using impedance technology, in MRC-5 cells (A) and in A549 cells (B). Normalized cell index values measured over 108 h are shown. (C, D) Cells were treated with capsaicin for 72 h, and cell viability was determined by WST-1 assay, in MRC-5 cells (C) and in A549 cells (D). Values (mean ± SE) are from three independent experiments performed in at least triplicates: (∗) $p < 0.05$ and (∗∗) $p < 0.01$ for A549 cells treated with capsaicin versis controls.

displaying the results as cell index values.[38] Using this approach, we found that MRC-5 cell growth was decreased by capsaicin at an early stage of exposure; however, cell growth gradually recovered, resulting in little overall inhibition at all concentrations tested (Figure 1A). In contrast, capsaicin induced a significant concentration-dependent decrease in cell growth in A549 cells; this inhibitory effect was much more evident than that in MRC-5 cells (Figure 1B). The greater responsiveness of A549 cells to capsaicin is reflected in IC_{50} values, which was determined to be 33.8 μM for A549 cells but could not be calculated in MRC-5 cells because the degree of inhibition was so low in these cells. We also tested cell viability using WST-1 assays and demonstrated that the viability of MRC-5 cells was not inhibited significantly by capsaicin (Figure 1C), whereas that of A549 cells was decreased considerably (to less than 76 and 60% of control values at 100 and 200 μM, respectively) (Figure 1D). The IC_{50} value for capsaicin in A549 cells determined on the basis of WST-1 assays was 146 μM and could not be calculated for MRC-5 cells due to a low degree of inhibition. These data suggested that capsaicin is cytotoxic in A549 cells but not in MRC-5 cells.

DOI: 10.1021/acs.jafc.5b02876
J. Agric. Food Chem. 2015, 63, 7361−7370

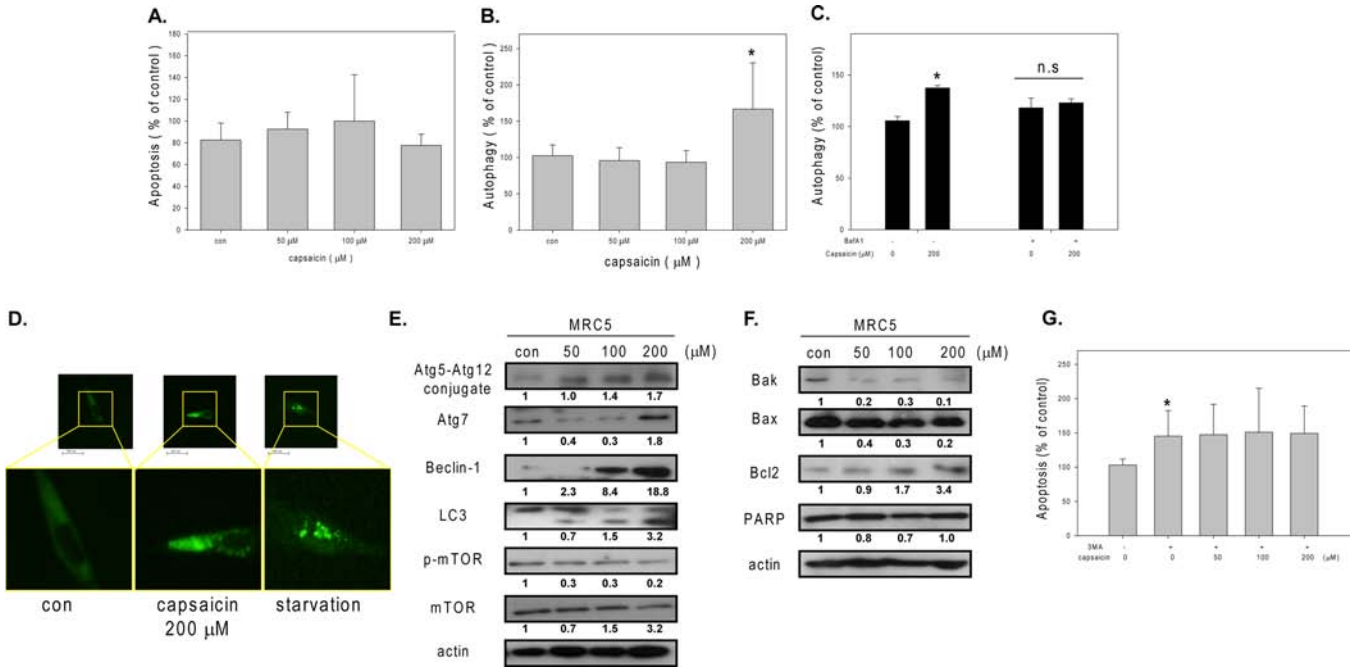

Figure 2. Capsaicin preferentially induces autophagy but not apoptosis in MRC-5 cells. (A) MRC-5 cells were treated with capsaicin or ethanol for 24 h. The percentage of apoptotic cells was determined by flow cytometry, and the results are expressed as a percentage relative to the control group. Values (mean ± SE) are from three independent experiments. No significant differences were observed. (B) Cells were treated with capsaicin or ethanol for 6 h. Autophagy was determined by AO staining using flow cytometry, and the results are expressed as a percentage relative to the control group. Values (mean ± SE) are from four independent experiments: (∗) $p < 0.05$ for MRC-5 cells treated with 200 μM capsaicin versus controls. (C) MRC-5 cells were pretreated with 0.1 μM BafA1 or not for 30 min before exposure to capsaicin for 6 h. The percentage of autophagic cells was assessed by flow cytometry, and the results are expressed as a percentage relative to the control group. Values (mean ± SE) are from three independent experiments: (∗) $p < 0.05$ for MRC-5 cells without BafA1 pretreatment treated with capsaicin versus controls. (D) MRC-5 cells were transiently transfected with EGFP-LC3 for 48 h and serum starved or treated with capsaicin or ethanol for 6 h. EGFP fluorescence was observed under a fluorescence microscopy. (E, F) MRC-5 cells were treated with capsaicin or ethanol for 24 h. Aliquots of cell lysates were separated by SDS-PAGE and analyzed by Western blotting; β-actin was used as internal control. Representative images from three experiments are shown. (G) MRC-5 cells were pretreated with 100 μM 3-MA or not for 1 h before exposure to capsaicin or ethanol for 24 h. The percentage of apoptotic cells was assessed by flow cytometry, and the results are expressed as a percentage relative to the control group. Values (mean ± SE) are from four independent experiments: (∗) $p < 0.05$ for MRC-5 cells without 3-MA pretreatment versus other groups.

Capsaicin Induces Autophagy in MRC5 Cells but Not Apoptosis. To determine whether programmed cell death is involved in the differential cellular responses to capsaicin, we analyzed cells for apoptotic subpopulations. Interestingly, little apoptotic effect was observed in capsaicin-exposed MRC-5 cells, indicating that MRC-5 cells were largely impervious to the apoptotic effect of capsaicin (Figure 2A). We also explored the possibility that capsaicin induces autophagy—a type II programmed cell death-related pathway—in these cells. Using AO staining for detection of acidic vesicular organelles, we found that 200 μM capsaicin significantly increased the population of MRC-5 cells undergoing autophagy at 6 h (Figure 2B). Pretreatment of MRC-5 cells with the autophagy inhibitor bafilomycin A1 (BafA1) has shown to reverse the capsaicin-induced autophagy (Figure 2C). To further explore autophagy in capsaicin-exposed MRC-5 cells, we exogenously expressed a fusion protein of enhanced green fluorescent protein and the autophagy marker microtubule associated light chain 3 protein (EGFP-LC3) and observed the fluorescence. We showed that capsaicin exposure resulted in autophagosomes formation as green punctuate dots, similar to that observed in serum-starved cells (Figure 2D). Moreover, protein analyses verified that important autophagy regulators, such as autophagy-related 7 (Atg7), Atg5−Atg12 conjugate, beclin-1, and cleaved LC3 II, were up-regulated, whereas phosphorylated and total mammalian target of rapamycin (mTOR) were down-regulated by capsaicin (Figure 2E). Expressions of apoptosis-related proteins also indicated a lack of apoptosis in capsaicin-exposed MRC-5 cells, pro-apoptotic Bak protein Bax were decreased, pro-survival Bcl-2 protein was increased, and a caspase-3-mediated poly(ADP-ribose) polymerase (PARP) cleavage was not detected (Figure 2F). Pretreatment of MRC-5 cells with the autophagy inhibitor 3-methyladenine alone indeed significantly enhanced apoptosis; however, it had little impact on capsaicin-induced apoptosis (Figure 2G).

Capsaicin Induces Cytotoxic Apoptosis in A549 Cells. To verify that transformed and noncancerous cells indeed exhibit differential cytotoxicity to capsaicin, lung carcinoma cells were used in this study. In A549 cells, a 24 h capsaicin exposure induced a significant, >2-fold, increase in apoptosis at 200 μM (Figure 3A). Western blot analyses also revealed that capsaicin triggered considerable up-regulation of the Bak and Bax as well as cleaved PARP, with concurrent down-regulation of Bcl-2 and survivin in capsaicin-exposed A549 cells (Figure 3B). However, we found a lack of capsaicin-induced autophagy at 6 h of exposure (Figure 3C). Changes in autophagy protein levels were less marked in A549 cells (Figure 3D). Moreover, pretreatment with z-VAD, a pan-caspase inhibitor, had little effect on capsaicin-induced autophagy (Figure 3E).

Capsaicin Modulates Intracellular NAD^+/NADH Ratio. An association between capsaicin-inhibited tumor-associated NADH oxidase (tNOX) activity and cytotoxic apoptosis has

DOI: 10.1021/acs.jafc.5b02876
J. Agric. Food Chem. 2015, 63, 7361−7370

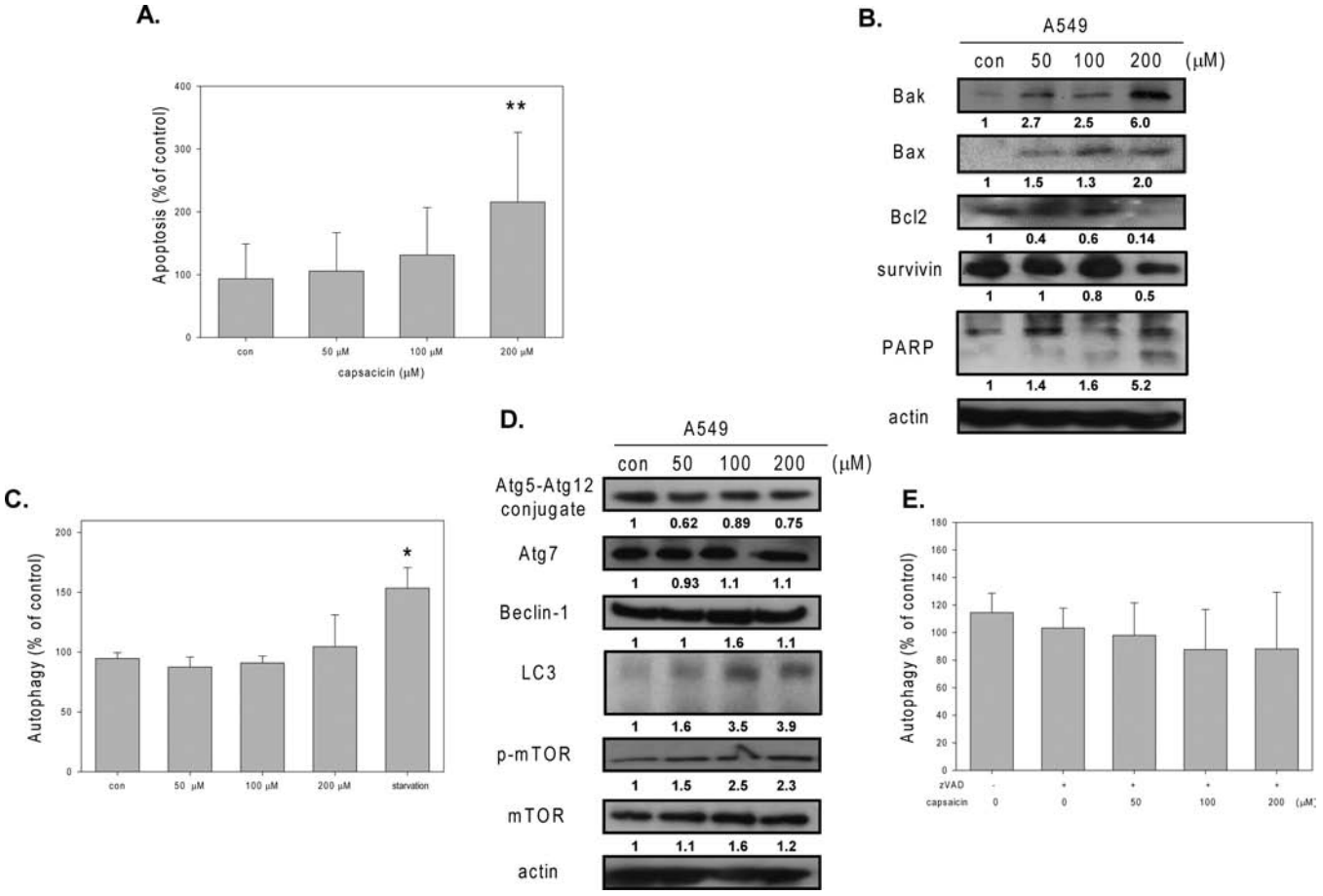

Figure 3. Capsaicin induces apoptosis but not autophagy in A549 cells. (A) A549 cells were treated with capsaicin or ethanol for 24 h. The percentage of apoptotic cells was determined by flow cytometry, and the results are expressed as a percentage relative to the control group. Values (mean ± SE) are from four independent experiments: (**) $p < 0.01$ for A549 cells treated with 200 μM capsaicin versus controls. (B, D) A549 cells were treated with capsaicin or ethanol for 6 or 24 h. Aliquots of cell lysates were separated by SDS-PAGE and analyzed by Western blotting. β-Actin was used as internal control. Representative images from three experiments are shown. (C) A549 cells were treated with capsaicin or ethanol for 6 h. Autophagy was determined by AO staining using flow cytometry, and the results are expressed as a percentage relative to the control group. Values (mean ± SE) are from three independent experiments: (*) $p < 0.05$ and (**) $p < 0.01$ for A549 cells treated with starvation or 200 μM capsaicin versus controls. (E) A549 cells were pretreated with 100 μM z-VAD for 1 h before exposure to capsaicin or ethanol for 6 h. The percentage of autophagic cells was assessed by flow cytometry, and the results are expressed as a percentage relative to the control group. Values (mean ± SE) are from three independent experiments. There were no significant differences in this experiment.

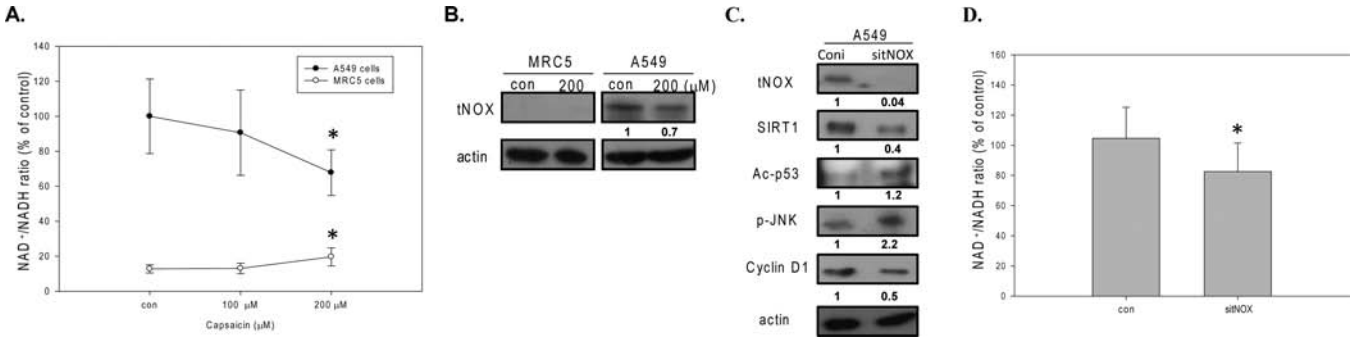

Figure 4. Modulation effects of capsaicin and tNOX-knockdown on cellular redox status and protein expression. (A) Cells were treated with ethanol or capsaicin, and NAD^+ and NADH in cell extracts were then quantified. The optical density at 450 nm was recorded and used to calculate the NAD^+/NADH ratio. Values (mean ± SE) are from three independent experiments: (*) $p < 0.05$ for cells treated with 200 μM capsaicin versus others. (B) Cells were treated with capsaicin or ethanol for 24 h. Aliquots of cell lysates were separated by SDS-PAGE and analyzed by Western blotting; β-actin was used as internal control. Representative images from three experiments are shown. (C) tNOX was down-regulated using siRNA. Aliquots of cell lysates were separated by SDS-PAGE and analyzed by Western blotting; β-actin was used as internal control. Representative images from three experiments are shown. (D) NAD^+ and NADH in control and tNOX-depleted A549 cell extracts were quantified. The optical density at 450 nm was recorded and used to calculate the NAD^+/NADH ratio. Values (mean ± SE) are from three independent experiments: (*) $p < 0.05$ for tNOX-depleted cells versus controls.

DOI: 10.1021/acs.jafc.5b02876
J. Agric. Food Chem. 2015, 63, 7361−7370

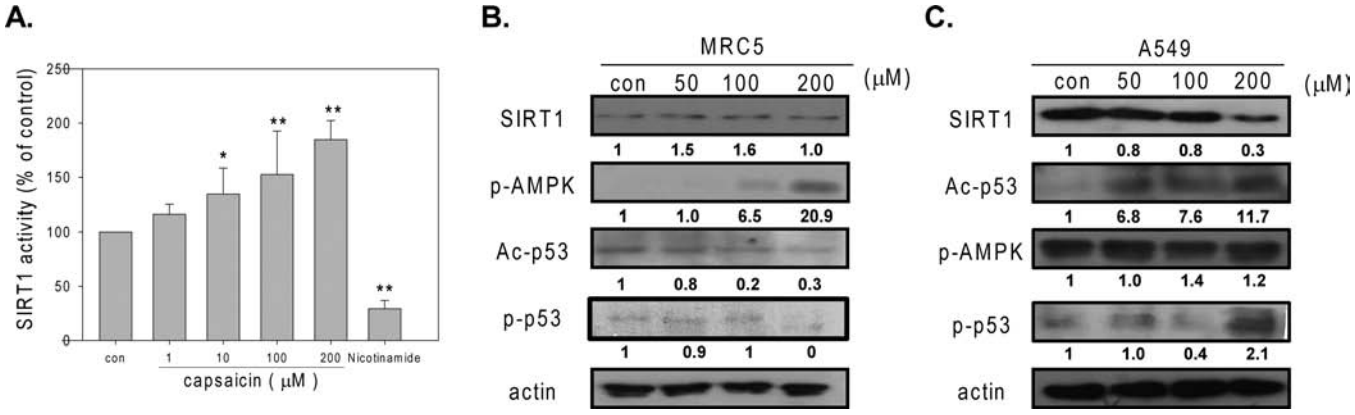

Figure 5. Modulation effects of capsaicin on SIRT1 in vitro activity and protein expression. (A) Samples were incubated with ethanol or capsaicin, and SIRT1 deacetylase activity in vitro was determined using a direct fluorescence assay kit. Nicotinamide was used as a control. Values (mean ± SE) are from three independent experiments performed in at least triplicates: (**) $p < 0.01$ and (*) $p < 0.05$ for samples treated with capsaicin or nicotinamide versus controls. (B, C) Cells were treated with capsaicin or ethanol for 24 h, in MRC-5 cells (B) and in A549 cells (C). Aliquots of cell lysates were separated by SDS-PAGE and analyzed by Western blotting; β-actin was used as internal control. Representative images from three experiments are shown.

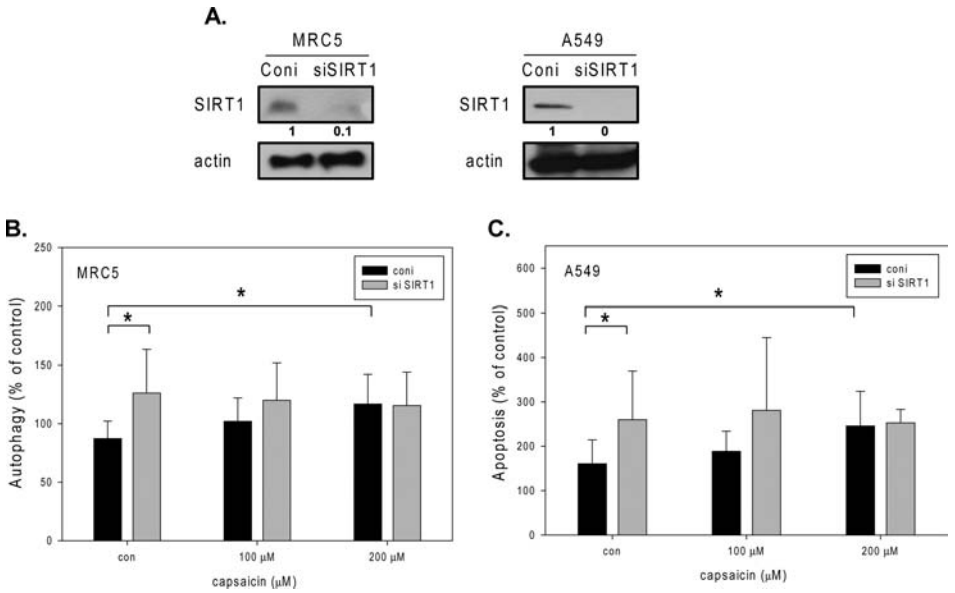

Figure 6. Effect of SIRT1 depletion on capsaicin-induced programmed cell death. (A) SIRT1 was down-regulated by siRNA, and cells were treated with ethanol or capsaicin. Aliquots of cell lysates were separated by SDS-PAGE and analyzed by Western blotting; β-actin was used as internal control. Representative images from three experiments are shown. (B) Control or SIRT1-depleted MRC-5 cells were treated with capsaicin or ethanol for 6 h. Autophagy was determined by AO staining using flow cytometry, and the results are expressed as a percentage relative to the control group. Values (mean ± SE) are from four independent experiments: (*) $p < 0.05$ for siRNA-control cells versus SIRT1-knockdown controls and also for siRNA-control cells treated with 200 μM capsaicin versus untreated controls. (C) Control and SIRT1-depleted A549 cells were treated with capsaicin or ethanol for 24 h. Apoptosis was determined by annexin V staining by flow cytometry, and the results are expressed as a percentage of apoptotic cells. Values (mean ± SE) are from three independent experiments: (*) $p < 0.05$ for siRNA-control cells versus SIRT1-knockdown controls and also for siRNA-control cells treated with 200 μM capsaicin versus untreated controls.

been previously established only in cancer/transformed cells.[1] This observation prompted us to examine whether the capsaicin-induced cytotoxicity in A549 cells involves tNOX and, if so, by what mechanism. NAD^+ is a biological oxidizing agent for many metabolic reactions, and tNOX oxidizes hydroquinones and NADH, converting the latter to the oxidized NAD^+ form.[33] Thus, it is reasonable to presume that a capsaicin-inhibited tNOX could potentially disturb cellular redox homeostasis and, consequently, disrupt cellular responses. In this regard, we found that the basal NAD^+/NADH ratio in A549 cells was much greater than that in MRC-5 cells, possibly reflecting endogenous tNOX activity in A549 cells (Figure 4A). Treatment of A549 cells with 200 μM capsaicin significantly decreased the NAD^+/NADH ratio but increased it in MRC-5 cells, although the change was relatively small compared with that in A549 cells (Figure 4A). These data support that tNOX oxidizes NADH to NAD^+ and capsaicin-inhibited tNOX resulted in a decrease in the intracellular NAD^+/NADH ratio in cancer cells. Moreover, capsaicin (200 μM) down-regulated tNOX expression in A549 cells, whereas tNOX expression was not detected in MRC-5 cells (Figure 4B), confirming tNOX expression in a cancerous, but not a nontransformed, line. We further found that targeting tNOX in A549 cells with siRNA (Figure 4C) decreased the NAD^+/

DOI: 10.1021/acs.jafc.5b02876
J. Agric. Food Chem. 2015, 63, 7361−7370

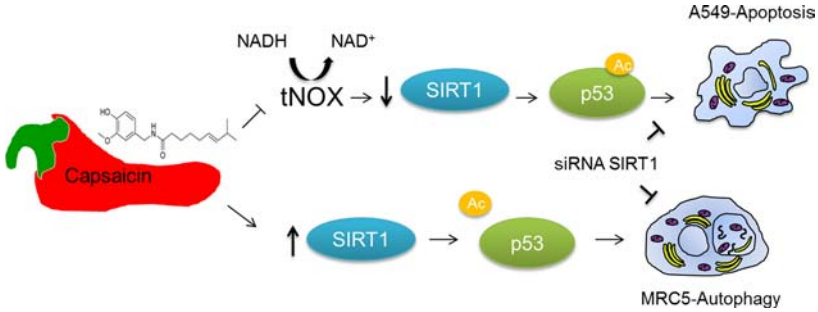

Figure 7. Schematic diagram of the mechanism of capsaicin-induced programmed cell death.

NADH ratio compared to A549 cells expressing control (scrambled) siRNA (Figure 4D). We also noted that tNOX-depleted A549 cells exhibited reduced silent mating type information regulation 1 (SIRT1) expression, whereas p53 acetylation and JNK phosphorylation were increased and cyclin D was attenuated (Figure 4C), confirming a tumor-promoting role of tNOX in cancer cells.

Capsaicin Inhibits SIRT1 Deacetylase Activity in A549 Cells but Enhances It in MRC-5 Cells. Given that NAD^+ is also a cofactor for SIRT1 deacetylase, we were interested in determining whether the opposing effects of capsaicin on the NAD^+/NADH ratio in A549 and MRC-5 cells affected SIRT1 activity. Utilizing an in vitro assay with recombinant SIRT1, we found that capsaicin effectively stimulated its activity at concentrations of 10−200 μM, whereas nicotinamide, a SIRT1 inhibitor, significantly decreased SIRT1 activity in vitro (Figure 5A). We also found that 200 μM capsaicin had little effect on SIRT1 expression in MRC-5 cells (Figure 5B). Thus, in the absence of a change in SIRT1 expression, the higher in vitro SIRT1 activity by capsaicin (Figure 5A) together with the capsaicin-induced increased in intracellular NAD^+/NADH ratio (Figure 4A) led to enhanced SIRT1 deacetylase activity. This interpretation is supported by the decrease in the acetylation level of p53 and enhancement of adenosine monophosphate-activated protein kinase (AMPK) phosphorylation/activation, an activator of SIRT1 (Figure 5B). It is documented that deacetylation of p53 induces autophagy,[39] and we also found that capsaicin reduced p53 acetylation accompanying the up-regulation of Atg5, Atg7, becline-1, cleaved LC3 II, and autophagy (Figure 2). Interestingly, exposure of A549 cells to 200 μM capsaicin reduced SIRT1 protein expression (Figure 5C). Alongside the decrease in intracellular NAD^+/NADH ratio in capsaicin-exposed A549 cells (Figure 4A), we found that the p53 acetylation level was noticeably augmented (Figure 5C), possibly by the decreased SIRT1 acetylase activity. Thus, capsaicin induced acetylated/activated/phosphorylated p53 (Figure 5C), and, in turn, up-regulated apoptotic Bax and Bak; this, together with down-regulation of Bcl-2, resulted in apoptosis in A549 cells (Figure 3). Furthermore, small interfering RNA (siRNA) effectively decreased SIRT1 expression in both lines (Figure 6A). In SIRT1-depleted MRC-5 cells, capsaicin-induced autophagy was diminished (Figure 6B), whereas capsaicin-induced apoptosis was reduced in SIRT1-knockdown A549 cells (Figure 6C), demonstrating a key role for SIRT1 in the regulation of capsaicin-mediated programmed cell death-related pathways.

DISCUSSION

Capsaicin acts on an array of cellular targets, several of which have been identified, and initiates a number of signaling pathways. Transient receptor potential vanilloid type 1 (TRPV1) is the most-often mentioned protein targets of capsaicin that belongs to a member of the TRP family of nonselective cation channels.[40] Several studies have suggested that capsaicin exerts its anticancer actions through interaction with the TRPV1, although capsaicin also acts through TRPV1 as a cocarcinogen.[41,42] Here, we present evidence demonstrating that capsaicin modulates SIRT1 deacetylase activity; in particular, depending on the cellular context, capsaicin decreases the NAD^+/NADH ratio and increases p53 acetylation, resulting in enhanced cytotoxic apoptosis (A549 cells), or increases the NAD^+/NADH ratio and SIRT1 deacetylase activity toward p53, leading to survival autophagy (MRC-5 cells). These pathways are summarized in Figure 7.

One major finding of this study is our clarification of the molecular mechanisms underlying the differential effect of capsaicin on cancer and noncancer cells. Capsaicin has long been considered as a chemopreventive agent by virtue of its inhibitory effect on cancer cell survival and proliferation as well its induction of apoptosis.[15,43,44] Interestingly, noncancerous cells exhibit greater tolerance to capsaicin compared to cancer cells, although the basis for this selective cytotoxicity is uncertain.[15] Consistent with the reports of others, our study provides support for the idea that capsaicin induces different mechanisms leading to distinct outcomes depending on cell type and cellular context.[1,4,14] Our results confirmed that capsaicin preferentially induces cytotoxicity in A549 human lung cancer cells but not in MRC-5 cells normal human lung tissue, as supported by the observed IC_{50} value of 33.5 μM (based on cell impedance measurements) for A549 cells, but unmeasurable IC_{50} value in MRC-5 cells. A similar phenomenon was also reported in H-*ras*-transformed MCF10A and their parental noncancerous MCF10A cells.[14] The current study further demonstrated that capsaicin acts through SIRT1 to selectively induce two types of programmed cell death-like pathways: protective autophagy in noncancerous cells but cytotoxic apoptosis in cancer cells.

Another significant finding of this study is the demonstration of a regulatory role of SIRT1 in capsaicin-induced programmed cell death. SIRT1 belongs to the sirtuin protein family of NAD^+-dependent deacetylases that target histones and nonhistone proteins.[45,46] To our knowledge, Lee et al.[47] is first to focus on the links between SIRT1 and capsaicin. Although these researchers found that capsaicin acted through inhibition of apoptosis to exert a neuroprotective effect against glutamate-induced toxicity, they found no significant effect of capsaicin on SIRT1 mRNA levels. Thus, it remained unclear whether capsaicin affected SIRT1 deacetylase activity and its downstream target proteins. In this study, we found that capsaicin reduced SIRT1 expression in A549 cells (Figure 5B), although

DOI: 10.1021/acs.jafc.5b02876
J. Agric. Food Chem. 2015, 63, 7361−7370

we have not examined whether capsaicin-induced SIRT1 down-regulation is at the translational or transcriptional level at this point. It is suggested that p53 enhances microRNA-34a expression and promotes apoptosis[48] and that SIRT1 is one of the direct target genes of microRNA-34a.[49] Consistent with our results (Figure 5C), it is possible that capsaicin induces p53 activation, leading to microRNA-34a expression and SIRT1 down-regulation in A549 cells. The lack of inhibitory effect of capsaicin on SIRT1 expression in MRC-5 cells was perhaps due to less activation of p53 (Figure 5B); however, it remains unconfirmed at this point.

Interestingly, activation of AMPK, an important activator for SIRT1, was found to be associated with capsaicin-induced apoptosis in cancer cells.[11,50] However, whether capsaicin-induced AMPK activation modulates SIRT1 activity and subsequent apoptosis was not examined further in these previous studies. A most recent report has demonstrated that capsaicin increases FOXO-1 acetylation through the modulation of SIRT deacetylase activity, leading to apoptosis in pancreatic cancer cells.[51] All of this evidence provides a rationale to explore the role of SIRT1 in capsaicin-induced programmed cell death, as shown in our present study; capsaicin modulates SIRT1 deacetylase activity, leading to apoptosis in A549 cancer cells but autophagy in MRC-5 cells. By dissecting the different pathways triggered by capsaicin, we present evidence that the intracellular NAD^+/NADH ratio contributes to the divergent effects of capsaicin in noncancer and cancer cell lines. NAD^+ plays an essential role in many metabolic reactions, and it has recently emerged that NAD^+ acts as a metabolic regulator, in part, through regulation of SIRT family.[52] Given the metabolic centrality of NAD, NAD^+/NADH ratios must be well regulated by several complex systems to maintain redox homeostasis. In this context, we here provide evidence suggesting that tNOX also participates in modulating the cellular NAD^+/NADH ratio in cancer cells. Thus, it is not surprising that tNOX also plays a role in capsaicin-induced apoptosis in this system. In fact, we previously discovered that capsaicin has divergent effects on the growth of gastric cancer cells that parallel its effects on tNOX expression, apoptosis in association with reduced tNOX expression in SNU-1 gastric cancer cells, and little apoptosis accompanied by insignificant changes in tNOX in the TMC-1 metastatic gastric carcinoma line.[4] However, whether the intracellular NAD^+/NADH ratio also contributed to the different cellular responses between these two gastric cancer lines was not examined. Experiments utilizing tNOX-knockdown cells showed that tNOX-depletion decreased the intracellular NAD^+/NADH ratio compared to that in control cells (Figure 5), further confirming a regulatory role of tNOX in maintaining the NAD^+/NADH redox status. Our results thus provide yet another scenario in which capsaicin regulates intracellular NAD^+/NADH ratio and SIRT1 activity in A549 cancer cells, in this case through tNOX protein. In contrast, the lack of tNOX expression in the noncancer MRC-5 line resulted in an attenuated inhibitory effect of capsaicin on the intracellular NAD^+/NADH ratio that acted concurrently with capsaicin-induced SIRT1 activity (measured in vitro) to ultimately deacetylate p53 and induce autophagy.

Notwithstanding being generally considered a chemopreventive agent, capsaicin has demonstrated mutagenic properties[53] and tumor-promoting effect.[42,54−58] Moreover, data from epidemiologic studies suggest that capsaicin may exert dual effects—antitumor or tumor-promoting—depending on the dose.[59] For example, capsaicin functions as a cocarcinogen through EGFR signaling in the TPA-induced skin cancer model.[60] Erin et al. also reported that capsaicin promotes a more aggressive gene expression phenotype and represses expression of pro-apoptotic proteins in breast cancer cells,[61] supporting the idea that capsaicin acts on other targets to activate unanticipated pathways, subsequently leading to tumorigenesis. A study from our own laboratory has shown that low concentrations of capsaicin up-regulate tNOX expression in colon cancer cells in conjunction with enhanced cell proliferation and migration.[62] Consistent with our findings, Waning et al. also present a precedent for the reinforcing effect of capsaicin on cell migration.[63] Much remains to be learned regarding the cellular targets of capsaicin and the molecular mechanisms initiated by capsaicin that mediate its effects, from cell death to sustained cell survival.

We have elucidated the differential effects of capsaicin utilizing cell lines from lung tissues addressing not only the role of tNOX in cancer cells but also the signal pathways leading to two types of programmed cell death. Our results demonstrated, for the first time, that intracellular NAD^+/NADH ratio and SIRT1 deacetylase activity are central to the regulation of capsaicin-induced programmed cell deaths in cancer and noncancerous cell lines, specifically, apoptosis in A549 cancer cells but survival autophagy in MRC-5 cells. The findings of this study assist us in understanding the biological function of capsaicin and should provide a rational framework for the further development of improved chemopreventive strategies.

AUTHOR INFORMATION

Corresponding Author

*(P.J.C.) Mail: Institute of Biomedical Sciences, National Chung Hsing University, Taichung 40227, Taiwan. Phone: +886 4 22840896. Fax: +886 4 22853469. E-mail: pjchueh@dragon.nchu.edu.tw.

Present Address

[Δ]Department of Chemical and Biomolecular Engineering, Johns Hopkins University, Baltimore, MD 21218, USA.

Author Contributions

Y.-H.L. and P.J.C. conceived and designed the experiments. Y.-H.L. H.-Y.C., and L.J.S. performed the experiments. Y.-H.L. H.-Y.C., L.J.S., and P.J.C. analyzed the data. Y.-H.L. and H.-Y.C contributed reagents/materials/analysis tools. Y.-H.L. and P.J.C. wrote the paper.

Notes

The authors declare no competing financial interest.

ACKNOWLEDGMENTS

We thank Dr. Tamotsu Yoshimori at Osaka University in Japan for providing pEGFP-LC3 plasmid.

REFERENCES

(1) Morré, D. J.; Chueh, P. J.; Morré, D. M. Capsaicin inhibits preferentially the NADH oxidase and growth of transformed cells in culture. *Proc. Natl. Acad. Sci. U. S. A.* **1995**, *92*, 1831−1835.

(2) Ito, K.; Nakazato, T.; Yamato, K.; Miyakawa, Y.; Yamada, T.; Hozumi, N.; Segawa, K.; Ikeda, Y.; Kizaki, M. Induction of apoptosis in leukemic cells by homovanillic acid derivative, capsaicin, through oxidative stress: implication of phosphorylation of p53 at Ser-15 residue by reactive oxygen species. *Cancer Res.* **2004**, *64*, 1071−1078.

(3) Lee, S. H.; Richardson, R. L.; Dashwood, R. H.; Baek, S. J. Capsaicin represses transcriptional activity of beta-catenin in human colorectal cancer cells. *J. Nutr. Biochem.* **2012**, *23*, 646−655.

DOI: 10.1021/acs.jafc.5b02876
J. Agric. Food Chem. 2015, 63, 7361−7370

(4) Wang, H. M.; Chuang, S. M.; Su, Y. C.; Li, Y. H.; Chueh, P. J. Down-regulation of tumor-associated NADH oxidase, tNOX (ENOX2), enhances capsaicin-induced inhibition of gastric cancer cell growth. *Cell Biochem. Biophys.* **2011**, *61*, 355−366.
(5) Huh, H. C.; Lee, S. Y.; Lee, S. K.; Park, N. H.; Han, I. S. Capsaicin induces apoptosis of cisplatin-resistant stomach cancer cells by causing degradation of cisplatin-inducible Aurora-A protein. *Nutr. Cancer* **2011**, *63*, 1095−1103.
(6) Lu, H. F.; Chen, Y. L.; Yang, J. S.; Yang, Y. Y.; Liu, J. Y.; Hsu, S. C.; Lai, K. C.; Chung, J. G. Antitumor activity of capsaicin on human colon cancer cells in vitro and colo 205 tumor xenografts in vivo. *J. Agric. Food Chem.* **2010**, *58*, 12999−13005.
(7) Pramanik, K. C.; Boreddy, S. R.; Srivastava, S. K. Role of mitochondrial electron transport chain complexes in capsaicin mediated oxidative stress leading to apoptosis in pancreatic cancer cells. *PLoS One* **2011**, *6*, e20151.
(8) Zhang, R.; Humphreys, I.; Sahu, R. P.; Shi, Y.; Srivastava, S. K. In vitro and in vivo induction of apoptosis by capsaicin in pancreatic cancer cells is mediated through ROS generation and mitochondrial death pathway. *Apoptosis* **2008**, *13*, 1465−1478.
(9) Ip, S. W.; Lan, S. H.; Lu, H. F.; Huang, A. C.; Yang, J. S.; Lin, J. P.; Huang, H. Y.; Lien, J. C.; Ho, C. C.; Chiu, C. F.; Wood, W. G.; Chung, J. G. Capsaicin mediates apoptosis in human nasopharyngeal carcinoma NPC-TW 039 cells through mitochondrial depolarization and endoplasmic reticulum stress. *Hum. Exp. Toxicol.* **2012**, *31*, 539−549.
(10) Lin, S.; Zhang, J.; Chen, H.; Chen, K.; Lai, F.; Luo, J.; Wang, Z.; Bu, H.; Zhang, R.; Li, H.; Tong, H. Involvement of endoplasmic reticulum stress in capsaicin-induced apoptosis of human pancreatic cancer cells. *Evidence-Based Complement. Altern. Med.: eCAM* **2013**, *2013*, 629750.
(11) Kim, Y. M.; Hwang, J. T.; Kwak, D. W.; Lee, Y. K.; Park, O. J. Involvement of AMPK signaling cascade in capsaicin-induced apoptosis of HT-29 colon cancer cells. *Ann. N. Y. Acad. Sci.* **2007**, *1095*, 496−503.
(12) Pramanik, K. C.; Srivastava, S. K. Apoptosis signal-regulating kinase 1-thioredoxin complex dissociation by capsaicin causes pancreatic tumor growth suppression by inducing apoptosis. *Antioxid. Redox Signaling* **2012**, *17*, 1417−1432.
(13) Macho, A.; Calzado, M. A.; Munoz-Blanco, J.; Gomez-Diaz, C.; Gajate, C.; Mollinedo, F.; Navas, P.; Munoz, E. Selective induction of apoptosis by capsaicin in transformed cells: the role of reactive oxygen species and calcium. *Cell Death Differ.* **1999**, *6*, 155−165.
(14) Kang, H. J.; Soh, Y.; Kim, M. S.; Lee, E. J.; Surh, Y. J.; Kim, H. R.; Kim, S. H.; Moon, A. Roles of JNK-1 and p38 in selective induction of apoptosis by capsaicin in ras-transformed human breast epithelial cells. *Int. J. Cancer* **2003**, *103*, 475−482.
(15) Bley, K.; Boorman, G.; Mohammad, B.; McKenzie, D.; Babbar, S. A comprehensive review of the carcinogenic and anticarcinogenic potential of capsaicin. *Toxicol. Pathol.* **2012**, *40*, 847−873.
(16) Maiuri, M. C.; Zalckvar, E.; Kimchi, A.; Kroemer, G. Self-eating and self-killing: crosstalk between autophagy and apoptosis. *Nat. Rev. Mol. Cell Biol.* **2007**, *8*, 741−752.
(17) Rubinstein, A. D.; Kimchi, A. Life in the balance − a mechanistic view of the crosstalk between autophagy and apoptosis. *J. Cell Sci.* **2012**, *125*, 5259−5268.
(18) Gordy, C.; He, Y. W. The crosstalk between autophagy and apoptosis: where does this lead? *Protein Cell* **2012**, *3*, 17−27.
(19) Wajant, H. The Fas signaling pathway: more than a paradigm. *Science* **2002**, *296*, 1635−1636.
(20) Er, E.; Oliver, L.; Cartron, P. F.; Juin, P.; Manon, S.; Vallette, F. M. Mitochondria as the target of the pro-apoptotic protein Bax. *Biochim. Biophys. Acta, Bioenerg.* **2006**, *1757*, 1301−1311.
(21) Kuwana, T.; Mackey, M. R.; Perkins, G.; Ellisman, M. H.; Latterich, M.; Schneiter, R.; Green, D. R.; Newmeyer, D. D. Bid, Bax, and lipids cooperate to form supramolecular openings in the outer mitochondrial membrane. *Cell* **2002**, *111*, 331−342.
(22) Lee, H. J.; Wang, C. J.; Kuo, H. C.; Chou, F. P.; Jean, L. F.; Tseng, T. H. Induction apoptosis of luteolin in human hepatoma HepG2 cells involving mitochondria translocation of Bax/Bak and activation of JNK. *Toxicol. Appl. Pharmacol.* **2005**, *203*, 124−131.
(23) Jiang, X.; Wang, X. Cytochrome C-mediated apoptosis. *Annu. Rev. Biochem.* **2004**, *73*, 87−106.
(24) Vander Heiden, M. G.; Thompson, C. B. Bcl-2 proteins: regulators of apoptosis or of mitochondrial homeostasis? *Nat. Cell Biol.* **1999**, *1*, E209−E216.
(25) Yang, Z.; Klionsky, D. J. Eaten alive: a history of macroautophagy. *Nat. Cell Biol.* **2010**, *12*, 814−822.
(26) White, E. Deconvoluting the context-dependent role for autophagy in cancer. *Nat. Rev. Cancer* **2012**, *12*, 401−410.
(27) Li, L.; Ishdorj, G.; Gibson, S. B. Reactive oxygen species regulation of autophagy in cancer: implications for cancer treatment. *Free Radical Biol. Med.* **2012**, *53*, 1399−1410.
(28) Oh, S. H.; Lim, S. C. Endoplasmic reticulum stress-mediated autophagy/apoptosis induced by capsaicin (8-methyl-*N*-vanillyl-6-nonenamide) and dihydrocapsaicin is regulated by the extent of c-Jun NH_2-terminal kinase/extracellular signal-regulated kinase activation in WI38 lung epithelial fibroblast cells. *J. Pharmacol. Exp. Ther.* **2009**, *329*, 112−122.
(29) Chien, C. S.; Ma, K. H.; Lee, H. S.; Liu, P. S.; Li, Y. H.; Huang, Y. S.; Chueh, S. H. Dual effect of capsaicin on cell death in human osteosarcoma G292 cells. *Eur. J. Pharmacol.* **2013**, *718*, 350−360.
(30) Yoon, J. H.; Ahn, S. G.; Lee, B. H.; Jung, S. H.; Oh, S. H. Role of autophagy in chemoresistance: Regulation of the ATM-mediated DNA-damage signaling pathway through activation of DNA-PKcs and PARP-1. *Biochem. Pharmacol.* **2012**, *83*, 747−757.
(31) Choi, C. H.; Jung, Y. K.; Oh, S. H. Autophagy induction by capsaicin in malignant human breast cells is modulated by p38 and extracellular signal-regulated mitogen-activated protein kinases and retards cell death by suppressing endoplasmic reticulum stress-mediated apoptosis. *Mol. Pharmacol.* **2010**, *78*, 114−125.
(32) Morré, D. J. NADH oxidase: a multifunctional ectoprotein of the eukaryotic cell surface. In *Plasma Membrane Redox Systems and Their Role in Biological Stress and Disease*; Asard, H., Bérczi, A., Caubergs, R., Eds.; Kluwer Academic Publishers: Dordrecht, The Netherlands, 1998; pp 121−1561.
(33) Chueh, P. J. Cell membrane redox systems and transformation. *Antioxid. Redox Signaling* **2000**, *2*, 177−187.
(34) Liu, S. C.; Yang, J. J.; Shao, K. N.; Chueh, P. J. RNA interference targeting tNOX attenuates cell migration via a mechanism that involves membrane association of Rac. *Biochem. Biophys. Res. Commun.* **2008**, *365*, 672−677.
(35) Wu, Z.; Zeng, Y.; Zhong, M.; Wang, B. Targeting A549 lung adenocarcinoma cell growth and invasion with protease-activated receptor1 siRNA. *Mol. Med. Rep.* **2014**, *9*, 1787−1793.
(36) Su, Y. C.; Lin, Y. H.; Zeng, Z. M.; Shao, K. N.; Chueh, P. J. Chemotherapeutic agents enhance cell migration and epithelial-to-mesenchymal transition through transient up-regulation of tNOX (ENOX2) protein. *Biochim. Biophys. Acta, Gen. Subj.* **2012**, *1820*, 1744−1752.
(37) Hu, D.; Wu, J.; Xu, L. F.; Zhang, R. B.; Chen, L. P. A method for the establishment of a cell line with stable expression of the GFP-LC3 reporter protein. *Mol. Med. Rep.* **2012**, *6*, 783−786.
(38) Ke, N.; Wang, X.; Xu, X.; Abassi, Y. A. The xCELLigence system for real-time and label-free monitoring of cell viability. *Methods Mol. Biol.* **2011**, *740*, 33−43.
(39) Contreras, A. U.; Mebratu, Y.; Delgado, M.; Montano, G.; Hu, C. A.; Ryter, S. W.; Choi, A. M.; Lin, Y.; Xiang, J.; Chand, H.; Tesfaigzi, Y. Deacetylation of p53 induces autophagy by suppressing Bmf expression. *J. Cell Biol.* **2013**, *201*, 427−437.
(40) Nagy, I.; Santha, P.; Jancso, G.; Urban, L. The role of the vanilloid (capsaicin) receptor (TRPV1) in physiology and pathology. *Eur. J. Pharmacol.* **2004**, *500*, 351−369.
(41) Amantini, C.; Ballarini, P.; Caprodossi, S.; Nabissi, M.; Morelli, M. B.; Lucciarini, R.; Cardarelli, M. A.; Mammana, G.; Santoni, G. Triggering of transient receptor potential vanilloid type 1 (TRPV1) by capsaicin induces Fas/CD95-mediated apoptosis of urothelial cancer

DOI: 10.1021/acs.jafc.5b02876
J. Agric. Food Chem. 2015, 63, 7361−7370

cells in an ATM-dependent manner. *Carcinogenesis* **2009**, *30*, 1320−1329.
(42) Bode, A. M.; Dong, Z. The two faces of capsaicin. *Cancer Res.* **2011**, *71*, 2809−2814.
(43) Gupta, S. C.; Kim, J. H.; Prasad, S.; Aggarwal, B. B. Regulation of survival, proliferation, invasion, angiogenesis, and metastasis of tumor cells through modulation of inflammatory pathways by nutraceuticals. *Cancer Metastasis Rev.* **2010**, *29*, 405−434.
(44) Surh, Y. J. More than spice: capsaicin in hot chili peppers makes tumor cells commit suicide. *J. Natl. Cancer I* **2002**, *94*, 1263−1265.
(45) Imai, S.; Armstrong, C. M.; Kaeberlein, M.; Guarente, L. Transcriptional silencing and longevity protein Sir2 is an NAD-dependent histone deacetylase. *Nature* **2000**, *403*, 795−800.
(46) Vaziri, H.; Dessain, S. K.; Eagon, E. N.; Imai, S. I.; Frye, R. A.; Pandita, T. K.; Guarente, L.; Weinberg, R. A. hSIR2(SIRT1) functions as an NAD-dependent p53 deacetylase. *Cell* **2001**, *107*, 149−159.
(47) Lee, J. G.; Yon, J. M.; Lin, C.; Jung, A. Y.; Jung, K. Y.; Nam, S. Y. Combined treatment with capsaicin and resveratrol enhances neuroprotection against glutamate-induced toxicity in mouse cerebral cortical neurons. *Food Chem. Toxicol.* **2012**, *50*, 3877−3885.
(48) Chang, T. C.; Wentzel, E. A.; Kent, O. A.; Ramachandran, K.; Mullendore, M.; Lee, K. H.; Feldmann, G.; Yamakuchi, M.; Ferlito, M.; Lowenstein, C. J.; Arking, D. E.; Beer, M. A.; Maitra, A.; Mendell, J. T. Transactivation of miR-34a by p53 broadly influences gene expression and promotes apoptosis. *Mol. Cell* **2007**, *26*, 745−752.
(49) Mohan, M.; Kumar, V.; Lackner, A. A.; Alvarez, X. Dysregulated miR-34a-SIRT1-acetyl p65 axis is a potential mediator of immune activation in the colon during chronic simian immunodeficiency virus infection of Rhesus macaques. *J. Immunol.* **2015**, *194*, 291.
(50) Ying, H.; Wang, Z.; Zhang, Y.; Yang, T. Y.; Ding, Z. H.; Liu, S. Y.; Shao, J.; Liu, Y.; Fan, X. B. Capsaicin induces apoptosis in human osteosarcoma cells through AMPK-dependent and AMPK-independent signaling pathways. *Mol. Cell. Biochem.* **2013**, *384*, 229−237.
(51) Pramanik, K. C.; Fofaria, N. M.; Gupta, P.; Srivastava, S. K. CBP-mediated FOXO-1 acetylation inhibits pancreatic tumor growth by targeting SirT. *Mol. Cancer Ther.* **2014**, *13*, 687−698.
(52) Lin, S. J.; Guarente, L. Nicotinamide adenine dinucleotide, a metabolic regulator of transcription, longevity and disease. *Curr. Opin. Cell Biol.* **2003**, *15*, 241−246.
(53) Nagabhushan, M.; Bhide, S. V. Mutagenicity of chili extract and capsaicin in short-term tests. *Environ. Mutagen.* **1985**, *7*, 881−888.
(54) Malagarie-Cazenave, S.; Olea-Herrero, N.; Vara, D.; Diaz-Laviada, I. Capsaicin, a component of red peppers, induces expression of androgen receptor via PI3K and MAPK pathways in prostate LNCaP cells. *FEBS Lett.* **2009**, *583*, 141−147.
(55) Toth, B.; Gannett, P. Carcinogenicity of lifelong administration of capsaicin of hot pepper in mice. *In Vivo* **1992**, *6*, 59−63.
(56) Agrawal, R. C.; Wiessler, M.; Hecker, E.; Bhide, S. V. Tumour-promoting effect of chilli extract in BALB/c mice. *Int. J. Cancer* **1986**, *38*, 689−695.
(57) Serra, I.; Yamamoto, M.; Calvo, A.; Cavada, G.; Baez, S.; Endoh, K.; Watanabe, H.; Tajima, K. Association of chili pepper consumption, low socioeconomic status and longstanding gallstones with gallbladder cancer in a Chilean population. *Int. J. Cancer* **2002**, *102*, 407−411.
(58) Archer, V. E.; Jones, D. W. Capsaicin pepper, cancer and ethnicity. *Med. Hypotheses* **2002**, *59*, 450−457.
(59) Lopez-Carrillo, L.; Lopez-Cervantes, M.; Robles-Diaz, G.; Ramirez-Espitia, A.; Mohar-Betancourt, A.; Meneses-Garcia, A.; Lopez-Vidal, Y.; Blair, A. Capsaicin consumption, *Helicobacter pylori* positivity and gastric cancer in Mexico. *Int. J. Cancer* **2003**, *106*, 277−282.
(60) Hwang, M. K.; Bode, A. M.; Byun, S.; Song, N. R.; Lee, H. J.; Lee, K. W.; Dong, Z. Cocarcinogenic effect of capsaicin involves activation of EGFR signaling but not TRPV1. *Cancer Res.* **2010**, *70*, 6859−6869.
(61) Erin, N.; Zhao, W.; Bylander, J.; Chase, G.; Clawson, G. Capsaicin-induced inactivation of sensory neurons promotes a more aggressive gene expression phenotype in breast cancer cells. *Breast Cancer Res. Treat.* **2006**, *99*, 351−364.
(62) Liu, N. C.; Hsieh, P. F.; Hsieh, M. K.; Zeng, Z. M.; Cheng, H. L.; Liao, J. W.; Chueh, P. J. Capsaicin-mediated tNOX (ENOX2) up-regulation enhances cell proliferation and migration in vitro and in vivo. *J. Agric. Food Chem.* **2012**, *60*, 2758−2765.
(63) Waning, J.; Vriens, J.; Owsianik, G.; Stuwe, L.; Mally, S.; Fabian, A.; Frippiat, C.; Nilius, B.; Schwab, A. A novel function of capsaicin-sensitive TRPV1 channels: involvement in cell migration. *Cell Calcium* **2007**, *42*, 17−25.

DOI: 10.1021/acs.jafc.5b02876
J. Agric. Food Chem. 2015, 63, 7361−7370

mechanisms for the observed reduction of total cholesterol levels in serum. Other studies carried out using other mushroom species such as *G. frondosa* mentioned hepatic upregulation of the *Abcg5/8* genes (genes encoding cholesterol transporters, ATP-binding cassette subfamily G proteins, involved in cholesterol excretion from the liver to the bile or in reverse cholesterol transport from the enterocyte to the intestinal lumen).[15] Mushroom DF fractions include mainly by water-insoluble polysaccharides, with β-glucans and chitins being higher in concentrations, whereas the levels of water-soluble polysaccharides are usually lower than 10% (depending on species).[1]

However, the described molecular studies on edible mushroom DF were carried out using cholesterol-free or standard diets; therefore, animals showed no hypercholesterolemia or altered cholesterol-related biochemical parameters. Functional foods with hypocholesterolemic properties (such as products enriched in phytosterols, cereal β-glucans, etc.) are usually recommended by physicians/nutritionists to people with slight to moderate hypercholesterolemia; thus, if a new functional product (based on mushroom DF) is intended to be developed, then the effect of such a fraction should be tested on individuals with certain level of hypercholesterolemia. Moreover, other reports indicated that when hypercholesterolemic animals were regularly fed with whole fruiting bodies, lowering of cholesterol in serum was noticed.[11]

Thus, in order to study whether DF fraction obtained from edible mushrooms can be used as a hypocholesterolemic ingredient to design novel functional foods and study their influence at the molecular level under cholesterol-altered physiological conditions, the modulation of mRNA expression of genes related to cholesterol metabolism was investigated using two models of hypercholesterolemic mice and low-density arrays (LDA). First, a preliminary in vitro study was carried out using Caco-2 cell cultures to select one DF fraction out of the three most consumed mushrooms (*A. bisporus*, *P. ostreatus*, and *L. edodes*) to reduce the number of mice and assays. Then, two different in vivo experiments were carried out in order to compare the effect of a mushroom DF fraction with two hypocholesterolemic drugs.

MATERIALS AND METHODS

Raw Material and Preparation of the Dietary Fiber-Enriched Extracts. Fresh fruiting bodies of *A. bisporus* L. (Imbach) Fungisem H-15, *P. ostreatus* (Jacq. Ex Fr.) Kummer strain Gurelan H-107, and *L. edodes* S. (Berkeley) from Sylvan 4312 from the first flush were harvested, cut in slices, lyophilized, and ground until a dry powder was obtained following the procedure described by Gil-Ramírez et al.[16] Resulting mushroom powders were utilized as starting material to extract the DF. DF-enriched fractions from the three mushroom species were prepared according to the method of Jeurink et al.[17]

Standards and Reagents. Solvents such as hexane (95%), chloroform, and methanol (HPLC-grade) were obtained from LAB-SCAN (Gliwice, Poland). Potassium hydroxide, ascorbic acid, BHT (2,6-di-*tert*-butyl-*p*-cresol), cholesterol, cholic acid, ergosterol, congo red, and hexadecane were purchased from Sigma-Aldrich (Spain). Simvastatin was obtained from Cinfa Laboratories (Spain) and ezetimibe (Ezetrol) from Merck Sharp & Dohme (Spain). Schizophyllan was purchased from Contripo Biotech S.R.O. (Czech Republic). All other reagents and solvents used were of analytical grade.

β-Glucan Content of DF Fractions. The β-glucan content of the obtained DF fractions (50 mg) was evaluated in duplicate by a β-glucan determination kit specific for mushrooms (Megazyme, Spain) as described in Palanisamy et al.[18] The amount of β-(1 → 3)(1 → 6)-glucans was also determined following the method of Nitschke et al.[19] using a red congo concentration of 0.08% (w/v) and schizophyllan as standard curve; chitins concentrations were determined as described in Palanisamy et al.[18]

In Vitro Digestion. Obtained DF fractions were submitted to an in vitro digestion according to Palanisamy et al.[18] Briefly, the extracts were digested in 1 mL of 0.01 M HCl for 1 h at 37 °C with gentle agitation (Orbital incubator S150, Stone, UK). Afterward, the sample pH was adjusted to 6.3 with 0.1 mL of 0.1 M NaOH. Then, 4 mL of bile extract (14.3 mg in Tris-maleate buffer, pH 6.3) and 5 mL of pancreatin (10 mg in tris-maleate buffer, pH 6.3) were added, and the mixture was incubated for 1 h at 37 °C. After digestion, the samples were added to Caco-2 cultures. A control sample was prepared following the same digestion protocol but without the addition of DF fractions.

Caco-2 Cell Cultures. Human colorectal adenocarcinoma cell line Caco-2 (ATCC HTB-37) obtained from the ATCC (Rockville, MD, USA) were maintained in Dulbecco's modified Eagle's medium (DMEM) with high glucose content (4.5 g/L) and supplemented with 10% fetal bovine serum, 1% penicillin−streptomycin, and 1% nonessential amino acids. First, the cytotoxicity was evaluated using 3-(4,5-dimethylthiazol)-2,5-diphenyl tetrazolium bromide (MTT) according the method published by Mosmann et al.[20] Then, cells were seeded at a density of 3.3×10^5 cell/mL and were allowed to generate a monolayer for 21 days before experiments. The digested DF fractions were applied at subtoxic concentrations (4 μL/mL) and left incubating at 37 °C and 5% CO_2 for 1 or 24 h. Afterward, cells were separated from the membranes by incubation at 37 °C during 30 min with Triton 0.1% and submitted to RNA extraction. Four replicates per sample were carried out.

Animals and Diets. Male C57BL/6JRj mice were purchased from Janvier SAS (Le Genest, France). Mice were maintained in temperature-, humidity-, and light-controlled conditions (24 ± 2 °C, 40−60% humidity, 12:12 h light: dark cycle) and had free access to water and food. They were randomly divided into five groups. Normal control group (NC, $n = 6$) was fed a standard diet (Safe Rodent Diet A04, France), and the hypercholesterolemic control group (HC, $n = 8$) was fed a high-cholesterol diet. The treated groups ($n = 8$) were given a high-cholesterol diet supplemented with their corresponding mushroom extract or control drug and were identified as follows: PDF (*Pl. ostreatus* DF fraction), SV (simvastatin, as a positive control for inhibition of cholesterol biosynthesis), and EZ (ezetimibe as a positive control for inhibition of cholesterol absorption). The animal intervention was carried out following two experimental settings in order to evaluate whether PDF might act as a palliative agent (sequential supplementation) or preventive agent (simultaneous supplementation) against diet-induced hypercholesterolemia. In the sequential supplementation, mice were fed high-cholesterol diet for 4 weeks (from 5 to 9 weeks of age), followed by another 4 weeks of high-cholesterol diet plus mushroom extract (from 10 to 13 weeks of age), whereas in the simultaneous supplementation, mice were simultaneously fed a high-cholesterol diet and the mushroom extract for 4 weeks (from 10 to 13 weeks of age). The composition of diets, the dose per day of mushroom extract, drug, or β-glucans as well as the energy that was received by the mice daily is shown in Table 1. Body weight was registered before the experimental feeding period and at the end of the experiments. Wet mass of the liver was also registered. Animal studies were approved by our institution's Animal Welfare and Ethics Committee and were carried out according to Spanish and European legislation (RD 53/2013, 2010/63/EU, respectively).

Feces, Plasma, and Liver Lipid Analyses, Tissue Collection. At the end of the experiments, mice were sacrificed by intracardiac exsanguination under anesthesia with 1.5% isoflurane, and plasma was stored at −80 °C before use. Jejunum, ileum, cecum, and liver samples were removed, immediately frozen in liquid nitrogen, and stored at −80 °C. Feces were collected at the beginning and at the end of the experimental feeding period and maintained at −20 °C until further use. Cholesterol extraction from the stored feces (300 mg) and analysis by GC-MS were carried out as described in Gil-Ramírez et al.[16] Plasma levels of total cholesterol, triglyceride, HDL cholesterol, and LDL cholesterol were measured in duplicate for each sample using

DOI: 10.1021/acs.jafc.5b02942
J. Agric. Food Chem. 2015, 63, 7371−7380

Table 1. Composition of Diets[a]

components	NC	HC	PDF	SV	EZ
carbohydrates (%)	59.9	59.9	59.9	59.9	59.9
proteins (%)	16.1	16.1	16.1	16.1	16.1
lipids (%)	3.1	3.1	3.1	3.1	3.1
fibers[b] (%)	3.9	3.9	3.9	3.9	3.9
mineral mixture[c] (%)	5.1	5.1	5.1	5.1	5.1
moisture (%)	11.9	8.9	7.4	8.9	8.9
cholesterol (%)	0.0	2.0	2.0	2.0	2.0
cholic acid (%)	0.0	1.0	1.0	1.0	1.0
mushroom extract or drug (%)	0.0	0.0	1.5	0.025	0.005
mushroom extract or drug (mg/mouse/day)	0.0	0.0	60.0	1.0	0.2
β-glucans (%)	n.m.	n.m.	0.6	n.m.	n.m.
β-glucans (mg/mouse/day)	n.m.	n.m.	24.0	n.m.	n.m.
energy (kcal/mouse/day)	13.37	14.39	14.39	14.39	14.39

[a]NC, normal control; HC, hypercholesterolemic control; PDF: *Pleurotus ostreatus* DF fraction; SV: simvastatin; EZ: ezetimibe; n.m.: not measured. [b]β-glucans excluded. [c]A04 mineral mixture.

a Covas C311 Auto analyzer (Roche, Spain). Cholesterol and triglyceride were extracted from the liver and analyzed in duplicate according to the manufacturer's protocol by colorimetric kits (BioVision Inc., CA, USA).

Statistical Analysis for Biochemical Data. All values were expressed as mean ± SD. The SPSS v15.0 software (Lead Technologies, IL, USA) was used to determine whether the variables differed among treatment groups. The effects of treatments were assessed by one-way ANOVA followed by Tukey's test when the ANOVA identified significant treatment effects. Differences with $P < 0.05$ were considered statistically significant.

RNA Extraction from Cells and Mice Tissues and Quantitative Real-Time PCR for LDA. Total RNA from cell cultures or mice tissues was extracted by magnetic bead technology using a pureLinkTM Total RNA kit TRIzol Plus RNA Kit (Invitrogen, CA, USA) in an iPrepTM Purification Instrument (Invitrogen) programmed with an iPrepTM total RNA card (Invitrogen) according to manufacturer instructions. The RNA concentration was determined by spectrophotometry at 260 nm, and the purity of the extracted RNA was calculated from ratio of absorbance at 260/280 nm and 260/230 nm in a NanoDrop ND-1000 (NanoDrop Technologies Inc., Wilmington, DE, USA). A 400 ng amount of total RNA from each sample was reverse transcribed using the High Capacity cDNA Reverse Transcription Kit (Applied Biosystems, MA, USA). The obtained cDNA (100 μL per port) were loaded into microfluid cards designed for low-density array (LDA), and the microfluid cards were run in a 7900HT Fast Real-Time PCR system (Applied Biosystems, MA, USA). Amplification conditions were 50 °C for 2 min, 94.5 °C for 10 min, followed by 40 cycles with 97 °C with 30 s and 59.7 °C for 1 min. The microfluid card was constructed using human and mouse commercially available assays for several genes related to the cholesterol metabolism, some internal standards, and housekeeping genes that are described in detail elsewhere.[21] The cholesterol-related genes were ABCA1 (ATP-binding cassette, sub-family A, member 1), ABCG5 and ABCG8 (ATP-binding cassette, subfamily G (WHITE), members 5 and 8), ACAT1 and ACAT2 (acetyl-CoA acetyltransferase 1 and 2), APOB (apolipoprotein B), DGAT1 and DGAT2 (diacylglycerol O-acyltransferase 1 and 2), FDFT1 farnesyl-diphosphate farnesyltransferase 1), HMGCR (3-hydroxy-3-methylglutaryl-CoA reductase), LDLR (low-density lipoprotein receptor), MTTP (microsomal triglyceride transfer protein), NPC1L1 (Niemann-Pick C1-like 1), NR1H3 and NR1H4 (nuclear receptor subfamily 1, group H, member 3 and 4), SOAT1 and SOAT2 (sterol O-acyltransferase 1 and 2), SREBF1 and SREBF2 (sterol regulatory element binding transcription factor 1 and 2). Comparative analysis of each of these genes was performed using specialized computer programs SDS2.3 and RQ 2.1 (Applied Biosystems).

Gene Expression Statistical Data Analysis. The expression of each gene was measured at least in duplicate, and each biological group included a minimum of three replicates. To control for potential outliers, Grubb's test was applied to technical replicates with a threshold of 0.05. Biological replicates were quality controlled using the median absolute deviation test (MAD test). Samples of the same biological group with a MAD score higher than 3 were removed from the analysis. Genorm algorithm[22] was used to identify the most stable reference genes for normalization. Genes GUSB and HPRT1 were found to be the most stably expressed in Caco-2 cell cultures. In the mouse tissue samples, genes *Hprt1* and *Polr2a* were the most stably expressed in cecum and liver tissues; *Gusb* and *Polr2a* were the most stably expressed in jejunum and ileum tissues. Relative gene expression levels were calculated by using the 2-ΔΔCT method;[23] using these, we identified most stable genes as internal control genes in each group. Statistical significance of the results was assessed using a Limma test, and Benjamini–Hochberg false discovery rate procedure was subsequently applied. Adjusted P values lower than 0.05 were considered significant. All these calculations were carried out with Real Time StatMiner 4.5 (Integromics S.L, Spain).

RESULTS

Modulation of the mRNA Expression Pattern in Caco-2 Cell Cultures. First, three mushroom species (*A. bisporus*, *L. edodes*, and *P. ostreatus*) were selected because they showed in vitro bile-acid-binding capacity, and this ability could be related to hypocholesterolemic activities.[18] Then, digestates of the mushroom DF fractions were applied to Caco-2 cells to investigate their influence on cholesterol-related gene expression. Results indicated that 1 h after application only digested DF fraction from *A. bisporus* and *P. ostreatus* were able to induce significant overexpression of NR1H4 (Figure 1a). Moreover, the digestate of the *A. bisporus* DF fraction upregulated the ACAT2 gene and downregulated the MTTP and SOAT2 genes. However, when the treated cells were incubated for 24 h, overexpression of other genes was induced by the digestates obtained from the DF fractions of *L. edodes* and particularly of *P. ostreatus* (Figure 1b), acting differently than those of *A. bisporus* that showed no effect. Both digestates were able to induce significant overexpression of the NPC1L1 gene directly involved in cholesterol absorption. Digestates from the DF fraction of *L. edodes* induced mRNA LDLR expression, whereas those from *P. ostreatus* induced mRNA expression of other cholesterol-related genes such as DGAT1, FDFT1, SOAT1, and SREBF1 and inhibited mRNA expression of SOAT2.

The fractions of the three mushroom species contained similar polysaccharide compositions,[18] including chitin content lower than β-glucans content. However, those β-glucans apparently showed different solubilities (Table 2). The DF fraction of *A. bisporus* contained lower β-(1,3)(1,6)-glucans concentration than the other two DF fractions, and they were not soluble in KOH. β-(1,3)(1,6)-glucans from the *L. edodes* DF fraction were mainly soluble in alkalis, whereas those of the *P. ostreatus* DF fraction were more soluble in KOH than in NaOH.

Effect of Mushroom Extract on Body and Liver Weight and Fecal Cholesterol Excretion. Food intake was approximately 4 g/day per mouse throughout the experimental feeding period in all groups, with no significant difference among groups (data not shown). No differences were noticed in initial body weight (Table 3). The normal control group gained weight over the feeding period in the sequential and simultaneous experiments. As expected, the remaining groups showed a slight tendency to lose weight because diets supplemented with cholate and cholesterol induced even higher

DOI: 10.1021/acs.jafc.5b02942
J. Agric. Food Chem. 2015, 63, 7371−7380

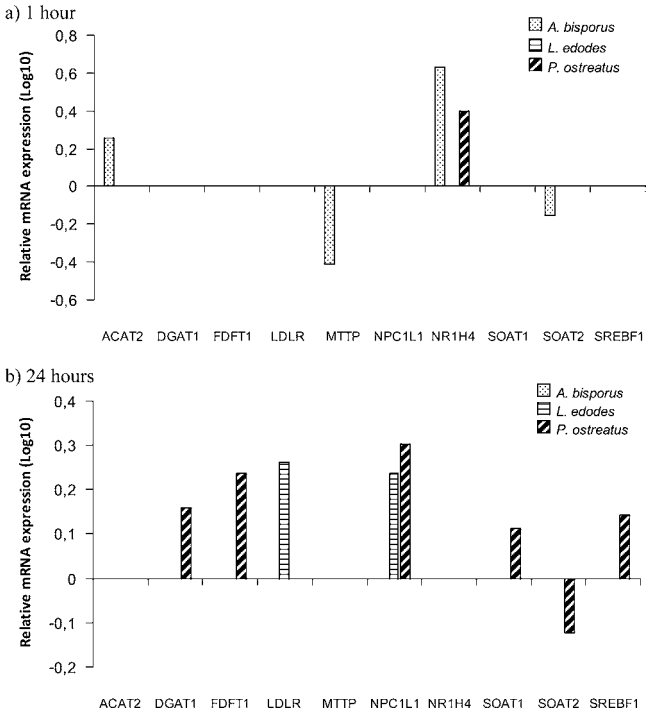

Figure 1. Relative mRNA expression (log 10) of Caco-2 cells' cholesterol-related genes after (a) 1 h and (b) 24 h application of the digested DF fraction obtained from *A. bisporus*, *L. edodes*, or *P. ostreatus*. Indicated genes are only those noted as significant ($P < 0.05$) compared with their controls (addition of the digestion product without DF addition). The expression of each gene was measured at least in duplicate, and each biological group included a minimum of three replicates. A few genes did not pass the quality control either in the target or the control group; therefore, their expression level was omitted in the figure.

weight loss in C57BL/6J mice.[24] No significant differences in final body weight of the treated groups was noticed compared with that of the hypercholesterolemic control group either in the sequential or simultaneous experiment, except for the simvastatin group where a significantly lower final body weight was recorded compared to those of all other groups. In the sequential experiment, liver weight was significantly increased in the hypercholesterolemic controls and the treated groups, except the simvastatin group, compared with that of the normal control group. Similar results for liver-to-body-weight ratio were observed, with a significant increase in all groups compared to that of the normal control group. In the simultaneous experiment, liver weight was also significantly increased in the hypercholesterolemic controls compared with that of the normal control group, and liver-to-body-weight ratio was significantly increased in the hypercholesterolemic controls and PDF group. The simvastatin and ezetimibe groups showed a significantly lower liver weight compared with that of hypercholesterolemic controls. Similar results for liver-to-body-weight ratio were observed, although only the ezetimibe group reached statistical significance.

No cholesterol was detected in feces of normal controls, but hypercholesterolemic controls significantly increased their cholesterol excretion in either the sequential or simultaneous supplementation compared with normal controls. In the sequential experiment, no significant difference in cholesterol excretion was noticed between hypercholesterolemic controls and the treated groups, except for mice fed the PDF extract where a significantly lower cholesterol excretion was observed. In the simultaneous experiment, the slightly higher cholesterol excretion was significant for the ezetimibe group compared with that of hypercholesterolemic controls but not for mice fed with PDF. No differences were noticed in mice treated with simvastatin with respect to hypercholesterolemic controls.

Modulation of the Lipid Profile of Plasma and Liver in the Animal Intervention. *Sequential Supplementation.* Plasma cholesterol levels increased 3.3-fold in hypercholesterolemic controls compared with normal controls (Table 4). In mice fed PDF or treated with simvastatin, plasma cholesterol levels remained unchanged compared with those in hypercholesterolemic controls, whereas a reduction reaching normal levels was observed in the ezetimibe group. There was no significant difference in the plasma HDL levels between normal controls and hypercholesterolemic controls. No significant differences between mice fed the PDF or treated with simvastatin and hypercholesterolemic controls were observed, although interestingly the mushroom DF extract slightly increased HDL levels by 9% compared to that of hypercholesterolemic controls. Ezetimibe induced a significant reduction. The LDL levels were markedly increased by 6.6-fold in hypercholesterolemic controls compared with normal controls but remained unchanged in mice fed PDF or treated with simvastatin with respect to hypercholesterolemic controls. Reduction was noticed with the administration of ezetimibe compared with hypercholesterolemic controls. In addition to the plasma lipid profile, two atherogenic indexes were calculated: total cholesterol/HDL and LDL/HDL ratios. Compared with normal controls, the total cholesterol/HDL and the LDL/HDL ratios were significantly increased in hypercholesterolemic controls by 2.1- and 5.3-fold, respectively. It is noteworthy that a slight and not significant negative balance in both indexes was improved in mice fed PDF compared with hypercholesterolemic controls mainly because of the increase in HDL levels. A significant reduction in both indexes was noticed in the ezetimibe group but not in the simvastatin group. Hypercholesterolemic controls and treated groups showed a reduction in plasma triglyceride levels compared to normal controls. However, when compared to hypercholesterolemic controls, treated groups showed quite similar plasma triglyceride levels.

Liver cholesterol levels were significantly increased by 4.9-fold in hypercholesterolemic controls compared with normal controls. In contrast with the lacking effect of PDF on total plasma cholesterol, a 21% reduction in liver cholesterol levels

Table 2. Total β-Glucan Concentrations of the DF Fractions Obtained from the Three Mushroom Species and Their Distribution as β-(1,3)(1,6)-Glucans or Chitins

		β-(1,3)(1,6)-glucans (mg/100 mg; dw)				
DF fractions	total β-glucans (mg/100 mg; dw)	KOH fraction	HCl fraction	NaOH fraction	total	chitins (mg/100 mg; dw)
A. bisporus	25.87 ± 7.87	0.0 ± 0.01	1.01 ± 0.03	1.04 ± 0.06	2.05 ± 0.14	6.67 ± 2.23
L. edodes	38.41 ± 6.50	2.54 ± 0.44	0.76 ± 0.11	2.89 ± 0.17	6.19 ± 1.01	9.13 ± 1.76
P. ostreatus	39.87 ± 11.53	2.94 ± 0.54	0.00 ± 0.00	2.57 ± 0.60	5.51 ± 1.61	6.10 ± 3.56

DOI: 10.1021/acs.jafc.5b02942
J. Agric. Food Chem. 2015, 63, 7371−7380

Table 3. Effects of Mushroom Extract on Body and Liver Weight and Fecal Cholesterol Excretion[a]

variable	NC	HC	PDF	SV	EZ
			Sequential Supplementation		
initial BW (g)	19.27 ± 0.84	20.06 ± 0.71	19.36 ± 0.54	19.30 ± 0.60	19.82 ± 0.92
final BW (g)	25.07 ± 0.69	18.97 ± 1.07[b]	18.68 ± 1.18[b,d]	15.48 ± 1.52[b,c,e]	19.52 ± 0.93[b]
LW (g)	1.25 ± 0.15	1.62 ± 0.13[b]	1.83 ± 0.15[b,d,e]	1.46 ± 0.31	1.56 ± 0.22[b]
LW/BW (%)	4.99 ± 0.62	8.54 ± 0.56[b]	9.80 ± 0.63[b,e]	9.43 ± 1.34[b,e]	7.99 ± 1.15[b]
cholesterol (mg/g feces)	n.d.	61.83 ± 0.47[b]	52.36 ± 4.62[b,c]	65.40 ± 7.41[b]	60.20 ± 14.74[b]
			Simultaneous Supplementation		
initial BW (g)	23.46 ± 0.65	23.29 ± 0.50	23.14 ± 0.62	23.25 ± 0.58	23.27 ± 0.68
final BW (g)	24.71 ± 0.54	21.85 ± 0.57[b]	20.28 ± 1.22[b,d]	14.98 ± 0.73[b,c,e]	20.39 ± 1.66[b]
LW (g)	1.27 ± 0.15	1.68 ± 0.31[b]	1.53 ± 0.14[d]	0.96 ± 0.10[c]	1.26 ± 0.20[c]
LW/BW (%)	5.14 ± 0.63	7.69 ± 1.44[b]	7.54 ± 0.59[b,e]	6.41 ± 0.44	6.18 ± 0.63[c]
cholesterol (mg/g feces)	n.d.	58.47 ± 2.10[b]	64.10 ± 8.41[b]	59.51 ± 7.96[b]	65.12 ± 2.58[b,c]

[a]NC, normal control; HC, hypercholesterolemic control; PDF: *Pleurotus ostreatus* DF fraction; SV: simvastatin; EZ: ezetimibe. BW, body weight; LW, liver weight; n.d., not detected. [b]$P < 0.05$ vs NC. [c]$P < 0.05$ vs HC. [d]$P < 0.05$ vs SV. [e]$P < 0.05$ vs EZ.

Table 4. Plasma and Liver Lipid Profiles in Mice Treated for 4 Weeks with PDF, Simvastatin, or Ezetimibe Simultaneously with High-Cholesterol Diet after 4 Weeks of High-Cholesterol Diet Alone (Sequential Supplementation)[a]

variable	NC	HC	PDF	SV	EZ
			Plasma Level (mg/dL)		
TC	65.33 ± 26.63	214.25 ± 97.30[b]	207.14 ± 36.71[b,e]	156.29 ± 31.80[b,e]	59.43 ± 19.03[c]
HDL	59.80 ± 25.07	89.70 ± 27.97	98.06 ± 17.93[e]	81.90 ± 21.92	47.91 ± 10.49[c]
LDL	23.40 ± 11.03	155.03 ± 77.38[b]	152.66 ± 28.07[b,e]	102.51 ± 24.01[b,e]	23.40 ± 14.94[c]
TC/HDL	1.10 ± 0.07	2.31 ± 0.38[b]	2.12 ± 0.16[b,e]	1.95 ± 0.21[b,e]	1.22 ± 0.16[c]
LDL/HDL	0.31 ± 0.13	1.65 ± 0.35[b]	1.57 ± 0.17[b,e]	1.35 ± 0.22[b,e]	0.46 ± 0.23[c]
TG	72.00 ± 20.00	47.25 ± 8.41[b]	39.43 ± 10.05[b]	46.29 ± 11.04[b]	43.43 ± 8.30[b]
			Liver Level (mg/g liver)		
TC	0.22 ± 0.09	1.09 ± 0.23[b]	0.86 ± 0.46[b]	1.44 ± 0.43[b,e]	0.45 ± 0.20[c]
TG	4.49 ± 0.87	3.72 ± 0.61	2.29 ± 0.60[b,c,d,e]	0.78 ± 0.18[b,c]	0.88 ± 0.52[b,c]

[a]NC, normal control; HC, hypercholesterolemic control; PDF: *Pleurotus ostreatus* DF fraction; SV: simvastatin; EZ: ezetimibe. TC, total cholesterol; HDL, high-density lipoprotein cholesterol; LDL, low-density lipoprotein cholesterol; TG, triglyceride. The results are mean ± SD of six (NC group) or eight (remaining groups) mice on each diet and were analyzed by one-way ANOVA and the Tukey's procedure. The assays were performed in duplicate for each sample. [b]$P < 0.05$ vs NC. [c]$P < 0.05$ vs HC. [d]$P < 0.05$ vs SV. [e]$P < 0.05$ vs EZ.

compared to hypercholesterolemic controls was observed, although it did not reach statistical significance. Simvastatin had no effect, whereas ezetimibe produced a significant reduction compared with hypercholesterolemic controls. No significant differences in liver triglyceride levels were detected between hypercholesterolemic and normal controls. Treated groups showed a significant reduction with respect to normal and hypercholesterolemic controls, and mice treated with simvastatin or ezetimibe showed significant lower values compared with those of mice fed PDF.

Simultaneous Supplementation. Plasma cholesterol levels increased 1.9-fold in hypercholesterolemic controls compared to normal controls (Table 5). No significant difference was noticed between PDF and hypercholesterolemic control group. Simvastatin and ezetimibe produced a significant reduction, with ezetimibe being the most effective. Plasma HDL levels were increased in hypercholesterolemic controls compared with normal controls. No significant difference in plasma HDL levels was observed between PDF and hypercholesterolemic control group, whereas treatment with simvastatin or ezetimibe induced a significant reduction. A 16-fold increase in plasma LDL levels was observed in hypercholesterolemic controls compared with normal controls. Mice fed with PDF showed no significant changes compared with hypercholesterolemic controls, whereas simvastatin and ezetimibe groups showed significant reductions. The total cholesterol/HDL ratio was moderately increased ($P = 0.071$) in hypercholesterolemic controls compared with normal controls. No significant differences between hypercholesterolemic controls and treated groups were observed. An 11.3-fold increase in the LDL/HDL ratio was noticed in hypercholesterolemic controls compared with normal controls. Similar values were observed in the treated groups except for the ezetimibe group where a significant reduction compared with hypercholesterolemic controls was recorded. Plasma triglyceride levels were reduced in hypercholesterolemic controls compared to normal controls, and compared to hypercholesterolemic controls, similar plasma triglyceride levels were observed in the treated groups.

There was no significant difference in liver cholesterol levels between normal and hypercholesterolemic controls. Liver cholesterol levels in the simvastatin group were significantly higher than those in the hypercholesterolemic control group, but no significant differences in the PDF or ezetimibe groups were observed compared with hypercholesterolemic controls. No significant differences in liver triglyceride levels were detected between normal and hypercholesterolemic controls or between PDF group and hypercholesterolemic controls. Liver triglyceride levels in mice treated with simvastatin or ezetimibe were significantly lower than those in hypercholesterolemic controls.

Modulation of the mRNA Expression Pattern in the Animal Intervention. *Sequential Supplementation.* In the jejunum, PDF induced overexpression of 10 genes, particularly

DOI: 10.1021/acs.jafc.5b02942
J. Agric. Food Chem. 2015, 63, 7371−7380

Table 5. Plasma and Liver Lipid Profile in Mice Treated for 4 Weeks with PDF, Simvastatin, or Ezetimibe Simultaneously with High-Cholesterol Diet (Simultaneous Supplementation)[a]

variable	NC	HC	PDF	SV	EZ
			Plasma Level (mg/dL)		
TC	120.86 ± 18.58	226.57 ± 16.64[b]	209.00 ± 40.33[b,d,e]	132.00 ± 13.37[c]	95.00 ± 14.14[c]
HDL	84.69 ± 17.11	118.11 ± 13.07[b]	97.50 ± 21.36[d,e]	64.35 ± 9.81[c]	64.35 ± 17.57[c]
LDL	10.03 ± 3.81	160.46 ± 25.42[b]	143.00 ± 29.46[b,d,e]	91.65 ± 17.30[b,c,e]	34.13 ± 16.11[c]
TC/HDL	1.45 ± 0.15	1.93 ± 0.20	2.16 ± 0.18[b,e]	2.10 ± 0.44[b]	1.58 ± 0.51
LDL/HDL	0.12 ± 0.04	1.36 ± 0.13[b]	1.48 ± 0.11[b,e]	1.47 ± 0.43[b,e]	0.62 ± 0.57[c]
TG	161.43 ± 49.42	50.29 ± 3.73[b]	38.00 ± 4.20[b]	42.00 ± 12.54[b]	68.50 ± 14.88[b]
			Liver Level (mg/g liver)		
TC	0.65 ± 0.23	0.98 ± 0.38	1.39 ± 0.21[b,e]	1.94 ± 0.64[b,c,e]	0.59 ± 0.42
TG	3.03 ± 0.85	2.35 ± 0.69	3.47 ± 0.97[d,e]	0.38 ± 0.18[b,c]	1.03 ± 0.51[b,c]

[a]NC, normal control; HC, hypercholesterolemic control; PDF: *Pleurotus ostreatus* DF fraction; SV: simvastatin; EZ: ezetimibe; TC, total cholesterol; HDL, high-density lipoprotein cholesterol; LDL, low-density lipoprotein cholesterol; TG, triglyceride. The results are mean ± SD of six (NC group) or eight (remaining groups) mice on each diet and were analyzed by one-way ANOVA and the Tukey's procedure. The assays were performed in duplicate for each sample. [b]$P < 0.05$ vs NC. [c]$P < 0.05$ vs HC. [d]$P < 0.05$ vs SV. [e]$P < 0.05$ vs EZ.

Fdft1, *Abca1* and *Npc1l1*. On the contrary, it inhibited the expression of *Nr1h4* and *Srebf2* to a degree similar to that induced by simvastatin and ezetimibe. Treatment with either simvastatin or ezetimibe inhibited the expression of *Srebf1*, and simvastatin further inhibited other genes such as *Fdft1*, *Hmgcr*, *Ldlr*, *Npc1l1*, and *Nr1h3* (Figure 2a). No significant changes induced by PDF or the two drugs were observed in the ileum (data not shown). However, a higher transcriptional regulation was found in the cecum, with PDF being the one that modulated the expression of more genes, whereas simvastatin showed no effect, suggesting a response for the accumulation of the indigestible DF fraction in the large intestine (Figure 2b). PDF induced upregulation of *Abcg5*, *Acat1*, *Dgat1*, *Ldlr*, and *Srebf1*, whereas the expression of *Hmgcr* and *Nr1h4* were slightly decreased. Ezetimibe induced upregulation of *Abcg5* and downregulation of *ApoB* and *Fdft1*. In the liver, PDF inhibited *Dgat1*, *Ldlr*, and *Nr1h4* expression to a degree similar to that induced by simvastatin and induced overexpression of *Acat1*, *Srebf1*, and *Srebf2*. Simvastatin inhibited the expression of *Abcg8*, *Ldlr*, *Nr1h4*, and *Dgat1*/2 (Figure 2c). Ezetimibe inhibited expression of *Abcg8* and *Dgat1*.

Simultaneous Supplementation. In the jejunum, PDF induced *Fdft1* overexpression (Figure 3a) at levels similar to those induced by sequential supplementation (Figure 2a) and *Srebf2* overexpression. Simvastatin induced overexpression of *Abcg8*, whereas ezetimibe did not induce statistically significant changes. In the ileum, PDF did not modify the gene expression profile (Figure 3b). Simvastatin induced upregulation of *Abca1*, *Fdft1*, and *Nr1h3* genes and downregulation of *ApoB*, whereas ezetimibe induced *Dgat1* and *Nr1h3* upregulation. In the cecum, *Dgat1* and *Soat2* expression were upregulated by PDF and simvastatin, respectively (Figure 3c). The hepatic expression profile was largely modulated by PDF and drugs with a clear tendency to downregulate rather than upregulate cholesterol-related genes (Figure 3d). PDF increased *Acat1* and *Srebf2* expression and decreased the expression levels of eight genes. Simvastatin slightly increased expression levels of *ApoB* and decreased expression levels of nine genes, particularly *Fdft1*. Ezetimibe increased and decreased expression levels of, respectively, 3 and 10 genes. *Abcg5*, *Fdft1*, *Ldlr*, *Nr1h3*, and *Nr1h4* were downregulated by PDF, simvastatin, and ezetimibe.

DISCUSSION

To select the more interesting DF fraction regarding its potential hypocholesterolemic effect, in vitro gene expression studies were carried out before in vivo studies. The DF fractions obtained from *A. bisporus*, *P. ostreatus*, and *L. edodes* mushrooms were submitted to in vitro digestion and applied to Caco-2 cultures in order to mimic in vivo conditions. The expression profiles of cholesterol-related genes in Caco-2 cells were different depending on the DF fraction assayed with *P. ostreatus* being the one that showed larger transcriptional changes. DF digestion can induce conformational changes in β-glucans structure, influencing their solubility, or can stimulate partial liberation of more water-soluble oligosaccharides,[18,25] modifying their biological properties.[26] Thus, the different DF fractions' effects at the transcriptional level could be due to the different solubilities and conformations formed in the DF digestates. PDF induced transcriptional changes in the short and longer terms because NR1H4 mRNA was upregulated after 1 h whereas FDFT1 and NPC1L1 genes were upregulated after 24 h. These results might suggest a possible cholesterol-lowering effect because on one hand FXR activation lowers plasma cholesterol in mice[27] and on the other hand the retarded activation of genes that enhance cholesterol biosynthesis (FDFT1) and cholesterol absorption (NPC1L1) suggests a compensatory response to the reduced available cholesterol in the cells 24 h after application of *P. ostreatus* digestate. Taking into account these observations together with the fact that *Pleurotus* is one of the genera that have been target of more studies describing its hypocholesterolemic properties, PDF was selected for in vivo studies.

In the sequential supplementation, PDF administration did not improve plasma and liver cholesterol levels and slightly reduced fecal cholesterol, indicating that the extract was not able of acting as a palliative agent. However, increased plasma and liver cholesterol levels as a consequence of reduced fecal cholesterol excretion were also not observed. In contrast, concomitant overexpression of *Npc1l1*, *Abcg5*, and *Abcg8* in the jejunum makes difficult a clear explanation because *Npc1l1* upregulation could be associated with enhanced intestinal cholesterol absorption and therefore reduction of fecal cholesterol excretion[28] but not upregulation of *Abcg5* and *Abcg8* genes, which can stimulate effect opposite that of *Npc1l1*. Mice fed PDF showed slightly higher (not significant) HDL levels compared with those of hypercholesterolemic controls. Elevation in

DOI: 10.1021/acs.jafc.5b02942
J. Agric. Food Chem. 2015, 63, 7371−7380

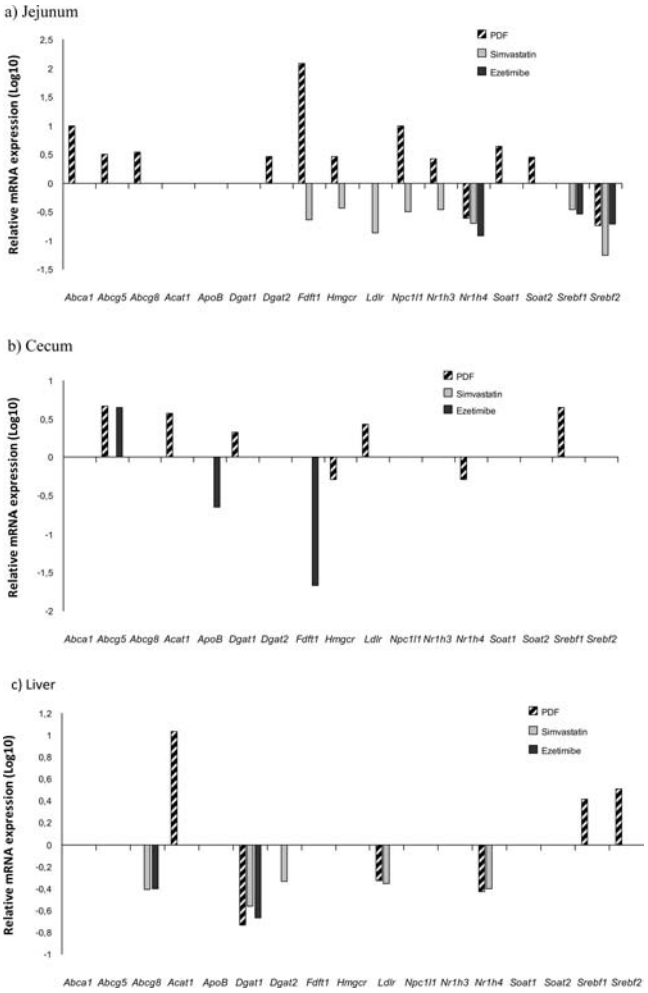

Figure 2. Relative mRNA expression (log 10) of cholesterol-related genes in (a) jejunum, (b) cecum, and (c) liver of mice treated for 4 weeks with PDF, simvastatin, or ezetimibe simultaneously with high-cholesterol diet after 4 weeks of high-cholesterol diet alone (sequential supplementation). Indicated genes are only those noted as significant ($P < 0.05$) compared with hypercholesterolemic mice at 8 weeks as control. The expression of each gene was measured at least in duplicate, and each biological group included a minimum of three replicates. A few genes did not pass the quality control either in the target or the control group; therefore, their expression level was omitted in the figure.

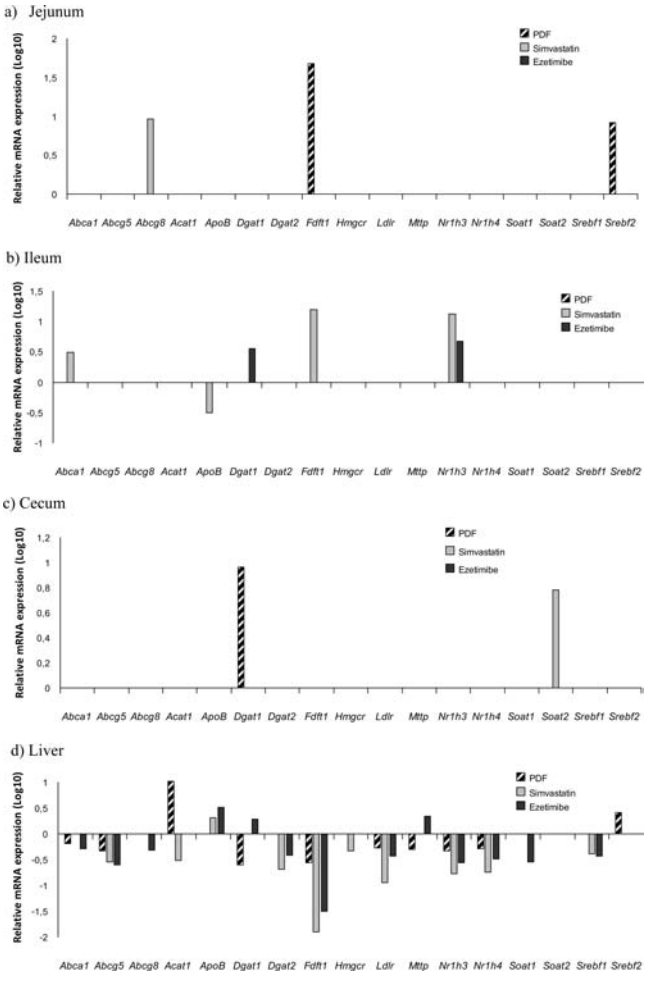

Figure 3. Relative mRNA expression (log 10) of cholesterol-related genes in (a) jejunum, (b) ileum, (c) cecum, and (d) liver of mice treated for 4 weeks with PDF, simvastatin, or ezetimibe simultaneously with high-cholesterol diet (simultaneous supplementation). Indicated genes are only those noted as significant ($P < 0.05$) compared with hypercholesterolemic mice at 4 week as control. The expression of each gene was measured at least in duplicate, and each biological group included a minimum of three replicates. Few genes did not pass the quality control either in the target or the control group; therefore, their expression level was omitted in the figure.

HDL levels occurs through an increase in liver production of *apoAI*,[29] and *Abca1* overexpression in the jejunum was associated with enhanced *apoAI* and HDL plasma levels in mice.[30] Thus, the slight (not significant) increase of HDL levels induced by PDF might be related to the enhanced jejunal *Abca1* expression, and the weakness of that effect might likely be due to the lower HDL production in jejunum compared to liver.

Diet supplementation with PDF and control drugs decreased triglyceride in the liver but not hepatomegaly (measured as liver-to-body-weight ratio) induced by high-cholesterol diet. Parallel to that reduction, hepatic *Dgat1* downregulation in the three experimental groups was observed, suggesting that the reduced hepatic triglyceride accumulation could be induced by inhibition of triglyceride synthesis. Another hepatic triglyceride-lowering pathway is the one induced by cholic acid. In mouse models of hypertriglyceridemia, cholic acid reduces hepatic expression of *Srebp-1c* via *Nr1h4* upregulation.[31] In contrast, *Srebf1* upregulation and *Nr1h4* downregulation were observed in mice fed PDF, which rules out regulation of liver triglyceride via that pathway. Reduction of liver triglyceride by simvastatin or ezetimibe was also not associated with that pathway. Therefore, results suggest a common effect for PDF, simvastatin, and ezetimibe for reducing liver triglyceride by inhibition of triglyceride synthesis mediated via *Dgat1* downregulation. Triglyceride accumulation in the liver caused by lifestyle-related diseases can result in more serious diseases. In this line, administration of *A. bisporus* prevents hepatic steatosis in mice,[32] and *Panellus serotinus* ameliorates nonalcoholic fatty liver disease in obese, diabetic mice.[33,34] Thus, PDF could be of interest to develop new therapeutic approaches preventing hepatic triglyceride accumulation. In addition to that effect, PDF showed a trend to reduce hepatic cholesterol (21%), although it did not reach statistical significance. Cholesterol-lowering effects in the liver can be directly induced by inhibition of synthesis (statins) or indirectly by decreasing enterohepatic circulation of bile acids

DOI: 10.1021/acs.jafc.5b02942
J. Agric. Food Chem. 2015, 63, 7371−7380

(bile acid sequestrants) that in turn results in increased bile acid synthesis and then decreased hepatic cholesterol.[35] Concerning the first case, neither PDF nor control drugs influenced *Fdft1* or *Hmgcr* expression in the liver, suggesting a lack of transcriptional effect on cholesterol synthesis. However, mice fed PDF showed hepatic overexpression of *Srebf-2* (gene encoding *Srebp2* protein), and *Srebp2* overexpression induces upregulation of *Fdft1* and *Hmgcr* in liver of mice fed a high-protein/low-carbohydrate diet.[36] Differences between the diet used by Sakakura et al. and those used in the models of this work could explain that apparent controversy. Regarding the second case, PDF induced downregulation of jejunal *Nr1h4* expression. In this line, the classical mechanism of action for the bile acid sequestrants is mediated by blocking apical bile acid uptake in the ileum, which results in downregulation of *Nr1h4* and its target genes[37], suggesting that the uptake of bile acids in the jejunum could be similarly blocked. Further studies assessing intestinal transport of bile acids are needed to confirm this possibility. The association between reduced liver cholesterol and reduced jejunal *Nr1h4* expression was more clearly noticed for ezetimibe but not for simvastatin where despite reduced jejunal *Nr1h4* a lack of effect on liver cholesterol was noticed.

In contrast with the effect of PDF in the sequential supplementation, no significant changes in fecal cholesterol excretion were noticed in the simultaneous supplementation. Lack of significant influence on cholesterol excretion in feces as compared with the hypercholesterolemic controls was also previously reported in hypercholesterolemic rats given powder of *P. ostreatus* fruiting bodies.[38] Although these slight changes were not directly associated with jejunal regulation of genes involved in cholesterol absorption or reverse cholesterol transport, *Srebf2* and *Fdft1* overexpression induced by PDF in the jejunum might be related, with a possible enhancing of cholesterol synthesis in the small intestine.

The hypocholesterolemic effect of edible mushrooms, particularly *P. ostreatus*, have been evidenced by animal trials,[11,39,40] and some of them pointed out mushroom DF from other mushrooms as having potential responsibility for the observed effects[12,13,41] although not all.[42,43] Rats administrated powdered *P. ostreatus* fruiting bodies (including similar amounts of DF than PDF) under similar experimental setting to the simultaneous supplementation but for a longer period of time did have lowering of plasma and liver cholesterol after 8[44] and 10 weeks.[42] Either the lower experimental time set for this experiment or different extract concentration could be the reason for the lack of significant hypocholesterolemic activity because in the latter reports a higher mushroom fiber dose (5 vs 1.5%) and normocholesterolemic condition instead of diet-induced hypercholesterolemia were utilized. Regarding the tissue-specific transcriptional regulation, no large changes were observed except for the liver. However, it is wise to notice that *Fdft1* upregulation was noticed in the jejunum of both mice models as well as in Caco-2 cells after PDF administration. Overexpression of the genes encoding enzymes might sometimes be related to reduction or insufficient enzyme activity; thus, perhaps PDF administration could inhibit or impair the normal squalene synthase function in enterocytes acting at post-transcriptional levels. However, more studies are needed to confirm this possibility. In liver, the administration of PDF or the two control drugs downregulated most of the genes. Interestingly, the hepatic expression of *Abcg5*, *Fdft1*, *Ldlr*, *Nr1h3*, and *Nr1h4* genes was downregulated by PDF, simvastatin, and ezetimibe. However, these changes do not mirror those observed in hepatic cholesterol or triglyceride levels. Concerning *Abcg5* expression in the liver, the heterodimer conformed by *Abcg5* and *Abcg8* is necessary for cholesterol excretion into bile,[45,46] and their overexpression promotes this phenomena.[47] Therefore, the physiological significance of downregulation of *Abcg5* gene alone is difficult to interpret. Although simvastatin and ezetimibe downregulated hepatic *Srebf1* and its target gene *Fdft1*[36] and PDF downregulated *Fdft1*, no correlation with changes in hepatic cholesterol levels was observed. Similarly, the *Ldlr* downregulation induced by PDF, simvastatin, and ezetimibe was not correlated with changes in plasmatic LDLc. However, the downregulation of *Dgat2* gene by simvastatine or ezetimibe suggests a possible association with the reduction of hepatic triglyceride levels observed.

PDF induced a downregulation of *Dgat1* mRNA similar to that induced by simvastatin or ezetimibe in liver, suggesting a possible relation between their reduced hepatic triglyceride levels and inhibition of triglyceride synthesis in the sequential supplementation. Thus, PDF may be useful in limiting hepatic triglyceride accumulation. The biochemical data recorded in plasma and liver for mice treated with PDF showed no significant changes in the cholesterol metabolism and no relation with the transcriptional changes observed. Once the hypercholesterolemia was induced in mice, administration of PDF or simvastatin was unable to revert that status. Thus, it seems that doses of fungal DF fractions similar to those effective in normocholesterolemic models for lowering cholesterol levels are ineffective in hypercholesterolemic mice. However, a mushroom extract that can modulate the transcription of genes involved in the cholesterol homeostasis in a manner similar to that of hypocholesterolemic drugs promotes further studies in a dose-dependent experimental setting to investigate in more detail its potential as a hypercholesterolemia preventive agent. Studies with higher doses are currently being developed to clarify the effect of mushroom DF fractions on lipid metabolism.

AUTHOR INFORMATION

Corresponding Authors

*Tel.: +34-912071032. Fax: +34-912071512. E-mail: juanvictor.caz@salud.madrid.org.

*Tel.: +34-910017922. Fax: +34-910017905. E-mail: cristina.soler@uam.es.

Author Contributions

V.C. and A.G.-R. contributed equally to this work.

Funding

This research was supported by AGL2010-21537 national R+D program from the Spanish Ministry of Science and Innovation and ALIBIRD-CM S2009/AGR-1469 regional program from the Community of Madrid (Spain).

Notes

The authors declare no competing financial interest.

ACKNOWLEDGMENTS

CTICH (Centro Tecnológico de Investigación del Champiñón de La Rioja, Autol, Spain) is acknowledged for the cultivation and supplying of the mushroom fruiting bodies, and Maria Navarro-Rubio is thanked for her technical assistance.

ABBREVIATIONS

DF, dietary fiber; PDF, *Pleurotus ostreatus* DF fraction; TC, total cholesterol; HDL, high-density lipoprotein cholesterol;

DOI: 10.1021/acs.jafc.5b02942
J. Agric. Food Chem. 2015, 63, 7371−7380

LDL, low-density lipoprotein cholesterol; TG, triglyceride; LDA, low-density array

REFERENCES

(1) Cheung, P. C. K. Mini-review on edible mushrooms as source of dietary fiber: preparation and health benefits. *Food Science and Human Wellness.* **2013**, *2*, 162−166.

(2) Zacherl, C.; Eisner, P.; Engel, K.-H. In vitro model to correlate viscosity and bile acid-binding capacity of digested water-soluble and insoluble dietary fibres. *Food Chem.* **2011**, *126*, 423−428.

(3) Galisteo, M.; Duarte, J.; Zarzuelo, A. Effects of dietary fibers on disturbances clustered in the metabolic syndrome. *J. Nutr. Biochem.* **2008**, *19*, 71−84.

(4) Drozdowski, L. A.; Reimer, R. A.; Temelli, F.; Bell, R. C.; Vasanthan, T.; Thomson, A. B. R. b-glucan extracts inhibit the in vitro intestinal uptake of long-chain fatty acids and cholesterol and downregulate genes involved in lipogenesis and lipid transport in rats. *J. Nutr. Biochem.* **2010**, *21*, 695−701.

(5) Kaczmarczyk, M.; Miller, M. J.; Freund, G. G. The health benefits of dietary fiber: beyond the usual suspects of type 2 diabetes mellitus, cardiovascular disease and colon cancer. *Metab., Clin. Exp.* **2012**, *61*, 1058−1066.

(6) Parnell, J. A.; Reimer, R. A. Effect of prebiotic fibre supplementation on hepatic gene expression and serum lipids: a dose-response study in JCR:LA-cp rats. *Br. J. Nutr.* **2010**, *103*, 1577−1584.

(7) Chen, J.; Huang, X. F. The effect of diets enriched in beta-glucans on blood lipoprotein concentrations. *J. Clin. Lipidol.* **2009**, *3*, 154−158.

(8) Mazur, A.; Felgines, C.; Nassir, F.; Bayle, D.; Gueux, E.; Remesy, C.; Rayssiguier, Y.; Cardot, P. Apolipoprotein B gene expression in rat intestine. The effect of dietary fiber. *FEBS Lett.* **1991**, *284*, 63−65.

(9) Hu, Y. B.; Wang, Z.; Xu, S. Y. Corn bran dietary fibre modified by xylanase improves the mRNA expression of genes involved in lipids metabolism in rats. *Food Chem.* **2008**, *109*, 499−505.

(10) Aida, F. M. N. A.; Shuhaimi, M.; Yazid, M.; Maaruf, A. G. Mushroom as a potential source of prebiotics: a review. *Trends Food Sci. Technol.* **2009**, *20*, 567−575.

(11) Gil-Ramirez, A.; Soler-Rivas, C. The use of edible mushroom extracts as bioactive ingredients to design novel functional foods with hypocholesterolemic activities. In *Mushrooms: Cultivation, Antioxidant Properties and Health Benefits*; Pesti, G., Ed.; Nova Science Publishers, Inc.: Hauppauge, NY, 2014; pp 43−73.

(12) Fukushima, M.; Nakano, M.; Morii, Y.; Ohashi, T.; Fujiwara, Y.; Sonoyama, K. Hepatic LDL Receptor mRNA in Rats Is Increased by Dietary Mushroom (Agaricus bisporus) Fiber and Sugar Beet Fiber. *J. Nutr.* **2000**, *130*, 2151−2156.

(13) Fukushima, M.; Ohashi, T.; Fujiwara, Y.; Sonoyama, K.; Nakano, M. Cholesterol-Lowering effects of maitake (Grifola frondosa) fiber, shiitake (Lentinus edodes) fiber, and enokitake (Flammulina velutipes) fiber in rats. *Exp. Biol. Med. (Maywood)* **2001**, *226*, 758−765.

(14) Sato, M.; Tokuji, Y.; Yoneyama, S.; Fujii-Akiyama, K.; Kinoshita, M.; Ohnishi, M. Profiling of Hepatic Gene Expression of Mice Fed with Edible Japanese Mushrooms by DNA Microarray Analysis: Comparison among Pleurotus ostreatus, Grifola frondosa, and Hypsizigus marmoreus. *J. Agric. Food Chem.* **2011**, *59*, 10723−10731.

(15) Sato, M.; Tokuji, Y.; Yoneyama, S.; Fujii-Akiyama, K.; Kinoshita, M.; Chiji, H.; Ohnishi, M. Effect of dietary maitake (Grifola frondosa) mushrooms on plasma cholesterol and heptatic gene expression in cholesterol-fed mice. *J. Oleo Sci.* **2013**, *62*, 1049−1058.

(16) Gil-Ramírez, A.; Aldars-García, L.; Palanisamy, M.; Jiverdeanu, R. M.; Ruiz-Rodríguez, A.; Marín, F. R.; Reglero, G.; Soler-Rivas, C. Sterols enriched fractions obtained from Agaricus bisporus fruiting bodies and by-products by compressed fluid technologies (PLE and SFE). *Innovative Food Sci. Emerging Technol.* **2013**, *18*, 101−107.

(17) Jeurink, P. V.; Noguera, C. L.; Savelkoul, H. F. J.; Wichers, H. J. Immunomodulatory capacity of fungal proteins on the cytokine production of human peripheral blood mononuclear cells. *Int. Immunopharmacol.* **2008**, *8*, 1124−1133.

(18) Palanisamy, M.; Aldars-García, L.; Gil-Ramírez, A.; Ruiz-Rodríguez, A.; Marín, F. R.; Reglero, G.; Soler-Rivas, C. Pressurized water extraction of β-glucan enriched fractions with bile acids-binding capacities obtained from edible mushrooms. *Biotechnol. Prog.* **2014**, *30*, 391−400.

(19) Nitschke, J.; Altenbach, H. J.; Malolepszy, T.; Mölleken, H. A new method for the quantification of chitin and chitosan in edible mushrooms. *Carbohydr. Res.* **2011**, *346*, 1307−1310.

(20) Mosmann, T. Rapid colorimetric assay for cellular growth and survival: application to proliferation and cytotoxicity assays. *J. Immunol. Methods* **1983**, *65*, 55−63.

(21) Gil-Ramírez, A.; Caz, V.; Martin-Hernandez, R.; Marín, F. R.; Largo, C.; Rodríguez-Casado, A.; Tabernero, M.; Ruiz-Rodríguez, A.; Reglero, G.; Soler-Rivas, C. Modulation of cholesterol-related gene expression by ergosterol and ergosterol-enriched extracts obtained from Agaricus bisporus. *Eur. J. Nutr.* **2015**, 10.1007/s00394-015-0918-x

(22) Vandesompele, J.; De Preter, K.; Pattyn, F.; Poppe, B.; Van Roy, N.; De Paepe, A.; Speleman, F. Accurate normalization of real-time quantitative RT-PCR data by geometric averaging of multiple internal control genes. *Genome Biol.* **2002**, *3*, research0034.1.

(23) Pfaffl, M. W. A new mathematical model for relative quantification in real-time RT-PCR. *Nucleic Acids Res.* **2001**, *29*, 45e.

(24) Ikemoto, S.; Takahashi, M.; Tsunoda, N.; Maruyama, K.; Itakura, H.; Kawanaka, K.; Tabata, I.; Higuchi, M.; Tange, T.; Yamamoto, T. T.; Ezaki, O. Cholate inhibits high-fat diet-induced hyperglycemia and obesity with acyl-CoA synthetase mRNA decrease. *Am. J. Physiol.* **1997**, *273*, E37−E45.

(25) Harish Prashanth, K. V.; Tharanathan, R. N. Chitin/chitosan: modifications and their unlimited application potential − an overview. *Trends Food Sci. Technol.* **2007**, *18*, 117−131.

(26) Barsanti, L.; Passarelli, V.; Evangelista, V.; Frassanito, A. M.; Gualtieri, P. Chemistry, physico-chemistry and applications linked to biological activities of β-glucans. *Nat. Prod. Rep.* **2011**, *28*, 457−466.

(27) Zhang, Y.; Lee, F. Y.; Barrera, G.; Lee, H.; Vales, C.; Gonzalez, F. J.; Willson, T. M.; Edwards, P. A. Activation of the nuclear receptor FXR improves hyperglycemia and hyperlipidemia in diabetic mice. *Proc. Natl. Acad. Sci. U. S. A.* **2006**, *103*, 1006−1011.

(28) Sudhop, T.; Reber, M.; Tribble, D.; Sapre, A.; Taggart, W.; Gibbons, P.; Musliner, T.; von Bergmann, K.; Lütjohann, D. Changes in cholesterol absorption and cholesterol synthesis caused by ezetimibe and/or simvastatin in men. *J. Lipid Res.* **2009**, *50*, 2117−2123.

(29) Sahoo, D.; Trischuk, T. C.; Chan, T.; Drover, V. A.; Ho, S.; Chimini, G.; Agellon, L. B.; Agnihotri, R.; Francis, G. A.; Lehner, R. ABCA1-dependent lipid efflux to apolipoprotein A-I mediates HDL particle formation and decreases VLDL secretion from murine hepatocytes. *J. Lipid Res.* **2004**, *45*, 1122−1131.

(30) Joyce, C. W.; Amar, M. J.; Lambert, G.; Vaisman, B. L.; Paigen, B.; Najib-Fruchart, J.; Hoyt, R. F., Jr.; Neufeld, E. D.; Remaley, A. T.; Fredrickson, D. S.; Brewer, H. B., Jr.; Santamarina-Fojo, S. The ATP binding cassette transporter A1 (ABCA1) modulates the development of aortic atherosclerosis in C57BL/6 and apoE-knockout mice. *Proc. Natl. Acad. Sci. U. S. A.* **2002**, *99*, 407−412.

(31) Watanabe, M.; Houten, S. M.; Wang, L.; Moschetta, A.; Mangelsdorf, D. J.; Heyman, R. A.; Moore, D. D.; Auwerx, J. Bile acids lower triglyceride levels via a pathway involving FXR, SHP, and SREBP-1c. *J. Clin. Invest.* **2004**, *113*, 1408−1418.

(32) Kanaya, N.; Kubo, M.; Liu, Z.; Chu, P.; Wang, C.; Yuan, Y. C.; Chen, S.; et al. Protective effects of white button mushroom (Agaricus bisporus) against hepatic steatosis in ovariectomized mice as a model of postmenopausal women. *PLoS One* **2011**, *6*, e26654.

(33) Inoue, N.; Inafuku, M.; Shirouchi, B.; Nagao, K.; Yanagita, T. Effect of Mukitake mushroom (Panellus serotinus) on the pathogenesis of lipid abnormalities in obese, diabetic ob/ob mice. *Lipids Health Dis.* **2013**, *12*, 18−23.

(34) Inafuku, M.; Nagao, K.; Nomura, S.; Shirouchi, B.; Inoue, N.; Nagamori, N.; Nakayama, H.; Toda, T.; Yanagita, T. Protective effects of fractional extracts from Panellus serotinus on non-alcoholic fatty

DOI: 10.1021/acs.jafc.5b02942
J. Agric. Food Chem. 2015, 63, 7371−7380

liver disease in obese, diabetic db/db mice. *Br. J. Nutr.* **2012**, *107*, 639−646.
(35) Catapano, A. L.; Reiner, Z.; De Backer, G.; Graham, I.; Taskinen, M. R.; Wiklund, O.; Agewall, S.; Alegria, E.; Chapman, M.; Durrington, P.; Erdine, S.; Halcox, J.; Hobbs, R.; Kjekshus, J.; Perrone Filardi, P.; Riccardi, G.; Storey, R. F.; Wood, D. European Society of Cardiology (ESC); European Atherosclerosis Society (EAS). ESC/EAS Guidelines for the management of dyslipidaemias The Task Force for the management of dyslipidaemias of the European Society of Cardiology (ESC) and the European Atherosclerosis Society (EAS). *Atherosclerosis* **2011**, *217*, 3−46.
(36) Sakakura, Y.; Shimano, H.; Sone, H.; Takahashi, A.; Inoue, N.; Toyoshima, H.; Suzuki, S.; Yamada, N. Sterol regulatory element-binding proteins induce an entire pathway of cholesterol synthesis. *Biochem. Biophys. Res. Commun.* **2001**, *286*, 176−183.
(37) Dawson, P. A.; Lan, T.; Rao, A. Bile acid transporters. *J. Lipid Res.* **2009**, *50*, 2340−2357.
(38) Alam, N.; Yoon, K. N.; Lee, T. S.; Lee, U. Y. Hypolipidemic activities of dietary *Pleurotus ostreatus* in hypercholesterolemic rats. *Mycobiology* **2011**, *39*, 45−51.
(39) Anandhi, R.; Annadurai, T.; Anitha, T. S.; Muralidharan, A. R.; Najmunnisha, K.; Nachiappan, V.; Thomas, P. A.; Geraldine, P. Antihypercholesterolemic and antioxidative effects of an extract of the oyster mushroom, *Pleurotus ostreatus*, and its major constituent, chrysin, in Triton WR-1339-induced hypercholesterolemic rats. *J. Physiol. Biochem.* **2013**, *69*, 313−323.
(40) Ravi, B.; Renitta, R. E.; Prabha, M. L.; Issac, R.; Naidu, S. Evaluation of antidiabetic potential of oyster mushroom (*Pleurotus ostreatus*) in alloxan-induced diabetic mice. *Immunopharmacol. Immunotoxicol.* **2013**, *35*, 101−109.
(41) Jeong, S. C.; Jeong, Y. T.; Yang, B. K.; Islam, R.; Koyyalamudi, S. R.; Pang, G.; Cho, K. Y.; Song, C. H. White button mushroom (*Agaricus bisporus*) lowers blood glucose and cholesterol levels in diabetic and hypercholesterolemic rats. *Nutr. Res. (N. Y., NY, U. S.)* **2010**, *30*, 49−56.
(42) Bobek, P.; Ozdin, L.; Kuniak, L. Effect of oyster mushroom and isolated b-glucan on lipid peroxidation and on the activities of antioxidative enzymes in rats fed the cholesterol diet. *J. Nutr. Biochem.* **1997**, *8*, 469−471.
(43) Seto, S.W.; Lam, T. Y.; Tam, H. L.; Au, A. L. S.; Chan, S. W.; Wu, J. H.; Yu, P. H. F.; Leung, G. P. H.; Ngai, S. M.; Yeung, J. H. K.; Leung, P. S.; Lee, S. M. Y.; Kwan, Y. W. Novel hypoglycemic effects of *Ganoderma lucidum* water-extract in obese/diabetic (+db/+db) mice. *Phytomedicine* **2009**, *16*, 426−436.
(44) Bobek, P.; Ondreicka, R.; Klvanova, J.; Ozdin, L. Oyster mushroom (*Pleurotus ostreatus*) decreases serum and liver cholesterol and increases cholesterol 7alpha-hydroxylase activity and fecal excretion of neutral sterols and bile acids in hypercholesterolemic rats. *Nutr. Res. (N. Y., NY, U. S.)* **1994**, *14*, 1683−1688.
(45) Yu, L.; Hammer, R. E.; Li-Hawkins, J.; Von Bergmann, K.; Lutjohann, D.; Cohen, J. C.; Hobbs, H. H. Disruption of Abcg5 and Abcg8 in mice reveals their crucial role in biliary cholesterol secretion. *Proc. Natl. Acad. Sci. U. S. A.* **2002**, *99*, 16237−16242.
(46) Graf, G. A.; Yu, L.; Li, W. P.; Gerard, R.; Tuma, P. L.; Cohen, J. C.; Hobbs, H. H. ABCG5 and ABCG8 are obligate heterodimers for protein trafficking and biliary cholesterol excretion. *J. Biol. Chem.* **2003**, *278*, 48275−48282.
(47) Yu, L.; Li-Hawkins, J.; Hammer, R. E.; Berge, K. E.; Horton, J. D.; Cohen, J. C.; Hobbs, H. H. Overexpression of ABCG5 and ABCG8 promotes biliary cholesterol secretion and reduces fractional absorption of dietary cholesterol. *J. Clin. Invest.* **2002**, *110*, 671−680.

DOI: 10.1021/acs.jafc.5b02942
J. Agric. Food Chem. 2015, 63, 7371−7380

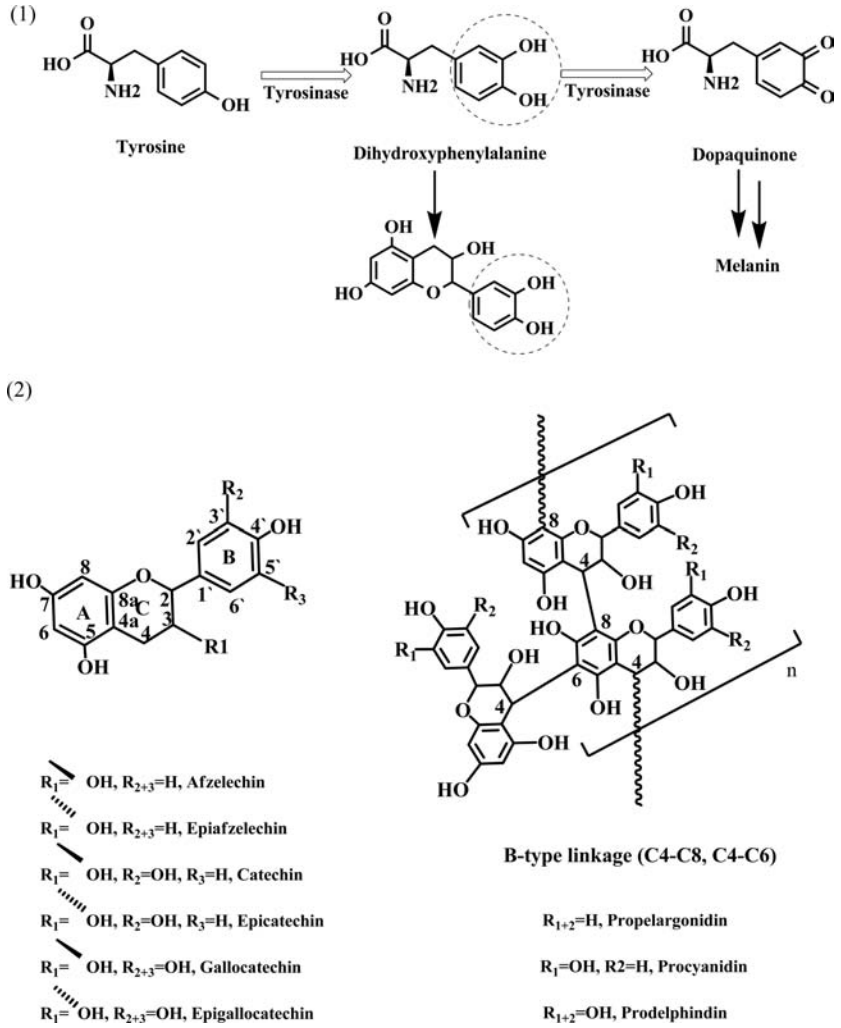

Figure 1. Chemical structures of proanthocyanidins, flavan-3-ol monomer units, and substrates of tyrosinase. (1) Processes of melanogensis and structural similarity between epicatechin/catechin and L-DOPA. (2) Chemical structures of flavan-3-ol monomer units and proanthocyanidins.

Amberlite IRP-64 cation-exchange resin, cesium chloride, 2,5-dihydroxybenzoic acid, and all HPLC standards were purchased from Sigma-Aldrich (St. Louis, MO). Arbutin was obtained from Aladdin (Shanghai, China). The fresh fruits of avocado were picked from the trees growing in Xiamen University (Xiamen, China) in August 2012. They were immediately washed, freeze-dried, ground, and stored at −20 °C before further processes.

Extraction and Purification of Avocado Proanthocyanidins. Powders (10.0 g) of the avocado fruit were ultrasonically extracted 3 times with acetone/water (70:30, v/v, each 200 mL) solution at 25 °C. Simultaneously, 0.1% ascorbic acid was added to prevent the oxidation of proanthocyanidins. Petroleum ether and ethyl acetate were then selected as an extractant to eliminate chlorophyll, lipophilic compounds, and low-molecular-weight phenolics. The remaining aqueous fraction was chromatographed on a Sephadex LH-20 column (50 × 1.5 cm inner diameter), which was eluted successively with 50% methanol/water and 70% acetone/water. The fraction of 70% acetone/water was retained; acetone was eliminated; and then the aqueous fraction freeze-dried to obtain purified proanthocyanidins.

MALDI−TOF MS Analysis. The MALDI−TOF MS spectra were obtained through a Bruker Reflex III (Germany). The experiment was completed according to the conditions and steps previously described.[4] As the irradiation source, a pulsed nitrogen laser (337 nm) would last 3 ns. Cs^+ and 2,5-dihydroxybenzoic acid were selected as the cationization and matrix, respectively. The sample solutions (10 mg/mL), the cesium chloride solution (1.52 mg/mL), and the matrix solution (10 mg/mL) were mixed at a volumetric ratio of 1:1:3.

Reversed-Phase HPLC−ESI−QTRAP MS Analysis after Thiolysis Reaction. Reversed-phase HPLC−ESI−QTRAP MS analysis was completed in the method described by Zhou et al.[7] Proanthocyanidins were thiolysis-degraded in the presence of benzyl mercaptan, and then the degradation products were injected into an Agilent 1200 system (Agilent, Santa Clara, CA) interfaced to a QTRAP 3200 (Applied Biosystems, Foster City, CA) with a 250 × 4.6 mm inner diameter, 5.0 mm Hypersil ODS column (Elite, Dalian, China). The mean degree of polymerization (mDP) was calculated on the basis of the following equation:

$$\text{mDP} = (\text{total area of the extender units}) / (\text{total area of the terminal units}) + 1$$

Enzyme Assay. L-Tyrosine was selected as a substrate of monophenolase, and 3,4-dihydroxyphenylalanine was used as a substrate of diphenolase. The final concentrations of the enzyme were 16.67 and 3.33 mg/mL for the monophenolase and diphenolase analyses, respectively. The experiment was repeated 3 times. Their results were expressed in IC_{50} value (μg/mL). The inhibition type depended upon the Lineweaver−Burk plot. Arbutin was selected as a positive control. The procedure and conditions for the enzyme reaction were carried out as described in our previous study.[4]

Fluorescence Quenching Analysis. The fluorescence test of tyrosinase and proanthocyanidins was performed on a fluorescence spectrophotometer (Varian Cary Eclipse). Sample solution, tyrosinase solution, and sodium phosphate buffer (pH 6.8) were mixed at a

DOI: 10.1021/acs.jafc.5b03099
J. Agric. Food Chem. 2015, 63, 7381−7387

volumetric ratio of 1:2:7 (v/v/v). The final reaction total volume was 3 mL. The analysis was carried out with an excitation wavelength of 290 nm at 25 °C. The Stern–Volmer equation describes fluorescence quenching[13]

$$F_0/F = 1 + K_q\tau_0[Q] = 1 + K_{SV}[Q]$$

where F_0 and F are the fluorescence intensities in the presence and absence of the quencher, respectively, K_q is the bimolecular quenching constant, τ_0 (10^{-8} s) is the lifetime of the fluorophore in the absence of the quencher, [Q] is the concentration of the quencher, and K_{SV} is the Stern–Volmer quenching constant.

There exist two types of fluorescence quenching mechanisms: static and dynamic.[14] When the type was static, the apparent binding constant (K_A) and the binding affinity (n) are estimated by the following equation:[15]

$$\log[(F_0 - F)/F] = \log K_A + n \log[Q]$$

The fluorescence assays of L-tyrosine/3,4-dihydroxyphenylalanine and proanthocyanidins were also performed on a fluorescence spectrophotometer (Varian Cary Eclipse). In brief, L-tyrosine (12 mM) or 3,4-dihydroxyphenylalanine (0.5 mM) solution, sample solution, and sodium phosphate buffer (pH 6.8) were mixed at a volumetric ratio of 1:1:3 (v/v/v) at 25 °C. The mixture was preincubated for 30 s before fluorescence spectra analysis. The excitation wavelength was 290 nm. The experiment was repeated 3 times.

Determination of Cu^{2+} Chelating Activity. A total of 100 μL of copper sulfate solution with different concentrations (25, 50, and 100 μM) and 100 μL of sample (1 mg/mL) solution were added to sodium phosphate buffer (50 mM, pH 6.8). The final volume was 1 mL, and the mixture was then shaken well and kept at 25 °C for 1 min prior to ultraviolet–visible (UV–vis) and fluorescence quenching analyses.

Molecular Docking of Tyrosinase with Ligands. Protein–ligand docking was completed by Molecular Operation Environment (MOE) 2010 software. In present study, we selected the structure of the oxy-tyrosinase of *Streptomyces castaneoglobisporus* as the initial model for docking simulations. ChemBioDraw Utra 12.0 was used to prepare the three-dimensional (3D) structures of the ligands. The structure models of the protein and ligands were energy-minimized before docking. Then, hydrogens were added to the protein and ligands. The refinement module of molecular docking was set to force field and retains scoring set to 10. The docking poses ranged according to the MM/GBVI binding free energy scoring. The binding mode was judged by the docked conformation, which had the lowest energy value.

Statistical Analysis. SPSS 19.0 was applied to the calculations. Results of antityrosinase analyses were indicated as the mean ± standard deviation.

RESULTS AND DISCUSSION

MALDI–TOF MS Analysis. The MALDI–TOF MS technique is an effective method for the characterization of proanthocyanidins in food science.[4,7,16,17] It has the potency to distinguish molecular weight differences because of the hydroxylation pattern in the B ring (Δ 16 Da), 3-*O*-galloylation (Δ 152 Da), or A-type linkage (Δ 2 Da).[16] Figure 2A displayed the MALDI–TOF mass spectra of avocado fruit proanthocyanidins, recorded as Cs^+ adducts in the reflection mode. Peaks increased equably from 999.00 Da (3-mers) to the 6183.42 Da (21-mers) at a distance of 288 Da, which was in accordance with the addition of one (epi)catechin. Therefore, it could be concluded that the main constitute unit is (epi)catechin. For each multiple, masses of 16 Da higher and lower were also detected in spectra when they were enlarged (Figure 2A). These masses were heteropolymers of repeating constitution units, which indicated the presence of (epi)gallocatechin and (epi)afzelechin. These results further demonstrated the coexistence of procyanidins, prodelphinidins, and propelargonidins in avocado fruit proanthocyanidins, which were dominated by procyanidins. However, in comparison to procyanidins, there were few prodelphinidins and propelargonidins. Besides the series of peaks described above, mass signals following the main groups of peaks at a distance of 152 and 132 Da were detected (Figure 2A). The 152 Da mass distance was in accordance with the addition of one galloyl group at the heterocyclic C ring.[18] The 132 Da mass distance may be produced by the substitution of a pentoside[18] or synchronous attachment of two Cs^+ and the absence of a proton $[M + 2Cs^+ - H]^+$.[19] Specifically, mass signals following the main groups of

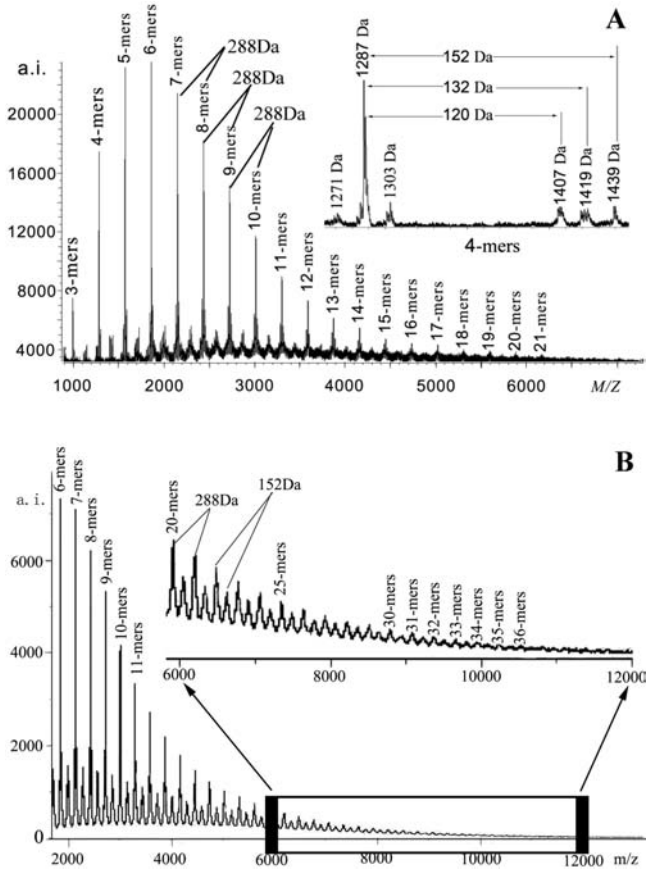

Figure 2. MALDI–TOF positive-ion (Cs^+) mode mass spectra of avocado proanthocyanidins in the (A) reflectron mode and (B) linear mode. The *y* axis represents absolute intensity (ai), that is, the number of ions of each species that reach the detector.

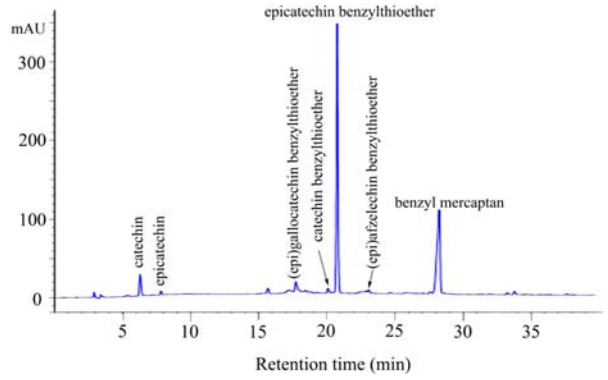

Figure 3. Reversed-phase HPLC–ESI–QTRAP MS chromatograms of proanthocyanidins from avocado after thiolytic degradation.

DOI: 10.1021/acs.jafc.5b03099
J. Agric. Food Chem. 2015, 63, 7381–7387

Table 1. Effects of Avocado Proanthocyanidins on the Activity of Mushroom Tyrosinase for the Oxidation of L-Tyr and L-DOPA[a]

	monophenolase	diphenolase		
sample	IC_{50} (μg/mL)	IC_{50} (μg/mL)	inhibition	inhibition type
proanthocyanidins	40 ± 1.2	19.5 ± 0.6 a	reversible	competitive
arbutin	not detected	1442.9 ± 2.77 b	reversible	competitive

[a]Values are expressed as the mean of triplicate determinations ± standard deviation. Different letters in the same column show significant differences from each other at the $p < 0.05$ level.

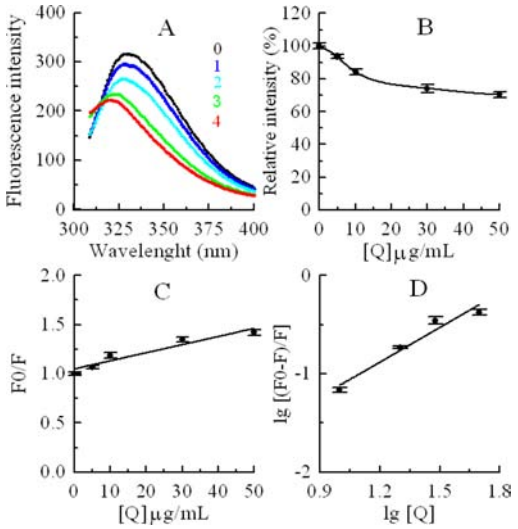

Figure 4. Changes in intrinsic tyrosinase fluorescence at different concentrations of avocado pulp proanthocyanidins. (A) Emission spectra 0, 1, 2, 3, and 4 of tyrosinase in the presence of proanthocyanidins are 0, 5, 10, 30, and 50 μg/mL, respectively. (B) Maximum florescence intensity changes. (C) Stern–Volmer plot describes the tyrosinase quenching caused by association with the quencher. (D) Plot of $\log[(F_0 - F)/F]$ against $\log[Q]$ for tyrosinase and various concentrations of the quencher. F_0 and F are the fluorescence intensities before and after the addition of the quencher.

peaks at a distance of 120 Da were also found in the mass spectrum. Additionally, the degree of polymerization of these compounds varied from 3-mers to 21-mers under the reflection mode, with the most intensity in 6-mers. However, the linear MALDI–TOF MS technique allowed for the test of avocado fruit proanthocyanidins up to 36-mers (Figure 2B). These results revealed structural heterogeneity and complexity of avocado fruit proanthocyanidins. The structures of proanthocyanidins extracted from avocado fruit were therefore successfully analyzed by employing MALDI–TOF MS for the first time.

Analysis of Proanthocyanidins by Reversed-Phase HPLC–ESI–QTRAP MS after Thiolysis Reaction. Avocado fruit proanthocyanidins were depolymerized by thiolysis reaction, which was proven to be a powerful method.[16,17,20] Benzylmercaptan was selected as the nucleophile. The result of the thiolysis reaction showed that terminal units were released as free monomers, but extender units were released as benzylthioether adducts.[21] Figure 3 showed that the dominant peak detected was epicatechin benzylthioether, while the other five smaller peaks were catechin, epicatechin, (epi)gallocatechin benzylthioether, catechin benzylthioether, and (epi)afzelechin benzylthioether. These results indicated that avocado fruit proanthocyanidins were mainly constituted of procyanidins, which were composed of an epicatechin unit. These results agreed well with the findings completed by the MALDI–TOF MS method. Besides, mDP of the proanthocyanidin polymers was calculated to be 12.3 ± 0.8. In fact, depolymerization by phenolysis (phloroglucinol) was also an efficient approach to determine the mDP of proanthocyanidins. Proanthocyanidin oligomers of 15 strawberry cultivars were depolymerized by phenolysis, and their mDP (3.4–5.8) was estimated.[22]

Effects of Avocado Fruit Proanthocyanidins on Monophenolase Activity. Effects of avocado fruit proanthocyanidins on monophenolase activity, where L-tyrosine was catalyzed by monophenolase, were first studied (see Figure 1-I of the Supporting Information). When the monophenolase activity was tested, a lag period (lag time) was observed. After the lag time, the monophenolase activity reached a steady-state rate, which was estimated by extrapolation of the linear portion of the product accumulation curve to the abscissa. Increasing concentrations of the avocado fruit proanthocyanidins not only extended the lag time (see Figure 1-III of the Supporting Information) but also decreased obviously the steady-state rate (see Figure 1-II of the Supporting Information). IC_{50} of proanthocyanidins on monophenolase activity was calculated as 40 ± 1.2 μg/mL (Table 1). Arbutin had little effect on the monophenolase activity (Table 1). The lag time was extended by 36 ± 0.8 s when the concentration of the proanthocyanidins was increased to 80 μg/mL. These results showed that avocado fruit proanthocyanidins were efficient inhibitors of monophenolase.

Effect of Avocado Fruit Proanthocyanidins on Diphenolase Activity. Effects of avocado fruit proanthocyanidins on oxidation of L-3,4-dihydroxyphenylalanine (L-DOPA) catalyzed by diphenolase were investigated. The results showed that diphenolase activity was obviously reduced with increasing the concentration of the inhibitor, but it was not completely suppressed (see Figure 2-I of the Supporting Information). IC_{50} of proanthocyanidins on diphenolase activity was estimated to be 19.5 ± 0.6 μg/mL (Table 1). IC_{50} of arbutin was 1442.9 ± 2.77 μg/mL (Table 1). The molecular weight of proanthocyanidins was markedly larger than that of arbutin, and avocado fruit proanthocyanidins might therefore be considered as excellent tyrosinase inhibitors.

Table 2. Stern–Volmer Equation for the Interaction between Quenchers and Tyrosinase

quencher	type of quenching	K_{SV} $(\mu g/mL)^{-1}$	K_q $(\mu g\ mL^{-1}\ s^{-1})^{-1}$	K_A $(\mu g/mL)^{-1}$	n
proanthocyanidins	static	$(8 \pm 0.2) \times 10^{-3}$	$(8 \pm 0.2) \times 10^{5}$	$(5 \pm 0.4) \times 10^{-3}$	1.17 ± 0.02

DOI: 10.1021/acs.jafc.5b03099
J. Agric. Food Chem. 2015, 63, 7381–7387

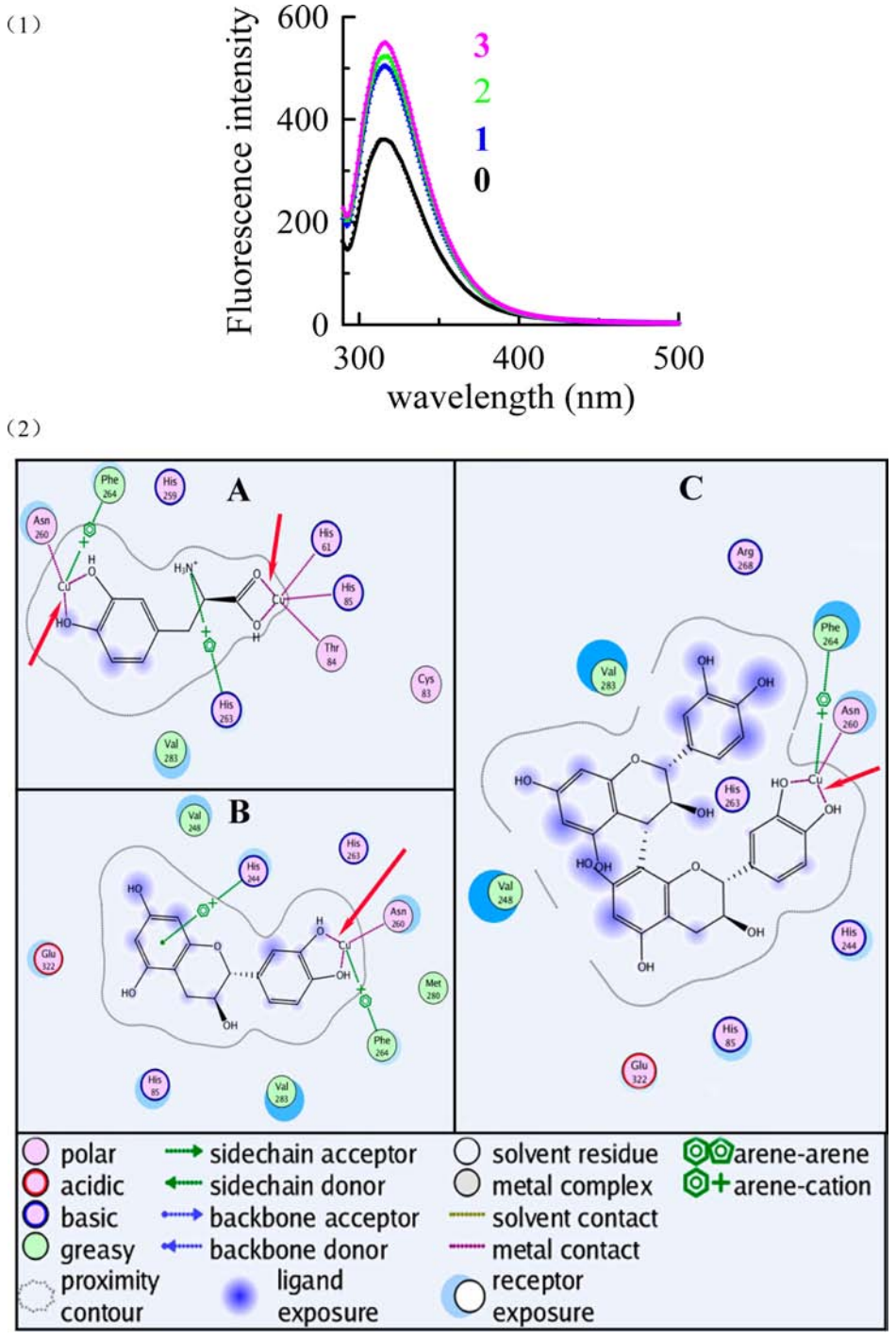

Figure 5. (1) Interaction of Cu^{2+} and proanthocyanidins. (2) Binding mode found from the ligand with tyrosinase residues using the lowest energy docked method. The receptor exposure differences were shown by the size and intensity of the turquoise discs surrounding the residues. The red arrows indicated the interaction of the ligand and the copper iron. Panels A, B, and C represented L-DOPA, epicatechin, and procyanidin dimer, respectively.

The inhibition mechanism of the avocado fruit proanthocyanidins on diphenolase activity was studied. It was revealed in Figure 2-II of the Supporting Information that, with the different concentrations of proanthocyanidins, the enzyme activity relied heavily on its concentration. The plots of the residual enzyme activity versus the concentrations of enzyme at different concentrations of proanthocyanidins gave a family of straight lines, which passed through the origin, indicating that the inhibition of the enzyme by proanthocyanidins was reversible. With the proanthocyanidin concentrations increased gradually, the slopes of the lines were descending.

The kinetic behavior of diphenolase in the process of oxidation of L-DOPA was then studied. The oxidation of L-DOPA catalyzed by diphenolase followed Michaelis–Menten kinetics. Plot of $1/v$ versus $1/[S]$ gave a family of lines with a fixed intercept on the y axis but with different slopes. These lines intersected on the y axis, which indicated that avocado

DOI: 10.1021/acs.jafc.5b03099
J. Agric. Food Chem. 2015, 63, 7381−7387

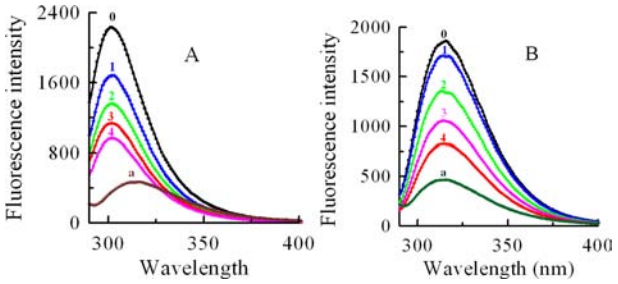

Figure 6. (A) Relative fluorescence intensities of L-tyrosine in solution with different concentrations of proanthocyanidins. The concentrations of proanthocyanidins of curves 0, 1, 2, 3, and 4 were 0, 10, 30, 40, and 80 μg/mL. (B) Relative fluorescence intensities of 3,4-dihydroxyphenylalanine in solution with different concentrations of proanthocyanidins. The concentrations of proanthocyanidins of curves 0, 1, 2, 3, and 4 were 0, 20, 30, 40, and 50 μg/mL, respectively. Curve a was the fluorescence intensity of proanthocyanidins when their concentration was 80 μg/mL.

fruit proanthocyanidins were competitive-type inhibitors (see Figure 2-III of the Supporting Information and Table 1).

Plant extracts have attracted more and more attention because of their potent tyrosinase inhibition activity.[23−25] In comparison to extracts obtained from *Aloe vera* L. gel,[23] red koji,[24] kiwifruit pericarp,[4] and fruit stone of Chinese hawthorn,[17] avocado fruit proanthocyanidins could better inhibit monophenolase and diphenolase activities. It could be speculated that strong inhibition of avocado fruit proanthocyanidins on the enzyme might mainly derive from structural similarity between the proanthocyanidin substrate of tyrosinase. In addition, a high polymer of avocado proanthocyanidins was considered as a important fator for the efficient inhibition. In our previous study, the proanthocyanidins with higher mDP showed better antityrosinase activity.[4] In comparison to synthesized compounds, tyrosinase inhibitors obtained from natural sources have attracted more and more attention because of the food and cosmetic demands.[26] Because of fact that proanthocyanidins are already in use for different medicinal properties, it is apparent that these compounds could well be applied in food, cosmetic, and pharmaceutical industries.

Analysis of Fluorescence Quenching of Tyrosinase with Avocado Fruit Proanthocyanidins. Fluorescence quenching was used to evaluate the interaction of ligand (proanthocyanidins) and tyrosinase by using a Varian Cary Eclipse fluorescence spectrophotometer. Figure 4A showed the fluorescence emission spectra of tyrosinase with different concentrations of avocado fruit proanthocyanidins. The results showed that enzyme gave a strong emission peak at 337 nm and decreased inversely with an increasing concentration of proanthocyanidins (Figure 4B). Figure 4C, the Stern−Volmer plot, was selected to measure the Stern−Volmer quenching constants of the proanthocyanidins. The results showed a good linear Stern−Volmer plot with K_q and K_{SV} values of $(8 \pm 0.2) \times 10^5$ $(\mu g\ mL^{-1}\ s^{-1})^{-1}$ and $(8 \pm 0.2) \times 10^{-3}$ $(\mu g/mL)^{-1}$, respectively (Figure 4C and Table 2). Because of the fact that the K_{SV} for dynamics cannot be larger than 100 L/M,[15] the K_{SV} that we obtained demonstrated that the type of fluorescence quenching mechanism between tyrosinase and avocado fruit proanthocyanidins was static. Figure 4D showed the plot of $\log[(F_0 - F)/F]$ against $\log[Q]$. From the intercept and the slope of this graph, values of K_A and n were calculated to be $(5 \pm 0.4) \times 10^{-3}$ $(\mu g/mL)^{-1}$ and 1.17 ± 0.02, respectively (Table 2).

Interaction of Cu^{2+} and Proanthocyanidins. Interaction between proanthocyanidins and Cu^{2+} were investigated using fluorescence analysis. The intrinsic fluorescence intensity of avocado fruit proanthocyanidins increased with the addition of Cu^{2+} (part 1 of Figure 5). The Cu^{2+} concentrations for curves 0, 1, 2, and 3 were 0, 25, 50, and 100 μM, respectively. The results revealed the binding of Cu^{2+} and proanthocyanidins.

Molecular Docking. To better understand the mechanism of the potent antityrosinase activities of the proanthocyanidins, molecular docking were carried out using MOE. Interactions of the ligands (L-DOPA, epicatechin, and procyanidin dimer) and the virtual enzyme catalytic center were simulated. The results revealed that L-DOPA (panel A in part 2 of Figure 5), (epi)catechin (panel B in part 2 of Figure 5), and proanthocyanidin dimer (panel C in part 2 of Figure 5) could chelate with copper irons of tyrosinase. The results obtained from docking simulations were a good supplement of the interaction experiment between Cu^{2+} and proanthocyanidins. The results revealed that the copper ion chelating ability of proanthocyanidins with an adjacent hydroxyl group on the B ring may be a significant mechanism to explain their inhibitory potency on the tyrosinase.

Fluorescence Quenching Analysis between the Substrate of Tyrosinase and Avocado Fruit Proanthocyanidins. The interaction between the proanthocyanidins and substrate of tyrosinase was investigated using the fluorescence quenching method. The result showed that intrinsic fluorescence intensity of L-tyrosine and 3,4-dihydroxyphenylalanine decreased distinctly with the addition of proanthocyanidins (Figure 6). The fluorescence intensity of L-tyrosine was reduced by 56.8% when the proanthocyanidin concentration reached 80 μg/mL (curve 4 in Figure 6A). Concentrations of curves 0, 1, 2, 3, and 4 were 0, 20, 30, 40, and 80 μg/mL, respectively (Figure 6A). The fluorescence intensity of 3,4-dihydroxyphenylalanine reduced by 74.9% when the proanthocyanidin concentration reached 50 μg/mL (curve 4 in Figure 6B). Concentrations of curves 0, 1, 2, 3, and 4 were 0, 20, 30, 40, and 50 μg/mL, respectively (Figure 6B). However, blue or red shifts were not found in the experiment. This indicated that the conformations of L-tyrosine and 3,4-dihydroxyphenylalanine were unchanged. Curves labeled "a" were fluorescence emission spectra of proanthocyanidins with a concentration at 80 μg/mL.

These results strongly proved that proanthocyanidins were the effective binding agents of L-tyrosine and 3,4-dihydroxyphenylalanine. Because of this, proanthocyanidins could efficiently stop the oxidation of the substrate. This could also make it clear that proanthocyanidins have a strong inhibitory effect on the tyrosinase catalytic reaction.

In conclusion, this study demonstrated that avocado fruit proanthocyanidins were comprised of homo- and heteropolymers of procyanidins, prodelphinidins, propelargonidins, and procyanidin gallate with a degree of polymerization up to 36-mers. They possessed structural heterogeneity in monomer units, substituent, and degree of polymerization. The results obtained from the enzyme assay revealed that these compounds were a potent, reversible, and competitive-type antityrosinase agent. Interactions of proanthocyanidins (particularly high polymer) with a substrate and dicopper catalytic center of tyrosinase were important mechanisms to explain their efficient inhibition. Structural similarity between proanthocyanidins and

DOI: 10.1021/acs.jafc.5b03099
J. Agric. Food Chem. 2015, 63, 7381−7387

the substrate of tyrosinase was the foundation of strong interactions. These findings played a significant role in both screening and designing great potential tyrosinase inhibitors. Our study revealed that proanthocyanidins purified from avocado fruit may have possible applications in agriculture, food, pharmaceutical, and cosmetic industries.

■ ASSOCIATED CONTENT

Supporting Information

The Supporting Information is available free of charge on the ACS Publications website at DOI: 10.1021/acs.jafc.5b03099.

Inhibition effect of avocado proanthocyanidins on monophenolase activity of mushroom tyosinase (Figure 1) and inhibitory effect (I), inhibitory mechanism (II), and inhibitory type (III) of avocado proanthocyanidins on the diphenolase reaction (Figure 2) (PDF)

■ AUTHOR INFORMATION

Corresponding Authors

*E-mail: chaiweiming@jxnu.edu.cn.

*E-mail: yiyuanpeng@jxnu.edu.cn.

Funding

The present investigation was supported by the Natural Science Foundation of China (21162012, 21362014, and 31260082), the Science and Technology Foundation of JianXi Province (20122BAB203007), and the Open Project Program of Key Laboratory of Functional Small Organic Molecule, Ministry of Education, Jiangxi Normal University (KLFSKF-201419).

Notes

The authors declare no competing financial interest.

■ REFERENCES

(1) Gowda, L. R.; Paul, B. Diphenol activation of the monophenolase and diphenolase activities of field bean (*Dolichos lablab*) polyphenol oxidase. *J. Agric. Food Chem.* **2002**, *50*, 1608−1614.

(2) Friedman, M. Food browning and its prevention: an overview. *J. Agric. Food Chem.* **1996**, *44*, 631−653.

(3) Pan, Z. Z.; Li, H. L.; Yu, X. J.; Zuo, Q. X.; Zheng, G. X.; Shi, Y.; Liu, X.; Lin, Y. M.; Liang, G.; Wang, Q.; Chen, Q. X. Synthesis and antityrosinase activities of alkyl 3, 4-dihydroxybenzoates. *J. Agric. Food Chem.* **2011**, *59*, 6645−6649.

(4) Chai, W. M.; Shi, Y.; Feng, H. L.; Xu, L.; Xiang, Z. H.; Gao, Y. S.; Chen, Q. X. Structure characterization and anti-tyrosinase mechanism of polymeric proanthocyanidins fractionated from kiwifruit pericarp. *J. Agric. Food Chem.* **2014**, *62*, 6382−6389.

(5) Aron, P. M.; Kennedy, J. A. Flavan-3-ols: nature, occurrence and biological activity. *Mol. Nutr. Food Res.* **2008**, *52*, 79−104.

(6) Xiao, J.; Ni, X.; Kai, G.; Chen, X. A review on structure-activity relationship of dietary polyphenols inhibiting α-amylase. *Crit. Rev. Food Sci. Nutr.* **2013**, *53*, 497−506.

(7) Zhou, H. C.; Lin, Y. M.; Wei, S. D.; Tam, N. F. Y. Structural diversity and antioxidant activity of condensed tannins fractionated from mangosteen pericarp. *Food Chem.* **2011**, *129*, 1710−1720.

(8) Dixon, R. A.; Xie, D. Y.; Sharma, S. B. Proanthocyanidins - a final frontier in flavonoid research? *New Phytol.* **2005**, *165*, 9−28.

(9) Gómez López, V. M. Characterization of avocado (*Persea americana Mill.*) varieties of very low oil content. *J. Agric. Food Chem.* **1998**, *46*, 3643−3647.

(10) Rodríguez-Carpena, J. G.; Morcuende, D.; Andrade, M. J.; Kylli, P.; Estévez, M. Avocado (*Persea americana Mill.*) phenolics, in vitro antioxidant and antimicrobial activities, and inhibition of lipid and protein oxidation in porcine patties. *J. Agric. Food Chem.* **2011**, *59*, 5625−5635.

(11) Kosińska, A.; Karamać, M.; Estrella, I.; Hernández, T.; Bartolomé, B.; Dykes, G. A. Phenolic compound profiles and antioxidant capacity of *Persea americana Mill.* peels and seeds of two varieties. *J. Agric. Food Chem.* **2012**, *60*, 4613−4619.

(12) Rodríguez-Sánchez, D. G.; Pacheco, A.; García-Cruz, M. I.; Gutiérrez-Uribe, J. A.; Benavides-Lozano, J. A.; Hernández-Brenes, C. Isolation and structure elucidation of avocado seed (*Persea americana*) lipid derivatives that inhibit *Clostridium sporogenes* endospore germination. *J. Agric. Food Chem.* **2013**, *61*, 7403−7411.

(13) Eftink, M. R.; Ghiron, C. A. Fluorescence quenching studies with proteins. *Anal. Biochem.* **1981**, *114*, 199−227.

(14) Li, Y.; He, W.; Liu, J.; Sheng, F.; Hu, Z.; Chen, X. Binding of the bioactive component jatrorrhizine to human serum albumin. *Biochim. Biophys. Acta, Gen. Subj.* **2005**, *1722*, 15−21.

(15) Zhao, Y.; Cao, Y.; Han, F. M.; Chen, Y. Study on the interaction between cinnamic acid and human serum albumin by fluorescence quenching method. *Spectrosc. Spectral Anal. (Beijing, China)* **2008**, *28*, 904−907.

(16) Li, C. M.; Leverence, R.; Trombley, J. D.; Xu, S. F.; Yang, J.; Tian, Y.; Reed, J. D.; Hagerman, A. E. High molecular weight persimmon (*Diospyros kaki L.*) proanthocyanidin: a highly galloylated, A-linked tannin with an unusual flavonol terminal unit, myricetin. *J. Agric. Food Chem.* **2010**, *58*, 9033−9042.

(17) Chai, W. M.; Chen, C. M.; Gao, Y. S.; Feng, H. L.; Ding, Y. M.; Shi, Y.; Zhou, H. T.; Chen, Q. X. Structural analysis of proanthocyanidins isolated from fruit stone of Chinese hawthorn with potent antityrosinase and antioxidant activity. *J. Agric. Food Chem.* **2014**, *62*, 123−129.

(18) Reed, J. D.; Krueger, C. G.; Vestling, M. M. MALDI-TOF mass spectrometry of oligomeric food polyphenols. *Phytochemistry* **2005**, *66*, 2248−2263.

(19) Xiang, P.; Lin, Y.; Lin, P.; Xiang, C.; Yang, Z.; Lu, Z. Effect of cationization reagents on the matrix-assisted laser desorption/ionization time-of-flight mass spectrum of Chinese gallotannins. *J. Appl. Polym. Sci.* **2007**, *105*, 859−864.

(20) Fu, C.; Loo, A. E. K.; Chia, F. P. P.; Huang, D. Oligomeric proanthocyanidins from mangosteen pericarps. *J. Agric. Food Chem.* **2007**, *55*, 7689−7694.

(21) Meagher, L.; Lane, G.; Sivakumaran, S.; Tavendale, M.; Fraser, K. Characterization of condensed tannins from Lotus species by thiolytic degradation and electrospray mass spectrometry. *Anim. Feed Sci. Technol.* **2004**, *117*, 151−163.

(22) Buendía, B.; Gil, M. I.; Tudela, J. A.; Gady, A. L.; Medina, J. J.; Soria, C.; López, J. M.; Tomás-Barberán, F. A. HPLC-MS analysis of proanthocyanidin oligomers and other phenolics in 15 strawberry cultivars. *J. Agric. Food Chem.* **2010**, *58*, 3916−3926.

(23) Gupta, S. D.; Masakapalli, S. Mushroom tyrosinase inhibition activity of *Aloe vera L. gel* from different germplasms. *Chin. J. Nat. Med.* **2013**, *11*, 616−620.

(24) Wu, L. C.; Chen, Y. C.; Ho, J. A. A.; Yang, C. S. Inhibitory effect of red koji extracts on mushroom tyrosinase. *J. Agric. Food Chem.* **2003**, *51*, 4240−4246.

(25) Zhuang, J. X.; Hu, Y. H.; Yang, M. H.; Liu, F. J.; Qiu, L.; Zhou, X. W.; Chen, Q. X. Irreversible competitive inhibitory kinetics of cardol triene on mushroom tyrosinase. *J. Agric. Food Chem.* **2010**, *58*, 12993−12998.

(26) Lee, S. Y.; Baek, N.; Nam, T. G. Natural, semisynthetic and synthetic tyrosinase inhibitors. *J. Enzyme Inhib. Med. Chem.* **2015**, *0*, 1−13.

DOI: 10.1021/acs.jafc.5b03099
J. Agric. Food Chem. 2015, 63, 7381−7387

from bovine mammary gland. Later, ficoll and sucrose density gradient centrifugations were proven to obtain a high purification of the PM fraction from lactating bovine mammary gland.[12] Differential velocity centrifugation has been used to isolate the membrane fraction of mammary tissues from Holstein cows.[13] Recently, proteomics technologies have been successfully applied to reveal proteome profiles of lactating bovine mammary tissue,[13−15] milk fat globule membrane,[16] and cultured mammary epithelial cells from humans[17] and *Bos indicus*,[18] but it has not been used to elucidate the proteome profile of PM from lactating bovine mammary gland.

Therefore, this experiment was designed to isolate and identify the PM of bovine mammary gland by discontinuous sucrose density gradient centrifugation and by liquid chromatography−tandem mass spectrometry (LC-MS/MS), respectively. Investigating the composition of PM proteins in the mammary gland of lactating cows, and subsequent identification of regulatory proteins involved in synthesis and secretion pathways of milk components on the subcellular level, would extend our understanding of the milk synthesis and secretion mechanisms of the bovine mammary gland.

MATERIALS AND METHODS

Preparation of Plasma Membranes of the Bovine Mammary Gland. Plasma membranes were isolated from bovine mammary gland homogenates by discontinuous sucrose density gradient centrifugation. Twelve mammary gland tissue blocks were obtained from the right or left fore-quarter of the mammary gland of four female Holstein-Friesian dairy cows (500−530 kg, 6 years old) in their fourth parity and midlactation period. This experiment was conducted according to the animal care guidelines of the Animal Care Committee, Institute of Subtropical Agriculture, The Chinese Academy of Sciences, Changsha city, Hunan province, China (no. KYNEAAM-2013-0009). Three technical replicates per cow were prepared for the isolation of plasma membranes. Approximately 6−8 g of fresh, mixed mammary gland tissue was weighed for each technical replicate and washed in ice-cold 0.9% NaCl, until the blood, milk, and connective tissues were removed. The tissue samples were then minced in 5 volumes of ice-cold homogenization buffer (0.25 M sucrose, 10 mM HEPES, pH 7.5) and homogenized by a Fisher Scientific PowerGen 125 homogenizer (Thermo Fisher Scientific Inc., USA). The homogenate was filtered through one layer of nylon gauze, and the filtrates were centrifuged at $1000g_{max}$ for 20 min in a Himac CR21 centrifuge (Hitachi High Technology, Japan). The resulting pellet was resuspended in 3 mL of buffer A (0.3 M sucrose, 50 mM Tris-HCl, 3 mM $MgCl_2$, pH 7.5) and 9 volumes of buffer B (1.98 M sucrose, 50 mM Tris-HCl, 3 mM $MgCl_2$, pH 7.5) to achieve a concentration of 1.8 M sucrose. Thirty milliliters of suspension liquids was transferred into one each of SW28 rotor tubes and overlaid with buffer C (0.25 M sucrose, 10 mM HEPES, 1 mM EDTA, pH 7.5) to fill the tubes. They were then centrifuged at $70900g_{av}$ for 90 min in a Beckman Optima L-XP100 ultracentrifuge (Beckman Coulter Inc., USA). The band at the interface was collected, resuspended in buffer C, and centrifuged at $20000g_{max}$ for 10 min. The resulting pellet was resuspended in a 1.45 M sucrose solution mixed with buffers C and D (2.4 M sucrose, 10 mM HEPES, pH 7.5), overlaid with enough buffer C to fill the SW28 rotor tubes, and then centrifuged at $68400g_{av}$ for 80 min. The pellicle at the interface was resuspended in buffer C and centrifuged at $17600g_{max}$ for 10 min. Isometric buffer C and buffer D were added into the pellet to bring the final concentration of sucrose to 1.35 M, the solution was transferred into an NVT100 rotor tube, overlaid with enough buffer C, and centrifuged at $231000g_{av}$ for 60 min. The purified plasma membranes were collected from the interface, washed in buffer C and then 10 mM HEPES (pH 7.5), and then centrifuged at $40000g_{max}$ for 10 min. All operations were performed at 4 °C, and a piece of protease inhibitor cocktail tablet (Roche Diagnostics GmbH, Mannheim, Germany) was added into every centrifugation tube in each step. The PM fractions were stored in a final volume of 2 mL at −80 °C.

Electron Microscopy. Fresh PM (0.1 mL) and 3% glutaraldehyde in PBS were mixed, incubated overnight at 4 °C, and centrifuged at 14500*g* for 15 min. The resulting pellets were fixed in 2% OsO_4, dehydrated through a graded series of ethanol (50, 70, 90, and 100% in turn) and acetone (100%), embedded in Epon overnight at 37 °C, and then solidified at 60 °C for 48 h. After cooling, the samples were sliced into thin sections with thickness of 70 nm and observed under a transmission electron microscope (Hitachi JSM-1230; JEOL, Tokyo, Japan) at 100 kV.

Western Blotting. Proteins of the homogenates and PM fractions were solubilized in a lysis buffer (LB1: 5 M urea, 2 M thiourea, 10% glycerol, 50 mM Tris-HCl, 2.0% OG, 2.5% SB3-10, 1 mM PMSF, pH 8.0), incubated at 37 °C for 30 min and room temperature for 1 h, respectively. Then the suspension was centrifuged at 20000*g* for 1 h, and the concentration of protein in the supernatant was determined by RC DC protein assay kit (catalog 500-0120, Bio-Rad, Hercules, CA, USA). The extracted proteins were separated by sodium dodecyl sulfate−polyacrylamide gel electrophoresis (SDS-PAGE) and then transferred to polyvinylidene fluoride membranes (Bio-Rad, USA). The membranes were blocked overnight at 4 °C and then incubated with anti-Na^+/K^+-ATPase α1 subunit (Novus Biologicals, LLC, Littleton, CO, USA), anti-flotillin-1 (Santa Cruz Biotechnology, Inc., Santa Cruz, CA, USA), and anti-prohibitin and anti-actin (Abcam, Hong Kong, China) for 2.5−3 h at room temperature. After being washed three times with PBST (0.1% Tween 20 in PBS), the membranes were incubated with peroxidase-conjugated goat anti-mouse, anti-rabbit, and donkey anti-goat IgG (H + L) for 1.5 h, washed three times with PBST, and detected by WesternBright ECL Western Blotting HRP Substrate (APGBio, Shanghai, China). Densitometric analysis of immunoblots was performed using an AlphaImager 2200 digital imaging system (Digital Imaging System, Kirchheim, Germany). Experiments were performed in triplicate and replicate three times.

Enzyme Activity Determination. The determination of organelle marker enzyme activity of the purified PM fractions was performed according to the standard protocols of the following kits: the 5′-nucleotidase assay kit (A041, Nanjing, China), the bovine Na^+/K^+-ATPase ELISA kit (catalog no. CSB-eq 027407BO, Wuhan, China), the bovine monoamine oxidase, succinodehydrogenase, aryl sulfatase, β1,4-GTase ELISA kits (JRDUN Biotechnology Co. Ltd., Shanghai, China), and the bovine NADPH cytochrome *c* reductase assay kit (BGI, Guangdong, China).

Preparation of PM-Associated Proteins. To compare the solubilization efficiency of PM proteins, two lysis buffers (one is LB1 as previously described; the other is LB2, containing 4% SDS, 10 mM Tris-HCl, 20% glycerol, and 100 mM dithiothreitol, pH 6.8) were used to dissolve the pooled PM fractions isolated from 12 homogenates. The isolation procedure of proteins and determination of protein concentration were the same as that of LB1. The isolated proteins were used for further in-solution digestion and SDS-PAGE separation. The PM proteins were separated by 6% SDS-PAGE and then stained by Coomassie brilliant blue R250 solution (Zomanbio, Beijing, China) overnight. Each protein gel lane was divided into four to five equal parts and removed by a sterilized knife.

In-Gel Digestion of Samples. Protein slices in fresh Coomassie brilliant blue R250-stained gel were excised and destained twice with 200 μL of 50 mM NH_4HCO_3 and 50% acetonitrile (ACN). Then 200 μL of 10 mM dithiothreitol (DTT) in 50 mM NH_4HCO_3 was added for protein reduction at 56 °C. After the removal of supernatant, 40 μL of 55 mM iodoacetamide in 100 mM NH_4HCO_3 was immediately added for protein alkylation in the dark. Finally, protein slices were dried twice with 200 μL of ACN. Afterward, the dried pieces of gels were incubated with ice-cold digestion solution (12.5 ng/μL trypsin and 20 mM NH_4HCO_3) for 20 min and then transferred into a 37 °C incubator for digestion overnight. Finally, peptides in the supernatant were collected after extraction twice with 200 μL of extract solution (5% formic acid in 50% ACN).

DOI: 10.1021/acs.jafc.5b02231
J. Agric. Food Chem. 2015, 63, 7388−7398

Table 1. Enzyme Activities in Homogenates and Isolated Plasma Membranes (PMs) from Bovine Mammary Gland

enzyme	homogenates	PMs	relative specific activity[a]
protein (8) mg/mL	2.10 ± 0.550	1.11 ± 0.370	
5′-nucleotidase, U/mg protein (6)	0.143 ± 0.053	1.58 ± 0.694	11.3 ± 2.49
Na^+/K^+-ATPase, ng/mg protein/h (7)	0.182 ± 0.053	1.64 ± 0.464	9.09 ± 0.920
monoamine oxidase, U/mg protein (8)	0.071 ± 0.019	0.282 ± 0.141	2.37 ± 0.015
NADPH cytochrome *c* reductase, nmol/min (7)	4.14 ± 1.19	47.8 ± 17.1	11.3 ± 1.89
succinodehydrogenase, IU/mg protein (10)	4.11 ± 0.842	6.31 ± 1.07	1.54 ± 0.103
aryl sulfatase	ND[b]	ND	
β1,4-GTase, U/mg protein	ND	ND	

[a]Relative specific activities were calculated as the ratio of the specific activity of the plasma membranes to that of the homogenates. The specific activity of the homogenates was normalized to 1. [b]ND, not detectable.

In-Solution Digestion of Samples. The membrane proteins isolated by LB1 and LB2 were in-solution digested using the method previously described[19] with minor modification. In each experiment, the concentrated proteins were heated at 100 °C for 10 min. After the sample was cooled to room temperature on ice, DTT was introduced into the solution to reach a final concentration of 10 mM, and the sample was incubated at 57 °C for 30 min. To prevent disulfide bond formation, cysteine residues were alkylated by iodoacetamide, which was added to the sample solution at 20 mM final concentration. The 30 min incubation in the dark, and at room temperature, was performed for cysteine derivatization. The reaction was quenched by the addition of DTT at a 10 mM final concentration in solution for 10 min. After iodoacetamide deactivation, the sample solution was diluted 10-fold with 50 mM NH_4HCO_3 buffer. Trypsin was added to the sample at a ratio of (1:50) and incubated overnight at 37 °C. All digested peptide mixtures were passed over a C18 column to remove extra DTT and salt. Tryptic peptides were eluted from the column with 80% ACN in 0.1% trifluoroacetic acid, and the peptide solution was divided equally. Thereafter, each aliquot was dried in a vacuum centrifuge for later use.

Strong Cation Exchange (SCX) Chromatography. The peptide mixtures from in-gel and in-solution digestion were fractionated by SCX chromatography on a 20AD high-performance liquid chromatography (HPLC) system (Shimadzu, Kyoto, Japan) using a polysulfethyl column (2.1 × 100 mm, 5 um, 200 Å; Nest Group, Southborough, MA, USA). The mixed sample was diluted with a loading buffer (10 mM KH_2PO_4 in 25% ACN, pH 2.6) and loaded onto the column. Buffer A was identical in composition to the loading buffer, and buffer B was formatted using buffer A containing 350 mM KCl. Separation was performed using a linear binary gradient of 0−80% buffer B in buffer A at a flow rate of 200 μL/min for 60 min. The absorbance at 214 and 280 nm was monitored, and a total of 40 SCX fractions were collected along the gradient.

Automated Nano-LC-ESI-MS/MS Analysis of Peptides. All of the eluted fractions and extracted solutions mentioned above were dried thoroughly using a vacuum centrifuge and then resuspended with 40 μL of 5% ACN in 0.1% formic acid, separated by Nano-LC, and analyzed by online electrospray tandem mass spectrometry as follows. The experiments were performed on an LC-20AD system (Shimadzu) connected to an LTQ Orbitrap mass spectrometer (Thermo Electron, Bremen, Germany) equipped with an online nanoelectrospray ion source (Michrom Bioresources, Auburn, CA, USA). The separation of the peptides took place in a 15 cm reverse phase column (100 μm i.d., Michrom Bioresources). The peptide mixtures were injected onto the trap column with a flow of 60 μL/min, subsequently eluted with a gradient of 5−45% solvent B (95% ACN in 0.1% formic acid) over 90 min, and then injected into the mass spectrometer at a constant column-tip flow rate of 500 nL/min. Eluted peptides were analyzed by MS and data-dependent MS/MS acquisition, selecting the eight most abundant precursor ions for MS/MS with a dynamic exclusion duration of 1 min.

Database Searching. The .mzXML files in the LTQ Orbitrap mass spectrometer were converted to.mgf files by MassMatrix Mass Spec Data File Conversion Tools and submitted for database sequence searches using ProteinPilot software (version 4.0, Applied Biosystems). The following parameters were set in the searching: trypsin as enzyme, fixed modification of carbamidomethyl-labeled cysteine, no special factors, biological modification, thorough identification search, SwissProt database. Other parameters, such as tryptic cleavage specificity, precursor ion mass accuracy, and fragment ion mass accuracy, were built-in functions of ProteinPilot software, and the Paragon method was adopted. The detected protein threshold was set at 1.3, responding to the minimum identification probability of ≥0.95, and the competitor error margin was 2.00.

Data Analysis and Bioinformatics. Swiss-Prot accession numbers of identified proteins were submitted to the retrieve ID/mapping tool of UniProt (http://www.uniprot.org) to generate FASTA formatted protein sequences. The prediction of transmembrane helices in identified proteins was carried out using the transmembrane hidden Markov model (TMHMM) algorithm, available at http://www.cbs.dtu.dk/servies/TMHMM. The average hydrophobicity for identified proteins was calculated using ProtParam software (http://us.expasy.org) by submitting each protein accession. The proteins exhibiting positive grand average of hydropathicity (GRAVY) values were recognized as hydrophobic, and those with negative values were deemed hydrophilic.[20] The subcellular location and function of all the identified proteins were elucidated by gene ontology (GO) component and function terms respectively, which were online annotated by DAVID Bioinformatics Resources 6.7 (http://david.abcc.ncifcrf.gov) against the background of *Bos taurus*. Functional enrichment analyses of cellular components, molecular functions, and biological processes were also performed via DAVID database. In the enrichment analysis, modified Fisher's exact tests and false-discovery rate were used for statistical analysis. The significantly ($p < 0.05$ and false-discovery rate <5%) enriched GO categories were investigated. The enriched pathways were analyzed by Ingenuity Pathway Analysis (content version: 17199142), choosing Ingenuity Knowledge Base as reference set and mammary gland as tissue.

RESULTS

Purity and Identification of Plasma Membranes. The PM fraction was located at the interface of the 0.25 M/1.35 M sucrose gradient. The protein yield of the plasma membranes was 0.185 mg/g of mammary gland. As shown in Table 1, the activities of various marker enzymes localized to the PM or subcellular organelles suggested that the Na^+/K^+-ATPase and 5′-nucleotidase activities were 9- and 11-fold greater in the plasma membranes than in the homogenates, respectively. Marker enzyme activities for outer mitochondrial membranes (monoamine oxidase), mitochondria (succinodehydrogenase), lysosomes (aryl sulfatase), and Golgi (β1, 4-GTase) were not significantly enriched in the plasma membranes compared to the homogenates. However, NADPH cytochrome *c* reductase activity in the plasma membranes, an endoplasmic reticulum marker, was enriched 11-fold in comparison with the homogenates.

DOI: 10.1021/acs.jafc.5b02231
J. Agric. Food Chem. 2015, 63, 7388−7398

The quality of the PM was morphologically evaluated by transmission electron microscopy (Figure 1). The predominant

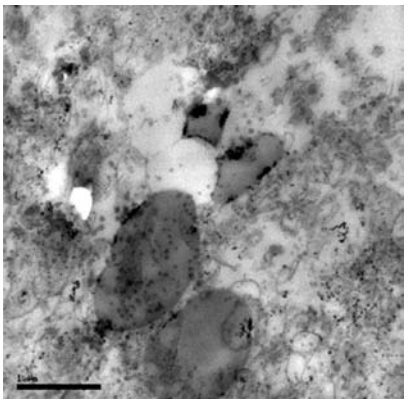

Figure 1. Electron micrographs of isolated plasma membranes from bovine mammary gland. The predominant structures in this fraction were membrane sheets and irregular vesicles. Bar, 1 μm × 30000.

structures in the final PM fraction were small, closed, and irregular membrane vesicles. Occasional mitochondrial membranes and endoplasmic reticulum membranes were also observed.

The purity of the plasma membranes was further examined by Western blotting using antibodies against organelle-specific protein markers (Figure 2). To estimate the degree of

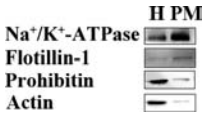

Figure 2. Western blotting analysis of the plasma membranes (PM) isolated by subcellular fractionation. Eighty micrograms of the mammary gland homogenate and plasma membrane proteins were separated by 12% SDS-PAGE and transferred to PVDF membranes. The blots were probed with antibodies against organelle-specific proteins: anti-Na^+/K^+-ATPase and anti-flotillin-1 for plasma membranes (PM); anti-prohibitin for mitochondria; anti-actin for cytoplasm. H represents homogenates.

enrichment of plasma membranes, we detected the PM-specific proteins Na^+/K^+-ATPase and flotillin-1 and found that these proteins were enriched about 4- and 5-fold, respectively, in PM in comparison with mammary gland homogenate. Meanwhile, both mitochondria and cytoplasm-specific proteins prohibitin and actin were about 14-fold less in PM than in mammary gland homogenate.

Separation and Identification of PM Proteins. The overall separation profiles of PM proteins isolated by two different lysis buffers are shown in Figure 3. The staining patterns of the two samples were similar for most bands, but differences in the intensities of a few bands were apparent. Gel slices cut from SDS-PAGE gel and proteins isolated by lysis buffers were digested in gel and in solution, respectively, separated by SCX chromatography, and further analyzed by automated Nano-LC-ESI-MS/MS. As shown in Table 2, PM protein yield of LB1 was 4.5-fold greater than that of LB2. The total number of nonredundant proteins identified from LB1 and LB2 was 872 (Supporting Information Supplementary Table 1). Of these 445 were found in LB1 and 575 were found in LB2; therefore, there were 381 proteins in common. Eight-

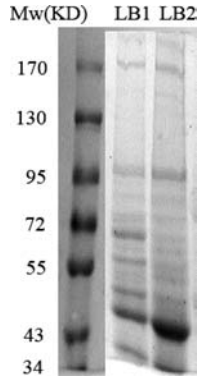

Figure 3. SDS-PAGE analysis of the proteins isolated from LB1 and LB2. Eighty micrograms of isolated proteins were separated by SDS-PAGE.

Table 2. Comparison between LB1 and LB2 and Total Identified Proteins

parameter	LB1[a]	LB2	total
protein yield, mg/g mammary gland	0.156	0.035	
no. of proteins identified	445	575	872
no. of proteins with TM[b] ≥ 1, %	132 (29.7)	182 (31.7)	195 (22.4)
no. of proteins with GRAVY[c] > 0, %	99 (22.2)	124 (21.6)	143(16.4)
no. of proteins with plasma membrane-associated locations, %	135 (30.3)	162 (28.2)	215 (24.7)

[a]LB, lysis buffer. [b]TM, transmembrane domain. [c]GRAVY, grand average of hydropathicity.

hundred and sixty-two of the 872 proteins were recognized by DAVID, and the remaining 10 proteins were not recognized and defined as unknown proteins. The transmembrane domains of the identified proteins were predicted with TMHMM. One-hundred and ninety-five (22.4%) were integral membrane proteins with at least one predicted transmembrane domain, and the percentage of these within LB2 (31.7%) was slightly greater than that of LB1 (29.7%). The GRAVY index represented the hydrophobicity property of proteins. One-hundred and forty-three (16.4%) proteins had positive values, and the percentage of LB1 (22.2%) was greater than that of LB2 (21.6%). Two-hundred and fifteen proteins (24.7%) of 872 identified proteins belonged to the PM proteins according to their GO annotations and the published literature; 30.3 and 28.2% of all identified proteins were from LB1 and LB2, respectively, including a list of known PM marker proteins such as sodium/potassium-transporting ATPase subunit α-1, flotillin-1, vesicle-associated membrane proteins, and 5′-nucleotidase.

Protein Classification and Enrichment Analysis. Among the identified proteins, 215 (30.6%) proteins were classified as PM proteins, with a smaller number classified as proteins in mitochondria (25.2%), endoplasmic reticulum (7.7%), Golgi apparatus (2.4%), nuclei (6.4%), and ribosome (7.6%). There were 20.1% unknown proteins without cellular component terms (Figure 4a).

The PM-associated proteins were further classified according to their molecular functions. As Figure 4b displays, 100 proteins (47.4%) and 41 proteins (19.4%) were binding proteins and transporter molecules, respectively, 32 proteins (15.2%)

DOI: 10.1021/acs.jafc.5b02231
J. Agric. Food Chem. 2015, 63, 7388−7398

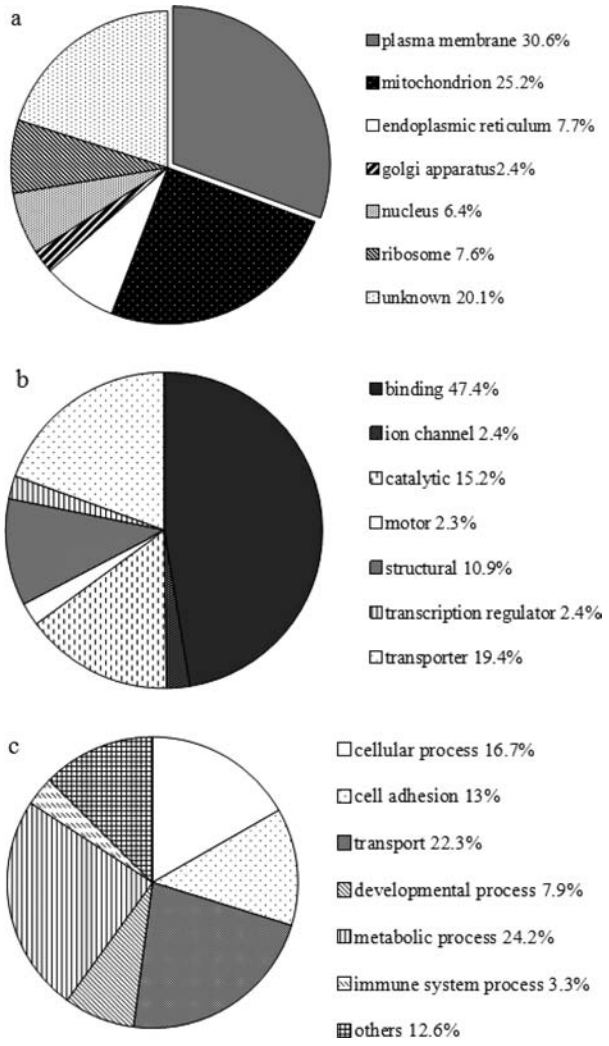

Figure 4. Classification of proteins identified in isolated bovine mammary gland plasma membrane. The subcellular localization of the identified proteins (a), functional characterization of plasma membrane proteins (b), and biological processes of plasma membrane proteins (c) were classified by GO terms annotated by DAVID Bioinformatics Resources 6.7 against the background of *Bos taurus*.

corresponded to catalytic activity, and 23 proteins (10.9%) were associated with structural proteins. Other proteins were involved in ion channel activity (2.4%), motor activity (2.3%), and transcription regulator activity (2.4%).

The PM proteins were also classified into several categories according to their DAVID annotation (Figure 4c): 36 (16.7%) proteins were involved in cellular processes, 28 (13%) in cell adhesion, 48 (22.3%) in transport, 17 (7.9%) in developmental process, 52 (24.2%) in metabolic process, 7 (3.3%) in immune system process, and 27 (12.6%) in apoptosis, cell cycle, generation of precursor metabolites, and response to stimulus. Seventy-five of 215 PM proteins had transmembrane domains and were involved in various processes associated with milk synthesis and secretion (Table 3), such as nutrient (glucose, amino acids, and fatty acids) transport, endocytosis, lactation, and synthesis of steroid and phospholipid.

To access the enrichment degree of plasma membranes and to explore over-represented biological functions associated with the PM proteins, DAVID was used to characterize potential biological functions in the PM proteome of bovine mammary gland. With respect to cellular components, the top 10 cellular component terms were significantly over-represented, including PM, vesicle, melanosome, pigment granule, cytoplasmic membrane-bounded vesicle, cytoplasmic vesicle, membrane-bounded vesicle, PM part, internal side of PM, and cell surface (Figure 5a).

Similar to the cellular components, the top 10 over-represented molecular function terms were typically associated with the PM, including enzyme binding, GTP binding, guanyl ribonucleotide binding, guanyl nucleotide binding, calcium-dependent phospholipid binding, unfolded protein binding, cytoskeletal protein binding, purine nucleotide binding, purine ribonucleotide binding, and ribonucleotide binding (Figure 5b).

In biological processes, the top 10 enriched terms were vesicle-mediated transport, protein localization, protein transport, cell adhesion, cellular protein localization, intracellular transport, small GTPase mediated signal transduction, membrane organization, establishment of protein localization, and biological adhesion (Figure 5c).

The identified PM proteins were involved in 74 pathways according to the pathway analysis. The top 15 pathways that were significantly enriched included caveolae-mediated endocytosis signaling, leukocyte extravasation signaling, clathrin-mediated endocytosis signaling, RhoGDI signaling, ephrin receptor signaling, signaling by Rho family GTPases, ephrin B signaling, virus entry via endocytic pathways, aldosterone signaling in epithelial cells, lipid antigen presentation by CD1, eNOS signaling, remodeling of epithelial adherens junctions, sertoli cell sertoli cell junction signaling, PPARα/RXRα activation, and tight junction signaling (Figure 5d).

DISCUSSION

Discontinuous sucrose gradient centrifugation, with its advantage of a reproducible and wide range of applications, was employed in this study to isolate the plasma membranes from lactating bovine mammary gland. However, this method often encounters difficulties in separating particular domains of PM from other cellular organelles, and from each other,[21] which also appeared in the current study. The sheet-like plasma membranes were low in relative activities of marker enzymes and protein yield (0.185 mg per g wet tissue). This was greater than the yield of 0.032 mg obtained from plasma membranes isolated from lactating cow mammary gland,[12] but less than that of isolated PM from lactating rat mammary gland by two-phase polymer partitioning (0.3 ± 0.1 mg).[5] The marker enzymes used in the present study, 5′-nucleotidase and Na^+/K^+-ATPase, are considered to be reliable as PM markers of lactating mammary cells.[12] Their activities in the PM were only 9 or 11 times greater than in the homogenates; perhaps the contamination of cytoplasmic proteins originating from the outer mitochondrial membranes caused this result. Western blotting results also confirmed that the plasma membranes were relatively enriched as indicated from an increased amount of PM marker proteins Na^+/K^+-ATPase and flotillin-1 and a lower amount of mitochondria and cytoplasm-specific proteins prohibitin and actin. All of these results indicate that plasma membranes isolated from bovine mammary gland and purified by discontinuous sucrose gradient centrifugation can be used for identification of proteins specific to the PM.

In the current investigation, two different detergents were employed to solubilize more PM proteins. LB1 contains zwitterionic detergent SB3-10 and nonionic detergent *n*-octyl-β-D-glucopyranoside (OG), and LB2 contains ionic detergent

DOI: 10.1021/acs.jafc.5b02231
J. Agric. Food Chem. 2015, 63, 7388−7398

Table 3. Characterization of Identified PM Proteins with Transmembrane Domain

protein name	accession	TM[a]	predicted function[b]
3-ketodihydrosphingosine reductase	Q2KIJ5	1	oxidation reduction
5′-nucleotidase	Q05927	1	negative regulation of inflammatory response
activated leukocyte cell adhesion molecule	Q9BH13	1	cell adhesion
adipocyte plasma membrane-associated protein	Q3T0E5	1	arylesterase activity
amine oxidase [flavin-containing] A	P21398	1	regulation of neurotransmitter levels
aminopeptidase N	P79098	1	ion binding
aquaporin 1 (Colton blood group)	P47865	6	water transport
ATP-binding cassette subfamily G member 2	Q4GZT4	6	xenobiotic transport; protein dimerization activity
β-1,4-galactosyltransferase 1	P08037	1	epithelial cell development
BOLA class I histocompatibility antigen, α chain BL3-7	P13753	2	immune response
butyrophilin subfamily 1 member A1	P18892	1	secretion of milk-fat droplets
cadherin-1	Q6R8F2	1	regulation of cell death
carbonic anhydrase 4	Q95323	1	one-carbon metabolic proces
catechol *O*-methyltransferase	A7MBI7	1	regulation of neurotransmitter levels
cation-independent mannose-6-phosphate receptor	P08169	1	glycoprotein binding
caveolin-1	P79132	1	MAPKKK cascade
caveolin-2	Q66WT7	2	protein dimerization activity
CD36 molecule (thrombospondin receptor)	P26201	2	regulator of fatty acid transport
CD46 molecule, complement regulatory protein	Q6VE48	1	adaptive immune response
CD81 molecule	Q3ZCD0	4	positive regulation of cell proliferation; signal transduction
CD9 molecule	P30932	4	negative regulation of cell proliferation
claudin-3	Q765N9	4	response to oxygen levels
claudin-4	Q6BBL6	4	cell adhesion
claudin-7	Q3B7N4	4	structural molecule activity
cytochrome *b*-245 heavy chain	O46522	6	generation of precursor metabolites and energy
cytochrome *b*5	P00171	1	generation of precursor metabolites and energy
desmocollin-2 (fragment)	P33545	1	calcium ion binding
disintegrin and metalloproteinase domain-containing protein 10	Q10741	1	regulation of cell growth
DnaJ homologue subfamily C member 5	Q29455	1	regulation of cell death
dolichyl-diphosphooligosaccharide−protein glycosyltransferase subunit STT3A	Q2KJI2	13	protein amino acid glycosylation
dysferlin	A6QQP7	1	plasma membrane repair,calcium ion binding
dystroglycan	O18738	1	epithelium development
epithelial cell adhesion molecule	Q3T0L5	1	positive regulation of cell proliferation
inositol 1,4,5-trisphosphate receptor type 1	Q9TU34	6	cellular calcium ion homeostasis
integrin α-V	P80746	1	endocytosis
integrin β-1	P53712	1	positive regulation of cell proliferation
integrin β-2	P32592	1	regulation of protein amino acid phosphorylation
integrin β-6	Q8SQB8	1	inflammatory response; multicellular organismal development
intercellular adhesion molecule 1	Q95132	1	cell adhesion
leukocyte surface antigen CD47	Q9N0K1	5	positive regulation of cell proliferation
lysophospholipid acyltransferase 5	Q3SZL3	9	phospholipid biosynthetic process
lysosomal-associated membrane protein 1	Q05204	1	granzyme-mediated apoptotic signaling pathway
membrane primary amine oxidase	Q9TTK6	1	copper/calcium binding
membrane-associated progesterone receptor component 1	Q17QC0	1	steroid binding
mucin 15, cell surface associated	Q8MI01	1	−
mucin-1	Q8WML4	2	−
peptidyl-prolyl cis−trans isomerase B	P80311	1	protein folding
platelet/endothelial cell adhesion molecule	P51866	1	regulation of cell migration
polymeric immunoglobulin receptor	P81265	1	−
protein disulfide-isomerase A4	Q29RV1	1	cell redox homeostasis
protein S100-A10	P60902	1	calcium ion binding
proteolipid protein 2	Q6Y1E2	4	cytokine binding
receptor accessory protein 6	Q32LG5	2	regulation of intracellular transport
sigma nonopioid intracellular receptor 1	Q58DH7	1	steroid biosynthetic process
sodium/potassium-transporting ATPase subunit α-1	Q08DA1	10	ATP biosynthetic process
sodium/potassium-transporting ATPase subunit β-3	Q3T0C6	1	ATP biosynthetic process
solute carrier family 1, member 1	Q95135	8	neuronal/epithelial high affinity glutamate transporter
solute carrier family 1, member 5	Q95JC7	9	neutral amino acid transporter
solute carrier family 16, member 1	Q3MHW6	11	monocarboxylic acid transporter
solute carrier family 2, member 3	P58352	12	glucose transporter

DOI: 10.1021/acs.jafc.5b02231
J. Agric. Food Chem. 2015, 63, 7388−7398

Table 3. continued

protein name	accession	TM[a]	predicted function[b]
solute carrier family 44, member 3	A5PK40	8	−
stromal interaction molecule 1	Q58CP9	1	positive regulation of calcium ion transport
suppressor of tumorigenicity 14 protein homologue	Q0IIH7	1	serine-type endopeptidase activity
synaptojanin 2 binding protein	Q3T0C9	1	endocytosis
Toll-like receptor 2	Q9SLA9	1	regulation of cytokine production
transmembrane 9 superfamily member 1	A4IFE9	9	autophagy
transmembrane emp24 domain-containing protein 1	Q2TBK5	1	protein transport
transmembrane emp24-like trafficking protein 10 (yeast)	Q5E971	2	regulated secretory pathway
transmembrane protein 168	A0JNG0	11	−
very-long-chain enoyl-CoA reductase	Q3ZCD7	5	steroid biosynthetic process
vesicle-associated membrane protein 8	Q3T0Y8	1	regulation of endocytosis
vesicle-associated membrane protein 3 (cellubrevin)	Q2KJD2	1	Ca^{2+}-dependent exocytosis
vesicle-associated membrane protein-associated protein A	Q0VCY1	1	signal transducer activity
vesicle-associated membrane protein-associated protein B	A2VDZ9	1	sphingolipid de novo biosynthesis
V-type proton ATPase 116 kDa subunit a isoform 1	Q29466	6	inorganic cation transmembrane transporter activity

[a]TM, transmembrane domain. [b]The predict function of PM proteins was noted by the molecular function or biological process of the Gene Ontology annotation. −, the protein had no Gene Ontology annotation.

SDS and reductive agent DTT. Although the protein yield of LB1 was slightly greater than that of LB2, the number of total identified proteins, PM proteins, transmembrane proteins, and hydrophobic proteins was less than that of LB2 (Table 2). It could be suggested that the solubilization efficiency of LB2 was higher than that of LB1; thus, LB2 was more suitable for the extraction of PM proteins of the mammary gland.

1D-SDS-PAGE was applied in this study because of its high loading capacity and high solubilizing power of hydrophobic membrane proteins.[22] Finally, 215 of the identified 872 proteins were PM proteins. If 20.1% unknown proteins were deducted, the proportion of PM proteins would be greater. Janjanam et al.[18] had identified 111 and 37 PM proteins of mammary epithelial cells by 1D-Gel-LC-MS/MS and 2DE-MS/MS, respectively. It was reported that around 9.1% of 700 protein spots detected by 2DE-MS/MS were localized to PM in the rat mammary gland.[23] Peng et al.[15] and Yang et al.[13] had identified 160 and 183 membrane proteins by 1D-Gel-RPLC-MS/MS and 1D-Gel-LC-MS, respectively. Therefore, 1D-SDS-PAGE combined with LC-MS/MS had its advantage of high-throughput identification for PM-associated proteins.

In the proteomic maps of PM fractions (Supplementary Table 1), many proteins were associated with metabolic pathways and involved in lactation-associated function such as staphylococcal nuclease domain-containing protein 1, annexin A5, and Rab GDP dissociation inhibitor 2. Signorelli et al.[24] reported that in lactating sheep there was an increased expression of these three proteins at the lactation peak, which was in agreement with their basic cellular functions in relationship to higher milk yield. Staphylococcal nuclease domain-containing protein 1 was increased in humans in response to lactogenic hormones.[25] Apolipoprotein A-I observed in this study's PM fractions has been involved in delivering cholesterol to milk fat globules,[26] and the highest expression of this protein occurred at midlactation.[24] The eukaryotic translation elongation factor 2 was also present in the PM fractions. It has been reported that the main limiting factor in the protein synthesis at the end of lactation was the availability of this protein.[24,26] The enzymes of the pentose phosphate pathway (transketolase), the tricarboxylic acid cycle (cytosolic NADP-isocitrate, succinate dehydrogenase, and malate dehydrogenase), and de novo lipogenesis (fatty acid synthase and fatty acid-binding proteins) were also identified in the PM fractions. These proteins provide a substantial fraction of the reducing equivalents of NADPH and long-chain fatty acids taken up from blood, needed for lipid synthesis in the mammary gland.[27−31]

We also detected 5 of 10 enzymes involved in glycolysis, including hexokinase, triosephosphate isomerase, glyceraldehyde-3-phosphate dehydrogenase, ADP-dependent glucokinase, and enolase. This suggests that our lactating bovine mammary glands provide the necessary precursors for the energy-generating pathway required for milk synthesis and secretion. Additionally, we also identified six proteins participating in milk secretion and lactation regulation, including β-casein, κ-casein, lactotransferrin, xanthine dehydrogenase, butyrophilin A1, and fatty acid synthase.

We compared the proteome profile of our PM fractions with the proteome profiles of mammary tissues and cells. Of 215 proteins and 188 PM proteins reported in lactating mammary tissue of Friesian cows,[14,15] 83 proteins (39%) and 48 proteins (26%) matched our data. Seventy-four proteins (25%) of 297 proteins identified in bovine milk fat globule membrane[31] and 138 proteins (28%) of 497 proteins reported in bovine mammary epithelial cells[18] matched our data, respectively. Relatively less coverage of our data with data from other groups can be attributed to the different lactation period of mammary glands and the fact that the mammary tissue may represent a mixed-cell population that constitutes adipose and stromal tissue, epithelial tissue, macrophages, and lymphocytes.[32] It would appear that some newly identified PM-associated proteins of lactating bovine mammary gland have not been reported earlier.

The PM proteins were further classified according to their functional characterization (Figure 4b,c). The main groups identified were binding and transport proteins, including annexin proteins (ANXA2, ANXA6, ANXA7, ANXA9, ANXA11), heat shock proteins, integrin, RAS oncogene family members, S100 calcium binding proteins, and solute carrier (SLC) families and members (SCL1A1, SLC1A5, SLC2A3, SLC16A1, SLC25A1, SLC44A3). Different types of annexins identified in the bovine mammary gland in midlactation have roles in various cellular functions including cell proliferation,[33] secretion of milk components,[34] apoptosis,[35] and other

DOI: 10.1021/acs.jafc.5b02231
J. Agric. Food Chem. 2015, 63, 7388−7398

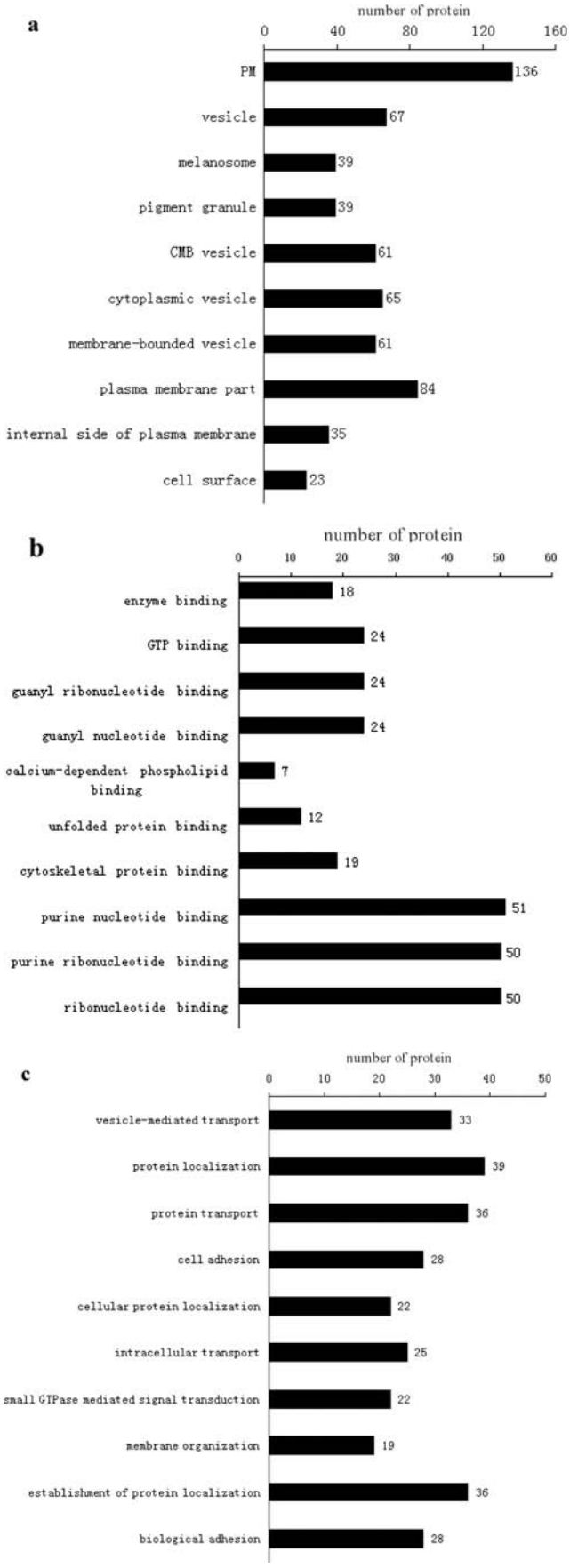

Figure 5. continued

DOI: 10.1021/acs.jafc.5b02231
J. Agric. Food Chem. 2015, 63, 7388−7398

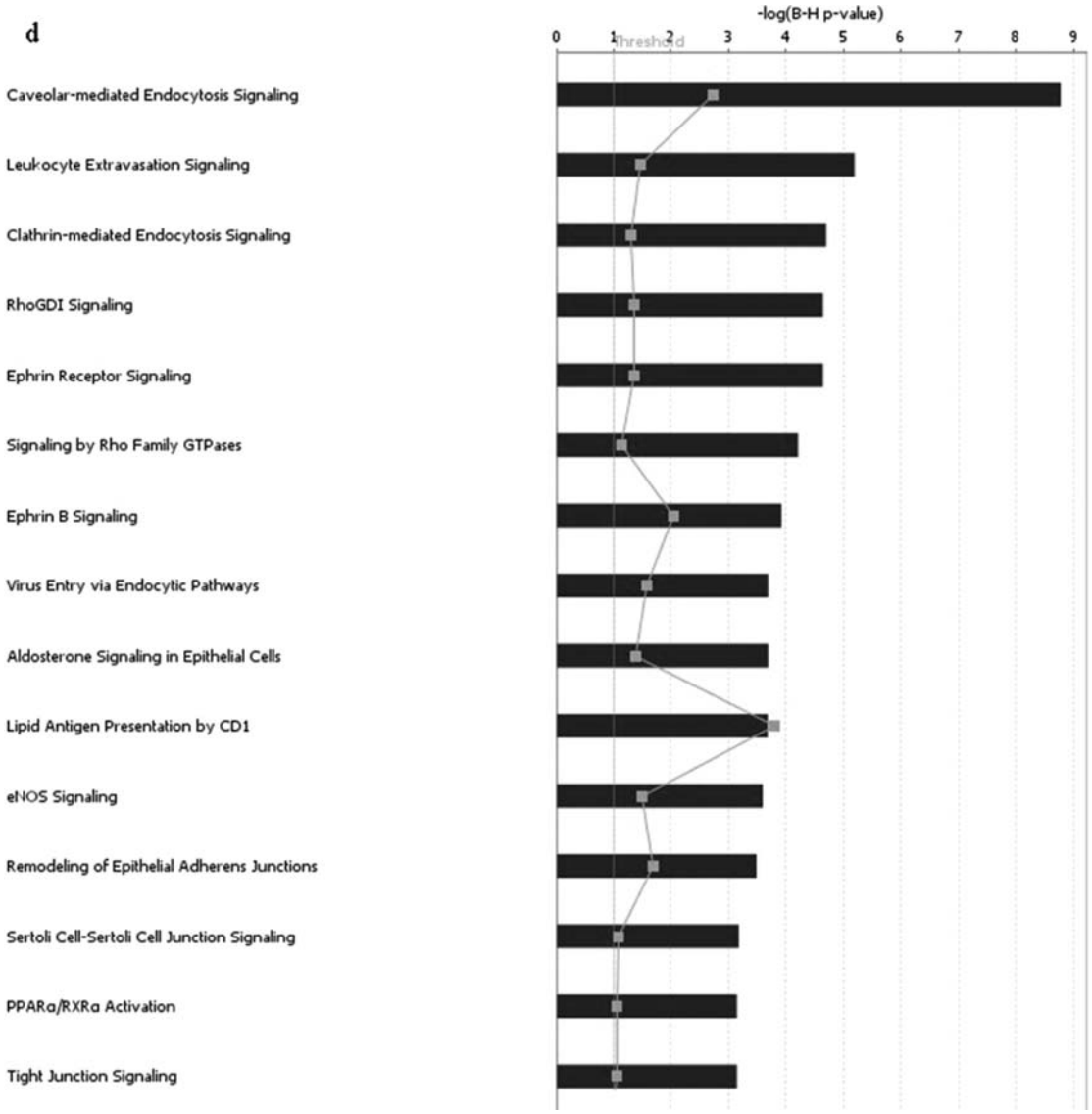

Figure 5. Enriched cellular components, molecular functions, biological processes, and pathways in the plasma membrane proteome. The over-representation of each category is determined by p value ($\leq$0.05). Each general category is organized by GO algorithms, and only top 10 categories are shown: enriched cellular components in plasma membrane proteome (a), enriched molecular functions in plasma membrane proteome (b), enriched biological processes in plasma membrane proteome (c), and enriched pathways in plasma membrane proteome (d). PM, plasma membrane; CMB, cytoplasmic membrane-bound; ARVC, arrhythmogenic right ventricular cardiomyopathy.

essential signaling events during lactation. SLC1A1 (EAAC1) and SLC1A5 (ASCT2) mediated transport of L-Glu, L-Asp, and D-Asp and Na^+-dependent exchange of small neutral amino acids such as Ala, Ser, Cys, and Thr, respectively,[36] implying that SLC1A1 and SLC1A5 play important roles in providing materials for milk protein synthesis. Physiological functions regarding other SLC families and members expressed in mammary gland are not characterized yet and need to be investigated in the future.

DAVID was used to identify enriched cellular component terms such as PM, vesicle, PM part, internal side of PM, and cell surface (Figure 5a). Functions such as binding (Figure 5b) and transport and adhesion (Figure 5c) were typically associated with the PM proteins. We found that six CD antigen proteins (CD9, CD36, CD47, CD166, PECAM1, ICAM1) were included in the cell adhesion terms. These cell surface molecules often act as receptors or ligands, which usually initiate a signal cascade. Yonezawa et al.[37] have demonstrated that CD36 facilitated the movement of fatty acids across the PM in bovine mammary gland. Also, the expression of CD36 mRNA in the bovine mammary gland has been shown to increase during lactation[38] and stimulated by octanoate in the bovine mammary epithelial cells,[37] demonstrating that CD36 expression could be related to physiological variations of lipid transport and metabolism within the cell. The relationship between the expressions of other CD antigen proteins and biological function in mammary gland has not been reported; therefore, there is an area for further investigation.

In the investigation of the significantly enriched pathways (Figure 5d), it was found that integrin β1 was involved in eight signal pathways. Integrins mediate adhesion-induced phosphorylation events that trigger activation of numerous signaling intermediates such as FAK, Src, ILK, p130CAS, PI3K, JNK, and MARK and regulated Rho-family GTPases, which are central for the control of actin cytoskeleton organization, contractility,

DOI: 10.1021/acs.jafc.5b02231
J. Agric. Food Chem. 2015, 63, 7388−7398

and cell shape changes.[27] It was also reported that β1 integrins were critical for the alveolar morphogenesis of a glandular epithelium and for the maintenance of its differentiated function.[27] β1 integrins and activation of FAK were essential for ductal morphogenesis, and Rac and ILK appeared to be major mediators of integrin signaling in the regulation of mammary luminal cell lactogenic differentiation.[27] Myoepithelial cell contractile activity in lactation required α3β1 integrin-mediated activation of Rac, FAK, and PAK1.[39] In the bovine mammary gland, milk accumulation decreased the mRNA expression of integrins (β1, α5, α6) involved in cell−extracellular matrix communication and was associated with the induction of apoptosis.[27] The integrin-induced intracellular signal transduction in bovine mammary gland remains to be further characterized.

In summary, the PM fractions isolated from lactating bovine mammary gland by discontinuous sucrose gradient centrifugation were relatively enriched. Eight hundred and seventy-two nonredundant proteins were identified by 2D-Nano-LC-ESI LTQ-Orbitrap MS/MS, wherein 215 proteins belonged to the PM. Bioinformatic analysis revealed that the main groups of the PM proteins had functions related to binding, transport, and catalysis and were predicted to be involved in caveolae-mediated endocytosis, leukocyte extravasation, aldosterone signaling in epithelial cells, and remodeling of epithelial adherens junctions. The results of this study provide the proteome profile of PM from bovine mammary tissue in vivo. This profile will be helpful to further elucidate the composition and functions of PM proteins and provide more knowledge about the molecular events taking place in the lactating bovine mammary gland.

■ ASSOCIATED CONTENT

Supporting Information

The Supporting Information is available free of charge on the ACS Publications website at DOI: 10.1021/acs.jafc.5b02231.

Proteins identified by Nano-LC-ESI-MS/MS (Table S1) (PDF)

■ AUTHOR INFORMATION

Corresponding Author

*(Z.T.) Phone: + 86 731 84619702. E-mail: zltan@isa.ac.cn.

Funding

We thank the National Natural Science Foundation of China (Grants 31001023, 31402112, 31101741, 31320103917), the National Science and Technology Support Program (Grant 2012BAD12B02), the project "Strategic Priority Research Program − Climate Change: Carbon Budget and Relevant Issues" of the Chinese Academy of Sciences (Grant XDA05020700), the K. C. Wong Education Foundation of CAS, and the CAS Visiting Professorship for Senior International Scientists (Grant 2010T2S13) for joint financial support.

Notes

The authors declare no competing financial interest.

■ ABBREVIATIONS USED

PM, plasma membrane; LB, lysis buffer; LC-MS/MS, liquid chromatography−tandem mass spectrometry; 1D, one-dimensional; SDS-PAGE, sodium dodecyl sulfate−polyacrylamide gel electrophoresis; 2DE, two-dimensional gel electrophoresis; ELISA, enzyme-linked immunosorbent assay; ECL, enhanced chemiluminescence; DTT, dithioerythritol; SCX, strong cation exchange

■ REFERENCES

(1) Akers, R. M. *Lactation and the Mammary Gland*; Wiley-Blackwell: Chichester, UK, 2002.

(2) Rudolph, M. C.; McManaman, J. L.; Phang, T.; Russell, T.; Kominsky, D. J.; Serkova, N. J.; Stein, T.; Anderson, S. M.; Neville, M. C. Metabolic regulation in the lactating mammary gland: a lipid synthesizing machine. *Physiol. Genomics* **2007**, *28*, 323−336.

(3) Hopkins, A. L.; Groom, C. R. The druggable genome. *Nat. Rev. Drug Discovery* **2002**, *1*, 727−730.

(4) Kirat, D.; Kato, S. Monocarboxylate transporter genes in the mammary gland of lactating cows. *Histochem. Cell Biol.* **2009**, *132*, 447−455.

(5) Keenan, T. W.; Valivullah, H. M.; Dunlevy, J. T. Isolation of plasma-membranes from mammary-gland by 2-phase polymer partitioning. *Anal. Biochem.* **1989**, *177*, 194−198.

(6) Watarai, H.; Hinohara, A.; Nagafune, J.; Nakayama, T.; Taniguchi, M.; Yamaguchi, V. Plasma membrane-focused proteomics: dramatic changes in surface expression during the maturation of human dendritic cells. *Proteomics* **2005**, *5*, 4001−4011.

(7) Shin, B. K.; Wang, H.; Yim, A. M.; Le Naour, F.; Brichory, F.; Jang, J. H.; Zhao, R.; Puravs, E.; Tra, J.; Michael, C. W.; Misek, D. E.; Hanash, S. M. Global profiling of the cell surface proteome of cancer cells uncovers an abundance of proteins with chaperone function. *J. Biol. Chem.* **2003**, *278*, 7607−7616.

(8) Zhang, H.; Li, X. J.; Martin, D. B.; Aebersold, R. Identification and quantification of N-linked glycoproteins using hydrazide chemistry, stable isotope labeling and mass spectrometry. *Nat. Biotechnol.* **2003**, *21*, 660−666.

(9) Liu, Z.; Xu, B.; Nameta, M.; Zhang, Y.; Magdeldin, S.; Yoshida, Y.; Yamamoto, K.; Fujinaka, H.; Yaoita, E.; Tasaki, M.; Nakagawa, Y.; Saito, K.; Takahashi, K.; Yamamoto, T. Profiling of kidney vascular endothelial cell plasma membrane proteins by liquid chromatography-tandem mass spectrometry. *Clin. Exp. Nephrol.* **2013**, *17*, 327−337.

(10) Huggins, J. W.; Carraway, K. L. Purification of plasma membranes from rat mammary gland by a density perturbation procedure. *J. Supramol. Struct.* **1976**, *5*, 59−63.

(11) Keenan, T. W.; Morre, D. J.; Olson, D. E.; Yunghans, W. N.; Patton, S. Biochemical and morphological comparison of plasma membrane and milk fat globule membrane from bovine mammary gland. *J. Cell Biol.* **1970**, *44*, 80−93.

(12) Kanno, C.; Hattori, H.; Yamauchi, K. Isolation and characterization of plasma membrane from lactating bovine mammary gland. *Biochim. Biophys. Acta, Biomembr.* **1982**, *689*, 121−134.

(13) Yang, Y. X.; Cao, S. Z.; Zhang, Y.; Zhao, X. X. Proteomic approach analysis of mammary membrane proteins expression profiles in Holstein cows. *Asian−Australas. J. Anim. Sci.* **2009**, *22*, 885−892.

(14) Beddek, A. J.; Rawson, P.; Peng, L.; Snell, R.; Lehnert, K.; Ward, H. E.; Jordan, T. W. Profiling the metabolic proteome of bovine mammary tissue. *Proteomics* **2008**, *8*, 1502−1515.

(15) Peng, L. F.; Rawson, P.; McLauchlan, D.; Lehnert, K.; Snell, R.; Lordan, T. W. Proteomic analysis of microsomes from lactating bovine mammary gland. *J. Proteome Res.* **2008**, *7*, 1427−1432.

(16) Cebo, C. Milk fat globule membrane proteomics: a 'snapshot' of mammary epithelial cell biology. *Food Technol. Biotechnol.* **2012**, *50*, 306−314.

(17) Jacobs, J. M.; Mottaz, H. M.; Yu, L. R.; Anderson, D. J.; Moore, R. J.; Chen, W. N. U.; Auberry, K. J.; Strittmatter, E. F.; Monroe, M. E.; Thrall, B. D.; Camp, D. G.; Smith, R. D. Multidimensional proteome analysis of human mammary epithelial cells. *J. Proteome Res.* **2004**, *3*, 68−75.

(18) Janjanam, J.; Jamwal, M.; Singh, S.; Kumar, S.; Panigrahi, A. K.; Hariprasad, G.; Jena, M. K.; Anand, V.; Kumar, S.; Kaushik, J. K.; Dang, A. K.; Mukesh, M.; Mishra, B. P.; Srinivasan, A.; Reddy, V. S.; Mohanty, A. K. Proteome analysis of functionally differentiated bovine (*Bos indicus*) mammary epithelial cells isolated from milk. *Proteomics* **2013**, *13*, 3189−3204.

DOI: 10.1021/acs.jafc.5b02231
J. Agric. Food Chem. 2015, 63, 7388−7398

(19) Sun, B. Y.; Ranish, J. A.; Utleg, A. G.; White, J. T.; Yan, X. W.; Lin, B. Y.; Hood, L. Shotgun glycopeptide capture approach coupled with mass spectrometry for comprehensive glycoproteomics. *Mol. Cell. Proteomics* **2007**, *6*, 141−149.
(20) Kyte, J.; Doolittle, R. F. A simple method for displaying the hydropathic character of a protein. *J. Mol. Biol.* **1982**, *157*, 105−132.
(21) Josic, D.; Clifton, J. G. Mammalian plasma membrane proteomics. *Proteomics* **2007**, *7*, 3010−3029.
(22) Rabilloud, T. Membrane proteins and proteomics: love is possible, but so difficult. *Electrophoresis* **2009**, *30*, S174−S180.
(23) Betancourt, A. M.; Mobley, J. A.; Russo, J.; Lamartiniere, C. A. Proteomic analysis in mammary glands of rat offspring exposed in utero to bisphenol A. *J. Proteomics* **2010**, *73*, 1241−1253.
(24) Signorelli, F.; Cifuni, G. F.; Miarelli, M. Differentially expressed mammary proteins during lactation in dairy sheep. *Livest. Sci.* **2012**, *149*, 224−231.
(25) Paukku, K.; Yang, J.; Silvennoinen, O. Tudor and nuclease-like domains containing protein p100 function as coactivators for signal transducer and activator of transcription 5. *Mol. Endocrinol.* **2003**, *17*, 1805−1814.
(26) Christophersen, C. T.; Karlsen, J.; Nielsen, M. O.; Riis, B. Eukaryotic elongation factor-2 (eEF-2) activity in bovine mammary tissue in relation to milk protein synthesis. *J. Dairy Res.* **2002**, *69*, 205−212.
(27) Clegg, R. A.; Barber, M. C.; Pooley, L.; Ernens, I.; Larondelle, Y.; Travers, M. T. Milk fat synthesis and secretion: molecular and cellular aspects. *Livest. Prod. Sci.* **2001**, *70*, 3−14.
(28) Chakravarty, B.; Gu, Z. W.; Chirala, S. S.; Wakil, S. J.; Quiocho, F. A. Human fatty acid synthase: structure and substrate selectivity of the thioesterase domain. *Proc. Natl. Acad. Sci. U. S. A.* **2004**, *101*, 15567−15572.
(29) Hertzel, A. V.; Bernlohr, D. A. The mammalian fatty acid-binding protein multigene family: molecular and genetic insights into function. *Trends Endocrinol. Metab.* **2000**, *11*, 175−180.
(30) Jones, P. D.; Carne, A.; Bass, N. M.; Grigor, M. R. Isolation and characterization of fatty-acid binding-proteins from mammary tissue of lactating rats. *Biochem. J.* **1988**, *251*, 919−925.
(31) Affolter, M.; Grass, L.; Vanrobaeys, F.; Casado, B.; Kussmann, M. Qualitative and quantitative profiling of the bovine milk fat globule membrane proteome. *J. Proteomics* **2010**, *73*, 1079−1088.
(32) Maningat, P. D.; Sen, P.; Rijnkels, M.; Sunehag, A. L.; Hadsell, D. L.; Bray, M.; Haymond, M. W. Gene expression in the human mammary epithelium during lactation: the milk fat globule transcriptome. *Physiol. Genomics* **2009**, *37*, 12−22.
(33) Grewal, T.; Enrich, C. Annexins − modulators of EGF receptor signalling and trafficking. *Cell. Signal.* **2009**, *21*, 847−858.
(34) Hong, K.; Duzgunes, N.; Papahadjopoulos, D. Role of synexin in membrane-fusion. Enhancement of calcium-dependent fusion of phospholipid-vesicles. *J. Biol. Chem.* **1981**, *256*, 3641−3644.
(35) Monastyrskaya, K.; Babiychuk, E. B.; Draeger, A. The annexins: spatial and temporal coordination of signaling events during cellular stress. *Cell. Mol. Life Sci.* **2009**, *66*, 2623−2642.
(36) Kanai, Y.; Hediger, M. A. The glutamate/neutral amino acid transporter family SLC1: molecular, physiological and pharmacological aspects. *Pfluegers Arch.* **2004**, *447*, 469−479.
(37) Yonezawa, T.; Yonekura, S.; Sanosaka, M.; Hagino, A.; Katoh, K.; Obara, Y. Octanoate stimulates cytosolic triacylglycerol accumulation and CD36 mRNA expression but inhibits acetyl coenzyme A carboxylase activity in primary cultured bovine mammary epithelial cells. *J. Dairy Res.* **2004**, *71*, 398−404.
(38) Spitsberg, V. L.; Matitashvili, E.; Gorewit, R. C. Association and coexpression of fatty-acid-binding protein and glycoprotein CD36 in the bovine mammary gland. *Eur. J. Biochem.* **1995**, *230*, 872−878.
(39) Raymond, K.; Cagnet, S.; Kreft, M.; Janssen, H.; Sonnenberg, A.; Glukhova, M. A. Control of mammary myoepithelial cell contractile function by $\alpha 3\beta 1$ integrin signalling. *EMBO J.* **2011**, *30*, 1896−1906.

DOI: 10.1021/acs.jafc.5b02231
J. Agric. Food Chem. 2015, 63, 7388−7398

Table 1. Primers Used in qRT-PCR Reactions

gene name	accession number	primer sequences (5′ → 3′)	T_m (°C)	product length (bp)
MPK3	NC015443	F: GGAGTTTTCTGATGTTTACATTGCT	59.2	343
		R: ATATTCTCGTTCTCTACGTTTGGC	59.3	
MPK6	NC015442	F: GGAGACACGTGAGGAAGTAGCT	57.8	233
		R: GCTGTTGGTTGGAATGAATAATC	58.4	
PR1a1	NC015438	F: TGCTGGTGCTGTGAAGATGTG	60.1	81
		R: CAGACTTTACCTGGAGCACACG	60.0	
PR5	NM001247232	F:TGAAAAAATTACCAAAATAATAAGCA	58.0	104
		R: GTTGAAGGGAGACATACATAACACAC	59.2	
UBI3	X58253	F: AGGTTGATGACACTGGAAAGGTT	60.6	150
		R: AATCGCCTCCAGCCTTGTTGTA	60.0	

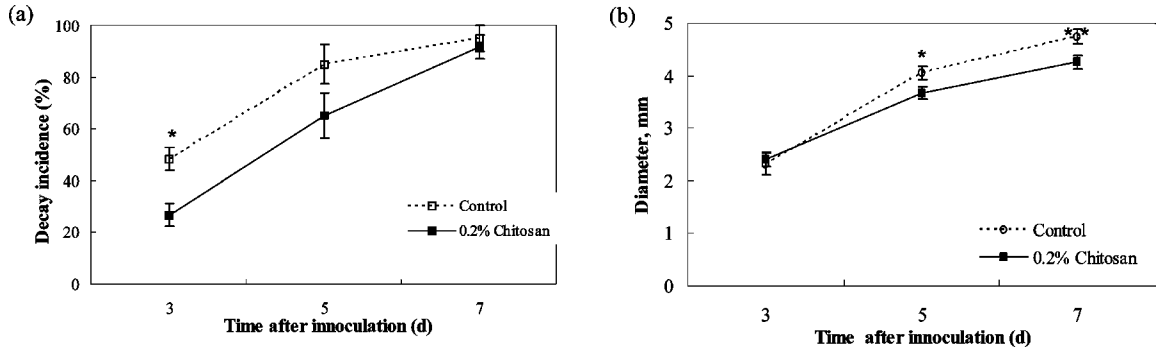

Figure 1. (a) Disease incidence and (b) lesion diameter of cherry tomato fruits inoculated with *B. cinerea*. Cherry tomato fruits treated with 1% acetate solution serviced as the control. Statistical significance of the difference was confirmed according to Duncan's multiple range test at $p < 0.05$ (*, $p < 0.05$; **, $p < 0.01$).

with a sterile nail at the equator on two opposite sides, dipped in 0.2% of chitosan solution for 5 min, and then air-dried on a clean bench. A total of 5 μL of spore suspension of *B. cinerea* was injected into each wound. Because acetate could also attribute to the inhibition of fruit decay,[20] we used the fruit treated with 1% acetate solution (pH was adjusted to 5.0) as the control.

Treated fruits were put in 200 × 130 × 50 mm plastic boxes with tap water to maintain a high relative humidity (about 80%) and stored at 22 °C. Decay incidence of tomato fruit was determined 3, 5, and 7 days after inoculation. After storage, the disease symptoms and severity (lesion diameter) were recorded. Disease incidence (%) was calculated as follows:

$$\text{disease incidence (\%)} = \frac{\text{number of infected wounds}}{\text{total wounds per replicate}} \times 100$$

Each treatment contained three replicates with 10 fruits per replicate, and the experiment was repeated 3 times.

Determination of the Malondialdehyde (MDA) Content and POD Activity in Tomato Fruit Tissue. To determine the MDA content, we conducted two treatments for cherry tomato fruit samples: (i) dipped in 0.2% chitosan solution for 5 min and air-dried, and 1 g of fruit tissue was collected 0, 3, 5, and 7 days after treatment; (ii) immersed in 0.2% chitosan solution for 10 min, 20 min, 30 min, 1 h, 2 h, and 3 h, and 1 g of fruit tissue was collected immediately. Tissue samples were homogenized in 5 mL of 100 mM ice-cold sodium phosphate buffer (pH 6.4) containing 0.1 g of polyvinyl polypyrrolidone (Sigma-Aldrich, St. Louis, MO). The MDA content was determined as the description of Song et al.[21] POD activity was determined according to Liu et al. and expressed as units mg^{-1} of protein, where 1 unit was expressed as the increase rate of absorbency per mass of protein per minute.[11] The protein content was determined using bovine serum albumin (Sigma-Aldrich, St. Louis, MO) as the standard.[22] Fruit treated with 1% acetate solution (pH 5.0) serviced as the control. Each treatment contained three replicates with three fruits per replicate, and the experiment was repeated 3 times.

Detection of Hydrogen Peroxide in Tomato Epidermal Peel. Cherry tomato was immersed in 0.2% chitosan solution for 10 min, 20 min, 30 min, 1 h, 2 h, and 3 h. Then, the tomato epidermal peel was collected immediately for H_2O_2 detection and total mRNA extraction. For H_2O_2 determination, peel samples were stained with 10 μM 2′,7′-dichlorodihydrofluorescein diacetate (H_2DCFDA, Invitrogen) for 30 min in darkness at 30 °C as the description of Liu et al.[23] H_2O_2 accumulation was examined on a laser confocal microscopy (FV1000, Olympus) at 488 nm excitation and 520 nm emission. For total mRNA extraction, peel samples were stored at −80 °C. Relative gene expressions would be detected in the total mRNA sample. Fruit treated with 1% acetate solution (pH 5.0) serviced as the control. Each treatment contained three replicates with three fruits per replicate, and the experiment was repeated 3 times.

RNA Extraction and Real-Time Quantitative Reverse Transcription Polymerase Chain Reaction (qRT-PCR). The tomato peel samples stored at −80 °C were milled using liquid nitrogen, and total mRNA was extracted using Trizol reagent (Invitrogen) according to the instruction of the manufacturer. About 100 ng of mRNA was used for cDNA synthesis. Real-time qRT-PCR was performed using the cDNA, and the gene-specific primers used were presented in Table 1. Real-time qRT-PCR was performed using Transgen Supermix (TransGen Biotech, Beijing, China) in a StepOne Plus real-time PCR system (Applied Biosystems). The PCR conditions were as follows: 95 °C for 30 s, followed by 40 cycles of 95 °C for 5 s and 60 °C for 15 s. Melting curve analyses of amplification products were performed at the end of the PCR reaction. The melting cycle was 95 °C for 15 s, 60 °C for 1 min, and 95 °C for 15 s. The expression level was normalized by the internal control gene UBI3, using the $2^{-\Delta\Delta C_T}$ method.[24]

Statistical Analysis. All statistical analyses were performed using SAS 9.2 (Cary, NC). Data were analyzed by one-way analysis of variation (ANOVA). Mean separations were performed by Duncan's multiple range tests. Least square means (LSMEANS) and standard errors of least-squares means (SEM) were calculated using the LSMEANS. Differences at $p < 0.05$ were considered to be significant.

DOI: 10.1021/acs.jafc.5b01566
J. Agric. Food Chem. 2015, 63, 7399−7404

RESULTS AND DISCUSSION

Effects of Chitosan on Postharvest Diseases of Cherry Tomato Fruit. Results in Figure 1a showed that chitosan at the concentration of 0.2% could control gray mold caused by *B. cinerea* notably 3 days after innoculation ($p < 0.05$). The disease incidence was reduced by 44.7%. However, at 5 days after innoculation, the difference was not significant ($p > 0.05$). A previous study showed that chitosan at the concentration of 0.05% could significantly inhibit the decay of citrus fruit caused by *B. cinerea*.[25] Liu et al. reported that 0.5% of chitosan could significantly decrease decay incidence of tomato fruit after 3 days of storage at 25 °C.[11] It suggested that chitosan inhibits the tomato gray mold depending upon the dosage. The lesion diameter on the fruit was also observed, and it was lower on the chitosan treatment than the control after 5 days of storage (Figure 1b), in accordance with previous studies that chitosan could reduce decay on fruits.[10,26]

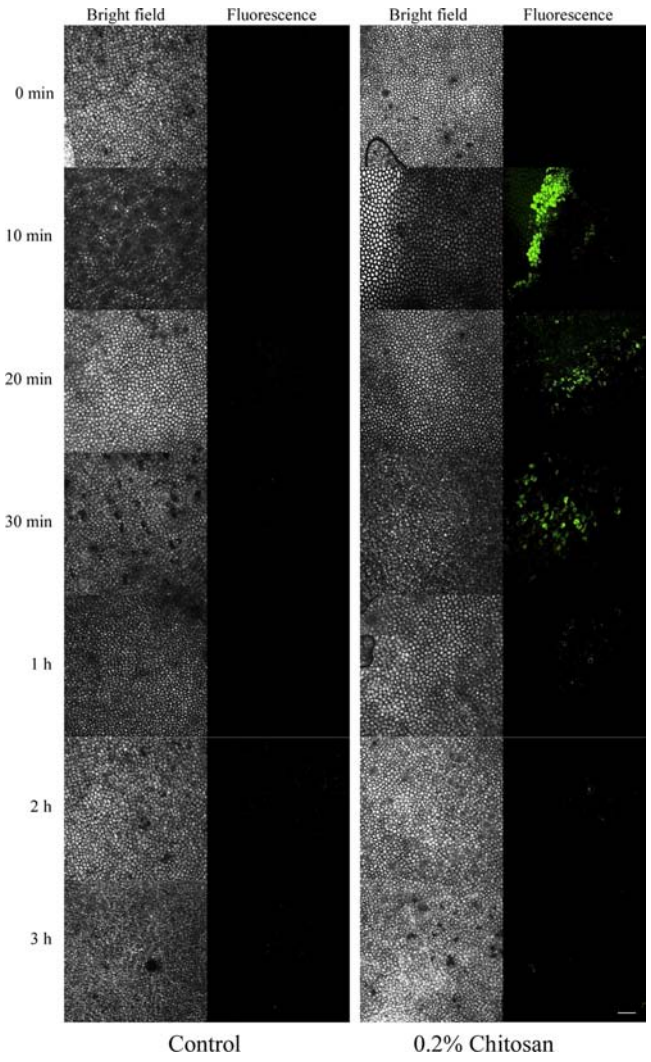

Figure 2. H_2O_2 accumulation in cherry tomato epidermal peel with chitosan. Peels were stained with H_2DCFDA and observed with a laser confocal microscopy at 488 nm excitation and 520 nm emission. Cherry tomato treated with 1% acetate solution serviced as the control. Bar = 150 μm.

Effect of Chitosan on ROS Accumulation in Cherry Tomato Fruit Epidermal Peel. Chitosan was recognized by receptors localized on the cell surface as the attack of fungal pathogens, and then ROS was stimulated.[27,28] This is one of the earliest cellular responses following successful pathogen recognition.[29] ROS include H_2O_2 and other chemical forms, such as superoxide anion, hydroxyl radical, and peroxyl radical; among them, H_2O_2 is most stable, although it lasts for no more than 1 s in fresh tissue.[30]

ROS accumulation has already been observed in *Arabidopsis* treated with chitosan.[31−33] A similar result was observed in sycamore cultured cells.[34] In this study, while cherry tomato was treated with 0.2% chitosan for 10 min, H_2O_2 accumulation in the epidermal peel could be observed; in 20 and 30 min, the fluorescence signal of H_2O_2 remained strong (Figure 2). However, the H_2O_2 level was reduced significantly in the treatments in 1 h; and in 3 h, it could hardly be detected (Figure 2). This result indicated that, in the mature tomato fruit peel, H_2O_2 was stimulated as an early response to chitosan. Zeng et al. reported that, in the navel orange fruit treated with chitosan, the H_2O_2 content significantly increased and, subsequently, inhibited the postharvest decay.[35] The increase

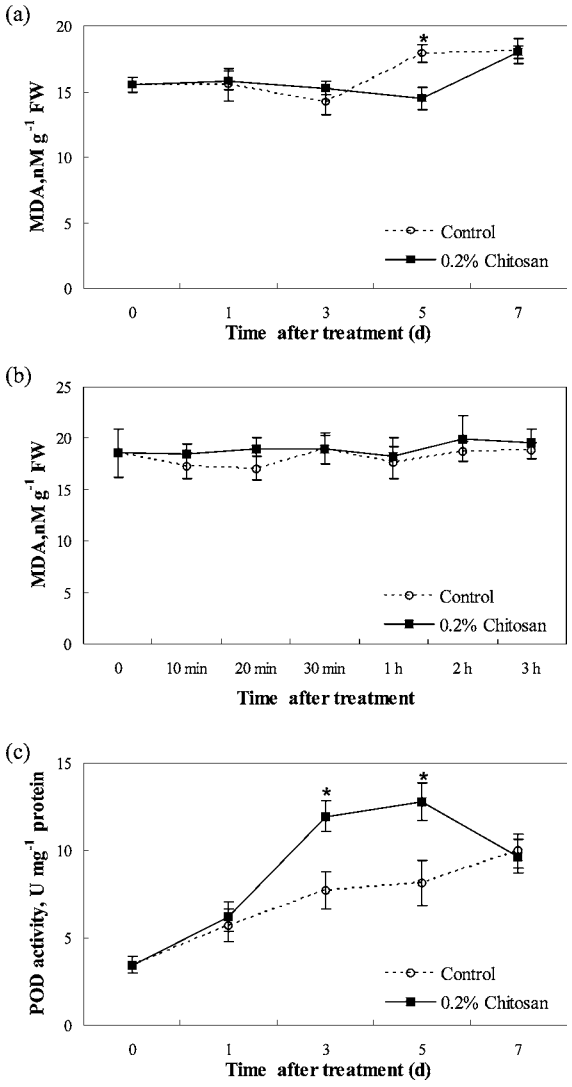

Figure 3. (a and b) MDA production and (c) POD activity in cherry tomato treated with chitosan. Cherry tomato treated with 1% acetate solution serviced as the control. Statistical significance of the difference was confirmed according to Duncan's multiple range test at $p < 0.05$ (*, $p < 0.05$).

DOI: 10.1021/acs.jafc.5b01566
J. Agric. Food Chem. 2015, 63, 7399−7404

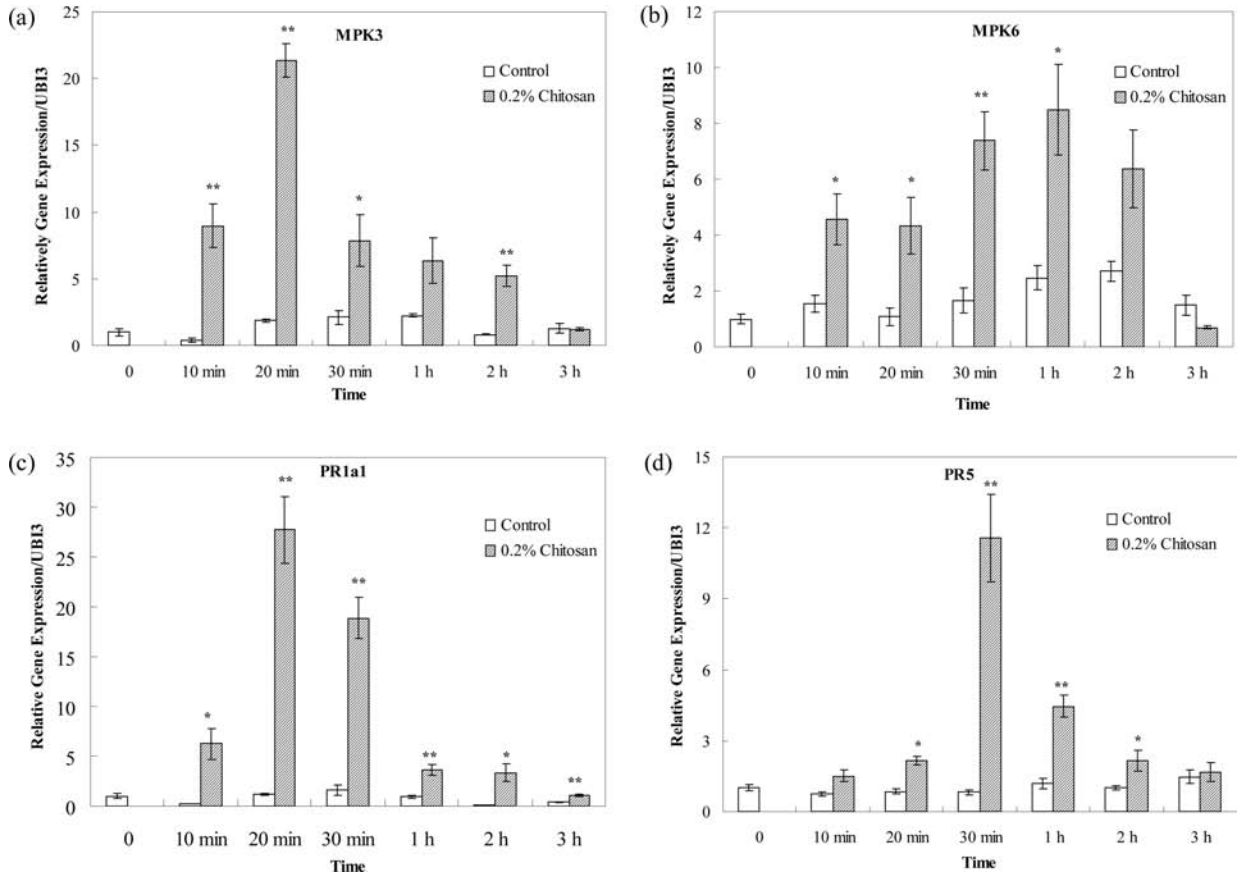

Figure 4. Relative expression of (a) *MPK3*, (b) *MPK6*, (c) *PR1a1*, and (d) *PR5* in cherry tomato epidermal peel treated with chitosan. *UBI3* was used as the internal control gene. Cherry tomato treated with 1% acetate solution serviced as the control. Statistical significance of the difference was confirmed according to Duncan's multiple range test at $p < 0.05$ (*, $p < 0.05$; **, $p < 0.01$).

of the H_2O_2 content was believed to promote resistance of apple fruit to *Penicillium expansum*.[36] Therefore, the improvement of the H_2O_2 level might serve as an important signaling molecule to activate plant defense-related genes in cherry tomato fruit.

Effect of Chitosan on the MDA Content and POD Activity in Cherry Tomato Fruit Tissue. In the past, ROS was always considered to contribute to the senescence of harvested fruit.[37,38] ROS in peach petals induced by *Monilinia fructicola* resulted in oxidative damage in host tissues,[23] which might enhance the infection by necrotrophic pathogen. Therefore, the content of ROS must be maintained at a nontoxic level, and ROS producing/scavenging enzymes were involved in the maintaining of this balance.[39]

MDA, a decomposition product of polyunsaturated fatty acid hydroperoxides, is often used as a marker for monitoring lipid peroxidation caused by oxidative damage.[40] In our study, the MDA content in fruit treated by chitosan was not different with the control (panels a and b of Figure 3; $p > 0.05$), indicating that the instantaneous H_2O_2 accumulated in the epidermal peel had no effect on the oxidation of fruit tissue. After 5 days of storage, the MDA content was even lower than that in the control ($p < 0.05$). This might be ascribed to the increasing activities of catalase and POD, which were crucial for suppressing the toxic ROS level.[30]

Figure 3c showed that the POD activity was enhanced notably with the addition of chitosan ($p < 0.05$), in agreement with the previous studies on tomato, sweet cherry, and peach.[11,41,42] After 3 days, POD activity in chitosan treatment was significantly higher than that in the control ($p < 0.05$); this might explain the decrease of the MDA content 5 days after treatment. However, it was reduced after 7 days and had no difference compared to the control ($p > 0.05$). In the control, the POD activity also increased markedly during storage, in agreement with a previous report that the POD activity was increased dramatically in grape fruit treated with deionized water at pH 5.6.[26]

Effect of Chitosan on *MPK3*/*MPK6* and *PR* Transcripts in Cherry Tomato Fruit Epidermal Peel. MAPK cascades are major components downstream of receptors that can rapidly transduce stress signals into intracellular responses in all eukaryotes.[15] MAPK cascade activation is one of the earliest signaling events while the plant interacts with PAMPs. Many of the known PAMPs were shown to activate MAPKs, e.g., flagellin,[43] peptidoglycan,[44] and chitin.[45,46] PAMPs are recognized by pattern recognition receptors on the plasma membrane, and intracellular immune responses are immediately initiated.[47] Several chitin/chitosan receptors have been identified in *Arabidopsis*.[48−50] The cascades mainly composed of a MAPK kinase kinase, a MAPK kinase, and a MAPK link upstream receptors to downstream targets involved in the regulation of development, growth, and programmed cell death and in responses to a diversity of environmental stimuli.[15]

MPK3 and *MPK6* are key players and make positive effects in the defense response to bacterial and fungal pathogens. They show a high level of functional redundancy.[15] In this experiment, the relative expression level of *MPK3* was induced 10 min after treatment, reached the highest level at 20 min,

DOI: 10.1021/acs.jafc.5b01566
J. Agric. Food Chem. 2015, 63, 7399−7404

which was 11 times higher than that in the control ($p < 0.05$), and reduced to the basal level 3 h after treatment (Figure 4a). The expression of *MPK6* was also induced in 10 min ($p < 0.05$) and reached the highest level at 1 h. At 3 h after treatment, the expression level of *MPK6* was significantly decreased (Figure 4b).

The activated MPK3/MPK6 is followed by a series of modifications of the cell, including the synthesis of pathogen-induced synthesis of PR proteins (e.g., β-1,3-glucanases and chitinases),[15,51] lignin deposition,[52] and phytoalexin (e.g., camalexin) synthesis.[53] *PR* genes play an important role in plant defense responses and have been widely used as a marker of downstream immune signaling.[54] They are classified into 17 families.[55] In our study, *PR1a1* and *PR5* were selected to detect the defense response in tomato fruit peel. The expression of *PR1a1* was also induced in 10 min ($p < 0.05$) and reached the highest level at 20 min, about 24 times higher than the control ($p < 0.01$; Figure 4c), while the expression of *PR5* was induced in 20 min ($p < 0.05$) and reached the highest level at 30 min ($p < 0.01$; Figure 4d). This might be one of the reasons that the disease severity was notably lower on fruits treated by chitosan. Additionally, we had also determined two other *PR* genes, *PR-P2* and *PR-P4*; however, they were not induced (data not shown), indicating that not all *PR* genes were induced in response to the chitosan-triggered defense.

The regulation of the *PR1* gene is considered to depend upon the salicylic acid signaling pathway and correlated with the onset of systemic acquired resistance.[54] It was reported that salicylic acid improved the activities of the main defense-related enzymes, including phenylalanine ammonia-lyase, POD, chitinase, and β-1,3-glucanase in jujube fruit and, consequently, enhanced the fruit resistance.[56]

In conclusion, this study showed that 0.2% of chitosan could induce the accumulation of ROS and the expressions of *MPK3*, *MPK6*, *PR1*, and *PR5* genes in cherry tomato peel. The result suggested that the MAPK signaling pathway was possibly activated in the cherry tomato fruit treated with chitosan. This might be one of the molecular mechanisms that the resistance to fungal pathogens of fruit was enhanced by chitosan. However, the complete cascade stimulated by chitosan on tomato contains the specific MAPK kinase kinase, and MAPK kinase upstream of MPK3/MPK6 should be further identified.

AUTHOR INFORMATION

Corresponding Author

*Telephone: 86-187-0983-2886. Fax: +86-551-6290-1516. E-mail: liuyongsheng1122@hfut.edu.cn.

Funding

The authors thank the China Postdoctoral Science Foundation (113-471015) and the National Natural Science Foundation of China (31461143008).

Notes

The authors declare no competing financial interest.

REFERENCES

(1) Zhang, H.; Li, R.; Liu, W. Effects of chitin and its derivative chitosan on postharvest decay of fruits: A review. *Int. J. Mol. Sci.* **2011**, *12*, 917−934.

(2) Droby, S.; Wisniewski, M.; Macarisin, D.; Wilson, C. Twenty years of postharvest biocontrol research: is it time for a new paradigm? *Postharvest Biol. Technol.* **2009**, *52*, 137−145.

(3) Sharma, R. R.; Singh, D.; Singh, R. Biological control of postharvest diseases of fruits and vegetables by microbial antagonists: A review. *Biol. Control* **2009**, *50*, 205−221.

(4) Badawy, M. E. I.; Rabea, E. I. Potential of the biopolymer chitosan with different molecular weights to control postharvest gray mold of tomato fruit. *Postharvest Biol. Technol.* **2009**, *51*, 110−117.

(5) Ge, L.; Zhang, H.; Chen, K.; Ma, L.; Xu, Z. Effect of chitin on the antagonistic activity of Rhodotorula glutinis against *Botrytis cinerea* in strawberries and the possible mechanisms involved. *Food Chem.* **2010**, *120*, 490−495.

(6) Romanazzi, G.; Feliziani, E.; Santini, M.; Landi, L. Effectiveness of postharvest treatment with chitosan and other resistance inducers in the control of storage decay of strawberry. *Postharvest Biol. Technol.* **2013**, *75*, 24−27.

(7) Jiang, Y.; Li, Y. Effects of chitosan coating on postharvest life and quality of longan fruit. *Food Chem.* **2001**, *73*, 139−143.

(8) Ali, A.; Zahid, N.; Manickam, S.; Siddiqui, Y.; Alderson, P. G.; Maqbool, M. Effectiveness of submicron chitosan dispersions in controlling anthracnose and maintaining quality of dragon fruit. *Postharvest Biol. Technol.* **2013**, *86*, 147−153.

(9) Wang, L.; Wu, H.; Qin, G.; Meng, X. Chitosan disrupts *Penicillium expansum* and controls postharvest blue mold of jujube fruit. *Food Control* **2014**, *41*, 56−62.

(10) Lu, H.; Lu, L.; Zeng, L.; Fu, D.; Xiang, H.; Yu, T.; Zheng, X. Effect of chitin on the antagonistic activity of *Rhodosporidium paludigenum* against *Penicillium expansum* in apple fruit. *Postharvest Biol. Technol.* **2014**, *92*, 9−15.

(11) Liu, J.; Tian, S.; Meng, X.; Xu, Y. Effects of chitosan on control of postharvest diseases and physiological responses of tomato fruit. *Postharvest Biol. Technol.* **2007**, *44*, 300−306.

(12) de Oliveira, C. E.; Magnani, M.; de Sales, C. V.; de Souza Pontes, A. L.; Campos-Takaki, G. M.; Stamford, T. C.; de Souza, E. L. Effects of post-harvest treatment using chitosan from *Mucor circinelloides* on fungal pathogenicity and quality of table grapes during storage. *Food Microbiol.* **2014**, *44*, 211−219.

(13) Zhang, D.; Quantick, P. C. Antifungal effects of chitosan coating on fresh strawberries and raspberries during storage. *J. Hortic. Sci. Biotechnol.* **1998**, *73*, 763−767.

(14) Romanazzi, G.; Nigro, F.; Ippolito, A.; Di Venere, D.; Salerno, M. Effects of pre- and postharvest chitosan treatments to control storage grey mould of table grapes. *J. Food Sci.* **2002**, *67*, 1862−1867.

(15) Pitzschke, A.; Schikora, A.; Hirt, H. MAPK cascade signalling networks in plant defence. *Curr. Opin. Plant Biol.* **2009**, *12*, 421−426.

(16) Lin, W.; Hu, X.; Zhang, W.; John Rogers, W.; Cai, W. Hydrogen peroxide mediates defence responses induced by chitosans of different molecular weights in rice. *J. Plant Physiol.* **2005**, *162*, 937−944.

(17) Hamel, L. P.; Miles, G. P.; Samuel, M. A.; Ellis, B. E.; Séguin, A.; Beaudoin, N. Activation of stress-responsive mitogen-activated protein kinase pathways in hybrid poplar (*Populus trichocarpa* × *Populus deltoides*). *Tree Physiol.* **2005**, *25*, 277−288.

(18) Lizama-Uc, G.; Estrada-Mota, I. A.; Caamal-Chan, M. G.; Souza-Perera, R.; Oropeza-Salín, C.; Islas-Flores, I.; Zúñiga-Aguilar, J. J. Chitosan activates a MAP-kinase pathway and modifies abundance of defense-related transcripts in calli of *Cocos nucifera* L. *Physiol. Mol. Plant Pathol.* **2007**, *70*, 130−141.

(19) Grant-Downton, R. T.; Terhem, R. B.; Kapralov, M. V.; Mehdi, S.; Rodriguez-Enriquez, M. J.; Gurr, S. J.; van Kan, J. A. L.; Dewey, F. M. A novel *Botrytis* species is associated with a newly emergent foliar disease in cultivated. *PLoS One* **2014**, *9*, e89272.

(20) Sholberg, P. L.; Shephard, T.; Randall, P.; Moyls, L. Use of measured concentrations of acetic acid vapour to control postharvest decay in d'Anjou pears. *Postharvest Biol. Technol.* **2004**, *32*, 89−98.

(21) Song, H.; Fan, P.; Li, Y. Overexpression of organellar and cytosolic AtHSP90 in *Arabidopsis thaliana* impairs plant tolerance to oxidative stress. *Plant Mol. Biol. Rep.* **2009**, *27*, 342−349.

(22) Bradford, M. N. A rapid and sensitive method for the quantitation of microgram quantities of protein using the principle of protein−dye binding. *Anal. Biochem.* **1976**, *72*, 248−254.

DOI: 10.1021/acs.jafc.5b01566
J. Agric. Food Chem. 2015, 63, 7399−7404

(23) Liu, J.; Macarisin, D.; Wisniewski, M.; Sui, Y.; Droby, S.; Norelli, J.; Hershkovitz, V. Production of hydrogen peroxide and expression of ROS-generating genes in peach flower petals in response to host and non-host fungal pathogens. *Plant Pathol.* **2013**, *62*, 820−828.
(24) Livak, K. J.; Schmittgen, T. D. Analysis of relative gene expression data using real-time quantitative PCR and the $2^{-\Delta\Delta Ct}$ Method. *Methods* **2001**, *25*, 402−408.
(25) Chien, P. J.; Sheu, F.; Lin, H. R. Coating citrus (Murcott tangor) fruit with low molecular weight chitosan increases postharvest quality and shelf life. *Food Chem.* **2007**, *100*, 1160−1164.
(26) Meng, X.; Li, B.; Liu, J.; Tian, S. Physiological responses and quality attributes of table grape fruit to chitosan preharvest spray and postharvest coating during storage. *Food Chem.* **2008**, *106*, 501−508.
(27) Bradley, D. J.; Kjellbom, P.; Lamb, C. J. Elicitor- and wound-induced oxidative cross-linking of a proline-rich plant cell wall protein: A novel, rapid defense response. *Cell* **1992**, *70*, 21−30.
(28) Bueter, C. L.; Specht, C. A.; Levitz, S. M. Innate sensing of chitin and chitosan. *PLoS Pathog.* **2013**, *9*, e1003080.
(29) Torres, M. A.; Jones, J. D. G.; Dangl, J. L. Reactive oxygen species signaling in response to pathogens. *Plant Physiol.* **2006**, *141*, 373−378.
(30) Sharma, P.; Jha, A. B.; Dubey, R. S.; Pessarakli, M. Reactive oxygen species, oxidative damage, and antioxidative defense mechanism in plants under stressful conditions. *J. Bot.* **2012**, *2012*, 1−26.
(31) Khokon, M. A. R.; Uraji, M.; Munemasa, S.; Okuma, E.; Nakamura, Y.; Mori, I. C.; Murata, Y. Chitosan-induced stomatal closure accompanied by peroxidase-mediated reactive oxygen species production in *Arabidopsis*. *Biosci., Biotechnol., Biochem.* **2010**, *74*, 2313−2315.
(32) Povero, G.; Loreti, E.; Pucciariello, C.; Santaniello, A.; Di Tommaso, D.; Di Tommaso, G.; Kapetis, D.; Zolezzi, F.; Piaggesi, A.; Perata, P. Transcript profiling of chitosan-treated *Arabidopsis* seedlings. *J. Plant Res.* **2011**, *124*, 619−629.
(33) Feng, H.; Xia, W.; Shan, C.; Zhou, T.; Cai, W.; Zhang, W. Quaternized chitosan oligomers as novel elicitors inducing protection against *B. cinerea* in *Arabidopsis*. *Int. J. Biol. Macromol.* **2015**, *72*, 364−369.
(34) Malerba, M.; Crosti, P.; Cerana, R. Defense/stress responses activated by chitosan in sycamore cultured cells. *Protoplasma* **2012**, *249*, 89−98.
(35) Zeng, K.; Deng, Y.; Ming, J.; Deng, L. Induction of disease resistance and ROS metabolism in navel oranges by chitosan. *Sci. Hortic.* **2010**, *126*, 223−228.
(36) Torres, R.; Valentines, M. C.; Usall, J.; Viñas, I.; Larrigaudiere, C. Possible involvement of hydrogen peroxide in the development of resistance mechanisms in 'Golden Delicious' apple fruit. *Postharvest Biol. Technol.* **2003**, *27*, 235−242.
(37) Qin, G.; Meng, X.; Wang, Q.; Tian, S. Oxidative damage of mitochondrial proteins contributes to fruit senescence: a redox proteomics analysis. *J. Proteome Res.* **2009**, *8*, 2449−2462.
(38) Tian, S.; Qin, G.; Li, B. Reactive oxygen species involved in regulating fruit senescence and fungal pathogenicity. *Plant Mol. Biol.* **2013**, *82*, 593−602.
(39) Baxter, A.; Mittler, R.; Suzuki, N. ROS as key players in plant stress signaling. *J. Exp. Bot.* **2014**, *65*, 1229−1240.
(40) Bailly, C.; Benamar, A.; Corbineau, F.; Côme, D. Changes in malondialdehyde content and in superoxide dismutase, catalase and glutathione reductase activities in sunflower seeds as related to deterioration during accelerated aging. *Physiol. Plant.* **1996**, *97*, 104−110.
(41) Dang, Q. F.; Yan, J. Q.; Li, Y.; Cheng, X. J.; Liu, C. S.; Chen, X. G. Chitosan acetate as an active coating material and its effects on the storing of *Prunus avium* L. *J. Food Sci.* **2010**, *75*, S125−131.
(42) Ma, Z.; Yang, L.; Yan, H.; Kennedy, J. F.; Meng, X. Chitosan and oligochitosan enhance the resistance of peach fruit to brown rot. *Carbohydr. Polym.* **2013**, *94*, 272−277.
(43) Asai, T.; Tena, G.; Plotnikova, J.; Willmann, M. R.; Chiu, W. L.; Gomez-Gomez, L.; Boller, T.; Ausubel, F. M.; Sheen, J. MAP kinase signalling cascade in *Arabidopsis* innate immunity. *Nature* **2002**, *415*, 977−983.
(44) Gust, A. A.; Biswas, R.; Lenz, H. D.; Rauhut, T.; Ranf, S.; Kemmerling, B.; Götz, F.; Glawischnig, E.; Lee, J.; Felix, G.; Nürnberger, T. Bacteria-derived peptidoglycans constitute pathogen-associated molecular patterns triggering innate immunity in *Arabidopsis*. *J. Biol. Chem.* **2007**, *282*, 32338−32348.
(45) Wan, J.; Zhang, S.; Stacey, G. Activation of a mitogen-activated protein kinase pathway in *Arabidopsis* by chitin. *Mol. Plant Pathol.* **2004**, *5*, 125−135.
(46) Kaku, H.; Nishizawa, Y.; Ishii-Minami, N.; Akimoto-Tomiyama, C.; Dohmae, N.; Takio, K.; Minami, E.; Shibuya, N. Plant cells recognize chitin fragments for defense signaling through a plasma membrane receptor. *Proc. Natl. Acad. Sci. U. S. A.* **2006**, *103*, 11086−11091.
(47) Zipfel, C. Pattern-recognition receptors in plant innate immunity. *Curr. Opin. Immunol.* **2008**, *20*, 10−16.
(48) Miya, A.; Albert, P.; Shinya, T.; Desaki, Y.; Ichimura, K.; Shirasu, K.; Narusaka, Y.; Kawakami, N.; Kaku, H.; Shibuya, N. CERK1, a LysM receptor kinase, is essential for chitin elicitor signaling in *Arabidopsis*. *Proc. Natl. Acad. Sci. U. S. A.* **2007**, *104*, 19613−19618.
(49) Liu, T.; Liu, Z.; Song, C.; Hu, Y.; Han, Z.; She, J.; Fan, F.; Wang, J.; Jin, C.; Chang, J.; Zhou, J. M.; Chai, J. Chitin-induced dimerization activates a plant immune receptor. *Science* **2012**, *336*, 1160−1164.
(50) Cao, Y.; Liang, Y.; Tanaka, K.; Nguyen, C. T.; Jedrzejczak, R. P.; Joachimiak, A.; Stacey, G. The kinase LYK5 is a major chitin receptor in *Arabidopsis* and forms a chitin-induced complex with related kinase CERK1. *eLife* **2014**, *3*, e03766.
(51) Djamei, A.; Pitzschke, A.; Nakagami, H.; Rajh, I.; Hirt, H. Trojan horse strategy in *Agrobacterium* transformation: Abusing MAPK defense signaling. *Science* **2007**, *318*, 453−456.
(52) Morse, A. M.; Whetten, R. W.; Dubos, C.; Campbell, M. M. Post-translational modification of an R2R3-MYB transcription factor by a MAP Kinase during xylem development. *New Phytol.* **2009**, *183*, 1001−1013.
(53) Ren, D.; Liu, Y.; Yang, K. Y.; Han, L.; Mao, G.; Glazebrook, J.; Zhang, S. A fungal-responsive MAPK cascade regulates phytoalexin biosynthesis in *Arabidopsis*. *Proc. Natl. Acad. Sci. U. S. A.* **2008**, *105*, 5638−5643.
(54) Durrant, W. E.; Dong, X. Systemic acquired resistance. *Annu. Rev. Phytopathol.* **2004**, *42*, 185−209.
(55) van Loon, L. C.; Rep, M.; Pieterse, C. M. J. Significance of inducible defense-related proteins in infected plants. *Annu. Rev. Phytopathol.* **2006**, *44*, 135−162.
(56) Cao, J.; Yan, J.; Zhao, Y.; Jiang, W. Effects of postharvest salicylic acid dipping on *Alternaria* rot and disease resistance of jujube fruit during storage. *J. Sci. Food Agric.* **2013**, *93*, 3252−3258.

DOI: 10.1021/acs.jafc.5b01566
J. Agric. Food Chem. 2015, 63, 7399−7404

multilayer microcapsules based on TA and synthetic polymers (poly-*N*-vinylpyrrolidone) via hydrogen-bonding interaction, for drug encapsulation, controlled delivery, and long-term storage. TA−protein interactions are essentially physical: hydrophobic and hydrogen bond mediated.[7] The tannin affinities for human salivary proline-rich proteins (PRP) were found to be related to astringency,[12] and tannin−gliadin interactions for haze formation[13] had been investigated extensively. For PRP, including gliadin[13] and kafirin,[14] hydrogen bonds between the hydroxyl groups of tannins and the carbonyl groups of proteins are believed to be involved in the complexation of the proteins and tannins. PRP can also interact with pentagalloyl glucose of TA via hydrophobic interactions with the pyrrolidine ring of proline. Below the tannin critical micelle concentration (CMC), the protein polypeptides surround the tannins; above the tannin CMC, tannins act as bridges to cross-link the polypeptides for forming aggregates or agglomerates of proteins.[15]

Stabilization of the oil−water interface with colloidal particles, which leads to the formation of Pickering emulsions, is known to display long-term stability against coalescence, and the potentials for texture modification, calorie and fat reduction, and bioactive compound delivery have emerged.[16] As compared to conventional emulsifiers, the main benefits of Pickering emulsions are high physical/chemical stabilities. The particle-stabilized interface can be modified after emulsion formation to bring additional functionality; this modification of interfacial properties can be in response to a trigger, and Pickering emulsions can serve as templates for preparing materials that could not be obtained from conventional emulsions.[16] Studies on protein-based particles used as Pickering emulsion stabilizers are still scarce, although they show clearly a growing research field. Zein, a major protein of corn, is capable of forming self-assembled nanoparticles to stabilize Pickering emulsion due to its amphiphilic character. Therefore, zein-based particles possess promising potential to serve as food-grade Pickering emulsion stabilizers in the food industry. de Folter and co-workers have employed unmodified zein colloidal particles to stabilize Pickering emulsion, but it was very unstable to creaming and the aqueous phase was turbid.[17] Fortunately, we have reported the stabilization of oil−water interfaces with zein complex colloidal particles.[18,19] Our findings showed that the complexation of zein particles and the surfactant sodium stearate (SS) was due to nonspecific hydrophobic interaction, which resulted in enhanced adsorption and accumulation of zein particles at the oil−water interface. The resultant Pickering emulsions exhibited superior stability against both coalescence and creaming.[18] More recently, we fabricated dual-functional zein/chitosan complex particles (ZCP), which were loaded with antioxidant curcumin, and further prepared antioxidant Pickering emulsions via manipulation of the interface framework. The combination of steric hindrance from ZCP-based interfacial architecture and interfacial cargo of curcumin gave rise to emulsions with favorable oxidative stability.[19] However, modifiers such as SS and chitosan are either synthetic or have a poor organoleptic acceptation, which limit their application in food formulations. Moreover, emulsions stabilized by zein−SS complexes presented oil droplets in the top phase after a few days of storage. In this work, TA, a natural polyphenol, was used as an efficient tool to control the self-assembly behavior of zein, so as to fabricate stable and edible zein/TA colloidal particles (ZTP) and consequently prepare stable Pickering emulsions. Interestingly, the results indicated that the complexation of zein and TA was due to noncovalent interaction (mainly hydrogen bonding), which was more specific than the hydrophobic interaction in zein−SS complexes. Because of the multiple biological properties of TA, including antioxidant and antibacterial properties, these emulsions might inherently possess excellent chemical stability and some health benefits, and they could be developed as novel functional food ingredients.

MATERIALS AND METHODS

Materials. Zein (purity is around 88−96%), tannic acid, and fluorescent dyes (Nile Red and Nile Blue A) were purchased from Sigma-Aldrich, Inc. (St. Louis, MO, USA). α-Zein is the major component of zein, which has two subtypes, Z19 and Z22, confirmed by SDS-PAGE. Corn oil was obtained in a local supermarket (Guangzhou, China). Other chemicals were of analytical grade.

Colloidal Particle Synthesis. The zein colloidal particles were prepared via an antisolvent precipitation technique,[19] with modification. In brief, an aliquot of 2.5 g of zein powder was dispersed in 100 mL of a 70:30 ethanol/water (v/v) solution and stirred using a magnetic stirrer for 2 h, then stored overnight at 4 °C to allow complete hydration. Zein stock solutions with different TA concentrations (expressed as zein/TA ratios, 1:0−1:0.5 w/w) at different pH values (3.0, 5.0, 7.0; the pH was adjusted with 2 mol/L HCl and 2 mol/L NaOH) were heated in a water bath at 55 °C for 50 min with slow stirring. The preheated zein−TA solutions (10 mL) were quicklyt poured into 25 mL of Millipore water (18.2 MΩ·cm) under continued stirring (1000 rpm). After 15 min of stirring, the ethanol in zein−TA solutions were further removed, and preconcentration of colloidal particle was performed by using an RV 10 digital rotary evaporator (IKA-Works Inc., Germany). Finally, the zein concentration in the solutions (8.3 mL) was 3% (w/v). The obtained solutions were centrifuged at 4000*g* for 10 min to remove insoluble aggregates, and then they were stored at 4 °C for further use. For field emission scanning electron microscope (FE-SEM) observation and contact angle measurement, the resultant ZTP colloidal particles were lyophilized for 24 h (Christ Delta 1-24 LSC, Martin Christ, Germany) and then ground into homogeneous powders.

Particle Size and Zeta (ζ)-Potential Measurements. The ZTP colloidal particles were diluted to 1 mg/mL with Millipore water, and the pH was adjusted to 3.5; then the particle size, ζ-potential, and polydispersity index (PDI) were measured using a Nano ZS Zetasizer instrument (Malvern Instruments, Worcestershire, UK). All measurements were carried out at 25 °C, and the results are reported as averages of three readings.

Morphology Observation. The morphology of the freeze-dried ZTP powders was observed by FE-SEM. The powder samples were loosely glued onto a conductive adhesive mounted on a stainless steel stage, subsequently coated with a thin conductive gold and platinum layer using a sputter coater (Hummer XP, Anatech, Union City, CA, USA). They were observed with a Zeiss Merlin FE-SEM (Zeiss, Oberkochen, Germany).

Contact Angle Measurement. The three-phase contact angle (θ_{ow}) of colloidal particles was measured using an OCA 20 AMP (Dataphysics Instruments GmbH, Germany), which was described in our previous research.[18] The ZTP powders were prepared as pellets of 13 mm in diameter and 2 mm in thickness, and the pellets were placed into an optical glass cuvette containing purified corn oil. Next, a drop of pH 3.5 Milli-Q water (5 μL) was deposited on the surface of the pellets using a high-precision injector. After 4 min for equilibration, the drop image was photographed using a high-speed video camera, and the profile of the droplet was numerically solved and fitted to the Laplace−Young equation. Contact angles were measured on each of four pellets per sample, and three measurements were performed for each pallet.

Circular Dichroism (CD) Spectroscopy. A Chirascan spectropolarimeter (Applied Photophysics Ltd., UK) was used for monitoring the configuration of zein in 70% (v/v) aqueous ethanol after heating with TA. The samples were diluted to 0.1 mg/mL by 70% (v/v)

DOI: 10.1021/acs.jafc.5b03113
J. Agric. Food Chem. 2015, 63, 7405−7414

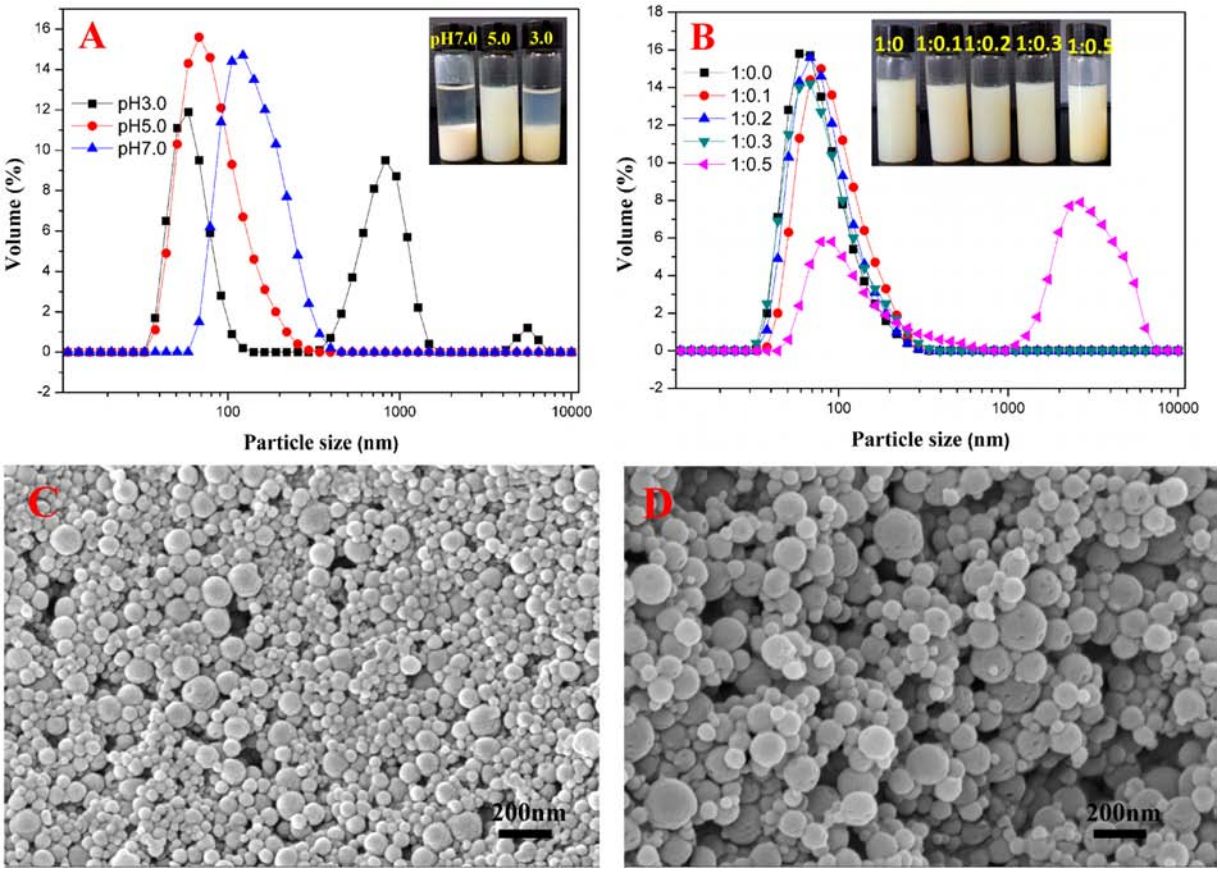

Figure 1. Size distribution and morphology of the zein/TA complex colloidal particle (ZTP) prepared at (A) various pH values (3.0, 5.0, and 7.0) with a zein/TA ratio of 1:0.2 and (B) various zein/TA ratios (from 1:0 to 1:0.5 w/w) at pH 5.0. FE-SEM images showed the ZTP prepared at pH 5.0 (C) and 7.0 (D) with the same zein/TA ratio of 1:0.2.

aqueous ethanol solution with different pH values (3.0, 5.0, 7.0), which was also used as the reference buffer. The CD spectroscopy was recorded from 190 to 260 nm in a 1 mm path length quartz cuvette, expressed as mean residue ellipticity in deg cm^2 $dmol^{-1}$. From the CD spectra, fractional contents of the secondary structure (α-helix, β-sheet, β-turn, and random coil) of the zein−TA complex in 70% (v/v) aqueous ethanol were calculated according to the CONTIN/LL program in CD Pro software.

Small-Angle X-ray Scattering (SAXS). SAXS experiments were performed using a SAXSess camera (Anton-Paar, Graz, Austria) to collect information about the structure parameters and the shape of zein/TA complexes in 70% (v/v) aqueous ethanol solutions. A PW3830 X-ray generator with a long fine-focus sealed glass X-ray tube (PAN Alytical Almelo, The Netherlands) was operated at 40 kV and 50 mA. The samples with a zein concentration of 1.0 wt % were filled into a capillary of 1 mm diameter and 0.01 mm wall thickness. The capillary was placed in a TCS 120 temperature-controlled sample holder unit (Anton Paar) along the line-shaped X-ray beam in the evacuated camera housing. A shot exposure period of 900 s was used to acquire the scattering data. The sample-to-detector distance was 261.2 mm, and the temperature was kept at 25.0 °C. Data analyses were done by Guinier methods. The overall radius of gyration (R_g) calculated from the initial slope of a Guinier plot as $\ln(I(q))$ against q^2, where $I(q)$ is the scattering intensity and $q = (4\pi/\lambda)\sin(\theta/2)$ is the modulus of the scattering vector with θ the scattering angle and λ the wavelength of the X-ray beam. The limit of Guinier plots is usually defined as $qR_g < 1$. The $I(0)$ was evaluated at very small angles, and the intensity is represented as $I(q) = I(0)\exp(-1/3(qR_g)^2)$. If one of the particle dimensions is much larger than other two dimensions, the radius of gyration of the cross-section (R_c) is obtained in a larger q range than that used in the R_g analyses and calculated from the slope of the cross-section plots as $\ln(I(q)q)$ against q^2 ($qR_c < 1$). Moreover, if the observed asymmetric particles are approximated by a rectangular prism with edges of a, b, and c (b and $c \ll a$), knowledge of R_g and R_c gives edge a with the largest length from the equation $a^2 = 12(R_g^2 - R_c^2)$.[21]

Fourier Transform Infrared Spectroscopy (FTIR). The FTIR spectra of ZTP powder were recorded at 400−4000 cm^{-1} using a Bruker VERTEX 70 spectrometer (Germany) equipped with a narrow-band mercury cadmium telluride detector with a resolution of 2 cm^{-1}.

Preparation of Pickering Emulsion. The Pickering emulsions were prepared by resultant zein/TA colloidal particles with different concentrations (0.25−1.5 wt %). All emulsions were prepared by homogenizing the mixture of 50 v % corn oil and 50 v % corresponding concentration particle suspensions. In brief, corn oil (5 mL) was added to the particle suspensions (5 mL) in a glass vial, and the resultant mixtures were sheared using an Ultra-Turrax T10 homogenizer (IKA-Works Inc., Germany) at 23000 rpm for 2 min at room temperature to yield Pickering emulsions.

Droplet Size Distribution of Emulsion. The oil droplet size distribution of emulsions was determined using a Malvern MasterSizer 3000 (Malvern Instruments Ltd., Worcestershire, UK). The samples were diluted with deionized water. The refractive indices of water and corn oil were taken as 1.33 and 1.52, respectively. Droplet size measurements were reported as the volume-average diameter, $d_{4,3} = \Sigma n_i d_i^4 \Sigma n_i d_i^3$, where n_i is the number of particles with diameter d_i. All of the experiments were performed in three replicates.

Confocal Laser Scanning Microscopy (CLSM). The microstructure of emulsions was observed with a Leica TCS SP5 confocal laser scanning microscope (Leica Microsystems Inc., Heidelberg, Germany). The emulsions were dyed with a mixed fluorescent dye solution consisting of 1 mg/mL Nile Red and 1 mg/mL Nile Blue A. The stained emulsions were placed on concave slides and covered with

DOI: 10.1021/acs.jafc.5b03113
J. Agric. Food Chem. 2015, 63, 7405−7414

coverslips. They were observed with a 100× oil immersion lens and an argon krypton laser having an excitation line of 488 nm and a helium neon laser (He/Ne) with excitation at 633 nm.

Rheology of Emulsion Gels. The dynamic oscillatory measurement of Pickering emulsion gels was performed at 25 °C with the frequency ranging from 1 to 10 rad/s (all of the measurements were conducted within the linear viscoelastic region), using a Haake RS600 rheometer (Thermo Electron Co., Waltham, MA, USA) between two parallel plates (d = 35 mm) with a gap of 1.0 mm. The elastic (G') and loss (G'') moduli as a function of the frequency were recorded. All of the experiments were performed in three replicates.

Statistics. Statistical analyses were performed using an analysis of variance (ANOVA) procedure of the SPSS 21.0 statistical analysis program, and the differences between means of the trials were detected by a least significant difference (LSD) test ($P \leq 0.05$).

RESULTS AND DISCUSSION

Preparation of Zein−TA Complex Colloidal Particles (ZTP). Compared with the traditional antisolvent approach that was used to fabricate zein colloidal particles,[18,19] we adopted a modified method to prepare ZTP. In brief, both zein and TA were dissolved in 70% (v/v) aqueous ethanol solution and heated to enhance their interaction, rather than directly diluting the aqueous ethanol solution of zein with TA aqueous solution. Heating can unravel some α-helical chain structures of zein by breaking hydrogen bonds, followed by realignment and reorganization into a β-sheet conformation.[21] It can be hypothesized that hydrogen bonds of α-helical structures and β-sheets may be broken during incubation, leading to the formation of random coils, which may provide complexation sites for TA to interact. The complexation sites are probably the carbonyl groups of the polypeptide, which hydrogen bond with the hydroxyl groups of the TA.[22] Due to the protonation, neutralization, and ionization of TA in solutions under varied pH, TA exhibited the capability to facilitate hydrogen-bonded interaction with macromolecules through pH-dependent regulation.[11,17] Therefore, the colloidal stability of ZTP was explored at pH 3.0, 5.0, and 7.0, respectively. Figure 1 shows the morphology and size distribution of ZTP formed at different pH values and TA concentrations (expressed as zein/TA ratio). Table 1 shows the mean size, polydispersity (PDI), and ζ-potential values of ZTP as a function of pH and zein/TA ratio. Unlike the ZTP prepared at pH 3.0 and 7.0, which showed severe aggregation, greater particle size (~200 nm, determined by FE-SEM), and multiple-modal size distribution (PDI ≈ 0.74, pH 3.0), the ZTP prepared at pH 5.0 with intermediate TA concentration (zein/TA wt/wt = 1:0.2) exhibited colloidal stable, nanosized (~99 nm), and nearly monodisperse size distribution (PDI ≈ 0.11). FE-SEM images (Figure 1C,D) further confirmed that the particles formed at pH 5.0 were relatively small and well dispersed, whereas ZTP particles formed at pH 7.0 were aggregated clusters. The ZTP prepared at pH 5.0 with zein/TA ratios of 1:0.2 actually possessed much higher ζ-potential (about +51 mV), which contributed to the strong electrostatic repulsion among particles. However, when the zein/TA ratio was increased from 1:0.3 to 1:0.5, the ζ-potential of ZTP declined to +35 mV and the particle dispersions became unstable (Figure 1B; Table 1), indicating that the excess TA resulted in the aggregation and complex precipitation of ZTP. Moreover, the ζ-potentials of TA colloidal particles (prepared via an antisolvent precipitation technique stated under Materials and Methods; TA concentration in ethanol aqueous of 5 mg/mL) prepared at pH 3.0, 5.0, and 7.0 and finally adjusted to a pH of 3.5 were +9.32, −2.67, and −4.26 mV (data not shown), respectively.

Zein is positively charged below its isoelectric point (pI 6.2).[23] After the antisolvent and evaporation procedure, the pH of the ZTP dispersion decreased from pH 5.0 to 3.48 (data not shown). The protonation of zein at such a pH resulted in a strong positive surface charge on colloidal particles (about +51 mV); thus, this long-range electrostatic repulsion was able to stabilize zein in water, which was its poor solvent.[17] However, the final pH of ZTP formed at pH 3.0 was much lower (about 2.85; data not shown), and these particles had lower surface charge (+33 mV), leading to colloidal instability and precipitation. Recently, Kharlampieva and co-workers[11,24] studied the TA−poly(*N*-vinylpyrrolidone) (TA−PVPON) multilayer microcapsules formed at pH 5.0 and 7.4, respectively. They found that TA was in its neutral and partially protonated form at pH 5.0, and this facilitated strong hydrogen-bonding interactions between the hydroxyl groups on TA and the carbonyl groups on the pyrrolidone rings in PVPON. This complexation further suppressed the ionization of TA, resulting in the improvement of their drug encapsulation and long-term storage.[11,24] In a similar way, hydrogen-bonding interaction between protonated TA and zein might dominate in the ZTP formed at pH 5.0. At pH 3.0 and 7.0, TA was in partial ionization of hydroxyl groups, leading to the formation of electrostatic complexes with low surface charge and unstable colloidal dispersions.

The interfacial wettability of the particles plays a crucial role for the preparation of emulsions stabilized by particles or Pickering emulsions. The near-neutral wettability (θ_{ow} ~ 90°) can facilitate efficient packing of particles at the oil−water interface and create a steric barrier against the coalescence of oil droplets. The wettability of the zein particles had been successfully modified by ionic surfactant, sodium stearate, via hydrophobic interaction[18] or by a positively charged polysaccharide, chitosan, via weak electrostatic interaction,[19] as we reported previously. In this study we tried to tune the wettability of zein particles via modulating the hydrogen-bonding interaction between TA and zein. Figure 2 shows typical images of water droplets deposited to zein films immersed in corn oil. The wettability of zein particles expressed as oil-in-water three-phase contact angles (θ_{ow}) was calculated,[19] which is shown in the insets of Figure 2. The θ_{ow} of bare zein particles formed at pH 5.0 was around 107.13°, which was consistent with our previous result (θ_{ow} ~ 112.7°).[19] These particles actually did not favor interfacial particle adsorption and formation of oil-in-water Pickering emulsion. The ZTP

Table 1. Mean Size, PDI, and ζ-Potential of ZTP Prepared under Varied pH and Zein/TA Ratios[a]

sample	mean size (nm)	PDI	mean ζ-potential (mV)
pH (zein/TA (w/w) = 1:0.2)			
3.0	249.45 ± 12.95a	0.74 ± 0.05a	33.35 ± 1.65b
5.0	99.12 ± 0.37c	0.11 ± 0.00b	51.50 ± 0.50a
7.0	148.75 ± 5.65b	0.14 ± 0.00b	33.05 ± 0.15b
zein/TA (w/w) (pH 5.0)			
1:0.0	96.27 ± 0.87c	0.09 ± 0.01c	57.10 ± 3.10a
1:0.1	109.00 ± 1.20b	0.15 ± 0.03b	56.90 ± 1.50a
1:0.2	99.12 ± 0.37bc	0.11 ± 0.00bc	51.50 ± 0.50ab
1:0.3	103.80 ± 1.00bc	0.16 ± 0.01b	49.35 ± 1.55b
1:0.5	202.95 ± 7.05a	0.57 ± 0.01a	35.55 ± 0.45c

[a]Mean values in table followed by different lower case letters are significantly different at $P \leq 0.05$ by Duncan's multiple-range tests.

DOI: 10.1021/acs.jafc.5b03113
J. Agric. Food Chem. 2015, 63, 7405−7414

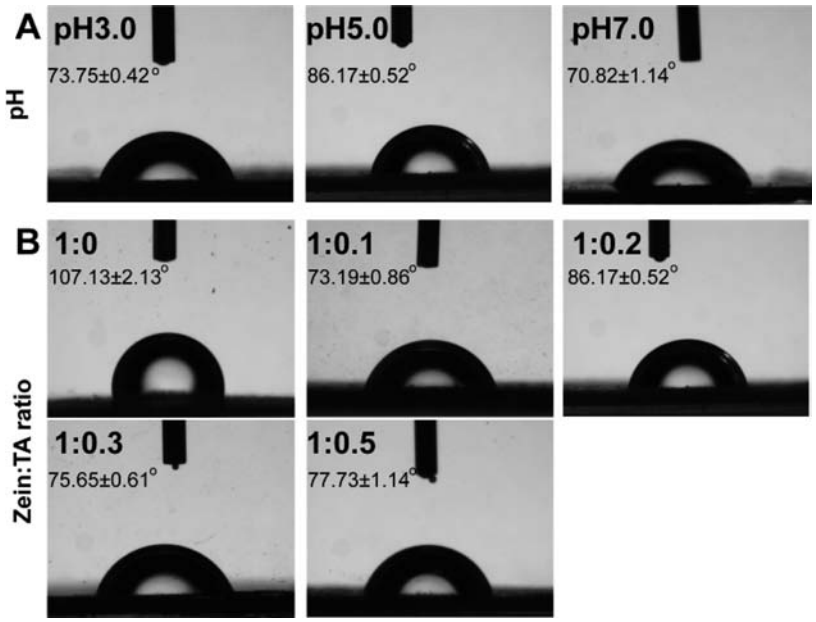

Figure 2. Oil-in-water three-phase contact angles (θ_{ow}) of zein particles with different pH values and TA concentrations: (A) ZTP prepared at different pH values with the same zein/TA ratio of 1:0.2 (w/w); (B) ZTP prepared at pH 5.0 with different zein/TA ratios. θ_{ow} values (insets) were determined for corn oil phases.

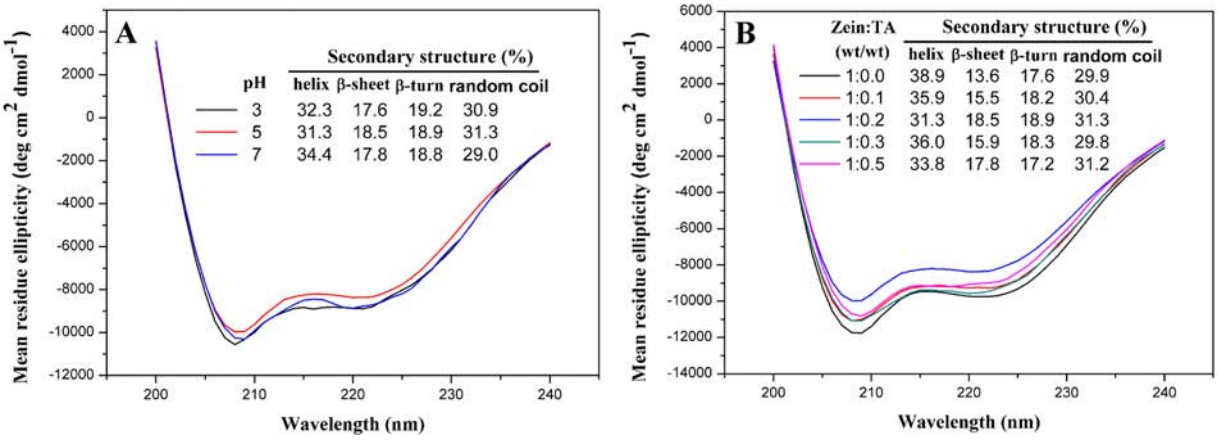

Figure 3. CD spectra of zein in 70% (v/v) aqueous ethanol with different pH values (A) and TA concentrations: (A) with different pH at the same zein/TA ratio of 1:0.2 (w/w); (B) with different zein/TA ratios at pH 5.0. (Insets) Fractional contents of the secondary structure in zein after heat treatment.

formed at pH 3.0 and 7.0 as well as at pH 5.0 with excess TA concentrations (zein/TA ratios of 1:0.3−1:0.5) had much lower θ_{ow} (70−77°) and surface charge (+30 mV) concurrently. These implied that the excess TA and ionization of TA facilitated the formation of electrostatic complexes. In contrast, the ZTP formed at pH 5.0 with a zein/TA ratio of 1:0.2 had near-neutral wettability ($\theta_{ow} \sim 86°$) without decreasing their surface charge significantly, suggesting that this ZTP could be utilized to yield stable Pickering emulsion. These interactions might be dominated by hydrogen bonding between the carbonyl moieties of zein and the hydroxyl groups of the neutral TA at acidic pH and caused an increase in the hydroxyl groups at the surface of zein particles, thereby lessening their hydrophobic characteristics.

Structure Characterization of Zein/TA Complexes and Particles. The structure and conformation of α-zein in various solutions had been extensively studied.[25−27] The consensus is that α-zein in aqueous ethanol solution exists as an extended oblong structure with an axial ratio of 6:1−12:1, which was evidenced by SAXS experiments.[25,27] The extended configuration of zein in protic solvents could provide increased accessibility to the reactive sites of protein for TA, thus modifying their functionality. The secondary structure of zein in 70% (v/v) aqueous ethanol was monitored in the far-ultraviolet (UV) region. The CD profiles of zein with different pH values and TA concentrations are shown in Figure 3. The fractional contents of secondary structure (α-helix, β-sheet, β-turn, and random coil) of zein were calculated, and they are shown in the insets of Figure 3. First, because the CD spectrum of TA was almost the same as that of the buffer (70:30 v/v ethanol/water solutions), TA did not have its own CD pattern to interfere with zein (data not shown). The CD spectra of zein exhibited the characteristics of α-helix with two strong negative ellipticity values at around 208 and 222 nm. CD ellipticity at 222 nm has been widely used to estimate α-helix content in proteins.[27] Compared to the complexes at pH 5.0, a slight

DOI: 10.1021/acs.jafc.5b03113
J. Agric. Food Chem. 2015, 63, 7405−7414

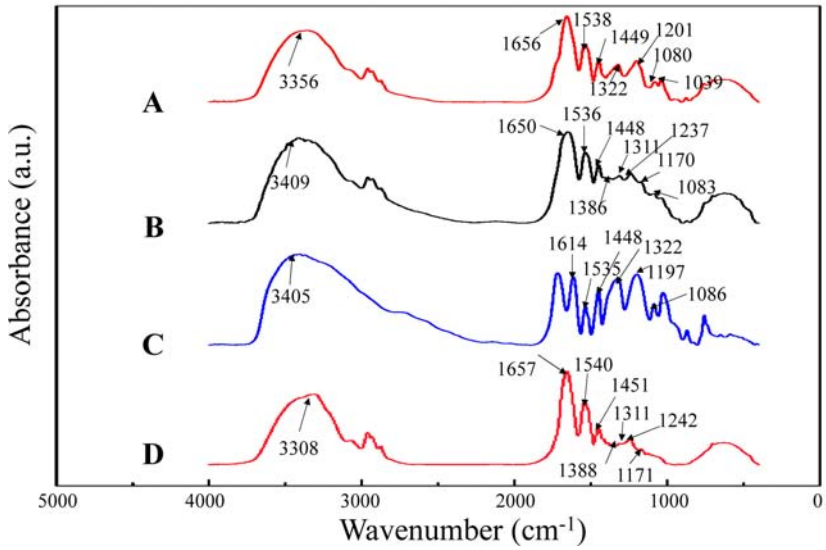

Figure 4. FTIR spectra of zein/TA complex colloidal particle (prepared at pH 5.0 with a zein/TA ratio of 1:0.2) (A), zein/TA physical mixture (mixed the zein and TA powder with a zein/TA ratio of 1:0.2) (B), TA (C), and zein particle (D).

Table 2. Structural Parameters of Zein−TA Complex in 70% (v/v) Aqueous Ethanol Obtained by SAXS[a]

	pH (zein/TA = 1:0.2 w/w)			zein/TA (w/w, pH 5.0)				
	3.0	5.0	7.0	1:0.0	1:0.1	1:0.2	1:0.3	1:0.5
R_g (nm)	2.50	3.25	5.63	2.90	2.24	3.25	2.35	2.17
a (nm)	8.66	11.25	19.50	10.03	7.76	11.25	8.15	7.61
$I(0)$	0.45	0.67	1.01	0.52	0.38	0.67	0.42	0.45

[a] R_g, overall radius of gyration of zein; a, longest edge in an elongated rectangular prism, which approximates the asymmetric particles of zein; $I(0)$, extrapolation of intensity to an angle of zero.

increase of α-helix content and decrease of β-sheet for zein/TA complexes at pH 3.0 and 7.0 were observed, but the difference was not significant (Figure 3A). Cabra et al.[21] found that the secondary structure of zein in aqueous ethanol solutions strongly depended on the pH on the basis of CD measurements. It was also shown that the α-helix and β-sheet contents at pH 5.0 were around 33 and 12%, which were similar to our results. Huang and co-workers[27] compared the dissolution behavior of α-zein in aqueous ethanol with that in acetic acid solutions by SAXS, which indicated that the protonation of acetic acid imposed on zein. The positive surface charges of zein and reduction of hydrophobic interaction with the presence of the acetate solvation layer, which was able to provide long-range electrostatic repulsion, enhanced the solution stability of zein. As a weak acid, TA completely protonates and ionizes at pH 3.0 and 7.0, respectively.[11] Therefore, the increase of α-helix content at pH 3.0 and 7.0 might contribute to the formation of electrostatic complexes between zein and protonated or ionized TA.

Figure 3B clearly shows evidence for a conformational change of zein in aqueous ethanol solution that was induced by TA binding. It can be seen that binding of TA causes an obvious transformation from α-helix to β-sheet configuration of zein at pH 5.0, and the greatest shift generated on the zein−TA complexes with intermediate TA concentration (a zein/TA ratio of 1:0.2). The protein interaction with polyphenol driven by hydrophobic attraction and enhanced with hydrogen-bonding network had been well confirmed.[28] The interaction between milk β-lactoglobulin (β-LG)[29] and tea tannins (epigallocatechin gallate, EGCG) was studied in detail,[27] which indicated that the β-LG conformation was altered in the presence of EGCG with an increase in β-sheet and α-helix, which helped to enhance the structural stabilization of protein. The conformational change of zein due to the TA binding is dependent on the TA concentration. When the zein/TA ratio was increased to 1:0.3−1:0.5, the fractional contents of the secondary structure in zein were close to that of pure zein (Figure 4B), implying that the binding model of zein and TA would be changed. Recent findings indicated that for native unfolded protein, such as β-casein[30] and PRP,[15] interactions with tannin were dependent on the colloidal state and the concentration of tannins. Small tannins below their CMC generate a conformational change of the protein surrounding or "wrapping" the tannins. However, larger tannins with high concentration led to aggregation and complex precipitation by a bridging effect. Zein, which is a proline-rich protein, adopts an extended and flexible conformation in aqueous ethanol solution,[21,27] and its binding with TA might comply with the similar model.

SAXS experiments suggested that α-zein in aqueous ethanol solution existed as an extended oblong structure with an axial ratio of 6:1.[27] In this study, SAXS was used to monitor the possible changes of the contour structure of zein in aqueous ethanol with TA binding. On the basis of Guinier plots for the oblong structure of zein, the structural parameters, including overall gyration radius (R_g), the longest edge in an elongated particle (a), and the extrapolation of intensity to an angle of zero $I(0)$ of zein, were calculated and are shown in Table 2. It was noteworthy that there was a little difference in R_g and $I(0)$ values of zein/TA complexes when compared with those of

DOI: 10.1021/acs.jafc.5b03113
J. Agric. Food Chem. 2015, 63, 7405−7414

pure zein. R_g values of zein in all ethanol solutions at pH 5.0 with different zein/TA ratios are between 2.17 and 3.25 nm, which were equal to or even less than that of pure zein (2.90 nm), indicating that the TA binding at pH 5.0 did not disturb the contour structure of zein in aqueous ethanol, although small changes were recorded in its secondary structure (Figure 3). A similar result was observed for β-casein.[30] Small tannins could increase the number of proteins per micelle without changing their size, leading to compaction of micelles. In the case of pH 7.0, the R_g and a values of zein/TA complexes increased significantly. They were nearly twice greater than those of the ZTP prepared at pH 3.0 and 5.0, indicating the formation of complex aggregates. This might explain why the ZTP formed at pH 7.0 was larger than that formed at pH 5.0 (Figure 1; Table 1).

FTIR spectra of zein colloidal particles, which were used to characterize the noncovalent interaction of zein and TA, are shown in Figure 4. The absorption peak at 3308 cm^{-1} is assigned to the N—H stretching vibration of the amide I from zein, whereas the absorptions at 1657 and 1540 cm^{-1} are attributed to C═O of amide I and C—N—H of amide II of zein, respectively (Figure 4D).[31] Wide bands in the range of 3600−3100 cm^{-1} are attributed to O—H stretching of the phenolic or hydroxyl group of TA (Figure 4C).[32,33] Both C═O and N—H bonds were involved in the hydrogen bonding between different elements contributing to the secondary structure of zein. For ZTP (Figure 4A), the absorption at 1657 cm^{-1} related to the C═O bond (amide I) of zein overlapped the TA band at 1614 cm^{-1} (aromatic C═O bonds). Therefore, only a single band at 1656 cm^{-1} was observed, and the new component at 3356 cm^{-1} appeared. Collectively, the results revealed the hydrogen-bonding interaction in nature for the zein/TA complex colloidal particles. For the zein/TA physical mixture (mixture of the zein and TA powder with a zein/TA ratio of 1:0.2), the absorbance peaks at 1386, 1311, 1237, and 1170 cm^{-1} were almost similar to those of the zein particle and the peaks at 1448 and 869 cm^{-1} were similar to those of TA, but all peaks above were significantly different from those of the ZTP. Moreover, the range below 1500 cm^{-1} is significant for deformation, bending, and ring vibrations, which can be very specific for a substance or for different types of substitution; thus, this range is frequently referred to as the "fingerprint region" of a spectrum.[34]

Pickering Emulsions and Gels Prepared by ZTP. As shown in Figure 5, Pickering emulsions prepared by using bare zein colloidal particle and ZTP (prepared at pH 5.0) as stabilizers were compared in terms of storage stability. The bare zein colloidal particle was actually not a good emulsifier for Pickering emulsions, which showed severe aggregation and oil release on the top phase of fresh emulsions. In contrast, the emulsions stabilized by ZTP showed no sign of oil separation even after 30 days of storage. Actually, these emulsions immediately transformed from the liquid state to the solid state and exhibited arrested dynamics. This further contributed to the long-term stabilization action (Figure 5). Interestingly, it could be seen that the emulsion stabilized by ZTP with relatively low particle volume fractions (0.25−1.0 wt %/v) showed creaming and serum release, but significant increase of the serum in the bottom phase was not observed in the prolonged 30 days of storage, which had been observed in typical Pickering emulsion stabilized by zein/chitosan particles (ZCP).[23] Nevertheless, emulsions prepared with high particle fractions (1.0−1.5 wt %/v) exhibited homogeneous gels

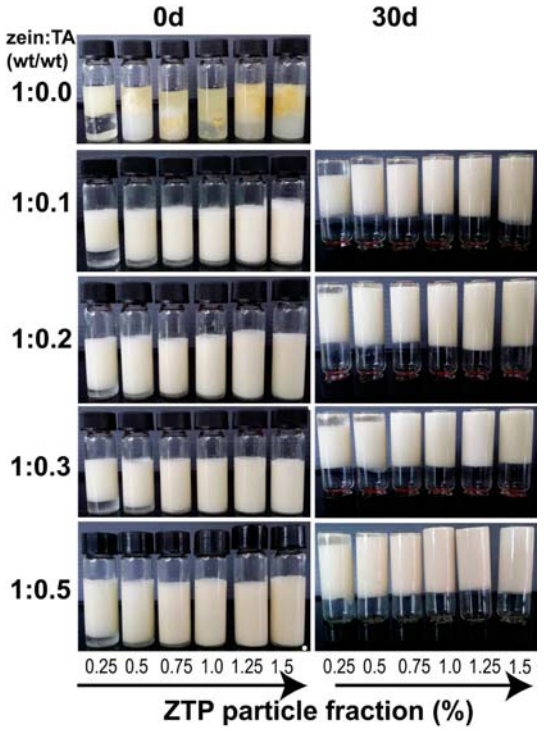

Figure 5. Visual observation of fresh emulsion gels prepared by ZTP with varied zein/TA ratios by different particle concentrations (0.25−1.5%, w/v) for fresh (0 days) and 30 days of storage. ZTP was prepared at pH 5.0.

without creaming and phase separation after 30 days of storage. These homogeneous emulsion gels are remarkable given the formation of protein continuous networks.

CLSM was used to characterize the microstructure of emulsions prepared with ZTP by different particle fractions, and the obtained images are shown in Figure 6. Droplets were rendered visible by the fluorescent protein particles (labeled in red) that covered the oil droplets (labeled in green). For the emulsions stabilized solely by zein particles, few protein molecules were absorbed around the oil droplets. In contrast, the interfacial protein network around the oil droplets was

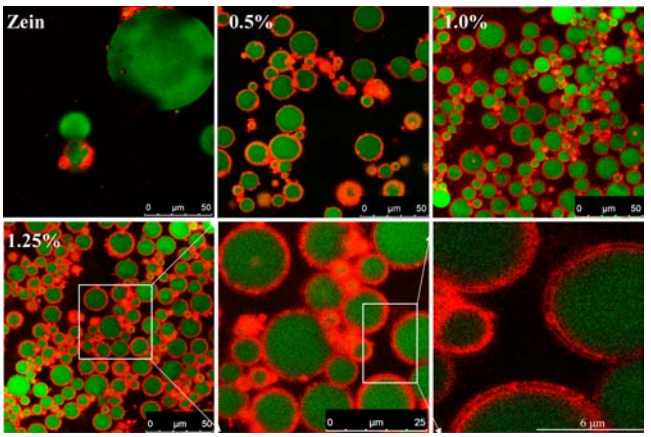

Figure 6. CLSM images of the emulsions stabilized by pure zein colloidal particles (1.5% w/v) and ZTP with different particles contents (0.5, 1.0, and 1.25% w/v). Protein was stained red and the oil phase, green. ZTP was prepared at pH 5.0 with a zein/TA ratio of 1:0.2.

DOI: 10.1021/acs.jafc.5b03113
J. Agric. Food Chem. 2015, 63, 7405−7414

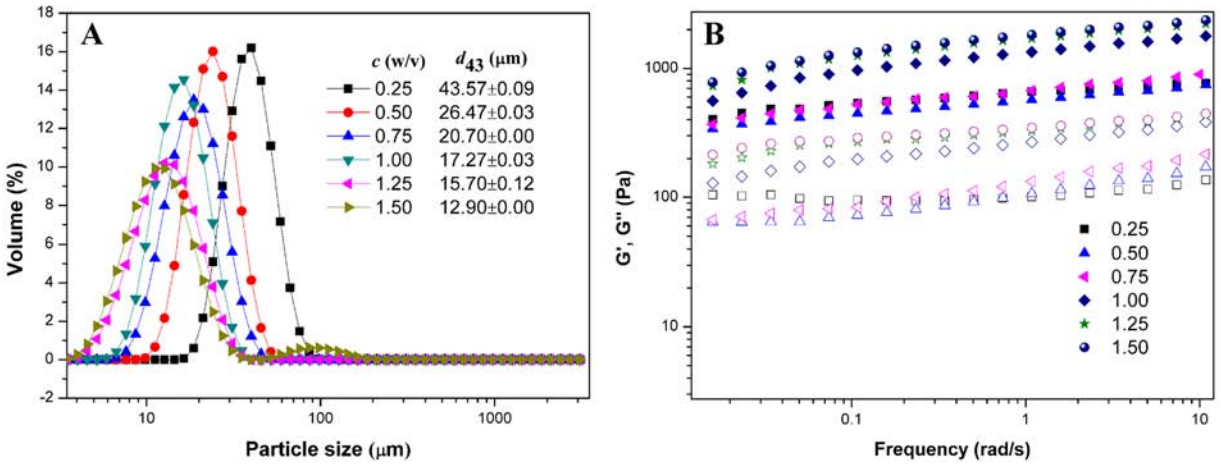

Figure 7. Droplet size distribution profiles (A) and rheological property (B) of Pickering emulsion gels prepared by ZTP with different particle fractions: storage moduli, G' (solid symbols) and loss moduli, G'' (open symbols). ZTP was prepared at pH 5.0 with a zein/TA ratio of 1:0.2.

found in the emulsions stabilized by ZTP, confirming the formation of an oil-in-water (O/W) Pickering emulsion. Furthermore, higher magnification confocal images clearly showed that the multilayer interfacial architecture was formed on the oil−water surface. These microstructures were typically hierarchical, which probably arose from the predominantly LbL assembly behavior of zein particles and TA.[24,35] We previously found that the ZCP could facilitate the formation of particle-based interfacial network architecture, and the ultrastable Pickering emulsions finally formed. However, to the best of our knowledge, this was the first observation of this ordered morphological signature on the oil−water interface, which implied a possibility to fabricate hierarchical interface microstructure via modulation of the noncovalent interaction between hydrophobic protein and natural polyphenol.

The droplet size distributions and the mean droplet diameter (d_{43}) for emulsions stabilized by ZTP were measured to assess the emulsifying ability and physical stability, which are shown in Figure 7A. The oil droplets in fresh emulsions prepared with ZTP had approximately uniform size with a very narrow peak in their distribution, which remained unchanged even after 30 days of storage, confirming their long-term storage stability against coalescence (data not shown). In addition, the mean droplet diameter (d_{43}) showed the particle fraction-dependent behavior. It decreased with increase of the ZTP fraction. This behavior was further supported by the CLSM observation (Figure 6). We believe these results can be attributed to the competition for surface space of oil droplets with more surface-active TA micelles. As a hydrolyzed tannin, TA is actually an amphiphilic polyphenol, which can self-assemble to form micelles when their concentration is above the CMC (about 10 mM for hydrolyzed tannins).[15,36] Accordingly, TA might form micelles with high ZTP fractions, resulting in interfacial particle displacement, and, consequently, decrease the size of oil droplets. Our previous findings showed that the amphiphilic stevioside (STE) micelles, competitively adsorbed on the oil−water interface with soy protein isolate (SPI), formed a mixed interfacial layer, resulting in a decrease in particle size and evident enhancement in the physical stability of SPI-based emulsions.[6] Moreover, the emulsion stabilized with zein alone showed oil release on the top phase, which was not suitable to evaluate the diameter, so we did not show its diameter.

There are two kinds of protein-based emulsion gels. One is emulsion-filled protein gel, in which oil droplets act as filler particles incorporated in the continuous protein network. The other is protein-stabilized emulsion gels or particulate gels in which protein molecules on the surface connect together and form a network. Both of these two types have totally different rheological behaviors.[37] We therefore investigated the rheological properties of the Pickering emulsion gels, which are presented in Figure 7B using frequency sweep tests. In all cases, the storage modulus (G') slightly but progressively increased with the increase of particle fractions, indicating their noncovalent "physical" cross-links in nature.[37] The increased intermolecular noncovalent cross-links among ZTP particles strengthened the gel network. The G' of emulsion gels with low particle fraction (0.25−0.75% w/v) showed less frequency dependence, which was the hallmark of particulate gels,[38] whereas the G' of the emulsion gels with high particle fraction (1.0−1.5% w/v) showed more frequency dependence. Hence, it can be concluded that the shift of gelling model from particulate gels to protein-based emulsion gels occurs with the increase of the colloidal particle loading, which involves cross-linking of the continuous phase. The enhanced reactivity of ZTP was due to the complexation of zein and TA, and it would be a key to explain the formation of Pickering emulsion gels. At high particle fractions, excess ZTP might trigger cross-links via hydrogen-bonded interaction and form a continuous network among and around the well-dispersed oil droplets (as active filler particles), leading to the formation of strong emulsion gels.

DISCUSSION

The novel colloidal structure, which is based on food-grade materials and formed via modulation of noncovalent interactions, has emerged with potential as a functional ingredient for the formulation and delivery of bioactive molecules or enhancement in the functionality of food biopolymers.[1,2] In this study the novel zein/TA complex colloidal particle (ZTP) based on the antisolvent approach and the hydrogen-bonding interaction between zein and TA was successfully generated. These complex colloidal particles with tuned wettability and enhanced interfacial reactivity can be utilized for the preparation of stable Pickering emulsions gels by one-step homogenization. To better understand the underlying mech-

DOI: 10.1021/acs.jafc.5b03113
J. Agric. Food Chem. 2015, 63, 7405−7414

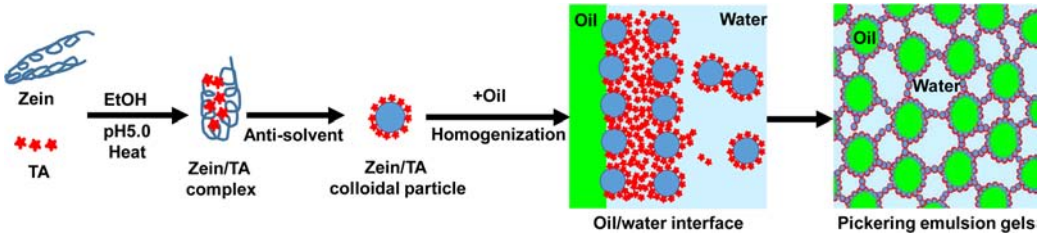

Figure 8. Schematic mechanism for the formation of the Pickering emulsions gels prepared with zein/TA complex colloidal particles.

anism of ZTP-stabilized Pickering emulsion gels, we propose a schematic illustration to explain the formation pathway of Pickering emulsion gels, shown in Figure 8.

The protonation and ionization of TA are both critical to understanding the colloidal behavior with protein,[11,24] which can be modulated efficiently via changing the pH and ionic strength of the solution. Furthermore, the colloidal state of TA affects the nature of their interaction with proteins,[15,39] especially for proline-rich proteins such as zein. Zein adopted an extended configuration in aqueous ethanol solution,[25,27] which exhibited a different tannin binding model compared with compacted protein in aqueous solution. TA in the neutral and partially protonated form at pH 5.0 with intermediate TA concentration facilitated strong hydrogen-bonding interactions between the hydroxyl groups on TA and the carbonyl moieties on the pyrrolidone rings of the proline-rich domain in zein. This specific interaction generated a conformational change of zein without altering their supramolecular structure (Figure 3; Table 2). The TA binding consequently affected the self-assembly behavior of zein during the antisolvent process, leading to the formation of zein colloidal particles that were coated or "wrapped" by TA (Figure 8). This complexation further suppressed the ionization of TA,[11] and it caused an increase in the hydroxyl group on the surface of zein particles at acidic pH (~3.48), thereby lessening their hydrophobic characteristics without decreasing surface charge (+51 mV) significantly (Table 1). The hydrogen-bonded zein/TA complex colloidal particle, evidenced by FTIR, with near-neutral wettability (Figure 2) and enhanced reactivity (due to the neutral TA coating), was capable of facilitating the multilayer interfacial architecture on the oil−water surface of the oil droplets (Figure 6), resulting in the formation of Pickering emulsion. In addition, the hydrogen-bonding interaction further triggered cross-links between the colloidal particles to form a continuous network among and around the oil droplets, leading to the formation of stable Pickering emulsion gels.

In conclusion, stable colloidal particles with near-neutral wettability and high interfacial reactivity, which is fabricated by modulating the noncovalent interactions between small molecules (TA) and macromolecules (zein), can be used as building blocks with reaction activity to form novel edible Pickering emulsion gels with orderly interfacial architecture. This study implies a possibility to fabricate hierarchical interface microstructure via modulation of the noncovalent interaction between hydrophobic protein and natural polyphenol.

AUTHOR INFORMATION

Corresponding Author

*(X.-Q.Y.) Phone: +86 20 87114262. Fax: +86 20 87114263. E-mail: fexqyang@scut.edu.cn, fexqyang@163.com.

Funding

This research was supported by grants from the Special Fund for Agro-scientific Research in the Public Interest (Grant 201303071), the Chinese National Natural Science Foundation (No. 31371744, 21406077), and the Project of National Key Technology Research and Development Program for the National High Technology Research and Development Program of China (863 Program: 2013AA102208).

Notes

The authors declare no competing financial interest.

REFERENCES

(1) McClements, D. J.; Decker, E. A.; Park, Y.; Weiss, J. Structural design principles for delivery of bioactive components in nutraceuticals and functional foods. *Crit. Rev. Food Sci. Nutr.* **2009**, *49*, 577−606.

(2) Patel, A.; Velikov, K. P. Colloidal delivery systems in foods: a general comparison with oral drug delivery. *LWT-Food Sci. Technol.* **2011**, *44*, 1958−1964.

(3) Wan, Z. L.; Wang, L. Y.; Wang, J. M.; Yuan, Y.; Yang, X. Q. Synergistic foaming and surface properties of a weakly interacting mixture of soy glycinin and biosurfactant stevioside. *J. Agric. Food Chem.* **2014**, *62*, 6834−6843.

(4) Patel, A. R.; ten-Hoorn, J. S.; Hazekamp, J.; Blijdenstein, T. B.; Velikov, K. P. Colloidal complexation of a macromolecule with a small molecular weight natural polyphenol: implications in modulating polymer functionalities. *Soft Matter* **2013**, *9*, 1428−1436.

(5) Patel, A. R.; Seijen-ten-Hoorn, J.; Heussen, P. C.; Drost, E.; Hazekamp, J.; Velikov, K. P. Straightforward preparation of organic colloidal particles by harnessing spontaneous non-covalent interactions of active molecules from natural origin. *J. Colloid Interface Sci.* **2012**, *374*, 150−156.

(6) Wan, Z. L.; Wang, L. Y.; Wang, J. M.; Zhou, Q.; Yuan, Y.; Yang, X. Q. Synergistic interfacial properties of soy protein-stevioside mixtures: relationship to emulsion stability. *Food Hydrocolloids* **2014**, *39*, 127−135.

(7) Van Buren, J. P.; Robinson, W. B. Formation of complexes between protein and tannic acid. *J. Agric. Food Chem.* **1969**, *17*, 772−777.

(8) Kim, T.; Silva, J.; Kim, M.; Jung, Y. Enhanced antioxidant capacity and antimicrobial activity of tannic acid by thermal processing. *Food Chem.* **2010**, *118*, 740−746.

(9) Nakashima, H.; Murakami, T.; Yamamoto, N.; Sakagami, H.; Tanuma, S.-i.; Hatano, T.; Yoshida, T.; Okuda, T. Inhibition of human immunodeficiency viral replication by tannins and related compounds. *Antiviral Res.* **1992**, *18*, 91−103.

(10) Taylor, J.; Bean, S. R.; Ioerger, B. P.; Taylor, J. R. Preferential binding of sorghum tannins with γ-kafirin and the influence of tannin binding on kafirin digestibility and biodegradation. *J. Cereal Sci.* **2007**, *46*, 22−31.

(11) Liu, F.; Kozlovskaya, V.; Zavgorodnya, O.; Martinez-Lopez, C.; Catledge, S.; Kharlampieva, E. Encapsulation of anticancer drug by hydrogen-bonded multilayers of tannic acid. *Soft Matter* **2014**, *10*, 9237−9247.

(12) Zanchi, D.; Poulain, C.; Konarev, P.; Tribet, C.; Svergun, D. Colloidal stability of tannins: astringency, wine tasting and beyond. *J. Phys.: Condens. Matter* **2008**, *20*, 494224.

DOI: 10.1021/acs.jafc.5b03113
J. Agric. Food Chem. 2015, 63, 7405−7414

(13) Siebert, K. J.; Troukhanova, N. V.; Lynn, P. Y. Nature of polyphenol-protein interactions. *J. Agric. Food Chem.* **1996**, *44*, 80−85.
(14) Emmambux, M.; Stading, M.; Taylor, J. Sorghum kafirin film property modification with hydrolysable and condensed tannins. *J. Cereal Sci.* **2004**, *40*, 127−135.
(15) Cala, O.; Dufourc, E. J.; Fouquet, E.; Manigand, C.; Laguerre, M.; Pianet, I. The colloidal state of tannins impacts the nature of their interaction with proteins: the case of salivary proline-rich protein/procyanidins binding. *Langmuir* **2012**, *28*, 17410−17418.
(16) Berton-Carabin, C. C.; Schroen, K. Pickering emulsions for food applications: background, trends, and challenges. *Annu. Rev. Food Sci. Technol.* **2015**, *6*, 263−97.
(17) de Folter, J. W.; van Ruijven, M. W.; Velikov, K. P. Oil-in-water Pickering emulsions stabilized by colloidal particles from the water-insoluble protein zein. *Soft Matter* **2012**, *8*, 6807−6815.
(18) Gao, Z. M.; Yang, X. Q.; Wu, N. N.; Wang, L. J.; Wang, J. M.; Guo, J.; Yin, S. W. Protein-based Pickering emulsion and oil gel prepared by complexes of zein colloidal particles and stearate. *J. Agric. Food Chem.* **2014**, *62*, 2672−2678.
(19) Wang, L. J.; Hu, Y. Q.; Yin, S. W.; Yang, X. Q.; Lai, F. R.; Wang, S. Q. Fabrication and characterization of antioxidant Pickering emulsions stabilized by zein/chitosan complex particles (ZCPs). *J. Agric. Food Chem.* **2015**, *63*, 2514−2524 20..
(20) Matsushima, N.; Danno, G.-i.; Takezawa, H.; Izumi, Y. Three-dimensional structure of maize α-zein proteins studied by small-angle X-ray scattering. *Biochim. Biophys. Acta, Protein Struct. Mol. Enzymol.* **1997**, *1339*, 14−22.
(21) Cabra, V.; Arreguin, R.; Vazquez-Duhalt, R.; Farres, A. Effect of temperature and pH on the secondary structure and processes of oligomerization of 19 kDa alpha-zein. *Biochim. Biophys. Acta, Proteins Proteomics* **2006**, *1764*, 1110−1118.
(22) Byaruhanga, Y. B.; Emmambux, M. N.; Belton, P. S.; Wellner, N.; Ng, K. G.; Taylor, J. R. N. Alteration of kafirin and kafirin film structure by heating with microwave energy and tannin complexation. *J. Agric. Food Chem.* **2006**, *54*, 4198−4207.
(23) Shukla, R.; Cheryan, M. Zein: the industrial protein from corn. *Ind. Crops Prod.* **2001**, *13*, 171−192.
(24) Kozlovskaya, V.; Kharlampieva, E.; Drachuk, I.; Cheng, D.; Tsukruk, V. V. Responsive microcapsule reactors based on hydrogen-bonded tannic acid layer-by-layer assemblies. *Soft Matter* **2010**, *6*, 3596−3608.
(25) Momany, F. A.; Sessa, D. J.; Lawton, J. W.; Selling, G. W.; Hamaker, S. A.; Willett, J. L. Structural characterization of α-zein. *J. Agric. Food Chem.* **2006**, *54*, 543−547.
(26) Forato, L. A.; Doriguetto, A. C.; Fischer, H.; Mascarenhas, Y. P.; Craievich, A. F.; Colnago, L. A. Conformation of the Z19 prolamin by FTIR, NMR, and SAXS. *J. Agric. Food Chem.* **2004**, *52*, 2382−2385.
(27) Li, Y.; Li, J.; Xia, Q.; Zhang, B.; Wang, Q.; Huang, Q. Understanding the dissolution of α-zein in aqueous ethanol and acetic acid solutions. *J. Phys. Chem. B* **2012**, *116*, 12057−12064.
(28) Haslam, E. Polyphenol-protein interactions. *Biochem. J.* **1974**, *139*, 285−288.
(29) Kanakis, C.; Hasni, I.; Bourassa, P.; Tarantilis, P.; Polissiou, M.; Tajmir-Riahi, H. A. Milk β-lactoglobulin complexes with tea polyphenols. *Food Chem.* **2011**, *127*, 1046−1055.
(30) Zanchi, D.; Narayanan, T.; Hagenmuller, D.; Baron, A.; Guyot, S.; Cabane, B.; Bouhallab, S. Tannin-assisted aggregation of natively unfolded proteins. *EPL* **2008**, *82*, 58001.
(31) Forato, L. A.; Bicudo, T. D. C.; Colnago, L. A. Conformation of α zeins in solid state by Fourier transform IR. *Biopolymers* **2003**, *72*, 421−426.
(32) Pantoja-Castro, M. A.; González-Rodríguez, H. Study by infrared spectroscopy and thermogravimetric analysis of tannins and tannic acid. *Rev. Latinoam. Quim.* **2011**, *39*, 107−112.
(33) Erdem, P.; Bursali, E. A.; Yurdakoc, M. Preparation and characterization of tannic acid resin: study of boron adsorption. *Environ. Prog. Sustainable Energy* **2013**, *32*, 1036−1044.
(34) Schmitt, J.; Flemming, H.-C. FTIR-spectroscopy in microbial and material analysis. *Int. Biodeterior. Biodegrad.* **1998**, *41*, 1−11.
(35) Kim, B. S.; Lee, H.-i.; Min, Y.; Poon, Z.; Hammond, P. T. Hydrogen-bonded multilayer of pH-responsive polymeric micelles with tannic acid for surface drug delivery. *Chem. Commun.* **2009**, 4194−4196.
(36) Pianet, I.; André, Y.; Ducasse, M.-A.; Tarascou, I.; Lartigue, J.-C.; Pinaud, N. L.; Fouquet, E.; Dufourc, E. J.; Laguerre, M. Modeling procyanidin self-association processes and understanding their micellar organization: a study by diffusion NMR and molecular mechanics. *Langmuir* **2008**, *24*, 11027−11035.
(37) Dickinson, E. Emulsion gels: the structuring of soft solids with protein-stabilized oil droplets. *Food Hydrocolloids* **2012**, *28*, 224−241.
(38) Lee, M. N.; Chan, H. K.; Mohraz, A. Characteristics of Pickering emulsion gels formed by droplet bridging. *Langmuir* **2012**, *28*, 3085−3091.
(39) Ma, W.; Baron, A.; Guyot, S.; Bouhallab, S.; Zanchi, D. Kinetics of the formation of β-casein/tannin mixed micelles. *RSC Adv.* **2012**, *2*, 3934−3941.

DOI: 10.1021/acs.jafc.5b03113
J. Agric. Food Chem. 2015, 63, 7405−7414

ethanol, the reaction between cyanate and ethanol was studied as a model. Therefore, herein we describe the kinetic aspects of this reaction and use density functional theory (DFT) calculations to discuss potential mechanistic pathways.

MATERIALS AND METHODS

Reagents. The reagents and solvents used were of analytical or chromatographic grade and were purchased from Sigma-Aldrich (Steinheim, Germany), Mallinckrodt Baker (Paris, KY, USA), and Carlo Erba (Milano, Italy). The water used was previously distilled and then deionized using a Milli-Q system (Millipore, Bedford, MA, USA).

Reference Cachaça. One commercial, nonaged cachaça sample (200 L), which was provided and certified by a major producer, was used as a model (reference) solution during the experiments. Selected constituents were evaluated in terms of their initial concentrations in this matrix (Table S1, Supporting Information).

Ethyl Carbamate Analysis. The samples were analyzed using a gas chromatograph system equipped with a mass selective detector (GC-MS) using electron impact (70 eV) as an ionization source. The mass spectrometer was operated in selected ion monitoring (SIM) mode (m/z 62), and propyl carbamate was added as an internal standard.[10] The oven temperature program was as follows: 90 °C (2 min), followed by an increase to 150 °C at 10 °C/min (0 min) and then an increase to 230 °C at 40 °C/min (10 min). A HP-FFAP (50 m, 0.2 mm, 0.3 μm, Agilent Technologies, Santa Clara, CA, USA) capillary column was used in the EC separation. The inlet and detector interface temperatures were 250 and 230 °C, respectively. Sample aliquots of 1.0 μL were injected into the gas chromatograph system in the splitless mode.

Copper and Iron Ion Analysis. Copper and iron ions were determined using methodology described in the literature.[9] The analysis was performed using inductively coupled plasma atomic emission spectroscopy (Optima 3000 model dual view, PerkinElmer, Santa Clara, CA, USA). The calibration curves were constructed using an external standard method.

Photochemical Experiments. The irradiation of commercial cachaças and the aqueous ethanolic model solutions was performed in a photochemical bench (model 68805 Universal) equipped with a 200 W xenon lamp with interference filters (Oriel Instruments, Irvine, CA, USA). The intensity of the incident radiation was 1.3×10^{-7} einstein/min, which was calculated using a chemical actinometer (K_3[Fe(C_2O_4)$_3$], tris(oxalato)ferrate(III) of potassium, 0.2 mol/L), as previously described.[20]

Kinetic Experiments. Unless otherwise indicated, the kinetic experiments were carried out using a previously described cachaça model solution. During the kinetic studies, potassium cyanate was added to this solution, and the formation of EC was monitored. These analyses were performed as a function of the following parameters: alcoholic degree; pH; addition of salts of copper, iron, and EDTA; influence of light (photochemical irradiation bench); and temperature. In the experiments, the solution pH was controlled using an acetic acid/sodium acetate buffer system. Half-life ($t_{1/2}$) data were calculated from plots of ethyl carbamate concentration ([EC]) as a function of reaction time. $t_{1/2}$ was defined as the time corresponding to the formation of half of the maximum urethane concentration ($[EC]_\infty$).[21,22]

The experiments were carried out under pseudo-first-order conditions (excess of ethanol), and the rate constant k_{obs} (observed rate constant) was calculated from plots of $\ln([EC]_\infty - [EC]_t)$ versus time.[21,22] These plots were linear for at least 3 half-lives. To calculate the kinetic parameters, the temperature was controlled at ±0.2 °C using a thermostat, and the experiments were run at 15, 25, and 35 °C. The activation parameters ($\Delta G_1^{\ddagger}$, $\Delta H_1^{\ddagger}$, and $\Delta S_1^{\ddagger}$) were determined graphically.[21,22]

Preparation, Storage, and Analysis of Model Solutions Fortified with Potassium Cyanate. All cachaça model solutions were obtained using the reference cachaça (Table S1) and buffered using an acetic acid/sodium acetate buffer system. These solutions were spiked with a stock solution of potassium cyanate and stored in 28 mL glass bottles (vials), sealed with rubber septa and aluminum, and kept in the dark (wrapped in aluminum foil). During the kinetic experiments, the pH, the contents of copper(II) and iron(II), the alcoholic concentration of the cachaça, and the temperature (25 °C) were kept constant, except when the influences of these parameters were evaluated separately. During the experiments, aliquots of the cachaça model solution were collected with the aid of a glass syringe.

Decay of the Cyanate Ion. The cyanate concentration decay was monitored using two different procedures that have been described in the literature.[19,23] Both methods involve the reaction between cyanate ion and 2-aminobenzoic acid in the presence of HCl to form 2,4-(1*H*,3*H*)-quinazolinedione. The choice of method was based on the sensitivity required. One method uses the light absorption,[23] whereas the other uses the fluorescence[19] of the derivatization reaction product. The absorbance measurements were performed at 310 nm (ε = 412 L/mol cm) on a UV−visible spectrophotometer (model U-3501, Hitachi, Tokyo, Japan) with a 10 cm path length cylindrical quartz cell. The fluorescence measurements were carried out on a model F-4500 fluorescence spectrophotometer (Hitachi, Tokyo, Japan); 310 nm was used as the excitation wavelength, and the maximum emission was observed at 410 nm. The emission spectra were recorded over a range of 320−600 nm at a resolution of 240 nm/min using a 5 nm slit and a 1 cm quartz cell.

Cyanate Influence in the Formation of Ethyl Carbamate. Model solutions of cachaça (50 mL) were prepared at final cyanate ion concentrations of $(0.5-4.5) \times 10^{-5}$ mol/L. Subsequently, the influence of the OCN^- ion on the formation and evolution of EC levels was evaluated at 25 °C. On the basis of the analytical results (linearity, reproducibility, and repeatability)[24] obtained for the EC levels in these experiments, a concentration of approximately 2.1×10^{-5} mol/L of KOCN was selected for further experiments.

Influence of pH on the Ethyl Carbamate Formation. The pH measurements were carried out in an Ion Analyzer Radiometer Analytical model PHM250 (MeterLab, Villeurbanne, France). Model solutions of spirits (50 mL) were prepared with the following pH values: 3.0 ± 0.1, 3.9 ± 0.1, 5.3 ± 0.1, and 6.0 ± 0.1. The pH was decreased and increased with hydrochloric acid (1.0×10^{-2} mol/L) and sodium hydroxide (1.0×10^{-2} mol/L) solutions, respectively. These solutions were fortified with approximately 2.1×10^{-5} mol/L of KOCN, and their EC contents were subsequently analyzed at 25 °C.

Influence of Light in the Formation of Ethyl Carbamate. Cachaça model solutions (50 mL) were prepared with approximately 2.1×10^{-5} mol/L KOCN. One of these solutions was protected from light (wrapped in aluminum foil and kept in the dark), whereas the others were exposed to radiation in a photochemical bench with appropriate filters (250−500 nm). Subsequently, these solutions were analyzed for their EC contents at 25 °C.

Influence of Alcohol Content in the Formation of Ethyl Carbamate. Two new standard solutions with alcohol levels of 13.3% v/v (2.3 mol/L ethanol) and 24.4% v/v (4.2 mol/L) were prepared by diluting the reference cachaça, which had an alcohol content of 48% v/v (8.2 mol/L ethanol), with distilled water. These solutions were fortified with approximately 2.1×10^{-5} mol/L KOCN and subsequently analyzed for EC content at 25 °C. Then, aqueous ethanolic solutions were prepared with different alcohol concentrations (1.70−91.5% v/v), fortified with 2.1×10^{-5} mol/L KOCN, and analyzed for their EC contents at 35 °C. The alcoholic strength was decreased and increased using deionized water and ethanol (99.5% v/v), respectively.

Molecular Energies and Structures Calculations. The reaction between cyanate and ethanol was modeled using ab initio DFT[25,26] calculations with a B3LYP[27] exchange correlation function. The all-electron 6-31+G(d,p)[28−30] basis set function was used to describe the electronic structures of the studied systems.

An isomeric equilibrium reaction (Scheme 1, path A) was considered for the corresponding acid species cyanic acid (HOCN) and isocyanic acid (HNCO). Both of these species can react with ethanol (EtOH) according to the mechanism (B, C) in Scheme 1, forming ethyl carbamate (EC). A hydrolysis reaction (D) was also considered.

DOI: 10.1021/acs.jafc.5b03146
J. Agric. Food Chem. 2015, 63, 7415−7420

Scheme 1. Studied Reactions Using DFT/B3LYP Conformations: (A) Isocyanic to Cyanic Acid Isomerization; EC Formation through Isocyanic Acid (B) and Ethanol Reaction and Cyanic Acid (C) and Ethanol Reaction and Isocyanic Acid Hydrolysis (D) Yielding CO_2 and NH_3

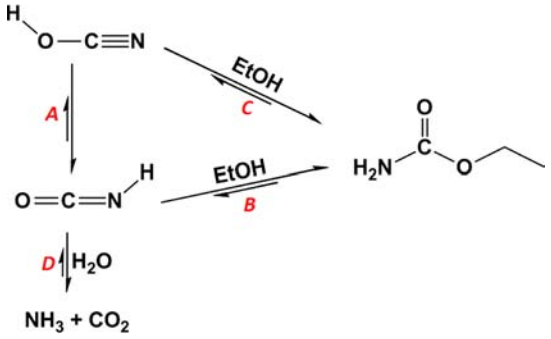

The reaction pathway was proposed on the basis of the potential energy surface (PES) scanning[31] considering a free gas phase system, a solvated model with integral equation formalism to the polarization continuum model[32] (IEFPCM), and explicit solvent effects, with solvent molecule inclusion in the calculation matrix designed to maximize hydrogen bond stabilization. The PES stationary points were confirmed via a vibrational mode calculation.[31] The minimal energy structure does not show imaginary frequencies, and the saddle points were confirmed by a QST3[33] model, revealing a unique imaginary frequency with displacement that corresponds to the atoms shown in the pathway, also confirmed with an intrinsic reaction coordinate[34] (IRC) method.

RESULTS AND DISCUSSION

The addition of cyanate either to an aqueous ethanolic solution or to cachaça leads to the formation of EC. This phenomenon is clearly reproducible if a second addition of cyanate is carried out at the end of the reaction. As can be observed in Figure 1,

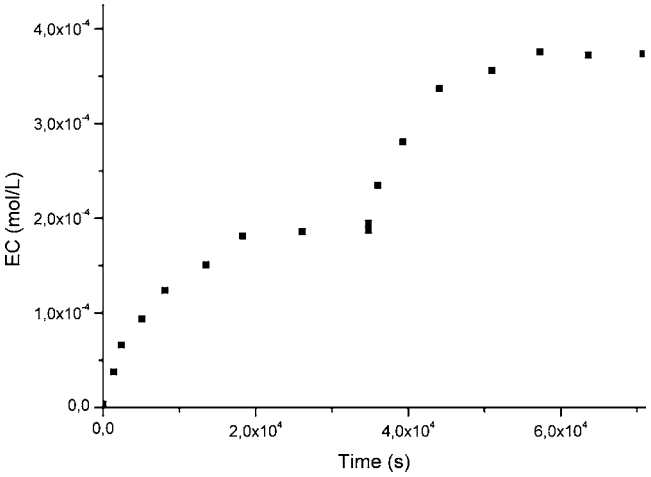

Figure 1. EC formation at 25 °C, as a function of the time in aqueous ethanolic solution (48% v/v, pH 4.5) after successive additions of 5.0 × 10^{-3} mol/L KOCN.

both plots of EC concentration versus time exhibit the same half-life values. However, no significant EC formation was observed when arginine, citrulline, or carbamyl phosphate, which are all possible EC precursors,[1] was added to the same solutions (at concentrations up to 5.0 × 10^{-3} mol/L) instead of cyanate (Figure S1). Only a very small amount of EC is formed as a consequence of the addition of urea or cyanide. This residual EC formation is <0.5% of the EC formed when an equal molar concentration of cyanate is added and was attributed to the presence of traces of cyanate in the urea and cyanide. As depicted in Figure 2, cyanate consumption, which was monitored using UV−vis or fluorescence spectrophotometry, occurs simultaneously with ethyl carbamate formation, which was observed via GC-MS.

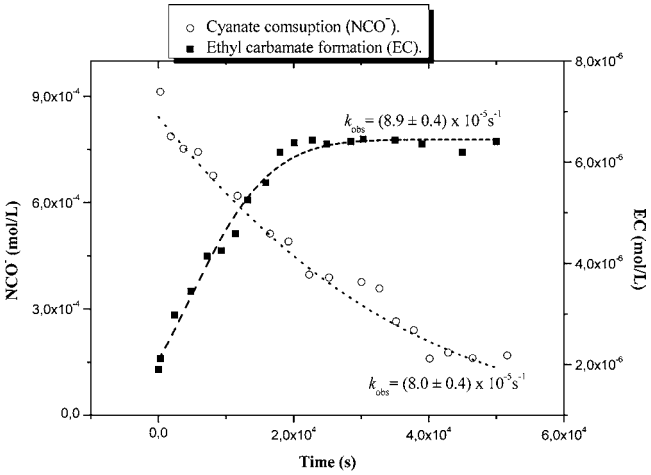

Figure 2. Consumption of the cyanate ion (○) and EC formation (■) as a function of the time in cachaças model solutions fortified with cyanate 4.1 × 10^{-4} mol/L KOCN (○) and 2.1 × 10^{-5} mol/L KOCN (■), at 25 °C and pH 4.5.

Tables 1 and 2 summarize the stoichiometry and kinetic data for the cyanate/ethanol reaction under a wide range of experimental conditions.

Table 1. Effect of Different KOCN Concentrations on Ethyl Carbamate Formation in the Cachaça Model Solution (48% v/v, pH 4.5 at 25 °C)

$[OCN^-]_{added}$ (mol/L)	$[EC]_{formed}$ (mol/L)	k_{obs} (s^{-1})	$t_{1/2}$ (s)
0.5 × 10^{-5}	0.2 × 10^{-5}	8.5 × 10^{-5}	8.4 × 10^3
0.8 × 10^{-5}	0.3 × 10^{-5}	9.3 × 10^{-5}	7.6 × 10^3
2.1 × 10^{-5}	0.6 × 10^{-5}	8.6 × 10^{-5}	8.1 × 10^3
4.5 × 10^{-5}	1.5 × 10^{-5}	9.1 × 10^{-5}	7.8 × 10^3

According to Table 1, the final EC content depends on the cyanate ion concentration that is added to the ethanolic solution (48%) and indicates that around 0.3 mol of EC is formed per mole of added cyanate (≈32%) when all other experimental parameters are kept constant. For whiskey, a "rule of thumb" proposed for use in distilleries is to calculate the potential of EC formation in the beverage as 32% of the total amount of EC precursors.[7] The hydrolysis of HNCO in water can occur in parallel with the formation of EC. Under comparable experimental conditions, this competitive reaction takes place 3.6 times (k_{obs} = 2.9 × 10^{-4} s^{-1} at 25 °C)[35] faster than EC formation, which may account for the above-mentioned EC yield with respect to the available cyanate.

According to Table 2, the EC yield increases as the ethanol concentration ([EtOH]) increases, reaching a maximum value of around 0.3 when [EtOH] is equal to 9.8 mol/L (57.5% v/v) and then remaining constant until [EtOH] = 15.7 mol/L (91.5% v/v). Furthermore, in our experiments, the ethyl

DOI: 10.1021/acs.jafc.5b03146
J. Agric. Food Chem. 2015, 63, 7415−7420

Table 2. Concentrations of Ethyl Carbamate (EC) Formed, Observed Rate Constants (k_{obs}), and Half-Life ($t_{1/2}$) at Different Temperatures (°C), Alcoholic Degrees (% v/v), and pH Values in Cachaça Model Solutions Fortified with 2.1×10^{-5} mol/L KOCN

temperature (°C)	alcoholic degree (% v/v)	pH	$[EC]_{formed}$ (mol/L)	k_{obs} (s^{-1})	$t_{1/2}$ (s)
15	48.0	4.5	6.5×10^{-6}	3.7×10^{-5}	2.0×10^{4}
25	48.0	4.5	6.2×10^{-6}	8.6×10^{-5}	8.1×10^{3}
35	48.0	4.5	6.4×10^{-6}	3.6×10^{-4}	2.1×10^{3}
25	48.0	3.0	6.0×10^{-6}	7.5×10^{-4}	8.8×10^{2}
25	48.0	3.9	6.4×10^{-6}	4.4×10^{-4}	1.7×10^{3}
25	48.0	5.3	6.1×10^{-6}	3.5×10^{-5}	1.9×10^{4}
25	48.0	6.0	6.3×10^{-6}	1.4×10^{-5}	5.5×10^{4}
25	13.3	4.5	1.9×10^{-6}	9.0×10^{-5}	7.7×10^{3}
25	24.4	4.5	4.0×10^{-6}	9.2×10^{-5}	7.6×10^{3}
35	1.70	4.5	3.4×10^{-8}	4.1×10^{-4}	1.7×10^{3}
35	2.00	4.5	1.9×10^{-7}	4.2×10^{-4}	1.6×10^{3}
35	4.54	4.5	4.2×10^{-7}	4.4×10^{-4}	1.6×10^{3}
35	5.26	4.5	4.0×10^{-7}	4.3×10^{-4}	1.6×10^{3}
35	10.6	4.5	1.7×10^{-6}	3.6×10^{-4}	1.9×10^{3}
35	22.4	4.5	3.0×10^{-6}	3.6×10^{-4}	1.9×10^{3}
35	35.0	4.5	4.8×10^{-6}	4.2×10^{-4}	1.8×10^{3}
35	57.5	4.5	7.2×10^{-5}	4.3×10^{-4}	1.7×10^{3}
35	70.0	4.5	7.1×10^{-5}	3.6×10^{-4}	2.1×10^{3}
35	83.1	4.5	7.3×10^{-5}	3.6×10^{-4}	2.0×10^{3}
35	91.5	4.5	7.3×10^{-5}	3.6×10^{-4}	2.0×10^{3}

carbamate yield was not sensitive to the solution pH in the range of 3.0−6.0 (Table 2).

Neither the addition of 5.0×10^{-3} mol/L Cu(II), Fe(II), or EDTA nor the irradiation of the solution with 250−500 nm light (Table S2) leads to a noticeable change in the EC yield or the rate of ethyl carbamate formation.

Within the limits of experimental error, the rate constant values (k_{obs}) for cyanate ion decay $(8.0 \pm 0.4) \times 10^{-5}$ s^{-1} and EC formation $(8.9 \pm 0.4) \times 10^{-5}$ s^{-1} were in agreement with the corresponding values reported in the literature,[19,35] which were determined using different techniques and by monitoring cyanate concentration and formed product (EC) (Table 2 and Figure 2).

The observed rate constants are independent of ethanol concentration in the range from 2.9×10^{-2} to 15.7 mol/L but increase as the temperature increases (Table 2). In the pH range of 3.0−6.0, the rates decrease as the solution pH increases (Table 2). When the solution pH exceeds 7, the rate of EC formation was estimated to be $<10^{-7}$ s^{-1}, indicating the relevance of the protonated form of cyanate in this reaction.

The effect of temperature on EC formation was evaluated using kinetic data as a function of temperature (Table 2) to calculate the activation parameters as follows: $\Delta H_1^{\ddagger} = 19.4 \pm 1$ kcal/mol, $\Delta S_1^{\ddagger} = -12.1 \pm 1$ cal/K, and $\Delta G_1^{\ddagger} = 23.0 \pm 1$ kcal/mol.

EC is formed via a reaction between ethanol and cyanate. However, it is interesting to recall that under the experimental conditions described in Table 2, the rate of this reaction is independent of ethanol and cyanate concentrations and is equal to $(8.9 \pm 0.4) \times 10^{-5}$ s^{-1} at 25 °C. These observations would suggest a reaction in which an intermediate is formed, the concentration of which would be dependent on the presence in the medium of a protonated form of cyanate as the rate-determining step. Indeed, four isomers of cyanic acid are described: HNCO, HOCN, HONC, and HCNO. Isocyanic acid (HNCO, $pK_a = 3.7$) and cyanic acid (HOCN, $pK_a < 3.0$) are the most abundant and exist in a tautomeric equilibrium.[36−38] On the basis of infrared spectra of the vapor and liquid, it was inferred that the acid was primarily HNCO, containing <0.2% of HOCN. Furthermore, the formation of HNCO is favored as the temperature increases.[36] According to our DFT calculations, in water or ethanolic solutions, isocyanic acid is more stable than the corresponding HOCN isomer in terms of free energy (ΔG_{eq}) by 23.6 ± 2 kcal/mol. The isomerization barrier is $\Delta G_1^{\ddagger} = 24.9 \pm 1$ kcal/mol when the IEFPCM effect is considered and solvent molecules (three molecules of water or ethanol) are explicitly considered in the matrix.

Considering that the typical pH value found in cachaça is approximately 4.5, both HNCO and HOCN could be considered as potential active precursors for EC formation. However, HNCO is likely the most relevant precursor because of its abundance under the experimental conditions.[36]

EC formation was investigated using reaction modeling between ethanol and both isocyanic (Figure 3) and cyanic acids

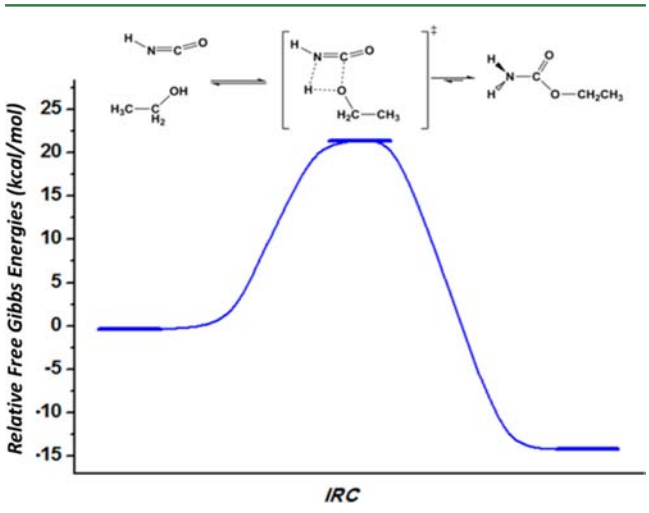

Figure 3. EC formation reaction pathway through isocyanic acid and ethanol: relative free Gibbs energies considering explicit solvent model (−).

(Figure 4). Considering the isocyanic acid pathway, the reaction is straightforward; the activation parameters $\Delta G_1^{\ddagger}$, $\Delta H_1^{\ddagger}$, and $\Delta S_1^{\ddagger}$ were calculated to be 21.5×10^{-3}, 14.6×10^{-3}, and -23.1×10^{-3} kcal/mol, respectively (Table 3), and the ΔG_{eq}, ΔH_{eq}, and ΔS_{eq} are thus -14.1×10^{-3}, 19.0×10^{-3}, and 16.9×10^{-3} kcal/mol, respectively.

When cyanic acid is considered as the active form, the mechanism appears to be more complex, as can be observed in the reaction sequence shown in Figure 4.

For this case, in the first step, one molecule of HOCN associates with one molecule of CH_3CH_2OH, and a proton is transferred from the oxygen atom of the ethanol to the nitrogen atom of HOCN.

In the next step, the proton bonded to the oxygen atom of the cyanic acid migrates to the nitrogen atom, yielding ethyl carbamate. The activation parameters $\Delta G_1^{\ddagger}$, $\Delta H_1^{\ddagger}$, and $\Delta S_1^{\ddagger}$ in this case are 41.8×10^{-3}, 34.4×10^{-3}, and 23.0×10^{-3} kcal/mol, respectively. From Table 3, the reaction between ethanol and isocyanic acid is more favorable than the reaction with cyanic acid by 20.3 kcal/mol. Furthermore, there is very good

DOI: 10.1021/acs.jafc.5b03146
J. Agric. Food Chem. 2015, 63, 7415−7420

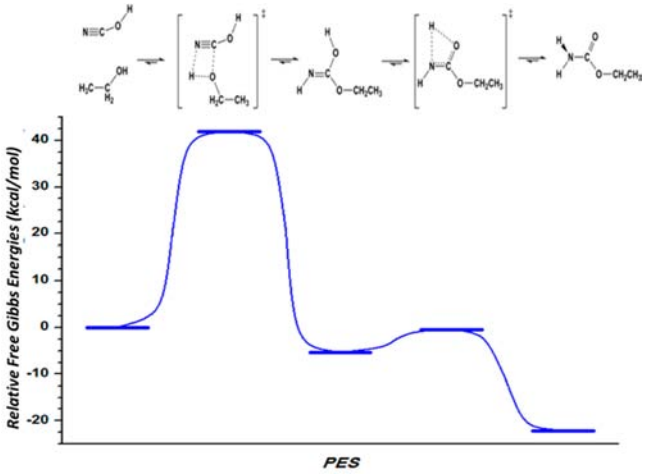

Figure 4. EC formation reaction pathway through cyanic acid and ethanol: relative free Gibbs energies considering explicit solvent model (−).

Table 3. Kinetic and Thermodynamic Parameters of the Studied Reactions: Experimental (Exptl), DFT Gas Phase (Gas), DFT with IEFPCM Solvent Model (IEFPCM), and DFT IEFPCM with Explicit Solvent (ES)

reaction		$\Delta G_1^{\ddagger}$ (kcal mol^{-1})	ΔG_{eq} (kcal mol^{-1})
HNCO ⇌ HOCN	Exptl		
	Gas	90.6	27.6
	IEFPCM	82.5	23.6
	ES	24.9	22.1
HNCO + EtOH ⇌ EC	Exptl	23.0	
	Gas	40.1	−10.6
	IEFPCM	37.8	−14.1
	ES	21.5	−14.1
HOCN + EtOH ⇌ EC	Exptl		
	Gas	48.1	−39.7
	IEFPCM	49.0	−36.7
	ES	41.8	−23.4
HNCO + H_2O ⇌ CO_2 + NH_3	Exptl	22.4	
	Gas	40.4	−16.3
	IEFPCM	41.8	−13.7
	ES	24.0	−17.6

agreement between the calculated reaction parameters of the isocyanic acid pathway and the experimental ones determined for EC formation (Table 3).

The formation of EC in freshly distilled sugar cane spirit is not sensitive to light irradiation (250-550 nm) or to the presence of copper and iron salts or EDTA. This reaction reaches completion in <10 days. However, distilled whiskey is reported to be sensitive to light irradiation, and the reaction has been shown to reach completion after 3−4 weeks.[7] Thus, it is unlikely that these differences could be satisfactorily explained on the basis of the experimental conditions (temperature and alcoholic degree) alone. These observations suggest that comparing the chemistry of these beverages is not as straightforward a process as might be initially assumed. Because cachaça and whiskey are produced using different raw materials (sugar cane vs malt and grains) processed in different ways, they are expected to present some differences in their final chemical compositions[39] and, therefore, in their respective carbamate precursor profiles. According to our experimental data, the active precursor in sugar cane spirit is likely cyanate. The presence of cyanate in the spirit can be explained as a consequence of the degradation of urea during the wine distillation process.[1] Urea can also be formed by arginine degradation during fermentation,[1] and cyanate could be transferred to the distillate as acid vapors of HOCN or HNCO. Because the reaction occurs between ethanol and cyanate, although this study was performed in cachaça and water−ethanol model solutions, the findings described here could be extended to other distillates and to ethanol production. Finally, EC can be reduced or eliminated in cachaça and whiskey by a simple redistillation.

■ ASSOCIATED CONTENT

Supporting Information

The Supporting Information is available free of charge on the ACS Publications website at DOI: 10.1021/acs.jafc.5b03146.

Figure S1 and Tables S1 and S2 (PDF)

■ AUTHOR INFORMATION

Corresponding Author

*(D.W.F.) Phone/fax: + 55-16-33739976. E-mail: douglas@iqsc.usp.br.

Funding

This work was financially supported by several Brazilian agencies (CAPES, CNPq, and FAPESP).

Notes

The authors declare no competing financial interest.

■ ACKNOWLEDGMENTS

This paper is dedicated to Professor Fernando Valadares Novaes, the first one to describe the presence of ethyl carbamate in cachaças.

■ ABBREVIATIONS USED

ABV, alcohol by volume; [EC], ethyl carbamate concentration (mol/L); DFT, density functional theory; HP-FFAP, capillary column for gas chromatography; EDTA, ethylenediaminetetraacetic acid, $C_{10}H_{16}N_2O_8$; EtOH, ethanol; PES, potential energy surface; IRC, intrinsic reaction coordinate; IEFPCM, integral equation formalism to the polarization continuum model; UV−vis, ultraviolet−visible; GC-MS, gas chromatograph system equipped with a mass selective detector; SIM, selected ion monitoring

■ REFERENCES

(1) European Food Safety Authority (EFSA).. Ethyl carbamate and hydrocyanic acid in food and beverages. *EFSA J.* **2007**, *551*, 1−44.

(2) Jiao, Z.; Dong, Y.; Chen, Q. Ethyl carbamate in fermented beverages: presence, analytical chemistry, formation mechanism, and mitigation proposals. *Compr. Rev. Food Sci. Food Saf.* **2014**, *13*, 611−626.

(3) Cook, R.; McCaig, N.; McMillan, J. M. B.; Lumsden, W. B. Ethyl carbamate formation in grain-based spirits. Part III. The primary source. *J. Inst. Brew.* **1990**, *96*, 233−244.

(4) Riffkin, H. L.; Wilson, R.; Howie, D.; Muller, S. B. Ethyl carbamate formation in the production of pot still whisky. *J. Inst. Brew.* **1989**, *95*, 115−119.

DOI: 10.1021/acs.jafc.5b03146
J. Agric. Food Chem. 2015, 63, 7415−7420

(5) Galinaro, C. A.; Franco, D. W. Formação de carbamato de etila em aguardentes recém-destiladas; proposta para seu controle. *Quim. Nova* **2011**, *34*, 996−1000.
(6) Bruno, S. N. F.; Vaitsman, D. S.; Kunigami, C. N.; Brasil, M. G. Influence of the distillation processes from Rio de Janeiro in the ethyl carbamate formation in Brazilian sugar cane spirits. *Food Chem.* **2007**, *104*, 1345−1352.
(7) Aylott, R. I.; Cochrane, G. C.; Leonard, M. J.; MacDonald, L. S.; MacKenzie, W. M.; McNeish, A. S.; Walker, D. A. Ethyl carbamate formation in grain based spirits part i: post-distillation ethyl carbamate formation in maturing grain whisky fermented foods and beverages. *J. Inst. Brew.* **1990**, *96*, 213−221.
(8) Aresta, M.; Boscolo, M.; Franco, D. W. Copper(II) catalysis in cyanide conversion into ethyl carbamate in spirits and relevant reactions. *J. Agric. Food Chem.* **2001**, *49*, 2819−2824.
(9) Reche, R. V.; Neto, A. F. L.; Da Silva, A. A.; Galinaro, C. A.; De Osti, R. Z.; Franco, D. W. Influence of type of distillation apparatus on chemical profiles of Brazilian cachaças. *J. Agric. Food Chem.* **2007**, *55*, 6603−6608.
(10) Andrade-Sobrinho, L. G. De; Boscolo, M.; Lima-Neto, B. dos S.; Franco, D. W. Carbamato de etila em bebidas alcoólicas (cachaça, tiqueira, whisky and grape). *Quim. Nova* **2002**, *25*, 1074−1077.
(11) Alcarde, A. R.; de Souza, L. M.; Bortoletto, A. M. Ethyl carbamate kinetics in double distillation of sugar cane spirit. *J. Inst. Brew.* **2012**, *118*, 27−31.
(12) Santiago, W. D.; Cardoso, M. D. G.; Zacaroni, L. M.; Rodrigues, L. M. A.; Duarte, F. C.; Ribeiro, C.; de Fatima e Silva Ribeiro, C.; Nelson, D. L. Multivariate analysis for the characterization of physico-chemical profiles of cachaça produced in copper stills over a period of six years in Minas Gerais state. *J. Inst. Brew.* **2015**, *121*, 244−250.
(13) Bortoletto, A. M.; Alcarde, A. R. Assessment of chemical quality of Brazilian sugar cane spirits and cachaças. *Food Control* **2015**, *54*, 1−6.
(14) Lachenmeier, D. W.; Lima, M. C. P.; Nóbrega, I. C. C.; Pereira, J. A. P.; Kerr-Corrêa, F.; Kanteres, F.; Rehm, J. Cancer risk assessment of ethyl carbamate in alcoholic beverages from Brazil with special consideration to the spirits cachaça and tiquira. *BMC Cancer* **2010**, *10*, 266.
(15) Nóbrega, I. C. C.; Pereira, J. A. P.; Paiva, J. E.; Lachenmeier, D. W. Ethyl carbamate in pot still cachaças (Brazilian sugar cane spirits): influence of distillation and storage conditions. *Food Chem.* **2009**, *117*, 693−697.
(16) De Almeida Lima, U.; Teixeira, C. G.; Bertozzi, J. C.; Serafim, F. A. T.; Alcarde, A. R. Influence of fast and slow distillation on ethyl carbamate content and on coefficient of non-alcohol components in Brazilian sugarcane spirits. *J. Inst. Brew.* **2012**, *118*, 305−308.
(17) Riachi, L. G.; Santos, A.; Moreira, R. F. A.; De Maria, C. A. B. A review of ethyl carbamate and polycyclic aromatic hydrocarbon contamination risk in cachaça and other Brazilian sugarcane spirits. *Food Chem.* **2014**, *149*, 159−169.
(18) Francisco, I. A.; Pinotti, M. H. P. Cyanogenic glycosides in plants. *Braz. Arch. Biol. Technol.* **2000**, *43*, 487−492.
(19) Ohe, T. H. K.; Da Silva, A. A.; Rocha, T.; da, S.; De Godoy, F. S.; Franco, D. W. A fluorescence-based method for cyanate analysis in ethanol/water media: correlation between cyanate presence and ethyl carbamate formation in sugar cane spirit. *J. Food Sci.* **2014**, *79*, 1950−1955.
(20) Simoni, D. D. A.; Andrade, J. C. de; Faigle, J. F. G.; Simoni, J. de A. Um experimento com propostas múltiplas para um laboratório de química geral. *Quim. Nova* **2002**, *25*, 1034−1039.
(21) Laidler, K. J. *Chemical Kinetics*, 3rd ed.; McGraw-Hill: New York, 1987.
(22) Monk, P. *Physical Chemistry: Understanding Our Chemical World*; Wiley: Chichester, UK, 2004.
(23) Guilloton, M.; Karst, F. A spectrophotometric determination of cyanate using reaction with 2-aminobenzoic acid. *Anal. Biochem.* **1985**, *149*, 291−295.
(24) Meier, P. C.; Zund, R. E. *Statistical Methods in Analytical Chemistry*, 2nd ed.; Wiley: New York, 1993; Vol. 153.
(25) Hohenberg, P.; Kohn, W. Inhomogeneous electron gas. *Phys. Rev.* **1964**, *136* (3B), B864−B871.
(26) Kohn, W.; Sham, L. J. Self-consistent equations including exchange and correlation effects. *Phys. Rev.* **1965**, *140* (4A), A1133A113810.1103/PhysRev.140.A1133
(27) Becke, A. Density functional thermochemistry. III. The role of exact exchange. *J. Chem. Phys.* **1993**, *98*, 5648−5652.
(28) Ditchfield, R.; Hehre, W. J.; Pople, J. A. Self-consistent molecular-orbital methods. IX. An extended gaussian-type basis for molecular-orbital studies of organic molecules. *J. Chem. Phys.* **1971**, *54*, 724.
(29) Clark, T.; Chandrasekhar, J.; Spitznagel, G. W.; Schleyer, P. V. R. Efficient diffuse function-augmented basis sets for anion calculations. III. The 3-21+G basis set for first-row elements, Li−F. *J. Comput. Chem.* **1983**, *4*, 294−301.
(30) Frisch, M. J.; Pople, J. A.; Binkley, J. S. Self-consistent molecular orbital methods 25. Supplementary functions for Gaussian basis sets. *J. Chem. Phys.* **1984**, *80*, 3265.
(31) Foresman, J. B.; Frisch, A. E. *Exploring Chemistry with Electronic Structure Method*, 2nd ed.; Gaussian Inc.: Pittsburgh, PA, USA, 1996.
(32) Cancès, E.; Mennucci, B.; Tomasi, J. A new integral equation formalism for the polarizable continuum model: theoretical background and applications to isotropic and anisotropic dielectrics. *J. Chem. Phys.* **1997**, *107*, 3032.
(33) Hratchian, H. P.; Schlegel, H. B. Finding minima, transition states, and following reaction pathways on ab initio potential energy surfaces. *Theory and Applications of Computational Chemistry: The First Forty Years*; Elsevier: Amsterdam, The Netherlands, 2005; pp 195−249.
(34) Fukui, K. The path of chemical reactions—the IRC approach. *Acc. Chem. Res.* **1981**, *14*, 363−368.
(35) Da Silva, A. A.; Ohe, T. H. K.; Franco, D. W. Decaimento de íons cianato e a formação de carbamato de etila. *Quim. Nova* **2013**, *36*, 1101−1103.
(36) Amell, A. R. Kinetics of the hydrolysis of cyanic acid. *J. Am. Chem. Soc.* **1956**, *78*, 6234−6238.
(37) Adamczyk, K.; Dreyer, J.; Pines, D.; Pines, E.; Nibbering, E. T. J. Ultrafast protonation of cyanate anion in aqueous solution. *Isr. J. Chem.* **2009**, *49*, 217−225.
(38) Zabardast, A.; Kakan, A. Theoretical study of hydrogen bonded clusters of water and cyanic acid: hydrogen bonding in terms of the molecular structure. *Polyhedron* **2008**, *27*, 2973−2977.
(39) Cardoso, D. R.; De Andrade-Sobrinho, L. G.; Leite-Neto, A. F.; Reche, R. V.; Isique, W. D.; Ferreira, M. M. C.; Lima-Neto, B. S.; Franco, D. W. Comparison between cachaca and rum using pattern recognition methods. *J. Agric. Food Chem.* **2004**, *52*, 3429−3433.

DOI: 10.1021/acs.jafc.5b03146
J. Agric. Food Chem. 2015, 63, 7415−7420

acetylvulgarine, and echivulgarine *N*-oxide.[1,14] The full structural elucidation of echivulgarine, including its absolute configuration, is presented herein.

MATERIALS AND METHODS

General. The optical rotation was obtained using an Autopol II polarimeter (Rudolph Research Analytical, Hackettstown, NJ), while the CD spectrum was recorded on a Chirascan CD spectrometer (Applied Photophysics, Surrey, U.K.) using a 1 cm quartz cell. Nuclear magnetic resonance (NMR) spectra were recorded using a DirectDrive 600 NMR spectrometer equipped with a cryogenically cooled probe (Agilent Technologies, Santa Clara, CA) operating at 600, 150, and 60 MHz for ^{1}H, ^{13}C, and ^{15}N nuclei, respectively. Spectra were acquired using standard Agilent pulse sequences (^{1}H, s2pul; ^{13}C, s2pul; COSY, gCOSY; ^{1}H−^{13}C HSQC, HSQCAD; ^{1}H−^{13}C HMBC, gHMBCAD; ^{1}H−^{15}N HMBC, CIGARAD; two-dimensional NOESY, NOESY) and were internally referenced to the residual solvent peak ($CDCl_3$, 7.26 ppm for ^{1}H and 77.0 ppm for ^{13}C). HRESI-MS data were acquired using an Agilent Technologies 6530 Q-TOF instrument in positive and negative ion modes with MS/MS data generated using Ar as a collision gas using energies of 10−50 V. The relative ionization responses of various DHPA analytes were determined with an AB Sciex Triple Quad 6500 instrument (AB Sciex, Framingham, MA) operating in positive electrospray ionization MRM mode. Quantitative proton NMR (qNMR) using 1,4-dinitrobenzene as an internal standard was used to calibrate solutions of echivulgarine for use as reference material in quantitative LC−MS/MS analysis. When monitored by LC−MS/MS in MRM mode, associated *N*-oxides, including echivulgarine *N*-oxide, were detected (sum of impurity peak areas of <1%).

Pollen Material. Bee pollen granules (280 g), containing a high proportion of dark blue granules (estimated level of 50%), were obtained from Central Otago, New Zealand. The blue granules were presumed to originate from *E. vulgare*, which is a common plant found in this region.

Extraction and Isolation. The pollen was extracted with 30% methanol in 0.025 M sulfuric acid (2 × 850 mL) and filtered under vacuum. The acidic filtrate was washed twice by being shaken with hexane. Small aliquots of the acidic methanol (25 mL) were purified using 0.5 g Bond Elute Plexa PCX cation exchange cartridges (Agilent Technologies) based on the method of Boppré.[14] Ammoniated methanol eluates from multiple SPE cartridges were combined and concentrated under reduced pressure. Further purification was achieved via semipreparative HPLC using a 250 mm × 9.4 mm (inside diameter), 5 μm, Zorbax Eclipse XDB-C18 column (Agilent Technologies). Mobile phases were 0.1% formic acid in water (A) and 0.1% formic acid in 95% methanol (B), starting at 50% B with a gradient to 100% B from 8 to 12 min. The column flow rate was 3.0 mL/min. The fraction containing echivulgarine and its *N*-oxide was collected from 6 to 8 min. Fractions collected from multiple runs were combined and evaporated to dryness. These were chemically reduced to the tertiary base using indigo carmine redox resin.[16] Additional cleanup was achieved by dissolving the dry extract in 10 mL of dichloromethane and loading onto a 1 g silica SepPak cartridge (Waters Corp., Milford, MA). The cartridge was washed with dichloromethane (10 mL) and tertiary base alkaloids eluted with 25% methanol in chloroform (10 mL) to give echivulgarine (**2**) (11 mg).

Echivulgarine, ***2****.* White amorphous solid: $[\alpha]_D^{20}$ −75.5 (*c* 0.03, CH_2Cl_2); ^{1}H, ^{13}C, and ^{15}N ($CDCl_3$) (Table 1); HRESIMS *m*/*z* 480.2606 $[M + H]^+$ (calcd for $C_{25}H_{38}NO_8$, *m*/*z* 480.2592), *m*/*z* 502.2421 $[M + Na]^+$ (calcd for $C_{25}H_{37}NO_8Na$, *m*/*z* 502.2411); HRESIMS/MS *m*/*z* 322.1656 (calcd for $C_{17}H_{24}NO_5$, *m*/*z* 322.1649), *m*/*z* 220.1334 (calcd for $C_{13}H_{18}NO_2$, *m*/*z* 220.1338), *m*/*z* 120.0806 (calcd for $C_8H_{10}N$, *m*/*z* 120.0819), *m*/*z* 83.0490 (calcd for C_5H_7O, *m*/*z* 83.0497).

Computational Methods. A conformational analysis of all four possible diastereoisomers of echivulgarine (**2a**−**2d**) was performed with the Boltzmann jump method (SP4, 3000 steps, 300 K, 60° root-mean-square deviation) as implemented in the AMMP package with the Vega ZZ graphical frontend.[17] After duplicate structures had been removed, the obtained conformers were fully optimized using hybrid density functional theory (DFT) with Gaussian 09.[18] The 1996 hybrid functional of Perdew, Burke, and Ernzerhof[19−22] was employed for all calculations in combination with Alrichs' basis set, i.e., PBE0/def2-SVP, and Grimme's empirical D3 correction with Becke−Johnston damping (D3BJ).[23,24] Solvent effects were considered through the polarizable continuum model (PCM) in the integral equation formalism variant (IEFPCM)[25] with Cramer and Truhlar's SMD parameter set.[26] Dichloromethane was used as a solvent in all the calculations. All conformers were confirmed to be minima on the potential energy surface at the PBE0-D3BJ/def2-SVP/SMD_{CCl2H2} level through the calculation of harmonic force constants. NMR calculations were performed using the same level of theory. The DP4 statistical analysis[27] was employed to distinguish between different diastereomers. Theoretical electronic circular dichroism (ECD) spectra were calculated using time-dependent density functional theory (TDDFT) with the same level of theory (24 excited states).[28]

Table 1. NMR Data ($CDCl_3$) of Echivularine, 2

position	δ_C/δ_N [a]	δ_H [b]	multiplicty, *J* (Hz)
1	132.7	–	–
2	126.7	5.82	br s
3	61.5	4.29 (β)	d (15.3)
		3.53 (α)	ddd (15.5, 4.3, 2.1)
4	−310.8	–	–
5	53.9	3.78 (β)	m
		2.87 (α)	ddd (12.3, 10.3, 6.0)
6	34.3	2.30 (β)	m
		2.24 (α)	dd (14.0, 6.0)
7	72.7	5.57	br t (3.4)
8	76.3	4.82	br s
9	61.7	4.65	d (13.4)
		4.62	d (13.5)
1′	173.6	–	–
2′	83.5	–	–
3′	72.3	5.49	q (6.2)
4′	15.4	1.38	d (6.7)
5′	73.6	–	–
6′	26.7	1.24	s
7′	25.2	1.39	s
1″	166.2	–	–
2″	127.6	–	–
3″	139.0	6.04	qq (7.3, 1.7)
4″	15.9	1.93	dq (7.3, 1.6)
5″	20.6	1.77	m
1‴	166.5	–	–
2‴	126.5	–	–
3‴	141.0	6.14	qq (7.4, 1.5)
4‴	15.9	1.93	dq (7.3, 1.6)
5‴	20.7	1.78	m

[a]At 150 MHz (^{13}C) or 60 MHz (^{15}N; indirect detection). [b]Operating at 600 MHz.

RESULTS AND DISCUSSION

A protonated molecular ion consistent with the empircal formula $C_{25}H_{38}NO_8$ was detected at *m*/*z* 480.2606 (calcd at *m*/*z* 480.2592) using an accurate mass ESI-Q-TOF-MS instrument. Confirmation of all the carbons and nitrogen was obtained via the ^{13}C and ^{15}N NMR spectra obtained from echivulgarine (Table 1). Of the 37 protons required by the molecular formula, 35 were attached to carbon (Figure 1), based upon the multiplicity-edited ^{1}H−^{13}C HSQC experiment, leaving two exchangeable protons.

DOI: 10.1021/acs.jafc.5b02402
J. Agric. Food Chem. 2015, 63, 7421−7427

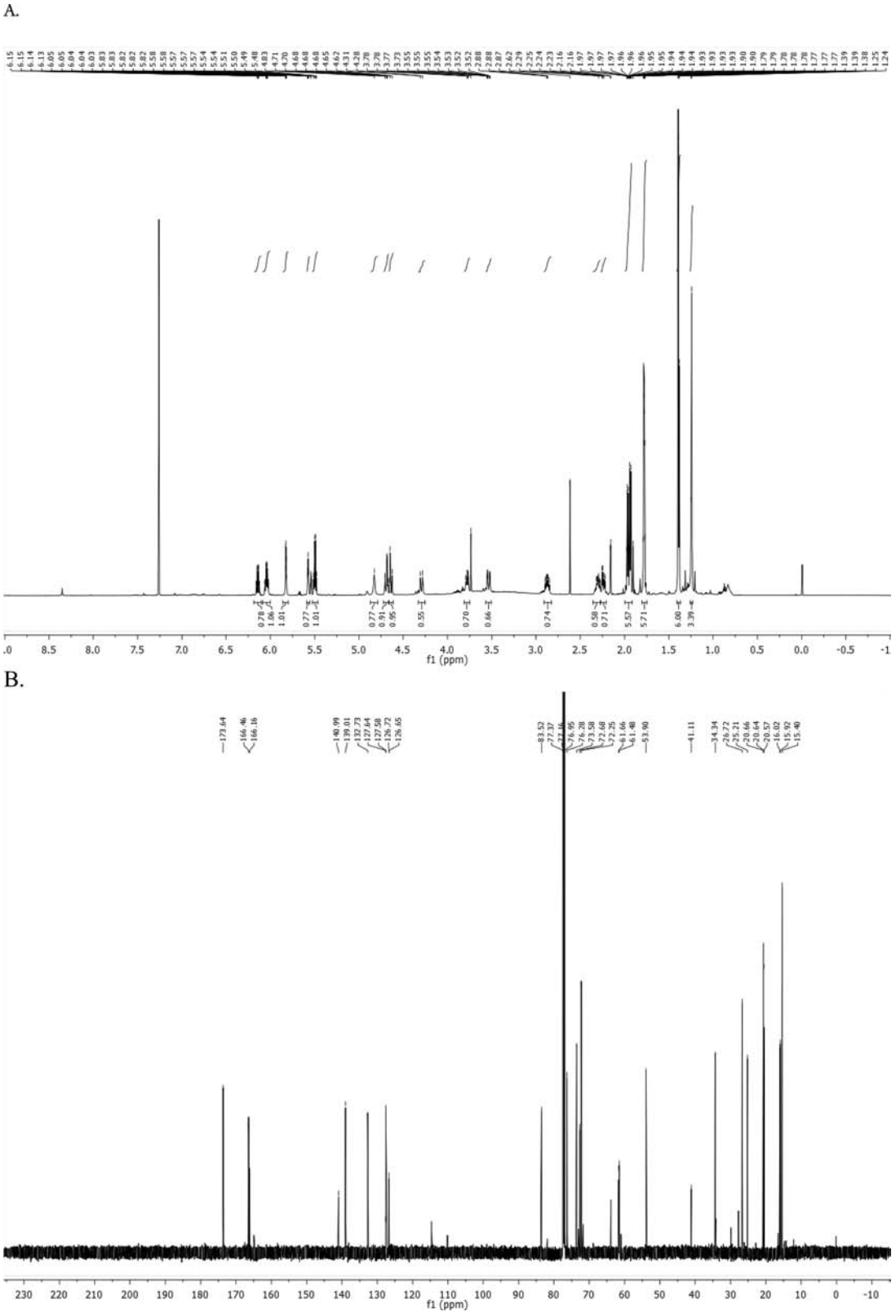

Figure 1. (A) ^{1}H (600 MHz) and (B) ^{13}C (150 MHz) NMR spectra of echivulgarine, **2** ($CDCl_3$).

The core necine base skeleton was rapidly established from a combination of $^{1}H-^{1}H$ COSY and both $^{1}H-^{13}C$ and $^{1}H-^{15}N$ HMBC spectra (Figure 2), in complete agreement with data compiled in reviews of the NMR data of DHPAs.[1,29] COSY and HMBC correlations were also used to establish the presence of one 5-hydroxytrachelanthyl and two angelyl fragments. Key HMBC correlations linked the various side-chain moieties to the necine base core. In particular, H-7 showed an HMBC correlation to C-1‴, while H_2-9 correlated with C-1′, as did quartet methine H-3′. A key and intense HMBC correlation was

DOI: 10.1021/acs.jafc.5b02402
J. Agric. Food Chem. 2015, 63, 7421−7427

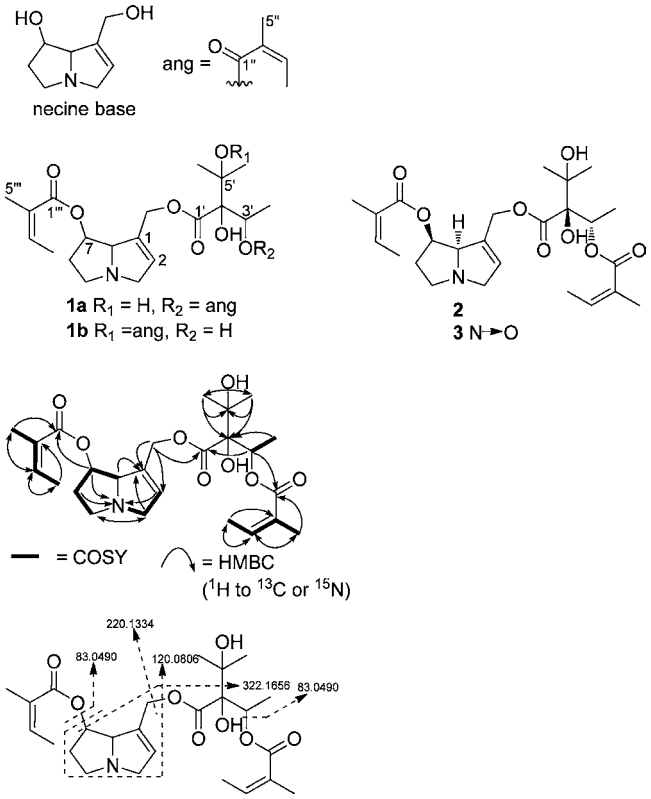

Figure 2. Key two-dimensional NMR correlations and MS/MS fragments confirming the planar structure of echivulgarine, **1a**.

observed between H-3′ and C-1″ of the second angelic acid group, finalizing the planar structure of echivulgarine as **1a** and thereby establishing the placement of this ester functionality that could not be determined during previous MS^n studies.[14] Finally, the planar structure of **1a** (Figure 2) established by NMR was corroborated by high-mass accuracy MS/MS experiments conducted with a Q-TOF instrument. As an ion trap mass spectrometer was not available, the fragments observed by Boppré could not be corroborated,[14,15] but those observed (Figure 2) were consistent with the structure proposed.

The final structural feature of echivulgarine to be established was the overall relative and absolute configurations of the molecule. Colegate et al.[30] have indicated that individual NMR measurements can be unreliable for the assignment of relative configuration within the family of DHPA diesters. Various researchers have obtained conflicting results when trying to use nuclear Overhauser effect (NOE) data alone to relate the configuration of C-7 and C-8, as well as configurations within the side-chain esters. Moreover, scalar couplings between mutually coupled protons can be unreliable for confirming relative configurations around five-membered rings. Chemical shift arguments can therefore be a useful guide for assisting in assigning the relative relationship between substituents at C-7 and C-8. Accordingly, the proton resonances noted for echivulgarine were all consistent with the trends noted[30] for a *syn* relationship between H-7 and H-8, although the signals for H_2-6 to H-8 resonate approximately 0.2 ppm downfield of those reported previously.[30] Such a *syn* relationship would result in the 7*R**, 8*R** relative configuration as previously assumed. This proposed relative configuration was supported by observation of multiple through-space interactions via a two-dimensional NOESY experiment (Figure 3). A key through-space NOE

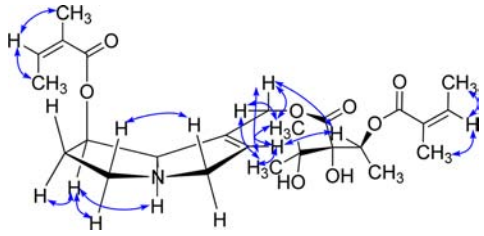

Figure 3. Key NOE correlations establishing the relative configuration of the necine base core of echivulgarine, **2**.

correlation was noted between H-7 and H-8, confirming the expected *cis* fusion of the two five-membered rings within the pyrrolizidine core. Fortuitously, this correlation was corroborated by the cofacial NOE correlations noted between both H-7 and H-8 and the deshielded resonances of methylenes H_2-5 and H_2-6, and also supported by correlations between the shielded proton resonances of methylenes H_2-3 and H_2-5 (Figure 3).

Unfortunately, significant issues for resolving the relative configurations at C-2′ and C-3′ of the 5-hydroxytrachelanthyl side chain precluded the establishment of their spatial relationship using NOE or coupling constant data. Furthermore, no clear trend in the ^1H or ^{13}C chemical shifts could differentiate among the four possible diastereomers of the side chain. We therefore undertook a detailed computational study to elucidate the relative configuration of the side chain, and the absolute configuration of the compound as a whole.

To get insight into the absolute configuration of echivulgarine, **2**, TDDFT ECD calculations were performed and the results compared with the experimental CD spectrum of the compound obtained in dichloromethane. For this purpose, all four possible side-chain diastereomers of **2**, i.e., 2′*R*,3′*R*-echivulgarine (**2a**), 2′*R*,3′*S*-echivulgarine (**2b**), 2′*S*,3′*R*-echivulgarine (**2c**), and 2′*S*,3′*S*-echivulgarine (**2d**), were taken into account. A conformational analysis was applied to each diastereomer using molecular mechanics. Then, after duplicates had been carefully removed, the energetically lowest-lying 40, 49, 48, and 49 conformers for **2a**−**2d**, respectively, were optimized using DFT at the PBE0-D3BJ/def2-SVP/SMD_{CCl2H2} level. The energies obtained at this level of theory were then used to determine their relative contributions (Boltzmann distribution at 298.15 K) to the solution phase mixture. The most strongly contributing conformers (accounting for >99.0%) were selected for ECD calculations. The resulting computed ECD spectra were summed and Boltzmann averaged using SpecDis[31] and compared with the experimental ECD spectra (Figures 4). By careful comparison, the best match of the calculated to the experimental CD spectrum was that of **2b**, with both exhibiting negative Cotton

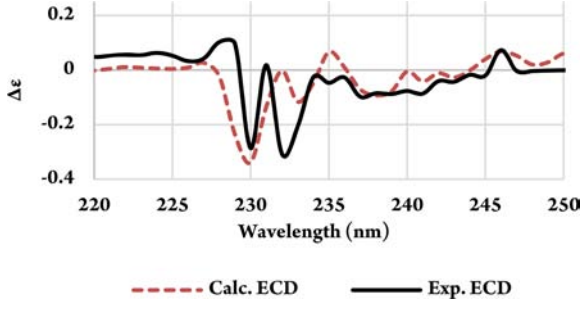

Figure 4. Comparison of the experimental (dichloromethane) and calculated ECD spectra of 2′*R*,3′*S*-echivulgarine, **2**.

DOI: 10.1021/acs.jafc.5b02402
J. Agric. Food Chem. 2015, 63, 7421−7427

effects at 230 nm. The lowest-energy conformer of **2b** (92.74% Boltzmann weight) is shown in Figure 5. This structure has a

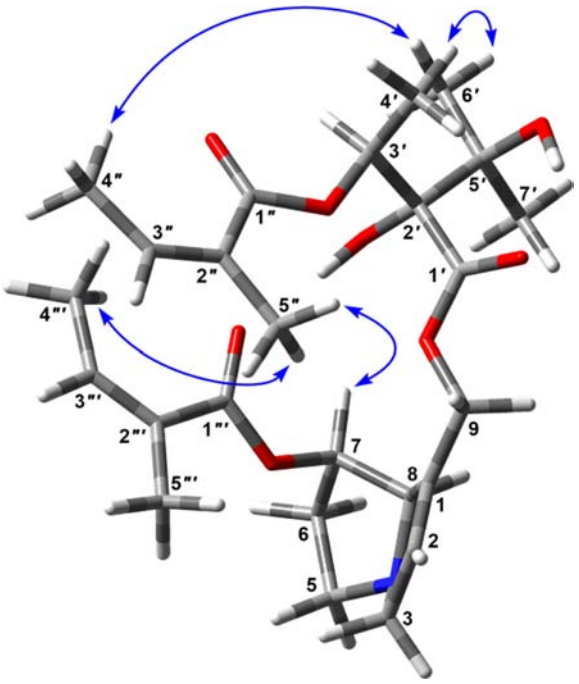

Figure 5. Lowest-energy conformer predicted for 7*R*,8*R*,2′*R*,3′*S*-echivulgarine, **2b**.

twisted geometry with an intramolecular hydrogen bond between the C-2′ hydroxyl group and the C-1‴ oxygen. This geometry is also supported by the key NOE correlations noted between H-4‴ and H-5″, H-7 and H-5″, and H-4‴ and H-6′, all of which were supportive of structure **2b**. Therefore, the absolute configuration of echivulgarine, **2**, was proposed to be 7*R*,8*R*,2′*R*,3′*S*, although this proposal would require further experiments such as X-ray crystallography or total synthesis to confirm this assignment.

To further verify the results, DP4 statistical analysis[27] was also applied to differentiate further among the different possible diastereomers of this highly flexible molecule. For this purpose, the previously selected conformers were subjected to NMR calculations at the PBE0-D3BJ/def2-SVP/SMD_{CCl2H2} level of theory. The Boltzmann-averaged NMR data of all calculated conformers and the experimental data were subjected to DP4 analysis, which also predicted the structure of **2b** to be the most probable candidate when both the ^{13}C and ^{1}H NMR data were used in the analysis. Overall, the combination of experimental and calculated NMR and ECD data all supported the same conclusion, an absolute configuration of 7*R*,8*R*,2′*R*,3′*S* for **2**. We also tentatively suggest that the structure of echivulgarine *N*-oxide, **3**,[14,15] be reassigned to reflect the complete planar and configurational assignments presented here for the parent tertiary amine, although such an inference would need to be confirmed by in-depth spectroscopic investigation of an authentic sample of this compound.

Given that different natural product congeners vary dramatically in ionization response (Table 2), and that this depends upon the type of mass spectrometer ion source, industry reliance upon mass spectrometric detection, identification and subsequent "quantitation" of newly discovered DHPAs may be risky. The toxic contributions of each DHPA to any food product would need to be assessed individually. Unfortunately, a paucity of material prevented the evaluation of the actual toxicity of **2** at this time.

Table 2. Relative MRM Ion Responses of Various DHPAs

compound name	precursor ion (m/z)	product ion (m/z)	sensitivity relative to echimidine ion 1
echimidine *N*-oxide ion 1	414.1	254.0	0.13
echimidine *N*-oxide ion 2	414.1	352.0	0.04
echimidine ion 1	398.1	120.1	1.00
echimidine ion 2	398.1	220.1	0.27
echivulgarine ion 1	480.1	120.1	1.45
echivulgarine ion 2	480.1	55.1	0.31
heliotrine ion 1	314.1	138.1	2.12
heliotrine ion 2	314.1	156.1	0.43
heliotrine *N*-oxide ion 1	330.1	172.1	2.00
heliotrine *N*-oxide ion 2	330.1	80.0	0.41
lycopsamine ion 1	300.1	94.1	0.49
lycopsamine ion 2	300.1	156.1	0.39
retrorsine ion 1	352.0	120.1	0.11
retrorsine ion 2	352.0	138.1	0.08
retrorsine *N*-oxide ion 1	368.0	118.1	0.20
retrorsine *N*-oxide ion 2	368.0	94.1	0.22
senecionine *N*-oxide ion 1	352.0	118.1	0.26
senecionine *N*-oxide ion 2	352.0	94.2	0.27
senecionine ion 1	336.1	120.1	0.32
senecionine ion 2	336.1	138.1	0.21
seneciphylline ion 1	334.0	120.1	0.23
seneciphylline ion 2	334.0	94.1	0.14
seneciphylline *N*-oxide ion 1	350.0	118.0	0.16
seneciphylline *N*-oxide ion 2	350.0	94.0	0.20
senkirkine ion 1	366.1	168.1	0.94
senkirkine ion 2	366.1	150.1	0.44

In the future, a potentially better approach to the global assessment of total DHPA concentration within a foodstuff could be the use of quantitative NMR (qNMR).[32] In fact, the use of ^{1}H NMR spectroscopy as a possible tool for pyrrolizidine alkaloid quantitation in *Senecio* plant species was first applied in 1979.[33] Since then, recent advances in NMR technology, specifically higher-field-strength magnets and cryogenically cooled and/or capillary probes, have allowed for significant increases in spectral dispersion and sensitivity, making such an instrumental approach more useful. NMR has the benefit of not varying significantly in response to congener composition, and the dynamic range is insensitive to widely varying concentrations of the metabolite.[32] Several works by the Molinski group[34−36] have shown that complete structural elucidation of complex marine macrolides is possible with as little as 7 μg, equating to concentrations of <30 nM. As an extension of these studies, they have also developed a methodology for qNMR determinations using the ^{13}C satellites detected in coupled ^{1}H NMR spectra to quantitate metabolites in the range of 1−200 nM.[37] Moreover, qNMR has very recently been used to determine the concentrations of azaspiracids, potent dinoflagellate toxins, for subsequent determination of LC−MS/MS ion response factors.[38] Consequently, the integra-

DOI: 10.1021/acs.jafc.5b02402
J. Agric. Food Chem. 2015, 63, 7421−7427

tion of various conserved DHPA resonances within a ^{1}H NMR spectrum and relating those to the area of an internal standard resonance (or resonances) would give an unbiased view of overall DHPA concentration. The overall DHPA content would give a measure of potential toxicity far more reliable than that of LC−MS measures of compounds with widely varying response factors, especially when calculating concentrations for regulatory reasons. We are currently evaluating the use of qNMR in such a fashion as a viable alternative for measuring DHPA content.

■ ASSOCIATED CONTENT

Supporting Information

The Supporting Information is available free of charge on the ACS Publications website at DOI: 10.1021/acs.jafc.5b02402.

Full experimental details regarding the isolation of echivulgarine, **2**, including experimental and calculated NMR, MS, MS/MS, and CD spectral data (PDF)

■ AUTHOR INFORMATION

Corresponding Author

*Telephone: +64 4 463 5117. Fax: +64 4 463 5249. E-mail: rob.keyzers@vuw.ac.nz.

Notes

E.C. is an employee of AsureQuality Ltd. All other authors declare no competing financial interests.

■ ACKNOWLEDGMENTS

We gratefully thank Dr. P. Northcote (Victoria University of Wellington) for assistance in acquiring the ^{1}H−^{15}N HMBC data and Dr. D. Stirling (AsureQuality Ltd.) for support of the project. We gratefully acknowledge Dr. J. Tallon (Robinson Research Institute, Victoria University of Wellington) for the use of his CD spectrometer. The considered comments and references suggested by several anonymous referees were valuable to the improvement of the manuscript, and the referees are thanked accordingly.

■ REFERENCES

(1) El-Shazly, A.; Wink, M. Diversity of pyrrolizidine alkaloids in the Boraginaceae: Structures, distribution, and biological properties. *Diversity* **2014**, *6*, 188−282.

(2) Robertson, J.; Stevens, K. Pyrrolizidine alkaloids. *Nat. Prod. Rep.* **2014**, *31*, 1721−1788.

(3) Mattocks, A. R. Toxicity of pyrrolizidine alkaloids. *Nature* **1968**, *217*, 723−727.

(4) Mattocks, A. R. Acute hepatotoxicity and pyrrolic metabolites in rats does with pyrrolizidine alkaloids. *Chem.-Biol. Interact.* **1972**, *5*, 227−242.

(5) White, I. N. H.; Mattocks, A. R.; Butler, W. H. The conversion of the pyrrolizidine alkaloid retrorsine to pyrrolic derivatives *in vivo* and *in vitro* and its acute toxicity to animal species. *Chem.-Biol. Interact.* **1973**, *6*, 207−218.

(6) Culvenor, C. C. J.; Dann, A. T.; Dick, A. T. Alkylation as the mechanism by which the hepatotoxic pyrrolizidine alkaloids act on cell nuclei. *Nature* **1962**, *195*, 570−573.

(7) Culvenor, C. C.; Edgar, J. A.; Jago, M. V.; Outteridge, A.; Peterson, J. E.; Smith, L. M. Hepato- and pneumotoxicity of pyrrolizidine alkaloids and derivatives in relation to molecular structure. *Chem.-Biol. Interact.* **1976**, *12*, 299−324.

(8) Smith, L. M.; Culvenor, C. C. J. Plant sources of hepatotixic pyrrolizidine alkaloids. *J. Nat. Prod.* **1981**, *44*, 129−152.

(9) Chou, M. W.; Wang, Y.-P.; Yan, J.; Yang, Y.-C.; Beger, R. D.; Williams, L. D.; Doerge, D. R.; Fu, P. P. Riddelliine *N*-oxide is a phytochemical and mammalian metabolite with genotoxic activity that is comparable to the parent pyrrolizidine alkaloid riddelliine. *Toxicol. Lett.* **2003**, *145*, 239−247.

(10) Molyneux, R. J.; Johnson, A. E.; Olsen, J. D.; Baker, D. C. Toxicity of pyrrolizidine alkaloids from Riddell groundsel (*Senecio riddellii*) to cattle. *Am. J. Vet. Res.* **1991**, *52*, 146−151.

(11) Dübecke, A.; Beckh, G.; Lüllmann, C. Pyrrolizidine alkaloids in honey and bee pollen. *Food Addit. Contam., Part A* **2011**, *28*, 348−358.

(12) Culvenor, C. C. J.; Edgar, J. A.; Smith, L. W. Pyrrolizidine alkaloids in honey from *Echium plantagineum* L. *J. Agric. Food Chem.* **1981**, *29*, 958−960.

(13) Bodi, D.; Ronczka, S.; Gottschalk, C.; Behr, N.; Skibba, A.; Wagner, M.; Lahrssen-Wiederholt, M.; Preiss-Weigert, A.; These, A. Determination of pyrrolizidine alkaloids in tea, herbal drugs and honey. *Food Addit. Contam., Part A* **2014**, *31*, 1886−1895.

(14) Boppré, M.; Colegate, S. M.; Edgar, J. A. Pyrrolizidine alkaloids of *Echium vulgare* honey found in pure pollen. *J. Agric. Food Chem.* **2005**, *53*, 594−600.

(15) Beales, K. A.; Betteridge, K.; Colegate, S. M.; Edgar, J. A. Solid-phase extraction and LC-MS analysis of pyrrolizidine alkaloids in honeys. *J. Agric. Food Chem.* **2004**, *52*, 6664−6672.

(16) Colegate, S. M.; Edgar, J. A.; Knill, A. M.; Lee, S. T. Solid-phase extraction and HPLC-MS profiling of pyrrolizidine alkaloids and their N-oxides: a case study of *Echium plantagineum*. *Phytochem. Anal.* **2005**, *16*, 108−119.

(17) Pedretti, A.; Villa, L.; Vistoli, G. VEGA: a versatile program to convert, handle and visualize molecular structure on Windows-based PCs. *J. Mol. Graphics Modell.* **2002**, *21*, 47−49.

(18) Frisch, M. J.; Trucks, G. W.; Schlegel, H. B.; Scuseria, G. E.; Robb, M. A.; Cheeseman, J. R.; Scalmani, G.; Barone, V.; Mennucci, B.; Petersson, G. A.; Nakatsuji, H.; Caricato, M.; Li, X.; Hratchian, H. P.; Izmaylov, A. F.; Bloino, J.; Zheng, G.; Sonnenberg, J. L.; Hada, M.; Ehara, M.; Toyota, K.; Fukuda, R.; Hasegawa, J.; Ishida, M.; Nakajima, T.; Honda, Y.; Kitao, O.; Nakai, H.; Vreven, T.; Montgomery, J. A., Jr.; Peralta, J. E.; Ogliaro, F.; Bearpark, M.; Heyd, J. J.; Brothers, E.; Kudin, K. N.; Staroverov, V. N.; Kobayashi, R.; Normand, J.; Raghavachari, K.; Rendell, A.; Burant, J. C.; Iyengar, S. S.; Tomasi, J.; Cossi, M.; Rega, N.; Millam, J. M.; Klene, M.; Knox, J. E.; Cross, J. B.; Bakken, V.; Adamo, C.; Jaramillo, J.; Gomperts, R.; Stratmann, R. E.; Yazyev, O.; Austin, A. J.; Cammi, R.; Pomelli, C.; Ochterski, J. W.; Martin, R. L.; Morokuma, K.; Zakrzewski, V. G.; Voth, G. A.; Salvador, P.; Dannenberg, J. J.; Dapprich, S.; Daniels, A. D.; Farkas, Ö.; Foresman, J. B.; Ortiz, J. V.; Cioslowski, J.; Fox, D. J. *Gaussian 09*, revision D.01; Gaussian Inc.: Wallingford, CT, 2010.

(19) Perdew, J. P.; Burke, K.; Ernzerhof, M. Generalized gradient approximation made simple. *Phys. Rev. Lett.* **1996**, *77*, 3865−3868.

(20) Handy, N. C.; Cohen, A. J. Left-right correlation energy. *Mol. Phys.* **2001**, *99*, 403−412.

(21) Hoe, W.-M.; Cohen, A. J.; Handy, N. C. Assessment of a new local exchange functional OPTX. *Chem. Phys. Lett.* **2001**, *341*, 319−328.

(22) Adamo, C.; Barone, V. Toward reliable density functional methods without adjustable parameters: The PBE0 model. *J. Chem. Phys.* **1999**, *110*, 6158−6170.

(23) Grimme, S.; Antony, J.; Ehrlich, S.; Krieg, H. A consistent and accurate ab initio parametrization of density functional dispersion correction (DFT-D) for the 94 elements H-Pu. *J. Chem. Phys.* **2010**, *132*, 154104.

(24) Grimme, S.; Ehrlich, S.; Goerigk, L. Effect of the damping function in dispersion corrected density functional theory. *J. Comput. Chem.* **2011**, *32* (7), 1456−1465.

(25) Tomasi, J.; Mennucci, B.; Cammi, R. Quantum mechanical continuum solvation models. *Chem. Rev.* **2005**, *105*, 2999−3094.

(26) Marenich, A. V.; Cramer, C. J.; Truhlar, D. G. Universal solvation model based on solute electron density and on a continuum model of the solvent defined by the bulk dielectric constant and atomic surface tensions. *J. Phys. Chem. B* **2009**, *113*, 6378−6396.

(27) Smith, S. G.; Goodman, J. M. Assigning stereochemistry to single diastereoisomers by GIAO NMR calculation: The DP4 probability. *J. Am. Chem. Soc.* **2010**, *132*, 12946−12959.

DOI: 10.1021/acs.jafc.5b02402
J. Agric. Food Chem. 2015, 63, 7421−7427

(28) Stratmann, R. E.; Scuseria, G. E.; Frisch, M. J. An efficient implementation of time-dependent density-functional theory for the calculation of excitation energies of large molecules. *J. Chem. Phys.* **1998**, *109*, 8218−8224.
(29) Roeder, E. Carbon-13 NMR spectroscopy of pyrrolizidine alkaloids. *Phytochemistry* **1990**, *29*, 11−29.
(30) Colegate, S. M.; Gardner, D. R.; Davis, T. Z.; Betz, J. M.; Panter, K. E. Dehydropyrrolizidine alkaloids in two *Cryptantha* species: Including two new open chain diesters one of which is amphoteric. *Phytochem. Anal.* **2013**, *24*, 201−212.
(31) Bruhn, T.; Schaumlöffel, A.; Hemberger, Y.; Bringmann, G. SpecDis: Quantifying the comparison of calculated and experimental electronic circular dichroism spectra. *Chirality* **2013**, *25*, 243−249.
(32) Pauli, G. F.; Chen, S.-N.; Simmler, C.; Lankin, D. C.; Gödecke, T.; Jaki, B. U.; Friesen, J. B.; McAlpine, J. B.; Napolitano, J. G. Importance of purity evaluation and the potential of quantitative ^{1}H NMR as a purity assay. *J. Med. Chem.* **2014**, *57*, 9220−9231.
(33) Molyneux, R. J.; Johnson, A. E.; Roitman, J. N.; Benson, M. E. Chemistry of toxic range plants. Determination of pyrrolizidine alkaloid content and composition in *Senecio* species by nuclear magnetic resonance spectroscopy. *J. Agric. Food Chem.* **1979**, *27*, 494−499.
(34) Dalisay, D. S.; Rogers, E. W.; Edison, A. S.; Molinski, T. F. Structure elucidation at the nanomole scale. 1. Trisoxazole macrolides and thiazole-containing cyclic peptides from the nudibranch *Hexabranchus sanguineus*. *J. Nat. Prod.* **2009**, *72*, 732−738.
(35) Dalisay, D. S.; Molinski, T. F. Structure elucidation at the nanomole scale. 2. Hemi-phorboxazole A from *Phorbas* sp. *Org. Lett.* **2009**, *11*, 1967−1970.
(36) Dalisay, D. S.; Molinski, T. F. Structure elucidation at the nanomole scale. 3. Phorbasides G-I from *Phorbas* sp. *J. Nat. Prod.* **2010**, *73*, 679−682.
(37) Dalisay, D. S.; Molinski, T. F. NMR quantitation of natural products at the nanomole scale. *J. Nat. Prod.* **2009**, *72*, 739−744.
(38) Kilcoyne, J.; Twiner, M. J.; McCarron, P.; Crain, S.; Giddings, S.; Foley, B.; Rise, F.; Hess, P.; Wilkins, A.; Miles, C. O. Structure elucidation, relative LC-MS response and *in vitro* toxicity of azaspiracids 7−10 isolated from mussels (*Mytilus edulis*). *J. Agric. Food Chem.* **2015**, *63*, 5083−5091.

DOI: 10.1021/acs.jafc.5b02402
J. Agric. Food Chem. 2015, 63, 7421−7427

addition to these, the other carotenoids that have been identified so far are phytoene, phytofluene, ζ-carotene, γ-carotene, and neurosporene.[12,18,19]

Even if the chromatographic behavior and the UV-vis absorption spectrum offer valuable clues for the identification of carotenoids, the MS detection has recently been combined with DAD to enhance identification power and sensitivity of their LC analysis in complex matrices.[20−27] Besides molecular weight, MS can provide molecular structure information, based on fragmentation patterns, to support the UV−vis identification of structural and geometrical isomers[11,28−30] as well as that of epoxidized forms.[31]

This work has aimed at developing an effective analytical approach, based on the HPLC-DAD-QqQ$_{LIT}$ hyphenation, to profile carotenoids occurring in five of the most known Italian tomato varieties: 'Tangerine', 'Pachino', 'Datterino', 'Camone', and 'San Marzano'. Six carotenoids, whose authentic standards are commercially available and moderately expensive, were used as model compounds to predict the behavior of carotenes and xanthophylls toward the chromatographic retention on a C_{30} stationary phase and the chemical ionization at atmospheric pressure. The product ion scan spectra (PIS) of these six compounds and the enhanced product ion (EPI) spectra of untargeted carotenoids, obtained by planning an adequate IDA experiment, allowed us to select MRM transitions useful (i) to support the LC-DAD identification of major carotenoids, (ii) to screen carotenoids occurring at low concentrations with high sensitivity, and (iii) to discriminate among structural isomers by using, for the first time, the ion ratio. Compared to the previous LC-DAD-MS methods,[11,28−31] the developed approach has made possible the acquisition of a large number of experimental data to realize a large-scale screening by using a minimum number of analytical standards; since the latter ones are very expensive and/or difficult to find, our approach also offers a considerable economical and practical advantage.

All data on the composition of the different varieties of tomatoes will be presented and discussed in this paper along with the results related to the method development.

EXPERIMENTAL SECTION

Chemicals and Materials. *all-trans-β*-Carotene, *all-trans*-lutein, *all-trans*-zeaxanthin, *all-trans-β*-cryptoxanthin, and *all-trans*-lycopene were provided by Aldrich-Fluka-Sigma Chemical (Milan, Italy). *all-trans-γ*-Carotene was acquired from CaroteNature GmbH (Ostermundigen, Switzerland). All standards had a purity grade ≥90% and were used without further purification.

Butylated hydroxytoluene (BHT), provided by Aldrich-Fluka-Sigma Chemical, was used as antioxidant both in standard solutions and during the several steps of extraction procedure. Acetonitrile and methanol were RS-Plus grade (special grade reagents); 2-propanol, hexane, and chloroform were RS grade (elevated purity grade); absolute ethanol was RPE grade (analytical grade). All of these solvents, potassium hydroxide (KOH), magnesium carbonate, and sodium sulfate were purchased from Carlo Erba (Milan, Italy). Distilled water, used in the extraction procedure based on the cold saponification, was further purified by passing it through a Milli-Q Plus apparatus (Millipore, Bedford, MA, USA).

Diatomaceous earth SPE-ED MATRIX 38 was purchased from Applied Separations (Allentown, PA, USA). Syringe-like polypropylene tubes (i.d. 26 mm, 75 mL capacity) and polyethylene frits were from Alltech (Deerfield, IL, USA).

Standard Solutions. After a stability study was performed over a period of 30 days, the individual stock solutions of the six carotenoids were prepared fortnightly by dissolving the weighed amounts (OHAUS DV215CD Discovery Semi-Micro and Analytical Balance 81 g/210 g capacity, 0.01 mg/0.1 mg readability) in chloroform containing 0.1% (w/v) BHT at the following concentrations:

- 1 μg/μL, for *all-trans-β*-carotene and *all-trans*-lycopene
- 0.5 μg/μL, for *all-trans*-lutein (sonicating for 6 min at 30 °C), *all-trans*-zeaxanthin, *all-trans-β*-cryptoxanthin
- 0.2 μg/μL for *all-trans-γ*-carotene

Working multistandard solutions were prepared from the individual stock solutions by diluting in methanol with 0.1% (w/v) BHT to obtain concentrations suitable for the several studies and experiments. When unused, all preparations were degassed with nitrogen and stored in amber glass flasks at −18 °C in the dark. Authentic standards were stored at −80 °C.

Tomato and Passata Samples. The five tomato varieties ('Tangerine', 'Pachino', 'Datterino', 'Camone', 'San Marzano') selected for this study were purchased from some supermarkets and green-groceries of Rome. The passata of 'San Marzano' tomatoes was homemade or bought from local grocery stores.

Tangerine tomato owes its orange color to the prevalence of *cis*-lycopenes that, in its GMO variants, accumulate prevalently as prolycopene; in this work, we have studied the wild type.[32] 'Pachino' is a protected geographical indication (GPI) variety, produced in a restricted area of Sicily; we have considered the cherry type, characterized by small, sweet, and bright red fruits. Also the 'Datterino' variety has small fruits, but they have an elongated form and a superior sweetness. The 'Camone' variety was introduced in the mid-1980s in the south of Sardinia; its fruits are red-green, crispy, and suitable for salads. Finally, the 'San Marzano' tomato is an Italian variety with protected designation of origin (PDO), and it is famous worldwide because its red pulpy fruits are particularly suitable for making passata. The passata preparation provides few fundamental steps: blanching of tomatoes in boiling water for 20 to 30 s, squeezing of the peeled fruits, sieving to separate the juice from the skins and flesh, bottling of the juice, and finally, sterilization at 95−100 °C.

Sample Treatment. A whole fruit was homogenized in an Ultra-Turrax homogenizer (Janke & Kunkle, Staufenim Breisgau, Germany), adding magnesium carbonate (in a ratio of 10:1, w/w) to neutralize the released organic acids and BHT (in a ratio of 10:0.1, w/w), in order to prevent isomerization and degradation of carotenoids. Tomato passata, ready to be used, was only spiked with BHT at the specified ratio.

Two different extraction procedures were used to exclude the potential formation of artifacts: overnight cold saponification and matrix solid phase dispersion (MSPD). In both procedures, the analytes were shielded from UV light by using low actinic glass tubes and plastic tubes wrapped with aluminum foil; for the same reason, all operations were performed in subdued light. Protection from oxygen was ensured by the addition of BHT to the solvents (0.1% (w/v)).

Overnight Cold Saponification. A 4 g aliquot of homogenized tomato was transferred into a 50 mL polypropylene centrifuge tube with a screw-cap (falcon). Six milliliters of absolute ethanol containing BHT and 1 mL of 50% (w/v) aqueous KOH were poured into the centrifuge tube. After flushing with oxygen-free nitrogen, the falcon was promptly closed and placed in a water bath kept at 25 °C, under magnetic stirring overnight (15 h).

At the end of the incubation period, the digest was diluted with 3 mL of Milli-Q water and the analytes were extracted with 4 mL of hexane with 0.1% (w/v) BHT. The extraction was repeated six times. After the addition of each aliquot, the mixture was stirred for 5 min, vortexed for 5 min, and then, centrifuged at 6000 rpm for 10 min to facilitate the separation of the insoluble residue, aqueous phase, and organic phase. Afterward, the combined hexane layers were washed with 8 mL portions of Milli-Q water; two washings were enough to remove alkalis completely (no color was observed on phenolphthalein addition). At this point, the extract was collected into a glass tube with conical bottom (i.d. 2 cm), evaporated up to 100 μL in a water bath kept at 30 °C under a slow nitrogen flow, and diluted to a final volume of 200 μL with 2-propanol:hexane (75:25, v/v) solution containing 0.1% (w/v) BHT. Eventually, after sonication for 10 min at 25 °C, 40 μL was injected into the HPLC-DAD-QqQ$_{LIT}$ system.

DOI: 10.1021/acs.jafc.5b02910
J. Agric. Food Chem. 2015, 63, 7428−7439

Matrix Solid Phase Dispersion. Owing to the high water content of tomato fruit and passata, MSPD was performed by using diatomaceous earth, as a dispersing medium, in combination with sodium sulfate, a highly hygroscopic salt.

For each experiment, 4 g of sample, 6 g of diatomaceous earth, and 2 g of Na_2SO_4 were placed into a ceramic mortar and pounded with a pestle until the achievement of an evenly colored powder. At this point, the extraction cartridge was prepared by filling large-diameter syringe-like polypropylene tubes with a layer of C_{18} sorbent (0.4 g) and a layer of the solid mixture, in this order. Polyethylene frits were placed below and above the chromatographic bed.

The analytes were eluted with 15 mL of methanol, 5 mL of 2-propanol, and 20 mL of hexane, with the aid of vacuum. The eluates were collected into a 50 mL falcon and centrifuged at 6000 rpm for 10 min. The supernatant was poured out into a glass tube with conical bottom (i.d. 2 cm) and evaporated up to 200 μL in a water bath kept at 25 °C under a gentle flow of nitrogen. The extract was then sonicated for 2 min, transferred into an Eppendorf tube, and centrifuged (Centric150, Tehtnica, Slovenia) at 4000 rpm for 5 min. Forty microliters was injected into the chromatographic column for the HPLC-DAD-QqQ$_{LIT}$ analysis.

Instrumentation. *Liquid Chromatography.* Liquid chromatography was performed by means of a micro HPLC series 200 (PerkinElmer, Norwalk, CT, USA) equipped with an autosampler, a vacuum degasser, and a column oven.

The analytes were separated on a ProntoSIL C30 column (4.6 mm i.d. × 250 mm, 3 μm particle size) from Bischoff Chromatography (Leonberg Germany) protected by a guard column of the same type (4.0 × 10 mm, 5 μm) under nonaqueous reversed-phase (NARP) conditions and with the column kept at 19 °C. In separating carotenoids, phase A was methanol and phase B a mixture 2-propanol/hexane 50:50 v/v. The elution profile was as follows: after the first minute in isocratic mode at 100% of eluent A, phase B was linearly increased from 0% to 50% in 20 min and then from 50% to 99.5% in 0.1 min; finally, phase B was maintained at 99.5% for 10 min. Flow rate of the mobile phase was 1 mL/min, and it was entirely introduced into the DAD-MS detection system. Phase B was also used to wash the autosampler injection device.

Diode Array Detection. Carotenoids were identified by a series 200 model (PerkinElmer) diode array detector, equipped with a flow Z cell (12 μL volume; optical path of 10 mm), coupled online between the chromatographic column and the mass spectrometer. The LC-DAD chromatograms were acquired by selecting the 450 nm wavelength (λ_{max} of *all-trans-β*-carotene, *all-trans*-zeaxanthin, and *all-trans-β*-cryptoxanthin) and a bandwidth of 10 nm. The UV−vis spectra were recorded in the range of 200−700 nm. The software packages used for running the instrument and acquiring spectral data were Totalchrom Navigator 6.3.1 and Iris (PerkinElmer) respectively.

Mass Spectrometry. The analytes were also identified by means of a 4000 Qtrap (AB SCIEX, Foster City, CA, USA) mass spectrometer. Detection was performed in positive ionization, placing the APCI probe in the Turbo V source and setting a needle current (NC) of 3 μA and a probe temperature of 450 °C. High-purity nitrogen was used as curtain (40 psi) and collision gas (4 mTorr), whereas air was used as nebulizer (55 psi) and makeup gas (30 psi).

A preliminary mass axis calibration of each quadrupole mass-analyzer, Q_1 and Q_3, was carried out by infusion of a polypropylene glycol solution at 10 μL/min. Unit mass resolution was established and kept in the each mass-resolving quadrupole by maintaining a full width at half-maximum (fwhm) of approximately 0.7 ± 0.1 u.

The APCI-Q1-full scan spectrum and the PIS spectra of *all-trans*-lutein, *all-trans*-zeaxanthin, *all-trans-β*-cryptoxanthin, *all-trans-β*-carotene, *all-trans-γ*-carotene, and *all-trans*-lycopene were acquired by working in flow injection analysis (1−10 ng injected; 1 mL/min of flow rate).

Structural information on untargeted carotenoids in the real samples was obtained by acquiring an IDA scan cycle, including an enhanced-mass scan (EMS) as the survey scan, an enhanced-resolution (ER) scan to obtain high resolution m/z values for the precursor ions of interest, and dependent EPI scan. With the threshold of the ion intensity at 10000 counts per second (cps), the IDA criteria were set to allow the most abundant ions in the EMS to trigger EPI scans. The EMS scan was carried out from m/z 500 to m/z 610 at 100 ms of dwell time. The EPI scan was in the range m/z 100−610, scanned at 4000 Da/s, under a collision energy (CE) of 60 eV with a CE spread of 20 eV (60 ± 20 eV).

A sensitive LC-DAD-MRM screening of carotenoids in real samples was performed selecting two MRM transitions per carotenoid on the basis of the fragmentation spectra previously acquired; when such fragmentation spectra were not available, two theoretical MRM transitions were "guessed" by using ChemBioDraw Ultra 12.0.

The software used for running the instrument and acquiring LC-MS data was Analyst 1.5.1 (AB Sciex).

RESULTS AND DISCUSSION

Selection of Nonaqueous Reversed-Phase Chromatographic Conditions as a Compromise between Requirements of Separation and MS Detection. The NARP chromatography has often been used for the separation of carotenoids and fat-soluble vitamins.[30,33] This technique makes use of C_{18} or C_{30} columns and of poorly polar mobile phases. The triacontyl stationary phase is superior to the octadecyl one for shape selectivity, which significantly improves at subambient temperature. A typical nonaqueous mobile phase consists of a polar solvent (for instance, acetonitrile or methanol) and a solvent of lower polarity (for example, dichloromethane) to solubilize the analytes and to adjust the eluting strength of the mobile phase. It is well-known that the APCI ionization process uses the mobile-phase vapor as reactant gas in addition to the nebulizer gas and makeup gas; nevertheless, the composition of a nonaqueous mobile phase is, in general, not completely suitable to support APCI ionization. For this reason, our chromatographic conditions were selected as a compromise between requirements of separation and MS detection. The six model compounds were used to refine the separative conditions which included the use of

- a C_{30} analytical column, kept at 19 °C to enhance shape selectivity and efficiently solve structural and geometrical isomers
- methanol and a mixture 2-propanol:hexane (50:50, v/v) as mobile phase. Hexane is not involved in the acid−base reactions during APCI ionization, but it was indispensable to reduce the retention time of carotenes (especially lycopene) and to avoid peak broadening phenomena due to longitudinal diffusion. Both alcohols participate in the acid−base reactions; in particular, in order to assist the ionization of the analytes with high capacity factors, a percentage of 0.5% methanol was maintained in the final part of the chromatographic run.

The chromatographic selectivity was adjusted by modulating the polarity difference between stationary phase and mobile phase: the smaller was the difference, the higher was the selectivity. Selecting this mobile phase we have achieved good results in terms of resolution.

Identification Criteria of Carotenoids by HPLC-DAD-QqQ$_{LIT}$. The model compounds were also used to study their APCI ionization and fragmentation, and to forecast the chromatographic retention of untargeted carotenoids on the triacontyl-bonded stationary phase. Table 1 shows the parameters applied for their identification in tomato and passata samples (retention time, two MRM transitions for each analyte, ion ratio).

Expected Retention Time. The expected retention time is an important parameter to support the UV−vis/MS identification of a specific carotenoid. In this work, it has been deduced both on

DOI: 10.1021/acs.jafc.5b02910
J. Agric. Food Chem. 2015, 63, 7428−7439

Table 1. LC-MRM Parameters Used for the Identification of the Six Model Carotenoids

carotenoid	retention time: mean ± SD[a] (min)	MRM transitions	ion ratio:[b] mean ± SD[a]	DP[c] (V)	CE[d] (eV)
all-trans-lutein	10.6 ± 0.4	551.5/175	0.6 ± 0.1	55	40
		551.5/135			30
all-trans-zeaxanthin	11.2 ± 0.4	569.6/175	0.5 ± 0.1	30	60
		569.6/119			40
all-trans-β-cryptoxanthin	13.8 ± 0.4	553.5/175	1.3 ± 0.1	30	70
		553.5/119			60
all-trans-β-carotene	17.9 ± 0.5	537/177	1.5 ± 0.1	70	30
		537/119			60
all-trans-γ-carotene	20.4 ± 0.5	537/177	0.8 ± 0.1	70	30
		537/119			60
all-trans-lycopene	26.8 ± 0.5	537/177	0.4 ± 0.1	70	30
		537/119			60

[a]Standard deviation. [b]The ion ratio was calculated as follows: I_r = (intensity$_{(\text{MRM on the first line})}$/intensity$_{(\text{MRM on the second line})}$. [c]Declustering potential. [d]Collision energy.

the basis of the chromatographic behavior of the six model compounds under the NARP conditions, described in the Liquid Chromatography section, and on the basis on data from the literature.[33] The following elution patterns have been considered for the prediction of retention times:

(i) The increase of molecular weight or the conjugation extension corresponds to longer retention time.

(ii) The retention time decreases as the number of hydroxyl and/or epoxy groups increases, because the increase of polarity prevails over the corresponding increase of the chromophore length; therefore, among β,β-type carotenoids, zeaxanthin elutes before β-cryptoxanthin, which, in turn, elutes before β-carotene. This behavior has allowed us to simplify the carotenoid identification, subdividing each LC-DAD-MS chromatogram into three regions: the first one including xanthophylls with two and more than two polar groups (t_r up to 12 min); the second one comprising xanthophylls with only one polar group (t_r between ∼12 and 15 min); finally, the third one encompassing carotenes (t_r between ∼15 and 26 min). Within each of these ranges, further considerations can be made to postulate the retention times. For example:
- Comparing the chromatographic behavior of the pairs lutein/zeaxanthin and α-carotene/β-carotene (mixed carotenes from carrots; purchased Aldrich-Fluka-Sigma Chemical, Milan, Italy), it can be deduced that β,ε-carotenoids have a lower retention time than β,β-carotenoids.
- A bicyclic carotenoid elutes before a monocyclic carotenoid that, in turn, elutes before an acyclic carotenoid; for example, β-carotene (bicyclic β,β) elutes before the γ-carotene (β,ψ-carotene), which in turn elutes before lycopene (ψ,ψ-carotene).

(iii) The molecule shape can affect the retention of carotenoids, sometimes representing an exception to the rule in the point (i). For example:
- 5,8-Epoxycarotenoids (mutatoxanthin) elute later than the 5,6-epoxycarotenoids (antheraxanthin, taraxanthin), although 5,8-epoxycarotenoids have a shorter chromophore. This happens because the 5,8-epoxide group affects the molecule shape and exerts a deep interaction with the stationary phase despite of the less extensive conjugation length.[33]
- A *cis* double bond affects the elution order of equal length chromophores, depending on its location in the system of conjugated double bonds.[33] The 15-*cis*-isomers are the least retained because their molecules are more twisted than the 13-*cis*- and 13,9-di-*cis* isomers. On the other hand, carotenoids with peripheral *cis* double bonds (9-*cis*- and 9,9′-di-*cis*-isomers for bicyclic carotenoids; 5-*cis*-isomers for monocyclic and acyclic carotenoids) are more retained than the *all-trans* isomers which, thus, elute between the next-to-central and the peripheral geometrical isomers.

MS Identification Criteria. On the basis of what was observed in this work and described in previous papers[20,34] and reviews,[30,35,36] it can be stated that both carotenes and xanthophylls show $[M + H]^+$ as base peak on APCI(+)-full scan mass spectra. For *all-trans*-β-carotene, *all-trans*-γ-carotene, and *all-trans*-lycopene, such an ion is observed at m/z 537; when

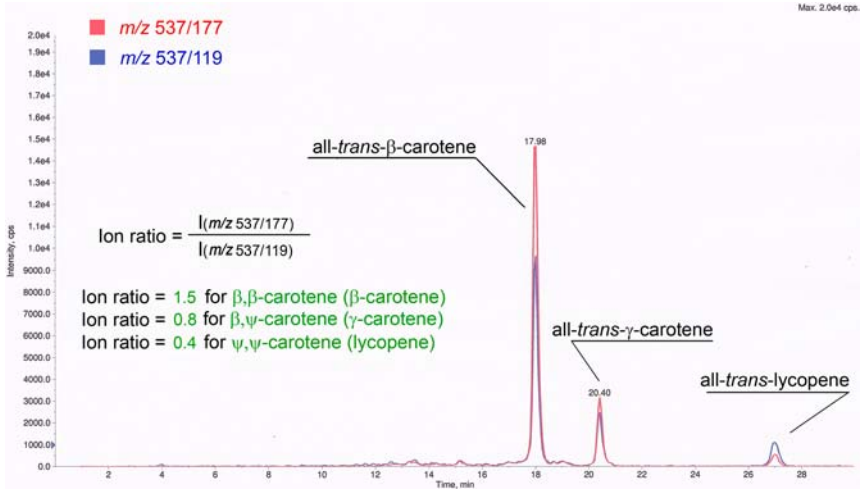

Figure 1. Relative abundance of two MRM transitions, shared by isomeric carotenes, is an effective parameter to distinguish and identify *all-trans*-β-carotene, *all-trans*-γ-carotene, *all-trans*-lycopene, and the related families of geometrical isomers in real samples (see also Figure 4).

DOI: 10.1021/acs.jafc.5b02910
J. Agric. Food Chem. 2015, 63, 7428−7439

selected as precursor ion in MS/MS experiments, it exhibits a similar fragmentation pattern with two series of fragment ions: the first series is originated from breaking the double bonds (C7−C8, C9−C10, C11−C12, C13−C14, and C15−C15′) and generates intense product ions at m/z 137 and m/z 177; the second series is due to the cleavage of single bonds (C6−C7, C10−C11, C12−C13, and C14−C15) and produces an abundant ion at m/z 119. The main distinctions between the PIS spectra of these three structural isomers consist of the different intensities of the common fragment ions.

Besides $[M + H]^+$, xanthophylls also show the dehydrated ion $[MH - H_2O]^+$. Zeaxanthin and β-cryptoxanthin are β,β-carotenols and exhibit $[M + H]^+$ as base peak, while lutein is a β,ε-carotenol and has $[MH - H_2O]^+$ as base peak. In general, all carotenols with a hydroxyl group in an allylic position (for example lutein and α-cryptoxanthin) lose a water molecule, producing an intense fragment ion which is stabilized by mesomeric effects.[35] We have exploited this behavior to distinguish isomeric xanthophylls from each other such as lutein from zeaxanthin or lutein epoxide from antheraxanthin. Product ions common to all xanthophylls are the fragments at m/z 135 and m/z 175, corresponding to a dehydrated terminal ring with cleavage at the C7−C8 bond and the C9−C10 bond, respectively: these ions can be considered diagnostic for this carotenoid class. Like β-carotene, γ-carotene, and lycopene, also lutein and zeaxanthin are structural isomers which share similar fragmentation pattern; nevertheless, unlike carotenes, lutein exhibits two exclusive fragment ions at m/z 495 and m/z 430.[37] However, their intensity is too low to detect lutein (and to distinguish it from zeaxanthin) at the concentrations naturally occurring in tomato samples. To this end, the abundant ion at m/z 119 is more useful despite its lower specificity.

Relying on the PIS spectra, we have selected the two most intense MRM transitions to identify each model compound as well as their isomeric unknowns (sharing the same ion currents). Although there is no unique fragment to differentiate carotenes that are structural isomers, we have found a simple but efficacious solution to this problem: the relative abundance between the two MRM transitions, shared *all-trans*-β-carotene, *all-trans*-γ-carotene, and *all-trans*-lycopene, provides a characteristic ion ratio (see Table 1 and Figure 1) which we have used successfully to distinguish the three carotenes and their families of geometrical isomers in the real samples (see the paragraph entitled Characterization of the Carotenoid Fraction of Some Italian Varieties of Tomatoes).

For carotenoids that are not isomers of the six model compounds, the MRM transitions have been deduced from the EPI spectra acquired by the IDA experiments. When the sensitivity of the IDA analysis was poor, theoretical MRM transitions were inferred by using the Fragmentation Tools, provided by the software ChemBioDraw 12.0.

In general, the MRM scan mode is particularly effective in the identification of low-abundance compounds. Moreover, the partial specificity of MRM ion currents of isomeric carotenoids is advantageous because it allows their screening without having the availability of all the authentic standards, but on the condition that their chromatographic separation is guaranteed. To this aim, we used the model compounds also to verify the complete chromatographic separation of the isomeric groups lycopene/γ-carotene/β-carotene and lutein/zeaxanthin. A good resolution was achieved as a result of the chromatographic selectivity related to the small polarity difference between nonaqueous reversed mobile phase and C_{30} stationary phase.

In this work, the UV−vis data have been correlated with the MS data, considering that the retention times on the LC-MS chromatogram are about 0.8 min later compared to those on the corresponding LC-DAD chromatogram.

UV−Vis Identification Criteria. Carotenoids are characterized by a strong absorption in the UV−vis region of electromagnetic spectrum due to the extensive conjugated double-bond system. The majority of these compounds exhibit a three-peak spectrum[5,7] whose fine structure and absorption maxima allow the chromophore identification. In this work, the experimental UV−vis data have been compared to both the literature data and theoretical data. The latter has been obtained by applying the Fieser rules,[38] which allows foreseeing the wavelength of the central peak (λ_{II} or λ_{max}) on the basis of the hypothesized structure:

$$\lambda_{max} = 114 + 5M + n(48 - 1.7n) - 16.5R_{endo} - 10R_{exo}$$
for carotenes (1)

$$\lambda_{max} = 114 + 5M + n(55.5 - 2.1n) - 16.5R_{endo}$$
for carotenals and carotenic acids (2)

$$\lambda_{max} = 118 + 5M + n(48 - 1.7n) - 23R_{endo}$$
for epoxycarotenoids (3)

where n = number of conjugated double bonds; M = number of alkyl or alkyl-like substituents on the conjugated system; R_{endo} = number of rings with endocyclic double bonds in the conjugated system; R_{exo} = number of rings with exocyclic double bonds.

Such rules are valid only if the polyene moiety contain more than 4 conjugated double bonds.

In all cases, the degree of fine structure has been expressed as the percentage ratio between the heights of the peaks II and III, measured from baseline (i.e., % III/II).

The identification of a *cis* isomer[5] has relied on the comparison between its absorption spectrum and that of the corresponding *all-trans* isomer. The following differences have been evaluated: (i) a decrease of % III/II; (ii) a hypochromic effect; (iii) a hypsochromic shift of about 2−6 nm for mono-*cis* isomers, 10 nm for di-*cis* isomers, and 50 nm for poli-*cis* isomers; (iv) the appearance of a *cis*-peak (peak B) in the UV region. Since the height of the *cis*-peak increases as the *cis*-double bond becomes closer and closer at the center of the conjugated system, the *Q*-ratio has been used as parameter to establish the position of such a bond.[7] This parameter has been calculated as the ratio between the heights of the peaks II and B, measured from the baseline of spectrum; in the literature, it is sometimes calculated also as (B/II).

Extraction of Carotenoids from Tomato Fruits and Passata. In this work, the extraction of carotenoids from the real samples has been achieved by applying two different extraction methodologies: (a) cold saponification and (b) MSPD. The definitive conditions were established after optimizing several parameters including sample amount, type of extractants, and volume of extractants.

In general, hot saponification is one of the most used procedures to extract carotenoids from foods because it allows the effective removal of lipids and chlorophylls. In alkaline media, carotenoids are quite stable, but isomerization and degradation can occur to an extent depending on the applied conditions, especially for xanthophylls.[39] To avoid these processes, we applied milder conditions by digesting the real samples overnight

DOI: 10.1021/acs.jafc.5b02910
J. Agric. Food Chem. 2015, 63, 7428−7439

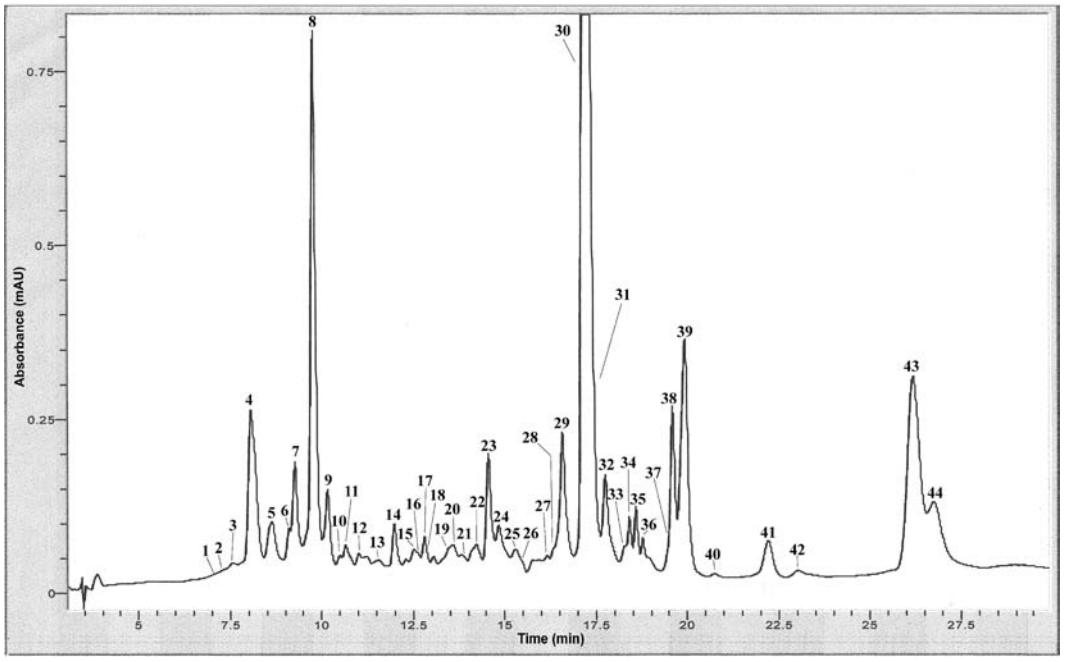

Figure 2. LC-DAD chromatogram, acquired at 450 nm, of a saponified extract from 'Wild Tangerine' tomato.

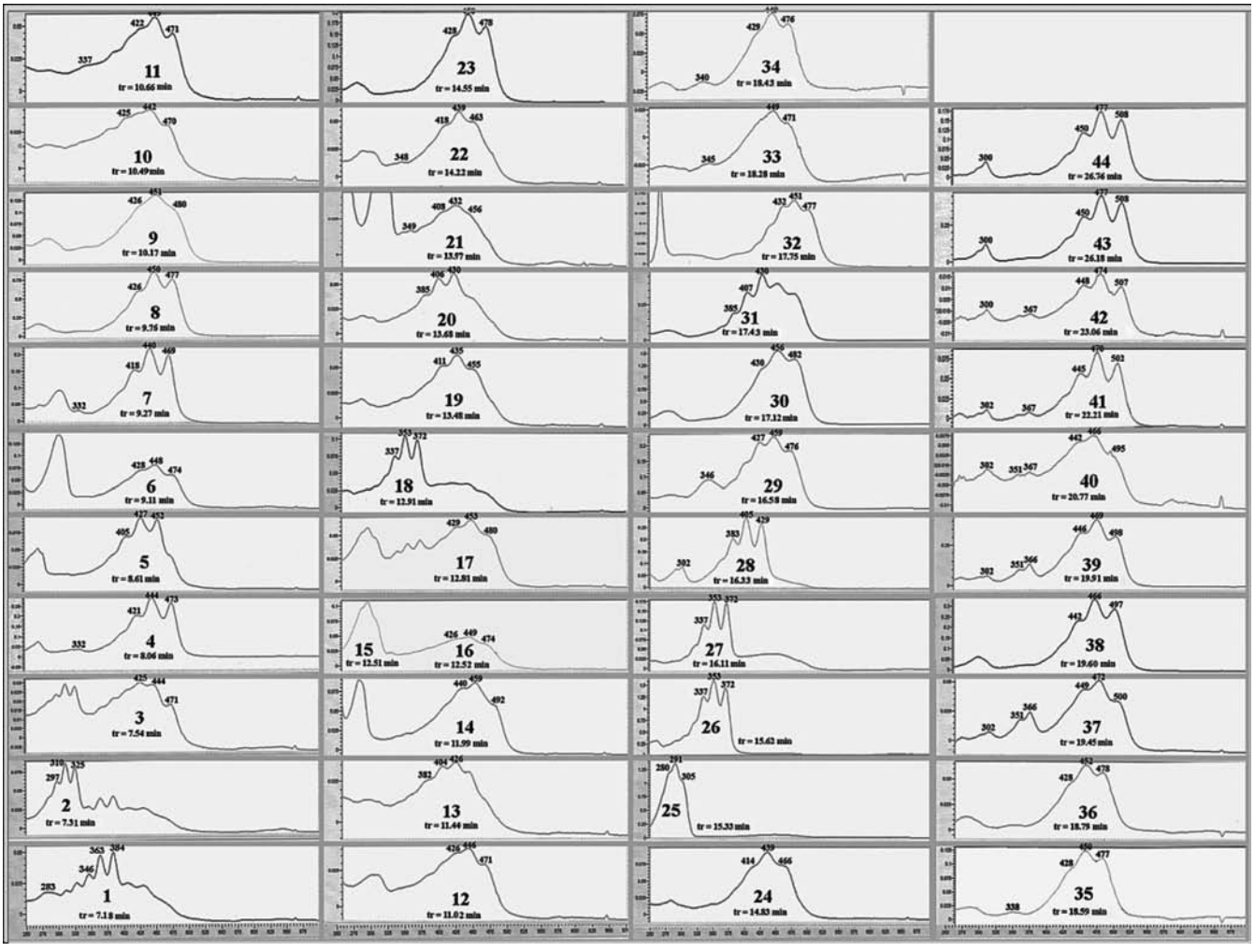

Figure 3. UV−vis absorption spectra (200−700 nm) extracted from the corresponding chromatographic peaks of Figure 2.

DOI: 10.1021/acs.jafc.5b02910
J. Agric. Food Chem. 2015, 63, 7428−7439

Table 2. LC-UV/Vis Data Used for the Identification of Carotenoids in 'Wild Tangerine' Tomato and Other Tomato Varieties

peak no.	LC-DAD retention times (min)	identified carotenoids	calcd λ_{max} [a] (nm)	λ (nm) obsd[b]	λ (nm) lit.[c]	(III/II) % obsd[b]	(III/II) % lit.[c]	Q-ratio (II/B) obsd[b]	Q-ratio (II/B) lit.[c]
1	7.18	9-*cis*-valenciaxanthin	368−364	283, 346, 363, 384	282, 348, 366, 388	102			
2	7.31	*cis*-phytofluene diepoxide	319	297, 310, 325		73			
3	7.54	deepoxyneoxanthin or trollein	442.5	425, 444, 471	420, 442, 469				
4	8.06	9-*cis*-antheraxanthin	443−439	332, 421, 444, 473	325, 417, 440, 468[d]	75	63[d]	3.3	7[d]
5	8.61	9-*cis*- mutatoxanthin	430−426	310, 405, 427, 452	310, 405, 427, 452[d]	81	78[d]	4.1	
6	9.11	zeaxanthin epoxide	447	428, 448, 474					
7	9.27	9-*cis*-lutein epoxide or *cis*-taraxanthin	440−436	332, 418, 440, 469	420, 440, 470[e]	78		6[e]	
8	9.76	*all-trans*-lutein	448	426, 450, 477	422, 445, 474	57	60		
9	10.17	*all-trans*-zeaxanthin	453	426, 451, 480	428, 450, 478	25	25		
10	10.49	*cis*-β-cryptoxanthin 5,6-epoxide	443−439	425, 442, 470		20			
11	10.66	9-*cis*-lutein	446−442	337, 422, 444, 471	418, 441, 469[f]	22	58[f]		
12	11.02	9′-*cis*-lutein	446−442	426, 446, 471	335, 417, 441, 469[f]	−22	60[f]		
13	11.44	*all-trans*-ζ-carotene diepoxide	401	382, 404, 426					
14	11.99	apo-10′-lycopenal	454	440, 459, 492	460[g]				
15	12.51	phytoene epoxide	[h]	280, 290, 302	275, 285, 296				
16	12.52	*cis*-β-cryptoxanthin	447−451	326, 426, 449, 474					
17	12.81	*all-trans*-β-cryptoxanthin	453	429, 453, 480	425, 449, 476	25	25		
18	12.91	phytofluene epoxide	341	337, 353, 372		82			
19	13.60	prolycopene		411, 435, 460	414, 436, 463				
20	13.69	9,15,9′-tri-*cis*-ζ-carotene		289, 385, 406, 430	377, 399, 424[i]		76[i]	2.3	4.2[i]
21	14.00	di-*cis*-γ-carotene-epoxide		408, 432, 456					
22	14.22	di-*cis*-γ-carotene-1,2-epoxide		418, 439, 463					
23	14.55	*all-trans*-β-carotene-5,6-epoxide	445	428, 450, 478	422, 445, 472	38			
24	14.83	tri-*cis*-γ-carotene		414, 439, 466					
25	15.33	15-*cis*-phytoene	[h]	280, 291, 302	276, 285, 297				
26	15.62	15-*cis*-phytofluene	350−346	262, 337, 353, 372		89		1.7	
27	16.11	*all-trans*-phytofluene	352	337, 353, 372	331, 347, 367[i]	97	91[i]		
28	16.33	15-*cis*-ζ-carotene	396−392	292, 302, 383, 405, 429		92		1.3	
29	16.58	13-*cis*-β-carotene	451−447	346, 427, 450, 476	339, 422, 445, 470[i]	10	5[i]	2.4	2.6[i]
30	17.12	*all-trans*- β-carotene	453	430, 456, 482	425, 450, 477	25	25		
31	17.43	*all-trans*-ζ-carotene	398	385, 407, 430	378, 401, 426[i]		102[i]		
32	17.75	9-*cis*-β-carotene or neo-β-carotene	451−447	347, 451, 477	340, 424, 446, 474[i]	22	29[i]	4.1	10[i]
33	18.28	15,15′-di-*cis*-lycopene		345, 449, 471		22		3.7	
34	18.43	9′-*cis*-γ-carotene	463−459	340, 428, 452, 478		33		5.5	
35	18.59	9-*cis*-γ-carotene	463−459	338, 428, 450, 477		30		5.8	
36	18.79	13,15-di-*cis*-lycopene		340, 428, 452, 478		33		5.5	
37	19.45	15-*cis*-lycopene	474−470	351, 366, 449, 472, 500	362, 446, 470, 500[j]			1.7	1.6[j]
38	19.60	*all-trans*-γ-carotene	465	442, 466, 497	437, 462, 494	53	40		
39	19.91	13-*cis*-lycopene	474−470	351, 366, 446, 469, 498	362, 440, 470, 508[j]	18		2.7	1.8[j]
40	20.77	9,13-di-*cis*-lycopene	466	351, 367 442, 466, 495	344, 434, 464, 494[j]			2.0	
41	22.21	9-*cis*-lycopene	474−470	367, 445, 470, 502	362, 446, 470, 500[k]	67		4.6	4.2[k]
42	23.06	5-*cis*-lycopene-epoxide	478−474	367, 448, 474, 507		44		2.6	
43	26.18	*all-trans*-lycopene	476	300, 450, 477, 508	452, 476, 506[j]	75	76[j]		
44	26.76	5-*cis*-lycopene	476	300, 367, 450, 477, 508	344, 446, 476, 506[j]	71	76[j]		20[j]

[a] λ_{max} was calculated by using the Fieser rules as explained in the UV−Vis Identification Criteria paragraph. [b] In this work, the solvents used for the carotenoid separation and, therefore, for the acquisition of the UV-vis spectra were methanol, 2-propanol, and hexane. [c] The majority of the UV−vis data have been taken from ref 5; references different from ref 5 are given explicitly next to the corresponding datum. [d] See ref 44. [e] See ref 45. [f] See ref 46. [g] Reference 47 reports λ_{max}, but does not show the UV−vis spectrum. [h] For polyenes with less than 4 conjugated double-bonds, the Fieser rules cannot be applied. [i] See ref 42. [j] See ref 13. [k] See ref 48.

DOI: 10.1021/acs.jafc.5b02910
J. Agric. Food Chem. 2015, 63, 7428−7439

Table 3. LC-MS and LC-MS/MS Data Used for the Identification of Carotenoids in 'Wild Tangerine' Tomato and Other Tomato Varieties

				LC-IDA method		LC-MRM method
peak no.	LC-MS retention time[a] (min)	identified carotenoids	monoisotopic mass[b] (u)	EMS data (*m/z*)	EPI data[d] (*m/z*)	MRM transitions (*m/z*)
1		9-*cis*-valenciaxanthin	412, 2977	[c]		413/221[e]
						413/181
2		*cis*-phytofluene diepoxide	576, 4906	$[M + H]^+$ = 577.5		577.5/503[e]
						557.5/429
3		deepoxyneoxanthin or trollein	584, 4229			585.4/567.5[e]
						567.5/549.5
4	8.84	9-*cis*-antheraxanthin	584, 4229	$[MH - H_2O]^+$ = 567.4	$[MH\text{-}2H_2O]^+$ = 549.4; $[MH - 56]^+$= 529; 221; 181	567.4/221
						567.4/181
5	9.39	9-*cis*- mutatoxanthin	584, 4229	$[M + H]^+$ = 585.4	$[MH\text{-}H_2O]^+$ = 567.4; $[MH\text{-}2H_2O]^+$ = 549.4; $[MH - 92]^+$= 493; 221;181	585.4/221
						585.4/181
6		zeaxanthin epoxide	584, 4229	$[M + H]^+$ = 585.4		585.4/221[e]
						585.4/135
7	10.05	9-*cis*-lutein epoxide or *cis*-taraxanthin	584, 4229	$[MH - H_2O]^+$ = 567.4	$[MH\text{-}H_2O]^+$ = 567.4; $[MH - 92]^+$= 493; 221	567.4/221
						567.4/175
8	10.54	*all-trans*-lutein	568, 4280	$[MH - H_2O]^+$ = 551.4	$[MH-2H_2O]^+$= 533; 175; 135;119	551.4/135
						551.4/175
9	10.95	*all-trans*-zeaxanthin	568, 4280	$[M + H]^+$ = 569.4	$[MH\text{-}H_2O]^+$ = 551.4; 175; 135;119	569.4/119
						569.4/175
10	11.27	*cis*-β-cryptoxanthin 5,6-epoxide	568, 4280			569.4/181[e]
						569.5/221
11	11.43	9-*cis*-lutein	568, 4280			551.4/135
						551.4/175
12	11. 80	9′-*cis*-lutein	568, 4280			551.4/135
						551.4/175
13	12.22	*all-trans*-ζ-carotene diepoxide	572, 4593	$[M + H]^+$ = 573.5	317, 243, 173, 135, 119	573.5/119[e]
						573.5/135
14	12.77	apo-10′-lycopenal	376, 2766	[c]		377/308[e]
						377/69
15	13.24	phytoene epoxide	560, 4957	$[M + H]^+$ = 561.5		553.5/135[e]
						553.5/69
16	13.30	*cis*-β-cryptoxanthin	552, 4331	$[M + H]^+$ = 553.4		553.5/119
						553.5/175
17	13.81	*all-trans*-β-cryptoxanthin	552, 4331	$[M + H]^+$ = 553.4		553.5/119
						553.5/175
18	13.69	phytofluene epoxide	558.4800	$[M + H]^+$ = 559.5		559.5/109[e]
						559.5/69
19	14.37	prolycopene	536, 4382	$[M + H]^+$ = 537.4	321; 177; 137; 119	537.5/119
						537.5/177
20	14.47	9,15,9′-tri-*cis*-ζ-carotene	540, 4695			541.5/173[e]
						541.5/69
21	14.66	di-*cis*-γ-carotene-epoxide	552, 4331	$[M + H]^+$ = 553.4		553.5/119[e]
22	15.00	di-*cis*-γ-carotene-1,2-epoxide	552, 4331	$[M + H]^+$ = 553.4	$[MH-H_2O]^+$= 535.5; 119	553.5/119
23	15.32	*all-trans*-β-carotene-5,6-epoxide	552, 4331	$[M + H]^+$ = 553.4	$[MH-H_2O]^+$= 535.5; 135; 119	553.5/135
						553.5/119
24	15.61	tri-*cis*-γ-carotene	536, 4382	$[M + H]^+$ = 537.4	321; 177; 137; 119	537.5/119
						537.5/177
25	16.11	15-*cis*-phytoene	544, 5008	$[M + H]^+$ = 545.5	203; 177; 109	545.5/177
						545.5/109
26	16.40	15-*cis*-phytofluene	542, 4852	$[M + H]^+$ = 543.5	461; 173; 137; 109	543.5/173
						543.5/109
27	16.89	*all-trans*-phytofluene	542, 4852	$[M + H]^+$ = 543.5	461; 173; 137; 109	543.5/173
						543.5/109
28	17.11	15-*cis*-ζ-carotene	540, 4695	$[M + H]^+$ = 541.5	173; 123.5	541.5/173
						541.5/123.5

DOI: 10.1021/acs.jafc.5b02910
J. Agric. Food Chem. 2015, 63, 7428−7439

Table 3. continued

peak no.	LC-MS retention time[a] (min)	identified carotenoids	monoisotopic mass[b] (u)	LC-IDA method: EMS data (m/z)	LC-IDA method: EPI data[d] (m/z)	LC-MRM method: MRM transitions (m/z)
29	17.35	13-*cis*-β-carotene	536, 4382	$[M + H]^+$ = 537.4	203; 177; 137; 121; 119	537.5/119 537.5/177
30	17.97	*all-trans*- β-carotene	536, 4382	$[M + H]^+$ = 537.4	321; 177; 137; 119	537.5/119 537.5/177
31	18.21	*all-trans*-ζ-carotene	540, 4695	$[M + H]^+$ = 541.5	173; 123.5	541.5/173 541.5/123.5
32	18.51	9-*cis*-β-carotene or neo-β-carotene	536, 4382	$[M + H]^+$ = 537.4	321; 177; 137; 119	537.5/119 537.5/177
33	19.1	15,15′-di-*cis*-lycopene	536, 4382	$[M + H]^+$ = 537.4	321; 177; 137; 119	537.5/119 537.5/177
34	19.21	9′-*cis*-γ-carotene	536, 4382	$[M + H]^+$ = 537.4	209; 177; 157; 137; 119; 109	537.5/119 537.5/177
35	19.44	9-*cis*-γ-carotene	536, 4382	$[M + H]^+$ = 537.4	209; 177; 157; 137; 119; 109	537.5/119 537.5/177
36	19.57	13,15-di-*cis*-lycopene	536, 4382	$[M + H]^+$ = 537.4		537.5/119 537.5/177
37	20.23	15-*cis*-lycopene	536, 4382	$[M + H]^+$ = 537.4	468; 209; 171; 157; 119	537.5/119 537.5/177
38	20.36	*all-trans*-γ-carotene	536, 4382	$[M + H]^+$ = 537.4	209; 177; 157; 137; 119; 109	537.5/119 537.5/177
39	20.68	13-*cis*-lycopene	536, 4382	$[M + H]^+$ = 537.4	468; 209; 171; 157; 119	537.5/119 537.5/177
40	21.53	9,13-di-*cis*-lycopene	536, 4382	$[M + H]^+$ = 537.4		537.5/119 537.5/177
41	22.97	9-*cis*-lycopene	536, 4382	$[M + H]^+$ = 537.4	468; 209; 171; 157; 119	537.5/119 537.5/177
42	23.80	5-*cis*-lycopene-epoxide	552, 4331	$[M + H]^+$ = 553.4		553.5/135[e] 553.5/119
43	27.01	*all-trans*-lycopene	536, 4382	$[M + H]^+$ = 537.4	468; 209; 171; 157; 119	537.5/119 537.5/177
44	27.55	5-*cis*-lycopene	536, 4382	$[M + H]^+$ = 537.4	169; 145; 107	537.5/119 537.5/177

[a]The retention times on the LC-MS chromatogram appear with a delay of about 0.78 min compared to the corresponding LC-DAD chromatogram. [b]Monoisotopic masses have been calculated by Chem & Bio Draw 12.0. [c]The mass range of the EMS experiment includes m/z values from 500 to 610. [d]Only the most intense or characteristic fragment ions have been listed. [e]For these compounds the MRM transitions are theoretical.

at room temperature with the minimal amount of KOH (established comparing the results obtained with 0.5, 1.0, and 2 mL of KOH). Compared to MSPD, the advantages of this procedure (see the detailed conditions in the corresponding paragraph) are several: (i) a very clean extract; (ii) slightly superior yields; (iii) the achievement of a greater enrichment factor; (iv) simplification of the carotenoid analysis by hydrolyzing esters of carotenols with fatty acids.

MSPD is a valuable technique for a mild and rapid isolation of carotenoids from foods (especially for solid samples). Its extraction efficiency without the formation of artifacts during the sample preparation process has been already verified previously.[20,40]

The comparison of the LC-DAD-MS chromatograms, acquired after applying the two different extraction protocols, is an easy and quick way to deduce the occurrence of esterified carotenols in real matrices. When this comparison was performed for the tomato samples, the matching between the LC-DAD-MS chromatograms has proved the absence of bound carotenols as well as of artifacts during the saponification.

Characterization of the Carotenoid Fraction of Some Italian Varieties of Tomatoes. The developed method was applied to the analysis of the previously mentioned tomato varieties (see Tomato and Passata Samples paragraph). Like a representative example, Figure 2 depicts the LC-DAD chromatogram of a sample of 'Wild Tangerine' tomato, after cold saponification. Figure 3 shows the UV−vis spectra extracted from each chromatographic peak of Figure 2, while Tables 2 and 3 summarize the LC-DAD and LC-MS data used for the identification of carotenoids in the 'Tangerine' tomato as well as in the other tomato varieties.

Most of the assignments comply with the biosynthetic sequence of carotenoids in plants and confirm the supposition that the biosynthetic pathway involves *cis* configurations of the precursor (15-*cis*-phytoene) and the intermediates (*cis* isomers of ζ-carotene and lycopene).[41,42] For almost all the analyzed varieties, we have observed the presence of phytoene only in the 15-*cis* configuration and of phytofluene in the 15-*cis* and *all-trans* forms.

9,15,9′-Tri-*cis*-ζ-carotene is the intermediate that follows 15-*cis*-phytoene in the biosynthetic pathway.[42] In this work, we have

DOI: 10.1021/acs.jafc.5b02910
J. Agric. Food Chem. 2015, 63, 7428−7439

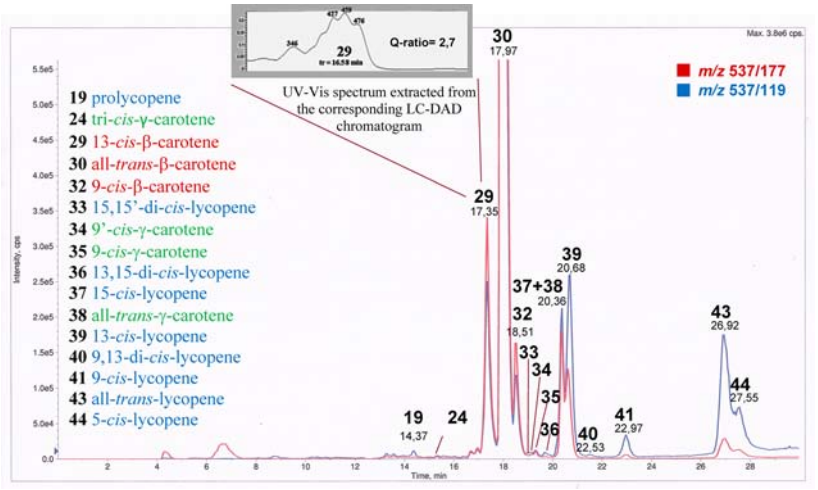

Figure 4. LC-MRM profiles of a saponified extract from 'Wild Tangerine' tomato: the ion currents m/z 537/177 and m/z 537/119 are shared by *all-trans*-lycopene, *all-trans*-β-carotene, *all-trans*-γ-carotene, and their corresponding *cis* isomers; each family of geometrical isomers can easily be distinguished on the basis of the characteristic ion ratio (see Table 1 and Figure 1).

identified 9,15,9′-tri-*cis*-ζ-carotene along with 15-*cis*-ζ-carotene and *all-trans*-ζ carotene in all tomato varieties. The *all-trans* isomer was prevalent only in the passata samples, probably because of the isomerization of 15-*cis*-ζ-carotene to the more stable *all-trans* isomer during the tomato processing. Neurosporene, another intermediate in the synthesis of lycopene,[42] was never detected in any of the analyzed varieties.

Prolycopene is known as the final product of the desaturation reactions that a specific isomerase converts into *all-trans*-lycopene;[41] subsequent cyclizations of *all-trans*-lycopene create a series of carotenes that have one or two rings of β-type and/or of ε-type. Unlike their precursors, lycopene, γ-carotene and β-carotene occur as *all-trans*-carotenes in wild-type tomato fruits; nevertheless, we have also observed their geometrical isomers and epoxidic forms in the 'Wild Tangerine' variety and passata (Tables 2 and 3). Figure 4 depicts the MRM profiles shared by lycopene, β-carotene, and γ-carotene, for a saponified sample of 'Wild Tangerine' tomato. These ion currents, together with the UV−vis data (Table 2; Figure 3), were used to identify 16 carotenes including three geometrical isomers of β-carotene, nine geometrical isomers of lycopene, and four geometrical isomers of γ-carotene. As an example, the peak 29 has been ascribed to 13-*cis*-β-carotene for the following reasons:

- the ion ratio value (ion ratio = $(I_{(m/z\ 537/177)}/I_{(m/z\ 537/119)})$ = 1.5) indicates that it is one of the geometrical isomers of β-carotene (Table 1; Figure 2)
- the retention time suggests that it is a next-to-central *cis*-isomer, because it elutes before the *all-trans* form
- the Q-ratio, calculated as (II/B) = 2.4, is in agreement with the data of the literature (Table 2); the hypsochromic shift of λ_{II} of 6 nm (from 456 nm for *all-trans*-β-carotene to 450 nm for the unknown) and the decrease in the intensity of peak III reinforce the attribution

Similarly, the peaks 37 and 39 have been attributed to 13-*cis* and 15-*cis* isomers of lycopene. The peaks 43 and 44 have been assigned to *all-trans*-lycopene and 5-*cis*-lycopene, respectively; the peak assignment has been based on the retention time of the authentic standard of *all-trans*-lycopene in solvent and on the occurrence of *cis*-peak at 367 nm detected only for the unknown 44. It is interesting to highlight that 5-*cis*-lycopene (peak 44), 13-*cis*-β-carotene (peak 29), and 9-*cis*-β-carotene (peak 32) were detected only in the extracts of 'Wild Tangerine' tomato and passata of 'San Marzano' tomatoes (probably due to the isomerization of *all-trans* forms during tomato processing). In the other tomato varieties, *all-trans*-lycopene and *all-trans*-β-carotene did not accompany the above-mentioned geometrical isomers.

The presence of γ-carotene in tomato and tomato products has previously been reported by Tonucci et al.[18] and Kimura et al.,[19] based on the online acquisition of UV−visible spectra without peak verification using more specific techniques. In this work, the occurrence of *all-trans*-γ-carotene (peak 38 of Figure 4) has been confirmed by using its authentic standard (Table 1; Figure 1); the key element of the identification has been the matching of the retention time, the perfect overlapping of the UV−vis spectra (λ_I, λ_{II}, λ_{III}, and % III/II), and the MS data. Even if *all-trans*-γ-carotene coelutes with 15-*cis*-lycopene (peak 37 + 38), their UV−vis spectra are perfectly distinguishable (see spectra 37 and 38 of Figure 3); moreover, the ion ratio close to 1 (compare Figure 1 and Figure 4) indicates that *all-trans*-γ-carotene is more abundant than 15-*cis*-lycopene.

Apo-lycopenals are hypothesized to be lycopene metabolites in mammals; nevertheless, they have recently been found in raw tomato and processed tomato products,[43] suggesting that these compounds may also be absorbed from food. In this work, the occurrence of apo-10′-lycopenal (peak 14) has been supposed on the basis of the UV−vis spectrum (Figure 2), the correspondence with the λ_{max} calculated according to the Fieser rule modified for aldehydes (eq 2; Table 2), and the LC-MRM profile obtained by acquiring the m/z 377/308 ion current (Table 3). For this compound, the two theoretical MRM transitions, listed in Table 3, have been deduced by hypothesizing an allylic cleavage of the C4−C5 bond.

Finally, among the xanthophylls identified in the 'Wild Tangerine' tomato, relevant for abundance were *all-trans*-lutein and 9-*cis*-antheraxanthin, followed by *cis*-lutein epoxide and *all-trans*-zeaxanthin. A series of *cis* isomers of low intensity were observed in particular for lutein, together with epoxides of zeaxanthin and β-cryptoxanthin (Tables 2 and 3). Traces of valenciaxanthin, a norcarotenoid occurring in some orange varieties, were found in the 'Pachino' tomato along with antheraxanthin and mutatoxanthin, all of them in the 9-*cis*-configuration. Usually, epoxidic forms are difficult to identify

DOI: 10.1021/acs.jafc.5b02910
J. Agric. Food Chem. 2015, 63, 7428−7439

using only the UV−vis detection (UV−Vis Identification Criteria paragraph, eq 3); LC-MS supports their LC-DAD identification since fragments at m/z 352, 221, and 181 indicate the presence of an epoxy group in a ring with a hydroxyl,[30] while fragment ions at m/z 165 and m/z 205 are characteristic of an epoxy group as the only substituent in the β-ring.[30] In passata and raw tomatoes, we also have identified epoxides of some carotenes (Tables 2 and 3).

In conclusion, the approach described in this paper has allowed us to realize a large-scale screening of carotenoids with the support of few authentic standards by exploiting the versatility of the LC-DAD-QqQ_{LIT} hyphenation. The identification power of this hyphenated technique is quite strong when all data (retention time; λ_I, λ_{II}, λ_{III}; % III/II; Q-ratio; m/z of pseudomolecular ion; fragmentation spectrum; relative abundance between the MRM transitions) are available, otherwise the assignment has to be considered tentative. Our methodology has been proved to be time-saving, because it can collect a large number of data with few analytical steps, and money-saving, because it uses a small number of standards commercially available at a reasonable cost. The 'Wild Tangerine' tomato has shown a number of carotenoids significantly larger than those of other analyzed varieties (up to forty-four compounds). In passata from 'San Marzano' fruits, some *cis*-forms of β-carotene and lycopene have been found particularly abundant since they were probably formed during the manufacturing process (isomerization due to the heat treatment and/or the occurrence of the organic acids freed during the squeezing step). The presence of *cis*-isomers in food has recently been revalued due to the superior bioavailability of these carotenoid forms.[9−11]

This study has not examined the effect of geographic area, the season, the ripening grade, and other variability parameters which can potentially affect the concentrations of these micronutrients. In the future, such an analytical approach could be extended to the comprehensive characterization of antioxidants in the genetically engineered varieties of tomato, enriched with anthocyanins to enhance the anticancer power of these fruits that, in the wild types, is only due to the carotenoids.

■ ASSOCIATED CONTENT

Supporting Information

The Supporting Information is available free of charge on the ACS Publications website at DOI: 10.1021/acs.jafc.5b02910.

Characteristics of the tomatoes, list of identified carotenoids, LC-MS distinction of lutein and zeaxanthin, structures of selected carotenoids, and EPI spectra (PDF)

■ AUTHOR INFORMATION

Corresponding Author

*Fax: + 39-06-490631. E-mail: alessandra.gentili@uniroma1.it.

Notes

The authors declare no competing financial interest.

■ ABBREVIATIONS USED

QqQ_{LIT}, hybrid triple quadrupole-linear ion trap mass spectrometer; DAD, diode array detection; APCI-MS, atmospheric pressure chemical ionization-mass spectrometry; IDA, information dependent acquisition; EMS, enhanced-mass scan; ER, enhanced-resolution; EPI, enhanced product ion; MRM, multiple reaction monitoring; LC, liquid chromatography; λ_{max}, wavelength of maximum absorption; PIS, product ion scan spectra; BHT, butylated hydroxytoluene; MSPD, matrix solid phase dispersion; NARP, nonaqueous reversed-phase; CE, collision energy

■ REFERENCES

(1) Gómez-Romero, M.; Arráez-Román, D.; Segura-Carretero, A.; Fernández-Gutiérrez, A. Analytical determination of antioxidants in tomato: Typical components of the Mediterranean diet. *J. Sep. Sci.* **2007**, *30*, 452−461.

(2) Rao, A. V.; Agarwal, S. Role of Antioxidant Lycopene in Cancer and Heart Disease. *J. Am. Coll. Nutr.* **2000**, *19*, 563−569.

(3) Khachik, F.; Carvalho, L.; Bernstein, P. S.; Muir, G. J.; Zhao, D. Y.; Katz, N. B. Chemistry, Distribution, and Metabolism of Tomato Carotenoids and Their Impact on Human Health. *Exp. Biol. Med.* **2002**, *227*, 845−851.

(4) Britton, G. Structure and properties of carotenoids in relation to function. *FASEB J.* **1995**, *9*, 1551−1558.

(5) Britton, G., Liaaen-Jensen, S., Pfander, H., Eds. *Carotenoids Handbook*; Birkhäuser Verlag: Basel, Switzerland, 2008.

(6) Gruszecki, W. I.; Strzałka, K. Carotenoids as modulators of lipid membrane physical properties. *Biochim. Biophys. Acta, Mol. Basis Dis.* **2005**, *1740*, 108−115.

(7) Rodriguez-Amaya, D. B.; Kimura, M. *HarvestPlus Handbook for Carotenoid Analysis*; Technical Monograph 2; HarvestPlus: Washington, DC. http://www.harvestplus.org/sites/default/files/tech02.pdf (accessed February 23, 2015).

(8) Gentili, A. The Chemistry of Vitamin A. In *Vitamin A and Carotenoids: Chemistry, Analysis, Function and Effects*; Preedy, V. R., Ed.; Food and Nutritional Components in Focus; RSC Publishing: Cambridge, U.K., 2012; pp 73−89. DOI: 10.1039/9781849735506-00073.

(9) Boileau, T. W. M.; Boileau, A. C.; Erdman, J. W., Jr. Bioavailability of all-trans and cis-isomers of Lycopene. *Exp. Biol. Med.* **2002**, *227*, 914−919.

(10) Schierle, J.; Bretzel, W.; Bühler, I.; Faccin, N.; Hess, D.; Steiner, K.; Schüep, W. Content and isomeric ratio of lycopene in food and human blood plasma. *Food Chem.* **1997**, *59*, 459−465.

(11) Fang, L.; Pajkovic, N.; Wang, Y.; Gu, C.; van Breemen, R. B. Quantitative analysis of lycopene isomers in human plasma using high-performance liquid chromatography−tandem mass spectrometry. *Anal. Chem.* **2003**, *75*, 812−817.

(12) Khachik, F.; Goli, M. B.; Beecher, G. R.; Holden, J.; Lusby, W. R.; Tenorio, M. D.; Barrera, M. R. Effect of food preparation on qualitative and quantitative distribution of major carotenoid constituents of tomatoes and several green vegetables. *J. Agric. Food Chem.* **1992**, *40*, 390−398.

(13) Lin, C. H.; Chen, B. H. Determination of carotenoids in tomato juice by liquid chromatography. *J. Chromatogr. A* **2003**, *1012*, 103−109.

(14) Li, H.; Deng, Z.; Liu, R.; Loewen, S.; Tsao, R. Ultra-performance liquid chromatographic separation of geometric isomers of carotenoids and antioxidant activities of 20 tomato cultivars and breeding lines. *Food Chem.* **2012**, *132*, 508−517.

(15) Gama, J. J. T.; Tadiotti, A. C.; Sylos, C. M. Comparison of carotenoid content in tomato, tomato pulp and ketchup by liquid chromatography. *Alimentos e Nutrição Araraquara* **2009**, *17*, 353−358.

(16) Huang, X. Y.; Liu, Y. W.; Di, D. L.; Liu, J. X.; Li, C. An improved LC-DAD method for simultaneous determination of lutein, β-carotene and lycopene in tomato and its products. *Chromatographia* **2010**, *71*, 331−334.

(17) Motilva, M. J.; Macià, A.; Romero, M. P.; Labrador, A.; Domínguez, A.; Peiró, L. Optimisation and validation of analytical methods for the simultaneous extraction of antioxidants: Application to the analysis of tomato sauces. *Food Chem.* **2014**, *163*, 234−243.

(18) Tonucci, L. H.; Holden, J. M.; Beecher, G. R.; Khachik, F.; Davis, C. S.; Mulokozi, G. Carotenoid content of thermally processed tomato-based food products. *J. Agric. Food Chem.* **1995**, *43*, 579−586.

(19) Kimura, M.; Rodriguez-Amaya, D. Carotenoids of tomato and tomato paste: verification of the occurrence of γ-carotene. *Rev. Inst. Adolfo Lutz* **2003**, *62*, 21−26.

DOI: 10.1021/acs.jafc.5b02910
J. Agric. Food Chem. 2015, 63, 7428−7439

(20) Gentili, A.; Caretti, F. Evaluation of a method based on liquid chromatography−diode array detector−tandem mass spectrometry for a rapid and comprehensive characterization of the fat-soluble vitamin and carotenoid profile of selected plant foods. *J. Chromatogr. A* **2011**, *1218*, 684−697.
(21) Hsu, B. Y.; Pu, Y. S.; Inbaraj, B. S.; Chen, B. H. An improved high performance liquid chromatography−diode array detection−mass spectrometry method for determination of carotenoids and their precursors phytoene and phytofluene in human serum. *J. Chromatogr. B: Anal. Technol. Biomed. Life Sci.* **2012**, *899*, 36−45.
(22) Gentili, A.; Caretti, F.; Bellante, S.; Ventura, S.; Canepari, S.; Curini, R. Comprehensive profiling of carotenoids and fat-soluble vitamins in milk from different animal species by LC-DAD-MS/MS hyphenation. *J. Agric. Food Chem.* **2013**, *61*, 1628−1639.
(23) Kao, T. H.; Loh, C. H.; Inbaraj, B. S.; Chen, B. H. Determination of carotenoids in *Taraxacum formosanum* by HPLC−DAD−APCI-MS and preparation by column chromatography. *J. Pharm. Biomed. Anal.* **2012**, *66*, 144−153.
(24) Giuffrida, D.; Dugo, P.; Torre, G.; Bignardi, C.; Cavazza, A.; Corradini, C.; Dugo, G. Characterization of 12 *Capsicum* varieties by evaluation of their carotenoid profile and pungency determination. *Food Chem.* **2013**, *140*, 794−802.
(25) Kurz, C.; Carle, R.; Schieber, A. HPLC-DAD-MS^n characterisation of carotenoids from apricots and pumpkins for the evaluation of fruit product authenticity. *Food Chem.* **2008**, *110*, 522−530.
(26) Dugo, P.; Herrero, M.; Kumm, T.; Giuffrida, D.; Dugo, G.; Mondello, L. Comprehensive normal-phase reversed-phase liquid chromatography coupled to photodiode array and mass spectrometry detection for the analysis of free carotenoids and carotenoid esters from mandarin. *J. Chromatogr. A* **2008**, *1189*, 196−206.
(27) Inbaraj, B. S.; Lu, H.; Hung, C. F.; Wu, W. B.; Lin, C. L.; Chen, B. H. Determination of carotenoids and their esters in fruits of *Lycium barbarum* Linnaeus by HPLC− DAD−APCI−MS. *J. Pharm. Biomed. Anal.* **2008**, *47*, 812−818.
(28) Crupi, P.; Milella, R. A.; Antonacci, D. Simultaneous HPLC-DAD-MS (ESI+) determination of structural and geometrical isomers of carotenoids in mature grapes. *J. Mass Spectrom.* **2010**, *45*, 971−980.
(29) Lech, K.; Witowska-Jarosz, J.; Jarosz, M. Saffron yellow: characterization of carotenoids by high performance liquid chromatography with electrospray mass spectrometric detection. *J. Mass Spectrom.* **2009**, *44*, 1661−1667.
(30) Rivera, S. M.; Canela-Garayoa, R. Analytical tools for the analysis of carotenoids in diverse materials. *J. Chromatogr. A* **2012**, *1224*, 1−10.
(31) Matsubara, A.; Uchikata, T.; Shinohara, M.; Nishiumi, S.; Yoshida, M.; Fukusaki, E.; Bamba, T. Highly sensitive and rapid profiling method for carotenoids and their epoxidized products using supercritical fluid chromatography coupled with electrospray ionization-triple quadrupole mass spectrometry. *J. Biosci. Bioeng.* **2012**, *113*, 782−787.
(32) Isaacson, T.; Ronen, G.; Zamir, D.; Hirschberg, J. Cloning of tangerine from tomato reveals a carotenoid isomerase essential for the production of β-carotene and xanthophylls in plants. *Plant Cell* **2002**, *14*, 333−342.
(33) Meléndez-Martínez, A. J.; Escudero-Gilete, M. L.; Vicario, I. M.; Heredia, F. J. Separation of structural, geometrical and optical isomers of epoxycarotenoids using triacontyl-bonded stationary phases. *J. Sep. Sci.* **2009**, *32*, 1838−1848.
(34) Van Breemen, R. B.; Huang, C. R.; Tan, Y.; Sander, L. C.; Schilling, A. B. Liquid chromatography/mass spectrometry of carotenoids using atmospheric pressure chemical ionization. *J. Mass Spectrom.* **1996**, *31*, 975−981.
(35) Rivera, S. M.; Christou, P.; Canela-Garayoa, R. Identification of carotenoids using mass spectrometry. *Mass Spectrom. Rev.* **2014**, *33*, 353−372.
(36) Bijttebier, S. K.; D'Hondt, E.; Hermans, N.; Apers, S.; Voorspoels, S. Unraveling ionization and fragmentation pathways of carotenoids using orbitrap technology: a first step towards identification of unknowns. *J. Mass Spectrom.* **2013**, *48*, 740−754.
(37) Van Breemen, R. B.; Dong, L.; Pajkovic, N. D. Atmospheric pressure chemical ionization tandem mass spectrometry of carotenoids. *Int. J. Mass Spectrom.* **2012**, *312*, 163−172.
(38) Fieser, L. F. Absorption spectra of carotenoids; structure of vitamin A. *J. Org. Chem.* **1950**, *15*, 930−943.
(39) Larsen, E.; Christensen, L. P. Simple saponification method for the quantitative determination of carotenoids in green vegetables. *J. Agric. Food Chem.* **2005**, *53*, 6598−6602.
(40) Glaser, T.; Lienau, A.; Zeeb, D.; Krucker, M.; Dachtler, M.; Albert, K. Qualitative and quantitative determination of carotenoids steroisomers in a variety of spinach samples by use of MSPD before HPLC-UV, HPLC-APCI-MS, and HPLC-NMR on-line coupling. *Chromatographia* **2003**, *57*, S19−S25.
(41) Giuliano, G.; Giliberto, L.; Rosati, C. Carotenoid isomerase: a tale of light and isomers. *Trends Plant Sci.* **2002**, *7*, 427−429.
(42) Breitenbach, J.; Sandmann, G. ζ-Carotene *cis* isomers as products and substrates in the plant poly-*cis* carotenoid biosynthetic pathway to lycopene. *Planta* **2005**, *220*, 785−793.
(43) Kopec, R. E.; Riedl, K. M.; Harrison, E. H.; Curley, R. W., Jr; Hruszkewycz, D. P.; Clinton, S. K.; Schwartz, S. J. Identification and quantification of apo-lycopenals in fruits, vegetables, and human plasma. *J. Agric. Food Chem.* **2010**, *58*, 3290−3296.
(44) Chisté, R. C.; Mercadante, A. Z. Identification and quantification, by HPLC-DAD-MS/MS, of carotenoids and phenolic compounds from the Amazonian Fruit *Caryocar villosum*. *J. Agric. Food Chem.* **2012**, *60*, 5884−5892.
(45) Cano, M. P.; de Ancos, B. Carotenoid and carotenoid ester composition in mango fruit as influenced by processing method. *J. Agric. Food Chem.* **1994**, *42*, 2737−2742.
(46) Cervantes-Paz, B.; Yahia, E. M.; Ornelas-Paz, J. D. J.; Gardea-Béjar, A. A.; Ibarra-Junquera, V.; Pérez-Martínez, J. D. Effect of heat processing on the profile of pigments and antioxidant capacity of green and red Jalapeño Peppers. *J. Agric. Food Chem.* **2012**, *60*, 10822−10833.
(47) Liu, A. G.; Erdman, J. W., Jr. Lycopene and apo-10′-lycopenal do not alter DNA methylation of GSTP1 in LNCaP cells. *Biochem. Biophys. Res. Commun.* **2011**, *412*, 479−482.
(48) Lee, M. T.; Chen, B. H. Separation of lycopene and its cis isomers by liquid chromatography. *Chromatographia* **2001**, *54*, 613−617.

DOI: 10.1021/acs.jafc.5b02910
J. Agric. Food Chem. 2015, 63, 7428−7439

MCs are present in fish tissue in two different forms: (1) the free fraction consisting of the dissolved and reversibly bound MCs to tissues and (2) the covalently bound fraction associated with PP or cysteine-containing peptides within tissues. Extracting the bound fraction has been a challenge for tissue extraction procedures in fish exposed to MCs.[15] Conventional extraction methods involve organic solvents using aqueous or acidified methanol (MeOH). However, solvent extraction yielded poor recovery values because only the free fraction of MCs was recovered and detected.[16] A different approach was explored to analyze the total MCs in fish tissue via Lemieux oxidation (Figure 1) in order to release the oxidative product of Adda, 2-methyl-3-methoxy-4-phenylbutyric acid (MMPB).[15,17,18] Common to all congeners, MMPB makes it possible to quantify the total MCs and has been successfully used for analyses in water by our research group and other laboratories.[19−22] As for fish tissue analysis, a method was proposed using trypsinization followed by Lemieux oxidation and SPE cleanup, and MMPB was detected using liquid chromatography coupled with mass spectrometry (LC-MS).[15,17,18] However, the results from oxidation recoveries, SPE extraction efficiency, and signal recovery from matrix effects gave poor values. Moreover, the global procedures were laborious: up to 20 h of sample preparation was required for the trypsinization step and long LC-MS analysis times with over 40 min runs.[15]

We have developed a new approach to detect total MCs (free and protein-bound) in fish tissues. First, the tissue was digested with sodium hydroxide followed by Lemieux oxidation. A different SPE procedure was proposed to enhance recovery values and decrease the amount of salts in the extracts. Finally, the MMPB moiety was analyzed using a technology known as laser diode thermal desorption (LDTD) coupled with atmospheric pressure chemical ionization (APCI), and the detection was done with a high-resolution mass spectrometer, the Q-Exactive (HRMS). The LDTD has ultrafast analysis times (<15 s/sample), works with small amount of samples (2−10 μL) per analysis, and requires only a small volume of solvents because there is no liquid chromatography. In a previous study, the LDTD was successfully used to analyze MMPB in water samples with a triple-quadrupole mass spectrometer detector (MS/MS).[20] Anatoxin-A was also detected with this technology for its direct determination in water using both MS/MS and HRMS.[23,24] The LDTD was also successfully applied to small molecules in different matrices, including wastewater, sludge, sediment, soil, and biological matrices.[25−30] For this method, the Q-Exactive was chosen for two reasons: the sensitivity is higher than that of a standard triple quadrupole, thus giving better limits of detection and quantification; and the selectivity is better because the mass spectrometer enables precursor fragmentation and exact mass detection. Indeed, this hybrid Orbitrap detector combines a quadrupole precursor selection with a high-energy collisional dissociation cell (HCD), making it possible to fragment selected precursor ions. Also, with a resolving power of up to 140,000 full width at half-maximum (fwhm) at m/z 200, the mass accuracy obtained with the Q-Exactive is between 1 and 3 ppm.[31]

The objective of this study was to develop a new analytical method for the detection of all the MC variants and to improve their extraction in fish tissue to get a more realistic quantification for prudent risk management. By applying this method to samples of fish exposed to cyanotoxins, we aimed to determine the possible undervaluation from their quantification by conventional analytical methods based on the analysis of individual MCs using available standards.

MATERIALS AND METHODS

Chemicals, Reagents, and Stock Solutions. 2-Methyl-3-methoxy-4-phenylbutyric acid sodium salt (MMPB, purity ≥ 94%) was purchased from Wako Pure Chemical Industries, Ltd. (Osaka, Japan). 4-Phenylbutyric acid (4-PB, purity ≥ 99%) was obtained from Sigma-Aldrich (Oakville, ON, Canada). Ampules of certified standard solutions of microcystin-LR (MC-LR, 10.2 μM aqueous methanol (1:1, v/v)) were obtained from the Certified Reference Materials Program (NRC, Halifax, NS, Canada). Potassium permanganate ($KMnO_4$, purity ≥ 99.0%), sodium (meta)periodate ($NaIO_4$, purity ≥9 9.0%), sodium bisulfite (purity ≥ 95%), sodium hydroxide (NaOH, purity ≥ 98%), hydrochloric acid (HCl, ACS reagent 37%), and sulfuric acid standard solution (1.000 M) were obtained from Sigma-Aldrich. All solvents were of high-performance liquid chromatography (HPLC) grade from Fisher Scientific (Whitby, ON, Canada). Deionized/distilled water (dd-H_2O) was used for recovery evaluation. Individual stock standard solutions were prepared in methanol (MeOH) at a concentration of 100 mg L^{-1} and kept at −20 °C for 12 months for the MMPB standards and a maximum of 6 months for the 4-PB standards, according to compound stability.[20] Compressed air (Ultra Zero Certified grade; ≤2 ppm of water) was used as a carrier gas for the LDTD desorption and obtained from MEGS Specialty Gases, Inc. (St-Laurent, QC, Canada).

Fish Tissue Samples. Environmental samples were provided by the monitoring program of the Ministère du Développement durable, de l'Environnement et de la Lutte aux changements climatiques (MDDELCC), Québec provincial environment ministry (Québec, QC, Canada), as part of an MC project to monitor fish in natural lakes where cyanobacterial blooms occur. Fish were caught on August 20, 2009, and on October 14 and 15, 2009, in three different lakes in the province of Québec, Canada: Lac Vert, Lac Roxton, and Lac Noir. All three lakes were affected by cyanobacterial blooms. Eight different species were caught and kept at −20 °C until homogenization and analysis: rainbow smelt, white sucker, brook trout, yellow perch, walleye, pike, brown bullhead, and lake whitefish. The analysis was first performed by the government monitoring program of the Centre d'expertise en analyze environnementale du Québec (CEAEQ). Fish tissue (muscle and whole fish) was weighed and dried using diatomaceous earth, followed by slow elution with acidified MeOH with formic acid. The solvent was evaporated, and the samples were reconstituted in the mobile phase and filtered using 0.2 μm nylon filters submitted to ultracentrifugation. An aliquot was used for LC-MS/MS analysis. Four microcystins were quantified: MC-LA, MC-LR, MC-RR, and MC-YR.

NaOH Digestion and Lemieux Oxidation. Frozen homogenized fish tissue was used instead of freeze-dried tissue to make direct comparisons with MCs previously found in the samples using the CEAEQ's standard analytical procedure. Thus, 1 g of wet weight and homogenized fish tissue was submitted to a freeze−thaw lysis three times to break the remaining cells and leach the toxins. The tissues were then digested in 5 mL of NaOH solution (50 mM) for 2 h. The pH was adjusted to 9 using an HCl solution (100 mM), and oxidants were added in solution with $KMnO_4$ (50 mM) and $NaIO_4$ (50 mM). The reaction was conducted at room temperature for 2 h in the absence of light. Saturated $NaHSO_3$ solution was added until the purple color turned white to quench the reaction. A 10% sulfuric acid solution was used to acidify the solution (pH ∼2).

Solid Phase Extraction (SPE) Procedures. Before the SPE step, suspensions were transferred in centrifuge tubes and submitted to sonication for 15 min. They were then centrifuged for 15 min at 3000 rpm, and the supernatants were filtered using 0.2 μm nylon filters from Whatman (Florham Park, NJ, USA) prior to extraction. A polymeric hydrophobic sorbent consisting of styrene−divinylbenzene (Strata SDB-L) was used as an SPE cartridge from Phenomenex (Torrance, CA, USA) with a 500 mg bed mass and a volume of 6 mL. The

DOI: 10.1021/acs.jafc.5b02318
J. Agric. Food Chem. 2015, 63, 7440−7449

Table 1. Parameters of HRMS Detection

compd	chem formula	calcd exact mass (m/z)	exptl exact mass (m/z)	NCE[a] (%)	mass accuracy[b] (ppm)	confirmation ion[c] (m/z)
MMPB	$C_{12}H_{16}O_3-H$[d]	207.10212	207.1019	25	1.2	208.1042
	$C_9H_{11}O$[e]	135.08099	135.0808		1.5	135.0829
	C_7H_7[f]	91.05478	91.0547		1.1	91.0571
4-PB	$C_{10}H_{12}O_2-H$	163.07590	163.0756	30	1.7	163.0780
	C_7H_7	91.05478	91.0546		1.5	91.0568

[a]Fragmentation energy for precursor ion in HCD cell. [b]Accuracy of average measured mass. [c]Second abundant ion in isotopic pattern. [d]Precursor ion. [e]Quantification ion (most abundant MS/MS transition). [f]Confirmation ion (second most abundant MS/MS transition).

procedure was carried out using a 12-position manifold from Phenomenex. The SPE was performed with the filtered aliquots of sample supernatants with the pH already adjusted to 2. The SPE cartridges were conditioned with 5 mL of methanol (MeOH) for sorbent activation followed by 5 mL of acidified water with 0.1% formic acid (HPLC grade). The samples were then loaded on the cartridge columns by gravity. The cartridges were washed twice with 5 mL of water with 0.1% formic acid containing 10% MeOH (v/v). Elution was performed with 5 mL of MeOH into glass conical-bottom centrifuge tubes. The eluates were completely dried under a gentle stream of nitrogen at room temperature with a nine-port Reacti-Vap unit (Pierce, Rockford, IL, USA). The dried fractions were then reconstituted in acetonitrile (ACN) and directly submitted to LDTD-APCI-HRMS detection.

LDTD-APCI-HRMS. Compound desorption was achieved with a T-960 LDTD-APCI ionization interface model, and the instrument was controlled using LazSoft 4.0 software (Phytronix Technologies, Québec, QC, Canada) integrated with Excalibur 2.2 software (Thermo Fisher Scientific, Waltham, MA, USA). The LDTD instrument was described in previous work.[20,29,30] In this experiment, 4 μL aliquots from extract samples were spotted into a LazWell 96-well sample metal plate. After complete solvent drying at 40 °C for 5 min, the back of the sample well was heated by an infrared laser (980 nm, 20 W, continuous) in the LDTD instrument. The sample was desorbed, and a carrier gas flow of 2 L min^{-1} was then set at a temperature of 50 °C to avoid temperature variations and transfer the gas phase molecules to negative APCI ionization followed by HRMS detection. Finally, the laser power is expressed as a percentage, and the laser pattern was optimized to the following settings: 2 s at 0%, 2 s ramping from 0 to 40%, 1 s hold at 40%, 0.1 s from 40 to 0%, and 2 s hold at 0%, with a total desorption time of 7 s per sample. APCI in negative mode is within these parameters: ion sweep gas, 0.3; sheath gas, auxiliary gas, and skimmer offset set to 0 (all arbitrary values); vaporizer temperature, 0 °C; and capillary temperature, 350 °C.

The detection was performed using a Q-Exactive mass spectrometer controlled by Excalibur 2.3 software (Thermo Fisher Scientific). Instrument calibration in negative mode was done every 5 days to avoid mass shifts in detection with a direct infusion of a LTQ Velos ESI Negative Ion Calibration Solution (Pierce Biotechnology Inc., Rockford, IL, USA). The Q-Exactive parameters were selected toward mass resolution and accuracy for better quantification, sensitivity, and selectivity. The targeted ion fragmentation (t-MS^2) mode was used for MMPB quantification, and normalized collision energy (NCE) was optimized. Standard solutions of MMPB and 4-PB at a concentration of 100 μg L^{-1} were directly infused with a syringe at a flow rate of 0.01 mL min^{-1}. The fragment ions and their NCE were chosen using Q-Exactive Tune 2.3 software (Thermo Fisher Scientific). The precursor ions were filtered by the quadrupole, which operates at an isolation width of 0.4 amu. The optimized collision energies, precursor ions, and fragment ions are presented in Table 1. A resolving power of 17500 fwhm at m/z 200 was used with an automatic gain control (AGC) target set at 1×10^5 ions for a maximum injection time of 50 ms. For more technical details, please refer to previous studies.[23,32−34]

Method Validation. Data treatment was carried out using Excalibur 2.3 software (Thermo Fisher Scientific). The method validation was done according to the recommendations of the validation protocol for environmental chemistry analysis from the MDDELCC ministry guidelines. The two fragment ions with the highest signal intensity were selected as the quantification and confirmation ions. The quantification ion was used to establish the method limits of detection and quantification. Compound confirmation could be done with the ratio of their relative intensities to avoid false positives. The second most abundant ion from the isotopic pattern and the isotopic ratio with <10% intensity variations were used for confirmation. A mass tolerance window was set to 5 ppm (±2.5 ppm) for the extracted masses from acquisition to get a good selectivity in data analysis. The reaction recovery yield values for fish tissue digestion and oxidation were evaluated using a blank matrix, which consisted of fish that were not in contact with cyanobacterial bloom at three MMPB concentrations: 25, 250, and 1000 μg kg^{-1}. The fish tissue was spiked with MC-LR and the corresponding MMPB concentrations prior to digestion and oxidation. To obtain a relevant matrix with interactions between the fish tissue and the added MC, the blank homogenates were incubated for 3 h prior to the extraction procedure. The mean peak area values were compared with those obtained by spiking the digested and oxidized fish tissue with MMPB before SPE. The recovery values of the SPE method and the matrix effects were also evaluated using blank fish tissue at three concentrations: 25, 250, and 1000 μg kg^{-1}. Extraction recoveries were determined with the mean peak area of MMPB spiked prior to extraction in matrix-containing (blank fish tissue) samples compared to matrix-containing samples spiked postextraction. The matrix effects were evaluated with the mean peak area of MMPB spiked prior to extraction in matrix-containing samples compared to spiked matrix-free (dd-H_2O) samples prior to extraction. All recovery values were evaluated in triplicate, and the results are reported as percentages. A seven-point internal calibration curve was prepared with blank fish tissue by standard addition with concentration levels ranging from 15 to 2500 μg kg^{-1}. The concentration of internal standard (IS) 4-PB was selected at 500 μg kg^{-1} for its capacity for signal correction (data not shown). The method detection limit (MDL) and method quantification limit (MQL) were established by calculating 3 and 10 times the standard deviation of the mean value of six spiked blank fish tissue samples containing approximately 5 times the estimated concentration for detection limit (15 μg kg^{-1}), respectively. Accuracy—expressed as relative error (RE %)—and interday/intraday—expressed as the relative standard deviation (RSD %)—were determined with three different concentrations on the linearity range (25, 250, and 1 000 μg kg^{-1}, $n = 6$) in blank fish tissue samples. Intraday repeatability was estimated over 3 weeks. Statistical comparison was used when needed with the Statistical Package for Social Sciences (SPSS 21.0, Chicago, IL, USA) for Windows. ANOVA and Tukey's post hoc tests were used with statistical significance defined as $P < 0.05$.

RESULTS AND DISCUSSION

Digestion and Oxidation. The extraction of total MCs through MMPB from biological matrices was previously explored with the use of trypsinization and Lemieux oxidation followed by SPE cleanup.[15,18] For higher extraction efficiency, our study first considered the possibility of NaOH as a digestion reagent to break down the tissue and thus allow the free and bound MCs to react to Lemieux oxidation and then be

DOI: 10.1021/acs.jafc.5b02318
J. Agric. Food Chem. 2015, 63, 7440−7449

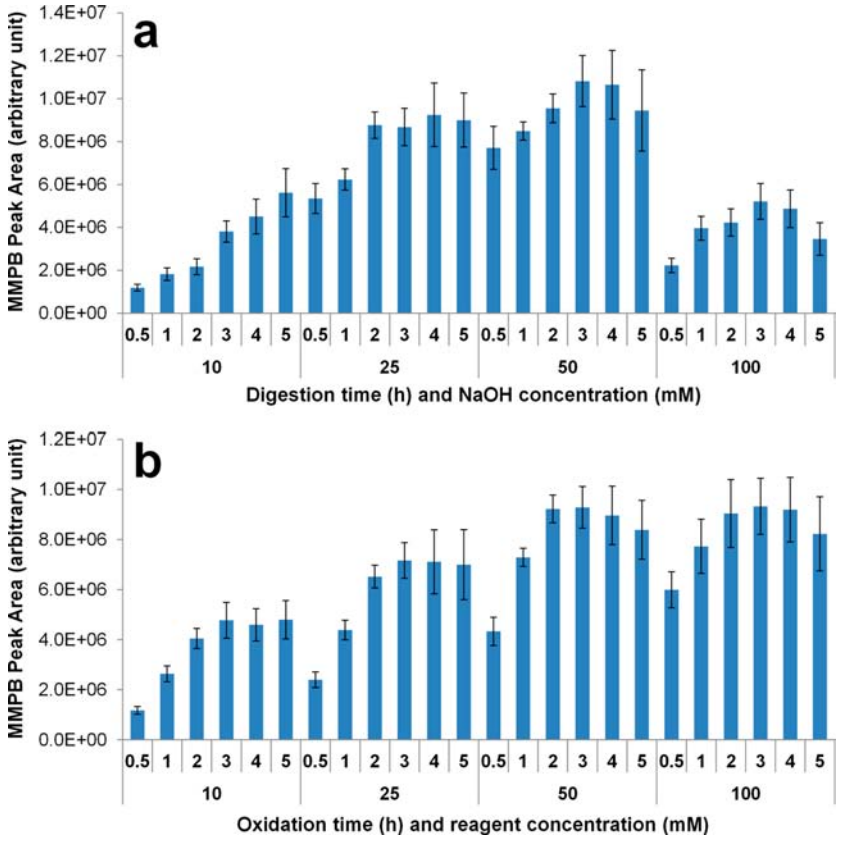

Figure 2. Optimization of (a) the digestion and (b) the oxidation by varying the reaction time (first *x*-axis) and the reagent concentration (second *x*-axis). $KMnO_4$ and $NaIO_4$ concentrations were identical during the oxidation. Vertical error bars represent standard deviations from the mean (n = 3).

Table 2. Validation Parameters Using Internal Calibration with Three Different Concentrations (n = 6)

concn (μg kg^{-1})	accuracy RE (%)	intraday RSD (%)	interday RSD (%)	digestion/oxidation recovery ± SD (%)	SPE recovery ± SD (%)	signal recovery from matrix effects ± SD (%)
25	10	6	7	70 ± 7	91 ± 6	92 ± 7
250	6	4	5	75 ± 9	95 ± 9	90 ± 10
1000	5	5	9	72 ± 6	98 ± 7	93 ± 9

converted to MMPB. MCs are known to be stable in a wide range of pH as well as high temperatures and sunlight.[35] Because MCs can withstand higher alkaline and acidic pH, NaOH was then used as a digestion agent for fish tissue without affecting MC stability. The optimization was developed by spiking MC-LR in blank fish tissue before the digestion and oxidation with the corresponding MMPB concentration (1000 μg kg^{-1}) recovered after SPE cleanup, and this concentration was chosen for its higher signal intensity and therefore easier optimization. Different NaOH concentrations between 10 and 100 mM were studied and submitted to different digestion periods ranging from 30 min to 5 h (n = 3). The results are shown in Figure 2a. The optimal results were 50 mM NaOH used for 2 h, which yielded in higher MMPB signals and less variability. Longer digestion durations did not significantly increase the MMPB signal (P > 0.05), and the faster digestion time was therefore preferred. Finally, higher concentrations enhance salt concentration in solution and can reduce LDTD desorption due to the presence of a salt layer in the wells and may also induce ion suppression during the charge transfer of APCI ionization.[30,36,37]

Lemieux oxidation was previously used in bloom water matrices in a previous work and was optimized according to three parameters: pH, oxidation time, and reagent concentration. The reaction medium was alkaline with a pH of 9 with 100 mM HCl after digestion. This was set as the most efficient pH value used for MC oxidation in previous studies. However, because the oxidation takes place in fish tissue, reagent concentration and oxidation time were reassessed to obtain the best reaction yield. $KMnO_4$ and $NaIO_4$ were tested with concentrations between 10 and 100 mM, and each concentration was tested for an oxidation time between 30 min and 5 h (n = 3). The results are shown in Figure 2b. The optimal values were the use of 50 mM reagents at a reaction time of 2 h. Reaction conditions were similar to those in the previous study, with a reaction time of 2 h instead of 1 h being the only difference. The lower reaction time and reagent concentrations were selected for faster sample preparation and to limit ion suppression from ionization due to the high amount of salts in the matrix. The digestion and oxidation reaction recovery values were determined together, using blank fish tissue spiked before digestion with MC-LR, and the results were compared with blank fish tissue spiked after oxidation with the

DOI: 10.1021/acs.jafc.5b02318
J. Agric. Food Chem. 2015, 63, 7440−7449

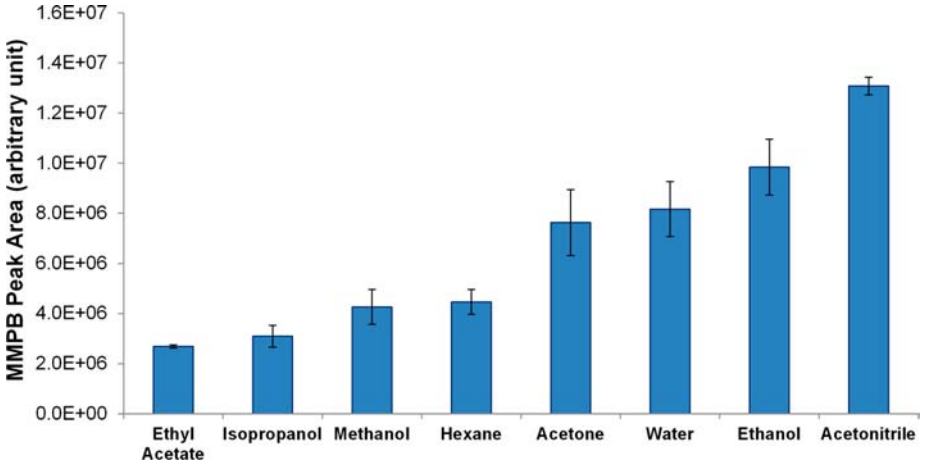

Figure 3. Effect of different solvents used for post SPE sample reconstitution and LDTD desorption after sample deposition in wells on MMPB mean peak area. Vertical error bars represent standard deviations from the mean (n = 6).

corresponding MMPB concentrations (25, 250, and 1000 μg kg^{-1}). Recovery yield values are shown in Table 2 with their respective standard deviations (SD) and values ranging from 70 to 75%. These results represent a significant improvement as compared to previous studies using trypsinization prior to Lemieux oxidation with results ranging from 5 to 40%.[17,18]

Sample Cleanup and Elution. A SPE cleanup was developed to isolate MMPB and 4-PB from the reaction mixtures. Extensive cleanup was necessary because of the fish tissue, which constitutes a highly complex matrix, and the high amounts of salts in the digestion and oxidations steps.[17] Indeed, the presence of proteins, lipids, and salts can induce ion suppression during APCI ionization due to charge transfer limitations and thus affect signal intensity.[37] In the analysis of MMPB in animal tissues, reverse phase or ion-exchange SPE sorbents are generally used for cleanup.[15,17,18] In this study, SDB-L sorbent was tested to enhance MMPB recovery and limit the elution of contaminants from the matrix. The SDB-L SPE targets hydrophobic and aromatic analytes, which is appropriate for MMPB because its structure includes an aromatic cycle. The pK_a of MMPB being 4.63, the molecule is in neutral state in acidic conditions and can be adsorbed on the SDB-L sorbent. As for the procedure, SPE sorbents were washed twice with 5 mL of H_2O with 0.1% formic acid 10% MeOH to eliminate a maximum of interfering compounds and salts from the matrix. The elution step was done with 5 mL of MeOH because the compounds did not need a change of polarity to be released from the sorbent. The recovery values for the SPE procedure were evaluated using blank fish tissues spiked before SPE, and the mean peak area values were compared to blank fish tissue spiked after SPE. The recovery results were deemed satisfactory (ranging from 91 to 98%) and are shown in Table 2 for the three concentration levels (25, 250, and 1000 μg kg^{-1}). The matrix effects were determined by comparing the mean peak area of targeted compounds in matrix-containing samples spiked before extraction as compared to dd-H_2O spiked before extraction. The signal recoveries are shown in Table 2 and ranged from 90 to 93%, illustrating that the MMPB signal is not significantly affected by the matrix.

LDTD-APCI-HRMS. Different parameters were optimized to improve signal intensity for optimal MMPB detection by LDTD-APCI-HRMS. Several parameters from the LDTD desorption had to be reassessed. Indeed, in earlier work, an analytical method was developed and optimized to analyze MMPB by LDTD-APCI-MS/MS in lake water. However, fish tissue is a completely different matrix, and the LDTD desorption may be affected if parameters such as deposition solvent, volume of deposition, laser power, and laser pattern are not optimized. In this case, the carrier gas flow was not studied because changing the parameter did not lead to improvement. The different optimizations were done with postextraction blank fish tissue spiked with 100 μg L^{-1} MMPB (n = 6).

First, the deposition solvent will affect compound desorption by LDTD depending on its solubility and on how the dried solvent will create layers of nanocrystals constituted of the analytes and the matrix.[30] Therefore, deposition solvents were tested as solvents of reconstitution after the SPE cleanup and included ethyl acetate, isopropanol, methanol, hexane, acetone, water, ethanol, and acetonitrile. As the results demonstrate in Figure 3, the optimal deposition solvent was acetonitrile (ACN). Indeed, the use of ACN considerably reduces the amount of proteins and amino acids available in the samples by their precipitation, thus reducing matrix complexity. Second, deposition volumes were evaluated to maximize the amount of analytes submitted to desorption, thus increasing the signal intensity. Figure S1 in the Supporting Information shows the results, and a volume of 4 μL yields a significantly higher signal intensity ($P < 0.05$) with a lower variability. With higher deposition volumes, higher variability is observed followed by a signal decrease. This is explained by the higher mass of analyte, which is concomitant with a higher presence of interfering compounds that can reduce LDTD desorption and also affect APCI ionization with ion suppression. Third, the laser power is the amount of energy transferred to the back of the well of the LDTD plate expressed as a percentage (of maximum) and which influences the analytes' desorption rate. Laser power values were studied between 10 and 60% because higher power can burn the well, thus inducing compound degradation or fragmentation. The results in Figure S2 show that 40% is the optimal laser power for higher MMPB desorption with minimal signal variability.

The laser pattern was studied, including the laser ramp time enhancement followed by the laser plateau time. The laser ramp time influences the shape of the LDTD peak and, by the same token, the number of acquisition data points per peak. Because LDTD desorption is fast, the HRMS detection can often lack data acquisition points for low-variability quantification (the criteria being at least seven points).[34] The laser

DOI: 10.1021/acs.jafc.5b02318
J. Agric. Food Chem. 2015, 63, 7440−7449

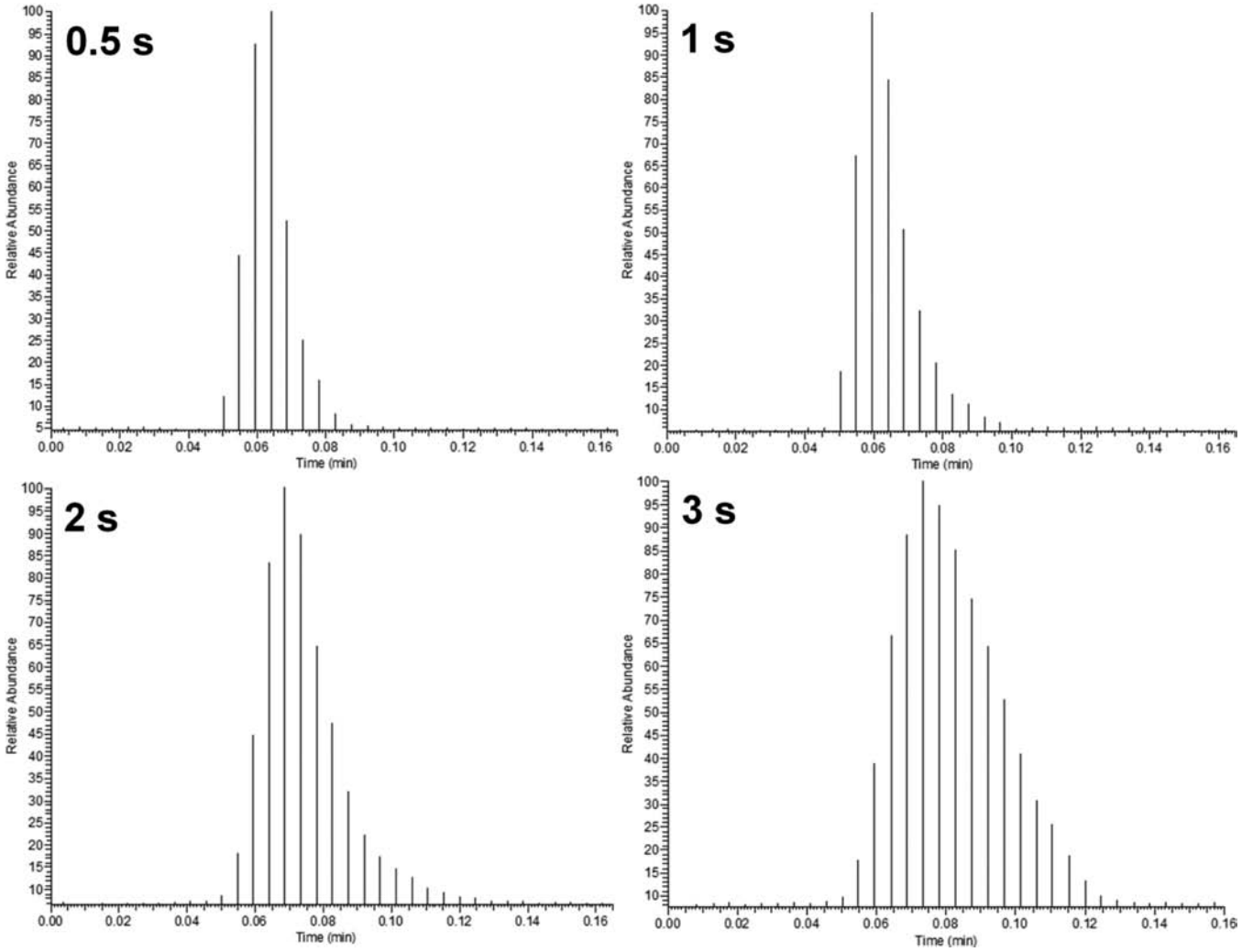

Figure 4. Number of data acquisition points for LDTD peaks of MMPB with different laser ramp times.

plateau time influences the amount of compound that will desorb and the signal stability. The two parameters were evaluated together by varying them between 0.5 and 3 s (Figure S3). The optimal values were a laser ramp time of 2 s with a laser plateau time of 1 s yielding more than 10 data acquisition points in a peak width of about 5 s (Figure 4). Higher laser plateau times caused signal instability and higher variability. The phenomenon also occurred with higher laser ramp time, at >3 s, when the beginning of a peak distortion was observed and caused higher signal variability. With 4 s of laser ramp time, peak distortion is obvious, causing much higher signal variability (Figure S4). No significant enhancement was observed with higher laser plateau and ramp time ($P > 0.05$).

Method Validation. The evaluation of the LDTD-APCI-HRMS method was done according to these parameters: linearity, sensitivity, accuracy, precision, selectivity, and matrix effects, which were previously discussed under Sample Cleanup and Elution. Due to the unavailability of isotopically labeled MMPB, 4-PB was used as the internal standard based on previous studies.[17,20] All validation parameters were evaluated using spiked blank fish tissue to take matrix effects into account. A seven-point standard addition calibration curve spiked prior to the SPE procedure was used with a linear dynamic range between 15 and 2 500 $\mu g\ kg^{-1}$ analyzed in triplicate. The optimal concentration of 4-PB used as signal variation correction was set at 500 $\mu g\ kg^{-1}$ depending on the lowest variability throughout the calibration linearity range (data not shown). Ultimately, correlation coefficients showed a good linearity with $R^2 > 0.999$. The method detection limit and method quantification limit (MDL and MQL) were 2.7 and 8.2 $\mu g\ kg^{-1}$, which are comparable to previous work. Figure S5 shows a sample LDTD peak signal obtained around the MQL (8 $\mu g\ kg^{-1}$).[17] Table 2 summarizes the validation parameters determined at three concentrations from the linearity range (25, 250, and 1000 $\mu g\ kg^{-1}$). Values from the accuracy expressed as the relative errors (RE %) and from intraday and interday precisions expressed as relative standard deviations (RSD %) were ≤10%, which means that the method was both selective and precise.

Fish Tissue Samples. The method was applied to determine the total MCs present in 49 samples of fish tissue caught in three different lakes of the province of Québec, Canada, where cyanobacterial blooms occurred during the growing season. Tables 3 and S1 present the results obtained using three different analytical methods. The results from the method developed in this study are presented first. Then, the same samples were submitted to LDTD-APCI-MS/MS analysis using a previously developed method for total MCs in lake water.[20] The purpose here was to compare the sensitivity and selectivity of MS/MS detection with HRMS detection using

DOI: 10.1021/acs.jafc.5b02318
J. Agric. Food Chem. 2015, 63, 7440−7449

Table 3. Comparison of Results from Fish Samples with Detected MCs above Method Detection Limit Using Three Detection Methods

sample	location	fish species	fish part	total MC via MMPB and HRMS[a] (μg kg^{-1}) (RSD %)	total MC via MMPB and MS/MS[b] (μg kg^{-1}) (RSD %)	total MC with standards[c] (μg kg^{-1})
1	Lac Vert	rainbow smelt	no head/ viscera	**11.9 (7)**[d]	10.3 (9)	nd[e]
2	Lac Vert	white sucker	whole	8.7 (8)	7.5 (12)	nd
3	Lac Vert	white sucker	whole	**13.2 (6)**	11.9 (11)	2.0
4	Lac Vert	white sucker	whole	**9.5 (10)**	8.1 (11)	nd
6	Lac Vert	brook trout	muscle	5.0 (10)	nd	nd
7	Lac Vert	brook trout	muscle	4.5 (9)	nd	nd
9	Lac Roxton	yellow perch	muscle	4.0 (10)	nd	nd
11	Lac Roxton	yellow perch	muscle	3.1 (11)	nd	nd
14	Lac Roxton	yellow perch	muscle	5.2 (9)	nd	nd
17	Lac Noir	yellow perch	muscle	4.5 (7)	nd	nd
18	Lac Noir	yellow perch	muscle	7.3 (11)	6.9 (12)	nd
20	Lac Noir	yellow perch	muscle	2.7 (12)	nd	nd
22	Lac Noir	walleye	muscle	4.4 (8)	nd	nd
24	Lac Noir	walleye	muscle	2.9 (10)	nd	nd
27	Lac Noir	walleye	muscle	3.4 (9)	nd	nd
33	Lac Noir	brown bullhead	muscle	3.8 (9)	nd	nd
35	Lac Noir	brown bullhead	muscle	5.2 (8)	nd	nd
38	Lac Noir	lake whitefish	muscle	7,1 (8)	nd	nd
40	Lac Noir	lake whitefish	muscle	6,2 (9)	nd	nd
41	Lac Noir	lake whitefish	muscle	5.9 (7)	nd	nd
44	Lac Noir	lake whitefish	muscle	7.3 (10)	nd	nd
45	Lac Noir	lake whitefish	muscle	4.5 (11)	nd	nd
46	Lac Noir	lake whitefish	muscle	3.0 (9)	nd	nd
49	Lac Noir	yellow perch	muscle	3.7 (11)	nd	nd

[a]Total microcystins determined via MMPB using LDTD-APCI-HRMS. [b]Total microcystins determined via MMPB using LDTD-APCI-MS/MS. [c]Microcystins determined via the summation of all microcystins for which standards allowed detection and quantification (i.e., MC-LA, MC-LR, MC-RR, and MC-YR) using LC-MS/MS. [d]Values in bold represent concentrations above the MQL. [e]nd, not detected.

LDTD-APCI technology. Finally, CEAEQ results using a standard analytical method for MCs in fish tissue are presented for the same samples. Of the 49 samples (Table S1), 24 had a positive response to MCs, including 22 that were above the detection limit (Table 3). Concentrations varied between 2.7 and 13.2 μg kg^{-1} of fresh fish tissues weight. Four samples (1−4) had relatively higher detected concentrations, which could be explained by the type of fish tissue. Indeed, three of these samples from a bottom feeder, the white sucker, included the viscera known to concentrate higher amount of MCs, but that are not generally consumed by fisherman. Interestingly, the second highest concentration was for a headed and gutted rainbow smelt, these small fish are eaten as is. Smelt's preferred habitat is the metalimnion, which is also the habitat of the blue green algae *Planktothrix* responsible for the Lac Vert's contamination by MCs. Smelt consume crustacean, zooplankton and insect larvae that are themselves algae consumers. Only four results were above the estimated MQL values, although yellow perch and lake whitefish were quite close. Of the 24 samples with positive MC detection, only 5 were detected using the LDTD-APCI-MS/MS technique with relative differences in values of −13% on average. This difference was explained by the different response of matrix effects using MS/MS, for which the signal recovery was 82%. The detection and quantification limits of the method were 6.8 and 20.4 μg kg^{-1}, respectively. Whereas these values are comparable with those obtained in previous studies, the use of HRMS offered better sensitivity (i.e., 2.7 and 8.2 μg kg^{-1}, respectively), which supports the choice of our detection method.

Using the CEAEQ's standard analytical method, only one sample showed the positive detection of MCs at 2.0 μg kg^{-1} of MC-YR congener. This value represents 15% of the recovered total MCs from the same sample. The detection limit of each studied MC variant was 1 μg kg^{-1}, and detection method sensitivity therefore cannot explain this discrepancy. Two reasons may explain the substantial underestimation of MCs. First, it is possible that the extraction method may not be able to release the covalently bound MCs from the tissue. Williams et al. provided experimental evidence, using Lemieux oxidation, MMPB-GC/MS, radiolabeled MMPB, and MeOH extraction-PPase, to demonstrate that a substantial amount of MCs was covalently bound in vivo.[38,39] MeOH extraction actually recovered ≈24% of the total MC-LR measured with MMPB in the liver of salmon intraperitoneally injected. This underestimation is similar to what this study obtained for whole fish in the only sample with a detection using the conventional extraction method. Other authors estimated that as much as 60−90% of total MCs could be covalently bound.[38−41] Second, other variants and variant isomers present in the samples could have been missed altogether. Indeed, some tissue samples from the same lake and date had MC detections suspected by CEAEQ to be YR isomer (data not shown). Due to the absence of appropriate standards for LC-MS/MS, the CEAEQ analytical laboratory could not certify the identification and concentration of the suspected isomer, although its characteristics were so close to the available standard that it was deemed with a very high probability to be an isomer of MC-YR. As was recently demonstrated with total MCs in water,[20] this study also illustrates the inherent risk of relying on a limited number of

DOI: 10.1021/acs.jafc.5b02318
J. Agric. Food Chem. 2015, 63, 7440−7449

standards when the total MC contamination in tissue is assessed. Our results show the importance of analyzing total MCs in fish tissue using proper sample preparation and extraction methods along with selective and sensitive detection methods.

Risk Assessment. The maximum lifetime TDI for humans (i.e., 0.04 μg/kg/day) set out by the WHO has been used in several exposure scenarios to estimate the potential risk for fish consumers. Scenarios aiming to protect at-risk groups (e.g., children[42] or important consumers of locally caught fish[43]) are expected to be the most stringent. Assuming that no exposure would come from drinking water or recreational exposure, the TDI would transfer to ≈8 μg kg^{-1} of fish for a 60 kg adult who consumes 300 g of fish per day, on average,[43,44] or to ≈24 μg kg^{-1} for those who consume 100 g per day.[45] Some of the results presented in Table 3 would then exceed the TDI if fish consumption is high enough. These results are noteworthy because only 1 of the 49 samples was over the detection limit (i.e., 1 μg kg^{-1}) of the initial LC-MS/MS analysis. However, it was observed that only three samples were detected above the estimated MQL (8.2 μg kg^{-1}). Although further studies are required to improve sensitivity, the findings here were satisfactory for MCs detection around the WHO's TDI.

Likewise, assuming that 15% of the total MCs were detected in studies analyzing only unbound concentrations, several studies including this one would have MC levels above the WHO's TDI using our method.[45−49] Overall these results suggest that certain groups may be at a higher risk than previously estimated and that more research on the toxicity of total MCs is needed.

Moreover, the WHO has classified MCs as a "possible human carcinogenic" (class II-B).[50] It is therefore important to enhance our ability to estimate the total concentration from all sources of exposure to this class of pollutants because cancer may develop after a long latency period and possibly at relatively low exposure levels.

Although the variants, isomers, conjugates, and covalently bound MCs probably all have different toxicological properties that have yet to be understood, a method to analyze quickly total MCs is nevertheless essential to make prudent exposure measurements while research progresses. Furthermore, this new method for total MCs in tissue would be helpful in a tiered approach to screen out samples that do not contain these toxins, enabling resource allocation where other variants could be playing an unnoticed role in toxicity. Although many studies have explored the availability of MCs in aquatic animal consumption after cooking and digestion, the bioavailability and toxicity of bound MCs are still poorly understood.[51−53] However, findings showed that serious risk to animal and human health is most likely possible and that contamination monitoring could prevent eventual poisoning cases. It would therefore be beneficial to understand the fate, transportation, and accumulation of MCs in the food web, with or without other analyses and assays.[54]

In conclusion, a new approach to detect total microcystins in fish tissue has been demonstrated and validated using LDTD-APCI-HRMS. MCs are known to covalently bind with animal tissue, and effective sample preparation is therefore necessary to analyze both free and bound fractions and the possible MC congeners. We explored the possibility of using sodium hydroxide as a digestive agent for fish tissue prior to a well-known oxidation step, Lemieux oxidation, for total MC analysis. A new approach for sample cleanup was also explored using an SDB-L SPE cartridge for recovery enhancement and eliminating the salts present in solution. The use of LDTD-APCI has already been reported for the analysis of MMPB in water, but HRMS detection with the Q-Exactive was chosen for better sensitivity and selectivity. The use of LDTD-APCI-HRMS enabled ultrafast analysis times at 10 s per sample. Digestion and oxidation were optimized, and recoveries ranged from 70 to 75%, respectively. SPE recoveries ranged from 86 to 103%, and signal recoveries from matrix effects ranged from 90 to 93%. An internal calibration was used with 4-PB, and the validated method gave linear correlation coefficients (R^2) of 0.999; MDL and MQL were 2.7 and 8.2 μg kg^{-1}, respectively. Accuracy and interday/intraday variation coefficients for target compounds were below 10%. Interday and intraday precisions were evaluated below 10%. Of a total of 49 fish samples from lakes with HABs, 25 (51%) had a positive response for total microcystins with concentrations ranging from 2.9 to 13.2 μg kg^{-1} fresh weight in tissue. Using standardized extraction and LC-MS/MS methods, only one sample (2%) had a microcystin response with a concentration of 2 μg kg^{-1} of MC-YR. For that sample, the total MCs were 7 times higher than the initial value. These results suggest that MC concentration in fish tissues could be significantly underestimated using standard analytical methods and that a suitable extraction method combined with total MC detection is required for prudent risk management.

■ ASSOCIATED CONTENT

Supporting Information

The Supporting Information is available free of charge on the ACS Publications website at DOI: 10.1021/acs.jafc.5b02318.

Figures S1−S5 and Table S1 (PDF)

■ AUTHOR INFORMATION

Corresponding Author

*(S.S.) Phone: (514) 343-6749. Fax: (514) 343-7586. E-mail: sebastien.sauve@umontreal.ca. Mail: Université de Montréal, Departement of Chemistry, CP 6128 Centre-Ville, Montréal, QC H3C 3J7, Canada.

Funding

This research was carried out with the financial support of the Fond de recherche Québec−Nature et technologies and the Natural Sciences and Engineering Research Council of Canada (NSERC).

Notes

The authors declare no competing financial interest.

■ ACKNOWLEDGMENTS

We thank Thermo Fisher Scientific and Phytronix Technologies for their support as well as Paul B. Fayad and Sung Vo Duy for their technical and scientific expertise.

■ REFERENCES

(1) Codd, G. A.; Morrison, L. F.; Metcalf, J. S. Cyanobacterial toxins: risk management for health protection. *Toxicol. Appl. Pharmacol.* **2005**, *203*, 264−272.

(2) McLean, T. I.; Sinclair, G. A. Harmful algal bloom. In *Environmental Toxicology*; Springer: New York, 2013; pp 319−360.

(3) Christoffersen, K. Ecological implications of cyanobacterial toxins in aquatic food webs. *Phycologia* **1996**, *35*, 42−50.

(4) Qiu, T.; Xie, P.; Ke, Z.; Li, L.; Guo, L. In situ studies on physiological and biochemical responses of four fishes with different

DOI: 10.1021/acs.jafc.5b02318
J. Agric. Food Chem. 2015, 63, 7440−7449

trophic levels to toxic cyanobacterial blooms in a large Chinese lake. *Toxicon* **2007**, *50*, 365−376.
(5) Metcalf, J. S.; Codd, G. A. Cyanotoxins. In *Ecology of Cyanobacteria II*; Springer: New York, 2012; pp 651−675.
(6) Rinehart, K. L.; Harada, K.; Namikoshi, M.; Chen, C.; Harvis, C. A.; Munro, M. H. G.; Blunt, J. W.; Mulligan, P. E.; Beasley, V. R.; Dahlem, A. M.; Carmichael, W. W. Nodularin, microcystin, and the configuration of adda. *J. Am. Chem. Soc.* **1988**, *110*, 8557−8558.
(7) Puddick, J.; Prinsep, M. R.; Wood, S. A.; Kaufononga, S. A.; Cary, S. C.; Hamilton, D. P. High levels of structural diversity observed in microcystins from microcystis CAWBG11 and characterization of six new microcystin congeners. *Mar. Drugs* **2014**, *12*, 5372−5395.
(8) Bortoli, S.; Volmer, D. Account: Characterization and identification of microcystins by mass spectrometry. *Eur. Mass Spectrom.* **2014**, *20*, 1−19.
(9) del Campo, F. F.; Ouahid, Y. Identification of microcystins from three collection strains of *Microcystis aeruginosa*. *Environ. Pollut.* **2010**, *158*, 2906−2914.
(10) Pearson, L.; Mihali, T.; Moffitt, M.; Kellmann, R.; Neilan, B. On the chemistry, toxicology and genetics of the cyanobacterial toxins, microcystin, nodularin, saxitoxin and cylindrospermopsin. *Mar. Drugs* **2010**, *8*, 1650−1680.
(11) Svirčev, Z.; Baltić, V.; Gantar, M.; Juković, M.; Stojanović, D.; Baltić, M. Molecular aspects of microcystin-induced hepatotoxicity and hepatocarcinogenesis. *J. Environ. Sci. Health C* **2010**, *28*, 39−59.
(12) Žegura, B.; Štraser, A.; Filipič, M. Genotoxicity and potential carcinogenicity of cyanobacterial toxins—a review. *Mutat. Res., Rev. Mutat. Res.* **2011**, *727*, 16−41.
(13) Chorus, I.; Bartram, J. In *Toxic Cyanobacteria in Water: A Guide to Their Public Health Consequences, Monitoring, and Management*; E & FN Spon: Germany, 1999.
(14) World Health Organization. Cyanobacterial toxins: microcystin-LR in drinking-water. In *Background Document for Development of WHO Guidelines for Drinking-Water Quality*, 2nd ed.; World Health Organization: Geneva, Switzerland, 2003.
(15) Cadel-Six, S.; Moyenga, D.; Magny, S.; Trotereau, S.; Edery, M.; Krys, S. Detection of free and covalently bound microcystins in different tissues (liver, intestines, gills, and muscles) of rainbow trout (*Oncorhynchus mykiss*) by liquid chromatography-tandem mass spectrometry: method characterization. *Environ. Pollut.* **2014**, *185*, 333−339.
(16) Smith, J. L.; Boyer, G. L. Standardization of microcystin extraction from fish tissues: a novel internal standard as a surrogate for polar and non-polar variants. *Toxicon* **2009**, *53*, 238−245.
(17) Ott, J. L.; Carmichael, W. W. LC/ESI/MS method development for the analysis of hepatotoxic cyclic peptide microcystins in animal tissues. *Toxicon* **2006**, *47*, 734−741.
(18) Neffling, M. R.; Lance, E.; Meriluoto, J. Detection of free and covalently bound microcystins in animal tissues by liquid chromatography-tandem mass spectrometry. *Environ. Pollut.* **2010**, *158*, 948−952.
(19) Wang, C.; Tian, C.; Tian, Y.; Feng, B.; We, S.; Li, Y.; Wu, X.; Xiao, B. A sensitive method for the determination of total microcystins in water and sediment samples by liquid chromatography with fluorescence detection. *Anal. Methods* **2015**, *7*, 759−765.
(20) Roy-Lachapelle, A.; Fayad, P. B.; Sinotte, M.; Deblois, C.; Sauve, S. Total microcystins analysis in water using laser diode thermal desorption-atmospheric pressure chemical ionization-tandem mass spectrometry. *Anal. Chim. Acta* **2014**, *820*, 76−83.
(21) Suchy, P.; Berry, J. Detection of total microcystin in fish tissues based on lemieux oxidation and recovery of 2-methyl-3-methoxy-4-phenylbutanoic acid (MMPB) by solid-phase microextraction gas chromatography-mass spectrometry (SPME-GC/MS). *Int. J. Environ. Anal. Chem.* **2012**, *92*, 1443−1456.
(22) Wu, X.; Xiao, B.; Li, R.; Wang, Z.; Chen, X.; Chen, X. Rapid quantification of total microcystins in cyanobacterial samples by periodate-permanganate oxidation and reversed-phase liquid chromatography. *Anal. Chim. Acta* **2009**, *651*, 241−247.
(23) Roy-Lachapelle, A.; Solliec, M.; Sinotte, M.; Deblois, C.; Sauvé, S. High resolution/accurate mass (HRMS) detection of anatoxin-A in lake water using LDTD−APCI coupled to a Q-Exactive mass spectrometer. *Talanta* **2015**, *132*, 836−844.
(24) Lemoine, P.; Roy-Lachapelle, A.; Prévost, M.; Tremblay, P.; Solliec, M.; Sauvé, S. Ultra-fast analysis of anatoxin-A using laser diode thermal desorption-atmospheric pressure chemical ionization-tandem mass spectrometry: validation and resolution from phenylalanine. *Toxicon* **2013**, *61*, 165−174.
(25) Solliec, M.; Massé, D.; Sauvé, S. Analysis of trimethoprim, lincomycin, sulfadoxin and tylosin in swine manure using laser diode thermal desorption-atmospheric pressure chemical ionization-tandem mass spectrometry. *Talanta* **2014**, *128*, 23−30.
(26) Darwano, H.; Duy, S. V.; Sauvé, S. A new protocol for the analysis of pharmaceuticals, pesticides, and hormones in sediments and suspended particulate matter from rivers and municipal wastewaters. *Arch. Environ. Contam. Toxicol.* **2014**, *66*, 582−593.
(27) Boisvert, M.; Fayad, P. B.; Sauvé, S. Development of a new multi-residue laser diode thermal desorption atmospheric pressure chemical ionization tandem mass spectrometry method for the detection and quantification of pesticides and pharmaceuticals in wastewater samples. *Anal. Chim. Acta* **2012**, *754*, 75−82.
(28) Viglino, L.; Prévost, M.; Sauvé, S. High throughput analysis of solid-bound endocrine disruptors by LDTD-APCI-MS/MS. *J. Environ. Monit.* **2011**, *13*, 583−590.
(29) Segura, P. A.; Tremblay, P.; Picard, P.; Gagnon, C.; Sauvé, S. High-throughput quantitation of seven sulfonamide residues in dairy milk using laser diode thermal desorption-negative mode atmospheric pressure chemical ionization tandem mass spectrometry. *J. Agric. Food Chem.* **2010**, *58*, 1442−1446.
(30) Fayad, P. B.; Prévost, M.; Sauvé, S. Laser diode thermal desorption/atmospheric pressure chemical ionization tandem mass spectrometry analysis of selected steroid hormones in wastewater: method optimization and application. *Anal. Chem.* **2010**, *82*, 639−645.
(31) Thermo Fisher Scientific. In *Q Exactive*, revision C-1288120, 2012.
(32) Solliec, M.; Roy-Lachapelle, A.; Sauve, S. Quantitative performance of liquid chromatography coupled to Q-Exactive high resolution mass spectrometry (HRMS) for the analysis of tetracyclines in a complex matrix. *Anal. Chim. Acta* **2015**, *853*, 415−424.
(33) Fedorova, G.; Randak, T.; Lindberg, R. H.; Grabic, R. Comparison of the quantitative performance of a Q-Exactive high-resolution mass spectrometer with that of a triple quadrupole tandem mass spectrometer for the analysis of illicit drugs in wastewater. *Rapid Commun. Mass Spectrom.* **2013**, *27*, 1751−1762.
(34) Zhang, Y.; Hao, Z.; Kellmann, M.; Huhmer, A. *HR/AM Targeted Peptide Quantitation on a Q Exactive MS: A Unique Combination of High Selectivity, Sensitivity and Throughput*, Application Note: 554; Thermo Fisher Scientific, 2012.
(35) Song, W.; De La Cruz, A. A.; Rein, K.; O'Shea, K. E. Ultrasonically induced degradation of microcystin-LR and-RR: Identification of products, effect of pH, formation and destruction of peroxides. *Environ. Sci. Technol.* **2006**, *40*, 3941−3946.
(36) Badjagbo, K.; Picard, P.; Moore, S.; Sauvé, S. Direct atmospheric pressure chemical ionization-tandem mass spectrometry for the continuous real-time trace analysis of benzene, toluene, ethylbenzene, and xylenes in ambient air. *J. Am. Soc. Mass Spectrom.* **2009**, *20*, 829−836.
(37) Sangster, T.; Spence, M.; Sinclair, P.; Payne, R.; Smith, C. Unexpected observation of ion suppression in a liquid chromatography/atmospheric pressure chemical ionization mass spectrometric bioanalytical method. *Rapid Commun. Mass Spectrom.* **2004**, *18*, 1361−1364.
(38) Williams, D. E.; Craig, M.; Dawe, S. C.; Kent, M. L.; Holmes, C. F.; Andersen, R. J. Evidence for a covalently bound form of microcystin-LR in salmon liver and dungeness crab larvae. *Chem. Res. Toxicol.* **1997**, *10*, 463−469.
(39) Williams, D. E.; Craig, M.; Dawe, S. C.; Kent, M. L.; Andersen, R. J.; Holmes, C. F. ^{14}C-labelled microcystin-LR administered to Atlantic salmon via intraperitoneal injection provides in vivo evidence

DOI: 10.1021/acs.jafc.5b02318
J. Agric. Food Chem. 2015, 63, 7440−7449

for covalent binding of microcystin-LR in salmon livers. *Toxicon* **1997**, *35*, 985−989.
(40) Nasri, H.; El Herry, S.; Bouaïcha, N. First reported case of turtle deaths during a toxic *Microcystis* spp. bloom in Lake Oubeira, Algeria. *Ecotoxicol. Environ. Saf.* **2008**, *71*, 535−544.
(41) Lance, E.; Josso, C.; Dietrich, D.; Ernst, B.; Paty, C.; Senger, F.; Bormans, M.; Gérard, C. Histopathology and microcystin distribution in *Lymnaea stagnalis* (Gastropoda) following toxic cyanobacterial or dissolved microcystin-LR exposure. *Aquat. Toxicol.* **2010**, *98*, 211−220.
(42) Weirich, C. A.; Miller, T. R. Freshwater harmful algal blooms: toxins and children's health. *Curr. Probl. Pediatr. Adolesc. Health Care* **2014**, *44*, 2−24.
(43) Dyble, J.; Gossiaux, D.; Landrum, P.; Kashian, D. R.; Pothoven, S. A kinetic study of accumulation and elimination of microcystin-LR in yellow perch (*Perca flavescens*) tissue and implications for human fish consumption. *Mar. Drugs* **2011**, *9*, 2553−2571.
(44) Deblois, C. P.; Mochon, A.; Juneau, P. Toxines de cyanobactéries dans les perchaudes: Analyse exploratoire dans quatre lacs du bassin de la rivière Yamaska. *Le Naturaliste Canadien* **2008**, *132*, 56−59.
(45) Poste, A. E.; Hecky, R. E.; Guildford, S. J. Evaluating microcystin exposure risk through fish consumption. *Environ. Sci. Technol.* **2011**, *45*, 5806−5811.
(46) Schmidt, J. R.; Shaskus, M.; Estenik, J. F.; Oesch, C.; Khidekel, R.; Boyer, G. L. Variations in the microcystin content of different fish species collected from a eutrophic lake. *Toxins* **2013**, *5*, 992−1009.
(47) Jia, J.; Luo, W.; Lu, Y.; Giesy, J. P. Bioaccumulation of microcystins (MCs) in four fish species from Lake Taihu, China: assessment of risks to humans. *Sci. Total Environ.* **2014**, *487*, 224−232.
(48) Amrani, A.; Nasri, H.; Azzouz, A.; Kadi, Y.; Bouaïcha, N. Variation in cyanobacterial hepatotoxin (microcystin) content of water samples and two species of fishes collected from a shallow lake in Algeria. *Arch. Environ. Contam. Toxicol.* **2014**, *66*, 379−389.
(49) Zhang, D.; Xie, P.; Liu, Y.; Chen, J.; Liang, G. Bioaccumulation of the hepatotoxic microcystins in various organs of a freshwater snail from a subtropical Chinese lake, Taihu Lake, with dense toxic *Microcystis* blooms. *Environ. Toxicol. Chem.* **2007**, *26*, 171−176.
(50) Grosse, Y.; Baan, R.; Straif, K.; Secretan, B.; El Ghissassi, F.; Cogliano, V. Carcinogenicity of nitrate, nitrite, and cyanobacterial peptide toxins. *Lancet Oncol.* **2006**, *7*, 628−629.
(51) Papadimitriou, T.; Kagalou, I.; Stalikas, C.; Pilidis, G.; Leonardos, I. D. Assessment of microcystin distribution and biomagnification in tissues of aquatic food web compartments from a shallow lake and evaluation of potential risks to public health. *Ecotoxicology* **2012**, *21*, 1155−1166.
(52) Freitas, M.; Azevedo, J.; Carvalho, A. P.; Campos, A.; Vasconcelos, V. Effects of storage, processing and proteolytic digestion on microcystin-LR concentration in edible clams. *Food Chem. Toxicol.* **2014**, *66*, 217−223.
(53) Guzmán-Guillén, R.; Prieto, A. I.; Moreno, I.; Soria, M. E.; Cameán, A. M. Effects of thermal treatments during cooking, microwave oven and boiling, on the unconjugated microcystin concentration in muscle of fish (*Oreochromis niloticus*). *Food Chem. Toxicol.* **2011**, *49*, 2060−2067.
(54) Schmidt, J. R.; Wilhelm, S. W.; Boyer, G. L. The fate of microcystins in the environment and challenges for monitoring. *Toxins* **2014**, *6*, 3354−3387.

DOI: 10.1021/acs.jafc.5b02318
J. Agric. Food Chem. 2015, 63, 7440−7449

Table 1. Multiplex LC-MS/MS Method Information for the Quantitation of AAD-12, 2mEPSPS, and PAT Proteins from Soybean Tissues

protein	peptide	charge state	MS/MS transition (m/z)	collision energy (V)	peptide molecular weight (Da)	protein molecular weight (kD)
AAD-12	AAYDALDEATR[b]	(+2)	598.3/704.4	26	1195	32
	AAYDALDEATR[a]	(+2)	598.3/591.3	32	1195	
	AAYDALDEATR[c]	(+2)	603.3/601.3	32	1205	
	IGGGDIVAISNVK[d]	(+2)	621.9/631.4	29	1242	
2mEPSPS	EISGTVK[b]	(+2)	367.2/491.3	18	733	47.5
	EISGTVK[a]	(+2)	367.2/404.3	18	733	
	EISGTVK[c]	(+2)	371.2/499.3	18	741	
	DVASWR[d]	(+2)	367.2/519.3	15	733	
PAT	TEPQTPQEWIDDLER[b]	(+2)	928.9/1300.6	52	1857	21
	TEPQTPQEWIDDLER[a]	(+2)	928.9/813.9	38	1857	
	TEPQTPQEWIDDLER[c]	(+2)	933.9/818.9	38	1867	
	SVVAVIGLPNDPSVR[d]	(+2)	761.9/784.4	33	1522	

[a]Quantitation peptide, MS/MS transition used for quantitation. [b]Quantitation peptide, MS/MS transition used for confirmation. [c]Heavy labeled peptide internal standard. [d]Confirmation peptide, used to confirm digestion completeness.

previous literature.[22,23] To demonstrate signature peptide quantitation by LC-MS/MS as a suitable multiplex platform to quantify multiple proteins within a single analysis, we report a comprehensive development and validation of a multiplex LC-MS/MS method for the determination of the aryloxyalkanoate dioxygenase (AAD-12), 5-enol-pyruvylshikimate-3-phosphate synthase (2mEPSPS), and phosphinothricin acetyltransferase (PAT) herbicide-tolerant proteins in Enlist E3 soybean tissues.

MATERIALS AND METHODS

Materials. Soybean plants were grown in a Dow AgroSciences greenhouse (Indianapolis, IN), and leaf, root, and seed tissues were lyophilized, ground to a fine powder, then stored at −80 °C. Recombinant protein standards were expressed in and purified from *Pseudomonas fluorescens* (>95% purity), and aliquots were stored at −80 °C for single usage with protein concentrations assessed by amino acid analysis using acid hydrolysis, automated OPA/FMOC derivatization, and C18 reverse-phase separation with fluorescence detection. Synthetic peptides representative of natural abundance peptides from each protein, defined as surrogate peptides, and heavy-labeled peptide internal standards (L-lysine-$^{13}C_6$,$^{15}N_2$ or L-arginine-$^{13}C_6$,$^{15}N_4$, depending on protein sequence) were obtained from New England Peptide (Gardner, MA). Phosphate-buffered saline containing 0.05% Tween 20 (PBST) was obtained from Teknova (Hollister, CA). Casein was purchased from SurModics (Eden Prairie, MN). Albumin chicken egg (OVA), polyvinylpyrrolidone (PVP), and HPLC solvents were obtained from Sigma-Aldrich (St. Louis, MO). Ammonium bicarbonate, dithiothreitol, and formic acid were obtained from Fisher Scientific (USA). Sequencing-grade trypsin was purchased frozen from Promega Corporation (Madison, WI).

LC-MS/MS Method Overview. All surrogate peptide LC-MS/MS method development and validation was carried out at Dow AgroSciences (Indianapolis, IN). Briefly, a total of 1.5 mL of PBST and two metal beads were added per 15 mg of lyophilized soybean leaf, root, or seed tissue weighed into low-binding microcentrifuge tubes. Samples were extracted in a bead grinder (Geno/Grinder, Swedesboro, NJ) at 1500 strokes per minute for 3 min followed by centrifugation at 4 °C and >3000 rpm for 10 min. A total of 100 μL of supernatant was transferred to a clean microcentrifuge tube with the addition of 7.5 mM dithiothreitol (DTT) and incubated at 95 °C for 45 min followed by cooling at 4 °C. After the samples were cooled to room temperature, 60 μL of 50 mM ammonium bicarbonate, 20 μL of heavy-isotope-labeled peptide internal standard, and 5 μg of trypsin enzyme (enzyme/substrate ratio ≈ 1:75 (w/w), on the basis of BCA assay results for total extractable protein content from respective tissues) were added. The synthetic natural abundance peptide reference standards were spiked into control soybean tissue and processed in the same manner as the unknown samples. The samples and peptide reference standards were incubated overnight at 37 °C, followed by quenching with formic acid/H_2O (50:50, v/v). The samples were centrifuged at >3000 rpm for 10 min to pellet any undigested insoluble particulate, followed by LC-MS/MS analysis. Quantitation of detected surrogate peptides was carried out with linear regression and $1/x^2$ weighting, followed by conversion into respective protein concentrations using the following equation and information found in Table 1.

$$\text{Protein Concentration} = \text{Detected Peptide Concentration} \times \left(\frac{\text{Protein Molecular Weight}}{\text{Peptide Molecular Weight}}\right)$$

The LC-MS/MS system included an AB Sciex 4000 QTRAP with turbo ion-spray source and Waters Acquity H-Class UPLC. The autosampler temperature was kept at 4 °C during analysis. A total of 5 μL of sample was injected onto an Acquity UPLC BEH130 C18 1.7 μm (2.1 mm × 50 mm) column set at 50 °C. The reverse phase analysis was carried out using an organic mobile phase (MPB) acetonitrile containing 0.1% formic acid and the aqueous mobile phase (MPA) was water containing 0.1% formic acid. The LC flow rate was 0.5 mL/min with a linear gradient from 0.1% MPB to 28% MPB over 6 min, followed by 100% MPB for 1 min to wash the column, and 0.1% MPB for 1 min to re-equilibrate the column. The needle wash and seal wash contained 50:50 methanol/water with no detected carryover between samples.

The mass spectrometer was operated in positive ion mode with ion-spray voltage of 5500 V and temperature set at 450 °C. MS/MS transitions and collision energy for each peptide can be found in Table 1. Other relevant instrument parameters included curtain gas of 35 psi, ion-source gas 1 and 2 of 55

DOI: 10.1021/acs.jafc.5b03083
J. Agric. Food Chem. 2015, 63, 7450−7461

psi, collision gas set to medium, entrance potential of 10 V, declustering potential of 80 V, and collision cell exit potential of 15 V.

LC-MS/MS Method Validation. *Extraction Efficiency.* Extraction efficiency (EE) was evaluated by repeatedly extracting transgenic soybean tissue samples containing AAD-12, 2mEPSPS, and PAT proteins and determining the amount of protein from each extraction. After extraction, the samples were centrifuged and the supernatant transferred to a new vial, and the extraction of the pellet was repeated. Each extract was analyzed for surrogate peptide concentrations by LC-MS/MS, and the levels of transgenic proteins in the extracts and the pellet were confirmed by Western blotting. The extraction efficiency for each protein in each tissue was calculated as the percentage of peptide detected in the first extraction relative to the peptide found in all soluble extractions by the following equation:

$$\mathrm{EE} = \left(\frac{\text{Amount of peptide recovered in 1st extraction}}{\text{Sum of peptide recovered from all extractions}}\right) \times 100$$

Western Blotting. Briefly, 750 μL of Laemmli buffer was added to each pelleted tissue after the fifth serial extraction and extracted with the Geno Grinder at 1500 strokes/min for 3 min followed by centrifugation at 4 °C and > 3000 rpm for 5 min. The first and fifth extraction supernatants were diluted 1:2 into 2× concentrated Laemmli buffer; all prepared solutions were heated at 95 °C for 10 min, loaded onto a gel along with recombinant protein standards with XT MES running buffer, and separated by electrophoresis for approximately 1 h at 160 V. Each gel was transferred to a nitrocellulose membrane, washed 3 times with PBST, and incubated with each corresponding primary antibody in PBST overnight at 4 °C with gentle shaking. After primary antibody incubation, the membranes were washed 3 times with PBST. The membranes were then incubated with respective HRP-conjugated secondary antibodies prepared in blocking solution for 1 h at room temperature with gentle shaking. After incubation with secondary antibodies, the membranes were washed 3 times with PBST. The membranes were exposed to X-ray film after addition of chemilumenscence substrate to the membrane.

Accuracy. Method accuracy was assessed by determining the recovery of surrogate peptides (described in Table 1) produced from the digestion of AAD-12, 2mEPSPS, and PAT recombinant proteins that had been fortified into non-GE control soybean tissues at the proposed limit of quantitation (LOQ), a midrange concentration, and a high-range concentration for each protein. Briefly, control soybean tissue (leaf, root, or seed depending on which matrix was being evaluated) was extracted with PBST, and the supernatant was pooled together. Each pooled tissue extract was then fortified with all three proteins, denatured, digested, and analyzed by LC-MS/MS. Recovery was determined as a percentage of fortified recombinant proteins via the following equation:

$$\%\ \text{Recovery} = \frac{\text{Detected Peptide Concentration} \times \left(\frac{\text{Protein Molecular Weight}}{\text{Peptide Molecular Weight}}\right)}{\text{Theoretical Protein Fortification Concentration}} \times 100$$

Precision and Ruggedness. Precision and ruggedness were determined by evaluating the recovery of surrogate peptides produced from the digestion of AAD-12, 2mEPSPS, and PAT recombinant proteins that had been fortified into control soybean tissues at the LOQ and midrange and high-range concentrations for each protein across multiple days.

Peptide Stability. Digested peptide stability was examined over the course of 5 days. A sample set of non-GE control tissues fortified with AAD-12, 2mEPSPS, and PAT recombinant proteins at the LOQ and midrange and high-range concentrations was digested, and analyzed along with reference peptide standards prepared in control tissue by LC-MS/MS (day 0). The reference standard peptides and fortified tissue samples were stored at 4 °C for 5 days and reanalyzed using the same instrument parameters as the day 0 analysis. The difference in recovery of peptides from day 0 to 5 was assessed.

Sensitivity. The preliminary quantitative range for the LC-MS/MS multiplex assay was empirically defined on the basis of assay parameters such as analyte signal intensity, background noise intensity, matrix contributions, and analyte stability from an overnight digest. Three times the signal-to-noise ratio and ten times the signal-to-noise ratio of peptide standard response to digested control sample were used to define limit of detection (LOD) and LOQ, respectively (Table 2). The calibration standard range was defined to be at least 20% above and below the quantitative range for all proteins with acceptable correlation coefficients ≥0.995.

Table 2. AAD-12, 2mEPSPS, and PAT Quantitative Range Comparison for Individual ELISA and Multiplex LC-MS/MS Methods

	LC-MS/MS		ELISA	
protein	LOQ (ng/mg)	ULOQ (ng/mg)	LOQ (ng/mg)	ULOQ (ng/mg)
AAD-12	6.60	165.00	1.00	10.00
2mEPSPS	12.20	305.00	8.00	200.00
PAT	6.50	163.00	0.12	0.60

Interlaboratory Method Assessment. An independent assessment of the LC-MS/MS method was carried out at Critical Path Services, LLC (Garnet Valley, PA). Control soybean tissues described in the Materials section were fortified with recombinant AAD-12, 2mEPSPS, and PAT proteins at the LOQ and midrange and high-range concentrations and analyzed following the method described in the LC-MS/MS Method Overview section. The LC-MS/MS analysis was carried out on an Agilent 1290 UHPLC coupled to an Agilent 6410B mass spectrometer.

ELISA and LC-MS/MS Comparison. Leaf tissue containing AAD-12, 2mEPSPS, and PAT proteins from nine individual soybean plants was analyzed using ELISA and LC-MS/MS. The leaf samples were analyzed by LC-MS/MS following the analytical method described in the LC-MS/MS Method Overview section. Individual sandwich-based ELISA methods were developed and validated under good laboratory practice guidelines for each protein. For each ELISA method described below, a total of 1.5 mL of respective extraction buffer and two metal beads were added to 15 mg of soybean leaf tissue and extracted in a Geno/Grinder at 1500 strokes per minute for 3 min and then centrifuged at 4 °C and >3000 rpm for 5 min. The assays were measured using purified recombinant protein as standards with quadratic regression.

The AAD-12 protein was extracted from soybean leaf tissue with PBST buffer with 0.75% ovalbumin. The extract was centrifuged; the aqueous supernatant was collected, diluted, and assayed using a specific AAD-12 ELISA kit (Envirologix,

DOI: 10.1021/acs.jafc.5b03083
J. Agric. Food Chem. 2015, 63, 7450−7461

Portland Maine). An aliquot of the diluted sample was incubated with enzyme-conjugated anti-AAD-12 protein monoclonal antibody in the wells of an anti-AAD-12 polyclonal-antibody-coated plate. At the end of the incubation period, the unbound reagents were removed from the plate by washing with PBST followed by incubation of enzyme conjugate with an enzyme substrate. The reaction was quenched with acid, and the absorbance was read at 450 nm minus absorbance at 650 nm using a plate reader.

The 2mEPSPS protein was extracted from soybean leaf tissue with a PBST and 2× casein (PBST/casein). The extract was centrifuged; the aqueous supernatant was collected, diluted with PBST/casein, and assayed using a specific 2mEPSPS ELISA kit made in-house at Dow AgroSciences. An aliquot of the diluted sample was incubated in the wells of an anti-2mEPSPS polyclonal-antibody-coated plate, and then the unbound samples were removed from the plate by washing with PBST. An excess amount of enzyme-conjugated anti-2mEPSPS monoclonal antibody was subsequently added to the wells. At the end of the incubation period, the unbound reagents were removed from the plate by washing with PBST. Subsequent addition of an enzyme substrate generated a colored product. The reaction was quenched with acid, and the absorbance was read at 450 nm minus absorbance at 650 nm using a plate reader.

The PAT protein was extracted from soybean leaf tissue with a buffer consisting of PBST and 1% polyvinylpyrrolidone (PBST/PVP). The extract was centrifuged; the aqueous supernatant was collected, diluted and assayed using a specific PAT ELISA kit (Envirologix, Portland Maine). An aliquot of the diluted sample was incubated with enzyme-conjugated anti-PAT monoclonal antibody in the wells of an anti-PAT polyclonal-antibody-coated plate in a sandwich ELISA format. At the end of the incubation period, the unbound reagents are removed from the plate by washing with PBST. The presence of PAT was detected by incubating the antibody-bound enzyme conjugate with an enzyme substrate, generating a colored product. The reaction was quenched with acid, and the absorbance was read at 450 nm minus absorbance at 650 nm using a plate reader.

RESULTS AND DISCUSSION

Method Development. *Target Peptide Selection.* Traditional bottom-up proteomics employs a protease of known cleavage specificity and a protein's primary sequence to cleave high-molecular-weight proteins into smaller peptide chains of predicted sequence suitable for analysis by tandem mass spectrometry.[24] These peptides are defined as surrogate peptides and are representative of the target proteins.[25] The enzyme trypsin was chosen for this assay because of its high specificity to cleave at the C terminus of lysine and arginine residues. For method development, all possible tryptic peptides for each target protein from a theoretical digestion were considered and surveyed using specific criteria during the peptide selection process. Initial selection criteria required 6–20 amino acids in length because fewer than 4 residues can lead to nonspecific identification.[26] Peptide residues susceptible to modification such as those produced from N-terminal cleavage or residues prone to oxidation such as methionine and cysteine were excluded from selection. Digested recombinant protein standards were analyzed using a targeted information-dependent acquisition (IDA) in the mass spectrometer to determine relative fragmentation ratios and highest abundance MS/MS fragment ions for each tryptic peptide candidate. Using the most abundant MS/MS fragmentation ions and considering charge state, peptides were further profiled for sensitivity and reproducibility from an overnight digestion and minimal isobaric interference in comparison to control tissue (specificity). Two surrogate peptides were chosen per protein for further optimization representing different locations of the protein sequence to prevent missed identification during analysis caused by truncation. One peptide was defined as the quantitation peptide with the second peptide serving as a confirmation peptide during quantitation (Table 1).

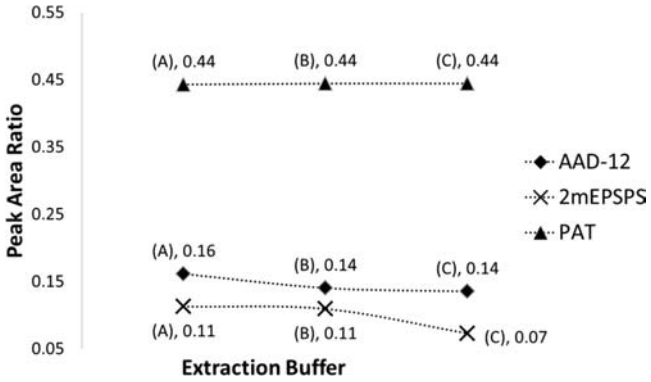

Figure 1. Example extraction buffer evaluation for leaf tissue using (A) PBST, (B) 50 mM Tris(hydroxymethyl)aminomethane hydrochloride, or (C) 50 mM ammonium bicarbonate. A 15 mg sample of soybean leaf tissue containing AAD-12, 2mEPSPS, and PAT proteins was extracted with each respective buffer, digested, and analyzed by LC-MS/MS. Peptide response from the overnight digest was plotted (peak area ratio) versus individual extraction buffers for each protein. The optimized amount of tissue per volume buffer and buffer choice for the multiplex LC-MS/MS method was 15 mg lyophilized tissue per 1.5 mL PBST.

Extraction. The LC-MS/MS extraction mirrored individual ELISA methods for AAD-12, 2mEPSPS, and PAT to incorporate direct comparison of the assays. PBST is the base component of each of the ELISA methods. Tissue containing AAD-12, 2mEPSPS, and PAT proteins was extracted with different extraction buffers offering a large range of biochemical properties (PBST, 50 mM Tris(hydroxymethyl)aminomethane hydrochloride (pH 8.0), or 50 mM ammonium bicarbonate), digested, and analyzed by LC-MS/MS. Results demonstrated little change in peptide response, confirming PBST as suitable for extraction for all three proteins in the multiplex method (Figure 1). Many ELISA extraction buffer components (nonvolatile detergents such as Tween 20, surfactants, etc.) are less favorable for extended LC-MS/MS analysis.[27] Because surrogate peptide analysis decouples from accepted ELISA methodology, further optimization of extraction buffers to reduce surfactants and detergents or removal of these components all together before analysis can improve sensitivity for detection by LC-MS/MS. The optimized amount of tissue per volume buffer and buffer choice for the multiplex LC-MS/MS method was 15 mg lyophilized tissue per 1.5 mL PBST.

Digestion. The underlying foundation for surrogate peptide analysis relies on protease digestion that is 100% efficient in order for the resulting peptide fragments to be present in equal molar amounts compared to the original target protein prior to digestion. Proteins can differ greatly in their susceptibility to proteolysis, and this requires a digestion protocol that is optimal for all proteins in a multiplex analysis for accurate

DOI: 10.1021/acs.jafc.5b03083
J. Agric. Food Chem. 2015, 63, 7450–7461

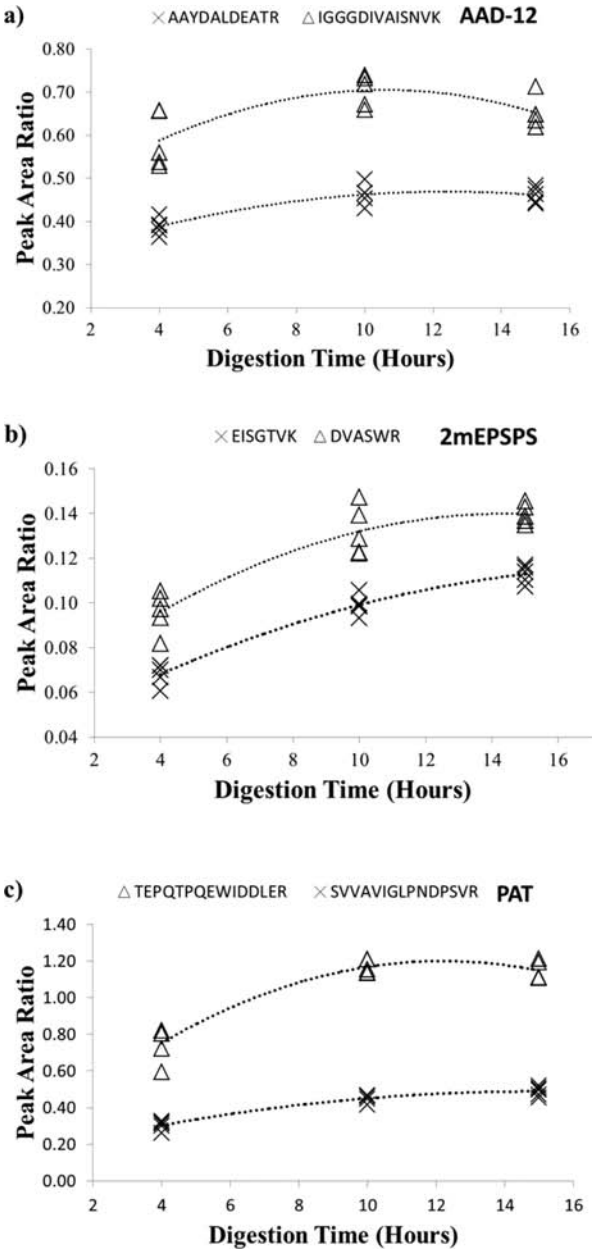

Figure 2. – Time-course digestion efficiency evaluation for (a) AAD-12, (b) 2mEPSPS, and (c) PAT. Digestion was monitored (peak area ratios plotted versus digestion time) for individual replicates and quenched with acid at 4, 10, and 15 h time points to simulate an overnight digestion. An enzyme–substrate ratio of 1:75 used in the method demonstrated digestion completeness at the 12 h digestion time because longer digestion time did not improve detection and the signal was stable at time points representative of an overnight digestion.

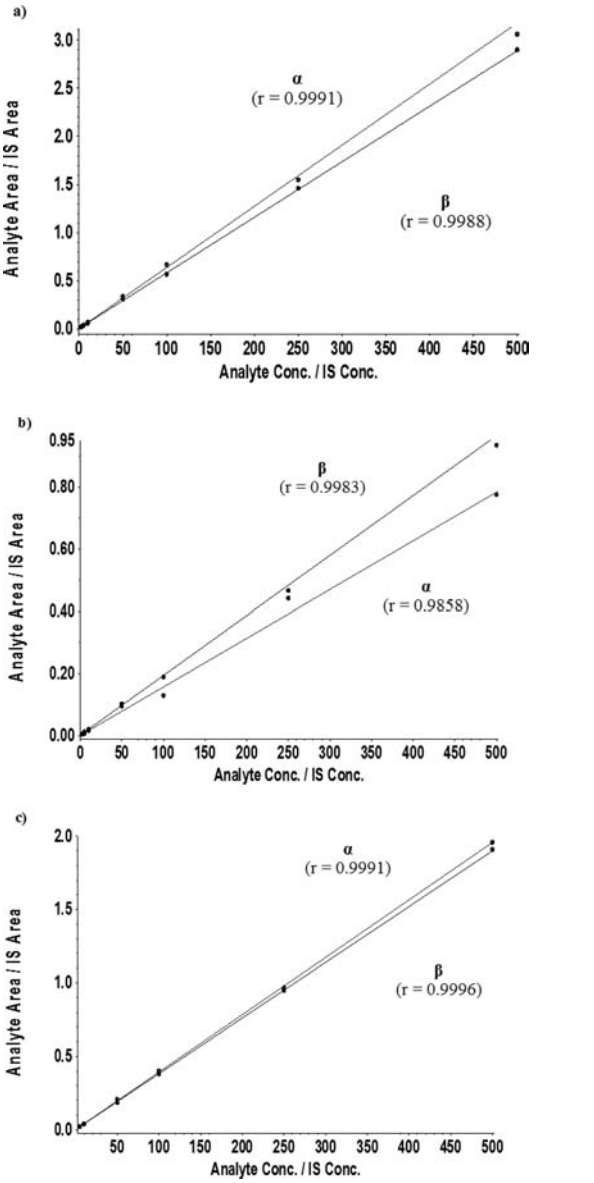

Figure 3. Example calibration curves for (a) AAD-12 (AAYDALDEATR, 598.3/704.4), (b) 2mEPSPS (EISGTVK, 367.2/404.3), and (c) PAT (TEPQTPQEWIDDLER, 928.9/813.9) from two separate multiplex analyses carried out on separate days. The calibration curve labeled "α" was prepared in PBST and the calibration curve labeled "β" was prepared in digested soybean control leaf tissue. Good linearity was observed for AAD-12 and PAT in both analysis formats (panels a and c). 2mEPSPS observed peptide loss caused by surface absorption to lab materials during sample preparation, affecting both signal intensity and linearity (panel b). Linearity of the 2mEPSPS calibration curve was recovered when prepared in digested control tissue.

measurements. Prior to digestion, proteins were denatured to primary structure at high temperatures and reduced in the presence of DTT to allow for efficient proteolytic cleavage. Optimized conditions were found to be 95 °C for 45 min because lower temperature and time incurred lower accuracy from recombinant protein spike recovery. The trypsin concentration, peptide stability over a particular digest time interval, and buffer selection (pH) were key variables in the digestion development. A trypsin enzyme–substrate ratio of 1:75 enabled 100% digestion efficiency because increasing the concentration of trypsin did not increase detected peptide response from the overnight digestion. Detergents, such as Tween 20 used in the extraction buffer, can impact enzymatic digestion efficiency and downstream LC-MS/MS analysis.[28] To minimize these effects and achieve an optimal digestion condition for trypsin (pH 7.5–8.5), the denatured supernatant was diluted into 50 mM ammonium bicarbonate prior to addition of trypsin enzyme for the overnight digestion.

A time-course evaluation for digestion efficiency has been documented in literature to demonstrate digestion completeness;[29] the abundance of target signal and stability of signal

DOI: 10.1021/acs.jafc.5b03083
J. Agric. Food Chem. 2015, 63, 7450–7461

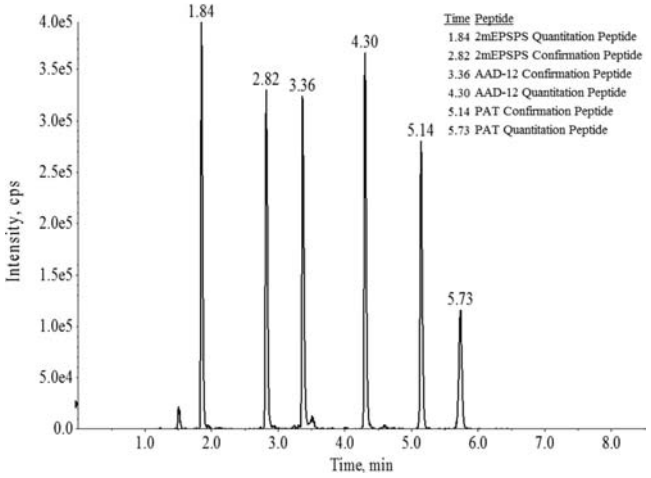

Figure 4. Typical total ion chromatogram (TIC) of a 250 ng/mL peptide standard to demonstrate the detection of AAD-12, 2mEPSPS, and PAT quantitation and confirmation of surrogate peptides in a single analysis.

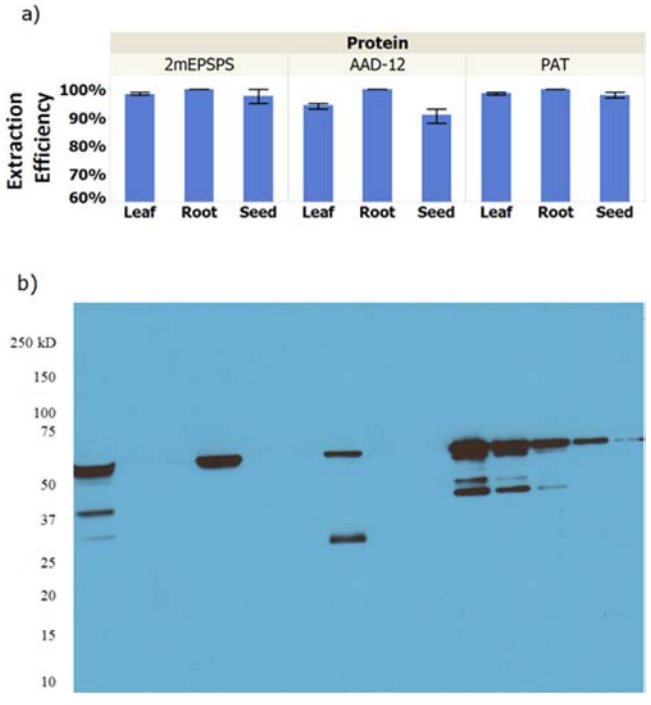

Figure 5. (a) Summary of extraction efficiency for three biological replicates of leaf, root, and seed tissues expressing AAD-12, 2mEPSPS, and PAT serial extracted 5 times each, calculated with the equation EE = ((Amount of peptide recovered in first extraction)/(Sum of peptide recovered from all extractions)) × 100 applied. (b) Example Western blot confirmation for extraction efficiency, 2mEPSPS ∼ 47.5 kDa. (PAT and AAD-12 Western blots can be found in the Supporting Information.) An immunoreactive band of the expected 47.5 kDa size is observed in lanes 10−14, representing the 2mEPSPS recombinant protein standard at concentrations of 2000, 1000, 500, 100, and 50 ng/mL, respectively. Some cross-reactivity with nontarget plant proteins was observed at lower molecular weights; however, the 47.5 kDa immunoreactive band is detected in the first extraction, represented in lanes 1 (leaf), 4 (root), and 7 (seed). No immunoreactivity is observed in lanes 2 (leaf), 5 (root), and 8 (seed), representing the fifth serial extraction or in lanes 3 (leaf), 6 (root), and 9 (seed), representing the pelleted tissue after the fifth serial extraction, which is evidence supporting effective extraction.

over the length of time of the digest were considered. Individual replicates were extracted in PBST, digested, and quenched with acid at three time points (4, 10, and 15 h to simulate an overnight digestion), and peak area ratios were plotted versus digestion time (Figure 2). Confidence in digestion completeness can be inferred because longer digestion time did not improve detection and the signal was stable at time points representative of an overnight digestion. An enzyme−substrate ratio of 1:75 and 12 h digestion time were selected for the method.

Reference Standards. Representative synthetic peptides were chosen as reference standards instead of recombinant proteins that are commonly used in ELISA analysis. Digested recombinant protein standards may provide a linear quantitative range; however, because of reliance on proteolysis, some intrinsic variability will exist from analysis to analysis, adding complexity to interpretation of results. Once completeness of digestion and peptide stability have been validated for a particular trypsin concentration and digestion time interval, the use of synthetic peptide standards may offer a more straightforward approach to quantifying incurred peptide residues from proteolysis. Initially, the reference peptide standards were prepared in extraction buffer; however, peptide loss was observed that was due to surface absorption of more hydrophobic peptides to labware during the sample preparation affecting the accuracy of the standard curve (Figure 3).[30] To overcome these effects, reference standards were prepared in digested control soybean matrix in which native proteins provide a protective medium to minimize peptide surface absorption. Proteins such as bovine serum albumin or ovalbumin are commonly used as buffer additives with the same intent as the digested control matrix. Further characterization of materials used during sample treatment may allow for the standard curve to be prepared in extraction buffer alone, simplifying the analytical procedure.

Multiplexing Assay. The multiplex detection of AAD-12, 2mEPSPS, and PAT surrogate peptides in reference standards and unknown samples was carried out by tandem mass spectrometry. Selected reaction monitoring (SRM) refers to the selectivity of tandem mass spectrometry where a precursor ion (in this case, a peptide) with a specific mass-to-charge ratio (m/z) is identified and fragmented into one or more product ions or MS/MS transitions. SRM LC-MS/MS-based detection is specific by virtue of chromatographic separation (Figure 4) and selective MS/MS detection. A second layer of specificity is produced from monitoring multiple product ions per peptide, defined as a confirmation ratio.[31] The confirmation ratio represents the relative abundance between two product ions derived from the same precursor ion, demonstrating real-time validation of results. Further specificity from the method is obtained from the addition of a structurally identical heavy-labeled peptide internal standard (HIS) to normalize all samples and reference standards and to reduce the impact of common technical pitfalls such as signal suppression or enhancement (matrix effects) and ion drift, among others. The precursor and product ions of the HIS should coelute with those of the natural abundance peptide, producing a peak area ratio.[32] The peak area ratio in the unknown sample is interpolated to the peak area ratios produced from the reference standard curve for a quantitative result. The use of peak area ratios of unknown samples to reference standards normalizes results across different analytical runs and instruments because the quantitation is not strictly limited to the

DOI: 10.1021/acs.jafc.5b03083
J. Agric. Food Chem. 2015, 63, 7450−7461

Table 3. Spike Recovery Results of Recombinant AAD-12, 2mEPSPS, and PAT Proteins Fortified into Control Soybean Leaf, Root, and Seed Tissues Performed over Multiple Days

			day 1				day 2				recovery across days				
protein	tissue	protein spike (ng/mg)	mean (ng/mg)[a]	std dev.	range (ng/mg)[a]	CV (%)	mean (ng/mg)[a]	std dev.	range (ng/mg)[a]	CV (%)	mean (%)[b]	range (%)[b]	CV (%)	*N*	LOQ std dev.(3×, 10×)[c]
AAD12	leaf	6.60	7.03	0.10	6.96−7.15	1	6.30	0.73	5.46−6.75	12	101	83−108	9	6	0.61 (1.83, 6.10)
		33.00	34.45	0.67	33.74−35.08	2	37.31	2.03	35.88−39.63	5	109	102−120	6	6	
		165.00	162.01	6.69	154.51−167.36	4	171.56	11.90	157.99−180.22	7	101	94−109	6	6	
	root	6.60	6.07	0.81	5.38−6.96	13	5.85	0.36	5.44−6.11	6	90	82−105	10	6	0.57 (1.71, 5.70)
		33.00	38.56	1.17	37.76−39.90	3	38.29	0.97	37.49−39.36	3	116	114−121	3	6	
		165.00	200.66	1.64	199.23−202.44	1	203.87	9.36	196.82−214.49	5	123	119−130	3	6	
	seed	6.60	6.31	0.16	6.16−6.48	3	7.31	0.05	7.26−7.36	1	103	93−112	8	6	0.56 (1.68, 5.60)
		33.00	33.65	1.01	32.94−34.81	3	34.63	2.41	32.13−36.95	7	103	97−112	5	6	
		165.00	150.67	8.34	141.92−158.53	6	162.90	4.76	157.46−166.29	3	95	86−101	6	6	
2mEPSPS PAT	leaf	12.20	13.09	0.95	12.51−14.19	7	13.20	1.01	12.12−14.13	8	108	99−116	7	6	0.88 (2.64, 8.80)
		61.00	59.29	3.11	55.73−61.43	5	68.15	5.37	62.53−73.23	8	104	91−120	10	6	
		305.00	294.42	11.63	281.24−303.27	4	312.35	4.25	307.81−316.23	1	99	92−104	4	6	
	root	12.20	13.28	2.13	10.82−14.52	16	10.87	3.55	6.87−13.67	33	99	56−119	24	6	2.94 (8.82, 29.40)
		61.00	63.03	3.94	58.91−66.75	6	64.22	16.04	49.06−81.00	25	104	80−133	16	6	
		305.00	291.83	12.16	284.48−305.87	4	312.35	24.00	287.72−335.68	8	99	83−110	7	6	
	seed	12.20	13.26	1.37	12.38−14.48	10	10.54	3.40	6.74−13.28	32	98	55−122	23	6	2.76 (8.28, 27.60)
		61.00	53.22	2.29	51.71−55.86	4	58.49	5.19	54.24−64.28	9	92	85−105	8	6	
		305.00	266.55	2.45	263.74−268.28	1	282.97	5.24	277.35−287.72	2	90	86−94	4	6	
PAT	leaf	6.50	6.58	0.09	6.48−6.65	1	5.95	0.43	5.48−6.34	7	96	84−102	7	6	0.45 (1.35, 4.50)
		32.50	33.93	1.55	32.57−35.62	5	29.36	1.53	27.82−30.87	5	97	86−110	9	6	
		162.50	147.77	5.10	142.49−152.67	3	136.83	3.39	133.44−140.23	2	88	82−94	5	6	
	root	6.50	6.04	0.21	5.81−6.22	3	6.08	0.31	5.72−6.29	3	93	88−97	4	6	0.24 (0.72, 2.40)
		32.50	31.06	3.75	27.14−34.60	12	36.53	3.44	32.57−38.79	12	104	84−119	13	6	
		162.50	151.16	5.80	144.75−156.06	4	177.54	4.08	174.15−182.07	4	101	89−112	9	6	
	seed	6.50	5.49	0.16	5.37−5.68	3	5.42	0.58	4.90−6.05	11	84	75−93	7	6	0.38 (1.14, 3.80)
		32.50	37.54	1.67	36.53−39.47	4	30.01	1.16	29.18−31.32	4	104	90−121	13	6	
		162.50	160.20	5.34	156.06−166.24	3	142.86	11.99	130.05−153.8	8	93	80−102	8	6	

[a]Results represent detected surrogate peptides converted into protein concentrations represented as dry tissue weight (ng/mg). [b]Accuracy was indicated as percentage peptide recovery converted into protein concentrations from recombinant protein fortifications. [c]LOD or LOQ statistical confirmation using 3 or 10 times the standard deviation from the LOQ detected response.

DOI: 10.1021/acs.jafc.5b03083
J. Agric. Food Chem. 2015, 63, 7450−7461

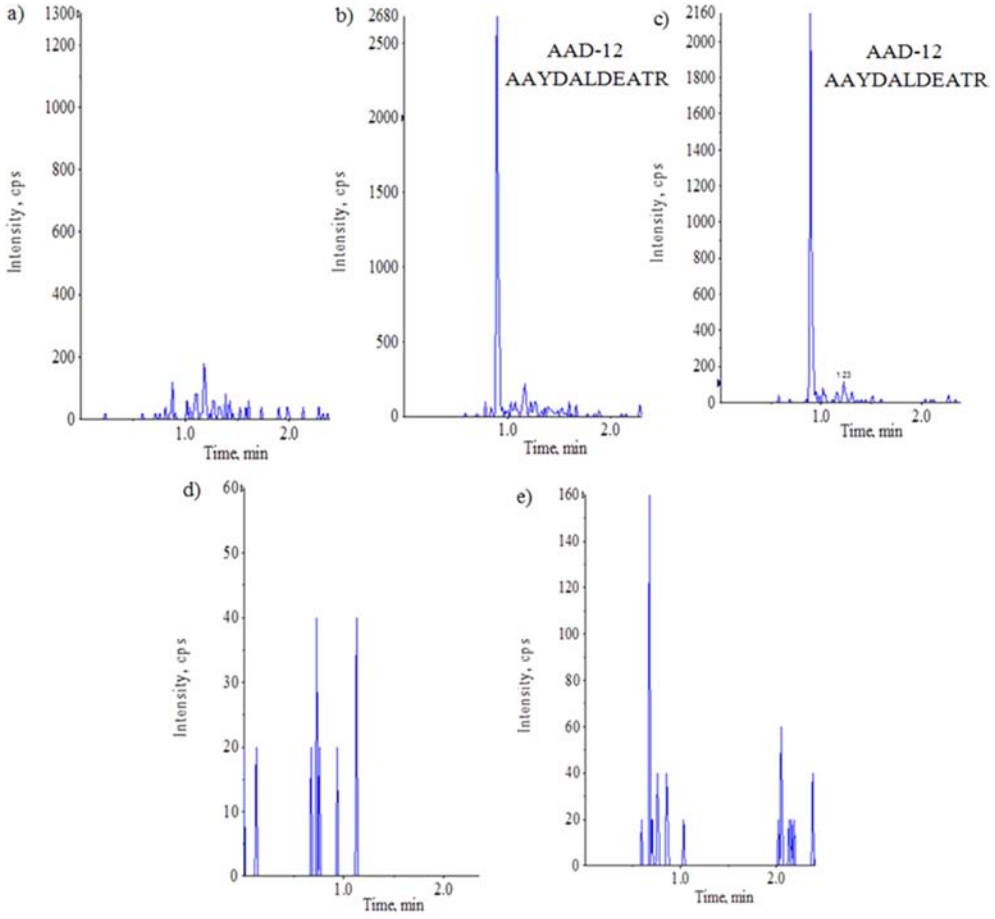

Figure 6. Example specificity assessment for AAYDALDEATR during AAD-12 peptide selection: (a) control tissue, (b) tissue containing AAD-12, (c) digested recombinant AAD-12 protein standard, (d) digested recombinant 2mEPSPS standard, and (e) digested recombinant PAT protein standard. The AAYDALDEATR peptide (0.90 min) is present in tissue expressing AAD-12 and the recombinant protein standard and absent in digested control leaf tissue and 2mEPSPS and PAT recombinant protein standards.

intensity of signal, leading to more reproducible data and a greater degree in confidence for interpretation of results. Although only one peptide is typically reported for quantitation results, two peptides are monitored per protein in the analytical method to confirm complete digestion during sample analysis.

Method Validation Results. *Extraction Efficiency (EE).* The extraction was found to be effective with efficiencies for all proteins ranging between 90 and 100% for all tissues (Figure 5a). Western blotting was used to qualitatively confirm the extraction results and demonstrated that the surrogate peptides were truly representative of intact AAD-12, 2mEPSPS, and PAT proteins in plant extracts (Figure 5b). No immunoreactivity was observed in the last serial extraction supernatant or in the pelleted tissue after the last extraction, which is evidence supporting effective extraction.

Accuracy. Good recovery of surrogate peptides from intact recombinant protein fortifications reinforces complete digestion and supports the use of synthetic peptide reference standards as a calibration source. The assay accuracy was indicated as percentage peptide recovery from recombinant protein fortifications carried out across multiple days. The accuracy of the multiplex method is acceptable for AAD-12, 2mEPSPS, and PAT with observed mean recoveries for all tissues between 70 and 123% (Table 3).

Precision and Ruggedness. Precision of the multiplex method was evaluated across two separate analyses for each tissue. To avoid any potential loss during extraction impacting precision results, control samples were extracted with buffer, pooled together, and fortified with recombinant protein standards. The precision results showed in general CVs $\leq$ 20% for both inter- and intraday analysis for all three proteins (Table 3).

Specificity/Matrix Effects. Specificity is the ability of an analytical method to differentiate a target analyte from other components in a complex matrix. Evaluations for ELISA commonly address assay specificity by spiking nontarget proteins into control tissue at a range of concentrations to determine the level of immunoreactive cross-reactivity and through comparison of standard curves prepared in different dilutions of extracted control tissue to standard curves prepared in buffer to assess matrix effects. Surrogate peptide LC-MS/MS specificity should be addressed during peptide selection in method development with evaluation of recombinant protein standards fortified into control tissue, unfortified control tissues, and tissues containing the protein of interest (Figure 6). Following peptide selection, assay specificity is not as great of an issue with LC-MS/MS because of HIS being used to normalize all samples (not as the quantitation source) and the aforementioned chromatographic separation coupled to MS/MS detection.

Peptide Stability. In addition to peptide stability from an overnight digestion (evaluated from the time-course digestion

DOI: 10.1021/acs.jafc.5b03083
J. Agric. Food Chem. 2015, 63, 7450−7461

Table 4. Digested surrogate peptide stability for AAD-12, 2mEPSPS, and PAT evaluated over 5 days

AAD-12 Average Recovery Results (%)[a]							
		leaf		root		seed	
fortification	N	day 0	day 5	day 0	day 5	day 0	day 5
LOQ	3	106	76	92	103	111	102
midrange	3	104	111	117	113	105	105
high-range	3	98	101	122	113	99	100
2mEPSPS Average Recovery Results (%)[a]							
		leaf		root		seed	
fortification	N	day 0	day 5	day 0	day 5	day 0	day 5
LOQ	3	107	99	109	86	109	112
midrange	3	97	98	103	100	87	102
high-range	3	96	86	96	99	87	95
PAT Average Recovery Results (%)[a]							
		leaf		root		seed	
fortification	N	day 0	day 5	day 0	day 5	day 0	day 5
LOQ	3	101	92	93	79	83	113
midrange	3	104	100	96	92	92	88
high-range	3	91	87	93	97	88	83

[a]AAD-12, 2mEPSPS, and PAT recombinant proteins fortified into leaf, root, and seed control tissues analyzed on Day 0. Fortified tissues and reference peptide standards were stored at 4 °C and reanalyzed on Day 5.

and fortification experiments), digested peptide stability in storage conditions over a length of time was assessed to incorporate sample reinjection and instrument issues, among other factors. The digested AAD-12, 2mEPSPS, and PAT recombinant proteins in control tissue were confirmed to be stable for at least 5 days when stored at 4 °C with acceptable mean recoveries of 70−120% (Table 4).

Sensitivity. The LOD is defined as the analyte concentration that gives a significant difference from the analyte-free sample. The quantitative range is generally defined as the highest and lowest concentrations which can be determined with an acceptable degree of accuracy. The quantitative range was proposed during method development to encompass the general protein levels observed in transgenic plants rather than reflecting the true assay quantitative range. The dynamic range of LC-MS instrumentation has been shown to span 3−5 orders of magnitude,[33] which can be further optimized to increase the defined upper range of quantitation for the assay. The targeted LOD and LOQ (Table 2) for each protein were empirically defined on the basis of assay parameters such as peptide signal intensity and signal-to-noise ratio. In addition to accuracy of recovery, the LOD and LOQ were also verified by statistical approaches[34] using 3 and 10 times the standard deviation, respectively, from the LOQ recovery results for each protein (Table 3). The statistically calculated LOD and LOQ results were less than the target LOD and LOQ results for AAD-12 and PAT in all tissues as well as leaf tissue for 2mEPSPS (Table 3). Statistical calculations of 2mEPSPS were slightly higher for root and seed because of low recovery in one sample from each analysis, potentially caused by the previously mentioned peptide absorption to materials during sample preparation. Overall, the results provide appropriate estimates of the quantitative range of the assay.

Interlaboratory Validation. Independent laboratory assessment of accuracy and precision of the LC-MS/MS method was carried out with AAD-12, 2mEPSPS and PAT recombinant proteins fortified into non-GE control tissues by Critical Path Services, LLC. Recovery results were comparable to data obtained from the full validation carried out by Dow AgroSciences (Tables 3 and 5) and demonstrated LC-MS/MS as a robust workflow incorporating different analysts and instrumentation (vendor, ionization source, and detector) with reproducible results. In addition, minimal optimization was carried out to the original MS/MS instrument parameters during the independent laboratory assessment, yielding similar results between laboratories and demonstrating the ease of transferring the methodology (as has been previously documented in literature).[35]

Table 5. Independent Laboratory Accuracy and Precision Assessment for the Multiplex LC-MS/MS Detection of AAD-12, 2mEPSPS, and PAT Proteins in Soybean Tissues

			recovery[a]		
protein	tissue	protein spike (ng/mg)	mean (%)	range (%)	CV (%)
AAD12	leaf	6.60	83	70−97	17
		33.00	87	67−98	20
		165.00	92	81−110	17
	root	6.60	70	60−81	15
		33.00	90	86−97	7
		165.00	87	86−88	1
	seed	6.60	100	85−127	24
		33.00	74	71−78	5
		165.00	78	73−83	6
2mEPSPS	leaf	12.20	80	74−87	8
		61.00	75	68−78	8
		305.00	85	73−91	12
	root	12.20	69	65−71	5
		61.00	76	72−83	8
		305.00	96	94−99	3
	seed	12.20	74	62−81	14
		61.00	65	62−68	5
		305.00	74	71−77	4
PAT	leaf	6.50	70	64−75	7
		32.50	77	73−83	7
		162.50	80	72−90	11
	root	6.50	107	102−116	7
		32.50	86	77−98	13
		162.50	89	84−97	8
	seed	6.50	75	71−79	6
		32.50	62	57−67	8
		162.50	63	60−66	4

[a]Interlaboratory method evaluation carried out by Critical Path Services, LLC. Results indicate recovery (%) of recombinant proteins (detected surrogate peptide converted into protein concentrations) fortified into soybean leaf, root, and seed tissues at the LOQ, midrange, and high-range concentrations.

ELISA and LC-MS/MS Comparison. ELISA immunochemistry uses antibodies highly specific to target proteins. Quantitation depends on a single signal produced most commonly from the addition of an enzyme substrate to a specific antibody sandwich containing target protein, producing a colored product. The resulting colored product, measured via optical density, is proportional to the concentration of protein in the sample, which is correlated to the optical densities produced from reference standards. In contrast, SRM LC-MS/MS-based detection is specific by virtue of the chromatographic separation and selective MS/MS detection. SRM LC-MS/MS

DOI: 10.1021/acs.jafc.5b03083
J. Agric. Food Chem. 2015, 63, 7450−7461

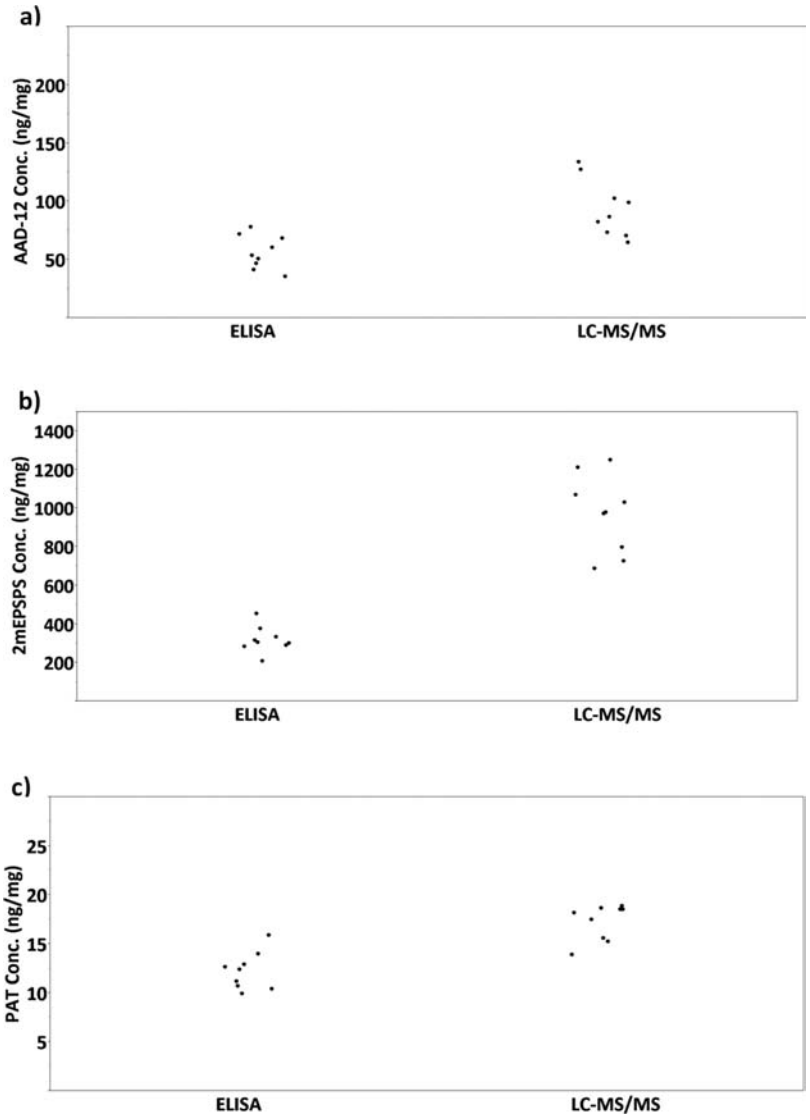

Figure 7. Results (ng/mg) for (a) AAD-12, (b) 2mEPSPS, and (c) PAT proteins in leaf tissue from nine individual soybean plants analyzed by surrogate peptide LC-MS/MS and ELISA.

employs multiple signals to evaluate the concentration of target analyte such as MS/MS confirmation ratios, peak area ratios, and monitoring multiple peptides representing multiple areas of the protein sequence, providing greater confidence in obtained results.[36] The samples and natural abundance peptide reference standards are standardized by virtue of HIS, increasing the precision and accuracy across multiple analysis compared to ELISA. In addition to multiplex capability, the increased dynamic range of LC-MS/MS compared to ELISA (generally 3−5 orders of magnitude compared to 2−3) allows for fewer reanalyses of samples because of the need for sample dilution into the reference standard range. The LOQ for LC-MS/MS was comparable to that of the individual ELISA assays (Table 2).

ELISA measures immunoreactivity of intact proteins by largely depending on protein conformation, whereas surrogate peptide LC-MS/MS measures total abundance of denatured linear peptide chains where unstable protein in tissues will have less impact on quantitation results. Because of the complexity and intrinsic variability of biological analysis that is present in addition to typical analytical challenges, perfect agreement between two vastly different technologies such as ELISA and LC-MS/MS is not expected; however, correlation of the data does support validation of surrogate peptides representative of intact proteins. Nine individual plants were analyzed for AAD-12, 2mEPSPS, and PAT protein levels by ELISA and LC-MS/MS (Figure 7). The LC-MS/MS results were consistently higher likely because of the detection of native and denatured forms of the protein; however, the data demonstrated that both results were comparable for AAD-12 and PAT. Further work is needed for 2mEPSPS to understand the larger than expected difference between ELISA and LC-MS/MS results that in addition to detecting both native and denatured forms of the protein can be explained by the aforementioned surface absorption of reference standard peptides to labware or a larger portion of 2mEPSPS population in a denatured form that would not be detected by ELISA.[37]

This research demonstrates a multiplex format specifically identifying three proteins in a single injection with high confidence. The signature peptides defined in the multiplex LC-MS/MS method were validated to represent intact proteins because the accuracy of target peptide mean recovery values

DOI: 10.1021/acs.jafc.5b03083
J. Agric. Food Chem. 2015, 63, 7450−7461

from recombinant AAD-12, 2mEPSPS, and PAT proteins fortified into three different types of matrices fell between 70 and 123% across different analysts, laboratories, and instrumentation and because data correlated well with ELISA. The ease of transfer of the method with reproducible results and the ability to quantify multiple proteins from a single injection make LC-MS/MS a suitable technology to quantify transgenic proteins in GE crops.

■ ASSOCIATED CONTENT

Supporting Information

The Supporting Information is available free of charge on the ACS Publications website at DOI: 10.1021/acs.jafc.5b03083.

Protein sequences, possible tryptic peptides, selectivity assessment during peptide selection, method validation data (including extraction efficiency, recovery, and peptide stability), and independent method assessment recoveries. (PDF)

■ AUTHOR INFORMATION

Corresponding Author

*Phone: (317) 337-4864. E-mail: rhill1@dow.com.

Notes

The authors declare the following competing financial interest(s): R.C.H., T.J.O., G.S., and B.S. are employees of Dow AgroSciences, LLC, a wholly owned subsidiary of The Dow Chemical Company, which develops transgenic crops and produces insecticides, herbicides, and fungicides for agricultural applications and residential pest control. Critical Path Services, LLC was contracted by Dow AgroSciences to perform the independent laboratory validation.

■ ACKNOWLEDGMENTS

We thank Jeff Gilbert and John Lawry for helpful comments and discussions as well as the Dow AgroSciences immunochemistry group for the ELISA data generated in this study. Enlist E3 soybeans were jointly developed by Dow AgroSciences and M.S. Technologies, L.L.C.

■ REFERENCES

(1) Juma, C.; Gordon, K. Taking Root: Global Trends in Agricultural Biotechnology. Discussion Paper; Belfer Center for Science and International Affairs, Harvard University: Cambridge, MA, 2015. (http://belfercenter.ksg.harvard.edu/publication/24899/taking_root.html, accessed March 18, 2015).

(2) Westcott, P.; Trostle, R. Long-Term Prospects for Agriculture Reflect Growing Demand for Food, Fiber, and Fuel. United States Department of Agriculture, Economic Research Service: Washington, D.C., 2012. (http://www.ers.usda.gov/amber-waves/2012-september/long-term-prospects-for-agriculture.aspx#.VOeTB3zF98E, accessed March 18, 2015).

(3) Naranjo, S. Impacts of Bt Transgenic Cotton on Integrated Pest Management. *J. Agric. Food Chem.* **2011**, *59*, 5842−5851.

(4) Brookes, G. Weed Control Changes and Genetically Modified Herbicide Tolerant Crops in the USA 1996−2012. *GM Crops & Food* **2014**, *5*, 321−332.

(5) Lepping, M. D.; Herman, R. A.; Potts, B. L. Compositional Equivalence of DAS-444Ø6−6 (AAD-12 + 2mEPSPS + PAT) Herbicide-Tolerant Soybean and Nontransgenic Soybean. *J. Agric. Food Chem.* **2013**, *61*, 11180−11190.

(6) Dryzga, M. D.; Yano, B. L.; Andrus, A. K.; Mattsson, J. L. Evaluation of the Safety and Nutritional Equivalence of a Genetically Modified Cottonseed Meal in a 90-Day Dietary Toxicity Study in Rats. *Food Chem. Toxicol.* **2007**, *45*, 1994−2004.

(7) International Service for the Acquisition of Agri-Biotech Applications. *Stacked Traits in Biotech Crops*; ISAAA Pocket K No. 42; March 2013. (http://www.isaaa.org/resources/publications/pocketk/42/).

(8) Nicolia, A.; Manzo, A.; Veronesi, F.; Rosellini, D. An Overview of the last 10 years of genetically engineered crop safety. *Crit. Rev. Biotechnol.* **2014**, *34*, 77−88.

(9) Shan, G.; Embrey, S. K.; Schafer, B. W. A highly specific Enzyme-linked immunosorbent assay for the detection of Cry1Ac insecticidal crystal protein in transgenic WideStrike cotton. *J. Agric. Food Chem.* **2007**, *55*, 5974−5959.

(10) Shan, G.; Embrey, S. K.; Herman, R. A.; McCormick, R. W. Cry1F Protein not Detected in Soil After Three Years of Transgenic Bt Corn (1507 Corn) Use. *Environ. Entomol.* **2008**, *37*, 255−262.

(11) Shan, G. *Immunoassays in Agricultural Biotechnology*; John Wiley & Sons, Inc.: Hoboken, NJ, 2011; pp 1−4.

(12) Lundry, D. R.; Burns, J. A.; Nemeth, M. A.; Riordan, S. G. Composition of Grain and Forage from Insect-Protected and Herbicide-Tolerant Corn, Mon 89034 x TC1507 x MON 88017 x DAS-59122−7 (SmartStax), Is Equivalent to That of Conventional Corn (Zea mays L.). *J. Agric. Food Chem.* **2013**, *61*, 1991−1998.

(13) Lipton, C. R.; Dautlick, J. X.; Grothaus, G. D.; Hunst, P. L.; Magin, K. M.; Mihaliak, C. A.; Rubio, F. M.; Stave, J. W. Guidelines for the Validation and Use of Immunoassays for Determination of Introduced Proteins in Biotechnology Enhanced Crops and Derived Food Ingredients. *Food Agric. Immunol.* **2000**, *12*, 153−164.

(14) Grothaus, G. D.; Bandla, M.; Currier, T.; Giroux, R.; Jenkins, G. R.; Lipp, M.; Shan, G.; Stave, J. W.; Pantella, V. Immunoassay as an Analytical Tool in Agricultural Biotechnology. *J. AOAC Int.* **2006**, *89*, 913−928.

(15) Zhou, S.; Song, Q.; Tang, Y.; Naidong, W. Critical Review of Development, Validation, and Transfer for High Throughput Bioanalytical LC-MS/MS Methods. *Curr. Pharm. Anal.* **2005**, *1*, 3−14.

(16) Palandra, J.; Finelli, A.; Zhu, M.; Masferrer, J.; Neubert, H. Highly Specific and Sensitive Measurements of Human and Monkey Interleukin 21 Using Sequential Protein and Tryptic Peptide Immunoaffinity LC-MS/MS. *Anal. Chem.* **2013**, *85* (11), 5522−5529.

(17) Sack, C.; Smoker, M.; Chamkasem, N.; Thompson, R.; Satterfield, G.; Masse, C.; Mercer, G.; Neuhaus, B.; Cassias, I.; Chang, E.; Lin, Y.; MacMahon, S.; Wong, J.; Zhang, K.; Smith, R. E. Collaborative Validation of the QuEChERs Procedure for the Determination of Pesticides in Food by LC-MS/MS. *J. Agric. Food Chem.* **2011**, *59* (12), 6383−6411.

(18) Chamkasem, N.; Ollis, L. W.; Harmon, T.; Lee, S.; Mercer, G. Analysis of 136 Pesticides in Avocado Using a Modified QuEChERS Method with LC-MS/MS and GC-MS/MS. *J. Agric. Food Chem.* **2013**, *61* (10), 2315−2329.

(19) Gardner, M. S.; Voyksner, R. D.; Haney, C. A. Analysis of Pesticides by LC-Electrospray-MS with Postcolumn Removal of Nonvolatile Buffers. *Anal. Chem.* **2000**, *72*, 4659−4666.

(20) Lerch, R. N.; Ferrer, I.; Thurman, E. M.; Zablotowicz, R. M. Identification of Trifluralin Metabolites in Soil Using Ion-Trap LC/MS/MS. In *Liquid Chromatography/Mass Spectrometry, MS/MS and Time of Flight MS*; Ferrer, I., Thurman, E. M., Eds.; American Chemical Society: Washington, D.C., 2003; Chapter 17, pp 291−310.

(21) Vargo, J. D. Determination of Chloroacetanilide and Chloroacetamide Herbicides and Their Polar Degradation Products in Water by LC/MS/MS. In *Liquid Chromatography/Mass Spectrometry, MS/MS and Time of Flight MS*; Ferrer, I., Thurman, E. M., Eds.; American Chemical Society: Washington, D.C., 2003; Chapter 14, pp 238−255.

(22) Hu, X. T.; Owens, M. A. Multiplexed Protein Quantification in Maize Leaves by Liquid Chromatography Coupled with Tandem Mass Spectrometry; An Alternative Tool to Immunoassays for Target Protein Analysis in Genetically Engineered Crops. *J. Agric. Food Chem.* **2011**, *59*, 3551−3558.

(23) Zhang, H.; Liu, Q.; Zimmerman, L. J.; Ham, A. L.; Slebos, R. J.; Rahman, J.; Kikuchi, T.; Massion, P.; Carbone, D.; Billheimer, D.; Liebler, D. Methods for Peptide and Protein Quantitation by Liquid

DOI: 10.1021/acs.jafc.5b03083
J. Agric. Food Chem. 2015, 63, 7450−7461

Chromatography-Multiple Reaction Monitoring Mass Spectrometry. *Mol. Cell. Proteomics* **2011**, *10*, M110.006593.
(24) Zhang, Y.; Fonslow, B. R.; Shan, B.; Baek, M.; Yates, J. R. Protein Analysis by Shotgun/Bottom-up Proteomics. *Chem. Rev.* **2013**, *113*, 2343−2394.
(25) Lesur, A.; Varesio, E.; Domon, B.; Hopfgartner, G. Peptides Quantification by Liquid Chromatography with Matrix-Assisted Laser Desorption/Ionization and Selected Reaction Monitoring Detection. *J. Proteome Res.* **2012**, *11* (10), 4972−4982.
(26) Lowenthal, M. S.; Liang, Y.; Phinney, K.; Stein, S. E. Quantitative Bottom-Up Proteomics Depends on Digestion Conditions. *Anal. Chem.* **2014**, *86* (1), 551−558.
(27) Yeung, Y.; Stanley, E. R. Rapid Detergent Removal from Peptide Samples with Ethyl Acetate for Mass Spectrometry Analysis. *Curr. Protoc. Protein Sci.* **2010**, *16* (12), 1.
(28) Kolsrud, H.; et al. A critical review of trypsin digestion for LC-MS based proteomics. *Integrative Proteomics* **2012**, 73.
(29) van den Broek, I.; Smit, N.; Romijn, F.; van der Laarse, A.; et al. Evaluation of Interspecimen Trypsin Digestion Efficiency Prior to Multiple Reaction Monitoring-Based Absolute Protein Quantification with Native Protein Calibrators. *J. Proteome Res.* **2013**, *12*, 5760−5774.
(30) Goebel-Stengel, M.; Stengel, A.; Taché, Y.; Reeve, J. R., Jr. The importance of using the optimal plastic and glassware in studies involving peptides. *Anal. Biochem.* **2011**, *414* (1), 38−46.
(31) Bernert, J. T.; Turner, W. E.; Pirkle, J. L.; Sosnoff, C. S.; Akins, J. R.; Waldrep, M. K.; Ann, Q.; Covey, T. R.; Whitfield, W. E.; Gunter, E. W.; Miller, B. B.; Patterson, D. G.; Needham, L. L.; Hannon, W. H.; Sampson, E. J. Development and validation of sensitive method for determination of serum cotinine in smokers and nonsmokers by liquid chromatography/atmospheric pressure ionization tandem mass spectrometry. *Clin. Chem.* **1997**, *43* (12), 2281−2291.
(32) Cohen Freue, G. V.; Borchers, C. H. Multiple Reaction Monitoring (MRM) Principles and Application to Coronary Artery Disease. *Circ.: Cardiovasc. Genet.* **2012**, *5*, 378.
(33) Lu, Q.; Zheng, X.; McIntosh, T.; Davis, H.; Nemeth, J. F.; Pendley, C.; Wu, S.; Hancock, W. S. Development of different analysis platforms with LC-MS for pharmacokinetic studies of protein drugs. *Anal. Chem.* **2009**, *81* (21), 8715−8723.
(34) Keith, L. H.; Crummett, W.; Deegan, J.; Libby, R. A.; Taylor, J. K.; Wentler, G. Principles of environmental analysis. *Anal. Chem.* **1983**, *55*, 2210−2218.
(35) Addona, T. A.; Abbatiello, S. E.; Schilling, B.; Skates, S. J.; Mani, D. R.; Bunk, D. M.; Spiegelman, C. H.; Zimmerman, L. J.; Ham, A. J.; Keshishian, H.; Hall, S. C.; Allen, S.; Blackman, R. K.; Borchers, C. H.; Buck, C.; Cardasis, H. L.; Cusack, M. P.; Dodder, N. G.; Gibson, B. W.; Held, J. M.; Hiltke, T.; Jackson, A.; Johansen, E. B.; Kinsinger, C. R.; Li, J.; Mesri, M.; Neubert, T. A.; Niles, R. K.; Pulsipher, T. C.; Ransohoff, D.; Rodriguez, H.; Rudnick, P. A.; Smith, D.; Tabb, D. L.; Tegeler, T. J.; Variyath, A. M.; Vega-Montoto, L. J.; Wahlander, A.; Waldemarson, S.; Wang, M.; Whiteaker, J. R.; Zhao, L.; Anderson, N. L.; Fisher, S. J.; Liebler, D. C.; Paulovich, A. G.; Regnier, F. E.; Tempst, P.; Carr, S. A. Multi-site assessmentof the precision and reproducibility of multiple reaction monitoring-based measurements of proteins in plasma. *Nat. Biotechnol.* **2009**, *27*, 633−641.
(36) Aebersold, R.; Burlingame, A.; Bradshaw, R. A. Western Blots versus Selected Reaction Monitoring Assays: Time to Turn the Tables? *Mol. Cell. Proteomics* **2013**, *12*, 2381−2382.
(37) Shan, G. *Immunoassays in Agricultural Biotechnology*; John Wiley & Sons, Inc.: Hoboken, NJ, 2011; pp 197−198.

DOI: 10.1021/acs.jafc.5b03083
J. Agric. Food Chem. 2015, 63, 7450−7461

JOURNAL OF AGRICULTURAL AND FOOD CHEMISTRY

Addition/Correction

pubs.acs.org/JAFC

Correction to A 90 Day Safety Assessment of Genetically Modified Rice Expressing Cry1Ab/1Ac Protein Using an Aquatic Animal Model

Hao-Jun Zhu, Yi Chen, Yun-He Li, Jia-Mei Wang, Jia-Tong Ding, Xiu-Ping Chen,* and Yu-Fa Peng*

J. Agric. Food Chem. **2105**, *63* (14), 3627−3633. DOI: 10.1021/jf5055547

The *t* values in the far right columns of Tables 5 and 6 on page 3630 should be *F* values.

Table 5. Absolute and Relative Organ Weights and Intestinal Lengths in *X. laevis* Froglets Fed Test versus Control Diets[a]

	HH1	MH63	control	statistics[b]
		Absolute Measurements		
body (g)	27.7 ± 2.17	27.4 ± 2.40	27.9 ± 1.67	$F = 0.07$; $p = 0.93$
heart (g)	0.14 ± 0.01	0.14 ± 0.02	0.15 ± 0.02	$F = 0.41$; $p = 0.66$
liver (g)	1.70 ± 0.16	1.60 ± 0.16	1.64 ± 0.07	$F = 0.17$; $p = 0.84$
spleen (g)	0.03 ± 0.00	0.03 ± 0.00	0.03 ± 0.00	$F = 0.02$; $p = 0.98$
lung (g)	0.16 ± 0.01	0.16 ± 0.01	0.16 ± 0.02	$F = 0.07$; $p = 0.94$
kidney (g)	0.21 ± 0.03	0.21 ± 0.03	0.22 ± 0.01	$F = 0.16$; $p = 0.85$
fat body (g)	1.84 ± 0.14	1.82 ± 0.21	1.73 ± 0.06	$F = 0.20$; $p = 0.82$
ovary (g)	0.12 ± 0.02 (16)	0.11 ± 0.01 (13)	0.12 ± 0.02 (19)	$F = 0.11$; $p = 0.90$
testis (g)	0.05 ± 0.01 (16)	0.04 ± 0.01 (19)	0.05 ± 0.01 (13)	$F = 0.95$; $p = 0.39$
intestinal length (cm)	15.1 ± 1.11	15.0 ± 1.30	16.2 ± 1.76	$F = 1.94$; $p = 0.15$
		Relative Values[c]		
heart	0.51 ± 0.05	0.49 ± 0.04	0.52 ± 0.06	$F = 0.60$; $p = 0.55$
liver	6.06 ± 0.14	5.75 ± 0.20	5.70 ± 0.15	$F = 2.00$; $p = 0.14$
spleen	0.10 ± 0.01	0.11 ± 0.01	0.10 ± 0.01	$F = 0.75$; $p = 0.48$
lung	0.56 ± 0.04	0.58 ± 0.05	0.56 ± 0.04	$F = 0.27$; $p = 0.76$
kidney	0.74 ± 0.05	0.76 ± 0.07	0.77 ± 0.04	$F = 0.63$; $p = 0.54$
fat body	6.56 ± 0.22b	6.49 ± 0.39ab	6.00 ± 0.26a	$F = 3.99$; $p = 0.02$
ovary	0.44 ± 0.06 (16)	0.42 ± 0.06 (13)	0.48 ± 0.09 (19)	$F = 0.73$; $p = 0.49$
testis	0.18 ± 0.03 (16)	0.16 ± 0.02 (19)	0.17 ± 0.01 (13)	$F = 0.60$; $p = 0.55$
intestinal length	0.56 ± 0.02	0.58 ± 0.08	0.63 ± 0.02	$F = 2.47$; $p = 0.09$

[a]Data presented as group mean values ± SD ($n = 32$, except for ovaries and testes, where n is given in parentheses). Different Roman lower case letters in the same row indicate a statistical difference of $p < 0.05$. [b]One-way ANOVA, $p < 0.05$. [c]Relative values expressed as g or cm per 100 g of body weight.

Table 6. Liver Function, Kidney Function, and Fat Metabolism in *X. laevis* Froglets Fed Test versus Control Diets ($n = 24$)

indices	HH1	MH63	control	statistics[a]
		Liver Function		
AKP (U/g protein)	195 ± 12.6	193 ± 31.1	167 ± 12.1	$F = 0.81$; $p = 0.45$
ALB (g/L)	7.31 ± 0.55	7.22 ± 0.58	7.04 ± 0.72	$F = 0.73$; $p = 0.49$
ALT (U/g protein)	860 ± 181	902 ± 224	813 ± 36.7	$F = 0.55$; $p = 0.58$
AST (U/g protein)	443 ± 66.5	432 ± 65.1	405 ± 22.0	$F = 0.75$; $p = 0.48$
BUN (mg/L)	1.82 ± 0.08	1.79 ± 0.08	1.72 ± 0.08	$F = 2.71$; $p = 0.08$
CHE (U/mg protein)	1.41 ± 0.15	1.40 ± 0.10	1.34 ± 0.12	$F = 0.06$; $p = 0.94$
TP (g/L)	9.27 ± 0.48	8.90 ± 0.21	9.10 ± 0.25	$F = 1.28$; $p = 0.28$
		Kidney Function		
BUN (mg/L)	3.49 ± 0.11	3.32 ± 0.18	3.36 ± 0.48	$F = 0.47$; $p = 0.63$
CR (μmol/L)	23.9 ± 4.07	25.1 ± 3.30	20.3 ± 5.56	$F = 2.82$; $p = 0.07$
GLU (μmol/g protein)	30.6 ± 4.34	28.25 ± 3.74	29.75 ± 0.82	$F = 0.74$; $p = 0.48$
		Fat Metabolism		
TC (mmol/L)	0.66 ± 0.05	0.69 ± 0.10	0.67 ± 0.16	$F = 0.19$; $p = 0.83$
TG (mmol/L)	2.32 ± 0.34	2.11 ± 0.10	2.06 ± 0.68	$F = 0.79$; $p = 0.46$

[a]One-way ANOVA, $p < 0.05$.

Published: August 12, 2015

ACS Publications © 2015 American Chemical Society

DOI: 10.1021/acs.jafc.5b03809
J. Agric. Food Chem. 2015, 63, 7462−7462

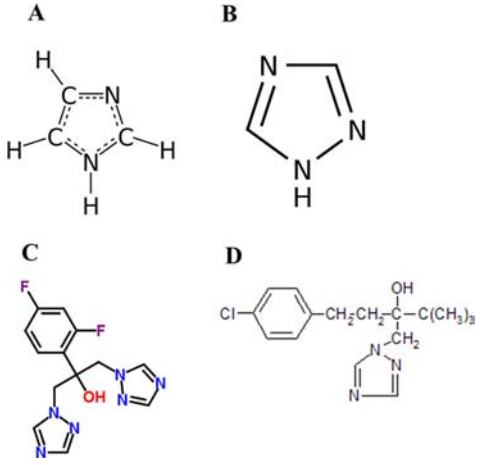

Figure 1. Chemical struture of (A) imidazole, (B) 1,2,4-triazole, (C) fluconazole, and (D) tebuconazole.

States, less than 5% of the total crop area is treated with these compounds. In the European Union, the situation of the Netherlands stands out in particular, because the utilization of azole fungicides has almost doubled since the mid-1990s.[13] Several reasons are usually forwarded to justify the use of azoles in agriculture, in particular, the fact that these compounds are not expensive and that they exhibit broad spectrum activity. However, because azoles are very stable molecules, they can persist active in the soil and water for several months[14] as well as in several fruits and vegetables.[15−17] Although the azole residues detected in many samples do not reach health hazard toxic levels, the amount could vary considerably. Data from the literature show that considerable quantities of azole residues could persist in some food products for a long time.[5]

Farmers have been strongly encouraged to follow guidelines aiming to reduce the probability of developing resistance to agricultural antifungals, to minimize its extent, and/or to increase the chance that any developed resistance would still be reversible. Such practices include the rotating use of antifungal products with different modes of action as well as the preferential practice of a limited number of interventions using higher dosages as opposed to more frequent applications with lower dosages. This does not, however, imply that the use of antifungal substances in agriculture should not be closely monitored, considering the risk of accumulation of azoles in the soils (the half-life time of azoles is usually longer than 1 year) and because the newer compounds may also be at the origin of resistance development.

USE OF AGRICULTURAL AZOLE FUNGICIDES IN PORTUGAL

In the particular case of Portugal, there is a real need to promote agriculture and invest in training farmers. According to the results of the Agricultural Census report,[18] the social characterization of the Portuguese family farm population consists of 793 000 individuals representing, 7% of the resident population. The rural population aged considerably between 1999 and 2009; the average age increased from 46 to 52 years. The educational level is rather low; 40% of subjects only attended the first cycle, and 22% have no schooling. However, despite these social indicators, significant improvements were registered during the 10 year period under study; illiteracy rate decreased by 7%, and the frequency of senior secondary cycle and higher education increased by 3%. At the present, the typical profile of the Portuguese farmer nowadays is a 63-year-old male, having just completed the first cycle of basic education, only having practical agricultural training, and working in agricultural activities about 22 h per week.

By December 31, 2012, 907 PPP, based on 248 active substances, were available in Portugal.[19] The largest volume of these substances available at the national market belong to the fungicides group, followed by herbicides and insecticides, representing the remaining products about 15% of the total PPP marketed. According to the Agricultural Statistics report, the ratio between sales of PPP/agricultural area used was in 2008, 2009, and 2010 of 4.6, 3.8, and 3.8, respectively. In the case of the total sales volume being subtracted with the value of sulfur and derivates, this ratio corresponds to values of 1.9, 2.0, and 1.9, respectively.[19]

Sales figures of PPP at the national level constitute an indicator that can provide an estimation about the use of such products in Portugal. The amount of PPP sold in Portugal during 2012 corresponded to a total of 12 462 237 kg, expressed as active substances. The fungicides contributed to about 68.3% of the total of active substances sold, whereas sulfur represented 49.8% of the total sales and 71.4% of all of the fungicides sold. Figure 2 depicts an overview of fungicide

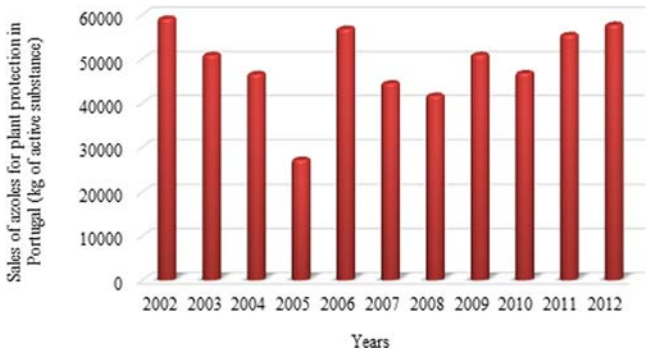

Figure 2. Sales of fungicides in Portugal between 2002 and 2012.[20]

sales by chemical group in Portugal between 2002 and 2012. Overall, a decrease in fungicide sales was registered from 2008 until 2012.[20] With respect to azoles, a consecutive decrease in sales was registered between 2002 and 2005; however, after 2006, the values started to increase again, reaching a peak in 2012 (Figure 3).[20]

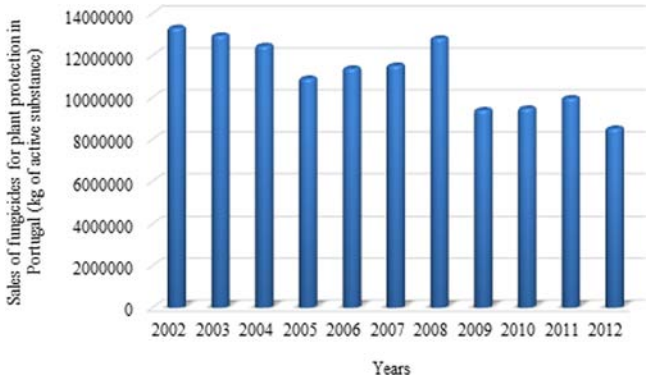

Figure 3. Sales of agricultural azole in Portugal between 2002 and 2012.[20]

DOI: 10.1021/acs.jafc.5b02728
J. Agric. Food Chem. 2015, 63, 7463−7468

MODE OF ACTION OF AZOLE DRUGS

Concerning the mode of action, all of the azole drugs interact and target the same active site in fungal enzyme; thus, agricultural azole fungicides share the mode of action with medical azoles.[21] This results in a fungistatic rather than fungicidal effect; in this sense, the terminology often used in agriculture "fungicides" is ambiguous.

This class of compounds are sterol demethylation inhibitors (SBIs) and impair the synthesis of ergosterol.[5,21] Azole drugs interfere with the activity of fungal lanosterol 14α-demethylase, an enzyme responsible for the transformation of lanosterol in ergosterol. Ergosterol is an important compound of the fungal cytoplasmatic membrane; the impairment of its metabolism induces cell membrane disorganization and decreases fungal growth. Moreover, fungal growth arrest can also result from the accumulation of toxic ergosterol precursors.[22]

The available SBIs—fungicides can be classified into four classes according to their respective target sites, which are membrane-bound enzymes, namely, thiocarbamates or allylamines (squalene epoxidase), inhibithors of C_{14} demethylation or DMIs, amines (Δ^{14} reduction or $\Delta^{8} \rightarrow \Delta^{7}$ isomerization), and hydroxyanilides (C_4 demethylation). However, several resistance mechanisms to SBIs have been described. The two major mechanisms involve either alterations of the target enzyme, which result in a reduced affinity to fungicides, or a decrease of the intracellular drug accumulation, which is linked to an overexpression of membrane transporter proteins, usually, namely, effux pumps.

HYPOTHETICAL LINK BETWEEN AZOLE USE IN AGRICULTURE AND HUMAN HEALTH

Several reports claim that antibiotic resistance can be a natural occurrence in the soil. In fact, microorganisms inhabiting soil have to strive for energy sources; it is known that some bacteria and fungi develop the ability to produce antibiotic compounds to destroy their competitors. Such microorganisms are thus naturally immune to the effects of their own excretions.[23]

The development of resistance to azoles among plant fungal pathogens is complex and generally progressing in small steps. First descriptions date from a long time ago and claim that some plant pathogens acquired azole resistance following agricultural exposure.[24] Data from the literature describe resistance or tolerance to triazole fungicides for pathogens of crops, such as wheat, barley, and strawberry.[25] While, in Portugal, resistance to triazoles in vineyard powdery mildew has been detected in the past,[26] still recent studies describe this situation.[27]

Over the last 2 decades, clinically important fungal infections have become more prevalent because medical progress allows for the survival of an increasing number of immunocompromised patients. However, resistance to antifungal drugs also became a critical medical problem.

It has been proposed that there may be a direct relation between the development of resistance to azole fungicides used in agricultural practice and the development of resistance to azole antifungals observed in clinical settings.[28] Exposure of a microorganism to any antibiotic involves a risk of emergence of resistance through the process of selection. The knowledge about the rate and extent of the emergence of resistant organisms[29] and whether this resistance is reversible or not is a very relevant issue to clinical medicine. Resistance depends upon a variety of factors and conditions, including the mechanisms of action of the compound, the target site(s) in the organism and their number, the risk of resistance transference between individual organisms and species, and the mechanism of such resistance.

Resistance in fungi and the mechanisms involved in its development and transmission differ to some extent from those seen in bacteria. There is no evidence that the genes that confer resistance to fungi can be transferred horizontally, a key difference with bacteria. There are two forms of resistance, primary (or intrinsic) and secondary. In primary resistance, the fungal organism cannot be inhibited even by high concentrations of an antifungal drug. For example, *Aspergillus fumigatus* is intrinsically resistant to fluconazole and does not respond at all to this drug. Similarly, *Candida krusei* and *Candida glabrata* isolates are often intrinsically resistant to fluconazole. Conversely, fluconazole resistance in *Candida albicans* can emerge *de novo* during prolonged treatment, which is an example of secondary resistance.[30]

There are at least three different mechanisms by which antifungal drug resistance might arise. They can involve increased efflux of drug, altered target demethylase sites, and availability of alternative pathways for the synthesis of cell membrane sterols. *C. krusei* shows intrinsic resistance to fluconazole largely as a result of the last mentioned mechanism.

There is also evidence that, in clinical settings, the adoption of some therapeutic strategies to treat patients over long periods or to prevent infection through antifungal prophylaxis can result in selection of resistant organisms, of either the same or different species. Several studies have shown that a strong and persistent antimicrobial pressure upon a microbial population will undoubtedly lead to the selection of resistant clones, particularly whenever the antimicrobial agent induces a static effect instead of a biocidal effect.[23] This situation can happen in fungi submitted to azole pressure. Because azoles represent first line clinical antifungals, the topic of azole resistance is of great medical relevance. Azole resistance can thus hypothetically result from exposure to azole compounds, which can happen *in vivo* (azole-treated patients) or as a result of the presence of these compounds in the environment, namely, agriculture use.[31] The massive use of azoles in agriculture could stress susceptible species of the fungal flora, both in nature but also at human endogenous niches. This disturbance in the fungal flora ecology could result in changes among the population of medically important fungi; human fungi pathogens may thus persist and thrive.[5] In this situation, health risks might increase seriously. In addition, new resistance mutations could also develop in the environment. Studies addressing the epidemiology of invasive fungal infections are of high relevance to determine the hipothetical impact of anthropogenic activities upon the susceptibility profile of yeast and filamentous fungi and also to report any emergent species. In Portugal, two studies conducted at the same institution, within a 10 year interval, revealed several relevant differences not only in susceptibility patterns but, most importantly, with regard to species distribution.[29,32]

Invasive aspergillosis is a very dangerous opportunistic fungal infection. The conidia of *Aspergillus* spp. usually become airborne from soil or decaying organic matter, and patients become infected usually by inhalation from such a reservoir.[13] In 2009, Snelders and co-workers provided for the first time evidence that patients with invasive aspergillosis as a result of azole-resistant *A. fumigatus* might have acquired the organism from the environment.[31] According to this study, resistant

DOI: 10.1021/acs.jafc.5b02728
J. Agric. Food Chem. 2015, 63, 7463−7468

strains of *A. fumigatus* to medical azoles were found in the soil and compost from areas nearby the admission hospital.[31] The dominance of a single resistance mechanism and the genetic homology between the clinical and environmental isolates suggested that the acquisition of azole-resistant isolates from the environment was the most important infection route.

Azole resistance among *A. fumigatus* isolates was not only found in Dutch hospitals;[33] resistant isolates were also detected in several European countries, such as Spain,[34] Belgium,[35] Denmark,[36] Sweden,[37] and France.[38]

Human and animal fungal pathogens, such as *Coccidioides*, *Histoplasma*, *Aspergillus*, and *Cryptococcus*, also thrive in the environment, including plants and food products. It should also be stressed that only a few yeast species are endogenous to the flora of healthy humans; in most occasions, the fungal pathogens are taken up from the environment. Thus, environmental-resistant isolates could have developed antifungal resistance following a prolonged environmental-selective azole pressure. Therefore, the probability that an individual might be exposed to environmental-resistant fungal organisms is real and high. Nevertheless, the stress of residual azoles that might be present in vegetables and other food products upon the endogenous native fungal flora of humans should not be neglected and may also contribute to the emergence of antifungal resistance at endogenous niches.

In the case of *A. fumigatus*, it was concluded that two distinct models of resistance might have developed. One of them occurs following long time exposure to azole treatment, as might occur in clinical settings, supported by several possible genetic mutations, and the other model is facilitated by a single mechanism, TR/L98H mutation, that occurs in environmental isolates under the selective pressure of agricultural azole fungicides. This kind of mutation started spreading worldwide and has nowadays also been described outside Europe.[39] A very recent study conducted in France describes a clinical case of a French farmer who developed invasive aspergillosis caused by an azole-resistant *A. fumigatus* with the TR34/L98H mutation following hematopoietic stem cell transplantation.[40] This farmer had worked in fungicide-sprayed fields from where *A. fumigatus* TR34/L98H isolates were also recovered. This study supports the assumption that humans might indeed be infected with environmental azole-resistant isolates.

Measures to control this problem should be adopted, in particular in the Netherlands, where the TR/L98H mutation became endemic.[5] Interestingly, in Portugal, back in 2007, Araújo et al.[41] compared the antifungal susceptibility profile of different *Aspergillus* species recovered from environmental and clinical sources and found high minimal inhibitory concentration (MIC) levels of clinical antifungals among environmental strains.

Verweij and co-workers reported cross-resistance between azole drugs, which constitutes a very relevant clinical issue, with relatively few therapeutic options available in the case of invasive *Aspergillus* infections.[42] More recently, several studies demonstrated the development of cross-resistance between agricultural and medical azoles.[13,21] Faria-Ramos and co-workers[43] clearly demonstrated that exposure of clinically relevant molds and yeast organisms to azoles used in agriculture does result in the emergence of cross-resistance to clinical azoles, which may not be reversible.

Additional research efforts aiming to reduce the emergence of fungicide resistance are urgently needed, in both agriculture and medical settings. Because the mechanisms providing the basis for fungicide resistance are likely to be conserved between plant and human pathogens, plant pathologists and medical microbiologists should develop effective strategies counteracting the development of antifungal resistance, in a concerted action.

PORTUGUESE NATIONAL STRATEGIE PLAN FOR A SUSTAINABLE USE OF PPP

The Directive no. 2009/128/EC is an innovation in the context of the European Community legislation about PPP; for the first time, legislation was provided about the use of PPP, to protect human health and the environment from possible risks inherent to its use.

To operationalize the implementation of this Directive at the national level, the law no. 26/2013 was published; it regulates the distribution, sales, and application of PPP by professional users as well as adjuvants for PPP and also sets the monitoring procedures for the use of PPP. Together with the law no. 86/2010 (which establishes a mandatory inspection scheme of PPP and its application using equipment authorized for professional use), it constitutes the transposition into national legal order of that European Community law.

The article 51 of this law envisaged the creation of National Action Plans. These plans aimed at reducing the risks and effects of the use of PPP on human health and the environment and to promote the development of integrated protection technical alternatives to reduce dependence of the use of conventional PPP.

The Portuguese National Plan has been prepared with the collaboration of various agents, from either public or private sector, without which would not have been possible to achieve the intended goals. It must also be pointed out that the implementation of this plan will only be effective with the committed collaboration of all of the agents involved in manufacture, storage, sale, and use of PPP as well as those responsible for managing the effects and risks associated with the use of PPP. The correct application of PPP can be encouraged by the training of professionals, appropriate counselling at the point of sale, and monitoring/supervision of compliance by professional users. In the act of sale, adequate information about the use of PPP and the risks and safety instructions regarding human health should be provided to buyers, to enable the adequate management of the risks inherent to the products concerned.

The protection of professionals configures primarily a matter of safety and health regarding the professional handling field use and application of pesticides. Risks may include not only acute intoxication but also chronic and subchronic risks resulting from prolonged exposure. The lines of action chosen for this intervention area are (i) protection of professional users (commercial and storage settings), (ii) reduction of exposure, and (iii) limitation of the use of certain PPP.[44]

The main measure of protection regarding non-professional users is restricting its access to a limited category of PPP. In any case, buyers should be provided awareness of the risks associated with PPP use and about promotion of good general practices regarding its use.

To assess the progress made in reducing the risks and adverse effects of the use of PPP, to both human health and the environment, monitoring plans should be in place so that, on the basis of a sample of professional users and predefined criteria, it will be possible to assess the progresses resulting the

DOI: 10.1021/acs.jafc.5b02728
J. Agric. Food Chem. 2015, 63, 7463−7468

implementation of the general principles of integrated protection.

In addition, it should be emphasized the relevance of the contribution of scientific research and field application of the most recently available scientific and technological information in improving resources and instruments available to the professional users, including complementary or alternative means of use of PPP.

In conclusion, fungicide-based plant protection is at present indispensable for efficient and large-scale crop production. Notably, modern fungicides should exhibit negligible acute toxicity, and the regulations for fungicide application should ensure the availability of safe food. Because long time periods and enormous financial investments are required to develop new fungicides, serious efforts must be taken to prevent emergence of fungicide resistance. This is particularly important because fungicides with novel modes of action are rarely found and resistance to single-target fungicides may occur within the first few years of its field use.

The key to prevent or at least delay the onset of development of fungicide resistance in agriculture is the preparation of efficient fungicide mixtures as well as the rotation between fungicides with different modes of action during a crop campaign. The recommendations are to maintain highly efficient fungicides in the market, precluding the use of monofungicides, to keep its use above a threshold allowing for quantitative resistance to develop. The strategy adopted during the last few decades was to apply single-target fungicides, resulted in a strong selective pressure for mutants with a modified fungicide-binding site. Because fungicides with more than one target are not easy to overcome by mutations, the focus in fungicide screening should also be directed toward identifying multi-site inhibitors. After having such fungicides available, the risk of rapid occurrence of qualitative resistance might be strongly and effectively reduced. Nevertheless, particular attention should be devoted to the assessment of the development of cross-resistance to clinical antifungals, strict monitoring of the emergence of fungal strains with resistance mechanisms, and variations in species distribution regarding both plant and human pathogens, which should be implemented.

AUTHOR INFORMATION

Corresponding Author

*Telephone: +351936320962. E-mail: maria.manuel.azevedo2011@gmail.com.

Funding

Isabel Faria-Ramos is supported by Fundação para a Ciência e Tecnologia (FCT) Ph.D. Grant SFRH/BD/91155/2012.

Notes

The authors declare no competing financial interest.

REFERENCES

(1) Price, C. L.; Parker, J. E.; Warrilow, A. G.S.; Kelly, D. E.; Kelly, S. L. Azole fungicides − understanding resistance mechanisms in agricultural fungal pathogens. *Pest Manage. Sci.* **2015**, *71*, 1054−1058.

(2) Lucas, J. Resistance of Qol fungicides. Implications for cereal disease management in Europe. *Pestic. Outlook* **2003**, *14*, 268−270.

(3) Chambers, J. E.; Greim, H.; Kendall, R. J.; Segner, H.; Sharpe, R. M.; Van Der Kraak, G. Human and ecological risk assessment of a crop protection chemical: a case study with the azole fungicide epoxiconazole. *Crit. Rev. Toxicol.* **2014**, *44* (2), 176−210.

(4) Matthews, G. A. *Pesticide Application Methods*, 3rd ed.; Blackwell Science: Oxford, U.K., 2000.

(5) Hof, H. Critical annotations to the use of azole antifungals for plant protection. *Antimicrob. Agents Chemother.* **2001**, *45*, 2987−2990.

(6) Lelièvre, L.; Groh, M.; Angebault, C.; Maherault, A. C.; Didier, E.; Bougnoux, M. E. Azole resistant *Aspergillus fumigatus*: an emerging problem. *Med. Mal. Infect* **2013**, *43*, 139−45.

(7) https://en.wikipedia.org/wiki/Imidazole#/media/File:Imidazole_2D_full_aromatic.svg. (Accessed July 8, 2015).

(8) http://www.sigmaaldrich.com/catalog/product/aldrich/333662?lang=pt&region=PT&gclid=CJS1mfbmycYCFXQatAodotkEgA. (Accessed July 8, 2015).

(9) Hof, H. Is there a serious risk of resistance development to azoles among fungi due to the widespread use and long-term application of azole antifungals in medicine? *Drug Resist. Updates* **2008**, *11*, 25−31. Fluconazole - http://www.chemspider.com/Chemical-Structure.3248.html. (Accessed August 24, 2015).

(10) Dijksterhuis, J.; Houbraken, J.; Samson, R. A. Fungal spoilage of crops and food. In *The Mycota: Agricultural Applications*; Kempken, F., Eds.; Springer-Verlag: Berlin, Germany, 2013; Vol. *11*, pp 35−56. Tebuconazole - http://www.sinoharvest.com/products/Tebuconazole.shtml. (Accessed August 24, 2015).

(11) Barth, M.; Hankinson, T. R.; Zhuang, H.; Breidt, F. Microbiological spoilage of fruits and vegetables. In *Compendium of the Microbiological Spoilage of Foods and Beverages, Food Microbiology and Food Safety*; Sperber, W. H., Doyle, M. P., Eds.; Springer-Verlag: New York, 2009; pp 135−183, DOI: 10.1007/978-1-4419-0826-1_6.

(12) European Commision, Health and Consumer Protection Directorate-General. *Opinion on Azole Antimycotc Resistance Adopted by the Scientific Steering Committee at Its Meeting 27−28 June 2002*; European Commision, Health and Consumer Protection Directorate-General: Luxembourg, 2002; http://ec.europa.eu/food/fs/sc/ssc/out278_en.pdf). (Accessed Dec 20, 2014).

(13) Verweij, P. E.; Snelders, E.; Kema, G. H.; Mellado, E.; Melchers, W. J. Azole resistance in *Aspergillus fumigatus*: a side effect of environmental fungicide use? *Lancet Infect. Dis.* **2009**, *9* (12), 789−795.

(14) Tomlim, C. D. S. *The Pesticide Manual*, 11th ed.; British Crop Protection Council: Surrey, U.K., 1997.

(15) Garland, S. M.; Menary, R. C.; Davies, N. W. Dissipation of propiconazole and tebuconazole in peppermint crops (*Mentha piperita* (Labiatae)) and their residues in distilled oils. *J. Agric. Food Chem.* **1999**, *47*, 294−298.

(16) Hamey, P. Y.; Harris, C. A. The variation of pesticide residues in fruits and vegetables and the associated assessment of risk. *Regul. Toxicol. Pharmacol.* **1999**, *30*, S34−S41.

(17) Trösken, E. R.; Bittner, N.; Volkel, W. Quantitation of 13 azole fungicides in wine samples by liquid chromatography-tandem mass spectrometry. *J. Chromatogr. A* **2005**, *1083*, 113−19.

(18) Eurostat. *Agricultural Census Report in Portugal*; Eurostat: Luxembourg, 2012; http://ec.europa.eu/eurostat/statisticsexplained/index.php/Agricultural_census_in_Portugal (Accessed Jan 20, 2015).

(19) Direcção-Geral de Alimentação e Veterinária (DGAV). *Plano de Ação Nacional para o Uso Sustentável dos Produtos Fitofarmacêuticos. Contexto Nacional da Utilização de Produtos Fitofarmacêuticos*; DGAV: Lisbon, Portugal, 2013; Vol. *2*, http://www.dgv.min-agricultura.pt/xeov21/attachfileu.jsp?look_parentBoui=6321372&att_display=n&att_download=y (Accessed Jan 20, 2015).

(20) Direção Geral de Agricultura e Desenvolvimento Rural (DGADR). *Vendas de Produtos Fitofarmacêuticos em Portugal 2002−2012*; http://www.dgadr.mamaot.pt/. (Accessed Jan 20, 2015).

(21) Snelders, E.; Camps, S. M. T.; Karawajczyk, A.; Schaftenaar, G.; Kema, G. H. J.; Van der Lee, H. A.; et al. Triazole fungicides can induce cross-resistance to medical triazoles in *Aspergillus fumigatus*. *PLoS One* **2012**, *7* (3), e31801.

(22) White, T. C.; Marr, K. A.; Bowden, R. A. Clinical, Cellular, and Molecular Factors That Contribute to Antifungal Drug Resistance. *Clin. Microbiol. Rev.* **1998**, *11* (2), 382−402.

DOI: 10.1021/acs.jafc.5b02728
J. Agric. Food Chem. 2015, 63, 7463−7468

(23) Davies, J.; Davies, D. Origins and Evolution of Antibiotic Resistance. *MMBR* **2010**, *74* (3), 417−433.
(24) Russell, P. E. Fungicide resistance: occurrence and management. *J. Agric. Sci.* **1995**, *124*, 317−323.
(25) Serfling, A.; Wohlrab, J.; Deising, H. B. Treatment of a clinically relevant plant-pathogenic fungus with an agricultural azole causes cross-resistance to medical azoles and potentiates caspofungin efficacy. *Antimicrob. Agents Chemother.* **2007**, *51* (10), 3672−6.
(26) Steva, H.; Clerjeau, M. Cross-resistance to sterol biosynthesis inhibitor fungicides in strains of Uncinula necator isolated in France and Portugal. *Meded. Fac. Landbouwwet. Rijksuniv. Gent* **1990**, *55*, 983−988.
(27) Lago, M.; Aguiar, A.; Natário, A.; Fernandes, C.; Faria, M.; Pinto, E. Does fungicide application in vineyards induce resistance to medical azoles in Aspergillus species? Environ. *Environ. Monit. Assess.* **2014**, *186* (9), 5581−93.
(28) Laxminarayan, R.; Mills, A. J.; Breman, J. G.; Measham, A. R.; Alleyne, G.; Claeson, M.; Jha, P.; Musgrove, P.; Chow, J.; Shahid-Salles, S.; Jamison, D. T. Advancement of global health: key messages from the Disease Control Priorities Project. *Lancet* **2006**, *367*, 1193−1208.
(29) Faria-Ramos, I.; Neves-Maia, J.; Ricardo, E.; Santos-Antunes, J.; Silva, A. T.; Costa-de-Oliveira, S.; Cantón, E.; Rodrigues, A. G.; Pina-Vaz, C. Species distribution and in vitro antifungal susceptibility profiles of yeast isolates from invasive infections during a Portuguese multicenter survey. *Eur. J. Clin. Microbiol. Infect. Dis.* **2014**, *33* (12), 2241−7.
(30) Perea, S.; Lopez-Ribot, J. L.; Kirkpatrick, W. R.; et al. Prevalence of molecular mechanisms of resistance to azole antifungal agents in *Candida albicans* strains displaying high-level fluconazole resistance isolated from human immunodeficiency virus-infected patients. *Antimicrob. Agents Chemother.* **2001**, *45*, 2676−2684.
(31) Snelders, E.; Huis in 't Veld, R. A.; Rijs, A. J.; Kema, G. H.; Melchers, W. J.; Verweij, P. E. Possible environmental origin of resistance of *Aspergillus fumigatus* to medical triazoles. *Appl. Environ. Microbiol.* **2009**, *75* (12), 4053−4057.
(32) Costa-de-Oliveira, S.; Pina-Vaz, C.; Mendonca, D.; Gonçalves Rodrigues, A. A first Portuguese epidemiological survey of fungaemia in a university hospital. *Eur. J. Clin. Microbiol. Infect. Dis.* **2008**, *27*, 365−374.
(33) Snelders, E.; van der Lee, H. A. L.; Kuijpers, J. M.; Rijs, A. J. M. M.; Varga, J.; Samson, R. A.; Mellado, E.; et al. Emergence of azole resistance in *Aspergillus fumigatus* and spread of a single resistance mechanism. *PLoS Med.* **2008**, *5* (11), e219.
(34) Mellado, E.; Garcia-Effron, G.; Alcázar-Fuoli, l.; Melchers, W. J.; Verweij, P. E.; Cuenca Estrella, M.; Rodriguez-Tudela, J. L. A new *Aspergillus fumigatus* resistance mechanism conferring *in vitro* cross-resistance to azole antifungals involves a combination of *cyp5A* alterations. *Antimicrob. Agents Chemother.* **2007**, *51*, 1897−1904.
(35) Lagrou, K.; De Vleeschouwer, J.; Meerseman, W.; Dupont, L.; Verleden, G.; Melchers, W. J. G.; Verweij, P. E.; Maertens, J. Triazole resistance among clinical *Aspergillus fumigatus* isolates. *Proceedings of the 3th Advances Against Aspergillosis*; Miami Beach, FL, Jan 16−19, 2008.
(36) Arendrup, M. C.; Perkhofer, S.; Howard, S. J.; Garcia-Effron, G.; Vishukumar, A.; Perlin, D.; Lass-Flörl, C. Establishing in *vitro- in vivo* correlations for *Aspergillus fumigatus*: the challenge of azoles vs echinocandins. *Antimicrob. Agents Chemother.* **2008**, *52*, 3504−3511.
(37) Chryssanthou, E. *In vitro* susceptibility of respiratory isolates of *Aspergillus species* to itraconazole and amphotericin B acquired resistance to itraconazole. *Scand. J. Infect. Dis.* **1997**, *29*, 509−512.
(38) Dannaoui, E.; Borel, E.; Monier, M. F.; Piens, M. A.; Picot, S.; Persat, F. Acquired itraconazole resistance in *Aspergillus fumigatus*. *J. Antimicrob. Chemother.* **2001**, *47*, 333−340.
(39) Chowdhary, A.; Kathuria, S.; Randhawa, H. S.; Gaur, S. N.; Klaassen, C. H.; Meis, J. F. Isolation of multiple-triazole-resistant *Aspergillus fumigatus* strains carrying the TR/L98H mutations in the *cyp51* A gene in India. *J. Antimicrob. Chemother.* **2012**, *67* (2), 362−6.
(40) Rocchi, S.; Daguindau, E.; Grenouillet, F.; Deconinck, E.; Bellanger, A. P.; Garcia-Hermoso, D.; Bretagne, S.; Reboux, G.; Millon, L. Azole-resistant *Aspergillus fumigatus* isolate with the TR34/L98H mutation in both a fungicide-sprayed field and the lung of a hematopoietic stem cell transplant recipient with invasive aspergillosis. *J. Clin. Microbiol.* **2014**, *52* (5), 1724−6.
(41) Araujo, R.; Pina-Vaz, C.; Rodrigues, A. G. Susceptibility of environmental versus clinical strains of pathogenic Aspergillus. *Int. J. Antimicrob. Agents* **2007**, *29* (1), 108−11.
(42) Verweij, P. E.; Howard, S. J.; Melchers, W. J.; Denning, D. W. Azole-resistance in *Aspergillus*: proposed nomenclature and break-points. *Drug Resist. Updates* **2009**, *12*, 141−147.
(43) Faria-Ramos, I.; Farinha, S.; Neves-Maia, J.; Tavares, P. R.; Miranda, I. M.; Estevinho, L. M.; Pina-Vaz, C.; Rodrigues, A. G.; et al. Development of cross-resistance by *Aspergillus fumigatus* to clinical azoles following exposure to prochloraz, and agricultural azole. *BMC Microbiol.* **2014**, *14*, 155.
(44) Direcção-Geral de Alimentação e Veterinária (DGAV). *Plano de Ação Nacional para o Uso Sustentável dos Produtos Fitofarmacêuticos. Estabelecimento e Implementação*; DGAV: Lisbon, Portugal, 2013; Vol. *1*, http://ec.europa.eu/food/plant/pesticides/sustainable_use_pesticides/docs/nap_portugal_pt.pdf.

DOI: 10.1021/acs.jafc.5b02728
J. Agric. Food Chem. 2015, 63, 7463−7468

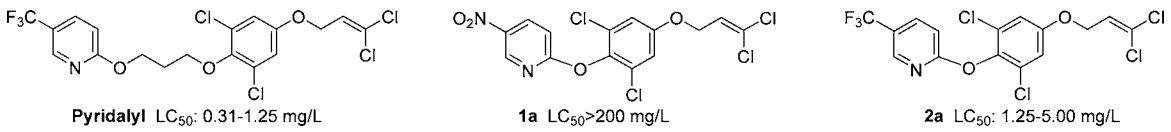

Figure 1. Pyridalyl, NO_2 and CF_3 analogue quantitative structure−activity profiles.

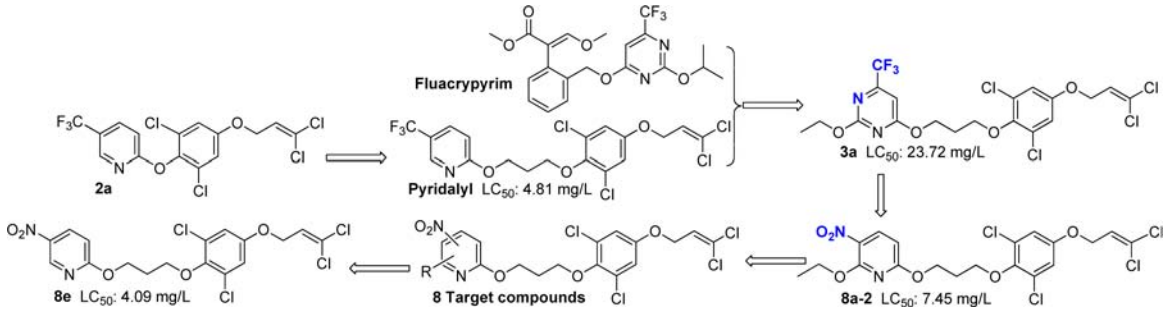

Figure 2. Design strategies of the target compounds containing nitropyridyl.

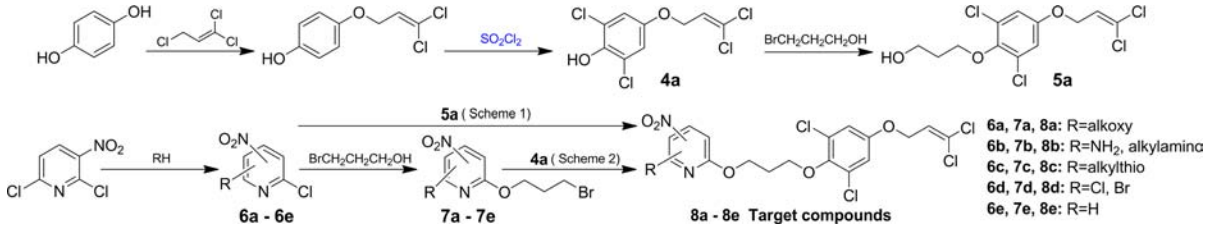

Figure 3. Synthetic pathways for the novel nitropyridyl-based dichloropropene ethers.

suggested that the trifluoromethyl group on the 5-position was required, our other works on nitropyridyl-based compounds indicated that hydrogen exhibited insecticidal activities similar or stronger than that with 6-alkoxy. Therefore, **8a-2** was optimized by replacing the ethoxy with hydrogen to give **8e**. Bioassay results indicated that **8e** exhibited insecticidal activities against major agricultural pests such as *M. separata*, *P. xylostella*, and *P. litura* at levels similar to that of Pyridalyl. The design strategies of all compounds are shown in Figure 2.

MATERIALS AND METHODS

Unless otherwise noted, reagents and solvents were used as received from commercial suppliers. NMR spectra were obtained with a Varian INOVA-300 spectrometer using tetramethylsilane (TMS) as the internal standard and deuteriochloroform ($CDCl_3$) as the solvent. LC-MS were recorded with an Agilent 1260/6120 series and GC-MS with an Agilent 7890-5975C series. Uncorrected melting points were taken in a WRS-1A digital melting points apparatus. Elemental analyses were obtained with a Vario EL III from Elementar.

Synthesis. The general synthetic methods for the target compounds **8** are shown in Figure 3. Representative procedures are given below. Yields were not optimized. All reactions were carried out under a protective atmosphere of dry nitrogen or utilizing a calcium chloride tube.

*2,6-Dichloro-4-(3,3-dichloroallyloxy)phenol (**4a**).* 1,1,3-Trichloropropene (27.6 g, 190 mmol) in *N*,*N*-dimethylformamide (DMF; 30 mL) was added dropwise to a solution of hydroquinone (23.1 g, 210 mmol) and potassium carbonate (30.4 g, 220 mmol) in DMF (100 mL) at room temperature. After 6−8 h of stirring, the reaction was poured into ice−water (500 mL) and extracted with ethyl acetate (2 × 250 mL). The combined ethyl acetate extracts were washed with water and dried with anhydrous sodium sulfate. Then the solvent was removed using a rotary evaporator. The residue was separated by silica gel column chromatography with petroleum ether and ethyl acetate (10:1 by volume) as eluant to give 99.5% (GC) 4-((3,3-dichloroallyl)-oxy)phenol, 26.2 g (63.0%). Sulfuryl dichloride (35.0 g, 260 mmol) was added dropwise to the solution of 4-((3,3-dichloroallyl)oxy)-phenol (26.2 g, 120 mmol) and triethylamine (0.70 g, 7.0 mmol) in toluene (150 mL) at 90−100 °C. The reaction was stirred for 8−10 h. After the extra sulfuryl dichloride was removed, the resulting solution was poured into ice−water (500 mL), washed with saturated sodium hydrogen carbonate solution and then water, and dried with anhydrous sodium sulfate. The solvent was removed to give 95.5% (GC) **4a**: 26.6 g (73.7%).

*2,6-Dichloro-4-(3,3-dichloroallyloxy)phenyl 3-Hydroxypropyl Ether (**5a**).* 3-Bromopropanol (2.02 g, 14.5 mmol) in DMF (20 mL) was added dropwise to a solution of **4a** (2.88 g, 10 mmol) and potassium carbonate (2.00 g, 14.5 mmol) in DMF (60 mL) at room temperature. The reaction mixture was stirred for 26−28 h, after which the reaction was poured into ice−water (150 mL) and extracted with ethyl acetate (2 × 100 mL). The combined ethyl acetate extracts were washed with water and dried with anhydrous sodium sulfate. Then the solvent was removed using a rotary evaporator. The residue was separated by silica gel column chromatography with petroleum ether and ethyl acetate (10:1 by volume) as eluant to give 96.0% (GC) **5a**: 2.14 g (59.4%).

*6-Chloro-2-ethoxy-3-nitropyridine (**6a-2**).* Ethanol (2.40 g, 52.0 mmol) in toluene (10 mL) was added dropwise to a solution of 60% sodium hydride (4.48 g, 112 mmol) in toluene (80 mL) at 0 °C and stirred for 30−45 min. 2,6-Dichloro-3-nitropyridine (10.0 g, 52.0 mmol) in toluene (40 mL) was added dropwise to the reaction mixture. After 2−4 h of stirring at room temperature, the reaction was poured into ice−water (250 mL) and extracted with toluene (2 × 150 mL). The combined toluene extracts were washed with water and dried with anhydrous sodium sulfate. The solvent was removed to give a residue, 9.80 g. Separation by silica gel column chromatography with petroleum ether and ethyl acetate (100:1−50:1 by volume) as eluant gave 95.2% (GC) **6a-2**: 7.92 g (71.7%); GC-MS (EI, 70 eV) (*m*/*z*) 202 (50% M^+), 174 (70% $M^+ - 28$), 158 (100% $M^+ - 44$), 117 (60% $M^+ - 85$); ^{1}H NMR ($CDCl_3$) δ 1.45 (3H, t, J = 7.2 Hz, CH_3), 4.55 (2H, q, J = 7.2 Hz, CH_2), 7.01 (1H, d, J = 8.1 Hz, Py H), 8.24 (1H, d, J = 8.1 Hz, Py H).

DOI: 10.1021/acs.jafc.5b02279
J. Agric. Food Chem. 2015, 63, 7469−7475

*2-Chloro-6-ethoxy-3-nitropyridine (**6a′-2**).* Sodium ethanolate (4.10 g, 60 mmol) in ethanol (20 mL) was added dropwise to a solution of 2,6-dichloro-3-nitropyridine (11.6 g, 60 mmol) in ethanol (40 mL) at 0 °C. After 4−5 h of stirring at room temperature, the reaction was poured into ice−water (350 mL) and extracted with ethyl acetate (2 × 100 mL). The combined ethyl acetate extracts were washed with water and dried with anhydrous sodium sulfate. Then the solvent was removed using a rotary evaporator to give a residue, which was then recrystallized from petroleum ether and ethyl acetate to give 97.0% (GC) **6a′-2**: 5.62 g (44.7%); GC-MS (EI, 70Ev) (*m*/*z*) 202 (30% M^+), 187 (100% $M^+ - 15$), 174 (60% $M^+ - 28$), 158 (60% $M^+ - 44$), 117 (30% $M^+ - 85$); ^{1}H NMR δ($CDCl_3$) 1.40 (3H, t, *J* = 7.2 Hz, CH_3), 4.44 (2H, q, *J* = 7.2 Hz, CH_2), 6.74 (1H, d, *J* = 8.7 Hz, Py H), 8.24 (1H, d, *J* = 8.7 Hz, Py H).

*2-(3-Bromopropoxy)-6-ethoxy-3-nitropyridine (**7a′-2**).* **6a′-2** (2.02 g, 10 mmol) in tetrahydrofuran (THF; 20 mL) was added dropwise to a solution of 60% sodium hydride (0.52 g, 13 mmol) in THF (30 mL) at 0 °C and stirred for 15−30 min. 3-Bromopropanol (1.39 g, 10.0 mmol) in THF (15 mL) was then added dropwise. The reaction mixture was stirred at room temperature for 2−3 h, after which the reaction was treated as described for the synthesis of **5a**. The residue was separated by silica gel column chromatography with petroleum ether and ethyl acetate (50:1 by volume) as eluant to give 98.9% (GC) **7a′-2**: 2.00 g (64.9%); GC-MS (EI, 70 eV) (*m*/*z*) 304 (60% M^+), 289 (15% $M^+ - 15$), 169 (100% $M^+ - 135$), 156 (75% $M^+ - 148$), 140 (65% $M^+ - 164$); ^{1}H NMR ($CDCl_3$) δ 1.40 (3H, t, *J* = 7.05 Hz, CH_3), 2.36−2.42 (2H, m, CH_2), 3.67 (2H, t, *J* = 6.15 Hz, CH_2), 4.43 (2H, q, *J* = 7.1 Hz, CH_2), 4.62 (2H, t, *J* = 6.0 Hz, CH_2), 6.35 (1H, d, *J* = 8.7 Hz, Py H), 8.32 (1H, d, *J* = 8.7 Hz, Py H).

*2,6-Dichloro-4-(3,3-dichloroallyloxy)phenyl 3-[6-Ethoxy-5-nitro-2-pyridyloxy] propyl Ether (**8a-2**).* **5a** (0.88 g, 2.54 mmol) in THF (10 mL) was added dropwise to a solution of **6a-2** (0.52 g, 2.54 mmol) and 60% sodium hydride (0.12 g, 3.00 mmol) in THF (20 mL) at 0 °C and then stirred for 8−10 h at 20−30 °C. The reaction mixture was poured into ice−water (120 mL) and extracted with ethyl acetate (2 × 50 mL). The combined ethyl acetate extracts were washed with water and dried with anhydrous sodium sulfate. After the solvent was removed, the crude product was separated by silica gel column chromatography using petroleum ether and ethyl acetate (200:1 to 100:1 by volume) as eluant to give 95.7% (HPLC) **8a-2** as an oil: 0.38 g, yield 28.0%; LC-MS (APCI, Pos) (*m*/*z*) 511 ($M^+ + 1$); calcd for $C_{19}H_{18}Cl_4N_2O_6$ C 44.56, H 3.54, N 5.47; found C 44.65, H 3.59, N 5.42; ^{1}H NMR ($CDCl_3$, 300 MHz) δ 1.45 (3H, t, *J* = 7.1 Hz), 2.26−2.34 (2H, m), 4.10 (2H, t, *J* = 5.9 Hz), 4.54 (2H, q, *J* = 7.1 Hz), 4.56 (2H, t, *J* = 6.3 Hz), 4.57 (2H, d, *J* = 6.6 Hz), 6.09 (1H, t, *J* = 6.2 Hz), 6.34 (1H, d, *J* = 8.7 Hz), 6.84 (2H, s), 8.31 (1H, d, *J* = 9.0 Hz); ^{13}C NMR ($CDCl_3$, 75 MHz) δ 14.39, 29.34, 63.76, 64.15, 65.41, 69.66, 115.19, 120.55, 124.43, 124.93, 126.53, 129.58, 138.61, 145.53, 154.00, 157.03, 164.93.

*2,6-Dichloro-4-(3,3-dichloroallyloxy)phenyl 3-[6-Ethoxy-3-nitro-2-pyridyloxy]propyl Ether (**8a′-2**).* **7a′-2** (1.62 g, 5.30 mmol) in THF (10 mL) was added dropwise to a solution of 60% sodium hydride (0.26 g, 6.50 mmol) and **4a** (1.53 g, 5.30 mmol) in THF (20 mL) at 0 °C. The reaction mixture was stirred for 25−30 min at 0 °C and then for 10−12 h at 20−30 °C. The reaction was then treated as described for the synthesis of **8a-2** to give 96.6% (HPLC) **8a′-2** as an oil: 1.05 g, yield 37.6%; LC-MS (APCI, Pos)(m/z0) 511 (M^++1); calc for $C_{19}H_{18}Cl_4N_2O_6$ C 44.56, H 3.54, N 5.47; found C 44.59, H 3.50, N 5.52; ^{1}H NMR ($CDCl_3$, 300 MHz) δ 1.39 (3H, t, *J* = 7.1 Hz), 2.31−2.39 (2H, m), 4.17 (2H, t, *J* = 5.9 Hz), 4.41 (2H, q, *J* = 7.1 Hz), 4.56 (2H, d, *J* = 6.3 Hz), 4.75 (2H, t, *J* = 6.3 Hz), 6.09 (1H, t, *J* = 6.2 Hz), 6.32 (1H, d, *J* = 8.7 Hz), 6.82 (2H, s), 8.31 (1H, d, *J* = 8.7 Hz); ^{13}C NMR ($CDCl_3$, 75 MHz) δ 14.36, 29.37, 63.45, 64.27, 65.44, 69.73, 102.56, 115.18, 124.50, 124.90, 126.26, 129.58, 138.54, 145.54, 154.00, 157.03, 165.05.

The syntheses of **8a′-1**, **8a-3**−**8a-10**, **8b-1**−**8b-10**, **8c′-1**, **8c-2**−**8c-4**, **8d-1**−**8d-4**, **8e′**, and **8e** with ≥95.0% purity (HPLC) were similar to that of **8a-2** or **8a′-2**, and their structures are supported by spectroscopic data in Tables 1 and 2.

Biological Assay.[11−14] *Test Insects.* Stock colonies of test insects were reared in a conditioned room maintained at 25 (±1)°C, 60 (±5)% relative humidity, and 14:10 h light/dark.

Test Compounds. Stock solution of every test compound was prepared in DMF or acetone at a concentration of 1.0 g L^{-1} and then diluted to the required test concentrations (1−500 mg L^{-1}) with water containing 0.2% Tween 80.

Activity against M. separats. Ten third-instar of *M. separata* and five pieces of corn fragments were placed in a Petri dish and sprayed with test solutions using a potter sprayer. After air-drying, the dishes were kept in a room for normal cultivation. Mortality was determined 72 h after treatment. A control group was tested with the solvent only. The test was run three times, and results were averaged. Data were subjected to probit analysis, and the median lethal concentrations (LC_{50}) value of tested compounds were calculated (95% FL).[15]

Activity against Plutella xylostella or Prodenia litura. Cabbage leaves were dipped into test solutions for 10 s. After air-drying, five leaves were put into a Petri dish with 10 third-instar of test insects, kept in a room for normal cultivation. Mortality was assessed 72 h after treatment. A control group was tested with the solvent only. The test was run four times. Data were treated as described for *M. separata*.

RESULTS AND DISCUSSION

Chemistry. The synthesis scheme shown in Figure 3 provides moderate yields of the test compounds. The structures of all synthesized compounds were analyzed and confirmed by ^{1}H NMR and MS. Due to the structural similarity of compounds **8**, only some representative compounds, such as **8a′-1**, **8a-2**, **8a′-2**, **8b-2**, **8e**, and **8e′**, were analyzed and confirmed by ^{13}C NMR and **8a-2**, **8a′-2** and **8e** by elemental analysis. Table 1 summarizes the chemical structures, MS data, and physical characteristics of compounds **8**. NMR and elemental analysis data are listed in Table 2.

Due to the presence of the nitro group on the pyridyl ring, we expected to observe positional isomers on compounds **8**. Selective synthesis of positional isomers of **6** can be achieved by selecting different solvents. In aprotic solvent, the reaction of 2,6-dichloro-3-nitropyridine and nucleophilic alcohol yields mostly 3-NO_2 product **6a′**; in protic solvent, however, the same reaction gives mainly 5-NO_2 product **6a**. Also in protic solvent, the reaction of 2,6-dichloro-3-nitropyridine and nucleophilie amine or thiol gives 3-NO_2 product **6b′** or **6c′**.

Positional isomers may be differentiated with ^{1}H NMR data. Because NO_2 is a strongly electron-withdrawing group, when NO_2 is on the ortho position of $-OCH_2CH_2CH_2O-$ (defined as 3-NO_2), the maximum value of δ_H in $-OCH_2CH_2CH_2O-$ is usually ≥4.75 ppm; however, when NO_2 is on the para position of $-OCH_2CH_2CH_2O-$ (defined as 5-NO_2), the maximum value of δ_H in $-OCH_2CH_2CH_2O-$ is often <4.75 ppm. For example, δ_H = 4.56 for **8a-2** and δ_H = 4.75 for **8a′-2**.

Another way to identify positional isomers of compounds **8** is to study the ^{1}H NMR or GC-MS of their corresponding intermediate **6** and **7**. In ^{1}H NMR, the hydrogen on the ortho position of chlorine on the pyridyl ring has a lower chemical shift value than the hydrogen on the ortho position of alkoxy, alkylthio, or alkylamino on the pyridyl ring. For example, δ_H = 7.01 for **6a-2** and δ_H = 6.74 for **6a′-2**. In GC-MS, when the alkoxy locates between the nitro group and the nitrogen atom in the pyridyl ring, the base peak is usually $M^+ -$ alkoxy + 1 or $M^+ -$ alkyl + 1 because alkoxy or alkyl can be removed easily. For example, the base peak of **6a-2** is 158 ($202 - OCH_2CH_3 + 1$), but the base peak of **6a′-2** is 187 ($202 - CH_3$).

Insecticidal Activity. All compounds prepared were evaluated for initial activity against *M. separata* at 100 mg/L by typical assay above, and LC_{50} was calculated through further

DOI: 10.1021/acs.jafc.5b02279
J. Agric. Food Chem. 2015, 63, 7469−7475

Table 1. Chemical Structures, MS, Physical Characteristics, Insecticidal Activity against *M. separata* at 100 mg/L, and LC_{50} (3 Days) of Compounds 8

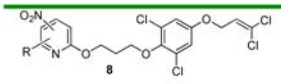

No.	NO_2	R	formula	MS	mp (°C)	100 mg/L	20 mg/L	regression equation	r	LC_{50} mg/L
8a'-1	3-NO_2	6-OCH_3	$C_{18}H_{16}Cl_4N_2O_6$	496	oil	0[a]	0	-[c]	-	> 40
8a-2	5-NO_2	6-OCH_2CH_3	$C_{19}H_{18}Cl_4N_2O_6$	510	oil	100	100	Y=2.6262+2.77x	0.993	7.45
8a'-2	3-NO_2	6-OCH_2CH_3	$C_{19}H_{18}Cl_4N_2O_6$	510	oil	0[a]	0	-	-	> 40
8a-3	5-NO_2	6-$OCH_2CH_2CH_3$	$C_{20}H_{20}Cl_4N_2O_6$	524	oil	100	100	Y=-0.9779+4.5542x	0.9439	9.78
8a-4	5-NO_2	6-$OCH(CH_3)_2$	$C_{20}H_{20}Cl_4N_2O_6$	524	oil	100	100	Y=0.1333+6.5171x	0.9528	5.58
8a-5	5-NO_2	6-$O(CH_2)_3CH_3$	$C_{21}H_{22}Cl_4N_2O_6$	538	viscous solid	100	100	Y=1.5059+3.7473x	0.9974	8.58
8a-6	5-NO_2	6-$OCHCH_3CH_2CH_3$	$C_{21}H_{22}Cl_4N_2O_6$	538	oil	100	9[a]	-	-	> 20
8a-7	5-NO_2	6-$OC(CH_3)_3$	$C_{21}H_{22}Cl_4N_2O_6$	538	viscous solid	100	11	-	-	> 20
8a-8	5-NO_2	6-$O(CH_2)_4CH_3$	$C_{22}H_{24}Cl_4N_2O_6$	552	viscous solid	100	45	Y=1.4715+2.4428x	0.9988	27.83
8a-9	5-NO_2		$C_{22}H_{22}Cl_4N_2O_6$	550	oil	30	0	-	-	> 100
8a-10	5-NO_2		$C_{23}H_{24}Cl_4N_2O_6$	564	oil	80	17[b]	-	-	> 20
8b-1	5-NO_2	6-$NHCH_3$	$C_{18}H_{17}Cl_4N_3O_5$	495	81.7-83.2	100	100	Y=-0.0586+4.901x	0.9721	10.77
8b-2	5-NO_2	6-$NHCH_2CH_3$	$C_{19}H_{19}Cl_4N_3O_5$	509	36.0-36.9	100	100	Y=1.0031+4.6838x	0.9629	7.13
8b-3	5-NO_2	6-$NH(CH_2)_2CH_3$	$C_{20}H_{21}Cl_4N_3O_5$	523	63.2-64.5	100	27	Y=0.7600+3.4073x	1.0000	17.48
8b-4	5-NO_2	6-$NHCH(CH_3)_2$	$C_{20}H_{21}Cl_4N_3O_5$	523	62.4-66.1	100	100	Y=1.3962+3.7704x	0.9270	9.03
8b-5	5-NO_2	6-$NH(CH_2)_3CH_3$	$C_{21}H_{23}Cl_4N_3O_5$	537	61.6-64.1	100	30	Y=-2.8521+5.5649x	0.9738	25.76
8b-6	5-NO_2	6-$NHCH_2CH{=}CH_2$	$C_{20}H_{19}Cl_4N_3O_5$	521	52.6-55.0	100	43	Y=-2.5045+5.9926x	0.9534	17.88
8b-7	5-NO_2	6-$NHCH_2C{\equiv}CH$	$C_{20}H_{17}Cl_4N_3O_5$	519	76.4-97.4	100	53	Y=-1.9984+5.7114x	0.9699	16.80
8b-8	5-NO_2	6-NHC_6H_5	$C_{23}H_{19}Cl_4N_3O_5$	557	74.9-76.2	0[a]	0	-	-	> 40
8b-9	5-NO_2	6-$NHCH_2C_6H_5$	$C_{24}H_{21}Cl_4N_3O_5$	571	oil	100	37	Y=1.8561+2.5131x	0.9869	17.82
8b-10	5-NO_2	6-NH_2	$C_{17}H_{15}Cl_4N_3O_5$	481	yellow solid	100	< 50	Y=-1.0132+4.3627x	0.9037	16.47
8c'-1	3-NO_2	6-SCH_3	$C_{18}H_{16}Cl_4N_2O_5S$	512	89.9-91.1	20	0	-	-	> 100
8c-2	5-NO_2	6-SCH_2CH_3	$C_{19}H_{18}Cl_4N_2O_5S$	526	viscous solid	100	87	Y=2.9291+2.144x	0.9081	9.24
8c-3	5-NO_2	6-$S(CH_2)_2CH_3$	$C_{20}H_{20}Cl_4N_2O_5S$	540	viscous solid	100	73	Y=2.2714+2.6178x	0.9854	11.02
8c-4	5-NO_2	6-$SCH(CH_3)_2$	$C_{20}H_{20}Cl_4N_2O_5S$	540	oil	100	3.3	-	-	> 20
8d-1	5-NO_2	3-Cl	$C_{17}H_{13}Cl_5N_2O_5$	500	oil	100	100	Y=2.3223+2.9004x	0.9826	8.37
8d-2	5-NO_2	6-Cl	$C_{17}H_{13}Cl_5N_2O_5$	500	oil	0	0	-	-	> 100
8d-3	5-NO_2	3-Br	$C_{17}H_{13}BrCl_4N_2O_5$	544	viscous solid	100	-	Y=0.9814+2.8266x	0.9586	26.41
8d-4	5-NO_2	6-Br	$C_{17}H_{13}BrCl_4N_2O_5$	544	oil	0	0			> 500
8e	5-NO_2	H	$C_{17}H_{14}Cl_4N_2O_5$	466	oil	100	100	Y=3.2727+2.8259x	0.9888	4.09
8e'	3-NO_2	H	$C_{17}H_{14}Cl_4N_2O_5$	466	oil	-	-	Y=-0.5573+2.7648x	0.9657	102.3
Pyridalyl						100	100	Y=2.8967+3.0826x	0.9948	4.81

[a]40 mg/L. [b]12.5 mg/L. [c]No test.

assay in which five to six different concentrations were used and are listed in Table 1. A few representative compounds were evaluated against *P. xylostella* and *P. litura*, and LC_{50} values of **8a-2** and **8e** are listed in Table 3. The activities of Pyridalyl are also shown in Tables 1 and 3.

As shown in Table 1, all compounds **8** except **8a-9**, **8a-10**, **8d-2**, **8d-4**, and **8′** exhibit 100% insecticidal activity against *M. separata* at 100 mg/L, and some compounds have shown potent insecticidal activities when compared with commercial insecticides. For example, **8a-2**, **8a-4**, **8a-5**, **8b-2**, **8d-1**, and **8e** have LC_{50} (mg L^{-1}) values of 7.45, 5.58, 8.58, 7.13, 8.37, and 4.09, respectively. Particularly, the LC_{50} value of **8e** is at the same level as that of Pyridalyl.

Apparent Structure–Activity Relationship. The general structure of compounds **8** (Figure 3) was optimized through the R moiety and the position of the nitro group. Different choices of R and position of NO_2 can greatly affect insecticidal activity (Table 1).

When the nitro group was kept on the 5-position, the insecticidal activity against *M. separata* was influenced by the nature of the R group. Changing the R group from 6-alkoxy to 6-alkylamino or 6-alkylthio maintained or slightly reduced the insecticidal activity. For example, the insecticidal activities were correlated as follows: **8c-2** < **8b-2** ≈ **8a-2**, **8b-3** < **8c-3** < **8a-3**, **8c-4** < **8b-4** < **8a-4**. For 6-substituted analogues, the results in Table 1 show that a C_2–C_3 saturated alkyl chain was required for the development of optimal insecticidal activity, and there was no obvious relationship between activity and the number of carbon atoms in alkyl; for 3-substituted analogues, the insecticidal activities of the corresponding compounds increased. For example, the insecticidal activities of **8d-1** and **8d-3** were stronger than those of **8d-2** and **8d-4**, respectively; for R = H, the resulting compound **8e** showed the highest activity among compounds **8** and possessed levels of insecticidal activity comparable to that of Pyridalyl. When the position of the nitro group was changed from 5-NO_2 to 3-NO_2 and R was kept constant, the insecticidal activity of the corresponding compound decreased as illustrated by the orders **8a′-2** ≪ **8a-2** and **8e′** ≪ **8e**.

In general, for compounds **8** the activity order of NO_2 is 5-NO_2 ≫ 3-NO_2. The activity order of R is H > 6-$OCH(CH_3)_2$ > 6-OCH_2CH_3, 6-$NHCH_2CH_3$ > 6-$O(CH_2)_3CH_3$, 3-Cl > 6-$O(CH_2)_2CH_3$, 6-$NHCH(CH_3)_2$, 6-SCH_2CH_3 > 6-$NHCH_3$,

DOI: 10.1021/acs.jafc.5b02279
J. Agric. Food Chem. 2015, 63, 7469–7475

Table 2. ^{1}H NMR Data of the Synthesized Nitropyridyl-Based Dichloropropene Ethers

no.	^{1}H NMR ($CDCl_3$, 300 MHz) and ^{13}C NMR ($CDCl_3$, 75 MHz), δ; elemental analysis
8a′-1	^{1}H NMR: 2.34−2.40 (2H, m), 4.01 (3H, s), 4.12 (2H, t, J = 6.0 Hz), 4.56 (2H, d, J = 6.6 Hz), 4.79 (2H, t, J = 6.0Hz), 6.09 (1H, t, J = 6.3 Hz), 6.35 (1H, d, J = 9.0 Hz), 6.82 (2H, s), 8.32 (1H, d, J = 9.0 Hz); ^{13}C NMR: 29.40, 54.63, 64.35, 65.48, 69.74, 102.67, 115.25, 124.50, 124.90, 126.26, 129.69, 138.63, 145.69, 154.00, 157.05, 165.35
8a-3	^{1}H NMR: 1.04 (3H, t, J = 7.5 Hz), 1.84−1.91 (2H, m), 2.28−2.34 (2H, m), 4.12 (2H, t, J = 6.15 Hz), 4.46 (2H, t, J = 6.6 Hz), 4.58 (2H, d, J = 6.6 Hz), 4.67 (2H, t, J = 6.3 Hz), 6.11 (1H, t, J = 6.0 Hz), 6.34 (1H, d, J = 9.0 Hz), 6.82 (2H, s), 8.33 (1H, d, J = 8.7 Hz)
8a-4	^{1}H NMR: 1.44 (6H, d, J = 6.3 Hz), 2.26−2.34 (2H, m), 4.11 (2H, t, J = 5.85 Hz), 4.60 (2H, d, J = 6.3 Hz), 4.65 (2H, t, J = 4.2 Hz), 5.44−5.52 (1H, m), 6.11 (1H, t, J = 6.3 Hz), 6.32 (1H, d, J = 8.7 Hz), 6.81 (2H, s), 8.31 (1H, d, J = 8.7 Hz)
8a-5	^{1}H NMR: 0.95 (3H, t, J = 7.5 Hz), 1.48−1.55 (2H, m), 1.80−1.85 (2H, m), 2.28−2.32 (2H, m), 4.12 (2H, t, J = 6.0 Hz), 4.50 (2H, t, J = 6.6 Hz), 4.58 (2H, d, J = 6.3 Hz), 4.65 (2H, t, J = 6.3 Hz), 6.11 (1H, t, J = 6.3 Hz), 6.34 (1H, d, J = 8.7 Hz), 6.84 (2H, s), 8.32 (1H, d, J = 8.7 Hz)
8a-6	^{1}H NMR: 1.00 (3H, t, J = 7.5 Hz), 1.40 (3H, d, J = 6.6 Hz), 1.70−1.89 (2H, m), 2.26−2.34 (2H, m), 4.12 (2H, t, J = 6.0 Hz), 4.58 (2H, d, J = 6.3 Hz), 4.65 (2H, t, J = 6.3 Hz), 5.22−5.34 (1H, m), 6.11 (1H, t, J = 6.3 Hz), 6.32 (1H, d, J = 9.0 Hz), 6.84 (2H, s), 8.31 (1H, d, J = 8.7 Hz)
8a-7	^{1}H NMR: 1.68 (9H, s), 2.30−2.32 (2H, m), 4.13 (2H, t, J = 5.85 Hz), 4.57 (2H, d, J = 6.3 Hz), 4.62 (2H, t, J = 6.6 Hz), 6.11 (1H, t, J = 6.3 Hz), 6.31 (1H, d, J = 9.0 Hz), 6.84 (2H, s), 8.24 (1H, d, J = 8.7 Hz)
8a-8	^{1}H NMR: 0.92 (3H, t, J = 6.9 Hz), 1.39−1.59 (4H, m), 1.82−1.87 (2H, m), 2.28−2.32 (2H, m), 4.12 (2H, t, J = 6.0 Hz), 4.49 (2H, t, J = 6.6 Hz), 4.58 (2H, d, J = 6.6 Hz), 4.67 (2H, t, J = 6.3 Hz), 6.11 (1H, t, J = 6.3 Hz), 6.34 (1H, d, J = 8.7 Hz), 6.84 (2H, s), 8.32 (1H, d, J = 8.7 Hz)
8a-9	^{1}H NMR: 1.60−2.05 (8H, m), 2.26−2.36 (2H, m), 4.12 (2H, t, J = 5.85 Hz), 4.58 (2H, d, J = 6.0 Hz), 4.67 (2H, t, J = 6.45 Hz), 5.54−5.59 (1H, m), 6.11 (1H, t, J = 6.3 Hz), 6.31 (1H, d, J = 8.7 Hz), 6.84 (2H, s), 8.29 (1H, d, J = 9.0 Hz)
8a-10	^{1}H NMR:1.40−1.97 (10H, m), 2.25−2.33 (2H, m), 4.12 (2H, t, J = 5.85 Hz), 4.58 (2H, d, J = 5.7 Hz), 4.64 (2H, t, J = 6.45 Hz), 5.26−5.28 (1H, m), 6.11 (2H, t, J = 6.15 Hz), 6.31 (1H, d, J = 9.0 Hz), 6.84 (2H, s), 8.30 (1H, d, J = 8.7 Hz)
8b-1	^{1}H NMR: 2.22−2.34 (2H, m), 3.15(3H, d, J = 5.1 Hz), 4.12 (2H, t, J = 5.85 Hz), 4.58 (2H, d, J = 6.3 Hz), 4.69 (2H, t, J = 6.3 Hz), 6.05 (1H, t, J = 9.0 Hz), 6.12 (1H, t, J = 6.0 Hz), 6.84 (2H, s), 8.30 (1H, d, J = 9.0 Hz), 8.640 (1H, s)
8b-2	^{1}H NMR: 1.29 (3H, t, J = 7.2 Hz), 2.25−2.33 (2H, m), 3.60−3.69 (2H, m), 4.10 (2H, t, J = 6.0 Hz), 4.57 (2H, d, J = 6.3 Hz), 4.64 (2H, t, J = 6.3 Hz), 6.02 (1H, t, J = 9.3 Hz), 6.09 (1H, t, J = 6.3 Hz), 6.82 (2H, s), 8.27 (1H, d, J = 9.3 Hz), 8.65 (1H, s); ^{13}C NMR: 14.65, 29.31, 36.14, 63.75, 65.39, 69.82, 100.40, 115.14, 121.64, 124.44, 124.85, 129.59, 138.88, 145.56, 153.16, 153.93, 166.52; Anal. Calcd for $C_{19}H_{19}Cl_4N_3O_5$ C 44.64, H 3.75, N 8.22; found C 44.64, H 3.82, N 8.16
8b-3	^{1}H NMR: 1.00 (3H, t, J = 7.5 Hz), 1.65−1.75 (2H, m), 2.25−2.33 (2H m), 3.55−3.61 (2H, m), 4.13 (2H, t, J = 5.85 Hz), 4.57 (2H, d, J = 6.3 Hz), 4.64 (2H, t, J = 5.55 Hz), 6.03(1H, d, J = 9.3 Hz), 6.11(1H, t, J = 6.15 Hz), 6.84 (2H, s), 8.29 (1H, d, J = 9.3 Hz), 8.73 (1H, s)
8b-4	^{1}H NMR: 1.25 (6H, d), 2.25−2.34 (2H, m), 4.12 (2H, t, J = 6.0 Hz), 4.43−4.48 (1H, m), 4.58 (2H, d, J = 6.0 Hz), 4.66 (2H, t, J = 6.0 Hz), 6.03 (1H, d, J = 9.0 Hz), 6.12 (1H, t, J = 6.3 Hz), 6.84 (2H, s), 8.29 (1H, d, J = 9.3 Hz), 8.60 (1H, s)
8b-5	^{1}H NMR: 0.97 (3H, t, J = 7.2 Hz), 1.37−1.49 (2H, m), 1.62−1.72 (2H, m), 2.25−2.36 (2H, m), 3.57−3.65 (2H, m), 4.10 (2H, t, J = 6.0 Hz), 4.58 (2H, d, J = 6.0 Hz), 4.68 (2H, t, J = 6.0 Hz), 6.03 (1H, d, J = 9.3 Hz), 6.11 (1H, t, J = 6.15 Hz), 6.84 (2H, s), 8.29 (1H, d, J = 9.3 Hz), 8.72 (1H, s)
8b-6	^{1}H NMR: 2.26−2.32 (2H, m), 4.11 (2H, t, J = 5.85 Hz), 4.23−4.28 (2H, m), 4.57 (2H, d, J = 6.6 Hz), 4.65 (2H, t, J = 6.3 Hz), 5.16−5.31 (2H, m), 5.91−5.99 (1H, m), 6.06 (1H, d, J = 9.0 Hz), 6.11 (1H, t, J = 6.3 Hz), 6.84 (2H, s), 8.30 (1H, d, J = 9.0 Hz), 8.75 (1H, s)
8b-7	^{1}H NMR: 2.24 (1H, t, J = 2.4 Hz), 2.29−2.38 (2H, m), 4.12 (2H, t, J = 6.0 Hz), 4.38−4.40 (2H, m), 4.58 (2H, d, J = 6.0 Hz), 4.71 (2H, t, J = 6.3 Hz), 6.11 (1H, t, J = 6.3 Hz), 6.12 (1H, d, J = 9.0 Hz), 6.84(2H, s), 8.32 (1H, d, J = 9.0 Hz), 8.65 (1H, s)

J. Agric. Food Chem. 2015, 63, 7469−7475
DOI: 10.1021/acs.jafc.5b02279

Table 2. continued

no.	^{1}H NMR ($CDCl_3$, 300 MHz) and ^{13}C NMR ($CDCl_3$, 75 MHz), δ; elemental analysis
8b-8	^{1}H NMR: 2.25−2.39 (2H, m), 4.09 (2H, t, J = 5.85 Hz), 4.58 (2H, d, J = 6.3 Hz), 4.63 (2H, t, J = 6.45 Hz), 6.11 (1H, t, J = 6.15 Hz), 6.22 (1H, d, J = 9.0 Hz), 6.83 (2H, s), 7.23−7.67 (5H, m), 8.42 (1H, d, J = 9.0 Hz), 10.64 (1H, s)
8b-9	^{1}H NMR: 2.18−2.26 (2H, m), 4.07 (2H, t, J = 5.85 Hz), 4.57 (2H, t, J = 6.0 Hz), 4.58 (2H, d, J = 6.3 Hz), 4.81 (2H, d, J = 5.7 Hz), 6.09 (1H, d, J = 9.0 Hz), 6.10 (1H, t, J = 6.15 Hz), 6.84 (2H, s), 7.28−7.37 (5H, m), 8.30 (1H, d, J = 9.0 Hz), 9.02 (1H, s)
8b-10	^{1}H NMR: 2.25−2.33 (2H, m), 4.11 (2H, t, J = 5.7 Hz), 4.58 (2H, d, J = 6.6 Hz), 4.60 (2H, t, J = 5.7 Hz), 6.12 (1H, t, J = 6.6 Hz), 6.16 (1H, d, J = 9.3 Hz), 6.84 (2H, s), 8.30 (1H, d, J = 9.3 Hz)
8c′-1	^{1}H NMR: 2.34−2.38 (2H, m), 2.62 (3H, s), 4.19 (2H, t, J = 5.85 Hz), 4.59 (2H, d, J = 6.3 Hz), 4.85 (2H, t, J = 6.3 Hz), 6.11(1H, t, J = 6.3 Hz), 6.83 (2H, s), 6.88 (1H, d, J = 8.7 Hz), 8.17(1H, d, J = 8.7 Hz)
8c-2	^{1}H NMR: 1.38 (3H, t, J = 7.2 Hz), 2.30−2.36 (2H, m), 3.22 (2H, q, J = 7.2 Hz), 4.13 (2H, t, J = 5.85 Hz), 4.59 (2H, d, J = 6.3 Hz), 4.73 (2H, t, J = 6.3 Hz), 6.11 (1H, t, J = 6.3 Hz), 6.54 (1H, d, J = 9.0 Hz), 6.84 (2H, s), 8.41 (1H, d, J = 9.0 Hz)
8c-3	^{1}H NMR: 1.07 (3H, t, J = 7.5 Hz), 1.72−1.85 (2H, m), 2.28−2.36 (2H, m), 3.18 (2H, t, J = 7.2 Hz), 4.14 (2H, t, J = 6.3 Hz), 4.58 (2H, d, J = 6.0 Hz), 4.72 (2H, t, J = 6.3 Hz), 6.11 (1H, t, J = 6.3 Hz), 6.45 (1H, d, J = 9.0 Hz), 6.84 (2H, s), 8.40 (1H, d, J = 9.0 Hz)
8c-4	^{1}H NMR: 1.43 (6H, d, J = 6.9 Hz), 2.28−2.36 (2H, m,), 4.07−4.17 (1H, m,), 4.13 (2H, t, J = 5.7 Hz), 4.58 (2H, d, J = 6.6 Hz), 4.72 (2H, t, J = 6.45 Hz), 6.11 (1H, t, J = 6.3 Hz), 6.50 (1H, d, J = 9.0 Hz), 6.85 (2H, s), 8.40 (1H, d, J = 9.0 Hz)
8d-1	^{1}H NMR: 2.36−2.41 (2H, m), 4.18 (2H, t, J = 6.0 Hz), 4.68 (2H, d, J = 6.3 Hz), 4.82 (2H, t, J = 6.0 Hz), 6.17 (1H, t, J = 6.3 Hz), 6.84 (2H, s), 8.45 (1H, d, J = 2.7 Hz), 8.99 (1H, d, J = 2.4 Hz)
8d-2	^{1}H NMR: 2.30−2.38 (2H, m), 4.18 (2H, t, J = 6.0 Hz), 4.57 (2H, d, J = 6.0 Hz), 4.80 (2H, t, J = 6.3 Hz), 6.11 (1H, t, J = 6.3 Hz), 6.83 (2H, s), 7.02 (1H, d, J = 8.1 Hz), 8.26 (1H, d, J = 8.1 Hz)
8d-3	^{1}H NMR: 2.27−2.35 (2H, m), 4.13 (2H, t, J = 6.0 Hz), 4.61 (2H, d, J = 6.3 Hz), 4.69 (2H, t, J = 6.3 Hz), 6.14 (1H, t, J = 6.2 Hz), 6.82 (2H, s), 8.61 (1H, d, J = 2.7 Hz), 8.99 (1H, d, J = 2.7 Hz)
8d-4	^{1}H NMR: 2.30−2.40 (2H, m), 4.18 (2H, t, J = 6.0 Hz), 4.57 (2H, d, J = 6.3 Hz), 4.80 (2H, t, J = 6.0 Hz), 6.11 (1H, t, J = 6.0 Hz), 6.82 (2H, s), 7.22 (1H, d, J = 8.4 Hz), 8.13 (1H, d, J = 8.1 Hz)
8e′	^{1}H NMR: 2.30−2.38 (2H, m), 4.18 (2H, t, J = 6.0 Hz), 4.57 (2H, d, J = 6.3 Hz), 4.81(2H, t, J = 6.0 Hz), 6.09 (1H, t, J = 6.3 Hz), 6.82 (2H, s), 7.01(1H, dd, J = 8.1, 4.8 Hz), 8.25 (1H, dd, J = 8.1, 1.8 Hz), 8.39 (1H, dd, J = 4.8, 1.8 Hz); ^{13}C NMR: 29.41, 64.15, 65.45, 69.74, 115.18, 116.34, 124.51, 124.89, 129.70, 133.95, 134.91, 145.74, 153.43, 153.93, 156.28
8e	^{1}H NMR: 2.28−2.36 (2H, m), 4.12 (2H, t, J = 6.0 Hz), 4.57 (2H, d, J = 6.3 Hz), 4.70 (2H, t, J = 6.3 Hz), 6.09 (1H, t, J = 6.3 Hz), 6.82 (1H, d, J = 9.0 Hz), 6.83 (2H, s), 8.34 (1H, dd, J = 9.0 Hz, 2.7 Hz), 9.09 (1H, d, J = 2.7 Hz); ^{13}C NMR: 29.39, 64.29, 65.40, 69.74, 111.22, 115.16, 124.43, 124.96, 129.66, 133.85, 139.30, 144.88, 145.62, 153.97, 167.05; Anal. Calcd for $C_{17}H_{14}Cl_4N_2O_5$ C 43.62, H 3.01, N 5.98; found C 43.64, H 3.00, N 6.00.

DOI: 10.1021/acs.jafc.5b02279
J. Agric. Food Chem. 2015, 63, 7469−7475

Table 3. LC_{50} against *P. xylostella* and *P. litura* of 8a-2, 8e, and Pyridalyl (3 Days)

no.	$Y = a + bx$	r	LC_{50}(mg/L)
	P. xylostella		
8a-2	$Y = 2.6262 + 2.77x$	0.993	7.07
8e	$Y = 4.0618 + 1.4006x$	0.9964	4.68
pyridyl	$Y = 3.9255 + 1.6996x$	0.9880	4.29
	P. litura		
8a-2	$Y = -3.1505 + 4.6849x$	0.9659	54.92
8e	$Y = 2.8096 + 2.0033x$	0.9734	11.66
pyridyl	$Y = 2.8738 + 2.1177x$	0.9942	10.07

6-$S(CH_2)_2CH_3$ > 3-NH_2, 6-$NHCH_2CH{\equiv}CH$, 6-$NH(CH_2)_2CH_3$, 6-$NHCH_2CH{=}CH_2$, 6-$NHCH_2C_6H_5$.

The above results demonstrate that besides the trifluoromethyl group in Pyridalyl,[6] a nitro group on the 5-position of the pyridyl ring is also viable for the development of optimal insecticidal activity when the chain between the phenyl ring and the pyridyl ring is $-OCH_2CH_2CH_2O-$. Further studies on the biological activity and structure−activity relationships of this series of compounds are in progress.

Aiping Liu[†,§]
Wanqi Yu[#]
Minhua Liu[†]
Jianjun Bai[†]
Weidong Liu[†]
Xingping Liu[†]
Hui Pei[†]
Li Hu[†]
Mingzhi Huang*[,†,⊥]
Xiaoguang Wang*[,†]

[†]National Engineering Research Center for Agrochemicals, Hunan Research Institute of Chemical Industry, Changsha 410007, People's Republic of China
[§]Hunan Province Key Laboratory for Agrochemicals, Changsha 410014, People's Republic of China
[#]Department of Chemistry, Carleton College, Northfield, Minnesota 55057, United States
[⊥]Hunan Haili Chemical Industry Company Ltd., Changsha 410007, People's Republic of China

AUTHOR INFORMATION

Corresponding Authors

*(M.Z. Huang) Phone: 86-731-85357883. E-mail: huang-mz@163.com.
*(X.G. Wang) Phone: 86-731-85357859. E-mail: Wang5999@163.com.

Funding

Financial support was provided by the National Natural Science Foundation of China (21272062 and 21572050).

Notes

The authors declare no competing financial interest.

REFERENCES

(1) Picardi, P.; Massardo, P.; Bettarini, F.; Longoni, A. New chlorinated juenile hormone analoguse and their activity. *Pestic. Sci.* **1980**, *11*, 423−431.
(2) Quistad, B. G.; Cerf, C. D.; Kramer, J. S.; Bergot, B. J.; Schooley, A. D. Design of novel insect and juvenile hormones: allylic alcohol derivatives. *J. Agric. Food Chem.* **1985**, *33*, 47−50.
(3) Wei, T. L.; Xu, M. C.; Liu, X. P.; Pei, H.; Zuo, J. J.; Yu, Y. Y.; Xiang, J.; Lin, X. M.; Liu, A. P. Synthesis and insecticidal activity of dichloroallyl ethers containing pyrimidine group. *Fine Chem. Intermediates* **2012**, *42* (1), 14−17.
(4) Sakamoto, N.; Matsuo, S.; Suzuki, M.; Hirose, T.; Tsushima, K.; Umeda, K. Prepartion of dihalopropene insecticides and acaricides. European Patent Application EP 785923, 1997.
(5) Saito, S.; Isayama, S.; Sakamoto, N.; Umeda, K.; Kasamatsu, K. Pyridalyl: a novel insecticidal agent for controlling lepidopterous pests. *Proceedings, Brighton Crop Protection Conference—Pests and Diseases*; BCPC: Farnham, Surrey, UK, 2002; pp 33−38
(6) Sakamoto, N.; Saito, S.; Hirose, T.; Suzuki, M.; Matsuo, S.; Izumi, K.; Nagatomi, T.; Ikegami, H.; Umeda, K.; Tsushima, K.; Matsuo, N. The discovery of pyridalyl: a novel insecticidal agent for controlling lepidopterous pests. *Pest Manage. Sci.* **2004**, *60*, 25−34.
(7) Sakamoto, N.; Suzuki, M.; Tsushima, K.; Umeda, K. Preparation of substituted phenyl-containing dihalopropene insecticides and acaricides. European Patent Application EP 722430, 1996.
(8) Sakamoto, N.; Suzuki, M.; Nagatomi, T.; Tsushima, K.; Umeda, K. Preparation of dihalopropene aryl ethers as insecticides and acaricides. European Patent Application EP 648729, 1995.
(9) Welch, J. T.; Eswarakrishnan, S. *Fluorine in Bioorganic Chemistry*, 10th ed.; Wiley: New York, 1991.
(10) Banks, R. E., Smart, B. E., Tatlow, J. C., Eds. *Organofluorine Chemistry: Principles and Commercial Applications*, 10th ed.; Plenum Press: New York, 1994.
(11) Liu, A. P.; Ou, X. P.; Huang, M. Z.; Wang, X. G.; Liu, X. P.; Wang, Y. J.; Chen, C.; Yao, J. R. Synthesis and insecticidal activities of novel oxime-ether pyrethroids. *Pest Manage. Sci.* **2005**, *61*, 166−170.
(12) Liu, A. P.; Wang, X. G.; Ou, X. M.; Huang, M. Z.; Chen, C.; Liu, S. D.; Huang, L.; Liu, X. P.; Zhang, C. L.; Zhen, Y. Q.; Ren, Y. G.; He, L.; Yao, J. R. Synthesis and fungicidal activities of novel Bis-(trifluoromethyl)phenyl-based strobilurins. *J. Agric. Food Chem.* **2008**, *56*, 6562−6566.
(13) Liu, A. P.; Wang, X. G.; Chen, C.; Pei, H.; Mao, C. H.; Wang, Y. J.; Liu, X. P.; Hu, Z. B.; Huang, L.; He, H. J.; Ou, X. M.; Huang, M. Z.; Yao, J. R. The discovery of HNPC-A3066: a novel strobilurin acaricide. *Pest Manage. Sci.* **2009**, *65*, 229−234.
(14) Liu, A. P.; Wang, X. G.; Ou, X. M.; Huang, M. Z.; Pei, H.; Liu, X. P.; Liu, S. D. The discovery of insecticide sufluoxime. *Fine Chem. Intermediates* **2011**, *41* (5), 1−6.
(15) Bliss, C. The calculation of the dosage-mortality curve. *Ann. Appl. Biol.* **1935**, *22*, 134−167.

DOI: 10.1021/acs.jafc.5b02279
J. Agric. Food Chem. 2015, 63, 7469−7475

Table 1. Pear Cultivars Studied and Resistance to *Psylla pyri*

Cultivar	Country of Origin	Pedigree	Ripening	Resistance
		EUROPEAN CULTIVARS (*Pyrus communis*)		
Bella di Giugno	Italy	unknown	−50	Moderately resistant
Turandot	Italy	Guyot x Bella di Giugno	−35	Susceptible
Moldovàs early	Moldovas autochthonous	unknown	−29	Moderately- high resistant
Coscia	Italy	unknown	−25	Moderately resistant
Ilinjača	Serbian autochthonous	unknown	−25	Moderately resistant
Carmen	Italy	Guyot x Bella di Giugno	−22	Moderately resistant
Butirra precoce Morettini	Italy	Coscia x Williams'	−21	Susceptible
Precoce de Trevoux	France	unknown	−19	Susceptible
Santa Maria	Italy	Williams' x Coscia	−15	Highly susceptible
Williams'	England	unknown	20th August	Susceptible
Jeribasma	Serbian autochthonous	unknown	25	Higher resistant
Abbé Fétel	France	unknown	26	Moderately resistant
Packhams Triumph	Australia	Uvedale's St. Germain x Williams'	34	Susceptible
Beurre Bosc	Belgium	unknown	36	Susceptible
Alexander Lucas	France	Chance seedling	40	Moderately high resistant
Poire de Cure	France	unknown	47	Moderately resistant
		ORIENTAL PEARS (*Pyrus pyrifolia*)		
Niitaka	Japan	Amanogawa x Immamura-Aki	+25	Very high resistant
Kumoi	Japan	Ishiiwase x Yakumo	+10	Very high resistant
Chojuro	Japan	Chance seeedling	+21	Very high resistant
Shinsui	Japan	Kikusui x Kimizuka wase	+2	Very high resistant
Nijisseiki	Japan	Chance seeedling	+10	Very high resistant
Kieffer	USA	*P. pyrifolia* x Williams'	+50	Very high resistant

and development of the insects.[15] Thus, the composition of single polyphenols in plant tissues may be influenced by nutrition, cultivars, rootstock, growing technology, and pathogen attack.[16,17] However, Mikulič Petkovšek et al.[18] found that leaf development had no effect on polyphenolic content. In pear fruit, the predominant phenolic constituents are chlorogenic, caffeic, *p*-coumaroylquinic and *p*-coumaric acids, arbutin, and a number of procyanidins and flavonol glycosides.[19]

Plant resistance to phytophagous insects[20] can be achieved through antixenosis (insect deterrence) or inhibition of insect growth, development, reproduction, and survival (antibiosis), or alternatively, the plant may acquire an increased ability for herbivore tolerance.[21] Although both antixenosis and antibiosis are generally associated with resistant pear genotypes, some of these expressed only one of the two traits, suggesting genetic independence.[4]

Resistance of deciduous trees to phloem feeding insects is hypothesized to result from a combination of constitutive and induced physical and chemical defenses.[22] Despite the fact that a comprehensive knowledge concerning pear foliar phenolics is recognized as mandatory for understanding their involvement in defense mechanisms, little is known about their composition. Therefore, our aim was to study the preformed or constitutive content of polyphenols in leaves of pear cultivars of diverse origin and with different resistance to psylla. Furthermore, we sought to clarify whether one or several of the phenolic compounds in pear leaves are putatively involved in pear resistance to psylla. To this end, the most important foliar pear polyphenols were defined using principal component analysis (PCA). Conclusions from this study can provide us guidance in future pear breeding programs.

MATERIALS AND METHODS

Plant Material. The plant material for comparison was obtained from a five-year-old pear orchard in Grocka (44° 66′ N and 20° 72′ E) near Belgrade, Serbia. In this experimental orchard, 22 pear cultivars (Table 1) were chosen according to their different resistance to psylla and origin. Using data in the literature[23,24] and after empirical observation, the cultivars were divided into two groups, where the first included 16 cultivars of *P. communis*, and the second consisted of five cultivars of *P. pyrifolia* and one interspecific hybrid (*P. pyrifolia* x *P. communis*). Planting distance was 4 × 1.2 m, and Quince BA29 was used as the rootstock. The soil is classified as Eutric Cambisol. The trees were trained in spindle bush shape and were grown under nonirrigated standard cultural conditions.

Each cultivar was represented by three plants, with each replicate being composed of 20 leaves, sampled from a single tree randomly from all around the canopy. Leaves were gathered on the same day, from the median section of one-year branches at the end of June, when fully formed. None of the leaves had any disease or pest symptoms, so there were no induced plant responses. After collection, leaves were air-dried for 10 days and kept in a dark ventilated place. The leaves were then bagged and stored at room temperature until the analysis. All data presented in the tables are means of three replicates.

Reagents and Standards. Acetonitrile and formic acid (both of MS grade), methanol (HPLC grade), hydrochloric acid, sodium carbonate, sodium acetate, sodium hydroxide, and Folin-Ciocalteu reagent were purchased from Merck (Darmstadt, Germany). Ultrapure water (Thermofisher Scientific, Bremen, Germany) was used to prepare standard solutions and blanks. Syringe filters (13 mm, PTFE membrane 0.45 μm) were purchased from Supelco (Bellefonte, PA, USA).

2,2-Diphenyl-1-picrylhydrazyl (DPPH) and phenolic standards (gallic, protocatechuic, chlorogenic, *p*-hydroxybenzoic, gentisic, caffeic, ellagic, *p*-coumaric and ferulic acids; aesculin, epicatechin, catechin, rutin, naringin, umbelliferone, quercetin, and *trans*-resveratrol) were purchased from Fluka AG (Buch, Switzerland).

Preparation of Standard Solutions. A 1000 mg/L stock solution of a mixture of each phenolic standard was prepared in methanol. Dilution of the stock solution with methanol yielded working solutions at concentrations of 0.025, 0.050, 0.100, 0.250, 0.500, 0.750, and 1.000

DOI: 10.1021/acs.jafc.5b03394
J. Agric. Food Chem. 2015, 63, 7476−7486

mg/L. Calibration curves were obtained by plotting the peak areas of the standards against their concentration. Calibration curves revealed good linearity, with R^2 values exceeding 0.99 (peak areas vs concentration).

Preparation of Sample Extracts. To prepare leaf samples for measurement of total phenolic content (TPC), radical scavenging activity (RSA) and UHPLC-MS/MS Orbitrap analysis, 2 g of dry leaves (lamina with midrib and lateral veins) were ground into powder and extracted three times with 100 mL of a mixture of methanol/water (70/30) containing 0.1% HCl in an ultrasonic bath for 1 h at room temperature. The residue after evaporation was dissolved in a mixture of methanol/water as described by Pavlović et al.[25]

UHPLC–MS/MS Orbitrap Analysis of Polyphenolic Compounds. The compounds of interest were separated using a liquid chromatography system. This consisted of a quaternary Accela 600 pump and Accela Autosampler connected to a linear ion trap-orbitrap hybrid mass spectrometer (LTQ OrbiTrap XL) with a heated-electrospray ionization probe, HESI-II (ThermoFisher Scientific, Bremen, Germany).

Separation was achieved on a 100 × 2.1 mm i.d., 1.7 μm, Syncronis C18 analytical column (ThermoFisher Scientific, Bremen, Germany). The mobile phase consisted of (A) water + 0.1% formic acid and (B) acetonitrile + 0.1% formic acid. A linear gradient program at a flow rate of 0.300 mL/min was used as follows: 0.0–1.0 min 5% B, 1.0–12.0 min from 5% to 95% B, 12.0–12.2 min from 95% to 5% B, then 5% B for 3 min. The injection volume was 5 μL.

The mass spectrometer was operated in negative mode. HESI–source parameters were described previously.[26] Phenolics were identified and quantitated according to the corresponding spectrometric characteristics of reference standards: mass spectra, accurate mass, characteristic fragmentation, and characteristic retention time. Xcalibur software (version 2.1) was used for instrument control, data acquisition, and data analysis. The generated MS/MS spectra were processed by ToxID software (version 2.1.1). Quantitative analysis was done according to the exact mass search method (±5 ppm) by comparing the retention times and exact mass of available standards.

Full scan analysis was employed for detection of the monoisotopic masses of deprotonated unknown compounds, while the MS/MS experiment provided fragmentation pathways. Unknown compounds were identified on the basis of their monoisotopic mass and MS/MS fragmentation, and confirmed using previously reported MS fragmentation data. This exact mass search of unknown compounds was based on high resolution MS analysis (OrbiTrap), online database searching and prediction of MS/MS fragmentation and fragmentation pathway using Mass Frontier 6.0 software (ThermoFisher Scientific, Bremen, Germany).

Determination of TPC and DPPḢ Radical Scavenging Activity. The total phenolic content in leaf extracts was determined as described by Singleton and Rossi[27] using the Folin-Ciocalteu reagent. The TPC values were expressed as grams of gallic acid equivalent (GAE) per kilogram dry weight (DW), based on a standard curve for 20–100 mg of gallic acid/L. The radical scavenging activity of the leaf extracts was measured employing the DPPḢ method of Pavlović et al.[25] The Trolox calibration curve was plotted as a function of the percentage inhibition of the DPPH radical. The results are expressed as millimoles of Trolox equivalents per kilogram of sample (mM TE/kg).

Statistical Analysis. Data for all measurements made in triplicate are expressed as the mean ± standard error (SE). One-way analysis of variance (ANOVA) was used to evaluate the experimental data, followed by Tukey's test to detect significant differences ($p \leq 0.05$) between the mean values. Pearson's coefficient of correlation between values for TPC, RSA and the content of phenolic compounds was also determined. These analyses were performed with the statistical program MS Excel (Microsoft Office 2007 Professional). PCA was carried out employing the PLS_Tool Box software package for MATLAB (Version 7.12.0). All data were group-scaled prior to PCA. The singular value decomposition algorithm (SVD) and a 0.95 confidence level for Q and T2 Hotelling limits for outliers were chosen.

RESULTS AND DISCUSSION

Determination of Total Phenolic Content and DPPḢ Scavenging Activity. Samples were characterized by determination of total phenolic content (TPC) and radical scavenging activity (RSA) as shown in Table 2. TPC values ranged from 27.03 ('Kumoi') to 56.93 g of GAE per kg of DW in 'Coscia' cultivar. Generally, European pear cultivars (*P. communis*), which are susceptible to psylla, had somewhat higher TPC values (43.04 g of GAE per kg DW) than *P. pyrifolia* cultivars (38.06 g of GAE per kg DW). Although it is generally known that pest resistance is influenced by polyphenols, total phenolic levels may not be as important as high levels of one or a few specific compound(s) that exhibit activity toward *C. pyri*. The results for RSA ranged from 0.15 ('Precoce de Trevoux') to 0.35 mmol TE/g DW ('Coscia'). ANOVA showed a statistically significant difference between RSA values obtained for *P. communis* and *P. pyrifolia* cultivars ($P < 0.001$; $F = 92.15$; $F_{crit} = 1.80$). Similarly, a statistically significant difference was found between *P. communis* and *P. pyrifolia* cultivars for total phenolics ($P < 0.001$; $F = 540.87$; $F_{crit} = 1.80$). Therefore, Tukey's test was used to determine the significance of differences ($P \leq 0.05$) between individual samples (Table 2).

Table 2. Total Phenolic Content and Radical Scavenging Activity[a]

Cultivar	TPC, g GAE/kg DW	RSA, mmol TE/kg DW
European cultivars (*Pyrus communis*)		
Bella di Giungo	52.84 ± 1.08^{c}	0.31 ± 0.01^{bc}
Turandot	34.11 ± 1.48^{i}	0.24 ± 0.01^{fgh}
Moldova's early	48.33 ± 1.95^{e}	0.29 ± 0.01^{cde}
Coscia	56.93 ± 0.94^{b}	0.35 ± 0.01^{a}
Ilinjača	29.45 ± 1.88^{l}	0.19 ± 0.00^{ijk}
Carmen	49.99 ± 1.75^{de}	0.31 ± 0.00^{bc}
Butirra precoce Morettini	31.12 ± 0.34^{kl}	0.22 ± 0.01^{hij}
Precoce de Trevoux	39.38 ± 0.73^{gh}	0.15 ± 0.02^{l}
Santa Maria	59.60 ± 0.40^{a}	0.33 ± 0.01^{ab}
Williams'	50.79 ± 0.60^{cd}	0.28 ± 0.01^{cde}
Jeribasma	32.83 ± 0.00^{ijk}	0.19 ± 0.01^{jk}
Abbé Fétel	50.49 ± 0.87^{de}	0.28 ± 0.02^{cde}
Packham's Triumphy	39.34 ± 0.54^{gh}	0.23 ± 0.02^{gh}
Beurre Bosc	44.33 ± 0.07^{f}	0.28 ± 0.02^{def}
Alexander Lucas	30.78 ± 0.27^{kl}	0.18 ± 0.01^{k}
Piore de Cure	38.34 ± 1.68^{h}	0.24 ± 0.01^{fgh}
Oriental pears (*Pyrus pyrifolia*)		
Niitaka	33.54 ± 0.95^{ij}	0.27 ± 0.01^{de}
Kumoi	27.03 ± 0.61^{m}	0.19 ± 0.01^{jk}
Chojuro	31.63 ± 0.59^{jkl}	0.17 ± 0.02^{kl}
Shinsui	44.16 ± 0.27^{f}	0.27 ± 0.03^{efg}
Nijisseiki	51.13 ± 1.19^{cd}	0.30 ± 0.00^{cd}
Kieffer	40.91 ± 0.34^{g}	0.22 ± 0.02^{hi}

[a]Different letters in the same column denote a significant difference according to Tukey's test, $p < 0.05$.

Analysis of Phenolic Compounds. A UHPLC system coupled to an OrbiTrap MS was utilized in order to obtain a comprehensive profile of individual phenolic compounds (Figure 1, Table 3). A total of 17 compounds were quantitated by comparing retention times and MS spectra with available standards (Table 4). The results showed that the analyzed leaf samples contained roughly the same types of phenolics,

DOI: 10.1021/acs.jafc.5b03394
J. Agric. Food Chem. 2015, 63, 7476–7486

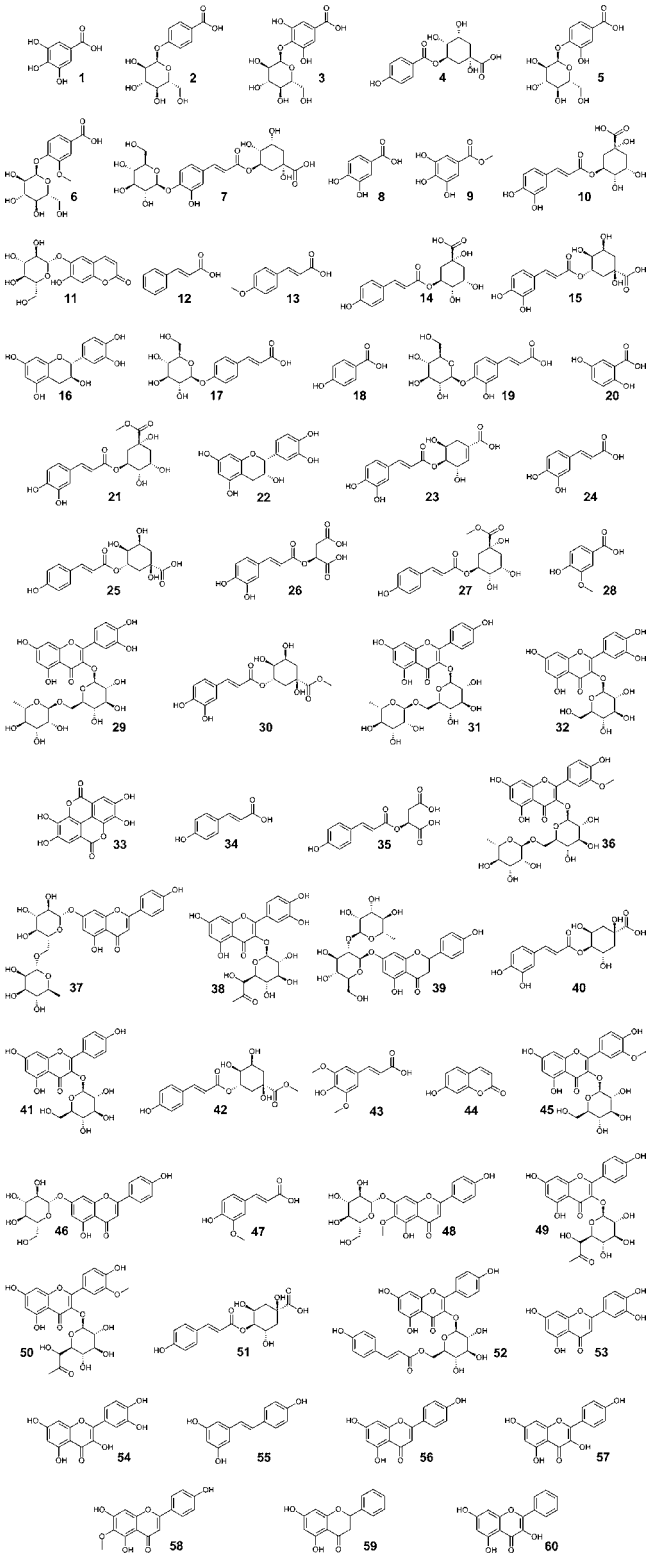

Figure 1. Structures of phenolic compounds found in pear leaf samples. Glycosylation position is uncertain.

although differences in concentration of individual compounds were detected between cultivars.

Chlorogenic (5-*O*-caffeoylquinic) acid was the most abundant phenolic compound, accounting for an average of 44% of the total polyphenolics quantitated in leaves of all pear cultivars, which is consistent with the findings of Colarič et al.[28] In addition, pear leaves stored significant amounts of *p*-coumaric acid (20%), ferulic acid (15%), and rutin (10%).

Among the hydroxybenzoic acids, we measured gentisic acid, protocatechuic acid, gallic acid, and *p*-hydroxybenzoic acid. Together they accounted for 5% of the total quantitated phenolics. In resistant (Oriental) pear cultivars, the mean value for *p*-hydroxybenzoic acid ranged from 5.37 ('Nijisseiki') to 133.22 mg/kg DW ('Niitaka'). In *P. pyrifolia* cultivars, its level was 45% higher than in European cultivars. Conversely, mean values for protocatechuic acid and gallic acid in European cultivars were 41% and 40%, respectively, higher than in Oriental ones. It was interesting to note that 'Santa Maria', a highly susceptible cultivar, accumulated large quantities of gentisic acid (36.88 mg/kg DW), i.e. ∼11-fold higher than the average for all other cultivars examined. This can be explained by the fact that gentisic acid has a role as an intermediary signal in compatible plant−pathogen interactions, where it can act as a defensive component of the antipathogenic response, with progressive accumulation showing correlation with disease development.[29] 'Santa Maria' had probably been attacked previously by some pathogen (viroids, viruses, fungi, or bacteria), which had induced such a reaction.

Hydroxycinnamic acids (chlorogenic acid, caffeic acid, ferulic acid, and *p*-coumaric acid) were other major phenolic compounds detected in the pear leaves. The total content showed a wide range; from 722.63 mg/kg DW ('Ilinjača') to 2227.91 mg/kg DW ('Williams') and varied from 61% in 'Ilinjača' up to 95% of the total quantitated phenols in 'Nijisseiki'. As previously documented, the main hydroxycinnamic acid found here was chlorogenic acid. This compound was most abundant in almost all cultivars, except for 'Santa Maria', 'Williams', 'Kieffer', and 'Precoce de Trevoux', where *p*-coumaric acid showed predominance. The level of chlorogenic acid in European cultivars was between 477.63 mg/kg DW ('Santa Maria') and 1185.99 mg/kg DW ('Coscia'), while in Oriental cultivars it varied from 358.22 mg/kg DW ('Kumoi') to 765.56 mg/kg DW ('Nijisseiki').

Thus, Oriental pears stored 42% lower levels of chlorogenic acid than European pears, which confirm the results of Cui et al.[30] and Gunen et al.,[31] who reported that European pears are a much better source of this compound. Leiss et al.[32] claimed that chlorogenic acid acts as a feeding deterrent and a growth inhibitor for various leafhoppers, aphids, and thrips. European cultivars that stored higher amounts of chlorogenic acid showed moderate resistance to psylla ('Alexander Lucas', 'Bella di Giugno', 'Carmen', 'Moldova's early', 'Abbé Fétel', 'Coscia', etc.), while some with low values ('Santa Maria', 'Butirra Precoce Morettini', and 'Precoce de Trevoux') were highly susceptible. The only exception was 'Jeribasma', sharing both a moderate level of chlorogenic acid and high resistance to psylla, a combination of traits which resembles that of Oriental pears. This favors the supposition that one of the progenitors of this cultivar must have been *P. pyrifolia*, which agrees with the conclusion of Bell and Stuart.[23]

P. pyrifolia and *P. communis* cultivars stored different amounts of caffeic and *p*-coumaric acid. The mean values for caffeic and *p*-coumaric acid in European cultivars were 32% and 29%, respectively, which were higher than those in Oriental cultivars (Table 4). The concentration of ferulic acid, another compound belonging to this group, was very cultivar dependent, with 'Bella di Giugno' showing the lowest value (18.05 mg/kg DW) and 'Nijisseiki' having the highest concentration (412.92 mg/kg DW). In Oriental pears the

DOI: 10.1021/acs.jafc.5b03394
J. Agric. Food Chem. 2015, 63, 7476−7486

Table 3. Polyphenolics Identified in the Pear Leaf Samples in Negative Ionization Mode

No.	t_R, min	Compound name	Molecular formula, $[M-H]^-$	Calculated mass, $[M-H]^-$	Exact mass, $[M-H]^-$	Δm, Da	MS/MS Fragments, (% MS/MS Base Peak)
1	2.70	Gallic acid[a]	$C_7H_5O_5^-$	169.01425	169.01343	0.82	125(100)
2	3.25	*p*-Hydroxybenzoic acid 4-*O*-hexoside	$C_{13}H_{15}O_8^-$	299.07724	299.07574	1.50	137(100)
3	3.72	Gallic acid 4-*O*-hexoside	$C_{13}H_{15}O_{10}^-$	331.06707	331.06549	1.58	313(100), 168(50), 150(10), 125(20)
4	3.98	*p*-Hydroxybenzoylquinic acid	$C_{14}H_{15}O_8^-$	311.07724	311.07535	1.89	137(100)
5	4.05	Protocatechuic acid 4-*O*-hexoside	$C_{13}H_{15}O_9^-$	315.07216	315.07004	2.12	153(100), 109(10)
6	4.15	Vanillic acid 4-*O*-hexoside	$C_{14}H_{17}O_9^-$	329.08781	329.08572	2.09	167(100)
7	4.34	Chlorogenic acid 4-*O*-hexoside	$C_{22}H_{27}O_{14}^-$	515.14008	515.13776	2.32	353(100), 341(5), 323(10), 191(90)
8	4.45	Protocatechuic acid[a]	$C_7H_5O_4^-$	153.01933	153.01860	0.73	125(5), 109(100)
9	4.53	Methyl gallate	$C_8H_7O_5^-$	183.02990	183.02843	1.47	168(5), 165(15), 139(10), 125(100)
10	4.57	3-*O*-Caffeoylquinic acid	$C_{16}H_{17}O_9^-$	353.08781	353.08487	2.94	191(100), 179(40), 173(5), 135(10)
11	4.83	Aesculin[a]	$C_{15}H_{15}O_9^-$	339.07216	339.07056	1.60	177(100)
12	4.85	Cinnamic acid	$C_9H_7O_2^-$	147.04515	147.04398	1.17	103(100)
13	5.02	*p*-Methoxycinnamic acid	$C_{10}H_9O_3^-$	177.05572	177.05446	1.26	162(100)
14	5.04	3-*O*-*p*-Coumaroylquinic acid	$C_{16}H_{17}O_8^-$	337.09289	337.09036	2.53	191(10), 173(10), 163(100), 119(10)
15	5.07	5-*O*-Caffeoylquinic acid[a]	$C_{16}H_{17}O_9^-$	353.08781	353.08472	3.09	191(100), 179(5)
16	5.08	Catechin[a]	$C_{15}H_{13}O_6^-$	289.07176	289.07013	1.63	245(100), 231(10), 205(40), 179(20)
17	5.14	*p*-Coumaric acid 4-*O*-hexoside	$C_{15}H_{17}O_8^-$	325.09289	325.09042	2.47	163(100), 145(20), 119(10)
18	5.26	*p*-Hydroxybenzoic acid[a]	$C_7H_5O_3^-$	137.02442	137.02377	0.65	93(100)
19	5.34	Caffeic acid 4-*O*-hexoside	$C_{15}H_{17}O_9^-$	341.08781	341.08551	2.30	179(100), 135(10)
20	5.35	Gentisic acid[a]	$C_7H_5O_4^-$	153.01933	153.01859	0.74	125(10), 109(100)
21	5.39	Methyl 3-*O*-caffeoylquinate	$C_{17}H_{19}O_9^-$	367.10346	367.10059	2.87	193(20), 161(100), 135(10)
22	5.47	Epicatechin[a]	$C_{15}H_{13}O_6^-$	289.07176	289.07004	1.72	245(100), 231(10), 205(40), 179(20)
23	5.50	4-*O*-Caffeoylshikimic acid	$C_{16}H_{15}O_8^-$	335.07724	335.07465	2.59	291(20), 179(100), 161(80), 135(30)
24	5.52	Caffeic acid[a]	$C_9H_7O_4^-$	179.03498	179.03415	0.83	135(100)
25	5.65	5-*O*-*p*-Coumaroylquinic acid	$C_{16}H_{17}O_8^-$	337.09289	337.08997	2.92	191(100), 179(5), 163(10)
26	5.71	Caffeoylmalic acid	$C_{13}H_{11}O_8^-$	295.04594	295.04306	2.88	179(100), 135(5), 133(65), 115(5)
27	5.80	Methyl 3-*O*-*p*-coumaroylquinate	$C_{17}H_{19}O_8^-$	351.10854	351.10593	2.61	163(5), 145(100), 119(10), 117(10)
28	5.82	Vanillic acid	$C_8H_7O_4^-$	167.03498	167.03363	1.35	152(100), 123(90), 108(20)
29	5.91	Rutin[a]	$C_{27}H_{29}O_{16}^-$	609.14611	609.14154	4.57	343(10), 301(100), 300(40), 271(10)
30	5.93	Methyl 5-*O*-caffeoylquinate	$C_{17}H_{19}O_9^-$	367.10346	367.10031	3.15	193(50), 179(100), 161(20), 135(40)
31	5.93	Kaempferol 3-*O*-rutinoside	$C_{27}H_{29}O_{15}^-$	593.15119	593.14789	3.30	285(100)
32	6.14	Quercetin 3-*O*-hexoside	$C_{21}H_{19}O_{12}^-$	463.08820	463.08459	3.61	301(100), 300(30)
33	6.20	Ellagic acid[a]	$C_{14}H_5O_8^-$	300.99899	300.99747	1.52	301(50), 284(30), 257(100), 229(70)
34	6.24	*p*-Coumaric acid[a]	$C_9H_7O_3^-$	163.04007	163.03925	0.82	119(100)
35	6.28	*p*-Coumaroylmalic acid	$C_{13}H_{11}O_7^-$	279.05103	279.04865	2.38	163(100)
36	6.31	Isorhamnetin 3-*O*-rutinoside	$C_{28}H_{31}O_{16}^-$	623.16176	623.15729	4.47	315(100), 314(10), 300(20), 299(5)
37	6.32	Apigenin 7-*O*-rutinoside	$C_{27}H_{29}O_{14}^-$	577.15573	577.15277	2.96	269(100)
38	6.33	Quercetin 3-*O*-(6″-*O*-acetyl)-hexoside	$C_{23}H_{21}O_{13}^-$	505.09876	505.09485	3.91	463(20), 301(100), 300(50)
39	6.38	Naringin[a]	$C_{27}H_{31}O_{14}^-$	579.17193	579.16870	3.23	459(100), 313(10), 271(40), 235(10)
40	6.48	4-*O*-Caffeoylquinic acid	$C_{16}H_{17}O_9^-$	353.08781	353.08465	3.16	191(60), 179(75), 173(100), 135(15)
41	6.49	Kaempferol 3-*O*-hexoside	$C_{21}H_{19}O_{11}^-$	447.09329	447.08966	3.63	327(20), 285(85), 284(100), 255(20)
42	6.50	Methyl 5-*O*-*p*-coumaroylquinate	$C_{17}H_{19}O_8^-$	351.10854	351.10614	2.40	163(100), 145(5), 119(15)
43	6.52	Sinapic acid	$C_{11}H_{11}O_5^-$	223.06120	223.06013	1.07	208(100), 179(50), 177(30), 164(40)

DOI: 10.1021/acs.jafc.5b03394
J. Agric. Food Chem. 2015, 63, 7476−7486

Table 3. continued

No.	t_R, min	Compound name	Molecular formula, $[M-H]^-$	Calculated mass, $[M-H]^-$	Exact mass, $[M-H]^-$	Δm, Da	MS/MS Fragments, (% MS/MS Base Peak)
44	6.56	Umbelliferone[a]	$C_9H_5O_3^-$	161.02442	161.02364	0.78	133(100), 117(10)
45	6.57	Isorhamnetin 3-*O*-hexoside	$C_{22}H_{21}O_{12}^-$	477.10385	477.10031	3.54	449(5), 357(20), 315(45), 314(100)
46	6.58	Apigenin 7-*O*-hexoside	$C_{21}H_{19}O_{10}^-$	431.09837	431.09543	2.94	269(100), 268(10)
47	6.66	Ferulic acid[a]	$C_{10}H_9O_4^-$	193.05063	193.04961	1.02	178(30), 149(40), 134(100)
48	6.70	Hispidulin 7-*O*-hexoside	$C_{22}H_{21}O_{11}^-$	461.10894	461.10626	2.68	446(70), 299(100), 298(10), 284(5)
49	6.72	Kaempferol 3-*O*-(6″-*O*-acetyl)-hexoside	$C_{23}H_{21}O_{12}^-$	489.10385	489.10095	2.90	285(100), 284(5)
50	6.83	Isorhamnetin 3-*O*-(6″-*O*-acetyl)-hexoside	$C_{24}H_{21}O_{13}^-$	519.11441	519.11133	3.08	315(100), 314(15), 300(5)
51	6.92	4-*O*-*p*-Coumaroylquinic acid	$C_{16}H_{17}O_8^-$	337.09289	337.09015	2.74	191(5), 173(100), 163(10)
52	7.61	Kaempferol 3-*O*-(6″-*O*-*p*-coumaroyl)-hexoside	$C_{30}H_{25}O_{13}^-$	593.13006	593.12695	3.11	447(10), 307(5), 285(100)
53	7.76	Luteolin[a]	$C_{15}H_9O_6^-$	285.04046	285.03860	1.86	241(100), 199(70), 175(85), 151(30)
54	7.81	Quercetin[a]	$C_{15}H_9O_7^-$	301.03538	301.03314	2.24	273(20), 257(20), 179(100), 151(70)
55	7.94	*trans*-Resveratrol[a]	$C_9H_7O_3^-$	227.07137	227.06946	1.91	185(100), 159(30), 143(20)
56	8.43	Apigenin[a]	$C_{15}H_9O_5^-$	269.04555	269.04391	1.64	225(100), 201(25), 183(20), 151(30)
57	8.54	Kaempferol[a]	$C_{15}H_9O_6^-$	285.04046	285.03839	2.07	285(100), 229(50), 185(50), 151(65)
58	8.60	Hispidulin	$C_{16}H_{11}O_6^-$	299.05611	299.05389	2.22	285(10), 284(100)
59	10.01	Pinocembrin[a]	$C_{15}H_{11}O_4^-$	255.06628	255.06450	1.78	213(100), 187(15), 151(35)
60	10.10	Galangin[a]	$C_{15}H_9O_5^-$	269.04555	269.04395	1.60	241(50), 227(80), 213(90), 197(100)

[a]Confirmed using available standards; all the other compounds were identified based on MS/MS data.

mean ferulic acid concentration was 54% higher than in the European cultivars. This was expected since ferulic acid was reported to be a factor in resistance of peanut species to thrips.[33]

Catechin was detected only in four pear cultivars ('Carmen', 'Beurre Bosc', 'Williams', and 'Kieffer'), where amounts varied from 1.04 mg/kg DW in 'Kieffer' to 15.80 mg/kg DW in 'Williams'. Among highly resistant cultivars (Oriental), only 'Kieffer', which is a hybrid of *P. pyrifolia*, and 'Williams', contained small quantities of catechin, while in others this compound could not be detected. In contrast, the susceptible cultivar 'Williams' stored relatively large quantities of catechin. Epicatechin was found in half of the cultivars (Table 4). The content was rather variable, ranging from 1.15 mg/kg DW in 'Niitaka' up to 91.21 mg/kg DW in 'Williams'.

From the flavonol group only rutin and quercetin were quantitated in pear leaves. Rutin showed quite a wide range, from 6.31 mg/kg DW in 'Shinsui' to 541.98 mg/kg DW in 'Precoce de Trevoux'. The mean value for this compound in European cultivars was 317.64 mg/kg DW compared to 33.02 mg/kg DW for Oriental cultivars. Namely, *P. communis* stored ~90% more rutin than *P. pyrifolia*. Such results were predicted, since rutin has been shown to be a phago- and oviposition stimulant.[15] Determination of quercetin content disclosed that some cultivars did not store this compound. The leaves of the cultivar 'Santa Maria', which is highly susceptible to psylla, accumulated the highest level of quercetin (239.40 mg/kg DW). Clearly, the role that flavonols play in defending plants against insect attack is complex and probably species (cultivar)-specific.

Aesculin showed a relatively wide concentration range among cultivars, from 2.76 in 'Alexander Lucas' to 10.63 mg/kg DW in 'Shinsui'. In general, cultivars of *P. pyrifolia* had ~32% more of this coumarin glucoside than cultivars originating from *P. communis*. The situation regarding naringin, a flavanone glycoside, was almost the same. Oriental pears had a 56% higher level of this compound than European pears. According to Atteyat et al.[34] naringin can be used as a botanical insecticide leading to significant mortality of nymphs and adults of the woolly apple aphid, *Eriosoma lanigerum* (Hausmann).

Umbelliferone, a natural coumarin, was present in ten cultivars. Within Oriental pears, umbelliferone was not detected, except for trace quantities in 'Nijiieseiki' (0.07 mg/kg DW). Moreover, some European cultivars also did not store any ('Poire de Cure', 'Ilinjača', 'Carmen', 'Beurre Bosc', 'Moldova's early', 'Abbé Fétel', 'Bella di Giungo', and 'Coscia'), while 'Williams' accumulated the largest amount (10.92 mg/kg DW). 'Kieffer' probably inherited this trait intermediately, as the level of umbelliferone was between those for Oriental pears and 'Williams'.

The stilbene phytoalexin, *trans*-resveratrol, was undetectable only in 'Coscia'. In European cultivars, levels ranged from 7.64 mg/kg DW ('Beurre Bosc') to 62.16 mg/kg DW ('Williams'), and in Oriental ones, from 22.92 mg/kg DW ('Nijiieseiki') to 54.47 mg/kg DW ('Kieffer'). In Oriental pears the mean value for *trans*-resveratrol was 22% higher than in European pears. According to Wang et al.,[35] levels of *trans*-resveratrol were found to be affected by genotype, cultural practices, and environmental conditions.

In the absence of standards, a total of 43 phenolic compounds were identified based on the search for $[M-H]^-$ deprotonated molecules and their fragmentation. The retention times (t_R, min), molecular formula, calculated and exact masses

DOI: 10.1021/acs.jafc.5b03394
J. Agric. Food Chem. 2015, 63, 7476−7486

Table 4. Content of Polyphenolic Compounds (mg/kg DW) Quantitated in Pear Leaf Samples

	Polyphenolic compounds[a]																
	1	8	11	15	16	18	20	22	24	29	33	34	39	44	47	54	55
European cultivars (*Pyrus communis*)																	
Bella di Giungo	8.05	14.41	8.43	957.95	-	4.90	2.72	-	58.37	300.30	-	8.74	-	-	18.05	60.91	9.26
Turandot	4.34	33.38	7.38	859.22	-	69.32	0.53	24.29	27.70	366.51	-	759.10	-	4.22	157.25	-	30.27
Moldova's early	2.98	12.59	6.29	1026.20	-	83.94	0.77	56.36	37.51	394.99	-	7.86	-	-	30.17	2.68	31.52
Coscia	2.95	10.91	5.34	1185.90	-	8.48	1.95	-	78.61	236.07	-	142.66	1.60	-	63.24	54.95	-
Ilinjača	7.06	20.24	5.08	670.97	-	111.95	0.75	-	17.19	273.28	3.88	9.57	0.33	-	24.90	-	41.68
Carmen	5.43	5.71	5.73	1116.60	4.82	87.93	0.84	58.33	47.86	280.08	-	244.34	0.27	-	163.82	1.01	31.33
Butirra precoce Morettini	4.07	13.09	4.76	563.33	-	44.84	0.44	-	37.30	355.15	2.83	340.12	-	2.93	112.39	4.48	51.52
Precoce de Trevoux	4.03	16.88	5.91	680.81	-	22.27	1.01	-	19.66	541.98	-	941.19	-	4.28	249.73	18.48	26.02
Santa Maria	3.28	6.69	4.17	477.63	-	10.69	36.88	-	68.44	159.14	-	489.42	0.32	0.45	129.18	239.40	19.62
Williams'	6.51	30.41	4.10	840.45	15.80	18.56	1.80	91.21	31.66	363.23	-	1075.10	0.13	10.92	280.75	0.90	62.16
Jeribasma	6.70	30.40	3.58	775.10	-	17.31	0.44	4.68	48.52	223.09	3.94	84.84	0.16	1.95	141.35	-	49.03
Abbé Fétel	6.33	5.87	4.09	1184.20	-	18.72	0.57	10.43	31.58	251.18	-	169.55	-	-	104.04	0.76	29.92
Packham's Triumphy	5.16	16.05	8.08	855.88	-	7.44	0.50	2.38	12.84	379.39	-	402.58	0.23	4.27	95.88	0.68	55.40
Beurre Bosc	4.70	3.29	7.68	729.43	3.40	6.66	0.62	29.12	26.14	392.40	-	8.62	1.73	-	24.01	0.11	7.64
Alexander Lucas	6.71	12.84	2.76	950.93	-	17.12	0.36	21.26	14.50	248.19	4.00	529.10	-	3.09	266.47	-	43.06
Piore de Cure	8.88	38.25	5.68	768.84	-	53.07	0.62	-	32.69	317.21	4.23	493.87	-	-	112.36	-	7.95
Oriental pears (*Pyrus pyrifolia*)																	
Niitaka	4.96	6.06	9.37	444.35	-	133.22	0.56	1.15	20.34	19.19	-	63.92	2.67	-	206.31	-	47.47
Kumoi	4.37	14.44	4.76	358.16	-	74.75	0.28	-	18.53	11.29	-	105.18	0.43	-	277.62	-	34.74
Chojuro	3.37	7.20	8.24	382.98	-	119.03	0.21	-	21.30	14.65	-	119.15	-	-	236.67	8.10	32.67
Shinsui	-	3.32	10.63	610.12	-	8.37	5.74	-	39.36	6.31	-	246.13	0.40	-	231.64	13.50	45.00
Nijisseiki	2.70	11.46	10.54	765.56	-	5.37	1.38	-	34.14	11.76	-	332.02	0.17	0.07	412.92	8.26	22.92
Kieffer	4.03	18.08	5.90	398.05	1.04	57.26	10.98	4.28	16.57	134.92	-	651.8	0.43	5.27	258.32	10.06	54.47

[a]Number of compounds corresponding to Figure 1 and Table 3.

DOI: 10.1021/acs.jafc.5b03394
J. Agric. Food Chem. 2015, 63, 7476−7486

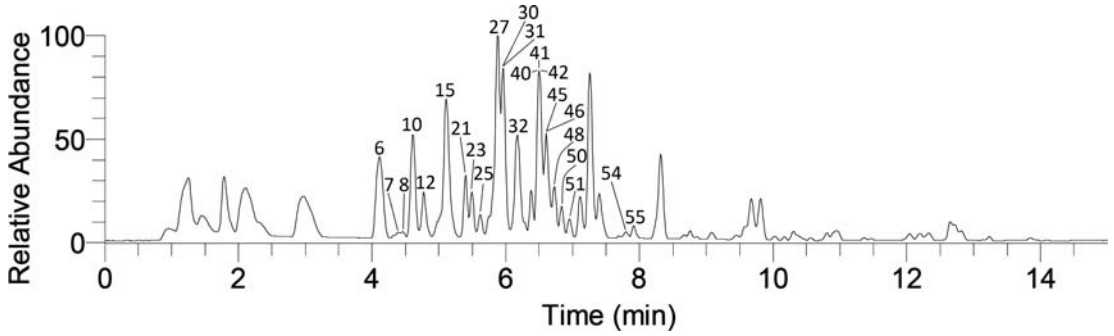

Figure 2. Base peak chromatogram of "Shinsui" pear leaf extract. Number of compounds corresponding to Figure 1 and Table 3.

([M−H]$^-$, m/z), mass accuracy errors, as well as major MS/MS fragment ions are summarized in Table 3. As the exact nature of the sugar moiety could not be ascertained, tentative structures of identified phenolics are given in Figure 1. A selected base peak chromatogram of a representative leaf extract ('Shinsui') is shown in Figure 2. Peak identification was based on published chromatographic and MS/MS data. In this section an explanation is given on fragmentation utilized for the identification of individual phenolic compounds. The total intensities of individual phenolics obtained from the full scan spectra were used for semiquantitative comparison of their contents in the pear leaf samples.

Examination of mass spectra for our pear leaf extracts revealed numerous phenolic acids and their derivatives. Hydroxycinnamic acids were identified as free acids (cinnamic and sinapic acid), while derivatives were esters with organic acids (malic, quinic, and shikimic acid) and glycosides. All derivatives were characterized on the basis of their exact mass fragmentation pattern recorded in the available literature.[36] *p*-Hydroxybenzoic acid 4-*O*-hexoside and *p*-hydroxybenzoyl-quinic acid were identified in all investigated samples, showing an MS/MS base peak fragment at m/z = 137.

Identification of flavonol and flavone glycosides was largely based on the MS/MS data (Table 3).[37] In the analyzed leaf extracts it was possible to identify hexosides (loss of 162 Da), acetyl-hexosides (loss of 204 Da), rutinosides (loss of 308 Da), and one derivative of *p*-coumaroyl-hexoside. Regarding flavonol glycosides, derivatives of kaempferol, quercetin, and isorhamnetin were found, giving MS/MS base peaks belonging to the deprotonated aglycones at m/z 285, 301, and 315, respectively. Kaempferol 3-*O*-(6″-*O*-*p*-coumaroyl)-hexoside at 7.61 min with the molecular ion at m/z 593 produced an MS/MS base peak at m/z 285 ([kaempferol−H]$^-$) and a secondary MS/MS peak at m/z 307 ([M−kaempferol]$^-$).[38] The compound at 8.60 min, with the molecular ion at m/z 299, and the MS/MS base peak at m/z 284 (obtained by elimination of a methyl group) were tentatively identified as the flavone hispidulin. Furthermore, we identified hispidulin 7-*O*-hexoside (t_R = 6.70 min, m/z 461) with an MS/MS base peak at m/z 299 and a secondary MS/MS peak at m/z 446.[39] Another two apigenin glycosides were also found (apigenin 7-*O*-rutinoside and apigenin 7-*O*-hexoside), both of them showing an MS/MS base peak at m/z 269, which is the mass of deprotonated apigenin.[37] Confirmation for traces of flavonoid aglycones (luteolin, apigenin, kaempferol, pinocembrin, and galangin) was based on data for standards and fragmentation published in the literature.[26]

Although kaempferol was present in the leaves of all tested pear cultivars, its derivate, kaempferol 3-*O*-(6″-*O*-*p*-coumaroyl)-hexoside, and hispidulin were found in almost all *P. pyrifolia* cultivars together with 'Jeribasma'. The former was not detected in 'Nitaka', and the latter in 'Kumoi' and 'Chojuro' cultivars. A similar situation was observed for apigenin 7-*O*-rutinoside, which was present in the same cultivars (Oriental pear cultivars and 'Jeribasma'), as previously. The flavone pinocembrin was detected in cultivars with different psylla susceptibility, from the susceptible cultivar 'Precoce de Trevoux' to the fully resistant 'Chojuro' and 'Shinsui', which leads to the conclusion that this polyphenol could be cultivar dependent.

The most intriguing results are related to the presence of apigenin, a polyphenol connected with insect resistance.[40] This compound was found in the most susceptible cultivar 'Santa Maria', in resistant 'Jeribasma', and in Oriental pears (except 'Kumoi'). There is a possibility that its production is genetically coded, but we believe that this compound is synthesized in response to some kind of stress, not necessarily due to psylla but probably in reaction to some other pest or environmental stress, since it has already been shown to display strong effects against pathogenic fungi.[41] Thus, Potters et al.[42] recorded that synthesis of apigenin can occur in response to some environmental stresses, such as high UV-B and/or UV-A + UV-B radiation in genotypes with large, thin leaf blades, as in 'Santa Maria'.

Civolani et al.[43] examined pear cultivars resistant to *C. pyri* and excluded the existence of surface (trichomes, repellent volatiles, color or toughness of leaf surface), epidermis/mesophyll, and mesophyll/phloem resistance but strongly supported the hypothesis that factors located in phloem sap are responsible for pear resistance. Resistant selections mainly exhibit pronounced nymphal antibiosis, expressed by lower honeydew emission, increased development time, and marked nymphal mortality.[44] Since we examined whole leaf compounds, not just those from the midrib and lateral veins, we are not sure which leaf tissue in *P. pyrifolia* cultivars stored elevated levels of *p*-hydroxybenzoic acid, ferulic acid, naringin, aesculin, kaempferol 3-*O*-rutinoside, apigenin, apigenin 7-*O*-rutinoside, and hispidulin. Considering the findings of Butt et al.,[44] it seems likely that the psylla would sense these compounds during probing, but phloem specific compounds would be more important for inhibition of feeding and antibiosis than whole leaf compounds. Also, according to Hilker and Meiners[45] ovipositional antixenosis is the most important plant defense against herbivorous insects. Horton and Krysan[46] showed that psylla ovipositional activity is more selective than settling and probing activity. Psylla can colonize and feed on nonoptimal hosts, such as *Malus* spp., but they do not lay eggs.

Principal Component Analysis. This part of our study aimed to determine which polyphenolics could be responsible for differentiation of European and Oriental pear leaf samples.

DOI: 10.1021/acs.jafc.5b03394
J. Agric. Food Chem. 2015, 63, 7476−7486

Chemical markers, such as polyphenolics, have been proposed to be useful for classifying pear leaves according to their variety.[47] Several studies have considered relations between different pear species and polyphenolic profiles and have indicated the usefulness of polyphenols as biomarkers.[30,48]

The total intensities of all characterized phenolic compounds, obtained from the full scan spectra processed through ToxID software, were used as variables together with total phenolic content and the radical scavenging activity for PCA. The initial matrix 22 (the number of pear leaf samples) × 62 (total intensities of phenolics, TPC, and RSA) was processed using the covariance matrix with autoscaling. PCA resulted in seven PCs explaining 75.0% of the variation of the data set. The first principal component accounted for 25.2%, the second 11.7%, and the third component 10.6% of the total variance. In Figure 3A (PCA scatter plot) it is evident that the cultivars were clustered in two main groups along the PC1 axis. The first group included six cultivars originating from *P. pyrifolia* and one interspecies hybrid (*P. pyrifolia* x *P. communis*). The loading plot (Figure 3B) revealed the most influential variables

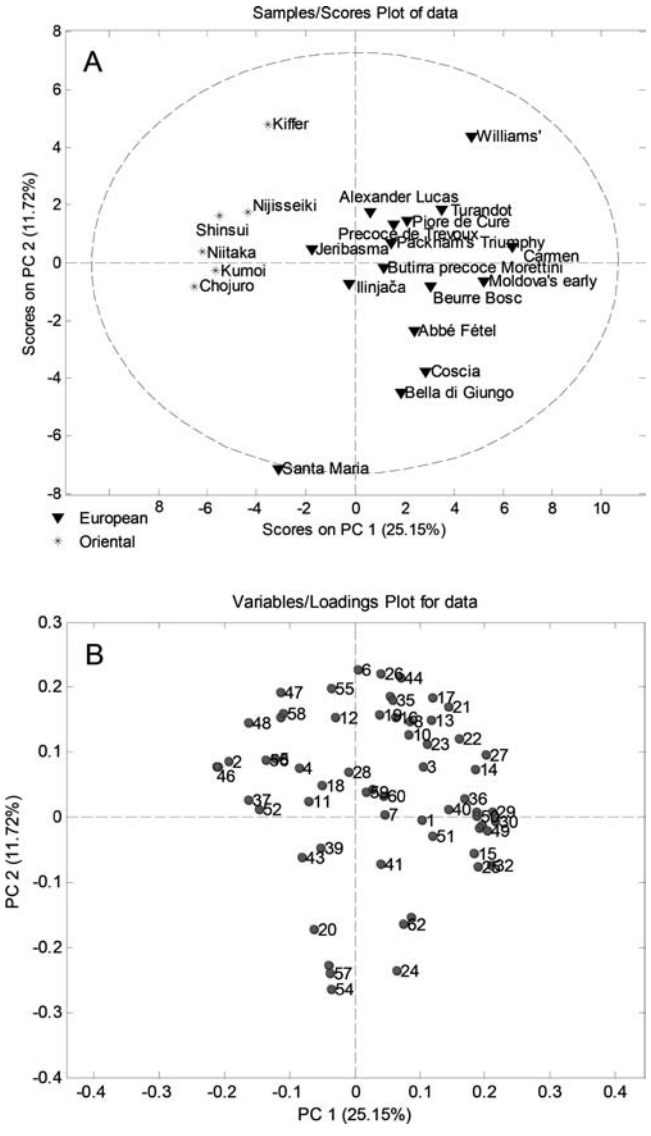

Figure 3. (A) PC scores plot of pear leaf samples; (B) Loadings plot of pear leaf samples.

responsible for classifying the pear leaf samples into two groups. Phenolic compounds that discriminate five cultivars originating from *P. pyrifolia* and the interspecies hybrid (*P. pyrifolia* x *P. communis*) from European cultivars are *p*-hydroxybenzoic acid 4-*O*-hexoside, kaempferol 3-*O*-rutinoside, apigenin 7-*O*-rutinoside, apigenin 7-*O*-hexoside, ferulic acid, hispidulin 7-*O*-hexoside, and kaempferol 3-*O*-(6″-*O*-*p*-coumaroyl)-hexoside. Higher contents of total phenolics, RSA values, and caffeic acid were the most influential in distinguishing 'Coscia' and 'Bella di Giungo' from the other varieties, and the separation was achieved along PC2.

The specific polyphenolic profile of cultivar 'Jeribasma' (named 'Eribasma' in some previous studies) in some respects resembled Oriental cultivars and most probably has *P. pyrifolia* as one of its ancestors.[23] Extremely high levels of quercetin and gentisic acid and the presence of kaempferol and methyl gallate, among other coumpounds, made cultivar 'Santa Maria' an outlier.

Correlations. Relationships between TPC, RSA, and the quantitated phenolic compounds were examined using Pearson correlation analysis. The close correlation between TPC and RSA ($r = 0.855$, $P < 0.001$) suggests that the antioxidant activity of leaves is derived mainly from their phenolic compounds. Significant correlations between some phenolic acids (chlorogenic acid, gentisic acid, and caffeic acid) and quercetin, on the one hand, and between some phenolic acids and TPC ($r = 0.455–0.703$, $P = 0.000–0.033$), on the other, suggest that those polyphenols represent the most important components of TPC. Regarding quercetin, the results were predictable, since it is well-known that it is a powerful antioxidant.[49] Also, some phenolic compounds, such as chlorogenic acid, caffeic acid, and quercetin, were found to be positively correlated with RSA ($r = 0.456$, $r = 0.721$, and $r = 0.446$, respectively, $P = 0.000–0.038$), which is similar to the findings of Sánchez et al.[50] for pear phenolics and antioxidant activity. However, *trans*-resveratrol, a phenolic compound that indicates stress, was negatively related with RSA ($r = -0.427$, $P = 0.047$). Among all phenolics investigated, caffeic acid, *p*-hydroxybezoic acid, and naringin did not correlate with any other polyphenolic components, indicating that those traits are genetically and/or physiologically independent.

This study attempted to discriminate a wide variety of preformed polyphenolics in pear leaves that can be sensed by an adult female, which will process the information and decide whether to initiate egg-laying and/or feeding. Although chlorogenic acid was found to be the predominant polyphenolic compound, followed by ferulic acid and *p*-coumaric acid, in leaves of all tested pear cultivars, *P. pyrifolia* and *P. communis* cultivars in most cases contained roughly the same types of phenolics. However, Oriental pears stored much more *p*-hydroxybenzoic acid, ferulic acid, aesculin, and naringin than European cultivars. We hypothesized that the levels of those four polyphenolics, together with the presence of kaempferol 3-*O*-rutinoside, apigenin, apigenin 7-*O*-rutinoside, and hispidulin, which were exclusively found in resistant pear cultivars, are most probably responsible for pear resistance to psylla. We assume that these results will be investigated further in bioassays of psylla against specific compounds.

Correlation analysis showed the genetic independence of caffeic acid, *p*-hydroxybenzoic acid, and naringin, when compared with the other compounds detected. If so, genes that code the synthesis of those substances could be easily inherited in some future planned hybridization. This analysis of

DOI: 10.1021/acs.jafc.5b03394
J. Agric. Food Chem. 2015, 63, 7476–7486

pear leaves represents a contribution to numerous studies aimed at discovering possible relations between chemical content and plant responses against insects. Thus, our findings could be used as a basis for further investigations of resistance mechanisms at the metabolic and chemical levels. Finally, our results may provide guidance in future pear breeding programs and early seedling selection, because it is possible to recognize ideal combinations of foliar phenolics as a natural defense mechanism against insects. Since phloem specific compounds important for inhibiting psylla feeding and ovipositional antixenosis still remain unidentified, subsequent studies should incorporate other specific phenolics as well as the ratios between them. Besides resistance assays (psylla against specific compounds), new experiments should include analysis of other compounds, such as types and amounts of nitrogenous compounds, especially amino-acids, which directly influence the growth and fecundity of psylla.

■ ASSOCIATED CONTENT

Supporting Information

The Supporting Information is available free of charge on the ACS Publications website at DOI: 10.1021/acs.jafc.5b03394.

Table of intensities obtained from the full scan spectra for identified polyphenols in pear leaf samples; and the correlation matrix of quantitated polyphenols, TPC, and RSA (PDF)

■ AUTHOR INFORMATION

Corresponding Author

*Tel: +381112615315/ext. 457. Fax: +381112199805. E-mail: fotiric@agrif.bg.ac.rs.

Notes

The authors declare no competing financial interest.

■ ACKNOWLEDGMENTS

This study was supported by the Ministry of Education, Science and Technological Development of the Republic of Serbia (projects No. TR 31063 and No. 172017) and FP7 Project AREA 316004. Also, the authors wish to thank Dr. Judith Anna Nikolić for proofreading of the article.

■ REFERENCES

(1) Hancock, J. F.; Lobos, G. A. Pears. In: *Temperate Fruit Crop Breeding: Germplasm to Genomics*; Hancock, J. F., Ed.; Springer: Netherlands, 2008; pp 299−335.

(2) Bellini, E.; Nin, S. Breeding for new traits in pear. *Acta Hortic.* **2002**, *596*, 217−224.

(3) Nin, S.; Ferri, A.; Sacchetti, P.; Giordani, E. Pear resistance to psylla (*Cacopsylla pyri*). A review. *Riv. Ortoflorofruttic. Ital.* **2012**, *26*, 59−74.

(4) Bell, R. L.; Puterka, G. L. Modes of host plant resistance to pear psylla: a review. *Acta Hortic.* **2004**, *663*, 183−188.

(5) Bell, R. L. Fruit quality of pear psylla-resistant parental germplasm. *HortScience* **2014**, *49*, 138−140.

(6) Horton, D. R.; Landolt, P. J. Attraction of male pear psylla, *Cacopsylla pyricola*, to female-infested pear shoots. *Entomol. Exp. Appl.* **2007**, *123*, 177−183.

(7) Ullman, D. E.; McLean, D. L. Feeding behavior of the winter-form pear psylla, *Psylla pyricola* (Homoptera: Psyllidae), on reproductive and transitory host plants. *Environ. Entomol.* **1988**, *17*, 675−678.

(8) Horton, D. R. Oviposition by overwintering morph of pear psylla (Homoptera:Psyllidae) with information on conditioning. *Environ. Entomol.* **1990**, *19*, 357−361.

(9) Horton, D. R.; Krysan, J. L. Host acceptance behavior of pear psylla (Homoptera: Psyllidae) affected by plant species, host deprivation, habituation, and egg load. *Ann. Entomol. Soc. Am.* **1991**, *84*, 612−627.

(10) Civolani, S.; Leis, M.; Grandi, G.; Garzo, E.; Pasqualini, E.; Musacchi, S.; Chicca, M.; Castaldelli, G.; Rossi, R.; Tjallingii, W. F. Stylet penetration of *Cacopsylla pyri*; an electrical penetration graph (EPG) study. *J. Insect Physiol.* **2011**, *57*, 1407−1419.

(11) Hildebrand, M.; Dickler, E.; Geider, K. Occurrence of *Erwinia amylovora* on insects in a fire blight orchard. *J. Phytopathol.* **2000**, *148*, 251−256.

(12) Seemüller, E.; Schneider, B. '*Candidatus* Phytoplasma mali', '*Candidatus* Phytoplasma pyri' and '*Candidatus* Phytoplasma prunorum', the causal agents of apple proliferation, pear decline and European stone fruit yellows, respectively. *Int. J. Syst. Evol. Microbiol.* **2004**, *54*, 1217−1226.

(13) Usha Rani, P.; Jyothsna, Y. Biochemical and enzymatic changes in rice as a mechanism of defense. *Acta Physiol. Plant.* **2010**, *32*, 695−701.

(14) War, A. R.; Paulraj, M. G.; Ahmad, T.; Buhroo, A. A.; Hussain, B.; Ignacimuthu, S.; Sharma, H. C. Mechanisms of plant defense against insect herbivores. *Plant Signaling Behav.* **2012**, *7*, 1306−1320.

(15) Simmonds, M. S. J. Flavonoid-insect interactions: recent advances in our knowledge. *Phytochemistry* **2003**, *64*, 21−30.

(16) Mikulič Petkovšek, M.; Štampar, F.; Veberič, R. Increased phenolic content in apple leaves infected with the apple scab pathogen. *J. Plant Pathol.* **2008**, *90*, 49−55.

(17) Veberič, R.; Trobec, M.; Herbinger, K.; Hofer, M.; Grill, D.; Stampar, F. Phenolic compounds in some apple (*Malus domestica* Borkh) cultivars of organic and integrated production. *J. Sci. Food Agric.* **2005**, *85*, 1687−1694.

(18) Mikulič Petkovšek, M.; Štampar, F.; Veberič, R. Seasonal changes in phenolic compounds in the leaves of scab-resistant and susceptible apple cultivars. *Can. J. Plant Sci.* **2009**, *89*, 745−753.

(19) Oleszek, W.; Amiot, M. J.; Aubert, S. Y. Identification of some phenolics in pear fruit. *J. Agric. Food Chem.* **1994**, *42*, 1261−1265.

(20) Painter, R. H. The economic value and biologic significance of insect resistance in plants. *J. Econ. Entomol.* **1941**, *34*, 358−367.

(21) Walling, L. L. The myriad plant responses to herbivores. *J. Plant Growth Regul.* **2000**, *19*, 195−216.

(22) Eyles, A.; Jones, W.; Riedl, K.; Herms, D. A.; Cipollini, D.; Schwartz, S.; Chan, K.; Herms, D. A.; Bonello, P. Comparative phloem chemistry of Manchurian (*F. mandshurica*) and two North American ash species (*F. americana* and *F. pennsylvanica*). *J. Chem. Ecol.* **2007**, *33*, 1430−1448.

(23) Bell, R. L.; Stuart, L. C. Resistance in Eastern European *Pyrus* germplasm to pear psylla nymphal feeding. *HortScience* **1990**, *25*, 789−791.

(24) Benedek, P.; Szabó, T.; Nyéki, J.; Soltész, M.; Szabó, Z.; Konrád-Németh, C. Susceptibility of European pear genotypes in a gene bank to pear psylla damage and possible exploitation of resistant varieties in organic farming. *Int. J. Hortic. Sci.* **2010**, *16*, 95−101.

(25) Pavlović, A.; Dabić, D.; Momirović, N.; Dojčinović, B.; Milojković-Opsenica, D.; Tešić, Ž.; Natić, M. Chemical composition of two diffrent extracts of berries harvested in Serbia. *J. Agric. Food Chem.* **2013**, *61*, 4188−4194.

(26) Gašić, U.; Kečkeš, S.; Dabić, D.; Trifković, J.; Milojković-Opsenica, D.; Natić, M.; Tešić, Z. Phenolic profile and antioxidant activity of Serbian polyfloral honeys. *Food Chem.* **2014**, *145*, 599−607.

(27) Singleton, V. L.; Rossi, J. A. Colorimetry of total phenolics with phosphomolybdic-phosphotungstic acid reagents. *Am. J. Enol. Vitic.* **1965**, *16*, 144−158.

(28) Colarič, M.; Štampar, F.; Hudina, M. Changes in sugars and phenolics concentrations of Williams pear leaves during the growing season. *Can. J. Plant Sci.* **2006**, *86*, 1203−1208.

(29) Bellés, J. M.; Garro, R.; Pallás, V.; Fayos, J.; Rodrigo, I.; Conejero, V. Accumulation of gentisic acid as associated with systemic infections but not with the hypersensitive response in plant-pathogen interactions. *Planta* **2006**, *223*, 500−511.

DOI: 10.1021/acs.jafc.5b03394
J. Agric. Food Chem. 2015, 63, 7476−7486

(30) Cui, T.; Nakamura, K.; Ma, L.; Li, J.; Kayahara, H. Analysis of arbutin and chlorogenic acid the major phenolic constituents in Oriental pear. *J. Agric. Food Chem.* **2005**, *53*, 3882−3887.
(31) Gunen, Y.; Misirli, A.; Gulcan, R. Leaf phenolic content of pear cultivars resistant or susceptible to fire blight. *Sci. Hortic. (Amsterdam, Neth.)* **2005**, *105*, 213−221.
(32) Leiss, K. A.; Maltese, F.; Choi, Y. H.; Verpoorte, R.; Klinkhamer, P. G. L. Identification of chlorogenic acid as a resistance factor for thrips in *Chrysanthemum*. *Plant Physiol.* **2009**, *150*, 1567−1575.
(33) Yang, G.; Espelie, K. E.; Todd, J. W.; Culbreath, A. K.; Pittman, R. N.; Demski, J. W. Cuticular lipids from wild and cultivated peanuts and the relative resistance of these peanut species to fall armyworm and thrips. *J. Agric. Food Chem.* **1993**, *41*, 814−818.
(34) Atteyat, M.; Abu-Romann, S.; Abu-Darwish, M.; Ghabeish, I. Impact of flavonoids against woolly apple aphid *Eriosoma lanigerum* (Hausmann) and its sole parasitoid *Aphelinus mali* (Hald.). *J. Agric. Sci.* **2012**, *4*, 227−236.
(35) Wang, S. Y.; Chen, C. T.; Wang, C. Y.; Chen, P. Resveratrol content in strawberry fruit is affected by preharvest conditions. *J. Agric. Food Chem.* **2007**, *55*, 8269−8274.
(36) Karaköse, H.; Jaiswal, R.; Kuhnert, N. Characterization and quantification of hydroxycinnamate derivatives in *Stevia rebaudiana* leaves by LC-MS^n. *J. Agric. Food Chem.* **2011**, *59*, 10143−10150.
(37) Álvarez-Fernández, M. A.; Cerezo, A. B.; Cañete-Rodríguez, A. M.; Troncoso, A. M.; García-Parrilla, M. C. Composition of nonanthocyanin polyphenols in alcoholic-fermented strawberry products using LC-MS (QTRAP), high-resolution MS (UHPLC-Orbitrap-MS), LC-DAD, and antioxidant activity. *J. Agric. Food Chem.* **2015**, *63*, 2041−2051.
(38) Felipe, D. F.; Brambilla, L. Z.; Porto, C.; Pilau, E. J.; Cortez, D. A. Phytochemical analysis of *Pfaffia glomerata* inflorescences by LC-ESI-MS/MS. *Molecules* **2014**, *19*, 15720−15734.
(39) Spínola, V.; Pinto, J.; Castilho, P. C. Identification and quantification of phenolic compounds of selected fruits from Madeira Island by HPLC-DAD-ESI-MS^n and screening for their antioxidant activity. *Food Chem.* **2015**, *173*, 14−30.
(40) Goławska, S.; Łukasik, I.; Goławski, A.; Kapusta, I.; Janda, B. Alfalfa (*Medicago sativa* L.) apigenin glycosides and their effect on the pea aphid (*Acyrthosiphon pisum*). *Polish J. Environ. Stud.* **2010**, *19*, 913−919.
(41) Saleem, M.; Nazir, M.; Ali, M. S.; Hussain, H.; Lee, Y. S.; Riaz, N.; Jabbar, A. Antimicrobial natural products: An update on future antibiotic drug candidates. *Nat. Prod. Rep.* **2010**, *27*, 238−254.
(42) Potters, G.; Pasternak, T. P.; Guisez, Y.; Jansen, M. A. Different stresses, similar morphogenic responses: Integrating a plethora of pathways. *Plant, Cell Environ.* **2009**, *32*, 158−169.
(43) Civolani, S.; Grandi, G.; Chicca, M.; Pasqualini, E.; Fano, E. A.; Musacchi, S. Probing behaviour of *Cacopsylla pyri* on a resistant pear selection. *J. Appl. Entomol.* **2013**, *137*, 365−375.
(44) Butt, B. A.; Stuart, L. C.; Bell, R. L. Feeding longevity and development of pear pscaugella (Homoptera: Psyllidae) nymphs on resistant and susceptible pear genotypes. *J. Econ. Entomol.* **1989**, *82*, 458−461.
(45) Hilker, M.; Meiners, T. How do plants 'notice' attack by herbivorous arthropods? *Biol. Rev.* **2010**, *85*, 267−280.
(46) Horton, D. R.; Krysan, J. L. Probing and oviposition-related activity of summerform pear psylla (Homoptera: Psyllidae) on host and non-host substrates. *Environ. Entomol.* **1990**, *19*, 1463−1468.
(47) Westwood, M. N. Pear germplasm of the new national clonal repository: it's evaluation and uses. *Acta Hortic.* **1982**, *124*, 57−66.
(48) Li, X.; Wang, T.; Zhou, B.; Gao, W.; Cao, J.; Huang, L. Chemical composition and antioxidant and anti-inflammatory potential of peels and flesh from 10 different pear varieties (Pyrus spp.). *Food Chem.* **2014**, *152*, 531−538.
(49) Wang, H.; Cao, G.; Prior, R. L. Total antioxidant capacity of fruits. *J. Agric. Food Chem.* **1996**, *44*, 701−705.
(50) Galvis Sánchez, A. C.; Gil-Izquierdo, A.; Gil, M. I. Comparative study of six pear cultivars in terms of their phenolic and vitamin C contents and antioxidant capacity. *J. Sci. Food Agric.* **2003**, *83*, 995−1003.

DOI: 10.1021/acs.jafc.5b03394
J. Agric. Food Chem. 2015, 63, 7476−7486

their adsorptivity on the surface of a tongue.[16−20] This retention of fat on the tongue can cause residual taste perception (i.e., aftertaste) of flavor compounds that they are interacting but to varying extents.[21]

In this study a systematic approach was used to mechanistically understand the relationship between salt release behavior and perception as affected by biopolymer−salt interactions. The objectives of this study were to specifically evaluate the extent of protein−salt interactions at different solution concentrations and to characterize interfacial effects when biopolymers are structured around nanoscale lipid droplets on salt transport and perception. We modified a chromatography column with a porcine tongue to simulate salt transport in the mouth. Analytical results for salt transport and adsorptivity were then correlated with sensory evaluation to elucidate the mechanisms controlling the perception of saltiness in such colloidal systems. In the subsequent paper we investigated the effects of lipid−protein−salt interactions on the hydration rate, and subsequent salt release, from low-moisture (i.e., freeze-dried) samples.

MATERIALS AND METHODS

Materials. Sodium caseinate (Na-cas) and sodium chloride (NaCl) (USP grade) were both purchased from Sigma-Aldrich (St. Louis, MO, USA). Corn oil was purchased from a local supermarket. The porcine tongues were obtained from the meat laboratory at the University of Minnesota (St. Paul, MN, USA). In all sample preparations and experiments, sodium-free nanopure water was used. In house deionized water was further purified by using a Barnstead Nanopure Diamond water purification system (Thermo Scientific, Dubuque, IA, USA) to obtain nanopure water. Protein solutions (0−10 wt %) were prepared by overnight stirring in nanopure water at room temperature. Emulsions at different protein/lipid ratios were prepared using a hot homogenization technique.[22] Briefly, hot protein solutions (1−5 wt %) were mixed with corn oil (0−20 wt %) using a high-speed blender to form a coarse emulsion. The emulsion premix was then passed through a microfluidizer (M-110Y Microfluidizer, Microfluidics, Newton, MA, USA) at ca. 60−65 °C (3 passes at 1200 bar). After the samples cooled to room temperature, salt was added and stirred for 4−5 h.

Analytical Measurements. Salt adsorptivity and retention on a model tongue surface were evaluated by using a modified gel permeation chromatography column accompanied by a porcine tongue (Figure 1). The front section of the fresh porcine tongue was cut as a disk (2.1 cm in diameter and 0.2−0.3 cm in thickness) and kept frozen at −20 °C until used. The thawed tongue pieces were then placed on the bottom plunger surface covering the base. Then, aliquots of samples (ca. 0.15 mL) were added to the tongue surface, and the top plunger was adjusted to about 0.1−0.2 cm above the tongue, leaving a negligible amount of empty space above the tongue surface. Salted protein solutions and oil-in-water emulsions were then washed from the tongue surface using an HPLC system (Shimadzu 10A series, Columbia, MD, USA) with nanopure water at a rate of 5 mL/min. The effluent was collected at 1 min intervals by a fraction collector. Each fraction was analyzed for sodium concentrations using an atomic absorption spectrometer (AAS) (PerkinElmer Inc., Waltham, MA, USA) coupled with a K−Na lumina hallow cathode lamp (PerkinElmer Inc.) and for dissolved solids using an evaporative light scattering detector (ELSD) (PL-ELSD 2100 Ice, Agilent, Santa Clara, CA, USA). The fractions from the column effluent were diluted in water to be within the dynamic range of the instrument. The ELSD was calibrated using reference dispersions with various protein and lipid concentrations similar to that measured for the sample fractions.

Particle Size Measurements. The average hydrodynamic diameter of the emulsions was determined by dynamic light scattering. The samples were diluted to ca. 1:100 with nanopure water, and then the particle size was analyzed using a Delsa Nano C Particle Analyzer (Beckman, Brea, CA, USA). The measurement was performed at 25 °C and at a 165° scattering angle. Mean hydrodynamic diameter was calculated on the basis of size distribution by weight, assuming a log-normal distribution. Ten individual size measurement runs were performed, with each run recording 100 size events. The droplet size (i.e., Sauter mean diameter) of the emulsions was found to be 0.2 μm.

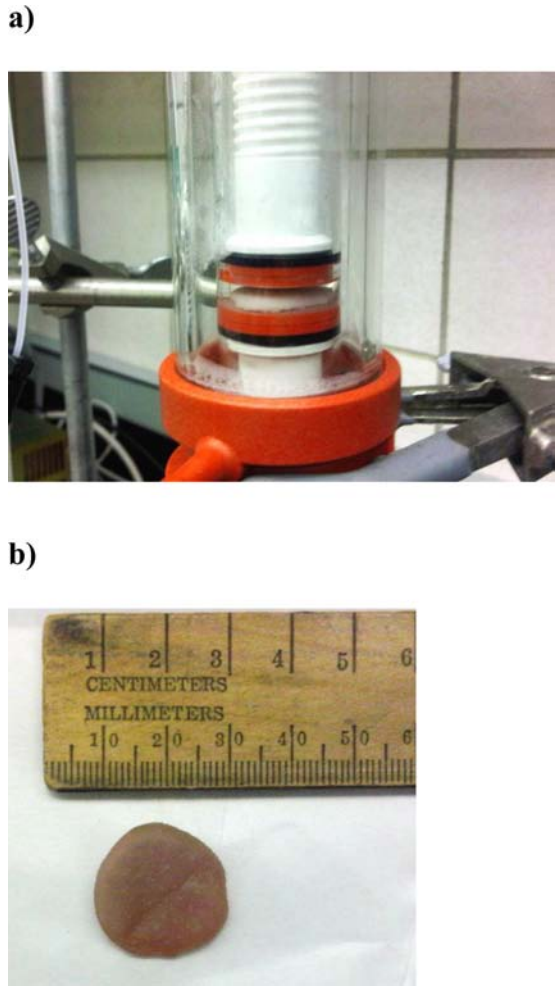

Figure 1. Picture of the chromatography column modified to work with circular porcine tongue (2.1 cm) and coupled to an HPLC system.

Sensory Analysis. A trained descriptive analysis panel of 11 panelists evaluated the salty intensity of the samples. Panelists were trained on a 15-point intensity scale, with NaCl reference solutions at 0.2, 0.35, 0.5, 0.64, and 0.75% corresponding to intensity scores of 2.5, 5, 8.5, 12, and 15, respectively. The panelists were trained during 12 1-h sessions over a period of 3 weeks. The performance of the panelists was assessed using blind references during training.

Samples were evaluated in triplicate using a randomized block design. Four samples were evaluated each session. The samples were served in 20 mL plastic cups, coded in random three-digit codes. During the sample evaluation the panelists were instructed to pour 10 mL of sample onto their tongue, hold for 5 s, and then expectorate the sample back into a container (time zero for aftertaste analysis) for further analysis of the residual sodium. Panelists rated the saltiness aftertaste intensity at 0, 15, 30, 60, 120, 180, 240, and 300 s after expectorating the sample. Panelists waited 10 min between samples. Water and unsalted crackers were used as palate cleansers.

Panelists were classified into two groups on the basis of their rating of saltiness intensity after rinsing their mouth with a 1% salt solution and waiting 1 min prior to evaluation. High and low saliva flow rates were classified for those who rated saltiness at <2 and >2 at 1 min after sample introduction, respectively.

DOI: 10.1021/acs.jafc.5b02311
J. Agric. Food Chem. 2015, 63, 7487−7493

Statistical Analysis. Results were evaluated for statistical significance using a t test for a pairwise comparison of two samples at $\alpha = 0.05$. All samples were prepared and analyzed in triplicate.

RESULTS AND DISCUSSION

It is known that the salty taste of food is produced by the transduction of the sodium ions via epithelial sodium channels, albeit all of the cellular mechanisms related to the perception of saltiness are still under investigation.[23] To taste sodium ions they need to be released from the food to be adsorbed on the surface of the tongue to start electrochemical signaling producing the sensation of saltiness. However, during consumption food products typically have very short retention time in the oral cavity, limiting the available sodium contributing to the salty taste. In a food matrix such ions can interact with other larger molecules, especially biopolymers (e.g., proteins), via electrostatic interactions, and as a result affect their transport kinetics and retention on the surface of the tongue. In the current study our goal was to focus on the nature of interactions between protein and salt molecules affecting the transport kinetics of salt ions in aqueous solutions and, in turn, mechanisms that influence salt perception. The delivery profile of sodium in protein−salt solutions was initially investigated using a tongue surface in a modified chromatography column coupled to an HPLC system (Figure 1). As the first step, we validated the performance of the designed tongue−column system to study the transport kinetics of sodium. Simple aqueous solutions of sodium chloride (0.5−10 wt %) were injected onto the column−tongue system, and the adsorptivity of sodium on the tongue surface was monitored from the effluent (Figure 2). The first data point in the sodium concentration versus time graph corresponds to the sodium concentration in the first fraction of the effluent (0−1 min). The linear relationship reported between the initial concentrations of the salt solutions and the sodium concentrations in the first fraction collected from the tongue−column system indicated that this design was working as expected, and therefore it was deemed suitable to study the transport kinetics of sodium. The rate of sodium removal from the tongue's surface was very fast, being quantitatively depleted within 2 min. In the next step, we investigated the effects of dissolved protein on sodium retention on the tongue's surface.

Three protein−salt solutions consisting of 1, 5, and 10% protein at a constant 1% NaCl level were made using sodium caseinate, the sodium salt of the major protein in milk. The intrinsic levels of sodium in sodium caseinate were negligible with regard to the amount of NaCl added to the samples. It is highly soluble in water and often used in low-fat product formulations. Addition of the protein was predicted to bind the sodium ions via electrostatic interactions and change the availability of sodium to the aqueous phase during consumption and subsequently alter salt perception. The sodium concentration in the aqueous effluent as monitored from the model tongue system (Figure 1) for the three protein solutions is shown in Figure 3. As seen in Figure 3a, the sodium concentrations in the first minute of the effluent decreased with increasing protein concentrations, specifically for the 5 and 10% protein solutions. The release of sodium in the effluent for the 1% protein solution was similar to that for the pure salt solution (no protein), indicating there were not sufficient protein interactions at this dosage level to alter the initial salt amount washed off the tongue system. Protein−salt interactions largely depend on the anionic charged segments of the

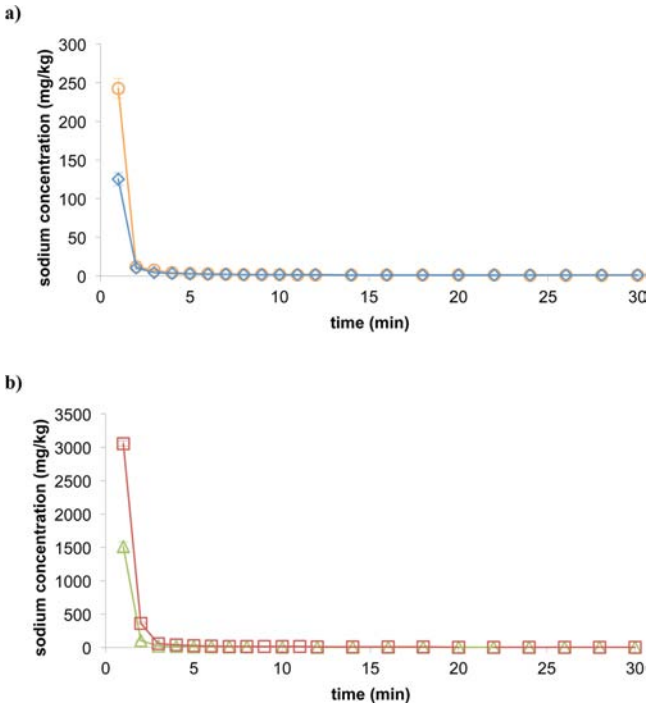

Figure 2. Sodium concentrations in the effluent after (a) 0.5% (diamonds) and 1% (circles) salt solutions and (b) 5% (triangles) and 10% (squares) salt solutions were washed from the model tongue surface (5 mL/min) as collected in fractions at 1 and 2 min intervals (13−30 min). The bars on the data show standard deviation. The straight lines between data points are merely used to aid in visual analysis.

available protein and would increase with higher concentration of protein in these solutions (i.e., higher protein/salt ratio) as well as with the charge potential of the proteins. After this initial minute, the higher protein samples reported higher sodium concentrations in the effluent over time (Figure 3b). For example, from 1 to 4 min the amount of sodium in the effluent was approximately 2 times higher for the 5 and 10% protein solutions in comparison to the 1 or 0% protein solutions. The increased release of sodium over time from the higher protein solution could be explained by protein adhesion to the tongue's surface that would serve as a salt reservoir and release sodium over time into the aqueous phase.

Other researchers have also reported salt perception was influenced by polymer−salt interactions based on various mechanisms. Rosett et al. showed that the charge on the biopolymer was more important to determine the perception of salty taste, rather than the viscosity.[5] Oral processing has also been reported to modify food−tastant interactions. For example, it has been shown that saliva amylase can break down large starch molecules, decreasing the apparent viscosity of the solutions but also the mixing efficiency, which limits the molecular diffusion of salt and reduces the salt perception.[24] De Jongh and Janssen reported the retention time of liquid foods in the oral cavity increased when the viscosity was increased (by protein and carbohydrate addition) and likewise altered taste perception.[20]

The noted influence of the protein/salt ratio on the sodium transport behavior in Figure 3 could potentially be confounded by the change in the sample solids content on molecular diffusion.

DOI: 10.1021/acs.jafc.5b02311
J. Agric. Food Chem. 2015, 63, 7487−7493

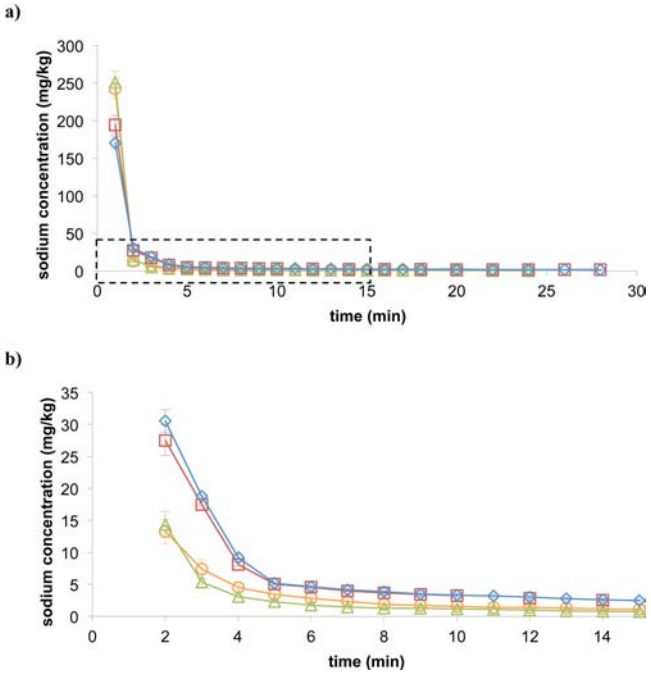

Figure 3. (a) Sodium concentrations in the effluent of 1% salt solutions containing 0% (circles), 1% (triangles), 5% (squares), and 10% (diamonds) casein after washing from the model tongue surface (5 mL/min) as collected in fractions at 1 min intervals. (b) The dashed area from the top graph was zoomed for better resolution from 1 to 15 min. The bars on the data show standard deviation. The straight lines between data points are merely used to aid in visual analysis.

To further ascertain if changes in the solids content affected the sodium release profiles in Figure 3, sodium release was monitored from two protein solutions at 5 and 10% that were formulated at the same protein/salt ratio of 10:1 (Figure 4).

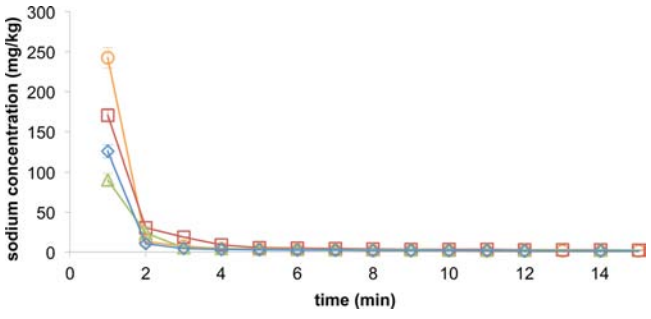

Figure 4. Sodium concentrations in the effluent of 0.5% salt solutions containing 0% (diamonds) and 5% (triangles) casein and 1.0% salt solutions containing 0% (circles) and 10% (squares) casein after washing from the model tongue surface (5 mL/min) as collected in fractions at 1 min intervals. The bars on the data show standard deviation. The straight lines between data points are merely used to aid in visual analysis.

For both the 5 and 10% protein solutions the decreases in sodium concentration in the first fraction (0−1 min) relative to the corresponding salt solution were effectively the same ($p > 0.05$). The sodium concentrations reported in the first fractions for the 5 and 10% were significantly smaller ($p > 0.05$) and 1.39 ± 0.03 and 1.42 ± 0.02 times less than the corresponding pure salt solutions. An effective diffusivity (k_{eff}) constant was also calculated assuming pseudo-first-order kinetics for the fractions between 1 and 6 min (i.e., k_{eff} was calculated from the slope). Similarly, k_{eff} was not statistically different for 10% (0.81 s^{-1}) and 5% (0.82 s^{-1}) protein solutions at the same protein/salt ratio (10:1), although the solution thicknesses were different. However, when the salt concentration in the 5% protein solution was increased to a protein/salt ratio of 5:1 (1% salt, Figure 3), both the sodium concentration change in the first fraction (1.31 ± 0.02%) and the k_{eff} (0.86 s^{-1}) were significantly larger than for the 10:1 ratio. These findings indicate viscosity effects from the protein added to the solutions were not an important factor that influenced the difference in salt delivery reported between the 5 and 10% protein solutions in Figure 3 and supported protein ionic binding as an important mechanism of salt delivery.

The extent of ionic protein−salt interactions would be governed by the accessibility of the ionic groups to the aqueous phase. To investigate this concept, protein−salt interactions in emulsion systems were characterized using casein and oil colloid systems. When oil is emulsified with caseinate, the hydrophilic protein segments (volume fraction is about 0.9) surround the outside of the oil droplets as a dense outer layer that is approximately 1 nm in thickness, whereas a diffuse hydrophobic segment (volume fraction is about 0.1) forms an inner layer in the oil droplet that can extend up to 10 nm in thickness.[25] Moreover, proteins on these lipid droplets are known to have a net negative charge around neutral pH (i.e., pH above their isoelectric point).[26] It has been shown that such interfacial structures of caseinate can affect the distribution profiles of small molecules and cause localization around the droplets' interface.[22] This electrostatic charge around the droplets could further affect the rate of ion exchange between the aqueous phase and the droplet surface. For example, the oxidation of protein-stabilized omega-3-enriched oil-in-water emulsions can be inhibited at pH below the p*I* of proteins (i.e., due to cationic properties of the emulsion droplets).[27,28] In a similar manner, the net negative charge around the droplet can attract cationic sodium ions and serve to enhance the localization of sodium ions around the charged outer layer segments of the caseinate molecules on the lipid droplets.

The release of sodium from the aqueous emulsion systems is illustrated in Figure 5. Two different emulsion formulations of 1% protein−4% lipid and 2.5% protein−2.5% lipid were compared to a 5% protein aqueous solution and a aqueous salt solution, all at 1% salt. The sodium concentration in the first fraction of the effluent (0−1 min) was significantly reduced for the emulsion systems compared to the 5% protein solution, even though the percent protein levels in the emulsions were comparatively lower in amount. Additionally, the emulsion with 4% lipid and 1% protein reported a lower salt concentration (at 0−1 min) compared to the 2.5% lipid and 2.5% protein emulsion. Although the emulsion systems had a lower percent protein, when the lipid amount increased relative to the percent protein, a higher interfacial area is expected that ultimately enhanced the exposure of the anionic groups in the aqueous phase and thus the ionic interactions with sodium. The release of sodium from the emulsion systems from 1 to 14 min is further shown in a magnified view in Figure 5b and showed similar trends as Figure 3b. Samples that lowered the salt concentration the most in the first minute had the highest release of sodium after this first minute, in this case the 1% protein−4% lipid sample.

DOI: 10.1021/acs.jafc.5b02311
J. Agric. Food Chem. 2015, 63, 7487−7493

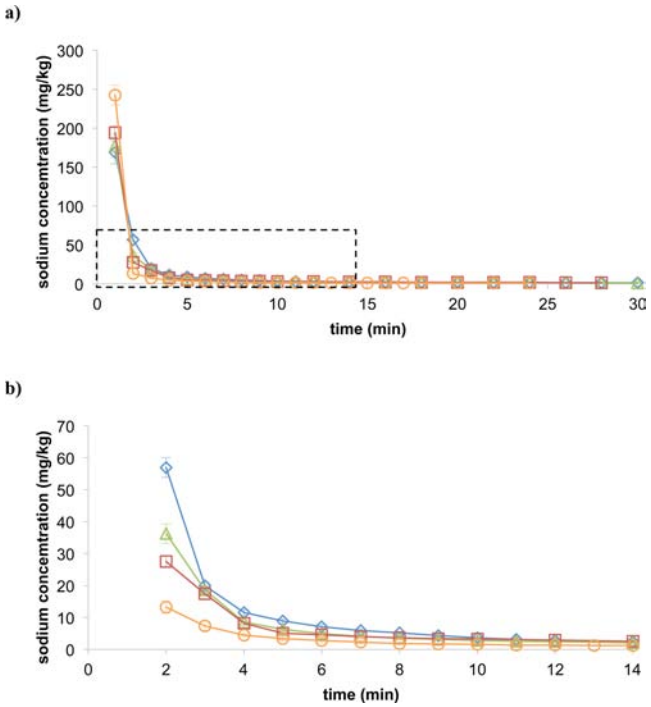

Figure 5. (a) Sodium concentrations in the effluent of emulsions (5% organic phase) compared to that of the 1% salt solution (circles) after washing from the model tongue surface (5 mL/min) as collected in fractions at 1 min intervals. The emulsified phase was formulated as 1% protein−4% lipid (diamonds), 2.5% protein−2.5% lipid (triangles), or 5% protein−0% lipid (squares). (b) The dashed area from the top graph was zoomed for better resolution for fractions between 1 and 14 min. The bars on the data show standard deviation. The straight lines between data points are merely used to aid in visual analysis.

To further single out the interfacial effects of emulsions on sodium interactions (i.e., as a function of surface area and number of droplets), sodium release rates from emulsions with the same protein content (5%) and different lipid concentrations (5 and 20 wt %) at 1% salt were compared (Figure 6). Similar results were obtained; the droplet surface area increased (by increasing the lipid content) and the initial release rate decreased. Therefore, the electrostatic interactions between protein and salt molecules were enhanced by conferring the anionic properties of the proteins to the aqueous phase of the emulsified droplets. The higher retained sodium was then washed off the tongue surface at a higher rate over time.

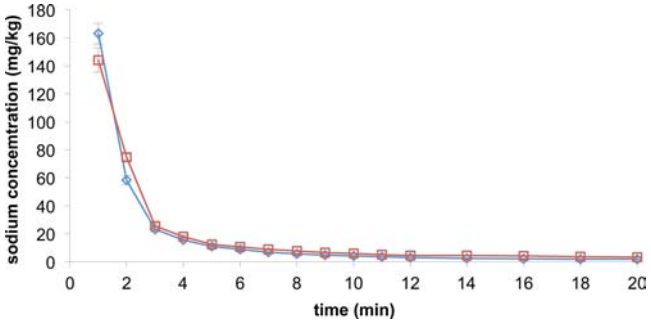

Figure 6. Sodium concentrations in the effluent of emulsions stabilized with 5% casein and containing 5% (diamonds) or 20% (squares) lipid, after washing from the model tongue surface (5 mL/min) as collected in fractions at 1 min intervals. The bars on the data show standard deviation. The straight lines between data points are merely used to aid in visual analysis.

On the basis of the observed influence of protein on the retention of salt and corresponding higher amounts of salt released over time (compared to aqueous salt) in the model tongue column (Figures 3 and 5), the protein material was suggested to adhere to the tongue's surface and function as a salt reservoir and release salt with continued washing. To further examine the interaction of the protein in the tongue column, the total solute concentration in the effluent was also measured from 0 to 14 min by using an ELSD, and the data are shown in Figure 7. Review of the solute concentration in the effluent over time confirmed our previous statement that the organic phase (i.e., protein) adhered to the tongue's surface. In parallel, the highest absorptivity (i.e., slowest diffusivity) was observed for the emulsions with the highest lipid concentrations. Consequently, this supported our statement that the protein material functioned as a reservoir of sodium that released sodium over time into the aqueous phase.

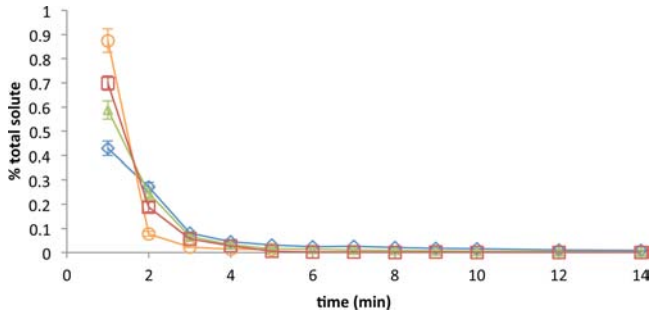

Figure 7. Total solute concentration in the effluent of emulsions after washing from the model tongue surface (5 mL/min) as collected in fractions at 1 min intervals and analyzed by evaporative light scattering detector. Samples consisted of 1% salt solution (circles), 1% protein−4% lipid (diamonds), 2.5% protein−2.5% lipid (triangles), and 5% protein−0% lipid (squares). The bars on the data show standard deviation. The straight lines between data points are merely used to aid in visual analysis.

Sensory descriptive analysis of the salt intensity was further conducted on the protein−salt solutions (Figure 8) as well as the emulsion systems (Figure 9) to extrapolate the analytical data to human perception. For the sensory evaluations, the panelists were classified into two groups, low and high saliva flow rates. For the protein solution (Figure 8), the sensory data were in agreement with analytical results (Figure 3). With increasing protein content of the salt solutions, a lower salt intensity rating was reported for the initial time period with a corresponding higher salt intensity afterward (aftertaste). For example, in the low saliva flow regimen, the salty taste of the salt solution (no protein) disappeared within 120 s, whereas there was still a residual salty taste lingering after 180 s for the 10% casein solution. Although the salty ratings in both groups with high and low saliva flow rates followed the same trend, the time−salt intensity curves more clearly separated at the low saliva flow regimen. Therefore, we further discussed the sensory ratings of this group for the emulsion samples.

The presence of colloidal lipid considerably changed the perception of saltiness (Figure 9). Interestingly the initial intensities of the emulsions at a constant 5% organic content were not significantly different ($p < 0.05$) from that of the 1% salt solution itself (Figure 9a) in contrast to the analytical data

DOI: 10.1021/acs.jafc.5b02311
J. Agric. Food Chem. 2015, 63, 7487−7493

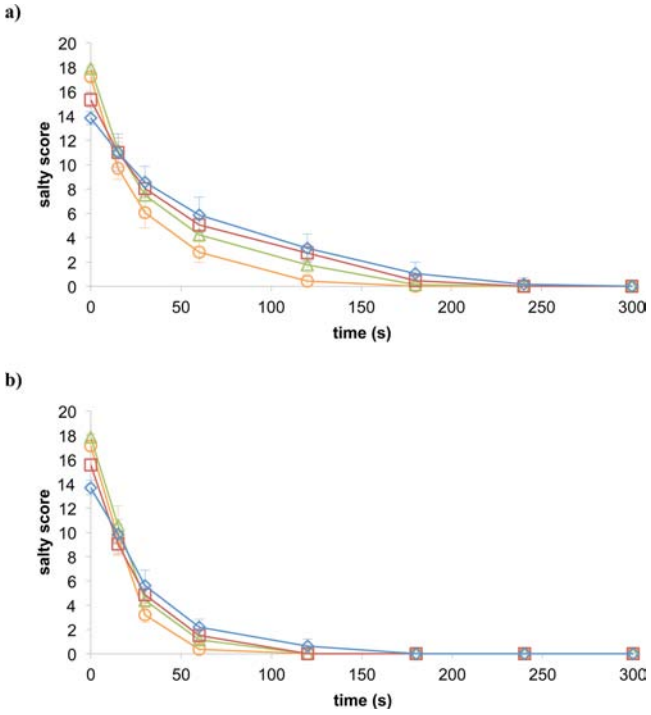

Figure 8. Time–intensity plot for salty intensity rating of 1% salt solutions containing 0% (circles), 1% (triangles), 5% (squares), and 10% (diamonds) casein for (a) low saliva flow rates and (b) high saliva flow rates. The bars on the data show standard deviation. The straight lines between data points are merely used to aid in visual analysis.

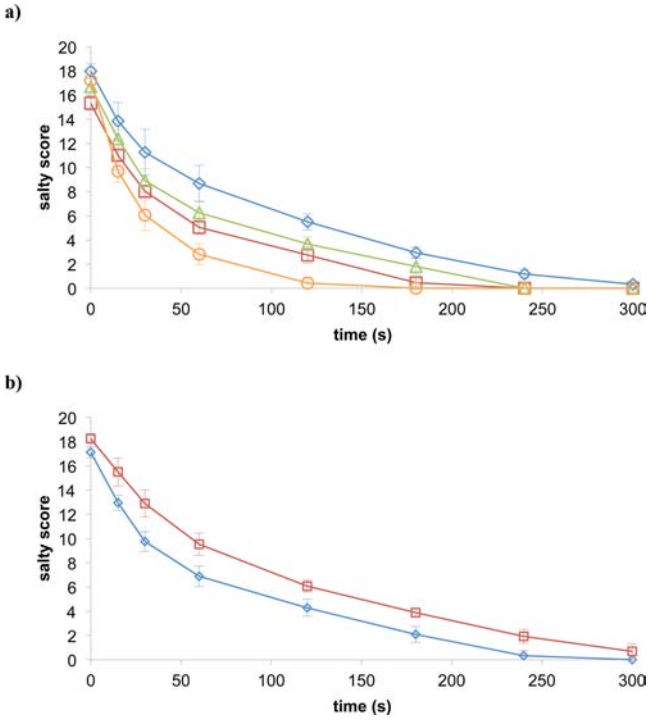

Figure 9. Time–intensity plot for salty intensity rating of 1% salt emulsions for samples formulated as (a) 5% total organic phase containing 1% protein–4% lipid (diamonds), 2.5% protein–2.5% lipid (triangles), 5% protein–0% lipid (squares), 1% salt solution (circles) and (b) 5% protein with 5% lipid (diamonds) or 20% lipid (squares). The bars on the data show standard deviation. The straight lines between data points are merely used to aid in visual analysis.

(Figure 5a). The nanoscale dimensions of lipid droplets may have facilitated sodium availability on the tongue's surface. However, increasing the lipid concentrations caused higher salt intensity aftertaste, which was in line with the analytical data (Figure 5b). Emulsion samples with the same amount of protein (5%) at two lipid concentrations (5 and 20%) were compared for their time course salt intensity behaviors (Figure 9b). The sensory results followed the same trend as the analytical data (Figure 4): increasing the number of lipid droplets provides more interface for proteins, further enhancing the salt–protein interactions and resulting in longer salty aftertaste.

In this study, we showed that protein–salt interactions could play an important role in determining the transport properties of sodium in solutions. We designed an analytical system to study sodium retention on a tongue surface and compared the results to sensory analysis. Overall, our data supported the importance of intermolecular interactions (i.e., electrostatic interactions) in determining the perception of salty taste. These results can serve as a guideline to control sodium availability, and subsequently its perception, when food products are formulated for lower sodium content while enhancing salt perception. In the following paper, we studied the effect of protein–salt interactions on the salt perception and the hydration rates of low-moisture samples as a function of lipid levels.

AUTHOR INFORMATION

Corresponding Author

*(D.G.P.) E-mail: dgp@umn.edu. Phone: (612) 624-3201. Fax: (612) 625-5272.

Funding

This research was supported by the Flavor Research and Education Center, Department of Food Science and Nutrition, University of Minnesota.

Notes

The authors declare no competing financial interest.

REFERENCES

(1) Cutler, J. A.; Follmann, D.; Allender, P. S. Randomized trials of sodium reduction: an overview. *Hypertension* **1997**, *65*, 643S–651S.

(2) Kilcast, D.; Angus, F. *Reducing Salt in Foods: Practical Strategies*; Woodhead Publishing: Boca Raton, FL, USA, 2007.

(3) Osborn, S. Salt reduction innovations. *World Food Ingred.* **2013**, *April/May*, 18–20.

(4) Phan, V. A.; Yven, C.; Lawrence, G.; Chabanet, C.; Reparet, J. M.; Salles, C. In vivo sodium release related to salty perception during eating model cheeses of different textures. *Int. Dairy J.* **2008**, *18*, 956–963.

(5) Rosett, T. R.; Kendregan, S. L.; Klein, B. P. Fat, protein, and mineral components of added ingredients affect flavor qualities of tomato soups. *J. Food Sci.* **1997**, *62* (1), 190–193.

(6) Busch, J. L. H. C.; Tournier, C.; Knoop, J. E.; Kooyman, G.; Smit, G. Temporal contrast of salt delivery in mouth increases salt perception. *Chem. Senses* **2009**, *34*, 341–348.

(7) Le Reverend, B. J. D.; Norton, I. T.; Bakalis, S. Modelling the human response to saltiness. *Food Funct.* **2013**, *4*, 880–888.

(8) Lauverjat, C.; Deleris, I.; Trelea, I. C.; Salles, C.; Souchon, I. Salt and aroma compound release in model cheeses in relation to their mobility. *J. Agric. Food Chem.* **2009**, *57*, 9878–9887.

(9) Lemieux, L.; Simard, R. E. Bitter flavor in dairy products. I. A review of the factors likely to influence its development, mainly in cheese manufacture. *Lait* **1991**, *71*, 599–636.

(10) Roy, G. General ingredient or process approaches to bitterness inhibition and reduction in oral pharmaceuticals. In *Modifying*

DOI: 10.1021/acs.jafc.5b02311
J. Agric. Food Chem. 2015, 63, 7487–7493

Bitterness: Mechanism, Ingredients, and Applications; Roy, G., Ed.; CRC Press: Boca Raton, FL, USA, 1997; pp 285−320.
(11) Sohi, H.; Sultana, Y.; Khar, R. K. Taste masking technologies in oral pharmaceuticals: recent developments and approaches. *Drug Dev. Ind. Pharm.* **2004**, *30* (5), 429−448.
(12) Shamil, S.; Wyeth, L. J.; Kilcast, D. Flavour release and perception in reduced-fat foods. *Food Qual. Prefer.* **1992**, *3*, 51−60.
(13) Metcalf, K. L.; Vickers, Z. M. Taste intensitie of oil-in-water emulsions with varying fat content. *J. Sens. Stud.* **2002**, *17*, 379−390.
(14) Geurts, T. J.; Walstra, P.; Mulder, P. Transport of salt and water during salting of cheese. 1. Analysis of the processes involved. *Neth. Milk Dairy J.* **1974**, *28*, 102−129.
(15) Lynch, J.; Liu, Y. H.; Mela, D. J.; MacFie, H. J. H. A time-intensity study of the effect of oil mouthcoatings on taste perception. *Chem. Senses* **1993**, *18*, 121−129.
(16) Rietberg, M. R.; Rousseau, D.; Duizer, L. Sensory evaluation of sodium chloride-containing water-in-oil emulsions. *J. Agric. Food Chem.* **2012**, *60*, 4005−4011.
(17) Dresselhuis, D. M.; Stuart, M. A. C.; van Aken, G. A.; Schipper, R. G.; de Hoog, E. H. A. Fat retention at the tongue and the role of saliva: adhesion and spreading of "protein-poor" versus "protein-rich" emulsions. *J. Colloid Interface Sci.* **2008**, *321* (1), 21−29.
(18) Dresselhuis, D. M.; van Aken, G. A.; de Hoog, E. H. A; Stuart, M. A. C. Direct observation of adhesion and spreading of emulsion droplets at solid surfaces. *Soft Matter* **2008**, *4*, 1079−1085.
(19) de Jongh, H. H. J.; Janssen, A. M.; Weenen, H. Differential retention of emulsion components in the mouth after swallowing: ATR FTIR measurements of oral coatings. In *Food Lipids: Chemistry, Flavor, and Texture*; Shahidi, F., Weenen, H., Eds.; American Chemical Society: Washington, DC, USA, 2006; pp 87−94.
(20) de Jongh, H. H. H.; Janssen, A. M. Differential clearance kinetics of adhered layer constituents from the oral cavity as modulator for afterfeel of dressings: ATR FT-IR measurements of localized oral coatings. *J. Texture Stud.* **2007**, *38* (1), 70−86.
(21) Lauverjat, C.; Deleris, I.; Trelea, I. C.; Salles, C.; Souchon, I. Salt and aroma compound release in model cheeses in relation to their mobility. *J. Agric. Food Chem.* **2009**, *57*, 9878−9887.
(22) Yucel, U.; Elias, R. J.; Coupland, J. N. Solute distribution and stability in emulsion-based delivery systems: an EPR study. *J. Colloid Interface Sci.* **2012**, *377*, 105−113.
(23) Gilbertson, T. A.; Damak, S.; Margolskee, R. F. The molecular physiology of taste transduction. *Curr. Opin. Neurobiol.* **2000**, *10* (4), 519−527.
(24) Ferry, A. L. S.; Mitchell, J. R.; Hort, J.; Hill, S. E.; Taylor, A. J.; Lagarrigue, S.; Valles-Pamies, B. In-mouth amylase activity can reduce perception of saltiness in starch-thickened foods. *J. Agric. Food Chem.* **2006**, *54*, 8869−8873.
(25) Leermakers, F. A. M.; Atkinson, P. J.; Dickinson, E.; Horne, D. S. Self-consistent-field modeling of adsorbed β-casein: effects of pH and ionic strength on surface coverage and density profile. *J. Colloid Interface Sci.* **1996**, *178*, 681−693.
(26) Dalgleish, D. G.; Srinivasan, M.; Singh, M. J. Surface properties of oil-in-water emulsion droplets containing casein and Tween-60. *J. Agric. Food Chem.* **1995**, *43*, 2351−2355.
(27) Donnelly, J. L.; Decker, E. A.; McClements, D. J. Iron-catalyzed oxidation of Menhaden oil as affected by emulsifiers. *J. Food Sci.* **1998**, *63* (6), 997−1000.
(28) McClements, D. J.; Decker, E. A. Lipid oxidation in oil-in-water emulsions: impact of molecular environment on chemical reactions in heterogeneous food systems. *J. Food Sci.* **2000**, *65* (8), 1270−1282.

DOI: 10.1021/acs.jafc.5b02311
J. Agric. Food Chem. 2015, 63, 7487−7493

maximum intensity profiles and enhancing the overall salt perception.[4,13] This effect may also depend on the initial salt content.

Previously we showed that ionic interactions between cationic sodium ions and anionic sodium caseinate molecules can affect sodium transport to the tongue and its absorptivity on the surface of the tongue to enhance the perception of saltiness and create a longer aftertaste.[6] Such interactions can be further modified via interfacial effects in emulsions. The overall objective of this study is to expand this knowledge and to further understand the influence of protein in low-moisture systems on sodium release during hydration and perceived saltiness intensity. The effect of the emulsion-associated interfacial properties of a protein on sodium delivery was similarly investigated, and analytical results were compared to sensory analyses.

MATERIALS AND METHODS

Materials. Sodium caseinate (Na-cas) and sodium chloride (NaCl) (USP grade) were both purchased from Sigma-Aldrich (St. Louis, MO, USA). Corn oil was purchased from a local supermarket. The porcine tongues were obtained from the meat laboratory at the University of Minnesota (St. Paul, MN, USA). All sample preparations and experiments used in house deionized water that was further purified by the Barnstead Nanopure Diamond water purification system (Thermo Scientific, Dubuque, IA, USA) to obtain nanopure water.

Protein solutions (0−5 wt %) and oil-in-water emulsions (0−20 wt % corn oil) were prepared as described in the previous paper.[6] Briefly, protein solutions were prepared by overnight stirring in nanopure water at room temperature. Emulsions at different protein/lipid ratios were prepared using a hot homogenization technique, where a coarse emulsion premix was passed three times at 1200 bar through a microfluidizer (M-110Y Microfluidizer, Microfluidics, Newton, MA, USA) at ca. 60−65 °C. After the samples cooled to room temperature, salt was added and stirred for 4−5 h. Then, samples were frozen at −20 °C and dried by lyophilization (at 100 mT) using a Virtis Freezemobile 35EL (SP Scientific, Warminster, PA, USA).

Analytical Measurements. Salt adsorptivity and retention on a porcine tongue surface were evaluated by using the modified GPC column−tongue setup coupled to an HPLC system as previously described.[6] Briefly, total mass equivalents (same amount of total mass for each sample, 7.5 mg) or salt equivalents (i.e., same amount of salt but various total mass, i.e., 1.5 mg of salt) of freeze-dried powders of protein solutions and oil-in-water emulsions were placed directly and homogeneously on the surface of the tongue, and the column was sealed by fixing the top plunger at 0.1−0.2 cm above the tongue surface. Powder samples were then washed from the tongue's surface using an HPLC system (Shimadzu, Columbia, MD, USA) with nanopure water at a rate of 5 mL/min. The effluent was collected at 1 min intervals using a fraction collector. Each fraction was analyzed for sodium concentrations using an atomic absorption spectrometer (AAS) (PerkinElmer Inc., Waltham, MA, USA) coupled with a K−Na lumina hallow cathode lamp (PerkinElmer Inc.) and for dissolved solids using an evaporative light scattering detector (ELSD) (PL-ELSD 2100 Ice, formerly Polymer Laboratories, presently Agilent, Santa Clara, CA, USA). Fractions were diluted in water to be within the dynamic range of the instrument, and the ELSD was calibrated using reference dispersions with various protein and lipid concentrations similar to those measured for the sample fractions.

Sensory Analysis. A trained descriptive analysis panel of 11 panelists evaluated the salty intensity of the samples. Panelists were trained on a 15-point intensity scale with NaCl reference solutions at 0.2, 0.35, 0.5, 0.64, and 0.75% corresponding to intensity scores of 2.5, 5, 8.5, 12, and 15, respectively. The panelists were trained during 12 1-h sessions over a period of 3 weeks. The performance of the panelists was assessed using blind references during training.

The samples were evaluated in triplicate using a randomized block design. Three samples were evaluated each session. For the sample evaluation panelists were instructed to put 0.1 g of sample on the center of their tongue, and the timer was started as time zero. Panelists rated the saltiness intensity at 0, 10, 20, 30, 60, 120, 180, 240, and 300 s. The dissolution time of the powder (i.e., time needed to completely hydrate the powder in the mouth) and the final time for complete removal of the salty taste were also recorded. Panelists waited 10 min between samples. Water and unsalted crackers were used as palate cleansers.

Statistical Analysis. Results were evaluated for statistical significance using a t test for a pairwise comparison of two samples at $\alpha = 0.05$. All samples were prepared and analyzed in triplicate.

RESULTS AND DISCUSSION

In a preceding study, we demonstrated that the presence of protein can affect the transport kinetics of sodium from aqueous salt solutions and, likewise, salt perception.[6] The extent of these interactions could further be enhanced by promoting the availability of charged segments of the protein via interfacial effects as seen in nanoemulsions. In the current study, we investigated the effects of such intermolecular interactions in low-moisture systems during hydration on salt release and consequently on the perception of saltiness. A modified chromatography column coupled to an HPLC system as described in the preceding paper was utilized to model sodium release and hydration and in parallel samples were evaluated by sensory analysis.[6]

Sodium release from freeze-dried powders derived from protein solutions (5% Na-cas) of various salt concentrations (0.5, 1, and 10% NaCl) at 10:1, 5:1, and 1:2 protein/salt ratios during hydration wsd analyzed. The sodium release profiles for samples at equivalent mass are shown in Figure 1a. The samples with excess salt (i.e., 1:2 protein/salt ratio) showed a monotonous decrease of salt concentration in the effluent, whereas when the ratio of protein to salt increased, a different behavior was observed. The sodium concentration in the effluent of samples with 10:1 and 5:1 protein/salt ratios first increased followed by a subsequent decrease over time. This noted difference in sodium release between the samples with excess sodium to protein versus the samples with excess protein to salt was likely due to amount of free sodium (i.e., fraction not associated with the protein). The sodium less associated with protein more readily hydrated and dissolved.

Additionally, we considered that the presence of salt likely influenced the hydration rates of proteins. The configurations of proteins are modified in aqueous solutions by salt ions, which can be approximated by the Hofmesiter series.[14,15] Recent research indicated direct ion−macromolecule interactions determine the solubility and hydration capacity of the macromolecules, in contrast to earlier models that assumed the water structure is modified by the salt ions.[16] Consequently, it is likely that protein−salt interactions altered the hydration rates of the powders in the current study and contributed to the release profile noted for the samples with excess protein to salt composition in Figure 1a.

A similar trend was also observed when the total mass of sample placed on the tongue's surface was adjusted to provide equivalent sodium contents for each sample at different protein/salt ratios (Figure 1b). These findings indicated sample size or changing the amount of protein between samples (5:1 or 10:1) was not affecting the sodium release profile. Consequently, the sodium ions more associated with the proteins limited the release of sodium and became available only after the protein was hydrated. These findings are in agreement with Lauverjat et al.,[9] who showed that casein

DOI: 10.1021/acs.jafc.5b02312
J. Agric. Food Chem. 2015, 63, 7494−7498

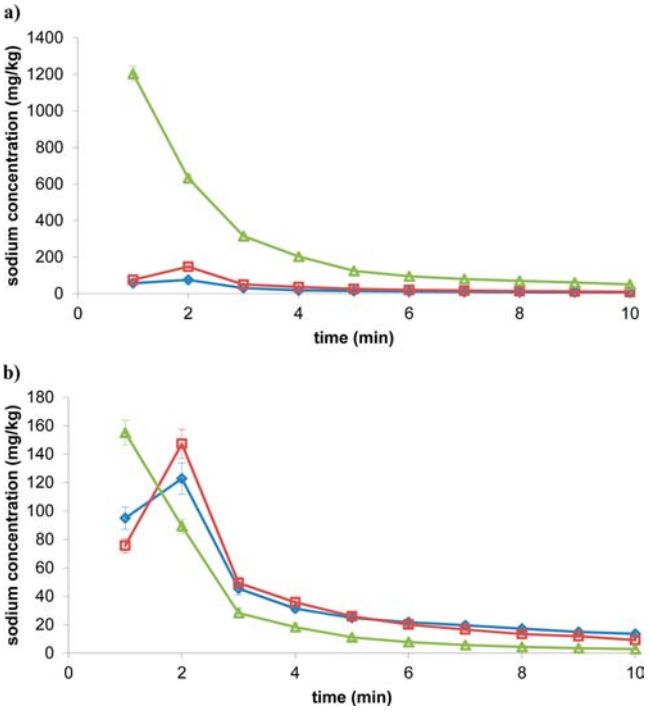

Figure 1. Sodium concentrations in the effluent of protein powders with 10:1 (90.9% protein, 9.1% salt) (diamonds), 5:1 (83.3% protein, 16.7% salt) (squares), and 1:2 (33.3% protein, 66.7% salt) (triangles) casein/salt (w/w) ratios for (a) total mass equivalents (7.5 mg sample) and (b) equivalent sodium amounts (1.5 mg), after washing from the model tongue surface (5 mL/min) as collected in fractions at 1 min and at 2 min intervals (after 12 min). The bars on the data show standard deviation. The straight lines between data points are merely used to aid in visual analysis.

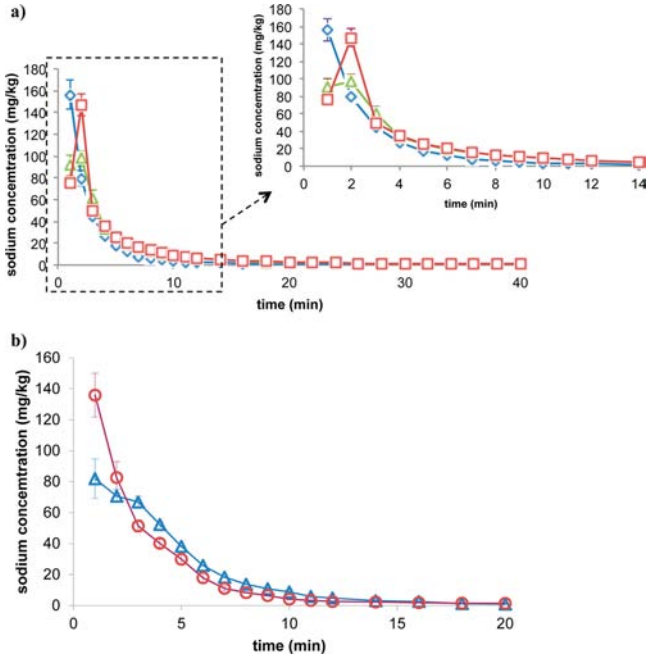

Figure 2. Sodium concentrations in the effluent of emulsion powders for total mass equivalents (7.5 mg sample) of (a) constant organic phase/salt ratio (5:1) where organic phase formulated at 5:0 (83% protein, 0% lipid, 17% salt) (squares), 1:1 (41.5% protein, 41.5% lipid, 17% salt) (triangles), and 1:4 (17% protein, 67% lipid, 17% salt) (diamonds) protein/lipid ratios (the dashed area was zoomed for higher resolution from 1 to 15 min as shown in the inset) and (b) the same protein/salt ratio (5:1) but with various protein/lipid contents as 1:1 (45.5% protein, 45.5% lipid, 9% salt) (triangles) from 5% protein−5% lipid emulsions and 1:4 (19.2% protein, 77% lipid, 3.8% salt) (circles) from 5% protein−20% lipid emulsions, after washing from the model tongue surface (5 mL/min) as collected in fractions at 1 min and at 2 min intervals (after 12 min). The bars on the data show standard deviation. The straight lines between data points are merely used to aid in visual analysis.

molecules in cheese could bind sodium ions, slowing the mobility and release during hydration. In the following part of the current study, we further investigated the influence of modifying the protein structure through interfacial effects in the presence of colloidal lipids on subsequent sodium delivery during hydration.

The release of sodium during hydration of the freeze-dried emulsions with a constant protein/salt (5:1) ratio and changing lipid levels is shown in Figure 2b. Increasing the lipid concentration would increase the protein interfacial area and expose more of the hydrophilic segments of the protein to the aqueous phase of the emulsion.[17] Indeed, the casein structure around lipid droplets was described earlier on the basis of neutron scattering measurements as a diffuse hydrophilic protein layer, which can extend up to 10 nm from the droplet surface as compared to a dense inner hydrophobic layer with a 1 nm thickness.[18] Therefore, the diffuse protein structure formed around the lipid droplets is anticipated to enhance the availability of protein material to water to hydrate more quickly and the associated sodium ions and ultimately increase sodium release during hydration of the sample. The results in Figure 2 were in agreement with this hypothesis; the dried emulsion sample at the higher lipid level resulted in a faster release of sodium during the initial hydration step when compared to the lower lipid content sample. A delayed release rate was also observed for the lower lipid content sample, indicating that when the protein was less structured at the interface, the salt−protein interactions reduced the immediate availability of sodium but also prolonged its retention on the tongue surface.

In a similar way, Lawrence et al. showed that sodium ions associate with anionic liposome matrixes, which can enhance the salt release and subsequent salty taste perception in cheese products.[19] Similar results were observed when the sample size was held constant but the protein and fat levels were altered (see Figure 2a). At a lower protein to fat ratio, more protein would be structured at the interface. As expected, the 1:4 protein/lipid emulsion samples had a higher initial sodium release than the 1:1 protein/lipid emulsion samples or the protein salt mixtures.

In addition to sodium concentration measurements, total dissolution kinetics were also evaluated by analyzing the solute concentration in the effluent of freeze-dried emulsions with constant organic phase/salt (5:1) ratio by using ELSD (Figure 3). In parallel with sodium measurements, the fastest dissolution rate was observed for powder with 4:1 versus the 1:1 lipid/protein ratio, and the pure protein powder had the lowest initial release of solutes. The powder with 1:1 protein/lipid ratio showed S-shape two-stage dissolution kinetics. Initially, the lipid particle portion of the powder dissolved quickly, and the dissolution rate slowed as the protein fraction not structured around the lipid droplet dominated.

The localization of sodium in a food product is of critical importance in determining the molecular mobility of sodium and therefore the availability for perception. We further

DOI: 10.1021/acs.jafc.5b02312
J. Agric. Food Chem. 2015, 63, 7494−7498

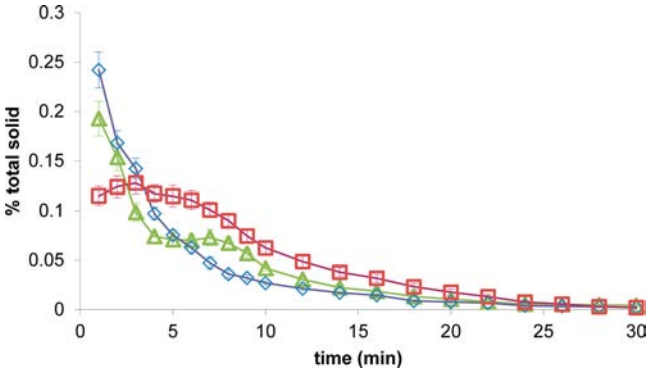

Figure 3. Total solute concentration change as percentage of initial solute concentration in the effluent of dried emulsion powders containing 1% salt after washing from the model tongue surface (5 mL/min) as collected in fractions at 1 min and at 2 min intervals (after 10 min) and as analyzed by ELSD. The powders are formulated as 5:0 (83% protein, 0% lipid, 17% salt) (squares), 1:1 (41.5% protein, 41.5% lipid, 17% salt) (triangles), and 1:4 (17% protein, 67% lipid, 17% salt) (diamonds) protein/lipid ratios. The bars on the data show standard deviation. The straight lines between data points are merely used to aid in visual analysis.

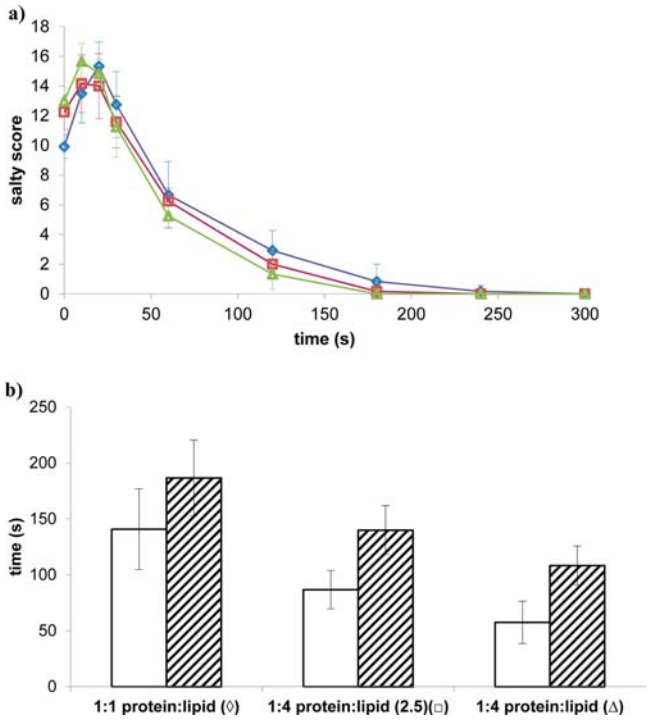

Figure 4. (a) Time–intensity plot for salty intensity rating of emulsion powders at low saliva flow rates, formulated as (at constant protein/salt ratio) 1:1 protein/lipid ratio (45.5% protein, 45.5% lipid, 9% salt) (diamonds) and 4:1 protein/lipid ratio (19.2% protein, 77% lipid, 3.8% salt) (triangles) with total mass equivalents (0.1 g) and 4:1 protein/lipid ratio (19.2% protein, 77% lipid, 3.8% salt) (squares) with equivalent sodium amounts to 1:1 protein/lipid (the amount tested is 2.5 times more than constant organic phase/salt ratio samples). The straight lines between data points are merely used to aid in visual analysis. (b) Dissolution time for the powder in the mouth (white bars) and final time for the salty taste to disappear (shaded bars). The bars on the data show standard deviation.

evaluated the effects of the hydration rates of the emulsion powders on saltiness perception using a trained sensory panel. Panelists rated the saltiness intensity of the emulsion powders over a period of 5 min (Figure 4a). In general, the time–salt intensity curves followed the same pattern of release as the analytical results (Figure 2). The initial intensity of the powder with 1:4 protein/lipid ratio (19.2% protein, 77% lipid, and 3.8% salt) was higher than that for 1:1 protein/lipid ratio (45.5% protein, 45% lipid, and 9% salt). This higher initial intensity was due to faster dissolution rates, which also served to decrease the retention of the powder on the tongue over time and, hence, the faster removal of the salty taste (i.e., shorter time for the residual taste). The sample weight of the 1:4 protein/lipid ratio was also increased 2.5 times for evaluation to have the equivalent amount of salt as in the 1:1 protein/lipid sample. Although the amount of powder consumed slightly affected the dissolution behavior, the profile of the salt time–intensity curve was similar to the lower sample size: the higher the lipid content, the faster the dissolution with higher initial intensity (Figure 4a).

To confirm the relationship between the dissolution rates of the powders and residual salty taste, we asked the panelists to record the time required for complete dissolution of the powders and final time for the salty taste to disappear (Figure 4b). These results are in agreement with previous observations that samples with longer dissolution times resulted in longer salty aftertaste. Increasing the lipid levels (i.e., number of lipid nanoparticles) resulted in shorter powder dissolution times. Moreover, a greater degree of difference was observed between the dissolution time and final time for saltiness perception between the samples with 1:4 and 1:1 protein/lipid ratios, likely because after the lipid particles hydrated, the resulting emulsified droplets have higher adsorption on the tongue than the protein material that is not emulsified, as previously discussed.[6]

The localization of sodium in our samples was shown to affect molecular mobility and therefore availability for perception. In the preceding study we showed that the extent of ionic interactions between sodium and caseinate were enhanced when the protein was structured around the lipid droplets, when the protein was at a net negative charge.[6] In the present study, we showed that such protein structure around the lipid droplets can be a powerful tool to enhance the hydration rates of powders to control sodium release from low-moisture food products and control the perception of salty taste. Therefore, when integrated to formulations of low-moisture foods, such systems can allow more sodium ions to reach sodium channels before swallowing to contribute to the salty taste.

AUTHOR INFORMATION

Corresponding Author

*(D.G.P.) E-mail: dgp@umn.edu. Phone: (612) 624-3201. Fax: (612) 625-5272.

Funding

This research was supported by the Flavor Research and Education Center, Department of Food Science and Nutrition, University of Minnesota.

Notes

The authors declare no competing financial interest.

DOI: 10.1021/acs.jafc.5b02312
J. Agric. Food Chem. 2015, 63, 7494–7498

REFERENCES

(1) Cutler, J. A.; Follmann, D.; Allender, P. S. Randomized trials of sodium reduction: an overview. *Am. J. Clin. Nutr.* **1997**, *65*, 643S−651S.

(2) U.S. Department of Agriculture and U.S. Department of Health and Human Services. *Dietary Guidelines for Americans 2010*, 7th ed.; U.S. Government Printing Office: Washington, DC, USA, 2010.

(3) Kilcast, D.; Angus, F. *Reducing Salt in Foods: Practical Strategies*; Woodhead Publishing: Boca Raton, FL, USA, 2007.

(4) Osborn, S. Salt reduction innovations. *World Food Ingred.* **2013**, *April/May*, 18−20.

(5) Gilbertson, T. A.; Damak, S.; Margolskee, R. F. The molecular physiology of taste transduction. *Curr. Opin. Neurobiol.* **2000**, *10* (4), 519−527.

(6) Yucel, U.; Peterson, D. G. Effect of protein-lipid-salt interactions on sodium availability in the mouth and consequent perception of saltiness: in solutions. *J. Agric. Food Chem.* **2015**, DOI: 10.1021/acs.jafc.5b02311.

(7) Kuo, W.-Y.; Lee, Y. Effect of food matrix on saltiness perception-implications for sodium reduction. *Compr. Rev. Food Sci. Food Saf.* **2014**, *13*, 906−923.

(8) Ruusunen, M.; Simolin, M.; Puolanne, E. The effect of fat content and flavor enhancers on the perceived saltiness of cooked 'bologna-type' sausages. *J. Muscle Foods* **2001**, *12* (2), 107−120.

(9) Lauverjat, C.; Deleris, I.; Trelea, I. C.; Salles, C.; Souchon, I. Salt and aroma compound release in model cheeses in relation to their mobility. *J. Agric. Food Chem.* **2009**, *57*, 9878−9887.

(10) Phan, V. A.; Yven, C.; Lawrence, G.; Chabanet, C.; Reparet, J. M.; Salles, C. In vivo sodium release related to salty perception during eating model cheeses of different textures. *Int. Dairy J.* **2008**, *18*, 956−963.

(11) Busch, J. L. H. C.; Tournier, C.; Knoop, J. E.; Kooyman, G.; Smit, G. Temporal contrast of salt delivery in mouth increases salt perception. *Chem. Senses* **2009**, *34*, 341−348.

(12) Le Reverend, B. J. D.; Norton, I. T.; Bakalis, S. *Food Funct.* **2013**, *4*, 880−888.

(13) Rama, R.; Chiu, N.; da Silva, M. C.; Hewson, L.; Hort, J.; Fisk, I. D. Impact of salt crystal size on in-mouth delivery of sodium and saltiness perception from snack foods. *J. Texture Stud.* **2013**, *44*, 338−345.

(14) Shimizu, S.; McLaren, W. M. The Hofmeister series and protein−salt interactions. *J. Chem. Phys.* **2006**, *124* (23), 1−4.

(15) Bostrom, M.; Williams, D. R. M.; Ninham, B. W. Why the properties of proteins in salt solutions follow a Hofmeister series. *Curr. Opin. Colloid Interface Sci.* **2004**, *9*, 48−52.

(16) Zhang, Y.; Cremer, P. S. Interactions between macromolecules and ions: the Hofmeister series. *Curr. Opin. Chem. Biol.* **2006**, *10*, 658−663.

(17) Yucel, U.; Elias, R. J.; Coupland, J. N. Solute distribution and stability in emulsion-based delivery systems: an EPR study. *J. Colloid Interface Sci.* **2012**, *377*, 105−113.

(18) Leermakers, F. A. M.; Atkinson, P. J.; Dickinson, E.; Horne, D. S. Self-consistent-field modeling of adsorbed β-casein: effects of pH and ionic strength on surface coverage and density profile. *J. Colloid Interface Sci.* **1996**, *178* (2), 681−693.

(19) Lawrence, G.; Buchin, S.; Achilleos, C.; Berodier, F.; Septier, C.; Courcoux, P.; Salles, C. In vivo sodium release and saltiness perception in solid lipoprotein matrices. 1. Effect of composition and texture. *J. Agric. Food Chem.* **2012**, *60*, 5287−5298.

DOI: 10.1021/acs.jafc.5b02312
J. Agric. Food Chem. 2015, 63, 7494−7498

butanal, 2-methylfuran, 2-methylpropanal, 2-nonanone, 2-pentylfuran, 2,3,5-trimethylpyrazine, 3-mercaptohexanol, 3-methylbutanal, 3-methylbutyl acetate, 3-methylbutanoate, 5-methyl-2-furfural, 6-methyl-5-hepten-2-one, acetaldehyde, acetic acid, benzaldehyde, benzothiazole, benzyl alcohol, butanal, butyl acetate, camphor, *cis*-jasmone, *cis*-linaloloxide, dihydroactinidiolide, dimethyl disulfide, dimethyl sulfide, dimethyl sulfoxide, dimethyl trisulfide, (*E*)-2-heptenal, (*E*)-2-hexenal, (*E*)-2-pentenal, (*E*,*E*)-2,4-heptadienal, (*E*,*E*)-2,4-hexadienal, ethyl acetate, (*E*)-2-octenal, ethanethiol, furan, furfural, geraniol, heptanal, heptanoic acid, heptanol, hotrienol, hexanal, hexanoic acid, hexanol, indole, methanethiol, methyl benzoate, methyl hexanoate, methyl jasmonate, methyl salicylate, nerolidol, nonanal, octanal, octanoic acid, pentanal, propanal, propanethiol, phenyl acetaldehyde, phenylethyl alcohol, (*R*)-(−)-linalool, *S*-methyl thioacetate, *trans*-linalooloxide, (*Z*)-3-hexen-1-ol, and (*Z*)-4-heptenal were purchased from Alfa Aesar Corporation (Tianjin, China). Furfurylthiol, methional, methionol, and C_6−C_{30} *n*-alkane standard were purchased from Sigma-Aldrich Corporation (Shanghai, China). All of the chemical standards used above were of GC quality.

Sample Preparation. Twenty grams of oolong tea was weighed and placed in a prewarmed tea pot, and 1000 mL of 80 °C distilled water was added. The tea was brewed for 5 min and swirled 10 times clockwise while brewing. Then, the tea was poured through a porcelain strainer into a prewarmed porcelain bowl. These samples were stored in a refrigerator (4 °C) after the tea infusions had cooled down to room temperature.

Solid Phase Microextraction (SPME) Absorption of Aroma Compounds. The manual SPME holder, together with 20 mL vials, Teflon covers, and one 75 μm divinylbenzene-carboxyl-polydimethylsiloxane (DVB-CAR-PDMS) fiber, were purchased from Supelco, Inc. (Bellefonte, PA, USA). Before chemical absorption, the fiber was preconditioned for 30 min on an Agilent 6890 gas chromatograph (Agilent Technologies, USA) with the injector temperature of 250 °C.

The main parameters that were known to influence the methodology were investigated, such as fiber, extraction time, extraction temperature, and sample volume. According to the results obtained (data not shown), optimized SPME experimental conditions were established, i.e., 30 min of extraction time, and a sample volume of 5 g. It is worth pointing out that the volatile compounds in tea infusions were very likely artifacts formed during the heat impact. Therefore, the extraction temperature was set at 25 °C. Then 5 g portions of the treated samples were transferred to the vials and sealed with a Teflon cover. The vials were kept at 25 °C on a water bath for 30 min with shaking at regular intervals. After the SPME fiber had been exposed in the upper space of the bottle for 30 min, it was then withdrawn and directly introduced to the GC injector for desorption and analysis.

Calibration of Standard Curves. To obtain a matrix similar to that of tea infusion, model solution was prepared containing 25 mg/g caffeine, 5 mg/g (+)-catechin (C), 5 mg/g (−)-epicatechin (EC), 10 mg/g (−)-epicatechin gallate (ECG), 20 mg/g (−)-epigallocatechin (EGC), 10 mg/g (−)-gallocatechin gallate, 40 mg/g (−)-epigallocatechin gallate (EGCG), 4 mg/g theanine, 0.8 mg/g Glu, 0.5 mg/g Pro, 0.5 mg/g Val, and 0.5 mg/g Ser in Milli-Q deionized water.[6,13,14]

A standard stock solution was prepared containing 50 mg/kg methanethiol, 5 mg/kg ethanethiol, 2 mg/kg propanethiol, 1500 mg/kg dimethyl sulfide, 10 mg/kg dimethyl trisulfide, 150 mg/kg dimethyl sulfoxide, 10 mg/kg dimethyl disulfide, 0.1 mg/kg 3-mercaptohexanol, 1 mg/kg *S*-methyl thioacetate, 2 mg/kg benzothiazole, 1 mg/kg methionol, 2 mg/kg methional, and 0.1 mg/kg furfurylthiol in Milli-Q deionized water. The standard stock solution was then diluted with water to 1:2, 1:10, 1:20, 1:50, and 1:200 strengths. In order to construct the calibration curves, 0.01 g of each of those diluted solutions of sulfur compounds and 0.01 g of the internal standard solution containing 2 mg/kg of dipropyl disulfide were introduced to the 5 g of model solution in a 20 mL vial, which was extracted by SPME, as was performed for the tea infusions.

The standard curves were shown in the research, where *y* represented the peak area ratio (peak area of sulfur volatile standard/peak area of internal standard) and *x* represented the concentration ratio (concentration of sulfur volatile standard/concentration of internal standard). The calibration curves were obtained from Chemstation software (Agilent Technologies Inc.) and used for calculation of volatiles in tea infusions. Quantitation of other volatile compounds was carried out by standard curves obtained by each compound from six different concentrations in water with the internal standard of 2-octanol (0.01 g of 5 mg/kg).

GC−MS Identification of Aroma Compounds. The analyses were performed using a Hewlett-Packard 7890 GC with a 5975 mass selective detector (MSD) (Agilent Technologies) instrument operating under electron ionization (EI) mode (70 eV, ion source temperature 230 °C) with the quadrupole in a scanning mode (scan range was *m*/*z* 30−450 at a scan rate of 1 scan/s). Separation of compounds was achieved on Innowax-Wax (60 m × 0.25 mm i.d. × 0.25 μm film thickness, Agilent Technologies) and DB-5 (60 m × 0.25 mm i.d. × 0.25 μm film thickness, Agilent Technologies). Helium (purity = 99.999%) was used as a carrier with a constant flow velocity of 1 mL/min. The quadrupole mass filter was at 150 °C. The oven temperature was held at 40 °C for 6 min, then ramped to 100 °C at the rate of 2 °C/min, and ramped at the rate of 5 °C/min to 230 °C for the last 10 min.

The volatile compounds were identified by comparing retention indices and authentic standards, or with mass spectra in the Wiley and NIST11 libraryies. The RIs were determined via sample injection with a homologous series of alkanes (C5−C30) (Sigma-Aldrich).

Gas Chromatography−FPD. Gas chromatography equipped with a 5380 FPD detector from Agilent (Santa Clara, CA) was used in the sulfur mode. Separation of compounds was achieved on Innowax-Wax (60 m × 0.25 mm i.d. × 0.25 μm film thickness, Agilent Technologies, USA) and DB-5 (60 m × 0.25 mm i.d. × 0.25 μm film thickness, Agilent Technologies, USA). The oven temperature was held at 40 °C for 6 min, then ramped to 100 °C at the rate of 2 °C/min, and ramped at the rate of 5 °C/min to 230 °C for the last 10 min. GC was operated in a constant flow mode (1 mL/min) with helium as the carrier gas. The FPD detector was set at 250 °C, and the photomultiplier tube (PMT) voltage was set at 500 V. The sulfur-containing compounds were confirmed by comparison with authentic standards on both columns, RI value matching, and aroma descriptor. The quantification method was identical to the GC analysis as described in the above section. The samples were run in triplicate.

GC−Olfactometry Analysis. GC−olfactometry analysis was carried out on an Agilent 6890N GC equipped with flame ionization detection (FID) system and an olfactometer (Gerstel, Inc., Baltimore, MD). The Innowax (60 m × 0.25 mm i.d. × 0.25 μm film thickness, Agilent Technologies, USA) and DB-5 (60 m × 0.25 mm i.d. × 0.25 μm film thickness, Agilent Technologies, USA) were used. The oven temperature was held at 40 °C for 6 min, then ramped to 100 °C at the rate of 2 °C/min, and ramped at the rate of 5 °C/min to 230 °C for the last 10 min. The column effluent was split 1:1 into the FID and the heated sniffing port (250 °C) using two deactivated and uncoated fused silica capillaries. The column carrier gas was nitrogen at a constant flow rate of 2 mL/min. A panel of ten trained panelists (5 males and 5 females) evaluated the effluents enriched with purified, humidified air (120 mL/min). Each of the panelists was trained before sensory analysis in order to get familiar with an odor description by using solutions of artificial odorants. The aroma-active compounds perceived by ten panelists were recorded as the time for onset and end while sniffing the effluent from the sniffing mask. The panelists were also required to note the perceived odor characteristic and intensity. With the same time, the computer automatically recorded the retention time and sniffing time of aroma-active compound individually. The odor intensities were evaluated using a 6-point intensity scale from 0 to 5; "0" was none, "3" was moderate, and "5" was extreme. The experiment was replicated in triplicate by each panelist. Finally, the aroma intensity was the average from ten panelists.

Odor Activity Values (OAV). The contribution of each odor to the overall fruit wine aroma was evaluated by the odor activity value, which was measured as the ratio of the concentration of each compound to its detection threshold. The threshold values were taken from information available in the references.

DOI: 10.1021/acs.jafc.5b02358
J. Agric. Food Chem. 2015, 63, 7499−7510

Table 1. GC−O Identified Aroma-Active Compounds in Tea Infusions with the Method of Aroma Intensity

no.[a]	name	RI[b] Innowax	RI[b] DB-5	aroma description	DHP[c]	TGY[c]	DDWL[c]	identification basis[d]
1	methanethiol	696	502	sulfur, gasoline, garlic	0.8ab[e]	0.5b	2.2a	RI, Std, AD, FPD
2	acetaldehyde	714	<500	pungent, ether	np[f]	2.6	1.5	RI, Std, AD
3	dimethyl sulfide	716	505	cabbage, sulfur, corn, molasses	2.3b	2.7b	3.4a	RI, Std, AD, FPD
4	propanal	750	506	solvent, pungent	np	0.7	2.5	RI, Std, AD
5	2-methylpropanal	821	662	pungent, malt, green	2.2ab	1.8b	3.0a	RI, Std, AD
6	butanal	832	596	pungent, green	np	1.4	1.7	RI, Std, AD
7	3-methylbutanal	910	650	malt	np	2.6	3	RI, Std, AD
8	2-methylbutanal	912	641	cocoa, almond	2.0a	2.4a	2.2a	RI, Std, AD
9	pentanal	935	732	almond, malt, pungent	2.2b	2.2b	2.6a	RI, Std, AD
10	2,3-butanedione	970	593	butter	2.3	np	2.3	RI, Std, AD
11	1-penten-3-one	973	680	fish, pungent	2.2	1.2	np	RI, Std, AD
12	2,3-pentanedione	1054	700	cream, butter	2.7	np	2.2	RI, Std, AD
13	dimethyl disulfide	1071	785	onion, cabbage, putrid	3.3a	2.8a	3.1a	RI, Std, AD, FPD
14	hexanal	1084	801	grass, tallow, fat	3.4b	4.1a	4.3a	RI, Std, AD
15	(*E*)-2-pentenal	1131	754	grass, tomato	3.0b	2.7c	4.0a	RI, Std, AD
16	1-penten-3-ol	1157	686	butter, pungent	3.7a	2.8b	3.5a	RI, Std, AD
17	unknown1	1165	806	fish,fat	2.2	np	np	−
18	heptanal	1174	903	fat, citrus, rancid	3.1b	4.0a	4.2a	RI, Std, AD
19	(*E*)-2-hexenal	1192	844	green, leaf	3.1b	3.4b	4.3a	RI, Std, AD
20	(*Z*)-4-heptenal	1230	902	biscuit, cream	2	2.3	np	RI, Std, AD
21	1-pentanol	1255	766	balsamic	np	0.8	2.2	RI, Std, AD
22	octanal	1280	1006	fat, lemon, green	2.2ab	1.7b	2.7a	RI, Std, AD
23	2,5-dimethylpyrazine	1302	905	cocoa, roasted nut	3.6a	3.6a	3.0b	RI, Std, AD
24	(*E*)-2-heptenal	1315	957	soap, fat	2.3c	3.8b	4.2a	RI, Std, AD
25	2,3-octanedione	1320	960	cream, butter, wax	1.9	np	1.7	RI, Std, AD
26	6-methyl-5-hepten-2-one	1336	974	sweet, fruity	3.4a	3.8a	3.2a	RI, Std, AD
27	unknown2	1345	954	grass, citrus	np	1.5	1.7	−
28	hexanol	1360	851	resin, flower, green	np	2	1.2	RI, Std, AD
29	(*Z*)-3-hexen-1-ol	1378	858	grass	3.2a	3.0a	3.4a	RI, Std, AD
30	nonanal	1385	1104	fat, citrus, green	2.4a	2.3a	2.9a	RI, Std, AD
31	2,3,5-trimethylpyrazine	1395	1000	roast, potato, must	0.8a	0.6a	0.5a	RI, Std, AD
32	(*E*,*E*)-2,4-hexadienal	1405	910	green	2.6	np	2.1	RI, Std, AD
33	(*E*)-2-octenal	1411	1060	green, nut, fat	2.0b	2.7a	2.5ab	RI, Std, AD
34	*cis*-linaloloxide	1420	1070	flower	3.2a	2.7b	3.0a	RI, Std, AD
35	1-octen-3-ol	1426	982	mushroom	1.6ab	1.8a	1.2b	RI, Std, AD
36	furfurylthiol	1432	912	coffee, roast	4	3.7	np	RI, Std, AD, FPD
37	unknown3	1443	1011	flower, wood	2.3	1.1	np	−
38	furfural	1455	829	bread, almond, sweet	3.4a	2.5b	1.5c	RI, Std, AD
39	methional	1458	909	cooked potato	4.1	3.9	np	RI, Std, AD, FPD
40	*trans*-linalooloxide	1465	1212	flower, wood	3.5a	1.9b	2.2b	RI, Std, AD
41	(*E*,*E*)-2,4-heptadienal	1470	1011	nut, fat	2.3b	2.8ab	3.7a	RI, Std, AD
42	2-acetylfuran	1490	893	balsamic	2.7	np	np	RI, Std, AD
43	benzaldehyde	1495	960	almond, burnt sugar	3.2a	3.3a	2.0b	RI, Std, AD
44	(*R*)-(−)-linalool	1537	1100	flower, lavender	3.6b	4.3a	3.2b	RI, Std, AD
45	dimethyl sulfoxide	1576	1228	garlic	2.0b	3.2a	2.8ab	RI, Std, AD, FPD
46	5-methyl-2-furfural	1598	978	almond, caramel, burnt sugar	3.2a	2.4b	1.7c	RI, Std, AD
47	unknown4	1611	1121	flower	np	1.3	1.1	−
48	hotrienol	1623	1101	hyacinth	2.6a	2.7a	2.7a	RI, Std, AD
49	phenyl acetaldehyde	1625	1049	hawthorne, honey, sweet	1.4b	2.2a	1.6b	RI, Std, AD
50	methionol	1723	978	sweet, potato	4.1	3.9	np	RI, Std, AD, FPD
51	methyl salicylate	1745	1234	peppermint	3.2a	2.9a	2.8a	RI, Std, AD
52	unknown5	1776	1322	nut, wood	np	1.3	1.1	−
53	*β*-damascenone	1813	1386	apple. rose, honey	4.1a	4.0a	3.7a	RI, Std, AD
54	geraniol	1847	1276	rose, geranium	4.2a	3.5b	3.8b	RI, Std, AD
55	3-mercaptohexanol	1875	1527	passionfruit, grapefruit	3.5	3.2	np	RI, Std, AD, FPD
56	phenylethyl alcohol	1925	1118	honey, spice, rose, lilac	1.5b	1.4b	2.2a	RI, Std, AD
57	*β*-ionone	1932	1493	violet, flower, raspberry	3.2	3.2	np	RI, Std, AD
58	benzothiazole	1950	1240	gasoline, rubber	np	np	4.1	RI, Std, AD, FPD
59	*cis*-jasmone	1959	1370	jasmine	3.7a	3.5a	3.3a	RI, Std, AD

DOI: 10.1021/acs.jafc.5b02358
J. Agric. Food Chem. 2015, 63, 7499−7510

Table 1. continued

no.[a]	name	RI[b] Innowax	RI[b] DB-5	aroma description	DHP[c]	TGY[c]	DDWL[c]	identification basis[d]
60	methyl jasmonate	1974	1626	jasmine	3.8a	3.7a	3.8a	RI, Std, AD
61	nerolidol	2009	1539	wood, flower	4.4a	4.1a	3.8a	RI, Std, AD
62	dihydroactinidiolide	2400	1489	musk	4.0a	3.6a	3.8a	RI, Std, AD
63	indole	2450	1292	mothball, burnt	4.0a	4.2a	4.5a	RI, Std, AD

[a]Code for the volatile compounds detected in the tea infusions. [b]Retention index of compounds on DB-5 and Innowax Column. [c]The lowercase letters (a−c) following the values in the DHP, TGY, and DDWL entries in the same row are significantly different according to the Duncan test ($p < 0.05$). [d]Method of identification: RI, retention index; Std, confirmed by authentic standards; AD, aroma descriptor; PFD, flame photometric detector. [e]The aroma intensities were evaluated by GC−O. [f]Not perceived.

Sensory Analysis. Quantitative descriptive analyses (QDA) were performed for evaluating three types of samples by ten assessors (5 females and 5 males). All the assessors were previously trained in the ability to recognize, describe, and discriminate different aroma qualities. Each of them completed 150 h of specific training with tea infusions. Five sensory attributes were commonly selected to describe the overall aroma by the panelists: "roast", "sweet", "green and grassy", "sulfur", and "floral". These five aroma terms were defined as the following aromas: 2,3,5-trimethylpyrazine for "roast" attribute, β-damascenone for "sweet" note, hexanal for "green and grassy" attribute, dimethyl sulfide for "sulfur" attribute, and geraniol for "floral" attribute. After the training period, the respective samples (10 g) were placed in capped glasses with different three-digit numbers for the sensory assessors. Each assessor rated the intensity of the five attributes on a ten-point scale (0, none; 5, moderate; 10, very strong), and the results were averaged for each sensory note and plotted in a radar diagram. The sensory evaluations of each sample were performed in triplicate at room temperature (20 ± 1 °C).

Statistical Analysis. The data were processed with analysis of variance (ANOVA). ANOVA and Duncan's multiple range tests were applied to the data to determine significant differences ($P < 0.05$). The correlation analysis was employed to show the correlations between attribute variables and the aroma-active volatile profile. All statistical analyses were operated using XLSTAT ver.7.5 (Addinsoft, New York, NY, USA).

RESULTS AND DISCUSSION

GC−O Results for Tea Infusions. The results of aroma intensity (AI) testing of the compounds are summarized in Table 1. The aroma compounds were confirmed by comparison with authentic standards on columns, RI, and aroma descriptor. Application of the GC−O to the tea infusions revealed forty-three, forty-five, and forty-eight aroma-active compounds (AI ≥ 2) in the TGY, DHP, and DDWL infusions, respectively. There were five unidentified volatile compounds that were found in samples. The differences in the number of aroma-active compounds in the tea infusions were mainly caused by concentration differences thereof. As seen in Table 1, the DHP infusions contained more aroma-active compounds than other samples. The compounds having the highest AI (4.4) were nerolidol for DHP infusions, (*R*)-(−)-linalool and (*E*)-2-heptenal (4.3) for TGY infusions, and indole and nerolidol (4.5) for DDWL infusions.

Aldehydes and alcohols were important classes of aroma-active compounds in the three types of tea infusions. Odor threshold values are generally lower than concentrations of those compounds; thus, they have an important potential effect on the overall aroma of a sample.[15] Aldehydes and alcohols are generally characterized by intense sensory description by panelists and are associated with greenery, freshly mown grass, green plants, citrusy, fatty, and sweet notes. The total numbers of aroma-active aldehydes and alcohols were nineteen, twenty, and eighteen, and four, six, and six in DHP, TGY, and DDWL infusions, respectively. Of those aroma-active compounds, hexanal, heptanal, (*E*)-2-hexenal, (*E*)-2-heptenal, (*Z*)-3-hexen-1-ol, and 1-penten-3-ol were the most powerful aroma-active compounds contributing to the aroma profile of tea infusions. The result was consistent with previous investigations, which presented aldehydes with six to ten carbons as being perceived as having green, fatty, or tallow aromas. This green aroma is sometimes referred to as a fresh note, and the chemicals responsible are predominantly C6 alcohols and aldehydes, preferably unsaturated.[6] From Table 1, DDWL infusions exhibited the highest AI of those aldehydes among the three types of samples. As the degree of fermentation increased, the concentrations of those compounds with grassy and green aromas gradually declined. This might have been associated with the withering process of the teas. During this process, a series of biochemical and chemical reactions occurred. As a result, many low-boiling point compounds with green aromas are transformed and volatilized.[6]Besides those aroma compounds, (*E,E*)-2,4-heptadienal and (*E,E*)-2,4-hexadienal, which exhibited relatively high AIs among all the samples, also exerted a significant influence on the aroma of the tea infusions. The result was consistent with that arising from a recent study on green teas.[16] (*E,E*)-2,4-Heptadienal and (*E,E*)-2,4-hexadienal are mostly derived from lipid degradation during manufacture.

Terpenes were another significant class of aroma-active compounds found in the three types of tea infusions. In total, six aroma-active terpenes were found in these three types of samples. Of the aroma-active compounds, nerolidol, (*R*)-(−)-linalool, geraniol, *cis*-linaloloxide, hotrienol, β-ionone, and *trans*-linalool oxide were the most powerful aroma-active compounds contributing to the aroma profile of tea infusions. Nerolidol was responsible for rose and apple aromas, which presented the highest AIs in the DHP infusions (4.4). Therefore, nerolidol might be a major contributor to the characteristic floral aroma note common to the DPH cultivar investigated. β-Damascenone, which might be responsible for the sweet-like and fruity odor, exhibited a high AI (4.1) in the DHP infusions. The result was consistent with a recent study which shows that β-damascenone, with its extremely low human odor perception threshold (0.05 μg/kg),[17] exerted a significant influence on black tea aroma.[16] Given this conclusion, β-damascenone was also likely to enhance the fruity aroma of tea. In addition, the AIs of (*R*)-(−)-linalool found in samples were high enough to be considered representative of an active compound, suggesting that floral characteristics may encapsulate the dominant tea infusion aroma. The AIs of nerolidol, β-damascenone, and (*R*)-(−)-linalool were dominant in DHP infusion teas. This might have resulted from different tea varieties, various manufacturing processes, or cultivation practices. The formation of those

DOI: 10.1021/acs.jafc.5b02358
J. Agric. Food Chem. 2015, 63, 7499−7510

Table 2. Result of Recovery (%) and RSD (%) in Model Solution and Tea Infusions for 13 Volatile Sulfur Compounds

		model solution		DHP		TGY		DDWL	
code	compd	recovery	RSD	recovery	RSD	recovery	RSD	recovery	RSD
1	methanethiol	90.4 (5)[a]	9.35	113 (50)	8.33	91.5 (5)	9.68	85.6 (5)	7.99
2	dimethyl sulfide	96.7 (10)	11.4	95.7 (10)	9.66	112 (10)	10.6	82.2 (1000)	6.76
3	ethanethiol	114 (5)	7.45	95.5 (5)	9.84	83.8 (1)	8.21	88.6 (1)	9.51
4	propanethiol	96.4 (2)	9.17	101.7 (2)	9.02	–[b]		–	
5	dimethyl disulfide	112 (5)	8.19	104 (2)	10.5	92.3 (10)	8.61	81.3 (10)	6.37
6	*S*-methyl thioacetate	81.9 (0.5)	11.4	77.7 (0.2)	7.92	85.0 (0.2)	8.56	79.4 (1)	7.93
7	dimethyl trisulfide	91.1 (2)	8.88	109 (2)	10.1	86.5 (2)	9.40	106 (2)	7.22
8	furfurylthiol	107 (0.05)	7.57	77.9 (0.05)	10.3	78.5 (0.05)	6.94	–	
9	methional	85.9 (2)	7.39	86.7 (2)	6.69	91.2 (2)	8.86	–	
10	dimethyl sulfoxide	113 (10)	10.5	91.8 (10)	10.4	85.6 (10)	7.74	86.7 (100)	6.81
11	methionol	90.0 (1)	8.00	86.8 (1)	7.57	98.4 (1)	7.39	–	
12	3-mercaptohexanol	82.2 (0.02)	8.65	101.3 (0.02)	8.10	99.4 (0.02)	7.35	–	
13	benzothiazole	83.8 (1)	9.68	–		–		98.2 (1)	5.16

[a]The amounts (μg/kg) of each analyte used in the spike experiments. [b]Recovery was not calculated because concentration data of compound was not available in the sample.

Table 3. Concentrations and Standard Deviation of Volatile Sulfur Compounds in Tea Infusions (μg/kg)

		RI			DHP		TGY		DDWL	
code	compound	Innowax	DB-5	identification	av	SD[a]	av	SD	av	SD
1	methanethiol	700	500	FPD, RI, Std	49.9a[b]	6.55	4.45b	0.662	2.96b	0.230
2	dimethyl sulfide	716	521	FPD, RI, Std	7.81b	0.511	37.2b	2.660	1.45×10^3a	159
3	ethanethiol	722	508	FPD, RI, Std	5.05a	0.420	1.32b	0.141	1.06b	0.131
4	propanethiol	863	616	FPD, RI, Std	1.85	0.290	–[c]		–	
5	dimethyl disulfide	1071	710	FPD, RI, Std	5.63a	0.330	4.39b	0.691	3.05c	0.450
6	*S*-methyl thioacetate	1078	727	FPD, RI, Std	0.270b	0.040	0.201c	0.021	0.591a	0.0702
7	dimethyl trisulfide	1355	978	FPD, RI, Std	1.99c	0.110	2.69b	0.212	5.26a	0.370
8	furfurylthiol	1432	912	FPD, RI, Std	0.050a	0.0100	0.0322b	0.000	–	
9	methional	1468	909	FPD, RI, Std	1.46a	0.130	0.811b	0.080	–	
10	dimethyl sulfoxide	1580	839	FPD, RI, Std	4.05c	0.540	22.7b	2.301	121a	12.2
11	methionol	1723	989	FPD, RI, Std	0.811a	0.060	0.122b	0.011	–	
12	3-mercaptohexanol	1875	1127	FPD, RI, Std	0.021b	0.00212	0.0411a	0.000	–	
13	benzothiazole	1950	1240	FPD, RI, Std	–		–		1.12	0.110

[a]SD: standard deviation. [b]Values with different superscript roman letters (a–c) in the same row are significantly different according to the Duncan test ($p < 0.05$). [c]Not detected.

compounds was the result of material transformation and enzymolysis of aroma precursors. The formation of intercellular channels promoted contact between substrate and enzymes and the release of the enzymes, which were largely related to aroma compounds.[18]

Ketones were also an important class of aroma-active compound in the three types of tea infusions. The total numbers of aroma-active ketone compounds were eight, four, and seven in the three types of samples, respectively. Within these aroma-active compounds, *cis*-jasmone, 6-methyl-5-hept-en-2-one, β-ionone, 2,3-butanedione, and 2,3-pentanedione were the most powerful aroma-active compounds contributing to the aroma profile of the tea infusions. Unsaturated fatty acid is oxidatively degraded to small molecules of ketone compounds with fatty oxidase.[19] Macromolecular ketone is produced by β-carotene oxidation and degradation. During fermentation, low boiling point ketone compounds were transformed and high boiling point compounds gradually accumulated. 2,3-Butanedione and 2,3-pentanedione accounted for the typical butter note present in the tea infusions. The DHP infusions exhibited higher AIs (2.3 and 2.7) for these compounds than the DDWL infusions. Interestingly, those compounds were not perceived from GC–O in TGY infusions. However, it does not mean that those were absent from the TGY infusions.

It should be noted that methyl jasmonate and indole might be important aroma-active compounds in tea infusions. The AIs of methyl jasmonate were similar in the three types of samples. Methyl jasmonate contributed to the tea having floral odors.[20] Indole, which might be considered an animal-like aroma, exhibited the highest AI (4.5) in the DDWL infusions and the lowest AI (4.0) in the DHP infusions. This compound might positively strengthen the overall nature of the tea aroma.[21]

Stabilization of VSCs in Tea Infusions. It has been reported that sulfur compounds are extremely reactive and artifacts can be formed during analysis.[22,23] In this work, all standards were tested individually for stability during sample extraction and analysis. Most of the compounds were stable and only gave a single chromatographic peak. The chromatogram data of VSCs are shown in the Supporting Information. It was noteworthy that methanethiol could be easily oxidized to form dimethyl disulfide and dimethyl trisulfide, probably due to the presence of oxygen and transition metals.[23,24] As a result, it was unreliable to quantify VSCs in food. Thus, some measurements should be taken to prevent the formation of artifacts. The pretreatment of the instrument was indispensable to the

DOI: 10.1021/acs.jafc.5b02358
J. Agric. Food Chem. 2015, 63, 7499–7510

analysis of sulfur compounds. In this experiment, the GC injection port was deactivated with bis(trimethylsilyl)-trifluoroacetamide. Finally, sulfur standards were checked individually and only single peaks were detected: this indicated that artifact formation was prevented under this experimental condition. The observation was consistent with previous studies.[25−27] Furthermore, a recovery study was performed to investigate the influence of model solution and tea infusions on the recovery of 13 VSCs, which were detected in tea infusions. For the model solution, and real tea infusions, recoveries ranged from 88.3% to 104% for all compounds with relative standard deviations (RSD) below 10% for all compounds (Table 2). The result demonstrated that this method was reliable when quantifying those VSCs.

As shown in Table 3, thirteen sulfur volatiles were detected in this investigation: these were identified on the basis of their retention index in two dissimilar columns compared with standard chemicals and aroma descriptor. A sulfur-specific FPD response indicated that the peaks detected did contain sulfur. On the basis of their chemical structure, these compounds included thioesters, sulfides, polysulfides, heterocyclic forms, and thio forms.

Qualitatively, eight, eleven, and twelve sulfur compounds were identified in DDWL, TGY, and DHP infusions, respectively. Among these compounds, seven compounds were present in all samples. The observed differences in the sulfur compounds present in tea infusions obtained from the different cultivars and manufacturing processes were both quantitative and qualitative. Quantitatively, dimethyl sulfide, dimethyl disulfide, and dimethyl sulfoxide were the predominant volatile compounds, followed by methanethiol and dimethyl trisulfide. The result demonstrated that sulfide, sulfides, and polysulfides presented relatively higher contents in samples than other sulfur compounds. It was noteworthy that the 3-mercaptohexanol and furfurylthiol presented trace contents in the samples. Dimethyl sulfide, dimethyl disulfide, and dimethyl trisulfide have been reported in tea, wine, tomato, and onions.[11,16,28−30] Dimethyl sulfide described as an "asparagus", "corn", and "molasses" aroma was considered a beneficial compound in low concentrations.

The formation of dimethyl sulfide happens during leaf maturation and fermentation and is caused by a yeast mechanism involving cleavage of *S*-methyl-L-methionine to homoserine and dimethyl sulfide.[31,32] Among samples, dimethyl sulfide was identified at a concentration of between 7.81 μg/kg for DHP infusions and 1.45 × 10^3 μg/kg for DDWL infusions. The different concentrations of dimethyl sulfide between these samples might be ascribable to the variety, manufacture, fermentation process, and even small differences in withering conditions, such as withering temperature and withering time. The result agreed with data from a previous investigation,[6] which showed that the aroma composition and their quantities in different types of teas varied widely. It is well-known that the degree of fermentation of DDWL (10 to 20%) was generally lower than in DHP (60 to 80%). Thus, the aroma of DDWL was close to green tea, which contained a significant amount of dimethyl sulfide. The same corroborating results were also obtained by previous research,[33] which indicated that dimethyl sulfide contributed significantly to the aroma properties of green tea. Furfurylthiol, named "coffee aldehyde", has been found in roasted coffee, meat, wheat bread, and popcorn.[34] Concentrations of furfurythiol were almost two times as high in sample DHP infusions (0.05 μg/kg) compared to sample TGY infusions (0.03 μg/kg). It was worth noting that the low concentrations of aroma compounds might influence the perceived aroma intensity in samples due to their low detection thresholds (0.01 μg/kg).[26] On the other hand, methanethiol, ethanethiol, and propanethiol were responsible for sulfur, gasoline, and garlic aromas being detected. The relatively high contents of those compounds in sample DHP infusions (49.9, 5.05, and 1.85 μg/kg) suggested that these compounds were related to the tea manufacturing process. Along with the degree of fermentation being increased, those compounds might be gradually released from the tea leaves by enzymatic reactions. The other important VSC was methional, with its distinctive potato odors.[11] The absence of methional in DDWL infusions, and its presence in DHP and TGY infusions, was a clear indication that fermentation had liberated this compound due to degradation of the nonvolatile sulfur-containing amino acid, such as methionine.[35] 3-Mercaptohexanol has been previously reported in grapefruit and red wine, with passionfruit and grapefruit odors.[36] It is worth noting that 3-mercaptohexanol was of particular importance to tea aroma due to its extremely low threshold (60 ng/kg) of detection.[36]

Quantitative Analysis of Volatile Compounds. The concentrations and odor-activity values (OAVs) of volatile compounds obtained by GC−MS are presented in Table 4. The major volatile constituents of the tea infusions were heptanal (6.70 × 10^3 to 9.60 × 10^3 μg/kg), (*R*)-(−)-linalool (628−868 μg/kg), benzaldehyde (2.18 × 10^3− to 3.66 × 10^3 μg/kg), 1-penten-3-ol (1.56 × 10^3 to 2.39 × 10^3 μg/kg), and 5-methyl-2-furfural (1.63 × 10^3−3.60 × 10^3 μg/kg). The AIs and OAVs of these compounds were greater than 1, which were considered as odor-active compounds in tea infusions.

On the other hand, β-damascenone (3.74 × 10^{-2} to 7.66 × 10^{-2} μg/kg), indole (3.84−5.52 μg/kg), 3-methylbutanal (2.40 × 10^{-2} to 70.7 μg/kg), and octanal (19.2−91.4 μg/kg) were present at low concentrations (<100 μ g/kg). Despite their low levels, these compounds might have a significant impact on tea infusion aroma because of their low odor detection threshold values.

In this study, OAVs were calculated using odor detection thresholds determined in water, which was appropriate because tea infusions were mainly an aqueous product. From Table 4, volatile compounds like 2-methylpropanal (230−455), 3-methylbutanal (1−353), 2-methylbutanal (34−68), nerolidol (108−184), (*E*)-2-heptenal (148−294), hexanal (134−230), octanal (28−131), β-damascenone (29−59), indole (96−138), 6-methyl-5-hepten-2-one (34−67), (*R*)-(−)-linalool (63−87), and dimethyl sulfide (7−1320) presented relatively higher OAVs than those of other compounds, indicating the importance of these compounds in the overall aroma of tea infusions.

Generally, many compounds like nerolidol, (*R*)-(−)-linalool, β-damascenone, indole, hexanal, and (*E*)-2-hexenal presented both high AIs and high OAVs, which confirmed the positive relationship between GC−O and OAV. However, volatile compounds like 2-methylpropanal, pentanal, heptanal, (*Z*)-3-hexen-1-ol and nonanal that had high AI but a relatively low OAV, which could be related to the difference of thresholds in air and water.

Although GC−O is a useful technique for screening odor-active compounds, it does not provide information about the contribution of individual compounds to the overall aroma. The reason might be that these odorants were detected based

DOI: 10.1021/acs.jafc.5b02358
J. Agric. Food Chem. 2015, 63, 7499−7510

Table 4. Average Values (Mean ± Standard Deviation) (μg/kg) and OAVs of Aroma Compounds Detected in Tea Infusions

			RI[b]		concn (μg/kg)									OAV		
no.	compd[a]	source	Innowax	DB-5	DHP[c]	SD	TGY[c]	SD	DDWL[c]	SD	identification basis[d]	thresholds (μg/kg)	ref[e]	DHP	TGY	DDWL
1	methanethiol	1[g]	696	502	4.99 × 10a	4.49	4.45b	4.65×10^{-1}	2.96c	3.09×10^{-1}	RI, Std, MS	4	47	13	1	1
2	acetaldehyde	1	714	<500	8.52b	8.26×10^{-1}	9.43b	1.09	2.54 × 10a	2.95	RI, Std, MS	10	47	1	1	3
3	dimethyl sulfide	1	716	505	7.81c	8.59×10^{-1}	3.72 × 10b	3.15	1.45×10^{3}a	1.23×10^{2}	RI, Std, MS	1.1	47	7	34	1320
4	propanal	1	750	506	6.48b	7.91×10^{-1}	1.78 × 10b	1.74	1.92×10^{2}a	1.88 × 10	RI, Std, MS	81	47	<1	<1	2
5	furan	1	774	500	2.11ab	1.89×10^{-1}	2.37b	2.44×10^{-1}	9.87a	1.01	RI, Std, MS	11	47	<1	<1	1
6	2-methylpropanal	1	821	662	2.50×10^{2}b	2.57 × 10	1.61×10^{2}c	1.50 × 10	3.19×10^{2}a	2.97 × 10	RI, Std, MS	0.7	42	357	230	456
7	2-methylfuran	1	824	595	8.47a	9.15×10^{-1}	2.4b	1.99×10^{-1}	8.22a	6.80×10^{-1}	RI, Std, MS	3500	47	<1	<1	<1
8	butanal	1	832	596	1.86c	1.82×10^{-1}	4.09 × 10b	3.46	6.25 × 10a	5.29	RI, Std, MS	17	47	<1	2	4
9	ethyl acetate	1	628	907	4.24b	3.68×10^{-1}	2.4c	2.38×10^{-1}	1.15 × 10ba	1.14	RI, Std, MS	6200	43	<1	<1	<1
10	3-methylbutanal	1	910	650	2.40×10^{-1}c	2.14×10^{-2}	4.47 × 10b	4.71	7.07 × 10a	7.46	RI, Std, MS	0.2	43	1	224	354
11	2-methylbutanal	1	912	641	3.44 × 10c	3.58	6.79 × 10a	6.90	4.69 × 10b	4.76	RI, Std, MS	1	40	34	68	47
12	2-ethylfuran	1	925	717	1.86a	2.06×10^{-1}	1.90a	1.50×10^{-1}	1.52b	1.20×10^{-1}	RI, Std, MS	2.3	40	1	1	1
13	pentanal	1	935	732	1.21×10^{2}c	1.29 × 10	1.29×10^{2}b	1.13 × 10	2.51×10^{2}a	2.19 × 10	RI, Std, MS	12	47	10	11	21
14	2,3-butanedione	1	970	593	9.32 × 10a	7.74	7.21c	6.51×10^{-1}	6.99 × 10b	6.31	RI, Std, MS	15	42	6	<1	5
15	1-penten-3-one	1	973	680	6.21 × 10a	5.71	4.24 × 10b	4.31	1.44c	1.47×10^{-1}	RI, Std, MS	23	47	3	2	<1
16	2,3-pentanedione	1	1054	700	1.82×10^{2}a	1.73 × 10	2.09c	1.72×10^{-1}	1.52×10^{2}b	1.26 × 10	RI, Std, MS	29	47	6	<1	5
17	dimethyl disulfide	1	1071	785	5.63a	6.02×10^{-1}	4.39b	4.63×10^{-1}	3.05c	3.22×10^{-1}	RI, Std, MS	1.1	41	5	4	3
18	butyl acetate	1	1075	808	2.03a	1.76×10^{-1}	1.78b	1.53×10^{-1}	1.69b	1.91×10^{-1}	RI, Std, MS	58	40	<1	<1	<1
19	hexanal	1	1084	801	6.03×10^{2}c	6.69 × 10	7.96×10^{2}b	7.79 × 10	1.04×10^{3}a	8.58 × 10	RI, Std, MS	4.5	43	134	177	230
20	3-methylbutyl acetate	1	1129	876	1.50c	1.45×10^{-1}	3.28a	3.57×10^{-1}	2.80b	2.66×10^{-1}	RI, Std, MS	2	47	1	2	1
21	(*E*)-2-pentenal	1	1131	754	2.00×10^{3}a	2.20×10^{2}	1.90×10^{3}b	1.50×10^{2}	5.1×10^{3}a	5.12×10^{2}	RI, Std, MS	310	47	6	6	17
22	1-penten-3-ol	1	1157	686	2.39×10^{3}a	2.92×10^{2}	1.56×10^{3}c	1.43×10^{2}	2.16×10^{3}b	1.97×10^{2}	RI, Std, MS	400	45	6	4	5
23	2-heptanone	1	1169	893	2.12b	1.89×10^{-1}	2.40a	2.31×10^{-1}	1.64c	1.33×10^{-1}	RI, Std, MS	140	47	<1	<1	<1
24	heptanal	1	1174	903	6.70×10^{3}c	6.90×10^{2}	8.43×10^{3}b	7.35×10^{2}	9.6×10^{3}a	7.95×10^{2}	RI, Std, MS	550	47	12	15	18
25	methyl hexanoate	1	1185	988	1.87b	2.02×10^{-1}	1.88b	1.45×10^{-1}	2.44a	2.36×10^{-1}	RI, Std, MS	87	47	<1	<1	<1
26	(*E*)-2-hexenal	1	1192	844	8.05×10^{2}c	7.89 × 10	1.05×10^{3}b	8.31 × 10	1.47×10^{3}a	1.52×10^{2}	RI, Std, MS	82	47	10	13	18
27	2-pentylfuran	1	1223	989	2.11a	1.84×10^{-1}	1.84b	1.70×10^{-1}	1.65c	1.64×10^{-1}	RI, Std, MS	5.9	40	<1	<1	<1
28	(*Z*)-4-heptenal	1	1230	902	6.06 × 10b	5.39	8.48 × 10a	8.38	8.22c	6.35×10^{-1}	RI, Std, MS	10	47	6	8	1
29	1-pentanol	1	1255	766	1.91×10^{2}c	1.98 × 10	1.22×10^{3}b	1.17×10^{2}	8.27×10^{3}a	7.08×10^{2}	RI, Std, MS	5000	44	0	0	2
30	octanal	1	1280	1006	5.93 × 10b	6.58	1.92 × 10c	1.42	9.14 × 10a	8.07	RI, Std, MS	0.7	43	85	28	131
31	2,5-dimethylpyrazine	1	1302	905	1.88×10^{2}a	2.01 × 10	1.75×10^{2}b	1.43 × 10	1.33×10^{2}c	1.32 × 10	RI, Std, MS	20	47	9	9	7
32	(*E*)-2-heptenal	1	1315	957	1.93×10^{3}c	1.60×10^{2}	2.86×10^{3}b	2.42×10^{2}	3.83×10^{3}a	3.09×10^{2}	RI, Std, MS	13	47	148	220	294
33	2,3-octanedione	1	1320	960	1.91 × 10a	1.75	4.46c	4.24×10^{-1}	1.48 × 10b	1.53	RI, Std, MS	–[f]		–	–	–
34	6-methyl-5-hepten-2-one	1	1336	974	1.72×10^{3}b	1.64×10^{2}	3.36×10^{3}a	2.60×10^{2}	1.77×10^{3}b	1.40×10^{2}	RI, Std, MS	50	44	34	67	35
35	hexanol	1	1360	851	7.25 × 10c	7.75	1.26 × 10^{3}a	1.25×10^{2}	8.28×10^{2}b	7.59 × 10	RI, Std, MS	500	47	0	3	2
36	(*Z*)-3-hexen-1-ol	1	1378	858	1.22×10^{2}c	1.06×10^{2}	1.33×10^{3}b	1.95×10^{2}	1.57×10^{3}a	1.51×10^{2}	RI, Std, MS	70	47	17	19	22
37	2-nonanone	1	1380	1088	3.60a	4.00×10^{-1}	2.27b	2.43×10^{-1}	1.41c	1.23×10^{-1}	RI, Std, MS	130	47	<1	<1	<1
38	nonanal	1	1385	1104	1.53×10^{2}b	2.02 × 10	1.58×10^{2}b	1.95 × 10	2.94×10^{2}a	2.28 × 10	RI, Std, MS	40	33	4	4	7
39	2,3,5-trimethylpyrazine	1	1395	1000	1.31×10^{2}a	1.92 × 10	1.22×10^{2}ab	1.58 × 10	1.12×10^{2}b	8.83	RI, Std, MS	297	41	<1	<1	<1

J. Agric. Food Chem. 2015, 63, 7499−7510
DOI: 10.1021/acs.jafc.5b02358

Table 4. continued

			RI[b]		concn (μg/kg)									OAV		
no.	compd[a]	source	Innowax	DB-5	DHP[c]	SD	TGY[c]	SD	DDWL[c]	SD	identification basis[d]	thresholds (μg/kg)	ref[e]	DHP	TGY	DDWL
40	(*E*,*E*)-2,4-hexadienal	1	1405	910	3.11×10^2a	3.33×10	3.82×10c	4.49	1.56×10^2b	1.44×10	RI, Std, MS	94.8	45	3	<1	2
41	(*E*)-2-octenal	1	1411	1060	7.78c	9.61×10^{-1}	2.64×10a	2.76	1.64×10b	1.62	RI, Std, MS	3	47	3	9	5
42	*cis*-linalooloxide	1	1420	1070	1.53×10^3a	1.98×10^2	1.41×10^3b	1.50×10^2	1.43×10^3b	1.36×10^2	RI, Std, MS	320	46	5	4	4
43	1-octen-3-ol	1	1426	982	1.62×10b	1.90	2.38×10a	2.96	1.54×10b	1.14	RI, Std, MS	1.5	41	11	16	10
44	heptanol	1	925	1273	1.90a	1.98×10^{-1}	1.94a	0.26	1.50b	1.23×10^{-1}	RI, Std, MS	3	43	1	1	<1
45	furfural	1	1455	829	7.27×10^2a	7.77×10	5.49×10^2b	7.05×10	4.56×10^2c	3.86×10	RI, Std, MS	282	47	3	2	2
46	*trans*-linalooloxide	1	1465	1212	1.34×10^3a	1.67×10^2	5.02×10^2c	5.00×10	6.22×10^2b	5.93×10	RI, Std, MS	320	47	4	2	2
47	acetic acid	1	1467	600	2.21×10c	2.94	3.21×10b	3.54	1.14×10a	8.84×10^{-1}	RI, Std, MS	22000	41	<1	<1	<1
48	(*E*,*E*)-2,4-heptadienal	1	1470	1011	1.10×10^2c	1.41×10	1.38×10^2b	1.58×10	2.33×10^2a	2.31×10	RI, Std, MS	56	47	2	2	4
49	2-ethyl-1-hexanol	1	1490	1024	1.29b	1.28×10^{-1}	1.99a	2.55×10^{-1}	1.95a	2.08×10^{-1}	RI, Std, MS	1280	47	<1	<1	<1
50	2-acetylfuran	1	1490	893	1.48×10^3a	1.63×10^2	1.22×10^2c	1.17×10	1.23×10^2b	1.52×10	RI, Std, MS	15025.2	40	<1	<1	<1
51	camphor	1	1492	1149	1.81b	2.07×10^{-1}	2.99a	3.98×10^{-1}	1.77b	2.30×10^{-1}	RI, Std, MS	460	47	<1	<1	<1
52	benzaldehyde	1	1495	960	2.36×10^3b	3.03×10^2	3.66×10^3a	3.82×10^2	2.18×10^3b	2.56×10^2	RI, Std, MS	750.9	40	3	5	3
53	(*R*)-(−)-linalool	1	1537	1100	3.14×10^3	3.28×10^2	4.43×10^3	5.03×10^2	3.39×10^3	3.55×10^2	RI, Std, MS	10	44	63	87	68
54	1-octanol	1	1553	1072	2.78a	3.70×10^{-1}	1.51b	1.27×10^{-1}	1.26b	1.35×10^{-1}	RI, Std, MS	110	44	<1	<1	<1
55	dimethyl sulfoxide	1	1576	1228	4.05c	4.45×10^{-1}	2.28×10b	2.23	1.21×10^2a	1.51×10	RI, Std, MS	–		–	–	–
56	5-methyl-2-furfural	1	1598	978	3.60×10^3a	2.89×10^2	2.91×10^3b	2.99×10^2	1.63×10^3c	2.18×10^2	RI, Std, MS	500	47	7	6	3
57	hotrienol	1	1623	1101	1.84×10^2c	1.71×10	2.59×10^2b	2.41×10	2.94×10^2a	3.73×10	RI, Std, MS	110	44	2	2	3
58	methyl benzoate	1	1624	1107	1.89a	1.84×10^{-1}	1.55b	1.28×10^{-1}	1.95a	1.94×10^{-1}	RI, Std, MS	73	41	<1	<1	<1
59	phenyl acetaldehyde	1	1625	1049	7.12c	6.28×10^{-1}	1.05×10a	8.91×10^{-1}	9.34b	1.03	RI, Std, MS	4	47	2	3	2
60	3-methylbutanoate	1	1645	1060	2.02b	1.58×10^{-1}	2.59a	2.56×10^{-1}	2.19b	2.50×10^{-1}	RI, Std, MS	60	47	<1	<1	<1
61	α-terpineol	1	1670	1185	3.19×10a	2.56	2.21×10b	2.33	3.17×10a	4.08	RI, Std, MS	330	44	<1	<1	<1
62	methyl salicylate	1	1745	1234	1.53×10^3a	1.44×10^2	9.26×10^2c	9.41×10	1.04×10^3b	1.09×10^2	RI, Std, MS	40	44	38	23	26
63	β-damascenone	1	1813	1386	7.66×10^{-2}a	7.65×10^{-3}	5.29×10^{-2}b	4.17×10^{-3}	3.74×10^{-2}c	4.32×10^{-3}	RI, Std, MS	0.0013	47	59	41	29
64	geraniol	1	1847	1276	2.54×10^2a	2.45×10	1.83×10^2b	1.60×10	1.84×10^2b	2.47×10	RI, Std, MS	40	44	6	5	5
65	hexanoic acid	1	1871	977	1.45×10b	1.08	2.23×10a	2.01	2.31×10a	3.24	RI, Std, MS	1840	47	<1	<1	<1
66	benzyl alcohol	1	1902	1039	1.75c	1.45×10^{-1}	3.32a	3.37×10^{-1}	2.48b	3.16×10^{-1}	RI, Std, MS	100	45	<1	<1	<1
67	phenylethyl alcohol	1	1925	1118	1.12×10^2b	9.60	9.86×10b	8.15	1.44×10^2a	1.63×10	RI, Std, MS	60	47	2	2	2
68	β-ionone	1	1932	1493	1.36×10^2b	1.31×10	1.56×10^2a	1.65×10	4.01c	4.64×10^{-1}	RI, Std, MS	7	44	19	22	1
69	heptanoic acid	1	1945	1083	1.21c	9.46×10^{-2}	1.75b	1.71×10^{-1}	2.02a	2.73×10^{-1}	RI, Std, MS	3000		<1	<1	<1
70	2-acetylpyrrole	1	1950	1393	1.28a	1.28×10^{-1}	2.34b	2.56×10^{-1}	1.92b	2.77×10^{-1}	RI, Std, MS	170000	44	<1	<1	<1
71	*cis*-jasmone	1	1959	1370	1.06×10b	1.25	4.57×10a	5.43	6.58c	9.15×10^{-1}	RI, Std, MS	–		–	–	–
72	methyl jasmonate	1	1974	1626	3.19×10^2a	3.33×10	3.13×10^2a	3.38×10	3.26×10^2a	3.52×10	RI, Std, MS	70	47	5	4	5
73	nerolidol	1	2009	1539	1.84×10^3a	1.97×10^2	1.58×10^3b	1.52×10^2	1.08×10^3c	1.30×10^2	RI, Std, MS	10	47	184	158	108
74	octanoic acid	1	2083	1279	2.12c	2.64×10^{-1}	3.13a	3.06×10^{-1}	2.57b	3.17×10^{-1}	RI, Std, MS	1900	47	<1	<1	<1
75	dihydroactinidiolide	1	2400	1489	3.15×10a	4.20	1.06×10c	1.22	1.52×10b	2.11	RI, Std, MS	–		–	–	–
76	indole	1	2450	1292	3.84c	4.93×10^{-1}	4.30b	5.25×10^{-1}	5.52a	6.24×10^{-1}	RI, Std, MS	0.04	47	96	108	138

[a]Aroma compounds detected in the tea infusion. [b]Retention indices of compounds on DB-5 and Innowax Column. [c]The lowercase letters (a−c) following the values in the DHP, TGY, and DDWL entries in the same row are significantly different according to the Duncan test ($p < 0.05$). [d]Method of identification: MS, mass spectrum comparison using Wiley library; RI, retention index in agreement with literature value; Std, confirmed by authentic standards. [e]Reference number. [f]The detection threshold was not found in reference. [g]Authentic standards were obtained from Alfa Aesar Corporation (Tianjin, China). All of the chemical standards used above were of GC quality.

J. Agric. Food Chem. 2015, 63, 7499−7510
DOI: 10.1021/acs.jafc.5b02358

on odor activity in air without considering interactions with the food matrix. For this reason, the use of OAVs may provide a better assessment of the odor activities of compounds as long as the quantitative data and the odor detection thresholds are accurate. However, the accuracy of identification of aroma-active compounds in tea infusions with GC−O or OAV methods should be further verified by other methods, such as aroma recombination.

Sensory Analysis. Sensory analysis was performed by an evaluation of the organoleptic qualities of tea infusions, using five descriptors including "roast", "sweet", "green and grassy", "sulfur", and "floral" aromas. ANOVA was used to distinguish different tea samples by their sensory evaluation scores. Statistical analysis showed that the "roast", "sweet", "green and grassy", "sulfur", and "floral" attributes were significantly different ($p < 0.05$) (Figure 1).

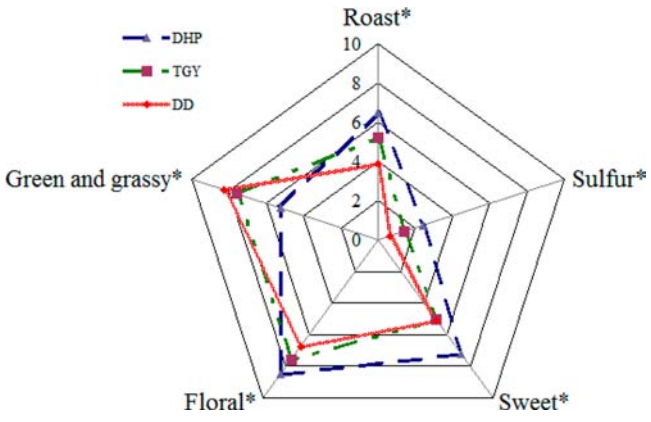

Figure 1. Aroma profiles of tea infusions obtained from DHP, TGY, and DDWL infusion samples. In sensorial parameters indicated with an (*) a difference among some trials is verified for $p < 0.05$.

The total roast attribute intensity for DHP infusions was 6.5 compared to 3.9 for DDWL infusions. The major compounds involved in this aroma category included 2,5-dimethylpyrazine, 2,3,5-trimethylpyrazine, and furfurylthiol. 2,5-Dimethylpyrazine and 2,3,5-trimethylpyrazine were typically associated with roast aromas, as described from GC−O. Those compounds might have been produced by the Maillard reaction occurring during fermentation. A previous study finds that these compounds are derived from amino acids and sugars.[37]

"Sweet" was an important flavor attribute for tea infusions: the DHP infusions returned the highest score (7.2) in this category compared to 5.0 in the TGY infusions. The major aroma-active compounds in the sweet category included 6-methyl-5-hepten-2-one and β-damascenone; the β-damascenone was considered to have been the characteristic sweet aroma. Although 6-methyl-5-hepten-2-one greatly contributed to the fruity aroma, it could enhance the perception of sweetness in tea infusions.[16]

"Green/grassy" was also a typical aroma attribute in tea infusions. It exhibited the highest aroma intensity in DDWL infusions (8.3) and lowest intensity in DHP infusions (5.2). It was mainly composed of aldehydes and alcohols such as hexanal, heptanal, octanal, nonanal, (*E*)-2-hexenal, (*E*)-2-heptenal, (*E*)-2-octenal, 1-pentanol, 1-penten-3-ol, and (*Z*)-3-hexen-1-ol. Previous research found that the fermentation method could cause a change of volatile flavor component in terms of quality and quantity, and it the fermentation process can probably cause the loss of grassy/green aromas.[6,38]

The DHP infusions were rated as having the highest value (2.4) in the "sulfur" attribute category, whereas TGY infusions returned a low sensory evaluation score (0.6). The major aroma-active compounds included dimethyl sulfide, dimethyl disulfide, methionol, methional, and 3-mercaptohexanol. Traditionally, these sulfur compounds were typically associated with a negative sensory contribution to tea samples; however, those compounds might improve the aroma quality of teas when present in appropriate amounts. Although sulfur compounds presented common sulfur aroma, those compounds exhibited characteristic aroma themselves, e.g., dimethyl sulfide with cabbage, corn, and molasses aroma; methional with its distinctive cooked potato aroma; 3-mercaptohexanol with passionfruit and grapefruit aroma.[36]

"Floral" was also a typical aroma attribute in tea infusions. It had its highest aroma intensity in DHP infusions (8.5) and lowest in DDWL infusions (6.7). It was mainly composed of terpenes and ketones such as β-ionone, nerolidol, *cis*-jasmone, methyl jasmonate, and (*R*)-(−)-linalool. "Floral" was a characteristic aroma of oolong tea, which was one of the important indications for distinguishing it from other types of tea.

Correlation Analysis. Correlation analysis could be manipulated to further illustrate the relationships between the volatile compounds and sensory attributes. From Table 5, positive correlations were found between "roast" attribute and 2,5-dimethylpyrazine ($r = 0.996$), furfurylthiol ($r = 0.994$), furfural ($r = 0.983$), and 5-methyl-2-furfural ($r = 0.986$); "sulfur" attribute and methanethiol ($r = 0.908$), dimethyl disulfide ($r = 0.908$), furfurylthiol ($r = 0.984$), and methional ($r = 0.992$); "sweet" attribute and 6-methyl-5-hepten-2-one ($r = 0.955$), β-damascenone ($r = 0.990$), geraniol ($r = 0.920$), and nerolidol ($r = 0.918$); "floral" attribute and hotrienol ($r = 0.973$), geraniol ($r = 0.999$), phenylethyl alcohol ($r = 0.937$), β-ionone ($r = 0.958$), methyl jasmonate ($r = 0.956$), and nerolidol ($r = 0.918$); and "green and grassy" attribute and butanal ($r = 0.990$), hexanal ($r = 0.932$), (*E*)-2-pentenal ($r = 0.965$), heptanal ($r = 0.981$), (*E*)-2-hexenal ($r = 0.990$), (*E*)-2-heptenal ($r = 0.951$), and (*Z*)-3-hexen-1-ol ($r = 0.999$). The result was partly according to the analysis of GC−O and sensory analysis. On the other hand, negative correlations were found between "roast" attribute and (*Z*)-3-hexen-1-ol ($r = -0.981$) and hotrienol ($r = -0.972$); "sulfur" attribute and butanal ($r = -0.921$), 3-methylbutanal ($r = -0.916$), (*E*,*E*)-2,4-heptadienal ($r = -0.933$), and hotrienol ($r = -0.986$); "sweet" attribute and butanal ($r = -0.921$), 3-methylbutanal ($r = -0.912$), hexanol ($r = -0.946$), hotrienol ($r = -0.945$), and phenyl acetaldehyde ($r = -0.952$); "floral" attribute and hexanal ($r = -0.998$), (*E*)-2-hexenal ($r = -0.988$), and (*E*,*E*)-2,4-heptadienal($r = -0.954$); and "green and grassy" attribute and methanethiol ($r = -0.982$), dimethyl disulfide ($r = -0.946$), *cis*-linaloloxide ($r = -0.926$), furfural ($r = -0.992$), *trans*-linalooloxide ($r = -0.939$), and geraniol ($r = -0.917$). Positive as well as negative correlations suggest that the perception of an aromatic note was influenced not only by the presence of a few compounds whose aroma forms the attribute but also by the presence of other odorants that affect negatively in the perception of such aromatic attribute.[39]

DOI: 10.1021/acs.jafc.5b02358
J. Agric. Food Chem. 2015, 63, 7499−7510

Table 5. Correlation Observed between the Volatile Compounds and Sensory Attributes

no.	compd	roast	sulfur	sweet	floral	green and grassy
1	methanethiol	0.878	0.908	0.600	0.880	−0.982
2	dimethyl sulfide	−0.877	−0.432	−0.480	−0.875	0.688
3	propanal	−0.894	−0.861	−0.512	−0.892	0.714
4	2-methylpropanal	−0.443	−0.380	0.109	−0.439	0.147
5	butanal	−0.299	−0.995	−0.921	−0.799	0.990
6	3-methylbutanal	−0.399	−0.996	−0.916	−0.899	0.988
7	2-methylbutanal	−0.364	−0.427	−0.808	−0.369	0.632
8	pentanal	−0.390	−0.486	−0.516	−0.894	0.717
9	2,3-butanedione	0.258	0.324	0.738	0.263	−0.542
10	1-penten-3-one	0.698	0.597	0.723	0.698	−0.875
11	2,3-pentanedione	0.149	0.216	0.658	0.153	−0.444
12	dimethyl disulfide	0.760	0.996	0.833	0.670	−0.946
13	hexanal	−0.698	−0.240	−0.810	−0.998	0.932
14	(*E*)-2-pentenal	−0.854	−0.816	−0.439	−0.851	0.965
15	1-penten-3-ol	0.258	0.324	0.738	0.263	−0.346
16	heptanal	−0.599	−0.430	−0.899	−0.549	0.981
17	(*E*)-2-hexenal	−0.569	−0.398	−0.753	−0.988	0.990
18	(*Z*)-4-heptenal	0.672	0.620	0.168	0.669	−0.413
19	octanal	−0.447	−0.385	0.104	−0.443	0.152
20	2,5-dimethylpyrazine	0.996	0.593	0.649	0.496	−0.821
21	(*E*)-2-heptenal	−0.800	−0.330	−0.841	−0.440	0.951
22	6-methyl-5-hepten-2-one	−0.020	−0.088	0.955	−0.024	0.325
23	hexanol	−0.623	−0.676	−0.946	−0.627	0.833
24	(*Z*)-3-hexen-1-ol	−0.981	−0.397	−0.723	−0.498	0.999
25	nonanal	−0.882	−0.848	−0.491	−0.880	0.696
26	(*E*,*E*)-2,4-hexadienal	0.563	0.618	0.892	0.566	−0.789
27	(*E*)-2-octenal	−0.460	−0.520	−0.866	−0.464	0.710
28	*cis*-linaloloxide	0.766	0.808	0.859	0.769	−0.926
29	1-octen-3-ol	0.090	0.022	−0.460	0.086	0.219
30	furfurylthiol	0.994	0.984	0.778	0.399	−0.691
31	furfural	0.983	0.793	0.789	0.798	−0.992
32	methional	0.730	0.992	0.810	0.889	−0.793
33	*trans*-linalooloxide	0.789	0.829	0.869	0.792	−0.939
34	(*E*,*E*)-2,4-heptadienal	−0.696	−0.933	−0.646	−0.954	0.819
35	benzaldehyde	0.115	0.046	−0.438	0.110	0.195
36	(*R*)-(−)-linalool	−0.193	−0.259	−0.690	−0.197	0.484
37	5-methyl-2-furfural	0.986	0.873	0.743	0.493	−0.889
38	hotrienol	−0.972	−0.986	−0.945	0.973	0.440
39	phenyl acetaldehyde	−0.637	−0.688	−0.952	−0.641	0.843
40	methyl salicylate	0.762	0.804	0.699	0.765	−0.792
41	*β*-damascenone	0.494	0.540	0.990	0.891	−0.798
42	geraniol	0.854	0.888	0.920	0.999	−0.917
43	phenylethyl alcohol	−0.686	−0.634	−0.186	0.937	0.430
44	*β*-ionone	0.801	0.758	0.352	0.958	−0.579
45	methyl jasmonate	−0.562	−0.504	−0.029	0.956	0.282
46	nerolidol	0.499	0.497	0.918	0.988	−0.599
47	indole	0.651	0.598	0.141	0.648	−0.388

■ ASSOCIATED CONTENT

Supporting Information

The Supporting Information is available free of charge on the ACS Publications website at DOI: 10.1021/acs.jafc.5b02358.

VSC chromatograms (PDF)

■ AUTHOR INFORMATION

Corresponding Author

*School of Perfume and Aroma Technology, Shanghai Institute of Technology, 100 Haiquan Road, Shanghai, 201418, People's Republic of China. Tel: 0086-021-60873424. Fax: 0086-021-54487207. E-mail: flavorsit@163.com.

Funding

This research was funded by the Natural Science Foundation of Shanghai Institute of Technology (Grant YYY-11067), the National Natural Science Foundation of China (Grants 21476140 and 21306114), The National Key Technology R&D Program (2011BAD23B01), and Shanghai Engineering Technology Research Center of Fragrance and Flavor (15DZ2280100).

Notes

The authors declare no competing financial interest.

DOI: 10.1021/acs.jafc.5b02358
J. Agric. Food Chem. 2015, 63, 7499−7510

ABBREVIATIONS USED

GC−MS, gas chromatography−mass spectrometry; FPD, flame photometric detection; PMT, photomultiplier tube; GC−O, gas chromatography−olfactometry; VSC, volatile sulfur compound; DDWL, Dongdingwulong; TGY, Tieguanyin; DHP, Dahongpao; FID, flame ionization detection; SPME, solid phase microextraction; DVB-CAR-PDMS, divinylbenzene-carboxyl-polydimethylsiloxane

REFERENCES

(1) Owuor, P. O.; Obanda, M.; Nyirenda, H. E.; Mandala, W. L. Influence of region of production on clonal black tea chemical characteristics. *Food Chem.* **2008**, *108*, 263−271.

(2) Chen, Q.; Sun, C.; Ouyang, Q.; Wang, Y.; Liu, A.; Li, H.; Zhao, J. Classification of different varieties of Oolong tea using novel artificial sensing tools and data fusion. *LWT - Food Sci. Technol.* **2015**, *60*, 781−787.

(3) Chen, Y. J.; Kuo, P. C.; Yang, M. L.; Li, F. Y.; Tzen, J. T. C. Effects of baking and aging on the changes of phenolic and volatile compounds in the preparation of old Tieguanyin oolong teas. *Food Res. Int.* **2013**, *53*, 732−743.

(4) Xing, G. Research on the connection between main component of tea and degree of fermentation. *J. Hebei Univ.* **2013**, *33*, 24−28.

(5) Chen, S.; Wang, D.; Xu, Y. Characterization of odor-active compounds in sweet-type Chinese rice wine by aroma extract dilution analysis with special emphasis on sotolon. *J. Agric. Food Chem.* **2013**, *61*, 9712−9718.

(6) Wang, K.; Liu, F.; Liu, Z.; Huang, J.; Xu, Z.; Li, Y.; Chen, J.; Gong, Y.; Yang, X. Comparison of catechins and volatile compounds among different types of tea using high performance liquid chromatograph and gas chromatograph mass spectrometer. *Int. J. Food Sci. Technol.* **2011**, *46*, 1406−1412.

(7) Chen, Y.; Jiang, Y.; Duan, J.; Shi, J.; Xue, S.; Kakuda, Y. Variation in catechin contents in relation to quality of 'Huang Zhi Xiang' Oolong tea (*Camellia sinensis*) at various growing altitudes and seasons. *Food Chem.* **2010**, *119*, 648−652.

(8) Cho, J. Y.; Mizutani, M.; Shimizu, B. I.; Kinoshita, T.; Ogura, M.; Tokoro, K.; Lin, M. L.; Sakata, K. Chemical profiling and gene expression profiling during the manufacturing process of Taiwan oolong Tea "Oriental Beauty". *Biosci., Biotechnol., Biochem.* **2007**, *71*, 1476−1486.

(9) Mottram, D. S.; Mottram, H. R. An overview of the contribution of sulfur-containing compounds to the aroma in heated foods. In *Heteroatomic Aroma Compounds*; ACS Symposium Series; American Chemical Society: Washington, DC, 2002; Vol. *826*, pp 73−92. DOI: 10.1021/bk-2002-0826.ch004.

(10) Cadwallader, K.; Potts, D.; Brisske-BeVier, L.; Mirarefi, S. Contribution of volatile sulfur compounds to the characteristic aroma of roasted garlic. In *Volatile Sulfur Compounds in Food*; ACS Symposium Series; American Chemical Society: Washington, DC, 2011; Vol. *1068*, pp 137−151. DOI 10.1021/bk-2011-1068.ch007.

(11) Du, X.; Song, M.; Baldwin, E.; Rouseff, R. Identification of sulphur volatiles and GC-olfactometry aroma profiling in two fresh tomato cultivars. *Food Chem.* **2015**, *171*, 306−314.

(12) McGorrin, R. J. The significance of volatile sulfur compounds in food flavors. *Volatile Sulfur Compounds in Food* **2011**, *1068*, 3−31.

(13) Liu, X. The Research on the oolong tea manipulating handicraft and quality of high fragrance breed dangui. Dissertation for Master's Degree, Fujian Agriculture and Forestry University, 2007.

(14) Shao, Z. Simultaneous determination six components in oolong tea by HPLC. *Chin Pharm. J.* **2014**, *49*, 2201−2205 [In Chinese].

(15) Kesen, S.; Kelebek, H.; Selli, S. Characterization of the key aroma compounds in Turkish olive oils from different geographic origins by application of aroma extract dilution analysis (AEDA). *J. Agric. Food Chem.* **2014**, *62*, 391−401.

(16) Qin, Z.; Pang, X.; Chen, D.; Cheng, H.; Hu, X.; Wu, J. Evaluation of Chinese tea by the electronic nose and gas chromatography−mass spectrometry: Correlation with sensory properties and classification according to grade level. *Food Res. Int.* **2013**, *53*, 864−874.

(17) Sun, S. Y.; Che, C. Y.; Sun, T. F.; Lv, Z. Z.; He, S. X.; Gu, H. N.; Gao, Y. Evaluation of *sequential inoculation* of *Saccharomyces cerevisiae* and *Oenococcus oeni* strains on the chemical and aromatic profiles of cherry wines. *Food Chem.* **2013**, *138*, 2233−2241.

(18) Zhang, W. T.; Zhang, L. Z.; Wang, D. L. Research advances in the effect of processing technology of oolong tea aroma components. *Chinese Tea* **2014**, *10*, 10−13 [In Chinese].

(19) Ravichandran, R.; Parthiban, R. Lipid occurrence, distribution and degradation to flavour volatiles during tea processing. *Food Chem.* **2000**, *68*, 7−13.

(20) Yang, Z.; Baldermann, S.; Watanabe, N. Recent studies of the volatile compounds in tea. *Food Res. Int.* **2013**, *53*, 585−599.

(21) Katsuno, T.; Kasuga, H.; Kusano, Y.; Yaguchi, Y.; Tomomura, M.; Cui, J.; Watanabe, N. Characterisation of odorant compounds and their biochemical formation in green tea with a low temperature storage process. *Food Chem.* **2014**, *148*, 388−395.

(22) Block, E.; Calvey, E. M. Facts and artifacts in allium chemistry. *Sulfur Compounds in Foods, Am. Chem. Soc.* **1994**, *564*, 63−79.

(23) Haberhauer-Troyer, C.; Crnoja, M.; Rosenberg, E.; Grasserbauer, M. Surface characterization of commercial fibers for solid-phase microextraction and related problems in their application. *Fresenius' J. Anal. Chem.* **2000**, *366*, 329−331.

(24) Chin, H. W.; Lindsay, R. C. Ascorbate and transition-metal mediation of methanethiol oxidation to dimethyl disulfide and dimethyl trisulfide. *Food Chem.* **1994**, *49*, 387−392.

(25) Vazquez-Landaverde, P. A.; Torres, J. A.; Qian, M. C. Quantification of trace volatile sulfur compounds in milk by solid-phase microextraction and gas chromatography−pulsed flame photometric detection. *J. Dairy Sci.* **2006**, *89*, 2919−2927.

(26) Burbank, H. M.; Qian, M. C. Volatile sulfur compounds in Cheddar cheese determined by headspace solid-phase microextraction and gas chromatograph-pulsed flame photometric detection. *J. Chromatogr. A* **2005**, *1066*, 149−157.

(27) Fang, Y.; Qian, M. C. Sensitive quantification of sulfur compounds in wine by headspace solid-phase microextraction technique. *J. Chromatogr. A* **2005**, *1080*, 177−185.

(28) Gürbüz, O.; Rouseff, J.; Talcott, S. T.; Rouseff, R. Identification of Muscadine Wine Sulfur Volatiles: Pectinase versus Skin-Contact Maceration. *J. Agric. Food Chem.* **2013**, *61*, 532−539.

(29) Soto, V. C.; Maldonado, I. B.; Jofré, V. P.; Galmarini, C. R.; Silva, M. F. Direct analysis of nectar and floral volatile organic compounds in hybrid onions by HS-SPME/GC-MS: Relationship with pollination and seed production. *Microchem. J.* **2015**, *122*, 110−118.

(30) Colina-Coca, C.; Gonzalez-Pena, D.; Vega, E.; de Ancos, B.; Sanchez-Moreno, C. Novel approach for the determination of volatile compounds in processed onion by headspace gas chromatography-mass spectrometry (HS-GC-MS). *Talanta* **2013**, *103*, 137−144.

(31) Swiegers, J. H.; Bartowsky, E. J.; Henschke, P. A.; Pretorius, I. S. Yeast and bacterial modulation of wine aroma and flavour. *Aust. J. Grape Wine Res.* **2005**, *11*, 139−173.

(32) Ribéreau-Gayon, P.; Glories, Y.; Maujean, A.; Dubourdieu, D. *Handbook of Enology: The Chemistry of Wine and Stabilization and Treatments*; 2000; Vol. *2*.

(33) Tontul, I.; Torun, M.; Dincer, C.; Sahin-Nadeem, H.; Topuz, A.; Turna, T.; Ozdemir, F. Comparative study on volatile compounds in Turkish green tea powder: Impact of tea clone, shading level and shooting period. *Food Res. Int.* **2013**, *53*, 744−750.

(34) Tominaga, T.; Blanchard, L.; Darriet, P.; Dubourdieu, D. A Powerful Aromatic Volatile Thiol, 2-Furanmethanethiol, Exhibiting Roast Coffee Aroma in Wines Made from Several Vitis vinifera Grape Varieties. *J. Agric. Food Chem.* **2000**, *48*, 1799−1802.

(35) Herbst-Johnstone, M.; Nicolau, L.; Kilmartin, P. A. Stability of varietal thiols in commercial sauvignon blanc wines. *Am. J. Enol. Vitic.* **2011**, *62*, 495−502.

(36) Coetzee, C.; du Toit, W. J. A comprehensive review on Sauvignon blanc aroma with a focus on certain positive volatile thiols. *Food Res. Int.* **2012**, *45*, 287−298.

DOI: 10.1021/acs.jafc.5b02358
J. Agric. Food Chem. 2015, 63, 7499−7510

(37) Kato, M.; Shibamoto, T. Variation of Major Volatile Constituents in Various Green Teas from Southeast Asia. *J. Agric. Food Chem.* **2001**, *49*, 1394−1396.
(38) Wang, L. F.; Lee, J. Y.; Chung, J. O.; Baik, J. H.; So, S.; Park, S. K. Discrimination of teas with different degrees of fermentation by SPME−GC analysis of the characteristic volatile flavour compounds. *Food Chem.* **2008**, *109*, 196−206.
(39) Liang, H. Y.; Chen, J. Y.; Reeves, M.; Han, B. Z. Aromatic and sensorial profiles of young Cabernet Sauvignon wines fermented by different Chinese autochthonous *Saccharomyces cerevisiae* strains. *Food Res. Int.* **2013**, *51*, 855−865.
(40) Giri, A.; Osako, K.; Okamoto, A.; Ohshima, T. Olfactometric characterization of aroma active compounds in fermented fish paste in comparison with fish sauce, fermented soy paste and sauce products. *Food Res. Int.* **2010**, *43*, 1027−1040.
(41) Feng, Y.; Su, G.; Zhao, H.; Cai, Y.; Cui, C.; Sun-Waterhouse, D.; Zhao, M. Characterisation of aroma profiles of commercial soy sauce by odour activity value and omission test. *Food Chem.* **2015**, *167*, 220−228.
(42) Jelen, H.; Majcher, M.; Ginja, A.; Kuligowski, M. Determination of compounds responsible for tempeh aroma. *Food Chem.* **2013**, *141*, 459−465.
(43) Birch, A. N.; Petersen, M. A.; Arneborg, N.; Hansen, Å. S. Influence of commercial baker's yeasts on bread aroma profiles. *Food Res. Int.* **2013**, *52*, 160−166.
(44) Joshi, R.; Gulati, A. Fractionation and identification of minor and aroma-active constituents in Kangra orthodox black tea. *Food Chem.* **2015**, *167*, 290−298.
(45) Qian, M. C.; Wang, Y. Seasonal variation of volatile composition and odor activity value of'Marion'(*Rubus spp. hyb*) and'Thornless Evergreen'(*R. laciniatus L.*) Blackberries. *J. Food Sci.* **2005**, *70*, C13−C20.
(46) Pino, J. A.; Mesa, J. Contribution of volatile compounds to mango (*Mangifera indica L.*) aroma. *Flavour Fragrance J.* **2006**, *21*, 207−213.
(47) van Gemert, L. J. Compilations of Odour Threshold Values in Air, Water and Other Media; Van Setten Kwadraat: Houten, The Netherlands, 2003.

DOI: 10.1021/acs.jafc.5b02358
J. Agric. Food Chem. 2015, 63, 7499−7510

using the VIDEO-Sniff method (vocabulary−intensity−duration of elementary odors by sniffing),[13] a hybrid olfactometry method combining detection frequency, intensity, and descriptive vocabulary of the judges, and their quantitation by HS-SPME-GC-MS/PFPD.

To date, and to the authors' knowledge, there is no publication reporting the comparative study of differently manufactured Swiss Tilsit cheeses using olfactometry and with a focus on VSC odor impact and quantitation.

MATERIALS AND METHODS

Chemicals. Chemical compounds were purchased from Sigma-Aldrich Chemie GmbH (Buchs, Switzerland) and Alfa Aesar GmbH & Co KG (Karlsruhe, Germany): acetic acid (Aldrich 320099), 2-acetyl-2-thiazoline (Aldrich W381718), allyl sulfide (Aldrich A35801), benzaldehyde (Aldrich W212709), benzyl alcohol (Aldrich 305197), bis(methylthio)methane (Aldrich W387800), butane-2,3-dione (Aldrich B85307), butan-2-one (Aldrich 360473), butanoic acid (Aldrich W222119), carbon disulfide (Aldrich 335266), decan-2-one (Aldrich W510637), (2*E*,4*E*)-deca-2,4-dienal (Aldrich W313505), dimethyl disulfide (Aldrich W353604), 2,5-dimethylpyrazine (Aldrich W327204), dimethyl sulfide (Aldrich W274623), dimethyl sulfone (Aldrich M81705), dimethyl sulfoxide (Aldrich D8418), dimethyl trisulfide (Aldrich W327506), ethanol (Aldrich 02860), ethyl butanoate (Aldrich W242705), ethyl hexanoate (Aldrich W243906), 4-ethylguaiacol (Aldrich W243604), ethyl isobutyrate (Aldrich W242802), ethyl methyl sulfide (Aldrich 238317), ethyl octanoate (Aldrich W244902), hexanal (Aldrich 115606), hexanoic acid (Aldrich W255904), 3-methylbutyl acetate (Aldrich W205532), methanethiol (Aldrich 742805), 3-methylbutanal (Aldrich W269204), 3-methylbutanoic acid (Aldrich W310204), 3-methylbutan-2-ol (Aldrich 110949), 3-methylindole (Aldrich W301912), methyl isothiocyanate (Aldrich 112771), 2-methylpropanoic acid (Aldrich W222216), 5-methylnonan-5-ol (Aldrich S505021), 4-methylpentanoic acid (Aldrich 277827), *S*-methyl thioacetate (Aldrich CDS001513), 2-methyltetrahydrothiophen-3-one (Aldrich W351202), methyl thiocyanate (Aldrich 722197), 3-(methylthio)propanal (Aldrich W274704), nonanal (Aldrich W278203), δ-octalactone (Aldrich w321405), octanal (Aldrich W279706), octanoic acid (Aldrich W279900), oct-1-en-3-ol (Aldrich W280518), oct-1-en-3-one (Aldrich W351504), oct-3-en-2-one (Aldrich W341606), pentanoic acid (Aldrich W310107), phenol (Aldrich P1037), potassium thiocyanate (Aldrich 207799), polyethylene glycol 200 (P3015), 2-phenylethanol (Aldrich 77861), pentane-2,3-dione (Aldrich W284106), α-pinene (Aldrich 147524), sodium sulfide nonahydrate (Aldrich 208043), sulfuric acid 98% (Aldrich 320501), tridecan-2-one (Aldrich W338818), undecan-2-one (Aldrich W309311), and *m*-xylene (Aldrich 95670).

Carbonyl sulfide was prepared according to the method of Svoronos and Bruno.[16] The solution was stored at −80 °C during a maximum of 1 week.

Hydrogen sulfide was prepared according to the method of Vazquez-Landaverde et al.[17] The solution was stored at 4 °C during a maximum of 1 week.

A stock solution of 1% methanethiol was prepared by bubbling gas in cold (4 °C) polyethylene glycol 200. The solution was stored at −20 °C during a maximum of 1 week.

Cheese Samples. Ten pieces of Swiss Tilsit cheese of each type and of similar commercial size and weight (approximately 200 g) were obtained from a supermarket located in Bern, Switzerland (Table 1). The cheeses were kept at 4 °C in vacuum-sealed plastic bags for a maximum of 1 month until analysis.

Sample Preparation. The samples for all analyses were obtained on the basis of a procedure described by Burbank and Qian.[7] In the present study, 2 cm of rind and cheese were removed from all sides of the cheese to provide a sample as homogeneous as possible. The sample was then finely cut with a ceramic knife to avoid contact with metal, thus limiting the oxidation of sulfur compounds. Cut cheese (2.00 ± 0.10 g) was placed in 20 mL HS vials (Interchim, Montluçon, France). For calibration curves, cut cheese was homogenized together with 10 μL of an internal standard solution containing ethyl methyl sulfide (2 mg kg^{-1}) dissolved in polyethylene glycol 200. The mixture was homogenized using a glass pestle. The vials were placed in an ice bath at 0 °C to cool the exothermic reaction when 4.00 ± 0.10 g of $CaCl_2$ was added to each mixture. Three replicates per sample were prepared. To prevent oxidation, the vials were flushed with argon for 5 s with two needles to create an "argon stream" in the vial after it had been hermetically sealed with a blue silicone/Teflon septum (Interchim).

Table 1. Description of Cheeses (www.Tilsiter.ch, 2014)

	green Tilsit	red Tilsit	yellow Tilsit
thermal treatment	pasteurized milk	partially thermized milk	pasteurized milk with higher fat content
fat in dry matter (FDM)	at least 45% FDM	at least 45% FDM	at least 55% FDM
approx fat content in 100 g	28 g	29.5 g	33 g
ripening time	30−60 days	70−110 days	30−75 days
taste perception	mild aroma, slightly sour	rich, spicy, pungent	creamy, slightly sour, mild aroma

Solid-Phase Microextraction (SPME) and Chromatography. *Identification and Quantitation of VSCs by GC-MS/PFPD.* Samples were extracted using a 1 cm carboxen/polydimethylsiloxane (CAR/PDMS) 85 μm StableFlex fiber (Supelco, Bellefonte, PA, USA) per the manufacturer's recommendation, and the literature[9,18−22] revealed that this coating is the best solution for the extraction of highly volatile sulfur compounds, such as carbonyl sulfide, hydrogen sulfide, or methanethiol from foodstuffs.

The fiber was conditioned according to the supplier's recommendations (300 °C for 60 min). The analyses were realized using an MPS2 autosampler equipped with Maestro1 software, V.1.4.8.14/3.5 (Gerstel, Sursee, Switzerland), a Trace GC Ultra GC coupled with a DSQ II mass selective detector (MSD) (Thermo Finnigan, Milan, Italy), and a PFPD (OI Analytical, College Station, TX, USA).

The headspace was extracted for 120 min at 60 °C with an agitation rate of 250 rpm without preheating. Bound volatiles were desorbed for 1 min at 250 °C in the injector, which was in the splitless mode for 30 s, and then the split valve was opened (split flow = 80 mL min^{-1}). Volatile compounds were separated on a TRB-FFAP fused silica capillary column (100% polyethylene glycol PEG with nitroterephthalic acid, bonded and cross-linked, 30 m × 0.32 mm, 1.0 μm film; Teknokroma, Barcelona, Spain) with helium as the carrier gas at a constant flow of 2.1 mL min^{-1} (37 cm s^{-1}).

The oven temperature was programmed as follows: 5 min at 35 °C, then heated to 150 °C at a rate of 10 °C min^{-1}, held for 1 min, and then heated to 220 °C at a rate of 20 °C min^{-1}, with a final hold time of 5 min. The settings of the PFPD were as follows: 250 °C, voltage at 540 V, ignitor current at 2.6 A, trigger level at 300, range at 10, and attenuation at 32 with flow rates of air1 at 17 mL min^{-1}, H_2 at 14 mL min^{-1}, and air2 at 10 mL min^{-1}. The MS settings were as follows: transfer line at 230 °C, source temperature at 230 °C, and analytes monitored in SCAN mode between 30 and 150 amu without solvent delay.

Calibration curves were established by the method of standard additions in the cheese matrix. One hundred microliters of calibration solution prepared in polyethylene glycol 200 was added to the matrix as given in Table 3, together with 10 μL of the internal standard solution containing ethyl methyl sulfide (2 mg kg^{-1}) to correct variations during the extraction.

The detector response signals were integrated using the Xcalibur 2.0.7 software (Thermo Fisher Scientific AG, Reinach, Switzerland). The NIST/EPA/NIH mass spectral library (NIST11) version 2.0 g (NIST, Gaithersburg, MD, USA) was used for peak identification. The PFPD signal was used to trace the VSCs in the chromatogram.

Gas Chromatography−Olfactometry. Odor-active compounds were analyzed using a two-way odor detection port (ODP2; Gerstel) connected to a 6890N Agilent gas chromatograph (2W-GC-O) coupled with a 5973N MSD (Agilent Technology, Santa Clara, CA, USA) and a

DOI: 10.1021/acs.jafc.5b02536
J. Agric. Food Chem. 2015, 63, 7511−7521

Table 2. Distribution of Vocabulary Items by 8 GC-O Sniffers in 11 Classes

odor class	odor descriptors
buttery-cheesy	acid, animalic, buttery, caramel, creamy, butyric acid, cheese, cheesy, rancid, raclette cheese, sweaty, vomit, propionic acid, cooked milk, Tilsit, ripe, pungent, cheesy surface, diacetyl, old socks, cellar
earthy-undergrowth	earthy, mushrooms, forest, musty, old wardrobe, pine green, champignons
empyreumatic	bread, burned, roasted, cooked, smoked
floral-fruity	floral, fresh gum, fruity, strawberry, sweet, mint, pineapple, rose, vanilla, artificial fruit, rubbery, citrus, honey, terpene, cooked apple, cherry, fresh fruit, wine
green-fatty	fatty, green, fresh vegetable, grass, plant, oil, persil, old fat, wax, colored pencil, basilica, fresh-cut grass, cut grass, bee wax, vitamin supplier
malty-chemical	chemical, malty, cleaning product, plastic, gum, solvent, urine, acetic acid, medical like a hospital, glass cleaner, alcoholic, cork
meaty	bouillon, cooked meat, ham
nutty	cooked nut, chestnut, nutty
spicy	sesame-spicy, spicy
sulfur	garlic, gas, potatoes, putrid, methanethiol, onion, sulfury, pungent, rotten, decomposed, compost, moldy
undefined	?, nd, warm, unpleasant, unknown

PFPD (OI Analytical) and equipped with an MPS2 autosampler and the Maestro1 software, V.1.4.8.14/3.5 (Gerstel, Sursee, Switzerland).

For GC-O analyses, volatile organic compounds were extracted using a 2 cm 50/30 μm divinylbenzene/carboxen/polydimethylsiloxane (DVB/CAR/PDMS) StableFlex fiber (Supelco). To obtain a representative evaluation of the odor of the samples in olfactometry, a DVB/CAR/PDMS fiber is suitable for the extraction of volatile and semivolatile compounds and was reported to give good odor representativeness for dairy products.[23] The fiber was conditioned according to the supplier's recommendations (270 °C for 60 min).

The cheese headspace was extracted for 16 h at 45 °C with an agitation rate of 250 rpm without preheating. The SPME extraction time was optimized for an optimal olfactory analysis to obtain clearly perceivable odorant signals.[9] The absence of artifact formation was checked using 16 h as the incubation time and only 45 min for the extraction, and the results were compared with short incubation and extraction conditions (5 min incubation, 45 min extraction). Bound volatiles were desorbed for 1 min at 250 °C in the injector, which was in the splitless mode for 30 s; then the split valve was opened (split flow = 80 mL min^{-1}). Volatile compounds were separated on a TRB-FFAP fused silica capillary column (60 m × 0.32 mm, 0.5 μm film; Teknokroma) with helium as the carrier gas at a constant flow of 2.3 mL min^{-1} (39 cm s^{-1}).

The oven temperature was programmed as follows: 5 min at 35 °C, then heated to 150 °C at a rate of 10 °C min^{-1}, held for 1 min, and then heated to 220 °C at a rate of 20 °C min^{-1} with a final hold time of 5 min.

The olfactometric ports were provided by Gerstel and are designed for two panelists to detect volatile compounds simultaneously. The dimensions and capillaries after the GC separation were adapted to obtain an optimal and timely synchronized signal between the physical detectors and the two sniffers.[24] The sample is split through deactivated silica capillaries into the proportions MSD/PFPD/ODP/ODP 1:1:1.5:1.5, corresponding to flow rates of 0.46 mL min^{-1}/0.46 mL min^{-1}/0.69 mL min^{-1}/0.69 mL min^{-1}. The transfer line for each ODP is heated at 220 °C to prevent the condensation of volatiles in the capillaries.

Olfactory analyses were performed by a trained panel of eight sniffers. A single individual response is by definition not reproducible, and a minimum of eight sniffers is required to obtain a reliable aromagram.[25,26] Panelists are equipped with a microphone and must simultaneously press a button and comment on the odor they perceive while indicating its intensity on a scale from 1 to 5, 1 being barely perceptible and 5 being a very strong odor. Comments are registered and processed at the end of each session with AcquiSniff version 6.5.9 (INRA, Clermont-Ferrand, France).

The aromagrams were computed using the VIDEO-Sniff method and the AcquiSniff software. All vocabulary employed by the judges was sorted into the 11 olfactory classes (Table 2).[27]

The settings of the PFPD were as follows: 250 °C, voltage at 540 V, ignitor current at 2.6 A, trigger level at 300, range at 10, and attenuation at 32 with the flow rates air1 at 17 mL min^{-1}, H_2 at 14 mL min^{-1}, and air2 at 10 mL min^{-1}. The MSD settings were as follows: transfer line at 230 °C, source temperature at 230 °C, and the analytes were monitored in SCAN mode between 30 and 150 amu without solvent delay.

The detectors' response signals were integrated using Chemstation Data Analysis software version E.02.00.493 (Agilent Technologies). Aromagrams were recorded and processed using the VIDEO-Sniff method and AcquiSniff Software, as described in the literature.[13] The NIST/EPA/NIH mass spectral library (NIST11) version 2.0g (NIST) was used for peak identification.

GC−Olfactometry Panel Training. GC-O is used to identify odor-active compounds with the aid of the human nose.[13] It is not necessary to be specially trained to participate as an olfactometry panelist. However, it is very convenient for data processing to work with panelists who are familiar with odors and use the same language. For this, all panelists were trained statically for 4 months to memorize 17 odorant molecules (ethyl isobutyrate, 3-methylbutyl acetate, oct-1-en-3-ol, oct-1-en-3-one, pentane-2,3-dione, 2-phenylethanol, 3-methylindole, α-pinene, allyl sulfide, dimethyl trisulfide, butanoic acid, 4-ethylguaiacol, 3-(methylthio)propanal, 2-acetyl-2-thiazoline, nonanal, (2*E*,4*E*)-deca-2,4-dienal, and 3-methylbutanal) of 10 different odor families commonly present in cheese and dairy products (buttery-cheesy, empyreumatic, floral-fruity, green-fatty, malty-chemical, meaty, spicy, nutty, sulfur, and earthy-undergrowth). After successful completion, they were familiarized with the GC-O setup and trained three times using a standard solution containing the 17 molecules. Panel performance was monitored through regular training, and information was recorded in a database.

Determination of "Average Odor Activity Values by Sniffing ($aOAV_{sniff}$)" Using Gas Chromatography−Olfactometric Detection Limits of the Compounds (GCO_t) and "Average Absolute Quantified Amounts (aAQA)". GC-O detection limits of target VSCs (GCO_t)[28] were determined by the injection of several standard solutions of pure compounds at known concentrations, using a dilution factor of 2, until the molecule was no longer identifiable by the panelists with the same GC-O method as described above and used in all applications. The procedure was repeated with two trained panelists, and the average values for each compound were used. The method was successfully verified using two different GC-O units to confirm the feasibility of the technique.

During sniffing analyses of the cheeses, aAQA were determined by MS quantitation as described to ensure that these data correspond to the run during which olfactometric perception was recorded. Finally and according to the classical concept of OAV,[29] $aOAV_{sniff}$ values are calculated by dividing the aAQA by the GCO_t (Table 3).

Statistical Analysis. Olfactory charts and statistics were realized using AcquiSniff version 6.5.9 (INRA, Clermont-Ferrand, France).

RESULTS AND DISCUSSION

Olfactometry Evaluation. A total of 36 odorant zones were perceived during the sniffing of the three kinds of Tilsit cheese by the eight panelists. Red Tilsit showed the most odorant zones in the aromagram with 31 odorant zones, followed by yellow Tilsit with 29 odorant zones and green Tilsit with 25 odorant zones.

DOI: 10.1021/acs.jafc.5b02536
J. Agric. Food Chem. 2015, 63, 7511−7521

Table 3. Concentration of VSCs in Swiss Tilsit Cheese Sample

compound[b]	calibration concn (μg kg^{-1})	regression eq	R^2	LOD[c] (μg kg^{-1})	LOQ[d] (μg kg^{-1})	ions monitored (m/z)	Tilsit cheese sample[a] (μg kg^{-1})			aAQA[e] (ng)	GCO_t[f] (ng)	$aOAV_{sniff}$[g] (−)
							green	red	yellow			
COS	0.1, 1, 10, 100, 1000	$Y = 4905.3x$	0.9990	0.180	0.610	32, 44, 60*[h]	$119.1^{\pm 21.3}$	$191.0^{\pm 80.4}$	$311.0^{\pm 29.6}$	NA[i]	odorless	NA
H_2S	0.1, 1, 10, 100, 1000	$Y = 4398.9x$	0.9988	2.500	8.400	33, 34,* 35	$163.0^{\pm 58.0}$	$147.0^{\pm 19.6}$	$89.0^{\pm 10.6}$	0.7	12	<1
MeSH	1, 10, 100, 1000, 10000	$Y = 50337x$	0.9976	0.040	0.140	45, 47, 48*	$40.0^{\pm 5.1}$	$226.0^{\pm 57.4}$	$605.0^{\pm 14.4}$	24	0.06	400
CS_2	0.1, 1, 10, 100, 1000	$Y = 3 \times 10^6 x$	0.9997	0.002	0.008	38, 44, 76*	$4.9^{\pm 0.6}$	$0.4^{\pm 0.1}$	$2.9^{\pm 0.3}$	4.6	67	<1
DMS	0.1, 1, 10, 100, 1000	$Y = 260362x$	1.0000	5.710	19.050	47, 61, 62*	<LOQ	$33^{\pm 2.7}$	$32.4^{\pm 0.9}$	1.8	1.0	1.8
MeSAc	0.01, 0.1, 1, 10, 100	$Y = 2 \times 10^6 x$	1.0000	0.003	0.011	43, 75, 90*	$0.3^{\pm 0.03}$	$1.0^{\pm 0.25}$	$0.6^{\pm 0.04}$	2.3	5.0	0.46
DMDS	0.1, 1, 10, 100, 1000	$Y = 2 \times 10^6 x$	1.0000	0.008	0.025	61, 79, 94*	$2.8^{\pm 0.3}$	$87.0^{\pm 34.1}$	$50.8^{\pm 1.0}$	35	10	3.5
MITC	0.01, 0.1, 1, 10, 100	$Y = 332975x$	0.9999	0.108	0.360	70, 72,* 73	$0.5^{\pm 0.1}$	$2.7^{\pm 0.4}$	$0.6^{\pm 0.1}$	0.005	2400	<1
bis(methylthio)methane	0.01, 0.1, 1, 10, 100	$Y = 863876x$	1.0000	0.018	0.059	45, 61, 108*	$0.07^{\pm 0.04}$	$0.73^{\pm 0.09}$	$0.72^{\pm 0.03}$	0.3	0.1	3
MTC	0.01, 0.1, 1, 10, 100	$Y = 2 \times 10^6 x$	1.0000	0.075	0.250	70, 72,* 73	<LOQ	<LOQ	<LOQ	<LOQ	1930	<1
DMTS	0.01, 0.1, 1, 10, 100	$Y = 726994x$	0.9995	0.039	0.130	79, 111, 126*	$0.4^{\pm 0.05}$	$3.0^{\pm 0.75}$	$4.5^{\pm 0.49}$	0.3	0.002	150
3-(methylthio)propanal	0.1, 1, 10, 100, 1000	$Y = 10469x$	0.9993	2.115	7.050	61, 76, 104*	<LOQ	$8.7^{\pm 1.9}$	<LOQ	2.0	0.08	25
2-methyltetrahydrothiophen-3-one	0.01, 0.1, 1, 10, 100	$Y = 276000x$	0.9959	0.487	1.624	60, 88, 116*	$11.1^{\pm 1.8}$	$1.6^{\pm 0.21}$	$3.5^{\pm 0.21}$	1.6	100	<1
DMSO	1, 10, 100, 1000, 10000	$Y = 445.49x$	0.9782	5.715	19.050	45, 63, 78*	$897.0^{\pm 195.6}$	$523.0^{\pm 80.0}$	$645.0^{\pm 55.3}$	NA	odorless	NA
Me_2SO_2	10, 100, 1000, 10000, 100000	$Y = 338.78x$	0.9994	1.077	3.590	63, 79, 94*	$1561.0^{\pm 369.1}$	$1536.0^{\pm 216.8}$	$2631.0^{\pm 474.7}$	NA	odorless	NA
sum of all quantified VSCs							2800	2761	4377			
sum of odor-active VSCs detected in GC-O							54.4	327.0	664.5			

[a]Green = 45% fat in dry matter (FDM), 30−60 days ripening time; red = 45% FDM, 70−110 days ripening time; yellow = 55% FDM, 30−75 days ripening time. [b]COS = carbonyl sulfide; H_2S = hydrogen sulfide; MeSH = methanethiol; CS_2 = carbon disulfide; DMS = dimethyl disulfide; MeSAc = methyl thioacetate; DMDS = dimethyl disulfide; MTC = methyl thiocyanate; MITC = methyl isothiocyanate, DMTS = dimethyl trisulfide; DMSO = dimethyl sulfoxide; Me_2SO_2 = dimethyl sulfone. [c]LOD = limit of detection = 3σ/S. σ = standard deviation of the analyte. [d]LOQ = limit of quantitation = 10σ/S. [e]aAQA = average absolute quantified amount, determined during a sniffing run. [f]GCO_t = gas chromatography−olfactometric detection limits of the compounds determined with pure reference compounds. [g]$aOAV_{sniff}$ = average odor activity values by sniffing, determined using the GCO_t and the aAQA of a VSC found during sniffing analyses in the sample. [h]* = quantitation ion. [i]NA = not available.

J. Agric. Food Chem. 2015, 63, 7511−7521
DOI: 10.1021/acs.jafc.5b02536

Altogether, 41 odorant compounds were found to be responsible for the 36 odorant zones and could be identified by combining odor, linear retention indices (LRI), PFPD, and quadrupole mass spectrometer (qMS) information. The results are presented in Table 4. A minimum of 50% of the panelists detected 17 odorant zones in the red Tilsit, 15 odorant zones in the yellow Tilsit, and 13 odorant zones in the green Tilsit. Detection frequency of <50% is generally considered as noise,[30] but molecules detected by <50% of the panel might also contribute to the overall odor of a sample. The aromagrams of the three cheeses are given in Figure 1.

A common core of odorant compounds of the three Tilsit cheeses with a detection frequency of at least 50% consists of hexanal (peak 6 in Figure 1; odor descriptors: green, grass, floral; GC-O-VIDEO-Sniff characteristics in all three cheeses such as the mean intensity × detection frequency value and detection frequency in percentage are given in Table 4), octanal (peak 12; fruity), butane-2,3-dione (peak 4; buttery, creamy, cheesy), non-8-en-2-one$^{t(std)}$ (peak 10; cooked potatoes, earthy, roasted, meaty, salty meat; ^{t} = tentatively identified, e.g. reference compound not injected ($^{t(std)}$) or odor descriptor ($^{t(Odor)}$) or reference compound not exactly matching and/or no detection by MS ($^{t(MS)}$)), 3-methylbutan-2-ol$^{t(Odor)}$ (peak 8; plastic, fatty, chemical, solvent, gum), butanoic acid (peak 31; cheesy, rancid), 3-methylbutanoic acid (peak 32; cheesy, rancid raclette cheese), MeSH (peak 1; cheesy, old socks, cabbage, cellar, rancid, putrid), DMDS (peak 7; pungent, sulfur), bis(methylthio)methane (peak 13; animalic, cheesy, sulfury, garlic, onion, rancid), DMTS (peak 17; garlic, sulfury, gas, metallic), and 3-(methylthio)propanal (peak 23; boiled potatoes, sulfury).

Two odor-active compounds, oct-1-en-3-one (peak 14; earthy, mushrooms, green) and 2-methylpropanoic acid (peak 26; green, fatty, fruity, rancid), were perceived in both red and yellow Tilsit with a detection frequency of at least 50%. Acetic acid (peak 21; chemical, green, fresh, acid, pungent, spicy) was perceived in both yellow and green Tilsit.

Some compounds were found exclusively in one of the cheeses with a detection frequency of at least 50% and lower than 50% in the other ones. Red Tilsit contains a wider variety of such compounds, with five specific odor-active compounds that were found only in red Tilsit: 3-methylbutanal (peak 3; burned, cooked, roasted, spicy), octa-3,5-dien-2-one$^{t(std)}$ (peak 28; floral, earthy), ethyl butanoate (peak 5; fruity, floral), 2-methyltetrahydrothiophen-3-one$^{t(odor\ threshold)}$ (peak 27; cheesy, sulfur, pungent), and *m*-xylene$^{t(odor)}$ (peak 9; roasted, fatty, old oil, bread). Two specific odor-active compounds were detected exclusively in yellow Tilsit, undecan-2-one (peak 30; floral, fresh, fruity, mint) and 2,3-dimethyl-5-(1-propenyl)pyrazine$^{t(std)}$ (peak 29; green, cut grass, plant), and one specific odor-active compound was detected exclusively in green Tilsit, 2,5-dimethylpyrazine (peak 15; mushroom, green).

In addition, 18 compounds were perceived with a detection frequency of panelists <50% but could be easily identified by LRI, qMS, or odor. Again, red Tilsit shows a greater number of these odorant compounds with 14 such molecules, of which 3 were exclusively perceived in red Tilsit. Yellow Tilsit contains 12 molecules, including 2 specific compounds, and green Tilsit contains the least, with only 9 molecules without specific compounds. The following compounds were identified with a detection frequency of <50%: nonanal$^{t(odor)}$ (peak 16; fruity, cooked, roasted, vanilla, honey), benzaldehyde (peak 25; sesame-spicy, fatty, green, oily, animalic), butan-2-one (peak 2; burned plastic, plastic), decan-2-one (peak 24; cooked, roasted, boiled potatoes), oct-3-en-2-one (peak 18; mushrooms), tridecan-2-one$^{t(odor)}$ (peak 34; wax, fatty), δ-octalactone (peak 38; fatty, green, floral, fruity, creamy, buttery), 5-methylnonan-5-ol (peak 20, green, chemical, earthy), benzyl alcohol (peak 37; urine, wax, fruity, ball pen), phenol (peak 39; plastic), ethyl hexanoate (peak 11; fruity, sweet), ethyl octanoate$^{t(odor)}$ (peak 19; wine, cork, chemical), hexanoic acid (peak 36; cheesy, sweaty), pentanoic acid (peak 33; cheesy, rancid), octanoic acid (peak 40; cheesy, rancid, fatty, ham), 4-methylpentanoic acid (peak 35; cheesy, rancid), and 2,6-diethylpyrazine$^{t(LRI,\ std)}$ (peak 22; chemical, green, sulfury, plastic).

The coelution of odor-active compounds complicates the identification of an odorant zone. A coelution example with hexanal (green, grass) and DMDS (pungent, sulfur), described using both green and pungent descriptors, illustrates the difficulty of identifying the compound using only the odor perception descriptors given by the panelists.

Distribution according to the number of citations of the odor families shows that the dominant odor family contributing to the odor of the different cheeses is "cheesy-buttery", as expected (citation percentages: green Tilsit, 42%; red Tilsit, 41%; and yellow Tilsit, 33%). It is followed by the "sulfur" family (green Tilsit, 24%; yellow Tilsit, 20%; and red Tilsit, 14%), the "malty-chemical" family (red Tilsit, 13%; yellow Tilsit, 12%; and green Tilsit, 5%), and the "fatty-green" family, especially in red and yellow Tilsit (yellow Tilsit, 12%; red Tilsit, 10%; and green Tilsit, 8%). Other odor families also contribute to the overall flavor but to a lesser extent, especially in green Tilsit. The "cheesy-buttery" and "sulfur" families together account for >50% of all odor citations in all three cheeses (green Tilsit, 66%; red Tilsit, 55%; and yellow Tilsit, 53%).

The citation percentages of the dominant class "buttery-cheesy" depicted in yellow in the aromagram (Figure 1) are very similar for the green and red Tilsit (41−42%) and are a little less predominant in the yellow Tilsit (33%). The "buttery-cheesy" odor zones are mainly evoked by three compounds: butanoic acid (cheesy, rancid), 3-methylbutanoic acid (cheesy, rancid, raclette cheese), and butane-2,3-dione (buttery, creamy, cheesy). These odorant compounds were detected by at least 50% of the panelists (Table 4).

The odor class "sulfur" depicted in blue represents 24% of total detected odor zones in green Tilsit, despite a lower overall sulfur compound concentration (Table 3). This might be explained by the nature of the matrix as well as the distribution and release of the compounds.

The "fatty-green" class depicted in green represents 10−12% in red and yellow Tilsit and is less frequently evoked in green Tilsit (8%). However, a single strong "fatty-green" odor zone evoked due to hexanal (green, grass, and floral) was more intense in the green Tilsit (Table 4, peak 6).

The class "malty-chemical" shown in brown is less represented in green Tilsit and is mainly due to three compounds (3-methylbutanal, benzaldehyde, and 5-methylnonan-5-ol), which seem to be mainly present in red and yellow Tilsit.

The "fruity-floral" class shown in pink is slightly more frequent in red Tilsit and comes from the presence of esters, such as ethyl butanoate (fruity, floral) or ethyl hexanoate (fruity, sweet).

"Spicy" notes depicted in violet are present in the form of acetic acid (chemical, green, fresh, acid, pungent, spicy) in all cheeses, and benzaldehyde (spicy, fatty, green, oily, animalic) is present only in red and yellow Tilsit.

The "earthy-undergrowth" notes shown in dark green come from the perception of mushroom notes. The compounds

DOI: 10.1021/acs.jafc.5b02536
J. Agric. Food Chem. 2015, 63, 7511−7521

Table 4. Potent Odorants Identified in Swiss Tilsit by HS-SPME-2W-GC-O-MS

no.[d]	LRI[a] DB-5MS	LRI[a] TRB-FFAP	compound[e]	odor description[f]	mean intensity[b] × detection frequency green	mean intensity[b] × detection frequency red	mean intensity[b] × detection frequency yellow	detection frequency[c] % green	detection frequency[c] % red	detection frequency[c] % yellow	identification[g]
1	464	647	methanethiol	cheesy, old socks, cabbage, cellar, rancid, putrid	3.0	2.7	3.6	88	88	100	LRI, odor, qMS, PFPD, std
2	595	901	butan-2-one	burned plastic, plastic	0.5		1.2	25		38	LRI, odor[lit], qMS, std
3	652	913	3-methylbutanal	burned, cooked, roasted, spicy		0.9	0.5		50	25	LRI, odor, qMS, std
4	588	981	butane-2,3-dione	buttery, creamy, cheesy	1.7	1.8	1.5	50	50	50	LRI, odor, qMS, std
5	799	1039	ethyl butanoate	fruity, floral	0.8	1.6		38	63		LRI, odor, qMS, std
6, 7	800/745	1101/1093	hexanal/dimethyl disulfide	green, grass, floral, pungent, sulfur	2.6	3.2	1.9	88	88	75	LRI, odor, qMS, PFPD, std
8	680	1121	3-methylbutan-2-ol[t]	plastic, fatty, chemical, solvent, gum	2.1	2.3	1.8	63	75	75	LRI, qMS, std
9	870	1156	*m*-xylene[t]	roasted, fatty, old oil, bread		1.5			50		LRI, qMS, std
10	ND[h]	1157	non-8-en-2-one[t]	cooked potatoes, earthy, roasted, meaty, salty meat	2.1	2.9	1.9	75	88	63	odor, qMS
11	1000	1249	ethyl hexanoate	fruity, sweet		0.8			38		LRI, odor, qMS, std
12	1002	1304	octanal	fruity	1.1	1.4	2.9	50	50	88	LRI, odor, qMS, std
13	908	1326	bis(methylthio)methane	animalic, cheesy, sulfury, garlic, onion, rancid	1.1	1.4	2.9	50	50	88	LRI, odor, qMS, PFPD, std
14	976	1332	oct-1-en-3-one	earthy, mushrooms, green	1.2	1.9	1.8	38	50	50	LRI, odor, qMS, std
15	911	1336	2,5-dimethylpyrazine	mushroom, green	1.5		0.6	50		25	LRI, odor, qMS, std
16	1105	1406	nonanal	fruity, cooked, roasted, vanilla, honey	0.6	0.9	0.4	25	25	25	LRI, odor[lit], qMS, std
17	973	1428	dimethyl trisulfide	garlic, sulfury, gas, metallic	3.2	3.0	3.2	88	88	88	LRI, odor, qMS, PFPD, std
18	727	1439	oct-3-en-2-one	mushrooms		0.5			13		LRI, odor[lit], qMS, std
19	1198	1453	ethyl octanoate[t]	wine, cork, chemical			0.8			25	LRI, qMS, std
20	1086	1465	5-methylnonan-5-ol	chemical, fruity, sulfury		1.1	1.2		38	38	LRI, odor, qMS, std
21	725	1472	acetic acid	chemical, green, fresh, acid, pungent, spicy	2.0	1.4	1.8	63	38	50	LRI, odor, qMS, std
22	ND	1475	2,6-diethylpyrazine[t]	chemical, green, sulfury, plastic			1.1			38	odor, qMS
23	906	1486	3-(methylthio)propanal	boiled potatoes, sulfury	2.8	2.6	2.0	75	75	50	LRI, odor, qMS, PFPD, std
24	1184	1505	decan-2-one	cooked, roasted, boiled potatoes	0.8	0.9	0.8	25	38	25	LRI, odor, qMS, std
25	964	1575	benzaldehyde	sesame-spicy, fatty, green, oily, animalic		1.0	0.9		38	38	LRI, odor[lit], qMS, std
26	757	1587	2-methylpropanoic acid	green, fatty, fruity, rancid	1.0	1.8	2.0	25	50	50	LRI, odor, qMS, std
27, 28	992/1067	1588	2-methyltetrahydrothiophen-3-one[t] + octa-3,5-dien-2-one[t(std)]	cheesy, floral, sulfur, pungent, earthy	0.5	1.2		25	50		LRI, odor, qMS, PFPD, std
29, 30	ND/1295	ND/1625	2,3-dimethyl-5-(1-propenyl)pyrazine[t(std)] + undecan-2-one	green, cut grass, floral, fresh, fruity, plant, mint	0.5	1.1	1.4	25	38	50	LRI, odor, qMS, std
31	791	1647	butanoic acid	cheesy, rancid	3.5	2.6	2.4	88	88	63	LRI, odor, qMS, std
32	842	1689	3-methylbutanoic acid	cheesy, rancid, raclette cheese	3.5	3.4	2.6	100	88	63	LRI, odor, qMS, std
33	883	1753	pentanoic acid	cheesy, rancid			0.9			38	LRI, odor, qMS, std
34, 35	958/1497	1824/1836	4-methylpentanoic acid + tridecan-2-one[t(odor)]	wax, fatty, cheesy, rancid	1.3	1.0	1.1	38	38	38	LRI, odor, qMS, std
36	980	1868	hexanoic acid	cheesy, sweaty	0.9	0.6	1.1	25	25	38	LRI, odor, qMS, std
37	1025	1917	benzyl alcohol	urine, wax, fruity, ball pen	0.5	1.0	0.9	25	38	38	LRI, odor[lit], qMS, std
38, 39	1284/974	2035/2041	δ-octalactone + phenol	fatty, green, plastic, floral, fruity, creamy, buttery	0.8	0.6		25	38		LRI, odor[lit], qMS, std

J. Agric. Food Chem. 2015, 63, 7511−7521
DOI: 10.1021/acs.jafc.5b02536

Table 4. continued

no.[d]	LRI[a] DB-5MS	LRI[a] TRB-FFAP	compound[e]	odor description[f]	mean intensity[b] × detection frequency green	mean intensity[b] × detection frequency red	mean intensity[b] × detection frequency yellow	detection frequency[c] % green	detection frequency[c] % red	detection frequency[c] % yellow	identification[g]
40	1155	2073	octanoic acid	cheesy, rancid, fatty, ham		0.5	0.6		25	25	LRI, odor, qMS, std
41	ND	2098	unknown	sweet, pineapple		0.4			25		
sum					40.2	48.0	45.8				

[a]LRI on nonpolar (DB-5MS) and polar (TRB-FFAP) stationary phases, determined with a series of *n*-alkanes (C5−C25). [b]Mean intensity given by eight judges (on a scale from 1 to 5). [c]Detection frequency over eight judges. [d]Peak number according to Figure 1. [e]Compounds are listed in elution order on a TRB-FFAP column. [f]Description of odors given by the judges. [g]Identification methods: LRI = linear retention index, odor = comparison of the odor descriptors of the reference compound to the judges' descriptions, $odor^{lit}$ = comparison of the judges' descriptions to the literature, qMS = mass spectrum obtained by quadrupole mass spectrometry, std = reference compounds injection. [t]Tentatively identified (reference compounds not injected $^{(std)}$ or odor descriptor of reference compound not exactly matching $^{(odor)}$ and/or no detection by MS $^{(MS)}$; superscript precisions are given for, e.g., coelutions where the identification column does not provide all information, and in the text. [h]ND = not determined.

responsible were partially identified (Table 4: non-8-en-2-one$^{t(std)}$, oct-1-en-3-one, oct-3-en-2-one, and octa-3,5-dien-2-one$^{t(std)}$). Two additional specific aroma-active zones with a strong "earthy-undergrowth" note are present only in green Tilsit between peaks 21 and 23 and between peaks 37 and 38 (Figure 1). Due to the very low amount in the sample, these molecules could not be identified.

The class "nutty" shown in orange contributes to 1% of all detected items in cheeses. This odor class was described by the panelists as cooked nut, chestnut, and nutty. The very low concentrations in the cheeses did not allow for identification by conventional detectors in the present study.

Calculation of Average Odor Activity Values by Sniffing ($aOAV_{sniff}$). The olfactory impact of a compound depends on both its concentration in a sample and its odor threshold. In general, to account for these two parameters, the literature refers to the odor activity value (OAV), which is the ratio of the concentration of a compound to its odor threshold, to describe how strongly an odorant compound is perceived by the human nose.[29] The odor threshold values are usually taken from the literature and are determined in a simple matrix, such as water, oil, or air, using a static method. It is therefore difficult to apply such OAVs, especially to a complex matrix such as cheese.

However, the odor perception threshold is the lowest concentration of a compound that can be perceived in a matrix. It is different from the odor recognition threshold at which an odorant is both perceived and its odor recognized/identified/described. In general, perception thresholds are 2−5 times lower than identification thresholds.[31] Sniffing analysis is a dynamic method, and the panelists are trained to detect and describe odorant zones. However, for both perception and identification, the compound concentration has to be higher than the respective thresholds, and the time during which the thresholds are high enough might be too short for the panelists to react, or the panelists might be exhaling and thus miss the stimulus. This is why it is preferable to work with identification thresholds, which ensure that the determined OAV is truly the one of the target compounds, and not with perception thresholds.

Therefore, we decided not to employ the classic concept used in the literature, but to determine such gas chromatography−olfactometric detection limits as GCO_t for target odorant VSCs[28] and use them for $aOAV_{sniff}$ calculations: $aOAV_{sniff}$ values of target odorant VSCs were calculated by dividing the average absolute quantified amount (aAQA) of a VSC found during sniffing analyses in the sample by the GCO_t and are given in Table 3.

The $aOAV_{sniff}$ can help to estimate the potential odor impact a compound might have on the overall odor profile. As it is based on the theory of the classical OAV, an $aOAV_{sniff}$ with a high value is a strong indication that the compound contributes greatly to the cheese aroma.[29]

Sulfur Profiles of the Three Swiss Tilsit Cheeses. A total of 21 VSCs were detected by GC-PFPD in the studied cheeses: 21 in yellow Tilsit, 18 in red, and 18 in green. Of these 21 compounds only 6 were found to be odorant by 2W-GC-O: 6 in green Tilsit, 6 in red Tilsit, and 5 in yellow Tilsit. Fifteen selected sulfur compounds were quantified at parts per billion (ppb) levels (Table 3).

MeSH, DMDS, bis(methylthio)methane, DMTS, and 3-(methylthio)propanal, all known for their low odor thresholds, were found at ppb levels in all three cheeses and were also detected by 2W-GC-O.

2-Methyltetrahydrothiophen-3-one$^{t(odor\ threshold)}$ was also detected in all cheeses and was confirmed by LRI, qMS, PFPD, and

DOI: 10.1021/acs.jafc.5b02536
J. Agric. Food Chem. 2015, 63, 7511−7521

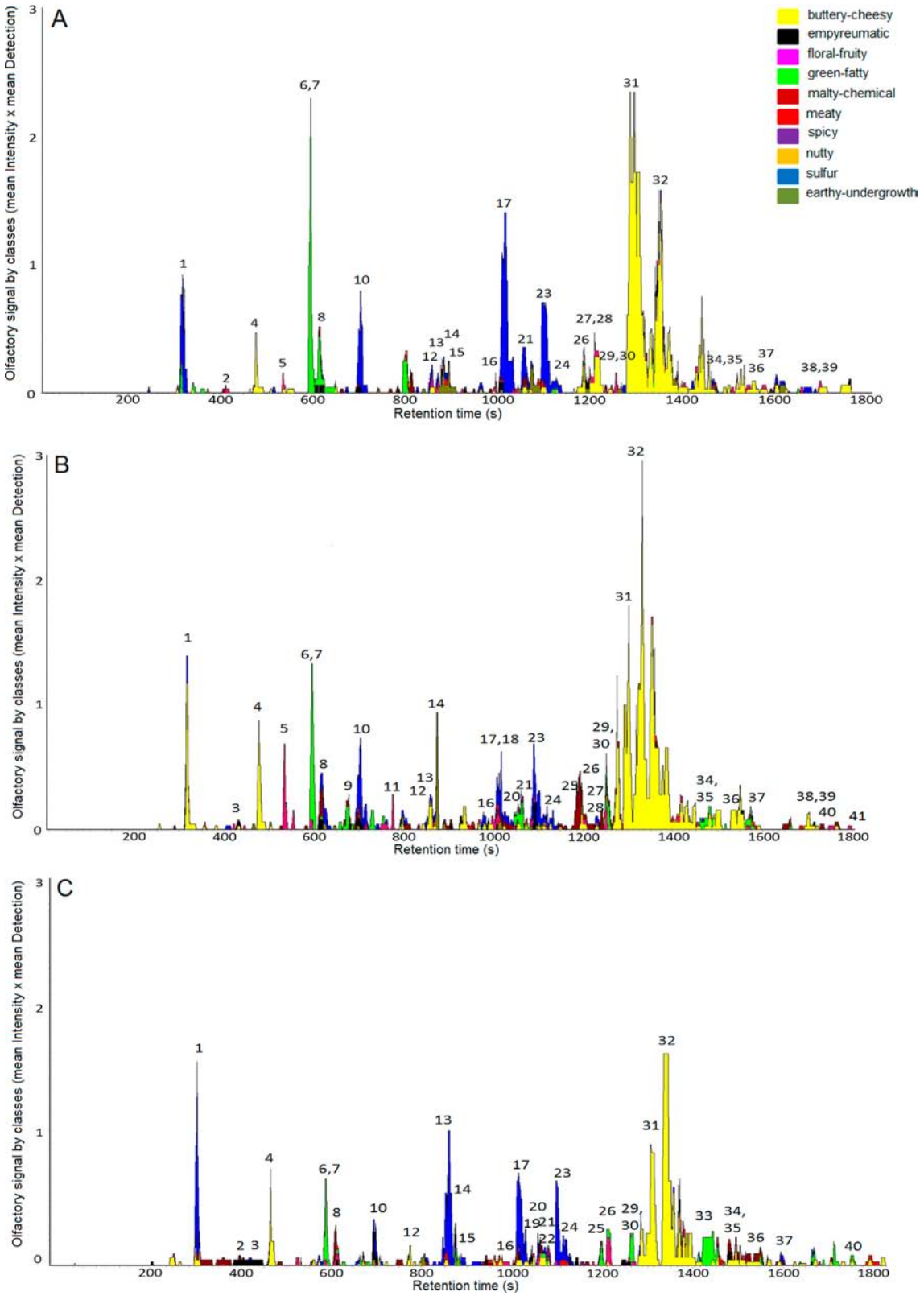

Figure 1. Mean olfactory signal by classes ($\overline{OSC}_{Int \times Det}$) of green (A), red (B), and yellow (C) Tilsit over eight judges. The signals are classified in 10 distinct odor families of the 11 families represented in Table 2. The family "undefined" is not represented in the aromagram. Labels corresponding to the peak numbers are given in Table 4. The compounds were separated on a TRB-FFAP capillary column.

odor specifications. Using its absolute quantified amount found during sniffing analyses in the samples and its GCO_t (100 ng) determined with the pure reference compound, an $aOAV_{sniff} < 1$ was calculated for 2-methyltetrahydrothiophen-3-one$^{t(\text{odor threshold})}$. Hence, it should in theory not be detectable by the panelists. Numerous reasons could explain why the compound was nevertheless smelled and confirmed by odor descriptor comparison; the following two hypotheses may be

DOI: 10.1021/acs.jafc.5b02536
J. Agric. Food Chem. 2015, 63, 7511−7521

proposed: (1) The molecule has an asymmetric carbon and hence two enantiomers exist. There are no stereochemistry specifications for the commercially available mixture used to determine the molecule properties (LRI, qMS, and odor specifications), and it might differ from the compound or enantiomer ratio found in the cheeses. (2) A synergistic effect or coelution, as octa-3,5-dien-2-one$^{t(std)}$ elutes at the same time. Further investigations will be needed to elucidate this question.

When the amounts (in $\mu g\ kg^{-1}$) of all the quantified VSCs are added, the total amount of quantified VSCs is 4377 $\mu g\ kg^{-1}$ in yellow Tilsit, 2800 $\mu g\ kg^{-1}$ in green Tilsit, and 2761 $\mu g\ kg^{-1}$ in red Tilsit. When only odorant VSCs detected during 2W-GC-O were considered, the overall amounts add up to 664.5 $\mu g\ kg^{-1}$, corresponding to 15.2% of the total quantified VSCs in yellow Tilsit; 327.0 $\mu g\ kg^{-1}$, corresponding to 11.8% in red Tilsit; and 54.4 $\mu g\ kg^{-1}$, corresponding to 1.9% in green Tilsit. COS, H_2S, CS_2, DMS, MeSAc, MTC, MITC, DMSO, and Me_2SO_2 were also quantified, but due to their high odor thresholds or odorless aspect, they were not considered.

Calibration curves on five points show correlation coefficients R^2 >0.97 for all quantified compounds. Of 15 compounds, 10 were above the quantitation limits (LOQ). DMS in green Tilsit was below the LOQ. MITC was below the LOQ in all Tilsits, and 3-(methylthio)propanal was below the LOQ in the green and yellow Tilsit.

The contribution of MeSH (odor description, Table 4: cheesy, old socks, cabbage, cellar, rancid, putrid) as the sulfur compound with an $aOAV_{sniff}$ of 400 is the most important in the studied cheeses. It was perceived with almost the same intensity in each of the cheeses. However, the quantified concentration of MeSH is higher in yellow Tilsit (15 times higher than in green Tilsit and 3 times higher than in red Tilsit). Its olfactory impact is so important that the signal covers DMS, which has a close retention time. The next most important VSC is DMTS (garlic, sulfury, gas, metallic), with an $aOAV_{sniff}$ of 150. Although its concentration is 11 times lower in green Tilsit than in yellow Tilsit, it was found to be more intense in the latter than in the other cheeses. The nature of the matrix can explain this phenomenon, as can the variability of the panelists. The samples were not measured on the same day, and the environment and the physical state of the panelists may influence the results. 3-(Methylthio)propanal (boiled potatoes, sulfury) with an $aOAV_{sniff}$ of 25 also contributes equally to the overall odor of all cheeses. It is difficult to evaluate the impact of DMDS (pungent, sulfur) in this experiment as it coeluted with hexanal (green, grass, floral) and its $aOAV_{sniff}$ is only 3.5. Bis-(methylthio)methane (animalic, cheesy, sulfury, garlic, onion, rancid) with an $aOAV_{sniff}$ of 3 has a strong impact in yellow Tilsit despite being present at the same concentration in the red Tilsit. The variability of the panelists can explain this difference.

The other quantified VSCs are odorless, such as COS, DMSO, and Me_2SO_2, or the $aOAV_{sniff}$ is <1 (H_2S, CS_2, MTC, MITC, and 2-methyltetrahydrothiophen-3-one$^{t(odor\ threshold)}$). Therefore, they do not directly affect the overall odor because their concentrations are below the odor threshold. However, they might still contribute due to synergistic effects, which were not evaluated in the present study.

Origin of Sulfur Compounds in a Cheese Matrix. Several VSCs were found to have an impact on the odor of the studied Swiss Tilsit cheeses. Their origin in a cheese matrix is of great interest, especially as variations in their concentrations may strongly influence the cheese's odor profile. VSCs in cheese originate from the enzymatic or nonenzymatic degradation of the amino acids cysteine and methionine by the action of microorganisms. Methionine, present in larger amounts in the cheese than cysteine, is the most important source of VSCs.[32,33] The vast majority of complex sulfur compounds derive from two major and highly reactive compounds, MeSH and H_2S. H_2S is formed by Strecker degradation of cysteine with diketones such as butane-2,3-dione and pentane-2,3-dione, or it can also be formed by thermal degradation of thiamin, during which the rearrangement of a thiazole group liberates H_2S.[34] Another metabolic pathway through the degradation of cysteine by the activity of cystathionine lyases of *Lactobacillus casei* can also explain the formation of H_2S in cheese.[35] MeSH is formed by Strecker degradation of methionine,[36] and a study carried out by Bogicevic et al.[35] shows the major role of deamination and dethiolation by lyases in cheese. Strains of *L. casei* with genes *ctl1* and *ctl2* present exhibited cystathionine lyase activity and broke down methionine. The presence and the formation of CS_2 is not well-defined. A high concentration is correlated with the heat treatment of milk, and the concentration of CS_2 decreases with storage time.[37] CS_2 may also be an extraction artifact due to the reaction of COS with the matrix.[16] This hypothesis was confirmed by internal laboratory tests. A large part of DMS can come from animal feed due to the nonenzymatic degradation at a pH of 7.5 of the *S*-methylmethionine sulfonium salt present in cattle feed.[34] MeSAc can be formed by *Brevibacterium linens*, but in general, the biosynthetic pathway involved in thioester production is not yet elucidated.[38] However, the combination of *Micrococcus* strains with *B. linens* shows a vastly higher concentration in MeSAc compared to when the strains are present separately in the cheese matrix. These microorganisms appear on the surface of the cheese after ripening periods of 2 and 3 weeks,[39,40] and their metabolites have been found to contribute to cheese flavor.[41] MeSH can react with free fatty acids to form *S*-methyl thioesters, such as MeSAc, and contribute to a cooked cauliflower aroma.[7] DMDS is the result of the Strecker degradation of methionine and the reaction of methionine with riboflavin. It also originates from the oxidation of MeSH during heat treatment of milk.[34] DMTS is mainly due to the oxidation of DMDS, the latter being a product of the oxidation of MeSH.[42] Oxidative reactions are accelerated by the presence of transition metals such as Cu(II) or Fe(III).[4] These metals are commonly present in low concentrations in cheese produced traditionally or industrially in production facilities, for example, in cheese kettles. The formation of 3-(methylthio)propanal requires the decarboxylation of 4-methylthio-2-ketobutyrate, and this reaction can be carried out by *Lactococcus lactis* strains.[36] DMSO is an intermediate oxidation step of DMS, the final oxidation product being Me_2SO_2.[34] MTC and MITC can be produced by a few *Pseudomonas* strains, which are naturally present in milk before heat treatment.[43] Bis(methylthio)methane can be formed through condensation or the aldol reaction of the MeSH with the formaldehyde. This compound has already been found in Gouda and Camembert cheeses.[44,45] 2-Methyltetrahydrothiophen-3-one$^{t(odor\ threshold)}$ has been found in many foodstuffs, such as coffee, whiskey, yogurt, and cheese. This molecule is formed by chemical reactions or is produced by microorganisms. The microbial mechanism is still unknown.[46−48]

To conclude, quantitation of VSCs shows a clear difference in concentration between the cheeses. Red Tilsit made from partially thermized milk and yellow Tilsit made with pasteurized milk and a higher fat content contain the highest amounts of most of the target VSCs. This can, however, not be explained by a unique reason, but can be caused by several factors such as

DOI: 10.1021/acs.jafc.5b02536
J. Agric. Food Chem. 2015, 63, 7511−7521

treatment of the raw milk, a longer ripening time, and fat content and also by a wide variety of indigenous microflora in raw milk.

According to the literature, a higher fat content can affect the growth of microflora, enzymatic activity, partitioning, and matrix effects, thus influencing the concentration of VSCs.[49] The literature showed that flavor compound retention by lipids can be significant for sulfur compounds. A lipid concentration >10% in the matrix can decrease the release of sulfur compounds into the headspace by up to 20%.[50] In the present case, all cheeses contain >10% fat (between 28 and 33 g fat per 100 g of cheese), and despite this, no negative influence of fat content on VSC release was observed with the employed analytical protocol. The protein content, on the other hand, has not been found to influence flavor release in a cheese matrix[50] and was not evaluated in the present study.

GC-O analyses in the employed analytical conditions suggest that the overall odor of the studied Tilsit cheeses is mainly determined by cheesy-buttery odor notes, followed by sulfur, malty-chemical, and fatty-green odor zones. When all perceived odor zones in the cheeses were summed (mean intensity × detection frequency values, Table 4), green Tilsit had an overall value of 40.2, red Tilsit had an overall value of 48.0, and yellow Tilsit had an overall value of 45.8. These values illustrate that red Tilsit is the most flavorful cheese of the three samples, followed by yellow Tilsit. Green Tilsit, as expected, shows the least intense overall odor. Numerous odorant compounds were identified in all three cheeses, but the number of compounds that were found in only one of the cheeses and not in the others was higher for red Tilsit, which alone of the three cheeses had *m*-xylene$^{t(odor)}$, ethyl hexanoate, oct-3-en-2-one, and unknown peak 41.

With regard to VSCs, 2W-GC-O showed that MeSH, DMDS (coelution with hexanal), bis(methylthio)methane, DMTS, 3-(methylthio)propanal, and 2-methyltetrahydrothiophen-3-one$^{t(odor\ threshold)}$ (coelution with octa-3,5-dien-2-one$^{t(std)}$) were the only identified VSCs to have a strong impact on the odorant profile of the tested cheese samples. In total, the "sulfury" odor family represents up to 14% of the total odor profile. The aromagrams of the cheeses show differences, but the differences in VSCs were not as pronounced as one might expect on the basis of the quantitation results. This might be due to either the use of optimal analytical conditions for each technique or a limitation of the methodology: when the concentration of a given compound greatly exceeds the odor threshold, the panelist cannot rate the intensity of the perceived odor stronger than the maximum of the employed scale (1−5), and detection frequency cannot exceed 100%. This is particularly the case for the most intense peaks and might explain why, despite clear differences in quantified VSC amounts, these are not directly translated in the aromagrams. However, when the number of times a certain odor family is perceived are counted, differences become more evident but are not congruent with the quantitation results.

Our work allowed for the clear differentiation of the three commercial Tilsit cheeses in terms of VSCs, odorant VSCs, and GC-O profiles. GC-O results confirm the general opinion that Tilsit cheese made from raw milk has a more intense and more diverse overall flavor than cheese manufactured with pasteurized milk. VSC quantitation could not be directly linked to this statement, as optimal analytical conditions were employed for each technique and other factors, such as limitation of GC-O methodology, but also fabrication process, fat content, and ripening time are likely to have an impact. Further research, including practice trials, is necessary to determine the precise causes of the differences found in this study, and future results should be combined with sensory profiling information.

AUTHOR INFORMATION

Corresponding Author

*(P.F.) Phone: +41 (0) 58 463 82 60. Fax +41 (0) 58 463 82 27. E-mail: pascal.fuchsmann@agroscope.admin.ch.

Notes

The authors declare no competing financial interest.

ACKNOWLEDGMENTS

We gratefully acknowledge all panelists for their participation and René Badertscher, Cornelia Bär, and René Imhof for revision of the manuscript.

REFERENCES

(1) Beuvier, E.; Buchin, S. Raw milk cheeses. *Cheese: Chem. Phys. Microbiol.* **2014**, *1*, 319−345.

(2) Rehman, S.-U.; McSweeney, P. L. H.; Banks, J. M.; Brechany, E. Y.; Muir, D. D.; Fox, P. F. Ripening of Cheddar cheese made from blends of raw and pasteurised milk. *Int. Dairy J.* **2000**, *10*, 33−44.

(3) Yang, W. T.; Min, D. B. Dynamic headspace analyses of volatile compounds of Cheddar and Swiss cheese during ripening. *J. Food Sci.* **1994**, *59*, 1309−1312.

(4) Landaud, S.; Helinck, S.; Bonnarme, P. Formation of volatile sulfur compounds and metabolism of methionine and other sulfur compounds in fermented food. *Appl. Microbiol. Biotechnol.* **2008**, *77*, 1191−1205.

(5) Harper, J.; Kocaoglu-Vurma, N.; Wick, C.; Elekes, K.; Langford, V. Volatile sulfur compounds in Swiss cheese using selected ion flow tube mass spectrometer (SIFT-MS). *Volatile Sulfur Compounds in Food* **2011**, 153−181.

(6) Burbank, H.; Qian, M. C. Volatile sulfur compounds in Cheddar cheese determined by headspace solid-phase microextraction and gas chromatograph-pulsed flame photometric detection. *J. Chromatogr. A* **2005**, *1066*, 149−157.

(7) Burbank, H.; Qian, M. C. Development of volatile sulfur compounds in heat-shocked and pasteurized milk cheese. *Int. Dairy J.* **2008**, *18*, 811−818.

(8) Bloes-Breton, S.; Bergère, J. L. Production de composé soufrés volatiles par Micrococcaceae et des bactéries corynéformes d'origine fromagère. *Lait* **1997**, *77* (5), 543−560.

(9) Frank, D. C.; Owen, C. M.; Patterson, J. Solid phase microextraction (SPME) combined with gas- chromatography and olfactometry-mass spectrometry for characterization of cheese aroma compounds. *Lebensm. Wiss. Technol.* **2004**, *37* (2), 139−154.

(10) Curioni, P. M. G.; Bosset, J. O. Key odorants in various cheese types as determined by gas chromatography-olfactometry. *Int. Dairy J.* **2002**, *12*, 959−984.

(11) Smit, G.; Smit, B. A.; Engels, W. J. M. Flavour formation by lactic acid bacteria and biochemical flavour profiling of cheese products. *FEMS Microbiol. Rev.* **2005**, *29* (3), 591−610.

(12) Grosch, W. Evaluation of the key odorants of foods by dilution experiments, aroma models and omission. *Chem. Senses* **2001**, *26* (5), 533−545.

(13) Berdagué, J. L.; Tournayre, P.; Cambou, S. Novel multi-gas chromatography-olfactometry device and software for the identification of odour-active compounds. *J. Chromatogr. A* **2007**, *1146*, 85−92.

(14) Delahunty, C. M.; Eyres, G.; Dufour, J. P. Review: Gas chromatography-olfactometry. *J. Sep. Sci.* **2006**, *29*, 2107−2125.

(15) Cheskis, S.; Atar, E.; Amirav, A. Pulsed-flame photometer: a novel gas chromatography detector. *Anal. Chem.* **1993**, *65*, 539−555.

(16) Svoronos, P. D. N.; Bruno, T. J. Carbonyl sulfide: a review of its chemistry and properties. *Ind. Eng. Chem. Res.* **2002**, *41*, 5321−5336.

(17) Vazquez-Landaverde, P. A.; Torres, J. A.; Qian, M. C. Quantification of trace volatile sulfur compounds in milk by solid-phase microextraction and gas chromatography-pulsed flame photometric detection. *J. Dairy Sci.* **2006**, *89* (8), 2919−2927.

DOI: 10.1021/acs.jafc.5b02536
J. Agric. Food Chem. 2015, 63, 7511−7521

(18) Roberts, D. D.; Pollien, P.; Milo, C. Solid-phase microextraction method development for headspace analysis of volatile flavor compounds. *J. Agric. Food Chem.* **2000**, *48*, 2430−2437.
(19) Pinho, O.; Ferreira, M. Discriminate analysis of the volatile fraction from "Terrincho" ewe cheese: correlation with flavour characteristics. *Int. Dairy J.* **2004**, *14* (5), 455−464.
(20) Lestremau, F.; Andersson, F. A. T.; Desauziers, V.; Fanlo, J. L. Evaluation of solid-phase microextraction for time-weighted average sampling of volatile sulfur compounds at ppb concentrations. *Anal. Chem.* **2003**, *75*, 2626−2632.
(21) Lecanu, L.; Ducruet, V.; Jouquand, C.; Gratadoux, J. J.; Feigenbaum, A. Optimization of headspace solid-phase microextraction (SPME) for the odor analysis of surface-ripened cheese. *J. Agric. Food Chem.* **2002**, *50* (13), 3810−3817.
(22) Hill, P. G.; Smith, R. M. Determination of sulphur compounds in beer using headspace solid-phase microextraction and gas chromatographic analysis with pulsed flame photometric detection. *J. Chromatogr. A* **2000**, *872* (1−2), 203−213.
(23) Breme, K.; Schlichtherle-Cerny, H.; Eugster-Meier, E.; Dubois, A.; Braun, M. Evaluation of odour representativeness of HS-SPME extracts of fruit yoghurt by direct-GC-olfactometry. *Advances and Challenges in Flavor Chemistry & Biology: Proceedings of the 9th Wartburg Symposium*; Deutsche Forschungsanstalt für Lebensmittelchemie: Freising, Germany, 2011; pp 343−347
(24) Boeker, P.; Haas, T.; Lammers, P. S. Theory and practice of a variable dome splitter for gas chromatography-olfactometry. *J. Chromatogr. A* **2013**, *1286*, 200−207.
(25) van Ruth, S. M.; O'Connor, C. H. Evaluation of three gas chromatography-olfactometry methods: comparison of odour intensity-concentration relationships of eight volatile compounds with sensory headspace data. *Food Chem.* **2001**, *74* (3), 341−347.
(26) Pollien, P.; Fay, L. B.; Baumgartner, M.; Chaintreau, A. First attempt of odorant quantitation using gas chromatography-olfactometry. *Anal. Chem.* **1999**, *71* (23), 5391−5397.
(27) Tournayre, P.; Berdague, J. L. Gas chromatography-olfaction analyse device and method. WO 2005/001470 A2, 2005.
(28) Ferreira, V.; Ardanuy, M.; Lopez, R.; Cacho, J. F. Relationship between flavor dilution values and odor unit values in hydroalcoholic solutions: role of volatility and practical rule for its estimation. *J. Agric. Food Chem.* **1998**, *46*, 4341−4346.
(29) Grosch, W. Determination of potent odourants in food by aroma extract dilution analysis (AEDA) and calculation of odour activity values (OAVs). *Flavour Fragrance J.* **1994**, *9* (1), 147−158.
(30) Varlet, V.; Knockaert, C.; Prost, C.; Serot, T. Comparison of odor-active volatile compounds of fresh and smoked salmon. *J. Agric. Food Chem.* **2006**, *54*, 3391−3401.
(31) Spengler, J. D.; Samet, J. M.; McCarthy, J. F. *Indoor Air Quality Handbook*; McGraw-Hill: New York, 2001; 21.3; ISBN 9780074455494
(32) Nimni, M. E.; Han, B.; Cordoba, F. Are we getting enough sulfur in our diet? *Nutr. Metab.* **2007**, *4* (24), 1−12.
(33) Bogicevic, B.; Irmler, S.; Portmann, R.; Meile, L.; Berthoud, H. Characterization of the cysK2-ctl1-cysE2 gene cluster involved in sulfur metabolism in *Lactobacillus casei*. *Int. J. Food Microbiol.* **2012**, *152*, 211−219.
(34) Al-Attabi, Z.; D'Arcy, B. R.; Deeth, H. C. Volatile sulphur compounds in UHT milk. *Crit. Rev. Food Sci. Nutr.* **2009**, *49*, 28−47.
(35) Bogicevic, B.; Fuchsmann, P.; Breme, K.; Portmann, R.; Guggenbühl, B.; Irmler, S. A preliminary study on the effect of *Lactobacillus casei* expressing cystathionine lyase1/cystathionine lyase2 on Cheddar cheese and the formation of sulphur-containing compounds. *Int. Dairy J.* **2013**, *33* (2), 97−103.
(36) Marilley, L.; Casey, M. G. Flavours of cheese products: metabolic pathways, analytical tools and identification of producing strains. *Int. J. Food Microbiol.* **2004**, *90* (2), 139−159.
(37) Vazquez-Landaverde, P. A.; Torres, J. A.; Qian, M. C. Effect of high-pressure-moderate-temperature processing on the volatile profile of milk. *J. Agric. Food Chem.* **2006**, *54*, 9184−9192.
(38) Cuer, A.; Dauphin, G.; Kergomard, A.; Dumont, J. P.; Adda, J. Production of *S*-methylthioacetate by *Micrococcus* cheese strains. *Agric. Biol. Chem.* **1979**, *43*, 1783−1784.
(39) Rea, M. C.; Gorges, S.; Gelsomino, R.; Brennan, N. M.; Mounier, J.; Vancanneyt, M.; Scherer, S.; Swings, J.; Cogan, T. M. Stability of the biodiversity of the surface consortia of Gubbeen, a red-smear cheese. *J. Dairy Sci.* **2007**, *90* (5), 2200−2210.
(40) Roth, E.; Miescher Schwenninger, S.; Hasler, M.; Eugster-Meier, E.; Lacroix, C. Population dynamics of two antilisterial cheese surface consortia revealed by temporal temperature gradient gel electrophoresis. *BMC Microbiol.* **2010**, *10* (74), 1−14.
(41) Cuer, A.; Dauphin, G.; Kergomard, A.; Dumont, J. P.; Adda, J. Production of *S*-methylthioacetate by *Brevibacterium linens*. *Appl. Environ. Microbiol.* **1979**, *38* (2), 332−334.
(42) Chin, H. W.; Lindsay, R. C. Ascorbate and transition-metal mediation of methanethiol oxidation to dimethyl disulfide and dimethyl trisulfide. *Food Chem.* **1994**, *49*, 387−392.
(43) Morales, P.; Fernández-García, E.; Nuñez, M. Volatile compounds produced in cheese by *Pseudomonas* strains of dairy origin belonging to six different species. *J. Agric. Food Chem.* **2005**, *53*, 6835−6843.
(44) Dumont, J. P.; Roger, S.; Adda, J. L'arôme du camembert: autres composés mineurs mis en évidence. *Lait* **1976**, *56*, 559−560.
(45) Sloot, D.; Harkes, P. D. Volatile trace components in Gouda cheese. *J. Agric. Food Chem.* **1975**, *23* (2), 356−357.
(46) Nawrath, T.; Gerth, K.; Müller, R.; Schulz, S. The biosynthesis of the aroma volatile 2-methyltetrahydrothiophen-3-one in the bacterium Chitinophaga Fx7914. *ChemBioChem* **2010**, *11*, 1914−1919.
(47) Cheng, H. Volatile flavour compounds in yogurt: a review. *Crit. Rev. Food Sci. Nutr.* **2010**, *50*, 938−950.
(48) Ott, A.; Fay, L. B.; Chaintreau, A. Determination and origin of the aroma impact compounds of yogurt flavor. *J. Agric. Food Chem.* **1997**, *45* (3), 850−858.
(49) Drake, M. A.; Miracle, R. E.; McMahon, D. J. Impact of fat reduction on flavor and flavor chemistry of Cheddar cheeses. *J. Dairy Sci.* **2010**, *93*, 5069−5081.
(50) Gijs, L.; Piraprez, G.; Perpete, P.; Spinnler, E.; Collin, S. Retention of sulfur flavours by food matrix and determination of sensorial data independent of the medium composition. *Food Chem.* **2000**, *69* (3), 319−330.

DOI: 10.1021/acs.jafc.5b02536
J. Agric. Food Chem. 2015, 63, 7511−7521

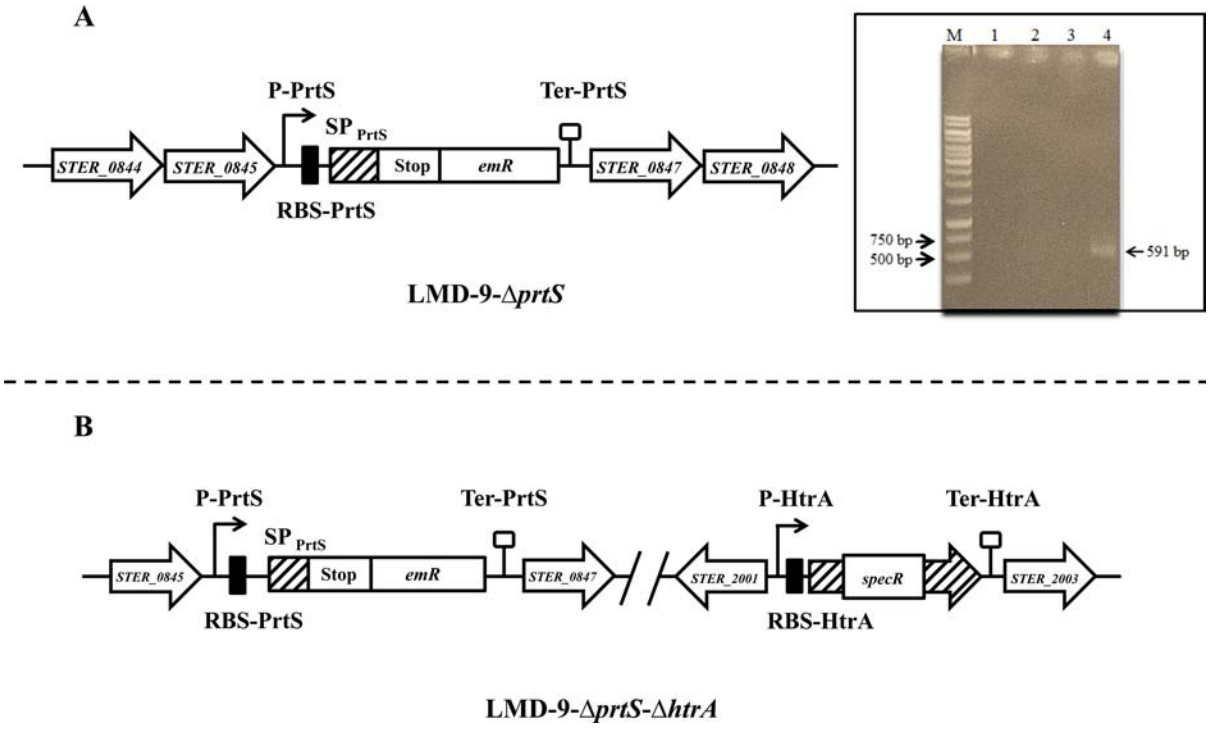

Figure 1. Schematic representation of construction of (A) *S. thermophilus* LMD-9-Δ*prtS* strain and (B) *S. thermophilus* LMD-9-Δ*prtS*-Δ*htrA* strain. P-PrtS: *prtS* promoter region. RBS-PrtS: *prtS* ribosome binding site. SP_{PrtS}: PrtS signal peptide. Stop: sequence containing multiple stop codons. Ter-PrtS: *prtS* terminator region. P-HtrA: *htrA* promoter region. RBS-HtrA: *htrA* ribosome binding site. Ter-HtrA: *htrA* terminator region. *emR*: erythromycin resistance gene. *specR*: spectinomycin resistance gene. The inset reveals the PCR amplification of *prtS* gene. M: DNA molecular weight marker. Lanes 1, 2, 3, and 4 indicate PCR product obtained from the genomic DNA of *S. thermophilus* CNRZ1066, LMD-9-Δ*prtS*, LMD-9-Δ*prtS*-Δ*htrA*, and LMD-9, respectively.

the growth of $PrtS^-$ strains, since these strains acidified their growth medium at a rate similar to $PrtS^+$ strains when this medium contained a mixture of peptides, i.e., bactotryptone.[7] Contrariwise, such cell-associated extracellular peptidase activities might be undesirable for the stability of milk-derived peptides carrying a given biological activity, eventually added to the fermented milk products or produced from milk proteins by the PrtS activity during the fermentation process. This hypothesis is reinforced by a current study in which Hafeez and colleagues[11] revealed hydrolysis of several milk-derived bioactive peptides by cell-associated extracellular peptidases of *S. thermophilus* strains.

Isracidin corresponds to the 1−23 fragment of bovine α_{s1}-casein (CN) and is released by chymosin digestion of this casein. It exhibits an antimicrobial activity against different bacteria such as *Escherichia coli* and staphylococci.[12,13] It could be applied as a biopreservative in the dairy products due to its inherent antimicrobial properties.[14] Besides this, isracidin has been widely employed as a substrate to determine cleavage specificities of the surface proteases of different LAB.[15,16] Indeed, relatively large peptide size and presence of three proline residues make isracidin an ideal substrate for this purpose, as certain enzymes are unable to hydrolyze peptide bonds involving proline residue. Thereby, Fernandez-Espla and colleagues[6] determined the cleavage preference of the purified PrtS of *S. thermophilus* CNRZ 385 on isracidin, showing that PrtS displayed a specificity that was intermediate between the specificities of $PrtP_I$-type and $PrtP_{III}$-type cell-envelope proteases of *Lactococcus lactis*. Knowing that *S. thermophilus* strains also possess cell-associated extracellular peptidases and hydrolyze different bioactive peptides of smaller size,[11] we have chosen to use isracidin as substrate to study the proteolytic effect of PrtS and cell-associated extracellular peptidases (strain $PrtS^+$ phenotype) as well as that of cell-associated extracellular peptidases alone (strain $PrtS^-$ phenotype), on this peptide.

Therefore, first, we determined the contribution of PrtS activity of LMD-9 strain, among all of the other proteolytic activities present at the cell surface, in the hydrolysis of isracidin, and we investigated the subsequent evolution of the peptides formed by a kinetics approach. Second, in order to investigate the level of hydrolysis of isracidin by known cell-associated extracellular peptidase activities (aminopeptidase and X-prolyl dipeptidyl peptidase), two mutant strains, i.e., Δ*prtS* and Δ*prtS*-Δ*htrA*, constructed from strain LMD-9, were incubated with the peptide. In addition, the level of hydrolysis of isracidin by the strain CNRZ1066 that does not naturally display any PrtS activity has been studied.

MATERIALS AND METHODS

Bacterial Strains, Growth Conditions, and Construction of Mutants. *S. thermophilus* CNRZ1066 came from the CNRZ (Centre National de Recherches Zootechniques, INRA, Jouy-en-Josas, France) while *S. thermophilus* LMD-9 (ATCC BAA-491) came from ATCC (American Type Culture Collection, Manassas, VA, USA) collections. Their genomes have been entirely sequenced.[17,18]

S. thermophilus LMD-9-Δ*prtS* mutant used in this study was obtained in a previous study.[19] Briefly, it was planned to replace the ORF of *prtS* gene by a fragment consisting of the ORF of *prtH* gene fused with the ORF of an erythromycin resistance (*emR*) gene. During this mutant construction, a clone presenting the LMD-9-Δ*prtS* sequence was obtained (Figure 1A).

To construct *S. thermophilus* LMD-9-Δ*prtS*-Δ*htrA* mutant strain, *htrA* gene (locus_tag: *STER_RS09790*; NCBI Accession Number:

DOI: 10.1021/acs.jafc.5b01647
J. Agric. Food Chem. 2015, 63, 7522−7531

NC_008532.1) located between positions 1854162 and 1855397 on the *S. thermophilus* LMD-9 chromosome was replaced by *specR* gene that encodes spectinomycin adenyltransferase. For this purpose, *htrA* (upper and down) and *specR* fragments were amplified form genomic DNA of *S. thermophilus* LMD-9-Δ*prtS* mutant strain and pSET4s plasmid, respectively, as described by Hafeez et al.[11] The overlap extension polymerase chain reaction was carried out using the above three amplicons, and then *S. thermophilus* LMD-9-Δ*prtS* mutant strain was transformed with final amplicon (Figure 1B).[11]

The strains were conserved at −80 °C in sterile reconstituted skim milk (10%). They were grown overnight at 42 °C by inoculation (1%) in fresh sterile reconstituted skim milk (10%), and the precultures were then inoculated at 1% in LM17 medium (M17[20] broth supplemented with 20 g/L lactose) and incubated at 42 °C. When required, erythromycin was added to the culture media at final concentration of 5 μg/mL as selection pressure for LMD-9-Δ*prtS* and both erythromycin and spectinomycin at concentrations of 2.5 and 150 μg/mL, respectively, to select LMD-9-Δ*prtS*-Δ*htrA* mutant strain.

Polymerase Chain Reaction Analysis for Detection of *prtS* Gene. The presence or the absence of PrtS was determined using forward and reverse primer pairs of *prtS* gene and genomic DNA of *S. thermophilus* LMD-9, as well as mutant strains, i.e., LMD-9-Δ*prtS* and LMD-9-Δ*prtS*-Δ*htrA*, and of *S. thermophilus* CNRZ1066 as template.

Chromosomal DNA of *S. thermophilus* strains were purified from 50 mL LM17 cultures after growth to an optical density at 650 nm (OD_{650nm}) of about 1.0 as described by Fischer et al.[21] The standard polymerase chain reaction (PCR) was conducted in a Mastercycler Pro thermocycler (Eppendorf, Hamburg, Germany) to detect the *prtS* gene. The forward (5′-CAATTCCATCTGTCTTCATTC-3′) and reverse (5′-CCGTTGTTAATTGTGTTGAGT-3′) primers used to amplify an internal fragment of the *prtS* gene were synthesized by Eurogentec (Serain, Belgium). The PCR reaction was performed in a final reaction volume of 20 μL consisting of 0.5 units of *Taq* DNA polymerase (Thermo Fisher Scientific, Villebon-sur-Yvette, France), 1× *Taq* buffer, 0.2 mM of each deoxyribonucleotide triphosphate (dNTP), 1.5 mM of $MgCl_2$, 0.5 μM of each primer, and about 100 ng of purified DNA as template. PCR amplification was carried out under the following conditions: initial denaturation step at 95 °C for 3 min, 30 cycles consisting of denaturation at 95 °C for 30 s, annealing at 58 °C for 30 s, and an extension at 72 °C for 60 s followed by a single 10 min final elongation at 72 °C. As expected, after agarose gel electrophoresis, the single nucleotide band with the anticipated molecular mass of the *prtS* gene was detected only in *S. thermophilus* LMD-9 (Figure 1 inset). This thus confirmed that the *prtS* gene is absent from the genome of LMD-9-Δ*prtS*, LMD-9-Δ*prtS*-Δ*htrA*, and CNRZ1066 strains.

Evaluation of Cell Lysis. In order to verify cell integrity in the pH 6.5, 12.5 mM potassium phosphate/acetate buffer (PAB), the activity of intracellular peptidases, potentially liberated by a cell lysis during cell incubation in the medium, was measured using the lysine-*para*-nitroanilide (Lys-*p*-NA) chromogenic substrate (Sigma-Aldrich France, Saint-Quentin Fallavier, France). The substrate was prepared at 2 mM as described elsewhere,[8] whereas the samples were prepared as follows: the log phase (OD_{650nm} = 1.00 ± 0.05) cells of each *S. thermophilus* strain grown in LM17 medium were centrifuged at 3100*g* for 10 min at 20 °C and resuspended in PAB to the initial OD_{650nm} of about 1 preceded by two washings with PAB. A part of the resuspended cells was frozen at −20 °C while the other part was incubated at 42 °C with shaking at 200 rpm (revolutions per min). After 0, 2, and 6 h incubation, cells were removed by centrifugation at 12000*g* for 5 min at 20 °C and the supernatant obtained was filtered through a sterile 0.22-μm filter (Merck Millipore, Darmstadt, Germany) to obtain cell free filtrate. Frozen cell suspensions of *S. thermophilus* were thawed on ice and disrupted by sonication 3 × 1 min, power 5, and active cycle 50% with a Vibra-cell (Fisher Scientific SAS, Illkirch, France). The cell lysate was recovered by centrifugation at 13400*g* for 10 min at 4 °C and used as such as positive control of intracellular peptidase activity, as intracellular peptidases have the ability to hydrolyze Lys-*p*-NA substrate. 100 μL volume samples of both cell free filtrate and cell lysate (intracellular proteins) were added to 1 mL of the substrate and incubated 1 h at 37 °C. The hydrolysis of Lys-*p*-NA was determined by measuring absorbance at 410 nm using BioSpectrometer Basic (Eppendorf France S.A.S., Le Pecq, France).

Isracidin Preparation. α_{s1}-CN from sodium caseinate was first purified by batch fractionation according to the method of Miclo et al.[22] and then hydrolyzed with rennet from *Mucor meihei*, type II (Sigma-Aldrich), as described by Lahov and Regelson[12] with some modifications to get pure isracidin. Crude isracidin was separated from the residual α_{s1}-CN by solid phase extraction (SPE) using Plus C_{18} Sep-Pak cartridges (Waters, Milford, MA, USA) as follows: the cartridges were equilibrated with 5 mL of solvent A (5% acetonitrile and 0.1% trifluoroacetic acid in water) at a flow rate of approximately 1 mL/min. The α_{s1}-CN hydrolysate (2 mL) prepared at 5 mg/mL in solvent A was loaded onto the cartridges. The salts were removed by washing the cartridges with 5 mL of solvent A while the crude isracidin was eluted with 5 mL of solvent B (30% acetonitrile and 0.1% trifluoroacetic acid in water). The liquid chromatography−mass spectrometry analysis (LC/ESI-MS/MS; see below) showed that the crude isracidin was a mixture of 1−23 and 3−23 peptides in a molar ratio 10:1 (data not shown). This crude isracidin was then injected into Uptisphere C_{18} column (length and internal diameter 250 × 10 mm, particle size 5 μm, porosity 10 nm; Interchim, Montluçon, France) connected to an Alliance high-performance liquid chromatography (HPLC) unit (Waters) to get pure 1−23 peptide. A linear gradient of 25−38% acetonitrile in water in the presence of 0.1% trifluoroacetic acid was applied at a flow rate of 3.0 mL/min and at 30 °C. Finally, isracidin was detected with a photodiode array detector 996 (Waters) at 215 nm, collected, and lyophilized.

Hydrolysis of Isracidin. *S. thermophilus* strains were grown to the exponential phase (OD_{650nm} of 1.00 ± 0.05) in LM17 medium with or without antibiotic(s). The cells were harvested by centrifugation at 3100*g* for 10 min at 20 °C and the resulting cell pellet was washed twice with PAB, followed by resuspension of the cells to obtain the initial OD_{650nm} of 1.00 ± 0.05 in the same buffer. Crude and pure isracidin solutions prepared in the PAB were then added to the cell suspensions to a final concentration of 20 nmol/mL and incubated at 42 °C with shaking at 200 rpm. A sample (500 μL) was aliquoted immediately, and other samples of the same volume were collected after 10, 20, 45, 60, 120, 180, 240, and 360 min of incubation. The hydrolysis reaction was stopped by adding 15 μL of trifluoroacetic acid to each sample. The cells were removed by filtration through a 0.45-μm filter (Phenomenex, Le Pecq, France), and the hydrolysis products were stored at −20 °C until the LC/ESI-MS/MS analysis. The experiments were done in duplicate. Stability of the isracidin in PAB was checked in the same conditions without bacteria.

Identification of Peptides by LC/ESI-MS/MS. The peptide fragments resulting from isracidin hydrolysis were analyzed by reversed-phase HPLC on an Ultimate 3000 system (Thermo Fisher Scientific/Dionex) coupled to electrospray ionization tandem mass spectrometry (RP-HPLC/ESI-MS/MS) using a spectrometer equipped with a linear trap quadripole ion trap mass analyzer LQT-XL (Thermo Fisher Scientific). Peptides were separated using a C_{18} Alltima reversed-phase column (length and inner diameter 150 × 2.1 mm, 5-μm porosity; Grace/Alltech, Darmstadt, Germany) equipped with a C_{18} Alltima precolumn (7.5 × 2.1 mm, 5-μm porosity; Grace/Alltech) at 25 °C. The peptides were eluted using a linear gradient of 5−60% acetonitrile in water in the presence of 0.1% (v/v) trifluoroacetic acid for 60 min at a flow rate of 0.2 mL/min and quantified with a double photodiode array detector (Thermo Fischer Scientific/Dionex). Peptides were detected by photodiode array detector and by mass spectrometric detector allowing UV semiquantification at 214 nm and also accurate MS semiquantification due to specific screening of peptide ions, seen on single ion parent chromatograms (SIC). To perform the quantification by UV detection at 214 nm, the molar extinction coefficient of each identified peptide was calculated according to Kuipers and Gruppen.[23]

The mass spectrometry was conducted under the following conditions: ESI positive ionization mode was used; spray voltage was set at 4.5 kV; source gases were set (in arbitrary units per min) for sheath gas, auxiliary gas, and sweep gas at 20, 5, and 5, respectively;

DOI: 10.1021/acs.jafc.5b01647
J. Agric. Food Chem. 2015, 63, 7522−7531

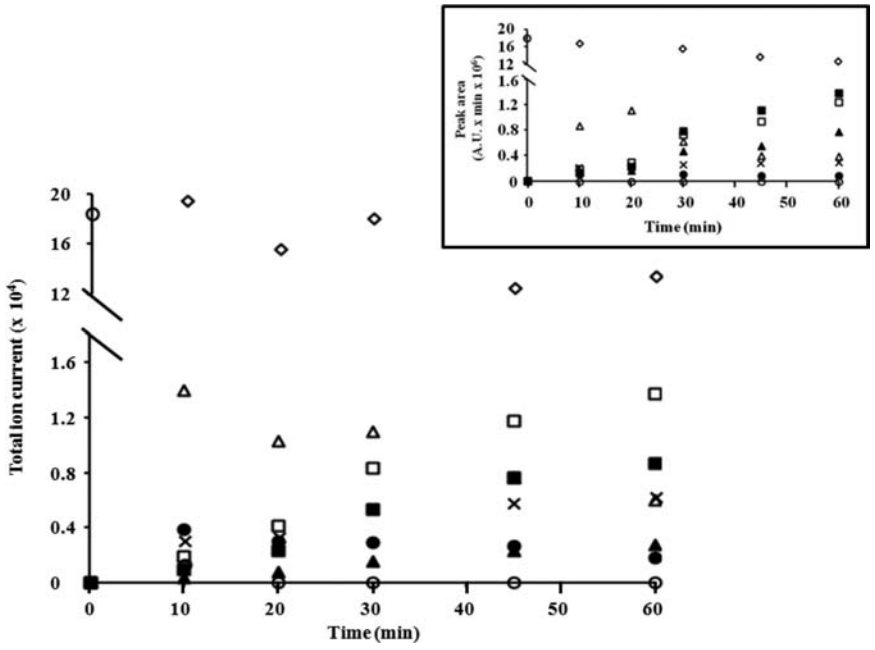

Figure 2. Hydrolysis kinetics of isracidin (empty circle) by *S. thermophilus* LMD-9 with generation of fragments ([1]RPKHPIK[7], filled triangle; [1]RPKHPIKH[8], filled square; [1]RPKHPIKHQ[9], empty square; [1]RPKHPIKHQGLPQ[13], cross; [1]RPKHPIKHQGLPQEVL[16], empty triangle; [1]RPKHPIKHQGLPQEVLN[17], empty diamond; and [1]RPKHPIKHQGLPQEVLNENLL[21], filled circle) analyzed by using single parent ion chromatograms. Isracidin (20 nmol/mL) was incubated at 42 °C under shaking at 200 rpm with log phase cells of this bacterial strain in phosphate/acetate buffer 12.5 mM, pH 6.5. The inset indicates similar hydrolysis kinetics of isracidin after peak area integration at 214 nm corrected by the molar extinction coefficients according to Kuipers and Gruppen.[23] A.U.: absorption unit.

capillary temperature was set at 250 °C; capillary voltage at 26 V; tube lens, split lens, and front lens voltages at 90 V, −42 V, and −5.75 V, respectively. The ion optics parameters were optimized by automatic tuning using a standard solution of the dipeptide Val-Trp at 0.1 g/L infused in mobile phase (50% acetonitrile in water and in the presence of 0.1% trifluoroacetic acid) at a flow rate of 5 μL/min. Full scan MS spectra were repeatedly performed from 100 to 2000 *m/z* during the time of the run and, second, automatized MS/MS scans were realized in order to identify the peptides with certainty. The peptide masses were given with a precision of 0.01%.

RESULTS

Hydrolysis of Isracidin by Surface Proteolytic System of *S. thermophilus* LMD-9. The ability of the surface proteolytic system of *S. thermophilus* LMD-9 to hydrolyze isracidin was evaluated. For this, the pure isracidin was incubated with nongrowing log phase cells of LMD-9 strain in PAB at pH 6.5 and 42 °C. It was determined by MS screening of isracidin corresponding to $[M + 2H]^{2+}$ double charged parent ion that about 99% of the isracidin was already lost after 10 min incubation and that no intact peptide was detected after 20 min (Figure 2). This hydrolysis was attributed to the proteolytic activity of the LMD-9 strain and not to an eventual instability of the peptide since isracidin was not hydrolyzed when incubated without cells in the PAB under the same conditions.

The degradation products were then analyzed by RP-HPLC/ESI-MS/MS, and the peptides identified are listed in Table 1. It was observed that the cell-associated proteolytic system of *S. thermophilus* LMD-9 cleaved the isracidin at K^7–H^8, H^8–Q^9, Q^9–G^{10}, Q^{13}–E^{14}, L^{16}–N^{17}, N^{17}–E^{18}, and L^{21}–R^{22} peptide bonds. Hydrolysis kinetics revealed that a large quantity (determined by peak area integration using single parent ion chromatogram) of peptide 1−17 was present just after a 10-min exposure of isracidin to the nonproliferating cells of LMD-9 strain (Figure 2) followed by smaller quantity of the peptide 1−16. The quantity of both peptides decreased throughout 1 h of incubation, unlike the peptides 1−8, 1−9, and 1−13, the quantity of which increased slowly and consistently. On the other hand, the increase in the quantity of peptides 1−7 and 1−21 was noted at much lower intensity during 1 h incubation (Figure 2). According to the results of Fernandez-Espla et al.,[6] who reported the preferential cleavage sites of purified PrtS on the pure isracidin, and to those of Miclo et al.,[1] who analyzed hydrolysis of the 1−23 region of the α_{s1}-CN by cells of various strains of *S. thermophilus*, the cleavage sites observed in this study could be attributed to the protease PrtS. Indeed, these authors reported that the PrtS cleaved the bonds N^{17}–E^{18} and L^{16}–N^{17} most preferably followed by the bonds H^8–Q^9 and Q^9–G^{10}. The bonds Q^{13}–E^{14} and L^{21}–R^{22} are cleaved to a

Table 1. Identification by RP-HPLC/ESI-MS/MS of Peptide Fragments Generated upon 1-h Incubation of Isracidin with *S. thermophilus* LMD-9 in Phosphate/Acetate Buffer 12.5 mM, pH 6.5

		mass (Da)	
peptide fragment	sequence	obsd	theor
1−7	RPKHPIK	874.7	874.6
1−8	RPKHPIKH	1012.0	1011.7
1−9	RPKHPIKHQ	1140.0	1139.7
1−13	RPKHPIKHQGLPQ	1535.0	1534.9
1−16	RPKHPIKHQGLPQEVL	1876.3	1876.1
1−17	RPKHPIKHQGLPQEVLN	1991.0	1990.1
1−21	RPKHPIKHQGLPQEVLNENLL	2460.0	2459.4
17−23	NENLLRF	904.6	904.5
18−23	ENLLRF	790.6	790.4
22−23	RF	321.3	321.2

DOI: 10.1021/acs.jafc.5b01647
J. Agric. Food Chem. 2015, 63, 7522−7531

medium and lesser extent, respectively. Hydrolysis of the bond K^7-H^8 was reported only by Miclo et al.,[1] who used bacterial cells and not purified PrtS. Only slight differences in the evolution of the quantity of the peptides (appeared or disappeared) were observed as a function of time when quantified using either single parent ion chromatograms or absorbance at 214 nm by taking into account the different molar extinction coefficients (Figure 2 inset).

Hydrolysis of Isracidin by Cell-Associated Extracellular Peptidases. To assess the contribution of cell-associated extracellular peptidases in hydrolysis of isracidin, strains without cell surface PrtS activity (CNRZ1066, LMD-9-Δ*prtS*, and LMD-9-Δ*prtS*-Δ*htrA*) were used. The purpose of deleting *htrA* gene was to remove all the surface protease activities of LMD-9 strain whether they make part of the proteolytic system or not. The isracidin was incubated individually for 6 h with the resting intact cells of these three strains. The hydrolysis of the peptide was less important than with the LMD-9 strain since 50% of isracidin was intact after 1 h of hydrolysis by CNRZ1066 and 78% by LMD-9 mutants. The released peptides were identified by RP-HPLC/ESI-MS/MS (Table 2) and seemed to be the result of different cell-associated extracellular peptidase activities and were grouped into five different categories. The Figure 3 presents an overview of the different categories of peptides generated according to the different exopeptidase activities highlighted for the three $PrtS^-$ strains. The category A included all those peptides, which resulted from isracidin cleavage at $L^{21}-R^{22}$, $N^{19}-L^{20}$, $N^{17}-E^{18}$, $V^{15}-L^{16}$, $Q^{13}-E^{14}$, Q^9-G^{10}, and K^7-H^8 peptide bonds (Figure 3). This thus indicated the consecutive removal of dipeptides from the C-terminal of the isracidin, indicating a peptidyl dipeptidase activity (for informations on this kind of activity see http://www.brenda-enzymes.org). The presence of the C-terminal dipeptide $^{22}RF^{23}$ was highlighted, but no other dipeptides were found by mass spectrometry analysis. On the other hand, peptidyl dipeptidase activity was not observed when a Pro residue was encountered at a potential cleavage site, as in the case of $L^{11}-P^{12}$, P^5-I^6, and R^1-P^2 peptide bonds. The peptides, whose release involved the cleavage of these bonds, as peptide 1−9 by example, were formed by previous action of other enzymes (see below). The type of cleavage leading to the release of peptides belonging to category A referred to a peptidyl dipeptidase activity and was observed for each of the three *S. thermophilus* strains exhibiting a $PrtS^-$ phenotype, i.e., CNRZ1066 as well as both LMD-9-Δ*prtS* and LMD-9-Δ*prtS*-Δ*htrA*. Furthermore, the release of the C-terminal Phe residue as well as of peptides whose number of residues was an even number (category B; Table 2) revealed a carboxypeptidase activity that might act in a recurrent manner. The existence of the peptides 1−14, 1−16, and 1−20 might also reveal a combined action of peptidyl dipeptidase and carboxypeptidase activities. As an example, the peptide 1−20 might be formed by the successive action of the peptidyl dipeptidase activity at peptide bond $L^{21}-R^{22}$ of isracidin (formation of peptide 1−21) followed by the action of carboxypeptidase activity at peptide bond $L^{20}-L^{21}$ (Figure 3). The peptides 1−14 and 1−16 seemed to be generated in a similar manner, whereas the release of carboxyl-terminal Phe residue might be produced likewise or by the action of the aminopeptidase activity mentioned below (see peptides belonging to category C) on the dipeptide $^{22}RF^{23}$. Both peptidyl dipeptidase and carboxypeptidase activities were associated with the cell wall because no such activities were observed in cell free filtrate obtained even after 6 h incubation of the bacterial cells in PAB (data not shown). This thus confirmed the absence of cell lysis which could have led to the release of intracellular peptidases in the incubation buffer. To our knowledge, peptidyl dipeptidase and carboxypeptidase activities associated with the cell wall have never been reported before in this bacterium.

Table 2. Isracidin Fragments Identified by RP-HPLC/ESI-MS/MS from 0- to 6-h Exposure to *S. thermophilus* LMD-9-Δ*prtS*, LMD-9-Δ*prtS*-Δ*htrA*, and CNRZ1066 in Phosphate/Acetate Buffer 12.5 mM, pH 6.5

peptide fragment	sequence	mass (Da) obsd	mass (Da) theor
	Category A		
1−21	RPKHPIKHQGLPQEVLNENLL	2460.0	2459.4
1−19	RPKHPIKHQGLPQEVLNEN	2233.7	2233.2
1−17	RPKHPIKHQGLPQEVLN	1991.0	1990.1
1−15	RPKHPIKHQGLPQEV	1763.0	1763.0
1−13	RPKHPIKHQGLPQ	1535.0	1534.9
1−9	RPKHPIKHQ	1140.0	1139.7
1−7	RPKHPIK	874.7	874.6
22−23	RF	321.3	321.2
	Category B		
23−23	F	165.0	165.1
1−20	RPKHPIKHQGLPQEVLNENL	2346.0	2346.3
1−16	RPKHPIKHQGLPQEVL	1876.3	1876.1
1−14	RPKHPIKHQGLPQE	1664.0	1663.9
	Category C		
4−23	HPIKHQGLPQEVLNENLLRF	2382.0	2381.3
7−23[a]	KHQGLPQEVLNENLLRF	2304.2	2304.1
8−23	HQGLPQEVLNENLLRF	1907.0	1906.0
9−23	QGLPQEVLNENLLRF	1768.6	1768.9
10−23	GLPQEVLNENLLRF	1640.5	1640.9
11−23[a]	LPQEVLNENLLRF	1583.9	1583.9
14−23	EVLNENLLRF	1245.5	1245.7
15−23	VLNENLLRF	1116.5	1116.6
16−23	LNENLLRF	1017.0	1017.6
17−23	NENLLRF	904.0	904.5
18−23	ENLLRF	790.0	790.4
	Category D		
1−2	RP	271.0	271.2
4−5	HP	252.0	252.1
3−23	KHPIKHQGLPQEVLNENLLRF	2509.0	2509.4
6−23	IKHQGLPQEVLNENLLRF	2147.0	2147.2
13−23[a]	QEVLNENLLRF	1373.8	1373.7
	Category E		
3−21[a]	KHPIKHQGLPQEVLNENLL	2206.3	2206.2
4−21	HPIKHQGLPQEVLNENLL	2078.0	2078.1
8−21	HQGLPQEVLNENLL	1602.0	1602.8
14−21	EVLNENLL	942.0	942.5
18−21	ENLL	487.0	487.3

[a]Identified in the case of CNRZ1066 with crude isracidin (mixture of peptides 1−23 and 3−23 in a ratio 10:1) as substrate; the crude isracidin was not tested with the LMD-9 mutant strains.

The second main group is the category C, which is composed of peptides generated by an aminopeptidase activity. Table 2 shows all the peptides identified by mass spectrometry that were the result of consecutive removal of N-terminal amino acids. Peptides ending with the Phe^{23} residue and the first residue of which corresponded to the 3rd to the 18th residue of isracidin were recovered except for peptides 2−23, 5−23, and 12−23. In the case of the latter three peptides, the

DOI: 10.1021/acs.jafc.5b01647
J. Agric. Food Chem. 2015, 63, 7522−7531

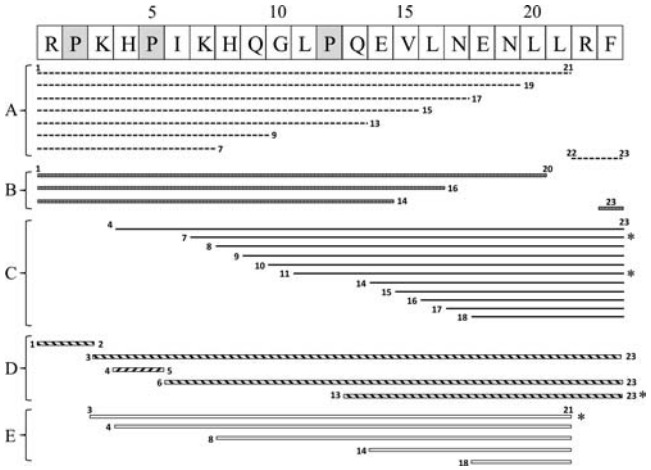

Figure 3. Peptides identified by RP-HPLC/ESI-MS/MS released from 0- to 6-h contact of isracidin with PrtS$^-$ strains, i.e., *S. thermophilus* CNRZ1066, LMD-9-Δ*prtS*, and LMD-9-Δ*prtS*-Δ*htrA* in phosphate/acetate buffer 12.5 mM, pH 6.5. The peptides were obtained as a result of peptidyl dipeptidase activity (class A), carboxypeptidase activity (class B), aminopeptidase activity (class C), X-prolyl-dipeptidyl peptidase activity (class D), and a combination of previous activities (class E). Peptides with an asterisk symbol were identified with CNRZ1066 with crude isracidin (mixture of peptides 1−23 and 3−23 in a ratio 10:1) as substrate; the crude isracidin was not tested with LMD-9-Δ*prtS* and LMD-9-Δ*prtS*-Δ*htrA*.

aminopeptidase activity was blocked due to the presence of a proline residue at the carboxyl side or P1′ position (according to the nomenclature of Schechter and Berger)[24] of the bonds R^1−P^2, H^4−P^5, and L^{11}−P^{12}. Initially the aminopeptidase activity was detected upon incubation of *S. thermophilus* CNRZ1066 with the crude isracidin, which contains, in addition to 1−23, a low amount of fragment 3−23 (in a molar ratio 10:1 between the two peptides). Under these conditions, all the peptides belonging to category C (Figure 3) were found as hydrolysis of peptide 3−23 did not need the cleavage of the first bond of isracidin involving a Pro residue. Meanwhile, the existence of the dipeptides 1−2 and 4−5 (category D) showed that the isracidin was also cleaved by an X-prolyl dipeptidyl peptidase activity, which removed dipeptides containing proline residue and allowed aminopeptidase activity to continue downstream of these proline residues. However, the dipeptide 11−12 was not identified in our experimental conditions. The release of this peptide needed the cleavage of numerous bonds by the conjugated actions of (i) the aminopeptidase and X-prolyl dipeptidyl peptidase activities and (ii) peptidyl dipeptidase and/or carboxypeptidase activities on the polypeptide chain. The unknown relative rates and residue preferences of these activities do not allow to predict if the generation of this peptide is possible.

The presence of certain peptides indicated that they were produced due to action of two or more peptidase activities. All the PrtS$^-$ strains of *S. thermophilus*, i.e., CNRZ1066, LMD-9-Δ*prtS*, and LMD-9-Δ*prtS*-Δ*htrA*, produced these peptides, and they are listed in category E (Figure 3).

Kinetic Approach To Distinguish PrtS Activity from Exopeptidase Activities. Through three examples of selected peptides (1−13, 1−17, and 22−23), kinetics of isracidin degradation showed that all four *S. thermophilus* strains, i.e., CNRZ1066, LMD-9, LMD-9-Δ*prtS*, and LMD-9-Δ*prtS*-Δ*htrA*, were able to cleave isracidin at N^{17}−E^{18}, Q^{13}−E^{14}, and L^{21}−R^{22} peptide bonds, but differently (Figure 4). As shown in Figure 4A, the peptide 1−17 was produced in substantially high amount by LMD-9 strain and seemed likely to be the result of PrtS activity, whereas in the case of the PrtS$^-$ phenotype strains

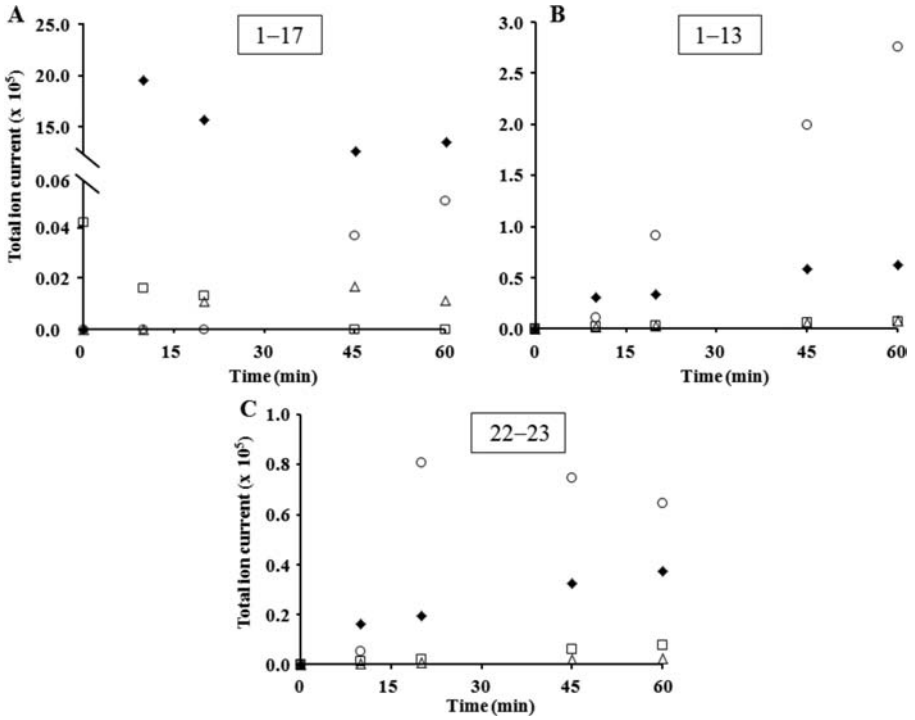

Figure 4. Distinct release pattern of peptide fragments (A) 1−17, (B) 1−13, and (C) 22−23 by cell-associated extracellular proteolytic activities of *S. thermophilus* strains LMD-9 (filled diamond), LMD-9-Δ*prtS* (empty square), LMD-9-Δ*prtS*-Δ*htrA* (empty triangle), and CNRZ1066 (empty circle) upon 6-h incubation with isracidin in phosphate/acetate buffer 12.5 mM, pH 6.5.

DOI: 10.1021/acs.jafc.5b01647
J. Agric. Food Chem. 2015, 63, 7522−7531

such as CNRZ1066 and LMD-9 mutant strains, a minor quantity was produced as a result of action of peptidyl dipeptidase and/or carboxypeptidase activities. In contrast, the peptides 1−13 and 22−23 were generated in greater quantities by peptidase activities of CNRZ1066 strain than by PrtS and/or peptidase activities of the strain LMD-9 (Figures 4B and 4C). However, among the PrtS$^-$ phenotype, peptidase activities leading to generation of peptides 1−13 and 22−23 in strain CNRZ1066 appeared to be much higher than in both mutant strains of LMD-9.

DISCUSSION

Isracidin is a substrate widely used to determine cleavage specificities of the surface proteases of different LAB.[15,16] In the present study, the impact of surface protease PrtS as well as exopeptidase activities of *S. thermophilus* on the degradation of isracidin was explored, as it has been shown that the 1−23 N-terminal region of α_{s1}-CN is sensitive toward proteolytic attack of *S. thermophilus* (such as the LMD-9 strain) and other LAB strains that possess the main cell wall-associated protease.[1,6,15,16]

Isracidin was completely hydrolyzed after exposure to the intact cells of *S. thermophilus* LMD-9. It has been reported by Fernandez-Espla et al.[6] that the purified PrtS of *S. thermophilus* CNRZ385 preferentially and primarily cleaved isracidin at N^{17}−E^{18} and L^{16}−N^{17} peptide bonds, and we have found similar results upon exposure of isracidin to the cells of *S. thermophilus* LMD-9. In another study the same results were obtained with the highly acidifying *S. thermophilus* strains PB302, PB385, 4F44, and ATE19PB8.[1] Hence, it appeared that the proteolytic activity toward isracidin highlighted for *S. thermophilus* LMD-9 was overwhelmingly due to the activity of PrtS. Nevertheless some differences were noted, as the hydrolysis of peptide bond L^{21}−R^{22} to a medium extent in this study whereas this bond appeared to be poorly hydrolyzed by PrtS of the strain CNRZ385.[6] Moreover K^7−H^8, H^8−Q^9, and Q^9−G^{10} peptide bonds were poorly hydrolyzed, in the present study, while they appeared to be preferred cleavage sites of PrtS in other studies,[1,6] although the peptide bond K^7−H^8 was not hydrolyzed by PrtS of strain CNRZ385.[6] The perceptible difference in the preference of some peptide bond hydrolysis might be explained by the difference in pH of incubation buffer. This observation is consistent with the previous findings that pH of the medium is one of the factors that alter the preference for bonds in the 1−23 fragment of α_{s1}-CN, which can even result in a completely changed specificity.[15,25] As shown in Figure 5, the cleavage preference of the PrtS protease for the peptide bonds N^{17}−E^{18} and L^{16}−N^{17} remains unchanged regardless of the pH tested. However, PrtS has pronounced cleavage preference toward K^7−H^8, H^8−Q^9, and Q^9−G^{10} peptide bonds at pH 7.5 compared to pH 6.5, since no hydrolysis of K^7−H^8 peptide bond is observed at pH 8.0. Contrariwise, the weak hydrolysis of the peptide bond between the residues L^{21} and R^{22} is reported at pH 8.0 and 5.2. The peptide bond Q^{13}−E^{14} is cleaved by PrtS in a similar way at all tested pH except 5.2 (Figure 5). In conclusion, the hydrolysis of a maximum of peptide bonds in the isracidin was observed at a pH (6.5−7.5) close to the initial pH of the milk fermentation process. This emphasizes that the sensitivity of the peptide toward PrtS can be modulated in the fermented products by changing the pH.

Having a relatively large chain length, isracidin appeared to be a suitable substrate for further unveiling the potential

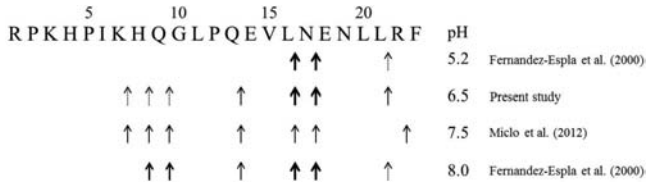

Figure 5. Cleavage site preferences of *S. thermophilus* LMD-9 nonproliferating cells (Miclo et al.[1] and this study) and of purified PrtS of *S. thermophilus* CNRZ 385 (Fernandez-Espla et al.[6]) on isracidin at different pH. In the case of work of Miclo et al.,[1] the peptide bond 22−23 is cut preferably instead of bond 21−22 as α_{s1}-casein and not isracidin is the substrate. The relative cleavage rates are indicated by large (major site), medium (medium site), and dotted (minor site) arrows except for Miclo et al.,[1] where the cleavage rates are not given.

exopeptidase activities acting both at the N-terminal and C-terminal extremities. Moreover, the presence of three proline residues in the 1−12 N-terminal region of isracidin permitted us to highlight the X-prolyl dipeptidyl peptidase and aminopeptidase activities simultaneously as the latter is inhibited by proline residues. Two mutant strains of LMD-9 devoid of PrtS or both PrtS and HtrA, i.e., LMD-9-Δ*prtS* and LMD-9-Δ*prtS*-Δ*htrA*, were used in this study. The LMD-9-Δ*prtS* strain permitted highlighting of peptidase activities associated with cell that were masked in the presence of PrtS in LMD-9 wild type strain, whereas the LMD-9-Δ*prtS*-Δ*htrA* strain helped to conclude that observed hydrolysis was not due to the protease HtrA, another surface protease, which is involved in the hydrolysis of extracellular misfolded proteins. The strain CNRZ1066 represented naturally PrtS$^-$ phenotype and provided the means to evaluate the variability of the surface exopeptidase system by comparison with the LMD-9 mutant strains.

When one or the other LMD-9 mutant strains was incubated with isracidin, hydrolysis of isracidin occurred in a similar way. The LMD-9 mutant strains displayed exopeptidase activities such as carboxypeptidase, peptidyl dipeptidase, aminopeptidase, and X-prolyl dipeptidyl peptidase that could act simultaneously or successively in an undefined order. Moreover, almost similar peptidase activities were shown by *S. thermophilus* CNRZ1066 after exposure to the isracidin. All these activities were cell-associated extracellular activities as no peptidase activity was observed in cell free filtrate.

In this study, the identified carboxypeptidase activity was observed only on some of the peptides released after peptidyl dipeptidase activity as evidenced by the absence of the peptide 1−22. The poor carboxypeptidase and higher peptidyl dipeptidase activity could be the result of nonoptimal reaction conditions for carboxypeptidase, or of specificity of carboxypeptidase toward peptide bonds, or of relative velocity of the enzymatic activities or a combination of these hypotheses. It has been stated that the internal carboxypeptidase and dipeptidase of *Lactobacillus casei* NCDO 151 require different pH and temperature for their optimal activity.[26] Macedo and workers[27] also detected lower carboxypeptidase activity than the corresponding dipeptidase activity in the intracellular enzymatic extracts of *Lactobacillus paracasei* subsp. *paracasei* ESB230 and *Lactococcus lactis* subsp. *lactis* ESB117. However, to our knowledge, only one study highlighted the presence of intracellular carboxypeptidase activity in *S. thermophilus*.[28] Moreover, Kang and colleagues[29] reported the predicted presence of a membrane carboxypeptidase, and the gene of

DOI: 10.1021/acs.jafc.5b01647
J. Agric. Food Chem. 2015, 63, 7522−7531

this peptidase is present in the genome of many strains of *S. thermophilus* available in databases. This carboxypeptidase corresponds to low molecular mass penicillin binding protein that cross-links disaccharide chains of peptidoglycan by peptide bridges. The presence of an arginine carboxypeptidase[30] and of a dipeptidyl carboxypeptidase (peptidyl dipeptidase)[31] associated with the cell wall has also been reported in *Streptococcus mitis* ATCC 15909 and *Streptococcus gordonii* FSS2, respectively.

To our knowledge, no cell-associated extracellular peptidyl dipeptidase activity was ever reported in *S. thermophilus*. The peptide bonds $L^{11}-P^{12}$, P^5-I^6, or R^1-P^2 were not hydrolyzed by peptidyl dipeptidase activity, as no fragment corresponding to such a hydrolysis was generated (Figure 3). This might be correlated to the presence of proline residue. Indeed, Dasarathy et al.[32] have reported that peptides containing a proline residue at ultimate or penultimate position are not hydrolyzed by the extracellular peptidyl dipeptidase-4 of *Pseudomonas maltophilia*. Contrarily, hydrolysis at P^2-K^3 and P^5-I^6 peptide bonds leading to the generation of the dipeptides 1−2 and 4−5 seemed more likely to be the result of X-prolyl dipeptidyl peptidase activity rather than that of peptidyl dipeptidase. With regard to aminopeptidase and X-prolyl dipeptidyl peptidase activities, recently, the presence of cell-associated extracellular aminopeptidase and X-prolyl dipeptidyl peptidase activities has been described in two *S. thermophilus* strains, i.e., LMD-9 and CNRZ1066.[11] Similarly, aminopeptidase activity in the growth medium of *S. thermophilus*, *Lactobacillus delbrueckii* subsp. *bulgaricus*, and *Bifidobacteria* has also been detected.[33] Moreover, different cell wall-associated aminopeptidases such as those from *Lactobacillus helveticus* ITGL1,[34] *Lactobacillus lactis*,[35] and *Lactococcus lactis* subsp. *cremoris*[36] have been purified and characterized. Besides, *Streptococcus suis* and *S. gordonii* FSS2 also possess extracellular and cell wall-associated arginine aminopeptidase activity.[37,38]

However, in the present study, the aminopeptidase activity on the isracidin was exhibited only after the action of the X-prolyl dipeptidyl peptidase, showing that the presence of proline residue as the second residue of the peptide precluded the aminopeptidase activity. Recently, the absence of hydrolysis of the β-casomorphin-7 (YPFPGPI) by cell-associated extracellular aminopeptidase of *S. thermophilus* has been reported due to the presence of proline residue at position P1′.[11] Moreover, a cell-associated peptidase activity has been described after exposure of the antihypertensive dodecapeptide (FFVAPFPEVFGK) of bovine α_{s1}-casein to *Lactobacillus delbrueckii* subsp. *bulgaricus*. Similarly, the cell-associated peptidase activity was not observed once a proline residue was encountered at position P1′.[39] The presence of extracellular and cell-wall X-prolyl-dipeptidyl peptidase activity has already been described in *Lactococcus lactis* subsp. *cremoris*,[40] *Lactococcus lactis* subsp. *lactis* IFPL359,[41] and *Streptococcus gordonii* FSS2.[42]

This study provides new insights into the surface proteolytic system of *S. thermophilus*. Indeed, *S. thermophilus* possesses the well-known PrtS activity that is essentially pH-dependent, indispensable for milk fermentation and may also be involved in increasing the functional properties of fermented products by releasing bioactive peptides from milk proteins. Besides this activity, this bacterium also displays a broad range of exopeptidase activities associated with the cell. In the absence of PrtS, four distinct exopeptidase activities, i.e., carboxypeptidase, peptidyl dipeptidase, aminopeptidase, and X-prolyl dipeptidyl peptidase, were identified. The existence of cell-associated extracellular carboxypeptidase and peptidyl dipeptidase activities in both $PrtS^+$ and $PrtS^-$ phenotypes of *S. thermophilus* has been highlighted for the first time. This indicated that the surface proteolytic system of *S. thermophilus* is more complex than reported in previous studies. Now, it is clear that these cell-associated extracellular peptidase activities may play a role for the $PrtS^-$ phenotypes of *S. thermophilus* in the use of milk caseins to generate free amino acids, vital for bacterial growth. Nevertheless, this growth is slower because the proteolytic activity of these peptidases is weaker than that of PrtS as it was shown in this study where the presence of PrtS concealed peptidase activities. Second, the desirability of the *S. thermophilus* strains in certain cheeses could be associated with its cell-associated extracellular peptidase activities, as they may be involved in the degradation of bitter peptides comprising proline or hydrophobic residues (Leu, Phe), where the released amino acids ultimately act as flavor precursors. The detection of the *S. thermophilus* cell-associated extracellular peptidases should motivate further biochemical and genetic studies to understand completely their role in milk fermentation, which is still not clear.

AUTHOR INFORMATION

Corresponding Author

*Tel: +33 383684269. Fax: +33 383684274. E-mail: Laurent.Miclo@univ-lorraine.fr.

Notes

The authors declare no competing financial interest.

ACKNOWLEDGMENTS

The authors thank Chantal Poirson for her technical assistance.

ABBREVIATIONS USED

ATCC, American Type Culture Collection; EDTA, ethylenediaminetetraacetic acid; ESI, electrospray ionization; HPLC, high performance liquid chromatography; HtrA, high temperature requirement A protease; Lys-*p*-NA, lysine-*para*-nitroanilide; MS, mass spectrometry; PAB, potassium phosphate/acetate buffer; PCR, polymerase chain reaction; PrtS, cell-wall associated protease of *S. thermophilus*; RP, reversed-phase; rpm, revolutions per min; SPE, solid phase extraction; TEA, trishydroxymethylaminomethane-acetate-EDTA

REFERENCES

(1) Miclo, L.; Roux, E.; Genay, M.; Brusseaux, E.; Poirson, C.; Jameh, N.; Perrin, C.; Dary, A. Variability of hydrolysis of β-, α_{s1}-, and α_{s2}-caseins by 10 strains of *Streptococcus thermophilus* and *resulting* bioactive peptides. *J. Agric. Food Chem.* **2012**, *60*, 554−565.

(2) Pastink, M. I.; Teusink, B.; Hols, P.; Visser, S.; de Vos, W. M.; Hugenholtz, J. Genome-scale model of *Streptococcus thermophilus* LMG18311 for metabolic comparison of lactic acid bacteria. *Appl. Environ. Microbiol.* **2009**, *75*, 3627−3633.

(3) Hols, P.; Hancy, F.; Fontaine, L.; Grossiord, B.; Prozzi, D.; Leblond-Bourget, N.; Decaris, B.; Bolotin, A.; Delorme, C.; Ehrlich, S. D.; Guedon, E.; Monnet, V.; Renault, P.; Kleerebezem, M. New insights in the molecular biology and physiology of *Streptococcus thermophilus* revealed by comparative genomics. *FEMS Microbiol. Rev.* **2005**, *29*, 435−463.

(4) Savijoki, K.; Ingmer, H.; Varmanen, P. Proteolytic systems of lactic acid bacteria. *Appl. Microbiol. Biotechnol.* **2006**, *71*, 394−406.

(5) Shahbal, S.; Hemme, D.; Renault, P. Characterization of a cell envelope-associated proteinase activity from *Streptococcus thermophilus* H-Strains. *Appl. Environ. Microbiol.* **1993**, *59*, 177−182.

DOI: 10.1021/acs.jafc.5b01647
J. Agric. Food Chem. 2015, 63, 7522−7531

(6) Fernandez-Espla, M. D.; Garault, P.; Monnet, V.; Rul, F. *Streptococcus thermophilus* cell wall-anchored proteinase: release, purification, and biochemical and genetic characterization. *Appl. Environ. Microbiol.* **2000**, *66*, 4772−4778.
(7) Galia, W.; Perrin, C.; Genay, M.; Dary, A. Variability and molecular typing of *Streptococcus thermophilus* strains displaying different proteolytic and acidifying properties. *Int. Dairy J.* **2009**, *19*, 89−95.
(8) Chang, O. K.; Perrin, C.; Galia, W.; Saulnier, F.; Miclo, L.; Roux, E.; Driou, A.; Humbert, G.; Dary, A. Release of the cell-envelope protease PrtS in the growth medium of *Streptococcus thermophilus* 4F44. *Int. Dairy J.* **2012**, *23*, 91−98.
(9) Poquet, I.; Saint, V.; Seznec, E.; Simoes, N.; Bolotin, A.; Gruss, A. HtrA is the unique surface housekeeping protease in *Lactococcus lactis* and is required for natural protein processing. *Mol. Microbiol.* **2000**, *35*, 1042−1051.
(10) Christensen, J. E.; Dudley, E. G.; Pederson, J. A.; Steele, J. L. Peptidases and amino acid catabolism in lactic acid bacteria. *Antonie van Leeuwenhoek* **1999**, *76*, 217−246.
(11) Hafeez, Z.; Cakir-Kiefer, C.; Girardet, J.-M.; Jardin, J.; Perrin, C.; Dary, A.; Miclo, L. Hydrolysis of milk-derived bioactive peptides by cell-associated extracellular peptidases of *Streptococcus thermophilus*. *Appl. Microbiol. Biotechnol.* **2013**, *97*, 9787−9799.
(12) Lahov, E.; Regelson, W. Antibacterial and immunostimulating casein-derived substances from milk: casecidin, isracidin peptides. *Food Chem. Toxicol.* **1996**, *34*, 131−145.
(13) Hayes, M.; Ross, R. P.; Fitzgerald, G. F.; Hill, C.; Stanton, C. Casein-derived antimicrobial peptides generated by *Lactobacillus acidophilus* DPC6026. *Appl. Environ. Microbiol.* **2006**, *72*, 2260−2264.
(14) Somkuti, G. A.; Paul, M. Enzymatic fragmentation of the antimicrobial peptides casocidin and isracidin by *Streptococcus thermophilus* and *Lactobacillus delbrueckii* ssp. *bulgaricus*. *Appl. Microbiol. Biotechnol.* **2010**, *87*, 235−242.
(15) Exterkate, F. A.; Alting, A. C.; Slangen, C. J. Specificity of two genetically related cell-envelope proteinases of *Lactococcus lactis* subsp. *cremoris* towards α_{s1}-casein-(1−23)-fragment. *Biochem. J.* **1991**, *273*, 135−139.
(16) Sadat-Mekmene, L.; Genay, M.; Atlan, D.; Lortal, S.; Gagnaire, V. Original features of cell-envelope proteinases of *Lactobacillus helveticus*. A review. *Int. J. Food Microbiol.* **2011**, *146*, 1−13.
(17) Bolotin, A.; Quinquis, B.; Renault, P.; Sorokin, A.; Ehrlich, S. D.; Kulakauskas, S.; Lapidus, A.; Goltsman, E.; Mazur, M.; Pusch, G. D.; Fonstein, M.; Overbeek, R.; Kyprides, N.; Purnelle, B.; Prozzi, D.; Ngui, K.; Masuy, D.; Hancy, F.; Burteau, S.; Boutry, M.; Delcour, J.; Goffeau, A.; Hols, P. Complete sequence and comparative genome analysis of the dairy bacterium *Streptococcus thermophilus*. *Nat. Biotechnol.* **2004**, *22*, 1554−1558.
(18) Makarova, K.; Slesarev, A.; Wolf, Y.; Sorokin, A.; Mirkin, B.; Koonin, E.; Pavlov, A.; Pavlova, N.; Karamychev, V.; Polouchine, N.; Shakhova, V.; Grigoriev, I.; Lou, Y.; Rohksar, D.; Lucas, S.; Huang, K.; Goodstein, D. M.; Hawkins, T.; Plengvidhya, V.; Welker, D.; Hughes, J.; Goh, Y.; Benson, A.; Baldwin, K.; Lee, J. H.; Diaz-Muniz, I.; Dosti, B.; Smeianov, V.; Wechter, W.; Barabote, R.; Lorca, G.; Altermann, E.; Barrangou, R.; Ganesan, B.; Xie, Y.; Rawsthorne, H.; Tamir, D.; Parker, C.; Breidt, F.; Broadbent, J.; Hutkins, R.; O'Sullivan, D.; Steele, J.; Unlu, G.; Saier, M.; Klaenhammer, T.; Richardson, P.; Kozyavkin, S.; Weimer, B.; Mills, D. Comparative genomics of the lactic acid bacteria. *Proc. Natl. Acad. Sci. U. S. A.* **2006**, *103*, 15611−15616.
(19) Lecomte, X.; Gagnaire, V.; Briard-Bion, V.; Jardin, J.; Lortal, S.; Dary, A.; Genay, M. The naturally competent strain *Streptococcus thermophilus* LMD-9 as a new tool to anchor heterologous proteins on the cell surface. *Microb. Cell Fact.* **2014**, *13*, 82.
(20) Terzaghi, B. E.; Sandine, W. E. Improved medium for lactic streptococci and their bacteriophages. *Appl. Microbiol.* **1975**, *29*, 807−813.
(21) Fischer, G.; Decaris, B.; Leblond, P. Occurrence of deletions, associated with genetic instability in *Streptomyces ambofaciens*, is independent of the linearity of the chromosomal DNA. *J. Bacteriol.* **1997**, *179*, 4553−4558.
(22) Miclo, L.; Perrin, E.; Driou, A.; Papadopoulos, V.; Boujrad, N.; Vanderesse, R.; Boudier, J. F.; Desor, D.; Linden, G.; Gaillard, J.-L. Characterization of α-casozepine, a tryptic peptide from bovine α_{s1}-casein with bezodiazepine-like activity. *FASEB J.* **2001**, *15*, 1780−1782.
(23) Kuipers, B. J. H.; Gruppen, H. Prediction of molar extinction coefficients of proteins and peptides using UV absorption of the constituent amino acids at 214 nm to enable quantitative reverse phase high-performance liquid chromatography-mass spectrometry analysis. *J. Agric. Food Chem.* **2007**, *55*, 5445−5451.
(24) Schechter, I.; Berger, A. On the size of the active site in proteases. I. Papain. *Biochem. Biophys. Res. Commun.* **1967**, *27*, 157−162.
(25) Exterkate, F. A.; Alting, A. C. The conversion of the α_{s1}-casein-(1−23)-fragment by the free and bound form of the cell-envelope proteinase of *Lactococcus lactis* subsp. *cremoris* under conditions prevailing in cheese. *Syst. Appl. Microbiol.* **1993**, *16*, 1−8.
(26) El Soda, B. M.; Desmazeaud, M. J.; Bergere, J.-L. Peptide hydrolases of *Lactobacillus casei*: isolation and genreal properties of various peptidase activities. *J. Dairy Res.* **1978**, *45*, 445−455.
(27) Macedo, A. C.; Vieira, M.; Pocas, R.; Malcata, F. X. Peptide hydrolase system of lactic acid bacteria isolated from Serra da Estrela cheese. *Int. Dairy J.* **2000**, *10*, 769−774.
(28) Deutsch, S. M.; Molle, D.; Gagnaire, V.; Piot, M.; Atlan, D.; Lortal, S. Hydrolysis of sequenced β-casein peptides provides new insight into peptidase activity from thermophilic lactic acid bacteria and highlights intrinsic resistance of phosphopeptides. *Appl. Environ. Microbiol.* **2000**, *66*, 5360−5367.
(29) Kang, X.; Ling, N.; Sun, G.; Zhou, Q.; Zhang, L.; Sheng, Q. Complete genome sequence of *Streptococcus thermophilus* strain MN-ZLW-002. *J. Bacteriol.* **2012**, *194*, 4428−4429.
(30) Linder, L. E.; Sund, M.-L.; Lonnies, H. Isolation and purification of cell wall-associated arginine carboxypeptidase from *Streptococcus mitis* ATCC 15909. *Curr. Microbiol.* **1994**, *28*, 91−96.
(31) Harty, D. W. S.; Hunter, N. Carboxypeptidase activity common to viridans group streptococci cleaves angiotensin I to angiotensin II: an activity homologous to angiotensin-converting enzyme (ACE). *Microbiology* **2011**, *157*, 2143−2151.
(32) Dasarathy, Y.; Stevens, J.; Fanburg, B. L.; Lanzillo, J. J. A peptidyl dipeptidase-4 from *Pseudomonas maltophilia*: purification and properties. *Arch. Biochem. Biophys.* **1989**, *270*, 255−266.
(33) Shihata, A.; Shah, N. P. Proteolytic profiles of yogurt and probiotic bacteria. *Int. Dairy J.* **2000**, *10*, 401−408.
(34) Blanc, B.; Laloi, P.; Atlan, D.; Gilbert, C.; Portalier, R. Two cell-wall associated aminopeptidases from *Lactobacillus helveticus* and the purification and characterization of APII from strain ITGLl. *J. Gen. Microbiol.* **1993**, *139*, 1441−1448.
(35) Eggimann, B.; Bachmann, M. Purification and partial characterization of an aminopeptidase from *Lactobacillus lactis*. *Appl. Environ. Microbiol.* **1980**, *40*, 876−882.
(36) Geis, A.; Bockelmann, W.; Teuber, M. Simultaneous extraction and purification of a cell wall-associated peptidase and β-casein specific protease from *Streptococcus cremoris* AC1. *Appl. Microbiol. Biotechnol.* **1985**, *23*, 79−84.
(37) Goldstein, J. M.; Nelson, D.; Kordula, T.; Mayo, J. A.; Travis, J. Extracellular arginine aminopeptidase from *Streptococcus gordonii* FSS2. *Infec. Immun.* **2002**, *70*, 836−843.
(38) Jobin, M.-C.; Grenier, D. Identification and characterization of four proteases produced by *Streptococcus suis*. *FEMS Microbiol. Lett.* **2003**, *220*, 113−119.
(39) Paul, M.; Somkuti, G. A. Degradation of milk-based bioactive peptides by yogurt fermentation bacteria. *Lett. Appl. Microbiol.* **2009**, *49*, 345−450.
(40) Kiefer-Partsch, B.; Bockelmann, W.; Geis, A.; Teuber, M. Purification of an X-prolyl-dipeptidyl aminopeptidase from the cell wall proteolytic system of *Lactococcus lactis* subsp. *cremoris*. *Appl. Microbiol. Biotechnol.* **1989**, *31*, 75−78.
(41) Requena, T.; Pelaez, C.; Fox, P. F. Peptidase and proteinase activity of *Lactococeus lactis*, *Lactobacillus casei* and *Lactobacillus plantarum*. *Z. Lebensm.-Unters. Forsch.* **1993**, *196*, 351−355.

DOI: 10.1021/acs.jafc.5b01647
J. Agric. Food Chem. 2015, 63, 7522−7531

(42) Goldstein, J. M.; Banbula, A.; Kordula, T.; Mayo, J. A.; Travis, J. Novel extracellular X-prolyl dipeptidyl-peptidase (DPP) from *Streptococcus gordonii* FSS2: an emerging subfamily of viridans streptococcal X-prolyl DPPs. *Infec. Immun.* **2001**, *69*, 5494−5501.

DOI: 10.1021/acs.jafc.5b01647
J. Agric. Food Chem. 2015, 63, 7522−7531

anthocyanin profiles of cranberry have also been applied as authenticity markers.[21]

Whereas methods for the separation and detection of anthocyanins are established and usually well-reported, sample preparations, including the different extraction techniques, vary considerably, and frequently, their description lacks detail. Besides classic approaches, such as Soxhlet, liquid–liquid, and solid–liquid extractions, some new extraction techniques have emerged in the last few decades. These include ultrasound-assisted extraction (UAE), microwave-assisted extraction, and accelerated solvent extraction (ASE).[22,23] The great variety of extraction methods inevitably raises the question of comparability of the corresponding results. This problem is addressed in the present study by comparing the influence of ASE and UAE on the profile of anthocyanins in bilberry, lowbush blueberry, and American cranberry extracts of lyophilized berries. In addition, fresh samples of the named fruits were investigated applying UAE. Finally, the established method influences on the anthocyanin profiles were interrelated with the natural profile diversity by comparison to a data set of 26 bilberry and blueberry samples using a linear discriminant analysis. It should be emphasized that the scope of the study was the assessment of the anthocyanin profiles and not the optimization of anthocyanin yields.

MATERIALS AND METHODS

Chemicals. Ultrapure water was obtained from a Synergy purification system (Millipore, Molsheim, France). High-performance liquid chromatography (HPLC)-grade acetonitrile and acetic acid were from VWR (Mannheim, Germany). Formic acid (≥98%) was purchased from Sigma-Aldrich (St. Louis, MO). Methanol was from Th. Geyer (Renningen, Germany). Diatomaceous earth (Chromabond XTR) and regenerated cellulose filters (Chromafil RC-20/15 MS) were supplied by Macherey-Nagel (Düren, Germany). Malvidin 3-*O*-glucoside (≥87%) was obtained from Phytoplan (Heidelberg, Germany).

Samples. Wild bilberries (*Vaccinium myrtillus* L.; n = 21) and lowbush blueberries (*Vaccinium angustifolium* Ait.; n = 5) were mainly collected manually in Germany and Poland between 2013 and 2014 or harvested in Ukraine and Canada between 2009 and 2014 and provided by Rudolf Wild GmbH & Co. KG (Eppelheim, Germany), Faethe Labor GmbH (Paderborn, Germany), and Haus Rabenhorst O. Lauffs GmbH & Co. KG (Unkel, Germany). American cranberries (*V. macrocarpon* Ait.; n = 1) harvested in the U.S.A. in 2012 were obtained from Haus Rabenhorst O. Lauffs GmbH & Co. KG (Unkel, Germany). All samples were stored at −20 °C until freeze-drying or extraction.

Freeze-Drying Protocol. Freeze-drying was conducted using an Alpha 2-4 LSC freeze-dryer (Christ, Osterode, Germany) at 0.070 mbar for 3 days with a condenser temperature of −90 °C.

Extraction Methods. *Sonication.* Fresh berry material (6 g) or lyophilized berry powder (1.2 g) were filled in centrifuge tubes in three replicate samples and treated with 20 mL of extraction solvent consisting of methanol/water/acetic acid (A, 20:75:5; B, 80:15:5, v/v/v). The suspension was homogenized with an Ultra-Turrax and, afterward, placed upright into a sonication bath (1100 W) for 10 min. Subsequently, the samples were centrifuged at 10947*g* for 10 min, and the supernatant was decanted. The residue was extracted again under the same conditions, excluding the homogenization step, with 10 mL of extraction solvent. Finally, the supernatants were pooled and made up to 50 mL with water. This solution was used for ultrahigh-pressure liquid chromatography (UHPLC) analysis after membrane filtration (0.2 μm) with regenerated cellulose.

Accelerated Solvent Extraction. Lyophilized berry powder was extracted using an accelerated solvent extractor model ASE 350 (Thermo Scientific, Inc., Braunschweig, Germany). For this purpose, 0.2 g of lyophilized berry powder was mixed with diatomaceous earth and packed into a 10 mL stainless-steel extraction cell. The cells were prepared with two cellulose filters on the bottom and top of the cells. The same extraction solvents as mentioned before were used, and each sample was extracted in triplicate. Extraction parameters were 5 min static time, 3 cycles, 40 °C, and 100% flush volume. Finally, all extracts were adjusted to 25 mL with water and used for UHPLC analysis after membrane filtration with regenerated cellulose.

UHPLC–Mass Spectrometry (MS) Identification of Anthocyanins. The identification of anthocyanins was conducted on a Waters Aquity I-Class system (Milford, MA) coupled with a Thermo Scientific, Inc. LTQ-XL ion trap mass spectrometer (Braunschweig, Germany). The column was a Kinetex C-18, 1.7 μm particle size (150 × 2.1 mm) (Phenomenex, Inc., Aschaffenburg, Germany) equipped with a security guard cartridge of the same material (2.1 × 5 mm, 1.7 μm). At a flow rate of 0.4 mL/min, the following gradient was used: 0 min, 4% B; 4 min, 4% B; 8 min, 4.5% B; 14 min, 7% B; 20 min, 15% B; 25 min, 30% B; 25.1 min, 100% B; 27.9 min, 100% B; 28 min, 4% B; and 32 min, 4% B, where eluent A was water/formic acid (95:5, v/v) and eluent B was acetonitrile/formic acid (95:5, v/v). The experimental conditions of MS were as follows: The capillary was set to a temperature of 300 °C during positive electrospray ionization (ESI) and a voltage of 180 V. The source voltage was maintained at 4 kV at a current of 100 μA. The tube lens was adjusted to 110 V. Nitrogen was used as sheath, auxiliary, and sweep gas at a flow of 45, 10, and 3 arbitrary units, respectively. Collision-induced dissociation spectra were obtained at 35 eV using helium as the collision gas.

UHPLC–Diode Array Detector (DAD) Quantification of Anthocyanins. Anthocyanin quantification was performed on a Nexera UFLC system (Shimadzu, Kyoto, Japan) equipped with two high-pressure gradient pumps LC-30AD, a degasser DGU-20A5R, an autosampling unit SIL-30AD (cooled to 10 °C, injecting 2 μL), a column oven CTO-20AC (at 40 °C), and a DAD SPD-M20A. The column, gradient, and solvent were the same as for the identification. Anthocyanins were detected at 520 nm and quantified as malvidin 3-*O*-glucoside equivalents by external calibration. The mean standard deviations of all triplicate determinations ranged from 1 to 10% and were, therefore, considered acceptable for repeatable and precise quantification (see Table 1 of the Supporting Information). The total anthocyanin content was calculated as the sum of individual anthocyanins.

Statistics. For statistical and discriminant analyses, the software XLSTAT was used. An analysis of variation (ANOVA) with a Dunn–Sidak post-hoc test as a result of heterogeneity of variances was performed to determine significant differences. The level of significance was defined as $p \leq 0.05$.

RESULTS AND DISCUSSION

Because ASE and UAE have overcome most problems of conventional extraction methods, such as Soxhlet and maceration, they are of increasing importance for the extraction of bioactive compounds, such as polyphenols, for further analysis.[24] UAE is based on the principle of cavitation, which means the production, growth, and collapse of bubbles in the extraction solvent and sample material.[25] In contrast, ASE uses high pressure to keep solvents liquid above their boiling point,[26] which facilitates the extractability of the analytes. Among the broad range of extraction techniques, UAE and also ASE were extensively reviewed by Azmir et al. According to these authors, both methods are applied for the extraction of a broad range of different polyphenols. In particular, the extraction of anthocyanins from berry fruits was shown by Monrad et al. and Santos et al.[27,28] The extraction conditions chosen in the present study are based on applications of ASE and UAE reported for polyphenol extraction. Briefly, both polar[29,30] and unpolar[31,32] solvents had been applied for the extraction of anthocyanins. Furthermore, acidified solvents were used because of the higher anthocyanin stability and

DOI: 10.1021/acs.jafc.5b02255
J. Agric. Food Chem. 2015, 63, 7532–7538

extractability at low pH values.[33] Accordingly, two acidified extraction solvents with different polarities were applied in this study. Preliminary work had revealed no significant influence of the extraction time on the target analytes during ASE, and thus, the extraction time for UAE was adjusted to the total time of the ASE methods (approximately 25 min). Besides the extraction of lyophilized berry material, also the application of fresh berries had previously been reported and was therefore investigated as well using UAE as the manufacturer suggested, applying only dry sample materials in ASE. As reference extraction conditions, the application of UAE with 80% methanol on fresh berries was chosen, with the purpose to retain the anthocyanin profile as natural as possible using unprocessed berries. Moreover, sonication baths are more common than accelerated solvent extractors, and the majority of publications showed that less polar solvents are most efficient for the anthocyanin extraction.

For fast and reliable quantification of anthocyanins, a UHPLC−DAD method was developed that is capable of separating 15 individual anthocyanins from bilberry fruits within 20 min and requires only 8 mL of solvent per chromatographic run. Conventional HPLC methods are either not suitable for the separation of all anthocyanins present in bilberries or require more time and solvent.[31,34,35] In addition, thus far, only few UHPLC−DAD methods have been reported that show similar separation capabilities.[36,37]

Anthocyanin Content of Bilberry and Lowbush Blueberry in UAE and ASE Extracts. The 15 anthocyanins were individually quantified after application of two different extraction techniques and extraction solvents to determine the influence of the extraction technique (UAE versus ASE) and solvent composition (20 versus 80% acidified methanol) on the yields. The anthocyanins were identified according to their absorption spectra,[38] order of elution[31] (Figure 1), and

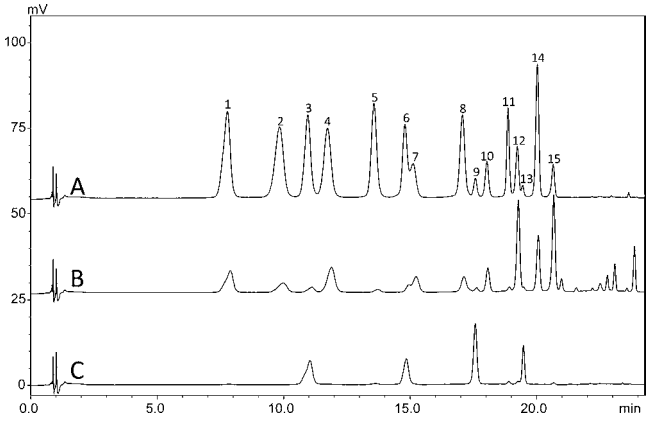

Figure 1. UHPLC−DAD chromatogram (520 nm) of the fruit extracts under reference conditions (80% methanol, fresh berries, UAE): (A) bilberry, (B) lowbush blueberry, and (C) American cranberry, for (1) dp-3-gal, (2) dp-3-glu, (3) cy-3-gal, (4) dp-3-ara, (5) cy-3-glu, (6) pt-3-gal, (7) cy-3-ara, (8) pt-3-glu, (9) pn-3-gal, (10) pt-3-ara, (11) pn-3-glu, (12) mv-3-gal, (13) pn-3-ara, (14) mv-3-glu, and (15) mv-3-ara.

UHPLC−MS experiments. For this purpose, masses and fragmentations of anthocyanins previously reported were used.[39] For bilberries, the contents of total anthocyanins ranged from 15.9 to 200.1 mg/g of dry weight (DW) and from 4.5 to 26.2 mg/g of DW for lowbush blueberries, respectively (see Table 1 of the Supporting Information). These results are in accordance with previously published concentrations.[30,32,40]

The wide range of concentrations are related to differing extraction conditions. For bilberry, the total amount of anthocyanins using 80% methanol as the extraction solvent is significantly higher than the corresponding amounts after application of 20% methanol. For lyophilized berries, ASE yields a significantly higher anthocyanin amount than the corresponding UAE method. As expected, the anthocyanin contents of lowbush blueberries are considerably lower than those of bilberries. The total anthocyanin contents after extraction of lyophilized berries with 20 and 80% methanol are about 2-fold higher using ASE compared to UAE, respectively. With regard to the extraction solvent, the extraction with 80% methanol leads to higher total anthocyanin amounts than the respective extraction with 20% methanol.

Differences in Anthocyanin Profiles of Bilberries. Anthocyanin profiles indicated by the percentage of each compound contributing to the sum of all anthocyanins were used to compare the different extraction methods (see Table 2 of the Supporting Information). To interrelate those methods, correlation coefficients considering the whole anthocyanin profile of all 15 anthocyanins were calculated, leading to high correlations between 0.995 and 0.976. To visualize how the different extraction conditions influence the individual anthocyanins, spider web plots were used. They efficiently reveal the effects of different extraction solvents, techniques, and materials. Figure 2 illustrates these effects for all individual

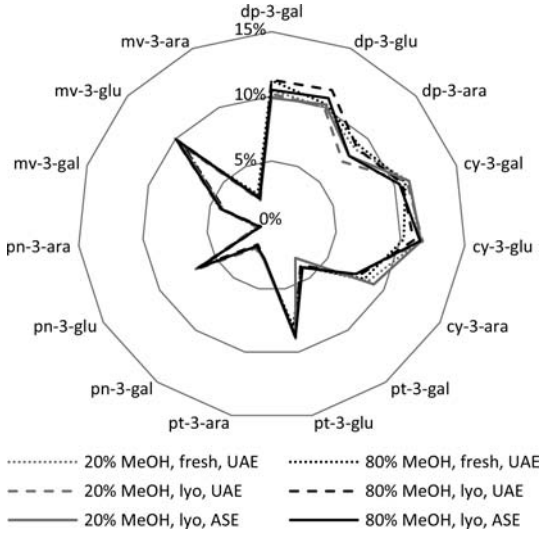

Figure 2. Anthocyanin proportions of bilberry after different extraction methods. UAE, ultrasound-assisted extraction; ASE, accelerated solvent extraction; fresh, fresh berries; and lyo, lyophilized berries.

anthocyanins in bilberry, whereby the aglycones are arranged according to their polarity (dp > cy > pt > pn > mv). It is obvious that the anthocyanins are not affected equally. Although the overall profiles are similar as reflected in good correlation coefficients and the variation of the extraction methods show only little effect especially on less polar anthocyanins, more polar anthocyanins show significant variances. Apparently, the delphinidin glycosides as well as cyanidin glucoside and arabinoside are affected most. In particular, the application of 80% methanol leads to higher delphinidin glycoside proportions, whereas cyanidin glycoside

DOI: 10.1021/acs.jafc.5b02255
J. Agric. Food Chem. 2015, 63, 7532−7538

proportions are lower compared to proportions after the usage of 20% methanol as the extraction solvent. Besides these compounds, which are altered considerably in proportions, other anthocyanins are not subjected to method-induced profile variations. Especially cyanidin and malvidin galactosides as well as petunidin and peonidin arabinosides are not affected significantly by any extraction conditions. It is interesting to note that comparing the results of different extraction conditions to the reference method (80% methanol, fresh berries, UAE), a glycoside-type-derived pattern can be found. Almost all extraction conditions lead to higher proportions of anthocyanin glucosides compared to the reference methods, whereas arabinosides and galactosides tend to show lower relative amounts (see Table 2 of the Supporting Information).

Obviously, the changes in the anthocyanin profile as affected by the extraction method are inconsistent and show different variabilities. Moreover, a trend toward greater variabilities in terms of more polar anthocyanins of bilberries can be observed. Consequently, the differing patterns exhibit that profile changes are caused by different extraction techniques (ASE versus UAE) as well as by different solvent composition (20 versus 80% methanol).

Differences in Anthocyanin Profiles of Lowbush Blueberries. The anthocyanin profiles of lowbush blueberries were used to interrelate the effects of all six extraction methods. They showed good correlations between 0.906 and 0.998, which means that the anthocyanin profiles are very similar. However, the variabilities of all individual anthocyanins are not homogeneous, meaning that all anthocyanins are individually affected (Figure 3). While dp glycosides reveal significantly

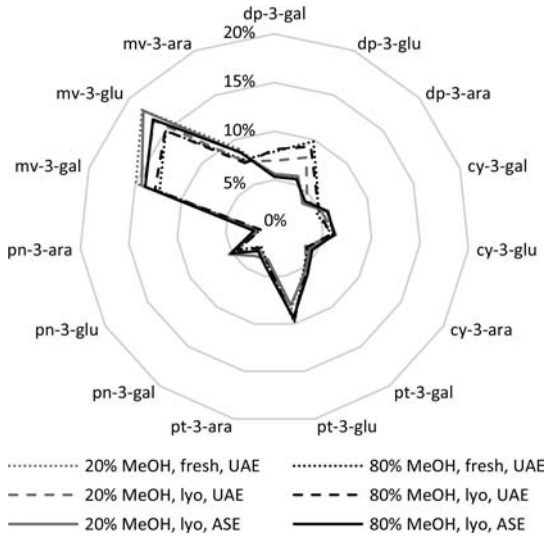

Figure 3. Anthocyanin proportions of lowbush blueberry after different extraction methods. UAE, ultrasound-assisted extraction; ASE, accelerated solvent extraction; fresh, fresh berries; and lyo, lyophilized berries.

higher proportions after UAE compared to ASE, all other anthocyanins are either not affected or show lower proportions. With regard to equal extraction techniques with different solvents, it can be stated that, in terms of ASE, the pt glucoside proportion is significantly higher and mv glucoside is significantly lower when 80% methanol is used instead of 20% methanol. In contrast, the application of 80% methanol in UAE leads to higher dp glycoside and lower mv glycoside proportions than the usage of 20% methanol. The extraction of fresh berry material shows the same trend to a greater extent considering the extraction solvent effects. These results reveal that individual anthocyanins are differently affected by different extraction methods. Apparently, dp as the most polar and mv as the most abundant aglycones are affected most in lowbush blueberries as the variability between all extraction methods reveals. In contrast, proportions of all other aglycones seem to be much more robust against method variations (see Table 2 of the Supporting Information).

Interestingly, the individual differences of lowbush blueberry anthocyanins are not in line with those of the individual differences determined for bilberry anthocyanins. Obviously, profile variations as a result of differing extraction methods are plant-dependent and not generally consistent and, thus, not predictable.

Anthocyanin Contents of American Cranberry in UAE and ASE Extracts. Six major anthocyanins in American cranberry were identified by their absorption spectra, order of elution, and characteristic fragmentation patterns.[39] They were individually quantified after application of the two extraction methods and solvents. The contents of total anthocyanin range from 1.51 to 2.20 mg/g of DW, which is in accordance with the results described by Pappas and Schaich (see Table 1 of the Supporting Information).[18]

Differences in Anthocyanin Profiles of American Cranberry after ASE and UAE. The application of ASE and UAE with different extraction solvents results in very similar anthocyanin yields, whereas slightly higher contents were obtained via ASE and 80% methanol.

Even the anthocyanin profiles are very similar, indicated by very high correlation coefficients between 0.994 and 0.997 (Figure 4). Nevertheless, the post-hoc analysis shows significant differences as a result of very low standard deviations of each method. When 80% methanol is used instead of 20% methanol, a significant decrease in the cy galactoside proportion during ASE and an increased cy arabinoside proportion via UAE can be observed. These differences can only be noticed for fresh fruits. The anthocyanin profile of lyophilized berry material is

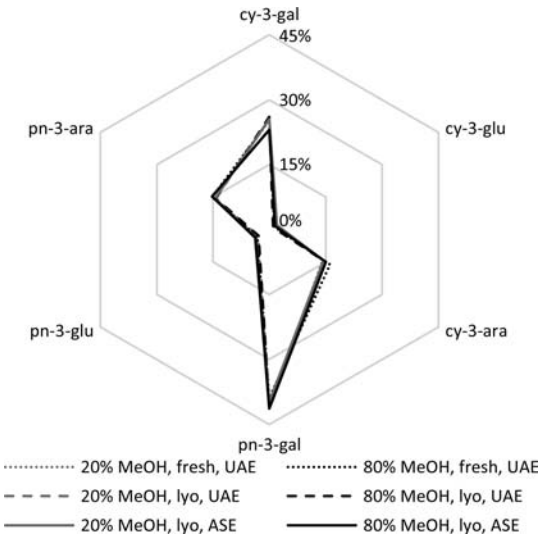

Figure 4. Anthocyanin proportions of American cranberry after different extraction methods. UAE, ultrasound-assisted extraction; ASE, accelerated solvent extraction; fresh, fresh berries; and lyo, lyophilized berries.

DOI: 10.1021/acs.jafc.5b02255
J. Agric. Food Chem. 2015, 63, 7532−7538

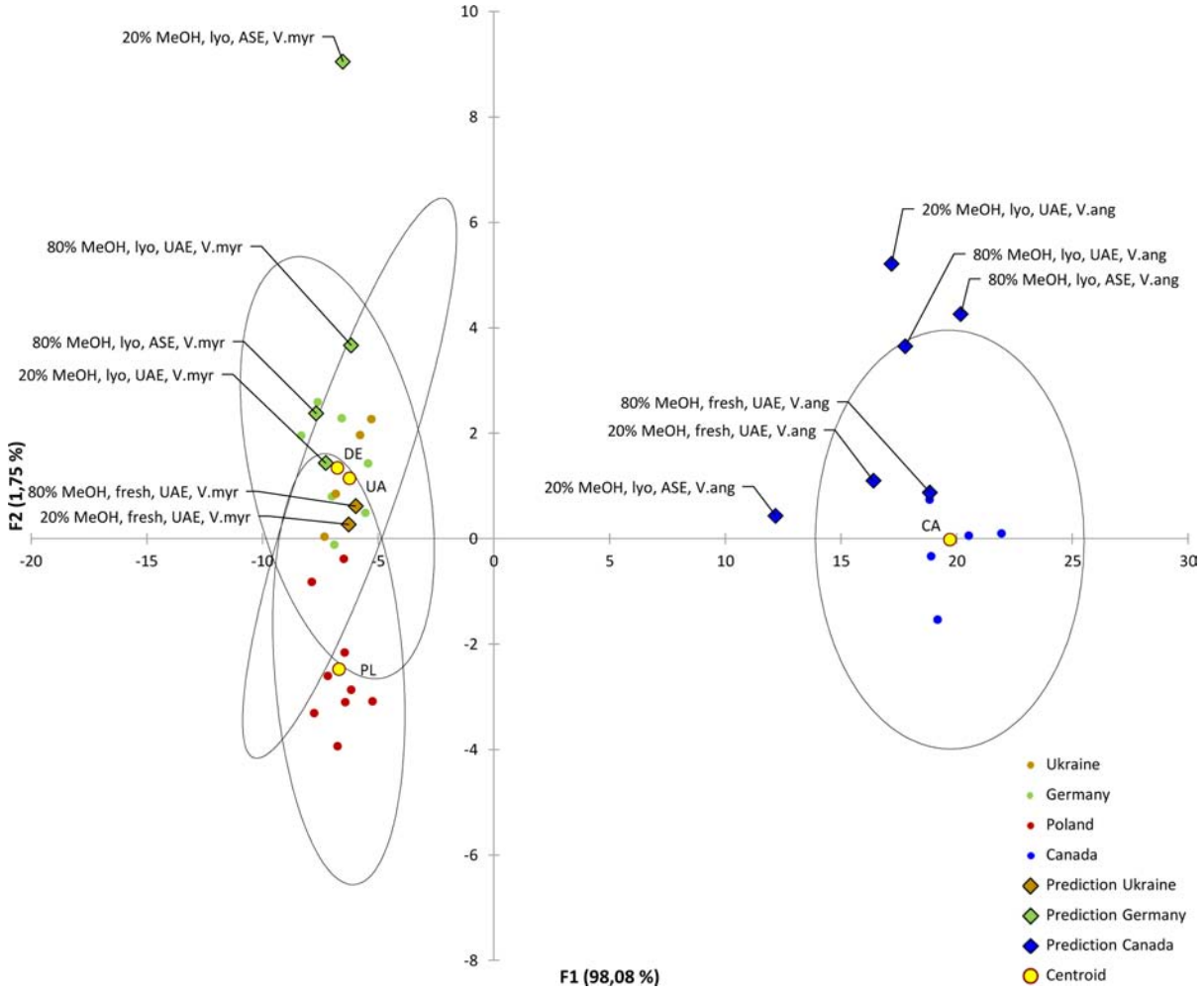

Figure 5. LDA of bilberry and lowbush blueberry samples from different origins extracted under reference conditions (80% methanol, fresh berries, UAE) and prediction of samples extracted under various extraction conditions. UAE, ultrasound-assisted extraction; ASE, accelerated solvent extraction; fresh, fresh berries; and lyo, lyophilized berries.

not affected by the extraction solvent using UAE. Therefore, the effects of the investigated extraction methods on the anthocyanin profile of American cranberry seem to be negligible.

Differences in Anthocyanin Profiles of Bilberries and Lowbush Blueberries from Various Origins. Because authenticity data are often based on specific profiles of individual compounds, the acquisition of the corresponding data has to be reproducible and should ensure good comparability. Several studies investigated whether there are typical fingerprints according to varieties,[31] geographical origins,[19,41,42] and climatic conditions.[43] Some of these authors showed that botanical differences and external factors could be correlated to ratios of certain individual compounds. It could be of great interest to interrelate such findings, performing a meta-analysis. However, the comparison might be critical, because different extraction methods were applied.

To classify the profile variations induced by different extraction methods, 21 bilberry (*V. myrtillus*) cultivars from Germany, Poland, and Ukraine as well as 5 lowbush blueberry (*V. angustifolium*) cultivars from Canada were analyzed. The average total anthocyanin content in bilberries from Germany, Poland, and Ukraine was 6.0 ± 0.3, 6.4 ± 0.8, and 5.2 ± 0.6 mg/g of fresh weight (FW), respectively. Canadian lowbush blueberries had a total anthocyanin content of 1.5 ± 0.2 mg/g of FW. To obtain comparable anthocyanin profiles, this set of authentic samples was extracted with the reference method applying UAE with 80% methanol on fresh berries (see Table 3 of the Supporting Information). For evaluation of the results, linear discriminant analysis (LDA) was performed. The LDA subdivides the multivariate space in as many subspaces as previous classes (CA, DE, PL, and UA) were defined. The resulting orthogonal discriminant functions are linear combinations with a maximized between class variance and a minimized within class variance. Figure 5 shows the result of a two-dimensional LDA of the authentic data set. It is obvious that samples from Canada related to the species *V. angustifolium* can be easily discriminated along F1 (explaining 98.08% of the total variances) from the group of European samples related to the species *V. myrtillus*. However, the samples from Germany, Poland, and Ukraine cannot be separated well. A slight differentiation along F2 can be observed, but the interclass variances are too high, leading to overlapping confidence ellipses. As seen in Table 3 of the Supporting Information, dp and cy glycosides show the greatest variations, while pt glycosides reveal the most consistent proportions. This may be of interest if authenticity markers shall be chosen from the anthocyanin profile. Compounds that are incorporated in

DOI: 10.1021/acs.jafc.5b02255
J. Agric. Food Chem. 2015, 63, 7532−7538

constant amounts should be preferred to those that are constrained to natural fluctuations to obtain robust authenticity information. In addition, high variances between samples of the same species but different growing conditions prove that geological factors as well as climate conditions apparently influence the biosynthesis of anthocyanins and, thus, the profiles. However, the results obtained from the data set analyzed also show that anthropogenic borders do not need to go along with these differences. Therefore, a differentiation of European samples solely based on the anthocyanin profile is barely reasonable.

Extraction Method Induced Profile Variations versus Natural Variations. As mentioned above, anthocyanin profiles are subjected to considerable variations as a result of different extraction conditions. To assess the relevance of these variations, the results of the application of different extraction methods have to be evaluated in the context of naturally occurring between species differences and interspecies variances. As the different extraction methods were applied to a Ukrainian *V. myrtillus* and a Canadian *V. angustifolium* sample, the anthocyanin profiles obtained were assigned to one of the classes of the discriminant analysis derived from the authentic data set using the prediction of the discriminant function. It becomes apparent that samples extracted under reference conditions are assigned correctly and are located close to the centroid of the respective class, which validates the discriminant function. Anthocyanin profiles of samples extracted under non-reference conditions, however, vary widely, indicating considerable method effects. In terms of the predicted Ukrainian samples, only those samples extracted from fresh berries are assigned to the correct origin. Here, it has to be stressed that the calculated discriminant function is not capable of differentiating the different European origins but allocate only samples to the species *V. myrtillus* or *V. angustifolium*. The method-dependent variations are so predominant that some predictions even fall out of the respective area of confidence, meaning that they cannot be assigned to one of the classes with a probability greater than 95%. Especially samples extracted under conditions, which differ a lot from the reference conditions, show greater distances from the centroids to which they are supposed to be assigned. Nevertheless, all predictions regarding the species assignment are correct. This is because a discriminant analysis only enables a "hard" classification, meaning that a predicted sample must be assigned to the most likely class, independent from how low the probability.

In conclusion, the current study addresses one of the crucial problems regarding the comparability of authenticity data sets. Different techniques and solvents applied for the extraction of bilberry, lowbush blueberry, and American cranberry anthocyanins resulted in considerably altered yields and peak ratios. In particular, peak proportions of more polar compounds, such as dp and cy, were affected by the applied extraction conditions, whereas other compounds, such as pt glycosides, are only marginally influenced.

Comparing the differences caused by the extraction method to the natural differences within a set of 26 bilberry and lowbush blueberry samples of different origins revealed that profile variations induced by the extraction method are in a similar scale to profile variations as a result of geographic and climatic differences. LDA could not differentiate between bilberry samples of different European origins, but prediction models allocated differently extracted samples outside of the area of confidence. Application of different methods for the extraction could lead to a false allocation of samples. On the one hand, samples with a very similar genuine profile could be considered as different. On the other hand, actually different samples could erroneously be allocated as similar.

Possible correlations between anthocyanin profiles and individual origins may not be accounted for by assumed intrinsic profile differences but rather reasoned on disparate sample preparations. Furthermore, the results for the different fruits are not completely consistent regarding the resulting profile differences after ASE and UAE and, hence, do not inevitably demonstrate systematic differences between the investigated extraction methods but rather illustrate plant-specific differences. In view of these results, a cautious review not only of the analytical methods but also of the sample preparation applied, in particular extraction methods, is a prerequisite for the reliable comparison of analytical data in general and authenticity data in particular.

■ ASSOCIATED CONTENT

Supporting Information

The Supporting Information is available free of charge on the ACS Publications website at DOI: 10.1021/acs.jafc.5b02255.

Anthocyanin proportions of individual anthocyanins resulting from all extraction parameters and origins (Tables 1−3) (PDF)

■ AUTHOR INFORMATION

Corresponding Author

*Telephone: +49-228-734462. Fax: +49-0-228-734429. E-mail: fabian.weber@uni-bonn.de.

Funding

This research project was financially supported by the German Ministry of Economics and Technology (via AiF) and the Forschungskreis der Ernährungsindustrie e.V., Bonn (FEI), Project AiF 16645N.

Notes

The authors declare no competing financial interest.

■ ACKNOWLEDGMENTS

The authors gratefully thank Haus Rabenhorst O. Lauffs GmbH & Co. KG, Rudolf Wild GmbH & Co. KG, and Faethe Labor GmbH for providing the berry material.

■ ABBREVIATIONS USED

ara, arabinoside; ASE, accelerated solvent extraction; cy, cyanidin; dp, delphinidin; DW, dry weight; FW, fresh weight; gal, galactoside; glu, glucoside; mv, malvidin; pn, peonidin; pt, petunidin; UAE, ultrasound-assisted extraction

■ REFERENCES

(1) El Gharras, H. Polyphenols: food sources, properties and applications - a review. *Int. J. Food Sci. Technol.* **2009**, *44*, 2512−2518.

(2) Motilva, M.-J.; Serra, A.; Macià, A. Analysis of food polyphenols by ultra high-performance liquid chromatography coupled to mass spectrometry: An overview. *J. Chromatogr. A* **2013**, *1292*, 66−82.

(3) Arts, I. C. W.; Hollman, P. C. H. Polyphenols and disease risk in epidemiologic studies. *Am. J. Clin. Nutr.* **2005**, *81*, 317S−325S.

(4) Dai, Q. I.; Borenstein, A. R.; Wu, Y.; Jackson, J. C.; Larson, E. B. Fruit and vegetable juices and Alzheimer's disease: the Kame project. *Am. J. Med.* **2006**, *119*, 751−759.

DOI: 10.1021/acs.jafc.5b02255
J. Agric. Food Chem. 2015, 63, 7532−7538

(5) Hooper, L.; Kroon, P. A.; Rimm, E. B.; Cohn, J. S.; Harvey, I.; Le Cornu, K. A.; Ryder, J. J.; Hall, W. L.; Cassidy, A. Flavonoids, flavonoid-rich foods, and cardiovascular risk: A meta-analysis of randomized controlled trials. *Am. J. Clin. Nutr.* **2008**, *88*, 38−50.
(6) Pan, M.-H.; Lai, C.-S.; Ho, C.-T. Anti-inflammatory activity of natural dietary flavonoids. *Food Funct.* **2010**, *1*, 15.
(7) de Pascual-Teresa, S.; Moreno, D. A.; García-Viguera, C. Flavanols and anthocyanins in cardiovascular health: A review of current evidence. *Int. J. Mol. Sci.* **2010**, *11*, 1679−1703.
(8) Scalbert, A.; Andres Lacueva, C.; Arita, M.; Kroon, P.; Manach, C.; Urpi-Sarda, M.; Wishart, D. Databases on food phytochemicals and their health-promoting effects. *J. Agric. Food Chem.* **2011**, *59*, 4331−4348.
(9) Abad-García, B.; Berrueta, L. A.; Garmón-Lobato, S.; Urkaregi, A.; Gallo, B.; Vicente, F. Chemometric characterization of fruit juices from Spanish cultivars according to their phenolic compound contents: I. Citrus fruits. *J. Agric. Food Chem.* **2012**, *60*, 3635−3644.
(10) Fügel, R.; Carle, R.; Schieber, A. Quality and authenticity control of fruit purées, fruit preparations and jams - a review. *Trends Food Sci. Technol.* **2005**, *16*, 433−441.
(11) Häkkinen, S.; Heinonen, M.; Kärenlampi, S.; Mykkänen, H.; Ruuskanen, J.; Törrönen, R. Screening of selected flavonoids and phenolic acids in 19 berries. *Food Res. Int.* **1999**, *32*, 345−353.
(12) Jungfer, E.; Zimmermann, B. F.; Ruttkat, A.; Galensa, R. Comparing procyanidins in selected *Vaccinium* species by UHPLC-MS^2 with regard to authenticity and health effects. *J. Agric. Food Chem.* **2012**, *60*, 9688−9696.
(13) Schieber, A.; Keller, P.; Streker, P.; Klaiber, I.; Carle, R. Detection of isorhamnetin glycosides in extracts of apples (*Malus domestica* cv. "Brettacher") by HPLC-PDA and HPLC-APCI-MS/MS. *Phytochem. Anal.* **2002**, *13*, 87−94.
(14) Zhang, Y.; Krueger, D.; Durst, R.; Lee, R.; Wang, D.; Seeram, N.; Heber, D. International multidimensional authenticity specification (IMAS) algorithm for detection of commercial pomegranate juice adulteration. *J. Agric. Food Chem.* **2009**, *57*, 2550−2557.
(15) Filip, M.; Vlassa, M.; Copaciu, F.; Coman, V. Identification of anthocyanins and anthocyanidins from berry fruits by chromatographic and spectroscopic techniques to establish the juice authenticity from market. *J. Planar Chromatogr.–Mod. TLC* **2012**, *25*, 534−541.
(16) Cho, M. J.; Howard, L. R.; Prior, R. L.; Clark, J. R. Flavonoid glycosides and antioxidant capacity of various blackberry, blueberry and red grape genotypes determined by high-performance liquid chromatography/mass spectrometry. *J. Sci. Food Agric.* **2004**, *84*, 1771−1782.
(17) Kalt, W.; Forney, C. F.; Martin, A.; Prior, R. L. Antioxidant capacity, vitamin C, phenolics, and anthocyanins after fresh storage of small fruits. *J. Agric. Food Chem.* **1999**, *47*, 4638−4644.
(18) Pappas, E.; Schaich, K. M. Phytochemicals of cranberries and cranberry products: characterization, potential health effects, and processing stability. *Crit. Rev. Food Sci. Nutr.* **2009**, *49*, 741−781.
(19) Primetta, A. K.; Jaakola, L.; Ayaz, F. A.; Inceer, H.; Riihinen, K. R. Anthocyanin fingerprinting for authenticity studies of bilberry (*Vaccinium myrtillus* L.). *Food Control* **2013**, *30*, 662−667.
(20) Leahy, M.; Speroni, J.; Starr, M. Latest developments in cranberry health research. *Pharm. Biol. (London, U. K.)* **2002**, *40*, 50−54.
(21) Obón, J. M.; Díaz-García, M. C.; Castellar, M. R. Red fruit juice quality and authenticity control by HPLC. *J. Food Compos. Anal.* **2011**, *24*, 760−771.
(22) Ignat, I.; Volf, I.; Popa, V. I. A critical review of methods for characterisation of polyphenolic compounds in fruits and vegetables. *Food Chem.* **2011**, *126*, 1821−1835.
(23) Wang, L.; Weller, C. L. Recent advances in extraction of nutraceuticals from plants. *Trends Food Sci. Technol.* **2006**, *17*, 300−312.
(24) Azmir, J.; Zaidul, I.; Rahman, M. M.; Sharif, K. M.; Mohamed, A.; Sahena, F.; Jahurul, M.; Ghafoor, K.; Norulaini, N.; Omar, A. Techniques for extraction of bioactive compounds from plant materials: A review. *J. Food Eng.* **2013**, *117*, 426−436.
(25) Doktycz, S.; Suslick, K. Interparticle collisions driven by ultrasound. *Science* **1990**, *247*, 1067−1069.
(26) Richter, B. E.; Jones, B. A.; Ezzell, J. L.; Porter, N. L.; Avdalovic, N.; Pohl, C. Accelerated solvent extraction: A technique for sample preparation. *Anal. Chem.* **1996**, *68*, 1033−1039.
(27) Monrad, J. K.; Howard, L. R.; King, J. W.; Srinivas, K.; Mauromoustakos, A. Subcritical solvent extraction of anthocyanins from dried red grape pomace. *J. Agric. Food Chem.* **2010**, *58*, 2862−2868.
(28) Santos, D. T.; Veggi, P. C.; Meireles, M. A. A. Optimization and economic evaluation of pressurized liquid extraction of phenolic compounds from jabuticaba skins. *J. Food Eng.* **2012**, *108*, 444−452.
(29) Arapitsas, P.; Sjöberg, P. J.; Turner, C. Characterisation of anthocyanins in red cabbage using high resolution liquid chromatography coupled with photodiode array detection and electrospray ionization-linear ion trap mass spectrometry. *Food Chem.* **2008**, *109*, 219−226.
(30) Lätti, A. K.; Riihinen, K. R.; Kainulainen, P. S. Analysis of anthocyanin variation in wild populations of bilberry (*Vaccinium myrtillus* L.) in Finland. *J. Agric. Food Chem.* **2008**, *56*, 190−196.
(31) Müller, D.; Schantz, M.; Richling, E. High performance liquid chromatography analysis of anthocyanins in bilberries (*Vaccinium myrtillus* L.), blueberries (*Vaccinium corymbosum* L.), and corresponding juices. *J. Food Sci.* **2012**, *77*, C340−C345.
(32) Nicoue, E. É.; Savard, S.; Belkacemi, K. Anthocyanins in wild blueberries of quebec: Extraction and identification. *J. Agric. Food Chem.* **2007**, *55*, 5626−5635.
(33) Kalt, W.; McDonald, J. E.; Donner, H. Anthocyanins, phenolics, and antioxidant capacity of processed lowbush blueberry products. *J. Food Sci.* **2000**, *65*, 390−393.
(34) Juadjur, A.; Winterhalter, P. Development of a novel adsorptive membrane chromatographic method for the fractionation of polyphenols from bilberry. *J. Agric. Food Chem.* **2012**, *60*, 2427−2433.
(35) Prior, R. L.; Lazarus, S. A.; Cao, G.; Muccitelli, H.; Hammerstone, J. F. Identification of procyanidins and anthocyanins in blueberries and cranberries (*Vaccinium* Spp.) using high-performance liquid chromatography/mass spectrometry. *J. Agric. Food Chem.* **2001**, *49*, 1270−1276.
(36) Díaz-García, M.; Obón, J.; Castellar, M.; Collado, J.; Alacid, M. Quantification by UHPLC of total individual polyphenols in fruit juices. *Food Chem.* **2013**, *138*, 938−949.
(37) Yamamoto, M.; Yamaura, K.; Ishiwatari, M.; Shimada, M.; Kado, S.; Seki, H.; Shimada, N.; Ueno, K. Degradation index for quality evaluation of commercial dietary supplements of bilberry extract. *J. Food Sci.* **2013**, *78*, S477−S483.
(38) Faria, A.; Oliveira, J.; Neves, P.; Gameiro, P.; Santos-Buelga, C.; de Freitas, V.; Mateus, N. Antioxidant properties of prepared blueberry (*Vaccinium myrtillus*) extracts. *J. Agric. Food Chem.* **2005**, *53*, 6896−6902.
(39) Wu, X.; Prior, R. L. Systematic identification and characterization of anthocyanins by HPLC-ESI-MS/MS in common foods in the United States: fruits and berries. *J. Agric. Food Chem.* **2005**, *53*, 2589−2599.
(40) Dinkova, R.; Heffels, P.; Shikov, V.; Weber, F.; Schieber, A.; Mihalev, K. Effect of enzyme-assisted extraction on the chilled storage stability of bilberry (*Vaccinium myrtillus* L.) anthocyanins in skin extracts and freshly pressed juices. *Food Res. Int.* **2014**, *65*, 35−41.
(41) Åkerström, A.; Jaakola, L.; Bång, U.; Jäderlund, A. Effects of latitude-related factors and geographical origin on anthocyanidin concentrations in fruits of *Vaccinium myrtillus* L. (bilberries). *J. Agric. Food Chem.* **2010**, *58*, 11939−11945.
(42) Rieger, G.; Müller, M.; Guttenberger, H.; Bucar, F. Influence of altitudinal variation on the content of phenolic compounds in wild populations of *Calluna vulgaris*, *Sambucus nigra*, and *Vaccinium myrtillus*. *J. Agric. Food Chem.* **2008**, *56*, 9080−9086.
(43) Hohtola, A.; Jaakola, L.; Määttä-Riihinen, K.; Kärenlampi, S. Activation of flavonoid biosynthesis by solar radiation in bilberry (*Vaccinium myrtillus* L.) leaves. *Planta* **2004**, *218*, 721−728.

DOI: 10.1021/acs.jafc.5b02255
J. Agric. Food Chem. 2015, 63, 7532−7538

evidenced between whole cells and cell walls. Seed and skin tannins exhibited a high affinity for whole yeast cells, associated with high adsorption levels (between 300 and 700 mg g^{-1} for average degree of polymerization (aDP) 21 skin tannins) and low reversibility (about 20%). By contrast, adsorption remained very low and mostly reversible with cell walls (on the order of 50 mg g^{-1} for aDP 21 skin tannins, with 60% reversibility). Experiments were repeated with red wine polyphenols. Adsorption primarily concerned oligomeric and polymeric tannins and pigments. That of monomers was very small. Once again, wine tannin and pigment sorption strongly differed between whole cells and cell walls, with maximum adsorbed amounts around 350 and 20−30 mg g^{-1}, respectively. This last point was quite unexpected and led us to wonder about the exact part played by cell walls in the adsorption of wine polyphenols. We suggested that grape and wine tannins, even those with high molecular weight, were able to diffuse quite easily through the wall network of dead cells and that the differences observed were related to their accumulation in the periplasmic space and/or their interactions with cell membrane.

The aim of the present work was to identify the location of polyphenol compounds in yeast cells. This was achieved through scanning electron microscopy, light epifluorescence, and confocal microscopy.

MATERIALS AND METHODS

Purification of Grape Skin Tannins and Red Wine Polyphenols. The grape skin tannin fraction was extracted from the skin of Muscat berries according to the procedure proposed by Mane.[20] It was further purified by extractions with hexane, followed by adsorption on a styrene/divinylbenzene Diaion resin and chromatography on a Toyopearl TSK HW-50 (F) gel (Tosoh Corp., Tokyo, Japan), as described in detail previously.[19] This procedure allowed the recovery of a high molecular weight tannin fraction, which was freeze-dried and stored at −80 °C before use. The composition of the fraction was determined by UPLC after acid-catalyzed cleavage in the presence of thioglycolic acid.[21] Its mean degree of polymerization was 20.1 ± 0.7, and its percentage of epigallocatechin units was 16.8 ± 1.2%. The yield of the depolymerization reaction was 73.9%. This fraction was named skin21.

The red wine polyphenol fraction (WP) was purified from a Merlot wine by chromatography on a styrene/divinylbenzene Diaion resin and analyzed as detailed in our previous work.[19] This fraction contained residual polysaccharides and nitrogenous compounds, which represented about 15% of the dry weight. Its polyphenol composition was as follows: 29.3 mg g^{-1} anthocyanins, 7.7 mg g^{-1} flavan-3-ol monomers, 32.7 mg g^{-1} phenolic acids, 24.2 mg g^{-1} stilbenes, 5.9 mg g^{-1} flavonols, and 95.0 mg g^{-1} tannins. The average degree of polymerization and composition of the tannins, determined by phloroglucinolysis, were aDP, 7.3 ± 1.1; epigallocatechin units (EgC), 24.2 ± 2.3%; and epicatechin-gallate (Ec-G), 3.3 ± 0.3%. The yield of the depolymerization reaction was very low (around 13%). This was attributed to the presence in this fraction of a large amount of derived pigments and tannins. The latter are formed by chemical reactions during winemaking and aging and are resistant to usual depolymerization methods.[1,21,22]

Yeast Cells and Preparation of Yeast Cell Walls. The yeast strain used was a commercial *S. cerevisiae* strain (Lallemand, Montreal, Canada), commonly used in enology. The yeast biomass (Y), the inactivated yeast (IY), and the yeast inactivated after autolysis (A-IY) were produced by the manufacturer according to the protocols described previously.[19] The yeast biomass was produced in aerobic conditions. Part of this biomass was frozen at −20 °C and conserved as such until further use. The viability of the cells was determined before interaction experiments. Results obtained by flow cytometry (1%) and growth on Petri plates (2.4%) indicated that most cells in Y were dead. Another part of the biomass (IY) was inactivated by thermal treatment (70 °C, 15 min). The last part (A-IY) was first submitted to autolysis (pH 5.5 at 55 °C for 20 h), and cells were recovered by centrifugation and inactivated in the same conditions as IY. Both IY and A-IY were spray-dried and stored at 4 °C. Cell walls (CW) were purified at the laboratory from the biomass Y by mechanical disruption,[19] according to the protocol described by Dallies et al.[23] The cell wall suspension obtained was heated (72 °C, 15 min) to remove residual enzymatic activities. The suspension was then stored at 4 °C in the presence of sodium azide (0.02% w/v) until use. Cell walls represented around 20% of the whole cell dry weight, which was in accordance with literature data.[24,25] Neutral sugars represented 80% of their dry weight, and Kjeldahl analyses indicated a nitrogen content of about 2% (w/w).

Sorption Experiments. Suspensions were prepared as described in Mekoue Nguela et al.[19] Briefly, yeast cells (Y, IY, or A-IY) (2×10^8 cells mL^{-1}) or yeast cell walls (CW) (0.88 mg mL^{-1}) were suspended in a model wine (12% ethanol, 2 g L^{-1} tartaric acid, 50 mM NaCl, pH adjusted to 3.5 with KOH, 25 mg L^{-1} SO_2). An equal volume of grape skin tannins or wine polyphenol pool solution (8 mg mL^{-1} in model wine) was added to yeast cells or yeast cell wall suspensions, and the mixtures were gently stirred for 24 h. Suspensions were then centrifuged and the pellets recovered. Centrifugation conditions were 1500*g* for 5 min at 5 °C and 10000*g* for 5 min at 5 °C for yeast whole cells and cell walls, respectively. Pellets were washed four times with 1 mL of PBS buffer to remove the nonsorbed polyphenols and resuspended in 1 mL of the same buffer. Yeast cells and yeast cell walls suspended in the same conditions in a model wine without polyphenol served as controls.

Light and Epifluorescence Microscopy. Samples and controls were observed under normal light and epifluorescence. Imaging was performed with a Zeiss Axiophot microscope using a DAPI filter (DAPI = 4′6-diamidino-2-phenylindole; λ_{exc} = 340−380 nm, λ_{em} = 425−800 nm).

Confocal Microscopy. Confocal imaging was performed with a Zeiss Axiovert microscope 200 M 510 META fitted with a Plan-Apochromat ×40/1.2 W Zeiss objective. Excitations were obtained for tannins with a 405 nm blue diode, and emissions were collected for tannins with a (505−550 nm bandpass) filter.[26] For images acquired in lambda scanning mode, the emission spectra were obtained on sample regions of interest (ROIs) by spectral acquisition (lambda stack, excitation at 405 nm). The detection bandwidth was set to collect emissions from 400 to 750 nm, using an array of 32 photomultiplier tube (PMT) detectors, each with a 10.7 nm bandwidth. The method of linear unmixing was applied with advanced iterative and one residual channel.

Transmission Electron Microscopy (TEM). PBS was removed from the samples and controls, and the pellets were resuspended in a solution of 2% acrolein and 2% glutaraldehyde in cacodylate buffer (0.05 M, pH 7) for 12 h at 4 °C.[27] They were then rinsed several times in cacodylate buffer and postfixed in a 1% osmic acid for 2 h in the dark and at room temperature. After two rinses in cacodylate buffer, the samples were dehydrated in a graded series of acetone solutions (30−100%) at room temperature. They were then embedded in EmBed 812 using automated microwave tissue processor for electronic microscopy (Leica EM AMW). Thin sections (70 nm; Leica-Reichert Ultracut E) were collected at different levels of each block. These sections were stained sequentially with uranyl acetate and lead citrate. They were then observed using a Hitachi 7100 transmission electron microscope with 75 kV accelerating voltage in the Centre de Ressources en Imagerie Cellulaire de Montpellier (France).

RESULTS AND DISCUSSION

Epifluorescence and Confocal Microscopy. Untreated yeast cells (Y) were observed in light microscopy (Figure 1A) as regular spheres (average diameter = 3 μm). Yeast cells after contact with grape skin tannins (treated cells) showed the same morphology as untreated cells and formed stacks (Figure 1B). Untreated yeast cells exhibited no fluorescence (Figure 1C), whereas treated ones fluoresced strongly in blue (Figure 1D).

DOI: 10.1021/acs.jafc.5b02241
J. Agric. Food Chem. 2015, 63, 7539−7545

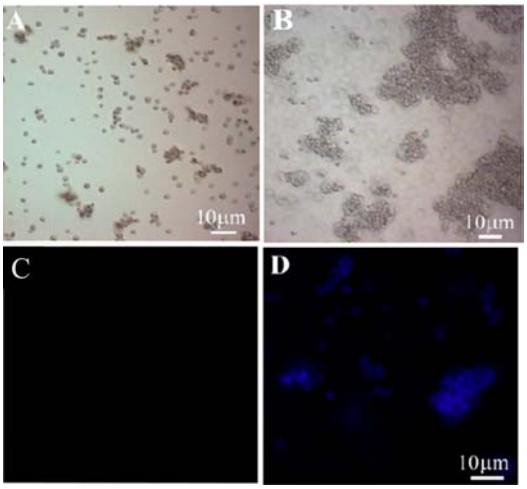

Figure 1. Views of untreated (A, C) and treated (B, D) yeast cells with grape skin tannins under light and epifluorescence microscopy (λ_{exc} = 340−380 nm, λ_{em} = 425−800 nm).

This fluorescence was within the range of that of tannins in the applied experimental conditions.

Confocal microscopy was performed on yeast cells (Y), inactivated yeasts (IY, A-IY), and yeast cell walls (CW) (Figure 2). Untreated yeast cells and inactivated yeasts showed an extremely faint and almost invisible blue fluorescence; the same was observed for purified cell walls (Figure 2). After contact with skin21 (grape skin tannins), yeast cells and inactivated yeasts showed an intense blue fluorescence in their inner core (Figure 2); some plasmolyzed cells were observed with Y, and they showed, in addition to their fluorescent core, a corona fluorescing in blue. Cell walls exhibited a blue fluorescence and were devoid of internal content. With Y and CW, some scarce residual fluorescent cytoplasmic elements were observed (Figure 2). An examination of treated cells (Y) by confocal spectral analysis revealed particles (diameter = 3 μm) (Figure 3A) exhibiting an autofluorescence emission spectrum (Figure 3B) with several maxima in the 500−600 nm range. Spectral analysis of this fluorescence in comparison with purified grape tannins[26] indicated this was due to tannins.

Thus, after contact with skin21, the yeast biomass (Y) and the inactivated yeasts (IY and A-IY) showed a strong blue fluorescence in their cytoplasm. This indicated the presence of tannins inside the cells. Another site of fluorescence, the cell wall, was identified on plasmolyzed cells and purified cell walls.

Transmission Electron Microscopy. TEM was performed on yeast cell biomass (Y) and yeast cell wall (CW) without and after contact with grape skin tannins (Figure 4) or with wine polyphenol pool (Figure 5). Untreated yeast cells (Y) appeared typical, in comparison with published TEM images[28−30] being spherical and with the electron-dense fibrillary network of the cell wall (thickness = 200 nm) evident (Figures 4A−C and 5A−C). At higher magnification (Figures 4B,C and 5B,C), the distinction of regions within the cell wall became evident. Yeast cell wall is described as a two-layered structure made of β-(1→3) and β-(1→6)-glucans, mannoproteins, and chitin, which can be covalently linked to form higher order complexes.[25,31] TEM views showed the more electron-dense outer brush-like layer enriched in mannoprotein, over the more electron transparent microfibrillar glucan-rich layer.[30,32] In particular, one must note the regular design of mannoproteins bound to the outer face of the cell wall; it appears as fibers extending from the wall. Within

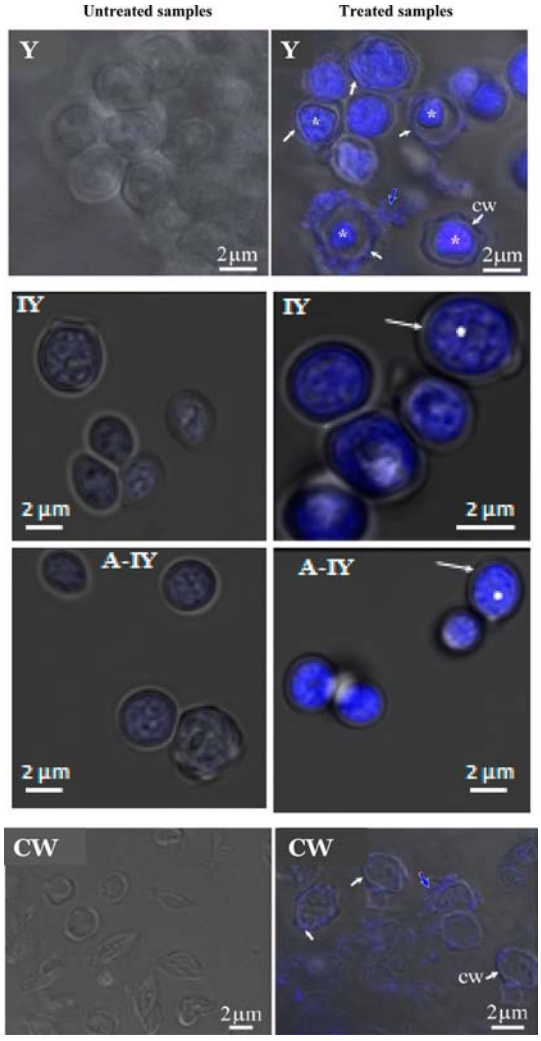

Figure 2. Confocal images of untreated and treated yeast cells (Y, IY, A-IY) and untreated and treated yeast cell walls (CW) with grape skin tannins. Asterisk focuses on fluorescent cytoplasm; white arrows, cell walls; blue arrow, remnants of cytoplasm out of the cells; Y, whole yeast cells; IY, inactivated yeast cells; A-IY, yeast inactivated after autolysis. λ_{exc} = 405 nm, λ_{em} = 505−550 nm.

yeast cells, plasma membrane and ultrastructure granular elements were visible.

Following exposure to grape tannins (Figure 4) or wine polyphenols (Figure 5), cells and cell walls, compared with untreated cells, showed obvious differences at their cell wall and cytoplasm levels. The outer brush-like layer of cell walls appeared as electron-dense aggregated elements (Figures 4D−F and 5D−F). Another major difference was observed in the cytoplasm of polyphenol-treated cells: indeed, and contrary to untreated cells, the entire cytoplasm appeared as highly electron-dense. Finally, at the junction between the cytoplasm and the cell wall, an electron-dense thin layer was visible (Figure 5D−F). The enhanced electron-dense character observed in the outer mannoprotein layer and within the cytoplasm can be attributed to the presence of tannins. Indeed, postfixation of samples for TEM observations was performed with osmic acid, and the tendency of osmium to strongly stain tannins has been evidenced.[26] Whereas the grape skin tannin fraction consists only of flavan-3-ol polymers with an aDP of 21, red wine polyphenols consist of a complex mixture of native

DOI: 10.1021/acs.jafc.5b02241
J. Agric. Food Chem. 2015, 63, 7539−7545

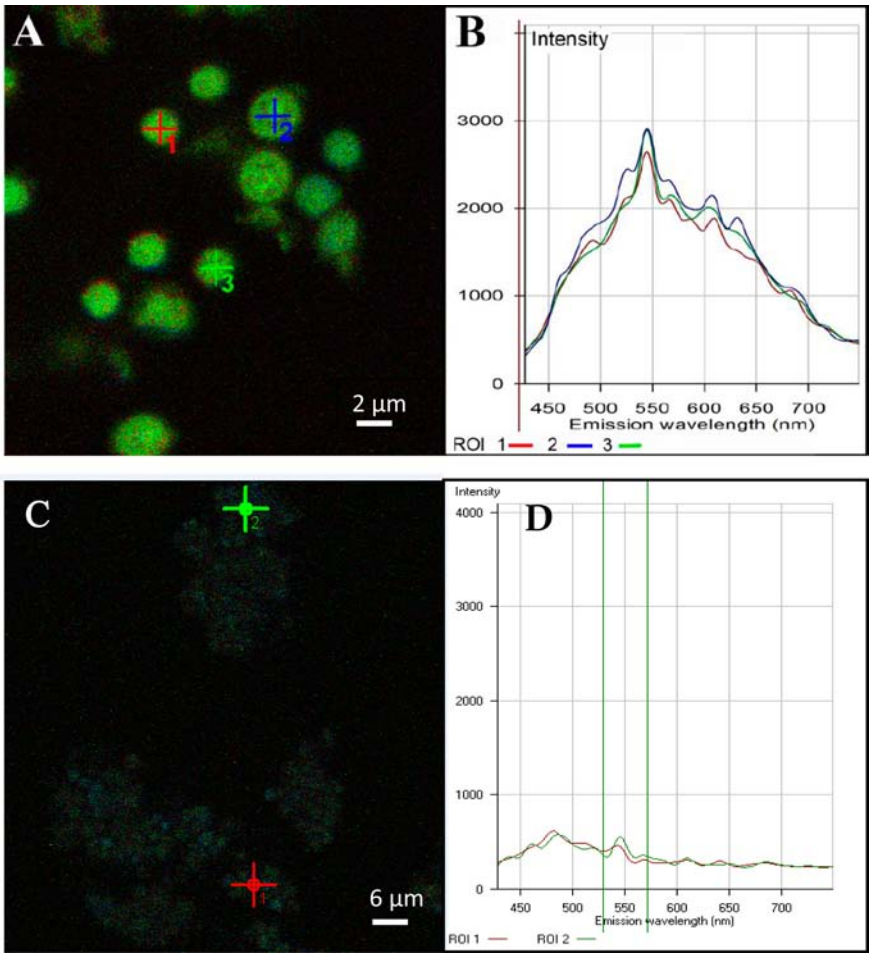

Figure 3. (A) Confocal image of yeast cells treated with grape skin tannins and (B) spectral analysis showing their autofluorescence emission spectrum (λ_{em} = 430−800 nm range), similar to that of grape tannins.[26] ROI, region of interest. (C) Untreated yeast cells (control) and (D) spectral analysis showing their autofluorescence emission spectrum.

polyphenols monomers (mainly phenolic acids, flavanol monomers, and anthocyanins) and tannins, along with so-called derived pigments and tannins formed during wine-making.[1,3,21,22] We evidenced previously that interactions between red wine polyphenols and yeast cells or cell walls mainly concerned oligomeric and polymeric forms.[19] Thus, TEM observations confirmed that interactions between yeast cells and native or derived condensed tannins/pigments occur not only in the cell wall but also with their cytoplasmic components.

Plasmolysis of some yeast cells was helpful for description of interactions between tannins and mannoproteins. On intact cells, mannoproteins bound to the outer face of the plasma membrane were hardly visible, the plasma membrane being stuck to the wall (Figure 5A,B); after contact with tannins, only a fine osmophilic layer appressed between the wall and plasmalemma was visible (Figure 5D−F). After plasmolysis, fine structures were unveiled in the space generated: on treated cells, mannoproteins were seen attached by GP1 anchor (glycosyl-phosphatidylinositol)[25] to the outer face of the plasmalemma (Figure 6A−C). The inner mannoproteins formed large aggregated electron-dense structures still attached through their GPI anchor to the plasmalemma (Figure 6B,D). In this area, we noted that, under the influence of plasmolysis tearing force, the mannoproteins were cleaved, a large proportion remaining attached to the inner face of the wall. Interactions of the plasmalemma proteins with tannins were also well visible on plasmolyzed yeast cells (Figure 6C). The weakly electron-opaque cell wall [mainly β-(1→3)-glucan and chitin] did not show any typical structure.

Tannin and Red Wine Polyphenol Interactions with Dead/Inactivated Yeast Cells and Cell Walls. These results evidenced that interactions between yeast cells and grape or wine tannins are not necessarily limited to cell walls when dealing with dead and/or inactivated cells. Grape tannins and wine tannins/pigments are liable to enter the periplasmic space through the cell wall and to interact with the cell membrane and its cytoplasmic content. According to their average degree of polymerization, a 3 nm average hydrodynamic volume could be estimated for aDP 21:[33] thus, the polysaccharide wall in our study was permeable to molecules of this size. These observations explained the very large differences observed in our previous work[19] between whole cells and cell walls regarding their ability to bind grape and red wine tannins. Indeed, adsorption isotherms evidenced that the amount of polyphenols adsorbed at concentrations corresponding to those found in red wines was about 10-fold higher with whole cells (nonviable yeast biomass and inactivated cells) than with cell walls. In addition, the reversibility of the interactions was also much more important with cell walls.

The property of tannins to form complexes with proteins is well-known.[34,35] Proteins relevant to the yeast wall include

DOI: 10.1021/acs.jafc.5b02241
J. Agric. Food Chem. 2015, 63, 7539−7545

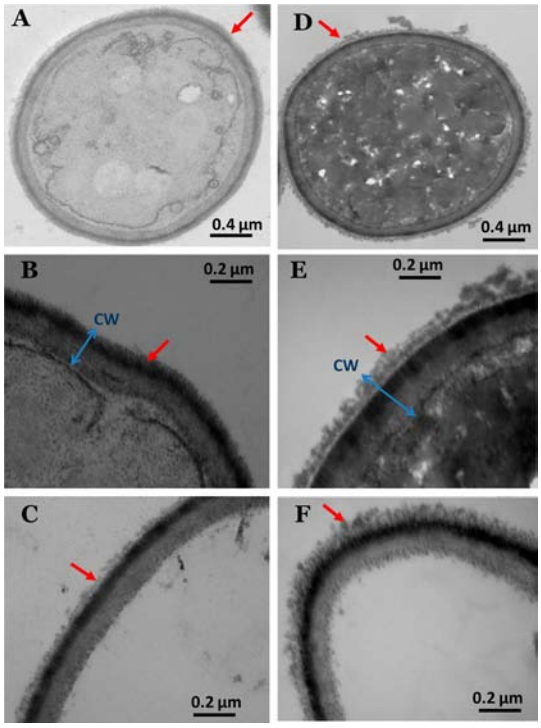

Figure 4. TEM images at diverse magnifications of (A–C) untreated and (D–F) treated yeast cells (Y) and cell walls (CW) with grape skin tannins. Red arrows, mannoproteins; blue arrows, cell wall thickness.

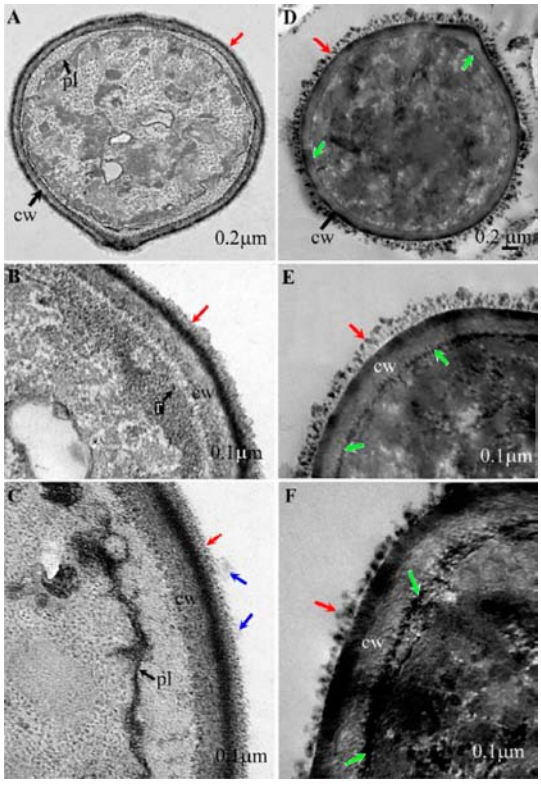

Figure 5. TEM images at diverse magnifications of (A–C) untreated and (D–F) treated yeast cells (Y) and cell walls (CW) with wine polyphenol pool. Red arrows, mannoproteins; blue arrows, antennary oligo(manno)-saccharides; pl, plasma membrane.

hydrolases or transglycosidases, nonenzymatic mating agglutinins, flocculins, and β-(1→3)-glucan cross-connectors. Most, if

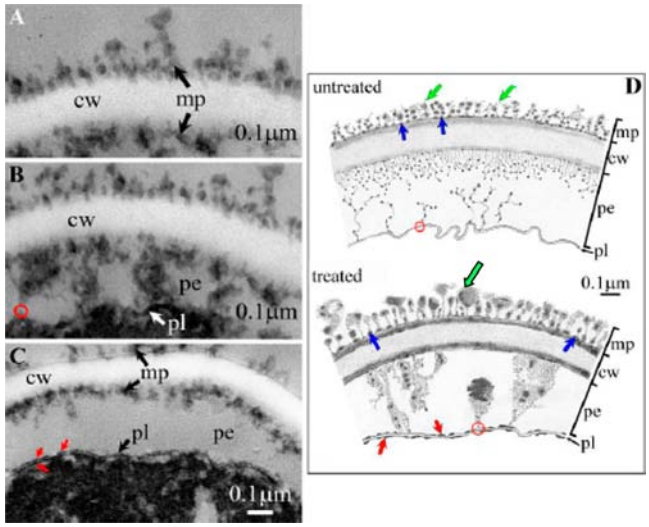

Figure 6. TEM images of (A) treated yeast cell wall with wine polyphenol pool, showing aggregated outer and inner mannoproteins, (B, C) a treated cell showing the plasmalemma, and (D) drawing of plasmolyzed outer region of untreated and treated yeast cells. cw, polysaccharidic cell wall; mp, mannoproteins; pe, periplasm; pl, plasmalemma; red circles, GPI anchor; blue arrows, contrasted knots in the inner layer of mannoproteins; green arrows, contrasted knots at the outer layer of mannoproteins; red arrows, clumps of clotted plasmalemma proteins; on scale.

not all, of the proteins in these two groups are glycosylated. The third group consists of single-pass plasma membrane proteins, mechanosensors that detect cell wall stress.[25] TEM observations evidenced that among cell wall constituents (mannoproteins, proteins, β-glucans, and chitin), mannoproteins are likely primarily involved in the interaction with tannins. This observation is in accordance with previous works evidencing interactions in solution between mannoproteins and tannins or tannin aggregates.[36−38] Considering whole cells and cytoplasmic constituents, it can be supposed that interactions occur with the proteins of the plasmalemma or of other cell membranes or with cytoplasmic proteins. Indeed, proteins represent between 40 and 50% of the yeast cell dry weight.[39] The much higher reversibility of the interactions between cell walls and tannins compared to that observed with whole yeast cells and tannins can be related to the high glycosylation level of mannoproteins: it has been demonstrated that mannosylated yeast invertase presents a 10-fold lower ability to bind red wine tannins than bovine serum albumin.[36]

Potential Implications in Winemaking. The present results have several potential implications in winemaking and aging. The latter concerns first the role of yeast-derived products, especially inactivated yeasts and yeast cell walls, and their use in red winemaking for their potential impact on wine mouthfeel and color stability. Although the exact mechanisms are not solved yet, this impact has mainly been attributed to interactions between mannoproteins and wine tannins. Interactions may occur in solution, due to the release of mannoproteins from cell walls,[15,40,41] or at the interface, due to tannin interactions with mannoproteins located in the outer layer of walls.[10,15] Interactions between condensed grape skin tannins or red wine tannins/derived pigments and mannoproteins in the cell walls have been evidenced here by TEM for the first time. They induce aggregate formation in the initially brush-like structure of the outer mannoprotein layer. However,

DOI: 10.1021/acs.jafc.5b02241
J. Agric. Food Chem. 2015, 63, 7539−7545

when dealing with whole dead or inactivated cells, most of the interactions (about 90%) occur with the yeast cellular constituents. It can then be expected that a quite different impact on red wine polyphenol composition will be obtained depending on the exact structure and composition of the yeast-derived product used:[17] inactivated yeast, yeast inactivated after autolysis treatment and autolysis conditions, yeast walls or hulls. Indeed, autolysis may strongly affect the yeast cell wall composition and cytoplasmic content[42−45] and thus their interactions with wine polyphenols. The autolyzed and inactivated yeast (A-IY) used in our study did not present changes in their ultrastructure detectable by TEM, and only small differences were observed between IY and A-IY in their interactions with red wine polyphenols.[19] Besides the degree of autolysis, also the yeast strain and culture conditions have a potential impact on the composition of the yeast-derived products that deserves to be further explored.[12,17]

Inactivated cells and cell walls are proposed as wine quality enhancers to replace aging on lees. Cell growth conditions used to produce yeast biomass and yeast-derived products strongly differ from those found in winemaking. This may induce different behavior of dead cells toward their interactions with wine polyphenols by comparison to the yeast biomass Y used in our work. However, for a close initial tannin concentration, the amount of polyphenols adsorbed by the yeast biomass Y in our study was similar to that adsorbed by yeast lees in the previous work of Mazauric et al.[10,15] In that case, lees were obtained after alcoholic fermentation in a model must and the strain was not the one used in the present study. This tends to indicate that results obtained in the present work are not related only to the strain and its growth conditions (aerobiosis versus anaerobiosis). This will need to be further explored. Likewise, we focused in the present work on condensed tannins and red wine polyphenols. Although their phenolic compositions are very different, white and rosé wines also contain flavan-3-ol oligomers and derived pigments that can develop physicochemical interactions with yeast cells. For instance, it has been hypothesized that direct interactions between small flavan-3-ols and yeast cytoplasmic membrane lipids could explain the protective effect of yeast lees toward polyphenol oxidation in white wines. Thus, it will be of importance to identify the exact sites of interaction between white and rosé polyphenols and yeast cells to better understand the mechanisms involved in the impact of yeasts and yeast-derived products on wine quality.

AUTHOR INFORMATION

Corresponding Author

*(A.V.) E-mail: vernhet@supagro.fr.

Notes

The authors declare no competing financial interest.

ACKNOWLEDGMENTS

We are grateful to Dr. Chantal Cazevieille [Centre de Ressources en Imagerie Cellulaire (CRIC), Université Montpellier I, Montpellier, France] and Elodie Jublanc (INRA, Montpellier, France) for their technical assistance in transmission electron and confocal microscopy, respectively. We thank Stephanie Carrillo for the purification of skin tannins.

ABBREVIATIONS

aDP, average degree of polymerization; A-IY, autolyzed and inactivated yeast; CW, cell wall; IY, inactivated yeast; skin 21, grape skin tannins with an average degree of polymerization of 21; TEM, transmission electron microscopy; WP, wine polyphenols; Y, yeast biomass

REFERENCES

(1) Fulcrand, H.; Dueñas, M.; Salas, E.; Cheynier, V. Phenolic reactions during winemaking and aging. *Am. J. Enol. Vitic.* **2006**, *57*, 289−297.

(2) Morata, A.; Gómez-Cordovés, M. C.; Calderón, F.; Suárez, J. A. Effects of pH, temperature and SO_2 on the formation of pyranoanthocyanins during red wine fermentation with two species of *Saccharomyces*. *Int. J. Food Microbiol.* **2006**, *106*, 123−129.

(3) Fulcrand, H.; Cameira Dos Santos, P. J.; Sarni-Manchado, P.; Cheynier, V.; Fabre-bonvin, J. Structure of new anthocyanin-derived wine pigments. *J. Chem. Soc., Perkin Trans. 1* **1996**, 735−739.

(4) Salmon, J.-M.; Fornairon-bonnefond, C.; Mazauric, J.-P. Interactions between wine lees and polyphenols: influence on oxygen consumption capacity during simulation of wine aging. *J. Food Sci.* **2002**, *67*, 1604−1609.

(5) Bonilla, F.; Mayen, M.; Merida, J.; Medina, M. Yeasts used as fining treatment to correct browning in white wines. *J. Agric. Food Chem.* **2001**, *49*, 1928−1933.

(6) Razmkhab, S.; Lopez-Toledano, A.; Ortega, J. M.; Mayen, M.; Merida, J.; Medina, M. Adsorption of phenolic compounds and browning products in white wines by yeasts and their cell walls. *J. Agric. Food Chem.* **2002**, *50*, 7432−7437.

(7) Morata, A.; Gómez-Cordovés, M. C.; Suberviola, J.; Bartolomé, B.; Colomo, B.; Suárez, J. A. Adsorption of anthocyanins by yeast cell walls during the fermentation of red wines. *J. Agric. Food Chem.* **2003**, *51*, 4084−4088.

(8) Merida, J.; Lopez-Toledano, A.; Marquez, T.; Millan, C.; Ortega, J. M.; Medina, M. Retention of browning compounds by yeasts involved in the winemaking of sherry type wines. *Biotechnol. Lett.* **2005**, *27*, 1565−1570.

(9) Vasserot, Y.; Caillet, S.; Maujean, A. Study of anthocyanin adsorption by yeast lees. Effect of some physicochemical parameters. *Am. J. Enol. Vitic.* **1997**, *48*, 433−437.

(10) Mazauric, J.-P.; Salmon, J.-M. Interactions between yeast lees and wine polyphenols during simulation of wine aging: I. Analysis of remnant polyphenolic compounds in the resulting wines. *J. Agric. Food Chem.* **2005**, *53*, 5647−5653.

(11) Marquez, T.; Millan, C.; Salmon, J.-M. Plasma membrane sterols are involved in yeast's ability to adsorb polyphenolic compounds resulting from wine model solution browning. *J. Agric. Food Chem.* **2009**, *57*, 8026−8032.

(12) Loira, I.; Vejarano, R.; Morata, A.; Ricardo-da-Silva, J. M.; Laureano, O.; González, M. C.; Suárez-Lepe, J. A. Effect of *Saccharomyces* strains on the quality of red wines aged on lees. *Food Chem.* **2013**, *139*, 1044−1051.

(13) Rodrigues, A.; Ricardo-Da-Silva, J. M.; Lucas, C.; Laureano, O. Effect of winery yeast lees on touriga nacional red wine color and tannin evolution. *Am. J. Enol. Vitic.* **2013**, *64*, 98−109.

(14) Palomero, F.; Morata, A.; Benito, S.; Gonzalez, M.; Suarezlepe, J. Conventional and enzyme-assisted autolysis during ageing over lees in red wines: influence on the release of polysaccharides from yeast cell walls and on wine monomeric anthocyanin content. *Food Chem.* **2007**, *105*, 838−846.

(15) Mazauric, J.-P.; Salmon, J.-M. Interactions between yeast lees and wine polyphenols during simulation of wine aging: II. Analysis of desorbed polyphenol compounds from yeast lees. *J. Agric. Food Chem.* **2006**, *54*, 3876−3881.

(16) Pozo-Bayón, Á. M.; Andújar-Ortiz, I.; Moreno-Arribas, M. V. Scientific evidences beyond the application of inactive dry yeast preparations in winemaking. *Food Res. Int.* **2009**, *42*, 754−761.

(17) Pozo-Bayón, Á. M.; Andújar-Ortiz, I.; Alcaide-Hidalgo, J. M.; Martin-Alvarez, P. J.; Moreno-Arribas, M. V. Characterization of commercial inactive dry yeast preparations for enological use based on their ability to release soluble compounds and their behavior toward

DOI: 10.1021/acs.jafc.5b02241
J. Agric. Food Chem. 2015, 63, 7539−7545

aroma compounds in model wines. *J. Agric. Food Chem.* **2009**, *57*, 10784−10792.
(18) Del Barrio-Galán, R.; Pérez-Magariño, S.; Ortega-Heras, M.; Guadalupe, Z. Polysaccharide characterization of commercial dry yeast preparations and their effect on white and red wine composition. *LWT−Food Sci. Technol.* **2012**, *48*, 215−223.
(19) Mekoue Nguela, J.; Sieczkowski, N.; Roi, S.; Vernhet, A. Sorption of grape proanthocyanidins and wine polyphenols by yeasts, inactivated yeasts, and yeast cell walls. *J. Agric. Food Chem.* **2015**, *63*, 660−670.
(20) Mane, C. *Phénomènes Oxydants et Composés Phénoliques Dans Les Vins Blancs de Champagne: Developpements Methodologiques Pour L'analyse Des Polymères*. Ph.D. Thesis, Centre International d'Etudes Supérieures en Sciences Agronomiques "Montpellier SupAgro", 2007.
(21) Mouls, L.; Fulcrand, H. UPLC-ESI-MS study of the oxidation markers released from tannin depolymerization: toward a better characterization of the tannin evolution over food and beverage processing. *J. Mass Spectrom.* **2012**, *47*, 1450−1457.
(22) Poncet-Legrand, C.; Cabane, B.; Bautista-Ortín, A.-B.; Carrillo, S.; Fulcrand, H.; Pérez, J.; Vernhet, A. Tannin oxidation: intra- versus intermolecular reactions. *Biomacromolecules* **2010**, *11*, 2376−2386.
(23) Dallies, N.; François, J.; Paquet, V. A new method for quantitative determination of polysaccharides in the yeast cell wall. Application to the cell wall defective mutants of *Saccharomyces cerevisiae*. *Yeast* **1998**, *14*, 1297−1306.
(24) Klis, F. M.; Boorsma, A.; De Groot, P. W. J. Cell wall construction in *Saccharomyces cerevisiae*. *Yeast* **2006**, *23*, 185−202.
(25) Orlean, P. Architecture and biosynthesis of the *Saccharomyces cerevisiae* cell wall. *Genetics* **2012**, *192*, 775−818.
(26) Brillouet, J.-M.; Romieu, C.; Schoefs, B.; Solymosi, K.; Cheynier, V.; Fulcrand, H.; Verdeil, J.-L.; Conéjéro, G. The tannosome is an organelle forming condensed tannins in the chlorophyllous organs of Tracheophyta. *Ann. Bot.* **2013**, *112*, 1003−1014.
(27) Parham, R. A.; Kaustinen, H. M. Differentiation of tannin, lipid, and starch in cultured plant cells. *Inst. Pap. Chem. Appleton, Wisconsin* **1975**, *16*, 1−9.
(28) Osumi, M. The ultrastructure of yeast: cell wall structure and formation. *Micron* **1998**, *29*, 207−233.
(29) Kapteyn, J. C.; Van Den Ende, H.; Klis, F. M. The contribution of cell wall proteins to the organization of the yeast cell wall. *Biochim. Biophys. Acta, Gen. Subj.* **1999**, *1426*, 373−383.
(30) Tudela, R.; Gallardo-Chacón, J. J.; Rius, N.; López-Tamames, E.; Buxaderas, S. Ultrastructural changes of sparkling wine lees during long-term aging in real enological conditions. *FEMS Yeast Res.* **2012**, *12*, 466−476.
(31) Klis, F. M.; Brul, S.; De Groot, P. W. J. Covalently linked wall proteins in Ascomycetous fungi. *Yeast* **2010**, *27*, 489−493.
(32) Hagen, I.; Ecker, M.; Lagorce, A.; Francois, J. M.; Sestak, S.; Rachel, R.; Grossmann, G.; Hauser, N. C.; Hoheisel, J. D.; Tanner, W.; et al. Sed1p and Srl1p are required to compensate for cell wall instability in *Saccharomyces cerevisae* mutants defective in multiple GPI-anchored mannoproteins. *Mol. Microbiol.* **2004**, *52*, 1413−1425.
(33) Zanchi, D.; Konarev, P. V.; Tribet, C.; Baron, A.; Svergun, D. I.; Guyot, S. Rigidity, conformation, and solvation of native and oxidized tannin macromolecules in water-ethanol solution. *J. Chem. Phys.* **2009**, *130*, 245103−245116.
(34) Hagerman, A. E.; Butler, L. G. The specificity of proanthocyanidin-protein interactions. *J. Biol. Chem.* **1981**, *256*, 4494−4497.
(35) Charlton, A. J.; Baxter, N. J.; Lokman Khan, M.; Moir, A. J. G.; Haslam, E.; Davies, A. P.; Williamson, M. P. Polyphenol/peptide binding and precipitation. *J. Agric. Food Chem.* **2002**, *50*, 1593−1601.
(36) Rowe, J. D.; Harbertson, J. F.; Osborne, J. P.; Freitag, M.; Lim, J.; Bakalinsky, A. T. Systematic identification of yeast proteins extracted into model wine during aging on the yeast lees. *J. Agric. Food Chem.* **2010**, *58*, 2337−2346.
(37) Riou, V.; Vernhet, A.; Doco, T.; Moutounet, M. Aggregation of grape seed tannins in model wine-effect of wine polysaccharides. *Food Hydrocolloids* **2002**, *16*, 17−23.
(38) Poncet-Legrand, C.; Gautier, C.; Cheynier, V.; Imberty, A. Interactions between flavan-3-ols and poly(L-proline) studied by isothermal titration calorimetry: effect of the tannin structure. *J. Agric. Food Chem.* **2007**, *55*, 9235−9240.
(39) Wiederhold, E.; Veenhoff, L. M.; Poolman, B.; Slotboom, D. J. Proteomics of *Saccharomyces cerevisiae* organelles. *Mol. Cell. Proteomics* **2010**, *9*, 431−445.
(40) Doco, T.; Brillouet, J. M.; Moutounet, M. Evolution of grape (Carignan Noir cv) and yeast polysaccharides during fermentation and post-maceration. *Am. J. Enol. Vitic.* **1996**, *47*, 108−110.
(41) Escot, S.; Feuillat, M.; Dulau, L.; Charpentier, C. Release of polysaccharides by yeasts and the influence of released polysaccharides on colour stability and wine astringency. *Aust. J. Grape Wine Res.* **2001**, *7*, 153−159.
(42) Babayan, T. L.; Bezrukov, M. G. Autolysis in yeasts. *Acta Biotechnol.* **1985**, *2*, 129−136.
(43) Charpentier, C.; Feuillat, M. Yeast autolysis. *Wine Microbiology and Biotechnology*; Fleet, G., Ed.; Harwood Academic: Chur, Switzerland 1992; pp 225−242.
(44) Guilloux-Benatier, M.; Chassagne, D. Comparison of components released by fermented or active dried yeasts after aging on lees in a model wine. *J. Agric. Food Chem.* **2003**, *51*, 746−751.
(45) Tanguler, H.; Erten, H. Utilisation of spent brewer's yeast for yeast extract production by autolysis: the effect of temperature. *Food Bioprod. Process.* **2008**, *86*, 317−321.

DOI: 10.1021/acs.jafc.5b02241
J. Agric. Food Chem. 2015, 63, 7539−7545

(octadecatrienoic acid) found in tung oil using UV spectrophotometry at 273 nm. The CAT assay has several advantages over the ORAC assay.

First, the CAT assay was performed under a heterogeneous system (oil-in-water emulsions). Thus, the effect of the locations of antioxidants in O/W emulsions (antioxidant partitioning) on their antioxidative performance has been incorporated into the model. Second, the amount of antioxidants used in the CAT assay was approximately 100 times less than that of the substrate. Under this condition, the reaction kinetic had a realistic trend in terms of natural antioxidant phenomena.[9]

Recently, the CAT assay has been used in many research experiments to explore an optimum degree of lipophilization of phenolic compounds[16] using AAPH (a water-soluble peroxyl radical initiator) to accelerate lipid oxidation in oil-in-water emulsions. However, due to the complexity of lipid oxidation in emulsion systems, locations of free radicals in the system could be differently partitioned not only into the water phase, but also into the oil/lipid interfacial region and/or the lipid core at which lipid oxidation was hypothesized to occur in emulsions. Thus, it is worthy of investigating the influence of using a lipid-soluble free radical initiator on antioxidant behaviors in the CAT-based assay as an additional complementary method to the original CAT assay using different ways to initiate lipid oxidation.

In this research, the apolar radical-initiated conjugated autoxidizable triene (ApoCAT) assay, a modified CAT assay, was proposed by using a lipid soluble free radical azo initiator (dimethyl 2,2′-azobis(2-methylpropionate) so-called V601or AIBME) instead of AAPH. According to chemical information, AIBME is a non-nitrile azo initiator which is very insoluble in water. It was hypothesized that the ApoCAT assay may be more relevant to autoxidation of oil-in-water emulsions, since it was believed that lipid oxidation in O/W emulsions occurs at the interface of oil droplets[17,18] instead of acceleration from the aqueous phase.

In addition, these two assays may be suitable for studying combinations of antioxidants. It was reported that the locations of antioxidants in O/W emulsions also impacted the overall antioxidative performances of combined antioxidants, resulting in different interaction behaviors, such as synergistic, additive, and antagonistic effects.[19]

This research aimed to investigate the effects of hydrophilic and lipophilic peroxyl radical initiators on the antioxidative performances of some synthetic antioxidants and natural extracts, to study the relationship between the CAT and ApoCAT assays, and to explore antioxidant interactions using these assays.

MATERIALS AND METHODS

Chemicals and Materials. Ethylenediaminetetraacetic acid (EDTA), 2,4,6-tris(2-pyridyl)-s-triazine (TPTZ), silicic acid, Folin-Ciocalteau's reagent, sodium carbonate, ferric chloride, tung oil, Brij 35, ascorbic acid, ascorbyl palmitate, gallic acid, lauryl gallate, and mixed tocopherols were purchased from Sigma-Aldrich (St. Louis, USA). Hydrochloric acid was purchased from Fisher Scientific (Loughborough, UK). Absolute ethanol was purchased from RCI Labscan (Thailand). 2,2′-Azobis-2-methylpropanimidamide, dihydrochloride (AAPH),dimethyl 2,2′-azobis(2-methylpropionate) (AIBME) or V601 and activated charcoal were purchased from Wako Chemical (Japan). Miglyol812N, a medium chain triglyceride (MCT) mixture, was purchased from Sasol Germany Gmbh (Witten,Germany). Commercial grape seed (95% oligomeric proanthocyanidins; OPC) and rosemary (60% carnosic acid) extracts were purchased from Changsha Nutramax Inc. (Changsha, China). Commercial green tea extract was purchased from Specialty Natural Products Co., Ltd. (Chonburi, Thailand). All commercial extracts were processed without any additive and carriers. Double-distilled and deionized water was used for the preparation of all solutions. All organic solvents used were analytical grade.

Total Phenolic Content (TPC) Assay. Total phenolic contents of antioxidants and plant extracts were determined by the method of Deetae et al. (2012)[8] with some modifications. The reaction was performed in a 96-well microplate. Briefly, 30 microliter of sample was mixed with 150 μL of Folin-Ciocalteau's reagent (10-times dilution). Then, 7.5% w/v of sodium carbonate (120 μL) was added. The mixtures were kept in the dark for 30 min. The absorbance of mixture was recorded at 765 nm using a microplate reader (SpectraMax 190, Molecular Devices, USA). Gallic acid was used as a standard phenolic compound. In the case of synthetic antioxidants, result is expressed as millimole of gallic acid per one mole of antioxidant (mmole GAE/mol antioxidant). In the case of natural extracts, result is expressed as mg of gallic acid per one gram of antioxidants (mg GAE/g extract).

ABTS Radical Scavenging Activity Assay. Free radical scavenging activity of antioxidants and plant extracts was performed according to the ABTS assay described by Deetae et al. with some modification.[8] ABTS cation radical ($ABTS^{\bullet+}$) was generated by reacting 10 mL of 7 mM ABTS stock solution with 179 μL of 140 mM potassium persulfate. Then, the mixture was incubated at room temperature for 16 h. $ABTS^{\bullet+}$ solution was diluted to obtain an absorbance of 0.7 at a wavelength of 734 nm before use. Twenty microliters of samples were added into 280 μL of $ABTS^{\bullet+}$ solution in a microplate. The mixtures were mixed using the microplate mixer, and then incubated in the dark at room temperature for 6 min. The absorbance of mixture was then read at 734 nm by a microplate reader (Spectra Max 190, Molecular Devices, USA). Ascorbic acid was used as a standard phenolic compound. In the case of synthetic antioxidants, result is expressed as millimole of ascorbic acid per one mole of antioxidant (mmole ascorbic acid/mol antioxidant). In the case of natural extracts, result is expressed as mg of ascorbic acid per one gram of antioxidants (mg ascorbic acid/g extract).

Ferrous Reducing Antioxidant Power (FRAP) Assay. Ferric reducing antioxidant power (FRAP) assay was performed using a method described by Deetae et al. with some modification.[8] Shortly, FRAP reagent was freshly prepared by mixing 300 mM acetate buffer (pH 3.6), 10 mM TPTZ in 40 mM HCl, and 20 mM $FeCl_3.6H_2O$ at the ratio of 10:1:1. Sample (30 μL) was added into 270 μL of FRAP reagent in a 96-well microplate. The microplate was kept in the dark at 37 °C for 8 min. The absorbance of the mixture was measured at 595 nm using a microplate reader (SpectraMax 190, Molecular Devices, USA). Ascorbic acid was used as a standard phenolic compound. In the case of synthetic antioxidants, result is expressed as millimole of ascorbic acid per one mole of antioxidant (mmole ascorbic acid/mol antioxidant). In the case of natural extracts, result is expressed as mg of ascorbic acid per one gram of antioxidants (mg GAE/g extract).

Oxygen Radical Absorbance Capacity (ORAC) Assay. Oxygen radical absorbance capacity (ORAC) assay was performed according to Nkhili et al.[10] Briefly, a series of varying concentrations of antioxidant was prepared. Twenty microliters of samples were added into a 96-well black microplate (Eppendorf). Then, 160 μL of 78 nM fluorescein in PBS solution (pH 7.2) was added. The mixture was incubated at 37 °C for 5 min in the dark. The reaction started when 12 mM AAPH (20 μL) was added. Fluorescent intensity of the mixture was recorded using a fluorescent microplate reader (SpectraMax M5, Molecular Devices, USA) with an excitation wavelength of 485 nm and an emission wavelength of 520 nm at 2 min intervals for 3 h in kinetic mode.

Conjugated Autoxidizable Triene (CAT) Assay. Conjugated autoxidizable triene (CAT) assay was assessed as described by Laguerre and co-workers[20] with some modification. Conjugated triene triacylglycerols in tung oil was used as a substrate and UV probe for monitoring the progress of the oxidation reaction. Polar compounds of tung oil were stripped by using a method explained by Boon et al.[21] Briefly, silicic acid (100 g) was washed three times with a total of 3 L of distilled water followed by drying at 110 °C for 20 h.

A chromatographic column (3.0 cm internal diameter and 35 cm height) was then packed sequentially with 22.5 g of silicic acid followed

DOI: 10.1021/acs.jafc.5b02493
J. Agric. Food Chem. 2015, 63, 7546−7555

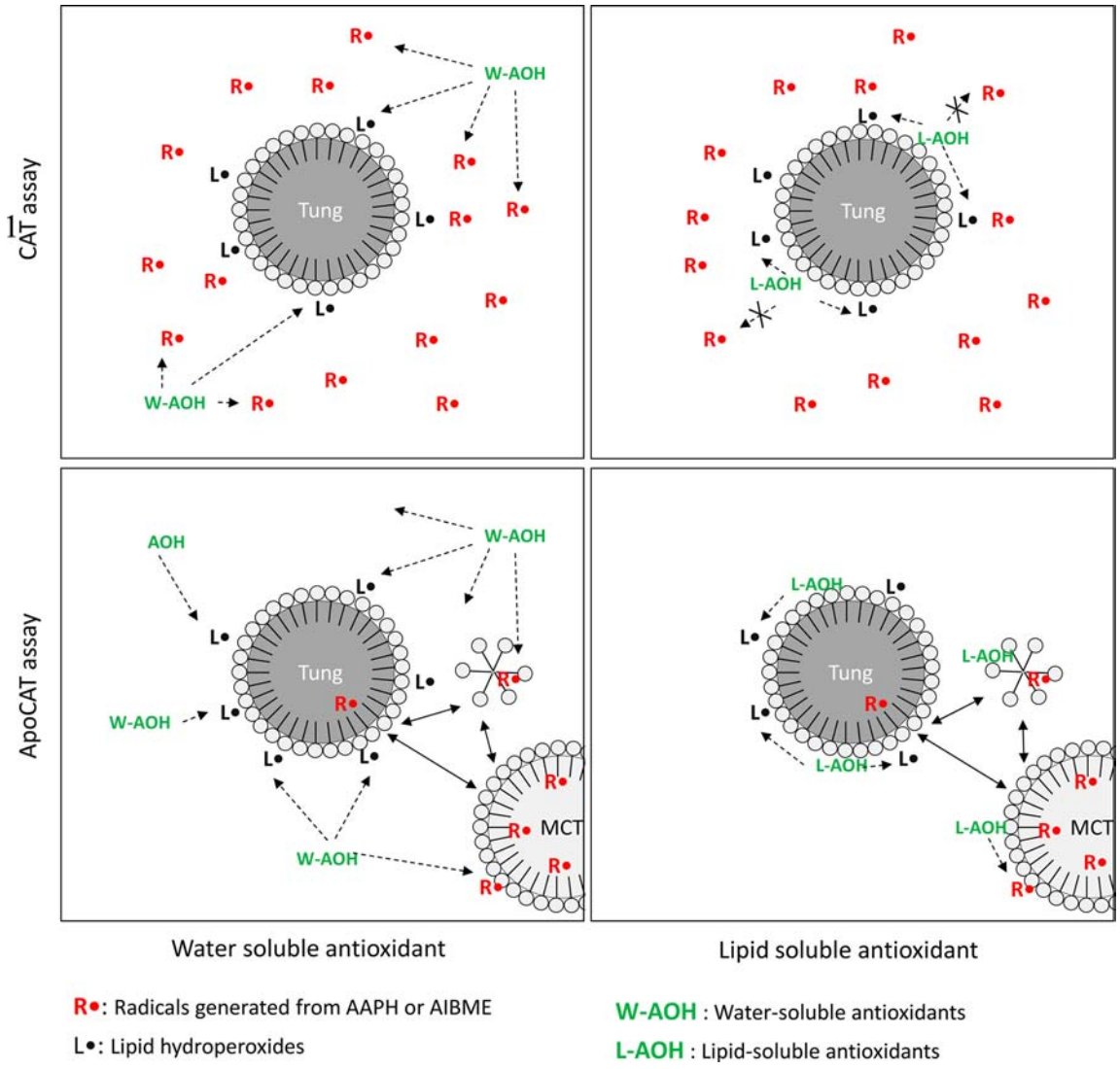

Figure 1. Proposed mechanisms of oxidants and antioxidants in the CAT and ApoCAT assays.

by 5.625 g of activated charcoal and then another layer of silicic acid (22.5 g). Tung oil (30 g) was dissolved in 30 mL of *n*-hexane and passed through the column. Tung oil was eluted with addition of *n*-hexane (270 mL). The collected triacylglycerols were held in an ice bath, and covered with aluminum foil to inhibit lipid oxidation. The solvent in stripped tung oil was removed using a vacuum rotary evaporator (BÜCHI Rotavapor R-114, Switzerland) at 37 °C, and traces of the remaining solvent were removed by flushing with nitrogen. The stripped tung oil was transferred into small vials, and stored at −80 °C until performing an experiment.

The CAT assay was performed with two main steps as the following details. First, for emulsion preparation, 25 mL of PBS solution (pH 7.2) containing 34 μM Brij 35 was added into a beaker containing 6(±0.5) mg of stripped tung oil. Oil-in-water emulsions were made by homogenizing the mixture at 6,500 rpm for 90 s (Ultra-Turrax T25 basic, IKA Werke, Germany). The emulsion was then centrifuged using a centrifuge (Model 5810 R, Eppendorf, Germany) at 10,000 g, 10 °C for 5 min in order to remove the unstable part (large oil droplets), providing more homogeneous size distribution of O/W emulsions.

Second, a series of different concentrations of samples in PBS solution (50 μL) was transferred to a UV-Star 96-well microplate (Costar, Corning, USA), followed by addition of the prepared emulsion (125 μL). The samples were mixed at 1,200 rpm, 37 °C for 5 min using a microplate mixer (Thermomixer R, Eppendorf, Germany). After mixing, the samples were immediately mixed with 25 μL of 8 mM AAPH solution in PBS solution and recorded at 273 nm at 1 min intervals for 3 h using a microplate reader (SpectraMax 190, Molecular Devices, USA). Trolox was used as a standard antioxidant to compare against other treatments.

The CAT value, expressed as mg of trolox per one gram (or mole) of an antioxidant, was calculated from a relationship between net protection areas under the curve (AUC) and concentrations of antioxidants compared to trolox (6-hydroxy-2,5,7,8-tetramethylchroman-2-carboxylic acid).

Apolar Radical-Initiated Conjugated Autoxidizable Triene (ApoCAT) Assay. The ApoCAT assay was adapted from the original CAT assay described by Laguerre et al.[20] Instead of using AAPH, the lipid-soluble free radical initiator, dimethyl 2,2′-azobis (2-methylpropionate), was used. All procedures were performed as described in the CAT assay except for the preparation of free radical initiator.

In brief, MCT oil-in-water emulsion was prepared exactly the same way as described in tung oil-in-water emulsion. MCT emulsion solutions was mixed directly with the lipid-soluble free radical initiator to obtain a final concentration of 8 mM dimethyl 2,2′-azobis (2-methylpropionate) in MCT oil-in-water emulsion. Twenty-five milliliters of V601 loaded MCT oil-in-water emulsion were mixed with 125 μL of tung oil-in-water emulsions and 50 μL of samples in PBS solution to start the oxidation reaction.

Calculation of Antioxidant Interaction Indexes in the CAT and ApoCAT Assays. Interaction indexes of combined effects between α-tocopherol (lipid soluble) and water-soluble antioxidants were

DOI: 10.1021/acs.jafc.5b02493
J. Agric. Food Chem. 2015, 63, 7546−7555

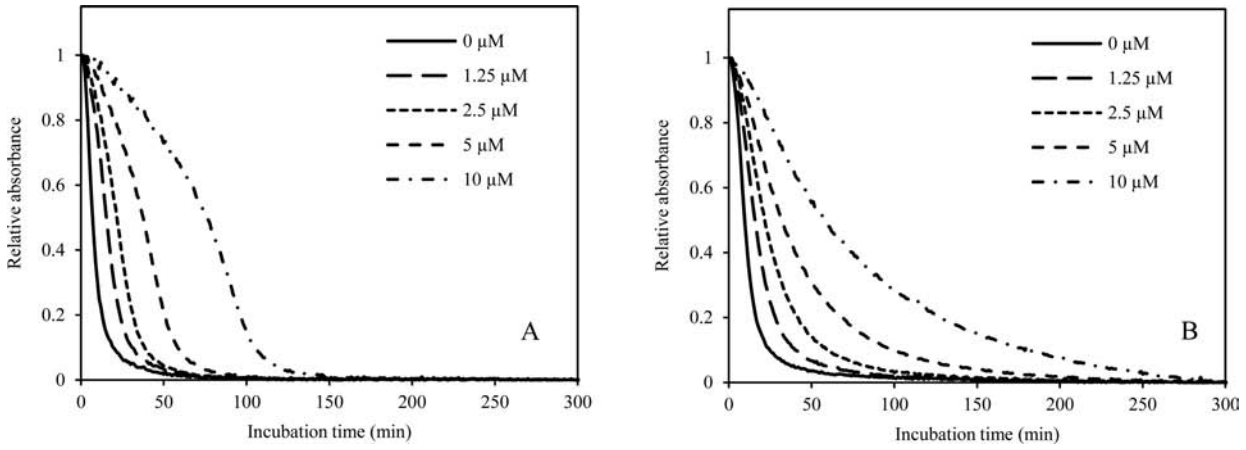

Figure 2. Kinetic decay of conjugated triene in the CAT (left) and the ApoCAT (right) assays treated with trolox (A and B).

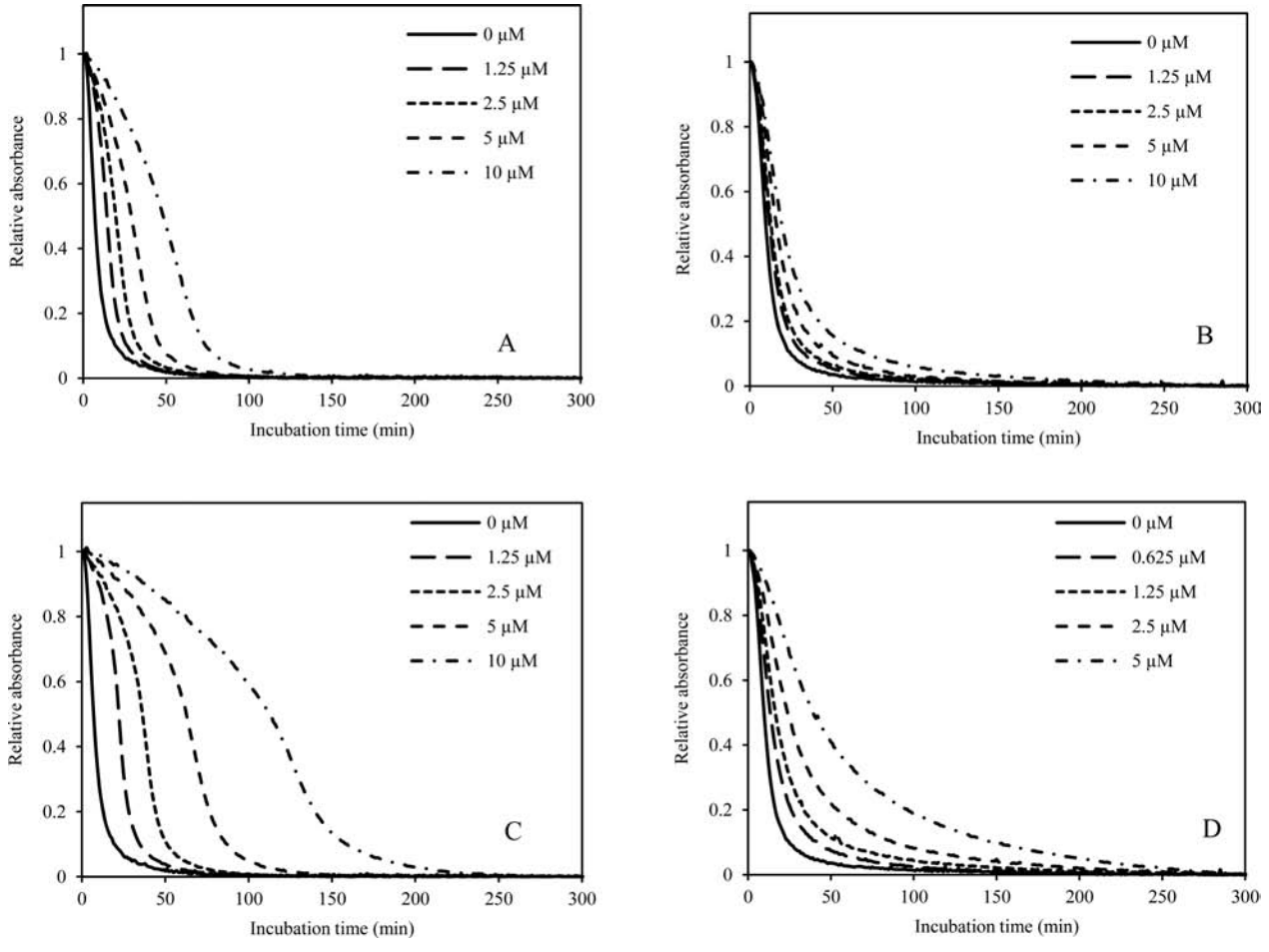

Figure 3. Kinetic decay of conjugated triene in the CAT (left) and the ApoCAT (right) assays treated with gallic acid (A and B) and lauryl gallate (C and D).

investigated using the CAT and the ApoCAT assays. Different ratios of water to lipid soluble antioxidants (1:3, 1:1, 3:1, 5:1, and 7:1) were prepared in ethanolic solution based on molar mass basis of antioxidants. To estimate the interaction indexes, individual and combined antioxidants were performed in the same 96-well microplate. Antioxidant capacities of individual antioxidant could be observed directly. For the expected antioxidant capacities of the combination, it could be estimated as described in the following equation.

$$\text{Interaction Index} = \frac{\text{Observed CAT value of the combination}}{\text{Expected CAT value of the combination}} = \frac{\textit{the CAT value of combined } (A + B)}{\textit{the CAT value of } A \times F1 + \textit{the CAT value of } B \times F2}$$

Where, A and B represent α-tocopherol and another antioxidant, respectively. Individual CAT or ApoCAT values of A and B were used to calculate the expected CAT or ApoCAT of the combined A and B. F1and F2 represent fractions of the combination. For example, a ratio between antioxidants was 3 to 1. The F1 and F2 are 3/4 and 1/4,

DOI: 10.1021/acs.jafc.5b02493
J. Agric. Food Chem. 2015, 63, 7546−7555

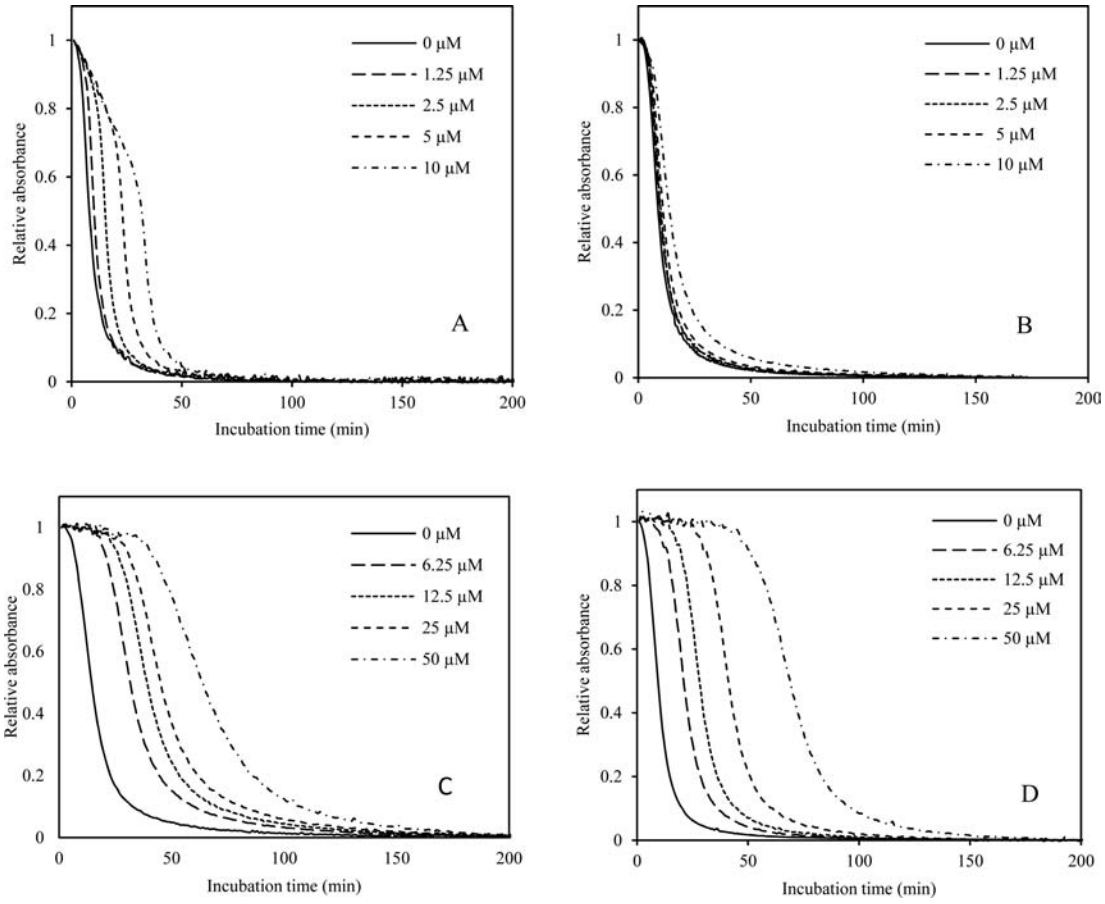

Figure 4. Kinetic decay of conjugated triene in the CAT (left) and the ApoCAT (right) assays treated with ascorbic acid (A and B) and ascorbyl palmitate (C and D).

respectively. Interaction indexes were expressed as synergistic (>1), additive (≈1) and antagonistic (<1) antioxidant effects.

Statistical Analysis. All analyses were performed on triplicate samples. In all cases, comparisons of the means were performed using Duncan's multiple-range tests. A significance level of $p < 0.05$ was defined as being statistically different. All calculations were performed using SPSS18.0 (http://www.spss.com; SPSS Inc., Chicago, IL).

RESULTS AND DISCUSSION

Effect of Hydrophilic and Lipophilic Azo Radical Initiators on Antioxidant Capacities in the CAT Assay. Water-soluble (AAPH) and lipid soluble (AIBME) azo radical initiators were used to investigate the influences of different oxidant locations in the CAT assay on the antioxidant capacities of a variety of antioxidants. Instead of using water-soluble AAPH, the ApoCAT assay has been developed by using lipid-soluble AIBME in the original CAT assay. One of the problems in the development of the ApoCAT assay was finding a suitable delivery system for the incorporation of AIBME into the tung oil emulsions. To avoid large impacts on antioxidant distributions in the emulsion system from using solvents and surfactants, AIBME incorporated MCT oil-in-water emulsions were prepared using the same protocol as that for the tung oil emulsions. It was observed that using ethanol as a solvent to dissolve AIBME impacted on the emulsion stability of tung oil emulsions (data not shown). Hence, using excess surfactant concentrations could change the distribution of antioxidants in the systems, as previously reported by Panya et al. that the antioxidant activity of medium-chain alkyl ester (4−12 carbons) antioxidants (rosmarinic acid) decreased, while the activity of the ong-chain alkyl ester (20 carbons) antioxidant rosmarinic acid was improved by the addition of Tween 20.[15]

Figure 1 demonstrates proposed mechanisms of oxidants and antioxidants in the CAT and ApoCAT assays. In the CAT assay, water-soluble antioxidants are supposed to be mainly distributed in the water phase, so they have high possibility to react with radicals generated in the water phase. Because of the limitation of lipid soluble antioxidants to dissolve in water, lipid soluble antioxidants could only react with radicals generated near the oil/water interfacial regions.

However, in the case of the ApoCAT assay, lipid-soluble radicals and nonpolar antioxidants could be partitioned into several hydrophobic regions, such as lipid cores of tung and MCT oil droplets, micelles, and the oil/water interfaces. As a result, lipid-soluble antioxidants could mainly inactivate free radicals generated in the lipid phase, while water-soluble antioxidants could only interact with lipid-soluble radicals at the interfacial regions. It should be noted that dynamic exchanges of lipid soluble radicals and antioxidants between the tung oil and MCT oil emulsion droplets could be also facilitated by surfactants due to the formation of micelles.

As illustrated in Figure 2, without addition of Trolox, oxidation rates of tung oil-in-water emulsions in the ApoCAT assay were slightly slower than that of the CAT assay. At the same concentration of Trolox, the oxidation rates of tung oil emulsions of the ApoCAT assay were also slower than what was observed in the CAT assay. As a result, the net protection areas against various concentrations of Trolox observed in the ApoCAT assay

DOI: 10.1021/acs.jafc.5b02493
J. Agric. Food Chem. 2015, 63, 7546−7555

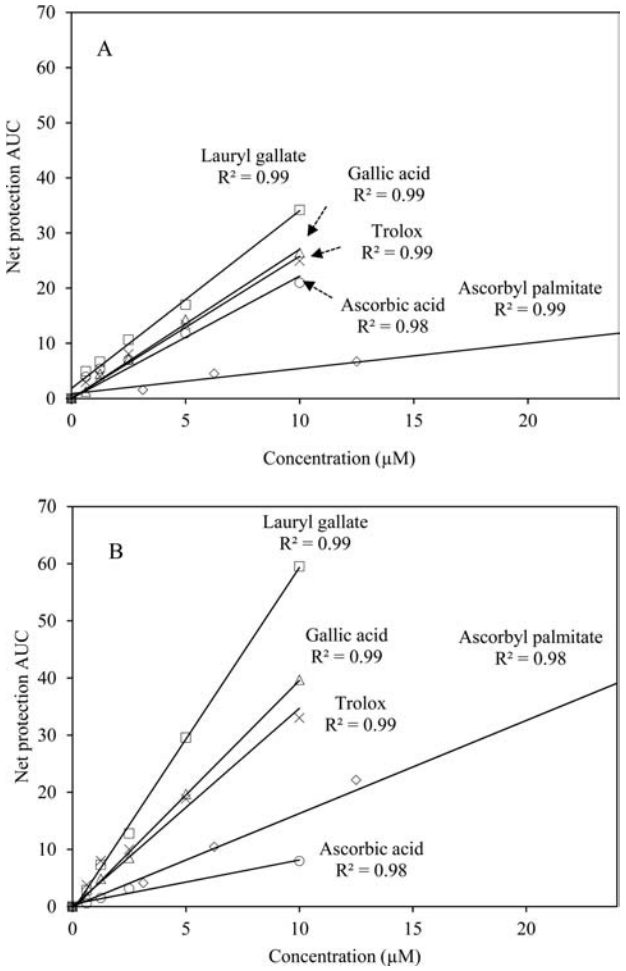

Figure 5. Area under the curve (AUC) vs concentrations of antioxidants in the CAT (A) and ApoCAT (B) assays.

was higher than that observed in the CAT assay. This could be due to the 10 h half-life decomposition temperature of AIBME is 66 °C, while that of AAPH is 44 °C. Thus, in general, the radical generation rate of AIBME is slower than that of AAPH under the same experiment condition.

From a kinetic point of view, Trolox exhibited different behaviors in both assays. Trolox could suppress oxidation more effective in the CAT assay than in the ApoCAT assay, as indicated by larger oxidation lag phase and/or slower initial oxidation rates. Laguerre and co-workers[9] have also reported that Trolox exhibited retarder behavior in the CAT assay. However, it was noted that, in this research, Trolox showed a pure retarder behavior (with an insignificant oxidation lag phase) in the ApoCAT assay. Results implied that a water-soluble antioxidant could exhibit higher antioxidant activity in the CAT assay than that observed in the ApoCAT assay.

The relationships between the CAT and ApoCAT assays were investigated using several water-and lipid-soluble antioxidants. The kinetics of absorbance bleaching in the presence of water-soluble (gallic acid and ascorbic acid) and lipid soluble (lauryl gallate and ascorbyl palmitate) antioxidants performed in the CAT and ApoCAT assays are shown in Figures 3 and 4, respectively. The results suggested that there was a strong influence of oxidant locations on the oxidation behaviors of water-and lipid-soluble antioxidants, as indicated by changes in the decay kinetics of tung oil emulsions with several antioxidants.

In the ApoCAT assay, gallic acid exhibited as a strong retarder as a result of the faster decay rate of the oxidation in comparison with what was observed in the CAT assay. The same was true in the case of lauryl gallate. In the CAT assay, lauryl gallate showed a significant lag phase, while, in the ApoCAT assay, lauryl gallate did not exhibit any lag phase. As illustrated in Figure 4, similar results were observed for ascorbic acid and ascorbyl palmitate. Ascorbic acid exhibited higher antioxidant activity in the CAT assay (Figure 4A) than in the ApoCAT assay (Figure 4B). However, ascorbyl palmitate showed higher antioxidant activity in the ApoCAT assay (Figure 4D) than in the CAT assay (Figure 4C). It should be noted that ascorbyl palmitate exhibited as a strong chain-breaker due to a significant lag phase.

From these results, it should be noted that the kinetic behaviors of antioxidants, as indicated by lag times and net protective areas under the curve (AUC), were changed according to how the systems were accelerated. This could be due to the fact that antioxidant partitioning was different in the CAT and ApoCAT systems. It was postulated that water-soluble antioxidants, mostly distributed in aqueous phase, could be able to mainly react with radicals generated in the aqueous phase and near the oil/water interface of tung oil emulsions, in the case of the CAT assay, and of both tung oil and MCT oil emulsions, in the case of ApoCAT. In comparison with the CAT assay, aqueous antioxidants in the ApoCAT model may have less chance to react with aqueous phase radicals, so decreases in the antioxidant performance of water-soluble antioxidants were observed, resulting in shorter or insignificant oxidation lag phases.

In the case of lipid soluble lauryl gallate (12 carbons), its oxidation lag time was clearly observed in the CAT assay, while it was not found in the ApoCAT assay. These results were different in comparison with ascorbyl palmitate (16 carbons), with an oxidation lag time being longer in the ApoCAT assay than in the CAT assay. It was hypothesized that this could be due to the fact that the polarity of ascorbyl palmitate was lower than that of lauryl gallate, so the distribution of ascorbyl palmitate should be mainly associated with the emulsion droplets. However, the antioxidant performance of lauryl gallate had dramatically

Table 1. Comparisons of Antioxidant Capacities of Synthesized Antioxidants[a]

Antioxidants	TPC Gallic acid equivalents	ABTS Ascorbic acid equivalents	FRAP Ascorbic acid equivalents	ORAC Trolox equivalents	CAT Trolox equivalents	ApoCAT Trolox equivalents
Ascorbic acid	0.59 ± 0.00a	1.00*	1.00*	0.95 ± 0.02b	0.56 ± 0.04c	0.19 ± 0.01d
Ascorbyl palmitate	0.39 ± 0.01c	0.74 ± 0.02c	1.23 ± 0.01b	0.96 ± 0.05b	0.17 ± 0.00c	0.56 ± 0.02b
Gallic acid	1.00*	3.39 ± 0.09a	2.99 ± 0.06a	1.46 ± 0.00c	0.67 ± 0.08b	0.31 ± 0.05c
Lauryl gallate	0.56 ± 0.01b	1.22 ± 0.05b	0.90 ± 0.03c	0.23 ± 0.05a	1.75 ± 0.12a	3.27 ± 0.12a

[a]Means within a column with different letters are significantly different ($p < 0.05$). The * indicates the value of approximately 1 due to the antioxidant being used as the standard.

DOI: 10.1021/acs.jafc.5b02493
J. Agric. Food Chem. 2015, 63, 7546−7555

Table 2. Comparisons of Antioxidant Capacities of Natural Antioxidant Extracts[a-]

Antioxidants	TPC (mg gallic acid/g sample)	ABTS (mg ascorbic acid/g sample)	FRAP (mg ascorbic acid/g sample)	ORAC (mg trolox/g sample)	CAT (mg trolox/g sample)	ApoCAT (mg trolox/g sample)
Mixed tocopherols	268.5 ± 5.3b	344.2 ± 6.9a	360.6 ± 2.6b	60.0 ± 14.1a	503.9 ± 31.5c	723.9 ± 41.5ab
Green tea extract	40.0 ± 0.9d	50.9 ± 0.0c	58.9 ± 0.9d	536.2 ± 29.3b	195.9 ± 13.3d	314.7 ± 25.5c
Grape seed extract	365.0 ± 24.8a	253.4 ± 1.2b	582.8 ± 7.8a	2101.7 ± 97.7c	670.2 ± 34.0b	640.9 ± 57.3b
Rosemary extract	178.9 ± 0.0c	45.8 ± 0.10c	174.7 ± 6.5c	2402.1 ± 79.4d	736.2 ± 45.7a	782.4 ± 57.7a

[a-]Means within a column with different letters are significantly different ($p < 0.05$).

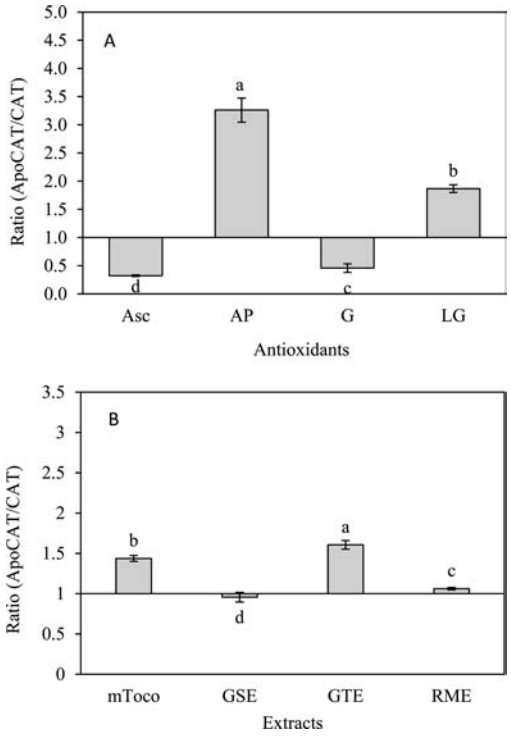

Figure 6. Ratio of antioxidant capacity of pure chemical antioxidants between the CAT and the ApoCAT assays. Synthetic antioxidants are ascorbic acid (Asc), ascorbyl palmitate (AP), gallic acid (G) and lauryl gallate (LG). Natural crude antioxidants are mixed tocopherol (mToco), grape seed extract (GSE), green tea extract (GTE), and rosemary extract (RME). Values are the means of three replicates. The different letters (a, b, c, and d) of interaction index obtained from different ratios of the same assay indicate significant differences ($p < 0.05$).

changed in both assays. The results suggested that the majority of lauryl gallate molecules may be distributed in the water phase instead of in oil droplets

The relationships between the net AUC of selected antioxidants in the CAT and the ApoCAT assays are shown in Figure 5A and B, respectively. The results suggested that the AUC of the ApoCAT assay was higher than that of the CAT assay. This could be due to the slower oxidation rate of the AIBME in comparison to the AAPH because the 10 h half-life decomposition temperature of AIBME (66 °C) was higher than that of AAPH (44 °C). In addition, the same concentrations of AAPH and AIBME were used in both assays.

The results suggested that the ApoCAT assay showed a strong impact on the antioxidant activities of nonpolar antioxidants (ascorbyl palmitate and lauryl gallate) in the same manner. For instance, it was noticed that the antioxidant activities of ascorbic acid and ascorbyl palmitate were strongly impacted. Ascorbic acid exhibited a strong antioxidant activity in the CAT assay, while it showed a poor antioxidant activity in the ApoCAT assay. On the contrary, ascorbyl palmitate exhibited higher antioxidant activity in the ApoCAT assay than in the CAT assay. Overall, it could be concluded that nonpolar antioxidants performed better in the ApoCAT assay than in the CAT assay, and vice versa.

Comparisons of the Performance of the CAT and ApoCAT Assays to Those of Conventional Antioxidant Activity Assays. As illustrated in Table 1, antioxidant capacities of ascorbic acid, gallic acid and their esters were investigated in TPC, ABTS, FRAP, ORAC assays in comparisons with the CAT and the ApoCAT assays. It should be noted that TPC, ABTS, FRAP and ORAC assays were considered as homogeneous systems, while the CAT and the ApoCAT assays were concerned as heterogeneous systems. Results showed that ascorbic acid and gallic acid exhibited higher antioxidant capacities than their ester forms in TPC, ABTS, FRAP, and ORAC assays. Hence, the solubility of antioxidants in the aqueous systems should be one of the important factors affecting on the overall antioxidant activities.

However, in the CAT assay, ascorbyl palmitate exhibited lower antioxidant capacity than ascorbic acid, while lauryl gallate showed higher antioxidant capacity than gallic acid, based on trolox equivalents. Results indicated that the cutoff effect could be observed in ascorbyl palmitate. Laguerre and co-workers[9,22] explained the cutoff effect in several heterogeneous systems that too low polarity of an antioxidant may impact on the locations of the antioxidant, distributing into the lipid core inside and/or self-aggregation outside emulsion droplets. However, in the case of the ApoCAT assay, it was noted that a different antioxidant behavior was observed. Ascorbyl palmitate exhibited higher antioxidant capacity than ascorbic acid, based on trolox equivalents.

In addition, these models were performed on various commercial antioxidant extracts as shown in Table 2. Based on homogeneous models, TPC, ABTS and FRAP assays showed a similar antioxidant behavior that green tea extract had the lowest antioxidant capacity followed by rosemary extract, mixed tocopherol and/or grape seed extract. On the contrary, the obtained results from the ORAC assay differed from other assays. In this model, mixed tocopherol had the lowest antioxidant capacity followed by green tea, grape seed, and rosemary extracts, respectively.

The CAT and the ApoCAT assays showed a similar antioxidant pattern that green tea had the lowest antioxidant capacities, while rosemary extract had the highest antioxidant capacity. To understand the effect of oxidant locations, the ApoCAT/CAT ratios of tested antioxidants were calculated as illustrated in Figure 6. It should be noted that the higher the

DOI: 10.1021/acs.jafc.5b02493
J. Agric. Food Chem. 2015, 63, 7546−7555

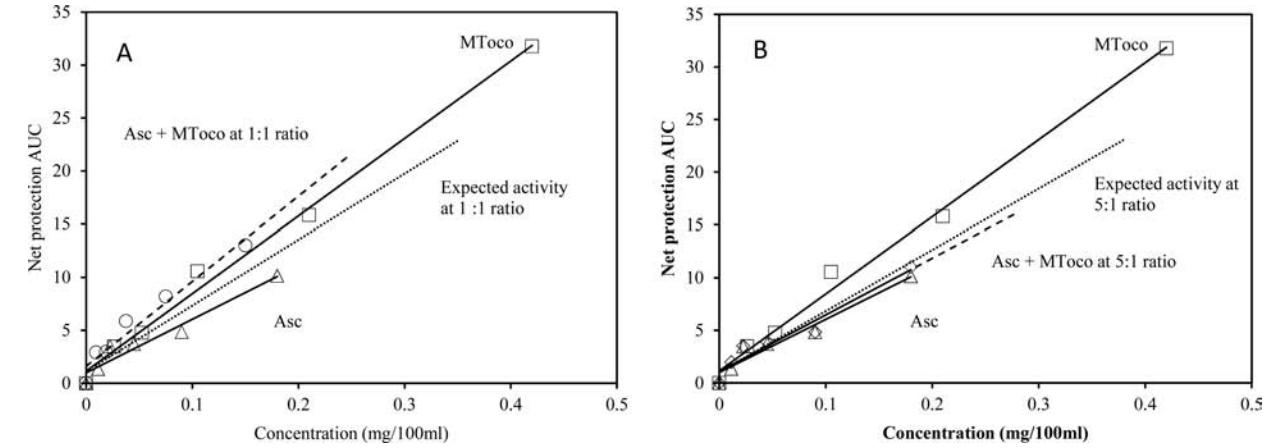

Figure 7. Demonstration of estimating interaction index of ascorbic acid and α-tocopherol at the ratio of 1 to 1 and 5 to 1 in the CAT assay.

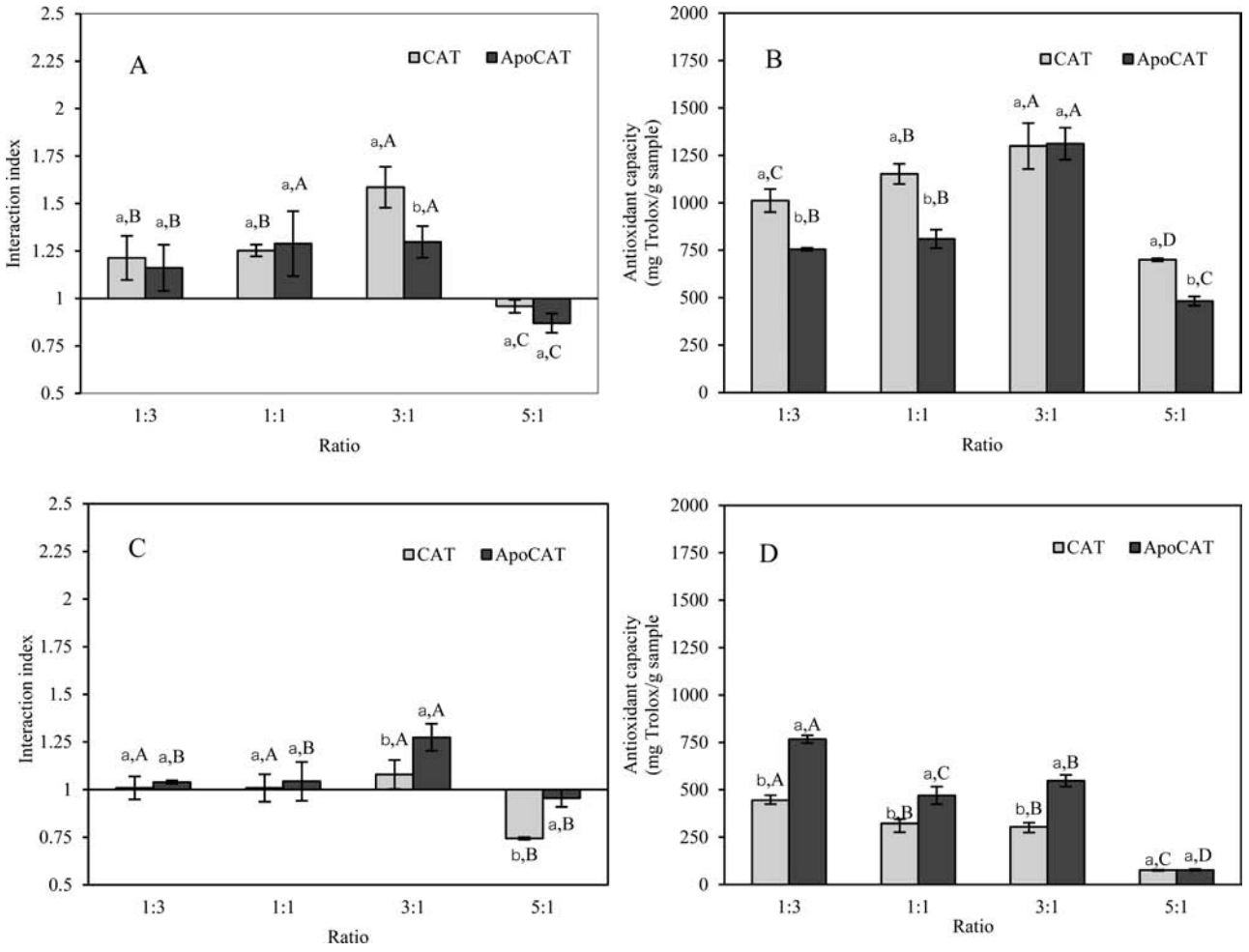

Figure 8. Antioxidant interactions (left) and capacities (right) between selected antioxidants and mixed tocopherols in both CAT and ApoCAT assays. Combination of ascorbic acid and mixed tocopherols (A and B), and combination of green tea extract and mixed tocopherols (C and D). Values are the means of three replicates. The different letters (a and b) of interaction index from the CAT and the ApoCAT assays at the same ratio indicate significant differences ($p < 0.05$). The different letters (A, B, C, and D) of interaction index obtained from different ratios of the same assay indicate significant differences ($p < 0.05$).

ApoCAT/CAT ratio, the better antioxidative performance of an antioxidant was observed in a lipid phase radical-initiating system. As shown in Figure 6A, all ester forms had higher ApoCAT/CAT ratios than their acid forms. For example, ascorbyl palmitate showed an improved performance in the ApoCAT assay, while ascorbic acid showed the opposite trend. In addition, the same was true for gallic acid and its ester.

Overall, the ApoCAT/CAT ratio could provide more information on the characteristics of antioxidants preferring free radicals in water and/or lipid phases. This concept was also applied for characterizing some commercial antioxidants and

DOI: 10.1021/acs.jafc.5b02493
J. Agric. Food Chem. 2015, 63, 7546−7555

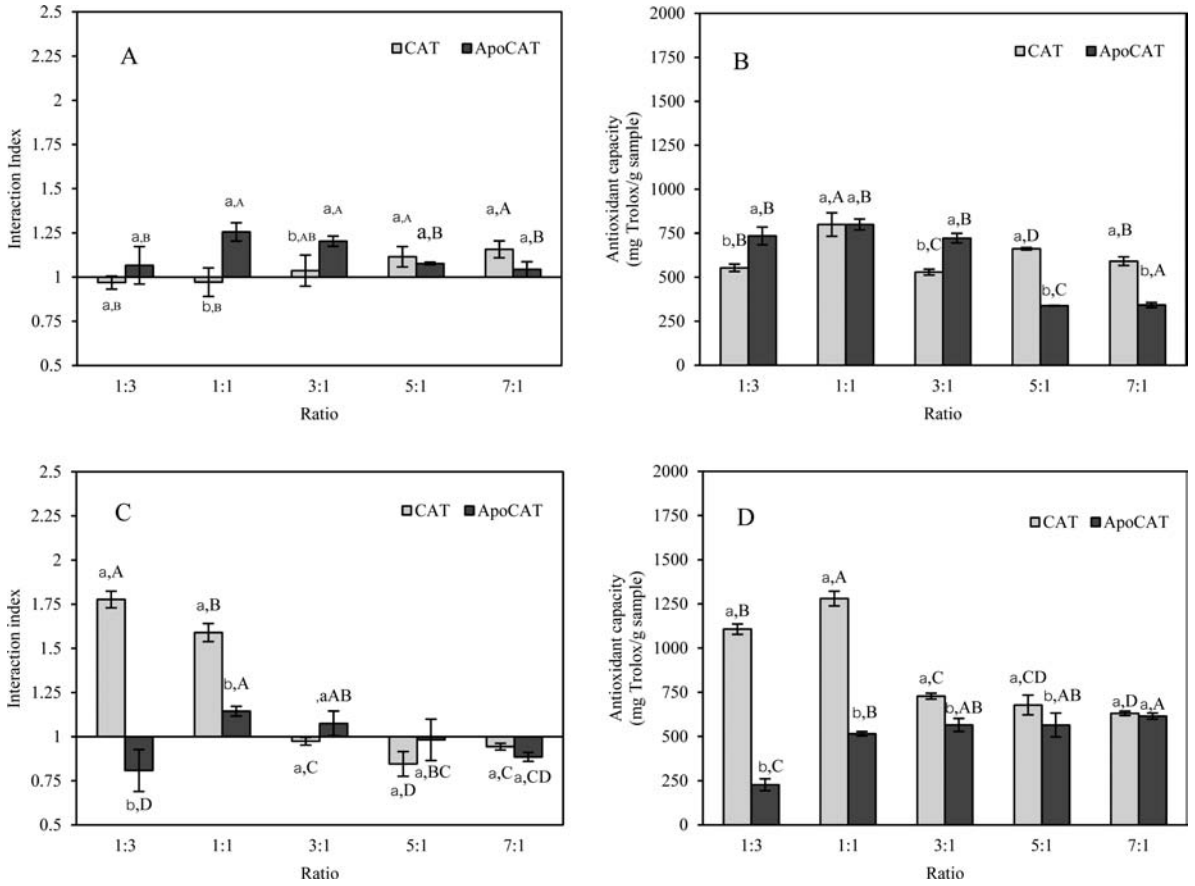

Figure 9. Antioxidant interactions (left) and capacities (right) between selected antioxidants and mixed tocopherol in both CAT and ApoCAT assays. Combination of grape seed extract and mixed tocopherol (A and B), and combination of rosemary extract and mixed tocopherol (C and D). Values are the means of three replicates. The different letters (a and b) of interaction index from the CAT and the ApoCAT assays at the same ratio indicated significant differences ($p < 0.05$). The different letters (A, B, C, and D) of interaction index obtained from different ratios of the same assay indicate significant differences ($p < 0.05$).

natural plant extracts as shown in Figure 6B. As expected, mixed tocopherols performed better in the ApoCAT assay, since they are lipid soluble antioxidants. Interestingly, the performances of green tea and rosemary extracts have also been increased, while grape seed extract showed no significant difference in both assays. The results suggested that mixed tocopherols, green tea extract, and rosemary extract could be good antioxidant candidates for preventing oxidation in oil-in-water emulsion systems.

Investigation of Antioxidant Interactions Using the CAT and the ApoCAT Assays. The combined effects of selected antioxidants were investigated using the CAT and ApoCAT assays at various ratios. Figure 7 shows linear relationships between observed individual and combined antioxidants, and expected combined antioxidants of various ratios of ascorbic acid/α-tocopherol mixtures based on mass basis. Results indicated that increasing the ratio of ascorbic acid to α-tocopherol from 1:1 to 5:1 changed antioxidant interactions from synergism to antagonism. In the case of a synergistic effect, the observed slope of the antioxidant activity was higher than the expected slope of the antioxidant activity, and vice versa for the antagonistic effect. Using this calculation, the relationships between ratios of polar and nonpolar antioxidants, and antioxidant interactions in O/W emulsions could be investigated.

As shown in Figures 8 and 9, increasing the ratios of various polar antioxidants to mixed tocopherol (nonpolar antioxidant) resulted in altered antioxidant interactions and overall antioxidant capacities. Depending on antioxidants and evaluation methods, the optimal combination ratios to obtain the highest antioxidant synergy and capacities could be different. As illustrated in Figure 8, combining ascorbic acid or green tea with α-tocopherol exhibited the highest interaction index at a 3:1 ratio. It should be noted that increasing the ratio further than this level resulted in an antagonistic effect (at 5:1 ratio).

Similar behaviors of the combinations were observed in the combined effects of grape seed and rosemary extracts. For the combinations with grape seed extract, the optimal ratios for synergy were observed around 1:1 to 3:1 ratios; however, for rosemary extract, the highest synergy was observed at 1:3 ratios. It was noted that the combination with ascorbic acid (Figure 8A) and rosemary (Figure 9A) extracts exhibited similar combination behaviors in such a way that the CAT assay provided a significantly higher interaction index in comparison with the ApoCAT assay. However, green tea (Figure 8C) and grape seed (Figure 9C) extracts exhibited a weak synergy in the ApoCAT assay higher than in the CAT assay.

Overall, results demonstrated that the performance of antioxidants could be improved by a combined strategy between water-and lipid-soluble antioxidants. It was hypothesized that water-soluble antioxidants could provide active prevention against radicals generated from AAPH in the water phase in addition to passive prevention of the radicals generated at the oil-in-water interface of the emulsion droplets. This could explain

DOI: 10.1021/acs.jafc.5b02493
J. Agric. Food Chem. 2015, 63, 7546−7555

why the strong synergy was strongly observed in the CAT assay rather than the ApoCAT assay.

However, due to the complexity of antioxidant mechanisms, it is impossible to explain antioxidant interactions using a simple explanation. Several reports showed that antioxidant regeneration was one of the important mechanisms to obtain a strong antioxidant synergy. By principle, the primary antioxidant is regenerated by the secondary antioxidant based on differences in their reduction potentials. For instance, ascorbic acid is able to regenerate α-tocopherol, which is more active in the system.[23] In addition, several compounds were reported to exhibit some antioxidant interactions with α-tocopherol, such as β-carotene, amino acids, peptides, and phospholipids.[24−30]

AUTHOR INFORMATION

Funding

We would like to express our thanks to Ri-BIOTEC (Grant No. P13-00445), Young Scientist and Technologist Program (YSTP), NSTDA (Grant No. SP-56-BT05), and Thailand Research Fund (Grant No. TRG5780061) for supporting this research project.

Notes

The authors declare no competing financial interest.

REFERENCES

(1) Gonzalez, E. A.; Nazareno, M. A. Antiradical action of flavonoid-ascorbate mixtures. *Lwt-Food Science and Technology* **2011**, *44* (2), 558−564.

(2) Liu, D. H.; Shi, J.; Ibarra, A. C.; Kakuda, Y.; Xue, S. J. The scavenging capacity and synergistic effects of lycopene, vitamin E, vitamin C, and beta-carotene mixtures on the DPPH free radical. *Lwt-Food Science and Technology* **2008**, *41* (7), 1344−1349.

(3) Hidalgo, M.; Sanchez-Moreno, C.; de Pascual-Teresa, S. Flavonoid-flavonoid interaction and its effect on their antioxidant activity. *Food Chem.* **2010**, *121* (3), 691−696.

(4) Chen, J.; Shi, J.; Macnaughton, L.; Kakuda, Y.; Xue, S. J.; Ma, Y.; Zhang, M.; Jiang, Y. The scavenging capacity of combinations of lycopene, B-carotene, vitamin e, and vitamin c on the free radical 2,2-diphenyl-1-picrylhydrazyl (DPPH). *J. Food Biochem.* **2009**, *33* (2), 232−245.

(5) Hiramoto, K.; Miura, Y.; Ohuki, G.; Kato, T.; Kikigawa, K. Are water-soluble natural antioxidants: synergistic in combination with alpha-tocopherol. *J. Oleo Sci.* **2002**, *51* (9), 569−576.

(6) Parker, T. L.; Miller, S. A.; Myers, L. E.; Miguez, F. E.; Engeseth, N. J. Evaluation of synergistic antioxidant potential of complex mixtures using oxygen radical absorbance capacity (ORAC) and electron paramagnetic resonance (EPR). *J. Agric. Food Chem.* **2010**, *58* (1), 209−17.

(7) Freeman, B. L.; Eggett, D. L.; Parker, T. L. Synergistic and Antagonistic Interactions of Phenolic Compounds Found in Navel Oranges. *J. Food Sci.* **2010**, *75* (6), C570−C576.

(8) Deetae, P.; Parichanon, P.; Trakunleewatthana, P.; Chanseetis, C.; Lertsiri, S. Antioxidant and anti-glycation properties of Thai herbal teas in comparison with conventional teas. *Food Chem.* **2012**, *133* (3), 953−959.

(9) Laguerre, M.; Lopez-Giraldo, L. J.; Lecomte, J.; Barea, B.; Cambon, E.; Tchobo, P. F.; Barouh, N.; Villeneuve, P. Conjugated autoxidizable triene (CAT) assay: a novel spectrophotometric method for determination of antioxidant capacity using triacylglycerol as ultraviolet probe. *Anal. Biochem.* **2008**, *380* (2), 282−90.

(10) Nkhili, E.; Brat, P. Reexamination of the ORAC assay: effect of metal ions. *Anal. Bioanal. Chem.* **2011**, *400* (5), 1451−1458.

(11) Ou, B.; Hampsch-Woodill, M.; Flanagan, J.; Deemer, E. K.; Prior, R. L.; Huang, D. J. Novel fluorometric assay for hydroxyl radical prevention capacity using fluorescein as the probe. *J. Agric. Food Chem.* **2002**, *50* (10), 2772−2777.

(12) Laguerre, M.; Wrutniak-Cabello, C.; Chabi, B.; Giraldo, L. J. L.; Lecomte, J.; Villeneuve, P.; Cabello, G. Does hydrophobicity always enhance antioxidant drugs? A cut-off effect of the chain length of functionalized chlorogenate esters on ROS-overexpressing fibroblasts. *J. Pharm. Pharmacol.* **2011**, *63* (4), 531−540.

(13) Laguerre, M.; Giraldo, L. J.; Lecomte, J.; Figueroa-Espinoza, M. C.; Barea, B.; Weiss, J.; Decker, E. A.; Villeneuve, P. Chain length affects antioxidant properties of chlorogenate esters in emulsion: the cutoff theory behind the polar paradox. *J. Agric. Food Chem.* **2009**, *57* (23), 11335−42.

(14) Panya, A.; Laguerre, M.; Lecomte, J.; Villeneuve, P.; Weiss, J.; McClements, D. J.; Decker, E. A. Effects of chitosan and rosmarinate esters on the physical and oxidative stability of liposomes. *J. Agric. Food Chem.* **2010**, *58* (9), 5679−5684.

(15) Panya, A.; Laguerre, M.; Bayrasy, C.; Lecomte, J.; Villeneuve, P.; McClements, D. J.; Decker, E. A. An Investigation of the Versatile Antioxidant Mechanisms of Action of Rosmarinate Alkyl Esters in Oil-in-Water Emulsions. *J. Agric. Food Chem.* **2012**, *60* (10), 2692−2700.

(16) Laguerre, M.; Lopez Giraldo, L. J.; Lecomte, J.; Figueroa-Espinoza, M. C.; Barea, B.; Weiss, J.; Decker, E. A.; Villeneuve, P. Relationship between hydrophobicity and antioxidant ability of "phenolipids" in emulsion: a parabolic effect of the chain length of rosmarinate esters. *J. Agric. Food Chem.* **2010**, *58* (5), 2869−76.

(17) Waraho, T.; McClements, D. J.; Decker, E. A. Mechanisms of lipid oxidation in food dispersions. *Trends Food Sci. Technol.* **2011**, *22* (1), 3−13.

(18) McClements, D. J.; Decker, E. A. Lipid oxidation in oil-in-water emulsions: Impact of molecular environment on chemical reactions in heterogeneous food systems. *J. Food Sci.* **2000**, *65* (8), 1270−1282.

(19) Panya, A.; Kittipongpittaya, K.; Laguerre, M.; Bayrasy, C.; Lecomte, J.; Villeneuve, P.; McClements, D. J.; Decker, E. A. Interactions between α-Tocopherol and Rosmarinic Acid and Its Alkyl Esters in Emulsions: Synergistic, Additive, or Antagonistic Effect? *J. Agric. Food Chem.* **2012**, *60* (41), 10320−10330.

(20) Laguerre, M.; López-Giraldo, L. J.; Lecomte, J.; Baréa, B.; Cambon, E.; Tchobo, P. F.; Barouh, N.; Villeneuve, P. Conjugated autoxidizable triene (CAT) assay: A novel spectrophotometric method for determination of antioxidant capacity using triacylglycerol as ultraviolet probe. *Anal. Biochem.* **2008**, *380* (2), 282−290.

(21) Boon, C. S.; Xu, Z.; Yue, X.; McClements, D. J.; Weiss, J.; Decker, E. A. Factors affecting lycopene oxidation in oil-in-water emulsions. *J. Agric. Food Chem.* **2008**, *56* (4), 1408−1414.

(22) Laguerre, M.; Bayrasy, C.; Panya, A.; Weiss, J.; McClements, D. J.; Lecomte, J.; Decker, E. A.; Villeneuve, P. What Makes Good Antioxidants in Lipid-Based Systems? The Next Theories Beyond the Polar Paradox. *Crit. Rev. Food Sci. Nutr.* **2013**, *55* (2), 183−201.

(23) Fukuzawa, K.; Ikebata, W.; Sohmi, K. Location, antioxidant and recycling dynamics of alpha-tocopherol in liposome membranes. *J. Nutr. Sci. Vitaminol.* **1993**, *39*, S9−S22.

(24) Gardner, H. W.; Kleiman, R.; Weisleder, D.; Inglett, G. E. Cysteine adds to lipid hydroperoxide. *Lipids* **1977**, *12* (8), 655−660.

(25) Lambelet, P. S. F.; Loliger, J. Radical exchange reactions between vitamin E and vitamin C and phospholipids in autoxidizing polyunsaturated lipids. *Free Radical Res.* **1994**, *20* (1), 1−10.

(26) Sims, R. J.; Fioriti, J. A. Methional as an antioxidant for vegetable-oils. *J. Am. Oil Chem. Soc.* **1977**, *54* (1), 4−7.

(27) Terao, J.; Yamauchi, R.; Murakami, H.; Matsushita, S. Inhibitory effects of tocopherols and beta-carotene on singlet oxygen-initiated photo-oxidation of methyl linoleate and soybean oil. *J. Food Process. Preserv.* **1980**, *4* (1−2), 79−93.

(28) Burton, G. W.; Ingold, K. U. Beta-carotene - An unusual type of lipid antioxidant. *Science* **1984**, *224* (4649), 569−573.

(29) Kennedy, T. A.; Liebler, D. C. Peroxyl radical scavenging by beta-carotene in lipid bilayers - effect of oxygen partial-pressure. *J. Biol. Chem.* **1992**, *267* (7), 4658−4663.

(30) Palozza, P.; Krinsky, N. I. Beta-carotene and alpha-tocopherol are synergistic antioxidants. *Arch. Biochem. Biophys.* **1992**, *297* (1), 184−187.

DOI: 10.1021/acs.jafc.5b02493
J. Agric. Food Chem. 2015, 63, 7546−7555

importance because it reacts with electrophilic or oxidizing species before they interact with critical cellular constituents such as nucleic acids or proteins.[8] Gardiner et al.[9] reported that RNA profiling of DON-treated barley spikes showed strong up-regulation of gene transcripts encoding glutathione-*S*-transferases and cysteine synthases. Suggested structures for DON−GSH conjugates include addition of GSH on the double bond at C-9[3,9] and nucleophilic attack on the hydroxylated C-7 atom or at the carbonyl carbon at C-8.[9] Frühmann et al.[10] proposed that DON−GSH is broken down in planta, resulting in methylthiodeoxynivalenol as the final product. They synthesized methylthiodeoxynivalenol and showed that their product was a mixture of the C-8 hemiketal and ketone, produced via addition of thiourea to the double bond of DON.

Here we report studies using mercaptoethanol as a model thiol for reaction with DON and other trichothecenes to identify the reaction pathways for DON with thiols. We also show that the same pathways are important for reaction of DON with a wide variety of thiols including cysteine and glutathione. In contrast to earlier reports, we identified the epoxide group as an important target for thiol addition to DON.

MATERIALS AND METHODS

Chemicals and Reagents. HPLC grade water and acetonitrile were obtained from Thermo Fisher Scientific (Waltham, MA, USA). Ammonium formate (Fluka, puriss. p.a. for HPLC), deoxynivalenol (DON) (≥98%), lipopolysaccharide (LPS) from *Escherichia coli*, CD_3CN (99.95 atom % D), 5.0 mm Wilmad NMR tubes, sodium carbonate (pro analysis), 2-mercaptoethanol (≥99.0%), 2-aminoethanethiol (≥98%), sodium methanethiolate (technical grade (>90%)), sodium 2-mercaptoethanesulfonate (≥98%), L-cysteine (≥98%), and reduced L-glutathione (≥98%) were from Sigma-Aldrich (Steinheim, Germany). Phosphate-buffered saline (pH 7.3, 0.172 M) was prepared from ready-to-use tablets (Oxoid, Hampshire, UK). Sodium bicarbonate (pro analysis, Merck, Darmstadt, Germany) and sodium carbonate were used to prepare 0.2 M buffers at pH 9.2 and 10.7. Buffer pH was measured at ambient temperature with a Mettler Delta 320 pH meter. Solutions of T-2 tetraol (50.3 μg/mL) and de-epoxy-DON 50.5 μg/mL) in acetonitrile were from Biopure (Romer Laboratories, Tulln, Austria). Standards of norDON B and norDON C were provided by Institute of Food Chemistry, Münster, Germany. Alamar Blue and human TNF-α Cytoset were from Invitrogen (Life Technologies, Carlsbad, CA, USA), and human IL-1β/IL-1F2 Duoset was from R&D Systems (Minneapolis, MN, USA). RPMI 1640, culture medium, penicillin/streptomycin, fetal bovine serum (EU standard, FBS), and PBS were from Lonza (Verviers, Belgium). Phorbol-12-myristate-13-acetate (PMA) was from Calbiochem (La Jolla, CA, USA). Hydrogen peroxide (30%) was from Merck.

Reaction of Trichothecenes with Thiols. All reactions were conducted in 2 mL HPLC vials and monitored by LC-MS or LC-HRMS.

Procedure 1. Aliquots (0.33 μmol) of the stock solutions of DON, de-epoxy-DON, and T-2 tetraol in acetonitrile were evaporated under a stream of N_2 at 60 °C and dissolved in carbonate buffer (pH 10.7; 1.0 mL), and mercaptoethanol 0.5 μL (7.13 μmol) was then added. The vials were flushed with argon, sealed, and placed in the autosampler set to 25 °C. Reactions (together with thiol-free controls) were followed by LC-MS (method A1), half-hourly for the first 8 h and then at 1−2 day intervals thereafter for 1 month. The reaction of DON with mercaptoethanol was also carried out in buffer at pH 9.2 and 7.3.

Procedure 2a. Mercaptoethanol (10 μL, 142 μmol) was added to DON (1.0 mg, 3.3 μmol) in buffer (1 mL; pH 10.7), and the reaction was followed by LC-MS for ca. 3 weeks (method A1), by which time DON was absent and the peak intensity of **1a**/**1b** was equal to that of **2b** (Figure S1).

Procedure 2b. Mercaptoethanol (15 μL, 210 μmol) was added to DON (1.5 mg, 5.1 μmol) in buffer (1.5 mL; pH 10.7), and the reaction was followed by LC-MS for 14 days, by which time the peak intensities of **2a** and **2b** were about equal and dominated the chromatogram (Figure S2a).

Procedure 3. Solutions of other thiols (71.3 mM, 1 mL) (i.e., other than mercaptoethanol) in buffer (pH 10.7) were added to solid DON (100 μg, 0.33 μmol), and reactions were monitored by one or more LC-MS methods (methods A1, A2, B1, or B2) for 3 weeks.

Oxidation of 1a/1b. Hydrogen peroxide (30%, 50 μL) was added to an aliquot (150 μL) of the reaction mixture obtained from the procedure 1 containing **1a**/**1b**. Reaction was followed for 1 h, when **1a**/**1b** were no longer detectable.

LC-MS. HPLC was performed using an Atlantis T3 column (150 × 2.1 mm, 3 μm; Waters). The flow rate was 0.3 mL/min, and the injection volume was 1.5 μL. Mobile phase A was 5 mM ammonium formate in MeCN/water (19:1), and mobile phase B was aqueous ammonium formate (5 mM). Gradient 1: Separation was performed by elution with a linear gradient of 5−15% A over 15 min and then to 100% A at 20 min, with a 3 min hold followed by a return to 5% A with a 3 min hold to equilibrate the column. Gradient 2: This was identical to gradient 1 except that the gradient started and ended with 0.5% A (instead of 5% A). Gradient 3 was identical to gradient 1, apart from the mobile phase containing 2.5 mM ammonium formate and 2.5 mM formic acid.

Method A1. A Finnigan Surveyor HPLC system was used with gradient 1 and interfaced to an LTQ linear ion trap mass spectrometer (Thermo Fisher Scientific) operated in negative ionization full scan mode (m/z 180−600) and fitted with an electrospray ionization (ESI) interface. This method was used to monitor the reactions of DON, T-2 tetraol, and de-epoxy-DON with mercaptoethanol, as well as reactions of DON with sodium methanethiolate and sodium 2-mercaptoethanesulfonate. Capillary voltage and tube lens offset were tuned with continuous infusion of DON (10 μg/mL) in acetonitrile into a mobile phase composed of 10% A. The spray voltage was set to 3 kV, the sheath gas and auxiliary gas flow rates were 58 and 11 units, respectively, and the capillary temperature was 250 °C

The MS^n (n = 2−5) fragmentation of DON was studied using collision-induced dissociation in the ion trap by directly infusing 10 μg/mL DON in acetonitrile into a mobile phase composed of 10% A, via the instrument syringe pump (5 μL/min). The ESI settings were as described above. Individual precursor ions were selected with an isolation width of 2 m/z, the activation Q was set to 0.25, and the activation time was set to 30 ms. The collision energy was chosen such that the intensity of the precursor ion was <10% relative peak intensity. Product spectra were recorded for 30 s.

Method A2. Method A2 was performed as for method A1, except that gradient 2 was used for elution and the MS was run in positive mode for m/z 100−1000 in order to monitor the reaction of DON with 2-aminoethanethiol, glutathione, or cysteine.

Method B1. A Waters Acquity UPLC (Milford, MA, USA) used with gradient 1 was interfaced to a Q Exactive Fourier-transform high-resolution mass spectrometer (Thermo Fisher Scientific) and used for analysis of the products from the reactions of DON, T-2 tetraol, and de-epoxy-DON with mercaptoethanol and of DON with sodium methanethiolate and sodium 2-mercaptoethanesulfonate. A heated electrospray interface was used for ionization with a spray voltage of 3.8 kV and a temperature of 300 °C. The mass spectrometer was run in the negative full-scan mode in the mass range m/z 150−600. The mass resolution was set to 70000 at m/z 200. Other important interface parameters included a capillary temperature of 250 °C, a sheath gas flow rate of 55 units, and an auxiliary gas flow rate of 25 units.

For targeted MS/MS, $[M + HCOO]^-$ ions of mercaptoethanol derivatives were selected and subjected to higher energy collisional dissociation at a normalized collision energy of 35 eV. The resolution was set to 17500 at m/z 200, and the product ions were scanned in the mass range m/z 50−365, 50−445, or 50−525 (as appropriate).

Method B2. Method B2 was as described for method B1 except that gradient 2 was used for elution and the MS was run in positive mode

DOI: 10.1021/acs.jafc.5b02864
J. Agric. Food Chem. 2015, 63, 7556−7566

for m/z 100−1000 in order to monitor the reaction of DON with 2-aminoethanethiol, glutathione, or cysteine.

Method C. Preparative LC-MS was performed by injecting portions (150 μL) onto an Atlantis T3 column (250 × 10 mm, 5 μm; Waters). The column was eluted with a Shimadzu LC-20AD pump (Shimadzu Corp., Kyoto, Japan) at 3 mL/min. A portion of the column effluent (0.1%) was continuously split into an LCQ Fleet ion trap mass spectrometer (Thermo Fisher), whereas individual fractions containing target compounds were collected manually.

Purification of DON−Mercaptoethanol Derivatives. Reaction mixtures from pocedures 2A and 2B were fractionated on Strata-X SPE columns (500 mg; Phenomenex, Torrance, CA, USA). The SPE column was conditioned with methanol (10 mL) and then water (10 mL), and the reaction mixture was applied. The columns were eluted with 5 mL each of 0, 5, 10, 15, 20, 25, 40, and 50% MeOH in water and then finally with MeOH. The 40 and 50% MeOH fractions from procedure 2A contained **1a**/**1b** and **2a**/**2b** and were combined and evaporated to ca. 1 mL under a stream of N_2. The components were purified by preparative LC-MS (method C) using a linear gradient of water (A) and acetonitrile (B) (from 5 to 21% B over 17 min, then 100% B for 3 min, and finally to 5% B for 5 min to equilibrate the column), with **1a**/**1b** eluting at 14.5 min and **2a**/**2b** (ca. 1:5 by NMR) at 16.8 min.

When the mixture obtained from procedure 2B was chromatographed by SPE (as above), the 40% MeOH fraction contained **2a**/**2b**. This material was concentrated to 1 mL as above and purified by preparative LC-MS (method C) using isocratic elution with 21% MeCN in water, with **2a**/**2b** (ca. 1:1 by NMR) coeluting at 6.6 min (Figure S2b).

NMR Spectroscopy. 1-D (^{1}H, SELTOCSY, SELROESY, ^{13}C, JMOD, DEPT135) and 2-D (COSY, TOCSY, HSQC, HMBC, NOESY, ROESY) NMR experiments were conducted with Bruker Avance AV 600 MHz and AVII 600 MHz NMR spectrometers equipped with 5 mm CP-TCI (^{1}H/^{13}C, ^{15}N−^{2}H) triple-resonance inverse cryoprobes with *Z*-gradient coils. Compounds were dissolved in CD_3CN in 5.0 mm Wilmad NMR tubes. Data were recorded and processed using Bruker TOPSPIN (version 2.1 and 3.0) software, and chemical shifts, determined at 25 °C, are reported relative to internal CHD_2CN (1.96 ppm) and CD_3CN (118.26 ppm).[11]

Cell Culture and Treatments. The human acute monocyte leukemia cell line (THP-1) was obtained from the European collection of cell cultures (ECACC) and grown in RPMI 1640 supplemented with 10% heat-inactivated FBS, penicillin (100 U/mL), and streptomycin (100 μg/mL). The cells were cultured at 37 °C under 5% CO_2 in a humidified incubator and kept in a logarithmic growth phase at (5−15) × 10^5 cells/mL through routine subculturing, according to standard ECACC protocol. The passage number was kept below 20. DON and its derivatives were dissolved in PBS and applied to the cells at a final concentration of 4 μM.

Proliferation. THP-1 cells (monocytes) were seeded at 150,000 cells/cm^2 and, following exposure to DON and the conjugates, the metabolic activity of the cells was measured using the Alamar Blue assay according to the manufacturer's protocol. The dark blue oxidized form of Alamar Blue is reduced to a highly fluorescent form in functional mitochondria,[12] and the measured fluorescence intensity is thus proportional to the number of viable cells. The fluorescence (585 nm) was quantified using a VICTOR^2 Multilabel Counter (PerkinElmer, Boston, MA, USA).

Cytokine Measurement, ELISA. Secreted cytokines were measured with an enzyme-linked immunosorbent assay (ELISA). THP-1 cells were seeded at 260,000/cm^2 and differentiated into macrophages by treatment with PMA (50 ng/mL) for 24 h. The medium was then replaced, and the cells were rested for 24 h before exposure. The cells were then treated with LPS (0.05 ng/mL) for 3 h, followed by toxin exposure for an additional 24 h. The medium was harvested and centrifuged (500*g*, 4 °C, 10 min) to remove cell debris. Levels of TNF-α and IL-1β in supernatants were measured by ELISA, using human TNF-α Cytoset or human IL-1β/IL-1F2 Duoset, respectively, according to the manufacturers' guidelines. The absorbances were measured using a plate reader (TECAN Sunrise, Phoenix Research Products, Hayward, CA, USA) equipped with analyzing software (Magellan VI).

Statistical Analysis. Data analyses were performed using Sigma Plot version 13.0. Statistical significance ($p < 0.05$) was assessed using one-way-ANOVA, followed by Dunnett's post-test.

RESULTS AND DISCUSSION

Reaction of DON, De-epoxy-DON, and T-2 tetraol with Mercaptoethanol. Initial experiments followed the reaction of DON using LC-MS (method A1, gradient 3) for up to 1 month, with mercaptoethanol as a model thiol under neutral and weakly basic conditions (procedure 1). Mercaptoethanol was used because it was expected to produce DON derivatives with retention times and ionization properties similar to those of DON itself, thereby facilitating monitoring of the reaction and its products by LC-MS. At pH 10.7 there was rapid formation of **1d** and **1e** (Figure 2) with a mass difference of 78 Da relative to the formate adduct of DON, corresponding to a single addition of mercaptoethanol. The broad peak observed for **1e** was suspected to be caused by the presence of formic acid in gradient 3; however, use of a neutral eluent (gradient 1) did not appreciably sharpen this peak. After 30 min, peaks corresponding to **1a**/**1b** (not resolved) and **1c** were also detected with the same m/z (Figure 2), along with **2a** and **2b** (Figure 2) exhibiting a mass difference of 156 Da

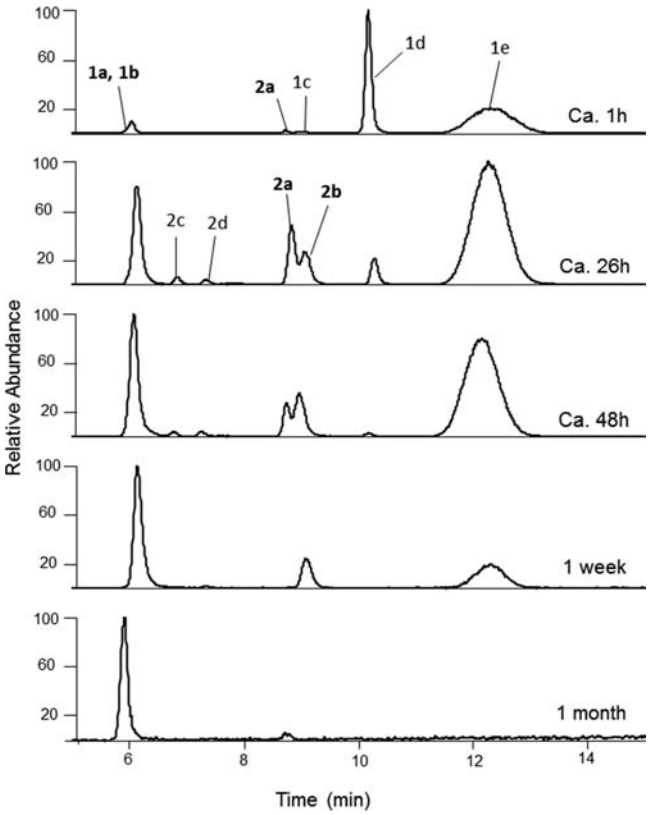

Figure 2. LC-MS extracted ion chromatograms (m/z 419 + m/z 497) from the reaction of DON with mercaptoethanol (method A1, pH 10.7, 25 °C). Adduct peaks are annotated 1 (m/z 419) or 2 (m/z 497) to indicate the number of mercaptoethanol units adducted to DON and with lower case letters then used to indicate separate peaks. Peaks labeled with bold text refer to adducts with structures determined by NMR spectroscopy (Figure 4). Note, a small drift in retention time occurred toward the end of the study.

DOI: 10.1021/acs.jafc.5b02864
J. Agric. Food Chem. 2015, 63, 7556−7566

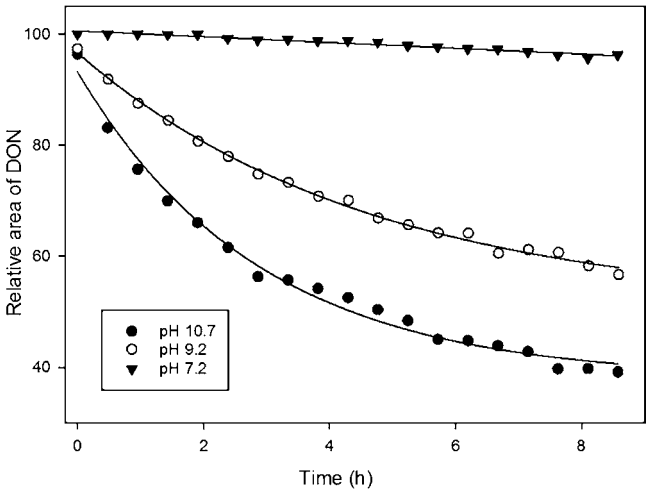

Figure 3. Change in the concentration of DON (measured by LC-MS, as a percentage of the total concentration of DON derivatives) with time upon treatment with mercaptoethanol at 30 °C at selected pH values. Lines show data fitted to exponential decay curves (pseudo-first-order kinetics).

relative to DON (corresponding to the addition of two molecules of mercaptoethanol). The ratios of these peaks continued to change over time, with **1a**/**1b** becoming more prevalent until they were the only compounds remaining in the mixture. Initially, four peaks corresponding to addition of two molecules of mercaptoethanol were detected, but **2c** and **2d** were minor and were no longer detectable after 1 week. Products **2a** and **2b** were the prominent double-addition conjugates, but **2a** disappeared in less than a week, leaving **2b** as the most prominent double-addition conjugate. However, **2b** also slowly disappeared with time, so that after 1 month the major peak was from **1a**/**1b**. The intensity of the LC-MS peak from DON gradually decreased as the reaction progressed (Figure 3) and was no longer detectable after 3 weeks.

We anticipated that thiol addition was most likely to occur reversibly at the C-10 carbon of the α,β-unsaturated ketone in DON and irreversibly at the epoxy group in DON. To test this hypothesis, we compared the reactions of DON, T-2 tetraol, and de-epoxy-DON with mercaptoethanol (Figure S17). In T-2 tetraol the C-8 carbon is hydroxylated, resulting in a 9,10-double bond that is not conjugated, whereas in de-epoxy-DON the epoxide ring has been reduced to an olefinic methylene (Figure 1). The reaction of T-2 tetraol was followed for 10 days by LC-MS (method A1), during which time just one new, later-eluting peak appeared, corresponding to addition of one mercaptoethanol molecule. LC-HRMS analysis (method B1) of this peak revealed it had m/z 421.1541, corresponding to $C_{18}H_{29}O_9S^-$ ([T-2 tetraol + HSEtOH + HCOO]$^-$, Δ 0.9 ppm) (Figures S3). Similarly, the reaction mixture containing de-epoxy-DON gave in total four peaks with m/z 403.1437−403.1443 corresponding to $C_{18}H_{27}O_8S^-$ ([de-epoxy-DON + HSEtOH + HCOO]$^-$, Δ 1.2−2.9 ppm). After 10 h of reaction, an earlier-eluting peak had almost the same intensity as de-epoxy-DON, whereas a later-eluting peak was higher in intensity (Figure S4a), and two other peaks had very low intensities. After 10 days, analysis revealed de-epoxy-DON was the most intense peak, with the later-eluting mercaptoethanol adduct now having an intensity 4 times lower than that of de-epoxy-DON (Figure S4b), indicating reversibility of the reaction. In contrast, reanalysis of the T-2 tetraol reaction after 10 days revealed the same two peaks as detected early in the reaction, but with the mercaptoethanol adduct having increased in intensity relative to T-2 tetraol. No double adducts of mercaptoethanol with de-epoxy-DON or T-2 tetraol were detectable at any stage of the reactions. These observations are consistent with reversible Michael addition of thiols to the conjugated double bond in type B trichothecenes and a slower irreversible addition of thiols to C-13 on the 12,13-epoxy group of trichothecenes (Figures 11 and S17).

These results suggested that **1c**, **1d**, and **1e** were products from Michael addition of mercaptoethanol to the 9,10-double bond of DON, whereas the relatively early eluting **1a**/**1b** was attributable to addition of mercaptoethanol to the epoxy group in DON.

During the reaction of DON with mercaptoethanol under basic conditions, several minor products with masses similar to that of DON were detected by LC-HRMS. The same products were also observed in thiol-free control samples, and these appeared to be identical to those reported earlier by Bretz et al.,[13] thought to be products from degradation of DON under basic conditions. Two of the degradation products, norDON B and norDON C,[13] were confirmed in the DON−mercaptoethanol reaction mixtures using authentic standards. Because these DON degradation reactions compete with the thiol addition, higher concentrations of thiols were used in the semipreparative reactions to reduce the reaction time and thereby minimize the effect of the degradation reactions.

Minor peaks affording ions with a 16 Da higher mass (m/z 435), relative to the DON−mercaptoethanol adducts, were also detected during the reaction, suggesting the presence of sulfoxide derivatives. Addition of H_2O_2 to an aliquot of a reaction mixture containing **1a**/**1b** resulted in rapid oxidation, affording products with the same masses and retention times as the putative sulfoxide derivatives (Figure S5). This indicates that m/z 435 peaks are due to the sulfoxides of thiol adducts **1a**/**1b**. Similar autoxidation was also seen with DON derivatives of the other thiols including cysteine or glutathione. Purified DON conjugates were therefore stored under argon to minimize the autoxidation.

Preparative Synthesis and Purification. DON and mercaptoethanol were reacted on a semipreparative scale to identify the major products. Two reactions were followed by LC-MS: one was stopped by SPE when almost equal ratios of **1a**/**1b** and **2b** were present (procedure 2a) and the other when the ratios of **2a** and **2b** were identical (procedure 2b). Fractionation of the reaction mixtures by SPE followed by semipreparative LC-MS afforded pure mixtures of **1a** together with **1b** and of **2a** together with **2b**.

Structural Elucidation. NMR structural elucidation of major products was done on mixtures of **1a** and **1b**, and of **2a** and **2b**, in CD_3CN, with DON used for spectral comparison. LC-HRMS showed a single peak for **1a**/**1b**, with m/z 419.1383 consistent with $C_{18}H_{27}O_9^-$ (DON + HSEtOH + HCOO]$^-$), indicating the addition of one molecule of mercaptoethanol to DON. However, NMR spectroscopy revealed the presence of two isomeric compounds (Table 1) in a ratio of 5:1. Three of the most diagnostic pairs of signals were methyl singlets at 1.27 and 1.24 ppm (H-14), methyl triplets at 1.74 and 1.81 ppm (H-16), and signals due to olefinic protons (both doublets of quartets) at 5.35 and 6.44 ppm (H-10). The presence of an olefinic proton in **1a** and **1b** indicated the presence of a double bond and thus showed that mercaptoethanol had not been added to C-10.

DOI: 10.1021/acs.jafc.5b02864
J. Agric. Food Chem. 2015, 63, 7556−7566

Table 1. ^{1}H and ^{13}C NMR Assignments (δ) for DON, 1a, 1b, 2a, and 2b in CD_3CN

	DON		1a		1b		2a		2b	
atom	^{1}H[a]	^{13}C	^{1}H[a]	^{13}C	^{1}H[a]	^{13}C	^{1}H[a]	^{13}C	^{1}H[a]	^{13}C
2	3.51 (d, 4.5)	81.4	3.72 (d, 4.5)	81.6	3.76 (d, 4.5)	80.9	3.78 (d, 4.5)	80.9	3.81 (d, 4.5)	83.1
3	4.34 (dq, 11.1, 4.4)	69.4	4.55 (dq, 10.5, 4.3)	70.5	4.52 (dq, 10.6, 4.5)	70.3	4.50 (dq, 10.5, 4.3)	70.4	4.58 (dq, 10.6, 4.4)	70.8
4[b]	2.30 (dd, 14.6, 4.4)	44.3	1.42 (dd, 13.8, 3.7)	45.9	1.91 (dd, 14.0, 3.2)	44.5	1.50 (dd, 14.2, 3.5)	45.9	1.48 (dd, 13.8, 3.8)	46.9
	1.95 (dd, 14.6,11.1)		1.97 (dd, 13.8, 10.7)[c]		2.06 (dd,14.0, 10.6)		2.00 (dd,14.2, 10.4)		1.99 (dd,13.8, 10.6)	
5	–	46.7	–	50.8	–	50.9	–	50.4	–	51.0
6	–	53.1	–	51.8	–	53.4	–	54.1	–	55.4
7	4.80 (d, 2.9)	75.2	3.92 (d, 3.8)	77.7	4.71 (d, 2.7)	75.2	3.94 (d, 5.8)	72.9	3.95 (d, 5.4)	78.8
8	–	200.7	–	104.7	–	200.4		107.7	–	106.6
9	–	136.0	–	142.4	–	134.9	1.80 (dq, 9.2, 7.0)[d]	46.3	1.78 (dq, 12.0, 6.5)[d]	44.2
10	6.60 (dq, 5.9, 1.6)	139.6	5.35 (dq, 3.7, 1.6)	122.9	6.44 (dq, 5.3, 1.5)	139.7	2.41 (dd, 9.2, 6.6)	52.0	2.77 (dd, 12.0, 7.2)[d]	50.2
11	4.86 (d, 5.9)	70.9	4.81 (dq, 3.7, 1.6)	77.0	4.94 (d, 5.3)	71.8	4.48 (d, 6.6)	85.9	4.62 (d, 7.2)	76.5
12	–	66.7	–	81.7	–	81.4	–	81.6	–	81.3
13	3.03 (d, 4.4)	47.8	2.99 (d, 13.7)	36.3	2.98 (d, 13.2)	37.7	2.94 (d, 13.8)	36.2	3.09 (d, 13.7)	37.0
	3.05 (d, 4.4)		3.55 (d, 13.7)		3.54 (d, 13.2)		3.54 (d, 13.8)		3.63 (d, 13.7)	
14	1.05 (s)	14.6	1.27 (s)	15.8	1.24 (s)	15.7	1.23 (s)	16.3	1.22 (s)	15.6
15[b]	3.70 (dd, 11.9, 4.9)	61.7	3.31 (d, 8.7)	70.0	3.61 (dd, 11.7, 5.2)	64.8	3.52 (d, 8.3)	71.6	3.49 (d, 8.1)	70.3
	3.67 (dd, 11.9, 5.7)		4.09 (d, 8.7)		3.87 (dd, 11.7, 6.5)		4.11 (d, 8.3)		4.16 (d, 8.1)	
16	1.82 (dd, 1.6, 0.9)	15.3	1.74 (t, 1.7)	16.2	1.81 (t, 1.4)	15.5	1.13 (d, 6.9)	17.4	1.12 (d, 6.5)	13.3
1′	–		2.71 (dt, 3.1, 6.2)	37.0	2.69 (dt, 1.6, 6.2)	37.2	2.74 (m)	36.8	2.73 (m)	37.1
2′	–		3.68 (m)	62.0	3.64 (m)	61.9	3.72 (m)	62.3	3.71 (m)	62.03[e]
1″	–	–	–		–	–	2.69 (dt, 13.8, 6.3)[b]	35.6	2.66 (dt, 13.5, 6.4)	35.1
							3.00 (dt, 13.7, 6.2)		2.90 (dt, 13.5, 6.4)	
2″	–	–	–		–	–	3.66 (m)	62.00[e]	3.62 (m)	61.9
3-OH	3.25 (br d, 4.4)		3.13 (d, 4.4)		3.15 (d, 4.7)		3.14 (d, 4.5)		3.31 (d, 4.3)	
7-OH	3.79 (d, 2.9)		4.17 (bs)				3.50 (d, 5.8)[f]		4.10 (br s)	
12-OH	ND[g]		ND		ND		ND		ND	
2′−OH	ND		3.06 (t, 5.2)		ND		3.16 (t, 5.5)		3.11 (t, 4.8)[f]	
2″−OH	ND		ND		ND		3.12 (t, 6.6)[f]		3.08 (t, 6.4)	
15-OH	2.70 (br t, 5.5)		ND		2.66 (t, 6.2)		ND		ND	

[a]In the format: chemical shift in ppm (multiplicity, coupling constants in Hz). [b]Orientation of the protons was distinguishable (except for H-15 of DON and **1b**), and they are presented in the order α-H and β-H. [c]Resonance hidden under solvent signal. [d]Coupling constant measured from the HSQC spectra. [e]Shifts to two decimal places due to very close, but distinguishable resonances. [f]Coupling constants measured from TOCSY spectra. [g]ND, not detected.

Examination of the COSY and TOCSY spectra of the major isomer (**1a**) revealed a number of relatively short spin systems corresponding to H-16/H-10/H-11, H-2/H-3/3-OH/H-4α/H-4β/H-14, H-13a/H-13b, H-7/7-OH, H-15α/H-15β, and H-1′/H-2′/2-OH. The corresponding protonated carbon resonances were assigned from HSQC correlations, and connections between spin systems were established via correlations observed in HMBC spectra. Of particular note were HMBC correlations from the methyl triplet at 1.74 ppm (H-16) to 104.7 (C-8), 142.4 (C-9), and 122.9 (C-10) ppm and from H-15α/H-15β (3.31 and 4.09 ppm) to 104.7 (C-8), 77.7 (C-7), 50.8 (C-5), and 51.8 ppm (C-6). The latter established **1a** as a C-8 hemiketal derivative generated by intramolecular addition of the oxygen atom on C-15 to the C-8 carbonyl. Furthermore, correlations observed in the HMBC spectra from H-13a/H-13b (2.99/3.55 ppm) and C-1′ (37.0 ppm) and between H-1′ (2.71 ppm) and C-13 (36.3 ppm), showed attachment of the mercaptoethanol moiety at C-13 as a result of nucleophilic attack on the epoxy group of DON.

Examination of the corresponding spectra of the minor component (**1b**) revealed similar spin systems and correlations. Notable differences from **1a** included the presence in **1b** of HMBC correlations of the methyl protons at 1.81 ppm (H-16) to carbon signals at 200.7 (C-8), 134.9 (C-9), and 139.7 (C-10) ppm (Figure S6). Also, the COSY/TOCSY spectra of **1b** included a spin system corresponding to H-15α/H-15β/15-OH. The multiplicity of the signals from the H-15 resonances in **1b** (doublet of doublets) was consistent with ^{3}J coupling to the 15-OH proton, in contrast to **1a**, where H-15 resonances were observed as a pair of doublets due to the absence of a 15-OH. These results revealed the minor component (**1b**) to be the ketone analogue of **1a** (Figure 4). These observations are in accord with the known keto−hemiketal equilibration of type-B

DOI: 10.1021/acs.jafc.5b02864
J. Agric. Food Chem. 2015, 63, 7556−7566

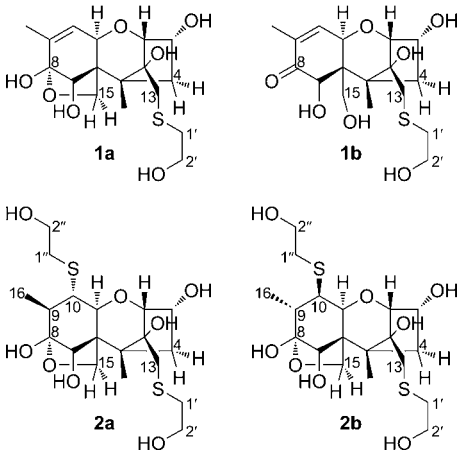

Figure 4. Structures of the major products purified from the reaction of DON with mercaptoethanol. **1a** and **1b** are the ketone and hemiketal pair resulting from addition of mercaptoethanol to the epoxide ring of DON, whereas **2a** and **2b** are a pair of diastereoisomers of the hemiketal form of adducts of mercaptoethanol to both the double bond and the epoxide ring of DON.

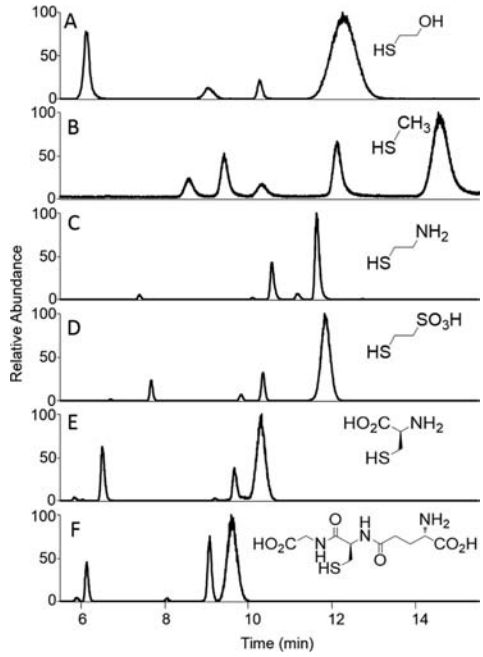

Figure 6. Extracted ion LC-MS chromatograms at the specified value of m/z for monoadducts of DON after reaction with various thiols at pH 10.7: (A) mercaptoethanol at 24 h, m/z 419.1381 ($[DON + HSCH_2CH_2OH + HCOO]^-$), negative ion mode; (B) sodium methanethiolate at 7 h, m/z 389 ($[DON + HSCH_3 + HCOO]^-$), negative ion mode; (C) 2-aminoethanethiol at 6 h, m/z 374.1632 ($[DON + HSCH_2CH_2NH_3]^+$), positive ion mode; (D) sodium 2-mercaptoethanesulfonate at 18 h, m/z 437.0945 ($[DON + HSCH_2CH_2SO_3]^-$), negative ion mode; (E) cysteine at 46 h, m/z 418.1530 ($[DON + CYS + H]^+$), positive ion mode; (F) glutathione at 48 h, m/z 604.2171 ($[DON + GSH + H]^+$), positive ion mode.

trichothecenes,[14] with the hemiketal form appearing to be favored by derivatization of the 9,10-olefinic group.[5,10,15]

Compounds **2a** and **2b** were isolated twice as a mixture, once in an approximate 1:1 ratio and once in a 1:5 ratio, which facilitated identification of NMR signals associated with the two components (Figure S7). LC-HRMS showed that **2a** and **2b** afforded ions with m/z 497.1524 and 497.1523, respectively, corresponding to $C_{20}H_{33}O_{10}S_2^-$ (Δ 0.7 and 0.6 ppm, respectively), consistent with the addition of two mercaptoethanol molecules to DON (i.e., $[DON + (HSEtOH)_2 + HCOO]^-$). The COSY, TOCSY, and SELTOCSY NMR spectra were used to identify spin systems corresponding to H-16/H-9/H-10/H-11, H-2/H-3/3-OH/H4α/H-4β/H-14, H-15α/H-15β, H-7/7-OH, H-13a/H-13b, H-1′/H-2′/2′-OH, and H-1a″/H-1b″/H-2″/2″-OH for both **2a** and **2b**. Protonated carbon resonances were assigned from correlations in HSQC spectra, whereas HMBC correlations were used to assign nonprotonated carbon resonances and to connect the spin systems. Correlations observed in the ROESY and SELROESY spectra established the relative stereochemistries in **2a** and **2b**. In contrast to **1a**/**1b** and DON, the NMR spectra of **2a** and **2b** lacked resonances attributable to olefinic protons or carbons, indicating thiol addition to C-10 in **2a** and **2b**. Consistent with this, the H-16 methyl resonances of **2a** and **2b** were shifted upfield relative to DON and **1a**/**1b** and appeared as doublets (J = 7 Hz), indicating the presence of a proton at C-9. The H-9 signal in **2a** and **2b** was further coupled (COSY) to H-10 as well as to the H-16 methyl, establishing that addition of a mercaptoethanol molecule had occurred at C-10 (Michael

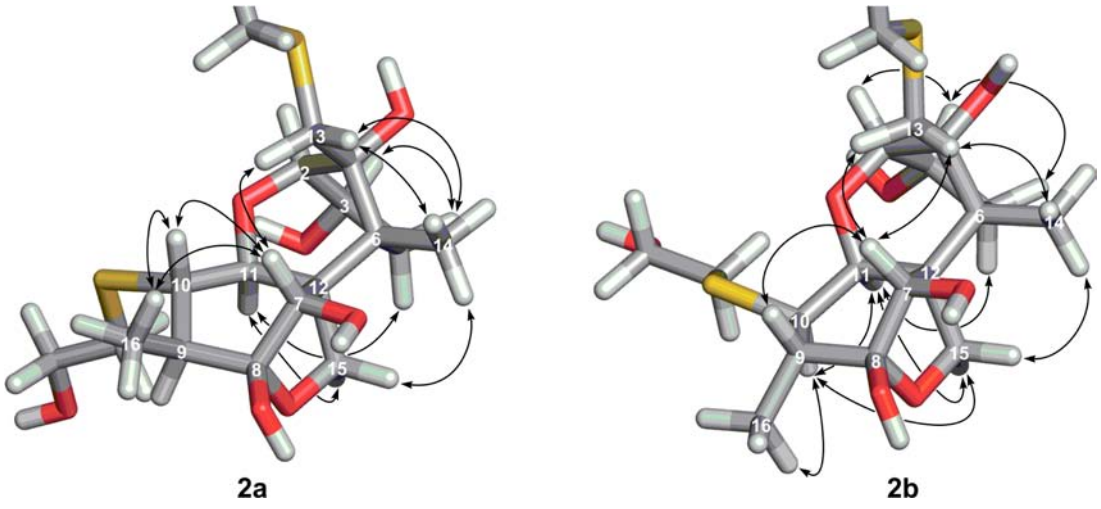

Figure 5. 3D models of **2a** and **2b**, showing selected structurally significant correlations (arrows) observed in ROESY and SELROESY NMR spectra.

DOI: 10.1021/acs.jafc.5b02864
J. Agric. Food Chem. 2015, 63, 7556−7566

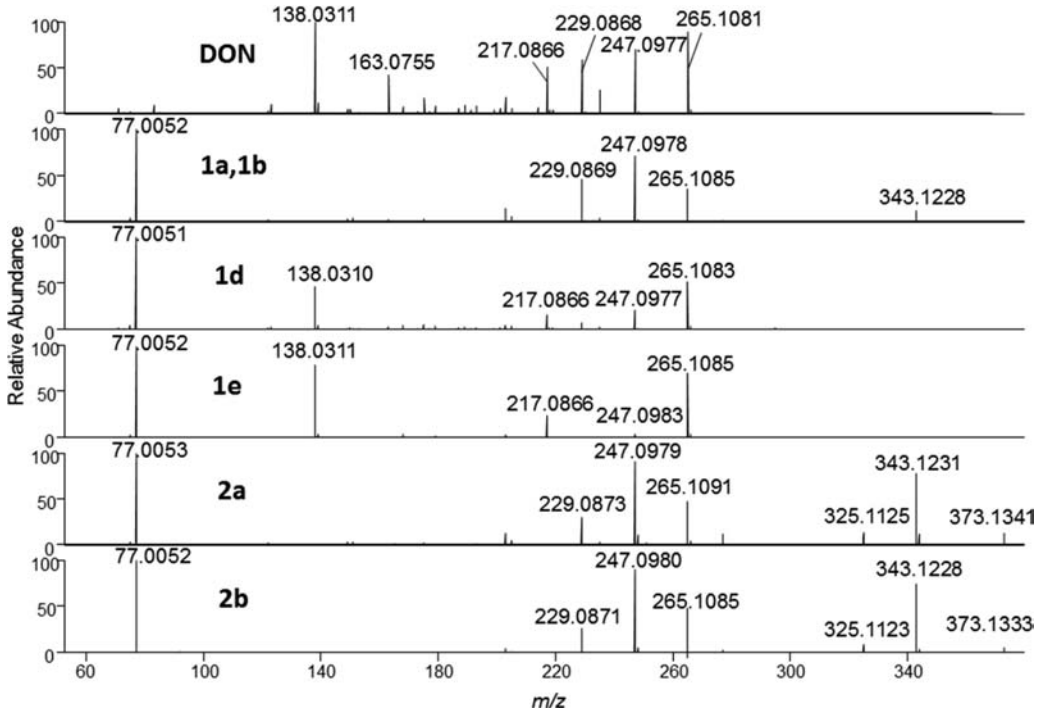

Figure 7. Product ion mass spectra from LC-HRMS^2 of the formate adduct ions of DON and its mercaptoethanol derivatives **1a**/**1b** (derivatized at the epoxide), **1d** and **1e** (Michael addition at C-10) and **2a** and **2b** (both epoxide and Michael addition). The prominent ion at *m*/*z* 77.0052 appears to correspond to $HOCH_2CH_2S^-$ (Δ 19 ppm) and is present in the spectra of all mercaptoethanol adducts regardless of the position of attachment of the thiol.

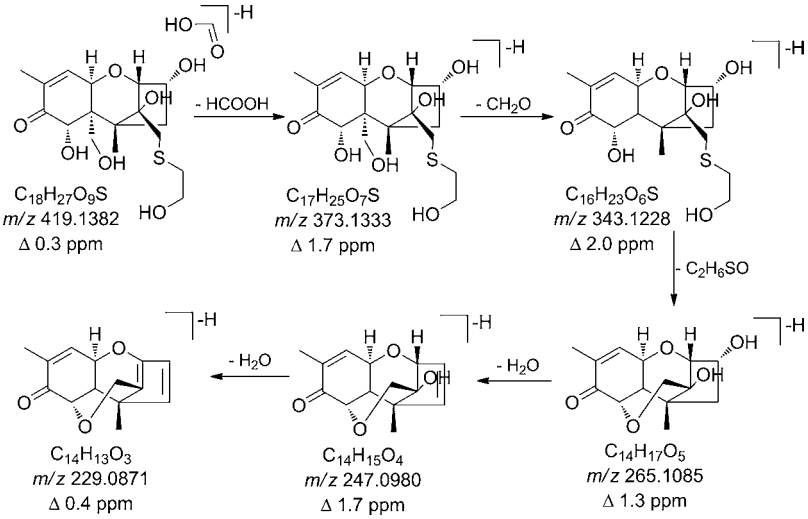

Figure 8. Possible negative ion mass spectral fragmentation pathway for mercaptoethanol adducts of the epoxide group of DON. The *m*/*z* values were measured by LC-HRMS.

addition) of DON. This conclusion was supported by HMBC correlations observed between H-10 (2.41/2.77 ppm) and both C-16 (17.4/13.3 ppm) and C-1″ (35.6/35.1 ppm) (Figure S8). No carbonyl resonances were observed in the ^{13}C, JMOD, or HMBC spectra of **2a** and **2b**. However, the HMBC spectra showed that both H-16 (1.13/1.12 ppm) and H-15 (3.51/4.11 and 3.49/4.16) correlated with a hemiketal carbon (C-8, 107.7/106.6 ppm) for both **2a** and **2b**. Furthermore, the H-15 doublets showed no TOCSY correlations to a 15-OH, indicating that **2a** and **2b** were both hemiketals (Figure 4). Correlations from H-13a (2.94/3.09 ppm) to C-2 (80.9/83.1 ppm), C-12 (81.6/81.3 ppm), C-5 (50.4/51.0 ppm), and C-1′ 36.8/37.1 ppm) confirmed the presence of a mercaptoethanol moiety at C-13 of **2a** and **2b**. Thus, **2a** and **2b** have the same skeleton and differ only in their stereochemistries at C-9 and C-10, which is reflected in the differing ^3J coupling constants for this spin system (Table 1). The stereochemistries at C-9 and C-10 were established from ROESY (Figure S9) and SELROESY NMR experiments (Figure 5). For **2a**, the ROESY spectra showed correlations between H-7 and both H-16 (not observed for **2b**) and H-10, locating H-10 and the 16-methyl together with H-7 on the β-face of the molecule. In the case of **2b**, however, H-7 showed a ROESY correlation to H-9, whereas H-10 showed ROESY correlations to H-11, H-15α (3.49 ppm),

DOI: 10.1021/acs.jafc.5b02864
J. Agric. Food Chem. 2015, 63, 7556−7566

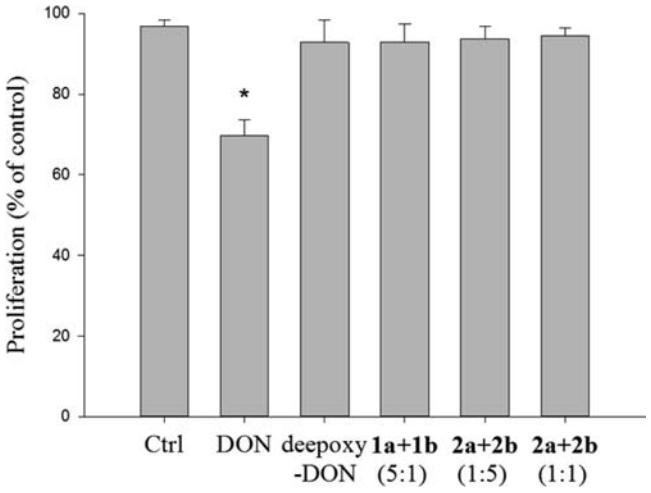

Figure 9. Proliferation of THP-1 cells after treatment with 4 μM DON or its derivatives for 24 h, measured with Alamar Blue. Data represent mean ± SD of three independent experiments. (*) Significantly different from control (one-way-ANOVA with Dunnett's post-test, $p < 0.05$). Two samples with different ratios of **2a** and **2b** were tested.

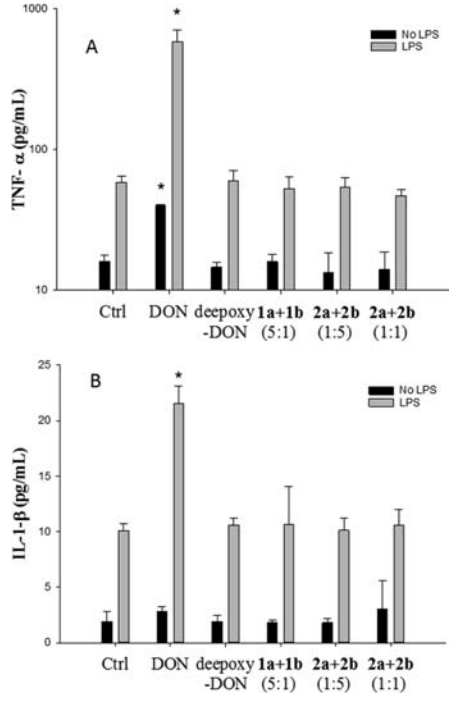

Figure 10. Cytokine secretion measured by ELISA in THP-1 cells treated for 3 h with LPS (0.05 ng/mL) followed by treatment with DON and its derivatives (4 μM) for 24 h. Data represent the mean ± SD of three independent incubations. (*) Significantly different from control (one-way-ANOVA with Dunnett's post-test, $p < 0.05$). Two samples with different ratios of **2a** and **2b** were tested.

and H-16. This locates H-10 and the 16-methyl group on the α-face and H-9 on the β-face of **2b**. This situation places the 16-methyl and mercaptoethanol substituents attached at C-9 and C-10, respectively, equatorially on the ring in both **2a** and **2b** (Figures 5 and Figure S10) and would be expected to result in the least steric crowding in this region of these molecules. Thus, **2a** and **2b** have the structures shown in Figure 4.

Reaction of DON with Other Thiols. A set of experiments was carried out to see if DON reacted similarly with other thiols, including the biologically relevant amino acid cysteine and the tripeptide glutathione. Reactions were monitored for 1 week by LC-MS (Figure 6) and the chromatograms all showed peaks corresponding to the addition of a single thiol molecule to DON. The chromatograms displayed patterns of broad and sharp, later- and earlier-eluting peaks similar to those observed from the mercaptoethanol reaction (Figure 2). A wider array of thiol addition products formed in a shorter time for the reactions with smaller thiols, presumably as a consequence of reduced steric hindrance. Double conjugates were also present in all of the reaction mixtures (Figure S11). When mixtures were analyzed after aproximately 45 days at room temperature, there was only one early-eluting peak present having a mass that corresponded to addition of a single thiol (data not shown) believed to be analogous to the identified **1a**/**1b** epoxide adducts in the DON−mercaptoethanol reaction.

LC-HRMS and LC-MS^n. We studied the MS characteristics and fragmentation patterns of DON and its mercaptoethanol derivatives using LC-HRMS and LC-HRMS^2 as well as multiple-stage ion trap LC-MS^n. Upon electrospray ionization in the negative ion mode, **1a**−**1e** afforded formate adducts with m/z 419.1382−419.1384, corresponding to an elemental composition of $C_{18}H_{27}O_9S^-$ (Δ 0.3−0.5 ppm), whereas **2a**−**2d** afforded formate adducts with m/z 497.1523−497.1524 corresponding to an elemental composition of $C_{20}H_{33}O_{10}S_2^-$ (Δ 0.5−0.7 ppm). The formate adducts of **1a**/**b**, **1d**/**1e**, and **2a** and **2b** showed different fragmentation patterns during LC-HRMS^2 (Figure 7), attributable to different fragmentation pathways for the epoxide conjugates and Michael addition products, potentially allowing the two types of addition products to be distinguished by MS alone. To understand these differences, the fragmentation spectra of the mercaptoethanol adducts were compared to those of DON (Figure 7). The fragmentation pathways of DON were studied in more detail by multiple-stage ion trap MS^n (Figure S12). Fragmentation of the deprotonated molecular ions of DON (m/z 295), obtained from collision-induced MS^2 fragmentation of the corresponding formate adduct (m/z 341), primarily yielded m/z 265 (loss of CH_2O). Further fragmentation of m/z 265 (MS^4) yielded m/z 247 (loss of H_2O), m/z 217 (loss of H_2O and CH_2O), and m/z 138 as the most abundant product ions. The two losses of CH_2O during MS fragmentation of DON are attributable to cleavage of the CH_2OH side chain at C-6 and cleavage of the epoxide, as proposed previously.[16] The m/z 138 fragment appears to be a rare radical anion and has earlier been suggested to be the result of cleavage through the B-ring of the molecule.[16] An m/z 138.0311 product ion was present in the LC-HRMS^2 spectra of the DON, **1d** and **1e**, but not in compounds where mercaptoethanol was known to be added to the epoxy group (**1a**/**1b**, **2a**, and **2b**) (Figure 7). Additionally, HRMS^2 analysis of de-epoxy-DON did not reveal the presence of a m/z 138.0311 fragment (Figure S13). The foregoing information suggests that the formation of the m/z 138 fragment ion is associated with the presence of an intact 12,13-epoxy group, and **1d** and **1e** are thus suspected to be Michael adducts of mercaptoethanol at C-10 of DON. Another diagnostic feature that may assist in distinguishing between a Michael addition product and a reaction product from monoaddition of mercaptoethanol to the epoxy group is the presence of an m/z 343.1228 product ion ($C_{16}H_{23}O_6S^-$, Δ 2.9 ppm) in the LC-HRMS^2 spectra of the epoxide conjugates (Figure 7). These ions are formed by loss of formate and of CH_2O, presumably from the C-6 position of the molecular ion.

DOI: 10.1021/acs.jafc.5b02864
J. Agric. Food Chem. 2015, 63, 7556−7566

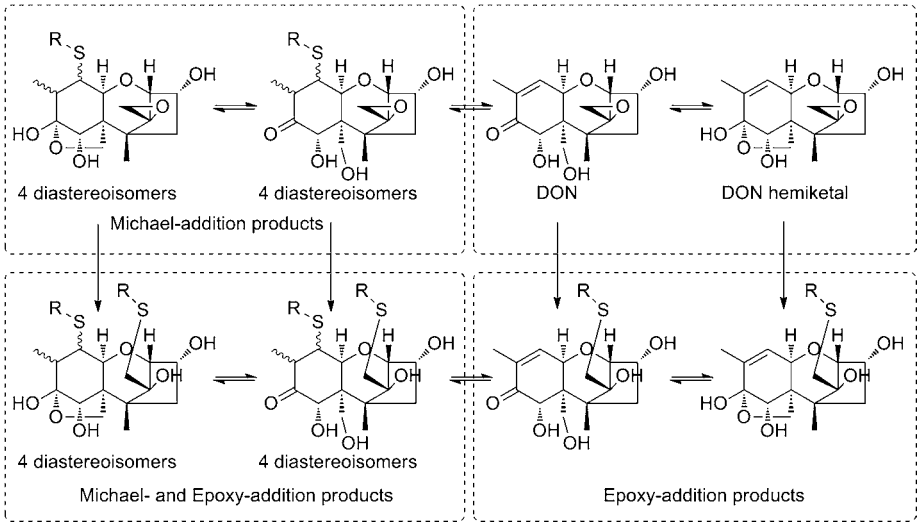

Figure 11. Generalized scheme showing proposed reaction of DON with a thiol (RSH) under basic conditions, as well as hemiketal−ketone equilibration at C-8.

In the LC-MS^n spectra, fragmentation of m/z 343 (MS^4) afforded m/z 265 (loss of 78 Da, corresponding to the mass of mercaptoethanol), m/z 247 (additional loss of H_2O), and m/z 229 (further loss of H_2O). Formation of the m/z 265 ion could occur via linkage of the 7-OH group and C-13 during the mercaptoethanol elimination to form a six-membered ring (Figure 8).

Cellular Effects. DON is able to cause cellular effects, such as inflammation and toxicity, through its ability to target ribosomes and to cause ribotoxic stress.[17] Because de-epoxy-DON does not affect ribosomes, it has been proposed that the 12,13-epoxy group is critical for DON's action on ribosomes.[17] To compare the effects of DON, de-epoxy-DON, and mercaptoethanol derivatives **1a**/**1b** and **2a**/**2b** on proliferation of THP-1 monocytes, we used the Alamar Blue assay, as previous studies[18] showed toxicity of DON with Alamar Blue in different cell lines. THP-1 cells were treated with DON, de-epoxy-DON, and purified mixtures of **1a**/**1b** and **2a**/**2b** for 24 h. DON decreased the proliferation of THP-1 monocytes, but de-epoxy-DON and DON−mercaptoethanol adducts **1a**/**1b** and **2a**/**2b** did not (Figure 9). These results support the epoxide moiety as an important structural feature for the toxicity of DON.

DON induces the expression of several pro-inflammatory cytokines, such as TNFα, IL-1b, IL-6, and IL-8,[19] and pretreatment (i.e., priming) with LPS potentiates this effect.[20,21] To examine pro-inflamatory responses induced by DON, de-epoxy-DON, and mercaptoethanol derivatives **1a**/**1b** and **2a**/**2b**, we analyzed the levels of TNF-α and IL-1β secretion by PMA-differentiated macrophages, with and without LPS priming. Regardless of the absence or presence of LPS, there was an increase in TNF-α in response to DON, but not to any of the derivatives (Figure 10A), although the sensitivity was higher with LPS present. Similarly, DON increased the release of IL-1β in LPS-primed cells, whereas de-epoxy-DON, **1a**/**1b**, and **2a**/**2b** did not (Figure 10B), although cells that were not treated with LPS did not show an IL-1β response to any of the compounds, including DON.

Thus, DON, but not de-epoxy-DON or mercaptoethanol derivatives **1a**/**1b** and **2a**/**2b**, reduced proliferation of THP-1 monocytes and induced pro-inflammatory responses in PMA-differentiated LPS-primed THP-1 macrophages. The lack of toxic responses to **1a**/**1b** and **2a**/**2b** (both of which involve derivatization of the 12,13-epoxy group of DON) supports the involvement of the epoxy group in the toxicity of trichothecenes—a hypothesis hitherto based solely on observations with de-epoxy-DON. Whereas all of the mecaptoethanol adducts isolated in the present study were derivatized at C-13 of the epoxy group of DON and were nontoxic, previous studies[22,23,10] have also demonstrated reduced toxicity for Michael addition products of DON.

Effect of pH on Reaction Rate. DON and mercaptoethanol were reacted at pH 7.3, 9.2, and 10.7, and the reaction was monitored by LC-MS. Neither DON nor mercaptoethanol contain acidic or basic groups, so DON and its mercaptoethanol derivatives can be expected to have similar responses in LC-MS. This makes it possible to estimate the proportions of DON and its reaction products by integrating areas under the peaks in the LC-MS chromatograms. We used a large excess of the thiol and observed pseudo-first-order reaction kinetics and followed the depletion of DON by plotting the relative peak area over time (Figure 3). However, the reaction kinetics are expected to be more complex, with several reversible reaction equilibria including Michael addition of the thiol to the double bond and hemiketal−ketone exchange (Figure 11). Furthermore, autoxidation of the thiol to form the disulfide can be expected to reduce the thiol concentration over time. Therefore, the reaction of DON with mercaptoethanol displayed pseudo-first-order kinetics only for the first few hours. Nevertheless, a dramatic increase in reaction rate was observed when the pH was increased from 7.2 to 9.2, with a further increase when the pH was increased to 10.7. These observations support nucleophilic attack by the thiolate ion as the dominant reaction mechanism, as the pK_a of mercaptoethanol has been reported to be approximately 9.7.[24] Regardless of the pH, there was always the same progression in the formation of the reaction products, as shown in Figure 2, and even at physiological pH adducts **1d** and **1e** appeared first. Attack of thiolate on the 12,13-epoxy group is expected to be essentially irreversible, whereas thiolate attack on C-10 of DON (Michael addition) should be reversible. In contrast, attack of thiolate on the isolated double bond in DON hemiketal is not expected, and

DOI: 10.1021/acs.jafc.5b02864
J. Agric. Food Chem. 2015, 63, 7556−7566

isomerization of the thia-Michael addition products of DON to their hemiketal forms should hinder the elimination of thiol from C-10. The reaction scheme shown in Figure 11 thus accounts for the products identified in the reaction and, together with the well-known autoxidation of thiols to disulfides,[25] for the presence of only epoxy adducts **1a** and **1b** at extended reaction times. The late-eluting broad peak in the LC-MS analyses (Figures 2 and 6) may be due to on-column ketone−hemiketal isomerization, as this peak partially resolved when the mercaptoethanol addition products of DON were analyzed without the presence of formic acid in the mobile phase (data not shown).

Thus, DON and other trichothecenes have been shown to react with several natural and synthetic thiolates via Michael addition to C-10 of the α,β-unsaturated ketone and addition to C-13 of the 12,13-epoxy group. These reactions occurred rapidly in weakly basic conditions, but proceeded even at physiological pH, and could potentially result in the formation of adducts with cysteine-containing proteins or peptides even in the absence of enzymatic catalysis. None of the products from the reaction of DON with mercaptoethanol in which the thiol had been conjugated with the epoxy group showed any signs of toxicity in vitro.

■ ASSOCIATED CONTENT

Supporting Information

The Supporting Information is available free of charge on the ACS Publications website at DOI: 10.1021/acs.jafc.5b02864.

LC-HRMS chromatograms of all reactions described between DON, T-2 tetraol, de-epoxy-DON, and thiols; table including accurate mass data, calculated elemental compositions, and difference from the calculated exact mass; structures of **1a**, **1b**, **2a**, and **2b**, showing selected HMBC and NOE correlations; ^{1}H NMR spectra of two purified mixtures of **2a** and **2b**, showing their ratios; selected region of the ROESY NMR spectrum for **2a** and **2b** diagnostic for determining their stereochemistries; selected region of the HSQC NMR spectrum of **2a** and **2b** showing how coupling constants were measured for the signals overlapping in the ^{1}H spectrum; proposed fragmentation pathway of DON−mercaptoethanol Michael adducts; MS^n data for DON (PDF)

■ AUTHOR INFORMATION

Corresponding Author

*(A. Stanic) E-mail: ana.stanic@vetinst.no, ana.stanic.hr@gmail.com.

Funding

This work was part of the project "Mycotoxins and toxigenic fungi in Norwegian pig farming: consequences for animal health and possible intervention strategies" funded by the Research Council of Norway (project 225332) and cofinanced by Animalia, Lantmännen and Felleskjøpet Fôrutvikling.

Notes

The authors declare no competing financial interest.

■ ACKNOWLEDGMENTS

We thank Hans-Ulrich Humpf from the Institute of Food Chemistry, University of Münster, Germany, for kindly providing us with standards for breakdown products of DON (norDONs).

■ ABBREVIATIONS USED

COSY, correlation spectroscopy; DEPT, distortionless enhancement of polarization transfer; DON, deoxynivalenol; GSH, glutathione; ELISA, enzyme-linked immunosorbent assay; ESI, electrospray ionization; FBS, fetal bovine serum; HMBC, heteronuclear multiple-bond correlation; HPLC, high-performance liquid chromatography; HRMS, high-resolution mass spectrometry; HSQC, heteronuclear single-quantum coherence:; IL-1β, interleukin-1 beta; JMOD, J-modulated spin−echo; LPS, lipopolysaccharide; MS, mass spectrometry; NMR, nuclear magnetic resonance; NOESY, nuclear Overhauser spectroscopy; PMA, phorbol-12-myristate-13-acetate; ROESY, rotating frame Overhauser spectroscopy; SELTOCSY, selective total correlation spectroscopy; SPE, solid phase extraction; TOCSY, total correlation spectroscopy; TNF-α, tumor necrosis factor alpha

■ REFERENCES

(1) Berthiller, F.; Crews, C.; Dall'Asta, C.; Saeger, S. D.; Haesaert, G.; Karlovsky, P.; Oswald, I. P.; Seefelder, W.; Speijers, G.; Stroka, J. Masked mycotoxins: a review. *Mol. Nutr. Food Res.* **2013**, *57*, 165−186.

(2) Alassane-Kpembi, I.; Kolf-Clauw, M.; Gauthier, T.; Abrami, R.; Abiola, F. A.; Oswald, I. P.; Puel, O. New insights into mycotoxin mixtures: the toxicity of low doses of type B trichothecenes on intestinal epithelial cells is synergistic. *Toxicol. Appl. Pharmacol.* **2013**, *272*, 191−198.

(3) Kluger, B.; Bueschl, C.; Lemmens, M.; Berthiller, F.; Haubl, G.; Jaunecker, G.; Adam, G.; Krska, R.; Schuhmacher, R. Stable isotopic labelling-assisted untargeted metabolic profiling reveals novel conjugates of the mycotoxin deoxynivalenol in wheat. *Anal. Bioanal. Chem.* **2013**, *405*, 5031−5036.

(4) Young, J. C. Formation of sodium bisulfite addition products with trichothecenones and alkaline hydrolysis of deoxynivalenol and its sulfonate. *J. Agric. Food Chem.* **1986**, *34*, 919−923.

(5) Schwartz, H. E.; Hametner, C.; Slavik, V.; Greitbauer, O.; Bichl, G.; Kunz-Vekiru, E.; Schatzmayr, D.; Berthiller, F. Characterization of three deoxynivalenol sulfonates formed by reaction of deoxynivalenol with sulfur reagents. *J. Agric. Food Chem.* **2013**, *61*, 8941−8948.

(6) Warth, B.; Fruhmann, P.; Wiesenberger, G.; Kluger, B.; Sarkanj, B.; Lemmens, M.; Hametner, C.; Frohlich, J.; Adam, G.; Krska, R.; Schuhmacher, R. Deoxynivalenol-sulfates: identification and quantification of novel conjugated (masked) mycotoxins in wheat. *Anal. Bioanal. Chem.* **2015**, *407*, 1033−1039.

(7) Kluger, B.; Bueschl, C.; Lemmens, M.; Michlmayr, H.; Malachova, A.; Koutnik, A.; Maloku, I.; Berthiller, F.; Adam, G.; Krska, R.; Schuhmacher, R. Biotransformation of the mycotoxin deoxynivalenol in *Fusarium* resistant and susceptible near isogenic wheat lines. *PLoS One* **2015**, *10*, 19.

(8) Pompella, A.; Visvikis, A.; Paolicchi, A.; De Tata, V.; Casini, A. F. The changing faces of glutathione, a cellular protagonist. *Biochem. Pharmacol.* **2003**, *66*, 1499−1503.

(9) Gardiner, S. A.; Boddu, J.; Berthiller, F.; Hametner, C.; Stupar, R. M.; Adam, G.; Muehlbauer, G. J. Transcriptome analysis of the barley−deoxynivalenol interaction: evidence for a role of glutathione in deoxynivalenol detoxification. *Mol. Plant−Microbe Interact.* **2010**, *23*, 962−976.

(10) Fruhmann, P.; Weigl-Pollack, T.; Mikula, H.; Wiesenberger, G.; Adam, G.; Varga, E.; Berthiller, F.; Krska, R.; Hametner, C.; Frohlich, J. Methylthiodeoxynivalenol (MTD): insight into the chemistry, structure and toxicity of thia-Michael adducts of trichothecenes. *Org. Biomol. Chem.* **2014**, *12*, 5144−5150.

(11) Gottlieb, H. E.; Kotlyar, V.; Nudelman, A. NMR chemical shifts of common laboratory solvents as trace impurities. *J. Org. Chem.* **1997**, *62*, 7512−7515.

(12) Springer, J. E.; Azbill, R. D.; Carlson, S. L. A rapid and sensitive assay for measuring mitochondrial metabolic activity in isolated neural tissue. *Brain Res. Protoc.* **1998**, *2*, 259−263.

DOI: 10.1021/acs.jafc.5b02864
J. Agric. Food Chem. 2015, 63, 7556−7566

(13) Bretz, M.; Beyer, M.; Cramer, B.; Knecht, A.; Humpf, H. U. Thermal degradation of the *Fusarium* mycotoxin deoxynivalenol. *J. Agric. Food Chem.* **2006**, *54*, 6445−6451.
(14) Jarvis, B. B.; Mazzocchi, D. B.; Ammon, H. L.; Mazzola, E. P.; Flippen-Anderson, J. L.; Gilardi, R. D.; George, C. F. Conformational effects in trichothecenes: structures of 15-hydroxy C4 and C8 ketones. *J. Org. Chem.* **1990**, *55*, 3660−3662.
(15) Burrows, E. P.; Szafraniec, L. L. Hypochlorite-promoted transformations of trichothecenes, 3. Deoxynivalenol. *J. Nat. Prod.* **1987**, *50*, 1108−1112.
(16) Liu, Z.-Y.; Yu, C.-H.; Wan, L.; Sun, Z.-L. Fragmentation study of five trichothecenes using electrospray hybrid ion trap/time-of-flight mass spectrometry with accurate mass measurements. *Int. J. Mass Spectrom.* **2012**, *309*, 133−140.
(17) Maresca, M. From the gut to the brain: journey and pathophysiological effects of the food-associated trichothecene mycotoxin deoxynivalenol. *Toxins* **2013**, *5*, 784−820.
(18) Ivanova, L.; Skjerve, E.; Eriksen, G. S.; Uhlig, S. Cytotoxicity of enniatins A, A1, B, B1, B2 and B3 from *Fusarium avenaceum*. *Toxicon* **2006**, *47*, 868−876.
(19) Arunachalam, C.; Doohan, F. M. Trichothecene toxicity in eukaryotes: cellular and molecular mechanisms in plants and animals. *Toxicol. Lett.* **2013**, *217*, 149−158.
(20) Islam, Z.; Pestka, J. J. LPS priming potentiates and prolongs proinflammatory cytokine response to the trichothecene deoxynivalenol in the mouse. *Toxicol. Appl. Pharmacol.* **2006**, *211*, 53−63.
(21) Pestka, J.; Zhou, H. R. Toll-like receptor priming sensitizes macrophages to proinflammatory cytokine gene induction by deoxynivalenol and other toxicants. *Toxicol. Sci.* **2006**, *92*, 445−455.
(22) Young, J. C.; Trenholm, H. L.; Friend, D. W.; Prelusky, D. B. Detoxification of deoxynivalenol with sodium bisulfite and evaluation of the effects when pure mycotoxin or contaminated corn was treated and given to pigs. *J. Agric. Food Chem.* **1987**, *35*, 259−261.
(23) Schwartz-Zimmermann, H. E.; Wiesenberger, G.; Unbekannt, C.; Hessenberger, S.; Schatzmayr, D.; Berthiller, F. Reaction of (conjugated) deoxynivalenol with sulphur reagents − novel metabolites, toxicity and application. *World Mycotoxin J.* **2014**, *7*, 187−197.
(24) Serjeant, E. P.; Dempsey, B. *Ionisation Constants of Organic Acids in Aqueous Solution*; Pergamon Press: New York, 1979; p 34.
(25) Koundal, K. R.; Sawhney, S. K.; Sinha, S. K. Oxidation of 2-mercaptoethanol in the presence of tris buffer. *Phytochemistry* **1983**, *22*, 2183−2184.

DOI: 10.1021/acs.jafc.5b02864
J. Agric. Food Chem. 2015, 63, 7556−7566

MS) without derivatization has also been reported on a variety of stationary phases, such as reversed phase,[34−36] hydrophilic interaction chromatography (HILIC),[37−39] mixed-mode,[40] and ion exchange.[41] Only a handful of these published methods have employed a stable isotope-labeled analogue of leucine for quantitative analysis, and of those which did, none has achieved satisfactory chromatographic separation between the isobaric amino acids leucine and isoleucine.[40−42]

The work described herein reports the development and validation of a new, direct, quantitative, and confirmatory analytical method based on LC−MS without derivatization for the analysis of HMB, KIC, HICA, and free leucine in human breast milk. The applicability of the developed method was demonstrated by carrying out (for the first time) a mini-survey of the presence and abundance of these four analytes in human breast milk, collected at various stages of lactation.

MATERIALS AND METHODS

Safety. Methanol and formic acid should be dispensed in a hood, and appropriate laboratory safety glasses, coat, and gloves should be worn.

Chemicals and Reagents. L-Leucine (≥99.5%), L-leucine-5,5,5-d_3 (99 atom % D), L-isoleucine (pure), *trans*-4-hydroxy-L-proline (≥99%), α-ketoisocaproic acid (also known as 4-methyl-2-oxovaleric acid or 2-keto-4-methylpentanoic acid) (≥98% by titration), α-hydroxyisocaproic acid (also known as 2-hydroxyisocaproic acid) (99%), and formic acid (≥96%) were purchased from Sigma-Aldrich Corp. (St. Louis, MO). Calcium β-hydroxy-β-methylbutyrate monohydrate (≥99.5%) was supplied by Lonza Group (Basel, Switzerland). 3,4-Methyl-$^{13}C_3$-3-hydroxyisovaleric acid (99% purity, 99 atom % ^{13}C) was purchased from Cambridge Isotope Laboratories, Inc. (Andover, MA). Sodium 2-keto-4-methyl-d_3-pentanoate (99 atom % D) was purchased from CDN Isotopes (Pointe-Claire, Quebec, Canada). Methanol (LC−MS grade) was purchased from Fisher Scientific (Fair Lawn, NJ). Laboratory deionized water was purified through a Milli-Q (EMD Milipore, Millerica, MA) water purification system.

Stock Solutions and Calibration Standards. Individual stock solutions of HMB and 2-keto-4-methyl-d_3-pentanoic acid (KIC-d_3) were prepared at concentrations of ca. 1000 mg/L by dissolving the corresponding calcium and sodium salts, respectively, in 0.1% formic acid. Individual stock solutions of L-leucine (leucine), L-leucine-5,5,5-d_3 (leucine-d_3), 3,4-methyl-$^{13}C_3$-3-hydroxyisovaleric acid ($^{13}C_3$-HMB), KIC, and HICA were prepared at concentrations of ca. 1000 mg/L in Milli-Q water. Stock solutions were prepared fresh every 30 days and were determined to be stable when stored at +5 °C during this time period.

An intermediate stock solution containing 2 mg/L HMB, 2 mg/L KIC, 1 mg/L HICA, and 10 mg/L leucine was prepared in Milli-Q water. An intermediate internal standard stock solution containing 4 mg/L $^{13}C_3$-HMB, 10 mg/L KIC-d_3, and 200 mg/L leucine-d_3 was prepared in Milli-Q water.

Calibration standards containing 2, 4, 10, 20, 100, and 200 μg/L of HMB, 2, 4, 10, 20, 100, and 200 μg/L of KIC, 1, 2, 5, 10, 50, and 100 μg/L of HICA, 10, 20, 50, 100, 500, and 1,000 μg/L of leucine, and 20 μg/L each of $^{13}C_3$-HMB, 50 μg/L each of KIC-d_3, and 100 μg/L each of leucine-d_3 were prepared in Milli-Q water.

Samples. Pooled, mature (lactation stage III) human breast milk and six samples of human breast milk from individual donors (lactation stages I, II, and III) was purchased from BioreclamationIVT (Westbury, NY). Samples were received in frozen state and were kept at −20 °C until analysis.

Sample Preparation. After thawing at ambient temperature and vortexing, 0.5 mL of human breast milk or water (for method blanks) was pipetted into a 2 mL Eppendorf centrifuge tube. Appropriate aliquots of spiking solution were added [for quality control (QC) accuracy determination], followed by 25 μL of the intermediate internal standard stock solution. After brief vortexing, 0.75 mL of methanol was added. The tube was capped, shaken for 30 s, and centrifuged at 3000 rpm for 5 min at ambient temperature.

For analysis of HMB, KIC, and HICA, a 250 μL portion of the supernatant was transferred to a clean 2 mL Eppendorf centrifuge tube, followed by the addition of 750 μL of 0.1% formic acid in water. The tube was vortexed briefly, and its content was filtered through a 0.2 μm pore size polytetrafluoroethylene (PTFE) syringe filter into a 2 mL autosampler vial.

For analysis of leucine, a 25 μL portion of the supernatant was transferred to a clean 2 mL Eppendorf centrifuge tube, followed by the addition of 975 μL of 0.1% formic acid in water. The tube was vortexed briefly, and its content was filtered through a 0.2 μm pore size PTFE syringe filter into a 2 mL autosampler vial.

Samples were also prepared for confirmatory analysis on a HILIC column. For this purpose, 100 μL of human breast milk was added to 900 μL of acetonitrile. After brief vortexing, the extract was filtered through a 0.2 μm pore size PTFE syringe filter into a 2 mL autosampler vial.

Instrumentation. Analysis was performed on a Waters ACQUITY ultra-performance liquid chromatograph coupled to a Xevo TQ-S triple quadrupole mass spectrometer. Chromatographic separation was carried out on an ACQUITY UPLC HSS C18, 1.8 μm, 2.1 × 100 mm column (Waters Corp., Milford, MA), operated at 40 °C at a flow rate of 0.3 mL/min with a mobile phase system consisting of 0.1% formic acid in water/0.1% formic acid in methanol. The injection volume was 10 μL. For analysis of HMB, KIC, and HICA, the following gradient program was used: 0−2 min, 15% B; 2−3 min, 15−30% B; 3−6 min, 30% B; 6−9 min, 100% B; and 9−12 min, 15% B. For analysis of leucine, the following gradient program was used: 0−2 min, 0% B; 2−7 min, 0−100% B; 7−9 min, 100% B; and 9−12 min, 0% B.

The mass spectrometer was operated in both positive (leucine) and negative (HMB, KIC, and HICA) electrospray ionization (ESI) mode with both quadrupoles tuned for unit resolution. Selected operating parameters were as follows: capillary voltage, 3.5 kV; cone voltage, 20 V; desolvation temperature, 350 °C; desolvation gas (N_2), 800 L/h; cone gas (N_2), 250 L/h; and collision gas (Ar), 0.15 mL/min. One multiple reaction monitoring (MRM) transition was recorded for each compound (Table 1).

Table 1. MRM Transitions Used for Considered Analytes and Internal Standards

compound	polarity	MRM	CE[a] (eV)	dwell (s)
HMB	ESI^-	117 > 59	10	0.1
$^{13}C_3$-HMB	ESI^-	120 > 59	10	0.1
KIC	ESI^-	129 > 129	5	0.1
KIC-d_3	ESI^-	132 > 132	5	0.1
HICA	ESI^-	131 > 85	10	0.1
leucine	ESI^+	132 > 86	7	0.4
leucine-d_3	ESI^+	135 > 89	10	0.4

[a]CE = collision energy.

Confirmatory analysis was carried out on an ACQUITY UPLC HILIC, 1.7 μm, 2.1 × 150 mm column (Waters Corp., Milford, MA). The mobile phase consisted of 10 mM ammonium acetate in 10:90 water/acetonitrile (isocratic) at 0.3 mL/min and 40 °C. The injection volume was 10 μL.

RESULTS AND DISCUSSION

Method Development. Sample preparation consisted of a two-step extraction−dilution approach, i.e., protein precipitation with methanol, followed by further dilution with 0.1% formic acid to achieve compatibility with the starting mobile phase composition. The dilution factor incurred along the extraction procedure from human breast milk to final extract was 10 for the analysis of HMB, KIC, and HICA and 100 for the analysis of leucine. The separate analysis of leucine after

DOI: 10.1021/acs.jafc.5b02563
J. Agric. Food Chem. 2015, 63, 7567−7573

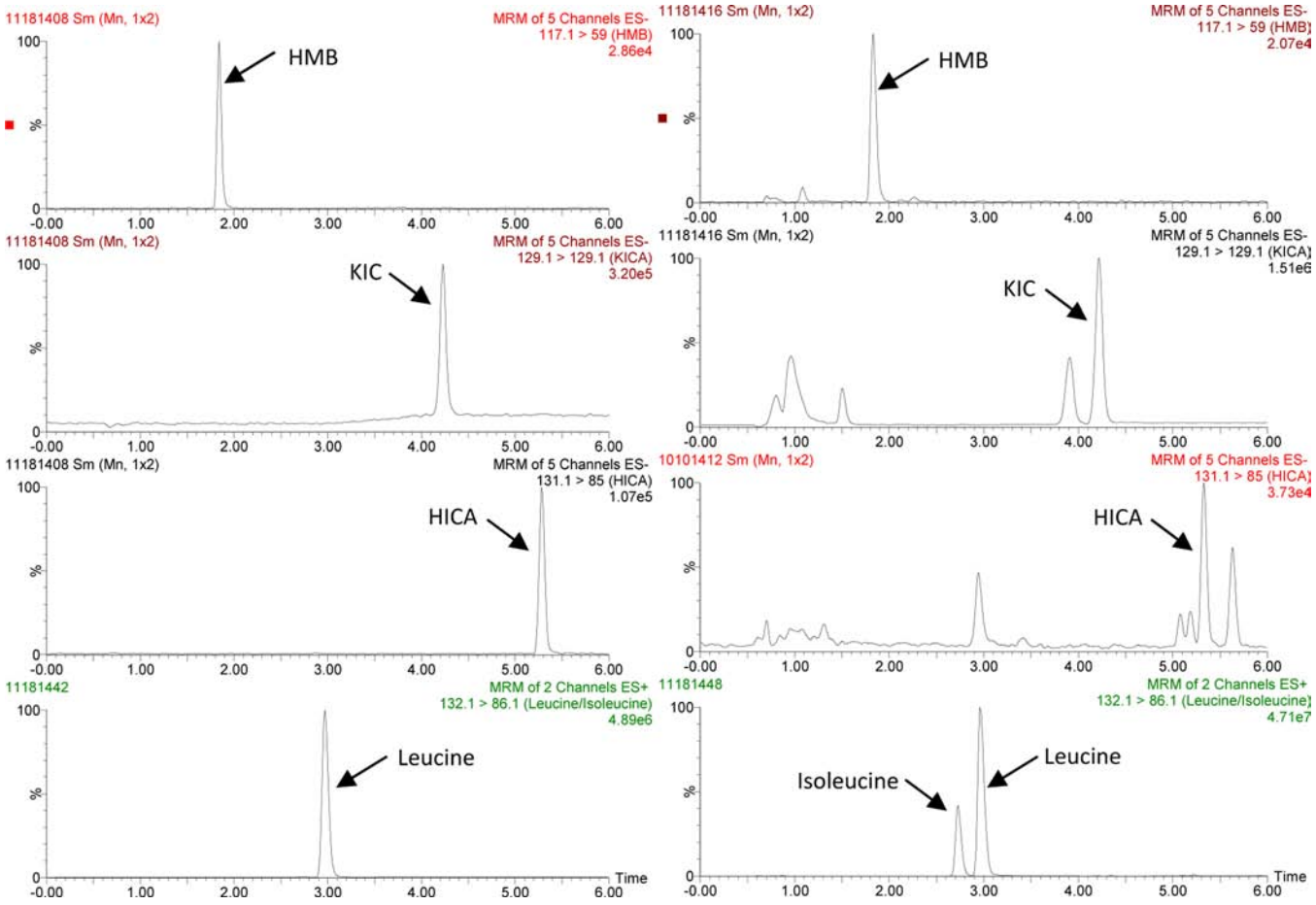

Figure 1. MRM chromatograms of HMB, KIC, HICA, and leucine in (left panel) neat standard solution and (right panel) human breast milk extract.

Table 2. Summary of Method Validation Data (Accuracy and Precision) for HMB, KIC, HICA, and Leucine in Human Breast Milk

					precision (% RSD)		
analyte	QC level	concentration	unit	accuracy (%)	within run	between run	overall
HMB	background	47.3	μg/L	N/A	7.3	4.4	8.5
	QCL	100		109	2.9	4.3	5.2
	QCM	400		109	2.2	4.9	5.4
	QCH	1500		115	2.2	5.2	5.6
KIC	background	13.3[a]	μg/L	N/A	N/A	N/A	N/A
	QCL	60		95.1	3.0	4.7	5.6
	QCM	300		88.9	2.5	6.2	6.7
	QCH	1500		94.6	1.7	6.2	6.4
HICA	background	16.9	μg/L	N/A	2.9	2.7	3.9
	QCL	30.0		111	2.3	5.4	5.9
	QCM	150		117	1.7	6.3	6.6
	QCH	750		115	2.6	4.2	5.0
leucine	background	7.05	mg/L	N/A	5.3	7.7	9.3
	QCL	10.0		98.1	4.4	7.6	8.8
	QCM	35.0		102	3.3	6.1	6.9
	QCH	70.0		98.9	1.8	6.2	6.5

[a]Estimated concentration (below the LOQ).

100-fold dilution of human breast milk was necessary as a result of two factors: (i) the naturally occurring concentrations of leucine in human breast milk are ca. 3 orders of magnitude higher than its metabolites HMB, KIC, and HICA, and (ii) after 100-fold dilution, the concentration of methanol in the final extract is reduced to 1.5%, achieving compatibility with the starting mobile phase for the analysis of leucine, which is 100% aqueous. The use of 100% aqueous mobile phase during the first 2 min of the analysis is necessary to achieve adequate separation between isobaric leucine and isoleucine. Isobaric hydroxyproline eluted in the column void volume (ca. 0.7 min), and hence, it did not interfere with the determination of

DOI: 10.1021/acs.jafc.5b02563
J. Agric. Food Chem. 2015, 63, 7567−7573

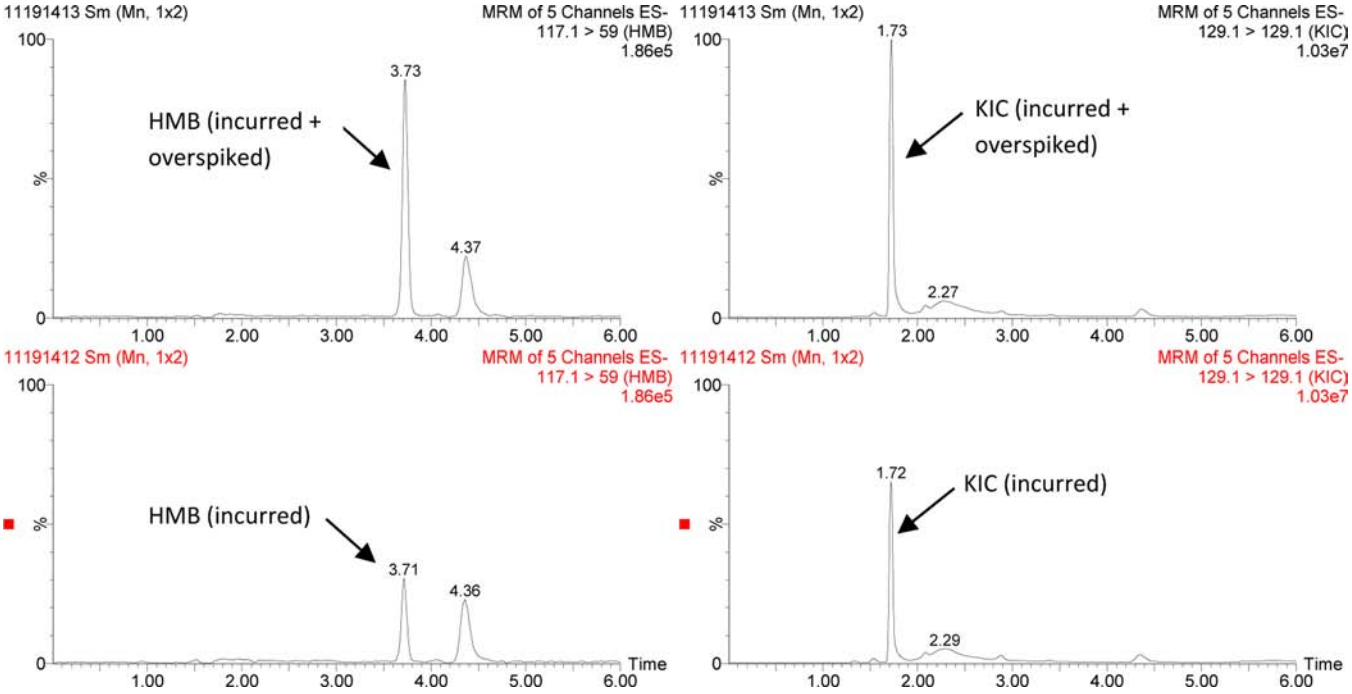

Figure 2. Orthogonal confirmation of HMB and KIC in human breast milk extract by HILIC.

leucine. Both isoleucine and hydroxyproline are naturally occurring amino acids in human breast milk. One single aliquot of 0.5 mL of human breast milk is used for both analyses, which are carried out using the same chromatographic column and the same mobile phase system employing different gradients. Representative chromatograms of all analytes in neat standard solution and in human breast milk extract are shown in Figure 1.

Because of the low molecular weight of considered analytes, one single MRM transition was available for each analyte. KIC and its isotopically labeled analogue KIC-d_3 did not undergo any significant fragmentation in the collision cell. Hence, their pseudo-molecular ions $[M - H]^-$ at m/z 129 and 132, respectively, were used for quantitation (Table 1). Stable isotope-labeled internal standards were used for the quantitation of HMB, KIC, and leucine. HICA, which lacks a commercially available stable isotope-labeled analogue was quantified using $^{13}C_3$-HMB as an internal standard. Confirmatory analysis of selected analytes was attempted on alternative stationary phases with orthogonal selectivity (e.g., HILIC).

Method Validation. Calibration standards were analyzed at the beginning and end of each run. A linear regression model ($1/x$ weighted) was used. Coefficients of determination (R^2) were ≥0.99. Residuals were ≤20% at the lowest calibration level and ≤15% at all other levels.

An analyte-free blank human breast milk matrix was not available. Hence, analytes were spiked into human breast milk at appropriate concentrations on top of incurred concentrations. Three core validation runs consisting of a minimum of five replicates each at low, medium, and high QC spiking levels (QCL, QCM, and QCH) were conducted on 3 different days. A minimum of five replicate analyses were also performed with no spiking to assess the background (incurred) concentrations of analytes. Overall, 68 data points each were collected for HMB, KIC, and HICA. For leucine, overall, 72 data points were collected, of which 2 were rejected as outliers (accuracy outside of the 80−120% range).

Accuracy (relative to the sum of incurred and spiked concentrations), within-day precision, between-day precision, and overall (intermediate) precision were calculated as described in ref 43 and are summarized in Table 2. Accuracy and overall (intermediate) precision were 89−117% and <10% relative standard deviation (RSD), respectively, for all analytes at all three QC levels. The use of a stable isotope-labeled internal standard in the present method significantly improved precision of results for HMB compared to the method reported previously,[21] in which an analogue internal standard was used. Acceptable accuracy and precision were obtained even for HICA, which lacked a stable isotope-labeled internal standard. The consistent performance of the method in terms of accuracy and precision over 3 core validation runs have demonstrated its ruggedness.

LOQs for HMB, KIC, and HICA in human breast milk were 20, 20, and 10 μg/L, respectively. These concentrations corresponded to the lowest calibration levels used for each compound, after the 10-fold dilution incurred during sample extraction. LOQ for leucine in human breast milk was 1 mg/L, corresponding to the lowest calibration level after the 100-fold dilution incurred during sample extraction.

The matrix effect was evaluated by comparing the average peak areas of the internal standards $^{13}C_3$-HMB, KIC-d_3, and leucine-d_3 in sample extracts and neat calibration standards, respectively. The matrix effect was not significant (<15%) for $^{13}C_3$-HMB and leucine-d_3. For KIC-d_3, a positive matrix effect of ca. 30% was noticed; however, this did not adversely affect quantitation.

Extract stability was determined by reanalyzing an entire core validation run after maintaining the samples on the autosampler tray for 48 h at ambient temperature. The run met accuracy and precision criteria described above. The stability of individual stock solutions was also established over 30 days at +5 °C.

DOI: 10.1021/acs.jafc.5b02563
J. Agric. Food Chem. 2015, 63, 7567−7573

Confirmatory Analysis of HMB and KIC in Human Breast Milk by Orthogonal Chromatography. Confirmatory analysis of HMB and KIC was carried out by HILIC, which is orthogonal to reversed-phase chromatography. This is justified because both HMB and KIC have low molecular masses, and hence, only one MRM transition was available for monitoring each analyte. Both HMB and KIC were confirmed in human breast milk on the HILIC column by the retention time agreement between the peaks of incurred and overspiked analytes (Figure 2). Because HICA was present only in trace amounts in human breast milk and because of its less than ideal peak shape on the HILIC column, no further confirmation was possible. Leucine is a major natural component of human breast milk, and further confirmation was not deemed necessary.

Survey of HMB, KIC, HICA, and Leucine in Human Breast Milk. To demonstrate the applicability of the method, six samples of human breast milk collected from individual donors at various stages of lactation (I, II, and III, corresponding to 0−7, 8−21, and >21 days, respectively) were analyzed for HMB, KIC, HICA, and free leucine. Results of this survey (averages of duplicate analyses) are summarized in Table 3.

Table 3. Results of the Survey of Concentrations of HMB, KIC, HICA, and Leucine in Six Samples of Human Breast Milk from Various Stages of Lactation

sample number	stage of lactation	HMB (μg/L)	KIC (μg/L)	HICA (μg/L)	leucine (mg/L)
1	I	62.4	93.5	<10.0	10.7
2	I	164	1057	<10.0	88.5
3	II	42.1	<20.0	<10.0	2.07
4	II	55.9	23.5	<10.0	4.03
5	III	46.0	<20.0	<10.0	2.63
6	III	44.6	33.9	<10.0	2.88

Concentrations of HMB in human breast milk were between 42 and 164 μg/L. All samples contained higher concentrations of HMB than reported previously in bovine whole milk (20−29 μg/L).[21] One sample of stage I (colostral) human breast milk contained a particularly high concentration of HMB (164 μg/L) compared to all other samples. Concentrations of KIC varied from below the LOQ (<20 μg/L) to 1057 μg/L. The same particular sample of stage I (colostral) human breast milk mentioned previously contained the highest concentration of KIC as well. A small trace of HICA below the LOQ (<10 μg/L) was present in all six samples surveyed. However, HICA was present at a quantifiable level (17 μg/L) in the pooled human breast milk sample used for method validation (Table 2). The concentration of free leucine ranged between 2.1 and 88.5 mg/L, with the highest concentration being determined in the same particular sample of stage I (colostral) human breast milk referred to above.

To our knowledge, this is the first report on the presence and abundance of leucine metabolites HMB, KIC, and HICA in human breast milk. Concentrations of free leucine in human breast milk (determined by a derivatization approach) have been reported previously by several authors and were in the range of 1.7−253 mg/L.[30−33] Our findings reported herein for free leucine are in agreement with those published in previous reports.

Along with our previous report,[21] this is the first description of the development and comprehensive validation of a direct, quantitative, and confirmatory method based on LC−MS without derivatization for the analysis of leucine metabolites HMB, KIC, and HICA in a biological matrix. It is also the first report on the direct and quantitative analysis of leucine in a biological matrix by stable isotope dilution mass spectrometry, where the need for the chromatographic resolution of leucine from isobaric isoleucine has been adequately addressed. The presence and abundance of HMB, KIC, and HICA in human breast milk is being reported here for the first time. The concentrations of HMB, KIC, and leucine present in human breast milk could potentially affect rates of protein synthesis, protein breakdown, and consequently, infant growth.

AUTHOR INFORMATION

Corresponding Author

*Telephone: +1-614-624-6309. Fax: +1-614-727-6309. E-mail: stefan.ehling@abbott.com.

Author Contributions

†Stefan Ehling and Todime M. Reddy contributed equally to this work.

Notes

The authors declare no competing financial interest.

ACKNOWLEDGMENTS

The authors thank Daniel Schmitz, Director of Analytical Research and Services, Abbott Nutrition, for his guidance and support. The authors also thank Dr. Jeffrey Baxter, Dr. Steven Davis, and Dr. Sean Garvey for helpful discussions during the preparation of the manuscript.

ABBREVIATIONS USED

ESI, electrospray ionization; GC−MS, gas chromatography−mass spectrometry; HICA, α-hydroxyisocaproic acid; HILIC, hydrophilic interaction chromatography; HMB, β-hydroxy-β-methylbutyric acid; HPLC, high-performance liquid chromatography; KIC, α-ketoisocaproic acid; LC−MS, liquid chromatography−mass spectrometry; LOQ, limit of quantitation; MRM, multiple reaction monitoring; PTFE, polytetrafluoroethylene; QC, quality control; RSD, relative standard deviation

REFERENCES

(1) Anthony, J. C.; Anthony, T. G.; Kimball, S. R.; Jefferson, L. S. Signaling pathways involved in translational control of protein synthesis in skeletal muscle by leucine. *J. Nutr.* **2001**, *131*, 856S−860S.

(2) Suryawan, A.; Jeyapalan, A. S.; Orellana, R. A.; Wilson, F. A.; Nguyen, H. V.; Davis, T. A. Leucine stimulates protein synthesis in skeletal muscle of neonatal pigs by enhancing mTORC1 activation. *Am. J. Physiol. Endocrinol. Metab.* **2008**, *295*, E868−E875.

(3) Anthony, J. C.; Anthony, T. G.; Kimball, S. R.; Vary, T. C.; Jefferson, L. S. Orally administered leucine stimulates protein synthesis in skeletal muscle of postabsorptive rats in association with increased eIF4F formation. *J. Nutr.* **2000**, *130*, 139−145.

(4) Churchward-Venne, T. A.; Burd, N. A.; Mitchell, C. J.; West, D. W.; Philp, A.; Marcotte, G. R.; Baker, S. K.; Baar, K.; Phillips, S. M. Supplementation of a suboptimal protein dose with leucine or essential amino acids: effects on myofibrillar protein synthesis at rest and following resistance exercise in men. *J. Physiol.* **2012**, *590*, 2751−2765.

(5) Atherton, P. J.; Smith, K.; Etheridge, T.; Rankin, D.; Rennie, M. J. Distinct anabolic signalling responses to amino acids in C2C12 skeletal muscle cells. *Amino Acids* **2010**, *38*, 1533−1539.

DOI: 10.1021/acs.jafc.5b02563
J. Agric. Food Chem. 2015, 63, 7567−7573

(6) Suryawan, A.; Hawes, J. W.; Harris, R. A.; Shimomura, Y.; Jenkins, A. E.; Hutson, S. M. A molecular model of human branched-chain amino acid metabolism. *Am. J. Clin. Nutr.* **1998**, *68*, 72−81.
(7) Escobar, J.; Frank, J. W.; Suryawan, A.; Nguyen, H. V.; Van Horn, C. G.; Hutson, S. M.; Davis, T. A. Leucine and alpha-ketoisocaproic acid, but not norleucine, stimulate skeletal muscle protein synthesis in neonatal pigs. *J. Nutr.* **2010**, *140*, 1418−1424.
(8) Van Koevering, M.; Nissen, S. Oxidation of leucine and alpha-ketoisocaproate to beta-hydroxy-beta-methylbutyrate in vivo. *Am. J. Physiol.* **1992**, *262*, E27−31.
(9) Mock, D. M.; Stratton, S. L.; Horvath, T. D.; Bogusiewicz, A.; Matthews, N. I.; Henrich, C. L.; Dawson, A. M.; Spencer, H. J.; Owen, S. N.; Boysen, G.; Moran, J. H. Urinary excretion of 3-hydroxyisovaleric acid and 3-hydroxyisovaleryl carnitine increases in response to a leucine challenge in marginally biotin-deficient humans. *J. Nutr.* **2011**, *141*, 1925−1930.
(10) Nissen, S.; Sharp, R. L.; Panton, L.; Vukovich, M.; Trappe, S.; Fuller, J. C., Jr. Beta-hydroxy-beta-methylbutyrate (HMB) supplementation in humans is safe and may decrease cardiovascular risk factors. *J. Nutr.* **2000**, *130*, 1937−1945.
(11) Wheatley, S. M.; El-Kadi, S. W.; Suryawan, A.; Boutry, C.; Orellana, R. A.; Nguyen, H. V.; Davis, S. R.; Davis, T. A. Protein synthesis in skeletal muscle of neonatal pigs is enhanced by administration of beta-hydroxy-beta-methylbutyrate. *Am. J. Physiol.: Endocrinol. Metab.* **2014**, *306*, E91−E99.
(12) Wilkinson, D. J.; Hossain, T.; Hill, D. S.; Phillips, B. E.; Crossland, H.; Williams, J.; Loughna, P.; Churchward-Venne, T. A.; Breen, L.; Phillips, S. M.; Etheridge, T.; Rathmacher, J. A.; Smith, K.; Szewczyk, N. J.; Atherton, P. J. Effects of leucine and its metabolite β-hydroxy-β-methylbutyrate on human skeletal muscle protein metabolism. *J. Physiol.* **2013**, *591*, 2911−2923.
(13) Mirza, K. A.; Pereira, S. L.; Voss, A. C.; Tisdale, M. J. Comparison of the anticatabolic effects of leucine and Ca-beta-hydroxy-beta-methylbutyrate in experimental models of cancer cachexia. *Nutrition* **2014**, *30*, 807−813.
(14) Deutz, N.; Pereira, S.; Hays, N.; Oliver, J.; Edens, N.; Evans, C.; Wolfe, R. Effect of β-hydroxy-β-methylbutyrate (HMB) on lean body mass during 10 days of bed rest in older adults. *Clin. Nutr.* **2013**, *32*, 704−712.
(15) Columbus, D. A.; Fiorotto, M. L.; Davis, T. A. Leucine is a major regulator of muscle protein synthesis in neonates. *Amino Acids* **2015**, *47*, 259.
(16) Lang, C. H.; Pruznak, A.; Navaratnarajah, M.; Rankine, K. A.; Deiter, G.; Magne, H.; Offord, E. A.; Breuille, D. Chronic alpha-hydroxyisocaproic acid treatment improves muscle recovery after immobilization-induced atrophy. *Am. J. Physiol.: Endocrinol. Metab.* **2013**, *305*, E416−E428.
(17) Mero, A. A.; Ojala, T.; Hulmi, J. J.; Puurtinen, R.; Karila, T. A.; Seppala, T. Effects of alfa-hydroxy-isocaproic acid on body composition, DOMS and performance in athletes. *J. Int. Soc. Sports Nutr.* **2010**, *7*, 1.
(18) Davis, T. A.; Fiorotto, M. L.; Nguyen, H. V.; Reeds, P. J. Enhanced response of muscle protein synthesis and plasma insulin to food intake in suckled rats. *Am. J. Physiol.* **1993**, *265*, R334−340.
(19) Johnson, M. J.; Wootton, S. A.; Leaf, A. A.; Jackson, A. A. Preterm birth and body composition at term equivalent age: a systematic review and meta-analysis. *Pediatrics* **2012**, *130*, E640−E649.
(20) Belfort, M. B.; Gillman, M. W.; Buka, S. L.; Casey, P. H.; McCormick, M. C. Preterm infant linear growth and adiposity gain: trade-offs for later weight status and intelligence quotient. *J. Pediatr.* **2013**, *163*, 1564−1569.
(21) Ehling, S.; Reddy, T. M. Investigation of the presence of beta-hydroxy-beta-methylbutyric acid and alpha-hydroxyisocaproic acid in bovine whole milk and fermented dairy products by a validated liquid chromatography-mass spectrometry method. *J. Agric. Food Chem.* **2014**, *62*, 1506−1511.
(22) Matsukawa, T.; Hasegawa, H.; Shinohara, Y.; Hashimoto, T. Gas chromatographic-mass spectrometric determination of alpha-ketoisocaproic acid and [2H7]alpha-ketoisocaproic acid in plasma after derivatization with N-phenyl-1,2-phenylenediamine. *J. Chromatogr., Biomed. Appl.* **2001**, *751*, 213−220.
(23) Kienle, M. G.; Magni, F. Simultaneous quantification of plasma levels of alpha-ketoisocaproate and leucine by gas chromatography-mass spectrometry. *Methods Enzymol.* **2000**, *324*, 62−73.
(24) Magni, F.; Arnoldi, L.; Galati, G.; Kienle, M. G. Simultaneous determination of plasma levels of alpha-ketoisocaproic acid and leucine and evaluation of alpha-[1−13C]ketoisocaproic acid and [1−13C]-leucine enrichment by gas chromatography-mass spectrometry. *Anal. Biochem.* **1994**, *220*, 308−314.
(25) Calder, A. G.; Smith, A. Stable isotope ratio analysis of leucine and ketoisocaproic acid in blood plasma by gas chromatography/mass spectrometry. Use of tertiary butyldimethylsilyl derivatives. *Rapid Commun. Mass Spectrom.* **1988**, *2*, 14−16.
(26) Nissen, S.; Van Huysen, C.; Haymond, M. W. Measurement of plasma alpha-ketoisocaproate concentrations and specific radioactivity by high-performance liquid chromatography. *Anal. Biochem.* **1981**, *110*, 389−392.
(27) Horber, F. F.; Kahl, J.; Lecavalier, L.; Krom, B.; Haymond, M. W. Determination of leucine and alpha-ketoisocaproic acid concentrations and specific activity in plasma and leucine specific activities in proteins using high-performance liquid chromatography. *J. Chromatogr., Biomed. Appl.* **1989**, *495*, 81−94.
(28) Milley, J. R.; Sweeley, J. C. High-performance liquid chromatographic measurement of leucine and alpha-ketoisocaproate in whole blood: Application to fetal protein metabolism. *J. Chromatogr., Biomed. Appl.* **1993**, *613*, 23−33.
(29) Keen, R. E.; Nissenson, C. H.; Barrio, J. R. Analysis of femtomole concentrations of alpha-ketoisocaproic acid in brain tissue by precolumn fluorescence derivatization with 4,5-dimethoxy-1,2-diaminobenzene. *Anal. Biochem.* **1993**, *213*, 23−28.
(30) Chuang, C. K.; Lin, S. P.; Lee, H. C.; Wang, T. J.; Shih, Y. S.; Huang, F. Y.; Yeung, C. Y. Free amino acids in full-term and pre-term human milk and infant formula. *J. Pediatr. Gastroenterol. Nutr.* **2005**, *40*, 496−500.
(31) Valentine, C. J.; Morrow, G.; Fernandez, S.; Gulati, P.; Bartholomew, D.; Long, D.; Welty, S. E.; Morrow, A. L.; Rogers, L. K. Docosahexaenoic Acid and Amino Acid Contents in Pasteurized Donor Milk are Low for Preterm Infants. *J. Pediatr.* **2010**, *157*, 906−910.
(32) Zhang, Z.; Adelman, A. S.; Rai, D.; Boettcher, J.; Lonnerdal, B. Amino acid profiles in term and preterm human milk through lactation: a systematic review. *Nutrients* **2013**, *5*, 4800−4821.
(33) Baldeon, M. E.; Mennella, J. A.; Flores, N.; Fornasini, M.; San Gabriel, A. Free amino acid content in breast milk of adolescent and adult mothers in Ecuador. *SpringerPlus* **2014**, *3*, 104.
(34) Kıvrak, I.; Kıvrak, S.; Harmandar, M. Free amino acid profiling in the giant puffball mushroom (*Calvatia gigantea*) using UPLC−MS/MS. *Food Chem.* **2014**, *158*, 88−92.
(35) Nimbalkar, M. S.; Pai, S. R.; Pawar, N. V.; Oulkar, D.; Dixit, G. B. Free amino acid profiling in grain Amaranth using LC-MS/MS. *Food Chem.* **2012**, *134*, 2565−2569.
(36) Ozcan, S.; Senyuva, H. Z. Improved and simplified liquid chromatography/atmospheric pressure chemical ionization mass spectrometry method for the analysis of underivatized free amino acids in various foods. *J. Chromatogr. A* **2006**, *1135*, 179−185.
(37) Guo, S.; Duan, J.-a.; Qian, D.; Tang, Y.; Qian, Y.; Wu, D.; Su, S.; Shang, E. Rapid determination of amino acids in fruits of Ziziphus jujuba by hydrophilic interaction ultra-high-performance liquid chromatography coupled with triple-quadrupole mass spectrometry. *J. Agric. Food Chem.* **2013**, *61*, 2709−2719.
(38) Yao, X.; Zhou, G.; Tang, Y.; Pang, H.; Qian, Y.; Guo, S.; Mo, X.; Zhu, S.; Su, S.; Qian, D.; Jin, C.; Qin, Y.; Duan, J.-a. Direct determination of underivatized amino acids from Ginkgo biloba leaves by using hydrophilic interaction ultra high performance liquid chromatography coupled with triple quadrupole mass spectrometry. *J. Sep. Sci.* **2013**, *36*, 2878−2887.
(39) Gökmen, V.; Serpen, A.; Mogol, B. A. Rapid determination of amino acids in foods by hydrophilic interaction liquid chromatography

DOI: 10.1021/acs.jafc.5b02563
J. Agric. Food Chem. 2015, 63, 7567−7573

coupled to high-resolution mass spectrometry. *Anal. Bioanal. Chem.* **2012**, *403*, 2915−2922.
(40) Lowenthal, M. S.; Yen, J.; Bunk, D. M.; Phinney, K. W. Certification of NIST standard reference material 2389a, amino acids in 0.1 mol/L HCl − quantification by ID LC-MS/MS. *Anal. Bioanal. Chem.* **2010**, *397*, 511−519.
(41) Thiele, B.; Füllner, K.; Stein, N.; Oldiges, M.; Kuhn, A. J.; Hofmann, D. Analysis of amino acids without derivatization in barley extracts by LC−MS−MS. *Anal. Bioanal. Chem.* **2008**, *391*, 2663−2672.
(42) Sanchez, C. L.; Cubero, J.; Sanchez, J.; Franco, L.; Rodriguez, A. B.; Rivero, M.; Barriga, C. Screening for human milk amino acids by HPLC-ESI-MS/MS. *Food Anal. Methods* **2012**, *5*, 312−318.
(43) Thermo Electron Corporation. *Watson LIMS 7.3 User Manual r1*; Thermo Electron Corporation: Waltham, MA, 2006; p 365.

DOI: 10.1021/acs.jafc.5b02563
J. Agric. Food Chem. 2015, 63, 7567−7573

nowadays mandatory for accredited WADA laboratories,[9,10] it is applied in the food safety arena to a minor extent.[11]

The first aim of the presented research was to develop a common analytical backbone able to provide carbon isotopic measurements for main metabolites of 17β-testosterone (βT), namely, etiocholanolone (Etio) and 17α-testosterone (αT), and of 17β-estradiol (βE2), namely, 17α-estradiol (αE2), thus allowing the simultaneous detection of the abuse of synthetic homologues of androgenic and estrogenic steroid hormones. The second aim was to apply the validated method for an experimental study involving treatment of a bull and a heifer, determining the detection window capability of the analytical approach and allowing a direct comparison with other strategies including the monitoring of steroid esters in blood.

MATERIALS AND METHODS

Chemicals. All reagents and solvents were of analytical grade and were provided by Sigma-Aldrich (Bornem, Belgium). The solvents for liquid chromatography were of LC- and HPLC-grade from Biosolve (Valkenswaard, The Netherlands). 17β-Testosterone acetate was supplied by Sigma-Aldrich (Bornem, Belgium). Other steroids were obtained from Steraloids (Wilton, NY, USA). SPE C_{18} cartridges were provided by Achrom (Zulte, Belgium). *Escherichia coli* β-glucuronidase was from Roche Diagnostics GmbH (Mannheim, Germany). Dry pyridine and acetic anhydride were from Sigma-Aldrich (Bornem, Belgium).

Sample Description. *Animal Experiment.* One male bovine and one female bovine (Belgian white-and-red breed), aged 22 and 19 months and weighing 310 and 269 kg, respectively, were used for an administration study. After arrival at the farm until the end of the experiment, they were fed with a typical feed concentrate (2.0 kg daily), which contained mainly C3-plant material with added vitamins and minerals, and had access to dried grass, chopped corn and water ad libitum. It needs to be noted that the amount of chopped corn, consumed by the animals, was significantly larger than that of the feed concentrate and the dried grass. After 21 days, they were treated with a single intramuscular injection into the dorsal neck muscles, containing 1 mg kg^{-1} bw testosterone (administered as 1.194 mg kg^{-1} 17β-testosterone propionate (βTP)) and 0.2 mg kg^{-1} bw estradiol (administered as 0.276 mg kg^{-1} 17β-estradiol-3-benzoate (βE2B)) as an oil based preparation. Urine samples were collected before and during the first 28 days after administration and stored frozen at −21 °C. When all the samples were collected, they were stored at −85 °C in a monitored temperature environment until assay.

The animal experiment was performed at the Department of Veterinary Medicine of Ghent University (B), in line with the guidelines of the ethical committee, with approval code EC2011/163.

Compliant Samples. Eleven urine samples of nontreated pregnant cows were collected at different farms. Additionally, 12 urine samples from animals, a priori nontreated according to routine analyses, were added to obtain a sufficiently large reference population. The samples were stored at −85 °C in a monitored temperature environment until assay.

Spiked Samples. A urine sample which contained low concentrations of AEdiol (12.4 μg L^{-1}), Etio (3.5 μg L^{-1}), αE2 (not present), and αT (0.45 μg L^{-1}) was spiked with these substances at 100 μg L^{-1} and divided into eight subsamples to be used during the method validation.

GC-MS/C/IRMS Sample Preparation and Analysis. To provide adequate GC-MS/C/IRMS data, an extensive sample preparation is necessary to definitely avoid signal interferences that may generate inaccuracy in the $^{13}C/^{12}C$ measurement. After hydrolysis for 15 h with β-glucuronidase at 37 °C and pH 6.8, the urine samples, with a volume of 10 mL, were brought onto a C_{18} solid phase extraction (SPE) column, washed with 6 mL of H_2O and 5 mL of H_2O/acetonitrile (ACN) (80/20; v/v), and finally eluted with 8 mL of H_2O/ACN (10/90; v/v). Then, two subsequent liquid−liquid extractions (LLEs) with 4 mL of *n*-pentane/diethyl ether (92.5:7.5; v/v) at different pH values (pH 14 and pH 5.2) were performed to separate estrogenic and androgenic steroids. The extracts are further purified using reversed phase HPLC-fractionation followed by a normal phase for particular fractions containing target compounds. The four obtained fractions containing the isolated targeted analytes (αE2, AEdiol, Etio, and αT) are eventually acetylated overnight at room temperature with pyridine and acetic anhydride before separate injection into the GC-MS/C/IRMS, with noretiocholanolone being added as internal standard. Details of the sample preparation procedure and instrumental setup are described in a previous published work.[12] However, a limited number of adjustments, described below, have been introduced in the original analytical backbone to include a wider range of steroid metabolites, including those of 17β-testosterone.

Sample Preparation. The volume of the glycerol solution, used as a keeper after the LLE steps, was reduced from 100 to 30 μL. Medroxyprogesterone replaced fluoxymesterone as the internal standard in the estrogen fraction during reversed phase HPLC. Finally, progesterone was used as internal standard during the normal phase HPLC step instead of medroxyprogesterone. Because of the weak UV-detector response for Etio, a progesterone standard was used instead to determine the adequate fractionation windows during the HPLC steps.

HPLC/UV. For the reversed phase HPLC, the C_{18} functionalized precolumn and analytical column were replaced by Kinetex (Security Guard Ultra C18 for 2.1 mm ID) and Kinetex C_{18} columns (XB-C18; 250 mm × 4.6 mm; 5 μm), respectively. The chromatographic conditions were slightly altered: column temperature was changed from 40 to 50 °C, flow rate from 0.6 mL min^{-1} to 0.8 mL min^{-1}, and mobile phase composition from 37:63 to 35:65 (A:B; v/v), with H_2O/MeOH (95:5; v/v) as solvent A and MeOH as solvent B.

The normal phase HPLC-setup, using two diol functionalized columns in series (LiChrospher Diol; 250 mm × 4 mm; 5 μm) and a constant mobile phase of isooctane/isopropanol (85:15; v/v), was left unchanged.

GC-MS/C/IRMS. The T-pieces, used to split the sample after the GC-column to the mass spectrometer and isotope ratio mass spectrometer for simultaneous detection, were replaced by SilFlows (SGE Analytical Science). The RXI 5 SIL MS column (Restek −30 m; 0.25 mm i.d.; 0.25 μm df) GC-column was replaced by an Optima 17MS column (Machery Nagel −30 m; 0.25 mm i.d.; 0.25 μm df). The injection and GC program were adapted accordingly. The initial injector temperature was set at 100 °C, which was held for 0.10 min with a vent flow of 20 mL min^{-1}. The temperature was raised at 8 °C min^{-1} and held at 320 °C for 2 min during sample transfer on column. The initial GC oven temperature was 110 °C, which was held for 1.5 min. The temperature was then subsequently raised to 220 °C at 30 °C min^{-1}, to 270 °C at 6 °C min^{-1}, and to 300 °C at 2 °C min^{-1}. Finally, the temperature was raised to 330 °C at 50 °C min^{-1} and held for 3 min. The carrier gas was helium at a constant flow rate of 1.2 mL min^{-1}. The injection volume of 8 μL was left unchanged.

LC-MS/MS Sample Preparation and Analysis. *LC-MS/MS Analysis.* The quantitative analyses performed in this study were carried out on a Thermo Accela HPLC system coupled to a Thermo TSQ Quantum Ultra triple quadrupole mass spectrometer.

The LC was equipped with a C_{18} column (Kinetex C18; 2.1 mm × 150 mm; 1.7 μm) at a temperature of 70 °C. Solvent A was prepared by adding 400 μL of acetic acid to 1600 g of MeOH. For the preparation of solvent B, 1600 g of H_2O was mixed with 320 g of MeOH and 400 μL of acetic acid. Initially, the mobile phase composition was set at 35:65 (A:B; v/v). Between 1 and 4 min, the composition was linearly increased to 50:50 (A:B; v/v). During the following minute, the composition changed to 75:25 (A:B; v/v). After a final rapid increase in 10 s, the mobile phase was held at 95:5 (A:B; v/v).

The triple quadrupole was operated in the electrospray ionization mode, and the signals were recorded in the selected reaction monitoring mode (SRM). Prior to sample analysis, a solvent blank and two standard solutions containing 20 ng mL^{-1} of the analytes (αE2, αT, AEdiol, and Etio) in H_2O/MeOH (56:44; v/v) were injected, all with added internal standard (1 ng mL^{-1} of 17β-

DOI: 10.1021/acs.jafc.5b02746
J. Agric. Food Chem. 2015, 63, 7574−7581

testosterone-d_2 and 40 ng mL^{-1} of 17β-estradiol-d_3). This was done to calculate the one-point calibration curve covering 0 to 40 ng mL^{-1}.

Sample Preparation. The sample preparation protocol used for this analysis, was very similar to the protocol used prior to the GC-MS/C/IRMS described above but adapted to a sample volume of 5 mL and omitting a number of steps. Since there was no need to isolate the different analytes for quantification, the alkaline LLE and the two HPLC-purifications were unnecessary. Also, there was no need to derivatize the compounds. Thus, the sample preparation consists of a hydrolysis with β-glucuronidase, followed by one SPE and one LLE purification step. Finally, the extract was reconstituted in 125 μL of MeOH/H_2O (80:20; v/v) of which 10 μL was injected into the LC-MS/MS. Samples were spiked at 2 ng mL^{-1} with 17β-testosterone-d_2 and at 80 ng mL^{-1} with 17β-estradiol-d_3 to serve as internal standards for the quantification of the androgens and estrogens, respectively.

Analysis of the Preparation. The administered βE2B and βTP were dissolved separately in methanol to prepare standard solutions of 10 ng μL^{-1}. Next, 100 μL of each solution was hydrolyzed using 2 mL of 1 M NaOH in MeOH. After 15 min at 65 °C, 8 mL of 2 M formic acid in H_2O was added to stop the hydrolysis. Then, the samples were brought onto a SPE C_{18} column, washed with 6 mL of H_2O, and eluted two times with 4 mL of MeOH. The eluate was evaporated to dryness under a nitrogen stream at 37 °C and reconstituted into 40 μL of MeOH and 70 μL of H_2O. Afterward, a reversed phase HPLC fractionation and an acetylation step were performed identical to those used during the preparation of the urine samples. Finally, the samples were reconstituted into 80 μL of isooctane and analyzed with GC-MS/C/IRMS.

RESULTS AND DISCUSSION

Used Analytical Strategies. *GC-MS/C/IRMS Method.* The primary objective of the current research was to develop a method allowing the detection of βT abuse. On the basis of the literature,[7,13,14] Etio and αT were retained as diagnostic markers of βT administration.

During the two HPLC steps, separate fractions for both metabolites were successfully collected, resulting in very pure extracts suitable for IRMS analysis, as illustrated in Figure 1.

Finally, in combination with the already included fractions from a previous study,[12] the method allows for the simultaneous detection of estrogen and androgen abuse, with αE2 as a metabolite of βE2 and AEdiol as endogenous reference compound (ERC) for both βE2 and βT. The extraction yield for αT and Etio was between 36 and 69%, and between 31 and 71%, respectively, which is very similar to the yield of AEdiol and αE2 that was previously published.[12]

HPLC-MS/MS Method. While performing the analysis for the routine detection of estrogen abuse in 2013, it became clear that the majority of the received urine samples did not contain a sufficient quantity of αE2 to provide an IRMS measurement within the linear range. This is in line with findings from the literature, placing an average concentration of αE2 at around 6000 pg mL^{-1} for heifers and less than 500 pg mL^{-1} for bulls.[15,16] Therefore, a quantitative screening method with a similar but severely simplified sample preparation was initially developed to assess which samples contained more than 20 ng mL^{-1} necessary to provide IRMS-analysis within the linear range, filtering out large numbers of samples and avoiding unnecessary work.

Afterward, when including the testosterone metabolites into the method, the quantitative screening gained a second functionality. Because of the low UV-absorption of Etio, it was not possible to determine the adequate dilution of this fraction for IRMS analysis based on UV-detection during the straight phase HPLC fractionation, as is done for the other analytes. However, it was possible to determine the dilution and provide measurements within the linear range based on the LC-MS/MS output.

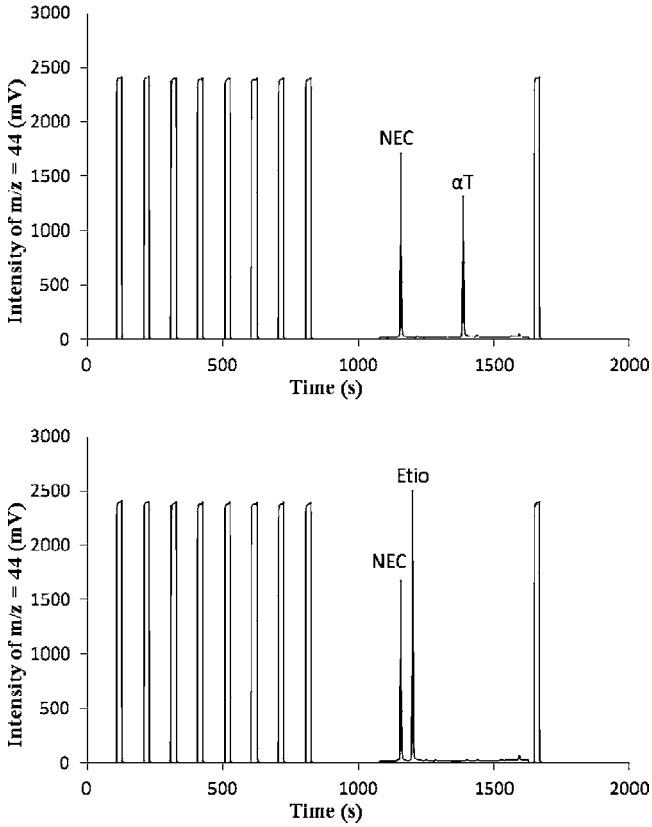

Figure 1. IRMS chromatograms (m/z = 44) of a compliant bovine urine sample, showing the internal standard noretiocholanolone acetate (NEC), 17α-testosterone (αT) (above), and etiocholanolone (Etio) (below).

Finally, it must be pointed out that, although this method provides accurate and reproducible results in the lower concentration range, a linear calibration curve only provided a perfect match (R^2 > 0.99) up to 50 ng mL^{-1}. Concentrations between 50 and 100 ng mL^{-1}, mentioned with regard to the animal experiment, should be considered as an approximation, whereas even higher concentrations must be interpreted as "elevated". Still, these data were found valuable to include.

Hydrolysis of the Steroid Preparations. The existence of steroid preparations having $\delta^{13}C_{VPDB}$ values similar to endogenous steroids has recently been reported for sports doping products.[17−20] To ensure that the $\delta^{13}C_{VPDB}$ values of the preparations used during the animal experiment were not within the endogenous range, the preparations were analyzed prior to treatment. An alkaline hydrolysis protocol for preparations, based on present experience at the laboratory and similar to published methods,[18,20] was used. To confirm complete hydrolysis of the preparations and avoid any potential influence on the $\delta^{13}C_{VPDB}$ values, the absence of intact steroid esters was verified by UV-detection during the HPLC-separation. The measured $\delta^{13}C_{VPDB}$ values, corrected for the acetate moieties, after hydrolysis were −32.13‰ and −31.70‰ for βE2 and βT, respectively, which is significantly different from endogenous values and should allow for the detection of the administration.

DOI: 10.1021/acs.jafc.5b02746
J. Agric. Food Chem. 2015, 63, 7574−7581

Method Validation. The method validation was performed similar to the previous study,[12] and the most important results are summarized in Table 1 and Figure 2.

Table 1. Summary of the Method Validation Results of 5-Androstene-3β,17α-diol (AEdiol), 17α-Estradiol (αE2), 17α-Testosterone (αT), and Etiocholanolone (Etio)

validation parameter	AEdiol (ERC)	αE2	αT	Etio
intermediate precision (‰) (sample standard deviation (n = 8))	0.21	0.35	0.35	1.05
mean difference between spiked water samples and standards (‰) (n = 8)	0.18	0.66	0.33	0.61
linear range (ng of analyte on column) (min−max)	7.5−50	15−80	10−80	10−80
AMDIS "net match" factor (specificity)	94	90	94	99
AMDIS "purity" factor	91	88	81	87

The validation results for AEdiol and αE2 were comparable to those obtained during the previous study, and for αT, similar results were obtained. For Etio, however, two results stand out. First, the intermediate precision was noticeably higher than that for the other compounds. Still, similar and even higher values have been considered acceptable both in published methods for sports doping control[21,22] and lifestock control,[23,24] although reported for other steroids or matrices. For the determination of the intermediate precision during the initial validation, the 8 spiked urine subsamples were analyzed two by two in four separate measurement series, performed by three different analysts over a time span of three months. To reevaluate the result for Etio afterward, the measurements of the compliant control sample for routine analyses, analyzed in 14 different measurement series over a time span of eight months, were assessed. The calculated intermediate precision based on these data (n = 14) was 0.76‰, which is significantly better.

Second, the noncompliance $\Delta^{13}C_{VPDB}$ threshold value, based on 21 measurements from untreated cows, executed in five series of measurements over a time span of four months, was 3.47‰, which is above the 3‰ threshold value usually applied, as is displayed in Figure 2. Remarkably, similar observations have been made with regard to sports doping control, where a number of reference population studies indicated that a 3‰ threshold is too low in certain cases.[21,22] Because of these observations, the new guidelines of the World Anti Doping Agency (WADA) include that each laboratory for sports doping control must perform a reference population study to determine a laboratory specific threshold value, which must be used in case it is higher than the WADA fixed threshold.[10] Additionally, the fixed threshold for the metabolite Etio in human urine was elevated to 4‰. The presented findings suggest that a similar precaution must be used for the analysis of bovine urine. Therefore, the applied threshold for routine analysis was fixed at 3‰ for the couples αE2-AEdiol and αT-AEdiol, and at 4‰ for Etio-AEdiol.

Specificity of the method was verified according to legal criteria,[3] and the absence of impurities and coelutions was verified by inspection of the MS data. Additionally, AMDIS, specialized software to evaluate peak purity and identification of the analyte peaks, was used for this purpose.

Finally, the trueness was evaluated by the injection of standards of dehydroepiandrosterone acetate and 17β-testosterone acetate with known and certified $\delta^{13}C_{VPDB}$ values. These standards were included into the five series of measurement, performed for the method validation, and allowed to verify the absence of a system bias. The mean difference between the certified and the measured $\delta^{13}C_{VPDB}$ values was 0.88‰ and 0.25‰ for dehydroepiandrosterone acetate and 17β-testosterone acetate, respectively.

Results of the Animal Experiment. An administration study was required to assess the capability of the developed method to detect steroid abuse in cattle and to adequately evaluate the pharmacokinetics and the detection window after administration. To be able to observe gender differences, male and female animals were treated. Prior to treatment, the diet of both animals was kept constant for 3 weeks, to ensure stable $\delta^{13}C_{VPDB}$ values for the ERCs during the experiment. Finally, the animals were treated with 400 mg of βT and 80 mg of βE2, injected as a propionate and benzoate ester, respectively. While a typical approved dosage in the USA, administered by implant, is 20−45 mg per animal for βE2 and 140−200 mg for βT,[25] laboratory experience with the analysis of injection sites indicated dosages sometimes up to several hundred milligrams more. The selected treatment holds the middle ground between both scenarios.

Effect of the Treatment on Measured $\delta^{13}C_{VPDB}$ Values. The $\delta^{13}C_{VPDB}$ values of the four measured analytes in the urine samples after treatment are displayed in Figure 3.

The measured $\delta^{13}C_{VPDB}$ values of AEdiol remain stable after treatment at −15.49 ± 0.49‰ and −14.80 ± 0.57‰ in the male and female, respectively, confirming the functionality as a reference compound for both androgens and estrogens, as already described elsewhere.[6,13] This enriched level for endogenous values fits well with the reported measurements from cattle fed with a diet containing a high percentage of maize.[6,13] As expected, gender does not influence the endogenous $^{13}C/^{12}C$ ratio of the ERC significantly.

Already the first day after treatment, the $\delta^{13}C_{VPDB}$ of the metabolites of both βE2 and βT approached their lowest values,

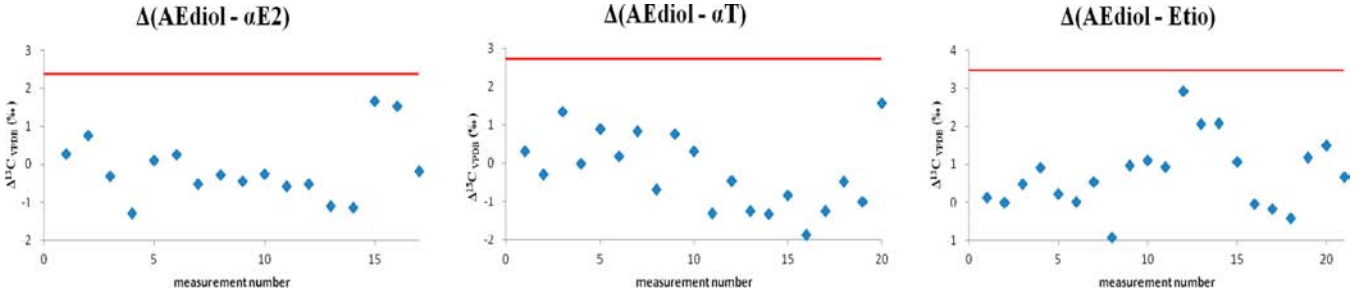

Figure 2. $\Delta^{13}C_{VPDB}$ values (expressed in ‰) of 17α-estradiol (αE2) (left), 17α-testosterone (αT) (middle), and etiocholanolone (Etio) (right), with 5-androstene-3β,17α-diol (AEdiol) as the endogenous reference compound, from a compliant control population.

DOI: 10.1021/acs.jafc.5b02746
J. Agric. Food Chem. 2015, 63, 7574−7581

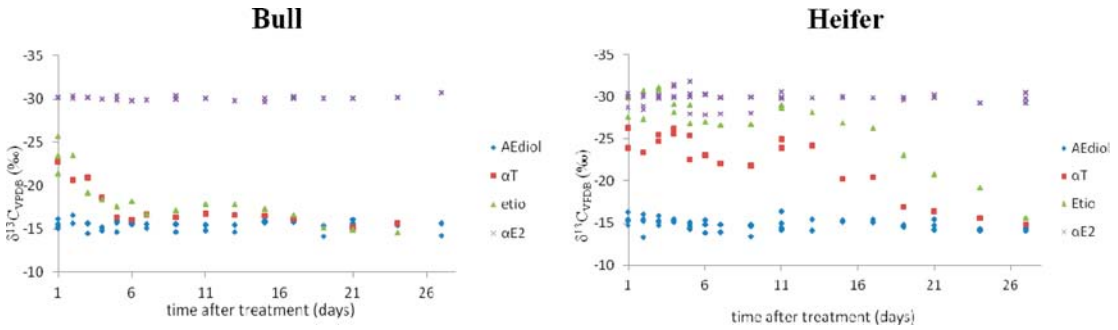

Figure 3. $\delta^{13}C_{VPDB}$ values (expressed in ‰) of 5-androstene-3β,17α-diol (AEdiol), 17α-estradiol (αE2), 17α-testosterone (αT), and etiocholanolone (Etio) in the urine samples from a bull (left) and a heifer (right) after treatment with 17β-testosterone propionate and 17β-estradiol benzoate.

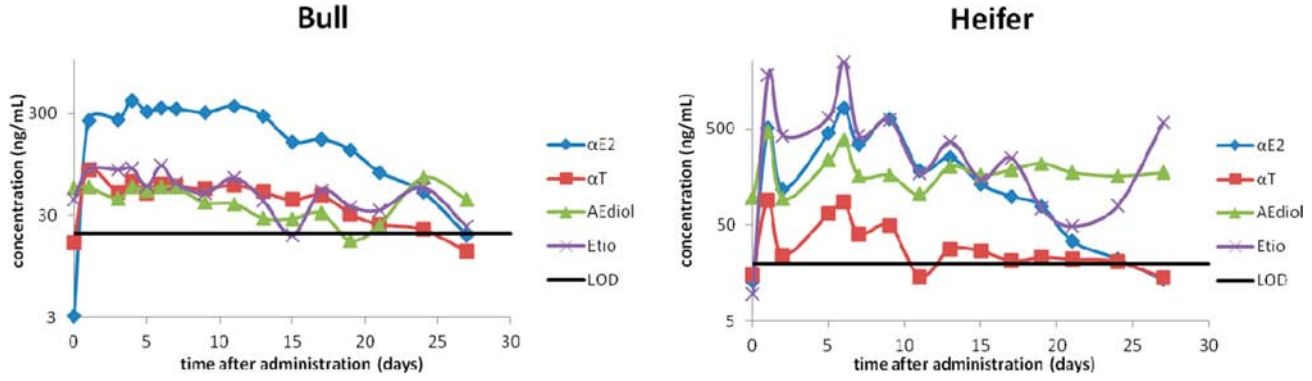

Figure 4. Concentrations (expressed in ng mL^{-1}), measured with LC-MS/MS, of 5-androstene-3β,17α-diol (AEdiol), 17α-estradiol (αE2), 17α-testosterone (αT), and etiocholanolone (Etio) in the urine samples from a bull (left) and a heifer (right) after treatment with 17β-testosterone propionate and 17β-estradiol benzoate.

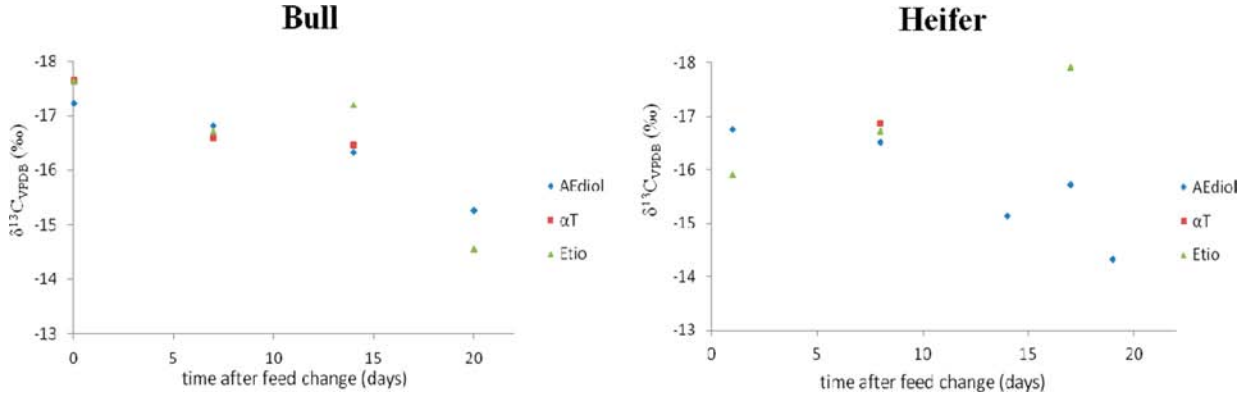

Figure 5. $\delta^{13}C_{VPDB}$ values (expressed in ‰) of 5-androstene-3β,17α-diol (AEdiol), 17α-testosterone (αT), and etiocholanolone (Etio) in the urine samples from a bull (left) and a heifer (right) after changing the feed composition.

contrary to previous testosterone administration studies, in which a more gradual decline over a time span of several days was described.[7,26,27] This difference can be contributed to the currently used preparation, 17β-testosterone propionate, which is known to have a more rapid and shorter lasting effect because of the short carbon chain length of the ester, as opposed to 17β-testosterone enanthate, although influence of other factors such as age, weight, or type of feed of the animals cannot be excluded.

The $\delta^{13}C_{VPDB}$ values of αE2 remain stable after injection, at −30.13 ± 0.24‰ and −29.90 ± 0.70‰ for the male and female, respectively. The small difference in value between the used preparation and the urine samples indicate a very low endogenous production of estrogens, and therefore, the treatment remained visible until the end of the experiment, 27 days after administration.

However, regarding the androgen metabolites, differences between both animals are more pronounced. The difference between the injected testosterone $\delta^{13}C_{VPDB}$ value and the more depleted $\delta^{13}C_{VPDB}$ value in the various female urine samples is close to zero for both Etio and αT. It would indicate that the contribution of the endogenous steroids in the female is insignificant versus the concentration of exogenous residues. For the male, the relative concentration contribution of the endogenous steroids is rather high as attested by the difference observed between $\delta^{13}C_{VPDB}$ values of the injected testosterone

DOI: 10.1021/acs.jafc.5b02746
J. Agric. Food Chem. 2015, 63, 7574−7581

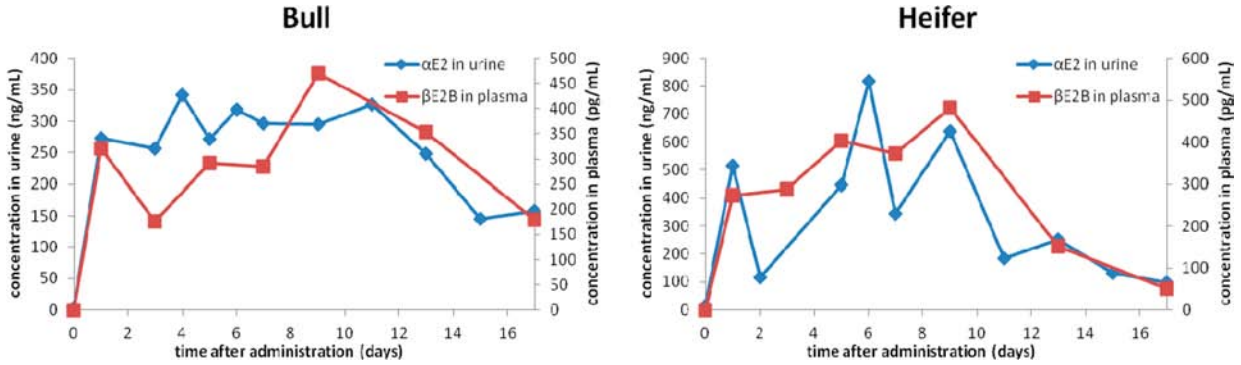

Figure 6. Concentrations of 17β-estradiol benzoate (βE2B) in plasma (expressed in pg mL^{-1}) and 17α-estradiol (αE2) in urine (expressed in ng mL^{-1}) from a bull (left) and a heifer (right) after treatment with 17β-testosterone propionate and 17β-estradiol-3-benzoate. Adapted with permission from ref 30. Copyright 2013 Elsevier B.V.

and the most depleted level of Etio found in the urine samples after treatment (6‰).

As a consequence, while βTP treatment could be proven up to 24 days after injection in the female, this was limited to 3 days for the male. However, since βE2 was proven to be a more powerful growth promoter in male animals than βT, both substances can be expected to be administered together to enhance the effects.[28] Still, the detection of βE2 administration has its boundaries as well. While endogenous dilution determines the detection window for the androgens, it is limited for the estrogens by their abundance in the urine samples (Figure 4). While the results 27 days after administration still indicate the administration in both animals, the measurements are just below the linear range of the IRMS and would have been discarded during routine analysis.

When evaluating the results for both testosterone metabolites, the carbon enrichment was prolonged in Etio, compared to αT for which the $^{13}C/^{12}C$ ratio returned to the endogenous value within 2 days after treatment in the bull, making it a less suitable metabolite in male animals.[13] In the heifer, however, the $\Delta^{13}C_{VPDB}$ value for αT remained above the threshold for up to 17 days, thus proving its usefulness.

Effect of the Feeding on Measured $\delta^{13}C_{VPDB}$ Values. After the animals were obtained, their feeding regime was kept constant during the entire experiment. The treatment was only performed after 21 days to ensure that the measurements of the ERC after treatment were stable and reflected the current diet. Urine samples were collected during this adaptation period as well, whose the results are displayed in Figure 5. In the samples from the bull, an upward trend in measured $\delta^{13}C_{VPDB}$ values is visible, which corresponds with the described effect of an enlarged portion of maize in the feed.[24,26] The values of both the ERC and the metabolites shift simultaneously, with the $\Delta^{13}C_{VPDB}$ values never exceeding 0.89‰. However, this trend is not very pronounced since apparently, the previous diet already contained a significant portion of C4 plant material, and for the heifer, this trend was only visible for AEdiol. Unfortunately, the four target analytes could not be measured simultaneously in any of the samples before treatment, and for αE2, none of the samples contained a sufficient amount to provide an adequate result.

Comparison to Other Detection Methods. As an alternative to the analysis of urine samples with IRMS, abuse of synthetic homologues of naturally occurring steroid hormones in cattle can also be proven by the detection of the intact steroid esters, used for the treatment, in hair or blood samples, using other mass spectrometric techniques.[29] During the administration study, serum samples were collected at different times from both animals for the detection and quantification of βTP and βE2B using ultrahigh performance liquid chromatography/tandem mass spectrometry. The used method, as well as the obtained results from these and other treated animals, were discussed by Kaabia et al.[30] The amount of βE2B in the serum samples increases rapidly already 1 day after injection and only starts decreasing between 9 and 13 days after injection in both animals. A good correspondence can be observed between the kinetic curve of βE2B in serum and the concentration of αE2 in the urine samples of both animals (Figure 6). βE2B remained detectable up to 17 days after administration. Unfortunately, no βTP was detected in the samples from the bull. However, in samples from three other heifers which received a similar treatment, βTP remained detectable up to 2 days, indicating a high esterase activity.

Thus, the detection window for the administration of both substances was wider when using the GC-MS/C/IRMS approach, while the difference between both analyses was most pronounced when looking at testosterone abuse in the heifer, which could be detected up to 17 days longer compared to the analysis of the serum samples. However, it is expected that the IRMS detection windows will become narrower as the relative portion of C3 plant material in the feed increases, whereas it is unlikely that a dietary change would affect the presence of the administered steroid esters in serum. Also, the analytical method for the analysis of the plasma samples is significantly less complex and time-consuming than the sample preparation prior to IRMS analysis.

As mentioned above, a third way to undisputedly demonstrate the abuse of synthetic homologues of naturally occurring steroid hormones is by detection of the intact steroid esters in hair. Unfortunately, no hair samples were analyzed during the current study. However, detection methods using GC-MS/MS and LC-MS/MS and results from administration studies with esters of βT and βE2 are available.[29,31−33]

Regarding a single intramuscular βE2B administration, detection windows from 2 weeks up to 70 days have been reported.[29,31] Regarding βTP, no data could be produced on the successful detection of its incorporation into bovine hair after treatment, although this could have been due to the low dosage used in the study.[33] Nevertheless, in studies using other esters of testosterone, detection windows similar to those reported above for βE2B were observed, up to 70 days after treatment.[29,33] Even though this method offers great

DOI: 10.1021/acs.jafc.5b02746
J. Agric. Food Chem. 2015, 63, 7574−7581

perspectives due to its large detection windows, the result is highly variable and influenced by additional factors such as pigmentation of the hair and sampling distance from the injection site. It is clear that GC-MS/C/IRMS is an excellent technique for the detection of abuse of homologues of naturally occurring steroids and that the presented method is functioning well. However, the inclusion of additional ERCs would provide an even more powerful result, and since different steroids are often abused together, the addition of metabolites of other substances to the analysis would broaden the scope and detection possibilities. Still, as illustrated by this study, the technique is limited by both the abundance of steroids in urine samples and the required complex sample preparation. Therefore, this technique is complementary to the detection of steroid esters in blood, for which a far less laborious and time-consuming sample preparation can be used, and in hair, which could offer a larger time frame for detection.

■ ASSOCIATED CONTENT

Supporting Information

The Supporting Information is available free of charge on the ACS Publications website at DOI: 10.1021/acs.jafc.5b02746.

Sample preparation overview and additional results of the treated animals (PDF)

■ AUTHOR INFORMATION

Corresponding Author

*Tel: 0032478551161. E-mail: geert.janssens@favv.be.

Notes

The authors declare no competing financial interest.

■ REFERENCES

(1) European Council. Council Directive 96/22/EC of 29 April 1996 concerning the prohibition on the use in stock farming of certain substances having a hormonal or thyrostatic action and of β-agonist and repealing Directives 81/602/EEC, 88/146/EEC and 88/299/EEC. *Off. J. Eur. Commun.* **1996**, *L125*, 3−9.

(2) European Council. Council Directive 96/23/EC of 29 April 1996 on measures to monitor certain substances and residues thereof in live animals and animal products and repealing Directives 85/358/EEC and 86/469/EEC and Decisions 89/187/EEC and 91/664/EEC. *Off. J. Eur. Commun.* **1996**, *L125*, 10−32.

(3) European Commission. Commission Decision 2002/657/EC of 12 August 2002 implementing Council Directive 96/23/EC concerning the performance of analytical methods and the interpretation of results. *Off. J. Eur. Commun.* **2002**, *L221*, 8−36.

(4) Courtheyn, D.; Le Bizec, B.; Brambilla, G.; De Brabander, H. F.; Cobbaert, E.; Van de Wiele, M.; Vercammen, J.; De Wasch, K. Recent developments in the use and abuse of growth promoters. *Anal. Chim. Acta* **2002**, *473*, 71−82.

(5) Le Bizec, B.; Pinel, G.; Antignac, J. P. Review: Options for veterinary drug analysis using mass spectrometry. *J. Chromatogr. A* **2009**, *1216*, 8016−8034.

(6) Buisson, C.; Hebestreit, M.; Preiss Weigert, A.; Heinrich, K.; Fry, H.; Flenker, U.; Banneke, S.; Prevost, S.; André, F.; Schaenzer, W.; Houghton, E.; Le Bizec, B. Application of stable carbon isotope analysis to the detection of 17β-estradiol administration to cattle. *J. Chromatogr., A* **2005**, *1093*, 69−80.

(7) Ferchaud, V.; Le Bizec, B.; Monteau, F.; André, F. Determination of the exogenous character of testosterone in bovine urine by gas chromatography-combustion-isotope ratio mass spectrometry. *Analyst* **1998**, *123*, 2617−2620.

(8) Sterk, S. S.; Blokland, M. H.; De Rijke, E.; Van Ginkel, L. A. EURL reflection paper: natural growth promoting substances in biological samples. *Research Report RIKILT* **2014**, 1−68.

(9) Piper, T.; Emery, C.; Saugy, M. Recent developments in the use of isotope ratio mass spectrometry in sports drug testing. *Anal. Bioanal. Chem.* **2011**, *401*, 433−447.

(10) World Anti Doping Agency. WADA technical document − TD2014IMRS. 2014. https://wada-main-prod.s3.amazonaws.com/pdfpreview/ce72cd2b20418a2b6fe3d45bcaed2620.jpg.

(11) Janssens, G.; Courtheyn, D.; Mangelinckx, S.; Prévost, S.; Bichon, E.; Monteau, F.; De Poorter, G.; De Kimpe, N.; Le Bizec, B. Use of Isotope Ratio Mass Spectrometry to differentiate between endogenous steroids and synthetic homologues in cattle: a review. *Anal. Chim. Acta* **2013**, *772*, 1−15.

(12) Janssens, G.; Mangelinckx, S.; Courtheyn, D.; Prévost, S.; De Poorter, G.; De Kimpe, N.; Le Bizec, B. Application of gas chromatography-mass spectrometry/combustion/isotope ratio mass spectrometry (GC-MS/C/IRMS) to detect the abuse of 17β-estradiol in cattle. *J. Agric. Food Chem.* **2013**, *61*, 7242−7249.

(13) Hebestreit, M.; Flenker, U.; Buisson, C.; André, F.; Le Bizec, B.; Fry, H.; Lang, M.; Preiss Weigert, A.; Heinrich, K.; Hird, S.; Schänzer, W. Application of stable carbon isotope analysis to the detection of testosterone administration to cattle. *J. Agric. Food Chem.* **2006**, *54*, 2850−2858.

(14) Angeletti, R.; Contiero, L.; Gallina, G.; Montesissa, C. The urinary ratio of testosterone to epitestosterone: a good marker of illegal treatment also in cattle? *Vet. Res. Commun.* **2006**, *30* (Suppl. 1), 127−131.

(15) Scarth, J. P.; Clarke, A.; Teale, P.; Mill, A.; Macarthur, R.; Kay, J. Detection of endogenous steroid abuse in cattle: results from population studies in the UK. *Food Addit. Contam., Part A* **2011**, *28*, 44−61.

(16) Biddle, S.; Teale, P.; Robinson, A.; Bowman, J.; Houghton, E. Gas chromatography−mass spectrometry/mass spectrometry analysis to determine natural and post-administration levels of oestrogens in bovine serum and urine. *Anal. Chim. Acta* **2007**, *586*, 115−121.

(17) Cawley, A.; Collins, M.; Kazlauskas, R.; Handelsman, D. J.; Heywood, R.; Longworth, M.; Arenas-Queralt, A. Stable isotope ratio profiling of testosterone preparations. *Drug Test. Anal.* **2010**, *2*, 557−567.

(18) Forsdahl, G.; Östreicher, C.; Koller, M.; Gmeiner, G. Carbon isotope ratio determination and investigation of seized testosterone preparations. *Drug Test. Anal.* **2011**, *3*, 814−819.

(19) Brooker, L.; Cawley, A.; Drury, J.; Edey, C.; Hasick, N.; Goebel, C. Stable carbon isotope ratio profiling of illicit testosterone preparations − domestic and international seizures. *Drug Test. Anal.* **2014**, *6*, 996−1001.

(20) Hullstein, I.; Sagredo, C.; Hemmersbach, P. Carbon isotope ratios of nandrolone, boldenone, and testosterone preparations seized in Norway compared to those of endogenously produced steroids in a Nordic reference population. *Drug Test. Anal.* **2014**, *6*, 1163−1169.

(21) Piper, T.; Mareck, U.; Geyer, H.; Flenker, U.; Thevis, M.; Platen, P.; Schänzer, W. Determination of $^{13}C/^{12}C$ ratios of endogenous urinary steroids: method validation, reference population and application to doping control purposes. *Rapid Commun. Mass Spectrom.* **2008**, *22*, 2161−2175.

(22) Piper, T.; Riemann, P.; Opfermann, G.; Marck, U.; Geyer, H.; Vajiala, G.; Flenker, U.; Schänzer, W. Determination of $^{13}C/^{12}C$ ratios of urinary epitestosterone and its main metabolites 5α- and 5β-androstane-3α,17α-diol. *Drug Test. Anal.* **2009**, *1*, 576−586.

(23) Mason, P. M.; Hall, S. E.; Gilmour, I.; Houghton, E.; Pillinger, C.; Seymour, M. A. The use of stable carbon isotope analysis to detect the abuse of testosterone in cattle. *Analyst* **1998**, *123*, 2405−2408.

(24) Balizs, G.; Jainz, A.; Horvatovich, P. Investigation of the feeding effect on the $^{13}C/^{12}C$ isotope ratio of the hormones in bovine urine using gas chromatography/combustion isotope ratio mass spectrometry. *J. Chromatogr. A* **2005**, *1067*, 323−330.

(25) FDA website: http://www.ecfr.gov/cgi-bin/text-idx?c=ecfr&SID=f44bc2af7b4ac5a3adf170a9e18b9842&rgn=div5&view=text&node=21:6.0.1.1.11&idno=21#21:6.0.1.1.11.0.1.56.

(26) Ferchaud, V.; Le Bizec, B.; Monteau, F.; André, F. Characterization of exogenous testosterone in livestock by gas chromatography/

DOI: 10.1021/acs.jafc.5b02746
J. Agric. Food Chem. 2015, 63, 7574−7581

combustion/isotope ratio mass spectrometry: influence of feeding and age. *Rapid Commun. Mass Spectrom.* **2000**, *14*, 652−656.
(27) Prévost, S.; Nicol, T.; Monteau, F.; André, F.; Le Bizec, B. GC/C/IRMS to control the misuse of androgens in breeding animals: new derivatization method applied to testosterone metabolites and precursors in urine samples. *Rapid Commun. Mass Spectrom.* **2001**, *15*, 2509−2514.
(28) Heitzman, R. J. The effectiveness of anabolic agents in increasing rate of growth in farm animals; report on experiments in cattle. *Environ. Qual. Saf. Suppl.* **1976**, *5*, 89−98.
(29) Stolker, A. A. M.; Groot, M. J.; Lasaroms, J. J. P.; Nijrolder, W. J. M.; Blokland, M. H.; Riedmaier, I.; Becker, C.; Meyer, H. H. D.; Nielen, M. W. F. Detectability of testosterone esters and estradiol benzoate in bovine hair and plasma following pour-on treatment. *Anal. Bioanal. Chem.* **2009**, *395*, 1075−1087.
(30) Kaabia, Z.; Dervilly-Pinel, G.; Hanganu, F.; Cesbrond, N.; Bichon, E.; Popot, M. A.; Bonnaire, Y.; Le Bizec, B. Ultra high performance liquid chromatography/tandem mass spectrometry based identification of steroid esters in serum and plasma: An efficient strategy to detect natural steroids abuse in breeding and racing animals. *J. Chromatogr., A* **2013**, *1284*, 126−140.
(31) Rambaud, L.; Bichon, E.; Cesbron, N.; André, F.; Le Bizec, B. Study of 17 ß-estradiol-3-benzoate, 17α-methyltestosterone and medroxyprogesterone acetate fixation in bovine hair. *Anal. Chim. Acta* **2005**, *532*, 165−176.
(32) Rambaud, L.; Monteau, F.; Deceuninck, Y.; Bichon, E.; André, F.; Le Bizec, B. Development and validation of a multi-residue method for the detection of a wide range of anabolic steroids in hair using gas chromatography-tandem mass spectrometry. *Anal. Chim. Acta* **2007**, *586*, 93−104.
(33) Nielen, M. W. F.; Lasaroms, J. J. P.; Mulder, P. P. J.; Van Hende, J.; Van Rhijn, J. A.; Groot, M. J. Multi residue screening of intact testosterone esters and boldenone undecylenate in bovine hair using liquid chromatography electrospray tandem mass spectrometry. *J. Chromatogr. B: Anal. Technol. Biomed. Life Sci.* **2006**, *830*, 126−134.

DOI: 10.1021/acs.jafc.5b02746
J. Agric. Food Chem. 2015, 63, 7574−7581

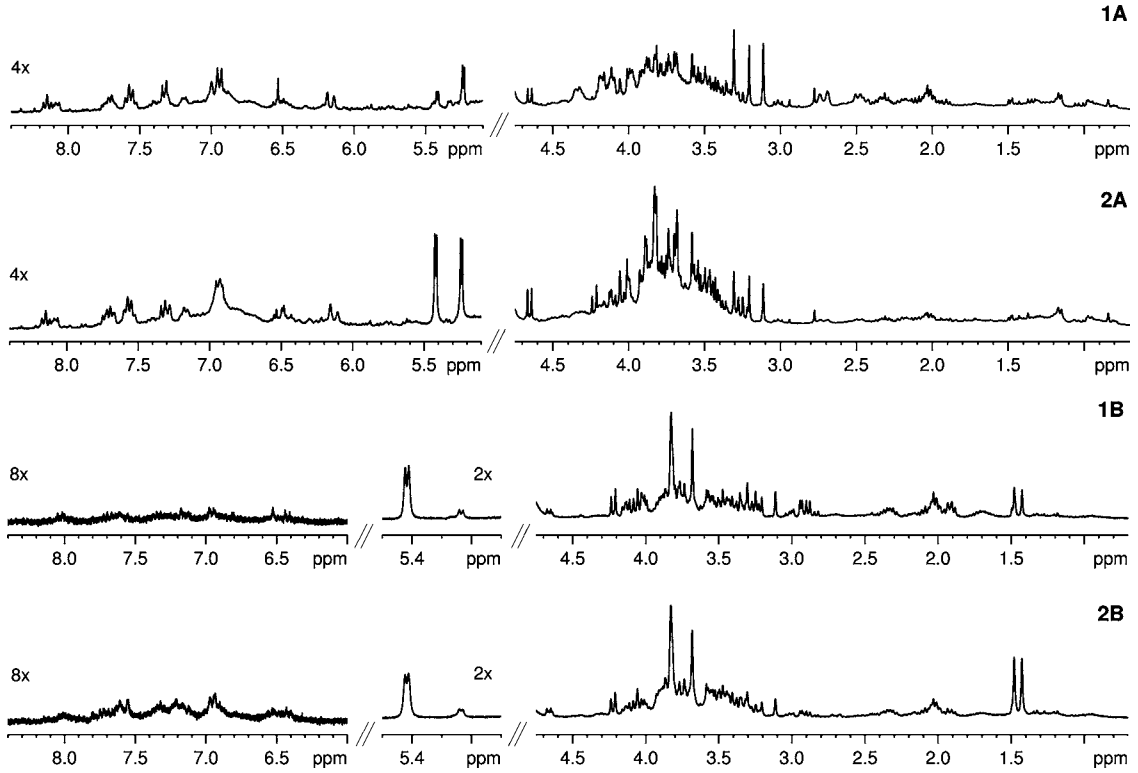

Figure 1. Representative ^{1}H NMR spectral profile of the extracts from the asymptomatic (1) and symptomatic (2) leaves (A) and roots (B).

combination of NMR and chemometrics can help to identify metabolic patterns in plants under stress conditions such as those caused by diseases.

In this context, the present work aimed to apply NMR and chemometrics to the metabolomic evaluation of HLB-affected leaves and roots in the asymptomatic and symptomatic stages of the disease.

MATERIALS AND METHODS

Plant Material. Leaf and secondary root samples of symptomatic (SYM) and asymptomatic (ASY) HLB-affected trees were collected in August 2012 from a 6-year-old grove with Valencia sweet orange (*Citrus sinensis* L. Osbeck) on Rangpur Lime rootstock (*Citrus limonia* Osbeck) in a commercial citrus orchard near Taquaritinga in the central part of São Paulo state. All trees received normal grove management, pest control, and fertilization.

The SYM plants showed the typical yellowish asymmetrical chlorosis of the leaves, as well as small and lopsided fruits, whereas the ASY plants showed normal shoots, leaves, and fruits. Samples from roots were collected on the same side of the canopy from which leaf samples were taken. All samples (the SYM and ASY groups) were subjected to a titer estimation of *Ca.* Liberibacter asiaticus using quantitative real-time PCR (qPCR).

A total of 10 neighboring orange trees in the same planting row were collected: 5 SYM and 5 ASY biological samples. About 40 leaves and a piece of secondary root per tree were sampled. Among five ASY biological samples, one plant did not show a detectable level of bacterium in the leaves by qPCR analysis, but it showed a detectable level of bacterium in roots (in this study) and fruits (data not shown). The same case occurred for one root. As reported by Chin and co-workers,[13] the bacteria are not evenly distributed throughout the tree; thus, false negatives can occur in qPCR. Therefore, the negative samples for *Ca.* Liberibacter asiaticus are highlighted in the principal component analysis (PCA) figures (Figures 2A and 3A) as ASY-ND (nondetected HLB in the ASY samples), but they belong to the ASY group.

Sample Preparation and qPCR Analysis. The sample preparation and analysis by qPCR were performed according to the procedure outlined by Coletta-Filho et al.[7] The qPCR data showed averaged cycle threshold (Ct) values of 23.6 ± 1.3 for the SYM leaves and 36.3 ± 2.3 for the ASY leaves, whereas the Ct values for roots were 31.6 ± 3.9 for the SYM samples and 38.8 ± 0.7 for the ASY samples. Samples with Ct value ≥40 were negative for *Ca.* Liberibacter asiaticus.

Sample Preparation and NMR Analysis. Each biological sample was independently analyzed, with three technical replicates. For each replicate, 80 mg of leaves or roots was manually macerated for 2 min. Extractions were performed with 1 mL of TMSP-d_4/D_2O 0.05% solution in phosphate buffer (KH_2PO_4/Na_2HPO_4) at pH 5.4 and sonicated for 20 min. The extracts were centrifuged, filtered, and maintained at approximately 1 °C until the NMR analyses were performed. The extracts were directly inserted into 5 mm NMR tubes.

The ^{1}H NMR measurements were obtained using a Bruker DPX 300 (7.05 T) spectrometer, which operated at 300.13 MHz for ^{1}H. The ^{1}H NMR spectra were acquired at 20 °C using a composite pulse presaturation sequence to suppress the solvent signal (D_2O), with 128 scans, 65,536 points, an acquisition time of 3.64 s, a relaxation delay of 2 s, and a spectral window of 30 ppm. The spectra were processed with 65,536 points in the Fourier transformation and subjected to exponential multiplication of 0.30 Hz with manual phase and baseline corrections. Two-dimensional experiments (gHSQC, gHMBC, and gTOCSY) were conducted at the default parameters to further support compound identification.

Principal Component Analysis and Statistical Analysis. The ^{1}H NMR spectra were introduced into the AMIX program (3.8 Bruker) and subjected to exploratory analyses using PCA. The 0.75−8.26 ppm proton region of the leaf extracts and the 0.70−8.10 ppm proton region of root extracts were evaluated; the region between 4.60 and 5.20 ppm, which corresponds to the deuterated water signal, was excluded. Buckets were constructed through a simple rectangular format with 0.04 ppm of width and integrated, normalizing by the sum of the absolute intensities. The samples were mean-centered, and Pareto scaling preprocessing was applied for leaves and roots.

Statistical analyses were performed using the integration values from the signals with high loadings in PCA relative to the TMSP-d_4 signal in the ^{1}H NMR spectra. Student's t test was applied to assess the differences between the means of the ASY and SYM groups. PCA and

DOI: 10.1021/acs.jafc.5b03598
J. Agric. Food Chem. 2015, 63, 7582−7588

Table 1. NMR Chemical Shift Assignments of the Compounds Identified in Extracts from Leaves and Roots

compound	assignment	δ ^{1}H	multiplicity [J(Hz)]	δ ^{13}C	part of the plant[a]	
					leaves	roots
		Amino Acids				
proline	α-CH	4.13	m[c]	64.3	D	ND
	β-CH_2	2.27−2.37	m		D	D
	γ-CH_2	1.97−2.14[b]	m	26.8	D	D
	δ-CH	3.34	m	49.0	D	ND
	δ'-CH	3.42	m	49.0	D	ND
valine	γ-CH_3	0.99	d [7.04]		D	ND
	γ'-CH_3	1.05	d [7.04]	20.6	D	ND
leucine	α-CH	3.75		58.8	D	ND
	β-CH_2	1.71			D	ND
	γ-CH	1.71			D	ND
	δ, δ'-CH_3	0.96		24.4	D	ND
tyrosine	H-2, H-6	7.20		126.3	D	ND
	H-3, H-5	6.94		118.7	D	ND
alanine	α-CH	3.77			D	ND
	β-CH_3	1.48	d [7.28]		D	D
threonine	γ-CH_3	1.33	d [6.7]		D	D
	α-CH	3.60			D	ND
	β-CH	4.25			D	ND
tryptophan	H-2	7.56			D	ND
	H-5	7.71			D	ND
proline betaine	CH_3	3.11[b]	s	48.8	D	D
	CH_3	3.30	s	55.1	D	D
γ-aminobutyric acid (gaba)	α-CH_2	2.31		37.0	D	ND
	γ-CH_2	3.01	t [7.50]	42.1	D	ND
		Carbohydrates				
α-glucose	C1H	5.24	d [3.74]	95.1	D	D
β-glucose	C1H	4.65	d [7.90]	99.0	D	D
sucrose	C1H	5.42[b]	d [3.84]		D	D
	C7H	4.22	d [8.74]		D	D
	C10H	3.68			D	D
	C11/12H	3.81−3.84	m		D	D
		Organic Acids				
malate	α-CH	4.31−4.33	m	73.0	D	ND
	β-CH	2.44		44.8	D	ND
	β'-CH	2.70[b]		44.8	D	ND
fumaric acid		6.53	s		D	ND
		Other Compounds				
choline	CH_3	3.20	s	56.7	D	D

[a]D, detected; ND, nondetected. [b]Signal used to quantify the compound. [c]m, multiplet; d, doublet; s, singlet; t, triplet.

statistical analyses were performed with a 95% confidence level. A P value below 0.05 was used to indicate statistical significance.

RESULTS AND DISCUSSION

Identification of Metabolites in the Leaves and Roots.

The ASY and SYM leaves and roots had similar spectral profiles but different signal intensities (Figure 1). The ^{1}H NMR spectra associated with the two-dimensional experiments and the literature[16−19] supported the identification of carbohydrates, amino acids, organic acids, and other compounds. The identified metabolites and their chemical shifts are reported in Table 1.

Multivariate Analysis by PCA in the Leaves and Roots.

The changes caused by HLB in the leaves and roots of the citrus plants were evaluated using PCA, which enabled the observation of the natural clustering of the samples and unsupervised pattern recognition. The ASY and SYM leaves were distinguished on the

DOI: 10.1021/acs.jafc.5b03598
J. Agric. Food Chem. 2015, 63, 7582−7588

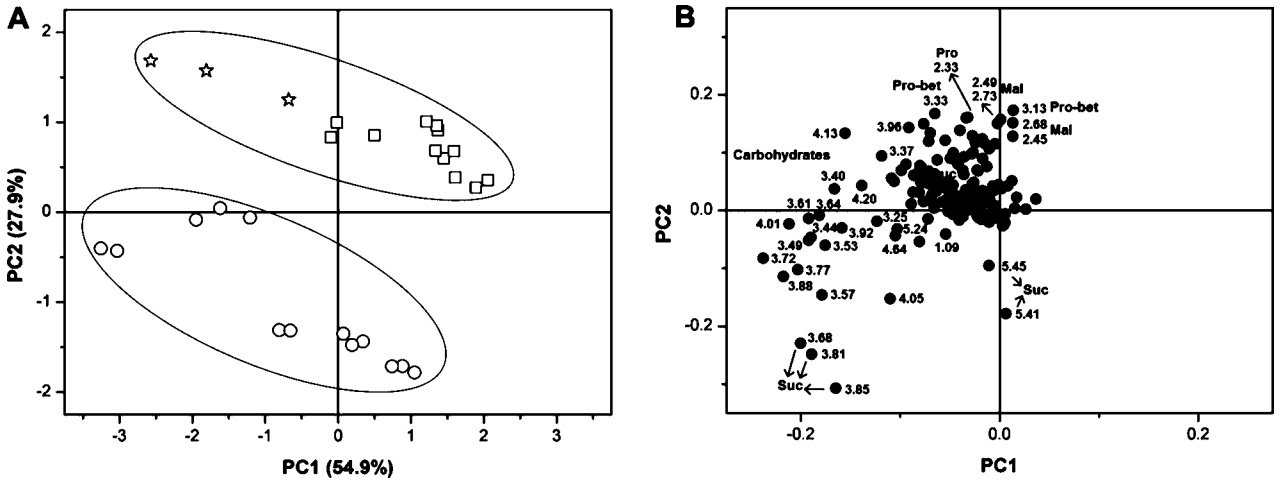

Figure 2. PCA score (A) and loading (B) plots from ^{1}H NMR spectra of the extracts from nondetected HLB (☆) and asymptomatic (□) and symptomatic (○) leaves. Mal, malate; Pro, proline; Pro-bet, proline betaine; Suc, sucrose.

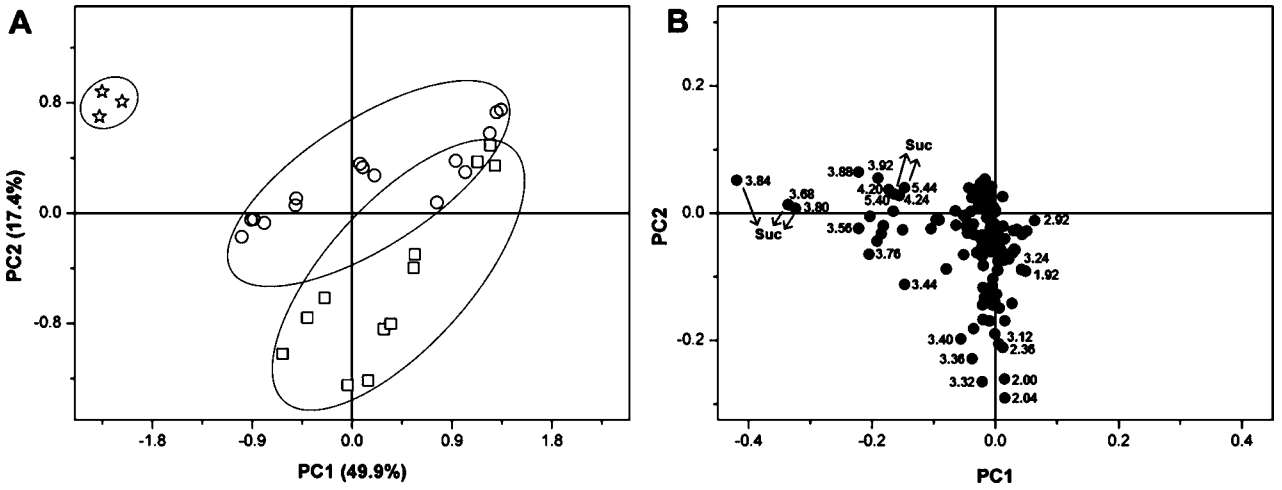

Figure 3. PCA score (A) and loading (B) plots from ^{1}H NMR spectra of the extracts from nondetected HLB (☆) and asymptomatic (□) and symptomatic (○) roots. Suc, sucrose.

score plot (Figure 2A). The characteristic spectral region of carbohydrates was responsible for the disposition of the SYM samples in the negative PC1 values, which included the signals related to sucrose (Figure 2B). The loadings that corresponded to malate and proline betaine were important for allocating the ASY samples to the more positive values of PC2. The ASY-ND scores are close to those of the ASY leaves, although they were allocated to the positive PC2 axis because of the greater contribution of proline, proline betaine, and malate and the smaller contribution of sucrose.

In Figure 3A, the roots of the asymptomatic plants were indistinguishable from those of symptomatic ones. However, there was a tendency of separation between these groups of samples. The ASY-ND roots were detached from the HLB-affected ones on the PC1 axis. The sucrose signals were the variables responsible for allocating the ASY-ND roots to the more negative values of PC1 (Figure 3B).

Figure 4 illustrates the relative proportion of highlighted metabolites in the loading plots (sucrose, proline betaine, malate, and proline), which are responsible for the separation of the ASY and SYM samples. The SYM leaves had a higher sucrose content than the ASY ones (Figure 4A1; $P = 4.77 \times 10^{-5}$), although the ASY and SYM roots were not significantly different in terms of sucrose content (Figure 4A2; $P = 0.086$). The SYM leaves showed a significant decrease in the proline betaine and malate contents (Figure 4A3,A4; $P = 3.71 \times 10^{-9}$ and $P = 2.18 \times 10^{-6}$, respectively), whereas the proline contents were not significantly different between the ASY and SYM leaves (Figure 4A5; $P = 0.65$).

Role of Sucrose, Proline Betaine, Proline, and Malate in HLB-Affected Citrus. Our results indicate that sucrose is an important metabolite for evaluating HLB-affected leaves. Sucrose is the principal source of energy that is transported by the phloem in plants, whereas starch is a stable source of energy that can be stored in the plants. Several studies have indicated the accumulation of starch in HLB-affected trees.[8,10,20,21] However, starch accumulation is detrimental to the plants because of the large volume that it occupies, which disintegrates the thylakoid membrane and causes chlorosis of the leaves.[9]

The starch and sucrose formations occur simultaneously, so an increase in sucrose concentration may cause a source−sink metabolic imbalance. The transcriptome data from young HLB-infected leaves also show that the genes involved in both sucrose metabolism and starch biosynthesis were up-regulated.[22]

Fan et al. found no significant difference in sucrose content between asymptomatic and symptomatic leaves; however, both

DOI: 10.1021/acs.jafc.5b03598
J. Agric. Food Chem. 2015, 63, 7582−7588

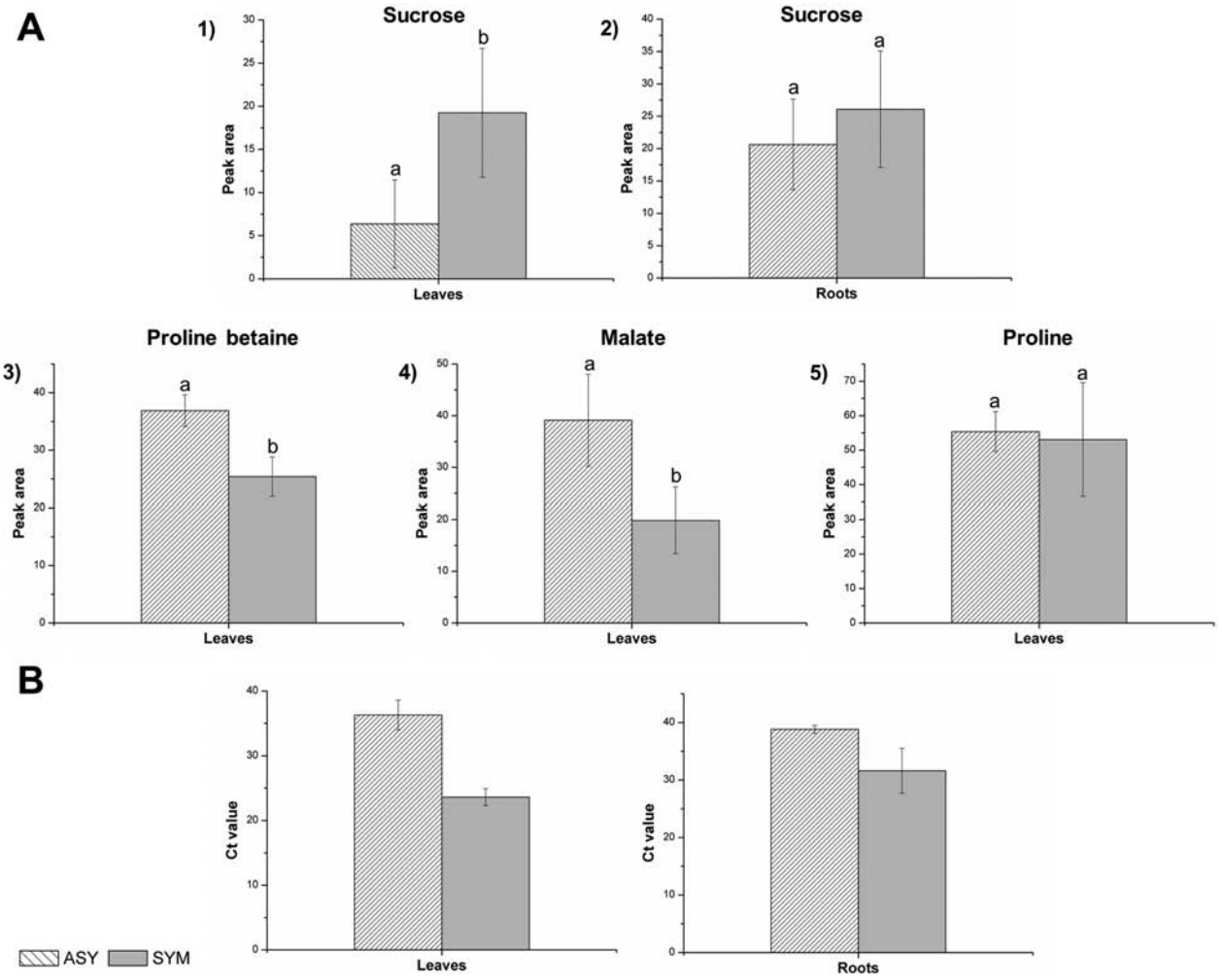

Figure 4. (A) Relative ratio (obtained by integration from signal of the compound in the ^{1}H NMR spectra normalized by TMSP-d_4 signal) of sucrose in the extracts from leaves (1) and roots (2); proline betaine (3), malate (4), and proline (5) in the extracts from leaves. Data are displayed as a mean of relative ratio ± standard deviation. Different letters on bars indicate significant differences ($P < 0.05$). (B) Averaged cycle threshold (Ct) values from qPCR for ASY and SYM leaves and roots.

types of leaves were sampled from infected plants with HLB symptoms.[11] In our case, the asymptomatic leaves were collected from asymptomatic plants; thus, we observed a sucrose accumulation in the SYM leaves (Figure 4A1). The high concentration of sucrose in the SYM leaves suggests that this metabolite cannot be normally transported to other parts of the plant. For the roots, this accumulation was not observed (Figure 4A2) because the phloem vessel was blocked by the *Ca.* Liberibacter spp. bacteria, which alters the transport of sucrose to all parts of the plant.

Proline betaine is commonly found in the Rutaceae species and can be formed by consecutive methylations of proline.[23] Proline and proline betaine are traditionally considered nontoxic compatible osmolytes[24] and are generally associated with the osmotic adjustment and protection of subcellular structures during abiotic[23,25−28] and biotic stresses.[29]

We detected a decrease in proline betaine content in the SYM leaves (Figure 4A3), whereas no significant variation was observed for proline (Figure 4A5). Proline betaine has not been reported in HLB-affected citrus leaves,[30] but it has been observed in juices of HLB-affected oranges with negligible variation.[12,13] As noted by Seifi et al.,[31] the redox-regulating potential of proline may be important in its defense against pathogens, but the pathogens can also exploit these mechanisms to induce susceptibility. Lower proline levels were found in the juices from asymptomatic and symptomatic fruits.[13] These results are different from the findings of Cevallos-Cevallos et al.,[30] who reported significantly higher concentrations of this amino acid in HLB-affected leaves.

Despite the observed accumulation of proline in response to the abiotic and biotic stresses in many plant species, the metabolic alterations in proline and proline betaine content in the HLB-symptomatic leaves remain unclear and may indicate a specific plant−pathogen relationship that specifically modifies this metabolic pathway. Therefore, further studies on the precursors, cofactors, expression, and activities of the key enzymes in the metabolism and catabolism of proline and proline betaine are necessary to understand and characterize the role of these amino acids in the citrus response to HLB infection in different tissues and stages of disease development.

Malate is reported to be a substrate that performs various functions in the cells,[32] which include supplying carbon skeletons for the biosynthesis of amino acids.[33] It is an important intermediary component in the citric acid cycle,[34] and variations in malate content have been associated with the plant response to stress conditions.[35] Malate can be formed from phosphoenolpyr-

DOI: 10.1021/acs.jafc.5b03598
J. Agric. Food Chem. 2015, 63, 7582−7588

uvate, which is a product of glycolysis. Phosphoenolpyruvate is carboxylated by the action of the PEP carboxylase enzyme to produce oxaloacetate, which is reduced to malate by the action of malate dehydrogenase.[36] An important functionality in plants is the action of the NAD-malic enzyme, which converts malate to pyruvate. Consequently, malate plays an important role in maintaining the activities of the citric acid cycle and in the production of some amino acids.[37]

In our study, a decrease in malate content was observed in the SYM leaves (Figure 4A4). This result suggests that HLB significantly changes the essential metabolic processes and affects normal plant development. The change in malate content may indicate the greater consumption of this metabolite to maintain the normal functions of the citric acid cycle, which suggests that other substrates may be consumed for the plant defense.

Relationship between NMR Metabolic Profiles and qPCR. It is possible to relate the observed changes in metabolic profiles with the quantity of bacteria in the samples (Figure 4). The performed NMR analyses in this work show that greater sucrose content in the leaves (Figure 4A1) is observed when the symptoms are observable, that is, when there is a high bacterial concentration (Ct value of 23.6 ± 1.3 for the SYM leaves, Figure 4B). Thus, the HLB-affected leaves with a low quantity of bacteria that do not show any symptoms (Ct value of 36.3 ± 2.3 for the ASY leaves, Figure 4B) do not display sucrose accumulation, although they are already infected with the disease.

Meanwhile, equivalent sucrose content was detected in both the ASY and SYM HLB-affected roots (Figure 4A2). Therefore, even in the ASY roots (Ct value of 38.8 ± 0.7, Figure 4B), HLB sufficiently alters the phloem to inhibit the transport of sucrose from the leaves to the roots, as expected for the SYM roots (Ct value of 31.6 ± 3.9, Figure 4B).

The proline betaine and malate contents (Figures 4A3,A4) show an inversely proportional decrease with the level of bacteria in the leaves (Figure 4B). The plant response can be observed in the SYM leaves because of a reduction in content of these compounds, which may be associated with their catabolism for plant defense.

In summary, our data show modifications in the metabolic profiles of the leaves and less pronounced changes in the roots, which proves that NMR and chemometrics approaches are effective techniques for the metabolomic study of HLB-affected plants. An increase in sucrose content in the leaves and the negligible changes of this metabolite in the roots demonstrate the collapse of the phloem transportation, which is caused by *Ca.* Liberibacter asiaticus. The decrease in proline betaine and malate contents suggests that these compounds are associated with response mechanisms. This study provides important results to further the understanding of the progression of HLB in citrus trees, which can be helpful in developing strategies to control HLB in the future.

AUTHOR INFORMATION

Corresponding Author

*(G.B.A.) Mail: Universidade Federal de Mato Grosso do Sul, Instituto de Química, Av. Filinto Muller 1555, CP 549, CEP 79074-460, Campo Grande, MS, Brazil. Phone: +55 67 3345-3577. Fax: +55 67 3345-3552. E-mail: glaucia.alcantara@ufms.br.

Funding

This research was supported by Coordenação de Aperfeiçoamento de Pessoal de Nível Superior (CAPES), Fundação de Apoio ao Desenvolvimento do Ensino, Ciência e Tecnologia do Estado de Mato Grosso do Sul (FUNDECT), and Fundação Araucária.

Notes

The authors declare no competing financial interest.

ABBREVIATIONS USED

ASY, asymptomatic; ASY-ND, nondetected HLB in the ASY samples; Ct, averaged cycle threshold from qPCR data; gHMBC, gradient heteronuclear multiple-bond correlation; gHSQC, gradient heteronuclear single-quantum coherence; gTOCSY, gradient total correlation spectroscopy; HLB, huanglongbing; NMR, nuclear magnetic resonance; PCA, principal component analysis; qPCR, quantitative real-time polymerase chain reaction; SYM, symptomatic; TMSP-d_4, 2,2,3,3-d_4-3-(trimethylsilyl)-propionic acid sodium salt

REFERENCES

(1) Texeira, D. C.; Ayres, A. J.; Kitajima, E. W.; Tanaka, F. A. O.; Danet, J. L.; Jagoueix-Eveillard, S.; Saillard, C.; Bové, J. M. First report of a huanglongbing-like disease of citrus in Sao Paulo State, Brazil, and association of a new Liberibacter species, "*Candidatus* Liberibacter americanus", with the disease. *Plant Dis.* **2005**, *89*, 107.

(2) Coletta-Filho, H. D.; Takita, M. A.; Targon, M. L. P. N.; Machado, M. A. Analysis of the 16S rDNA sequences from citrus-huanglongbing bacteria reveal a different "*Ca.* Liberibacter" strain associated to the citrus disease in Sao Paulo, Brazil. *Plant Dis.* **2005**, *89*, 848−852.

(3) Halbert, S. E. The discovery of huanglongbing in Florida. Proceedings of 2nd International Citrus Canker and Huanglongbing Research Workshop; http://freshfromflorida.s3.amazonaws.com/2nd_International_Canker_Huanglongbing_Research_Workshop_2005.pdf (accessed Oct 16, 2014).

(4) Garnier, M.; Bové, J. M. Structure trilamellaire des deux membranes qui entourent les organismes procaryotes associés à la maladie du "greening" des agrumes. *Fruits* **1977**, *32*, 749−752.

(5) Bové, J. M. Huanglongbing: a destructive, newly-emerging, century-old disease of citrus. *J. Plant Pathol.* **2006**, *88*, 7−37.

(6) da Graça, J. V. Citrus greening disease. *Annu. Rev. Phytopathol.* **1991**, *29*, 109−136.

(7) Coletta-Filho, H. D.; Carlos, E. F.; Alves, K. C. S.; Pereira, M. A. R.; Boscariol-Camargo, R. L.; Souza, A. A.; Machado, M. A. In planta multiplication and graft transmission of *Candidatus* Liberibacter asiaticus revealed by real-time PCR. *Eur. J. Plant Pathol.* **2010**, *126*, 53−60.

(8) Fan, J.; Chen, C.; Achor, D. S.; Brlansky, R. H.; Li, Z.; Gmitter, F. G., Jr. Differential anatomical responses of tolerant and susceptible citrus species to the infection of '*Candidatus* Liberibacter asiaticus'. *Physiol. Mol. Plant Pathol.* **2013**, *83*, 69−74.

(9) Folimonova, S. Y.; Robertson, C. J.; Garnsey, S. M.; Gowda, S.; Dawson, W. O. Examination of the responses of different genotypes of citrus to huanglongbing (citrus greening) under different conditions. *Phytopathology* **2009**, *99*, 1346−1354.

(10) Etxeberria, E.; Gonzalez, P.; Achor, D.; Albrigo, G. Anatomical distribution of abnormally high levels of starch in HLB-affected Valencia orange trees. *Physiol. Mol. Plant Pathol.* **2009**, *74*, 76−83.

(11) Fan, J.; Chen, C.; Brlansky, R. H.; Gmitter, F. G., Jr; Li, Z. G. Changes in carbohydrate metabolism in *Citrus sinensis* infected with '*Candidatus* Liberibacter asiaticus'. *Plant Pathol.* **2010**, *59*, 1037−1043.

(12) Cevallos-Cevallos, J. M.; Futch, D. B.; Shilts, T.; Folimonova, S. Y.; Reyes-De-Corcuera, J. I. GC-MS metabolomic differentiation of selected citrus varieties with different sensitivity to citrus huanglongbing. *Plant Physiol. Biochem.* **2012**, *53*, 69−76.

(13) Chin, E. L.; Mishchuk, D. O.; Breksa, A. P.; Slupsky, C. M. Metabolite signature of *Candidatus* Liberibacter asiaticus infection in two citrus varieties. *J. Agric. Food Chem.* **2014**, *62*, 6585−6591.

(14) Slisz, A. M.; Breksa, A. P., III; Mishchuk, D. O.; McCollum, G.; Slupsky, C. M. Metabolomic analysis of citrus infection by '*Candidatus*

DOI: 10.1021/acs.jafc.5b03598
J. Agric. Food Chem. 2015, 63, 7582−7588

Liberibacter' reveals insight into pathogenicity. *J. Proteome Res.* **2012**, *11*, 4223−4230.
(15) Kim, H. K.; Choi, Y. H.; Verpoorte, R. NMR-based plant metabolomics: where do we stand, where do we go? *Trends Biotechnol.* **2011**, *29*, 267−275.
(16) Bharti, S. K.; Bhatia, A.; Tewari, S. K.; Sidhu, O. P.; Roy, R. Application of HR-MAS NMR spectroscopy for studying chemotype variations of *Withania somnifera* (L.) Dunal. *Magn. Reson. Chem.* **2011**, *49*, 659−667.
(17) Pérez, E. M. S.; Iglesias, M. J.; Ortiz, F. L.; Pérez, I. S.; Galera, M. M. Study of the suitability of HRMAS NMR for metabolic profiling of tomatoes: application to tissue differentiation and fruit ripening. *Food Chem.* **2010**, *122*, 877−887.
(18) Piccioni, F.; Capitani, D.; Zolla, L.; Mannina, L. NMR metabolic profiling of transgenic maize with the Cry1A(b) gene. *J. Agric. Food Chem.* **2009**, *57*, 6041−6049.
(19) Son, H.; Hwang, G.; Ahn, H.; Park, W.; Lee, C.; Hong, Y. Characterization of wines from grape varieties through multivariate statistical analysis of ^{1}H NMR spectroscopic data. *Food Res. Int.* **2009**, *42*, 1483−1491.
(20) Kim, J.; Sagaram, U. S.; Burns, J. K.; Li, J.; Wang, N. Response of sweet orange (*Citrus sinensis*) to '*Candidatus* Liberibacter asiaticus' infection: microscopy and microarray analyses. *Phytopathology* **2009**, *99*, 50−57.
(21) Schneider, H. Anatomy of greening-diseased sweet orange shoots. *Phytopathology* **1968**, *58*, 1155−1160.
(22) Martinelli, F.; Reagan, R. L.; Uratsu, S. L.; Phu, M. L.; Albrecht, U.; Zhao, W.; Davis, C. E.; Bowman, K. D.; Dandekar, A. M. Gene regulatory networks elucidating huanglongbing disease mechanisms. *PLoS One* **2013**, *8*, e74256.
(23) Trinchant, J.; Boscari, A.; Spennato, G.; Van de Sype, G.; Le Rudulier, D. Proline betaine accumulation and metabolism in alfalfa plants under sodium chloride stress. Exploring its compartmentalization in nodules. *Plant Physiol.* **2004**, *135*, 1583−1594.
(24) Rhodes, D.; Hanson, A. D. Quaternary ammonium and tertiary sulfonium compounds in higher plants. *Annu. Rev. Plant Physiol. Plant Mol. Biol.* **1993**, *44*, 357−384.
(25) Itai, C.; Paleg, L. G. Responses of water-stressed *Hordeum distichum* L. and *Cucumis sativus* to proline and betaine. *Plant Sci. Lett.* **1982**, *25*, 329−335.
(26) Hanson, A. D.; Rathinasabapathi, B.; Rivoal, J.; Burnet, M.; Dillon, M. O.; Gage, D. A. Osmoprotective compounds in the Plumbaginaceae: a natural experiment in metabolic engineering of stress tolerance. *Proc. Natl. Acad. Sci. U. S. A.* **1994**, *91*, 306−310.
(27) Hare, P. D.; Cress, W. A. Metabolic implications of stress-induced proline accumulation in plants. *Plant Growth Regul.* **1997**, *21*, 79−102.
(28) Campos, M. K. F.; Carvalho, K.; Souza, F. S.; Marur, C. J.; Pereira, L. F. P.; Bespalhok Filho, J. C.; Vieira, L. G. E. Drought tolerance and antioxidant enzymatic activity in transgenic 'Swingle'citrumelo plants over-accumulating proline. *Environ. Exp. Bot.* **2011**, *72*, 242−250.
(29) Szabados, L.; Savouré, A. Proline: a multifunctional amino acid. *Trends Plant Sci.* **2010**, *15*, 89−97.
(30) Cevallos-Cevallos, J. M.; García-Torres, R.; Etxeberria, E.; Reyes-De-Corcuera, J. I. GC-MS analysis of headspace and liquid extracts for metabolomic differentiation of citrus Huanglongbing and zinc deficiency in leaves of 'Valencia' sweet orange from commercial groves. *Phytochem. Anal.* **2011**, *22*, 236−246.
(31) Seifi, H. S.; Van Bockhaven, J.; Angenon, G.; Hofte, M. Glutamate metabolism in plant disease and defense: friend or foe? *Mol. Plant−Microbe Interact.* **2013**, *26*, 475−485.
(32) Martinoia, E.; Rentsch, D. Malate compartmentation-responses to a complex metabolism. *Annu. Rev. Plant Physiol. Plant Mol. Biol.* **1994**, *45*, 447−467.
(33) Schulze, J.; Tesfaye, M.; Litjens, R. H. M. G.; Bucciarelli, B.; Trepp, G.; Miller, S.; Samac, D.; Allan, D.; Vance, C. P. Malate plays a central role in plant nutrition. *Plant Soil* **2002**, *247*, 133−139.
(34) de Andrade, L. R. M.; Ikeda, M.; do Amaral, L. I. V.; Ishizuka, J. Organic acid metabolism and root excretion of malate in wheat cultivars under aluminium stress. *Plant Physiol. Biochem.* **2011**, *49*, 55−60.
(35) Schaaf, J.; Walter, M. H.; Hess, D. Primary metabolism in plant defense. *Plant Physiol.* **1995**, *108*, 949−960.
(36) Heldt, H.; Piechulla, B. *Plant Biochemistry*; Academic Press: San Diego, CA, USA, 2004.
(37) Naik, M. S.; Nicholas, D. J. D. Malate metabolism and its relation to nitrate assimilation in plants. *Phytochemistry* **1986**, *25*, 571−576.

DOI: 10.1021/acs.jafc.5b03598
J. Agric. Food Chem. 2015, 63, 7582−7588

and its recent developments using columns with smaller particle size and enabling increased resolution. Structural information can be obtained online on the basis of UV−visible, mass, and nuclear magnetic resonance spectra. However, extraction, sample cleaning, fractionation, and compound isolation are often essential steps in the development of analytical procedures. Solid phase extraction (SPE) and liquid chromatography on various solid phases and centrifugal partition chromatography have proven very helpful for the isolation of polyphenol fractions and purification. Purification of anthocyanins has been achieved by combining SPE with supramolecular complex formation.[7]

Tentative identifications can be reasonably proposed on the basis of relative retention times, UV−visible spectra, and mass spectra, including fragmentation patterns obtained through multiple stages of ionization/fragmentation in MS/MS or MS^n experiments and accurate mass determination provided by high-resolution mass spectrometers such as Fourier transform ion cyclotron resonance (FT-ICR) MS. Chemotaxonomic information and common structural patterns within families of molecules can provide important clues for data interpretation. However, formal identification requires the use of nuclear magnetic resonance (NMR), involving a combination of ^1H, ^{13}C, and two-dimensional homo- and heteronuclear techniques. LC-NMR can be performed online in the stopped-flow mode, but it suffers from a lack of sensitivity. To overcome this problem, a solid phase extraction (SPE) or lyophilization step can be introduced after the HPLC to concentrate the analytes and replace the elution solvent with a deuterated solvent for NMR analysis.

Moreover, for compounds containing asymmetric carbons, the absolute configuration needs to be determined. Indeed, enantiomeric purity is crucial, especially for medical applications, as the activity or toxicity of a compound may be specific of a given chirality. Electron circular dichroism (ECD) spectroscopy and vibrational circular dichroism (VCD) spectroscopy are the most universal techniques for the determination of absolute configuration, especially when X-ray techniques cannot be applied.[8] Progress in computational technologies allows ECD and VCD spectra to be predicted by using quantum mechanics calculations based on density functional theory (DFT) and the absolute configuration established by comparing calculated and experimental spectra. Another strategy using chiral ionic liquids (CILs) as chiral solvating agents in NMR has been proposed.

High-Throughput Profiling and Metabolomics. Paralleling the development of other omics approaches, metabolomics profiling of polyphenol composition in plants, foods, and biological fluids, including targeted and nontargeted approaches, has become very important in studies related to plant, animal, and human metabolism, plant varietal selection, product authentication, etc. Applications of targeted and untargeted methods to study tea composition have been recently reviewed.[9]

Mass spectrometry is commonly used for high-throughput polyphenol profiling in metabolomics or authentication studies. MS analysis after direct flow injection[10] or after UPLC separation with a 2 min gradient elution[11] provided fingerprints of wine polyphenols. New approaches involving interpretation of high-resolution MS data using petroleomics-inspired strategies are starting to emerge.[12] Structures arising from cascade oxidation reactions were thus proposed for theaflavins, a major but poorly characterized polyphenol fraction of black tea. However, these approaches are restricted to rather low molecular weight compounds and provide only putative identification. NMR, especially ^1H NMR, is also widely used for untargeted metabolomics, but detection of secondary metabolites such as polyphenols can be hindered by the presence of more abundant components. The use of two-dimensional NMR increases signal discrimination and facilitates assignment. High-resolution diffusion-ordered spectroscopy (HR-DOSY) NMR, giving access to diffusion data as an additional dimension, appears very promising for the analysis of phenolic compounds in complex mixtures without prior separation.[13]

Quantitative Analysis. Quantitative analysis is classically performed on the basis of HPLC peak areas after spectrophotometric or fluorometric detection, using external calibration. Although some papers report quantitation based on mass signal intensities, multiple reaction monitoring (MRM) based on MS/MS fragmentation of a selected parent mass followed by monitoring of a specific fragment allows increased sensitivity and selectivity and thus appears as the method of choice for mass spectrometric quantitation. A common limitation to these quantitative approaches is the lack of suitable standards. Indeed, molar absorption coefficients as well as ionization and fragmentation efficiency in mass spectrometry may vary widely within a molecular family so that expression as standard equivalent is usually not accurate. Moreover, a matrix effect can result in signal enhancement or suppression and should be carefully checked in method validation. Quantitative NMR (qNMR) enables universal quantitation of analytes from the integration of ^1H signals, reflecting the molar proportions of nuclei and/or molecules present in the solution. Absolute measurements of seven catechins and of other constituents present in green tea samples could thus be obtained by using an internal calibrant.[14]

Poorly Resolved Polymers. The focus on well-known (e.g., commercially available as standards, spectra available in databases) or easily detected compounds often leads the immersed part of the polyphenol iceberg, that is, unresolved polymers and unextractable polyphenols, being overlooked. Indeed, resolution in liquid chromatography becomes limiting as the sample complexity increases, especially for the analysis of polymers. Gel permeation chromatography (GPC), also called size exclusion chromatography (SEC), has been applied for the molecular weight separation of tannins[15] and of pigments derived from anthocyanins and tannins,[16] but interpretation is limited by the lack of suitable calibration standards. The use of a multiangle laser light scattering detector (MALLS) associated with a concentration detector (e.g., UV) enables determination of the average size and absolute mass of the molecules. MALLS can be hyphenated to SEC and to asymmetric flow field-flow fractionation (AF4) that separates macromolecules according to their size for molecular weight determination.[17]

Complex polyphenol fractions can be characterized by mass spectrometry (Oliveira et al., in this issue). Molecular distribution of proanthocyanidins has been studied by matrix-assisted laser desorption ionization (MALDI) and electrospray ionization (ESI) MS. Higher molecular weight polymers are underestimated by both methods, especially in the presence of lower molecular weight compounds. However, ESI-MS, after optimization, has proven suitable for analyzing tannins with average degrees of polymerization below 26,[18] whereas MALDI-MS analysis of tannin complexes with bovine serum albumin combined with fractionation provided information on the molecular weight distribution of very large and polydisperse

DOI: 10.1021/acs.jafc.5b01173
J. Agric. Food Chem. 2015, 63, 7589−7594

tannins.[19] Both qualitative and quantitative information can also be obtained by NMR analysis. Other approaches are based on the analysis of the products released after acid-catalyzed depolymerization or hydrolysis. HPLC analysis after acid-catalyzed cleavage in the presence of a nucleophile (e.g., thiolysis, phloroglucinolysis) provides qualitative and quantitative information on proanthocyanidin composition. However, high reaction yield is essential to ensure the reliability of qualitative data such as average degree of polymerization. Further information can be obtained by acidic and alkaline hydrolysis, releasing sugar and acyl groups, respectively, from complex phenolic structures. Hydrolysis of wine polyphenols provided evidence of acylation with various acids and confirmed that acetaldehyde and anthocyanins are involved in polymer formation.[20] However, half of the composition remained uncharacterized. The development of methods to determine the composition of polymers including reaction products formed during processing thus remains a major challenge.

Unextractable Compounds. The identification of unextractable polyphenols is even more challenging. This includes lignins and hydroxycinnamates involved in cell wall polymer cross-linking, especially in cereals[21] but also other types of polyphenols that are found in both extractable and unextractable fractions. Nonextractable polyphenols exceed extractable ones in many plant-derived foods and, therefore, may represent a major proportion of the polyphenol dietary intake, as recently concluded in a study on the Spanish diet.[22] This material can be released by performing thiolysis, butanolysis, or hydrolysis on the extraction residue or analyzed by ^{13}C solid state NMR.[23] Considerable variations were reported in proanthocyanidin extractability from plant foods, from totally extractable (in plum) to totally unextractable (in banana).[24] Large differences are also observed between studies. This may result from differences in the preparation of the plant material (e.g., frozen versus freeze-dried), in the analysis method (thiolysis versus butanolysis), and in the calibration standards used.[25] Acidic hydrolysis also released hydroxycinnamic and benzoic acids from fruit unextractable fraction.[22] Finally, these methods proved inefficient for archeological samples. A more drastic pyrolysis method involving a thermally assisted hydrolysis−methylation followed by gas chromatography—mass spectrometry analysis released phenolic markers that can serve as signature compounds for the detection of wine traces in ceramics.[26]

■ CHEMICAL REACTIVITY AND TRANSFORMATIONS

Chemical reactivity and transformations of polyphenols are basic and very important topics of the conference.

During biosynthesis and storage in plant tissues and in food-processing systems, reactions of phenolic compounds, sometimes also involving other compounds (e.g., acetaldehyde), occur to give varieties of new compounds, including pigments.

Tea leaves give various products, including green tea, black tea, oolong tea, and others, because of differences in production processes. Studies on the transformation of tea polyphenols, promoted by the progress of instrumental analytical methodologies, were one of the most important and attractive topics. Theaflavin and theasinensin are known to be major polyphenol components in black tea. The structure of theasinensins seemed to be a simple dimer of epigallocatechin gallate (EGCG); however, this compound was not obtained by a radical coupling of EGCG, but produced from an unstable precursor. Tanaka reported in his plenary lecture that in vitro oxidation of EGCG using a pear polyphenol oxidase yielded the theasinensin precursor, dehydrotheasinensin A. He revealed that theasinensins were formed by oxido-reductive disproportionation reaction.[27] The formation mechanism of oolongtheanins was reported to occur by oxidation of EGCG by $CuCl_2$.[28,29] Pigment compositions of red grape pomace (Oliveira et al., in this issue) and of apple juice (Le Deun et al., in this issue) have also been presented.

Curcumin, an ingredient of turmeric, also attracted attention because of its wide variety of activities; many preclinical studies are going on. This compound exists as a mixture of tautomers and is very unstable. To evaluate the metabolism of curcumin by identification of its degradation products, isotopically labeled curcumin was synthesized. Schneider's group synthesized hexadeuterated curcumin and $^{14}C_2$-labeled curcumin and, using these compounds, they found new metabolites, bicyclopentadione derivatives by LC-MS and NMR analysis (Schneider et al., in this issue). Synthetic studies of curcumin analogues are also useful for clinical studies. Synthesis of C_5-curcuminoids and structure−activity relationships on antitumor activities are reported. A designed probe connected to biotin allowed the identification of the target protein as a KH-type splicing regulatory protein.

The synthesis of chemical probes of bioactive polyphenols that can be used for searching the target protein is very important for pharmaceutical studies to clarify the mode of action. The number of studies in this area is increasing, as illustrated in the conference. Quideau and his group presented a molecular design of affinity-based probes of flavonoids and studies of polyphenol−protein interactions. They synthesized biotinylated catechins to capture leucoanthocyanidin dioxygenase, a key enzyme of anthocyanidin biosynthesis.[30] Kan et al. also reported the synthesis of hapten probe and fluorescent catechin and theaflavin probes.[31] They synthesized a positron emitting tomography (PET) probe containing ^{11}C, the half-life period of which is 20 min. The PET imaging study of nobiletin and EGCG using rat clarified the distribution of the compounds in living organisms.[31]

Other synthetic studies of polyphenols are now promoted by developing new reagents and reactions. Pohjoispää and Wähälä reported deuteration of polyphenol (in this issue), Ohmori and Suzuki presented biosynthesis-inspired isoflavone synthesis and procyanidin oligomer synthesis,[32] and Yamada et al. established synthesis of ellagitannins containing a highly oxygenated diaryl ether residue, C−O digallates.[33]

On the subject of wood polyphenols, the number of studies has increased and much new progress has been reported. Miyakoshi presented in his plenary lecture the oxidative polymerization mechanism of Japanese urushi lacquer, involving a first-stage enzyme (laccase) catalyzed oxidation and a second-stage autoxidation. He also presented the potential of the hybrid lacquer, which is obtained by silication of natural lacquer, as more stable and robust.[34] Many researchers in wood chemistry attended the conference, and reports on the biosynthesis of lignin using imaging mass analysis,[35] synthetic studies, and model reactions were presented. A new research area on materials science of polyphenols should be developed with a tight discussion in ICP.

In the biosynthesis of glucosylated and acylated flavonoids, Ozeki et al. reported a new glucose and acyl donor, acylglucose, as a "Zwitter donor". Up to now, the glucosyl donor of

DOI: 10.1021/acs.jafc.5b01173
J. Agric. Food Chem. 2015, 63, 7589−7594

flavonoids has been considered to be UDP-glucose; however, sinapoyl-glucose and *p*-hydroxybenzoyl-glucose are now proposed as new donors.[36,37]

PHYSICOCHEMICAL PROPERTIES AND ACTIVITIES

In the conference, recent advances in the chemical aspects of polyphenols as plant and food pigments were discussed. In addition to reactions leading to new pigments as discussed above, multiple copigmentation interactions and complexation of metal ions with pigments change the hue of colors. Recent studies with advanced analytical methods show that the color finally observed is a consequence of the co-occurrence of different phenolic compounds that interact with anthocyanins and other organic molecules and inorganic ions that modulate these physicochemical interactions.[38] The transformation and stabilization of anthocyanins, depending on pH change and the presence of copigments, have been interesting subjects in flower coloration. Stabilization of anthocyanins with clathrate compounds, cucurbit[7]uril, and β-cyclodextrin, was reported by Pina (Basílio et al., in this issue). Kondo presented the suppression of hydration reaction of anthocyanins by molecular stacking and metal complexation to give a stable blue flower petal coloration. Oyama et al. reported the structure of elusive blue pigment of hydrangea and, using a synthetic quinic acid ester, the interaction between anthocyanin chromophores and copigments was clarified (in this issue). Multiple copigmentation in anthocyanin−flavanol−flavonol mixtures and its implication in the color of red wines was also studied (Gordillo et al., in this issue).

Although the chemical process of interaction of tannins with proteins is well-known and has been used for industrial processes for a long time, it is still a matter of active scientific research as these interactions are very relevant for food organoleptic properties (astringency, mouthfeel, bitterness, etc.), food and feed antinutritional properties, crop protection against herbivores, and health effects through interaction with human proteins and receptors.

With regard to sensory-related aspects, astringency has long been studied and has been directly associated with interactions of tannins with saliva proteins. There are advances in the knowledge of the relationship between chemical features of polymeric and oligomeric polyphenols and the astringency (mouthfeel) sensation. This field will continue advancing as the analytical methods available, and the genetic characterization of the individuals with different polymorphisms affecting taste, allow a better study of this food-quality related phenomenon.[39]

It was also shown that some polyphenols that can be absorbed after dietary intake interact with serum proteins, and this can be a mode of transportation of polyphenols through the bloodstream to different systemic tissues. The analysis of these associations with the true circulating metabolites and the release of the polyphenols under specific physiological conditions (i.e., inflammation) is also a matter of active research.[40]

The interaction of specific polyphenols with receptors, enzymes, and transporters is also providing evidence of the mechanisms explaining the physiological effects of polyphenols in humans and other animals.[41]

In addition to proteins, evidence was provided about polyphenols interacting with other biological molecules such as lipids and carbohydrates. A study was presented on the effect of polyphenols protecting lipids and proteins from oxidation and degradation during transit through the gastrointestinal tract and the adsorption of polyphenols on cellulose and interaction with nondigestible saccharides such as fructo-oligosaccharides that modulate the effects of polyphenols on rat intestinal cells.

Polyphenols can also be degraded through different mechanisms, including oxidation, during technological processing, storage, and digestion, and the degradation metabolites can also show significant biological effects, positive or negative, that need to be considered. This was clearly illustrated for the turmeric phenolic pigment, curcumin. Little is known of the activity of these degradation products, and the study of this topic in the future is warranted.

Polyphenols can also interact with other relevant food chemical processes, as is the case of the Maillard reaction that has sensory and safety implications. These indirect effects of polyphenols have to be considered to understand relevant chemical processes occurring in complex foods.

Another important field of research regarding polyphenol properties is the study of the role of polyphenols in human health. In this field advances in bioavailability and metabolism, in the mechanisms of action, and in the evidence of health effects in animal models and humans have been reported.[42]

In the bioavailability and metabolism of polyphenols, factors affecting absorption, metabolism, and excretion and intra-individual and interindividual variability were reviewed.[43] For some phenolic compounds, pharmacokinetic studies are still needed, as there is evidence that genetic polymorphisms involved in polyphenol transport and metabolism have a relevant impact on the types and amounts of metabolites present in circulation and in urine.[43]

The interindividual variability of polyphenol metabolites present in plasma and urine after the intake of different polyphenols (isoflavones, lignanes) that has been described previously[44] is now been correlated with human gut microbiota composition and/or genetic polymorphisms, and it will be potentially associated with specific health effects, although the evidence about this is still scarce.

In vivo studies with animal models (mice and rats) or clinical studies show physiological effects of some dietary polyphenols but also show the large interindividual variation mentioned above that divides the participants in the studies into responders and nonresponders.[45] The presented in vivo studies on the effect of polyphenols on cardiovascular health and cognitive function were particularly relevant.

As was highlighted in previous polyphenols meetings,[38,46] for mechanistic studies, the need to use the polyphenol metabolites that reach the target tissues and at the concentrations found in vivo was agreed upon. This approach is not always followed but should be encouraged to reach conclusions that are biologically significant and not simply a nice laboratory exercise. Different types of cells were used for these mechanistic studies going from intestinal cells to neuronal cells.

The interaction of polyphenols with microbes is becoming a hot topic, not only for the role of polyphenols as antimicrobial agents but also for their activity as modulators of the human gut microbiota, which has been correlated with a dozen relevant human diseases.[47,48] In addition, gut-colonizing microbes metabolize dietary polyphenols, leading to metabolites that are often better absorbed than the precursors and, in addition, show interesting health effects including anti-inflammatory and phytoestrogen-like effects.[48]

DOI: 10.1021/acs.jafc.5b01173
J. Agric. Food Chem. 2015, 63, 7589−7594

THE 27TH INTERNATIONAL CONFERENCE ON POLYPHENOLS AND 8TH TANNIN CONFERENCE

These conferences have been held jointly, for the first time in their history, in Nagoya, Japan, during September 2014 and hosted 500 participants from 35 countries. ICP 2014 was divided into six topics: (1) Chemistry, Physicochemistry, and Materials Science; (2) Biosynthesis, Genetics, and Metabolic Engineering; (3) Plant and Ecosystem, Lignocellulose Biomass; (4) Food, Nutrition, and Health; (5) Natural Medicine and Kampo; (6) Tannins and Their Functions. An additional feature of ICP 2014 was that papers on lignin chemistry were also presented. As previously mentioned, lignin was one of the major targets of polyphenol research in the early days. Now in relation to biomass and ecosystems, and the development of new materials, the significance of this topic deserves special attention. Chemical studies of polyphenols must be the platform and basis of all the scientific research of polyphenols. In this special issue, a selection of high-quality original research presented at ICP 2014 is published. Now the countdown to ICP 2016, which will be organized by Prof. Karl Stich, in Vienna, Austria, from July 11−15, 2016, is on.

Véronique Cheynier*

UMR1083 Sciences pour l'œnologie, INRA, 2 place Viala, 34060 Montpellier cedex, France

Francisco A. Tomas-Barberan

Research group on Quality, Safety and Bioactivity of Plant Foods, CEBAS-CSIC, P.O. Box 164, Espinardo, Murcia 30100, Spain

Kumi Yoshida

Graduate School of Information Science, Nagoya University, Chikusa, Nagoya 464-8601, Japan

AUTHOR INFORMATION

Notes

The authors declare no competing financial interest.

ACKNOWLEDGMENTS

We thank the former and current Editors-in-Chief Prof. Jim Seiber and Dr. Thomas Hofmann and the JAFC editorial office for the opportunity to publish this special issue, as well as all submitting authors and reviewers for their invaluable contributions.

DEDICATION

This paper is dedicated to Professor Edwin Haslam, whose work on polyphenols has been and still is an inspiration for all polyphenol scientists

REFERENCES

(1) Yoshida, K.; Oyama, K. I.; Kondo, T. Chemistry of flavonoids in color development. In *Recent Advances in Polyphenol Research*, 1st ed.; Cheynier, V., Sarni-Manchado, P., Quideau, S., Eds.; Wiley-Blackwell: Hoboken, NJ, USA, 2012; Vol. 3, pp 99−130.

(2) (a) *Recent Advances in Polyphenol Research*; Daayf, F., Lattanzio, V., Eds.; Wiley-Blackwell: Chichester, UK, 2008; Vol. 1. (b) *Recent Advances in Polyphenol Research*; Santos-Buelga, C., Escribano-Bailon, M. T., Lattanzio, V., Eds.; Wiley-Blackwell: Chichester, UK, 2010; Vol. 2. (c) *Recent Advances in Polyphenol Research*; Cheynier, V., Sarni-Manchado, P., Quideau, S., Eds.; Wiley-Blackwell: Hoboken, NJ, USA, 2012; Vol. 3. *Recent Advances in Polyphenol Research*; Romani, A., Lattanzio, V., Quideau, S. Eds.; Wiley-Blackwell: Hoboken, NJ, USA, 2014; Vol. 4.

(3) Haslam, E.; Cai, Y. Plant polyphenols (vegetable tannins)-gallic acid metabolism. *Nat. Prod. Rep.* **1994**, *11*, 41−66.

(4) Quideau, S.; Deffieux, D.; Douat-Casassus, C.; Pouységu, L. Plant polyphenols: chemical properties, biological activities, and synthesis. *Angew. Chem., Int. Ed.* **2011**, *50*, 586−621.

(5) Chen, H.-C.; Song, J.; Wang, J. P.; Lin, Y.-C.; Ducoste, J.; et al. Systems biology of lignin biosynthesis in *Populus trichocarpa*: heteromeric 4-coumaric acid: coenzyme A ligase protein complex formation, regulation, and numerical modeling. *Plant Cell* **2014**, *26*, 876−893.

(6) Cheynier, V.; Comte, G.; Davies, K.; Lattanzio, V.; Martens, S. Plant phenolics: recent advances on their biosynthesis, genetics, and ecophysiology. *Plant Physiol. Biochem.* **2013**, *72* (SpecialIssue), 1−20.

(7) Asada, T.; Tamura, H. Isolation of bilberry anthocyanins 3-glycosides bearing ortho-dihydroxy groups on the B ring by forming aluminium complex and their antioxidant activity. *J. Agric. Food Chem.* **2012**, *60*, 10634−10640.

(8) Li, X.-C.; Ferreira, D.; Ding, Y. Determination of absolute configuration of natural products: theoretical calculation of electronic circular dichroism as a tool. *Curr. Org. Chem.* **2010**, *14* (16), 1678−1697.

(9) Daglia, M.; Antiochia, R.; Sobolev, A. P.; Mannina, L. Untargeted and targeted methodologies in the study of tea (*Camellia sinensis* L.). *Food Res. Int.* **2014**, *63*, 275−289.

(10) Mazerolles, G.; Preys, S.; Bouchut, C.; Meudec, M.; Fulcrand, H.; Souquet, J. M.; Cheynier, V. Combination of several mass spectrometry ionization modes: a multiblock analysis for a rapid characterization of the red wine polyphenolic composition. *Anal. Chim. Acta* **2010**, *678*, 195−202.

(11) Delcambre, A.; Saucier, C. High-throughput oenomics: shotgun polyphenomics of wines. *Anal. Chem.* **2013**, *85*, 9736−9741.

(12) Kuhnert, N.; Drynan, J. W.; Obuchowicz, J.; Clifford, M. N.; Witt, M. Mass spectrometric characterization of black tea thearubigins leading to an oxidative cascade hypothesis for thearubigin formation. *Rapid Commun. Mass Spectrom.* **2010**, *24*, 3387−3404.

(13) Nilsson, M.; Duarte, I. F.; Almeida, C.; Delgadillo, I.; Goodfellow, B. J.; Gil, A. M.; Morris, G. A. High-resolution NMR and diffusion-ordered spectroscopy of Port wine. *J. Agric. Food Chem.* **2004**, *52*, 3736−3743.

(14) Napolitano, J. G.; Goedecke, T.; Lankin, D.; Jaki, B.; McAlpine, J.; Chen, S.-N.; Pauli, G. F. Orthogonal analytical methods for botanical standardization: determination of green tea catechins by qNMR and LC-MS/MS. *J. Pharm. Biomed. Anal.* **2014**, *93*, 59−67.

(15) Stringano, E.; Gea, A.; Salminen, J. P.; Mueller-Harvey, I. Simple solution for a complex problem: proanthocyanidins, galloyl glucoses and ellagitannins fit on a single calibration curve in high performance-gel permeation chromatography. *J. Chromatogr., A* **2011**, *1218*, 7804−7812.

(16) Bindon, K.; Kassara, S.; Hayasaka, Y.; Schulkin, A.; Smith, P. Properties of wine polymeric pigments formed from anthocyanin and tannins differing in size distribution and subunit composition. *J. Agric. Food Chem.* **2014**, *62*, 11582−11593.

(17) Vernhet, A.; Dubascoux, S.; Cabane, B.; et al. Characterization of oxidized tannins: comparison of depolymerization methods, asymmetric flow field-flow fractionation and small-angle X-ray scattering. *Anal. Bioanal. Chem.* **2011**, *401*, 1559−1569.

(18) Mouls, L.; Mazauric, J. P.; Sommerer, N.; Fulcrand, H.; Mazerolles, G. Comprehensive study of condensed tannins by ESI mass spectrometry: average degree of polymerisation and polymer distribution determination from mass spectra. *Anal. Bioanal. Chem.* **2011**, *400*, 613−623.

(19) Mouls, L.; Hugouvieux, V.; Mazauric, J. P.; Sommerer, N.; Mazerolles, G.; Fulcrand, H. How to gain insight into the polydispersity of tannins: a combined MS and LC study. *Food Chem.* **2014**, *165*, 348−353.

(20) Wollmann, N.; Hofmann, T. Compositional and sensory characterization of red wine polymers. *J. Agric. Food Chem.* **2013**, *61*, 2045−2061.

DOI: 10.1021/acs.jafc.5b01173
J. Agric. Food Chem. 2015, 63, 7589−7594

(21) Ralph, J. Hydroxycinnamates in lignification. *Phytochem. Rev.* **2010**, *9*, 65−83.
(22) Arranz, S.; Silvan, J. M.; Saura-Calixto, F. Nonextractable polyphenols, usually ignored, are the major part of dietary polyphenols: a study on the Spanish diet. *Mol. Nutr. Food Res.* **2010**, *54*, 1646−1658.
(23) Reid, D. G.; Bonnet, S. L.; Kemp, G.; van der Westhuizen, J. H. Analysis of commercial proanthocyanidins. Part 4: Solid state ^{13}C NMR as a tool for in situ analysis of proanthocyanidin tannins, in heartwood and bark of quebracho and acacia, and related species. *Phytochemistry* **2013**, *94*, 243−248.
(24) Hellstrom, J.; Torronen, A. R.; Mattila, P. H. Proanthocyanidins in common food products of plant origin. *J. Agric. Food Chem.* **2009**, *57*, 7899−7906.
(25) Cheynier, V. Phenolic compounds, from plants to foods. *Phytochem. Rev.* **2012**, *11*, 153−177.
(26) Garnier, N.; Richardin, P.; Cheynier, V.; Regert, M. Characterization of tetramethylammo-nium hydroxide thermochemolysis products of polyphenols from modern and archeological vine derivatives using gas chromatography. *Anal. Chim. Acta* **2003**, *493*, 137−157.
(27) Matsuo, Y.; Hayashi, T.; Saito, Y.; Kouno, I.; Tanaka, T. Structure of enzymatic oxidation products of epigallocatechin. *Tetrahedron* **2013**, *69*, 8952−8958.
(28) Hirose, S.; Tomatsu, K.; Yanase, E. Isolation of key intermediates during formation of oolongtheanins. *Tetrahedron Lett.* **2013**, *54*, 7040−7043.
(29) Ogawa, K.; Hirose, S.; Yamamoto, H.; Shimada, M.; Nagaoka, S.; Yanase, E. Synthesis of oolongtheanins and their inhibitory activity on micellar cholesterol solubility *in vitro*. *Bioorg. Med. Chem. Lett.* **2015**, *25*, 749−752.
(30) Carrie, H.; Tran, D. T.; Rousseau, S.; Chaignepain, S.; Schmitter, J.-M.; Deffieux, D.; Quideau, S. New affinity-based probes for capturing flavonoid-binding proteins. *Chem. Commun.* **2014**, *50*, 9387−9389.
(31) Shimizu, T.; Asakawa, T.; Harada, N.; Fukumoto, D.; Tsukada, H.; Asai, T.; Yamada, S.; Kan, T. Use of positron emission tomography for real-time imaging of biodistribution of green tea catechin. *PLoS One* **2014**, *9*, e85520.
(32) Ohmori, J.; Suzuki, K. Synthetic strategies and tactics for catechin and related polyphenols. In *Recent Advances in Polyphenol Research*, 1st ed.; Romani, A., Lattanzio, V., Quideau, S., Eds.; Wiley-Blackwell: Hoboken, NJ, USA, 2014; Vol. 4, pp 371−410.
(33) Hirokane, T.; Hirata, Y.; Ishimoto, T.; Nishii, K.; Yamada, H. A unified strategy for the synthesis of highly oxygenated diaryl ethers featured in ellagitannins. *Nat. Commun.* **2014**, *5*, 3478. Awarded "GP Ragai Ibrahim Award" in ICP2014.10.1038/ncomms4478
(34) Lu, R.; Yoshida, T.; Miyakoshi, T. Oriental lacquer: a natural polymer. *Polym. Rev.* **2013**, *53*, 153−191.
(35) Aoki, D.; Kuroda, K.; Hanaya, Y.; Saito, K.; Takama, R.; Matsushita, Y.; Fukushima, K. Development of the cryo-TOF-SIMS/SEM system and application for topochemical analysis of plant biomolecules. *Mokuzai Gakkaishi* **2013**, *59*, 367−374.
(36) Miyahara, T.; Sakiyama, R.; Ozeki, Y.; Sasaki, N. Acyl-glucose-dependent glucosyltransferase catalyzes the final step of anthocyanin formation in *Arabidopsis*. *J. Plant Physiol.* **2013**, *170*, 619−624.
(37) Nishizaki, Y.; Yasunaga, M.; Okamoto, E.; Okamoto, M.; Hirose, Y.; Yamaguchi, M.; Ozeki, Y.; Sasaki, N. *p*-Hydroxybenzoyl-glucose is a "Zwitter donor" for the biosynthesis of polyacyl-anthocyanin in delphinium. *Plant Cell* **2013**, *25*, 4150−4165.
(38) Santos-Buelga, C.; Mateus, N.; De Freitas, V. Anthocyanins. Plant pigments and beyond. *J. Agric. Food Chem.* **2014**, *62*, 6879−6884.
(39) Soares, S.; Kohl, S.; Thalmann, S.; Mateus, N.; Meyerhof, W.; De Freitas, V. Different phenolic compounds activate distinct human bitter taste receptors. *J. Agric. Food Chem.* **2013**, *61*, 1525−1533.
(40) Ishikawa, A.; Kuwabata, K.; Miki, S.; Shiba, Y.; Minekawa, S.; Nishikawa, T.; Mukai, R.; Terao, J.; Kawai, Y. Mitochondrial disfunction leads to deconjugation of quercetin glucuronides in inflammatory macrophages. *PLoS One* **2013**, *8*, e80843.
(41) Alvarez, A. I.; Vallejo, F.; Barrera, B.; Merino, G.; Prieto, J. G.; Tomás-Barberán, F.; Espin, J. C. Reeevaluation of the roles of ABCG2 in the disposition of genistein. *Drug Metab. Dispos.* **2012**, *40*, 2219−2220.
(42) Visioli, F.; Lastra, C. A. D. L.; Andrés-Lacueva, C.; Aviram, M.; Calhau, C.; Cassano, A.; D'Archivio, M.; Faria, A.; Feve, G.; Fogliano, V.; Llorach, R.; Vitaglione, P.; Zoratti, M.; Edeas, M. Polyphenols and human health: a prospectus. *Crit. Rev. Food Sci. Nutr.* **2011**, *51*, 524−546.
(43) Bolca, S.; Van de Wiele, T.; Possemiers, S. Gut metabotypes govern health affects of dietary polyphenols. *Curr. Opin. Biotechnol.* **2013**, *24*, 220−225.
(44) Bolca, S.; Possemiers, S.; Herregat, A.; Huybrechts, I.; Heyerick, A.; de Vriese, S.; Verbruggen, M.; Depypere, H.; De Keukeliere, D.; Bracke, M.; De Henauw, S.; Verstraete, W.; Van de Wilele, T. Microbial and dietary factors are associated with the equol producer phenotype in early postmenaopausal women. *J. Nutr.* **2007**, *137*, 2242−2246.
(45) Brink, E.; Coxam, V.; Robins, S.; Wahala, K.; Cassidy, A.; Branca, R. Long-term consumption of isoflavone-enriched foods does not affect bone mineral desnity, bone metabolism, and hormonal status in early postmenaopusal women: a randomized, double blind, placebo controlled study. *Am. J. Clin. Nutr.* **2008**, *87*, 761−770.
(46) Tomás-Barberán, F. A.; Andrés-Lacueva, C. Polyphenols and health: current state and progress. *J. Agric. Food Chem.* **2012**, *60*, 8773−8775.
(47) De Vos, W. M.; de Vos, E. A. Role of the intestinal microbiome in health and disease: from correlation to causation. *Nutr. Rev.* **2012**, *70*, S45−56.
(48) Tomás-Barberán, F. A.; Mine, Y. A key to understanding the effects of food bioactives in health. Gut microbiota. *J. Agric. Food Chem.* **2013**, *61*, 9755−9757.

DOI: 10.1021/acs.jafc.5b01173
J. Agric. Food Chem. 2015, 63, 7589−7594

chromatography (GC) with various detection systems. By far the predominant and most popular applications for analyzing lignans and other phytoestrogens are the (HP)LC-MS methods. In contrast to GC-MS, LC-MS has the advantage that it is not necessary to prepare volatile derivatives and that conjugated forms, such as the glycosides, can be analyzed as well.[26−28] However, the phytoestrogen contents are usually very low in biological matrices, and these techniques remain largely qualitative unless authentic standards are available. Thus, isotopically and isomerically pure polydeuterated lignans and other phytoestrogens are needed as references for the quantitation of these compounds in biological samples. The use of structural analogues as internal standards, rather than authentic isotope labeled isotopologues (i.e., substances that differ only in isotopic composition, e.g., CH_3OH, CD_3OH, CH_2DOH), is undesirable because the former will have different behaviors in sample preparation as well as different retention times and ionization properties compared with the analytes. An authentic stable isotope labeled analogue of a compound is essentially identical to the compound of interest except for mass.

One of the most reliable and sensitive methods of quantification is based on the addition of a stable isotope analogue of the analyte of interest into a sample at a known concentration. The technique is called stable isotope dilution (SID).[29] Because the analyte and its isotopologue possess almost identical chemical and physical properties, the isotopic ratios remain stable, as they are affected equally by variations in extraction, sample preparation, injection, and instrument parameters.[30] In the ion chromatogram, the analyte and its labeled analogue usually have the same retention time. Thus, all of the losses during sample preparation can be corrected for and the analytes reliably identified and quantified.

REQUIREMENTS FOR THE INTERNAL STANDARDS

In quantitation methods, internal standards are used to take into account all of the losses during the process and the behavior of the compounds during the measurement. A stable, chemically, isomerically, and isotopically pure isotopologue of the analyte is the optimal standard. As the physicochemical properties of an isotope labeled analogue are very similar to those of the analyte, no separation takes place during the process: the analyte and its labeled analogue have the same retention times in chromatography but different m/z values in mass spectrometry.

Labeled compounds that are used as internal standards in quantitative analytical techniques such as GC-MS and LC-MS must fulfill certain important criteria. First, the compounds and the labels must remain stable during the entire sample preparation procedure and analysis. Second, there cannot be any unlabeled species present in the standard. Third, the labeled analogue and the analyte should have a difference of at least 3 units, or more if the analyte contains elements other than C, H, O, and N, in the M^+ m/z value to avoid overlap with the internal standard.[31] On the other hand, it has been suggested that for internal standards an optimal number of deuteriums would be from three to five, as more deuteriums in the molecule may cause chromatographic separation between the standard and the analyte.[32,33] However, no chromatographic separation of a deuterated compound from the corresponding unlabeled compound has been reported for lignans.

LABELS FOR LIGNANS

Apart from radioactive labels, the possible labels for lignans are ^{18}O, ^{13}C, and D, the heavier stable isotopes of oxygen, carbon, and hydrogen, respectively. ^{18}O-labeled compounds are used to study reaction mechanisms,[34,35] but they could also be used as stable isotope labeled analogues for quantitative determinations. $^{16}O/^{18}O$ exchange is limited to compounds such as carboxylic acids that contain functional groups prone to facile oxygen exchange reactions.[36] Oxygen labeling has been used also when reactive phenols, for example, resorcinol moieties, are present, but the labeling conditions required were quite harsh (180 °C for 16 h), the yields were low, and protecting groups were needed.[37] To the best of our knowledge, no ^{18}O-labeled lignans have been synthesized apart from those in our mechanistic studies.[35]

In the literature there are some examples of carbon-labeled lignan precursors[38] that have been used to examine the biosynthesis and mechanisms of formation of lignans and neolignans.[18,24,39] The nonradioactive isotope of carbon, ^{13}C, might be considered as an optimal, general-purpose label because the isotope effects with ^{13}C are small (compared with $^{18}O/^{16}O$ and D/H), it can be used to label the fairly stable carbon backbone of lignans, and it cannot be exchanged for ^{12}C under ordinary conditions. However, the stability advantage is offset by the necessity of total or partial synthesis using expensive ^{13}C-labeled reagents or starting materials. Only one total synthesis of stable ^{13}C-labeled lignan derivatives has been reported in the literature.[40,41] After the first ^{13}C label was introduced, this synthesis took 11 or 12 steps to obtain the final triply labeled target, and although the yields for most of the steps are very good, the overall yields were 0.3−2%.[40,41]

On the other hand, deuterium labeling provides by far the most important route to stable isotope labeled standards in organic analysis. This is a result from the wide distribution of hydrogen in the target material, the ease of H/D exchange in most cases, and the cheap and ready availability of deuterated solvents and reagents. Furthermore, depending on the functional groups of the target molecules, it is often possible to acquire the desired label without any synthesis by performing simple exchange reactions on the native molecules in deuterated solvents.[36] The various deuteration reagents and solvents, such as D_2O, CH_3OD, DCl, D_2SO_4, and NaOD for deuterium exchange, and the reducing agents $LiAlD_4$ and $NaBD_4$, used in total synthesis approaches, are readily available and less costly than ^{18}O- and ^{13}C-labeled reagents.

As a result of the isotope effects, deuterated analogues may have certain defects as internal standards. There may be a small separation of the deuterated internal standard and its endogenous protium form during chromatography.[42] Ion fragmentation is sensitive to the kinetic isotope effect, but differences in ionization efficiency between labeled and unlabeled compounds are very small and become unmeasurable when the labeling site is remote from the charge center, even in the case of deuterium.[43] Yet, structural analogues are even less representative of the endogenous compounds because, in addition to differences in retention time, the structural analogue can show different absorption loss.[42] Thus, exchange−deuteration has remained the most important labeling method for obtaining stable isotope labeled compounds.

DOI: 10.1021/acs.jafc.5b00214
J. Agric. Food Chem. 2015, 63, 7595−7605

CHARACTERIZATION OF THE DEUTERATED COMPOUNDS

Isotopic purity is an important feature of an isotope-labeled compound. However, in the literature and in the catalogs of commercial suppliers there are no established practices on how to define or measure the isotopic purity, isotope distribution, or isotope content. In this paper, the isotope distribution is determined by NMR and the isotopic purity is indicated as the percentage of the most abundant D species, determined from the molecular ion region in EI mass spectra by comparison with those of the undeuterated compounds.

The number of deuterium atoms in a product as well as the isotopic purity is determinable by MS. The isotopic purities of deuterated compounds may be determined from the ion clusters in the molecular ion region in the EI or ESI mass spectra by comparison with those of undeuterated compounds. For the native butyrolactone and tetrahydrofuran type lignans the M − 1 and M − 2 peaks usually are very small (2−5% of the intensity of the molecular ion peak) or totally absent (Figure 2).[44] For flavonoids, which may have intense M − 1 and M − 2 fragments, an equation to determine the isotopic purity is reported.[45]

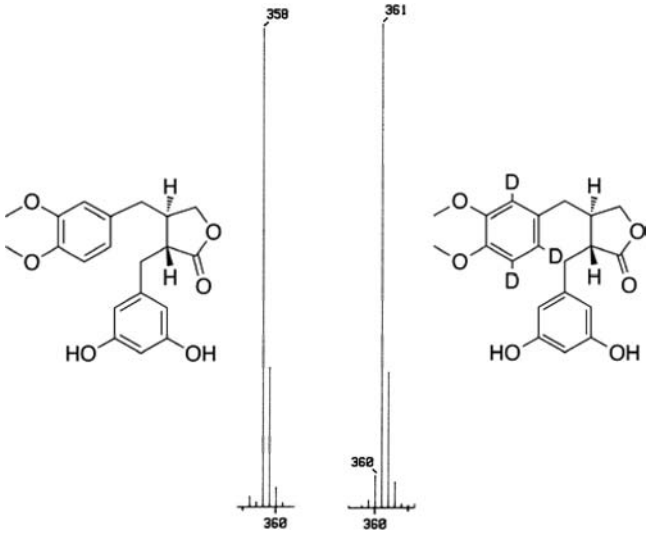

Figure 2. Molecular ion regions of an unlabeled butyrolactone type lignan (M = 358) and its stable deuterium-labeled D_3 analogue (M = 361).[44]

The locations of the deuterium atoms can be established from ^1H and ^{13}C NMR studies. In the ^{13}C NMR spectrum, the carbon atom bearing a deuterium atom produces a low-intensity triplet (instead of the relatively intensive aromatic C−H singlet) because the spin of deuterium is 1 (Figure 3). The ^1H NMR spectra of deuterium-labeled compounds are the same as for unlabeled compounds, with the exception that the aromatic deuterons cannot be seen and the coupling patterns of the protons attached to the adjacent carbons are simplified (Figure 4).

DEUTERATED LIGNANS

Introducing Deuteriums via Reduction. In the literature there are some reports of the introduction of deuterium into the lignan skeleton via reduction. The first reported synthesis for deuterium-labeled lignans was a multistep total synthesis for D_2-enterolactone and D_2- and D_4-enterodiol,[48,49] utilizing the method based on Pelter et al.'s synthesis of *trans*-dibenzylbutyrolactones via tandem conjugate addition.[50] The Michael addition−alkylation method was modified by using D_2-butenolide D_2-**3** as starting material to produce D_2-enterolactone D_2-**4** (Figure 5). Deuterium-labeled enterodiol was available in two forms: D_2-**5**, either by reducing unlabeled enterolactone **4** with $LiAlD_4$ or by reducing labeled enterolactone D_2-**4** with $LiAlH_4$, and D_4-**5** by reducing the labeled lactone D_2-**4** with $LiAlD_4$.

Neidigh et al. synthesized monodeutero-labeled podophyllotoxin precursors from podorhizone by using $NaBD_4$ as a reducing agent.[51]

A two-step synthesis[52] of symmetrically substituted butyrolactone lignans was applied to prepare hexadeuterated benzyl protected derivatives of matairesinol **6** (Figure 6).[53] The first step is the formation of a fulgenic acid **7** by the Stobbe condensation of 4-benzyloxy-3-methoxybenzaldehyde **8** and dimethyl succinate **9**. The second, deuteration step is a ruthenium-catalyzed ring closure with simultaneous deuteration, giving the benzyl protected D_6-matairesinol derivatives *trans*-D_6-**6** and *cis*-D_6-**6** in a 10:1 ratio (the yield of the reaction was not mentioned).

Labeling via H/D Exchange of Aromatic Protons. All of the other syntheses for deuterium-labeled lignans are based on H/D exchange within the complete molecular framework. In the case of lignans, the exchangeable protons are in the aromatic rings, and the benzylic or α-carbonyl sites remain unaffected.

The first efforts to deuterate aromatic compounds were in 1934, three years after the discovery of the heavy hydrogen isotope.[54] Horiuti and Polanyi heated benzene in 3% heavy water in the presence of a nickel catalyst.[55] Later in the same year Ingold et al. introduced deuterium into the aromatic nucleus by means of ordinary electrophilic reagents, namely, concentrated aqueous sulfuric acid (without heterogeneous catalysis).[56] They also proposed that the mechanism of the exchange is an electrophilic aromatic substitution[57] and proved the theory with comparison of the efficiencies of some acidic and basic deuterating agents and the influence of some aromatic substituents.[58,59] In lignans the aromatic substituents usually are hydroxy and/or methoxy groups.[60] When an electrophilic substitution reaction, such as deuteration, is performed, the existing substituents determine which position the new group will take and whether the reaction will be slower or faster than that with benzene. Both hydroxy and methoxy are *ortho*−*para* directing and activating groups.[61]

The first deuterium exchange within a lignan skeleton was performed with DBr (PBr_3 in D_2O, Figure 7).[62] The protons of phenolic groups were replaced with deuterons by D_2O treatment before the deuteration procedure, and the predeuterated enterolactone **10** was labeled with deuterium by exchange in DBr−D_2O to give the hexadeuterated enterolactone D_6-**4**. Aromatic protons that are *ortho* or *para* to the directing and activating phenolic OH groups were exchanged, whereas the protons that are *meta* to OH remained unaffected. The H/D treatment was repeated to ascertain complete deuteration and >90% isotopic purity. After final exchange, the reaction products were treated with a large excess of H_2O or ethanol to restore the protic hydroxy groups.

Deuterated phosphoric acid D_3PO_4 was used to synthesize a D_6 derivative of matairesinol **11** (Figure 8).[21] Matairesinol **11** was first predeuterated with CH_3COOD, made from freshly

DOI: 10.1021/acs.jafc.5b00214
J. Agric. Food Chem. 2015, 63, 7595−7605

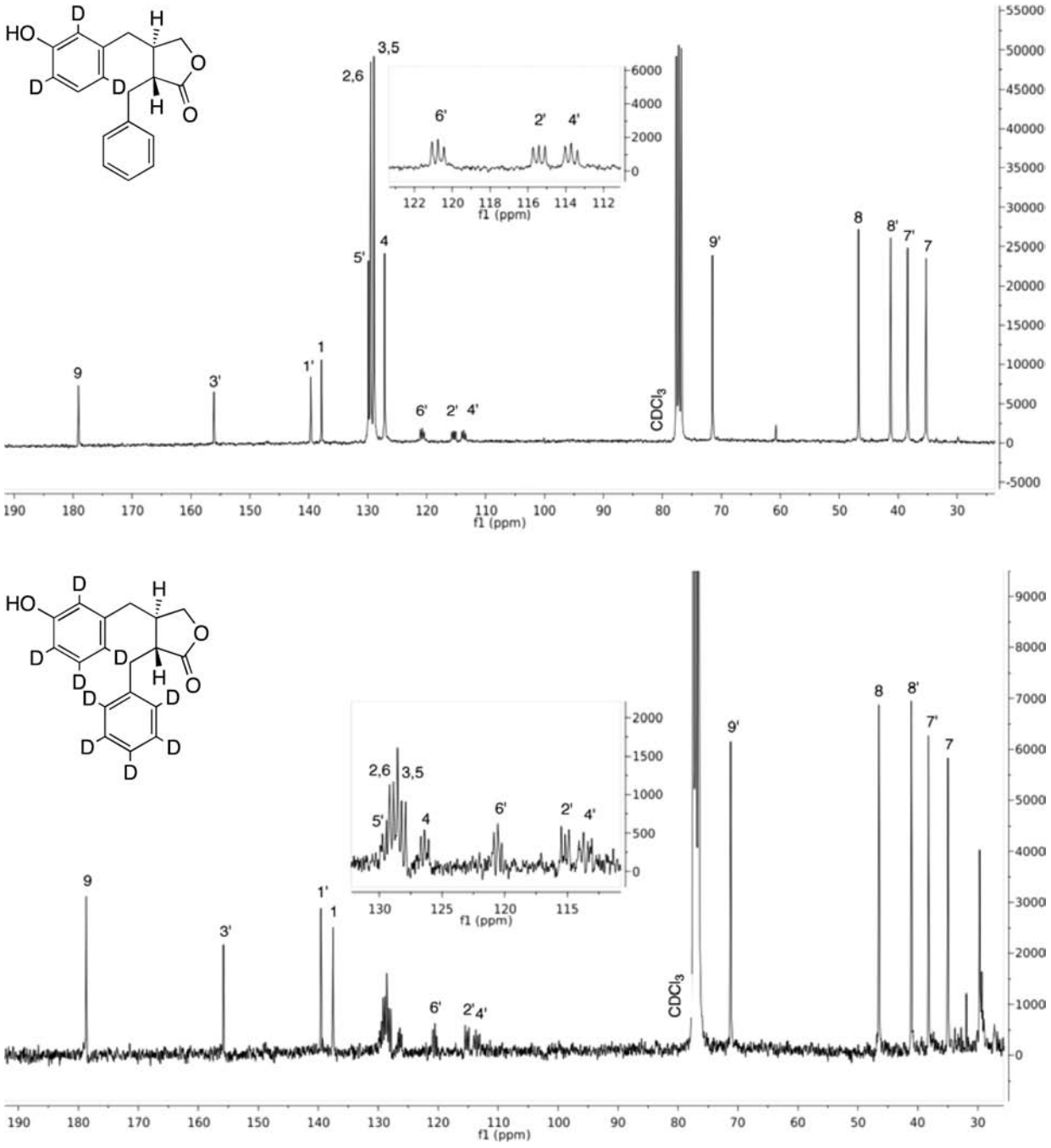

Figure 3. ^{13}C NMR spectra of D_3- and D_9-labeled 3′-hydroxylignano-9,9′-lactones (in $CDCl_3$).[44,46,47] The C−H singlets for deuterated sites are replaced by low-intensity C−D triplets (expanded).

distilled acetic anhydride by slow addition to heavy water and stirring the solution under argon for 2 h. The phenolic protons were exchanged with deuteriums by dissolving matairesinol in labeled acetic acid, leaving it to stand for several hours and finally evaporating the solvent. The labeled phosphoric acid D_3PO_4 was prepared by adding D_2O to P_2O_5. Predeuterated matairesinol was added to deuterated phosphoric acid under argon, and the reaction mixture was stirred at 80 °C for 3 days. Deuteration and workup were repeated three times. The isotopic purity was estimated from the mass spectrum to be 95% for D_6-**11** and 5% for the D_5 derivative.

Neidigh et al. prepared a <20 mg portion of hexadeutero-labeled matairesinol D_6-**17** by stirring the unlabeled lignan with $DClO_4$ (68% in D_2O) in THF/$CDCl_3$ at room temperature in only 4 h.[51]

An effective method using the deuterated phosphoric acid−boron trifluoride complex $D_3PO_4{\cdot}BF_3/D_2O$ was developed in our group initially to synthesize a stable deuterium-labeled isoflavone genistein[63] and, later, also other related compounds.[64−66] Originally tetradeuterogenistein was synthesized by refluxing predeuterated genistein **12** in CF_3COOD for 2 days to obtain D_4-genistein [6,8,3′,5′-D_4]-**12** in 75% yield and >90% isotopic purity ("a" in Figure 9).[21] However, it was found later that the most highly activated 6- and 8-site labels were unstable during the ID-GC-MS-SIM analytical procedure and were lost to some extent, making the [6,8,3′,5′-D_4]-**12**

DOI: 10.1021/acs.jafc.5b00214
J. Agric. Food Chem. 2015, 63, 7595−7605

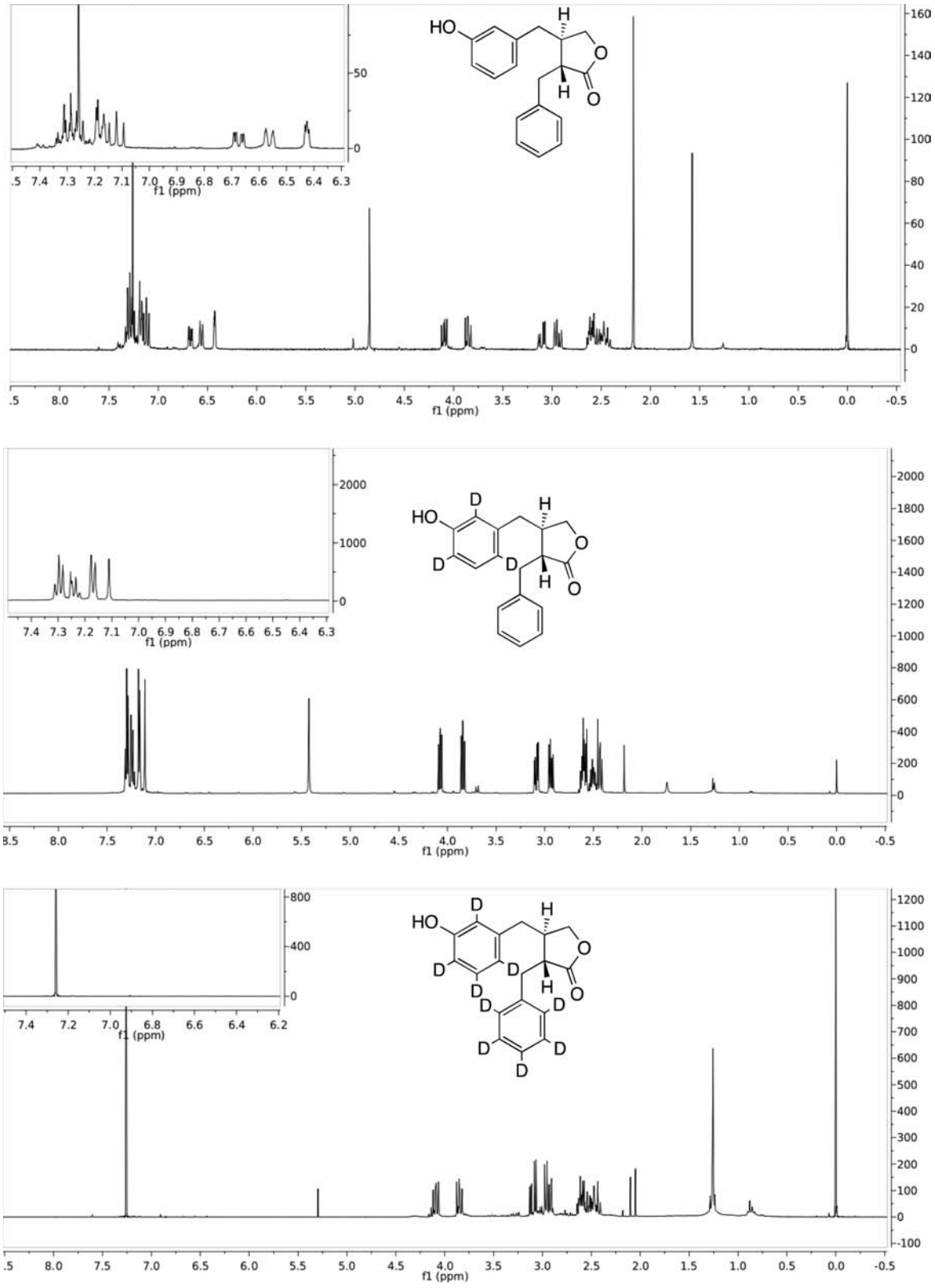

Figure 4. ^{1}H NMR spectra of unlabeled, D_3-labeled, and D_9-labeled 3′-hydroxylignano-9,9′-lactone (in $CDCl_3$).[44,46,47] In the expanded aromatic region it is clearly seen that proton signals are lacking when the aromatic positions are deuterated.

unsuitable as an internal standard. In fact, the labile deuterium labels at sites 6 and 8 were readily exchanged back to hydrogens, and the two remaining deuteriums at sites 3′ and 5′, although stable, were not enough to avoid the interference of fairly intense M + 1, M + 2, and M + 3 ions of the natural isotopes of the unlabeled compounds in mass spectra (as discussed above). Thus, several reagents were tested to overcome the problem. For example, D_3PO_4, which was used

DOI: 10.1021/acs.jafc.5b00214
J. Agric. Food Chem. 2015, 63, 7595−7605

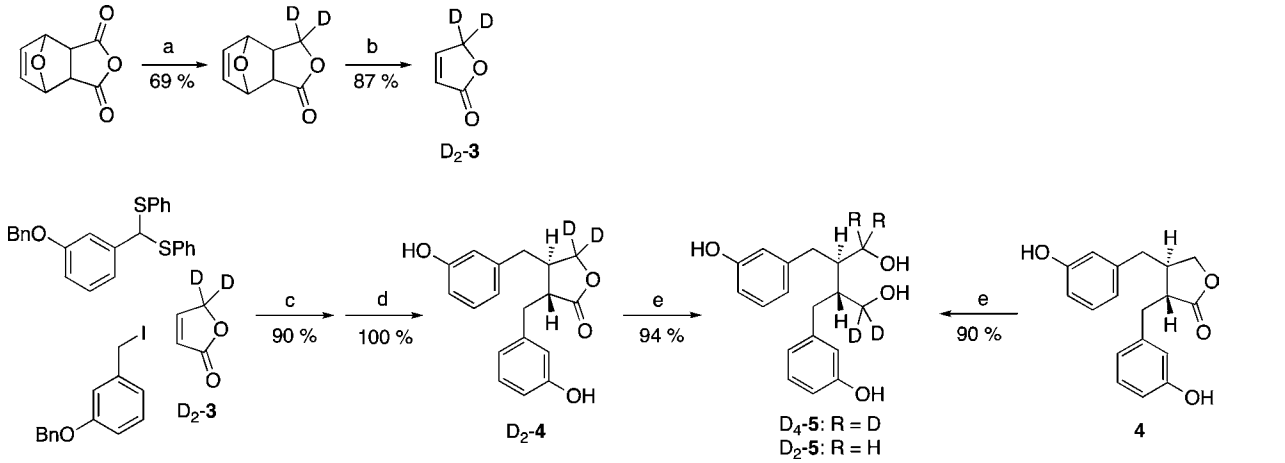

Figure 5. First reported deuterolabeled lignans.[48] Reagents and conditions: (a) $NaBD_4$, DMF, 0 °C; (b) 21 mbar, 200 °C; (c) (i) *n*-BuLi, THF, −78 °C, (ii) TMEDA; (d) Raney Ni, EtOH, reflux; (e) $LiAlD_4$, THF.[49]

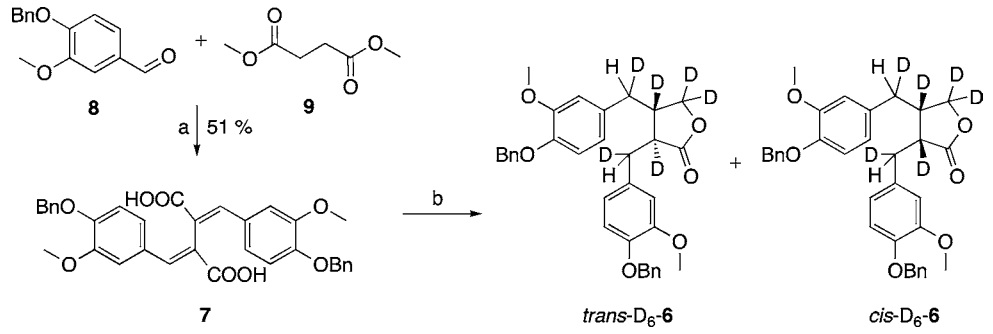

Figure 6. Reagents and conditions: (a) NaH, toluene; (b) D_2, $Ru_4H_4(CO)_8(PBu_3)_4$, 48 h, 180 °C.[53]

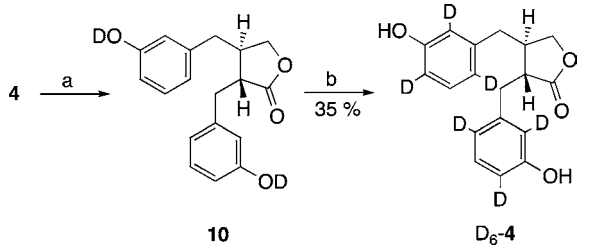

Figure 7. Reagents and conditions: (a) D_2O; (b) (i) PBr_3, D_2O, reflux, 5 h; (ii) H_2O.[62]

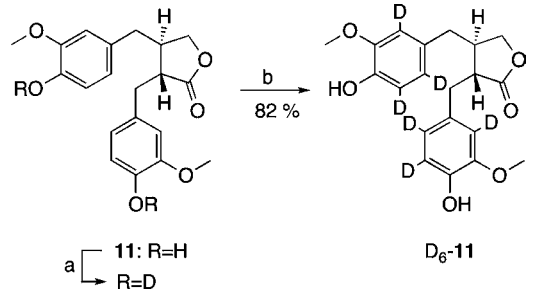

Figure 8. Reagents and conditions: (a) CH_3COOD; (b) (i) D_3PO_4, 80 °C, 9 days in total, (ii) H_2O.[21]

for deuteration of the lignan matairesinol **17** to good effect,[21] could exchange only a third of the ring A protons and none from the B ring. However, the deuterated phosphoric acid−boron trifluoride complex $D_3PO_4{\cdot}BF_3/D_2O$ was active enough to exchange all of the aromatic ring protons ("b" in Figure 9).[63] After the removal of the labile 6- and 8-labels ("c" in Figure 9) an isotopically pure and stable [2′,3′,5′,6′-D_4]-isotopologue of tetradeuterogenistein d_4-**12** was obtained.[45]

The deuteration reagent $D_3PO_4{\cdot}BF_3/D_2O$ is used also to deuterate various lignans. The reagent is freshly prepared by dissolving dry P_2O_5 in D_2O at 0 °C, and the resulting deuterated phosphoric acid is saturated with BF_3 gas bubbling through the acid at room temperature. Treatment of matairesinol **11** worked as expected to give the hexadeuterated matairesinol D_6-**11** much more quickly than with D_3PO_4 alone (Figure 10), that is, in 20 h instead of 9 days.[67] Additionally, the reaction with enterolactone **4** was remarkably found to give the fully aryl deuterated D_8-**4** (Figure 10).[68] All eight aromatic protons, even from the nonactivated C-5 and C-5′ sites, were exchanged at room temperature, giving D_8-labeled product in >99% isotopic purity. No exchange was observed at the *α*-carbonyl or benzylic sites.[47]

The use of dielectric microwave heating has been increasingly utilized in organic synthesis since the pioneering works of Gedye[69] and Giguere[70] in 1986. Despite being commonly employed in laboratory work, microwave techniques had not been reported in the synthesis or labeling of lignans until very recently.[71−73] It was found that the use of 35% DCl in D_2O and the ionic liquid 1-butyl-3-methylimidazolium chloride, [bmim]-Cl, as a cosolvent under microwave irradiation is a fast and high-yielding deuteration method for polyphenolic compounds including lignans.[71,74] The reaction times were shortened significantly (from several days to 40 min). The selectivities were not different from those observed under conventional heating.

DOI: 10.1021/acs.jafc.5b00214
J. Agric. Food Chem. 2015, 63, 7595−7605

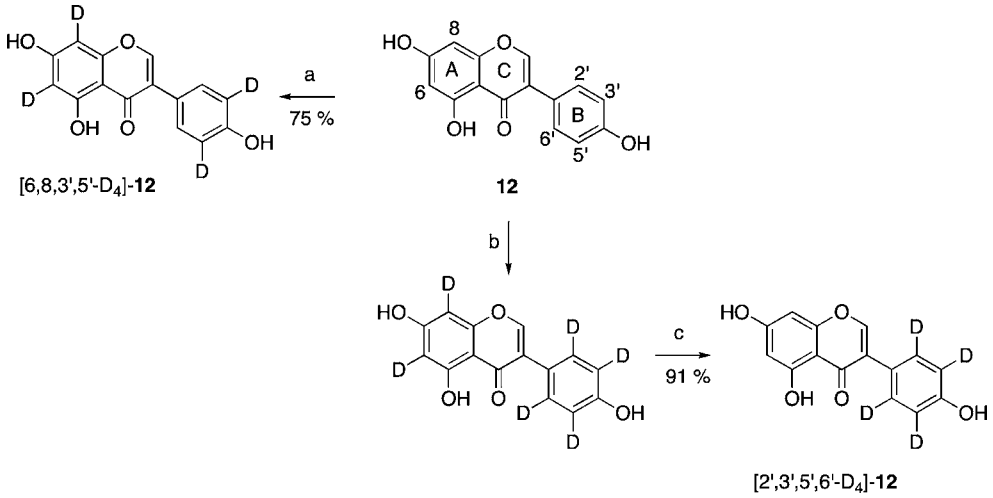

Figure 9. Reagents and conditions: (a) CF_3COOD;[21] (b) (i) D_2O/acetone, (ii) $D_3PO_4{\cdot}BF_3/D_2O$, 55 °C, 3 days, (iii) H_2O/EtOH; (c) 1% CH_3COCl in MeOH, reflux, 30 min.[63]

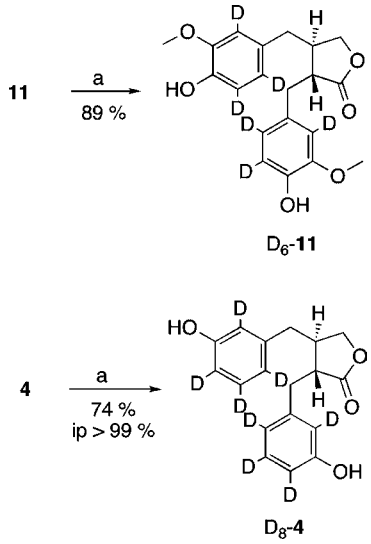

Figure 10. Reagents and conditions: (a) (i) D_2O/acetone, (ii) $D_3PO_4{\cdot}BF_3/D_2O$, room temperature, 20 h; (iii) H_2O.[67,68]

Lignans have been shown to be susceptible to heating.[44] The method using DCl/D_2O together with microwave heating works well for lignans even at lower temperatures (40 °C) and in some cases also without an ionic liquid solvent. Several tetrahydrofuran and butyrolactone type lignans were deuterated.[46]

SELECTIVITIES IN ELECTROPHILIC AROMATIC DEUTERATION

Relative Ease of H/D Exchange at Various Aromatic Positions. When $D_3PO_4{\cdot}BF_3/D_2O$ was used for the isoflavones daidzein and dihydrodaidzein, the degree of deuteration could be modulated by the reaction temperature.[64,66] In the case of isoflavonoids[64] and flavones,[65] raising the temperature to 55 °C does not seem to diminish the yields, but the lignan framework is found to be more fragile.[44] Hence, the deuteration reactions were carried out at room temperature. It is also interesting that within the lignan skeleton, all of the aromatic sites undergo exchange at room temperature (Figure 10),[47,68] whereas in the case of the isoflavone daidzein, only three positions were deuterated at room temperature in 3 days. Repeating the reaction deuterated the fourth position, and raising the temperature to 55 °C deuterated the fifth position.[64]

Deuteration using the highly acidic $D_3PO_4{\cdot}BF_3/D_2O$ also exchanges protons to deuteriums at the less reactive aromatic sites, giving, for example, a fully aryl deuterated derivative of 3′-hydroxylignano-9,9′-lactone **13** (D_9-**13**, Figure 11).[47] The other reported acidic methods, however, work in a more conventional way. For example, DCl in D_2O exchanges protons of **13** at the substituted B-ring only and at the activated sites *ortho* and *para* to the hydroxy group (Figure 11).[46]

As the deuteration reagent $D_3PO_4{\cdot}BF_3/D_2O$ was found to be very efficient in labeling isoflavones and especially lignans, exchanging protons for deuterium even at the unactivated aromatic positions of the lignan skeleton (see D_8-**4** in Figure 10 and D_9-**13** in Figure 11), several new deuterium-labeled

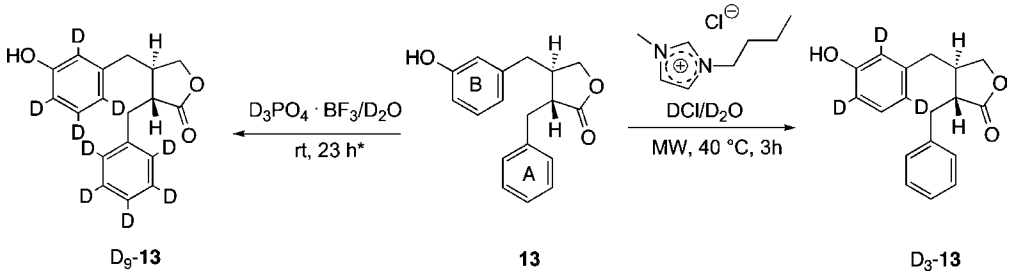

Figure 11. Deuteration of 3-hydroxylignano-9,9′-lactone **13**.[46,47] * The deuteration reaction was repeated with fresh reagent until the isotopic purity was >85%.

DOI: 10.1021/acs.jafc.5b00214
J. Agric. Food Chem. 2015, 63, 7595−7605

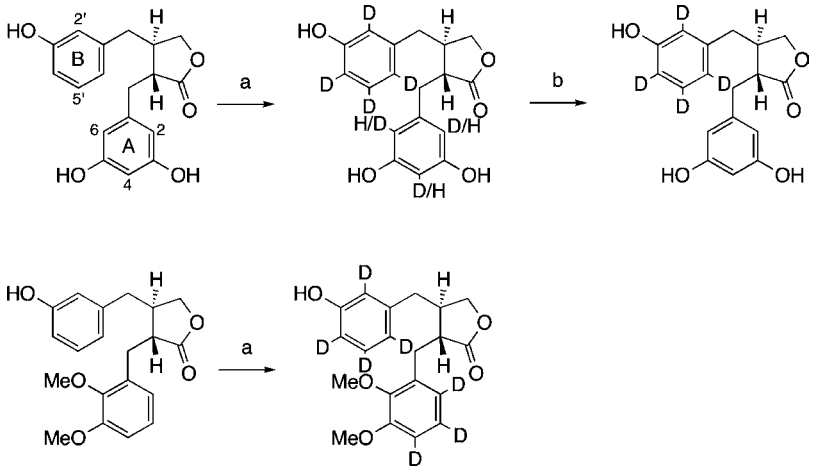

Figure 12. Synthesis of stable deuterated lignano-9,9′-lactones. Reagents and conditions: (a) (i) $D_3PO_4{\cdot}BF_3/D_2O$ (freshly prepared), room temperature; (ii) H_2O; (b) CH_3COCl, MeOH, reflux.[47]

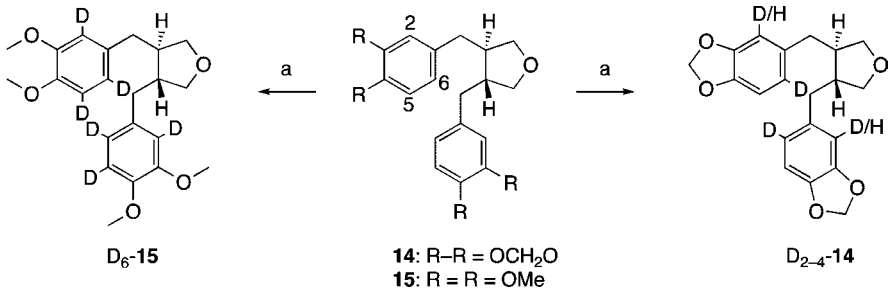

Figure 13. Deuteration of dehydroxycubebin **14** and brassilignan **15**. Reagents and conditions: (a) (i) 35% DCl in D_2O, [bmim]Cl, MW, 40 °C; (ii) H_2O.[46]

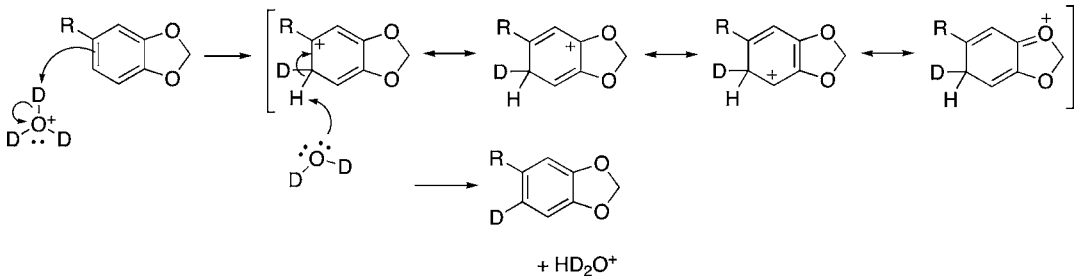

Figure 14. Mechanism of H/D exchange. R is for the rest of the lignan molecule.

lignanolactones were synthesized to examine the influence of the substitution pattern on the deuteration order.[47,75]

The exchange order of hydrogens, that is, the relative ease of H/D exchange at the various aromatic positions, was determined by following the progress of the deuteration reaction by ^1H NMR. In addition, electrostatic potential (ESP) charges were calculated to study the relative reactivities of the aromatic protons. The observed reactivities were compared with the calculated reactivities and found to be in good agreement.[47] The very inactive 5-position in the 3-hydroxyphenyl moiety (see 5′ in Figure 12) was tardy in reacting and in some cases needed several repetitions with fresh deuteration reagent. On the other hand, the presence of the two *meta*-substituted hydroxy or methoxy groups in ring A highly activated the aromatic sites 2, 4, and 6 (Figure 12). Because of the strong activation at these sites (2, 4, and 6), back exchange from deuterium to hydrogen occurred to some extent during quenching of the deuteration reaction into a large volume of ice-cold water (0.5 L water/100 mg lignan).[44] Thus, when the deuteration had reached a satisfactory level, that is, the isotopic purity was >85%, the remaining labile deuterium labels were selectively back exchanged to hydrogens in refluxing 0.5−1% CH_3COCl in methanol ("b" in Figure 12). This approach of deuteration with $D_3PO_4{\cdot}BF_3/D_2O$ and subsequently removal of the labile deuteriums in CH_3COCl/MeOH was very efficient in synthesizing labeled lignans possessing three to nine deuteriums in the aromatic rings. The deuterated lignans were isomerically and isotopically pure (>85% isotopic purity), and the yields were good (81−97%).[47] These deuterated standards have been successfully used in quantitating lignan contents in food samples.[76]

Aberrant Selectivity in Deuteration of Methylenedioxy Substituted Compounds. The deuteration of several butyrolactone and tetrahydrofuran type lignans with DCl in D_2O gave the expected behavior, exchanging protons to deuteriums at all of the activated positions (see D_3-**13** in

DOI: 10.1021/acs.jafc.5b00214
J. Agric. Food Chem. 2015, 63, 7595−7605

Figure 11). However, dehydroxycubebin **14** gave unexpected results (Figure 13).[46] The deuteration was only partial, giving a mixture of di-, tri-, and tetradeuterated products D_{2-4}-**14**. In contrast, brassilignan **15**, a close analogue of dehydroxycubebin, was successfully hexadeuterated with >97% isotopic purity.

As mentioned above, the mechanism of the H/D exchange is an ordinary electrophilic aromatic substitution,[57] where hydroxy and alkoxy groups are *ortho*−*para* directing and activating. The methylenedioxy substituent, however, causes aberrant selectivity. In the model compound 1,3-benzodioxole (1,2-methylenedioxybenzene, Figure 14: R = H) the positions *meta*/*para* to the methylenedioxy substituent were fully deuterated, whereas the *ortho* positions were only partially deuterated.[46] The higher *para*-selectivity of 1,3-benzodioxole in electrophilic aromatic substitution, in comparison to its cyclohomologues or veratrole, has been observed and rationalized by a distortion of the aromatic ring when annelated to a small ring and by quasiaromatic nature of the heterocyclic ring.[77]

The deuteration mechanism takes place in two steps: first, the electrophile attacks, giving rise to positively charged resonance stabilized intermediate, and the leaving group departs in the second step (Figure 14). Simultaneous attack and departure mechanisms are not known.[61] With regard to the mechanism, computational studies suggested another, conformation-dependent factor responsible for the deviant behavior preventing the complete deuteration of **14**.[46] The calculations imply that under the reaction conditions, the tetrahydrofuran type lignans prefer π-stacked, so-called sandwich, conformations, suggesting that the first reaction step, that is, addition of the deuterium, occurs from the solvent-exposed face of the molecule where the steric pressure is weaker, and the second step, that is, departure of the protium, occurs from the internal face. The first step is possible for both structures **14** and **15**; however, the second step of the electrophilic aromatic substitution is sterically prevented for one of the dehydroxycubebin **14** conformers. Presumably, due to interactions with the rigid methylenedioxy substituent, there is increased coplanarity between the aromatic rings of **14**, compared to **15**, which has two freely rotating methoxy groups.[46]

The butyrolactone and tetrahydrofuran type lignan structures undergo electrophilic aromatic substitution in deuteration reactions under acidic conditions. The degree of reactivity and selectivity of the deuteration is generally straightforward and predictable, enabling isotopically pure and stable polylabeled analogues to be prepared. However, some aberrant behavior is detected. The deuteration reagent $D_3PO_4{\cdot}BF_3/D_2O$ has the remarkable ability to exchange protons even at the unactivated aromatic positions, completely inaccessible with the other reported methods. Additionally, methylenedioxy substituents may cause unexpected deficiencies in the degree and orientation of atomatic deuteration, particularly in polycyclic aromatics.

AUTHOR INFORMATION

Corresponding Author

*(K.W.) E-mail: kristiina.wahala@helsinki.fi. Phone: +358 9 191 50356.

Notes

The authors declare no competing financial interest.

REFERENCES

(1) Begum, A. N.; Nicolle, C.; Mila, I.; Lapierre, C.; Nagano, K.; Fukushima, K.; Heinonen, S.-M.; Adlercreutz, H.; Rémésy, C.; Scalbert, A. Dietary lignins are precursors of mammalian lignans in rats. *J. Nutr.* **2004**, *134*, 120−127.

(2) Milder, I. E. J.; Arts, I. C. W.; van de Putte, B.; Venema, D. P.; Hollman, P. C. H. Lignan contents of Dutch plant foods: a database including lariciresinol, pinoresinol, secoisolariciresinol and matairesinol. *Br. J. Nutr.* **2005**, *93*, 393−402.

(3) Smeds, A. I.; Eklund, P. C.; Willför, S. M. Content, composition and stereochemical characterisation of lignans in berries and seeds. *Food Chem.* **2012**, *134*, 1991−1998.

(4) Adlercreutz, H. Phytoestrogens and breats cancer. *J. Steroid Biochem. Mol. Biol.* **2003**, *83*, 113−118.

(5) Cvejić, J.; Bursać, M.; Atanacković, M. Phytoestrogens: "estrogen-like" phytochemicals. *Stud. Nat. Prod. Chem.* **2012**, *38*, 1−35.

(6) Adlercreutz, H. Lignans and human health. *Crit. Rev. Clin. Lab. Sci.* **2007**, *44*, 483−525.

(7) Webb, A. L.; McCullough, M. L. Dietary lignans: potential role in cancer prevention. *Nutr. Cancer* **2005**, *51*, 117−131.

(8) Boccardo, F.; Puntoni, M.; Guglielmini, P.; Rubagotti, A. Enterolactone as a risk factor for breast cancer: a review of the published evidence. *Clin. Chim. Acta* **2006**, *365*, 58−67.

(9) Velentzis, L. S.; Cantwell, M. M.; Cardwell, C.; Keshtgar, M. R.; Leathem, A. J.; Woodside, J. V. Lignans and breast cancer risk in pre- and post-menopausal women: meta-analyses of observational studies. *Br. J. Cancer* **2009**, *100*, 1492−1498.

(10) Buck, K.; Zaineddin, A. K.; Vrieling, A.; Linseisen, J.; Chang-Claude, J. Meta-analyses of lignans and enterolignans in relation to breast cancer risk. *Am. J. Clin. Nutr.* **2010**, *92*, 141−153.

(11) Qun, Q.; Wedick, N. M.; Pan, A.; Townsend, M. K.; Cassidy, A.; Franke, A. A.; Rimm, E. B.; Hu, F. B.; van Dam, R. M. Gut microbiota metabolites of dietary lignans and risk of type 2 diabetes: a prospective investigation in two cohorts of U.S. women. *Diabetes Care* **2014**, *37*, 1287−1295.

(12) Valsta, L. M.; Kilkkinen, A.; Mazur, W.; Nurmi, T.; Lampi, A.-M.; Ovaskainen, M.-L.; Korhonen, T.; Adlercreutz, H.; Pietinen, P. Phyto-oestrogen database of foods and average intake in Finland. *Br. J. Nutr.* **2003**, *89*, S31−S38.

(13) Thompson, L. U.; Boucher, B. A.; Liu, Z.; Cotterchio, M.; Kreiger, N. Phytoestrogen content of foods consumed in Canada, including isoflavones, lignans and coumestans. *Nutr. Cancer* **2006**, *54*, 184−201.

(14) Peñalvo, J. L.; Adlercreutz, H.; Uehara, M.; Ristimäki, A.; Watanabe, S. Lignan content of selected foods from Japan. *J. Agric. Food Chem.* **2008**, *56*, 401−409.

(15) Schwartz, H.; Sontag, G. Analysis of lignans in food samples − impact of sample preparation. *Curr. Bioact. Compd.* **2011**, *7*, 156−171.

(16) Smeds, A. I.; Eklund, P. C.; Sjöholm, R. E.; Willför, S. M.; Nishibe, S.; Deyama, T.; Holmbom, B. Quantification of a broad spectrum of lignans in cereals, oilseeds and nuts. *J. Agric. Food Chem.* **2007**, *55*, 1337−1346.

(17) Moss, G. P. Nomenclature of lignans and neolignans. IUPAC Recommendations 2000. *Pure Appl. Chem.* **2000**, *72*, 1493−1523.

(18) Sakakibara, N.; Suzuki, S.; Umezawa, T.; Shimada, M. Biosynthesis of yatein in *Anthriscus sylvestris*. *Org. Biomol. Chem.* **2003**, *1*, 2474−2485.

(19) Saarinen, N. M.; Penttinen, P. E.; Smeds, A. I.; Hurmerinta, T. T.; Mäkelä, S. I. Structural determinants of plant lignans from growth of mammary tumors and hormonal responses in vivo. *J. Steroid Biochem. Mol. Biol.* **2005**, *93*, 209−219.

(20) Sakakibara, N.; Nakatsubo, T.; Suzuki, S.; Shibata, D.; Shimada, M.; Umezawa, T. Metabolic analysis of the cinnamate/monolignol pathway in *Carthamus tinctorius* seeds by a stable-isotope-dilution method. *Org. Biomol. Chem.* **2007**, *5*, 802−815.

(21) Adlercreutz, H.; Fotsis, T.; Bannwart, C.; Wähälä, K.; Brunow, G.; Hase, T. Isotope dilution gas chromatographic-mass spectrometric method for the determination of lignans and isoflavonoids in human

DOI: 10.1021/acs.jafc.5b00214
J. Agric. Food Chem. 2015, 63, 7595−7605

urine, including identification of genistein. *Clin. Chim. Acta* **1991**, *199*, 263−278.
(22) Milder, I. E. J.; Arts, I. C. W.; Venema, D. P.; Lasaroms, J. J. P.; Wähälä, K.; Hollman, P. C. H. Optimization of a liquid chromatography−tandem mass spectrometry method for quantification of the plant lignans secoisolariciresinol, matairesinol, lariciresinol and pinoresinol in foods. *J. Agric. Food Chem.* **2004**, *52*, 4643−4651.
(23) Peñalvo, J. L.; Haajanen, K. M.; Botting, N.; Adlercreutz, H. Quantification of lignans in food using isotope dilution gas chromatography/mass spectrometry. *J. Agric. Food Chem.* **2005**, *53*, 9342−9347.
(24) Tazaki, H.; Taguchi, D.; Hayashida, T.; Nabeta, K. Stable isotope-labeling studies on the oxidative coupling of caffeic acid *via o*-quinone. *Biosci., Biotechnol., Biochem.* **2001**, *65*, 2613−2621.
(25) Harmatha, J.; Buděšínský, M.; Trka, A. The structure of yatein. Determination of the positions, and configurations of benzyl groups in lignans of the 2,3-dibenzylbutyrolactone type. *Collect. Czech Chem. Commun.* **1982**, *47*, 644−663.
(26) Hoikkala, A. A.; Schiavoni, E.; Wähälä, K. Analysis of phytoestrogens in biological matrices. *Br. J. Nutr.* **2003**, *89*, S5−S18.
(27) Richards, D. P.; Sojo, L. E.; Keller, B. O. Quantitative analysis with modern bioanalytical mass spectrometry and stable isotope labeling. *J. Labelled Compd. Radiopharm.* **2007**, *50*, 1124−1136.
(28) Schwartz, H.; Sontag, G. Analysis of lignans in food samples − impact of sample preparation. *Curr. Bioact. Compd.* **2011**, *7*, 156−171.
(29) Heumann, K. G. Isotope dilution mass spectrometry of inorganic and organic substances. *Fresenius' Z. Anal. Chem.* **1986**, *325*, 661−666.
(30) Barron, D.; Smarrito-Menozz, C.; Fumeaux, R.; Viton, F. Synthesis of dietary phenolic metabolites and isotopically labeled dietary phenolics. *Flavonoids and Related Compounds: Bioavailability and Function*; Oxidative Stress and Disease 30; CRC Press: Boca Raton, FL, USA, 2012; pp 233−280.
(31) Wähälä, K.; Rasku, S.; Parikka, K. Deuterated phytoestrogen flavonoids and isoflavonoids for quantitation. *J. Chromatogr. B: Anal. Technol. Biomed. Life Sci.* **2002**, *777*, 111−122.
(32) Dehennin, L.; Reiffsteck, A.; Scholler, R. Simple methods for the synthesis of twenty different, highly enriched deuterium labelled steroids, suitable as internal standards for isotope dilution mass spectrometry. *Biol. Mass Spectrom.* **1980**, *7*, 493−499.
(33) De Leenheer, A. P.; Lefevere, M. F.; Lambert, W. E.; Colinet, E. S. Isotope-dilution mass spectrometry in clinical chemistry. *Adv. Clin. Chem.* **1985**, *24*, 111−161.
(34) Sykes, P. *A Guidebook to Mechanism in Organic Chemistry*, 6th ed.; Longman: New York, 1986; pp 46−47.
(35) Raffaelli, B.; Pohjoispää, M.; Hase, T.; Cardin, C. J.; Gan, Y.; Wähälä, K. Stereochemistry and rearrangement reactions of hydroxylignanolactones. *Org. Biomol. Chem.* **2008**, *6*, 2619−2627.
(36) Leis, H. J.; Fauler, G.; Windischhofer, W. Stable isotope labeled target compounds: preparation and use as internal standards in quantitative mass spectrometry. *Curr. Org. Chem.* **1998**, *2*, 131−144.
(37) Leis, H. J.; Gleispach, H.; Nitsche, V.; Malle, E. Quantitative determination of terbutaline and orciprenaline in human plasma by gas chromatography/negative ion chemical ionization/mass spectrometry. *Biol. Mass Spectrom.* **1990**, *19*, 382−386.
(38) Beejmohun, V.; Grand, E.; Lesur, D.; Mesnard, F.; Fliniaux, M.-A.; Kovensky, J. Synthesis and purification of [1,2-$^{13}C_2$]coniferin. *J. Labelled Compd. Radiopharm.* **2006**, *49*, 463−470.
(39) Davin, L. B.; Wang, C.-Z.; Helms, G. L.; Lewis, N. G. [^{13}C]-Specific labeling of 8-2′ linked (−)-*cis*-blechnic, (−)-*trans*-blechnic and (−)-brainic acids in the fern *Blechnum spicant*. *Phytochemistry* **2003**, *62*, 501−511.
(40) Haajanen, K.; Botting, N. P. Synthesis of multiply ^{13}C-labeled furofuran lignans using ^{13}C-labeled cinnamyl alcohols as building blocks. *Steroids* **2006**, *71*, 231−239.
(41) Fryatt, T.; Botting, N. P. The synthesis of multiply ^{13}C-labelled plant and mammalian lignans as internal standards for LC-MS and GC-MS analysis. *J. Labelled Compd. Radiopharm.* **2005**, *48*, 951−969.
(42) Ciccimaro, E.; Blair, I. A. Stable-isotope dilution LC-MS for quantitative biomarker analysis. *Bioanalysis* **2012**, *2*, 311−341.
(43) Mamer, O. A. Stable isotope dilution techniques. *J. Chromatogr., Biomed. Appl.* **1996**, *682*, 182−183.
(44) Pohjoispää, M. *Deuterium Labelling and Rearrangement Studies of Lignans*. Ph.D. thesis, University of Helsinki, 2014; http://urn.fi/URN:ISBN:978-951-51-0049-8.
(45) Rasku, S. Deuteration of flavonoids. Ph.D. thesis, University of Helsinki, 2000.
(46) Pohjoispää, M.; Mera-Adasme, R.; Sundholm, D.; Heikkinen, S.; Hase, T.; Wähälä, K. Capricious selectivity in electrophilic deuteration of methylenedioxy substituted aromatic compounds. *J. Org. Chem.* **2014**, *79*, 10636−10640.
(47) Leppälä, E.; Pohjoispää, M.; Koskimies, J.; Wähälä, K. Synthesis of new deuterium-labelled lignanolactones. *J. Labelled Compd. Radiopharm.* **2008**, *51*, 407−412.
(48) Setchell, K. D. R.; Lawson, A. M.; McLaughlin, L. M.; Patel, S.; Kirk, D. N.; Axelson, M. Measurement of enterolactone and enterodiol, the first mammalian lignans, using stable isotope dilution and gas chromatography mass spectrometry. *Biomed. Mass Spectrom.* **1983**, *10*, 227−235.
(49) Kirk, D. N.; McLaughlin, L. M.; Lawson, A. M.; Setchell, K. D. R.; Patel, S. K. Synthesis of the [^{2}H]-labelled urinary lignans enterolactone and enterodiol. *J. Chem. Soc., Perkin Trans. 1* **1985**, 35−37.
(50) Pelter, A.; Satyanarayana, P.; Ward, R. S. A short efficient synthesis of *trans*-dibenzylbutyrolactones exemplified by the synthesis of di-*O*-methyl compound X (HPMF) and an anti-tumour extractive. *Tetrahedron Lett.* **1981**, *22*, 1549−1550.
(51) Neidigh, K. A.; Kingston, D. G. I.; Lewis, N. G. Synthesis of stereospecifically deuterated matairesinol, podorhizol, epipodorhizol and yatein. *J. Nat. Prod.* **1994**, *57*, 791−800.
(52) Bambagiotti-Alberti, M.; Coran, S. A.; Vincieri, F. F.; Mulinacci, N.; Pieraccini, G. M. L. New synthetic route to butanolide lignans by a ruthenium complex catalyzed hydrogenation of the corresponding Stobbe's fulgenic acids. *Heterocycles* **1988**, *27*, 2185−2196.
(53) Frediani, P.; Rosi, L.; Frediani, M.; Bartolucci, G.; Bambagiotti-Alberti, M. A convenient route to the synthesis of isotopomeric dihydro-2(3H)furanones. *J. Agric. Food Chem.* **2007**, *55*, 3877−3883.
(54) Urey, H. C.; Brickwedde, F. G.; Murphy, G. M. A hydrogen isotope of mass 2. *Phys. Rev.* **1932**, *39*, 164−165.
(55) Horiuti, J.; Polanyi, M. Catalytic interchange of hydrogen between water and ethylene and between water and benzene. *Nature* **1934**, 377−378.
(56) Ingold, C. K.; Raisin, C. G.; Wilson, C. L. Direct introduction of deuterium into benzene without heterogenous catalysis. *Nature* **1934**, 734.
(57) Ingold, C. K.; Raisin, C. G.; Wilson, C. L. Structure of benzene. Part II. Direct introduction of deuterium into benzene and the physical properties of hexadeuterobenzene. *J. Chem. Soc.* **1936**, 915−925.
(58) Ingold, C. K.; Raisin, C. G.; Wilson, C. L. Direct introduction of deuterium into aromatic nucleus. Part I. Qualitative comparison of the efficiencies of some acidic deuterating agents and of the influence of some aromatic substituents. *J. Chem. Soc.* **1936**, 1637−1643.
(59) Best, A. P.; Wilson, C. L. Direct introduction of deuterium into the aromatic nucleus. Part II. Orientation by certain substituents. *J. Chem. Soc.* **1938**, 28−29.
(60) Ayres, D. C.; Loike, J. D. *Lignans: Chemical, Biological and Clinical Properties*; Cambridge University Press: Cambridge, UK, 1990.
(61) Smith, M. B.; March, J. *March's Advanced Organic Chemistry: Reactions, Mechanisms, And Structure*, 5th ed.; Wiley: New York, 2001; Chapter 11.
(62) Wähälä, K.; Mäkelä, T.; Bäckström, R.; Brunow, G.; Hase, T. Synthesis of the [^{2}H]-labelled urinary lignans, enterolactone and enterodiol, and the phytoestrogen daidzein and its metabolites equol and *O*-demethylangolensin. *J. Chem. Soc., Perkin Trans. 1* **1986**, 95−98.
(63) Wähälä, K.; Rasku, S. Synthesis of d_4-genistein, a stable deutero labeled isoflavone, by a perdeuteration − selective dedeuteration approach. *Tetrahedron Lett.* **1997**, *38*, 7287−7290.

DOI: 10.1021/acs.jafc.5b00214
J. Agric. Food Chem. 2015, 63, 7595−7605

(64) Rasku, S.; Wähälä, K.; Koskimies, J.; Hase, T. Synthesis of isoflavonoid deuterium labeled polyphenolic phytoestrogens. *Tetrahedron* **1999**, *55*, 3445−3454.
(65) Rasku, S.; Wähälä, K. Synthesis of deuterium labeled polyhydroxy flavones and 3-flavonols. *Tetrahedron* **2000**, *56*, 913−916.
(66) Rasku, S.; Wähälä, K. Synthesis of d_6-daidzein. *J. Labelled Compd. Radiopharm.* **2000**, *43*, 849−853.
(67) Rasku, S.; Mazur, W.; Adlercreutz, H.; Wähälä, K. Synthesis of deuterated plant lignans for gas chromatography−mass spectrometry analysis. *J. Med. Food* **1999**, *2*, 103−105.
(68) Leppälä, E.; Wähälä, K. Synthesis of $[^2H_8]$-enterolactone and $[^2H_{10}]$-enterodiol. *J. Labelled Compd. Radiopharm.* **2004**, *47*, 25−30.
(69) Gedye, R.; Smith, F.; Westaway, K.; Ali, H.; Baldisera, L.; Laberge, L.; Rousell, J. The use of microwave ovens for rapid organic synthesis. *Tetrahedron Lett.* **1986**, *27*, 279−282.
(70) Giguere, R. J.; Bray, T. L.; Duncan, S. M.; Majetich, G. Application of commercial microwave ovens to organic synthesis. *Tetrahedron Lett.* **1986**, *27*, 4945−4948.
(71) Hakala, U.; Wähälä, K. Expedient deuterolabeling of polyphenols in ionic liquids−DCl/D_2O under microwave irradiation. *J. Org. Chem.* **2007**, *72*, 5817−5819.
(72) Mont, N.; Mehta, V. P.; Appukkuttan, P.; Beryozkina, T.; Toppet, S.; Van Hecke, K.; Van Meervelt, L.; Voet, A.; DeMaeyer, M.; Van der Eycken, E. Diversity oriented microwave-assisted synthesis of (−)-staganacin aza-analogues. *J. Org. Chem.* **2008**, *73*, 7509−7516.
(73) Mondière, A.; Pousse, G.; Bouyssi, D.; Balme, G. Efficient rhodium-catalyzed conjugate addition of arylboronic acids to unsaturated furano esters for the highly stereoselective synthesis of four natural trisubstituted furanolignans. *Eur. J. Org. Chem.* **2009**, *25*, 4225−4229.
(74) Pohjoispää, M.; Hakala, U.; Silvennoinen, G.; Wähälä, K. Expedient deuterolabelling of lignans using ionic liquid−DCl/D_2O under microwave heating. *J. Label. Compd. Radiopharm.* **2010**, *53*, 429−430.
(75) Pohjoispää, M.; Leppälä, E.; Wähälä, K. Synthesis of stable deuterium labelled lignan derivatives and studies of H/D exchange at the aromatic sites. *J. Labelled Compd. Radiopharm.* **2007**, *50*, 521−522.
(76) Milder, I. E. J.; Arts, I. C. W.; Venema, D. P.; Lasaroms, J. P.; Wähälä, K.; Hollman, P. C. H. Optimization of a liquid chromatogaphy-tandem mass spectrometry method for quantification of the plant lignans secolariciresinol, matairesinol, lariciresinol, and pinoresinol in foods. *J. Agric. Food Chem.* **2004**, *52*, 4643−4651.
(77) Daukšas, V. K.; Purvaneckas, G. V.; Udrėnaitė, E. B.; Gineitytė, V. L.; Barauskaitė, A. V. Relative reactivity of the aromatic ring in benzo-1,3-dioxole, its cyclohomologues and veratrole. *Heterocycles* **1981**, *15*, 1395−1404.

DOI: 10.1021/acs.jafc.5b00214
J. Agric. Food Chem. 2015, 63, 7595−7605

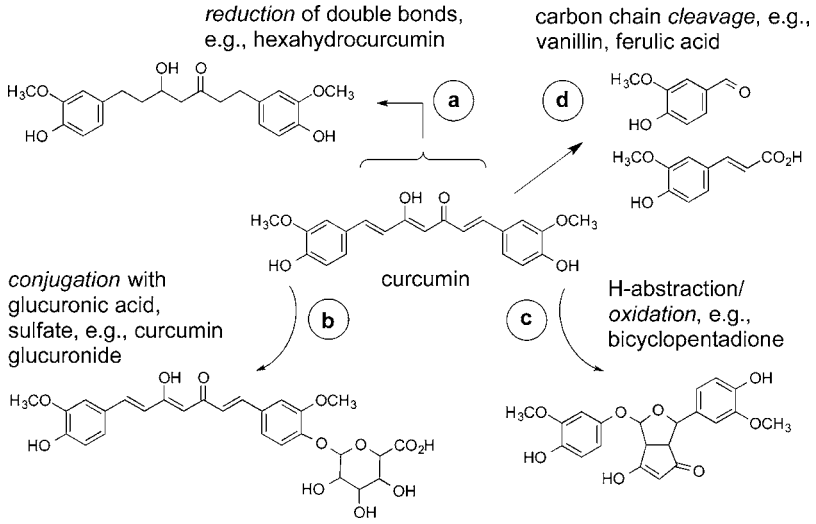

Figure 2. Metabolic and degradation pathways of curcumin: (a) reduction; (b) conjugation; (c) oxidation; (d) cleavage.

the in vivo and in vitro biological activities of curcumin will be discussed in the following.

DEGRADATION OF CURCUMIN IN CELL CULTURE

Although the chemical instability of curcumin is widely recognized, this fact is less considered in the interpretation of studies with cultured cells in vitro. Curcumin degrades quickly at physiological pH but more slowly when incubated in the presence of serum or with cultured cells.[24] Protein increases the half-life of curcumin from a few minutes to 1−2 h.[24] Nevertheless, there is sufficient time for curcumin to degrade during a typical 4−8 h incubation before cultured cells are harvested and analyzed. When cells have been treated with curcumin for several hours, it is impossible to decide whether the observed effects are due to curcumin or its degradation products. Unless interpreted with a consideration of what active or inactive metabolites of curcumin may be formed (or not) during an assay, results can be misleading and give only limited insight into the in vivo biological activity of curcumin.

Similar considerations are relevant for studies claiming that the mechanism of action of curcumin is due to the induction of oxidative stress ("reactive oxygen species", ROS) in cells. In many instances, the role of curcumin-induced ROS has been shown indirectly, that is, by addition of a reducing antioxidant, for example, *N*-acetylcysteine, that abolished the effects of curcumin.[25−29] The action of the antioxidant, however, is not only to reduce ROS formation but also to delay or prevent degradation of curcumin. Thus, unless specific probes against ROS are used rather than a general antioxidant, it is not possible to decide whether effects caused by curcumin are mediated by the induction of oxidative stress or its degradation products.

Another facet of curcumin that is not sufficiently considered is its heterogeneity as a natural product. "Curcumin" is used to describe the chemically pure compound or an extract from the turmeric rhizome that is enriched in curcuminoids, that is, a mixture of curcumin, demethoxycurcumin (DMC), and bisdemethoxycurcumin (BDMC). Their relative abundance in commercial extracts is about 80:15:5. Whether pure curcumin or a mixture of curcuminoids is used in an assay is relevant not only because curcumin, DMC, and BDMC may have distinct activities but also because the stability of the mixture is different from that of the pure compounds.[30]

THE DEGRADATION IS AN AUTOXIDATION

For many years cleavage of the heptadienedione chain reported by Wang and co-workers in the late 1990s was considered the prevailing degradation reaction, resulting in vanillin, ferulic acid, and feruloylmethane as products.[24] Meanwhile, there is evidence from revisiting the degradation reaction that chain cleavage is only a very minor pathway[31] and thus irrelevant for understanding the biological effects of curcumin in vitro. Interestingly, vanillin, ferulic acid, and feruloylmethane were described to be minor products already in the original paper by Wang and co-workers, and the major product detected was tentatively identified as *trans*-6-(4′-hydroxy-3′-methoxyphenyl)-2,4-dioxo-5-hexenal, the assignment being uncertain because NMR data were not available.[24] In hindsight, the identification of the major product was probably incorrect, and the major product detected by Wang and co-workers was likely the bicyclopentadione product of autoxidative transformation of curcumin.[16]

The degradation of curcumin in buffer is a spontaneous, free radical-driven incorporation of O_2 that meets the criteria of an autoxidative process (Figure 3).[16] The major product of the autoxidation of curcumin is a bicyclopentadione, formed by oxygenation and double cyclization of the heptadienedione

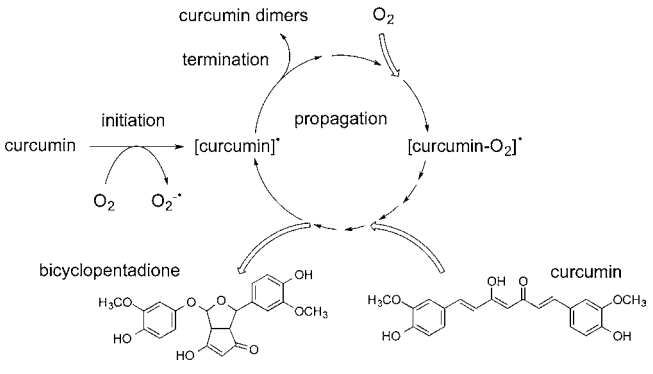

Figure 3. Degradation of curcumin is an autoxidation to a bicyclopentadione.

DOI: 10.1021/acs.jafc.5b00244
J. Agric. Food Chem. 2015, 63, 7606−7614

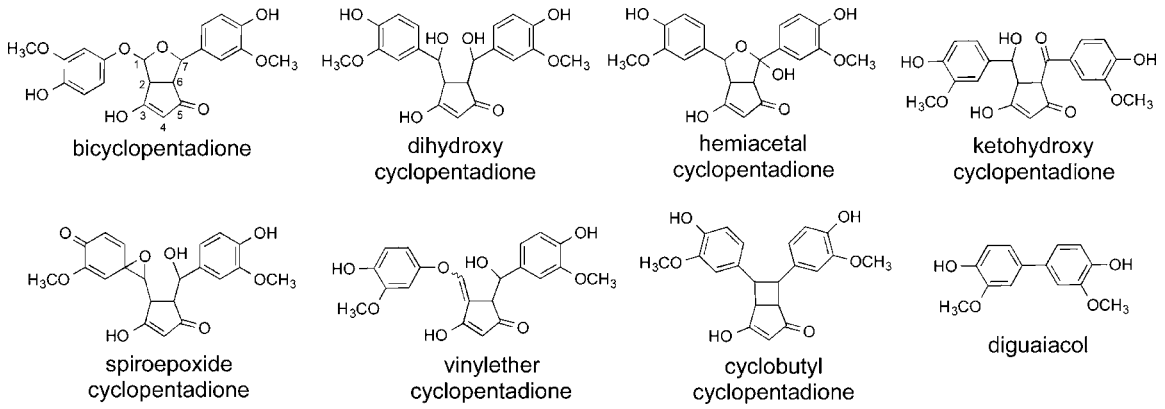

Figure 4. Products of autoxidation of curcumin.

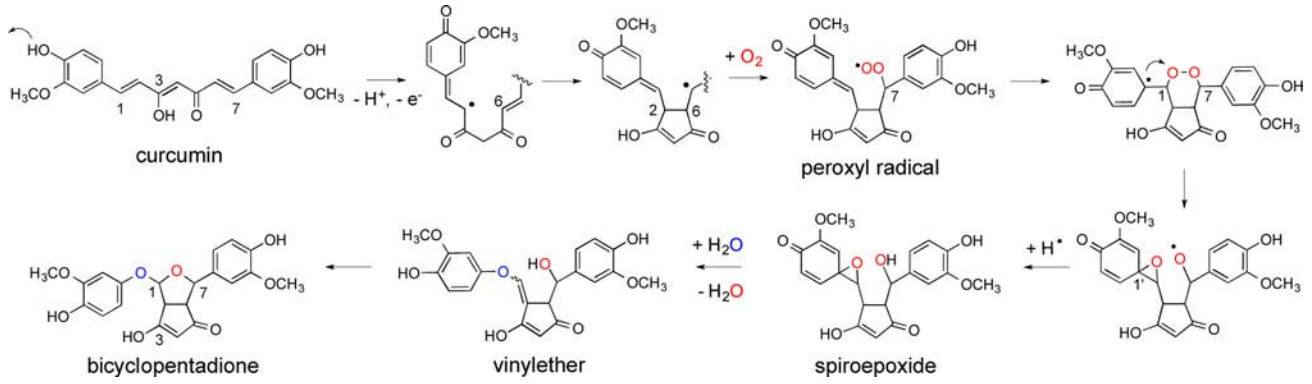

Figure 5. Proposed mechanism for the formation of the bicyclopentadione during autoxidation of curcumin.

chain connecting the two methoxyphenol rings of curcumin.[16] This complex transformation is the result of incorporation of O_2 and further rearrangement through several key intermediates.[32] Autoxidation is initiated by O_2 serving as the initial electron acceptor. The propagation results in a 1:1 molar reaction of curcumin with molecular oxygen: for every molecule of curcumin converted, one molecule of oxygen is consumed.[16] Thus, the terms "degradation" and "autoxidation" are equivalent in describing the spontaneous transformation of curcumin in vitro.

■ PRODUCTS OF OXIDATIVE TRANSFORMATION

We analyzed the degradation products of curcumin using [$^{14}C_2$]curcumin as tracer for RP-HPLC analyses.[32] We isolated seven novel compounds and determined their structures using LC-MS, HR-MS, and NMR analyses (Figure 4). Six products had oxygen substitutions at C-1 and C-7 of the former heptadienedione chain. The oxygen atoms were present in hydroxy, keto, epoxy, ether, and hemiketal moieties. Two products that did not incorporate oxygen were a cyclobutylcyclopentadione and diguaiacol, an obvious cleavage product. Two of the isolated products, the spiroepoxide and the vinylether cyclopentadiones, were intermediates in the reaction to the bicyclopentadione. The others were end products formed in addition to the bicyclopentadione. Neither vanillin nor ferulic acid was formed in sufficient amount to be detected by the radiodetector.[32] Vanillin, however, can be detected as a minor product when a more sensitive UV diode array detector is used.[31]

An explanation of why these novel products have not been described before is probably their minor abundance (e.g., the cyclobutylcyclopentadiones and diguaiacol) combined with unexpectedly high polarity on RP-HPLC, especially in the case of the dihydroxy, ketohydroxy, and hemiketal cyclopentadiones, and sensitivity to acid. Even brief exposure of the spiroepoxide and vinylether to acidic pH will result in transformation to the bicyclopentadione. Unless precautions are undertaken, the newly identified products undergo further reaction, are not extracted, or elute in the void volume if standard extraction procedures and RP-HPLC conditions are employed.[32]

Depending on reaction time and sample workup different product profiles of curcumin autoxidation reactions were obtained. Reactions conducted for longer than 4 h followed by acidification and extraction (solid-phase or liquid/liquid) gave the bicyclopentadione diastereomers as the almost exclusive products with little to no curcumin remaining.[31] Shorter reaction times, between 30 min and 4 h, followed by acidification and extraction also gave the bicyclopentadiones as major products and, in addition, several smaller unidentified peaks were detected.[16] If reactions are shortened to 20−45 min and injected directly on RP-HPLC (without acidification and extraction), the chromatograms show prominent products that are more polar than the bicyclopentadiones.[32] These peaks comprise the spiroepoxide and vinylether as major products and the dihydroxy, ketohydroxy, and hemiketal cyclopentadiones as minor products.

Time course experiments established that at physiological pH the spiroepoxide has a longer half-life than curcumin. Whether this holds true under more physiological conditions is not clear. The spiroepoxide is electrophilic and subject to reaction with thiols.[32]

DOI: 10.1021/acs.jafc.5b00244
J. Agric. Food Chem. 2015, 63, 7606−7614

MECHANISM OF OXIDATIVE TRANSFORMATION

Curcumin and the bicyclopentadione are structurally very different. It is obvious that the degradation must involve a series of discrete reactions resulting in double cyclization and oxygenation of the heptadienedione chain (Figure 5).[32] The two methoxyphenol rings are required for the reaction but participate only indirectly by facilitating certain reaction steps (see below).[30]

Because the molecular weight of the bicyclopentadione is increased by 32 mass units compared to that of curcumin, it seemed plausible that O_2 would be inserted during the autoxidation and end up in the bicyclopentadione. It was quite surprising then that one ^{18}O from $H_2{}^{18}O$ was incorporated into the bicyclopentadione when degradation reactions of curcumin were conducted in labeled buffer.[32] Thus, although it is true that O_2 is inserted into curcumin during autoxidation, only one of the two oxygen atoms remains in the final product.

The initiating event of the autoxidation is hydrogen abstraction from one of the phenolic hydroxyls to form a phenoxyl radical.[16] The hydrogen abstraction likely occurs as a two-step process of proton loss in the slightly alkaline medium (pH 7.4−8) followed by electron transfer[33,34] from the phenolate anion to molecular oxygen, which is reduced to superoxide.[16] H abstraction can also be catalyzed by peroxidases with curcumin acting as a cosubstrate, providing an electron to reduce a peroxide. As expected, the addition of H_2O_2 to the peroxidase-catalyzed transformation of curcumin resulted in a large increase of the enzymatic turnover rate.[16]

The 1,2-*E* double-bond conjugated to the methoxyphenol ring enables delocalization of the radical to C-2 of the chain, leaving the aromatic ring oxidized to a quinone methide. The C-2 radical performs a 5-*exo* cyclization with the 6-*E* double bond to form the cyclopentadione ring that is present in all products except for diguaiacol.[32] The carbon-centered radical is now localized at C-7 where it reacts with O_2 to a peroxyl radical. The peroxyl radical is poised to quench the unstable quinone methide by forming a C-1/C-7 endoperoxide. This brings the radical back to the semiquinone ring. The tertiary radical reacts with the endoperoxide in an intramolecular homolytic substitution reaction (S_Hi).[35,36] S_Hi results in cleavage of the endoperoxide O−O bond to give an epoxide (C-1/C-1′-spiroepoxide) and an alkoxyl radical at C-7. Reduction of the alkoxyl radical results in a spiroepoxide cyclopentadione. The reduction may occur as a hydrogen abstraction from curcumin and propagate the free radical chain reaction. The spiroepoxide is the earliest product in the degradation pathway that has been isolated, compatible with being the first nonradical product in the proposed mechanism (Figure 5).[32]

Although hydrolysis of the epoxide by nucleophilic attack of the C-7 hydroxyl could directly lead to the bicyclopentadione,[16] this does not occur.[32] Instead, the spiroepoxide is transformed to a vinylether as the immediate precursor to the bicyclopentadione. Unexpectedly, the opening of the spiroepoxide also involves the exchange of the epoxide oxygen (that is derived from O_2) for an oxygen from H_2O. These results can be explained by a mechanism in which the electron-donating effect of the *m*-methoxy group of the spiroepoxide triggers S_N1 opening of the epoxide that is facilitated by hydrogen bonding with the cyclopentadione hydroxyl (Figure 6).[32] Addition of water to the *o*-quinone intermediate results in a vicinal diol that

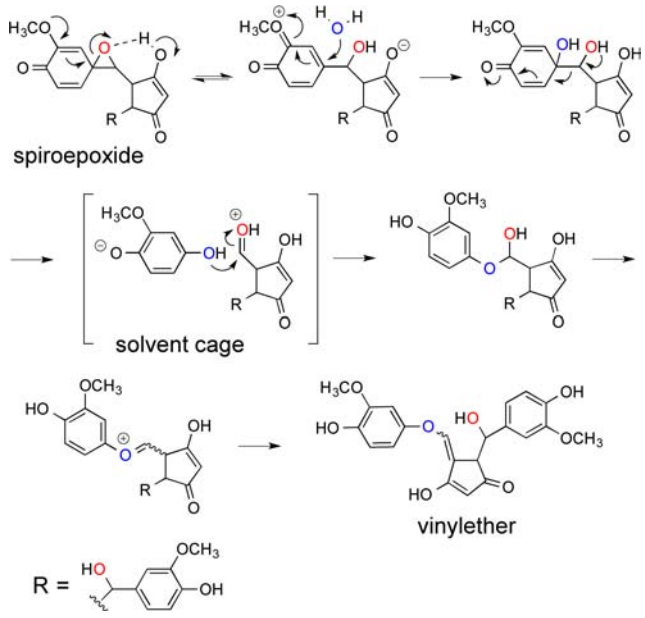

Figure 6. Proposed mechanism of the exchange of water during transformation of the spiroepoxide to the vinylether.

undergoes C−C bond cleavage, driven by rearomatization of the ring, to an aldehyde and methoxyhydroquinone. The two molecules are in a solvent cage and instantly recombine to a hemiacetal that loses water (containing the original epoxide oxygen) on the way to the vinylether.

The byproducts of the autoxidation are formed by alternative reactions of intermediates in the proposed mechanism:[32]

(i) Cyclobutyl cyclopentadione: The peroxyl radical can undergo *β*-fragmentation (i.e., the loss of O_2 to regain the C-7 carbon radical) at a rate that is fast enough to enable 4-*exo* cyclization with C-1 to form the cyclobutyl ring. Although the rates for these steps have not been determined, the formation of the cyclobutyl product indicates that the quinone methide intermediates have a considerable lifetime to undergo alternative reactions, especially with nucleophilic protein or small molecule thiols.

(ii) Dihydroxy, ketohydroxy, and hemiketal cyclopentadiones: The endoperoxide radical intermediate is a branching point from which not only the spiroepoxide emerges. Reduction of the tertiary radical gives a covalently complete endoperoxide, which is predicted but has not been confirmed by isolation (Figure 7). The curcumin endoperoxide is unstable and opens to the ketohydroxy cyclopentadione in a Kornblum−DeLaMare rearrangement.[37] The ketohydroxy cyclopentadione is in equilibrium with its hemiketal form. Reduction of the endoperoxide gives the dihydroxy cyclopentadione. These reactions are reminiscent of the reactions of the cyclooxygenase-derived prostaglandin endoperoxide PGH_2 and its transformations to prostaglandins PGD_2, PGE_2, and $PGF_{2\alpha}$.[38]

(iii) Diguaiacol: The mechanism of formation of diguaiacol is uncertain. Most likely, it involves cleavage of the carbon bond connecting the methoxyphenol ring to the heptadienedione chain. Such a cleavage could be facilitated by, for example, further oxygenation of the endoperoxide radical as has been described to occur during chain cleavage of lipid hydroperoxides.[39,40]

DOI: 10.1021/acs.jafc.5b00244
J. Agric. Food Chem. 2015, 63, 7606−7614

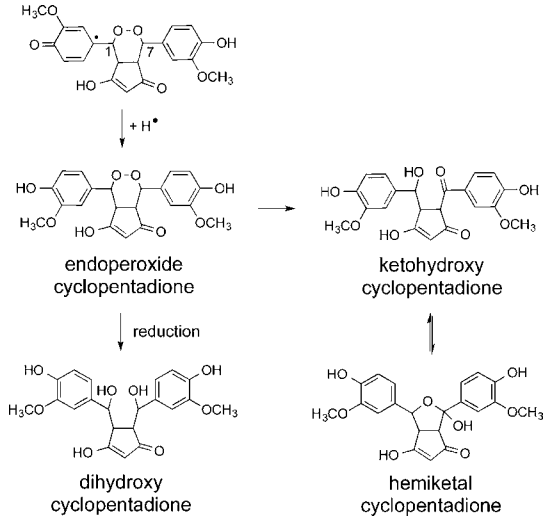

Figure 7. Formation of dihydroxy, ketohydroxy, and hemiketal cyclopentadiones from a proposed endoperoxide intermediate.

(iv) Vanillin: Trace amounts of vanillin detected in RP-HPLC/UV diode array analyses might be formed by C−C bond cleavage of the alkoxyl radical intermediate. Cleavage is competing with reduction of the alkoxyl radical to the spiroepoxide by H abstraction from curcumin. This origin of vanillin is compatible with data by Wang and co-workers, who noted that vanillin was increased when curcumin was incubated in buffer for an extended time.[24] Upon prolonged incubation, the reaction will run out of curcumin as a hydrogen donor, and the alkoxyl radical may be prone to undergo cleavage into vanillin.

OXIDATIVE TRANSFORMATION OF DMC AND BDMC: ROLE OF THE *m*-METHOXY GROUP

The less abundant curcuminoids DMC and BDMC also can be oxidatively transformed.[30] There were, however, two important differences in the oxidation of DMC and BDMC compared to curcumin. First, the rate of autoxidation of DMC was markedly reduced such that its half-life is in the range of hours rather than minutes (Table 1). This trend was enhanced in BDMC that did not autoxidize at all. Second, whereas DMC formed the expected demethoxy bicyclopentadione, BDMC formed a bisdemethoxy spiroepoxide when forced to oxidize. The bisdemethoxy spiroepoxide was stable and did not further transform to a bisdemethoxy bicyclopentadione analogue.[30]

The mixture of curcuminoids as it is present in turmeric extract was more stable to autoxidation than predicted on the basis of the relative abundance of curcumin, DMC, and BDMC in the mixture. Thus, not only are DMC and BDMC more stable toward autoxidation, they also appear to protect curcumin from autoxidation.[30]

These findings point toward a crucial role of the methoxy groups in determining the stability of the curcuminoids toward

Table 1. Structures, Autoxidation, and Products of Curcumin and Analogues

Compound/structure	Autoxidation (approx. $t_{1/2}$)	Main product
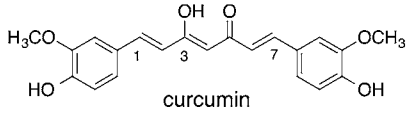 curcumin	fast (minutes)	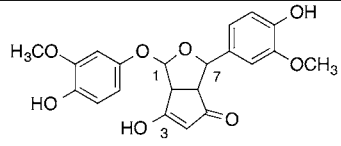 bicyclopentadione
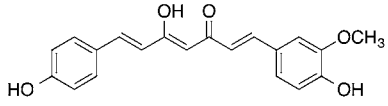 demethoxycurcumin (DMC)	slow (hours-days)	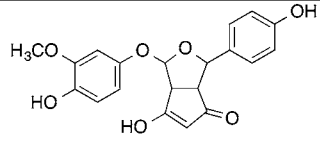 demethoxybicyclopentadione
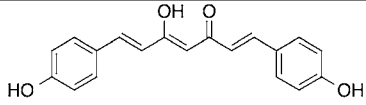 bisdemethoxycurcumin (BDMC)	stable; requires enzymatic or chemical oxidation	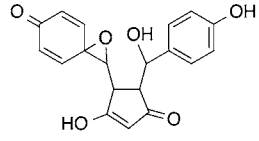 bisdemethoxyspiroepoxide
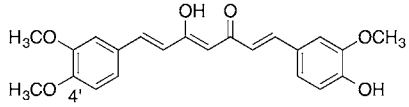 4'-O-methylcurcumin	slow (hours-days)	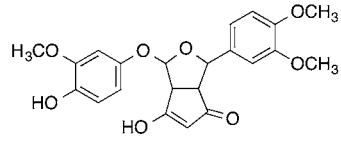 methylbicyclopentadione
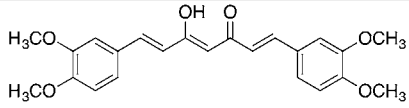 4',4"-O-dimethylcurcumin	stable	N/A

DOI: 10.1021/acs.jafc.5b00244
J. Agric. Food Chem. 2015, 63, 7606−7614

autoxidation as well as the product profile (Table 1). The electron-donating effect of the methoxy group facilitates transfer of an electron from the phenolate anion to molecular oxygen. The lack of one methoxy group in DMC significantly slows the rate of electron transfer (hydrogen abstraction), although loss of the methoxy group and hydrogen abstraction occur on opposite ends of the molecule. BDMC, lacking both methoxy groups, is stable toward autoxidation. BDMC can be forced to oxidize using horseradish peroxidase/H_2O_2 or the oxidizing agent potassium ferricyanide.[30]

The methoxy group also affects the hydrolysis of the spiroepoxide. The contribution of the methoxy group to S_N1 hydrolysis of the epoxide moiety was discussed above.[32] It can be deduced that in a DMC spiroepoxide (which is predicted to be formed but has not been isolated) the methoxy group is in the ring that forms the epoxide and thus is positioned to induce hydrolysis of the epoxide. Lack of both methoxy groups in the BDMC spiroepoxide (which has been isolated) considerably increases stability, and the compound was stable to acid treatment to pH 3. It is less stable, however, in organic solvent, where it quickly decomposes to a mixture of products that have not been identified.[30]

As the site of the initial H abstraction, the phenolic hydroxyl also plays a key role in the disposition of curcumin and analogues toward autoxidation. Chemical modification to eliminate the abstractable hydrogen compromises autoxidation (Table 1). Substitution of one phenolic hydroxyl by a methoxy group (4′-*O*-methylcurcumin) greatly enhances stability, although oxidation can still be achieved enzymatically (HRP or cyclooxygenase-2/H_2O_2) or chemically (potassium ferricyanide). The product is a bicyclopentadione with the additional methyl group in the aromatic ring connected to C-7.[32] As expected, methylation of both phenolic hydroxyls (4′,4″-*O*-dimethylcurcumin) abolished oxidative transformation entirely.[16]

DOES AUTOXIDATION OCCUR IN VIVO?

Autoxidation is a prominent reaction when curcumin is incubated with cultured cells in vitro. Whether autoxidation also occurs in vivo is a crucial question for its biological relevance. Because so far there is no evidence that oxidative transformation of curcumin does indeed occur in vivo, it is worthwhile to consider factors relevant to this question:

(i) Curcumin is usually consumed as turmeric extract, containing also the minor curcuminoids DMC and BDMC. DMC and BDMC contribute to the stability of curcumin in vitro.[30] Whether the presence of DMC and BDMC in turmeric extract results in stabilization of curcumin in vivo remains an open question.

(ii) Albumin and protein in general increase the stability of curcumin toward autoxidation.[24] There is little doubt that the abundance of cellular protein in vivo enhances the stability of curcumin toward autoxidation.

(iii) Glucuronidation of curcumin at the phenolic hydroxyl is a major phase II metabolic pathway in vivo. Glucuronidation contributes to enhancing the stability of curcumin by blocking the free hydroxyl required for autoxidative transformation (O.N.G., P.B.L., and C.S., unpublished results).

(iv) Peroxidases can utilize curcumin as reducing cosubstrate, which may result in enzyme-catalyzed oxidative transformation in vivo.[16]

(v) Oxidative stress at inflammatory sites may contribute to oxidative transformation of curcumin.

(vi) Oxidative transformation to the bicyclopentadione proceeds through several reactive electrophilic intermediates. In vivo, these will be subject to interception by cellular antioxidant defense mechanisms such as adduction with glutathione and *N*-acetylcysteine.[32] As long as the cellular antioxidant defense is functional, only a small fraction of reaction intermediates is predicted to "make it" past the antioxidant barrier and form the bicyclopentadione. Thus, any bicyclopentadione detected in vivo might only be the tip of an iceberg and indicate that oxidative transformation may be an abundant metabolic pathway.

(vii) The glutathione or *N*-acetylcysteine adducts of the quinone methide and spiroepoxide reaction intermediates could be more appropriate markers of oxidative transformation of curcumin than the bicyclopentadione.

(viii) The reaction intermediates will adduct not only to small soluble thiols but also to reactive cysteine residues in proteins. Covalent adduction to protein may be a major mechanism by which oxidative metabolites of curcumin exert biological effects.

Thus, there are a number of factors that imply that oxidative transformation might or might not occur in vivo. We consider this an open question that we plan to address by careful analysis of in vivo samples.

PUTTING METABOLISM, AUTOXIDATION, AND BIOLOGICAL ACTIVITY TOGETHER

How does oxidative transformation relate to the structure–function of curcumin? Curcumin can act as a metal chelator, antioxidant, and Michael acceptor (Figure 8).[41−47] The metal

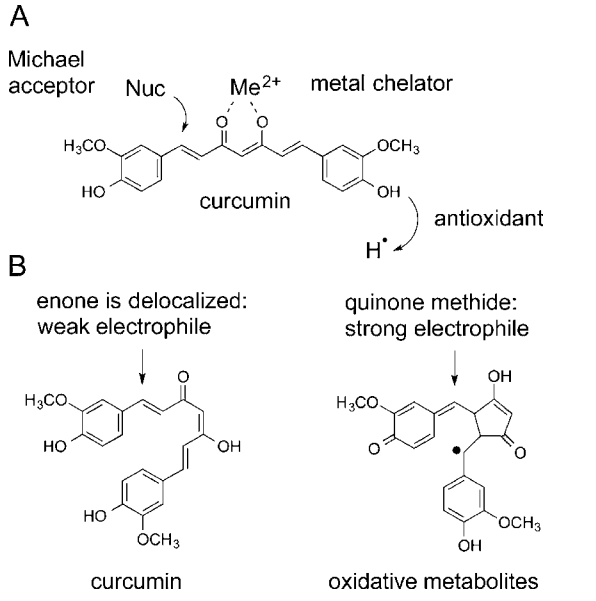

Figure 8. Structure–activity features of curcumin and its quinone methide.

chelating activity of the β-diketo moiety may be disturbed by the formation of the more rigid cyclopentadione ring, which is also more nucleophilic (acidic) than the β-diketo moiety of curcumin.

The antioxidant activity of curcumin is dependent on how readily a hydrogen can be abstracted from the phenolic hydroxyl by a lipid peroxyl radical *and* whether the resulting curcumin radical is less prone to initiate a new lipid

DOI: 10.1021/acs.jafc.5b00244
J. Agric. Food Chem. 2015, 63, 7606−7614

peroxidation chain in turn.[48] The hydrogen abstraction is the initiation of curcumin autoxidation with the resulting radical reactions as described in Figure 5. Dimerization of two curcumin quinone methide radicals has been described as a mechanism of termination.[49] The same group also identified linoleate peroxyl radical coupling products with curcumin.[50] These studies were performed in organic solvent (where curcumin does not autoxidize), and it would be interesting to analyze equivalent reactions in aqueous medium.

The Michael acceptor activity is undoubtedly influenced by autoxidation of curcumin. We hypothesize that it is even dependent on autoxidation.[51] The 1,3-enone (α,β-unsaturated carbonyl) in curcumin is only a weak electrophile because it is part of a delocalized system that spans the entire molecule. Oxidative transformation, specifically the initial hydrogen abstraction and delocalization of the radical into the heptadienedione chain, forms a quinone methide as a strong electrophile (Figure 8). As discussed above, the quinone methide has a considerable lifetime, and because it is present in three distinct intermediates (before and after 5-*exo* cyclization and in the peroxyl radical; cf. Figure 5), it possesses a range of reactivities that can be anticipated to react with different strength cellular nucleophiles. Interestingly, in either case (i.e., in curcumin or its quinone methide) the electrophilic carbon is the same, namely C-1.

A second electrophilic species formed in the autoxidation is the spiroepoxide. HPLC-isolated spiroepoxide readily formed a covalent adduct with *N*-acetylcysteine that was detected in LC-MS analyses.[32] A similar adduct was formed in peroxidase-catalyzed oxidation reactions of curcumin conducted in the presence of *N*-acetylcysteine. Interestingly, ions representing adducts of curcumin or the quinone methide with *N*-acetylcysteine were not detected.[32] These findings support our interpretation of the effect of *N*-acetylcysteine as inhibiting curcumin autoxidation and scavenging reactive electrophiles rather than counteracting ROS formation as a cellular response.

Because oxidative transformation is abundant under cell culture conditions, its products and intermediates need to be considered as mediators of biological effects. We hypothesize that the quinone methide and/or the spiroepoxide are the functional electrophiles in reactions where curcumin is proposed to form a covalent adduct with nucleophilic protein cysteine residues.[52−57] The hypothesis is also indirectly supported by the crucial role of quinone methides as the acting principle in many anticancer drugs as well as toxic DNA methylating agents.[58−60] The requirement for oxidative transformation has clearly been shown for the topoisomerase IIα poisoning activity of curcumin.[61] Neither 4′,4″-*O*-dimethylcurcumin (which does not autoxidize; Table 1) nor reaction conditions that prevented autoxidation of curcumin resulted in poisoning of topoisomerase IIα. The quinone methide intermediates were suggested as the electrophiles binding to active site cysteines, although the spiroepoxide could not be ruled out.[61]

Another pertinent example for Michael adduction is the anti-inflammatory activity of curcumin, especially when effects on the NF-κB pathway are invoked.[62−64] Both NF-κB and its upstream kinase, IKKβ, are targets of curcumin, and both are inhibited by small molecule electrophiles adducting covalently to regulatory cysteines in critical regions of the protein. A Michael type adduction by curcumin via its enone has been invoked as mechanism, whereas we suggest that the quinone methide is the adducting electrophile. This mechanism of adduct formation requires oxidative transformation of curcumin to form the reactive electrophile. This is a crucial difference because conditions for oxidative transformation may not be met in vivo, which could result in a discrepancy between in vitro and in vivo effects. There is an expanding number of proteins that are redox-regulated through strategically placed cysteines that undergo reversible redox cycling to sulfenic acids and can be adducted by small molecule electrophiles.[65] Identification of which of these might be cellular targets of curcumin will require proteomics approaches.

A second reason why oxidative transformation is relevant for understanding the biological activity of curcumin is the surprising number of products formed (Figure 4). When added to cultured cells, curcumin rapidly changes from a single molecule to a family of diverse chemotypes. It is not unreasonable to suggest that the free radical, quinone methide, endoperoxide, alkoxyl radical, dihydroxy, hemiacetal, ketohydroxy, spiroepoxy, vinylether, and other cyclopentadiones each have a distinct set of cellular targets. Together, these products and their biological activities may add up to the "polypharmacology" of curcumin. We are at the beginning of understanding the remarkable transformations of curcumin in vitro and in vivo. Future studies will show which of the many biological effects of curcumin are due to the parent and which are due to its degradation products.

AUTHOR INFORMATION

Corresponding Author

*(C.S.) Mail: Department of Pharmacology, RRB514, 23rd Avenue S at Pierce, Nashville, TN 37232, USA. E-mail: claus.schneider@vanderbilt.edu.

Present Address

†(O.N.G.) Covance Laboratories, Madison, WI, USA.

Funding

This work was supported by Awards CA159382, AT006896, and GM076592 by NCI, NCCIH, and NIGMS, respectively, of the National Institutes of Health (NIH) to C.S. O.N.G. acknowledges support by training grant 2T32GM07628 from NIGMS and a predoctoral fellowship award (F31AT007287) from NCCIH of the NIH. The initial phase of this work was supported by pilot awards from the Vanderbilt Institute in Chemical Biology, the Vanderbilt DDRC (P30DK058404), and the NCI SPORE in GI Cancer (5P50CA095103). The content is solely the responsibility of the authors and does not necessarily represent the official views of the NIH.

Notes

The authors declare no competing financial interest.

REFERENCES

(1) Wright, L. E.; Frye, J. B.; Gorti, B.; Timmermann, B. N.; Funk, J. L. Bioactivity of turmeric-derived curcuminoids and related metabolites in breast cancer. *Curr. Pharm. Design* **2013**, *19*, 6218−6225.

(2) Park, W.; Amin, A. R.; Chen, Z. G.; Shin, D. M. New perspectives of curcumin in cancer prevention. *Cancer Prev. Res. (Phila.)* **2013**, *6*, 387−400.

(3) Howells, L. M.; Mahale, J.; Sale, S.; McVeigh, L.; Steward, W. P.; Thomas, A.; Brown, K. Translating curcumin to the clinic for lung cancer prevention: evaluation of the preclinical evidence for its utility in primary, secondary, and tertiary prevention strategies. *J. Pharmacol. Exp. Ther.* **2014**, *350*, 483−494.

(4) Lopresti, A. L.; Maes, M.; Maker, G. L.; Hood, S. D.; Drummond, P. D. Curcumin for the treatment of major depression: a randomised,

DOI: 10.1021/acs.jafc.5b00244
J. Agric. Food Chem. 2015, 63, 7606−7614

double-blind, placebo controlled study. *J. Affect. Disord.* **2014**, *167*, 368−375.
(5) Brondino, N.; Re, S.; Boldrini, A.; Cuccomarino, A.; Lanati, N.; Barale, F.; Politi, P. Curcumin as a therapeutic agent in dementia: a mini systematic review of human studies. *Sci. World J.* **2014**, *2014*, No. 174282.
(6) Chin, D.; Huebbe, P.; Pallauf, K.; Rimbach, G. Neuroprotective properties of curcumin in Alzheimer's disease − merits and limitations. *Curr. Med. Chem.* **2013**, *20*, 3955−3985.
(7) Anand, P.; Thomas, S. G.; Kunnumakkara, A. B.; Sundaram, C.; Harikumar, K. B.; Sung, B.; Tharakan, S. T.; Misra, K.; Priyadarsini, I. K.; Rajasekharan, K. N.; Aggarwal, B. B. Biological activities of curcumin and its analogues (congeners) made by man and Mother Nature. *Biochem. Pharmacol.* **2008**, *76*, 1590−1611.
(8) Heger, M.; van Golen, R. F.; Broekgaarden, M.; Michel, M. C. The molecular basis for the pharmacokinetics and pharmacodynamics of curcumin and its metabolites in relation to cancer. *Pharmacol. Rev.* **2014**, *66*, 222−307.
(9) Esatbeyoglu, T.; Huebbe, P.; Ernst, I. M.; Chin, D.; Wagner, A. E.; Rimbach, G. Curcumin-from molecule to biological function. *Angew. Chem., Int. Ed. Engl.* **2012**, *51*, 5308−5332.
(10) Cottart, C. H.; Nivet-Antoine, V.; Beaudeux, J. L. Review of recent data on the metabolism, biological effects, and toxicity of resveratrol in humans. *Mol. Nutr. Food Res.* **2014**, *58*, 7−21.
(11) Tome-Carneiro, J.; Gonzalvez, M.; Larrosa, M.; Yanez-Gascon, M. J.; Garcia-Almagro, F. J.; Ruiz-Ros, J. A.; Tomas-Barberan, F. A.; Garcia-Conesa, M. T.; Espin, J. C. Resveratrol in primary and secondary prevention of cardiovascular disease: a dietary and clinical perspective. *Ann. N.Y. Acad. Sci.* **2013**, *1290*, 37−51.
(12) Sak, K. Site-specific anticancer effects of dietary flavonoid quercetin. *Nutr. Cancer* **2014**, *66*, 177−193.
(13) Shirakami, Y.; Shimizu, M.; Moriwaki, H. Cancer chemoprevention with green tea catechins: from bench to bed. *Curr. Drug Targets* **2012**, *13*, 1842−1857.
(14) Pan, M. H.; Huang, T. M.; Lin, J. K. Biotransformation of curcumin through reduction and glucuronidation in mice. *Drug Metab. Dispos.* **1999**, *27*, 486−494.
(15) Vareed, S. K.; Kakarala, M.; Ruffin, M. T.; Crowell, J. A.; Normolle, D. P.; Djuric, Z.; Brenner, D. E. Pharmacokinetics of curcumin conjugate metabolites in healthy human subjects. *Cancer Epidemiol. Biomarkers Prev.* **2008**, *17*, 1411−1417.
(16) Griesser, M.; Pistis, V.; Suzuki, T.; Tejera, N.; Pratt, D. A.; Schneider, C. Autoxidative and cyclooxygenase-2 catalyzed transformation of the dietary chemopreventive agent curcumin. *J. Biol. Chem.* **2011**, *286*, 1114−1124.
(17) Tan, S.; Rupasinghe, T. W.; Tull, D. L.; Boughton, B.; Oliver, C.; McSweeny, C.; Gras, S. L.; Augustin, M. A. Degradation of curcuminoids by in vitro pure culture fermentation. *J. Agric. Food Chem.* **2014**, *62*, 11005−11015.
(18) Hassaninasab, A.; Hashimoto, Y.; Tomita-Yokotani, K.; Kobayashi, M. Discovery of the curcumin metabolic pathway involving a unique enzyme in an intestinal microorganism. *Proc. Natl. Acad. Sci. U.S.A.* **2011**, *108*, 6615−6620.
(19) Ireson, C.; Orr, S.; Jones, D. J.; Verschoyle, R.; Lim, C. K.; Luo, J. L.; Howells, L.; Plummer, S.; Jukes, R.; Williams, M.; Steward, W. P.; Gescher, A. Characterization of metabolites of the chemopreventive agent curcumin in human and rat hepatocytes and in the rat in vivo, and evaluation of their ability to inhibit phorbol ester-induced prostaglandin E2 production. *Cancer Res.* **2001**, *61*, 1058−1064.
(20) Ireson, C. R.; Jones, D. J.; Orr, S.; Coughtrie, M. W.; Boocock, D. J.; Williams, M. L.; Farmer, P. B.; Steward, W. P.; Gescher, A. J. Metabolism of the cancer chemopreventive agent curcumin in human and rat intestine. *Cancer Epidemiol. Biomarkers Prev.* **2002**, *11*, 105−111.
(21) Hoehle, S. I.; Pfeiffer, E.; Solyom, A. M.; Metzler, M. Metabolism of curcuminoids in tissue slices and subcellular fractions from rat liver. *J. Agric. Food Chem.* **2006**, *54*, 756−764.
(22) Aggarwal, B. B.; Deb, L.; Prasad, S. Curcumin differs from tetrahydrocurcumin for molecular targets, signaling pathways and cellular responses. *Molecules* **2014**, *20*, 185−205.
(23) Wu, J. C.; Tsai, M. L.; Lai, C. S.; Wang, Y. J.; Ho, C. T.; Pan, M. H. Chemopreventative effects of tetrahydrocurcumin on human diseases. *Food Funct.* **2014**, *5*, 12−17.
(24) Wang, Y. J.; Pan, M. H.; Cheng, A. L.; Lin, L. I.; Ho, Y. S.; Hsieh, C. Y.; Lin, J. K. Stability of curcumin in buffer solutions and characterization of its degradation products. *J. Pharm. Biomed. Anal.* **1997**, *15*, 1867−1876.
(25) Das, R.; Roy, A.; Dutta, N.; Majumder, H. K. Reactive oxygen species and imbalance of calcium homeostasis contributes to curcumin induced programmed cell death in *Leishmania donovani*. *Apoptosis: Int. J. Programmed Cell Death* **2008**, *13*, 867−882.
(26) Hail, N., Jr. Mitochondrial reactive oxygen species affect sensitivity to curcumin-induced apoptosis. *Free Radical Biol. Med.* **2008**, *44*, 1382−1393.
(27) Choi, H.; Chun, Y. S.; Shin, Y. J.; Ye, S. K.; Kim, M. S.; Park, J. W. Curcumin attenuates cytochrome P450 induction in response to 2,3,7,8-tetrachlorodibenzo-*p*-dioxin by ROS-dependently degrading AhR and ARNT. *Cancer Sci.* **2008**, *99*, 2518−2524.
(28) Wan, R.; Mo, Y.; Zhang, X.; Chien, S.; Tollerud, D. J.; Zhang, Q. Matrix metalloproteinase-2 and -9 are induced differently by metal nanoparticles in human monocytes: the role of oxidative stress and protein tyrosine kinase activation. *Toxicol. Appl. Pharmacol.* **2008**, *233*, 276−285.
(29) Khan, M. A.; Gahlot, S.; Majumdar, S. Oxidative stress induced by curcumin promotes the death of cutaneous T-cell lymphoma (HuT-78) by disrupting the function of several molecular targets. *Mol. Cancer Ther.* **2012**, *11*, 1873−1883.
(30) Gordon, O. N.; Luis, P. B.; Ashley, R. E.; Osheroff, N.; Schneider, C. Oxidative transformation of demethoxy- and bisdemethoxycurcumin: products, mechanism of formation, and poisoning of human topoisomerase IIα. *Chem. Res. Toxicol.* **2015**, DOI: 10.1021/acs.chemrestox.5b00009.
(31) Gordon, O. N.; Schneider, C. Vanillin and ferulic acid: not the major degradation products of curcumin. *Trends Mol. Med.* **2012**, *18*, 361−363 (author reply 363−364).
(32) Gordon, O. N.; Luis, P. B.; Sintim, H. O.; Schneider, C. Unraveling curcumin degradation. Autoxidation proceeds through spiroepoxide and vinylether intermediates en route to the main bicyclopentadione. *J. Biol. Chem.* **2015**, *290*, 4817−4828.
(33) Litwinienko, G.; Ingold, K. U. Abnormal solvent effects on hydrogen atom abstraction. 2. Resolution of the curcumin antioxidant controversy. The role of sequential proton loss electron transfer. *J. Org. Chem.* **2004**, *69*, 5888−5896.
(34) Litwinienko, G.; Ingold, K. U. Solvent effects on the rates and mechanisms of reaction of phenols with free radicals. *Acc. Chem. Res.* **2007**, *40*, 222−230.
(35) Porter, N. A.; Zuraw, P. J.; Sullivan, J. A. Peroxymercuration-demercuration of lipid hydroperoxides. *Tetrahedron Lett.* **1984**, *25*, 807−810.
(36) Schneider, C.; Boeglin, W. E.; Brash, A. R. Identification of two cyclooxygenase active site residues, leucine-384 and glycine-526, that control carbon ring cyclization in prostaglandin biosynthesis. *J. Biol. Chem.* **2004**, *279*, 4404−4414.
(37) Kornblum, N.; DeLaMare, H. E. The base catalyzed decomposition of a dialkyl peroxide. *J. Am. Chem. Soc.* **1951**, *73*, 880−881.
(38) Hamberg, M.; Samuelsson, B. Oxygenation of unsaturated fatty acids by the vesicular gland of sheep. *J. Biol. Chem.* **1967**, *242*, 5344−5354.
(39) Schneider, C.; Boeglin, W. E.; Yin, H.; Porter, N. A.; Brash, A. R. Intermolecular peroxyl radical reactions during autoxidation of hydroxy and hydroperoxy arachidonic acids generate a novel series of epoxidized products. *Chem. Res. Toxicol.* **2008**, *21*, 895−903.
(40) Schneider, C.; Porter, N. A.; Brash, A. R. Routes to 4-hydroxynonenal: fundamental issues in the mechanisms of lipid peroxidation. *J. Biol. Chem.* **2008**, *283*, 15539−15543.

DOI: 10.1021/acs.jafc.5b00244
J. Agric. Food Chem. 2015, 63, 7606−7614

(41) Minear, S.; O'Donnell, A. F.; Ballew, A.; Giaever, G.; Nislow, C.; Stearns, T.; Cyert, M. S. Curcumin inhibits growth of *Saccharomyces cerevisiae* through iron chelation. *Eukaryot. Cell* **2011**, *10*, 1574−1581.
(42) Jiao, Y.; Wilkinson, J. t.; Christine Pietsch, E.; Buss, J. L.; Wang, W.; Planalp, R.; Torti, F. M.; Torti, S. V. Iron chelation in the biological activity of curcumin. *Free Radical Biol. Med.* **2006**, *40*, 1152−1160.
(43) Ak, T.; Gulcin, I. Antioxidant and radical scavenging properties of curcumin. *Chem.−Biol. Interact.* **2008**, *174*, 27−37.
(44) Jiao, Y.; Wilkinson, J. t.; Di, X.; Wang, W.; Hatcher, H.; Kock, N. D.; D'Agostino, R., Jr.; Knovich, M. A.; Torti, F. M.; Torti, S. V. Curcumin, a cancer chemopreventive and chemotherapeutic agent, is a biologically active iron chelator. *Blood* **2009**, *113*, 462−469.
(45) Masuda, T.; Hidaka, K.; Shinohara, A.; Maekawa, T.; Takeda, Y.; Yamaguchi, H. Chemical studies on antioxidant mechanism of curcuminoid: analysis of radical reaction products from curcumin. *J. Agric. Food Chem.* **1999**, *47*, 71−77.
(46) Amolins, M. W.; Peterson, L. B.; Blagg, B. S. Synthesis and evaluation of electron-rich curcumin analogues. *Bioorg. Med. Chem.* **2009**, *17*, 360−367.
(47) Dinkova-Kostova, A. T.; Abeygunawardana, C.; Talalay, P. Chemoprotective properties of phenylpropenoids, bis(benzylidene)-cycloalkanones, and related Michael reaction acceptors: correlation of potencies as phase 2 enzyme inducers and radical scavengers. *J. Med. Chem.* **1998**, *41*, 5287−96.
(48) Schneider, C. Chemistry and biology of vitamin E. *Mol. Nutr. Food Res.* **2005**, *49*, 7−30.
(49) Masuda, T.; Toi, Y.; Bando, H.; Maekawa, T.; Takeda, Y.; Yamaguchi, H. Structural identification of new curcumin dimers and their contribution to the antioxidant mechanism of curcumin. *J. Agric. Food Chem.* **2002**, *50*, 2524−2530.
(50) Masuda, T.; Maekawa, T.; Hidaka, K.; Bando, H.; Takeda, Y.; Yamaguchi, H. Chemical studies on antioxidant mechanism of curcumin: analysis of oxidative coupling products from curcumin and linoleate. *J. Agric. Food Chem.* **2001**, *49*, 2539−2547.
(51) Gordon, O.; Schneider, C. Spice of Life. *Chem. Ind.−London* **2014**, *78*, 36−39.
(52) van Iersel, M. L.; Ploemen, J. P.; Lo Bello, M.; Federici, G.; van Bladeren, P. J. Interactions of α,β-unsaturated aldehydes and ketones with human glutathione S-transferase P1-1. *Chem.−Biol. Interact.* **1997**, *108*, 67−78.
(53) Jurrmann, N.; Brigelius-Flohe, R.; Bol, G. F. Curcumin blocks interleukin-1 (IL-1) signaling by inhibiting the recruitment of the IL-1 receptor-associated kinase IRAK in murine thymoma EL-4 cells. *J. Nutr.* **2005**, *135*, 1859−1864.
(54) Fang, J.; Lu, J.; Holmgren, A. Thioredoxin reductase is irreversibly modified by curcumin: a novel molecular mechanism for its anticancer activity. *J. Biol. Chem.* **2005**, *280*, 25284−25290.
(55) Jung, Y.; Xu, W.; Kim, H.; Ha, N.; Neckers, L. Curcumin-induced degradation of ErbB2: A role for the E3 ubiquitin ligase CHIP and the Michael reaction acceptor activity of curcumin. *Biochim. Biophys. Acta* **2007**, *1773*, 383−390.
(56) Pullakhandam, R.; Srinivas, P. N.; Nair, M. K.; Reddy, G. B. Binding and stabilization of transthyretin by curcumin. *Arch. Biochem. Biophys.* **2009**, *485*, 115−119.
(57) Marcu, M. G.; Jung, Y. J.; Lee, S.; Chung, E. J.; Lee, M. J.; Trepel, J.; Neckers, L. Curcumin is an inhibitor of p300 histone acetylatransferase. *Med. Chem.* **2006**, *2*, 169−174.
(58) Tomasz, M.; Lipman, R.; Chowdary, D.; Pawlak, J.; Verdine, G. L.; Nakanishi, K. Isolation and structure of a covalent cross-link adduct between mitomycin C and DNA. *Science* **1987**, *235*, 1204−1208.
(59) Thompson, D. C.; Thompson, J. A.; Sugumaran, M.; Moldeus, P. Biological and toxicological consequences of quinone methide formation. *Chem.−Biol. Interact.* **1993**, *86*, 129−162.
(60) Awad, H. M.; Boersma, M. G.; Boeren, S.; Van Bladeren, P. J.; Vervoort, J.; Rietjens, I. M. Quenching of quercetin quinone/quinone methides by different thiolate scavengers: stability and reversibility of conjugate formation. *Chem. Res. Toxicol.* **2003**, *16*, 822−831.
(61) Ketron, A. C.; Gordon, O. N.; Schneider, C.; Osheroff, N. Oxidative metabolites of curcumin poison human type II topoisomerases. *Biochemistry* **2013**, *52*, 221−227.
(62) Jobin, C.; Bradham, C. A.; Russo, M. P.; Juma, B.; Narula, A. S.; Brenner, D. A.; Sartor, R. B. Curcumin blocks cytokine-mediated NF-κB activation and proinflammatory gene expression by inhibiting inhibitory factor I-κB kinase activity. *J. Immunol.* **1999**, *163*, 3474−3483.
(63) Plummer, S. M.; Holloway, K. A.; Manson, M. M.; Munks, R. J.; Kaptein, A.; Farrow, S.; Howells, L. Inhibition of cyclo-oxygenase 2 expression in colon cells by the chemopreventive agent curcumin involves inhibition of NF-κB activation via the NIK/IKK signalling complex. *Oncogene* **1999**, *18*, 6013−6020.
(64) Pan, M. H.; Lin-Shiau, S. Y.; Lin, J. K. Comparative studies on the suppression of nitric oxide synthase by curcumin and its hydrogenated metabolites through down-regulation of IκB kinase and NFκB activation in macrophages. *Biochem. Pharmacol.* **2000**, *60*, 1665−1676.
(65) Lo Conte, M.; Carroll, K. S. The redox biochemistry of protein sulfenylation and sulfinylation. *J. Biol. Chem.* **2013**, *288*, 26480−26488.

DOI: 10.1021/acs.jafc.5b00244
J. Agric. Food Chem. 2015, 63, 7606−7614

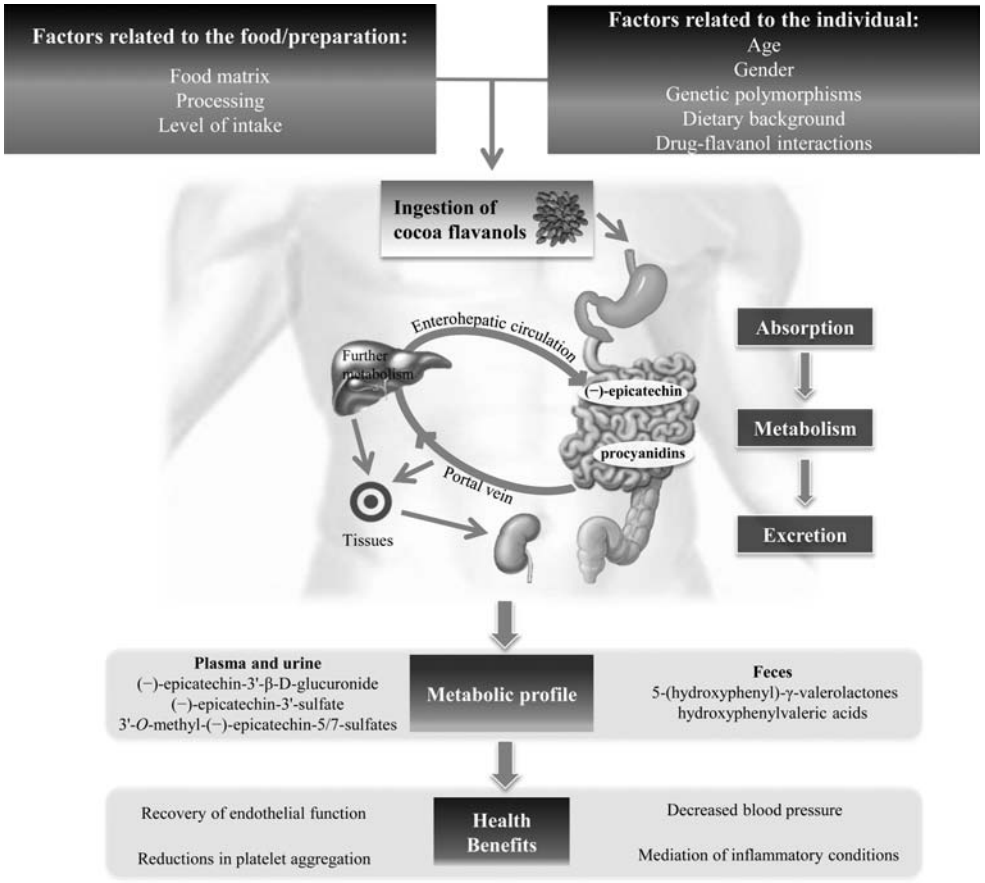

Figure 1. Schematic describing the main factors affecting the absorption, metabolism, and excretion of cocoa flavanols, together with the health benefits mediated by the circulating (−)-epicatechin metabolites.

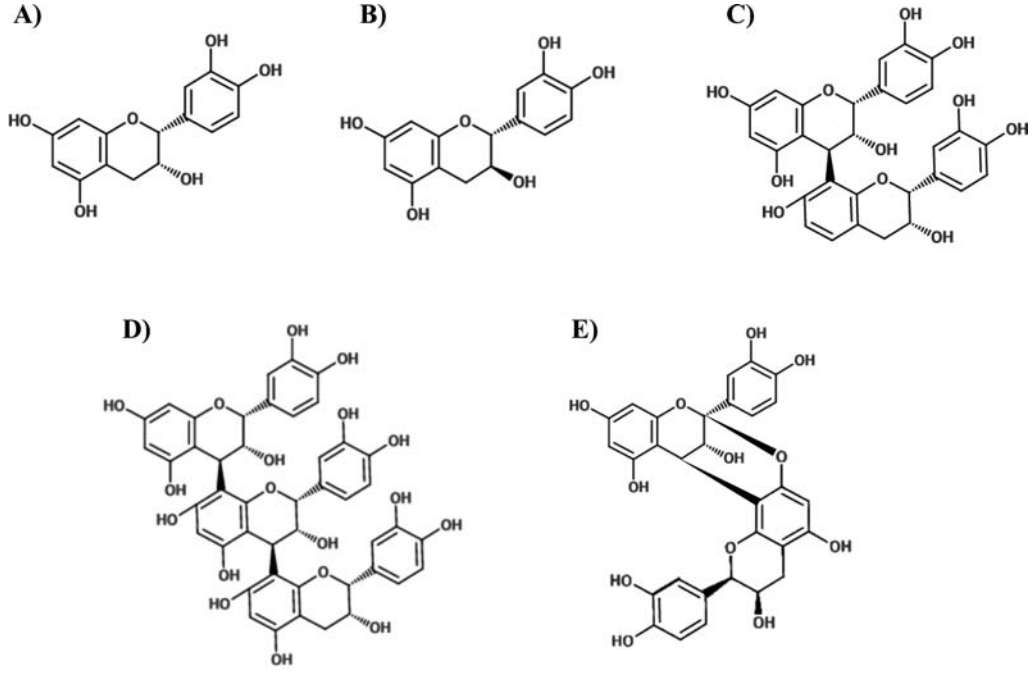

Figure 2. Chemical structures of (A) (−)-epicatechin, (B) (+)-catechin, (C) procyanidin dimer B2, (D) procyanidin trimer C1, and (E) procyanidin tetramer A2.

The polyphenol content of cocoa consists predominately of flavanols (monomeric forms: (−)-epicatechin, (+)-epicatechin, (−)-catechin, and (+)-catechin), procyanidins (oligomeric and polymeric derivatives of flavanols characterized by their degree of polymerization (DP), also named proanthocyanidins), and, to a lesser extent, anthocyanins.[10] The term "cocoa flavanols"

DOI: 10.1021/acs.jafc.5b00443
J. Agric. Food Chem. 2015, 63, 7615−7623

Table 1. Bioavailability and Pharmacokinetics of Epicatechin after Consumption of Cocoa Flavanols in Humans[a]

reference	source	n	intake	C_{max} (nM)	t_{max} (h)	AUC (nM·h)	urinary excretion[b] (% of EC intake)
Richelle et al., 1999[40]	chocolate	8	82 mg EC	383	2.0	1535	–[f]
	chocolate	8	164 mg EC	700	2.6	3688	–
Baba et al., 2000[34]	cocoa	5	220 mg (−)-EC	4920	2.0	–	29.8
	chocolate	5	220 mg (−)-EC	4770	2.0	–	25.3
Rein et al., 2000[39]	chocolate	10	137 mg EC	257	2.0	–	–
Wang et al., 2000[44]	chocolate	13	35 mg (−)-EC	133	2.0	500	–
	chocolate	13	69 mg (−)-EC	258	2.0	1000	–
	chocolate	10	104 mg (−)-EC	355	2.0	1500	–
Holt et al., 2002[29]	cocoa	5	323 mg EC+C	5920	2.0	–	–
Schramm et al., 2003[36]	cocoa	6	1.53 mg EC+C/kg BW (115 mg/75 kg)	1021	1.6[c]	4230	–
Natsume et al., 2003[33]	pure (−)-EC	4	1000 mg (−)-EC	21599[d]	–	–	–
Schroeter et al., 2003[58]	cocoa	12	5.44 mg EC+C/kg BW (408 mg/75 kg)	–	–	8888	–
Roura et al., 2005[48]	cocoa	5	54 mg (−)-EC	626	–	–	–
Schroeter et al., 2006[49]	cocoa	10	174 mg EC	2750[c]	2.0	–	–
Neukam et al., 2007[46]	cocoa	10	61 mg EC	63	1.0	–	–
Roura et al., 2007[47]	cocoa	21	28.2 mg (−)-EC	330	2.0	–	–
Taubert et al., 2007[43]	chocolate	22	5.1 mg EC	13	1.3	43	–
Balzer et al., 2008[45]	cocoa	10	16.8 mg EC	194[e]	–	–	–
	cocoa	10	78.9 mg EC	529[e]	–	–	–
	cocoa	10	203 mg EC	964[e]	–	–	–
Loke et al., 2008[77]	pure (−)-EC	12	200 mg (−)-EC	2870	–	–	–
Neilson et al., 2009[38]	chocolate	6	27 mg EC	32	2.3	121	–
	cocoa	6	27 mg EC	43	0.9	132	–
Mullen et al., 2009[35]	cocoa	9	6.7 mg (−)-EC	143[d]	1.0–1.4	296[d]	18.3
Spadafranca et al., 2010[42]	chocolate	20	58 mg EC	362	–	–	–
Ottaviani et al., 2011[32]	pure (−)-EC	7	1.5 mg (−)-EC/kg BW (112 mg/75 kg)	889	2.0	–	3
Rodriguez-Mateos et al., 2012[41]	chocolate	15	58 mg EC	608	2.0	1672	–
Ottaviani et al., 2012[7]	cocoa	10	1.8 mg (−)-EC/kg BW (135 mg/75 kg)	1234[d]	2.0	–	–
Ottaviani et al., 2012[8]	cocoa	12	1.8 mg (−)-EC/kg BW (135 mg/75 kg)	880	2.0	–	5.1[c]
Actis-Goretta et al., 2012[6]	chocolate	5	79 mg (−)-EC	873[d]	3.2–3.8	4154[d]	21

[a] C_{max}, maximum plasma concentration; t_{max}, time to reach maximum concentration; AUC, area under the curve of the concentration over time; EC, epicatechin; C, catechin; BW, body weight. [b] Urine collected over a 24 h period. [c] Data interpreted visually from a graph. [d] Values represent total epicatechin metabolites summed by the author. [e] Values derived by subtracting baseline values. [f] –, unavailable data in the manuscript.

includes both the monomeric forms (mainly (−)-epicatechin and to a lesser extent (+)-catechin) and the oligomeric procyanidins ranging from dimers to decamers (DP 2–10) (Figure 2). The average intake of cocoa flavanols has been recently estimated in Europe at 105 mg/day,[11] below the 200 mg/day considered by EFSA to be sufficient to help maintain normal endothelium-dependent vasodilation.[12] The primary flavanol in cocoa beans is (−)-epicatechin, ranging from 0.1 to 13.5 mg/g, with lower levels of (+)-catechin,[13−15] whereas oligomeric and polymeric procyanidin content ranges from 18 to 27 mg/g and from 9 to 16 mg/g, respectively.[16] In milk and dark chocolates, the epicatechin content (both enantiomers, (−) and (+) forms) has been reported between 0.18 and 1.25 mg/g, with catechin between 0.05 and 0.40 mg/g and oligomeric and polymeric procyanidin content around 1.1–11.2 and 0.8–7.0 mg/g, respectively.[16−18] The flavanol monomer content of chocolate is predominantly in the (−) form, accounting for approximately 95 and 89% of EC and catechin present, respectively.[18] Considering that cocoa beans do not contain (−)-catechin, it has been reported that the presence of this stereoisomer in chocolate might be due to the epimerization of (−)-epicatechin to (−)-catechin during processing.[14,19]

ADME

After oral intake, (−)-EC is exposed to enterocytes[20,21] in the small intestine, where they enter via passive diffusion[22] and are rapidly metabolized. The aglycone undergoes phase II enzymatic metabolism forming sulfate, glucuronide, and methylated sulfate/glucuronide metabolites through the respective actions of sulfotransferases (SULTs), uridine-5′-diphosphate glucuronosyltransferases (UGTs), and catechol-*O*-methyltransferases (COMTs).[23,24] Once absorbed, any unmetabolized (−)-EC undergoes rapid glucuronidation, sulfation, and O-methylation in the liver. Although a degree of enterohepatic recirculation was initially proposed,[25] recent intestinal perfusion studies have reported only a relatively modest elimination of (−)-EC via the bile.[26] Procyanidins were suggested to undergo depolymerization in the gastrointestinal (GI) tract, resulting in monomers,[27] although subsequent studies have indicated that this is unlikely and that they are very poorly absorbed, if at all, in humans.[8,28] Indeed, to date, only flavanol dimers have been detected in human plasma and in very low amounts compared with monomers.[29] However, once in the large intestine, procyanidins together with flavanol monomers undergo rapid C-ring fission induced by the gut microbiome, yielding a host of smaller phenolic acids and 5-(hydroxyphenyl)-γ-valerolactones.[8,9,30] These are absorbed and further metabolized in the liver prior to their renal excretion.

DOI: 10.1021/acs.jafc.5b00443
J. Agric. Food Chem. 2015, 63, 7615−7623

The pharmacokinetics of (−)-EC in blood and urine following cocoa flavanol consumption has been extensively studied in numerous human intervention trials (Table 1), although it should be noted that the accurate identification and quantification of flavanols have been limited for several reasons. First, the analytical methodology used often fails to capture the full metabolic profile, for example, by failing to profile flavanol metabolite stereoisomers. Added to this, a lack of reference standards has made it difficult to accurately standardize flavanol metabolite characterization in different studies. Instead, it has been necessary to report total flavanol absorption based on the hydrolysis of sulfates of (methyl)epicatechins using enzymes to convert the conjugated forms to aglycones. It is now known that such an approach is flawed due to the ineffective cleavage of flavanol conjugates under experimental conditions and has led to an underestimation of total EC bioavailability.[31] The stereochemical configuration of flavanols has also been reported to play a crucial role with regard to the absorption and metabolism of cocoa flavanols. The oral bioavailability of the stereoisomers has been studied and indicated that flavanol monomeric enantiomers significantly differed from each other with regard to their levels of nonmethylated metabolites present in plasma and urine ((−)-epicatechin > (+)-epicatechin = (+)-catechin > (−)-catechin).[32]

Generally, in the majority of human trials the amounts of monomers epicatechin and catechin consumed by the volunteers ranged between 20 and 300 mg, a level that leads to maximum plasma concentrations of epicatechin and catechin of around 30 and 5000 nM, between 0.9 and 3.2 h after consumption (Table 1). Only one study has reported maximum concentrations of around 21 μM after consumption of 1 g of EC, an amount unlikely to be relevant to dietary intake even following the consumption of a high-flavanol diet.[33]

With respect to the precise metabolic profile, access to chemically synthesized EC metabolites has allowed the identity of the major flavanol metabolites to be elucidated.[6,7] After consumption of a cocoa flavanol drink containing 1.8 mg of (−)-epicatechin/kg of body weight, the conjugates (−)-epicatechin-3′-β-D-glucuronide, (−)-epicatechin-3′-sulfate, and 3′-*O*-methyl-(−)-epicatechin-5/7-sulfate were the major in vivo metabolites found in the circulation 2 h after intake, accounting for 46, 28, and 17% of all plasma flavanol metabolites, respectively, whereas (−)-epicatechin-5-sulfate and (−)-epicatechin-7-sulfate (representing 3.1 and 1.1%, respectively) were present at lower levels.[7] These data are in agreement with another human trial in which volunteers consumed dark chocolate containing 79 mg of (−)-epicatechin. In this case, 3′-*O*-methyl-(−)-epicatechin-4-sulfate and (−)-epicatechin-4′-β-D-glucuronide were also identified, accounting for 7 and 4% of all metabolites detected in the bloodstream.[6] The urinary excretion of structurally related EC metabolites has been reported between 21 and 30% of the ingested dose over a period of 24 h, of which >80% was excreted in the first 8−10 h,[6,34,35] with the exception of two studies that reported <6% of total intake.[7,8] The elimination of epicatechin metabolites is quite rapid ($t_{1/2} \approx 2-4$ h), and their accumulation in the blood or tissues is thought unlikely to occur.[6,36]

It has been reported that 45% of parent (−)-EC ingested is neither absorbed nor metabolized in the upper GI tract,[26] but passes to the large intestine where the actions of the resident bacteria lead to the generation of microbial metabolites that appear in circulation and urine at later time points (6−48 h). After regular cocoa flavanol intake, analysis of 24 h urine revealed a significant level of glucuronide and sulfate conjugates of 5-(3′,4′-dihydroxyphenyl)-γ-valerolactone and 5-(3′-methoxy-4′-hydroxyphenyl)-γ-valerolactone.[9] Such metabolites may be generated from both monomeric and oligomeric flavanols, and data indicate that intake of monomeric flavanols or procyanidins (degree of polymerization ranging from 2 to 10) results in urinary levels of γ-valerolactone metabolites representing 43 and 54% of intake, respectively.[8] The excretion of phenolic acids, mainly vanillic, ferulic, 3,4-dihydroxyphenylacetic, and 3-hydroxyphenylacetic acids, is also known to be increased 6−48 h after flavanol intake,[9,37] with vanillic acid showing a different peak excretion between 0 and 3 h.[30] In plasma, glucuronide conjugates of dihydroxyphenylvalerolactones were increased after regular cocoa intake,[9] whereas a recent study also reported an enhancement of circulating total phenolic acids between 0 and 6 h after consumption of a cocoa−nut cream containing 176 μmol (51.1 mg) of EC and catechin.[37]

In summary, although there are a number of studies relating to the absorption, metabolism, and excretion of cocoa flavanols, only very recently has the precise and detailed profile of flavanol ADME been elucidated due to developments in analytical techniques and the availability of authentic flavanol metabolites. Much is known about structure microbiota-derived catabolites, but data relating to the extent to which specific bacterial profiles may alter the generation of smaller phenolic metabolites are presently lacking.

FACTORS AFFECTING FLAVANOL ADME

The extent to which (−)-EC is absorbed/metabolized from cocoa and other flavanol-rich foods in the small intestine, yielding structurally related epicatechin metabolites, depends on numerous variables including (1) the structure of the food matrix, including its physical state and macronutrient composition; (2) the processing steps that the flavanol-containing foodstuff has been subjected to, notably heating, fermenting, etc.; (3) the interactions of flavanols with other nutrient and non-nutrient components (nutrient−nutrient interactions); (4) the level of intake; and (5) individual genetic polymorphisms in relevant metabolic enzymes, most notably, SULTs, GST, and COMT. The current data available regarding the influence of these factors on the ADME of cocoa flavanols are limited, and there are some discrepancies that exist among individual studies, again mainly due to the differences in analytical methodology and study design.

Food Matrix Effects. The main food matrix factors influencing flavanol absorption in vivo include its physical state and its macronutrient composition. Flavanols are not typically consumed as purified supplements but rather in complex matrices both natural (plant material, typically fruits and vegetables) or as formulated/manufactured products. Thus, flavanol interactions with, or binding to, other nutrients/non-nutrients may significantly influence the accessibility of flavanols to the intestinal lumen and thus their potential to undergo transfer across it. As such, the kinetics of flavanol absorption/metabolism is thought to be heavily influenced by the food delivery system.

Physical State. Most of the studies investigating the absorption and metabolism of EC after consumption of chocolate (solid confection)[6,34,38−44] or cocoa (liquid beverage)[7,34,35,44−49] have reported similar plasma flavanol concentrations and times to reach the maximum concentration (t_{max}) between 1 and 2 h, although in some cases the number of time

DOI: 10.1021/acs.jafc.5b00443
J. Agric. Food Chem. 2015, 63, 7615−7623

points evaluated was limited. To our knowledge, only two studies have assessed the effect of physical structure on EC bioavailability comparing solid versus liquid matrix delivery of flavanols. Comparison of solid (solid chocolate) and liquid (cocoa drink) in five volunteers has indicated no significant effect of food matrix with respect to t_{max} for the appearance of EC metabolites in the circulation (2 h for both). Despite this, at 1 h after consumption, the plasma concentrations of total nonmethylated epicatechin metabolites were significantly higher in the cocoa drink group, suggesting a subtle effect of matrix on flavanol O-methylation.[34] In contrast, total flavanol (AUC) and maximum concentration (C_{max}) were observed to be significantly higher following intake of a cocoa drink compared to that of solid chocolate.[38] Additionally, the time to reach the maximum concentration was 0.9 ± 0.1 h for beverages and 2.3 ± 0.8 h for chocolate confection, although these differences were not significant. Two recent studies in healthy volunteers have reported a t_{max} of 2 h after intake of a cocoa drink[7] and a t_{max} around 3.2−3.8 h after solid chocolate consumption.[6] Taken all together, these data suggest faster absorption rates and earlier peak plasma concentrations of EC from liquid food matrices relative to solid chocolate, probably due to a rapid digestive release and rapid stomach-emptying from liquids compared to solids.

Macronutrient Composition. Carbohydrate-, lipid-, or protein-rich meals have been reported to have a pronounced effect on the metabolism of many xenobiotics.[50,51] As such, it is hypothesized that such macronutrients may also influence the efficacy and profile of flavanols from different foods/beverages. Although information regarding lipid−flavanol interactions remains scarce, carbohydrates and, in particular milk proteins, have been relatively well studied for their potential to affect flavanol absorption and metabolism.

(a) Lipid Effects. To our knowledge, only one study has investigated the effect of coconsumption of lipids (delivered as butter; 28.6 g of fat), which suggested that lipid−flavanol interactions do not influence total flavanol absorption of total plasma flavanols.[36] However, future larger scale pharmacokinetic studies are warranted and required well-characterized lipid and food matrix controls.

(b) Carbohydrate Effects. Carbohydrate interactions are important because in many flavanol-containing foods/beverages there are commonly high levels of sugars present. Data have suggested that codelivery of flavanols in a matrix containing carbohydrate may increase flavanol absorption in rats[52] and humans.[36,38,41] For example, the co-administration of sugar with a flavanol-rich cocoa resulted in significant increases in plasma C_{max} (18%) and AUC (22%) of epicatechin plus catechin and accelerated their renal elimination.[36] Similarly, the consumption of a sucrose-containing hard chocolate resulted in a 20% higher C_{max} and 21% greater AUC for total plasma flavanols compared to a maltitol-containing equivalent, although the O-methylation pattern of conjugated metabolites was unaffected by sugar type.[41] Additionally, human endothelial function has been shown to be increased to a higher degree (although not significantly) following the consumption of a sugar-sweetened cocoa beverage compared to that observed with a sugar-free cocoa drink.[53] In contrast, no significant differences in the plasma flavanol pharmacokinetics were observed after ingestion of a high-sucrose-containing hard chocolate compared with a low-sucrose control dark chocolate containing the same amount of flavanols,[38] although the methodology used here was capable of resolving only pure EC and catechin and not their conjugated metabolites, which may explain the lack of significance. On the basis of the available evidence, it seems plausible that carbohydrate-rich meals may act to enhance flavanol absorption without influencing metabolism, although further research is required to confirm such initial observations.

(c) Protein and Milk Effects. Flavanols, and in particular flavanol oligomers, have been suggested to interact with proteins in a manner that might, in turn, result in altered bioavailability/bioefficacy of dietary flavanols.[54] In vitro data have demonstrated that β-lactoglobulin, a major milk protein, can stably bind to epicatechin and catechin via covalent bonding.[55] Co-intervention with meat (beef steak; 47.7 g of protein) with cocoa flavanols was observed not to affect either the AUC or the C_{max} for total plasma flavanols when compared to the intake of cocoa alone, although the rate of elimination was significantly faster.[56]

Unlike the levels of carbohydrate and protein, the fat composition in milk varies widely, and thus it is a major confounding factor in determining the specific effects of milk protein on flavanol absorption. Indeed, there has been controversy regarding the effects of milk on the bioavailability of flavanols. On the one hand, the consumption of 100 g of dark chocolate with 200 mL of milk significantly reduced the (−)-EC levels in plasma (calculated as AUC) compared with the consumption of dark chocolate lacking milk.[57] In contrast, two studies report no impact of milk protein on plasma flavanol concentrations following intake of either a cocoa flavanol beverage[58] or hard chocolate.[38] As the former study was not performed under isocaloric and isolipidemic conditions, it is conceivable that other components in the matrix might be responsible for the differences on flavanol absorption. More recent data tend to support the latter observations that whole milk[35,47,56] and skimmed milk[59] do not influence flavanol absorption.

With regard to the urinary excretion, only a couple of studies have evaluated the effect of milk on the flavanol metabolite excretion profile in urine with contradictory results. Milk co-administration with flavanol-containing cocoa did not significantly affect the total amount of (−)-epicatechin metabolites excreted in the urine, although the metabolite profile indicated high levels of sulfation relative to glucuronidation over the first 6 h of urinary excretion.[60] In contrast, milk was observed to significantly decrease the urinary excretion of epicatechin plus catechin metabolites following administration of a cocoa−milk-containing beverage.[35] However, it should be noted that the lipid content was different between products, and protein content was not described. Thus, it remains unclear as to which particular compounds were causing the reduced flavanol absorption. The influence of milk on flavanol absorption in the colon has also been investigated, showing that, of 15 phenolic acids assessed, the urinary excretion of 3,4-dihydroxyphenylacetic, protocatechuic, 4-hydroxybenzoic, 4-hydroxyhippuric, hippuric, caffeic, and ferulic acids decreased when milk was co-administered, whereas urinary concentrations of vanillic and phenylacetic acids were increased.[61]

In conclusion, it appears that milk does not have an overall effect on the absorption of cocoa flavanols, but it might have a small impact on the profile of metabolites produced and their excretion. Further research is necessary, in particular, studies with well-characterized milk−cocoa interventions.

Processing Effects. Although the evidence regarding the influence of cocoa processing on the pharmacokinetics of

DOI: 10.1021/acs.jafc.5b00443
J. Agric. Food Chem. 2015, 63, 7615−7623

flavanols is scarce, there is evidence to suggest that a significant decrease of monomeric flavanols and procyanidins occurs during fermentation, drying, roasting, and alkalization.[13−15,62,63] Fermentation (from 4−5 days to 10 days) results in reductions in EC levels of around 80% compared with that of unfermented beans,[14,63] whereas drying of cocoa beans has been shown to lead to lesser losses of around 14%.[15] When cocoa beans are roasted for 30 min at 45 °C and the temperature is steadily increased, data report that EC degradation occurs at roast temperatures above 70 °C, with only around 18% of epicatechin remaining following roasting at 120 °C.[63] However, roasting data are variable with another study reporting less significant losses at 140−150 °C (73, 43, and 70% for total EC, procyanidin B1, and procyanidin B2, respectively).[15] With regard to the impact of alkalization, the analysis of commercially available cocoa powders with various degrees of alkali processing resulted in a 40% reduction in total flavanols for those lightly alkalized (pH 6.5−7.2), a 22% reduction for medium alkalized (pH 7.2−7.6), and an 11% decrease for heavily alkalized cocoa powders (pH ≥7.61).[62] In agreement with these data, alkalization of natural cocoa powder at pH 7.2 resulted in losses of 67% for (−)-epicatechin, 36% for (+)-catechin, and 69 and 67% for dimer B2 and trimer C1, respectively.[13]

To our knowledge, only one study has investigated the impact of cocoa processing on flavanol absorption in vivo. In that study, 10 healthy volunteers consumed a nonalkalized, medium-alkalized, or heavily alkalized cocoa, and, as expected, reductions in flavanol content in the cocoa resulted in reduced levels of total plasma flavanols.[64] In addition to flavanol losses, significant interconversion of flavanol stereoisomers also occurs during cocoa processing. Notably, a large increase in (−)-catechin, a stereoisomer not naturally present in cocoa, has been reported following fermentation, roasting, and alkalization of cocoa beans, presumably due to the epimerization of (−)-epicatechin to (−)-catechin.[14,65] In support of this, (−)-catechin has been measured in 23 commercially available chocolate samples, with an average ratio of 1:0.1 (−)-catechin/(+)-catechin.[18] Because the preferred order of absorption has been recently ranked as (−)-epicatechin > (+)-catechin > (−)-catechin,[66] such epimerization together with other processing techniques is likely to greatly affect the bioavailability and bioactivity of cocoa flavanols.

Drug−Flavanol Interactions. As described previously, flavanols are substrates of phase II conjugation enzymes and thus share a metabolic pathway similar to that of many drugs.[23,24,67] However, the extent to which flavanols may alter drug metabolism in vivo is currently unknown, although a few studies have shown that flavanols may modulate the activity of phase II enzymes in vitro.[68−70] Notably, EC has been shown to inhibit the enzyme UGT2B17, albeit at concentrations above those that are physiologically possible.[69] EC and catechin have also been observed to inhibit human SULT1A1 and SULT1A3 with IC_{50} values in the micromolar range.[70] Catechin and EC, however, appear unable to influence P-glycoprotein drug transporter activity in intestinal cells.[68] Although these in vitro studies suggest that EC might be able to alter drug metabolism, results without in vivo confirmation should be interpreted with caution. A recent in vitro study investigating the cellular uptake and metabolism of EC and its major in vivo metabolites showed that the conjugates formed in the cells only account for one of the four major metabolites in human plasma, suggesting that the in vitro models do not accurately reflect the in vivo situation.[21] In vitro studies with both parental flavanols and their metabolites at physiologically relevant concentrations and human in vivo studies investigating potential drug−flavanol interactions are warranted.

Intake. The influence of the intake level of overall absorption and metabolism has also been investigated. Consumption of 27, 53, and 80 g of chocolate resulted in measured plasma EC levels (C_{max} and AUC) that increased in an intake-dependent fashion.[44] The same trend was observed in another study providing 40 and 80 g of chocolate, although in this case t_{max} was slightly delayed from 2 to 2.6 h, respectively.[40] Together the data suggest that there is a good correlation between intake and C_{max} (R^2 = 0.954), considering the diversity of the study conditions (Figure 3). When 1 g of pure (−)-EC

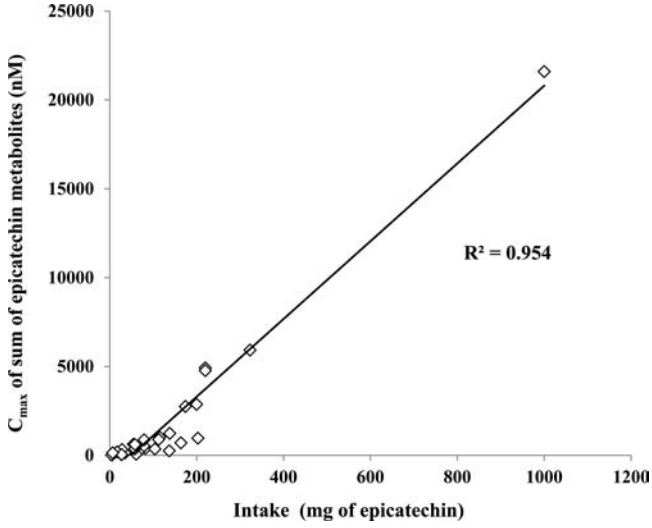

Figure 3. Linear correlation between plasma concentrations of epicatechin metabolites (expressed as C_{max}) and intake of epicatechin for 22 studies shown in Table 1.

was consumed, plasma concentrations of total EC metabolites were 6269 ng/mL (≈21.56 μM) at 1 h after consumption,[33] whereas consumption of only 6.7 mg of (−)-EC from a cocoa drink resulted in C_{max} values of 143 nM.[35] The average C_{max}, normalized to the ingestion of 1 mg of EC, indicates that 9.4 ± 1.3 nM of total EC metabolites is present in the circulation per milligram of EC consumed (Table 1). As such, it appears that the saturation of (−)-EC absorption does not occur in this dosage range. However, it remains unclear as to how increasing amounts of (−)-EC intake might influence the overall pattern of flavanol metabolism. For example, in rats it has been reported that increased (−)-EC methylation occurs at higher intake levels.[71] To what extent this may occur in humans remains to be established.

Genetic Polymorphisms. Interindividual variability in the absorption and metabolism of cocoa flavanols is thought to be at least partially caused by genetic polymorphisms, in particular, in phase II enzymes involved in flavanol metabolism. A single nucleotide polymorphism (SNP) in the gene encoding for COMTs, which is responsible for flavanol O-methylation, involves a single G to A transition that result in a change from valine to methionine.[72] In this polymorphism (COMT Val^{158}Met) the variant allele COMT-Met (also called COMT-A) has shown a 40% reduction of enzymatic activity compared with the wild type allele COMT-Val (also named

DOI: 10.1021/acs.jafc.5b00443
J. Agric. Food Chem. 2015, 63, 7615−7623

COMT-G) in in vitro studies.[73] Thus, polymorphisms such as the COMT Val[158]Met might result in modified flavanol O-methylation relative to other forms of the enzyme. Although there are no studies addressing this issue specifically for cocoa flavanols, studies have investigated the effect of COMT Val[158]Met polymorphism on flavanol absorption and metabolism following green tea consumption. In a cross-sectional analysis with 660 subjects, men possessing the low-activity genotype (COMT-AA) had lower urinary levels of five tea polyphenol metabolites, including epigallocatechin, *O*-methyl-epigallocatechin, EC, and valerolactones, relative to the other genotypes (COMT-GG and COMT-AG).[74] In contrast, in an intervention study investigating the same polymorphism with 10 volunteers harboring allele COMT-A and 10 volunteers with the wild type allele COMT-G, no significant differences in the plasma catechin concentrations were observed between COMT groups following intake of a decaffeinated green tea extract,[75] although significantly lower urinary levels of 4′-*O*-methylepigallocatechin during the first 5.5 h were reported in the COMT-AA group (lowest activity genotype).[76]

Further large-scale pharmacokinetics studies are warranted to expand these investigations along with studies designed to assess the impact of other polymorphic variants of phase II drug-metabolizing enzymes such as UGTs and SULTs.

SUMMARY AND FUTURE RESEARCH

Current literature strongly supports the notion that the consumption of cocoa flavanols is causally related to benefits in the cardiovascular function. Importantly, the large majority of circulating flavanols are present in the form of their phase II metabolites, which are likely to mediate these effects. Despite their being a number of dietary intervention studies reporting the absorption, metabolism, and excretion of flavanols, only very few report the precise structures, profile, and quantification of flavanol metabolites in the systemic circulation in humans. Further research is required to conclude on the pharmacokinetic profiles of microbiota-derived catabolites, such as valerolactones and phenolic acids, and ultimately whether these may underpin biological activity in humans.

The extent to which (−)-EC is absorbed/metabolized from cocoa depends on numerous factors. The food matrix influences flavanol bioavailability in different ways, with EC absorption from liquid food matrices occurring more rapidly than that observed for solid chocolate. The codelivery of flavanols in a carbohydrate matrix may also increase flavanol absorption. In contrast, lipids, proteins, and milk appear not to influence overall flavanol absorption, although milk may affect the metabolic profile of flavanol metabolites generated. Further investigation is also required to establish how intake level, common food-processing techniques, drugs, and genetic polymorphisms influence the absorption, metabolism, and excretion of cocoa flavanols in humans. Finally, the influence of age, sex, reproductive status, and/or dietary background on flavanol intake/health markers should be a focus of immediate future research. Such data will help to define a minimum amount of flavanols necessary to achieve population-based health benefits and thus contribute to the creation of flavanol-specific dietary guidelines and recommendations.

AUTHOR INFORMATION

Corresponding Author

*(J.P.E.S.) Phone: 004411837868724. Fax: 00441183788709. E-mail: j.p.e.spencer@reading.ac.uk.

Funding

M.E.A. thanks Fundación Alfonso Martín Escudero for a postdoctoral fellowship.

Notes

The authors declare no competing financial interest.

ABBREVIATIONS USED

ADME, absorption, metabolism, distribution, and excretion; AUC, area under the curve; C_{max}, maximum concentration; EC, epicatechin; t_{max}, time to reach the maximum concentration

REFERENCES

(1) Rothwell, J. A.; Pérez-Jiménez, J.; Neveu, V.; Medina-Ramon, A.; M'Hiri, N.; Garcia Lobato, P.; Manach, C.; Knox, K.; Eisner, R.; Wishart, D.; Scalbert, A. Phenol-Explorer 3.0: a major update of the Phenol-Explorer database to incorporate data on the effects of food processing on polyphenol content. Database, 10.1093/database/bat070, 2013; available from http://www.phenol-explorer.eu.

(2) Manach, C.; Scalbert, A.; Morand, C.; Remesy, C.; Jimenez, L. Polyphenols: food sources and bioavailability. *Am. J. Clin. Nutr.* **2004**, *79*, 727−747.

(3) Heiss, C.; Keen, C. L.; Kelm, M. Flavanols and cardiovascular disease prevention. *Eur. Heart J.* **2010**, *31*, 2583−2592.

(4) Galleano, M.; Oteiza, P. I.; Fraga, C. G. Cocoa, chocolate, and cardiovascular disease. *J. Cardiovasc. Pharmacol.* **2009**, *54*, 483−490.

(5) Fernandez-Murga, L.; Tarin, J. J.; Garcia-Perez, M. A.; Cano, A. The impact of chocolate on cardiovascular health. *Maturitas* **2011**, *69*, 312−321.

(6) Actis-Goretta, L.; Leveques, A.; Giuffrida, F.; Romanov-Michailidis, F.; Viton, F.; Barron, D.; Duenas-Paton, M.; Gonzalez-Manzano, S.; Santos-Buelga, C.; Williamson, G.; Dionisi, F. Elucidation of (−)-epicatechin metabolites after ingestion of chocolate by healthy humans. *Free Radical Biol. Med.* **2012**, *53*, 787−795.

(7) Ottaviani, J. I.; Momma, T. Y.; Kuhnle, G. K.; Keen, C. L.; Schroeter, H. Structurally related (−)-epicatechin metabolites in humans: assessment using de novo chemically synthesized authentic standards. *Free Radical Biol. Med.* **2012**, *52*, 1403−1412.

(8) Ottaviani, J. I.; Kwik-Uribe, C.; Keen, C. L.; Schroeter, H. Intake of dietary procyanidins does not contribute to the pool of circulating flavanols in humans. *Am. J. Clin. Nutr.* **2012**, *95*, 851−858.

(9) Urpi-Sarda, M.; Monagas, M.; Khan, N.; Llorach, R.; Lamuela-Raventos, R. M.; Jauregui, O.; Estruch, R.; Izquierdo-Pulido, M.; Andres-Lacueva, C. Targeted metabolic profiling of phenolics in urine and plasma after regular consumption of cocoa by liquid chromatography-tandem mass spectrometry. *J. Chromatogr., A* **2009**, *1216*, 7258−7267.

(10) Wollgast, J.; Anklam, E. Review on polyphenols in *Theobroma cacao*: changes in composition during the manufacture of chocolate and methodology for identification and quantification. *Food Res. Int.* **2000**, *33*, 423−447.

(11) Vogiatzoglou, A.; Mulligan, A. A.; Luben, R. N.; Lentjes, M. A.; Heiss, C.; Kelm, M.; Merx, M. W.; Spencer, J. P.; Schroeter, H.; Kuhnle, G. G. Assessment of the dietary intake of total flavan-3-ols, monomeric flavan-3-ols, proanthocyanidins and theaflavins in the European Union. *Br. J. Nutr.* **2014**, *111*, 1463−1473.

(12) EFSA Panel on Dietetic Products, N. a. A. N. Scientific Opinion on the substantiation of a health claim related to cocoa flavanols and maintenance of normal endothelium-dependent vasodilation pursuant to Article 13(5) of Regulation (EC) No. 1924/2006. *EFSA J.* **2012**, *10* (7), 2809 [21 pp].

(13) Andres-Lacueva, C.; Monagas, M.; Khan, N.; Izquierdo-Pulido, M.; Urpi-Sarda, M.; Permanyer, J.; Lamuela-Raventos, R. M. Flavanol and flavonol contents of cocoa powder products: influence of the manufacturing process. *J. Agric. Food Chem.* **2008**, *56*, 3111−3117.

(14) Hurst, W. J.; Krake, S. H.; Bergmeier, S. C.; Payne, M. J.; Miller, K. B.; Stuart, D. A. Impact of fermentation, drying, roasting and Dutch

DOI: 10.1021/acs.jafc.5b00443
J. Agric. Food Chem. 2015, 63, 7615−7623

processing on flavan-3-ol stereochemistry in cacao beans and cocoa ingredients. *Chem. Cent. J.* **2011**, *5*, 53.
(15) Mazor Jolić, S.; Radojčić Redovniković, I.; Marković, K.; Ivanec Šipušić, Đ.; Delonga, K. Changes of phenolic compounds and antioxidant capacity in cocoa beans processing. *Int. J. Food Sci. Technol.* **2011**, *46*, 1793−1800.
(16) Gu, L.; House, S. E.; Wu, X.; Ou, B.; Prior, R. L. Procyanidin and catechin contents and antioxidant capacity of cocoa and chocolate products. *J. Agric. Food Chem.* **2006**, *54*, 4057−4061.
(17) Miller, K. B.; Stuart, D. A.; Smith, N. L.; Lee, C. Y.; McHale, N. L.; Flanagan, J. A.; Ou, B.; Hurst, W. J. Antioxidant activity and polyphenol and procyanidin contents of selected commercially available cocoa-containing and chocolate products in the United States. *J. Agric. Food Chem.* **2006**, *54*, 4062−4068.
(18) Cooper, K. A.; Campos-Gimenez, E.; Jimenez Alvarez, D.; Nagy, K.; Donovan, J. L.; Williamson, G. Rapid reversed phase ultra-performance liquid chromatography analysis of the major cocoa polyphenols and inter-relationships of their concentrations in chocolate. *J. Agric. Food Chem.* **2007**, *55*, 2841−2847.
(19) Kothe, L.; Zimmermann, B. F.; Galensa, R. Temperature influences epimerization and composition of flavanol monomers, dimers and trimers during cocoa bean roasting. *Food Chem.* **2013**, *141*, 3656−3663.
(20) Donovan, J. L.; Crespy, V.; Manach, C.; Morand, C.; Besson, C.; Scalbert, A.; Remesy, C. Catechin is metabolized by both the small intestine and liver of rats. *J. Nutr.* **2001**, *131*, 1753−1757.
(21) Rodriguez-Mateos, A.; Toro-Funes, N.; Cifuentes-Gomez, T.; Cortese-Krott, M.; Heiss, C.; Spencer, J. P. Uptake and metabolism of (−)-epicatechin in endothelial cells. *Arch. Biochem. Biophys.* **2014**, *559*, 17−23.
(22) Crozier, A.; Clifford, M. N.; Ashihara, H. Occurrence, structure and role in the human diet. In *Plant Secondary Metabolites*; Wiley: Hoboken, NJ, USA, 2008; pp 305−309.
(23) Kuhnle, G.; Spencer, J. P.; Schroeter, H.; Shenoy, B.; Debnam, E. S.; Srai, S. K.; Rice-Evans, C.; Hahn, U. Epicatechin and catechin are O-methylated and glucuronidated in the small intestine. *Biochem. Biophys. Res. Commun.* **2000**, *277*, 507−512.
(24) Shali, N. A.; Curtis, C. G.; Powell, G. M.; Roy, A. B. Sulphation of the flavonoids quercetin and catechin by rat liver. *Xenobiotica* **1991**, *21*, 881−893.
(25) Donovan, J. L.; Manach, C.; Faulks, R. M.; Kroon, P. A. Absorption and metabolism of dietary plant secondary metabolites. In *Plant Secondary Metabolites*; Blackwell Publishing: Oxford, UK, 2007; pp 303−351.
(26) Actis-Goretta, L.; Leveques, A.; Rein, M.; Teml, A.; Schafer, C.; Hofmann, U.; Li, H.; Schwab, M.; Eichelbaum, M.; Williamson, G. Intestinal absorption, metabolism, and excretion of (−)-epicatechin in healthy humans assessed by using an intestinal perfusion technique. *Am. J. Clin. Nutr.* **2013**, *98*, 924−933.
(27) Spencer, J. P. E.; Chaudry, F.; Pannala, A. S.; Srai, S. K.; Debnam, E.; Rice-Evans, C. Decomposition of cocoa procyanidins in the gastric milieu. *Biochem. Biophys. Res. Commun.* **2000**, *272*, 236−241.
(28) Rios, L. Y.; Bennett, R. N.; Lazarus, S. A.; Remesy, C.; Scalbert, A.; Williamson, G. Cocoa procyanidins are stable during gastric transit in humans. *Am. J. Clin. Nutr.* **2002**, *76*, 1106−1110.
(29) Holt, R. R.; Lazarus, S. A.; Sullards, M. C.; Zhu, Q. Y.; Schramm, D. D.; Hammerstone, J. F.; Fraga, C. G.; Schmitz, H. H.; Keen, C. L. Procyanidin dimer B2 [epicatechin-(4β-8)-epicatechin] in human plasma after the consumption of a flavanol-rich cocoa. *Am. J. Clin. Nutr.* **2002**, *76*, 798−804.
(30) Rios, L. Y.; Gonthier, M. P.; Remesy, C.; Mila, I.; Lapierre, C.; Lazarus, S. A.; Williamson, G.; Scalbert, A. Chocolate intake increases urinary excretion of polyphenol-derived phenolic acids in healthy human subjects. *Am. J. Clin. Nutr.* **2003**, *77*, 912−918.
(31) Saha, S.; Hollands, W.; Needs, P. W.; Ostertag, L. M.; de Roos, B.; Duthie, G. G.; Kroon, P. A. Human O-sulfated metabolites of (−)-epicatechin and methyl-(−)-epicatechin are poor substrates for commercial aryl-sulfatases: implications for studies concerned with quantifying epicatechin bioavailability. *Pharmacol. Res.* **2012**, *65*, 592−602.
(32) Ottaviani, J. I.; Momma, T. Y.; Heiss, C.; Kwik-Uribe, C.; Schroeter, H.; Keen, C. L. The stereochemical configuration of flavanols influences the level and metabolism of flavanols in humans and their biological activity in vivo. *Free Radical Biol. Med.* **2011**, *50*, 237−244.
(33) Natsume, M.; Osakabe, N.; Oyama, M.; Sasaki, M.; Baba, S.; Nakamura, Y.; Osawa, T.; Terao, J. Structures of (−)-epicatechin glucuronide identified from plasma and urine after oral ingestion of (−)-epicatechin: differences between human and rat. *Free Radical Biol. Med.* **2003**, *34*, 840−849.
(34) Baba, S.; Osakabe, N.; Yasuda, A.; Natsume, M.; Takizawa, T.; Nakamura, T.; Terao, J. Bioavailability of (−)-epicatechin upon intake of chocolate and cocoa in human volunteers. *Free Radical Res.* **2000**, *33*, 635−641.
(35) Mullen, W.; Borges, G.; Donovan, J. L.; Edwards, C. A.; Serafini, M.; Lean, M. E.; Crozier, A. Milk decreases urinary excretion but not plasma pharmacokinetics of cocoa flavan-3-ol metabolites in humans. *Am. J. Clin. Nutr.* **2009**, *89*, 1784−1791.
(36) Schramm, D. D.; Karim, M.; Schrader, H. R.; Holt, R. R.; Kirkpatrick, N. J.; Polagruto, J. A.; Ensunsa, J. L.; Schmitz, H. H.; Keen, C. L. Food effects on the absorption and pharmacokinetics of cocoa flavanols. *Life Sci.* **2003**, *73*, 857−869.
(37) Vitaglione, P.; Barone Lumaga, R.; Ferracane, R.; Sellitto, S.; Morello, J. R.; Reguant Miranda, J.; Shimoni, E.; Fogliano, V. Human bioavailability of flavanols and phenolic acids from cocoa-nut creams enriched with free or microencapsulated cocoa polyphenols. *Br. J. Nutr.* **2013**, *109*, 1832−1843.
(38) Neilson, A. P.; George, J. C.; Janle, E. M.; Mattes, R. D.; Rudolph, R.; Matusheski, N. V.; Ferruzzi, M. G. Influence of chocolate matrix composition on cocoa flavan-3-ol bioaccessibility in vitro and bioavailability in humans. *J. Agric. Food Chem.* **2009**, *57*, 9418−9426.
(39) Rein, D.; Lotito, S.; Holt, R. R.; Keen, C. L.; Schmitz, H. H.; Fraga, C. G. Epicatechin in human plasma: in vivo determination and effect of chocolate consumption on plasma oxidation status. *J. Nutr.* **2000**, *130*, 2109s−2114s.
(40) Richelle, M.; Tavazzi, I.; Enslen, M.; Offord, E. A. Plasma kinetics in man of epicatechin from black chocolate. *Eur. J. Clin. Nutr.* **1999**, *53*, 22−26.
(41) Rodriguez-Mateos, A.; Jose Oruna-Concha, M.; Kwik-Uribe, C.; Vidal, A.; Spencer, J. P. Influence of sugar type on the bioavailability of cocoa flavanols. *Br. J. Nutr.* **2012**, *108*, 2243−2250.
(42) Spadafranca, A.; Martinez Conesa, C.; Sirini, S.; Testolin, G. Effect of dark chocolate on plasma epicatechin levels, DNA resistance to oxidative stress and total antioxidant activity in healthy subjects. *Br. J. Nutr.* **2010**, *103*, 1008−1014.
(43) Taubert, D.; Roesen, R.; Lehmann, C.; Jung, N.; Schomig, E. Effects of low habitual cocoa intake on blood pressure and bioactive nitric oxide: a randomized controlled trial. *JAMA, J. Am. Med. Assoc.* **2007**, *298*, 49−60.
(44) Wang, J. F.; Schramm, D. D.; Holt, R. R.; Ensunsa, J. L.; Fraga, C. G.; Schmitz, H. H.; Keen, C. L. A dose-response effect from chocolate consumption on plasma epicatechin and oxidative damage. *J. Nutr.* **2000**, *130*, 2115s−2119s.
(45) Balzer, J.; Rassaf, T.; Heiss, C.; Kleinbongard, P.; Lauer, T.; Merx, M.; Heussen, N.; Gross, H. B.; Keen, C. L.; Schroeter, H.; Kelm, M. Sustained benefits in vascular function through flavanol-containing cocoa in medicated diabetic patients a double-masked, randomized, controlled trial. *J. Am. Coll. Cardiol.* **2008**, *51*, 2141−2149.
(46) Neukam, K.; Stahl, W.; Tronnier, H.; Sies, H.; Heinrich, U. Consumption of flavanol-rich cocoa acutely increases microcirculation in human skin. *Eur. J. Nutr.* **2007**, *46*, 53−56.
(47) Roura, E.; Andres-Lacueva, C.; Estruch, R.; Mata-Bilbao, M. L.; Izquierdo-Pulido, M.; Waterhouse, A. L.; Lamuela-Raventos, R. M. Milk does not affect the bioavailability of cocoa powder flavonoid in healthy human. *Ann. Nutr. Metab.* **2007**, *51*, 493−498.
(48) Roura, E.; Andres-Lacueva, C.; Jauregui, O.; Badia, E.; Estruch, R.; Izquierdo-Pulido, M.; Lamuela-Raventos, R. M. Rapid liquid

DOI: 10.1021/acs.jafc.5b00443
J. Agric. Food Chem. 2015, 63, 7615−7623

chromatography tandem mass spectrometry assay to quantify plasma (−)-epicatechin metabolites after ingestion of a standard portion of cocoa beverage in humans. *J. Agric. Food Chem.* **2005**, *53*, 6190−6194.
(49) Schroeter, H.; Heiss, C.; Balzer, J.; Kleinbongard, P.; Keen, C. L.; Hollenberg, N. K.; Sies, H.; Kwik-Uribe, C.; Schmitz, H. H.; Kelm, M. (−)-Epicatechin mediates beneficial effects of flavanol-rich cocoa on vascular function in humans. *Proc. Natl. Acad. Sci. U.S.A.* **2006**, *103*, 1024−1029.
(50) Jones, A. W.; Jonsson, K. A.; Kechagias, S. Effect of high-fat, high-protein, and high-carbohydrate meals on the pharmacokinetics of a small dose of ethanol. *Br. J. Clin. Pharmacol.* **1997**, *44*, 521−526.
(51) Lentz, K. A. Current methods for predicting human food effect. *AAPS J.* **2008**, *10*, 282−288.
(52) Neilson, A. P.; Sapper, T. N.; Janle, E. M.; Rudolph, R.; Matusheski, N. V.; Ferruzzi, M. G. Chocolate matrix factors modulate the pharmacokinetic behavior of cocoa flavan-3-ol phase II metabolites following oral consumption by Sprague-Dawley rats. *J. Agric. Food Chem.* **2010**, *58*, 6685−6691.
(53) Njike, V. Y.; Faridi, Z.; Shuval, K.; Dutta, S.; Kay, C. D.; West, S. G.; Kris-Etherton, P. M.; Katz, D. L. Effects of sugar-sweetened and sugar-free cocoa on endothelial function in overweight adults. *Int. J. Cardiol.* **2011**, *149*, 83−88.
(54) Ferruzzi, M. G.; Bordenave, N.; Hamaker, B. R. Does flavor impact function? Potential consequences of polyphenol-protein interactions in delivery and bioactivity of flavan-3-ols from foods. *Physiol. Behav.* **2012**, *107*, 591−597.
(55) Gallo, M.; Vinci, G.; Graziani, G.; De Simone, C.; Ferranti, P. The interaction of cocoa polyphenols with milk proteins studied by proteomic techniques. *Food Res. Int.* **2013**, *54*, 406−415.
(56) Schramm, D. D.; Karim, M.; Schrader, H. R.; Holt, R. R.; Kirkpatrick, N. J.; Polagruto, J. A.; Ensunsa, J. L.; Schmitz, H. H.; Keen, C. L. Food effects on the absorption and pharmacokinetics of cocoa flavanols. *Life Sci.* **2003**, *73*, 857−869.
(57) Serafini, M.; Bugianesi, R.; Maiani, G.; Valtuena, S.; De Santis, S.; Crozier, A. Plasma antioxidants from chocolate. *Nature* **2003**, *424*, 1013.
(58) Schroeter, H.; Holt, R. R.; Orozco, T. J.; Schmitz, H. H.; Keen, C. L. Nutrition: milk and absorption of dietary flavanols. *Nature* **2003**, *426*, 787−788 (discussion 788).
(59) Keogh, J. B.; McInerney, J.; Clifton, P. M. The effect of milk protein on the bioavailability of cocoa polyphenols. *J. Food Sci.* **2007**, *72*, S230−S233.
(60) Roura, E.; Andres-Lacueva, C.; Estruch, R.; Lourdes Mata Bilbao, M.; Izquierdo-Pulido, M.; Lamuela-Raventos, R. M. The effects of milk as a food matrix for polyphenols on the excretion profile of cocoa (−)-epicatechin metabolites in healthy human subjects. *Br. J. Nutr.* **2008**, *100*, 846−851.
(61) Urpi-Sarda, M.; Llorach, R.; Khan, N.; Monagas, M.; Rotches-Ribalta, M.; Lamuela-Raventos, R.; Estruch, R.; Tinahones, F. J.; Andres-Lacueva, C. Effect of milk on the urinary excretion of microbial phenolic acids after cocoa powder consumption in humans. *J. Agric. Food Chem.* **2010**, *58*, 4706−4711.
(62) Miller, K. B.; Hurst, W. J.; Payne, M. J.; Stuart, D. A.; Apgar, J.; Sweigart, D. S.; Ou, B. Impact of alkalization on the antioxidant and flavanol content of commercial cocoa powders. *J. Agric. Food Chem.* **2008**, *56*, 8527−8533.
(63) Payne, M. J.; Hurst, W. J.; Miller, K. B.; Rank, C.; Stuart, D. A. Impact of fermentation, drying, roasting, and Dutch processing on epicatechin and catechin content of cacao beans and cocoa ingredients. *J. Agric. Food Chem.* **2010**, *58*, 10518−10527.
(64) Oruna-Concha, M. J.; Rodriguez-Mateos, A.; Kwik-Uribe, C.; Mottram, D. S.; Gibson, G. R.; Spencer, J. P. E. Absorption, metabolism and vascular effects of alkalised cocoa. *Proceedings of the Nutrition Society*, 70 (OCE4), E224 2011; Summer Meeting, July 4−6, 2011.
(65) Kofink, M.; Papagiannopoulos, M.; Galensa, R. (−)-Catechin in cocoa and chocolate: occurrence and analysis of an atypical flavan-3-ol enantiomer. *Molecules* **2007**, *12*, 1274−1288.
(66) Ottaviani, J. I.; Momma, T. Y.; Heiss, C.; Kwik-Uribe, C.; Schroeter, H.; Keen, C. L. The stereochemical configuration of flavanols influences the level and metabolism of flavanols in humans and their biological activity in vivo. *Free Radical Biol. Med.* **2011**, *50*, 237−244.
(67) Vaidyanathan, J.; Walle, T. Transport and metabolism of the tea flavonoid (−)-epicatechin by the human intestinal cell line Caco-2. *Pharm. Res.* **2001**, *18*, 1420−1425.
(68) Cermak, R.; Wolffram, S. The potential of flavonoids to influence drug metabolism and pharmacokinetics by local gastrointestinal mechanisms. *Curr. Drug Metab.* **2006**, *7*, 729−744.
(69) Jenkinson, C.; Petroczi, A.; Barker, J.; Naughton, D. P. Dietary green and white teas suppress UDP-glucuronosyltransferase UGT2B17 mediated testosterone glucuronidation. *Steroids* **2012**, *77*, 691−695.
(70) Huang, C.; Chen, Y.; Zhou, T.; Chen, G. Sulfation of dietary flavonoids by human sulfotransferases. *Xenobiotica* **2009**, *39*, 312−322.
(71) Baba, S.; Osakabe, N.; Natsume, M.; Muto, Y.; Takizawa, T.; Terao, J. Absorption and urinary excretion of (−)-epicatechin after administration of different levels of cocoa powder or (−)-epicatechin in rats. *J. Agric. Food Chem.* **2001**, *49*, 6050−6056.
(72) Weinshilboum, R. M.; Otterness, D. M.; Szumlanski, C. L. Methylation pharmacogenetics: catechol *O*-methyltransferase, thiopurine methyltransferase, and histamine *N*-methyltransferase. *Annu. Rev. Pharmacol. Toxicol.* **1999**, *39*, 19−52.
(73) Chen, J.; Lipska, B. K.; Halim, N.; Ma, Q. D.; Matsumoto, M.; Melhem, S.; Kolachana, B. S.; Hyde, T. M.; Herman, M. M.; Apud, J.; Egan, M. F.; Kleinman, J. E.; Weinberger, D. R. Functional analysis of genetic variation in catechol-*O*-methyltransferase (COMT): effects on mRNA, protein, and enzyme activity in postmortem human brain. *Am. J. Hum. Genet.* **2004**, *75*, 807−821.
(74) Inoue-Choi, M.; Yuan, J. M.; Yang, C. S.; Van Den Berg, D. J.; Lee, M. J.; Gao, Y. T.; Yu, M. C. Genetic association between the COMT genotype and urinary levels of tea polyphenols and their metabolites among daily green tea drinkers. *Int. J. M. Epidemiol. Genet.* **2010**, *1*, 114−123.
(75) Miller, R. J.; Jackson, K. G.; Dadd, T.; Nicol, B.; Dick, J. L.; Mayes, A. E.; Brown, A. L.; Minihane, A. M. A preliminary investigation of the impact of catechol-*O*-methyltransferase genotype on the absorption and metabolism of green tea catechins. *Eur. J. Nutr.* **2012**, *51*, 47−55.
(76) Miller, R. J.; Jackson, K. G.; Dadd, T.; Mayes, A. E.; Brown, A. L.; Lovegrove, J. A.; Minihane, A. M. The impact of the catechol-*O*-methyltransferase genotype on vascular function and blood pressure after acute green tea ingestion. *Mol. Nutr. Food Res.* **2012**, *56*, 966−975.
(77) Loke, W. M.; Hodgson, J. M.; Proudfoot, J. M.; McKinley, A. J.; Puddey, I. B.; Croft, K. D. Pure dietary flavonoids quercetin and (−)-epicatechin augment nitric oxide products and reduce endothelin-1 acutely in healthy men. *Am. J. Clin. Nutr.* **2008**, *88*, 1018−1025.

DOI: 10.1021/acs.jafc.5b00443
J. Agric. Food Chem. 2015, 63, 7615−7623

Scheme 1. Representation of the Network of Chemical Reactions for Malvidin 3-Glucoside (Oenin)

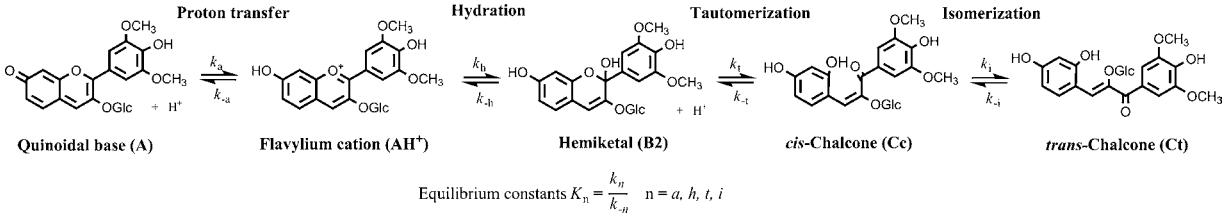

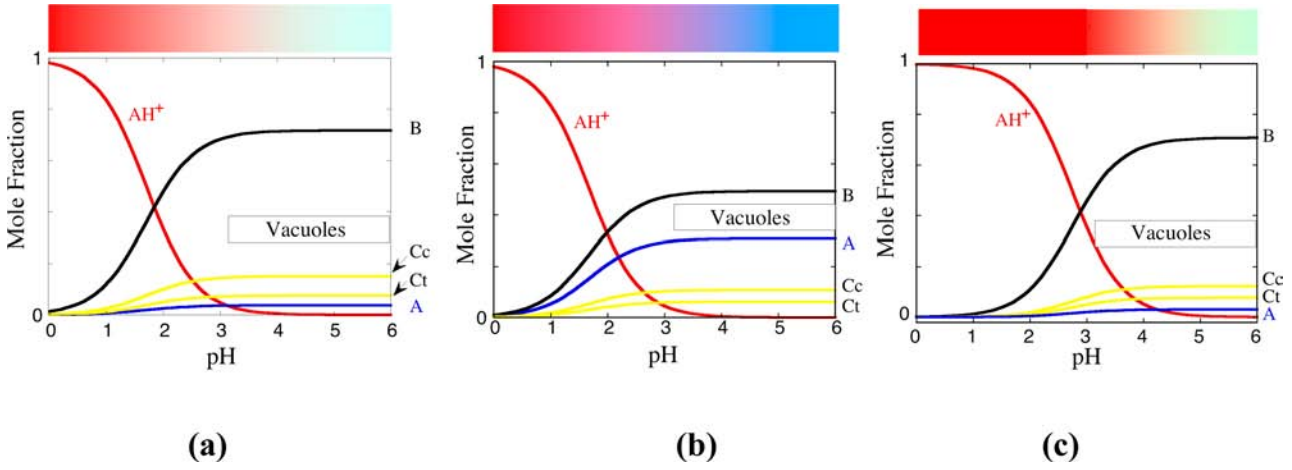

Figure 1. Mole fraction distribution of the several multistate species of malvidin 3,5-diglucoside: (a) free (pK_{ap} = 1.7); (b) simulation in the case of copigmentation (1:1) with **A** for a copigment concentration of 0.1 M and an association constant, K_{cp} = 100 M^{-1}; (c) same as (b) but when exclusive copigmentation with $\mathbf{AH}^+$ occurs. The upper bands simulate the color as a function of pH. Reprinted with permission from ref 7. Copyright 2000 Elsevier.

of the blue color. In the case of the blue color, beautiful work from Goto, Kondo, and Yoshida has been reported in recent decades.[8−10] The blue color is achieved by means of supramolecular structures involving anthocyanins, flavone, and metals, the first bearing a cathecol unit to allow the metal binding. Additionally, the fraction of colored species at moderately acidic or neutral pH values can be augmented through the formation of adducts with colorless organic aromatic compounds (copigments) driven by $\pi-\pi$ stacking, hydrophobic, and charge-transfer interactions.[11−16]

A simple model considering the possibility of an adduct formation (1:1) with species **A** and another compound (copigment 0.1 M) with association constant K_{cp} = 100 M^{-1} is reported in Figure 1b. The mole fraction distribution of species **A** increases dramatically. On the other hand, the adduct with the same constant involving the flavylium cation gives rise to a shift of the pH domain of the red color toward higher pH values. Summarizing, anthocyanins are not able to give color in plants unless they participate in more or less complex structures.

The red and blue colors of anthocyanins can also be accomplished by self-aggregation.[17,18] Increasing the total concentration of the anthocyanin, the domain of the red flavylium is shifted toward higher pH values and the mole fraction distribution of the blue quinoidal base increases.[17]

Cucurbit[*n*]urils and cyclodextrins are macrocyclic molecules with tridimensional hydrophobic cavities capable of forming inclusion complexes with molecules and ions of suitable size, shape, and charge/polarity. Whereas cyclodextrins are formed by α-(1,4)-linked maltooligosaccharides with α-, β-, and γ-cyclodextrin consisting of six, seven, and eight glucose units, respectively, cucurbit[*n*]urils are composed of *n* glycouril units linked by methylene bridges. Due to their structural characteristics, cyclodextrins display higher selectivity for hydrophobic and neutral molecules, whereas cucurbiturils preferentially bind organic cations.[19] However, it should be stressed that cucurbiturils also show high affinity for neutral organic molecules with stability constants that can be orders of magnitude higher than those found for cyclodextrins.[20] With respect to their applications as food additives, cyclodextrins were demonstrated to be fit for human consumption and are applied to improve the stability of flavors, colorants, vitamins, etc.[21] To the best of our knowledge, the safety of cucurbiturils as food additives has not been explored, but these compounds were shown to display low toxicity, and their use as drug delivery vehicles has been suggested.[22] If their use as compatible food additives is demonstrated, they present some advantages with respect to cyclodextrins related to the usually higher stability of their inclusion complexes, which translates into better performance and lower quantity of material required to achieve full complexation.

In this work positive and negative copigmentation effects in anthocyanins analogues are mimicked by host−guest interaction with cucurbit[7]uril (CB7) and (2-hydroxypropyl)-β-cyclodextrin (2-HP-β-CD). The effect of these hosts on the degradation rate of anthocyanidins was also investigated.

MATERIALS AND METHODS

Materials and Stock Solutions. Cucurbit[7]uril (CB7) and 7-hydroxyflavylium were available from previous studies.[23,24] (2-Hydroxypropyl)-β-cyclodextrin (2-HP-β-CD, Sigma-Aldrich) and pelargonidin and cyanidin chlorides (Extrasynthese, France) were obtained from commercial suppliers. Stock solution of 7-hydroxyflavylium was prepared in 0.1 M of HCl, whereas stock solutions of

DOI: 10.1021/acs.jafc.5b00765
J. Agric. Food Chem. 2015, 63, 7624−7629

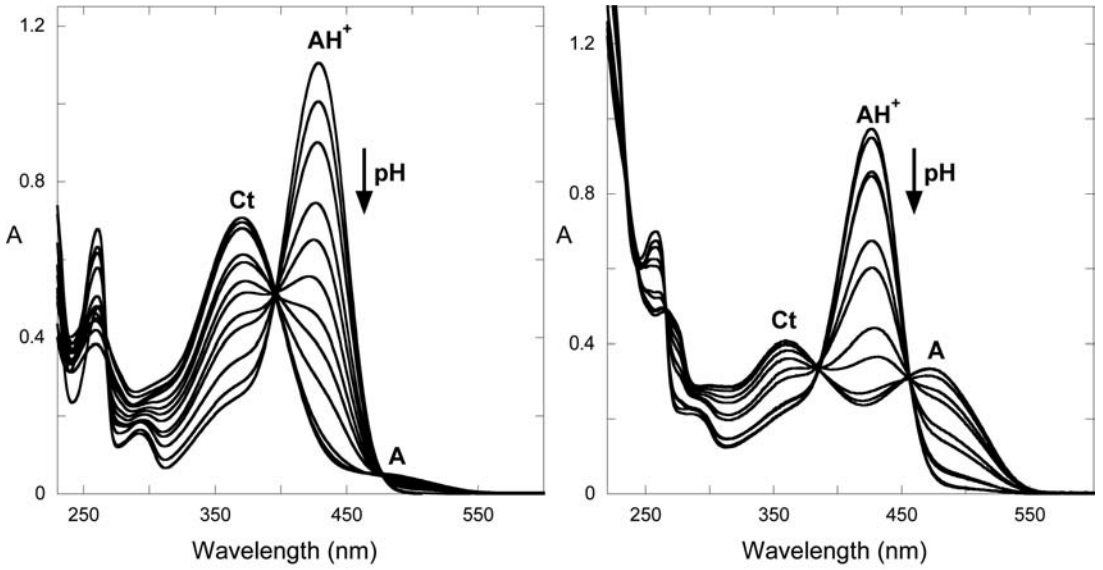

Figure 2. Spectral variations of the model compound 7-hydroxyflavylium (1.7×10^{-2} mM) as a function of pH: (a) in the absence of CB7; (b) in the presence of [CB7] = 1 mM.

pelargonidin and cyanidin were prepared in ethanol/concentrated HCl 99:1 (v/v) to avoid degradation and stored at 4 °C. Under these conditions the cationic flavylium form is the main species and the colorants remain stable for several weeks as monitored by UV−vis spectroscopy. Stock solutions of CB7 and 2-HP-β-CD were prepared in high-purity Milli-Q water.

Methodology. Equilibrated solutions of 7-hydroxyflavylium were prepared by adding 0.5 mL of the stock solution at pH 1 to a cuvette containing 0.5 mL of 0.1 M NaOH and 2 mL of universal buffer of Theorell and Stenhagen at the desired pH and concentration.[25] A similar procedure was used for experiments performed in the presence of host molecules. The final concentration of Na^+ was 0.045 M in all cases. Solutions were allowed to equilibrate overnight, and the UV−vis absorbance spectra were recorded in a Cary 100 spectrophotometer (Varian). Superposition of the UV−vis spectra registered after some hours (ca. 6−8) confirmed that the system was equilibrated.

The degradation kinetics of anthocyanidins was studied by UV−vis spectroscopy. An aliquot of the anthocyanidin stock solution was added to a cuvette containing the required amounts of NaOH to neutralize the acid contained in the aliquot and universal buffer at the desired pH. The spectral acquisition was immediately started. The final contents of ethanol in the cuvettes were 2 and 10% for pelargonidin and cyanidin, respectively. Observed rate constants were obtained from the variation of the absorbance versus time data.

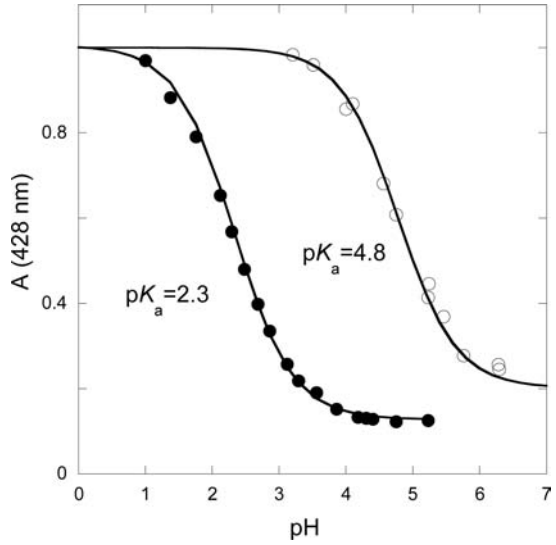

Figure 3. pH dependence of the normalized absorption of the model compound 7-hydroxyflavylium as a function of pH: (●) in the absence of CB7; (○) in the presence of [CB7] = 1 mM.

RESULTS AND DISCUSSION

Effect of the Host in the Final Equilibrium of 7-Hydroxyflavylium. Figure 2 reports the spectral variations of the model compound 7-hydroxyflavylium as a function of pH in the absence (a) and presence (b) of cucurbit[7]uril (CB7) = 1 mM. Inspection of these curves clearly indicates that the absorption band appearing around 477 nm, characteristic of the quinoidal base, increases dramatically in the presence of CB7 and the pK'_a is shifted from 2.3 to 4.8 (Figure 3). Both data show that in the presence of CB7, $\mathbf{AH^+}$ is stabilized in comparison with **CB** (eq 5), and identical stabilization occurs for **A** in its partition with **B**, **Cc**, and **Ct**. In conclusion, CB7 stabilizes preferentially the species that give color, similarly to the copigmentation effect described for anthocyanins and related compounds.[11−16] This result suggests that the heterogeneities in cell vacuoles could in some way modulate the color, which depends on the composition of the cells' environment where the anthocyanins are located and the organization of anthocyanins within vacuole.[26] The copigmentation models in homogeneous solution are thus one simple approximation of a more complex phenomenon.

Identical behavior was reported for the compound 3′,4′,7-trihydroxyflavylium in the presence of CB7, but both effects were smaller.[27]

The mimicking of the copigmentation effect can be visualized in Figure 4. Increasing quantities of CB7 were added (up to 2.5 mM) to the model compound 7-hydroxyflavylium at pH 4 (a)

DOI: 10.1021/acs.jafc.5b00765
J. Agric. Food Chem. 2015, 63, 7624−7629

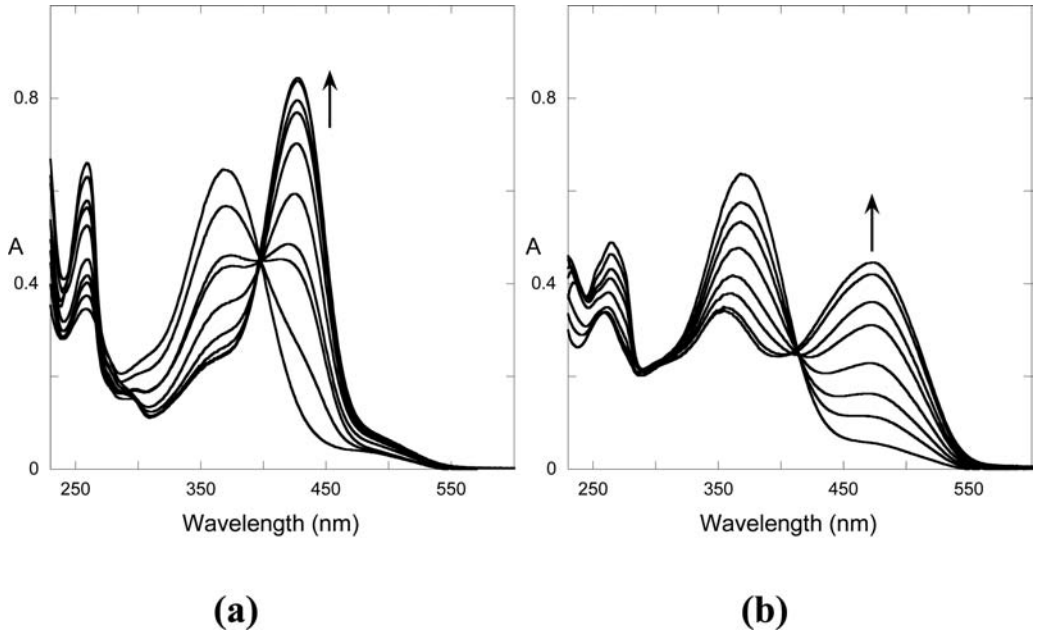

Figure 4. Mimicking copigmentation effect with the model compound 7-hydroxyflavylium in the presence of added CB7 up to 2.5 mM at pH 4 (a) and pH 6 (b).

and 6 (b), and the solutions were allowed to equilibrate in the dark.

In Figure 4a the addition of the host has a dramatic effect shifting the multistate system toward the flavylium cation. The same experiment carried out at pH 6 (Figure 4b) leads to the appearance of the quinoidal base.

The interaction of flavylium derivatives with another host, β-CD, leads to a completely different behavior.[28] Previous results have shown that the pK'_a of the model compound 3′,4′,7-trihydroxyflavylium decreases from 3.1 to 2.2 in the presence of this host at 4.8 mM, indicating that **CB** is stabilized in comparison with $\mathbf{AH}^+$. Moreover, whereas in the absence of β-cyclodextrin (β-CD) the composition of **CB** is approximately 90% **Ct** and 10% **A**, in the presence of β-CD 4.8 mM becomes 97% **Ct** and 3% **A**. With regard to the kinetic processes of the network, β-CD increases the rate constant of the flavylium cation hydration to give the hemiketal and decreases the reverse rate constant (dehydration). Identical results were reported for the compound 4,7-dihydroxyflavylium,[29] as well as 4′-(2-hydroxyethoxy)-7-hydroxyflavylium.[30] In this last example the encapsulation of this guest into the host was observed by induced circular dichroism.

The interaction of the natural compound dracoflavylium (7,4-dihydroxy-5-methylflavylium, a dye from the resin of dragon's blood (*Dracaena draco*), with 2-HP-β-CD was also reported.[31] The pK'_a changes from 3.8 to 2.4 (host 16 mM) and the composition of **CB** = 63% **A** + 37% **Ct** to **CB** = 13% **A** + 87% **Ct**.

The observation that cyclodextrins promote discoloration in anthocyanins, the so-called anti-copigmentation effect,[32−34] was previously reported. Our findings confirm that the same is observed for the model compounds.

Effect of the Host in Anthocyanidin Degradation. Anthocyanidins are known to suffer a relatively fast degradation in aqueous solution. Profiting the preferential stabilization of the flavylium cation by CB7, the kinetics of the degradation process of pelargonidin was studied as a function of pH. UV−vis titration of pelargonidin with CB7 at pH 1.0 is compatible with a 1:1 association with constant $(4.5 \pm 0.3) \times 10^3\ M^{-1}$. The pH-dependent bell-shaped curve for the disappearance of pelargonidin (Figure 5) is similar to the one found for cyanidin.[4]

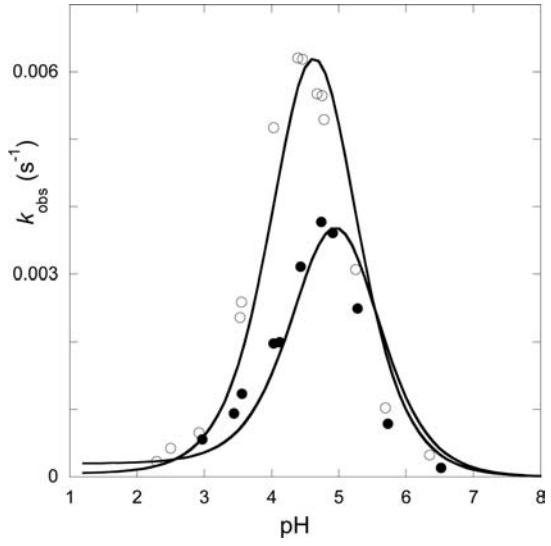

Figure 5. Rate constant for pelargonidin disappearance as a function of pH: (○) in the absence of cucurbit[7]uril; (●) in the presence of CB7 = 1.9 mM.

One minute after preparation at moderately acidic pH values, for example, pH 4.6, 35% of the anthocyanidin is already decomposed. This behavior is compatible with a sequence of chemical reactions as reported in eq 6[4,5] and is accounted for by eq 7, where k_{dis} is the rate of the anthocyanidin decomposition, the other rate and equilibrium constants being defined in Scheme 1.[4,5]

DOI: 10.1021/acs.jafc.5b00765
J. Agric. Food Chem. 2015, 63, 7624−7629

$$\mathbf{A} \underset{H^+}{\overset{\text{equilibrium}\ K_a}{\rightleftharpoons}} \mathbf{AH}^+ \underset{k_{-h}H^+}{\overset{k_h}{\rightleftharpoons}} \mathbf{B} \underset{k_{-t}}{\overset{\text{equilibrium}\ k_t}{\rightleftharpoons}} \mathbf{Cc(Ct)} \xrightarrow{k_{dis}} \text{products} \quad (6)$$

$$k_{obs} = \frac{\frac{[H^+]}{[H^+]+K_a} K_h K_t k_{dis}}{[H^+] + \frac{K_t k_{dis}}{k_{-h}}} \quad (7)$$

The experimental data (Figure 5) can be fitted with eq 7 (Table 1). The bell-shaped curve was also observed for the reversible transformation of some flavylium derivatives to the respective *trans*-chalcones.[35] In that case the low-pH branch of the curve is controlled by the isomerization, whereas the descending part is controlled by the hydration. Evidence that the degradation of anthocyanidins takes place via chalcones and that the same equation used to account for the reversible processes can be used if the isomerization constant is substituted by the degradation rate constant ,k_{dis}, was reported previously.[4,5] The fitting parameters are reported in Table 1 for pelargonidin.

Table 1. Fitting Parameters of Equation 7 for Pelargonidin in the Absence and Presence of CB7

[CB7]	pK_a	$K_h K_t k_{dis}$/M (s^{1-})	$K_t k_{dis}/k_{-h}$/M	k_h (s^{-1})
	3.8	1.4×10^{-6}	8×10^{-6}	0.18
1.9 mM	4.8	3.5×10^{-7}	3.0×10^{-5}	0.012

The effect of CB7 in the protection of the pelargonidin degradation is relatively modest. This is due to the existence of two contradictory effects, both accounted for by eq 7: (i) by one side the hydration (k_h) is reduced ca. 15 times, contributing to slow the process; (ii) by the other the decreasing of the acidity constant (K_a) accelerates the observed rate constant.

The effect of 2-HP-β-CD in the degradation of anthocyanidins was checked with cyanidin (Figure 6). In this case two opposing effects are expected: (i) the hydration rate constant is expected to increase, leading to an increase of the observed rate in eq 7; (ii) increasing of the acidity constant (K_a) will have an opposite effect (Table 2).

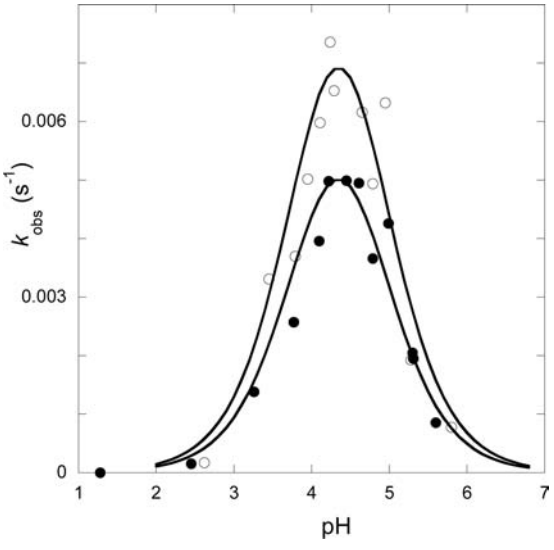

Figure 6. Rate constant for the cyanidin disappearance as a function of pH (10% ethanol): (○) in the absence of 2-HP-β-CD; (●) in the presence of 10 mM 2-HP-β-CD.

Table 2. Fitting Parameters of Equation 7 for Cyanidin in the Absence and Presence of 2-HP-β-CD

[2-HP-β-CD]	pK_a	$K_h K_t k_{dis}$/M (s^{-1})	$K_t k_{dis}/k_{-h}$/M	k_h (s^{-1})
	4.8	1.6×10^{-6}	1.4×10^{-4}	0.011
10 mM	4.4	8×10^{-7}	4×10^{-5}	0.02

Previous studies based on NMR data have shown that the two hosts here reported are able to form inclusion complexes with flavylium derivatives.[23,27−33] The different behavior of flavylium derivatives upon interaction with CB7 and β-CD can be attributed to the nature of the cavities: curcubit[7]uril exhibits a negative charge density, whereas β-CD is essentially neutral.[19]

The interaction of anthocyanins models with curcubit[7]uril and β-CD mimics the copigmentation or the so-called anti-copigmentation effect, respectively. At the pH of the vacuoles the dominant species is the colorless hemiketal, and thus the appearance of color implies a shift of the flavylium multistate system toward flavylium cation or quinoidal base, respectively, for the red and blue. Our results suggest the possibility of using cucurbiturils possessing the adequate cavity dimension to form inclusion complexes with anthocyanins. Preliminary data suggest that cucurbiturils have low toxicity and can be used as drug delivery vehicles to profit from the anthocyanins' antioxidant properties.[22]

AUTHOR INFORMATION

Corresponding Authors

*(N.B.) E-mail: nuno.basilio@fct.unl.pt. Phone: +351 212 948 355. Fax: +351 212 948 550.

*(F.P.) E-mail: fp@fct.unl.pt. Phone: +351 212 948 355. Fax: +351 212 948 550.

Funding

This work was supported by Fundação para a Ciência e Tecnologia (FCT) through Research Unit UID/QUI/50006/2013 and Project PTDC/QUI-QUI/117996/2010. N.B. thanks FCT for Grant SFRH/BPD/84805/2012.

Notes

The authors declare no competing financial interest.

REFERENCES

(1) A direct pH jump is obtained by addition of base to an equilibrated solution of the flavylium cation, $\mathbf{AH}^+$ (pH ≤1), whereas a reverse pH jump is obtained upon addition of acid to an equilibrated solution at moderately acidic (or even basic) pH values. Usually the spectral changes are monitored by means of a stopped flow apparatus, unless the kinetics is slow enough to permit the use of a common spectrophotometer.

(2) Oliveira, C. M.; Ferreira, A. C. S.; De Freitas, V.; Silva, A. M. S. Oxidation mechanisms occurring in wines. *Food Res. Int.* **2011**, *44*, 1115−1126.

(3) Fulcrand, H.; Benabdeljalil, C.; Rigaud, J.; Cheynier, V.; Moutounet, M. A new class of wine pigments generated by reaction between pyruvic acid and grape anthocyanins. *Phytochemistry* **1998**, *47*, 1401−1407.

(4) Cabrita, L.; Petrov, V.; Pina, F. On the thermal degradation of anthocyanidins: cyanidin. *RSC Adv.* **2014**, *4*, 18939−18944.

(5) Furtado, P.; Figueiredo, P.; Das Neves, H. C.; Pina, F. Photochemical and thermal degradation of anthocyanidins. *J. Photochem. Photobiol., A* **1993**, *75*, 113−118.

DOI: 10.1021/acs.jafc.5b00765
J. Agric. Food Chem. 2015, 63, 7624−7629

(6) Remy, S.; Fulcrand, H.; Labarbe, B.; Cheynier, V.; Moutounet, M. First confirmation in red wine of products resulting from direct anthocyanin-tannin reactions. *J. Sci. Food Agric.* **2000**, *80*, 745−751.
(7) Melo, M. J.; Moncada, M.; Pina, F. On the red colour of raspberry (*Rubus idaeus*). *Tetrahedron Lett.* **2000**, *41*, 1987−1991.
(8) Yoshida, K.; Mori, M.; Kondo, T. Blue flower color development by anthocyanins: from chemical structure to cell physiology. *Nat. Prod. Rep.* **2009**, *26*, 884−915.
(9) Goto, T.; Kondo, T. Structure and molecular stacking of anthocyanins—flower color variation. *Angew. Chem., Int. Ed. Engl.* **1991**, *30*, 17−33.
(10) Yoshida, K.; Kondo, T.; Okazaki, Y.; Katou, K. Cause of blue petal colour. *Nature* **1995**, *373*, 291.
(11) Dangles, O.; Saito, N.; Brouillard, R. Kinetic and thermodynamic control of flavylium hydration in the pelargonidin-cinnamic acid complexation. origin of the extraordinary flower color diversity of Pharbitis nil. *J. Am. Chem. Soc.* **1993**, *115*, 3125−3132.
(12) Mistry, T. V.; Cai, Y.; Lilley, T. H.; Haslam, E. Polyphenol interactions. Part 5. Anthocyanin co-pigmentation. *J. Chem. Soc., Perkin Trans. 2* **1991**, *34*, 1287.
(13) Houbiers, C.; Lima, J. C.; Maçanita, A. L.; Santos, H. Color stabilization of malvidin 3-glucoside: self-aggregation of the flavylium cation and copigmentation with the Z-chalcone form. *J. Phys. Chem. B* **1998**, *102*, 3578−3585.
(14) Boulton, R. The copigmentation of anthocyanins and its role in the color of red wine: a critical review. *Am. J. Enol. Vitic.* **2001**, *52*, 67−87.
(15) Ferreira da Silva, P.; Lima, J. C.; Freitas, A. A.; Shimizu, K.; Maçanita, A. L.; Quina, F. H. Charge-transfer complexation as a general phenomenon in the copigmentation of anthocyanins. *J. Phys. Chem. A* **2005**, *109*, 7329−7338.
(16) Sousa, A.; Araújo, P.; Cruz, L.; Brás, N. F.; Mateus, N.; De Freitas, V. Evidence for copigmentation interactions between deoxyanthocyanidin derivatives (oaklins) and common copigments in wine model solutions. *J. Agric. Food Chem.* **2014**, *62*, 6995−7001.
(17) Leydet, Y.; Gavara, R.; Petrov, V.; Diniz, A. M.; Parola, A. J.; Lima, J. C.; Pina, F. The effect of self-aggregation on the determination of the kinetic and thermodynamic constants of the network of chemical reactions in 3-glucoside anthocyanins. *Phytochemistry* **2012**, *83*, 125−135.
(18) Fernandes, A.; Brás, N. F.; Mateus, N.; Freitas, V. A study of anthocyanin self-association by NMR spectroscopy. *New J. Chem.* **2015**, *39*, 2602.
(19) Lee, J. W.; Samal, S.; Selvapalam, N.; Kim, H.-J.; Kim, K. Cucurbituril homologues and derivatives: new opportunities in supramolecular chemistry. *Acc. Chem. Res.* **2003**, *36*, 621−630.
(20) Assaf, K. I.; Nau, W. M. Cucurbiturils: from synthesis to high-affinity binding and catalysis. *Chem. Soc. Rev.* **2015**, *44*, 394−418.
(21) Szente, L.; Szejtli, J. Cyclodextrins as food ingredients. *Trends Food Sci. Technol.* **2004**, *15* (3-4), 137−142.
(22) Oun, R.; Floriano, R. S.; Isaacs, L.; Rowan, E. G.; Wheate, N. G. The ex vivo neurotoxic, myotoxic and cardiotoxic activity of cucurbituril-based macrocyclic drug delivery vehicles. *Toxicol. Res.* **2014**, *3*, 447−455.
(23) Basílio, N.; Laia, C. A. T.; Pina, F. Excited-state proton transfer in confined medium. 4-methyl-7-hydroxyflavylium and β-naphthol incorporated in cucurbit[7]uril. *J. Phys. Chem. B* **2015**, *119*, 2749−2757.
(24) Pina, F.; Melo, M. J.; Parola, A. J.; Maestri, M.; Balzani, V. pH-controlled photochromism of hydroxyflavylium ions. *Chem.−Eur. J.* **1998**, *4*, 2001−2007.
(25) Küster, W. F.; Thiel, A. *Tabelle per le Analisi Chimiche e ChimicoFisiche*, 12th ed.; Hoepli: Milan, Italy, 1982.
(26) Conn, S.; Zhang, W.; Franco, C. Anthocyanic vacuolar inclusions (AVIs) selectively bind acylated anthocyanins in *Vitis vinifera* L. (grapevine) suspension culture. *Biotechnol. Lett.* **2003**, *25*, 835−839.
(27) Basilio, N.; Pina, F. Flavylium network of chemical reactions in confined media: modulation of 3′,4′,7-trihydroxyflavylium reactions by host−guest interactions with cucurbit[7]uril. *ChemPhysChem* **2014**, *15*, 2295−2302.
(28) Basilio, N.; Fernandes, A.; De Freitas, V.; Gago, S.; Pina, F. Effect of β-cyclodextrin on the chemistry of 3′,4′,7-trihydroxyflavylium. *New J. Chem.* **2013**, *37*, 3166−3173.
(29) Petrov, V.; Stanimirov, S.; Petrov, I. K.; Fernandes, A.; De Freitas, V.; Pina, F. Emptying the β-cyclodextrin cavity by light. Photochemical removal of the *trans*-chalcone of 4′,7-dihydroxyflavylium. *J. Phys. Chem. A* **2013**, *117*, 10692−10701.
(30) Gago, S.; Basilio, N.; Fernandes, A.; De Freitas, V.; Quintas, A.; Pina, F. Photochromism of the complex between 4′-(2-hydroxyethoxy)-7-hydroxyflavylium and β-cyclodextrin, studied by ^{1}H NMR, UV-vis, continuous irradiation and circular dichroism. *Dyes Pigm.* **2014**, *110*, 106−112.
(31) Lopes-Costa, T.; Basílio, N.; Pedrosa, J. M.; Pina, F. Photochromism of the natural dye 7,4′-dihydroxy-5-methoxyflavylium (dracoflavylium) in the presence of hydroxypropyl-β-cyclodextrin. *Photochem. Photobiol. Sci.* **2014**, *13*, 1420−1426.
(32) Dangles, O.; Stoeckel, C.; Wigand, M. C.; Brouillard, R. Two very distinct types of anthocyanin complexation: copigmentation and inclusion complexation. *Tetrahedron Lett.* **1992**, *33*, 5227−5230.
(33) Dangles, O.; Wigand, M. C.; Brouillard, R. Anthocyanin anti-copigment effect. *Phytochemistry* **1992**, *31*, 3811−3812.
(34) Fernandes, A.; Ivanova, G.; Brás, N. F.; Mateus, N.; Ramos, M. J.; Rangel, M.; De Freitas, V. Structural characterization of inclusion complexes between cyanidin-3-*O*-glucoside and β-cyclodextrin. *Carbohydr. Polym.* **2014**, *102*, 269−277.
(35) Pina, F.; Melo, M. J.; Laia, C. A. T.; Parola, A. J.; Lima, J. C. Chemistry and applications of flavylium compounds: a handful of colours. *Chem. Soc. Rev.* **2012**, *41*, 869−908.

DOI: 10.1021/acs.jafc.5b00765
J. Agric. Food Chem. 2015, 63, 7624−7629

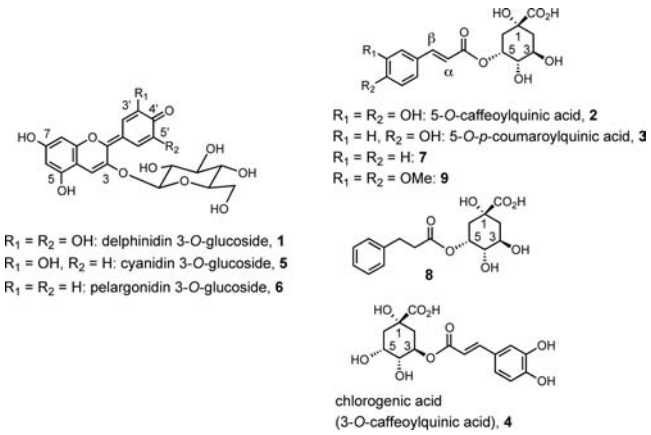

Figure 2. Structures of anthocyanins (**1**, **5**, **6**) and copigments (**2**−**4**, **7**−**9**).

with significant diferences.[16,17] We also quantified the contents of **1**−**4** and the Al^{3+} in blue and red cells. The equivalents of 5-*O*-acylquinic acids (**2** and **3**) and Al^{3+} compared to **1** in the blue cells were 12.8 and 1 equiv, respectively, significantly higher than those in the red cells (3.6 and 0.03 equiv).[18] To obtain structural information on the blue complex, we synthesized various natural and unnatural copigments.[17,19−21] Using the unnatural copigment for reproduction experiments, the essential structural components of the copigment for blue coloration were determined to be the 1-COOH, 1-OH, and 5-*O*-aromatic acyl groups in the quinate.[17,19,20] However, the molecular structure of the blue metal complex pigment in hydrangea remains obscure.

Many blue flower colorations are due to metal coordination to the anthocyanins,[22−25] and these metal complex pigments are categorized into two types; one is a stoichiometric supramolecule named metalloanthocyanin found in blue dayflower,[24,26−29] blue cornflower,[30−33] and blue salvias;[34−36] and the other comprises nonstoichiometoric pigments found in hydrangea,[15,19,20,24] tulip,[37] and blue poppy.[38,39] Detailed chemical structures of the former were determined by X-ray crystallographic analysis as commelinin[28,29] from dayflower and protocyanin from cornflower.[33] In metalloanthocyanins, the metal ions coordinate only to di-OH groups at the B-ring of the anthocyanidin chromophore, not to the copigments.[24,25,28,29,32,33] However, in the blue complex of the hydrangea sepals, the ratio of each component in not stoichiometric, but fluctuates within a certain range. In addition, Al^{3+} may have some interactions with both the anthocyanin and the copigment.[17,19,20] The Al^{3+} complex with **1** appears blue; however, this complex is not water-soluble, but MeOH- and EtOH-soluble,[19,40,41] and copigments **2** and **3** have a solubilizing effect on the **1**−Al^{3+} complex in water with some coordination to Al^{3+}.[19,20]

To clarify the basis of such a curious character of the hydrangea-blue complex and to obtain its structural information and the chemical mechanism of the blue color development, we attempted to reconstruct the same blue color as the sepals according to the physiological data of the colored vacuoles.[16,18,42] The previous experiments reported that the color of the blue solution changed with the difference in pH, composition of copigments, and equivalents of Al^{3+} to anthocyanin (**1**).[6,18,42] Furthermore, it was indicated that the hydrangea-blue pigment exists only in aqueous solutions; any crystallization trials of the blue complex pigment composed of **1**, **2**, or **3**, and Al^{3+} as in the same procedure for commelinin[26−29] and protocyanin[33] failed.[17,19] These results strongly suggest that in the aqueous solution each component of the hydrangea-blue complex might be under equilibrium and the molar ratio changes under the condition. In the living vacuoles the concentration of **1** and copigments is very high, approximately 5−20 mM,[18,42] suggesting that general solution chemistry may not hold true. In this study we examined the mixing conditions for their reconstruction, and the obtained solutions were evaluated by visible absorption spectrum, circular dichroism (CD), and nuclear magnetic resonance (NMR) spectrometry. We will discuss the special arrangement of **1** and **2** in the complex.

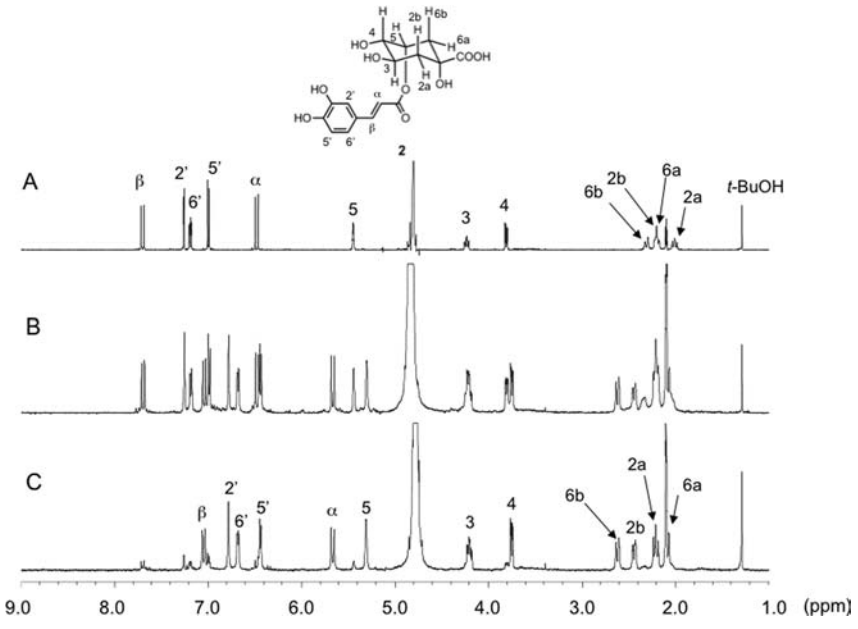

Figure 3. ^1H NMR spectra of **2** coexisting with various concentrations of Al^{3+} in deuterated acetate buffer: (A) 0 mM; (B) 2.5 mM; (C) 5 mM.

DOI: 10.1021/acs.jafc.5b02368
J. Agric. Food Chem. 2015, 63, 7630−7635

MATERIALS AND METHODS

General. The visible absorption spectrum was recorded on a V-560 spectrometer (JASCO, Japan), and CD was measured with a J-720 spectrometer (JASCO, Japan). ^{1}H NMR spectra were recorded in a tube (5.0 mm i.d.) on a ECA-500 (^{1}H, 500 MHz; ^{13}C, 125 MHz; JEOL, Japan). Chemical shifts for ^{1}H NMR were reported on a scale relative to the shignal of *t*-BuOH (δ 1.29). Measurement of pH was carried out with a D-21 pH meter (HORIBA, Japan) with a LAQUA 9618 electrode. The adjustment of the electrode was carried out using the standard buffer of pH 7 and 4, and the value of pD in deuterated buffer solution was noted as addition of 0.4 to the recorded value.

Plant Materials. The blue cultivar of *H. macrophylla* cv. Narumi Blue was donated by Okumura Farm (Toyoake, Aichi) and cultivated in a greenhouse (daytime, approximately 25 °C; nighttime, >10 °C) of the Botanical Garden, Nagoya University Museum, before use.

Materials. Delphinidin 3-*O*-glucoside, **1**, cyanidin 3-*O*-glucoside, **5**, and pelargonidin 3-*O*-glucoside, **6**, were isolated from the seed coat of *Phaseolus coccineus*, *Glycine max*, and *Phaseolus vulgaris*, respectively.[43] 5-*O*-Caffeoylquinic acid, **2**, 5-*O*-*p*-coumaroylquinic acid, **3**, 5-*O*-cinnamoylquinic acid, **7**, 5-*O*-(3-phenylpropionyl)quinic acid, **8**, and 5-*O*-(3′,4′-dimethoxycinnamoyl)quinic acid, **9**, were synthesized according to our procedures.[21] Chlorogenic acid (3-*O*-caffeoylquinic acid), **4**, was purchased (Tokyo Chemical Industry Co., Ltd. (TCI), Japan). $AlNH_4(SO_4)_2{\cdot}12H_2O$ was purchased (Nacalai Tesque, Inc., Japan). All commercially available reagents and solvents were used directly without further purification.

^{1}H NMR Measurement of Al^{3+} Complex of 5-*O*-Caffeoylquinic acid, 2. **2** was dissolved in D_2O and dried up in vacuo. To the residue were added D_2O and deuterated $AlNH_4(SO_4)_2$ (0.5 and 1.0 equiv to **2**) at the concentration of **2** as 5 mM. The pH of the mixture was adjusted to be 3.6 (pD 4.0) by addition of CD_3COOD and/or NaOD−D_2O. After the addition of *t*-BuOH as an internal standard, the mixture was filtered by using a cartridge (pore size, 0.45 μm), and ^{1}H NMR was recorded.

Procedure of Blue Pigment Reconstruction. Trifluoroacetic acid (TFA) salt of **1** (1.77 mg, 3 μmol, TFA salt), **2** (1−3 equiv to **1**), and a trivalent metal salt (1−4 equiv to **1**) were dissolved in a deuterated buffer solution (206 μL of CD_3COOD, 175 μL of 2 M NaOD, and 214 μL of D_2O), and then the solution was adjusted to pH 4.0 (pD 4.4) by the addition of 2 M NaOD. The visible absorption spectrum and CD were measured in a quartz cell (0.1 mm path length). For the ^{1}H NMR measurements, *t*-BuOH was added as an internal standard.

RESULTS AND DISCUSSION

Complexation of Copigment with Al^{3+}. In the hydrangea-blue complex, it was suggested that copigment 5-*O*-caffeoylquinic acid, **2**, also might coordinate to Al^{3+} in aqueous solution. Therefore, we first measured ^{1}H NMR of **2** coexisting with Al^{3+} in D_2O at pD 4.0 (Figure 3). By addition of 0.5 equiv of Al^{3+} (2.5 mM) to **2** (5 mM) the signals became complicated (Figure 3B), and when the amount of Al^{3+} was increased to 1.0 equiv (5 mM) to **2** (5 mM), the signals converged to a simpler one (Figure 3C). Compared with the spectra of Figure 3A,C, the spectrum of Figure 3B (0.5 equiv of Al^{3+} to **2**) seemed to be just a 1:1 mixture of the spectra of Figure 3A and 3C. Therefore, it was concluded that addition of 1 equiv of Al^{3+} might give **2**−Al^{3+} complex completely and addition of 0.5 equiv of Al^{3+} might give a half amount of **2**−Al^{3+} with remaining noncomplexed **2**. In the spectrum of **2**−Al^{3+} (Figure 3C) signals attributable to caffeoyl residue shifted upfield. The signals of quinic acid (H-2a,b and H-6a,b) also shifted slightly compared with those of H-3,4,5. These results indicated that the chelating position might be at the catechol part of the caffeoyl residue and 1-OH and 1-COOH of quinic acid. In contrast, 5-*O*-*p*-coumaroylquinic acid, **3**, and 3-*O*-caffeoylquinic acid, **4**, did not show such a phenomenon under coexisting with Al^{3+}. Thus, the formation of Al^{3+} complex of copigment in D_2O at pH 4.0 (pD 4.4) was a special phenomenon

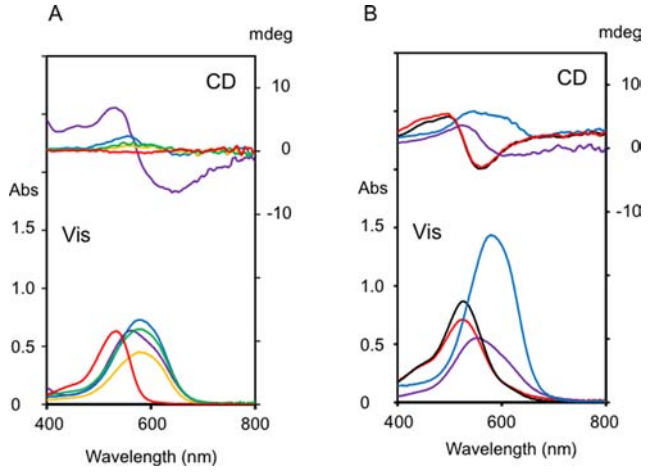

Figure 4. Visible absorption spectra and CD of the mixtures of **1** coexisting with copigment **2** and Al^{3+} for reconstruction of hydrangea-blue complex. (A) Spectra in various concentrated buffer solutions: purple line, 1 M; blue line, 6 M; orange line, 10 M; green line, 11.6 M; red line, in acetic acid. (B) Spectra of the various combination mixtures in 6 M deuterated acetate buffer: red line, without any copigment or metal ion; purple line, **1** (5 mM) and Al^{3+} (5 mM); black line, **1** (5 mM) and **2** (10 mM); blue line, **1** (5 mM), **2** (10 mM), and Al^{3+} (10 mM).

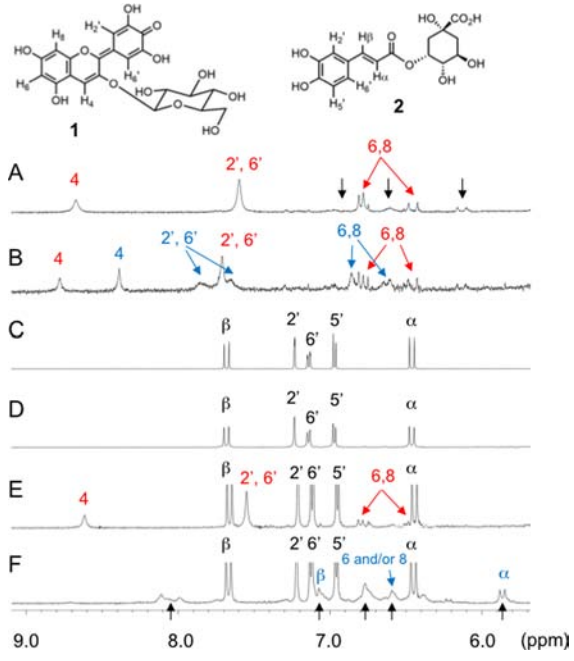

Figure 5. ^{1}H NMR of the various combinations of **1**, copigment **2**, and Al^{3+} in 6 M deuterated acetate buffer: (A) **1** (5 mM); (B) **1** (5 mM) and Al^{3+} (5 mM); (C) **2** (5 mM); (D) **2** (5 mM) and Al^{3+} (10 mM); (E) **1** (5 mM) and **2** (10 mM); (F) **1** (5 mM), **2** (10 mM), and Al^{3+} (10 mM).

observed only with **2**, which has a catechol moiety on the axial acyl substituent.

Reconstruction Conditions for the Same Blue Color as Hydrangea Sepals. We surveyed the combination of components and mixing conditions.[15,18−20,42] To analyze the structure and spatial arrangement of components in the hydrangea-blue complex, measurements of visible absorption spectrum, CD, and ^{1}H NMR should give useful information. To evaluate whether the same complex as the hydrangea-blue complex is reproduced or not, those spectra were compared. At

DOI: 10.1021/acs.jafc.5b02368
J. Agric. Food Chem. 2015, 63, 7630−7635

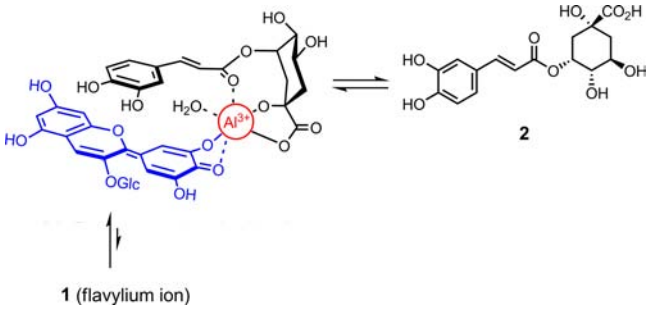

Figure 6. Schematic model of hydrangea-blue complex composed of **1**, **2**, and Al^{3+} in aqueous solution.

first the chelating position in the anthocyanin component was studied by using **1**, cyanidin 3-*O*-glucoside, **5**, and pelargonidin 3-*O*-glucoside, **6**, which have different numbers of OH groups on the B-ring (Figure 1). In 200 mM acetate buffer (pH 4) **1**, **5**, and **6** (3 mM) were mixed with **2** (3 mM) and Al^{3+} (6 mM). Delphinidin 3-*O*-glucoside, **1**, and cyanidin 3-*O*-glucoside, **5**, gave bathochromic shift in visible absorption spectrum; however, the mixture of pelargonidin 3-*O*-glucoside, **6**, did not show such a blue shift, but the color was red, supporting the previous report that Al^{3+} is chelating to the *o*-dihydroxy group at the B-ring of anthocyanin.[15,19] In ^{1}H NMR spectra of the lower field, the signals of **1** and **5** seemed very broad, but those of **6** were sharp and assigned it in the flavylium cation form. In the **1**−**2**−Al^{3+} and **5**−**2**−Al^{3+} complexes the signals of **2** seemed to be two sets, similar to Figure 3B, indicating that the Al^{3+} complex of **2** also existed in the solution. These complex ^{1}H NMR spectra made it very difficult to analyze the structure; therefore, we reexamined the mixing condition.

To clarify the effect of copigment in hydrangea-blue complex composed of **1**, **2**, and Al^{3+}, comparison of ^{1}H NMR spectra of the hydrangea-blue complex with the simple **1**−Al^{3+} complex is essential. However, previously the **1**−Al^{3+} complex was reported to be insoluble in aqueous buffer;[19,40,41] then, the ^{1}H NMR spectrum was recorded only in CD_3OD. We found that a concentrated acetate buffer (>6 M) could solubilize both the hydrangea-blue complex and simple **1**−Al^{3+} complex. In addition, in 6 M buffer, the **2**−Al^{3+} complex did not form and the signals of **2** became simple. Therefore, we optimized the concentration of the buffer and the ratio of each component, **1**, **2**, and Al^{3+}, by reproduction experiments (Figure 4). The concentration of anthocyanin **1** was fixed at 5 mM, which was nearly the same as that in the sepal cells,[18,42] and other conditions were evaluated with the obtained spectra by the similarity between the visible absorption spectrum and the CD to those of the colored cells, which specifically included the value of λ_{max}, the absorbance, and the curve shape (Figure 1).[16−18] As shown in Figure 4A, all of the spectra of **1** (5.0 mM) with 1 equiv of **2** and 4 equiv of Al^{3+} with differing concentrations of buffer (1−11.6 M) exhibited a blue color with a λ_{max} of approximately 580 nm, but in acetic acid, the mixture was red (λ_{max} 533 nm). However, the CD in a 1 M buffer solution showed a negative exiton-type Cotton effect, indicating the different arrangement of anthocyanins: existence of self-association of anthocyanins, **1**, with an anticlockwise stacking manner. After optimization experiments, the ratio of **1**, **2**, and Al^{3+} to **1** was determined to be 1:2:2 (Figure 4B, blue line).

Using the optimized condition, visible absorption spectrum and CD were compared to analyze the structure of hydrangea-blue complex (Figure 4B). **1** in the buffer solution was red (λ_{max} at 527 nm) and in CD, a negative exciton-type Cotton effect was observed, indicating anticlockwise stacking of the chromophores (Figure 4B, red line). When 1 equiv of Al^{3+} was added to **1**, the visible absorption spectrum exhibited a bathochromic shift (λ_{max} at 558 nm) with a negative exciton-type Cotton effect (Figure 4B, purple line), indicating that the anthocyanidin chromophores still self-associate in an anticlockwise stacking manner in the Al^{3+} complexed state. The mixture of **1** and **2** exhibited no bathochromic shift but a small effect on increase in absorbance with the same exciton-type Cotton effect (Figure 4B, black line). The visible spectrum of blue complex pigment composed of **1**, **2**, and Al^{3+} showed very high intensity at its λ_{max} compared with the other mixture mentioned above (Figure 4B, blue line). In the CD, the exciton-type negative Cotton effect disappeared. This indicates that no self-association exists in the solution of hydrangea-blue complex and that copigmentation between **1** and **2** became stronger than the mixture of **1** and **2**. The arrangement of each component resulted in the increase of population of the blue anhydrobase anion form.

To optimize the reconstruction condition suitable for ^{1}H NMR measurements, the replacement of the metal ions with other ions of the same valency and copigments with unnatural synthetic ones was carried out. We reconstructed the blue complex by mixing various trivalent metal ions (Sc^{3+}, Ga^{3+}, In^{3+}, La^{3+}, Yb^{3+}, and Bi^{3+}); however, only Ga^{3+} gave a blue solution with a low absorbance (λ_{max} 580 nm), and other ions did not give stable blue solutions. This result indicated that Al^{3+} is essential for the formation of hydrangea-blue complex. We previously reported that the aromatic plane of the 5-acyl group of **2** is also essential for reconstruction of the hydrangea-blue complex.[17,19,20] To re-examine these phenomena in the 6 M buffer conditions, reconstruction experiments using other copigments, **4**, **7**, **8**, and **9**, were carried out (Figure 1). It was confirmed that the conjugated system of the 5-*O*-acyl group in the copigment was crucial for the reconstruction of the natural-type hydrangea-blue complex. Furthermore, the oxygen atoms at the aromatic ring of the cinnamate residue may not be directly involved in coordination to Al^{3+} but instead assist in the stabilization of the blue complex pigment.

^{1}H NMR Analysis of Blue Complex Pigment. Using the optimized reconstruction conditions, the hydrangea-blue complex was analyzed by ^{1}H NMR. In the NMR spectrum the signals of sugar residues were very complicated and thus not assignable; therefore, only the signals at lower field attributable to aromatic protons were analyzed. To obtain structural information on hydrangea-blue complex, solutions of **1**, **2**, **1**−Al^{3+} complex, a mixture of **1** and **2**, and **2** and Al^{3+} at pD 4.4 were measured and the signals were compared (Figure 5). In addition, various 2D NMR experiments were carried out.

The ^{1}H NMR spectrum of **1** showed typical signals of the flavylium cation form of delphinidin nucleus (Figure 5A); in the aromatic region very broad H-4 (8.67 ppm) and H-2′ and H-6′ (7.60 ppm) peaks as well as two sets of H-6 and H-8 peaks were observed. However, the intensity of the visible absorption spectrum is low (Figure 4B, red line), and several broad signals (Figure 5A, black arrows) suggested that **1** may exist under an equilibrium mixture of the pseudobase−flavylium cation−quinonoidal base form.[44,45] Very broad signals at 7.0, 6.6, and 6.1 ppm could be assigned as signals of the pseudobase.[44,45] In a dilute solution (<0.05 mM) at pH 4, the anthocyanidin monoglycoside typically adopts the pseudobase form, but in the highly concentrated, 5 mM, solution, the flavylium cation form is stabilized by self-association of the chromophores. This

DOI: 10.1021/acs.jafc.5b02368
J. Agric. Food Chem. 2015, 63, 7630−7635

indicates that the equilibrium constant between the pseudobase−flavylium cation−quinonoidal base form may change depending on concentration.

In previous studies, a simple Al^{3+} complex of **1** was not water-soluble and the ^1H NMR spectrum was recorded in organic solvent such as CD_3OD.[19,40,41] In our study we found 6 M acetate buffer as a new solvation system and could measure the **1**−Al^{3+} complex in aqueous solution for the first time. In the ^1H NMR spectrum of **1** with 1 equiv of Al^{3+}, the additional signals to Figure 5A appeared, and those signals were assigned as protons of the **1**−Al^{3+} complex (Figure 5B). The signal of H-4 (Figure 5B, blue numbers) was determined by NOESY correlation between the anomeric proton of the sugar. The NOESY correlation between H-4 (red) and H-4 (blue) and between H-2′,6′ (red) and H-2′,6′ (blue) suggested that **1** may attain equilibrium of the flavylium cation−quinonoidal base−quinonoidal base anion by adding 1 equiv of Al^{3+} to **1**.

Figure 5C,D shows the ^1H NMR of copigment **2**. The signals of **2** were very sharp and easily assignable (Figure 5C). The addition of Al^{3+} did not induce remarkable spectral changes in **2** (Figure 5D), indicating that 2 equiv of Al^{3+} in 6 M acetate buffer had no effect. It was concluded that Al^{3+} may not coordinate with **2**, although in a diluted buffer **2** forms a complex with Al^{3+} and gave a complex signal. The results of mixing **1** (5 mM) and **2** (10 mM) are shown in Figure 5E. In the ^1H NMR spectrum the signals for H-4, H-2′, H-6′, H-6, and H-8 of **1** shifted slightly upfield, but no such shift was observed with the signals of **2**. This upfield shift could be the copigmentation effect by hydrophobic interaction between the chromophore of **1** and the caffeic acid ring of **2**. This indicated that **1** and **2** may interact with one another, but this interaction is not strong.

The ^1H NMR spectrum of the hydrangea-blue complex composed with **1** (5 mM), **2** (10 mM), and Al^{3+} (10 mM) showed a completely different spectrum attributable to the signals of delphinidin chromophore (Figure 5F). There were no similar signals found in Figure 5A (flavylium cation form) and Figure 5B (Al^{3+} complex of **1**). However, the signals of **2** were almost the same as found in Figure 5C−E. Concerning the signals of delphinidin chromophore, new, broad signals appeared at approximately 8.0, 7.1, 6.8, 6.6, and 5.9 ppm (Figure 5F, black arrows). Among these signals, a broad peak at 6.6 ppm disappeared after 1 day. It was hard to find the signals attributable to H-6 and H-8; however, the protons of 5-OH free anthocyanin rapidly changed with D in D_2O.[45] Using this phenomenon, we assigned the signals. Thus, this signal was assigned to H-6 and/or H-8 of **1**. As mentioned above, the major signals of **2** were sharp and remained unchanged, but the newly appeared signals at 5.9 and 7.1 ppm were assigned as H-α and H-β, respectively, by COSY and the *J* values (16.0 Hz). These signals were also shifted upfield, indicating that the anisotropic effect caused by stacking with **1** may occur.

For the study of blue coloration of hydrangea we investigated reconstruction conditions and obtained the same blue complex, the hydrangea-blue complex, which was composed of **1**, **2**, and Al^{3+} in a ratio of 5:10:10 mM. In a 6 M deuterated acetate buffer, ^1H NMR spectra of the blue complex were measured and several aromatic protons were assigned. In the blue solution, multiple anthocyanin and copigment signals were observed, indicating that the complex structure is not fixed but instead under equilibrium. It was clarified that the blue anhydrobase anion form of delphinidin 3-glucoside, **1**, is formed by complexation with Al^{3+} and the complex is stabilized by nonflavonoid copigment, **2**, which also chelates to Al^{3+} (Figure 6). However, the whole supramolecular structure may not be a static structure but instead a fluctuating structure in equilibrium state. The combination of **1**, **2**, and Al^{3+} may construct a very unique and special coordination structure, and this imparts a very elusive character to hydrangea blue.

■ ASSOCIATED CONTENT

Supporting Information

^1H NMR of metal complex solutions (**1**−**2**−Al^{3+}, **5**−**2**−Al^{3+}, and **6**−**2**−Al^{3+}) (Figure S1); difference in visible and CD spectra of the mixture of various trivalent metal ions with **1** and **2** (Figure S2); synthesis of **9** (Figure S3); difference in visible and CD spectra of the structure of the copigment mixture of **4**, **7**, **8**, and **9** with **1** and Al^{3+} (Figure S4); ^1H NMR spectrum of the mixed solution with delphinidin 3-*O*-glucoside, **1**, and Al^{3+} (Figure S5); NOESY NMR spectrum of the mixed solution with delphinidin 3-*O*-glucoside, **1**, and Al^{3+} (Figure S6); ^1H NMR of time-dependent change of delphinidin 3-*O*-glucoside, **1** (Figure S7); ^1H NMR of time-dependent change of the mixed solution with delphinidin 3-*O*-glucoside, **1**, and Al^{3+} (Figure S8); ^1H NMR of time-dependent change of the mixed solution with delphinidin 3-*O*-glucoside, **1**, **2**, and Al^{3+} (Figure S9); COSY NMR spectrum of the mixed solution with delphinidin 3-*O*-glucoside, **1**, copigment **2**, and Al^{3+} (Figure S10); characterization of new compounds and experimental procedures. The Supporting Information is available free of charge on the ACS Publications website at DOI: 10.1021/acs.jafc.5b02368.

■ AUTHOR INFORMATION

Corresponding Author

*(K.Y.) Phone: +81-52-789-5638. Fax: +81-52-789-5638. E-mail: yoshidak@is.nagoya-u.ac.jp.

Funding

This work was financially supported by the Ministry of Education, Culture, Sports, Science and Technology, Japan ((B) No. 24380062, Creative Scientific Research No. 16GS0206, and Global COE in Chemistry, Nagoya University).

Notes

The authors declare no competing financial interest.

■ ACKNOWLEDGMENTS

We thank Kazushi Koga (Graduate School of Bioagricultural Sciences, Nagoya University) for the NMR measurement.

■ ABBREVIATIONS USED

CD, circular dichroism; NMR, nuclear magnetic resonance; TFA, trifluoroacetic acid; NOESY, nuclear Overhauser effect spectroscopy; COSY, correlation spectroscopy

■ REFERENCES

(1) Francis, F. J. Food colorants: anthocyanins. *Crit. Rev. Food Sci. Nutr.* **1989**, *28*, 273−314.

(2) Jian He, J.; Giusti, M. M. Anthocyanins: natural colorants with health-promoting properties. *Annu. Rev. Food Sci. Technol.* **2010**, *1*, 163−187.

(3) Chenery, E. M. The problem of the blue hydrangea. *J. R. Hortic. Soc.* **1937**, *62*, 604−620.

(4) Allen, R. C. Influence of aluminum on the flower color of *Hydrangea macrophylla* DC. *Boyce Thompson Inst.* **1943**, *13*, 221−242.

(5) Ma, J. F.; Ryan, P. R.; Delhaize, E. Aluminium tolerance in plants and the complexing role of organic acids. *Trends Plant Sci.* **2001**, *6*, 273−278.

DOI: 10.1021/acs.jafc.5b02368
J. Agric. Food Chem. 2015, 63, 7630−7635

(6) Yoshida, K.; Ito, D.; Shinkai, Y.; Kondo, T. Change of color and components in sepals of chameleon hydrangea during maturation and senescence. *Phytochemistry* **2008**, *69*, 3159−3165.
(7) Lawrence, W. J. C.; Price, J. R.; Robinson, G. M.; Robinson, R. Survey of anthocyanins. V. *Biochem. J.* **1938**, *32*, 1661−1667.
(8) Robinson, G. M.; Robinson, R. The colloid chemistry of leaf and flower pigments and the precursors of the anthocyanins. *J. Am. Chem. Soc.* **1939**, *61*, 1606−1607.
(9) Hayashi, K.; Abe, Y. Studien über anthocyane, XXIII. Papierchromatographische übersicht der anthocyane im pflanzeneich. I. *Misc. Rep. Res. Inst. Nat. Resour.* **1958**, *29*, 1−8.
(10) Asen, S.; Siegelman, H. W.; Stuart, N. W. Anthocyanin and other phenolic compounds in red and blue sepals of *Hydrangea macrophylla* var. Merveille. *Proc. Am. Soc. Hortic. Sci.* **1957**, *69*, 561−569.
(11) Asen, S.; Siegelman, H. W. Effect of aluminum on absorption spectra of the anthocyanin and flavonols from sepals of *Hydrangea macrophylla* var. Merveille. *Proc. Am. Soc. Hortic. Sci.* **1957**, *70*, 478−481.
(12) Kinraide, T. Identity of the rhizotoxic aluminium species. *Plant Soil* **1991**, *134*, 167−178.
(13) Takeda, K.; Kubota, R.; Yagioka, C. Copigments in the blueing of sepal colour of *Hydrangea macrophylla*. *Phytochemistry* **1958**, *24*, 1207−1209.
(14) Takeda, K.; Kariuda, M.; Itoi, H. Blueing of sepal colour of *Hydrangea macrophylla*. *Phytochemistry* **1958**, *24*, 2251−2254.
(15) Takeda, K.; Yamashita, T.; Takahashi, A.; Timberlake, C. F. Stable blue complexes of anthocyanin-aluminium-3-*p*-coumaroyl- or 3-caffeoyl-quinic acid involved in the blueing of *Hydrangea* flower. *Phytochemistry* **1990**, *29*, 1089−1091.
(16) Yoshida, K.; Toyama-Kato, Y.; Kameda, K.; Kondo, T. Sepal color variation of *Hydrangea macrophylla* and vacuolar pH measured with a proton-selective microelectrode. *Plant Cell Physiol.* **2003**, *44*, 262−268.
(17) Kato, Y. *Chemical Studies on Blue Sepal-Color Development of Hydrangea by Using Molecular-Designed Co-pigments*. Thesis, Nagoya University, 2006.
(18) Ito, D.; Shinkai, Y.; Kato, Y.; Kondo, T.; Yoshida, K. Chemical studies on different color development in blue- and red-colored sepal cells of *Hydrangea macrophylla*. *Biosci., Biotechnol., Biochem.* **2009**, *73*, 1054−1059.
(19) Kondo, T.; Toyama-Kato, Y.; Yoshida, K. Essential structure of co-pigment for blue sepal-color development of hydrangea. *Tetrahedron Lett.* **2005**, *46*, 6645−6649.
(20) Toyama-Kato, Y.; Kondo, T.; Yoshida, K. Synthesis of designed acylquinic acid derivatives involved in blue color development of hydrangea and their co-pigmentation effect. *Heterocycles* **2007**, *72*, 239−254.
(21) Oyama, K.-I.; Watanabe, N.; Yamada, T.; Suzuki, M.; Sekiguchi, Y.; Kondo, T.; Yoshida, K. Efficient and versatile synthesis of 5-*O*-acylquinic acids with a direct esterification using a *p*-methoxybenzyl quinate as a key intermediate. *Tetrahedron* **2015**, *71*, 3120−3130.
(22) Goto, T.; Kondo, T. Structure and molecular stacking of anthocyanins − flower color variation. *Angew. Chem., Int. Ed. Engl.* **1991**, *30*, 17−33.
(23) Brouillard, R.; Dangles, O. Flavonoids and flower color. In *The Flavonoids Advances in Research since 1986*; Harborne, J. B., Ed.; Chapman & Hall: London, UK,1994; pp 565−588.
(24) Yoshida, K.; Mori, M.; Kondo, T. Blue flower color development by anthocyanins: from chemical structure to cell physiology. *Nat. Prod. Rep.* **2009**, *26*, 884−915.
(25) Yoshida, K.; Oyama, K.-I.; Kondo, T. Chemistry of flavonoids in color development. In *Recent Advances in Polyphenol Research*; Cheynier, V., Sarni-Manchado, P., Quideau, S., Eds.; Wiley: Chichester, UK, 2012; Vol. 3, pp 99−129.
(26) Hayashi, K.; Abe, Y.; Mitsui, S. Blue anthocyanin from flowers of *Commelina*, the crystallisation and some properties thereof. Studies on anthocyanins. XXX. *Proc. Jpn. Acad.* **1958**, *34*, 373−378.
(27) Mitsui, S.; Hayashi, K.; Hattori, S. Commelinin, a crystalline blue metallo-anthocyanin from the flowers of *Commelina*. *Proc. Jpn. Acad.* **1959**, *35*, 169−174.
(28) Kondo, T.; Yoshida, K.; Nakagawa, A.; Kawai, T.; Tamura, H.; Goto, T. Structural basis of blue-colour development in flower petals from *Commelina communis*. *Nature* **1992**, *358*, 515−518.
(29) Shiono, M.; Matsugaki, N.; Takeda, K. Structure of commelinin, a blue complex pigment from the bue flowers of *Commelina communis*. *Proc. Jpn. Acad., Ser. B* **2008**, *84*, 452−456.
(30) Bayer, E. Natürliche und synthetische Anthocyan-Metallkomplexe. *Chem. Ber.* **1958**, *91*, 1115−1122.
(31) Kondo, T.; Ueda, M.; Tamura, H.; Yoshida, K.; Isobe, M.; Goto, T. Composition of protocyanin, a self-assembled supramolecular pigment from the blue cornflower *Centaurea cyanus*. *Angew. Chem., Int. Ed. Engl.* **1994**, *33*, 978−979.
(32) Kondo, T.; Ueda, M.; Isobe, M.; Goto, T. A new molecular mechanism of blue color development with protocyanin, a supramolecular pigment from corn flower *Centaurea cyanus*. *Tetrahedron Lett.* **1998**, *39*, 8307−8310.
(33) Shiono, M.; Matsugaki, N.; Takeda, K. Structure of the blue cornflower pigment. *Nature* **2005**, *436*, 791.
(34) Takeda, K.; Yanagisawa, M.; Kifune, T.; Kinoshita, T.; Timberlake, C. F. A blue pigment complex in flowers of *Salvia patens*. *Phytochemistry* **1994**, *35*, 1167−1169.
(35) Kondo, T.; Oyama, K.-I.; Yoshida, K. Chiral molecular recognition on formation of a metalloanthocyanin: a supramolecular metal complex pigment from blue flower of *Salvia patens*. *Angew. Chem., Int. Ed.* **2001**, *40*, 894−897.
(36) Mori, M.; Kondo, T.; Yoshida, K. Cyanosalvianin, a supramolecular blue metalloanthocyanin, from petals of *Salvia uliginosa*. *Phytochemistry* **2008**, *69*, 3151−3158.
(37) Shoji, K.; Miki, N.; Nakajima, N.; Momonoi, K.; Kato, C.; Yoshida, K. Perianth bottom-specific blue color development in tulip cv. Murasakizuisho requires ferric ions. *Plant Cell Physiol.* **2007**, *48*, 243−251.
(38) Tanaka, M.; Fujimori, T.; Uchida, I.; Yamaguchi, S.; Takeda, K. A malonylated anthocyanin and flavonols in blue *Meconopsis* flowers. *Phytochemistry* **2001**, *56*, 373−376.
(39) Kumi Yoshida, K.; Kitahara, S.; Ito, D.; Kondo, T. Ferric ions involved in the flower color development of the Himalayan blue poppy *Meconopsis grandis*. *Phytochemistry* **2006**, *67*, 992−998.
(40) Dangles, O.; Elhabiri, M.; Brouillard, R. Kinetic and thermodynamic investigation of the aluminium-anthocyanin complexation in aqueous solution. *J. Chem. Soc., Perkin Trans. 2* **1994**, 2587−2596.
(41) Schreiber, H. D.; Jones, A. J.; Lariviere, C. M.; Mayhew, K. M.; Cain, J. B. Role of aluminium in red-to-blue color changes in *Hydrangea macrophylla* sepals. *BioMetals* **2011**, *24*, 1005−1015.
(42) Ito, D. *Chemical Studies on Sepal-Color Variation of Hydrangea by Using Single Cell-Analytical Method*. Thesis, Nagoya University, 2009.
(43) Yoshida, K.; Sato, Y.; Okuno, R.; Kameda, K.; Isobe, M.; Kondo, T. Structural analysis and measurement of anthocyanins from colored seed coats of *Vigna*, *Phaseolus*, and *Glycine* legumes. *Biosci., Biotechnol., Biochem.* **1996**, *60*, 589−593.
(44) Cheminat, A.; Brouillard, R. PMR investigation of 3-*O*-(β-D-glucosyl)malvidin structural transformations in aqueous solutions. *Tetrahedron Lett.* **1986**, *27*, 4457−4460.
(45) Yanamala, N.; Tirupula, K. C.; Balem, F.; Klein-Seetharaman, J. pH-Dependent interaction of rhodopsin with cyanidin-3-glucoside. 1. Structural aspects. *Photochem. Photobiol.* **2009**, *85*, 454−462.

NOTE ADDED AFTER ASAP PUBLICATION

There were errors in Figure 6 and the TOC graphic in the version of this article published June 2, 2015. The correct version published June 24, 2015.

DOI: 10.1021/acs.jafc.5b02368
J. Agric. Food Chem. 2015, 63, 7630−7635

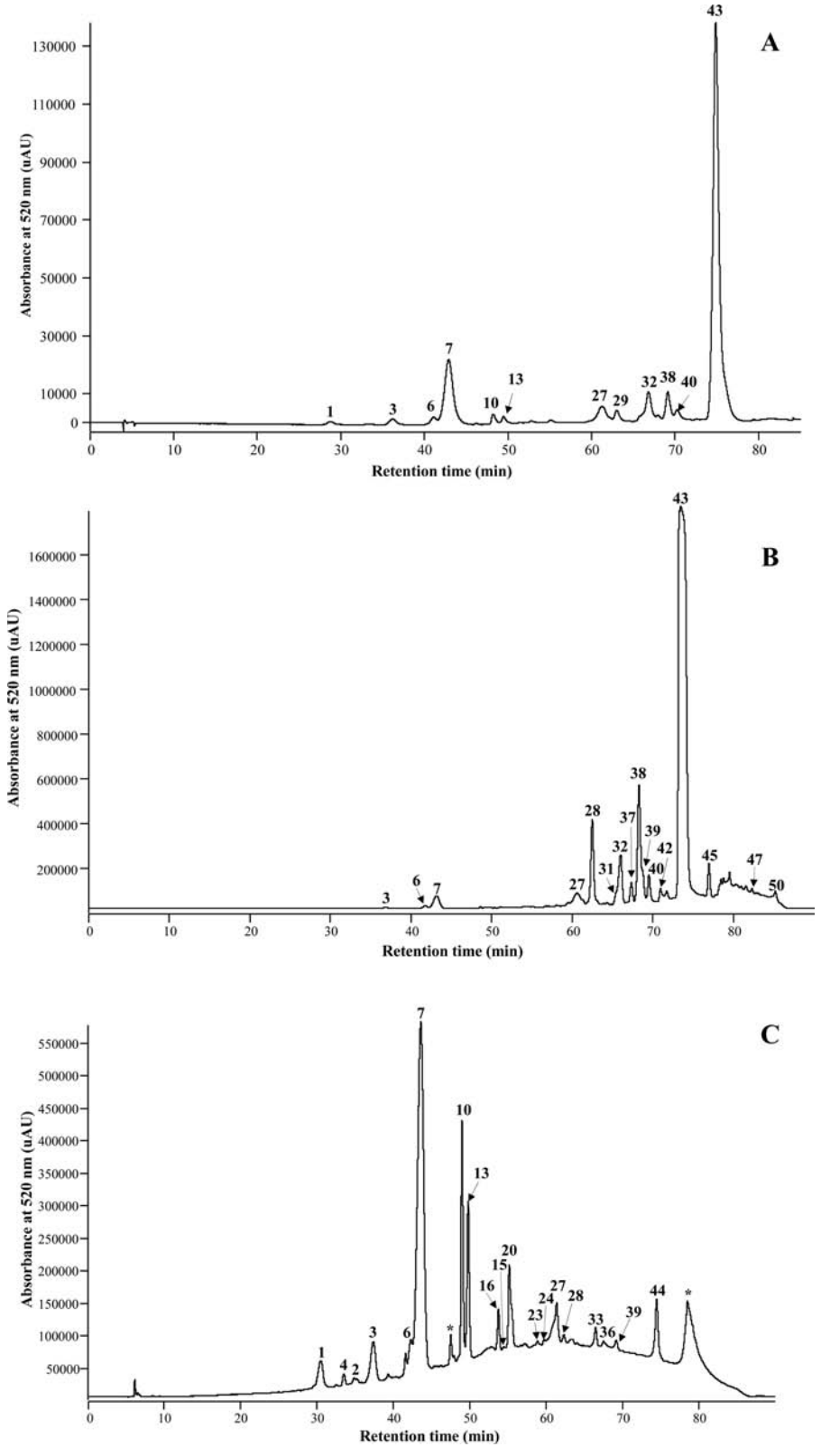

Figure 1. (A) Chromatogram at 520 nm obtained from the LC-DAD/MS from the red GP extract 1; (B) chromatogram at 520 nm obtained from the LC-DAD/MS from the isoamylic alcohol fraction and (C) aqueous fraction of the red GP extract 2. ∗, unidentified peak.

The solution was sonicated in an ice bath for 30 min, and then the solids were filtered using glass wool. A similar extract (extract 2) was obtained, but in this case the solution was sonicated for 18 h.

Purification of the Grape Pomace Extracts. Organic solvents were removed from the previous extracts 1 and 2 by evaporation in a rotoevaporator under vacuum, and the resulting aqueous extract (200 mL) was submitted to a liquid−liquid extraction procedure with 2 × 200 mL of hexane. After rotoevaporation of the hexane, the residue was analyzed by HPLC-DAD/MS. The proteins present in the aqueous fraction were precipitated in cold methanol (1:50) and then removed by

DOI: 10.1021/acs.jafc.5b00256
J. Agric. Food Chem. 2015, 63, 7636−7644

Table 1. Molecular Ion in the Positive-Ion Mode and Respective Fragments MS^2 and MS^3 Obtained by API-LC-ESI-MS/MS of Several Anthocyanins and Anthocyanin-Derived Compounds Detected in Red Grape Pomace (Extract 2)

compound	RT (min)	$[M^+]$	$[MS^2]$	$[MS^3]$	identity
1	29.52	465	303		delphinidin-3-*O*-glucoside
2	35.52	449	287		cyanidin-3-*O*-glucoside
3	36.50	479	317		petunidin-3-*O*-glucoside
4	33.65	1477			malvidin-3-*O*-glucoside trimer
5	39.13	655	493	331	malvidin-3,5-*O*-diglucoside
6	41.54	463	301		peonidin-3-*O*-glucoside
7	42.92	493	331		malvidin-3-*O*-glucoside
8	45.09	657	495		unknown
9	47.32	487	325		pyranopeonidin-3-*O*-glucoside
10	48.36	561	399		carboxypyranomalvidin-3-*O*-glucoside
11	48.53	625	331		malvidin-3-*O*-caftaric acid
12	48.65	547	385		carboxypyranopetunidin-3-*O*-glucoside
13	49.10	517	355		pyranomalvidin-3-*O*-glucoside
14	51.53	801	331		malvidin-3-*O*-coumaroylglucoside-5-*O*-glucoside
15	52.95	809	519	357	malvidin-3-*O*-glucoside-(8,8)-methylmethyne-catechin
16	53.28	603	399		carboxypyranomalvidin-3-*O*-acetylglucoside
17	54.07	663	369		methylpyranomalvidin-3-*O*-caftaric acid
18	54.49	521	317		petunidin-3-*O*-acetylglucoside
19	54.67	627	303		delphinidin-3-*O*-caffeoylglucoside
20	55.18	531	369		methylpyranomalvidin-3-*O*-glucoside
21	56.89	809	519	357	malvidin-3-*O*-glucoside-(8,8)-methylmethyne-epicatechin
22	58.30	693	385		carboxypyranopetunidin-3-*O*-coumaroylglucoside
23	58.79	1623			monocoumaroyl malvidin-3-*O*-glucoside trimer
24	59.08	723	399		carboxypyranomalvidin-3-*O*-caffeoylglucoside
25	59.60	927	619		unknown
26	59.98	479	303		unknown
27	60.04	535	331		malvidin-3-*O*-acetylglucoside
28	61.79	679	355		pyranomalvidin-3-*O*-caffeoylglucoside
29	62.24	611	303		delphinidin-3-*O*-coumaroylglucoside
30	63.23	649	341		pyranopetunidin-3-*O*-coumaroylglucoside
31	65.65	625	301		peonidin-3-*O*-caffeoylglucoside
32	65.43	655	331		malvidin-3-*O*-caffeoylglucoside
33	65.88	707	399		carboxypyranomalvidin-3-*O*-coumaroylglucoside
34	66.52	663	369		unknown
35	66.83	663	339		methylpyranopeonidin-3-*O*-caffeoylglucoside
36	67.15	693	369		carboxypyranopeonidin-3-*O*-caffeoylglucoside
37	67.33	595	287		cyanidin-3-*O*-coumaroylglucoside
38	67.95	625	317		petunidin-3-*O*-coumaroylglucoside
39	68.69	663	355		pyranomalvidin-3-*O*-coumaroylglucoside
40	69.42	639	331		malvidin-3-*O*-*cis*-coumaroylglucoside
41	70.74	671	331		malvidin-3-*O*-galloylglucoside
42	70.77	955	665	357	malvidin-3-*O*-coumaroylglucoside-(8,8)-methylmethyne-catechin
43	73.19	639	331		malvidin-3-*O*-*trans*-coumaroylglucoside
44	73.99	677	369		methylpyranomalvidin-3-*O*-coumaroylglucoside
45	76.75	1315			unknown
46	78.44	609	447		pyrano-malvidin-3-*O*-glucoside-phenol
47	82.59	909	601	449	unknown
48	82.85	813	505		ninylpyrano-malvidin-3-*O*-coumaroylglucoside-pyrogallol
49	83.01	1277			malvidin-3-*O*-coumaroylglucoside dimer
50	85.43	755	447		pyrano-malvidin-3-*O*-coumaroylglucoside-phenol

centrifugation. The aqueous fractions (extracts 1 and 2) without proteins were lyophilized and then analyzed by LC-DAD/MS and MALDI-TOF.

Fractionation of the Grape Pomace Extracts. One gram of GP extract 1 was applied on top of a C18 (20 g) column, and different fractions were obtained by elution with water acidified with formic acid (1%), ethyl ether, ethyl acetate, and aqueous solution with increasing percentages of methanol (10, 30, 60, and 100%, v/v) acidified with formic acid. Additionally, 100 mg of the same extract was fractionated by TSK Toyopearl 40-HW(S) column chromatography using different aqueous solvents with increasing percentages of methanol (0, 10, 20, 30, and 100%, v/v). The obtained fractions were analyzed by LC-DAD/MS and MALDI-TOF.

One gram of extract 2 dissolved in 200 mL of water was submitted to a liquid−liquid extraction procedure with ethyl acetate (3 × 200 mL) and isoamyl alcohol (2 × 200 mM). All of the fractions were analyzed by LC-DAD/MS.

LC-DAD/MS. The anthocyanin and anthocyanin-derived compound composition of each fraction was evaluated by LC-DAD/MS. An Accela series liquid chromatograph, equipped with a 150 × 4.6 mm i.d., 5 μm, LicroCART reversed-phase C18 column was used, and detection was carried out between 200 and 600 nm using an Accela PDA detector. The mass detection was performed using an LTQ Orbitrap XL mass spectrometer (Thermo Fischer Scientific, Bremen, Germany) controlled by LTQ Tune Plus 2.5.5 and Xcalibur 2.1.0. Solvents were (A) H_2O/HCOOH (99:1) and (B) HCOOH/H_2O/CH_3CN (1:69:30). The gradient was performed using an Accela 600 Pump and consisted of 20−85% B for 70 min at a flow rate of 0.3 mL/min. The column was washed with 100% B for 10 min and then stabilized with the initial conditions for another 10 min. The capillary voltage of the electrospray ionization (ESI) was set to 3100 V, and the capillary temperature was 275 °C. The sheath gas flow rate (nitrogen) was set to 5 (arbitrary units as provided by the software settings). The capillary voltage was 49 V and the tube lens voltage 250 V. Spectra were recorded in positive-ion mode between m/z 50 and 2000. The mass spectrometer was programmed to do a series of three scans: a full scan mass, a zoom scan of the most intense ion in the first scan (selected ion monitoring, SIM), and a MS-MS of the most intense ion using relative collision energies of 30 and 60 V.

MALDI-TOF (Matrix-Assisted Laser Desorption Ionization−Time of Flight) Analysis. The different GP fractions were analyzed by MALDI-TOF using an UltrafleXtreme mass spectrometer (Bruker, Bremen, Germany) operating in positive reflectron ion detection mode with laser SmartBeamIII and under FlexCompass 1.4 software control (Bruker Daltonics, Germany). For each sample the laser power was adjusted to 55%, the detector gain 4.0× (2410 V), and the mass range between 200 and 3500.

For the sample preparation, a tIAA (*trans*-3-indolacrylic acid) matrix (≥98.5%, Sigma-Aldrich, USA), 50 mg/mL, was prepared in an aqueous solution of 70% (v/v) acetone. Moreover, each grape pomace fraction was prepared in the same solvent in a concentration of 5 mg/mL. The polyphenolic fractions eluted from the Toyopearl column were mixed with the matrix solution at volumetric ratios of (1:2). The analyte/matrix mixture was first deionized with Dowex 50X8-400 cation exchange resin (Supelco), equilibrated in 70% aqueous acetone (v/v). Positive ion mode was used for the detection of anthocyanins. Two microliters from each sample (after mixing with the matrix and the resin) was applied onto a stainless steel target plate (MTP 394 target plate ground steel BC, Bruker Daltonics) and fully air-dried. For each assay, three sample spot replicates were analyzed, and samples were spotted in triplicate.

RESULTS AND DISCUSSION

GP Anthocyanic Profile by LC-DAD/MS. According to the LC-DAD analysis of the red GP extract 1, without using any

DOI: 10.1021/acs.jafc.5b00256
J. Agric. Food Chem. 2015, 63, 7636−7644

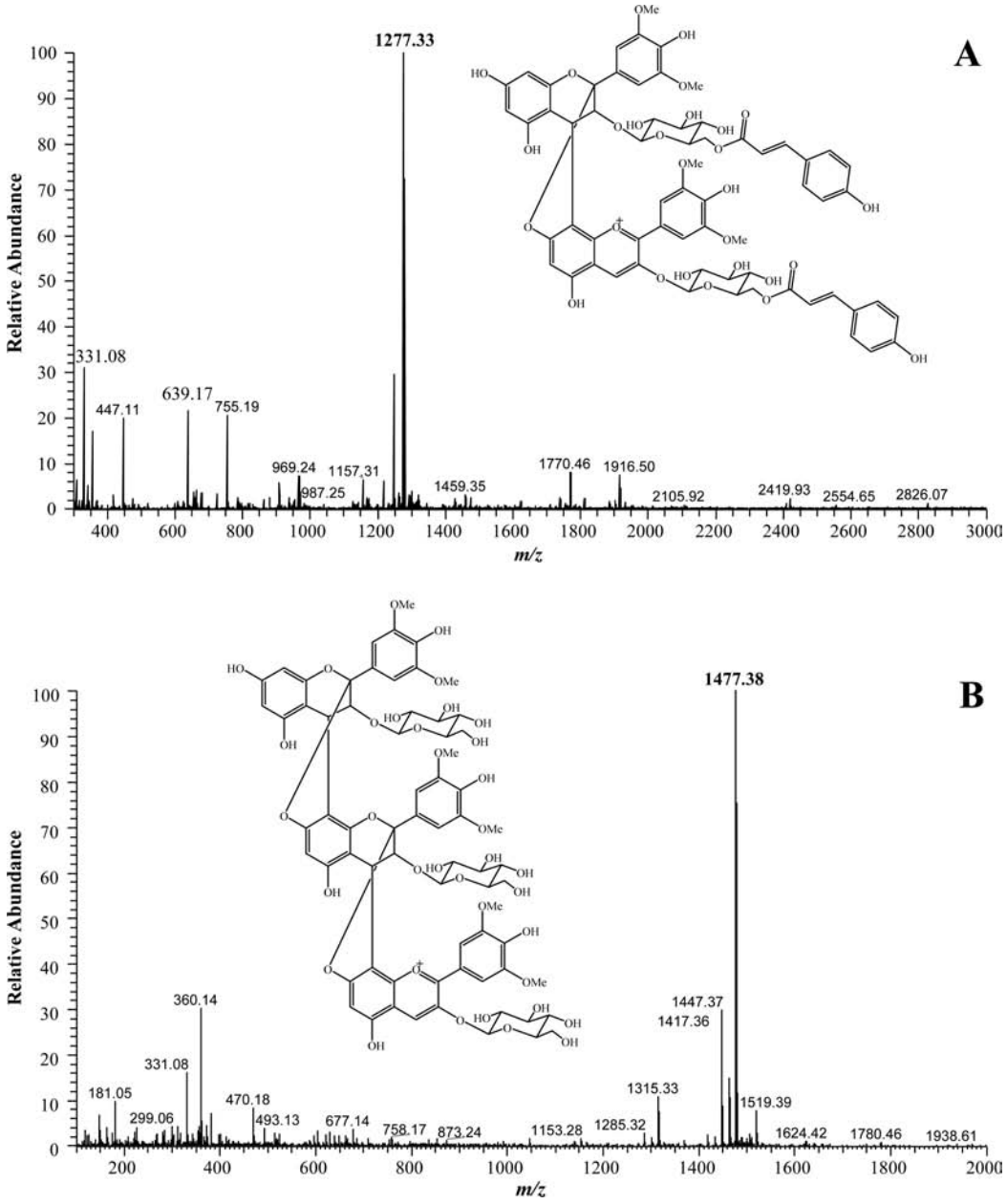

Figure 2. ESI-MS analysis performed in the positive-ion mode of a GP fraction (60% (v/v) methanol) showing the presence of anthocyanin dimers and trimers: (A) full mass spectrum (*m*/*z* 1277) of the malvidin-3-*O*-coumaroylglucoside dimer (**49**); (B) full mass spectrum (*m*/*z* 1477) of the malvidin-3-*O*-glucoside trimer (**4**).

previous fractionation methodology it was possible to observe in the chromatogram recorded at 520 nm the presence of 12 peaks (Figure 1A). The main compound was identified by its UV−visible spectra, retention time, ion mass (*m*/*z* 639) in the positive ion mode, and fragmentation pattern (MS^2 331) and was attributed to malvidin-3-*O*-coumaroylglucoside (peak 43) (Figure 1 and Table 1). The area of malvidin-3-*O*-coumaroylglucoside represents around 65% of the total area. The chromatographic profile (Figure 1) of the GP extract is quite different from one that is usually observed in grapes and young red wines, where, generally, malvidin-3-*O*-glucoside is the main anthocyanin present with the coumaroyl-derivative being the second most intense, especially in the Douro region.[13] The appearance of this chromatographic profile can be due to the specificities of the winemaking process, or it can be explained by the lower solubility of the coumaroyl derivative in aqueous solution, slowing or limiting its diffusion to the hydroalcoholic solution during the fermentation/winemaking process. In addition to the malvidin-3-*O*-coumaroylglucoside pigment, other peaks were detected in the same GP extract corresponding to the four nonacylated anthocyanin-3-*O*-glucosides mainly present in grapes and red wines (delphinidin, petunidin, peonidin, and malvidin) and to some of their acetylated, coumaroylated, and caffeoylated derivatives (Figure 1 and Table 1). The presence of the A- and B-type vitisin compounds was also observed (peaks 10 and 13, respectively) (Figure 1 and Table 1). Moreover, the detection of a compound (peak 40) (Figure 1) with the same ion mass as the malvidin-3-*O*-coumaroylglucoside (*m*/*z* 639) (peak 43) in the positive ion mode was observed. Similarly to what was reported in the literature by Monagas et al.[14] and Núñez et al.,[15] in grapes and wines from *Vitis vinifera* this can be attributed to the occurrence of the *cis* isomer of the

DOI: 10.1021/acs.jafc.5b00256
J. Agric. Food Chem. 2015, 63, 7636−7644

malvidin-3-*O*-(6-*p*-coumaroyl)-glucoside (**40**) in GP that is present in smaller amounts when compared with the *trans* isomer.

To obtain fractions with different chemical compositions and therefore better characterize the GP extract polyphenolic composition, a fractionation methodology was developed. First, the anthocyanin and anthocyanin-derived compounds from extract 1 were separated in a reverse phase C-18 resin and eluted with solvents that present different polarities, namely, ethyl ether, ethyl acetate, water, and aqueous solutions with increasing percentages of methanol. With the less polar solvent (ethyl ether) it was possible to remove the chlorophylls and the hydrophobic fractions, but due to its lack of solubility in water or methanolic solvents, this fraction was not analyzed by LC-DAD/MS. No additional peaks were detected in those fractions obtained from the fractionation of the GP with C-18 resin or with Toyopearl HW-40(S) gel when compared to direct analysis of the GP extract (extract 1). The main exception was the fraction eluted with 60% (v/v) methanol, where it was possible to detect by LC-MS in positive-ion mode the presence of the malvidin-3-*O*-coumaroylglucoside dimer (**49**) (*m*/*z* 1277) and the malvidin-3-*O*-glucoside trimer (**4**) (*m*/*z* 1477) (Figure 2), both already reported in the literature to be present in red grapes and wines.[16−18] The possibility of detecting anthocyanins self-assembling by LC-MS made us think that these signals detected in fraction 60% (v/v) methanol could be due to the auto-association of malvidin-3-*O*-coumaroylglucoside and malvidin-3-*O*-glucoside, respectively, leading to the formation of the dimer and trimer. To confirm that dimer and trimer are isolated compounds and not products formed during the anthocyanins' autoassociation, MALDI-TOF analysis was used, and the results are discussed below.

However, the high complexity of the red GP was recognized after the LC-DAD/MS analysis of GP extract 2, where the solid/solvent contact time was increased to 18 h. In this extract >50 different anthocyanin and anthocyanin-derived compounds were detected and most of them identified (Table 1). In this extract the five anthocyanin-monoglucosides (delphinidin, cyanidin, petunidin, peonidin, and malvidin), two acetylglucoside derivatives (petunidin and malvidin), five coumaroyl derivatives, and three caffeoyl-derivatives (delphinidin, peonidin, and malvidin) were identified on the basis of their ion mass, fragmentation patterns (Table 1), and UV−visible spectra (data not shown). The presence of these anthocyanins in GP is not surprising because they are present in red grapes and therefore are also expected to be present in the resulting red GP.[19,20] Additionally, in the mass spectrum in the positive-ion mode was detected an ion mass at *m*/*z* 655 (peak 5) and two fragments *m*/*z* 493 (− 162 amu) and *m*/*z* 331 (− 2 × 162 amu). The fragmentation pattern is in agreement with the presence of the malvidin aglycone (*m*/*z* 331) and two glucose moieties (− 2 × 162 amu) as is observed in malvidin-3,5-diglucoside (malvin). This is also corroborated by the retention time that is smaller (RT 39.13 min) than the one observed for malvidin-3-glucoside (RT 42.92 min) as is expected for a diglucoside (more polar) in a reverse phase C-18 column. The presence of malvin is not expected to occur in *Vitis vinifera* grapes but only in other *Vitis* sp. Even though its occurrence in *V. vinifera*-based GP has never been reported in the literature, Baldi et al. and Heier et al. have detected small amounts of anthocyanin-3,5-diglucosides in *V. vinifera* L. grapes and wines.[20,21] Moreover, the same ion mass (*m*/*z* 655) was observed later in the mass chromatogram (RT 65.43 min), but in this case the fragmentation pattern

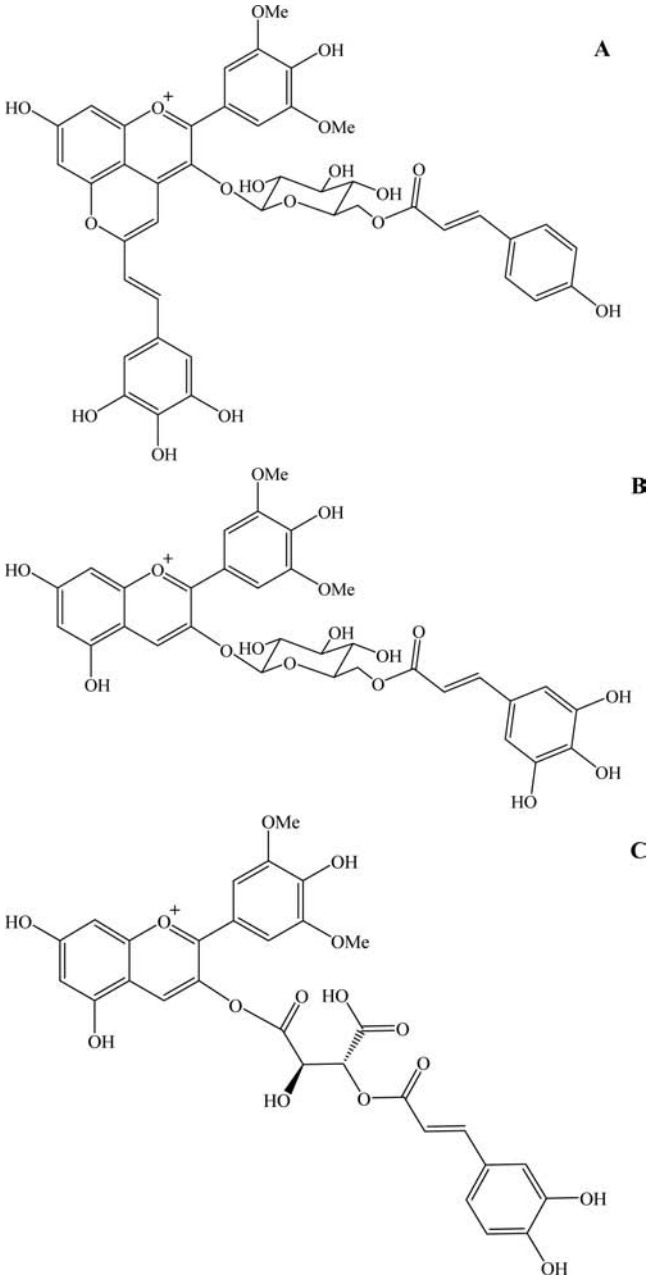

Figure 3. Hypothetic structures of the compounds (A) **48** (vinyl-pyranomalvidin-3-*O*-coumaroylglucoside-pyrogallol), (B) **41** (malvidin-3-*O*-galloylglucoside), and (C) **11** (malvidin-3-*O*-caftaric acid) detected by LC-MS in the positive-ion mode in GP extract 2.

was *m*/*z* 331 (corresponding to the loss of a caffeoylglucoside moiety, − 324 amu) and by this was attributed to the malvidin-3-*O*-caffeoylglucoside (**32**). Furthermore, seven A-type vitisins (petunidin-, peonidin-, and malvidin-based, nonacylated, acetylated, coumaroylated, and caffeoylated) were also detected in red GP and identified by comparison with their known fragmentation patterns (Table 1) reported in the literature.[22−24] Similarly, five B-type vitisins and three methyl-pyranoanthocyanins were also identified on the basis of their fragmentation patterns (Table 1).[25,26] The typical fragmentation pattern of A- and B-type vitisins is the loss of their sugar moiety that can be in their nonacylated (glucose − 162 amu) or acylated (acetylglucose − 204 amu, coumaroylglucose − 308 amu, or caffeoylglucose − 324 amu) forms giving origin to the

DOI: 10.1021/acs.jafc.5b00256
J. Agric. Food Chem. 2015, 63, 7636−7644

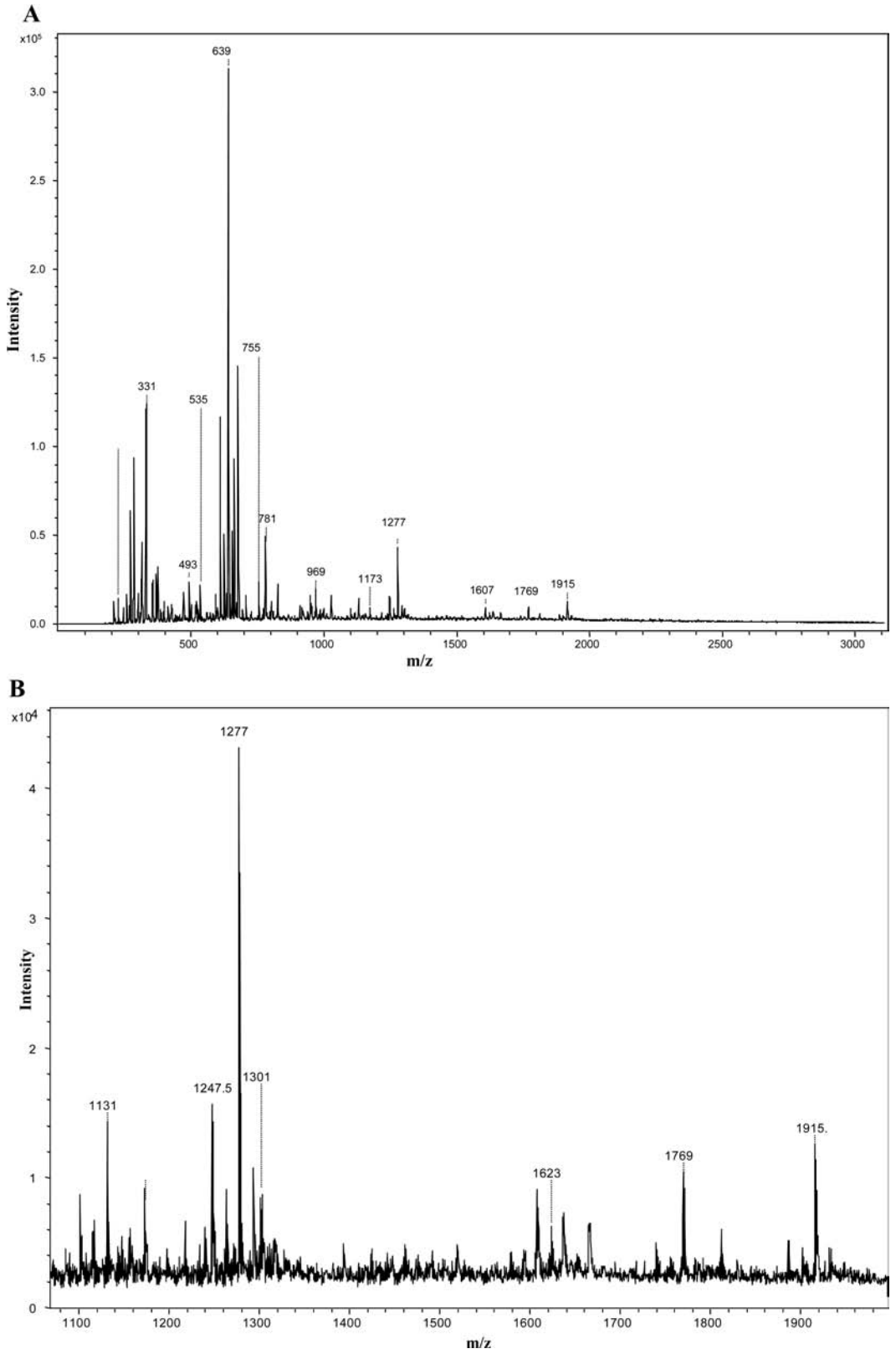

Figure 4. (A) MALDI-TOF analysis in the positive ion mode of the red GP extract (extract 1); (B) same analysis from m/z 1000 to 2000.

respective A and vitisin aglycones (m/z 399 and 355, respectively for the malvidin-derived compounds). The presence of these anthocyanin-derived pigments, although expected, has never been reported in the literature for grape pomace.

Besides, anthocyanin-derived compounds containing a catechin moiety were also detected in GP. These compounds belong to the family of the malvidin-methylmethine-catechin pigments and were identified by their ion mass (m/z 809) and characteristic fragmentation patterns (m/z 519 and 357)

DOI: 10.1021/acs.jafc.5b00256
J. Agric. Food Chem. 2015, 63, 7636−7644

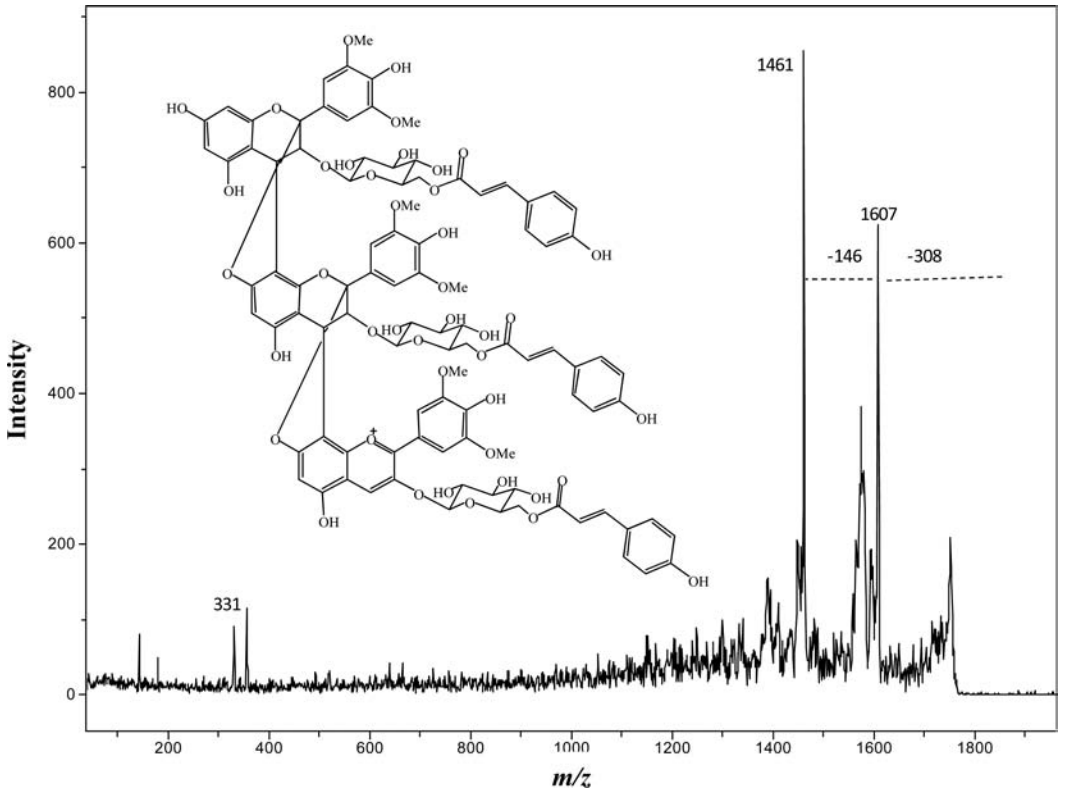

Figure 5. MALDI-TOF-TOF fragmentation of the ion at m/z 1915.

according to the data reported in the literature.[27] These ion mass and fragmentation patterns were observed for two compounds (**15** and **21**) (Table 1), and two explanations can be given for this. First, the malvidin-methylmethine-catechin pigment has an asymmetric carbon in the methylmethine group, and this way two enantiomers are possibly present. Another explanation is the possibility of formation of a similar compound but in this case with (−)-epicatechin instead of (+)-catechin. As (+)-catechin and (−)-epicatechin are isomers, the same ion mass and fragmentation patterns are expected to occur in (−)-epicatechin-based pigments. The unequivocal identification of these compounds is not possible to achieve through LC-MS spectrometry, and only by using NMR spectroscopy could the structure be confirmed. The coumaroyl derivative of this compound was also found to occur in GP (**42**) (Table 1). Moreover, the presence of two pyranomalvidin compounds with a phenol moiety was also detected and identified by LC-DAD/MS in the GP extract, namely, the pyranomalvidin-3-*O*-glucoside-phenol (**46**) and the respective coumaroyl derivative (**50**). The ion mass detected at 82.85 min with m/z 813 and fragment m/z 505 could be identified as a vinylpyranomalvidin-3-*O*-coumaroylglucoside-pyrogallol (**48**) (Figure 3A; Table 1) with a structure similar to that of B-type portisins but that has never been described in the literature. However, this is only a hypothetical structure because no full characterization by NMR has been performed on the compound due to its small concentration in GP. On the other hand, the ion mass m/z 671 detected in GP extract with a fragment at m/z 331 was attributed to the malvidin-3-*O*-galloylglucoside (**41**) (Figure 3B; Table 1). The galloylated derivative of anthocyanins has never been described in the literature. However, this identification is based on only the fragmentation pattern of the molecule as the full characterization of the compound by NMR was not possible. Additionally, small amounts of the malvidin-3-*O*-caftaric acid (**11**) (Figure 3C; Table 1) were also detected in the GP extract. Moreover, some compounds with known fragmentation patterns, namely, loss of glucose or retro-Diels–Alder (RDA) fragmentation, indicate the presence of a flavanol moiety was also observed; nevertheless, the identity of these compounds was not achieved. Their ion masses are not reported in the literature, and using only mass spectrometry it is not possible to fully identify these anthocyanin-derived compounds. Additionally, the small amounts of the compounds present in the GP extract make its full characterization by NMR nearly impossible to accomplish. These compounds are indicated in Table 1 as "unknown".

MALDI-TOF. The use of the mass spectrometry MALDI-TOF technique to characterize the oligomeric nature of the GP extract was of crucial importance because the presence of the oligomeric anthocyanin ion masses (m/z 1277, 1477, 1623, and 1915) in the ESI-MS could be due to a self-assembling mechanism that sometimes is possible to observe when the concentration of the sample is high in this mass spectrometry technique. In MALDI-TOF stacking has not been reported to occur.

Figure 4 shows the MALDI-TOF analysis of the GP extract (extract 1). It can be observed that the ion at m/z 639 is the most intense, which is in agreement with Figure 1, malvidin-3-*O*-coumaroylglucoside (compound **43**).

Figure 4B shows a series of masses that could correspond to oligomeric coumaroylated anthocyanins: the ion at m/z 1131 might be a monocoumaroylated malvidin-3-*O*-glucoside dimer, the ion at m/z 1277 could correspond to the malvidin-3-*O*-coumaroylglucoside dimer (compound **49**, Table 1), the ion at m/z 1623 could be a monocoumaroylated malvidin-3-*O*-glucoside trimer (compound **23**, Table 1), the ion at m/z 1769 might be dicoumaroylated malvidin-3-*O*-glucoside trimer, and finally the ion at m/z 1915 could correspond to a trimer of

DOI: 10.1021/acs.jafc.5b00256
J. Agric. Food Chem. 2015, 63, 7636−7644

malvidin 3-*O*-coumaroylglucoside. The latter in its nonacylated glucoside form has already been detected in a young Port wine.[18]

MALDI-TOF-TOF fragmentation of the ion at *m*/*z* 1915 gave fragments at *m*/*z* 1607 (−308), *m*/*z* 1461, and *m*/*z* 331 (Figure 5). The loss of 308 mass units corresponds to a glucose acylated with a coumaric acid, and the loss of 146 mass units corresponds to a coumaric acid moiety; therefore, it can be concluded that these fragmentations confirm the suspected nature of the trimer.

MALDI-TOF has already been used in the analysis of oligomeric food polyphenols,[28] mainly procyanidins; however, it is not commonly used in anthocyanin analysis because monomeric anthocyanins have a molecular weight of around 500 mass units, which is a difficult mass range for MALDI-TOF analysis. However, oligomeric pigments containing both anthocyanins and flavanols have already been detected by MALDI-TOF to occur in cranberry fruit.[28,29] Nevertheless, to our knowledge, this is the first study in which MALDI-TOF was used for the analysis of oligomeric anthocyanins.

One of the late-eluting fractions (obtained with 100% organic solvent in low-pressure chromatography with Toyopearl HW-40(S) gel) was particularly enriched in less hydrophilic pigments. This fraction was mainly composed of coumaroyl derivatives of anthocyanins (monomers and oligomers).

Grape pomace is an interesting source of anthocyanin-based pigments (both native and derived), as >50 different anthocyanin-based compounds were detected in this study. Oligomeric anthocyanins with coumaroylated derivatives of malvidin were detected by means of mass spectrometry for the first time in this work, and the influence of oligomeric anthocyanins on wine color remains unknown; these oligomeric anthocyanins (malvidin-3-*O*-glucoside trimer) have already been detected in young Port wine; however, the less hydrophilic nature of oligomeric coumaroylated anthocyanins raises the question of their extractability in wine. Moreover, recently the equilibrium forms of malvidin-3-*O*-glucoside trimer present in grape skins were studied in aqueous solution at different pH values through UV−visible spectroscopy. It was observed that the reactivity of this compound is strongly dominated by acid−base chemistry, with the hydration reaction accounting for <10% of the overall reactivity.[30] This indicates that polymerization may be a natural stabilization mechanism for the red color of anthocyanins.

AUTHOR INFORMATION

Corresponding Authors

*(E.S.) E-mail: esalas@uach.mx. Fax: (52) 6142366000. Phone: (52) 6142366000, ext. 4286.

*(J.O.) E-mail: joana.silva.oliveira@gmail.com.

Funding

This work received financial support from FEDER funds through COMPETE, POPH/FSE, QREN, and FCT (Fundação para a Ciência e Tecnologia) from Portugal and through Ph.D. SFRH/BD/70053/2010 and postdoctoral SFRH/BPD/65400/2009 scholarships. E.S. thanks the Consejo Nacional de Ciencia y Tecnologia (CONACYT, Mexico) for providing Grant 204199.

Notes

The authors declare no competing financial interest.

ACKNOWLEDGMENTS

We thank Silvia Maia for the LC-DAD/MS and MALDI-TOF analyses.

ABBREVIATIONS USED

GP, grape pomace; MALDI-TOF, matrix-assisted laser desorption ionization−time of flight; RT, retention time

REFERENCES

(1) Lu, Y.; Foo, L. Y. The polyphenol constituents of grape pomace. *Food Chem.* **1999**, *65*, 1−8.

(2) Amico, V.; Napoli, E. M.; Renda, A.; Ruberto, G.; Spatafora, C.; Tringali, C. Constituents of grape pomace from the Sicilian cultivar 'Nerello Mascalese'. *Food Chem.* **2004**, *88*, 599−607.

(3) Fontana, A. R.; Antoniolli, A.; Bottini, R. Grape pomace as a sustainable source of bioactive compounds: extraction, characterization, and biotechnological applications of phenolics. *J. Agric. Food Chem.* **2013**, *61*, 8987−9003.

(4) Sousa, E. C.; Uchoa-Thomaz, A. M. A.; Carioca, J. O. B.; De Morais, S. M.; De Lima, A.; Martins, C. G.; Alexandrino, C. D.; Ferreira, P. A. T.; Rodrigues, A. L. M.; Rodrigues, S. P.; Silva, J. D.; Rodrigues, L. L. Chemical composition and bioactive compounds of grape pomace (*Vitis vinifera* L.), Benitaka variety, grown in the semiarid region of northeast Brazil. *Food Sci. Technol.* **2014**, *34*, 135−142.

(5) Monrad, J. K.; Howard, L. R.; King, J. W.; Srinivas, K.; Mauromoustakos, A. Subcritical solvent extraction of anthocyanins from dried red grape pomace. *J. Agric. Food Chem.* **2010**, *58*, 2862−2868.

(6) Metivier, R. P.; Francis, F. J.; Clydesdale, F. M. Solvent extraction of anthocyanins from wine pomace. *J. Food Sci.* **1980**, *45*, 1099−1100.

(7) Vergara-Salinas, J. R.; Vergara, M.; Altamirano, C.; Gonzalez, A.; Perez-Correa, J. R. Characterization of pressurized hot water extracts of grape pomace: chemical and biological antioxidant activity. *Food Chem.* **2015**, *171*, 62−69.

(8) Gonzalez-Centeno, M. R.; Comas-Serra, F.; Femenia, A.; Rossello, C.; Simal, S. Effect of power ultrasound application on aqueous extraction of phenolic compounds and antioxidant capacity from grape pomace (*Vitis vinifera* L.): experimental kinetics and modeling. *Ultrason. Sonochem.* **2015**, *22*, 506−514.

(9) Xu, C. M.; Yagiz, Y.; Hsu, W. Y.; Simonne, A.; Lu, J.; Marshall, M. R. Antioxidant, antibacterial, and antibiofilm properties of polyphenols from muscadine grape (*Vitis rotundifolia* Michx.) pomace against selected foodborne pathogens. *J. Agric. Food Chem.* **2014**, *62*, 6640−6649.

(10) de Sa, M.; Justino, V.; Spranger, M. I.; Zhao, Y. Q.; Han, L.; Sun, B. S. Extraction yields and anti-oxidant activity of proanthocyanidins from different parts of grape pomace: effect of mechanical treatments. *Phytochem. Anal.* **2014**, *25*, 134−140.

(11) Li, Y.; Ma, R. J.; Xu, Z. Z.; Wang, J. H.; Chen, T.; Chen, F.; Wang, Z. F. Identification and quantification of anthocyanins in Kyoho grape juice-making pomace, Cabernet Sauvignon grape winemaking pomace and their fresh skin. *J. Sci. Food Agric.* **2013**, *93*, 1404−1411.

(12) Boonchu, T.; Utama-Ang, N. Optimization of extraction and microencapsulation of bioactive compounds from red grape (*Vitis vinifera* L.) pomace. *J. Food Sci. Technol.* **2015**, *52*, 783−792.

(13) Mateus, N.; Machado, J. M.; de Freitas, V. Development changes of anthocyanins in *Vitis vinifera* grapes grown in the Douro Valley and concentration in respective wines. *J. Sci. Food Agric.* **2002**, *82*, 1689−1695.

(14) Monagas, M.; Núñez, V.; Bartolomé, B.; Gómez-Cordovés, C. Anthocyanin-derived pigments in Graciano, Tempranillo, and Cabernet Sauvignon wines produced in Spain. *Am. J. Enol. Vitic.* **2003**, *54*, 163−169.

(15) Núñez, V.; Monagas, M.; Gomez-Cordovés, M. C.; Bartolomé, B. *Vitis vinifera* L. cv. Graciano grapes characterized by its anthocyanin profile. *Postharvest Biol. Technol.* **2004**, *31*, 69−79.

(16) Vidal, S.; Meudec, E.; Cheynier, V.; Skouroumounis, G.; Hayasaka, Y. Mass spectrometric evidence for the existence of oligomeric anthocyanins in grape skins. *J. Agric. Food Chem.* **2004**, *52*, 7144−7151.

(17) Salas, E.; Duenas, M.; Schwarz, M.; Winterhalter, P.; Cheynier, V.; Fulcrand, H. Characterization of pigments from different high speed

DOI: 10.1021/acs.jafc.5b00256
J. Agric. Food Chem. 2015, 63, 7636−7644

countercurrent chromatography wine fractions. *J. Agric. Food Chem.* **2005**, *53*, 4536−4546.
(18) Oliveira, J.; da Silva, M. A.; Jorge Parola, A.; Mateus, N.; Brás, N. F.; Ramos, M. J.; de Freitas, V. Structural characterization of a A-type linked trimeric anthocyanin derived pigment occurring in a young Port wine. *Food Chem.* **2013**, *141*, 1987−1996.
(19) Segade, S. R.; Vazquez, E. S.; Rodriguez, E. I. V.; Martinez, J. F. R. Influence of training system on chromatic characteristics and phenolic composition in red wines. *Eur. Food Res. Technol.* **2009**, *229*, 763−770.
(20) Baldi, A.; Romani, A.; Mulinacci, N.; Vincieri, F. F.; Casetta, B. HPLC/MS application to anthocyanins of *Vitis vinifera* L. *J. Agric. Food Chem.* **1995**, *43*, 2104−2109.
(21) Heier, A.; Blaas, W.; Droß, A.; Wittkowski, R. Anthocyanin analysis by HPLC/ESI-MS. *Am. J. Enol. Vitic.* **2002**, *53*, 78−86.
(22) Oliveira, J.; Fernandes, V.; Miranda, C.; Santos-Buelga, C.; Silva, A.; de Freitas, V.; Mateus, N. Color properties of four cyanidin-pyruvic acid adducts. *J. Agric. Food Chem.* **2006**, *54*, 6894−6903.
(23) Mateus, N.; Silva, A. M. S.; Vercauteren, J.; de Freitas, V. Occurrence of anthocyanin-derived pigments in red wines. *J. Agric. Food Chem.* **2001**, *49*, 4836−4840.
(24) Bakker, J.; Timberlake, C. F. Isolation, identification, and characterization of new color-stable anthocyanins occurring in some red wines. *J. Agric. Food Chem.* **1997**, *45*, 35−43.
(25) Oliveira, J.; de Freitas, V.; Mateus, N. A novel synthetic pathway to vitisin B compounds. *Tetrahedron Lett.* **2009**, *50*, 3933−3935.
(26) He, J.; Santos-Buelga, C.; Silva, A. M. S.; Mateus, N.; De Freitas, V. Isolation and structural characterization of new anthocyanin-derived yellow pigments in aged red wines. *J. Agric. Food Chem.* **2006**, *54*, 9598−9603.
(27) Bakker, J.; Picinelli, A.; Bridle, P. Model solutions: color and composition changes during ageing. *Vitis* **1993**, *32*, 111−118.
(28) Reed, J. D.; Krueger, C. G.; Vestling, M. M. MALDI-TOF mass spectrometry of oligomeric food polyphenols. *Phytochemistry* **2005**, *66*, 2248−2263.
(29) Christian, G. K.; Martha, M. V.; Jess, D. R. Matrix-assisted laser desorption-ionization time-of-flight mass spectrometry of anthocyanin-poly-flavan-3-ol oligomers in cranberry fruit *Vaccinium macrocarpon* and spray-dried cranberry juice. In *Red Wine Color*; American Chemical Society: Washington, DC, USA, 2004; Vol. 886, pp 232−246.
(30) Oliveira, J.; Bras, N. F.; da Silva, M. A.; Mateus, N.; Parola, A. J.; de Freitas, V. Grape anthocyanin polymerization: a putative mechanism for red color stabilization? *Phytochemistry* **2014**, *105*, 178−185.

DOI: 10.1021/acs.jafc.5b00256
J. Agric. Food Chem. 2015, 63, 7636−7644

colorless flavonoids and anthocyanins when these compounds coexist together in a complex food matrix such as red wines.

In red wine, copigmentation occurs in a "multiple" way, and more than one copigment can interact simultaneously with anthocyanins. Under these conditions, it is expected that there will be competition between the copigments and pigments in the same solution.[4] The preference or order for these associations could result in positive or negative synergies on the color and color stability, as has been previously reported for other important properties of phenolic compounds such as antioxidant activity.[18−20]

Studies focused on the mechanism of these multiple interactions in model solutions and its effects on copigmentation are scarce,[21,22] and some aspects are still not well understood such as the possible additive, synergistic, or antagonistic effects among the components present in multiple mixtures and the way to quantify the extent of the process.

From a sensory point of view, the objective assessment of copigmentation seems to be critical for understanding the relationship between grape composition and color in young red wines.[21] It is assumed that positive effects of copigmentation include greater color stability and also quantitative and qualitative color changes. Therefore, an adequate description of the color variations caused by copigmentation requires considering the changes produced in the entire visible spectral curve (380−770 nm), and not only in its visible λ_{max} portion. The color characterization of the multiple copigmentation process in the CIELAB color space by differential colorimetry provides the opportunity of assessing this phenomenon in a global way by considering the modifications in the whole visible spectrum, and conclusions related to the later color stability could be extracted. Research into the industrial evaluation of color variations based on differential colorimetry has shown significant progress in recent years.[23−25] The CIELAB color attributes lightness, chroma, and hue, and their related color-difference formulas are widely used for industrial applications that require accurate measurement of color changes related to perception and acceptability. Nonetheless, there is very little previous information about the application of differential colorimetry into the study of copigmentation.[14,26] Recently, differential colorimetry has led to a new point of view in the knowledge of the chemistry of the anthocyanin color and to the interpretation of the copigmentation effects on its visual assessment, both in model solutions and in wines.[9,15,22,27]

Thus, with the aim to further the knowledge of the copigmentation interactions and their implication in the chemical and colorimetric stability of the color of red wine anthocyanins, we have studied the combined effect of anthocyanin−flavanol−flavonol ternary mixtures by differential colorimetry. The levels of flavanols and flavonols in the multiple mixtures were modified to simulate the effect of applying such enological procedures as adding white skins (flavonols) or seeds (flavanols) during the vinification of red wines. The pigment considered in this study represents the main anthocyanin of red grapes and wines (malvidin-3-glucoside). The copigment (+)-catechin was selected as it is one of the main monomeric flavanols present in grape seed, and quercetin-3-β-D-glucoside was representative of flavonols present in grape skin.

MATERIALS AND METHODS

Chemicals and Standards. Malvidin-3-glucoside (≥97%) was purchased from Extrasynthese (Genay, France). The copigments (+)-catechin (≥96%) and quercetin-3-β-D-glucoside (≥90%) were purchased from Sigma-Aldrich (Madrid, Spain). All chromatographic solvents (acetonitrile and formic acid) were of HPLC grade (Merck, Darmstadt, Germany). Purified water was obtained from a NANOpure Diamond system (Barnsted Inc., Dubuque, IA, USA). All other chemicals (methanol, tartaric acid, and sodium chloride) were of analytical grade and supplied by Panreac Química (Barcelona, Spain).

Preparation of Ternary Copigmented Solutions. All copigmented solutions used were prepared in a wine-like medium containing 5 g/L tartaric acid in 12% ethanol with ionic strength adjusted to 0.2 M by the addition of sodium chloride and pH adjusted to 3.6 with NaOH.

Two copigmented solutions based on binary combinations of malvidin-3-glucoside with (+)-catechin (MC) and malvidin-3-glucoside with quercetin-3-β-D-glucoside (MQ) were prepared at the same pigment/copigment concentration (200:200 mg/L). MC and MQ solutions were filtered (0.45 μm Millipore-AP20 filters) and stored closed in darkness at 25 °C for 2 h to reach equilibrium. Then, quercetin-3-β-D-glucoside was added in concentrations 50, 100, and 200 mg/L to three aliquots of the MC solution to obtain the following ternary mixtures: MC+Q50, MC+Q100, and MC+Q200. In the same way (+)-catechin was added in concentrations of 50, 100, and 200 mg/L to three aliquots of the MQ solution to obtain the following ternary mixtures: MQ+C50, MQ+C100, and MQ+C200.

All of the copigmented solutions, in both binary and ternary combinations, were prepared in triplicate and stored closed in darkness at 25 °C. The final anthocyanin concentration was the same in all cases (200 mg/L). Samples (n = 24) were taken periodically for the colorimetric and chemical analysis at 2, 24, and 72 h and at 1, 2, and 3 weeks.

HPLC-DAD Analysis. The content of malvidin-3-glucoside in the model solutions and its evolution over the storage period were evaluated by HPLC-DAD using a Hewlett-Packard 1200 series liquid chromatograph (Palo Alto, CA, USA), equipped with a quaternary pump, column heater, UV−vis diode array detector, automatic injector, and ChemStation software. A Zorbax SB C18 column (4.6 mm × 250 mm, 4.6 μm particle size) thermostated at 38 °C was used. The solvents used were (A) acetonitrile/formic acid/water (3:10:87) and (B) acetonitrile/formic acid/water (50:10:40). The elution profile was as follows: 0−5 min, 94% A; 5−7.5 min, 70% A; 7.5−12.5 min, 60% A; 12.5−16 min, 55% A; 16−19 min, 50% A; 19−20 min, 94% A. The flow rate was 1 mL/min, and the injection volume was 50 μL. UV−vis spectra were recorded from 200 to 800 nm with a bandwidth of 2.0 nm. The quantification was performed at 525 nm by HPLC-DAD using calibration curves of malvidin-3-glucoside standard. All analyses were carried out in duplicate, and results were expressed as milligrams per liter.

Analysis of Copigmentation by Colorimetric Measurements. The absorption spectra (380−770 nm) of all solutions were recorded at constant intervals ($\Delta\lambda$ = 2 nm) with a Hewlett-Packard UV−vis HP8453 spectrophotometer, using 5 mm path length glass cells and distilled water as a reference. The CIELAB parameters were calculated from the absorption spectra by using the original software CromaLab,[28] following the recommendations of the Commission International de L'Eclariage: CIE 1964 10° Standard Observer and the Standard Illuminant D65, corresponding to natural daylight.[29] CIELAB parameters were calculated: L^* (the correlate of lightness; ranging from 0, black, to 100, white) and two color coordinates, a^* (which takes positive values for reddish colors and negative values for greenish ones) and b^* (positive for yellowish colors and negative for bluish ones). From these coordinates, other color parameters are defined: the hue angle (h_{ab}, the correlate of chromaticity or tone, and the chroma C^*_{ab}, the correlate of saturation or intensity of color). Moreover, L^*, C^*_{ab}, and h_{ab} can be distinguished as quantitative or qualitative parameters as they indicate quantitative (L^* and C^*_{ab}) or qualitative (h_{ab}) attributes of color.

The color changes of solutions induced by copigmentation and their color stability over the storage period were evaluated by differential colorimetry according to the methodology described in Gordillo et al.,[15] which is based on the application of various different

DOI: 10.1021/acs.jafc.5b00181
J. Agric. Food Chem. 2015, 63, 7645−7653

Table 1. Mean Values and Standard Deviations (n = 3) of Colorimetric Parameters (L^*, a^*, b^*, C^*_{ab}, h_{ab}) Obtained in MC and MQ Binary Solution and Their Respective Ternary Copigmented Solutions after the Addition of Increasing Concentrations of Quercetin-3-β-O-glucoside to MC and (+)-Catechin to MQ, at 2 h and 3 Weeks of Storage (25 °C)[a]

	MC solutions[b]				MQ solutions[c]			
	binary mixture	multiple mixture			binary mixture	multiple mixture		
	MC	MC+Q50	MC+Q100	MC+Q200	MQ	MQ+C50	MQ+C100	MQ+C200
				2 h of Storage				
L^*	73.1 ± 0.1 a	71.4 ± 0.4 b	67.0 ± 2.6 c	64.3 ± 0.6 c	65.2 ± 0.1 a	65.2 ± 0.5 a	64.7 ± 0.1 a	65.1 ± 0.4 a
a^*	42.5 ± 0.1 a	44.0 ± 0.6 b	45.6 ± 0.8 b	47.2 ± 0.3 c	47.6 ± 0.6 a	48.2 ± 0.6 a	47.7 ± 0.3 a	47.9 ± 0.3 a
b^*	−4.4° ± 0.1 a	−6.3° ± 0.5 b	−7.9° ± 1.6 b	−11.8° ± 0.6 c	−11.1° ± 0.1 a	−11.3° ± 0.1 a	−11.5° ± 0.1 a	−12.2° ± 0.1 b
C^*_{ab}	42.7 ± 0.1 a	44.5 ± 0.6 b	46.2 ± 1.1 b	48.6 ± 0.4 c	48.7 ± 0.6 a	49.7 ± 0.6 a	49.1 ± 0.1 a	49.5 ± 0.3 a
h_{ab}	−5.8° ± 0.1 a	−8.2° ± 0.6 b	−9.3° ± 1.9 b	−13.9° ± 0.6 c	−13.3° ± 0.1 a	−13.3° ± 0.1 a	−13.6° ± 0.2 a	−14.3° ± 0.2 b
total color	50.1 ± 0.2 a	52.9 ± 0.3 b	56.1 ± 0.7 c	60.3 ± 0.3 d	60.4 ± 0.3 a	60.1 ± 1.0 a	60.3 ± 0.2 a	60.7 ± 0.5 a
				3 Weeks of Storage				
L^*	81.5 ± 0.1 a	72.8 ± 0.2 b	69.8 ± 0.4 c	67.3 ± 0.3 d	64.5 ± 0.5 a	66.4 ± 0.2 b	66.8 ± 0.1 b	66.9 ± 0.2 b
a^*	32.2 ± 0.4 a	36.7 ± 0.1 b	39.6 ± 0.5 c	45.4 ± 0.2 d	47.5 ± 0.1 a	44.5 ± 0.3 b	42.0 ± 0.2 c	41.7 ± 0.2 c
b^*	5.6° ± 0.3 a	2.9° ± 0.1 b	1.4° ± 0.1 c	−2.5° ± 0.1 d	−7.5° ± 0.1 a	−6.8° ± 0.1 b	−5.8° ± 0.1 c	−4.5° ± 0.2 d
C^*_{ab}	32.3 ± 0.3 a	36.7 ± 0.1 b	39.6 ± 0.5 c	45.6 ± 0.2 d	48.1 ± 0.1 a	45.4 ± 0.3 b	42.4 ± 0.1 c	41.8 ± 0.2 c
h_{ab}	6.6° ± 0.4 a	2.8° ± 0.4 b	1.9° ± 0.2 c	−3.4° ± 0.1 d	−8.9° ± 0.2 a	−8.8° ± 0.1 a	−7.3° ± 0.1 b	−6.7° ± 0.2 b
total color	36.2 ± 0.4 a	45.7 ± 0.1 b	49.8 ± 0.2 c	56.1 ± 0.1 d	60.2 ± 0.2 a	55.9 ± 0.4 b	54.0 ± 0.2 c	53.3 ± 0.3 d

[a]Different letters in the same row indicate significant differences (p < 0.05; Tukey test) between binary and ternary mixtures for each MC and MQ solution, respectively. [b]MC, Mv 3-glc/ (+)-cat (200:200 mg/L); MC+Q50, MC+Q100, MC+Q200, MC solution, +50, +100, +200 mg/L of querc 3-glc. [c]MQ, Mv 3-glc/querc 3-glc (200:200 mg/L); MQ+C50, MQ+C100; MQ+C200, MQ solution +50,+100,+200 mg/L of (+)-cat.

color-difference formulas. The color difference between pairs of samples was computed as the Euclidean distance between two points in the three-dimensional CIELAB space by means of the CIE76 color difference formulas: $\Delta E^*_{ab} = [(\Delta L^*)^2 + (\Delta a^*)^2 + (\Delta b^*)^2]^{1/2}$. Also, on the basis of ΔE^*_{ab} the parameter total color was calculated as the color difference between the color of each sample (L^*, a^*, and b^*) and distilled water, which correspond with an achromatic reference (L^* = 100, a^* = 0, b^* = 0), as follows:

$$\text{Total color: } [(L^* - 100)^2 + (a^* - 0)^2 + (b^* - 0)^2]^{1/2} \quad (1)$$

The trend of the changes in each individual color attribute between pairs of samples was evaluated by means of the absolute lightness, chroma, and hue differences (ΔL^*, ΔC^*_{ab}, Δh_{ab}). Also, the relative contribution of each color attribute that makes a given color difference value (ΔE^*_{ab}) was calculated as the quadratic differences of lightness, chroma, and hue ($\%\Delta^2 L$, $\%\Delta^2 C$, and $\%\Delta^2 H$), expressed as percentages:

$$\text{rel contribution (\%) of lightness: } \%\Delta^2 L = [(\Delta L^*)^2/(\Delta E^*_{ab})^2] \times 100$$

$$\text{rel contribution (\%) of chroma: } \%\Delta^2 C = [(\Delta C^*_{ab})^2/(\Delta E^*_{ab})^2] \times 100$$

$$\text{rel contribution (\%) of hue: } \%\Delta^2 H = [(\Delta h)^2/(\Delta E^*_{ab})^2] \times 100$$

ΔH is mathematically deduced from $\Delta H = [(\Delta E^*_{ab})^2 - ((\Delta L)^2 + (\Delta C)^2)]^{1/2}$.

Statistical Analysis. All statistical analyses were performed using Statistica v.8.0 software.[30] Univariate analysis of variance (Tukey test, p < 0.05.) was applied to establish statistical differences for the anthocyanin concentration and the colorimetric characteristic between binary and multiple copigmented solutions.

RESULTS AND DISCUSSION

Effect of Multiple Copigmentation on Color Characteristics by Differential Colorimetry. Table 1 shows the influence of increasing concentrations of quercetin-3-β-O-glucoside and (+)-catechin on the colorimetric parameters (L^*, a^*, b^*, C^*_{ab}, and h_{ab}) and total color of MC and MQ solutions, respectively, at 2 h after their preparation. Results showed that the two copigments studied have quite different abilities to interact with malvidin-3-glucoside in multiple copigmentation conditions. In particular, the addition of quercetin-3-β-D-glucoside caused an immediate increase in the total color of the MC solutions, which reflects the preferential binding between quercetin-3-β-D-glucoside and the flavylium ions and the shift of the equilibrium toward the colored forms. The magnitude of this effect, expressed as the relative increases of the Total color, was significantly (p < 0.05) correlated with the quercetin-3-β-D-glucoside concentration. Specifically, the Total color was increased by 5, 12, and 20% at 50, 100, and 200 mg/L of quercetin-3-β-D-glucoside. Thus, quercetin-3-β-D-glucoside was demonstrated to have a strong affinity for malvidin-3-glucoside in the presence of (+)-catechin. Also, the addition of quercetin-3-β-D-glucoside to MC solutions produced a progressive decrease in lightness and hue values (L^* and h_{ab}), followed by an increase of chroma (C^*_{ab}), which means a gradual and significant intensification of the color.

In contrast, the addition of (+)-catechin did not greatly influence the colorimetric characteristics of MQ solutions at any tested level, with the exception of the b^* and hue values, which were significantly (p < 0.05) decreased at 200 mg/L. These slight variations observed in the qualitative attributes of color (b^* and hue values) denote a bluish effect. In any case, no statistically significant differences were found in the total color, chroma, and lightness (quantitative attributes) between MC and MQ+C solutions, indicating similar color intensity in both binary and ternary mixtures. Thus, in comparison to quercetin-3-β-D-glucoside, (+)-catechin was demonstrated to have a much lower affinity for malvidin-3-glucoside in multiple conditions.

The different abilities of quercetin-3-β-D-glucoside and (+)-catechin to modify the copigmentation equilibrium in multiple conditions can be explained in terms of their specific binding strengths and concentrations resulting in variable effects in color.[4] With respect to the MQ solutions, our results suggest that the strong interaction initially established between quercetin-3-β-D-glucoside and malvidin-3-glucoside prevents the subsequent binding with (+)-catechin. As expected, quercetin-3-β-D-glucoside offers larger extended π conjugation that makes the molecule more planar and facilitates the $\pi-\pi$ interactions to form stable copigmentation complexes,[16,31] so the availability of the flavylium ion to interact with (+)-catechin could be strongly

DOI: 10.1021/acs.jafc.5b00181
J. Agric. Food Chem. 2015, 63, 7645−7653

Table 2. Color, Lightness, Chroma, and Hue Differences (ΔE^*_{ab}, ΔL^*, ΔC^*_{ab}, Δh_{ab}) between Binary and Ternary Copigmented Solutions after the Addition of Increasing Concentrations of Quercetin-3-β-*O*-glucoside to MC Solutions and (+)-Catechin to MQ Solutions, Calculated as Mean Values at 2 h and 3 Weeks of Storage (25 °C)

	MC solutions[a]			MQ solutions[b]		
	MC+Q50/MC	MC+Q100/MC	MC+Q200/MC	MQ+C50/MQ	MQ+C100/MQ	MQ+C200/MQ
			2 h of Storage			
ΔE^*_{ab}	2.9	7.7	12.4	0.6	1.2	1.1
ΔL^*	−1.7	−6.1	−8.8	0.0	−0.5	−0.1
ΔC^*_{ab}	+1.8	+3.5	+5.9	+1.0	+0.4	+0.8
Δh_{ab}	−2.4°	−3.5°	−8.1°	0.0°	−0.3°	−1.0°
			3 Weeks of Storage			
ΔE^*_{ab}	10.0	17.2	20.6	3.8	6.0	6.7
ΔL^*	−8.7	−11.7	−14.2	+1.9	+2.3	+2.4
ΔC^*_{ab}	+4.4	+7.3	+13.3	−2.7	−5.7	−6.3
Δh_{ab}	−3.8°	−4.7°	−10.0°	+0.1°	+1.6°	+2.1°

[a]MC, Mv 3-glc/ (+)-cat (200:200 mg/L); MC+Q50, MC+Q100, MC+Q200, MC solution +50, +100, +200 mg/L of querc 3-glc. [b]MQ, Mv 3-glc/ querc 3-glc (200:200 mg/L); MQ+C50, MQ+C100, MQ+C200, MQ solution +50,+100,+200 mg/L of (+)-cat.

limited. Similar results were obtained by Rustioni et al.,[17] who concluded that some flavonols are capable of displacing flavanols when they coexist in competitive equilibrium.

However, the opposite effect occurred when increasing concentrations of quercetin-3-β-D-glucoside were added to MC solutions. In this case, the initial copigmentation effect observed between malvidin-3-glucoside and (+)-catechin was comparatively weaker (note that the total color of MC was much lower than that of MQ). This fact probably favored the later interaction of the quercetin-3-β-D-glucoside with the anthocyanin chromophore, which gradually forced the global copigmentation equilibrium to a greater extent.

To establish whether the observed changes in the CIELAB parameters were visually relevant, color variations between binary and ternary copigmented solutions were calculated and expressed as colorimetric differences ΔE^*_{ab} (see Table 2, data referred to 2 h). Also, in an attempt of understand the significance of the color changes, the absolute lightness, chroma, and hue differences (ΔL^*, ΔC^*_{ab}, and Δh_{ab}) were calculated. According to Martinez et al.,[24] ΔE^*_{ab} around 3 units indicates, approximately, color differences appreciable to the human eye (as an average observer). On the basis of this premise, the most perceptible color changes were produced when quercetin-3-β-D-glucoside was added to the MC solutions. This color variation became more perceptible with higher concentrations of quercetin-3-β-D-glucoside, which was consistent with the effects observed in the total color and the magnitude of copigmentation. Specifically, the tendency was always toward higher decreases of ΔL^* and Δh_{ab} (negative values), which correspond to visually increasing darkening and bluish effects. Simultaneously, chroma differences ΔC^*_{ab} tended toward higher increases (positive values), resulting in more saturated solutions. Thus, it could be verified that in multiple copigmentation conditions quercetin-3-β-D-glucoside makes an important contribution to color intensity and tonality. In contrast, the color variations induced by (+)-catechin can be considered negligible at all of the concentrations tested as ΔE^*_{ab} values in all color pairs were <2 units. Similarly, ΔL^*, ΔC^*_{ab}, and Δh_{ab} showed relatively minor changes. This fact confirms again the greater difficulty of (+)-catechin binding malvidin-3-glucoside in the presence of quercetin-3-β-D-glucoside.

Moreover, by comparing the relative contributions of lightness ($\%\Delta^2 L$), chroma ($\%\Delta^2 C$), and hue ($\%\Delta^2 H$) to each color difference (ΔE^*_{ab}) it was possible to evaluate which color attribute was the most influenced (Figure 1). Taking into account only solutions with the largest perceptible color changes (MC+Q100 and MC+Q200), it can be observed that quercetin-3-β-D-glucoside induced similar color effects independently of the concentration tested. Results showed that the lightness was the most overall influential parameter ($\%\Delta^2 L \sim 50\%$), whereas the weights of the chroma and hue modifications were in general comparatively lower, but similar among them ($\%\Delta^2 C$ and $\%\Delta^2 H$ ~25%).

Effect of Multiple Copigmentation on Color Stability by Differential Colorimetry. The evolution of the total color of solutions during the 3 weeks of storage in darkness at 25 °C is shown in Figure 2, where the mean value and standard deviation of samples are included. It can be observed that the addition of quercetin-3-β-D-glucoside is more effective in maintaining the total color of the MC solutions than the addition of (+)-catechin to the MQ solutions. As shown in Figure 2A, the Total color hardly decreased in MC binary solutions after 2 weeks of storage (around 28%), whereas in the ternary solutions containing 50, 100, and 200 mg/L of quercetin-3-β-D-glucoside the total color losses were 13.6, 10.4, and 4%, respectively. Contrary to that, higher decreases of total color were observed in MQ+C ternary solutions as the (+)-catechin ratio increased in the mixtures (Figure 2B).

The assessment of changes in the CIELAB parameters during storage was also decisive to establish the copigment having the greatest impact on the stability of the quantitative (L^* and C^*_{ab}) or qualitative (h_{ab}) color attributes (Figures 3 and 4). As can be observed, the chroma values decreased in all solutions over time while the hue values increased toward positive values. This means that the color variation that took place during stabilization in both binary and ternary mixtures was due to a decrease of the quantity of color and bluish hue (h_{ab} nearer to 0°, redness color).[10]

In particular, quercetin-3-β-D-glucoside was shown to better preserve the lightness than chroma and hue of MC+Q ternary solutions (Figure 3). Independently of the concentration tested, the global variations of lightness values were always below 3.5% after 3 weeks of storage (Figure 3A). On the other hand, the evolution of chroma and hue (Figure 3B,C) suggests a greater stabilization effect at the highest concentration of quercetin-3-β-D-glucoside because the global losses of the quantity of color and bluish hues were less intense at 200 mg/L.

DOI: 10.1021/acs.jafc.5b00181
J. Agric. Food Chem. 2015, 63, 7645−7653

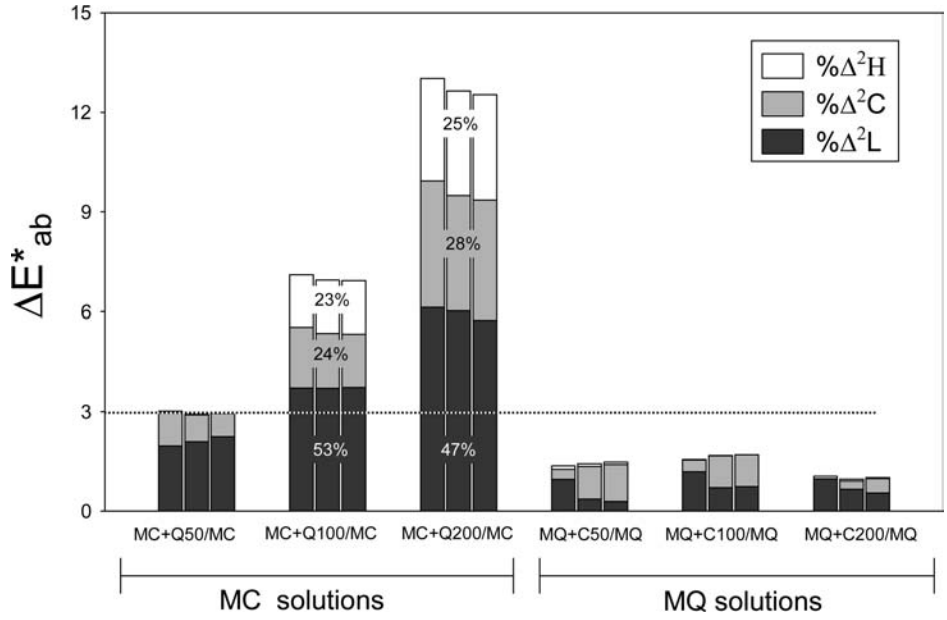

Figure 1. Color differences (ΔE^*_{ab}), with the relative contribution of lightness, chroma, and hue ($\%\Delta^2L$, $\%\Delta^2C$, $\%\Delta^2H$), between binary and ternary copigmented solutions after the addition of increasing concentrations of quercetin-3-β-*O*-glucoside to MC solution and (+)-catechin to MQ solutions, calculated at 2 h (25 °C).

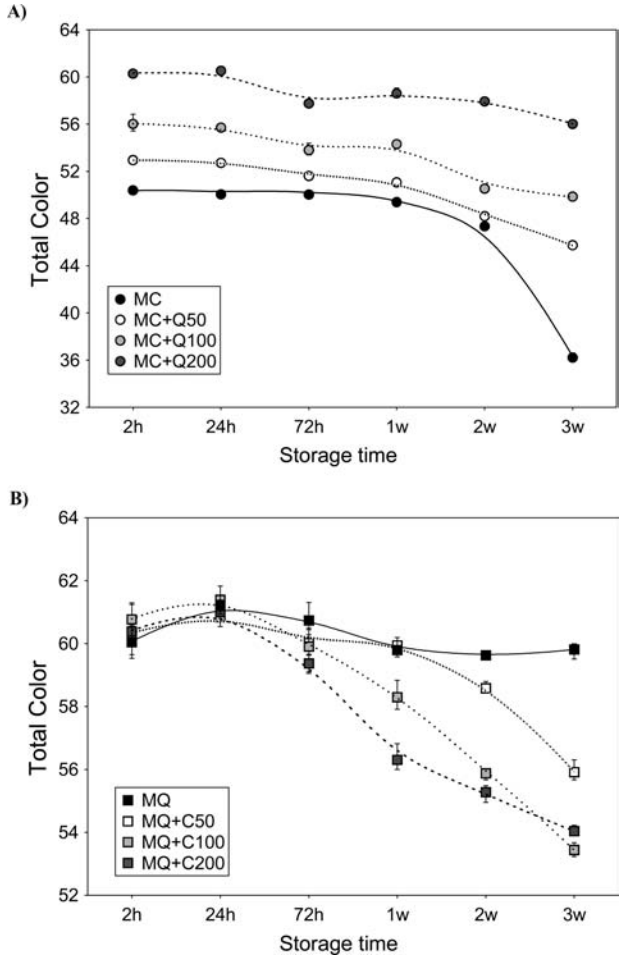

Figure 2. Influence of increasing concentrations of quercetin-3-β-*O*-glucoside and (+)-catechin on the evolution of the total color of MC and MQ binary and ternary solutions, respectively, over the storage period at 25 °C: (A) MC solutions; (B) MQ solutions.

(+)-Catechin showed a lower protective effect on the quantitative attributes of color, especially for chroma variations (Figure 4A,B). During storage, the chroma values notably decreased about 13% with concentrations of (+)-catechin up to 100 mg/L. Thus, surprisingly, the binary solution MQ showed greater color stability over time than in the presence of increasing concentrations of (+)-catechin. These results highlight that adding copigments does not always lead to a stabilizing effect, but depends on the type of copigments as well as on its concentration.

Furthermore, the assessment of the color differences (ΔE^*_{ab}) occurring at 24 and 72 h and at 1, 2, and 3 weeks, in relation to samples taken at 2 h, provides an objective evaluation of the chromatic stability for each solution over time (Figure 5). The lower values of ΔE^*_{ab} during storage in MC+Q ternary solutions than in MC binary solutions indicate lower color variation and, thus, higher color stability (Figure 5A). Considering the whole period of storage, the lowest color differences corresponded to MC+Q200 and MC+Q100 solutions compared to MC+Q50 and MC (ΔE^*_{ab} = 9.8, 10.5, 12.1, and 16.4, respectively). In contrast, growing ΔE^*_{ab} values in MQ+C ternary solutions relative to those in MQ binary solution indicate higher color variation and, thus, lower color stability (Figure 5B). Nevertheless, this negative effect seemed to greatly depend on the (+)-catechin concentration in the mixtures. It can be observed that the color modification experienced by MQ+C50 solution was not easily detectable ($\Delta E^*_{ab} < 3$)[24] until the end of the storage period. This means that (+)-catechin does not cause important color destabilization in multiple conditions at low concentrations (50 mg/L in our conditions). However, at (+)-catechin concentrations up to 100 mg/L, ΔE^*_{ab} values were detectable from the first weeks of storage.

As a consequence of the different color stabilities over time, MC+Q and MQ+C ternary solutions could be differentiated at the end of storage period in terms of luminosity, intensity, and chromaticity from their respective MC and MQ binary solutions (Table 1). Specifically, MC+Q solutions showed

DOI: 10.1021/acs.jafc.5b00181
J. Agric. Food Chem. 2015, 63, 7645−7653

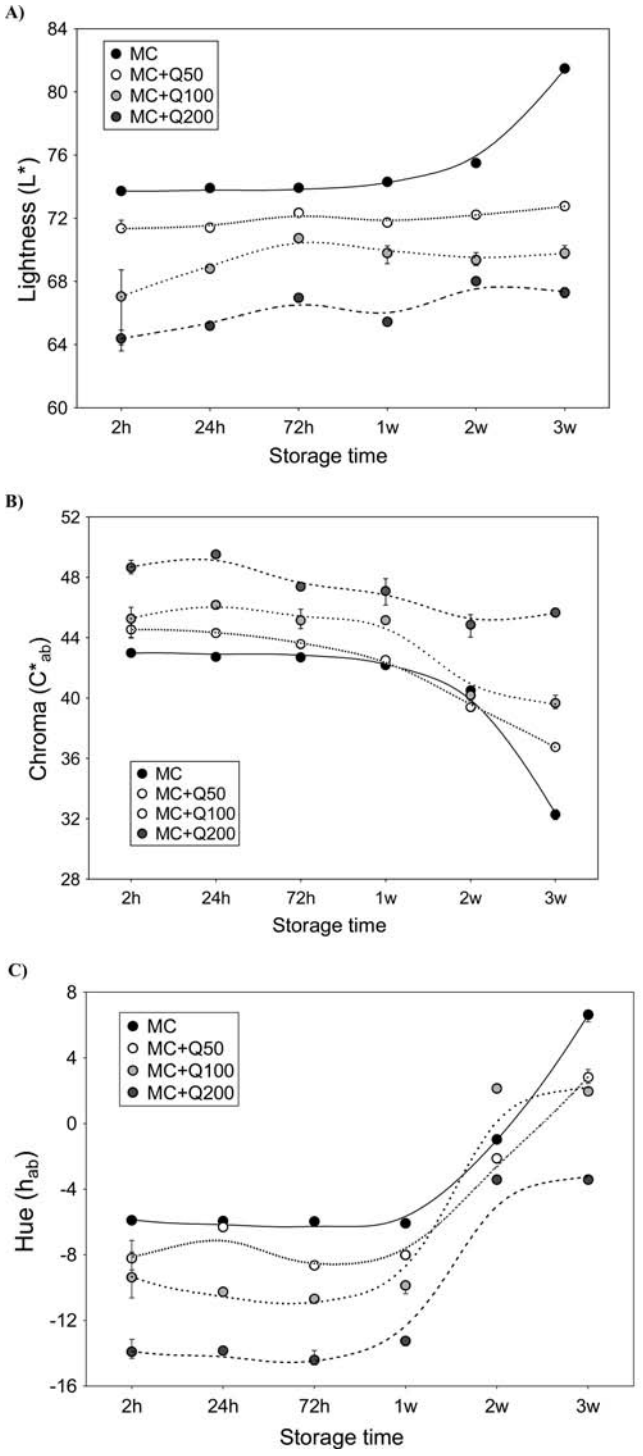

Figure 3. Influence of increasing concentrations of quercetin-3-β-*O*-glucoside on the evolution of the CIELAB colorimetric parameters of MC binary and ternary solution over the storage period at 25 °C in darkness: (A) lightness, L^*; (B) chroma, C^*_{ab}; (C) hue, h_{ab}.

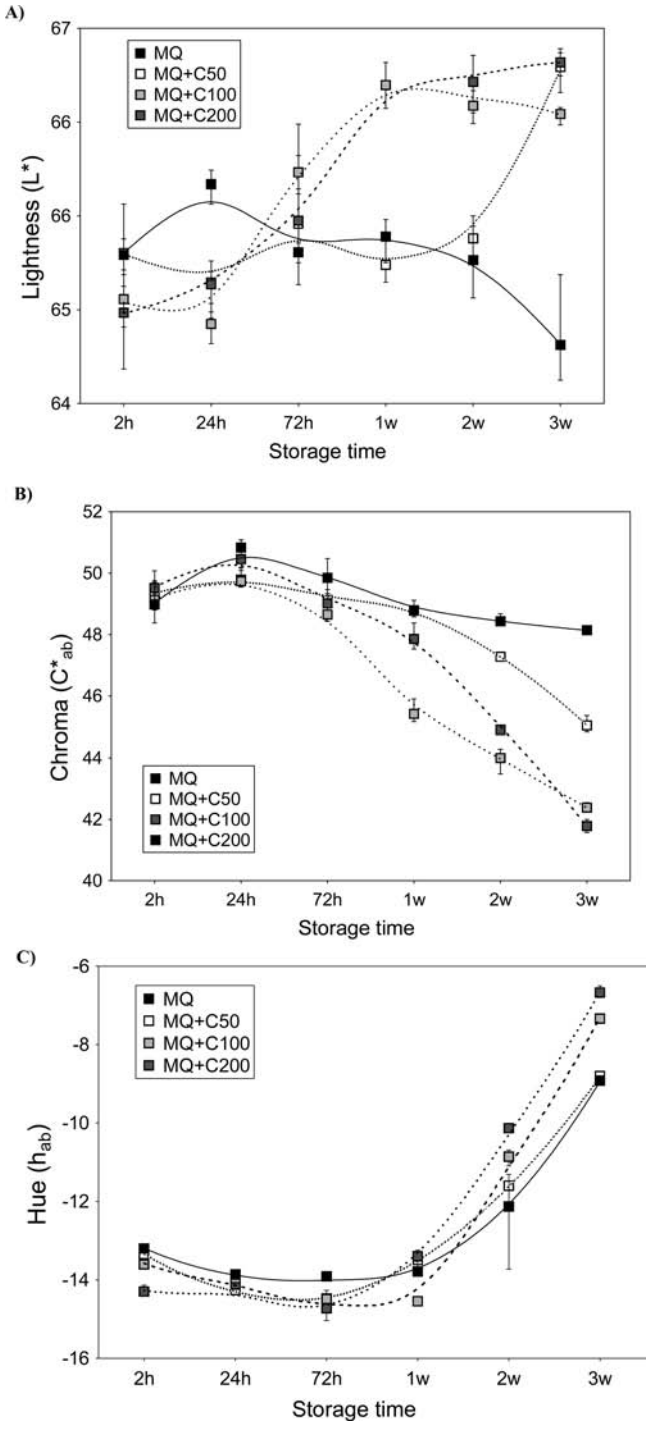

Figure 4. Influence of increasing concentrations of (+)-catechin on the evolution of the CIELAB colorimetric parameters of MQ binary and ternary solution over the storage period at 25 °C in darkness: (A) lightness, L^*; (B) chroma, C^*_{ab}; (C) hue, h_{ab}.

significantly lower values of L^* and hue but higher values of total color and C^*_{ab} than MC solution. In terms of detectable color variations[24] (Table 2), the highest color difference value was obtained between MC and MC+Q200 solutions (ΔE^*_{ab} = 20.6). The negative values of lightness and hue differences found among them (ΔL^* = −14.2, Δh_{ab} = −10.0°), but positive chroma difference (ΔC^*_{ab} = +13.3), means that MC +Q200 solutions had darker and more intense color with more bluish hue than MC solutions.

On the other hand, MQ+C solutions showed significantly higher values of L^* but lower total color and C^*_{ab} than MQ solutions (Table 1). In this case, the trend of the lightness and chroma differences among pairs of solutions was the opposite. Positive values for ΔL^* and negative values for ΔC^*_{ab} indicate that the final color of MQ+C solutions was lighter and less saturated than that of MQ solution. Again, the color differences were most appreciable with the highest concentration of (+)-catechin (MC+Q100 and MC+Q200 solutions).

DOI: 10.1021/acs.jafc.5b00181
J. Agric. Food Chem. 2015, 63, 7645−7653

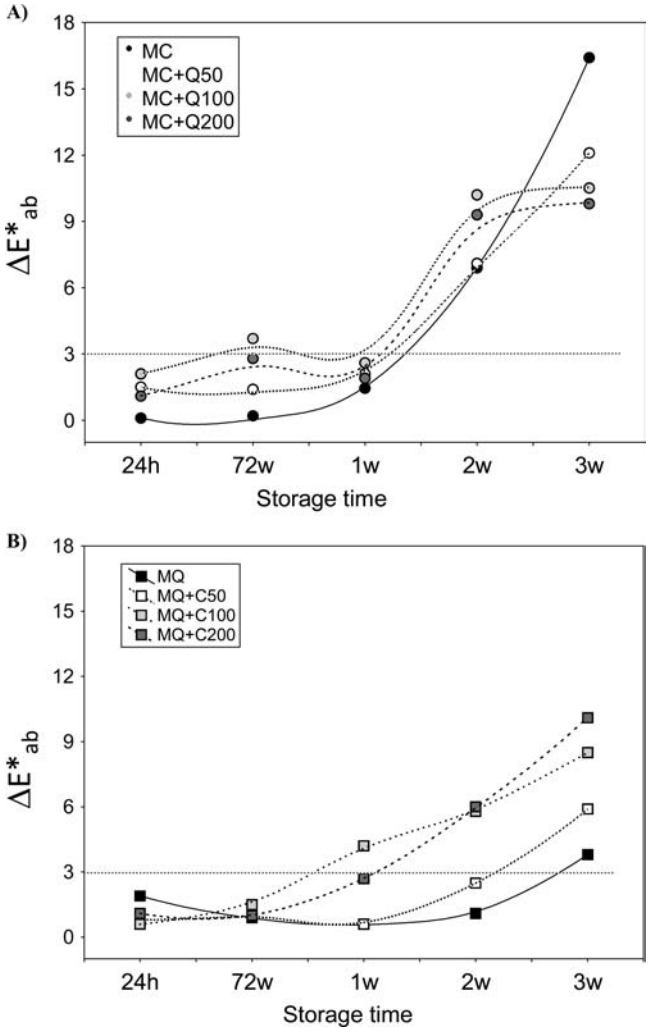

Figure 5. Influence of increasing concentrations of quercetin-3-β-*O*-glucoside and (+)-catechin on the color variation (ΔE^*_{ab}) of MC and MQ binary and ternary solutions, respectively, over the storage period at 25 °C: (A) MC solutions; (B) MQ solutions.

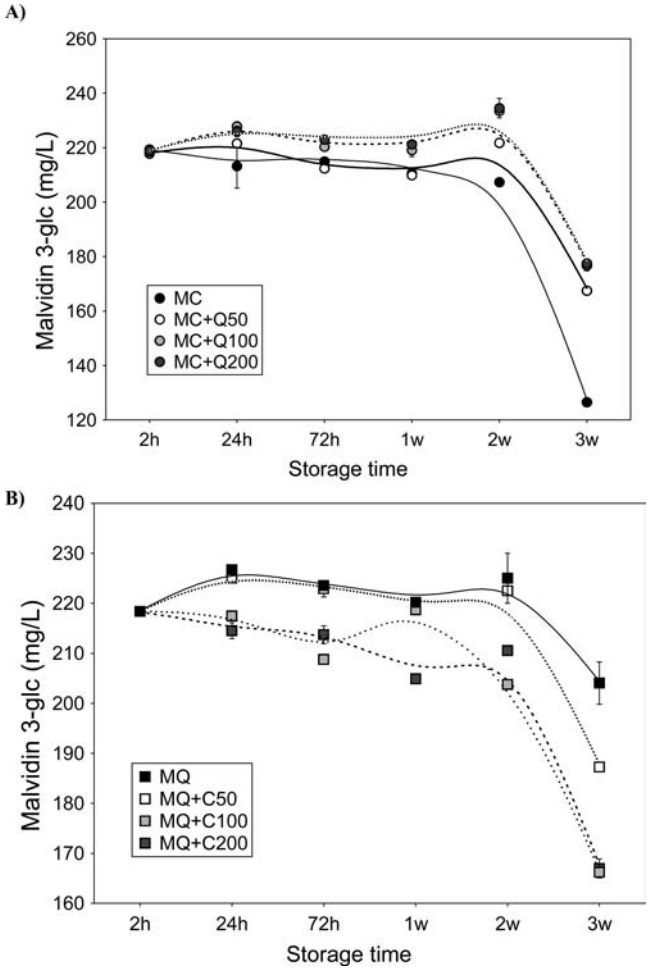

Figure 6. Influence of increasing concentrations of quercetin-3-β-*O*-glucoside and (+)-catechin on the evolution of the malvidin-3-glucoside content of MC and MQ binary and ternary solutions, respectively, over the storage period at 25 °C: (A) MC solutions; (B) MQ solutions.

Thus, with the whole set of data taken into account, it was confirmed that the addition of increasing amounts of quercetin-3-β-D-glucoside to MC binary mixtures led to MC+Q ternary solutions with more stable color that kept their intensity and vivid bluish tonalities for a longer time, which represent color characteristics highly appreciated in young red wines. In contrast, the addition of increasing amounts of (+)-catechin to MQ binary mixtures led to MQ+C ternary solutions with less stable color that maintain their vivid red intensity for only a short time, so their value as potential additives in the wine industry could be rather questionable because the minimization of color fluctuation is essential to maintain the global quality of wines.

Effect of Multiple Copigmentation Interactions on Chemical Stability. Figure 6 shows the changes in the concentration of malvidin-3-glucoside (mg/L ± SD) in solutions over time. Although the presence of the copigments does not impede the loss of the anthocyanin content, the protective effects of quercetin-3-β-D-glucoside and (+)-catechin in multiple conditions were quite different. As observed in Figure 6A, the content of malvidin-3-glucoside in MC and MC+Q solutions is maintained more or less constant during the first 2 weeks of storage. After this, the amount of malvidin-3-glucoside declines dramatically, the rate of degradation being less intense in the presence of quercetin-3-β-D-glucoside. The global content of malvidin-3-glucoside decreased over the whole storage period by 42% in MC binary solutions. In comparison, the anthocyanin degradation was notably reduced to 24, 19.5, and 19% with the addition of 50, 100, and 200 mg/L of quercetin-3-β-D-glucoside, respectively. These observations confirm that quercetin-3-β-D-glucoside behaved as a protective copigment in multiple conditions by preventing excessive pigment loss. In general terms, the higher the concentration of quercetin-3-β-D-glucoside in MC solution, the greater protective effects against anthocyanin degradation, which was in accordance with the amplitude of the effects observed in color stability. Nevertheless, the positive effect of quercetin-3-β-D-glucoside cannot be raised to an unlimited extent because no further improvement in the anthocyanin stability was produced when its concentration exceeded a certain level (in our conditions, up to 100 mg/L). This observation was in agreement with previous studies.[2,32] The analysis of variance (ANOVA, Tukey test) revealed significant differences ($p < 0.05$) for the final levels of malvidin-3-glucoside between MC and MC+Q solutions. MC solution showed the lowest content in malvidin-3-glucoside (126.5 ± 0.2 mg/L). As expected, no statistically significant differences were found for the anthocyanin content between MC+Q100 and MC+Q200 solutions (176.7 ± 2.8 and

DOI: 10.1021/acs.jafc.5b00181
J. Agric. Food Chem. 2015, 63, 7645−7653

177.5 ± 0.3 mg/L, respectively) because the losses of malvidin-3-glucoside were very similar in both ternary solutions. Thus, the application of quercetin-3-β-D-glucoside as wine copigments appears to be promising because it tends to significantly improve the stability of the anthocyanins in multiple conditions over time.

On the other hand, the anthocyanin stability of MQ and MQ+C solutions during storage is presented in Figure 6B. It can be observed that the malvidin-3-glucoside degradation occurred more rapidly in the presence of (+)-catechin (MQ+C solutions), which is in accordance with the color evolution. In particular, more remarkable losses occurred from the earliest moment of storage at concentrations of (+)-catechin up to 100 mg/L (approximately by 24%). After 3 weeks of storage, significantly ($p < 0.05$) higher contents of malvidin-3-glucoside were found in MQ and MQ+C50 solutions (204.8 ± 5.9 and 187.3 ± 0.3 mg/L, respectively), whereas this value fell to 166.1 ± 1.2 and 166.9 ± 2.7 mg/L in MQ+C100 and MQ+C200 solutions. This fact seems to indicate that, at high concentrations, (+)-catechin can interfere with the existing malvidin-3-glucoside/quercetin-3-β-D-glucoside equilibrium, diminishing their chemical stability. This antagonistic effect, clearly potentiated with time in our conditions, was also observed by Rustioni et al.,[17] who demonstrated that certain combinations of copigments (especially those from seeds, as could be (+)-catechin) can negatively affect the global copigmentation equilibrium by breaking tannin−anthocyanin interactions.

In summary, this work has shown that quercetin-3-β-D-glucoside and (+)-catechin exhibit quite different abilities to interact with malvidin-3-glucoside in ternary mixtures depending on their specific binding strength and concentration, which have important consequences on the color and chemical stability during storage. Differential colorimetry has demonstrated the fundamental role of quercetin-3-β-D-glucoside as a potential wine additive due to its immediate copigmentation effect in multiple systems and higher potential for stabilization over time. Our findings also showed the greater difficulty of (+)-catechin binding to malvidin-3-glucoside in the presence of quercetin-3-β-D-glucoside and its lower potential to lead to chemical and colorimetric stabilization. It should be borne in mind, therefore, that certain flavonoid combinations do not always result in positive effects on color by multiple copigmentation but also could cause negative effects. In this sense, further studies need to be done to better understand the mechanisms involved in the anthocyanin−flavanol−flavonol multiple interactions under different conditions (pH, temperature, sulfites, etc.) as well as to strategically select appropriate flavonoid combinations that promote synergistic interactions and avoid antagonisms.

■ ASSOCIATED CONTENT

Ⓢ Supporting Information

Chemical structures of the pigment and copigments used and visible absorbance spectra of the solutions prepared for this study. This material is available free of charge via the Internet at http://pubs.acs.org.

■ AUTHOR INFORMATION

Corresponding Author

*(M.T.E.-B.) Phone: +34 923 294537. Fax: +34 923 294515. E-mail: escriban@usal.es.

Funding

This research was financially supported by the Spanish MICINN (Project ref AGL2011-30254-C02-01) and (Project ref AGL2011-30254-C02-02) and Consejería de Economía, Innovación, Ciencia y Empleo, Junta de Andalucía, Spain (Project P11-AGR-7843). F.J.R.-P. thanks VPPI-Universidad de Sevilla for a postdoctoral grant.

Notes

The authors declare no competing financial interest.

■ ACKNOWLEDGMENTS

We are indebted to Dr. Modesto Carballo (Biology Service, CITIUS, Universidad de Sevilla) for technical assistance.

■ REFERENCES

(1) Monagas, M.; Bartolome, B.; Gomez-Cordoves, C. Updated knowledge about the presence of phenolic compounds in wine. *Crit. Rev. Food Sci. Nutr.* **2005**, *45*, 85−118.

(2) Eiro, M. J.; Heinonen, M. Anthocyanin color behavior and stability during storage: effect of intermolecular copigmentation. *J. Agric. Food Chem.* **2002**, *50*, 7461−7466.

(3) Shikov, V.; Kammerer, D. R.; Mihalev, K.; Mollov, P.; Carle, R. Heat stability of strawberry anthocyanins in model solutions containing natural copigments extracted from rose (*Rosa damascena* Mill.) petals. *J. Agric. Food Chem.* **2008**, *56*, 8521−8526.

(4) Boulton, R. The copigmentation of anthocyanins and its role in the color of red wine: a critical review. *Am. J. Enol. Vitic.* **2001**, *52*, 67−87.

(5) Castañeda-Ovando, A.; Pacheco-Hernández, M.; Páez-Hernández, M.; Rodríguez, J. A.; Galán-Vidal, C. A. Chemical studies of anthocyanins: a review. *Food Chem.* **2009**, *113*, 859−871.

(6) Bakker, J.; Timberlake, C. F. Isolation, identification, and characterization of new color-stable anthocyanins occurring in some red wines. *J. Agric. Food Chem.* **1997**, *45*, 35−43.

(7) De Freitas, V.; Mateus, N. Chapter 3. Updating wine pigments. In *Recent Advances in Polyphenol Research*; Santos-Buelga, C., Escribano-Bailon, M. T., Lattanzio, V., Eds.; Wiley-Blackwell: Oxford, UK, 2010; Vol. 2.

(8) Schwarz, M.; Picazo-Bacete, J. J.; Winterhalter, P.; Hermosín-Gutiérrez, I. Effect of copigments and grape cultivar on the color of red wines fermented after the addition of copigments. *J. Agric. Food Chem.* **2005**, *53*, 8372−8381.

(9) García-Marino, M.; Escudero-Gilete, M. L.; Heredia, F. J.; Escribano-Bailón, M. T.; Rivas-Gonzalo, J. C. Color-copigmentation study by tristimulus colorimetry (CIELAB) in red wines obtained from Tempranillo and Graciano varieties. *Food Res. Int.* **2013**, *51*, 123−131.

(10) Gordillo, B.; Cejudo-Bastante, M. J.; Rodríguez-Pulido, F. J.; Jara-Palacios, M. J.; Ramírez-Pérez, P.; González-Miret, M. L.; Heredia, F. J. Impact of adding white pomace to red grapes on the phenolic composition and color stability of syrah wines from a warm climate. *J. Agric. Food Chem.* **2014**, *62*, 2663−2671.

(11) García-Marino, M.; Hernández-Hierro, J. M.; Rivas-Gonzalo, J. C.; Escribano-Bailón, M. T. Colour and pigment composition of red wines obtained from co-maceration of Tempranillo and Graciano varieties. *Anal. Chim. Acta* **2010**, *660*, 134−142.

(12) Cavalcanti, R. N.; Santos, D. T.; Meireles, M. A. A. Non-thermal stabilization mechanisms of anthocyanins in model and food systems − an overview. *Food Res. Int.* **2011**, *44*, 499−509.

(13) Baranac, J. M.; Petranovic, N. A.; Dimitric-Markovic, J. M. Spectrophotometric study of anthocyan copigmentation reactions. 2. Malvin and the nonglycosidized flavone quercetin. *J. Agric. Food Chem.* **1997**, *45*, 1694−1697.

(14) Berké, B.; De Freitas, V. A colorimetric study of oenin copigmented by procyanidins. *J. Sci. Food Agric.* **2007**, *87*, 260−265.

(15) Gordillo, B.; Rodríguez-Pulido, F. J.; Escudero-Gilete, M. L.; González Miret, M. L.; Heredia, F. J. Comprehensive colorimetric study of anthocyanic copigmentation in model solutions. Effects of pH and molar ratio. *J. Agric. Food Chem.* **2012**, *60*, 2896−2905.

DOI: 10.1021/acs.jafc.5b00181
J. Agric. Food Chem. 2015, 63, 7645−7653

(16) Teixeira, N.; Cruz, L.; Brás, N. F.; Mateus, N.; Ramos, M. J.; De Freitas, V. Structural features of copigmentation of oenin with different polyphenol copigments. *J. Agric. Food Chem.* **2013**, *61*, 6942−6948.
(17) Rustioni, L.; Bedgood, D. R.; Failla, O.; Prenzler, P. D.; Robards, K. Copigmentation and anti-copigmentation in grape extracts studied by spectrophotometry and post-column-reaction HPLC. *Food Chem.* **2012**, *132*, 2194−2201.
(18) Pinelo, M.; Manzocco, L.; Nuñez, M. J.; Nicoli, M. C. Interaction among phenols in food fortification: negative synergism on antioxidant capacity. *J. Agric. Food Chem.* **2004**, *52*, 1177−1180.
(19) Hidalgo, M.; Sánchez-Moreno, C.; Pascual-Teresa, S. Flavonoid-flavonoid interaction and its effect on their antioxidant activity. *Food Chem.* **2010**, *121*, 691−696.
(20) Ioannou, I.; Hafsa, I.; Salem Hamdi, S.; Charbonnel, C.; Ghoul, M. Review of the effects of food processing and formulation on flavonol and anthocyanin behaviour. *J. Food Eng.* **2012**, *111*, 208−217.
(21) González-Manzano, S.; Dueñas, M.; Rivas-Gonzalo, J. C.; Escribano-Bailón, M. T.; Santos-Buelga, C. Studies on the copigmentation between anthocyanins and flavan-3-ols and their influence in the colour expression of red wine. *Food Chem.* **2009**, *114*, 649−656.
(22) Jara-Palacios, M. J.; Gordillo, B.; González-Miret, M. L.; Hernanz, D.; Escudero-Gilete, M. L.; Heredia, F. J. Comparative study of the enological potential of different winemaking byproducts: implications in the antioxidant activity and color expression of red wine anthocyanins in a model solution. *J. Agric. Food Chem.* **2014**, *62*, 6975−6983.
(23) Liu, H.; Chen, Y.; Hao, Y.; Zheng, N.; Jia, A. The evaluation of lightness and chroma difference for images according to color difference formulae. *Appl. Mech. Mater.* **2012**, *130*, 3036−3040.
(24) Martínez, J. A.; Melgosa, M.; Pérez, M. M.; Hita, E.; Negueruela, A. I. Note. Visual and instrumental color evaluation in red wines. *Food Sci. Technol. Int.* **2001**, *7*, 439−444.
(25) Cejudo-Bastante, M. J.; Gordillo, B.; Hernanz, D.; Escudero-Gilete, M. L.; González-Miret, M. L.; Francisco J. Heredia, F. J. Effect of the time of cold maceration on the evolution of phenolic compounds and colour of Syrah wines elaborated in warm climate. *Int. J. Food Sci. Technol.* **2014**, *49*, 1886−1892.
(26) Gonnet, J. Colour effects of co-pigmentation of anthocyanin revisited − 3. A further description using CIELAB differences and assessment of matched colours using the CMC model. *Food Chem.* **2001**, *75*, 473−485.
(27) Gordillo, B.; López-Infante, M. I.; Ramírez-Pérez, P.; González-Miret, M. L.; Heredia, F. J. Influence of prefermentative cold maceration on the color and anthocyanic copigmentation of organic Tempranillo wines elaborated in a warm climate. *J. Agric. Food Chem.* **2010**, *58*, 6797−6803.
(28) Heredia, F. J.; Álvarez, C.; González-Miret, M. L.; Ramírez, A. CromaLab, análisis de color. Registro General de la Propiedad Intelectual, 2004.
(29) CIE. Technical Report Colorimetry; Commission Internationale de l'Eclairage Central Bureau: Vienna, Austria, 2004.
(30) StatSoft Inc. STATISTICA (data analysis software system), v 8; StatSoft Inc.: Tulsa, OK, USA, 2007.
(31) Gómez-Míguez, M.; Gonzalez-Manzano, S.; González-Miret, M. L.; Escribano-Bailón, M. T.; Heredia, F. J.; Santos-Buelga, C. Influence of different phenolic copigments on the color of malvidin 3-glucoside. *J. Agric. Food Chem.* **2006**, *54*, 5422−5429.
(32) Sun, J.; Cao, X.; Bai, W.; Liao, X.; Hua, X. Comparative analyses of copigmentation of cyanidin 3-glucoside and cyanidin 3-sophoroside from red raspberry fruits. *Food Chem.* **2010**, *120*, 1131−1137.

DOI: 10.1021/acs.jafc.5b00181
J. Agric. Food Chem. 2015, 63, 7645−7653

mechanical properties of grape skins and proanthocyanidin extractability were found by Rolle and co-workers,[10] who determined that denser grapes provided higher phenolic extraction and who also stated that thinner skins assisted proanthocyanidin extraction. Recently, Bindon and co-workers[11] found that ripening affects cell wall porosity and its ability to adsorb proanthocyanidins, thus limiting their extraction to maceration media. Ripening also has an influence on the molecular weight of the extracted compounds, which was higher in riper grapes.

Some studies have related ripeness degree to grape skin flavonol composition,[3,4,12,13] but little is known about the influence of ripening on the extraction behavior of these compounds.[5]

The aim of this study was to evaluate the influence of cell wall composition on the extraction of flavan-3-ols and flavonols from red grape skins during ripening. To achieve this goal, red grapes of *Vitis vinifera* L. cv. Tempranillo were harvested at three different ripeness stages (preharvest, harvest, and over-ripened) and three soluble solid contents (22, 24, and 26 °Brix) within each ripeness degree.

MATERIALS AND METHODS

Grape Samples. *V. vinifera* L. cv. Tempranillo red grape samples were collected from a vineyard located in Lleida (Spain), which is under the influence of the Mediterranean climate. The samples were collected at three different ripeness degrees: preharvest (22 days before harvest date), harvest, and over-ripened (20 days after harvest date). In the studied samples notations P, H, and O were used to indicate preharvest, harvest, and over-ripened, respectively. Thirty clusters were collected at each stage, and their grapes were sorted according to their density. The density of grapes was estimated by flotation of berries in different NaCl solutions (130−150, 150−170, and 170−190 g L^{-1}) corresponding to different solid content (22, 24, and 26 °Brix, respectively). As a result, nine samples were obtained, with three different solid content (22, 24, or 26 °Brix) within each sampling date (P, H, or O). Grape skins were manually separated from the whole grapes, and three subsamples were taken from each sample, one for the exhaustive methanolic extraction, another for the hydroalcoholic extraction, and the third for cell wall isolation and characterization.

Cell Wall Analysis. Cell wall material was isolated from grape skins as the 70% ethanol insoluble residue as previously described.[14] Noncellulosic polysaccharides, pectins' esterification degree, lignin, cellulose, protein, and total phenolic compounds in cell wall material were determined as described in our previous work.[15]

Briefly, noncellulosic polysaccharides (i.e., arabinogalactans, mannans, homogalacturonans, xyloglucans, arabinans, rhamnogalacturonans-I, and rhamnogalacturonans-II) were obtained using an iterative calculation methodology[16] from monosaccharide profiles. Monosaccharides were determined by gas chromatography−mass spectrometry (GC-MS) of their trimethylsilyl ester *O*-methyl glycolsyl derivates (TMS) obtained after acidic methanolysis and derivatization following a modification of the Guadalupe et al. procedure[17]

Pectin esterification degree was determined as described by Femenia et al.[18] using the spectrophotometric measurement as proposed by Blumenkrantz and Asboe-Hansen,[19] but using *o*-hydroxydiphenyl solution[20] and recording the absorbance at 520 nm after 5 min of reaction.

Cellulose was determined as glucose in accordance with Lurie et al.[21] using the phenol method proposed by DuBois et al. for its spectrophotometric determination.[22] Lignin was gravimetrically determined as Klason lignin,[18] following the Saeman procedure.[23]

Flavanol and Flavonol Extractions. *Exhaustive Methanolic Extraction.* Extraction was performed as previously described.[15,24] Briefly, 10 g of grape skins was macerated at 4 °C in methanol containing 0.1% of 12 M HCl until colorless. Methanolic phases were successively pooled, a few milliliters of water was added, and the extract was concentrated under vacuum at 30 °C until methanol was removed and finally made up to 100 mL with ultrapure water.

Hydroalcoholic Extraction. Extraction was performed as previously described.[15,24] Briefly, 10 g of grape skins was macerated in 100 mL of model wine solution (4 g L^{-1} tartaric acid, 12.5% ethanol, adjusted at pH 3.6 with 0.5 M NaOH). The vials were kept at 25 °C and in darkness throughout the experiment. At regular intervals (1, 3, 5, 7, and 9 days) 1500 μL of extraction medium was taken and subjected to chromatographic analyses.

Sample Preparation for Chromatographic Analyses. Samples were prepared as previously described.[25]

For flavonol analysis, the extract was diluted 1:1 with 0.1 M HCl, filtered through 0.45 μm pore size filters, and directly injected into the chromatographic system to determine flavonols as described in the following section.

For the flavan-3-ol analysis, samples were fractionated prior to chromatographic analysis following the procedure described by Gonzalez-Manzano et al.:[26] 1 mL of each extract diluted (1:1) with 0.1 M HCl was eluted through Oasis MCX (Waters Corp., Milford, MA, USA) cartridges previously conditioned with 2 mL of methanol and 2 mL of water. After a washing with 4 mL of ultrapure water, flavan-3-ols and phenolic acids were eluted with 8 mL of methanol, whereas anthocyanins and flavonols were retained in the cartridges. A small volume of water was added to the eluate and concentrated under vacuum at <30 °C until complete elimination of methanol. The aqueous residue was adjusted to a volume of 0.5 mL with ultrapure water, filtered (0.45 μm), and analyzed by HPLC-DAD-MS as described in the following section.

HPLC-DAD-MS Analyses. An Agilent 1200 series HPLC system (Agilent Technologies, Palo Alto, CA, USA) consisting of an autosampler, a quaternary pump, a vacuum degasser, a thermostated column compartment, and a diode array detector (DAD) and controlled by ChemStation software (version B.04.01; Agilent Technologies) was used for chromatographic analyses. The HPLC system was coupled to a hybrid triple-quadrupole/linear ion trap (QqLIT) mass spectrometer API 3200 QTrap (Applied Biosystems, Foster City, CA, USA) equipped with a Turbo V ionization source and controlled by Analyst software (version 1.5; Applied Biosystems) via the DAD cell outlet.

Flavonol analysis was performed as described elsewhere.[27] Briefly, an Aqua C18 column (4.6 mm × 150 mm, 5 μm particle size) thermostated at 35 °C was used. Solvents were (A) 0.1% trifluoroacetic acid and (B) 100% HPLC grade acetonitrile. The elution profile was as follows: isocratic 10% B for 3 min, from 10 to 15% B for 12 min, isocratic 15% B for 5 min, from 15 to 18% B for 5 min, from 18 to 30% B for 20 min, and from 30 to 35% B for 5 min. The flow rate was 0.5 mL min^{-1} and the injection volume, 100 μL. UV−vis spectra were recorded from 250 to 770 nm with a bandwidth of 2 nm. Flavonols were detected at 360 nm as the preferred wavelength. MS analysis was carried out in positive mode (ESI^+) as described elsewhere:[28] declustering potential (DP), 41 V; entrance potential (EP), 7.5 V; ion spray voltage (IS), 5000 V; ion source gas 1 (GS1), 40 psi; ion source gas 2 (GS2), 50 psi (600 °C); curtain gas (CUR), 20 psi; and collision gas (CAD), set as "high". Both quadrupoles were set at unit resolution. Mass method consisted of three mass experiments: full mass analysis (EMS mode, collision energy (CE) 10 V), MS^2 analysis (EPI mode, CE 25 V), and MS^3 analysis (CE 30 V, excitation energy (AF2) 50 V). Spectra were recorded between m/z 150 and 1100.

Flavan-3-ol chromatographic separation was performed on a reversed-phase column Spherisorb ODS-2 (150 × 4.6 mm, 3 μm) from Waters maintained at 25 °C. Mobile phases A and B were, respectively, 0.25% acetic acid in water and acetonitrile The following linear gradient was used to achieve the chromatographic separation: from 0 to 10% B in 5 min, from 10 to 14.5% B in 35 min, from 14.5 to 19% B in 5 min, from 19 to 55% B in 5 min, hold at 55% B for 5 min, from 55 to 80% B in 5 min, hold at 80% B for 3 min, from 80 to 0% B in 2 min, and hold at 0% B for 5 min. The flow rate and the injection volume were set at 0.5 mL min^{-1} and 100 μL, respectively. UV−vis

DOI: 10.1021/acs.jafc.5b00261
J. Agric. Food Chem. 2015, 63, 7654−7662

Table 1. Average Values for Cell Wall Components Determined in Grape Skins

	%	μg/mg cell wall material								μg/mg cell wall material	%	μg/mg cell wall material		
	MI[a]	mannans	RG-II[b]	RG-I[c]	HG[d]	XG[e]	AG[f]	arabinans	total PS[g]	lignin	esterification degree	cellulose	protein	polyphenols
P 22	5.20	8.43	11.05	17.29	175.67	52.21	56.36	65.13	386.14	298.97	8.41	31.85	103.73	109.55
P 24	2.90	12.17	16.41	21.68	220.28	75.56	73.58	86.31	505.99	463.92	85.35	34.64	105.11	144.88
P 26	4.50	6.79	12.82	14.40	146.31	52.20	47.26	58.26	338.03	375.00	9.14	33.05	148.07	105.83
H 22	4.50	8.52	17.33	18.90	192.04	68.53	52.04	75.13	432.48	505.05	69.26	43.80	138.04	181.49
H 24	2.00	11.38	16.89	20.06	203.87	91.41	62.19	84.02	489.82	490.00	62.85	36.81	137.79	176.53
H 26	3.40	10.62	16.87	20.11	204.36	90.08	52.66	91.42	486.13	312.50	83.07	39.50	119.88	157.23
O 22	3.80	8.18	18.52	17.76	180.44	62.22	46.92	72.43	406.46	84.21	41.28	38.38	170.43	163.29
O 24	2.50	8.65	14.98	17.59	178.72	55.83	49.84	78.20	403.82	375.00	52.82	40.84	132.82	185.39
O 26	1.30	9.22	16.21	17.90	181.90	65.20	57.02	76.44	423.89	145.83	11.54	43.68	120.92	154.08

[a]MI, total insoluble material. [b]RG-II, type II rhamnogalacturonans. [c]RG-I, type I rhamnogalacturonan. [d]HG, homogalacturonan. [e]XG, xyloglucans. [f]AG, arabinogalactans. [g]Total PS, total polysaccharide content.

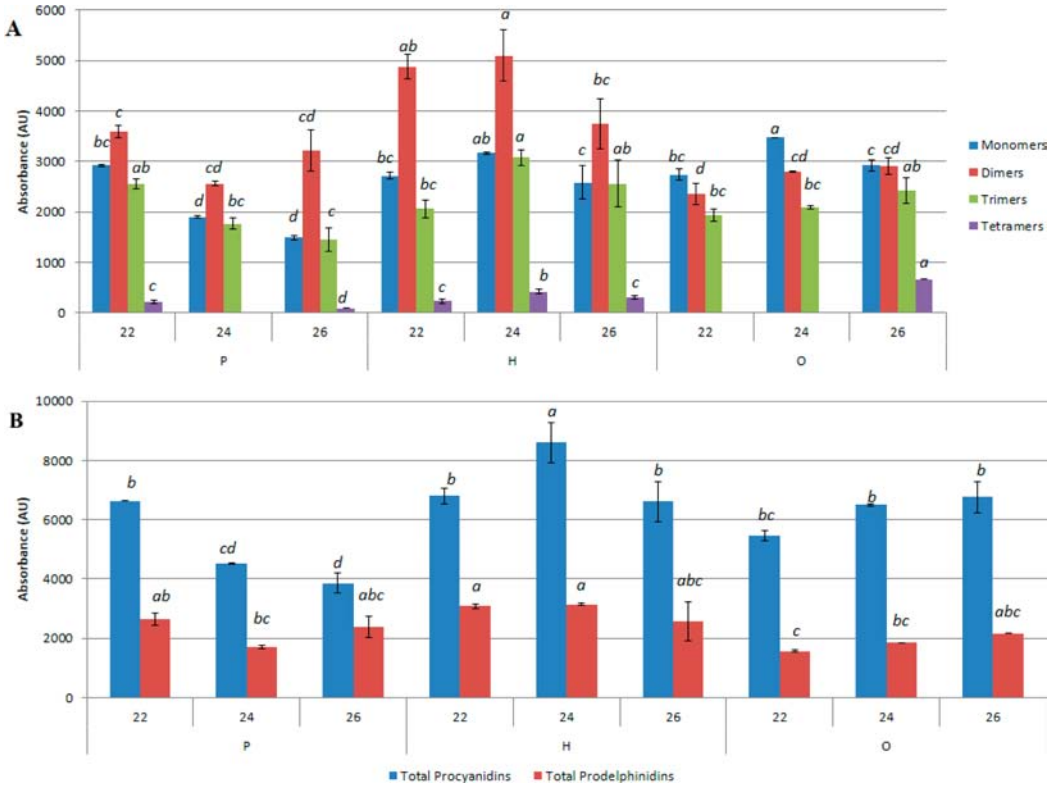

Figure 1. Total proanthocyanidin contents in exhaustive methanolic extracts grouped according to the number of subunits present in the molecule (A) and the structural characteristics (B). Within each group of compounds, different letters indicate statistical differences ($p < 0.05$) between samples by the Tukey HSD test.

spectra were recorded from 200 to 600 nm during acquisition at a selected wavelength of 280 nm.

The mass spectrometer was operated in the negative electrospray ionization (ESI) mode under the following specific conditions: IS, −4500 V; source temperature (TEM), 400 °C; CUR, 20 arbitrary units; GS1, 40 arbitrary units; GS2, 30 arbitrary units; DP, −40 V; EP, −7 V; and CE, −20 eV. Nitrogen (>99.98%) was employed as curtain, ion source, and collision gas. The detection was accomplished in the enhanced MS (EMS) full-scan mode, from m/z 100 to 1700, and in the enhanced product ion (EPI) mode to obtain the corresponding full-scan MS/MS spectra.

Extractabilities. Flavan-3-ol and flavonol extractabilities were calculated as percentages using the ratio between the DAD-HPLC peak areas obtained from hydroalcoholic and exhaustive methanolic extractions, as previously reported for anthocyanin extractability.[24]

Statistical Treatment. Principal components analysis (PCA), an unsupervised pattern recognition method, was used for data analysis. The IBM SPSS 21 for Windows software package (SPSS, Inc., Chicago, IL, USA) was used for data processing.

RESULTS AND DISCUSSION

Cell Wall Composition. Cell wall composition of grape skins harvested at different ripeness stages and with different soluble solid content within each stage has been detailed in our previous work.[15] Results obtained are in agreement with those reported in Ortega-Regules et al.[29] Cell wall composition is summarized in Table 1.

Flavan-3-ol and Flavonol Composition. Extracts obtained after exhaustive extraction of 10 g of grape skins were

DOI: 10.1021/acs.jafc.5b00261
J. Agric. Food Chem. 2015, 63, 7654−7662

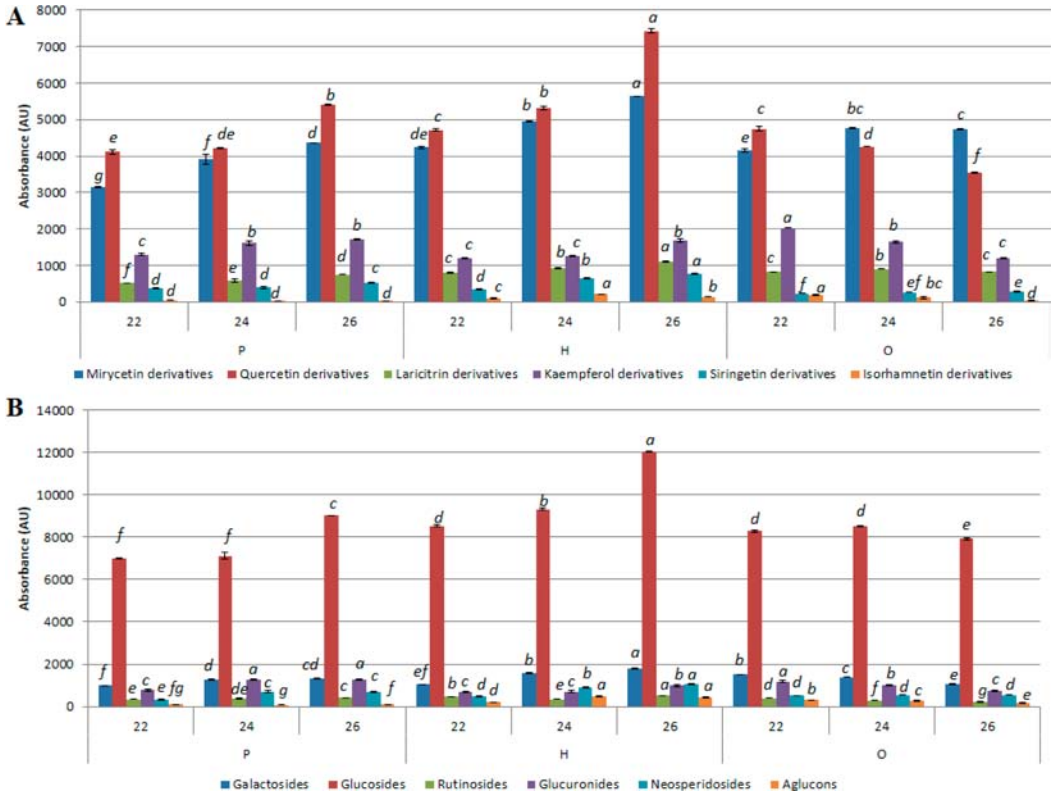

Figure 2. Flavonol total contents in exhaustive methanolic extracts grouped according to flavonol moiety (A) or the sugar moiety (B) present in the molecule. Within each group of compounds, different letters indicate statistical differences ($p < 0.05$) between samples by the Tukey HSD test.

analyzed to ascertain their flavanolic and flavonolic composition.

With regard to polymerization degree, as can be seen in Figure 1A, dimers were the most abundant compounds in preharvest and harvest samples, whereas monomers were, in general, the most abundant ones in over-ripened (O) samples. Trimers represented 20.9−28.4% of the proanthocyanidins quantified in the studied samples, being in all samples the third group in abundance, reaching levels similar to monomers in P 26, H 24, and H 26 samples. Tetramers were the least abundant oligomers in all of the studied samples, showing levels under quantification limits in three of the analyzed samples.

Flavan-3-ol compounds were classified according to their structure in two groups, procyanidins, which only catechin or epicatechin subunits present in their structure, or prodelphinidins, which present one or more gallocatechin or epigallocatechin subunits in their structure. Procyanidin and prodelphinidin contents in grape skins followed the same pattern (Figure 1B), increasing their level from preharvest to harvest and showing a slight decrease in over-ripened (O) samples, although these differences were not significant (Tukey HSD test, $\alpha = 0.05$) for several of the different samples. Despite higher prodelphinidin contents in harvest (H) samples, their percentages were bigger in preharvest (P) samples, varying from 27.5 to 38.3%, than in harvest samples, where they represented 26.8−31.2% of the quantified compounds. O samples presented the lowest percentages of this kind of compound. The abundance of prodelphinidins in red wines has been previously related to good maturity level of the grapes[30] and to the ability to produce high-quality wines.[31]

Up to 17 flavonol compounds were identified and quantified in the studied samples. They included quercetin, myricetin, kaempferol, laricitrin, syringetin, and isorhamnetin derivatives, esterified with different sugar moieties or in their nonglycosylated form. Figure 2A shows flavonol contents grouped as a function of the flavonol moiety present in the molecule for the nine analyzed samples. Flavonol content tended to increase as soluble solid content grew in preharvest and harvest samples, whereas over-ripened samples showed the opposite trend. The highest levels were reached in harvest samples, whereas preharvest and over-ripened samples showed quite lower levels. With regard to the kind of derivative, quercetin and myricetin derivatives were the most abundant compounds in all of the studied samples, as previously reported for Tempranillo grapes.[3,32] Quercetin derivatives were the most abundant found in seven of the nine analyzed samples, which is in agreement with the flavonol profile of the Tempranillo variety.[33] Myricetin derivatives were predominant in the two remaining samples, namely, O 24 and O 26. Kaempferol, laricitrin, syringetin, and isorhamnetin derivatives were also detected and quantified.

With regard to the sugar moiety linked to the flavonol moiety (Figure 2B), the most abundant derivatives were glucosylated compounds, displaying levels from 66.1 to 74.7%. Galactosides and glucuronides were also quite abundant, and small percentages of rutinosides, neosperidosides, and aglucons were also found.

Flavan-3-ol Extractabilities. In previous studies dealing with the average degree of polymerization of wine proanthocyanidins, we have determined in Tempranillo wines values varying from 2.9 to 4.3. That made us focus this extractability study on monomers and oligomers up to four.[26,34]

Up to 22 different flavanols were detected in our samples. Extractability statistical analyses were performed using the

DOI: 10.1021/acs.jafc.5b00261
J. Agric. Food Chem. 2015, 63, 7654−7662

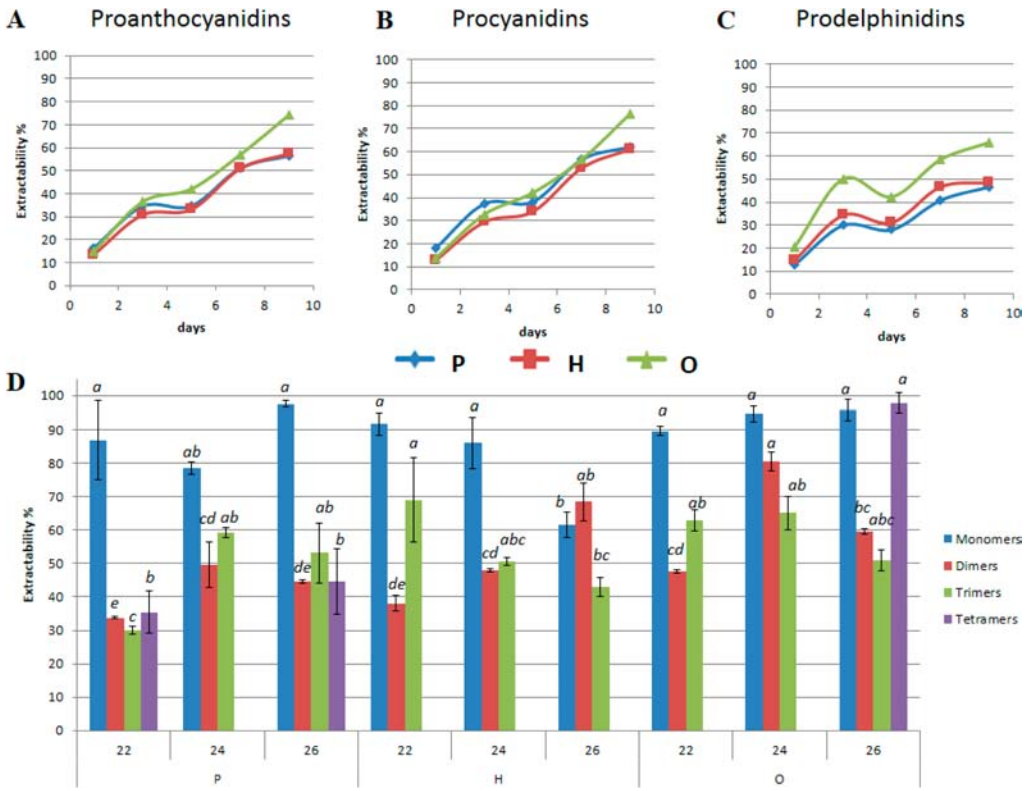

Figure 3. Percentage of extractability of proanthocyanidins (A), procyanidins (B), and prodelphindins (C) in samples with different ripeness degrees and percentage of extractability of flavanols grouped according to the number of subunits present in the molecule (D) on the last day of study. Within each group of compounds, different letters indicate statistical differences ($p < 0.05$) between samples by the Tukey HSD test.

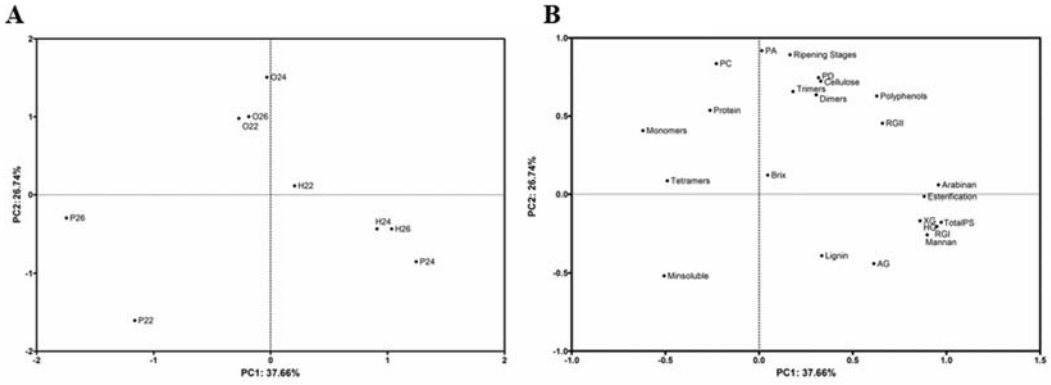

Figure 4. Projection of the samples on the plane defined by the first and second principal components (A) and the corresponding loading plot (B) for proanthocyanidin extractability. Minsoluble, insoluble material; Protein; Polyphenols; Lignin; Cellulose; AG, arabinogalactans; Mannans; HG, homogalacturonans; XG, xyloglucans; Arabinans; RGI, rhamnogalacturonans-I; RGII, rhamnogalacturonans-II; Total PS, total polysaccharide contents; Esterification, degree of esterification of pectins; Brix, soluble solid content; Ripening Stages; Total PA, maximum proanthocyanidin extractability; Total PC, maximum procyanidin extractability; Total PD, maximum prodelphinidin extractability; Monomers, extractability of monomers; Dimers, extractability of dimers; Trimers, extractability of trimers; Tetramers, extractability of tetramers.

compounds grouped as a function of their polymerization degree or their structural characteristics, i.e., procyanidins (polymers of catechin and/or epicatechin) and prodelphinidins (polymers of gallocatechin and/or epigallocatechin).

The maximum values obtained in our study for total proanthocyanidin extractability (Figure 3A) were reached the last day of the study in all samples. Llaudy et al. had observed that the amount of proanthocyanidin extracted to the maceration media from grape skins reached its maximum level after 4−5 days of maceration and then remained stable.[35] In our study, the extraction is extended (10 days), and it could be inferred that it would probably have increased if the maceration had been lengthened. This fact is especially noticeable in over-ripened samples, showing a steeper slope than preharvest and harvest samples, which presented very similar patterns (Figures 3A−C). As can be seen in Figure 3B,C, clear differences between procyanidin and prodelphinidin extractabilities can be observed. Prodelphinidin extractability increases with ripening, whereas this is not so evident for procyanidins. In fact, extractability of procyanidins in O samples is similar to that in H samples and even lower than that in P samples during the first days of the study.

DOI: 10.1021/acs.jafc.5b00261
J. Agric. Food Chem. 2015, 63, 7654−7662

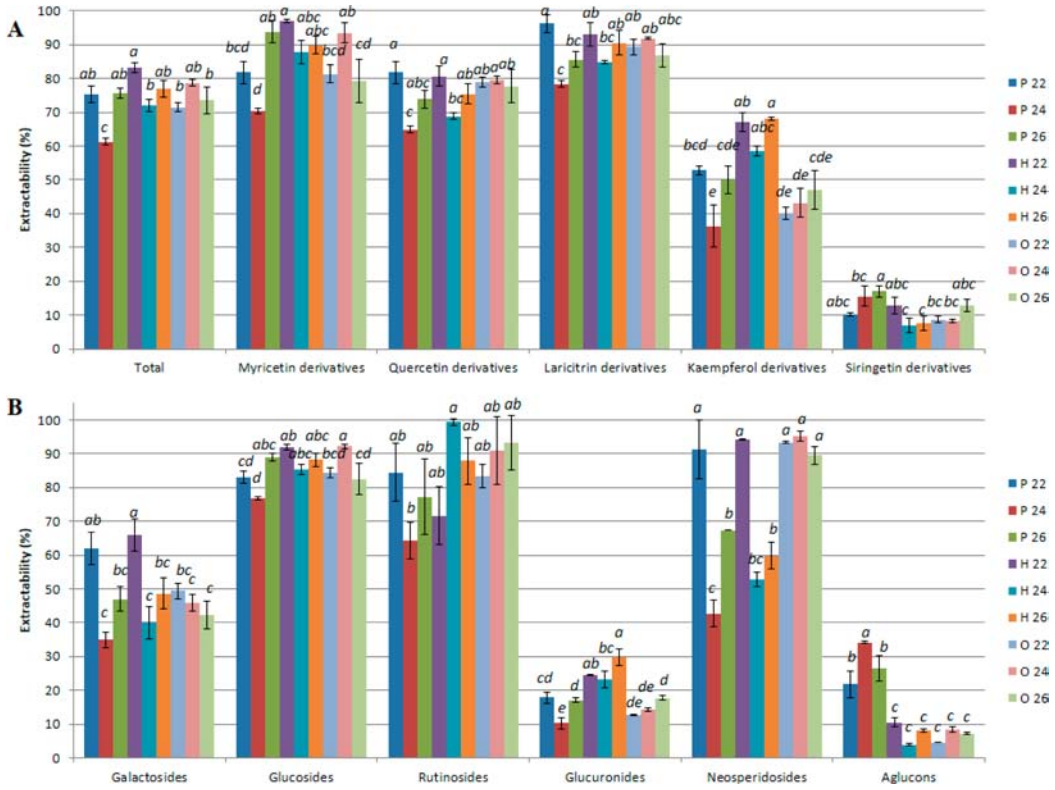

Figure 5. Percentages of extractability of flavonols, on the fifth day of study for the different samples, grouped according to the flavonol moiety (A) and the sugar moiety (B) present in the molecule. Within each group of compounds, different letters indicate statistical differences ($p < 0.05$) between samples by the Tukey HSD test.

Nevertheless, as extraction time increases, the extraction yield of procyanidins in O samples tends to be higher than in H and P samples, indicating that, during ripening, the cell walls become more porous and flavanols would be retained in these pores, reducing the extraction.[11] However, it should be assumed that once the pores are blocked, extractability could be favored due to structural degradation that may occur in over-ripened grapes. This would explain the behavior that we have observed, although further experiments need to be performed to confirm this hypothesis. Furthermore, it seems that the adsorbed flavanol compounds into the pores would consist mainly of procyanidins rather than prodelphinidins. In fact, the extraction of prodelphinidins seems to be faster the first days of the study, although afterward it tends to slow. This could be related to changes in the selectivity pattern of the pore of the cell walls that have been observed as the concentration of flavanols in the medium increases.[11] To our knowledge, no previous studies had evaluated the differences between procyanidin and prodelphinidin extractabilities.

No clear pattern is observed for soluble solid content (data not shown). The absence of a relationship between sugar content and proanthocyanidin extraction in hydroalcoholic media is in good agreement with previously reported studies.[8]

In relation to polymerization degree, as can be seen in Figure 3D, in general monomers were easily extracted in all samples, whereas dimers, trimers, and tetramers had variable behaviors. It is worth noting that tetramers are extracted only in three of the nine samples; this could indicate that the extraction of flavanols becomes more difficult as the polymerization degree increases.

PCA was conducted as unsupervised pattern recognition to observe relationships between proanthocyanidin extractabilities at the last day of the study, when maximum extraction levels were reached, stage of ripening, °Brix, and cell wall composition. The first principal component (PC 1) describes 37.66% of the variability in the data, and the second principal component (PC 2) describes 26.74% of the variability.

As can be seen in Figure 4, stage of ripening showed a clear positive relationship with total proanthocyanidin extractability and also with procyanidin and prodelphinidin extractabilities, whereas soluble solid content did not present any influence on the compound extraction. With regard to cell wall composition, total insoluble material displayed the biggest opposition to proanthocyanidin extractabilities. Some of the components of the cell wall showed a relationship with the proanthocyanidin extractabilities. This indicates that progression of ripening might cause changes in skin cell wall composition that could facilitate the release of proanthocyanidins. Those oppositions are quite stronger for total proanthocyanidins and total procyanidins, whereas they were weaker for prodelphinidin extractability. This behavior reflects a higher tendency of procyanidins to interact with components of cell walls than that of prodelphinidins.

Among cell wall constituents, some polysaccharide families exert an influence on proanthocyanidin total extractability and procyanidin extractability, namely, arabinogalactans (AG), mannans, RG-I, homogalacturonans (HG), xyloglucans (XG), and total polysaccharides content. All of these cell wall components displayed a negative relationship with proanthocyanidin extractabilities; thus, the higher the content of these compounds in the cell wall, the lower the proanthocyanidin extraction. The opposition to prodelphinidin extractability of those cell wall components is weaker than for procyanidins.

DOI: 10.1021/acs.jafc.5b00261
J. Agric. Food Chem. 2015, 63, 7654−7662

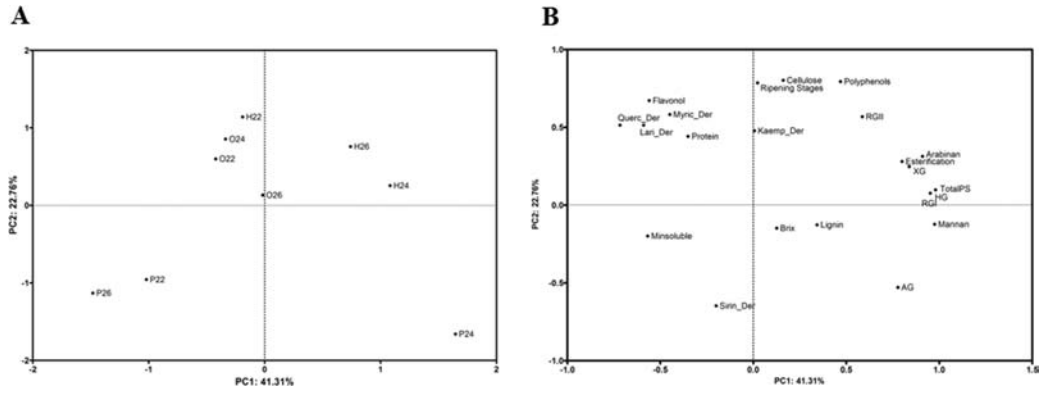

Figure 6. Projection of the samples on the plane defined by the first and second principal components (A) and the corresponding loading plot (B) for flavonol extractability. Minsoluble, insoluble material; Protein; Polyphenols; Lignin; Cellulose; AG, arabinogalactans; Mannans; HG, homogalacturonans; XG, xyloglucans; arabinans; RGI, rhamnogalacturonans-I; RGII, rhamnogalacturonans-II; total PS, total polysaccharide contents; Esterification, degree of esterification of pectins; Brix, soluble solid content; Ripening Stages; TotalFlavonol, maximum flavonol extractability; Querc-der, maximum extractability of quercetin derivatives; Myric-der, maximum extractability of myricitrin derivatives; Lari-der, maximum extractability of laricitrin derivatives; Kaempf-der, maximum extractability of kaempferol derivatives; Sirin-der, maximum extractability of siringitrin derivatives.

Orfila and Knox[36] reported that pit fields contain homogalacturonan. Therefore, a lower content in homogalacturonan is in accordance with the lesser presence of pores and, hence, with an increase in the proanthocyanidin extractability and mainly in procyanidin extractability. This would be in agreement with the negative correlation we have observed. Cellulose showed a strong positive relationship with prodelphinidin extraction and also with procyanidin and total proanthocyanidin extractabilities. Recently, it has been stated that cellulose presents a low affinity for proanthocyanidin binding,[37] whereas the galacturonan rich-fraction of cell wall material, obtained from grape skins, has a high propensity to associate with proanthocyanidins. The above-mentioned results for proanthocyanidin extraction confirm those observations; the higher amount of AG, RG-I, HG, and XG is related to a lesser proanthocyanidin extractability, whereas the higher the cellulose presence, the higher the proanthocyanidin extractability, probably due to the different ability of these polysaccharides to bind proanthocyanidins. With regard to the influence of cell wall composition on the extractability of compounds grouped on the basis of the number of subunits that make up the molecule, the extractability of dimers and trimers of proanthocyanidins displayed an opposition to total insoluble material and it was positively related to the presence of cellulose. The extractability of monomers and tetramers presented high opposition to total polysaccharide content and also to XG, HG, RG-I, and mannans. The above-mentioned results revealed that proanthocyanidin extractability is mainly influenced by harvest date and total insoluble material and to a lesser extent by some cell wall components. The pattern exhibited for proanthocyanidin extractability is quite similar to that previously reported for anthocyaninin extractability.[15]

Flavonol Extractabilities. Flavonol extractabilities reached their maximum at the fifth day of extraction (Figure 5), except for sample P 26, which reached the maximum at the third day of hydroalcoholic extraction, and samples P 24 and O 22, showing their maximum levels at the seventh day of extraction. H 24 extraction shows two maxima, the first one at the fifth day of extraction and the second one at the ninth day, although the percentages of extractability across the two maxima were very similar.

The pattern shown for flavonol extractability points out that flavonol are extracted from grape skins more slowly than anthocyanin compounds.[24] Quercetin, myricetin, and laringetin derivatives were more efficiently extracted than kaempferol or syringetin derivatives (Figure 5A), whereas isorhamnetin derivatives were not extracted in hydroalcoholic media. With regard to the sugar moiety in the molecule (Figure 5B), glucosides, rutinosides, and neosperidosides were more efficiently extracted than galactosides. Glucuronides and aglucons were the less extracted compounds to the hydroalcoholic maceration media.

PCA was conducted to establish relationships between flavonol extractabilities and cell wall composition. PC 1 described 41.31% of the variability observed in the data, and PC 2 described 22.76%. The projection of the samples in the plane defined by PC 1 and PC2 and the obtained loading plot are shown in Figure 6. This analysis revealed that ripening stage or soluble solid content was not related to total flavonol extractability. It showed also the lack of influence of the insoluble material contents on flavonol extractability. Some cell wall components presented a relationship with flavonol extractability; the presence of AG and mannans would decrease total flavonol extractability, whereas protein presence is positively related to total and major flavonol compounds (i.e., quercetin and myricetin derivatives) and to laricitrin derivative extractabilities. A possible explanation for the different behaviors shown for flavonol and other polyphenolic compounds extractabilities (anthocyanins and proanthocyanidins) is the different locations of the diverse polyphenolic compounds in the tissues; flavonol glucosides are located in epidermal cell layers in broad bean leaves,[38] and it is likely that they could be also located in epidermal layers in grape skins, bearing in mind that flavonols are related to UV protection, whereas anthocyanins and proanthocyanidins are located in hypodermal cell layers in grape skins.[39] Moreover, anthocyanins are accumulated inside cell vacuoles,[40] and proanthocyanidins have been found inside vacuoles, linked to proteins in the internal face of tonoplasts and also linked to cell wall polysaccharides.[39] It is possible that the extended release of proanthocyanidins from grape skins to the extraction media observed in this study is related to their different locations; thus, some of them are present as free forms, which would be

DOI: 10.1021/acs.jafc.5b00261
J. Agric. Food Chem. 2015, 63, 7654−7662

easily released during the first days of maceration, whereas there is also a linked fraction that would need a long maceration period to be loosened. Flavonol cellular location is not clear; some authors have determined the flavonol concentrations inside vacuoles, but other histochemical studies have suggested that they could be in cytoplasm as free forms in flower petals,[41] whereas other authors have pointed out the possibility of association between nucleus structures and flavonol compounds,[38,42] primarily due to the ability of these compounds to avoid cell damage caused by sunlight exposure.

Epidermal cells are covered by an external cuticule layer,[43] composed mainly of waxes, which could act as a barrier for flavonol extraction during winemaking. It is possible that the lack of a relationship between flavonol extraction and insoluble material might be due to the existence of this barrier on the outer surface of the epidermal cell layers, where flavonols are mainly located, whereas this barrier existence would not be related to proanthocyanidin or anthocyanin extraction because those compounds are located in hypodermal cells.

In conclusion, proanthocyanidin and flavonol extractabilities were influenced to some extent by cell wall composition, whereas ripening stage affected only proanthocyanidin extractability. Harvest samples presented the highest contents of both flavonols and flavan-3-ols. The extractions from grape skins were slower than those reported for anthocyanins, reaching their maxima in general on the fifth day for flavonol extraction and on the ninth day for proanthocyanidin extraction. To our knowledge, this is the first time that flavonol extractability throughout ripening has been studied. Flavan-3-ol extractability is increased with ripeness stage, whereas soluble solid contents had a negligible influence. Those differences between flavan-3-ol and flavonol extractabilities could be due to their different tissue and cellular locations in grape skins.

This study points out the importance of the maceration time for phenolic compound extraction during winemaking. This can help in the choice of the optimum maceration time to extract the desired amounts of phenolic compounds, reducing this time to avoid the complete extraction of proanthocyanidins and thus wine astringency or extending this maceration in the case of low phenolic content grapes.

AUTHOR INFORMATION

Corresponding Author

*(M.T.E.-B.) Phone: +34 923 294 537. Fax: +34 923 294 515. E-mail: escriban@usal.es.

Funding

We thank the Spanish MICINN (Projects ref AGL2011-30254-C02 and AGL2014-58486-C2-1-R) and the Project DEMETER program CENIT for financial support. N.Q.-M. and J.M.H.-H. also thank the Spanish MICINN for the FPI predoctoral scholarship and the Juan de la Cierva contract (JCI-2011-09201), respectively.

Notes

The authors declare no competing financial interest.

ACKNOWLEDGMENTS

We thank Bodegas Torres (Lleida, Spain) for supplying the grape samples.

REFERENCES

(1) Kennedy, J. A.; Hayasaka, Y.; Vidal, S.; Waters, E. J.; Jones, G. P. Composition of grape skin proanthocyanidins at different stages of berry development. *J. Agric. Food Chem.* **2001**, *49*, 5348−5355.

(2) Downey, M. O.; Harvey, J. S.; Robinson, S. P. Analysis of tannins in seeds and skins of Shiraz grapes throughout berry development. *Aust. J. Grape Wine Res.* **2003**, *9*, 15−27.

(3) Castillo-Munoz, N.; Gómez-Alonso, S.; García-Romero, E.; Hermosin-Gutiérrez, I. Flavonol profiles of *Vitis vinifera* red grapes and their single-cultivar wines. *J. Agric. Food Chem.* **2007**, *55*, 992−1002.

(4) Liang, N. N.; He, F.; Bi, H. Q.; Duan, C. Q.; Reeves, M. J.; Wang, J. Evolution of flavonols in berry skins of different grape cultivars during ripening and a comparison of two vintages. *Eur. Food Res. Technol.* **2012**, *235*, 1187−1197.

(5) Rusjan, D.; Korosec-Koruza, Z. A comparison of extraction methods for selected phenolic compounds from grape berry skins using liquid chromatography and spectrophotometry. *Acta Chim. Slov.* **2007**, *54*, 114−118.

(6) Canals, R.; Llaudy, M. C.; Valls, J.; Canals, J. M.; Zamora, F. Influence of ethanol concentration on the extraction of color and phenolic compounds from the skin and seeds of Tempranillo grapes at different stages of ripening. *J. Agric. Food Chem.* **2005**, *53*, 4019−4025.

(7) Romero-Cascales, I.; Ortega-Regules, A.; López-Roca, J. M.; Fernández-Fernández, J. I.; Gómez-Plaza, E. Differences in anthocyanin extractability from grapes to wines according to variety. *Am. J. Enol. Vitic.* **2005**, *56*, 212−219.

(8) Fournand, D.; Vicens, A.; Sidhoum, L.; Souquet, J.-M.; Moutounet, M.; Cheynier, V. Accumulation and extractability of grape skin tannins and anthocyanins at different advanced physiological stages. *J. Agric. Food Chem.* **2006**, *54*, 7331−7338.

(9) Mattivi, F.; Vrhovsek, U.; Masuero, D.; Trainotti, D. Differences in the amount and structure of extractable skin and seed tannins amongst red grape varieties. *Aust. J. Grape Wine Res.* **2009**, *15*, 27−35.

(10) Rolle, L.; Segade, S. R.; Torchio, F.; Giacosa, S.; Cagnasso, E.; Marengo, F.; Gerbi, V. Influence of grape density and harvest date on changes in phenolic composition, phenol extractability indices, and instrumental texture properties during ripening. *J. Agric. Food Chem.* **2011**, *59*, 8796−8805.

(11) Bindon, K. A.; Madani, S. H.; Pendleton, P.; Smith, P. A.; Kennedy, J. A. Factors affecting skin tannin extractability in ripening grapes. *J. Agric. Food Chem.* **2014**, *62*, 1130−1141.

(12) Liang, Z. C.; Sang, M.; Fan, P. G.; Wu, B. H.; Wang, L. J.; Duan, W.; Li, S. H. Changes of polyphenols, sugars, and organic acid in 5 *Vitis* genotypes during berry ripening. *J. Food Sci.* **2011**, *76*, C1231−C1238.

(13) Giovanelli, G.; Brenna, O. V. Evolution of some phenolic components, carotenoids and chlorophylls during ripening of three Italian grape varieties. *Eur. Food Res. Technol.* **2007**, *225*, 145−150.

(14) Apolinar-Valiente, R.; Romero-Cascales, I.; López-Roca, J. M.; Gómez-Plaza, E.; Ros-García, J. M. Application and comparison of four selected procedures for the isolation of cell-wall material from the skin of grapes cv. Monastrell. *Anal. Chim. Acta* **2010**, *660*, 206−210.

(15) Hernández-Hierro, J. M.; Quijada-Morín, N.; Martinez-Lapuente, L.; Guadalupe, Z.; Ayestarán, B.; Rivas-Gonzalo, J. C.; Escribano-Bailón, M. T. Relationship between skin cell wall composition and anthocyanin extractability of *Vitis vinifera* L. cv. Tempranillo at different grape ripeness degree. *Food Chem.* **2014**, *146*, 41−47.

(16) Arnous, A.; Meyer, A. S. Comparison of methods for compositional characterization of grape (*Vitis vinifera* L.) and apple (*Malus domestica*) skins. *Food Bioprod. Process.* **2008**, *86*, 79−86.

(17) Guadalupe, Z.; Martínez-Pinilla, O.; Garrido, Á.; Carrillo, J. D.; Ayestarán, B. Quantitative determination of wine polysaccharides by gas chromatography-mass spectrometry (GC-MS) and size exclusion chromatography (SEC). *Food Chem.* **2012**, *131*, 367−374.

(18) Femenia, A.; Sánchez, E. S.; Simal, S.; Rosselló, C. Effects of drying pretreatments on the cell wall composition of grape tissues. *J. Agric. Food Chem.* **1998**, *46*, 271−276.

DOI: 10.1021/acs.jafc.5b00261
J. Agric. Food Chem. 2015, 63, 7654−7662

(19) Blumenkrantz, N.; Asboe-Hansen, G. New method for quantitative determination of uronic acids. *Anal. Biochem.* **1973**, *54*, 484−489.
(20) Segarra, I.; Lao, C.; López-Tamames, E.; De La Torre-Boronat, M. C. Spectrophotometric methods for the analysis of polysaccharide levels in winemaking products. *Am. J. Enol. Vitic.* **1995**, *46*, 564−570.
(21) Lurie, S.; Levin, A.; Greve, L. C.; Labavitch, J. M. Pectic polymer changes in nectarines during normal and abnormal ripening. *Phytochemistry* **1994**, *36*, 11−17.
(22) DuBois, M.; Gilles, K. A.; Hamilton, J. K.; Rebers, P. A.; Smith, F. Colorimetric method for determination of sugars and related substances. *Anal. Chem.* **1956**, *28*, 350−356.
(23) Saeman, J. F.; Moore, W. E.; Mitchell, R. L.; Millett, M. A. Techniques for the determination of pulp constituents by quantitative paper chromatography. *Tappi* **1954**, *37*, 336−343.
(24) Hernández-Hierro, J. M.; Quijada-Morín, N.; Rivas-Gonzalo, J. C.; Escribano-Bailón, M. T. Influence of the physiological stage and the content of soluble solids on the anthocyanin extractability of *Vitis vinifera* L. cv. Tempranillo grapes. *Anal. Chim. Acta* **2012**, *732*, 26−32.
(25) Ferrer-Gallego, R.; Hernández-Hierro, J. M.; Rivas-Gonzalo, J. C.; Escribano-Bailón, M. T. Determination of phenolic compounds of grape skins during ripening by NIR spectroscopy. *LWT−Food Sci. Technol.* **2011**, *44*, 847−853.
(26) González-Manzano, S.; Santos-Buelga, C.; Pérez-Alonso, J. J.; Rivas-Gonzalo, J. C.; Escribano-Bailón, M. T. Characterization of the mean degree of polymerization of proanthocyanidins in red wines using liquid chromatography-mass spectrometry (LC-MS). *J. Agric. Food Chem.* **2006**, *54*, 4326−4332.
(27) García-Marino, M.; Hernández-Hierro, J. M.; Rivas-Gonzalo, J. C.; Escribano-Bailón, M. T. Colour and pigment composition of red wines obtained from co-maceration of Tempranillo and Graciano varieties. *Anal. Chim. Acta* **2010**, *660*, 134−142.
(28) Alcalde-Eon, C.; García-Estévez, I.; Ferreras-Charro, R.; Rivas-Gonzalo, J. C.; Ferrer-Gallego, R.; Escribano-Bailón, M. T. Adding oenological tannin vs. overripe grapes: effect on the phenolic composition of red wines. *J. Food Compos. Anal.* **2014**, *34*, 99−113.
(29) Ortega-Regules, A.; Romero-Cascales, I.; Ros-García, J. M.; López-Roca, J. M.; Gómez-Plaza, E. A first approach towards the relationship between grape skin cell-wall composition and anthocyanin extractability. *Anal. Chim. Acta* **2006**, *563*, 26−32.
(30) Ferrer-Gallego, R.; Hernández-Hierro, J. M.; Rivas-Gonzalo, J. C.; Escribano-Bailón, M. T. Influence of climatic conditions on the phenolic composition of *Vitis vinifera* L. cv. Graciano. *Anal. Chim. Acta* **2012**, *732*, 73−77.
(31) Kontoudakis, N.; Esteruelas, M.; Fort, F.; Canals, J. M.; De Freitas, V.; Zamora, F. Influence of the heterogeneity of grape phenolic maturity on wine composition and quality. *Food Chem.* **2011**, *124*, 767−774.
(32) Mattivi, F.; Guzzon, R.; Vrhovsek, U.; Stefanini, M.; Velasco, R. Metabolite profiling of grape: flavonols and anthocyanins. *J. Agric. Food Chem.* **2006**, *54*, 7692−7702.
(33) Alcalde-Eon, C.; García-Estevez, I.; Martín-Baz, A.; Rivas-Gonzalo, J. C.; Escribano-Bailón, M. T. Anthocyanin and flavonol profiles of *Vitis vinifera* L. cv Rufete grapes. *Biochem. Syst. Ecol.* **2014**, *53*, 76−80.
(34) Quijada-Morín, N.; Regueiro, J.; Simal-Gandara, J.; Tomás, E.; Rivas-Gonzalo, J. C.; Escribano-Bailón, M. T. Relationship between the sensory-determined astringency and the flavanolic composition of red wines. *J. Agric. Food Chem.* **2012**, *60*, 12355−12361.
(35) Llaudy, M. d. C.; Canals, R.; Canals, J. M.; Zamora, F. Influence of ripening stage and maceration length on the contribution of grape skins, seeds and stems to phenolic composition and astringency in wine-simulated macerations. *Eur. Food Res. Technol.* **2008**, *226*, 337−344.
(36) Orfila, C.; Knox, J. P. Spatial regulation of pectic polysaccharides in relation to pit fields in cell walls of tomato fruit pericarp. *Plant Physiol.* **2000**, *122*, 775−781.
(37) Ruiz-García, Y.; Smith, P. A.; Bindon, K. A. Selective extraction of polysaccharide affects the adsorption of proanthocyanidin by grape cell walls. *Carbohydr. Polym.* **2014**, *114*, 102−114.
(38) Hutzler, P.; Fischbach, R.; Heller, W.; Jungblut, T. P.; Reuber, S.; Schmitz, R.; Veit, M.; Weissenbock, G.; Schnitzler, J. P. Tissue localization of phenolic compounds in plants by confocal laser scanning microscopy. *J. Exp. Bot.* **1998**, *49*, 953−965.
(39) Braidot, E.; Zancani, M.; Petrussa, E.; Peresson, C.; Bertolini, A.; Patui, S.; Macri, F.; Vianello, A. Transport and accumulation of flavonoids in grapevine (*Vitis vinifera* L.). *Plant Signaling Behav.* **2008**, *3*, 626−32.
(40) Moskowitz, A. H.; Hrazdina, G. Vacuolar contents of fruit subepidermal cells from *Vitis* species. *Plant Physiol.* **1981**, *68*, 686−692.
(41) Markham, K. R.; Gould, K. S.; Ryan, K. G. Cytoplasmic accumulation of flavonoids in flower petals and its relevance to yellow flower colouration. *Phytochemistry* **2001**, *58*, 403−413.
(42) Grandmaison, J.; Ibrahim, R. K. Evidence for nuclear protein binding of flavonol sulfate esters in *Flaveria chloraefolia*. *J. Plant Physiol.* **1996**, *147*, 653−660.
(43) Pinelo, M.; Arnous, A.; Meyer, A. S. Upgrading of grape skins: significance of plant cell-wall structural components and extraction techniques for phenol release. *Trends Food Sci. Technol.* **2006**, *17*, 579−590.

DOI: 10.1021/acs.jafc.5b00261
J. Agric. Food Chem. 2015, 63, 7654−7662

Table 1. Variables

name of variable	meaning of variable	name of variable	meaning of variable
	anthocyanins (mg/g of skin)		**phenolic acids (mg/g of skin)**
Dp	total delphinidin derivatives	a_caftaric	total caftaric acids
Cy	total cyanidin derivatives	a_coutaric	total coutaric acids
Pt	total petunidin derivatives	a_fertaric	total fertaric acids
Pn	total peonidin derivatives	a_caffeic	total caffeic acids
Mv	total malvidin derivatives	a_coumaric	total coumaric acids and their glucoside derivatives
Monoglc	total anthocyanin monoglucosides	HC	total hydroxycinnamic acids
Acet	total anthocyanin acetylglucosides	HB	total hydroxybenzoic acids
Coumar	total anthocyanin coumaroylglucosides		**agronomic, biophysical, and technological variables**
Caffeo	total anthocyanin caffeoylglucosides	Leaf_area	total leaf area (m^2)
Acyl	total anthocyanin acylglucosides	Fresh_wood	total weight of fresh wood (kg)
Anthoc	total anthocyanins	Dry_wood	total weight of dry wood (kg)
	flavanols (mg/g of skin)	Grape_prod	total weight of bunches (kg)
Cs	catechin and epicatechin	Bunch_weight	average of the weight of bunches (g)
PC_dimer	dimers of procyanidins	Berry_weight	average of the weight of berries (g)
PC_trimer	trimers of procyanidins	Perc_skin	percentage (w/w) of berry skin
PC_tetra	tetramers of procyanidins	Perc_seed	percentage (w/w) of berry seeds
PC_gal	total of galloylated procyanidins	Brix	°Brix of grape must
PC_nongal	total of nongalloylated procyanidins	pH	pH of grape must
PC	total of catechins and procyanidins	Titratable_ac	titratable acidity of must (g/L of tartaric acid)
GCs	gallocatechin and epigallocatechin		**mechanical properties variables**
PD_dimer	dimers of prodelphinidins	Hardness	berry hardness by TPA test (N)
PD_trimers	trimers of prodelphinidins	Gumminess	berry gumminess by TPA test (N)
PD	total of gallocatechins and prodelphinidins	Chewiness	berry chewiness by TPA test (mJ)
PAC	total catechins, gallocatechins and proanthocyanidins	F_{sk}	berry skin break force (N)
		Sp_{sk}	berry skin thickness (μm)

istics of the soil.[20−22] As a result, important differences in the levels of acids, anthocyanins, and phenolics could be found within the same vineyard that can lead to variations in the composition and quality of wines.[23,24]

The numerous physiological and chemical changes that grape berries undergo during grape ripening induce modifications not only in their chemical composition but also in their texture features.[25] These textural modifications have been studied through the evaluation of the grape mechanical properties, which, in turn, have been correlated to grape quality.[26,27] A strong relationship between texture parameters and phenolic ripeness degree and grape variety has been reported.[28−30] In addition, these textural parameters have been demonstrated to be a useful tool to study phenolic extractability from grape skins.[31] However, studies in the literature about the relationship between grapevine-related characteristics, berry mechanical properties, and phenolic composition of grapes are scarce.

Due to the importance of phenolic compounds for wine organoleptic properties, phenolic composition has to be taken into account for the selection of harvest date. However, the harvest date is traditionally and chiefly selected on the basis of the technological maturity of grapes, which is related to the sugar concentration of grapes and therefore determines the alcohol content of wine. Nevertheless, the environmental and climatic conditions may cause technological maturity to be reached before phenolic maturity, and it seems that global climate change is going to increase this delay,[32] making it even more difficult to choose the appropriate harvest date to obtain high-quality wines. For this reason, knowledge about the detailed phenolic composition of grapes can be helpful in establishing strategies for harvest planning.

The purpose of this study was to evaluate the usefulness of parameters related to grapevine vigor and grape texture as indicative tools of the grape skin phenolic composition. Specifically, the main objective of this work was to study the relationship between the phenolic composition of *Vitis vinifera* L. cv. Tempranillo grape skins and the vigor-related grapevine characteristics. In addition, the relationship between texture properties of the berries and their phenolic composition has also been assessed.

MATERIALS AND METHODS

Samples. Thirteen different locations of a vineyard (100 ha) located in Zamora, Spain (coordinates 41°18′26″ N 5°21′45″ W), were selected on the basis of different orographic terrain features, such as orientation, altitude, and slope. For each location, all of the grapes (*V. vinifera* L. cv. Tempranillo) from two different grapevines were collected. All grape samples were collected on the same day at harvest time. Grape samples consisted of 300 berries randomly selected from all collected grapes.

Analysis of Phenolic Composition. Skins were manually separated from berries and extracted following Ferrer-Gallego and co-workers.[33] The detailed phenolic composition of grape skins (mg/g of skin) was analyzed by means of HPLC-DAD-MS. Grape skin extracts were directly analyzed for determining anthocyanin composition, whereas they were fractionated as explained below before analysis of flavanols. In both cases, HPLC analyses were performed in a Hewlett-Packard 1200 series HPLC (Agilent Technologies, Waldbronn, Germany). Mass spectrometry was carried out using an API 3200 Qtrap equipped with an ESI source and a triple-quadrupole linear ion trap mass analyzer that was controlled by Analyst 5.1 software (Applied Biosystems, Darmstadt, Germany). All of the analyses were performed in triplicate.

Anthocyanin composition was determined by using the methodology described by Alcalde-Eon and co-workers.[3] Twenty-three different anthocyanins were identified and quantified and grouped into 11 variables depending on the type of anthocyanidin and the type of anthocyanin derivative (see Table 1). Quantification was performed by HPLC-DAD using external calibration curves of standards of 3-*O*-

DOI: 10.1021/acs.jafc.5b00275
J. Agric. Food Chem. 2015, 63, 7663−7669

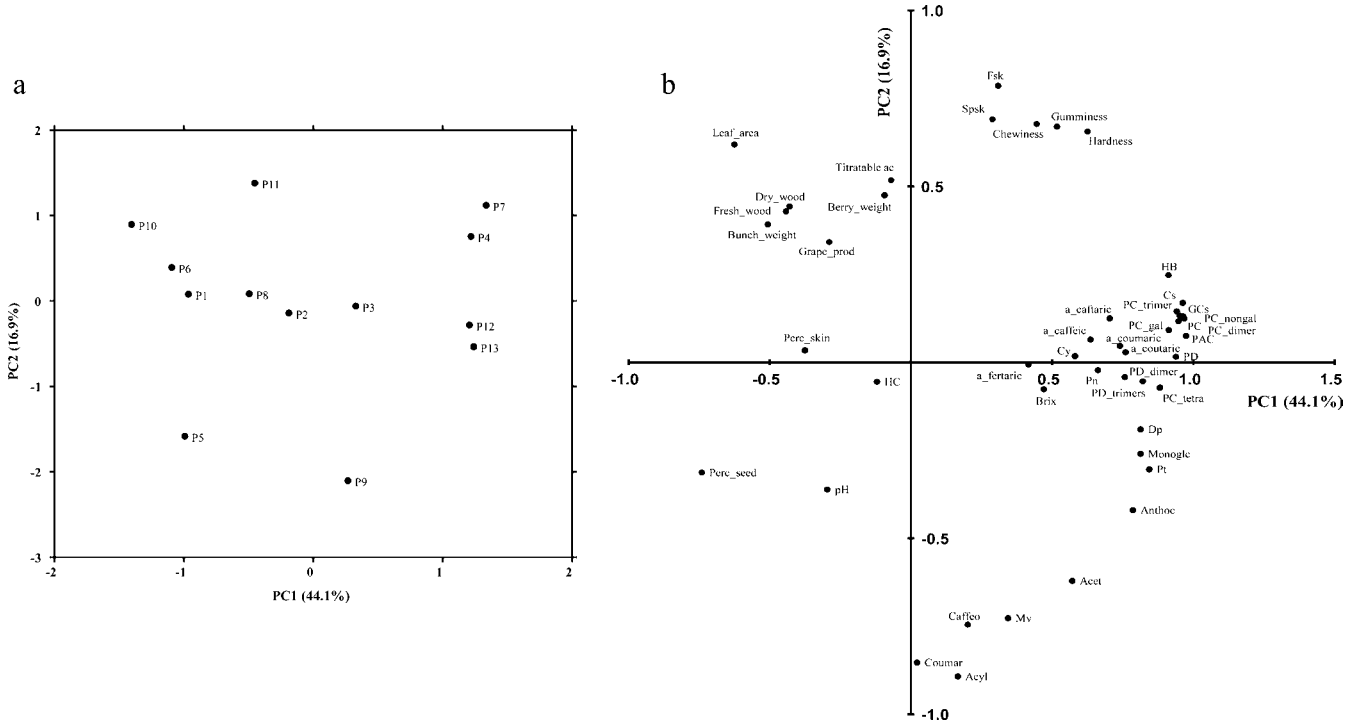

Figure 1. Representation of the samples in the score plot (a) and the variables in the loading plot (b) on the plane defined by the first and second principal components.

glucosides of delphinidin, cyanidin, petunidin, peonidin, and malvidin, purchased from Extrasynthèse (Lyon, France). Each determined anthocyanin was quantified using the calibration curve of the corresponding anthocyanin monoglucoside.

To analyze flavanols and phenolic acids, grape skin extracts were fractionated prior to HPLC-DAD-MS analysis with the objective of eliminating the anthocyanins. Fractionation was carried out according to the procedure described by González-Manzano and co-workers for wine samples.[34] Chromatographic analysis was performed following the methodology reported by Ferrer-Gallego and co-workers.[10] Detection was carried out at 280 nm (proanthocyanidins) and 330 nm (phenolic acids) as the preferred wavelengths. Quantification was performed by HPLC-DAD using external calibration curves of purchased standards except for standards of dimeric and trimeric procyanidins, which were isolated in our laboratory as described by González-Manzano and co-workers.[34] Nineteen different flavanols were determined and grouped into 12 variables depending on the type of flavanol and the polymerization degree (see Table 1). The calibration curves of catechin, dimeric procyanidin, and trimeric procyanidin were employed for quantifying catechin and epicatechin, dimeric procyanidins, and trimers and tetramers of procyanidins, respectively. Galloylated procyanidins were quantified using the epicatechin 3-*O*-gallate calibration curve, whereas gallocatechins and prodelphinidins were quantified using the gallocatechin calibration curve. Two hydroxybenzoic acids and 11 hydroxycinnamic acids and their tartaric esters or glucosidic derivatives were determined and grouped into seven variables (see Table 1). Hydroxybenzoic acids and hydroxycinnamic acids were quantified using the gallic acid and *p*-coumaric acid calibration curves, respectively.

Biophysical and Technological Variables. Eight different biophysical variables were studied (see Table 1), which were also determined at harvest time for each grapevine selected. Data are the average of the values determined for two grapevines of the same location. Leaf area (m^2) was the total leaf area of grapevine. To calculate this value, the number of long, medium-length, and short vine shoots of each grapevine was determined. Considering that long vine shoots have on average 20 knots with each having 4 big-size leaves, whereas medium-long ones have 12 knots with 3 medium-size leaves each and short vine shoots have 8 knots with 2 small-size leaves each, the total number of leaves of each size could be calculated. The average area of each kind of leaf was determined from the area of 10 leaves of each size, which was used to calculate the total leaf area. The grape production (kg) was the total weight of bunches of each grapevine. The average weight of bunches was calculated as the average of the weight of all bunches collected from the same grapevine. The average weight of berries was calculated from the weight of 50 different berries collected from the same grapevine. Moreover, the percentage (w/w) that skin and seeds represented in berry weight was also measured after manual separation of skin and seeds from berries. Grapevines were also pruned after leaf fall, allowing us to calculate the weight of fresh wood. The pruned wood was then dried for 72 h at 60 °C, and the weight of dried wood was determined.

°Brix and pH were directly measured in the grape must by using an optical refractometer and a pH-meter, respectively. Titratable acidity was calculated after acid−base titration of must employing 0.1 M NaOH and expressed as tartaric acid equivalents (g/L).[35]

Instrumental Mechanical Properties. The mechanical properties of the berries were assessed following the method of Letaief and co-workers.[36] A whole-berry texture profile analysis (TPA) double-compression test was carried out at a test speed of 1 mm/s until 25% of sample deformation (2 s waiting time between compressions), with the hardness (N), gumminess (N), and chewiness (mJ) parameters calculated from the force−distance curve.[36] Berry skin break force (F_{sk}, N) was evaluated with a puncture test on the intact berry performed at a test speed of 1 mm/s until 3 mm of sample deformation,[36] whereas the berry skin thickness (Sp_{sk}, μm) was assessed with a 0.2 mm/s compression of a piece of skin using a 2 mm flat cylindrical probe.[36] These parameters were determined by analyzing 30 randomly selected berries collected from the two grapevines of each location.

Statistical Analysis. Principal component analysis (PCA) was used for data analysis as an unsupervised pattern recognition method. The data matrix was constituted by the values determined for all 46 variables described in Table 1 for each selected location. Correlation analyses were carried out, and Pearson's coefficient and two-tailed *p* values were obtained. Backward stepwise multiple linear regression (MLR) was performed to assess the relationship between phenolic composition and the rest of variables. The coefficient of determination (R^2) and the significance (*p* value, bilateral) of the built models were

DOI: 10.1021/acs.jafc.5b00275
J. Agric. Food Chem. 2015, 63, 7663−7669

Table 2. Pearson's Coefficients of the Most Important Significant Correlation between Phenolic Composition of Grape Skins and Biophysical, Technological, and Texture Variables[a]

	Perc_seed	Leaf_area	Fresh_wood	Dry_wood	Bunch_weight	Berry_weight	F_{sk}	Hardness
Mv	ns	−0.691**	ns	ns	ns	ns	ns	ns
Monoglc	−0.600*	−0.561*	ns	ns	−0.577*	ns	ns	ns
Coumar	ns	−0.607*	−0.698**	−0.706**	ns	ns	−0.635*	ns
Caffeo	ns	ns	ns	ns	ns	−0.666*	ns	ns
Acyl	ns	−0.660*	−0.682*	−0.692**	ns	ns	−0.589*	ns
Anthoc	ns	−0.652*	ns	ns	−0.586*	ns	ns	ns
GCs	−0.825**	ns	ns	ns	ns	ns	ns	0.699**
PC_gal	−0.616*	−0.563*	ns	ns	ns	ns	ns	0.648*
PC_nongal	−0.792**	ns	ns	ns	ns	ns	ns	0.653*
PC	−0.764**	ns	ns	ns	ns	ns	ns	0.661*
PD	−0.782**	ns	ns	ns	ns	ns	ns	0.630*
PAC	−0.791**	ns	ns	ns	ns	ns	ns	0.660*
HB	−0.723**	ns	ns	ns	ns	ns	ns	0.678*

[a]See Table 1 for further information about variable meaning. ns, *, and ** indicate the level of significance (no significant, $p < 0.05$, and $p < 0.01$, respectively, $n = 26$).

studied. The software package IBM SPSS Statistics v. 21.0 (IBM, Armonk, NY, USA) was used for data processing.

RESULTS AND DISCUSSION

Study of Correlations. PCA was conducted as unsupervised pattern recognition technique to observe relationships between biophysical, technological, and texture variables and those related to phenolic composition. Figure 1 shows the projection of the samples on the plane defined by the first and second principal components and also the corresponding loadings plot. The first principal component (PC1) describes 44.15% of the variability, and the second principal component (PC2) describes 16.93% of the variability. As can be seen in Figure 1a, the distribution of samples into the score plot did not show any important grouping, thus pointing out the important differences among the selected grapevines (see also Table 1 in the Supporting Information), which will allow us to study possible correlations between the variables employed. Figure 1b shows the variables on the loadings plot. It can be observed that there is a strong opposition along PC1 between flavanol composition of grape skins and some of the biophysical variables studied, such as leaf area (Leaf_area), the average weight of bunch (Bunch_weight), the weight of fresh (Fresh_wood) and dry wood (Dry_wood), and the percentage (w/w) of seeds in total grape weight (Perc_seed). The latter variable also showed a clear negative relationship with the total anthocyanin content (Anthoc). Hence, it seems that it might be a negative relationship between the biophysical features of grapevine determined in this work and the phenolic composition of grapes. In the same way, the acyl derivatives of anthocyanins [mainly the coumaroyl derivatives (Coumar)] showed high negative values in PC2, in contrast to texture variables and leaf area, which showed high positive values in this PC. Thus, there also may be a negative relationship not only between the composition on anthocyanin acyl derivatives of grapes and their texture properties but also between the levels of these compounds and the biophysical features of grapevine. Moreover, from the low loading values obtained for °Brix in PC1 and in PC2 (<0.45 and > −0.08, respectively), it seems that this variable barely contributes to explain sample variability. This could be related to similarities on the sugar content (°Brix) of analyzed grapes (see Table 1 in the Supporting Information), which would indicate that all samples were collected at a similar status of technological maturity. However, phenolic composition is crucial for sample differentiation, which may point out important differences in the phenolic maturity of collected samples. These results indicate that grapes collected from the same vineyard at a similar status of technological maturity can show important differences in phenolic ripeness. These differences, as will be explained below, can be related to differences in grapevine vigor.

To assess the significance of these relationships, the correlation between all variables employed in the study was investigated by means of Pearson's coefficient and its significance. Table 2 shows the most important significant correlations between the phenolic composition of grape skins and the rest of the variables considered in this study. The phenolic composition did not show any significant correlations with the percentage (w/w) of skins (data not shown). However, they corroborate the negative relationship between the percentage (w/w) of seeds in relation to the whole grape (Perc_seed) and the flavanic composition of grape skins indicated in the PCA plotting (Figure 1b). This is in accordance with studies in the literature which have reported that skin weight was not a determining factor for anthocyanin potential of the berries but that seed weight seemed to significantly affect the grape composition.[37] All variables related to flavanic composition showed high negative coefficients of Pearson with Perc_seed variable. Among them, the total content of flavanols (PAC), as well as the total content of procyanidins (PC) and prodelphinidins (PD), showed Pearson's coefficients < −0.76. Moreover, these correlations are highly significant ($p < 0.01$). Thus, it seems that the heavier the seed, the lower amounts of flavanols in the skins. It might be possible that synthesis of flavanols in seeds and in skin could be competitive and that the highest weight of the seed reflects higher synthesis rate of flavanols in this part of the berry, at the expense of the synthesis in the grape skin. This negative correlation is also observed between total hydroxybenzoic acids content in grape skin and the percentage (w/w) of seeds. Because one of the two hydroxybenzoic acids (the major one) found in the skin is gallic acid, and this acid is also found in grape seeds, this negative correlation might be also due to the same reasons as those proposed for flavanols.

Total leaf area of grapevine also correlates negatively with phenolic composition of grape skin. Anthocyanin compounds

DOI: 10.1021/acs.jafc.5b00275
J. Agric. Food Chem. 2015, 63, 7663−7669

presented the highest negative Pearson's coefficients. Malvidin derivatives (Mv) and the acyl-derived anthocyanin (Acyl) levels were the most strongly correlated to leaf area. The acyl-derived, and, in particular, the coumaroyl-anthocyanin derivatives (Coumar), also showed a strong negative relationship with the weight of wood pruned from the grapevine (Fresh_wood and Dry_wood). These two variables, together with leaf area, could be related to vine vigor. Our results are consistent with those recently reported by Song and co-workers[17] which have found that as vine vigor decreased, total soluble solids in grapes and total phenolics and anthocyanins in wines increased, thus pointing out a negative relationship between vine vigor and grape phenolic composition. Moreover, vine vigor could be related to the grapevine water availability that in turn seems to affect the composition of grapes because an excess in water conditions has demonstrated to be more negative for anthocyanin contents than strong deficit conditions.[37]

A significant negative relationship could also be observed (Table 2) between the average weight of bunches (Bunch_weight) and the monoglucoside (Monoglc) and total anthocyanin (Antoc_total) contents. Moreover, the level of anthocyanin caffeoyl derivatives is also strongly correlated ($r = -0.666$, $p < 0.05$) to the average weight of berries (Berry_weight). Therefore, it seems that the heavier the bunches and berries were, the lower were the levels of anthocyanins (both total and monoglucoside and caffeoyl derivatives) the skins and, consequently, the berries showed. These results are in accordance with those reported in the literature showing that the total anthocyanin content (mg/berry) and anthocyanin concentration (mg/kg of berries and in mg/g of skin) were dependent on berry mass variation.[38] Likewise, it seems that the berries in which seeds accounted for a higher weight percentage (Perc_seed) show lower levels of monoglucosides, because a significant negative correlation ($r = -0.600$, $p < 0.05$) between these two variables was observed. It has been reported that berry weight is more related to seed weight than to skin and flesh weight,[37,38] so this might explain why both Berry_weight and Perc_seed variables showed a relationship with anthocyanin composition, whereas no relationship was found with Perc_skin variable. These correlations between physical features of berries and their phenolic composition might be explained because grape development occurs in two main stages. The first stage, comprising the flowering and green berry stages, and maybe even prior to that, during differentiation of the primordia,[39] seems critical in determining berry weight.[38] However, anthocyanin and sugar accumulation takes place in a second stage, from veraison to harvest. Thus, if the first stages were the most important, bunches, berries, and seeds could be heavier but grapes may show lower levels of anthocyanins.

Finally, a strong negative correlation was also observed between the texture features of grape and its phenolic composition. In particular, the berry skin break force (F_{sk}) and the levels of anthocyanidin−coumaroylglucosides ($r = -0.635$, $p < 0.05$) and of total acyl-derived anthocyanin ($r = -0.589$, $p < 0.05$) are negatively correlated (Table 2). These results are in accordance with those reported by Giacosa and co-workers,[40] who have observed in Shiraz grapes significantly lower values of F_{sk} in berries showing higher levels of coumaroyl-anthocyanin derivatives in its composition. These results are also consistent with other studies available in the literature pointing out the potential of the mechanical properties of berry skin (such as F_{sk} and Sp_{sk}) to predict the anthocyanin extractability.[29,31] Moreover, it has also been reported that cell-wall composition affects the anthocyanin extraction; in particular, the presence of higher amounts of glucose, rhamnose, 2-*O*-methylxylose, and lignin in the cell-wall composition would prevent anthocyanin extraction from grape skin.[41] Considering this, there might be a relationship between the cell-wall composition and the levels of coumaroyl-anthocyanin derivatives that may be explained by a possible interaction between the acyl-derived anthocyanins and some components of the grape cell wall, which in turn may determine the texture features of grapes. Further studies about the cell-wall and phenolic composition and texture features of berry skin must be carried out to assess this possibility.

Moreover, a significant positive correlation has been observed between berry hardness and its flavanic composition. It is worth noting the strong correlation between this texture parameter and the level of gallocatechin and epigallocatechin ($r = 0.699$, $p < 0.01$, Table 2). Thus, it seems that berry hardness might be indicative of the levels of flavanols in berry skin. Río Segade and co-workers[30] have reported that break force and thickness of berry skin can be considered mechanical properties adequate for the estimation of the degradability of the skin cell wall. Degradation is related to changes in the structure of the cell wall by depolymerization and formation of new cross-linking bridges[42] and to changes in its composition by loss of galactose and other pectic sugars such as arabinose and rhamnose.[30,43,44] Considering that these texture parameters could be related to cell-wall composition, the correlation found between flavanic composition and berry hardness might be explained, as in the case of acyl-derived anthocyanin, by a specific interaction of flavanols with some cell-wall components. In fact, Ruiz-García and co-workers[45] have pointed out that pectic polysaccharides have an important binding affinity for flavanols, whereas cellulose, due to a low porosity, showed less affinity for these compounds. Thus, both higher levels of flavanols and higher values of hardness of berries might be related to higher levels of cellulose in the cell wall. However, further specific studies about the relationship between cell-wall composition and texture features of berries must be carried out to assess this possibility.

Regression Studies. Considering the aforementioned correlations, different multiple linear regressions (MLR) were carried out to assess the influence of biophysical, technological, and texture variables employed in this work on the phenolic composition of grape skin. A backward-stepwise strategy was employed for MLR, in which all of the considered variables were used at the start of the process and then the least significant one is removed at each step. The model is refitted after each step including only the most significant variables. First, due to the correlation found between the amount of coumaroyl-anthocyanin derivatives and the texture parameters that pointed out a possible relationship between these compounds and cell-wall composition, the variable Coumar was selected as dependent variable, whereas the biophysical, technological, and texture variables described in Table 1 were used as independent variables. Among all of the variables considered, only the dry weight of pruned wood (Dry_wood), the berry skin break force (F_{sk}), and the berry skin thickness (Sp_{sk}) were considered statistically significant ($p < 0.05$) in the fitted final model. The values of the coefficient of determination (R^2), the nonstandardized coefficients (B), and the standardized coefficients (β) were obtained. The coefficient of determination ($R^2 = 0.856$) indicates that the proposed model

DOI: 10.1021/acs.jafc.5b00275
J. Agric. Food Chem. 2015, 63, 7663−7669

explains 85.6% of the variability of the levels of coumaroyl-anthocyanin derivatives, which supposed a good fit to the data. Table 3 shows the values of the regression constant and of the

Table 3. Results of the MLR Carried Out Using the Level of Coumaroyl-Glucoside Anthocyanins (Up) and of Total Flavanols (Down) as Dependent Variables

Dependent Variable: Coumaroyl-Glucoside Anthocyanins (Coumar, mg/g of Skin), R^2 = 0.856			
variable	nonstandardized coefficients (B)	standardized coefficients (β)	p value
Constant	1.934		<0.001
Dry_wood (kg)	−0.333	−0.741	<0.001
F_{sk} (N)	−0.715	−0.300	0.008
Sp_{sk} (mm)	−0.002	−0.352	0.006
Dependent Variable: Total Flavanols (PAC, mg/g of Skin), R^2 = 0.829			
variable	nonstandardized coefficients (B)	standardized coefficients (β)	p value
Constant	2.664		0.020
Leaf_area (m^2)	−8.331	−0.406	0.019
Perc_seed	−0.335	−0.507	0.001
Hardness (N)	0.181	0.310	0.009

β parameter for each variable, which could be considered the best estimation about its contribution to the model. As can be observed in the study of correlations, these three variables (Dry_wood, F_{sk} and Sp_{sk}) showed a negative relationship with the levels of coumaroyl-anthocyanin derivatives. The most important variable in the study was Dry_wood (β = −0.741), thus indicating the importance of grapevine vigor in the levels of these anthocyanin-derived compounds in grapes.

Considering the important role of flavanols in some organoleptic properties of wines such as astringency or color, MLR was also performed using the levels of total flavanols (PAC) as dependent variable and the biophysical, technological, and texture variables described in Table 1 as independent variables. Table 3 shows the result of fitting. The proposed model explained 82.9% of the variability of total flavanol levels (R^2 = 0.829), which indicates the goodness of data fitting. As can be observed in Table 3, the percentage (w/w) of seeds and leaf area showed a negative relationship, whereas berry hardness showed a positive relationship with flavanol content. The most important variable in this model is the percentage (w/w) of seeds, thus pointing out the importance of seed size on the flavanic composition of grape skins.

The proposed models indicated that there is a strong relationship between the biophysical parameters of grapevine (mostly vine vigor represented by leaf area, dry weight of pruned wood, and seed weight), the texture features (evaluated as instrumental mechanical properties) of berries, and the phenolic composition of grape skins. Although this study has been carried out in only one vintage, we have chosen a vineyard large enough to have important differences in orographic terrain features. This could be observed in the PCA and also in the high variability of variables that have been used in this work (see Table 1 in the Supporting Information). Thus, the results here presented set an important precedent because they establish the importance of agronomic parameters and texture properties for estimating the phenolic composition of grape skins. However, further studies involving different vineyards, grape cultivars, and vintages must be done to corroborate the quantitative relationship between these variables.

In conclusion, the results obtained pointed out an important relationship between the phenolic composition of grape skin, biophysical features of grapevines, and berry texture properties. Anthocyanin composition showed significant negative correlation with grapevine vigor-related parameters (such as leaf area and bunch weight), whereas the amount of flavanols of grape skins was negatively correlated with the percentage (w/w) of seeds. Moreover, the phenolic composition is also correlated to some mechanical properties of grapes. Berry skin break force showed a negative correlation with the coumaroyl-anthocyanin derivatives, whereas berry hardness was positively correlated to flavanic composition. Thus, a relationship between both acyl-derived anthocyanins and flavanols and grape cell-wall composition could be proposed. A significant regression was found between coumaroyl-anthocyanin derivatives and some biophysical (weight of pruned wood) and texture (berry skin break force and berry skin thickness) variables. Likewise, a significant regression was also found between flavanol levels and the percentage (w/w) of seeds, leaf area, and berry hardness. These results pointed out that grapevine vigor-related and texture parameters might be useful for estimating the phenolic composition of grape skins.

■ ASSOCIATED CONTENT

Supporting Information

Minimum, maximum, and average values and coefficients of variation of all the variables employed in this study. The Supporting Information is available free of charge on the ACS Publications website at DOI: 10.1021/acs.jafc.5b00275.

■ AUTHOR INFORMATION

Corresponding Author

*(M.T.E.-B.) Phone: +34 923294537. Fax: +34 923294515. E-mail: escriban@usal.es.

Funding

Thanks are due to the Spanish MICINN and FEDER (Projects ref AGL2011-30254-C02 and AGL2014-58486-C2-R) for financial support.

Notes

The authors declare no competing financial interest.

■ REFERENCES

(1) Moreno-Arribas, M. V.; Polo, M. C. *Wine Chemistry and Biochemistry*; Springer Science: New York, 2009.

(2) Alcalde-Eon, C.; Escribano-Bailón, M. T.; Santos-Buelga, C.; Rivas-Gonzalo, J. C. Changes in the detailed pigment composition of red wine during maturity and ageing − a comprehensive study. *Anal. Chim. Acta* **2006**, *563*, 238−254.

(3) Alcalde-Eon, C.; García-Estévez, I.; Ferreras-Charro, R.; Rivas-Gonzalo, J. C.; Ferrer-Gallego, R.; Escribano-Bailón, M. T. Adding oenological tannin vs. overripe grapes: effect on the phenolic composition of red wines. *J. Food Compos. Anal.* **2014**, *34*, 99−113.

(4) He, F.; Liang, N.-N.; Mu, L.; Pan, Q.-H.; Wang, J.; Reeves, M. J.; Duan, C.-Q. Anthocyanins and their variation in red wines I. Monomeric anthocyanins and their color expression. *Molecules* **2012**, *17*, 1571−1601.

(5) Dangles, O.; Saito, N.; Brouillard, R. Anthocyanin intramolecular copigment effect. *Phytochemistry* **1993**, *34*, 119−124.

(6) Gawel, R. Red wine astringency: a review. *Aust. J. Grape Wine Res.* **1998**, *4*, 74−95.

(7) Somers, T. C. Polymeric nature of wine pigments. *Phytochemistry* **1971**, *10*, 2175−2186.

DOI: 10.1021/acs.jafc.5b00275
J. Agric. Food Chem. 2015, 63, 7663−7669

(8) Kennedy, J. A.; Hayasaka, Y.; Vidal, S.; Waters, E. J.; Jones, G. P. Composition of grape skin proanthocyanidins at different stages of berry development. *J. Agric. Food Chem.* **2001**, *49*, 5348−5355.
(9) Escribano-Bailón, M. T.; Guerra, M. T.; Rivas-Gonzalo, J. C.; Santos-Buelga, C. Proanthocyanidins in skins from different grape varieties. *Z. Lebensm.-Unters. Forsch.* **1995**, *200*, 221−224.
(10) Ferrer-Gallego, R.; García-Marino, M.; Hernández-Hierro, J. M.; Rivas-Gonzalo, J. C.; Escribano-Bailón, M. T. Statistical correlation between flavanolic composition, colour and sensorial parameters in grape seed during ripening. *Anal. Chim. Acta* **2010**, *660*, 22−28.
(11) Bindon, K. A.; Smith, P. A.; Holt, H.; Kennedy, J. A. Interaction between grape-derived proanthocyanidins and cell wall material. 2. Implications for vinification. *J. Agric. Food Chem.* **2010**, *58*, 10736−10746.
(12) Kennedy, J. A. Grape and wine phenolics: observations and recent findings. *Cien. Invest. Agrar.* **2008**, *35*, 107−120.
(13) Fernández-López, J. A.; Hidalgo, V.; Almela, L.; López-Roca, J. M. Quantitative changes in anthocyanin pigments of *Vitis vinifera* cv Monastrell during maturation. *J. Sci. Food Agric.* **1992**, *58*, 153−155.
(14) Spayd, S. E.; Tarara, J. M.; Mee, D. L.; Ferguson, J. C. Separation of sunlight and temperature effects on the composition of *Vitis vinifera* cv. Merlot berries. *Am. J. Enol. Vitic.* **2002**, *53*, 171−182.
(15) Chorti, E.; Guidoni, S.; Ferrandino, A.; Novello, V. Effect of different cluster sunlight exposure levels on ripening and anthocyanin accumulation in Nebbiolo grapes. *Am. J. Enol. Vitic.* **2010**, *61*, 23−30.
(16) Guidoni, S.; Allara, P.; Schubert, A. Effect of cluster thinning on berry skin anthocyanin composition of *Vitis vinifera* cv. Nebbiolo. *Am. J. Enol. Vitic.* **2002**, *53*, 224−226.
(17) Song, J.; Smart, R. E.; Dambergs, R. G.; Sparrow, A. M.; Wells, R. B.; Wang, H.; Qian, M. C. Pinot Noir wine composition from different vine vigour zones classified by remote imaging technology. *Food Chem.* **2014**, *153*, 52−59.
(18) King, P. D.; Smart, R. E.; McClellan, D. J. Within-vineyard variability in vine vegetative growth, yield, and fruit and wine composition of Cabernet Sauvignon in Hawke's Bay, New Zealand. *Aust. J. Grape Wine Res.* **2014**, *20*, 234−246.
(19) Cortell, J. M.; Halbleib, M.; Gallagher, A. V.; Righetti, T. L.; Kennedy, J. A. Influence of vine vigor on grape (*Vitis vinifera* L. cv. Pinot Noir) anthocyanins. 1. Anthocyanin concentration and composition in fruit. *J. Agric. Food Chem.* **2007**, *55*, 6575−6584.
(20) Cortell, J. M.; Halbleib, M.; Gallagher, A. V.; Righetti, T. L.; Kennedy, J. A. Influence of vine vigor on grape (*Vitis vinifera* L. cv. Pinot noir) and wine proanthocyanidins. *J. Agric. Food Chem.* **2005**, *53*, 5798−5808.
(21) Dry, P. R.; Loveys, B. R. Factors influencing grapevine vigour and the potential for control with partial rootzone drying. *Aust. J. Grape Wine Res.* **1998**, *4*, 140−148.
(22) Johnson, L. F.; Bosch, D. F.; Williams, D. C.; Lobitz, B. M. Remote sensing of vineyard management zones: implications for wine quality. *Appl. Eng. Agric.* **2001**, *17*, 557−560.
(23) Lamb, D. W.; Weedon, M. M.; Bramley, R. G. V. Using remote sensing to predict grape phenolics and colour at harvest in a Cabernet Sauvignon vineyard: timing observations against vine phenology and optimizing image resolution. *Aust. J. Grape Wine Res.* **2004**, *10*, 46−54.
(24) Bramley, R. G. V.; Ouzman, J.; Boss, P. K. Variation in vine vigour, grape yield and vineyard soils and topography as indicators of variation in the chemical composition of grapes, wine and wine sensory attributes. *Aust. J. Grape Wine Res.* **2011**, *17*, 217−229.
(25) Rolle, L.; Siret, R.; Río Segade, S.; Maury, C.; Gerbi, V.; Jourjon, F. Instrumental texture analysis parameters as markers of table-grape and winegrape quality: a review. *Am. J. Enol. Vitic.* **2012**, *63*, 11−28.
(26) Rolle, L.; Gerbi, V.; Schneider, A.; Spanna, F.; Río Segade, S. Varietal relationship between instrumental skin hardness and climate for grapevines (*Vitis vinifera* L.). *J. Agric. Food Chem.* **2011**, *59*, 10624−10634.
(27) Giordano, M.; Zecca, O.; Belviso, S.; Reinotti, M.; Gerbi, V.; Rolle, L. Volatile fingerprint and physico-mechanical properties of 'muscat blanc' grapes grown in mountain area: a first evidence of the influence of water regimes. *Ital. J. Food Sci.* **2013**, *25*, 329−338.
(28) Maury, C.; Madieta, E.; Le Moigne, M.; Mehinagic, E.; Siret, R.; Jourjon, F. Development of a mechanical texture test to evaluate the ripening process of Cabernet Franc grapes. *J. Texture Stud.* **2009**, *40*, 511−535.
(29) Río Segade, S.; Orriols, I.; Giacosa, S.; Rolle, L. Instrumental texture analysis parameters as winegrapes varietal markers and ripeness predictors. *Int. J. Food Prop.* **2011**, *14*, 1318−1329.
(30) Río Segade, S.; Rolle, L.; Gerbi, V.; Orriols, I. Phenolic ripeness assessment of grape skin by texture analysis. *J. Food Compos. Anal.* **2008**, *21*, 644−649.
(31) Rolle, L.; Torchio, F.; Ferrandino, A.; Guidoni, S. Influence of wine-grape skin hardness on the kinetics of anthocyanin extraction. *Int. J. Food Prop.* **2012**, *15*, 249−261.
(32) Mira de Orduña, R. Climate change associated effects on grape and wine quality and production. *Food Res. Int.* **2010**, *43*, 1844−1855.
(33) Ferrer-Gallego, R.; Hernández-Hierro, J. M.; Rivas-Gonzalo, J. C.; Escribano-Bailón, M. T. Determination of phenolic compounds of grape skins during ripening by NIR spectroscopy. *LWT−Food Sci. Technol.* **2011**, *44*, 847−853.
(34) González-Manzano, S.; Santos-Buelga, C.; Pérez-Alonso, J. J.; Rivas-Gonzalo, J. C.; Escribano-Bailón, M. T. Characterization of the mean degree of polymerization of proanthocyanidins in red wines using liquid chromatography-mass spectrometry (LC-MS). *J. Agric. Food Chem.* **2006**, *54*, 4326−4332.
(35) OIV. *Recueil international des méthodes d'analyse des vins et des moûts*; Organisation Internationale de la Vigne et du Vin: Paris, France, 2008.
(36) Letaief, H.; Rolle, L.; Gerbi, V. Mechanical behavior of winegrapes under compression tests. *Am. J. Enol. Vitic.* **2008**, *59*, 323−329.
(37) Ferrer, M.; Echeverría, G.; Carbonneau, A. Effect of berry weight and its components on the contents of sugars and anthocyanins of three varieties of *Vitis vinifera* L. under different water supply conditions. *S. Afr. J. Enol. Vitic.* **2014**, *35*, 103−113.
(38) Barbagallo, M. G.; Guidoni, S.; Hunter, J. J. Berry size and qualitative characteristics of *Vitis vinifera* L. cv. Syrah. *S. Afr. J. Enol. Vitic.* **2011**, *32*, 129−136.
(39) Gray, J. D.; Coombe, B. G. Variation in Shiraz berry size originates before fruitset but harvest is a point of resynchronisation for berry development after flowering. *Aust. J. Grape Wine Res.* **2009**, *15*, 156−165.
(40) Giacosa, S.; Marengo, F.; Guidoni, S.; Rolle, L.; Hunter, J. J. Anthocyanin yield and skin softening during maceration, as affected by vineyard row orientation and grape ripeness of *Vitis vinifera* L. cv. Shiraz. *Food Chem.* **2015**, *174*, 8−15.
(41) Hernández-Hierro, J. M.; Quijada-Morín, N.; Martínez-Lapuente, L.; Guadalupe, Z.; Ayestaran, B.; Rivas-Gonzalo, J. C.; Escribano-Bailón, M. T. Relationship between skin cell wall composition and anthocyanin extractability of *Vitis vinifera* L. cv. Tempranillo at different grape ripeness degree. *Food Chem.* **2014**, *146*, 41−47.
(42) Hanlin, R. L.; Hrmova, M.; Harbertson, J. F.; Downey, M. O. Review: Condensed tannin and grape cell wall interactions and their impact on tannin extractability into wine. *Aust. J. Grape Wine Res.* **2010**, *16*, 173−188.
(43) Ortega-Regules, A.; Romero-Cascales, I.; Ros-García, J. M.; López-Roca, J. M.; Gómez-Plaza, E. A first approach towards the relationship between grape skin cell-wall composition and anthocyanin extractability. *Anal. Chim. Acta* **2006**, *563*, 26−32.
(44) Ortega-Regules, A.; Ros-García, J. M.; Bautista-Ortín, A. B.; López-Roca, J. M.; Gómez-Plaza, E. Changes in skin cell wall composition during the maturation of four premium wine grape varieties. *J. Sci. Food Agric.* **2008**, *88*, 420−428.
(45) Ruiz-García, Y.; Smith, P. A.; Bindon, K. A. Selective extraction of polysaccharide affects the adsorption of proanthocyanidin by grape cell walls. *Carbohydr. Polym.* **2014**, *114*, 102−114.

DOI: 10.1021/acs.jafc.5b00275
J. Agric. Food Chem. 2015, 63, 7663−7669

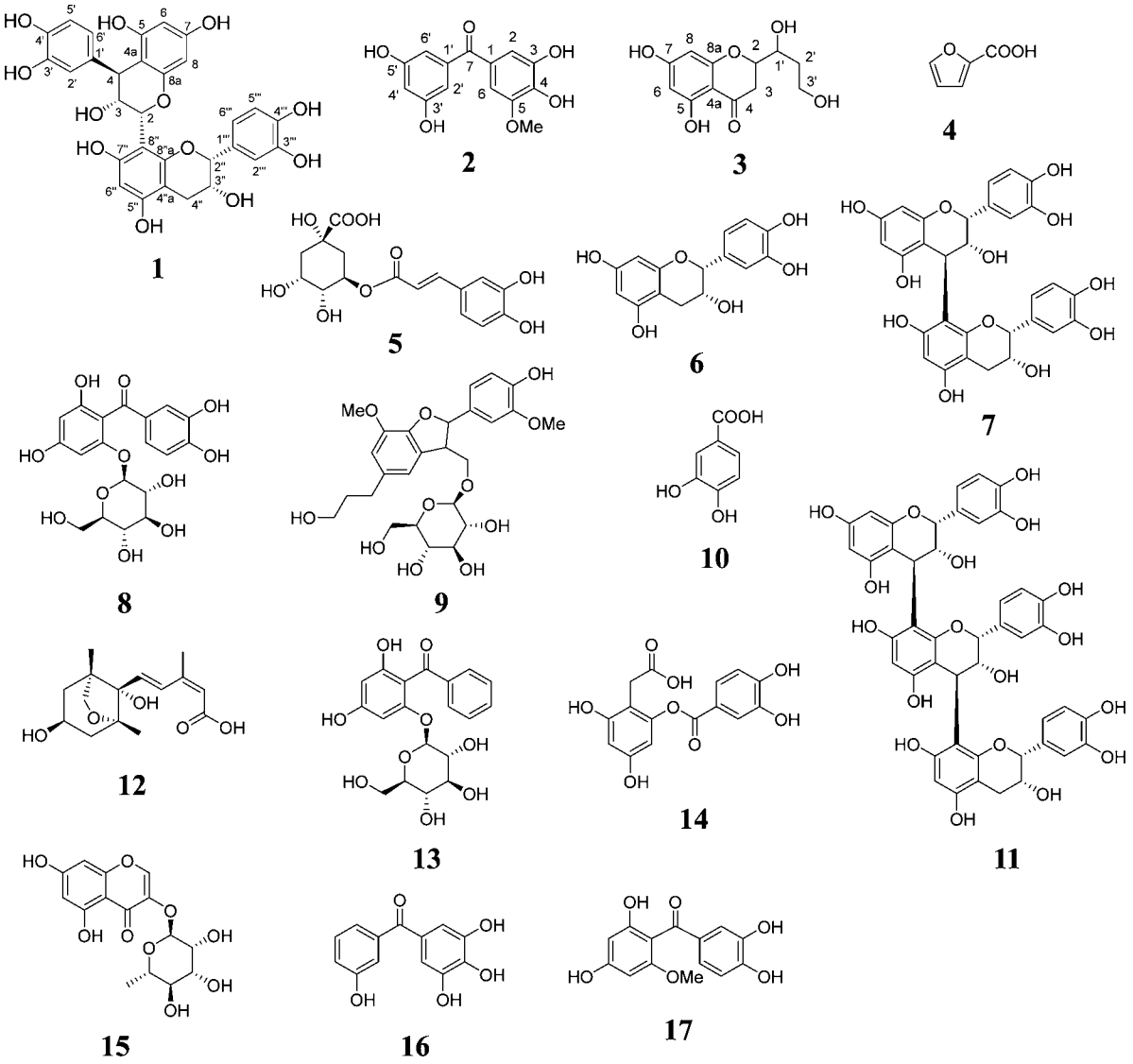

Figure 1. Structures of compounds (**1**–**17**) isolated from mangosteen (*Garcinia mangostana* L.) pericarp.

Healthcare Japan, Tokyo, Japan). Each authentic sample [procyanidin B2 (Extrasynthese, Lyon, France), procyanidin C1 (ChromaDex, Inc., Irvin, CA, USA), chlorogenic acid (Tokyo Chemical Industry, Tokyo, Japan), protocatechuic acid (Wako Pure Chemical Industries, Osaka, Japan)] was purchased from the manufacturer.

Isolation Procedure of Mangosteen Pericarp. The fruits of mangosteen were harvested in Chanthaburi province (eastern Thailand) and Nakhon Si Thammarat province (southern Thailand). The powdered dried mangosteen pericarps (600 kg) were extracted with hot water (90 °C, 5600 L) for 3 h, and the filtered concentrate was powdered with a spray-dryer after the addition of dextrin (to 25%) as diluent to yield hot water extract (92.1 kg). The hot water extract (100 g) was resuspended in water and subjected to liquid–liquid partition to yield *n*-hexane (65.5 mg), ethyl acetate (EtOAc) (2.6 g), *n*-butanol (*n*-BuOH) (12.5 g), and water extract. A part of the *n*-BuOH extract (9.0 g/12.5 g) was chromatographed over MCI-gel CHP20 (40 cm × 1.1 cm i.d.) eluted with water to methanol. The water eluate was further purified using YMC-gel ODS-AQ (40 cm × 1.1 cm i.d.) column chromatography to give six known compounds identified as 2-furancarboxylic acid, **4** (11.2 mg); chlorogenic acid, **5** (6.5 mg); epicatechin, **6** (12.4 mg); procyanidin B2, **7** (10.5 mg); rhodanthenone B, **8** (14.0 mg); and dihydrodehydrodiconiferyl alcohol 9-*O*-glucoside, **9** (2.0 mg) (Figure 1). The EtOAc extract (2.6 g) was chromatographed over a YMC-gel ODS-AQ (40 cm × 1.1 cm i.d.) column and eluted in a stepwise gradient mode with water–methanol. The water and 10% methanol eluate (960.5 mg) was separately chromatographed over Sephadex LH-20 (20 cm × 1.1 cm i.d.) yielding epicatechin, **6** (145.2 mg); procyanidin B2, **7** (28.7 mg); protocatechuic acid, **10** (11.9 mg); and procyanidin C1, **11** (7.4 mg). The 20% methanol eluate (297.4 mg) was further separated by column chromatography over Chromatorex ODS (20 cm × 1.1 cm i.d.) and Sephadex LH-20 (20 cm × 1.1 cm i.d.) to yield GM-3, **3** (1.0 mg); epicatechin, **6** (77.5 mg); dihydrophaseic acid, **12** (5.3 mg); garcimangosone D, **13** (2.7 mg); and 2-*O*-(3,4-dihydroxybenzoyl)-2,4,6-trihydroxyphenylacetic acid, **14** (2.4 mg). The 30% methanol eluate (215.4 mg) was further purified using Sephadex LH-20 (20 cm × 1.1 cm i.d.), Chromatorex ODS (20 cm × 1.1 cm i.d.), and MCI-gel CHP20 (20 cm × 1.1 cm i.d.) column chromatography to give GM-1, **1** (2.2 mg); GM-2, **2** (1.2 mg); garcimangosone D, **13** (2.2 mg); 2-*O*-(3,4-dihydroxybenzoyl)-2,4,6-trihydroxyphenylacetic acid, **14** (2.6 mg); eucryphin, **15** (2.6 mg); 3,4,5,3′-tetrahydroxybenzophenone, **16** (1.2 mg); and 4,6,3′,4′-tetrahydroxy-2-methoxybenzophenone, **17** (1.6 mg). Each structure of known compounds was inferred from the NMR and MS data or from a direct HPLC comparison with an authentic sample.

GM-1, 1: pale brown amorphous powder; $[\alpha]^{27}_{D}$ −42.5° (*c* 0.2, MeOH); ^{1}H NMR (methanol-d_4) δ 6.73 (1H, d, J = 8.5 Hz, H-5‴), 6.63 (1H, d, J = 8.0 Hz, H-5′), 6.60 (1H, d, J = 2.0 Hz, H-2‴), 6.59 (1H, d, J = 2.0 Hz, H-2′), 6.43 (1H, dd, J = 2.0, 8.5 Hz, H-6′), 6.16 (1H, dd, J = 2.0, 8.5 Hz, H-6‴), 5.99 (1H, s, H-6″), 5.93 (2H, s, H-6,

DOI: 10.1021/acs.jafc.5b01771
J. Agric. Food Chem. 2015, 63, 7670–7674

8), 5.63 (1H, br s, H-2), 4.68 (1H, br s, H-2″), 4.26 (1H, dd, J = 1.0, 2.5 Hz, H-3), 4.15 (1H, d, J = 2.5 Hz, H-4), 4.10 (1H, m, H-3″), 2.87 (1H, dd, J = 5.0, 17.0 Hz, H-4″), 2.70 (1H, dd, J = 1.5, 17.0 Hz, H-4″); ^{13}C NMR (methanol-d_4) δ 158.7 (C-5 or -8), 158.2 (C-7), 158.0 (C-5″), 157.8 (C-5 or -8), 157.3 (C-7″), 154.7 (C-8″a), 146.0 (C-3′), 145.7 (C-3‴), 145.3 (C-4‴), 144.4 (C-4′), 136.4 (C-1′), 131.6 (C-1‴), 120.9 (C-6′), 119.0 (C-6‴), 116.9 (C-2′), 116.8 (C-5‴), 116.5 (C-5′), 113.8 (C-2‴), 105.2 (C-8″), 102.1 (C-4a), 100.3 (C-4″a), 97.9 (C-6″), 96.8, 95.4 (each 1H, C-6,8), 80.0 (C-2″), 74.4 (C-3), 70.3 (C-2), 67.5 (C-3″), 45.7 (C-4), 29.6 (C-4″); HR-ESI-MS m/z 577.1343 $[M - H]^-$ (calculated for $C_{30}H_{26}O_{12}$ − H, 577.1352).

GM-2, **2***:* pale brown amorphous powder; ^{1}H NMR (acetone-d_6 + D_2O) δ 6.53 (2H, d, J = 2.0 Hz, H-2′, 6′), 6.45 (1H, t, J = 2.0 Hz, H-4′), 6.02 (1H, d, J = 2.0 Hz, H-2), 6.01 (1H, d, J = 2.0 Hz, H-6), 3.50 (3H, s, 5-OMe); ^{13}C NMR (acetone-d_6 + D_2O) δ 198.4 (C-7), 164.4 (C-4), 162.9 (C-3), 162.5 (C-5), 158.8 (2C, C-3′,5′), 143.8 (C-1′), 107.2 (2C, C-2′,6′), 106.9 (C-1), 106.3 (C-4″), 96.4 (C-2), 92.3 (C-6), 55.7 (5-OMe); HR-ESI-MS m/z 275.0565 $[M - H]^-$ (calculated for $C_{14}H_{12}O_6$ − H, 275.0561).

GM-3, **3***:* $[\alpha]^{27}_D$ +30.5° (c 0.2, MeOH); pale brown amorphous powder; ^{1}H NMR (acetone-d_6) δ 12.16 (1H, s, 5-OH), 5.94 (1H, d, J = 2.0 Hz, H-8), 5.90 (1H, d, J = 2.0 Hz, H-6), 4.42 (1H, dt, J = 3.5, 3.5, 13.0 Hz), 3.96 (1H, dt, J = 4.0, 4.0, 9.0 Hz, H-1′), 3.79 (2H, m, H-3′), 3.00 (1H, dd, J = 13.0, 17.5 Hz, H-3), 2.55 (1H, dd, J = 3.0, 17.5 Hz, H-3), 1.86 (2H, m, H-2′); ^{13}C NMR (acetone-d_6) δ 197.7 (C-4), 167.2 (C-7), 165.2 (C-5), 164.3 (C-8a), 103.2 (C-4a), 96.6 (C-6), 95.7 (C-8), 81.2 (C-2), 70.8 (C-1′), 59.8 (C-3′), 38.6 (C-3), 36.0 (C-2′); HR-ESI-MS m/z 253.0711 $[M - H]^-$ (calculated for $C_{12}H_{14}O_6$ − H, 253.0718).

RESULTS AND DISCUSSION

A hot water extract of mangosteen (*G. mangostana* L.) pericarp was successively partitioned with *n*-hexane, EtOAc, and *n*-BuOH to give respective extracts. The *n*-BuOH extract was subjected to successive column chromatography over MCI-gel CHP20 and YMC-gel ODS-AQ, yielding six known compounds identified as 2-furancarboxylic acid, **4**; chlorogenic acid, **5**; epicatechin, **6**; procyanidin B2, **7**; rhodanthenone B, **8**;[12] and dihydrodehydrodiconiferyl alcohol 9-*O*-glucoside, **9**.[9] The EtOAc extract was similarly separated by successive column chromatography over YMC-gel ODS-AQ, Sephadex LH-20, and Chromatorex ODS, yielding three new compounds (GM-1, -2, and -3), **1**−**3** along with 10 known compounds, which were characterized by NMR data or direct HPLC comparison with authentic samples as epicatechin, **6**; procyanidin B2, **7**; protocatechuic acid, **10**; procyanidin C1, **11**; dihydrophaseic acid, **12**; garcimangosone D, **13**;[9] 2-*O*-(3,4-dihydroxybenzoyl)-2,4,6-trihydroxyphenylacetic acid, **14**;[13] eucryphin, **15**;[14] 3,4,5,3′-tetrahydroxybenzophenone, **16**;[15] and 4,6,3′,4′-tetrahydroxy-2-methoxybenzophenone, **17**[16] (Figure 1). Among the known compounds, **4**, **8**, **9**, **11**, **14**, and **15** were for the first time isolated from mangosteen. Besides the reported xanthones and other low-polarity compounds, we demonstrated that the pericarp of mangosteen contains various types of benzophenones and procyanidins.

GM-1, **1**, was obtained as a pale brown amorphous powder with an assigned molecular formula of $C_{30}H_{26}O_{12}$ inferred from the high-resolution (HR)-ESI-MS data. The ^{1}H−^{1}H correlation spectroscopy (COSY) spectrum showed two pairs of ABX signals, two meta-coupled doublets, a singlet in the aromatic region, and three- and four-spin signals in the aliphatic region, thus suggesting **1** to be a dimeric flavonoid. The heteronuclear multiple-bond connectivity (HMBC) correlations (Figure 2) of H-2 to C-7″, -8″, and -8a″ and of H-4 to C-1′ and -4a indicated that **1** has a 4-aryl-2-flavanylbenzopyran skeleton. Furthermore,

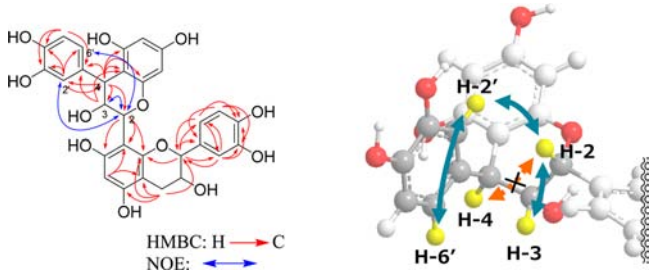

Figure 2. Heteronuclear multiple-bond connectivity (HMBC) correlations and the nuclear Overhauser effect (NOE) correlations of GM-1, **1**.

correlations of H-2 and H-2″ to C-8a″ proved that the intermolecular connection was in the 2→8″ position. The relative configuration of **1** was considered to have 2,3-*cis*-3,4-*trans* configurations on the basis of the nuclear Overhauser effect correlations of H-2 to H-2′, H-6′, and H-3, but no correlation between H-2 and H-4 (Figure 2). Additionally, small coupling constants (J = ca. 2 Hz) of H-2 and H-3 in the ^{1}H NMR spectrum indicated that the heterocyclic ring in **1** adopted the boat form similar to that of 4-aryl-2-flavanylbenzopyrans produced as the artifact from procyanidins under basic conditions.[17] With the co-occurrence of **1** with procyanidins B2 or C-1 taken into consideration, the 2-flavanyl moiety was tentatively assigned as (−)-epicatechin. On the basis of these spectroscopic data, the structure of GM-1 was established as **1** (Figure 1). Although artificial diastereoisomeric analogues of **1** were previously reported,[17] this is, to our knowledge, the first report of this type of compound to be isolated from a natural source.

GM-2, **2**, has the molecular formula $C_{14}H_{12}O_6$, as determined from the HR-ESI-MS data. The ^{1}H NMR spectrum showed three meta-coupled signals [a 2H-doublet (δ 6.53, J = 2.0 Hz), two 1H-doublets (δ 6.01 and 6.02, J = 2.5 Hz), and a 1H-triplet (δ 6.45, J = 2.0 Hz)] in the aromatic region. In the ^{13}C NMR spectrum, equivalent carbon signals assignable to C-2′,6′ (δ 107.2) and C-3′,5′ (δ 158.8) and a carbonyl carbon signal (δ 198.4) indicate that the structure of **2** is a benzophenone derivative. Additionally, the spectra indicated the presence of a methoxy group (δ_H 3.50, δ_C 55.7), which was located on a benzene ring (C-5) with nonequivalent protons. HMBC correlations (Figure 3) also supported the proposed structure. From the above spectroscopic data, the structure of **2** was elucidated as 3,4,3′,5′-tetrahydroxy-5-methoxybenzophenone.

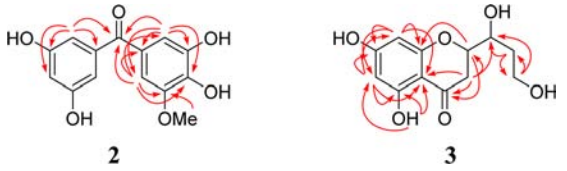

Figure 3. HMBC correlations of GM-2, **2**, and GM-3, **3** (HMBC: H → C).

GM-3, **3**, a pale brown amorphous powder, showed an $[M - H]^-$ ion peak at m/z 253.0711 in the HR-ESI-MS and was assigned the molecular formula $C_{12}H_{14}O_6$ (calculated for 253.0718, $C_{12}H_{14}O_6$ − H). The ^{1}H NMR spectrum of **3** showed a 1H-singlet at δ 12.2 (chelated −OH) and two meta-coupled 1H-doublets (δ 5.90 and 5.94, J = 2.0 Hz) in the aromatic region. In the aliphatic region, two pairs of methylene

DOI: 10.1021/acs.jafc.5b01771
J. Agric. Food Chem. 2015, 63, 7670−7674

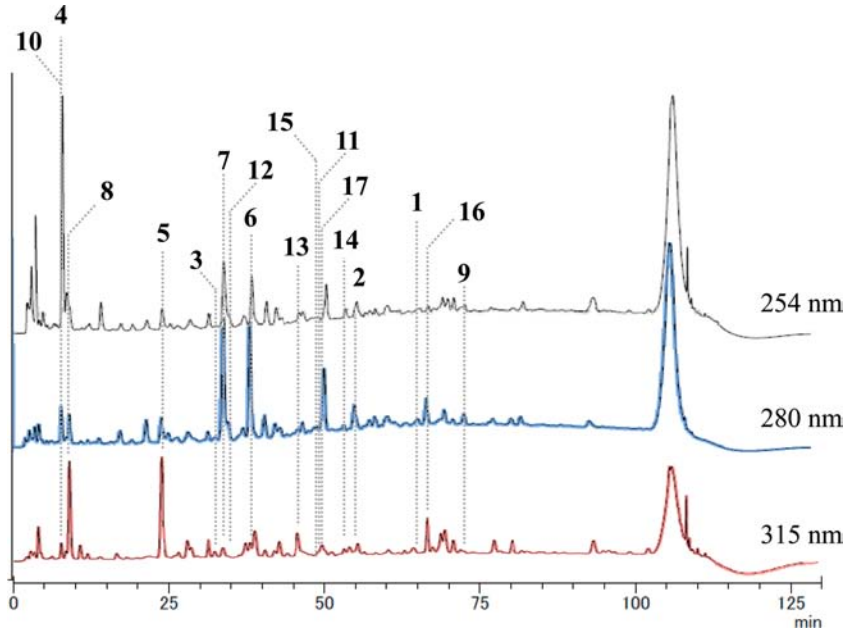

Figure 4. High-performance liquid chromatography (HPLC) profiles of hot water extract of mangosteen pericarp. The numbered peaks on the chromatogram correspond to the structure number in Figure 1: **1**, GM-1; **2**, GM-2; **3**, GM-3; **4**, 2-furancarboxylic acid; **5**, chlorogenic acid; **6**, epicatechin; **7**, procyanidin B2; **8**, rhodanthenone B; **9**, dihydrodehydrodiconiferyl alcohol 9-*O*-glucoside; **10**, protocatechuic acid; **11**, procyanidin C1; **12**, dihydrophaseic acid; **13**, garcimangosone D; **14**, 2-*O*-(3,4-dihydroxybenzoyl)-2,4,6-trihydroxyphenylacetic acid; **15**, eucryphin; **16**, 3,4,5,3′-tetrahydroxybenzophenone; **17**, 4,6,3′,4′-tetrahydroxy-2-methoxybenzophenone.

protons [δ 1.86 (2H, m, H-2′), 2.55 (1H, dd, J = 3.5, 17.5 Hz, H-3), and 3.00 (1H, dd, J = 13.0, 17.5 Hz, H-3)], an oxygen-bearing methylene [δ 3.79 (2H, m, H-3′)], and two oxygenated methines [δ 3.96 (1H, br dt, J = 4.0, 4.0. 9.0 Hz, H-1′), 4.42 (1H, dt, J = 3.5, 3.5, 13.0 Hz, H-2)] were confirmed from COSY and heteronuclear single-quantum coherence correlations. Furthermore, all of the aliphatic proton signals have relay correlations in ^{1}H−^{1}H COSY, and the location of the side chain was established from HMBC correlations of H-2 to C-8a and H-3 to C-4a (Figure 3). Additionally, ^{13}C NMR data also support this structure. From these results, the planar structure of GM-3 was identified as depicted in Figure 1.

Each peak on HPLC of the hot water extract of mangosteen pericarp was assigned by direct comparison with those of individual isolates as shown in Figure 4. Among polyphenolics detected at 280 nm, epicatechin, **6** and procyanidin B2, **7**, were major ingredients in the extract. On the other hand, benzophenones (**8**, **13**, and **16**) and chlorogenic acid (**5**) were readily distinguished from other phenolics by monitoring at 315 nm.

In the present study, along with 14 known compounds, we isolated 3 new compounds and elucidated their chemical structures. α-Mangostin and other xanthones that were known as representative bioactive components of mangosteen were not observed in the hot water extract of the pericarp because of their low polarity. These prenylated xanthones were effectively extracted with ethanol from the mangosteen pericarp. In traditional medicine, mangosteen pericarp is mainly decocted or macerated in water, thus preserving the bioactive properties of catechin and other polyphenols, which were revealed to be the major polar ingredients of the hot water extract. The componential analysis of water-soluble polar compounds would thus provide valuable information to discuss any function (e.g., antioxidant) of the pericarp arising from bioactive components other than xanthones and benzophenones.

■ ASSOCIATED CONTENT

Ⓢ Supporting Information

NMR spectra (^{1}H, ^{13}C, ^{1}H−^{1}H COSY, HSQC, HMBC, and NOESY) of GM-1, **1**, GM-2, **2**, and GM-3, **3**. The Supporting Information is available free of charge on the ACS Publications website at DOI: 10/1021/acs.jafc.5b01771.

■ AUTHOR INFORMATION

Corresponding Author

*(Y.A.) Phone: +81 89 925 7111. Fax: +81 89 926 7162. E-mail: amakura@cc.matsuyama-u.ac.jp.

Notes

The authors declare no competing financial interest.

■ REFERENCES

(1) Chen, L. G.; Yang, L. L.; Wang, C. C. Anti-inflammatory activity of mangostins from *Garcinia mangostana*. *Food Chem. Toxicol.* **2008**, *46*, 688−693.

(2) Hyung, W. R.; Jung, K. C.; Marcus, J. C.; Heung, J. Y.; Young, S. K.; Sunin, J.; Young, S. K.; Byong, W. L.; Ki, H. P. α-Glucosidase inhibition and antihyperglycemic activity of prenylated xanthones from *Garcinia mangostana*. *Phytochemistry* **2011**, *72*, 2148−2154.

(3) Palakawong, C.; Sophanodora, P.; Toivonen, P.; Delaquis, P. Optimized extraction and characterization of antimicrobial phenolic compounds from mangosteen (*Garcinia mangostana* L.) cultivation and processing waste. *J. Sci. Food Agric.* **2013**, *93*, 3792−800.

(4) Al-Massarani, S. M.; El Gamal, A. A.; Al-Musayeib, N. M.; Mothana, R. A.; Basudan, O. A.; Al-Rehaily, A. J.; Farag, M.; Assaf, M. H.; El Tahir, K. H.; Maes, L. Phytochemical, antimicrobial and antiprotozoal evaluation of *Garcinia mangostana* pericarp and α-mangostin, its major xanthone derivative. *Molecules* **2013**, *18*, 10599−10608.

(5) Doi, H.; Shibata, M. A.; Shibata, E.; Morimoto, J.; Akao, Y.; Iinuma, M.; Tanigawa, N.; Otsuki, Y. Panaxanthone isolated from pericarp of *Garcinia mangostana* L. suppresses tumor growth and

DOI: 10.1021/acs.jafc.5b01771
J. Agric. Food Chem. 2015, 63, 7670−7674

metastasis of a mouse model of mammary cancer. *Anticancer Res.* **2009**, *29*, 2485−2495.
(6) Akao, Y.; Nakagawa, Y.; Iinuma, M.; Nozawa, Y. Anti-cancer effects of xanthones from pericarps of mangosteen. *Int. J. Mol. Sci.* **2008**, *9*, 355−370.
(7) Balunas, M. J.; Su, B.; Brueggemeier, R. W.; Kinghorn, A. D. Xanthones from the botanical dietary supplement mangosteen (*Garcinia mangostana*) with aromatase inhibitory activity. *J. Nat. Prod.* **2008**, *71*, 1161−1166.
(8) Itoh, T.; Ohguchi, K.; Iinuma, M.; Nozawa, Y.; Akao, Y. Inhibitory effect of xanthones isolated from the pericarp of *Garcinia mangostana* L. on rat basophilic leukemia RBL-2H3 cell degranulation. *Bioorg. Med. Chem.* **2008**, *16*, 4500−4508.
(9) Huang, Y. L.; Chen, C. C.; Chen, Y. J.; Huang, R. L.; Shieh, B. J. Three xanthones and a benzophenone from *Garcinia mangostana*. *J. Nat. Prod.* **2001**, *64*, 903−906.
(10) Lyles, J. T.; Negrin, A.; Khan, S. I.; He, K.; Kennelly, E. J. In vitro antiplasmodial activity of benzophenones and xanthones from edible fruits of *Garcinia* species. *Planta Med.* **2014**, *80*, 676−681.
(11) Fu, C.; Loo, A. E.; Chia, F. P.; Huang, D. Oligomeric proanthocyanidins from mangosteen pericarps. *J. Agric. Food Chem.* **2007**, *55*, 7689−7694.
(12) Xu, M.; Zhang, M.; Wang, D.; Yang, C. R.; Zhang, Y. J. Phenolic compounds from the whole plants of *Gentiana rhodantha* (Gentianaceae). *Chem. Biodiversity* **2011**, *8*, 1891−1900.
(13) Hillenbrand, M.; Zapp, J.; Becker, H. Depsides from the petals of *Papaver rhoeas*. *Planta Med.* **2004**, *70*, 380−382.
(14) Tschesche, R.; Delhvi, S.; Sepulveda, S.; Breitmaier, E. Eucryphin, a new chromone rhamnoside from the bark of *Eucryphia cordifolia*. *Phytochemistry* **1979**, *18*, 867−869.
(15) Jiang, H. Z.; Quan, X. F.; Tian, W. X.; Hu, J. M.; Wang, P. C.; Huang, S. Z.; Cheng, Z. Q.; Liang, W. J.; Zhou, J.; Ma, X. F.; Zhau, Y. X. Fatty acid synthase inhibitors of phenolic constituents isolated from *Garcinia mangostana*. *Bioorg. Med. Chem. Lett.* **2010**, *20*, 6045−6047.
(16) Chiang, Y. M.; Kou, Y. H.; Oota, S.; Fukuyama, Y. Xanthones and benzophenones from the stems of *Garcinia multiflora*. *J. Nat. Prod.* **2003**, *66*, 1070−1073.
(17) Steynberg, J. P.; Bezuidenhoudt, B. C.; Burger, J. F.; Young, D. A.; Ferreira, D. Oligomeric flavanoids. Part 7. Novel base-catalysed pyran rearrangements of procyanidins. *J. Chem. Soc., Perkin Trans. 1* **1990**, 203−208.

DOI: 10.1021/acs.jafc.5b01771
J. Agric. Food Chem. 2015, 63, 7670−7674

when cellular integrity is disrupted. Indeed, plastidial polyphenol oxidases (PPOs) catalyze oxidation of vacuolar phenolic compounds in the presence of oxygen, generating colored *o*-quinones. These species are very unstable and are rapidly involved in nonenzymatic reactions,[18,19] thus forming secondary compounds, most of which are colorless, but some new pigments are produced. Differences in hue and intensity of browning appear to be related to apple phenolic content, speed of enzymatic reaction, and environmental factors such as pH, temperature, and the presence of reducing substances and metallic ions. Many studies have attempted to assess the correlation between browning intensity and phenolic content or PPO activity,[4,7] but there are some contradictory results in the literature.[14] The first difficulty was to find an adequate way of measuring the degree of browning. Amiot et al.[20,21] estimated the susceptibility of apples to browning by measuring the absorbance at 400 nm and the lightness (L^* parameter in the CIE Lab color system) of soluble and insoluble pigments, respectively. It can be noted that most studies were carried out in model solutions. Overall, research has highlighted the crucial role of the relative balance between hydroxycinnamic derivatives and flavanol monomers in oxidative browning.[21−24]

Multiple linear regression analysis has shown that both contribute to darkness (decrease in L^*) and yellowness (increase in b^*).[22] Chlorogenic acid is the best natural PPO substrate in apples.[25] Its oxidation leads to slightly yellow quinones, but secondary products are lighter, suggesting that they are not the most significant compounds involved in color development. Through coupled oxidation reduction reactions, chlorogenic acid quinones accelerate the degradation of flavanol monomers, of which the neo-formed products can be intensely colored[21−24,26] with absorbance maxima at 380 and 420 nm.[23] Some colored dimers are believed to be similar to dehydrodicatechin A.[27] In addition, procyanidins do not appear to be good PPO substrates; they have proved to result in PPO inhibition.[28] Nevertheless, Oleszek et al.[29] showed that enzymatic oxidation of procyanidins B2 and C1 could generate the same color intensity as catechins, but with a slower browning rate. Consequently, their contribution to the final coloration of juice should be considered. Moreover, dihydrochalcones play a role in this coloration despite their low concentration. First, as PPO substrates, they can directly lead to the formation of yellow compounds.[29,30] For example, Le Guernevé et al.[31] characterized, in a model solution, yellow phloridzin oxidation product (POPj), a pigment displaying a bright yellow color up to pH 5 and turning orange at higher pH.[32] This compound may contribute to the yellow color of apple juice. Second, phloretin glycosides may also have synergistic effects on color development when in the presence of chlorogenic acid or catechins[29,30] and could play a significant role in the complex color of real apple juice.

To our knowledge, no previous study has focused on identifying colored compounds present in real apple juices. Our aim was to investigate HPLC-DAD-MS profiles of yellow-orange pigments found in juices resulting from processing of four French cider apple varieties. The phenolic content in these varieties clearly differed, and juices covered a wide range of colors. We assessed varietal diversity of the chromophores and discussed the first structural elements regarding these natural pigments.

MATERIALS AND METHODS

Chemicals. Methanol and acetonitrile were of HPLC grade (Carlo Erba reagents, Val de Reuil, France). Acetic acid was of analytical grade (Carlo Erba reagents). Formic acid and sodium fluoride were purchased from NORMAPUR (VWR Prolabo, Fontenay sous Bois, France). Hydrochloric acid and sodium acetate were purchased from Emprove exp, Merck (Darmstadt, Germany). Ultrapure water was purified with a water purification system (PURELAB Classic model, Elga Véolia, Antony, France). Gelatin was obtained from Rousselot (Courbevoie, France). Phloroglucinol, (+)-catechin, (−)-epicatechin, 5-*O*-caffeoylquinic acid, *p*-coumaric acid, phloridzin, and avicularin (quercetin-3-*O*-arabinoside) phenolic standards were provided by Sigma-Aldrich (Lyon, France). Hyperoside (quercetin-3-*O*-galactoside), ideain chloride (cyanidin-3-*O*-galactoside chloride), procyanidin B1, and procyanidin B2 standards were obtained from Extrasynthèse (Genay, France).

Plant Material. French cider apples have various "taste types" that are described according to the acidity and total polyphenol content of the variety considered.[33] Here, four of the most grown French cider apple varieties were used to produce apple juices: 'Dous Moen' (bittersweet), 'Marie Ménard' (bitter), 'Petit Jaune' (sour), and 'Guillevic' (sharp). Fruits were picked in a local orchard (Iffendic, Brittany, France) in autumn 2012, except for 'Guillevic' fruits, which were picked in the Surzur orchard (Brittany, France). When technological ripeness was reached (50% of fruit had fallen to the ground), fruits were picked off the tree by hand to avoid bruising that causes flesh oxidation and deterioration. Fruits were kept at 10 °C until 100% starch regression (i.e., complete physiological ripeness) was confirmed using the visual iodine test.[34]

Oxidized and O_2-Deprived Juice Preparation. Juices were prepared according to two distinct procedures. In the first case, oxidation was promoted by the presence of air to generate colored juices, just like when cider-makers process their apples. In the second case, the presence of oxygen was avoided throughout all processing steps to prevent oxidation and thus limit juice browning. With regard to the oxidation processing mode, two 20 kg batches of ripe apples were pressed separately for each variety. After crushing, the grated apple flesh was vatted for 20 min in air and pressed at 2.5 bar with a hydraulic press (Hydropresse IT80, Fourage CTI, La Haye Fouassière, France) modified by Demoisy (Baune, France). Pectic substances were degraded enzymatically at 10 °C by adding 2.5 mL of pectinolytic enzyme preparation per hectoliter of crude juice (Endozym Pectofruit, Spindal, Gretz-Armainvilliers, France). The treated juice was stored overnight at 2 °C to let most of the crude juice particles settle. Must was then racked, microfiltered using 0.14 μm tangential filtration (Inside Céram membrane, 39 channels, hydraulic diameter of 2.5, Siva Diam, Nyons, France), and kept at −25 °C until use. For the O_2-deprived processing mode, ripe fruits were first placed under vacuum for 15 min to remove any air inside the fruits. The vacuum was then broken by incorporating pure CO_2. This operation was repeated once. All of the other processing steps were similar to the previous mode, but were achieved in an inert atmosphere with CO_2 or N_2 instead of O_2.

Solid Phase Polyphenol Extraction. Polyphenols were extracted from the juices using C18-solid phase extraction (5 g Sep-Pak Vac 20 cm^3 C18 cartridge, Waters, Milford, MA, USA). Silica sorbent was first preconditioned with 30 mL of methanol and 40 mL of acetic acid 1%, v/v. Potential residual polyphenol oxidase activity was inhibited in microfiltered juices by the addition of sodium fluoride (0.2 M). Juices were diluted twice with acidified water (acetic acid 1%) and then transferred to the solid phase. The sample volumes were adapted so as not to exceed the retention capacity of the solid phase. Forty milliliters of acetic acid 1%, v/v, was used to wash the cartridge and eliminate sugars. Polyphenols retained on the solid phase were then eluted with 40 mL of methanol/acetic acid 1%, 50/50, v/v. Purified phenolic extracts were concentrated under vacuum, frozen at −25 °C, and freeze-dried. Extracts were kept in a desiccator under argon atmosphere until analysis.

DOI: 10.1021/acs.jafc.5b00988
J. Agric. Food Chem. 2015, 63, 7675−7684

Table 1. CIE Lab Colorimetric Parameters Corresponding to the Different Apple Juices Produced in the Absence and in the Presence of Oxygen[a]

variety	oxidation type	L^*[b]		a^*[c]		b^*[d]		C^*[e]		h[f]	
Guillevic	O_2-[g]	100.1	*0.2*	−0.36	*0.05*	1.99	*0.09*	2.03	*0.09*	100	*1*
	O_2+[h]	97.3	*0.7*	−4.86	*0.06*	24.2	*0.3*	24.7	*0.3*	101.4	*0.2*
Petit Jaune	O_2-	99.8	*0.1*	−0.49	*0.06*	4.11	*0.06*	4.13	0.07	96.8	*0.8*
	O_2+	93.5	*0.3*	−1.09	*0.08*	40.7	*0.5*	40.8	0.5	91.5	*0.1*
Dous Moen	O_2-	99.6	*0.2*	−0.68	*0.04*	4.38	*0.10*	4.43	*0.10*	98.8	*0.5*
	O_2+	86.6	*0.4*	5.55	*0.37*	79.0	*0.9*	79.2	*1.0*	86.0	*0.2*
Marie Ménard	O_2-	99.3	*0.3*	−0.80	*0.07*	4.45	*0.04*	4.52	*0.05*	100.1	*0.8*
	O_2+	84.9	*0.2*	9.44	*0.40*	77.6	*0.9*	78.1	*1.0*	83.1	*0.2*

[a]Values in italics correspond to standard deviation (n = 3). [b]L^*, lightness. [c]a^*, green−red axis value. [d]b^*, blue−yellow axis value. [e]C^*, chroma. [f]h, hue value. [g]O_2-, oxygen-deprived juice. [h]O_2+, oxidized juice.

HPLC-DAD-MS Analysis of Yellow-Orange Colored Phenolic Compounds. Phenolic extracts were analyzed on a system composed of an SCM1000 degasser (Thermo Scientific, San Jose, CA, USA), an 1100 series binary high-pressure pump (Agilent Technologies, Palo Alto, CA, USA), and a Surveyor autosampler thermostated at 4 °C (Thermo Finnigan, San Jose, CA, USA). Two detectors were connected in series: a UV−visible diode array detector (model UV6000 LP, Thermo Finniga) and an ion trap mass spectrometer equipped with an electrospray ionization source (model LCQ Deca, Thermo Finnigan). The reversed-phase chromatography column used in this part of the work was a ZORBAX Eclipse XDB-C18 column (2.1 × 150 mm; 3.5 μm, Agilent Technologies) equipped with a ZORBAX Eclipse XDB-C8 precolumn (2.1 × 12.5 mm, 5 μm, Agilent Technologies). The analysis procedure was adapted from Guyot et al.[13] The oven was thermostated at 30 °C. Two microliters of sample was injected for analysis. The solvent system was a gradient of A (0.1% formic acid in ultrapure water) and B (0.1% formic acid in acetonitrile), which were filtered on 0.45 μm cellulose acetate and PTFE filters (VWR, Fontenay sous Bois, France), respectively, before use. An elution gradient was applied as follows with a flow rate of 0.2 mL/min: initial, 3% B; 0−5 min, 9% B, linear; 5−15 min, 16% B, linear; 15−45 min, 50% B, linear, followed by washing and reconditioning of the column. UV−visible detection covered the 240−600 nm wavelength range. Particular attention was paid to signals recorded at 420 nm as it corresponds to the response of yellow-orange compounds. The whole effluent was injected in an ESI source. Source parameters were negative ion mode, spray voltage (3.7 kV), capillary voltage (−70 V), sheath gas (67 arbitrary units), auxiliary gas (5 arbitrary units), and capillary temperature (240 °C). The nebulizing gas was nitrogen, and the damping gas was helium. MS spectra were acquired in full scan, negative ionization mode in the m/z 50−2000 range. The signals obtained correspond to the deprotonated molecule $[M - H]^-$. An MS/MS dependent-scan mode was also performed to obtain the daughter ion spectrum of the main molecular ions detected in full scan mode. For the MS/MS experiment, collision energy was selected arbitrarily as 35%. Data obtained were processed with 1.2 Xcalibur software (Finnigan Corp., San Jose, CA, USA).

Determination of CIE Lab Color Parameters. For apple juices, color was characterized using the Commission Internationale de l'Eclairage (CIE, International Commission on Illumination) color parameters. Absorbance spectra were measured at 5 nm intervals in the visible wavelength range, from 400 to 700 nm, with a spectrophotometer (SPECTROstar Nano, BMG Labtech, Ortenberg, Germany). The absorbance data were then converted into CIE L^*, a^*, and b^* parameters using mathematical processing, considering the illuminant D65 and 10° standard observer. They were also expressed and discussed in terms of lightness (L^*), chroma (C^*), and hue angle (h).

Gelatin Fining. Gelatin is a well-known fining agent, often used to remove part of the condensed tannins during beverage production.[33] Here, a gelatin solution and purified polyphenol extract from 'Dous Moen' oxidized juice were combined in 20 mM, pH 4.2, malate buffer. The final concentrations of gelatin and phenolic extract were 1 g/L. The incubation medium was placed at room temperature under mild stirring for the first 30 min and then without agitation for 15 min. After centrifugation for 30 min (4000 rpm, rotor model JA-10, Beckman Coulter, Villepinte, France), the supernatant was recovered and analyzed using HPLC-DAD-MS in the same conditions as described previously.

HPLC-DAD-MS Analysis of Native Polyphenols. Native polyphenols, including catechins, low molecular weight procyanidins, hydroxycinnamic acids, dihydrochalcones, and flavonols, were extracted using 1.2 mL of methanol acidified with 1% acetic acid, v/v. For each apple variety, extractions were performed in triplicate from 500 μL of freeze-dried juice. After homogenization, the extraction medium was placed in ice and ultrasonicated for 15 min. Samples were filtered on 0.45 μm PTFE filters (VWR) and analyzed using HPLC-DAD-MS. Dilutions with methanol/formic acid 0.5%, 50/50, v/v, were used if necessary to avoid saturation of the UV−visible detector. The HPLC system was the same as described above, but the chromatography column was a Hibar HR Purospher STAR RP-18 end-capped column (150 mm × 2.1 mm, 3 μm, Merck). The elution gradient used was initial, 3% B; 0−3 min, 7% B, linear; 3−21 min, 13% B, linear; 21−27 min, 13% B, linear, 27−41 min, 20% B, linear; 41−51 min, 45% B, linear, followed by washing and reconditioning of the column. Native compounds were identified by comparing the retention times, UV−visible spectra, and full MS spectra with those of available standards. Quantitation was performed by integrating peaks on UV−visible chromatograms at 280 nm for flavan-3-ols, procyanidins, and dihydrochalcones, at 320 nm for hydroxycinnamic acids, and at 350 nm for flavonols. (+)-Catechin, (−)-epicatechin, procyanidin B2, caffeoylquinic acid, phloridzin, and hyperoside were quantitated according to their own calibration curves. Quantitation of other compounds was carried out using a reference compound in the same phenolic class displaying a very similar UV−visible spectrum.

Determination of Total Procyanidin Concentration and Average Degree of Procyanidin Polymerization Using HPLC after Phloroglucinolysis. The phloroglucinolysis method was adapted from Kennedy and Jones.[35] The reactions were performed in triplicate on 500 μL of freeze-dried juice using 400 μL of methanol acidified with 0.3 N hydrochloric acid. After the addition of phloroglucinol (50 g/L) and ascorbic acid (10 g/L), the extraction medium was incubated at 50 °C for 30 min. The reaction was stopped by placing the vials in an ice bath and adding 1200 μL of sodium acetate (0.2 mM). Samples were filtered on 0.45 μm PTFE filters (VWR) and analyzed using HPLC-DAD-MS. Dilutions with methanol/formic acid 0.5%, 50/50, v/v, were used if necessary to avoid saturation of the UV−visible detector. The analysis system was the same as described for the native polyphenol analysis. The elution gradient used was initial, 3% B; 0−3 min, 7% B, linear; 3−21 min, 13% B, linear; 21−27 min, 13% B, linear; 27−30 min, 14.5% B, linear,

DOI: 10.1021/acs.jafc.5b00988
J. Agric. Food Chem. 2015, 63, 7675−7684

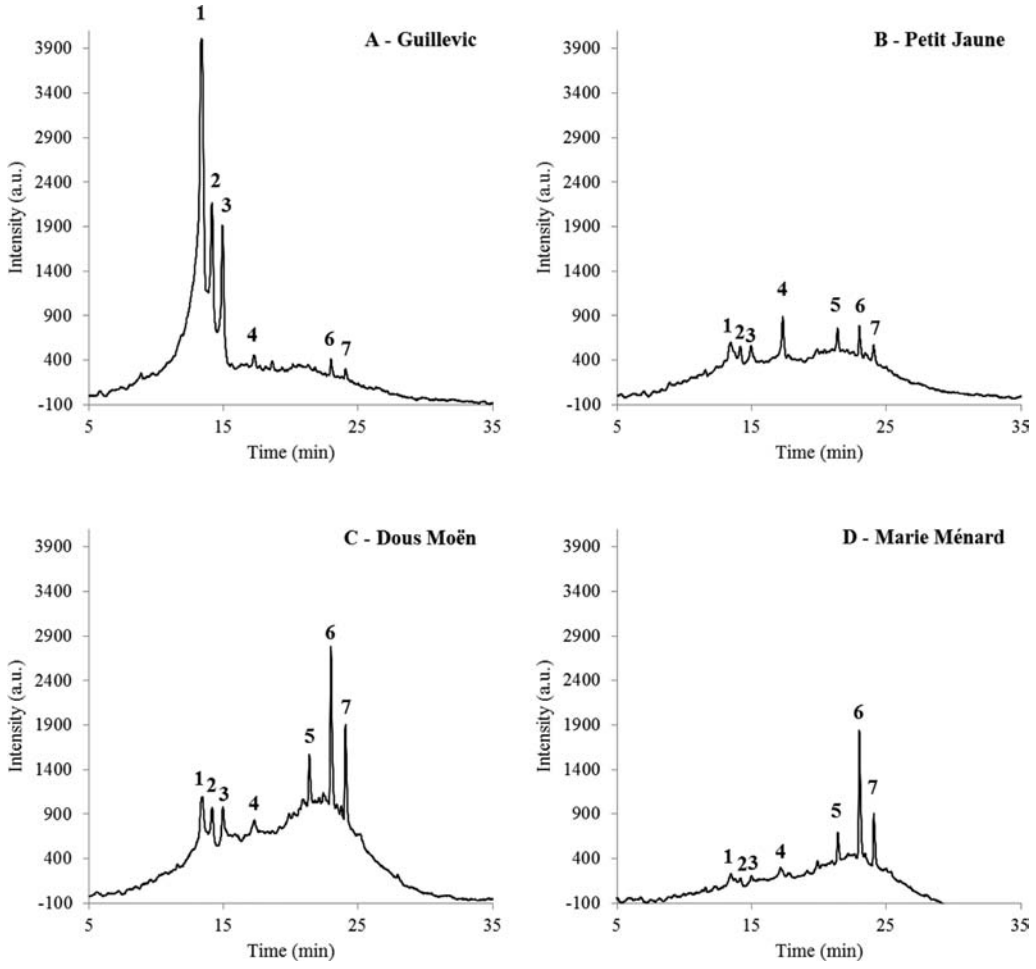

Figure 1. Reversed-phase UV−visible chromatograms at 420 nm of the four apple juice polyphenolic extracts. Fruit varieties used to produce oxidized juices are specified in bold. Numbers 1−7 designate colored compounds producing well-resolved peaks in HPLC.

followed by washing and reconditioning of the column. Peaks corresponding to apple procyanidin reaction products (i.e., (+)-catechin, (−)-epicatechin, and (−)-epicatechin phloroglucinol adduct) were integrated on the 280 nm chromatogram, and quantitation was performed using the corresponding calibration curves.

RESULTS AND DISCUSSION

Varietal Diversity of Cider Apple Juice Color. The four oxidized juices displayed contrasting colors, which is consistent with the range of coloration found in classical French cider products.[36] In contrast, the four juices deprived of oxidation were very bright, as shown by their very high lightness L^* values ranging between 99.3 and 100.1. These juices were almost colorless or very slightly colored, as revealed by their very low chroma C^* values (Table 1). Their "redness", expressed by positive a^* values, was close to 0. The "yellowness", expressed by positive b^* values, was noticeably different for 'Guillevic' juice, suggesting that the others were slightly yellower (b^* values of 2.0 for 'Guillevic' and ranging from 4.1 to 4.5 for 'Petit Jaune', 'Dous Moen', and 'Marie Ménard'). As expected, the considerable differences in the color parameters for the oxidized juices indicate the crucial role of enzymatic oxidation in the generation of apple juice coloration. In a previous study, Falguera et al.[37] described CIE Lab parameters of apple juices made from six different apple varieties. A comparison with our data highlights considerable disparity in the values obtained, particularly for L^* and a^*. This is probably related to the differences in apple processing and the use of dessert apple varieties that have different phenolic content and profiles from cider apple varieties. After oxidation, lightness values remained particularly high in our four juices, varying from 84.9 to 97.3, whereas L^* values of the six juices produced by Falguera et al.[37] ranged from 30.3 to 62.7. These low values could be explained by the fact that only centrifugation was performed before color measurement. Here, juices were microfiltered, leading to very bright, limpid products. In the present work, juices were produced in conditions very similar to the technological processing steps used in the French cider-making industry. Despite all of these variations, two conclusions were similar in both studies. First, the color of the juice differed substantially according to the apple variety. Second, all of the juices had higher yellowness than redness. Indeed, greater variations were observed for b^* values than for a^* values for all four oxidized apple juices. CIE L^*, a^*, b^*, C^*, and h values presented in Table 1 indicate that the four oxidized juices had an overall yellow hue, according to hue angle values, but highlight significant nuances. The shades are described more easily using the hue angle because this polar coordinate directly reflects the hue information on the juice, whereas a^* and b^* orthogonal parameters need to be described together to provide a complete picture of the color. Consequently, in the present study, the colors of the juices are described mainly according to the hue angle. The h value of

DOI: 10.1021/acs.jafc.5b00988
J. Agric. Food Chem. 2015, 63, 7675−7684

'Guillevic' juice was 101.4° (which corresponds to the a^* negative value of −4.9), higher than 90° (yellow hue), meaning that 'Guillevic' juice became greenish-yellow after oxidation. 'Dous Moen' (h value of 86.0°) and 'Marie Ménard' (h of 83.1°) juices had a more orangey-yellow hue. The latter is more orange as the hue angle is smaller. 'Petit Jaune' juice clearly had a dominant yellow hue, as the h value was very close to 90° (91.5°). In this case, with an a^* value close to 0 (−1.1), the yellow color of this juice was described directly by the positive value of b^* (40.7). With regard to C^* values, the colors of 'Marie Ménard' and 'Dous Moen' juices were 3 times more intense than the color of 'Guillevic' juice, for which the lightness remained close to 100 even after oxidation. Overall, the higher the C^* values, the lower the lightness values. The varietal differences in terms of hue and color intensity (indicated by chroma C^*) were related to the pigment content formed by polyphenol oxidation during fruit processing. The structures and relative concentrations of these chromophores are crucial in the final color of the juice.

HPLC-UV−Visible Profiles of Yellow-Orange Phenolic Compounds in Juices. Yellow-orange compounds absorb in the range of 400−450 nm. HPLC-UV−visible profiles of purified phenolic fractions of oxidized juices at 420 nm are presented in Figure 1. The four apple juices provided contrasting colored compound profiles. Although most polyphenol oxidation products formed during apple processing were colorless,[38] these chromatographic profiles clearly highlight two kinds of response at 420 nm: several well-defined peaks corresponding to yellow-orange compounds (peaks 1−7 on chromatograms A−D, Figure 1) and a globally unresolved absorbance hump. With regard to the well-resolved compounds, two groups of molecules were distinguished by their chromatographic behavior that reflected their polarity. Indeed, compounds **1**−**3** eluted early, contrary to compounds 5−**7**. Consequently, the polarity of the former was probably greater than the latter and produced wider chromatographic peaks. Compound **4** showed intermediate polarity. Its presence was particularly preponderant in 'Petit Jaune' juice, although it was also detected to a lesser extent in the other juices. The particular greenish-yellow coloration of 'Guillevic' juice discussed previously was clearly related to a specific profile of phenolic pigments (Figure 1A). It appeared less complex compared to the HPLC profiles of the other varieties, with the main pigments being polar compounds **1**−**3**, and the absorbance of the unresolved hump was lower (Figure 1A). 'Dous Moen' and 'Marie Ménard' extracts had very similar 420 nm HPLC profiles, in accordance with their rather similar color parameters (Table 1). In contrast with the 'Guillevic' colored compound profile, there was less of polar compounds **1**−**3** in 'Dous Moen' and 'Marie Ménard' than of the more apolar compounds **5**−**7** indicated by intense peaks at 420 nm. Moreover, the unresolved absorbance hump was well represented in these juices, which displayed a more orange hue than 'Guillevic' and 'Petit Jaune' juices. Consequently, it is suggested that more well-resolved apolar compounds and compounds responsible for the unresolved absorbance hump could be involved in the differences in hue observed. The absorbance maxima in the visible region of compounds **4**, **6**, and **7** (Table 2) shifted slightly (ca. 20 nm) to higher wavelengths in comparison with more polar compounds **1**−**3**. However, UV−visible spectra were acquired in acidified analytical conditions, meaning that pigments were in a different chemical environment from that of the juices. Consequently, this could alter slightly their optical properties measured by the diode array detector. Unfortunately, except for compound **1**, we did not succeed in obtaining clear MS data from the colored compounds displaying well-resolved peaks on 420 nm chromatograms. The structural characterization of compound **1** will be discussed later in a specific paragraph. It must be emphasized that colorless compounds were largely more concentrated than colored compounds in the purified phenolic fractions. Although it was not revealed on the 420 nm chromatograms, numerous coelutions occurred with colorless and UV-absorbing compounds. Thus, MS signals detected at retention times of colored compounds corresponded mainly to native colorless compounds and oxidation products coeluting at those retention times. Lea[27] proposed that some new colored compounds formed after oxidation of apple juices are similar to dehydrodicatechin A and are yellow dimers resulting from oxidative coupling of two catechin molecules.[39] However, the extracted ion chromatogram of the deprotonated molecule $[M - H]^-$ at m/z 575, which corresponds to the molecular ion of dehydrodicatechin A, did not indicate clear traces of this compound in the four oxidized juices studied here (data not shown). Indeed, ions at m/z 575 may also correspond to colorless oxidation products of procyanidin dimers or to product ions of procyanidin polymers that can be produced in the source of the mass spectrometer.[40] Further purification steps and optimized separation will be needed to obtain more information on the structure of these pigments formed in apple juices.

Table 2. Maximal Absorbance in the Visible Region (400−700 nm) of the Yellow Compounds Producing Well-Resolved Peaks on 420 nm Chromatograms

compound	RT (min)	λ_{max} (nm) in the visible region
1	13.17	417
2	13.95	418
3	14.73	419
4	17.10	437
5	21.20	424
6	22.80	437
7	23.88	433

Gelatin fining of the polyphenolic extract of 'Dous Moen' juice resulted in condensed tannin precipitation, and most of these procyanidins were colorless. However, as illustrated in Figure 2, the phenolic profile at 420 nm showed a clear decrease in absorbance of the previously described unresolved hump, suggesting that oxidized tannins were also partly responsible for the coloration of apple juices. In contrast, well-resolved peaks at 420 nm were not affected by gelatin fining, suggesting that those colored products do not have tanning properties. In the literature, "brown polymers" were often mentioned as being responsible for browning in crushed apple tissues.[41] However, to our knowledge, this formation of highly polymerized colored pigments has not been clearly demonstrated. Polymerization mechanisms are not likely to generate more conjugation in molecules and so should not lead directly to the formation of chromophores. Oleszek et al.[29] considered the role of procyanidin oxidation products in enzymatic browning phenomena. In a model solution, the authors showed that enzymatic oxidation of procyanidins B2 and C1 could lead to intense coloration even if the reaction rate was very slow. Nevertheless, these experiments were conducted in a model solution at pH 5.5, close to the optimal pH for PPO

DOI: 10.1021/acs.jafc.5b00988
J. Agric. Food Chem. 2015, 63, 7675−7684

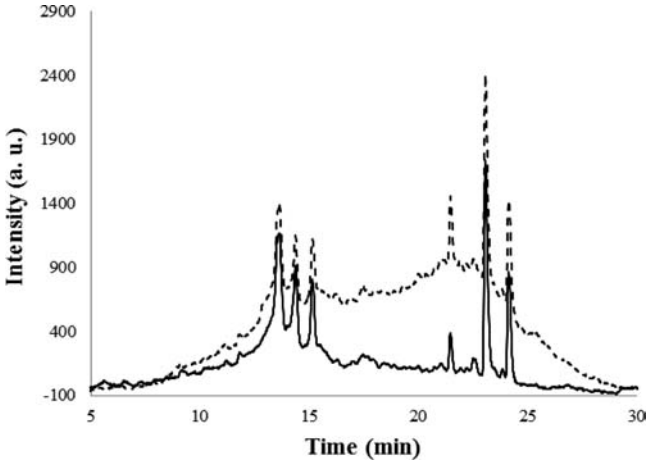

Figure 2. Reversed-phase UV−visible chromatograms at 420 nm of 'Dous Moen' phenolic extract before (dotted line) and after (solid line) gelatin fining.

activity. These pH conditions may favor autoxidation of polyphenols because they are much higher than pH values usually encountered in apple juice. In the present study, the colored oxidized tannins highlighted could result from the addition or coupling of some chromophores such as dehydrodicatechin A or dehydrotricatechin A to procyanidin oligomers and polymers. It could also explain why the deprotonated molecules corresponding to these chromophores were not directly detected in juices.

Flavanol Monomers, Hydroxycinnamic Acids, and Dihydrochalcones: The Main Phenolic Classes Containing Color Precursors. The diversity of apple juice colors is based on the diversity of colored oxidation products that can coexist in juices. These pigments are derived from native colorless polyphenols. Using multiple linear regression analysis, Goupy et al.[22] established that CIE L^*, a^*, and b^* values of an apple phenolic solution were correlated to both initial and oxidized amounts of phenolic classes. Here, native phenolic content of oxygen-deprived and oxidized juices were compared

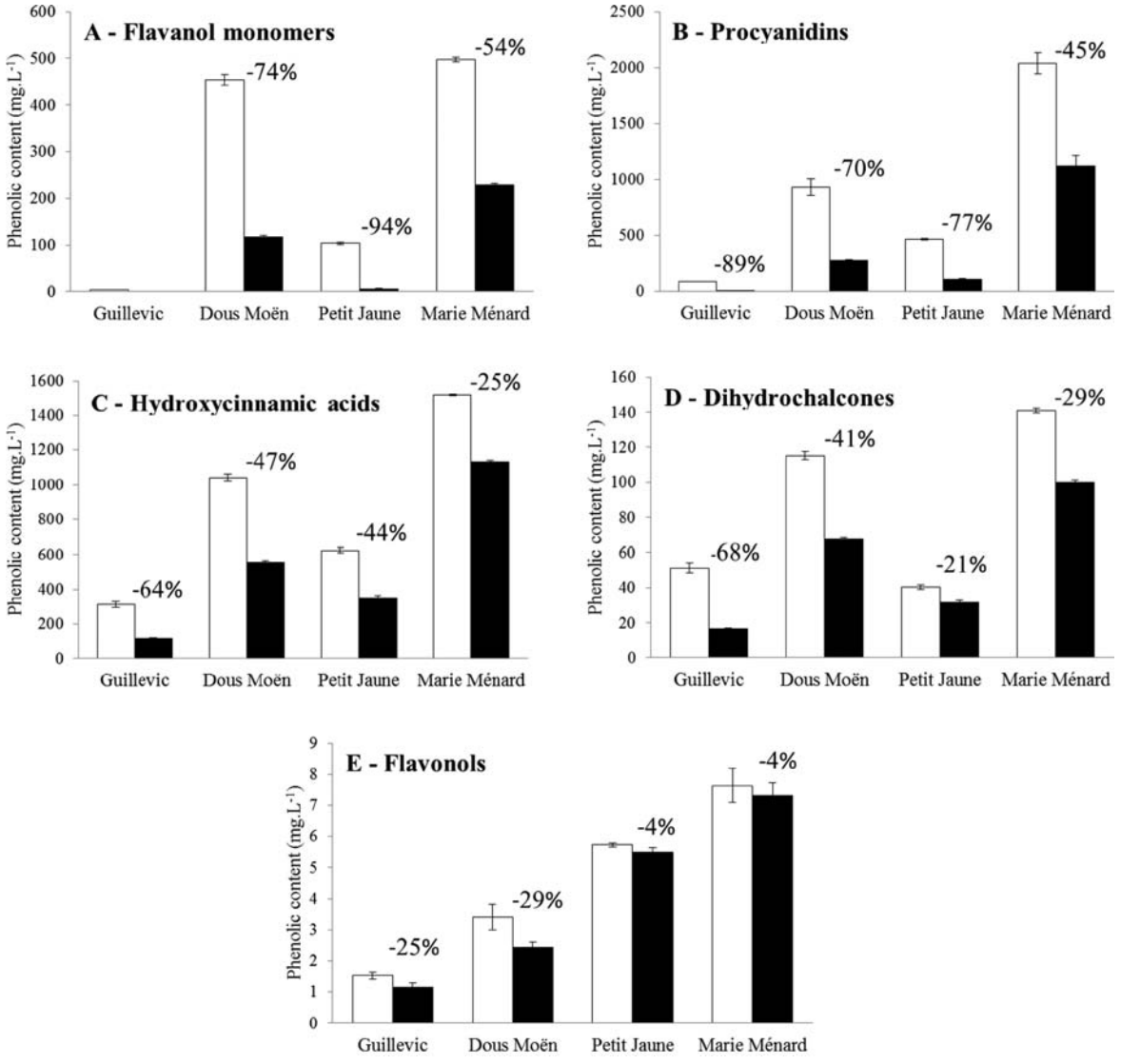

Figure 3. Comparison of content of different phenolic classes according to the oxidation conditions used to produce the French cider apple juices: (A) flavanol monomers; (B) procyanidins; (C) hydroxycinnamic acids; (D) dihydrochalcones; (E) flavonols. White bars correspond to O_2-deprived juices and black bars to oxidized juices. For each phenolic class, the difference in polyphenol content (expressed in %) between O_2-deprived and oxidized conditions is indicated above the black bars.

DOI: 10.1021/acs.jafc.5b00988
J. Agric. Food Chem. 2015, 63, 7675−7684

Table 3. Qualitative Parameters and Total Polyphenol Content for the Characterization of the Polyphenolic Profile in the Four French Cider Apple Juices Produced in the Absence (O_2−) and in the Presence (O_2+) of Oxygen

	variety							
	Guillevic		Petit Jaune		Dous Moen		Marie Ménard	
	O_2−	O_2+	O_2−	O_2+	O_2−	O_2+	O_2−	O_2+
PLZ[a]/XPL[b]	0.55	0.72	0.64	0.79	0.72	0.74	0.41	0.42
EPI[c]/CAT[d]			4.38	5.33	2.32	2.68	15.76	18.65
FA[e]/HCA[f]	0.30	0.09	0.92	0.33	1.33	0.72	1.67	1.19
CQA[g]/*p*CoQA[h]	1.55	0.98	14.85	9.43	6.30	3.92	18.09	14.06
DPn[i] PCA[j]	4.17	1.21	3.28	2.15	4.38	3.55	4.14	4.34
total polyphenol content (mg/L of juice)	460	140	1242	504	1881	1021	4204	2593

[a]PLZ, phloridzin. [b]XPL, phloretin xyloglucoside. [c]EPI, (−)-epicatechin. [d]CAT, (+)-catechin. [e]FA, flavanols. [f]HCA, hydroxycinnamic acids. [g]CQA, caffeoylquinic acids. [h]*p*CoQA, *p*-coumaroylquinic acids. [i]DPn, average degree of polymerization of procyanidins. [j]PCA, procyanidins.

by discussing the impact of oxidation within different phenolic classes (Figure 3 and Table 3). Details concerning specific compounds in these classes can be found in the Supporting Information. First of all, some varietal discrepancies were clearly noted in accordance with results of previous studies.[42] For example, the original colored profile of 'Guillevic' juice can be related to a distinctive native polyphenol composition. The amount of total polyphenols in this juice was low in comparison with the other varieties (Table 3), as it contained nearly 20 times less polyphenols than 'Marie Ménard' oxidized juice. Moreover, as shown in Figure 3B, the 'Guillevic' juices did not contain any flavanol monomers (i.e., (−)-epicatechin and (+)-catechin), which are known to act as precursors of oxidation products developing intense coloration.[23,24] In addition, 'Guillevic' juices contained very low concentrations of procyanidins (Figure 3B), which were shown to be involved in color formation, as revealed by the gelatin fining of 'Dous Moen' oxidized juices (Figure 2). Therefore, the absence of flavanols in 'Guillevic' juice could explain the considerable difference observed between its weakly saturated greenish-yellow hue and the orange-yellow hue of 'Dous Moen' and 'Marie Ménard' juices. This oxidized juice was also the only one with a CQA/pCoQA ratio below 1 (Table 3). This particular fraction of the hydroxycinnamic acid class could also be a factor of "color limitation". Indeed, *p*-coumaroylquinic acids could act as potential inhibitors of PPO as they are derived from *p*-coumaric acid, a molecule known to be an *o*-diphenolase inhibitor.[43]

For the other juices, the oxidation phenomenon strongly influenced flavanol content, particularly monomers. There was up to 94% less monomers in oxidized 'Petit Jaune' juice than in O_2-deprived juice (Figure 2A). The procyanidin content was also significantly lower, which may first be due to part of the oxidized tannins being adsorbed on parietal material during processing. Second, after oxidation, some procyanidins can become partly resistant to phloroglucinolysis, which could suggest an underestimation of the procyanidin content. Most of the oxidized polyphenols were colorless, but major classes affected by oxidation were probably involved in the generation of oxidized colored compounds. Hydroxycinnamic acids were also well represented in cider apple juices. This class is clearly affected by oxidation, but not to the same extent as flavanol monomers, as illustrated by the differences between O_2-deprived and oxidized juices (Figure 3C). These compounds seem to be more "protected" against oxidation, which can be explained by coupled oxidation−reduction reactions. Indeed, several authors[22−24,26,44] have mentioned the crucial role of the balance between hydroxycinnamic derivatives and flavanols in browning susceptibility. As the best PPO substrate, 5-*O*-caffeoylquinic acid, the major compound in this phenolic class in most apple varieties, generates *o*-quinones that can co-oxidize flavanol monomers. Through these reactions, caffeoylquinic acid *o*-quinones are regenerated as *o*-diphenolic forms with simultaneous oxidation of monomers leading to new compounds, some of which are highly colored products. Consequently, the data shown here seem to be consistent with results in the literature.

Interestingly, the significance of the dihydrochalcone class in the oxidation phenomenon is also highlighted in Figure 2. Indeed, even if the concentrations of these compounds are lower than those of flavanols and hydroxycinnamic derivatives, the dihydrochalcone content decreased by the same order of magnitude as hydroxycinnamic acids in oxidized juices, except for 'Petit Jaune', in which the content decreased less. Previous studies in model solutions have already shown that these molecules can result in yellowish products. Some synergistic effects on the browning rate have even been reported[29,30] when dihydrochalcones are in the presence of chlorogenic acids or flavanol monomers. In previous studies,[31,32] we characterized a yellow colorant consisting of a phloridzin oxidation product (POPj). The variations in dihydrochalcone content in the four juices indicated that the role of compounds in this class in the formation of color in apple juices must be particularly considered in the present study.

Finally, we noted that flavonols (i.e., a series of quercetin glycosides), localized mainly in the apple epidermis and known to be the only phenolic class displaying native yellow compounds, were found in very low quantities in juices (about 1−7 mg/L, Figure 3E). They did not appear to be the main compounds responsible for the color of apple juices.

Identification of a Yellow Compound Formed in Real Apple Juices: Yellow Pigment Phloretin Xyloglucoside Oxidation Product (PXGOPj) as Xyloglucose Analogue of POPj Colorant Previously Identified by Le Guernevé et al.[31] As previously specified, the juice obtained from the 'Guillevic' variety exhibited a singular native phenolic composition. Logically, it led to a particular profile of colored compounds and, consequently, to an oxidized juice with a very specific hue and saturation level. The greenish-yellow coloration of this juice appeared to be related mainly to the presence of three compounds (peaks 1, 2, and 3, Figure 1), also present in lower concentrations in the other juices studied. The MS signal corresponding to peak 1 revealed the existence of a product with a molecular weight of 598 Da ($[M - H]^-$ at m/z

DOI: 10.1021/acs.jafc.5b00988
J. Agric. Food Chem. 2015, 63, 7675−7684

A

RT (min)	λmax (nm)	$[M-H]^-$	Main product ions on MS/MS spectrum*
13.17	417	597	553 (100); 259 (79); 303 (26)

*Values in parentheses correspond to relative MS intensity

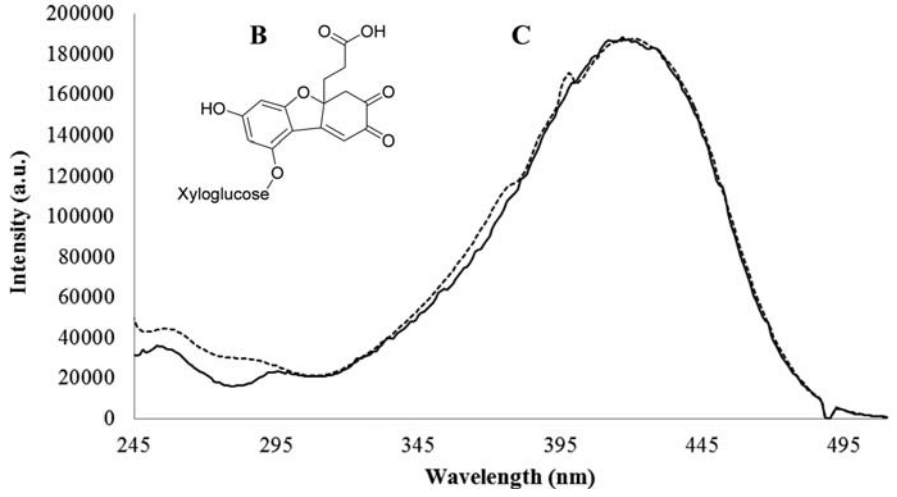

Figure 4. Identification of PXGOPj, a new yellow compound derived from phloretin xyloglucoside in cider apple juice: (A) LC-MS^n features; (B) hypothetical structure; (C) comparison of UV−visible spectra of POPj (dotted line) and PXGOPj (solid line).

597, see Figure 4A). The three main MS/MS product ions of the deprotonated molecule were detected at m/z 553, 259, and 303. Interestingly, this molecular weight and this fragmentation pattern were strictly in accordance with the xyloglucose analogue of the POPj molecule.[32] Indeed, the first product ion (m/z 553) corresponded to the loss of the free carboxylic group (− 44 amu). The MS/MS ion at m/z 259 (losses of 294 and 44 amu) could be obtained after the loss of the sugar moiety and the carboxylic group. Finally, the product ion at m/z 303 corresponded to the remaining phenolic part of the molecule after the loss of the sugar moiety. This new compound was named PXGOPj, and its proposed structure is illustrated in Figure 4B. Fromm et al.[45] previously suggested the formation of a POPj analogue pigment derived from phloretin xyloglucoside during the enzymatic oxidation of apple seed extracts. However, this compound was not clearly detected, and the authors concluded that it was coeluted with POPj in their analytical conditions. PXGOPj could be generated following the same reaction pathway as already described for POPj.[32] Thus, phloretin xyloglucoside could be oxidized by apple PPO involving both cresolase and catecholase activities coupled with intramolecular rearrangement, ring rearomatization, and addition of water.[32] As expected, the UV−visible spectrum of this xyloglucose analogue of POPj was very similar to the POPj spectrum (Figure 4C). Only the sugar moiety differs between both structures, which should not modify the electronic delocalization and, consequently, the chromophore is not modified. Theoretical calculations could be used to confirm this assertion. Interestingly, although phloridzin was significantly present in the oxygen-deprived juice, the extracted ion chromatogram at m/z 465, which corresponds to the POPj deprotonated molecule, revealed only the presence of traces of POPj in the oxidized 'Guillevic' juice (data not shown). This preferential formation of PXGOPj could be related to a higher affinity of polyphenol oxidase for phloretin xyloglucoside than for phloridzin. This would be in accordance with the observations of Oleszek et al.[29] Indeed, these authors showed that in a model solution phloretin xyloglucoside was more readily oxidized by PPO than phloridzin, even if both were PPO substrates. They also noted that enzymatic oxidation of these native dihydrochalcones resulted in yellowish products.

To conclude, the present paper proposed an initial exploration of yellow-orange compounds in apple juices produced in conditions very similar to those in the cider-making industry. The oxidized juices showed contrasting color parameters related to very contrasting phenolic profiles of colored compounds. The relative proportions of the different classes of native polyphenols appear to be important in relation to the final color. Flavanol monomers seem to play an essential role in oxidation, probably via direct enzymatic oxidation, but also with coupled oxidation−reduction reactions involving hydroxycinnamic acids. The significance of the dihydrochalcone class as a precursor of yellow oxidation products was clearly highlighted, and a pigment derived from phloretin xyloglucoside was identified.

The study of colored phenolic compounds encountered in apple juices is far from being accomplished. Further purification steps and attempts to optimize MS detection are still necessary to gain further insight into pigment structures. Moreover, this study focused on the initial phenolic composition of the juices to discuss color generation, but the physicochemical parameters of a beverage may also strongly influence the expression and stability of juice color. Indeed, factors such as pH, the presence of metallic ions, or copigmentation phenomena must not be neglected to understand the final coloration of a beverage.

■ ASSOCIATED CONTENT

Supporting Information

Detailed table of the different native phenolic compounds quantitated using HPLC-UV−visible in French cider apple O_2-

DOI: 10.1021/acs.jafc.5b00988
J. Agric. Food Chem. 2015, 63, 7675−7684

deprived and oxidized juices. The Supporting Information is available free of charge on the ACS Publications website at DOI: 10.1021/acs.jafc.5b00988.

AUTHOR INFORMATION

Corresponding Author

*(S.G.) Phone: 0033 2 23 48 52 09. Fax: 0033 2 23 48 52 10. E-mail: sylvain.guyot@rennes.inra.fr.

Funding

This work was supported by Région Bretagne, Région Pays de la Loire, and Pôle Agronomique Ouest, as part of an interregional CICHROM project.

Notes

The authors declare no competing financial interest.

ABBREVIATIONS USED

PPO, polyphenol oxidase; UV, ultraviolet; DAD, diode array detector; MS, mass spectrometry; POPj, phloridzin oxidation product (j for yellow); PXGOPj, phloretin xyloglucoside oxidation product (j for yellow); CQA, caffeoylquinic acids; *p*CoQA, *p*-coumaroylquinic acids

REFERENCES

(1) Francis, F. J. Quality as influenced by color. *Food Qual. Prefer.* **1995**, *6* (3), 149−155.

(2) Clydesdale, F. M. Color as a factor in food choice. *Crit. Rev. Food Sci. Nutr.* **1993**, *33* (1), 83−101.

(3) Clydesdale, F. M. Color perception and food quality1. *J. Food Qual.* **1991**, *14* (1), 61−74.

(4) Cheynier, V. Polyphenols in foods are more complex than often thought. *Am. J. Clin. Nutr.* **2005**, *81* (1), 223S−229S.

(5) Cheynier, V. Phenolic compounds: from plants to foods. *Phytochem. Rev.* **2012**, *11* (2−3), 153−177.

(6) Shoji, T. Polyphenols as natural food pigments: changes during food processing. *Am. J. Food Technol.* **2007**, *2* (7), 570−581.

(7) Robards, K.; Prenzler, P. D.; Tucker, G.; Swatsitang, P.; Glover, W. Phenolic compounds and their role in oxidative processes in fruits. *Food Chem.* **1999**, *66* (4), 401−436.

(8) Sanoner, P.; Guyot, S.; Marnet, N.; Molle, D.; Drilleau, J. F. Polyphenol profiles of French cider apple varieties (*Malus domestica* sp.). *J. Agric. Food Chem.* **1999**, *47* (12), 4847−4853.

(9) Awad, M. A.; de Jager, A.; van der Plas, L. H. W.; van der Krol, A. R. Flavonoid and chlorogenic acid changes in skin of 'Elstar' and 'Jonagold' apples during development and ripening. *Sci. Hortic.* **2001**, *90* (1−2), 69−83.

(10) Burda, S.; Oleszek, W.; Lee, C. Y. Phenolic compounds and their changes in apples during maturation and cold storage. *J. Agric. Food Chem.* **1990**, *38*, 945−948.

(11) Awad, M. A.; Wagenmakers, P. S.; de Jager, A. Effects of light on flavonoid and chlorogenic acid levels in the skin of 'Jonagold' apples. *Sci. Hortic.* **2001**, *88*, 289−298.

(12) Awad, M. A.; de Jager, A. Influences of air and controlled atmosphere storage on the concentration of potentially healthful phenolics in apples and other fruits. *Postharvest Biol. Technol.* **2003**, *27* (1), 53−58.

(13) Guyot, S.; Marnet, N.; Laraba, D.; Sanoner, P.; Drilleau, J.-F. Reversed-phase HPLC following thiolysis for quantitative estimation and characterization of the four main classes of phenolic compounds in different tissue zones of a French cider apple variety (*Malus domestica* var. Kermerrien). *J. Agric. Food Chem.* **1998**, *46* (5), 1698−1705.

(14) Nicolas, J. J.; Richard-Forget, F. C.; Goupy, P. M.; Amiot, M. J.; Aubert, S. Y. Enzymatic browning reactions in apple and apple products. *Crit. Rev. Food Sci. Nutr.* **1994**, *34* (2), 109−157.

(15) Gosch, C.; Halbwirth, H.; Stich, K. Phloridzin: biosynthesis, distribution and physiological relevance in plants. *Phytochemistry* **2010**, *71* (8−9), 838−843.

(16) Sadilova, E.; Stintzing, F. C.; Carle, R. Chemical quality parameters and anthocyanin pattern of red-fleshed Weirouge apples. *J. Appl. Bot. Food Qual.* **2006**, *80* (1), 82−87.

(17) Malec, M.; Le Quere, J. M.; Sotin, H.; Kolodziejczyk, K.; Bauduin, R.; Guyot, S. Polyphenol profiling of a red-fleshed apple cultivar and evaluation of the color extractability and stability in the juice. *J. Agric. Food Chem.* **2014**, *62* (29), 6944−6954.

(18) Nicolas, J. J.; Richard-Forget, F. C.; Goupy, P. M.; Amiot, M. J.; Aubert, S. Y. Enzymatic browning reactions in apple and apple products. *Crit. Rev. Food Sci. Nutr.* **1994**, *34* (2), 109−157.

(19) Macheix, J. J.; Sapis, J. C.; Fleuriet, A. Phenolic compounds and polyphenoloxidase in relation to browning in grapes and wines. *Crit. Rev. Food Sci. Nutr.* **1991**, *30* (3), 441−486.

(20) Amiot, M. J.; Fleuriet, A.; Cheynier, V.; Nicolas, J. Phenolic compounds and oxidative mechanisms in fruit and vegetables. In *Phytochemistry of Fruit and Vegetables. Proceedings of the Phytochemical Society of Europe*; Tomas-Barberan, F. A., Robins, R. J., Eds.; Clarendon Press: Oxford, UK, 1997; pp 51−85.

(21) Amiot, M. J.; Tacchini, M.; Aubert, S.; Nicolas, J. Phenolic composition and browning susceptibility of various apple cultivars at maturity. *J. Food Sci.* **1992**, *57* (4), 958−962.

(22) Goupy, P.; Amiot, M. J.; Richard-Forget, F.; Duprat, F.; Aubert, S.; Nicolas, J. Enzymatic browning of model solutions and apple phenolic extracts by apple polyphenoloxidase. *J. Food Sci.* **1995**, *60* (3), 497−505.

(23) Oszmianski, J.; Lee, C. Y. Enzymatic oxidative reaction of catechin and chlorogenic acid in a model system. *J. Agric. Food Chem.* **1990**, *38* (5), 1202−1204.

(24) Rouet-Mayer, M. A.; Ralambosoa, J.; Philippon, J. Roles of *o*-quinones and their polymers in the enzymic browning of apples. *Phytochemistry* **1990**, *29* (2), 435−440.

(25) Janovitz-Klapp, A. H.; Richard, F. C.; Goupy, P. M.; Nicolas, J. J. Kinetic studies on apple polyphenol oxidase. *J. Agric. Food Chem.* **1990**, *38* (7), 1437−1441.

(26) Richard-Forget, F.; Amiot, M. J.; Goupy, P.; Nicolas, J. Evolution of chlorogenic acid o-quinones in model solutions. In *Enzymatic Browning and Its Prevention*; Lee, C. Y., Whitaker, J. R., Eds.; American Chemical Society: Washington, DC, USA, 1994; pp 144−158.

(27) Lea, A. G. H. Farb- und Gerbstoffe in englischen Mostäpfeln. *Fluess. Obst* **1984**, *8*, 356−361.

(28) Le Bourvellec, C.; Le Quéré, J.-M.; Sanoner, P.; Drilleau, J.-F.; Guyot, S. Inhibition of apple polyphenol oxidase activity by procyanidins and polyphenol oxidation products. *J. Agric. Food Chem.* **2004**, *52* (1), 122−130.

(29) Oleszek, W.; Lee, C. Y.; Price, K. R. Apple phenolics and their contribution to enzymatic browning reactions. *Acta Soc. Bot. Pol.* **1989**, *58* (2), 273−283.

(30) Oszmianski, J.; Lee, C. Y. Enzymatic oxidation of phloretin glucoside in model system. *J. Agric. Food Chem.* **1991**, *39* (6), 1050−1052.

(31) Le Guernevé, C.; Sanoner, P.; Drilleau, J.-F.; Guyot, S. New compounds obtained by enzymatic oxidation of phloridzin. *Tetrahedron Lett.* **2004**, *45* (35), 6673−6677.

(32) Guyot, S.; Serrand, S.; Le Quéré, J. M.; Sanoner, P.; Renard, C. M. G. C. Enzymatic synthesis and physicochemical characterisation of phloridzin oxidation products (POP), a new water-soluble yellow dye deriving from apple. *Innovative Food Sci. Emerging Technol.* **2007**, *8* (3), 443−450.

(33) Lea, A. G. H. Cidermaking. In *Fermented Beverage Production*; Lea, A. G. H., Piggott, J. R., Eds.; Springer: New York, 1995; pp 66−96.

(34) *Pomme-Poire, De la Récolte au Conditionnement: Outils Pratiques*; Vaysse, P., Landry, P., Eds.; CTIFL: Paris, France, 2004.

(35) Kennedy, J. A.; Jones, G. P. Analysis of proanthocyanidin cleavage products following acid-catalysis in the presence of excess phloroglucinol. *J. Agric. Food Chem.* **2001**, *49* (4), 1740−1746.

(36) Alonso-Salces, R. M.; Guyot, S.; Herrero, C.; Berrueta, L. A.; Drilleau, J.-F.; Gallo, B.; Vicente, F. Chemometric classification of

DOI: 10.1021/acs.jafc.5b00988
J. Agric. Food Chem. 2015, 63, 7675−7684

Basque and French ciders based on their total polyphenol contents and CIELab parameters. *Food Chem.* **2005**, *91*, 91−98.
(37) Falguera, V.; Gatius, F.; Ibarz, A.; Barbosa-Canovas, G. V. Changes on colour parameters caused by high-pressure processing of apple juice made from six different varieties. *Int. J. Food Sci. Technol.* **2012**, *47* (10), 2158−2164.
(38) Guyot, S.; Bernillon, S.; Poupard, P.; Renard, C. M. G. C. Multiplicity of phenolic oxidation products in apple juices and ciders, from synthetic medium to commercial products. In *Recent Advances in Polyphenol Research*; Daayf, F., Lattanzio, V., Eds.; Wiley-Blackwell: Oxford, UK, 2008; Vol. 1, pp 278−292.
(39) Weinges, K.; Mattauch, H. Der chemische Konstitutionsbeweis des Dehydro-dicatechins A. *Chem. Zeit* **1971**, *95* (3), 155−156.
(40) Poupard, P.; Sanoner, P.; Baron, A.; Renard, M. G. C.; Guyot, S. Characterization of procyanidin B2 oxidation products in an apple juice model solution and confirmation of their presence in apple juice by high-performance liquid chromatography coupled to electrospray ion trap mass spectrometry. *J. Mass Spectrom.* **2011**, *46*, 1186−1197.
(41) Lozano, J. E. Food products, deterioration by browning. In *Fruit Manufacturing: Scientific Basis, Engineering Properties, and Deteriorative Reactions of Technological Importance*; Lozano, J. E., Ed.; Springer: New York, 2006; pp 163−174.
(42) Guyot, S.; Marnet, N.; Sanoner, P.; Drilleau, J.-F. Variability of the polyphenolic composition of cider apple (*Malus domestica*) fruits and juices. *J. Agric. Food Chem.* **2003**, *51* (21), 6240−6247.
(43) Walker, J. R.; Wilson, E. L. Studies on the enzymic browning of apples. Inhibition of apple *o*-diphenol oxidase by phenolic acids. *J. Sci. Food Agric.* **1975**, *26* (12), 1825−1831.
(44) Amiot, M. J.; Aubert, S.; Nicolas, J.; Goupy, P.; Aparicio, P. Phenolic composition and browning susceptibility of various apple and pear cultivars at maturity. *Groupe Polyphenols, Bull. Liaison* **1992**, *16* (2), 48−51.
(45) Fromm, M.; Loos, H. M.; Bayha, S.; Carle, R.; Kammerer, D. R. Recovery and characterisation of coloured phenolic preparations from apple seeds. *Food Chem.* **2013**, *136* (3−4), 1277−1287.

DOI: 10.1021/acs.jafc.5b00988
J. Agric. Food Chem. 2015, 63, 7675−7684

the influence of different parameters such as ethanol, pH, and glucose on their uptake. After ingestion, anthocyanin bioactivity in vivo will be dependent on the cumulative biological effect of native and resulting metabolites; thus, the research in this field is of crucial importance.

The purpose of this work was to explore the gastric absorption of red wine anthocyanins using an in vitro human stomach cell model, MKN-28, previously developed.[16] The influence of ethanol, glucose, pH, and pre-exposure to red wine on their transport was also performed.

Theoretical studies were conducted to study the interaction between anthocyanins and GLUT receptors. Two different conformations of GLUT receptors and different anthocyanin equilibrium forms were considered.

MATERIALS AND METHODS

Red Wine Extract. The red wine was a table red wine from 2012 made from the traditional Douro varieties (Touriga Nacional, Touriga Franca, Tinta Barroca, Tinto Cão, and Tinta Roriz) and was provided by Sogevinus Fine Wines, S.A. Ethanol was removed through rotative evaporation at 30 °C under vacuum. The dealcoholized wine was purified by reverse phase C-18 silica gel to eliminate all sugars and recover the wine phenolics. The eluents were acidic water (HCl 2% (v/v)) for conditioning of stationary phase and acidic methanol (HCl 2% (v/v)) for eluting. A new evaporation was made to remove methanol from the wine. The resulting wine extract was freeze-dried and stored at −20 °C until use.

Cell and Culture Conditions. Human cancer cell line from stomach, MKN-28, was grown as monolayers and maintained at 37 °C in an atmosphere of 5% CO_2 and 90% relative humidity. For routine maintenance, cells were cultured in 22.1 cm^2 tissue culture dishes as monolayers and maintained in RPMI 1640 AQmedia (Sigma, Germany), supplemented with 10% fetal calf serum (FCS) (Biowhittaker, Lonza, Belgium) and 1% of antibiotic/antimycotic solution (100 units/mL of penicillin, 100 mg/mL of streptomycin, and 0.25 mg/mL of amphotericin B) (Sigma). Cells were harvested by trypsinization (0.25%, w/v, trypsin−$EDTA_4$−Na) once a week.

Transport Studies. Transport experiments were performed according to previously published methods.[4,16] Briefly, MKN-28 cells were plated on 12-well transwell inserts (0.4 μm pore size tissue culture inserts (Corning Costar, Corning, NY, USA)). Cells were cultured at 37 °C in an atmosphere of 5% CO_2, and the medium was changed every 2 days. At 7 days MKN-28 cells were fully confluent and differentiated, so experiments were initiated at that time. Experiments were conducted only in MKN-28 cell monolayers that showed a TEER > 150 Ω·cm^2 (determined at 37 °C).

In transport experiments HBSS, pH 7.4, was the main component of the basolateral medium. In the gastric cell model the apical medium was acidified to 5.0 by adding solid 2-(*N*-morpholino)ethanesulfonic acid (MES) to give a concentration of 25 mM and then adjusting the pH with 5 M HCl.

Medium was removed and cells were washed with Hanks' medium, pH 7.4. Compound solution in Hanks, with a final concentration of 50 μg/mL, was added to the apical side of the cells and Hanks containing 2% FBS was added to the basolateral compartment.

Transepithelial transport was followed as a function of time. A total of 150 μL was taken from the basolateral side and replaced by fresh medium (Hanks containing 2% FBS) at 30, 60, and 120 min of incubation and also at 180 min for the MKN-28 cell line. Each time sample (150 μL) was acidified with HCl to a final concentration of 0.06 M. All samples, from both apical and basolateral sides, were acidified and frozen (−18 °C) to ensure that the cumulative amounts of each compound that were later quantified were not altered during sample delay until uHPLC analysis. Red wine anthocyanins were quantified using the malvidin-3-glucoside calibration curve Abs (520 nm) = 8.725 × concn (μM), R^2 = 0.9789.

Transport efficiency percentages were calculated as ((compound concentrations at the basolateral side overtime)/(compound concentrations at the apical side at 0 h)) × 100.

uHPLC Analysis. uHPLC analysis of the anthocyanins was performed on a Dionex Ultimate 3000 (Thermo Scientific) equipped with a Hypersil GOLD 50 × 2.1 mm i.d. (particle size = 1.9 μm) reversed phase C18 column (Thermo Scientific); detection was carried out at 520 nm using a diode array detector. The solvents were (A) H_2O/HCOOH (9.5:0.5) and (B) CH_3CN. The gradient consisted of 94.5−64% A for 7 min, 64−20% A for 3 min, 20−0% A for 0.1 min, 100% B for 3 min, and 94.5% A for 3 min at a flow rate of 0.5 mL/min.

RNA Isolation and qRT-PCR. Total RNA from cells was isolated using RNA-STAT 60 reagent (AMS Biotechnology, Oxon, UK) according to the manufacturer's instructions. Purity of RNA samples was confirmed with absorbance ratios 260/280 nm superior to 1.8. RNA samples were treated with DNaseI (RQ1 RNase-free DNase, Promega, Portugal). cDNA was synthesized from 5 μg of treated mRNA with an NZY First-Strand cDNA Synthesis Kit (NZYTech, Lisboa, Portugal).

Quantitative real-time polymerase chain reaction (qRT-PCR) was run on Lightcycler96 (Roche Diagnostics, USA). Ten microliter reactions were set on 96-well plates using 0.2 μM of each primer (Table 1) and 5 μL of FastStart Essential DNA Green Master (Roche Diagnostics, USA). Cycling conditions were as follows: denaturation (95 °C for 10 min), amplification and quantification (95 °C for 10 s, annealing temperature (AT) for 10 s, and 72 °C for 10 s, with a single fluorescence measurement at the end of the 72 °C for 10 s segment) repeated for 45 cycles, and a final melting at 95 °C 10 s, 65 °C 60 s, and 97 °C for 1 s. The following human-specific primers were used: HPRT-1 (AT = 59 °C) sense 5′ TGCTGACCTGCTGGATTACA 3′ and antisense 5′ TTTATGTCCCCTGTTGACTGG 3′. Data were analyzed using LightCycler 96 SW analysis software v1.1. The C_q values obtained were transformed into relative quantification data using $2^{(-\Delta C_q)}$.[20]

Table 1. Sequences (Forward and Reverse) and Annealing Temperature (AT) for Each Primer

transporter	primer	sequence	AT (°C)
GLUT1	forward	5′ GAT GAT GCG GGA GAA GAA GGT 3′	65
	reverse	5′ ACA GCG TTG ATG CCA GAC AG 3′	
GLUT2	forward	5′ CAG GAC TAT ATT GTG GGC TAA 3′	65
	reverse	5′ CTG ATG AAA AGT GCC AAG T 3′	
GLUT3	forward	5′ CTT CCC CTC CGC TGC TCA CTA 3′	64
	reverse	5′ CAA AAG TCC TGC CAC GGG TCT 3′	
SGLT1	forward	5′ TGG CAA TCA CTG CCC TTT A 3′	60
	reverse	5′ TGC AAG GTG TCC GTG TAA AT 3′	
hMCT1	forward	5′ CAC CGT ACA GCA ACT ATA CG 3′	60
	reverse	5′ CAA TGG TCG CCT CTT GTA GA 3′	
hSMCT1	forward	5′ CTC CCG GTG TTC TAC AAA CTG 3′	65
	reverse	5′ GGG CAG GGG CAT AAA TAA C 3′	

Anthocyanin/GLUT1 Computational Methods. Two crystallographic structures, extracted from the Protein DataBank (PDB), were

DOI: 10.1021/acs.jafc.5b00412
J. Agric. Food Chem. 2015, 63, 7685−7692

used: (i) an outward-facing conformation of *Escherichia coli*'s D-xylose:, H1 symporter (XylE) complexed with D-glucose (PDB code 4GBZ, resolution = 2.89 Å); and (ii) an inward-facing conformation of the human GLUT1 (hGLUT1) receptor (PDB code 4PYP, resolution = 3.17 Å).[21] The former structure is a homologue to the well-known human glucose transporters GLUT1−4. All of these receptors contain a typical major facilitator superfamily fold of 12 transmembrane segments (TMs), with amino and carboxy termini both located on the intracellular side. The 12 TMs are organized into three distinct domains—the N, C, and ICH domains. TM7 and TM10 belonging to the C domain are both discontinuous helices, which may facilitate conformational changes during substrate transport.[22]

Molecular docking studies were conducted with three different anthocyanins (Cy3glc, Dp3glc, and Mv3glc) in hemiketal, flavilium cation, and anionic quinoidal base forms. The structures were modeled with the GaussView software (Carnegie Office Park Gaussian Inc., Pittsburgh, PA, USA). The receptor PDB structures were protonated with the X-Leap tool of the AMBER 12.0 software,[23] considering their physiological protonation state. The docking procedure was performed with VsLab[24] that uses the Autodock software.[25] A total of 50 poses were generated, employing a genetic algorithm. The docking pocket was defined by the AutoGrid tool. The box dimensions were 23.2 × 20.6 × 21.7 Å. The docking structures were ranked energetically, and the best scores were taken as starting structures for the subsequent molecular dynamics (MD) simulations.

In the MD simulations, the receptors were parametrized with the ff99SB force field from the AMBER software. The parameters for the anthocyanins were derived following a standard protocol[26] using the Antechamber module.[27] The parameters were derived from the GAFF force field,[28] and atomic single-point charges were calculated using the Gaussian 09 software[29] and employing the RESP algorithm.[30]

The MD simulations were performed with the AMBER 12.0 software. Counter ions were added to neutralize the overall charge of the system. The X-Leap program was used for this purpose. An explicit solvation model with TIP3P water molecules was used, filling a truncated rectangular box with a minimum of 12 Å distance between the box edges and the model. Each structure was minimized in two stages. Subsequently, a 100 ps equilibration followed by a 25 ns production MD simulation was carried out. The Langevin temperature equilibration scheme was used to maintain the temperature at 310.15 K,[31] and periodic boundary conditions were imposed. Bond lengths involving hydrogen atoms were constrained using the SHAKE algorithm,[32] and the equations of motion were integrated with a 2 fs time step using the Verlet leapfrog algorithm. The particle-mesh Ewald (PME) method was used to treat long-range interactions,[33] and the nonbonded interactions were truncated with a 10 Å cutoff. All of the MD results were analyzed with the Ptraj module of Amber 12.0.

Statistical Analysis. All values are expressed as the arithmetic means ± SEM. Statistical significance of the difference between various treatments was evaluated by two-way analysis of variance (ANOVA) and by one-way analysis of variance between each group for the different incubation times, followed by the Bonferroni's correction for multiple comparisons. Differences were considered to be statistically significant (*) when $p < 0.05$.

RESULTS AND DISCUSSION

Gastric Transport of Red Wine Anthocyanins. A human adenocarcinoma gastric cell line, MKN-28, was previously developed as a model of human gastric barrier, useful for examining mechanisms of nutraceuticals transport. The transport of anthocyanins was studied in this cell model, and it could be concluded that their transport efficiency increases with incubation time, although no differences were observed among the three anthocyanins studied (Dp3glc, Cy3glc, and Mv3glc).[16]

Besides the importance that this barrier has for anthocyanins due to their rapid appearance in plasma, the possible interference of food components in anthocyanin gastric absorption also deserves investigation because these compounds are consumed as part of a normal diet. In particular, red wine is composed by a complex mixture of polyphenols (anthocyanins, tannins, catechins, etc.), alcohol, and monosaccharides (glucose and frutose), so it is not surprising that the total anthocyanin absorption may be affected by some of these parameters.

All transport experiments were performed in a transwell plate system introducing the Hanks buffer, pH 5, in which the wine extract (50 μg/mL) was previously dissolved, in the donor chamber. The Hanks buffer, 2% SFB and pH 7.4, was placed in the receptor chamber. At predetermined intervals, aliquots of 150 μL were removed from the basolateral chamber and analyzed by HPLC-DAD.

The anthocyanin profile of the red wine extract used is composed by six main anthocyanins (Figure 1).

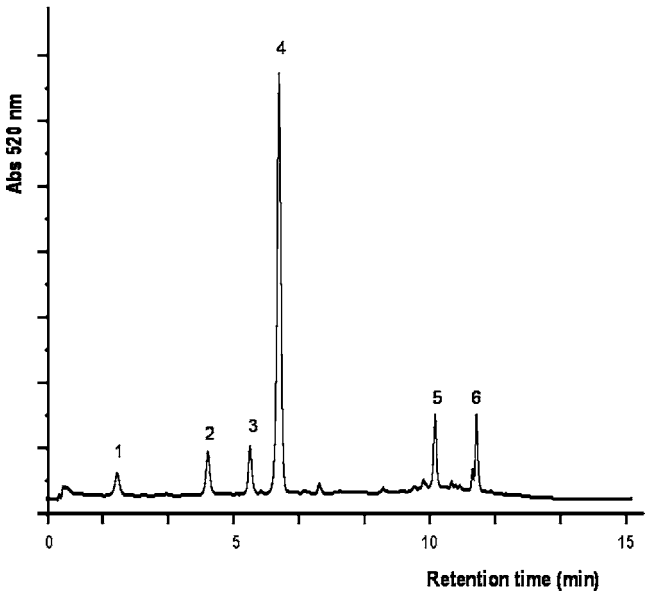

Figure 1. HPLC chromatogram of the red wine extract recorded at 520 nm. Peaks: 1, delphinidin-3-*O*-glucoside (Dp3glc); 2, petunidin-3-*O*-glucoside (Pt3glc); 3, peonidin-3-*O*-glucoside (Pn3glc); 4, malvidin-3-*O*-glucoside (Mv3glc); 5, malvidin-3-*O*-acetylglucoside (Mv3actglc); 6, malvidin-3-*O*-coumaroylglucoside (Mv3cumglc).

All anthocyanins present in the apical side of the transwell insert were detected in the basolateral side of this gastric barrier (data not shown).

Considering the ingestion of a glass of red wine containing 12% alcohol (v/v), this ethanol percentage will suffer a dilution within the gastric fluids, so the influence of 4% may be considered likely reliable in vivo. The effect of DMSO (wine stock solution solvent) and 4% ethanol (individually or co-administered) on the monolayer TEER was assayed. No effect was observed on cell viability or on monolayer integrity (data not shown).

In the presence of 4% ethanol no significant differences were observed in the transport efficiency of the total wine anthocyanins (Figure 2). There are some studies referring to anthocyanins that claim no influence of ethanol on their intestinal absorption[34,35]

The increase in the apical pH for values around 7.4 (similar to intestinal conditions) was associated with a reduction in the transport efficiency with statistical difference after 180 min

DOI: 10.1021/acs.jafc.5b00412
J. Agric. Food Chem. 2015, 63, 7685−7692

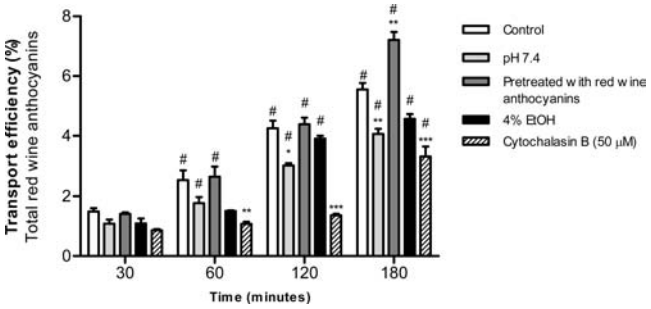

Figure 2. Transport efficiency of total red wine anthocyanins through MKN-28 barrier (apical → basolateral). The experiments were conducted with apical pH 5.0 and basolateral pH 7.4, unless otherwise indicated. The influence of 4% ethanol, pretreatment with red wine anthocyanins (3 h at third and fifth growing days), and apical pH (pH 5 vs 7.4) on total red wine transport efficiency was determined. Results are presented as transport efficiency (%) (mean ± SEM). Transport efficiency percentages were calculated as (compound concentrations at the basolateral side over time)/(compound concentrations at the apical side at 0 h) × 100. Significantly different from control for the same incubation time: ∗, $p < 0.05$; ∗∗, $p < 0.01$; ∗∗∗, $p < 0.001$. Significantly different between the different incubation times: #, $p < 0.001$.

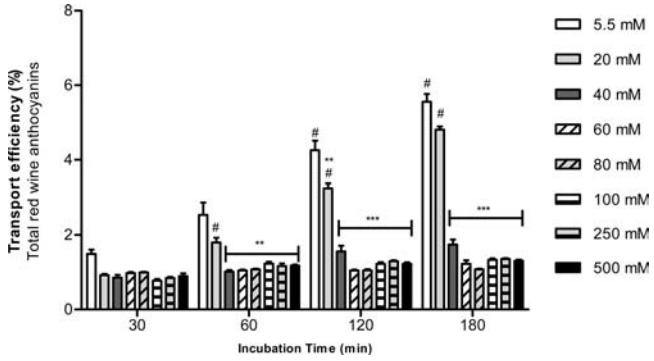

Figure 3. Transport efficiency of total red wine anthocyanins through MKN-28 barrier (apical → basolateral) in the presence of 20−500 mM D-glucose. Results are presented as transport efficiency (%) (mean ± SEM). Transport efficiency percentages were calculated as (compound concentrations at the basolateral side over time)/(compound concentrations at the apical side at 0 h) × 100. Significantly different from control for the same incubation time: ∗, $p < 0.05$; ∗∗, $p < 0.01$; ∗∗∗, $p < 0.001$. Significantly different between the different incubation times: #, $p < 0.001$.

(Figure 2). This result highlights the importance of pH on the anthocyanin transport efficiency that may be related not only to the main anthocyanin forms present but also to the influence on the possible transporters involved in their transport.

For the pretreatment study, transwell cells were incubated during 3 h with red wine anthocyanins (with the same concentration applied on the seventh day) at the third and fifth days postplating. After that incubation, the apical and basolateral medis were renewed. The pretreatment of the transwell system with anthocyanins during cell growth resulted in an increase in anthocyanin uptake for values above 30 min of incubation (Figure 2).

This result may be associated with a cellular adaptation to the presence of anthocyanins that could induce, for instance, an increase in the expression of some type of transporters.

Effect of D-(+)-Glucose. To evaluate the possible implication of glucose transporters in anthocyanin absorption, a range of glucose concentrations (5.5−500 mM) were co-administered to the apical side of the transwell system. According to the results obtained, for concentrations >40 mM glucose, the transport efficiency of anthocyanins is significantly decreased, remaining constant and around 1% during the 3 h of incubation time (Figure 3). This decrease in anthocyanin uptake may result from a competition for the same transporter. In fact, the presence of glucose in the anthocyanin moiety may account for the selective interaction between GLUTs and anthocyanins.

To test the possible implication of glucose transporters in anthocyanin absorption, besides adding their natural substrate, the effects of a glucose transporter inhibitor, cytocalasin B (50 μM), were also evaluated. For incubation time >60 min, the anthocyanins transport was significantly reduced (Figure 2). A similar behavior was observed in a previously work with the Caco-2 cell line.[4]

However, this is not the only molecular determining factor because all anthocyanin forms have glucose in their constitution, and it was seen that anthocyanin uptake was reduced by pH, which alters the anthocyanidin moiety and makes anthocyanin's access to the transporter core difficult. This will be studied by using a theoretical approach, as further discussed.

Characterization of Transporters Expression in MKN-28 Cell Line. Monocarboxylated transporter and organic anion transporter are expressed in intestine and liver but also in stomach.[36] To explore the possible involvement of transporters in the absorption across MKN-28, the expression of some transporters was evaluated by RT-PCR. It was concluded that not only MKN-28 expresses glucose transporters 1 (GLUT1) and 3 (GLUT3) but also monocarboxylated transporter 1 (MCT1) (Figure 4). The expression of glucose transporter 2 (GLUT2), sodium-coupled monocarboxylated transporter 1 (SMCT1), and sodium−glucose transporter 1 (SGLT1) was not observed.

Molecular Docking on XylE and hGLUT1 Receptors. A molecular docking of Cy3glc, Dp3glc, and Mv3glc on hemiketal, flavilium cation, and anionic quinoidal base forms against GLUT transporters was performed. Because the X-ray structure of XylE was complexed with a glucose (glc) molecule, a docking procedure using this unit was first performed to validate the protocol. Figure S1 in the Supporting Information (SI) shows the superimposition between the best docking result and the crystallographic geometry, in which a high similarity in the glc pose is observed with a root-mean-square deviation (RMSd) of 2.03 Å. This small RMSd value and the negative ΔG binding obtained for glucose (−6.6 kcal/mol) validates this docking procedure.

A similar process was applied to dock all anthocyanins into the XylE receptor. The values of ΔG binding obtained for all molecules are presented in Table 2. We observe that all negative free binding energy values were compatible with a favorable association between the polyphenols and XylE. Although all free energy values are similar, it was observed that the Cy3glc and Dp3glc molecules interact more strongly with the receptor than Mv3glc. This may be justified by the high number of hydroxyl groups present in the first two anthocyanins, which can establish strong hydrogen-bond interactions with the amino acids of the periplasmic side of the receptor.

It is also possible to see that all docking solutions of hemiketal forms bind to the periplasmic side of XylE by glucose

DOI: 10.1021/acs.jafc.5b00412
J. Agric. Food Chem. 2015, 63, 7685−7692

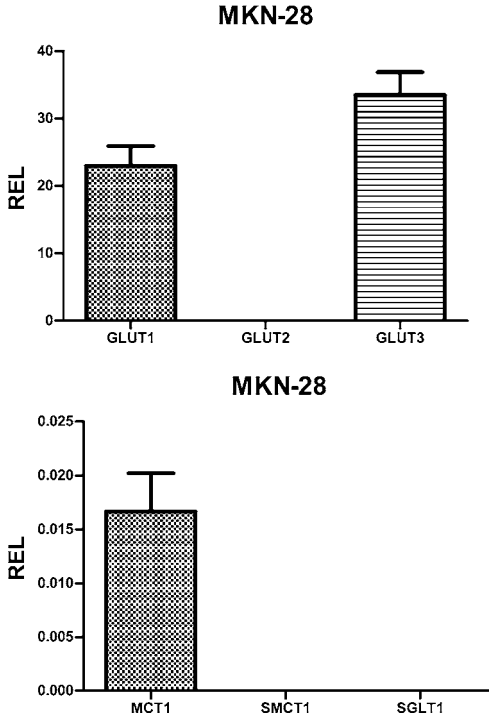

Figure 4. Transporter expression in MKN-28 cell line evaluated by qRT-PCR: glucose transporters 1 (GLUT1), 2 (GLUT2), and 3 (GLUT3), monocarboxylated transporter 1 (MCT1), sodium-coupled monocarboxylated transporter 1 (SMCT1); and sodium−glucose transporter 1 (SGLT1).

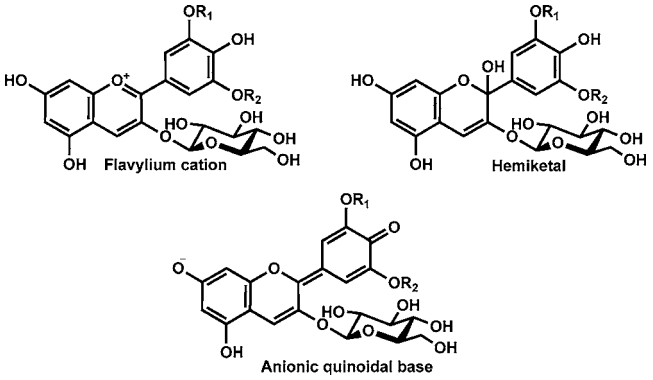

Figure 5. General structures of anthocyanins in flavylium cation, hemiketal, and anionic quinoidal base forms. R_1 and R_2 = H, OH, or OCH_3.

or the B ring, which suggests that both units have a key role in the entrance of anthocyanins. However, the flavilium cation form of anthocyanins appears to enter on XylE mainly by the AC moiety (Figure 5). This could be explained by the positive charge present in the C ring that is not found in the other forms.

Table 3 shows the values of ΔG binding obtained from the docking of the same anthocyanin molecules to the hGLUT1. In all protonation states, the AC moiety of anthocyanins is the one that interacts more deeply with the inward-facing conformation of hGLUT1. This fact reinforces the entrance by the opposite side (B and Glc groups) previously observed for the outward-facing conformation. These results suggest that there are two main conformations of anthocyanins during their entrance from the extracellular side to the outward-facing receptor, which implies that these compounds access the intracellular side mainly by the AC group. To summarize this, Figure 6 shows a proposal for the molecular mechanism by which the anthocyanins cross the cellular membrane through hGLUT receptors.

Figure 7 shows the main residues involved in the binding of anthocyanins to hGLUT1 receptor in both conformations (considering the corresponding residues of the outward-open form of XylE). In the literature, it was proposed that only the C domain is implied in the association of glucose to both XylE and hGLUT1, whereas the N domain works as a secondary place.[21,22] However, these docking results show that the residues involved in the binding of anthocyanins to hGLUT1 belong to both C and N domains. This could be explained due to the larger size of anthocyanins compared to glucose.

Molecular Dynamics (MD) Simulations. The two best docking solutions (S1 and S2) for each anthocyanin, in the three different protonation states, bound to the inward-open hGLUT1 were used as starting structures for the subsequent MD simulations. These two solutions were chosen because the anthocyanins can interact with the binding pocket by different groups (AC, B, or glc units). The unique exception was the Mv3glc hemiketal, in which the binding modes observed in S1 and S2 were very similar. Hence, MD simulations of 25 ns were carried out for the 17 different hGLUT1−anthocyanin complexes. The analysis of the results revealed that all anthocyanins remained in the binding pocket throughout the simulations. Figure S2 in the SI shows the superimposition of the initial pose and the average pose along the MD simulation for Cy3glc flavilium cation, in which we can see that both poses are similar. The same was observed for the other complexes. The RMSd values for the protein backbone complexed with the

Table 2. Values of $\Delta G_{binding}$ Obtained for the Anthocyanins Docked to the XylE Receptor[a]

ligand	$\Delta G_{binding}$ (kcal/mol)	internal group	ligand	$\Delta G_{binding}$ (kcal/mol)	internal group	ligand	$\Delta G_{binding}$ (kcal/mol)	internal group
hemiketal Cy S1	−9.07	B ring	cation Cy S1	−9.46	B ring	anion Cy S1	−9.18	AC ring
hemiketal Cy S2	−8.03	B ring	cation Cy S2	−9.45	AC ring	anion Cy S2	−8.22	B ring
hemiketal Dp S1	−8.13	Glc	cation Dp S1	−8.85	AC ring	anion Dp S1	−8.49	AC ring
hemiketal Dp S2	−7.09	B ring	cation Dp S2	−8.41	Glc	anion Dp S2	−7.87	Glc
hemiketal Mv S1	−7.36	Glc	cation Mv S1	−8.99	AC ring	anion Mv S1	−8.55	AC ring
hemiketal Mv S2	−6.35	Glc	cation Mv S2	−8.09	Glc	anion Mv S2	−7.43	Glc

[a]The most internal group of the polyphenols reaching the receptor is also depicted. S1 and S2 are the two best solutions obtained from the docking protocol.

DOI: 10.1021/acs.jafc.5b00412
J. Agric. Food Chem. 2015, 63, 7685−7692

Table 3. Values of $\Delta G_{binding}$ Obtained for the Anthocyanins Docked to the hGLUT1 Receptor[a]

ligand	$\Delta G_{binding}$ (kcal/mol)	internal group	ligand	$\Delta G_{binding}$ (kcal/mol)	internal group	ligand	$\Delta G_{binding}$ (kcal/mol)	internal group
hemiketal Cy S1	−11.71	AC ring	cation Cy S1	−10.96	AC ring	anion Cy S1	−10.78	B ring
hemiketal Cy S2	−10.26	AC ring	cation Cy S2	−10.01	AC ring	anion Cy S2	−9.86	AC ring
hemiketal Dp S1	−11.84	AC ring	cation Dp S1	−11.04	AC ring	anion Dp S1	−10.77	AC ring
hemiketal Dp S2	−10.11	Glc	cation Dp S2	−9.94	AC ring	anion Dp S2	−9.55	B ring
hemiketal Mv S1	−10.39	Glc	cation Mv S1	−9.35	AC ring	anion Mv S1	−9.56	AC ring
hemiketal Mv S2	−9.69	B ring	cation Mv S2	−9.34	AC ring	anion Mv S2	−8.55	B ring

[a]The most internal group of the polyphenols reaching the receptor is also depicted. S1 and S2 are the two best solutions obtained from the docking protocol.

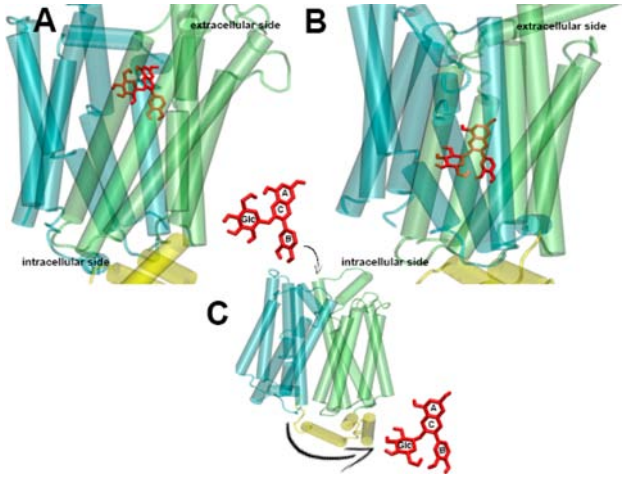

Figure 6. Proposal for the molecular mechanism by which the anthocyanins cross the cellular membrane through GLUT receptors.

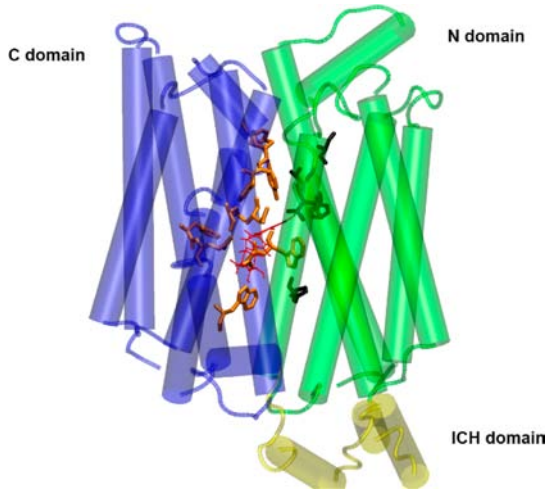

Figure 7. Representation of the main residues involved in the binding of anthocyanins to the hGLUT1 receptor. Cy3glc is represented with lines and colored in red; N, C, and ICH are represented in cartoons and colored in green, blue, and yellow, respectively; residues from N and C are represented in sticks and colored in black and orange, respectively.

anthocyanins during the MD simulations are represented in Figure S3 in the SI. It can be observed that these RMSd values are quite small (oscillating between 1.5 and 2.5 Å), which reveals the higher stability of the complexes. To obtain a measure of the movement of a subset of the system relative to the average structure over the whole simulation, the root-mean-square fluctuation (RMSf) values were also calculated for the protein, by residue, and are shown in Figure S4 in the SI. It was possible to observe an RMSf pattern conserved in all complexes. All of the residues within the binding pocket showed a minimal flexibility, which suggests that they maintain a rigid position during the simulation to reinforce the strong interaction with the several anthocyanins tested.

Structural information on the hGLUT1 binding pocket, in particular the hydrogen bonds established between the anthocyanins and the neighboring residues, were analyzed and are shown in Table S1. The van der Waals contacts established between the polyphenolic rings and the aliphatic side chains are also presented. It was seen that the main hydrogen bonds occur between the hydroxyl groups of anthocyanins and the side chains of Glu380, Asn317, Asn411, Asn415, Tyr292, and Thr30 residues. The major moiety of all anthocyanins involved in hydrogen-bond interactions seems to be glucose, which emphasizes its key role in anthocyanins transport. We have verified the presence of many hydrophobic interactions (stacking effect of $\pi-\pi$ interactions) between the rings of anthocyanins and the high number of aromatic residues present in the periplasmic side of hGLUT1 (Phe379, Trp412, Trp388, Phe72, Phe291, His160). Figure S5 in the SI exemplifies the main hydrophilic and hydrophobic interactions established between the hemiketal Cy3glc and the residues of hGLUT1. All of these interactions strongly contribute to the high stability of the complex formed between the anthocyanins and hGLUT1. Interestingly, Glu380 is the one that interacts with all anthocyanins by one of the shortest hydrogen bonds and has a high time occupancy during the MD simulations, which suggests that this residue has a key role in anthocyanin transport. This result agrees with the proposal by Deng et al.[21]

The number of water molecules within the periplasmic side of hGLUT1 during each MD simulation was also determined. The average numbers of water molecules within a radius of 3 and 5 Å around each anthocyanin were 6 and 9, which confirms that the binding pocket is highly accessible to the solvent. This solvation effect facilitates the binding of anthocyanins because they are highly water-soluble pigments.

These results obtained through computational studies do not superimpose with those obtained experimentally. Indeed, they show that all three forms of anthocyanins have similar affinities to hGLUT1, whereas a decrease of anthocyanin uptake was observed experimentally at pH 7.4. The information yielded from the theoretical studies constitutes very useful data to mechanistically understand the affinity between anthocyanins and glucose transporters. Nevertheless, other variables such as

DOI: 10.1021/acs.jafc.5b00412
J. Agric. Food Chem. 2015, 63, 7685−7692

cellular environment and biomembrane structural issues have to be taken into consideration in further studies.

■ ASSOCIATED CONTENT

Supporting Information

Additional figures obtained according to the docking protocol and the MD simulations described under Materials and Methods as well as a table of hydrogen-bond interactions between anthocyanins and the hGLUT1 receptor. This material is available free of charge via the Internet at http://pubs.acs.org.

■ AUTHOR INFORMATION

Corresponding Author

*(I.F.) E-mail: iva.fernandes@fc.up.pt. Phone: +351.220402562.

Funding

This work was supported by FCT (Fundação para a Ciência e Tecnologia) (POCI, FEDER, Programa Comunitário de Apoio), by one Post-Doc grant (SFRH/BPD/86173/2012), by one IF starting grant (IF/01355/2014), by a Ph.D. grant (PD/BD/106062/2015), and by one project grant (PTDC/AGR-TEC/2227/2012).

Notes

The authors declare no competing financial interest.

■ REFERENCES

(1) Renaud, S.; Gueguen, R. The French paradox and wine drinking. *Novartis Found. Symp.* **1998**, *216*, 208−217.

(2) German, J. B.; Walzem, R. L. The health benefits of wine. *Annu. Rev. Nutr.* **2000**, *20*, 561−593.

(3) Ruf, J. C. Overview of epidemiological studies on wine, health and mortality. *Drugs Exp. Clin. Res.* **2003**, *29*, 173−179.

(4) Faria, A.; Pestana, D.; Azevedo, J.; Martel, F.; De Freitas, V.; Azevedo, I.; Mateus, N.; Calhau, C. Absorption of anthocyanins through intestinal epithelial cells − putative involvement of GLUT2. *Mol. Nutr. Food Res.* **2009**, *53*, 1430−1437.

(5) Talavera, S.; Felgines, C.; Texier, O.; Besson, C.; Lamaison, J. L.; Remesy, C. Anthocyanins are efficiently absorbed from the stomach in anesthetized rats. *J. Nutr.* **2003**, *133*, 4178−4182.

(6) Zhao, Z.; Egashira, Y.; Sanada, H. Ferulic acid is quickly absorbed from rat stomach as the free form and then conjugated mainly in liver. *J. Nutr.* **2004**, *134*, 3083−3088.

(7) Green, B. G.; Dalton, P.; Cowart, B.; Shaffer, G.; Rankin, K.; Higgins, J. Evaluating the 'labeled magnitude scale' for measuring sensations of taste and smell. *Chem. Senses* **1996**, *21*, 323−334.

(8) Kavvada, K. M.; Murray, J. G.; Moore, V. A.; Coombes, A. G. A.; Hanson, P. J. A collagen IV matrix is required for guinea pig gastric epithelial cell monolayers to provide an optimal model of the stomach surface for biopharmaceutical screening. *J. Biomol. Screening* **2005**, *10*, 495−507.

(9) Lemieux, M.; Bouchard, F.; Gosselin, P.; Paquin, J.; Mateescu, M. A. The NCI-N87 cell line as a gastric epithelial barrier model for drug permeability assay. *Biochem. Biophys. Res. Commun.* **2011**, *412*, 429−434.

(10) Farrell, T. L.; Dew, T. P.; Poquet, L.; Hanson, P.; Williamson, G. Absorption and metabolism of chlorogenic acids in cultured gastric epithelial monolayers. *Drug Metab. Dispos.* **2011**, *39*, 2338−2346.

(11) Tracy, L. T. L. F.; Tristan, P. T. P. D.; Laure, L. P.; Peter, P. H.; Gary, G. W. Absorption and metabolism of chlorogenic acids in cultured gastric epithelial monolayers. *Drug Metab. Dispos.* **2011**, *39*, 2338−2346.

(12) Konishi, Y.; Zhao, Z.; Shimizu, M. Phenolic acids are absorbed from the rat stomach with different absorption rates. *J. Agric. Food Chem.* **2006**, *54*, 7539−7543.

(13) Crespy, V.; Morand, C.; Besson, C.; Manach, C.; Demigne, C.; Remesy, C. Quercetin, but not its glycosides, is absorbed from the rat stomach. *J. Agric. Food Chem.* **2001**, *50*, 618−621.

(14) Murota, K.; Terao, J. Quercetin appears in the lymph of unanesthetized rats as its phase II metabolites after administered into the stomach. *FEBS Lett.* **2005**, *579*, 5343−5346.

(15) El Mohsen, M. A.; Marks, J.; Kuhnle, G.; Moore, K.; Debnam, E.; Srai, S. K.; Rice-Evans, C.; Spencer, J. P. E. Absorption, tissue distribution and excretion of pelargonidin and its metabolites following oral administration to rats. *Br. J. Nutr.* **2006**, *95*, 51−58.

(16) Fernandes, I.; De Freitas, V.; Reis, C.; Mateus, N. A new approach on the gastric absorption of anthocyanins. *Food Funct.* **2012**, *3*, 508−516.

(17) He, J.; Wallace, T. C.; Keatley, K. E.; Failla, M. L.; Giusti, M. M. Stability of black raspberry anthocyanins in the digestive tract lumen and transport efficiency into gastric and small intestinal tissues in the rat. *J. Agric. Food Chem.* **2009**, *57*, 3141−3148.

(18) Passamonti, S.; Vrhovsek, U.; Mattivi, F. The interaction of anthocyanins with bilitranslocase. *Biochem. Biophys. Res. Commun.* **2002**, *296*, 631−636.

(19) Fernandes, I.; Faria, A.; Calhau, C.; de Freitas, V.; Mateus, N. Bioavailability of anthocyanins and derivatives. *J. Funct. Foods* **2014**, *7*, 54−66.

(20) Schmittgen, T. D.; Kenneth, J. L. Analyzing real-time PCR data by the comparative CT method. *Nat. Protoc.* **2008**, *3*, 1101−1108.

(21) Deng, D.; X, C.; Sun, P.; Wu, J.; Yan, C.; Hu, M.; Yan, N. Crystal structure of the human glucose transporter GLUT1. *Nature* **2014**, *510*, 121−125.

(22) Sun, L.; Zeng, X.; Yan, C.; Sun, X.; Gong, X.; Rao, Y.; Yan, N. Crystal structure of a bacterial homologue of glucose transporters GLUT1−4. *Nature* **2012**, *490*, 361−369.

(23) Case, D. A.; Darden, T. A.; Cheatham, T. E.; Simmerling, C. L.; Wang, J.; Duke, R. E.; Luo, R.; Walker, R. C.; Zhang, W.; Merz, K. M.; Roberts, B.; Hayik, S.; Roitberg, A.; Seabra, G.; Swails, J.; Goetz, A. W.; Kolossváry, I.; Kollman, P. A. AMBER 2012, 2012.

(24) Cerqueira, N. M. F. S. A.; Ribeiro, J.; Fernandes, P. A.; Ramos, M. J. VsLab − an implementation for virtual high-throughput screening using AutoDock and VMD. *Int. J. Quantum Chem.* **2011**, *111*, 1208−1212.

(25) Morris, G. M.; Huey, R.; Lindstrom, W.; Sanner, M. F.; Belew, R. K.; Goodsell, D. S.; Olson, A. J. AutoDock 4.2. *J. Comput. Chem.* **2009**, *16*, 2785−2791.

(26) Brás, N. F.; G, R.; Fernandes, P. A.; Mateus, N.; Ramos, M. J.; De Freitas, V. Understanding the binding of procyanidins to pancreatic elastase by experimental and computational methods. *Biochemistry* **2010**, *49*, 5097−5108.

(27) Wang, J.; Wang, W.; Kollman, P. A.; Case, D. A. Automatic atom type and bond type perception in molecular mechanical calculations. *J. Mol. Graphics Modell.* **2006**, *26*, 247−260.

(28) Wang, J.; Wolf, R. M.; Caldwell, J. W.; Kollman, P. A.; Case, D. A. Development and testing of a general AMBER force field. *J. Comput. Chem.* **2004**, *25*, 1157−1174.

(29) Frisch, M. J.; Trucks, G. W.; Schlegel, H. B.; Scuseria, G. E.; Robb, M. A.; Cheeseman, J. R.; Scalmani, G.; Barone, V.; Mennucci, B.; Petersson, G. A.; Nakatsuji, H.; Caricato, M.; Li, X.; Hratchian, H. P.; Izmaylov, A. F.; Bloino, J.; Zheng, G.; Sonnenberg, J. L.; Hada, M.; Ehara, M.; Toyota, K.; Fukuda, R.; Hasegawa, J.; Ishida, M.; Nakajima, T.; Honda, Y.; Kitao, O.; Nakai, H.; Vreven, T.; Montgomery, J. A., Jr.; Peralta, J. E.; Ogliaro, F.; Bearpark, M.; Heyd, J. J.; Brothers, E.; Kudin, K. N.; Staroverov, V. N.; Kobayashi, R.; Normand, J.; Raghavachari, K.; Rendell, A.; Burant, J. C.; Iyengar, S. S.; Tomasi, J.; Cossi, M.; Rega, N.; Millam, M. J.; Klene, M.; Knox, J. E.; Cross, J. B.; Bakken, V.; Adamo, C.; Jaramillo, J.; Gomperts, R.; Stratmann, R. E.; Yazyev, O.; Austin, A. J.; Cammi, R.; Pomelli, C.; Ochterski, J. W.; Martin, R. L.; Morokuma, K.; Zakrzewski, V. G.; Voth, G. A.; Salvador, P.; Dannenberg, J. J.; Dapprich, S.; Daniels, A. D.; Farkas, Ö.; Foresman, J. B.; Ortiz, J. V.; Cioslowski, J.; Fox, D. J. *Gaussian*; Gaussian, Inc.: Wallingford, CT, USA. 2009.

DOI: 10.1021/acs.jafc.5b00412
J. Agric. Food Chem. 2015, 63, 7685−7692

(30) Bayly, C. I.; Cieplak, P.; Cornell, W. D.; Kollman, P. A. A well-behaved electrostatic potential based method using charge restraints for deriving atomic charges: the RESP model. *J. Phys. Chem.* **1993**, *97*, 10269−10280.
(31) Izaguirre, J. A.; Catarello, D. P.; Wozniak, J. M.; Skeel, R. D. Langevin stabilization of molecular dynamics. *J. Chem. Phys.* **2001**, *114*, 2090−2098.
(32) Ryckaert, J. P.; Ciccotti, G.; Berendsen, H. J. C. Numerical-integration of Cartesian equations of motion of a system with constraints − molecular-dynamics of *n*-alkanes. *J. Comput. Phys.* **1977**, *23*, 327−341.
(33) Salomon-Ferrer, R.; Case, D. A.; Walker, R. C. An overview of the Amber biomolecular simulation package. *WIREs Comput. Mol. Sci.* **2012**, *3*, 198−210.
(34) Bub, A.; Watzl, B.; Heeb, D.; Rechkemmer, G.; Briviba, K. Malvidin-3-glucoside bioavailability in humans after ingestion of red wine, dealcoholized red wine and red grape juice. *Eur. J. Nutr.* **2001**, *40*, 113−120.
(35) Andlauer, W.; Stumpf, C.; Frank, K.; Furst, P. Absorption and metabolism of anthocyanin cyanidin-3-glucoside in the isolated rat small intestine is not influenced by ethanol. *Eur. J. Nutr.* **2003**, *42*, 217−223.
(36) Neuhoff, S.; Ungell, A.-L.; Zamora, I.; Artursson, P. pH-Dependent passive and active transport of acidic drugs across Caco-2 cell monolayers. *Eur. J. Pharm. Sci.* **2005**, *25*, 211−220.

DOI: 10.1021/acs.jafc.5b00412
J. Agric. Food Chem. 2015, 63, 7685−7692

because different intestinal enzymes exist in animals and humans, animal studies alone may not always be sufficient for predicting compound absorption in humans. There is no report on the absorption of *C. morifolium* in differentiated Caco-2 cells derived from human colorectal carcinoma, a vitro model of absorptive enterocytes. Therefore, we used the differentiated Caco-2 models, with animal in vivo studies, and they might be useful for the aim of predicting the absorption and metabolism in humans. As described above, flavonoids are generally metabolized to their conjugates in the gastrointestinal tract. Because most of these metabolites are not available from commercial sources, their direct analysis is precluded. Thus, in this study on luteolin conjugates in rat plasma and culture media, samples were treated with enzymes having glucuronidase/sulfatase activities to release the parent aglycone for HPLC, and for detailed qualitative analysis, untreated samples were applied to LC-MS.

MATERIALS AND METHODS

Chemicals. Luteolin, luteolin-7-*O*-β-glucoside, and myricetin were purchased from Extrasynthese (Genay, France). MEM nonessential amino acids (NEAA) and penicillin/streptomycin were obtained from Life Technologies (Carlsbad, CA, USA). Fetal bovine serum (FBS) and β-glucuronidase (type H-5 from *Helix pomatia* and type L-II from limpets) were purchased from Sigma-Aldrich (St. Louis, MO, USA). All other chemicals were obtained from Wako Pure Chemical Industries (Osaka, Japan), unless otherwise specified. HPLC solvents were all of analytical grade. The extraction of the dried *C. morifolium* flowers was performed as briefly described below. *C. morifolium* flowers (200 g) were homogenized in 2.0 L of methanol, incubated at 40 °C for 3 h twice, and evaporated.

Animals. Male Sprague−Dawley rats (7 weeks old; SLC, Hamamatsu, Japan) were housed in an air-conditioned room and given free access to MF commercial food pellets (Oriental Yeast Co., Tokyo, Japan) and tap water for 4 weeks before the experiments. After an overnight fast, the rats (11 weeks old) were intragastically administered the *C. morifolium* flower extract (1.7 g/kg body weight (bw)), equivalent to luteolin (22.8 μmol/kg bw) and luteolin-7-*O*-glucoside (58.3 μmol/kg bw), or propylene glycol as a vehicle control via intragastric intubation. At 0, 0.5, 1, 2, 3, and 6 h after administration, blood was collected from the vein into heparinized glass capillaries and centrifuged to obtain plasma. The rats were maintained and handled according to the Guidelines for the Regulation of Animal Experimentation Committee of the University of Shizuoka.

Cell Culture. Caco-2 human intestinal epithelial cells were purchased from the European Collection of Cell Cultures (Wiltshire, UK). Caco-2 cells were grown in EMEM supplemented with 10% heat-inactivated FBS, penicillin (100 U/mL), streptomycin (100 ng/mL), and NEAA at 37 °C under a humidified atmosphere of 95% air and 5% CO_2. To examine the bioavailability of luteolin and luteolin-7-*O*-glucoside, Caco-2 cells were seeded on cell culture inserts for a 12-well plate (Corning, Tewksbury, MA, USA) at a density of 3.4×10^4 cells/filter and used for experiments on days 15−20. The transepithelial electrical resistance (TEER) value of the monolayers was measured using a Millicell-ERS instrument (Millipore Corp., Bedford, MA, USA) according to the methods of Hidalgo et al.[23,24] and Murota et al.[23,24] After confirmation of differentiation by the TEER value (>600 Ω cm^2), the cells were pre-incubated with transport medium (Hank's balanced salt solution with Ca^{2+}, Mg^{2+}, and glucose; 500 μL in the apical compartment and 1500 μL in the basal compartment of the transwell system) for 30 min at 37 °C. The *C. morifolium* flower extract, luteolin, and luteolin-7-*O*-glucoside dissolved in transport medium were then added to the apical side of the cells at specified total concentrations. After incubation of the cells at 37 °C for the required times, the cell culture media from both compartments (apical and basal) were collected for investigation of the bioavailability.

Sample Preparation for HPLC and LC-MS Analysis. The collected plasma samples and medium samples with or without enzymatic deconjugation were treated as described below for determination of luteolin, luteolin glucoside, and conjugated metabolites using HPLC and LC-MS. Individual samples were divided into two aliquots. To hydrolyze conjugated luteolin metabolites, one aliquot of plasma sample was treated with *H. pomatia* β-glucuronidase type H-5 (200 U), which possesses β-glucuronidase, sulfatase, and glucosidase activities, and then incubated at pH 5.0 for 45 min at 37 °C in 0.5 M acetate buffer. Similarly, one aliquot of medium sample was treated with limpet β-glucuronidase type L-II (400−1400 U), which possesses β-glucuronidase and glucosidase activities in 0.1 M phosphate buffer (pH 5.0), and then incubated at pH 5.0 for 45 min at 37 °C in 0.1 M phosphate buffer. The resulting mixtures were acidified with an equivalent amount of 0.01 M oxalic acid. These conditions and the enzyme mixtures yielded the highest amounts of free luteolin from the plasma of *C. morifolium* flower extract-treated rats and from the medium treated with the *C. morifolium* flower extract, luteolin, and luteolin-7-*O*-glucoside in preliminary analyses. The other portions of the plasma and medium samples were retained without hydrolysis by β-glucuronidase and used for direct quantification of nonconjugated metabolites. These samples were also acidified with 0.01 M oxalic acid. After acidification, the hydrolyzed and unhydrolyzed samples were each mixed with myricetin as an internal standard and applied to a Sep-Pak C18 cartridge (Waters, Milford, MA, USA), which had been pretreated by passage with methanol. The cartridge was washed with 0.01 M oxalic acid, distilled water/methanol/0.5 M oxalic acid (88:10:2), and distilled water, and the methanol eluate was obtained. The eluate was evaporated to dryness, and the residue was dissolved in 20% acetonitrile/0.5% phosphoric acid for HPLC analysis and in methanol for LC-MS, respectively. After filtration (0.45 μm filter unit), the filtrate was applied to HPLC and LC-MS analysis.

HPLC Analysis. The sample was injected into an HPLC-electrochemical detection (ECD) system (model 5600A CA767 CoulArray Detector; ESA, Cambridge, MA, USA) equipped with a CAP CELL PAK C18 UG120 column (S-5 μm, 4.6 mm i.d. × 150 mm; Shiseido, Tokyo, Japan). The separation of the compounds was carried out by gradient elution. For detection of luteolin and luteolin-7-*O*-glucoside using the HPLC-ECD system, two gradient systems were employed. For system 1, solvent A was 20% acetonitrile/0.5% phosphoric acid and solvent B was 40% acetonitrile/0.5% phosphoric acid. The gradient program was as follows: 0−5 min, 0% B; 5−15 min, linear gradient to 100% B; 15−19 min, 100% B hold; 19−22 min, linear gradient to 0% B; flow rate, 0.8 mL/min. For system 2, solvents A and B were the same as in system 1, respectively, and the gradient program was as follows: 0−10 min, 0% B; 10−16 min, linear gradient to 10% B; 16−21 min, 10% B hold; 21−30 min, linear gradient to 25% B; 30−35 min, 25% B hold; 35−40 min, linear gradient to 50% B; 40−43 min, 50% B hold; 43−48 min, linear gradient to 100% B; 48−50 min, 100% B hold; 50−55 min, linear gradient to 0% B; flow rate, 0.8 mL/min. Electrochemical detection was performed with a coulometric electrode at 150 mV (for channel 1) and 200 mV (for channel 2).

LC-MS Analysis. For LC-MS analysis, the samples were injected onto Q Exactive (Thermo Fisher Scientific, Waltham, MA, USA). The mass spectrometer was operated in the negative-ion ESI mode with targeted selected ion monitering (SIM) mode for all LC-MS analytes. The samples were separated by UPLC (Accela; Thermo Fisher Scientific) equipped with an ACQUITY UPLC BEH C18 column (1.7 μm, 2.1 mm i.d. × 100 mm; Waters). Gradient elution was performed using a two-solvent system (solvent A, 0.1% formic acid; solvent B, acetonitrile containing 0.1% formic acid). The gradient program was as follows: 0−1 min, 2% B hold; 1−15 min, linear gradient to 98% B; flow rate, 0.3 mL/min.

RESULTS

Time-Dependent Changes in the Plasma Concentrations of Luteolin after Oral Administration of the *Chrysanthemum* Flower Extract. We quantified luteolin and luteolin-7-*O*-glucoside using HPLC-ECD, and representative

DOI: 10.1021/acs.jafc.5b00232
J. Agric. Food Chem. 2015, 63, 7693−7699

chromatograms for luteolin, luteolin-7-*O*-glucoside, and myricetin (internal standard) are shown in the Supporting Information (Supplemental Figure 1A). The peaks of luteolin, luteolin-7-*O*-glucoside, and myricetin were observed at 17.767, 11.167, and 14.733 min, respectively, using the system 1 program. On the basis of the analysis using this system, 1 g of *Chrysanthemum* flower extract contained luteolin and luteolin-7-*O*-glucoside at 13.4 and 34.3 μmol, respectively, giving 47.7 μmol of total luteolin in 1 g of the *Chrysanthemum* flower extract. To measure the total content of luteolin derivatives in plasma, we treated plasma samples with *H. pomatia* β-glucuronidase type H-5, which has hydrolysis activity against glucuronides and sulfates, and confirmed that this enzyme altered luteolin-7-*O*-glucoside to luteolin in preliminary analyses (data not shown).

We examined the time-dependent changes (0.5, 1, 2, 3, and 6 h) in the plasma luteolin concentration in rats administered the *Chrysanthemum* flower extract at 1.64 g/kg bw, equivalent to 81 μmol of total luteolin (Figure 1). In this experiment, the levels

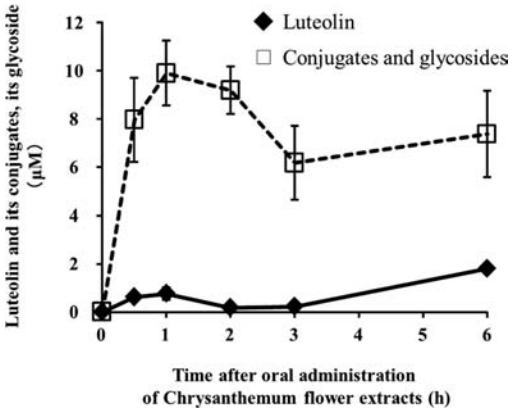

Figure 1. Time-dependent changes in luteolin derivatives in plasma from rats after oral administration of the *Chrysanthemum* flower extract. The concentrations of luteolin and its conjugates were measured in rat plasma after oral administration of the *C. morifolium* flower extract (1.7 g/kg body weight), equivalent to luteolin (22.8 μmol/kg body weight) and luteolin-7-*O*-glucoside (58.3 μmol/kg body weight). Plasma samples were treated with *H. pomatia* β-glucuronidase type H-5, which has hydrolysis activity against glucuronides, sulfates, and glucoside under the present experimental conditions. Thus, the glycosides and conjugates of luteolin were altered to luteolin aglycone. Data represent means ± SE (n = 4).

of free luteolin in plasma increased rapidly at 0.5 h after administration and reached the peak level at 1 h (0.76 ± 0.27 μM). Thereafter, the level of luteolin decreased at 2 h after administration, but increased again at 6 h (1.79 ± 0.17 μM). Meanwhile, the level of conjugated luteolin and luteolin-7-*O*-glucoside in plasma increased rapidly at 0.5 h after administration and reached the peak level at 1 h (9.88 ± 1.35 μM). Thereafter, the level of conjugated luteolin and luteolin-7-*O*-glucoside decreased but also increased again at 6 h after administration (7.35 ± 1.79 μM).

We presumed that the metabolites of luteolin and luteolin-7-*O*-glucoside included luteolin monoglucuronide, luteolin glucoside glucuronide, luteolin diglucuronide, luteolin glucoside sulfate, and luteolin glucuronide sulfate. The presence of these metabolites was confirmed by LC-MS in a qualitative manner. Figure 2A shows the mass chromatogram and mass spectrum of a rat plasma sample obtained 2 h after oral administration of the *Chrysanthemum* flower extract. Compared with the corresponding standard, luteolin-7-*O*-glucoside was identified in the plasma sample at 6.63 min (m/z 449.1033−449.1123). Meanwhile, as shown in Figure 2B, a prominent peak was observed at 6.73 min (m/z 463.0825−463.0917). This peak was possibly one of the presumed conjugates, luteolin monoglucuronide (MW 462.36). The other presumed conjugated metabolites were below the measurable limits.

Changes in Luteolin, Luteolin-7-*O*-glucoside, and Their Conjugated Metabolites in Caco-2 Cells Treated with the *Chrysanthemum* Flower Extract. To investigate the bioavailability in vitro, the *Chrysanthemum* flower extract was applied to the apical side (0.5 mL) of Caco-2 monolayers at a concentration equivalent to 5.0 nmol of total luteolin. As shown in Figure 3A, luteolin-7-*O*-glucoside decreased in the apical solution with incubation time (luteolin, from 0.50 ± 0.24 to 0.09 ± 0.02 nmol/well; luteolin-7-*O*-glucoside, from 4.22 ± 0.65 to 2.62 ± 0.45 nmol/well). Conjugated forms of luteolin in the apical solution appeared at 0.5 h, and their contents tended to increase in a time-dependent manner (from 1.00 ± 0.82 to 1.67 ± 0.65 nmol/well). As shown in Figure 3B, luteolin and luteolin-7-*O*-glucoside increased in the basolateral solution with incubation time (luteolin-7-*O*-glucoside, from 0.006 ± 0.001 to 0.016 ± 0.003 nmol/well; luteolin conjugates, from 0.013 ± 0.010 to 0.052 ± 0.009 nmol/well). Luteolin aglycone in the basolateral solution appeared at 0.5 h (0.016 ± 0.002 nmol/well) and was increased at 2 h (0.056 ± 0.005 nmol/well).

We presumed that the metabolite profile was the same as that observed in the animal experiments. Thereafter, the basolateral solution after 4.0 h of incubation was applied to LC-MS for qualitative analysis. Luteolin-7-*O*-glucoside was identified in the basolateral solution at 6.27 min (m/z 449.1033−449.1123) as shown in Supplemental Figure 2. Meanwhile, as shown in Supplemental Figure 3, prominent peaks were observed at 6.30, 6.78, and 6.97 min (m/z 463.0825−463.0917) and were possibly those of luteolin monoglucuronide (MW 462.36). Luteolin possesses four hydroxyl groups at the 3′-, 4′-, 5-, and 7-positions, and they are available for glucuronidation. Therefore, four types of luteolin monoglucuronides could possibly exist, and these prominent peaks were thought to be three of these monoglucuronides. Because each authentic sample was not commercially available, it was unclear which position of luteolin is a glucuronidation site at the present time. The other presumed conjugated metabolites were below the measurable limits.

Changes in Luteolin, Luteolin-7-*O*-glucoside, and Their Conjugated Metabolites in Caco-2 Cells Treated with Luteolin and Luteolin-7-*O*-glucoside. After luteolin was applied to the apical side of Caco-2 monolayers at the concentration of 10 μM, equivalent to 5.0 nmol of luteolin, both the apical and basolateral solutions were collected. In the apical solution, luteolin aglycone decreased in a time-dependent manner from 3.38 ± 0.22 to 1.40 ± 0.14 nmol/well, and luteolin conjugates tended to increase fom 1.18 ± 0.60 to 1.36 ± 0.34 nmol/well (Figure 4A). In the basolateral solution, luteolin aglycone appeared at 0.5 h (0.95 ± 0.27 nmol/well) and decreased to 0.62 ± 0.10 nmol/well with incubation time (Figure 4B). After application of luteolin-7-*O*-glucoside to the apical side, the detected luteolin-7-*O*-glucoside in the apical solution decreased to 3.66 ± 0.31 nmol/well at 4 h (Figure 5A). Luteolin aglycone tend to increase from 0.08 ± 0.01 to

DOI: 10.1021/acs.jafc.5b00232
J. Agric. Food Chem. 2015, 63, 7693−7699

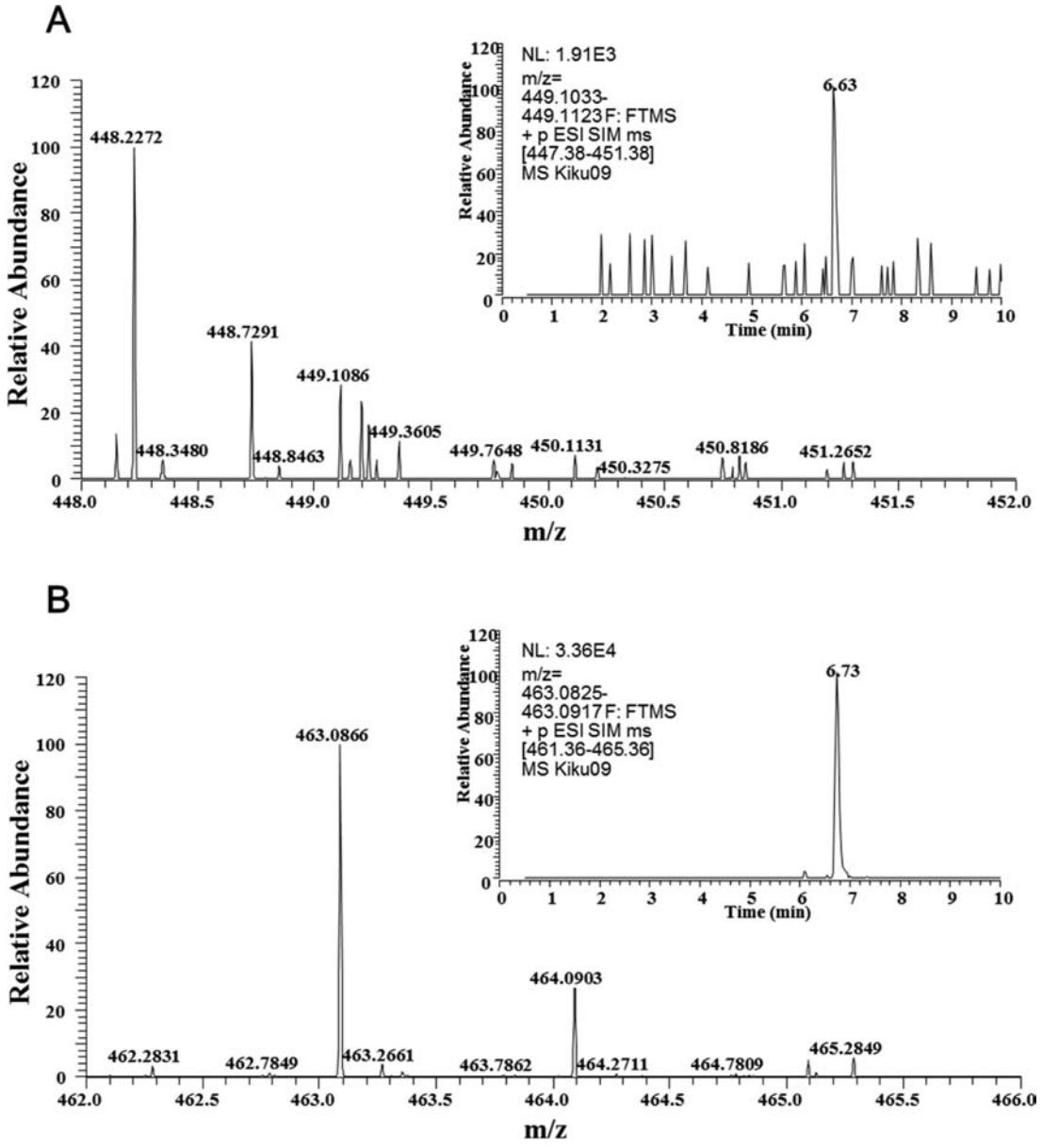

Figure 2. Mass chromatogram and mass spectrum of luteolin-7-*O*-glucoside (A) and luteolin monoglucuronide (B) in plasma from rats 2 h after administration of the *Chrysanthemum* flower extract: (A) mass chromatogram (*m*/*z* 449.1033−449.1123) and mass spectrum (time = 6.63 min); (B) mass chromatogram (*m*/*z* 463.0825−463.0917) and mass spectrum (time = 6.73−6.76 min).

0.12 ± 0.01 nmol/well in a time-dependent manner, and luteolin conjugates were not detected. As shown in Figure 5B, luteolin-7-*O*-glucoside, luteolin, and luteolin conjugates in the basolateral solution tend to increase in a time-dependent manner (luteolin-7-*O*-glucoside, from 0.052 ± 0.014 to 0.125 ± 0.030 nmol/well; luteolin, from 0.006 ± 0.001 to 0.018 ± 0.023 nmol/well; luteolin conjugates, from 0.006 ± 0.014 to 0.018 ± 0.023 nmol/well).

The basolateral solution after 1.0 h of incubation was obtained and applied to LC-MS for qualitative analysis. As shown in Supplemental Figure 4A, luteolin-7-*O*-glucoside was identified in the basolateral solution at 6.09 min (*m*/*z* 449.1033−449.1123). The peak of luteolin monoglucuronide was observed at 6.30 min (*m*/*z* 463.0825−463.0917; Supplemental Figure 4B). The other presumed conjugated metabolites were below the measurable limits.

DISCUSSION

The *Chrysanthemum* flower extract used in the present study contained luteolin and luteolin-7-*O*-*β*-glucoside. The data obtained with rats administered the *Chrysanthemum* flower extract showed that luteolin, luteolin glucuronide, and luteolin-7-*O*-*β*-glucoside were detected in plasma (Figures 1 and 2). Chen et al.[20] reported that luteolin was detected in the deconjugated plasma and urine samples when rats were administered a *Chrysanthemum* flower extract. Li et al.[25] showed that luteolin was detected in human plasma treatment with deconjugating enzyme after administration of a *Chrysanthemum* flower extract. In this study, we find results partly consistent with the knowledge reported previously because luteolin and luteolin glucuronide were detected, and we also newly found that luteolin glucoside can circulate without conjugation.

DOI: 10.1021/acs.jafc.5b00232
J. Agric. Food Chem. 2015, 63, 7693−7699

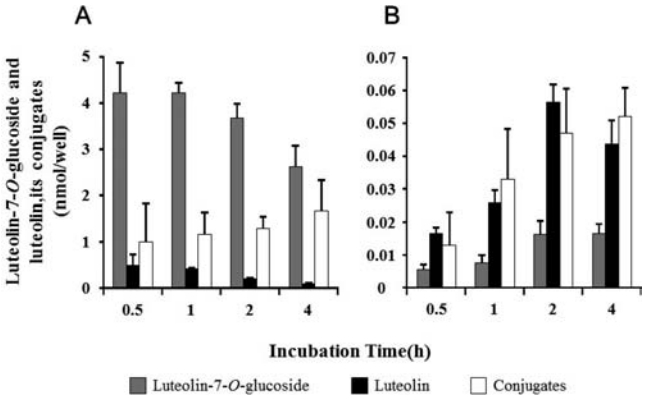

Figure 3. Amounts of luteolin derivatives in culture media from Caco-2 cells treated with the *Chrysanthemum* flower extract. Luteolin-7-*O*-glucoside, luteolin, and its conjugates in the apical solution (A) and basolateral solution (B) of Caco-2 cells treated with the *Chrysanthemum* flower extract, equivalent to luteolin (2.81 μM) and luteolin-7-*O*-glucoside (7.19 μM), are shown. The culture media were treated with limpet β-glucuronidase type L-II, which possesses β-glucuronidase and glucosidase activities in 0.1 M phosphate buffer (pH 5.0), and the conjugates of luteolin were altered to luteolin aglycone. Data represent means ± SD (n = 4−5).

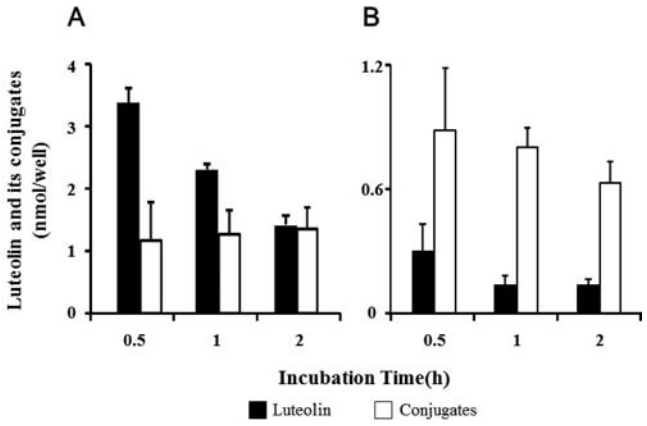

Figure 4. Amounts of luteolin derivatives in culture media from Caco-2 cells treated with luteolin. Luteolin and its conjugates in the apical solution (A) and basolateral solution (B) of Caco-2 cells treated with luteolin (10 μM) are shown. The culture media were treated with β-glucuronidase/sulfatase, and conjugates of luteolin were altered to luteolin aglycone. Data represent means ± SD (n = 5−6).

Glycosylated flavonoids are generally deglycosylated by luminal LPH and/or cleavage within the enterocytes by cytosolic β-glucosidase or bacterial flora in the intestine, followed by diffusion passively across the small intestine brush border.[12−15] According to Shimoi et al.,[26] aglycones of luteolin including the metabolite from the luteolin glycosides were absorbed without any conjugation or converted to glucuronides in the enterocytes of the digestive tract, leading to the appearance of luteolin and glucuronide conjugates in the circulatory system of rats and human. Thus, we showed that luteolin, luteolin glucoside, and luteolin monoglucuronide were detected, and these suggested the possibility that luteolin aglycone and glucoside might be absorbed and circulated with or without conjugation after administration of a *Chrysanthemum* flower extract, partly in agreement with the reported mechanism. Meanwhile, luteolin-7-*O*-glucoside was possibly absorbed also in other mechanisms through SGLT. Yin et al.[27]

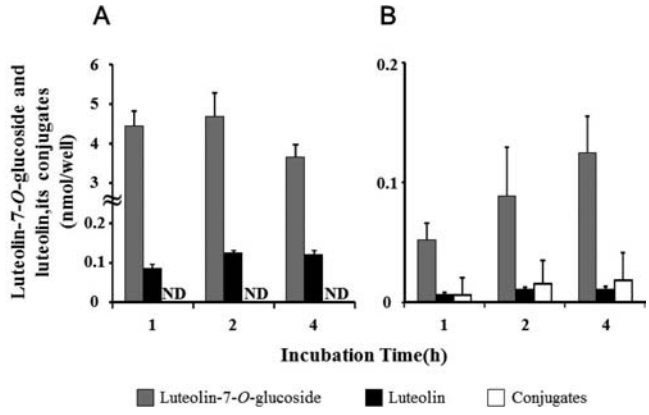

Figure 5. Amounts of luteolin derivatives in culture media from Caco-2 cells treated with luteolin-7-*O*-β-glucoside. Luteolin-7-*O*-glucoside, luteolin, and its conjugates in the apical solution (A) and basolateral solution (B) of Caco-2 cells treated with luteolin-7-*O*-β-glucoside (10 μM) are shown. The culture media were treated with β-glucuronidase/sulfatase, and conjugates of luteolin were altered to luteolin aglycone. Data represent means ± SD (n = 4−5).

investigated the metabolites in rats after administration of an *Ixeris sonchifoliain* (Bge.) extract, containing luteolin glucuronide and luteolin glucoside. They described that the glucuronide and glucoside of luteolin were detected in rat plasma, and a part of the luteolin-7-*O*-β-glucoside, which was not hydrolyzed by LPH and enterobacteria, was possibly absorbed through SGLT1 on the surface of intestinal cells, followed by its appearance in the plasma without conjugation.

As shown in Figure 1, the concentration of luteolin in rat plasma increased to the first and second peak levels at 1 and 6 h (0.76 ± 0.27 and 1.79 ± 0.17 μM), respectively, after dosing with the *Chrysanthemum* flower extract. Conjugated flavonoids are the substrates of efflux transporters (such as MPR2) and can be excreted to the bile and lumen, a phenomenon known as enterohepatic recycling.[20,25,28] This system may entail the reconversion of conjugates that are excreted by efflux transporters with subsequent hydrolysis by intestinal microflora and re-uptake. Otherwise, as described above, flavonoid glycoside is hydrolyzed to its aglycone by LPH in intestinal brush border cells and enterobacteria, and its aglycone is metabolized into conjugates.[12−15] Thus, we further proposed that the conjugates from the glycoside may appear later than those from the aglycone. These results were supported by the case of quercetin glycoside, and they showed that the concentrations of quercetin in rat plasma increased to the first and second peak levels at 30 min and 8 h, respectively, after dosing with αG-rutin, which consists of 4G-α-D-glucopyranosyl rutin and isoquercitrin.[29] However, because the mechanism remains unclear, and to elucidate this phenomena and underlying mechanisms in detail and confirm this speculation, further investigations focusing on kinetic bioavailability are required.

When differentiated Caco-2 cells were treated with the *Chrysanthemum* flower extract, luteolin aglycone, glucoside, and conjugates were detected in basolateral solution (Figure 3) as well as in the plasma from rat after administration of this extract, and luteolin conjugate and glucoside tend to increase in a time-dependent manner in the basolateral solution. Meanwhile, luteolin increased from 0.5 to 2 h there and decreased at 4 h, possibly because luteolin passed from the apical side to the basolateral side through the inside or tight junction of cells, and

DOI: 10.1021/acs.jafc.5b00232
J. Agric. Food Chem. 2015, 63, 7693−7699

luteolin was absorbed in cells again. After the differentiated Caco-2 cells were treated with luteolin-7-*O*-glucoside, luteolin glucoside in the apical solution decreased at 4 h, whereas luteolin aglycone tended to increase in a time-dependent manner and conjugates were not detected (Figure 5A). Previously, Chantret et al.[30] and Faria et al.,[31] reported that LPH was expressed in Caco-2 cells. Thus, we suggested the possibility that a part of the luteolin glucoside was hydrolyzed by LPH and that one part of the aglycone was not absorbed and accumulated in the apical solution, whereas the other part was absorbed into cells and secreted into the basolateral solution. Otherwise, Mukinda et al.[32] showed the possibility that luteolin-7-*O*-glucoside could be detected in the basolateral solution because the glucoside was absorbed through SGLT1 or passed through the intracellular tight junctions; this is in agreememt with the case in rat as described above. Therefore, the aglycone appeared in the basolateral solution (Figure 5B) and also because the glycoside from the absorbent through SGLT1 was hydrolyzed by intracellular glucosidase. This aglycone might be converted to conjugates detected in the basolateral solution. After treatment with luteolin in Caco-2 cells, luteolin was simply absorbed and conjugated as reported as the general mechanisms of flavonoid metabolism.[19] These results suggest that luteolin and luteolin glycoside from the *Chrysanthemum* flower extract might be absorbed and metabolized in the intestine.

Taken together, administration of the *Chrysanthemum* flower extract to rats and treatment-differentiated Caco-2 cells led to the detection of luteolin, luteolin glucoside, and luteolin glucuronide in the plasma and basolateral solution, respectively. Thus, when a *Chrysanthemum* flower extract is administered to humans, it is possible that luteolin glucoside is absorbed in the intestine without conjugation and circulated. Luteolin glucoside as well as luteolin have various beneficial effects.[5,6,30] In addition, as our group[31] showed, glucuronidase is released from stimulated neutrophils or certain injured cells, and subsequently deglucuronidates conjugated luteolin derivatives during inflammation. Thus, administration of the *C. morifolium* flower extract might possibly improve human health, and elucidation of the absorption and metabolism in humans should be clarified to assess the efficacy of this extract.

In conclusion, we showed that luteolin and luteolin monoglucoside were quickly absorbed into the plasma or basolateral solution and existed as the aglycone, monoglucoside, and monoglucuronide after administration of the *C. morifolium* flower extract to rats and differentiated Caco-2 cells. As described above, luteolin, luteolin glucoside, and glucuronide can exert biological functions in the human body.[5,6,33,34] The concentrations of these compounds in plasma also showed a secondary increase, meaning that intake of the *C. morifolium* flower extract led to retention of these compounds in the circulatory system for a long time.

■ ASSOCIATED CONTENT

Supporting Information

Supplemental Figure 1. HPLC chromatogram of the flavonoids. L7G, luteolin-7-*O*-glucoside (11.167 min); IS, internal standard (myricetin; 14.733 min); L, luteolin (17.767 min). Supplemental Figure 2. Mass chromatogram and mass spectrum of luteolin-7-*O*-glucoside in the culture medium of Caco-2 cells treated with the chrysanthemum flower extract. The mass chromatogram (m/z 449.1033−449.1123) (inset) and mass spectrum (time = 6.27 min) of luteolin-7-*O*-glucoside in the basolateral solution of Caco-2 cells treated with the chrysanthemum flower extract for 4 h are shown. Supplemental Figure 3. Mass chromatogram and mass spectrum of luteolin monoglucuronide in the culture medium of Caco-2 cells treated with the chrysanthemum flower extract. The mass chromatogram (m/z 463.0825−463.0917) (inset) and mass spectrum at time = 6.30 min (A), time = 6.78 min (B), and time = 6.97 min (C) of luteolin monoglucuronide in the basolateral solution of Caco-2 cells treated with the chrysanthemum flower extract for 4 h are shown. Supplemental Figure 4. Mass chromatogram and mass spectrum of luteolin-7-*O*-glucoside and luteolin monoglucuronide in culture media from Caco-2 cells treated with luteolin-7-*O*-β-glucoside. The mass chromatogram (m/z 449.1033−449.1123) and mass spectrum (time = 6.09 min) of luteolin-7-*O*-glucoside (A) and the mass chromatogram (m/z 463.0825−463.0917) and mass spectrum (time = 6.30 min) of luteolin monoglucuronide (B) in the basolateral solution of Caco-2 cell treated with luteolin-7-*O*-β-glucoside for 1 h are shown. This material is available free of charge via the Internet at http://pubs.acs.org.

■ AUTHOR INFORMATION

Corresponding Author

*(K.S.) Phone: 81-54-264-5787. Fax: 81-54-264-5787. E-mail: shimoi@u-shizuoka-ken.ac.jp.

Notes

The authors declare no competing financial interest.

■ ACKNOWLEDGMENTS

We thank Nisshin Pharma Inc. (Tokyo, Japan) for providing the *Chrysanthemum morifolium* flowers.

■ REFERENCES

(1) Miyazawa, M.; Hisama, M. Antimutagenic activity of flavonoids from *Chrysanthemum morifolium*. *Biosci., Biotechnol., Biochem.* **2003**, *67*, 2091−2099.

(2) Yoshikawa, M.; Morikawa, T.; Toguchida, I.; Harima, S.; Matsuda, H. Medicinal flowers. II. Inhibitors of nitric oxide production and absolute stereostructures of five new germacrane-type sesquiterpenes, kikkanols D, D monoacetate, E, F, and F monoacetate from the flowers of *Chrysanthemum indicum* L. *Chem. Pharm. Bull.* **2000**, *48*, 651−656.

(3) Ukiya, M.; Akihisa, T.; Yasukawa, K.; Kasahara, Y.; Kimura, Y.; Koike, K.; Nikaido, T.; Takido, M. Constituents of Compositae plants. 2. Triterpene diols, triols, and their 3-O-fatty acid esters from edible *Chrysanthemum* flower extract and their anti-inflammatory effects. *J. Agric. Food Chem.* **2001**, *49*, 3187−3197.

(4) Avula, B.; Wang, Y.-H.; Wang, M.; Avonto, C.; Zhao, J.; Smillie, T. J.; Rua, D.; Khan, I. A. Quantitative determination of phenolic compounds by UHPLC-UV-MS and use of partial least-square discriminant analysis to differentiate chemo-types of *Chamomile/Chrysanthemum* flower heads. *J. Pharm. Biomed. Anal.* **2014**, *88*, 278−288.

(5) Lin, Y.; Shi, R.; Wang, X.; Shen, H.-M. Luteolin, a flavonoid with potential for cancer prevention and therapy. *Curr. Cancer Drug Targets* **2008**, *8*, 634−646.

(6) Seelinger, G.; Merfort, I.; Schempp, C. M. Anti-oxidant, anti-inflammatory and anti-allergic activities of luteolin. *Planta Med.* **2008**, *74*, 1667−1677.

(7) Kuhnle, G.; Spencer, J. P.; Schroeter, H.; Shenoy, B.; Debnam, E. S.; Srai, S. K.; Rice-Evans, C.; Hahn, U. Epicatechin and catechin are O-methylated and glucuronidated in the small intestine. *Biochem. Biophys. Res. Commun.* **2000**, *277*, 507−512.

DOI: 10.1021/acs.jafc.5b00232
J. Agric. Food Chem. 2015, 63, 7693−7699

(8) Spencer, J. P.; Chowrimootoo, G.; Choudhury, R.; Debnam, E. S.; Srai, S. K.; Rice-Evans, C. The small intestine can both absorb and glucuronidate luminal flavonoids. *FEBS Lett.* **1999**, *458*, 224−230.
(9) Gee, J. M.; DuPont, M. S.; Day, A. J.; Plumb, G. W.; Williamson, G.; Johnson, I. T. Intestinal transport of quercetin glycosides in rats involves both deglycosylation and interaction with the hexose transport pathway. *J. Nutr.* **2000**, *130*, 2765−2771.
(10) Crespy, V.; Morand, C.; Besson, C.; Manach, C.; Démigné, C.; Rémésy, C. Comparison of the intestinal absorption of quercetin, phloretin and their glucosides in rats. *J. Nutr.* **2001**, *131*, 2109−2114.
(11) O'Leary, K. A.; Day, A. J.; Needs, P. W.; Mellon, F. A.; O'Brien, N. M.; Williamson, G. Metabolism of quercetin-7- and quercetin-3-glucuronides by an in vitro hepatic model: the role of human beta-glucuronidase, sulfotransferase, catechol-*O*-methyltransferase and multi-resistant protein 2 (MRP2) in flavonoid metabolism. *Biochem. Pharmacol.* **2003**, *65*, 479−491.
(12) Bokkenheuser, V. D.; Shackleton, C. H.; Winter, J. Hydrolysis of dietary flavonoid glycosides by strains of intestinal bacteroides from humans. *Biochem. J.* **1987**, *248*, 953−956.
(13) Day, A. J.; Cañada, F. J.; Díaz, J. C.; Kroon, P. A.; Mclauchlan, R.; Faulds, C. B.; Plumb, G. W.; Morgan, M. R.; Williamson, G. Dietary flavonoid and isoflavone glycosides are hydrolysed by the lactase site of lactase phlorizin hydrolase. *FEBS Lett.* **2000**, *468*, 166−170.
(14) Day, A. J.; Mellon, F.; Barron, D.; Sarrazin, G.; Morgan, M. R.; Williamson, G. Human metabolism of dietary flavonoids: identification of plasma metabolites of quercetin. *Free Radical Res.* **2001**, *35*, 941−952.
(15) Németh, K.; Plumb, G. W.; Berrin, J.-G.; Juge, N.; Jacob, R.; Naim, H. Y.; Williamson, G.; Swallow, D. M.; Kroon, P. A. Deglycosylation by small intestinal epithelial cell β-glucosidases is a critical step in the absorption and metabolism of dietary flavonoid glycosides in humans. *Eur. J. Nutr.* **2003**, *42*, 29−42.
(16) Walgren, R. A.; Lin, J. T.; Kinne, R. K.; Walle, T. Cellular uptake of dietary flavonoid quercetin 4′-β-glucoside by sodium-dependent glucose transporter SGLT1. *J. Pharmacol. Exp. Ther.* **2000**, *294*, 837−843.
(17) Day, A. J.; Gee, J. M.; DuPont, M. S.; Johnson, I. T.; Williamson, G. Absorption of quercetin-3-glucoside and quercetin-4′-glucoside in the rat small intestine: the role of lactase phlorizin hydrolase and the sodium-dependent glucose transporter. *Biochem. Pharmacol.* **2003**, *65*, 1199−1206.
(18) Wolffram, S.; Blöck, M.; Ader, P. Quercetin-3-glucoside is transported by the glucose carrier SGLT1 across the brush border membrane of rat small intestine. *J. Nutr.* **2002**, *132*, 630−635.
(19) Petri, N.; Tannergren, C.; Holst, B.; Mellon, F. A.; Bao, Y.; Plumb, G. W.; Bacon, J.; O'Leary, K. A.; Kroon, P. A.; Knutson, L.; Forsell, P.; Eriksson, T.; Lennernas, H.; Williamson, G. Absorption/metabolism of sulforaphane and quercetin, and regulation of phase II enzymes, in human jejunum in vivo. *Drug Metab. Dispos.* **2003**, *31*, 805−813.
(20) Chen, T.; Li, L.-P.; Lu, X.-Y.; Jiang, H.-D.; Zeng, S. Absorption and excretion of luteolin and apigenin in rats after oral administration of *Chrysanthemum morifolium* extract. *J. Agric. Food Chem.* **2007**, *55*, 273−277.
(21) Lu, X.-Y.; Sun, D.-L.; Chen, Z.-J.; Chen, T.; Li, L.-P.; Xu, Z.-H.; Jiang, H.-D.; Zeng, S. Relative contribution of small and large intestine to deglycosylation and absorption of flavonoids from *Chrysanthemun morifolium* extract. *J. Agric. Food Chem.* **2010**, *58*, 10661−10667.
(22) Li, L.-P.; Jiang, H.-D. Determination and assay validation of luteolin and apigenin in human urine after oral administration of tablet of *Chrysanthemum morifolium* extract by HPLC. *J. Pharm. Biomed. Anal.* **2006**, *41*, 261−265.
(23) Hidalgo, I. J.; Raub, T. J.; Borchardt, R. T. Characterization of the human colon carcinoma cell line (Caco-2) as a model system for intestinal epithelial permeability. *Gastroenterology* **1989**, *96*, 736−749.
(24) Murota, K.; Shimizu, S.; Chujo, H.; Moon, J. H.; Terao, J. Efficiency of absorption and metabolic conversion of quercetin and its glucosides in human intestinal cell line Caco-2. *Arch. Biochem. Biophys.* **2000**, *384*, 391−397.
(25) Li, L.; Jiang, H.; Wu, H.; Zeng, S. Simultaneous determination of luteolin and apigenin in dog plasma by RP-HPLC. *J. Pharm. Biomed. Anal.* **2005**, *37*, 615−620.
(26) Shimoi, K.; Okada, H.; Furugori, M.; Goda, T.; Takase, S.; Suzuki, M.; Hara, Y.; Yamamoto, H.; Kinae, N. Intestinal absorption of luteolin and luteolin 7-*O*-β-glucoside in rats and humans. *FEBS Lett.* **1998**, *438*, 220−224.
(27) Yin, L.; Shi, M.; Sun, Y.; Sun, X.; Meng, H.; Fawcett, J. P.; Yang, Y.; Gu, J. A Liquid chromatography-tandem mass spectrometric method for the simultaneous quantitation of five components of *Ixeris sonchifoliain* (Bge.) Hance in rat plasma and its application to a pharmacokinetic study. *J. Chromatogr. B: Anal. Technol. Biomed. Life Sci.* **2013**, *931*, 12−16.
(28) Ma, Y.; Li, P.; Chen, D.; Fang, T.; Li, H.; Su, W. LC/MS/MS quantitation assay for pharmacokinetics of naringenin and double peaks phenomenon in rats plasma. *Int. J. Pharm.* **2006**, *307*, 292−299.
(29) Shimoi, K.; Yoshizumi, K.; Kido, T.; Usui, Y.; Yumoto, T. Absorption and urinary excretion of quercetin, rutin, and αG-rutin, a water soluble flavonoid, in rats. *J. Agric. Food Chem.* **2003**, *51*, 2785−2789.
(30) Chantret, I.; Barbat, A.; Dussaulx, E.; Brattain, M. G.; Zweibaum, A. Epithelial polarity, villin expression, and enterocytic differentiation of cultured human colon carcinoma cells: a survey of twenty cell lines. *Cancer Res.* **1988**, *48*, 1936−1942.
(31) Faria, A.; Pestana, D.; Azevedo, J.; Martel, F.; de Freitas, V.; Azevedo, I.; Mateus, N.; Calhau, C. Absorption of anthocyanins through intestinal epithelial cells − putative involvement of GLUT2. *Mol. Nutr. Food Res.* **2009**, *53*, 1430−1437.
(32) Mukinda, J. T.; Syce, J. A.; Fisher, D.; Meyer, M. Effect of the plant matrix on the uptake of luteolin derivatives-containing *Artemisia afra* aqueous-extract in Caco-2 cells. *J. Ethnopharmacol.* **2010**, *130*, 439−449.
(33) Chiruvella, K. K.; Mohammed, A.; Dampuri, G.; Ghanta, R. G.; Raghavan, S. C. Phytochemical and antimicrobial studies of methyl angolensate and luteolin-7-*O*-glucoside isolated from callus cultures of *Soymida febrifuga*. *Int. J. Biomed. Sci.* **2007**, *3*, 269−278.
(34) Shimoi, K.; Saka, N.; Nozawa, R.; Sato, M.; Amano, I.; Nakayama, T.; Kinae, N. Deglucuronidation of a flavonoid, luteolin monoglucuronide, during inflammation. *Drug Metab. Dispos.* **2001**, *29*, 1521−1524.

DOI: 10.1021/acs.jafc.5b00232
J. Agric. Food Chem. 2015, 63, 7693−7699

into bile can be hydrolyzed to aglycones by intestinal bacteria, which have β-glucuronidase and arylsulfatase. The phase II conjugation of luteolin has been proven by the treatment of deconjugation with hydrochloric acid or β-glucuronidase/sulfatase. The concentrations of luteolin of samples hydrolyzed by hydrochloric acid and a mixture of β-glucuronidase and sulfatase were much higher than those in untreated samples.[13] The results suggested that sulfuric acid/glucuronic acid conjugates of luteolin are the major metabolites.[14] In addition, *O*-methylation is one of the metabolic pathways for the production of luteolin via catechol-*O*-methyltransferase (COMT) to produce chrysoeriol (3-*O*-methylation of luteolin) and diosmetin (4-*O*-methylation of luteolin).[15,16]

A previous report indicated that apigenin-7-*O*-glucoside can be enzymatically hydrolyzed to produce apigenin through β-glucosidase.[17,18] However, the metabolic mechanism of luteolin and luteolin-7-*O*-glucoside production is not entirely understood. In the present study, we first uncover that the flower of *D. morifolium* is a rich source of luteolin and luteolin-7-*O*-glucoside. To identify these two compounds from ethanolic and water extracts, the techniques of nuclear magnetic resonance (NMR), ^{1}H NMR and ^{13}C NMR, and mass spectrometry were used. Our hypothesis is that the luteolin-7-*O*-glucoside can be enzymatically hydrolyzed to produce luteolin by intestinal β-glucosidase, and then this is absorbed into the blood for circulation. To examine the pharmacokinetic mechanisms of luteolin and luteolin-7-*O*-glucoside, a parallel set of experiments was designed to study the effects of oral and intravenous administration of luteolin (10 mg/kg, iv; 100 mg/kg, po) and luteolin-7-*O*-glucoside (10 mg/kg, iv; 1 g/kg, po).

MATERIALS AND METHODS

Chemicals and Reagents. Luteolin and luteolin-7-*O*-glucoside were purified and isolated from the ethanolic extract of *D. morifolium* in our laboratory. HPLC grade methanol, acetonitrile, orthophosphoric acid (85%), and dimethyl sulfoxide were purchased from E. Merck (Darmstadt, Germany). Apigenin, apigenin-7-*O*-glucoside, and heparin were provided by Sigma-Aldrich Chemicals (St. Louis, MO, USA) and stored at room temperature. Triple-deionized water from Millipore (Bedford, MA, USA) was prepared for all aqueous solutions.

Isolation of Luteolin and Luteolin-7-*O*-glucoside. The flowers of *D. morifolium* were purchased from a drug store in Taipei, Taiwan, and identified by Dr. Lie-Chwen Lin, National Research Institute of Chinese Medicine, Taiwan. A voucher specimen (NHP-00861) has been deposited in the herbarium of the National Research Institute of Chinese Medicine. The dried flowers of *D. morifolium* (5.8 kg) were extracted with ethanol (40 L × 3), and the combined extract was evaporated under a vacuum for the EtOH extract. The ethanolic extract was partitioned successively between H_2O and EtOAc, followed by *n*-BuOH (each 1.5 L × 3). The resulting EtOAc fraction was separated on a Sephadex LH-20 column using MeOH for elution to produce 11 fractions, EA1−EA11. Fraction EA9 (2.4 g) was further purified on a Sephadex LH-20 column using acetone to give luteolin. The *n*-BuOH extract was suspended in $CHCl_3$. Throughout the filtration steps, the precipitates from the suspension were collected. The collected precipitates were dissolved in MeOH and subjected to Sephadex LH-20 with eluent of MeOH to obtain luteolin-7-*O*-glucoside. These isolated compounds were identified by spectral analysis and compared with the published literature.[19]

Spectroscopic Analysis. ^{1}H and ^{13}C NMR spectra were measured with a Varian Unity Inova-500 spectrometer with deuterated solvents (methanol-d_4, DMSO-d_6; Cambridge Isotope Laboratories, Tewksbury, MA, USA) as internal standards. The electrospray ionization technique used in mass spectrometry (ESIMS) was recorded on a Shimadzu LCMS-8030 mass spectrometer (Shimadzu, Kyoto, Japan).

Luteolin: light yellow powder; ^{1}H NMR (CD_3OD, 500 MHz) δ 6.19 (1H, d, *J* = 2.0 Hz, H-6), 6.42 (1H, d, *J* = 2.0 Hz, H-8), 6.52 (1H, s, H-3), 6.88 (1H, d, *J* = 8.5 Hz, H-5′), 7.36 (2H, m, H-2′, H-6′); ^{13}C NMR (CD_3OD, 125 MHz) δ 95.0 (C-8), 100.1 (C-6), 103.9 (C-3), 105.3 (C-10), 114.1 (C-2′), 116.8 (C-5′), 120.3 (C-6′), 123.7 (C-1′), 147.0 (C-3′), 151.0 (C-4′), 159.4 (C-9), 163.2 (C-5), 166.0 (C-2), 166.4 (C-7), 183.9 (C-4); ESIMS *m*/*z* 287 $[M + H]^+$.

Luteolin-7-O-glucoside: yellow powder; ^{1}H NMR (DMSO-d_6, 500 MHz) δ 5.05 (1H, d, *J* = 7.5 Hz, H-1″), 6.43 (1H, d, *J* = 2.0 Hz, H-6), 6.73 (1H, s, H-3), 6.78 (1H, d, *J* = 2.0 Hz, H-8), 6.89 (1H, d, *J* = 8.5 Hz, H-5′), 7.40 (1H, d, *J* = 2.0 Hz, H-2′), 7.43 (1H, dd, *J* = 8.5, 2.0 Hz, H-6′); ^{13}C NMR (DMSO-d_6, 125 MHz) δ 60.8 (C-6″), 69.7 (C-4″), 73.2 (C-2″), 76.5 (C-3″), 77.3 (C-5″), 94.9 (C-8), 99.7 (C-6), 100.1 (C-1″), 103.3 (C-3), 105.5 (C-10), 113.6 (C-2′), 116.1 (C-5′), 119.4 (C-6′), 121.5 (C-1′), 145.9 (C-3′), 150.1 (C-4′), 157.1 (C-9), 161.2 (C-5), 163.1 (C-7), 164.6 (C-2), 182.1 (C-4); ESIMS *m*/*z* 449 $[M + H]^+$.

HPLC-MS/MS Parameters. The HPLC-MS/MS system consisted of an LCMS-8030 triple-quadrupole mass spectrometer (Shimadzu) equipped with an electrospray ionization interface and coupled to a Shimadzu LC-20AD HPLC system. The HPLC system was equipped with two pumps, a system controller, an autosampler, a column oven, and an online degasser. Chromatographic separation of analytes was carried out using an Acquity BEH C_{18} column (100 × 2.1 mm, particle size = 1.7 mm; Waters, Ireland). The column temperature was maintained at 35 °C.

The mobile phase (A, 0.01% formic acid in deionized water; B, 0.01% formic acid in 100% methanol) was eluted at a flow rate of 0.2 mL/min. The gradient started at 50% of mobile phase B and was linearly run to 90% B over 3 min. Subsequently, the eluent composition was maintained for 3 min before it was decreased to 50% of mobile phase B. Then, the gradient was returned to the initial condition (50% B) in 1 min and equilibrated for 1 min. The total run time was 8 min, and the injection volume was 5 μL. The electrospray ion source was operated in positive ionization mode for the two compounds. The other parameters were as follows: DL temperature, 250 °C; heat block temperature, 400 °C; nebulizing gas flow, 3.0 L/min; drying gas flow, 15 L/min; CID gas, 230 kPa.

Animal Experiments. Adult male Sprague−Dawley rats were purchased from the laboratory Animal Center of National Yang-Ming University (Taipei, Taiwan). All animal experiments followed National Yang-Ming University guidelines and procedures. The protocol for this animal study has been approved by the Institutional Animal Care and Use Committee (IACUC, approval no. 990511) by the Institutional Animal Experimentation Committee of National Yang-Ming University.

Before surgery, the rats were allowed free access to food and water at all times. A conscious, freely moving rat model was used to minimize the stress caused by restraint or anesthesia and to simulate the pharmacokinetics in conscious states. During surgery, the rats were anesthetized with pentobarbital (50 mg/kg, ip); for the rats in the intravenous group, a polyethylene tube was implanted in the right jugular vein for blood sampling and in the left femoral vein for drug administration. The tubes crossed the subcutaneous tissue and were fixed at the dorsal neck region. The polyethylene tubes were filled with heparinized saline (20 units/mL) to prevent coagulation. After surgery, the rats were placed in experimental cages for 1 day until recovery from anesthesia. Food was not given for 12 h, and water was available at any time.

HPLC−Photodiode Array System and Sample Preparation. The HPLC system consisted of chromatographic pumps (LC-20AT; Shimadzu), an autosampler (SIL-20AC; Shimadzu), and a photodiode array detector (SPD-M20A; Shimadzu). All analytical samples were separated using a phenyl-hexyl column (150 mm × 4.6 mm i.d.; particle size = 5 μm, Phenomenex Luna, Torrance, CA, USA). The mobile phase of HPLC analysis consisted of two solvent compositions: 0.05 M NaH_2PO_4 and acetonitrile of 80:20, v/v, and 70:30, v/v, for luteolin and luteolin-7-*O*-glucoside, respectively. The pH of 0.05 M NaH_2PO_4 was adjusted to 2.6 by using orthophosphoric acid (85%). The flow rate for the mobile phase was set at 1.0 mL/min. The

DOI: 10.1021/jf505848z
J. Agric. Food Chem. 2015, 63, 7700−7706

temperature in the autosampler was set at 8 °C, the analytical volume was 20 μL of each sample, and the photodiode array detector was monitored at 350 nm.

The resulting plasma sample (100 μL) was mixed with 200 μL of internal standard solution (0.2 μg/mL dissolved in acetonitrile) for protein precipitation. The mixture was centrifuged at 13000*g* for 15 min at 4 °C. The supernatant was evaporated to dryness at 40 °C using a centrifugal evaporator. The dried residue was reconstituted in 100 μL of 20% acetonitrile and filtered by a 0.22 μm filter. An aliquot (20 μL) of the filtrate was applied to the HPLC system for analysis.

Method Validation of Linearity, Accuracy, and Precision. The process of method validation serves to demonstrate that the specific method used for quantification of an analyte in a particular biological sample is reliable and reproducible. Calibration standards were prepared from stock solutions of luteolin or luteolin-7-*O*-glucoside and then added into blank plasma to construct the spiked samples with concentrations of 1, 5, 10, 25, 50, 75, and 100 μg/mL. The standard stock solution of luteolin or luteolin-7-*O*-glucoside (1 mg/mL) was prepared in methanol, and working standard solutions were diluted using 50% (v/v) methanol. These spiked samples were processed as described under Materials and Methods, HPLC–Photodiode Array System and Sample Preparation.

The calibration curve was constructed from the peak area ratio of luteolin and luteolin-7-*O*-glucoside and their corrected internal standards of apigenin and apigenin-7-*O*-glucoside. The coefficient correlation values (r^2) of all calibration curves were required to be at least 0.995.

Six replications of the calibration curve were measured on the same day (intraday) for six continuous days (interday) to evaluate the precision and accuracy of this analytical method. The measure of accuracy describes the proximity of mean results (observed concentration, C_{obs}) from this analytical method to the true concentrations (nominal concentration, C_{nom}). The accuracy could be presented as bias, calculated as follows: bias (%) = $[(C_{obs} - C_{nom})/C_{nom}] \times 100$. The measure of precision represents the closeness of each individual analytical result. The precision, which could be quantified as relative standard deviation (RSD), was calculated as follows: RSD (%) = [standard deviation (SD)/C_{obs}] × 100.

The mean values for the accuracy and the precision must be within 15% of the actual value, except at the LLOQ, where it must not exceed the value by >20%. The method validation for this study was performed according to the guidance given by the U.S. Food and Drug Administration.[20]

Drug Administration. *Oral Administration of Luteolin or Luteolin-7-O-glucoside.* Pentobarbital sodium solution (50 mg/kg) was used to anesthetize rats via intraperitoneal administration. Surgical sites were shaved and cleaned with 70% ethanol solution. Then, the right jugular vein was catheterized with polyethylene tubing for blood sampling. The catheter was guided under the skin to the dorsal neck region and fixed.[21] After surgery, the rats were allowed to recover in a clean cage for at least 24 h before drug administration.

After the stabilization period, luteolin and luteolin-7-*O*-glucoside dissolved in dimethyl sulfoxide/water (1:1) were orally administered to the rats (n = 6) at doses of 100 mg/kg and 1 g/kg, respectively. A 250 μL blood sample was collected from the jugular vein at 0, 5, 15, 30, 60, 90, 120, 180, 240, and 360 min after drug administration. Blood samples were centrifuged at 8000*g* for 10 min at 4 °C to obtain plasma, and the resulting plasma was stored at −20 °C prior to analysis.

Pharmacokinetic Analysis and Statistics. Pharmacokinetic parameters, including maximum plasma concentration (C_{max}), time to reach the maximum concentrations (t_{max}), half-life ($t_{1/2}$), area under concentration–time curve (AUC), and oral clearance (CL), were estimated by a noncompartmental analysis using the pharmacokinetic program WinNonlin Standard Edition version 1.1 (Scientific Consulting, Apex, NC, USA). The bioavailability was calculated according to the following equation: bioavailability (%F) = $(AUC_{po}/dose_{po})/(AUC_{iv}/dose_{iv}) \times 100\%$. All results were expressed as the average mean ± standard deviation (SD). The statistical analyses were calculated using SPSS version 10.0 (SPSS, Chicago, IL, USA). Student's t test was used to compare the differences between groups, and a value of $P < 0.05$ was considered statistically significant.

RESULTS AND DISCUSSION

Isolation and Identification of Luteolin and Luteolin-7-*O*-glucoside. The luteolin-7-*O*-glucoside content was 4.19 and 6.56% in ethanolic and water extracts, respectively. However, the luteolin content was 0.19% in the ethanolic extract, and luteolin was not detected in the water extract. Luteolin was obtained as a light yellow powder. The ^{1}H spectrum of luteolin revealed the presence of a pair of meta-coupled aromatic protons (δ_H 6.19/6.42), an aromatic singlet (δ_H 6.52), and ABC-coupled aromatic protons (δ_H 6.88/7.35/7.36). In combination with the ^{13}C NMR data, which showed signals for a carbonyl group at δ_C 183.9 (C-4), six oxygenated quaternary carbons (δ_C 147.0, 151.0, 159.4, 163.2, 166.0, and 166.4), two sp^2 quaternary carbons (δ_C 105.3 and 123.7), and six sp^2 tertiary carbons (δ_C 95.0, 100.1, 103.9, 114.1, 116.8, and 120.3), and the ESIMS data, we were able to identify the molecules of luteolin[19] (Supporting Information, Figures S1 and S2).

When the ^{1}H spectrum of luteolin-7-*O*-glucoside was compared with that of luteolin, a difference was observed in the aliphatic region where there was an additional glucosyl moiety (δ 5.05/3.17–3.70) in luteolin-7-*O*-glucoside. This region was also associated with the ^{13}C NMR signals of luteolin-7-*O*-glucoside at δ_C 60.8, 69.7, 73.2, 76.5, 77.3, and 100.1 (Supporting Information, Figures S3 and S4). The ESIMS revealed the molecular ion at m/z 447 $[M - H]^-$, which is consistent with the molecular formula $C_{21}H_{20}O_{11}$. Upon further comparison with our previous study,[19] we were able to confirm the chemical structures of luteolin-7-*O*-glucoside and luteolin (Figure 1 and Figure S5).

Optimization of HPLC–Photodiode Array Conditions. An internal standard is a compound that can be used to correct for aliquot taking, instrumental performance, and, in the present study, should be similar in chemical structure to luteolin and luteolin-7-*O*-glucoside. On the basis of U.S. FDA guidelines,[20] an internal standard was used to facilitate quantification of the target analyte(s) during the development of the analysis method. To select a suitable internal standard, we surveyed PubMed and searched the available chemicals in our laboratory, which included apigenin and apigenin-7-*O*-glucoside, baicalein and baicalin, naringenin and naringin, quercetin and rutin, genistein and genistein, daidzein and daidzein, and the flavonoids and their correlated glycosides. Among the compounds tested, apigenin and apigenin-7-*O*-glucoside were found to be the most appropriate internal standards for correlated luteolin and luteolin-7-*O*-glucoside. Apigenin and apigenin-7-*O*-glucoside exhibited an appropriate retention time of within 15 min, a maximum absorbance at the UV wavelength of 350 nm, and a well-resolved peak shape, and they were previously reported to be highly stable.[22]

To optimize efficiency and resolution for liquid chromatography of the compound tested, the stationary phase of reversed C8, C18, and phenyl-hexyl column was examined. Successful separation and quantification of luteolin and luteolin-7-*O*-glucoside from blood, without other endogenous interfering peaks, was achieved using a phenyl-hexyl column in an optimal mobile phase containing 0.05 M NaH_2PO_4 and acetonitrile of 80:20, v/v, and 70:30, v/v, for luteolin and luteolin-7-*O*-glucoside, respectively. The pH value of the mobile phase plays an important role. After replication of the tests, it was found

DOI: 10.1021/jf505848z
J. Agric. Food Chem. 2015, 63, 7700–7706

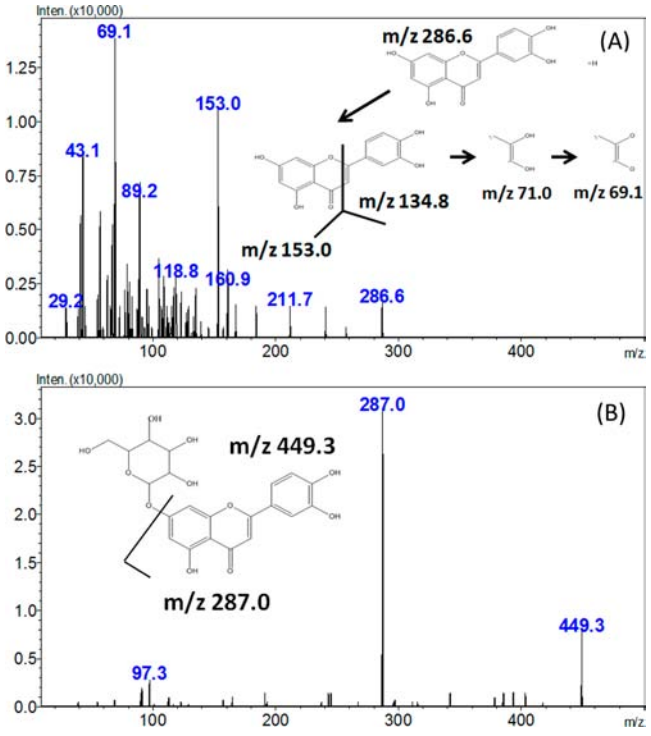

Figure 1. Chemical structures of (A) luteolin and (B) luteolin-7-*O*-glucoside and mass spectra of the analytes and their product ions in UPLC-MS/MS with electrospray in positive ion mode. The mass transitions of luteolin and luteolin-7-*O*-glucoside were m/z 286.6 → 69.1 and 449.3 → 287.0, respectively.

that the optimal pH value of the phosphate buffers (pH 2.6) could reduce the peak tailing of luteolin, luteolin-7-*O*-glucoside, and the internal standards without significant endogenous interference peaks. These results show that the analytical method used here is valid and reproducible. Our results are consistent with a previous study that the peak tailing of jaceosidin was severe in nonpolar columns.[23]

The analytical method established in this study was validated according to U.S. Food and Drug Administration guidelines for validation of bioanalytical methods.[20] Typical chromatograms of luteolin-7-*O*-glucoside and apigenin-7-*O*-glucoside (internal standard) in rat plasma after luteolin-7-*O*-glucoside administration (1 g/kg, po) are shown in Figure 2.

Validation of HPLC Assay. *Linearity, Accuracy, and Precision.* To evaluate linearity, the concentration of the calibration curve was derived from the peak area ratio of luteolin and luteolin-7-*O*-glucoside and their correlated internal standards, apigenin and apigenin-7-*O*-glucoside. The experimental results showed that the linearity range of luteolin and luteolin-7-*O*-glucoside in rat plasma was 0.125−2 μg/mL, and all of the coefficient correlation values (r^2) were >0.995.

The intraday and interday assays were carried out to evaluate the accuracy (as percent bias) and precision (as percent RSD) of luteolin and luteolin-7-*O*-glucoside (Supporting Information, Tables S1 and S2, n = 6). All of the bias and RSD values were <20%, which is the maximum acceptable value. These results revealed that this analytical method is reproducible.[20]

Pharmacokinetics of Luteolin. To describe the preclinical pharmacokinetics of luteolin, a single intravenous bolus of luteolin was administered via the femoral vein at a dose of 10 mg/kg, followed by a series of blood samplings at the designated time points of 5, 15, 30, 60, 90, 120, 180, 240, and 360 min after drug administration. The pharmacokinetic curves representing the changes in luteolin concentrations in the plasma across time are shown in Figure 3. The results suggested that the plasma concentration of luteolin was rapidly distributed and slowly decayed after luteolin administration in rats. The maximum concentration (C_{max}) of luteolin was 7.47 ± 3.78 μg/mL, and this concentration was observed at the first

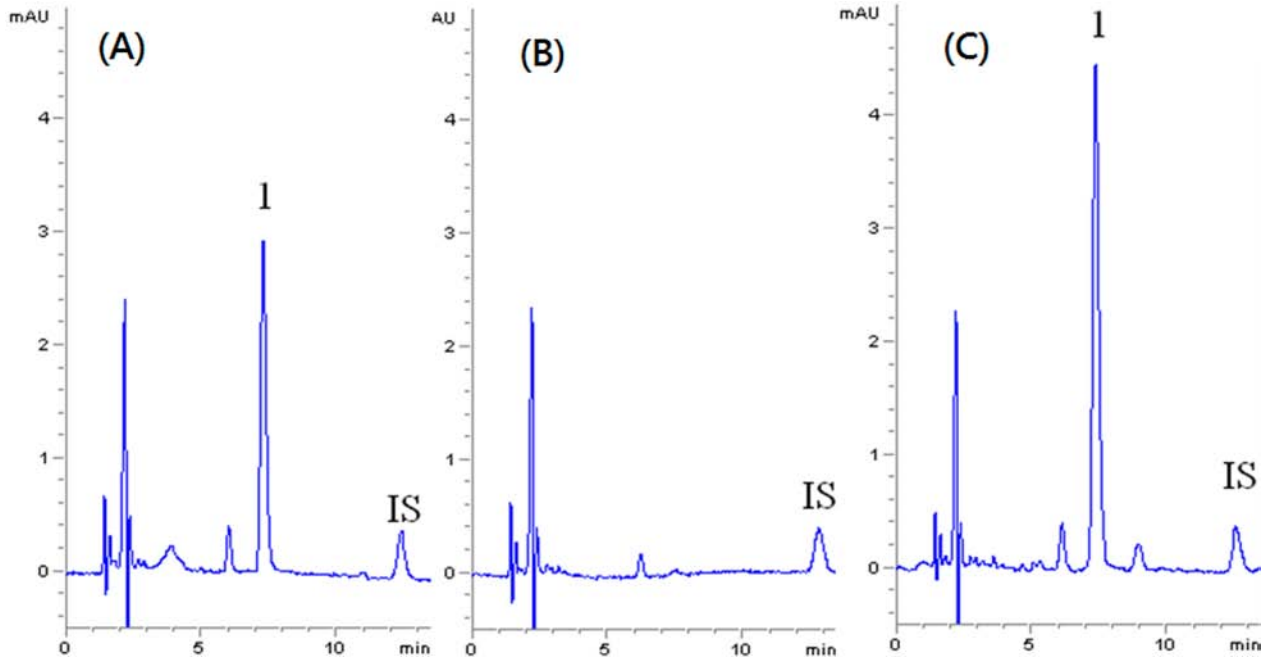

Figure 2. HPLC chromatograms of luteolin-7-*O*-glucoside in rat plasma for po administration of luteolin-7-*O*-glucoside: (A) standard luteolin-7-*O*-glucoside (2.5 μg/mL) and apigenin-*O*-glucoside (0.2 μg/mL); (B) blank plasma; (C) luteolin-7-*O*-glucoside (4.67 μg/mL) after po administration at 60 min. Peaks: 1, luteolin-7-*O*-glucoside; IS, internal standard (apigenin-7-*O*-glucoside).

DOI: 10.1021/jf505848z
J. Agric. Food Chem. 2015, 63, 7700−7706

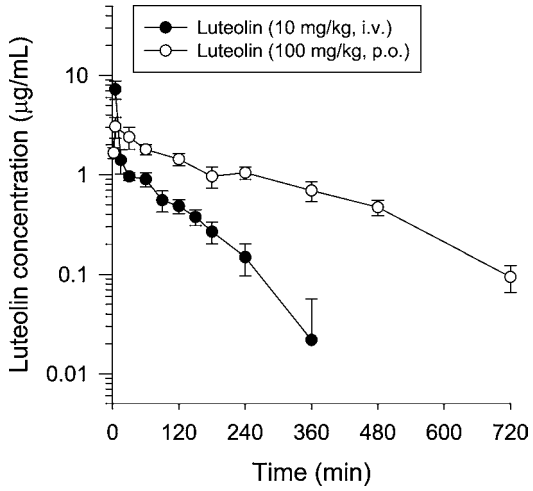

Figure 3. Concentration versus time profiles of luteolin in rat plasma after luteolin administration (10 mg/kg, iv; 100 mg/kg, po). Data are presented as the mean ± standard error, n = 6, for each group.

collected time point of 5 min after luteolin administration (10 mg/kg, iv). After this time point, the concentration of luteolin continually decreased up until the time point of 360 min after luteolin administration, at which time the concentration was undetectable.

When luteolin was given orally, the C_{max} of luteolin was 3.07 ± 0.72 μg/mL, and this concentration was observed at 5 min after luteolin administration (100 mg/kg, po). However, the luteolin concentration slowly decreased after oral administration, and the concentration of luteolin could still be detected up to 12 h after oral administration. The elimination half-lives of luteolin were 78 ± 14 and 132 ± 12 min for intravenous and oral administrations, respectively. The oral bioavailability of luteolin was 26 ± 6% on the basis of the doses used and the experimental animal model described above.

The pharmacokinetic profiles of the concentrations of luteolin in rat plasma versus time after oral administration of luteolin (10 mg/kg, iv; 100 mg/kg, po) are shown in Figure 3. There are multiple peaks at a t_{max} of 0.5 and at 4 h after oral administration of luteolin (100 mg/kg, po). This observance of multiple peaks suggested that enterohepatic circulation is a general phenomenon for the flavonoids,[24] such as luteolin and apigenin,[13] naringenin,[24] baicalein,[25] quercetin,[26] genistein,[27] and daidzein.[28] The concentration plateau appears at 1 and 4 h after luteolin intravenous and oral administration, respectively (Figure 3). This phenomenon reflects that the elimination half-time of luteolin by oral administration, 132 ± 12 h (Table 1), is relatively longer than it is by the route of intravenous

Table 1. Pharmacokinetic Parameters of Luteolin (10 mg/kg, iv; and 100 mg/kg, po)[a]

parameter	luteolin (10 mg/kg, iv)	luteolin (100 mg/kg, po)
C_{max} (μg/mL)	7.47 ± 3.78	3.07 ± 0.72
t_{max} (min)		290 ± 94
AUC (μg min/mL)	261 ± 33	611 ± 89
$t_{1/2}$ (min)	78 ± 14	132 ± 12
MRT (min)	66 ± 8	209 ± 12
CL (mL/min/kg)	41.3 ± 4.87	181 ± 25.5
oral bioavailability (%)		26 ± 6

[a]Data are presented as the mean ± SE (n = 6).

administration, 78 ± 14 h. Crespy et al. reported that the liver is the active site for the methylation of luteolin for additional biliary excretion and that a transporter system may be involved.[29] Then, the phase II methylated luteolins, chrysoeriol and diosmetin, have been identified, which was proved by the treatment of catechol-*O*-methyltransferase inhibitor, entacapone, in rat.[30,31] In the present study, we did not measure the precise nature of the metabolites from the hepatic conjugation. Consistently, we found that the multiple peaks may support the fate of enterohepatic circulation of luteolin.

With regard to the phase II metabolic mechanism of luteolin, we did not find the chromatographic peaks of metabolites in our analytical system. Luteolin can be found after luteolin-7-*O*-glucoside administration, but luteolin-7-*O*-glucoside was undetectable after luteolin administration (Figures 3 and 4).

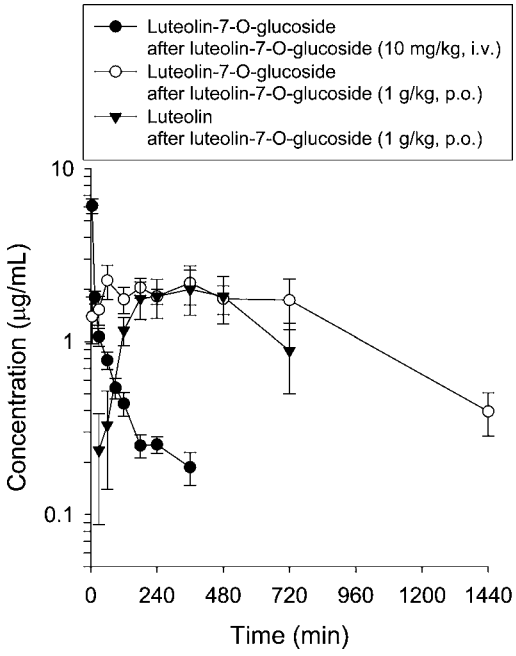

Figure 4. Concentration versus time profiles of luteolin-7-*O*-glucoside and luteolin in rat plasma after luteolin-7-*O*-glucoside administration (10 mg/kg, iv; 1 g/kg, po). Data are presented as the mean ± standard error, n = 6.

However, it has been shown that luteolin mainly undergoes conjugation by uridine diphosphoglucuronosyltransferases (UGTs), sulfotransferases (SULTs),[32] and COMT in vivo.[15,16] Because intestinal and hepatic first-pass effects are widely acknowledged to be responsible for low oral bioavailabilities of flavonoids, the oral bioavailabilities of luteolin and luteolin-7-*O*-glucoside were measured and found to be 26 ± 6 and 10 ± 2%, respectively (Tables 1 and 2).

Pharmacokinetics of Luteolin-7-O-glucoside. Luteolin-7-*O*-glucoside was hydrolyzed to luteolin in the gastrointestinal tract and absorbed into the systemic circulation (Figure 4). The AUCs of luteolin-7-*O*-glucoside were 229 ± 15 and 2109 ± 350 (min μg/mL) after administration of 10 mg/kg luteolin-7-*O*-glucoside, iv, and 1 g/kg, luteolin-7-*O*-glucoside, po, respectively (Figure 4). The oral bioavailability of luteolin-7-*O*-glucoside was approximately 10 ± 2%. In the group administered luteolin-7-*O*-glucoside orally, a biotransformed luteolin product was detected, but it was not detected in the

DOI: 10.1021/jf505848z
J. Agric. Food Chem. 2015, 63, 7700−7706

Table 2. Pharmacokinetic Parameters of Luteolin-7-*O*-glucoside (10 mg/kg, iv; and 1 g/kg, po)[a]

parameter	luteolin-7-*O*-glucoside (10 mg/kg, iv)	luteolin-7-*O*-glucoside (1 g/kg, po)	luteolin
C_{max} (μg/mL)	6.09 ± 0.59	3.04 ± 0.76	2.45 ± 0.55
t_{max} (min)		290 ± 94	280 ± 57
AUC (μg min/mL)	229 ± 15	2109 ± 350	1028 ± 253
$t_{1/2}$ (min)	87 ± 7	685 ± 193	
MRT (min)	84 ± 6	527 ± 25	356 ± 32
CL (mL/min/kg)	38.5 ± 2.7	540.2 ± 84.1	
oral bioavailability (%)		10 ± 2	

[a]Data are presented as the mean ± SE (n = 6).

group administered luteolin-7-*O*-glucoside intravenously. These results demonstrate that luteolin 7-*O*-β-glucoside was not readily absorbed alone and that luteolin glucuronides were detected after intestinal absorption.

To clarify the luteolin is the hydrolysis product of luteolin-7-*O*-glucoside, luteolin-7-*O*-glucoside was administered (1 g/kg, po). The concentration versus time curve showed that luteolin was detected in rat plasma after administration of luteolin-7-*O*-glucoside (1 g/kg, po) (Figure 4). It has been reported that intestinal bacteria can hydrolyze glucosides of flavonoids and produce aglycones.[33] Our data demonstrated that both luteolin and luteolin-7-*O*-glucoside can be detected after luteolin-7-*O*-glucoside administration (1 g/kg, po). The oral bioavailability of luteolin-7-*O*-glucoside was 10 ± 2% (Table 2), which suggested that luteolin-7-*O*-glucoside may first be hydrolyzed to luteolin by the bacteria that are present on the surface of the intestinal mucosa. β-Glycosidase is an enzyme that rapidly hydrolyzes glucosides, such as quercetin 3-*O*-glucoside, which had the highest percent of hydrolysis.[34] This phenomenon is consistent with our data that luteolin can be detected at the first collected time point of 5 min after luteolin-7-*O*-glucoside administration (1 g/kg, po). The maximum concentrations (C_{max}) of luteolin and luteolin-7-*O*-glucoside were found at 3.04 ± 0.76 and 2.45 ± 0.55 min after luteolin-7-*O*-glucoside administration (1 g/kg, po).

In conclusion, we first identified that the flower of *D. morifolium* Ramat Tzvel is a highly rich source of luteolin and luteolin-7-*O*-glucoside. We determined that the luteolin-7-*O*-glucoside contents in ethanolic and water extracts were 4.19 and 6.56%, respectively. However, the luteolin content was 0.19% in the ethanolic extract, and luteolin was not detected in the water extract. The oral bioavailability of luteolin was approximately 26 ± 6% after luteolin administration (10 mg/kg, i.v. and 100 mg/kg, p.o.). The oral bioavailability of luteolin-7-*O*-glucoside was approximately 10 ± 2% after luteolin-7-*O*-glucoside administration (10 mg/kg, iv; and 1 g/kg, po). Luteolin is one of the major metabolites present after oral administration of luteolin-7-*O*-glucoside, and we detected a biotransformed luteolin product, although this biotransformed product was not detected in the intravenous administration group. The transformation ratio (the AUC ratio of metabolite/parent compound) of luteolin to luteolin-7-*O*-glucoside was approximately 48.78 ± 0.12%. These results demonstrate that luteolin-7-*O*-glucoside is primarily hydrolyzed to luteolin in the gastrointestinal tract and absorbed into the systemic circulation. These results also imply that people who drink chamomile tea can also retain the benefits from luteolin, due to high transformation ratio of luteolin to luteolin-7-*O*-glucoside.

■ ASSOCIATED CONTENT

Supporting Information

Tables S1 and S2 and Figures S1−S5. This material is available free of charge via the Internet at http://pubs.acs.org.

■ AUTHOR INFORMATION

Corresponding Author

*(T.-H.T.) Mail: Institute of Traditional Medicine, School of Medicine, National Yang-Ming University, 155 Li-Nong Street Section 2, Taipei 112, Taiwan. Fax: (886-2) 2822 5044. Phone: (886-2) 2826 7115. E-mail: thtsai@ym.edu.tw.

Funding

This work was supported in part by research grants from the National Science Council (NSC102-2113-M-010-001-MY3) Taiwan and TCH 103-02 and TCH 10301-62-021 from Taipei City Hospital, Taipei, Taiwan.

Notes

The authors declare no competing financial interest.

■ REFERENCES

(1) Shim, S. Y.; Park, J. R.; Byun, D. S. 6-Methoxyluteolin from *Chrysanthemum zawadskii* var. *latilobum* suppresses histamine release and calcium influx via down-regulation of FcεRI α chain expression. *J. Microbiol. Biotechnol.* **2012**, *22* (5), 622−627.

(2) Chatterjee, A.; Sarkar, S.; Saha, S. K. Acacetin 7-*O*-β-D-galactopyranoside from *Chrysanthemum indicum*. *Phytochemistry* **1981**, *20*, 1760−1761.

(3) Beninger, C. W.; Abou-Zaid, M. M.; Kistner, A. L. E.; Hallett, R. H.; Iqbal, M. J.; Grodzinski, B.; Hall, J. C. A flavanone and two phenolic acids from *Chrysanthemum morifolium* with phytoxic and insect growth regulating activity. *J. Chem. Ecol.* **2003**, *30*, 579−596.

(4) Shimoi, K.; Masuda, S.; Furugori, M.; Esaki, S.; Kinae, N. Radioprotective effect of antioxidative flavonoids in γ-ray irradiated mice. *Carcinogenesis* **1994**, *15*, 2669−2672.

(5) Seelinger, G.; Merfort, I.; Schempp, C. M. Anti-oxidant, anti-inflammatory and anti-allergic activities of luteolin. *Planta Med.* **2008**, *74* (14), 1667−1677.

(6) Yasukawa, K.; Takido, M.; Takeuchi, M.; Nakagawa, S. Effect of chemical constituents from plants on 12-*O*-tetradecanoylphorbol-13-acetate-induced inflammation in mice. *Chem. Pharm. Bull.* **1989**, *37*, 1071−1073.

(7) Majumdar, D.; Jung, K. H.; Zhang, H.; Nannapaneni, S.; Wang, X.; Amin, A. R.; Chen, Z.; Chen, Z. G.; Shin, D. M. Luteolin nanoparticle in chemoprevention: in vitro and in vivo anticancer activity. *Cancer Prev. Res. (Phila.)* **2014**, *7* (1), 65−73.

(8) Yamamoto, H.; Sakakibara, J.; Nagatsu, A.; Sekiya, K. Inhibitors of arachidonate lipoxygenase from defatted perilla seed. *J. Agric. Food Chem.* **1998**, *46*, 862−865.

(9) Ferriola, P. C.; Cody, V.; Middleton, E., Jr. Protein kinase C inhibition by plant flavonoids. Kinetic mechanisms and structure-activity relationships. *Biochem. Pharmacol.* **1989**, *38*, 1617−1624.

(10) Nekohashi, M.; Ogawa, M.; Ogihara, T.; Nakazawa, K.; Kato, H.; Misaka, T.; Abe, K.; Kobayashi, S. Luteolin and quercetin affect the cholesterol absorption mediated by epithelial cholesterol transporter Niemann−Pick C1-like 1 in Caco-2 cells and rats. *PLoS One* **2014**, *9* (5), No. e97901.

(11) Sadzuka, Y.; Sugiyama, T.; Shimoi, K.; Kinae, N.; Hirota, S. Protective effect of flavonoids on doxorubicin-induced cardiotoxicity. *Toxicol. Lett.* **1997**, *92*, 1−7.

(12) Manach, C.; Morand, C.; Crespy, V.; Demigne, C.; Texier, O.; Regerat, F.; Remesy, C. Quercetin is recovered in human plasma as conjugated derivatives which retain antioxidant properties. *FEBS Lett.* **1998**, *426*, 331−336.

(13) Chen, T.; Li, L. P.; Lu, X. Y.; Jiang, H. D.; Zeng, S. Absorption and excretion of luteolin and apigenin in rats after oral administration

DOI: 10.1021/jf505848z
J. Agric. Food Chem. 2015, 63, 7700−7706

of *Chrysanthemum morifolium* extract. *J. Agric. Food Chem.* **2007**, *55*, 273−277.
(14) Li, L. P.; Jiang, H. D. Determination and assay validation of luteolin and apigenin in human urine after oral administration of tablet of *Chrysanthemum morifolium* extract by HPLC. *J. Pharm. Biomed. Anal* **2006**, *41*, 261−265.
(15) Chen, Z.; Chen, M.; Pan, H.; Sun, S.; Li, L.; Zeng, S.; Jiang, H. Role of catechol-*O*-methyltransferase in the disposition of luteolin in rats. *Drug Metab. Dispos.* **2011**, *39*, 667−674.
(16) Chen, Z.; Kong, S.; Song, F.; Li, L.; Jiang, H. Pharmacokinetic study of luteolin, apigenin, chrysoeriol and diosmetin after oral administration of *Flos Chrysanthemi* extract in rats. *Fitoterapia* **2012**, *83*, 1616−1622.
(17) Németh, K.; Plumb, G. W.; Berrin, J. G.; Juge, N.; Jacob, R.; Naim, H. Y.; Williamson, G.; Swallow, D. M.; Kroon, P. A. Deglycosylation by small intestinal epithelial cell β-glucosidases is a critical step in the absorption and metabolism of dietary flavonoid glycosides in humans. *Eur. J. Nutr.* **2003**, *42*, 29−42.
(18) Hostetler, G. L.; Ried, K. M.; Schwartz, S. J. Effects of food formulation and thermal processing on flavones in celery and chamomile. *Food Chem.* **2013**, *141* (2), 1406−1411.
(19) Lin, L. C.; Chou, C. J. Chemical constituents from *Pterocypsela formosana*. *Chin. Pharm. J.* **2002**, *54*, 181−185.
(20) U.S. FDA. *Guidance for Industry, Bioanalytical Method Validation*; U.S. Department of Health and Human Services, Food and Drug Administration Center for Drug Evaluation and Research (CDER): Washington, DC, USA, 2001.
(21) Thrivikraman, K. V.; Huot, R. L.; Plotsky, P. M. Jugular vein catheterization for repeated blood sampling in the unrestrained conscious rat. *Brain Res. Protoc.* **2002**, *10*, 84−94.
(22) Plazonić, A.; Bucar, F.; Males, Z.; Mornar, A.; Nigović, B.; Kujundzić, N. Identification and quantification of flavonoids and phenolic acids in burr parsley (*Caucalis platycarpos* L.), using high-performance liquid chromatography with diode array detection and electrospray ionization mass spectrometry. *Molecules* **2009**, *14* (7), 2466−2490.
(23) Song, W. Y.; Kim, N. J.; Kim, S. Y.; Lee, H. S. Liquid chromatography-tandem mass spectrometry for the determination of jaceosidin in rat plasma. *J. Pharm. Biomed Anal.* **2009**, *49* (2), 381−386.
(24) Ma, Y.; Li, P.; Chen, D.; Fang, T.; Li, H.; Su, W. LC/MS/MS quantitation assay for pharmacokinetics of naringenin and double peaks phenomenon in rats plasma. *Int. J. Pharm.* **2006**, *307* (2), 292−299 (Epub Nov 14, 2005).
(25) Zhang, L.; Lin, G.; Zuo, Z. Involvement of UDP-glucuronosyltransferases in the extensive liver and intestinal first-pass metabolism of flavonoid baicalein. *Pharm. Res.* **2007**, *24*, 81−89.
(26) Chen, X.; Yin, O. Q.; Zuo, Z.; Chow, M. S. Pharmacokinetics and modeling of quercetin and metabolites. *Pharm. Res.* **2005**, *22* (6), 892−901.
(27) Sfakianos, J.; Coward, L.; Kirk, M.; Barnes, S. Intestinal uptake and biliary excretion of the isoflavone genistein in rats. *J. Nutr.* **1997**, *127* (7), 1260−1268.
(28) Blaut, M.; Schoefer, L.; Braune, A. Transformation of flavonoids by intestinal microorganisms. *Int. J. Vitam. Nutr. Res.* **2003**, *73* (2), 79−87.
(29) Crespy, V.; Morand, C.; Besson, C.; Cotelle, N.; Vézin, H.; Demigné, C.; Rémésy, C. The splanchnic metabolism of flavonoids highly differed according to the nature of the compound. *Am. J. Physiol.* **2003**, *284* (6), G980−G988.
(30) Chen, Z.; Chen, M.; Pan, H.; Sun, S.; Li, L.; Zeng, S.; Jiang, H. Role of catechol-*O*-methyltansferase in the disposition of luteolin in rats. *Drug Metab. Dispos.* **2011**, *39*, 667−674.
(31) Chen, Z.; Kong, S.; Song, F.; Li, L.; Jiang, H. Pharmacokinetic study of luteolin, agigenin, chrysoeriol and diosmetin after oral administration of *Flos Chrysanthemi* extracted in rats. *Fitoterapia* **2012**, *83*, 1616−1622.
(32) Shimoi, K.; Okada, H.; Furugori, M.; Goda, T.; Takase, S.; Suzuki, M.; Hara, Y.; Yamamoto, H.; Kinae, N. Intestinal absorption of luteolin and luteolin 7-*O*-glucoside in rats and humans. *FEBS Lett.* **1998**, *438*, 220−224.
(33) Hawksworth, G.; Drasar, B. S.; Hill, M. J. Intestinal bacteria and the hydrolysis of glycosidic bonds. *J. Med. Microbiol.* **1971**, *4*, 451−459.
(34) Zhang, C. P.; Liu, G.; Hu, F. L. Hydrolysis of flavonoid glycosides by propolis β-glycosidase. *Nat. Prod Res.* **2012**, *26* (3), 270−273.

DOI: 10.1021/jf505848z
J. Agric. Food Chem. 2015, 63, 7700−7706

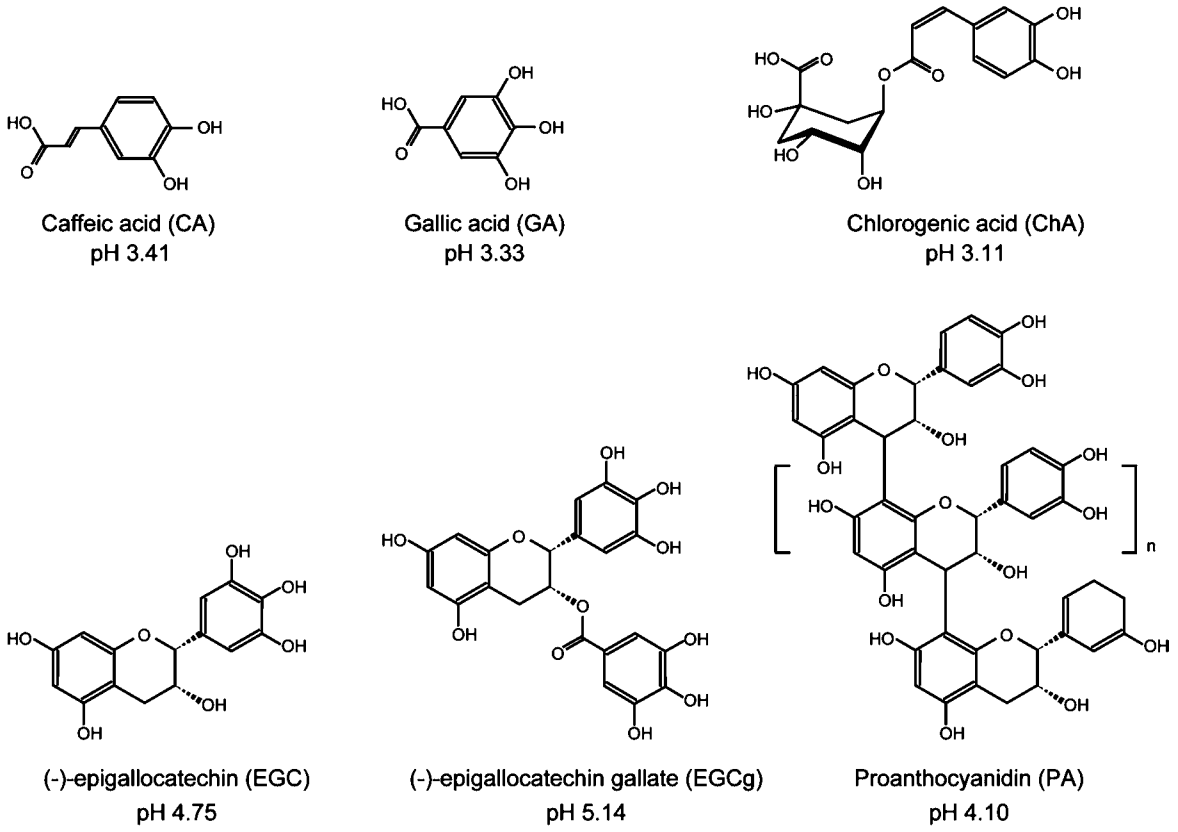

Figure 1. Structures of polyphenols used in the present study.

(Osaka, Japan); proanthocyanidin (PA; Leucoselect) from Indena (Milano, Italy); 5,5-dimethyl-1-pyrroline *N*-oxide (DMPO) from Labotec (Tokyo, Japan); chlorogenic acid (ChA) and 4-hydroxy-2,2,6,6-tetramethylpiperidine *N*-oxyl (TEMPOL) from Sigma-Aldrich (St. Louis, MO, USA). All other reagents used were of analytical grade.

Light Source. An experimental device equipped with a light-emitting diode (LED) with a wavelength of 400 nm (NHH105UV, Lustrous Technology, Shiji, Taiwan) was used according to our previous study.[14] The output power of the LED measured using a power meter (FieldMate, Coherent, Santa Clara, CA, USA) was set to be 400 mW/LED corresponding to an irradiance of 130 mW/cm^2 at a distance of 15 mm from the LED. A four-clear-sided methacrylate plastic cuvette containing the sample was placed in the experimental device. LED light irradiation was performed toward both sides of the plastic cuvette (total irradiance = 260 mW/cm^2).

Preparation of Polyphenol Solution. The structures of polyphenols used in the present study are shown in Figure 1. Each polyphenol was dissolved in pure water to be 1.1 mg/mL. On the preparation of CA, ChA, and EGC solutions, the tubes containing samples were put in hot water (90 °C) to heat them up and were agitated so that each polyphenol could be completely dissolved. CA, ChA, and EGC solutions were subjected to high-performance liquid chromatography (HPLC) using a Prominence HPLC system (Shimadzu, Kyoto, Japan) with a Shimpak-HRC ODS colum (5 μm, ø4.6 × 150 mm), and a Flex FX-15 HPLC system (PerkinElmer, Waltham, MA, USA) with a PerkinElmer Brownlee Supra column C18 (2.1 μm, ø2.1 × 100 mm). It was confirmed that the polyphenols were not decomposed by heating. The pH of each polyphenol solution measured using a pH meter (Seven Go SG2, Mettler Toledo, Greifensee, Switzerland) is also shown in Figure 1. The polyphenol solutions were used in the experiments without further pH adjustment.

Comparison of Bactericidal Activity of Photoirradiated Polyphenols. All bacterial species used in the present study were purchased from the Japan Collection of Microorganisms, RIKEN BioResource Center (Wako, Japan). Three different species of Gram-positive bacteria, *Enterococcus faecalis* JCM7783, *S. aureus* JCM 2413, and *Streptococcus mutans* JCM5705, and three different species of Gram-negative bacteria, *Aggregatibacter actinomycetemcomitans* JCM2434, *Escherichia coli* JCM5491, and *Pseudomonas aeruginosa* JCM6119, were used. A bacterial suspension was prepared in sterile physiological saline from a culture grown on brain−heart infusion (BHI) agar (Becton Dickinson Labware, Franklin Lakes, NJ, USA). *E. faecalis*, *S. aureus*, *E. coli*, and *P. aeruginosa* were cultured aerobically at 37 °C for 20 h, whereas *S. mutans* and *A. actinomycetemcomitans* were cultured anaerobically using Anaero Pack (Mitsubishi Gas Chemical Co., Tokyo, Japan) at 37 °C for 48 h before the preparation of bacterial suspension. In a plastic cuvette, 450 μL of polyphenol solution (CA, GA, ChA, EGC, EGCg, or PA) or pure water (PW) was mixed with 50 μL of the bacterial suspension to reach final concentrations of 1 mg/mL for polyphenol and approximately 10^7 colony-forming units (CFU)/mL for the bacteria. Then, the samples were exposed to LED light for 5 or 10 min. After irradiation, 50 μL of the sample was mixed with an equal volume of sterile catalase solution (5000 U/mL) to terminate the bactericidal effect of H_2O_2 generated by photo-oxidation of the polyphenol. A 10-fold serial dilution of the mixture was prepared using sterile physiological saline, and 10 μL of the diluted solution was seeded onto an agar plate. *P. aeruginosa* was seeded onto deoxycholate hydrogen sulfide lactose agar (Becton Dickinson Labware) to obtain colonies with an entire edge for counting, whereas the others were seeded onto BHI agar. The agar plates with each bacterial species were cultured in the same way as described above, and the CFU/mL was determined. In addition, a bacterial suspension that was kept for 10 min in a light-shielding box instead of being exposed to LED light was subjected to the same procedure. The bacterial initial count (inoculum size) in each assay was also evaluated by the viable counting method. All tests were performed in triplicate.

Bactericidal Effect of LED Light on Bacteria Pretreated with Polyphenols. An additional bactericidal assay was conducted to examine if polyphenols taken up by bacteria would exert bactericidal activity. *S. aureus* and *E. coli* were used as representative Gram-positive and -negative bacteria, respectively. In a microtube, 1800 μL of each

DOI: 10.1021/jf5058588
J. Agric. Food Chem. 2015, 63, 7707−7713

Table 1. Logarithmic Reduction of CFU/mL after Treatment with Each Polyphenol under Light-Shielding Condition for 10 min[a]

		CA	GA	ChA	EGC	EGCg	PA	PW
G(+)	*E. faecalis*	0.1	0.1	0.0	0.0	0.0	2.2**	0.0
	S. aureus	0.4	0.2	0.4	0.0	0.1	0.3	0.0
	S. mutans	0.8**	1.0**	1.5**	0.0	0.0	0.5**	0.0
G(−)	*A. actinomycetemcomitans*	1.5**	0.7	0.9*	0.2	3.5**	0.2	0.0
	E. coli	0.1	0.2**	0.4**	0.1	1.0**	0.1	0.0
	P. aeruginosa	2.7**	2.7**	2.8**	0.6**	1.0**	1.5**	0.6**

[a]Significant differences from the initial bacterial count are shown, $p < 0.05$ (*) and $p < 0.01$ (**). G(+), Gram-positive; G(−), Gram-negative; CA, caffeic acid; GA, gallic acid; ChA, chlorogenic acid; EGC, epigallocatechin; EGCg, epigallocatechin gallate; PA, proanthocyanidin; PW, pure water. Each value represents the mean of triplicate assays.

Table 2. Logarithmic Reduction of CFU/mL after LED Irradiation of Each Polyphenol for 5 min[a]

		CA	GA	ChA	EGC	EGCg	PA	PW
G(+)	*E. faecalis*	2.6**	0.0	1.0**	0.0	0.0	3.0**	0.0
	S. aureus	>5**	0.6**	1.0**	0.1	0.0	1.3**	0.0
	S. mutans	>5**	1.9**	>5**	0.3	0.4	1.5**	0.4
G(−)	*A. actinomycetemcomitans*	>5**	>5**	>5**	1.6**	3.0**	>5**	2.4**
	E. coli	>5**	2.2**	3.2**	0.2	1.1	0.9	0.3
	P. aeruginosa	>5**	>5**	>5**	2.1**	3.1**	3.8**	2.0**

[a]Significant differences from the initial bacterial count are shown, $p < 0.05$ (*) and $p < 0.01$ (**). G(+), Gram-positive; G(−), Gram-negative; CA, caffeic acid; GA, gallic acid; ChA, chlorogenic acid; EGC, epigallocatechin; EGCg, epigallocatechin gallate; PA, proanthocyanidin; PW, pure water. Each value represents the mean of triplicate assays.

polyphenol solution was mixed with 200 μL of the bacterial suspension to reach final concentrations of 1 mg/mL for polyphenol and approximately 10^9 CFU/mL for the bacteria. The mixture was incubated for 1 min at room temperature. Then, the bacteria were collected by centrifugation at 5000*g* at 4 °C for 10 min. Following the decantation of the supernatant, the pellet was resuspended in 1000 μL of sterile saline. The suspension was further diluted about 100 times with sterile saline to reach a final concentration of approximately 10^7 CFU/mL. An aliquot (500 μL) of the diluted suspension was put in a plastic cuvette and exposed to LED light for 10 min. After irradiation, determination of CFU/mL was performed in the same way as described above.

Oxidative DNA Damage. To examine if the photoirradiated polyphenol causes oxidative DNA damage in bacteria, biochemical analysis was performed. CA was used as a representative polyphenol, and *S. aureus* and *E. coli* were used as representative Gram-positive and -negative bacteria, respectively. In a plastic cuvette, 1800 μL of CA solution was mixed with 200 μL of the bacterial suspension to reach final concentrations of 1 mg/mL for CA and approximately 10^9 CFU/mL for the bacteria. The sample was exposed to LED light for 5 min. After irradiation, 200 μL of sterile catalase solution (5000 U/mL) was added to the sample. Then, the bacteria were collected by centrifugation, and DNA was extracted using a commercial kit (Isoplant, Nippon Gene, Tokyo, Japan). Concentration of DNA was adjusted to 200 μg/mL by reading an absorbance at 260 nm using a spectrophotometer (Gene Quant 1300, GE Healthcare, Bukinghamshire, UK). The formation of 8-hydroxydeoxyguanosine (8-OHdG), which is a marker of oxidative DNA damage,[19] was analyzed using a commercial kit (OxiSelect Oxidative DNA Damage ELISA Kit, Cell Biolabs, San Diego, CA, USA). The 8-OHdG formation caused by photoirradiated CA [CA(+)L(+)] was compared to the treatment with CA alone [CA(+)L(−)], LED irradiation alone [CA(−)L(+)], and no treatment [CA(−)L(−)]. Under the CA(−) condition, pure water was added to the reaction system. Under the L(−) condition, the samples were kept in a light-shielding box.

H_2O_2 Determination. The H_2O_2 content of each polyphenol solution and pure water with or without the 10 min exposure to LED light was determined by the colorimetric method based on the peroxide-mediated oxidation of Fe^{2+} followed by the reaction of Fe^{3+} with xylenol orange.[20] In brief, 500 μL of reaction mixture consisting of 500 μM ammonium ferrous sulfate, 50 mM sulfuric acid, 200 μM xylenol orange, and 200 mM sorbitol was added to 500 μL of polyphenol solution with or without LED irradiation. The polyphenol solution was diluted with pure water beforehand as appropriate. After the 45 min incubation at room temperature, absorbance at 560 nm was read using a spectrophotometer (Gene Quant 1300). The assay was calibrated using a standard curve, which was obtained in the range between 0.25 and 5 μM H_2O_2. Because the sample was mixed with an equal volume of the reaction agent, the detection limit was 0.5 μM.

Electron Spin Resonance (ESR) Analysis of Hydroxyl Radicals. Qualitative and quantitative analyses of $^{\bullet}$OH generated by photoirradiation of polyphenol solution were performed using an ESR spin trapping technique according to our previous studies.[14,21] In brief, polyphenol solution was mixed with DMPO, a spin trap agent, in a plastic cuvette to reach final concentrations of 1 mg/mL for polyphenol and 300 mM for DMPO. Then, the sample was exposed to LED light for 1 min. After irradiation, the sample was transferred to a quartz cell for ESR spectrometry. The ESR spectrum was recorded on an X-band ESR spectrometer (JES-FA-100; JEOL, Tokyo, Japan). The measurement conditions for ESR were as follows: field sweep, 331.41−341.41 mT; field modulation frequency, 100 kHz; field modulation width, 0.1 mT; amplitude, 200; sweep time, 2 min; time constant, 0.03 s; microwave frequency, 9.420 GHz; and microwave power, 4 mW. TEMPOL (10 μM) was used as a standard to calculate the concentration of spin-trapped radicals, and the ESR spectrum of manganese (Mn^{2+}) held in the ESR cavity was used as an internal standard. The concentration of $^{\bullet}$OH was determined using digital data processing (JEOL).

Statistical Analyses. The statistical significance ($p < 0.05$) in the CFU/mL obtained in the bactericidal test was assessed by Dunnett's multiple-comparison test using the initial bacterial count as a control group. The analyses for the bactericidal test were performed following logarithmic conversion. When a colony was not detected, the value of the detection limit (10^2 CFU/mL) was used for the statistical analysis. Statistical significance ($p < 0.05$) in the 8-OHdG formation was assessed by using the Tukey−Kramer honest significant difference

DOI: 10.1021/jf5058588
J. Agric. Food Chem. 2015, 63, 7707−7713

Table 3. Logarithmic Reduction of CFU/mL after LED Irradiation of Each Polyphenol for 10 min[a]

		CA	GA	ChA	EGC	EGCg	PA	PW
G(+)	*E. faecalis*	4.0**	0.0	>5**	0.1	0.1	>5**	0.0
	S. aureus	>5**	2.9**	>5**	0.7	0.2	3.6**	0.2
	S. mutans	>5**	3.2**	>5**	0.6**	0.6**	4.6**	1.0**
G(−)	*A. actinomycetemcomitans*	>5**	>5**	>5**	2.7**	>5**	>5**	3.4**
	E. coli	>5**	>5**	>5**	1.0**	2.2**	1.6**	0.9**
	P. aeruginosa	>5**	>5**	>5**	3.8**	>5**	>5**	3.0**

[a]Significant differences from the initial bacterial count are shown, $p < 0.05$ (*) and $p < 0.01$ (**). G(+), Gram-positive; G(−), Gram-negative; CA, caffeic acid; GA, gallic acid; ChA, chlorogenic acid; EGC, epigallocatechin; EGCg, epigallocatechin gallate; PA, proanthocyanidin; PW, pure water. Each value represents the mean of triplicate assays.

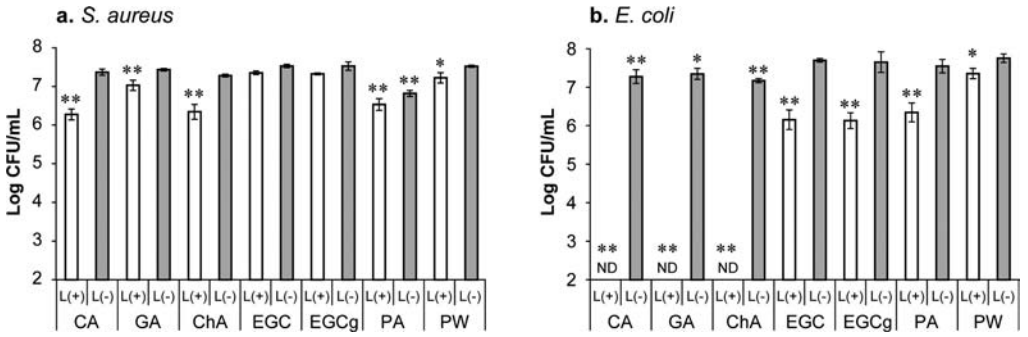

Figure 2. Bactericidal activity of a 1 min pretreatment with polyphenols against *S. aureus* (a) and *E. coli* (b). Each value represents the mean of triplicate assays with standard deviation. Significant differences from the CFU/mL of PW-L(−) are shown, $p < 0.05$ (*) and $p < 0.01$ (**). CA, caffeic acid; GA, gallic acid; ChA, chlorogenic acid; EGC, epigallocatechin; EGCg, epigallocatechin gallate; PA, proanthocyanidin; PW, pure water; L(+,−), with or without LED irradiation; ND, not detected.

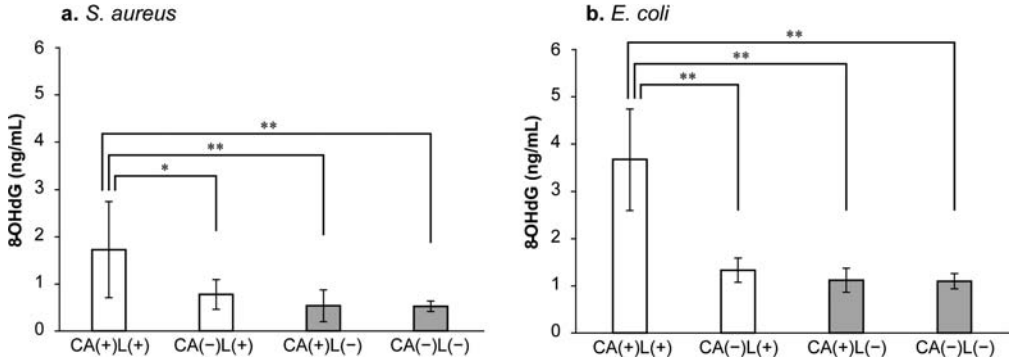

Figure 3. Formation of 8-OHdG in *S. aureus* (a) and *E. coli* (b) suspended in caffeic acid (CA) aqueous solution with or without LED irradiation. Each value represents the mean of sextuplicate assays with standard deviation. Significant differences are shown, $p < 0.05$ (*) and $p < 0.01$ (**). CA(+,−), with or without CA; L(+,−), with or without LED irradiation.

multiple-comparison test, and the yield of H_2O_2 and $^{\bullet}OH$ in each polyphenol solution with or without LED irradiation was assessed by Student's *t* test. When H_2O_2 was not detected, the value of the detection limit (0.5 μM) was used for the statistical analysis.

RESULTS

Bactericidal Assay. The logarithmic reduction of CFU/mL from the initial bacterial counts after each treatment is summarized in Tables 1−3. Under the light-shielding condition, certain bacterial species showed susceptibility to the polyphenols (Table 1). *E. faecalis* was killed by PA with a 2.2 log reduction of CFU/mL in 10 min, whereas the other polyphenols hardly killed the bacteria (Table 1). *A. actinomycetemcomitans* showed high susceptibility to EGCg and was killed with a 3.5 log reduction of CFU/mL (Table 1). Of the bacterial species used in the present study, *P. aeruginosa* was most susceptible to the polyphenols and was killed with a ≥1 log reduction of CFU/mL by CA, GA, ChA, EGCg, and PA (Table 1).

When exposed to LED light, the bactericidal activity of each polyphenol was enhanced in an irradiation time-dependent manner (Tables 2 and 3). Phenolic acids, such as CA, GA, and ChA, showed higher bactericidal activity than flavonoid, such as EGC and EGCg. In particular, photoirradiated CA and ChA killed all bacterial species with a ≥4 log reduction of CFU/mL within 10 min. Following CA and ChA, photoirradiated GA and PA showed relatively high bactericidal effect, although *E. faecalis* and *E. coli* were not effectively killed by GA and PA, respectively. LED irradiation alone (PW) also showed bactericidal activity, especially against *A. actinomycetemcomitans* and *P. aeruginosa*. Compared to PW, photoirradiated EGC showed no or only a little additional bactericidal effect.

DOI: 10.1021/jf5058588
J. Agric. Food Chem. 2015, 63, 7707−7713

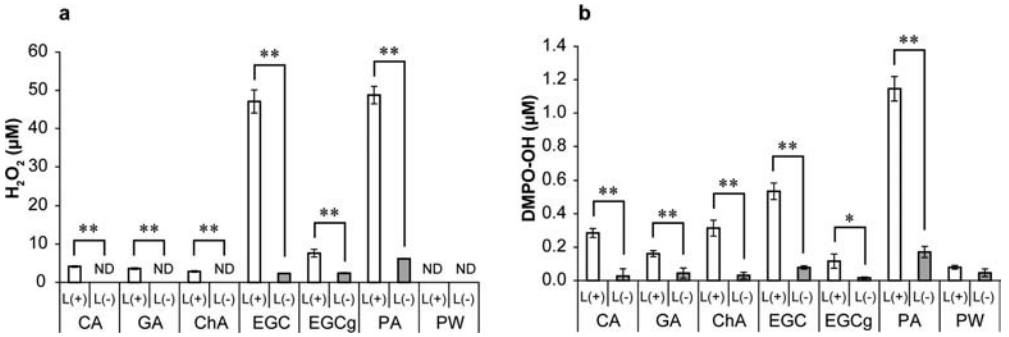

Figure 4. Quantification of H_2O_2 (a) and DMPO-OH, a spin adduct of hydroxyl radical (b), generated in each polyphenol solution with or without LED irradiation. Each value represents the mean of triplicate assays with standard deviation. Significant differences are shown, $p < 0.05$ (*) and $p < 0.01$ (**). CA, caffeic acid; GA, gallic acid; ChA, chlorogenic acid; EGC, epigallocatechin; EGCg, epigallocatechin gallate; PA, proanthocyanidin; PW, pure water; L(+,−), with or without LED irradiation; ND, not detected.

Although photoirradiated EGCg was effective against Gram-negative bacteria, it showed no additional bactericidal effect against Gram-positive bacteria. As a whole, Gram-negative bacteria tended to show higher susceptibility to the disinfection treatment than Gram-positive bacteria.

Bactericidal Effect of LED Light on Bacteria Pretreated with Polyphenols. When *S. aureus* was pretreated with polyphenols for 1 min followed by being exposed to LED light for 10 min, pretreatment with CA, GA, ChA, and PA significantly reduced the CFU/mL from the initial bacterial count (Figure 2a). However, the logarithmic reduction of CFU/mL in all cases was <2 log, which was lower than that obtained in the bactericidal assay where the bacteria suspended in each polyphenol solution were exposed to LED light. In the case of *E. coli* pretreated with each polyphenol, the bactericidal activity of each pretreatment was comparable to that observed in the bactericidal assay where the bacteria suspended in each polyphenol solution were irradiated. (Figure 2b). Pretreatment with CA, GA, and ChA killed the bacteria with a >5 log reduction of CFU/mL when exposed to LED light for 10 min. Pretreatment with EGC, EGCg, and PA followed by LED irradiation for 10 min also significantly reduced the CFU/mL, although the reduction was 1−2 log of CFU/mL. Pretreatment with CA, GA, and ChA without LED irradiation also significantly reduced the CFU/mL from the initial bacterial count, although the reduction was <1 log.

Oxidative DNA Damage. When *S. aureus* suspended in CA aqueous solution was exposed to LED light for 5 min [CA(+)L(+)], the 8-OHdG level significantly increased from the level observed in the no-treatment group [CA(−)L(−)] (Figure 3a). By contrast, treatment with CA alone [CA(+)-L(−)] and LED irradiation alone [CA(−)L(+)] did not elevate the 8-OHdG level. Similar to the case of *S. aureus*, photoirradiated CA significantly increased the 8-OHdG level in *E. coli*, although other conditions did not affect it(Figure 3b).

H_2O_2 Determination. H_2O_2 generation was observed in all polyphenol aqueous solutions used in the present study when irradiated, and the highest yield (approximately 50 μM) was recorded in the EGC and PA solutions, whereas H_2O_2 was not detected in PW regardless of LED irradiation (Figure 4a). In the EGC, EGCg, or PA solution, although H_2O_2 was also generated under the light-shielding condition, the yield of H_2O_2 was significantly lower than that generated in the same polyphenols with LED irradiation.

ESR Analysis of Hydroxyl Radicals. When the polyphenol aqueous solutions containing DMPO were exposed to LED light for 1 min, the ESR signal of DMPO-OH, a spin adduct of $^{\bullet}OH$, was detected. The presence of the spin adduct was confirmed by hyperfine coupling constants of $a_N = a_H = 1.49$ mT.[22] The yields of DMPO-OH generated in each polyphenol solution significantly increased by LED irradiation, whereas LED irradiation of PW did not increase the yield (Figure 4b). The highest yield of DMPO-OH (about 1 μM) was observed in photoirradiated PA, followed by EGC, ChA, CA, GA, and EGCg.

DISCUSSION

The newly developed disinfection technique applying edible polyphenols and blue light was evaluated in the present study. The antimicrobial activity of the polyphenols without LED irradiation against some bacterial species was observed as reported in the previous studies.[9−12] However, the bactericidal effect exerted within 10 min was rather weak (<1 log reduction of CFU/mL) with some exceptions. When bacteria suspended in PW were exposed to LED light, significant reductions of CFU/mL were also observed after 10 min of treatment except for *E. faecalis* and *S. aureus*. This finding agrees with earlier studies, which showed that ultraviolet or blue light could exert bactericidal action depending on the intensity and time of irradiation.[23,24] By comparing the bactericidal effect with different conditions, it was confirmed that photoirradiation enhanced the bactericidal activity of polyphenols. In particular, phenolic acids, such as CA and ChA, killed all bacterial species used in the present study with a ≥4 log reduction of CFU/mL when irradiated for 10 min. The photoirradiated GA and PA also exerted relatively high bactericidal activity, although they were not effective against *E. faecalis* and *E. coli*, respectively. By contrast, the bactericidal activity of photoirradiated flavonoids, such as EGC and EGCg, was limited. Especially, the bactericidal effect of EGC was almost equal to that of PW, which means EGC did not exert bactericidal effect additionally to that of LED irradiation alone.

In general, *E. faecalis* showed higher resistance to the disinfection treatment than other bacteria tested in the present study. It is known that *E. faecalis* is able to survive in hostile conditions and in many harsh environments, such as heat, acid, H_2O_2, hyperosmolarity, sodium hypochloride, and even ultraviolet irradiation.[25−28] Indeed, in our previous studies,[16,29] it has been demonstrated that *E. faecalis* is more resistant to the disinfection treatment based on photolysis of hydrogen peroxide than *S. aureus*, *S. mutans*, and *A. actinomycetemcomitans*. Therefore, it seems to be natural that *E. faecalis* is more

DOI: 10.1021/jf5058588
J. Agric. Food Chem. 2015, 63, 7707−7713

resistant to the disinfection treatment by photoirradiation of the polyphenols. The mechanism by which *E. faecalis* shows higher resistance to photoirradiated polyphenols should be further studied.

The results of quantitative analyses of H_2O_2 and $^{\bullet}OH$ showed that their yields in the polyphenol solutions significantly increased by LED irradiation. These findings are identical to the results of our previous studies, suggesting that the bactericidal activity of photoirradiated polyphenols would be attributable to oxidation by ROS.[14,15] However, when the yields of H_2O_2 were compared in each polyphenol solution, the photoirradiated EGC and PA showed the highest yield, followed by EGCg. Similarly, the photoirradiated PA showed the highest yield of $^{\bullet}OH$, followed by EGC. Because phenolic acids, such as CA, GA, and ChA, showed higher bactericidal activity than flavonoids, such as EGC and EGCg, a correlation was not observed between the yield of ROS and the bactericidal effect. This discrepancy suggests that there is another factor affecting the bactericidal activity other than the yield of the ROS.

One of the possible factors that affect the bactericidal activity of photoirradiated polyphenols is the affinity of polyphenols to bacterial cells as discussed in our previous studies.[14,15] When $^{\bullet}OH$ causes oxidative damage, it should be generated inside or in the vicinity of bacterial cells because it cannot diffuse long distances.[30,31] Thus, the affinity will be important in the mode of action. To verify the importance of affinity, an additional bactericidal assay was conducted. The bacteria were pretreated with the polyphenols for 1 min and were resuspended in saline so that only polyphenols incorporated into cytoplasm and/or bound to cytoplasmic membrane would exist. The result showed that both *S. aureus* and *E. coli* pretreated with the polyphenols could be killed when exposed to the LED light. This suggests that the polyphenols will be incorporated into cytoplasm and/or bound to cytoplasmic membrane as is the case with mammalian cells.[18] It was also demonstrated that the photoirradiation of Gram-negative *E. coli* pretreated with the polyphenols exerted comparable bactericidal effect to the photoirradiation of the bacteria suspended in the polyphenol solutions, whereas the former treatment was less effective against Gram-positive *S. aureus* than the latter. This finding indicates that the affinity of polyphenols to Gram-negative bacteria would be higher than to Gram-positive bacteria. This may explain why Gram-negative bacteria were more susceptible to the disinfection treatment than Gram-positive bacteria. In addition to the bactericidal assay, the biochemical assay for oxidative DNA damage demonstrated that photoirradiated CA increased the 8-OHdG level of *S. aureus* and *E. coli* but LED irradiation alone did not. This finding suggests that CA at least in part would penetrate into the cell. Furthermore, a higher 8-OHdG level was observed in *E. coli* than in *S. aureus*, suggesting that Gram-negative bacteria will take up CA more effectively than Gram-positive bacteria. The underlying mechanism by which polyphenols are incorporated into bacterial cells should be further studied.

Besides the bactericidal activity, we demonstrated that CA, ChA, and PA showed an accelerative effect on fibroblast proliferation.[18] Because fibroblast proliferation is one of the pivotal events for wound healing,[32−34] it can be expected that these polyphenols would contribute to acceleration of wound healing after the disinfection treatment. Furthermore, polyphenols can generally function as an antioxidant to terminate excessive oxidative damage and can exert a cytoprotective effect by improving intracellular oxidative stress response.[2,3,35] Because the polyphenols contained in plant foods are edible, the residual toxicity is likely to be negligible. Thus, treatment utilizing blue light and a polyphenol could be a novel disinfection treatment with a wide variety of applications.

AUTHOR INFORMATION

Corresponding Author

*(K.N.) Phone: +81-22-717-8299. Fax: +81-22-717-8299. E-mail: keisuke@m.tohoku.ac.jp.

Funding

This research was supported by JSPS KAKENHI, Grant-in-Aid for Young Scientists (B), 24791977, 2014, and the Ministry of Education, Science, Sports and Culture, Japan, Strategic Research Foundation Grant-in-Aid for Private Universities, S1312001.

Notes

The authors declare no competing financial interest.

ACKNOWLEDGMENTS

We are deeply grateful to Dr. Makiko Furuishi (PerkinElmer Japan Co., Ltd.) for her collaboration and technical advice.

ABBREVIATIONS USED

$^{\bullet}OH$, hydroxyl radical; DMPO, 5,5-dimethyl-1-pyrroline *N*-oxide; TEMPOL, 4-hydroxy-2,2,6,6-tetramethylpiperidine *N*-oxyl; LED, light-emitting diode; CFU, colony-forming units; ESR, electron spin resonance; CA, caffeic acid; GA, gallic acid; ChA, chlorogenic acid; EGC, epigallocatechin; EGCg, epigallocatechin gallate; PA, proanthocyanidin; PW, pure water; 8-OHdG, 8-hydroxydeoxyguanosine

REFERENCES

(1) Kondo, K.; Kurihara, M.; Miyata, N.; Suzuki, T.; Toyoda, M. Scavenging mechanisms of (−)-epigallocatechin gallate and (−)-epicatechin gallate on peroxyl radicals and formation of superoxide during the inhibitory action. *Free Radical Biol. Med.* **1999**, *27*, 855−863.

(2) Liu, Z.; Ma, L.; Zhou, B.; Yang, L.; Liu, Z. Antioxidative effects of green tea polyphenols on free radical initiated and photosensitized peroxidation of human low density lipoprotein. *Chem. Phys. Lipids* **2000**, *106*, 53−63.

(3) Yilmaz, Y.; Toledo, R. T. Major flavonoids in grape seeds and skins: antioxidant capacity of catechin, epicatechin, and gallic acid. *J. Agric. Food Chem.* **2004**, *52*, 255−260.

(4) Heim, K.; Tagliaferro, A.; Bobilya, D. Flavonoid antioxidants: chemistry, metabolism and structure-activity relationships. *J. Nutr. Biochem.* **2002**, *13*, 572−584.

(5) Hanasaki, Y.; Ogawa, S.; Fukui, S. The correlation between active oxygens scavenging and antioxidative effects of flavonoids. *Free Radical Biol. Med.* **1994**, *16*, 845−850.

(6) Ahmad, N.; Gupta, S.; Mukhtar, H. Green tea polyphenol epigallocatechin-3-gallate differentially modulates nuclear factor κB in cancer cells versus normal cells. *Arch. Biochem. Biophys.* **2000**, *376*, 338−346.

(7) Williamson, G.; Manach, C. Bioavailability and bioefficacy of polyphenols in humans. II. Review of 93 intervention studies. *Am. J. Clin. Nutr.* **2005**, *81*, 243S−255S.

(8) Khan, N.; Mukhtar, H. Tea polyphenols for health promotion. *Life Sci.* **2007**, *81*, 519−533.

(9) Hatano, T.; Kusuda, M.; Inada, K.; Ogawa, T. O.; Shiota, S.; Tsuchiya, T.; Yoshida, T. Effects of tannins and related polyphenols on methicillin-resistant *Staphylococcus aureus*. *Phytochemistry* **2005**, *66*, 2047−2055.

(10) Kusuda, M.; Inada, K.; Ogawa, T. O.; Yoshida, T.; Shiota, S.; Tsuchiya, T.; Hatano, T. Polyphenolic constituent structures of

DOI: 10.1021/jf5058588
J. Agric. Food Chem. 2015, 63, 7707−7713

Zanthoxylum piperitum fruit and the antibacterial effects of its polymeric procyanidin on methicillin-resistant *Staphylococcus aureus*. *Biosci., Biotechnol., Biochem.* **2006**, *70*, 1423−1431.
(11) Xu, L.; Liu, R.; Li, D.; Tu, S.; Chen, J. An in vitro study on the dental caries preventing effect of oligomeric procyanidins in sorghum episperm. *Food Chem.* **2011**, *126*, 911−916.
(12) Cushnie, T. P.; Lamb, A. J. Antimicrobial activity of flavonoids. *Int. J. Antimicrob. Agents* **2005**, *26*, 343−356.
(13) Iwasawa, A.; Niwano, Y.; Mokudai, T.; Kohno, M. Antiviral activity of proanthocyanidin against feline calicivirus used as a surrogate for noroviruses, and coxsackievirus used as a representative enteric virus. *Biocontrol Sci.* **2009**, *14*, 107−111.
(14) Nakamura, K.; Yamada, Y.; Ikai, H.; Kanno, T.; Sasaki, K.; Niwano, Y. Bactericidal action of photo-irradiated gallic acid via reactive oxygen species formation. *J. Agric. Food Chem.* **2012**, *60*, 10048−10054.
(15) Nakamura, K.; Shirato, M.; Ikai, H.; Kanno, T.; Sasaki, K.; Kohno, M.; Niwano, Y. Photo-irradiation of proanthocyanidin as a new disinfection technique via reactive oxygen species formation. *PLoS One* **2013**, *8*, No. e60053.
(16) Ikai, H.; Nakamura, K.; Shirato, M.; Kanno, T.; Iwasawa, A.; Sasaki, K.; Niwano, Y.; Kohno, M. Photolysis of hydrogen peroxide, an effective disinfection system via hydroxyl radical formation. *Antimicrob. Agents Chemother.* **2010**, *54*, 5086−5091.
(17) Silhavy, T. J.; Kahne, D.; Walker, S. The bacterial cell envelope. *Cold Spring Harbor Perspect. Biol.* **2010**, *2*, No. a000414.
(18) Tsuruya, M.; Niwano, Y.; Nakamura, K.; Kanno, T.; Nakashima, T.; Egusa, H.; Sasaki, K. Acceleration of proliferative response of mouse fibroblasts by short-time pretreatment with polyphenols. *Appl. Biochem. Biotechnol.* **2014**, *174*, 2223−2235.
(19) Kasai, H. Analysis of a form of oxidative DNA damage, 8-hydroxy-2′-deoxyguanosine, as a marker of cellular oxidative stress during carcinogenesis. *Mutat. Res.* **1997**, *387*, 147−163.
(20) Jiang, Z.; Woollard, A.; Wolff, S. Hydrogen peroxide production during experimental protain glycation. *FEBS Lett.* **1990**, *268*, 69−71.
(21) Nakamura, K.; Kanno, T.; Ikai, H.; Sato, E.; Mokudai, T.; Niwano, Y.; Ozawa, T.; Kohno, M. Reevaluation of quantitative ESR spin trapping analysis of hydroxyl radical by applying sonolysis of water as a model system. *Bull. Chem. Soc. Jpn.* **2010**, *83*, 1037−1046.
(22) Buettner, G. R. Spin trapping: ESR parameters of spin adducts. *Free Radical Biol. Med.* **1987**, *3*, 259−303.
(23) Hamamoto, A.; Mori, M.; Takahashi, A.; Nakano, M.; Wakikawa, N.; Akutagawa, M.; Ikehara, T.; Nakaya, Y.; Kinouchi, Y. New water disinfection system using UVA light-emitting diodes. *J. Appl. Microbiol.* **2007**, *103*, 2291−2298.
(24) Vermeulen, N.; Keeler, W. J.; Nandakumar, K.; Leung, K. T. The bactericidal effect of ultraviolet and visible light on *Escherichia coli*. *Biotechnol. Bioeng.* **2008**, *99*, 550−556.
(25) Giard, J. C.; Hartke, A.; Flahaut, S.; Benachour, A.; Boutibonnes, P.; Auffray, Y. Starvation-induced multiresistance in *Enterococcus faecalis* JH2-2. *Curr. Microbiol.* **1996**, *32*, 264−271.
(26) Giard, J. C.; Hartke, A.; Flahaut, S.; Boutibonnes, P.; Auffray, Y. Glucose starvation response in *Enterococcus faecalis* JH2-2: survival and protein analysis. *Res. Microbiol.* **1997**, *148*, 27−35.
(27) Hartke, A.; Giard, J. C.; Laplace, J. M.; Auffray, Y. Survival of *Enterococcus faecalis* in an oligotrophic microcosm: changes in morphology, development of general stress resistance, and analysis of protein synthesis. *Appl. Environ. Microbiol.* **1998**, *64*, 4238−4245.
(28) Oliveira, D. P.; Gomes, B. P.; Zaia, A. A.; Souza-Filho, F. J.; Ferraz, C. C. Ex vivo antimicrobial activity of several bleaching agents used during the walking bleach technique. *Int. Endod. J.* **2008**, *41*, 1054−1058.
(29) Shirato, M.; Ikai, H.; Nakamura, K.; Hayashi, E.; Kanno, T.; Sasaki, K.; Kohno, M.; Niwano, Y. Synergistic effect of thermal energy on bactericidal action of photolysis of H_2O_2 in relation to acceleration of hydroxyl radical generation. *Antimicrob. Agents Chemother.* **2012**, *56*, 295−301.
(30) Roots, R.; Okada, S. Estimation of life times and diffusion distances of radicals involved in X-ray-induced DNA strand breaks of killing of mammalian cells. *Radiat. Res.* **1975**, *64*, 306−320.
(31) Guo, Q. Q.; Yue, Q. L.; Zhao, J. J.; Wang, L.; Wang, H. S.; Wei, X. L.; Liu, J. F.; Jia, J. B. How far can hydroxyl radicals travel? An electrochemical study based on a DNA mediated electron transfer process. *Chem. Commun.* **2011**, *47*, 11906−11908.
(32) Singh, D.; Choi, S. M.; Zo, S. M.; Painuli, R. M.; Kwon, S. W.; Han, S. S. Effect of extracts of *Terminalia chebula* on proliferation of keratinocytes and fibroblasts cells: an alternative approach for wound healing. *Evidence-Based Complement. Alternat. Med.* **2014**, *2014*, No. 701656.
(33) Niwano, Y.; Koga, H.; Sakai, A.; Kanai, K.; Hamaguchi, H.; Uchida, M.; Tachikawa, T. Wound healing effect of malotilate in rats. *Arzneimittelforschung* **1996**, *46*, 450−455.
(34) Niwano, Y.; Koga, H.; Kanai, K.; Hamaguchi, H.; Yamaguchi, H. Wound healing effect of the new imidazole antimycotic lanoconazole in rats. *Arzneimittelforschung* **1996**, *46*, 218−223.
(35) Kurauchi, M.; Niwano, Y.; Shirato, M.; Kanno, T.; Nakamura, K.; Egusa, H.; Sasaki, K. Cytoprotective effect of short-term pretreatment with proanthocyanidin on human gingival fibroblasts exposed to harsh environmental conditions. *PLoS One* **2014**, *9*, No. e113403.

DOI: 10.1021/jf5058588
J. Agric. Food Chem. 2015, 63, 7707−7713

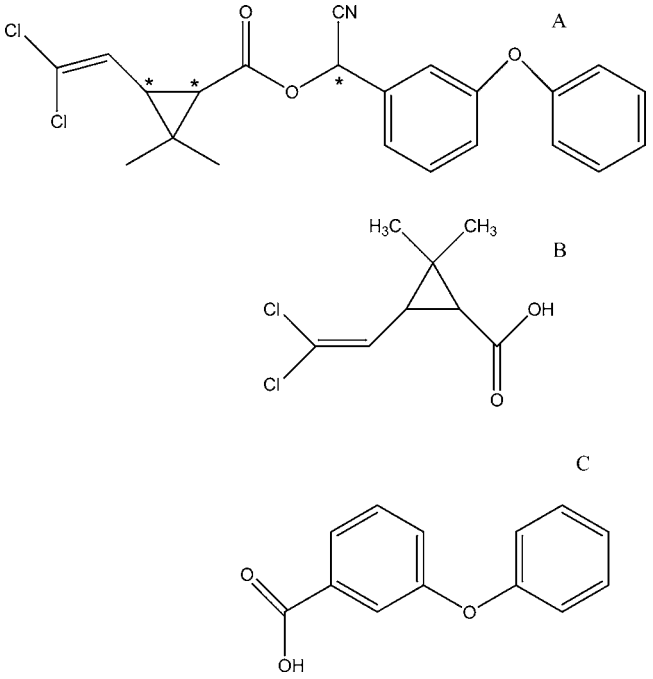

Figure 1. Chemical structures of α-cypermethrin and its metabolites: (A) α-cypermethrin, (B) *cis*-DCCA, and (C) 3-PBA.

ecotoxicity assays according to the Organisation for Economic Co-operation and Development (OECD) guidelines (OECD 1984) and is also used to survey the quality of the terrestrial environment. Traditional ecotoxicity assays and risk assessments have routinely focused on individual chemicals.[20] However, earthworms in soil are usually exposed to a variety of pollutants simultaneously. Therefore, toxicity assays using mixtures of contaminants may better reflect the real-world exposures. Studies about the toxicity of α-cypermethrin have been studied by Diao et al.[21] Little information regarding the toxicity of the metabolites and the combined acute toxicity of α-cypermethrin and its metabolites to earthworms has been reported.

The individual enantiomers of chiral pesticides may show differences in bioactivity, toxicity, metabolism, bioaccumulation, and degradation behaviors.[22,23] α-Cypermethrin is manufactured and applied to agro-ecosystems as racemic forms. The enantioselective environmental behavior of α-cypermethrin in the environment has not been considered for human health and ecological risk assessment. The formation of the metabolites *cis*-DCCA and 3-PBA influences non-target organisms and is also an important issue and should also be considered.

In this study, the enantiomers of α-cypermethrin were separated and the enantioselective transformation of α-cypermethrin in five soils was investigated. The toxicity of *cis*-DCCA and 3-PBA and the combined acute toxicity of *cis*-DCCA, 3-PBA, and α-cypermethrin to earthworms were also determined. This result may be applied to understand the risks of α-cypermethrin application.

2. MATERIALS AND METHODS

2.1. Chemicals and Reagents. The insecticide of α-cypermethrin [≥98.5% purity, enriched in (+)-1*R*-*cis*-*S* and (−)-1*S*-*cis*-*R*] was provided by the Institute for the Control of Agrochemicals, Ministry of Agriculture (ICAMA, Beijing, China). 1,1,1,3,3,3-Hexafluoroisopropanol (HFIP), *N*,*N*-diisopropylcarbodiimide (DIC), 3-phenoxybenzoic acid (3-PBA, 98%), and internal standard (chlorpyrifos, 98%) were purchased from Sigma−Aldrich Corp. (St. Louis, MO). *cis*-DCCA (98%) was purchased from Chem Service (West Chester, PA). Water was purified by a Milli-Q system. Isopropanol, *n*-hexane, and ethyl acetate (analytical grade) were purchased from commercial sources, distilled, and filtered through a 0.45 μm filter membrane before use. All other chemicals and solvents were of analytical grade and purchased from commercial sources.

2.2. Chiral Separation. The high-performance liquid chromatography (HPLC) analysis was performed on an Agilent 1200 Series HPLC system (Agilent Technology) equipped with a G1322A degasser, G1311A pump, G1314B variable wavelength detector (VWD), and G1329A ALS. An AT-930 heater and cooler column attemperator (Tianjin Automatic Science Instrument Co., Ltd., China) was used to control the column temperature. The signal was processed by Agilent ChemStation software. The enantiomers of α-cypermethrin were separated on a Chiralcel OD column (250 × 4.6 mm, Daicel Chemical Industries, Tokyo, Japan) using *n*-hexane and isopropanol in a 98:2 (v/v) ratio at a 0.5 mL/min flow rate (Figure 2A). The injection volume was 20 μL, and the ultraviolet (UV) detection wavelength was 230 nm. The chromatographic separation was conducted at 20 °C. No enantiomerization was observed for α-cypermethrin under this analytical condition.

2.3. Gas Chromatography (GC) Analysis. Agilent 6890N GC with an electron capture detector (ECD, Agilent Technologies, Palo Alto, CA) was used for quantitative analysis of α-cypermethrin and its metabolites. The detection was performed using a HP-5 capillary column (30 m × 0.25 mm inner diameter and 0.25 um film thickness). Nitrogen (>99.999%) was used as a carrier gas at a constant flow rate of 1.0 mL/min. The operating conditions were as follows: the column was held initially at a temperature of 100 °C for 10 min, then ramped at 5 °C/min to 155 °C, held at 155 °C for 5 min, ramped at 15 °C/

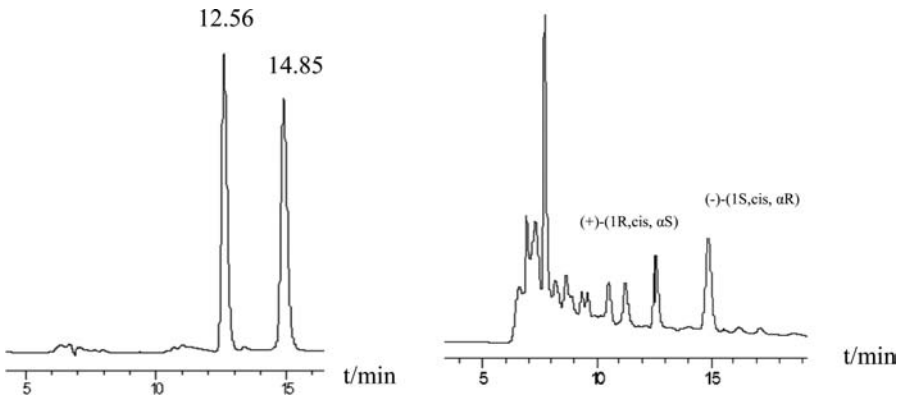

Figure 2. (A) Typical chromatograms of the chiral separation of α-cypermethrin and (B) enantioselective degradation of α-cypermethrin in soil 1 after 42 days.

DOI: 10.1021/acs.jafc.5b03148
J. Agric. Food Chem. 2015, 63, 7714−7720

Table 1. Physicochemical Properties of the Soils

number	site	particle size			texture	pH (water)	C_{org} (%)
		sand (%)	silt (%)	clay (%)			
1	Hunan	24.0	44.0	36.0	clay loam	5.18	1.15
2	Heilongjiang	48.0	28.0	24.0	loam	5.79	15.04
3	Beijing	61.2	8.0	30.8	sandy loam	8.14	2.51
4	Hainan	73.2	16.0	10.8	sandy loam	8.17	5.43
5	Neimeng	69.2	12.0	18.8	sandy loam	7.85	6.55

min to 290 °C, and held at 290 °C for 5 min. The total analysis time was 45 min. The temperature of the detector was set at 300 °C.

2.4. Sample Extraction. All of the samples were thawed for about 15 min at room temperature. Soil samples were mixed with 5 g of anhydrous sodium sulfate in a 50 mL polypropylene centrifuge tube, and 25 mL of ethyl acetate was added for extraction. The tube was vortexed for 3 min, exposed to ultrasonic vibration for 10 min, and then centrifuged at 3500 rpm for 5 min. The extraction was repeated following the same step, and the liquid phase was combined. The combined extracts were filtered through 5 g of anhydrous sodium sulfate for dehydration, evaporated to dryness *in vacuo* rotary at 35 °C, and reconstituted to 1 mL with acetonitrile. The solution was divided into two parts: (1) A total of 750 μL was evaporated to dryness under a stream of nitrogen and diluted to 250 μL with *n*-hexane, and a 20 μL aliquot was injected into HPLC for enantioselectivity determination. (2) A total of 250 μL was used for derivatization for GC analysis. The derivatization was conducted in a 5 mL centrifuge tube, with 30 μL of HFIP solution and 10 μL of DIC solution. After thorough mixing, the tube was placed in the oscillator. Derivatization was exposed to ultrasonic vibration for 10 min. After reaction, 500 μL of ultrapure water and 500 μL of *n*-hexane were added to the tube, vortexed for 5 min, and then centrifuged at 3500 rpm for 5 min. A total of 1 μL of *n*-hexane solution was subjected for GC/ECD analysis.

2.5. Method Validation. The GC method described above was validated for the quantitative analysis of α-cypermethrin and its metabolites in soils. Good linearities were observed in the range of 0.015−6 mg/kg for α-cypermethrin and in the range of 0.025−0.3 mg/kg for its two metabolites, with mean coefficients of determination (R^2) higher than 0.993. The average recoveries for α-cypermethrin at levels between 0.015 and 6 mg/kg ranged between 77.8 and 94.8% in the five soils, with relative standard deviation (RSD) below 10%, and the average recoveries of its metabolites at levels between 0.020 and 0.3 mg/kg ranged between 78.4 and 95.0% based on an acceptable RSD below 10%. The limits of detection (LODs) for α-cypermethrin, *cis*-DCCA, and 3-PBA in the tested soils were 0.003, 0.008, and 0.008 mg/kg, respectively, and the corresponding limits of quantitation (LOQs) were 0.015, 0.025, and 0.025 mg/kg, respectively.

2.6. Degradation of α-Cypermethrin in Soils. Five test soils from different agriculture regions (0−10 cm) of China that had not been treated with cypermethrin in the last 5 years were used in this study. Their major properties were shown in Table 1. Test soils were adjusted to a water content of 25% and maintained in the darkness at room temperature for 7 days to activate the microorganisms. To add the pesticide to the soil evenly, 10 g of soil was first placed into a 1000 mL Erlenmeyer flask and 0.5 mL of racemic α-cypermethrin solution (3000 μg/mL, acetone) was added. After the solvent was evaporated, another 290 g of soil was added gradually and stirred thoroughly to a spiked concentration of 5 μg/g (each enantiomer). The flasks were sealed with sterile cotton plugs and stored at 25 °C in the dark for 42 days. The moisture content in each flask was checked gravimetrically at each sampling point. The loss of water by evaporation was compensated by adding distilled water. Triplicate samples were removed from each treatment at different time intervals (0, 7, 14, 21, 28, 35, and 42 days) and immediately transferred to a freezer (−20 °C).

2.7. Acute Toxicity of *cis*-DCCA, 3-PBA, and α-Cypermethrin. According to the OECD guideline 207, the acute toxicity of *cis*-DCCA and 3-PBA to earthworms was tested by a paper contact toxicity assay (OECD 1984). Before the assay, the earthworms were rinsed with tap water and dried by absorbent paper, following a depuration period of 24 h on wet filter paper under dark, to evacuate the gut content of the earthworms. A series of concentrations, 10.0, 30.0, 50.0, 70.0, and 100.0 ng/cm^2 *cis*-DCCA and 3-PBA and 80.0, 159.0, 475.0, 632.0, and 790.0 ng/cm^2 α-cypermethrin, were spiked on filter papers (5.5 × 11.5 cm) by adding *cis*-DCCA, 3-PBA, and α-cypermethrin acetone solutions. Controls were set with the solvent acetone. The filter papers spiked with the test substance were placed in a flat-bottomed glass vial (3.6 cm in diameter and 8 cm in length), and 1 mL of deionized water was added to each vial. A total of 10 replicates were performed for each treatment. The earthworms were placed on the filter papers and kept at 20 ± 2 °C. Mortality was checked after an incubation period of 48 h, and on the basis of that, LC_{50} values were calculated by SPSS, version 18.0 (SPSS, Inc., Chicago, IL).

2.8. Combined Toxicity of *cis*-DCCA, 3-PBA, and α-Cypermethrin. After the LC_{50} values of *cis*-DCCA, 3-PBA, and α-cypermethrin were measured, two kinds of combined toxicity were determined: the binary combination of cis-DCCA + 3-PBA and the ternary combination of *cis*-DCCA + 3-PBA + α-cypermethrin. We chose the modified toxic unit (TU) approach to model the combined toxicity according to the literature.[24] In the TU model, a value of 1 TU is defined as the 50% lethal concentration (LC_{50}) value of the chemical. A series of the sum of the TU (∑TU) was used to set the concentrations of each component at proportions of their respective LC_{50} in the mixture. Therefore, the summations of the concentrations were set equivalent to five levels: ∑0.2 TU, ∑0.5 TU, ∑1.0 TU, ∑2.0 TU, and ∑4.0 TU for *cis*-DCCA + 3-PBA and ∑0.3 TU, ∑0.75 TU, ∑1.5 TU, ∑3.0 TU, and ∑6.0 TU for *cis*-DCCA + 3-PBA + α-cypermethrin. For example of a binary mixture of *cis*-DCCA + 3-PBA, 3.7 ng/cm^2 *cis*-DCCA (0.1 TU) and 5.0 ng/cm^2 3-PBA (0.1 TU) made the mixture of ∑0.2 TU. Therefore, to determine the combined toxicity of *cis*-DCCA + 3-PBA, the series concentrations were 3.7 + 5.0, 9.2 + 12.5, 18.4 + 24.9, 36.7 + 49.8, and 73.4 + 99.6 ng/cm^2, and for the determination of the combined toxicity of *cis*-DCCA + 3-PBA + α-cypermethrin, the concentrations were 3.7 + 5.0 + 19.5, 9.2 + 12.5 + 48.8, 18.4 + 24.9 + 97.6, 36.7 + 49.8 + 195.2, and 73.4 + 99.6 + 390.4 ng/cm^2. The calculation of $LC_{50\ mix}$ (50% lethal concentration of the mixture) was conducted by SPSS, version 18.0. The mixture exhibits synergism, additive, or antagonism effects if the determined $LC_{50\ mix}$ values were lower than 1 TU, equal to 1 TU, or greater than 1 TU, respectively.

2.9. Data Analysis. Degradation curves (concentration in soils versus incubation time) were regressed by Excel 2010 (Microsoft). The first-order polynomial regression analysis model was used to describe the dissipation process for α-cypermethrin enantiomers in the soils. It was assumed that the degradation of α-cypermethrin in five soils followed pseudo-first-order kinetics. The corresponding rate constants (k) were calculated according to the equation $C = C_0e^{-kt}$. The starting point of regressive functions was the maximum value of the enantiomer concentrations in the soils and then decreased in the following days. The half-life ($T_{1/2}$, day) was estimated from equation $T_{1/2} = \ln 2/k = 0.693/k$.

The enantiomeric fraction [EF = (+)/(+) + (−)][25] was used to express the enantioselectivity of a pair of enantiomers. Here, (+) and (−) were peak areas of the (+) and (−) enantiomers of α-cypermethrin. The EF values ranged from 0 to 1, with EF = 0.5 representing the racemic mixture.

DOI: 10.1021/acs.jafc.5b03148
J. Agric. Food Chem. 2015, 63, 7714−7720

3. RESULTS AND DISCUSSION

3.1. Enantioselective Degradation in Soils. Table 2 showed the first-order rate constant, half-life ($t_{1/2}$), and coefficient (R^2), and the results showed that there was great difference in the persistence and enantioselectivity of α-cypermethrin in the soils. The half-lives of the enantiomers ranged from 12.7 to 47.1 days in the soils, with R^2 of 0.8951−0.9837, and the persistence of α-cypermethrin in soil 2 was about 2−3 times longer than that in the others. The observed differences in the persistence of α-cypermethrin in the five soils may be due to the organic carbon content. Soil 2 had the highest organic carbon content among the five soils, which might decrease the dissipation of α-cypermethrin. Soils 1 and 5 had similar pH values; however, the degradation rate of α-cypermethrin in the two soils was totally different, suggesting no significant association between pH values and the degradation rate.

Table 2. First-Order Rate Constants, k, Half-Life ($t_{1/2}$), Coefficient (R^2), and the Enantioselectivity (ES) Values of the Degradation of α-Cypermethrin in Soils

soil	α-cypermethrin enantionmer	k (day^{-1})	$t_{1/2}$ (day)	R^2	ES
soil 1	(−)-(1*S*,*cis*,α*R*)	−0.052	14.40	0.9593	0.046
	(+)-(1*R*,*cis*,α*S*)	−0.057	13.30	0.9580	
soil 2	(−)-(1*S*,*cis*,α*R*)	−0.017	47.08	0.9091	0.227
	(+)-(1*R*,*cis*,α*S*)	−0.027	28.39	0.9837	
soil 3	(−)-(1*S*,*cis*,α*R*)	−0.039	16.56	0.9545	0.103
	(+)-(1*R*,*cis*,α*S*)	−0.048	12.70	0.9668	
soil 4	(−)-(1*S*,*cis*,α*R*)	−0.029	22.21	0.9664	0.134
	(+)-(1*R*,*cis*,α*S*)	−0.038	17.53	0.9717	
soil 5	(−)-(1*S*,*cis*,α*R*)	−0.053	17.12	0.8971	0.070
	(+)-(1*R*,*cis*,α*S*)	−0.051	14.42	0.9248	

The data showed that the two enantiomers dissipated at different rates in the five kinds of soils. The changes of EFs with time have been shown in Figure 3, which increased from the initial value of 0.50 with time in all of the soils, illustrating obvious enantioselectivity with (+)-(1*R*,*cis*,α*S*) being degraded faster than that with (−)-(1*S*,*cis*,α*R*). Figure 2B shows a typical chromatogram of the enantioselective degradation of α-cypermethrin in soil 1 after 42 days of incubation.

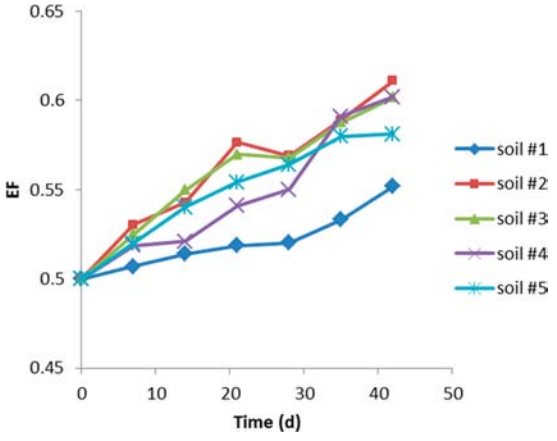

Figure 3. EF curves for the degradation of α-cypermethrin in the five soils.

Li et al. have reportd the enantioselctive degradation of β-cypermethrin in a Tianjin alkaline soil, and the results showed that significant enantioselectivity occurred during the 30 day incubation period, with the enantiomeric ratio (ER) values of one pair of enantiomers of (1*R*,*cis*,α*S*) and (1*S*,*cis*,α*R*) changing from the initial of 1.00 to the final of 0.79.[26] The dissipation of cypermethrin has also been reported in a soil at ambient temperature under aerobic conditions, and the enantiomers of (1*R*,*cis*,α*S*) and (1*S*,*cis*,α*R*) were measured separately, which had half-lives of 63 and 71 days, respectively.[27] The results indicated an enrichment of (1*S*,*cis*,α*R*) in the soils during the degradation process, which were similar to the results in this work.

Enantiomeric selectivity is also a measurement of enantioselectivity, defined as ES = $(k_R - k_S)/(k_S + k_R)$ [where k_R and k_S are rate constants of (+)-(1*R*,*cis*,α*S*) and (−)-(1*S*,*cis*,α*R*) α-cypermethrin in degradation regression equations]. Positive values (0 < ES < 1) indicate a more rapid degradation of (−)-(1*S*,*cis*,α*R*), whereas negative values (−1 < ES < 0) indicate a more rapid dissipation of (+)-(1*R*,*cis*,α*S*), and ES value of 0 shows that the dissipation is not enantioselective. The ES values of α-cypermethrin ranged from 0.0702 to 0.227, showing obvious enantioselectivity in all of the soils, with (+)-(1*R*,*cis*,α*S*) being degraded faster (Table 2). It was found that ES values were positively related to soil organic carbon content after correlation analysis (R^2 = 0.781). Consequently, it can be concluded that the enantioselectivity dissipation of α-cypermethrin was dependent upon the organic carbon content, which may affect chiral signatures by influencing the activity of the microbial community or the level of enzymes in soils.[28] It has been reported that high organic matters in soil increased cypermethrin persistence, which was similar to the result in this experiment.[29]

Some studies reported the enantiomer selectivity of toxicity of cypermethrin. The acute toxicity was measured for the individual enantiomer of α-cypermethrin, and the enantiomer of (+)-(1*R*,*cis*,α*S*) was more toxic than (−)-(1*S*,*cis*,α*R*).[21] The incubation in this paper revealed that (+)-(1*R*,*cis*,α*S*) degraded faster than (−)-(1*S*,*cis*,α*R*), which indicates that enrichment of (−)-(1*S*,*cis*,α*R*) may relieve the toxicity from α-cypermethrin to the earthworm. In addition, in aquatic toxicity, (+)-(1*R*,*cis*,α*S*) was also more toxic than (−)-(1*S*,*cis*,α*R*).[23] Therefore, it is essential to assess the toxicity of pesticide on an enantiomeric level.

3.2. Formation of *cis*-DCCA and 3-PBA. The two metabolites of α-cypermethrin were both detected during its dissipation in the five soils (Figure 4). *cis*-DCCA maintained a higher concentration than 3-PBA through the experimental periods maybe because of the faster degradation of 3-PBA in the soils. *cis*-DCCA could be detected at the 7th day in all of the soils, and the concentration increased with time or was kept at a steady level until the last sample point of 42 day. The final concentrations of *cis*-DCCA in soils 3, 4, and 5 with pH > 7 were 0.59, 0.50, and 0.34 μg/kg, respectively, at the 42nd day, which were higher than the concentrations of 0.11 and 0.17 μg/kg in soils 1 and 5 with pH < 7, respectively. It indicated that *cis*-DCCA was easily generated in alkaline soils.

3-PBA could also be detected at the 7th day in all of the soils. The concentrations increased with time in 1 and 2 soils, reaching a level around 0.11 mg/kg, but only a small amount was found in soil 3 and was undetectable after 21 days. In soils 4 and 5, the highest level appeared at about 14 day at concentrations of 0.13 and 0.31 mg/kg, respectively, and then it

DOI: 10.1021/acs.jafc.5b03148
J. Agric. Food Chem. 2015, 63, 7714−7720

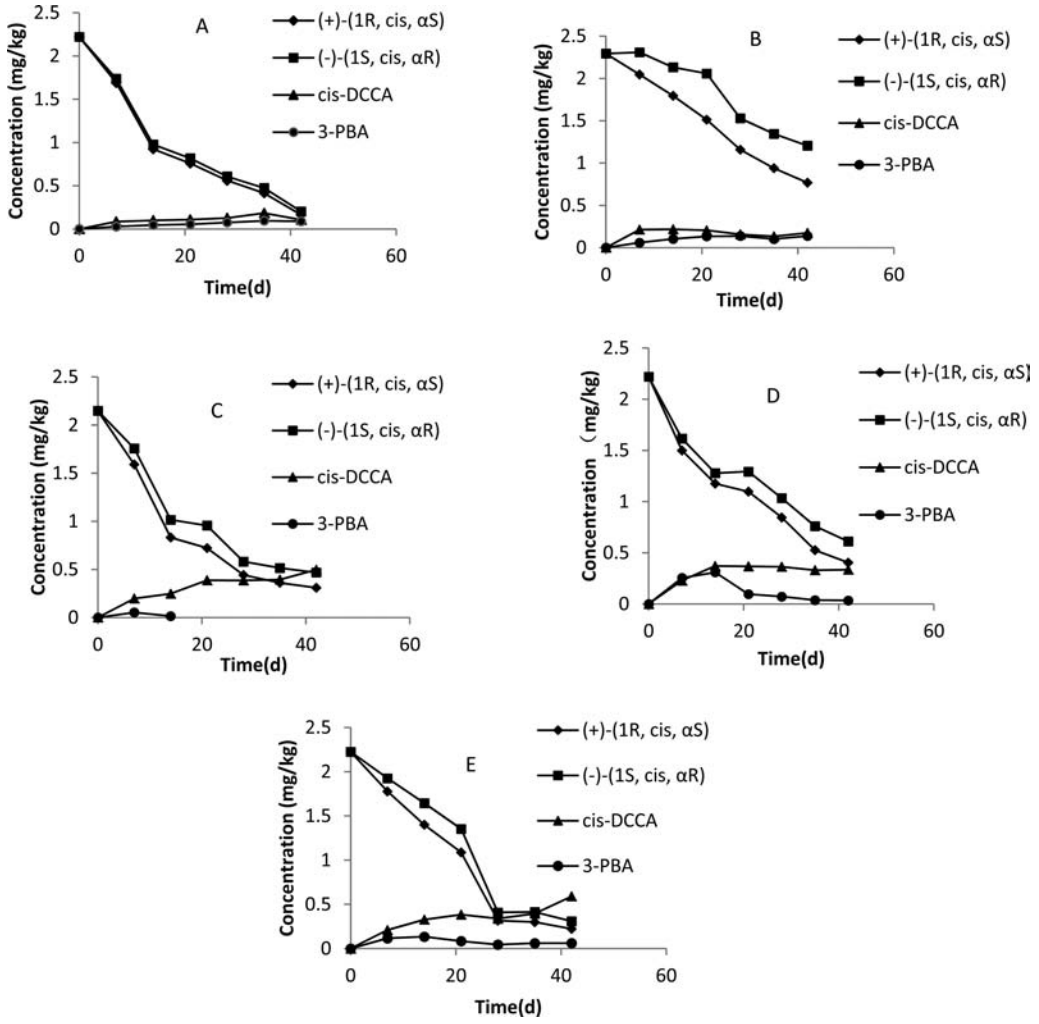

Figure 4. Degradation curves of α-cypermethrin enantiomers and the formation of its metabolites in the five soils.

underwent further degradation. It was found that 3-PBA was more slowly generated and degraded in soils 1 and 2 with pH < 7 than in soils 4 and 5 with pH > 7. It has been reported that the degradation half-life of 3-PBA in Guangzhou soil was 123.7 days,[30] which was much slower than the degradation in soils 3, 4 and 5. This might be caused by the different soil properties. The metabolites were relatively persistent in the soils, which might be a potential problem to the environment for cypermethrin application.

Some epidemiological studies have revealed that 3-PBA has adverse impact on health, such as sperm DNA damage[31] and effect on male reproductive hormone levels,[15] and a number of studies have reported the detection of 3-PBA and *cis*-DCCA in humans. Berkowitz et al. detected 3-PBA in urine samples from pregnant women from ethnic groups (Caucasian, African American, and Hispanic) in New York City, and generally, high levels of 3-PBA (median = 19.3 μg/g of creatinine) were found.[32] Another study in China indicated that the levels of urinary pyrethroid metabolites (3-PBA, *cis*-DCCA, and *trans*-DCCA) were higher than those from the general population of developed countries.[33] Humans may contact those metabolites by a variety of approaches, of which transfer of those from soils by the food chain may be a part.

3.3. Acute Toxicity Assay. By the filter paper contact test, the acute toxicity to earthworm was measured for *cis*-DCCA and 3-PBA. The LC_{50} values for *cis*-DCCA, 3-PBA, and α-cypermethrin were 36.72, 49.81, and 195.22 ng/cm^2, respectively (Table 3). Similar toxicity of α-cypermethrin to earthworm has been reported with the calculated LC_{50} value of 165.61 ng/cm^2.[21] Therefore, the results indicated that the two metabolites were more toxic to the earthworm than the parent compound α-cypermethrin.

Table 3. Calculated LC_{50} Values of *cis*-DCCA, 3-PBA, and α-Cypermethrin for Earthworm

chemicals	48 h LC_{50} (ng/cm^2)	95% confidence intervals	R^2
α-cypermethrin	195.22	138.12−275.94	0.9639
cis-DCCA	36.72	28.76−46.87	0.9794
3-PBA	49.81	37.07−66.89	0.9951

The rate and amount of the metabolites produced varied among the soils. Application of α-cypermethrin to alkaline soils (3, 4, and 5) might be more dangerous to the terrestrial community because more metabolites are produced. In the acidic soils, the metabolites degraded slowly and would last longer, also posing a potential threat to soil animals.

Fast degradation of most pesticides in the environment makes its terrestrial risks acceptable under practical uses. However, evaluations of the ecological risk of corresponding

DOI: 10.1021/acs.jafc.5b03148
J. Agric. Food Chem. 2015, 63, 7714−7720

metabolites are limited at present. Some metabolites may be more persistent and toxic than their parent compounds, which may pose a more detrimental effect on the environment.

The combined toxicities of *cis*-DCCA + 3-PBA and *cis*-DCCA + 3-PBA + α-cypermethrin on earthworms were determined. The combined effect was defined as either concentration additive ($LC_{50\ mix}$ = 1 TU), antagonistic (greater than additive, $LC_{50\ mix}$ > 1 TU), or synergetic (less than additive, $LC_{50\ mix}$ < 1 TU) effects. The $LC_{50\ mix}$ values for *cis*-DCCA + 3-PBA and *cis*-DCCA + 3-PBA + α-cypermethrin were 1.82 TU (1.14−2.90, 95% limits) and 1.72 TU (1.19−2.50, 95% limits), respectively. This result indicated that the combined effect of α-cypermethrin and the two metabolites was antagonistic.

Therefore, it is necessary to evaluate the toxicity of the metabolites and the combined toxicity when assessing the environmental risks from pesticides.

AUTHOR INFORMATION

Corresponding Author

*Telephone/Fax: +8610-62731294. E-mail: liudh@cau.edu.cn.

Notes

The authors declare no competing financial interest.

ACKNOWLEDGMENTS

This work was supported by the National Natural Science Foundation of China (Contract Grant 21307155).

REFERENCES

(1) Casida, J. E.; Quistad, G. B. Golden age of insecticide research: Past, present, or future? *Annu. Rev. Entomol.* **1998**, *43*, 1−16.

(2) Liu, W.; Gan, J. J.; Qin, S. Separation and aquatic toxicity of enantiomers of synthetic pyrethroid insecticides. *Chirality* **2005**, *17* (Suppl), S127−33.

(3) Naumann, K. *Synthetic Pyrethroid Insecticides: Structures and Properties*; Springer-Verlag: Berlin, Germany, 1990; pp 116−141.

(4) Weston, D. P.; Asbell, A. M.; Hecht, S. A.; Scholz, N. L.; Lydy, M. J. Pyrethroid insecticides in urban salmon streams of the Pacific Northwest. *Environ. Pollut.* **2011**, *159*, 3051−3056.

(5) Weston, D. P.; Holmes, R. W.; Lydy, M. J. Residential runoff as a source of pyrethroid pesticides to urban creeks. *Environ. Pollut.* **2009**, *157*, 287−294.

(6) Zhang, C.; Jia, L.; Wang, S. H.; Qu, J.; Li, K.; Xu, L. L.; Shi, Y. H.; Yan, Y. C. Biodegradation of beta-cypermethrin by two Serratia spp. with different cell surface hydrophobicity. *Bioresour. Technol.* **2010**, *101*, 3423−3429.

(7) Jin, Y. X.; Zheng, S. S.; Fu, Z. W. Embryonic exposure to cypermethrin induces apoptosis and immunotoxicity in zebrafish (Danio rerio). *Fish Shellfish Immunol.* **2011**, *30*, 1049−1054.

(8) Ansari, R. A.; Rahman, S.; Kaur, M.; Anjum, S.; Raisuddin, S. In vivo cytogenetic and oxidative stress-inducing effects of cypermethrin in freshwater fish, Channa punctata Bloch. *Ecotoxicol. Environ. Saf.* **2011**, *74*, 150−156.

(9) Wang, H.; Wang, S. F.; Ning, H.; Ji, Y. L.; Zhang, C.; Zhang, Y.; Yu, T.; Ma, X. H.; Zhao, X. F.; Wang, Q.; Liu, P.; Meng, X. H.; Xu, D. X. Maternal Cypermethrin Exposure During Lactation Impairs Testicular Development and Spermatogenesis in Male Mouse Offspring. *Environ. Toxicol.* **2011**, *26*, 382−394.

(10) McKinlay, R.; Plant, J. A.; Bell, J. N. B.; Voulvoulis, N. Endocrine disrupting pesticides: implications for risk assessment. *Environ. Int.* **2008**, *34*, 168−183.

(11) Zhang, C.; Wang, S. H.; Yan, Y. C. Isomerization and biodegradation of beta-cypermethrin by Pseudomonas aeruginosa CH7 with biosurfactant production. *Bioresour. Technol.* **2011**, *102*, 7139−7146.

(12) Sakata, S.; Yoshimura, J.; Nambu, K.; Mikami, N.; Yamada, H. Degradation and leaching behavior of the pyrethroid insecticde fenpropathrin in soils. *J. Pestic. Sci.* **1990**, *15*, 363−373.

(13) Tyler, C. R.; Beresford, N.; van der Woning, M.; Sumpter, J. P.; Tchorpe, K. Metabolism and environmental degradation of pyrethroid insecticides produce compounds with endocrine activities. *Environ. Toxicol. Chem.* **2000**, *19*, 801−809.

(14) Sun, H.; Xu, X. L.; Xu, L. C.; Song, L.; Hong, X.; Chen, J. F.; Cui, L. B.; Wang, X. R. Antiandrogenic activity of pyrethroid pesticides and their metabolite in reporter gene assay. *Chemosphere* **2007**, *66*, 474−479.

(15) Han, Y.; Xia, Y. K.; Han, J. Y.; Zhou, J. P.; Wang, S. L.; Zhu, P. F.; Zhao, R. C.; Jin, N. Z.; Song, L.; Wang, X. R. The relationship of 3-PBA pyrethroids metabolite and male reproductive hormones among non-occupational exposure males. *Chemosphere* **2008**, *72*, 785−790.

(16) Meeker, J. D.; Barr, D. B.; Hauser, R. Pyrethroid insecticide metabolites are associated with serum hormone levels in adult men. *Reprod. Toxicol.* **2009**, *27*, 155−160.

(17) Xie, W. J.; Zhou, J. M.; Wang, H. Y.; Chen, X. Q. Effect of nitrogen on the degradation of cypermethrin and its metabolite 3-phenoxybenzoic acid in soil. *Pedosphere* **2008**, *18*, 638−644.

(18) Duan, X.-Q.; Zheng, J.-W.; Zhang, J.; Hang, B.-J.; He, J.; Li, S.-P. Characteristics of a 3-phenoxybenzoic acid degrading-bacterium and the construction of a engineering bacterium. *Huanjing Kexue* **2011**, *32*, 240−246.

(19) Knaak, J. B.; Dary, C. C.; Zhang, X. F.; Gerlach, R. W.; Tornero-Velez, R.; Chang, D. T.; Goldsmith, R.; Blancato, J. N. Parameters for Pyrethroid Insecticide QSAR and PBPK/PD Models for Human Risk Assessment. *Rev. Environ. Contam. Toxicol.* **2012**, *219*, 1−114.

(20) Barata, C.; Baird, D. J.; Nogueira, A. J. A.; Soares, A.; Riva, M. C. Toxicity of binary mixtures of metals and pyrethroid insecticides to Daphnia magna Straus. Implications for multi-substance risks assessment. *Aquat. Toxicol.* **2006**, *78*, 1−14.

(21) Diao, J. L.; Xu, P.; Liu, D. H.; Lu, Y. L.; Zhou, Z. Q. Enantiomer-specific toxicity and bioaccumulation of alpha-cypermethrin to earthworm Eisenia fetida. *J. Hazard. Mater.* **2011**, *192*, 1072−1078.

(22) Hegeman, W. J. M.; Laane, R. Enantiomeric enrichment of chiral pesticides in the environment. *Rev. Environ. Contam. Toxicol.* **2002**, *173*, 85−116.

(23) Liu, W. P.; Gan, J. J.; Qin, S. Separation and aquatic toxicity of enantiomers of synthetic pyrethroid insecticides. *Chirality* **2005**, *17*, S127−S133.

(24) Marking, L. L. *Fundamentals of Aquatic Toxicology: Methods and Applications*; Hemisphere: New York, 1985; pp 164−176.

(25) Harner, T.; Wiberg, K.; Norstrom, R. Enantiomer fractions are preferred to enantiomer ratios for describing chiral signatures in environmental analysis. *Environ. Sci. Technol.* **2000**, *34*, 218−220.

(26) Li, Z. Y.; Zhang, Z. C.; Zhang, L.; Leng, L. Stereo and enantioselective degradation of beta-Cypermethrin and beta-Cyfluthrin in soil. *Bull. Environ. Contam. Toxicol.* **2008**, *80*, 335−339.

(27) Qin, S. J.; Budd, R.; Bondarenko, S.; Liu, W. P.; Gan, J. Y. Enantioselective degradation and chiral stability of pyrethroids in soil and sediment. *J. Agric. Food Chem.* **2006**, *54*, 5040−5045.

(28) Berger-Preiss, E.; Levsen, K.; Leng, G.; Idel, H.; Sugiri, D.; Ranft, U. Indoor pyrethroid exposure in homes with woollen textile floor coverings. *Int. J. Hyg. Environ. Health* **2002**, *205*, 459−472.

(29) Chapman, R. A.; Harris, C. R. Persistence of 4 pyrethroid insecticides in a mineral and an organic soil. *J. Environ. Sci. Health, Part B* **1981**, *16*, 605−615.

(30) Chen, S.; Geng, P.; Xiao, Y.; Hu, M. Bioremediation of β-cypermethrin and 3-phenoxybenzaldehyde contaminated soils using Streptomyces aureus HP-S-01. *Appl. Microbiol. Biotechnol.* **2012**, *94*, 505−515.

(31) Meeker, J. D.; Barr, D. B.; Hauser, R. Human semen quality and sperm DNA damage in relation to urinary metabolites of pyrethroid insecticides. *Hum. Reprod.* **2008**, *23*, 1932−1940.

(32) Berkowitz, G. S.; Obel, J.; Deych, E.; Lapinski, R.; Godbold, J.; Liu, Z. S.; Landrigan, P. J.; Wolff, M. S. Exposure to indoor pesticides

DOI: 10.1021/acs.jafc.5b03148
J. Agric. Food Chem. 2015, 63, 7714−7720

during pregnancy in a multiethnic, urban cohort. *Environ. Health Perspect.* **2002**, *111*, 79−84.
(33) Qi, X. J.; Zheng, M. L.; Wu, C. H.; Wang, G. Q.; Feng, C.; Zhou, Z. J. Urinary pyrethroid metabolites among pregnant women in an agricultural area of the Province of Jiangsu, China. *Int. J. Hyg. Environ. Health* **2012**, *215*, 487−495.

DOI: 10.1021/acs.jafc.5b03148
J. Agric. Food Chem. 2015, 63, 7714−7720

insulin resistance and the lipid profile in rats with diet-induced obesity.[15] Many previous studies have reported that triterpenoid saponins from *P. grandiflorum* exhibit a variety of pharmacological activities, such as anti-inflammatory, anticancer, immune-enhancing, and hepatoprotective effects.[16] Platycodin D (Figure 1), a bioactive compound of *P. grandiflorum*, has been reported to possess anti-inflammatory, neuroprotective, apoptosis-inducing, and antiadipogenic properties.[17,18] However, there has been no study of the influence of *P. grandiflorum* on brown adipocyte differentiation and mitochondria biogenesis.

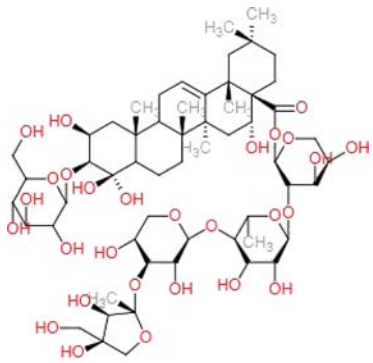

Figure 1. Structure of platycodin D.

In the present study, we investigated the effect of *P. grandiflorum* ethanolic extract (PG) on the differentiation of primary brown adipocytes and compared the antiadipogenic effects of PG and platycodin D in 3T3-L1 cells.

MATERIALS AND METHODS

Preparation of PG. PG was prepared as described previously.[19] Briefly, 1 kg of *P. grandiflorum* was extracted with 80% ethanol for 2 h 20 min using a heating mantle. The solvents were filtered and evaporated under reduced pressure (rotary evaporator model NE-1, Japan), and the remnant was then freeze-dried (freeze-dryer FD-1, Japan) at −56 °C and 9 mm Torr to acquire extracts of the herbal sample.

Reagents. Dulbecco's modified Eagle's medium (DMEM), penicillin−streptomycin, and fetal bovine serum (FBS) were purchased from Gibco RL (Grand Island, NY, USA). Insulin, 3-isobutylmethyxanthine, dexamethasone, indomethacin, 3,3′,5-triiodo-L-thyronine and Oil Red O powder were from Sigma Chemical Co. (St Louis, MO, USA).

HPLC Analysis. The HPLC was equipped with a vacuum degasser, a quaternary pump, and an automatic sample injection system. Chromatographic separation was performed on a Nucleosil C18 (150 mm × 4.6 mm, 5 μm, Teknokroma, Barcelona, Spain). Samples were separated using acetonitrile and phosphate buffer (50:50 v/v), pH 5.5, as the mobile phase at a flow rate of 1.0 mL/min at ambient temperature. Initial elution was performed by acetonitrile−aqueous ammonium acetate 20:80 (v/v). After 10 min, the linear gradient reached 60% acetonitrile.

Cell Culture and Differentiation. Murine 3T3-L1 mouse embryo fibroblasts were obtained from the American Type Culture Collection (Rockwill, MD, USA). Cells were cultured and differentiated as described in our previous study.[20] On day 2, PG was prepared in a differentiation medium at concentrations of 10, 50, and 100 μg/mL. Brown preadipocytes were isolated from the interscapular BAT of mice (age late fetal to postnatal 2−3 days), cultured, and differentiated as described previously.[21] On day 2, PG was prepared in a differentiation medium at concentrations of 10, 50, and 100 μg/mL.

Cytotoxicity Assay. Cell viability was measured using a Cell Proliferation MTS kit (Promega Co., Maddison, WI, USA) as described previously.[20]

Oil Red O staining. Intracellular lipid accumulation was measured using Oil Red O, based on the study of Ramirez-Zacarias et al.[22] as previously described.[20]

RNA Extraction and Real-Time Reverse Transcription Polymerase Chain Reaction (RT-PCR). Total RNA extraction, cDNA synthesis, and the real-time RT-PCR analyses were performed as described previously.[20] The primers used in the experiments are shown in Table 1.

Protein Extraction and Western Blot Analysis. The Western blot analyses were performed as described previously.[20] The antibodies against PPARγ, AMPKα, and pAMPKα were from Cell signaling Technology (Beverly, MA, USA), and the antibodies against C/EBPα, UCP1, PGC1α, and glyceraldehyde-3-phosphate dehydrogenase

Table 1. Sequences of Oligonucleotide Primers (5′ to 3′) for Real-Time RT-PCR[a]

strand (direction)	5′ to 3′ oligonucleotide sequences
	Mouse PPARγ
sense (forward)	TTT TCA AGG GTG CCA GTT TC
antisense (reverse)	TTA TTC ATC AGG GAG GCC AG
	Mouse C/EBPα
sense (forward)	GCC GAG ATA AAG CCA AAC AA
antisense (reverse)	CCT TGA CCA AGG AGC TCT CA
	Mouse Lipin-1
sense (forward)	CGC CAA AGA ATA ACC TGG AA
antisense (reverse)	TGA AGA CTC GCT GTG AAT GG
	Mouse Adiponectin
sense (forward)	AGA CCT GGC CAC TTT CTC CTC ATT
antisense (reverse)	AGA GGA ACA GGA GAG CTT GCA ACA
	Mouse SIRT1
sense (forward)	AGT TCC AGC CGT CTC TGT GT
antisense (reverse)	GAT CCT TTG GAT TCC TGC AA
	Mouse PRDM16
sense (forward)	TGG GCT CAC TAC CCT ACC AC
antisense (reverse)	GAC TTT GGC TCA GCC TTG AC
	Mouse UCP1
sense (forward)	AAC TGT ACA GCG GTC TGC CT
antisense (reverse)	TAA GCC GGC TGA GAT CTT GT
	Mouse PGC1α
sense (forward)	AAT GCA GCG GTC TTA GCA CT
antisense (reverse)	TGT TGA CAA ATG CTC TTC GC
	Mouse SIRT3
sense (forward)	TCG AAG GAA AGA TGT GGT CC
antisense (reverse)	ATC TGT CCT GTC CAT CCA GC
	Mouse NRF
sense (forward)	CCA CGT TGG ATG AGT ACA CG
antisense (reverse)	CAG ACT CGA GGT CTT CCA GG
	Mouse CytC
sense (forward)	TTG TTC AGA AGT GTG CCC AG
antisense (reverse)	CCA GGT GAT GCC TTT GTT CT
	Mouse GAPDH
sense (forward)	AAC TTT GGC ATT GTG GAA GG
antisense (reverse)	GGA TGC AGG GAT GAT GTT CT

[a]PPARγ, peroxisome proliferator-activated receptor γ; C/EBPα, CCAAT enhancer binding protein α; SIRT1, silent mating type information regulation 2 homologue 1; PRDM16, PR domain containing 16; UCP1, uncoupling protein 1; PGC1α, PPARγ-coactivator 1 α; SIRT3, silent mating type information regulation 2 homologue 3; NRF, nuclear respiratory factor 1; CytC, cytochrome C; GAPDH, glyceraldehyde-3-phosphate dehydrogenase.

DOI: 10.1021/acs.jafc.5b01908
J. Agric. Food Chem. 2015, 63, 7721−7730

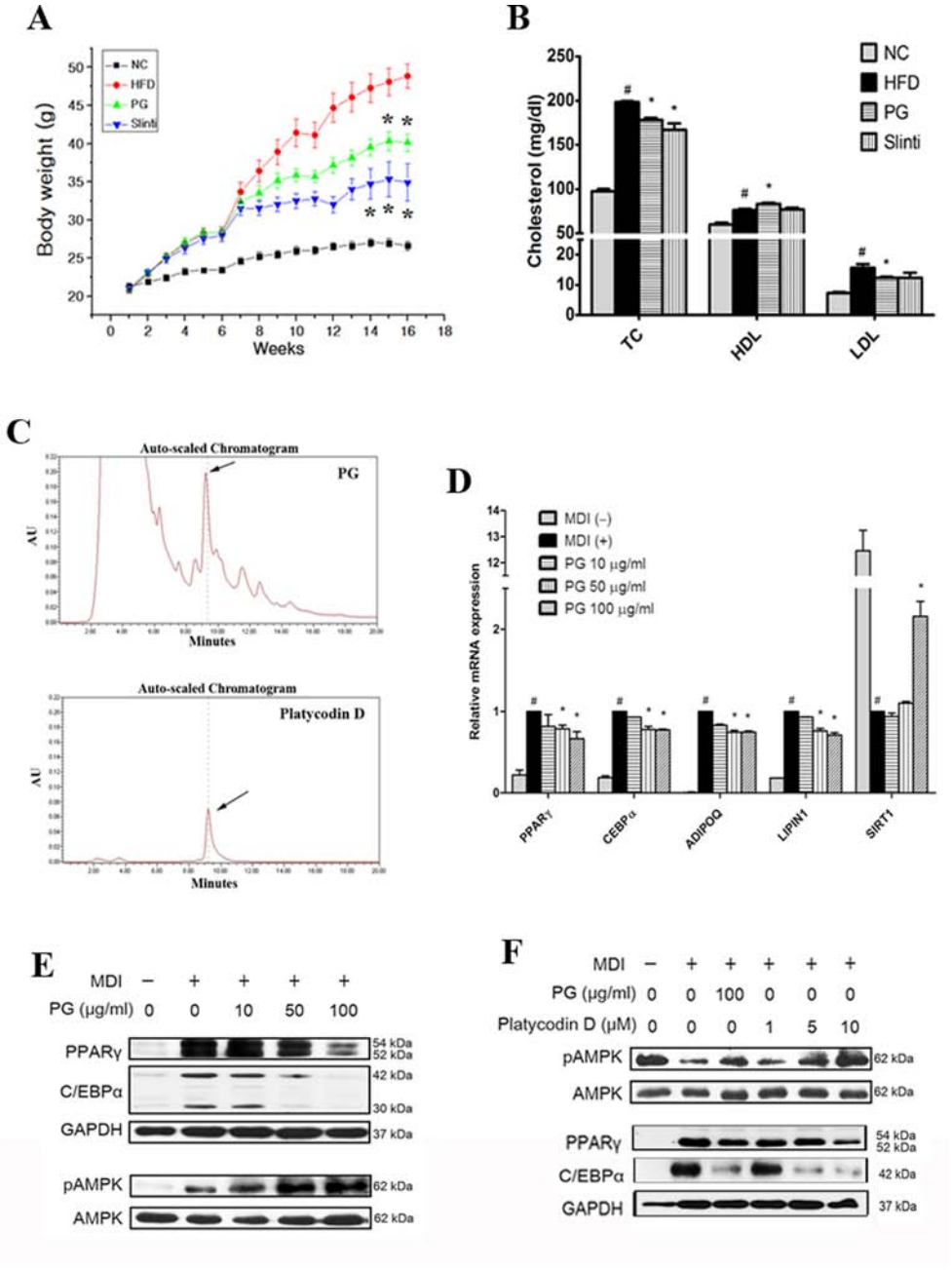

Figure 2. PG attenuates weight gain in HFD-induced obese mice and modulates key transcriptional regulators in 3T3-L1 cells. Mice (n = 5 per group) were administrated PG extract (100 mg/(kg·day)) with a high-fat-diet (HFD) for 12 weeks. Normal control group (NC) was fed normal chow diet. Slinti (5 mg/(kg·day)) was administrated as a positive control. Changes in (A) body weight and (B) serum levels of total, HDL, and LDL cholesterol were measured. (C) HPLC chromatogram of PG. Each peak displays PG (above) and platycodin D (below). PG was extracted with 80% ethanol. (D) The mRNA of PPARγ, C/EBPα, adiponectin, lipin-1, and SIRT1 were analyzed by real-time RT-PCR. (E) PPARγ, C/EBPα, and pAMPK protein levels were analyzed by a Western blot analysis. (F) Effect of PG on PPARγ, C/EBPα, and pAMPK was compared with effect of platycodin D by a Western blot analysis. Results were expressed relative to GAPDH. Values are mean ± SEM of data from three separate experiments. (A, B) $^{\#}p < 0.05$, significantly different from NC; $^{*}p < 0.05$, significantly different from HFD. (D) $^{\#}p < 0.05$ vs MDI-undifferentiated control cells; $^{*}p < 0.05$ vs MDI-differentiated control cells.

(GAPDH) were purchased from Santa Cruz Biotechnology (Santa Cruz, CA, USA).

Mitochondrial Microscopic Analysis. The mitochondrial analysis was performed as described previously.[21]

Ethics Statement. All procedures used in animal experiments were performed according to a protocol approved by the Animal Care and Use Committee of the Institutional Review Board of the Kyung Hee University (confirmation number, KHUASP (SE)-13-012).

High-Fat-Diet (HFD)-Induced Obese Mice Study. Male 4-week-old C57BL/6J mice were purchased from Daehan Biolink Co. (Eumsung, Korea) and maintained for 1 week prior to experiments. All animals were maintained under a 12 h light−dark cycle in a pathogen-free animal facility. Mice were provided with a laboratory diet and water *ad libitum*. To induce obesity, the mice were fed a HFD (Rodent Diet D12492, Research Diet, New Brunswick, NJ, USA) consisting of 60% fat in accordance with previously published reports.[23] Normal mice were fed a commercial standard chow diet (CJ Feed Co., Ltd., Seoul, Korea). The mice were fed a HFD for 4 weeks before administration with PG or Slinti, a green tea extract used as a positive control (Myoungmoon Pharm. Co., Ltd., Seoul, Korea). The mice

DOI: 10.1021/acs.jafc.5b01908
J. Agric. Food Chem. 2015, 63, 7721−7730

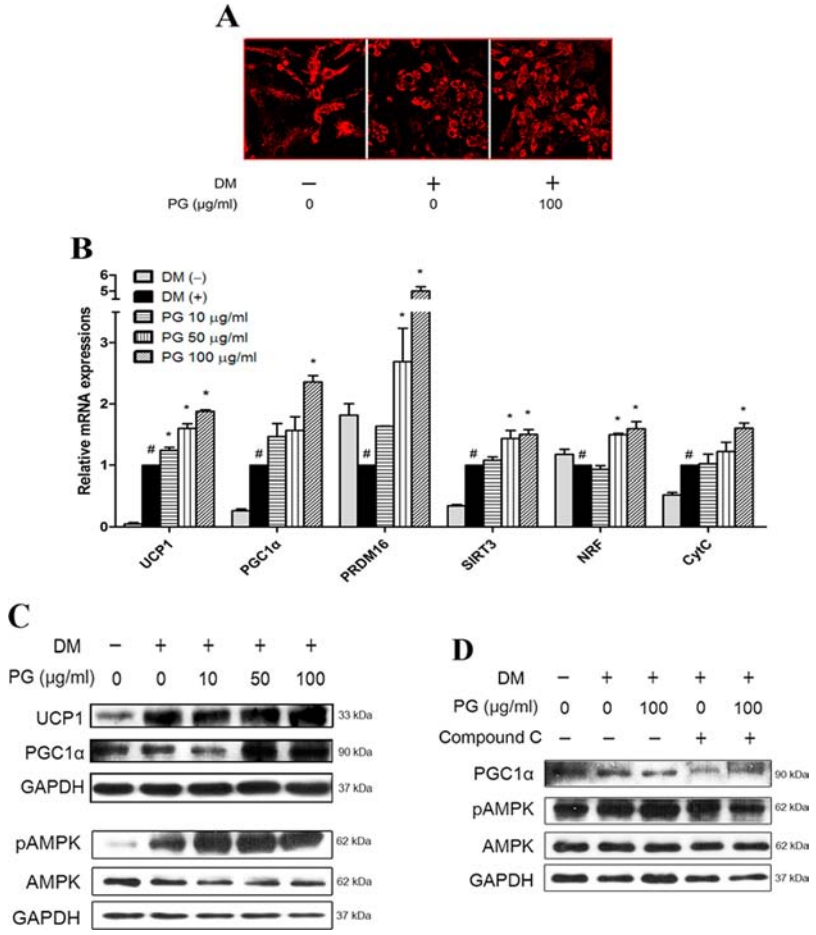

Figure 3. PG increases expressions of mitochondria-related factors in primary brown adipocytes. (A) Mitochondrial abundance in primary brown adipocytes was analyzed by MitoTracker Red staining. (B) The mRNA of UCP-1, PGC1α, PRDM16, SIRT3, NRF, and CytC were analyzed by real-time RT-PCR. (C) UCP1, PGC1α, and pAMPK protein levels were analyzed by a Western blot analysis. (D) Effects of PG with or without cotreatment of compound C on PGC1α and pAMPK were analyzed by a Western blot analysis. Results were expressed relative to GAPDH. Values are mean ± SEM of data from three separate experiments. (B) $^{\#}p < 0.05$ vs DM-undifferentiated control cells; $^{*}p < 0.05$ vs DM-differentiated control cells.

were randomly divided into four groups (n = 5 per group) that were fed a normal diet, a HFD, a HFD plus PG, or a HFD plus Slinti, for 16 weeks. Body weight and food intake were measured three times per week.

***db/db* Mice Study.** Male 5-week-old *Lepr*$^{-/-}$ (*db/db*) mice and age matched nondiabetic (ND) heterozygous mice (both derived from a C57BL/6J background) were purchased from Daehan Biolink Co. (Eumsung, Korea) and maintained for 1 week prior to experiments. All animals were maintained under a 12 h light−dark cycle in a pathogen-free animal facility. All mice were provided with a laboratory diet and water *ad libitum*. Healthy mice were randomly allocated into three groups as follows (n = 5 per group): an ND group, a *db/db* group, and a *db/db* group administered platycodin D. The control groups (ND and *db/db* group) were orally administered distilled water, while the experiment group was orally administered platycodin D prepared in distilled water (5 mg/kg of body weight) five times per week for 5 weeks. Body weight and food intake were measured three times per week.

Hematoxylin and Eosin Staining. After the *db/db* mice were sacrificed, the liver tissues were collected, washed in saline, fixed in 10% formalin, and then dehydrated using grades 70%, 80%, 90%, 95%, and 100% ethanol. After clearing in two changes of xylene, the samples were impregnated with molten paraffin wax, then embedded and blocked out. The tissues were then cut into 4−5 μm sections and stained with hematoxylin and eosin. Microscopic examinations were performed and photographs were taken under a regular light microscope (Olympus Co., Tokyo, Japan).

Serum Analysis. At the end of the treatment, the animals were anesthetized, and serum was separated immediately after blood sampling by centrifugation at 4000g for 30 min. The serum was stored at −70 °C until being used for assays. Aspartate aminotransferase (AST), alanine aminotransferase (ALT), total cholesterol (TC), high-density lipoprotein (HDL) cholesterol, and low-density lipoprotein (LDL) cholesterol were assayed at the Seoul Medical Science Institute (Seoul Clinical Laboratories, Seoul, Korea).

Statistical Analysis. All data, expressed as mean ± SEM, were processed statistically using the software SPSS 12 for Windows (SPSS Inc., Chicago, IL, USA). A value with $p < 0.05$ was considered to indicate statistical significance.

RESULTS

PG Attenuates Weight Gain in HFD-Induced Obese Mice and Modulates Key Transcriptional Regulators Level and the Phosphorylation of AMPK in 3T3-L1 Cells. In the present study, we investigated the effect of PG on primary cultured brown adipocytes, 3T3-L1 cells, and the HFD-induced obesity animal model. First, in order to investigate the antiobesity effects of PG *in vivo*, mice were fed HFD for 4 weeks before administration with PG. The HFD significantly increased the mouse body weights at 4 weeks compared with weights in the standard diet group. After induction of obesity, the mice were subdivided into four groups

DOI: 10.1021/acs.jafc.5b01908
J. Agric. Food Chem. 2015, 63, 7721−7730

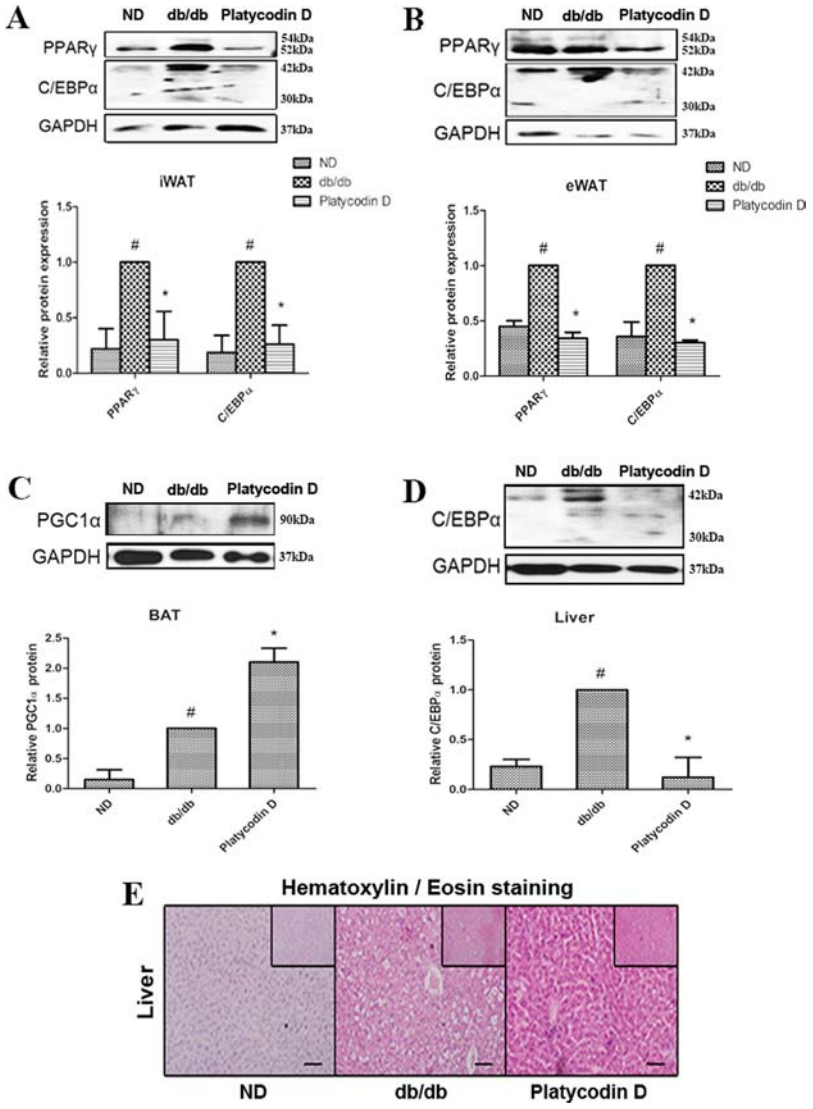

Figure 4. Platycodin D improves adipogenic-related factors and mitochondrial biogenesis factors in *db/db* mice. (A,B) After the study termination, protein expression levels of PPARγ and C/EBPα were measured in iWAT and eWAT. (C) The protein expression level of PGC1α, a thermogenic and mitochondrial biogenesis gene, was measured in BAT. (D) The protein expression level of C/EBPα was measured in liver. Results were expressed relative to GAPDH. (E) Paraffin sections of liver from nondiabetic (ND) mice, *db/db* mice, and *db/db* mice treated with platycodin D at 5 mg/kg were stained with hematoxylin and eosin (H&E), and the histological changes were observed at 200× (scale bar = 100 μm). Values are mean ± SEM of data from three separate experiments. (A−D) $^{\#}p < 0.05$ significantly different from ND; $^{*}p < 0.05$ significantly different from *db/db*.

(n = 5 per group): a normal diet group with vehicle treatment, a 60% HFD group with vehicle treatment, a 60% HFD group with Slinti (5 mg/(kg·day)) treatment as a positive control, and a 60% HFD group with PG (100 mg/(kg·day)). PG significantly suppressed body weight gain compared with the HFD group ($p < 0.05$). The HFD group gained 48.84 ± 1.61 g of weight, while the PG and Slinti groups gained 40.14 ± 0.75 g and 34.89 ± 2.42 g, respectively (Figure 2A). Administration of PG had no effect on food intake compared with the HFD (not shown). The changes in the blood plasma parameters after the 16 week experiment were measured. PG significantly attenuated the levels of TC and LDL cholesterol ($p < 0.05$) (Figure 2B).

A HPLC chromatogram revealed that platycodin D was a major constituent of PG (Figure 2C). To determine the cytotoxicity of PG, 3T3-L1 cells were treated with various concentrations of PG, and the cell viability was measured by an MTS assay. Treatment with 10−100 μg/mL of PG did not cause significant cytotoxic effects ($p < 0.05$; Figure S1A). Due to this result, further treatments were conducted at concentrations of 10, 50, and 100 μg/mL. Next, to investigate the effects of PG on preadipocyte differentiation, the lipid accumulation was measured by an Oil Red O staining assay. As shown in Figure S1C, 100 μg/mL of PG suppressed lipid accumulation in 3T3-L1 adipocytes at levels that were statistically significant ($p < 0.05$), suggesting that PG inhibits adipogenesis in 3T3-L1 cells.

Adipocyte differentiation accompanies the changes in expression of various adipogenic and lipogenic genes. PPARγ and C/EBPα are well recognized adipogenic genes known to have roles in the early stage of adipogenesis.[24,25] Lipin-1 is also required at the early step in adipocyte differentiation for induction of the adipogenic gene transcription.[26] To investigate the antiadipogenic mechanism of PG, its effects on mRNA expression levels of PPARγ, C/EBPα, lipin-1, adiponectin, and SIRT1 were examined. Fully differentiated 3T3-L1 cells were exposed for 48 h to various concentrations of PG. Expressions

DOI: 10.1021/acs.jafc.5b01908
J. Agric. Food Chem. 2015, 63, 7721−7730

of both adipogenic genes, PPARγ and C/EBPα, were significantly decreased by PG treatment ($p < 0.05$). PG also suppressed the expression of adiponectin and lipin-1 in a dose-dependent manner. In addition, SIRT1, an important regulator of preadipocyte differentiation and adipogenesis, was significantly increased by PG ($p < 0.05$; Figure 2D).

We demonstrated that PG treatment resulted in a dose-dependent suppression of PPARγ and C/EBPα. AMPK, a key player in energy homeostasis,[27] was activated by PG during differentiation, because the level of phosphorylated AMPKα was increased while the level of total AMPKα was unchanged (Figure 2E). To compare the effects of PG and platycodin D, AMPK phosphorylation was investigated by Western blotting. Platycodin D at 5 μM showed similar effects to 100 μg/mL of PG on AMPK activation. In addition, platycodin D at 5 μM exhibited decreased expression of PPARγ and C/EBPα, similarly to effects of 100 μg/mL of PG (Figure 2F).

PG Increases the Expression of Mitochondria-Related Genes in Primary Brown Adipocytes and Induces the Differentiation of Primary Brown Adipocytes via the AMPK Signal Pathway. We also investigated the effects of PG on differentiation of primary brown adipocytes. The amount of brown adipose tissue in adult humans has been reported to be highly correlated with their degree of obesity, indicating that brown adipocytes may play an important role in the prevention and treatment of obesity.[28,29] Before any further experiments, we first performed an MTS assay in order to evaluate the cell toxicity of PG on brown adipocytes. A cell viability assay demonstrated that PG (10−100 μg/mL) did not show any cytotoxicity ($p < 0.05$; Figure S1B). Since the activity and number of mitochodria is a typical difference between white and brown adipocytes, the mitochondrial abundance was analyzed. Brown preadipocytes isolated from mice interscapular brown fat were induced to differentiate into mature brown adipocytes. Mitochondria in mature brown adipocytes and adipocyte morphology were then quantified using Mito-Tracker fluorescence images. As a result, PG-treated cells showed stronger staining than control cells (Figure 3A). In addition, to investigate the effects of PG on differentiation of primary brown adipocytes, the level of mitochondia-related genes was measured by real-time RT- PCR. The mRNA of UCP1, PGC1α, PRDM16, SIRT3, NRF, and CytC was significantly increased in a dose-dependent manner by PG ($p < 0.05$) (Figure 3B). Similarly, the proteins of UCP1, PGC1α, and pAMPK were increased by PG (Figure 3C). Brown adipocytes exhibited significant decreases in PGC1α and pAMPK protein expressions by the AMPK inhibitor compound C, which was successfully restored by PG treatment (Figure 3D). These results clearly suggest that PG induces the differentiation of primary brown adipocytes via the AMPK signal pathway.

Platycodin D Modulates Adipose Tissue Metabolism and Alters Histologic Changes of the Livers in *db/db* Mice. To confirm the effects of platycodin D on adipose tissue metabolism *in vivo*, mice were administrated platycodin D for 5 weeks. Platycodin D reduced the protein expression levels of PPARγ and C/EBPα, the adipogenic-related markers in inguinal WAT (iWAT) and epididymal WAT (eWAT) (Figure 4A,B). Also, the protein expression level of C/EBPα in liver was decreased by platycodin D (Figure 4D). Treatment with platycodin D increased the protein expression levels of PGC1α, a specific marker involved in mitochondrial biogenesis in interscapular BAT of *db/db* mice (Figure 4C). Histology of the liver tissues showed that the triglyceride content of the liver in the platycodin D group was lower than the *db/db* group (Figure 4E). These results suggest that platycodin D is an important regulator of adipose tissue metabolism and decreases steatosis in the liver tissue.

DISCUSSION

Obesity has become an epidemic in developed countries and is also rapidly spreading in many developing countries.[30] The rates of obesity and overweight have been continuing to grow in adults, and unfortunately the situation has been worsening by penetrating into the child and adolescent populations.[7] Adipose tissue plays a critical role in energy homeostasis as both an energy reserve and an endocrine organ in animals.[7,31] Obesity is defined as an excessive growth of adipose tissue mass.[32] There are two types of adipose tissues, WAT and BAT, which are primarily composed of white and brown adipocytes, respectively. White adipocytes primarily function as a depot of triglycerides as energy reservoirs, while brown adipocytes generate heat energy at the expense of ATP generation due to their high expression of UCP1.[33−35] Most obesity related studies have focused on the differentiation of white adipocytes; thus the molecular differentiation mechanism of brown adipocytes has not been investigated thoroughly yet.[29,36,37] In the present study, we investigated the effects of PG on obesity in brown/white preadipocytes.

P. grandiflorum has been used as a traditional medicine for treating bronchitis, asthma, pulmonary tuberculosis, hyperlipidemia, and hypercholesterolemia in Asia. It contains numerous triterpenoid saponins, carbohydrates, and fibers.[38,39]

Many studies have focused on the identification of the biological activities of *P. grandiflorum* including anti-inflammation, antihyperlipidemia, antiobesity, and apoptosis.[40−42] Reportedly, *P. grandiflorum* water extract (PWE) significantly reduced plasma TC and TG concentrations, as well as body weight and adipose tissue weight. PWE also decreased the size of subcutaneous adipocytes. Furthermore, the up-regulation of FABP mRNA expression induced by a high-fat feeding was significantly repressed by PWE treatment.[15] Also, *P. grandiflorum* ameliorates obesity and insulin resistance in obese mice via reductions of adipocyte differentiation, followed by the activation of AMPK/ACC pathways.[43] Considering the reports, PG may be useful in the prevention and improvement of obesity.

PPARγ and C/EBPα are known to be regulated in early stages during adipocyte differentiation.[44] PPARγ is viewed as a master regulator of adipogenesis, since expression of PPARγ is sufficient to induce adipogenesis in the absence of extracellular hormones and, on the other hand, deficiency of PPARγ prevents preadipocytes from differentiating into mature adipocytes.[45] C/EBPα, a member of the basic region leucine zipper family of transcription factors, is involved in adipogenesis and hepatic glucose and lipid metabolism.[5,46] In the present study, PG treatment resulted in reduced expression of PPARγ and C/EBPα at both the mRNA and protein levels in 3T3-L1 cells. These results clearly indicated that PG is a potent inhibitor for adipocyte differentiation via the PPARγ and C/EBPα signaling cascade.

Lipin-1 exists in three isoforms, lipin-1α, -1β, and -1γ, and in most cell types, lipin-1 is distributed throughout the cell, because the 1β isoform predominantly exists in the cytoplasm and the 1α isoform mostly in the nucleus, while lipin-1γ is mainly localized in lipid droplets.[47] Adiponectin, an adipocytokine secreted by the adipose tissue, has been confirmed to

DOI: 10.1021/acs.jafc.5b01908
J. Agric. Food Chem. 2015, 63, 7721−7730

regulate glucose metabolism both *in vivo* and *in vitro*.[5] A decrease in the blood level of adiponectin with excessive body fat deposition was reported, while circulating adiponectin is raised with body fat loss, revealing that there is a close connection between adiponectin and body fat deposition.[5,48,49] We found that PG can inhibit adipocyte differentiation through suppression of lipin-1 and adiponectin. SIRT1 has numerous beneficial metabolic effects against those associated with a HFD, and this has been highlighted in SIRT1 deficient and gain of function mouse models. Also, SIRT1 exerts effects similar to those of AMPK on cellular energy metabolism and mitochondrial biogenesis.[50,51] AMPK regulation of fatty acid metabolism and mitochondrial content in response to pharmacological activation as well as exercise has grown AMPK into a potential therapeutic target for treatment of obesity and type 2 diabetes.[52,53] Our results demonstrated that PG significantly down-regulated lipin-1 and adiponectin mRNA expression in 3T3-L1 adipocyte differentiation. PG also significantly up-regulated the expressions of SIRT1 and AMPK during 3T3-L1 adipocyte differentiation. Interestingly, activation of AMPK and SIRT1 by PG seemed to inhibit adipocyte differentiation. Thus, we suggest that PG has a beneficial role in obesity by activating the AMPK/SIRT1 signaling pathway.

Platycodin D, a naturally occurring saponin in the roots of *P. grandiflorum*, has various pharmacological activities, including anti-inflammatory, antihyperlipidemic, and antiobesity.[18,54−56] In this study, we compared the effects of PG and platycodin D in the differentiation of adipocytes. When compared, inhibition rate of PG and platycodin D on lipid accumulation was similar in 100 μL/mL PG and 5 μM platycodin D (36.59% and 41.01%, respectively). In AMPK phosphorylation, 100 μL/mL PG also showed similar effect to that of 5 μM platycodin D on the AMPK activation. These results indicate that similar to PG, platycodin D inhibits adipogenesis in obesity.

Mitochondrial homeostasis is crucial for maintaining proper energy supply and function of tissues. The abundance of mitochondria in a cell is determined by biogenesis, fission/fusion, and mitophagy.[57,58] PGC1α is an important factor in mitochondrial biogenesis and function and is regulated by an acetylation/deacetylation reaction.[59] Also, PGC1α is a transcriptional coactivator that plays a major role in the acquisition of the specific brown adipocyte phenotype. Because of the important role of PGC1α in the differentiation process of brown fat, the stimulatory effects of PG on PGC1α gene transcription suggested that PG might also be able to enhance brown adipocyte differentiation. PGC1α coactivates with nuclear receptors and transcription factors and thereby activates genes involved in thermogenesis, lipid oxidation, and mitochondrial oxidation, which are associated with the specific thermogenic function of BAT.[14,60] In mice, its presence at very high levels in the inner membrane of brown fat cell mitochondria is determined by brown adipocyte precursor cell differentiation along a pathway involving the critical dual presence of PGC1α and PRDM16.[61] PRDM16 is a critical regulator of brown adipocyte development. Downregulation of PRDM16 in brown adipocytes promotes their fate switch to myoblasts.[62,63] PRDM16 drives expression of the browning and thermogenic gene program. Overexpression of PRDM16 in adipose lineage resulted in more energy expenditure, which improved glucose metabolism and enhanced insulin sensitivity.[63] The sirtuins (SIRT1−-SIRT7) are a family of nicotinamide adenine dinucleotide (NAD^+)-dependent protein deacetylases[64,65] and regulate multiple cellular processes, including metabolic homeostasis.[66] SIRT3 is a mitochondrial sirtuin that regulates fatty acid oxidation during fasting and ATP production.[8] We showed that PG significantly up-regulated the major factor expressions of brown adipocytes including PGC1α, PRDM16, SIRT3, and NRF. These genes are largely known to be involved in the regulation of thermogenesis and mitochondrial oxidation. The present findings, that PG up-regulated these genes and it was also associated with a large number of mitochondria, suggest the beneficial effect of PG on mitochondrial biogenesis, thermogenesis, and differentiation in primary cultured brown adipocytes.

We also performed an animal study to confirm the effect of PG *in vivo* using the concentration 100 mg/(kg·day). We showed that the body weight of PG fed mice was decreased in 100 mg/(kg·day). The serum TC and LDL cholesterol were decreased in PG treated mouse. In addition, HDL cholesterol was increased in PG treated mice. The serum levels of AST and ALT indicated that PG did not induce any toxicity (Figure S2). In the present study, we demonstrated the effect of PG on diet-induced obesity improvement and treatment.

Lepr$^{-/-}$ (*db/db*) mice are leptin receptor deficient and develop obesity, hyperglycemia, insulin resistance, and dyslipidemia by 4−8 weeks of age.[67] Two different types of adipose tissue have been described: BAT, composed mainly of brown adipocytes, and WAT, defined by a majority of white adipocytes, both tissues being able to accumulate lipids in intracellular droplets.[68] We performed a *db/db* mouse study to confirm the histologic change in the liver and adipose tissue metabolism induced by platycodin D *in vivo*. As shown in Figure 4, these results clearly suggest that platycodin D regulates the protein expression levels of several adipogenic- and thermogenic-factors in tissues related to metabolism. Therefore, this study provides the evidence that platycodin D is also able to exhibit an antiobesity activity in *db/db* mice.

Taken together, our results indicate that PG suppressed the adipogenesis of white adipocytes and stimulated the differentiation of brown adipocytes through modulation of mitochondria-related genes both *in vitro* and *in vivo*. Thus, our results suggest the potential of their usage for obesity treatment. However, further studies targeting the therapeutic pathways of PG and platycodin D on white/brown adipogenesis and thermogenesis are required, not only to clarify the effects of both materials but also to clarify the understanding of the mechanism link between WAT and BAT function, which is possibly due to AMPK signaling based on our study.

■ ASSOCIATED CONTENT

Supporting Information

The Supporting Information is available free of charge on the ACS Publications website at DOI: 10.1021/acs.jafc.5b01908.

PG inhibition of lipid accumulation in 3T3-L1 cells and PG reduction of AST and ALT levels in HFD-induced obese mice (PDF)

■ AUTHOR INFORMATION

Corresponding Author

*Tel: +82 961 9262. E-mail: jyum@khu.ac.kr.

Author Contributions

Hye-Lin Kim, Yunu Jung, Dong-Hyun Youn, JongWook Kang, and Hyewon Park performed the *in vitro* and *in vivo*

DOI: 10.1021/acs.jafc.5b01908
J. Agric. Food Chem. 2015, 63, 7721−7730

experiments and analyzed the data. Hye-Lin Kim and Mi-Young Jeong collected the data and undertook the statistical analyses. Hye-Lin Kim and Jinbong Park wrote the manuscript. Jae-Young Um designed and supervised the study, including editing of the manuscript. All authors contributed to and have approved the final manuscript.

Funding

This work was supported by the National Research Foundation of Korea (NRF) grant funded by the Korea government (NRF-2013R1A2A2A03006068 and NRF-2010-0022450).

Notes

The authors declare no competing financial interest.

■ ABBREVIATIONS USED

PPARγ, peroxisome proliferator-activated receptor γ; C/EBPα, CCAAT-enhancer-binding protein α; AMPK, AMP-activated protein kinase; SIRT1, silent mating type information regulation 2 homologue 1; PRDM16, PR domain containing 16; UCP1, uncoupling protein 1; PGC1α, PPARγ-coactivator 1 α; SIRT3, silent mating type information regulation 2 homologue 3; NRF, nuclear respiratory factor 1; CytC, cytochrome C; GAPDH, glyceraldehyde-3-phosphate dehydrogenase; DMEM, Dulbecco's modified Eagle's medium; FBS, fetal bovine serum; IBMX, 3-isobutylmethylxanthine; DEX, dexamethasone; TC, total cholesterol; LDL, low-density lipoprotein; HDL, high-density lipoprotein

■ REFERENCES

(1) Nakagami, H. The mechanism of white and brown adipocyte differentiation. *Diabetes Metab. J.* **2013**, *37*, 85−90.

(2) Student, A. K.; Hsu, R. Y.; Lane, M. D. Induction of fatty acid synthetase synthesis in differentiating 3T3-L1 preadipocytes. *J. Biol. Chem.* **1980**, *255*, 4745−4750.

(3) Morrison, R. F.; Farmer, S. R. Hormonal signaling and transcriptional control of adipocyte differentiation. *J. Nutr.* **2000**, *130*, 3116S−3121S.

(4) Yan, J.; Yang, H.; Gan, L.; Sun, C. Adiponectin-impaired adipocyte differentiation negatively regulates fat deposition in chicken. *J. Anim. Physiol. Anim. Nutr.* **2014**, *98*, 530−537.

(5) Bauche, I. B.; El Mkadem, S. A.; Pottier, A. M.; Senou, M.; Many, M. C.; Rezsohazy, R.; Penicaud, L.; Maeda, N.; Funahashi, T.; Brichard, S. M. Overexpression of adiponectin targeted to adipose tissue in transgenic mice: impaired adipocyte differentiation. *Endocrinology* **2007**, *148*, 1539−1549.

(6) Ugrankar, R.; Liu, Y.; Provaznik, J.; Schmitt, S.; Lehmann, M. Lipin is a central regulator of adipose tissue development and function in Drosophila melanogaster. *Mol. Cell. Biol.* **2011**, *31*, 1646−1656.

(7) He, Y.; Li, Y.; Zhao, T.; Wang, Y.; Sun, C. Ursolic acid inhibits adipogenesis in 3T3-L1 adipocytes through LKB1/AMPK pathway. *PLoS One* **2013**, *8*, e70135.

(8) Nogueiras, R.; Habegger, K. M.; Chaudhary, N.; Finan, B.; Banks, A. S.; Dietrich, M. O.; Horvath, T. L.; Sinclair, D. A.; Pfluger, P. T.; Tschop, M. H. Sirtuin 1 and sirtuin 3: physiological modulators of metabolism. *Physiol. Rev.* **2012**, *92*, 1479−1514.

(9) Cohen, H. Y.; Miller, C.; Bitterman, K. J.; Wall, N. R.; Hekking, B.; Kessler, B.; Howitz, K. T.; Gorospe, M.; de Cabo, R.; Sinclair, D. A. Calorie restriction promotes mammalian cell survival by inducing the SIRT1 deacetylase. *Science* **2004**, *305*, 390−392.

(10) Picard, F.; Kurtev, M.; Chung, N.; Topark-Ngarm, A.; Senawong, T.; Machado De Oliveira, R.; Leid, M.; McBurney, M. W.; Guarente, L. Sirt1 promotes fat mobilization in white adipocytes by repressing PPAR-gamma. *Nature* **2004**, *429*, 771−776.

(11) Giralt, A.; Villarroya, F. SIRT3, a pivotal actor in mitochondrial functions: metabolism, cell death and aging. *Biochem. J.* **2012**, *444*, 1−10.

(12) Schmidt, S. F.; Mandrup, S. Gene program-specific regulation of PGC-1{alpha} activity. *Genes Dev.* **2011**, *25*, 1453−1458.

(13) Chaturvedi, R. K.; Hennessey, T.; Johri, A.; Tiwari, S. K.; Mishra, D.; Agarwal, S.; Kim, Y. S.; Beal, M. F. Transducer of regulated CREB-binding proteins (TORCs) transcription and function is impaired in Huntington's disease. *Hum. Mol. Genet.* **2012**, *21*, 3474−3488.

(14) Giralt, A.; Hondares, E.; Villena, J. A.; Ribas, F.; Diaz-Delfin, J.; Giralt, M.; Iglesias, R.; Villarroya, F. Peroxisome proliferator-activated receptor-gamma coactivator-1alpha controls transcription of the Sirt3 gene, an essential component of the thermogenic brown adipocyte phenotype. *J. Biol. Chem.* **2011**, *286*, 16958−16966.

(15) Park, Y. S.; Yoon, Y.; Ahn, H. S. Platycodon grandiflorum extract represses up-regulated adipocyte fatty acid binding protein triggered by a high fat feeding in obese rats. *World J. Gastroenterol.* **2007**, *13*, 3493−3499.

(16) Qin, H.; Du, X.; Zhang, Y.; Wang, R. Platycodin D, a triterpenoid saponin from Platycodon grandiflorum, induces G2/M arrest and apoptosis in human hepatoma HepG2 cells by modulating the PI3K/Akt pathway. *Tumor Biol.* **2014**, *35*, 1267−1274.

(17) Choi, J. H.; Yoo, K. Y.; Park, O. K.; Lee, C. H.; Won, M. H.; Hwang, I. K.; Ryu, S. Y.; Kim, Y. S.; Yi, J. S.; Bae, Y. S.; Kang, I. J. Platycodin D and 2″-O-acetyl-polygalacin D2 isolated from Platycodon grandiflorum protect ischemia/reperfusion injury in the gerbil hippocampus. *Brain Res.* **2009**, *1279*, 197−208.

(18) Lee, H.; Bae, S.; Kim, Y. S.; Yoon, Y. WNT/beta-catenin pathway mediates the anti-adipogenic effect of platycodin D, a natural compound found in Platycodon grandiflorum. *Life Sci.* **2011**, *89*, 388−394.

(19) Kim, K.-S.; Yang, H.; Choi, E.-K.; Shin, M.; Kim, K.-H.; Um, J.; Lee, B.-C.; Jang, H.-J. The effects of complex herbal medicine composed of Cornus fructus, Dioscoreae rhizoma, Aurantii fructus, and Mori folium in obese type-2 diabetes mice model. *Orient. Pharm. Exp. Med.* **2013**, *13*, 69−75.

(20) Kim, H. L.; Sim, J. E.; Choi, H. M.; Choi, I. Y.; Jeong, M. Y.; Park, J.; Jung, Y.; Youn, D. H.; Cho, J. H.; Kim, J. H.; Hwang, M. W.; Jin, J. S.; Hong, S. H.; Cho, H. W.; Um, J. Y. The AMPK pathway mediates an anti-adipogenic effect of fruits of Hovenia dulcis Thunb. *Food Funct.* **2014**, *5* (11), 2961−8.

(21) Jeong, M. Y.; Kim, H. L.; Park, J.; Jung, Y.; Youn, D. H.; Lee, J. H.; Jin, J. S.; So, H. S.; Park, R.; Kim, S. H.; Kim, S. J.; Hong, S. H.; Um, J. Y. Rubi Fructus (Rubus coreanus) activates the expression of thermogenic genes in vivo and in vitro. *Int. J. Obes.* **2015**, *39*, 456−64.

(22) Ramirez-Zacarias, J. L.; Castro-Munozledo, F.; Kuri-Harcuch, W. Quantitation of adipose conversion and triglycerides by staining intracytoplasmic lipids with Oil red O. *Histochemistry* **1992**, *97*, 493−497.

(23) Liu, Y.; Dang, H.; Li, D.; Pang, W.; Hammock, B. D.; Zhu, Y. Inhibition of soluble epoxide hydrolase attenuates high-fat-diet-induced hepatic steatosis by reduced systemic inflammatory status in mice. *PLoS One* **2012**, *7*, e39165.

(24) Rosen, E. D.; Walkey, C. J.; Puigserver, P.; Spiegelman, B. M. Transcriptional regulation of adipogenesis. *Genes Dev.* **2000**, *14*, 1293−1307.

(25) Chen, Y. C.; Zeng, X. Y.; He, Y.; Liu, H.; Wang, B.; Zhou, H.; Chen, J. W.; Liu, P. Q.; Gu, L. Q.; Ye, J. M.; Huang, Z. S. Rutaecarpine analogues reduce lipid accumulation in adipocytes via inhibiting adipogenesis/lipogenesis with AMPK activation and UPR suppression. *ACS Chem. Biol.* **2013**, *8*, 2301−2311.

(26) Zhang, P.; Takeuchi, K.; Csaki, L. S.; Reue, K. Lipin-1 phosphatidic phosphatase activity modulates phosphatidate levels to promote peroxisome proliferator-activated receptor gamma (PPAR-gamma) gene expression during adipogenesis. *J. Biol. Chem.* **2012**, *287*, 3485−3494.

(27) Lowell, B. B. PPARgamma: an essential regulator of adipogenesis and modulator of fat cell function. *Cell* **1999**, *99*, 239−242.

(28) Virtanen, K. A.; Lidell, M. E.; Orava, J.; Heglind, M.; Westergren, R.; Niemi, T.; Taittonen, M.; Laine, J.; Savisto, N. J.;

DOI: 10.1021/acs.jafc.5b01908
J. Agric. Food Chem. 2015, 63, 7721−7730

Enerback, S.; Nuutila, P. Functional brown adipose tissue in healthy adults. *N. Engl. J. Med.* **2009**, *360*, 1518−1525.
(29) Choi, H. R.; Kim, W. K.; Kim, E. Y.; Han, B. S.; Min, J. K.; Chi, S. W.; Park, S. G.; Bae, K. H.; Lee, S. C. Dual-specificity phosphatase 10 controls brown adipocyte differentiation by modulating the phosphorylation of p38 mitogen-activated protein kinase. *PLoS One* **2013**, *8*, e72340.
(30) Prentice, A. M. The emerging epidemic of obesity in developing countries. *Int. J. Epidemiol.* **2006**, *35*, 93−99.
(31) Bae, K. H.; Kim, W. K.; Lee, S. C. Involvement of protein tyrosine phosphatases in adipogenesis: new anti-obesity targets? *BMB Rep.* **2012**, *45*, 700−706.
(32) Farmer, S. R. Transcriptional control of adipocyte formation. *Cell Metab.* **2006**, *4*, 263−73.
(33) Gesta, S.; Tseng, Y. H.; Kahn, C. R. Developmental origin of fat: tracking obesity to its source. *Cell* **2007**, *131*, 242−256.
(34) Spiegelman, B. M.; Flier, J. S. Obesity and the regulation of energy balance. *Cell* **2001**, *104*, 531−543.
(35) Tormos, K. V.; Anso, E.; Hamanaka, R. B.; Eisenbart, J.; Joseph, J.; Kalyanaraman, B.; Chandel, N. S. Mitochondrial complex III ROS regulate adipocyte differentiation. *Cell Metab.* **2011**, *14*, 537−544.
(36) Kim, W. K.; Choi, H. R.; Park, S. G.; Ko, Y.; Bae, K. H.; Lee, S. C. Myostatin inhibits brown adipocyte differentiation via regulation of Smad3-mediated beta-catenin stabilization. *Int. J. Biochem. Cell Biol.* **2012**, *44*, 327−334.
(37) Rosen, E. D.; MacDougald, O. A. Adipocyte differentiation from the inside out. *Nat. Rev. Mol. Cell Biol.* **2006**, *7*, 885−896.
(38) Tada, A.; Kaneiwa, Y.; Shoji, J.; Shibata, S. Studies on the saponins of the root of Platycodon grandiflorum A. De Candolle. I. Isolation and the structure of platycodin-D. *Chem. Pharm. Bull.* **1975**, *23*, 2965−2972.
(39) Kim, J. Y.; Moon, K. D.; Seo, K. I.; Park, K. W.; Choi, M. S.; Do, G. M.; Jeong, Y. K.; Cho, Y. S.; Lee, M. K. Supplementation of SK1 from Platycodi radix ameliorates obesity and glucose intolerance in mice fed a high-fat diet. *J. Med. Food* **2009**, *12*, 629−636.
(40) Kim, J. Y.; Hwang, Y. P.; Kim, D. H.; Han, E. H.; Chung, Y. C.; Roh, S. H.; Jeong, H. G. Inhibitory effect of the saponins derived from roots of Platycodon grandiflorum on carrageenan-induced inflammation. *Biosci., Biotechnol., Biochem.* **2006**, *70*, 858−864.
(41) Zhao, H. L.; Sim, J. S.; Shim, S. H.; Ha, Y. W.; Kang, S. S.; Kim, Y. S. Antiobese and hypolipidemic effects of platycodin saponins in diet-induced obese rats: evidences for lipase inhibition and calorie intake restriction. *Int. J. Obes.* **2005**, *29*, 983−990.
(42) Han, L. K.; Zheng, Y. N.; Xu, B. J.; Okuda, H.; Kimura, Y. Saponins from platycodi radix ameliorate high fat diet-induced obesity in mice. *J. Nutr.* **2002**, *132*, 2241−2245.
(43) Lee, C. E.; Hur, H. J.; Hwang, J. T.; Sung, M. J.; Yang, H. J.; Kim, H. J.; Park, J. H.; Kwon, D. Y.; Kim, M. S. Long-Term Consumption of Platycodi Radix Ameliorates Obesity and Insulin Resistance via the Activation of AMPK Pathways. *Evid. Based Complement. Alternat. Med.* **2012**, *2012*, 759143.
(44) Armani, A.; Mammi, C.; Marzolla, V.; Calanchini, M.; Antelmi, A.; Rosano, G. M.; Fabbri, A.; Caprio, M. Cellular models for understanding adipogenesis, adipose dysfunction, and obesity. *J. Cell. Biochem.* **2010**, *110*, 564−572.
(45) Tang, Q. Q.; Lane, M. D. Adipogenesis: from stem cell to adipocyte. *Annu. Rev. Biochem.* **2012**, *81*, 715−736.
(46) Qiao, L.; Schaack, J.; Shao, J. Suppression of adiponectin gene expression by histone deacetylase inhibitor valproic acid. *Endocrinology* **2006**, *147*, 865−874.
(47) Sembongi, H.; Miranda, M.; Han, G. S.; Fakas, S.; Grimsey, N.; Vendrell, J.; Carman, G. M.; Siniossoglou, S. Distinct roles of the phosphatidate phosphatases lipin 1 and 2 during adipogenesis and lipid droplet biogenesis in 3T3-L1 cells. *J. Biol. Chem.* **2013**, *288*, 34502−34513.
(48) Coppola, A.; Marfella, R.; Coppola, L.; Tagliamonte, E.; Fontana, D.; Liguori, E.; Cirillo, T.; Cafiero, M.; Natale, S.; Astarita, C. Effect of weight loss on coronary circulation and adiponectin levels in obese women. *Int. J. Cardiol.* **2009**, *134*, 414−416.
(49) Ouchi, N.; Kihara, S.; Funahashi, T.; Matsuzawa, Y.; Walsh, K. Obesity, adiponectin and vascular inflammatory disease. *Curr. Opin. Lipidol.* **2003**, *14*, 561−566.
(50) Philp, A.; Chen, A.; Lan, D.; Meyer, G. A.; Murphy, A. N.; Knapp, A. E.; Olfert, I. M.; McCurdy, C. E.; Marcotte, G. R.; Hogan, M. C.; Baar, K.; Schenk, S. Sirtuin 1 (SIRT1) deacetylase activity is not required for mitochondrial biogenesis or peroxisome proliferator-activated receptor-gamma coactivator-1alpha (PGC-1alpha) deacetylation following endurance exercise. *J. Biol. Chem.* **2011**, *286*, 30561−30570.
(51) Fullerton, M. D.; Steinberg, G. R. SIRT1 takes a backseat to AMPK in the regulation of insulin sensitivity by resveratrol. *Diabetes* **2010**, *59*, 551−553.
(52) O'Neill, H. M.; Holloway, G. P.; Steinberg, G. R. AMPK regulation of fatty acid metabolism and mitochondrial biogenesis: implications for obesity. *Mol. Cell. Endocrinol.* **2013**, *366*, 135−151.
(53) Viollet, B.; Andreelli, F. AMP-activated protein kinase and metabolic control. *Handb. Exp. Pharmacol.* **2011**, 303−330.
(54) Ahn, K. S.; Noh, E. J.; Zhao, H. L.; Jung, S. H.; Kang, S. S.; Kim, Y. S. Inhibition of inducible nitric oxide synthase and cyclooxygenase II by Platycodon grandiflorum saponins via suppression of nuclear factor-kappaB activation in RAW 264.7 cells. *Life Sci.* **2005**, *76*, 2315−2328.
(55) Lee, H.; Kang, R.; Kim, Y. S.; Chung, S. I.; Yoon, Y. Platycodin D inhibits adipogenesis of 3T3-L1 cells by modulating Kruppel-like factor 2 and peroxisome proliferator-activated receptor gamma. *Phytother. Res.* **2010**, *24* (Suppl 2), S161−167.
(56) Zhao, H. L.; Cho, K. H.; Ha, Y. W.; Jeong, T. S.; Lee, W. S.; Kim, Y. S. Cholesterol-lowering effect of platycodin D in hypercholesterolemic ICR mice. *Eur. J. Pharmacol.* **2006**, *537*, 166−173.
(57) Virbasius, J. V.; Scarpulla, R. C. Activation of the human mitochondrial transcription factor A gene by nuclear respiratory factors: a potential regulatory link between nuclear and mitochondrial gene expression in organelle biogenesis. *Proc. Natl. Acad. Sci. U. S. A.* **1994**, *91*, 1309−1313.
(58) Rehman, H.; Krishnasamy, Y.; Haque, K.; Thurman, R. G.; Lemasters, J. J.; Schnellmann, R. G.; Zhong, Z. Green tea polyphenols stimulate mitochondrial biogenesis and improve renal function after chronic cyclosporin a treatment in rats. *PLoS One* **2013**, *8*, e65029.
(59) Kitada, M.; Koya, D. SIRT1 in Type 2 Diabetes: Mechanisms and Therapeutic Potential. *Diabetes Metab. J.* **2013**, *37*, 315−325.
(60) Liang, H.; Ward, W. F. PGC-1alpha: a key regulator of energy metabolism. *Adv. Physiol. Educ.* **2006**, *30*, 145−151.
(61) Seale, P.; Kajimura, S.; Yang, W.; Chin, S.; Rohas, L. M.; Uldry, M.; Tavernier, G.; Langin, D.; Spiegelman, B. M. Transcriptional control of brown fat determination by PRDM16. *Cell Metab.* **2007**, *6*, 38−54.
(62) Seale, P.; Bjork, B.; Yang, W.; Kajimura, S.; Chin, S.; Kuang, S.; Scime, A.; Devarakonda, S.; Conroe, H. M.; Erdjument-Bromage, H.; Tempst, P.; Rudnicki, M. A.; Beier, D. R.; Spiegelman, B. M. PRDM16 controls a brown fat/skeletal muscle switch. *Nature* **2008**, *454*, 961−967.
(63) Liu, W.; Bi, P.; Shan, T.; Yang, X.; Yin, H.; Wang, Y. X.; Liu, N.; Rudnicki, M. A.; Kuang, S. miR-133a regulates adipocyte browning in vivo. *PLoS Genet.* **2013**, *9*, e1003626.
(64) Imai, S.; Armstrong, C. M.; Kaeberlein, M.; Guarente, L. Transcriptional silencing and longevity protein Sir2 is an NAD-dependent histone deacetylase. *Nature* **2000**, *403*, 795−800.
(65) Hirschey, M. D.; Shimazu, T.; Huang, J. Y.; Schwer, B.; Verdin, E. SIRT3 regulates mitochondrial protein acetylation and intermediary metabolism. Cold Spring Harb. *Cold Spring Harbor Symp. Quant. Biol.* **2011**, *76*, 267−277.
(66) Finkel, T.; Deng, C. X.; Mostoslavsky, R. Recent progress in the biology and physiology of sirtuins. *Nature* **2009**, *460*, 587−591.
(67) Giesbertz, P.; Padberg, I.; Rein, D.; Ecker, J.; Höfle, A. S.; Spanier, B.; Daniel, H. Metabo lite profiling in plasma and tissues of ob/ob and db/db mice identifies novel markers of ob esity and type 2 diabetes. *Diabetologia* **2015**, *58*, 2133.

DOI: 10.1021/acs.jafc.5b01908
J. Agric. Food Chem. 2015, 63, 7721−7730

(68) Mathers, C.; Stevens, G.; Mascarenhas, M. *Global Health Risks: Mortality and Burden of Disease Attributable to Selected Major Risks*; World Health Organization: Geneva, Switzerland, 2009.

DOI: 10.1021/acs.jafc.5b01908
J. Agric. Food Chem. 2015, 63, 7721−7730

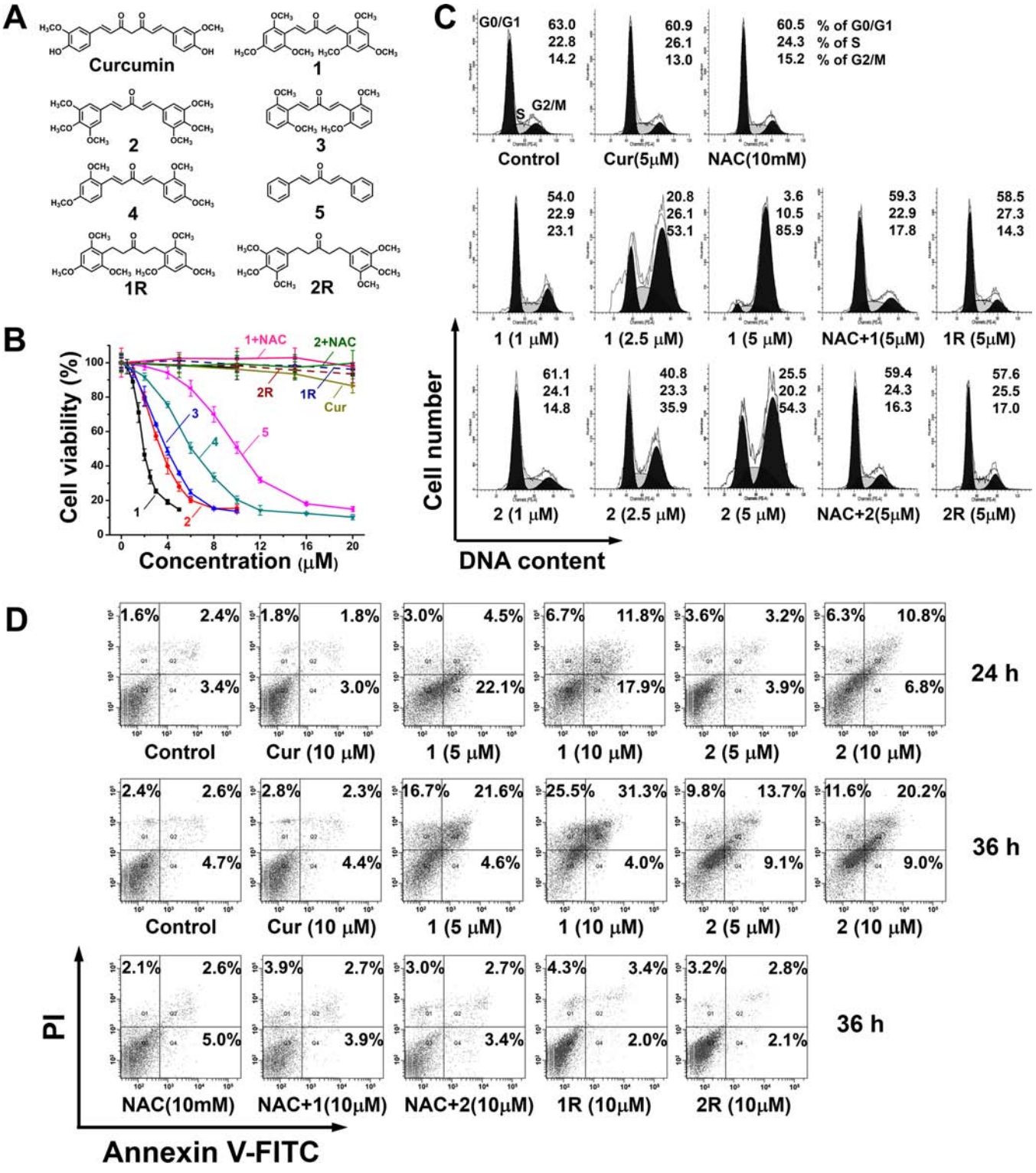

Figure 1. Cytotoxicity of compounds **1** and **2** toward NCI-H460 cells is mediated by the G2/M cell cycle arrest. (A) Chemical structures of curcumin (Cur) and its analogues. (B) Cytotoxicity of Cur and its active analogues. Cells (3×10^3/well) were treated with the test compounds at serial concentrations for 48 h in the absence or presence of 1 h of pretreatment with NAC, and cell viability was measured by the SRB assay as described under Materials and Methods. Data represent the mean ± SD of three experiments. (C) Michael acceptor- and ROS-dependent G2/M arrest induced by compounds **1** and **2** in NCI-H460 cells. Cells (4×10^5/well) were treated with the test compounds at the indicated concentrations for 24 h in the absence or presence of 1 h of pretreatment with NAC and subjected to cell cycle analyses. Representative histograms from three repeat experiments are shown to depict cell cycle distribution. (D) Apoptosis induced by compounds **1** and **2**. Cells (3×10^5/well) were treated with the test compounds with indicated concentrations for 24 or 36 h in the absence or presence of 1 h of pretreatment with NAC and subjected to annexin V-FITC/PI double-staining assay. Cells show four different cell populations marked as follows: necrotic cells (upper left, Q1), late apoptotic cells (upper right, Q2), live cells (lower left, Q3), and early apoptotic cells (lower right, Q4). Data are representative of three independent experiments.

DOI: 10.1021/acs.jafc.5b02011
J. Agric. Food Chem. 2015, 63, 7731−7742

substituted diarylpentadienone displays significantly increased cytotoxicity and apoptosis-inducing activity in A549 cells via ROS-mediated mechanisms; this compound could effectively and irreversibly modify the TrxR on the basis of its electrophilicity, geometry, and good cellular uptake and convert this antioxidant enzyme into a ROS promoter, resulting in a burst of intracellular ROS and collapse of the redox buffering system.[24] Additionally, we have also noted from published data that two symmetrical hexamethoxy-diarylpentadienones, **1**[20,21] and **2**[19,21,23] (Figure 1A), are more potent in inducing cancer cell death than curcumin. However, the action mechanisms are unclear. As part of our research project in pro-oxidant-mediated cancer chemoprevention,[6−8,24] we thus selected the two compounds to investigate their cytotoxic mechanisms. To probe the structure−activity relationships (SAR) and possibility of Michael acceptor-dependent redox intervention, we also synthesized their analogues **3**−**5** and reduced compounds **1R** and **2R** that lack the Michael acceptor units (Figure 1A). On the basis of preliminary screening experiments, we found that all of the test cell lines, including human hepatoma (HepG2 and SMMC-7721) and lung carcinoma (A549 and NCI-H460) cells, showed more significant response to compounds **1** and **2** than curcumin, with the NCI-H460 being the most sensitive cancer cell line for all of the test compounds. Additionally, we noted with interest that the cytotoxicity of compounds **1** and **2** toward NCI-H460 cells was mainly mediated by inducing cell cycle arrest. This is different from our previous results[24] showing that pro-apoptosis ability of another series of diarylpentadienones was responsible for their cytotoxicity in A549 cells. More interestingly, in comparison with compound **2**, compound **1** displayed a relatively weak ability to generate ROS but an increased cell cycle arrest activity and cytotoxicity in NCI-H460 cells. Therefore, we report herein the detailed mechanistic study on the cytotoxicity of compounds **1** and **2** toward NCI-H460 cells, with emphasis placed on elucidating Michael acceptor-dependent redox intervention, clarifying why compound **1** is a stronger G2/M cell cycle arrest agent than compound **2** and emphasizing the possibility of multiple targets involved in the processes.

MATERIALS AND METHODS

Materials. Roswell Park Memorial Institute (RPMI)-1640, sulforhodamine B (SRB), 2′,7′-dichlorofluorescin diacetate (DCFH-DA), L-glutathione reduced (GSH), L-glutathione oxidized (GSSG), glutathione reductase (GR), 2-vinylpyridine, 5,5′-dithiobis(2-nitrobenzoic acid) (DTNB), TrxR (from rat liver), Triton X-100, BSA, anti-α-tubulin-FITC antibody, and 4′,6-diamidino-2-phenylindole dihydrochloride (DAPI) were purchased from Sigma-Aldrich (St. Louis, MO, USA). NADPH was from Roche Diagnostics GmbH (Mannheim, Germany). BCA protein assay kit, anti-fade mounting medium, radioimmunoprecipitation assay buffer, and PMSF were from Beyotime Institute of Biotechnology (Jiangsu, China). Antibodies against p53, p21, cyclin B1, cyclin-dependent kinase 1 (Cdk1), glyceraldehyde 3-phosphate dehydrogenase (GAPDH), and TrxR1 were from Cell Signaling Technology (Beverly, MA, USA). The antibody against Cdc25C was purchased from Millipore (Billerica, MA, USA). TRFS-green was a generous gift from Prof. Jianguo Fang (State Key Laboratory of Applied Organic Chemistry, Lanzhou University). DNs-CV, a highly fluorogenic probe for glutathione *S*-transferases (GSTs), was synthesized as previously reported by Zhang.[25] Curcumin and compound **5** were prepared in our previous study.[24,26] All other chemicals were of the highest quality available.

Synthesis. Compounds **1**−**4** were synthesized from appropriate benzaldehydes and acetone under alkaline conditions, and compounds **1R** and **2R** were synthesized by catalytic hydrogenation of **1** and **2** over Pd/C according to our previous works.[24,26] Their structures were characterized by mp; IR, ^{1}H NMR, and ^{13}C NMR spectra; and HRMS (ESI) /MS (EI) analysis.

(1E,4E)-1,5-Bis(2,4,6-trimethoxyphenyl)penta-1,4-dien-3-one ***(1):*** yellow solid; yield 71%; mp 222−224 °C; IR (KBr) 2943, 2834, 1626, 1550, 1458, 1336, 1206, 1149, 1118, 1028 cm^{-1}; ^{1}H NMR (400 MHz, CD_3Cl, 25 °C, TMS) δ 3.86 (s, 6H), 3.91 (s, 12H), 6.14 (s, 4H), 7.48 (d, J = 16 Hz, 2 H), 8.14 (d, J = 16 Hz, 2 H); ^{13}C NMR (100 MHz, CD_3Cl, 25 °C, TMS) δ 55.6 (2C), 56.0 (4C), 90.8 (4C), 107.0 (2C), 126.7 (2C), 133.7 (2C), 161.7 (4C), 162.9 (2C), 192.7 (1C); HRMS (ESI) m/z calcd for $C_{23}H_{26}O_7$ $[M + H]^+$ 415.1751, found 415.1746, error = 1.2 ppm.

(1E,4E)-1,5-Bis(3,4,5-trimethoxyphenyl)penta-1,4-dien-3-one ***(2):*** yellow solid; yield 75%; mp 128−130 °C; IR (KBr) 2940, 2837, 1622, 1582, 1502, 1457, 1414, 1314, 1276, 1238, 1123 cm^{-1}; ^{1}H NMR (400 MHz, DMSO-d_6, 25 °C, TMS) δ 3.71 (s, 6H), 3.85 (s, 12H), 7.13 (s, 4H), 7.32 (d, J = 16 Hz, 2 H), 7.71 (d, J = 16 Hz, 2 H); ^{13}C NMR (100 MHz, DMSO-d_6, 25 °C, TMS) δ 56.1 (4C), 60.2 (2C), 106.1 (4C), 125.2 (2C), 130.3 (2C), 139.6 (2C), 142.9 (2C), 153.2 (4C), 188.3 (1C); HRMS (ESI) m/z calcd for $C_{23}H_{26}O_7$ $[M + H]^+$ 415.1751, found 415.1748, error = 0.7 ppm.

(1E,4E)-1,5-Bis(2,6-dimethoxyphenyl)penta-1,4-dien-3-one ***(3):*** yellow solid; yield 69%; mp 152−154 °C; IR (KBr) 2939, 2834, 1641, 1570, 1472, 1324, 1258, 1178, 1107, 1028 cm^{-1}; ^{1}H NMR (400 MHz, DMSO-d_6, 25 °C, TMS) δ 3.90 (s, 12H), 6.73 (d, J = 8 Hz, 4 H), 7.36 (d, J = 8 Hz, 2 H), 7.47 (d, J = 16 Hz, 2 H), 8.02 (d, J = 16 Hz, 2 H); ^{13}C NMR (100 MHz, DMSO-d_6, 25 °C, TMS) δ 56.0 (4C), 104.2 (4C), 111.5 (2C), 128.2 (2C), 132.1 (2C), 132.9 (2C), 159.8 (4C), 190.3 (1C); HRMS (ESI) m/z calcd for $C_{21}H_{22}O_5$ $[M + H]^+$ 355.1540, found 355.1538, error = 0.6 ppm.

(1E,4E)-1,5-Bis(2,4-dimethoxyphenyl)penta-1,4-dien-3-one ***(4):*** yellow solid; yield 77%; mp 140−142 °C; IR (KBr) 2947, 2838, 1643, 1613, 1581, 1499, 1462, 1326, 1268, 1186, 1112, 1031 cm^{-1}; ^{1}H NMR (400 MHz, DMSO-d_6, 25 °C, TMS) δ 3.83 (s, 6H), 3.89 (s, 6H), 6.61 (d, J = 8 Hz, 2 H), 6.63 (s, 2 H), 7.15 (d, J = 16 Hz, 2 H), 7.73 (d, J = 8 Hz, 2 H), 7.86 (d, J = 16 Hz, 2 H); ^{13}C NMR (100 MHz, DMSO-d_6, 25 °C, TMS) δ 55.5 (2C), 55.8 (2C), 98.4 (2C), 106.3 (2C), 115.9 (2C), 123.9 (2C), 130.0 (2C), 136.8 (2C), 159.8 (2C), 162.8 (2C), 188.2 (1C); HRMS (ESI): m/z calcd for $C_{21}H_{22}O_5$ $[M + H]^+$ 355.1540, found 355.1546, error = 1.7 ppm.

1,5-Bis(2,4,6-trimethoxyphenyl)pentan-3-one ***(1R):*** white solid; yield 21%; mp 73−75 °C; IR (KBr) 3002, 2943, 2839, 1710, 1600, 1500, 1462, 1359, 1237, 1203, 1158, 1120, 1029 cm^{-1}; ^{1}H NMR (400 MHz, DMSO-d_6, 25 °C, TMS) δ 2.49 (t, J = 8 Hz, 4H), 2.76 (t, J = 8 Hz, 4H), 3.78 (s, 18H), 6.21 (s, 4 H); ^{13}C NMR (100 MHz, DMSO-d_6, 25 °C, TMS) δ 18.2 (2C), 43.9 (2C), 55.5 (2C), 56.0 (4C), 91.5 (4C), 110.0 (2C), 159.6 (4C), 160.8 (2C), 206.1 (1C); MS (EI) m/z 419.0 $[M + H]^+$.

1,5-Bis(3,4,5-trimethoxyphenyl)pentan-3-one ***(2R):*** white solid; yield 36%. mp 79−81 °C; IR (KBr) 2998, 2938, 2839, 1718, 1586, 1509, 1457, 1421, 1329, 1241, 1179, 1118, 1001 cm^{-1}; ^{1}H NMR (400 MHz, DMSO-d_6, 25 °C, TMS) δ 2.72 (t, J = 8 Hz, 4H), 2.85 (t, J = 8 Hz, 4H), 3.82 (s, 6H), 3.84 (s, 12H), 6.39 (s, 4 H); ^{13}C NMR (100 MHz, DMSO-d_6, 25 °C, TMS) δ 30.2 (2C), 44.7 (2C), 56.1 (4C), 60.9 (2C), 105.3 (4C), 136.4 (2C), 136.8 (2C), 153.2 (4C), 209.0 (1C); MS (EI) m/z 419.3 $[M + H]^+$.

Cell Culture. NCI-H460 (human non-small cell lung cancer) cells, obtained from the Shanghai Institute of Biochemistry and Cell Biology, Chinese Academy of Sciences, were cultured in RPMI-1640 medium supplemented with fetal bovine serum (10%, v/v), $NaHCO_3$ (2 g/L), glutamine (2 mM), penicillin (100 kU/L), and streptomycin (100 kU/L) and maintained in a humidified 5% CO_2 atmosphere at 37 °C.

Cytotoxicity Assay. The SRB assay was used to determine cytotoxicity of the test compounds against NCI-H460 cells. The cells (3×10^3/well) treated with graded concentrations of the test compounds for 48 h were fixed with trichloroacetic acid and stained with SRB (0.4%) for 30 min. When necessary, the cells were pretreated with NAC (10 mM) for 1 h before the test compounds were added. Cells were washed with acetic acid (1%) and added to

DOI: 10.1021/acs.jafc.5b02011
J. Agric. Food Chem. 2015, 63, 7731−7742

Tris base solution (10 mM) for absorbance measurements at 570 nm using a microplate reader (Bio-Rad model 550). The cell viability was expressed as the percentage of the control.

Cell Cycle and Apoptosis Analysis. The cell cycle distribution and induction of apoptosis in NCI-H460 cells treated with the test compounds for the indicated durations were analyzed using a FACSCanto flow cytometer (Becton-Dickinson, San Jose, CA, USA), as described in detail in our previous work.[27] A total of 10000 cells were acquired per sample, and data were analyzed using FACSDiva software in both cell cycle and cell apoptosis assays. When necessary, the cells were pretreated with NAC (10 mM) for 1 h before the test compounds were added.

Intracellular ROS Assay. NCI-H460 cells (4×10^5/well), incubated with the test compounds (5 or 10 μM) for 3 or 9 h, were harvested, stained with DCFH-DA (3 μM) for 30 min at 37 °C in the dark, then washed with PBS, and subjected to immediate analysis by flow cytometry. When necessary, the cells were pretreated with NAC (10 mM) for 1 h before the test compounds were added. The ROS levels were calculated relative to the intensity of FITC fluorescence and expressed as fold increase relative to control.

Intracellular Glutathione Assay. A modified GR-DTNB recycling assay method was used to measure intracellular glutathione levels.[28] Briefly, NCI-H460 cells (4×10^5/well) treated with the test compounds were harvested, resuspended in ice-cold HCl (10 mM, 500 μL), and lysed by three freeze−thaw cycles. When necessary, the cells were pretreated with NAC (10 mM) for 1 h before the test compounds were added. The protein concentrations were determined by the BCA protein assay reagent kit. Precooled 5-sulfosalicylic acid (6.5%, 120 μL) was added to the 460 μL residual lysates, vortexed, and kept at 4 °C for 10 min. After centrifugation (8000*g*, 4 °C, 15 min), the supernatant was divided into two groups: one as the total GSH sample (no treatment) and the other as the GSSG sample (100 μL of supernatant added with 5 μL of 2-vinylpyridine, shaken for 1 h to dislodge the GSH). For the total GSH assay, the test solutions containing 5 μL of sample, 35 μL of PBS, and 200 μL of assay buffer (1 mM DTNB, 340 μM NADPH, in PBS) were pre-incubated in a 96-well plate for 5 min and then added to 40 μL of GR (8.5 IU/mL, in PBS). The absorbance change at 412 nm was monitored for 5 min using an Infinite M200 microplate reader (Tecan Group Ltd., Männedorf, Switzerland), whereas for the GSSG assay, the test solutions contained 40 μL of sample and 200 μL of assay buffer. Intracellular total GSH and GSSG concentrations were estimated using a GSH or GSSG standard curve, respectively, and normalized to the determined protein concentrations. Intracellular GSH concentration was calculated from the following formula: [GSH] = [total GSH] − 2[GSSG]. Results were expressed as the percentage of the control.

In Vitro and Intracellular TrxR-Inhibitory Activity Assays. The NADPH-reduced TrxR (120 nM) was incubated with the test compounds (50 μM) in TE buffer (50 mM Tris-HCl, pH 7.4, 1 mM EDTA, 100 μL) for 1 h and added to a mixture of DTNB (2.25 mM) and NADPH (200 μM) in TE buffer (800 μL). TrxR activity was calculated by measuring the slope for the linear increase in absorbance at 412 nm in the initial 90 s using a TU-1901 UV−vis spectrophotometer (Beijing Purkinje General Instrument Co. Ltd., Beijing, China).[29] The inhibitory activity was expressed as a percentage of the control.

Intracellular TrxR-inhibitory activity was imaged in living cells using a fluorescent probe for mammalian TrxR, TRFS-green, kindly provided by Prof. Fang from Lanzhou University, China.[30] NCI-H460 cells seeded on glass coverslips at 2×10^5 cells/coverslip were treated with the test compounds (30 μM) for 4 h and incubated with TRFS green (5 μM) in fresh medium for another 3 h. When necessary, the cells were pretreated with NAC (10 mM) for 1 h before the test compounds were added. The coverslips were rinsed with PBS and inverted onto glass slides with anti-fade mounting medium. The fluorescence images were acquired by a fluorescent microscope Leica DM 4000B (Leica Microsystems CMS GmbH, Wetzlar, Germany) with a ×40 objective lens.

NADPH Oxidase Activity Assay. NADPH-reduced TrxR (120 nM), NADPH (200 μM) in TE buffer (200 μL), was incubated with the test compounds (50 μM) for 30 min at room temperature. After incubation, the rate of oxidation of NADPH was determined by measuring the absorbance decay at 340 nm using an Infinite M200 microplate reader.[13] The activity was expressed as fold increase relative to control.

Western Blot Analysis. NCI-H460 cells (2×10^6 cells/dish) treated with the test compounds (2.5, 5 μM) for 24 h were lysed with the immunoblotting assay buffer containing 1% PMSF at 4 °C. Protein, 40 μg/lane, was used for SDS-PAGE and electroblotted onto PVDF membrane (Bio-Rad Laboratories, Hercules, CA, USA) at 4 °C. The membranes were blocked with 5% skim milk followed by incubation with appropriate primary antibody at 4 °C overnight, then washed, and probed with the corresponding horseradish peroxidase-conjugated secondary antibodies for 1 h at room temperature. The signals were finally detected using an enhanced ImageQuant chemiluminescence system (GE Healthcare, Pittsburgh, PA, USA).

Whole Cell Analysis of Tubulin Polymerization. Whole cell analysis of tubulin polymerization was conducted according to the established procedures.[31] Specifically, NCI-H460 cells (4×10^5/well) incubated with the test compounds for 24 h were harvested, fixed in 4% paraformaldehyde for 10 min, and then pelleted (500*g*, 8 min), followed by 10 min of permeabilization in ice-cold 90% methanol at −20 °C. When necessary, the cells were pretreated with NAC (10 mM) for 1 h before the test compounds were added. The permeablized cells were washed with microtubule stabilizing buffer consisting of 80 mM Pipes (pH 6.8), 1 mM $MgCl_2$, 5 mM EDTA, and 0.5% Triton X-100 and blocked in antibody diluting solution containing PBS (pH 7.4), 0.2% Triton X-100, 2% BSA, and 0.1% NaN_3 for 1 h. The cells were then incubated with anti-α-tubulin-FITC antibody (1:50 diluted) in the dark for 3 h and subjected to analysis by flow cytometry.

Intracellular GST-Inhibitory Activity Assays. The GST activity was evaluated in NCI-H460 cells by imaging experiments using DNs-CV, a previously reported fluorescent probe for GSTs.[25] NCI-H460 cells seeded on glass coverslips at 2×10^5 cells/coverslip were treated with or without the test compounds (30 μM) for 4 h followed by their removal and incubation with DNs-CV (2 μM) in serum-free medium without phenol red at 37 °C for 30 min. The cells were then fixed with 2% formaldehyde for 15 min and stained with 0.5 μg/mL DAPI for 10 min at room temperature. The coverslips were rinsed with PBS and inverted onto glass slides with anti-fade mounting medium. The fluorescence images were captured using a fluorescent microscope Leica DM 4000B (Leica Microsystems CMS GmbH) with a ×40 objective lens.

Cellular Uptake Assay. NCI-H460 cells seeded in 100 mm dishes at 2×10^6 cells/dish were treated with the test compounds (30 μM) for 0.5, 1, 2, 4, 6, or 8 h. After incubation, the medium was aspirated, and the cells were rapidly washed three times with excess ice-cold PBS, collected by trypsin, and further washed with medium and PBS in turns by centrifuging. Ice-cold methanol (500 μL) was then added and incubated for 10 h at 4 °C to lyse the cells. The cell lysates were centrifuged for 10 min at 10000 rpm at 4 °C, and the compound concentrations in the supernatants were then measured using an M850 fluorescence spectrophotometer (Hitachi, Japan; curcumin, Ex = 422 nm, Em = 536 nm; compounds **1** and **2**, Ex = 366 nm, Em = 512 nm).[32] The uptake was expressed as nanomoles per million cells.

Statistical Analysis. Data are expressed as the mean ± SD. Statistical comparisons among the results were performed using analysis of variance. Significant differences ($P < 0.05$) between the means of two groups were analyzed by Student's *t* test.

RESULTS

Cytotoxicity of Compounds 1 and 2 Was Mediated by G2/M Cell Cycle Arrest. We initially assessed the cytotoxicity of curcumin and its analogues (**1**−**5**) toward NCI-H460 cells by the SRB assay. The IC_{50} values (concentration of the test agent that is required for 50% inhibition of the cell viability)

DOI: 10.1021/acs.jafc.5b02011
J. Agric. Food Chem. 2015, 63, 7731−7742

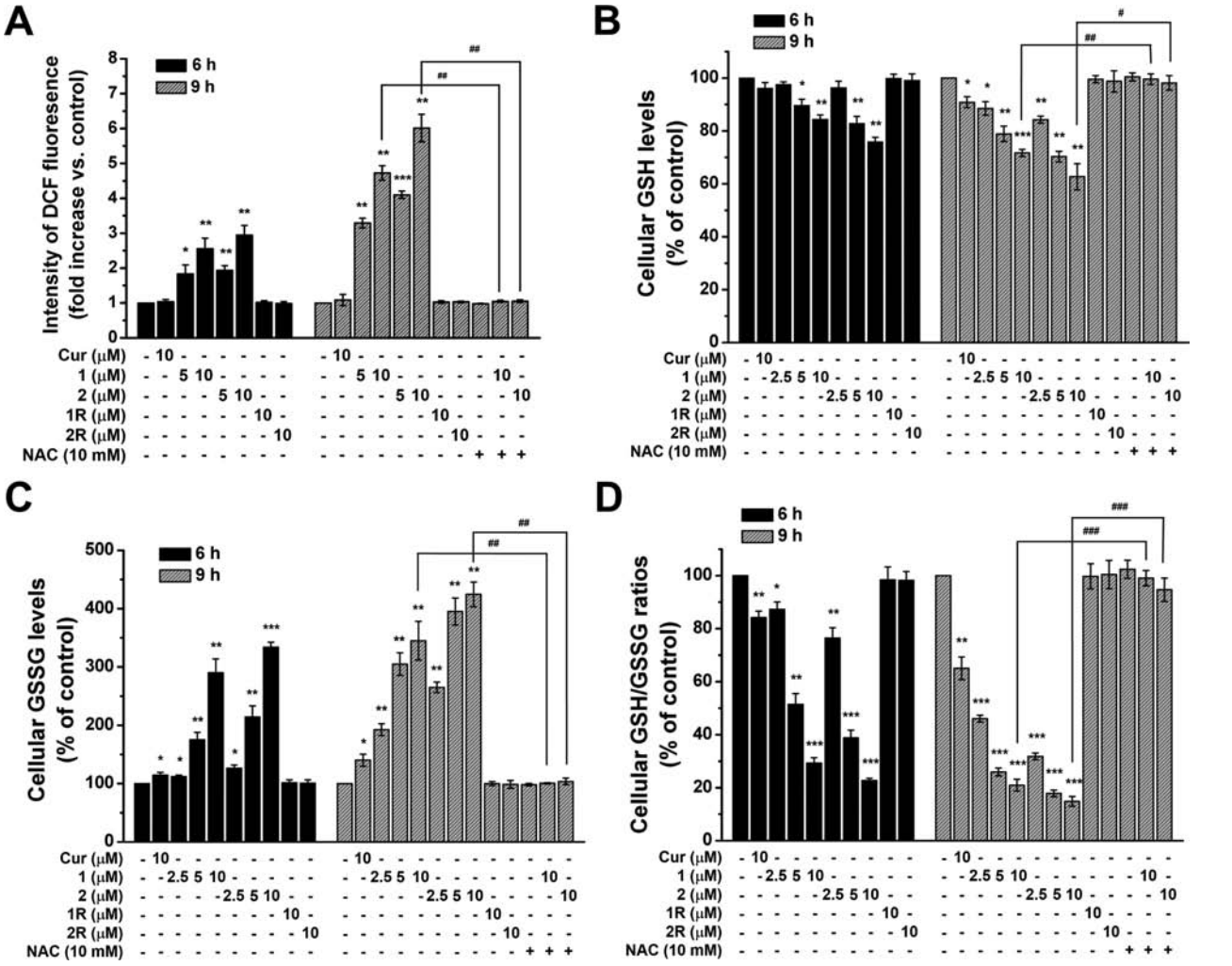

Figure 2. Compounds **1** and **2** cause ROS accumulation associated with imbalance of cellular redox homeostasis (A) ROS accumulation induced by curcumin (Cur) and its active analogues in NCI-H460 cells. Cells (4×10^5/well) were treated with the test compounds at the indicated concentrations for 6 or 9 h in the absence or presence of 1 h of pretreatment with NAC and subjected to DCFH-DA staining assay. (B–D) Alterations of intracellular GSH levels (B), GSSG levels (C), and GSH/GSSG ratios (D) induced by Cur and its active analogues. Cells (4×10^5/well) were treated with the test compounds with indicated concentrations for 6 or 9 h in the absence or presence of 1 h of pretreatment with NAC and subjected to intracellular glutathione assay as described under Materials and Methods. Data are expressed as the mean ± SD, $n = 3$: (*) $P < 0.05$, (**) $P < 0.01$, and (***) $P < 0.001$ versus control; (#) $P < 0.05$, (##) $P < 0.01$, amd (###) $P < 0.001$.

were obtained from a series of dose–response curve (Figure 1B). All of the tested monocarbonyl compounds (**1**–**5**) were more cytotoxic than the leading curcumin (IC_{50} = 38.5 ± 1.1 μM), with the IC_{50} values being 1.9 ± 0.1, 3.4 ± 0.1, 3.8 ± 0.2, 6.1 ± 0.3, and 9.8 ± 0.3 μM, respectively. Among the test compounds, the symmetrical hexamethoxy-diarylpentadienones (**1** and **2**) were the most active ones and displayed 20- and 11-fold more potent activity than curcumin, respectively. In contrast, their reduced analogues **1R** and **2R**, where the Michael acceptor units are completely abolished, showed no obvious effect on the cell viability (IC_{50} > 100 μM; Figure 1B), Additionally, pretreatment of *N*-acetylcysteine (NAC), acting as both a ROS scavenger and a sulfhydryl-containing nucleophile to react preferentially with the Michael acceptor units, almost completely abrogated the cytotoxicity induced by compounds **1** and **2** (Figure 1B). The above results indicate an indispensable role of the Michael acceptor units and the importance of ROS generation in determining the cytotoxicity of compounds **1** and **2**.

To investigate the possible mechanisms by which curcumin and its active analogues **1** and **2** exhibit cytotoxicity, we further analyzed their effects on cell cycle distribution by flow cytometry. As shown in Figure 1C, 24 h of treatment with compounds **1** and **2** induced a remarkable accumulation of cells in G2/M phase in a dose-dependent fashion. Specifically, compound **1** with increasing concentrations from 1 to 5 μM led to a successively increased accumulation of cells in G2/M phase, from ~23 to ~86% of the total cell count. However, under the same conditions, 5 μM curcumin exhibited no appreciable effect on the cell cycle distribution. The cell cycle arrest activity follows the sequence **1** > **2** > curcumin, in line with the results obtained by the cytotoxicity assay.

To further elucidate the cytotoxic mechanisms, we next conducted an apoptosis analysis by flow cytometry with annexin-V-FITC/propidium iodide (PI) double staining (Figure 1D). High-dose (10 μM) and long-duration (36 h) treatment with compounds **1** and **2** indeed caused obvious cell apoptosis and necrosis. However, under the conditions of low-dose (5 μM) and short-duration (24 h), they induced only a

DOI: 10.1021/acs.jafc.5b02011
J. Agric. Food Chem. 2015, 63, 7731–7742

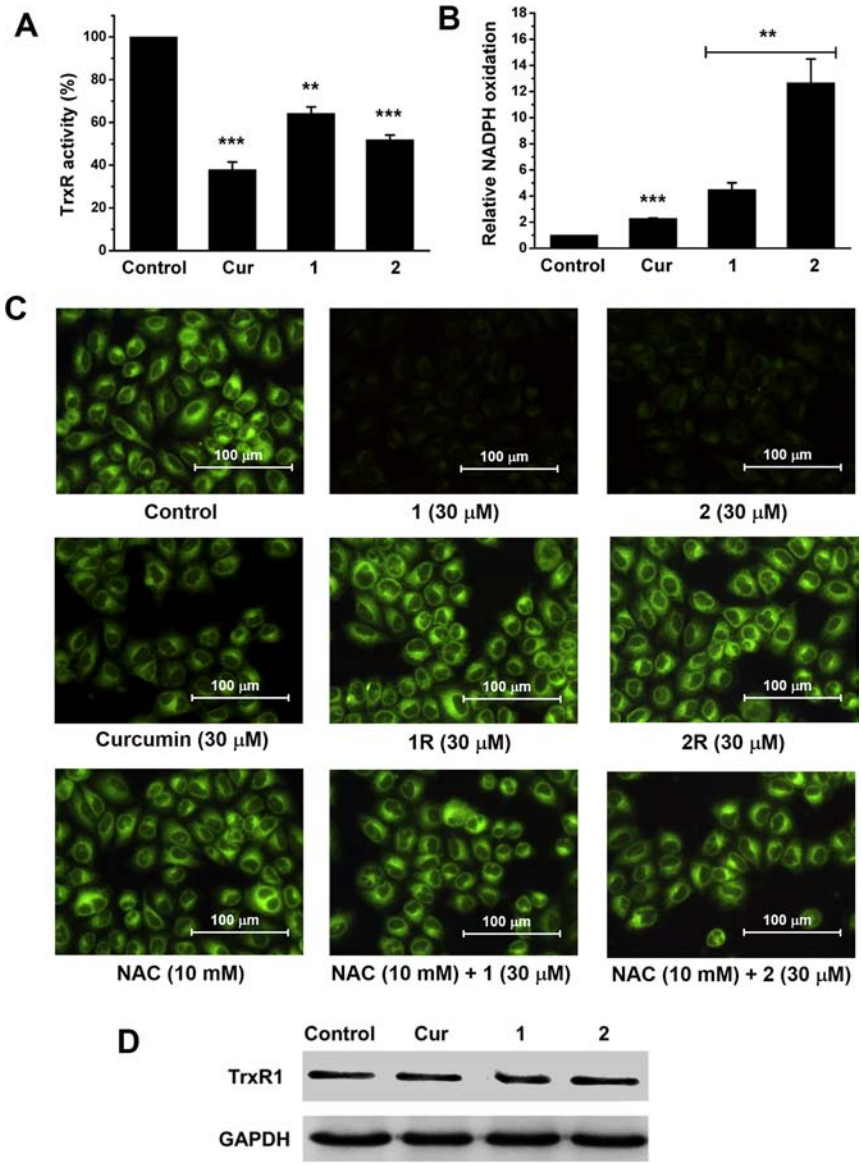

Figure 3. Inhibition of TrxR by curcumin (Cur) and its active analogues and NADPH oxidation induced by the resulting modified TrxR. (A) In vitro inhibition of TrxR by Cur and its analogues. NADPH-reduced TrxR was incubated with 50 μM compounds for 1 h, and the enzyme activity was determined by DTNB reduction assay as described under Materials and Methods. Data are expressed as the mean ± SD, n = 3: (**) $P < 0.01$ and (***) $P < 0.001$ versus control. (B) NADPH oxidase-like activity of the resulting modified TrxR. NADPH oxidation was monitored by a decrease of absorbance at 340 nm as described under Materials and Methods. Data are expressed as the mean ± SD, n = 3: (**) $P < 0.01$ and (***) $P < 0.001$ versus control. (C) Inhibition of TrxR by Cur and its analogues in NCI-H460 cells. Cells (2×10^5/well) were treated with the test compounds (30 μM) for 4 h in the absence or presence of 1 h of pretreatment with NAC, stained with TRFS-green (5 μM), a fluorescent probe for TrxR, and observed as described under Materials and Methods. Representative images are shown from three independent experiments. (D) No alteration in the TrxR1 protein levels in NCI-H460 cells induced by Cur and its analogues. Proteins were prepared from cells treated with the test compounds (30 μM) for 4 h and analyzed by Western blotting with an antibody against TrxR1.

small amount of apoptosis (Figure 1D), but induced significant G2/M phase arrest. The above results support the conclusion that the cytotoxicity of compounds **1** and **2** toward NCI-H460 cells is predominately mediated by G2/M cell cycle arrest, even though the arrest further triggers obvious cell apoptosis and necrosis in the case of high dose or long duration.

In line with the results obtained from the cytotoxicity assay, pretreatment of NAC reversed practically the cell cycle arrest and apoptosis induced by compounds **1** and **2**. Moreover, **1R** and **2R** were inactive in inducing cell cycle arrest and apoptosis (Figure 1C,D). The above results support an indispensable role of the Michael acceptor units and the importance of ROS generation in inducing cell cycle arrest and apoptosis.

Compounds 1 and 2 Caused ROS Accumulation and Imbalance of Cellular Redox Homeostasis. To further clarify the involvement of ROS in cell cycle arrest, we also measured the intracellular ROS levels by flow cytometry (Figure 2A). Treatment with either compound **1** or **2** caused dose- and time-dependently a substantial increase in DCFH-DA-reactive ROS, which reached a 6-fold increase in the case of 10 μM compound **2** after 9 h of treatment. In contrast, curcumin was almost inactive in increasing the ROS levels under the same conditions. Moreover, compound **1** and **2**-

DOI: 10.1021/acs.jafc.5b02011
J. Agric. Food Chem. 2015, 63, 7731−7742

enhanced DCF fluorescence intensity was entirely decreased to control group levels by pretreating the cells with NAC for 1 h (Figure 2A). This result coupled with the inactivity of **1R** and **2R** in inducing intracellular ROS accumulation (Figure 2A) emphasizes a dependence of ROS generation on the Michael acceptor units. Noticeably, compound **2** is a stronger ROS generator but a relatively weaker cell cycle arrest and cytotoxic agent than compound **1** (Figures 2A and 1C), implying that in addition to ROS generation, there must be other factors contributing to their cell cycle arrest activity and cytotoxicity. We will clarify this point in the following sections.

To investigate whether ROS generation was associated with the collapse of the cellular redox buffering system, we also determined the levels of reduced and oxidized glutathione (GSH and GSSG). Panels B and C of Figure 2 show a dose- and time-dependent decrease and increase for the GSH and GSSG levels, respectively, in the cells treated with compound **1** or **2**. A comparison of Figure 2B with Figure 2C clearly indicates that the alternation is much more pronounced in the GSSG levels than in the GSH levels. According to the measured GSH and GSSG levels, the GSH/GSSG ratios, an important index reflecting the cell redox status, were quantified. As shown in Figure 2D, the test compounds sharply decreased the ratios with the activity order **2** > **1** > curcumin. Obviously, the activity order accords with their ROS-generating ability, supporting a close connection between ROS generation and collapse of the intracellular redox buffering system. Likewise, pretreatment of NAC also abolished completely the change of the GSH and GSSH levels induced by compounds **1** and **2**; **1R** and **2R** were inactive in changing the GSH and GSSH levels (Figure 2B–D).

Compounds 1 and 2 Could Target TrxR To Generate ROS. The thioredoxin (Trx) system, consisting of NADPH, TrxR, and Trx, is pivotal for maintaining cellular redox balance.[33] In this system, TrxR catalyzes the NADPH-dependent reduction of Trx, which participates in many redox events.[33] It has been reported that curcumin could irreversibly modify TrxR by its Michael acceptor units, and the modified enzyme thereby exhibits the NADPH oxidase-like activity to generate ROS.[13] On the basis of the structure similarity among curcumin and its active analogues, we postulated that compounds **1** and **2** could trigger ROS accumulation likewise by inhibiting TrxR. To test this possibility, we assessed their TrxR-inhibitory activity in vitro by the DTNB reduction assay.[29] After incubation with compounds **1** and **2** for 1 h, the TrxR activity was reduced to ~60 and ~50% of control (Figure 3A), respectively. The lost activity was irrecoverable even after the test compounds were removed (data not shown), indicating an irreversible inhibition. Interestingly, compounds **1** and **2** were weaker in the TrxR-inhibitory activity in vitro than curcumin (Figure 3A), but the enzyme modified by them rather than by curcumin showed much higher NADPH oxidase-like activity (Figure 3B). Among the test compounds, compound **2** is the most active with a 12.7-fold increased oxidation of NADPH relative to the control, followed by compound **1**, whereas curcumin is the worst. The activity is fully in agreement with their ROS-generating ability in NCI-H460 cells. To further elucidate whether they can target intracellular TrxR, we employed a newly reported fluorescent probe (TRFS-green)[30] to image the TrxR activity in living NCI-H460 cells. On the basis of the bright green fluorescence intensity reflecting the intracellular TrxR activity (Figure 3C), we can conclude that after only 4 h of treatment, compounds **1** and **2** (30 μM) abrogate almost completely the intracellular TrxR activity and are approximately equipotent in the ability, whereas curcumin is obviously inferior to them. The intracellular TrxR-inhibitory activity order is completely different from that obtained from the in vitro DTNB reduction assay. Although the intracellular TrxR activity was significantly inhibited by the above compounds, the cytosolic TrxR1 protein levels remained unchanged (Figure 3D). Additionally, consistent with the results obtained from the ROS level assay, complete reversion of the intracellular TrxR-inhibitory activity of compounds **1** and **2** by NAC pretreatment as well as the inactivity of **1R** and **2R** (Figure 3C) was also observed, emphasizing that the Michael acceptor units are necessary for the activity.

Molecular Mechanisms for Compound 1- and 2-Mediated G2/M Cell Cycle Arrest. The progression through the cell cycle phase is orchestrated by promotion of cyclins, cyclin-dependent kinases (Cdks), and Cdc25 phosphatases as well as by inhibition of Cdk inhibitors such as p21.[34,35] To clarify the mechanisms for compound **1** and **2**-mediated G2/M cell cycle arrest in NCI-H460 cells, we examined their effects on expression of proteins that are critical for G2/M transition, including Cdk1, cyclin B1, Cdc25C, p21, and p53, by Western blotting (Figure 4). When the cells were treated with either

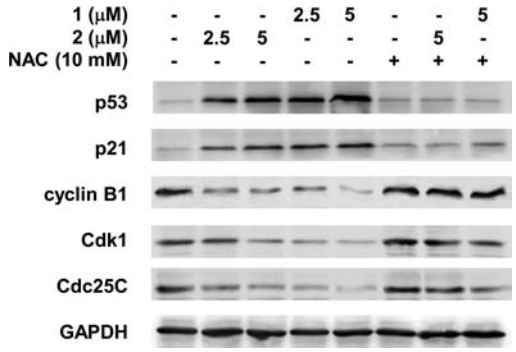

Figure 4. Alteration of G2/M cell cycle checkpoints induced by compounds **1** and **2** via a ROS- and Michael acceptor-dependent pathway. Proteins were prepared from cells (2×10^6 cells/dish) treated with the indicated concentrations of compounds for 24 h in the absence or presence of 1 h of pretreatment with NAC and subjected to Western blotting using corresponding antibodies. Data are representative of three independent experiments.

compound **1** or **2** for 24 h, a marked dose-dependent decrease of Cdk1, cyclin B1, and Cdc25C expression was observed. Conversely, the p53 and p21 expression increased in a dose-dependent manner. At the same concentration, both the inhibition and stimulation effects on protein express were much more pronounced by compound **1** than by compound **2**. This outcome is in accordance with their G2/M cell cycle arrest ability. In addition, pretreatment of NAC completely reversed the above changes in protein expression, highlighting a central role of the Michael acceptor units and ROS generation in regulating the expression of the redox active cell cycle regulatory proteins.

Inhibition of Tubulin Polymerization by Compound 1. As mentioned above, compound **2** is a stronger ROS generator but a relatively weaker G2/M cell cycle arrest agent than compound **1**. Therefore, we believe that as small molecular compounds, they can target not only TrxR to generate ROS but also other proteins related to cell cycle arrest by virtue of their Michael acceptor units. Microtubules, as key components of the

DOI: 10.1021/acs.jafc.5b02011
J. Agric. Food Chem. 2015, 63, 7731−7742

cytoskeleton, are composed of tubulin and are responsible for mitosis and cell division, and interfering with microtubule dynamics could induce cell cycle arrest during the M phase.[36,37] Some electrophiles such as 6-shagol[38] and dially trisulfide[39] can target sulfhydryl groups of cysteine residues (Cys-12β and Cys-354β) in tubulin, thereby perturbing tubulin polymerization, causing mitotic arrest and triggering cell death. To check whether compounds **1** and **2** affect tubulin polymerization, a flow cytometry method was employed to achieve a rapid and quantitative analysis of the whole cell tubulin polymerization levels. Paclitaxel and colchicine were used as reference compounds with known functions to stabilize and destabilize microtubules, respectively. As shown in Figure 5, compound **1**,

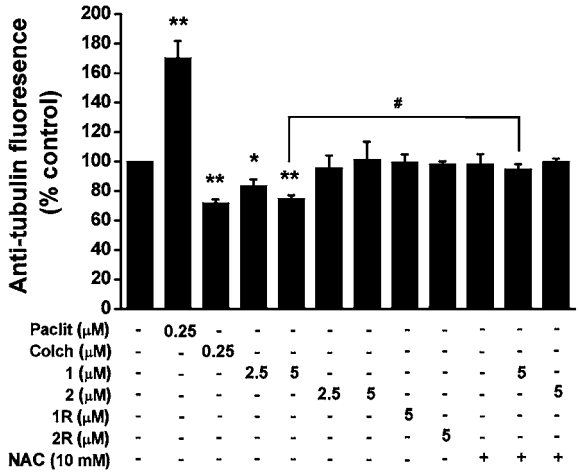

Figure 5. Effect of compounds **1** and **2** on tubulin polymerization in NCI-H460 cells. Cells (4×10^5/well) were treated with the test compounds at the indicated concentrations for 24 h in the absence or presence of 1 h of pretreatment with NAC and subjected to the whole cell tubulin quantitation analysis. Colchicine (Colch) and paclitaxel (Paclit) were used as references. Data are expressed as the mean ± SD, $n = 3$: (*) $P < 0.05$ and (**) $P < 0.01$ versus control; (#) $P < 0.05$.

acting like the microtubule destabilizer colchicine, obviously reduced the anti-tubulin fluorescence signal in a dose-dependent manner, indicating an inhibition of microtubule polymerization. In contrast, compounds **2** and **1R** failed to exhibit the effect. Furthermore, adding NAC almost blocked the inhibition of microtubule polymerization by compound **1**. These results reflect that the inhibitory activity of compound **1** against microtubule polymerization relies on not only the Michael acceptor units but also the installation mode of methoxy groups on the aromatic rings and is independent of ROS generation.

Higher GST-Inhibitory Activity by Compound 1 than by Compound 2. GSTs are a family of phase II detoxification enzymes that catalyze the conjugation of GSH to a broad spectrum of endogeneous and exogeneous electrophilic compounds, resulting in their removal from the cells.[40,41] GSTs have emerged as a promising therapeutic target because they are overexpressed in a wide variety of tumors and contribute to resistance to chemotherapeutics.[40,41] It has been reported that camptothecin-induced S or G2/M arrest of HeLa cells is intensified by silencing glutathione *S*-transferase P1 (GSTP1) gene.[42] Additionally, curcumin has also been identified as an inhibitor of human GSTs,[43] and its pro-apoptosis activity against K562 cells is mediated by inhibiting the GSTP1 expression at the level of transcription.[44] Therefore, to further elucidate the reason for the increased G2/M cell cycle arrest activity by compound **1** compared with compound **2**, we compared their GST-inhibitory activity together with that of curcumin in NCI-H460 cells by using GST (DNs-CV),[25] a red fluorescent probe applied to the imaging of GST activity in living cells. As illustrated in Figure 6, after only 4 h of treatment, compound **2** decreased obviously the fluorescence signal localized to an area adjacent to the nucleus, which reflects the intracellular GST activity, but to a lesser extent than compound **1** did. The order of intracellular GST-inhibitory activity further corresponds to the increased activity of compound **1** in the cell cycle arrest. Besides, the Michael acceptor-dependent effect of compounds **1** and **2** in relation to the GST-inhibitory activity was observed as evidenced by both complete blockage of their activity by NAC pretreatment and failure of **1R** and **2R** in exhibiting the activity.

Increased Cellular Uptake of Compound 1 Compared with Compound 2 and Curcumin. Considering that cellular uptake is also a probable factor in determining the cell cycle arrest activity apart from the ROS-generating ability, microtubule-destabilizing effect, and GST-inhibitory activity, we finally assayed intracellular concentrations of curcumin and its active analogues at different time points by fluorescence analysis of methanol extracted cell lysates. As shown in Figure 7, uptake of curcumin reached a maximum value after 2 h of incubation followed by its rapid decay during 8 h. Compound **2** was analogous to curcumin in the time course of uptake and decay, but appeared to exhibit a relatively rapid and high peak uptake. Notably, compound **1** exhibited the most efficient uptake, which was almost 6 times greater than that of compound **2**, and its decay occurred only after 4 h of incubation.

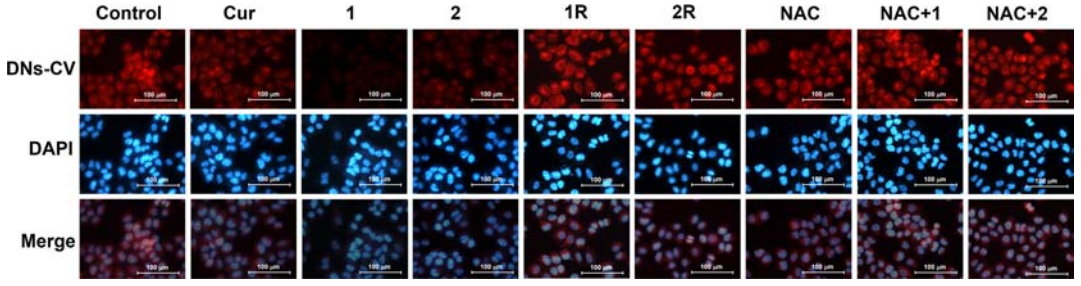

Figure 6. GST-inhibitory activity of curcumin (Cur) and its active analogues evaluated by fluorescence imaging of NCI-H460 cells. Cells (2×10^5/well) treated with the test compounds (30 μM) for 4 h were stained with a fluorescent probe for GSTs, DNs-CV (2 μM), for 30 min at 37 °C, and DAPI (0.5 μg/mL) was used to visualize the nuclei.

DOI: 10.1021/acs.jafc.5b02011
J. Agric. Food Chem. 2015, 63, 7731−7742

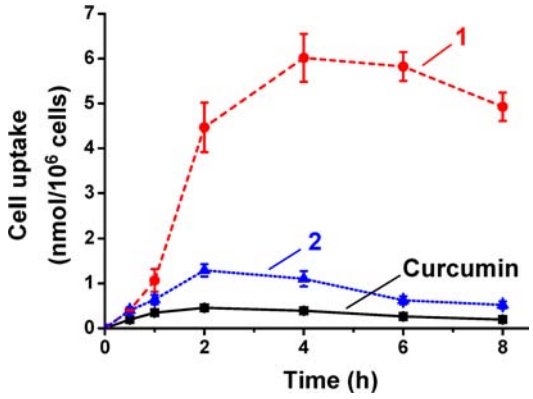

Figure 7. Cellular uptake of curcumin and its active analogues (30 μM) in NCI-H460 cells (2×10^6 cells/dish) estimated by fluorescence analysis of methanol extracted cell lysates.

DISCUSSION

The past two decades have witnessed much interest in investigating cancer chemoprevention and chemotherapy mechanisms of curcumin due to its multitargeted activity, selectivity, and safety for human use as a dietary molecule.[9−11] Like most polyphenols, although curcumin is a well-known natural antioxidant, it is also a pro-oxidant able to promote ROS generation under special conditions such as high concentrations[12,45−47] and in the presence of cupric ions.[48,49] Another efficient means of curcumin as a pro-oxidant is to covalently modify cysteine (selenocysteine) residues in redox-sensitive target proteins such as TrxR[13,14] by virtue of its Michael acceptor units. More importantly, the pro-oxidant property of curcumin is responsible for its apoptosis-inducing activity in various cancer cells and thus therapeutic effect.[12] In this study, we selected symmetrical hexamethoxy-diarylpentadienones, **1** and **2** (as the active and metabolically stable curcumin analogues) to investigate the cytotoxic mechanisms toward NCI-H460 cells from a chemical and biological point of view and tried to provide useful information for understanding the Michael acceptor-dependent redox intervention and designing curcumin-inspired anticancer agents by a pro-oxidant strategy.

The IC_{50} values of curcumin and compounds **1**−**5**, **1R**, and **2R** against NCI-H460 cells enable us to deduce the activity order **1** > **2** ∼ **3** > **4** > **5** > curcumin > **1R**, **2R** and allowed us to identify the following SAR: the Michael acceptor unit is necessary for the cytotoxicity, whereas the position and number of the methoxy groups on the aromatic rings further contribute to the activity. Abrogating the cytotoxicity of compounds **1** and **2** by NAC (Figure 1B), acting as both an antioxidant and a nucleophile, further supports the Michael acceptor-dependent cytotoxicity and contribution of ROS to the activity. Subsequently, in NCI-H460 cells, compounds **1** and **2** were identified as the G2/M cell cycle arrest agents to mediate the cytotoxicity via Michael acceptor- and ROS-dependent mechanisms (Figure 1C and 2A). Similarly, compound **2** has been previously found to induce G2/M cell cycle arrest in HCT116 cells.[19] Additionally, the dependency of ROS generation on the Michael acceptor units is supported by the fact that NAC blocks completely the stimulatory effect of compounds **1** and **2** on ROS generation; as well, **1R** and **2R** are inactive in inducing ROS accumulation (Figure 2A).

With regard to the ROS-generating mechanism, our data (Figure 3) show that compounds **1** and **2**, similar to curcumin,[13,14] could irreversibly inhibit TrxR depending on their Michael acceptor units, and the resulting covalently modified TrxR serves as an important source of ROS. The in vitro assay shows the weaker TrxR-inhibitory potency of compounds **1** and **2** relative to that of curcumin (curcumin > **1** > **2**; Figure 3A), but the higher NADPH oxidase-like activity of the TrxR modified by them than by curcumin (**2** > **1** > curcumin; Figure 3B). In contrast, the in vivo experiments suggest that compounds **1** and **2** are much more effective inhibitors of TrxR in NCI-H460 cells than curcumin (**1** ∼ **2** > curcumin; Figure 3C). The inconsistent results between the in vitro and in vivo TrxR-inhibitory activity are due, at least in part, to the increased cell uptake of compounds **1** and **2** compared with that of curcumin (Figure 7D). Notably, the SAR in the NADPH oxidase-like activity of the TrxR modified by curcumin and compounds **1** and **2**, as well as their in vivo TrxR-inhibitory activity, correlate well with their ROS-generating activity order (**2** > **1** > curcumin). The correlation also raises the possibility that TrxR is one of the targets by which compounds **1** and **2** promote ROS generation. Additionally, the cytosolic TrxR1 protein levels remained unchanged after cells were exposed to curcumin and its active analogues (Figure 3D), suggesting that the decrease of TrxR activity is mediated by directly inhibiting enzyme activity, instead of down-regulating protein expression. The above results also emphasize a broad substrate specificity of TrxR based on the following reasons: its penultimate selenocysteine residue locates at the flexible C-terminal tails and is thus easily accessible for inhibitors; its low pK_a value of 5.2 renders it easy to ionize at physiological pH, resulting in the formation of a highly active and nucleophilic selenolate.[33,50] Therefore, despite the different installation mode of methoxy groups on the aromatic rings, both compounds **1** and **2** could effectively target intracellular TrxR.

ROS generation and collapse of the intracellular redox buffering system (decrease in the GSH/GSSG ratios) induced by compounds **1** and **2** occurred almost simultaneously according to the time points of 6 and 9 h (Figure 2). This invites inevitably the following questions: Do ROS induce reduction of GSH, or does low GSH cause an increase in ROS generation? Currently, our cumulative data are not yet sufficient to clarify this point. However, the preferential reactivity of compounds **1** and **2** with TrxR at micromolar concentrations,[51] despite the presence of millimolar concentrations of GSH,[52] might result in the priority of ROS generation. The preferential reactivity is based on the fact that, as discussed above, selenocysteine is more easily ionized than GSH at physiological pH and nucleophilicity of the resulting selenolate is far stronger than that of thiolate. Furthermore, it could be also supported by our previous results showing that a double *o*-trifluoromethyl-substituted diarylpentadienone, structurally similar to compounds **1** and **2**, induced a dramatic increase in the GSSG levels, whereas it barely changed the GSH levels in A549 cells.[24] Besides, the almost simultaneous occurrence of ROS generation and collapse of the redox buffering system just reflects that the redox intervention style would be a vicious cycle, especially when the intervention occurs in such a double-effect pathway including both irreversibly inhibiting TrxR and converting it into a pro-oxidant.

Cell cycle progression is precisely regulated by cyclins, Cdks and Cdk inhibitors, and is also subject to a redox control fashion because ROS can influence the presence and activity of these proteins.[34,35] The G2/M phase transition and completion of the M phase require binding of cyclin B to Cdk1 and

DOI: 10.1021/acs.jafc.5b02011
J. Agric. Food Chem. 2015, 63, 7731−7742

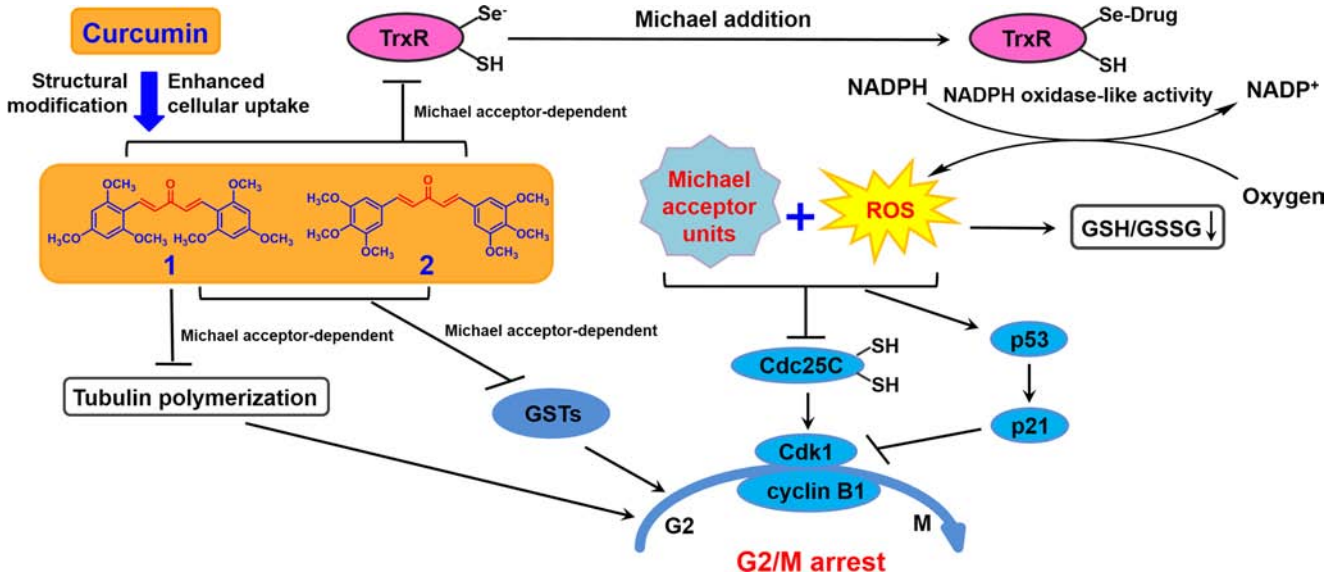

Figure 8. Mechanisms for the G2/M cell cycle arrest induced by compounds **1** and **2** in NCI-H460 cells.

subsequent Cdk1 activation.[34,35] Western blotting results reveal that both compounds **1** and **2** decrease dose-dependently the expression levels of cyclin B1 and Cdk1 (Figure 4). Additionally, p53 and p21 levels are up-regulated in the G2/M cell cycle arrest (Figure 4). It is generally agreed that p53, a multifunctional tumor suppressor, plays an important role in cell cycle arrest through its downstream mediator p21, especially under a stressed situation.[53] When the cellular redox state is shifted toward a more oxidative condition, the activity of the cyclin B1/Cdk1 complex can be inhibited through up-regulation of a p53-inducible cell cycle inhibitor p21,[54,55] thus causing the G2/M cell cycle arrest. Cdc25C phosphatase is another redox sensitive cell-cycle-regulatory protein that activates the cyclin B1/Cdk1 complex activity by dephosphorylating pThr14 and pTyr15 on Cdk1.[56] ROS can target the highly reactive cysteine 330 and 377 at the active site in Cdc25C, leading to the enzyme inactivation, and the ROS-inactivated Cdc25C is expected to prevent cell-cycle progression at the G2/M phase via inhibiting the cyclin B1/Cdk1.[56] A decrease of Cdc25C expression was also observed in the case of compounds **1** and **2** (Figure 4). In addition, all of the alterations of the regulatory proteins can be rescued by NAC (Figure 4). This further supports that compounds **1** and **2**, by virtue of their Michael acceptor units, can collapse the cell-cycle-regulatory system in NCI-H460 cells by both inducing a burst of ROS and directly modifying cysteine residues of the above redox-sensitive target proteins. The contribution of the latter can be deduced from the fact that compound **1**, compared with compound **2**, is more effective in inducing alteration in the cyclin B1, Cdk1, p53, p21, and Cdc25C expression, the G2/M cell cycle arrest activity, and, thus, the cytotoxicity but is relatively less effective in promoting ROS generation.

To clarify why compound **1**, compared with compound **2**, displays a relatively weak ability to generate ROS but increased cell cycle arrest activity and cytotoxicity, we turn to another target, tubulin/microtubule. Most microtubule-interfering agents cause cell cycle arrest during the M phase by either stabilizing or destabilizing tubulin.[36,37] Notably, compound **1** was an effective microtubule destabilizer, whereas compounds **2** and **1R** were ineffective (Figure 5). We can conclude from the SAR that both the Michael acceptor units and the installation mode of methoxy groups on the aromatic rings are indispensable for the inhibitory activity of compound **1** against microtubule polymerization. More importantly, compound **2** failed to display the effect despite its strong ROS-generating ability, clearly indicating that the microtubule-destabilizing effect of compound **1** is independent of ROS generation and contributes to its increased G2/M cell cycle arrest activity. Notably, the abrogative effect of NAC on the microtubule-destabilizing activity of compound **1** should be only due to its function as a nucleophile (not as an antioxidant) to react preferentially with the Michael acceptor acceptors of compound **1**, thereby inhibiting binding of compound **1** to active cysteine residues in tubulin.

Considering that camptothecin-induced S or G2/M arrest of HeLa cells is intensified by silencing the GSTP1 gene,[42] and curcumin-induced apoptosis of K562 cells is mediated by inhibiting the GSTP1 expression,[44] we also investigated the GST-inhibitory activity cucumin and its active analogues **1** and **2**. Our results show that the activity is Michael acceptor-dependent, and compound **1** is the most active, followed by compound **2**; curcumin is the worst (Figure 6). This provides another possible explanation for the increased G2/M cell cycle arrest activity of compound **1** despite its relatively weaker ROS-generating ability than that of compound **2**.

To sum up, in this work, the active curcumin analogues **1** and **2** were identified as the G2/M cell cycle arrest agents to mediate cytotoxicity toward NCI-H460 cells via Michael acceptor-dependent redox intervention. As summarized in Figure 8, they could act as dual-effective TrxR inhibitors, not only inactivating TrxR by their Michael acceptor units but also converting this antioxidant enzyme into a ROS promoter with a NADPH oxidase-like activity, leading to a burst in ROS associated with collapse of the redox buffering system. Depending on the Michael acceptor unit and ROS generation, they cause a final G2/M cell cycle arrest in NCI-H460 cells by decreasing the expression levels of cyclin B1 and Cdk1 via up-regulation of p53 and p21 and down-regulation of Cdc25C. Additionally, the increased cell cycle arrest activity of compound **1** compared with compound **2** is derived, at least in part, from its Michael acceptor-dependent microtubule-

DOI: 10.1021/acs.jafc.5b02011
J. Agric. Food Chem. 2015, 63, 7731−7742

destabilizing effect and greater GST-inhibitory activity, as well as its enhanced cellular uptake.

AUTHOR INFORMATION

Corresponding Author

*(B.Z.) E-mail: bozhou@lzu.edu.cn. Fax: +86-931-8915557.

Funding

This work was supported by the National Natural Science Foundation of China (Grant 21172101), the 111 Project, and the Fundamental Research Funds for the Central Universities (lzujbky-2015-51).

Notes

The authors declare no competing financial interest.

ACKNOWLEDGMENTS

We are grateful to Prof. Jianguo Fang (Lanzhou University) for the generous gift of TRFS-green.

REFERENCES

(1) Bindoli, A.; Rigobello, M. P. Principles in redox signaling: from chemistry to functional significance. *Antioxid. Redox Signal.* **2013**, *18*, 1557−1593.

(2) Trachootham, D.; Alexandre, J.; Huang, P. Targeting cancer cells by ROS-mediated mechanisms: a radical therapeutic approach? *Nat. Rev. Drug Discovery* **2009**, *8*, 579−591.

(3) Policastro, L. L.; Ibañez, I. L.; Notcovich, C.; Duran, H. A.; Podhajcer, O. L. The tumor microenvironment: characterization, redox considerations, and novel approaches for reactive oxygen species-targeted gene therapy. *Antioxid. Redox Signal.* **2013**, *19*, 854−895.

(4) Gupta, S. C.; Hevia, D.; Patchva, S.; Park, B.; Koh, W.; Aggarwal, B. B. Upsides and downsides of reactive oxygen species for cancer: The roles of reactive oxygen species in tumorigenesis, prevention, and therapy. *Antioxid. Redox Signal.* **2012**, *16*, 1295−1322.

(5) Wondrak, G. T. Redox-directed cancer therapeutics: molecular mechanisms and opportunities. *Antioxid. Redox Signal.* **2009**, *11*, 3013−3069.

(6) Fan, G.-J.; Jin, X.-L.; Qian, Y.-P.; Wang, Q.; Yang, R.-T.; Dai, F.; Tang, J.-J.; Shang, Y.-J.; Cheng, L.-X.; Yang, J.; Zhou, B. Hydroxycinnamic acids as DNA-cleaving agents in the presence of CuII ions: Mechanism, structure−activity relationship, and biological implications. *Chem.−Eur. J.* **2009**, *15*, 12889−12899.

(7) Liu, G.-Y.; Yang, J.; Dai, F.; Yan, W.-J.; Wang, Q.; Li, X.-Z.; Ding, D.-J.; Cao, X.-Y.; Zhou, B. CuII ions and the stilbene−chroman hybrid with a catechol moiety synergistically induced DNA damage, and cell cycle arrest and apoptosis of HepG2 cells: an interesting acid/base-promoted prooxidant reaction. *Chem.−Eur. J.* **2012**, *18*, 11100−11106.

(8) Wang, Q.; Qian, Y.-P.; Dai, F.; Lu, D.-L; Yan, W.-J.; Chen, Y.; Zhou, B. Ortho-dihydroxychalcones as cupric ion-dependent prooxidants: activity and mechanisms. *Food Chem.* **2013**, *141*, 1259−1266.

(9) Goel, A.; Jhurani, S.; Aggarwal, B. B. Multi-targeted therapy by curcumin: how spicy is it? *Mol. Nutr. Food Res.* **2008**, *52*, 1010−1030.

(10) Reuter, S.; Eifes, S.; Dicato, M.; Aggarwal, B. B.; Diederich, M. Modulation of anti-apoptotic and survival pathways by curcumin as a strategy to induce apoptosis in cancer cells. *Biochem. Pharmacol.* **2008**, *76*, 1340−1351.

(11) Ravindran, J.; Prasad, S.; Aggarwal, B. B. Curcumin and cancer cells: how many ways can curry kill tumor cells selectively? *AAPS J.* **2009**, *11*, 495−510.

(12) López-Lázaro, M. Anticancer and carcinogenic properties of curcumin: considerations for its clinical development as a cancer chemopreventive and chemotherapeutic agent. *Mol. Nutr. Food Res.* **2008**, *52*, S103−S127 and references therein..

(13) Fang, J.; Lu, J.; Holmgren, A. Thioredoxin reductase is irreversibly modified by curcumin. *J. Biol. Chem.* **2005**, *280*, 25284−25290.

(14) Cai, W.; Zhang, B.; Duan, D.; Wu, J.; Fang, J. Curcumin targeting the thioredoxin system elevates oxidative stress in HeLa cells. *Toxicol. Appl. Pharmacol.* **2012**, *262*, 341−348.

(15) Anand, P.; Thomas, S. G.; Kunnumakkara, A. B.; Sundaram, C. Biological activities of curcumin and its analogues (congeners) made by man and Mother Nature. *Biochem. Pharmacol.* **2008**, *76*, 1590−1611.

(16) Mosley, C. A.; Liotta, D. C.; Snyder, J. P. Highly active anticancer curcumin analogues. *Adv. Exp. Med. Biol.* **2007**, *595*, 77−103 and references therein..

(17) Liang, G.; Shao, L.; Wang, Y.; Zhao, C.; Chu, Y.; Xiao, J.; Zhao, Y.; Li, X.; Yang, S. Exploration and synthesis of curcumin analogues with improved structural stability both *in vitro* and *in vivo* as cytotoxic agents. *Bioorg. Med. Chem.* **2009**, *17*, 2623−2631.

(18) Adams, B. K.; Ferstl, E. M.; Davis, M. C.; Herold, M.; Kurtkaya, S.; Camalier, R. F.; Hollingshead, M. G.; Kaur, G.; Sausville, E. A.; Rickles, F. R.; Snyder, J. P.; Liotta, D. C.; Shoji, M. Synthesis and biological evaluation of novel curcumin analogs as anti-cancer and anti-angiogenesis agents. *Bioorg. Med. Chem.* **2004**, *12*, 3871−3883.

(19) Ohori, H.; Yamakoshi, H.; Tomizawa, M.; Shibuya, M.; Kakudo, Y.; Takahashi, A.; Takahashi, S.; Kato, S.; Suzuki, T.; Ishioka, C.; Iwabuchi, Y.; Shibata, H. Synthesis and biological analysis of new curcumin analogues bearing an enhanced potential for the medicinal treatment of cancer. *Mol. Cancer Ther.* **2006**, *5*, 2563−2571.

(20) Fuchs, J. R.; Pandit, B.; Bhasin, D.; Etter, J. P.; Regan, N.; Abdelhamid, D.; Li, C.; Lin, J.; Li, P. K. Structure−activity relationship studies of curcumin analogues. *Bioorg. Med. Chem. Lett.* **2009**, *19*, 2065−2069.

(21) Yamakoshi, H.; Ohori, H.; Kudo, C.; Sato, A.; Kanoh, N.; Ishioka, C.; Shibata, H.; Iwabuchi, Y. Structure−activity relationship of C5-curcuminoids and synthesis of their molecular probes thereof. *Bioorg. Med. Chem.* **2010**, *18*, 1083−1092.

(22) Kudo, C.; Yamakoshi, H.; Sato, A.; Nanjo, H.; Ohori, H.; Ishioka, C.; Iwabuchi, Y.; Shibata, H. Synthesis of 86 species of 1,5-diaryl-3-oxo-1,4-pentadienes analogs of curcumin can yield a good lead *in vivo*. *BMC Pharmacol.* **2011**, *11*, 1−9.

(23) Yamakoshi, H.; Kanoh, N.; Kudo, C.; Sato, A.; Ueda, K.; Muroi, M.; Kon, S.; Satake, M.; Ohori, H.; Ishioka, C.; Oshima, Y.; Osada, H.; Chiba, N.; Shibata, H.; Iwabuchi, Y. KSRP/FUBP2 is a binding protein of GO-Y086, a cytotoxic curcumin analogue. *ACS Med. Chem. Lett.* **2010**, *1*, 273−276.

(24) Dai, F.; Liu, G.-Y.; Li, Y.; Yan, W.-J.; Wang, Q.; Yang, J.; Lu, D.-L.; Ding, D.-J.; Lin, D.; Zhou, B. Insights into the importance for designing curcumin-inspired anticancer agents by the prooxidant strategy: the case of diarylpentanoids. *Free Radical Biol. Med.* **2015**, *85*, 127−137.

(25) Zhang, J.; Shibata, A.; Ito, M.; Shuto, S.; Ito, Y.; Mannervik, B.; Abe, H.; Morgenstern, R. Synthesis and characterization of a series of highly fluorogenic substrates for glutathione transferases, a general strategy. *J. Am. Chem. Soc.* **2011**, *133*, 14109−14119.

(26) Shang, Y.-J.; Jin, X.-L.; Shang, X.-L.; Tang, J.-J.; Liu, G.-Y.; Dai, F.; Qian, Y.-P.; Fan, G.-J.; Liu, Q.; Zhou, B. Antioxidant capacity of curcumin-directed analogues: structure−activity relationship and influence of microenvironment. *Food Chem.* **2010**, *119*, 1435−1442.

(27) Tang, J. J.; Fan, G. J.; Dai, F.; Ding, D. J.; Wang, Q.; Lu, D.-L.; Li, R.-R.; Li, X.-Z.; Hu, L.-M.; Jin, X.-L.; Zhou, B. Finding more active antioxidants and cancer chemoprevention agents by elongating the conjugated links of resveratrol. *Free Radical Biol. Med.* **2011**, *50*, 1447−1457.

(28) Vandeputte, C.; Guizon, I.; Genestie-Denis, I.; Vannier, B.; Lorenzon, G. A microtiter plate assay for total glutathione and glutathione disulfide contents in cultured/isolated cells: performance study of a new miniaturized protocol. *Cell Biol. Toxicol.* **1994**, *10*, 415−421.

(29) Nordberg, J.; Zhong, L.; Holmgren, A.; Arnér, E. S. J. Mammalian thioredoxin reductase is irreversibly inhibited by dinitrohalobenzenes by alkylation of both the redox active selenocysteine and its neighboring cysteine residue. *J. Biol. Chem.* **1998**, *273*, 10835−10842.

DOI: 10.1021/acs.jafc.5b02011
J. Agric. Food Chem. 2015, 63, 7731−7742

(30) Zhang, L.; Duan, D.; Liu, Y.; Ge, C.; Cui, X.; Sun, J.; Fang, J. Highly selective off-on fluorescent probe for imaging thioredoxin reductase in living cells. *J. Am. Chem. Soc.* **2014**, *136*, 226−233.
(31) Morrison, K. C.; Hergenrother, P. J. Whole cell microtubule analysis by flow cytometry. *Anal. Biochem.* **2012**, *420*, 26−32.
(32) Sun, J.; Bi, C.; Chan, H. M.; Sun, S.; Zhang, Q.; Zheng, Y. Curcumin-loaded solid lipid nanoparticles have prolonged *in vitro* antitumour activity, cellular uptake and improved *in vivo* bioavailability. *Colloids Surf., B* **2013**, *111*, 367−375.
(33) Lu, J.; Holmgren, A. Thioredoxin system in cell death progression. *Antioxid. Redox Signal.* **2012**, *17*, 1738−1747.
(34) Sarsour, E. H.; Kumar, M. G.; Chaudhuri, L.; Kalen, A. L.; Goswami, P. C. Redox control of the cell cycle in health and disease. *Antioxid. Redox Signal.* **2009**, *11*, 2985−3011.
(35) Verbon, E. H.; Post, J. A.; Boonstra, J. The influence of reactive oxygen species on cell cycle progression in mammalian cells. *Gene* **2012**, *511*, 1−6.
(36) Dumontet, C.; Jordan, M. A. Microtubule-binding agents: a dynamic field of cancer therapeutics. *Nat. Rev. Drug Discovery* **2010**, *9*, 790−803.
(37) Jordan, M. A.; Wilson, L. Microtubules as a target for anticancer drugs. *Nat. Rev. Cancer* **2004**, *4*, 253−265.
(38) Ishiguro, K.; Ando, T.; Watanabe, O.; Goto, H. Specific reaction of α,β-unsaturated carbonyl compounds such as 6-shogaol with sulfhydryl groups in tubulin leading to microtubule damage. *FEBS Lett.* **2008**, *582*, 3531−3536.
(39) Hosono, T.; Fukao, T.; Ogihara, J.; Ito, Y.; Shiba, H.; Seki, T.; Ariga, T. Diallyl trisulfide suppresses the proliferation and induces apoptosis of human colon cancer cells through oxidative modification of β-tubulin. *J. Biol. Chem.* **2005**, *280*, 41487−41493.
(40) McLellan, L. I.; Wolf, C. R. Glutathione and glutathione-dependent enzymes in cancer drug resistance. *Drug Resist. Updates* **1999**, *2*, 153−164.
(41) Townsend, D. M.; Tew, K. D. The role of glutathione-S-transferase in anti-cancer drug resistance. *Oncogene* **2003**, *22*, 7369−7375.
(42) Hara, T.; Ishii, T.; Fujishiro, M.; Masuda, M.; Ito, T.; Nakajima, J.; Inoue, T.; Matsuse, T. Glutathione S-transferase P1 has protective effects on cell viability against camptothecin. *Cancer Lett.* **2004**, *203*, 199−207.
(43) Hayeshi, R.; Mutingwende, I.; Mavengere, W.; Masiyanise, V.; Mukanganyama, S. The inhibition of human glutathione S-transferases activity by plant polyphenolic compounds ellagic acid and curcumin. *Food Chem. Toxicol.* **2007**, *45*, 286−295.
(44) Duvoix, A.; Morceau, F.; Delhalle, S.; Schmitz, M.; Schnekenburger, M.; Galteau, M.-M.; Dicato, M.; Diederich, M. Induction of apoptosis by curcumin: mediation by glutathione S-transferase P1-1. *Biochem. Pharmacol.* **2003**, *66*, 1475−1483.
(45) Kang, J.; Chen, J.; Shi, Y.; Jia, J.; Zhang, Y. Curcumin-induced histone hypoacetylation: the role of reactive oxygen species. *Biochem. Pharmacol.* **2005**, *69*, 1205−1213.
(46) Cao, J.; Jia, L.; Zhou, H.-M.; Liu, Y.; Zhong, L.-F. Mitochondrial and nuclear DNA damage induced by curcumin in human hepatoma G2 cells. *Toxicol. Sci.* **2006**, *91*, 476−483.
(47) McNally, S. J.; Harrison, E. M.; Ross, J. A.; Garden, O. J.; Wigmore, S. J. Curcumin induces heme oxygenase 1 through generation of reactive oxygen species, p38 activation and phosphatase inhibition. *Int. J. Mol. Med.* **2007**, *19*, 165−172.
(48) Ahsan, H.; Hadi, S. M. Strand scission in DNA induced by curcumin in the presence of Cu(II). *Cancer Lett.* **1998**, *124*, 23−30.
(49) Yoshino, M.; Haneda, M.; Naruse, M.; Htay, H. H.; Tsubouchi, R.; Qiao, S. L.; Li, W. H.; Murakami, K.; Yokochi, T. *Toxicol. In Vitro* **2004**, *18*, 783−789.
(50) Urig, S.; Becker, K. On the potential of thioredoxin reductase inhibitors for cancer therapy. *Semin. Cancer Biol.* **2006**, *16*, 452−465.
(51) Gromer, S.; Urig, S.; Becker, K. Thethioredoxin system-from sciencetoclinic. *Med. Res. Rev.* **2004**, *24*, 40−89.
(52) Dickinson, D. A.; Forman, H. J. Cellular glutathione and thiols metabolism. *Biochem. Pharmacol.* **2002**, *64*, 1019−1026.
(53) Chatterjee, S.; Kundu, S.; Sengupta, S.; Bhattacharyya, A. Divergence to apoptosis from ROS induced cell cycle arrest: effect of cadmium. *Mutat. Res., Fundam. Mol. Mech. Mutagen.* **2009**, *663*, 22−31.
(54) Jackson, J. G.; Pereira-Smith, O. M. p53 is preferentially recruited to the promoters of growth arrest genes p21 and GADD45 during replicative senescence of normal human fibroblasts. *Cancer Res.* **2006**, *66*, 8356−8360.
(55) O'Reilly, M. A. Redox activation of p21Cip1/WAF1/Sdi1: a multifunctional regulator of cell survival and death. *Antioxid. Redox Signaling* **2005**, *7*, 108−118.
(56) Rudolph, J. Redox regulation of the cdc25 phosphatases. *Antioxid. Redox Signal.* **2005**, *7*, 761−767.

DOI: 10.1021/acs.jafc.5b02011
J. Agric. Food Chem. 2015, 63, 7731−7742

of stored maize, *S. zeamais*,[14] have yet been performed. The aim of this investigation was to determine the antifungal effect of 10 recognized VOCs from cereal kernels on *F. verticillioides*, its mycotoxin production, and the insecticidal effects against its insect vector *S. zeamais*.

MATERIALS AND METHODS

Chemicals. The chemicals (2*E*)-2-hexenal (w256005, purity > 95%), (2*E*)-2-nonenal (255653, 97%), (2*E*,6*Z*)-2,6-nonadienal (w337706, > 96%), 1-pentanol (76929, > 99%), 1-hexanol (471402, > 99%), 1-butanol (281549, > 99%), 3-methyl-1-butanol (309435, > 99%), pentanal (w309818, > 97%), 2-decanone (w510637, > 98%), 3-decanone (268194, 98%), and propionic acid (101362192, 99.5%) were purchased from Sigma−Aldrich (Buenos Aires, Argentina). DDVP (dicholrvos, positive control, technical grade, > 98% purity) was purchased from Chemotécnica S.A (Buenos Aires, Argentina).

Fungal Strain. An isolate of *F. verticillioides* (Sacc) Niremberg (= *F. moniliforme* Sheldon teleomorph *Gibberella fujikuroi* (Sawada) Ito in Ito and Kimura[31] strain M3125 (provided by Dr. Robert Proctor, United States Department of Agriculture, Agricultural Research Service, National Center for Agricultural Utilization Research, Peoria, IL, United States)) was used for all experiments. This fumonisin-producing strain was isolated from maize in California.[32]

Inoculum Preparation. *F. verticillioides* M3125 was grown on Czapek-dox agar Petri plates for 7 days at 28 °C in the dark, to allow profuse sporulation. Then, sterile distilled water was added to each plate, and a conidia suspension was obtained by scraping the colony surface with a sterile Drigalsky spatula, which was then filtered through a cheesecloth. The conidial concentration (1×10^6 conidia/mL) was standardized using a hemocytometer.

Insects. *S. zeamais* (Motschulsky) were reared on sterilized whole maize grain in sealed containers. Insects were reared under controlled temperature and humidity (28 °C and 60−70%) and a light/dark regime of 12:12.[33] Adults of a strain of *S. zeamais* were obtained from Metán, Salta province, Argentina. The colony was maintained in our laboratory for one year without exposure to insecticides. The male and female weevils used in all the experiments were approximately 2 weeks old. All experiments were conducted in complete darkness in a climatic chamber (28 °C and 60−70% relative humidity).

Effect of Volatile Organic Compounds on Fungal Growth and Fumonisin Production. The antifungal activity of the VOCs was tested determining the radial growth of the fungal colony following a methodology proposed by Neri et al.[34] Briefly, a paper filter was placed on the inside cover of the maize meal extract agar (3%) Petri dish. The VOCs were added separately to 90 mm paper filter as pure liquid compounds, and the concentrations (0.03, 0.06, 0.13, 0.27, 0.53, 1.06, 2.12, and 4.24 mM) were expressed as 10^{-3} mol on filter paper per dish volume. A paper filter without VOCs was used as the control. Then, 10 μL of a conidial suspension (1×10^6 conidia/mL) of *F. verticillioides* M3125 was added aseptically to the center of the Petri dishes. The maize meal extract agar (3%) Petri dishes were then covered, wrapped in parafilm, and incubated in the dark at 28 °C. The colony diameter of *F. verticillioides* was measured after 7 days of incubation, and the colony area was calculated using the formula for the area of a circle ($\pi \times r^2$). The minimum inhibitory concentration (MIC) was defined as the lowest concentration of the VOCs at which no fungal growth was observed. To study the effects of the VOCs on FB_1 production, the inoculated plates were incubated in the dark at 28 °C for 28 days. After this incubation, the parafilm and filter papers were removed, and the agar in the experimental plates was dried for 96 h at 60 °C in a forced-air oven before being ground to a fine dry powder. Finally, 5 mL of water was added to the dried agar from each disk, and FB_1 was extracted by shaking the dried dishes with water for 120 min on an orbital shaker, with the mixture then being centrifuged at 5000 rpm for 15 min. The experiments were repeated twice in triplicate.[35]

Fumonisin B_1 Quantitation. The quantitation of the samples was performed following a methodology proposed by Shephard et al.[36] Briefly, samples (1000 μL) from the FB_1 extracts were diluted with acetonitrile/water (1:1), and then, an aliquot (50 μL) was derivatized prior to injection: during 3.5 min with 200 μL of a solution, which was prepared by adding 5 mL of 0.1 M sodium tetraborate and 50 μL of 2-mercaptoethanol to 1 mL of methanol containing 40 mg of *o*-phthaldialdehyde. Derivatized samples were analyzed using a PerkinElmer HPLC equipped with a fluorescence detector, with the wavelengths used for excitation and emission being 335 and 440 nm, respectively, and with an analytical reverse phase C_{18} column (150 mm × 4.6 mm internal diameter and 5 μm particle size) connected to a precolumn C_{18} (20 mm × 4.6 mm and 5 μm particle size). For the mobile phase, methanol and 0.1 M NaH_2PO_4 (75:25) were used, with the pH being set at 3.35 ± 0.2 with orthophosphoric acid and a flow rate of 1.5 mL/min. The quantitation of FB_1 was carried out by comparing the peak areas obtained from samples with those corresponding to the analytical standards of FB_1 (PROMEC, Program on mycotoxins and experimental carcinogenesis, Tygerberg, Republic of South Africa).

Insecticidal Assay. The insecticidal effect on *S. zeamais* was tested using a fumigant toxicity assay described by Huang et al.,[37] with some modifications. Briefly, different amounts of pure VOCs at concentrations corresponding to 20−600 μL/L air were placed onto Whatman filter paper disks of 2 cm diameter. Only the lowest concentrations were diluted in *n*-hexane, and in these cases, each filter paper disk was air-dried for 30 s and placed on the underside of the screw cap of a glass vial (30 mL). Ten adult *S. zeamais* were placed into each vial, and a nylon gauze piece was fitted 1 cm under the screw cap of each glass vial, to avoid direct contact of the weevils with the VOCs. The experiment was performed in five replicates twice per concentration, and control treatments were kept under the same conditions without pure compounds. DDVP was used as a positive control due to its high vapor pressure and known insecticide activity. Insect mortality was checked after 24 h, with the mortality percentages and lethal concentration (LC_{50}) values being calculated according to Finney.[38]

Repellent/Attraction Activity Bioassay. The behavioral response of *S. zeamais* adults to individual VOCs was tested in a two-choice olfactometer bioassay described by Herrera et al.[35] Briefly, two flasks (250 mL) were connected with a glass tube of 30 cm × 1 cm of diameter. In the middle (15 cm from the two flasks), a small hole was made of 1 cm × 1 cm. The connections between the two flasks and the tube were sealed with rubber plugs, which were covered with parafilm to prevent gas leakage. A filter paper of 2 cm diameter was placed within each flask where the compounds were added. Twenty insects, deprived of food for at least 4 h, were placed in the hole of the glass tube. These were then released and tested for 2 h in a climatic chamber, with the experiments being carried out between 10:00 and 16:00 h. The position of the flasks was changed at every replication, and the insects that did not show any response in the experiment were not used to calculate the response index (RI). Insects were given a choice between a specific dose of the test compound and the solvent (*n*-hexane) used as a control. The experiments were performed five times for each assay, with insects only being used once. For each experiment, an independent control (without any compound) showed that the movement of the beetles toward either flask was random (RI = −2.1 ± 7.5). Propionic acid was used as the positive control for repellent.[39]

In each trial, a RI was calculated by using the equation RI = $[(T - C)/\mathrm{Tot}] \times 100$, where T is number of insects responding to the treatment, C is number of insects responding to the control, and Tot is the total number of insects released.[40] Positive values of RI indicate attraction to the treatment, while negative values indicate repellence.

Statistical Analysis. Data were analyzed using InfoStat/Professional 2010p[41] at $p = 0.05$. Randomized complete block design was used for the experimental designs, and a one-way analysis of variance was used to study the experimental data. The Shapiro−Wilk test was utilized to test the normality of the experimental data, and comparisons between treatments were carried out using the Duncan test. Experimental data without a normal distribution were statistically analyzed by the Kruskal−Wallis nonparametric test (at $p < 0.05$). A pairwise comparison was used to compare means among treatment

DOI: 10.1021/acs.jafc.5b02315
J. Agric. Food Chem. 2015, 63, 7743−7749

ranges. The lethal concentrations (LC_{50} and LC_{95}) were calculated from dose−mortality values, using probit regression analysis by POLO−PLUS Software.[42] The significance of the mean RI in each treatment of the two-choice olfactometer bioassay was evaluated by the Student's *t* test for paired comparisons.[40] The chemical properties lipophilicity (log P: logarithm of the octanol/water partition coefficient) and the vapor pressure of the VOCs compounds were obtained from the ChemSpider database.[43]

RESULTS

Antifungal and Antimicotoxicogenic Activities. The inhibitory effects mediated by the VOCs on *F. verticillioides* growth was dose-dependent, with the most active compounds being the aldehydes: (2*E*)-2-nonenal, (2*E*)-2-hexenal, (2*E*, 6*Z*)-2,6-nonadienal, and pentanal, which exhibited MIC values of <0.03, 0.06, 0.06, and 0.53 mM, respectively (Table 1). Of the alcohols tested, 1-hexanol revealed the highest activity, while of the alkyl ketones, 3-decanone had a greater inhibitory effect on fungal growth than 2-decanone, at several concentrations. Treatments such as (2*E*)-2-hexenal (0.06 mM), 1-pentanol (4.24 mM), 1-hexanol (2.12 and 4.24 mM), pentanal (0.53 and 1.06 mM), 2-decanone (4.24 mM), and 3-decanone (2.12 and 4.24 mM) all caused a delay in the fungal growth, with no growth being observed on the seventh day. However, on the 28th day postinoculation, fungal growth was apparent, and the FB_1 concentration was determined. On the other hand, 1-pentanol showed a slight stimulatory effect on fungal growth at lower concentrations. The VOC effects on FB_1 production are presented in Table 2, where it can be observed that (2*E*)-2-hexenal, (2*E*)-2-nonenal, and (2*E*, 6*Z*)-2,6-nonadienal caused a total inhibition of mycelium growth, implying an absence of FB_1 production. 1-Hexanol (4.24 mM) and 1-butanol (0.53 mM and 4.24 mM) effectively inhibited fumonisin production by *F. verticillioides*.

Insecticidal and Repellent/Attraction Effects. The results of fumigant insecticidal activity of VOCs tested on *S. zeamais* are shown in Table 3. After 24 h exposure, the most active compounds were 2- and 3-decanone, with LC_{50} values of 50.4 and 54.6 μL/L, respectively. 1-Hexanol, 1-pentanol, 1-butanol, and (2*E*)-2-hexenal showed insecticide LC_{50} values between 224.1 and 306.6 μL/L, while (2*E*)-2-nonenal and pentanal did not show any insecticidal activity in the range of the evaluated concentrations (20−600 μL/L). The LC_{50} values of (2*E*,6*Z*)-2,6-nonadienal and 3-methyl-1-butanol could not be determined because they did not show a dose-dependent relationship. However, at a dose of 150 μL/L, the mortality was 98.0% (±4.5) for 3-methyl-1-butanol and 28.7% (±19.4) for (2*E*,6*Z*)-2,6-nonadienal (data not shown).

The behavioral responses of *S. zeamais* adults to VOCs are shown in Figure 1. All the compounds showed a repellent effect at 4 μL/L. Moreover, only (2*E*,6*Z*)-2,6-nonadienal showed repellent effects at 0.05 μL/L (0.31 μM), with a RI of −37.3 ± 14.0. On the other hand, 3-methyl-1-butanol and 1-butanol showed attractant effects at 0.4 μL/L.

DISCUSSION

The results obtained in the present work show the capacity of 10 natural VOCs present in the headspace volatiles of several cereal kernels[26,27,29,39,44] to affect the fungal growth of *F. verticillioides* and FB_1 production. In addition, these VOCs showed insecticidal and repellent effects against its insect vector *S. zeamais*. Our findings revealed that aldehydes had higher levels of antifungal activity than alcohols or alkyl ketones. In

Table 1. Antifungal Activity of VOCs against *F. verticillioides* M3125 in Maize Meal Extract Agar (3%) at 28 °C[a]

			inhibition of fungal growth[c] (%)							
compd	MIC[b] (mM)	MIC[b] (μL/L)	0.03 mM	0.06 mM	0.13 mM	0.27 mM	0.53 mM	1.06 mM	2.12 mM	4.24 mM
(2*E*)-hexenal	0.06	7.8	46.4 ± 2.6b	100[d]a	100[d]a	100[d]a	100[d]a	100[d]a	100[d]a	100[d]a
(2*E*)-nonenal	<0.03	<5.6	100[d]a	100[d]a	100[d]a	100[d]a	100[d]a	100[d]a	100[d]a	100[d]a
(2*E*,6*Z*)-nonadienal	0.06	10.6	53.9 ± 3.0b	100[d]a	100[d]a	100[d]a	100[d]a	100[d]a	100[d]a	100[d]a
pentanal	0.53	56.2	5.7 ± 4.3b	26.3 ± 6.1b	39.1 ± 0.2b	42.3 ± 7.5b	100[d]a	100[d]a	100[d]a	100[d]a
1-pentanol	4.24	460.7	2.8 ± 2.8b	−42.0 ± 0.2b	−42.0 ± 0.1b	−64.7 ± 0.1b	11.4 ± 0.2b	49.6 ± 13.3b	81.1 ± 8.8b	97.8 ± 0.9[d]a
1-hexanol	2.12	264.0	−0.1 ± 1.5b	18.8 ± 3.8b	21.3 ± 6.3b	34.6 ± 2.3b	54.2 ± 0.2b	89.5 ± 0.5b	99.8 ± 0.3[d]a	100[d]
3-methyl-1-butanol	>4.24	>460.7	−9.0 ± 4.6b	1.4 ± 0.2b	1.4 ± 0.1b	6.9 ± 5.5b	21.3 ± 2.7b	18.6 ± 0.1b	69.7 ± 5.8b	73.9 ± 1.5b
1-butanol	>4.24	>393.2	−0.1 ± 4.4b	28.8 ± 1.2b	30.0 ± 2.4b	26.4 ± 1.2b	31.6 ± 0.2b	32.8 ± 3.7b	46.6 ± 7.7b	78.3 ± 1.4b
2-decanone	>4.24	>797.7	0.1 ± 1.5b	42.8 ± 5.8b	3.0 ± 1.5b	13.3 ± 2.8b	62.3 ± 9.3b	81.9 ± 7.1b	92.9 ± 0.4[d]a	93.4 ± 2.7[d]a
3-decanone	>4.24	>797.7	−7.8 ± 3.2b	42.9 ± 1.2b	20.2 ± 4.1b	53.8 ± 1.0b	61.8 ± 0.9b	91.98 ± 1.3[d]a	95.2 ± 2.6[d]a	96.6 ± 1.1[d]a

[a]Values are expressed as mean ± standard deviation. Values having different letters are significantly different from each treatment. The experiments were performed twice in triplicate. [b]MIC: Minimum inhibitory concentration. [c]Inhibition of fungal growth was determined after 7 days of incubation. (−): Indicates fungal growth stimulation. [d]Indicates significant difference with the control according to the Kruskal−Wallis nonparametric test ($H = 249.27$. $P < 0.0001$). An all pairwise comparison was used to compare the means among treatments ranges.

DOI: 10.1021/acs.jafc.5b02315
J. Agric. Food Chem. 2015, 63, 7743−7749

Table 2. Effects of VOCs on FB_1 Production in Maize Meal Extract Agar (3%) at 28 °C[a]

	inhibition of FB_1 production (%)							
compd	0.03 mM	0.06 mM	0.13 mM	0.27 mM	0.53 mM	1.06 mM	2.12 mM	4.24 mM
(2*E*)-hexen[b]1	19.3 ± 60.7b	−5.7 ± 82.1b	ND	ND	ND	ND	ND	ND
(2*E*)-nonenal	ND	ND	ND	ND	ND	ND	ND	ND
(2*E*,6*Z*)-nonadienal	57.5 ± 16.4b	ND	ND	ND	ND	ND	ND	ND
pentanal	−25.2 ± 17.2b	47.8 ± 21.5b	−10.2 ± 15.6b	9.1 ± 15.9b	65.0 ± 10.5b	50.0 ± 27.7b	ND	ND
1- pentanol	38.3 ± 51.7b	3.4 ± 32.4b	63.6 ± 214.9b	−81.9 ± 79.6b	−3.8 ± 19.2b	12.5 ± 15.5b	−0.4 ± 20.0b	−110.6 ± 23.4b
1-hexanol	52.9 ± 86.0b	59.9 ± 31.9b	40.4 ± 51.6b	8.1 ± 18.9b	58.2 ± 37.4b	57.5 ± 20.0b	59.2 ± 8.2b	100.0 ± 14.13[b]a
3-methyl-1-butanol	64.3 ± 32.8b	21.1 ± 13.7b	34.2 ± 10.3b	58.9 ± 4.7b	64.3 ± 13.0b	36.3 ± 15.4b	39.5 ± 59.2b	−39.3 ± 24.0b
1-butanol	23.3 ± 9.5b	8.5 ± 19.3b	29.6 ± 11.8b	55.2 ± 4.8b	78.1 ± 4.1[b]a	57.6 ± 7.5b	26.5 ± 15.9b	73.8 ± 3.1[b]a
2-decanone	−71.0 ± 40.9b	16.1 ± 74.6b	22.3 ± 9.6b	27.1 ± 12.9b	38.7 ± 14.1b	−241.6 ± 64.2b	−8.2 ± 12.5b	−56.3 ± 27.3b
3-decanone	25.1 ± 5.4b	56.9 ± 9.3b	18.8 ± 27.3b	37.7 ± 8.1b	38.0 ± 23.8b	30.1 ± 27.0b	−85.9 ± 30.5b	−169.1 ± 79.1b

[a]Values are expressed as medians ± standard error. Values having different letters are significantly different from each treatment. The experiments were performed twice in triplicate. ND: Not determined. FB_1 inhibition was not determined because there was no fungal growth. (−): Indicates FB_1 stimulation. [b]Indicates significant difference with the control according to the Kruskal–Wallis nonparametric test ($H = 249.27$. $P < 0.0001$). An all pairwise comparison was used to compare the means among treatments ranges.

agreement, a previous report by Mita et al.[24] showed antifungal activity of C_6 and C_9 aldehydes against *A. carbonarius* and *F. proliferatum*, with (2*E*)-2-nonenal being the most effective compound. In addition, other studies reported high antifungal activity of (2*E*)-2-hexenal, (2*E*)-2-nonenal, and (2*E*,6*Z*)-2,6-nonadienal.[26−28,45] Moreover, the results presented here suggest that a relationship between the antifungal activity and the molecular properties, such as lipophilicity (log P) and vapor pressure, may exist in compounds with the same functional group. In the present work, the most active compound against *F. verticillioides* was (2*E*)-2-nonenal, which is the aldehyde with the highest lipophilic property. The relationship between log P and antifungal activity of plant phenolic compounds against *F. verticillioides* has been previously reported by Dambolena et al.[46] In the present study, (2*E*)-2-hexenal, (2*E*)-2-nonenal, and (2*E*, 6*Z*)-2,6-nonadienal also prevented FB_1 production because these compounds completely inhibited fungal growth at the tested concentrations. Previous investigations have reported aflatoxin B_1 being inhibited by (2*E*)-2-hexenal.[26,27] However, this compound did not have any effect on FB_1 production.[28]

Kernels fed on by insects provide a favorable environment for *F. verticillioides* growth and FB_1 production[43] and contribute to the dispersal of fungal spores. Hence, insect control could be considered a key strategy for controlling fungal growth in stored maize kernels. So, the repellent and insecticidal effects of VOCs against *S. zeamais*, an insect vector of *F. verticillioides* in stored maize, were also determined. The VOCs emitted by cereal grains are detected by the antennal sensila of the granary weevil and induce behavioral responses at different doses.[39,47] All the evaluated VOCs show repellent effects against *S. zeamais* at 4 μL/L; however, at very low concentrations (0.4 and 0.05 μL/L), the repellent effect was only shown by (2*E*,6*Z*)-2,6-nonadienal (one of the most antifungal compounds). In agreement with our results, Germinara et al.[39] demonstrated a repellent effect of diolefinic aldehydes, alkyl ketones, and the aliphatic alcohol 1-hexanol and the attractive effects of butyl alcohols on *S. granarius*. 2-Decanone and 3-decanone revealed strong fumigant activities against *S. zeamais*. On the other hand, the most antifungal and repellent compounds, (2*E*,6*Z*)-2,6-nonadienal and (2*E*)-2-nonenal, did not show strong fumigant toxicity against *S. zeamais* at the tested concentrations. However, Hubert et al.[30] reported insecticidal activity of (2*E*,6*Z*)-2,6-nonadienal and (2*E*)-2-nonenal (LD_{50} ranging 0.44−2.76 mg/g) against *S. granarius* and *S. oryzae* in fumigant assays.

Summing up, our results demonstrate that the different biological activities are mainly related with the functional group of the compounds tested, with the most active antifungal and insect repellent compounds being the aldehydes, while the most insecticidal compounds were the ketones. (2*E*,6*Z*)-2,6-Nonadienal demonstrated a complete inhibition of *F. verticillioides* growth and a repellent activity against its insect vector *S. zeamais*, thus preventing FB_1 occurrence, dispersion of fungal spores, and broken grains. These results reveal the strong potential for this compound to be used as a natural alternative to synthetic fungicides. In addition, LD_{50} values of aldehyde VOCs show slight toxicity (≤5 g/kg) in rats.[48] On the other hand, other evaluated VOCs showed a potential capacity to be used as a natural insecticidal (ketones) or as a lure for *S. zeamais* (alcohol). Therefore, the future use of VOCs opens up possibilities for a safer and economically viable option for the conservation of stored kernels and pest management.

DOI: 10.1021/acs.jafc.5b02315
J. Agric. Food Chem. 2015, 63, 7743−7749

Table 3. Fumigant Toxicity of VOCs against *S. zeamais* Adults after 24 h Exposure[a]

compd	LC_{50} (mM)	LC_{50} (μL/L)	95% confidence interval (μL/L)	LC_{95} (mM)	LC_{95} (μL/L)	95% confidence interval (μL/L)	slope ± SE	χ^{2b}	log P[c]	VP[c] (pascal) 25 °C
(2*E*)-2-hexenal	2.64	306.6	263.7−612.0	3.95	458.2	361.4−1678.2	5.44 ± 0.89	38.44	1.58	613.2
(2*E*)-2-nonenal	>3.62	>600							3.17	39.99
(2*E*,6*Z*)-2,6-nonadienal	ND	ND							2.6	39.99
pentanal	>5.64	>600							1.44	4239.6
1-pentanol	2.49	271.2	241.8−321.4	3.71	403.2	343.6−572.5	7.32 ± 1.02	23.48	1.41	373.3
1-hexanol	1.78	224.1	199.0−252.6	3.44	431.6	375.6−531.1	2.53 ± 0.85	3.29	1.94	119.99
3-methyl-1-butanol	ND	ND							1.22	559.95
1-butanol	3.18	291.6	260.9−354.9	5.21	477.0	394.9−727.6	5.33 ± 1.08	1.49	0.88	1133.2
2-decanone	0.26	50.4	46.4−55.5	0.35	66.2	59.8−80.7	13.53 ± 1.95	16.95	3.56	26.6
3-decanone	0.28	54.6	49.9−59.6	0.46	86.6	78.6−99.2	5.76 ± 0.84	1.46	3.56	26.6
DDVP		<0.06								

[a]Each value represents the mean of five times/concentration, each set up with 10 adults. ND: Not determined. LC: Lethal concentration. [b]χ^2: Chi-square value, significant at $P < 0.05$ level. [c]Values obtained from ChemSpider 2013, log P (logarithm of the octanol/water partition coefficient) and VP (vapor pressure).

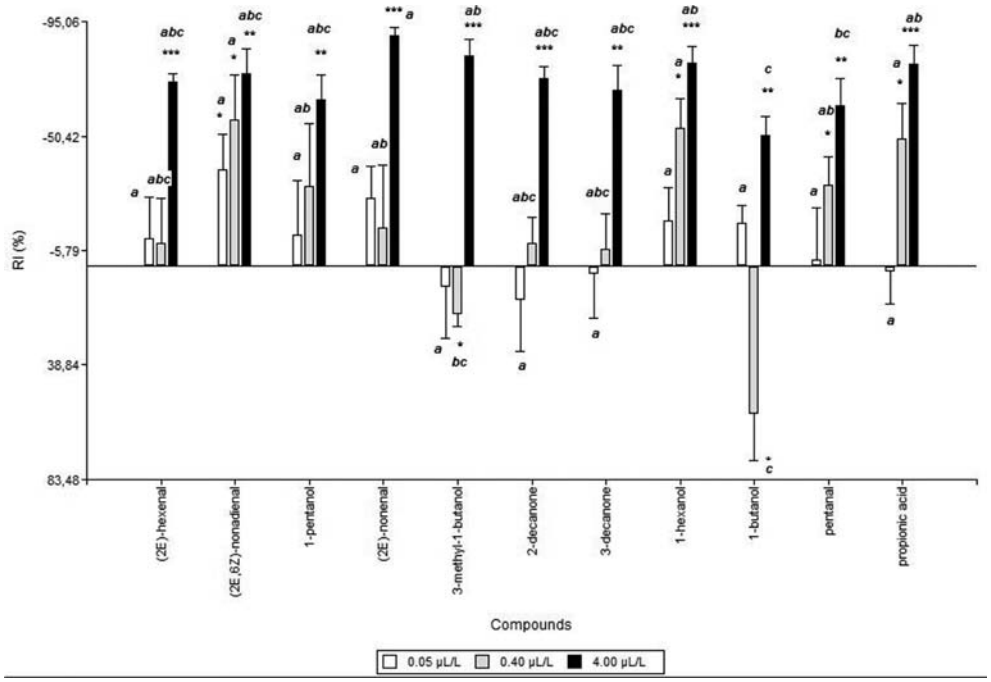

Figure 1. Behavioral responses of *S. zeamais* adults to VOCs. *$P \leq 0.05$; **$P < 0.01$; ***$P < 0.001$ (significant response to experimental stimulus; paired-sample *t* test). Values having different letters in the same column are significantly different from each other according to Duncan's multiple range test at $P \leq 0.05$ ($n = 5$). (+) values of RI indicate attraction. (−) values of RI indicate repellence.

AUTHOR INFORMATION

Corresponding Author

*Phone/fax: +54 0351 4334141; E-mail: jzygadlo@efn.uncor.edu.

Funding

This work was supported by grants from the CONICET PIP 11220120100661CO, FONCYT-PICT 2012-2146, and SECyT Universidad Nacional de Cordoba.

Notes

The authors declare no competing financial interest.

ACKNOWLEDGMENTS

We would like to thank native speaker Paul Hobson for revision of the manuscript, and Dra. Marcela Palacio for technical support. M.P.Z., R.P.P., J.S.D., and J.A.Z. are Career Members of Consejo Nacional de Investigaciones Científicas y Técnicas (CONICET), and J.M.H. has a fellowship from CONICET. The authors thank Robert H. Proctor for supplying a sample of *F. verticillioides* M3125 from the United States Department of Agriculture, Agricultural Research Service, National Center for Agricultural Utilization Research, Peoria, IL, USA.

REFERENCES

(1) SIIA. Sistema Integrado de Información Agropecuaria. Ministerio de Agricultura, Ganaderia y Pesca. http://old.siia.gov.ar/index.php/series-por-tema/usda (accessed February 28, 2014.

(2) Oerke, E. C. Crop losses to pest. *J. Agric. Sci.* **2006**, *144*, 31−43.

(3) Aulakh, J.; Regmi, A. *Post-harvest Food Losses Estimation-Development of Consistent Methodology*; Food and Agriculture Organization of the United Nations: Rome, Italy; http://www.fao.org/fileadmin/templates/ess/documents/meetings_and_workshops/

DOI: 10.1021/acs.jafc.5b02315
J. Agric. Food Chem. 2015, 63, 7743−7749

GS_SAC_2013/Improving_methods_for_estimating_post-harvest_losses/Final_PHLs_Estimation_6-13-13.pdf.
(4) Abass, A. B.; Ndunguru, G.; Mamiro, P.; Alenkhe, B.; Mlingi, N.; Bekunda, M. Post-harvest food losses in a maize-based farming system of semi-arid savannah area of Tanzania. *J. Stored Prod. Res.* **2014**, *57*, 49−57.
(5) Stockmann-Juvala, H.; Savolainen, K. A review of the toxic effects and mechanisms of action of fumonisin B_1. *Hum. Exp. Toxicol.* **2008**, *27*, 799−809.
(6) Theumer, M. G.; Canepa, M. C.; Lopez, A. G.; Mary, V. S.; Dambolena, J. S.; Rubinstein, H. R. Subchronic mycotoxicoses in Wistar rats: Assessment of the in vivo and in vitro genotoxicity induced by fumonisins and aflatoxin B_1, and oxidative stress biomarkers status. *Toxicology* **2010**, *268*, 104−110.
(7) Munkvold, G. P.; Desjardins, A. E. Fumonisins in maize: can we reduce their occurrence? *Plant Dis.* **1997**, *81*, 556−565.
(8) Martinez, M.; Moschini, R.; Barreto, D.; Bodega, J.; Comerio, R.; Forjan, H.; Piatti, F.; Presello, D. A.; Valentinuz, O. Environmental factors that affect the fumonisin content in maize grain. *Trop. Plant Pathol.* **2010**, *35*, 277−284.
(9) Lamboni, Y.; Hell, K. Propagation of mycotoxigenic fungi in maize stores by post-harvest insects. *Int. J. Trop. Insect Sci.* **2009**, *29*, 31−39.
(10) Nesci, A.; Barra, P.; Etcheverry, M. Integrated management of insect vectors of *Aspergillus flavus* in stored maize, using synthetic antioxidants and natural phytochemicals. *J. Stored Prod. Res.* **2011**, *47*, 231−237.
(11) Ferreira-Castro, F. L.; Potenza, M. R.; Rocha, L. O.; Correa, B. Interaction between toxigenic fungi and weevils in corn grain samples. *Food Control* **2012**, *26*, 594−600.
(12) Boyer, S.; Zhang, H.; Lemperiere, G. A review of control methods and resistance mechanisms in stored-product insects. *Bull. Entomol. Res.* **2012**, *102*, 213−229.
(13) Brent, K. J.; Hollomon, D. W. Fungicide Resistance: The Assessment of Risk. In *FRAC Monograph No. 2*; Global Crop Protection Federation: Brussels, Belgium, 1998; pp 1−48.
(14) Pimentel, M. A. G.; Faroni, L. R. D. A.; Guedes, R. N. C.; Sousa, A. H.; Tótola, M. R. Phosphine resistance in Brazilian populations of *Sitophilus zeamais* Motschulsky (Coleoptera: Curculionidae). *J. Stored Prod. Res.* **2009**, *45*, 71−74.
(15) Silva, L. B.; Reis, A. P.; Pereira, E. J. G.; Oliveira, M. G. A.; Guedes, R. N. C. Altered cysteine proteinase activity in insecticide-resistant strains of the maize weevil: Purification and characterization. *Comp. Biochem. Physiol., Part B: Biochem. Mol. Biol.* **2010**, *157*, 80−87.
(16) Correa, A. S.; Pereira, E. J. G.; Cordeiro, E. M. G.; Braga, L. S.; Guedes, R. N. C. Insecticide resistance, mixture potentiation and fitness in populations of the maize weevil (*Sitophilus zeamais*). *Crop Prot.* **2011**, *30*, 1655−1666.
(17) Sofos, J. N.; Beuchat, L. R.; Davidson, P. M.; Johnson, E. A. Naturally occurring antimicrobials in food, an interpretive summary. *Regul. Toxicol. Pharmacol.* **1998**, *28*, 71−72.
(18) Cook, S. P. Beetle (Coleoptera) diversity in mixed pine-hardwood stands in the Ouachita highlands five years following tree harvests. *Southwest Entomol.* **2002**, *27*, 269−276.
(19) Ukeh, D. A.; Woodcock, C. M.; Pickett, J. A.; Birkett, M. A. Identification of Host Kairomones from Maize, Zea mays, for the Maize Weevil. *J. Chem. Ecol.* **2012**, *38*, 1402−1409.
(20) Boue, S. M.; Shih, B. Y.; Carter-Wientjes, C. H.; Cleveland, T. E. Effect of Soybean Lipoxygenase on Volatile Generation and Inhibition of *Aspergillus flavus* Mycelial Growth. *J. Agric. Food Chem.* **2005**, *53*, 4778−4783.
(21) Cramer, A. C. J.; Mattinson, D. S.; Fellman, J. K.; Baik, B. K. Analysis of Volatile Compounds from Various Types of Barley-Cultivars. *J. Agric. Food Chem.* **2005**, *53*, 7526−7531.
(22) Germinara, G. S.; De Cristofaro, A.; Rotundo, G. Antennal olfactory responses to individual cereal volatiles in *Theocolax elegans* (Westwood) (Hymenoptera: Pteromalidae). *J. Stored Prod. Res.* **2009**, *45*, 195−200.
(23) Mosblech, A.; Feussner, I.; Heilmann, I. Oxylipins: Structurally diverse metabolites from fatty acid oxidation. *Plant Physiol. Biochem.* **2009**, *47*, 511−517.
(24) Mita, G.; Fasano, P.; De Domenico, S.; Perrone, G.; Epifani, F.; Iannacone, R.; Casey, R.; Santino, A. 9-Lipoxygenase metabolism is involved in the almond/*Aspergillus carbonarius* interaction. *J. Exp. Bot.* **2007**, *58*, 1803−1811.
(25) Cox, P. D.; Collins, L. E. Factors affecting the behaviour of beetle pests in stored grain, with particular reference to the development of lures. *J. Stored Prod. Res.* **2002**, *38*, 95−115.
(26) Cleveland, T. E.; Carter-Wientjes, C. H.; De Lucca, A. J.; Boue, S. M. Effect of soybean volatile compounds on *Aspergillus flavus* growth and aflatoxin production. *J. Food Sci.* **2009**, *74*, H83−H87.
(27) De Lucca, A. J.; Carter-Wientjes, C. H.; Boue, S.; Bhatnagar, D. Volatile trans-2-hexenal, a soybean aldehyde, inhibits *Aspergillus flavus* growth and aflatoxin production in corn. *J. Food Sci.* **2011**, *76*, M381−M386.
(28) Menniti, A. M.; Gregori, R.; Neri, F. Activity of natural compounds on *Fusarium verticillioides* and fumonisin production in stored maize kernels. *Int. J. Food Microbiol.* **2010**, *136*, 304−309.
(29) Germinara, G. S.; De Cristofaro, A.; Rotundo, G. Bioactivity of short-chain aliphatic ketones against adults of the granary weevil, *Sitophilus granarius* (L.). *Pest Manage. Sci.* **2012**, *68*, 371−377.
(30) Hubert, J.; Munzbergova, Z.; Santino, A. Plant volatile aldehydes as natural insecticides against stored-product beetles. *Pest Manage. Sci.* **2008**, *64*, 57−64.
(31) Leslie, J.; Summerel, B. A. Species concepts in *Fusarium*. In *The Fusarium Laboratory Manual*; Blackwell Publishing: Hoboken, NJ, 2006; Ch 9, pp 88−95.
(32) Leslie, J. F.; Plattner, R. D.; Desjardins, A. E.; Klittich, C. J. R. Fumonisin B_1 production by strains from different mating populations of *Gibberella fujikuroi* (*Fusarium* sectionLiseola). *Phytopathology* **1992**, *82*, 341−345.
(33) Food and Agriculture Organization of the United Nations (FAO). Método provisional para gorgojos adultos importantes en cereals almacenados con malatión o lindano, Método N° 15 de la FAO. In *Boletín Fitosanitario de la FAO*; FAO: Rome, Italy, 1974; Vol. *22*, pp 127−137.
(34) Neri, F.; Mari, M.; Brigati, S.; Bertolini, P. Fungicidal activity of plant volatile compounds for controlling *Monilinia laxa* in stone fruit. *Plant Dis.* **2007**, *91*, 30−35.
(35) Herrera, J. M.; Pizzolitto, R. P.; Zunino, M. P.; Dambolena, J. S.; Zygadlo, J. A. Effect of fungal volatile organic compounds on a fungus and an insect that damage stored maize. *J. Stored Prod. Res.* **2015**, *62*, 74−80.
(36) Shephard, G. S.; Marasas, W. F. O.; Leggott, N. L.; Yazdanpanah, H.; Rahimian, H.; Safavi, N. Natural occurrence of fumonisins in corn from Iran. *J. Agric. Food Chem.* **2000**, *48*, 1860−1864.
(37) Huang, Y.; Lam, S. L.; Ho, S. H. Bioactivities of essentialoil from *Elletaria cardamomum* (L.) Maton. to *Sitophilus zeamais* Motschulsky and Tribolium castaneum (Herbst). *J. Stored Prod. Res.* **2000**, *36*, 107−117.
(38) Finney, D. J. *Probit Analysis*; Cambridge University Press: London, 1971.
(39) Germinara, G. S.; De Cristofaro, A.; Rotundo, G. Behavioral responses of adult *Sitophilus granarius* to individual cereal volatiles. *J. Chem. Ecol.* **2008**, *34*, 523−529.
(40) Phillips, T. W.; Jiang, X. L.; Burkholder, W. E.; Phillips, J. K.; Tran, H. Q. Behavioral responses to food volatiles by two species of stored-product Coleoptera, *Sitophilus oryzae* (Curculionidae) and *Tribolium castaneum* (Tenebrionidae). *J. Chem. Ecol.* **1993**, *19*, 723−734.
(41) Di Rienzo, J.; Casanoves, F.; Balzarini, M. G.; Gonzalez, L.; Tablada, M.; Robledo, C. *Infostat*, versión 2010; Grupo Infostat: FCA, Universidad Nacional de Córdoba, Córdoba, Argentina, 2010.
(42) LeOra Software. *POLO-PLUS: A User's Guide to Probit or Logit Analysis*; LeOra Software: Berkeley, CA, 2002−2014.

DOI: 10.1021/acs.jafc.5b02315
J. Agric. Food Chem. 2015, 63, 7743−7749

(43) Chemspider Home Page. http://www.chemspider.com/ (accessed 03/28/2014).
(44) Buśko, M.; Jeleń, H.; Góral, T.; Chmielewski, J.; Stuper, K.; Szwajkowska-Michałek, L.; Tyrakowska, B.; Perkowski, J. Volatile metabolites in various cereal grains. *Food Addit. Contam., Part A* **2010**, *27*, 1574−1581.
(45) Gardini, F.; Lanciotti, R.; Guerzoni, M. E. Effect of trans-2-hexenal on the growth of *Aspergillus flavus* in relation to its concentration, temperature and water activity. *Lett. Appl. Microbiol.* **2001**, *33*, 50−55.
(46) Dambolena, J. S.; López, A. G.; Meriles, J. M.; Rubinstein, H.; Zygadlo, J. A. Inhibitory effect of 10 natural phenolic compounds on *Fusarium verticillioides*. A structure-property-activity relationship study. *Food Control* **2012**, *28*, 163−170.
(47) Trematerra, P.; Ianiro, R.; Athanassiou, C. G.; Kavallieratos, N. G. Behavioral responses of *Sitophilus zeamais* Motschulsky adults to conditioned grain kernels. *J. Stored Prod. Res.* **2013**, *53*, 77−81.
(48) Health Canada. Pesticide Label Search. http://www.hc-sc.gc.ca/cps-spc/pest/registrant-titulaire/tools-outils/label-etiq-eng.php (accessed 07/31/2015).

DOI: 10.1021/acs.jafc.5b02315
J. Agric. Food Chem. 2015, 63, 7743−7749

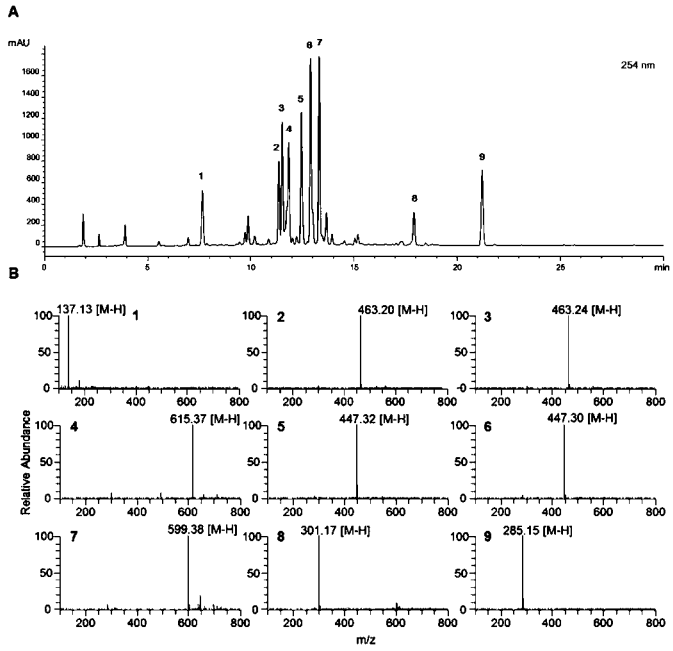

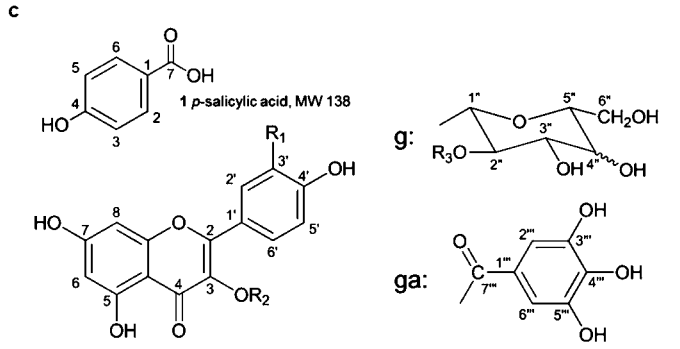

No	R_1	R_2	R_3	4"-	Compound Name	MW
2	OH	g	H	α	quercetin-3-O-β-galactoside	464
3	OH	g	H	β	quercetin-3-O-β-glucoside	464
4	OH	g	ga	β	quercetin-3-O-β-2"-galloylglucoside	616
5	H	g	H	α	kaempferol-3-O-β-galactoside	448
6	H	g	H	β	kaempferol-3-O-β-glucoside	448
7	H	g	ga	β	kaempferol-3-O-β-2"-galloylglucoside	600
8	OH	H	-	-	quercetin	302
9	H	H	-	-	kaempferol	286

Figure 1. (A) HPLC-UV chromatogram of EEDK. Retention times: compound **1**, 7.665 min; compound **2**, 11.350 min; compound **3**, 11.514 min; compound **4**, 11.828 min; compound **5**, 12.441 min; compound **6**, 12.889 min; compound **7**, 13.305 min; compound **8**, 17.918 min; compound **9**, 21.222 min. (B) MS spectra of major peaks (**1**−**9**). (C) Identified compounds.

Santa Cruz Biotechnology (Santa Cruz, CA, USA). Anti-GAPDH and glutathione peroxidase (GPx-1) antibodies were purchased from Cell Signaling Technology (Beverly, MA, USA). Alexa 488-conjugated anti-sheep, Alexa 594-conjugated anti-mouse, and Alexa 633-conjugated anti-sheep antibodies were purchased from Invitrogen (Carlsbad, CA, USA). A blocking solution was purchased from Dako (Santa Clara, CA, USA), and mounting medium was purchased from Vector Laboratories (Burlingame, CA, USA). Zoletil and Rumpun were purchased from Virbac Laboratories (Fort Worth, TX, USA) and Bayer (Newbury, UK), respectively, and used as anesthesia. All other chemicals and reagents were purchased from Sigma-Aldrich (St. Louis, MO, USA).

Plant Materials and Sample Preparation. *D. kaki* was collected in Gangneung, Gangwon province, Korea, in August 2013. A voucher specimen (D-521) was deposited at the KIST Gangneung Institute. Eight hundred grams of the dried *D. kaki* leaves was extracted three times with 7 L of ethanol at room temperature for 3 h in an ultrasonic cleaning bath (model RK 158s, Bandelin, Berlin, Germany) and filtered through Whatman no. 1 filter paper. The combined filtrate was concentrated to dryness by rotary evaporation at 40 °C to obtain 33 g (yield = 4.13%) of the ethanol extract of *D. kaki* leaves (EEDK). HPLC-PDA-MS analysis was applied using a Thermo Accela HPLC system and LCQ FLEET ion trap mass spectrometer (Thermo Fisher Scientific Inc., San Jose, CA, USA) for compound determinations in EEDK. The mobile phase consisted of 0.1% formic acid in water (solvent A) and 0.1% formic acid in acetonitrile (solvent B), which was used with a YMC-Triart C18 column (3 μm particle size, 150 mm × 4.6 mm i.d., YMC Co., Kyoto, Japan). A linear gradient (from 10 to 60% solvent B for 30 min) at a flow rate of 1 mL/min was used at 254 nm. The mass spectrometer conditions were as follows: negative ion mode; mass range, m/z 200−800; capillary voltage, 10.0 V; capillary temperature, 350 °C. The NMR spectra were recorded on a Varian 500 MHz NMR system (Varian, Palo Alto, CA, USA) at 500 MHz for ^{1}H NMR and 125 MHz for ^{13}C NMR in DMSO-d_6. Compounds **1**−**9** were purified by semipreparative HPLC.

Animals. Six-week-old male C57BL/6J mice weighing 20−25 g (Central Laboratory Animal Inc., Seoul, Korea) were housed at 23 ± 0.5 °C and 10% humidity, with a 12 h light−dark cycle. All animals were acclimated for at least 1 week, caged in groups of five or fewer, and fed a diet of animal chow and water ad libitum.

All animal studies were performed in a pathogen-free barrier zone at the KIST Gangneung Institute in accordance with the procedure outlined in the ARVO Statement for the Use of Animals in Ophthalmic and Vision Research. Procedures used in this study were approved by the Animal Care and Use Committee of the KIST Gangneung Institute (No. 2014-011).

MNU was used as a negative insult for retinal degeneration and was induced by a single intraperitoneal (ip) injection of 50 mg/kg MNU (50 mg/kg body weight) in C57BL/6J mice.[20] After the injection of MNU, EEDK was orally administered in doses of 10, 50, or 100 mg/(kg·day) for 4 weeks. Animals were examined at 1 and 4 weeks after the injection of MNU. Eyes were dissected and examined either for histological or Western blot analysis. Fixed eyes were cut into 4 μm slices and were then studied by staining with hematoxylin and eosin (H&E) or by immunofluorescence.

Spectral Domain Optical Coherence Tomography (SD-OCT). SD-OCT imaging was performed at 1 and 4 weeks after 50 mg/kg MNU treatment. The animals were anesthetized using a mixture of Zoletil (1.6 μg/g, Virbac Laboratories, Fort Worth, TX, USA) and Rumpun (0.05 μL/g, Bayer, Newbury, UK). Anesthetized animals were placed in front of the Spectral OCT system (Heidelberg Engineering, Germany) and analyzed as described previously.[21]

H&E Staining. H&E staining of the retina slides was performed using a standard procedure. Briefly, the retina slides were treated with hematoxylin buffer (0.1% hematoxylin and 10% ammonium) at room temperature. The slides were then washed three times with distilled water and dipped in 1% eosin Y solution. Next, the slides were washed twice with 95% alcohol and mounted. Histological analysis was evaluated under a CKX41 inverted phase contrast microscope (Olympus, Tokyo, Japan).

Western Blot Analysis. Proteins were separated on 10 or 12% SDS-PAGE gels and then transferred onto polyvinylidene difluoride (PVDF) membranes. The membranes were blocked at room temperature in 5% skim milk before overnight incubation at 4 °C with antibodies (diluted as indicated in PBS) against nestin (1:1000), GFAP (1:1000), GAPDH (1:2000), rhodopsin (1:1000), SOD-1 (1:1000), SOD-2 (1:1000), SOD-3 1 (1:1000), or GPx-1 (1:1000). Binding of the primary antibodies was detected following incubation with appropriate horseradish peroxidase-conjugated IgG secondary antibodies (diluted 1:5000) for 2 h at room temperature. The membranes

DOI: 10.1021/acs.jafc.5b02578
J. Agric. Food Chem. 2015, 63, 7750−7759

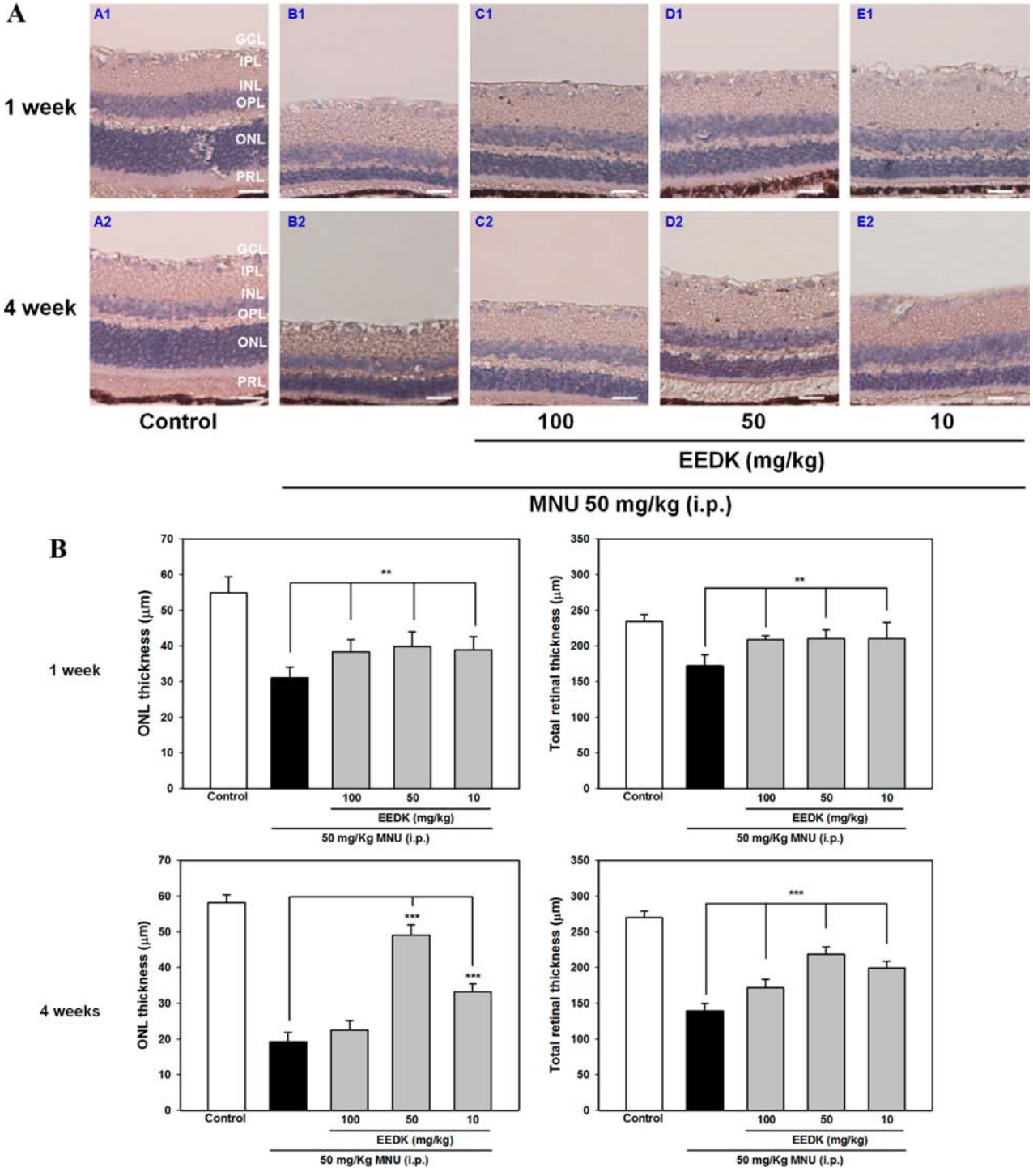

Figure 2. Histological evaluation in hematoxylin and eosin (H&E) staining. Panel A shows retinal cross sections of control (A1, A2), MNU-treated (B1, B2), MNU plus EEDK (100 mg/kg)-treated (C1, C2), MNU plus EEDK (50 mg/kg)-treated (D1, D2), and MNU plus EEDK (10 mg/kg)-treated (E1, E2) mice at 1 and 4 weeks, with or without MNU and/or EEDK treatment. Panel B shows total retinal thicknesses and outer layer thicknesses at the indicated time points. Scale bar = 50 μm. Experimental values are expressed as mean ± SEM. (**) $p < 0.01$ and (***) $p < 0.001$ from three independent experiments (n = 9 mice per group).

were developed using an enhanced chemiluminescence detection kit (Thermo Scientific, Waltham, MA, USA) and measured by densitometry using an LAS-4000 image reader and Multi Gauge 3.1 software (Fujifilm, Tokyo, Japan). GAPDH expression was detected as a loading control.

Immunofluorescence Staining. Paraffin-embedded retinal sections were deparaffinized and blocked in normal goat serum overnight at 4 °C. Subsequently, the sections were incubated with specific primary antibodies against nestin (diluted 1:200), GFAP (diluted 1:200), and rhodopsin (diluted 1:200) overnight at 4 °C. The sections were washed three times with PBST buffer (8 g/L NaCl, 0.2 g/L KCl, 1.44 g/L Na_2HPO_4, 0.24 g/L NaH_2HPO_4, and 0.1% Triton X-100) and incubated with matching secondary antibodies (Alexa 488-conjugated anti-sheep, Alexa 594-conjugated anti-mouse, and Alexa 633-conjugated anti-chicken antibodies; diluted 1:500) for 2 h at room temperature in the dark. The sections were washed with PBST, mounted, and

DOI: 10.1021/acs.jafc.5b02578
J. Agric. Food Chem. 2015, 63, 7750−7759

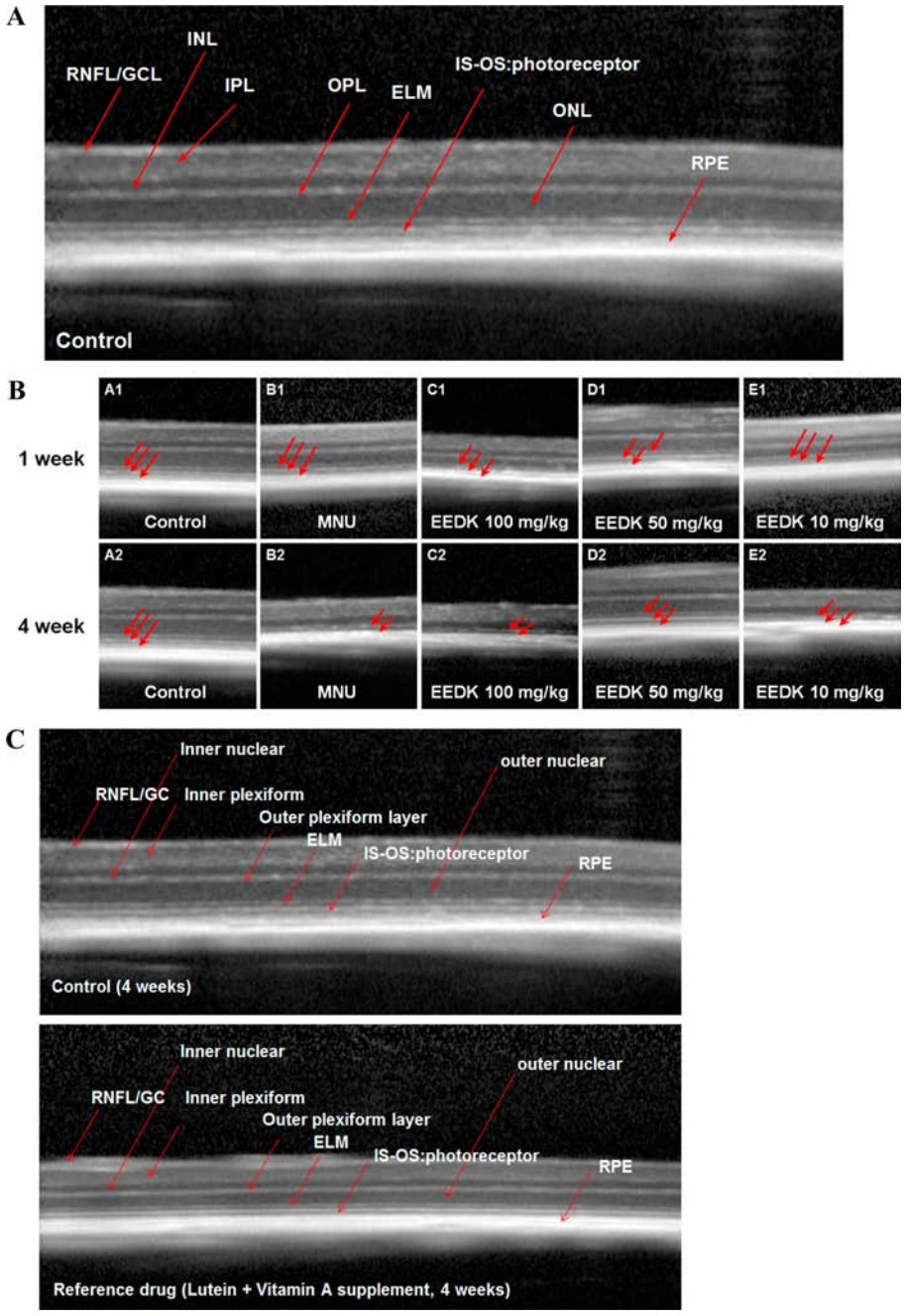

Figure 3. Evaluation of retinal thicknesses by optical coherence tomography. (A) SD-OCT cross-sectional image of a control retina. The following retinal layers were labeled: RNFL/GC, retinal nerve fiber layer/ganglion cell layer; IPL, inner plexiform layer; INL, inner nuclear layer; OPL, outer plexiform layer; ONL, outer nuclear layer; ELM, external limiting membrane; RPE, retinal pigment epithelium. (B) Representative images obtained from the experimental animal retina at 1 and 4 weeks after, with or without MNU and/or EEDK treatment: control (A1, A2), MNU-treated (B1, B2), MNU plus EEDK (100 mg/kg)-treated (C1, C2), MNU plus EEDK (50 mg/kg)-treated (D1, D2), and MNU plus EEDK (10 mg/kg)-treated (E1, E2). (C) Lutein plus vitamin A supplement used as reference drug (Bright lutein, Ildong Pharmaceutical, Korea). Reference drug group received lutein plus vitamin A supplement (0.2%/kg/day). Scale bar = 50 μm.

covered with a glass coverslip. Staining images were examined using a Leica TCS SP5 confocal microscope system (Leica, Wetzlar, Germany).

Cell Culture. Immortalized rat retinal precursor cells (R28 cells) were purchased from Kerafast (Kerafast, Inc., Boston, MA, USA). R28 cells were grown in 75 cm^2 culture flasks in low-glucose Dulbecco's modified Eagle's medium (DMEM; HyClone, Logan, UT, USA) supplemented with 10% (v/v) heat-inactivated fetal bovine serum (FBS; HyClone) and 100 U/mL penicillin/streptomycin (HyClone). Cultures were maintained at 37 °C in a humidified atmosphere containing 5% CO_2. The cells were passaged twice a week. R28 cells were pretreated with the indicated compounds for 1 h after 300 μM hydrogen peroxide (H_2O_2) was added to cultures for 24 h.

Cell Viability. R28 cell viabilities were determined by performing 3-(4,5-dimethylthiazol-2-yl)-2,5-diphenyltetrazolium bromide (MTT) assays. Briefly, MTT assays were performed by treating cells with MTT solution (0.5 mg/mL final concentration) for 1 h at 37 °C. After a 1 h incubation, the blue formazan crystals that formed in intact cells were solubilized with DMSO, and absorbance values at 570 and 590 nm were measured with a microplate reader (BioTek Instruments, Winooski, VT, USA). Results are expressed as the percent of MTT reduction.

DOI: 10.1021/acs.jafc.5b02578
J. Agric. Food Chem. 2015, 63, 7750−7759

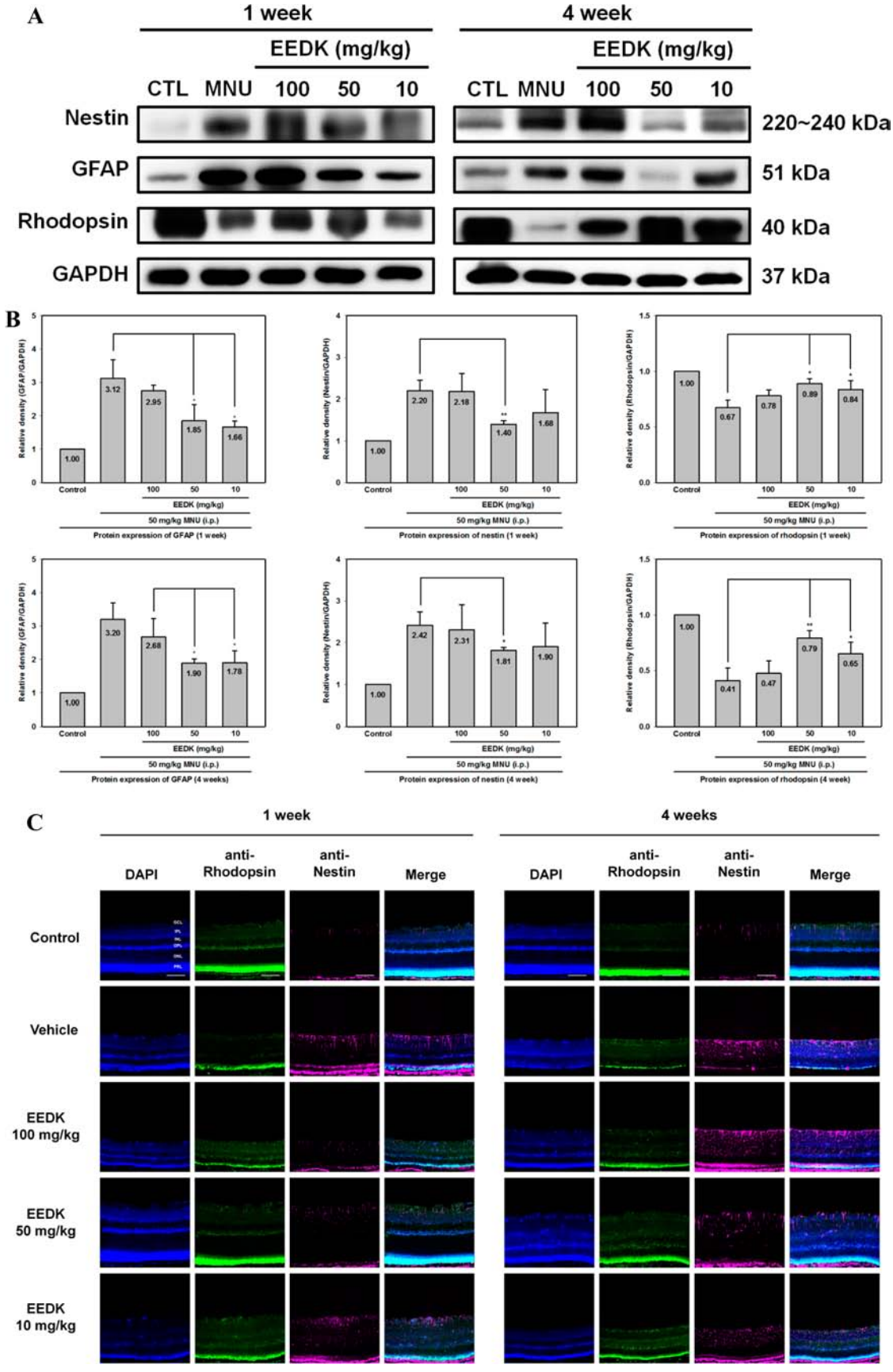

Figure 4. continued

DOI: 10.1021/acs.jafc.5b02578
J. Agric. Food Chem. 2015, 63, 7750−7759

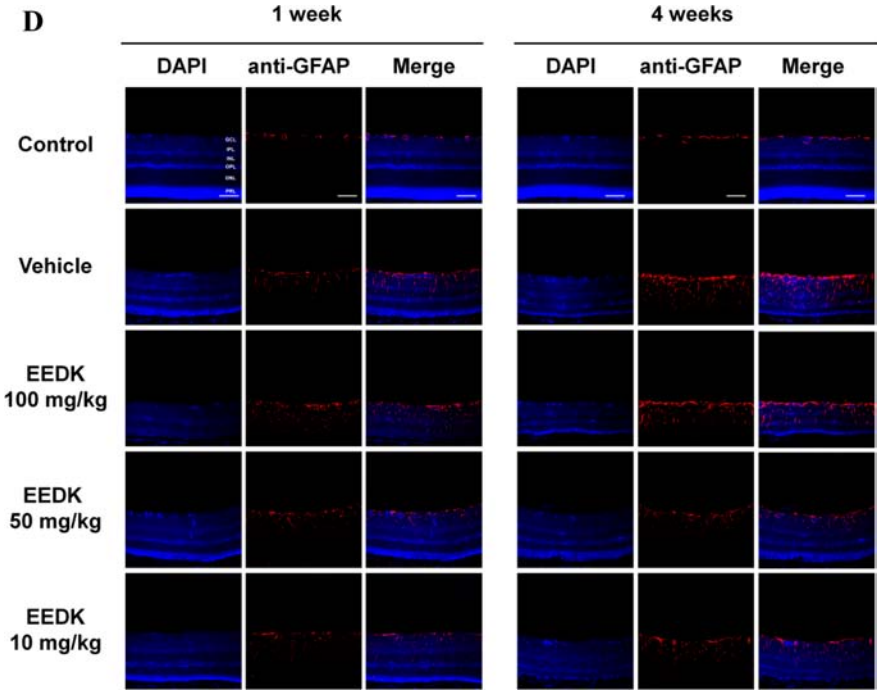

Figure 4. (A) Western blot analysis showing the effects of EEDK treatment on protein expression levels of nestin (Müller cell marker; ~220−240 kDa), glial fibrillary-acidic protein (GFAP; Müller cell and astrocyte marker; 51 kDa), rhodopsin (photoreceptor marker; 40 kDa), and GAPDH (loading control; 37 kDa) in C57BL/6J mice treated with 50 mg/kg MNU, at 1 and 4 weeks. (B) Quantification of relative protein levels. (C, D) Representative immunostaining images were stained with anti-netin (purple), anti-rhodopsin (green), and anti-GFAP (red) in the retina (nuclei were stained with DAPI) and obtained by confocal microscopy (original magnification, 630×). Retinal cross sections were from control, MNU-treated, MNU plus EEDK (100 mg/kg)-treated, MNU plus EEDK (50 mg/kg)-treated, and MNU plus EEDK (10 mg/kg)-treated mice at 1 and 4 weeks, with or without MNU and/or EEDK treatment. Scale bar = 50 μm. Experimental values are expressed as mean ± SEM. (*) $p < 0.05$ and (**) $p < 0.01$ from four independent experiments (n = 9 mice per group).

Assessment of ROS Production. To quantify intracellular ROS production, we used DCFH-DA as a probe for free radicals.[22] The R28 cells were seeded at a density of 5.0×10^3 cells per well into 96-well plates and incubated in a humidified atmosphere of 95% air and 5% CO_2 at 37 °C. Twenty-four hours later, the cell culture medium was replaced with DMEM containing 1% FBS. Superoxide radicals effectively oxidize nonfluorescent dichlorofluorescein (DCFH) to fluorescent dichlorofluorescein (DCF). The cells were loaded with the radical probe DCFH-DA (10 μM) through incubation for 20 min at 37 °C. Then, the cell culture medium was replaced to remove the excess probe. To generate radical species, we added KO_2 at 1 mM ($O_2^{\bullet-}$) to the radical probe-loading medium. Fluorescence was then measured after various durations, using excitation and emission wavelengths of 485 and 535 nm, respectively (Luminescence Spectrometer LS50B, PerkinElmer Ltd., Seer Green, UK).

Statistical Analysis. Experimental values were analyzed by Kruskal−Wallis and Mann−Whitney tests using the Bonferroni correction and are presented as the mean ± standard deviation. A result of $p < 0.05$ was considered to be statistically significant. Quantification of Western blotting results was performed using Fujifilm Multi Gauge software, version 3.0. All statistical analyses were performed using SPSS, version 16.0 (IBM Corp., Armonk, NY, USA).

RESULTS AND DISCUSSION

The chromatogram of EEDK showed nine major peaks (Figure 1). Peak 1 was identified as *p*-salicylic acid by mass (Figure 1) and NMR spectra. The major NMR peaks detected by ^{1}H NMR were 12.33 (1H, s, OH-7), 10.22 (1H, s, OH-4), 7.77 (2H, d, J = 8.7 Hz, H-2, 6), and 6.80 (2H, d, J = 8.7 Hz, H-3, 5), whereas the major peaks detected with ^{13}C NMR were 167.6 (C-7), 162.0 (C-4), 132.0 (C-2, 6), 121.9 (C-1), and 115.6 (C-3, 5). Peaks 2−9 were identified by MS as quercetin, kaempferol, or their glycoside, galactoside, or galloylated derivatives (Figure 1). The chromatograms and spectral data of peaks 2−9 were consistent with results with a previous study.[23]

The concentrations of compounds **1**−**9** in EEDK were measured as 0.8 ± 0.02 mg/g (**1**), 4.8 ± 0.08 mg/g (**2**), 10.6 ± 0.18 mg/g (**3**), 12.7 ± 1.24 mg/g (**4**), 9.4 ± 0.15 mg/g (**5**), 17.3 ± 0.27 mg/g (**6**), 17.2 ± 0.23 mg/g (**7**), 2.1 ± 0.03 mg/g (**8**), and 5.0 ± 0.08 mg/g (**9**).

To observe retinal degeneration caused by MNU treatment, we performed H&E staining of retinal tissues, as shown in Figure 2. The total thickness of the retinal layer and outer nuclear layer significantly decreased in the mouse group treated with MNU alone (Figure 2). However, the retinas of C57BL/6J mice administered EEDK were protected against MNU-induced retinal degeneration (Figure 2). During the observation period, the inner nuclear layer and ganglion cell layer appeared to be unaffected except in the MNU-treated group at 4 weeks post-MNU treatment. Our results also revealed that EEDK administration protected the outer retina against MNU-induced retinal degeneration. These results are consistent with those from a previous study demonstrating that MNU affects the outer layer by causing a reduction in the number of photoreceptors in the retina[24] and demonstrate protective effects of EEDK against retinal degeneration.

We observed further morphological changes in the retinas of live mice via SD-OCT scanning, as shown in Figure 3.[25]

SD-OCT is a noninvasive scanning technique that has been widely adopted clinically to assess retinal disorders involving changes in retinal thickness, structural changes, and edema, among others. SD-OCT enables accurate analysis because it can

DOI: 10.1021/acs.jafc.5b02578
J. Agric. Food Chem. 2015, 63, 7750−7759

provide cross-sectional images of retinas with high resolution. Recently, OCT has been used in many studies to evaluate changes occurring during retinal degeneration in small-animal model studies.[21]

Figure 3A shows an OCT image of a normal retina. The thickness of the outer retinal layer was slightly reduced in the MNU-treated group at 1 week, compared to the control group (Figure 3B). After 4 weeks, significant differences were found in retinal thickness between the control and MNU-treated groups (Figure 3B). However, MNU-induced retinal thinning was significantly attenuated by pretreatment with EEDK (Figure 3B). The reference drug lutein also showed a protective effect against MNU-induced retinal thinning (Figure 3C).

Western blot analysis was conducted to investigate the effects of EEDK treatment on nestin, GFAP, and rhodopsin expression in mouse retinal tissues after MNU-induced retinal degeneration. Nestin, a type VI intermediate filament protein, is expressed in stem cells and progenitor cells, as well as the related Müller cells that differentiate in the central nervous system.[26] The observed configuration of Müller cells and astrocytes has demonstrated that these glial cells help maintain the structural integrity of the retina.[27] Up-regulated nestin expression is often observed during late-stage pathology of neurodegenerative diseases.[28,29] As shown in Figure 4, nestin protein expression was considerably increased in the MNU-treated group at 1 week compared to the control group, but nestin expression was not increased at 4 weeks post-MNU treatment. This result may have been due to the low number of cells preserved in the whole retina.

Importantly, the elevation in nectin protein expression was significantly attenuated by EEDK administration (Figure 4A,B).

The results of recent studies have indicated that GFAP, a type III intermediate filament protein, is present in astrocytes and Müller cells in the retina. Increased GFAP expression is a reliable biomarker of retinal degeneration.[30] GFAP protein expression was up-regulated in a time-dependent manner after mice were treated with MNU alone, compared to the control group; this up-regulation was inhibited by EEDK administration (Figure 4A,B). The dose of 50 mg/kg EEDK showed a significant inhibition, compared with the MNU-treated group.

Rhodopsin is a photosensitive pigment in the rod-containing outer retinal layer and plays a key role in the visual system.[24] In the MNU-treated group, expression of the rhodopsin protein was down-regulated in a time-dependent manner compared to the control group. However, rhodopsin protein expression was maintained by EEDK administration (Figure 4A,B), and the photoreceptor tissue layer was well preserved by EEDK treatment. These results demonstrated that the protective effects of EEDK treatment on retinal degeneration might be related to the expression of retinal factors including nestin, GFAP, and rhodopsin during MNU-induced retinal degeneration.

To further evaluate the protective effects of EEDK on retinal degeneration, we analyzed nestin, GFAP, and rhodopsin expression by immunofluorescence staining, as shown in Figure 4C,D. Immunofluorescence staining revealed that the expression levels of nestin and GFAP, which are related to early signs of gliosis, were significantly increased in the MNU-treated group compared with the control group (Figure 4C,D). However, the 50 and 10 mg/kg EEDK-treated groups showed decreased nestin and GFAP protein expression compared with the MNU-treated group.

The loss of photoreceptor cells was evaluated by immunofluorescence staining for rhodopsin. The expression of rhodopsin was considerably decreased in the MNU-treated group relative to that observed in the control group (Figure 4C,D). In contrast, rhodopsin protein expression was preserved in the 50 and 10 mg/kg EEDK-treated groups (Figure 4C,D). As shown in Figures 2–4, the 100 mg/kg EEDK-treated groups showed no significant differences compared with the MNU-treated group. Thus, administration of EEDK can potentially confer a protective benefit, but a high dose may elicit retinotoxicity.

As observed by Western blot analysis, immunofluorescence staining demonstrated the capacity of EEDK to inhibit retinal degeneration by down-regulating nestin and GFAP expression and by up-regulating rhodopsin expression.

Cell viability assays were performed to confirm the protective effects of compounds **1**–**9** (Figure 5). As shown in Figure 5A,

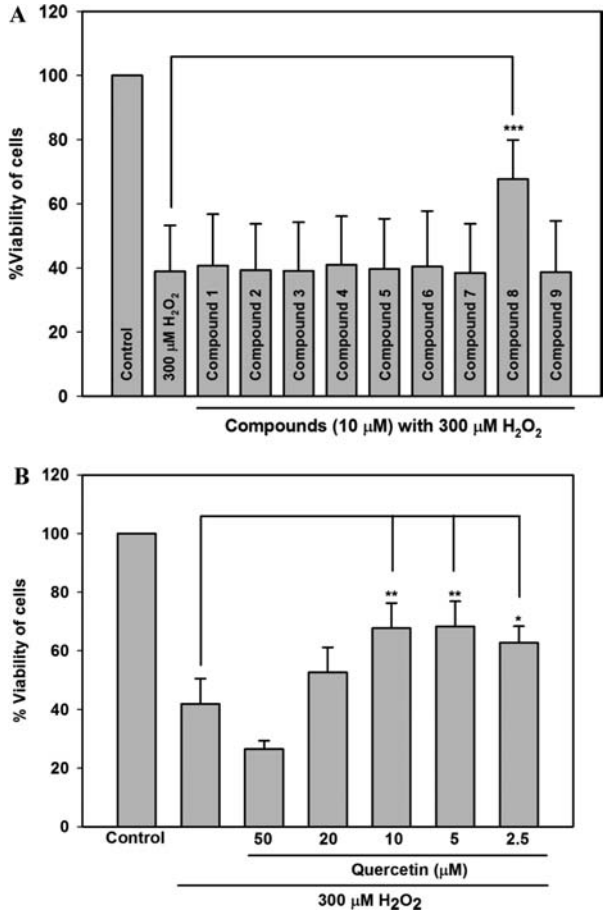

Figure 5. (A) Effects of nine compounds (10 μM concentration) isolated from an ethanol extract of *D. kaki* on R28 cell viability after treatment with 300 μM H_2O_2 for 24 h, as measured by the MTT assay. (B) Effects of compound **8** (quercetin) on H_2O_2-induced R28 cell death. Experimental values are expressed as a percentage of the viable cells with error bars indicating ± SEM from three independent experiments. (*) $p < 0.05$ and (**) $p < 0.01$ indicate statistically significant differences from the cells exposed to H_2O_2 alone.

only quercetin (10 μM; compound **8**) significantly inhibited H_2O_2-induced cell death (~65%) among compounds **1**–**9**. The inhibition of H_2O_2-induced cell death by quercetin occurred in a dose-dependent manner (Figure 5B).

Recently, Keiichi et al. reported that the administration of exogenous antioxidants such as α-tocopherol, ascorbic acid, Mn(III) tetrakis(4-benzoic acid) porphyrin, and α-lipoic acid protected against oxidative damages in an *rd1* mouse model.[31] Quercetin is known to possess antioxidant and free radical-scavenging activities.[32]

DOI: 10.1021/acs.jafc.5b02578
J. Agric. Food Chem. 2015, 63, 7750–7759

DCFH-DA was used as a radical probe to quantify intracellular ROS production. The intracellular ROS levels caused by $O_2^{\bullet-}$ were increased relative to the control by up to 360%. However, pretreating cells with EEDK and quercetin decreased the ROS levels in a dose-dependent manner (Figure 6A,B).

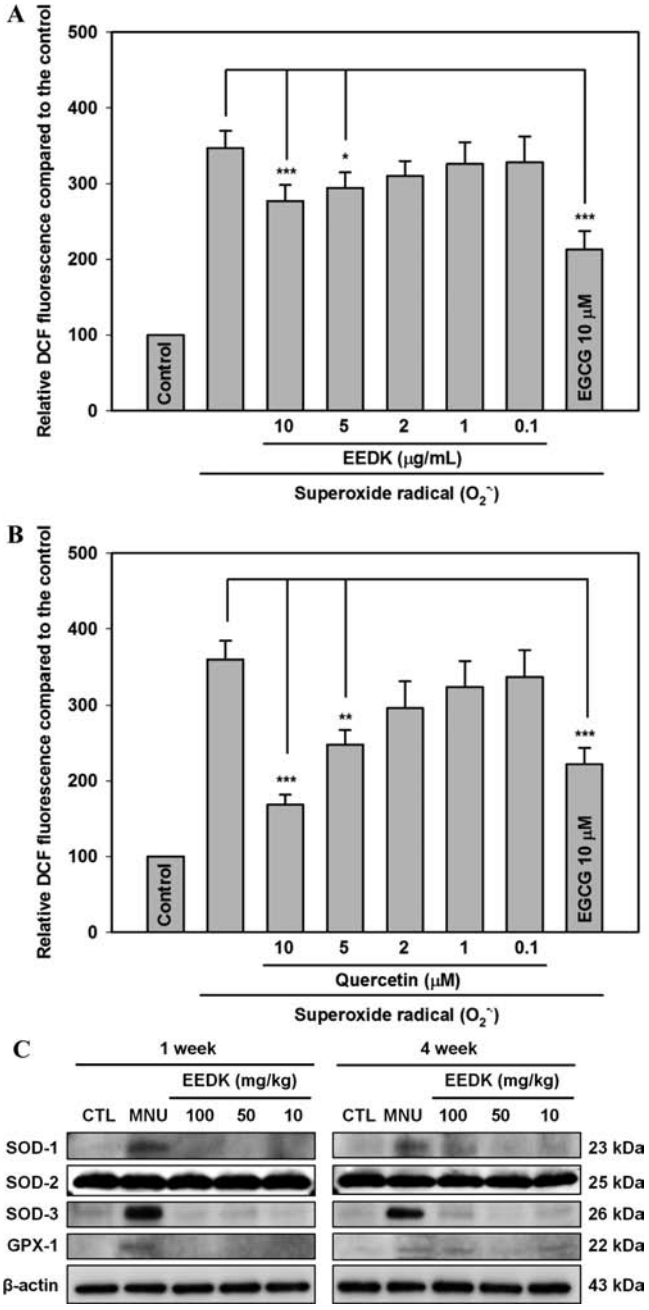

Figure 6. Capacity of EEDK or compound **8** (quercetin) to scavenge superoxide radical ($O_2^{\bullet-}$) in R28 cells. (A, B) The intracellular ROS level was determined on the basis of peroxide-sensitive DCF fluorescence. The results show that EEDK, compound **8** (quercetin), and EGCG as positive controls attenuated ROS production caused by superoxide radical, respectively. Experimental values are expressed as the mean ± SEM. (*) $p < 0.05$, (**) $p < 0.01$, and (***) $p < 0.001$ from four independent experiments. (C) Western blot analysis showing the effects of EEDK treatment on antioxidant associated protein expression levels of SOD-1 (Cu/Zn-SOD; 23 kDa), SOD-2 (mitochondrial SOD; 25 kDa), SOD-3 (extracellular SOD; 26 kDa), GPx-1 (glutathione peroxidase-1; 22 kDa), and β-actin (loading control; 43 kDa) in C57BL/6J mice treated with 50 mg/kg MNU, at 1 and 4 weeks.

The expression levels of antioxidant proteins such as SOD 1−3 and Gpx-1 induced by MNU in mouse retina were evaluated by Western blot analysis. Our results showed that SOD-1, SOD-3, and Gpx-1 expression levels were significantly inhibited by EEDK treatment (Figure 6C).

Endogenous antioxidant enzymes, including SODs, GPx, and catalase, served to reduce the oxidative stress of photoreceptors in retinas. Previous findings have shown that endogenous antioxidant enzymes up-regulated under oxidative stress conditions decreased ROS production and prevented cone cell death in several retinitis pigmentosa models.[33,34]

Therefore, the protective effects of EEDK in MNU-induced retinal degeneration may be due to its direct or indirect antioxidative properties.

In summary, our results showed that EEDK has protective effects against oxidative stress-induced cell death in vitro and considerably alleviated MNU-induced retinal degeneration in vivo. In particular, compound **8** (quercetin) could possibly be the acting compound due to antioxidative capacity. Quercetin glycosides, compounds **2**−**4**, did not show significant activity. However, it was known that flavonoid monoglucosides such as quercetin-3-*O*-*β*-glucoside are hydrolyzed by lactase phlorizin hydrolase[35] and cytosolic *β*-glucosidase[36,37] to be absorbed in the small intestine as aglycone forms. This demonstrates that compounds **2**−**4** (quercetin-3-*O*-*β*-galactoside, quercetin-3-*O*-*β*-glucoside, and quercetin-3-*O*-*β*-2″galloylglucoside) may be absorbed from the small intestine of humans as aglycone forms to exhibit antioxidative activity. Collectively, our findings indicate that EEDK may be useful as a potential agent for the prevention and treatment of retinal degeneration, such as with retinitis pigmentosa and AMD.

■ ASSOCIATED CONTENT

Supporting Information

The Supporting Information is available free of charge on the ACS Publications website at DOI: 10.1021/acs.jafc.5b02578.

^{1}H and ^{13}C NMR spectra of compound **1** and MS spectra of compounds **1**−**9** (PDF)

■ AUTHOR INFORMATION

Corresponding Author

*(S.H.J.) Phone: +82-33-650-3653. Fax: +82-33-650-3679. E-mail: shjung507@gmail.com.

Funding

This work was financially supported by an intramural grant (2Z04381) from the Korea Institute of Science and Technology (KIST), Republic of Korea.

Notes

The authors declare no competing financial interest.

■ ABBREVIATIONS USED

AMD, age-related macular degeneration; CAT, catalase; CNS, central nerve system; EEDK, ethanol extract of *Diospyros kaki*; ELM, external limiting membrane; GFAP, glial fibrillary acidic protein; GCL, ganglion cell layer; GSH, glutathione; GPx, glutathione peroxidase; INL, inner nuclear layer; IP, intraperitoneal; IPL, inner nuclear layer; MNU, *N*-methyl-*N*-nitrosourea; ONL, outer nuclear layer; RD-1, retinal degeneration-1 mice; RNFL/GC, retinal nerve fiber layer/ganglion cell layer; ROS, reactive oxygen species; RPE, retinal pigment epithelium; SD-OCT, spectral domain optical coherence tomography; SOD, superoxide dismutase

DOI: 10.1021/acs.jafc.5b02578
J. Agric. Food Chem. 2015, 63, 7750−7759

REFERENCES

(1) Cuenca, N.; Fernandez-Sanchez, L.; Campello, L.; Maneu, V.; De la Villa, P.; Lax, P.; Pinilla, I. Cellular responses following retinal injuries and therapeutic approaches for neurodegenerative diseases. *Prog. Retinal Eye Res.* **2014**, *43*, 17−75.

(2) Fletcher, A. E. Free radicals, antioxidants and eye diseases: evidence from epidemiological studies on cataract and age-related macular degeneration. *Ophthalmic Res.* **2010**, *44*, 191−198.

(3) Kiang, A. S.; Humphries, M. M.; Campbell, M.; Humphries, P. Antioxidant therapy for retinal disease. *Adv. Exp. Med. Biol.* **2014**, *801*, 783−789.

(4) Anderson, B., Jr. Ocular effects of changes in oxygen and carbon dioxide tension. *Trans. Am. Ophthalmol. Soc.* **1968**, *66*, 423−474.

(5) Brennan, L. A.; Kantorow, M. Mitochondrial function and redox control in the aging eye: role of MsrA and other repair systems in cataract and macular degenerations. *Exp. Eye Res.* **2009**, *88*, 195−203.

(6) Danulescu, R.; Costin, D. Use of blood markers in early diagnosis of oxidative stress in age related macular degeneration. *Rev. Med. Chir. Soc. Med. Nat. Iasi* **2012**, *116*, 1136−1142.

(7) Zampatti, S.; Ricci, F.; Cusumano, A.; Marsella, L. T.; Novelli, G.; Giardina, E. Review of nutrient actions on age-related macular degeneration. *Nutr. Res.* **2014**, *34*, 95−105.

(8) Klein, R.; Peto, T.; Bird, A.; Vannewkirk, M. R. The epidemiology of age-related macular degeneration. *Am. J. Ophthalmol.* **2004**, *137*, 486−495.

(9) Tsubura, A.; Lai, Y. C.; Miki, H.; Sasaki, T.; Uehara, N.; Yuri, T.; Yoshizawa, K. Review: Animal models of *N*-methyl-*N*-nitrosourea-induced mammary cancer and retinal degeneration with special emphasis on therapeutic trials. *In Vivo* **2011**, *25*, 11−22.

(10) Zulliger, R.; Lecaude, S.; Eigeldinger-Berthou, S.; Wolf-Schnurrbusch, U. E.; Enzmann, V. Caspase-3-independent photoreceptor degeneration by *N*-methyl-*N*-nitrosourea (MNU) induces morphological and functional changes in the mouse retina. *Graefe's Arch. Clin. Exp. Ophthalmol.* **2011**, *249*, 859−869.

(11) Prater, M. R.; Zimmerman, K. L.; Pinn, L. C.; Keay, J. M.; Laudermilch, C. L.; Holladay, S. D. Role of maternal dietary antioxidant supplementation in murine placental and fetal limb development. *Placenta* **2006**, *27*, 502−509.

(12) Usui, S.; Oveson, B. C.; Lee, S. Y.; Jo, Y. J.; Yoshida, T.; Miki, A.; Miki, K.; Iwase, T.; Lu, L.; Campochiaro, P. A. NADPH oxidase plays a central role in cone cell death in retinitis pigmentosa. *J. Neurochem.* **2009**, *110*, 1028−1037.

(13) Izuchi, R.; Takahashi, H.; Inada, Y. Preparing a carotenoid polyphenol-enriched extract from the peel of persimmon, *Diospyros kaki* L.f. *Biosci. Biotechnol. Biochem.* **2009**, *73*, 2793−2795.

(14) Ozen, A.; Colak, A.; Dincer, B.; Guner, S. A diphenolase from persimmon fruits (*Diospyros kaki* L., Ebenaceae). *Food Chem.* **2004**, *85*, 431−437.

(15) Ahn, H. S.; Jeon, T. I.; Lee, J. Y.; Hwang, S. G.; Lim, Y.; Park, D. K. Antioxidative activity of persimmon and grape seed extract: *in vitro* and *in vivo*. *Nutr. Res. (N. Y., NY, U. S.)* **2002**, *22*, 1265−1273.

(16) Katsube, T.; Tabata, H.; Ohta, Y.; Yamasaki, Y.; Anuurad, E.; Shiwaku, K.; Yamane, Y. Screening for antioxidant activity in edible plant products: comparison of low-density lipoprotein oxidation assay, DPPH radical scavenging assay, and Folin-Ciocalteu assay. *J. Agric. Food Chem.* **2004**, *52*, 2391−2396.

(17) Bei, W.; Zang, L.; Guo, J.; Peng, W.; Xu, A.; Good, D. A.; Hu, Y.; Wu, W.; Hu, D.; Zhu, X.; Wei, M.; Li, C. Neuroprotective effects of a standardized flavonoid extract from *Diospyros kaki* leaves. *J. Ethnopharmacol.* **2009**, *126*, 134−142.

(18) Age-Related Eye Disease Study Research. A randomized, placebo-controlled, clinical trial of high-dose supplementation with vitamins C and E and beta carotene for age-related cataract and vision loss: AREDS report 9. *Arch. Ophthalmol.* **2001**, *119*, 1439−1452.10.1001/archopht.119.10.1439

(19) Age-Related Eye Disease Study Research. A randomized, placebo-controlled, clinical trial of high-dose supplementation with vitamins C and E, beta carotene, and zinc for age-related macular degeneration and vision loss: AREDS report 8. *Arch. Ophthalmol.* **2001**, *119*, 1417−1436.10.1001/archopht.119.10.1417

(20) Jeong, E.; Paik, S. S.; Jung, S. W.; Chun, M. H.; Kim, I. B. Morphological and functional evaluation of an animal model for the retinal degeneration induced by *N*-methyl-*N*-nitrosourea. *Anat. Cell Biol.* **2011**, *44*, 314−323.

(21) Huber, G.; Beck, S. C.; Grimm, C.; Sahaboglu-Tekgoz, A.; Paquet-Durand, F.; Wenzel, A.; Humphries, P.; Redmond, T. M.; Seeliger, M. W.; Fischer, M. D. Spectral domain optical coherence tomography in mouse models of retinal degeneration. *Invest. Ophthalmol. Visual Sci.* **2009**, *50*, 5888−5895.

(22) Shimazawa, M.; Nakajima, Y.; Mashima, Y.; Hara, H. Docosahexaenoic acid (DHA) has neuroprotective effects against oxidative stress in retinal ganglion cells. *Brain Res.* **2009**, *1251*, 269−275.

(23) Kawakami, K.; Shibukura, Y.; Kanno, T.; Furuki, T.; Aketa, S.; Hirayama, M. Identification of 2″-galloylated flavonol 3-*O*-glycosides accumulating in developing leaves of persimmon. *Phytochem. Anal.* **2011**, *22*, 403−410.

(24) Wan, J.; Zheng, H.; Chen, Z. L.; Xiao, H. L.; Shen, Z. J.; Zhou, G. M. Preferential regeneration of photoreceptor from Muller glia after retinal degeneration in adult rat. *Vision Res.* **2008**, *48*, 223−234.

(25) Rosch, S.; Johnen, S.; Mataruga, A.; Muller, F.; Pfarrer, C.; Walter, P. Selective photoreceptor degeneration by intravitreal injection of *N*-methyl-*N*-nitrosourea. *Invest. Ophthalmol. Visual Sci.* **2014**, *55*, 1711−1723.

(26) Kawaguchi, A.; Miyata, T.; Sawamoto, K.; Takashita, N.; Murayama, A.; Akamatsu, W.; Ogawa, M.; Okabe, M.; Tano, Y.; Goldman, S. A.; Okano, H. Nestin-EGFP transgenic mice: visualization of the self-renewal and multipotency of CNS stem cells. *Mol. Cell. Neurosci.* **2001**, *17*, 259−273.

(27) Dahl, D. The radial glia of Muller in the rat retina and their response to injury. An immunofluorescence study with antibodies to the glial fibrillary acidic (GFA) protein. *Exp. Eye Res.* **1979**, *28*, 63−69.

(28) Xue, L.; Ding, P.; Xiao, L.; Hu, M.; Hu, Z. Nestin, a new marker, expressed in Muller cells following retinal injury. *Can. J. Neurol. Sci.* **2010**, *37*, 643−649.

(29) Valamanesh, F.; Monnin, J.; Morand-Villeneuve, N.; Michel, G.; Zaher, M.; Miloudi, S.; Chemouni, D.; Jeanny, J. C.; Versaux-Botteri, C. Nestin expression in the retina of rats with inherited retinal degeneration. *Exp. Eye Res.* **2013**, *110*, 26−34.

(30) Kohno, H.; Sakai, T.; Kitahara, K. Induction of nestin, Ki-67, and cyclin D1 expression in Muller cells after laser injury in adult rat retina. *Graefe's Arch. Clin. Exp. Ophthalmol.* **2006**, *244*, 90−95.

(31) Komeima, K.; Rogers, B. S.; Lu, L.; Campochiaro, P. A. Antioxidants reduce cone cell death in a model of retinitis pigmentosa. *Proc. Natl. Acad. Sci. U. S. A.* **2006**, *103*, 11300−11305.

(32) Hollman, P. C. H.; vanTrijp, J. M. P.; Buysman, M. N. C. P.; VanderGaag, M. S.; Mengelers, M. J. B.; deVries, J. H. M.; Katan, M. B. Relative bioavailability of the antioxidant flavonoid quercetin from various foods in man. *FEBS Lett.* **1997**, *418*, 152−156.

(33) Usui, S.; Komeima, K.; Lee, S. Y.; Jo, Y. J.; Ueno, S.; Rogers, B. S.; Wu, Z.; Shen, J.; Lu, L.; Oveson, B. C.; Rabinovitch, P. S.; Campochiaro, P. A. Increased expression of catalase and superoxide dismutase 2 reduces cone cell death in retinitis pigmentosa. *Mol. Ther.* **2009**, *17*, 778−786.

(34) Usui, S.; Oveson, B. C.; Iwase, T.; Lu, L.; Lee, S. Y.; Jo, Y. J.; Wu, Z.; Choi, E. Y.; Samulski, R. J.; Campochiaro, P. A. Overexpression of SOD in retina: need for increase in H_2O_2-detoxifying enzyme in same cellular compartment. *Free Radical Biol. Med.* **2011**, *51*, 1347−1354.

(35) Day, A. J.; Canada, F. J.; Diaz, J. C.; Kroon, P. A.; Mclauchlan, R.; Faulds, C. B.; Plumb, G. W.; Morgan, M. R. A.; Williamson, G. Dietary flavonoid and isoflavone glycosides are hydrolysed by the lactase site of lactase phlorizin hydrolase. *FEBS Lett.* **2000**, *468*, 166−170.

(36) Day, A. J.; DuPont, M. S.; Ridley, S.; Rhodes, M.; Rhodes, M. J. C.; Morgan, M. R. A.; Williamson, G. Deglycosylation of flavonoid and

DOI: 10.1021/acs.jafc.5b02578
J. Agric. Food Chem. 2015, 63, 7750−7759

isoflavonoid glycosides by human small intestine and liver beta-glucosidase activity. *FEBS Lett.* **1998**, *436*, 71−75.
(37) Ioku, K.; Pongpiriyadacha, Y.; Konishi, Y.; Takei, Y.; Nakatani, N.; Terao, J. *β*-Glucosidase activity in the rat small intestine toward quercetin monoglucosides. *Biosci. Biotechnol. Biochem.* **1998**, *62*, 1428−1431.

DOI: 10.1021/acs.jafc.5b02578
J. Agric. Food Chem. 2015, 63, 7750−7759

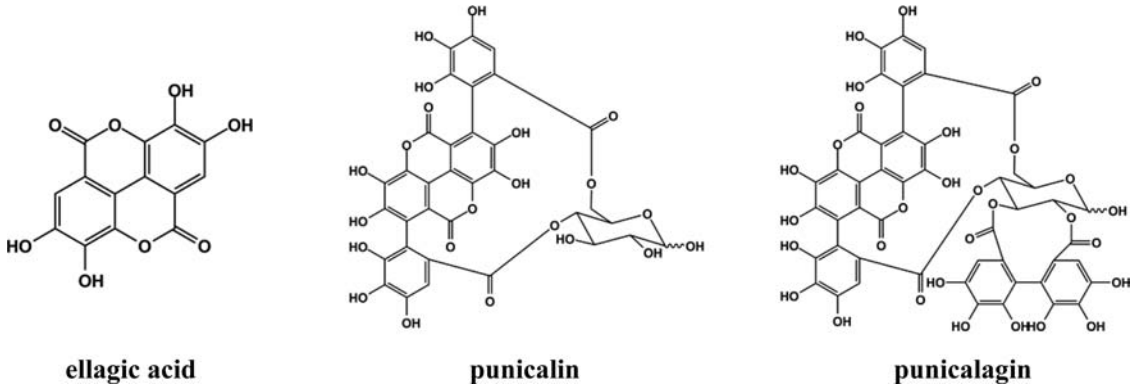

Figure 1. Structures of pomegranate polyphenols.

Table 1. Total Food Intake, Total Caloric Intake, and Final Body Weight of Diabetic Model Mice Fed with Normal (n = 13), HFS (n = 13), HFS + PFE (n = 13), and HFS + AG (n = 13) Diets[a]

parameter	normal	HFS	HFS+PFE	HFS+AG
total calorie intake (kcal)	1262 ± 18 a	1240 ± 25 a	1220 ± 27 a	1266 ± 40 a
total food intake (g)	318 ± 4.5 a	241 ± 4.9 b	240 ± 5.2 b	247 ± 7.7 b
body weight (g)	44.9 ± 0.76 a	48.6 ± 0.92 b	49.6 ± 1.1 b	49.3 ± 1.4 b

[a]Data are shown as the means ± SE. Values with different letters differed significantly at $p < 0.05$ (Tukey's test).

Pharma Co., Tokyo, Japan) once every 2 weeks. At the end of the feeding period, whole blood was collected from the postcaval vein to measure HbA1c using the enzymatic assay[17] (Norudia-HbA1c kit, Sekisui Medical Co., Ltd., Tokyo, Japan), serum AGEs using the ELISA assay (rat/mouse glyceraldehyde-derived AGE ELISA Kit, Up Well Co. Ltd., Fukuoka, Japan), and lipid peroxide using the thiobarbituric acid reactive substances assay[18] (Oxiselect TBARS Assay Kit, Cell Biolabs, Inc., San Diego, USA) according to the manufacturer's instructions. The present study was conducted in accordance with the Animal Experiment Guidelines of Josai University.

In Vitro Experiments. BSA (50 mg/mL) and sugar (100 mM glucose, 100 mM fructose, and 10 mM glyceraldehyde) were dissolved in 0.2 M phosphate buffer (pH 7.4). Each PFE-related sample was added to this solution to final concentrations of 10, 100, and 1000 μg/mL for PFE, and 10, 100, and 1000 μM for GA, EA, PC, and PG. The nonsupplemented BSA + sugar solution was used as a control. The mixture was incubated at 37 °C in total darkness: 15 days for the glucose-containing mixture, 5 days for the fructose-containing mixture, and 1 day for the glyceraldehyde-containing mixture. After incubation, the mixture was transferred to a 96-well black plate (Greiner Bio-One, Tokyo, Japan) to measure the fluorescence intensity (excitation = 370 nm, emission = 440 nm) using Spectra Max M2 (Molecular Devices, Sunnyvale, CA, USA). The rate of AGE formation was calculated as follows:

$$\text{AGE formation rate (\%)} = [\text{fluorescence intensity of sample (after incubation} - \text{before incubation)}]/[\text{fluorescence intensity of control (after incubation} - \text{before incubation)}] \times 100$$

Statistical Analysis. Statistical analysis was performed with StatMate III software (ATMS Co., Ltd., Tokyo, Japan). The data were analyzed by Dunnett's test and Tukey's test. Differences were considered significant at $p < 0.05$. The data are expressed as means ± SE.

RESULTS

Food Intake and Body Weight. To evaluate the antiglycation effect of PFE in vivo, glycation markers such as glycoalbumin, HbA1c, and serum AGEs of KK-A^y mice fed the sample (PFE with HFS) diet for 8 weeks after induction of hyperglycemia were analyzed. Table 1 shows total caloric intake and total food intake during the experimental diet, and body weight at the end of the experiment. Although the amount of food intake during the sample feeding was significantly lower in HFS-based groups (HFS, PFE, and AG) than the normal group, the total calorie consumption of all groups was virtually identical. The net intake of PFE was calculated as 1.5 mg/g/day. Final body weight was significantly higher in the HFS-based groups than in the normal group. There were no differences in caloric intake and weight gain between the HFS groups.

Blood Glucose, Glycation Products, and Lipid Peroxide Levels. The fasting blood glucose concentration was consistently higher in the HFS-based groups than in the normal group (Figure 2). Although the glycoalbumin levels of the HFS group tended to be higher than those of normal group, feeding of PFE and AG with HFS significantly decreased those levels

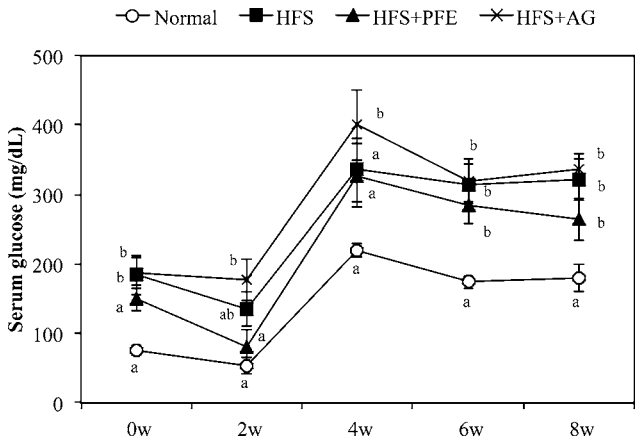

Figure 2. Fasting serum glucose levels in diabetic model mice fed with normal (n = 11−12), HFS (n = 12−13), HFS + PFE (n = 12−13), and HFS + AG (n = 11−13) diets. Data are shown as the means ± SE (n = 10−13), Tukey's test $p < 0.05$.

DOI: 10.1021/acs.jafc.5b02766
J. Agric. Food Chem. 2015, 63, 7760−7764

after 4 and 6 weeks, respectively (Figure 3A). PFE also significantly reduced HbA1c levels at 8 weeks as well as AG

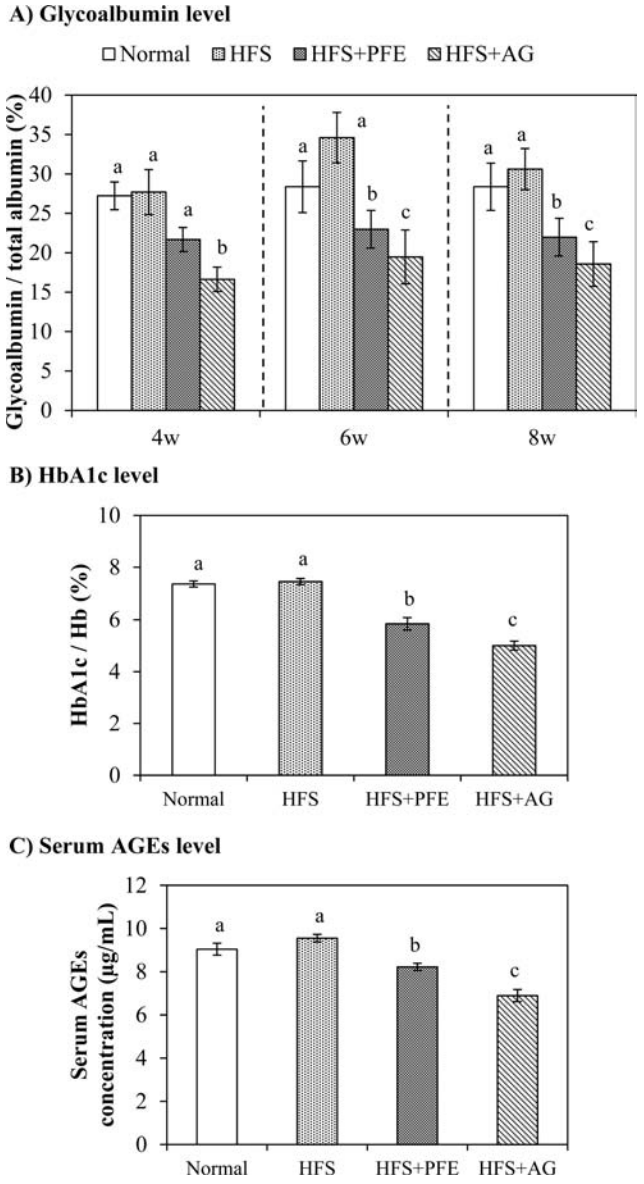

Figure 3. Serum glycation markers of (A) glycoalbumin levels (n = 11−13) at 4, 6, and 8 weeks, (B) hbA1c levels (n = 11−13) at 8 weeks, and (C) serum AGEs (n = 4) at 8 weeks in diabetic model mice fed normal, HFS, HFS + PFE, and HFS + AG diets. Data are shown as the means ± SE, Tukey's test $p < 0.05$.

(Figure 3B). Serum AGE concentration showed a trend similar to that of glycoalbumin and HbA1c (Figure 3C). Among significant increases in serum lipid peroxide in all HFS-based groups, PFE slightly suppressed the level as compared to HFS (p = 0.059) (Figure 4).

In Vitro Experiments. The AGE formation derived from BSA with glucose, fructose, and glyceraldehyde in vitro was concentration-dependently suppressed by addition of PFE and its components (Figure 5A−C). An even lower concentration of PFE (10 μg/mL) significantly suppressed the AGE formation from fructose and glyceraldehyde (Figure 5A). The anti-AGE-formation potency of the PFE components was similar in the assays using different sugars. The potency of EA

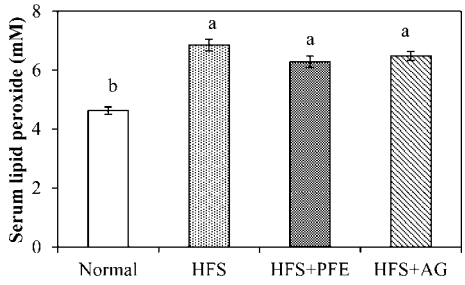

Figure 4. Serum lipid peroxide in diabetic model mice fed normal, HFS, HFS + PFE, and HFS + AG diets. Data are shown as the means ± SE (n = 10), Tukey's test $p < 0.05$.

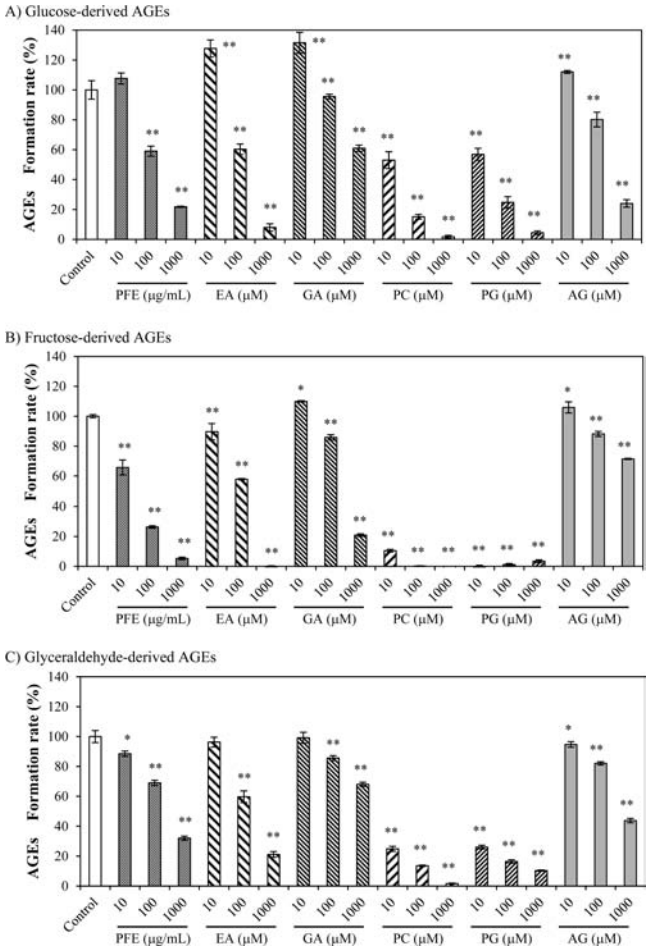

Figure 5. Antiglycation effects of PFE and its polyphenols on (A) glucose-derived, (B) fructose-derived, and (C) glyceraldehyde-derived AGE formation. Data are shown as the means ± SE (n = 3), Dunnett's test, *$p < 0.05$, **$p < 0.01$.

and GA was comparable to that of AG. PC and PG showed higher potency than EA and GA. The lowest concentration of PC and PG (10 μM) remarkably inhibited the AGE formation, especially with fructose (Figure 5B).

DISCUSSION

Most reports concerning the antiglycation effect of PFE have been performed in vitro, in which the suppression of AGE formation was via inhibition of the binding of proteins with sugars.[11−13] However, it has been unclear precisely what components of pomegranate contribute to this suppression.

DOI: 10.1021/acs.jafc.5b02766
J. Agric. Food Chem. 2015, 63, 7760−7764

Only one in vivo study reported that PFE inhibited collagen-derived AGEs in humans.[19] However, there has been no investigation about the antiglycation effects of pomegranate in vivo. Therefore, we have evaluated the antiglycation effects of pomegranate in type 2 diabetes model mice, in which it is relatively easy to induce conditions that promote glycation. Additionally, the effect of the individual components of PFE was investigated by an antiglycation in vitro assay. The results indicate that pomegranate contains several components that have the ability to suppress AGE formation in type 2 diabetic mice. Oral administration of PFE might not affect glucose absorption from meals in the intestine because there were no significant differences in caloric intake and body weight gain between HFS and HFS plus PFE. Higher levels of the fasting blood glucose concentration in the HFS plus PFE group indicate that PFE could not completely reverse the hyperglycemia. Therefore, the PFE-mediated reduction in HbA1c and glycoalbumin might be caused by inhibition of the reaction between the protein and glucose, that is, glycation. The accumulation of glycated albumin already started to decrease at 4 weeks after oral administration of PFE, also suggesting that PFE inhibited the early stages of glycation. The suppression of HbA1c by PFE also supports our hypothesis. The decreased accumulation of these glycation products probably resulted in the lower concentration of AGEs in PFE-fed mice. The additional benefit of PFE could be antioxidant effects that were observed as a slight decline in blood lipid peroxide levels. PFE and its constituent polyphenols have shown in vitro antiglycation effects as evaluated by the formation of glucose- and fructose-derived AGEs.[20,21] In this study, we revealed that PFE and its component polyphenols suppressed the generation of glyceraldehyde-derived AGEs in vitro, especially the ellagitannins PC and PG comparable to the antiglycation therapeutic aminoguanidine. Glyceraldehyde more easily reacts with protein than fructose and glucose,[2,22] and the glyceraldehyde-derived AGEs are thought to be highly toxic.[4] The anti-AGE-formation potency seemed to depend on the number of phenolic groups, suggesting that these polyphenols acted as an antioxidant in the latter stages of glycation in vitro. However, orally administered ellagitannins hardly transfer to the blood because of their relatively high molecular weight.[23−25] Ellagitannins like PC and PG are digested by gastric acid to EA, some of which will appear in the blood. The rest of EA is metabolized by intestinal bacteria into urolithin, which also will appear in the blood.[23,24,26,27]

Liu et al. reported that urolithin possessed antiglycation effect similar to aminoguanidine.[13] Therefore, the antiglycation effect of PFE shown in this in vivo study might be induced by these metabolites that had been degraded from ellagitannins in the digestive tract. Additionally, ellagitannins might contribute to the inhibition of exogenous AGE formation in the gastrointestinal tract. Further study is needed to clarify the mechanism of how the metabolites incorporated into the blood inhibit early stages of glycation.

AUTHOR INFORMATION

Corresponding Author

*1-1 Keyakidai, Sakado, Saitama 350-0295, Japan. Tel: +81 49 271 7249. Fax: +81 49 271 7249. E-mail: mwada@josai.ac.jp.

Funding

This work was supported by the subsidized projects support by Ministry of Agriculture, Forestry and Fisheries "Green and Water Environment Technology and Innovation Project, The 6th Industry Generation for Agriculture, Forestry and Fisheries Community Program 2014".

Notes

The authors declare the following competing financial interest(s): This work was supported by the subsidized projects support by Ministry of Agriculture, Forestry and Fisheries Green and Water Environment Technology and Innovation Project, The 6th Industry Generation for Agriculture, Forestry and Fisheries Community Program 2014.

REFERENCES

(1) Singh, R.; Barden, A.; Mori, T.; Beilin, L. Advanced glycation end-products: a review. *Diabetologia* **2001**, *44*, 129−146.

(2) Hodge, J. E. Chemistry of browning reactions in model systems. *J. Agric. Food Chem.* **1953**, *1*, 928−943.

(3) McPherson, J. D.; Shilton, B. H.; Walton, D. J. Role of fructose in glycation and cross-linking of proteins. *Biochemistry* **1988**, *27*, 1901−1907.

(4) Takeuchi, M.; Yamagishi, S. TAGE (toxic AGEs) hypothesis in various chronic diseases. *Med. Hypotheses* **2004**, *63*, 449−452.

(5) Ahmed, N. Advanced glycation endproducts-role in pathology of diabetic complications. *Diabetes Res. Clin. Pract.* **2005**, *67*, 3−21.

(6) Xie, J.; Méndez, J. D.; Méndez-Valenzuela, V.; Aguilar-Hernández, M. M. Cellular signalling of the receptor for advanced glycation end products (RAGE). *Cell. Signalling* **2013**, *25*, 2185−2197.

(7) Vasan, S.; Zhang, X.; Zhang, X.; Kapurniotu, A.; Bernhagen, J.; Teichberg, S.; Basgen, J.; Wagle, D.; Shih, D.; Terlecky, I.; Bucala, R.; Cerami, A.; Egan, J.; Ulrich, P. An agent cleaving glucose-derived protein crosslinks *in vitro* and *in vivo*. *Nature* **1996**, *382*, 275−278.

(8) Wu, C.-H.; Yen, G.-C. Inhibitory effect of naturally occurring flavonoids on the formation of advanced glycation endproducts. *J. Agric. Food Chem.* **2005**, *53*, 3167−3173.

(9) Liu, H.; Gu, L. Phlorotannins from brown algae (*Fucus Vesiculosus*) inhibited the formation of advanced glycation endproducts by scavenging reactive carbonyls. *J. Agric. Food Chem.* **2012**, *60*, 1326−1334.

(10) Qu, W.; Breksa, A. P., III; Pan, Z.; Ma, H. Quantitative determination of major polyphenol constituents in pomegranate products. *Food Chem.* **2012**, *132*, 1585−1591.

(11) Muthenna, P.; Akileshwari, C.; Reddy, G. B. Ellagic acid, a new antiglycating agent: its inhibition of Nε-(carboxymethyl)lysine. *Biochem. J.* **2012**, *442*, 221−230.

(12) Kokila, R.; Kumar, C.; Gowda, S. Antiglycation and antioxidant activity of polysaccharides isolated from fruit extract of pomegranate (*Punica Granatum*). *Pharmacologyonline* **2010**, *829*, 821−829.

(13) Liu, W.; Ma, H.; Frost, L.; Yuan, T.; Dain, J. A.; Seeram, N. P. Pomegranate phenolics inhibit formation of advanced glycation endproducts by scavenging reactive carbonyl species. *Food Funct.* **2014**, *5*, 2996−3004.

(14) Zhang, Y.; Wang, D.; Lee, R. P.; Henning, S. M.; Heber, D. Absence of pomegranate ellagitannins in the majority of commercial pomegranate extracts: implications for standardization and quality control. *J. Agric. Food Chem.* **2009**, *57*, 7395−7400.

(15) Miwa, I.; Okudo, J.; Maeua, K.; Okuda, G. Mutarotase effect on colorimetric determination of blood glucose with β-D-glucose oxidase. *Clin. Chim. Acta* **1972**, *37*, 538−540.

(16) Kouzuma, T.; Uemastu, Y.; Usami, T.; Imamura, S. Study of glycated amino acid elimination reaction for an improved enzymatic glycated albumin measurement method. *Clin. Chim. Acta* **2004**, *346*, 135−143.

(17) Ferri, S.; Kim, S.; Tsugawa, W.; Sode, K. Review of fructosyl amino acid oxidase engineering research: a glimpse into the future of hemoglobin A1c biosensing. *J. Diabetes Sci. Technol.* **2009**, *3*, 585−592.

(18) Song, Y. R.; You, S. J.; Lee, Y. M.; Chin, H. J.; Chae, D. W.; Oh, Y. K.; Joo, K. W.; Han, J. S.; Na, K. Y. Activation of hypoxia-inducible factor attenuates renal injury in rat remnant kidney. *Nephrol., Dial., Transplant.* **2010**, *25*, 77−85.

DOI: 10.1021/acs.jafc.5b02766
J. Agric. Food Chem. 2015, 63, 7760−7764

(19) Yagi, M.; Parengkuan, L.; Sugimura, H.; Shioya, N.; Matsuura, Y.; Nishida, N.; Nagatomo, A.; Yonei, Y. Anti-glycation effect of pomegranate (*Punica granatum* L.) extract: an open clinical study. *Glycative Stress Res.* **2014**, *1*, 60−67.
(20) Ni, Z.; Zhuge, Z.; Li, W.; Xu, H.; Zhang, Z.; Dai, H. Inhibitory effects of hydroxysafflor yellow A on the formation of advanced glycation end products *in vitro*. *Biol. Pharm. Bull.* **2012**, *35*, 2050−2053.
(21) Perez Gutierrez, R. M. Inhibition of advanced glycation end-product formation by *Origanum majorana* L. *in vitro* and in streptozotocin-induced diabetic rats. *Evid. Based. Complement. Alternat. Med.* **2012**, *2012*, 598638.
(22) Levi, B.; Werman, M. J. Long-term fructose consumption accelerates glycation and several. *J. Nutr.* **1998**, *128*, 1442−1449.
(23) Mertens-Talcott, S. U.; Jilma-Stohlawetz, P.; Rios, J.; Hingorani, L.; Derendorf, H. Absorption, metabolism, and antioxidant effects of pomegranate (*Punica Granatum* L.) polyphenols after ingestion of a standardized extract in healthy human volunteers. *J. Agric. Food Chem.* **2006**, *54*, 8956−8961.
(24) Seeram, N. P.; Lee, R.; Heber, D. Bioavailability of ellagic acid in human plasma after consumption of ellagitannins from pomegranate (*Punica granatum* L.) juice. *Clin. Chim. Acta* **2004**, *348*, 63−68.
(25) Bialonska, D.; Ramnani, P.; Kasimsetty, S. G.; Muntha, K. R.; Gibson, G. R.; Ferreira, D. The influence of pomegranate by-product and punicalagins on selected groups of human intestinal microbiota. *Int. J. Food Microbiol.* **2010**, *140*, 175−182.
(26) García-Villalba, R.; Beltrán, D.; Espín, J. C.; Selma, M. V.; Tomás-Barberán, F. a. Time course production of urolithins from ellagic acid by human gut microbiota. *J. Agric. Food Chem.* **2013**, *61*, 8797−8806.
(27) Clifford, M. N.; Scalbert, A. Review ellagitannins − nature, occurrence and dietary burden. *J. Sci. Food Agric.* **2000**, *80*, 1118−1125.

DOI: 10.1021/acs.jafc.5b02766
J. Agric. Food Chem. 2015, 63, 7760−7764

laboratory by a papain enzymatic method. Captopril was bought from YTHX Biotechnology Co., Ltd. (Beijing, China). RNAstore reagent, RNAprep pure Tissue Kit, FastQuant RT Kit, and SuperReal PreMix Plus (SYBR Green) Kit were purchased from Tiangen Bio Co., Ltd. (Beijing, China). The Rat Angiotensin Converting Enzyme Immuno Assay Kit, Angiotensin Type 1 Receptor ImmunoAssay Kit, Angiotensin Type 2 Receptor ImmunoAssay Kit, Angiotensin Converting Enzyme 2 ImmunoAssay Kit, Angiotensin II Immuno-Assay Kit, and Angiotensin-(1−7) ImmunoAssay Kit were from R&D Systems Inc. (Minneapolis, MN, USA).

Preparation of *S. platensis* Hydrolysates. *S. platensis* powder (10 g) was suspended by 30 mL of distilled water and stored at −80 °C, and then the suspension was thawed (frozen−thawed five times in total). After sonication for 3 min, the suspension was centrifuged at 6000*g* for 20 min at 4 °C and lyophilized. The protein content of the supernatant was determined by using a Total Protein Quantification Kit (Nanjing Jiancheng Bioengineering Institute, Nanjing, China). Before the hydrolysis reaction, 5.0 U of papain (Sigma Chemical Co., St. Louis, MO, USA) was added to 30 mL of redissolved protein solution (2% of substrate contained). The pH of the hydrolysis reaction system was adjusted to 7.0, and the reaction was performed at 70 °C for 9 h. Soon after the reaction was completed, the reaction system was transferred to 100 °C for 10 min to inactivate the enzyme. After centrifugation at 6000*g* for 10 min at 4 °C, the supernatant was ultrafiltered by 10000 and 5000 Da ultrafiltration membranes (Sartorius Co., Goettingen, Germany) successively. Finally, the products were lyophilized and stored at −20 °C. The percentages of IQP and VEP in SH were determined by RP-HPLC as 1.81 and 2.14%, respectively.

Animal Experiments and Blood Pressure Measurements. Eighty 5-week-old male SHRs were provided by Vital River Laboratories (Beijing, China). After 3 weeks of adaption to the environment and tail-cuff blood pressure measurement, SHRs were divided into five groups based on blood pressure (n = 16). Animals were kept in groups of five and maintained on a 12 h light/dark cycle under standard conditions at a temperature of 23 ± 2 °C, and a humidity of 60 ± 10%. The standard basal diet (HFK Bio., Beijing, China) according to the China National Standard (GB 14924.3-2001) and tap water were freely available. Systolic blood pressure (SBP), diastolic blood pressure (DBP), and heart rate (HR) were measured twice a week at 10:00 a.m. in the middle and at the end of the week from 9 to 16 weeks of age by a Kent Scientific CODA noninvasive blood pressure motoring system (Torrington, CT, USA) with a tail-cuff method. Before measurement, rats were kept on a warming pad for 10−15 min until pulsations in the tail artery were detectable. Given that the rats would be nervous during the measurements, the results of blood pressure were calculated and presented as weighted systolic blood pressure (WSBP) and diastolic blood pressure (WDBP), WSBP = SBP/HR × AveHR; WDBP = DBP/HR × AveHR, where AveHR is the mean heart rate of all SHRs measured in that time.[8] The body weights and diet and tap water intakes were measured twice a week. Between the 9th and 14th weeks of age at 9:00 a.m. every day, the five groups of SHRs were orally administered distilled water (negative control) 10 mL/kg/day, IQP 10 mg/kg/day, VEP 10 mg/kg/day, SH 10 mg/kg/day, or captopril (positive control) 10 mg/kg/day by a "passive swallow" gavage (filling the gavage needle in front of the esophagus to make a passive swallow instead of filling the needle directly into the stomach) to protect the rats' esophagus during the long-term experiment. From the 15th week of age, the treatments were withdrawn. At the end 11th, 14th, and 16th weeks of age, five or six rats per group were anesthetized and euthanized by 50 mg/kg pentobarbital (Sigma Chemical Co.). The left and right ventricles of the rats were separated and weighed. The left ventricular mass index (LVMI) and right ventricular mass index (RVMI) were calculated using the formulas LVMI (mg/g) = left ventricular mass (mg)/body weight (g) and RVMI (mg/g) = right ventricular mass (mg)/body weight (g).[11] Myocardial tissues were removed and stored in RNAstore reagent or in saline for 24 h at 4 °C, and then they were removed from the solutions and stored at −80 °C.

All rat experiments were performed in accordance with the Guidelines for the Care and Use of Laboratory Animals, Committee of Beijing Experimental Animal Care and Use, and were authorized by the Ethics Committee of the Beijing Experimental Animal Association.

Isolation of RNA, Reverse Transcription, and Quantitative Real-Time Polymerase Chain Reaction (qRT-PCR). Total RNA of myocardial tissues was extracted by using a Tiangen RNAprep pure Tissue Kit according to the manufacturer's guidelines, and the RNA concentrations and purities were determined by the ratios of A_{260}/A_{280} and A_{260}/A_{230} with a NanoDrop 2000 UV−vis spectrophotometer (NanoDrop Technologies, Wilmington, DE, USA). Reverse transcription for cDNA synthesis was done using a two-step method according to the instructions of the Tiangen FastQuant RT Kit with a 20 μL system to transcript 500 ng of cDNA in each sample, in which 2 μL of 10× Fast RT Buffer,1 μL of RT Enzyme Mix, and 2 μL of FQ-RT Primer Mix were mixed. Then the cDNA was stored at −20 °C. For qRT-PCR, a 20 μL qRT-PCR system with SYBR Green dye was set up following the instructions of the Tiangen SuperReal PreMix Plus (SYBR Green) Kit. A three-step procedure was followed for the qRT-PCR reaction using a CFX96 Touch Real-Time PCR Detection System (Bio-Rad Laboratories, Hercules, CA, USA) with 1 cycle of pre-denaturation at 95 °C for 15 min and 45 cycles of reaction, including denaturation at 95 °C for 10 s, annealing (different annealing temperatures were used for different genes, Table 1) for 20 s, and extension for 20 s at 72 °C. The primers for GAPDH, ACE, ACE2, AT1, AT2, and Mas were synthesized by Sangon Biotech Ltd. (Shanghai, China). GAPDH was used as a housekeeping gene. The sequences of real-time PCR primers are shown in Table 1.

Enzyme-Linked Immunosorbent Assay (ELISA). Myocardial tissues were homogenized in a glass homogenizer at 0 °C and then

Table 1. Primer Sequences and Annealing Temperatures for qRT-PCR

primer[a]	sequence	annealing temperature (°C)
GAPDH	sense: 5′-GGGCAAGGTCATCCCTGAGCTGAA-3′ antisense: 5′-GAGGTCCACCACCCTGTTGCTGTA-3′	55 or 60
ACE	sense: 5′-CACCGGCAAGGTCTGCTT-3′ antisense: 5′-CTTGGCATAGTTTCGTGAGGAA-3′	60
AT1	sense: 5′-CACAACCCTCCCAGAAAGTG-3′ antisense: 5′-AGGGCCATTTTGTTTTTCTG-3′	55
AT2	sense: 5′-GAACAGAATTACCCGTGACC-3′ antisense: 5′-ATGAATGCCAACACAACAGC-3′	60
ACE2	sense: 5′-ACCCTTCTTACATCAGCCCTAC-3′ antisense: 5′-GTACAAAACCTACCCCACATA-3′	55
Mas	sense: 5′-GACCAGCCCACAGTTACCAGTT-3′ antisense: 5′-CCAGGGTTCCCCTTCTGACT-3′	60

[a]ACE, angiotensin converting enzyme; AT1, angiotensin II type 1 receptor; AT2, angiotensin II type 2 receptor; ACE2, angiotensin converting enzyme 2.

DOI: 10.1021/acs.jafc.5b02801
J. Agric. Food Chem. 2015, 63, 7765−7774

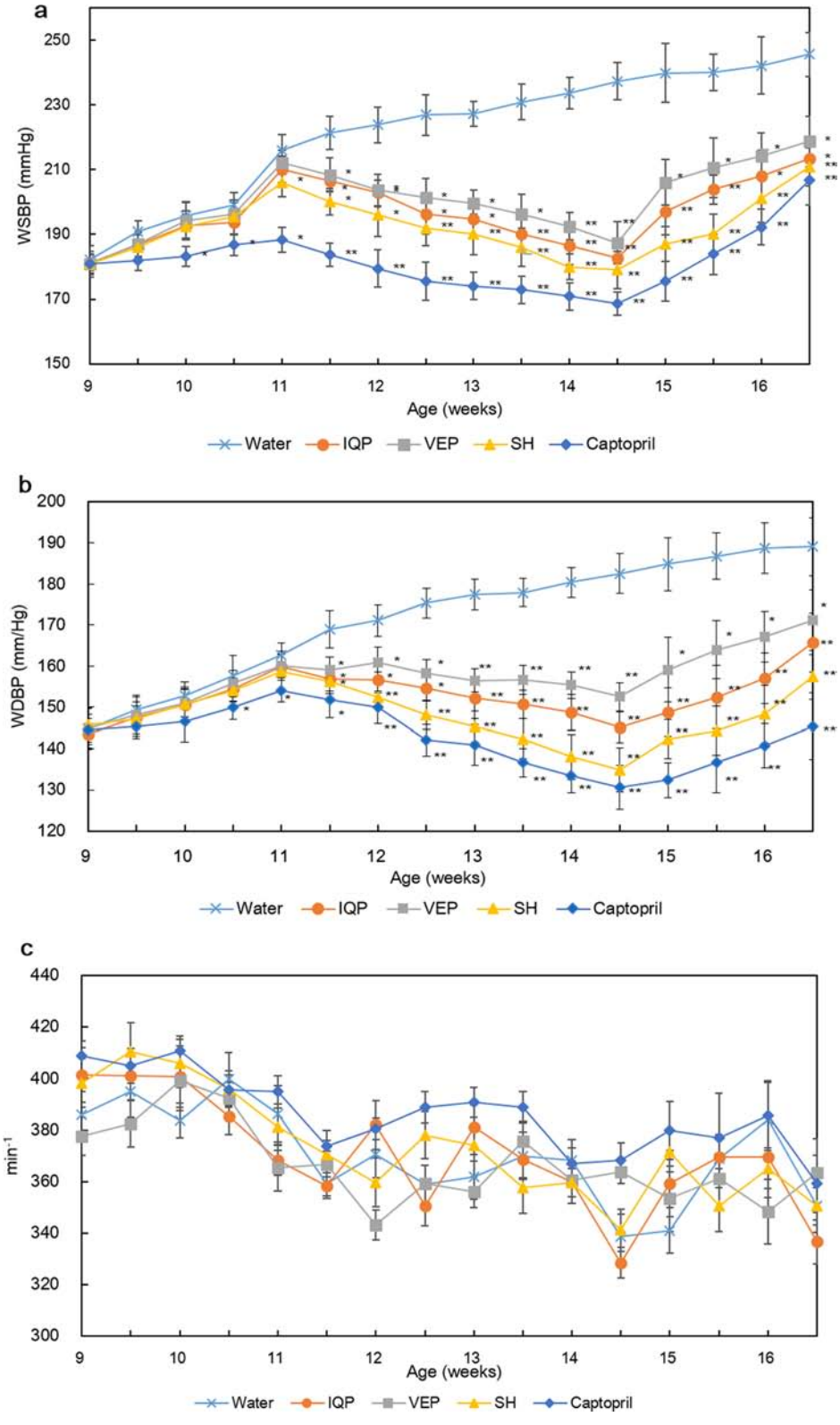

Figure 1. Blood pressure and heart rate changes of SHRs during the 8 week experimental period: (a) change of weighted SBP; (b) change of weighted DBP; (c) change of heart rate. The results are shown as means ± SE (9−11 weeks of age, n = 15; 12−14 weeks of age, n = 10; 15−16 weeks of age, n = 5): (∗) $p < 0.05$ and (∗∗) $p < 0.01$ versus the group fed distilled water. The "↓" represents the euthanasia time.

centrifuged at 3000g for 10 min at 4 °C. The total protein content of supernatants was measured by a Coomassie Brilliant Blue Total Protein Quantification Kit (Nanjing Jiancheng Bioengineering Institute). The protein/peptide contents of ACE, ACE2, AT1, AT2, Ang II, and Ang-(1−7) were assayed using R&D rat ELISA kits according to the manufacturer's instructions. Samples in 96-well microplates were read by a Multiskan MS ELISA reader (Helsinki, Finland) within 15 min after the reaction was stopped.

Western Blotting. Mas receptor protein concentrations were determined by Western blotting, and GAPDH was used as a reference.

DOI: 10.1021/acs.jafc.5b02801
J. Agric. Food Chem. 2015, 63, 7765−7774

The total protein of myocardial tissues was extracted by a Total Protein Extraction Kit (ProMab Biotechnologies, Albany, CA, USA), and the tissue lysates were heated at 100 °C for 10 min in a loading buffer. Equivalent amounts of total protein were separated on a 10% polyacrylamide gel in a 0.1% SDS buffer with SDS-PAGE. Then the proteins were transferred onto a nitrocellulose membrane (Pierce Chemical Co., Rockford, IL, USA). The membrane was blocked with nonfat dry milk (5%) in TBST buffer (20 mM Tris-HCl, pH 7.6, 137 mM NaCl, 0.5% Tween 20) for 2 h at 37 °C before the protein was incubated with MAS1L primary antibody (Abcam Inc., Cambridge, MA, USA) for the Mas receptor at a dilution of 1:500 for 2 h or GAPDH primary antibody (Santa Cruz Biotechnology, Santa Cruz, CA, USA) at a dilution of 1:800 for GAPDH. After four 5-min washes with TBST buffer, the membrane was probed by goat anti-rabbit IgG/HRP secondary antibody (Abcam Inc.) at a dilution of 1:4000 for Mas receptor or by goat anti-mouse IgG/HRP secondary antibody (Santa Cruz Biotechnology) at a dilution 1:8000 for GAPDH, followed by four 5-min washes with TBST buffer. Visualization was carried out by electrochemiluminescence (ECL) detection system (Bio-Rad Laboratories, Hercules, CA, USA). The content of Mas receptor protein was determined relative to GAPDH. Gel pro4.0 software (Media Cybernetics, Rockville, MD, USA) was used to analyze the integrated optical density (IOD) of the protein bands.

Statistical Analysis. The results are shown as means ± standard error (SE). One-way variance analysis (ANOVA) was estimated by SPSS 20.0 software (SPSS Inc., Chicago, IL, USA) followed by Scheffe test as a post hoc test. $P < 0.05$ between means was considered a significant difference, and $P < 0.01$ was considered a very significant difference.

RESULTS

Effects on SHR Blood Pressure. Changes in WSBP, WDBP, and heart rates of SHRs during the 8 week experimental period are shown in Figure 1. Before treatment, the mean WSBP was 181 ± 1 mmHg and the mean WDBP was 145 ± 1 mmHg. During 9−11 weeks of age, the blood pressure of all five groups increased, and there was no significant difference among the groups treated with distilled water (negative control), IQP, VEP, or SH. However, the group treated with captopril (positive control) showed a moderate increase in blood pressure and the lowest blood pressure by WSBP or WDBP. At the end of 11 weeks of age, the blood pressures of the treatment groups began to decrease compared with the negative control group. The captopril group had the lowest WSBP and WDBP, followed by the SH, IQP, and VEP groups. In addition, from the middle of 11 weeks of age, the other four groups showed significant differences in blood pressure compared with the negative control group. At 14 weeks of age, the IQP, VEP, SH, and captopril groups had 27, 25, 27, and 19 mmHg mean decreases in WSBP, respectively, and 15, 9, 24, and 21 mmHg decreases in WDBP, respectively, compared to blood pressure at 11 weeks of age, whereas the negative control group experienced a 16 mmHg increase in WSBP and a 14 mmHg increase in WDBP. When treatment was stopped at the start of the 15th week of age, the blood pressures of the IQP, VEP, SH, and captopril groups increased. However, they were still significantly lower than that of the negative control group. The WSBPs of the IQP, VEP, SH, and captopril groups had a mean lower value of 54, 50, 58, and 68 mmHg compared with the distilled water group at 14 weeks of age, whereas WDBPs were 38, 28, 48, and 52 mmHg, respectively. Throughout the experimental period, heart rates among the groups did not show significant differences (Figure 1c).

Growth Parameters of SHRs. In Figure 2, the body weights of SHRs at 9−16 weeks are shown. The body weights

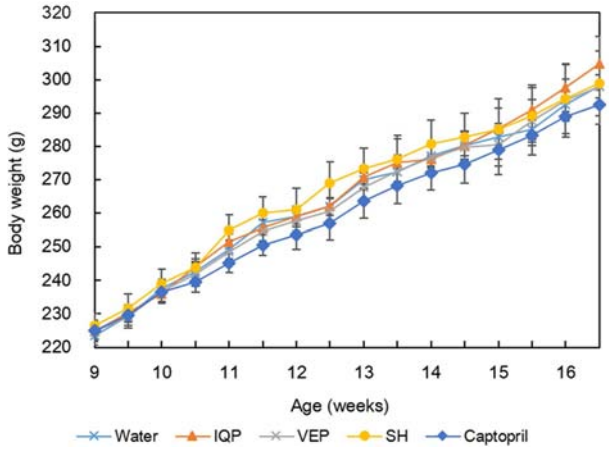

Figure 2. (a) Body weight changes of SHRs during the 8 week experimental period. The results are shown as means ± SE (9−11 weeks of age, $n = 15$; 12−14 weeks of age, $n = 10$; 15−16 weeks of age, $n = 5$).

of all SHR groups increased steadily, although the captopril group gained weight at a slower rate than other groups and the SH group gained weight at a faster rate. Tables 2 and 3 show the diet intake and water intake of SHRs during the experimental period. The diet intake was reduced at 10 weeks of age and then increased with slight fluctuations in the IQP group at 13 weeks, and at 14 weeks of age it was relatively higher but not significantly so. The results of water intake indicated that the captopril group drank the most water during 9−14 weeks of age, whereas the distilled water group drank the least. The other three groups had values between the positive and negative control groups, but were not significantly different. The trend of water intake also declined at 10 weeks of age, but then increased until 12 weeks of age and then showed a fluctuating pattern.

Left Ventricular Mass Index (LVMI) and Right Ventricular Mass Index (RVMI). LVMI and RVMI of SHRs euthanized at the end of 11, 14, and 16 weeks of age are shown in Figure 3. Both LVMI and RVMI of the negative control group were higher than the other groups and then were in the order VEP > IQP > SH > captopril. However, after the first 3 weeks, IQP, VEP, and SH groups showed no significant difference with the negative control group in RVMI but showed significant difference in LVMI. After 6 weeks of treatment, the differences in ventricular mass indices between the negative control group and other groups increased. However, when treatment was stopped for 2 weeks, the ventricular mass indices of the IQP, VEP, SH, and captopril groups were higher than during the treatment period. The LVMI of IQP, SH, and captopril groups still exhibited significant difference compared with the water group. However, only the captopril group and the SH group had significant differences compared with the water group in RVMI.

mRNA Expression Levels of ACE, ACE2, AT1, AT2, and Mas in the Myocardium of SHRs. The mRNA expression levels of ACE, ACE2, AT1, AT2, and Mas genes in the five groups were detected by qRT-PCR, and GAPDH was used as a housekeeping gene. The results are shown in Figure 4. The administration of IQP, VEP, SH, and captopril significantly lowered the mRNA expression levels of ACE and AT1 genes at 3 and 6 weeks of treatment, whereas significantly increased levels were observed for the ACE2, AT2, and Mas genes. The

DOI: 10.1021/acs.jafc.5b02801
J. Agric. Food Chem. 2015, 63, 7765−7774

Table 2. Diet Intake of SHRs during the Experimental Period (Grams/Rat/Week)[a]

	age (weeks)							
group	9 (n = 15)	10 (n = 15)	11 (n = 15)	12 (n = 10)	13 (n = 10)	14 (n = 10)	15 (n = 5)	16 (n = 5)
water	115.2 ± 1.1	108.3 ± 1.4	127.7 ± 1.9	130.6 ± 1.5	137.3 ± 1.5	137.5 ± 1.6	139.6 ± 1.5	142.4 ± 1.2
IQP	117.2 ± 1.8	109.3 ± 1.1	129.0 ± 1.8	132.2 ± 1.3	145.5 ± 1.5	147.4 ± 2.6	136.0 ± 1.4	141.0 ± 1.2
VEP	113.0 ± 0.9	105.7 ± 1.8	126.5 ± 2.3	133.2 ± 2.3	139.5 ± 1.7	143.2 ± 2.5	137.0 ± 2.1	148.0 ± 1.3
SH	118.6 ± 1.0	112.2 ± 1.8	129.3 ± 3.2	135.5 ± 1.1	140.5 ± 1.7	138.5 ± 0.8	137.3 ± 1.7	145.6 ± 1.3
captopril	114.5 ± 1.5	108.3 ± 1.4	127.5 ± 2.4	130.3 ± 1.7	139.5 ± 1.5	135.2 ± 1.3	134.9 ± 1.5	145.6 ± 1.4

[a]Data are expressed as means ± SE (standard error). IQP, Ile-Gln-Pro; VEP, Val-Glu-Pro; SH, *Spirulina platensis* hydrolysates; SHRs, spontaneously hypertensive rats.

Table 3. Water Intake of SHRs during the Experimental Period (Milliliters/Rat/Week)[a]

	age (weeks)							
group	9 (n = 15)	10 (n = 15)	11 (n = 15)	12 (n = 10)	13 (n = 10)	14 (n = 10)	15 (n = 5)	16 (n = 5)
water	153 ± 2	147 ± 2	171 ± 5	176 ± 7	152 ± 3	156 ± 3	146 ± 3	155 ± 2
IQP	157 ± 3	149 ± 2	179 ± 3[b]	188 ± 7[b]	161 ± 2[b]	163 ± 2[b]	146 ± 2	157 ± 3
VEP	156 ± 3	151 ± 2	179 ± 2[b]	185 ± 8[b]	168 ± 5[b]	168 ± 4[b]	147 ± 3	161 ± 5
SH	155 ± 3	151 ± 3	179 ± 4[b]	192 ± 5[b]	171 ± 2[b]	164 ± 2[b]	143 ± 2	153 ± 2
captopril	158 ± 4	155 ± 3[b]	181 ± 5[b]	194 ± 8[b]	172 ± 2[b]	170 ± 3[b]	145 ± 2	160 ± 3

[a]Data are expressed as means ± SE (standard error). IQP, Ile-Gln-Pro; VEP, Val- Glu-Pro; SH, *Spirulina platensis* hydrolysates; SHRs, spontaneously hypertensive rats. [b]$P < 0.05$ vs water group.

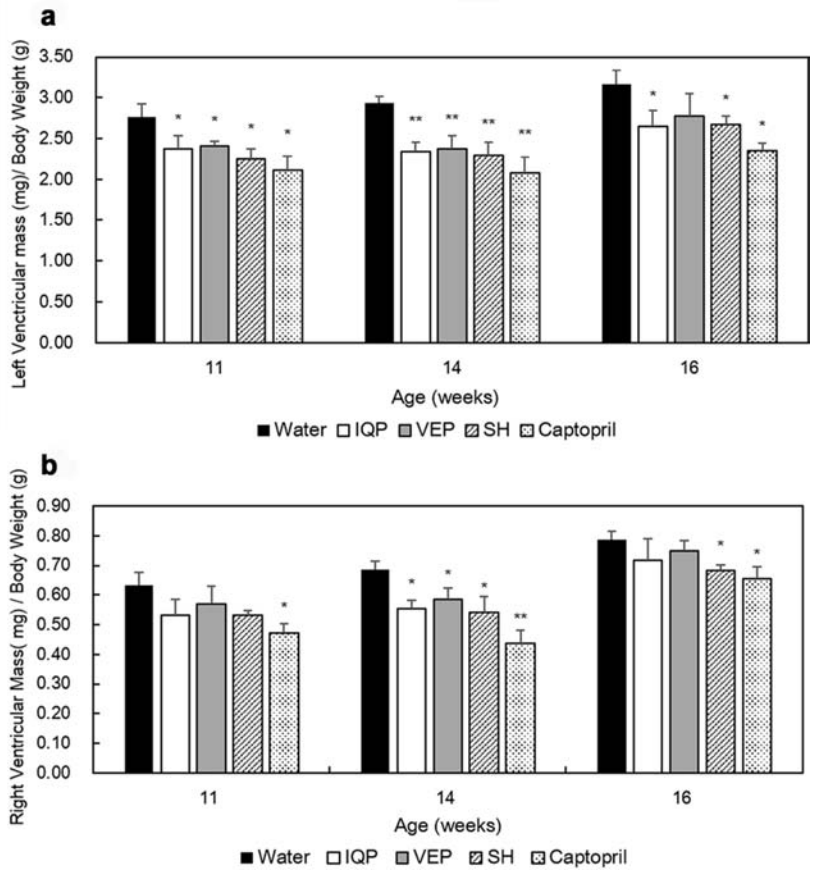

Figure 3. (a) Left ventricular mass index and (b) right ventricular mass index of SHRs euthanized at the end of 11, 14, and 16 weeks of age. The results are shown as means ± SE (n = 5): (*) $p < 0.05$ and (**) $p < 0.01$ versus the group fed distilled water.

trend of all gene expression after 6 weeks of treatment was slightly more significant than that after 3 weeks of treatment, and the differences in ACE, AT1, and AT2 gene expression were greater among the groups. After 6 weeks of treatment, the relative mRNA expression levels of the ACE gene and AT1 gene in the IQP, VEP, and SH groups were approximately 0.5-fold less than those of the negative control group. On the contrary, ACE2 gene and Mas gene expression levels were about 0.5-fold greater than those of the negative control group, whereas their AT2 gene expression levels were 1-fold greater

DOI: 10.1021/acs.jafc.5b02801
J. Agric. Food Chem. 2015, 63, 7765−7774

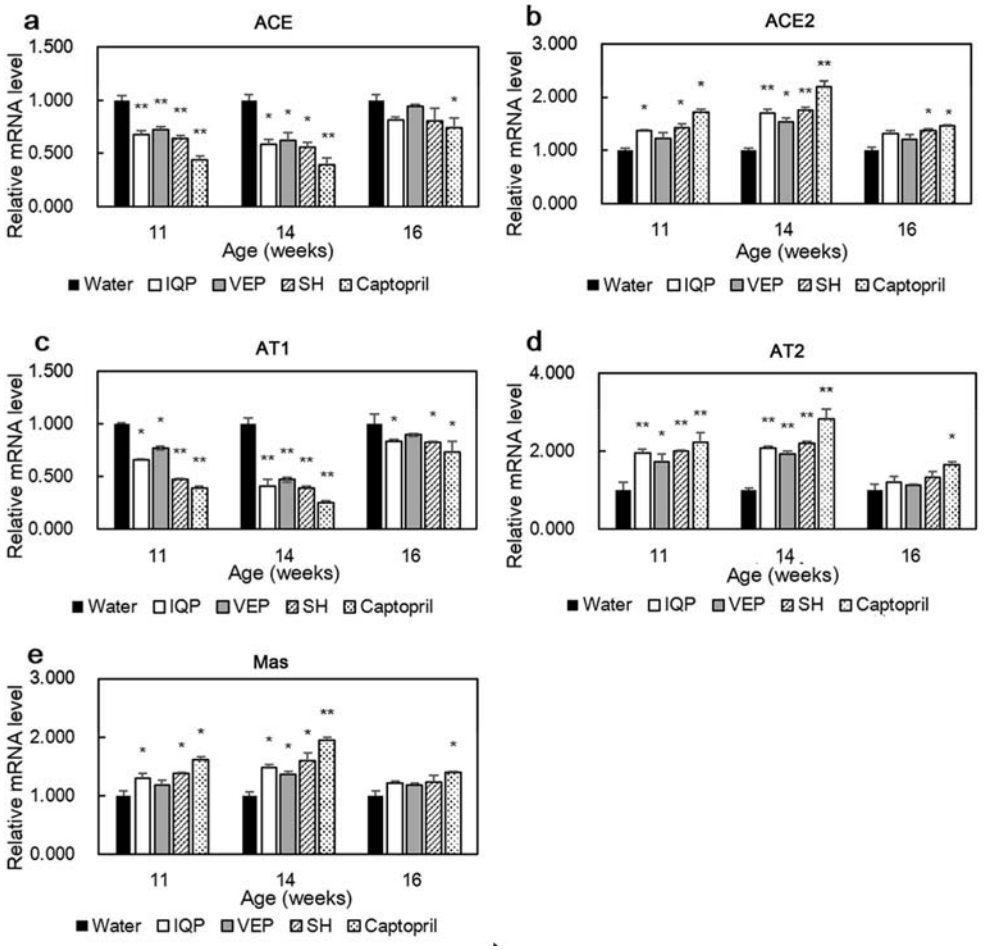

Figure 4. mRNA expression levels of (a) ACE, (b) ACE2, (c) AT1, (d) AT2, and (e) Mas genes at the end of different experimental periods. The gene expression of the group fed distilled water was used as a reference, and GAPDH was the housekeeping gene. The results are shown as relative level to the reference genes, as means ± SE (n = 5): (∗) $p < 0.05$ and (∗∗) $p < 0.01$ versus the group fed distilled water.

than that of the negative control group. The degree of treatment impact on mRNA expression levels was captopril > SH > IQP > VEP. When the treatments were stopped for 2 weeks, the differences among the groups became smaller.

Protein/Peptide Concentrations of ACE, ACE2, Ang II, Ang-(1−7), AT1, AT2, and Mas Receptor in the Myocardium of SHRs. The protein content of ACE, ACE2, AT1, and AT2 and the peptide content of Ang II and Ang-(1−7) were detected by ELISA (Figure 5), and the protein levels of Mas receptor were determined by Western blotting relative to that of GAPDH (Figure 6). The administration of IQP, VEP, SH, and captopril decreased the protein/peptide content of ACE, Ang II, and AT1, whereas increased content of ACE2, Ang-(1−7), AT2, and Mas receptor was observed after 3 and 6 weeks of treatment. This was similar to the trend for their mRNA expression levels. After 3 weeks of treatment, there were significant differences between the negative control group and the treatment groups in nearly all studied RAS substrates. As the treatment continued for another 3 weeks, the differences among the groups became more significant, and the withdrawal of the treatment reduced the difference in magnitude, although the trend remained the same. The degree of treatment impact on protein/peptide content was captopril > SH > IQP > VEP.

DISCUSSION

Anti-hypertensive peptides derived from foods have been a hot research topic in recent decades, and numerous studies have been performed to isolate the anti-hypertensive peptides from natural products to explore their in vitro and in vivo blood pressure regulatory characteristics and their anti-hypertensive mechanisms.

This study was based on previous studies of two *S. platensis*-isolated tripeptides, IQP and VEP.[6−9] IQP and VEP were isolated and purified by gel filtration chromatography and reverse-phase high-performance liquid chromatography and showed ACE inhibitory activity in vitro (IC_{50} = 5.77 ± 0.09 μM for IQP and IC_{50} = 27.36 ± 0.14 μM for VEP).[6,7] It was revealed that in 24 h and 1 week experiments, IQP and VEP demonstrated in vivo anti-hypertensive effects in SHRs, and some components of the RAS including renin, Ang, ACE, Ang II, AT1, and AT2 were influenced by treatment.[8,9] However, these studies were short-term experiments and mainly focused on the ACE−Ang II−AT1 axis. Long-term observation of blood pressure and regulation of the ACE−Ang II−AT1 and ACE2−Ang-(1−7)-Mas axes are required to complete the integrated evaluation of the anti-hypertensive effects of IQP and VEP. To compare the anti-hypertensive effects of these two tripeptides isolated from *S. platensis*, we used hydrolysates derived from *S. platensis* containing these two tripeptides, other peptides, or substrates as reference molecules.

DOI: 10.1021/acs.jafc.5b02801
J. Agric. Food Chem. 2015, 63, 7765−7774

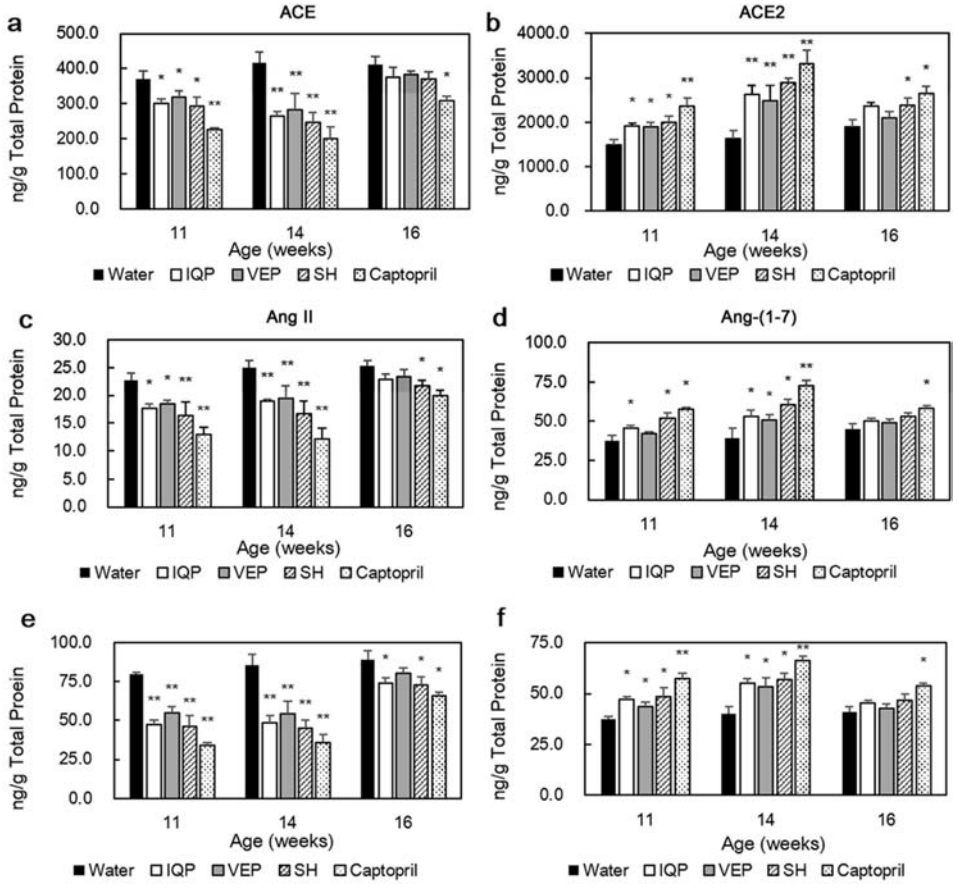

Figure 5. Protein/peptide concentrations of (a) ACE, (b) ACE2, (c) Ang II, (d) Ang-(1−7), (e) AT1, and (f) AT2 detected by ELISA at the end of different experimental periods. The results are shown as means ± SE (n = 5): (∗) $p < 0.05$, and (∗∗) $p < 0.01$ versus the group fed distilled water.

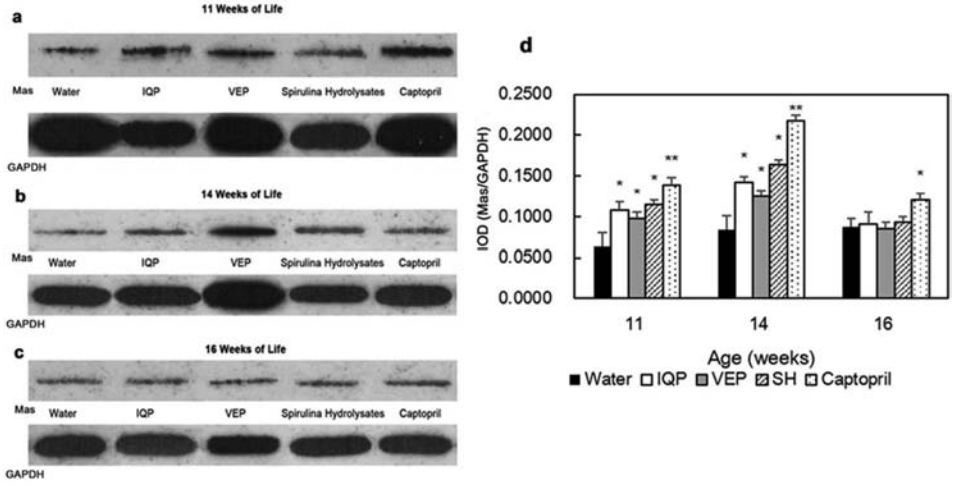

Figure 6. Protein levels of Mas receptor determined by Western blotting: protein bands from SHR samples at (a) 11, (b) 14, and (c) 16 weeks of age; (d) protein levels expressed as integrated optical density (Mas/GAPDH) of protein bands. The protein level of GAPDH was used as a reference. The results are shown as means ± SE (n = 5): (∗) $p < 0.05$ and (∗∗) $p < 0.01$ versus the group fed distilled water.

SHRs are often used for studies of the anti-hypertensive effects of foods and food protein-derived bioactive peptides because their hypertension patterns are similar to those in humans.[12,13] Male SHRs usually have a higher blood pressure than females of the same age, so they are easier to use for observation studies.[14] At the initial stages of SHR life, the blood pressure increases significantly and then stabilizes.[15,16] We also observed this pattern in the 3 weeks of adaption (data not shown) and first 3 weeks of treatment. However, the positive control group (captopril group) experienced a lower growth rate in both WSBP and WDBP compared with the other groups, and the negative control group showed a greater growth rate. After the end of 11 weeks of age, both the WSBP and WDBP of all groups excluding the negative control group began to decrease gradually and showed significant differences with the negative group ($P < 0.05$). This significance remained

DOI: 10.1021/acs.jafc.5b02801
J. Agric. Food Chem. 2015, 63, 7765−7774

until the end of the experiment, although the data of the IQP, VEP, SH, and captopril groups increased after the withdrawal of the treatment. We noticed that significant anti-hypertensive effects among the treatment groups appeared from the middle of 11 weeks of age in this study, which showed a delay of about 1 week compared to our short-term study.[8,9] The reason might be that the "passive swallow" method caused some deviation in daily actual intakes compared with direct gavaging into the stomach. Nonetheless, we suggest that such deviation would be more controllable than dissolving the treated compounds in daily drink water. Captopril is a well-known ACE-inhibitory drug for anti-hypertensive treatment in the clinic and showed the most prominent blood pressure lowering effect, followed by SH, IQP, and VEP. Saito et al.[17] found that in sake lee-derived ACE-inhibitory peptides, IYPRY had a higher in vivo SBP lowering effect than its hydrolyzed fragments IY, YP, and RY. Marczak et al.[18] also found similar results for anti-hypertensive peptides isolated from rapeseed. The subtilisin hydrolysates of rapeseed had a stronger anti-hypertensive effect than its fragmented peptides. Sipola et al.[19] compared the fermentative milk derived tripeptides, Iln-Pro-Pro (IPP) and Val-Pro-Pro (VPP), and sour milk containing these two peptides and found that sour milk had a more extensive SBP lowering effect than either IPP or VPP and proposed that there might be other anti-hypertensive factors such as electrolytes of calcium, magnesium, potassium, or sodium in the sour milk, which could regulate the blood pressure. Because *S. platensis* possesses abundant high-quality proteins, mineral substances, and other nutritional components, electrolytes and/or other unknown anti-hypertensive peptides in *S. platensis* hydrolysates alone or in combination might have contributed to the extensive attenuation of blood pressure in the SHRs. Furthermore, there were not very huge differences between the captopril group and other treated groups, although there is a huge difference between their IC_{50} values (2−15 nM for captopril).[20] It was reported that food-derived ACE inhibitory peptides might exert higher anti-hypertensive activities in vivo than their expected IC_{50} values in vitro compared to captopril.[8,21] This phenomenon might due to the higher affinity of ACE inhibitory peptides to target tissues and their slower elimination.[5,8,21,22]

Miguel et al.[15] reported that SHRs treated with captopril gained weight at a lower rate than the other groups, similar to the trend in the current study between 10 and 16 weeks of age, although this was not statistically significant. In contrast, the SH group gained weight at a slightly higher rate. The fluctuation of diet and water intake in the first 2 weeks of treatment might be caused by the SHRs' inadaptability to the administration. Diet intakes of the IQP, VEP, and SH groups were slightly higher than those of the other groups at 11−14 weeks of age. ACE-inhibitors have been proven to induce thirst and increase water intake in rats, and indeed the captopril group consumed the most water during the treatment period.[15] These factors might explain the increase of water intake of SHRs in the groups that had lower blood pressures.

During the pathogenesis of hypertension, long-term increased peripheral resistance and blood pressure can lead to changes in the compensatory structures of myocardial tissue, resulting in myocardial hypertrophy, myocardial fibrosis, and ventricular cavity expansion. Elevation of blood pressure can induce an increase in cardiac load, stretching of the myocardial fibers, hypoxia of myocardial tissue, accumulation of metabolites, and increased rate of protein synthesis, which can result in myocardial hypertrophy.[23] The high blood volume return to the right atrium and preload of the left atrium increased the left ventricular filling pressure, left ventricular volume, and cardiac output.[24] Increased left ventricular volume can cause left ventricular wall tension, causing the left ventricular mass to be elevated and produce a thicker myocardial wall to adapt to these changes.[25,26] Left ventricular hypertrophy predisposes the heart to congestive heart failure.[24] In SHRs, left ventricular hypertrophy is formed after approximately the 10th week of life.[27] Our study found that both the LVMI and RVMI of the IQP, VEP, SH, and captopril groups were lower than the negative control group after 6 weeks of treatment, indicating these peptides might inhibit myocardial hypertrophy. This result might be related to the anti-hypertensive effects of IQP, VEP, SH, and captopril. The study of Natsume et al.[28] showed that both the LVMI and RVMI of SHRs were lowered by treatment with captopril for 4 weeks. Besides, Horinaka and Frohlich[29] found celiprolol, a cardioselective β1 adrenergic receptor antagonist, could significantly reduce both the left and right ventricular mass in SHRs and discussed the effect of celiprolol as being similar to that of angiotensin enzyme inhibitors in SHRs. We also found that the anti-hypertensive and anticardiac hypertrophy effects of IQP and VEP in this study matched their IC_{50} values in vitro, suggesting that the IC_{50} of ACE inhibitory activities may also affect the cardiac function. However, the mechanisms of these functions require further study to explore the cardioprotective effects of these peptides.

The trends of change in protein/peptide content of RAS components were in accordance with their corresponding mRNA expression in the myocardium. Groups with lower blood pressure showed a down-regulation of the expression of ACE, Ang II, and AT1 but an up-regulation of ACE2, Ang-(1−7), Mas, and AT2. The trends in the regulation of ACE, Ang II, AT1, and AT2 in the IQP, VEP, and captopril groups were similar to that for the short-term regulation of IQP and VEP.[8,9] The regulatory trends of peptides on the ACE2-Ang-(1−7)-Mas axis were consistent with the regulation of adriamycin-induced heart failure rats treated by telmisartan and losartan, two Ang receptor blockers (ARBs) that prevent cardiotoxicity.[30] RAS plays a critical role in the cardiovascular system by influencing blood pressure regulation, electrolyte balance, water−electrolyte metabolism, vascular tone, and heart and kidney signaling.[31] Recent studies suggest RAS is regulated by two axes: the ACE−Ang II−AT1 axis and the ACE2−Ang-(1−7)−Mas axis.[10] The components of these two axes exist in many tissues, including the kidneys and heart.[10,32] At the beginning of RAS, renin hydrolyzes Ang into Ang I.[33] In the ACE−Ang II−AT1 axis, Ang II is synthesized from Ang I by ACE, and then Ang II binds to two major subtypes of receptors, AT1 and AT2.[10,33,34] The binding of Ang II to AT1 receptors mediates regional blood flow and leads to vasoconstriction and oxidative stress, and the combination of AT2 with Ang II conversely leads to lower blood pressure and inhibition of malignant cell proliferation.[35−37] Therefore, hyperactivity of the ACE−Ang II−AT1 axis can lead to CVDs, such as hypertension, stroke, and coronary heart disease.[36] In the ACE2−Ang-(1−7)−Mas axis, Ang-(1−7) is produced from ACE2 by cleaving Ang II, which then binds with the G protein-coupled receptor Mas, inducing the release of nitric oxide from endothelial cells and exerting vasodilative, antiproliferative, and anti-hypertensive functions.[10,38] The ACE2−Ang-(1−7)−Mas axis has an opposite effect from the ACE−Ang II−AT1 axis and plays a key role in blood pressure regulation and blood

DOI: 10.1021/acs.jafc.5b02801
J. Agric. Food Chem. 2015, 63, 7765−7774

vessel protection.[10,36,39] Furthermore, as elevated Ang II levels lead to infarcted hearts and other heart dysfunctions, ACE2, Ang-(1−7), and Mas receptor were contrarily reported to be associated with cardioprotective functions, and the elevated expression of Ang-(1−7) in failing heart tissue and the expression of its forming enzyme ACE2 are present in parallel to reduce heart dysfunction. Ang-(1−7) protects cardiac remodeling by decreasing hypertrophy and fibrosis, and Mas receptor prevents impaired heart functions in SHRs caused by high blood pressure.[38,40−43]

We studied the two axes in the myocardium and observed the countereffects of the ACE−Ang II−AT1 and ACE2−Ang-(1−7)−Mas axes (including the countereffects of AT1 and AT2), which were influenced by different treatment, and were related to the regulation of blood pressure in SHRs. After 3 weeks of treatment, there were differences in blood pressure regulation, mRNA expression levels, and protein/peptide content of the studied components in RAS among all of the groups. As the treatment time increased for another 3 weeks, the differences among the groups became more significant, and the withdrawal of the treatment for 2 weeks reduced the significance of the differences, although the general trends in blood pressure difference, mRNA expression levels, and protein/peptide concentrations of the substrates studied were maintained. However, we observed slightly more significant differences in mRNA expression levels and in protein/peptide content of the components of the ACE−Ang II−AT1 axis (including AT2) compared with the components of the ACE2−Ang-(1−7)−Mas axis. This suggested that the ACE−Ang II−AT1 axis might have a major role in myocardial RAS regulation compared with the ACE2−Ang-(1−7)−Mas axis.

In conclusion, this study suggests that the long-term oral intake of 10 mg/kg IQP, VEP, or SH can attenuate hypertension and myocardial hypertrophy in SHRs and regulate the RAS components that subsequently up-regulate the components in ACE2−Ang-(1−7)−Mas axis and AT2, while down-regulating the components in the ACE−Ang II−AT1 axis. Because most studies on the anti-hypertensive mechanisms of food-derived peptides have focused on the ACE−Ang II−AT1 axis, such as ACE-inhibitors, ARB, and renin inhibitors, the exploration of food-derived sources with ACE2 activation activity and with the ACE2−Ang-(1−7)−Mas axis has been limited. Our results revealed that bioactive tripeptides and hydrolysates derived from *S. platensis* can inhibit the ACE−Ang II−AT1 axis while activating the ACE2−Ang-(1−7)−Mas axis, and may serve as cardioprotective substrates. In addition to IQP and VEP, other peptides or substrates in SH might also show cardioprotective effects, and thus further studies should be dedicated to exploring the unknown components in *S. platensis* hydrolysates and their detailed regulatory mechanisms in the cardiovascular system.

AUTHOR INFORMATION

Corresponding Authors

*(D.R.) Phone: +86-10-62336700. Fax: +86-10-62338221. E-mail: rendifeng@bjfu.edu.cn.

*(J.L.) Phone: +86-10-53218278. Fax: +86-10-53218278. E-mail: johnljsmith@163.com.

Funding

This work was supported by grants from the National Natural Science Foundation of China (No. 31201339 and 31571772), the Special Fund for Forest Scientific Research in the Public Welfare (No. 201304805), the National High Technology Research and Development Program of China (863 Program, No. 2013AA102205), the Twelfth Five-Year National Science and Technology Support Program of China (No. 2012BAD33B04), the Cultivation Program of Hundred Talents in the Science and Technology Field in Beijing (No. Z131110000513026).

Notes

The authors declare no competing financial interest.

ABBREVIATIONS USED

IQP, Ile-Gln-Pro; VEP, Val-Glu-Pro; SH, *Spirulina platensis* hydrolysates; RAS, renin−angiotensin system; ACE, angiotensin converting enzyme; Ang, angiotensin; Ang I, angiotensin I; Ang II, angiotensin II; AT1, angiotensin II type 1 receptor; AT2, angiotensin II type 2 receptor; ACE2, angiotensin converting enzyme 2; Ang-(1−7), angiotensin-(1−7); ARB, angiotensin receptor blocker; SHR, spontaneously hypertensive rat; AveHR, average heart rate; WSBP, weighted systolic blood pressure; WDBP, weighted diastolic blood pressure; CVD, cardiovascular disease; LVMI, left ventricular mass index; RVMI, right ventricular mass index; qRT-PCR, quantitative real-rime polymerase chain reaction; ELISA, enzyme-linked immunosorbent assay; IOD, integrated optical density

REFERENCES

(1) World Health Organization (WHO). *World Health Statistics*, 2012; http://www.who.int/gho/publications/world_health_statistics/2012/en/ (accessed June 13, 2012).

(2) Udenigwe, C. C.; Mohan, A. Mechanisms of food protein-derived antihypertensive peptides other than ACE inhibition. *J. Funct. Foods* **2014**, *8*, 45−52.

(3) World Health Organizaion (WHO). *Controlling High Blood Pressure*; http://www.who.int/cardiovascular_diseases/en/ (accessed April 3, 2013).

(4) Patel, S. K.; Velkoska, E.; Freeman, M.; Wai, B.; Lancefield, T. F.; Burrell, L. M. From gene to protein-experimental and clinical studies of ACE2 in blood pressure control and arterial hypertension. *Front. Physiol.* **2014**, *5*, 227.

(5) Martínez-maqueda, D.; Beatriz, M.; Recio, I.; Hernández-ledesma, B. Antihypertensive peptides from food proteins: a review. *Food Funct.* **2012**, *4*, 350−361.

(6) Lu, J.; Ren, D. F.; Xue, Y. L.; Sawano, Y.; Miyakawa, T.; Tanokura, M. Isolation of an antihypertensive peptide from alcalase digest of spirulina platensis. *J. Agric. Food Chem.* **2010**, *58*, 7166−7171.

(7) Lu, J.; Ren, D. F.; Wang, J. Z.; Tanokura, M. Purification and characterization of an angiotensin I-converting enzyme inhibitory peptide derived from *Spirulina platensis*. *Shengwu Huaxue Yu Shengwu Wuli Jinzhan* **2010**, *37*, 568−574.

(8) Lu, J.; Sawano, Y.; Miyakawa, T.; Xue, Y. L.; Cai, M. Y.; Egashira, Y.; Ren, D. F.; Tanokura, M. One-week antihypertensive effect of Ile-Gln-Pro in spontaneously hypertensive rats. *J. Agric. Food Chem.* **2011**, *59*, 559−563.

(9) Lu, J.; Yang, Y.; Chen, L.; Ren, D. F.; Cai, M. Y.; Wang, J. Z.; Egashira, Y.; Tanokura, M. In vivo antihypertensive effect of Val-Glu-Pro in spontaneously hypertensive rats. *Shengwu Huaxue Yu Shengwu Wuli Jinzhan* **2011**, *38*, 353−360.

(10) Iwai, M.; Horiuchi, M. Devil and angel in the renin−angiotensin system: ACE−angiotensin II−AT1 receptor axis vs. ACE2−angiotensin-(1−7)−Mas receptor axis. *Hypertens. Res.* **2009**, *32*, 533−536.

(11) Geng, J.; Zhao, Z.; Kang, W.; Wang, W.; Zhang, Y.; Zhiming, G. Atorvastatin reverses cardiac remodeling possibly through regulation of protein kinase D/myocyte enhancer factor 2D activation in spontaneously hypertensive rats. *Pharmacol. Res.* **2010**, *61*, 40−47.

DOI: 10.1021/acs.jafc.5b02801
J. Agric. Food Chem. 2015, 63, 7765−7774

(12) Miguel, M.; López-Fandiño, R.; Ramos, M.; Aleixandre, A. Short-term effect of egg-white hydrolysate products on the arterial blood pressure of hypertensive rats. *Br. J. Nutr.* **2005**, *94*, 731−737.
(13) Sipola, M.; Finckenberg, P.; Korpela, R.; Vapaatalo, H.; Nurminen, M. L. Effect of long-term intake of milk products on blood pressure in hypertensive rats. *J. Dairy Res.* **2002**, *69*, 103−111.
(14) Silva-Antonialli, M. M.; Tostes, R. C. A.; Fernandes, L.; Fior-Chadi, D. R.; Akamine, E. H.; Carvalho, M. H. C.; Fortes, Z. B.; Nigro, D. A lower ratio of AT1/AT2 receptors of angiotensin II is found in female than in male spontaneously hypertensive rats. *Cardiovasc. Res.* **2004**, *62*, 587−593.
(15) Miguel, M.; López-Fandiño, R.; Ramos, M.; Aleixandre, A. Long-term intake of egg white hydrolysate attenuates the development of hypertension in spontaneously hypertensive rats. *Life Sci.* **2006**, *78*, 2960−2966.
(16) Cabassi, A.; Vinci, S.; Calzolari, M.; Bruschi, G.; Cavatorta, A.; Borghetti, A. The relationship between regional sympathetic activity and the onset of arterial hypertension in spontaneously hypertensive rats. *Cardiologia* **1997**, *42*, 393−396.
(17) Saito, Y.; Wanezaki, K.; Kawato, A.; Imayasu, S. Structure and activity of angiotensin I converting enzyme inhibitory peptides from sake and sake lees. *Biosci., Biotechnol., Biochem.* **1994**, *58*, 1767−1771.
(18) Marczak, E. D.; Usui, H.; Fujita, H.; Yang, Y.; Yokoo, M.; Lipkowski, A. W.; Yoshikawa, M. New antihypertensive peptides isolated from rapeseed. *Peptides* **2003**, *24*, 791−798.
(19) Sipola, M.; Finckenberg, P.; Santisteban, J.; Korpela, R.; Vapaatalo, H.; Nurminen, M.-L. Long-term intake of milk peptides attenuates development of hypertension in spontaneously hypertensive rats. *J. Physiol. Pharmacol.* **2001**, *52*, 745−754.
(20) Ben Henda, Y.; Labidi, A.; Arnaudin, I.; Bridiau, N.; Delatouche, R.; Maugard, T.; Piot, J. M.; Sannier, F.; Thiéry, V.; Bordenave-Juchereau, S. Measuring angiotensin-I converting enzyme inhibitory activity by micro plate assays: comparison using marine cryptides and tentative threshold determinations with captopril and losartan. *J. Agric. Food Chem.* **2013**, *61*, 10685−10690.
(21) Fujita, H.; Yoshikawa, M. LKPNM: a prodrug-type ACE-inhibitory peptide derived from fish protein. *Immunopharmacology* **1999**, *44*, 123−127.
(22) Hernández-Ledesma, B.; Del, M. C. M.; Recio, I. Antihypertensive peptides: production, bioavailability and incorporation into foods. *Adv. Colloid Interface Sci.* **2011**, *165*, 23−35.
(23) Cohn, J. N.; Ferrari, R.; Sharpe, N. Cardiac remodeling − concepts and clinical implications: a consensus paper from an international forum on cardiac remodeling. *J. Am. Coll. Cardiol.* **2000**, *35*, 569−582.
(24) Thakur, V. M.; Richards, R. M.; Reisin, E. M. Obesity, hypertension, and the heart. *Am. J. Med. Sci.* **2001**, *321*, 242−248.
(25) Messerli, F. H.; Sundgaard-Riise, K.; Reisin, E. D.; Dreslinski, G. R.; Ventura, H. O.; Oigman, W.; Frohlich, E. D.; Dunn, F. G. Dimorphic cardiac adaptation to obesity and arterial hypertension. *Ann. Intern. Med.* **1983**, *99*, 757−761.
(26) Chakko, S.; Mayor, M.; Allison, M. D.; Kessler, K. M.; Materson, B. J.; Myerburg, R. J. Abnormal left ventricular diastolic filling in eccentric left ventricular hypertrophy of obesity. *Am. J. Cardiol.* **1991**, *68*, 95−98.
(27) Arata, Y.; Geshi, E.; Nomizo, A.; Aoki, S.; Katagiri, T. Alterations in sarcoplasmic reticulum and angiotensin II receptor type 1 gene expression in spontaneously hypertensive rat hearts. *Jpn. Circ. J.* **1999**, *63*, 367−372.
(28) Natsume, T.; Kardon, M. B.; Pegram, B. L.; Frohlich, E. D. Ventricular performance in spontaneously hypertensive rats (SHR) with reduced cardiac mass. *Cardiovasc. Drugs Ther.* **1989**, *3*, 433−439.
(29) Horinaka, S.; Frohlich, E. D. Cardiovascular mass and ventricular function after celiprolol in Wistar-Kyoto and spontaneously hypertensive rats. *Cardiovasc. Res.* **1992**, *26*, 396−400.
(30) Zong, W. N.; Yang, X. H.; Chen, X. M.; Huang, H. J.; Zheng, H. J.; Qin, X. Y.; Yong, Y. H.; Cao, K.; Huang, J.; Lu, X. Z. Regulation of angiotensin-(1−7) and angiotensin II type 1 receptor by telmisartan and losartan in adriamycin-induced rat heart failure. *Acta Pharmacol. Sin.* **2011**, *32*, 1345−1350.
(31) Unger, T. The role of the renin-angiotensin system in the development of cardiovascular disease. *Am. J. Cardiol.* **2002**, *89*, 3−9.
(32) Murray, B.; Fitzgerald, R. Angiotensin converting enzyme inhibitory peptides derived from food proteins: biochemistry, bioactivity and production. *Curr. Pharm. Des.* **2007**, *13*, 773−791.
(33) Saleh, A. S.; Zhang, Q.; Shen, Q. Recent research in antihypertensive activity of food protein-derived hydrolyzates and peptides. *Crit. Rev. Food. Sci. Nutr.* **2014**, DOI: 10.1080/10408398.2012.724478.
(34) Bader, M.; Ganten, D. Update on tissue renin−angiotensin systems. *J. Mol. Med.* **2008**, *86*, 615−621.
(35) Ferreira, A. J.; Santos, R. A.; Bradford, C. N.; Mecca, A. P.; Sumners, C.; Katovich, M. J.; Raizada, M. K. Therapeutic implications of the vasoprotective axis of the renin-angiotensin system in cardiovascular diseases. *Hypertension* **2010**, *55*, 207−213.
(36) Ferreira, A.; Santos, R. Cardiovascular actions of angiotensin-(1−7). *Braz. J. Med. Biol. Res.* **2005**, *38*, 499−507.
(37) Bader, M. Tissue renin-angiotensin-aldosterone systems: targets for pharmacological therapy. *Annu. Rev. Pharmacol. Toxicol.* **2010**, *50*, 439−465.
(38) Santos, R. A. S; Ferreira, A. J.; Simões e Silva, A. C. Recent advances in the angiotensin-converting enzyme 2-angiotensin (1−7)-Mas axis. *Exp. Physiol.* **2008**, *93*, 519−527.
(39) Savoia, C.; D'Agostino, M.; Lauri, F.; Volpe, M. Angiotensin type 2 receptor in hypertensive cardiovascular disease. *Curr. Opin. Nephrol. Hypertens.* **2011**, *20*, 125−132.
(40) Huentelman, M. J.; Grobe, J. L.; Vazquez, J.; Stewart, J. M.; Mecca, A. P.; Katovich, M. J.; Ferrario, C. M.; Raizada, M. K. Protection from angiotensin II-induced cardiac hypertrophy and fibrosis by systemic lentiviral delivery of ACE2 in rats. *Exp. Physiol.* **2005**, *90*, 783−790.
(41) Diez-Freire, C.; Vázquez, J.; de Adjounian, M. F. C.; Ferrari, M. F.; Yuan, L.; Silver, X.; Torres, R.; Raizada, M. K. ACE2 gene transfer attenuates hypertension-linked pathophysiological changes in the SHR. *Physiol. Genomics* **2006**, *27*, 12−19.
(42) Johnston, C. I. Tissue angiotensin converting enzyme in cardiac and vascular hypertrophy, repair, and remodeling. *Hypertension* **1994**, *23*, 258−268.
(43) Danilczyk, U.; Penninger, J. M. Angiotensin-converting enzyme II in the heart and the kidney. *Circ. Res.* **2007**, *98*, 463−471.

DOI: 10.1021/acs.jafc.5b02801
J. Agric. Food Chem. 2015, 63, 7765−7774

compounds. Ethanol, as the major gastric acid stimulating constituent in wine, can be neglected because (i) the ethanol contents in red and white wines are similar and (ii) previous studies by Singer et al.[4] and Teyssen et al.[5] demonstrated that only fermented beverages such as beer and wine stimulate gastric acid output, whereas distilled alcoholic beverages with higher ethanol concentrations show very little or no effect.[4,5] Moreover, ethanol itself induced gastric acid secretion only in concentrations lower than those present in wine.[21] On the basis of these results, Teyssen and colleagues[22] fractionated fermented glucose and identified the organic acids maleic acid and succinic acid as strong stimulants of gastric acid secretion when administered to healthy subjects. Because the major organic acids in wine are tartaric, citric, malic, succinic, and lactic acid, one of our previous studies aimed to identify whether these constituents contribute to the stimulating effect of wine on gastric acid secretion.[3] All tested organic acids stimulated proton secretion, with malic acid in wine representative concentrations showing the most pronounced effect. Hydroxyl and carboxyl groups were proposed to be the functionally active groups of the organic acids.[3,22] Because these structural characteristics are shared by phenolic compounds as well, we hypothesized that phenolic constituents, which are present at higher concentrations in red wine as compared to white wine, contribute to the more pronounced effect of red wine on gastric acid secretion.

To our knowledge, no studies have investigated the effect of the phenolic compounds of wine on gastric acid secretion. However, we found one study in which the effect of phenolic compounds on proton secretion was tested; Ono and colleagues[23] measured [^{14}C]aminopyrine accumulation as an index of acid production in isolated parietal cells of guinea pigs. The isolated cells were stimulated with histamine or dibutyryl-cAMP and compared to cells treated with histamine or dibutyryl-cAMP combined with pentagalloylglucose (PGG) extracted from paeoniae radix or with gallic acid. The amount of [^{14}C]aminopyrine accumulation in the cells reflects the acid secretory state of the cells. PGG inhibited the histamine- or dibutyryl-cAMP-provoked effect in isolated parietal cells, whereas gallic acid, a compound also present in wine, had no effect.

The aim of this study was to identify whether the different effects of red wine versus white wine on mechanisms of gastric acid secretion can be explained by the different concentrations of malic and lactic acid and/or phenolic compounds. The secretory activity of four red wines and six white wines was tested using the well-established HGT-1 cell model.[3,7,16,18] The results on cellular proton secretion were correlated with the quantitated content of organic acids and phenolic compounds. The most promising compounds were tested individually and in a recombinate of all, which was added to a white wine sample that showed the least pronounced effect on proton secretion.

MATERIALS AND METHODS

Chemicals. DL-Lactic acid, L-malic acid, (+)-catechin, syringic acid, procyanidin B2, histamine, MTT reagent, and chemicals for the cell culture experiments, trypsin, glutamine, penicillin/streptomycin, and Dulbecco's modified Eagle's medium (DMEM) were purchased from Sigma-Aldrich. 1,5-Carboxy-seminaphtorhodafluor acetoxymethyl ester (SNARF-1-AM), nigericin, and fetal bovine serum were obtained from Invitrogen (Vienna, Austria). All other chemicals were obtained from Roth (Karlsruhe, Germany).

Samples. Wine samples were provided by the Federal College and Research Institute for Viticulture and Pomology, Klosterneuburg, Austria. A total of four red wine samples of the varieties "Blauer Burgunder" 2010 (R1), "Rösler" 2009 (R2), and "Cabernet Sauvignon-Merlot" 2009 (R3) produced by the Federal College and Research Institute for Viticulture and Pomology, Klosterneuburg, Austria, and "Zweigelt Reserve" 2009 (R4) produced by Rosner, Lower Austria, and a total of six white wine samples of the varieties "Grüner Veltliner" 2010 (W1) produced by Rosner, Lower Austria, "Gelber Muskateller" 2010 (W2), "Grüner Veltliner" 2010 (W3), "Chardonnay ice wine" 2009 (W4), "Chardonnay" 2010 (W5), and "Riesling" 2010 (W6) produced by the Federal College and Research Institute for Viticulture and Pomology, Klosterneuburg, Austria, were tested. For cell culture experiments, samples were diluted 1:100 in DMEM.

Cell Culture. For cell culture experiments, the human gastric tumor cell line HGT-1, obtained from Dr. C. Laboisse (Laboratory of Pathological Anatomy, Nantes, Frances), was used. They were cultured in DMEM with 4 g/L glucose, supplemented with 10% fetal bovine serum, 2% L-glutamine, and 1% penicillin/streptomycin under standard conditions at 37 °C, 95% humidity, and 5% CO_2.

Cell Vitality. Cytotoxic effects of wine samples were excluded by staining the cells with the yellow tetrazole MTT (3-(4,5-dimethylthiazol-2-yl)-2,5-diphenyltetrazolium bromide) reagent. A total of 100,000 cells per well were seeded in a 96-well plate and allowed to settle for 24 h. Afterward, the medium was discarded, and cells were treated with wine samples in a 1:100 dilution, individual compounds in wine-representative concentrations, and white wine (W6) in combination with a recombinate of catechin, procyanidin B2, and syringic acid added to DMEM for 30 min under standard conditions. Test samples were removed, and 100 μL of MTT-working solution, consisting of 1 part 5 mg/mL MTT solution and 5 parts DMEM, was added. In this assay, viable cells reduce the yellow tetrazole MTT to a purple formazan. After 15 min, the MTT solution was removed and the formazan was diluted in dimethyl sulfoxide. Absorbance was measured at 550 nm and at a reference wavelength of 690 nm using an Infinite 200 Pro Plate Reader (Tecan, Männderdorf, Switzerland). Cell viability was determined relative to medium-only treated control cells (untreated controls = 100%).

Intracellular pH Measurement in HGT-1 Cells. The intracellular pH was measured as a marker of proton secretion in HGT-1 cells by means of the pH-sensitive fluorescent dye SNARF-1-AM.[3,7,16,18] HGT-1 cells were seeded in a 96-well plate at a density of 100,000 viable cells per well under standard conditions at 37 °C, 95% humidity, and 5% CO_2 and allowed to settle for 24 h. Afterward, cells were washed once with Krebs−HEPES buffer (KRHB; 10 mM 4-(2-hydroxyethyl)-1-piperazineethanesulfonic acid (HEPES), 11.7 mM D-glucose, 4.7 mM KCl, 130 mM NaCl, 1.3 mM $CaCl_2$, 1.2 mM $MgSO_4$, and 1.2 mM KH_2PO_4, brought to a pH of 7.4 with 5 M KOH), and loaded with 3 μM SNARF-1-AM in KRHB for 30 min at standard conditions. The cells were washed twice and treated with either the wine samples or the wine constituents in wine representative concentrations or white wine (W6) in combination with a recombinate of catechin, procyanidin B2, and syringic acid in DMEM, all diluted 1:100, for 10 min at standard growth conditions. As positive control, 1 mM histamine was used. Afterward, the test substances were removed and the cells washed twice with KRHB, and 100 μL of KRHB per well was added prior to the measurement of fluorescence using an Infinite 200 Pro Plate Reader (Tecan, Männderdorf, Switzerland). Fluorescence was detected at 580 and 640 nm emission after excitation at 488 nm. The ratio between the two measured emission wavelengths was used to calculate the pH using a standard calibration curve. The calibration curve was generated by treating the cells with potassium buffer solutions of various pH values, ranging from 7.2 to 8.2 in the presence of 2 μM nigericin, to equilibrate intracellular and extracellular pH in the cells. The potassium buffer calibration solutions consisted of 20 mM NaCl, 110 mM KCl, 1 mM $CaCl_2$, 1 mM $MgSO_4$, 18 mM D-glucose, and 20 mM HEPES. The analyzed intracellular pH of the calibration solutions was fit to a linear regression. Using the intracellular pH, the intracellular H^+ concentration was calculated. The ratio between treated and medium-only/nontreated cells was calculated and $\log_2$ transformed to determine the intracellular proton index (IPX).[3,7,16,18] The lower the IPX, the stronger the proton secretion by the cell.

DOI: 10.1021/acs.jafc.5b02879
J. Agric. Food Chem. 2015, 63, 7775−7783

Quantitation of Wine Constituents and Parameters. *Analysis of General Wine Parameters.* Reducing substances, titratable acidity, volatile acidity, pH value, and free and total sulfurous acid were analyzed by means of standard methods as described by Eder and Brandes.[24] For reducing substances, the traditional iodometrical titration with Fehling reagent was applied. Titratable acids were determined potentiometrically with 0.1 N NaOH up to an end point of pH 7.0. The pH measurement was performed in the undiluted sample using a pH-sensitive electrode. For the determination of volatile acids, the acid content of water steam distillate was measured by titration with 0.01 N NaOH and phenolphthalein as indicator (pH 8.1). The effect of disturbing sulfurous acid was subtracted by extra iodometric titration. Free and total sulfurous acid were determined acidimetrically following the procedure described by Paul.[25]

Organic Acids. Quantitation of the major organic acids (tartaric, malic, lactic, citric, oxalic acid) was achieved by ionic chromatography as described by Prasnikar et al.[26] Succinic acid was quantified using an enzymatic kit from Megazyme International (Wicklow, Ireland) according to the protocol of the manufacturer.

Sugars, Glycerol, and Acetic Acid. Fructose, glucose, glycerol, acetic acid were analyzed enzymatically[27] using the Konelab 20 automatic system as described by Stojanović et al.[28]

Aromatic Phenols. The concentrations of aromatic phenols (vanillin, syringaldehyde, coniferylaldehyde, sinapaldehyde, and scopoletin) were determined after solid phase enrichment on a LiChrolut EN 200 mg, 3 mL, column (Merck) as described by Matejicek et al.[29] The SPE column was conditioned by subsequent washing with 3 mL of dichlormethane, 3 mL of methanol, and 3 mL of ethanol (13% (v/v) in water). Then 5 mL of the sample with internal standard (4-methoxybenzaldehyde) was slowly applied onto the column. After the column was washed with 2−3 volumes of ethanol (13% (v/v) in water), the column was dried by drawing nitrogen for 30 min. Finally, the phenols were eluted by twice adding 1 mL of dichloromethane. The eluate was dried on a rotavapor (240 mbar, 40 °C) and redissolved in 1 mL of HPLC solvent (0.5% formic acid, 10% methanol). Before injection into HPLC system, the eluate was purified by membrane filtration (Multoclear, 13 PVDF, 0.45 μm). HPLC was performed on a Rapid Resolution system (RR 1200 Agilent) equipped with a binary pump (SL, Agilent) and a diode array detector (DAD, Agilent) as well as a fluorescence detector (1260 Infinity FLD, Agilent). Separation was achieved on a reversed-phase column Zorbax SB-C-18 (150 × 2.1 mm, 1.8 μm) with gradient elution of (a) 0.5% formic acid and (b) methanol within 87 min. Flow rate was set at 0.25 mL/min and column oven temperature at 40 °C. Detection wavelengths were 260, 280, 290, 313, and 350 nm. Scopoletin was also detected using the FLD (excitation, 345 nm; emission, 460 nm). A volume of 5 μL of the filtered SPE eluate was injected for analysis of the phenolic acids (vanillic acid, syringic acid, ellagic acid, and gallic acid).

Phenolic Substances. The other phenolic substances (caftaric acid, *cis*- and *trans*-coutaric acid, fertaric acid, *p*-coumaric acid, ferulic acid, caffeic acid, catechin, epicatechin, tyrosol, and procyanidins B1 and B2) were analyzed with a modified HPLC method published by Vrhovsek et al.[30] The HPLC system consisted of a Rapid Resolution 1200 system with binary pump, DAD detector (Agilent) and a Poroshell 120 SB-C18 column (150 × 2.1, 2.7 μm; Agilent). A gradient elution with solvent (a) formic acid (0.5%) and (b) methanol and a flow rate of 0.2 mL/min was performed. Injection volume was 5 μL, and detection was at 280 and 320 nm.

Anthocyanins. Total monomeric anthocyanins were separated and detected by HPLC-UV, and the content was calculated as malvidol-3-glucoside as a reference compound, as described by Eder et al.[31] For the determination of the total phenol content, a photometric method using the Folin−Ciocalteu reagent was used as described by Linskens and Jackson.[32]

Gene Expression. A total of 100,000 HGT-1 cells per well were seeded in six-well plates and grown until confluence. Then the cells were treated with 10 mg/L DL-lactic acid and 10 mg/L L-malic acid for 5, 10, 15, 20, 25, and 30 min and harvested for RNA isolation using the RNeasy Mini Kit and SV Total RNA Isolation System (Promega, Madison, WI, USA). RNA quantity and quality were checked spectrophotometrically at 260 and 280 nm by calculation of the ratio of those wavelengths using the nanoquant plate for the Infinite 200 Pro Plate Reader (Tecan, Männderdorf, Switzerland). All cell samples had a ratio between 1.8 and 2.2. cDNA synthesis was carried out with the high-capacity RNA to cDNA Master Mix (Applied Biosystems, Munich, Germany) according to the manufacturer's protocol. Peptidylprolyl isomerase A (PPIA) was used as internal control. Primers for the H^+,K^+-ATPase α-subunit (*ATP4A*), the histamine H2 receptor (*HRH2*), the somatostatin receptor (*SSTR2*), and the acetylcholine receptor M3 (*CHRM3*) and *PPIA* were designed and validated previously[3,7,14,17] and were carried out as previously described.[3]

Statistical Analysis. The concentration of organic acids and phenolic compounds in wine was correlated to the IPX of the 10 wine samples using the correlation analysis after Spearman with SPSS 19.0.0 (IBM Statistics). Data below the limit of detection were replaced by the LOD/$\sqrt{2}$. Statistical analysis was performed using Excel 2007 (Microsoft), SigmaPlot software 11.0 (Systat Software). Outliers were excluded by Nalimov outlier analysis. Cytotoxic effects of the samples on HGT-1 cells compared to nontreated cells were determined with the two-tailed Student's *t* test and considered to be significant at $p < 0.05$. Significant differences in the data set of the intracellular pH measurements were determined by a one-way ANOVA with Holm−Sidak post hoc analysis or the two-tailed Student's *t* test as indicated in the figure captions. The two-way ANOVA with Holm−Sidak post hoc analysis was applied for analyzing time-dependent effects on gene expression. At least three biological replicates and two technical replicates were analyzed for each cell culture experiment. Data under Results as well as in diagrams are given as the mean ± SEM, unless indicated otherwise.

RESULTS

Cell Vitality of HGT-1 Cells after Treatment with Wine Samples and Wine Additions. We previously showed that red wine in concentrations higher than a 1:100 dilution caused cytotoxic effects in HGT-1 cells.[3] To exclude cytotoxic effects of the wine samples used in this study, we conducted an MTT assay using the same dilution (Table 1). The MTT assay is an indicator for the metabolic status of the cell. Data are represented as percent relative to nontreated cells. Lower values for sample-treated cells indicate a reduction of the metabolic status, which is an early indicator of cytotoxic effects. Neither the wine samples nor any of the individual wine constituents tested nor the combination of the white wine Riesling (W6) with the recombinate showed cytotoxic effects on HGT-1 cells.

Effect of Wine Samples on Proton Secretion in HGT-1 Cells. For studying the influence of the four red wines and six white wines on proton secretion in HGT-1 cells, cells were treated with 1:100 dilutions of each wine sample, and effects were compared to nontreated cells (control). Each wine sample itself stimulated proton secretion ($p < 0.001$, one-way ANOVA with Holm−Sidak post hoc test vs control) (Table 2). The red wine varieties "Blauer Burgunder" and "Roesler" showed the highest secretory activity ($p < 0.001$), with IPX values of −0.39 ± 0.02 and −0.37 ± 0.02, respectively. The white wine variety "Riesling" showed the least pronounced stimulation of the tested wines with an IPX of −0.10 ± 0.02. The average of the IPX values of the red wine samples was lower ($p < 0.016$) than that of the red wine samples (Figure 1), clearly demonstrating the more pronounced stimulating effect on proton secretion for red wines.

Characterization of Wines. All wines were produced in Lower Austria from the 2009 and 2010 vintages. The characteristics of the four red wines and six white wines are reported in Tables 2 and 3. Alcoholic strength was in the range of 13.0−14.1% for red and 11.8−13.1% for white wines. Titratable acidity was higher in white wines, ranging from 5.9 to 10.5 g/L, compared to red wines, ranging from 4.9 to 5.8 g/L. Organic acid

DOI: 10.1021/acs.jafc.5b02879
J. Agric. Food Chem. 2015, 63, 7775−7783

Table 1. Cell Vitality in Percent versus Nontreated Cells (Control: 100 ± 8%)[a]

	mean ± SD
red wines	
Blauer Burgunder 2010	100 ± 7
Rösler 2009	100 ± 7
Cabernet Sauvignon-Merlot 2009	100 ± 7
Zweigelt Reserve 2009 (Rosner)	97 ± 8
white wines	
Grüner Veltliner 2010 (Rosner)	109 ± 8 **
Gelber Muskateller 2010	102 ± 7
Grüner Veltliner 2010	120 ± 12 ***
Chardonnay Eiswein 2009	98 ± 9
Chardonnay 2010	106 ± 9
Riesling 2010	100 ± 15
recombinates	
recombinate 2	98 ± 5
Riesling 2010 + recombinate	106 ± 13
Riesling 2010 + recombinate 2	106 ± 12

[a]Wines were tested in a 1:100 dilution. The recombinate consisted of 0.8 mg/L (+)-catechin, 0.025 mg/L syringic acid, and 0.2 mg/L procyanidin B2. The concentrations were doubled in recombinate 2. Data are given as the mean ± SD, n = 3−6. (Statistics: one-way ANOVA with the Holm−Sidak post hoc test vs control; significant differences vs nontreated control cells are indicated by **, $p < 0.01$, and ***, $p < 0.001$.)

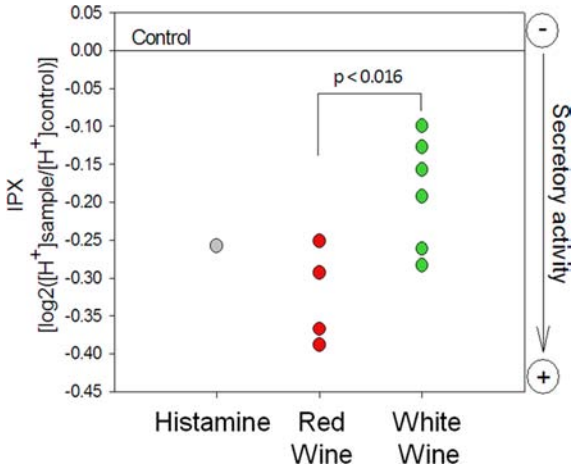

Figure 1. Intracellular proton index (IPX) means after treatment of HGT-1 cells with red wines or white wines (1:100 dilution). Means from n = 5−6, technical replicates = 3−6 (statistic: two-sided t test).

content mainly differed in the concentration of lactic and malic acid. Whereas lactic acid was only quantified in red wine samples in concentrations from 2 to 3.5 g/L, malic acid was only quantified in white wine samples in concentrations from 3.3−4.6 g/L.

Mean concentrations of total phenolics were higher in red wines, ranging from 1.11 to 1.84 g/L, compared to white wines, ranging from 0.05 to 0.09 g/L. Although several phenolic compounds were not detected in the majority of the white wine samples, caftaric acid and tyrosol were also quantified in white

Table 2. Characterization of Wine Samples[a]

	red wines				white wines					
parameter	R1	R2	R3	R4	W1	W2	W3	W4	W5	W6
IPX mean	−0.39	−0.37	−0.29	−0.25	−0.28	−0.26	−0.19	−0.16	−0.13	−0.10
IPX SEM	0.02	0.02	0.02	0.02	0.02	0.02	0.04	0.01	0.03	0.02
density (20 °C/20 °C)	1.00	1.00	0.99	0.99	0.99	0.99	0.99	1.07	0.99	0.99
alcohol (vol %)	13.0	13.4	13.7	14.1	12.0	12.7	12.8	11.8	13.1	12.4
pH	3.9	3.9	3.9	3.7	3.5	4.0	3.6	4.1	3.7	3.7
SO_2 acid										
free (mg/L)	38	23	28	19	23	32	17	19	23	26
total (mg/L)	129	97	81	65	57	121	100	143	74	99
glycerine (g/L)	8.3	8.3	8.5	9.3	5.7	5.6	6.0	20.2	6.2	5.9
red. compounds (g/L)	1.2	0.6	1.4	5.8	4.7	0.4	2.7	153	1.3	2.9
fructose (g/L)	0.5	0.4	0.4	2.6	2.3	0.5	2.0	96.9	0.8	2.6
glucose (g/L)	nd[b]	nd	nd	1.8	1.6	nd	0.2	53.1	nd	nd
titr acidity (g/L)	5.7	5.6	4.9	5.0	7.1	5.9	6.1	10.5	7.3	6.8
volatile acid (g/L)	1.4	1.5	1.1	0.7	0.5	0.4	0.6	1.6	0.1	0.3
tartaric acid (g/L)	1.4	1.3	1.2	2.0	2.7	0.3	1.6	0.6	1.0	1.0
malic acid (g/L)	nd	nd	nd	nd	3.8	4.6	3.3	5.5	4.6	4.5
lactic acid (g/L)	3.5	3.2	2.4	2.0	nd	nd	nd	nd	nd	nd
citric acid (g/L)	nd	nd	0.1	nd	0.2	nd	0.2	2.7	0.1	0.1
succinic acid (g/L)	0.6	0.7	0.8	0.6	0.3	0.4	0.3	0.4	0.4	0.3
acetic acid (g/L)	1.2	1.2	1.0	0.7	0.6	0.4	0.6	1.3	0.4	0.4
oxalic acid (mg/L)	nd	nd	nd	nd	nd	nd	nd	28	nd	nd

[a]R1, Blauer Burgunder 2010; R2, Rösler 2009; R3, Cabernet Sauvignon-Merlot 2009; R4, Zweigelt Reserve 2009 (Rosner); W1, Grüner Veltliner 2010 (Rosner); W2, Gelber Muskateller 2010; W3, Grüner Veltliner 2010; W4, Chardonnay Eiswein 2009; W5, Chardonnay 2010; W6, Riesling 2010. [b]nd, not detected.

DOI: 10.1021/acs.jafc.5b02879
J. Agric. Food Chem. 2015, 63, 7775−7783

Table 3. Contents of Phenolic Compounds and Amines in Wine Samples[a]

	red wines					white wines				
parameter	R1	R2	R3	R4	W1	W2	W3	W4	W5	W6
IPX mean	−0.39	−0.37	−0.29	−0.25	−0.28	−0.26	−0.19	−0.16	−0.13	−0.10
IPX SEM	0.02	0.02	0.02	0.02	0.02	0.02	0.04	0.01	0.03	0.02
phenols (g/L)	1.3	1.84	1.25	1.11	0.09	0.07	0.09	0.05	0.09	0.07
anthocyanins	98	49	123	11	nd[b]	nd	nd	nd	nd	nd
catechin	85.5	73.1	37.6	29.5	2	2.2	3.8	1.8	4.8	2.4
epicatechin	29.6	29.9	12.8	14.1	nd	nd	0.9	nd	1	nd
gallic acid	30.2	24.7	37.4	66.2	nd	0.1	0.5	1.6	0.2	0.1
procy B1	33.7	19.8	31.6	14.7	nd	1.2	2.2	nd	3.9	nd
procy B2	22	18.1	11.9	6.5	nd	nd	nd	nd	nd	nd
caffeic acid	18.2	15.9	5.3	12	1.7	1.7	2	3.5	1.9	2.1
caftaric acid	11.7	8.9	50.2	29.6	9.4	7.6	25.5	1.7	26.1	35.7
tyrosol	10.9	10.2	20	8.1	6.2	5.1	6.5	7.7	6.6	7.1
p-coumaric acid	6.3	11.6	5.1	5.1	1	1.2	1.2	1.9	2.4	1.3
ellagic acid	4.43	1.96	3.12	3.2	nd	nd	nd	nd	nd	nd
syringic acid	2.47	2.05	1.29	1.27	0.04	nd	0.02	0.05	0.02	0.03
syringaldehyde	0.22	0.33	0.28	0.06	nd	nd	nd	nd	nd	nd
cis-coutaric acid	0.4	0.5	2.8	1.3	1.2	1.6	0.9	0.4	1.3	1.2
trans-coutaric acid	1.9	2.3	14.7	6.7	2	2.4	2.5	0.5	3.7	4
vanillic acid	0.96	0.82	0.9	0.49	nd	nd	0.01	0.06	0.01	0.02
vanillin	0.14	0.15	0.13	0.04	nd	nd	nd	nd	nd	nd
fertaric acid	0.4	0.5	1.7	1.1	1.7	1.2	1.7	0.3	1.8	6.5
ferulic acid	1.9	1.9	1	0.8	0.8	0.6	0.8	0.9	0.8	0.9
scopoletin (μg/L)	63	146	35	21	nd	nd	nd	nd	nd	nd

[a]Results are expressed as mg/L. R1, Blauer Burgunder 2010; R2, Rösler 2009; R3, Cabernet Sauvignon-Merlot 2009; R4, Zweigelt Reserve 2009 (Rosner); W1, Grüner Veltliner 2010 (Rosner); W2, Gelber Muskateller 2010; W3, Grüner Veltliner 2010; W4, Chardonnay Eiswein 2009; W5, Chardonnay 2010; W6, Riesling 2010. [b] nd, not detected.

wines to nearly similar amounts as in red wine samples. Coniferylaldehyde and sinapaldehyde were not detected, either in white or in red wine. The phenolic compound with the highest amounts in wine samples was catechin, with concentrations ranging from 29.5 to 85.5 mg/L in red wines and from 1.8 to 4.8 mg/L in white wines.

Correlation between IPX and Wine Parameters. To determine which of the wine constituents quantified correlate with the stimulatory effect of wine samples on proton secretion in HGT-1 cells, the IPX data of the 10 wine samples were correlated with the amount of organic acids and phenolic compounds. Table 4 shows the results of the correlation analysis. Negative correlations indicating a pro-secretory effect were determined for lactic acid, procyanidins B1 and B2, ellagic acid, syringic acid, syringaldehyde, vanillic acid, and vanillin. According to the hypothesis that a higher amount of hydroxyl and carboxyl groups induces gastric acid secretion, we further investigated procyanidin B2 (10 hydroxyl groups) and syringic acid (1 hydroxyl and 1 carboxyl group). Because catechin (5 hydroxyl groups) showed the highest amount in the red wine samples of the measured phenolic compounds and is the parent structure of procyanidin B2 and several other phenolic compounds in wine, it has been included for further analysis. In addition, lactic and malic acid were investigated because both are present only either in white or in red wine.

Effect of DL-Lactic Acid and L-Malic Acid on Intracellular Proton Concentration. L-Malic and DL-lactic acid were tested in a concentration range quantified in the 10 wine samples, namely, 20−40 and 30−60 mg/L, respectively (Figure 2). Both organic acids stimulated proton secretion ($p < 0.001$) in HGT-1 cells in a concentration-dependent manner compared to nontreated cells (lactic acid, −0.30 ± 0.01 to −0.52 ± 0.02; malic acid, IPX ranging from −0.26 ± 0.03 to −0.44 ± 0.03).

Gene Expression of HGT-1 Cells after Treatment with Lactic Acid and Malic Acid. To gain a mechanistic insight into whether DL-lactic acid or L-malic acid affects the regulation of secretory-relevant genes, HGT-1 cells were treated with 10 mg/mL DL-lactic or L-malic acid over a time period of 30 min, and gene expression of *ATP4A*, *HRH2*, *SSTR2*, and *CHRM3* was determined by qPCR.

Gene expression of the target genes is presented as ratios normalized to the endogenous control *PPIA* (control = 1) (Figure 3). Treatment of HGT-1 cells with lactic acid or malic acid down-regulated expression of *ATP4A* and *HRH2* at 10 min (*ATP4A*, 0.57 ± 0.06 and 0.55 ± 0.06; *HRH2*, 0.66 ± 0.09 and 0.54 ± 0.08, respectively). None of the tested organic acids affected the expression levels of *CHRM3*. The main difference in effects between DL-lactic acid and L-malic acid were detected on expression levels of *SSTR2*. L-Malic acid reduced expression of *SSTR2* at 10 min (0.64 ± 0.08, $p < 0.01$). In contrast, DL-lactic acid increased mRNA expression of *SSTR2* at 25 min (1.29 ± 0.08, $p < 0.05$), an effect that was significantly different from that of L-malic acid at 25 min (0.95 ± 0.08, $p < 0.01$).

Effect of Catechin, Procyanidin B2, and Syringic Acid on Intracellular Proton Concentration. Catechin, syringic acid, and procyanidin B2 were tested in a wine representative concentration range. Catechin in the range of 0.1−1 mg/L stimulated proton secretion (IPX, −0.27 ± 0.03) as well as procyanidin B2 in the concentration range of 0.01−0.25 mg/L and syringic acid in the concentration range of 0.1−2.5 mg/L to

DOI: 10.1021/acs.jafc.5b02879
J. Agric. Food Chem. 2015, 63, 7775−7783

Table 4. Significant Results of the Correlation Analysis after Spearman between IPX Values and Phenolic Wine Compounds[a]

	all wines		
IPX mean vs	correlation coefficient	*P* two-ways	*n*
tartaric acid	−0.377	0.283	10
malic acid	**0.696***	**0.025**	**10**
lactic acid	**−0.792****	**0.006**	**10**
citric acid	0.483	0.157	10
succinic acid	−0.491	0.150	10
oxalic acid	0.290	0.416	10
acetic acid	−0.525	0.119	10
SO_2 total (acid)	0.006	0.987	10
phenols (g/L)	−0.763*	0.010	10
anthocyanins	−0.751*	0.012	10
catechin	**−0.588**	**0.074**	**10**
epicatechin	−0.600	0.067	10
gallic acid	−0.401	0.250	10
procy B1	−0.669*	0.034	10
procy B2	**−0.792****	**0.006**	**10**
caffeic acid	−0.474	0.166	10
caftaric acid	0.188	0.603	10
tyrosol	−0.455	0.187	10
p-coumaric acid	−0.463	0.177	10
ellagic acid	−0.683*	0.030	10
syringic acid	**−0.675***	**0.032**	**10**
syringaldehyde	−0.751*	0.012	10
cis-coutaric acid	0.116	0.749	10
trans-coutaric acid	0.261	0.467	10
vanillic acid	−0.659*	0.038	10
vanillin	−0.778**	0.008	10
fertaric acid	0.509	0.133	10
ferulic acid	−0.466	0.175	10
scopoletin (μg/L)	−0.673	0.033	10

[a]Significant differences are indicated by *, $p < 0.05$; **, $p < 0.01$. Compounds that were used for further analyzes are in boldface.

the highest extent, with IPX values of −0.17 ± 0.03 and −0.25 ± 0.05, respectively (Figure 4).

Enhancing the Stimulating Effect of White Wine on Proton Secretion via Addition of a Phenolic Recombinate. To verify that catechin, syringic acid, and procyanidin B2 can stimulate proton secretion in a complex wine matrix, a recombination of these substances in two concentrations was added to the white wine of the variety Riesling (W6). This wine showed the lowest pro-secretory activity (Table 2). Treatment of the cells with the W6 sample in combination with three phenolic compounds in concentrations representative for red wine led to IPX values of −0.14 ± 0.02 ($p < 0.05$), whereas treatment with a 2-fold addition of the recombinate (IPX, −0.16 ± 0.02) increased the proton secretion by 65 ± 21% ($p < 0.05$) compared to the cells treated with the white wine solely (IPX, −0.10 ± 0.02) (Figure 5).

DISCUSSION

In two previous studies, red wine was demonstrated to stimulate gastric acid secretion to a greater extent than white wine. However, because one of these studies was carried out in dogs with vagally denervated Haidenhain pouches[20] and in the other study only one red wine was tested versus one white wine in six

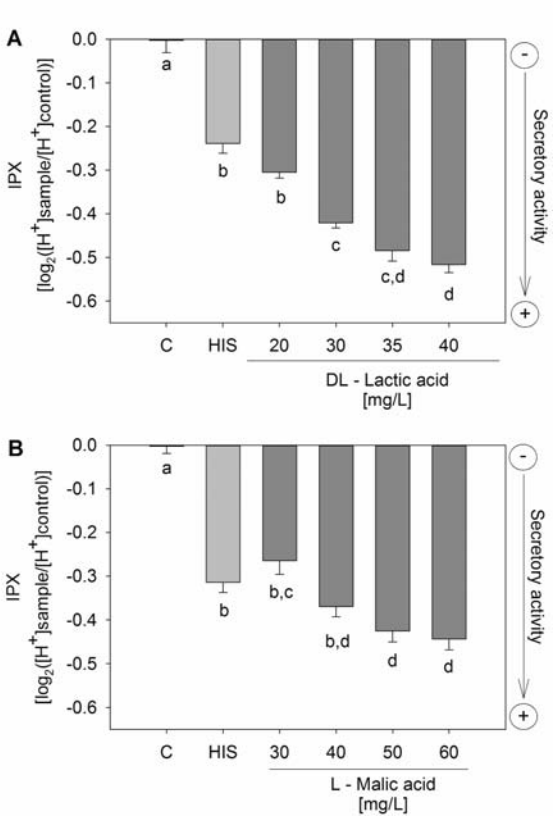

Figure 2. Intracellular proton index (IPX) of HGT-1 cells treated for 10 min with (A) DL-lactic acid and (B) L-malic acid in different wine representative concentrations. The control (C) was nontreated cells, and the positive control was 1 mM histamine (HIS). Data are displayed as the mean ± SEM, $n = 3$, tr = 4−6 (statistics: one-way ANOVA with the Holm−Sidak post hoc test; letters indicate significant differences between groups, $p < 0.05$).

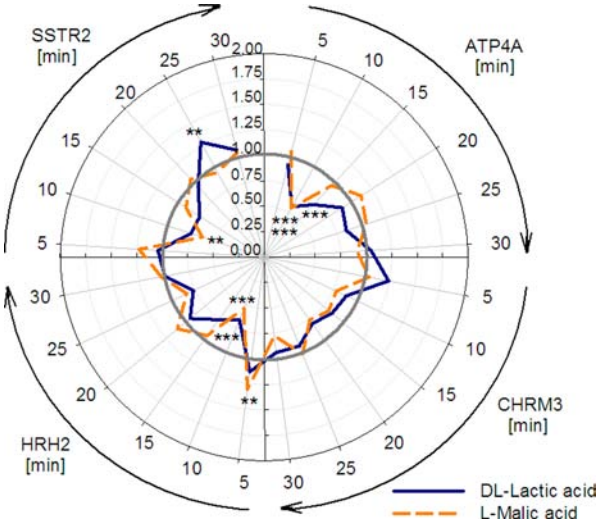

Figure 3. Time-dependent indices of gene expression for *ATP4A*, *CHRM3*, *HRH2*, and *SSTR2* in HGT-1 cells after treatment with 10 mg/L DL-lactic acid and 10 mg/L L-malic acid compared to nontreated cells. Data are displayed as mean values, $n = 3$, tr = 3 (statistics: two-way ANOVA with Holm−Sidak post hoc test; **, $p < 0.01$; ***, $p < 0.001$).

healthy subjects,[3] we hypothesized here that (i) the more pronounced effect of red wine is reproducible for a greater variety of wines and (ii) major quantitative differences in red and white

DOI: 10.1021/acs.jafc.5b02879
J. Agric. Food Chem. 2015, 63, 7775−7783

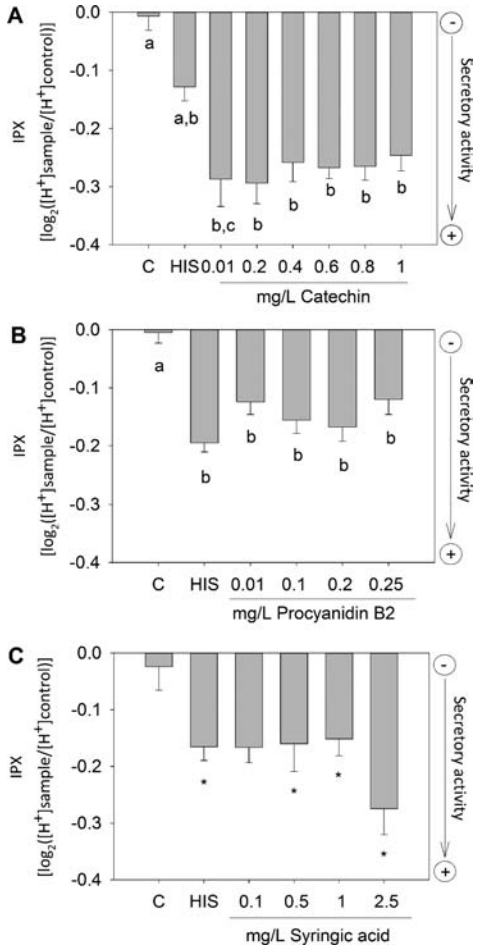

Figure 4. Intracellular proton index (IPX) of HGT-1 cells after treatment with (A) catechin, (B) procyanidin B2, (C) syringic acid in wine represantitive concentrations. The control (C) was nontreated cells and the positive control was 1 mM histamine (HIS). Data are displayed as mean ± SEM, n = 4, tr = 4-6, (statistics: one-way ANOVA with the Holm−Sidak post hoc test; letters indicate significant differences between groups, $p < 0.05$)

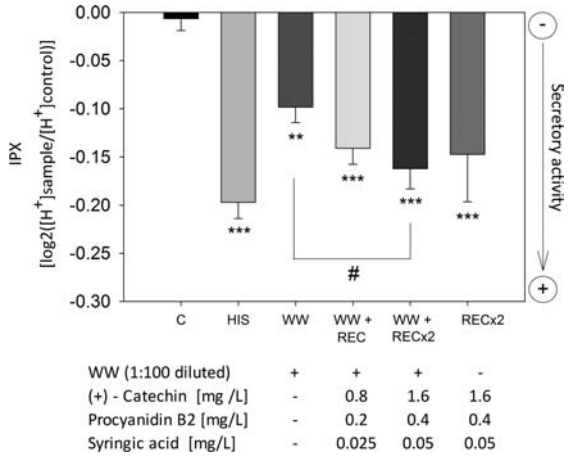

Figure 5. Intracellular proton index (IPX) of HGT-1 cells after treatment with white wine of the variety Riesling (2010) with or without recombinates of catechin, syringic acid, procyanidin B2 (REC) in red wine representative concentrations. The control (C) was nontreated cells and the positive control was 1 mM histamine (HIS). Data are displayed as mean ± SEM, n = 5-11, tr = 6, (statistics: one-way ANOVA with the Holm−Sidak post hoc test vs. Control; Student's t-test WW vs. WW + REC × 2, #, $p < 0.05$; **, $p < 0.01$; ***, $p < 0.001$)

wine contribute to this effect. Forty wine parameters were analyzed in four red wine samples and in six white wine samples. The major quantitative differences were analyzed for two classes of compounds: the organic acids malic acid and lactic acid, which were quantified in only white and red wine samples, respectively, and phenolic compounds. Correlation analysis between the quantitative data of the given constituents and the proton secretory activity of the 10 wine samples in parietal HGT-1 cells, a well-established cell culture model representing mechanisms of gastric acid secretion in humans,[3,7,16,18] revealed significant associations for the two organic acids as well as the phenolic compounds procyanidins B1 and B2, ellagic acid, syringic acid, syringaldehyde, vanillic acid, vanillin, and scopoletin. Because the red wine samples were, again, demonstrated to stimulate more pronounced proton secretion compared to the white wines, the contribution of malic acid, lactic acid, and selected phenolic compounds was studied.

In one of our previous studies, malic acid and lactic acid were identified to increase proton secretion in HGT-1 cells, independent of the ethanol content of the wine sample.[3] However, this finding was left on a descriptive level because no mechanistic data were provided. In this study, we were able to demonstrate that both organic acids regulate the mRNA expression of gene involved in proton secretion to a similar extent when tested in wine-representative concentrations, which is in line with their effect on proton secretion. However, the proton secretory activity of malic and lactic acid cannot chiefly account for the different effect of red versus white wine, because malic acid was only quantified in white wine, whereas lactic acid, in a similar concentration range, was quantified in red wine solely. This can be explained by the fact that the majority of red wines undergo malolactic fermentation, whereas this technology is less commonly used for the production of white wines.[33] In malolactic fermentation, a secondary fermentation after completion of the alcoholic fermentation, L-malic acid is transformed to the less sour L-lactic acid.[34] This reaction is used to reduce the acidic taste, to modify the organoleptic character, and to improve the microbial stability of wine.[33] Although the malolactic fermentation makes the red wine taste smoother, our findings suggest that this technology does not reduce its secretory potential.

Phenolic compounds were also hypothesized to contribute to the gastric acid secretory potential of red wine. This hypothesis was not only based on the quantitative differences of phenolic compounds in red versus white wine and their correlation with the effect on proton secretion. Previous results from Teyssen et al.[22] and our own group[3] suggest that the length of the carbon chain and the presence of carboxylic and hydroxyl groups are structural determinants for compounds to stimulate gastric acid secretion. Therefore, procyanidin B2 (10 hydroxyl groups, complex carbon molecule structure, bitter and astringent taste) and syringic acid (1 hydroxyl and 1 carboxyl group, astringent taste) as well as catechin as parent structure (10 hydroxyl groups, bitter taste, and astringent compound) were selected. For all three phenolic compounds, a contribution to bitter and/or astringent taste of wine has been reported.[35] To our knowledge, this is the first study that tested and demonstrated a stimulating effect of phenolic compounds on gastric acid secretion in wine-representative concentrations. Furthermore, when these compounds were added to the least active white wine (Riesling W6)

DOI: 10.1021/acs.jafc.5b02879
J. Agric. Food Chem. 2015, 63, 7775−7783

in concentrations 2-fold higher than those quantified in red wine, a significant increase in proton secretion was determined. This result clearly demonstrates that catechin and syringic acid as well as procyanidin B2 elicit a pro-secretory activity even when added to a complex solution such as white wine. Moreover, we suggest that the higher amount of phenolic compounds in red wine contributes to its higher stimulatory effect on gastric acid secretion compared to white wine. The majority of phenolic compounds in red wine are condensation products of flavan-3-ol units, which join to form oligomer structures (procyanidins) and polymers (condensed tannins). The monomers, epicatechin and catechin, are the most abundant units of procyanidins and condensed tannins.[36] Condensed tannins or higher oligomers of procyanidins are difficult to isolate or synthesize and, for most of them, not commercially available. However, in this study we showed that catechin, the monomer of procyanidins, and procyanidin B2, a dimer of epicatechin, stimulated proton secretion, indicating that the degree of polymerization might play a role in the proton secretory potential of procyanidins.

In conclusion, we have demonstrated that red wines stimulated mechanisms of gastric acid secretion more effectively than white wines. Furthermore, we showed for the first time that the organic acids DL-lactic acid and L-malic acid regulate gene expression relevant for gastric acid secretion. In addition, the phenolic constituents catechin, procyanidin B2, and syringic acid were demonstrated to stimulate proton secretion in gastric parietal cells and are suggested to contribute to the more pronounced effect of red wine on gastric acid secretion compared to white wine.

AUTHOR INFORMATION

Corresponding Author

*(V.S.) E-mail: veronika.somoza@univie.ac.at.

Funding

Financial support by the Austrian Federal Ministry of Economy, Family and Youth, and the Austrian National Foundation for Research, Technology and Development is also gratefully acknowledged.

Notes

The authors declare no competing financial interest.

ACKNOWLEDGMENTS

We thank Dr. C. L. Laboisse (Inserm 94-04, Faculté de Medicine, Nantes, France) for kindly providing the HGT-1 cells, clone 6.

REFERENCES

(1) Rubach, M.; Lang, R.; Bytof, G.; Stiebitz, H.; Lantz, I.; Hofmann, T.; Somoza, V. A dark brown roast coffee blend is less effective at stimulating gastric acid secretion in healthy volunteers compared to a medium roast market blend. *Mol. Nutr. Food Res.* **2014**, *58*, 1370.

(2) Cohen, M. M.; Debas, H. T.; Holubitsky, I. B.; Harrison, R. C. Caffeine and pentagastrin stimulation of human gastric secretion. *Gastroenterology* **1971**, *61* (4), 440−444 Is registered at pubmed: under the pubmed identification number: PMID: 4939934.

(3) Liszt, K. I.; Walker, J.; Somoza, V. Identification of organic acids in wine that stimulate mechanisms of gastric acid secretion. *J. Agric. Food Chem.* **2012**, *60*, 7022−7030.

(4) Singer, M. V.; Leffmann, C.; Eysselein, V. E.; Calden, H.; Goebell, H. Action of ethanol and some alcoholic beverages on gastric-acid secretion and release of gastrin in humans. *Gastroenterology* **1987**, *93*, 1247−1254 Is registered at pubmed: under the pubmed identification number: PMID: 3678743.

(5) Teyssen, S.; Lenzing, T.; González-Calero, G.; Korn, A.; Riepl, R. L.; Singer, M. V. Alcoholic beverages produced by alcoholic fermentation but not by distillation are powerful stimulants of gastric acid secretion in humans. *Gut* **1997**, *40*, 49−56.

(6) Peterson, W. L.; Barnett, C.; Walsh, J. H. Effect of intragastric infusions of ethanol and wine on serum gastrin concentration and gastric acid secretion. *Gastroenterology* **1986**, *91*, 1390−1395.

(7) Walker, J.; Hell, J.; Liszt, K. I.; Dresel, M.; Pignitter, M.; Hofmann, T.; Somoza, V. Identification of beer bitter acids regulating mechanisms of gastric acid secretion. *J. Agric. Food Chem.* **2012**, *60*, 1405−1412.

(8) Schubert, M. L. Gastric secretion. *Curr. Opin. Gastroenterol.* **2010**, *26*, 598−603.

(9) Katz, P. O.; Johnson, D. A. Control of intragastric pH and its relationship to gastroesophageal reflux disease outcomes. *J. Clin. Gastroenterol.* **2011**, *45*, 748−754.

(10) El-Serag, H. B.; Sweet, S.; Winchester, C. C.; Dent, J. Update on the epidemiology of gastro-oesophageal reflux disease: a systematic review. *Gut* **2014**, *63*, 871−880.

(11) Pehl, C.; Wendl, B.; Pfeiffer, A. White wine and beer induce gastro-oesophageal reflux in patients with reflux disease. *Aliment. Pharmacol. Ther.* **2006**, *23*, 1581−1586.

(12) Seidl, H.; Gundling, F.; Schepp, W.; Schmidt, T.; Pehl, C. Effect of low-proof alcoholic beverages on duodenogastro-esophageal reflux in health and GERD. *Neurogastroenterol. Motil.* **2011**, *23*, 145−150 e29.

(13) Konturek, S. J.; Brzozowski, T.; Konturek, P. C.; Schubert, M. L.; Pawlik, W. W.; Padol, S.; Bayner, J. Brain-gut and appetite regulating hormones in the control of gastric secretion and mucosal protection. *J. Physiol. Pharmacol.* **2008**, *59* (Suppl. 2), 7−31.

(14) Rubach, M.; Lang, R.; Hofmann, T.; Somoza, V. Time-dependent component-specific regulation of gastric acid secretion-related proteins by roasted coffee constituents. *Ann. N. Y. Acad. Sci.* **2008**, *1126*, 310−314.

(15) Carmosino, M.; Procino, G.; Casavola, V.; Svelto, M.; Valenti, G. The cultured human gastric cells HGT-1 express the principal transporters involved in acid secretion. *Pflugers Arch.* **2000**, *440*, 871−880.

(16) Weiss, C.; Rubach, M.; Lang, R.; Seebach, E.; Blumberg, S.; Frank, O.; Hofmann, T.; Somoza, V. Measurement of the intracellular ph in human stomach cells: a novel approach to evaluate the gastric acid secretory potential of coffee beverages. *J. Agric. Food Chem.* **2010**, *58*, 1976−1985.

(17) Rubach, M.; Lang, R.; Skupin, C.; Hofmann, T.; Somoza, V. Activity-guided fractionation to characterize a coffee beverage that effectively down-regulates mechanisms of gastric acid secretion as compared to regular coffee. *J. Agric. Food Chem.* **2010**, *58*, 4153−4161.

(18) Rubach, M.; Lang, R.; Seebach, E.; Somoza, M. M.; Hofmann, T.; Somoza, V. Multi-parametric approach to identify coffee components that regulate mechanisms of gastric acid secretion. *Mol. Nutr. Food Res.* **2012**, *56*, 325−335.

(19) Lang, R.; Bardelmeier, I.; Weiss, C.; Rubach, M.; Somoza, V.; Hofmann, T. Quantitation of *β-N*-akanoyl-5-hydroxytryptamides in coffee by means of LC-MS/MS-SIDA and assessment of their gastric acid secretion potential using the HGT-1 cell assay. *J. Agric. Food Chem.* **2010**, *58*, 1593−1602.

(20) Tsukimi, Y.; Ogawa, T.; Okabe, S. Pharmacological analysis of wine-stimulated gastric acid secretion in dogs. *J. Physiol. Paris* **2001**, *95*, 221−228.

(21) Teyssen, S.; González-Calero, G.; Korn, A.; Singer, M. V. Action of ethanol and some alcoholic beverages on gastric acid secretion in anaesthetized rats. *Alcohol Alcohol.* **1997**, *32*, 23−31.

(22) Teyssen, S.; Gonzalez-Calero, G.; Schimiczek, M.; Singer, M. V. Maleic acid and succinic acid in fermented alcoholic beverages are the stimulants of gastric acid secretion. *J. Clin. Invest.* **1999**, *103*, 707−713.

(23) Ono, K.; Sawada, T.; Murata, Y.; Saito, E.; Iwasaki, A.; Arakawa, Y.; Kurokawa, K.; Hashimoto, Y. Pentagalloylglucose, an antisecretory component of Paeoniae radix, inhibits gastric H+, K(+) ATPase. *Clin. Chim. Acta* **2000**, *290*, 159−167.

(24) Eder, R.; Brandes, W. *Weinanalysen im eigenen Betrieb: Grundparameter*; Verlag Eugen-Ulmer, Agrarverlag: Stuttgart, Germany, 2003.

DOI: 10.1021/acs.jafc.5b02879
J. Agric. Food Chem. 2015, 63, 7775−7783

(25) Paul, F. Die alkalimetrische Bestimmung der freien, gebundenen und gesamten schwefligen Säure mittels des Apparates von Lieb und Zacherl. *Mitt. Klosterneuburg* **1958**, *4a*, 225−234.
(26) Prasnikar, N.; Hann, S.; Eder, R. Orange-Weine − Erfassung der chemisch-physikalischen Zusammensetzung. *Dtsch. Lebensm. Rundsch.* **2014**, *110*, 383−390.
(27) Lafon-Lafourcade, S. Application des méthodes enzymatiques à l'analyse des mouts et des vins. *Ann. Nutr. Aliment.* **1978**, *32*, 969−974.
(28) Stojanović, N.; Rogić, D.; Stavljenić-Rukavina, A. Evaluation of the Konelab 20XT clinical chemistry analyser. *Clin. Chem. Lab. Med.* **2005**, *43*, 646−653.
(29) Matejícek, D.; Klejdus, B.; Mikes, O.; Sterbová, D.; Kubán, V. Application of solid-phase extraction for determination of phenolic compounds in barrique wines. *Anal. Bioanal. Chem.* **2003**, *377*, 340−345.
(30) Vrhovsek, U.; Wendelin, S.; Eder, R. Quantitative Bestimmung von Hydroxyzimtsäuren und Hydroxyzimtsäurederivaten (Hydroxycinnamaten) in Weißweinen mittels HPLC. *Mitt. Klosterneuburg* **1997**, *47*, 164−172.
(31) Eder, R.; Beyer, B.; Patzl-Fischerleitner; Wendelin, S.; Hann, S. Determination of pyranoanthocyane and malvidin-3-glucoside content in red wines of different vintages via LC-MS/ESI. *Mitt. Klosterneuburg* **2014**, *64*, 183−192.
(32) Linskens, H. F.; Jackson, J. F. *Wine Analysis. Modern Methods of Plant Analysis*; Springer Verlag: Heidelberg, Germany, 1988.
(33) Volschenk, H.; van Vuuren, H. J. J.; Viljoen-Bloom, M. Malic acid in wine: origin, function and metabolism during vinification. *S. Afr. J. Enol. Vitic.* **2006**, *27*, 123−136.
(34) Lerm, E.; Engelbrecht, L.; du Toit, M. Malolactic fermentation: the ABC's of MLF. *S. Afr. J. Eno. Vitic.* **2010**, *31*, 186−212.
(35) Hufnagel, J. C.; Hofmann, T. Orosensory-directed identification of astringent mouthfeel and bitter-tasting compounds in red wine. *J. Agric. Food Chem.* **2008**, *56*, 1376−1386.
(36) Waterhouse, A. L. Wine phenolics. *Ann. N. Y. Acad. Sci.* **2002**, *957*, 21−36.

DOI: 10.1021/acs.jafc.5b02879
J. Agric. Food Chem. 2015, 63, 7775−7783

Table 1. Chemical Structures of Dietary Flavonoids and Their Affinities for XO and XO Inhibitory Activities

Subclass	Name	Substitutions: OH	Substitutions: Others	α	Type	lgK_a
Flavones	Chrysin	5,7		0.50	com	6.84
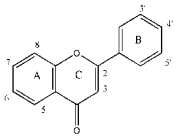	Apigenin	5,7,4'		1.20	com[19]	5.09
	Luteolin	5,7,3',4'		3.01	com[23]	3.80
	Baicalein	5,6,7		5.44	mix	6.70
	Baicalin	5,6	7-β-D-glucuronide	50.13	mix	3.36
Flavonols	Galangin	3,5,7		2.35	com	6.53
	Kaempferol	3,5,7,4'		5.76	com[10]	4.51
	Quercetin	3,5,7,3',4'		9.76	com[19]	5.76
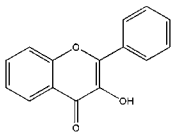	Morin	3,5,7,2',4'		21.87	mix[22]	5.25
	Myricetin	3,5,7,3',4',5'		35.75	mix[19]	4.95
	Diosmetin	5,7,3'	4'-o-methyl	12.24	mix	3.81
	Isorhamnetin	3,5,7,4'	3'-o-methyl	10.10	mix	3.84
	Hyperin	5,7,3',4'	3-o-galactose	41.04	mix	3.41
	Rutin	5,7,3',4'	3-α-L-rham-1,6-D-glc	57.29		3.01
Isoflavones	Genistein	5,7,4'		0.59	com[19]	4.72
Flavanone	Naringenin[b]	5,7,4'		140.41		4.55
	Silybin[b]	3,5,7		189.62	mix[9]	4.42
Others	Epicatechin[b]	—				3.05
	Phloretin[a]	—				4.54
	Curumin[a]	—				3.57

[a]Structure has no bicyclic benzopyranone ring. [b]C2−C3 is saturated, com = competitive, mix = mixcompetitive.

flavonoids on the basis of their structure[22] and concluded that the hydroxyl groups on the C-5 and C-7 of flavnoids were favorable for XO inhibition.[21,22] However, few investigations have examined the interactions of flavonoid−XO and the inhibitory activities of flavonoids against XO.

In this study, the inhibitory activities against XO of 20 flavonoids with C5−OH and C7−OH, which mimic the structural frame of xanthine (Figure 1), were determined

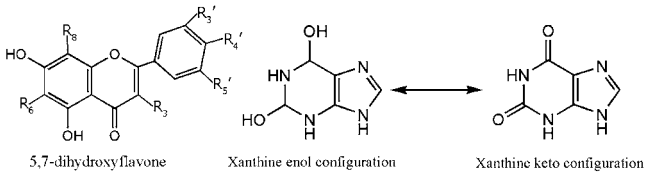

Figure 1. Comparison of structure similarities of xanthine enol form with 5,7-dihydroxylflavone. Structural similarity between xanthine enol form and 5,7-dihydroxylflavone suggests a similar binding location in XO allosteric center.

through UV spectrometry, and their binding affinities for XO were obtained by fluorescence titration method. With the application of molecular simulation, both the structure−activity relationship for inhibitory effects of flavonoids on XO and the relationship between the binding affinities and inhibitory activities were discussed. This study affords the opportunity to further explore the potential of these flavonoid-rich products for a successful application as gout-treating functional nutrients, especially by increasing their anti-XO effects and maintaining low side effects. It also provides new insights into clinical research of flavonoids as effective XO inhibitors.

MATERIALS AND METHODS

Materials. XO (35.7 units mL^{-1}, from bovine milk) and xanthine were both purchased from Sigma-Aldrich Co. (St. Louis, MO, USA) and then prepared as stock solutions with 50 M Tris-HCl buffer (pH 7.4). The stock solutions of XO and xanthine were freshly prepared just before the experiments. Luteolin, rutin, quercetin, morin, myricetin, myricetrin, and epicatechin were from Aladdin Reagent Int. (Shanghai, China). Chrysin, apigenin, galangin, kaempferol, diosmetin, hyperin, and curcumin were purchased from National Institute for the Control of Pharmaceutical and Biological Products (Beijing, China), and phloretin was from Shanghai Yuanye Bio-Technology Co., Ltd. They were all dissolved in absolute ethyl alcohol to prepare stock solutions (5.0×10^{-3} mol L^{-1}), and the final alcoholic concentrations in the experiments were <1%, thus avoiding effects on the structure and activity of XO. All other reagents were of analytical reagent grade, and fresh ultrapure water (18.2 MΩ cm) used throughout the study was produced by a Millipore Simplicity Water Purification System (Millipore, Molsheim, France).

Cell-free Enzyme Activity. A Shimadzu UV-2450 spectrophotometer (Shimadzu, Japan) with a 1.0 cm quartz cell was used in the enzyme activity assay. The inhibition of XO was measured by using the method described previously.[10] Briefly, an array of 2 mL mixtures of XO solution (75 nM), Tris-HCl buffer, and various concentrations of tested flavonoid solutions was incubated for 3 h at 37 °C. The reaction was started by adding substrate xanthine (the final concentration was 50 μM), and the absorbance of the mixture was measured spectrophotometrically by continuously recording uric acid formation at 290 nm every 5 s. The enzymatic activity assay without inhibitor was defined as 100%. Thus, the relative enzymatic activity (%) = (S_{sample})/

DOI: 10.1021/acs.jafc.5b03386
J. Agric. Food Chem. 2015, 63, 7784−7794

(S_{blank}) × 100%, where S_{sample} is the slope of the reaction kinetics equation obtained from the reaction with inhibitor and S_{blank} is the slope of the reaction kinetics equation obtained from the reaction without inhibitor. Allopurinol was used as the positive control. All assays were run in triplicate at minimum. The concentration of inhibitor required for 50% inhibition of XO activity (IC_{50}) was assessed by plotting the relative enzymatic activity against the corresponding inhibitor concentration.

Kinetic Analysis for Inhibitory Type. The same method as XO activity assay was used to determine the inhibitory type of flavonoids against XO.[23] The inhibition type of the tested flavonoids was analyzed by using the nonlinear regression Michaelis−Menten enzyme kinetics and the corresponding Lineweaver−Burk plots. Each concentration of the inhibitor (three different concentrations in each case) was mixed with four different concentrations of substrate. Each experiment was performed in triplicate.

Fluorescence Quenching Study of XO. The fluorescence spectra were recorded on a Hitachi spectrofluorometer (model F-7000, Hitachi, Japan) equipped with a 150 W xenon lamp and a thermostat bath. The excitation wavelength was 280 nm, and the excitation and emission bandwidths were both set at 2.5 nm. The fluorescence spectra of XO in the absence and presence of flavonoids were measured as reported earlier.[23]

Fluorescence Data Processing. To determine the quenching mechanism of flavonoid binding to XO, the fluorescence quenching data were described by the Stern−Volmer equation[24]

$$\frac{F_0}{F} = 1 + K_{SV}[Q] = 1 + K_q\tau_0[Q] \quad (1)$$

where F_0 and F represent the fluorescence intensities in the absence and presence, respectively, of flavonoids, [Q] is the concentration of flavonoids, K_q is the quenching rate constant, τ_0 is the average lifetime of the fluorophore in the absence of the quencher (its value for XO was 2.80×10^{-9} s),[10] and K_{SV} is the Stern−Volmer quenching constant. The binding constants (K_a) and the number of binding sites (n) were calculated according to the following formula:[25]

$$\log\frac{F_0 - F}{F} = n\log K_a - n\log\frac{1}{[Q_t] - n\frac{(F_0 - F)[P_t]}{F_0}} \quad (2)$$

All of the fluorescence data in this study were corrected for absorption of excitation light and reabsorption of emitted light according to the literature.[10]

Molecular Modeling. The molecular docking studies were carried out by the MGL tools 1.5.6 with AutoGrid4.0 and AutoDock4.0. It docked flexible ligand into the rigid protein conformationally and exhibited the detail of binding. The bovine milk XO (PDB code 3ETR) complexed with lumazine (substrate) was downloaded from the Protein Data Bank (http://www.rcsb.org/pdb). The 3D structures of ligands (flavonoids and allopurinol) were depicted in Chem3D Ultra 8.0. Before Gasteiger charges were assigned to the macromolecule file, all of the water molecules were removed and the hydrogen atoms were added. A dimension grid box (110 Å × 100 Å × 110 Å) was set up to enclose the active site with grid spacing of 0.37 Å. Docking calculations were performed with the default parameters except that the number of GA runs was set at 100 times. From the outcomes, the best-scoring docked model (the lowest docking energy) of the ligand was proposed as the feasible binding mode of the inhibitor in the active site of XO predicted by this program. The outputs were further rendered with Pymol to obtain visible combination models.

Statistical Analysis. All data for enzyme kinetic assays and plotting were obtained using Origin 8.0. Data were analyzed by one-way ANOVA for statistical significance using the SAS statistical package (SAS Institute, Cary, NC, USA). A p value of ≤0.05 was considered statistically significant.

RESULTS AND DISCUSSION

XO Inhibition. The inhibition of 20 flavonoids on XO was explored in vitro, and the results in the form of α (= $IC_{50(flavonoid)}/IC_{50(allopurinol)}$) are shown in Table 1. The inhibitory activities of flavonoids depended on their structures. The IC_{50} value of allopurinol was 2.93 μM. As a conclusion, it was possible to establish three distinct categories among all of the flavonoids studied. The first group was composed of the most active flavonoids with low α values (≤10). These compounds showed an inhibitory potency against XO in the micromolar range. The most active ones were chrysin and genistein (α values of 0.49 and 0.59, respectively) with α values below 1, indicating that less of these compounds was needed to inhibit XO compared with allopurinol. Additionally, quercetin (α = 9.76) and kaempferol (α = 5.76) were less active than apigenin (α = 1.20), which was consistent with previous results.[7,19,26] The second group referred to the flavonoids that expressed intermediate activity ($10 < \alpha \leq 50$). Most of them were flavonols, such as morin, myricetin, diosmetin, isorhamnetin, and hyperin. In the last group ($\alpha > 50$), compared with rutin (α = 57.29) and baicalin (α = 50.13), naringenin and silybin exhibited much weaker inhibition (α = 140.4 and 189.6, respectively). It could be found that these compounds all possessed a bulky substituent group. Phloretin, curcumin, and epicatechin did not even show XO inhibition activity.

Several studies have suggested the inhibitory ability of flavonoids on XO activity.[21,26,27] To further characterize the binding region in XO, the kinetic assay of some potent inhibitors ($\alpha \leq 50$) was conducted and Lineweaver−Burk double-reciprocal plots were applied. The results from the experiments and previous studies are summarized in Table 1. Allopurinol is a known competitive inhibitor. As shown in Figure 2a, inhibition of XO by chrysin was competitive, which was characterized by similar V_{max} and distinctly different K_m values, which was also seen for other flavones (apigenin and luteolin), suggesting binding of flavones to the XO active center, thereby replacing xanthine. Apigenin, kaempferol, and luteolin exhibited competitive inhibition (plot not shown), which conformed to the previous results that they could bind to XO at a single binding site and the binding was driven mainly by hydrophobic interactions.[10,23,28] Genistein and quercetin also exhibited competitive inhibition as reported previously.[19] Myricetin[19] showed mixed type inhibition (Figure 2b) as well as morin,[22] which can be concluded from different V_{max} and K_m values. These results indicated that some flavonoids are competitive or mixed competitive inhibitors of XO.

Quenching Effect of Flavonoids on XO Fluorescence. The fluorescence spectra of XO quenched by flavonoids were investigated. All flavonoids tested could quench the fluorescence of XO sharply with increasing concentrations. As representative cases, the fluorescence spectra of XO in the presence of chrysin (Figure 3a), phloretin (Figure 3b), myricetin (Figure 3c), and genistein (Figure 3d) are displayed. There were no obvious shifts in the peak at 340 nm of XO fluorescence for chrysin and genistein, whereas the maximum peak (λ_{em} = 340 nm) of XO fluorescence was obviously blue-shifted in the presence of phloretin and myricetin, suggesting that they were placed in a more hydrophobic environment;[29] that is, the molecular conformation of XO was affected. Individually, phloretin exhibited a slight affinity for XO, but it was a very weak inhibitor toward XO, and this feature could also be seen in the curumin−XO and epicatechin−XO systems.

DOI: 10.1021/acs.jafc.5b03386
J. Agric. Food Chem. 2015, 63, 7784−7794

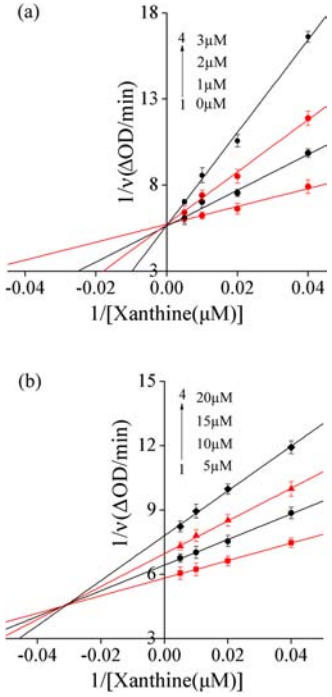

Figure 2. (a) Lineweaver–Burk plot for chrysin. The inhibition of XO by chrysin is competitive, as can be seen from similar V_{max} and distinctly different K_m values. (b) Lineweaver–Burk plot for myricetin. Inhibition of XO by myricetin shows mixed type inhibition, as can be concluded from different V_{max} and K_m values.

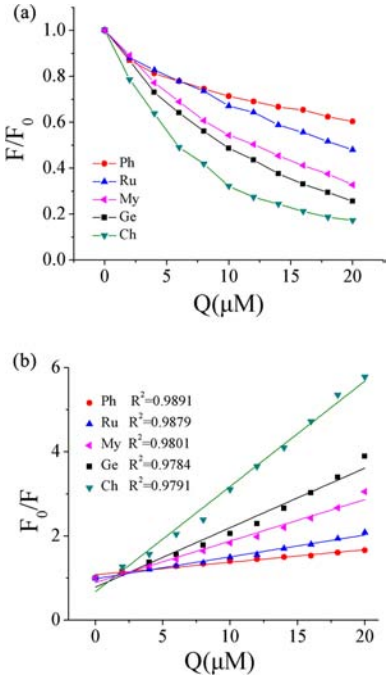

Figure 4. (a) Quenching ratio (F/F_0) of XO fluorescence spectra with addition of chrysin (Ch), myricetin (My), genistein (Ge), phloretin (Ph), and rutin (Ru). (b) Stern–Volmer plots for XO fluorescence quenching by these flavonoids at 298 K.

Moreover, different quenching ratios (F/F_0) of XO fluorescence with increasing flavonoid concentration were observed (Figure 4a). The fluorescence intensities of XO decreased sharply with increasing concentrations of chrysin, genistein, and myricetin, respectively, whereas the intensities of XO showed much slower decreasing rates with the addition of phloretin and rutin. Chrysin at 10.0 μM quenched the XO fluorescence by 69.4%; genistein, myricetin, and rutin quenched XO fluorescence by 51.9, 48.4, and 31.2%, respectively, but the corresponding concentration of phloretin quenched the XO

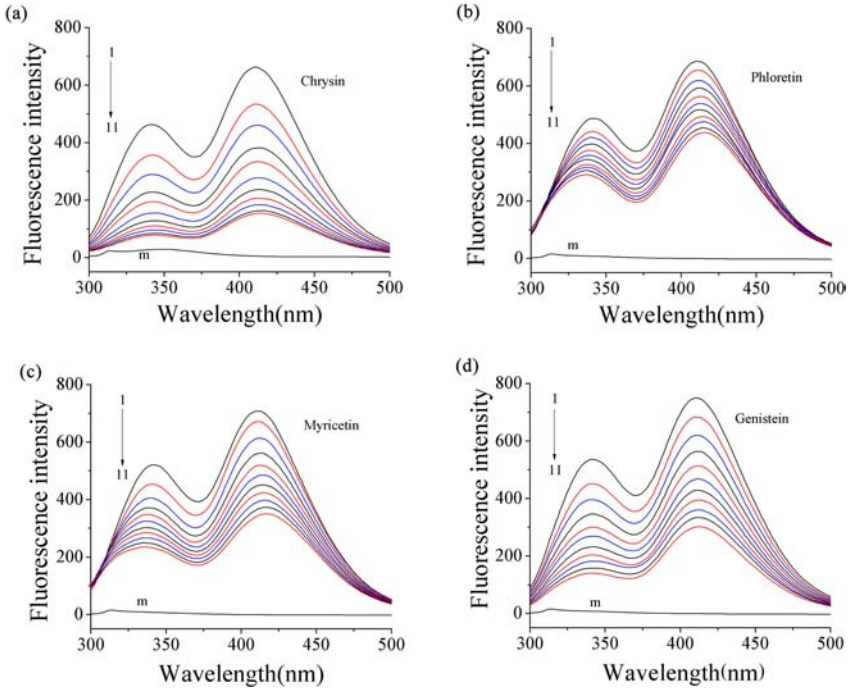

Figure 3. Quenching effects of chrysin (a), phloretin (b), myricetin (c), and genistein (d) on XO fluorescence spectra at 298 K. λ_{ex} = 280 nm. c(XO) = 0.5 μM. c(flavonoids) = 0, 2.0, 4.0, 6.0, 8.0, 10.0, 12.0, 14.0, 16.0, 18.0, and 20.0 μM for curves 1–11, respectively; curve m in every panel represents the individual spectrum of the corresponding flavonoid.

DOI: 10.1021/acs.jafc.5b03386
J. Agric. Food Chem. 2015, 63, 7784–7794

fluorescence by only 29.1%. These phenomena implied that the quenching of XO fluorescence might rely on the structures of flavonoids.

Figure 4b shows the Stern−Volmer plots for XO fluorescence quenching by chrysin, genistein, myricetin, rutin, and phloretin. The linear plots indicated that the K_{SV} and K_q values of XO fluorescence quenching by flavonoids could be assessed from eq 1. The calculated K_q values ($0.98-2.50 \times 10^{13}$ L mol^{-1} s^{-1}) were much higher than the maximum scatter collision quenching constant of various quenchers with a biopolymer (2.0×10^{10} L mol^{-1} s^{-1}), indicating that the fluorescence quenching of XO by flavonoid was probably initiated by static quenching resulting from the formation of the flavonoid−XO complex.[25,30] These results are in accordance with previous studies,[10,23] suggesting that the static fluorescence quenching of XO by morin, kaempferol, luteolin, and quercetin originated from the formation of the complexes.

Nature of Flavonoid−XO Noncovalent Interaction. Generally, the noncovalent interactions between flavonoids and proteins are caused by four major forms, namely, hydrogen bonding, van der Waals interaction, hydrophobic interaction, and electrostatic interaction.[29,30] The nature of the flavonoid−XO interaction was studied by investigating the molecular property−affinity relationship. Herein, the hydrogen bond acceptor/donor numbers and the lipophilicity of flavonoids were investigated. The relationships between the hydrogen bond acceptor/donor numbers (obtained from PubChem Public Chemical Database) of flavonoids and the affinities for XO (lg K_a) are shown in Figure 5a. The affinities for XO obviously decreased with increasing hydrogen bond acceptor numbers of flavonoids, which implied that the hydrogen-bonding force was not the main force in the binding of flavonoids to XO.[31]

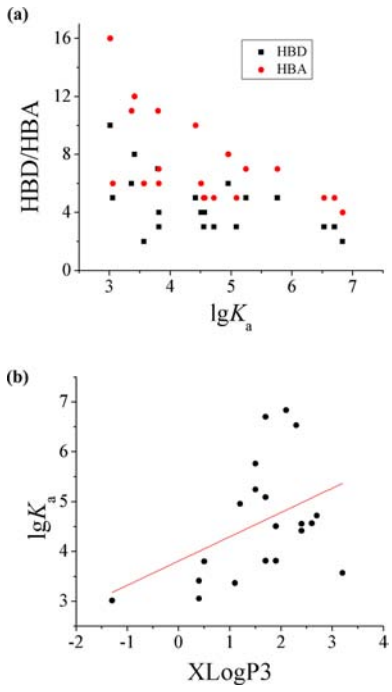

Figure 5. (a) Relationships of the hydrogen bond acceptor/donor number of flavonoids with the affinities (lg K_a) for XO. The hydrogen bond acceptor/donor numbers were taken from the PubChem Public Chemical Database. (b) Relationship of apparent binding constants (lg K_a) with partition coefficient (XLogP3) of flavonoids. The partition coefficient (XLogP3) was taken from the PubChem Public Chemical Database.

For an in-depth investigation of whether or not the lipophilicity played a main role in the binding of flavonoids to XO, the lipophilicity of the compounds under study was assessed by their partition coefficient values (XlgP3) according to the PubChem Public Chemical Database. As shown in Figure 5b, there was a relationship between XlgP3 values and lg K_a values for flavonoids. Generally, the binding affinities increased with an increase in the XLogP3 values. These results indicated that the hydrophobic force instead of lipophilicity may be the main acting force for driving the binding of flavonoids to XO, which was supported by the previous studies in some flavonoids.[32−34] In terms of these results, the noncovalent interaction between flavonoids and XO seemed to be different from the previously reported interaction of flavonoid−β-globulin[35] but similar to the interactions of flavonoid binding to serum albumin, hemoglobin,[29] common plasma proteins,[33] and milk proteins.[36]

Relationship between Affinities and XO Inhibitory Activities. XO is a dimer; each monomer contains an active site, which is believed to be surrounded by many amino acid residues.[37] Glu802, Glu1261, and Arg880 residues in the molybdenum center of the gorge play key roles in catalyzing xanthine oxidation,[38] whereas some residues at the entrance of the cavity, such as Leu648, Phe649, Phe914, Phe1009, Val1011, Phe1013, and Leu1014, modulate the entry of small molecules including substrates or inhibitors into the center.[10,23,37] For the inhibition on the catalytic activity of XO, flavonoids might directly enter the gorge to cover the active site or might just bind to the vicinity and hinder the entrance for xanthine. Thus, the relationship between the affinities for XO and their XO inhibition was discussed. Figure 6a shows that there was no obvious relationship between the affinities and inhibition for flavonoids,[39] but the inhibitory activities increased generally with the increasing affinities within the class of flavones and flavonols. These results might be due to the fact that the higher binding affinity increases the opportunity to enter and affect the catalytic site, whereas the inhibition finally rested with the direct interaction between the flavonoids and the active site. Interestingly, it was recently found that several clinically significant drug−enzyme complexes were similarly high-affinity active site-directed inhibitors that compete with substrates.[40]

Relationship between Topological Polar Surface Area (TPSA) and XO Inhibitory Activities. The TPSA is defined as the surface sum over all polar atoms. TPSA has been shown to be a descriptor characterizing passive molecular transport through membranes, which has been successfully used to predict the human intestinal absorption, bioavailability, Caco-2 monolayer permeability, and blood−brain barrier penetration.[41] It has been reported that molecules with a TPSA value of >140 Å^2 showed low human intestinal absorption and tended to be poor in permeating cell membranes.[42,43] The TPSA values were obtained from the PubChem Public Chemical Database. Figure 6b shows the relationship between TPSA and XO inhibitory activities of flavonoids. The relationship was not evident, but it might be roughly divided into four types considering their inhibitory activities. Type I was the most favorable group with high inhibitory activities (low α value) and penetration abilities (low TPSA), and type II was the less preferred group with good penetration abilities but low inhibitory activities (high α value). Although the flavonoids in type III group had great inhibitory activities on XO in vitro, little absorption may make them

DOI: 10.1021/acs.jafc.5b03386
J. Agric. Food Chem. 2015, 63, 7784−7794

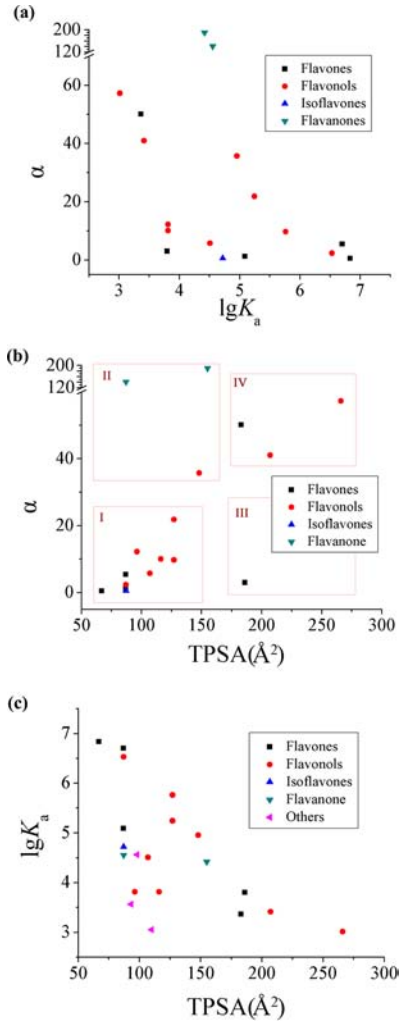

Figure 6. (a) Relationship of XO inhibitory activities (α) of flavonoids with affinities (lg K_a) for XO. (b) Relationship of TPSA with XO inhibitory activities (α) of flavonoids. (c) Relationship of TPSA with the affinities (lg K_a) of flavonoids for XO. The TPSA values were obtained online (www.molinspiration.com/cgi-bin/properties).

ineffective in treating gout. Type IV was supposed to be the most unfavorable inhibitor. Moreover, the binding affinity of flavonoids with XO was investigated (Figure 6c). TPSA values were found to generally decrease with increasing lg K_a flavonoids for XO, which was similar to the relationship as reported earlier between flavonoids and HSA.[35,43]

Structure–Activity of Flavonoids on XO Inhibition and Affinity for XO. *Hydroxylation.* Previous investigations have indicated that the patterns of the hydroxyl and methoxyl groups on the rings of flavonoids are involved in the bioactivities and binding affinities for proteins.[44−47] The effects of hydroxylation of flavonoids on their affinities for XO and XO inhibition are shown in Table 2. Baicalein with an extra C6−OH exhibited 9.84 times lower XO inhibition than chrysin, but their affinities did not change too much, indicating that the hydroxylation on the C6 (ring A) of flavones weakened the inhibitory activity obviously and the binding affinities slightly. Moreover, luteolin and quercetin with additional hydroxyl groups on position C3′ (ring B) showed 1.50 and 0.70 times lower inhibition than apigenin and kaempferol, respectively, whereas their affinity decreased by 0.25 and 0.28 times, respectively. Both the hydroxylation on C4′ (ring B) of chrysin (→apigenin) and galangin (→kaempferol) weakened their XO inhibition abilities by nearly 1.4 times. The hydroxylation on C5′ (ring B) of quercetin (→myricetin) decreased its inhibition and affinity by, respectively, 2.66 and 0.14 times.[48] These results indicated that the hydroxyl groups in the B ring may be particularly important for flavonoids in inhibiting XO and binding to XO. Consequently, the α values of galangin, kaempferol, quercetin, and myricetin increased gradually, indicating that the extra hydroxyl substituents in the B ring may be unfavorable for the inhibitory activity of flavonols. These results could be also concluded within flavones (Table 1). This may be explained by the fact that ring B was reported to stabilize in the hydrophobic region of XO;[26,28] therefore, the enhancive hydroxy groups were unfavorable for the stability of flavonols. Moreover, galangin (kaempferol) exhibited lower affinity and inhibition than chrysin (apigenin), implying that the presence of a hydroxyl group at position C3 of the flavone significantly reduced the ability to bind to XO as well as its inhibition on XO. This effect was also obtained in the inhibition of flavonoids toward lipoxygenase[39] and human aromatase (estrogen synthetase).[49]

Methylation. As shown in Table 2, the affinity of isorhamnetin for XO was weaker than that of its unmethoxylated form (kaempferol) by 0.37 times, indicating that an additional methoxy group at C5′ (ring B) decreased their binding affinities for XO. C4′-methylation of luteolin (→diosmetin) hardly affected the affinity for XO, with similar values of lg K_a, but in both conditions, their inhibition on XO obviously decreased. However, a previous study found that the methylation of hydroxyl groups in flavonoids enhanced their binding affinities for HSA by 2−16 times.[33] Here, the methylation of flavonoids exhibited great effect on the

Table 2. Effects of Hydroxylation and Methylation of Flavonoids on Their Affinities for XO and XO Inhibitory Activities

subclass	structural alteration	example	effects (times) affinity	activity
flavones	3′H → OH	apigenin → luteolin	0.25↓	1.50↓
	4′H → OH	chrysin → apigenin	0.25↓	1.41↓
	6H → OH	chrysin → baicalein	0.02↓	9.84↓
	3H → OH	chrysin → galangin	0.04↓	3.72↓
	4′OH → CH_3	luteolin → diosmetin	≈	3.07↓
flavonols	4′H → OH	galangin → kaempferol	0.31↑	1.45↓
	3′H → OH	kaempferol → quercetin	0.28↓	0.70↓
	5′H → OH	quercetin → myricetin	0.14↓	2.66↓
	5′H → OCH_3	kaempferol → isorhamnetin	0.37↓	0.75↓

DOI: 10.1021/acs.jafc.5b03386
J. Agric. Food Chem. 2015, 63, 7784−7794

inhibition toward XO, whereas the effect on the affinity for XO was uncertain.

Glycosylation. The dietary flavonoids in nature occur mostly as β-glycosides. The flavonols are found mainly as 3- and 7-*O*-glycoside, although the 4′-position may also be glycosylated in some plants.[29,32] As shown in Figure 7, compared with

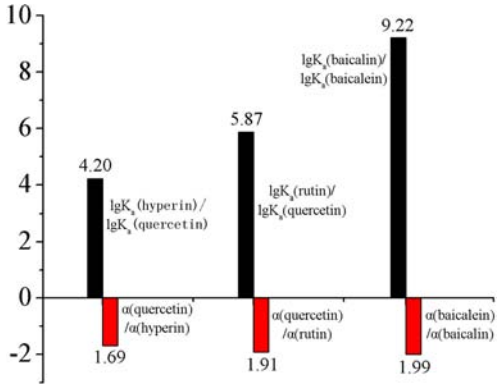

Figure 7. Effect of glycosylation of flavonoids on their affinities for XO and XO inhibitory activities.

quercetin, its galactoside (hyperin) showed a lower binding affinity and inhibition by 1.69 and 4.20 times, respectively. The inhibitions on XO of rutin and baicalin were about 5.87 and 9.22 times lower than that of quercetin and baicalein, respectively. Then by comparing their corresponding lg K_a, it was found that glycosylation of flavonoids lowered the affinity for XO depending on the conjugation site and the class of sugar moiety. The decreasing affinity for XO after glycosylation may be caused by the nonplanar structure; steric hindrance and hydrophilicity were other possible causes for the decreased affinity.[28,39] The behavior of depressed inhibition against XO could be explained by the fact that the increase in the size of the flavonoid compound may also increase the possibility of repulsive interactions in the active site, thus inhibiting the formation of the flavonoid−XO complex. Moreover, the presence of several hydroxyls in the galactoside group may act as an unstable element inside the highly nonpolar region, which finally resulted in a lower inhibitory activity and affinity, which was consistent with previous results. In addition, the previous studies reported that the glycosylation of dietary flavonoids decreased the affinities for plasma protein in vitro.[50] The present result that glycosylation decreased the inhibitory activities against XO was similar to the conclusion in a recent review that glycosylation of flavonoids decreased the inhibitory activities on both α-amylases and α-glucosidases.[51]

Hydrogenation of the C2═C3 Double Bond. The flavonoids with chromone (flavones, flavonols, and isoflavones) exhibited stronger inhibition with smaller values of α than those without (flavanone, others). The hydrogenation of the C2═C3 double bond decreased the inhibiting ability as well as the binding affinity of flavonoids. For example, naringenin showed a much higher α value and slightly lower lg K_a value than apigenin (Table 1), indicating that the hydrogenation of the C2═C3 of flavonoids decreased the inhibitory activities on XO more fiercely than the affinities for it. Phloretin and curumin without dual rings even showed no inhibition on XO, but still exhibited affinity. This may be because the C2═C3 double bond in conjugation with a 4-oxo group played an important role in the flavonoids in maintaining a plane molecular structure,[19] which was beneficial for inhibiting XO.[21,26] The fact that the benzopyran ring resembles the moieties of allopurinol (Figure 1) also might be a reason.[22] Generally, some of the structural elements that influence the inhibition of flavonoids against XO could be concluded. When the affinities and inhibitory activities were considered simultaneously, it was notable that the affinities of flavonoids changed consistently with the inhibitory activities, but not proportionally.

The typical structure properties of flavonoids affecting the inhibitory effect against XO are illustrated in Figure 8. The

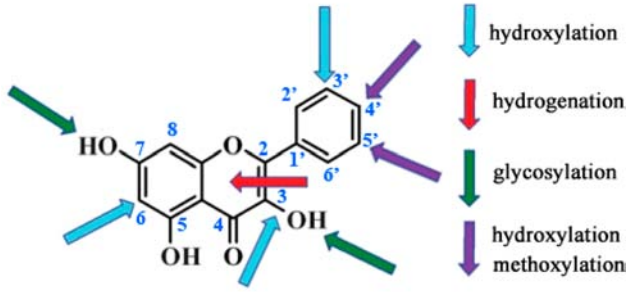

Figure 8. Structural elements that influence the inhibitions of 5,7-dihydroxyflavone to XO. The up arrows represent an increase in the inhibition; the down arrows represent a decrease in inhibition.

hydrogenation of the C2═C3 double bond on flavonoids decreased the inhibition on XO; hydroxylation of 3C (ring C) and the glycosylation of 3C—OH were unfavorable for the inhibition. The hydroxylation and methoxylation on ring B also decreased the inhibitory activity; moreover, the hydroxylation of 6C (ring A) and glycosylation of 7C—OH significantly decreased the inhibitory ability.

Computational Docking Analysis. From kinetic assay results, the active site of XO is specific for effective flavonoids, and the main focus will be the dockings of flavonoid into the Mo-pterin domain of XO. Herein, typical flavonoids (chrysin, apigenin, galangin, quercetin, rutin, genistein) were compared in their binding conformations to obtain conclusions on structural elements required for effective inhibition toward XO by performing a computational docking study. Allopurinol, as a well-known inhibitor, was used as a reference compound. Figure 9a shows allopurinol and flavonoids occupied the active cavity of XO (yellow), which was a long and narrow channel leading to the black catalytic site (Mo-pterin center). This once again supported that the mimic planar structure as xanthine was essential for potent inhibitory activity on XO.[19,22] The close-up views of computer-generated model (Figure 9b−e) reveal that all of the flavonoids plugged the channel (represented as Leu648, Phe649, Leu873, Phe914, Phe1009, Thr1010, Val1011, Phe1013, and Leu1014) and covered the access of designated substrate LUZ by interacting with the surrounding residues with different orientations. It was obvious that once the channel was mostly occupied by inhibitor, it might block the landing of substrate and ultimately prevent its oxidation. Figure 9b shows a close-up view of the active cavity of XO along with allopurinol. It docked in the Mo-pterin domain, showed a close position to LUZ, and formed hydrogen bonds with Lys 771 and Glu802.[52]

In Figure 9c, we superimposed two flavones of apigenin and chrysin, showing that their benzopyranone rings overlapped and both bound in the channel leading to the buried cofactor

DOI: 10.1021/acs.jafc.5b03386
J. Agric. Food Chem. 2015, 63, 7784−7794

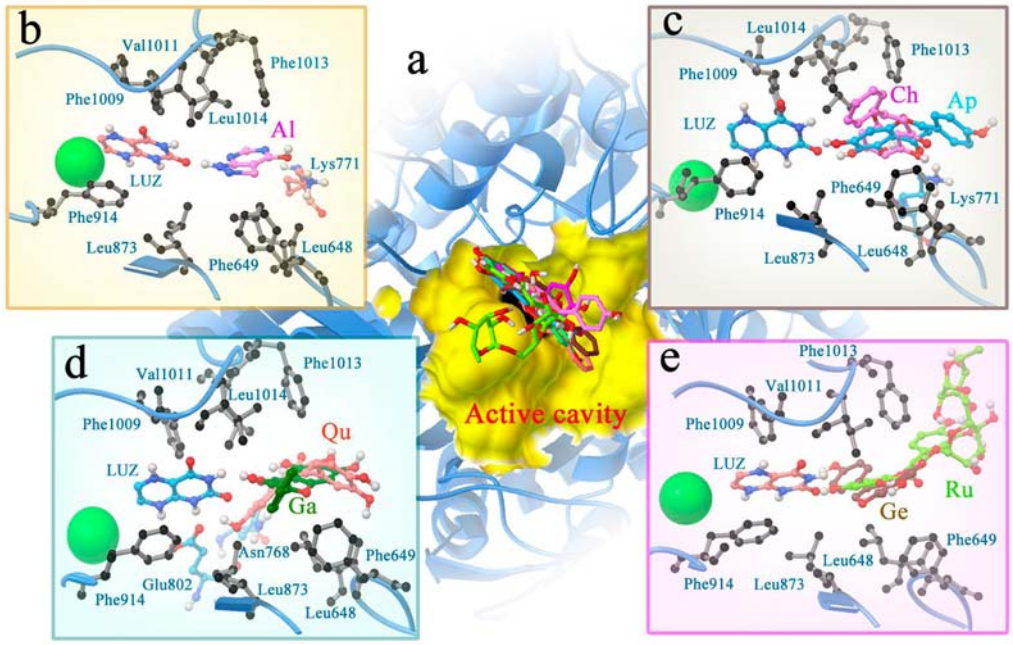

Figure 9. (a) Section view of flavonoids (stick) occupying the catalytic site cavity (surface view: yellow) of XO. The black domain is the surface of coenzyme factor (Mo-pterin cofactor). The close-up view of interaction of flavonoids with hydrophobic residues (shown in black ball and gray stick representation and labeled with their numbers) lining the access channel to Mo (green ball) center are shown as (b) allopurinol (Al), (c) chrysin (Ch) and apigenin (Ap), (d) galangin (Ga) and quercetin (Qu), and (e) geninstein (Ge) and rutin. Backbone segments are shown in cyan, and the residues of forming hydrogen bond with the corresponding flavonoids are in full color (Asn768, Glu802, Lys771).

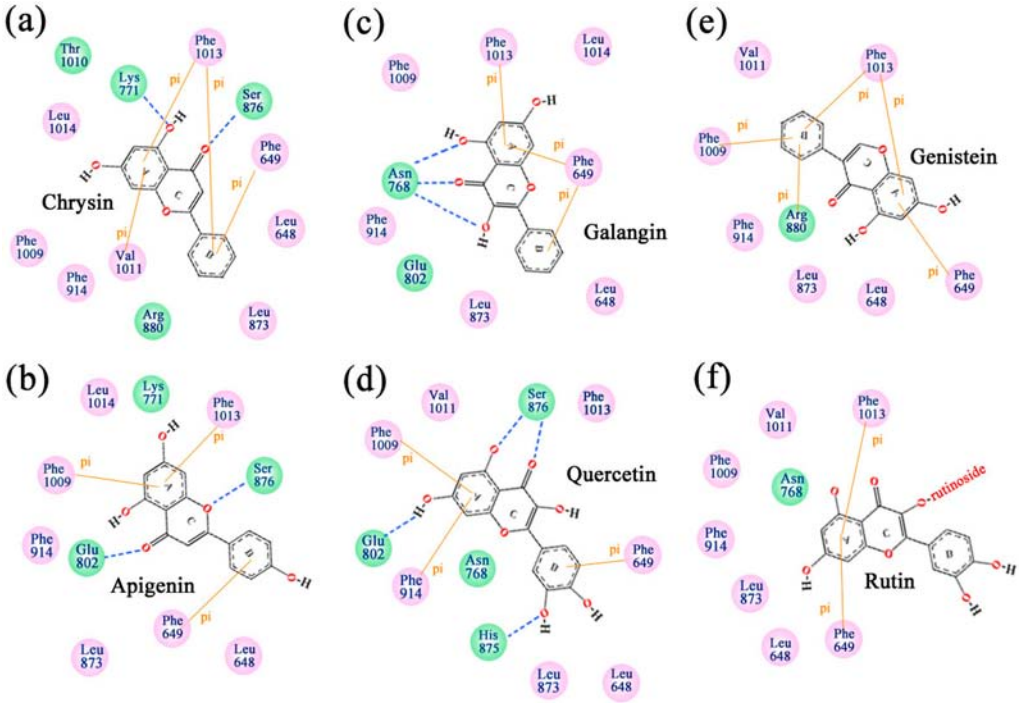

Figure 10. Key interactions of chrysin (a), apigenin (b), galangin (c), quercetin (d), genistein (e), and rutin (f) with the key residues in the active cavity of XO. Pink circles indicate hydrophobic amino acids, and green circles indicate hydrophilic amino acids. The blue short-dash lines indicate hydrogen bonds to side-chain residues. The orange lines represent π-interactions.

with slight difference. Chrysin showed hydrogen bonding of 5C—OH and 4C═O groups with side chain of Lys771 and Ser876 residues (Figure 10a), whereas hydrogen bonds were observed between 4C═O and the ether group of apigenin with the side chains of Glu802 and Lys771 residues, respectively (Figure 10b).

The overlay of binding poses of flavonol in the XO active site is displayed in Figure 9d; galangin and quercetin had almost identical binding modes at the active sites with each having ring A and C docked into the channel. Their polar 3C−OH stretched to the space surrounded by nonpolar Phe649, Leu648, and Leu1014. Thus, the weaker inhibition and

DOI: 10.1021/acs.jafc.5b03386
J. Agric. Food Chem. 2015, 63, 7784−7794

interaction of flavonol relative to flavone could be explained by the unsteadiness of polar hydroxyl in the hydrophobic region.[26] The destabilization of polar hydroxyl stretching into the hydrophobic region may cause the lower binding affinity; thus, the more hydroxyl groups in ring B within one subclass, the weaker inhibitory ability it exhibited (Table 1). The hydrogen bonds between 3C−OH of galangin and Asn768 residue (Figure 10c) and between 3′C−OH of quercetin and His875 residue (Figure 10d) might be the reason for their different orientations of ring B.

Three common features of binding with XO existing in both flavone and flavonol (Figure 10a−d) could be concluded. First, several hydrogen bonds and $\pi-\pi$ interactions existed in their docking into the active pockets.[37] For example, there were $\pi-\pi$ interactions between ring A and the aromatic residue of Phe1013 and Val1011; interactions between ring B and Phe1013 and Phe649 are shown in the chrysin−XO system (Figure 10a). Several hydrogen bonds were observed, including C5 hydroxyl bound to Lys771 (Figure 10a), Asn768 (Figure 10c), or Ser876 (Figure 10d) and C7 hydroxyl bound to Glu 802 (Figure 10d). This might support the previous result that C5 and C7 hydroxyl groups of flavonoid assist in the inhibitory activity against XO.[19,22] Second, the 4C═O group (ring C) of both flavonoids formed hydrogen bonds with the side chains of the residue within the cavity. A third significant feature of both flavonoids was shown by inserting ring A and ring C into the hydrophobic cavity instead of ring B. Additionally, each flavonoid docked into the active site of XO uniquely.

Genistein is a constitutional isomer of apigenin with a difference in the phenolic group substitution on ring C. The simulation revealed that the binding of genistein was in the opposite orientation to apigenin, with ring B inserting into the active site and approaching the Mo-center (Figure 9e). Herein, rutin had a comparable binding position to genistein with its benzopyranone bicyclic ring stretching beyond the hydrophobic pocket and ring C inserting into the Mo-pterin domain, but it exhibited fairly low affinity to the enzyme. These phenomena could be explained by the fact that the bulky rutinoside moiety located outside the active cavity, which was supposed to badly destabilize its binding; that is, the bulky rutinoside created a steric clash with the surrounding residues, thereby preventing productive binding to XO.[20] Moreover, the $\pi-$cation interactions of ring B (genistein) and the NH_2 of Arg880 (Figure 10e) and $\pi-\pi$ interactions between these flavonoids and Phe1013, Phe1009, and Phe649 (Figure 10e,f) also contributed to the tethering of the two flavonoids to the active sites. All together, our structural and experimental data indicated that these potent flavonoids occupy the active substrate-binding sites in the enzymatic pocket, although with different orientations, physically excluding the landing of substrate, further intervening in the xanthine oxidation activity of XO and hindering the redundant mechanism for uric acid.

In summary, this work reinforced flavonoids as effective inhibitors of XO in vitro. It was also possible to establish a structure−activity relationship for the inhibitory activity of flavonoids against XO. Data analysis indicated that the hydrophobic force was the main force of flavonoids to bind with XO. The inhibitory activities increased generally with increasing affinities within the class, especially for flavones and flavonols, which might be because the higher affinity increases the chance to enter the catalytic gorge, but the inhibition finally depends on the direct interaction between the flavonoid and the active site. The typical structure properties of flavonoids affecting the inhibitory effect against XO are illustrated in Figure 8. The hydrogenation of the C2═C3 double bond on flavonoids decreased the inhibition on XO, hydroxylation of C3 (ring C) and glycosylation of 3C−OH were unfavorable for the inhibition, and the hydroxylation and methoxylation on ring B also decreased the inhibitory activity; moreover, the hydroxylation of C6 (ring A) and glycosylation of 7C−OH siginificantly affected the inhibitiory ability.

The structure−activity relationship coupled with the results of computer modeling revealed several key factors of flavonoid binding in the active site of XO and inhibition against XO. Specifically, due to their mimic rings (A and C rings) of the xanthine (Figure 1), these compounds bound to the active site effectively. The C2═C3 that maintains a planar structure of flavonoids was essential for potent inhibitory activity on XO.[19,22] The hydroxyl moiety at C7 and C5 contributed favorable hydrogen bonds and interactions between inhibitors and the active site. However, C3−OH exhibited weaker inhibition, which could be due to the destabilization of polar hydroxyl stretching into the hydrophobic region of the active site and causing lower binding affinity. The methylation of flavonoids exhibited a great effect on the inhibition toward XO, whereas their effect on the affinity for XO was uncertain. The bully substitution of glycosyl on aromatic rings of flavonoids created a steric clash with the surrounding residues, hindering a lower binding affinity for XO. Generally, the occupancy of the active site by the potent flavonoids reduced the landing of substrate to the active sites and further intervened in the xanthine oxidation activity of XO and hindered the redundant mechanism for uric acid.

These results provide a molecular basis regarding the binding nature and structural requirements of phytochemical flavonoids to inhibit XO, which may be useful for developing new potential drugs for XO blockade. Thus, flavonoid-containing fruits and vegetables should be included in the diet of patients suffering gout. These examples also illustrate how knowledge of the inhibition mechanism can promote the development of novel therapies. However, the results from this in vitro study may be different from the results obtained from in vivo studies due to metabolic conversion processes; therefore, cell culture and animal studies including these chemicals should be further initiated. In fact, there was a study showing that flavonoids (genistein, apigenin, quercetin, rutin, and astilbin) had a significant effect on XO activities in vivo (serum XO).[20] However, it is still necessary to conduct more experiments in vitro and vivo to illuminate if the flavonoids are suitable candidates for replacing allopurinol for the treatment of gout.

AUTHOR INFORMATION

Corresponding Author

*(G.Z.) Phone: +86-791-88305234. Fax: +86-791-88304347. E-mail: gwzhang@ncu.edu.cn.

Notes

The authors declare no competing financial interest.

ACKNOWLEDGMENTS

This work was financially supported by the National Natural Science Foundation of China (No. 21167013, 31460422, and 31060210), the Natural Science Foundation of Jiangxi Province (20142BAB204001 and 20143ACB20006), the Joint Specialized Research Fund for the Doctoral Program of Higher Education (20123601110005), the Program of Jiangxi Provin-

DOI: 10.1021/acs.jafc.5b03386
J. Agric. Food Chem. 2015, 63, 7784−7794

cial Department of Science and Technology (20141BBG70092), and the Research Program of State Key Laboratory of Food Science and Technology of Nanchang University (SKLF-ZZA-201302).

REFERENCES

(1) Boban, M.; Kocic, G.; Radenkovic, S.; Pavlovic, R.; Cvetkovic, T.; Deljanin-Ilic, M.; Ilic, S.; Bobana, M. B.; Djindjic, B.; Stojanovic, D.; Sokolovic, D.; Jevtovic-Stoimenov, T. Circulating purine compounds, uric acid, and xanthine oxidase/dehydrogenase relationship in essential hypertension and end stage renal disease. *Renal Failure* **2014**, *36*, 613−618.

(2) Dawson, J.; Walters, M. Uric acid and xanthine oxidase: future therapeutic targets in the prevention of cardiovascular disease? *Br. J. Clin. Pharmacol.* **2006**, *62*, 633−644.

(3) Pacher, P.; Nivorozhkin, A.; Szabo, C. Therapeutic effects of xanthine oxidase inhibitors: renaissance half a century after the discovery of allopurinol. *Pharmacol. Rev.* **2006**, *58*, 87−114.

(4) Fukunari, A.; Okamoto, K.; Nishino, T.; Eger, B. T.; Pai, E. F.; Kamezawa, M.; Yamada, I.; Kato, N. Y-700 (1-(3-cyano-4-(2,2-dimethylpropoxy)phenyl)-1*H*-pyrazole-4-carboxylic acid): a potent xanthine oxidoreductase inhibitor with hepatic excretion. *J. Pharmacol. Exp. Ther.* **2004**, *311*, 519−528.

(5) Rees, F.; Hui, M.; Doherty, M. Optimizing current treatment of gout. *Nat. Rev. Rheumatol.* **2014**, *10*, 271−283.

(6) Arellano, F.; Sacristán, J. A. Allopurinol hypersensitivity syndrome: a review. *Ann. Pharmacother.* **1993**, *27*, 337−343.

(7) Malik, U. Z.; Hundley, N. J.; Romero, G.; Radi, R.; Freeman, B. A.; Tarpey, M. M.; Kelley, E. E. Febuxostat inhibition of endothelial-bound XO: implications for targeting vascular ROS production. *Free Radical Biol. Med.* **2011**, *51*, 179−184.

(8) Nagao, A.; Seki, M.; Kobayashi, H. Inhibition of xanthine oxidase by flavonoids. *Biosci., Biotechnol., Biochem.* **1999**, *63*, 1787−1790.

(9) Pauff, J. M.; Hille, R. Inhibition studies of bovine xanthine oxidase by luteolin, silibinin, quercetin, and curcumin. *J. Nat. Prod.* **2009**, *72*, 725−731.

(10) Wang, Y. J.; Zhang, G. W.; Pan, J. H.; Gong, D. M. Novel insights into the inhibitory mechanism of kaempferol on xanthine oxidase. *J. Agric. Food Chem.* **2015**, *63*, 526−534.

(11) Burda, S.; Oleszek, W. Antioxidant and antiradical activities of flavonoids. *J. Agric. Food Chem.* **2001**, *49*, 2774−2779.

(12) Ren, W.; Qiao, Z.; Wang, H.; Zhu, L.; Zhang, L. Flavonoids: promising anticancer agents. *Med. Res. Rev.* **2003**, *23*, 519−534.

(13) Kawai, M.; Hirano, T.; Higa, S.; Arimitsu, J.; Maruta, M.; Kuwahara, Y.; Ohkawara, T.; Hagihara, K.; Yamadori, T.; Shima, Y.; Ogata, A.; Kawase, I.; Tanaka, T. Flavonoids and related compounds as anti-allergic substances. *Allergol. Int.* **2007**, *56*, 113−123.

(14) Xie, Y.; Chen, X. Structures required of polyphenols for inhibiting advanced glycation end products formation. *Curr. Drug Metab.* **2013**, *14*, 414−431.

(15) Bastianetto, S.; Quirion, R. Natural extracts as possible protective agents of brain aging. *Neurobiol. Aging* **2002**, *23*, 891−897.

(16) Pietta, P. G. Flavonoids as antioxidants. *J. Nat. Prod.* **2000**, *63*, 1035−1042.

(17) Rathee, P.; Chaudhary, H.; Rathee, S.; Rathee, D.; Kumar, V.; Kohli, K. Mechanism of action of flavonoids as anti-inflammatory agents: a review. *Inflammation Allergy: Drug Targets* **2009**, *8*, 229−235.

(18) Kimura, Y.; Ito, H.; Ohnishi, R.; Hatano, T. Inhibitory effects of polyphenols on human cytochrome P450 3A4 and 2C9 activity. *Food Chem. Toxicol.* **2010**, *48*, 429−435.

(19) Lin, C. M.; Chen, C. S.; Chen, C. T.; Liang, Y. C.; Lin, J. K. Molecular modeling of flavonoids that inhibits xanthine oxidase. *Biochem. Biophys. Res. Commun.* **2002**, *294*, 167−172.

(20) Huang, J.; Wang, S.; Zhu, M.; Chen, J.; Zhu, X. Effects of genistein, apigenin, quercetin, rutin and astilbin on serum uric acid levels and xanthine oxidase activities in normal and hyperuricemic mice. *Food Chem. Toxicol.* **2011**, *49*, 1943−1947.

(21) Hayashi, T.; Sawa, K.; Kawasaki, M.; Arisawa, M.; Shimizu, M.; Morita, N. Inhibition of cow's milk xanthine oxidase by flavonoids. *J. Nat. Prod.* **1988**, *51*, 345−348.

(22) Van Hoorn, D. E.; Nijveldt, R. J.; Van Leeuwen, P. A.; Hofman, Z.; M'Rabet, L.; De Bont, D.; Van Norren, K. Accurate prediction of xanthine oxidase inhibition based on the structure of flavonoids. *Eur. J. Pharmacol.* **2002**, *451*, 111−118.

(23) Yan, J. K.; Zhang, G. W.; Hu, Y. T.; Ma, Y. D. Effect of luteolin on xanthine oxidase: inhibition kinetics and interaction mechanism merging with docking simulation. *Food Chem.* **2013**, *141*, 3766−3773.

(24) Li, X.; Wang, G.; Chen, D.; Lu, Y. Binding of ascorbic acid and α-tocopherol to bovine serum albumin: a comparative study. *Mol. BioSyst.* **2014**, *10*, 326−337.

(25) Wang, Y. Q.; Zhang, H. M.; Zhang, G. C.; Liu, S. X.; Zhou, Q. H.; Fei, Z. H.; Liu, Z. T. Studies of the interaction between paraquat and bovine hemoglobin. *Int. J. Biol. Macromol.* **2007**, *41*, 243−250.

(26) Da Silva, S. L.; Da Silva, A.; Honório, K. M.; Marangoni, S.; Toyama, M. H.; Da Silva, A. B. F. The influence of electronic, steric and hydrophobic properties of flavonoid compounds in the inhibition of the xanthine oxidase. *J. Mol. Struct.: THEOCHEM* **2004**, *684*, 1−7.

(27) Dew, T. P.; Day, A. J.; Morgan, M. R. Xanthine oxidase activity in vitro: effects of food extracts and components. *J. Agric. Food Chem.* **2005**, *53*, 6510−6515.

(28) Cos, P.; Ying, L.; Calomme, M.; Hu, J. P.; Cimanga, K.; Van Poel, B.; Pieters, L.; Vlietinck, A. J.; Berghe, D. V. Structure-activity relationship and classification of flavonoids as inhibitors of xanthine oxidase and superoxide scavengers. *J. Nat. Prod.* **1998**, *61*, 71−76.

(29) Xiao, J. B.; Huo, J. L.; Yang, F.; Chen, X. Q. Noncovalent interaction of dietary polyphenols with bovine hemoglobin in vitro: molecular structure/property-affinity relationship aspects. *J. Agric. Food Chem.* **2011**, *59*, 8484−8490.

(30) Wang, Y. P.; Zhang, G. W.; Wang, L. H. Potential toxicity of phthalic acid esters plasticizer: interaction of dimethyl phthalate with trypsin in vitro. *J. Agric. Food Chem.* **2015**, *63*, 75−84.

(31) Xu, C.; Chen, X. Molecular property-affinity relationship of the interaction between dietary polyphenols and bovine milk proteins. *Food Funct.* **2011**, *2*, 368−372.

(32) Xiao, J.; Zhao, Y.; Hui, W.; Yuan, Y.; Fan, Y.; Chao, Z.; Kai, G. Y. Non-covalent interaction of dietary polyphenols with total plasma proteins of type II diabetes: molecular structure/property−affinity relationships. *Integr. Biol.* **2011**, *3*, 1087−1094.

(33) Xiao, J.; Zhao, Y.; Yuan, Y.; Zhang, C.; Wang, H.; Yang, F.; Yamamoto, K. Noncovalent interaction of dietary polyphenols with common human plasma proteins. *J. Agric. Food Chem.* **2011**, *59*, 10747−10754.

(34) Xie, Y.; Xiao, J.; Kai, G.; Chen, X. Glycation of plasma proteins in type II diabetes lowers the non-covalent interaction affinities for dietary polyphenols. *Integr. Biol.* **2012**, *4*, 502−507.

(35) Yang, F.; Zhao, Y.; Kai, G.; Xiao, J. Interaction of dietary flavonoids with γ-globulin: molecular property-binding affinity relationship aspect. *Food Funct.* **2011**, *2*, 137−141.

(36) Courts, F. L.; Williamson, G. The c-glycosyl flavonoid, aspalathin, is absorbed, methylated and glucuronidated intact in humans. *Mol. Nutr. Food Res.* **2009**, *53*, 1104−1111.

(37) Okamoto, K.; Matsumoto, K.; Hille, R.; Eger, B. T.; Pai, E. F.; Nishino, T. The crystal structure of xanthine oxidoreductase during catalysis: implications for reaction mechanism and enzyme inhibition. *Proc. Natl. Acad. Sci. U. S. A.* **2004**, *101*, 7931−7936.

(38) Yamaguchi, Y.; Matsumura, T.; Ichida, K.; Okamoto, K.; Nishino, T. Human xanthine oxidase changes its substrate specificity to aldehyde oxidase type upon mutation of amino acid residues in the active site: roles of active site residues in binding and activation of purine substrate. *J. Biochem.* **2007**, *141*, 513−524.

(39) Ribeiro, D.; Freitas, M.; Tomé, S. M.; Silva, A. M.; Porto, G.; Cabrita, E. J.; Marques, M. M. B.; Eduarda Fernandes, E. Inhibition of LOX by flavonoids: a structure−activity relationship study. *Eur. J. Med. Chem.* **2014**, *72*, 137−145.

(40) Fang, P.; Yu, X.; Jeong, S. J.; Mirando, A.; Chen, K.; Chen, X.; Kim, S.; Francklyn, C. S.; Guo, M. Structural basis for full-spectrum

DOI: 10.1021/acs.jafc.5b03386
J. Agric. Food Chem. 2015, 63, 7784−7794

inhibition of translational functions on a tRNA synthetase. *Nat. Commun.* **2015**, *6*, 6402.
(41) Ertl, P.; Rohde, B.; Selzer, P. Fast calculation of molecular polar surface area as a sum of fragment-based contributions and its application to the prediction of drug transport properties. *J. Med. Chem.* **2000**, *43*, 3714−3717.
(42) Palm, K.; Stenberg, P.; Luthman, K.; Artursson, P. Polar molecular surface properties predict the intestinal absorption of drugs in humans. *Pharm. Res.* **1997**, *14*, 568−571.
(43) Xie, Y.; Yang, W.; Chen, X.; Xiao, J. Inhibition of flavonoids on acetylcholine esterase: binding and structure-activity relationship. *Food Funct.* **2014**, *5*, 2582−2589.
(44) Heim, K. E.; Tagliaferro, A. R.; Bobilya, D. J. Flavonoid antioxidants: chemistry, metabolism and structure-activity relationships. *J. Nutr. Biochem.* **2002**, *13*, 572−584.
(45) Jacob, V.; Hagai, T.; Soliman, K. Structure-activity relationships of flavonoids. *Curr. Org. Chem.* **2011**, *15*, 2641−2657.
(46) Zou, D.; Xie, A. Influence of polyphenol-plasma protein interaction on the antioxidant properties of polyphenols. *Curr. Drug Metab.* **2013**, *14*, 451−455.
(47) Xiao, J.; Kai, G.; Yamamoto, K.; Chen, X. Advance in dietary polyphenols as α-glucosidases inhibitors: a review on structure-activity relationship aspect. *Crit. Rev. Food Sci. Nutr.* **2013**, *53*, 818−836.
(48) Lin, C. M.; Chen, C. T.; Lee, H. H.; Lin, J. K. Prevention of cellular ROS damage by isovitexin and related flavonoids. *Planta Med.* **2002**, *68*, 365−367.
(49) Kao, Y. C.; Zhou, C.; Sherman, M.; Laughton, C. A.; Chen, S. Molecular basis of the inhibition of human aromatase (estrogen synthetase) by flavone and isoflavone phytoestrogens: a site-directed mutagenesis study. *Environ. Health Perspect.* **1998**, *106*, 85−92.
(50) Xiao, J.; Cao, H.; Wang, Y.; Zhao, J.; Wei, X. Glycosylation of dietary flavonoids decreases the affinities for plasma protein. *J. Agric. Food Chem.* **2009**, *57*, 6642−6648.
(51) Cao, H.; Chen, X. Structures required of flavonoids for inhibiting digestive enzymes. *Anti-Cancer Agents Med. Chem.* **2012**, *12*, 929−939.
(52) Truglio, J. J.; Theis, K.; Leimkühler, S.; Rappa, R.; Rajagopalan, K. V.; Kisker, C. Crystal structures of the active and alloxanthine-inhibited forms of xanthine dehydrogenase from *Rhodobacter capsulatus*. *Structure* **2002**, *10*, 115−125.

DOI: 10.1021/acs.jafc.5b03386
J. Agric. Food Chem. 2015, 63, 7784−7794

Molecular mechanisms of tumor cell proliferation inhibited by rBTI may be involved in the disorder of mitochondrial membrane potential and mitochondrial dysfunction. Thus, in this article, we will focus on the molecular mechanisms by which cells coordinate the mitochondria and mitophagy,[16] as induced by rBTI, and also examine the relationship between autophagy and reactive oxygen species (ROS).[17] Our results indicated that the rBTI directly targeted mitochondria, which caused a dose-dependent overproduction of ROS, leading to breakdown of mitochondrial membrane potential and ultimately mitophagy.

MATERIALS AND METHODS

Materials and Reagents. The rBTI was generated previously via cloning, protein expression, and one-step affinity purification in our laboratory.[18] The Hep G2 cells were obtained from the Biology Institute (Shanxi, China). Fetal bovine serum, penicillin, streptomycin, trypsin, and dimethyl sulfoxide (DMSO) were purchased from Sijiqing Company (Hangzhou, China). A superoxide dismutase (SOD) assay kit with WST-1, a catalase (CAT) assay kit, and a reduced glutathione assay kit were available from Nanjing Jiancheng Bioengineering Institute (Nanjing, China). A reactive oxygen species assay kit, an ATP assay kit, a mitochondrial membrane potential assay kit, a cell mitochondria isolation kit, cell lysis solution, and protein A+G agarose and Rabit IgG were obtained from Beyotime Institute of Biotechnology (Shanghai, China). TurboFect transfection reagent was purchased from Thermo Fisher Scientific (Massachusetts, US). Tom20 antibody (F-10) (sc-17764), Cox IV antibody (F-8) (sc-376731), ATG5 antibody (C-1) (sc-133158), p62 antibody (D-3) (sc-28359), and Tim23 antibody (sc-13298) were purchased from Santa Cruz Biotechnology, Inc. (California, US). Beclin 1 antibody (B6186) and LC3B antibody (L7543), monodansylcadeverine (MDC) (30432), and bafilomycin A1(B1793) were purchased from Sigma-Aldrich (St. Louis, MO). Cyto-ID Green Detection Kit was acquared from Enzo Life Sciences (Farmingdale, NY).

Cell Culture and Transfection. The human hepatoma cells (Hep G2) were cultured in Dulbecco's modified Eagle's medium (DMEM); supplemented with 10% fetal bovine serum (Hyclone, Logan, UT), 100 U/mL penicillin, and 100 g/mL streptomycin at 37 °C; and stored in a humidified 5% CO_2 atmosphere. The cells were cultured on tissue culture plates and harvested 24 h after plating when a confluent monolayer culture was achieved. Transfected Hep G2 cells were obtained by treatment with Turbo Fect transfection reagent according to the manufacturer's protocol.

Transmission Electron Microscopy (TEM). Hep G2 cells, treated or untreated with rBTI, were pelleted at 45 *g* and fixed in 1.5% PFA, 1.5% glutaraldehyde in 0.1 M cacodylate buffer, pH 7.4 overnight at 4 °C. For block contrasting, the samples were washed three times for 10 min each in cacodylate buffer and incubated for 2 h in the dark in 1% osmium tetroxide/cacodylate buffer. Samples were washed three times for 10 min each in cacodylate buffer and twice for 10 min each in distilled water, and then incubated overnight in the dark in half saturated uranylacetate solution. Uranylacetate was removed by washing two times for 10 min each with distilled water. Samples were prepared for embedding by dehydrating in acetone (two times for 10 min, 70%; two times for 10 min, 90%; and three times for 10 min, 100%) and by preincubating in 1:1 epoxy resin/acetone (1 h), 4:1 epoxy resin/acetone (1 h), and pure epoxy resin, overnight. Finally, the samples were embedded in epoxy resin and hardened at 40 °C for 20 h and 60 °C for 40 h. Ultrathin sections (50−70 nm) were then generated and placed on hexagonal copper grids. For sample contrasting, the sections were incubated with 5% uranylacetate in distilled water (10 min, 60 °C) and lead citrate (3 min, room temperature (RT)) then dried and analyzed by TEM.

Laser Scanning Confocal Fluorescence Microscopy. The detection of mitochondrial membrane potential was undertaken using a laser scanning confocal fluorescence microscope (Fluoview FV1000; Olympus, Japan) at λ_{ex} 488 and 600 nm. To investigate the mitochondrial membrane potential after rBTI treatment, Hep G2 cells were seeded onto glass coverslips in six-well plates (5×10^4 cells/well). The cells were treated with rBTI. After incubation with rBTI, cells were stained with the $\Delta\Psi_m$-specific probe JC-1 and autophagy marker MDC according to the manufacturer's protocol.

Fluorescence channels for different dyes were separated into different wells using sequential scanning to ensure there was no bleach from one channel. Samples were undertaken on a laser scanning confocal microscope with fluorescein isothiocyanate (FITC, green), tetramethyl rhodamine isothiocyanate (TRITC, red), and 4′,6-diamidino-2-phenylindole (DAPI, blue) channels. Confocal microscopy was conducted with an Olympus spectral confocal microscope using the XYZ mode and a 0.25/0.40 μm section height. For quantitative analysis, the fluorescence intensities were quantified by the ImageJ software (NIH, US) and the results were expressed as mean ± SEM.

Flow Cytometry. The Hep G2 cells were seeded on a 12-well plate at a density of $3-4 \times 10^4$ cells/well and incubated for 24 h at 37 °C. The cells were then treated with 50 μg/mL rBTI for 2 and 4 h. Hep G2 cells were trypsinized and collected by centrifugation. The analysis of ROS, mitochondrial membrane potential, and the autophagosomes were performed using the reactive oxygen species assay kit, mitochondrial membrane potential assay kit, and Cyto-ID green detection kit, according to the manufacturer's protocols. The cells were analyzed by flow cytometry using an excitation/emission of 488/520 nm.

Antioxidant Enzyme Activity Assay. The Hep G2 cells were seeded on a 6-well plate at 2×10^5 cells/well and incubated for 24 h at 37 °C. The cells were then treated with 50 μg/mL rBTI for different lengths of time. After incubation with rBTI, the growth medium was removed and the cells were washed twice with PBS. Then 100 μL of cell lysis solution was added to each well and MicroPette Plus was used to blow the liquid for 2−3 s. The cell debris and lysis solution were put into 1.5 mL eppendorf tubes, incubated on ice for 20 min, and centrifuged for 10 min at 13 500*g* at 4 °C before the supernatants were collected. The supernatant containing total cell protein was used for protein determination. Protein concentration in all samples was monitored by spectrophotometry using the BCA protein assay reagent. The supernatant was used only for SOD, CAT, and glutathione peroxidase (GSH) content assays.

SOD was evaluated using the superoxide dismutase assay kit. In this assay, WST-1 produces a water-soluble formazan dye upon reduction with a superoxide anion, which is a byproduct from the catalytic reaction of xanthine oxidase. The assay was performed in 96-well microplates according to the manufacturer's instruction. The absorbance was read at 450 nm using a plate reader.

CAT needed to be measured using the catalase assay kit. CAT activity can decompose H_2O_2 to produce water and oxygen. The unconverted H_2O_2 reacts with ammonium molybdate to produce a yellow product, the absorbance of which can be evaluated using a spectrophotometer. The assay was performed in 96-well microtiter plates according to the manufacturer's instructions, and the absorbance was read at 405 nm.

GSH content was evaluated using the glutathione reductase assay kit. Briefly, 40 μL of metaphosphoric acid was added into 10 μL of Hep G2 cell lysates. The mixtures was then centrifuged at 10 000 g for 10 min at 4 °C. The supernatant was used for both the GSH and oxidized glutathione (GSSG) assay. The total GSH level was monitored using a DTNB-GSSG recycling assay. The GSSG level was quantified using the total GSH assay, after supernatants were pretreated with 1% 1 mol/L 2-vinylpyridine solution to remove the reduced GSH.

MTT Assays. Hep G2 cells were seeded into 96-well microtiter plates at a density of 5×10^3 cells/mL in 100 μL of complete DMEM medium. The cells were allowed to adhere at different time points in fresh medium and then treated with 50 μg/mL rBTI and/or 3-MA for 12 or 24 h. Then, 20 μL of MTT (5 mg/mL) was added to the culture medium and the cells were incubated at 37 °C for an additional 4 h. The medium and MTT were removed, and 150 μL of dimethyl sulfoxide (DMSO) was added to each well. The plates were then

DOI: 10.1021/acs.jafc.5b02644
J. Agric. Food Chem. 2015, 63, 7795−7804

placed on a shaker for 5 min at room temperature. For each well, absorbance at 490 nm was measured using a microtiter plate ELISA reader (model 550; Bio-Rad, Hercules, CA).

Measurement of Cellular ATP. The ATP assay kit, based on the production of light from ATP and luciferin in the presence of luciferase, was used to measure ATP concentrations. Hep G2 cells were plated at a density of 2×10^5 cells/well in 6-well plates. After overnight incubation, the cells were treated with 50 μg/mL rBTI for different lengths of time. Following treatment, the medium was removed and the cells were washed twice with cold PBS, then 200 μL of cell lysis buffer was added to each well. The cells were then placed on ice for 20 min, then the lysate was cleared by centrifugation at 13 500*g* for 10 min at 4 °C and the supernatant (total cell lysate) was used immediately. ATP measurements were carried out using a luminometric assay, according to the manufacturer's instructions. The ATP concentration in the wells was determined using a standard curve and normalized to protein content.

Mitochondrial Morphology. Hep G2 cells transfected with the pDsRed2-Mito plasmid were seeded onto glass coverslips at a density of 2×10^5 cells/well in 6-well plates, each sample in triplicate. Following an overnight incubation, cells were treated with or without 50 μg/mL rBTI for different lengths of time. Following incubation, cells were fixed for 10 min at RT in 4% paraformaldehyde in 0.1 M PBS at pH 7.4. The cells were subsequently washed 3 times with 0.01 M PBS containing 0.85% NaCl at pH 7.4 and fixed in 4% paraformaldehyde.

Colocalization of FITC-BTI or LC3 with Mitochondria. The stable cell line (Hep G2/mito-RED) was transfected with pEGFP-LC3. Cells transfected with pEGFP-LC3 were incubated with 50 μg/mL rBTI, while the cells (Hep G2/mito-RED) were treated with FITC-rBTI for different lengths of time. Labeling of rBTI with FITC was carried out in accordance with the method published by Cui et al.[19] Following incubation with or without rBTI, we investigated the colocalization of mitochondria with rBTI or GFP-LC3. The transfected cells were maintained on coverslips in six-well plates overnight then left untreated or treated with 50 μg/mL rBTI for 4 h. The cells were then washed twice with PBS, and the cellular localization pattern of mitochondria was then photographed using confocal fluorescence microscopy.

Subcellular Fractionation. Subcellular fractionation of cells to separate mitochondrial and cytosolic fractions was carried out according to the instructions provided with the cell mitochondria isolation kit. Hep G2 cells collected from three 10 cm culture dishes with trypsination were washed once with PBS and then resuspended in 1 mL of mitochondria isolation buffer. After incubation on ice for 15 min to promote hypotonic swelling, cells were homogenized by 30 strokes with a glass homogenizer. The homogenate was centrifuged at 600*g* for 10 min at 4 °C, and the collected supernatant was transferred to a clean chilled tube for further centrifugation at 11 000 *g* for 15 min at 4 °C. The supernatant representing the cytosolic fraction was collected without any treatment and stored at −20 °C for later analysis. The resulting pellet representing the mitochondrial fraction was resuspended in 40 μL of mitochondria dissociation buffer.

Western Blot. Cells were collected and washed with PBS. Whole cellular proteins were extracted and cytosolic fractions were prepared according to the manufacturer's guidelines (Beyotime, China). The protein concentration in all samples was measured using the classic BCA assay. Equal amounts of sample lysates were subjected to 12% SDS-PAGE and then transferred onto PVDF membranes. The PVDF membranes were blocked with 5% nonfat milk in TBST buffer (20 mM Tris pH 7.5, 500 mM NaCl, 0.1% Tween-20) overnight at room temperature. The membranes were subsequently incubated with the relevant primary antibodies (1:1000 dilution) at 4 °C overnight and then with enzyme-linked secondary antibodies (1:10 000 dilution) for 1 h at room temperature. Immunoreactive bands were visualized with Enlight regents (Engreen, Beijing, China).

Immunoprecipitation. Hep G2 cells grown to a confluence of 90% were treated with 50 μg/mL of rBTI for 2 h and then washed once with PBS and lysed for 30 min on ice using NP-40 lysis buffer (Beyotime, Jiangsu, China). Cell lysates were then centrifuged at 12 000 *g* for 20 min. The soluble fraction was collected and the protein concentration was determined using the BCA protein assay kit (Beyotime, Jiangsu, China). Next, 1 mg of the extracted protein in lysis buffer was immunoprecipitated overnight with anti-Tom20 or anti-BTI antibody at 4 °C and then with protein A+G agarose beads for another 4 h. After that, the protein A+G agarose beads were washed three times with lysis buffer. The beads were then boiled in 1% SDS loading buffer for Western blotting with the indicated antibodies.

Statistical Analysis. Data were obtained from at least three independent experiments and presented as the mean ± SEM. Statistical evaluation of the results was performed by one-way ANOVA. Data represent ±standard error of the mean (SEM) from more than three independent experiments.

RESULTS AND DISCUSSION

rBTI Induces Mitophagy. To determine whether rBTI promotes autophagy and the type of autophagy, Hep G2 cells were incubated in medium containing either vehicle (control) or 50 μg/mL and 100 μg/mL rBTI for 12 h. Subsequently, cells were prepared for EM studies. Unequivocal evidence for autophagy was obtained from electron microscopy. Representative electron microphotographs of control and rBTI-treated cells are shown in Figure 1A. We found mitochondria inside an autophagosome structure in rBTI-treated Hep G2 cells, but not in untreated cells. Numerous membrane packaged structures were apparent inside the cells, and these structures could contain damaged mitochondria. When cells were treated with 100 ug/mL rBTI for 12 h, multiple autophagolysosome structures appeared in the cells. To confirm the effect of rBTI on autophagy, Hep G2 cells were transfected with pEGFP-LC3 and then incubated in medium containing either buffer or 50 μg/mL rBTI for different lengths of time. Following incubation, cells were examined by confocal microscopy. Representative microphotographs of autophagic activity stimulated by rBTI are presented in Figure 1B. rBTI strongly increased the LC3 protein conversion, as well as formation of GFP-LC3 punctate structures, indicating that rBTI induces autophagy (Figure 1B). At the same time, Hep G2 cells transfected with pDsRed2-Mito were used to monitor the changes of mitochondria induced by rBTI. When Hep G2/pDsRed2-Mito cells were treated with rBTI, mitochondria mainly existed in a form of Red-Mito punctate structures that could be clearly distinguished from the dispersed mitochondria seen in cells that were left untreated with rBTI (Figure 1B). Under rBTI treatment, mitochondria underwent fragmentation within a few hours; the mitochondrial pattern was disrupted, and the mitochondria partially disappeared.

Induction of autophagy was supported by MDC staining. Figure 1C shows clearly that control cells display very rare green fluorescent punctate structures, indicating a lack of acidic vesicular organelles. However, rBTI-treated cells showed an increase in the number of green fluorescent punctate structures at different time points post-treatment, when compared with the control. This indicates significant autophagic vesicle formation in Hep G2 cells exposed to rBTI. These autophagic vacuoles are then fused with lysosomes, and eventually the delivered contents are degraded by lysosome enzymes such as acid phosphatase and the mature form of cathepsin D.

We also investigated the alteration of mitochondrial proteins Cox IV and Tom20. Both of these proteins were decreased in rBTI-treated cells, whereas an ER protein GRP94 was not changed (Figure 1D). In particular, Hep G2 cells that had been treated with 100 μg/mL rBTI for 12 or 24 h showed significant reduction of Cox IV and Tom20, compared with cells treated

DOI: 10.1021/acs.jafc.5b02644
J. Agric. Food Chem. 2015, 63, 7795−7804

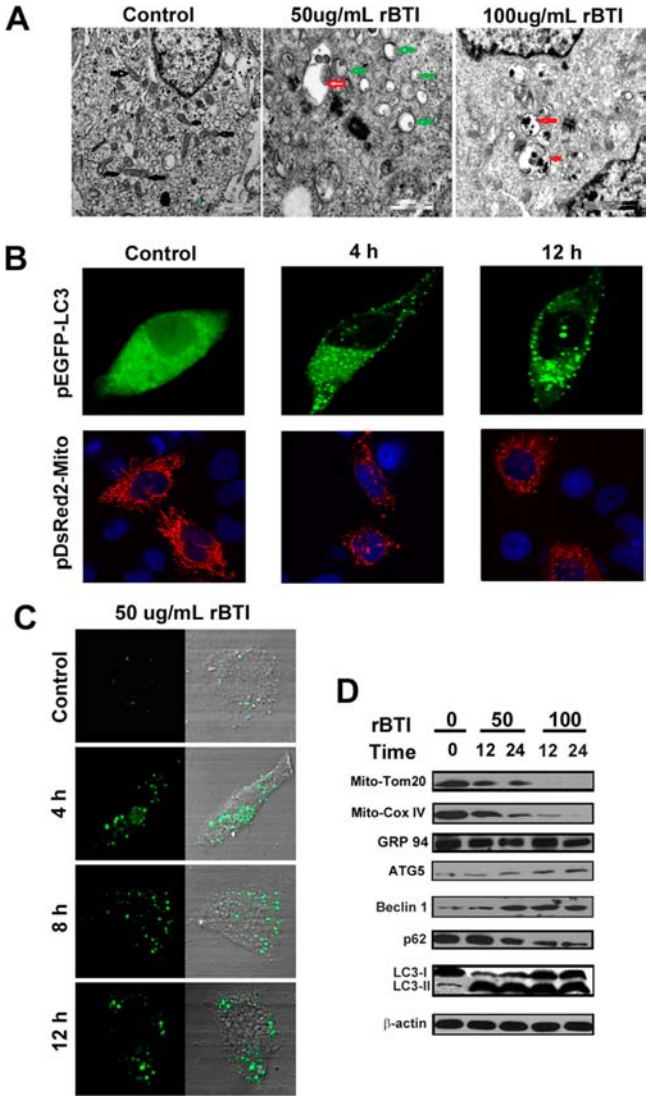

Figure 1. rBTI induces mitophagy. (A) Transmission electron microscopy pictures show rBTI-induced autophagic encapsulation of mitochondria. Hep G2 cells were treated with 50 μg/mL and 100 μg/mL rBTI for 12 h. Black arrow, mitochondria; green arrow, mitochondrial fragmentation; red arrow, autophagosome structures. (B) rBTI increases the number of GFP-LC3 punctate structures and induced mitochondrial fragmentation in Hep G2 cells. (C) MDC staining shows autophagy was activated in Hep G2 cells after treatment with rBTI. (D) Western blot was used to examine the mitochondrial protein and marker proteins involved in autophagy.

only with 50 μg/mL rBTI and the control group. Marker proteins involved in autophagy were also tested. As shown in Figure 1D, rBTI significantly increased the level of phosphatidylethanolamine-conjugated LC3-II, whereas unconjugated LC3-I levels were significantly decreased. Beclin-1, also known as the autophagy-related gene Atg 6, was also shown to be required for the initiation of autophagosome formation. Similar to LC3-II expression, beclin-1 levels were enhanced by rBTI treatment, and the autophagy substrate p62 was also reduced. Taking these data into account, we concluded that rBTI could induce the autophagic selective removal of mitochondria.

rBTI Depolarized Mitochondria and Increased ROS. We had an interest in understanding why autophagy induced by rBTI contributed to the degradation of mitochondria in Hep G2 cells. Therefore, first we tested the mitochondrial membrane potential (MMP) of Hep G2 cells under rBTI treatment. The cells were marked with JC-1; then, the mitochondrial membrane potential was analyzed by both flow cytometry and laser scanning confocal microscopy. The relative proportion of red and green fluorescent intensity indicates the mitochondrial depolarization ratio. Dramatic decline of mitochondrial potential was observed at the initial 4 h after rBTI treatment. Afterward, membrane depolarization was gradually recovered to the normal state, similar to that of the control at 24 h post-treatment (Figure 2A). The mitochondrial membrane potential was observed by laser scanning confocal microscopy following labeling of cells with JC-1 (Figure 2B). After 50 μg/mL of rBTI treatment for 2 and 4 h, mitochondria with normal MMP displayed red fluorescence, whereas those with abnormal MMP demonstrated green fluorescence. In this experiment, we observed an increase in green fluorescence but a decrease in red fluorescence in rBTI-treated cells.

It is well-known that ROS generation is correlated with depolarized mitochondrial membrane potential. Given that rBTI could quickly enter cells and negatively influence the mitochondrial membrane potential, we decided to examine the levels of cellular ROS after treatment with rBTI, utilizing H_2DCFH-DA staining and flow cytometry. Indeed, we observed a clear time-dependent increase in cellular ROS after treatment with 50 μg/mL rBTI. We found there was an increase in ROS production after treatment with rBTI for only 0.5 h, and ROS levels continuously increased for 2 h after exposure. ROS increased sharply between 2 and 4 h and reached a maximal level at 18 h. ROS levels then declined at 24 h, but were still higher than control levels (Figure 2C). Thus, rBTI is indeed a potent inducer of ROS. The relationship of mitochondrial membrane potential and ROS is shown in Figure 2D. Reduction of MMP and the consequent changes in ROS levels indicate a direct effect of rBTI rather than an indirect downstream effect.

rBTI Changed the Antioxidant System. Reactive oxygen species, including superoxide anions, hydroxyl radicals, and their byproducts, are toxic to diverse cell types as they can induce lipid peroxidation, DNA fragmentation, and protein oxidation. These reactive oxygen species can be scavenged by endogenous antioxidants including SOD, CAT, and glutathione peroxidase. In this study, the activities of SOD, CAT, and GSH in the cells were determined at various time points. As shown in Figure 3A, the activity of SOD in Hep G2 cells slowly increased after rBTI treatment for 0.5−6 h, with a peak value occurring at 8 h, although the activity at 18 and 24 h was still higher than that of the control group. CAT activity in Hep G2 cells showed no statistically significant difference after treatment with rBTI for 0−8 h, but the activity at 18 and 24 h slowly increased (Figure 3B). Total GSH level was significantly enhanced after rBTI treatment for 4−24 h, and at the same time the GSH/GSSG ratio also increased (Figure 3C,D). The significant increase in total GSH level and GSH/GSSG ratio also indicates that Hep G2 cells exposed to rBTI exhibited elevated antioxidant capacity.

Mild and Transient Oxidative Stress Induces Mitophagy. We were concerned with the role of ROS in regulating autophagy in Hep G2 cells under rBTI stress conditions. The amount of mitochondria undergoing autophagy was quantified by two assays using flow cytometry and confocal fluorescence microscopy. A Cyto-ID green detection kit−combined flow cytometric analysis was utilized to quantitatively determine the

DOI: 10.1021/acs.jafc.5b02644
J. Agric. Food Chem. 2015, 63, 7795−7804

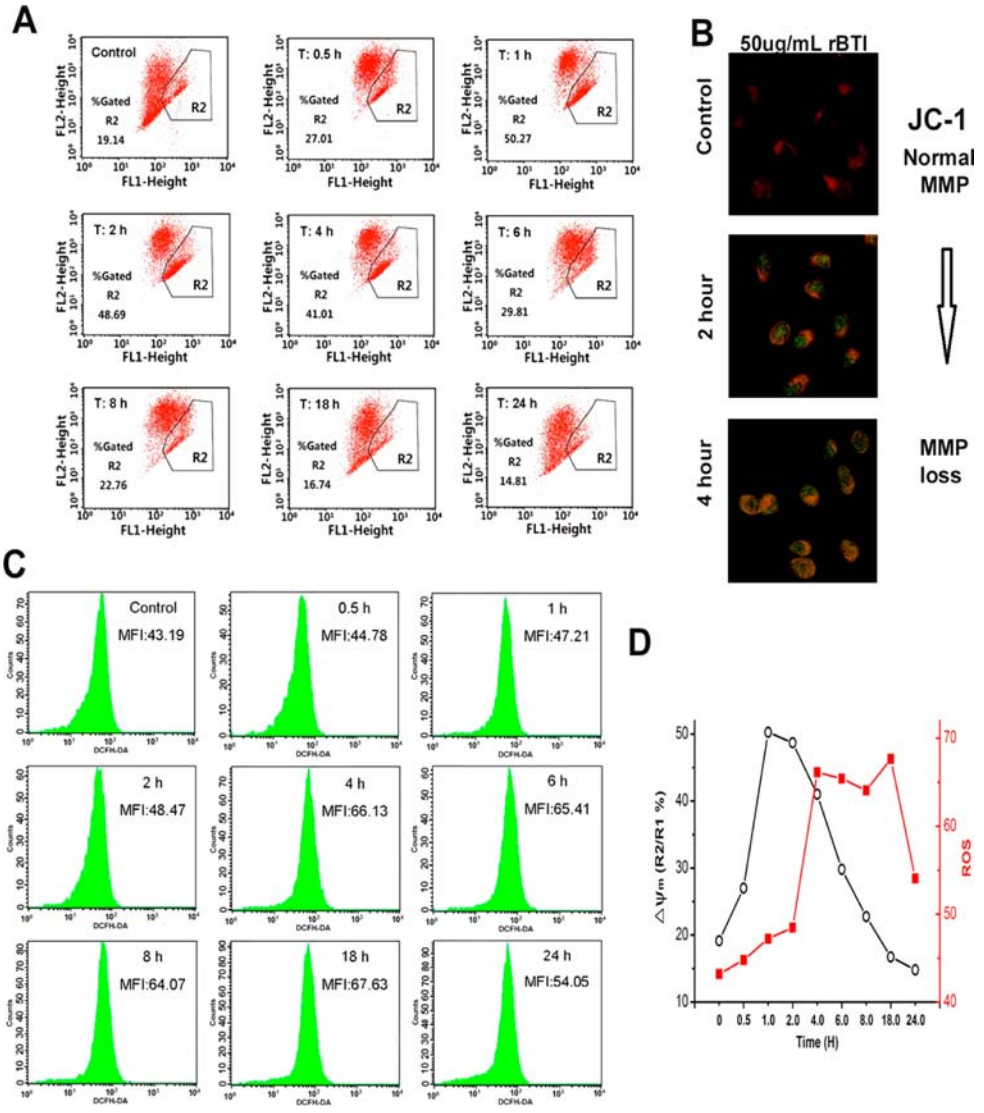

Figure 2. Effect of rBTI on mitochondrial membrane potential and ROS in Hep G2 cells. (A) Flow cytometry analysis of mitochondrial membrane potential. Cells were treated with 50 μg/mL rBTI for the indicated times, stained with JC-1, and then analyzed by flow cytometry. (B) Laser scanning confocal microscope analysis of mitochondrial membrane potential. Cells were treated with 50 μg/mL rBTI for 2 and 4 h, stained with anti-JC-1, and subjected to laser scanning confocal microscopy. (C) Flow cytometry analysis of intracellular ROS. Cells were treated with 50 μg/mL rBTI for the indicated times, stained with H_2DCFH-DA, and then analyzed by flow cytometry. (D) Graph showing the relationship between mitochondrial membrane potential and the level of ROS.

presence of autophagosome or autolysosome induced by rBTI in Hep G2 cells. After cells were incubated with rBTI and/or 3-MA and NAC, the average fluorescent intensity was measured by flow cytometry. The results showed that autophagy was significantly stimulated in Hep G2 cells when treated for 8 and 24 h. When Hep G2 cells were treated with rBTI combined with the autophagy inhibitor 3-MA and the ROS inhibitors NAC, respectively, the level of autophagy was dramatically decreased (Figure 4A). These results indicate that mild and transient ROS induced by rBTI were important signaling molecules required for the formation of autophagosomes.

LC3 has been considered an autophagosomal marker because of its localization and aggregation on autophagosomes. In this study, pEGFP-LC3 plasmid was transiently transfected into Hep G2 cells to determine if LC3 was involved in autophagy induced by rBTI. As shown in Figure 4B, rBTI-treated cells (at 8 and 24 h post-treatment) exhibited a significantly increased number of green LC3 punctate structures in the cytoplasm as compared to the nontreated control. In contrast, cells treated with rBTI and NAC or rBTI and 3-MA demonstrated apparently reduced numbers of GFP-LC3 puncta as compared to cells treated with rBTI alone. These data indicate decreasing ROS by NAC could reduce rBTI-mediated autophagy activation, which was comparable to the effect of 3-MA. In addition, ATP levels were reduced by rBTI treatment, indicating that the number of mitochondria was also reduced (Figure 4C). According to the results of MTT cytotoxicity assay, the inhibition rates of Hep G2 cells treated with either rBTI (50 μg/mL) or 3-MA alone were approximately 10% and 30% at 12 and 24 h post-treatments, respectively. However, the combined treatment could significantly reduce the inhibition rate. We also investigated the alteration of mitochondrial proteins Cox IV and Tom20 as well as the marker proteins involved in autophagy LC3 and P62 after Hep G2 cells were treated with rBTI (50 μg/mL), 3-MA/NAC alone, or combined with 3-MA/NAC for 24 h. The results showed

DOI: 10.1021/acs.jafc.5b02644
J. Agric. Food Chem. 2015, 63, 7795−7804

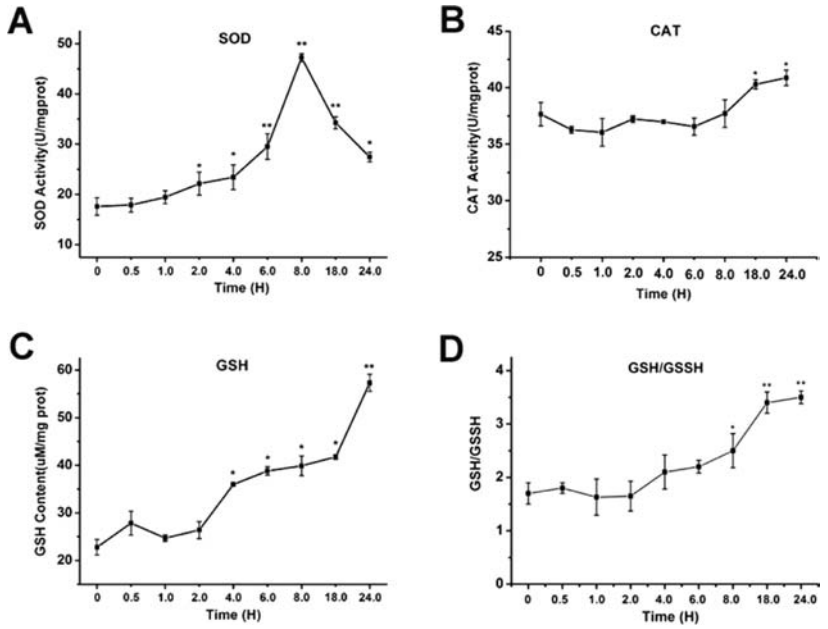

Figure 3. Analysis of antioxidant enzymes in Hep G2 cells. (A) Activity change of SOD. (B) Activity change of CAT. (C) Content change of GSH. (D) GSH/GSSG ratio in the Hep G2 cells. Cells were treated with 50 μg/mL rBTI for the indicated times (0, 0.5, 1, 2, 4, 6, 8, 12, and 24 h). After treatment, total cell lysates were prepared according to the protocol for each assay, and the activity/content of SOD, CAT, and GSH was measured. *, $P < 0.05$; **, $P < 0.01$ vs control group.

that 3-MA/NAC partly counteracted rBTI-mediated increment of autophagy activation as well as loss of mitochondrial outer membrane proteins Tom 20 and Cox IV (Figure 4E). Another antophagy inhibitor, bafilymocin A1, was used to check the autophagy flux. The result showed that autophagosome accumulation is due to autophagy induction rather than blockade of autophagic flux in the downstream steps (Figure 4F). Taken together, both assays show that mitophagy is induced by mild oxidative stress in rBTI-treated Hep G2 cells.

Subcellular Localization of rBTI. For immunofluorescence staining, transfected Hep G2 cells expressing pDsRed2-Mito were treated with FITC-BTI for 4 h and then fixed with 4% (w/v) paraformaldehyde for 10 min. In Figure 5A, the yellow color in the merged image indicates colocalization of FITC-BTI with mitochondria and that FITC-BTI and mitochondria mainly form punctate structures in the cytoplasm. This indicates that rBTI could target the mitochondria and induce mitochondrial fragmentation.

To further understand rBTI-mediated mitophagy, we investigated mitochondrial localization with LC3. Hep G2 cells transfected with pDsRed2-Mito and pEGFP-LC3 were incubated with or without rBTI; then, the colocalization of mitochondria with GFP-LC3 was examined. Consistently, treatment with rBTI increased colocalization of mitochondria with GFP-LC3, when compared to nontreated control. The yellow color in the merged image indicates colocalization of mitochondria and GFP-LC3 puntates (Figure 5B).

To support the immunofluorescence data, biochemical fractionation of crude extracts from Hep G2 cells was performed at 4 °C. Cytoplasmic and mitochondrial proteins were further analyzed by Western blot. As controls for proper cytosolic and mitochondrial separation, β-actin, p62, Tom 20, and Tim 23 were used as markers for the cytosol and mitochondria. In accordance with the immunofluorescent results, rBTI was found to be localized at both mitochondrial and cytoplasmic fractions (Figure 5C). An interesting phenomenon is that Tom 20 was found not only in the mitochondrial fraction but also in the cytoplasm when cells were treated with rBTI. Furthermore, by performing immunoprecipitation and Western blot assays, we found that rBTI specifically associates with Tom 20 (Figure 5D). Thus, Tom 20 may be the direct target of rBTI.

Mitochondria are essential regulators of cell death and respond to many different stress signals, including loss of growth factors, hypoxia, oxidative stress, and DNA damage. Mitochondria are a major source of ROS, which are byproducts of mitochondrial electron transport activity. Under normal conditions, cells develop a highly efficient antioxidant system that can neutralize ROS. However, destroyed mitochondria can produce excessive ROS at levels that exceed the capacity of the antioxidant system, which can result in cell death or autophagy. In recent years there has been much research showing that mitochondrial ROS signals affect signaling pathways and cellular processes. It is now recognized that mitochondrial ROS are required for the cellular response to hypoxia,[20] to regulate cell cycle progression,[21] to trigger E2F1-dependent apoptosis,[22] to regulate telomere stability,[23] and for organismal lifespan.[24] Additionally, signaling pathways such as Notch[25] and Akt[25] are now known to be modulated by mitochondrial ROS. In addition, ROS plays an important role in inducing autophagy in cells, but exactly how ROS regulates autophagy is unknown. ROS as signaling molecules can activate the protease Atg4B, which could cleave the C-terminus of LC3-I, an essential precursor to conversion of LC3-I to LC3-II.[26] Mitochondrial ROS could activate autophagy by activating AMPK, but independent of an increase in AMP/ATP ratio.[27]

In previous studies, we showed that rBTI has a strong cytotoxic effect on a wide variety of cancer cell lines, such as EC9706, Hep G2, HeLa, and other solid tumor cells, although the exact molecular mechanism is not certain. In this study, we utilized Hep G2 cells as an experimental model to evaluate the toxicity of rBTI and to investigate the effect of rBTI on

DOI: 10.1021/acs.jafc.5b02644
J. Agric. Food Chem. 2015, 63, 7795−7804

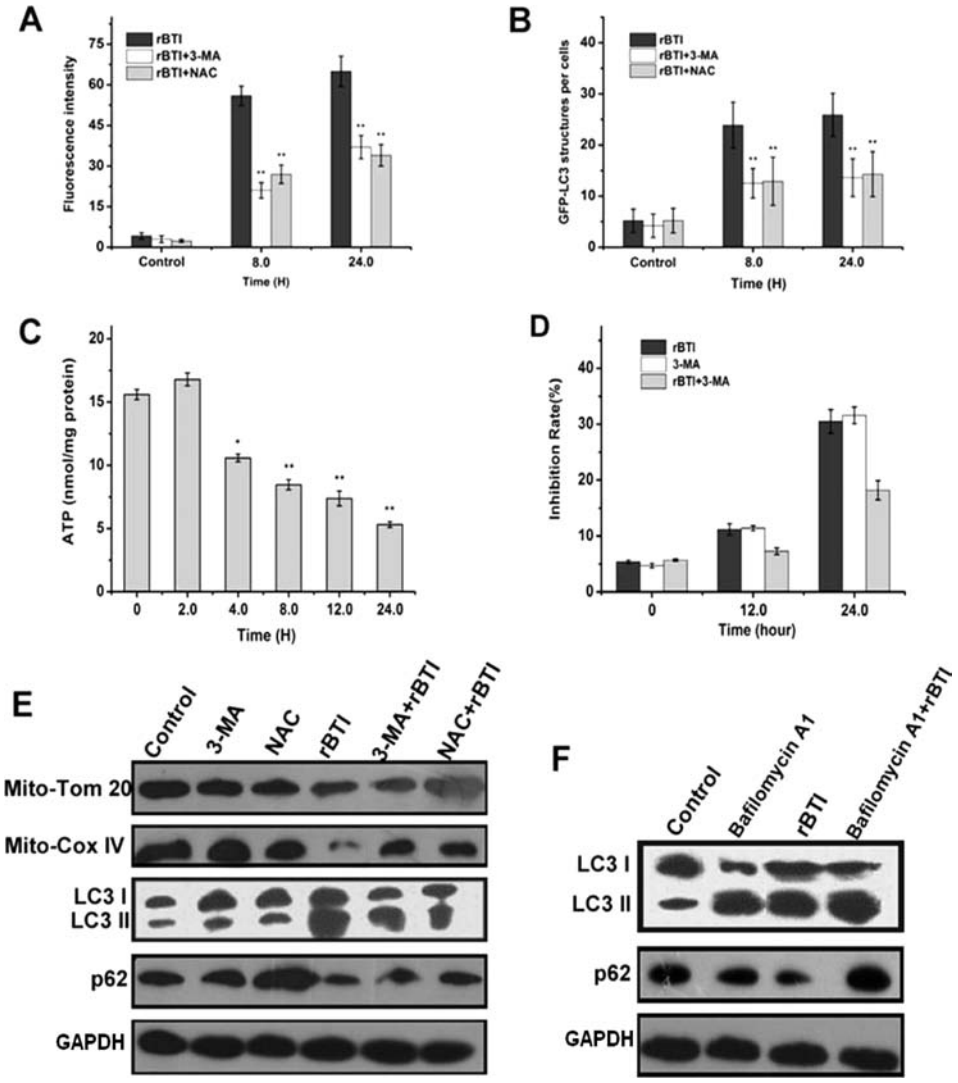

Figure 4. Mild and transient oxidative stress induced by rBTI-driven mitophagy. (A) Quantitative analysis of autophagy induced by rBTI was assessed by flow cytometry. Cells were incubated with rBTI and/or 3-MA and NAC; then, the average intensity of fluorescence was detected via flow cytometry. (B) Number of GFP-LC3 punctate structures in the cytoplasm. Hep G2/GFP-LC3 cells were exposed to rBTI and/or 3-MA, and NAC and autophagic GFP-LC3 punctate were counted in the pictures obtained from confocal microscopy at various time points. (C) Effect of rBTI on intracellular ATP levels in Hep G2 cells. Cells were treated with 50 μg/mL rBTI for different time points (2, 4, 8, 12, and 24 h) before measurement of ATP by a luminometric assay. (D) Cytotoxicity of rBTI. Hep G2 cells were treated with or without rBTI (50 μg/mL) and 3-MA for 12 or 24 h; then the cell viability was determined by standard MTT assay. (E) Effect of rBTI/3-MA/NAC on the level of autophagy and mitochondrial mass after rBTI treated. Hep G2 cells were treated with rBTI (50 μg/mL), 3-MA(2 mM)/NAC(1 mM) alone or combined with 3-MA/NAC for 24h, and then the level of Tom20, Cox IV, LC3 and p62 were analyzed by immunoblotting. (F) The level of autophagy in Hep G2 cells with or without rBTI (50 μg/mL) and Bafilomycin A1(10 nM). * $P < 0.05$, ** $P < 0.01$ vs control group.

mitochondrial function. Depending on the immunofluorescent staining, the autophagy level in Hep G2 was enhanced in those cells treated with rBTI. Taking into account the changes in mitochondrial morphology and the data from the Western blots, we concluded that rBTI could induce autophagic selective removal of dysfunctional mitochondria (Figure 1). We then studied the role of ROS in autophagy as well as the colocalization of rBTI and mitochondria in Hep G2 cells. We found that rBTI can directly target mitochondria to cause mitochondrial dysfunction and at the same time drive release of ROS from damaged mitochondria as signaling molecules to activate autophagy and quickly remove damaged mitochondria. Taken together, these results suggest that mitochondrial dysfunction plays an important role in mitophagy induced by rBTI.

ROS-scavenging enzymes include catalase, superoxide dismutase, monodehydroascorbate reductase, dehydroascorbate reductase, glutathione peroxidase, peroxiredoxin, ascorbate peroxidase, and glutathione reductase. Among these enzymes, SOD converts superoxide $O_2^{\bullet-}$ into H_2O_2, which is further detoxified into H_2O and O_2 by catalase or peroxidases.[28] In this study, we found an increasing trend of SOD activity after treatment with rBTI. Therefore, rBTI promotes Hep G2 cells to produce $O_2^{\bullet-}$. However, the detoxification of endogenous $O_2^{\bullet-}$ by SOD in different cellular compartments is always accompanied by the production of H_2O_2, which is toxic and often regulated by enzymes such as CAT and GSH-Px. As a consequence, we measured the increased content of GSH and an elevated ratio of GSH/GSSG in the treatment group, suggesting that cells can keep more glutathione in the reduced

DOI: 10.1021/acs.jafc.5b02644
J. Agric. Food Chem. 2015, 63, 7795−7804

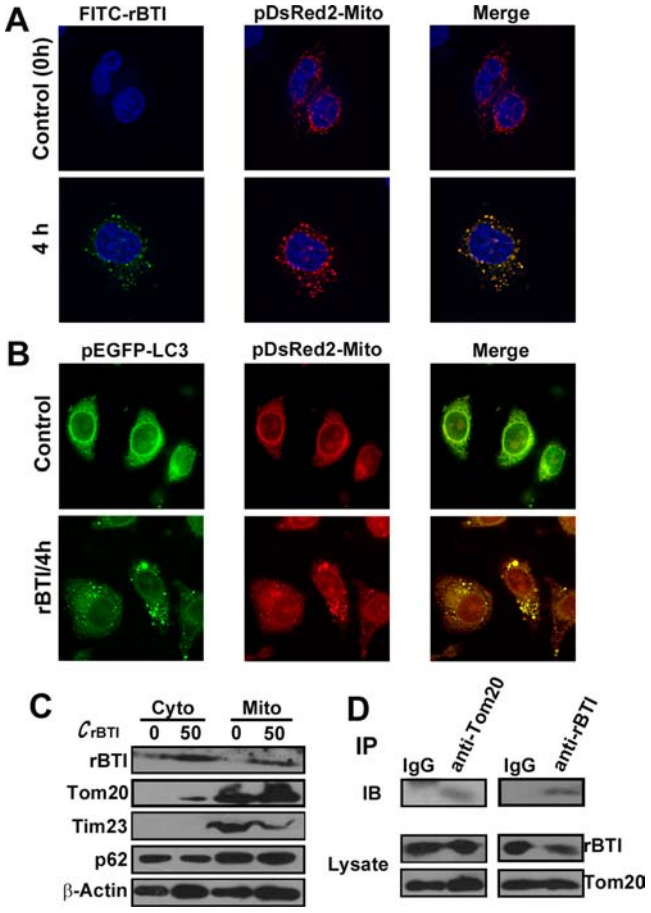

Figure 5. Mitochondrial targeting of rBTI in Hep G2 cells. (A) Colocalization of FITC-BTI with mitochondria. Cells transfected with pDsRed2-Mito are treated with FITC-BTI for 4 h and analyzed by confocal microscopy. (B) Colocalization of GFP-LC3 with mitochondria. Hep G2 cells were cotransfected with pDsRed2-Mito and pEGFP-LC3; after 24 h, thee cells were treated with 50 μg/mL rBTI for 4 h. (C) Western blot analysis of mitochondrial and cytosolic cell fractions. Mitochondrial and cytosolic fractions were obtained using a cell mitochondria isolation kit (Beyotime Institute of Biotechnology) after being treated with 50 μg/mL rBTI for 2 h in Hep G2 cells. These fractions were then analyzed by Western blot for the endogenous proteins Tom23, Tom20, and p62. β-Actin was used as a loading control, and rBTI in each fraction was also blotted. (D) Co-immunoprecipitation of rBTI with endogenous Tom 20 in Hep G2 cells after being treated with 50 μg/mL rBTI for 2 h in Hep G2 cells.

state by increasing enzymatic activity. When Hep G2 cells were treated with rBTI and NAC, the level of autophagy was drastically decreased. These results show that ROS induced by rBTI was mild and transient and that these kinds of ROS are important signaling molecules needed to induce the formation of autophagosomes.

Mitophagy promotes turnover of dysfunctional mitochondria that would otherwise damage the cell. Loss of mitochondrial membrane potential and mitochondrial fragmentation precede mitophagy,[4,29] suggesting that this plays a role in their selective uptake by autophagosomes. Indeed, mitochondrial depolarization plays a direct role in activating Parkin-dependent mitophagy by inducing PINK1 kinase stabilization at the OMM.[30,31] Mitochondrial membrane depolarization also induces proteolytic cleavage and degradation of the fusion protein Opa-1. This in turn decreases the size of mitochondria and is likely to favor uptake of mitochondria by phagophore membranes, while also linking mitochondrial turnover to loss of function.[32,33]

The duality of autophagy function in cancer (both pro- and antitumorigenic) makes it clinically questionable to generically target the entire autophagy process. Basal levels of mitophagy are important for maintaining cellular homeostasis and protecting cells against accumulation of dysfunctional mitochondria. However, enhanced levels of mitophagy can lead to excessive removal of mitochondria, loss of cardiac myocytes, and development of heart failure. Because tumor cells already produce increased ROS compared to normal cells,[34] the combined effect of increased ROS and reduced mitochondrial metabolism arising from inhibition of mitophagy may be synergistic and promote efficient tumor cell killing. Cancer cells decreased mitochondrial activity and instead shift to aerobic glycolysis for ATP production, a phenomenon known as the Warburg effect. An alternative approach may be to combine mitophagy inhibition with drugs that induce other forms of mitochondrial stress signaling, such as metformin that inhibits respiratory chain complex I or with antibiotics, such as tetracycline and doxcycline that inhibit mitochondrial protein translation, thereby inducing a "mitonuclear" protein imbalance and a mitochondrial unfolded protein response that might be predicted to depend on mitophagy to clear damaged and dysfunctional mitochondria.[35,36] With overwhelming mitochondrial damage, apoptosis becomes dominant, and inactivation of critical proteins of the autophagy pathway allow for cell death. Sodium valproate inhibits mitochondrial respiration and leads to mitochondrial dysfunction, oxidative stress, and increased cell death.[37] Shikonin could accumulate in the mitochondria of cancer cells, disrupt mitochondrial function, and lead to apoptosis.[38] Hence, drugs that induce mitochondrial dysfunction could have some potential for cancer treatment.

In summary, our results indicate that rBTI directly targets the mitochondria of cancer cells, disrupts mitochondrial function, and stimulates ROS production, resulting in mitophagy to remove dysfunctional mitochondria. In addition, rBTI could induce mitochondrial fragmentation and may therefore have potential as a mitochondria-penetrating peptide for use in the treatment of cancer.

AUTHOR INFORMATION

Corresponding Author

*Tel: +86 351 7019371. Fax: +86 351 7011499. E-mail: cuixiaodong@sxu.edu.cn.

Funding

This work was supported by the Natural Sciences Foundation of China (31171659 and 31300653) and the Science and Technology Committee of Shanxi Province (2014091028).

Notes

The authors declare no competing financial interest.

ABBREVIATIONS USED

rBTI, recombinant buckwheat trypsin inhibitor; DMSO, dimethyl sulfoxide; SOD, superoxide dismutase; CAT, catalase; GSH, reduced glutathione; GSSG, oxidized glutathione; ROS, reactive oxygen species; FITC, fluorescein isothiocyanate; TRITC, tetramethyl rhodamine isothiocyanate; DAPI, 4′,6-diamidino-2-phenylindole; JC-1, tetrechloro-tetraethyl-benzimidazol carbocyanine iodide; MDC, monodansyl-cadaverine; 3-MA, 3-methyladenine; NAC, *N*-acetyl-L-cysteine; LC3, microtubule-associated protein light chain 3

DOI: 10.1021/acs.jafc.5b02644
J. Agric. Food Chem. 2015, 63, 7795−7804

REFERENCES

(1) Cuervo, A. M. Autophagy: in sickness and in health. *Trends Cell Biol.* **2004**, *14* (2), 70−77.
(2) Rabinowitz, J. D.; White, E. Autophagy and metabolism. *Science* **2010**, *330* (6009), 1344−1348.
(3) Kaminskyy, V.; Zhivotovsky, B. Proteases in autophagy. *Biochim. Biophys. Acta, Proteins Proteomics* **2012**, *1824* (1), 44−50.
(4) Twig, G.; Elorza, A.; Molina, A. J.; Mohamed, H.; Wikstrom, J. D.; Walzer, G.; Stiles, L.; Haigh, S. E.; Katz, S.; Las, G.; Alroy, J.; Wu, M.; Py, B. F.; Yuan, J.; Deeney, J. T.; Corkey, B. E.; Shirihai, O. S. Fission and selective fusion govern mitochondrial segregation and elimination by autophagy. *EMBO J.* **2008**, *27* (2), 433−446.
(5) Lemasters, J. J. Selective mitochondrial autophagy, or mitophagy, as a targeted defense against oxidative stress, mitochondrial dysfunction, and aging. *Rejuvenation Res.* **2005**, *8* (1), 3−5.
(6) Youle, R. J.; Narendra, D. P. Mechanisms of mitophagy. *Nat. Rev. Mol. Cell Biol.* **2011**, *12* (1), 9−14.
(7) Okamoto, K.; Kondo-Okamoto, N. Mitochondria and autophagy: critical interplay between the two homeostats. *Biochim. Biophys. Acta, Gen. Subj.* **2012**, *1820* (5), 595−600.
(8) Lee, J.; Giordano, S.; Zhang, J. Autophagy, mitochondria and oxidative stress: cross-talk and redox signalling. *Biochem. J.* **2012**, *441* (2), 523−540.
(9) Park, S. J.; Shin, J. H.; Kim, E. S.; Jo, Y. K.; Kim, J. H.; Hwang, J. J.; Kim, J. C.; Cho, D. H. Mitochondrial fragmentation caused by phenanthroline promotes mitophagy. *FEBS Lett.* **2012**, *586* (24), 4303−4310.
(10) Turra, D.; Lorito, M. Potato type I and II proteinase inhibitors: modulating plant physiology and host resistance. *Curr. Protein Pept. Sci.* **2011**, *12* (5), 374−385.
(11) Palavalli, M. H.; Natarajan, S. S.; Wang, T. T.; Krishnan, H. B. Imbibition of soybean seeds in warm water results in the release of copious amounts of Bowman-Birk protease inhibitor, a putative anticarcinogenic agent. *J. Agric. Food Chem.* **2012**, *60* (12), 3135−3143.
(12) Chen, Y. W.; Huang, S. C.; Lin-Shiau, S. Y.; Lin, J. K. Bowman-Birk inhibitor abates proteasome function and suppresses the proliferation of MCF7 breast cancer cells through accumulation of MAP kinase phosphatase-1. *Carcinogenesis* **2005**, *26* (7), 1296−1306.
(13) Clemente, A.; Gee, J. M.; Johnson, I. T.; Mackenzie, D. A.; Domoney, C. Pea (Pisum sativum L.) protease inhibitors from the Bowman-Birk class influence the growth of human colorectal adenocarcinoma HT29 cells in vitro. *J. Agric. Food Chem.* **2005**, *53* (23), 8979−8986.
(14) Wang, Z. H.; Gao, L.; Li, Y. Y.; Zhang, Z.; Yuan, J. M.; Wang, H. W.; Zhang, L.; Zhu, L. Induction of apoptosis by buckwheat trypsin inhibitor in chronic myeloid leukemia K562 cells. *Biol. Pharm. Bull.* **2007**, *30* (4), 783−786.
(15) Li, Y. Y.; Zhang, Z.; Wang, Z. H.; Wang, H. W.; Zhang, L.; Zhu, L. rBTI induces apoptosis in human solid tumor cell lines by loss in mitochondrial transmembrane potential and caspase activation. *Toxicol. Lett.* **2009**, *189* (2), 166−175.
(16) Kubli, D. A.; Gustafsson, A. B. Mitochondria and mitophagy: the yin and yang of cell death control. *Circ. Res.* **2012**, *111* (9), 1208−1221.
(17) Scherz-Shouval, R.; Elazar, Z. ROS, mitochondria and the regulation of autophagy. *Trends Cell Biol.* **2007**, *17* (9), 422−427.
(18) Zhang, Z.; Li, Y.; Li, C.; Yuan, J.; Wang, Z. Expression of a buckwheat trypsin inhibitor gene in Escherichia coli and its effect on multiple myeloma IM-9 cell proliferation. *Acta Biochim. Biophys. Sin.* **2007**, *39* (9), 701−707.
(19) Cui, X.; Wang, Z.; Li, Y.; Li, C. Buckwheat trypsin inhibitor enters Hep G2 cells by clathrin-dependent endocytosis. *Food Chem.* **2013**, *141* (3), 2625−2633.
(20) Bell, E. L.; Klimova, T. A.; Eisenbart, J.; Moraes, C. T.; Murphy, M. P.; Budinger, G. R.; Chandel, N. S. The Qo site of the mitochondrial complex III is required for the transduction of hypoxic signaling via reactive oxygen species production. *J. Cell Biol.* **2007**, *177* (6), 1029−1036.
(21) Formentini, L.; Sanchez-Arago, M.; Sanchez-Cenizo, L.; Cuezva, J. M. The mitochondrial ATPase inhibitory factor 1 triggers a ROS-mediated retrograde prosurvival and proliferative response. *Mol. Cell* **2012**, *45* (6), 731−742.
(22) Raimundo, N.; Song, L.; Shutt, T. E.; McKay, S. E.; Cotney, J.; Guan, M. X.; Gilliland, T. C.; Hohuan, D.; Santos-Sacchi, J.; Shadel, G. S. Mitochondrial stress engages E2F1 apoptotic signaling to cause deafness. *Cell* **2012**, *148* (4), 716−726.
(23) Schroeder, E. A.; Raimundo, N.; Shadel, G. S. Epigenetic silencing mediates mitochondria stress-induced longevity. *Cell Metab.* **2013**, *17* (6), 954−964.
(24) Zarse, K.; Schmeisser, S.; Groth, M.; Priebe, S.; Beuster, G.; Kuhlow, D.; Guthke, R.; Platzer, M.; Kahn, C. R.; Ristow, M. Impaired insulin/IGF1 signaling extends life span by promoting mitochondrial L-proline catabolism to induce a transient ROS signal. *Cell Metab.* **2012**, *15* (4), 451−465.
(25) Hamanaka, R. B.; Glasauer, A.; Hoover, P.; Yang, S.; Blatt, H.; Mullen, A. R.; Getsios, S.; Gottardi, C. J.; DeBerardinis, R. J.; Lavker, R. M.; Chandel, N. S. Mitochondrial reactive oxygen species promote epidermal differentiation and hair follicle development. *Sci. Signaling* **2013**, *6* (261), ra8.
(26) Scherz-Shouval, R.; Shvets, E.; Fass, E.; Shorer, H.; Gil, L.; Elazar, Z. Reactive oxygen species are essential for autophagy and specifically regulate the activity of Atg4. *EMBO J.* **2007**, *26* (7), 1749−1760.
(27) Emerling, B. M.; Weinberg, F.; Snyder, C.; Burgess, Z.; Mutlu, G. M.; Viollet, B.; Budinger, G. R.; Chandel, N. S. Hypoxic activation of AMPK is dependent on mitochondrial ROS but independent of an increase in AMP/ATP ratio. *Free Radical Biol. Med.* **2009**, *46* (10), 1386−1391.
(28) Scherz-Shouval, R.; Elazar, Z. Regulation of autophagy by ROS: physiology and pathology. *Trends Biochem. Sci.* **2011**, *36* (1), 30−38.
(29) Rambold, A. S.; Kostelecky, B.; Elia, N.; Lippincott-Schwartz, J. Tubular network formation protects mitochondria from autophagosomal degradation during nutrient starvation. *Proc. Natl. Acad. Sci. U. S. A.* **2011**, *108* (25), 10190−10195.
(30) Matsuda, N.; Sato, S.; Shiba, K.; Okatsu, K.; Saisho, K.; Gautier, C. A.; Sou, Y. S.; Saiki, S.; Kawajiri, S.; Sato, F.; Kimura, M.; Komatsu, M.; Hattori, N.; Tanaka, K. PINK1 stabilized by mitochondrial depolarization recruits Parkin to damaged mitochondria and activates latent Parkin for mitophagy. *J. Cell Biol.* **2010**, *189* (2), 211−221.
(31) Vives-Bauza, C.; Zhou, C.; Huang, Y.; Cui, M.; de Vries, R. L.; Kim, J.; May, J.; Tocilescu, M. A.; Liu, W.; Ko, H. S.; Magrane, J.; Moore, D. J.; Dawson, V. L.; Grailhe, R.; Dawson, T. M.; Li, C.; Tieu, K.; Przedborski, S. PINK1-dependent recruitment of Parkin to mitochondria in mitophagy. *Proc. Natl. Acad. Sci. U. S. A.* **2010**, *107* (1), 378−383.
(32) Head, B.; Griparic, L.; Amiri, M.; Gandre-Babbe, S.; van der Bliek, A. M. Inducible proteolytic inactivation of OPA1 mediated by the OMA1 protease in mammalian cells. *J. Cell Biol.* **2009**, *187* (7), 959−966.
(33) Ehses, S.; Raschke, I.; Mancuso, G.; Bernacchia, A.; Geimer, S.; Tondera, D.; Martinou, J. C.; Westermann, B.; Rugarli, E. I.; Langer, T. Regulation of OPA1 processing and mitochondrial fusion by m-AAA protease isoenzymes and OMA1. *J. Cell Biol.* **2009**, *187* (7), 1023−1036.
(34) Sena, L. A.; Chandel, N. S. Physiological roles of mitochondrial reactive oxygen species. *Mol. Cell* **2012**, *48* (2), 158−167.
(35) Houtkooper, R. H.; Mouchiroud, L.; Ryu, D.; Moullan, N.; Katsyuba, E.; Knott, G.; Williams, R. W.; Auwerx, J. Mitonuclear protein imbalance as a conserved longevity mechanism. *Nature* **2013**, *497* (7450), 451−457.
(36) Durieux, J.; Wolff, S.; Dillin, A. The cell-non-autonomous nature of electron transport chain-mediated longevity. *Cell* **2011**, *144* (1), 79−91.
(37) Komulainen, T.; Lodge, T.; Hinttala, R.; Bolszak, M.; Pietilä, M.; Koivunen, P.; Hakkola, J.; Poulton, J.; Morten, K. J.; Uusimaa, J. Sodium valproate induces mitochondrial respiration dysfunction in HepG2 in vitro cell model. *Toxicology* **2015**, *331*, 47−56.

DOI: 10.1021/acs.jafc.5b02644
J. Agric. Food Chem. 2015, 63, 7795−7804

(38) Wiench, B.; Eichhorn, T.; Paulsen, M.; Efferth, T. Shikonin directly targets mitochondria and causes mitochondrial dysfunction in cancer cells. *Evid-Based. Compl. Alt.* **2012**, *2012*, 726025.

DOI: 10.1021/acs.jafc.5b02644
J. Agric. Food Chem. 2015, 63, 7795−7804

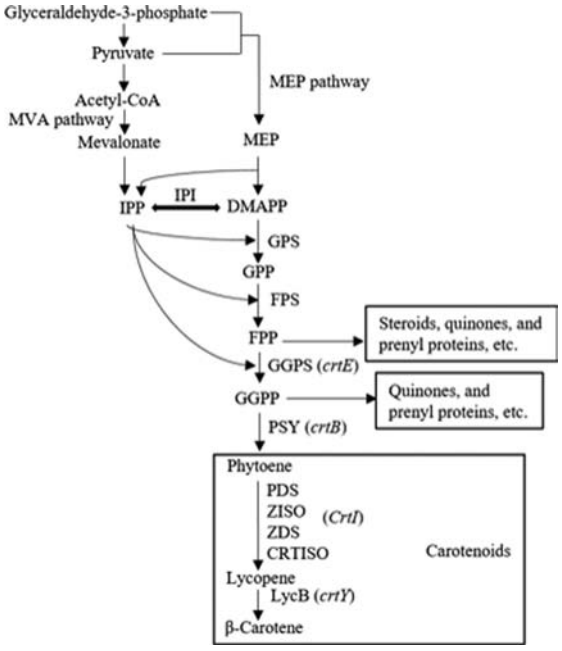

Figure 1. Isoprenoid biosynthetic pathway in the chloroplasts of plants and algae. IPP and DMAPP are synthesized using MVA and MEP pathways. MEP, 2-C-methyl-D-erythritol-4-phosphate; IPP, isopentenyl pyrophosphate; DMAPP, dimethylallyl pyrophosphate; GPP, geranyl diphosphate; FPP, farnesyl pyrophosphate; GGPP, geranylgeranyl diphosphate; IPI, isopentenyl pyrophosphate isomerase; GGPS, geranylgeranyl diphosphate synthase; PSY, phytoene synthase; PDS, phytoene desaturases; ZDS, ζ-carotene desaturases; ZISO, 15-cis-ζ-carotene isomerase; CRTISO, carotenoid isomerase; and LycB, lycopene β-cyclase. *CrtB*, *crtE*, *crtI*, and *crtY* encode the corresponding genes in bacteria.

The unique ability of *D. bardawil* to accumulate very large amounts of β-carotene under defined experimental conditions makes it an excellent choice for studying the intermediates of carotenoids. *PSY*[16] and *ZDS*[17] from *D. bardawil* and *PDS*[18] from *Dunaliella salina* have been isolated and characterized. In this study, *GGPS* from *D. bardawil* (*DbGGPS*) was first cloned and characterized. Then, heterologous expression using pET32a plasmid and functional complementation of *DbGGPS* using plasmids pACCRT-EIB and pACCAR16Δ*crtX* in *E. coli* were carried out to identify the cDNA encoding functional GGPS. This provides new gene sources for carotene genetic engineering and is helpful for understanding carotene biosynthesis.

MATERIALS AND METHODS

Algal Strains and Cultivation Conditions. The green algae *D. bardawil* was obtained from the Institute of Hydrobiology, Chinese Academy of Science. *D. bardawil* cells were grown in defined medium[19] containing 2 mol/L NaCl at 26 °C in a controlled chamber for 10−14 days and 8000 lx provided by cool-white fluorescent lamps, under a 16/8 h light/dark cycle with shaking at 96 rpm.

Bacterial Strains and Plasmids. *Escherichia coli* DH5α was used as the host for the multiplication of plasmids. The plasmids pACCRT-EIB and pACCAR16Δ*crtX*[8] were kindly provided by Norihiko Misawa, professor at Ishikawa Prefectural University, Japan.

Cloning of GGPS from *D. bardawil*. The total RNA was prepared from 8 mL of *D. bardawil* cells grown at the late log phase with Trizol reagent (Life Technology) according to the manufacture's instructions. The reverse transcription (RT) reaction was performed with the parameters set as 42 °C for 60 min followed by 70 °C for 5 min, according to the RevertAid First Strand cDNA Synthesis Kit (Thermo Scientific). To clone the *DbGGPS* cDNA, two degenerate primers (5′-ATGMGHTAYTCNBTDYTNGC-3′ and 5′-DSCRAT-RWAVTYNGCHARVSC-3′) were designed on the basis of the two conserved amino acid regions (upstream MRYSLLA and downstream AKYIGYR, Figure S1) from the GGPS protein sequences of several species (*Dunaliella viridis*, ADL16411.1; *Chlamydomonas reinhardtii*, XP_001703169.1; *Volvox carteri* f. *nagariensis*, XP_002953468.1; *Arabidopsis thaliana*, NP_195399.1; *Chrysanthemum boreale*, AGU91431.1; *Nicotiana tabacum*, ADD49734.1; *Croton sublyratus*, BAA86284.1; *Adonis palaestina*, AAV74395.1; *Taxus Canadensis*, AAD16018.1; *Cistus incanus* subsp. *Creticus*, AAM21638.1), then the expressed sequence tag (EST) of *DbGGPS* was acquired.

Then, on the basis of the switching mechanism at the 5′ end of the RNA transcript (SMART) technique, 5′-RACE PCR was performed using a modified oligo (dT) primer, 5′ SMARTer II A Oligonucleotide primer, and the SMARTScribe Reverse Transcriptase (a variant of MMLV RT) (BD Clontech). On the basis of the obtained EST of *DbGGPS*, two gene specific primers (5′-TCCTCTCCGTAC-ACCTTGTGGTTGGTGG-3′ and 5′-TGTCCCCTCCGACTAATT-CACAGGCAGC-3′) were designed to carry out the 5′ RACE-PCR. The following gradient PCR program was used: initial denaturalization at 95 °C for 3 min, followed by 5 cycles of 94 °C for 30 s and 72 °C for 3 min; another 5 cycles of 94 °C for 30 s, 70 °C for 30 s, and 72 °C for 3 min; a final 20 cycles of 94 °C for 30 s, 68 °C for 30 s, and 72 °C for 3 min; and last, 72 °C for 5 min. For nested PCR of 5′-RACE, the following PCR program was used: initial denaturalization at 95 °C for 3 min, followed by 25 cycles of 94 °C for 30 s, 68 °C for 30s, and 72 °C for 3 min; and last, 72 °C for 5 min.

3′-RACE was performed using the RNA PCR Kit (AMV) Ver. 3.0 (TaKaRa) according to the following protocol: RT reaction was implemented to synthesize the first strand of cDNA using Oligo dT-Adaptor Primer supplied. The first PCR of 3′-RACE was primed by a specific upstream primer (5′-TGCGGACGACGTGACAGTGGA-3′) and Oligo dT-Adaptor Primer supplied by the manufacturer. For nested PCR of 3′-RACE, the primers used were as follows: another specific upstream primer (5′-CCTCGCGTTCCAGGTGGTTGA-3′) and Adaptor Primer (5′-GTTTTCCCAGTCACGAC-3′). The PCR procedure was as follows: 1 cycle of 94 °C for 5 min; 30 cycles of 94 °C for 30 s, annealing temperature for 30 s, and 72 °C for 1 min/kb.

All of the amplified fragments were cloned to pCR2.1 vector (Life Technology) and transformed into *E. coli* DH5α for multiplication, then sequenced before further experiments.

Genomic DNA Isolation from *D. bardawil* and Manipulation. Genomic DNA extraction from *D. bardawil* cells in the log or late log phase was performed according to the E.Z.N.A.HP Plant DNA Kit. Genome walking was implemented with gene-specific primers to identify the genomic DNA of *DbGGPS* (as for the primers, data not shown). The initial PCR was fulfilled using gene-specific primers complemented with 3′-UTR of *DbGGPS* and genomic DNA as template. Subsequently, additional gene-specific primers were synthesized for genome walking on the basis of the initial PCR product. Genome walking was carried out by genome walking kit (TaKaRa). All the manipulations were on the basis of the user manual.

Bioinformatics Analysis. Sequence analysis was performed using BLAST software (http://blast.ncbi.nlm.nih.gov/). Component analysis of ACL was calculated using DNAStar software 7.1.0. Multiple alignments among similar enzymes were conducted using ClustalX 1.83. The open reading frame (ORF) of DbGGPS was predicted by ORF Finder on NCBI (http://www.ncbi.nlm.nih.gov/gorf/gorf.html). Physical and chemical features of DbGGPS were analyzed by the ProtParam tool (http://expasy.org/tools/protparam.html). Subcellular localization was predicted by TargetP 1.1 Server (http://www.cbs.dtu.dk/services/TargetP/). Conserved domains in DbGGPS were detected using the Conserved Domains Search tool (http://www.ncbi.nlm.nih.gov/Structure/cdd/wrpsb.cgi). Protein domains, families, and functional sites were predicted by Prosite (http://prosite.expasy.org/). The protein secondary structures were predicted by Phyre2 (http://www.sbg.bio.ic.ac.uk/phyre2/html/page.cgi?id=index). The 3D structure of DbGGPS was automatically predicted by 3D-JIGSAW Protein Comparative Modeling Server (http://bmm.can-

DOI: 10.1021/acs.jafc.5b02732
J. Agric. Food Chem. 2015, 63, 7805−7812

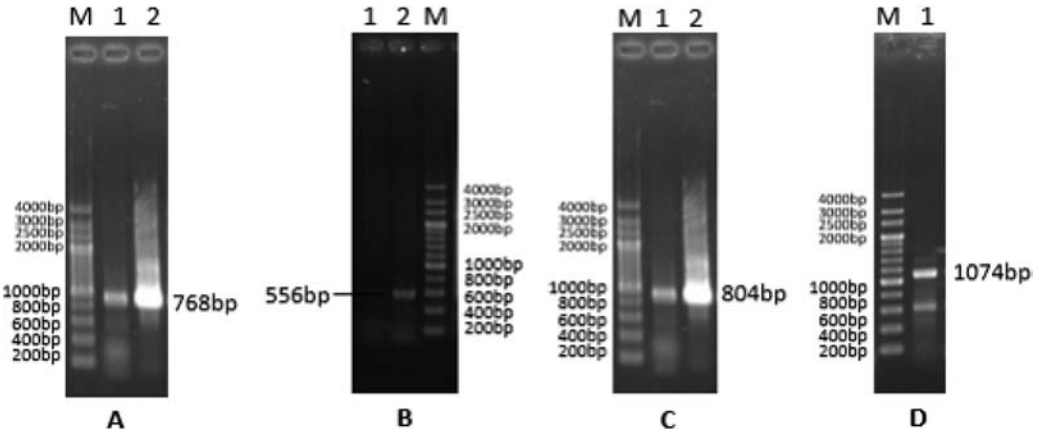

Figure 2. Isolation of *DbGGPS* cDNA. (A) *DbGGPS* EST. (B) 5′ end of the *DbGGPS* cDNA isolated by 5′ RACE. (C) 3′ end of the *DbGGPS* cDNA isolated by 3′ RACE. (D) Full-length *DbGGPS* ORF. Lane M, DNA ladder; lane 1, the first PCR products; and lane 2, the second PCR products.

cerresearchuk.org/~3djigsaw/), and the results were visualized by RasMol software 2.7.2.1.1.

Construction of Plasmid for DbGGPS Expression in *E. coli*. The coding region of a cDNA of DbGGPS was amplified by PCR using specific primers *Eco*RI-GGPS (5′-TCCGAATTCATG-GCCGCCCATCAAATGCA-3′) with an *Eco*RI site and *Xho*I-GGPS Rev (5′-GTGCTCGAGGTTTTGGCGGTAGCCAATGT-3′) with an *Xho*I site, respectively. The PCR product was purified, digested with *Eco*RI and *Xho*I, and then ligated to expression vector pET32a, which was predigested with the same restriction enzymes. The resulting recombinant plasmid pET32a-DbGGPS was then sequenced to confirm for the insertion of the ORF. Subsequently, the expression plasmid pET32a-DbGGPS was transformed into the host strain *E. coli* BL21 (DE3) for protein expression.

A single colony of *E. coli* BL21 cells harboring the expression plasmid pET32a-DbGGPS was inoculated at 37 °C in Luria−Bertani (LB) medium containing ampicillin (100 mg/L) and inoculated with shaking (200 rpm) at 37 °C until the optical density OD_{600} reached about 0.6. Then, the protein expression was induced by addition of IPTG (isopropyl-*β*-D-thiogalactoside) to a final concentration of 0.6 mM. The cultivation was continued for 4 h. The expression levels of the protein were assessed by analyzing total protein on SDS-PAGE followed by Coomassie Brilliant Blue R250 staining. A single colony of *E. coli* strain BL21 cells harboring the expression plasmid pET32a was used as control.

Functional Complementation Expression of DbGGPS in *E. coli*. The plasmid pACCRT-EIB contains the gene cluster *crtE*, *crtI* and *crtB*, and the *E. coli* DH5*α* harboring the plasmid pACCRT-EIB can produce lycopene. The plasmid pACCAR16Δ*crtX* contains the gene cluster *crtE*, *crtI*, *crtB* and *crtY*, and the *E. coli* DH5*α* harboring the plasmid pACCAR16Δ*crtX* can produce *β*-carotene.

The plasmids pAC-IBΔ*crtE* and pAC-IBYΔ*crtE*, where the *crtE* encoding GGPS had been deleted, were constructed in this study and used as the control. The linearized pAC-IBΔ*crtE* (or pAC-IBYΔ*crtE*) was amplified from pACCRT-EIB or pACCAR16Δ*crtX* by using the primers 5′-TCGGGCTGTCCTTATAAACGGA-3′ and 5′-TAAG-GATGCTGCATGAGCCATTTC-3′. The plasmids pAC-IBΔ*crtE* and pAC-IBYΔ*crtE* were constructed by incubation the linearized sequences with T4 DNA ligase (Takara) at 16 °C for 30 min, respectively, and then transformed in *E. coli* DH5*α*, respectively.

To test if *DbGGPS* encoded the anticipated functional protein, the plasmids pACCRT-*DbGGPS*-IB and pACCRT-*DbGGPS*-IBY were constructed from the corresponding plasmids pACCRT-EIB and pACCAR16Δ*crtX*, where *crtE* was replaced by *DbGGPS* using In-Fusion Enzyme (Clontech). The primers (5′-ATAAGGACAGCC-CGA**ATG**GCCGCCCATCAAATGCAGC-3′ and 5′-CATGCA-GCATCCTTA**CTA**GTTTTGGCGGTAGCCAATG-3′) for amplifying the *GGPS* sequence were designed with 15 bp (5′) extensions that are complementary to the ends of the linearized vector. The carotenoids were extracted from the transformants mentioned above.

Extraction of Carotenoids from *E. coli*. For *E. coli* cells biomass analysis, first *E. coli* cells (200 mL) were cultivated in LB medium with shaking (200 rpm) at 37 °C overnight. The absorbance values of the *E. coli* cultures (using blank medium diluted into different proportion; 1:1, 1:2, 1:5, 1:10, and 1:15) were read at 600 nm in a spectrophotometer, and a corresponding concentration of blank medium without *E. coli* was used as the control sample. For *E. coli* biomass dry weight measurement, an *E. coli* sample (100 mL) was harvested by centrifugation at 10 000 g for 2 min, washed twice with distilled water, and dried at 80 °C to a constant weight (24 h). Then, the relationship curve between *E. coli* OD_{600} and cell dry weight was obtained.

For extraction of carotenoids from *E. coli*, first *E. coli* samples (10 mL) were taken from each culture media after mixing thoroughly. Cells were harvested by centrifugation at 12 000 g for 2 min. Then, the cell pellets were washed twice with distilled water and mixed with 2 mL of acetone. The mixtures were shocked for 1 min and incubated for 15 min at 55 °C in the dark, then centrifuged for 20 min at 14 000 g to recover the supernatant with the pigment until colorless. Acetone extracts were collected and subsequently filtered through a 0.2 *μ*m hydrophobic fluorophore membrane (Sigma-Aldrich).

Analysis of Carotenoids. Carotenoid content was analyzed using the high-performance liquid chromatography (HPLC) method. Lycopene (or *β*-carotene) was separated using an Agilent HPLC system equipped with a Welch Ultimate XB-C18 column (250 mm × 4.6 mm, 120 Å) with an isocratic solvent system consisting of acetonitrile/methanol/isopropanol (45:10:45) at a flow rate of 1.2 mL/min at a wavelength of 473 (or 453) nm. The standards used were lycopene (95%) and *β*-carotene (95%), which were obtained from Sigma.

RESULTS

Isolation and Characterization of the *DbGGPS* cDNA. For the EST isolation of *DbGGPS*, according to the multiple sequences alignment result (Figure S1), a 768 bp fragment (Figure 2A) was isolated by RT-PCR reaction, and BLAST results showed high homology to *Dunaliella viridis GGPS* mRNA (HM114366.1) with 82% identity (632 identified nucleotides), indicating that the EST was from GGPS of *D. bardawil*. Furthermore, RACE manipulations were carried out to obtain the 5′ and 3′ ends of *DbGGPS* cDNA. Two fragments were recovered corresponding to the 5′ and 3′ ends, respectively, with lengths of 556 bp (Figure 2B) and 804 bp (Figure 2C). Sequence assembly revealed a 1814 bp cDNA of *DbGGPS*. ORF search found a 1074 bp (Figure 2D) coding

DOI: 10.1021/acs.jafc.5b02732
J. Agric. Food Chem. 2015, 63, 7805−7812

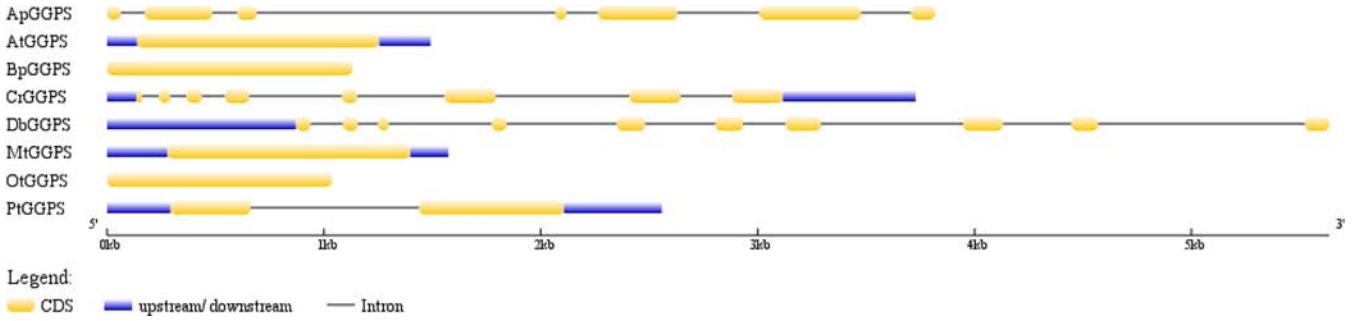

Figure 3. Distribution of exons and introns in the genomic DNA of GGPS. The sequences used for analysis are as follows: GGPS from microalgae, *DbGGPS* (in this study); ApGGPS, *Auxenochlorella protothecoides* (NW_011934251.1); BpGGPS, *Bathycoccus prasinos* (NC_024002.1) ; CrGGPS, *Chlamydomonas reinhardtii* (NW_001843980.1); OtGGPS, *Ostreococcus tauri* (NC_014437.1); GGPS from plants, AtGGPS, *Arabidopsis thaliana* (CP002687.1); MtGGPS, *Medicago truncatula*, (AC137839.19); and PtGGPS, *Populus trichocarpa* (NC_008475.2).

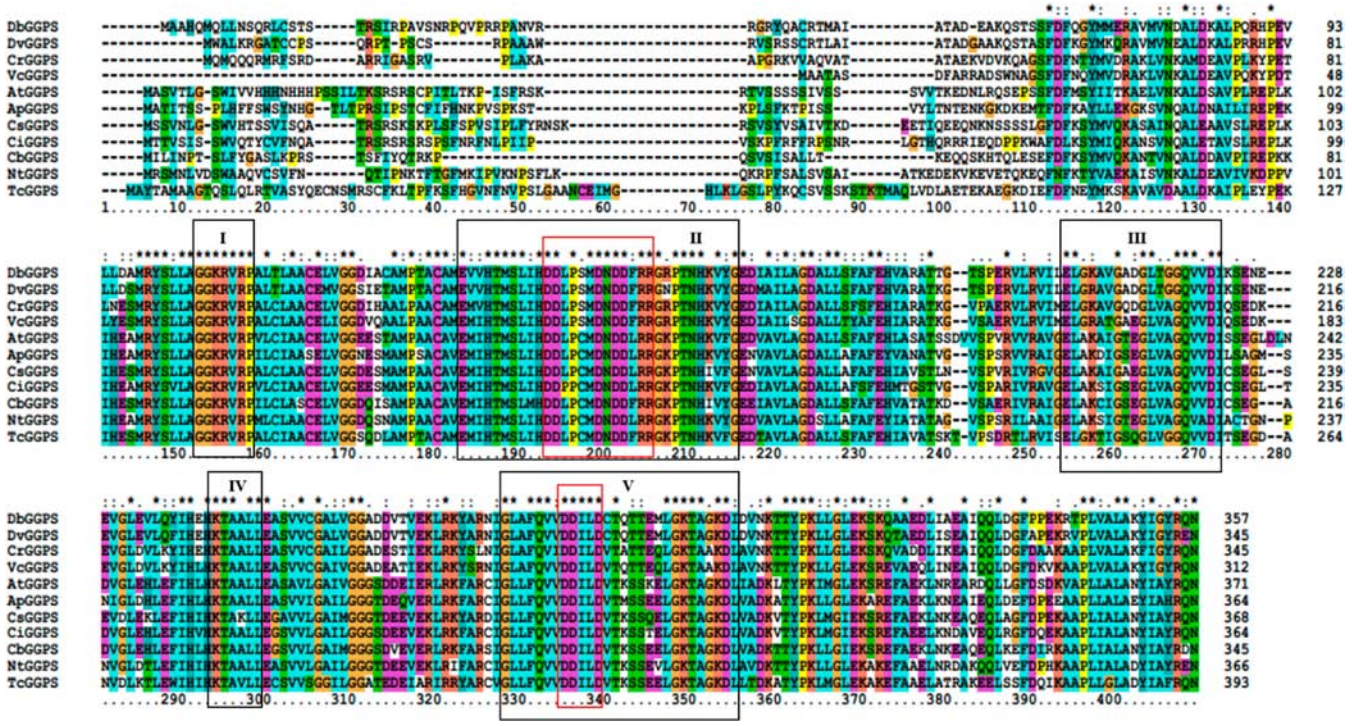

Figure 4. Alignment of amino acid sequences of DbGGPS and other algal and plant GGPSs. The following sequences were used for comparison: DbGGPS, GGPS from *D. bardawil* in this study; DvGGPS, *D. viridis* (HM114366.1); CrGGPS, *Chlamydomonas reinhardtii* (XP_001703169.1); VcGGPS, *Volvox carteri f. nagariensis* (XM_002953422.1); AtGGPS, *Arabidopsis thaliana* (NM_119845.3); ApGGPS, Adonis palaestina (AY661706.1); CsGGPS, *Croton sublyratus* (AB034249.1); CiGGPS, *Cistus incanus* (AF492022.1); CbGGPS, *Chrysanthemum boreale* (KC202428.1); NtGGPS, *Nicotiana tabacum* (GQ911583.1); and TcGGPS, *Taxus canadensis* (AF081514.1). The conserved domains were boxed in black and numbered (I, II, III, IV and V). The highly conserved aspartate-rich motif in the II and V domains of the GGPSs were boxed in red.

sequence (CDS) encoding 357 amino acids, which displayed 294 and 237 identical amino acids (88 and 77% homology, separately) with those of *D. viridis* and *C. reinhardtii*, respectively.

Analysis of the Genomic Structure of *DbGGPS*. The required genomic sequence of *DbGGPS* was 5636 bp. It contained a 4765 bp coding region (from ATG to TAA) and 871 bp upstream of the coding region. Analysis of the nucleotide sequence of the cloned genomic DNA fragment indicated that *DbGGPS* contained 10 exons interrupted by 9 introns, which is much more complicated than other algal and plant *GGPS* genes (Figure 3). As shown in Figure 3, some algal GGPS genomic DNA sequences were intron-rich (such as GGPS from *Auxenochlorella protothecoides*, *Chlamydomonas reinhardtii*, and *D. bardawil*), whereas some had no introns (such as GGPS from *Bathycoccus prasinos* and *Ostreococcus tauri*). Plant GGPS genomic DNA also seemed to be intronless, i.e., having no introns. The total length of the introns was 3691 bp, about 3.44-fold of the total length of exons (1074 bp). The average *DbGGPS* intron was about 410 bp in length. Each intron started with GT and ended with AG, belonging to the most common style of exon.

Sequence Analysis. On the basis of the analysis of the nucleotide sequence, we demonstrated that the *DbGGPS* full-length cDNA contained 1814 bp nucleotides with a 1074 bp long putative ORF, flanked by a 183 bp long 5′ untranslated region upstream of the start codon and a 557 bp long 3′ untranslated region after the stop codon. The 1074 bp putative ORF encoded a 357 amino acid peptide. Analysis by ProtParam

DOI: 10.1021/acs.jafc.5b02732
J. Agric. Food Chem. 2015, 63, 7805−7812

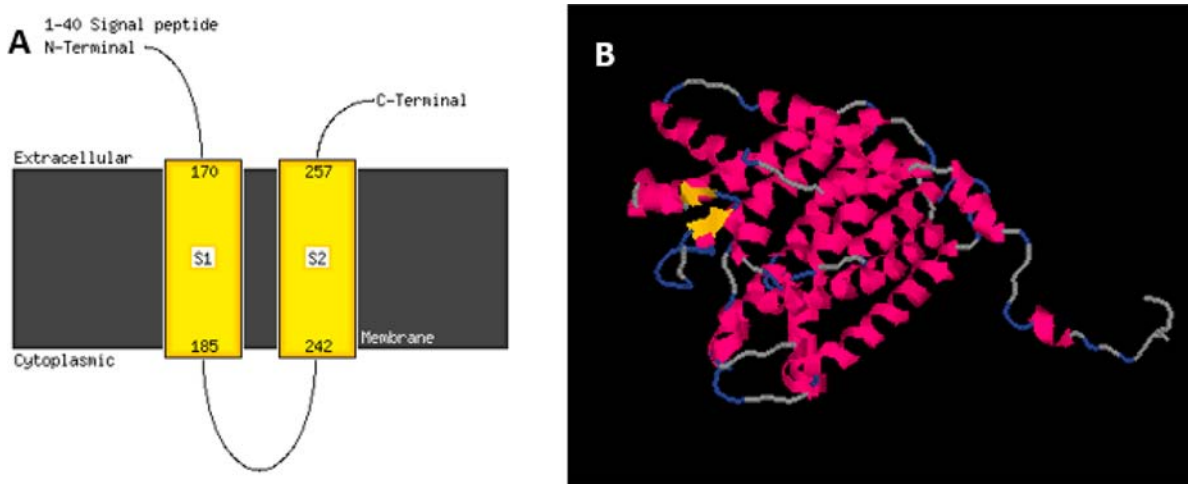

Figure 5. Schematic representations of transmembrane protein structure prediction and 3D model of the DbGGPS. (A) Transmembrane protein structure prediction of DbGGPS. (B) 3D model of the DbGGPS. Comparative modeling was performed using 3D-JIGSAW based on homologues of known structures automatically. The structures were visualized using RasMol version 2.7.2.1.1. The α-helix region of the putative protein is indicated with pink ribbons. Two TM-helix regions were indicated with yellow arrows. The loop regions are also indicated in the schematics.

tool revealed that the molecular weight of DbGGPS was 38.88 kDa and that the isoelectric point was 6.27.

The predicted amino acid sequence of DbGGPS has high similarity to other algal and plant GGPS (56−88%). Amino acid sequences of GGPSs from other algal and plant species were aligned according to the algorithm of the ClustalW, and the result was shown in Figure 4. Five domains (from I to V) found in the same relative locations as those described for prenyltransferases[20] were also identified in all the aligned sequences. Domains II and V contained aspartate-rich motifs (ARMs), referred to as the first ARM (FARM, $DD(X)_4D$) and the second ARM (SARM, $DD(X)_2D$)), respectively, that were proposed to be diphosphate-binding sites.[20] Domain II represented a longer region that contained highly conserved DD (Asp) and RR (Arg) dipeptides, $DD(X)_9RR$ (Figure 4). The DDXXD motif in domain V was the most conserved region and was proposed to be an allyl isoprenoid binding site.[21] Both $DD(X)_9RR$ and DDXXD motifs were important for the catalytic activity of GGPS.[21] In addition, two polyprenyl synthases signatures (at positions 143−159 and 275−287 in DbGGPS amino acid sequence) have been predicted by the Prosite tool, and they corresponded to ARMs. GGPS can be classified into three types on the basis of their amino acid sequences.[11] Type-I GGPS found in archaea have only two amino acids inserted in the FARM (DDXXD) and one aromatic amino acid residue at the fifth position upstream from the FARM. Plant and eubacterial (type-II) GGPS possess four amino acids inserted in the FARM. However, this type of GGPS lacks an aromatic amino acid residue at the fifth position upstream from the FARM. Type-III GGPS, found in eukaryotes (except plants), contain two inserted amino acids in the FARM and also lack an aromatic amino acid residue at the fifth position upstream from the FARM. Plant and algal GGPS are type-II GGPSs because the FARM is $DD(X)_4D$, as shown in Figure 4.

Conserved domains analysis using the NCBI Conserved Domain Database (Figure S2) showed that the deduced protein DbGGPS was conserved in substrate binding sites, active sites, catalytic center, and two aspartate-rich regions. However, there was little homology among the N termini of other GGPSs because these regions encoded plastidial transit peptides in which amino acid sequences varied much.[22] The predicted DbGGPS transit peptide was identified by TargetP, showing that DbGGPS had a 48 amino acid transit peptide at its N terminus to target to the plastids.

Protein Structure Prediction. The protein secondary structure was predicted by Phyre2. As shown (Figure S3), there were 70% α-helix regions, no β-sheet regions, 19% disordered regions, and 9% transmembrane (TM)-helix regions in DbGGPS. The schematic view of the transmembrane protein structure prediction was shown in Figure 5A. An ~40 amino acid signal peptide at the N terminus of DbGGPS was predicted, which was very close to the prediction of TargetP tool. Two TM-helix regions were at the positions 170−185 and 242−257 in DbGGPS amino acid sequence, which corresponded to the two yellow arrows in the 3D structure of DbGGPS predicted by 3D-JIGSAW (Figure 5B).

Heterologous Expression of DbGGPS in *E. coli* BL21 (DE3). To express DbGGPS, the gene was cloned into the plasmid pET32a to construct pET32a-DbGGPS. Upon induction by IPTG, DbGGPS was expressed as a major protein product in the total cellular protein (Figure 6). SDS-PAGE patterns of total cellular protein, visualized by Coomassie

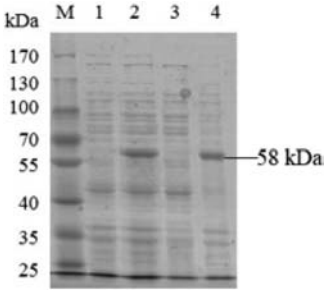

Figure 6. Expression of DbGGPS in pET32a vector analyzed by SDS-PAGE. M, molecular mass standards; lane 1, control (*E. coli* transformed with pET32a); lane 2, total protein extract of *E. coli* transformed with pET32a-GGPS after 4 h of IPTG induction; lane 3, soluble cytoplasmic fraction of *E. coli* transformed with pET32a-GGPS treated with IPTG; and lane 4, insoluble fraction of *E. coli* transformed with pET32a-GGPS treated with IPTG.

DOI: 10.1021/acs.jafc.5b02732
J. Agric. Food Chem. 2015, 63, 7805−7812

Table 1. Characteristic of Plasmids and Transformants

plasmids	genes	strain colors	HPLC results	carotenoid production (μg/g cell dry weight)
pACCRT-EIB	*crtE, crtI, crtB*	pink	lycopene	2385 ± 130
pAC-IBΔ*crtE*	*crtI, crtB*	nearly no pink	not detected	
pACCRT-*DbGGPS*-IB	*DbGGPS, crtI, crtB*	light pink	lycopene	528 ± 36
pACCAR16Δ*crtX*	*crtE, crtI, crtB, crtY*	yellow	β-carotene	1049 ± 73
pAC-IBYΔ*crtE*	*crtI, crtB, crtY*	nearly white	not detected	
pACCRT-*DbGGPS*-IBY	*DbGGPS, crtI, crtB, crtY*	pale yellow	β-carotene	107 ± 17

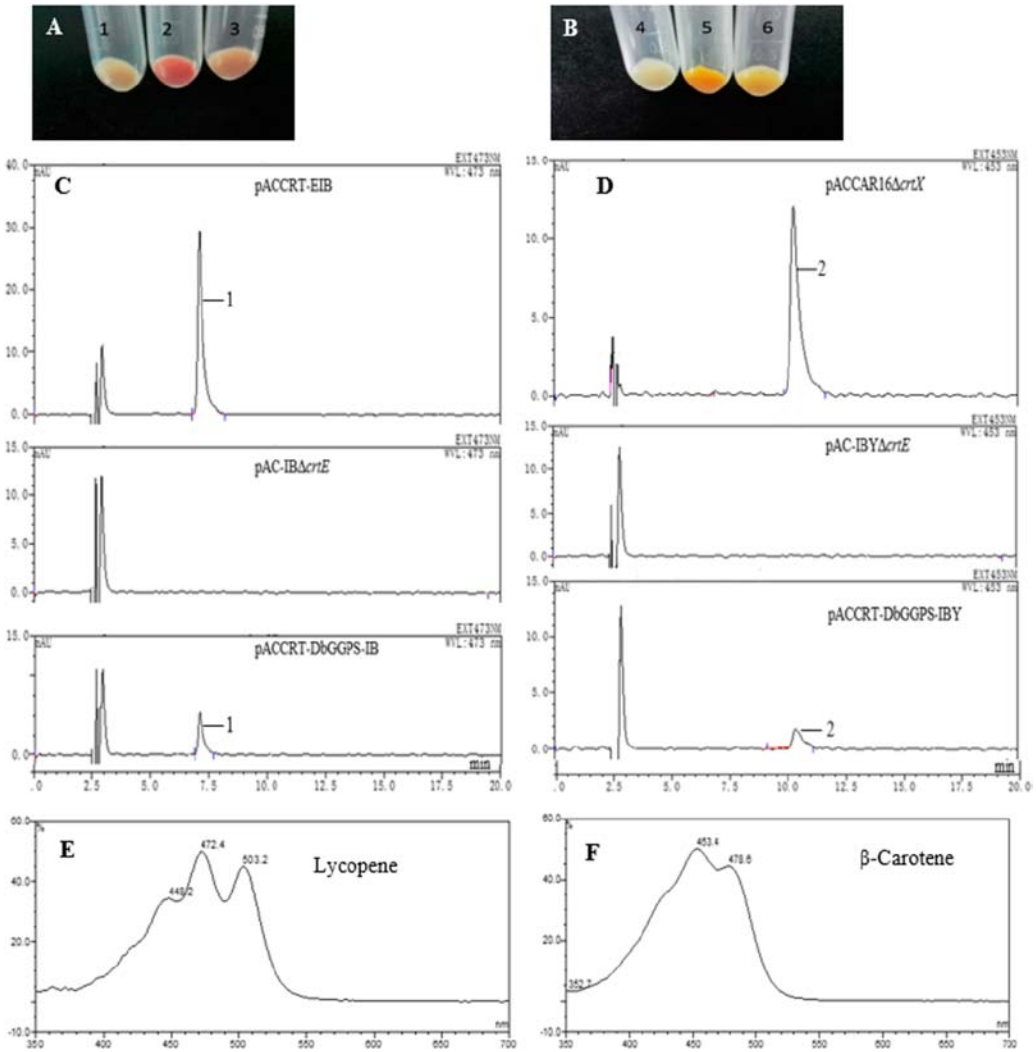

Figure 7. Carotenoid production of *E. coli* harboring different plasmids. (A) Lycopene production of *E. coli* harboring different plasmids: 1, pAC-IBΔ*crtE*; 2, pACCRT-EIB; and 3, pACCRT-*DbGGPS*-IB. (B) β-Carotene production of *E. coli* harboring different plasmids: 4, pAC-IBYΔ*crtE*; 5, pACCAR16Δ*crtX*; 6, pACCRT-*DbGGPS*-IBY. (C) *E. coli* cell extracts of lycopene production were analyzed by HPLC at a wavelength of 473 nm. Peak 1: lycopene. (D) *E. coli* cell extracts of β-carotene production were analyzed by HPLC at a wavelength of 453 nm. Peak 2: β-carotene. (E) Absorption spectrum of lycopene. The absorbance maximum of lycopene is at a wavelength of 473 nm. (F) Absorption spectrum of β-carotene. The absorbance maximum of β-carotene is at a wavelength of 453 nm.

Brilliant Blue R250 staining, showed that recombinant protein (pET32a-DbGGPPS) expression was achieved at 4 h after IPTG induction. The molecular weight of the expressed recombinant protein was estimated to be about 58 kDa fused with ~20 kDa of tags (two His·Tags, one Trx·Tag, and one S·Tag). Therefore, the size of expressed DbGGPS protein was predicted to be 38−39 kDa, which was in good agreement with that predicted by bioinformatics method (38.88 kDa). It was also found that the recombinant protein was expressed in insoluble fraction of the total bacterial cultures as an inclusion body. The expression and purification of the DbGGPPS protein would be a preparation for investigating its detailed function and facilitate the future research in *D. bardawil*.

Functional Complementation of DbGGPS in the *E. coli* Transformants. Functional activity of expressed GGPS was investigated by genetic complementation with the carotenogenic *crt* gene cluster. Carotenoids are produced in *E. coli* harboring a *crt* cluster gene from *E. uredovora*. Replacements of a *crt* gene with an unknown gene with the same activity can be used to determine the function of the gene. Herein, the

DOI: 10.1021/acs.jafc.5b02732
J. Agric. Food Chem. 2015, 63, 7805−7812

DbGGPS gene was used to replace *crtE* to construct the plasmids pACCRT-*DbGGPS*-IB and pACCRT-*DbGGPS*-IBY, and the plasmids pAC-IBΔ*crtE* and pAC-IBYΔ*crtE* were used as the control, respectively. All the plasmids were transformed into *E. coli* DH5α. The characteristics of the plasmids and the transformants has been listed in Table 1. The pink color of carotenoid was observed in the transformants *E. coli* DH5α/pACCRT-EIB and *E. coli* DH5α/pACCRT-*DbGGPS*-IB, and the carotenoids of the transformants were lycopene (Figure 7A). The yellow color of carotenoid was observed in the transformants *E. coli* DH5α/ pACCAR16Δ*crtX* and *E. coli* DH5α/pACCRT-*DbGGPS*-IBY, and the carotenoid produced by the transformants was β-carotene (Figure 7B). *E. coli* cells do not produce lycopene or β-carotene but can produce IPP and DMAPP, which are the essential precursors of carotenoids,[23] so a tiny bit of pink color was seen in *E. coli* DH5α/pAC-IBΔ*crtE*. However, no carotenoids could be detected in the transformants *E. coli* DH5α/pAC-IBΔ*crtE* and *E. coli* DH5α/pAC-IBYΔ*crtE* by HPLC (Table 1 and Figure 7C,D). All these results suggested that *DbGGPS* can substitute the *crtE* gene, and the coding region of a cDNA of *DbGGPS* encodes a functional GGPS. However, the lycopene production in *E. coli* DH5α/pACCRT-*DbGGPS*-IB was decreased by 77.86% relative to that in *E. coli* DH5α/pACCRT-EIB (Table 1 and Figure 7C). The β-carotene production in *E. coli* DH5α/pACCRT-*DbGGPS*-IBY was decreased by 89.80% relative to that in *E. coli* DH5α/pACCAR16Δ*crtX* (Table 1 and Figure 7D). These results indicated that that the function of DbGGPS expressed in *E. coli* was not as effective as that of *crtE* from *E. uredovora*.

DISCUSSION

Traditionally, GGPS enzymatic activity can be detected in *E. coli* cell extracts or by color complementation assay.[2] The gene encoding GGPS was constructed into a prokaryotic expression vector, such as pBluescript II SK(−)[13,24] and pQE30.[11] Then, the resulting plasmid and the plasmid carrying the *Erwinia uredovora crt* gene cluster from which the *crtE* gene (encoding GGPS) was deleted were used to cotransform into *E. coli*. The resultant *E. coli* transformant could produce carotenoid. One example was that carotenoid production was observed in *E. coli* harboring pACCAR25Δ*crtE* from *E. uredovora* and plasmid carrying *C. forskohlii* GGPS.[24] In this study, just one plasmid carrying the *E. uredovora crt* gene cluster in which the *crtE* gene (encoding GGPS) was replaced with *DbGGPS* was used to transform into *E. coli*, and the transformant still can produce corresponding carotenoids. Although we found that *E. coli* harboring the plasmid with *crtI*, *crtB*, *crtY* (or no *crtY*), and DbGGPS can produce fewer corresponding carotenoids than that harboring pACCRT-EIB and pACCAR16Δ*crtX*, *DbGGPS* has been verified to encode a functional protein and played an important role in carotenoid pathway flux.

As for the reason why fewer carotenoids were produced in *E. coli* harboring the plasmid with *crtI*, *crtB*, *crtY* (or no *crtY*), and *DbGGPS*, it may be that the SD sequence and promoter of the gene *crtE* cannot identify the expression of DbGGPS effectively. Codon optimization of *DbGGPS* or the eukaryotic expression system may solve this problem. (Over)expression of genes involved in carotenoid biosynthesis has been studied in detail in *E. coli*.[25−27] Recently, (over)expression of genes involved in carotenoid biosynthesis in yeast and algae have been paid attention. It was reported that expression of PSY from *Dunaliella salina* in *Chlamydomonas reinhardtii* under the control of the RBCS2 and HSP70A promoters caused the stable production of the corresponding PSY transcript and a significant increase in the content of carotenoids.[28] As for the overexpression of GGPS, it seemed to have a limitations of the carotenoid pathway.[29] It was reported that maximum astaxanthin biosynthesis could be achieved by engineered *Xanthophyllomyces dendrorhous* that overexpressed the enzyme GGPS in combination with advantageous cultivation conditions like dim light illumination of and enhanced air supply.[29]

In contrast, as a very first step toward the genetic manipulation of the terpenoid pathway, overexpression of GGPS is rarely manipulated alone. Among the genes involved in the carotenoid biosynthetic pathway, GGPS is a key gene that produces the general key precursor for carotenoid and a potential target for metabolic engineering. Besides carotenoids, FPP and GGPP are essential precursors for a variety of products including steroids, diterpenes, and quinones (Figure 1).[30] It was reported that the expressions of three key enzymes of the general isoprenoid pathway, IPI, FPS, and GGPS, resulted in an increase in the final carotenoid accumulation in *Mucor circinelloides*.[31] GGPS catalyzes the ultimate non-carotenoid-specific step in the pathway, participating not only in the synthesis of the carotenoids but also in that of the quinones and the prenyl groups of several proteins. It seems more important for enhancement of the IPP and DMAP supply, so genetic manipulation of GGPS is usually coupled with that of the enzyme IPI. The introduction of GGPS and IPI from *Blakeslea trispora* increased the β-carotene content in *E. coli* from 0.5 to 0.95 mg/g dry weight.[32] Another report has shown that genetic engineering of the complete carotenoid pathway (expression of the genes of 3-hydroxymethyl-3-glutaryl coenzyme A reductase, GGPS, phytoene synthase/lycopene cyclase, and astaxanthin synthase) resulted in extremely high astaxanthin accumulation in *Xanthophyllomyces dendrorhous*. This could also be achieved in algae like *Chlamydomonas* and *Dunaliella*.

We have successfully cloned the GGPS gene from the unicellular alga *Dunaliella bardawil*. GGPS catalyzed the production of GGPP, a key precursor for carotenoid biosynthesis. The successful isolation and verified activity of the DbGGPS gene will enable us to regulate an important step involved in carotenoids biosynthesis by genetic engineering in the future. Also, a new way to determine the function of the unknown gene involved in carotenoids biosynthesis was provided by replacing the *crt* gene from *E. uredovora* in the plasmid (pACCRT-EIB, pACCAR16Δ*crtX*, or pACCAR25Δ*crtX*) with an unknown gene.

ASSOCIATED CONTENT

Supporting Information

The Supporting Information is available free of charge on the ACS Publications website at DOI: 10.1021/acs.jafc.5b02732.

Multiple sequences alignment of GGPS from other algae and plants. Conserved domains in DbGGPS and protein similarity detected by NCBI Blastp. Protein secondary structure of DbGGPS predicted by Phyre2. (PDF)

AUTHOR INFORMATION

Corresponding Author

*E-mail: jgjiang@scut.edu.cn. Phone: +86-20-87113849. Fax: +86-20-87113849.

DOI: 10.1021/acs.jafc.5b02732
J. Agric. Food Chem. 2015, 63, 7805−7812

Funding

This project was supported by the National Natural Foundation of China (31171631 and 31571773), the Key Natural Science Foundation of Guangdong Province (2014A030311020), China, Guangdong Province Science and Technology Plan (2011B031200005 and 2013B010404009), China, and Guangdong Provincial Bureau of Ocean and Fishery Science and Technology (A201301C04), China.

Notes

The authors declare no competing financial interest.

REFERENCES

(1) Vershinin, A. Biological functions of carotenoids—diversity and evolution. *BioFactors* **1999**, *10*, 99−104.

(2) Zhu, F.; Suzuki, K.; Okada, K.; Tanaka, K.; Nakagawa, T.; Kawamukai, M.; Matsuda, H. Cloning and functional expression of a novel geranylgeranyl pyrophosphate synthase gene from Arabidopsis thaliana in Escherichia coli. *Plant Cell Physiol.* **1997**, *38*, 357−361.

(3) Ye, Z.-W.; Jiang, J.-G.; Wu, G.-H. Biosynthesis and regulation of carotenoids in Dunaliella: progresses and prospects. *Biotechnol. Adv.* **2008**, *26*, 352−360.

(4) Rohmer, M. The discovery of a mevalonate-independent pathway for isoprenoid biosynthesis in bacteria, algae and higher plants†. *Nat. Prod. Rep.* **1999**, *16*, 565−574.

(5) Hirschberg, J. Carotenoid biosynthesis in flowering plants. *Curr. Opin. Plant Biol.* **2001**, *4*, 210−218.

(6) Chen, Y.; Li, F.; Wurtzel, E. T. Isolation and characterization of the Z-ISO gene encoding a missing component of carotenoid biosynthesis in plants. *Plant Physiol.* **2010**, *153*, 66−79.

(7) Isaacson, T.; Ronen, G.; Zamir, D.; Hirschberg, J. Cloning of tangerine from tomato reveals a carotenoid isomerase essential for the production of β-carotene and xanthophylls in plants. *Plant Cell* **2002**, *14*, 333−342.

(8) Misawa, N.; Nakagawa, M.; Kobayashi, K.; Yamano, S.; Izawa, Y.; Nakamura, K.; Harashima, K. Elucidation of the Erwinia uredovora carotenoid biosynthetic pathway by functional analysis of gene products expressed in Escherichia coli. *J. Bacteriol.* **1990**, *172*, 6704−6712.

(9) Misawa, N.; Satomi, Y.; Kondo, K.; Yokoyama, A.; Kajiwara, S.; Saito, T.; Ohtani, T.; Miki, W. Structure and functional analysis of a marine bacterial carotenoid biosynthesis gene cluster and astaxanthin biosynthetic pathway proposed at the gene level. *J. Bacteriol.* **1995**, *177*, 6575−6584.

(10) Lin, J.; Jin, Y.; Zhou, X.; Wang, J. Molecular cloning and functional analysis of the gene encoding geranylgeranyl diphosphate synthase from Jatropha curcas. *Afr. J. Biotechnol.* **2010**, *9*, 3342−3351.

(11) Thabet, I.; Guirimand, G.; Guihur, A.; Lanoue, A.; Courdavault, V.; Papon, N.; Bouzid, S.; Giglioli-Guivarc'h, N.; Simkin, A. J.; Clastre, M. Characterization and subcellular localization of geranylgeranyl diphosphate synthase from Catharanthus roseus. *Mol. Biol. Rep.* **2012**, *39*, 3235−3243.

(12) Hefner, J.; Ketchum, R. E.; Croteau, R. Cloning and Functional Expression of a cDNA Encoding Geranylgeranyl Diphosphate Synthase fromTaxus canadensisand Assessment of the Role of this Prenyltransferase in Cells Induced for Taxol Production. *Arch. Biochem. Biophys.* **1998**, *360*, 62−74.

(13) Wang, Y.; Miao, Z.; Tang, K. Molecular cloning and functional expression analysis of a new gene encoding geranylgeranyl diphosphate synthase from hazel (Corylus avellana L. Gasaway). *Mol. Biol. Rep.* **2010**, *37*, 3439−3444.

(14) Sitthithaworn, W.; Kojima, N.; Viroonchatapan, E.; SUH, D.-Y.; Iwanami, N.; Hayashi, T.; Noji, M.; Saito, K.; Niwa, Y.; Sankawa, U. Geranylgeranyl diphosphate synthase from Scoparia dulcis and Croton sublyratus. Plastid localization and conversion to a farnesyl diphosphate synthase by mutagenesis. *Chem. Pharm. Bull.* **2001**, *49*, 197−202.

(15) Ben-Amotz, A.; Katz, A.; Avron, M. Accumulation of β-carotene in halotolerant alge: purification and characterization of β-carotene-rich globules from *Dunaliella bardawil* (chlorophyceae). *J. Phycol.* **1982**, *18*, 529−537.

(16) Lao, Y.-M.; Xiao, L.; Jiang, J.-G.; Zhou, S.-S. In silico analysis of phytoene synthase and its promoter reveals hints for regulation mechanisms of carotenogenesis in Duanliella bardawil. *Bioinformatics* **2011**, *27*, 2201−2208.

(17) Ye, Z.-W.; Liu, G.-N.; Jiang, J.-G. Structural and phylogenetic analysis of a novel ζ-carotene desaturase from Dunaliella bardawil, a unicellular alga that accumulates large amounts of β-carotene. *Limnol. Oceanogr.* **2011**, *56*, 133−138.

(18) Zhu, Y.-H.; Jiang, J.-G.; Yan, Y.; Chen, X.-W. Isolation and characterization of phytoene desaturase cDNA involved in the β-carotene biosynthetic pathway in Dunaliella salina. *J. Agric. Food Chem.* **2005**, *53*, 5593−5597.

(19) Ben-Amotz, A.; Avron, M. The biotechnology of cultivating the halotolerant alga *Dunaliella*. *Trends Biotechnol.* **1990**, *8*, 121−126.

(20) Sandmann, G. Carotenoid biosynthesis in microorganisms and plants. In *EJB Reviews 1994*; Springer: Berlin Heidelberg, Germany, 1995; pp 129−146.

(21) Carattoli, A.; Romano, N.; Ballario, P.; Morelli, G.; Macino, G. The Neurospora crassa carotenoid biosynthetic gene (albino 3) reveals highly conserved regions among prenyltransferases. *J. Biol. Chem.* **1991**, *266*, 5854−5859.

(22) Liao, Z.; Chen, M.; Gong, Y.; Guo, L.; Tan, Q.; Feng, X.; Sun, X.; Tan, F.; Tang, K. A new geranylgeranyl diphosphate synthase gene from Ginkgo biloba, which intermediates the biosynthesis of the key precursor for ginkgolides. *DNA Sequence* **2004**, *15*, 153−158.

(23) Rohmer, M.; Knani, M.; Simonin, P.; Sutter, B.; Sahm, H. Isoprenoid biosynthesis in bacteria: a novel pathway for the early steps leading to isopentenyl diphosphate. *Biochem. J.* **1993**, *295*, 517−524.

(24) Engprasert, S.; Taura, F.; Kawamukai, M.; Shoyama, Y. Molecular cloning and functional expression of geranylgeranyl pyrophosphate synthase from Coleus forskohlii Briq. *BMC Plant Biol.* **2004**, *4*, 18.

(25) Albrecht, M.; Misawa, N.; Sandmann, G. Metabolic engineering of the terpenoid biosynthetic pathway of Escherichia coli for production of the carotenoids β-carotene and zeaxanthin. *Biotechnol. Lett.* **1999**, *21*, 791−795.

(26) Yang, J.; Guo, L. Biosynthesis of β-carotene in engineered E. coli using the MEP and MVA pathways. *Microb. Cell Fact.* **2014**, *13*, 160.

(27) Li, X.-R.; Tian, G.-Q.; Shen, H.-J.; Liu, J.-Z. Metabolic engineering of Escherichia coli to produce zeaxanthin. *J. Ind. Microbiol. Biotechnol.* **2015**, *42*, 1−10.

(28) Couso, I.; Vila, M.; Rodriguez, H.; Vargas, M.; León, R. Overexpression of an exogenous phytoene synthase gene in the unicellular alga Chlamydomonas reinhardtii leads to an increase in the content of carotenoids. *Biotechnol. Prog.* **2011**, *27*, 54−60.

(29) Breitenbach, J.; Visser, H.; Verdoes, J. C.; van Ooyen, A. J.; Sandmann, G. Engineering of geranylgeranyl pyrophosphate synthase levels and physiological conditions for enhanced carotenoid and astaxanthin synthesis in Xanthophyllomyces dendrorhous. *Biotechnol. Lett.* **2011**, *33*, 755−761.

(30) Hemmi, H.; Noike, M.; Nakayama, T.; Nishino, T. An alternative mechanism of product chain-length determination in type III geranylgeranyl diphosphate synthase. *Eur. J. Biochem.* **2003**, *270*, 2186−2194.

(31) Csernetics, Á.; Nagy, G.; Iturriaga, E. A.; Szekeres, A.; Eslava, A. P.; Vágvölgyi, C.; Papp, T. Expression of three isoprenoid biosynthesis genes and their effects on the carotenoid production of the zygomycete Mucor circinelloides. *Fungal Genet. Biol.* **2011**, *48*, 696−703.

(32) Sun, J.; Sun, X.-X.; Tang, P.-W.; Yuan, Q.-P. Molecular cloning and functional expression of two key carotene synthetic genes derived from Blakeslea trispora into E. coli for increased β-carotene production. *Biotechnol. Lett.* **2012**, *34*, 2077−2082.

DOI: 10.1021/acs.jafc.5b02732
J. Agric. Food Chem. 2015, 63, 7805−7812

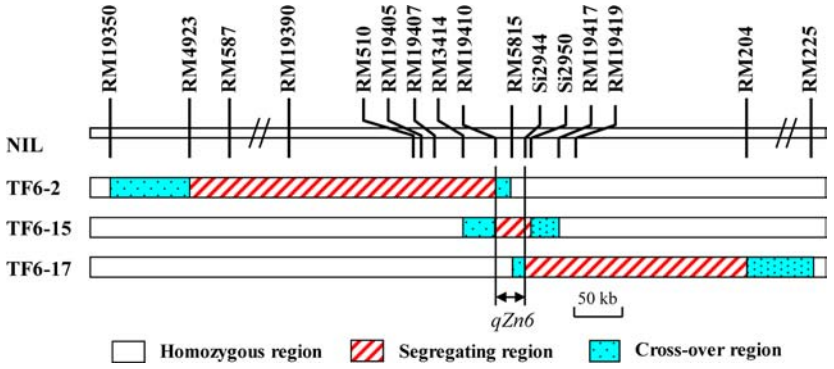

Figure 1. Genotypes of three sets of NILs, TF6-2, TF6-15, and TF6-17, in the interval RM19350−RM225 on the short arm of rice chromosome 6. The position of *qZn6* for the contents of seven elements in milled rice is indicated.

Table 1. Phenotypic Performance of the Contents of Seven Mineral Elements in Milled Rice of the ZS97/MY46 RIL Population

							parental mean	
trait[a]	mean	SD	CV	range	kurtosis	skewness	ZS97	MY46
P	1715.0	319.5	0.186	828.8−3250.0	3.32	1.00	2632.0	2390.0
K	1037.1	208.9	0.201	270.3−1622.0	0.55	−0.26	1262.0	1130.0
Mg	349.3	96.8	0.277	81.1−633.5	0.16	0.15	423.1	305.1
Ca	74.4	15.8	0.212	40.7−123.3	0.46	0.77	152.8	124.3
Zn	22.6	4.6	0.204	13.6−44.4	3.18	1.22	18.1	20.7
Mn	15.8	3.7	0.234	7.7−25.9	0.02	0.62	9.6	12.0
Cu	3.7	0.9	0.243	1.9−7.2	1.04	0.80	3.9	5.5

[a]The contents of the mineral elelments are presented as milligrams per kilogram in the milled rice. P, phosphorus; K, potassium; Mg, magnesium; Ca, calcium; Zn, zinc; Mn, manganese; and Cu, copper.

were selected for three generations based on genotyping of polymorphic markers located in the target QTL region. Three new RHs with sequential heterozygous segments, which jointly covered the entire QTL region, were identified. The three plants were each selfed to produce a NIL-F_2 population, from which 20 non-recombinant homozygous plants, including 10 maternal and 10 paternal homozygotes, were selected. Selfing seeds of these plants resulted in the development of three NIL sets, which were segregated in the intervals RM4923−RM19410, RM19410−Si2950, and Si2944−RM204 and named TF6-2, TF6-15, and TF6-17, respectively (Figure 1).

Field Experiments. The rice lines were planted in the paddy field at the China National Rice Research Institute, Hangzhou, Zhejiang, China. For each line, 12 plants were grown in one row with spacing of 16.7 cm between plants and 26.7 cm between rows. While 243 RILs were tested without replication, the NILs were planted in two replications with a randomized complete block design. Field management followed the normal agricultural practice. At maturity, seeds from five middle plants of each row were harvested.

Phenotype Determination. The grains were dried to a moisture content of about 13% and stored at room temperature for 3 months. They were then dehulled on a Satake Rice Machine (Satake Co., Tokyo, Japan). After polishing on a desktop rice miller (NSART, Sangyong Machinery Industry Co., Jungu, South Korea), the milled rice was ground into flour using a Cyclotec 1093 Sample Mill (Foss Tecator, Sweden) and passed through a 100-mesh sieve. The rice flour was stored at 4 °C.

Extraction of macro- and microelements was conducted by a digestion method. In briefly, about 0.50 g of rice flour and 5 mL of ultrapure nitric acid were added to a Teflon digestion vessel and then put on the microwave digestion instrument (CEM Mars, Matthews, NC). The digestion procedure was set as the followings: raising from room temperature to 120 °C, 0−5 min; holding at 120 °C, 6−7 min; raising from 120 to 180 °C, 8−17 min; and holding 180 °C, 18−32 min. After cooling to room temperature, the solution was transferred to a 50 mL volumetric flask and diluted to 50 mL with deionized water. The contents of P, K, Ca, Mg, Mn, Zn, and Cu were determined by inductively coupled plasma−atomic emission spectrometry (ICP−AES, Thermo Elemental, Franklin, MA) at the wavelengths of 213.6, 766.5, 183.8, 280.3, 257.6, 213.9, and 324.8 nm, respectively. The contents of elements were calibrated using the certified standards in rice flour samples (GBW10010, CRM Rice) obtained from the National Institute Center of Standards. Results were presented as milligrams per kilogram of rice flour. All of the determinations were conducted in duplication.

Marker Genotyping. A total of 16 DNA markers as shown in Figure 1 were used in the NIL development. Total DNA was extracted following the method of Zheng et al.[15] Polymerase chain reaction (PCR) amplification was performed according to Chen et al.,[16] and the products were visualized on 6% non-denaturing polyacrylamide gels using silver staining. All of the SSR markers were selected from the Gramene database (www.gramene.org). InDel markers Si2944 and Si2950 were designed according to the difference between ZS97 and MY46 detected by whole-genome re-sequencing. Primers used were 5′-AAACCACAAGATTAGGCTCTAAGT-3′ for Si2944-F and 5′-AAGTGAGGGAAACCACATTCTAC-3′ for Si2944-R and 5′-AGGCACTCACAACCATAAC-3′ for Si2950-F and 5′-TAGTACATGACAATGGAGCTATC-3′ for Si2950-R.

QTL Mapping. A linkage map has been constructed for the ZS97/MY46 RIL population, consisting of 256 DNA markers and spanning 1814.7 cM.[17,18] QTL analysis was performed with the Composite Interval Mapping (CIM) and Multiple Interval Mapping (MIM) of the Windows QTL Cartographer 2.5.[19] Candidate loci were selected with CIM using a threshold of log of odds (LOD) > 2.5 and tested with MIM using the Bayesian Information Criterion (BIC) default value $c(n) = \ln(n)$. Those showing significant effects were claimed as putative QTLs and designated as proposed by McCouch and the Committee on Gene Symbolization, Nomenclature and Linkage (CGSNL).[20]

For each of the three NIL sets, two-way analysis of variance (ANOVA) was conducted to test phenotypic differences between the two genotypic groups using SAS procedure general linear model (GLM) as described by Dai et al.[21] Given the detection of significant difference ($p < 0.05$), the same model was applied to estimate the

DOI: 10.1021/acs.jafc.5b02882
J. Agric. Food Chem. 2015, 63, 7813−7818

additive effect of the QTL and the proportion of phenotypic variance explained by the QTL.

RESULTS AND DISCUSSION

Phenotypic Performance of the RIL Population. Descriptive statistics of the mineral contents in milled rice of the ZS97/MY46 RIL population are presented in Table 1. Large variations with strong transgressive segregation were observed for all of the traits. While the contents in the female parent ZS97 were higher for macroelements (P, K, Mg, and Ca) and lower for microelements (Zn, Mn, and Cu) than in the male parent MY46, the parental differences were small compared to the variations among the RILs. Although the contents of macroelements were higher than that of microelements, the coefficients of variation were similar among the seven elements. In comparison to the mineral contents in brown rice determined for 304 *indica* landraces and 28 *indica* improved cultivars,[22] the contents in milled rice measured in our study were much smaller for P, K, Mg, Ca, and Cu but comparable for Zn. Consistent content of Zn in brown and milled rice was also found when more reports were compared,[6,9,11,23,24] along with the higher contents of P, K, Mg, Ca, and Cu in brown rice.[6,11,23] These results are in accordance with the understanding that most of the mineral elements are concentrated in the outer part of the rice grain but Zn has an relatively even distribution.[12,13,25,26] For the remaining element tested in our study, Mn, no consensus could be achieved because the content in brown rice had a large variation ranging from 7.3 to 35.0 mg/kg.[6,8,11,22,23]

Correlation coefficients between the contents of P, K, Ca, Mg, Mn, Zn, and Cu of the 243 RILs were all highly significant ($p < 0.01$), indicating the feasibility of improving these elements simultaneously in rice grain. The coefficients between the three elements having the largest contents, P, K, and Mg, were larger than those between the microelements. While the largest coefficient of 0.851 was observed between K and Mg, the lowest value of 0.213 was found between K and Cu (Table 2). In a previous QTL mapping for mineral contents using an interspecific cross,[6] all seven elements analyzed in our study were included and tested for 2 years. Of the 42 correlations between the seven elements, 24 were positively significant and the others were not significant. While correlations between the macroelements were all significant, Zn was not significantly correlated with other elements in 1 or 2 years and Cu was only significantly correlated with one element in 1 year. In another study using an inter-subspecific cross, positively significant correlations were found between P, Mn, Zn, and Cu, except that Mn was not significantly correlated with Zn and Cu.[10] It seems that positively significant correlations between the contents of different elements in rice grain are more achievable in populations that are less diverse.

Table 2. Coeffcients of Correlation between the Seven Traits in the RIL Population

trait[a]	K	Mg	Ca	Zn	Mn	Cu
P	0.621[b]	0.750[b]	0.515[b]	0.608[b]	0.495[b]	0.354[b]
K		0.851[b]	0.320[b]	0.268[b]	0.415[b]	0.213[b]
Mg			0.434[b]	0.353[b]	0.558[b]	0.258[b]
Ca				0.596[b]	0.689[b]	0.432[b]
Zn					0.448[b]	0.580[b]
Mn						0.415[b]

[a]The contents of the mineral elelments are presented as milligrams per kilogram in the milled rice. P, phosphorus; K, potassium; Mg, magnesium; Ca, calcium; Zn, zinc; Mn, manganese; and Cu, copper. [b]$p < 0.01$.

QTLs Detected in the RIL Population. A total of 20 QTLs distributed on six chromosomes were detected for the seven traits (Table 3 and Figure 2). The proportion of phenotypic variance explained by a single QTL (R^2) ranged from 4.2 to 11.8%.

For the contents of macroelements P, K, Mg, and Ca, the numbers of QTLs detected were 2, 3, 1, and 3, respectively. All of these QTLs, except *qCa5*, had the enhancing allele derived from the male parent MY46. Of the two QTLs for phosphorus content, *qP3* explained 11.8% of the phenotypic variance with an additive effect of 114.78 mg/kg, which were much larger than the values of 4.3% and 67.11 mg/kg estimated for *qP1*, respectively. It is also noted that the only QTL detected for magnesium content, *qMg3*, had the same location and allelic direction as *qP3*. The three QTLs for potassium content showed little difference in the magnitude, along with the three QTLs for calcium content. While the R^2 of *qK1*, *qK6.1*, and *qK6.2* ranged from 4.5 to 6.7% with the additive effects ranging from 45.19 to 55.06 mg/kg, the R^2 of *qCa5*, *qCa6* and *qCa10* ranged from 4.3 to 6.6% with the additive effects ranging from 3.33 to 4.27 mg/kg.

For the microelements Mn, Zn, and Cu, the numbers of QTLs detected were 4, 5, and 2, respectively. The QTL having the largest effect for manganese content, *qMn6*, was located at a region close to marker RM190 for the *Wx* gene on the short arm of chromosome 6, explaining 10.3% of the phenotypic variance, with the MY46 allele increasing the Mn content by 1.20 mg/kg. Two other QTLs, *qMn1.1* and *qMn1.2*, were linked in repulsion on the short arm of chromosome 1, having slightly lower effects compared to *qMn6*. The remaining QTL for this trait, *qMn11*, had a R^2 of 4.2%, with the MY46 allele decreasing the Mn content by 0.77 mg/kg.

All five QTLs for zinc content, except *qZn11*, had the enhancing allele derived from MY46. The QTL having the largest effect, *qZn3*, explained 11.7% of the phenotypic variance, with an additive effect of 1.59 mg/kg. The four other QTLs had R^2 ranging from 4.4 to 6.5% and additive effects ranging from 0.98 to 1.18 mg/kg. The two QTLs for copper content both had the enhancing allele derived from MY46. While *qCu6* located near RM190 had a R^2 of 11.2% and an additive effect of 0.31 mg/kg, the values estimated for *qCu10* were 7.4% and 0.25 mg/kg, respectively.

Two of the QTL regions described above were shown to be especially important. One was the RZ142−RZ613 interval on the long arm of chromosome 3, in which three QTLs were located, including *qMg3*, the only QTL detected for magnesium, and *qP3* and *qZn3*, the two QTLs having the largest effects for the contents of phosphorus and zinc in the ZS97/MY46 RIL population, respectively. The other was a region near the marker RM190 on the short arm of chromosome 6, in which five QTLs were located, including *qMn6* and *qCu6* having the largest effects for the contents of manganese and copper and *qK6.1*, *qCa6*, and *qZn6* that were associated with the contents of potassium, calcium, and zinc, respectively.

On the basis of the physical position of DNA markers linked to QTLs for mineral contents in rice grain, 12 of the QTLs detected in this study were coincident with those reported previously (Table 3). It is noteworthy that three members of

DOI: 10.1021/acs.jafc.5b02882
J. Agric. Food Chem. 2015, 63, 7813−7818

Table 3. QTLs Detected for the Contents of Seven Elements in Milled Rice

element	QTL	interval	LOD	A^a	R^2 (%)[b]	previous report[c]
P	*qP1*	RZ538−RG381	2.60	67.11	4.3	4, 6, and 7
	qP3	RZ142−RZ613	6.88	114.78	11.8	
K	*qK1*	RG472−RZ543	3.39	52.14	6.1	4
	qK6.1	RZ516−R1962	3.55	55.06	6.7	11
	qK6.2	RZ140−RZ405	2.82	45.19	4.5	
Mg	*qMg3*	RZ142−RZ613	4.61	27.60	7.8	
Ca	*qCa5*	C246−RM274	3.40	−4.27	6.5	
	qCa6	RM204−RM225	2.74	3.33	4.3	
	qCa10	RM171−RM1108	4.11	4.13	6.6	4 and 6
Mn	*qMn1.1*	RZ543−RG313	4.00	1.11	8.2	
	qMn1.2	RM1195−RM5359	4.85	−1.16	9.0	5 and 10
	qMn6	RZ516−R1962	5.66	1.20	10.3	
	qMn11	RG167−RM287	2.51	−0.77	4.2	7
Zn	*qZn1*	RM315−RZ538	2.64	1.02	4.8	8
	qZn3	RZ142−RZ613	5.98	1.59	11.7	11
	qZn5	RG119−RG346	3.04	1.05	5.0	4
	qZn6	RM204−RM225	4.18	1.18	6.5	4, 7, and 8
	qZn11	RM7557−RZ816	2.62	−0.98	4.4	5
Cu	*qCu6*	RM190−RZ516	5.63	0.31	11.2	6
	qCu10	RM1859−RM6704	2.78	0.25	7.4	

[a]Additive effect of replacing a maternal allele by a paternal allele. [b]Proportion of phenotypic variance explained by the given QTL. [c]Previous reports in which a QTL for the content of the same elelment in brown or milled rice was detected in a simliar location.

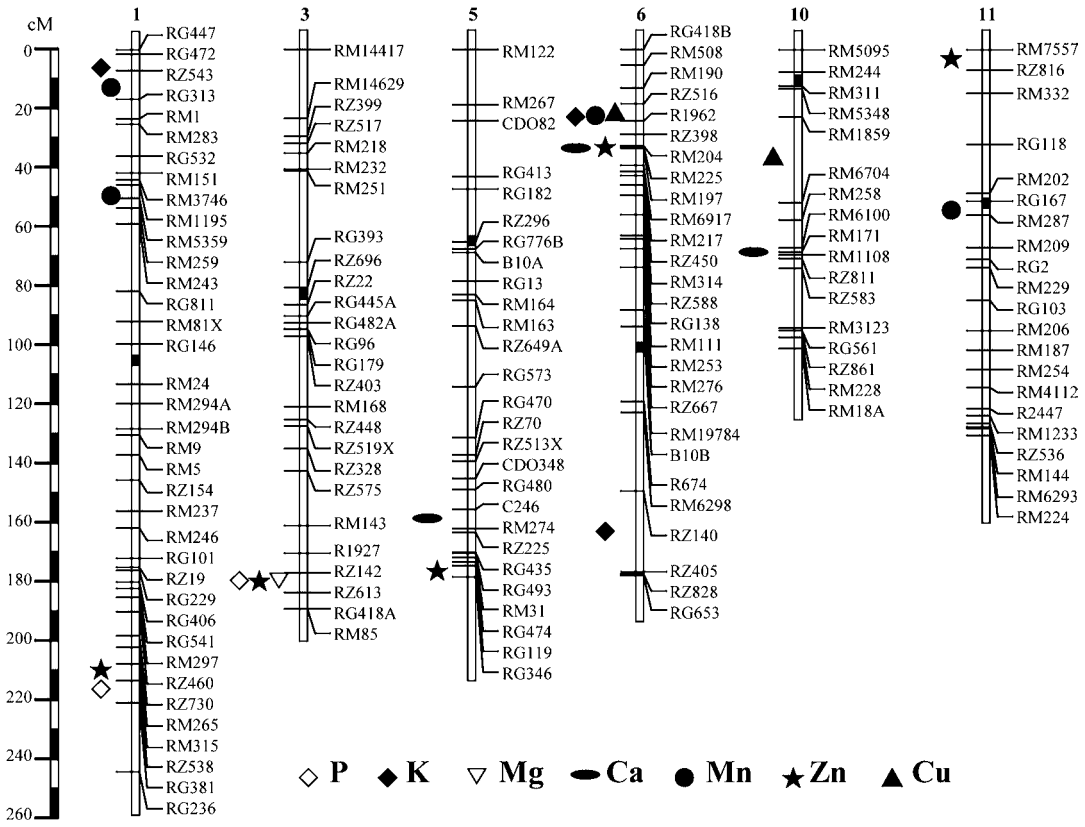

Figure 2. Genomic distribution of QTLs for mineral element contents in milled rice detected in the RIL population of ZS97/MY46.

the QTL cluster *qK6.1/qCa6/qMn6/qZn6/qCu6* have been previously detected, of which *qZn6* was detected for the Zn content in milled or brown rice in three studies[4,7,8] and *qK6.1* and *qCu6* were detected for the contents of K and Cu in brown rice as reported by Du et al.[11] and Garcia-Oliveira et al.,[6] respectively. Because this region was found to be associated with multiple mineral elements in a few independent studies, it was selected for validation and fine mapping.

QTL Fine Mapping Using NILs. Three sets of NILs with sequential segregating regions jointly covering the entire region flanked by RM4923 and RM204 (Figure 1) were used for QTL fine mapping. For NIL sets TF6-2, TF6-15, and TF6-17, which consisted of two homozygous genotypic groups differing in the

DOI: 10.1021/acs.jafc.5b02882
J. Agric. Food Chem. 2015, 63, 7813−7818

Table 4. QTL Effects Detected in the Three Sets of NILs

NIL name	segregating region	element	phenotype (mean ± SD) ZS97[a]	phenotype (mean ± SD) MY46[b]	P	A[c]	R^2 (%)[d]
TF6-2	RM4923−RM19410	Zn	18.0 ± 1.3	18.7 ± 1.7	0.0123	0.36	5.59
TF6-15	RM19410−Si2950	P	1370.5 ± 108.3	1883.9 ± 160.5	< 0.0001	257.23	73.22
		K	942.1 ± 90.0	1286.0 ± 134.3	< 0.0001	171.95	63.13
		Mg	305.7 ± 51.3	517.9 ± 64.9	< 0.0001	106.10	70.44
		Ca	59.3 ± 4.1	84.9 ± 10.9	< 0.0001	12.79	67.18
		Mn	20.4 ± 1.4	29.4 ± 2.3	< 0.0001	4.53	80.87
		Zn	20.1 ± 0.7	25.6 ± 1.3	< 0.0001	2.73	86.63
		Cu	4.3 ± 0.4	5.9 ± 0.4	< 0.0001	0.82	63.87
TF6-17	Si2944−RM204	P	1567.1 ± 105.9	1486.7 ± 138.5	0.0344	−40.00	10.52
		K	977.8 ± 82.1	926.6 ± 106. 8	0.0419	−25.63	7.08
		Mg	377.0 ± 50.2	344.9 ± 51.7	0.0337	−16.34	15.32
		Mn	23.8 ± 1.4	22.7 ± 1.6	0.0109	−0.56	13.03

[a]Zhenshan 97 homozygote. [b]Milyang 46 homozygote. [c]Additive effect of replacing a maternal allele by a paternal alelle. [d]Proportion of phenotypic variance explained by the given QTL.

regions of RM4923−RM19410, RM19410−Si2950, and Si2944−RM204, respectively, significant phenotypic differences between the two genotypes in the same NIL set would be an indication for allelic difference of a QTL within the segregating region.

Results of the two-way ANOVA are shown in Table 4. In NIL set TF6-15, highly significant effects ($p < 0.0001$) were detected for all seven traits, with the R^2 ranging from 63.13 to 86.63%. In agreement with the five QTLs detected in the RIL population, *qK6.1*, *qCa6*, *qMn6*, *qZn6*, and *qCa6*, the MY46 allele always acted for increasing the mineral contents in TF6-15. In NIL set TF6-2, a small effect with low significance ($p = 0.0123$) was detected for the zinc content and no significant effect was detected for the other six traits. Obviously, the major QTL detected in TF6-15 was not segregated in TF6-2. More work is needed to test whether a minor QTL for mineral contents is located in the segregating region of TF6-2. In NIL TF6-17, small effects with low significance ($p = 0.0419$−0.0109) were detected for the contents of four elements, P, K, Mg, and Mn, with the MY alleles always decreasing the contents. This indicates that a QTL having small effects for mineral content may locate in the segregating region of TF6-17.

On the basis of QTLs detected in the three NIL sets, it could be concluded that a major QTL having pleitropic effects for the contents of multiple elements was located in a region that was segregated in TF6-15 and homozygous in TF6-2 and TF6-17. As shown in Figure 1, this is a region flanked by RM19410 and Si2944, corresponding to a physical distance of 29.9 kb extending from 2 915 081 to 2 945 012 bp on chromosome 6 in the Michigan State University (MSU) Rice Genome Annotation Release 7 (http://rice.plantbiology.msu.edu/). Because the highest R^2 was detected for Zn, *qZn6* was chosen as the name for this QTL.

It is found that three annotated genes were located in the *qZn6* region, including *LOC_Os06g06300* and *LOC_Os06g06320* encoding phosphatidylethanolamine-binding proteins and *LOC_Os06g06310* encoding hypothetical proteins (http://rice.plantbiology.msu.edu/). This region was also located within a QTL region for hull silicon content, flag leaf length, and yield traits.[27,28] This suggested that the same QTL might be responsible for many traits, including mineral contents in milled rice, hull silicon content in the hull, and yield-related traits. Gene cloning is underway to determine the gene responsible for *qZn6*.

AUTHOR INFORMATION

Corresponding Author

*Telephone: +86-571-63370369. Fax: +86-571-63370364. E-mail: zhuangjieyun@caas.cn.

Funding

This work was supported by the Chinese 863 Program (2014AA10A604), the National Natural Science Foundation of China (31221004), and a research program of the China National Rice Research Institute (2014RG006-1).

Notes

The authors declare no competing financial interest.

ABBREVIATIONS USED

IL, introgression line; MY46, Milyang 46; QTL, quantitative trait locus; RH, residual heterozygote; RIL, recombinant inbred line; SSR, simple sequence repeat; ZS97, Zhenshan 97

REFERENCES

(1) Grusak, M. A. Enhancing mineral content in plant food products. *J. Am. Coll. Nutr.* **2002**, *21*, 178S−183S.

(2) Rawat, N.; Neelam, K.; Tiwari, V. K.; Dhaliwal, H. S. Biofortification of cereals to overcome hidden hunger. *Plant Breed.* **2013**, *132*, 437−445.

(3) Speich, M.; Pineau, A.; Ballereau, F. Minerals, trace elements and related biological variables in athletes and during physical activity. *Clin. Chim. Acta* **2001**, *312*, 1−11.

(4) Zhang, M.; Pinson, S. R. M.; Tarpley, L.; Huang, X.-Y.; Lahner, B.; Yakubova, E.; Baxter, I.; Guerinot, M. L.; Salt, D. E. Mapping and validation of quantitative trait loci associated with concentrations of 16 elements in unmilled rice grain. *Theor. Appl. Genet.* **2014**, *127*, 137−165.

(5) Lu, K.; Li, L.; Zheng, X.; Zhang, Z.; Mou, T.; Hu, Z. Quantitative trait loci controlling Cu, Ca, Zn, Mn and Fe content in rice grains. *J. Genet.* **2008**, *87*, 305−310.

(6) Garcia-Oliveira, A. L.; Tan, L.; Fu, Y.; Sun, C. Genetic identification of quantitative trait loci for contents of mineral nutrients in rice grain. *J. Integr. Plant Biol.* **2009**, *51*, 84−92.

(7) Norton, G. J.; Deacon, C. M.; Xiong, L. Z.; Huang, S. Y.; Meharg, A. A.; Price, A. H. Genetic mapping of the rice ionome in leaves and grain: identification of QTLs for 17 elements including arsenic, cadmium, iron and selenium. *Plant Soil* **2010**, *329*, 139−153.

(8) Norton, G. J.; Duan, G. L.; Lei, M.; Zhu, Y. G.; Meharg, A. A.; Price, A. H. Identification of quantitative trait loci for rice grain element composition on an arsenic impacted soil: influence of flowering time on genetic loci. *Ann. Appl. Biol.* **2012**, *161*, 46−56.

DOI: 10.1021/acs.jafc.5b02882
J. Agric. Food Chem. 2015, 63, 7813−7818

(9) Kumar, J.; Jain, S.; Jain, R. Linkage mapping for grain iron and zinc content in F_2 population derived from the cross between PAU201 and Palman 579 in rice (*Oryza sativa* L.). *Cereal Res. Commun.* **2014**, *42*, 389−400.
(10) Stangoulis, J. C. R.; Huynh, B.-L.; Welch, R. M.; Choi, E.-Y.; Graham, R. D. Quantitative trait loci for phytate in rice grain and their relationship with grain micronutrient content. *Euphytica* **2007**, *154*, 289−294.
(11) Du, J.; Zeng, D.; Wang, B.; Qian, Q.; Zheng, S.; Ling, H.-Q. Environmental effects on mineral accumulation in rice grains and identification of ecological specific QTLs. *Environ. Geochem. Health* **2013**, *35*, 161−170.
(12) Itani, T.; Tamaki, M.; Arai, E.; Horino, T. Distribution of amylase, nitrogen, and minerals in rice kernels with various characters. *J. Agric. Food Chem.* **2002**, *50*, 5326−5332.
(13) Wang, K. M.; Wu, J. G.; Li, G.; Zhang, D. P.; Yang, Z. W.; Shi, C. H. Distribution of phytic acid and mineral elements in three *indica* rice (*Oryza sativa* L.) cultivars. *J. Cereal Sci.* **2011**, *54*, 116−121.
(14) Du, J.-H.; Fan, Y.-Y.; Wu, J.-R.; Zhuang, J.-Y. Dissection of QTLs for yield traits on the short arm of rice chromosome 6. *Agric. Sci. China* **2008**, *7*, 513−520.
(15) Zheng, K.; Huang, N.; Bennett, J.; Khush, G. S. *PCR-Based Marker-Assisted Selection in Rice Breeding*; International Rice Research Institute (IRRI): Manila, Philippines, 1995; IRRI Discussion Paper Series 12.
(16) Chen, X.; Temnykh, S.; Xu, Y.; Cho, Y. G.; McCouch, S. R. Development of a microsatellite framework map providing genome-wide coverage in rice (*Oryza sativa* L.). *Theor. Appl. Genet.* **1997**, *95*, 553−567.
(17) Mei, D.-Y.; Zhu, Y.-J.; Yu, Y.-H.; Fan, Y.-Y.; Huang, D.-R.; Zhuang, J.-Y. Quantitative trait loci for grain chalkiness and endosperm transparency detected in three recombinant inbred line populations of *indica* rice. *J. Integr. Agric.* **2013**, *12*, 1−11.
(18) Zhang, Z.-H.; Guo, L.; Zhu, Y.-J.; Fan, Y.-Y.; Zhuang, J.-Y. Mapping of quantitative trait loci for heading date and plant height in two populations of *indica* rice. *Sci. Agric. Sin.* **2011**, *44*, 3069−3077.
(19) Wang, S.; Basten, C.; Zeng, Z. *Windows QTL Cartographer 2.5*; North Carolina State University: Raleigh, NC, 2011.
(20) McCouch, S. R. CGSNL (Committee on Gene Symbolization, Nomenclature and Linkage, Rice Genetics Cooperative). Gene nomenclature system for rice. *Rice* **2008**, *1*, 72−84.
(21) Dai, W.-M.; Zhang, K.-Q.; Wu, J.-R.; Wang, L.; Duan, B.-W.; Zheng, K.-L.; Cai, R.; Zhuang, J.-Y. Validating a segment on the short arm of chromosome 6 responsible for genetic variation in the hull silicon content and yield traits of rice. *Euphytica* **2008**, *160*, 317−324.
(22) Zeng, Y.; Wang, L.; Du, J.; Liu, J.; Yang, S.; Pu, X.; Xiao, F. Elemental content in brown rice by inductively coupled plasma atomic emission spectroscopy reveals the evolution of Asian cultivated rice. *J. Integr. Plant Biol.* **2009**, *51*, 466−475.
(23) Anandan, A.; Rajiv, G.; Eswaran, R.; Prakash, M. Genotypic variation and relationships between quality traits and trace elements in traditional and improved rice (*Oryza sativa* L.) genotypes. *J. Food Sci.* **2011**, *76*, H122−H130.
(24) Gregorio, G. B.; Senadhira, D.; Htut, T.; Graham, R. D. Breeding for trace mineral density in rice. *Food Nutr. Bull.* **2000**, *21*, 382−386.
(25) Lamberts, L.; De Bie, E.; Vandeputte, G. E.; Veraverbeke, W. S.; Derycke, V.; De Man, W.; Delcour, J. A. Effect of milling on colour and nutritional properties of rice. *Food Chem.* **2007**, *100*, 1496−1503.
(26) Liang, J.; Li, Z.; Tsuji, K.; Nakano, K.; Nout, M. J. R.; Hamer, R. J. Milling characteristics and distribution of phytic acid and zinc in long-, medium- and short-grain rice. *J. Cereal Sci.* **2008**, *48*, 83−91.
(27) Gong, J.-Y.; Wu, J.-R.; Wang, K.; Fan, Y.-Y.; Zhuang, J.-Y. Fine mapping of *qHUS6.1*, a quantitative trait locus for silicon content in rice (*Oryza sativa* L.). *Chin. Sci. Bull.* **2010**, *55*, 3283−3287.
(28) Shen, B.; Yu, W.-D.; Zhu, Y.-J.; Fan, Y.-Y.; Zhuang, J.-Y. Fine mapping of a major quantitative trait locus, *qFLL6. 2*, controlling flag leaf length and yield traits in rice (*Oryza sativa* L.). *Euphytica* **2012**, *184*, 57−64.

DOI: 10.1021/acs.jafc.5b02882
J. Agric. Food Chem. 2015, 63, 7813−7818

ammonia-lyase, chalcone synthase (CHS), chalcone isomerase (CHI), flavanone 3-hydroxylase (F3H), flavonoid 3′-hydroxylase, flavonol synthase (FLS), dihydroflavonol reductase (DFR), and leucoanthocyanidin dioxygenase.[16] Flavonols, anthocyanins, and proanthocyanidins share the same pathway before separating at the point of dihydroflavonol. Then, dihydroflavonols are biosynthesized to anthocyanins or flavonols by DFR or FLS, respectively. In *Arabidopsis*, AtMYB11, AtMYB12, and AtMYB111 activate the expressions of *CHS*, *CHI*, *F3H*, and *FLS1* without having a bHLH partner.[17] In grapevine, VvMYBF1 can regulate *VvFLS1* expression independent of the bHLH transcription factor.[18] However, in maize, *ZmFLS1* expression is controlled by a complex of MYB-bHLH transcription factors.[19] Altogether, these studies indicated that, in some plants, flavonol biosynthesis is regulated by MYB transcription factors with or without the collaboration of the bHLH transcription factor.

In *B. napus*, some flavonoid structural genes have been identified, such as *BnDFR* (GenBank DQ767950), *BnF3H-1* (GenBank DQ288239), *BnCHS* (GenBank DQ767948), and *BnC4H-1* (GenBank DQ485130). However, to the best of our knowledge, no studies on *FLS* genes in *B. napus* have been conducted. Therefore, we attempted to identify the *B. napus FLS* (*BnFLS*) gene, whose cDNA sequences were retrieved from expressed sequence tag (EST) data.[20] Transgenic *B. napus* plants that overexpress *BnFLS* (*BnFLS-ox*) show significantly higher flavonol accumulation than wild-type plants. In this study, we examined whether the cloned putative *BnFLS* is a real *FLS* gene of *B. napus*. To address this question, we overexpressed the *BnFLS* gene in *Arabidopsis atfls1-ko* mutant and found that this gene can complement the lack of the *AtFLS1* gene in terms of flavonol accumulation. By overexpression of the *BnFLS* gene, flavonol (kaempferol and quercetin) levels were recovered in the *atfls1-ko* mutant, while anthocyanin content was lower in this line (*BnFLS-ox/atfls1-ko*) than in *Arabidopsis* wild-type plants. In addition, we found that the higher endogenous flavonol levels of *BnFLS-ox* in vitro shoots correlated with slightly higher ROS scavenging activities. Thus, our results indicate that the *BnFLS* gene encodes for a BnFLS enzyme that can be manipulated to specifically increase flavonol accumulation in oilseed plants and other species such as *Arabidopsis*.

MATERIALS AND METHODS

Plant Materials and Growth Conditions. In this study, *B. napus* L. Hanla was used for all the experiments. Seeds were sterilized and germinated on Murashige and Skoog (MS) medium supplemented with 2% (w/v) sucrose and 0.4% (w/v) Phytagel (pH 5.8), and the following growth conditions were used: 23 °C and 16-h light/8-h dark cycle. For inducible abiotic-stress treatments, 5-day-old seedlings were submerged in MS medium supplemented with the indicated concentrations of sucrose, abscisic acid (ABA), gibberellic acid (GA_3), NaCl, and mannitol for 24 h before use.

RNA Extraction and RT-PCR. Total RNA was extracted from 3-week-old leaves of *B. napus* growing in amplification media, as described by Sánchez and Carbajosa.[21] First-strand cDNA was synthesized using M-MLV Reverse Transcriptase, according to the manufacturer's instructions (iNtRON Biotechnology, Inc., Republic of Korea). PCR was performed using the cDNA and specific primers (Supporting Table 1).

***BnFLS* Cloning and Transformation.** Full-length *BnFLS* cDNA was isolated from *B. napus* Hanla by using RT-PCR and cloned using the pCR8/GW/TOPO TA Cloning Kit (Invitrogen). *BnFLS* was then subcloned into *pEarleyGate202* vector[22] to generate the construct *35Spro:FLAG:BnFLS*.

Agrobacterium-mediated transformation of *B. napus* was conducted according to a previously reported protocol[23] with some modifications. A single colony of *Agrobacterium* was inoculated into 25 mL of LB containing 25 μg/mL of rifampicin and 50 μg/mL of kanamycin and cultured at 30 °C with shaking (200 rpm) for 48 h. *Agrobacterium* cells were spun down and resuspended in MS liquid medium supplemented with 2% sucrose to achieve OD_{650} = 0.5 for generating the infection medium. Cotyledons were cut from 4-day-old seedlings grown in the dark and submerged in the infection medium for 10 min. The infected explants were then regenerated in various types of media, namely, cocultivation medium (2 days), callus induction medium (2 days), shoot initiation medium (2 weeks), shoot outgrowth medium (3 weeks), selection medium (3 weeks), and root initiation medium (3 weeks). Subsequently, the T1 transgenic plants were transferred to soil and grown in green house to collect seeds. These in vitro transgenic plants were also cultured in amplification medium for 3 weeks before further use. Detailed information on all the above-mentioned media is listed in Supporting Table 2.

Measurement of Anthocyanin Levels. Anthocyanin levels were measured according to a previously described method with some modifications.[24] The samples were ground to a fine powder in liquid nitrogen and extracted with 250 μL of methanol and 1% (v/v) HCl at 4 °C overnight. Then, 250 μL of distilled water and 250 μL of chloroform were added to the extracted samples, and the mixtures were vortexed and centrifuged for 5 min at 9 000*g* to separate the anthocyanin-containing phase. The aqueous phase was collected, and OD was measured at 535 and 650 nm. Anthocyanin levels were calculated as $OD_{535} - OD_{650}$/fresh weight (grams).

High-Performance Liquid Chromatography. Three-week old shoots on amplification medium were analyzed by high-performance liquid chromatography (HPLC) using Ultimate 3000 HPLC system (Dionex, Sunnyvale, CA). The flavonol was analyzed on an YMC-Triart C18+ column (4.6 mm × 250 mm, 5 μm) (YMC, Kyoto, Japan) using a mobile phase consisting of 100% methanol and 0.1% formic acid for elution. The flow rate was 0.6 mL/min and injection volume was 10 μL. The temperature was set at 4.5 °C for autosampler and 30 °C for column oven. The UV detector was set at 360 nm. Quercetin and kaempferol were selected as the standard samples.

Antioxidant Activity Measured Using 2,2-Diphenyl-1-picrylhydrazyl (DPPH) Assay. Radical scavenging activity was measured using DPPH assay, as reported previously with some modifications.[25] About 250 mg of the samples were ground in liquid nitrogen and extracted with 1 mL of 70% (v/v) acetone by sonication for 10 min. The samples were then separated to collect the supernatant by a centrifuge and extracted twice more. The supernatants were combined, dried by evaporation, and 1 mL of ethanol was added for resuspension and centrifuged. Then, 100 μL of the supernatant was mixed with 100 μL of DPPH solution (200 μM in ethanol) and maintained for 20 min at room temperature. Radical scavenging activity was shown as the decrease in absorbance at 517 nm because of DPPH radicals from the blank test by using 100% ethanol.

3,3′-Diaminobenzidine (DAB) Staining. In situ detection of hydrogen peroxide was performed by staining with DAB (Sigma-Aldrich), according to an adaptation of a previously reported method.[26] Briefly, the samples were immersed in 1 mg/mL of DAB solution containing Tween 20 (0.05% v/v) and 10 mM sodium phosphate buffer (pH 7) and gently shaken for 4−6 h. The staining reaction was terminated and fixed in 3:1:1 ethanol/glycerol/acetic acid (bleaching solution) placed in a water bath at 95 °C for 15 min. The leaves were reimmersed in the bleaching solution until the chlorophyll was completely depleted and then visualized under white light and photographed.

DBPA Staining. Flavonol accumulation in root tips was observed using DPBA staining, as described previously[27] with some modifications. Briefly, seedlings were stained for 5−15 min by using saturated (0.25%, w/v) DPBA with 0.02% (v/v) Triton X-100 and were then washed three times in distilled water for 5 min. The samples were visualized using a confocal laser scanning microscope (LSM 700, Carl-Zeiss).

DOI: 10.1021/acs.jafc.5b02994
J. Agric. Food Chem. 2015, 63, 7819−7829

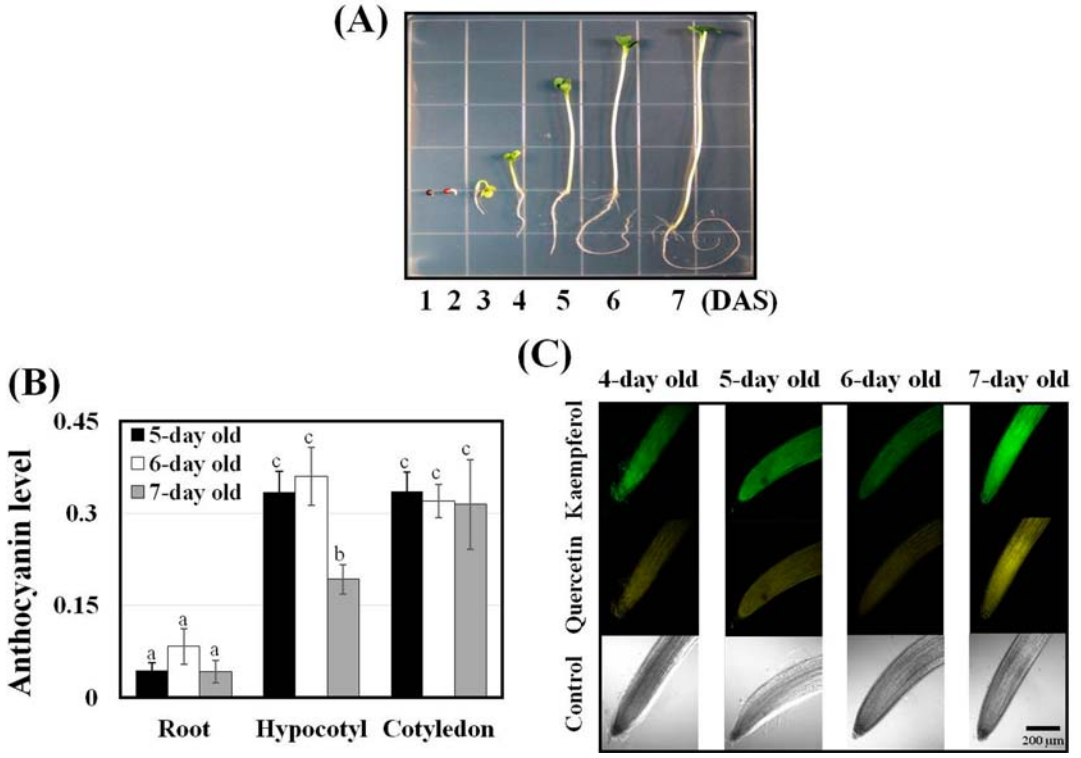

Figure 1. Wild-type *Brassica napus* seedlings and flavonoid accumulation. (A) 1- to 7-day-old *B. napus* L. Hanla seedlings (from left to right). (DAS: day after seeding). (B) Anthocyanin accumulation in various tissues (root, hypocotyls, and cotyledons) of 5-, 6-, and 7-day-old seedlings. Wild-type seedlings were grown under normal conditions for 5, 6, and 7 days and used for anthocyanin measurement. (C) Flavonol accumulation in *B. napus* seedlings. Wild-type seedlings were grown under normal conditions for 5, 6, and 7 days and used for flavonol detection. The experiment was repeated three times and Duncan's tests ($p < 0.05$) were performed. The letters above the columns indicate significant differences. Bars reflect standard errors.

Statistical Analyses. Statistical analyses were performed using Duncan's tests at 95% confidence level.

RESULTS

Flavonoid Accumulation in Wild-Type *B. napus* Seedlings. *B. napus* Hanla seeds were sown on MS medium for germination and grown for 7 days (Figure 1A). To investigate flavonoid accumulation in the oilseed plants, we first detected anthocyanin and flavonol levels in 5-, 6- and 7-day-old wild-type seedlings (Figure 1). As demonstrated in Figure 1B, the anthocyanin levels were not different between 5- and 6-day-old seedlings. Besides, while roots and cotyledons of the 5-, 6- and 7-day-old seedlings showed similar anthocyanin levels, hypocotyls of the 7-day-old seedlings accumulated a lesser amount of anthocyanin than younger seedlings (Figure 1B). Flavonol accumulation in the root tips of the seedlings was observed using DPBA staining. Root-tip tissues displayed green and yellow fluorescence because of kaempferol and quercetin accumulation, respectively. Flavonol levels in the root tips of 4- and 5-day-old seedlings showed no differences, while this accumulation decreased in 6-day-old seedlings and increased in 7-day-old seedlings (Figure 1C). Because anthocyanin accumulation was higher in hypocotyls of 5- and 6-day-old seedlings than in those of 7-day-old seedlings and flavonol accumulation was higher in root tips of 5-day-old seedlings than in those of 6-day-old seedlings, we chose 5-day-old seedlings for stress treatments. Five-day old seedlings were exposed to several stress conditions for 24 h and then used for measuring anthocyanin and flavonol accumulation. Anthocyanin levels increased in response to sucrose, ABA, NaCl, and mannitol treatments, but no difference was observed between GA_3 treatment results and control conditions (Figure 2A,B). In addition, flavonol levels in the root tips increased in response to sucrose, GA_3, NaCl, and mannitol treatments, but no difference was observed between ABA treatment results and control conditions (Figure 2C). These results suggest that flavonoid levels increased in response to salt and drought stress conditions in young *B. napus* seedlings.

Since flavonoids serve as antioxidants, we wanted to check whether stress treatment resulted in increased radical scavenging activity due to enhanced accumulation of flavonoids in *B. napus* seedlings. To measure radical scavenging activity, the DPPH assay was performed using 5-day-old wild-type seedlings grown under stress conditions. As shown in Figure 3, radical scavenging activity was slightly increased in response to NaCl and mannitol treatments, while sucrose, ABA, and GA_3 treatments showed no effects (Figure 3). On the basis of these results, we can conclude that the increase in flavonoid levels is positively correlated with higher radical scavenging activity in response to salt and drought stress conditions.

Isolation of *BnFLS* Gene from Wild-Type *B. napus* Seedlings. Overexpression of *AtPAP1* transcription factor has been reported to result in the enhancement of anthocyanin levels in transgenic *B. napus* plants.[2] Thus, in this study, we aimed to clone a *B. napus FLS* gene to test whether we can specifically increase flavonol levels in *B. napus* by manipulation of *BnFLS*, because flavonols can be used as antioxidants for food and medical purposes. For example, flavonols, including quercetin and kaempferol, are known to have antiproliferative effects on human cancer cells.[14] cDNA fragments of *BnFLS*

DOI: 10.1021/acs.jafc.5b02994
J. Agric. Food Chem. 2015, 63, 7819−7829

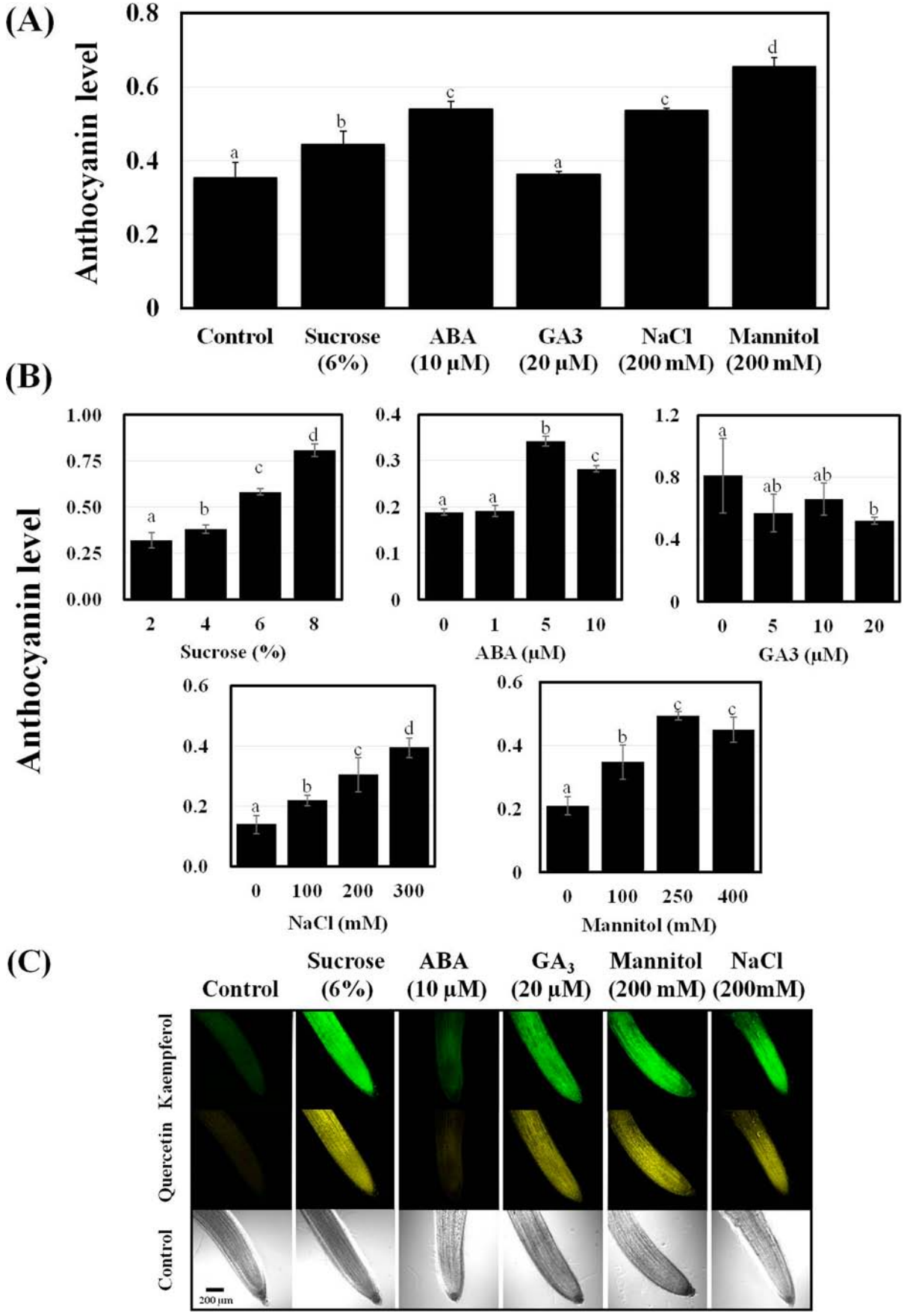

Figure 2. Flavonoid accumulation in *Brassica napus* seedlings in response to stress conditions. (A) Anthocyanin accumulation in 5-day-old seedlings in response to indicated stress conditions. (B) Anthocyanin accumulation in 5-day-old seedlings in response to sucrose, ABA, GA_3, NaCl, and

DOI: 10.1021/acs.jafc.5b02994
J. Agric. Food Chem. 2015, 63, 7819−7829

Figure 2. continued

mannitol. (C) Flavonol accumulation in the root tips of 5-day-old seedlings. The 5-day-old seedlings were grown under normal conditions and used for indicated treatments; control [MS liquid medium supplemented with 20 g/L of sucrose (2%)], ABA, sucrose, GA_3, NaCl, or mannitol with indicated concentrations in the figure. After 24 h, these seedlings were used for anthocyanin measurement and flavonol detection. The experiment was repeated three times and Duncan's tests ($p < 0.05$) were performed. The letters above the columns indicate significant differences. The letters ("ab" or "bc") above the columns indicate no significant difference with a, b, or c, respectively. Bars reflect standard errors.

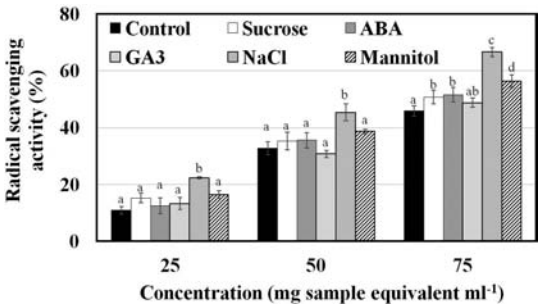

Figure 3. Radical scavenging activity of wild-type *Brassica napus* seedlings in response to various signals. The 5-day-old seedlings were grown under normal conditions and exposed to various signals; control [MS liquid medium supplemented with 20 g/L of sucrose (2%)], 10 μM ABA, 60 g/L sucrose, 20 μM GA_3, 200 mM NaCl, and 200 mM mannitol. After 24 h, these seedlings were subjected for DPPH assay to determine the radical scavenging activity. The experiment was repeated 3 times and Duncan's tests ($p < 0.05$) were performed. The letters above the columns indicate significant differences. The letters ("ab") above the column indicates no significant difference with a or b, respectively. Bars reflect standard errors.

from Expressed Sequence Tag (EST) data[20] were used to design a full-length specific primer pair for this gene. Total RNA was extracted from 5-day-old wild-type seedlings and used for synthesizing a first-strand cDNA library. PCR was performed using this primer set and the cDNA library. The PCR product was then cloned into TOPO vector (Invitrogen) and used to confirm the *BnFLS* sequence (Supporting Figure 1). The putative *BnFLS* sequence was translated to the amino acid sequence, and alignment results showed that BnFLS is highly homologous to BrFLS1 and AtFLS1 (Figure 4). Because the flavonol accumulation in root tips was altered in response to different treatments as shown in Figure 2C, we then examined whether *BnFLS* can be induced by these conditions (Figure 5). As shown in Figure 5, *BnFLS* was highly expressed in response to mannitol treatment. However, expression of *BnFLS* was slightly decreased by sucrose, GA_3, and NaCl treatments.

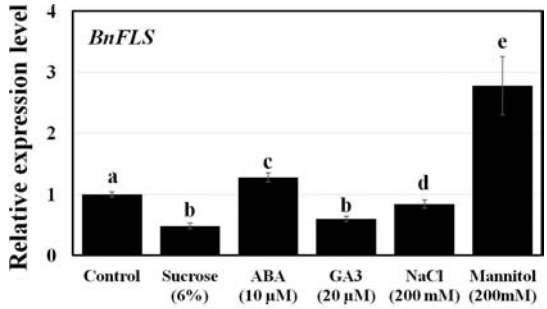

Figure 5. *BnFLS* expression in wild-type *Brassica napus* seedlings in response to various plant growth regulators and stress conditions. The 5-day-old seedlings were exposed to 6% sucrose, 10 μM ABA, 20 μM GA_3, 200 mM NaCl, and 200 mM mannitol for 24 h; mRNA was then extracted to produce cDNA for *qRT-PCR*. The control medium was 2% sucrose. The *BnACTIN* was used for internal control. The primer information was shown in Supporting Table 1.

```
BnFLS     MEIERVQDISSSSLHTEVIPLEFIRSEKEQPAITTFRGPVPAIPVVDLSDPDEESVARAV 60
BrFLS1    MEIERVQDISSSSLHTEAIPLEFIRSEKEQPAITTFRGPTPAIPVVDLSDPDEESVARAV 60
AtFLS1    MEVERVQDISSSSLLTEAIPLEFIRSEKEQPAITTFRGPTPAIPVVDLSDPDEESVRRAV 60
          **:*********** **.********************.*************** ***

BnFLS     VKASEEWGIFQVVNHGIPTELIKRLQEVGRTFFELPSSEKESVAKPADAKDIEGYGTKLQ 120
BrFLS1    VKASEEWGIFQVVNHGIPTELIKRLQEVGRTFFELPSAEKESVAKPVDAKDIEGYGTKLQ 120
AtFLS1    VKASEEWGLFQVVNHGIPTELIRRLQDVGRKFFELPSSEKESVAKPEDSKDIEGYGTKLQ 120
          ********:*************:***:***.******:******** *:***********

BnFLS     KEVEGKKAWVDHLFHRIWPPSCVNYSFWPKNPPEYREVNEEYALHVKKLSETLLGILSEG 180
BrFLS1    KEVEGKKAWVDHLFHRIWPPSCVNYSFWPKNPPEYREVNEEYALHVKKLSETLLGILSEG 180
AtFLS1    KDPEGKKAWVDHLFHRIWPPSCVNYRFWPKNPPEYREVNEEYAVHVKKLSETLLGILSDG 180
          *: ********************** ****************:**************:*

BnFLS     LGLRREALREGLGGDLVEYMMKINYYPPCPRPDLALGVPAHTDLSGITLLVPNEVPGLQV 240
BrFLS1    LGLRREALREGLGGDLAEYMMKINYYPPCPRPDLALGVPAHTDLSGITLLVPNEVPGLQV 240
AtFLS1    LGLKRDALKEGLGGEMAEYMMKINYYPPCPRPDLALGVPAHTDLSGITLLVPNEVPGLQV 240
          ***:*:**:*****:: .*********************************************

BnFLS     FKDDHWFDAEYIPSAVIVHIGDQILRLSNGRYKNVLHRTTVDKDRTRMSWPVFLEPHREM 300
BrFLS1    FKDDHWFDAEYIPSAVIVHIGDQILRLSNGRYKNVLHRTTVDKDRTRMSWPVFLEPHREM 300
AtFLS1    FKDDHWFDAEYIPSAVIVHIGDQILRLSNGRYKNVLHRTTVDKEKTRMSWPVFLEPPREK 300
          ********************************************:::*********** **

BnFLS     IVGPLPELISDGNPPKYKPFAFKDYSYRKLNKLPLD 336
BrFLS1    IVGPLPELISDDNPPKYKPFAFKDYSYRKLNKLPLD 336
AtFLS1    IVGPLPELTGDDNPPKFKPFAFKDYSYRKLNKLPLD 336
          ******** .*.****:******************
```

Name	Name	Score
BnFLS	AtFLS1	91.07
BnFLS	BrFLS1	98.21

Figure 4. Amino acid alignment among *Brassica napus, B. rapa*, and *Arabidopsis thaliana FLS1*. *BnFLS* cDNA sequence was translated to amino acid sequence and then aligned with *Brassica rapa* FLS1 (BrFLS1) and *Arabidopsis thaliana* FLS1 (AtFLS1).

DOI: 10.1021/acs.jafc.5b02994
J. Agric. Food Chem. 2015, 63, 7819−7829

Complementation Assay to Confirm That *BnFLS* Encodes a Functional FLS Enzyme by Using *Arabidopsis atfls1-ko* Mutant. Although we found that the BnFLS sequence was highly homologous to BrFLS1 and AtFLS1, we needed to examine whether this gene encodes a functional FLS protein. To address this, we introduced *BnFLS* into *Arabidopsis* wild-type (Col-0) and *atfls1-ko* mutant plants. Using the floral-dipping transformation method,[28] we obtained several transgenic plants on Col-0 (*BnFLS/Col-0* #1; #2) and *atfls1-ko* (*BnFLS/atfls1-ko* #1; #2) backgrounds. RT-PCR results confirmed *BnFLS* overexpression in these transgenic plants (Figure 6A). As shown in Figure 6B, flavonol accumulation was

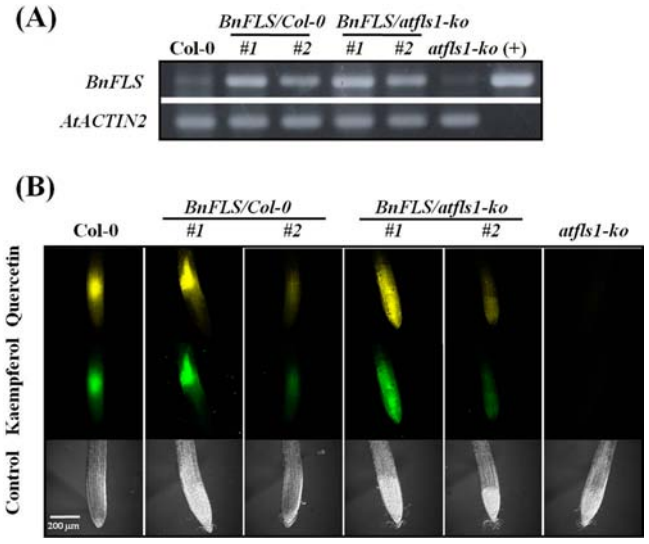

Figure 6. Functional complementation analysis of the *BnFLS*. (A) The *BnFLS* gene was introduced into *Arabidopsis* Col-0 (*BnFLS/Col-0*) as well as the *atfls1-ko* mutant seedlings (*BnFLS/atfls1-ko*) to examine whether this gene can recover the genetic defects of the *atfls1-ko* mutant. Seedlings of the wild-type (Col-0), *BnFLS/Col-0*, *BnFLS/atfls1-ko*, and *atfls1-ko* grown on 1/2× MS medium were used for RNA extraction and *RT-PCR* using specific primers (Supporting Table S1). *ACTIN2* was used as an internal control. (+) indicates the PCR product from bacterial plasmid containing the *BnFLS* gene. (B) Root tips of the wild-type (Col-0), *BnFLS/Col-0*, *BnFLS/atfls1-ko*, and *atfls1-ko* grown on 1/2× MS medium were used for the detection of flavonol by using DPBA staining. *BnFLC: BnFLS* transforms into Col-0; *BnFLf: BnFLS* transforms into *fls1-ko*. The 6-day-old seedlings grown under normal conditions were used for flavonol detection.

observed in root tips of 6-day-old seedlings by using DBPA staining; *BnFLS/Col-0* #1 showed higher flavonol accumulation than Col-0, but *BnFLS/Col-0* #2 showed decreased flavonol levels. In contrast, fluorescence of *atfls1-ko* was less intense, showing lower flavonol accumulation. However, the higher flavonol accumulation of *BnFLS/atfls1-ko* #1 and #2 than *atfls1-ko* confirmed that BnFLS serves as an FLS enzyme.

Generation of Transgenic Seedlings That Ectopically Express *BnFLS*. After confirming the flavonol synthase function of BnFLS, we decided to generate *B. napus* transgenic plants that overexpress the gene. To do this, the cDNA of *BnFLS* was cloned into *pEarleyGate202*,[22] in which the expression of this gene was driven by the cauliflower mosaic virus 35S promoter (*CaMV 35Spro*; Figure 7A). Next, the *35Spro:FLAG:BnFLS* construct was transformed into wild-type *B. napus* Hanla cotyledon samples, according to a method described by Bhalla and Singh.[23] The putative transgenic plants were confirmed using several methods (Figure 7). First, the putative transgenic plants were tested using instant strips that can detect the *BAR* gene product (Figure 7B). Real transgenic lines exhibited two bands instead of only one band, which is indicative of the wild-type as well as nontransgenic plants (Figure 7B). The putative transgenic plants were also examined using PCR with genomic DNA and PCR primers (Figure 7C and Supporting Table 1). In addition, RT-PCR was performed to show that these transgenic plants exhibited increased expression of *BnFLS* (Figure 7D). The expression levels of other genes involved in the flavonoid biosynthesis were similar in the wild type and transgenic *BnFLS-ox* plants (Supporting Figure 2).

Accumulation of Anthocyanins and Flavonols in *B. napus BnFLS-ox* Plants. Transgenic *BnFLS-ox* plants (T_1) were transferred onto amplification medium for further propagation (Supporting Table 2). After 3 weeks of growth on the amplification medium, around 5 new shoots were produced from the original shoot (Figure 8A). These shoots were separated and transferred to MS medium for further experiments. *In vitro* shoots of *Brassica* wild-type and *BnFLS-ox* (#1, #2, #3, and #4 lines) were transferred to MS medium supplemented with sucrose (2% or 6%) for growth and measurement of anthocyanin levels (Figure 8B). As shown in Figure 8B, anthocyanin levels of the wild-type and *BnFLS-ox* (#1, #2, #3, and #4) shoots were not significantly different in response to a low concentration of sucrose (2%). However, a higher concentration of sucrose (6%) increased anthocyanin accumulation in the wild-type samples, while there was no change in the *BnFLS-ox* shoots (Figure 8B). Next, we determined flavonol levels in the *in vitro* shoots by using HPLC (Figure 8C). The results showed that quercetin and kaempferol accumulation was higher in the *BnFLS-ox* line than in the wild-type, but sucrose treatment (6%) slightly decreased flavonol levels in comparison with control conditions (2%; Figure 8C). The transgenic shoots were transferred to MS medium and allowed to produce roots without adding any hormones in order to observe flavonol accumulation by using DPBA staining. As shown in Figure 8D, flavonol content in the *BnFLS-ox* (#1 #2, #3, and #4 lines) increased in comparison to the wild-type.

Next, we checked whether the *BnFLS-ox* plants have increased antioxidative ability because of enhanced flavonol levels. Leaves of the *BnFLS-ox* and wild-type plants growing in the amplification medium were used for DAB staining to check reactive oxygen species (ROS) levels. An intense brown stain indicated that the samples had high levels of ROS (Figure 9). ROS levels were higher in wild-type leaves than in the *BnFLS-ox* leaves, which indicated that the *BnFLS-ox* plants may have higher scavenging activity than the wild-type.

DISCUSSION

Anthocyanins and flavonols are biosynthesized using the flavonoid biosynthesis pathway. In this pathway, dihydroflavonols can be catalyzed to produce anthocyanins or flavonols by DFR or FLS, respectively. In a DFR-defective mutant, accumulation of flavonols is higher than that in wild-type plants,[29] whereas anthocyanin content is higher in the *atfls1-ko* mutant than in wild-type plants.[30,31] Therefore, it is important for plants to decide which enzymes need to be activated on the basis of the conditions. In this study, we cloned a newly isolated *B. napus FLS* and characterized transgenic plants that overexpressed this gene aiming for a high production of

DOI: 10.1021/acs.jafc.5b02994
J. Agric. Food Chem. 2015, 63, 7819−7829

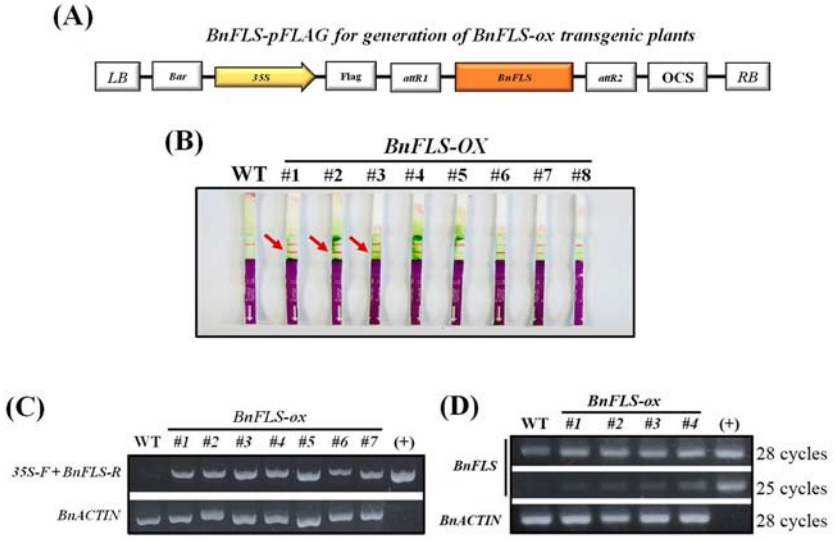

Figure 7. Generation of the *BnFLS* overxepressing transgenic *Brassica napus* plants (*BnFLS-ox*). (A) Construction map of the *35Spro:FLAG:BnFLS* plasmid for the generation of *BnFLS-ox* transgenic plants. *Bar*: Basta resistant gene; *35S*: cauliflower mosaic virus 35S promoter; FLAG: FLAG epitope tag for target proteins; *BnFLS*: *Brassica napus Flavonol Synthase* gene. (B) Selection method of real *BnFLS-ox* transgenic plants; the wild-type or nontransgenic plants showed only one band when instant basta detection strips were used, while real transgenic lines exhibited one additional band indicated with red arrows. (C) Genotyping of the *BnFLS-ox* transgenic plants by using PCR with genomic DNA and specific primers (Supporting Table 1). (D) Three-week-old *BnFLS-ox* transgenic plants were grown under normal conditions and used for RT-PCR to check for *BnFLS* expression level in two different PCR cycles. *BnACTIN* was used for internal control (primer information is listed in Supporting Table 1). (+) indicates the PCR product from bacterial plasmid containing the *BnFLS* gene. WT: wild type.

flavonols. In particular, we intended to redirect the flavonoid biosynthesis pathway by using genetic manipulation to increase the production of specific flavonoids, such as quercetin or kaempferol, in the oilseed plants.

Several genes that encode FLS enzymes have been isolated and characterized from various plant species, including *A. thaliana*,[32] *Ginkgo biloba*,[33] and *Glycine max*.[34] *Arabidopsis* is known to contain 6 *FLS* genes, while several other flavonoid biosynthesis enzymes are encoded by only 1 gene.[32,35] Flavonols such as kaempferol and quercetin exhibit variations in their accumulation levels and tissue specificities under different environmental circumstances, implying the involvement of various *FLS* genes.[17,36,37]

In the current study, anthocyanins accumulated more in the hypocotyls and cotyledons of the wild-type *B. napus* seedlings than in the roots (Figure 1B). This result was expected because it is well-established that anthocyanins have light-protection and light-filtration functions in plants. We observed that anthocyanin levels significantly decreased in 7-day-old seedlings, indicating the younger seedlings may be more active in producing anthocyanins. Young seedlings may be vulnerable to various types of biotic or abiotic agents, resulting in a high production of flavonoids to combat against these attacks like in other plant systems.[38] We observed that the levels of both anthocyanins and flavonols were significantly enhanced in the wild-type in response to several stresses (Figure 2). Interestingly, ABA increased anthocyanin levels but did not affect flavonol accumulation (Figure 2). In contrast, GA_3 did not alter anthocyanin levels but enhanced flavonol accumulation (Figure 2). These plant growth regulators are reported to control flavonoid biosynthesis by regulating the expression levels of certain transcription factor genes.[39,40] For instance, GA_3 inhibits the induction of *DFR* expression by sucrose but barely affects *FLS* expression, while ABA can increase *DFR* expression.[41] Several studies have reported that anthocyanin biosynthesis is promoted by UV-B light in *Arabidopsis thaliana*[42] and *B. rapa*.[43] In many cases, flavonoids serve antioxidants in stress tolerance. Flavonoids have been shown to function as excellent free radical scavengers because they are strongly reactive as hydrogen or electron donors.[44] Previous studies proposed that the radical scavenging activity of flavonoids can be determined by the number and location of the phenolic OH groups in their structure.[44] Overaccumulation of flavonols and anthocyanins was proposed to increase drought stress tolerance and antioxidant activity in *A. thaliana*.[44] This led us to examine radical scavenging activity in *B. napus* plants after stress treatment. Radical scavenging activity was higher in response to salt and drought stress conditions, which appears to be correlated with the increase in flavonoid accumulation in response to various stresses (Figures 2 and 3).

In *B. napus*, several structural genes for flavonoid biosynthesis, such as *BnF3′H*,[45] *BnIS*,[46] and transcription factor genes *BnTT2*,[47] *BnTT16*,[48] have been identified and studied, while no studies have been conducted on *BnFLS*. This prompted us to characterize *BnFLS* and generate *BnFLS-ox* transgenic plants to expand our understanding on the functions of FLS in *B. napus*. On the basis of gene expression data for *B. napus*,[20] we found 2 cDNA fragments of *BnFLS*, which is a homologue of *AtFLS1*. Alignment results of *BnFLS* and *AtFLS1* sequences helped us to deduce the full-length cDNA sequence of *BnFLS* (Supporting Figure 1). On the basis of this sequence, we designed a specific primer pair to amplify and clone *BnFLS* from *B. napus* cDNAs. The sequence of the cloned putative *BnFLS* was checked, and the open reading frame was confirmed to be 1011 bp (Supporting Figure 1). Then, *BnFLS* cDNA sequences were converted into amino acid sequences and aligned again with AtFLS1 and BrFLS1 amino acid sequences. This alignment indicated that BnFLS is highly homologous to BrFLS (98%) and AtFLS1 (91%) (Figure 4). The high homology between

DOI: 10.1021/acs.jafc.5b02994
J. Agric. Food Chem. 2015, 63, 7819−7829

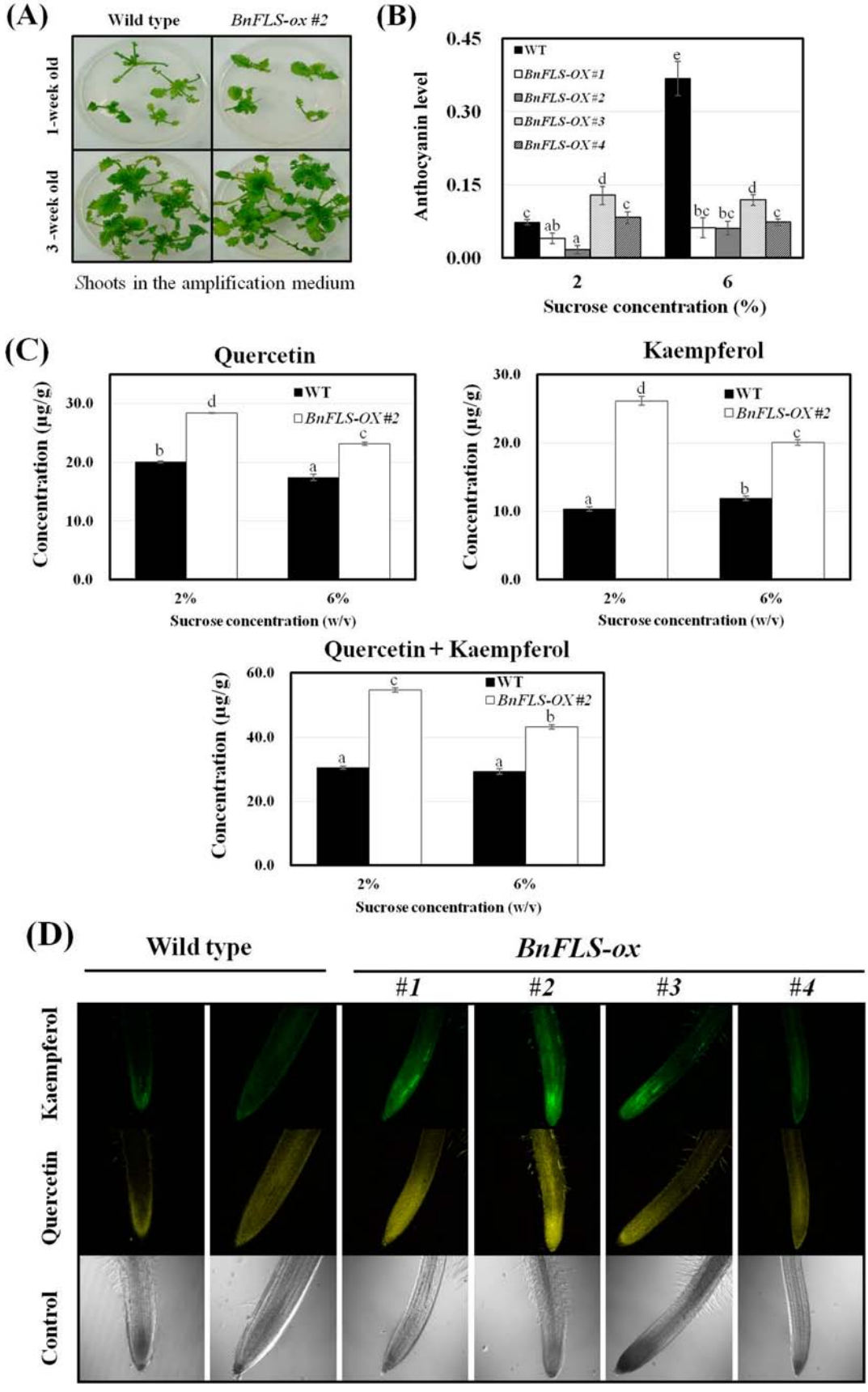

Figure 8. Flavonoid accumulation in wild type and the *BnFLS-ox* transgenic plants. (A) Growth phenotype of the wild type and *BnFLS-ox* #2 shoots growing in the amplification medium. (B) Anthocyanin levels in the wild type and *BnFLS-ox* shoots in response to 2 or 6% sucrose. (C) Flavonol (quercetin and kaempferol) levels in the wild type and *BnFLS-ox* #2 shoots in response to 2 or 6% sucrose. The 3-week-old transgenic plants grown under normal conditions were incubated in the liquid medium containing the indicated sucrose concentrations for 24 h. Then, these shoots were

DOI: 10.1021/acs.jafc.5b02994
J. Agric. Food Chem. 2015, 63, 7819−7829

Figure 8. continued

used for anthocyanin and flavonol detection. The experiment was repeated three times and Duncan's tests ($p < 0.05$) were performed. The letters above the columns indicate significant differences. The letters ("ab" or "bc") above the columns indicate no significant difference with a, b, or c, respectively. Bars reflect standard errors. (D) Flavonol accumulation in the root tips of in the wild type and *BnFLS-ox* lines. After growing for 3 weeks in the amplification medium, the roots were used for DPBA staining.

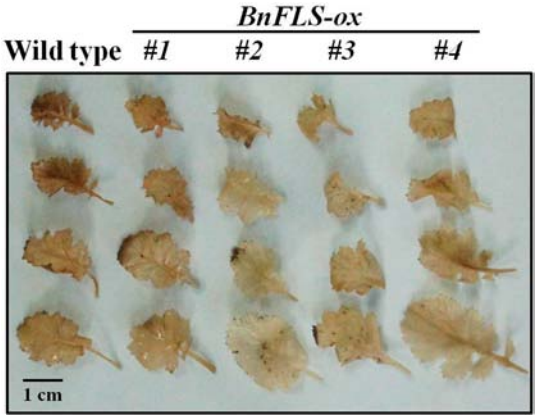

Figure 9. DAB staining of *BnFLS-ox* transgenic plants. Leaves of 3-week old wild type and *BnFLS-ox* (#1, #2, #3, #4 lines) shoots grown in the amplification medium were incubated in liquid medium supplemented with DAB reagent to visualize the ROS levels. Four separate leaves were examined.

BrFLS and BnFLS may be explained by the theory of origin of *B. napus*.[49,50] In addition, *BnFLS* cDNA was transformed into the *Arabidopsis fls1-ko* mutant and was shown to complement the flavonol-lacking phenotype of this mutant (Figure 6B). *Arabidopsis atfls1-ko* showed a strong reduction in flavonol content (Figure 6B) and accumulated higher levels of anthocyanins and glycosylated dihydroflavonols than the wild-type.[30,31,35] However, differences in substrate preference between the enzymes of different plant species or the expression of other flavonol synthase genes may be the reasons why flavonol accumulation in *BnFLS/Col-0* #2 and *BnFLS/atfls1-ko* #2 root tips were lower than that in Col-0.

To characterize the functions of *BnFLS*, we generated *BnFLS-ox* plants and confirmed the expression level of *BnFLS* in these transgenic plants by using RT-PCR (Figure 7C). In addition, we measured anthocyanin and flavonol levels in *BnFLS-ox* transgenic and wild-type seedlings (Figure 8). Higher expression of *BnFLS* in *BnFLS-ox* shoots was related to higher flavonol content (Figure 8C). Anthocyanin levels in 3-week-old seedlings of the wild-type were significantly increased in response to a high sucrose concentration (6%; Figure 8B). However, this high sucrose concentration could not succeed in promoting anthocyanin biosynthesis in the *BnFLS-ox* plants. Because DFR and FLS catalyze the same substrate, overexpression of *BnFLS* led to a higher accumulation of flavonols and resulted in lower anthocyanin levels in these transgenic plants (Figure 8). According to our observations, *BnFLS* overexpression confers increased antioxidative capability to transgenic oilseed plants, because ROS levels were decreased in the *BnFLS-ox* plants (Figure 9). Since high levels of flavonols as well as anthocyanins were suggested to be correlated with increased drought stress tolerance in *A. thaliana*,[44] it would be of great interest to examine *BnFLS-ox* plants in the future.

■ ASSOCIATED CONTENT

Supporting Information

The Supporting Information is available free of charge on the ACS Publications website at DOI: 10.1021/acs.jafc.5b02994.

Materials details and characterization (PDF)

■ AUTHOR INFORMATION

Corresponding Authors

*E-mail: lhojoung@korea.ac.kr. Phone: +82-2-3290-3006. Fax: +82-2-3290-3508.

*E-mail: sukwhan@chonnam.ac.kr. Phone: +82-62-530-2180. Fax: +82-62-530-2180.

Author Contributions

‖T.T.V. and C.Y.J. contributed equally.

Funding

This study was supported by a grant from the National Research Foundation of Korea (to Hojoung Lee, 2014; grant NRF-2014R1A1A3050272) and the Korea Institute of Planning and Evaluation for Technology in Food, Agriculture, Forestry and Fisheries (to H.L., 2012; grant #2012-112068-3).

Notes

The authors declare no competing financial interest.

■ ACKNOWLEDGMENTS

We would like to thank to Prof. Prem Bhalla and Dr. Dany Heang (Plant Molecular Biology and Biotechnology Laboratory, The University of Melbourne) for advising us the Canola genetic transformation technique. We would like to thank Dr. Christoph Ringli (Institute of Plant Biology, University of Zürich) for donating the *fls1-3* mutant seeds.

■ ABBREVIATIONS USED

DPPH, 2,2-diphenyl-1-picrylhydrazyl; ROS, reactive oxygen species; DAB, 3,3′-Diaminobenzidine

■ REFERENCES

(1) Fang, J.; Reichelt, M.; Hidalgo, W.; Agnolet, S.; Schneider, B. Tissue-specific distribution of secondary metabolites in rapeseed (*Brassica napus* L.). *PLoS One* **2012**, *7*, e48006.

(2) Li, X.; Gao, M.-J.; Pan, H.-Y.; Cui, D.-J.; Gruber, M. Y. Purple canola: Arabidopsis PAP1 increases antioxidants and phenolics in *Brassica napus* leaves. *J. Agric. Food Chem.* **2010**, *58*, 1639−1645.

(3) Charest, P.; Holbrook, L.; Gabard, J.; Iyer, V.; Miki, B. *Agrobacterium*-mediated transformation of thin cell layer explants from *Brassica napus* L. *Theor. Appl. Genet.* **1988**, *75*, 438−445.

(4) Moloney, M. M.; Walker, J. M.; Sharma, K. K. High efficiency transformation of *Brassica napus* using *Agrobacterium* vectors. *Plant Cell Rep.* **1989**, *8*, 238−242.

(5) Li, J.; Tan, X.; Zhu, F.; Guo, J. A rapid and simple method for *Brassica napus* floral-dip transformation and selection of transgenic plantlets. *Int. J. Biol.* **2010**, *2*, p127.

(6) Crozier, A.; Jaganath, I. B.; Clifford, M. N. Phenols, polyphenols and tannins: an overview. In *Plant Secondary Metabolites: Occurrence, Structure and Role in the Human Diet*, 1st ed.; Crozier, A., Clifford, M. N. and Ashihara, H., Eds.; Blackwell Publishing Ltd: Oxford, U.K., 2006; pp 1−24.

DOI: 10.1021/acs.jafc.5b02994
J. Agric. Food Chem. 2015, 63, 7819−7829

(7) Harborne, J. B.; Williams, C. A. Advances in flavonoid research since 1992. *Phytochemistry* **2000**, *55*, 481−504.
(8) Huits, H. S.; Gerats, A. G.; Kreike, M. M.; Mol, J. N.; Koes, R. E. Genetic control of dihydroflavonol 4-reductase gene expression in *Petunia hybrida*. *Plant J.* **1994**, *6*, 295−310.
(9) Bieza, K.; Lois, R. An Arabidopsis mutant tolerant to lethal ultraviolet-B levels shows constitutively elevated accumulation of flavonoids and other phenolics. *Plant Physiol.* **2001**, *126*, 1105−1115.
(10) Brown, D. E.; Rashotte, A. M.; Murphy, A. S.; Normanly, J.; Tague, B. W.; Peer, W. A.; Taiz, L.; Muday, G. K. Flavonoids act as negative regulators of auxin transport in vivo in Arabidopsis. *Plant Physiol.* **2001**, *126*, 524−535.
(11) Nicholson, R. L.; Hammerschmidt, R. Phenolic compounds and their role in disease resistance. *Annu. Rev. Phytopathol.* **1992**, *30*, 369−389.
(12) Dangles, O.; Fargeix, G.; Dufour, C. One-electron oxidation of quercetin and quercetin derivatives in protic and non protic media. *J. Chem. Soc., Perkin Trans. 2* **1999**, *2*, 1387−1396.
(13) Lee, B.-H.; Jeong, S.; Jung, S.; Lee, J.; Kim, J.; Yoon, I.; Choi, S.-H.; Lee, S.-M.; Chang, C.-G.; Kim, H.-C. Quercetin inhibits the 5-hydroxytryptamine type 3 receptor-mediated ion current by interacting with pre-transmembrane domain I. *Mol. Cells* **2005**, *20*, 69−73.
(14) Granado-Serrano, A. B.; Martín, M. A.; Bravo, L.; Goya, L.; Ramos, S. Quercetin induces apoptosis via caspase activation, regulation of Bcl-2, and inhibition of PI-3-kinase/Akt and ERK pathways in a human hepatoma cell line (HepG2). *J. Nutr.* **2006**, *136*, 2715−2721.
(15) Holton, T. A.; Cornish, E. C. Genetics and biochemistry of anthocyanin biosynthesis. *Plant Cell* **1995**, *7*, 1071.
(16) Pelletier, M. K.; Shirley, B. W. Analysis of flavanone 3-hydroxylase in Arabidopsis seedlings (Coordinate regulation with chalcone synthase and chalcone isomerase). *Plant Physiol.* **1996**, *111*, 339−345.
(17) Stracke, R.; Ishihara, H.; Huep, G.; Barsch, A.; Mehrtens, F.; Niehaus, K.; Weisshaar, B. Differential regulation of closely related R2R3-MYB transcription factors controls flavonol accumulation in different parts of the Arabidopsis thaliana seedling. *Plant J.* **2007**, *50*, 660−677.
(18) Czemmel, S.; Stracke, R.; Weisshaar, B.; Cordon, N.; Harris, N. N.; Walker, A. R.; Robinson, S. P.; Bogs, J. The grapevine R2R3-MYB transcription factor VvMYBF1 regulates flavonol synthesis in developing grape berries. *Plant Physiol.* **2009**, *151*, 1513−1530.
(19) Falcone Ferreyra, M. L.; Rius, S.; Emiliani, J.; Pourcel, L.; Feller, A.; Morohashi, K.; Casati, P.; Grotewold, E. Cloning and characterization of a UV-B-inducible maize flavonol synthase. *Plant J.* **2010**, *62*, 77−91.
(20) Trick, M.; Long, Y.; Meng, J.; Bancroft, I. Single nucleotide polymorphism (SNP) discovery in the polyploid *Brassica napus* using Solexa transcriptome sequencing. *Plant Biotechnol. J.* **2009**, *7*, 334−346.
(21) Oñate-Sánchez, L.; Vicente-Carbajosa, J. DNA-free RNA isolation protocols for *Arabidopsis thaliana*, including seeds and siliques. *BMC Res. Notes* **2008**, *1*, 93.
(22) Earley, K. W.; Haag, J. R.; Pontes, O.; Opper, K.; Juehne, T.; Song, K.; Pikaard, C. S. Gateway-compatible vectors for plant functional genomics and proteomics. *Plant J.* **2006**, *45*, 616−629.
(23) Bhalla, P. L.; Singh, M. B. *Agrobacterium*-mediated transformation of *Brassica napus* and *Brassica oleracea*. *Nat. Protoc.* **2008**, *3*, 181−189.
(24) Mancinelli, A. L. Photoregulation of anthocyanin synthesis VIII. Effect of light pretreatments. *Plant Physiol.* **1984**, *75*, 447−453.
(25) Tohge, T.; Matsui, K.; Ohme-Takagi, M.; Yamazaki, M.; Saito, K. Enhanced radical scavenging activity of genetically modified Arabidopsis seeds. *Biotechnol. Lett.* **2005**, *27*, 297−303.
(26) Bindschedler, L. V.; Dewdney, J.; Blee, K. A.; Stone, J. M.; Asai, T.; Plotnikov, J.; Denoux, C.; Hayes, T.; Gerrish, C.; Davies, D. R. Peroxidase-dependent apoplastic oxidative burst in Arabidopsis required for pathogen resistance. *Plant J.* **2006**, *47*, 851−863.
(27) Lewis, D. R.; Ramirez, M. V.; Miller, N. D.; Vallabhaneni, P.; Ray, W. K.; Helm, R. F.; Winkel, B. S.; Muday, G. K. Auxin and ethylene induce flavonol accumulation through distinct transcriptional networks. *Plant Physiol.* **2011**, *156*, 144−164.
(28) Clough, S. J.; Bent, A. F. Floral dip: a simplified method for *Agrobacterium*-mediated transformation of *Arabidopsis thaliana*. *Plant J.* **1998**, *16*, 735−473.
(29) Pelletier, M. K.; Burbulis, I. E.; Winkel-Shirley, B. Disruption of specific flavonoid genes enhances the accumulation of flavonoid enzymes and end-products in Arabidopsis seedlings. *Plant Mol. Biol.* **1999**, *40*, 45−54.
(30) Owens, D. K.; Alerding, A. B.; Crosby, K. C.; Bandara, A. B.; Westwood, J. H.; Winkel, B. S. Functional analysis of a predicted flavonol synthase gene family in Arabidopsis. *Plant Physiol.* **2008**, *147*, 1046−1061.
(31) Stracke, R.; De Vos, R. C.; Bartelniewoehner, L.; Ishihara, H.; Sagasser, M.; Martens, S.; Weisshaar, B. Metabolomic and genetic analyses of flavonol synthesis in *Arabidopsis thaliana* support the in vivo involvement of leucoanthocyanidin dioxygenase. *Planta* **2009**, *229*, 427−445.
(32) Pelletier, M. K.; Murrell, J. R.; Shirley, B. W. Characterization of flavonol synthase and leucoanthocyanidin dioxygenase genes in Arabidopsis (further evidence for differential regulation of "early" and "late" genes). *Plant Physiol.* **1997**, *113*, 1437−1445.
(33) Xu, F.; Li, L.; Zhang, W.; Cheng, H.; Sun, N.; Cheng, S.; Wang, Y. Isolation, characterization, and function analysis of a flavonol synthase gene from *Ginkgo biloba*. *Mol. Biol. Rep.* **2012**, *39*, 2285−2296.
(34) Takahashi, R.; Githiri, S. M.; Hatayama, K.; Dubouzet, E. G.; Shimada, N.; Aoki, T.; Ayabe, S-i.; Iwashina, T.; Toda, K.; Matsumura, H. A single-base deletion in soybean flavonol synthase gene is associated with magenta flower color. *Plant Mol. Biol.* **2007**, *63*, 125−135.
(35) Wisman, E.; Hartmann, U.; Sagasser, M.; Baumann, E.; Palme, K.; Hahlbrock, K.; Saedler, H.; Weisshaar, B. Knock-out mutants from an En-1 mutagenized *Arabidopsis thaliana* population generate phenylpropanoid biosynthesis phenotypes. *Proc. Natl. Acad. Sci. U. S. A.* **1998**, *95*, 12432−12437.
(36) Peer, W. A.; Brown, D. E.; Tague, B. W.; Muday, G. K.; Taiz, L.; Murphy, A. S. Flavonoid accumulation patterns of transparent testa mutants of Arabidopsis. *Plant Physiol.* **2001**, *126*, 536−548.
(37) Tohge, T.; Nishiyama, Y.; Hirai, M. Y.; Yano, M.; Nakajima, Ji.; Awazuhara, M.; Inoue, E.; Takahashi, H.; Goodenowe, D. B.; Kitayama, M. Functional genomics by integrated analysis of metabolome and transcriptome of Arabidopsis plants over-expressing an MYB transcription factor. *Plant J.* **2005**, *42*, 218−235.
(38) Stobiecki, M.; Kachlicki, P. Isolation and Identification of Flavonoids. In *The Science of Flavonoids*, 1st ed.; Erich, G., Ed.; Springer: New York, 2006; pp 97−122.
(39) Lai, B.; Li, X.-J.; Hu, B.; Qin, Y.-H.; Huang, X.-M.; Wang, H.-C.; Hu, G.-B. LcMYB1 Is a Key Determinant of Differential Anthocyanin Accumulation among Genotypes, Tissues, Developmental Phases and ABA and Light Stimuli in Litchi chinensis. *PLoS One* **2014**, *9*, e86293.
(40) Kadomura-Ishikawa, Y.; Miyawaki, K.; Takahashi, A.; Masuda, T.; Noji, S. Light and abscisic acid independently regulated FaMYB10 in Fragaria× ananassa fruit. *Planta* **2015**, *241*, 953−965.
(41) Loreti, E.; Povero, G.; Novi, G.; Solfanelli, C.; Alpi, A.; Perata, P. Gibberellins, jasmonate and abscisic acid modulate the sucrose-induced expression of anthocyanin biosynthetic genes in Arabidopsis. *New Phytol.* **2008**, *179*, 1004−1016.
(42) Suesslin, C.; Frohnmeyer, H. An Arabidopsis mutant defective in UV-B light-mediated responses. *Plant J.* **2003**, *33*, 591−601.
(43) Wang, Y.; Zhou, B.; Sun, M.; Li, Y.; Kawabata, S. UV-A light induces anthocyanin biosynthesis in a manner distinct from synergistic blue+ UV-B light and UV-A/blue light responses in different parts of the hypocotyls in turnip seedlings. *Plant Cell Physiol.* **2012**, *53*, 1470−1480.
(44) Nakabayashi, R.; Yonekura-Sakakibara, K.; Urano, K.; Suzuki, M.; Yamada, Y.; Nishizawa, T.; Matsuda, F.; Kojima, M.; Sakakibara,

DOI: 10.1021/acs.jafc.5b02994
J. Agric. Food Chem. 2015, 63, 7819−7829

H.; Shinozaki, K. Enhancement of oxidative and drought tolerance in Arabidopsis by overaccumulation of antioxidant flavonoids. *Plant J.* **2014**, *77*, 367−379.
(45) Xu, B.-B.; Li, J.-N.; Zhang, X.-K.; Wang, R.; Xie, L.-L.; Chai, Y.-R. Cloning and molecular characterization of a functional flavonoid 3′-hydroxylase gene from *Brassica napus*. *J. Plant Physiol.* **2007**, *164*, 350−363.
(46) Li, X.; Qin, J.-C.; Wang, Q.-Y.; Wu, X.; Lang, C.-Y.; Pan, H.-Y.; Gruber, M. Y.; Gao, M.-J. Metabolic engineering of isoflavone genistein in *Brassica napus* with soybean isoflavone synthase. *Plant Cell Rep.* **2011**, *30*, 1435−1442.
(47) Wei, Y.-L.; Li, J.-N.; Lu, J.; Tang, Z.-L.; Pu, D.-C.; Chai, Y.-R. Molecular cloning of *Brassica napus* TRANSPARENT TESTA 2 gene family encoding potential MYB regulatory proteins of proanthocyanidin biosynthesis. *Mol. Biol. Rep.* **2007**, *34*, 105−120.
(48) Chen, G.; Deng, W.; Peng, F.; Truksa, M.; Singer, S.; Snyder, C. L.; Mietkiewska, E.; Weselake, R. J. *Brassica napus* TT16 homologs with different genomic origins and expression levels encode proteins that regulate a broad range of endothelium-associated genes at the transcriptional level. *Plant J.* **2013**, *74*, 663−677.
(49) Parkin, I.; Sharpe, A.; Keith, D.; Lydiate, D. Identification of the A and C genomes of amphidiploid *Brassica napus* (oilseed rape). *Genome* **1995**, *38*, 1122−1131.
(50) Snowdon, R.; Friedrich, T.; Friedt, W.; Köhler, W. Identifying the chromosomes of the A-and C-genome diploid *Brassica* species *B. rapa* (syn. *campestris*) and *B. oleracea* in their amphidiploid *B. napus*. *Theor. Appl. Genet.* **2002**, *104*, 533−538.

DOI: 10.1021/acs.jafc.5b02994
J. Agric. Food Chem. 2015, 63, 7819−7829

compositional parameters and the evaluation of their organoleptic significance. Hence, the aim of this work was to characterize the formation of (i) key odorants, (ii) polyphenols, and (iii) lipid from the pistachio cultivar Uzun (*Pistacia vera*) under two different roasting conditions. Moreover, a purge-and-trap method for obtaining an aroma extract was optimized.

MATERIALS AND METHODS

Samples. The Uzun cultivar samples of *P. vera* pistachio nuts from Gaziantep, Turkey, were supplied by a local company. In the same factory, the pistachios were subjected to standard roasting processes to obtain single-roasted (160 °C for 20 min) and double-roasted (160 °C for 22 min) samples and then cooled for 10 min at room temperature. The three types of samples, raw, single-roasted, and double-roasted, were then stored in vacuum-sealed plastic bags prior to analysis. Raw nuts were used as the control to compare against the effect of two different roasting conditions.

Chemicals. Hexane, methanol, acetonitrile, formic acid, dichloromethane, and chloroform were purchased from LabScan (Dublin, Ireland) and Merck (Darmstad, Germany); potassium hydroxide and sodium sulfate-1-hydrate from Panreac (Barcelona, Spain); and 1,2,3-tritridecanoylglycerol (99%) and dilinolein (98%) from Sigma (St. Louis, USA). Reference milk fat butter CRM-519 (EU Commissions; Brussels, Belgium) was purchased from Fedelco Inc. (Madrid, Spain). FAME standards mix GLC-Nestlé36 and tritridecanoin (99%) were from Nu-Chek Prep, Inc. (Elysian, Minnesota, USA). Protocatechuic acid, catechin, chlorogenic acid, eriodictyol-7-*O*-glucoside, rutin, eriodictyol, and luteolin were purchased from Sigma-Aldrich (St. Louis, USA). *n*-Pentanal, α-pinene, 2,3-pentanedione, β-pinene, *N*-methylpyrrole, hexanal, (*E*)-2-pentenal, limonene, methyl pyrazine, styrene, ocimene, furfural, terpinolene, 2,5-dimethyl pyrazine, acetic acid, 2,6-dimethyl pyrazine, 2-ethylpyrazine, 2-ethyl-6-methylpyrazine, 2-ethyl-3-methylpyrazine, acetylfuran, trimethylpyrazine, 2-ethyl-3,5-dimethylpyrazine, 2-ethyl-3,6-dimethylpyrazine, 1-octen-3-ol, γ-butyrolactone, benzaldehyde, furfuryl alcohol, (−)-menthol, 1-methyl-2-pyrrolidinone, p-cymene-8-ol, hexanoic acid, benzyl alcohol, 2-phenylethanol, pyrrole-2-carboxaldehyde, 5-methyl-1*H*-pyrrole-2-carbaldehyde, octanoic acid, *p*-cresol, and 4-ethylphenol were purchased from Sigma-Aldrich (St. Louis, USA). Deionized water was obtained via the Milli-Q water purification system by Millipore Corp. (Saint-Quentin, France). For retention index calculation, mixtures C_8−C_{20} and C_{21}−C_{40} were purchased from Fluka. All other reagents used were of analytical grade.

Phenolic Compounds Analysis and Antioxidant Activity. Extraction of Phenolic Compounds. The extraction of phenolic compounds was carried out according to Tsantili et al.[11] after some modifications. The pistachio samples were ground (with seed coat) with a laboratory blender, and 5 g samples were prepared in duplicate. Each sample was extracted with 15 mL of 85% methanol by mixing with a magnetic stir bar for 2 h. The extract was separated and the solid was washed with 5 mL of 85% methanol. The two extracts were combined, filtered, and evaporated in a vacuum under 20 °C until the volume was reduced to 3 mL. Then, the extract was filtered through a 0.45-μm pore size membrane filter before injection.

HPLC Analysis of Phenolic Compounds. An Agilent 1100 HPLC system (Agilent Technologies, Palo Alto CA, USA) with a diode array detector operated by Windows NT based ChemStation software was used for the phenolic compounds analysis. Separation was performed on a Beckman Ultrasphere ODS column (Roissy, France; 4.6 mm × 250 mm, 5 μm). The mobile phase consisted of water with 5% formic acid (solvent A; v/v) and acetonitrile with 40% solvent A (solvent B; v/v). Phenolic compounds were eluted under the following conditions: 1 mL/min flow rate with the temperature set at 25 °C; isocratic conditions from 0 to 15 min with 0% solvent B; gradient conditions from 0% to 20% solvent B in 30 min; from 20% to 50% solvent B in 40 min; and from 50% to 100% solvent B until 5 min. The wavelengths of the diode array detector (DAD) were set at 280, 320, and 360 nm for monitoring phenolic compounds. The identification of the phenolic compounds was obtained by using authentic standards and by comparing the retention times and spectra.[11] Quantification was performed by external calibration with standards. Concentration was expressed as mg per 100 mg of pistachio sample.

Antioxidant Capacity (DPPH Assay). The electron donation ability of the extract was measured by bleaching of the purple-colored solution of 1,1-diphenyl-2-picrylhydrazyl (DPPH) radical according to the method of Tsantili et al.[11] An aliquot of 0.1 mL of the methanol/water phenolic extract of the pistachio samples (diluted 1/25) was added to 3.9 mL of DPPH solution in methanol (6×10^{-5} M). The mixture was shaken vigorously and left standing at room temperature for 30 min. The absorbance of the resulting solution was then measured at 515 nm after 30 min by a Shimadzu UV-1700 spectrophotometer (Kyoto-Japan). Results were expressed as Trolox equivalent antioxidant capacity. Trolox standard solutions were prepared at a concentration ranging from 1 to 50 μM.

Obtaining of Aroma Extract (Purge and Trap System) and Olfactometric Analysis. The purge and trap system used to carry out the extraction process consisted of a nitrogen source controlled by a flow-meter and connected to a splitter system to divide the flow in several channels in order to purge three samples at the same time. A standard 20 mL vial capped with a crimp cap with a septum was used to contain the solid sample. The needle of the source of N_2 and the cartridge were installed through the septum to purge and trap the aroma compounds. As adsorbent, 200 mg of Lichrolut EN resins from Merck was chosen as the most suitable material for aroma compounds retention according to the literature.[18,19] The temperature of the vial sample was controlled by a thermostated bath. The sample of pistachio, previously shelled and milled with a laboratory blender, was placed into a 20 mL vial (3 g in order to avoid the caking of the solid) removing oxygen from the headspace with nitrogen. The optimized conditions of the purge and trap method were the following: sample was preincubated at the optimized purging temperature (60 °C) for 10 min. The purge and trap process was carried out for 90 min with a nitrogen flow of 500 mL/min. After this was completed, the compounds retained in the cartridge were eluted with 6 mL of dichloromethane at very a slow flow. The eluate was dried with sodium sulfate and concentrated with a Dufton column until 200 μL remained (at 45 °C). β-Ionone and 2-octanol were used as internal standards. The samples were stored at −20 °C until GC analysis. The aroma compounds evaluated for the optimization of purge and trap method belong to different chemical families with a wide range of volatility, and they are presented in Table 1. The repeatability of the purge and trap method for the optimized conditions is also presented in Table 1. For the optimization all experiments were carried out in duplicate with the double roasted sample.

Table 1. Compounds Selected for Optimization of Purge-and-Trap Method

compound	LRI[a]	molecular weight	boiling point (°C)	log *P*[b]	RSD (%)[c]
limonene	1156	136	178	4.57	7.2
methylpyrazine	1194	94	137	0.21	2.1
furfural	1365	96	161.7	0.41	5.3
benzaldehyde	1420	106	179	1.48	3.7
γ-butyrolactone	1513	86	204	−0.64	5.7
octanoic acid	1957	144	239	3.05	17.9

[a]Linear retention index calculated based on DB-WAX phase. [b]Hydrophobic constant obtained from EPIWEB suite. [c]Repeatability of purge and trap optimized extraction method (n = 3).

GC-FID, GC-MS, and GC-MS-O Analyses of Aroma Compounds. The gas chromatography system consisted of an Agilent 6890 chromatograph equipped with a flame ionization detector (FID) (Wilmington, DE, USA), an Agilent 5973 mass selective detector (MSD) (Wilmington, DE, USA), and a Gerstel ODP-2 (Baltimore, MD, USA) sniffing port. This system allowed us to simultaneously obtain a FID signal, MS signal (for the identification), and the odor

DOI: 10.1021/acs.jafc.5b02576
J. Agric. Food Chem. 2015, 63, 7830−7839

characteristics of each compound detected in the sniffing port. The oven temperature of the DB-Wax column was first held at 40 °C (for 10 min) and then increased from 40 to 160 °C at a rate of 3 °C/min and then to 240 °C at 6 °C/min, with a final hold at 240 °C for 25 min. The pressure of the column was constant at 20.0 psi and 3 μL was injected in pulsed splitless mode. The MS (electronic impact ionization) conditions were ionization energy of 70 eV, mass range m/z of 33−350 amu in combined SCAN/SIM mode. Contents of volatile compounds were expressed as relative peak area to internal standard (β-ionone). Retention index were calculated by injection of commercial mixtures of alkanes.

Aroma Extract Dilution Analysis (AEDA). Olfactometric analysis was carried using two experienced sniffers. For AEDA, the concentrated aromatic extract (200 μL) of the pistachio samples was stepwise diluted 1:1 using dichloromethane as the solvent to obtain dilutions of 1:2, 1:4, 1:8, 1:16, with dilutions continuing through 1:512. Odor evaluation of the dilutions was continued until no odorant could be detected by GC-O. Each odorant was thus assigned a flavor dilution factor (FD factor) representing the last dilution in which the odorants was still detectable. The identification of aroma compounds was carried out by comparison with the mass spectra of commercial compounds (when available) and with the mass spectra of NIST library.

Lipid Profile Analysis. *Isolation of Lipids.* Shelled pistachios (40 g) were carefully cut into small pieces. Samples were then crushed into fine particles at 8000 rpm using an ultraturrax T25 (Ika-Werke, Staufen, Germany). A portion equaling 3 g was transferred into a 50 mL glass falcon tube (Vidrafoc, Barcelona, Spain), and lipids were isolated according to the Folch method modified by Iverson et al.[20] Finally, extracts were centrifuged (5 min, 8000g) to avoid impurities and chloroform removed by using rotatory evaporation. Then, lipids were accurately weighed. Extraction was carried out in triplicate.

Analysis of Triacylglycerols and Diacylglycerols. Triacylglycerols (TG) and diacylglycerols (DG) were analyzed on a CLARUS 400 gas chromatograph (PerkinElmer, Massachusetts, USA) equipped with FID detector and a Rtx-65TG column (30 m × 0.25 mm × 0.10 μm; Restek Corporation, Bellefonte, Pennsylvania, USA) using injector, detector, oven temperature and chromatographic conditions as prescribed by Fontecha et al.[21] Response factors were calculated by the injection of CRM-519 and dilinolein. Under these conditions, the limits of quantification (LOQ) were 1.14 mg TG/mL (R^2 = 0.9996) and 1.22 mg DG/mL (R^2 = 0.9993). Injections were performed in triplicate.

Analysis of Fatty Acid Methyl Esters. For the determination of the fatty acid composition, samples measuring 25 mg were added with tritridecanoin (200 μL, 1.24 mg/mL) and derivatized to fatty acid methyl esters (FAME) with 2 N methanolic KOH solution according to the International Dairy Federation procedure (ISO-IDF, 2002).[22] FAME were analyzed (1 μL; 1:10 split ratio) in a 6890 Agilent GLC (Palo Alto, California, USA) equipped with a MS detector (Agilent 5973N), fitted with a CPSil-88 capillary column (100 m × 0.25 mm id × 0.2 μm film thickness, Chrompack, Middelburg, Netherlands). The MS conditions were 250 °C transfer line temperature; 230 °C source temperature; 150 °C quad temperature; electron impact ionization of 70 eV; and scan operational mode, 50−550 Da. Oven temperature program and conditions were set according to Rodríguez-Alcalá et al.[23] Response factors were calculated by injection of GLC-Nestlé36. Under these conditions, the limit of quantification (LOQ) was 0.05 μg/mL (R^2: 0,9991). All analyses were carried out in triplicate.

Statistical Analysis. In a first instance all data were first subjected to an exploratory analysis to test normal distribution and homogeneity of variance. Thus, results regarding composition of volatiles and phenolics as well as antioxidant capacity were submitted to the one-way analysis of variance (ANOVA). Version 7.1 of STATISTICA for Windows was used for data processing (StatSoft, Inc., 2005, www.statsoft.com).

For the lipid profile, data were analyzed according to ANOVA with the Bonferroni test as a follow-up in order to evaluate statistical differences among groups using version 22 of IBM SPSS Statistics for Mac (IBM, Armonk, NY). For all the analysis the level of significance was set to $p < 0.05$, while $0.05 < p < 0.1$ was established as the trend.

RESULTS AND DISCUSSION

Phenolic Composition and Antioxidant Capacity of Pistachios. The phenolic acids and flavonoids identified in hydroalcoholic extracts of raw, single-roasted, and double-roasted pistachios are presented in Table 2. A total of seven phenolic compounds (protocatechuic acid, catechin, chlorogenic acid, eriodictyol-7-*O*-glucoside, rutin, eriodictyol, luteolin) were detected and quantified. The total phenolic content increased alongside the heat treatment in the samples, with the double-roasted nuts having the highest total phenolic compound content (42.4 mg/100 g fw). These results are in line with similar studies conducted using other types of nuts such as peanuts and almonds.[24,25] Thermal processing may release more bound phenolic acids from the breakdown of cellular constituents, although disruption of cell walls also releases the oxidative and hydrolytic enzymes that can destroy the antioxidants in fruits and vegetables.[26]

Table 2. Phenolic Compounds and Antioxidant Capacity of Pistachios (mg/100 g fw)[a]

compound	raw	single-roasted	double-roasted
protocatechuic acid	3.14 ± 0.26 a	3.96 ± 0.05 b	8.59 ± 0.33 c
catechin	4.81 ± 0.52 a	8.64 ± 1.48 b	8.72 ± 0.82 b
chlorogenic acid	4.96 ± 0.13	3.99 ± 0.78	5.79 ± 0.09
eriodictyol-7-*O*-glucoside	4.10 ± 0.42	3.64 ± 1.15	3.91 ± 0.35
rutin	3.01 ± 0.12 a	3.51 ± 0.10 b	5.43 ± 0.10 c
eriodictyol	2.17 ± 0.04	2.19 ± 0.01	2.67 ± 0.28
luteolin	0.78 ± 0.01 a	0.72 ± 0.02 a	1.22 ± 0.06 b
total	26.2 ± 1.2 a	32.4 ± 1.0 b	42.4 ± 1.9 c
antioxidant capacity (μmol of TE g of fw)	8.05 ± 0.21	9.76 ± 0.22	11.5 ± 2.0

[a]Different letters in a row for significant effect of processing ($p < 0.05$).

The phenolic acids in the pistachios were protocatechic acid and chlorogenic acid, positively identified by comparing their retention and UV−vis characteristics to commercial standards. Protocatechuic acid varied between 3.14−8.59 mg per 100 g of pistachios. Double-roasted nuts had almost three times as much protocatechuic acid as their raw and single-roasted counterparts, suggesting a liberation of protocatechuic acid during heat processing. Thus, double-roasted kernels contained significantly ($p < 0.05$) more protocatechuic acid than the other samples. Conversely, thermal processing did not affect the content of chlorogenic acid present in pistachio extracts, and there was no significance in the results obtained. In a previous study, Liu et al.[27] quantified the bioactives in the whole nut, nutmeat, and skin of California pistachios and found protocatechuic acid to be between 0.2 and 4.6 mg/100 g fw. Mandalari et al.[28] not only observed that protocatechuic acid concentration increased with heat treatment in pistachios, but also identified a small amount of chlorogenic acid solely in the salted and roasted nuts. The phenolic compounds may differ with respect to their binding status, dependent on specific aspects of their chemical structures. Thus, the most effective processes to release phenolic acids from plant tissues may not be the same.

Major flavonoids identified in the present study were catechin, eriodictyol-7-*O*-glucoside, and rutin, comprising

DOI: 10.1021/acs.jafc.5b02576
J. Agric. Food Chem. 2015, 63, 7830−7839

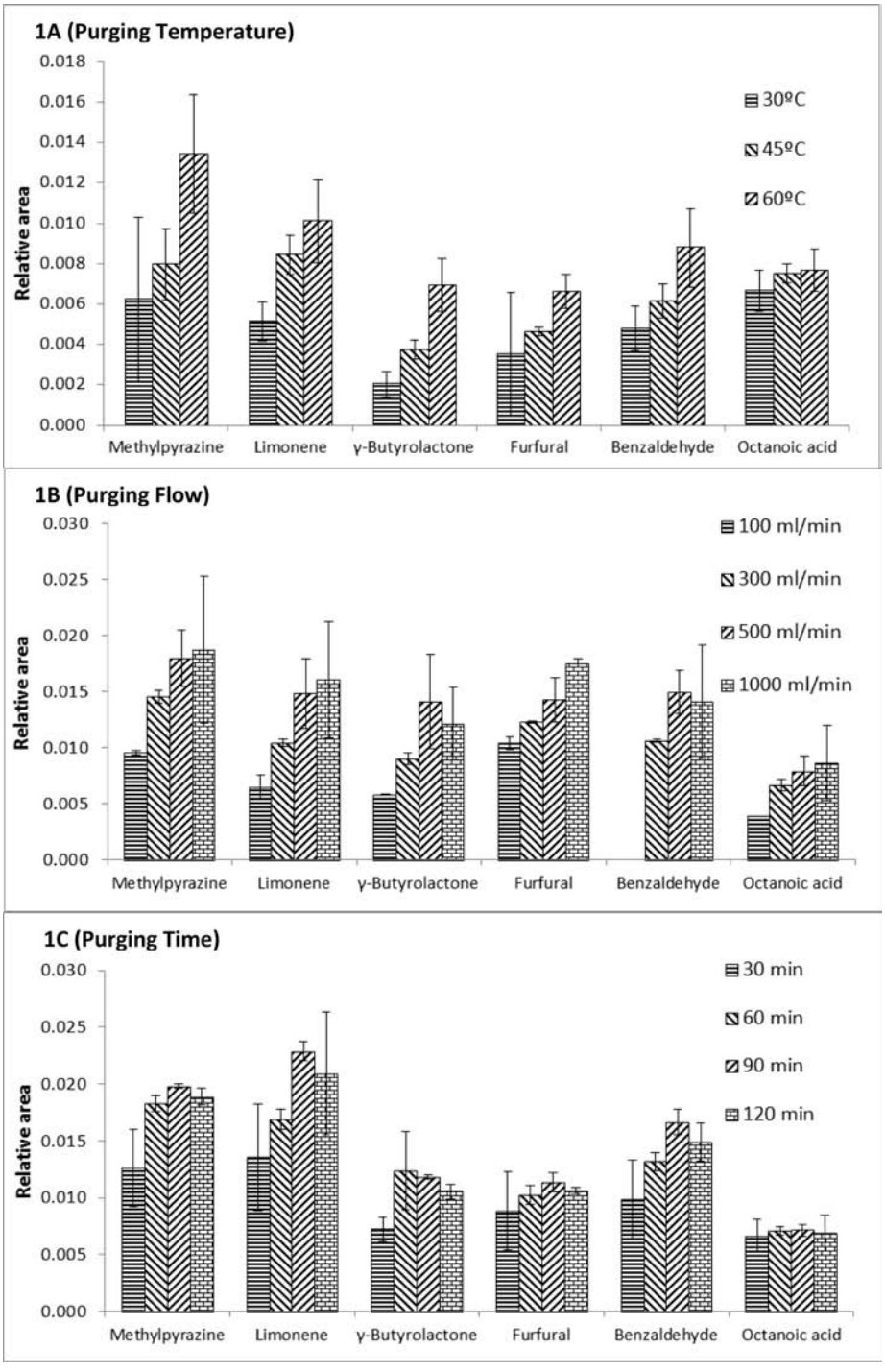

Figure 1. Optimization of the purge and trap method: effect of temperature (1A), nitrogen purging flow (1B), and purging time (1C) on recovery of volatiles from pistachio.

4.81−8.72 mg, 3.1−3.91 mg, and 3.01−5.43 mg per 100 g of pistachios, respectively. Our results shows that double-roasted samples had a 2-fold higher flavonoid content compared to raw and single-roasted nuts. It is well-established that flavonoids are effective natural antioxidants. The results obtained in the HPLC analysis suggest release and isomerization of such compounds during heat treatment of pistachios. Chandrasekara et al.[25] measured the effect of roasting on phenolic content and antioxidant properties of testa-containing and testa-free kernels of cashew nuts. These authors found the highest levels of flavonoids at high-temperature treatments, followed by low-temperature treatments, and last raw samples, which concurs with the present study. Furthermore, Tomanio et al.[8] and Martorana et al.[29] investigated the phenolic composition of pistachio seed and skin obtained from nuts grown in Bronte, Sicily. They quantified rutin as the major phenolic compound of the Bronte variety of *P. vera*.

The antioxidant potential of the pistachio samples was assessed by using the DPPH assay method (Table 2), revealing a slight trend of increasing DPPH values with the roasting process. Similarly, Chandrasekara et al.[25] mentioned that the antioxidant levels of cashew nuts increased as the roasting time

DOI: 10.1021/acs.jafc.5b02576
J. Agric. Food Chem. 2015, 63, 7830−7839

Table 3. Volatile Composition of Pistachio Samples[a]

LRI[b]	compounds	raw	single-roasted	double-roasted	identification[c]
960	*n*-pentanal	0.0161 + 0.0023 a	0.0617 + 0.0069 b	0.1597 + 0.0105 c	LRI,MS,std
978	2-methyl-3-pentanone	0.2271 ± 0.0367	0.2218 ± 0.0201	0.1916 ± 0.011	LRI,MS,tent
996	3-methyl-2-pentanone	0.6996 ± 0.1271	0.7028 ± 0.0687	0.6041 ± 0.0229	LRI,MS,tent
1010	*α*-pinene	3.0154 ± 0.051 a	4.8606 ± 0.2365 b	3.1398 ± 0.0566 a	LRI,MS,std
1018	2,3-pentanedione	0.0034 ± 0.0006 a	0.0192 ± 0.0003 b	0.1081 ± 0.0031 c	LRI,MS,std
1034	camphene	0.1624 ± 0.006 a	0.198 ± 0.0057 b	0.1743 ± 0.0032 a	LRI,MS,tent
1037	hexanal	0.0136 ± 0.0019 a	0.2092 ± 0.0068 c	0.1573 ± 0.0099 b	LRI,MS,std
1068	*β*-pinene	0.1821 ± 0.0012 a	0.3673 ± 0.0188 c	0.2345 ± 0.0121 b	LRI,MS,std
1075	*N*-methylpyrrole	0.0931 ± 0.0084 a	0.3909 ± 0.0343 b	0.7547 ± 0.0717 c	LRI,MS,std
1113	3-carene	0.201 ± 0.0093 a	0.2737 ± 0.0227 b	0.2503 ± 0.0249 ab	LRI,MS,tent
1119	(*E*)-2-pentenal	nd a	nd a	0.0092 ± 0.000 b	LRI,MS,std
1156	limonene	0.3238 ± 0.0364 a	0.5103 ± 0.0367 b	0.473 ± 0.0355 b	LRI,MS,std
1158	(2 + 3)-methyl-1-butanol	0.0259 ± 0.0017	0.0209 ± 0.0022	0.0191 ± 0.002	LRI,MS,tent
1185	styrene	0.0152 + 0.0026 a	0.0212 + 0.0007 ab	0.0266 + 0.0053 b	LRI,MS,std
1189	2-methyl-1-penten-3-ol	0.9405 ± 0.1701	0.9524 ± 0.0978	0.799 ± 0.0318	LRI,MS,tent
1194	methylpyrazine	0.0036 ± 0.005 a	0.0503 ± 0.0011 b	0.4717 ± 0.0027 c	LRI,MS,std
1203	ocimene	0.0939 ± 0.0047	0.1112 ± 0.0122	0.1215 ± 0.0198	LRI,MS,std
1211	3-methyl-1-penten-3-ol	0.705 ± 0.1259	0.71 ± 0.073	0.5934 ± 0.0209	LRI,MS,tent
1229	terpinolene	0.5662 ± 0.0288 a	0.9922 ± 0.0952 b	0.8935 ± 0.1659 b	LRI,MS,std
1252	2,5-dimethylpyrazine	nd a	0.148 ± 0.0026 b	1.2497 ± 0.0867 c	LRI,MS,std
1257	2,6-dimethyl-pyrazine	nd a	0.1481 ± 0.0026 b	0.1761 ± 0.006 c	LRI,MS,std
1259	2-ethylpyrazine	nd a	0.0146 ± 0.0006 b	0.1473 ± 0.007 c	LRI,MS,std
1272	2,3-dimethylpyrazine	nd a	nd a	0.1364 ± 0.0133 b	LRI,MS,tent
1311	2-ethyl-5-methylpyrazine	0.0029 ± 0.0007 a	0.017 ± 0.001 a	0.2152 ± 0.0258 b	LRI,MS,tent
1318	2-ethyl-6-methylpyrazine	0.0014 ± 0.0008 a	0.0582 ± 0.0037 a	0.5027 ± 0.0689 b	LRI,MS,std
1330	2-ethyl-3-methylpyrazine	0.0064 ± 0.0013 a	0.0062 ± 0.0008 a	0.0857 ± 0.0136 b	LRI,MS,std
1333	trimethylpyrazine	0.0014 ± 0.0007 a	0.0513 ± 0.0028 a	0.52 ± 0.0706 b	LRI,MS,std
1355	acetic acid	0.0805 ± 0.0097 a	0.216 ± 0.0127 b	0.5981 ± 0.0217 c	LRI,MS,std
1365	furfural	0.0049 ± 0.0016 a	0.0253 ± 0.0013 b	0.0578 ± 0.0015 c	LRI,MS,std
1376	2-ethyl-3,6-dimethylpyrazine	nd a	0.0489 ± 0.0026 a	0.535 ± 0.0902 b	LRI,MS,std
1384	1-octen-3-ol	nd a	0.0423 ± 0.0059 b	0.0654 ± 0.0043 c	LRI,MS, std
1390	2-ethyl-3,5-dimethylpyrazine	nd a	nd a	0.1318 ± 0.0226 b	LRI,MS, std
1405	acetylfuran	nd a	0.0044 ± 0.0001 b	0.0361 ± 0.0018 c	LRI,MS,std
1420	benzaldehyde	0.0133 ± 0.0037 a	0.0536 ± 0.002 b	0.0893 ± 0.003 c	LRI,MS,std
1425	ethylhexanol	0.2424 ± 0.0153	0.2025 ± 0.01	0.2215 ± 0.0849	LRI,MS,tent
1426	2-methyl-3,5-diethylpyrazine	nd a	0.009 ± 0.0007 a	0.0979 ± 0.0158 b	LRI,MS,tent
1429	camphor	0.0333 ± 0.0011 a	0.0698 ± 0.0042 b	0.0365 ± 0.0071 a	LRI,MS,tent
1457	2-methyl-6-(1-propenyl)-pyrazine	nd a	0.0115 ± 0.0014 a	0.0885 ± 0.0162 b	LRI,MS,tent
1513	*γ*-butyrolactone	0.0215 ± 0.001 a	0.1061 ± 0.0061 b	0.3622 ± 0.0286 c	LRI,MS,std
1516	5-methyl-1*H*-pyrrole-2-carbaldehyde	nd a	0.0085 + 0.0009a	0.0702 + 0.01b	LRI,MS,std
1551	isopropenylpyrazine	nd a	0.0097 ± 0.0008 a	0.1501 ± 0.029 b	LRI,MS,tent
1561	furfuryl alcohol	nd a	0.0079 ± 0.0003 b	0.0294 ± 0.0052 c	LRI,MS,std
1570	(−)-menthol	0.0949 ± 0.0125 b	0.1072 ± 0.0141 ab	0.0713 ± 0.0032 a	LRI,MS,std
1586	1-methyl-2-pyrrolidinone	nd a	0.0341 ± 0.0027 a	0.1915 ± 0.0282 b	LRI,MS,std
1613	*N*-acetyl-4(*H*)-pyridine	nd a	0.0608 ± 0.0065 a	0.535 ± 0.1386 b	LRI,MS,tent
1719	1-(2-furanylmethyl)-1*H*-pyrrole	nd a	nd a	0.0439 ± 0.0152 b	LRI,MS,tent
1729	*p*-propenylanisole	0.0374 ± 0.0155 a	0.0195 ± 0.0095 a	0.0728 ± 0.004 b	LRI,MS,tent
1745	hexanoic acid	0.0553 ± 0.0009 a	0.0862 ± 0.007 b	0.1196 ± 0.0032 c	LRI,MS,std
1755	*p*-cymen-8-ol	0.0352 ± 0.0023 a	0.0648 ± 0.0153 b	0.0754 ± 0.0059 b	LRI,MS,std
1766	benzyl alcohol	0.0121 ± 0.0021 a	0.0227 ± 0.0007 b	0.0228 ± 0.0028 b	LRI,MS,std
1802	2-phenylethanol	0.0569 ± 0.0299 a	0.0419 ± 0.0093 a	0.2072 ± 0.0779 b	LRI,MS,std
1894	pyrrole-2-carboxaldehyde	nd a	0.0086 ± 0.0023 a	0.0685 ± 0.0086 b	LRI,MS,std
1906	DL-pantolactone	nd a	0.0179 ± 0.0025 b	0.0542 ± 0.0101 c	LRI,MS,tent
1918	furaneol	nd a	0.0097 ± 0.0029 a	0.0583 ± 0.0161 b	LRI,MS,tent
1957	octanoic acid	0.0175 ± 0.0035	0.0112 ± 0.002	0.0226 ± 0.0076	LRI,MS,std
1963	*p*-cresol	0.0377 ± 0.0093	0.0281 ± 0.0099	0.0411 ± 0.007	LRI,MS,std
1969	*m*-cresol	0.0496 ± 0.0141	0.0317 ± 0.0131	0.0531 ± 0.0065	LRI,MS,tent
2053	3,4-dimethylphenol	0.075 ± 0.0216	0.0502 ± 0.0246	0.0818 ± 0.0122	LRI,MS,tent
2059	4-ethylphenol	0.0954 ± 0.029	0.0616 ± 0.0317	0.105 ± 0.0147	LRI,MS,std

[a]Volatile compounds (raw, single-roasted, and double-roasted) expressed in relative peak area to internal standard (*β*-ionone). Values with different letters in the same row are significant statistically ($p < 0.05$). [b]Linear retention index calculated based on DB-WAX phase. [c]Methods of identification:

DOI: 10.1021/acs.jafc.5b02576
J. Agric. Food Chem. 2015, 63, 7830−7839

Table 3. continued

LRI (linear retention index); MS tent. (tentatively identified by MS); std (chemical standard). When only MS or LRI is available for the identification of compounds, it must be considered as an attempt of identification.

and temperature increased. The differences in antioxidants among the three pistachio samples could be explained by their phenolic content and composition differences. Phenolic compounds with antioxidant properties are lost during the roasting of the nuts; nonetheless, the antioxidant levels of the nuts is partially restored by the development of compounds possessing more antioxidants.[30] These compounds were reported as the intermediate Maillard reaction products (MRPs), as well as the resultant melanoidins, characterized by high antioxidant levels and related to the presence of reduction-type structures. Together with oxidation, condensation, and complexation of polyphenol compounds, and following suit to protein and starch hydrolysis, the Maillard reaction involves not only the reduction of sugars and amino acids but also the production of carbonyl compounds from lipid oxidation.[31,32]

Optimization of Purge-and-Trap Method to Obtain Pistachio Aroma Extract. The initial conditions were chosen based on the literature[7,18] (60 °C for sample incubation, 300 mL/min of N_2 purge flow and 60 min purging time). The results of the optimization of each parameter, purge temperature, purge time, and nitrogen flow are presented in Figure 1 (*Y*-axis units are expressed as relative peak area to 2-octanol). As expected, an increase in peak areas from 30 to 60 °C was observed (Figure 1A) because most of the compounds presented have high boiling points (>115 °C). Although higher temperatures would produce more sensitive extractions, 60 °C was fixed as the maximum temperature to avoid any sample changes during testing time.[7] As observed in Figure 1B, the nitrogen purge flow generally increased the extraction efficiency between 100 mL/min and 500 mL/min. After 500 mL/min the extraction efficiency fluctuated slightly up and down until 1000 mL/min. In order to avoid loss of compounds or no retention on the cartridge, 500 mL/min was chosen. Finally, after the temperature and flow were fixed (60 °C and 500 mL/min N_2), the effect of purging time was evaluated (Figure 1C). As can be observed, the peak areas show a steady increase until 90 min and then either remain constant or experience a slight drop-off. On the basis of these results, optimal conditions were set with temperature at 60 °C and flow at 500 mL/min for 90 min.

In order to increase the sensitivity of the method in the olfactometric analysis, the dichloromethane extracts of two samples were combined, and the volume was reduced to 200 μL. Under these conditions, the error (Table 1) of the method is less than 10% for most of the compounds except for the less volatile octanoic acid (17.9%). These results showed that the method allowed aroma extraction of the volatile and semi-volatile compounds of pistachio with an acceptable repeatability. In the case of compounds with a high molecular weight, high boiling point, and high/low hydrophobic constant, the method showed some variations. However, the compounds with lower volatility and higher molecular weight would most likely have negligible significance at the sensory level.

Volatile Composition of Pistachios. The analysis of the aroma extracts by GC-MS and a deep study of the chromatograms has allowed tentative identification via mass spectrometry of numerous volatile compounds in the three sample types: raw, single-roasted, and double-roasted. The results are shown in Table 3 as relative peak areas to β-ionone. As can be seen, 39 compounds were identified in the raw sample (not roasted), while in single-roasted and double-roasted samples, 56 and 60 compounds were identified, respectively, indicating the importance of the roasting process on the number of compounds detected. The compounds were classified according their chemical characteristics: carbonyl compounds, terpenes, alcohols, phenols, furanic compounds, pyrazines, pyrroles, lactones, acids, phenolic, and benzene derivatives. Among them, only the volatile phenolics did not show any statistical differences created by the roasting process. Clearly, the increase in carbonyl compounds, pyrazines, pyrroles, and furanic compounds was related to the roasting process since these compounds are formed by Maillard reactions.[33]

With regard to the pyrazines, among the 16 detected in the double-roasted samples, only five were observed in the raw samples: methylpyrazine, trimethylpyrazine, 2-ethyl-5-methylpyrazine, 2-ethyl-6-methylpyrazine, and 2-ethyl-3-methylpyrazine. The production of pyrazines during the roasting process was also very significant in the nuts roasted a second time; indeed, most pyrazines increased between 8 and 15 times the amount identified in single-roasted samples. Our results are in accordance with Vazquez-Araujo et al.[34] and Agila et al.[35] who observed the strong effect of roasting time on pyrazine production in almonds. The number and type of pyrazines for single-roasted samples detected in our study are similar to the results in the GC-O study by Aceña et al.[7,36] in which pistachios were roasted at 160 °C for 20 min. However, Hojjati et al.[1] observed fewer differences in pyrazine levels for Iranian pistachios, both raw and roasted at 135 °C for 20 min, detecting only two pyrazines in the roasted samples that could be attributed to the less-intense roasting process. The sensory importance of pyrazines depends on the substituents of the molecule, as they are less potent with methyl groups than with ethyl ones.[33]

Like the pyrazines, most of the pyrroles and furans existed in virtually undetectable amounts in raw samples, subsequently increasing in amount over the course of the roasting process.[37] Thus, in raw samples, only the less volatile ones were detected, i.e., furfural and *N*-methylpyrrole; however, the levels of all these compounds increased with the roasting time but less dramatically than with pyrazines.[34] Furfural and derivatives generally possess caramel-like, sweet, and fruity notes, while pyrroles, depending on their substituents, could possess favorable (caramel-like, sweet, corn-like) or unfavorable notes.

In addition, another reaction related to the Maillard was the Strecker degradation of α-amino acids initiated by carbonyl compounds, producing an aldehyde and α-aminoketone. Although some aldehydes are highly volatile compounds and could be lost in the heating process through evaporation, our results showed an increase of the amount of aldehydes, including hexanal, pentanal, benzaldehyde, and (*E*)-2-pentenal, which may be due to their formation via Strecker degradation. Other compounds, such as short chain acids and lactones, were affected by roasting time since they also can be formed by Maillard reactions.[38]

DOI: 10.1021/acs.jafc.5b02576
J. Agric. Food Chem. 2015, 63, 7830−7839

Table 4. Aroma-Active Regions of Raw, Single-Roasted, and Double-Roasted Pistachio Samples

odor region	LRI[b]	odor description	FD Factor[a]			compound[c]
			raw	single-roasted	double-roasted	
1	960	solvent, rancid			2	*n*-pentanal
2	1185	burnt, toasted			4	styrene
3	1235	burnt, plastic			128	unknown
4	1242	chemical, solvent			2	an alcohol
5	1262−1269	popcorn, toasted	4	8	128	2,6-dimethyl pyrazine; 2-ethylpyrazine
6	1292	fatty, roasted			2	an alcohol
7	1346	popcorn, oily, toasted		4	4	unknown
8	1379	fatty, negative		8		unknown
9	1390	burnt			16	2-ethyl-3,5-dimethylpyrazine
10	1426	toasted		8	32	2-methyl-3,5-diethylpyrazine
11	1447	burnt, toasted		2		unknown
12	1475	popcorn, roasted		2	2	unknown
13	1516	popcorn		8	4	5-methyl-1*H*-pyrrole-2-carbaldehyde
14	1534	roasted			8	a pyrazine
15	1586	toasted, pharmacy			2	1-methyl-2-pyrrolidinone
16	1719	toasted, burnt			2	1-(2-furanylmethyl)-1*H*-pyrrole
17	1891	fatty		2		unknown
18	1914	phenolic		2		unknown
19	2059	plastic, chemical			8	4-ethylphenol

[a]FD factor is the highest dilution of the extract at which an odorant is determined by aroma extract dilution analysis. [b]Linear retention index calculated on DB-WAX capillary column. [c]Odor description as perceived by panelists during olfactometry.

The variation in the amount of other compounds in the raw samples, such as terpenes, benzene derivatives, and alcohols, is probably more related to a concentration effect in the sample through the loss of water and the subsequent evaporation of these compounds during roasting. Among them, it is remarkable that terpenes showed, in general, the highest values in single roasted samples. This group of compounds is the most interesting since numerous terpenes have been detected in oils of *P. vera* leaves[39] as well as in fruit pistachio oils and other edible nuts.[40] Among the nine terpene compounds detected in the present study were terpinolene, α-pinene, β-pinene, limonene, 3-carene, and camphene, which were detected in the Uzun variety of the raw Turkish pistachio,[2] in the raw and roasted Iranian pistachio,[1] and in the "Kerman" pistachio from California.[40]

Evaluation of the Aroma-Active Compounds of Pistachios. The results of the olfactometric analysis and the application of AEDA on the extracts of the three pistachio sample types (raw, single-roasted, and double-roasted) are presented in Table 4. As can be expected, the number of odor-active regions in the raw samples was much lower than in the roasted samples. Indeed, in raw samples, an odor-active region was detected only between LRI 1262 and 1269 with popcorn and toasted notes most likely associated with 2 pyrazines: 2,6-dimethyl-pyrazine and 2-ethylpyrazine having FD factors of 4. Although these two compounds were not identified in the chromatograms of the raw samples (Table 3), due to the sensitivity of the method, both compounds were detected in the other two sample types. It is remarkable that these two pyrazines were not detected in olfactometric analysis by other authors in raw samples of the pistachio (*P. vera*),[2] suggesting the probable existence of some thermic effects on the sample during harvesting and processing. Moreover, other studies undertaking chemical analyses have not detected pyrazines in raw pistachio samples (*P. vera* and *P. terebinthus*).[1,17]

The roasting process had a significant effect on the number of odor-active regions, with 9 regions observed for single-roasted samples and 15 for double-roasted samples. Single-roasted samples did not show a very high flavor dilution factor (FD), with a maximum value at 8 for four odor-active regions: 5 (popcorn/toasted), 8 (fatty/negative), 10 (toasted), and 13 (popcorn). The compounds responsible for these aroma regions could only be identified in some cases: region 5 was the same as that detected in the raw samples; region 10 was identified as 2-methyl-3,5-diethylpyrazine and camphor; and region 13 was identified as a pyrrole (5-methyl-1*H*-pyrrole-2-carbaldehyde). In addition, other regions at LRI 1346 (region 7) with a FD of 4, and several with FD of 2 (regions 11 and 12) which had aroma characteristics described as popcorn/toasted, are probably due to pyrazines or pyrrolic compounds, although the compounds were not identified.

Two regions at LRI 1891 and 1914 (regions 17 and 18) with fatty and phenolic notes, respectively, contained unknowns. Noteworthy those aroma notes detected in single-roasted samples that were not detected in double-roasted samples (regions 8, 11, 17, and 18). This could be due to compounds present in the original samples or generated during the roasting process in the first roasting and later degraded or evaporated away in the second roasting. Another possibility is the formation of these compounds in the first roasting and their subsequent transformation into others as roasting time is longer. Vazquez-Araujo et al.[34] studied the formation of toasty aroma notes in almonds and their volatile profile, observing that different roasting times are necessary to form different pyrazines and slight aroma loss at some points in the roasting process. In addition, the big differences in the odor thresholds of pyrazines is a function of their substituents (methyl or ethyl), which could significantly affect the quality and intensity of the aroma notes.[33]

As expected the double-roasted sample exhibited the highest flavor dilution factors. Thus, two regions presented a FD of 128: region 3 (burnt/plastic) and region 5 (popcorn/toasted). The compounds responsible for the notes in region 5 were 2,6-dimethylpyrazine and 2-ethylpyrazine, which were reported as

DOI: 10.1021/acs.jafc.5b02576
J. Agric. Food Chem. 2015, 63, 7830−7839

important contributors to roasted pistachio aroma.[36] In fact, 2,6-dimethylpyrazine has a very low odor threshold of 74 ng/L in air.[41] However, the significance of the 2-ethylpyrazine is expected to be lower because this compound has a higher odor threshold. On the other hand, the compounds of region 3 could not be identified. Odor region 10 (toasted) should be highlighted, with a FD of 32 and which was identified as camphor and 2-methyl-3,5-diethylpyrazine. Further, region 9 was characterized by a burnt note and a FD of 16. The last odor zone was identified as 2-ethyl-3,5-dimethylpyrazine. The pyrazine of region 9 showed a low odor threshold (0.011 ng/l of air)[41] and was detected by other authors[17,36] in roasted samples of *P. vera* and *P. terebinthus*. Two regions had a FD of 8. Specifically, region 14 was comprised of roasted notes probably due to a pyrazine, and, region 19, with both a plastic note and a chemical note were attributed to 3,4-dimethylphenol and 4-ethylphenol, the latter of which has also been detected through GC-O analysis of roasted pistachios.[7] Three more regions were identified with a FD of 4: region 2 had burnt and toasted notes identified as styrene; region 7 had a popcorn/oily/toasted notes; and region 13 had a popcorn note identified as a pyrrole. The remaining five regions had a FD of 2: region 1 had solvent and rancid notes identified as *n*-pentanal; region 4 had chemical and solvent notes probably due to alcohol; region 13, which was also detected in roasted samples; and regions 15 and 16 with toasted notes attributable to pyrrolic compounds.

Fatty Acid and Di- and Triacylglyceride Composition. Lipid content in the raw, single-roasted and double-roasted samples was 41.47 ± 0.85, 41.49 ± 0.75, and 41.96 g oil/100 g pistachio ($p > 0.05$), respectively.

DG and TG composition of the raw, single-roasted, and double-roasted pistachios is presented in Table 5. Contents of TG were 96.39 g/100 oil for raw samples, 96.49 g/100 oil for single-roasted samples, and 96.58 g/100 oil for double-roasted samples. In all of the samples assayed, TG CN54 was the main compound (74.87 g/100 oil for raw, 74.71 g/100 oil for single-roasted, and 74.69 g/100 oil for double-roasted), while TG CN52 and CN50 were lower. Two compounds were detected by DG composition, CN36 (0.50 g/100 oil for raw; 0.46 g/100 oil for single-roasted, and 0.48 g/100 oil for double-roasted) and DG CN38 (3.11 g/100 oil for raw, 3.05 g/100 oil for single-roasted, 2.94 g/100 oil for double-roasted). Holčapek et al.[42] reported the TG and DG composition of pistachio oil as equivalent carbon number ranging from 40 to 50 and 20 to 34, respectively. However, if TG and DG are calculated as CN, results are similar to those found in the current research study. The data revealed that TG in the assayed samples was not affected by processing. However, the results for DG CN38 ($0.05 < p < 0.1$) suggest that quantities were slightly reduced as a result of processing.

Table 5. Total Contents and Molecular Species Composition (%) of Di- and Triacylglycerides in the Assayed Pistachio Samples[a]

	raw	single-roasted	double-roasted	*p*
CN36	0.50 ± 0.01	0.46 ± 0.05	0.48 ± 0.02	0.43
CN38	3.11 ± 0.15	3.05 ± 0.15	2.94 ± 0.10	0.09
total DG	3.61 ± 0.16	3.51 ± 0.20	3.42 ± 0.12	0.39
CN50	2.07 ± 0.04	1.97 ± 0.39	2.10 ± 0.04	0.56
CN52	19.45 ± 0.19	19.82 ± 0.83	19.88 ± 0.24	0.25
CN54	74.87 ± 0.02	74.71 ± 1.32	74.60 ± 0.31	0.67
total TG	96.39 ± 0.16	96.49 ± 0.20	96.58 ± 0.12	0.39

[a]DG: diacylglycerides; TG: triacylglycerides; *p*: significance level ($p < 0.05$).

The analysis of fatty acid methyl esters (FAME) showed three main compounds (Table 6) which were palmitic (C16—72.50 mg/g oil for raw, 69.16 mg/g oil for single-roasted, and 73.85 mg/g oil for double-roasted), oleic (C18:1 c9—684.21 mg/g oil for raw, 691.60 mg/g oil for single-roasted, and 670.61 mg/g oil for double-roasted), and linoleic acid (C18:2 c9, c12—186.40 mg/g oil for raw, 186.68 mg/g oil for single-roasted, and 197.93 mg/g oil for double-roasted). Stearic (C18), palmitoleic (C16:1 c9), C18:1 c11 and α-linolenic acid (C18:3 c9, c12, c15) were also present by FAME analysis, demonstrating that the overall composition is similar to that reported elsewhere for pistachios in Turkey.[6]

In general terms, the fatty acid composition was stable after single roasting and double roasting. However, it was observed that double-roasted samples had significantly higher concentrations of elaidic acid (C18:1 t9, 0.12 mg/g oil) compared to raw (0.06 mg/g oil) and single-roasted (0.08 mg/g oil) samples. It was also observed that levels of oleic acid were lower ($p < 0.05$) in double-roasted samples than in the others.

The lipid composition of pistachios has a high concentration of unsaturated fatty acids. It is well-established that such compounds are prone to alteration by oxidative reactions. Thus, after drying Iranian pistachios at 70 °C, Kashani et al.[43] reported concentration levels of total free fatty acids associated with hydrolysis of TG, 1,3-DG, and phospholipids. The present study's results about DG CN38 are in line with those prior findings. In further investigations studying the effects of roasting (190 °C for 10 min), salting, and packing samples from Lebanon, it was concluded that thermal processing was the main factor leading to the production of hydroperoxides and total trans fatty acids.[44] On the other hand, studies focused on the possible effects of heating of butter (20—350 °C), found isomerization of oleic in elaidic acid explained through oxidation reactions.[45] Trans double bonds are more stable than cis bond when compared under the same conditions, with trans formation favored by temperature and time.[46] Other authors have[47,48] described that unsaturated fatty acids can be isomerized into cis/trans compounds at the intramolecular level,[49] catalyzed by thiyl radicals formed from thiols groups in proteins. The present results about variations in the amounts of oleic and elaidic are in line with the aforementioned studies. However, this is the first study describing exactly which trans compounds are involved in such changes.

In conclusion, the results obtained in this study showed the strong effect of roasting on the chemical composition of pistachios. The total amount of polyphenols increase with the roasting treatment; however, not all phenolic compounds demonstrated this behavior. In regard to the volatile composition and the aroma-active compounds, the effect of the roasting process on the number and intensity of the odor-active regions was clearly observed. Nevertheless, although the highest intensities were generally observed in double-roasted samples, in some cases odor regions in single-roasted samples had lower intensity than double-roasted samples. This observation can be used to optimize the roasting time in order to improve the organoleptic quality of the pistachios. Finally, the lipid analysis indicates that the roasting treatment of pistachio nuts reduced the concentration of DG CN38 and increased the amount of elaidic acid due to the isomerization of oleic acid by oxidative reactions.

DOI: 10.1021/acs.jafc.5b02576
J. Agric. Food Chem. 2015, 63, 7830—7839

Table 6. Fatty Acid Composition (mg/g oil) in the Assayed Pistachio Samples[a]

	raw	single-roasted	double-roasted	p
C14	0.78 ± 0.05	0.73 ± 0.01	0.80 ± 0.04	0.19
C15	0.06 ± 0.01	0.05 ± 0.01	0.06 ± 0.01	0.31
C16	72.50 ± 2.22	69.16 ± 1.98	73.85 ± 2.16	0.08
C16:1 t	0.47 ± 0.01	0.47 ± 0.04	0.48 ± 0.03	0.86
C16:1 c9	4.61 ± 0.14	4.34 ± 0.19	4.72 ± 0.16	0.07
C17	0.34 ± 0.01	0.32 ± 0.03	0.35 ± 0.01	0.23
C17:1	0.68 ± 0.03	0.65 ± 0.03	0.68 ± 0.02	0.28
C18	16.91 ± 0.23	17.35 ± 0.96	17.67 ± 0.22	0.34
C18:1 t9	0.06 ± 0.03 a	0.08 ± 0.03 a	0.12 ± 0.03 b	0.00
C18:1 t10	0.24 ± 0.01	0.23 ± 0.01	0.24 ± 0.02	0.68
C18:1 c9	684.21 ± 1.65 a	691.60 ± 8.55 a	670.61 ± 0.47 b	0.02
C18:1 c11	23.14 ± 0.38	22.87 ± 0.61	22.76 ± 0.25	0.57
C18:2 c9, t12	0.22 ± 0.04	0.22 ± 0.05	0.24 ± 0.01	0.71
C18:2 c9, c12	186.40 ± 0.71	186.68 ± 8.66	197.93 ± 1.46	0.05
C20	2.82 ± 0.13	3.00 ± 0.23	2.93 ± 0.13	0.46
C18:3 c9, c12, c15	1.75 ± 0.04	1.73 ± 0.06	1.73 ± 0.05	0.86
C20:1 c11	0.22 ± 0.03	0.24 ± 0.02	0.22 ± 0.03	0.54
C20:1 c13	2.63 ± 0.16	2.90 ± 0.07	2.62 ± 0.14	0.07
C22	1.26 ± 0.10	1.37 ± 0.17	1.27 ± 0.11	0.57
C23	0.27 ± 0.02	0.29 ± 0.01	0.26 ± 0.04	0.39
C24	0.42 ± 0.03	0.48 ± 0.06	0.42 ± 0.04	0.27
SFA	95.35 ± 1.94	92.75 ± 3.37	97.61 ± 1.70	0.13
MUFA	716.28 ± 1.29	718.61 ± 8.46	702.48 ± 0.28	0.01
PUFA	188.36 ± 0.72	188.64 ± 8.73	199.91 ± 1.45	0.054

[a] p: significance level. t: trans double bond; c: cis double bond. SFA: saturated fatty acids; MUFA: monounsaturated fatty acids; PUFA: polyunsaturated fatty acids. Different letters in a row for significant effect of processing ($p < 0.05$).

AUTHOR INFORMATION

Corresponding Author

*E-mail: sselli@cu.edu.tr; phone: + (90)-322-3386173; fax: + (90) 322 338 66 14).

Notes

The authors declare no competing financial interest.

ACKNOWLEDGMENTS

J.J.R.B. acknowledges the postdoctoral fellowship for the visiting scientists program, The Scientific and Technological Research Council of Turkey (TUBITAK-BIDEB, no: 2221). We thank Bethany J. Hausch from University of Illinois (UIUC) for proofreading the manuscript.

REFERENCES

(1) Hojjati, M.; Calin-Sanchez, A.; Razavi, S. H.; Carbonell-Barrachina, A. A. Effect of roasting on colour and volatile composition of pistachios (*Pistacia vera* L.). *Int. J. Food Sci. Technol.* **2013**, *48*, 437−443.

(2) Kendirci, P.; Onogur, T. Investigation of volatile compounds and characterization of flavor profiles of fresh pistachio nuts (*Pistacia vera* L.). *Int. J. Food Prop.* **2011**, *14*, 319−330.

(3) Venkatachalam, M.; Sathe, S. K. Chemical composition of selected edible nut seeds. *J. Agric. Food Chem.* **2006**, *54*, 4705−4714.

(4) Arena, E.; Campisi, S.; Fallico, B.; Maccarone, E. Distribution of fatty acids and phytosterols as a criterion to discriminate geographic origin of pistachio seeds. *Food Chem.* **2007**, *104*, 403−408.

(5) Tsantili, E.; Takidelli, C.; Christopoulos, M. V.; Lambrinea, E.; Rouskas, D.; Roussos, P. A. Physical, compositional and sensory differences in nuts among pistachio (*Pistachia vera* L.) varieties. *Sci. Hortic.* **2010**, *125*, 562−568.

(6) Satil, F.; Azcan, N.; Baser, K. H. C. Fatty Acid Composition of Pistachio Nuts in Turkey. *Chem. Nat. Compd.* **2003**, *39*, 322−324.

(7) Aceña, L.; Vera, L.; Guasch, J.; Busto, O.; Mestres, M. Determination of roasted pistachio (*Pistacia vera* L.) key odorants by headspace solid-phase microextraction and gas chromatography-olfactometry. *J. Agric. Food Chem.* **2011**, *59*, 2518−2523.

(8) Tomaino, A.; Martorana, M.; Arcoraci, T.; Monteleone, D.; Giovinazzo, C.; Saija, A. Antioxidant activity and phenolic profile of pistachio (*Pistacia vera* L., variety Bronte) seeds and skins. *Biochimie* **2010**, *92*, 1115−1122.

(9) Kucukoner, E.; Yurt, B. Some chemical characteristics of *Pistacia vera* varieties produces in Turkey. *Eur. Food Res. Technol.* **2003**, *217*, 308−310.

(10) Maskan, M.; Karatas, S. Storage stability of whole-split pistachio nuts (*Pistachia vera* L.) at various conditions. *Food Chem.* **1999**, *66*, 227−233.

(11) Tsantili, E.; Konstantinidis, K.; Christopoulos, M. V.; Roussos, P. A. Total phenolics and flavonoids and total antioxidant capacity in pistachio (*Pistachia vera* L.) nuts in relation to cultivars and storage conditions. *Sci. Hortic.* **2011**, *129*, 694−701.

(12) Raei, M.; Mortazavi, A.; Pourazarang, H. Effects of Packaging Materials, Modified Atmospheric Conditions, and Storage Temperature on Physicochemical Properties of Roasted Pistachio Nut. *Food Anal. Method.* **2010**, *3*, 129−132.

(13) Panahi, B.; Khezri, M. Effect of harvesting time on nut quality of pistachio (*Pistacia vera* L.) cultivars. *Sci. Hortic.* **2011**, *129*, 730−734.

(14) Shakerardekani, A.; Karim, R.; Ghazali, H. M.; Chin, N. L. Effect of roasting conditions on hardness, moisture content and colour of pistachio kernels. *Int. Food Res. J.* **2011**, *18*, 723−729, DOI: 10.2139/ssrn.1799189.

(15) Nikzadeh, V.; Sedaghat, N. Physical and Sensory Changes in Pistachio Nuts as Affected by Roasting Temperature and Storage. *Am.-Eurasian J. Agric. Environ. Sci.* **2008**, *4*, 478−483.

(16) Kashant, K.; Guy Valadon, L. R. Effect of salting and toasting on the carbohydrates and proteins of Iranian pistachio kernels. *J. Food Technol.* **1984**, *19*, 247−253.

(17) Gogus, F.; Ozel, M. Z.; Kocak, D.; Hamilton, J. F.; Lewis, A. C. Analysis of roasted and unroasted *Pistacia terebinthus* volatiles using

DOI: 10.1021/acs.jafc.5b02576
J. Agric. Food Chem. 2015, 63, 7830−7839

direct termal desorption-GCxGC−TOF/MS. *Food Chem.* **2011**, *129*, 1258−1264.
(18) San-Juan, F.; Pet'ka, J.; Cacho, J.; Ferreira, V.; Escudero, A. Producing Headspace Extracts for the Gas Chromatography-olfactometric evaluation of wine aroma. *Food Chem.* **2010**, *123*, 188−195.
(19) Ferreira, V., Cacho, J. Identification of impact odorants of wines. In *Wine Chemistry and Biochemistry*; Moreno-Arribas, M. V., Polo, M. C., Eds.; Springer: New York. 2009; pp 393−415.
(20) Iverson, S. J.; Lang, S. L.; Cooper, M. H. Comparison of the Bligh and Dyer and Folch methods for total lipid determination in a broad range of marine tissue. *Lipids* **2001**, *36*, 1283−1287.
(21) Fontecha, J.; Rios, J. J.; Lozada, L.; Fraga, M. J.; Juarez, M. Composition of goat's milk fat triglycerides analysed by silver ion adsorption-TLC and GC-MS. *Int. Dairy J.* **2000**, *10*, 119−128.
(22) ISO-IDF, I.S. 2002. Milk fat-Preparation of fatty acid methyl esters. ISO 15884:182, 2002.
(23) Rodríguez-Alcalá, L. M.; Calvo, M. V.; Fontecha, J. A quick, optimized method for routine analysis of essential and trans-octadecenoic acids in edible fats and oils by GLC. *J. Chromatogr. Sci.* **2013**, *51*, 70−80.
(24) Garrido, I.; Monagas, M.; Gomez-Cordoves, C.; Bartolomé, B. Polyphenols and antioxidant properties of almond skins: influence of industrial processing. *J. Food Sci.* **2008**, *73*, C106−C115.
(25) Chandrasekara, N.; Shahidi, F. Effect of Roasting on Phenolic Content and antioxidant activities of whole cashew nuts, kernels, and testa. *J. Agric. Food Chem.* **2011**, *59*, 5006−5014.
(26) Chism, G. W.; Haard, N. F. Characteristics of edible plant tissues. In *Food Chem.*, 3rd ed.; Fennema, O. R., Ed.; Dekker: New York. 1996; pp 943−1011.
(27) Liu, Y.; Blumberg, J. B.; Chen, C-Y.O. Quantification and bioaccessibility of california pistachio bioactives. *J. Agric. Food Chem.* **2014**, *62*, 1550−1556.
(28) Mandalari, G.; Bisignano, C.; Filocamo, A.; Chessa, S.; Saro, M.; Torre, G.; Faulks, R.; Dugo, P. Bioaccessibility of pistachio polyphenols, xanthophylls, and tocopherols during simulated human digestion. *Nutrition* **2013**, *29*, 338−344.
(29) Martorana, M.; Arcoraci, T.; Rizza, L.; Cristani, M.; Bonina, F. P.; Saija, A.; Trombetta, D.; Tomaino, A. In vitro antioxidant and in vivo photoprotective effect of pistachio (*Pistacia vera* L., variety Bronte) seed and skin extracts. *Fitoterapia* **2013**, *85*, 41−48.
(30) Oliviero, T.; Capuano, E.; Cammerer, B.; Fogliano, V. Influence of roasting on the antioxidant activity and hmf formation of a cocoa bean model systems. *J. Agric. Food Chem.* **2009**, *57*, 147−152.
(31) Hayase, F.; Hirashima, S.; Okamoto, G.; Kato, H. Scavenging of active oxygen by melanoidins. *Agric. Biol. Chem.* **1989**, *53*, 3383−3385.
(32) De Brito, E. S.; Pezoa Garcia, N. H.; Gallao, M. I.; Cortelazzo, A. L.; Fevereiro, P. S.; Braga, M. R. Structural and chemical changes in cocoa (*Theobroma cacao* L) during fermentation drying and roasting. *J. Sci. Food Agric.* **2001**, *81*, 281−288.
(33) Belitz, H. D., Grosch, W., Schieberle, P. *Food Chem.*, 4th extended ed.; Springer: Berlin, 2009; pp 340−400.
(34) Vazquez-Araujo, L.; Verdu, A.; Navarro, P.; Martinez-Sanchez, F.; Carbonell-Barrachina, A. Changes in volatile compounds and sensory quality during toasting of Spanish almonds. *Int. J. Food Sci. Technol.* **2009**, *44*, 2225−2233.
(35) Agila, A.; Barringer, S. Effect of Roasting Conditions on Color and Volatile Profile Including HMF Level in Sweet Almonds (*Prunus dulcis*). *J. Food Sci.* **2012**, *77*, C461−C468.
(36) Aceña, L.; Vera, L.; Guasch, J.; Busto, O.; Mestres, M. Comparative study of two extraction techniques to obtain representative aroma extracts for being analysed by gas chromatography-olfactometry application to roasted pistachio aroma. *J. Chromatogr. A* **2010**, *1217*, 7781−7787.
(37) Alasalvar, C.; Shahidi, F.; Cadwallader, K. R. Comparison of natural and roasted Turkish tombul hazelnut (*Corylus avellana* L.) volatiles and flavor by DHA/GC/MS and descriptive sensory analysis. *J. Agric. Food Chem.* **2003**, *51*, 5067−5072.
(38) Davidek, T.; Robert, F.; Devaud, S.; Vera, F. A.; Blank, I. Sugar fragmentation in the Maillard reaction cascade: Formation of short-chain carboxylic acids by a new oxidative alpha-dicarbonyl cleavage pathway. *J. Agric. Food Chem.* **2006**, *54*, 6677−6684.
(39) Duru, M. E.; Cakir, A.; Kordali, S.; Zengin, H.; Harmandar, M.; Izumi, S.; Hirata, T. Chemical composition and antifungal properties of essential oils of three Pistacia species. *Fitoterapia* **2003**, *74*, 170−176.
(40) Dragull, K.; Beck, J. J.; Merrill, G. B. Essential oil yield and composition of pistacia vera 'Kerman' fruits, peduncles and leaves grown in California. *J. Sci. Food Agric.* **2010**, *90*, 664−668.
(41) Wagner, R.; Czerny, M.; Bielohradsky, J.; Grosch, W. Structure-odour-activity relationships of alkylpyrazines. *Z. Lebensm Unters Forsch A* **1999**, *208*, 308−316.
(42) Holcapek, M.; Jandera, P.; Zderadicka, P.; Hruba, L. Characterization of triacylglycerol and diacylglycerol composition of plant oils using high-performance liquid chromatography − atmospheric pressure chemical ionization mass spectrometry. *J. Chromatogr A* **2003**, *1010*, 195−215.
(43) Kashani, G. G.; Valadon, L. R. G. Effect of salting and roasting on the lipids of Iranian pistachio kernels. *Int. J. Food Sci. Technol.* **1983**, *18*, 461−467.
(44) Yaacoub, R.; Saliba, R.; Nsouli, B.; Khalaf, G.; Birlouez-Aragon, I. Formation of lipid oxidation and isomerization products during processing of nuts and sesame seeds. *J. Agric. Food Chem.* **2008**, *56*, 7082−7090.
(45) Precht, D.; Molkentin, J.; Vahlendieck, M. Influence of the heating temperature on the fat composition of milk fat with emphasis on cis-/trans-isomerization. *Nahrung* **1999**, *43*, 25−33.
(46) Bruice, T. C.; Lightstone, F. C. Ground state and transition state contributions to the rates of intramolecular and enzymatic reactions. *Acc. Chem. Res.* **1999**, *32*, 127−136.
(47) Ferreri, C.; Costantino, C.; Perrotta, L.; Landi, L.; Mulazzani, Q. G.; Chatgilialoglu, C. Cis-trans isomerization of polyunsaturated fatty acid residues in phospholipids catalyzed by thiyl radicals. *J. Am. Chem. Soc.* **2001**, *123*, 4459−4468.
(48) Geißler, C.; Brede, O.; Reinhardt, J. cis−trans-Isomerization of unsaturated fatty acids during γ-irradiation of barley grains. *Radiat. Phys. Chem.* **2003**, *67*, 105−113.
(49) Christy, A. A. Evidence in the formation of conjugated linoleic acids from thermally induced 9t12t linoleic acid: a study by gas chromatography and infrared spectroscopy. *Chem. Phys. Lipids* **2009**, *161*, 86−94.

DOI: 10.1021/acs.jafc.5b02576
J. Agric. Food Chem. 2015, 63, 7830−7839

azine (IBMP) with a vegetative, green odor occur in many vegetables as aroma-relevant compounds[17] and also in *Vitis vinifera* varieties.[18] However, they can also contribute to earthy off-flavors in water,[19] fish,[20] and other foodstuffs.[6] IPMP is also known as major component contributing to the so-called 'ladybug taint' in wine, associated with beetles that are harvested together with the grapes.[21]

Further known substances capable of producing corky off-flavors in wine are other haloanisoles like 2,4,6-tribromoanisole (TBA), 2,3,4,6-tetrachloroanisole (TeCA), and pentachloroanisole (PCA).[8,22,23] Although their sensory characteristics are rather similar to TCA, they originate from the microbial degradation of halophenols (in pesticides or flame retardants) that then produce the potent haloanisoles. These compounds represent a contamination of the wine cellar and not the cork itself. However, migration may occur depending on storage and wine production conditions. Halogenation of phenolic compounds with further microbial transformation into potent haloanisoles is a well-known problem in general and can particularly be found in the wood processing industry.[24,25]

In plant anatomy, cork is part of the periderm in the bark system of the cork oak tree (*Quercus suber* L.) and consists primarily of suberin, lignin, and polysaccharides.[26] As a consequence of the halogenation of lignin, Kugler and Rapp[3] detected various chloroguaiacols and other chlorophenolic compounds in cork.

On the basis of the substantiated state of knowledge on the typical cork off-flavor as well as other musty substances, we wanted to identify compounds particularly responsible for atypical cork taint, an off-flavor that had not been fully characterized so far. Cork samples that had been considered off-odorous should be submitted to a purge and trap extraction followed by gas chromatography–olfactometry analysis (GC-O). Detected off-flavor regions in the chromatograms deviant from the control samples should be further processed by a set of multidimensional gas chromatographic methods to characterize the structural identity of the underlying chemical substances.

MATERIALS AND METHODS

Chemicals. Reference compounds used were 2,4,6-trichloroanisole, pentachloroanisole, 2,4,6-tribromoanisole, geosmin (100 μg/mL in methanol), 2-methylisoborneol (10 mg/mL in methanol), 3-isopropyl-2-methoxypyrazine, and 3-isobutyl-2-methoxypyrazine (Sigma–Aldrich, Steinheim, Germany); 2,3,4,6-tetrachloroanisole and 3,5-dichlorocatechol (LGC Promochem, Wesel, Germany); guaiacol (Fluka, Buchs, Switzerland); 3,5-dimethyl-2-methoxypyrazine (Bellen Chemistry Co. Ltd., Beijing, China); 1-octen-3-one (Alfa Aesar, Karlsruhe Germany); 1-octen-3-ol (BASF, Ludwigshafen, Germany); 2,6-dichloroanisole (Riedel-de Haën, Seelze, Germany); and 3,4,6-trichloroveratrole (kindly supplied by Professor Juha Knuutinen, University of Jyväskylä, Finland). Chlorophenolics standard mixtures regulated by U.S. Environmental Protection Agency (EPA) method 1653A were from Cambridge Isotope Laboratories (Andover, MA), comprising pentachlorophenol, tetrachlorocatechol, tetrachloroguaiacol, 2,3,4,6-tetrachlorophenol, 3,4,5-trichlorocatechol, 3,4,6-trichlorocatechol, 3,4,5-trichloroguaiacol, 3,4,6-trichloroguaiacol, 4,5,6-trichloroguaiacol, 2,4,5-trichlorophenol, and 2,4,6-trichlorophenol in methanol (EM-4181); 3,4,5-trichlorosyringol in acetone (EM-4182); 4-chlorocatechol, 4-chloroguaiacol, 4-chlorophenol, 3,4-dichlorocatechol, 3,6-dichlorocatechol, 4,5-dichlorocatechol, 3,4-dichloroguaiacol, 4,5-dichloroguaiacol, 4,6-dichloroguaiacol, 2,4-dichlorophenol, and 2,6-dichlorophenol in methanol (EM-4183); and 2-chlorosyringaldehyde, 5-chlorovanillin, 6-chlorovanillin, 2,6-dichlorosyringaldehyde, and 5,6-dichlorovanillin in acetone (EM-4184).

Reagents used for synthesizing further references were trimethylsilyldiazomethane (2 M in diethyl ether; Sigma–Aldrich) and 1,3-propylene glycol and *p*-toluenesulfonic acid (Fluka). Commercial chemicals were usually of analytical grade and used as such.

Synthesis of Reference Compounds. On the basis of multicomponent standard mixes containing chlorophenolic substances (EM-4181, EM-4182, EM-4183, and EM-4184), the corresponding *O*-methylated derivatives were synthesized by use of trimethylsilyldiazomethane (TMSD) according to Ranz et al.[27] An aliquot (40 μL) of the standard mixture (EM-4181, EM-4182, or EM-4183) with 250–1000 μg/mL of the chlorophenolic substances was mixed with TMSD (40 μL of 2 M in diethyl ether) and methanol (160 μL). After 2 h at 40 °C the reaction was complete as monitored by gas chromatography–mass spectrometry (GC-MS). 3,5-Dichlorocatechol was methylated accordingly. Chlorophenolic substances containing a carbonyl group (standard mixture EM-4184) yielded mixtures of reaction products. In this case the carbonyl group was protected as a cyclic acetal by use of 1,3-propylene glycol. Briefly, 1,3-propylene glycol (100 μL), a catalytic amount of *p*-toluenesulfonic acid, and molecular sieve were added to 50 μL of the standard mixture EM-4184 and kept at 45 °C overnight. The reaction mixture was then washed with a $NaHCO_3$ solution (4.8 g/L) and extracted with dichloromethane. The organic phase was used for *O*-methylation as described above. Thereafter, the carbonyl group was deprotected by adding 3 M hydrochloric acid (250 μL) to the organic solution, with agitation and heating at 50 °C until completion of the reaction (monitored by GC-MS). The dichloromethane phase was separated and used for characterization by GC. Linear retention indices (LRI), mass spectral data, and odor descriptions of the *O*-methylated derivatives are listed in Table S1 in Supporting Information.

Preselection of Conspicuous Cork Stoppers. In the industrial quality control process of raw natural cork stoppers (before processing, for example, coating and imprinting), sensory evaluation of cork stoppers was performed by three panelists experienced for years in assessing the odor of cork stoppers. A consistent vocabulary for odor descriptions of the cork stoppers had early been determined by repeatedly sniffing about 100 exemplary cork stoppers and comparing their individual odor descriptions. Technically, cork stoppers were moisturized by dipping in purified water, put in screw-top jars, and left overnight at room temperature. After the supernatant air was sniffed, cork stoppers were classified in a first step by their odor into four classes: no deviant odor (class 1), slightly deviant odor (class 2), strongly deviant odor (class 3A), and typical TCA taint (class 3B). Whereas cork stoppers of class 2 could be clearly distinguished from inconspicuous cork stoppers, the off-odor description was not further defined, also due to a high variability of subtle off-flavor notes. For our study of atypical cork taint, strongly deviant cork stoppers of class 3A were further sorted into the subgroups musty (dusty-musty), moldy (mildewed, 2-methylisoborneol-like, earthy, mushroom), cellarlike (wet cloth, musty wet cellar), earthy (woody, mossy, earthy), and green (vegetative, bell pepper, pea). The definition of these subgroups was done prior to analysis and was based on common and dominating subtle sensory notes (nuances). Cork stoppers of class 1 were used as inconspicuous control sample.

Extraction of Volatiles from Natural Cork Stoppers. The extraction of cork stoppers followed a standard quality control procedure applied in the cork industry to monitor TCA. In our case, six cork stoppers of each group were soaked in an aqueous solution of 10% (vol) ethanol (absolute) for 24 h at 40 °C, repeated three times. The combined cork soaks were transferred into a wide-neck glass bottle with a GLS 80 thread and a poly(tetrafluoroethylene) (PTFE) screw cap with connection ports (Bohlender GmbH, Grünsfeld, Germany). Volatiles were purged by bubbling nitrogen (purified by an activated charcoal inline filter) with a metal-frit sparger through the solution, similar to a setup previously described.[28] The purged gas passed a solid phase extraction (SPE) tube containing Lichrolut EN (0.4 g; Merck, Darmstadt, Germany) as sorbent via a self-made glass adapter. Each cork soak was purged for 7 h at 37 °C with a nitrogen flow of about 100 mL/min. The necessary purge time was evaluated in

DOI: 10.1021/acs.jafc.5b02793
J. Agric. Food Chem. 2015, 63, 7840–7848

a preliminary experiment, in which the SPE cartridge was changed every 100 min. Breakthrough of compounds was evaluated with a second cartridge connected in series. Trapped volatiles were then eluted with dichloromethane and the organic phase was kept at −25 °C overnight to remove moisture. Extracts obtained were finally concentrated to a volume of about 0.1 mL by use of a microdistillation apparatus according to Bemelmans.[29] These extracts containing the purgeable volatiles from the cork soaks were used for further analysis by various GC approaches.

Detection of Off-Flavor Compounds by Heart-Cut Multidimensional Gas Chromatography−Olfactometry. GC-O experiments (sniffings) were carried out by two panelists in separate runs using heart-cut multidimensional gas chromatography (H/C MDGC) utilizing a moving capillary stream switching (MCSS) device described previously.[30] Two GC instruments (model 8560, Mega II series) from C.E. Instruments (today ThermoFisher Scientific, Dreieich, Germany) were connected via a heated transfer line. The GC in the first dimension (^{1}D) was equipped with the MCSS device, allowing heart-cutting of GC fractions. For a first evaluation of odorous elution zones (odor or aroma events), sniffing occurred after separation in ^{1}D. Later, individual odor events were transferred onto the second dimension (^{2}D) separation column with a transfer window of the ^{1}D LRI ±25 units. The basic components of the MDGC system are outlined in the following sections.

First-Dimension System. The ^{1}D column configuration consisted of a 1 m × 0.32 mm i.d. phenylmethylsilylated precolumn (BGB Analytik, Rheinfelden, Germany) that was connected via a press-fit to a fused silica capillary column (20 m × 0.25 mm i.d.) coated with 0.5 μm of a poly(ethylene glycol) phase (ZB-Wax, Phenomenex, Aschaffenburg, Germany). The carrier gas used was helium with an inlet pressure of 70 kPa (*P*1) and a midpoint pressure of 47 kPa (*P*2). The actual inlet pressure for the ^{2}D column was given by the readout on the pressure gauge, *P*2*, and was at 30 kPa. A flame ionization detector (FID) was set to 250 °C and used as ^{1}D monitor detector when sniffing occurred after ^{2}D separation. For sniffing after ^{1}D separation, a sniffing adapter was installed instead of the FID, keeping the detector base temperature at 250 °C. Cork extracts (3 μL) were injected via a cold on-column injector. The oven temperature was programmed from 40 °C (5 min isothermal) at 8°/min to 250 °C (15 min isothermal). Control of the MCSS system as well as data processing was achieved by the Chromcard data acquisition software, version 2.2 (ThermoFisher).

Second-Dimension System. A deactivated fused silica capillary (1.5 m × 0.25 mm i.d., Phenomenex) was guided through a heated transfer line (200 °C), connecting the two GC ovens. The transfer capillary from the first oven was connected via a press-fit to the ^{2}D analytical column (11 m × 0.32 mm i.d. fused silica capillary) with 1 μm of 5% phenylmethylpolysiloxane (DB-5, Agilent, Waldbronn, Germany). At the end of the analytical column, the eluent flow was split via a Y-splitter connecting a deactivated fused silica capillary of 0.4 m × 0.25 mm i.d. (BGB Analytik) with the sniffing port and a 0.6 m × 0.22 mm i.d. (SGE, Victoria, Australia) leading to the FID, respectively. The sniffing port (detector base) was set to 250 °C and the FID was set to 280 °C. The oven temperature program was initiated via external event activation 1 s after the start signal of the ^{1}D oven. The oven temperature was raised from 35 °C (32 min isothermal) at 10°/min to 280 °C (5 min isothermal). LRIs were calculated by use of a series of *n*-alkanes (C10−C25). For determination of LRIs after ^{2}D separation, alkanes injected into ^{1}D were fully transferred into ^{2}D. Keeping the oven temperature in ^{2}D at 35 °C allowed cold trapping from C10 on, and following this transfer, oven temperature programming was done as in the analytical run.

Identification of Odorous Compounds. Retention indices after ^{1}D and ^{2}D separation of odor events, as well as their odor descriptions, were compared with those of reference compounds. Thus, tentatively identified substances were verified by injection of reference material, applying MDGC conditions as described in the previous section. The identification was further supported by additional analyses via MDGC-MS-MS and GC × GC-MS (described below). Odor events that could not be identified in this way demanded further specific sample enrichment and mass spectrometric detection. For this purpose, compounds eluting in the dedicated odor event zone (after H/C and ^{2}D separation) were trapped by use of thermodesorption tubes packed with polydimethylsiloxane (PDMS) foam (Gerstel, Mülheim an der Ruhr, Germany). PDMS foam was chosen due to its high capacity and known moderate bleed characteristics in thermodesorption applications compared to, for example, Tenax or other polymer-based sorbents. Good sorption properties for various aroma compounds have been demonstrated with solid phase microextraction (SPME) and stir bar sorptive extraction (SBSE) applications.[31] For higher sensitivity the Y-splitter was removed and a deactivated fused silica capillary of 0.6 m × 0.32 mm i.d. (BGB Analytik) was directly connected to the ^{2}D analytical column, guided through the heated detector base, and connected with the trap on top of the detector base with a homemade press-fit-type adapter made of a 6 mm i.d. polyethylene tube. In a separate GC (HP6890, Agilent) equipped with a MPS2 autosampler, a thermodesorption unit (TDU), and a cold injection system (CIS 4; all Gerstel), the trapped components were thermodesorbed at 250 °C for 10 min (in splitless mode) with a purge flow of 60 mL/min. The transferline between TDU and CIS was set to 300 °C. During thermodesorption, the CIS was set to −100 °C and operated in solvent vent mode. After thermodesorption, the CIS temperature was raised at 12°/s to 280 °C (1.5 min isothermal), with closed split valve for 2 min. The analytical column was a 30 m × 0.25 mm i.d. fused silica capillary column coated with 0.25 μm of 5% phenylmethylpolysiloxane (ZB-5, Phenomenex). Carrier gas used was helium at a constant flow rate of 1.2 mL/min. The oven temperature was raised from 50 °C (2 min isothermal) at 10°/min to 280 °C (5 min isothermal). MS acquisition was done with an Agilent MSD 5975 at 70 eV (EI+) in full-scan mode from *m*/*z* 29 to 400. Ion source and quadrupole were heated at 230 and 150 °C, respectively. The MS transfer line was set to 280 °C. Instrument control and MS data acquisition were performed via MSD ChemStation (version E.02.02.1431, Agilent) and Gerstel Maestro (version 1.4.23.11). Identification of unknowns was then based on mass spectra matching National Institute of Standards and Technology (NIST) library (version 2011), LRIs, and reference substances and also application of deconvolution algorithms (AMDIS software).

Methods for Specific Compound Identification. *Determination of 2,4,6-Trichloroanisole, 2,4,6-Tribromoanisole, and 2,3,4,6-Tetrachloroanisole.* Confirmation of haloanisoles in cork stoppers was done by analyzing the cork soaks, before purging, with the headspace (HS)-SPME-MDGC-electron capture detection (ECD) system described in an earlier work.[32]

Determination of Alkylmethoxypyrazines. Detection of alkylmethoxypyrazines (MDMP, IPMP, and IBMP) was achieved with the H/C enantio-MDGC-MS-MS system described previously.[33] Injection of the cork extracts (3 μL) was done in programmed temperature vaporizer (PTV) on-column mode (simile on-column liner, ThermoFisher Scientific) after attaching a 1 m × 0.53 mm i.d. phenylmethylsilylated precolumn (BGB Analytik) via a press-fit connector. PTV on-column injection was done at 50 °C (PTV temperature; 1 min hold) and then raised at 14.5°/s to 190 °C (0.5 min hold) and at 10°/s to 270 °C (hold during remaining runtime). The splitless time was 2 min. Temperature program, cut windows, and cryo time were adjusted accordingly.

Determination of Geosmin and 2-Methylisoborneol. Confirmation of GSM and MIB was done with the previously mentioned H/C MDGC-MS-MS system, modified as follows. The original 15 m ^{1}D column was replaced by a 30 m × 0.25 mm i.d. fused silica capillary column, coated with 0.25 μm of Stabilwax-MS (Restek, Bad Homburg, Germany). Inlet pressure was 197 kPa and midpoint pressure was 121 kPa (Deans' Switch). A ^{1}D column backflush (releasing the effluent through the PTV in split mode) was initiated after heart-cutting (24 min) by lowering the PTV inlet pressure to 15 kPa. Oven temperature was programmed from 50 °C (5 min isothermal) at 10°/min to 130 °C (0 min hold) and at 5°/min to 179 °C (155 °C for MIB). Then the temperature was lowered to 100 °C (80 °C for MIB) at 30°/min (2 min isothermal) before the ^{2}D GC separation started by raising the temperature to 150 °C at 5°/min and then to 190 °C at 30°/min (5

DOI: 10.1021/acs.jafc.5b02793
J. Agric. Food Chem. 2015, 63, 7840−7848

min hold). Cut windows and cryo time were adjusted accordingly. The optimized MS-MS transfers and collision energies were 182 → 112 (12 V), 182 → 97 (12 V) and 112 → 97 (12 V) for GSM and 107 → 65 (20 V), 107 → 91 (12 V), 135 → 91 (15 V), 135 → 107 (8 V), and 150 → 107 (12 V) for MIB.

Additional Compound Identification Supported by Comprehensive Multidimensional Gas Chromatography. A comprehensive multidimensional GC system (GC × GC) equipped with a PTV injector and a dual-jet carbon dioxide modulator (Trace GC × GC Ultra, ThermoFisher Scientific) was coupled to a quadrupole MS (DSQ, ThermoFisher Scientific). The analytical column system consisted of a 1 m × 0.53 mm i.d. phenylmethylsilylated fused silica capillary (BGB Analytik) used as a precolumn, a 30 m × 0.25 mm i.d. fused silica capillary column coated with a poly(ethylene glycol) phase of 0.5 μm (ZB-Wax, Phenomenex) as ^{1}D column, and a 2 m × 0.15 mm i.d. fused silica capillary coated with 0.25 μm of a 5% phenylmethylpolysiloxane phase (BPX-5, SGE) as ^{2}D column. Helium was used as carrier gas at a constant flow of 1.2 mL/min. Injection (3 μL) was done in PTV on-column mode at 50 °C (PTV temperature; 1 min hold), then raised at 14.5°/s to 260 °C (1 min hold) and at 10°/s to 270 °C (hold during remaining runtime). The splitless time was 2 min. The oven temperature was programmed from 50 °C (5 min isothermal) to 250 °C at 4.5°/min (5 min hold). Cryomodulation occurred on the last section of the ^{1}D column and was started after a delay time of 6 min. The modulation period was 6 s. The MS transfer line was set to 250 °C and the ion source was set to 240 °C. MS data acquisition was done in electron ionization (EI+) mode at 70 eV. The mass scan range was segmented into m/z 40−250 from 5 to 30 min and m/z 60−350 after 30 min. The scan rates were 16 and 13 Hz, respectively. Data acquisition was done with Xcalibur software (version 1.4, ThermoFisher Scientific), and processing of two-dimensional data was done with HyperChrom software version 2.5 (ThermoFisher Scientific). Compound identification was based on mass spectra matching NIST library (version 2011), LRI, and reference substances and application of deconvolution algorithms (AMDIS software) when required.

RESULTS AND DISCUSSION

Sample Selection and Preparation. About 150 000 individual natural cork stoppers were sensorially evaluated by trained panelists. As described in the Materials and Methods section, rejected cork stoppers were described either with a slightly deviant odor (class 2, 1.15%), a strong deviant odor (class 3A, 0.35%), or a typical TCA taint (class 3B, 0.04%). The cork stoppers classified as class 3B (typical TCA taint) represent only a minor part of those classified with adverse sensory properties. Within the strongly deviant cork group (class 3), class 3B is about a tenth of its sum. Already indicated by these numbers, the atypical off-odor seems to be a problem even more crucial to the industry than the typical TCA taint. Only cork stoppers from class 3A were further investigated (additionally subdivided into five groups) to determine the substantial base underlying these off-odors. The basic workflow of the various analytical approaches applied in this investigation is illustrated in Figure 1. Based on established analytical procedures, known haloanisoles responsible for musty cork taint (TCA, TBA, and TeCA) were analyzed by HS-SPME-MDGC-ECD from cork soaks. In order to target hitherto unknown compounds, volatiles were purged from pooled cork soaks and trapped on a sorbent material. Purge time for an individual extraction step was determined by detecting off-odors from trap extracts (each taken after 100 min) with sensory evaluation. After 400 min (four consecutive traps), off-odors could still be detected in the GC-O experiment. For practical reasons (working day), the overall purge time was set to 7 h for all samples.

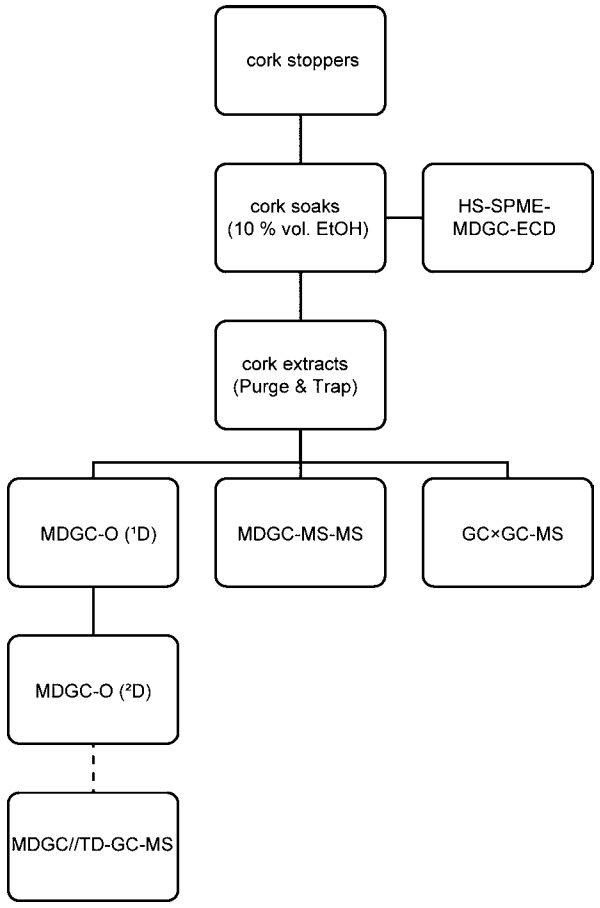

Figure 1. Workflow for identification of compounds responsible for atypical cork taint.

Olfactometric Analysis and Identification of Compounds Responsible for Off-Odors. Considering the complexity of a concentrated extract of a natural material such as cork, we expected coelution problems in standard one-dimensional GC-O. Therefore, we based our GC-O system on H/C MDGC-O with at first a ^{1}D GC-O experiment for detecting odorous elution zones in general. Such odor events were then individually transferred onto a second analytical column with different separation properties. The thus-reduced matrix allowed, in the following ^{2}D GC-O experiment, a more reliable detection of odorous events, as visualized with the example of Figure 2. The odor event with a ^{1}D LRI of 1442 that had been described with the sensory attributes 'nutty, musty, dusty' actually resulted in five odor events after ^{2}D separation and a number of additional non-odorous compounds producing a FID signal. This result reveals that GC-O odor events (particularly after a ^{1}D separation only) may be generated from a number of individual flavor compounds. Synergistic, antagonistic, or even suppressive effects can then influence the resulting odor sensation. Our approach with H/C MDGC-O thus provides a much higher resolution of odor events, eventually resulting in the sniffing of single components.

In general, sniffing of the cork extracts under investigation resulted in about 35−40 odor events per sample after ^{1}D separation. Compared to the extract from the control sample (class 1 cork stoppers), 4−8 odor events (depending on subgroup) were different with regard to musty or vegetative off-odors. The MDGC-O results after ^{1}D and ^{2}D sniffing are summarized in Table 1. Compounds responsible for the

DOI: 10.1021/acs.jafc.5b02793
J. Agric. Food Chem. 2015, 63, 7840−7848

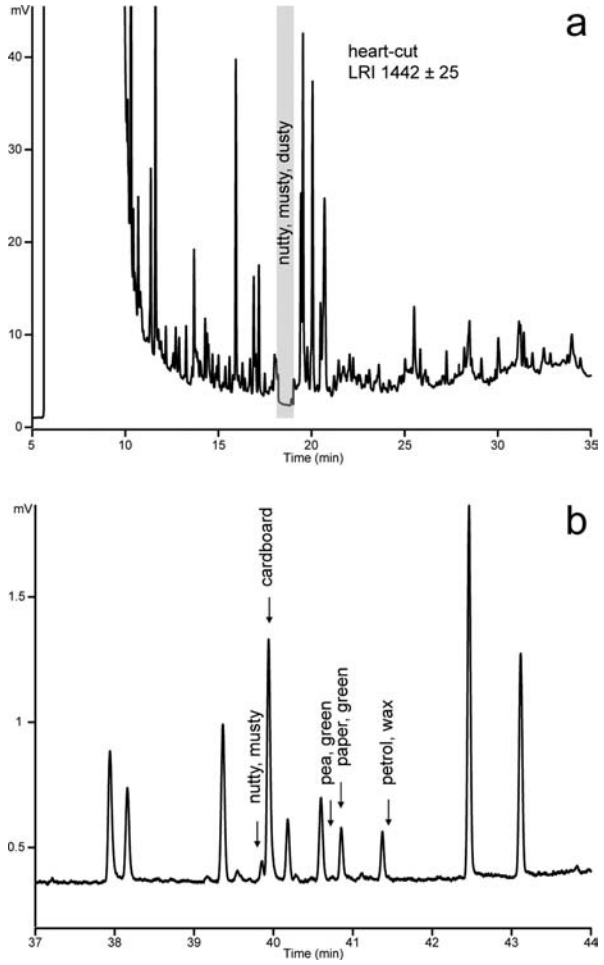

Figure 2. Enhanced resolution for determination of odorous zones responsible for cork taint after MDGC-O. (a) ^{1}D FID chromatogram with transfer of odor event. (b) Resulting ^{2}D FID chromatogram with indication of multiple odor events. Conditions were as described in the text.

individual odor events were tentatively identified by comparing the odor descriptions and LRIs on two stationary phases (ZB-Wax, DB-5) with those of authentic reference substances. Further confirmation was achieved by target analysis with established analytical methods such as MDGC-MS-MS or MDGC-ECD. The latter allows direct quantitation of TCA (and also TBA and TeCA) from the original cork soaks. Based on a previous work[2] suggesting guaiacol and 1-octen-3-one as compounds negatively affecting cork aroma, these two compounds could be confirmed in our study by use of GC × GC-MS as a supplementary method (see also Figure 1).

Although the investigated cork stoppers had been described with a musty odor deviant from TCA, this typical cork taint compound was perceived in all subgroups, including even the unaffected control cork stoppers. The intensity of the perceived TCA was highest in the moldy, musty, and cellarlike subgroups. This corresponds well with the analytical data obtained from the original cork soaks with TCA concentrations at 20 ng/L (moldy), 54 ng/L (musty), or 46 ng/L (cellarlike). The control sample was determined with <0.4 ng/L (limit of quantitation), whereas 0.7 and 11 ng/L were found in the green and earthy subgroups, respectively.

Another substance that was perceived in each extract was MDMP. This substance was first described as a compound associated with 'fungal must' in wine and found in cork stoppers by Simpson et al.[4] and was later confirmed by Prat et al.[5] and Chatonnet et al.[16] Besides, MDMP has not yet been described in other studies with respect to corky off-flavor. However, it was found among other alkylmethoxypyrazines as a potent and contributing off-flavor compound in wine related with the so-called 'ladybug taint'. Originally, this off-flavor was associated with a structural isomer of MDMP, 2,5-dimethyl-3-methoxypyrazine (DMMP).[34] Since retention properties on common stationary phases used for GC are almost identical for both isomers with furthermore non-distinguishable mass spectra, an unequivocal identification is critical. Such identification presupposes a chromatographic separation of MDMP and DMMP and also the availability of fully

Table 1. MDGC-O Analysis of Atypical Off-Flavor Compounds

			odor description of cork stoppers[a] (subgroups of class 3A)							
LRI[b] ZB-Wax	LRI[b] DB-5	odor description	control[c]	musty	moldy	cellarlike	earthy	green	compound	confirmed by
1313	999	mushroom, metallic	+	++	+	+	+	+	1-octen-3-one	GC × GC-MS
1441	1067	musty, moldy, nutty, earthy	(+)	+++	++	++	++	+	MDMP	MDGC-MS-MS, GC × GC-MS
1443	1102	green, pea, earthy	+	+	–	–	+	+++	IPMP	MDGC-MS-MS, GC × GC-MS
1536	1188	green, bell pepper	(+)	–	(+)	–	–	++	IBMP	MDGC-MS-MS
1618	1197	earthy, musty, camphoraceous	–	–	+++	+	–	(+)	MIB	MDGC-MS-MS
1736	1212	musty, TCA-like	–	–	–	+	–	–	unknown A[d]	
1865	1344	musty, TCA-like	+	++	++	+++	+	+	TCA	MDGC-ECD, GC × GC-MS
1889	1432	earthy, moldy, beetroot	–	–	+++	+++	+	++	GSM	MDGC-MS-MS
1908	1086	smoke, sweet, medicine	(+)	+	+	+	+	+	guaiacol	GC × GC-MS
2098	1435	musty, TCA-like	–	+	+	+	–	–	unknown B[d]	
2108	1530	musty, TCA-like	–	+	(+)	–	–	–	unknown C[d]	
2272	1474	musty, TCA-like	–	–	–	+	+	–	unknown D	
2272	1697	moldy, GSM-like	–	+	–	+	–	–	unknown E	

[a] +, weak; ++, strong; +++, very strong; (+), perceived only by one panelist; –, not perceived. [b] LRI, linear retention index. [c] Class 1 cork stoppers. [d] Identification as described in text.

DOI: 10.1021/acs.jafc.5b02793
J. Agric. Food Chem. 2015, 63, 7840–7848

characterized standards, as was outlined recently.[33] The origin of MDMP in cork is not yet fully understood. There is some evidence that microorganisms may produce MDMP.[5,15,16] Prat et al.[5] isolated microorganisms from cork and inoculated sterilized cork granules with bacterial or fungal suspensions. Resulting cork samples that were sensorially evaluated and described with vegetative and musty-earthy attributes contained MDMP, as was confirmed by GC-MS analysis. Chatonnet et al.[16] identified a bacterium capable of synthesizing high amounts of MDMP that is widespread in soil. A hypothetical contamination may occur during storage of cork barks or during cork stopper production in a process that has yet to be determined.

Besides MDMP and TCA, also 1-octen-3-one and guaiacol were present in all cork extracts and showed no distinct difference to the control. Both 1-octen-3-one and its reduced version 1-octen-3-ol are common metabolites of molds,[35] known to derive from enzymatic oxidation of unsaturated fatty acids. The ketone has a very low odor threshold in wine (20 ng/L in dry white wine)[2] that is 1000 times lower than the corresponding alcohol. Therefore, it is an important contributor to the off-flavor of affected wines or corks. It is well-known that widespread fungi like *Penicillium* species or *Botrytis cinerea* produce 1-octen-3-one and, among others, GSM and MIB.[36] During the production of cork stoppers, contamination with molds occurs, and thus contamination with such compounds can be explained. Guaiacol has already been described as a flavor-relevant compound affecting cork stoppers.[2] However, its odor threshold in wine is comparable to that of 1-octen-3-ol and its flavor contributes to smoky or medicinal attributes. Its production by degradation of vanillic acid with microorganisms isolated from cork has been described earlier.[37]

Within the moldy and cellarlike cork subgroups, GSM and MIB were the major contributing compounds, together with increased presence of TCA and also MDMP. Two other potent alkylmethoxypyrazines, IPMP and IBMP, were primarily found in cork stoppers with a green odor description. IPMP and IBMP are known for musty, earthy off-flavors in water and some foodstuffs.[6,19,20] Allen et al.[38] have already hypothesized the contamination of cork with IPMP in a situation where individual IPMP concentrations were found in different bottles of the same wine. Again, a synthesis by microorganisms was described earlier.[39] Migration of IPMP or IBMP from cork to wine and its potential for a negative effect on wine sensory properties has not been studied yet. One may assume similar defects as seen with the ladybug taint. However, if there is a negative influence, this cork stopper class can clearly be differentiated from musty- or moldy-type notes experienced with the other subgroups.

Further known compounds contributing to typical cork taint, like the haloanisoles TBA, TeCA, and PCA, were not detected by MDGC-O or further GC analyses, besides traces of PCA found in some extracts with GC × GC-MS. In principle, this could be expected as they are related to an anthropogenic entry into the environment (cellar and winery). Detection of traces of PCA in some cork stoppers may indicate that there might still be residues of pentachlorophenol, a biocide extensively used a few years ago also in cork forests.[3,40−42]

Identification of Unknown Compounds. In addition to the previously discussed odor events, there were five that remained unknown (unknowns A−E) after MDGC-O and comparison of LRIs of suspicious compounds known from literature. As a first identification step, visual comparison of GC × GC-MS chromatograms (control versus affected cork stoppers) in the conspicuous retention time ranges of the unknown compounds was performed. In some samples, recurring differences in the peak patterns corresponding to the retention of unknowns A−C could be detected and are shown as examples in Figure 3. A first comparison (NIST

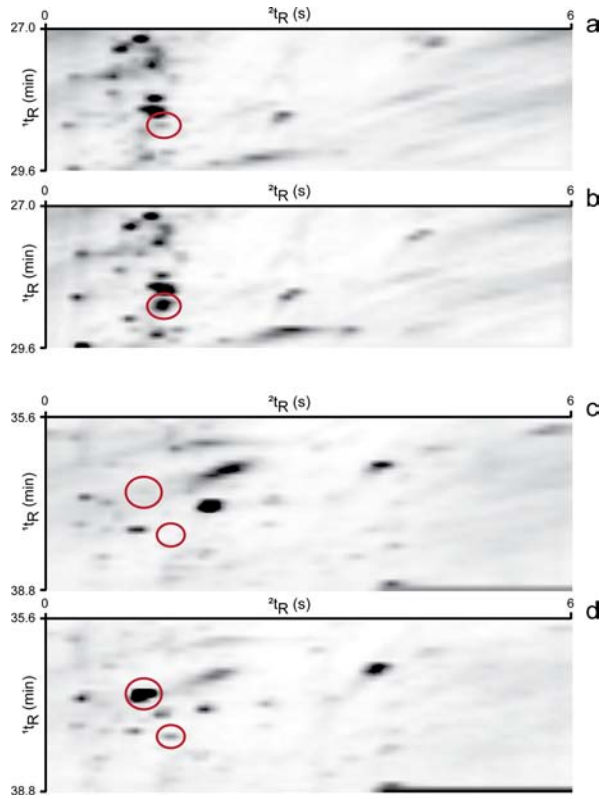

Figure 3. Comparison of GC × GC chromatograms (sections) of cork extracts. (a, c) Inconspicuous control samples; (b, d) tainted cork samples. Differences within peak patterns correspond to unknown odor events.

database) and interpretation of mass spectra obtained for the three highlighted peaks indicated the presence of chlorinated phenolic compounds. For further identification, the corresponding elution zones after MDGC were trapped and analyzed by thermal desorption (TD) GC-MS as described in the Materials and Methods section (MDGC//TD-GC-MS). Trace-level mass spectra interpretation was hindered by bleed produced from the sorbent used (PDMS). Subtraction of data obtained from a blank and application of deconvolution algorithms (AMDIS) finally yielded the corresponding mass spectra presented in Figure 4 that could also be observed with GC × GC-MS. Conclusive information for the remaining unknowns D and E could not be achieved. On the basis of the hypothesized presence of chlorophenolic compounds, we investigated structurally related compounds present in commercially available environmental contaminant standard mixtures. On the background that chlorophenols are *O*-methylated by microorganisms (as is known from the generation of TCA), we synthesized their *O*-methylated derivatives. In the case of aldehydes (5-chloro-, 6-chloro-, and 5,6-dichlorovanillin and 2-chloro- and 2,6-dichlorosyringaldehyde), intermediate protection of the carbonyl function was necessary before *O*-methylation. The corresponding chromato-

DOI: 10.1021/acs.jafc.5b02793
J. Agric. Food Chem. 2015, 63, 7840−7848

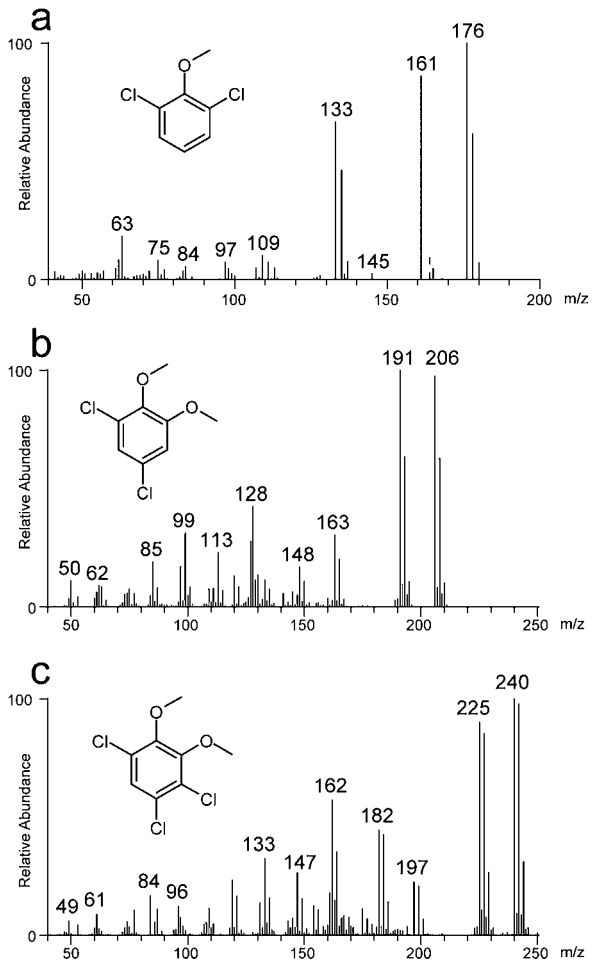

Figure 4. Mass spectra of chlorinated compounds identified after MDGC//TD-GC-MS analysis: (a) unknown A (2,6-dichloroanisole), (b) unknown B (3,5-dichloroveratrole), and (c) unknown C (3,4,6-trichloroveratrole). For detailed information, see text.

graphic (LRI on two different stationary phases), mass spectrometric, and sensory (GC-O) data were determined and are summarized in Table S1 (LRIs and MS data of chlorophenols are presented in Table S2). Since the synthesis of the *O*-methylated derivatives was based on a mixture of phenols, the correct assignment, particularly of isomeric compounds of the *O*-methylated products, was achieved by comparison of their LRIs with data published in the literature[43−46] (see also Supporting Information). Based on comparison of the two LRIs from MDGC-O, mass spectrometric, and sensory information, 2,6-dichloroanisole (unknown A), 3,5-dichloroveratrole (unknown B), and 3,4,6-trichloroveratrole (unknown C) could be identified and were verified with individual reference substances. Their chemical structures are similar to that of TCA, which may explain their comparable sensory properties.

Among the chlorinated compounds detected in cork stoppers were dichloroanisoles[1,47] and chloroveratroles.[1] A mono- and a dichloroveratrole (unassigned isomers) were also detected in the volatile fraction of microorganism cultures isolated from cork.[48] However, an exact identification of chloroveratrole isomers as well as sensory descriptions were not given earlier, so to the best of our knowledge, 3,4,6-trichloroveratrole and 3,5-dichloroveratrole are described here for the first time as a constituent of cork stoppers with off-flavor and were characterized by GC-O. Since Kugler and Rapp[3] found relatively high amounts of chloroguaiacols and 6-chlorovanillin in cork stoppers, we also considered these compounds but were not able to identify these in our samples.

The overall contribution of chlorinated compounds to today's cork taint situation was relativized in a review by Sefton and Simpson[9] due to the discontinuation of chlorine bleaching in the cork industry. However, in our results such chlorinated compounds were found, probably originating from the chlorination of lignin, then putting up the question of their origin. This is in accordance with the results of Sponholz and Muno.[40] They found trace amounts of pentachlorophenol and trichlorophenol even in non-chlorinated cork stoppers and suggested an environmental influence.

In addition to the previously mentioned compounds, we were able to detect isomers of dichlorophenol and dichloroanisole by targeted screening of the GC × GC chromatograms based on data published in Tables S1 and S2. However, they were not perceived by MDGC-O.

In general, such chlorinated substances are well-known to the wood processing industry as they are produced during the pulp bleaching process.[24,25,49] Chlorinated lignin is degraded to chlorocatechols and chloroguaiacols. Various microorganisms are then able to metabolize them to the corresponding *O*-methylated compounds, producing chloroveratroles.[49,50]

In conclusion, across the individual subgroups with atypical cork taints, the well-known TCA was present besides the hitherto not often described MDMP. Obviously, TCA is a good marker for cork taint in general, but analytical monitoring has to be extended by MDMP, particularly for the detection of atypical cork taint. Specific sensory subgroups showed high intensities of GSM and MIB (moldy and cellarlike) or of IPMP and IBMP (green), probably contributing with their potent individual flavor notes. Other compounds like 1-octen-3-one, guaiacol, and chlorinated compounds discussed above seem to play a minor role, possibly contributing to subtle sensory deviations. Future studies should investigate potential synergisms, as mostly mixtures of different compounds classes were found. Our results are in good agreement with compounds identified by Prat et al.[5] who also concluded that the diversity of microorganisms possibly found on the surface of corks generate their individual mix of substances. Based on some preliminary sensory trials performed in our laboratory, the reduced fruitiness perceived in wines seems to be associated with MDMP migrating from affected cork stoppers into the wine. In a future work this should be investigated in more detail. In this respect, further sensory studies based on recombination experiments are necessary to fully elucidate the role of the compounds described here.

■ ASSOCIATED CONTENT

Supporting Information

Tables S1−S2. The Supporting Information is available free of charge on the ACS Publications website at DOI: 10.1021/acs.jafc.5b02793.

Two tables listing chromatographic, MS, and sensory (GC-O) data for synthesized *O*-methylated chlorophenolic compounds and for chlorophenolic compounds contained in standard mixtures (PDF)

DOI: 10.1021/acs.jafc.5b02793
J. Agric. Food Chem. 2015, 63, 7840−7848

AUTHOR INFORMATION

Corresponding Author

*Phone 49-6321-671-289; fax 49-6321-671-375; e-mail hans-georg.schmarr@dlr.rlp.de.

Notes

The authors declare no competing financial interest.

ACKNOWLEDGMENTS

We are thankful to Rudolf Ohlinger GmbH for providing cork samples, for supporting sensory evaluation and categorization, and for helpful technical discussions and financial support. The donation of reference substances by Juha Knuutinen (University of Jyväskylä, Finland) is highly appreciated. Financial support from the Ministerium für Umwelt, Landwirtschaft, Ernährung, Weinbau und Forsten (MULEWF; Rheinland-Pfalz, Germany) is gratefully acknowledged. C. Legrum is grateful for the Ph.D. scholarship of the "Graduiertenförderung des Landes Rheinland Pfalz".

REFERENCES

(1) Buser, H. R.; Zanier, C.; Tanner, H. Identification of 2,4,6-trichloroanisole as a potent compound causing cork taint in wine. *J. Agric. Food Chem.* **1982**, *30*, 359−62.

(2) Amon, J. M.; Vandepeer, J. M.; Simpson, R. F. Compounds responsible for cork taint in wine. *Aust. N. Z. Wine Ind. J.* **1989**, *4*, 62−69.

(3) Kugler, D.; Rapp, A. Formation and development of volatile compounds in bark cork during cork stopper production. *Dtsch. Lebensm.-Rundsch.* **1997**, *93*, 174−177.

(4) Simpson, R. F.; Capone, D. L.; Sefton, M. A. Isolation and Identification of 2-Methoxy-3,5-dimethylpyrazine, a Potent Musty Compound from Wine Corks. *J. Agric. Food Chem.* **2004**, *52*, 5425−5430.

(5) Prat, C.; Trias, R.; Cullere, L.; Escudero, A.; Antico, E.; Baneras, L. Off-Odor Compounds Produced in Cork by Isolated Bacteria and Fungi: A Gas Chromatography-Mass Spectrometry and Gas Chromatography-Olfactometry Study. *J. Agric. Food Chem.* **2009**, *57*, 7473−7479.

(6) Maga, J. A. Musty/earthy aromas. *Food Rev. Int.* **1987**, *3*, 269−83.

(7) Simpson, R. F. Cork Taint in Wine: A Review of the Causes. *Aust. N. Z. Wine Ind. J.* **1990**, *5*, 286−296.

(8) Chatonnet, P.; Guimberteau, G.; Dubourdieu, D.; Boidron, J. Nature et origine des odeurs de 'moisi'dans les caves. Incidences sur la contamination des vins. *J. Int. Sci. Vigne Vin* **1994**, *28*, 131−151.

(9) Sefton, M. A.; Simpson, R. F. Compounds causing cork taint and the factors affecting their transfer from natural cork closures to wine − a review. *Aust. J. Grape Wine Res.* **2005**, *11*, 226−240.

(10) Lovell, R. T.; Broce, D. Cause of musty flavor in pond-cultured penaeid shrimp. *Aquaculture* **1985**, *50*, 169−174.

(11) Watson, S. B.; Brownlee, B.; Satchwill, T.; Hargesheimer, E. E. Quantitative analysis of trace levels of geosmin and MIB in source and drinking water using headspace SPME. *Water Res.* **2000**, *34*, 2818−2828.

(12) Gerber, N. N.; Lechevalier, H. A. Geosmin, a earthy-smelling substance isolated from actinomycetes. *Appl. Microbiol.* **1965**, *13*, 935−938.

(13) Dickschat, J. S.; Martens, T.; Brinkhoff, T.; Simon, M.; Schulz, S. Volatiles released by a Streptomyces species isolated from the North Sea. *Chem. Biodiversity* **2005**, *2*, 837−865.

(14) Ventura, F.; Quintana, J.; Gomez, M.; Velo-Cid, M. Identification of alkyl-methoxypyrazines as the malodorous compounds in water supplies from northwest spain. *Bull. Environ. Contam. Toxicol.* **2010**, *85*, 160−164.

(15) Mottram, D. S.; Patterson, R. L. S.; Warrilow, E. 2,6-Dimethyl-3-methoxypyrazine: a microbiologically-produced compound with an obnoxious musty odor. *Chem. Ind. (London)* **1984**, 448−449.

(16) Chatonnet, P.; Fleury, A.; Boutou, S. Origin and incidence of 2-methoxy-3,5-dimethylpyrazine, a compound with a "fungal" and "corky" aroma found in cork stoppers and oak chips in contact with wines. *J. Agric. Food Chem.* **2010**, *58*, 12481−12490.

(17) Murray, K. E.; Whitfield, F. B. Occurrence of 3-alkyl-2-methoxypyrazines in raw vegetables. *J. Sci. Food Agric.* **1975**, *26*, 973−86.

(18) Lacey, M. J.; Allen, M. S.; Harris, R. L. N.; Brown, W. V. Methoxypyrazines in Sauvignon blanc grapes and wines. *Am. J. Enol. Vitic.* **1991**, *42*, 103−108.

(19) Sung, Y.-H.; Li, T.-Y.; Huang, S.-D. Analysis of earthy and musty odors in water samples by solid-phase microextraction coupled with gas chromatography/ion trap mass spectrometry. *Talanta* **2005**, *65*, 518−524.

(20) Miller, A., 3rd; Scanlan, R. A.; Lee, J. S.; Libbey, L. M.; Morgan, M. E. Volatile compounds produced in sterile fish muscle (*Sebastes melanops*) by *Pseudomonas perolens*. *Appl. Microbiol.* **1973**, *25*, 257−261.

(21) Pickering, G.; Lin, J.; Riesen, R.; Reynolds, A.; Brindle, I.; Soleas, G. Influence of *Harmonia axyridis* on the Sensory Properties of White and Red Wine. *Am. J. Enol. Vitic.* **2004**, *55*, 153−159.

(22) Chatonnet, P.; Bonnet, S.; Boutou, S.; Labadie, M.-D. Identification and Responsibility of 2,4,6-Tribromoanisole in Musty, Corked Odors in Wine. *J. Agric. Food Chem.* **2004**, *52*, 1255−1262.

(23) Schäfer, V.; Jung, R. Nicht immer ist es der Korken. *Dtsch. Weinbau* **2010**, 14−18.

(24) Knuutinen, J. Analysis of chlorianted guaiacols in spent bleach liquor from a pulp mill. *J. Chromatogr. A* **1982**, *248*, 289−295.

(25) Brownlee, B. G.; MacInnis, G. A.; Noton, L. R. Chlorinated anisoles and veratroles in a Canadian river receiving bleached kraft pulp mill effluent. Identification, distribution, and olfactory evaluation. *Environ. Sci. Technol.* **1993**, *27*, 2450−5.

(26) Pereira, H. Chemical composition and variability of cork from *Quercus suber* L. *Wood Sci. Technol.* **1988**, *22*, 211−218.

(27) Ranz, A.; Korpecka, J.; Lankmayr, E. Optimized derivatization of acidic herbicides with trimethylsilyldiazomethane for GC analysis. *J. Sep. Sci.* **2008**, *31*, 746−752.

(28) Campo, E.; Ferreira, V.; Escudero, A.; Cacho, J. Prediction of the Wine Sensory Properties Related to Grape Variety from Dynamic-Headspace Gas Chromatography−Olfactometry Data. *J. Agric. Food Chem.* **2005**, *53*, 5682−5690.

(29) Bemelmans, J. M. H., Review of Isolation and Concentration Techniques. In *Progress in Flavour Research*, Land, D. G., Nursten, H. E., Eds.; Applied Science: London, 1979; pp 79−88.

(30) Schmarr, H.-G.; Ganß, S.; Sang, W.; Potouridis, T. Analysis of 2-aminoacetophenone in wine using a stable isotope dilution assay and multidimensional gas chromatography−mass spectrometry. *J. Chromatogr. A* **2007**, *1150*, 78−84.

(31) Seethapathy, S.; Gorecki, T. Applications of polydimethylsiloxane in analytical chemistry: A review. *Anal. Chim. Acta* **2012**, *750*, 48−62.

(32) Slabizki, P.; Schmarr, H.-G. Analysis of corky off-flavour compounds at ultra trace level with multidimensional gas chromatography-electron capture detection. *J. Chromatogr. A* **2013**, *1271*, 181−184.

(33) Slabizki, P.; Legrum, C.; Meusinger, R.; Schmarr, H.-G. Characterization and analysis of structural isomers of dimethyl methoxypyrazines in cork stoppers and ladybugs (*Harmonia axyridis* and *Coccinella septempunctata*). *Anal. Bioanal. Chem.* **2014**, *406*, 6429−6439.

(34) Cai, L.; Koziel, J. A.; O'Neal, M. E. Determination of characteristic odorants from *Harmonia axyridis* beetles using in vivo solid-phase microextraction and multidimensional gas chromatography-mass spectrometry-olfactometry. *J. Chromatogr. A* **2007**, *1147*, 66−78.

(35) Kaminski, E.; Stawicki, S.; Wasowicz, E. Volatile Flavor Compounds Produced by Molds of Aspergillus, Penicillium, and Fungi imperfecti. *Appl. Microbiol.* **1974**, *27*, 1001−1004.

DOI: 10.1021/acs.jafc.5b02793
J. Agric. Food Chem. 2015, 63, 7840−7848

(36) La Guerche, S.; Dauphin, B.; Pons, M.; Blancard, D.; Darriet, P. Characterization of some mushroom and earthy off-odors microbially induced by the development of rot on grapes. *J. Agric. Food Chem.* **2006**, *54*, 9193−9200.
(37) Alvarez-Rodriguez, M. L.; Belloch, C.; Villa, M.; Uruburu, F.; Larriba, G.; Coque, J.-J. R. Degradation of vanillic acid and production of guaiacol by microorganisms isolated from cork samples. *FEMS Microbiol. Lett.* **2003**, *220*, 49−55.
(38) Allen, M. S.; Lacey, M. J.; Boyd, S. J. Methoxypyrazines in Red Wines: Occurrence of 2-Methoxy-3-(1-methylethyl)pyrazine. *J. Agric. Food Chem.* **1995**, *43*, 769−772.
(39) Gallois, A.; Kergomard, A.; Adda, J. Study of the biosynthesis of 3-isopropyl-2-methoxypyrazine produced by *Pseudomonas taetrolens*. *Food Chem.* **1988**, *28*, 299−309.
(40) Sponholz, W. R.; Muno, H. Der Korkton - ein mikrobiologisches Problem? *Wein-Wiss.* **1994**, *49*, 17−22.
(41) Simpson, R. F.; Sefton, M. A. Origin and fate of 2,4,6-trichloroanisole in cork bark and wine corks. *Aust. J. Grape Wine Res.* **2007**, *13*, 106−116.
(42) Alvarez-Rodriguez, M. L.; Recio, E.; Coque, J. J. R. The analysis of natural cork stoppers in transversal sections as an effective tool to determine the origin of the taint by 2,4,6-trichloroanisole. *Eur. Food Res. Technol.* **2009**, *230*, 135−143.
(43) Korhonen, I. O. O. Gas-liquid chromatographic analyses. XXXI. Retention increments of isomeric chlorophenols on low-polarity (SE-30) and polar (FFAP) capillary columns. *J. Chromatogr.* **1984**, *315*, 185−200.
(44) Korhonen, I. O. O. Gas-liquid chromatographic analyses. XXVIII. Capillary column studies of chlorinated anisoles. *J. Chromatogr.* **1984**, *294*, 99−116.
(45) Korhonen, I. O. O.; Knuutinen, J.; Jaaskelainen, R. Gas-liquid chromatographic analyses. XXIV. Capillary column studies of the chlorinated veratroles (1,2-dimethoxybenzenes). *J. Chromatogr.* **1984**, *287*, 293−303.
(46) Spadone, J. C.; Takeoka, G.; Liardon, R. Analytical investigation of Rio off-flavor in green coffee. *J. Agric. Food Chem.* **1990**, *38*, 226−233.
(47) Pollnitz, A. P.; Pardon, K. H.; Liacopoulos, D.; Skouroumounis, G. K.; Sefton, M. A. The analysis of 2,4,6-trichloroanisole and other chloroanisoles in tainted wines and corks. *Aust. J. Grape Wine Res.* **1996**, *2*, 184−190.
(48) Caldentey, P.; Fumi, M. D.; Mazzoleni, V.; Careri, M. Volatile compounds produced by microorganisms isolated from cork. *Flavour Fragrance J.* **1998**, *13*, 185−188.
(49) Eriksson, K. E.; Kolar, M. C.; Ljungquist, P.; Kringstad, K. P. Studies on microbial and chemical conversions of chlorolignins. *Environ. Sci. Technol.* **1985**, *19*, 1219−24.
(50) Neilson, A. H.; Allard, A. S.; Hynning, P. A.; Remberger, M.; Landner, L. Bacterial methylation of chlorinated phenols and guaiacols: formation of veratroles from guaiacols and high-molecular-weight chlorinated lignin. *Appl. Environ. Microbiol.* **1983**, *45*, 774−783.

DOI: 10.1021/acs.jafc.5b02793
J. Agric. Food Chem. 2015, 63, 7840−7848

Scheme 1. Schematic Presentation of *V. parahaemolyticus* Detection Using a Colorimetric Aptasensor Based on HRP

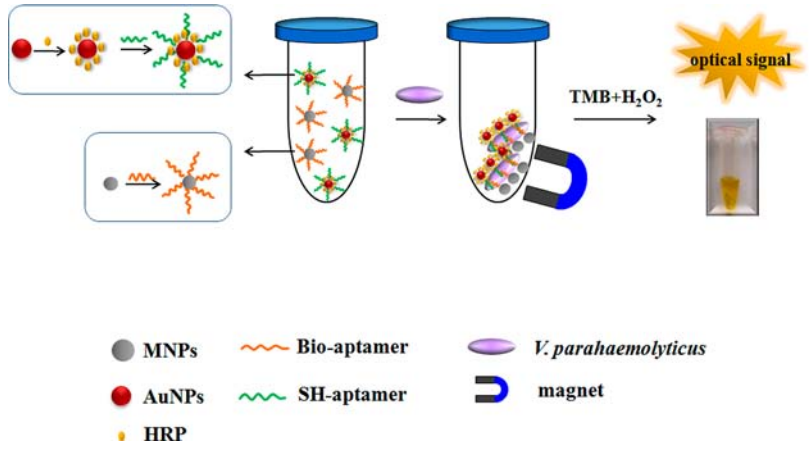

Gold nanoparticles (AuNPs) containing a large amout of horseradish peroxidase (HRP) and aptamer were used as signal amplifiers. MNPs−aptamer−target−aptamer−HRP−AuNPs sandwich complexes would be formed based on the recognition of aptamers and target. In the addition of TMB−H_2O_2, HRP on the sandwich complexes was catalyzed and generated an optical signal.

MATERIALS AND METHODS

Materials. Chloroauric acid ($HAuCl_4$), streptavidin, and 3,3′,5,5′-tetramethylbenzidine (TMB)−H_2O_2 were obtained from Sigma-Aldrich (St. Louis, MO, USA). HRP was purchased from Sangon Biotechnology (Shanghai, China). Trisodium citrate, 1,6-hexanediamine, anhydrous sodium acetate, $FeCl_3{\cdot}6H_2O$, glycol, 25% glutaraldehyde ($OHC(CH_2)_3CHO$), and polyethylene glycol (PEG) were of analytical grade and were purchased from Sinopharm Chemical Reagent Co., Ltd. (Shanghai, China). The *V. parahemolyticus* aptamer was prepared in our laboratory[17] and synthesized and purified by high-performance liquid chromatography (Sangon Biotechnology, Inc.). The sequences of *V. parahemolyticus* aptamers were 5′-SH-TCTAAA-AATGGGCAAAGAAACAGTGACTCGTTGAGATACT-3′ (apt 1) and 5′-bio-TCTAAAAATGGGCAAAGAAACAGTGACTCGTTG-AGATACT-3′ (apt 2).

Instrumentation. Transmission electron microscopy (TEM) images were acquired with JEM-2100HR (TEM, JEOL Ltd., Tokyo, Japan). FT-IR spectra of nanoparticles were measured on a Nicolet Nexus 470 Fourier transform infrared spectrophotometer (Thermo Electron Co., Boston, MA, USA). UV−vis spectra and absorbance were obtained using a UV-1800 spectrophotometer (Shimadzu Co., Kyoto, Japan).

Bacteria Strains. The *V. parahemolyticus* ATCC 17802 was kindly donated by the Animal, Plant and Food Inspection Centre, Jiangsu Entry-Exit Inspection and Quarantine Bureau (Nanjing, China). *V. parahemolyticus* was cultured in alkaline peptone with 3% NaCl (w/v) overnight past the logarithmic phase. One hundred microliters of the bacterial culture was diluted with medium and coated on the agar plates and cultured at 37 °C for 18 h to count colony-forming units (cfu). The rest of the bacteria were collected carefully by centrifugation at 3000 rpm and 4 °C and washed twice in a 1× binding buffer (50 mM Tris-HCl at pH 7.4, 5 mM KCl, 100 mM NaCl, and 1 mM $MgCl_2$) at room temperature.

Synthesis of HRP-Labeled AuNPs. Briefly, all glassware used in the experiment was cleaned with aqua regia (HNO_3/HCl, 3:1, v/v), rinsed thoroughly in ultrapure water, and dried prior to use. Half a milliliter of 1% $HAuCl_4$ solution and 49.5 mL of ultrapure water were heated to the boiling point for 10 min with continuous stirring. Then, 1.5 mL of 1% trisodium citrate was rapidly added, stirred, and boiled for 15 min. The solution color changed from gray to blue, then purple, and finally to wine red during this period. The heating source was removed, and the colloid was cooled to room temperature. HRP-labeled AuNPs were prepared according to the previous study, with slight modifications.[18] The prepared AuNPs (1 mL) were adjusted to pH 8.5 and mixed with 17.5 μL of HRP molecules (1 mg/mL) to incubate for 10 min at 25 °C under gentle shaking. Then, the mixed solution was allowed to stand overnight at 4 °C. After incubation with PEG (0.5%, w/v) for 30 min at 25 °C, the mixture was centrifuged (12000 rpm, 20 min) to remove the unbound HRP molecules and PEG and washed with PBS three times. The final deposition was suspended in 200 μL of PBS and stored at 4 °C for further use.

Synthesis of Aptamer-Functionalized HRP-Labeled AuNPs. HRP-labeled AuNPs modified by aptamer were prepared according to the literature with some modification.[19] This protocol was based on the Au−S interaction between the gold lattice and thiolated aptamer. Briefly, 10 μL of 10 μM apt 1 was added to 190 μL of the already prepared HRP-labeled AuNPs solution and reacted for 16 h. Then the HRP-labeled AuNPs−apt 1 complex was aged with salts (0.1 M NaCl, 10 mM phosphate, pH 7.0) for 40 h. The prepared complex was centrifuged at 12500 rpm for 15 min twice to remove the free aptamer. Then, the HRP-labeled AuNPs−apt 1 was dispersed in 200 μL of binding buffer for subsequent experiments.

Synthesis of MNPs and Aptamer-Functionalized MNPs. The amine-functionalized MNPs were prepared by a one-step solvothermal method according to ref 20. Typically, 6.5 g of 1,6-hexanediamine, 2.0 g of anhydrous sodium acetate, and 1.0 g of $FeCl_3{\cdot}6H_2O$ were dissolved in 30 mL of glycol to form a transparent solution with vigorous stirring at 50 °C. The mixture was subsequently transferred into a Teflon-lined autoclave and heated to 198 °C for 6 h. The product was cooled to room temperature and then washed with water and ethanol (two or three times) followed by drying at 50 °C.

The primary amine groups on the surface of MNPs were activated by glutaraldehyde, allowing amine groups on aptamer oligonucleotides to be covalently attached. Briefly, 1 mg of the MNPs was dispersed in 1 mL of 10 mM phosphate buffer solution (PBS, pH 7.4), and 0.25 mL of 25% glutaraldehyde was added into the solution. The reaction was continued for 2 h at room temperature with gentle shaking, followed by three washings with PBS. The resultant MNPs were dispersed in 1 mL of 10 mM PBS, and 50 μL of apt 2 (10 μM) was added and incubated for 2 h at 37 °C with gentle shaking. Next, the MNPs−apt 2 complexes were magnetically collected and rinsed twice with PBS.

Procedure for Analysis of *V. parahemolyticus*. In a typical experiment, 200 μL of AuNP−HRP−apt 1 and 150 μL of MNPs−apt 2 (1 mg/mL) were first mixed. Then, 50 μL of binding buffer containing various concentrations of *V. parahemolyticus* was added and incubated for 30 min at 37 °C with gentle shaking. After incubation, the magnetic beads were magnetically collected and rinsed with PBS twice. Then, 100 μL of TMB−H_2O_2 solution was added to each tube, and these tubes were incubated at 37 °C for 15 min with gentle shaking. Color development was stopped by adding 100 μL of

DOI: 10.1021/acs.jafc.5b03224
J. Agric. Food Chem. 2015, 63, 7849−7854

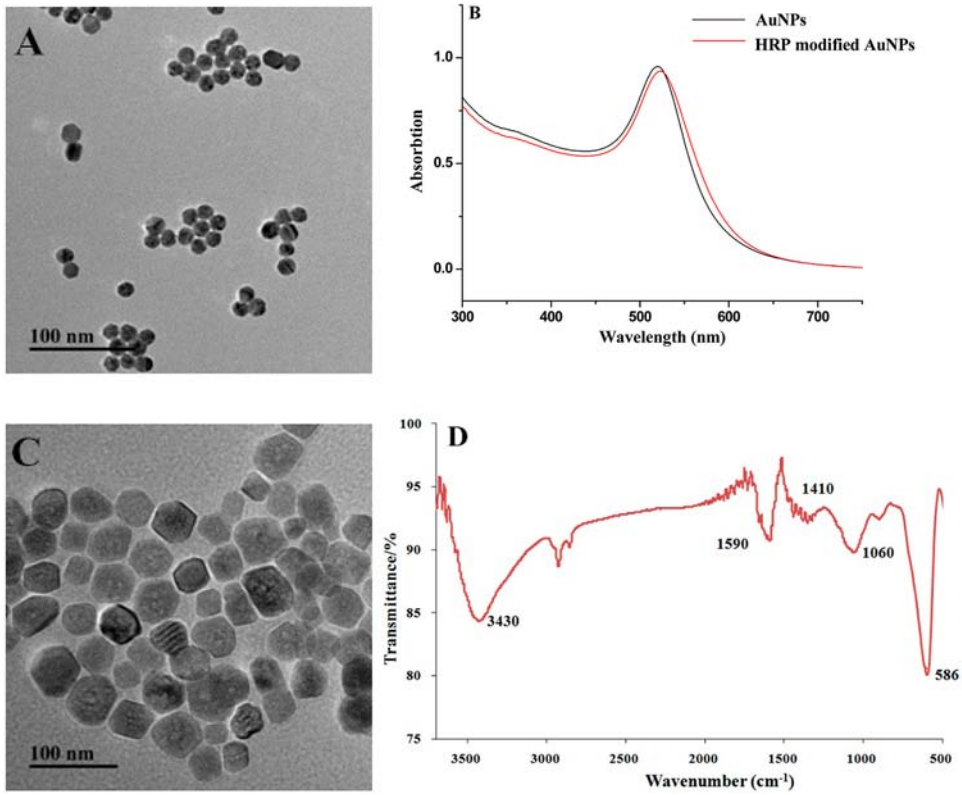

Figure 1. TEM image of AuNPs (A), the UV−vis spectrum of the AuNPs and HRP modified AuNPs (B); TEM image (C), and FT-IR spectrum of MNPs (D).

0.5 M sulfuric acid. After the magnetic separation, the absorbance at 450 nm of the supernatant was read with a UV spectrophotometer.

Real Sample Treatment. The water samples were collected from Tai Lake, the Yellow Sea, laboratory tap water, and groundwater in China, respectively. Then the water samples were filtered through a 0.45 μm filter. Different *V. parahemolyticus* concentrations were then added to the prepared samples for the experiments.

RESULTS AND DISCUSSION

Principle of the Aptasensor. Scheme 1 shows the principle of this developed aptasensor. MNPs were modified with aptamer to act as the capture probe. AuNPs were coated with a large amout of HRP and linked to aptamer to act as signal amplifiers. In the presence of target, aptamers on the surface of both MNPs and AuNPs bound with the target with high affinity and specificity, leading to the formation of MNPs−aptamer−target−aptamer−HRP−AuNPs sandwich complexes. With an extra magnetic field, unbound AuNPs−HRP−aptamer was removed. With the addition of TMB−H_2O_2, HRP on the sandwich complexes was catalyzed and generated an optical signal. With the carrier of AuNPs, a large amount of HRP could be loaded, resulting in an amplified signal, and the sensitivity would be improved.

Characteristics of AuNPs and MNPs. The morphology characteristics of AuNPs are shown in Figure 1A. The AuNPs are monodisperse and spherical with an average size of 15 nm. As shown in Figure 1B, the UV−vis spectrum of AuNPs solution (black line) exhibited a characteristic plasmon absorption peak at 520 nm. After modification of HRP on the surface, the UV−vis spectrum of the AuNP complex showed a small surface plasmon shift from 520 to 524 nm (red line). The shift after modification of AuNPs with HRP was

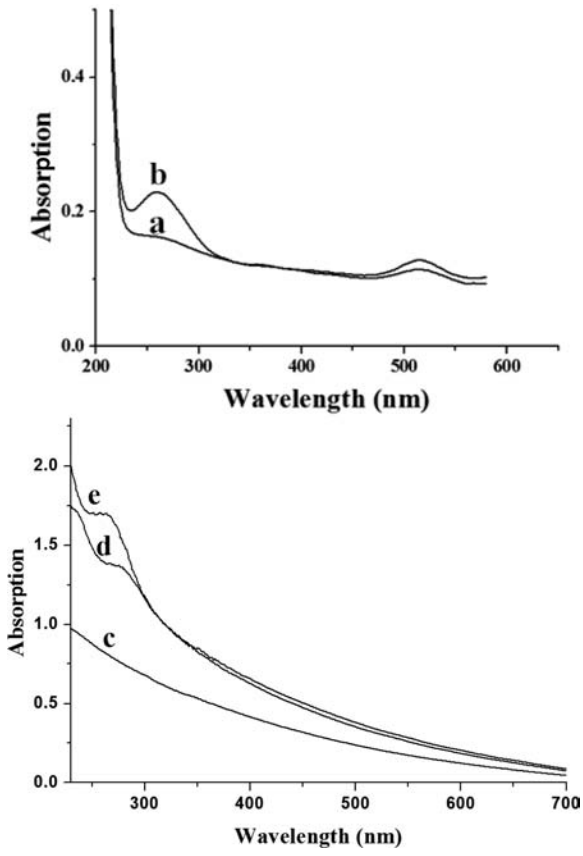

Figure 2. Absorption spectra of bare AuNPs-HRP (a), apt 1-functionalized AuNPs−HRP (b), bare MNPs (c), avidin conjugation to MNPs (d), and apt 2-functionalized MNPs (e).

DOI: 10.1021/acs.jafc.5b03224
J. Agric. Food Chem. 2015, 63, 7849−7854

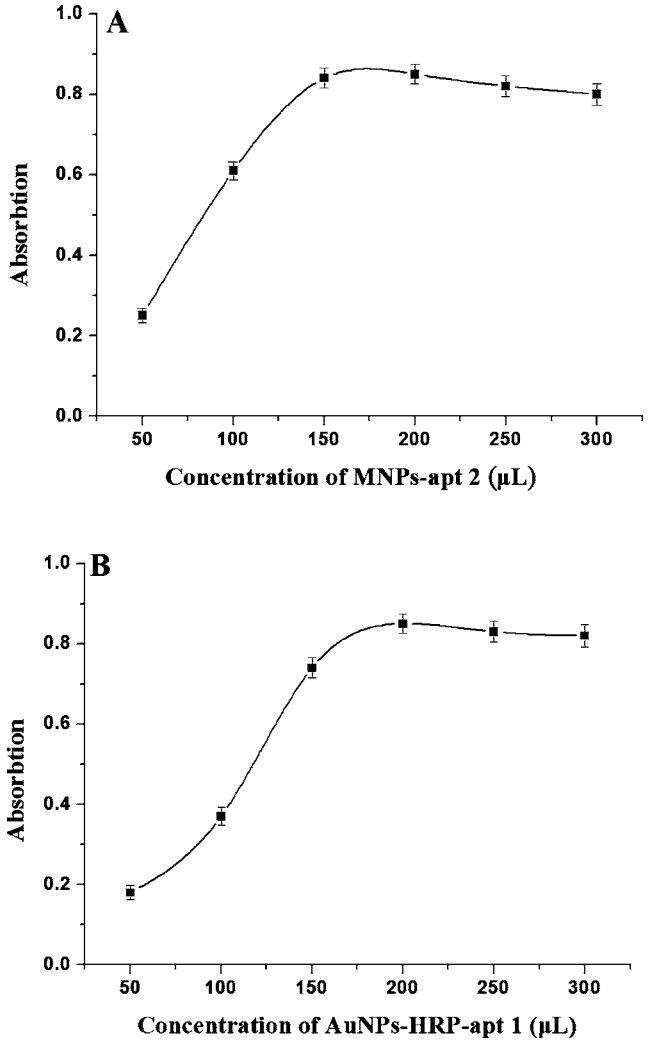

Figure 3. Optimization of MNPs−apt 2 concentration (A) and AuNPs−HRP−apt 1 complex concentration (B). (Concentration of *V. parahemolyticus* was 10^4 cfu/mL.)

attributed to changes in the particle size and the dielectric nature surrounding the AuNPs due to the presence of protein. Both results suggested successful immobilization of HRP onto the AuNPs.

The TEM and FT-IR techniques were used to obtain information about the as-synthesized MNPs. Figure 1C shows a TEM image of the MNPs, indicating a good dispersibility and morphology. Figure 1D shows the FT-IR spectra of MNPs. Formation of MNPs was confirmed by a strong IR band at 586 cm^{-1} that comes from the Fe−O vibrations. The bands around 1590, 1410, and 1060 cm^{-1} were NH bending mode and C−N stretching vibration, respectively. The results from FT-IR revealed that the MNPs have been functionalized with amino groups in the synthetic process.

Characteristics of the Nanoparticles Conjugated to Aptamer. We applied UV−vis spectrophotometer to validate the successful coupling of thiolated labeled aptamer (apt 1) to AuNPs−HRP through Au−S bonding and biotin-labeled aptamer (apt 2) to avidin-modified MNPs through biotin−avidin specific bonding. As shown in Figure 2A, AuNPs−HRP shows an absorbance peak at 524 nm (curve a); with the addition of apt 1, another peak at 260 nm, which is the characteristic absorption of DNA, has been observed (curve b).

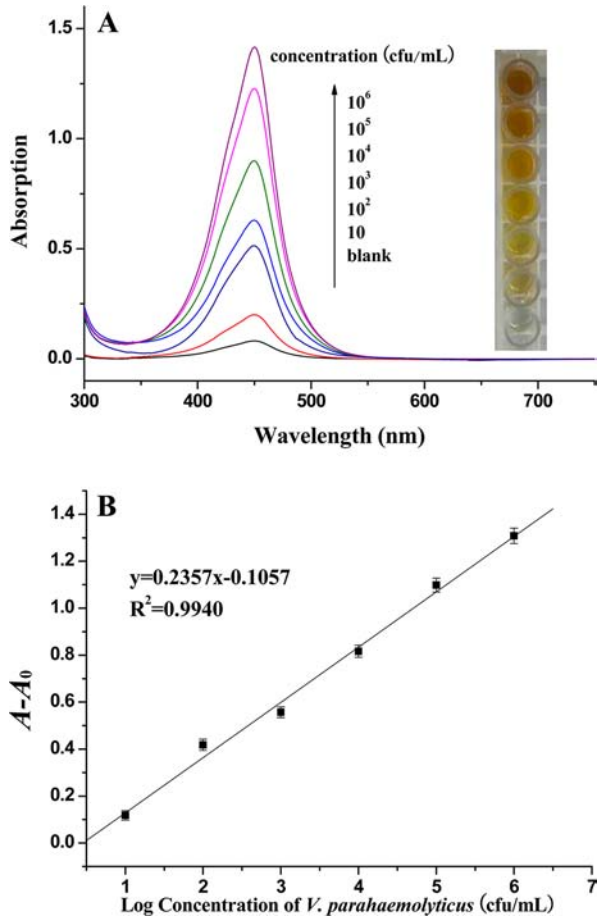

Figure 4. (A) Typical recorded output for the detection of different concentrations of bacteria by the developed method. (Inset) Color change by the naked eye. (B) Standard curve of the related absorbance ($A - A_0$) versus the concentrations of bacteria.

Similarly, no strong absorbance peak was detected for MNPs (curve c). After conjugation to avidin, a new absorption peak at approximately 280 nm, which is a characteristic absorption peak of avidin, was observed (curve d). With the subsequent addition of apt 2, the peak at 260 nm was also observed (curve e). These results demonstrate that aptamers were successfully coated on the nanoparticles.

Optimization for the Assay. According to the principle of the assay, experimental parameters such as the amount of aptamer functionalized MNPs and aptamer functionalized AuNPs−HRP complex would affect the signal response. The effect of the MNPs−apt 2 was first studied. As shown in Figure 3A, response signals increased with increasing MNPs−apt 2, and a maximum was attained at 150 μL (1 mg/mL). Further increase in MNPs−apt 2 concentration had very little additional beneficial effect. Therefore, an optimal volume of 150 μL of MNPs−apt 2 was chosen in subsequent experiments. Figure 3B shows optimization of the AuNPs−HRP−apt 1 complex concentration. The value of A_{450} was found to increase as the AuNPs−HRP−apt 1 complex concentration was increased until 200 μL, after which the A_{450} plateaued and remained constant. Therefore, 200 μL of the AuNPs−HRP−apt 1 complex was used for subsequent experiments.

Analytical Performance. Utilizing the optimal conditions in this system, the catalytic ability of the HRP-labeled AuNPs on TMB oxidation in the presence of different concentrations

DOI: 10.1021/acs.jafc.5b03224
J. Agric. Food Chem. 2015, 63, 7849−7854

of *V. parahemolyticus* was investigated. Results were evaluated in terms of $(A - A_0)$, where A_0 and A are the absorbance of the colorimetric aptasenosr method in the absence and presence of *V. parahemolyticus*, respectively. As displayed in Figure 4A, the absorbance was increased along with the *V. parahemolyticus* concentration. A clear change from light yellow to dark yellow could be obviously differentiated by the naked eye (inset A). As shown in Figure 4B, $A - A_0$ exhibits a good linear relationship with *V. parahemolyticus* in the concentration range from 10 to 10^6 cfu/mL. The linear regression equation of *V. parahemolyticus* is described as $Y = 0.2357x - 0.1057$ ($R^2 = 0.9940$), and the detection limit was found to be 10 cfu/mL.

Specificity, Interference, and Practical Performance of the Assay. To investigate the selectivity of the developed method, the AuNPs and MNPs complexes were employed to detect other pathogenic bacteria, including *Vibrio alginolyticus*, *Vibrio vulnificus*, *Vibrio mimicus*, *Escherichia coli*, *Salmonella typhimurium*, and *Staphylococcus aureus* at a concentration of 10^5 cfu/mL, which might affect the detection of *V. parahemolyticus* in real sample analysis. As shown in Figure 5, it is clearly seen

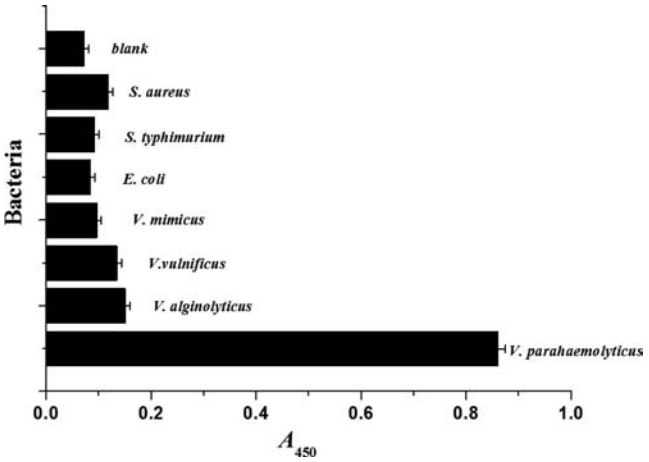

Figure 5. Specificity studies against other bacteria. Concentration of *V. parahemolyticus* was 10^4 cfu/mL, whereas the other concentrations were 10^5 cfu/mL.

that only *V. parahemolyticus* induces a dramatic increase of absorbance, whereas other species produced signals as low as the blank control. These results clearly demonstrated that the developed method is appropriate for the selective detection of *V. parahemolyticus*.

In addition, we examined the effect of a variety of possible interfering substances in this system. We used a range of proteins, small molecules, and ions to determine the selectivity for *V. parahemolyticus*. Under the optimized conditions (the concentration of *V. parahemolyticus* was set as 10^4 cfu/mL), none of the other interferents affected detection signals, even at concentrations as high as 2% bovine serum albumin, 10 μg/mL of immunoglobulin G, 100 mM resorcinol or microcystic toxins, and 500 mM Na^+, K^+, Pb^{2+}, or Cd^{2+}. Thus, the results clearly demonstrate that the developed method specifically identified *V. parahemolyticus* in a real environment.

The practical performance of the developed method was validated with four real water samples. The accuracy of this method was evaluated by determining the recoveries of *V. parahemolyticus* in the water samples by standard addition method. The water samples were spiked with *V. parahemolyticus* at the desired concentrations (2×10^2 and 2×10^3 cfu/mL) and were analyzed by standard culture and colony-counting method. Then, the spiked samples were analyzed by the colorimetric aptasensor method. As can be seen from Table 1, the recoveries of *V. parahemolyticus* in the four real water samples are between 92.0 and 102.0%. These results show that recoveries of *V. parahemolyticus* and the reproducibility are satisfactory.

In summary, we developed a colorimetric aptasensor to detect *V. parahemolyticus* in which AuNPs were used as carriers of HRP and aptamer, and MNPs−aptamer were used as supporting substrates for capture targets. The AuNPs−HRP−aptamer complex loaded a high amount of HRP amplification enzyme; thus, the developed assay based on the AuNPs complex exhibited improved sensitivity. This feature, as well as its convenient magnetic separation, made it a promising alternative to conventional pathogenic bacteria methods. This assay system displayed excellent specificity, sensitivity, and linearity for the quantitative detection of the target molecules, along with the production of a color signal that can be detected by the naked eye. In addition, this method has the potential to detect other bacteria by changing aptamers.

AUTHOR INFORMATION

Corresponding Author

*(N.D.) Phone/fax: +86-510-85917023. E-mail: duannuo@jiangnan.edu.cn.

Funding

This work was partialy supported by NSFC (31401576, 31401575), JUSRP11547, and BK20140155.

Notes

The authors declare no competing financial interest.

REFERENCES

(1) Xu, D.; Wang, Y.; Sun, L.; Liu, H.; Li, J. Inhibitory activity of a novel antibacterial peptide AMPNT-6 from *Bacillus subtilis* against *Vibrio parahaemolyticus* in shrimp. *Food Control* **2013**, *30*, 58−61.

(2) Joseph, S. W.; Colwell, R. R.; Kaper, J. B. *Vibrio parahaemolyticus* and related halophilic vibrios. *Crit. Rev. Microbiol.* **1982**, *10*, 77−124.

(3) Yeung, P. S.; Boor, K. J. Epidemiology, pathogenesis, and prevention of foodborne *Vibrio parahaemolyticus* infections. *Foodborne Pathog. Dis.* **2004**, *1*, 74−88.

(4) Su, Y. C.; Liu, C. *Vibrio parahaemolyticus*: a concern of seafood safety. *Food Microbiol.* **2007**, *24*, 549−558.

(5) Zhang, D. S.; Wang, T. Q.; Gu, J. N. Epidemiological analysis on food poisoning in Guangdong 2007−2011. *South China J. Prev Med.* **2013**, *39* (3), 74−76.

Table 1. Analysis of *V. parahaemolyticus* Cells in Spiked Water Samples by the Developed Method

sample	original value (cfu/mL)	spiked concentration (cfu/mL)	measured concentration (cfu/mL)	recovery (%)
Tai Lake	0	2.0×10^2	$(1.84 \pm 0.15) \times 10^2$	92.0
seawater	0	2.0×10^3	$(1.97 \pm 0.11) \times 10^3$	98.5
laboratory tap water	0	2.0×10^2	$(1.91 \pm 0.28) \times 10^2$	95.5
groundwater	0	2.0×10^3	$(2.04 \pm 0.16) \times 10^3$	102.0

DOI: 10.1021/acs.jafc.5b03224
J. Agric. Food Chem. 2015, 63, 7849−7854

(6) Kumar, B. K.; Raghunath, P.; Devegowda, D.; Deekshit, V. K.; Venugopal, M. N.; Karunasagar, I.; Karunasagar, I. Development of monoclonal antibody based sandwich ELISA for the rapid detection of pathogenic *Vibrio parahaemolyticus* in seafood. *Int. J. Food Microbiol.* **2011**, *145*, 244−249.
(7) Sakata, J.; Kawatsu, K.; Kawahara, R.; Kanki, M.; Iwasaki, T.; Kumeda, Y.; Kodama, H. Production and characterization of a monoclonal antibody against recombinant thermolabile hemolysin and its application to screen for *Vibrio parahaemolyticus* contamination in raw seafood. *Food Control* **2012**, *23*, 171−176.
(8) Zhao, G. Y.; Xing, F. F.; Deng, S. P. A disposable amperometric enzyme immunosensor for rapid detection of *Vibrio parahaemolyticus* in food based on agarose/nano-Au membrane and screen-printed electrode. *Electrochem. Commun.* **2007**, *9*, 1263−1268.
(9) Sun, W.; Zhang, Y. Y.; Ju, X. M.; Li, G. J.; Gao, H. W.; Sun, Z. F. Electrochemical deoxyribonucleic acid biosensor based on carboxyl functionalized grapheme oxide and ploy-L-lysine modified electrode for the detection of tlh gene sequence related to *Vibrio parahaemolyticus*. *Anal. Chim. Acta* **2012**, *752*, 39−44.
(10) Wang, L.; Zhang, J. X.; Bai, H. L.; Li, X.; Lv, P. T.; Guo, A. L. Specific detection of *Vibrio parahaemolyticus* by fluorescence quenching immunoassay based on quantum dots. *Appl. Biochem. Biotechnol.* **2014**, *173*, 1073−1082.
(11) Yi, M. Y.; Ling, L.; Neogi, S. B.; Fan, Y. S.; Tang, D. Y.; Yamasaki, S. J.; Shi, L.; Ye, L. Real time loop-mediated isothermal amplification using a portable fluorescence scanner for rapid and simple detection of *Vibrio parahaemolyticus*. *Food Control* **2014**, *41*, 91−95.
(12) Tuerk, C.; Gold, L. Systematic evolution of ligands by exponential enrichment: RNA ligands to bacteriophage T4 DNA polymerase. *Science* **1990**, *249*, 505−510.
(13) Ellington, A. D.; Szostak, J. W. In vitro selection of RNA that bind specific ligands. *Nature* **1990**, *346*, 818−822.
(14) Nimjee, S. M.; Rusconi, C. P.; Sullenger, B. A. Aptamers: an emerging class of therapeutics. *Annu. Rev. Med.* **2005**, *56*, 555−583.
(15) Nie, J.; Deng, Y.; Deng, Q. P.; Zhang, D. W.; Zhou, Y. L.; Zhang, X. X. A self-assemble aptamer fragment/target complex based high-throughput colorimetric aptasensor using enzyme linked aptamer assay. *Talanta* **2013**, *106*, 309−314.
(16) Park, H. Y.; Paeng, I. R. Development of direct competitive enzyme-linked aptamer assay for determination of dopamine in serum. *Anal. Chim. Acta* **2011**, *685*, 65−73.
(17) Duan, N.; Wu, S. J.; Chen, X. J.; Huang, Y. K.; Wang, Z. P. Selection and identification of a DNA aptamer targeted to *Vibrio parahaemolyticus*. *J. Agric. Food Chem.* **2012**, *60*, 4034−4038.
(18) Wu, W. H.; Li, J.; Pan, D.; Li, J.; Song, S. P.; Rong, M. G.; Li, Z. X.; Gao, J. M.; Lu, J. X. Gold nanoparticle-based enzyme-linked antibody-aptamer sandwich assay for detection of *Salmonella* Typhimurium. *ACS Appl. Mater. Interfaces* **2014**, *6*, 16974−16981.
(19) Wang, Y. L.; Wei, H.; Li, B. L.; Ren, W.; Guo, S. J.; Dong, S. J.; Wang, E. K. SERS opens a new way in aptasensor for protein recognition with high sensitivity and selectivity. *Chem. Commun.* **2007**, *48*, 5220−5222.
(20) Wang, L. Y.; Bao, J.; Wang, L.; Zhang, F.; Li, Y. One-pot synthesis and bioapplication of amine-functionalized magnetite nanoparticles and hollow nanoparticles. *Chem.−Eur. J.* **2006**, *12*, 6341−6347.

DOI: 10.1021/acs.jafc.5b03224
J. Agric. Food Chem. 2015, 63, 7849−7854

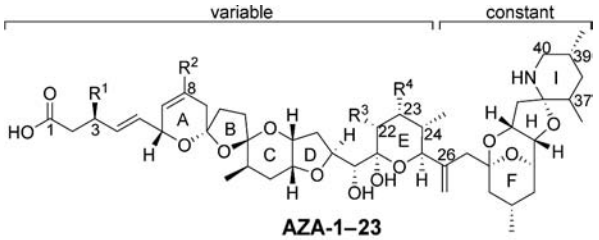

AZA-1–23

	R^1	R^2	R^3	R^4	C-37	MWt
AZA-1	H	H	CH_3	H	S	841.5
37-*epi*-AZA-1	H	H	CH_3	H	R	841.5
AZA-2	H	CH_3	CH_3	H	S	855.5
AZA-3	H	H	H	H	S	827.5
AZA-4	OH	H	H	H	S	843.5
AZA-5	H	H	H	OH	S	843.5
AZA-6	H	CH_3	H	H	S	841.5
AZA-7	OH	H	CH_3	H	S	857.5
AZA-8	H	H	CH_3	OH	S	857.5
AZA-9	OH	CH_3	H	H	S	857.5
AZA-10	H	CH_3	H	OH	S	857.5
AZA-11	OH	CH_3	CH_3	H	S	871.5
AZA-12	H	CH_3	CH_3	OH	S	871.5
AZA-13	OH	H	H	OH	S	859.5
AZA-14	OH	H	CH_3	OH	S	873.5
AZA-15	OH	CH_3	H	OH	S	873.5
AZA-16	OH	CH_3	CH_3	OH	S	887.5
AZA-17	H	H	CO_2H	H	S	871.5
AZA-19	H	CH_3	CO_2H	H	S	885.5
AZA-21	OH	H	CO_2H	H	S	887.5
AZA-23	OH	CH_3	CO_2H	H	S	901.5

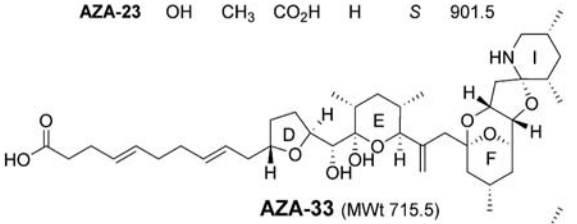

AZA-33 (MWt 715.5)

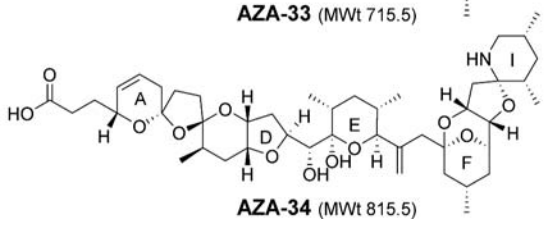

AZA-34 (MWt 815.5)

Figure 1. Structures of selected azaspiracids AZA-1–23 with variable functionality at R^1–R^4 (C-1, C-8, C-22, and C-23), AZA-33, and AZA-34. Note that 37-*epi*-AZA-1 differs stereochemically from AZA-1 at position 37.

Here we report the use of the polyclonal antibody against AZAs,[27] after further immunizations of the same sheep, to develop the first ELISA method for quantitation of these compounds in mussels at concentrations below the current regulatory limit.

MATERIALS AND METHODS

Materials. AZA-1 was from the Marine Institute, Ireland.[30] Bovine serum albumin (BSA), ovalbumin (OVA), L-cysteine, bromine (Br_2), and Freund's incomplete adjuvants were from Sigma-Aldrich (St. Louis, MO, USA). Cationized BSA (cBSA) was prepared according to standard methods.[31] Maxisorp immunoplates (96 flat-bottom wells) were from Nunc (Roskilde, Denmark), poly(vinylpyrrolidone) 25 (PVP) was from Serva Electrophoresis (Heidelberg, Germany), rabbit–anti-sheep horseradish peroxidase conjugate (anti-sheep–HRP) was from Zymed (now Invitrogen, Paisley, UK), and the HRP-substrate K-blue Aq. was from Neogen (Lexington, KY, USA). Certified reference materials (CRMs) of AZA-1, AZA-2, AZA-3, microcystin-LR, and okadaic acid were from the National Research Council of Canada (Halifax, NS, Canada). Quantitative laboratory reference materials (LRMs) of AZA-4–10, AZA-33, AZA-34, and 37-*epi*-AZA-1 were prepared as described by Kilcoyne et al.[32−34] Pinnatoxin G was from Cawthron Institute (Nelson, New Zealand). All other inorganic chemicals and organic solvents were of reagent grade or better. Plate-coating buffer was carbonate buffer (50 mM, pH 9.6). Phosphate-buffered saline (PBS) contained NaCl (137 mM), KCl (2.7 mM), Na_2HPO_4 (8 mM), and KH_2PO_4 (1.5 mM), pH 7.4. ELISA washing buffer (PBST) was 0.05% Tween 20 in PBS. Sample buffer was 10% MeOH (v/v) in PBST, and the antibody buffer consisted of 1% PVP (w/v) in PBST.

Immunogen. The synthetic AZA-hapten-1 was prepared and conjugated to cBSA as described by Forsyth et al.[27] Hapten-2 was prepared by using a novel synthetic route[35] and conjugated to cBSA in the same manner as for hapten-1 to form cBSA–hapten-2 (Figure 2).

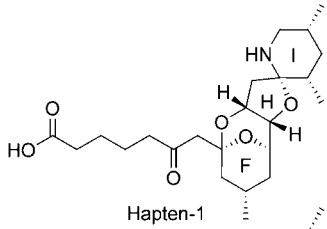

Hapten-1

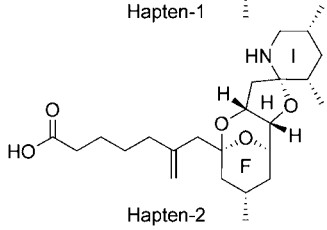

Hapten-2

Figure 2. Structures of hapten-1 and hapten-2 used for preparing immunogens and the initial plate-coating antigen. Both haptens consist of the constant region of AZAs (C-26–C-40).

The immunogen was washed through multiple centrifugations with PBS in a Vivaspin 5.0 mL concentrator with a 10000 MW cutoff (Sartorius Stedim Biotech GmbH, Goettingen, Germany) to remove unreacted hapten and excess reagents. The cBSA–hapten-2 was dispensed as aliquots (1 mg in 100 μL), lyophilized, and stored at −20 °C.

Plate Coating Antigen (OVA–BrAZA-1). Purified AZA-1 (40 μg) was dissolved in MeOH (100 μL), to which was added 50 μL of bromine solution (5 μL of Br_2 in 10 mL of MeOH). After 1 h, the solution was evaporated to dryness under a stream of nitrogen to remove solvent and residual bromine. The residue was dissolved in MeOH (100 μL) and added to a solution of ovalbumin (5 mg) in coating buffer (1 mL). After reaction for 18 h, 1 mL of 5 mg/mL L-cysteine in PBS was added to quench unreacted bromides for 2 h at 4 °C. The OVA–BrAZA-1 was washed, dispensed as aliquots (1 mg in 405 μL), lyophilized, and stored as for the immunogen.

Polyclonal Antibodies. Six sheep were immunized, three in New Zealand (Romney breed) and three in Norway (Nor X breed). The first six immunizations were with cBSA–hapten-1 (Figure 2),[27] followed by five immunizations with cBSA–hapten-2. During these 11 immunizations, the sheep were given three long resting periods to mature the immune response. Immunizations in New Zealand were, in general, performed as described by Briggs et al.[36] (300 μg of immunogen in 1.0 mL of water-in-oil emulsion) and those in Norway as described by Samdal et al.[37]

ELISA. Maxisorp immunoplates were coated overnight at ambient temperature with plate-coating antigen OVA–BrAZA-1 in coating buffer (100 μL/well) at 10 μg/mL. After incubation, the plates were washed four times with PBST. The plates were blocked for 1 h with 1% PVP in PBS (300 μL/well) and then washed twice with PBST.

DOI: 10.1021/acs.jafc.5b02513
J. Agric. Food Chem. 2015, 63, 7855−7861

Noncompetitive assays were used to estimate titers of the sera giving a maximum absorbance of 1.0. This was done by combining equal volumes (50 μL) of sample buffer (10% MeOH in PBST) and dilution series of antisera in antibody buffer (1% PVP in PBST) in wells and incubating for 1 h. After four washings with PBST, bound antibody was detected by adding anti-sheep−HRP conjugate diluted 1:3000 in antibody buffer (100 μL/well) for 2 h and then washing four times before the addition of the HRP substrate (100 μL/well). After 15 min, the reaction was stopped by adding 50 μL of 10% H_2SO_4, and absorbances were measured at 450 nm using a model 1420 Victor^2 plate reader (Wallac, Turku, Finland). All incubations were performed at ∼20 °C.

Competitive ELISAs were performed as described above, by adding appropriate amounts of standard or sample, and antiserum was added to the wells after blocking. Concentrated standards in MeOH, usually AZA-1 (1.31 μg/mL), were diluted in PBST to give a MeOH concentration of 10% and then in a 3-fold dilution series in sample buffer, giving standard concentrations of 0.0066−131 ng/mL. Shellfish extracts in MeOH were similarly diluted 10 times with PBST to adjust for the MeOH concentration, followed by a dilution series in sample buffer. All sample and standard dilutions were analyzed in duplicate wells. The remaining ELISA steps were as described for the noncompetitive ELISA.

Optimization. Optimal concentrations of plate-coating antigen (10 μg/mL), antiserum AgR367-11b (1:8700), and anti-sheep−HRP (1:3000) were determined by checkerboard titrations followed by optimization of the standard curve. Assay standard curves were calculated using logistic treatment of the data. The assay working range was defined as the linear region at 20−80% of maximal absorbance (A_{max}).

Cross-Reactivity. The relative specificity of the immunoassay toward the available AZAs, microcystin-LR, okadaic acid, and pinnatoxin G was determined by assaying a dilution series of each compound in sample buffer. The I_{50} values (molar concentration giving 50% inhibition) are expressed as a percent I_{50} relative to the AZA-1 CRM.

LC-MS/MS Analysis. Quantitation of AZA-1−3 and -6 was performed on a 2695 LC coupled to a Micromass triple-stage quadrupole (TSQ) Ultima (both from Waters, Manchester, UK) operated in multiple reaction monitoring (MRM) mode, with the following transitions: AZA-1, m/z 842.5 → 654.4 and 842.5 → 672.4; AZA-2 m/z 856.5 → 654.4 and 856.5 → 672.4; AZA-3 m/z 828.5 → 640.4 and 828.5 → 658.4; AZA-6 m/z 842.5 → 640.5 and 842.5 → 658.4. The cone voltage was 60 V, and the collision voltage was 40 V; the cone and desolvation gas flows were set at 100 and 800 L/h, respectively, and the source temperature was 150 °C.

Binary gradient elution was used, with phase A consisting of water and phase B of 95% acetonitrile in water (both containing 2 mM ammonium formate and 50 mM formic acid). Chromatography was performed with a 50 mm × 2.1 mm i.d., 3 μm, Hypersil BDS C8 column, with a 10 mm × 2.1 mm i.d. guard column of the same material (Thermo Scientific, Waltham, MA, USA). The gradient was from 30 to 90% B over 8 min at 0.25 mL/min, held for 5 min, then held at 100% B at 0.4 mL/min for 5 min, returned to the initial conditions, and held for 4 min to equilibrate the system. The injection volume was 5 μL, and the column and sample temperatures were 25 and 6 °C, respectively.

Mussel Extracts. AZA-contaminated raw mussel (*M. edulis*) samples, tested as part of the routine monitoring program in Ireland, were selected for analysis. The shellfish were shucked and homogenized using a Waring blender before extraction. Tissue samples were weighed (2 g) and duplicate samples sealed in 50 mL centrifuge tubes. One sample was placed in a water bath and heated to 90 °C for 10 min and then allowed to cool. Both samples were extracted by vortex mixing for 1 min with 9 mL of MeOH and centrifuged at 3950 *g* (5 min), and the supernatants were decanted into 25 mL volumetric flasks. The remaining pellet was further homogenized and extracted using an Ultra Turrax (IKA, Staufen, Germany) for 1 min with an additional 9 mL of MeOH and centrifuged at 3950 *g* for 5 min, and the supernatant was decanted into the same 25 mL volumetric flask, which was then brought to volume with MeOH. Extracts were analyzed by LC-MS/MS and ELISA.

Spiked Tissue Extracts. A mussel extract that had trace levels of AZAs (<0.1 ng/mL by LC-MS/MS) was spiked with an AZA-1 CRM at six concentrations ranging from 5 to 200 ng/mL.

RESULTS AND DISCUSSION

Hapten Synthesis, Conjugation, and Immunogen Preparation. A critical step in designing hapten chemistry to generate an immunoassay with appropriate specificity is deciding which substructures within the analyte should be recognized by the antibodies and which should not be recognized. Just as important, when one is dealing with numerous variants of AZA with modifications at several sites on the parent molecule, is to balance the preference of the antibodies for particular toxin variants to achieve uniform cross-reactivity.

Most AZAs have very similar structures, with all of the published analogues differing in the C3−C16 area and at C-22, C-23 and C-37 in the molecule (Figure 1). Therefore, with the aim of developing an ELISA with broad specificity to AZA-3, and the structurally conserved region C-26−C-40 appeared to be a favorable area to raise antibodies against. Furthermore, the scarcity of AZA-1 at the time, and the development of several partial syntheses of AZAs, made the constant C26−C40 area of the AZAs even more attractive as an immunogen. Subsequent attempts at raising antibodies against AZA-1 itself have encountered problems with toxicity.[28]

Two similar haptens were synthesized (Figure 2), representing the major structural elements of the AZA C26−C40 region (Figure 1). Hapten-1, an AZA fragment with a ketone at the position corresponding to C-26 in AZA-1, was synthesized and initially used for immunization.[27] Later, hapten-2, with an olefinic methylene instead of the ketone in hapten-1, was synthesized to resemble AZAs more closely[35] and used to continue the immunization program. Both haptens were conjugated to cBSA to make them immunogenic. Both immunogens present the structurally conserved region of AZAs (C-26−C-40) to the sheep's immune system, and it was hoped that this would result in antibodies specific to the C-26−C-40 moiety and therefore with good recognition for the wide range of known AZA variants.

Plate-Coating Antigen. For small molecules such as AZAs, ELISA format options are limited to competitive assays, where the antibody can bind either to the AZA on the plate-coating antigen (or on a reporter molecule) or to free AZAs in the sample. Because the assay is based on competition between the plate-coating antigen and the analyte for the antibody's binding sites, the plate-coating chemistry is important in the development of a competitive immunoassay, especially with polyclonal antisera. During assay development, several plate-coating antigens were prepared and tested. These initially used hapten-1, later hapten-2, and finally BrAZA-1 bound to OVA.

Precharacterization of AZA Antibodies. Between immunizations, antisera were screened by indirect ELISA for AZA-specific antibodies initially using OVA−hapten-1 and later OVA−hapten-2. Hapten-specific antibodies were detectable in each antiserum after the first booster injection. Antisera titers were determined by noncompetitive ELISA. Antiserum from sheep AgR367 gave the highest antibody titer (1:200,000) after four immunizations, whereas antisera from other sheep had much lower (5−200-fold) titers. Initial screening for competition, by addition of AZA-1, showed that acceptable standard

DOI: 10.1021/acs.jafc.5b02513
J. Agric. Food Chem. 2015, 63, 7855−7861

curves could be obtained using only antiserum AgR367 (I_{50} at 160 ng/mL). Therefore, this antiserum was used for assay development and optimization.

ELISA Optimization. The ELISA was optimized with 10% MeOH in all samples and standards to be compatible with standard methods for extraction and analysis of mussels for lipophilic algal toxins. To obtain maximum ELISA sensitivity, the assay conditions, such as the concentration of reagents, the blocking agent, and temperature, need to be optimized. Optimal concentrations of assay reagents were determined by checkerboard titrations and standard curves. Criteria used to evaluate optimization were A_{max}, working range (I_{20}–I_{80}), I_{50}, slope of the curve, and limit of quantitation (LOQ; I_{20} based on the mean of several assays and multiplied by the dilution factor (i.e., 10 for MeOH-extracts)). Note that AZAs in mussel tissue were diluted 12.5-fold during extraction with 100% MeOH, and the LOQ for AZAs in mussel tissue is therefore the assay I_{20} multiplied by 12.5 and then 10.

Assay optimization was carried out using bulk collections of antisera taken from sheep AgR367 after 4, 6, 10, and 11 immunizations (AgR367-4b, -6b, -10b, and -11b). Assay sensitivity was increased by using 1% PVP as the blocker, rather than 1% BSA, 1% OVA, 1% Superblock, or 1% casein. Furthermore, use of PVP as the blocker resulted in up to a 5-fold reduction in the amount of antiserum required for the assay.

Assay sensitivity and competition were improved by changing the plate-coating antigen from OVA–hapten-1 to OVA–hapten-2. The working range improved from 17–1054 to 4–62 ng/mL and the sensitivity (I_{50}) from 135 to 16 ng/mL, increasing assay sensitivity approximately 8-fold (using AgR367-4b). With OVA–BrAZA-1 as plate-coating antigen, the optimized assay (average of 13 assays) had a working range (I_{20}–I_{80}) of 0.45–8.6 ng/mL and the I_{50} was 1.9 ng/mL. This change to OVA–BrAZA-1 (and AgR367-11b) made the assay 8-fold more sensitive than with OVA–hapten-2 and 71-fold more sensitive than with OVA–hapten-1. This improved sensitivity may be due the antibodies' affinity for OVA–BrAZA-1 being closer to that for free AZAs (the analyte) than was the case for OVA–hapten-1 and OVA–hapten-2. This would be expected to lead to more effective competition by the analytes and, thus, higher assay sensitivity for AZAs. Standard curves obtained with the CRMs of AZA-1, AZA-2, and AZA-3 are shown in Figure 3.

Specificity. Reduction in the competitive ELISA signal upon addition of AZA-1 indicates competition, but does not show which other target analyte can bind to the antibodies. Often, ELISAs are aimed at recognizing one compound specifically. In this case, we aimed to develop an assay recognizing all AZAs containing the right-hand part of the AZA structure (C-26–C-40). Therefore, the response of the optimized assay to AZA-1–10, AZA-33, AZA-34, and 37-*epi*-AZA-1 (Figure 1), all of which are reported to be toxic,[34] was tested over a range of concentrations to determine cross-reactivity (Table 1). All AZA standards caused concentration-dependent inhibition of antibody binding. On the basis of I_{50} values, the molar cross-reactivities relative to AZA-1 were 75–140% for the CRMs of AZA-1, AZA-2, and AZA-, and 57–145% for LRMs of the remaining AZAs (Table 1). The antibodies in the assay therefore have a similar affinity for these other AZAs as they do for the reference standard, AZA-1. Similar tests with microcystin-LR (50 ng/mL), okadaic acid (1.4 μg/mL), and pinnatoxin G (1.0 μg/mL) resulted in no inhibition. Cross-reactivity to these toxins is <1% with the antibody, indicating that the antibody binds specifically to AZAs.

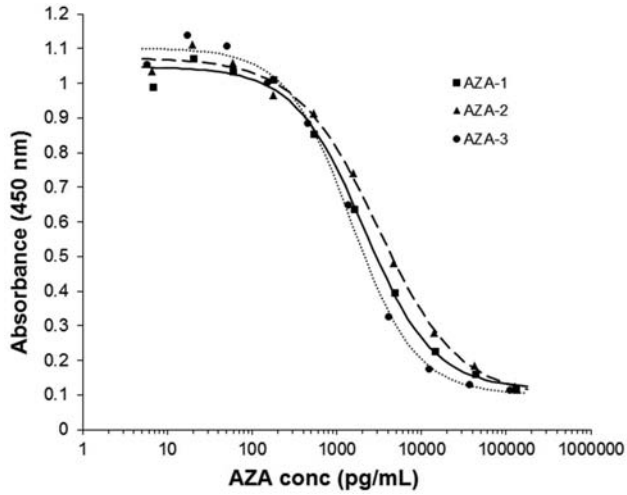

Figure 3. Standard curves obtained with CRMs of AZA-1, AZA-2, and AZA-3 in the AZA-ELISA using antibody AgR367-11b on plate coater OVA–BrAZA-1.

Table 1. Molar Cross-Reactivities of a Series of AZA Analogues in the AZA-ELISA

			assay range[a] (pg/mL)			
compound	origin	*n*	I_{20}	I_{80}	I_{50}	% CR[b]
AZA-1[c]	NRC	13	428	8047	1828	100
AZA-2[c]	NRC	6	504	14462	2666	75
AZA-3[c]	NRC	6	335	5228	1312	140
AZA-4[d]	MI	3	369	3658	1157	145
AZA-5[d]	MI	4	472	7558	1845	100
AZA-6[d]	MI	3	315	4595	1195	144
AZA-7[d]	MI	4	446	7642	1824	72
AZA-8[d]	MI	3	431	11202	2173	95
AZA-9[d]	MI	3	392	6186	1533	114
AZA-10[d]	MI	4	425	6497	1652	128
AZA-33[d]	MI	3	609	13289	2764	57
AZA-34[d]	MI	3	302	9364	1630	110
37-*epi*-AZA-1[d]	MI	3	440	15315	2586	77

[a] I_{20}, I_{50}, and I_{80} are the concentrations of analogue giving 20, 50, and 80% inhibition, respectively, of binding of antibody to the coating antigen (OVA–BrAZA-1). All values are corrected for AZA impurities in the standards. [b] Molar cross-reactivity; CR = 100 × (I_{50} AZA-1 CRM)/(I_{50} analogue). Intra-assay variation (CV) was 6–24% for I_{50} values based on 3–13 competition curves. [c] CRM. [d] LRM

Cross-reactivity studies indicated that recognition of analogues by antibodies in the ELISA was slightly reduced for AZA-2, AZA-7, AZA-33, and 37-*epi*-AZA-1 (Table 1), whereas it was slightly increased for AZA-3, AZA-4, AZA-6, and AZA-10. This may indicate that substitution of the methyl group at C-22 (R^3) for hydrogen slightly favors binding to the antibody, although AZA-5 does not show the same increase. The substituents at C-3, C-8, and C-23 (R^1, R^2, and R^4) seem to have less influence on antibody binding, which is as expected given that these substituents are not part of the C-26–C-40 present in the immunogens. A lack of standards of the other AZAs prevented characterization of the cross-reactivity of AZA-11 to AZA-32, but it is anticipated that the antibodies will recognize most of the known analogues, because they all

DOI: 10.1021/acs.jafc.5b02513
J. Agric. Food Chem. 2015, 63, 7855–7861

contain the C-26−C-40 region of the AZA (Figure 1). Furthermore, that the ELISA gave essentially identical results from cooked and uncooked mussels suggests that the 22-carboxy congeners AZA-17, -19, -21, and -23 also have similar cross-reactivities to their corresponding thermal degradation products (AZA-3, -6, -4 and -9, respectively).[38] Cross-reactivity with AZA-33 (57%) confirms that rings A−D are not included in the antibody binding site.

37-*epi*-AZA-1 is identical to AZA-1 except for a stereochemical change at C-37, where the methyl group is orientated axially (37*R*) instead of equatorially (37*S*) as in all the other AZA analogues. The ELISA cross-reactivity was 77% for 37-*epi*-AZA-1. This structural change is in the "constant region" and may explain the slightly lower response, but nevertheless suggests that antibody binding is not especially sensitive to stereochemistry at C-37.

The ELISA therefore appears to detect all of the reported AZA congeners. It should be noted, however, that although the assay estimates the total content of AZAs, this does not necessarily reflect the toxicity of the sample because different congener structures vary in toxicity.

Standards. The availability of reliable standards is critical for the development and validation of analytical methods. One obstacle in this study was the relatively limited array of AZA analogues that were available for cross-reactivity studies. The criteria for what constitutes a good standard may vary between analytical methods. For example, standards adequate for LC-MS may contain contaminating analogues that do not interfere with quantitation due to differences in mass and retention time. However, for antibody-based detection, contaminating AZA analogues can affect the response. Even for highly pure standards, all analytical methods require that standards are quantitatively accurate to produce reliable results. Consequently, cross-reactivity data should be regarded only as indicative, except where high-purity quantitatively verified standards have been used. When calculating cross-reactivities for the various AZA standards, the known impurities in the CRMs and LRMs were corrected for. However, because the AZA standards were relatively pure, these corrections resulted in only minor changes to the calculated cross-reactivities in Table 1.

Preliminary Validation. Preliminary investigations with methanolic extracts from mussels, scallops, oysters, and algal extracts showed minimal matrix effects (data not shown). The LOQ for total AZAs in whole shellfish was calculated to be 57 μg/kg (2 g extracted with 25 mL of MeOH).

AZA-1 was spiked into extracts of a natural sample of Irish mussel previously shown by LC-MS to contain only trace levels of AZAs. The sample was spiked with six concentrations of AZA-1 (Figure 4A). Analyses determined by the optimized ELISA and LC-MS/MS were compared with the calculated AZA-1 concentrations. The results for AZAs by ELISA and for AZA-1 by LC-MS/MS were very similar (Figure 4A), and the ELISA correlates well with LC-MS/MS (within ±20%) between 10 and 150 ng/mL (corresponding to 125−1875 μg/kg in whole shellfish). Both methods, however, appeared to underestimate the levels for very high concentrations (12−16 times the regulatory level of AZA-1). The average recovery by ELISA was 102%, well within the acceptable limits for assay recovery (100 ± 20%).

To confirm its applicability to real samples, the ELISA was used to analyze AZAs in 13 shellfish samples (*M. edulis*). Of these 13 samples, all were extracted as raw tissues and analyzed,

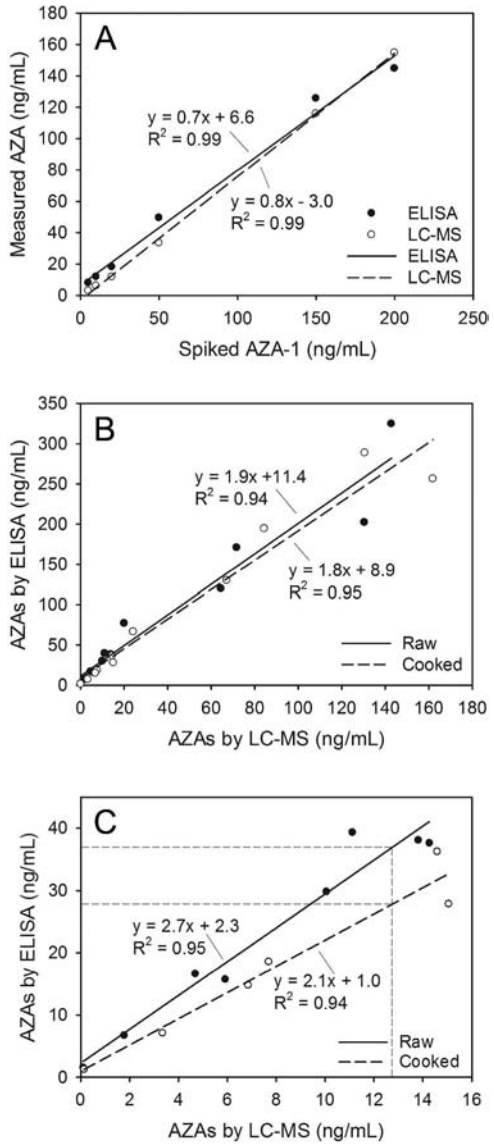

Figure 4. Comparison of total AZAs determined by ELISA and LC-MS/MS for samples of mussels (*M. edulis*): (A) spiking of a mussel sample with 5, 10, 20, 50, 150, and 200 ng/mL of AZA-1; (B) analysis of 13 raw (●) and 11 cooked (○) naturally contaminated samples for AZA-1, -2, -3, and -6 by LC-MS and for total AZAs by ELISA; (C) expansion of graph B showing the data from 0 to 16 ng/mL by LC-MS/MS, that is, close to and under the regulatory limit. The vertical dotted line at 12.8 ng/mL corresponds to the regulatory limit for AZA-1−3 in European shellfish.

whereas 11 were also extracted as cooked shellfish tissues, without changing the water content, and analyzed (Figure 4B,C). For comparison, all samples were also analyzed by ELISA for AZAs and by LC-MS for AZA-1, AZA-2, AZA-3, and AZA-6. Figure 4B shows results for all samples (13 raw and 11 cooked), whereas Figure 4C shows only results up to around the regulatory level of 160 μg/kg,[25] which corresponds to 12.8 ng/mL in the extracts (8 raw and 6 cooked samples). ELISA results were ∼2-fold those obtained by analysis with LC-MS/MS for AZA1−3 and AZA-6. Presumably this is due to the presence of minor AZAs that were not targeted in the LC-MS/MS analysis, because LC-MS/MS and the ELISA showed an excellent 1:1 correlation for AZA-1-spiked shellfish. Results by ELISA were essentially identical regardless of whether the

DOI: 10.1021/acs.jafc.5b02513
J. Agric. Food Chem. 2015, 63, 7855−7861

shellfish had been cooked or not, whereas LC-MS/MS results were ~20% lower for uncooked shellfish. This difference is attributable to the heat-promoted conversion of the mussel metabolites AZA-17 and AZA-19 (not analyzed for by LC-MS/MS), present in the uncooked tissue, into AZA-3 and AZA-6 (which were analyzed for) by cooking and suggests that the antibodies recognize AZA-17 and AZA-19 with approximately the same cross-reactivity as for AZA-3 and AZA-6.

The method used for extracting azaspiracids from mussels was unfortunately not well suited to the AZA-ELISA. Extraction with a lower volume of solvent, and containing a higher percentage of water (so that a smaller dilution of the extract was required), would be expected to considerably improve the LOQ of the ELISA for total AZAs in mussels.

In summary, we report the development of the first ELISA for the detection of AZAs. The antibodies were developed using two synthetic fragments of AZA, respectively hapten-1, as reported previously,[27] and with further immunizations with conjugates of the improved hapten-2.[35] In this paper we have applied the resulting antibodies to the development of an AZA-ELISA. This ELISA is specific for AZAs, with similar cross-reactivity to a broad range of AZA analogues, so that the total content of analogues and metabolites can be measured. The antiserum together with the plate-coating antigen (OVA−BrAZA-1) provides an ELISA with good sensitivity and broad specificity.

This ELISA for AZAs is a sensitive and rapid analytical method that uses inexpensive instrumentation and is suitable for use as a tool for shellfish toxin analysis. The broad specificity of the antibodies means that the ELISA provides an estimate of the total content of AZA analogues present in the sample. The AZA-ELISA detects all the analogues that the European Commission[26] currently require testing for, that is, AZA-1, AZA-2, and AZA-3 (with cross-reactivities of 100, 75, and 140%, respectively). In addition, the ELISA can also detect a wide range of other AZAs, including AZA-17 and AZA-19, which are converted to AZA-3 and AZA-6, respectively, during cooking. Thus, the assay detects all of the regulated AZAs, as well as some of their precursors, and in addition it detects other AZA metabolites such as AZA-4, AZA-5, and AZA-7−10, which are also known to be toxic.[33] Comparison of the ELISA and LC-MS should facilitate detection of new metabolites of AZAs in a similar manner as reported for yessotoxins.[39]

■ ASSOCIATED CONTENT

Supporting Information

The Supporting Information is available free of charge on the ACS Publications website at DOI: 10.1021/acs.jafc.5b02513.

ELISA inhibition curves on three different coaters, molar cross-reactivities of antiserum AgR367-11b with a series of AZA analogues (extended version), and tabulated impurities in the AZA standards (PDF)

■ AUTHOR INFORMATION

Corresponding Author

*(I.A.S.) Phone: +47 2321 6226. Fax: +47 2321 6201. E-mail: ingunn.samdal@vetinst.no.

Present Address

Δ(J.X.) Shanghai Hengrui Pharmaceutical Co., Ltd., No. 279 Wenjing Road, Minhang District, Shanghai City, People's Republic of China.

Funding

This study was supported by Grant 139593/140 from the Norwegian Research Council, by the BIOTOX project (partly funded by the European Commission, through the Sixth Framework Programme Contract 514074, priority Food Quality and Safety), by the European Union Seventh Framework Programme (FP7/2007-2013) under the ECsafe-SEAFOOD project (Grant Agreement 311820), and by the Norwegian Veterinary Institute. This study was also supported by the New Zealand Foundation for Research, Science and Technology (International Investment Opportunities Fund, Grant C10X0406. This publication was also made possible by Grant ES10615 from the National Institute of Environmental Health Sciences (NIEHS), NIH, USA (C.J.F.). Its contents are solely the responsibility of the authors and do not necessarily represent the official views of the NIEHS, NIH. Support was also received from the Marine Institute and the Marine Research Sub-Programme of the National Development Plan 2007-2013 (PBA/AF/08/001(01)), cofinanced under the European Regional Development Fund.

Notes

The authors declare no competing financial interest.

■ ACKNOWLEDGMENTS

Sheep for antibody development were provided and cared for by farm staff at AgResearch, Hamilton, New Zealand, and The Animal Production Experimental Centre at The Norwegian University of Life Sciences, Ås, Norway. Immunizations and blood sampling were done with assistance from Arne Flåøyen and Jens Børsum at the Norwegian Veterinary Institute and Colleen Podmore (including initial antiserum screening) at AgResearch. All animal experiments were in accordance with the three R's, laws, and regulations and approved by the AgResearch Ruakura Animal Ethics Committee (Application 11832) or the Norwegian Animal Research Authority. We thank Dr. Y. Ding for synthetic assistance. Standards of AZA-1−3 were kindly provided by M. A. Quilliam at National Research Council of Canada.

■ ABBREVIATIONS USED

AZA, azaspiracid; BSA, bovine serum albumin; BrAZA-1, brominated AZA-1; cBSA, cationized BSA; CRM, certified reference material; ELISA, enzyme-linked immunosorbent assay; HRP, horseradish peroxidase; LOQ, limit of quantitation; LRM, laboratory reference material; OVA, ovalbumin; PBS, phosphate-buffered saline; PBST, PBS with 0.05% Tween 20; PVP, poly(vinylpyrrolidone) 25

■ REFERENCES

(1) McMahon, T.; Silke, J. Winter toxicity of unknown aetiology in mussels. *Harmful Algal News* **1996**, *14*, 2 http://hab.ioc-unesco.org/index.php?option=com_content&view=article&id=22&Itemid=0.

(2) Satake, M.; Ofuji, K.; Naoki, H.; James, K. J.; Furey, A.; McMahon, T.; Silke, J.; Yasumoto, T. Azaspiracid, a new marine toxin having unique spiro ring assemblies, isolated from Irish mussels. *J. Am. Chem. Soc.* **1998**, *120*, 9967−9968.

(3) McMahon, T.; Silke, J. Re-occurrence of winter toxicity. *Harmful Algal News* **1998**, *17*, 12 http://hab.ioc-unesco.org/index.php?option=com_content&view=article&id=22&Itemid=0.

(4) Ofuji, K.; Satake, M.; McMahon, T.; Silke, J.; James, K. J.; Naoki, H.; Oshima, Y.; Yasumoto, T. Two analogs of azaspiracid isolated from mussels, *Mytilus edulis*, involved in human intoxication in Ireland. *Nat. Toxins* **1999**, *7*, 99−102.

DOI: 10.1021/acs.jafc.5b02513
J. Agric. Food Chem. 2015, 63, 7855−7861

(5) Ofuji, K.; Satake, M.; McMahon, T.; James, K. J.; Naoki, H.; Oshima, Y.; Yasumoto, T. Structures of azaspiracid analogs, azaspiracid-4 and azaspiracid-5, causative toxins of azaspiracid poisoning in Europe. *Biosci. Biotech. Biochem.* **2001**, *65*, 740−742.
(6) Nicolaou, K. C.; Koftis, T. V.; Vyskocil, S.; Petrovic, G.; Ling, T. T.; Yamada, Y. M. A.; Tang, W. J.; Frederick, M. O. Structural revision and total synthesis of azaspiracid-1, part 2: definition of the ABCD domain and total synthesis. *Angew. Chem., Int. Ed.* **2004**, *43*, 4318−4324.
(7) Nicolaou, K. C.; Vyskocil, S.; Koftis, T. V.; Yamada, Y. M. A.; Ling, T. T.; Chen, D. Y. K.; Tang, W. J.; Petrovic, G.; Frederick, M. O.; Li, Y. W.; Satake, M. Structural revision and total synthesis of azaspiracid-1, part 1: Intelligence gathering and tentative proposal. *Angew. Chem., Int. Ed.* **2004**, *43*, 4312−4318.
(8) Hess, P.; McCarron, P.; Krock, B.; Kilcoyne, J.; Miles, C. O. Azaspiracids: chemistry, biosynthesis, metabolism, and detection. In *Seafood and Freshwater Toxins. Phamacology, Physiology, and Detection*, 3rd ed.; Botana, L. M., Ed.; CRC Press: Boca Raton, FL, USA, 2014; pp 799−822.
(9) Magdalena, A. B.; Lehane, M.; Krys, S.; Fernandez, M. L.; Furey, A.; James, K. J. The first identification of azaspiracids in shellfish from France and Spain. *Toxicon* **2003**, *42*, 105−108.
(10) Aasen, J. A. B.; Torgersen, T.; Dahl, E.; Naustvoll, L. J.; Aune, T. *Confirmation of azaspiracids in mussels in Norwegian coastal areas, and full profile at one location*. In *Proceedings of 5th International Conference on Molluscan Shellfish Safety in 2004*; Henshilwood, K., Deegan, B., McMahon, T., Cusack, C., Keaveney, S., Silke, J., O'Cinneide, M., Lyons, D., Hess, P., Eds.; Galway, Ireland, 2006; pp 162−169.
(11) James, K. J.; Furey, A.; Lehane, M.; Ramstad, H.; Aune, T.; Hovgaard, P.; Morris, S.; Higman, W.; Satake, M.; Yasumoto, T. First evidence of an extensive northern European distribution of azaspiracid poisoning (AZP) toxins in shellfish. *Toxicon* **2002**, *40*, 909−915.
(12) Furey, A.; Moroney, C.; Magdalena, A. B.; Saez, M. J. F.; Lehane, M.; James, K. J. Geographical, temporal, and species variation of the polyether toxins, azaspiracids, in shellfish. *Environ. Sci. Technol.* **2003**, *37*, 3078−3084.
(13) Torgersen, T.; Bremnes, N. B.; Rundberget, T.; Aune, T. Structural confirmation and occurrence of azaspiracids in Scandinavian brown crabs (*Cancer pagurus*). *Toxicon* **2008**, *51*, 93−101.
(14) Amzil, Z.; Sibat, M.; Royer, F.; Savar, V. First report on azaspiracid and yessotoxin groups detection in French shellfish. *Toxicon* **2008**, *52*, 39−48.
(15) Taleb, H.; Vale, P.; Amanhir, R.; Benhadouch, A.; Sagou, R.; Chafik, A. First detection of azaspiracids in mussels in north west Africa. *J. Shellfish Res.* **2006**, *25*, 1067−1070.
(16) Twiner, M. J.; Rehmann, N.; Hess, P.; Doucette, G. J. Azaspiracid shellfish poisoning: a review on the chemistry, ecology, and toxicology with an emphasis on human health impacts. *Mar. Drugs* **2008**, *6*, 39−72.
(17) Alvarez, G.; Uribe, E.; Avalos, P.; Marino, C.; Blanco, J. First identification of azaspiracid and spirolides in *Mesodesma donacium* and *Mulinia edulis* from northern Chile. *Toxicon* **2010**, *55*, 638−641.
(18) Lopez-Rivera, A.; O'Callaghan, K.; Moriarty, M.; O'Driscoll, D.; Hamilton, B.; Lehane, M.; James, K. J.; Furey, A. First evidence of azaspiracids (AZAs): a family of lipophilic polyether marine toxins in scallops (*Argopecten purpuratus*) and mussels (*Mytilus chilensis*) collected in two regions of Chile. *Toxicon* **2010**, *55*, 692−701.
(19) Gu, H.; Luo, Z.; Krock, B.; Witt, M.; Tillmann, U. Morphology, phylogeny and azaspiracid profile of *Azadinium poporum* (Dinophyceae) from the China Sea. *Harmful Algae* **2013**, *21*−*22*, 64−75.
(20) Ueoka, R.; Ito, A.; Izumikawa, M.; Maeda, S.; Takagi, M.; Shinya, K.; Yoshida, M.; van Soest, R.; Matsunaga, S. Isolation of azaspiracid-2 from a marine sponge *Echinoclathria* sp. as a potent cytotoxin. *Toxicon* **2009**, *53*, 680−684.
(21) Krock, B.; Tillmann, U.; John, U.; Cembella, A. D. Characterization of azaspiracids in plankton size-fractions and isolation of an azaspiracid-producing dinoflagellate from the North Sea. *Harmful Algae* **2009**, *8*, 254−263.
(22) Tillmann, U.; Elbrachter, M.; Krock, B.; John, U.; Cembella, A. D. *Azadinium spinosum* gen. et sp nov (Dinophyceae) identified as a primary producer of azaspiracid toxins. *Eur. J. Phycol.* **2009**, *44*, 63−79.
(23) Krock, B.; Tillmann, U.; Voß, D.; Koch, B. P.; Salas, R.; Witt, M.; Potvin, É.; Jeong, H. J. New azaspiracids in *Amphidomataceae* (Dinophyceae). *Toxicon* **2012**, *60*, 830−839.
(24) Krock, B.; Tillmann, U.; Witt, M.; Gu, H. Azaspiracid variability of *Azadinium poporum* (Dinophyceae) from the China Sea. *Harmful Algae* **2014**, *36*, 22−28.
(25) EC. Commission decision of 15 March 2002 laying down detailed rules for the implementation of Council Directive 91/492/EEC as regards the maximum levels and the methods of analysis of certain marine biotoxins in bivalve molluscs, echinoderms, tunicates and marine gastropods. (2002/225/EC). *Off. J. Eur. Communities* **2002**, *L75*, 62−64.
(26) EC. Commission regulation (EU) No. 15/2011 of 10 January 2011 amending Regulation (EC) No. 2074/2005 as regards recognised testing methods for detecting marine biotoxins in live bivalve molluscs. *Off. J. Eur. Communities* **2011**, *L6*, 3−6.
(27) Forsyth, C. J.; Xu, J. Y.; Nguyen, S. T.; Samdal, I. A.; Briggs, L. R.; Rundberget, T.; Sandvik, M.; Miles, C. O. Antibodies with broad specificity to azaspiracids by use of synthetic haptens. *J. Am. Chem. Soc.* **2006**, *128*, 15114−15116.
(28) Frederick, M. O.; Marin, S. D.; Janda, K. D.; Nicolaou, K. C.; Dickerson, T. J. Monoclonal antibodies with orthogonal azaspiracid epitopes. *ChemBioChem* **2009**, *10*, 1625−1629.
(29) Rodriguez, L. P.; Vilarino, N.; Louzao, M. C.; Dickerson, T. J.; Nicolaou, K. C.; Frederick, M. O.; Botana, L. M. Microsphere-based immunoassay for the detection of azaspiracids. *Anal. Biochem.* **2014**, *447*, 58−63.
(30) Kilcoyne, J.; Keogh, A.; Clancy, G.; LeBlanc, P.; Burton, I.; Quilliam, M.; Hess, P.; Miles, C. O. Improved isolation procedure for azaspiracids from shellfish, structural elucidation of azaspiracid-6, and stability studies. *J. Agric. Food Chem.* **2012**, *60*, 2447−2455.
(31) Hermanson, G. T. *Bioconjugate Techniques*; Academic Press: San Diego, CA, USA, 1996.
(32) Kilcoyne, J.; McCarron, P.; Twiner, M. J.; Nulty, C.; Crain, S.; Quilliam, M. A.; Rise, F.; Wilkins, A. L.; Miles, C. O. Epimers of azaspiracids: isolation, structural elucidation, relative LC-MS response, and *in vitro* toxicity of 37-*epi*-azaspiracid-1. *Chem. Res. Toxicol.* **2014**, *27*, 587−600.
(33) Kilcoyne, J.; Nulty, C.; Jauffrais, T.; McCarron, P.; Herve, F.; Foley, B.; Rise, F.; Crain, S.; Wilkins, A. L.; Twiner, M. J.; Hess, P.; Miles, C. O. Isolation, structure elucidation, relative LC-MS response, and *in vitro* toxicity of azaspiracids from the dinoflagellate *Azadinium spinosum*. *J. Nat. Prod.* **2014**, *77*, 2465−2474.
(34) Kilcoyne, J.; Twiner, M. J.; McCarron, P.; Crain, S.; Giddings, S.; Wilkins, A. L.; Hess, P.; Miles, C. O. Structure elucidation, relative LC-MS and *in vitro* toxicity of azaspiracids 7−10 isolated from blue mussels (*Mytilus edulis*). *J. Agric. Food Chem.* **2015**, *63*, 5083−5091.
(35) Xu, J. *Progress towards the Total Synthesis of Azaspiracids*. Ph.D. thesis, Department of Chemistry, University of Minnesota, Minneapolis, MN, USA, 2006; pp 34−64.
(36) Briggs, L. R.; Miles, C. O.; Fitzgerald, J. M.; Ross, K. M.; Garthwaite, I.; Towers, N. R. Enzyme-linked immunosorbent assay for the detection of yessotoxin and its analogues. *J. Agric. Food Chem.* **2004**, *52*, 5836−5842.
(37) Samdal, I. A.; Ballot, A.; Løvberg, K. E.; Miles, C. O. Multihapten approach leading to a sensitive ELISA with broad cross-reactivity to microcystins and nodularin. *Environ. Sci. Technol.* **2014**, *48*, 8035−8043.
(38) McCarron, P.; Kilcoyne, J.; Miles, C. O.; Hess, P. Formation of azaspiracids-3,-4,-6, and-9 via decarboxylation of carboxyazaspiracid metabolites from shellfish. *J. Agric. Food Chem.* **2009**, *57*, 160−169.
(39) Miles, C. O.; Samdal, I. A.; Aasen, J. A. B.; Jensen, D. J.; Quilliam, M. A.; Petersen, D.; Briggs, L. M.; Wilkins, A. L.; Rise, F.; Cooney, J. M.; MacKenzie, A. L. Evidence for numerous analogs of yessotoxin in *Protoceratium reticulatum*. *Harmful Algae* **2005**, *4*, 1075−1091.

DOI: 10.1021/acs.jafc.5b02513
J. Agric. Food Chem. 2015, 63, 7855−7861

hydrolysis (e.g., neosolaniol, T2-triol, and T2-tetraol), oxidation (e.g., 3′-hydroxy-HT2 and 3′-hydroxy-T2), de-epoxidation (e.g., de-epoxy-3′-hydroxy-HT2, de-epoxy-T2-triol, and de-epoxy-HT2), and glucuronide conjugation of biotransformation products such as HT2 and neosolaniol.[9] De-epoxidation is an important detoxification mechanism and together with metabolic changes (e.g., conjugation) of the hydroxyl group at C-3 has the greatest impact on reducing the toxicity of trichothecenes.[10]

In plants, conjugation of xenobiotics with glucose, sulfate, glutathione, or amino acids constitute well-known and effective detoxification strategies.[3] The resulting metabolites are chemically distinct compounds produced by enzyme-catalyzed reactions, belonging to the so-called "masked mycotoxins".[11] Formation of glucosylated trichothecenes in artificially and naturally contaminated cereals was first shown for the type-B trichothecenes deoxynivalenol (DON)[12] and nivalenol,[13] followed by HT2 and T2.[14] Nonetheless, metabolic products similar to those reported in animals have been detected in T2-treated *Baccharis* spp., namely, HT2, 3′-hydroxy-HT2, and T2-tetraol.[15] To date, very limited information exists with regard to the metabolic fate of HT2 and T2 in cereal grains and natural occurrence of their plant-derived metabolites. In a recent survey study, HT-2 toxin-3-*O*-*β*-glucoside (HT2-3-Glc) was quantified in naturally contaminated barley, wheat, and oats, reaching concentrations of up to 300 μg/kg.[16]

To study the metabolism of xenobiotics *in planta* comprehensively, unbiased methods offer the chance to probe the entire metabolic space of the biological system under investigation. While liquid chromatography−high resolution mass spectrometry (LC-HRMS) methods are principally suited to measure hundreds of metabolites simultaneously, they come with the drawback of primarily detecting unspecific signals of nonbiological origin.[17] Stable isotope labeling (SIL)-assisted untargeted metabolomics may resolve several of these limitations. SIL workflows have been recently applied in conjunction with HRMS to investigate the metabolism of DON in wheat and identification of novel plant-derived DON-metabolites.[18] This approach has also been useful for the characterization of the fungal secondary metabolomes of *Aspergillus fumigatus*[19] and *F. graminearum*.[20]

The aim of this study was to investigate the *in planta* metabolic fate of T2 and HT2 in wheat. Putative identification of novel metabolites was performed with untargeted SIL-assisted metabolic profiling using LC-HRMS. Data were processed with MetExtract,[21] and annotation was based on accurate mass measurements as well as LC-HRMS/MS spectra.[22] Time course kinetics of the identified metabolites were also studied in two wheat lines ranging from the flowering stage until full ripening.

MATERIALS AND METHODS

Chemicals and Reagents. HPLC grade acetonitrile and methanol were obtained from VWR (Vienna, Austria), and formic acid (LC-MS grade) and TWEEN 20 were purchased from Sigma-Aldrich (Vienna, Austria). Ammonium formate solution (5 M) was provided by Agilent Technologies (Waldbronn, Germany). Water was purified successively by reverse osmosis using an ELGA Purelab Ultra-AN-MK2 system (Veolia Water, Vienna, Austria). Crystalline nonlabeled T2 (purity 85%) and HT2 (purity 92%), as well as uniformly labeled U-[$^{13}C_{24}$] T2 (purity 98%; degree of enrichment 99.6 atom % ^{13}C) and uniformly labeled U-[$^{13}C_{22}$] HT2 (purity 86%; degree of enrichment 99.3 atom % ^{13}C) standards were purchased from Romer Labs GmbH (Tulln, Austria). Solutions from lyophilized labeled and nonlabeled T2 (10.0 g/L) and HT2 (10.0 g/L) were prepared separately by dissolving the compounds in acetonitrile. Certified standard solutions of T2 and HT2 (100.4 mg/L and 100.6 mg/L, respectively, in acetonitrile) were also obtained from Romer Labs GmbH. The analytical standard of HT2-3-Glc was enzymatically produced from HT2 (Michlmayr et al., manuscript in preparation). 3-Acetyl-T2 was synthesized from T2 using acetic anhydride in dichloromethane/pyridine with 4-dimethylaminopyridine as catalyst. Stock solutions in acetonitrile were prepared and were stored in sealed vials at −20 °C until use.

Plant Materials. The plant experiments are described according to the Metabolomics Standard Initiative (MSI) for the Proposed Minimum Information Set for reporting plant biological experimental designs. For the metabolomics profiling experiment, the spring wheat (*Triticum aestivum* L.) variety "Remus" ("Sappo"/"Mex"/"Famos") was selected. The awn-free variety was developed at the Bavarian State Institute for Agronomy in Freising, Germany. It possesses well-adapted agronomic characteristics for cultivation in Central Europe but is highly susceptible to Fusarium head blight (FHB) and DON.[23,24] The time-course experiment was conducted on the wheat variety Remus and the FHB-resistant variety "CM-82036-1TP-10Y-OST-10Y-OM-OFC" (abbreviated to "CM-82036") which originated from the cross of the varieties "Sumai-3" and "Thornbird" and possess awns.[24] Seeds of Remus and CM-82036 were first germinated. No vernalization was required, but the wheat seedlings were routinely submitted to a cold treatment at 5 °C for 1 week to improve tillering. Pots (diameter 23 cm) were filled with 7 L of a substrate (consisting of 500 L heat-sterilized compost, 250 L peat, 10 kg sand, and 250 g rock flour). Five seedlings of the same wheat line were planted in each pot.

Experiments were conducted in a greenhouse with computer-controlled settings for light, temperature, and relative air humidity. Light intensity (outside dark) was 360 μmol/sm^2 at 1 m above the soil throughout the complete experiment. Relative air humidity was set between 60 and 70% during plant growth. Temperature (day/night) and duration of illumination (hours) varied according to the development stage of the plants: from planting until the end of tillering (stage 3 on the Feekes scale[25]), 12 °C/10 °C/12 h; end tillering to midstem extension when the ear starts to swell (stage 8), 14 °C/10 °C/14 h; mid stem extension to start heading (stage 10.1), 16 °C/14 °C/14 h; from the start of heading to the start of flowering (stage 10.51), 18 °C/14 °C/14 h; from the start of flowering (stage 10.51) until the end of the experiment, 20 °C/18 °C/16 h. In total, the seedlings needed 9−10 weeks to reach the flowering stage.

During the experiment, the pots were watered if required (typically three times/week). Water was applied until the substrate was completely wet and the water started to seep out through the holes in the bottom of the pot. The soil substrate contained sufficient minerals to support seedling growth. At the end of tillering (stage 5 on the Feekes scale), 2 g of a mineral fertilizer (COMPO Blaukorn ENTEC, Münster, Germany; N/P/K/Mg: 14/7/17/2) was applied per pot. To prevent mildew, the cabinet was treated twice during plant cultivation with sulfur overnight (sulfur evaporator, Nivola, Lisse, The Netherlands).

Treatment of Wheat Plants and Sampling. The experimental design was a completely randomized block with three biological replicates. Upon reaching the correct developmental stage (stage 10.51 on the Feekes scale), flowering ears were selected and individually labeled. Only one ear per plant was used in the experiment to prevent possible systemic effects of an earlier treated ear on other later flowering ears of the same plant. A woolen thread was used to label the lowest treated spikelet in the lower part of the ear (approx. 2/3 from the ear tip). In general, spikelets were treated by injecting 10 μL of the respective test solution into each of the outer floret (hence, 20 μL per spikelet) after placing the pipet tip in the spikelet using an electronic pipet Multipette Xstream (Eppendorf, Hamburg, Germany). After each treatment, the ear was covered for 24 h with a small transparent plastic bag internally wetted by spraying ca. 2 mL of bidistilled water with a handhold sprayer. This assured a high relative humidity promoting diffusion of the mycotoxins into the plant cells.

DOI: 10.1021/acs.jafc.5b02697
J. Agric. Food Chem. 2015, 63, 7862−7872

In the metabolic profiling experiment a 50:50 (v/v) mixture of ^{13}C-labeled and nonlabeled solutions of HT2 or T2 (in acetonitrile:water (50:50, v/v) and 1% TWEEN) was used. As controls, ears were treated with a mock solution containing only acetonitrile:water (50:50, v/v) and 1% TWEEN. At time point zero, two neighboring spikelets were treated, and 48 h later the second treatment on the same ears was performed using the next pair of adjacent spikelets located above those treated previously. At 96, 120, and 144 h after the first application, treatments on the same ear continued as described, always selecting the next pair of spikelets in acropetal direction. In total, 200 μg of the $^{12}C/^{13}C$ toxin mixture was applied per ear. Sampling was performed 24 h after the last round of toxin application by removing the ear with a surgical scissor and dividing the wheat ear into three parts, but only the middle part was later used for LC-MS analysis: lower part (upper part of the stem and nontreated spikelets in basipetal direction of the treated ones), middle part (spikelets treated with toxins), and upper part (spikelets above the treated spikelets). All samples were weighed, shock-frozen in liquid nitrogen, and stored at −80 °C until further processing.

For the time course study, wheat ears were treated with nonlabeled T2 or HT2 or with the mock solution (methanol:water (50:50, v/v) and 1% TWEEN) similar to the process described above. The only difference was that 10 pairs of neighboring spikelets were treated with 10 μL each in one treatment resulting in a single dose of 200 μg per ear. Samples were collected at eight time points (0 h, 6 h, 12 h, 1 day, 2 days, 3 days, 1 week, and at full ripening) in triplicate. Wheat ears were removed from the plants with a surgical scissor, weighed as a whole, and immediately frozen with liquid nitrogen to prevent any metabolic activity until analysis. All collected samples were stored at −80 °C until further processing.

Sample Preparation. The frozen wheat ears were ground into a fine powder using a ball mill (MM 301 Retsch, Haan, Germany). The samples were placed inside 10 mL stainless steel vessels, precooled with liquid nitrogen, and were milled for 30 s at 30 Hz. After homogenization, (100 ± 2) mg of wheat material were weighed into 1.5 mL Eppendorf tubes and extracted with 500 μL of acetonitrile:water:formic acid (79:20.9:0.1, v/v/v) for 90 min with 200 rpm at room temperature on a GFL3017 rotary shaker (Burgwedel, Germany). Afterward, the extracts were centrifuged for 10 min at 22 570*g* using an Awel centrifuge MF 48-R (Blein, France). The supernatants (ca. 200 μL) were transferred to HPLC vials containing microinserts. The time course samples were partly further diluted 1:10 or 1:50 (v/v) in acetonitrile:water (50:50, v/v) to allow quantification of target analytes.

UHPLC-QTOF-MS Analysis. Measurements were performed with a 1290 series ultra high performance liquid chromatography (UHPLC) system coupled to a 6550 iFunnel quadrupole time-of-flight (QTOF)-MS system (both Agilent Technologies, Waldbronn, Germany) equipped with an electrospray ionization (ESI) interface. Chromatographic separation was achieved on a reversed-phase Zorbax SB-C18 column (2.1 × 150 mm, 1.8 μm particle size; Agilent Technologies) kept at 30 °C. In the isotope-assisted, untargeted metabolic profiling experiment, gradient elution was carried out with water (solvent A) and methanol (solvent B), both containing 0.1% formic acid, and applying the following gradient 1: 0−0.5 min 10% B, 0.5−20 min linear gradient from 10 to 100% B, 20−22 min flushing at 100% B and column re-equilibration with the initial chromatographic conditions (10% B) from 22 to 25 min. During the first 2 min and after the 22 min point mark, the eluent flow was directed to the waste. The flow rate of the mobile phase was 0.25 mL/min, and the injection volume was set to 3 μL. To avoid carry over, the needle was flushed with acetonitrile:water (50:50, v/v) for 5 s immediately prior to injection. For the time course experiment, 5 mM ammonium formate was added to both solvents to promote the formation of ammonium adducts. Furthermore, gradient 2 was shortened to 10 min (0−0.5 min, 20% B; 0.5−6.0 min, 20−100% B; 6.0−8.0 min, 100% B; 8.0−8.1 min, 100−20% B; 8.1−10.0 min, 20% B) for faster analysis.

Full scan spectra were acquired in the range of m/z 50−1500 in positive and negative ESI modes at an acquisition rate of 3 spectra per second. The source conditions were set as follows: gas temperature, 130 °C; drying gas flow, 14 L/min; nebulizer, 30 psig; sheath gas temperature, 300 °C and flow, 10 L/min; capillary voltage, 4000 V; and nozzle voltage, 500 V. Targeted LC-HRMS/MS experiments for identification and characterization of the formed metabolites were performed with gradient 1, but 5 mM ammonium formate was added in the solvents to obtain ammonium adducts for improved fragmentation. An isolation width of m/z 1.3 was applied for precursor selection; the acquisition speed in MS/MS was set to 3 spectra per second, and the applied collision energies (5, 10, and 20 eV) depended on the analytes. The QTOF was tuned and calibrated prior to use on the same day, and during the run two reference masses (positive mode, m/z 121.0508 and 922.0098; negative mode, m/z 112.9855 and 966.0007) were constantly infused via a second nebulizer to ensure mass accuracy.

Data were acquired with Mass Hunter Data Acquisition version B.05.01, and evaluation of data was performed using Mass Hunter Qualitative and Quantitative Analysis version B.06.00 (all Agilent Technologies), as well as Excel 2010 (Microsoft Co., Redmond, WA).

Data Processing for Detection of HT2 and T2 Wheat Metabolites. Acquired raw, full-scan LC-HRMS data were centroided and converted to the mzXML format with MSConvert from the ProteoWizard package (version 3.0.3959; http://proteowizard.sourceforge.net/). The ^{13}C-enrichment (∼99.5%) and the applied nonlabeled to ^{13}C-labeled tracer ratio (∼1) were determined for the highly abundant $[M + Na]^+$ adducts of the T2 and HT2 tracers using TOPPView (version 1.10).[26] All biotransformation products of the T2 and HT2 tracer were expected to show a very similar ^{13}C-enrichment and nonlabeled-to-^{13}C-labeled ratio in the recorded LC-HRMS data. Successively, MetExtract[21] was utilized to screen for T2 and HT2 derived biotransformation products present as nonlabeled and partially ^{13}C-labeled ions. The principal processing steps of the software are as follows: Mass peak pairings of nonlabeled (M) and ^{13}C-labeled (M′) biotransformation product ions were searched for in each recorded mass spectrum (min intensity abundance, 500 counts; M:M′ ratio, 0.5−1.5). Each mass peak pairing had to have an m/z difference that corresponded to the number of labeled carbon atoms (max allowed relative m/z tolerance window, ± 4 ppm). The isotope patterns of both the nonlabeled and the partially ^{13}C-labeled ions were then tested against the determined number of labeled carbon atoms (one isotopolog tested; max allowed abundance deviation, ± 15%). Detected mass peak pairings were clustered (max m/z deviation of ions of a single cluster, ± 9 ppm; min number of detected mass peaks, 3), and for each cluster, both the extracted ion chromatogram (EIC) of the native and the EIC of the labeled biotransformation product ions were extracted (EIC window, ± 10 ppm). Chromatographic peaks were detected in both EICs using the wavelet algorithm of Du et al.[27] Only chromatographic peak pairs present in both EICs that eluted at the same retention time (max allowed deviation, ± 10 scans) and had a highly similar peak shape (min Pearson correlation coefficient, 0.85) were considered to be biotransformation product ions of both nonlabeled and ^{13}C-labeled T2 and HT2 tracers. Other also detected chromatographic peaks in either one of the EICs were discarded as these did not represent nonlabeled and ^{13}C-labeled biotransformation product ions of T2 and HT2 but other metabolites of wheat or contaminants. Finally, detected biotransformation product ions were convoluted into feature groups (max allowed retention time deviation, ± 10 scans; min Pearson correlation coefficient, 0.85), each representing one biotransformation product of T2 and HT2 in wheat. Ions assigned to a single group were investigated with respect to the presence of known mass increments between the detected ion species with the aim to annotate ion species. Commonly observed species during ESI positive mode were $[M + H]^+$, $[M + NH_4]^+$, $[M + Na]^+$, and $[M+K]^+$ ions, while in negative mode $[M-H]^-$, $[M + Cl]^-$, $[M + HCOO]^-$ ions were regularly detected.

Validation of the Method for Quantification Purposes. For those analytes for which analytical standards were available (T2, HT2, HT2-3-Glc, and 3-acetyl-T2), an in-house validation was performed. Mock samples of the variety Remus were weighed (100 ± 2 mg) using the biological triplicates and were spiked with a solution containing all target analytes in acetonitrile before extraction on one level

DOI: 10.1021/acs.jafc.5b02697
J. Agric. Food Chem. 2015, 63, 7862−7872

Table 1. Overview of Putative HT-2 Toxin (HT2) Metabolites Detected in Wheat Ears of the Variety Remus (Susceptible to Fusarium Head Blight)[a]

peak no.	RT (min)[b]	chemical formula[c]	ion species[d]	m/z[d]	mass accuracy (ppm)	^{13}C count	putative metabolite
1	5.2	$C_{23}H_{34}O_{12}$	$[M + Na]^+$	525.1940	−0.41	17	15-acetyl-T2-tetraol-glucoside***
2	10.2	$C_{28}H_{42}O_{14}$	$[M + Na]^+$	625.2461	−0.92	22	hydroxy-HT2-glucoside**
3	10.9	$C_{31}H_{44}O_{17}$	$[M + Na]^+$	711.2447	−3.33	22	hydroxy-HT2-malonyl-glucoside**
4	13.0	$C_{26}H_{40}O_{12}$	$[M+HCOO]^-$	589.2498	−0.64	20	T2-triol-glucoside**
5	13.2	$C_{28}H_{40}O_{13}$	$[M+HCOO]^-$	629.2446	−0.78	22	dehydro-HT2-glucoside**
6, 7	13.3, 14.0	$C_{34}H_{52}O_{18}$	$[M+HCOO]^-$	793.3135, 793.3135	−0.08, −0.08	22	HT2-diglucoside**,e
8	14.1	$C_{28}H_{42}O_{13}$	$[M + Na]^+$	609.2518	+0.00	22	HT2-3-glucoside*
9	14.3	$C_{31}H_{44}O_{16}$	$[M + Na]^+$	695.2505	−2.39	22	HT2-malonyl-glucoside**
HT2	14.9	$C_{22}H_{32}O_8$	$[M + Na]^+$	447.1992	+0.59	22	HT-2 toxin*
T2	16.0	$C_{24}H_{34}O_9$	$[M + Na]^+$	489.2098	+0.68	22	T-2 toxin (T2)*
10	16.2	$C_{24}H_{34}O_9$	$[M + Na]^+$	489.2083	−2.46	22	3-acetyl-HT2**

*Confirmation with standard by comparison of retention time, accurate mass, and HRMS/MS spectra. **Annotation with accurate mass and HRMS/MS spectra. ***Annotation with accurate mass and HRMS/MS spectra only in HT2-treated barley.[28] [a]Samples were collected after exposure to a mixture of 200 μg/ear $^{12}C/^{13}C$ HT2 (1:1, v/v) during days 1, 2, 3, 5, and 7 on the same ear, and annotation was performed with accurate mass measurements and HRMS/MS spectra. [b]Retention time. [c]Sum formula of neutral compound. [d]Accurate mass and ion species of the most abundant ion. [e]Structural isomers of HT2-diglucoside with presumably different conjugations of the glucose moiety.

Table 2. Overview of Putative T-2 Toxin (T2) Metabolites Detected in Wheat Ears of the Variety Remus (Susceptible to Fusarium Head Blight)[a]

peak no.	RT (min)[b]	chemical formula[c]	ion species[d]	m/z[d]	mass accuracy (ppm)	^{13}C count	putative metabolite
2	10.2	$C_{28}H_{42}O_{14}$	$[M + Na]^+$	625.2473	+1.00	22	hydroxy-HT2-glucoside**
3	10.9	$C_{31}H_{44}O_{17}$	$[M + Na]^+$	711.2459	−1.64	22	hydroxy-HT2-malonyl-glucoside**
4	13.0	$C_{26}H_{40}O_{12}$	$[M+HCOO]^-$	589.2497	−0.81	20	T2-triol-glucoside**
5	13.2	$C_{28}H_{40}O_{13}$	$[M+HCOO]^-$	629.2446	−0.79	22	dehydro-HT2-glucoside***
6, 7	13.3, 14.0	$C_{34}H_{52}O_{18}$	$[M+HCOO]^-$	793.3131, 793.3131	−0.63, −0.63	22	HT2-diglucoside**,e
8	14.2	$C_{28}H_{42}O_{13}$	$[M + Na]^+$	609.2519	+0.23	22	HT2-3-glucoside*
9	14.4	$C_{31}H_{44}O_{16}$	$[M + Na]^+$	695.2508	−1.95	22	HT2-malonyl-glucoside**
HT2	14.9	$C_{22}H_{32}O_8$	$[M + Na]^+$	447.1993	+0.81	22	HT-2 toxin (HT2)*
T2	16.0	$C_{24}H_{34}O_9$	$[M + Na]^+$	489.2096	+0.20	24	T-2 toxin*
11	17.3	$C_{26}H_{36}O_{10}$	$[M + Na]^+$	531.2187	−2.57	24	3-acetyl-T2*
12, 13	18.1, 18.4	$C_{34}H_{42}O_{12}$	$[M + Na]^+$	665.2561, 665.2561	−1.12, −1.12	24	feruloyl-T2**,f

*Confirmation with standard by comparison of retention time, accurate mass, and HRMS/MS-spectra. **Annotation with accurate mass and HRMS/MS-spectra. ***Annotation with accurate mass and HRMS/MS-spectra only in HT2-treated wheat samples. [a]Samples were collected after exposure to a mixture of 200 μg/ear $^{12}C/^{13}C$ T2 (1:1, v/v) during days 1, 2, 3, 5, and 7 on the same ear, and annotation was performed with accurate mass measurements and HRMS/MS spectra. [b]Retention time. [c]Sum formula of neutral compound. [d]Accurate mass and ion species of the most abundant ion. [e]Structural isomers of HT2-diglucoside with different conjugations of the glucose moiety. [f]Probably *trans*-feruloyl-T2 and *trans*-isoferuloyl-T2.

(1500 μg/kg, corresponding to 300 μg/L in the "undiluted" sample extract). The samples were stored overnight at room temperature to ensure solvent evaporation and to achieve equilibrium between the analytes and the matrix. The next day, the samples were extracted according to the procedure described above. Calculating ratios of the EIC (target $m/z \pm 30$ ppm) peak area achieved in these samples with those in a neat solvent standard (300 μg/L, mean value from triplicate analysis) multiplied with 100 resulted in the apparent recovery (R_A). For the evaluation of matrix effects (expressed as signal suppression or enhancement, SSE), mock samples of the same type (again in biological replicates) were extracted, and the raw extracts of the undiluted samples and 1:10 and 1:50 (v/v) diluted samples were spiked at a concentration of 300 μg/L. A comparison of EIC abundance values with the neat solvent standard (300 μg/L) provided the SSE values of the respective dilution. The extraction recovery was calculated by dividing R_A with the SSE of the undiluted sample and multiplying with 100. For the calculation of the corresponding relative standard deviation, the propagation of uncertainty was taken into account.

For the quantification of HT2, HT2-3-Glc, T2, and 3-acetyl-T2, neat solvent standards ranging from 3 to 300 μg/L for 3-acetyl-T2 and from 10 to 1000 μg/L for the other three compounds were prepared in acetonitrile−water (50:50, v/v). They were measured along with the different dilutions of the sample extracts, and calibration was performed using $1/x$ weighted calibration curves.

RESULTS AND DISCUSSION

HT2 and T2 Metabolite Annotation and Characterization. Raw UHPLC-QTOF-MS data derived from HT2- and T2-treated samples were processed by MetExtract, and the automatically generated features and feature groups were further manually inspected for false positives. Erroneously picked features, which by chance fulfilled MetExtract screening criteria, were easily recognized by certain characteristics such as imperfect coelution of assumed ^{12}C and ^{13}C EIC traces, a $^{12}C/^{13}C$ mass shift higher than the number of C atoms contained in the intact tracer, or implausible isotopolog intensity ratios. Finally, a total of 15 (HT2) and 16 (T2) feature groups (i.e., metabolites) including the native, non-modified toxins were obtained. Of those, 12 (HT2) and 13 (T2) feature groups were of sufficient intensity, enabling their further structural elucidation by MS/MS, verifying their tentative chemical structure (shown in Tables 1 and 2). Each of these feature groups consisted of up to 25 $^{12}C/^{13}C$ ion pairs

DOI: 10.1021/acs.jafc.5b02697
J. Agric. Food Chem. 2015, 63, 7862−7872

originating from adducts and/or in-source fragments that shared the same retention time and chromatographic peak shape. It is worth mentioning that in mock samples, no feature pairs corresponding to T2 or HT2 metabolic products were detected by automated data processing, demonstrating the high selectivity of the used isotope-assisted untargeted workflow. Annotation of biotransformation products was based on accurate m/z values, assumed ion species, number of toxin-derived ^{13}C atoms per metabolite ion, and LC-HRMS/MS spectral interpretations. The detailed structural characterization procedure is described in Meng-Reiterer, Varga, and co-workers[28] who performed a similar study on the metabolism of T2 and HT2 in barley. Briefly, characteristic fragments obtained from standard measurements (T2, HT2, HT2-3-Glc, and 3-acetyl-T2) or described in the literature were compared with those experimentally obtained here for the MetExtract derived metabolites. LC-HRMS/MS measurements of pairs of corresponding nonlabeled and labeled precursor provided further information. The LC-HRMS/MS spectra of the observed metabolites of HT2 and T2 in barley[28] were compared with those obtained in wheat and were shown to be identical. Figure 1 shows an overlay of EICs of all detected

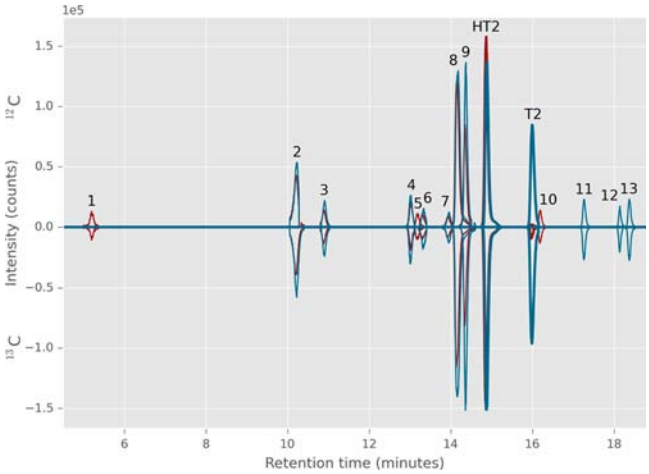

Figure 1. Overlaid extracted ion chromatograms (EICs) based on MetExtract data processing output showing the biotransformation products of a sample treated with a mixture of $^{12}C/^{13}C$-HT-2 toxin (red trace) and one treated with a mixture of $^{12}C/^{13}C$ T-2 toxin (blue trace). EICs of nonlabeled metabolites are displayed with positive intensity values; those of the corresponding labeled metabolites are displayed as negative intensities. Perfect coelution, similar peak shape, and $^{12}C/^{13}C$-intensities of EIC peaks verify the detected ions are truly tracer-derived metabolites.

biotransformation products, and Tables 1 and 2 provide a summary of the annotated metabolites in HT2- and T2-treated wheat ears of the variety Remus.

In the samples which had been treated with HT2 (m/z 447.1989, $[M + Na]^+$), a mass difference between the ^{12}C and ^{13}C ion pairs of 22.0738 Da (corresponding to the mass difference between 22 ^{12}C and ^{13}C atoms) signified that the conjugated metabolites contained the intact molecule of HT2. Formation of HT2-3-Glc (Table 1, peak 8), an already known monoglucosylated HT2 metabolite, was verified by measurements of an authentic standard and was also detected in T2-treated samples (Table 2, peak 8). Only one peak for the m/z ratio corresponding to HT2-3-Glc was found in the treated wheat samples. This peak was perfectly matching in retention time and HR MS/MS fragmentation with the authentic standard of HT-2 toxin-3-O-β-glucoside. Additionally, two tentative diglucosylated HT2 isomers (Table 1, peaks 6 and 7) with slightly different retention times were detected in the wheat samples. We postulate that because monoglucosylation of HT2 was found to occur only at C-3, the additional sugar moiety is most likely transferred by a different enzyme, presumably leading to β-1,4 or β-1,6 diglucosides. Likewise, HT2-malonyl-glucoside is formed by conjugation of malonic acid to the glucose moiety of HT2-3-Glc. In addition to the metabolites identified in barley,[28] also dehydro-HT2-glucoside was tentatively identified. Its HRMS/MS spectrum is provided as Figure S1 in Supporting Information. The absence of m/z 101.0608 and the occurrence of a fragment ion with m/z 99.0456 indicate the loss of two hydrogen atoms from the isovaleryl moiety, most likely after cleavage of water from hydroxy-HT2-glucoside. It should be noted that full structural elucidation of all detected metabolites would require purification and subsequent nuclear magnetic resonance (NMR) measurements, which was beyond the scope of this study.

The majority of the other metabolites were derived from HT2-3-Glc by additional conjugations and/or changes in the HT2 skeleton. Evaluation of mass shifts between corresponding $^{12}C/^{13}C$ feature pairs revealed that two metabolites contained less than 22 ^{13}C carbon atoms in their HT2 backbone (Table 1, peaks 1 and 4). These ions correspond to the putative metabolites 15-acetyl-T2-tetraol-glucoside (loss of the isovaleryl moiety at C-8) and T2-triol-glucoside (loss of the acetyl group at C-15). The fact that no 15-acetyl-T2-tetraol, T2-triol, or hydroxy-HT2 were detected even at the earlier time points indicates that the respective phase I type reactions hydrolysis, deacetylation, and oxidation, generally assumed to occur prior to conjugation of xenobiotics, took place after the conjugation of glucose to the HT2 backbone. Hence, direct conjugation of unaltered mycotoxins with plant constituents can result in metabolites susceptible to phase I reactions, under appropriate conditions, as has already been reported in the literature for pesticides.[29]

As previously described for HT2, metabolites containing the intact T2 carbon backbone (m/z 489.2095, $[M + Na]^+$) should reveal a mass difference of 24.0805 between the ^{12}C and ^{13}C ion pairs. Nevertheless, only three such biotransformation products were found. Putative metabolites including an intact T2 skeleton were 3-acetyl-T2 and two tentatively isomeric peaks of feruloyl-T2 (Table 2, peaks 11−13). As ferulic acid (4-hydroxy-3-methoxycinnamic acid) naturally exists majorly as *trans*-ferulic acid,[30] the second isomer is more likely isoferuloyl-T2 rather than a diastereomer of feruloyl-T2. It is worth mentioning that T2-glucoside could not be detected in this study as a biotransformation product of T2, although it has previously been documented in T2-contaminated wheat.[14,31] The majority of metabolites in T2-treated wheat were formed after deacetylation of the toxin to HT2 and further metabolism according to the same metabolic pathways.

***In Planta* Acetylation of HT2.** Many organisms, including plants, are capable of deacetylating T2 to HT2. However, with the $^{12}C/^{13}C$ experimental setup, we were able to show that wheat is also capable of acetylating HT2. The feature pair m/z 489.2083 (^{12}C)/511.2823 (^{13}C) recognized by MetExtract indicates the presence of 22 tracer-derived carbon atoms (as for the originally applied HT2), and the m/z value fits to the sum formula of the ^{13}C-HT2 backbone to which a nonlabeled acetyl

DOI: 10.1021/acs.jafc.5b02697
J. Agric. Food Chem. 2015, 63, 7862−7872

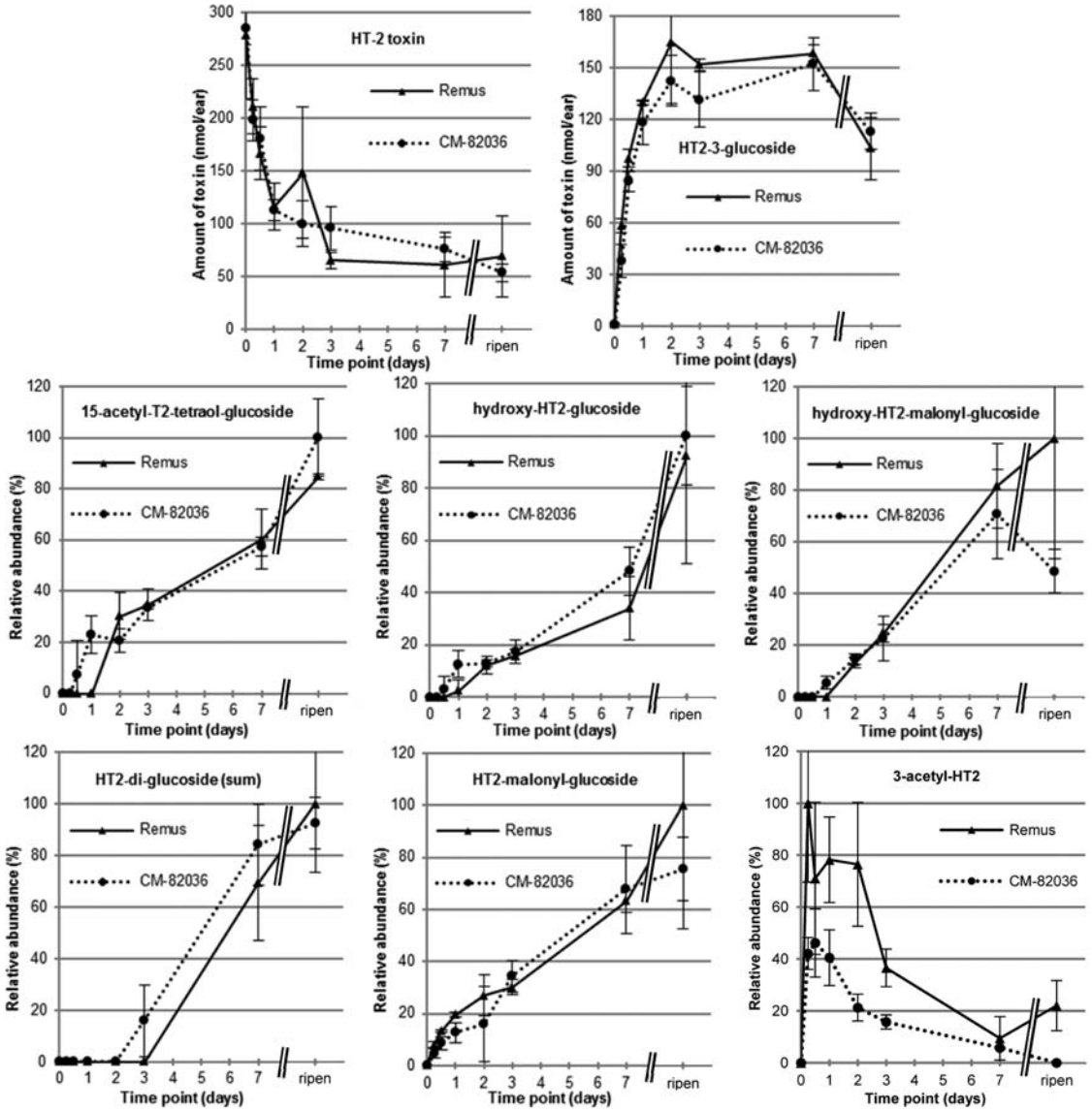

Figure 2. Results from the time course kinetics experiment. After exposure to a single dose of 200 μg/ear HT-2 toxin (HT2), the whole ears (n = 3) were harvested immediately after treatment (0 h), after 6 h, 12 h, 1 day, 2 days, 3 days, and 1 week, as well as at full ripening (ca. 8 weeks after treatment). For the parent toxin (HT2) and the major metabolite HT-2 toxin-3-glucoside, the absolute amounts (in nanomoles per ear) are provided together with the standard deviation of the biological triplicate. These values are based on quantitative measurements using the respective analytical standards and are corrected for matrix effects occurring during liquid chromatography−mass spectrometric analysis; the individual ear weights were taken into consideration. For all other metabolites no analytical standard was available; therefore, the relative abundances (in percent) are provided together with the standard deviation of the biological triplicate. Those values are based on the peak areas of the ammonium adduct (for 3-acetyl-HT-2 toxin the sodium adduct was used) multiplied with the individual ear weight. All values were set into correlation with the highest observed normalized area (usually the full ripening samples of Remus or CM-82036).

group has been conjugated ($^{13}C_{22}C_2H_{34}O_9$; calculated m/z for Na-adduct 511.2833). HT2 has two hydroxyl groups at positions C-3 and C-4, which might be acetylated, and T2 differs from HT2 only by the acetyl-group at position C-4. Because the obtained retention time of 16.2 min (Figure 1, peak 10) was close to, but did not match with those of a T2 standard (16.0 min), it was postulated that the acetyl moiety of this HT2 metabolite results from acetylation at the position C-3 instead of C-4. With MS/MS measurements (see Figure S2 in Supporting Information) it was not possible to determine differences in fragmentation between native T2 and the putative 3-acetyl-HT2. Quantification of the presumed 3-acetyl-HT2 using T2 as standard resulted in about 40 μg/kg that accounts for less than 0.4% of the applied HT2. In a similar study with barley,[28] no acetylated forms of HT2 could be confirmed. This acetylation reaction at C-3 can be regarded as a detoxification process because it has also been described to be a strategy employed by the trichothecene-producing fungus during toxin biosynthesis for self-protection.[32] Finally, it should be mentioned that the small EIC-peak (m/z 511.2832) at 16.0 min could be T2. However, the second isotopolog of ^{13}C-T2 (present as impurity of the ^{13}C-HT2 used for spiking) will also lead to this signal, rendering this assumption inconclusive. To sum up, the presence of an acetylated form of HT2 other than T2, (presumably) 3-acetyl-HT2, was confirmed in wheat samples. Whether also T2 might be formed from HT2 remains unclear on the basis of our data. In any case, the deacetylation of T2 in wheat is seemingly far faster, compared to the potential

DOI: 10.1021/acs.jafc.5b02697
J. Agric. Food Chem. 2015, 63, 7862−7872

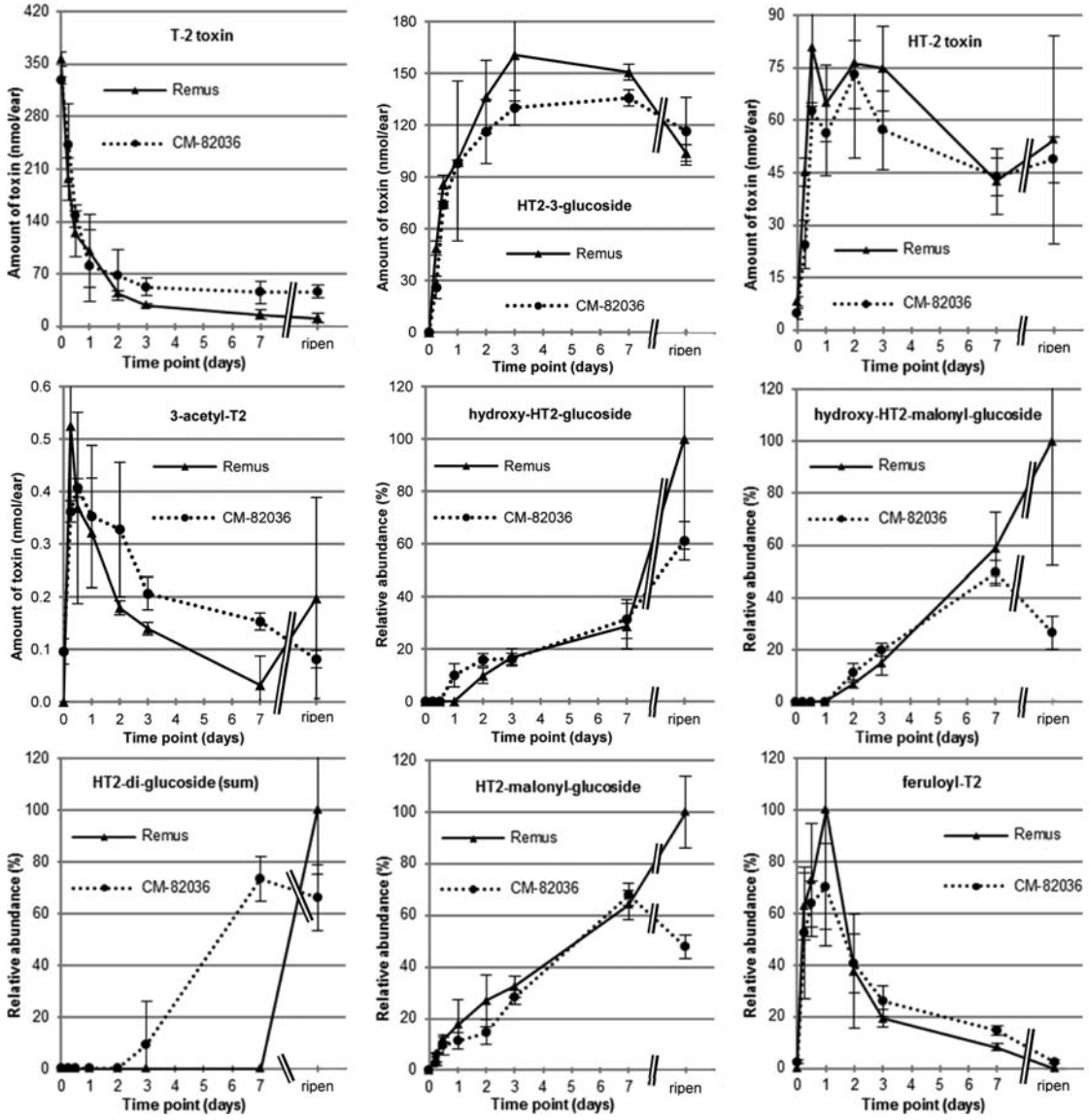

Figure 3. Results from the time course kinetics experiment. After exposure to a single dose of 200 μg/ear T-2 toxin (T2), the whole ears (n = 3) were harvested immediately after treatment (0 h), after 6 h, 12 h, 1 day, 2 days, 3 days, and 1 week, as well as at full ripening (ca. 8 weeks after treatment). For the parent toxin (T2), the two major metabolites HT-2 toxin and HT-2 toxin-3-glucoside, as well as 3-acetyl-T-2 toxin, the absolute amounts (in nanomoles per ear) are provided together with the standard deviation of the biological triplicate. These values are based on quantitative measurements using the respective analytical standards and are corrected for matrix effects occurring during liquid chromatography−mass spectrometric analysis; the individual ear weights were taken into consideration. For all other metabolites, no analytical standard was available; therefore, the relative abundances (in percent) are provided together with the standard deviation of the biological triplicate. Those values are based on the peak areas of the ammonium adduct multiplied with the individual ear weight. All values were set into correlation with the highest observed normalized area (usually the full ripening samples of Remus or CM-82036).

reverse acetylation of HT2, so that the potential occurrence of 3-acetyl HT2 or T2 after metabolization from HT2 in wheat is only marginal.

Method Validation. A small validation study was performed with wheat samples of the variety Remus to ensure absolute quantification for HT2, HT2-3-Glc, T2, and 3-acetyl-T2. Biological triplicates (1 day and full ripening) from mock samples were spiked on one level before extraction to obtain R_A. In the fully ripened samples, lower recoveries (56−124%) and higher relative standard deviations (up to 31%) were observed than in the samples harvested 1 day after treatment (74−132% and up to 3.5%, respectively; see Table S1 in Supporting Information). Additionally, different dilutions (undiluted, 1:10, and 1:50 (v/v)) of blank extracts of these biological triplicates were spiked on one level to assess matrix effects. For HT2 and HT2-3-Glc, some matrix enhancement was observed. The determined extraction recoveries (R_E) were approximately 100%; therefore, obtained quantitative values in the kinetic experiment were only corrected for SSE in the respective dilution. The SSE values obtained for the samples harvested after full ripening were used for the correction of both varieties. For all other time points the SSE values determined for the day 1 samples were used.

Time Course Kinetics and Metabolic Pathways. The kinetic profiles of T2 and HT2 metabolites were studied with a time course experiment conducted in wheat lines susceptible (Remus) and resistant (CM-82036) to FHB. Treated wheat ears did not show premature bleaching after a single exposure

DOI: 10.1021/acs.jafc.5b02697
J. Agric. Food Chem. 2015, 63, 7862−7872

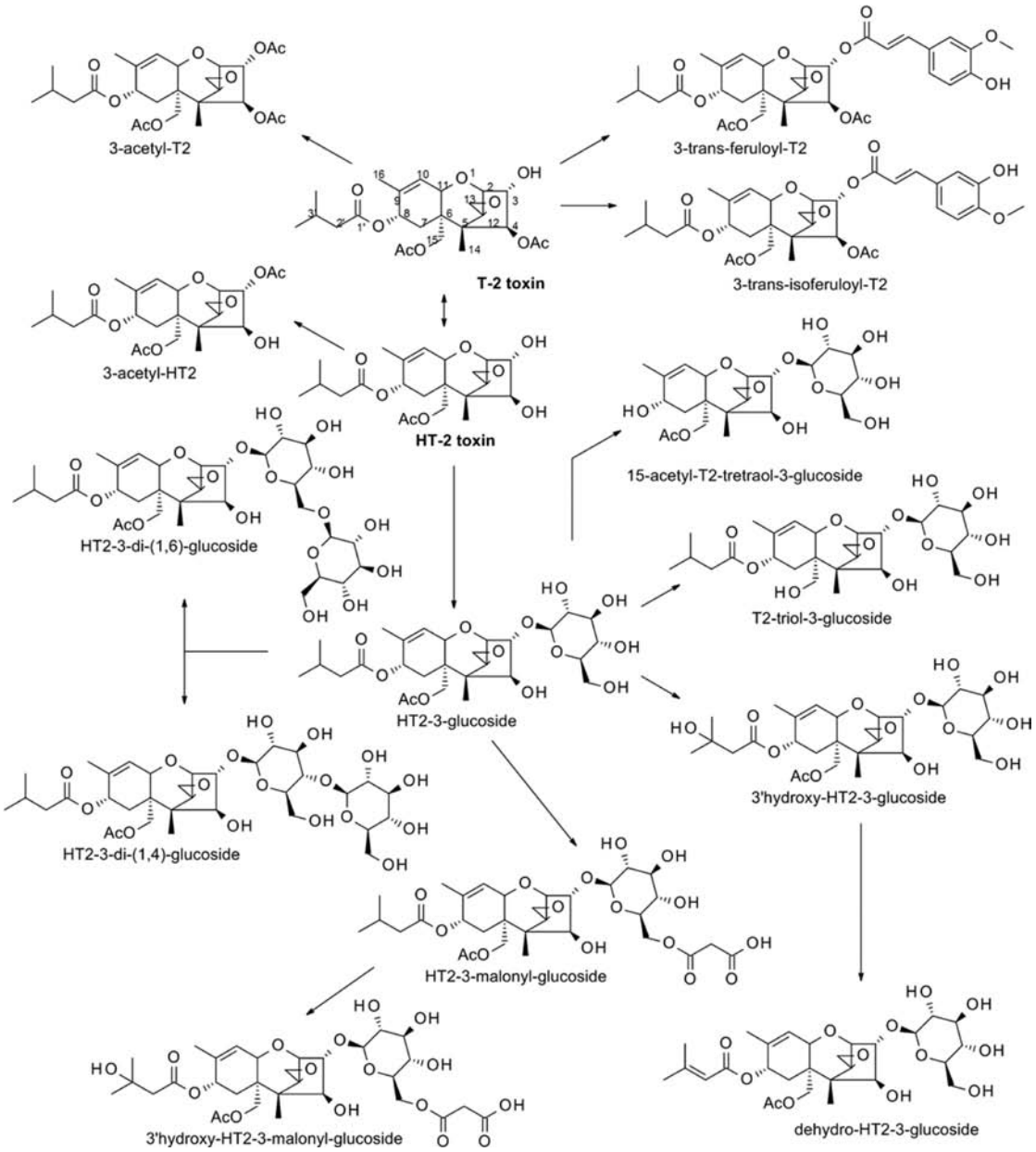

Figure 4. Proposed metabolic pathways of HT-2 toxin (HT2) and T-2 toxin (T2) in wheat.

to 200 μg of HT2 or T2, and in both wheat lines the same metabolites were determined. The kinetics of the major metabolites T2, HT2, and HT2-3-Glc in Remus and CM-82036 are illustrated in Figure 2 (HT2-treated sample) and Figure 3 (T2-treated sample). The absolute values were quantified with analytical standards, corrected for the observed SSE at the respective dilution, corrected for the individual ear weight, and calculated in nanomoles per ear. In T2-treated samples deacetylation of T2 to HT2 progresses rapidly, and already after 12 h only ca. 30% of the initially added toxin could be determined. This is in line with the study of Lattanzio et al.,[33] reporting the enzymatic hydrolysis of T2 to HT2 after 120 min of incubation in wheat (conversion rate 89%), as well as other cereals. At the same time, rapid glucosylation of HT2 to form HT2-3-Glc occurred. Biotransformation of HT2 was also activated at a very early stage, regardless of whether it originated from direct application or deacetylation of T2. HT2-3-Glc was the major metabolite 6 h after exposure and accounted for approximately 33% of the added toxin after a treatment time of 1 week. Another interesting observation is that HT2-3-Glc reached a maximum concentration between 3 days and 1 week, after which its concentration decreased until harvest because of further metabolization.

For all other metabolites, analytical standards were not available; thus, the data obtained from EIC integrated peak areas were corrected only for the individual ear weight. The values were set into correlation with the highest observed area (usually the full ripening samples of Remus or CM-82036) (HT2-treated samples in Figure 2, T2-treated samples in Figure 3). According to these findings, C3-acetylation of both toxins and (iso)ferulic acid conjugation of T2 are the immediate responses of plant detoxification mechanisms, apart from glucosylation. However, these compounds were further metabolized or covalently bound to plant matrix, as their concentration decreased over time. To accurately assess their abundance under field conditions at harvest, natural occurrence

DOI: 10.1021/acs.jafc.5b02697
J. Agric. Food Chem. 2015, 63, 7862−7872

studies in cereals for these compounds are necessary. Conjugations with an additional glucose moiety or malonic acid to existing HT2 monoglucosides occurred later. Hydrolysis of the acetyl group of HT2-3-Glc in C-15, leading to the formation of T2-triol glucoside, is presumably a consecutive later reaction as the compound was detectable only in ripened samples. The proposed metabolic pathway of HT2 and T2 metabolization is summarized in Figure 4.

The average weight of wheat ears of these two lines were significantly different. While CM-82036 ears on average weighed (0.92 ± 0.20) g, Remus ears weights were (1.61 ± 0.33) g on average. In addition, the ear weight (and the relative moisture content) changed over the investigated time frame. Therefore, data can be shown either as metabolite amounts per ear or as concentration (nanomoles of metabolite per gram of ear). Figures 2 and 3 represent data normalized to the weight of whole wheat ears. No significant differences in the amounts of HT2 and T2 metabolites in the two different wheat lines were determined. Another way of representing the same data would show that CM-82036 wheat plants more efficiently metabolize the toxins, as less biomass (of the treated ear) was able to produce approximately the same amount of metabolites. To compare the two wheat varieties in a truly quantitative manner it would be necessary to normalize the amount of added toxin relative to the different (dry) ears weights, which was beyond the scope of this study. Also, it should be mentioned that the applied toxins might not have had sufficient time to diffuse into the entire ear in the early time points.

Biological Role of Formed Metabolites and Toxicological Implications. According to these findings, the C12−C13 epoxy group of HT2 and T2 that is crucial for toxicity was not affected by wheat biotransformation. The conversion of T2 to HT2 is considered a detoxification step in mammals[8] and also shown for plants in an *Arabidopsis thaliana* detached leaf assay.[34] Formation of HT2-3-Glc was found to be the dominating biotransformation reaction of both HT2 and T2. Glucosylation of trichothecenes at the position C-3, with the anomeric carbon of glucose linked via a β-D-glucosidic bond, has been reported to greatly reduce phytotoxicity.[35]

Inhibition of the growth and spreading of *Fusarium* species due to antimicrobial properties of principal phenolic acids in grains and their role in cell wall thickening have been reported in the literature.[36,37] Our results concerning conjugation of T2 with ferulic acid might be another beneficial property of ferulic acid, assuming a largely decreased toxicity of the conjugate.

In contrast to DON metabolism in wheat,[18] no glutathione or other sulfur-containing conjugates of HT2 and T2 were detected in this study. This does obviously reflect the lack of an α,β-unsaturated carbonyl functionality at C-8 as T2 and HT2, a functionality that is presumed to be the primary conjugation target of glutathione,[38] in type B trichothecenes such as DON.

Although glucosylation of trichothecenes is considered a detoxification process, the resulting conjugates may be reactivated within the mammalian gastrointestinal tract, a fact that is currently regarded as the main health risk associated with masked mycotoxins.[39−41] In this context, limited and contradicting information is available concerning the toxic potential of type A trichothecene hydroxylation products, which could possibly emerge by microbial reactivation in the gut. Existing toxicological studies agree that 3′-hydroxy-HT2 is less toxic compared to its parent form,[42] whereas 3′-hydroxy-T2 has been reported as being more acutely toxic *in vivo* than T2.[43] These novel "activated" metabolites may constitute toxicologically relevant mycotoxin derivatives; thus, further investigations are required. Intestinal hydrolysis and uptake can vary for different conjugated forms. For instance, it has been shown that malonyl isoflavone glucosides are more effectively absorbed than nonmalonylated isoflavone glucosides in rats.[44] Therefore, thorough toxicokinetic and overall toxicological assessment of novel and known masked mycotoxins should be conducted.

In summary, the metabolism of HT2 and T2 mycotoxins in wheat was presented according to data obtained by untargeted metabolomics profiling and time course kinetic studies. Exposure of wheat to either HT2 or T2 primarily activates metabolic reactions involving hydroxylation, (de)acetylation, and various conjugations. HT2 is the major metabolite resulting from exposure to T2 which follows the same pathway to that of directly inoculated HT2. Metabolites such as HT2-malonyl-glucoside, hydroxy-HT2-glucoside, dehydro-HT2-glucoside, T2-triol-glucoside, as well as (iso)feruloyl-T2 were documented for the first time. The interested reader is referred to Meng-Reiterer and Varga et al.[28] for a detailed structural elucidation. Kinetic data revealed that detoxification progresses rapidly, resulting in the almost complete degradation of the toxins, within 1 week, after a single exposure in flowering wheat ears. No different metabolites were observed between the FHB-resistant wheat line CM-82036 and the FHB-susceptible wheat line Remus. Further investigations to compare the role of detoxification efficiency of wheat varieties in FHB resistance are required. Additional studies to assess the toxicological relevance and potential food safety concerns of the *in planta* metabolites emerging from T2 and HT2 mycotoxins are warranted.

■ ASSOCIATED CONTENT

Supporting Information

The Supporting Information is available free of charge on the ACS Publications website at DOI: 10.1021/acs.jafc.5b02697.

HRMS/MS spectra of the putative *in planta* HT2 metabolites dehydro-HT2-glucoside and 3-acetyl-HT-2 and results from the method validation (PDF)

■ AUTHOR INFORMATION

Corresponding Author

*E-mail: franz.berthiller@boku.ac.at. Phone: +43 2272/66280-413. Fax: +43 2272/66280-403.

Author Contributions

‖A.V.N. and E.V. contributed equally to the work.

Funding

The financial support by the Austrian Federal Ministry of Science, Research and Economy, the National Foundation for Research, Technology and Development of Austria, BIOMIN Holding GmbH, as well as the Austrian Science Fund (FWF, grants P26213-B22 and SFB F3706) is gratefully acknowledged. Furthermore, this work has been supported by the Finnish Funding Agency for Technology and Innovation (TEKES; Myco-DETECT Project 401/31/2011) and the Walter Ehrström Foundation. The production of the HT2-3-Glc was performed within a Vienna Science and Technology Fund project (WWTF LS12−012) and the synthesis of 3-acetyl-T2 was performed within the FWF project SFB F3701.

Notes

The authors declare no competing financial interest.

DOI: 10.1021/acs.jafc.5b02697
J. Agric. Food Chem. 2015, 63, 7862−7872

■ ACKNOWLEDGMENTS

The authors thank Imer Maloku for his support with the plant experiments.

■ ABBREVIATIONS USED

DON, deoxynivalenol; EFSA, European Food Safety Authority; EIC, extraction ion chromatogram; ESI, electrospray ionization; FHB, Fusarium head blight; HRMS, high resolution mass spectrometry; HT2, HT-2 toxin; HT2-3-Glc, HT-2 toxin-3-*O*-*β*-glucoside; LC, liquid chromatography; MS/MS, tandem mass spectrometry; MSI, Metabolomics Standard Initiative; NMR, nuclear magnetic resonance; QTOF, quadrupole time-of-flight; R_A, apparent recovery; R_E, extraction recovery; SIL, stable isotope labeling; SSE, signal suppression or enhancement; T2, T-2 toxin; TDI, tolerable daily intake; UHPLC, ultra high performance liquid chromatography

■ REFERENCES

(1) Desjardins, A. E.; Hohn, T. M. Mycotoxins in Plant Pathogenesis. *Mol. Plant-Microbe Interact.* **1997**, *10*, 147−152.
(2) Bottalico, A.; Perrone, G. Toxigenic *Fusarium* species and mycotoxins associated with head blight in small-grain cereals in Europe. *Eur. J. Plant Pathol.* **2002**, *108*, 611−624.
(3) Coleman, J. O. D.; Blake-Kalff, M. M. A.; Davies, T. G. E. Detoxification of xenobiotics by plants: chemical modification and vacuolar compartmentation. *Trends Plant Sci.* **1997**, *2*, 144−151.
(4) Krska, R.; Malachova, A.; Berthiller, F.; van Egmond, H. P. Determination of T-2 and HT-2 toxins in food and feed: an update. *World Mycotoxin J.* **2014**, *7*, 131−142.
(5) Rocha, O.; Ansari, K.; Doohan, F. M. Effects of trichothecene mycotoxins on eukaryotic cells: a review. *Food Addit. Contam.* **2005**, *22*, 369−378.
(6) European Food Safety Authority (EFSA) Panel on Contaminants in the Food Chain (CONTAM). Scientific Opinion on the risks for animal and public health related to the presence of T-2 and HT-2 toxin in food and feed. *EFSA Journal* **2011**, *9*, 12, 2481.
(7) Commission Recommendation 2013/165/EU of 27 March 2013 on the presence of T-2 and HT-2 toxin in cereals and cereal products *Off. J. Eur. Commun.* **2013**, *L 91*, 12−15.
(8) Wu, Q.; Dohnal, V.; Kuca, K.; Yuan, Z. Trichothecenes: Structure-Toxic Activity Relationships. *Curr. Drug Metab.* **2013**, *14*, 641−660.
(9) Dohnal, V.; Jezkova, A.; Jun, D.; Kuca, K. Metabolic Pathways of T-2 Toxin. *Curr. Drug Metab.* **2008**, *9*, 77−82.
(10) He, J.; Zhou, T.; Young, J. C.; Boland, G. J.; Scott, P. M. Chemical and biological transformations for detoxification of trichothecene mycotoxins in human and animal food chains: a review. *Trends Food Sci. Technol.* **2010**, *21*, 67−76.
(11) Rychlik, M.; Humpf, H.-U.; Marko, D.; Dänicke, S.; Mally, A.; Berthiller, F.; Klaffke, H.; Lorenz, N. Proposal of a comprehensive definition of modified and other forms of mycotoxins including "masked" mycotoxins. *Mycotoxin Res.* **2014**, *30*, 197−205.
(12) Berthiller, F.; Krska, R.; Dall'Asta, C.; Lemmens, M.; Adam, G.; Schuhmacher, R. Determination of DON-3-Glucoside in artificially and naturally contaminated wheat with LC-MS/MS. *Mycotoxin Res.* **2005**, *21*, 205−208.
(13) Nakagawa, H.; Ohmichi, K.; Sakamoto, S.; Sago, Y.; Kushiro, M.; Nagashima, H.; Yoshida, M.; Nakajima, T. Detection of a new *Fusarium* masked mycotoxin in wheat grain by high-resolution LC−Orbitrap MS. *Food Addit. Contam., Part A* **2011**, *28*, 1447−1456.
(14) Busman, M.; Poling, S. M.; Maragos, C. M. Observation of T-2 Toxin and HT-2 Toxin Glucosides from *Fusarium sporotrichioides* by Liquid Chromatography Coupled to Tandem Mass Spectrometry (LC-MS/MS). *Toxins* **2011**, *3*, 1554−1568.
(15) Mirocha, C. J.; Abbas, H. K.; Treeful, L.; Bean, G. T-2 Toxin and Diacetoxyscirpenol Metabolism by *Baccharis* spp. *Appl. Environ. Microbiol.* **1988**, *54*, 2277−2280.
(16) Nathanail, A. V.; Syvähuoko, J.; Malachová, A.; Jestoi, M.; Varga, E.; Michlmayr, H.; Adam, G.; Sieviläinen, E.; Berthiller, F.; Peltonen, K. Simultaneous determination of major type A and B trichothecenes, zearalenone and certain modified metabolites in Finnish cereal grains with a novel liquid chromatography-tandem mass spectrometric method. *Anal. Bioanal. Chem.* **2015**, *407*, 4745−4755.
(17) Theodoridis, G.; Gika, H. G.; Wilson, I. D. LC-MS-based methodology for global metabolite profiling in metabonomics/metabolomics. *TrAC, Trends Anal. Chem.* **2008**, *27*, 251−260.
(18) Kluger, B.; Bueschl, C.; Lemmens, M.; Michlmayr, H.; Malachova, A.; Koutnik, A.; Maloku, I.; Berthiller, F.; Adam, G.; Krska, R.; Schuhmacher, R. Biotransformation of the Mycotoxin Deoxynivalenol in Fusarium Resistant and Susceptible Near Isogenic Wheat Lines. *PLoS One* **2015**, *10*, e0119656.
(19) Cano, P. M.; Jamin, E. L.; Tadrist, S.; Bourdaud'hui, P.; Pean, M.; Debrauwer, L.; Oswald, I. P.; Delaforge, M.; Puel, O. New Untargeted Metabolic Profiling Combining Mass Spectrometry and Isotopic Labeling: Application on *Aspergillus fumigatus* Grown on Wheat. *Anal. Chem.* **2013**, *85*, 8412−8420.
(20) Bueschl, C.; Kluger, B.; Lemmens, M.; Adam, G.; Wiesenberger, G.; Maschietto, V.; Marocco, A.; Strauss, J.; Bödi, S.; Thallinger, G. G.; Krska, R.; Schuhmacher, R. A novel stable isotope labelling assisted workflow for improved untargeted LC−HRMS based metabolomics research. *Metabolomics* **2014**, *10*, 754−769.
(21) Bueschl, C.; Kluger, B.; Berthiller, F.; Lirk, G.; Winkler, S.; Krska, R.; Schuhmacher, R. MetExtract: a new software tool for the automated comprehensive extraction of metabolite-derived LC/MS signals in metabolomics research. *Bioinformatics* **2012**, *28*, 736−738.
(22) Kluger, B.; Bueschl, C.; Neumann, N.; Stückler, R.; Doppler, M.; Chassy, A. W.; Waterhouse, A. L.; Rechthaler, J.; Kampleitner, N.; Thallinger, G. G.; Adam, G.; Krska, R.; Schuhmacher, R. Untargeted Profiling of Tracer-Derived Metabolites Using Stable Isotopic Labeling and Fast Polarity-Switching LC−ESI-HRMS. *Anal. Chem.* **2014**, *86*, 11533−11537.
(23) Buerstmayr, H.; Lemmens, M.; Grausgruber, H.; Ruckenbauer, P. Scab Resistance of International Wheat Germplasm. *Cereal Res. Commun.* **1996**, *24*, 195−202.
(24) Lemmens, M.; Scholz, U.; Berthiller, F.; Dall'Asta, C.; Koutnik, A.; Schuhmacher, R.; Adam, G.; Buerstmayr, H.; Mesterházy, A.; Krska, R.; Ruckenbauer, P. The Ability to Detoxify the Mycotoxin Deoxynivalenol Colocalizes With a Major Quantitative Trait Locus for Fusarium Head Blight Resistance in Wheat. *Mol. Plant-Microbe Interact.* **2005**, *18*, 1318−1324.
(25) Large, E. C. Growth stages in cereals illustration of the Feekes scale. *Plant Pathol.* **1954**, *3*, 128−129.
(26) Sturm, M.; Kohlbacher, O. TOPPView: An Open-Source Viewer for Mass Spectrometry Data. *J. Proteome Res.* **2009**, *8*, 3760−3763.
(27) Du, P.; Kibbe, W. A.; Lin, S. M. Improved peak detection in mass spectrum by incorporating continuous wavelet transform-based pattern matching. *Bioinformatics* **2006**, *22*, 2059−2065.
(28) Meng-Reiterer, J.; Varga, E.; Nathanail, A. V.; Bueschl, C.; Rechthaler, J.; McCormick, S. P.; Michlmayr, H.; Malachová, A.; Fruhmann, P.; Adam, G.; Berthiller, F.; Lemmens, M.; Schuhmacher, R. Tracing the metabolism of HT-2 toxin and T-2 toxin in barley by isotope assisted untargeted screening and quantitative LC-HRMS analysis. *Anal. Bioanal Chem.*, in press, DOI: 10.1007/s00216-015-8975-9.
(29) Cole, D. J. Detoxification and Activation of Agrochemicals in Plants. *Pestic. Sci.* **1994**, *42*, 209−222.
(30) Sosulski, F.; Krygier, K.; Hogge, L. Free, Esterified, and Insoluble-Bound Phenolic Acids. 3. Composition of Phenolic Acids in Cereal and Potato Flours. *J. Agric. Food Chem.* **1982**, *30*, 337−340.
(31) McCormick, S. P.; Kato, T.; Maragos, C. M.; Busman, M.; Lattanzio, V. M. T.; Galaverna, G.; Dall-Asta, C.; Crich, D.; Price, N. P. J.; Kurtzman, C. P. Anomericity of T-2 Toxin-glucoside: Masked Mycotoxin in Cereal Crops. *J. Agric. Food Chem.* **2015**, *63*, 731−738.
(32) Alexander, N. The TRI101 story: engineering wheat and barley to resist Fusarium head blight. *World Mycotoxin J.* **2008**, *1*, 31−37.

DOI: 10.1021/acs.jafc.5b02697
J. Agric. Food Chem. 2015, 63, 7862−7872

(33) Lattanzio, V. M.; Solfrizzo, M.; Visconti, A. Enzymatic hydrolysis of T-2 toxin for the quantitative determination of total T-2 and HT-2 toxins in cereals. *Anal. Bioanal. Chem.* **2009**, *395*, 1325−1334.
(34) Desjardins, A. E.; McCormick, S. P.; Appell, M. Structure-Activity Relationships of Trichothecene Toxins in an *Arabidopsis thaliana* Leaf Assay. *J. Agric. Food Chem.* **2007**, *55*, 6487−6492.
(35) Poppenberger, B.; Berthiller, F.; Lucyshyn, D.; Sieberer, T.; Schuhmacher, R.; Krska, R.; Kuchler, K.; Glössl, J.; Luschnig, C.; Adam, G. Detoxification of the *Fusarium* Mycotoxin Deoxynivalenol by a UDP-glucosyltransferase from *Arabidopsis thaliana*. *J. Biol. Chem.* **2003**, *278*, 47905−47914.
(36) McKeehen, J. D.; Busch, R. H.; Fulcher, R. G. Evaluation of Wheat (*Triticum aestivum* L.) Phenolic Acids during Grain Development and Their Contribution to *Fusarium* Resistance. *J. Agric. Food Chem.* **1999**, *47*, 1476−1482.
(37) Gunnaiah, R.; Kushalappa, A. C.; Duggavathi, R.; Fox, S.; Somers, D. J. Integrated Metabolo-Proteomic Approach to Decipher the Mechanisms by Which Wheat QTL (*Fhb1*) Contributes to Resistance against *Fusarium graminearum*. *PLoS One* **2012**, *7*, e40695.
(38) Gardiner, S. A.; Boddu, J.; Berthiller, F.; Hametner, C.; Stupar, R. M.; Adam, G.; Muehlbauer, G. J. Transcriptome Analysis of the Barley-Deoxynivalenol Interaction: Evidence for a Role of Glutathione in Deoxynivalenol Detoxification. *Mol. Plant-Microbe Interact.* **2010**, *23*, 962−976.
(39) Dall'Erta, A.; Cirlini, M.; Dall'Asta, M.; Del Rio, D.; Galaverna, G.; Dall'Asta, C. Masked Mycotoxins Are Efficiently Hydrolyzed by Human Colonic Microbiota Releasing Their Aglycones. *Chem. Res. Toxicol.* **2013**, *26*, 305−312.
(40) De Angelis, E.; Monaci, L.; Mackie, A.; Salt, L.; Visconti, A. Bioaccessibility of T-2 and HT-2 toxins in mycotoxin contaminated bread models submitted to *in vitro* human digestion. *Innovative Food Sci. Emerging Technol.* **2014**, *22*, 248−256.
(41) Nagl, V.; Woechtl, B.; Schwartz-Zimmermann, H. E.; Hennig-Pauka, I.; Moll, W.-D.; Adam, G.; Berthiller, F. Metabolism of the masked mycotoxin deoxynivalenol-3-glucoside in pigs. *Toxicol. Lett.* **2014**, *229*, 190−197.
(42) Islam, Z.; Nagase, M.; Ota, A.; Ueda, S.; Yoshizawa, T.; Sakato, N. Structure-Function Relationship of T-2 Toxin and Its Metabolites in Inducing Thymic Apoptosis *in vivo* in Mice. *Biosci., Biotechnol., Biochem.* **1998**, *62*, 1492−1497.
(43) Yoshizawa, T.; Sakamoto, T.; Ayano, Y.; Mirocha, C. J. 3′-Hydroxy T-2 and 3′-Hydroxy HT-2 Toxins: New Metabolites of T-2 Toxin, a Trichothecene Mycotoxin, in Animals. *Agric. Biol. Chem.* **1982**, *46*, 2613−2615.
(44) Yonemoto-Yano, H.; Maebuchi, M.; Fukui, K.; Tsuzaki, S.; Takamatsu, K.; Uehara, M. Malonyl Isoflavone Glucosides Are Chiefly Hydrolyzed and Absorbed in the Colon. *J. Agric. Food Chem.* **2014**, *62*, 2264−2270.

DOI: 10.1021/acs.jafc.5b02697
J. Agric. Food Chem. 2015, 63, 7862−7872

glucose, lactate, glutamate/glutamine, and taurine, were proposed for diagnosing NAFLD at various stages.[3] Metabolomic analysis was also used to assess the effects of dietary cholesterol through NMR-based quantitative profiling of liver extracts from $LDLr^{-/-}$ mice. It was found that the levels of hepatic cholesterol, triglyceride (TG), oleic acid, polyunsaturated fatty acid (PUFA)/monounsaturated fatty acid (MUFA) ratio, long-chain polyunsaturated fatty acids, taurine, glutathione, methionine, and carnitine, which are related to fatty acid metabolism and mitochondrial function, were affected in the diet- and time-dependent progression from steatosis to NASH.[4]

Despite the different rodent models established and the few identified metabolites, there is still a need to further verify and identify more key metabolites involved in the pathogenesis and progression of NAFLD in an appropriate animal model that mimics the pathophysiological metabolism of human disease. The high-fat-diet (HFD)-fed C57BL/6J mouse model has been widely applied to investigate metabolic diseases, because it is susceptible to NAFLD development. This model provides an efficient metabolic system for the gradual development of obesity, insulin resistance, hepatic steatosis, and steatohepatitis, which better mimic the etiology and pathogenesis of NAFLD in humans, owing to integration among different environmental factors and multiple genes, as compared to focusing on a single-gene mutant phenotype.[7,8] However, to the best of our knowledge, there have been no previous metabolomic reports on the time-related NAFLD progression in HFD-fed C57BL/6J mice.

In the present study, ultrahigh-performance liquid chromatography coupled with quadrupole time-of-flight mass spectrometry (UHPLC−QTOF−MS) and gas chromatography−mass spectrometry (GC−MS) platform-based metabolomics was employed to analyze the serum metabolic profiles at various stages of NAFLD induced by 4, 8, 12, and 16 weeks of HFD feeding in C57BL/6J mice. On the basis of the results of pathophysiological parameters, potential metabolites, and metabolic pathway responses at the different time points of HFD feeding, we provide a well-established animal model and comprehensive profile of the metabolic changes that occur during the onset and progression of NAFLD. Our findings could help elucidate the metabolic mechanisms underlying the development of NAFLD induced by a HFD.

MATERIALS AND METHODS

Animal Model. Experiments were performed with 6-week-old male C57BL/6J mice (Laboratory Animal Center, National Taiwan University College of Medicine, Taipei, Taiwan) under controlled environmental conditions (temperature of 23 ± 2 °C, relative humidity of 50−70%, and 12 h light/dark cycle) with *ad libitum* access to food and water. Animal care and handling procedures were in accordance with an experimental protocol approved by the Institutional Animal Care and Use Committee (IACUC) of National Taiwan University (IACUC approval number NTU-101-EL-124) and complied with the guidelines described in the Animal Protection Law, amended on June 29, 2011, Hua-Zong-(1)-Yi-Tzi-10000136211, Council of Agriculture, Taiwan. After a 2 week adaptation period, all mice were randomly divided into two groups based on their diet. Control group mice were fed a normal diet containing 13.5% kcal fat (Laboratory Rodent Diet 5001, Lab Diet/PMI Nutrition International, Purina Mills LLC, Gray Summit, MO), while mice in the negative control group were fed a HFD with 60% kcal fat (D12492, Research Diets, Inc., New Brunswick, NJ). Food intake and body weight were recorded once a week. A total of 10−12 mice per group were fasted overnight and sacrificed by CO_2 asphyxiation at weeks 4, 8, 12, and 16 after commencing the diet administration.

Serological Analyses. Whole blood was immediately collected by cardiac puncture and then allowed to clot. After centrifugation at 1000*g* for 10 min at 4 °C, the resultant serum samples were separated and stored individually at −80 °C for subsequent analyses. Serum chemistry for aspartate aminotransferase (AST), alanine aminotransferase (ALT), total cholesterol (TC), and TG levels were subjected to biochemical testing with an automatic chemistry analyzer (SPOTCHEM EZ SP-4430, ARKRAY, Inc., Kyoto, Japan). The serum FFA concentration was measured using the enzyme-based FFA Quantification Kit (BioVision, San Francisco, CA), and the insulin level was determined using an enzyme-linked immunosorbent assay kit (Mercodia AB, Uppsala, Sweden).

Histopathological Examination. Liver and fat pads (subcutaneous, epididymal, and perirenal fat) were harvested, weighed, and photographed. Liver pathological analysis and semi-quantitative evaluation was carried out as previously described.[9] Briefly, paraffin-embedded and frozen sections of liver tissue were routinely processed for hematoxylin and eosin (H&E) and Oil Red O staining, respectively. Each H&E section was then scored for steatosis with morphometric analysis by an experienced pathologist. The degree of steatosis was graded from 1 to 5 according to severity: 1, minimal (<1%); 2, slight (1−25%); 3, moderate (26−50%); 4, moderate/severe (51−75%); and 5, severe/high (76−100%). Lastly, the remaining liver tissues were immediately frozen at −80 °C for further analysis.

Liver Enzymes and Inflammatory Cytokines. Samples of 300 mg liver tissues were homogenized in 3 mL of cold extraction buffer (8 mM KH_2PO_4, 12 mM K_2HPO_4, and 1.5% KCl at pH 7.4) for 10 min on ice and then centrifuged at 10000*g* for 30 min at 4 °C. The protein content in the liver homogenate was determined with a Bio-Rad protein assay (Hercules, CA). Hepatic TG, glutathione (GSH), glutathione peroxidase (GPx), glutathione reductase (GRd), catalase (CAT), and superoxide dismutase (SOD) were assayed by enzymatic colorimetric methods (Cayman Chemical Co., Ann Arbor, MI). Hepatic TC and lipid peroxidation were evaluated fluorometrically using the cholesterol and thiobarbituric acid-reactive substances (TBARS) assay kits (Cayman Chemical Co., Ann Arbor, MI), respectively. In addition, enzyme-linked immunosorbent assays were used for the quantitative detection of hepatic tumor necrosis factor-α (TNF-α), interleukin-1β (IL-1β), and interleukin-6 (IL-6) (eBioscience, Inc., San Diego, CA). All procedures complied with the manufacturer instructions.

Serum Sample Preparation. A 100 μL aliquot of each mouse serum sample was extracted for 2 min in 400 μL of ice-cold methanol using a Geno/Grinder 2010 Spex SamplePrep (Metuchen, NJ). Following centrifugation at 4 °C and 15000*g* and for 5 min, the remaining pellet was extracted twice with the same process. The serum extracts were pooled and evaporated using the Thermo SpeedVac SPD111V (Waltham, MA) for 4 h. For UHPLC−QTOF−MS analysis, the dried extracts were subsequently reconstituted in 200 μL of 50% methanol. After centrifugation at 15000*g* for 5 min, the resulting supernatant was filtered through a 0.22 μm Ministart RC 4 filter (Sartorius, Goettingen, Germany) and subjected to UHPLC−QTOF−MS analysis. For GC−MS, the dried residues were derivatized with trimethylsilylation through the subsequent addition of 10 μL of *O*-methylhydroxylamine hydrochloride (40 mg/mL in pyridine) and 90 μL of *N*,*O*-bis(trimethylsilyl)trifluoroacetamide containing 1% trimethylchlorosilane at 40 °C for 90 and 30 min, respectively. Finally, the derivatized samples were subjected to GC−MS analysis. For quality control, equal amounts of each sample aliquots were pooled and applied to monitor the stability of the analytical performance in the two platforms.

UHPLC−QTOF−MS Analysis. Chromatographic separations of the serum extracts were performed using an Agilent 1290 UHPLC system (Agilent Technologies, Santa Clara, CA) with an Acquity HSS T3 column (2.1 × 100 mm, 1.8 μm, Waters, Milford, MA) maintained at 40 °C. The mobile phases A and B were 0.1% formic acid in water and 0.1% formic acid in acetonitrile, respectively. The gradient elution program was initiated with 2% B for 1.5 min, linear gradient to 50% B in 7.5 min, linear gradient to 95% B in 5 min, and then held at 95% B

DOI: 10.1021/acs.jafc.5b02830
J. Agric. Food Chem. 2015, 63, 7873−7884

Table 1. Effect of HFD on Basal Characteristics and Serum Biochemical Parameters at Different Time Points after Induction[a]

	4 weeks		8 weeks		12 weeks		16 weeks	
	control	HFD	control	HFD	control	HFD	control	HFD
Basal Characteristics								
food consumption (g/day)	4.3 ± 0.7	3.4 ± 0.5	4.5 ± 0.5	3.1 ± 0.3	4.6 ± 0.6	3.3 ± 0.6	4.3 ± 0.7	3.0 ± 0.5
calorie intake (kcal/day)	13.1 ± 2.2	17.9 ± 0.8**	13.6 ± 1.5	16.1 ± 1.9**	14.0 ± 1.9	17.3 ± 3.3**	12.9 ± 2.2	16.0 ± 2.5**
body weight (g)	25.2 ± 2.0	34.2 ± 2.5***	28.0 ± 1.1	42.4 ± 2.3***	30.4 ± 1.7	49.4 ± 1.3***	31.5 ± 2.1	51.8 ± 3.1***
epididymal fat (g)	0.3 ± 0.1	1.7 ± 0.4***	0.4 ± 0.1	2.2 ± 0.3***	0.4 ± 0.1	1.9 ± 0.6***	0.4 ± 0.2	1.9 ± 0.6***
perirenal fat (g)	0.1 ± 0.0	0.6 ± 0.2***	0.1 ± 0.0	0.8 ± 0.1***	0.1 ± 0.1	1.3 ± 0.2***	0.1 ± 0.1	1.3 ± 0.2***
subcutaneous fat (g)	0.2 ± 0.0	0.8 ± 0.2***	0.2 ± 0.1	2.7 ± 0.7***	0.2 ± 0.1	3.6 ± 0.6***	0.3 ± 0.1	4.3 ± 0.6***
total fat (g)	0.5 ± 0.1	3.0 ± 0.7***	0.7 ± 0.2	5.8 ± 1.0***	0.8 ± 0.2	6.8 ± 0.9***	0.9 ± 0.3	7.5 ± 1.1***
relative total fat (%)	2.0 ± 0.3	8.9 ± 1.7***	2.3 ± 0.6	13.6 ± 1.7***	2.5 ± 0.7	13.8 ± 1.8***	2.7 ± 0.7	14.4 ± 1.8***
Serum Biochemical Parameters								
glucose (mg/dL)	214.8 ± 29.5	281.5 ± 14.6***	225.6 ± 13.5	274.7 ± 16.3***	213.1 ± 28.3	275.8 ± 19.5***	201.7 ± 25.9	266.3 ± 19.3***
insulin (ng/mL)	0.7 ± 0.4	0.7 ± 0.4	0.8 ± 0.4	1.3 ± 0.3*	0.9 ± 0.3	2.0 ± 0.4***	1.0 ± 0.4	2.3 ± 0.6***
FFA (nmol/μL)	0.6 ± 0.2	0.9 ± 0.4	0.9 ± 0.4	1.1 ± 0.5	0.8 ± 0.4	1.9 ± 0.4***	0.7 ± 0.1	1.8 ± 0.2***
TG (mg/dL)	93.2 ± 9.8	103.0 ± 18.6	88.5 ± 14.9	105.5 ± 8.7*	85.6 ± 12.2	115.9 ± 12.1***	81.4 ± 17.2	115.0 ± 15.0***
TC (mg/dL)	87.9 ± 15.1	181.0 ± 15.2***	86.3 ± 16.1	182.3 ± 18.0***	87.7 ± 18.9	233.1 ± 27.5***	81.0 ± 8.5	233.7 ± 16.1***
AST (IU/L)	115.5 ± 37.9	101.4 ± 21.4	109.8 ± 45.5	137.6 ± 49.4	120.8 ± 57.0	235.8 ± 82.1**	124.8 ± 37.7	278.3 ± 96.5***
ALT (IU/L)	37.5 ± 14.5	39.4 ± 11.2	47.4 ± 14.0	55.1 ± 14.1	41.8 ± 14.5	219.8 ± 46.8***	46.1 ± 10.1	236.6 ± 64.3***

[a]C57BL/6J mice were fed a normal diet or HFD for 4, 8, 12, and 16 weeks. The relative total fat is expressed as a percentage of body weight (total fat/final body weight × 100). Data are presented as mean ± SD (n = 10−12 mice per group). Comparison was made between HFD and their age-matched controls by Student's t test. *p < 0.05. **p < 0.01. ***p < 0.001. HFD, high-fat diet; FFA, free fatty acid; TG, triglyceride; TC, total cholesterol; AST, aspartate aminotransferase; and ALT, alanine aminotransferase.

DOI: 10.1021/acs.jafc.5b02830
J. Agric. Food Chem. 2015, 63, 7873−7884

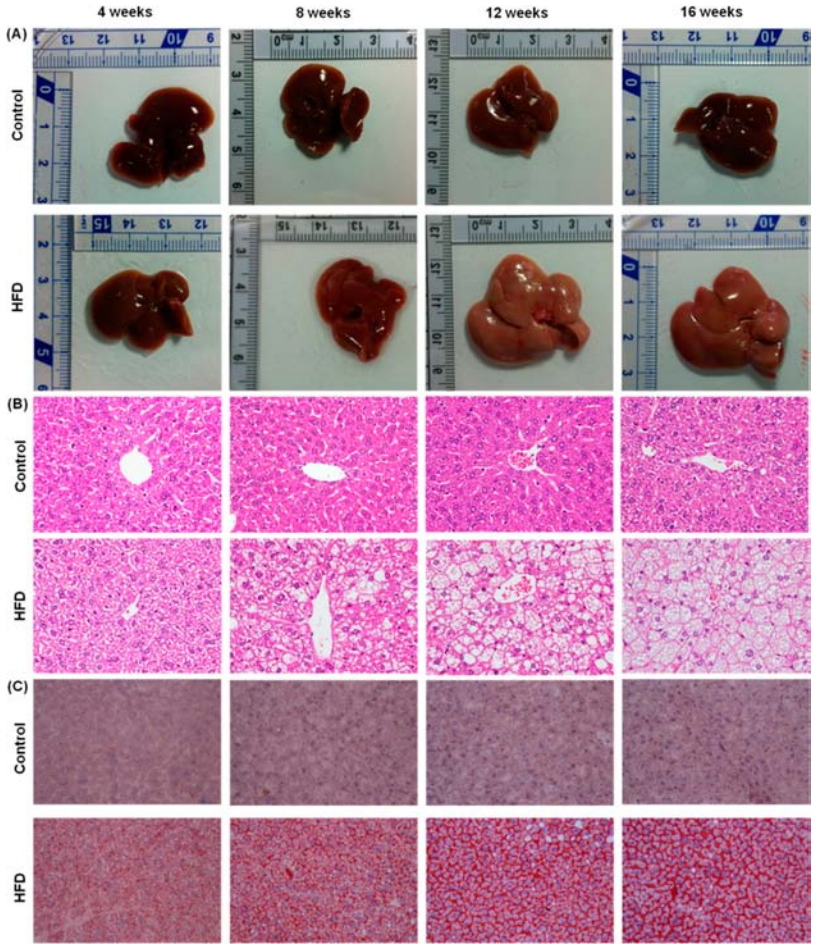

Figure 1. Effect of a HFD on liver histopathological alterations at different time points after induction: (A) liver morphology, (B) H&E stain, and (C) Oil Red O stain in C57BL/6J mice fed a normal diet or HFD for 4, 8, 12, and 16 weeks. Liver sections were stained with H&E and Oil Red O to visualize lipid droplets (in red). Representative images (400× magnification) of each group are shown. HFD, high-fat diet.

for 3 min. The flow rate was 0.3 mL/min, and the injected sample volume was 2 μL. The eluent was subsequently introduced into the Burker maXis QTOF mass spectrometer (Bruker Daltonics, Bremen, Germany) coupled to an electrospray ionization source, with capillary voltage set at 4500 V in positive- and negative-ion modes and end plate offset at 500 V. The parameters were used as follows: nebulizer pressure, 2.0 bar; dry gas temperature, 200 °C; and flow rate, 8 L/min. The full-scan mass range was from m/z 50 to 1500. To ensure accuracy and reproducibility, the mass instrument was calibrated with sodium formate before daily use with lock mass of hexakis between runs.

GC−MS Analysis. An Agilent 7890 GC system equipped with a 5975 quadrupole mass selective detector (MSD, Agilent, Santa Clara, CA) and a DB-5MS column (30 m × 0.25 mm inner diameter × 0.25 μm film thickness, Agilent, Santa Clara, CA) was employed to acquire metabolic profiles of the derivatized products. A total of 1 μL of the sample was injected in split mode (split ratio of 1:5) with an inlet temperature of 250 °C. Helium was used as the carrier gas in constant flow mode. The initial oven temperature was set to hold at 60 °C for 1 min, followed by a ramp to 325 °C at 10 °C/min, and finally held for 10 min. The mass spectrum was acquired in full-scan mode from m/z 50 to 550. Electron impact ionization at 70 V was operated with an ion source temperature of 250 °C.

Data Processing and Analysis. The UHPLC−QTOF−MS data were exported to True Ion Pick (TIPick) software for peak detection, alignment, and normalization as previously described.[10] For GC−MS data, all of the spectral processing was performed using the Automated Mass Spectral Deconvolution and Identification System (AMDIS) software. The acquired data from UHPLC−QTOF−MS and GC−MS were used to identify the compounds corresponding to those in the NTU MetaCore metabolomics chemical standards database and Fiehn library, respectively. Finally, the variables existing in at least 80% of either group were retained for further analysis.

Statistical Analysis. Principal component analysis (PCA) was carried out to discriminate visually the general structure of each data set based on their UHPLC−QTOF−MS or GC−MS metabolic profiles. The changes in peak intensity between two groups were compared by fold-change analysis. All pathophysiological data are presented as the mean ± standard deviation (SD). Statistical differences between the compared groups were assessed by the Student's t test, with p values less than 0.05 regarded as significant.

RESULTS

Animal Characteristics. The characteristics of C57BL/6J mice fed a normal diet or HFD (60% kcal from fat) for 4, 8, 12, and 16 weeks are shown in Table 1. Despite a higher food intake in control groups, the average daily caloric intake of mice in the HFD groups (16.0−17.9 kcal) were significantly higher ($p < 0.01$) than those of mice in the control groups (12.9−14.0 kcal) at all time points (4, 8, 12, and 16 weeks). The average body and fat pad weights of mice in each group showed increasing trends throughout the experimental period. After 4 weeks, HFD-fed mice immediately appeared obese, as reflected by marked enlargement of subcutaneous, epididymal, and perirenal fat pads in comparison to controls ($p < 0.001$). Noticeably, the epididymal and perirenal fat pads were slightly

DOI: 10.1021/acs.jafc.5b02830
J. Agric. Food Chem. 2015, 63, 7873−7884

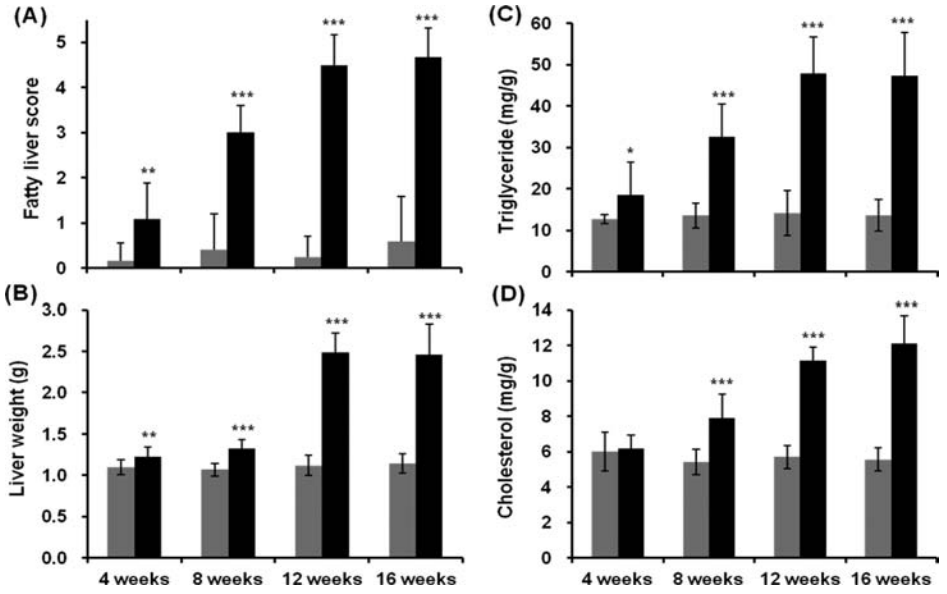

Figure 2. Effect of a HFD on hepatic lipid content at different time points after induction: (A) fatty liver score, (B) liver weight, (C) hepatic TG, and (D) cholesterol in C57BL/6J mice fed a normal diet or HFD for 4, 8, 12, and 16 weeks. Data are presented as the mean ± SD (n = 10−12 mice per group). Comparison was made between HFD and their age-matched controls by Student's t test: (∗) $p < 0.05$, (∗∗) $p < 0.01$, and (∗∗∗) $p < 0.001$. (Gray bars) Control and (black bars) HFD.

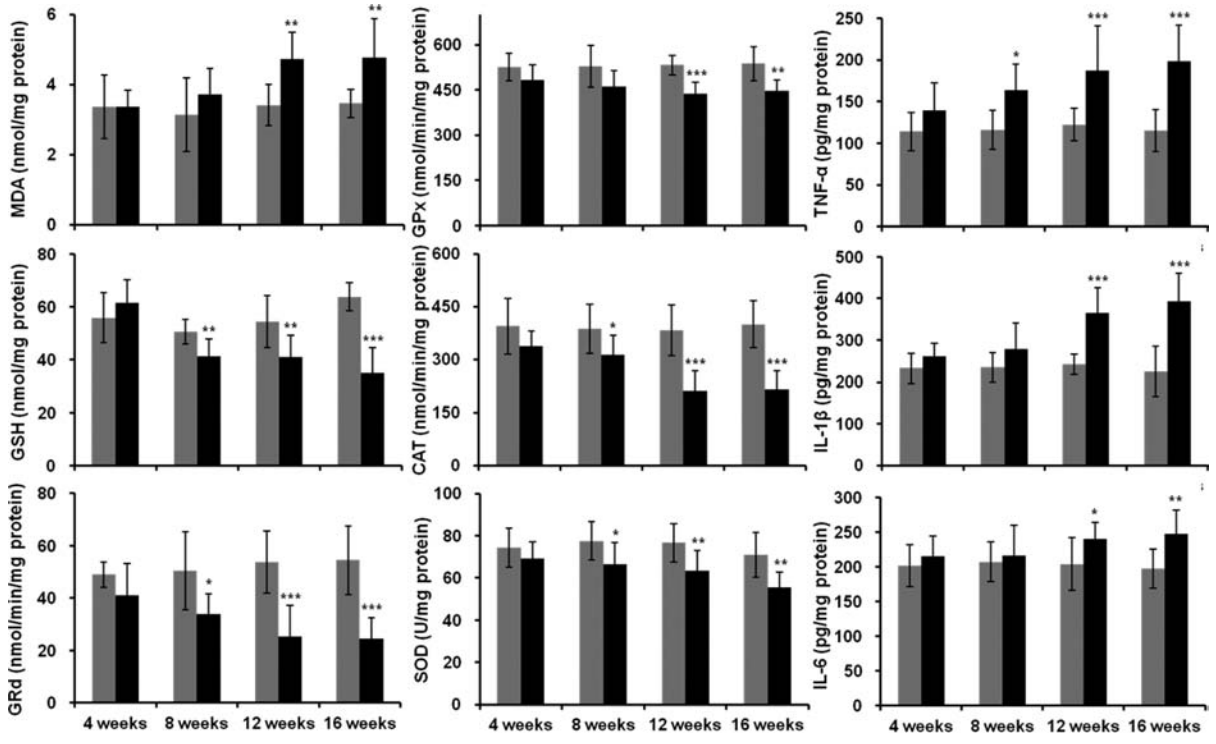

Figure 3. Effect of HFD on hepatic antioxidant capacity and pro-inflammatory cytokines at different time points after induction. C57BL/6J mice were fed a normal diet or HFD for 4, 8, 12, and 16 weeks. Data are presented as the mean ± SD (n = 10−12 mice per group). Comparison was made between HFD and their age-matched controls by Student's t test: (∗) $p < 0.05$, (∗∗) $p < 0.01$, and (∗∗∗) $p < 0.001$. (Gray bars) Control and (black bars) HFD. MDA, malondialdehyde; GSH, glutathione; SOD, superoxide dismutase; CAT, catalase; GPx, glutathione peroxidase; GRd, glutathione reductase; TNF-α, tumor necrosis factor-α; IL-1β, interleukin-1β; and IL-6, interleukin-6.

decreased in HFC mice after 12 weeks (−15.6%) and 16 weeks (−3.4%) of feeding, respectively, compared to previous weeks. However, the subcutaneous fat pads of HFD-fed mice increased continuously over time. We speculated that excess adipose tissue might accumulate in the subcutaneous tissues, liver, or other organs after 12 weeks on the HFD.

After 4 weeks, the HFD mice exhibited significantly higher serum concentrations of glucose ($p < 0.001$) and TC ($p < 0.001$) than those in the controls (Table 1). After 4 more weeks, the HFD-fed mice also developed hyperinsulinemia and hypertriglyceridemia, demonstrated by the markedly increase serum levels of insulin and TG, 1.6-fold ($p < 0.05$) and 1.2-fold

DOI: 10.1021/acs.jafc.5b02830
J. Agric. Food Chem. 2015, 63, 7873−7884

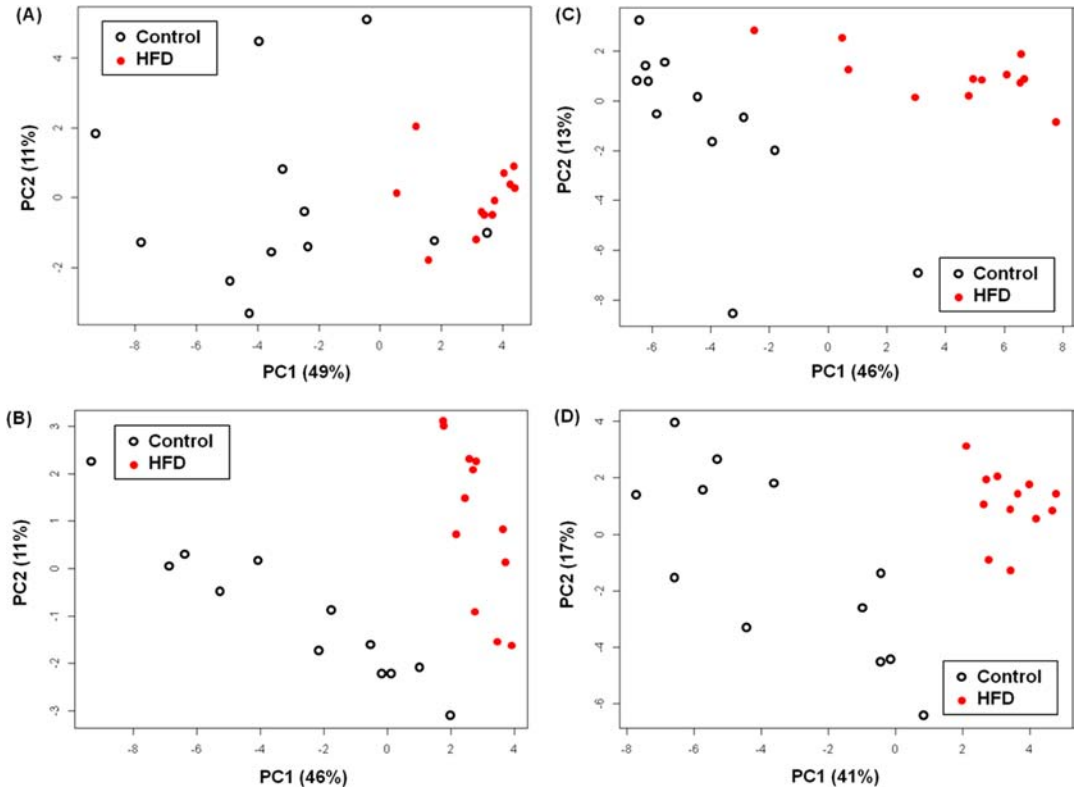

Figure 4. PCA score plots derived from the UHPLC−QTOF−MS spectrum of serum samples from control and HFD mice after (A) 4 weeks, (B) 8 weeks, (C) 12 weeks, and (D) 16 weeks of feeding. HFD, high-fat diet.

($p < 0.05$) the levels in controls, respectively. At the end of 12 and 16 weeks, the HFD group showed significantly higher serum levels of FFA ($p < 0.001$), AST ($p < 0.01$, or $p < 0.001$), and ALT ($p < 0.001$) than those in the controls, suggesting successful induction of the physiological indicators for NAFLD development.

Hepatic Steatosis and Histopathological Examination. Figure 1 shows that, in comparison to the control group, the macroscopic liver appearance of the HFD group indicated remarkable hepatomegaly with significant histopathological changes over time. Liver sections were evaluated by H&E staining and further staining with Oil Red O to visualize the lipid droplets of these vacuoles. Histopathological examinations revealed no abnormalities in control mice, whereas lipid vacuoles and lipid droplets accumulation progressively increased in the HFD-fed mice over the induction period. Correspondingly, the steatosis score indicated that macrovesicular fatty infiltration of hepatocytes was minimal (1.1), moderate (3.0), severe/high (4.5), and severe/high (4.7) after 4, 8, 12, and 16 weeks of HFD feeding, respectively (Figure 2). These morphological changes paralleled the significant increases in liver weight by 1.1-fold ($p < 0.01$), 1.2-fold, 2.2-fold, and 2.1-fold ($p < 0.001$), hepatic TG level by 1.5-fold ($p < 0.05$), 2.4-fold, 3.4-fold, and 3.5-fold ($p < 0.001$), and hepatic TC level by 1.0-fold (no significant difference), 1.5-fold, 2.0-fold, and 2.2-fold ($p < 0.001$) in the HFD-fed mice compared to those in controls at 4, 8, 12, and 16 weeks, respectively (Figure 2). Taken together, the maximal differences ($p < 0.001$) in both histopathological examination and hepatic biochemical parameters were observed after 8 weeks of HFD feeding.

Hepatic Oxidative Stress and Inflammation. As shown in Figure 3, none of the parameters of hepatic antioxidant capacity and pro-inflammatory cytokines were significantly different between the HFD and control groups after 4 weeks of feeding. At 8 weeks, HFD-fed mice showed noticeably reduced hepatic GSH levels ($p < 0.01$) and CAT, SOD, and GRd ($p < 0.05$) activities were reduced by 12.9−33.0%. In contrast, TNF-α content significantly increased by 29.0% ($p < 0.05$). At the end of 12 and 16 weeks, HFD induced oxidative stress and inflammation in the liver, as indicated by 16.7−49.5% inhibition of hepatic GSH, GPx ($p < 0.01$, or $p < 0.001$), SOD ($p < 0.01$), CAT, and GRd ($p < 0.001$) and 14.9−42.8% elevation of hepatic MDA ($p < 0.01$), TNF-α, IL-1β ($p < 0.001$), and IL-6 ($p < 0.05$, or $p < 0.01$).

Metabolomic Profile of Serum Extracts. Serum metabolomics based on UHPLC−QTOF−MS and GC−MS data was used to investigate the pathophysiological mechanism of HFD-induced hepatic steatosis in C57BL/6J mice at different time points (4, 8, 12, and 16 weeks). Among the normalized intensities of low-molecular-weight metabolites extracted from serum samples, a total of 244 and 101 distinct metabolites were identified by UHPLC−QTOF−MS and GC−MS, respectively. To discriminate the different metabolic profiles affecting the NAFLD mice at each time point, a PCA score plot was employed to visualize the sample distribution of the multivariate patterns. The two-dimensional scatter plot of the UHPLC−QTOF−MS spectrum was defined by the first and second principal components PC1 and PC2. As shown in Figure 4, PC1 discriminated the control and HFD groups after 4, 8, 12, and 16 weeks and explained 60, 57, 59, and 58% of the total variation, respectively. The serum PCA score plot from the GC−MS spectrum (Figure 5) was similar to that derived from the UHPLC−QTOF−MS data. The HFD group was clearly separated from their age-matched controls along PC1,

DOI: 10.1021/acs.jafc.5b02830
J. Agric. Food Chem. 2015, 63, 7873−7884

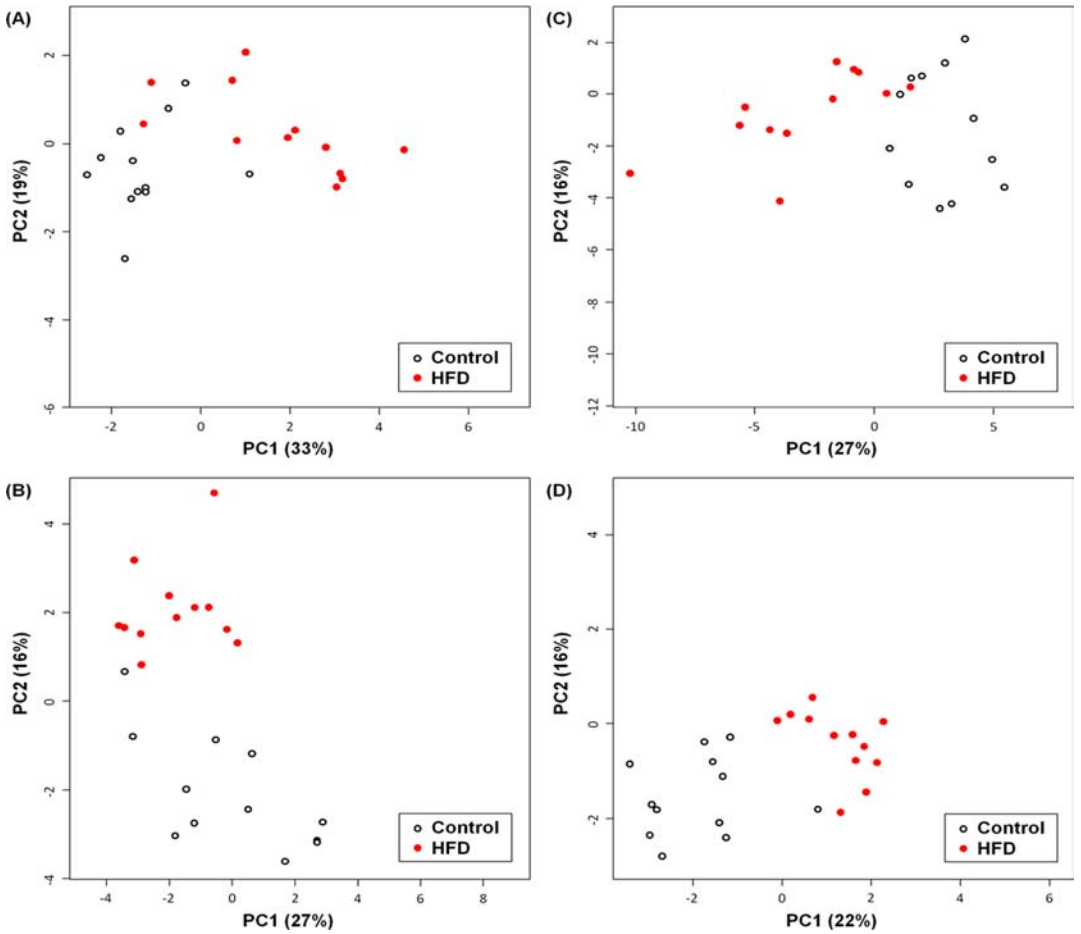

Figure 5. PCA score plots of serum GC−MS spectrum obtained from control and HFD mice after (A) 4 weeks, (B) 8 weeks, (C) 12 weeks, and (D) 16 weeks of feeding. HFD, high-fat diet.

while the mice fed the HFD for 8 weeks were discriminated from the control and other HFD groups by PC2. At 4, 8, 12, and 16 weeks of feeding, PC1 and PC2 together explained 52, 43, 43, and 38% of the total variance, respectively. These results indicated that the control and HFD groups were individually clustered and well-separated at all four time points. Therefore, metabolic variability exists in the mouse serum during long-term HFD intervention, confirming the validity of this animal model of NAFLD.

Potential Biomarkers and Metabolic Pathways. To further investigate the major alteration trends of all variables between the control and HFD-fed mice at each time point (4, 8, 12, and 16 weeks), the potential metabolites that were significant ($p < 0.05$) in the Student's t test were determined. Of various serum metabolites, 21 and 9 molecular species were assigned as the continually significant metabolites by UHPLC−QTOF−MS and GC−MS (Tables 2 and 3, respectively). To gain insight into the metabolic mechanism involved in the significantly different metabolites affected by the HFD during NAFLD onset and progression, the major metabolic pathways and possible physiological reactions of potential biomarkers were identified on the basis of the KEGG database, Human Metabolome Database (HMDB), and related references (Tables 2 and 3 and Figure 6).

A total of 11 metabolites were found to have changed significantly in the HFD mice relative to controls after 4 weeks of induction. These potential metabolites were D-xylose/D-ribose/D,L-arabinose, glucuronate, catechol, 4-coumarate, hippurate, L-kynurenine, kynurenate, 4-hydroxyproline, L-proline, L-lysine, and allantoin. This finding suggested that the early processes in NAFLD development are mainly associated with carbohydrate metabolism, hepatic biotransformation, collagen synthesis, and gut microbial metabolism. An additional 5 metabolites significantly changed after 8 weeks of induction, including *trans*-aconitic acid, α-ketoglutarate, L-glutamic acid, stearic acid, and sebacic acid, which are mainly correlated with impaired insulin secretion and lipid metabolism in the mid-term of NAFLD progression. In addition, 14 additional metabolites, including D-mannose, glycerol 3-phosphate, methylhippuric acid, palmitic acid, ketoleucine, 2-ketohexanoic acid, taurocholate, glycocholate, glycochenodeoxycholate, hydroxyphenyllactic acid, succinate, histamine, methionine, and L-tryptophan, were observed at the end of 12 and 16 weeks in the development of NAFLD. These metabolites are predominantly related to bile acid synthesis disorders, oxidative stress, inflammation, and mitochondrial dysfunction. These findings demonstrate the potential biomarkers that are closely associated with key metabolic pathways and that changed over time in the evolution of NAFLD.

DISCUSSION

We reported here the metabolomic assessment of serum from mice induced NAFLD by 4, 8, 12, and 16 weeks of HFD feeding through UHPLC−QTOF−MS and GC−MS analyses. Despite extensive research, there has been no systemic study of

DOI: 10.1021/acs.jafc.5b02830
J. Agric. Food Chem. 2015, 63, 7873−7884

Table 2. Potential Metabolites Detected by UHPLC−QTOF−MS between HFD and Control Mice[a]

metabolite	ion (m/z)	fold change (HFD/control)				metabolic pathway	physiological metabolism
		4 weeks	8 weeks	12 weeks	16 weeks		
D-xylose/D-ribose/D,L-arabinose	149.046	0.50**	0.62*	1.72**	0.54*	pentose and glucuronate interconversions	carbohydrate metabolism
glucuronate	193.035	0.47*	0.06***	0.54*	0.38**	pentose and glucuronate interconversions	hepatic biotransformation
catechol	109.030	0.11**	<0.01**	<0.01**	<0.01***	benzoate degradation	gut microbial metabolism
4-coumarate	163.040	0.34**	0.31**	0.41*	0.28**	phenylalanine metabolism	gut microbial metabolism
hippurate	180.060	<0.01***	<0.01*	<0.01***	<0.01***	phenylalanine metabolism	gut microbial metabolism
L-kynurenine	209.092	0.39**	0.23**	0.38**	0.18***	tryptophan metabolism	oxidation and inflammation
kynurenate	190.050	0.47*	0.35	0.39**	0.16***	tryptophan metabolism	oxidation and inflammation
sebacic acid	201.113	0.55	0.06***	<0.01*	<0.01**	fatty acid β-oxidation	lipid metabolism
methylhippuric acid	192.067	0.62	0.51	1.92**	1.50*	fatty acid β-oxidation	lipid metabolism
glycerol 3-phosphate	171.006	1.02	1.23	3.39***	1.70*	triacylglycerol biosynthesis	lipid metabolism
taurocholate	514.284	0.76	0.78	0.31**	0.09**	primary bile acid biosynthesis	bile acid synthesis
glycochenodeoxycholate	450.321	0.10	0.10	0.03***	<0.01*	primary bile acid biosynthesis	bile acid synthesis
glycocholate	466.316	0.61	0.03	0.03***	0.01**	primary bile acid biosynthesis	bile acid synthesis
D-mannose	179.056	1.10	1.22	2.81***	1.33*	mannose metabolism	carbohydrate metabolism
ketoleucine	129.056	0.93	1.01	3.25***	1.75***	leucine biosynthesis pathway	insulin secretion
2-ketohexanoic acid	129.056	0.95	1.07	3.31***	1.93***	norleucine biosynthesis pathway	insulin secretion
hydroxyphenyllactic acid	181.051	1.06	0.92	5.59***	1.71**	tyrosine metabolism	oxidation and inflammation
succinate	117.019	1.10	1.05	3.40***	1.40**	TCA cycle	oxidation and inflammation
histamine	112.087	1.04	0.82	0.15***	0.20**	histidine metabolism	oxidation and inflammation
methionine	150.058	0.95	1.01	1.49*	0.53*	cysteine and methionine metabolism	oxidation and inflammation
L-tryptophan	205.097	0.80	0.83	1.71**	0.71*	tryptophan metabolism	oxidation and inflammation

[a]C57BL/6J mice were fed a normal diet or HFD for 4, 8, 12, and 16 weeks. Fold change was calculated by dividing the mean of the peak intensity of each metabolite from HFD and control groups. Comparison was made between HFD and their age-matched controls by Student's t test. *$p < 0.05$. **$p < 0.01$. ***$p < 0.001$. HFD, high-fat diet.

DOI: 10.1021/acs.jafc.5b02830
J. Agric. Food Chem. 2015, 63, 7873−7884

Table 3. Potential Metabolites Detected by GC−MS between HFD and Control Mice[a]

metabolite	fold change (HFD/control) 4 weeks	8 weeks	12 weeks	16 weeks	metabolic pathway	physiological metabolism
4-hydroxyproline	0.73*	1.47*	0.61*	0.27***	proline biosynthesis	collagen synthesis
L-proline	1.48*	1.06	2.22**	1.50**	proline biosynthesis	collagen synthesis
L-lysine	3.72*	1.08	3.00**	2.92**	lysine metabolism	collagen synthesis
allantoin	0.29***	0.53**	0.22***	0.33***	purine metabolism	gut microbial metabolism
trans-aconitic acid	0.19	0.07**	<0.01***	<0.01**	gut microbial metabolism	gut microbial metabolism
α-ketoglutarate	0.91	0.44*	2.18*	1.90*	TCA cycle	insulin secretion
L-glutamic acid	0.80	1.62*	1.65*	0.73*	glutamate metabolism	insulin secretion
stearic acid	1.23	1.42*	1.64**	1.46***	fatty acid metabolism	lipid metabolism
palmitic acid	1.14	0.92	0.68*	1.31**	fatty acid metabolism	lipid metabolism

[a]C57BL/6J mice were fed a normal diet or HFD for 4, 8, 12, and 16 weeks. Fold change was calculated by dividing the mean of the peak intensity of each metabolite from HFD and control groups. Comparison was made between HFD and their age-matched controls by Student's *t* test. *$p < 0.05$. **$p < 0.01$. **$p < 0.001$. HFD, high-fat diet.

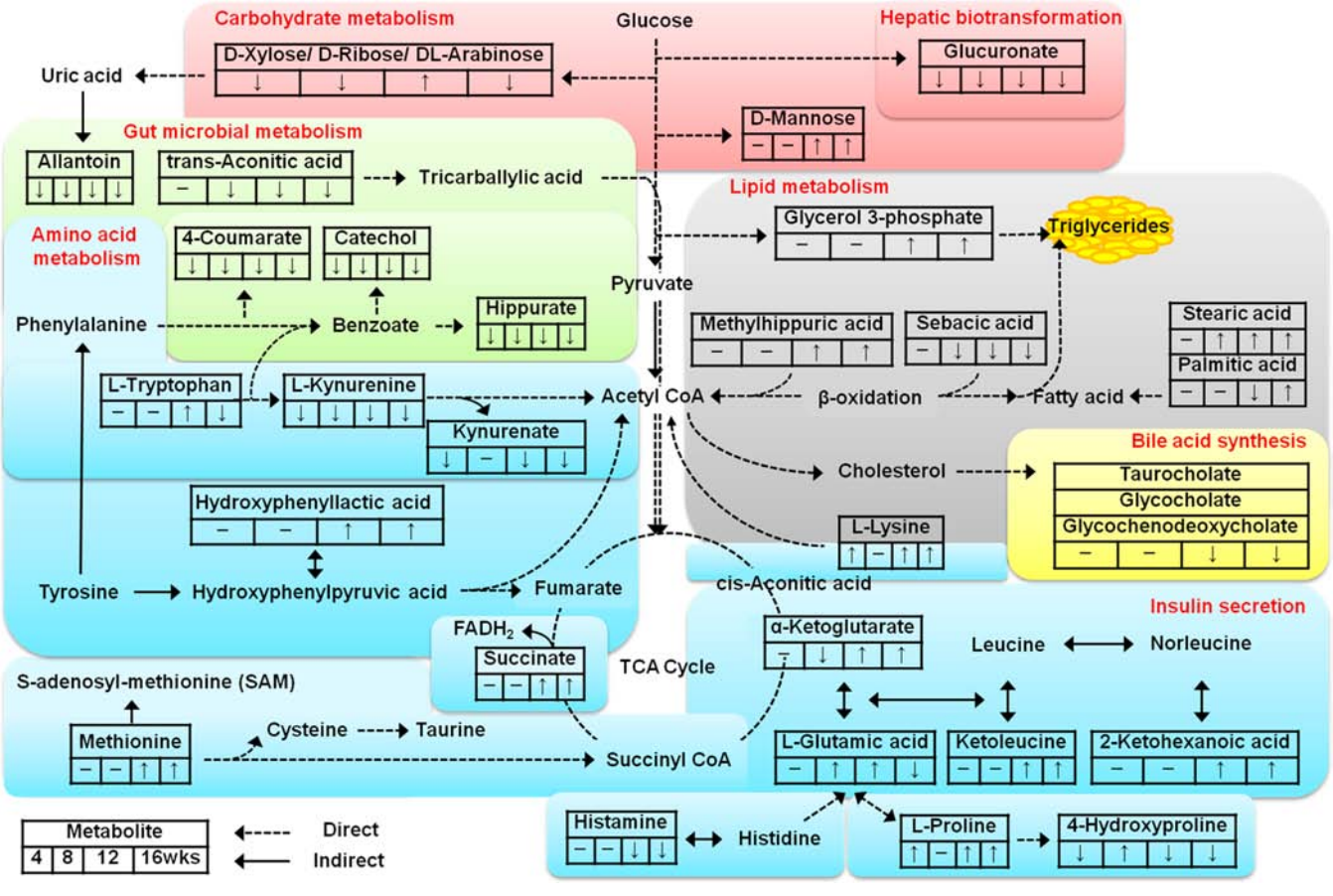

Figure 6. Major metabolic pathways in progressive NAFLD induced by HFD based on serum metabolite analysis. Solid and dashed arrows indicate the single and multiple steps involved between two metabolites, respectively. The up arrow (↑) indicates relative increase in signal. The down arrow (↓) indicates relative decrease in signal. The dash (−) represents no statistically significant difference. TCA, tricarboxylic acid.

pathophysiological characteristics and metabolic profiling in C57BL/6J mice fed a HFD to induce NAFLD development. Our results revealed that NAFLD onset and progression from early metabolic disturbances arise from minimal/moderate fatty infiltration (4 and 8 weeks) to alterations in various metabolic pathways following severe/high hepatic lipid accumulation (12 and 16 weeks). We identified a total of 30 potential biomarkers that were strongly associated with the development of NAFLD. Among these, 11 metabolites were identified to be mainly related to carbohydrate metabolism, hepatic biotransformation, gut microbial metabolism, and collagen synthesis, which are characteristics of a state of obesity, as well as high levels of serum glucose, TC, and hepatic TG during the onset of NAFLD (4 weeks). An additional 5 metabolites identified in the mid-term of NAFLD progression (8 weeks), which are chiefly involved in perturbation of lipid metabolism and insulin secretion, could be reflective of the pathophysiology associated with hyperinsulinemia, hyperlipidemia, and hepatic steatosis. In combination of the foregoing metabolic abnormalities, 14 additional metabolites that were predominantly correlated to abnormal bile acid synthesis, oxidative stress, and inflammation, representing hepatic inflammatory infiltration, were observed at

DOI: 10.1021/acs.jafc.5b02830
J. Agric. Food Chem. 2015, 63, 7873−7884

the end of 12 and 16 weeks of feeding in the development of NAFLD. Below, we discuss the reliable and abundant evidence for the potential biomarkers associated with the related metabolic disorder and their potential pathological roles.

In this study, we observed that D-ribose, D-xylose, D,L-arabinose, and D-mannose are associated with carbohydrate metabolism in HFD-induced NAFLD. These metabolites play various physiological roles, including control of pentolysis, biosynthesis of ribose-5-phosphate, glucuronate, and ascorbate, and functions of the ATP-binding cassette (ABC) transporters. Abnormal metabolism of carbohydrates and changes in metabolites, such as D-xylose, D,L-arabinose, and D-mannose, have been detected in patients with NAFLD or NASH.[11,12] Moreover, this study showed that glucuronate is involved in the hepatic biotransformation of HFD-induced NAFLD mice. Glucuronate normally participates in xenobiotic metabolism through glucuronidation.[13] Previous studies have suggested that HFD or NAFLD could interfere with hepatic glucuronidation.[14] In addition, glucuronate participates in ascorbic acid biosynthesis, which protects tissues from oxidation and promotes cholesterol metabolism. Furthermore, we noticed that 4-hydroxyproline, L-proline, and L-lysine are associated with collagen synthesis in HFD-induced NAFLD mice. 4-Hydroxyproline is the product of L-proline hydroxylation by the cofactor ascorbic acid. Excessive levels of L-proline and 4-hydroxyproline in the blood are potential indicators of increased collagen production in the liver.[15] Studies have confirmed that NAFLD can increase collagen synthesis in the liver, especially in patients with chronic hepatitis.[16] L-Lysine is not only important for collagen synthesis in the body but is also considered a precursor for carnitine biosynthesis in the liver. Normal L-lysine metabolism depends upon ascorbic acid, which is the electron donor for collagen hydroxylation and carnitine synthetase.[17] Excessive amounts of L-lysine have been linked with increased levels of TG and cholesterol.[18] Significant increases in lysine levels are found in mice with HFD-induced NAFLD.[4] Clinical metabolic studies have revealed significantly higher serum lysine levels in patients with NASH than in healthy subjects.[11]

This study revealed that hippurate, catechol, 4-coumarate, *trans*-aconitic acid, and allantoin are associated with the gut microbial metabolism in HFD-induced NAFLD. Food-derived amino acids, such as tryptophan, tyrosine, and phenylalanine, are metabolized by the gut microbiota to form benzoate. Benzoate is conjugated with glycine in the hepatic mitochondria via the phenylalanine metabolic pathway to form hippurate.[19] Catechol and 4-coumarate affect the degradation of aromatic compounds and the benzoate and phenylalanine metabolic pathways.[20,21] Studies have shown that HFD significantly reduced the gut microbial metabolites of hippurate, which is regarded as an indicator for assessing the risks of obesity and hepatic functional impairment.[11,22] In the intestinal tract, *trans*-aconitic acid is converted to tricarballylic acid by the gut microbiota. A rat model of HFD-induced obesity showed a significant change in *trans*-aconitic acid content,[23] which was assumed to be related to the influence of gut microbial metabolism. Allantoin is the product of uric acid catabolism in various organisms. Approximately one-third of the uric acid pool is excreted into the intestinal tract, where it is degraded by the gut microbiota to allantoin.[24] In comparison to the healthy control group, significantly lower levels of allantoin are found in the disease group, which is considered a biomarker of diet-induced obesity, NAFLD, and NASH.[25,26]

In the current study, we noticed that sebacic acid, methylhippuric acid, glycerol 3-phosphate, stearic acid, and palmitic acid are involved in lipid metabolism in HFD-induced NAFLD. A metabolite of fatty acid catabolism in the liver, sebacic acid is a straight-chain dicarboxylic acid with 10 carbon atoms. In the hepatic mitochondria and peroxisomes, medium-chain dicarboxylic acids mainly undergo β-oxidation, which is consistent with the oxidation of fatty acids.[27,28] Methylhippuric acid is a secondary metabolite of fatty acids, and an increased level of this metabolite is a diagnostic indicator of diseases associated with anomalous mitochondrial functions related to fatty acid β-oxidation. Significant changes in methylhippuric acid were detected in patients with chronic hepatitis.[29] In addition, a significantly increased level of methylhippuric acid was detected in a rat model of HFD-induced NAFLD, suggesting that methylhippuric acid affects the pathways of lipid metabolism.[25] Glycerol 3-phosphate is an intermediate of glycolysis. A HFD can promote esterification of a FFA, increase the glycerol 3-phosphate level in the liver tissues, and promote lipogenesis, eventually resulting in NAFLD.[30] Stearic and palmitic acids are the most common saturated fatty acids in the body, and high levels of these metabolites have been detected in the serum lipid profile of patients with NAFLD or NASH, indicating that metabolic disturbances affecting FFA may be an important factor in the pathogenesis and progression of diseases.[31,32]

This study showed that 2-ketohexanoic acid, ketoleucine, α-ketoglutarate, and L-glutamic acid participate in the regulation of insulin secretion in mice with HFD-induced NAFLD. 2-Ketohexanoic acid can directly inhibit the ATP-sensitive potassium channel in pancreatic β cells, thereby stimulating insulin secretion.[33] Ketoleucine is also believed to stimulate the release of insulin, which is the major factor responsible for the pathogenesis of obesity-induced insulin resistance.[34] Stimulation of insulin secretion by 2-ketohexanoic acid and ketoleucine can simultaneously increase the production of α-ketoglutarate in pancreatic β-cell mitochondria,[35] which enters the cytoplasm to indirectly stimulate insulin secretion. Therefore, α-ketoglutarate has also been viewed as an effective biomarker in the pathogenesis of diabetes and insulin resistance associated with NAFLD and NASH.[11,36,37] In addition, L-glutamic acid stimulates insulin secretion by promoting Ca^{2+}-dependent exocytosis.[38] Metabolic profiling studies have shown that the level of L-glutamic acid is strongly correlated with insulin resistance.[39] Studies on patients with NAFLD or NASH with significantly high insulin levels have revealed significantly higher serum glutamate levels than those in healthy subjects;[11] this finding suggests that serum L-glutamic acid is a possible biomarker of the progression of NAFLD and NASH.[3]

This study revealed that glycocholate, glycochenodeoxycholate, and taurocholate are associated with bile acid synthesis in HFD-induced NAFLD. In the hepatocytic microsomes and cytosol, cholesterol participates in primary bile acid biosynthesis to form primary conjugated bile acids, such as glycocholate, glycochenodeoxycholate, taurocholate, and taurochenodeoxycholate.[40] Studies have indicated that NAFLD and NASH may cause hepatic injury and inflammation, resulting in bile acid dysmetabolism and significant changes in blood metabolites of glycocholate, glycochenodeoxycholate, and taurocholate.[11,41]

We also observed dysregulation of several amino acids, including succinate, methionine, histamine, hydroxyphenyllactic acid, L-tryptophan, L-kynurenine, and kynurenate, which are

DOI: 10.1021/acs.jafc.5b02830
J. Agric. Food Chem. 2015, 63, 7873−7884

predominantly related to the oxidative stress and inflammation in HFD-induced NAFLD. Succinate is a key participant of the tricarboxylic acid (TCA) cycle. In HFD-induced NAFLD, a relatively high succinate level may cause disturbances in the mitochondrial TCA cycle,[25] thereby promoting increased oxidative stress, impairment of hepatic mitochondrial function, and the release of cytokines, eventually leading to hepatitis.[42] In hepatocytes, methionine is metabolized to *S*-adenosyl methionine, cysteine, and taurine, which regulate lipid metabolism, oxidative stress, and bile metabolism, respectively.[43] Patients with NAFLD or NASH tend to have aberrant methionine metabolism, which is considered a key mechanism of hepatic oxidative damage.[44] Histamine, produced by decarboxylation of histidine, is mainly present in mast cells and basophils as a chemical transmitter that regulates oxidative stress and inflammatory and immune responses.[45] An abnormal level of histamine disrupts energy metabolism and forms the basis of the pathogenesis of NASH.[46] As a metabolic product of tyrosine, hydroxyphenyllactic acid can promote the production of ROS in the mitochondria and neutrophils, resulting in increased oxidative stress.[47] Indeed, relatively high levels of hydroxyphenyllactic acid are found in patients with liver diseases.[48] L-Tryptophan is known to effectively alleviate hepatitis by reducing the levels of proinflammatory cytokines in patients with NASH.[49] Studies have shown that long-term chronic inflammation induced by a HFD can cause degradation of L-tryptophan in hepatic cells to L-kynurenine and kynurenate, which can regulate inflammatory damage;[50] these findings demonstrate that tryptophan metabolism is a key metabolic pathway in the inflammatory infiltration of the liver associated with NAFLD.[11,25]

The present study identified several key metabolites in major metabolic pathways involved in the development of NAFLD, similar to those observed in clinical cases of NAFLD. These metabolites could be considered as potential biomarkers for early risk assessment of NAFLD as well as improved monitoring and management of NAFLD-related disease. Moreover, these results provide comprehensive insights into the metabolic processes underlying the onset and progression of NAFLD induced by HFD.

AUTHOR INFORMATION

Corresponding Author

*Telephone: 886-2-33664129. Fax: 886-2-2362-0849. E-mail: lysheen@ntu.edu.tw.

Funding

This research work was partially funded by the National Science Council (NSC-102-2628-B-002-010-MY2) and the National Taiwan University (Aim for Top University Program 102R-7620), Taiwan.

Notes

The authors declare no competing financial interest.

ACKNOWLEDGMENTS

The authors thank Prof. Chih-Hsien Chiu for helpful discussions in animal experiments. The authors also thank Dr. Guan-Yuan Chen and Cheng-En Tan for technical support.

REFERENCES

(1) Abdelmalek, M. F.; Diehl, A. M. Mechanisms underlying nonalcoholic steatohepatitis. *Drug Discovery Today: Dis. Mech.* **2006**, *3*, 479−488.

(2) Oresic, M. Metabolomics, a novel tool for studies of nutrition, metabolism and lipid dysfunction. *Nutr., Metab. Cardiovasc. Dis.* **2009**, *19*, 816−824.

(3) Li, H.; Wang, L.; Yan, X.; Liu, Q.; Yu, C.; Wei, H.; Li, Y.; Zhang, X.; He, F.; Jiang, Y. A proton nuclear magnetic resonance metabonomics approach for biomarker discovery in nonalcoholic fatty liver disease. *J. Proteome Res.* **2011**, *10*, 2797−2806.

(4) Vinaixa, M.; Rodriguez, M. A.; Rull, A.; Beltran, R.; Blade, C.; Brezmes, J.; Canellas, N.; Joven, J.; Correig, X. Metabolomic assessment of the effect of dietary cholesterol in the progressive development of fatty liver disease. *J. Proteome Res.* **2010**, *9*, 2527−2538.

(5) Barr, J.; Vazquez-Chantada, M.; Alonso, C.; Perez-Cormenzana, M.; Mayo, R.; Galan, A.; Caballeria, J.; Martin-Duce, A.; Tran, A.; Wagner, C.; Luka, Z.; Lu, S. C.; Castro, A.; Le Marchand-Brustel, Y.; Martinez-Chantar, M. L.; Veyrie, N.; Clement, K.; Tordjman, J.; Gual, P.; Mato, J. M. Liquid chromatography-mass spectrometry-based parallel metabolic profiling of human and mouse model serum reveals putative biomarkers associated with the progression of nonalcoholic fatty liver disease. *J. Proteome Res.* **2010**, *9*, 4501−4512.

(6) Toye, A. A.; Dumas, M. E.; Blancher, C.; Rothwell, A. R.; Fearnside, J. F.; Wilder, S. P.; Bihoreau, M. T.; Cloarec, O.; Azzouzi, I.; Young, S.; Barton, R. H.; Holmes, E.; McCarthy, M. I.; Tatoud, R.; Nicholson, J. K.; Scott, J.; Gauguier, D. Subtle metabolic and liver gene transcriptional changes underlie diet-induced fatty liver susceptibility in insulin-resistant mice. *Diabetologia* **2007**, *50*, 1867−1879.

(7) Takahashi, Y.; Soejima, Y.; Fukusato, T. Animal models of nonalcoholic fatty liver disease/nonalcoholic steatohepatitis. *World J. Gastroenterol.* **2012**, *18*, 2300−2308.

(8) Anstee, Q. M.; Goldin, R. D. Mouse models in non-alcoholic fatty liver disease and steatohepatitis research. *Int. J. Exp. Pathol.* **2006**, *87*, 1−16.

(9) Lai, Y. S.; Chen, W. C.; Ho, C. T.; Lu, K. H.; Lin, S. H.; Tseng, H. C.; Lin, S. Y.; Sheen, L. Y. Garlic essential oil protects against obesity-triggered nonalcoholic fatty liver disease through modulation of lipid metabolism and oxidative stress. *J. Agric. Food Chem.* **2014**, *62*, 5897−5906.

(10) Ho, T. J.; Kuo, C. H.; Wang, S. Y.; Chen, G. Y.; Tseng, Y. J. True ion pick (TIPick): a denoising and peak picking algorithm to extract ion signals from liquid chromatography/mass spectrometry data. *J. Mass Spectrom.* **2013**, *48*, 234−242.

(11) Kalhan, S. C.; Guo, L.; Edmison, J.; Dasarathy, S.; McCullough, A. J.; Hanson, R. W.; Milburn, M. Plasma metabolomic profile in nonalcoholic fatty liver disease. *Metab., Clin. Exp.* **2011**, *60*, 404−413.

(12) Ji, G.; Wu, T.; Song, H. Y.; Wei, H. F.; Yang, M.; He, S. H. The glucose metabolism in metabolic syndrome patients with non-alcoholic fatty liver disease. *Global J. Gastroenterol. Hepatol.* **2014**, *2*, 19−28.

(13) King, C. D.; Rios, G. R.; Green, M. D.; Tephly, T. R. UDP-glucuronosyltransferases. *Curr. Drug Metab.* **2000**, *1*, 143−161.

(14) Osabe, M.; Sugatani, J.; Fukuyama, T.; Ikushiro, S.; Ikari, A.; Miwa, M. Expression of hepatic UDP-glucuronosyltransferase 1A1 and 1A6 correlated with increased expression of the nuclear constitutive androstane receptor and peroxisome proliferator-activated receptor alpha in male rats fed a high-fat and high-sucrose diet. *Drug Metab. Dispos.* **2008**, *36*, 294−302.

(15) Wu, G.; Bazer, F. W.; Burghardt, R. C.; Johnson, G. A.; Kim, S. W.; Knabe, D. A.; Li, P.; Li, X.; McKnight, J. R.; Satterfield, M. C.; Spencer, T. E. Proline and hydroxyproline metabolism: implications for animal and human nutrition. *Amino Acids* **2011**, *40*, 1053−1063.

(16) Murawaki, Y.; Kato, S.; Hirayama, C. Hepatic collagen synthesis in patients with alcoholic and nonalcoholic liver disease. *Gastroenterol Jpn.* **1991**, *26*, 465−471.

(17) Naidu, K. A. Vitamin C in human health and disease is still a mystery? An overview. *Nutr. J.* **2003**, *2*, 7.

(18) Yagasaki, K.; Matsumoto, M.; Fujisawa, K.; Kuboya, A.; Funabiki, R. Effect of dietary lysine on endogenous hyperlipidemia in nephrotic rats. *Biosci., Biotechnol., Biochem.* **1992**, *56*, 980−982.

DOI: 10.1021/acs.jafc.5b02830
J. Agric. Food Chem. 2015, 63, 7873−7884

(19) Nicholson, J. K.; Holmes, E.; Wilson, I. D. Gut microorganisms, mammalian metabolism and personalized health care. *Nat. Rev. Microbiol.* **2005**, *3*, 431−438.
(20) Shingler, V.; Powlowski, J.; Marklund, U. Nucleotide sequence and functional analysis of the complete phenol/3,4-dimethylphenol catabolic pathway of Pseudomonas sp. strain CF600. *J. Bacteriol.* **1992**, *174*, 711−724.
(21) Clayton, T. A. Metabolic differences underlying two distinct rat urinary phenotypes, a suggested role for gut microbial metabolism of phenylalanine and a possible connection to autism. *FEBS Lett.* **2012**, *586*, 956−961.
(22) Lees, H. J.; Swann, J. R.; Wilson, I. D.; Nicholson, J. K.; Holmes, E. Hippurate: the natural history of a mammalian-microbial cometabolite. *J. Proteome Res.* **2013**, *12*, 1527−1546.
(23) Kim, H. Y.; Lee, M. Y.; Park, H. M.; Park, Y. K.; Shon, J. C.; Liu, K. H.; Lee, C. H. Urine and serum metabolite profiling of rats fed a high-fat diet and the anti-obesity effects of caffeine consumption. *Molecules* **2015**, *20*, 3107−3128.
(24) Sorensen, L. B. Degradation of uric acid in man. *Metabolism* **1959**, *8*, 687−703.
(25) Li, J. J.; Yang, J.; Cui, W. X.; Chen, X. Q.; Chen, G. L.; Wen, X. D.; Wang, Q. Analysis of Therapeutic Effect of Ilex hainanensis Merr. Extract on Nonalcoholic Fatty Liver Disease through Urine Metabolite Profiling by Ultraperformance Liquid Chromatography/Quadrupole Time of Flight Mass Spectrometry. *Evid. Based Complement Alternat. Med.* **2013**, *2013*, 451975.
(26) Terashima, Y.; Nishiumi, S.; Minami, A.; Kawano, Y.; Hoshi, N.; Azuma, T.; Yoshida, M. Metabolomics-based search for therapeutic agents for non-alcoholic steatohepatitis. *Arch. Biochem. Biophys.* **2014**, *555*−*556*, 55−65.
(27) Chen, L.; Zhang, J.; Chen, W. N. Engineering the Saccharomyces cerevisiae beta-oxidation pathway to increase medium chain fatty acid production as potential biofuel. *PLoS One* **2014**, *9*, e84853.
(28) Mortensen, P. B. Formation and degradation of dicarboxylic acids in relation to alterations in fatty acid oxidation in rats. *Biochim. Biophys. Acta, Lipids Lipid Metab.* **1992**, *1124*, 71−79.
(29) Zhang, A.; Sun, H.; Han, Y.; Yan, G.; Wang, X. Urinary metabolic biomarker and pathway study of hepatitis B virus infected patients based on UPLC-MS system. *PLoS One* **2013**, *8*, e64381.
(30) Postic, C.; Girard, J. Contribution of de novo fatty acid synthesis to hepatic steatosis and insulin resistance: lessons from genetically engineered mice. *J. Clin. Invest.* **2008**, *118*, 829−838.
(31) de Almeida, I. T.; Cortez-Pinto, H.; Fidalgo, G.; Rodrigues, D.; Camilo, M. E. Plasma total and free fatty acids composition in human non-alcoholic steatohepatitis. *Clin. Nutr.* **2002**, *21*, 219−223.
(32) Puri, P.; Wiest, M. M.; Cheung, O.; Mirshahi, F.; Sargeant, C.; Min, H. K.; Contos, M. J.; Sterling, R. K.; Fuchs, M.; Zhou, H.; Watkins, S. M.; Sanyal, A. J. The plasma lipidomic signature of nonalcoholic steatohepatitis. *Hepatology* **2009**, *50*, 1827−1838.
(33) Lenzen, S.; Formanek, H.; Panten, U. Signal function of metabolism of neutral amino acids and 2-keto acids for initiation of insulin secretion. *J. Biol. Chem.* **1982**, *257*, 6631−6633.
(34) Isganaitis, E.; Woo, M.; Ma, H.; Chen, M.; Kong, W.; Lytras, A.; Sales, V.; Decoste-Lopez, J.; Lee, K. J.; Leatherwood, C.; Lee, D.; Fitzpatrick, C.; Gall, W.; Watkins, S.; Patti, M. E. Developmental programming by maternal insulin resistance: hyperinsulinemia, glucose intolerance, and dysregulated lipid metabolism in male offspring of insulin-resistant mice. *Diabetes* **2014**, *63*, 688−700.
(35) Lenzen, S.; Schmidt, W.; Rustenbeck, I.; Panten, U. 2-ketoglutarate generation in pancreatic B-cell mitochondria regulates insulin secretory action of amino acids and 2-keto acids. *Biosci. Rep.* **1986**, *6*, 163−169.
(36) Bain, J. R.; Stevens, R. D.; Wenner, B. R.; Ilkayeva, O.; Muoio, D. M.; Newgard, C. B. Metabolomics applied to diabetes research: moving from information to knowledge. *Diabetes* **2009**, *58*, 2429−2443.
(37) Rodriguez-Gallego, E.; Guirro, M.; Riera-Borrull, M.; Hernandez-Aguilera, A.; Marine-Casado, R.; Fernandez-Arroyo, S.; Beltran-Debon, R.; Sabench, F.; Hernandez, M.; del Castillo, D.; Menendez, J. A.; Camps, J.; Ras, R.; Arola, L.; Joven, J. Mapping of the circulating metabolome reveals alpha-ketoglutarate as a predictor of morbid obesity-associated non-alcoholic fatty liver disease. *Int. J. Obes.* **2015**, *39*, 279−287.
(38) Newsholme, P.; Brennan, L.; Rubi, B.; Maechler, P. New insights into amino acid metabolism, beta-cell function and diabetes. *Clin. Sci.* **2005**, *108*, 185−194.
(39) Cheng, S.; Rhee, E. P.; Larson, M. G.; Lewis, G. D.; McCabe, E. L.; Shen, D.; Palma, M. J.; Roberts, L. D.; Dejam, A.; Souza, A. L.; Deik, A. A.; Magnusson, M.; Fox, C. S.; O'Donnell, C. J.; Vasan, R. S.; Melander, O.; Clish, C. B.; Gerszten, R. E.; Wang, T. J. Metabolite profiling identifies pathways associated with metabolic risk in humans. *Circulation* **2012**, *125*, 2222−2231.
(40) Chiang, J. Y. Bile acid regulation of hepatic physiology: III. Bile acids and nuclear receptors. *Am. J. Physiol. Gastrointest. Liver Physiol.* **2003**, *284*, G349−356.
(41) Tanaka, N.; Matsubara, T.; Krausz, K. W.; Patterson, A. D.; Gonzalez, F. J. Disruption of phospholipid and bile acid homeostasis in mice with nonalcoholic steatohepatitis. *Hepatology* **2012**, *56*, 118−129.
(42) Begriche, K.; Massart, J.; Robin, M. A.; Bonnet, F.; Fromenty, B. Mitochondrial adaptations and dysfunctions in nonalcoholic fatty liver disease. *Hepatology* **2013**, *58*, 1497−1507.
(43) Gomez, J.; Caro, P.; Sanchez, I.; Naudi, A.; Jove, M.; Portero-Otin, M.; Lopez-Torres, M.; Pamplona, R.; Barja, G. Effect of methionine dietary supplementation on mitochondrial oxygen radical generation and oxidative DNA damage in rat liver and heart. *J. Bioenerg. Biomembr.* **2009**, *41*, 309−321.
(44) Kalhan, S. C.; Edmison, J.; Marczewski, S.; Dasarathy, S.; Gruca, L. L.; Bennett, C.; Duenas, C.; Lopez, R. Methionine and protein metabolism in non-alcoholic steatohepatitis: evidence for lower rate of transmethylation of methionine. *Clin. Sci.* **2011**, *121*, 179−189.
(45) Gill, D. S.; Fonseca, V. A.; Barradas, M. A.; Balliod, R.; Moorhead, J. F.; Dandona, P. Plasma histamine in patients with chronic renal failure and nephrotic syndrome. *J. Clin. Pathol.* **1991**, *44*, 243−245.
(46) Wang, K. Y.; Tanimoto, A.; Yamada, S.; Guo, X.; Ding, Y.; Watanabe, T.; Watanabe, T.; Kohno, K.; Hirano, K.; Tsukada, H.; Sasaguri, Y. Histamine regulation in glucose and lipid metabolism via histamine receptors: model for nonalcoholic steatohepatitis in mice. *Am. J. Pathol.* **2010**, *177*, 713−723.
(47) Levchuk, A. A.; Faron, R. A.; Khrustalev, S. A.; Raushenbakh, M. O. Effect of the carcinogenic tyrosine metabolite p-hydroxyphenyllactic acid on the ascorbic acid concentration in the organs and blood of mice. *Bull. Exp. Biol. Med.* **1986**, *102*, 1417−1418.
(48) Muting, D.; Wuzel, H.; Bucsis, L.; Flasshoff, H. J. Urinary p-hydroxyphenyllactic acid as indicator of hepatic encephalopathy in patients with hepatic cirrhosis. *Lancet* **1985**, *2*, 1365−1366.
(49) Celinski, K.; Konturek, P. C.; Slomka, M.; Cichoz-Lach, H.; Brzozowski, T.; Konturek, S. J.; Korolczuk, A. Effects of treatment with melatonin and tryptophan on liver enzymes, parameters of fat metabolism and plasma levels of cytokines in patients with non-alcoholic fatty liver disease–14 months follow up. *J. Physiol. Pharmacol.* **2014**, *65*, 75−82.
(50) Nagano, J.; Shimizu, M.; Hara, T.; Shirakami, Y.; Kochi, T.; Nakamura, N.; Ohtaki, H.; Ito, H.; Tanaka, T.; Tsurumi, H.; Saito, K.; Seishima, M.; Moriwaki, H. Effects of indoleamine 2,3-dioxygenase deficiency on high-fat diet-induced hepatic inflammation. *PLoS One* **2013**, *8*, e73404.

DOI: 10.1021/acs.jafc.5b02830
J. Agric. Food Chem. 2015, 63, 7873−7884

revealed that depression leads to an altered intestinal microbiota profile in OBx mice.

It is noted that anxiety and depression are generally considered to be correlated with stress. Increasing data show that stress has also been associated with changes in the GI microbiota via the sympathetic nervous system and adrenergic response. By deprivation of food, water, and bedding in mice inoculated with *Salmonella*, it was shown that environmental and dietary stresses significantly alter the gut microbiota in mice: stressed mice had lower levels of lactobacilli compared with control mice.[19] Maternal separation in rodents is a well-studied model of early-life stress. O'Mahony et al.[20] demonstrated that maternal separation stress causes marked population-based alterations in the fecal microbiota of separated animals, and such a disrupted microbiota can persist into adulthood. Bailey et al.[21] demonstrated that a prolonged restraint stressor significantly reduced microbial richness and diversity, such as a reduction in the family Porphyromonadaceae. Another study from this laboratory also showed that social disruption significantly changed the community structure of the microbiota, specifically, increasing the relative abundance of the genus *Clostridium* and decreasing the relative abundance of the genus *Bacteroides*.[22] In addition, it has been found that grid floor-induced stress significantly increased the relative abundance of *Odoribacter*, *Alistipes*, and an unclassified genus from the Coriobacteriaceae family.[23] These findings suggest that stress leads to anxiety/depression by altering the gut microbiota (Table 1) and that anxiety/depression influences the gut microbiota, which also affects anxiety and depression.

Table 1. Link between Microbiota and Brain Function

brain function	altered microbes	refs
stress	Porphyromonadaceae ↓	21
stress	*Clostridium* ↑, *Bacteroides* ↓	22
stress and anxiety	*Odoribacter* ↑, *Alistipes* ↑, Coriobacteriaceae ↑	23
autism	*Clostridium* ↑	27−29
	Akkermansia muciniphila ↓	30
	Sutterella ↑, *Ruminococcus torques* ↑	7, 31, 32
	Desulfovibrio ↑, *Bifidobacterium* ↓	
	Prevotella ↓, *Coprococcus* ↓, Veillonellaceae ↓	33

Gut Microbiota and Autism. Autism spectrum disorders (ASD) comprise a complex neurobiological disorder; its characteristics include impairment in social interaction and communication and restricted, repetitive, and stereotyped patterns of behavior, interests, and activities.[24] Genetic and environmental factors are involved in the pathogenesis of ASD. In particular, one potentially important environmental factor is abnormal intestinal microbiota, as GI disturbances are frequently reported in infants with ASD,[25] and there is a strong positive correlation between GI problems and ASD severity.[26] Indeed, altered compositions of the intestinal microbiota have been reported in several studies. Specifically, the *Clostridium* species were higher in the ASD patients compared to control.[27−29] Moreover, lower levels of the mucolytic bacterium *Akkermansia muciniphila*[30] and *Bifidobacterium* species,[31] higher levels of *Sutterella*, *Ruminococcus torques*, and *Desulfovibrio* species,[7,32] and significantly lower abundances of the genera *Prevotella*, *Coprococcus*, and unclassified Veillonellaceae[33] were found in ASD patients (Table 1).

Modulation of Gut Microbiota−Brain Axis for the Healthy Brain. The reported link of gut microbiota to brain health and disorders raises the question of how to modulate the microbiota for re-equilibration of the gut microbiota compositions altered by brain disorders. There is a growing body of evidence documenting the ability of probiotics, prebiotics, synbiotics, and other diets to normalize the dysbiotic microbiota associated with psychological disorders.[34]

Probiotics-Based Modulation. Although a complex relationship between gut microbiota and anxiety/depression exists, it is possible to improve anxiety and depression by probiotics modulation (Table 2). For example, Bercik et al.[35] indicated that *Bifidobacterium longum* normalized anxiety-like behavior induced by the noninvasive parasite *Trichuris muris* infection; Bravo et al.[36] showed that chronic treatment with *Lactobacillus rhamnosus* (JB-1) reduced the anxiety- and depression-related behavior in the *Trichuris muris*-infected mice.

Recently, using the maternal immune activation (MIA) mouse model of ASD in mouse offspring, Hsiao et al.[37] showed that oral administration of the human commensal *Bacteroides fragilis* reversed the abnormalities in gut permeability and ASD-related behaviors. Interestingly, these behavioral effects are not specific to *Bacteroides fragilis*, as *Bacteroides thetaiotaomicron* also significantly improves anxiety-like behavior, although *Enterococcus faecalis* does not exhibit anxiolytic action in MIA offspring.

Especially, ingestion of selected probiotics also exhibits effects on brain activity in humans. After 2 months of administration of *Lactobacillus casei* strain Shirota in chronic fatigue syndrome patients, there were significant rises in both *Lactobacillus* and *Bifidobacterium* and also a significant decrease in anxiety symptoms among those taking the probiotic versus controls.[38] The oral administration of *L. helveticus* R0052 and *B. longum* R0175 for 2 weeks was shown to alleviate anxiety and depressive symptoms in healthy volunteers, as measured by the Hopkins Symptom Checklist (HSCL-90), the Hospital Anxiety and Depression Scale (HADS), the Perceived Stress Scale, the Coping Checklist (CCL), and 24 h urinary free cortisol (UFC).[39] Similarly, after 4 weeks of consumption of a fermented milk product with probiotics (FMPP) (containing *Bifidobacterium animalis* subsp. *lactis*, *Streptococcus thermophiles*, *Lactobacillus bulgaricus*, and *Lactococcus lactis* subsp. *lactis*) by healthy women, Tillisch et al.[40] found that FMPP intake affected the activity of brain regions that control central processing of emotion and sensation, including affective, viscerosensory, and somatosensory cortices.

Several studies have spurred better understanding of the acting mechanisms of probiotics involved in gut−brain axis signaling. After exposure to *Bifidobacterium infantis*, the levels of brain-derived neurotrophic factor (BDNF) and *N*-methyl-D-aspartate (NMDA) receptor subunit 2a (NR2a) in the cortex and hippocampus were reduced in GF animals compared to SPF controls.[41] Likewise, the induced anxiety-like behavior in *Trichuris muris*-infected mice was still present after vagotomy, which was also associated with decreased hippocampal BDNF mRNA and increased circulating tumor necrosis factor-α and interferon-γ. When *Bifidobacterium longum* reversed the anxiety-like behavior in infected mice, the hippocampal BDNF expression was also restored, although the cytokines were not affected.[35] This means that visceral signals derived from bacterial colonization can be transmitted to the brain, and the anxiolytic actions of *Bifidobacterium infantis* and *Bifido-*

DOI: 10.1021/acs.jafc.5b02404
J. Agric. Food Chem. 2015, 63, 7885−7895

Table 2. Modulation of Brain Behaviors by Probiotics and Prebiotics

model	behavior tests	intervention	duration	effects	refs
Trichuris muris-infected mice	light/dark preference and step-down tests	*Bifidobacterium longum*	14 days	normalized anxiety behavior	35
Trichuris muris-infected BALB/c mice	open field, elevated plus maze, fear conditioning, stress-induced hyperthermia	*Lactobacillus rhamnosus* (JB-1)	28 days	reduced anxiety- and depression-related behavior	36
maternal immune activation C57BL/6N mice	open field, marble burying, social interaction, and adult ultrasonic vocalizations	*Bacteroides fragilis*, *Bacteroides thetaiotaomicron*	6−9 weeks	reversed autism spectrum disorder, improved anxiety-like behavior	37
chronic fatigue syndrome patients	Beck Depression and Beck Anxiety Inventories	*Lactobacillus casei*	8 weeks	decreased anxiety symptoms	38
Wistar rats and humans	conditioned defensive burying test, Hopkins Symptom Checklist, Hospital Anxiety and Depression Scale, Perceived Stress Scale, Coping Checklist	*Lactobacillus helveticus* R0052, *Bifidobacterium longum* R0175	14 days/30 days	reduced anxiety-like behavior in rats, alleviated psychological distress in humans	39
humans	brain response to an emotional faces attention task and resting brain activity	fermented milk product with probiotics (FMPP) (containing *Bifidobacterium animalis* subsp. *lactis*, *Streptococcus thermophiles*, *Lactobacillus bulgaricus*, and *Lactococcus lactis* subsp. *lactis*)	4 weeks	reduced task-related response of a distributed functional network containing affective, viscerosensory, and somatosensory cortices	40
humans	stress hormone, cortisol, and emotional processing	galactooligosaccharides	3 weeks	lowered cortisol awakening reactivity and increased attentional vigilance to positive versus negative stimuli	59

bacterium longum were mediated by a BDNF-dependent and cytokine-independent pathway.

However, in Sprague−Dawley rats treated for 14 days with *Bifidobacterium infantis*, Desbonnet et al.[42] showed that there are significant decreases of cytokines (IFN-γ, TNF-α, and IL-6), 5-HIAA concentration in the frontal cortex, and DOPAC in the amygdaloid cortex, but remarkable increases in plasma concentrations of tryptophan and kynurenic acid, in the *Bifidobacteria*-treated rats relative to controls. Moreover, the same team assessed the potential benefits of *Bifidobacterium infantis* in the rat maternal separation (MS) model of depression.[43] The results showed that Bifidobacteria treatment reversed behavioral deficits, restored basal noradrenaline (NA) concentrations, and normalized immune response; especially peripheral interleukin (IL)-6 release and amygdala corticotrophin-releasing factor mRNA levels were enhanced. These findings point to immune response-dependent antidepressant properties of *Bifidobacterium infantis*.

Wall et al.[44] reported that the administration of a *Bifidobacterium* strain to mice had a significant impact on the fatty acid composition of the brain. Significantly higher concentrations of arachidonic acid (ARA) and docosahexaenoic acid (DHA) were observed in mice receiving the bacteria for 8 weeks, compared to control mice. These fatty acids play a critical role in neurotransmission and protection against oxidative stress[45,46] and are also involved in the improvement of cognitive functions such as memory and learning.[47,48] These data indicate that probiotics are able to enhance brain function by modulating the metabolism of the host.

Bravo et al.[36] indicated that the reduced anxiety/depression effects in *Lactobacillus rhamnosus*-treated mice were accompanied by the reduction of corticosterone, the region-dependent alterations of γ-aminobutyric acid (GABA) and its receptors in the brain. Specifically, GABAB1b was up-regulated in cortical regions and down-regulated in the hippocampus, amygdala, and locus coeruleus; GABA(Aα2) was increased in the hippocampus but reduced in the prefrontal cortex and amygdala, compared to the control mice. However, these neurochemical and behavioral changes caused by *Lactobacillus rhamnosus* were not observed in vagotomized mice. This highlights that the vagus nerve is involved in the direct communication between the bacteria and the brain, supporting the important role of GABA-mediated signaling pathway in the bidirectional communication of the gut microbiota−brain axis.

Except for GABA secreted by certain strains of *Lactobacillus* and *Bifidobacterium*,[49] other important bacterial metabolites include norepinephrine produced by *Saccharomyces*, *Bacillus*, and *Escherichia*; serotonin produced by *Enterococcus*, *Streptococcus*, *Escherichia*, and *Candida* and dopamine from *Bacillus* and *Serratia*.[50] All of these neurotransmitters play a major role in the action of antidepression.

The administration of *L. helveticus* for 21 days can prevent high fat diet-induced anxiety-like behavior in wild type micel; however, in immunocompromised (IL-10 deficient) mice, high fat diet-induced anxiety-like behavior was not prevented by *L. helveticus* administration, demonstrating the importance of IL-10 signaling in the microbiota−brain communication pathway.[51]

In *Citrobacter rodentium*-infected mice, Gareau et al.[5] demonstrated that treatment with a combination of probiotics of *Lactobacillus rhamnosus* R0011 and *Lactobacillus helveticus* R0052 improved learning and memory behaviors; normalized the population of *Firmicutes* and *Eubacterium rectale* but elevated the levels of *Bacteroides*; restored hippocampal c-Fos and BDNF expression; and ameliorated serum corticosterone and colonic IFN-γ, but not TNF-α, levels. This reflects a BDNF- and IFN-dependent mechanism of action for probiotics to normalize the memory dysfunction occurring in *Citrobacter rodentium*-infected mice exposed to acute stress.

Hsiao et al.[37] reported that oral administration of *Bacteroides fragilis* and *Bacteroides thetaiotaomicron* significantly restored the relative abundance of the Lachnospiraceae family as well as unclassified Bacteriodales and normalized ASD-like behavior in MIA offspring. Importantly, on the basis of an altered serum metabolomic profile in MIA offspring, they found that *Bacteroides fragilis* changed back the abundance of 34% of the plasma metabolites, including 4-ethylphenylsulfate (4EPS), indolepyruvate, serotonin, glycolate, imidazole propionate, and *N*-acetylserine. Interestingly, the systemic administration of the single metabolite 4EPS (with a 46-fold increase) to

DOI: 10.1021/acs.jafc.5b02404
J. Agric. Food Chem. 2015, 63, 7885−7895

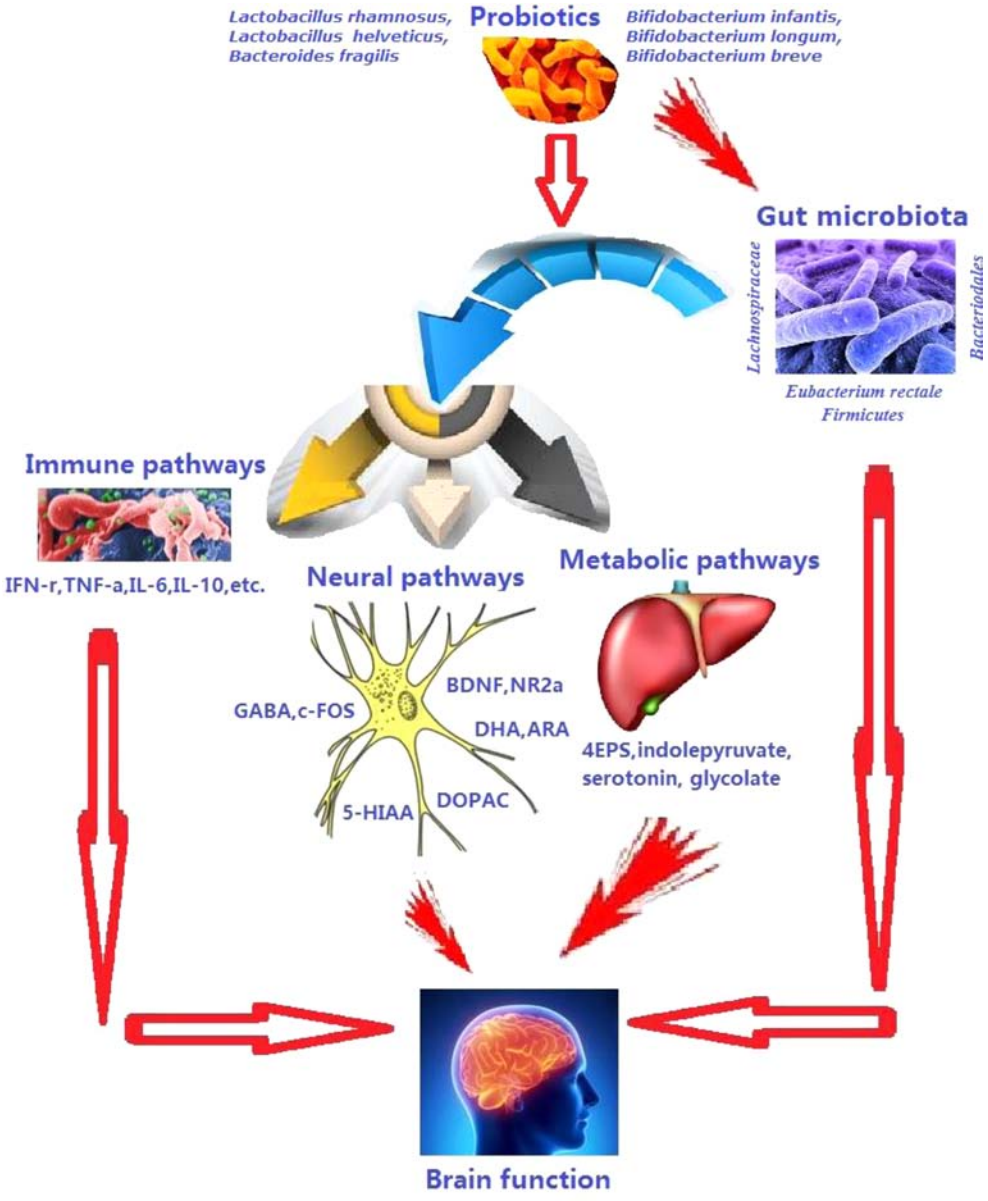

Figure 1. Proposed mechanism for probiotics-based modulation in the gut microbiota−brain axis. Probiotics modulate brain function by altering the composition of gut microbiota or regulating multiple signaling pathways including neural pathways, immune pathways, and metabolic pathways. INF-γ, interferon-gamma; TNF-α, (umor necrosis factor-alpha; IL-6, interleukin-6; IL-10, interleukin-10; BDNF, brain-derived neurotrophic factor; NMDA, *N*-methyl-D-aspartate; NR2a, receptor subunit 2a; GABA, gamma-aminobutyric acid; 5-HIAA, 5-hydroxyindoleacetic acid; DOPAC, dihydroxyphenylacetic acid; DHA, docosahexaenoic acid; ARA, arachidonic acid; 4EPS, 4-ethylphenylsulfate.

healthy mice is sufficient to induce anxiety-like behavior. It has been shown that commensal microbes are required for the production of serum 4EPS in mice; the precursor 4-ethylphenol is believed to be produced by several species of *Clostridium*;[52] the putative ASD biomarker *p*-cresol with a structure similar to that of 4EPS also derives from *Clostridium* species.[53] In addition, the elevated indolepyruvate in MIA offspring, which is also corrected by *Bacteroides fragilis* treatment, is reported to be produced by bacterial metabolism.[54] These findings suggest the critical role of the microbially modulated metabolism signaling pathway in modulating neurodevelopmental disorders.

Overall, as discussed above, the mechanisms of action are largely speculative and are not well-defined. On the basis of current knowledge, probiotics treatment alters the composition of gut microbiota, and multiple pathways may be involved in the conversation between gut microbiota and brain (Figure 1): vagus nerve-mediated pathways,[5,35,36,41] immune response-mediated pathways,[5,20−23] and metabolite-mediated pathways.[37]

Prebiotics-Based Modulation. It has been shown that varieties of polysaccharides can improve brain function in controlled human, animal, and in vitro studies after oral, systemic, and localized administration.[55] For example, ingestion of isolichenan, an α-glucan from the lichen *Cetrariella islandica*, reversed ethanol-induced memory impairment in mice.[56] Supplementation with a mixed polysaccharide product (Ambrotose complex) significantly improved cognitive function and mood in healthy middle-aged adults.[57] The oral administration of arabinoxylan from the yeast *Triticum aestivum* and β-glucan from barley were able to preserve memory in a mouse model of vascular dementia.[58]

A recent study explored the neuroendocrine and affective effects of two prebiotics (fructooligosaccharides, FOS, or

DOI: 10.1021/acs.jafc.5b02404
J. Agric. Food Chem. 2015, 63, 7885−7895

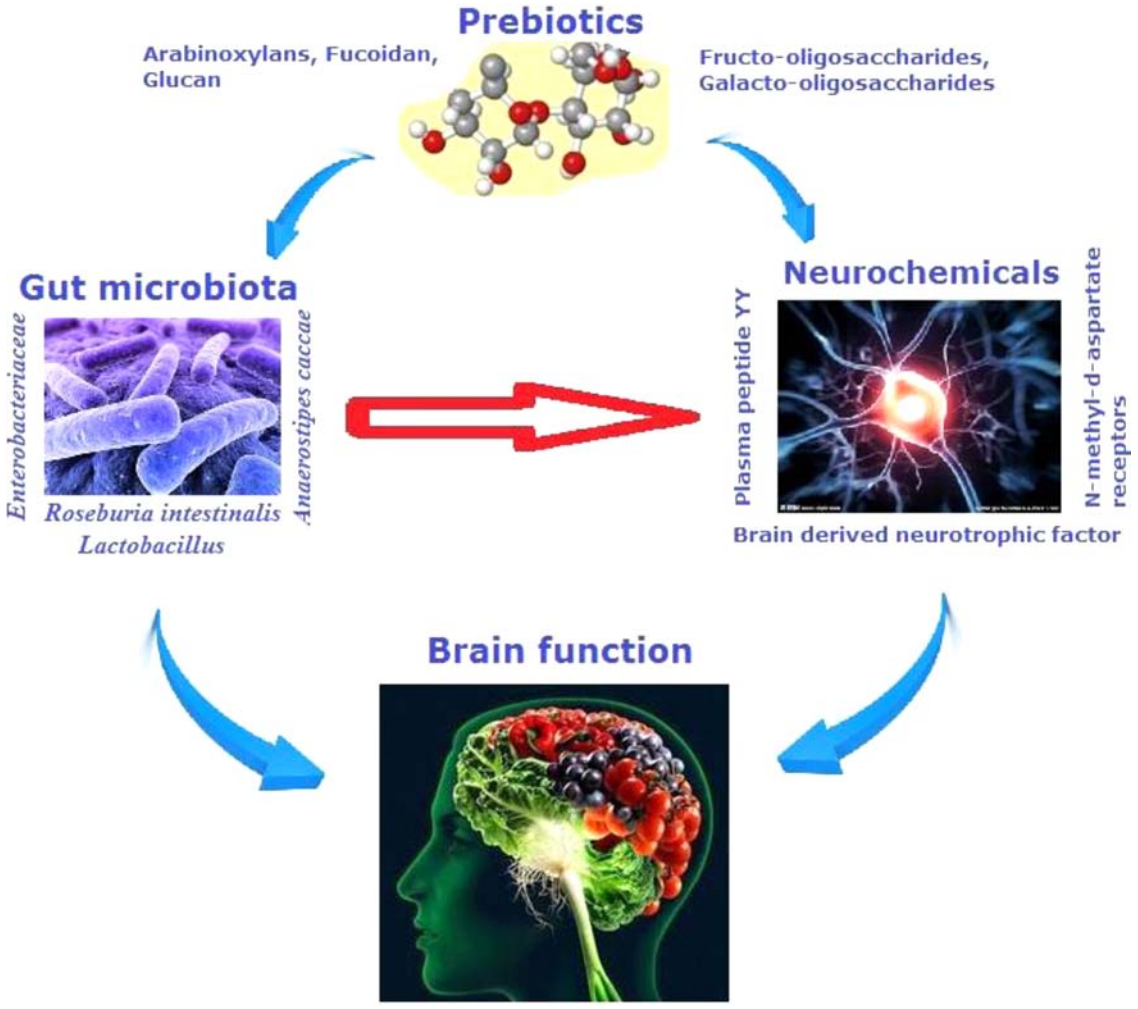

Figure 2. Proposed mechanism for prebiotics-based modulation in the gut microbiota–brain axis. Prebiotics modulate brain function by altering the composition of gut microbiota or influencing the production of neurochemicals.

Bimuno-galactooligosaccharides, B-GOS) in healthy human volunteers (Table 2).[59] Results revealed that no effects were found after the administration of FOS. In contrast, B-GOS lowered cortisol awakening reactivity and increased attentional vigilance to positive versus negative stimuli on the dot-probe task compared to the placebo group. The cortisol-awakening response is a reliable marker of HPA axis activity, which was increased in individuals at high risk of depression.[60] This indicates that B-GOS administration may have an antidepression effect by modulating the HPA axis.

Then, how do prebiotics act on the gut microbiota–brain axis? On the one hand, plant polysaccharides have major influences on gut microbiota. For example, the above-mentioned arabinoxylan was found to stimulate the growth of known butyrate producers (*Roseburia intestinalis*, *Eubacterium rectale*, *Anaerostipes caccae*);[61] fucoidan was reported to reduce the Enterobacteriaceae population in the newly weaned pig;[62] glucan, which is highly fermentable by the intestinal microbiota in the cecum and colon, can enhance the growth of *Lactobacillus* strains in the human intestine.[63] On the other hand, prebiotics directly influence signaling molecules in brain. In a recent study, Savignac et al.[64] revealed that prebiotics (FOS and galacto-oligosaccharides (GOS)) increased hippocampal BDNF and NR1 subunit expression, but did not alter amino acids associated with glutamate neurotransmission compared to controls. The intake of GOS also increased hippocampal NR2A subunits, frontal cortex NR1, and plasma peptide YY (PYY). This suggests that the prebiotics-mediated effect of the gut microbiota on brain chemistry is similar to that of probiotics, increasing brain BDNF expression probably through the involvement of gut hormones (Figure 2). However, the detailed mechanisms of prebiotic action, including how alterations in gut bacteria can affect these brain functions and behaviors, are not yet explored in these studies. Additional research is needed to determine whether these prebiotics-induced changes in brain physiology convincingly lead to cognitive and mood outcomes.

Moreover, compared with probiotics-based modulation, prebiotics could be advantageous to some extent, due to the presence of a survival problem in the GI tract for probiotics. In particular, genetic factors could have major impacts. For example, a single host gene, FUT2, is strongly associated with the diversity and composition of the human bifidobacterial population.[65] Specifically, several genotypes, including *Bifidobacterium bifidum*, *Bifidobacterium adolescentis*, and *Bifidobacterium catenulatum/pseudocatenulatum*, were absent or rarely colonized in the individuals without the FUT2 gene. On the other hand, probiotics are usually supplemented by one or several species at one time, whereas prebiotics supplementation

DOI: 10.1021/acs.jafc.5b02404
J. Agric. Food Chem. 2015, 63, 7885–7895

could stimulate a number of beneficial species simultaneously, which is good for their synergestic actions.

Diet-Based Modulation. Except for probiotics and prebiotics, diet can affect neural activity in the central nervous system. Hanstock et al.[66] reported that a fermentable carbohydrates-based diet increased anxiety and aggression behaviors in rats, and these effects were not related to the concentrations of dopamine and 5-HT in the brain, suggesting the mechanism of action could be neurotransmitter-independent. Haghpanah et al.[67] showed that oral administration of kefir (a fermented product of milk) can significantly improve spatial learning and consolidation of memory in rat. However, these studies did not examine the alterations in the bacterial populations. In fact, diet not only affects behavior but also alters the composition of the GI microbiota. For example, using male CF1 mice fed standard rodent chow (PP diet) or chow containing 50% lean ground beef (BD diet) for 3 months, Li et al.[68] showed that significantly higher bacterial diversity was observed in the BD group compared with the PP group. Three genera (*Atopobium*, *Bacteroidales*, and *Erysipelothrix*) were exclusively present in the PP group, whereas 12 genera (*Alistipes*, *Allobaculum*, *Chthoniobacter*, *Dorea*, *Eggerthella*, *Gemella*, *Leuconostoc*, *Proteus*, *Sarcina*, *Serratia*, *Staphylococcus*, and *Turicibacter*) were unique to the BP group. Furthermore, BD diet mice also displayed increased learning and memory behaviors as well as decreased levels of anxiety-like behavior compared to PP-fed animals. Notably, the nutritional components for both the PP and BD diets were approximately equal with the exception of taurine and fat, which were present at 18 and 1.5 times the concentrations in BD compared to PP diet, respectively. Although taurine improved learning behavior in aged mice[69] and high fat fed C57Bl/6ByJ mice increased learning and memory behaviors compared to regular chow fed mates,[70] it is not clear how BD diet-induced alterations in bacterial diversity lead to altered learning and memory behaviors.

FUTURE CHALLENGES

Selection of a Suitable Model or Strain for a Specific Behavior or Mood Is Essential. Except for the intrinsic complex in the gut microbiota−brain communication, one major impact factor is the use of different research methods, such as the selection of a suitable animal model or strain. For example, when using the bacterial infection method to induce anxiety-like behavior in animals, different infections will certainly lead to different anxiety models due to the different central sensing of GI infections. Indeed, acute infection with *Campylobacter jejuni* results in anxiety-like behavior by nonimmune responsive activation of vagal pathways,[71] whereas a recent study[36] reported that chronic *Trichuris muris*-infected mice exhibit anxiety-like behavior (present even after vagotomy), which is associated with decreased hippocampal BDNF and increased circulating tumor necrosis factor-α and interferon-γ, as well as the kynurenine, suggesting an inflammation-dependent and vagus nerve-independent pathway. Moreover, it is also possible to generate different anxiety models, even using the same bacterial species. For example, *Citrobacter rodentium* infection, an animal model of inflammatory bowel disease (IBD), induces anxiety-like behavior in mice during the early phase of infection (7−8 h post-infection), which is accompanied by unchanged plasma levels of the cytokines IFN-γ, TNF-α, and IL-12 and elevated c-Fos protein in vagal sensory ganglia.[72] These findings suggest that the behavioral effect is likely mediated by vagal sensory neurons, not by inflammation-related stress.[72] In another study,[5] *Citrobacter rodentium*-infected mice exhibit stress-induced memory dysfunction but no anxiety-like behavior during the late phase of infection (10 and 30 days post-infection), with decreased serum corticosterone, hippocampus BDNF, and c-Fos expressions; increased colonic IFN-γ and TNF-α levels; and altered gut microbiota (significantly elevated *Firmicutes*, Enterobacteriaceae, *Eubacteria rectale*, and *Bacteroides*), suggesting a neural and cytokine-mediated sensing pathway and highlighting the pronounced impacts of measuring behaviors at different time points.

On the other hand, the difference in the commonly used strains of mice (CD-1, MF1, NIH Swiss, C57BL6/J, and BALB/C) should be considered when using them to establish behavioral models. That is, BALB/c mice express more anxiety-like behavior and timidity and higher levels of serotonin and dopamine (may be genetically determined) in the colon than NIH Swiss mice, which are generally more gregarious and less timid.[13−15] It is imaginable that the results should be variable when investigating the effect of environmental factors on their behaviors, even under the same experimental conditions. Therefore, it is very important to identify the most suitable model or strain for a specific brain disorder model.

Strain−Strain Differences Are Important Factors for Modulating the Gut Microbiota−Brain Axis. Studies have supported a role of probiotics in modulating gut microbiota and improving brain behaviors, but the beneficial effects are divergent and are dependent on the strain. For example, Wall et al.[44] showed that reduced proportions of Eubacteriaceae (3 vs 12%) and increased proportions of Clostridiaceae (25 vs 12%) were observed in mice supplemented with *Bifidobacterium breve* DPC 6330 compared to mice supplemented with *Bifidobacterium breve* NCIMB 702258. Interestingly, administration of *Bifidobacterium breve* NCIMB 702258 was found to have a greater effect on the fatty acid composition of the brain; for instance, there were significantly higher concentrations of arachidonic acid (ARA) and docosahexaenoic acid (DHA) in the brain of mice supplemented with *B. breve* NCIMB 702258 than in the brain of mice supplemented with *B. breve* DPC 6330. Studies have indicated that ARA and DHA play important roles in neurogenesis and neurotransmission,[45,46] and their concentrations in the brain influence cognitive processes such as learning and memory.[47,48] Therefore, it is important to perform extensive studies on whether or not the strain-dependent differences in the compositions of gut microbiota and brain fatty acids or other neurochemicals result in remarkably functional consequences for the host.

Communication among the Gut, Gut Microbiota, and Brain. Although the existence of multiple signaling pathways including immune, neural, and metabolic pathways in the modulation of the gut microbiota−brain axis is discussed above, it is still challenging to fully understand how the gut, gut microbiota, and brain cooperate to maintain the functioning of the host.

The gut possesses its own nervous system, named the enteric nervous system (ENS). It is well-known that the ENS maintains constant and direct communication with the central nervous system (CNS) via nerves.[1] Therefore, the remaining issue is the communication between ENS or CNS and gut microbiota. Notably, the ENS is separated from gut microbiota by mucosal cell layers, which makes the intestinal commensal microbes inaccessible to ENS. Thus, there are two possibilities to realize

DOI: 10.1021/acs.jafc.5b02404
J. Agric. Food Chem. 2015, 63, 7885−7895

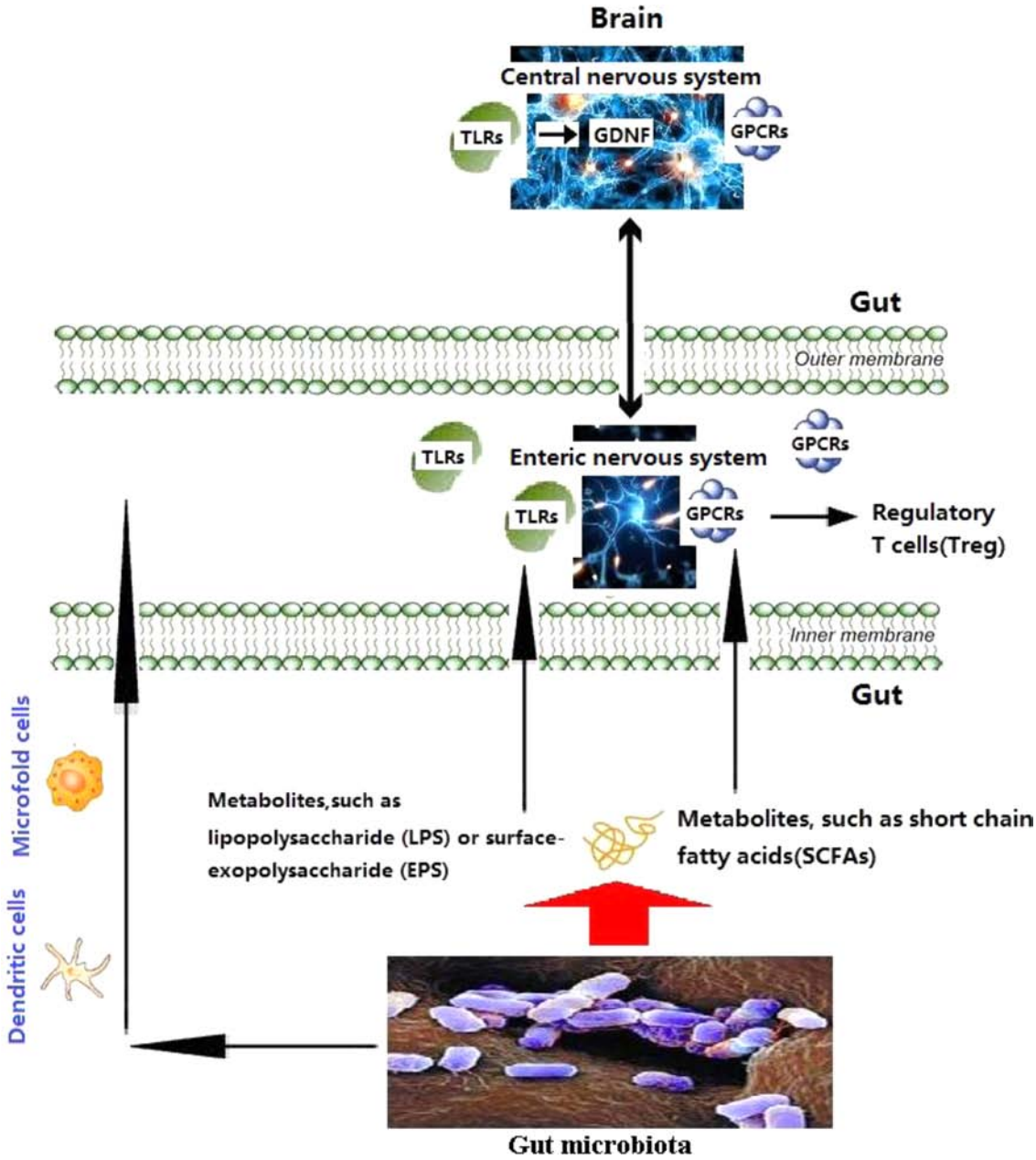

Figure 3. Communication among the gut, gut microbiota, and brain. The enteric nervous system (ENS) directly communicates with the central nervous system (CNS). The resident microbes translocate to the lamina propria from the intestinal lumen by the microfold cells and/or by dendritic cells. The microbiota-generated components, such as bacterial lipopolysaccharide (LPS), surface exopolysaccharide (EPS), and short-chain fatty acids (SCFAs), cross or bypass the epithelium to act directly on the ENS. The resident microbes or their metabolites are able to interact with some specific receptors such as Toll-like receptors (TLRs) and G-protein coupled receptors (GPCRs). The gut microbiota regulates the ENS by TLR signaling, stimulates the expression of a glial cell line-derived neurotrophic factor (GDNF), and increases the number of enteric neurons and glial cells. SCFAs regulate colonic regulatory T cell (cTreg) homeostasis by acting on GPCRs.

communication between gut microbiota and ENS: (1) the resident microbes translocate to the lamina propria from the intestinal lumen by microfold cells and/or dendritic cells, probably by direct entrance in disease state due to "leaky" intestinal wall; (2) the microbiota-generated components access the lamina propria. Indeed, bacterial lipopolysaccharide (LPS) or polysaccharide A (PSA) or surface-exopolysaccharide (EPS), short-chain fatty acids, glutamate, and so on, are able to cross or bypass the epithelium to act directly on the ENS.[73] After the resident microbes (probably secreted products or metabolites) or their products/metabolites translocate to the lamina propria, they are able to interact with some specific receptors, such as pattern recognition receptors including Toll-like receptors (TLRs) and G-protein coupled receptors (GPCRs).

TLRs are universally distributed in macrophages, endothelial cells, glia, and neurons.[74] In the immune system, TLRs recognize the invading microorganisms, and in the nervous system, TLRs recognize endogenous ligands released by undifferentiated or necrotic/injured cells; their activities are associated with brain disorders.[75] After interaction, the ENS and immune system are activated to release cytokines and neurohumoral mediators.[76] In fact, Brun et al.[77] revealed that gut microbiota regulate ENS integrity by TLR-2 signaling,

DOI: 10.1021/acs.jafc.5b02404
J. Agric. Food Chem. 2015, 63, 7885−7895

stimulate the expression of a glial cell line-derived neurotrophic factor (GDNF), and increase the number of enteric neurons and glial cells, hence facilitating the development and survival of many types of neurons. Depletion of gut microbiota significantly reduced the expression of GDNF in mice; TLR-2-deficient mice increased susceptibility to inflammation, whereas the severity of inflammation was reduced by administration of GDNF. This highlights the importance of the gut microbiota−TLR-2−GDNF axis in modulating the ENS and inflammation.

GPCRs are also universally expressed in many sites, including in the CNS, especially in the striatum,[78] and these receptors play a critical role in the regulation of metabolism, inflammation, neurological/psychiatric disorders, and other diseases.[79,80] Short-chain fatty acids (SCFAs) are produced by the gut microbiota during the fermentation of partially digestible or nondigestible polysaccharides. Except for inhibition of histone deacetylases (HDACs), another major SCFA signaling mechanism is activation of GPCRs. Especially, GPR43, GPR41, and GPR109A have been identified as receptors of SCFAs.[81] Smith et al.[82] reported that acetic acid, propionic acid, and butyric acid, the three most abundant microbial-derived SCFA, display an exciting role in regulating colonic regulatory T cell (cTreg) homeostasis and protecting against colitis by acting on GPR43. This is supported by Atarashi et al.,[83] who found that a rationally selected mixture of *Clostridia* strains from the human microbiota enhances Treg induction. In particular, De Vadder et al.[84] showed that SCFAs such as propionate from fermentation of gut microbiota on prebiotic GOS promote metabolic benefits on body weight and glucose control via a gut−brain neural circuit involving the fatty acid receptor GPR41. This highlights the importance of the gut microbiota−GPCRs−brain axis in regulating host functions.

Thus, although the exact mechanism describing the communication among gut, gut microbiota, and brain still warrants further study, it can be speculated that various axes of gut microbiota−receptors−brain could be responsible for the realization of many functions between the gut and brain (Figure 3), such as the gut microbiota−TLRs−brain axis for probiotics modulation and the gut microbiota−GPCRs−brain axis for prebiotics modulation.

Novel Technologies in the Gut Microbiota−Brain Axis. To extensively explore the detailed mechanism underlying the gut microbiota−brain axis, novel techniques are highly needed. One technology is functional magnetic resonance imaging (fMRI), which has shown the potential for studies of gut−brain signaling in humans over the past few years. For example, using fMRI, Van Oudenhove et al.[85] found that there was a significant fat−emotion interaction effect on the blood oxygen level-dependent signal (BOLD signal) in multiple regions of interest, including medulla/pons, midbrain, hypothalamus, thalamus, caudate head, putamen, cerebellum, AND right hippocampus, suggesting that fatty acid infusion attenuated the behavioral and neural responses to sad emotion induction in humans. By physiological/pharmacological MRI (phMRI), Jones et al.[86] revealed that intragastric dodecanoate caused strong bilateral activation of a matrix of CNS areas, including the brain stem, hypothalamus, and limbic areas, and ghrelin bolus decreased the BOLD signal in feeding-activated areas of the CNS. Very recently, Tillisch et al.[40] demonstrated that the reactivity of a widely distributed network of brain regions to an emotional attention task was reduced in women who had ingested FMPP, including primary interoceptive and somatosensory regions, prefrontal cortex, precuneus, basal ganglia, and the parahippocampal gyrus. This provides important clues for further exploring the mechanism of action.

Another technology is omics analysis (i.e., transcriptomics, proteomics, metabolomics, and systems biology). For example, transcriptomics, which is the study of the complete set of RNA transcripts produced in cells or tissues, was applied to explore in vivo mucosal responses of healthy adults to probiotics.[87,88] The results revealed that gene-regulatory networks and pathways were differentially induced in the human mucosa and were dependent on the preparations of living and heat-killed *Lactobacillus plantarum* bacteria and the specific species (*L. acidophilus*, *L. casei*, and *L. rhamnosus*). Transcriptomic comparisons of two breast milk-derived *Lactobacillus* (*L. reuteri* ATCC 55730 and ATCC PTA 6475) identified candidate genes involved in the survival and persistence in the gut, and genes responsible for immunomodulation and health-promoting factors such as antimicrobial agents and vitamins especially predicted a complete pathway for thiamin biosynthesis in strain 55730 for the first time.[89]

Proteomics is the large-scale study of the entire set of proteins produced or modified by an organism or system, which is largely an underexploited approach at the interface of gut microbiota and brain physiology.[90] In a *Trichuris muris*-infected mice model, Bercik et al.[36] showed that anxiety-like behavior was induced and CNS biochemistry was changed, and several proteins related to inflammation and neural function were identified by proteomic analysis. Using comparative proteomics, Kim et al.[91] investigated the response of *Bifidobacterium longum* subsp. *infantis* to different prebiotics. ATP-dependent sugar transport systems related to the consumption of different prebiotics was determined, providing molecular foundations for different prebiotics consumption in *B. infantis* and evidence for differential impacts on brain health.

Metabolomics is simultaneously analyzes hundreds to thousands of small-molecule metabolites in biological samples by an array of analytical techniques including mass spectrometry and high-resolution nuclear magnetic resonance spectroscopy. Real-time analysis of the small-molecule metabolites derived from the gut, microbes, and brain is increasingly useful for deciphering inherent and intimate gut microbiota−brain relationships.[92] Using capillary electrophoresis with time-of-flight mass spectrometry (CE-TOFMS), Matsumoto et al.[93] identified 196 metabolites from the cerebral metabolome in both GF and Ex-GF mice (inoculated with suspension of feces obtained from specific pathogen-free mice); among them, 38 metabolites differed significantly, and 10 of these metabolites are known to be involved in brain function. A novel relationship between gut microbiota and cerebral glycolytic metabolism was found. These findings suggest that the intestinal microbiota is closely connected with brain health and disease through the gut microbiota−brain axis. Indeed, an excellent study conducted by Hsiao et al.[37] supported this observation. In this study, MIA-associated changes in serum metabolites were profiled using gas chromatography−liquid chromatography with mass spectrometry (GC-LC/MS)-based metabolomics technology, demonstrating that 8% of all serum metabolites were significantly altered by MIA induction and 34% of all metabolites were significantly affected by *B. fragilis* treatment. Among them, 4-ethylphenylsulfate (4EPS) displayed a 46-fold increase in serum levels of MIA offspring and is completely restored by *B. fragilis* treatment. Strikingly, systemic administration of the single metabolite, 4EPS, to healthy mice is sufficient to induce

DOI: 10.1021/acs.jafc.5b02404
J. Agric. Food Chem. 2015, 63, 7885−7895

anxiety-like behavior. This highlights an important role of a single metabolite regulated by gut microbes in the molecular connections between the gut and the brain. It is believable that more metabolic signatures in the gut microbiota−brain axis can be identified when this method is applied to other neurodevelopmental disorders.

In summary, abnormalities of brain function are associated with the altered composition of the gut microbiota. The use of probiotics, prebiotics, and functional foods can partly or completely reverse the dysbiosis in the microbiota caused by some brain disorders. Multiple pathways are involved in the modulation of the gut microbiota−brain axis: vagus nerve-mediated pathways, immune response-mediated pathways, and metabolite-mediated pathways. The availability of novel techniques such as functional magnetic resonance imaging, metatranscriptomes, metaproteomics, and metabolomics will rapidly expand our knowledge on the complex mechanisms of action underlying the interactions between microbiota components and the host. A comprehensive understanding of the gut microbiota−brain axis may provide novel approaches for the prevention and treatment of brain dysfunctions.

AUTHOR INFORMATION

Corresponding Author

*(X.Z.) Mail: College of Light Industry and Food Sciences, South China University of Technology, 381 Wushan Road, Guangzhou 510640, China. Phone/fax: 86 20 87113848. E-mail: snow_dance@sina.com.

Notes

The authors declare no competing financial interest.

[‖]X.L. and S.C. are identifed as co-first authors.

REFERENCES

(1) Furness, J. B. Novel gut afferents: intrinsic afferent neurons and intestinofugal neurons. *Auton. Neurosci.* **2006**, *125*, 81−85.

(2) Grenham, S.; Clarke, G.; Cryan, J. F.; Dinan, T. G. Brain-gut-microbe communication in health and disease. *Front. Physiol.* **2011**, *7* (2), 94.

(3) Cryan, J. F.; Dinan, T. G. Mind-altering microorganisms: the impact of the gut microbiota on brain and behaviour. *Nat. Rev. Neurosci.* **2012**, *13* (10), 701−712.

(4) Neufeld, K. M.; Kang, N.; Bienenstock, J.; Foster, J. A. Reduced anxiety-like behavior and central neurochemical change in germ-free mice. *Neurogastroenterol. Motil.* **2011**, *23* (3), 255−264.

(5) Gareau, M. G.; Wine, E.; Rodrigues, D. M.; Cho, J. H.; Whary, M. T.; Philpott, D. J.; Macqueen, G.; Sherman, P. M. Bacterial infection causes stress-induced memory dysfunction in mice. *Gut* **2011**, *60* (3), 307−317.

(6) Dinan, T. G.; Cryan, J. F. Melancholic microbes: a link between gut microbiota and depression? *Neurogastroenterol. Motil.* **2013**, *25* (9), 713−719.

(7) Wang, L.; Christophersen, C. T.; Sorich, M. J.; Gerber, J. P.; Angley, M. T.; Conlon, M. A. Increased abundance of *Sutterella* spp. and *Ruminococcus torques* in feces of children with autism spectrum disorder. *Mol. Autism* **2013**, *4* (1), 42.

(8) Moloney, R. D.; Desbonnet, L.; Clarke, G.; Dinan, T. G.; Cryan, J. F. The microbiome: stress, health and disease. *Mamm. Genome.* **2014**, *25*, 4910.1007/s00335-013-9488-5

(9) Hill, C.; Guarner, F.; Reid, G.; Gibson, G. R.; Merenstein, D. J.; Pot, B.; et al. The International Scientific Association for Probiotics and Prebiotics consensus statement on the scope and appropriate use of the term probiotic. *Nat. Rev. Gastroenterol. Hepatol.* **2014**, *11*, 506−514.

(10) Hardy, H.; Harris, J.; Lyon, E.; Beal, J.; Foey, A. D. Probiotics, prebiotics and immunomodulation of gut mucosal defences: homeostasis and immunopathology. *Nutrients* **2013**, *5* (6), 1869−1912.

(11) Gibson, G. R.; Probert, H. M.; Van Loo, J.; Rastall, R. A.; Roberfroid, M. B. Dietary modulation of the human colonic microbiota: updating the concept of prebiotics. *Nutr. Res. Rev.* **2004**, *17*, 259−275.

(12) Kanauchi, O.; Andoh, A.; Mitsuyama, K. Effects of the modulation of microbiota on the gastrointestinal immune system and bowel function. *J. Agric. Food Chem.* **2013**, *61* (42), 9977−9983.

(13) Diaz Heijtz, R.; Wang, S.; Anuar, F.; Qian, Y.; Björkholm, B.; Samuelsson, A.; Hibberd, M. L.; Forssberg, H.; Pettersson, S. Normal gut microbiota modulates brain development and behavior. *Proc. Natl. Acad. Sci. U. S. A.* **2011**, *108* (7), 3047−3052.

(14) Bercik, P.; Denou, E.; Collins, J.; Jackson, W.; Lu, J.; Jury, J.; Deng, Y.; Blennerhassett, P.; Macri, J.; McCoy, K. D.; Verdu, E. F.; Collins, S. M. The intestinal microbiota affect central levels of brain-derived neurotropic factor and behavior in mice. *Gastroenterology* **2011**, *141* (2), 599−609.

(15) Conti, L. H.; Costello, D. G.; Martin, L. A.; White, M. F.; Abreu, M. E. Mouse strain differences in the behavioral effects of corticotropin-releasing factor (CRF) and the CRF antagonist alpha-helical CRF9−41. *Pharmacol., Biochem. Behav.* **1994**, *48* (2), 497−503.

(16) Kalinichev, M.; Bate, S. T.; Coggon, S. A.; Jones, D. N. Locomotor reactivity to a novel environment and sensitivity to MK-801 in five strains of mice. *Behav. Pharmacol.* **2008**, *19* (1), 71−75.

(17) Turnbaugh, P. J.; Ley, R. E.; Mahowald, M. A.; Magrini, V.; Mardis, E. R.; Gordon, J. I. An obesity-associated gut microbiome with increased capacity for energy harvest. *Nature* **2006**, *444* (7122), 1027−1031.

(18) Park, A. J.; Collins, J.; Blennerhassett, P. A.; Ghia, J. E.; Verdu, E. F.; Bercik, P.; Collins, S. M. Altered colonic function and microbiota profile in a mouse model of chronic depression. *Neurogastroenterol. Motil.* **2013**, *25* (9), 733−e575.

(19) Tannock, G. W.; Savage, D. C. Influences of dietary and environmental stress on microbial populations in the murine gastrointestinal tract. *Infect. Immun.* **1974**, *9*, 591−598.

(20) O'Mahony, S. M.; Marchesi, J. R.; Scully, P.; Codling, C.; Ceolho, A. M.; Quigley, E. M.; Cryan, J. F.; Dinan, T. G. Early life stress alters behavior, immunity, and microbiota in rats: implications for irritable bowel syndrome and psychiatric illnesses. *Biol. Psychiatry* **2009**, *65*, 263−267.

(21) Bailey, M. T.; Dowd, S. E.; Parry, N. M.; Galley, J. D.; Schauer, D. B.; Lyte, M. Stressor exposure disrupts commensal microbial populations in the intestines and leads to increased colonization by *Citrobacter rodentium*. *Infect. Immun.* **2010**, *78*, 1509−1519.

(22) Bailey, M. T.; Dowd, S. E.; Galley, J. D.; Hufnagle, A. R.; Allen, R. G.; Lyte, M. Exposure to a social stressor alters the structure of the intestinal microbiota: implications for stressorinduced immunomodulation. *Brain, Behav., Immun.* **2011**, *25*, 397−407.

(23) Bangsgaard Bendtsen, K. M.; Krych, L.; Sørensen, D. B.; Pang, W.; Nielsen, D. S.; Josefsen, K.; Hansen, L. H.; Sørensen, S. J.; Hansen, A. K. Gut microbiota composition is correlated to grid floor induced stress and behavior in the BALB/c mouse. *PLoS One* **2012**, *7* (10), e46231.

(24) Johnson, C. P.; Myers, S. M. Identification and evaluation of children with autism spectrum disorders. *Pediatrics* **2007**, *120*, 1183−1215.

(25) Coury, D. L.; Ashwood, P.; Fasano, A.; Fuchs, G.; Geraghty, M.; Kaul, A.; Mawe, G.; Patterson, P.; Jones, N. E. Gastrointestinal conditions in children with autism spectrum disorder: developing a research agenda. *Pediatrics* **2012**, *130* (Suppl.2), S160−S168.

(26) Adams, J. B.; Johansen, L. J.; Powell, L. D.; Quiq, D.; Rubin, R. A. Gastrointestinal flora and gastrointestinal status in children with autism − comparisons to neurotypical children and correlation with autism severity. *BMC Gastroenterol.* **2011**, *11*, 22−34.

(27) Parracho, H. M. R. T.; Bingham, M. O.; Gibson, G. R.; McCartney, A. L. Differences between the gut microflora of children

DOI: 10.1021/acs.jafc.5b02404
J. Agric. Food Chem. 2015, 63, 7885−7895

with autistic spectrum disorders and that of healthy children. *J. Med. Microbiol.* **2005**, *54*, 987−991.
(28) Song, Y.; Liu, C.; Finegold, S. M. Real-Time PCR Quantitation of Clostridia in feces of autistic children. *Appl. Environ. Microbiol.* **2004**, *70*, 6459−6465.
(29) Williams, B. L.; Hornig, M.; Buie, T.; Bauman, M. L.; Cho Paik, M.; Wick, I.; Bennett, A.; Jabado, O.; Hirschberg, D. L.; Lipkin, W. I. Impaired carbohydrate digestion and transport and mucosal dysbiosis in the intestines of children with autism and gastrointestinal disturbances. *PLoS One* **2011**, *6*, e24585.
(30) Wang, L.; Christophersen, C. T.; Sorich, M. J.; Gerber, J. P.; Angley, M. T.; Conlon, M. A. Low relative abundances of the mucolytic bacterium *Akkermansia muciniphila* and *Bifidobacterium* spp. in feces of children with autism. *Appl. Environ. Microbiol.* **2011**, *77*, 6718−6721.
(31) De Angelis, M.; Piccolo, M.; Vannini, L.; Siragusa, S.; De Giacomo, A.; Serrazzanetti, D. I.; Cristofori, F.; Guerzoni, M. E.; Gobbetti, M.; Francavilla, R. Fecal microbiota and metabolome of children with autism and pervasive developmental disorder not otherwise specified. *PLoS One* **2013**, *8*, e76993.
(32) Finegold, S. M.; Dowd, S. E.; Gontcharova, V.; Liu, C.; Henley, K. E.; Wolcott, R. D.; Youn, E.; Summanen, P. H.; Granpeesheh, D.; Dixon, D.; Liu, M.; Molitoris, D. R.; Green Iii, J. A. Pyrosequencing study of fecal microflora of autistic and control children. *Anaerobe* **2010**, *16*, 444−453.
(33) Kang, D. W.; Park, J. G.; Ilhan, Z. E.; Wallstrom, G.; Labaer, J.; Adams, J. B.; Krajmalnik-Brown, R. Reduced incidence of Prevotella and other fermenters in intestinal microflora of autistic children. *PLoS One* **2013**, *8*, e68322.
(34) Saulnier, D. M.; Ringel, Y.; Heyman, M. B.; Foster, J. A.; Bercik, P.; Shulman, R. J.; Versalovic, J.; Verdu, E. F.; Dinan, T. G.; Hecht, G.; Guarner, F. The intestinal microbiome, probiotics and prebiotics in neurogastroenterology. *Gut Microbes.* **2013**, *4* (1), 17−27.
(35) Bercik, P.; Verdu, E. F.; Foster, J. A.; Macri, J.; Potter, M.; Huang, X.; Malinowski, P.; Jackson, W.; Blennerhassett, P.; Neufeld, K. A.; Lu, J.; Khan, W. I.; Corthesy-Theulaz, I.; Cherbut, C.; Bergonzelli, G. E.; Collins, S. M. Chronic gastrointestinal inflammation induces anxiety-like behavior and alters central nervous system biochemistry in mice. *Gastroenterology* **2010**, *139* (6), 2102−2112.
(36) Bravo, J. A.; Forsythe, P.; Chew, M. V.; Escaravage, E.; Savignac, H. M.; Dinan, T. G.; Bienenstock, J.; Cryan, J. F. Ingestion of *Lactobacillus* strain regulates emotional behavior and central GABA receptor expression in a mouse via the vagus nerve. *Proc. Natl. Acad. Sci. U. S. A.* **2011**, *108* (38), 16050−16055.
(37) Hsiao, E. Y.; McBride, S. W.; Hsien, S.; Sharon, G.; Hyde, E. R.; McCue, T.; Codelli, JA4; Chow, J.; Reisman, S. E.; Petrosino, J. F.; Patterson, P. H.; Mazmanian, S. K. Microbiota modulate behavioral and physiological abnormalities associated with neurodevelopmental disorders. *Cell* **2013**, *155* (7), 1451−1463.
(38) Rao, A. V.; Bested, A. C.; Beaulne, T. M.; Katzman, M. A.; Iorio, C.; Berardi, J. M.; Logan, A. C. A randomized, double-blind, placebo-controlled pilot study of a probiotic in emotional symptoms of chronic fatigue syndrome. *Gut Pathog.* **2009**, *1*, 6.
(39) Messaoudi, M.; Lalonde, R.; Violle, N.; Javelot, H.; Desor, D.; Nejdi, A.; Bisson, J. F.; Rougeot, C.; Pichelin, M.; Cazaubiel, M.; Cazaubiel, J. M. Assessment of psychotropic-like properties of a probiotic formulation (*Lactobacillus helveticus* R0052 and *Bifidobacterium longum* R0175) in rats and human subjects. *Br. J. Nutr.* **2011**, *105* (5), 755−764.
(40) Tillisch, K.; Labus, J.; Kilpatrick, L.; Jiang, Z.; Stains, J.; Ebrat, B.; Guyonnet, D.; Legrain-Raspaud, S.; Trotin, B.; Naliboff, B.; Mayer, E. A. Consumption of fermented milk product with probiotic modulates brain activity. *Gastroenterology* **2013**, *144* (7), 1394−1401.
(41) Sudo, N.; Chida, Y.; Aiba, Y.; Sonoda, J.; Oyama, N.; Yu, X. N.; Kubo, C.; Koga, Y. Postnatal microbial colonization programs the hypothalamic-pituitary-adrenal system for stress response in mice. *J. Physiol. (Oxford, U. K.)* **2004**, *558*, 263−275.
(42) Desbonnet, L.; Garrett, L.; Clarke, G.; Bienenstock, J.; Dinan, T. G. The probiotic Bifidobacteria infantis: an assessment of potential antidepressant properties in the rat. *J. Psychiatr. Res.* **2008**, *43* (2), 164−174.
(43) Desbonnet, L.; Garrett, L.; Clarke, G.; Kiely, B.; Cryan, J. F.; Dinan, T. G. Effects of the probiotic Bifidobacterium infantis in the maternal separation model of depression. *Neuroscience* **2010**, *170* (4), 1179−1188.
(44) Wall, R.; Marques, T. M.; O'Sullivan, O.; Ross, R. P.; Shanahan, F.; Quigley, E. M.; Dinan, T. G.; Kiely, B.; Fitzgerald, G. F.; Cotter, P. D.; Fouhy, F.; Stanton, C. Contrasting effects of Bifidobacterium breve NCIMB 702258 and Bifidobacterium breve DPC 6330 on the composition of murine brain fatty acids and gut microbiota. *Am. J. Clin. Nutr.* **2012**, *95* (5), 1278−1287.
(45) Innis, S. M. Dietary (n-3) fatty acids and brain development. *J. Nutr.* **2007**, *137*, 855−859.
(46) Maekawa, M.; Takashima, N.; Matsumata, M.; Ikegami, S.; Kontami, M.; Hara, Y.; Kawashima, H.; Owada, Y.; Kiso, Y.; Yoshikawa, T.; et al. Arachidonic acid drives postnatal neurogenesis and elicits a beneficial effect on prepulse inhibition, a biological trait of psychiatric illnesses. *PLoS One* **2009**, *4*, e5085.
(47) Yurko-Mauro, K.; McCarthy, D.; Rom, D.; Nelson, E. B.; Ryan, A. S.; Blackwell, A.; Salem, N., Jr; Stedman, M. MIDAS Investigators. Beneficial effects of docosahexaenoic acid on cognition in age-related cognitie decline. *Alzheimer's Dementia* **2010**, *6*, 456−464.
(48) Henriksen, C.; Haugholt, K.; Lindgren, M.; Aurvåg, A. K.; Rønnestad, A.; Grønn, M.; Solberg, R.; Moen, A.; Nakstad, B.; Berge, R. K.; Smith, L.; Iversen, P. O.; Drevon, C. A. Improved cognitive development among preterm infants attributable to early supplementation of human milk with docosahexaenoic acid and arachidonic acid. *Pediatrics* **2008**, *121*, 1137−1145.
(49) Barrett, E.; Ross, R. P.; O'Toole, P. W.; Fitzgerald, G. F.; Stanton, C. Gamma-aminobutyric acid production by culturable bacteria from the human intestine. *J. Appl. Microbiol.* **2012**, *113* (2), 411−417.
(50) Lyte, M. Probiotics function mechanistically as delivery vehicles for neuroactive compounds: microbial endocrinology in the design and use of probiotics. *BioEssays* **2011**, *33* (8), 574−581.
(51) Ohland, C. L.; Kish, L.; Bell, H.; Thiesen, A.; Hotte, N.; Pankiv, E.; Madsen, K. L. Effects of Lactobacillus helveticus on murine behavior are dependent on diet and genotype and correlate with alterations in the gut microbiome. *Psychoneuroendocrinology* **2013**, *38* (9), 1738−1747.
(52) Nicholson, J. K.; Holmes, E.; Kinross, J.; Burcelin, R.; Gibson, G.; Jia, W.; Pettersson, S. Host-gut microbiota metabolic interactions. *Science* **2012**, *336*, 1262−1267.
(53) Persico, A. M.; Napolioni, V. Urinary p-cresol in autism spectrum disorder. *Neurotoxicol. Teratol.* **2013**, *36*, 82−90.
(54) Keszthelyi, D.; Troost, F. J.; Masclee, A. A. Understanding the role of tryptophan and serotonin metabolism in gastrointestinal function. *Neurogastroenterol. Motil.* **2009**, *21*, 1239−1249.
(55) Nelson, E. D.; Ramberg, J. E.; Best, T.; Sinnott, R. A. Neurologic effects of exogenous saccharides: a review of controlled human, animal, and in vitro studies. *Nutr. Neurosci.* **2012**, *15* (4), 149−162.
(56) Smriga, M.; Chen, J.; Zhang, J.-T.; Narui, T.; Shibata, S.; Hirano, E. Isolichenan, an alpha-glucan isolated from lichen Cetrariella islandica, repairs impaired learning behaviors and facilitates hippocampal synaptic plasticity. *Proc. Jpn. Acad., Ser. B* **1999**, *75* (7), 219−223.
(57) Talbott, S.; Talbott, J. Effect of beta 1,3/1,6 glucan on respiratory tract infection symptoms and mood state in marathon atheletes. *J. Sports Sci. Med.* **2009**, *8* (4), 509−515.
(58) Han, H. S.; Jang, J. H.; Jang, J. H.; Choi, J. S.; Kim, Y. J.; Lee, C.; et al. Water extract of *Triticum aestivum* L. and its components demonstrate protective effect in a model of vascular dementia. *J. Med. Food* **2010**, *13* (3), 572−578.
(59) Schmidt, K.; Cowen, P. J.; Harmer, C. J.; Tzortzis, G.; Errington, S.; Burnet, P. W. Prebiotic intake reduces the waking cortisol response and alters emotional bias in healthy volunteers. *Psychopharmacology (Berlin)* **2015**, *232* (10), 1793−1801.

DOI: 10.1021/acs.jafc.5b02404
J. Agric. Food Chem. 2015, 63, 7885−7895

(60) Mannie, Z. N.; Harmer, C. J.; Cowen, P. J. Increased waking salivary cortisol levels in young people at familial risk of depression. *Am. J. Psychiatry* **2007**, *164*, 617−621.
(61) Van den Abbeele, P.; Gérard, P.; Rabot, S.; Bruneau, A.; El Aidy, S.; Derrien, M.; Kleerebezem, M.; Zoetendal, E. G.; Smidt, H.; Verstraete, W.; Van de Wiele, T.; Possemiers, S. Arabinoxylans and inulin differentially modulate the mucosal and luminal gut microbiota and mucin-degradation in humanized rats. *Environ. Microbiol.* **2011**, *13* (10), 2667−2680.
(62) Walsh, A. M.; Sweeney, T.; O'Shea, C. J.; Doyle, D. N.; O'Doherty, J. V. Effect of dietary laminarin and fucoidan on selected microbiota, intestinal morphology and immune status of the newly weaned pig. *Br. J. Nutr.* **2013**, *110* (9), 1630−1638.
(63) Arena, M. P.; Caggianiello, G.; Fiocco, D.; Russo, P.; Torelli, M.; Spano, G.; Capozzi, V. Barley β-glucans-containing food enhances probiotic performances of beneficial bacteria. *Int. J. Mol. Sci.* **2014**, *15* (2), 3025−3039.
(64) Savignac, H. M.; Corona, G.; Mills, H.; Chen, L.; Spencer, J. P.; Tzortzis, G.; Burnet, P. W. Prebiotic feeding elevates central brain derived neurotrophic factor, *N*-methyl-D-aspartate receptor subunits and d-serine. *Neurochem. Int.* **2013**, *63* (8), 756−764.
(65) Wacklin, P.; Mäkivuokko, H.; Alakulppi, N.; Nikkilä, J.; Tenkanen, H.; Räbinä, J.; Partanen, J.; Aranko, K.; Mättö, J. Secretor genotype (FUT2 gene) is strongly associated with the composition of Bifidobacteria in the human intestine. *PLoS One* **2011**, *6*, e20113.
(66) Hanstock, T. L.; Clayton, E. H.; Li, K. M.; Mallet, P. E. Anxiety and aggression associated with the fermentation of carbohydrates in the hindgut of rats. *Physiol. Behav.* **2004**, *82* (2−3), 357−368.
(67) Haghpanah, T.; Sheibani, V.; Afarinesh, M. R. Effect of kefir consumption on spatial learning and memory consolidation in adult male rats. *Pharm. Sci.* **2012**, *18*, 43−50.
(68) Li, W.; Dowd, S. E.; Scurlock, B.; Acosta-Martinez, V.; Lyte, M. Memory and learning behavior in mice is temporally associated with diet-induced alterations in gut bacteria. *Physiol. Behav.* **2009**, *96* (4−5), 557−567.
(69) El Idrissi, A. Taurine improves learning and retention in aged mice. *Neurosci. Lett.* **2008**, *436*, 19−22.
(70) Tannenbaum, B. M.; Tannenbaum, G. S.; Anisman, H. Impact of life-long macronutrient choice on neuroendocrine and cognitive functioning in aged mice: differential effects in stressor-reactive and stressor-resilient mouse strains. *Brain Res.* **2003**, *985*, 187−197.
(71) Goehler, L. E.; Gaykema, R. P.; Opitz, N.; Reddaway, R.; Badr, N.; Lyte, M. Activation in vagal afferents and central autonomic pathways: early responses to intestinal infection with *Campylobacter jejuni*. *Brain, Behav., Immun.* **2005**, *19* (4), 334−344.
(72) Lyte, M.; Li, W.; Opitz, N.; Gaykema, R. P.; Goehler, L. E. Induction of anxiety-like behavior in mice during the initial stages of infection with the agent of murine colonic hyperplasia *Citrobacter rodentium*. *Physiol. Behav.* **2006**, *89* (3), 350−357.
(73) Anitha, M.; Vijay-Kumar, M.; Sitaraman, S. V.; Gewirtz, A. T.; Srinivasan, S. Gut microbial products regulate murine gastrointestinal motility via Toll-like receptor 4 signaling. *Gastroenterology* **2012**, *143* (4), 1006−1016.e4.
(74) McKernan, D. P.; Dennison, U.; Gaszner, G.; Cryan, J. F.; Dinan, T. G. Enhanced peripheral toll-like receptor responses in psychosis: further evidence of a pro-inflammatory phenotype. *Transl. Psychiatry* **2011**, *1*, e36.
(75) Paschon, V.; Takada, S. H.; Ikebara, J. M.; Sousa, E.; Raeisossadati, R.; Ulrich, H.; Kihara, A. H. Interplay between exosomes, microRNAs and Toll-like receptors in brain disorders. *Mol. Neurobiol.* **2015**, April 11 [Epub ahead of print, DOI: 10.1007/s12035-015-9142-1].
(76) Dockray, G. J. Enteroendocrine cell signalling via the vagus nerve. *Curr. Opin. Pharmacol.* **2013**, *13* (6), 954−958.
(77) Brun, P.; Giron, M. C.; Qesari, M.; Porzionato, A.; Caputi, V.; Zoppellaro, C.; Banzato, S.; Grillo, A. R.; Spagnol, L.; De Caro, R.; Pizzuti, D.; Barbieri, V.; Rosato, A.; Sturniolo, G. C.; Martines, D.; Zaninotto, G.; Palù, G.; Castagliuolo, I. Toll-like receptor 2 regulates intestinal inflammation by controlling integrity of the enteric nervous system. *Gastroenterology* **2013**, *145* (6), 1323−1333.
(78) Komatsu, H.; Maruyama, M.; Yao, S.; Shinohara, T.; Sakuma, K.; Imaichi, S.; Chikatsu, T.; Kuniyeda, K.; Siu, F. K.; Peng, L. S.; et al. Anatomical transcriptome of G protein-coupled receptors leads to the identification of a novel therapeutic candidate GPR52 for psychiatric disorders. *PLoS One* **2014**, *9* (2), e90134.
(79) Komatsu, H. Novel therapeutic GPCRs for psychiatric disorders. *Int. J. Mol. Sci.* **2015**, *16* (6), 14109−14121.
(80) Layden, B. T.; Angueira, A. R.; Brodsky, M.; Durai, V.; Lowe, W. L., Jr. Short chain fatty acids and their receptors: new metabolic targets. *Transl. Res.* **2013**, *161* (3), 131−140.
(81) Tan, J.; McKenzie, C1; Potamitis, M1; Thorburn, AN1; Mackay, CR2; Macia, L. The role of short-chain fatty acids in health and disease. *Adv. Immunol.* **2014**, *121*, 91−119.
(82) Smith, P. M.; Howitt, M. R.; Panikov, N.; Michaud, M.; Gallini, C. A.; Bohlooly-Y, M.; Glickman, J. N.; Garrett, W. S. The microbial metabolites, short-chain fatty acids, regulate colonic Treg cell homeostasis. *Science* **2013**, *341* (6145), 569−573.
(83) Atarashi, K.; Tanoue, T.; Oshima, K.; Suda, W.; Nagano, Y.; Nishikawa, H.; Fukuda, S.; Saito, T.; Narushima, S.; Hase, K.; Kim, S.; Fritz, J. V.; Wilmes, P.; Ueha, S.; Matsushima, K.; Ohno, H.; Olle, B.; Sakaguchi, S.; Taniguchi, T.; Morita, H.; Hattori, M.; Honda, K. Treg induction by a rationally selected mixture of Clostridia strains from the human microbiota. *Nature* **2013**, *500* (7461), 232−236.
(84) De Vadder, F.; Kovatcheva-Datchary, P.; Goncalves, D.; Vinera, J.; Zitoun, C.; Duchampt, A.; Bäckhed, F3; Mithieux, G. Microbiota-generated metabolites promote metabolic benefits via gut-brain neural circuits. *Cell* **2014**, *156* (1−2), 84−96.
(85) Van Oudenhove, L.; McKie, S.; Lassman, D.; Uddin, B.; Paine, P.; Coen, S.; Gregory, L.; Tack, J.; Aziz, Q. Fatty acid-induced gut-brain signaling attenuates neural and behavioral effects of sad emotion in humans. *J. Clin. Invest.* **2011**, *121* (8), 3094−3099.
(86) Jones, R. B.; McKie, S.; Astbury, N.; Little, T. J.; Tivey, S.; Lassman, D. J.; McLaughlin, J.; Luckman, S.; Williams, S. R.; Dockray, G. J.; Thompson, D. G. Functional neuroimaging demonstrates that ghrelin inhibits the central nervous system response to ingested lipid. *Gut* **2012**, *61* (11), 1543−1551.
(87) van Baarlen, P.; Troost, F. J.; van Hemert, S.; van der Meer, C.; de Vos, W. M.; de Groot, P. J.; Hooiveld, G. J.; Brummer, R. J.; Kleerebezem, M. Differential NF-kappaB pathways induction by *Lactobacillus plantarum* in the duodenum of healthy humans correlating with immune tolerance. *Proc. Natl. Acad. Sci. U. S. A.* **2009**, *106*, 2371−2376.
(88) van Baarlen, P.; Troost, F.; van der Meer, C.; Hooiveld, G.; Boekschoten, M.; Brummer, R. J.; Kleerebezem, M. Human mucosal in vivo transcriptome responses to three lactobacilli indicate how probiotics may modulate human cellular pathways. *Proc. Natl. Acad. Sci. U. S. A.* **2011**, *108* (Suppl. 1), 4562−4569.
(89) Saulnier, D. M.; Santos, F.; Roos, S.; Mistretta, T. A.; Spinler, J. K.; Molenaar, D.; Teusink, B.; Versalovic, J. Exploring metabolic pathway reconstruction and genome-wide expression profiling in *Lactobacillus reuteri* to define functional probiotic features. *PLoS One* **2011**, *6* (4), e18783.
(90) Lopes, L. V.; Kussmann, M. Proteomics at the interface of psychology, gut physiology and dysfunction: an underexploited approach that deserves expansion. *Expert Rev. Proteomics* **2011**, *8* (5), 605−614.
(91) Kim, J. H.; An, H. J.; Garrido, D.; German, J. B.; Lebrilla, C. B.; Mills, D. A. Proteomic analysis of *Bifidobacterium longum* subsp. infantis reveals the metabolic insight on consumption of prebiotics and host glycans. *PLoS One* **2013**, *8* (2), e57535.
(92) Xie, G.; Zhang, S.; Zheng, X.; Jia, W. Metabolomics approaches for characterizing metabolic interactions between host and its commensal microbes. *Electrophoresis* **2013**, *34* (19), 2787−2798.
(93) Matsumoto, M.; Kibe, R.; Ooga, T.; Aiba, Y.; Sawaki, E.; Koga, Y.; Benno, Y. Cerebral low-molecular metabolites influenced by intestinal microbiota: a pilot study. *Front. Syst. Neurosci.* **2013**, *7*, 9.

DOI: 10.1021/acs.jafc.5b02404
J. Agric. Food Chem. 2015, 63, 7885−7895

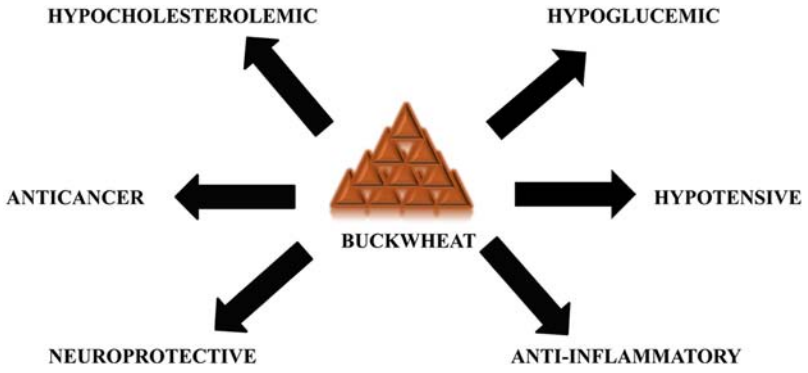

Figure 1. Simplified scheme summarizing the health benefits associated with buckwheat consumption.

Table 1. General Composition of Common and Tartary Buckwheat (BW) (A) Groats and (B) Sprouts

parameter	level (%) common BW	level (%) tartary BW
(A) Groats (Dry Matter)		
starch	54.50	57.40
soluble carbohydrates[a]	1.60	1.78
dietary fiber	7.0	10.60
protein	12.30	13.15
lipids	3.80	3.84
ash	2.0	2.70
other compounds[b]	18.40	10.53
(B) Sprouts (Fresh Weight)		
water	92.80	92.34
dietary fiber	0.70	0.73
protein	0.17	0.14
lipids	0.38	0.14
ash	0.68	0.49

[a]Including sucrose and fagopyritols. [b]Organic acids, phenolic compounds, tannins, phosphorylated sugars, nucleotides and nucleic acids, and unknown compounds.

broad spectrum of biological activities exerted by emodin, it may be an important bioactive factor in BW.[26]

Buckwheat proteins (BWPs) have a high biological value due to a well-balanced amino acid composition. They are rich in lysine, which is generally the first limiting amino acid in other plant proteins, and arginine. However, the content in glutamine and proline is much lower than in wheat,[27] and threonine and methionine are the first and second limiting amino acids, respectively. Thiamin-binding proteins isolated from BW may be used in the care of people who suffer from the lack of thiamin.[7] Furthermore, many researchers have reported that the low digestibility of BWPs and lysine/arginine and methionine/glycine rates are critical factors in determining the cholesterol-lowering effects of the plant proteins.[7,28]

The contents and composition of flavonoids are dissimilar in different BW species. Generally, the flavonoid content in *F. tataricum* (40 mg g^{-1}) is higher than in *F. esculentum* (10 mg g^{-1}), reaching concentrations of 100 mg g^{-1} in tartary BW flowers, leaves, and stems.[2] BW seeds (groats and hull) and sprouts are important sources of rutin (quercetin-3-rutinoside), and its content depends on the variety and growth conditions.[29,30] Tartary BW groats (BWG) contain more rutin (80.94 mg g^{-1} dm) than common BW (0.20 mg g^{-1} dm),[31,32] whereas tartary BW sprouts (BWS) possess 2.2-fold more rutin than common BWS.[33] Rutin has attracted increasing attention mainly due to its numerous beneficial effects observed in vitro and in vivo: anti-inflammatory, antidiabetic, hypocholesterolemic, antiatherosclerotic, and anticarcinogenic.[34] Its activity has been associated with its antioxidant capacity, although the precise mechanism of protection is not known. Quercitrin (quercetin-3-rhamnoside) is another glycoside present in BW at concentrations ranging from 0.01 to 0.05% dm in tartary BW and from 0.54 to 1.80% dm in common BW.[31,35] Isoquercetin (quercetin-3-glucoside) is present in BW hypocotyls (1.4 μM g^{-1} dm),[36] and it has been shown to exert antidiabetic and anticancer activities.[37−39] The aglycone quercetin is present in BWG (0.001 mg g^{-1} dm) and BW hull (0.009−0.029 mg g^{-1} dm) at lower concentration than rutin.[12,32] The flavone *C*-glycosides present in BW seedlings (vitexin, isovitexin, orientin, and homoorientin), the content of anthocyanins and proanthocyanins,[36] and the presence of squalene, epicatechin, and vitamin E (tocopherols)[40] make BW a good antioxidant source in the human diet.

Phenolic acids of BW also contribute to its antioxidant capacity. 4-Hydroxybenzoic (*p*-hydroxybenzoic), 3-(4-hydroxy-3-methoxyphenyl)-2-propenoic acid (ferulic), and 3,4-dihydroxybenzoic (protocatechuic) acids are prominent in the seeds of different cultivars of tartary BW, and other phenolics, including 4-hydroxycinnamic (*p*-coumaric), 3,4,5-trihydroxybenzoic (gallic), 3,4-dihydroxycinnamic (caffeic), 4-hydroxy-3-methoxybenzoic (vanillic), and 3,5-dimethoxy-4-hydroxybenzoic (syringic) acids, have been detected.[41] Several phenolic acids were described in the inflorescences of different varieties of BW: 3-(3,4-dihydroxycinnamoyl)quinic (chlorogenic), 4-methoxybenzoic (*p*-anisic), 2-hydroxybenzoic (salicylic), and methoxycinnamic acid.[42] The most abundant phytosterol in BW flour (BWF) is β-sitosterol (0.86 mg g^{-1} dm) followed by campesterol (0.11 mg g^{-1} dm) and stigmasterol (0.02 mg g^{-1} dm).[43]

BW is also an important source of vitamins. Total vitamin B content, including B_1 (thiamin, 2.2−3.3 μg g^{-1} dm), B_2 (riboflavin, 10.6 μg g^{-1} dm), B_3 (niacin, 18 μg g^{-1}), B_5 (pantothenic acid, 11 μg g^{-1}), and B_6 (piridoxine, 1.5 μg g^{-1}), is higher in tartary BW than in common BW, and the levels of vitamin C have been reported as 50 μg g^{-1} dm, reaching 250 μg g^{-1} dm in sprouts.[5,44,45] Along with vitamins, other compounds such as glutathione (1.10 mmol g^{-1} dm in BWG), phytic acid (35−38 mg g^{-1} dm in BW bran), carotenoids (2.10 mg g^{-1} dm in BW seeds), and melatonin (470 pg g^{-1} dm in BWG) have been detected and may contribute to the antioxidant activity of BW.[4,32]

Recently, γ-aminobutyric acid (GABA) and 2″-hydroxynicotianamine (2HN) have been found to serve as functional compounds in BW. Seeds and sprouts contain GABA, whereas

DOI: 10.1021/acs.jafc.5b02498
J. Agric. Food Chem. 2015, 63, 7896−7913

2HN has been recently identified in BWF. These compounds have been reported to reduce blood pressure in humans and to inhibit the angiotensin I converting enzyme (ACE) activity.[46−48]

HEALTH BENEFITS AND BUCKWHEAT

Antioxidant Activity. Increasing appreciation of the nutritional and functional properties of BW has also encouraged some investigations about its antioxidant properties. The antioxidant features of BW pseudocereals appear reflected in human intervention studies. There have been reported increases in the total antioxidant capacity of plasma samples from healthy donors after consuming 1.5 g of BW honey kg^{-1} (single dose, $n = 37$),[49] or when BW honey was added to water or black tea (160 g honey L^{-1}, $n = 25$)[50] as well as after BW-enriched wheat bread consumption.[51]

The biological antioxidant capacity of BW is further supported by in vivo experimental models fed a BWH-containing diet (0.75% in diet, 14 days),[52] a BW byproduct-enriched diet (15% for 4 weeks),[53] and 100 and 200 mg of BW kg^{-1} day^{-1} for 20 days.[54] The results showed increased activity of antioxidant enzymes, including superoxide dismutase (SOD), catalase (CAT), and gluthatione peroxidase (GSH-Px), and reduced lipid peroxidation parameters such as thiobarbituric acid reactive substances (TBARS), malondialdehyde (MDA), and fluorescent substance (FLS) in plasma samples, red blood cells, and several different organs (heart, kidney, liver, and brain). In contrast, total plasma antioxidant status and the activities of SOD and GSH-Px were unaltered in healthy rats fed a normal diet containing 30% expanded BW seeds or 5% of BWS for 4 weeks.[55]

In vitro antioxidant activity of BW has been assessed in relation to its phenolic content and composition[41,42,56−59] and compared to that of other cereals and pseudocereals.[60−63] In this sense, Zieliński and Kozłowska established the following hierarchy of antioxidant activity: BW > barley > oat > wheat ∼ rye.[64] The high antioxidant capacity of BW is connected with its high polyphenol content, especially rutin.[65,66] Liu et al. described the antioxidant effects of BWS in human hepatoma HepG2 cells, revealing that tartary and common BW had a positive effect on the production of intracellular peroxide and superoxide anions. Tartary BW was more effective than common BW, and this effect was associated with the higher concentration of rutin.[16] Studies by Zhou et al. also reported that BW honey showed protective effects on hydroxyl radical-induced DNA damage through is antioxidant activity.[67] These studies seem to indicate that BW may exert its beneficial effects through its antioxidant activity.

Hypocholesterolemic Activity. Increased cholesterol intake can induce oxidative stress and cause an increase in blood cholesterol level, leading to the up-regulation of low-density lipoproteins (LDL) and oxidized LDL (oxLDL), contributing to the development of chronic diseases such as atherosclerosis.[68] In vitro and in vivo studies have proposed that BW's protective effect against cardiovascular diseases may come from its ability to modulate the cholesterol (Ch) level.

The number of studies investigating the cholesterol-lowering activity of BW in humans is small (Table 2). The investigation carried out by Zhang et al. in 2007 is one of the biggest studies in relation to the consumption of BW and health: 3542 Mongolians in two adjacent counties of Inner Mongolia (China) were randomly sampled in a cross-sectional study to assess the association of hypertension, dyslipidemia, and hyperglycemia with lifetime consumption of BW seed as a staple food. The authors described a reduction of total cholesterol (TCh) (4%; $p < 0.05$), triglycerides (TG) (4.85%; $p > 0.05$), and LDL (9.05%; $p < 0.01$) and an increase of high-density lipoproteins (HDL) (6.9%; $p < 0.01$) in the participants who consumed BW ($n = 1628$) compared with the population who consumed corn ($n = 1914$). In addition to this, a decrease in blood glucose concentration (14.5%; $p < 0.01$) was also described in the group that consumed BW compared to the other group.[69] In 2011, Wieslander et al. performed a double-blind randomized crossover study with 62 healthy volunteers who were divided in two groups consuming four cookies elaborated either with tartary or with common BW for 4 weeks. A decrease in serum TCh (13.56%; $p < 0.001$) and HDL (15.44%; $p < 0.001$) and myeloperoxidase (MPO) (enzyme involved in oxidative stress and inflammation) was documented.[70]

The hypocholesterolemic effect of BW has also been observed in an important number of in vivo and in vitro studies to a similar extent. Early work investigating the hypocholesterolemic effect of BW consumption on animals dates back to the 1990s. In 1995, Kayashita et al. reported that BWP consumption by Sprague−Dawley rats reduced body fat content, decreased TCh, and increased the level of HDL in plasma compared to those groups that consumed soy protein or casein.[71] In a second study, lower Ch (14.4%; $p < 0.05$) and TG (38.1%; $p < 0.01$) levels in plasma and liver, respectively, were observed in rats fed a BWP-enriched diet compared with those fed a casein diet.[72] This hypocholesterolemic effect exerted by BWP was more effective in rats consuming Ch-containing diets than in those consuming Ch-free diets.[73]

It has been suggested that the Ch-lowering activity of BWP is mediated by its influence on fecal excretion of bile acids and neutral sterols. In 2001, Tomotake et al. found that Sprague−Dawley rats consuming BWP-enhanced Ch-free diets showed lower plasma TCh levels (11−22%) and higher fecal excretion of bile acids and neutral and acidic steroids relative to animals consuming a casein- or soy protein-enriched diet.[74] Studies investigating the effect of BWP in rats fed a high-Ch diet reported a Ch-lowering effect accompanied by higher fecal excretion of neutral sterols. Tomotake et al. also reported that a BWP-containing diet markedly suppressed gallstone formation compared with casein- and soy protein-enriched diets, and this effect was related to the lower level of Ch in gallbladder, plasma, and liver and the higher fecal excretion of bile acids and steroids.[75] This effect of BWP suppressing gallstone formation and enhancing excretion of bile acids and steroids was also observed in ddY mice and Sprague−Dawley rats fed a Ch-enhanced diet.[76] It has been suggested that the Ch-lowering effect and enhanced level of sterol secretion may be associated with the low digestibility of BWP.[77]

BW extracts (BWext) have also been reported to exhibit a hypocholesterolemic effect, reducing intestinal absorption of dietary Ch. In vitro studies have reported a decrease in the uptake of Ch micelles in Caco-2 cells in the presence of common BWPext.[78] This effect may be mediated by reducing the gut transit time after BW consumption.[79] Another possible mechanism was recently proposed by Yang et al., which investigated the Ch-lowering effect of the diet supplemented with tartary BWF, wheat, or rice in hamsters. BW (but not wheat and rice) reduced plasma as well as hepatic Ch levels and led to a greater neutral sterol excretion along with a down-regulation of intestinal acyl-CoA:Ch acyltransferatse 2 (ACAT2) and Niemann−Pick C1-like 1 (NPC1L1),[80] two intestinal transporters that have been suggested to play a critical role in cholesterol absorption.[81]

DOI: 10.1021/acs.jafc.5b02498
J. Agric. Food Chem. 2015, 63, 7896−7913

Table 2. Human, Animal, and in Vitro Studies Describing the Hypocholesterolemic Effect Related to Buckwheat Consumption[a]

Human Studies

population of study	intake; duration	foodstuff	parameters	effect	ref
healthy (n = 62 ♀)	group 1: four common BW cookies (daily) group 2: four tartary BW cookies (daily) 4 weeks (after 2 weeks, the groups switched their type of cookie)	BW cookies	MPO serum: TCh serum: HDL	↓ ↓ ↓	70
healthy (n = 12 ♂)	100 g of sieved BW preparation; 4 week dietary period	sieved BWF enriched diet	HDL HDL/Ch	↑ ↑	160
healthy (♂)	100 g of whole BW preparation; 4 and 12 weeks	whole BW flour	HDL HDL/Ch glucose tolerance	↑ ↑ ↑	161
healthy (n = 857 ♂)	group 1 (n = 319), 0 g/day group 2 (n = 207), <40 g/day group 3 (n = 161), 40−200 g/day Group 4 (n = 163), > 200 g/day.	BW	serum: TCh serum: LDL systolic and diastolic pressure HDL/TCh	↓ ↓ ↓ ↑	162

Animal Studies

model	dose; duration	assayed product	parameters	effect	ref
♂ Sprague−Dawley rats	38.1%; 3 weeks	BWPext	TG FFA TCh phospholipid HDL body fat content	↓ ↓ ↓ ↓ ↑ ↓	71
♂ Sprague−Dawley rats	323.1 g kg^{-1} (high-Ch diet); 3 weeks	BWPext	hepatic: TCh hepatic: HDL hepatic: TG hepatic: weight plasma: TCh	↓ ↓ ↑ ↓ ↓	73
♂ Sprague−Dawley rats	381 g kg^{-1}; 3 weeks	BWPext	hepatic: TG body fat content enz activity: G6PD enz activity: FA synthase fecal excretion: fat fecal excretion: N_2	↓ ↓ ↓ ↓ ↑ ↑	72
♂ Sprague−Dawley rats	307 g kg^{-1} (normal diet); 8 weeks	BWPext	plasma: TCh plasma: HDL fecal excretion: neutral steroids fecal excretion: acidic steroids fecal excretion: bile acids	↓ ↓ ↑ ↑ ↑	74
♂ Golden Syrian hamster	381g kg^{-1} (high-Ch diet); 2 weeks	BWPext	plasma: TCh plasma: TG plasma: phospholipids plasma: HDL plasma: HDL/TCh hepatic: Ch plasma: TCh plasma: phospholidis plasma: lithogenic index gallstone formation fecal excretion: Ch fecal excretion: bile acids fecal excretion: fecal steroids	↓ ↓ ↓ ↓ ↑ ↓ ↓ ↓ ↓ ↓ ↑ ↑ ↑	75

DOI: 10.1021/acs.jafc.5b02498
J. Agric. Food Chem. 2015, 63, 7896−7913

Table 2. continued

Animal Studies					
model	dose; duration	assayed product	parameters	effect	ref
♂ Sprague−Dawley rats	381 g kg^{-1} (high-Ch diet); 2 or 3 weeks	BWPext	plasma: HDL/TCh	↑	77
			plasma: phospholipids	↑	
			plasma: TCh	↓	
			plasma: TG	↓	
			liver: rel wt	↓	
			liver: Ch	↓	
			liver: phospholipids	↓	
♂ stroke-prone SHR (SHRSP)	34.4% in diet; 14 days	BWPext	atherogenic lipoproteins	↓	163
			antiatherogenic apoE-HDL	↑	
♂ Syrian Golden hamster	24% in diet; 6 weeks	BWF (tartary BW)	plasma: TCh	↓	80
			plasma: non-HDL	↓	
			gepatic: TCh	↓	
			fecal excretion: neutral sterol	↑	
			fecal excretion: acidic sterol[b]	↑	
			mRNA exp: NCPC1L1	↓	
			mRNA exp: ACAT2	↓	
♂ Sprague−Dawley rats and ♂ ddY mice	30.7% of BWP in the diet (rats fed a normal diet or high-Ch diet); 10 days 54.8% of protein BWF (mice fed a high-Ch diet); 27 days	BWPext and BWF protein (common BW)	serum: Ch serum: TG	↓	76
			serum: phospholipids	↓	
			hepatic: rel wt	↓	
			hepatic: Ch	↓	
			enz activity: FA synthase	↓	
			fat pad wt	↓	
			feces dry wt	↑	
			fecal excretion: N_2	↑	
			fecal excretion: bile acids	↑	
			fecal excretion: acid steroids	↑	
			fecal excretion: neutral steroids	↑	
			bile: Ch	↓	
			bile: phospholipids	↓	
			Ch-induced gallstone incidence	↓	
			lithogenic index	↓	
♂ Mongrel rabbits	0.25 g kg^{-1} day^{-1} (high-fat diet); 12 weeks	BWext (common BW)	hepatic: TG	↓	164
			plasma: MDA	↓	
			ascorbate free radicals	↑	
			serum testosterone	↑	
			insulin	↓	
C57BL/6 mice	100 and 200 mg kg^{-1} body wt (high-fat diet); 8 weeks	ethanol-germinated extBW	hepatic: Ch	↓	82
			hepatic: TG	↓	
			hepatic: wt	↓	
			serum: HDL	↑	
			serum: HDL/TCh	↑	
			mRNA exp: PPAR-γ	↓	
			mRNA exp: C/EBPα	↓	
KK-A^y mice	0.05 mg g^{-1} body weight; 6 weeks	bran powder (common BW)	blood glucose level	↓	83
			mRNA exp: ACC2	↓	
			mRNA exp: SCD1	↓	
			mRNA exp: FA synthase	↓	
			mRNA exp: ACC1[b]	↓	
			mRNA exp: SREBP-1c	↓	
			mRNA exp: ChREBP[b]	↓	

DOI: 10.1021/acs.jafc.5b02498
J. Agric. Food Chem. 2015, 63, 7896−7913

Table 2. continued

Animal Studies					
model	dose; duration	assayed product	parameters	effect	ref
♂ F344/DuCrj rats	50 g kg^{-1} diet (Ch-free diet); 4 weeks	BWS powder (common and tartary BW)	plasma: TCh	↓	84
			hepatic: TCh[b]	↓	
			fecal excretion: SCFA	↑	
			fecal excretion: bile acids	↑	
			fecal excretion: neutral steroids[b]	↑	
			fecal excretion: matter excretion	↑	
			mRNA exp: Ch 7-α-hydroxylase	↑	
			mRNA exp: HMG-CoA reductase	↑	
Syrian hamster	2.5 and 25% in the diet (high-fat and high-Ch diet); 4 weeks	BWS and seeds (common BW)	liver/body wt	↓	165
			liver wt	↓	
			serum: TCh	↓	
			serum: TG	↓	
			serum: LDL	↓	
			serum: LDL/HDL	↓	
			serum: TCh/HDL	↓	
			hepatic: TCh	↓	
♂ Sprague–Dawley rats and ♂ ddY mice	30.7% of common BWP and 43.7% of tartary BWP in the diet (high-Ch diet); 27 days	BWPext and BWF protein (common and tartary BW)	serum: Ch	↓	166
			hepatic: Ch	↓	
			liver rel wt	↓	
			feces dry wt	↑	
			fecal excretion: N_2	↑	
			fecal excretion: neutral sterols	↑	
			fecal excretion: bile acids	↑	
			bile: Ch	↓	
			bile: phospholipids	↓	
			bile: lithogenic index	↑	
			gallstone incidence	↓	
♂ Syrian hamster	1–5% in the diet (high-Ch diet); 4 weeks	sprouts (common BW)	antioxidant capacity	↑	167
			serum: LDL	↓	
			serum: TG	↓	
			serum: LDL/HDL	↓	
			serum: TCh/HDL	↓	
♂ pathogen-free Wistar rats	0.2–1 g kg^{-1} body weight (high-fat diet); 6 weeks	bran extract (tartary BW)	serum: TG	↓	168
			serum: TCh	↓	
			serum: HDL	↑	
			serum: MDA	↓	
			ApoB/ApoA1[b]	↑	
			antioxidant enzymes	↑	
			HDL/TCh	↑	
			atherogenic index	↓	
			hepatic: TG	↓	
			hepatic: TCh	↓	
			hepatic: SOD	↑	
			hepatic: MDA[b]	↓	
♂ Wistar rats	5% in the diet (high-fat diet); 13 weeks	BW leaf and flower mixture (common BW)	SFA	↓	169
			PUFA	↑	
			body wt gain	↓	
			plasma TCh, TG, LDL	↓	
			atherogenic index	↓	
			DPPH	↓	
			MDA	↓	

DOI: 10.1021/acs.jafc.5b02498
J. Agric. Food Chem. 2015, 63, 7896–7913

Table 2. continued

Animal Studies					
model	dose; duration	assayed product	parameters	effect	ref
♂ diabetic db/db and ♂ nondiabetic db/+ mice	5% in diet and 10% in diet; 21 days	sprouts (common BW)	HbA1c	↓	170
			liver: TCh	↓	
			liver: lipids	↓	
			liver: TG	↓	
			plasma: TCh	↓	
			plasma: HDL	↓	
			TBARS	↓	
			fecal bile acids	↑	
			atherogenic index	↓	
♂ Sprague–Dawley rats	5% in the diet (high-fat diet); 6 weeks	BW leaf and flower mixture	body wt gain	↓	171
			plasma: TG	↓	
			plasma: TCh	↓	
			plasma: HDL	↓	
			plasma: non-HLD	↓	
			HDL/TCh	↑	
			atherogenic index	↓	
			hepatic: TG	↓	
			hepatic: TCh	↓	
			hepatic: ACAT	↑	
			hepatic: HMG-CoA reductase	↑	
			fecal excretion: TG	↑	
			fecal excretion: acidic sterols	↑	
			epididymal adypocites size	↓	

In Vitro Studies					
test model	dose; duration	assayed product	parameters	effect	ref
human colon cancer cells (Caco-2)	0.2% (w/v); 30 min	BWPext (common BW)	Ch micelle uptake	↓	78

[a]Antiatheromatosus plaque formation index = HDL/TCh; arteriosclerotic index = ([TCh − HDL]/HDL); atherogenic index of plasma = log (TG/HDL); lithogenic index = (molar % of Ch/molar % of Ch at saturation); ↑, increase; ↓, decrease. Abbreviations: ACAT2, acyl-CoA:Ch acyltransferatse 2; ACC1 and 2: acetyl-coenzyme A carboxylase 1 and 2; ApoA1, apolipoprotein A1; ApoB, apolipoprotein B; ApoE, apolipoprotein E; BW, buckwheat; BWF, buckwheat flour; BWPext, buckwheat protein extract; C/EBPα, CCAAT/enhancer-binding protein-α; Ch, cholesterol; ChREBP, carbohydrate resopnsive element-binding protein; CPT, carnitine palmitoyltransferase; DPPH, 2,2-diphenyl-1-picrylhydrazyl; FA, fatty acid; FFA, free fatty acid; G6PDH, glucose-6-phosphate dehydrogenase; HbA1c, glycated hemoglobin A1c; HDL, high-density lipoprotein; HMG-CoA, 3-hydroxy-3-methylglutaryl-coenzyme A; LDL, low-density lipoprotein; MDA, malondialdehyde; MPO, myeloperoxidase; N_2, nitrogen; NPC1L1, Niemann–Pick C1-like 1; PPAR-γ, peroxisome proliferator-activated receptor-γ; PUFA, polyunsaturated fatty acids; SCD1, stearoyl-coenzyme A oxidase; SCFA, short-chain fatty acids; SFA, saturated fatty acid; SOD, superoxide dismutase; SREBP-1c, sterol regulatory element-binding protein 1c; TBARS, thiobarbituric acid reactive substances; TCh, total cholesterol; TG, triglycerides. [b]Not significant.

BW consumption also seems to have an effect on the activity and mRNA expression of enzymes involved in lipid metabolism. The intake of BWP exerted a lipid-lowering effect accompanied by a decrease in hepatic activities of glucose-6-phosphate dehydrogenase (G6PDH) and fatty acid (FA) synthase.[72,76] Other BWext, such as an ethanol extract of germinated BW rich in rutin, and BW bran extracts down-regulated mRNA expression of the adipogenic transcription factors peroxisome proliferator-activated receptor-γ (PPAR-γ), CCAAT/enhancer-binding protein-α (C/EBPα), sterol regulatory element-binding protein 1c (SREBP1c), and carbohydrate responsive element-binding protein (ChREBP) and of lipogenic genes acetyl-coenzyme a carboxylase 1 or 2 (ACC1 and 2), stearyl-coenzyme A oxidase (SCD1), and FA synthase.[82,83] Meanwhile, BWS has been shown to up-regulate the expression of Ch-7-α-hydroxylase and 3-hydroxy-3-methylglutaryl-coenzyme A (HMG-CoA).[84]

Antidiabetic Activity. Diabetes is a chronic disease caused by deficient insulin secretion or ineffective insulin activity, which lead to an increase in plasma glucose levels.[85,86] In the past few years there has been a considerable interest in the possibility of improving diabetic control by altering the glycemic impact of the carbohydrates ingested. A low glycemic index (GI) diet has been related to advantages in the prevention and treatment of diabetes.[87]

BW for dietary use is one way to prevent diabetes in China.[88] In the study of Skrabanja et al., 10 healthy volunteers consumed (single dose) boiled BW groats, bread enriched with 50% of BW groats, or white wheat bread. The postpandrial plasma glucose and insulin production were lower in volunteers who consumed BW products, especially BW groats, than those who consumed white wheat bread.[89] Su-Que et al. randomly recruited 10 type 2 diabetic subjects. All patients showed a decrease of 51% ($p < 0.05$) in the postpandrial 2 h plasma glucose after consumption of BW compared with those who consumed white wheat bread.[90] Reduction of energy consumption is an important consideration for those attempting to control glycemia. In the aforementioned study[89] the volunteers consuming BW products, especially groats, showed high postprandial satiety. Berti et al.

DOI: 10.1021/acs.jafc.5b02498
J. Agric. Food Chem. 2015, 63, 7896−7913

also described a positive effect of BW lasagna consumption on energy intake and time satiety in healthy volunteers.[91] In a single-blind, controlled, crossover study conducted by Stringer et al., the efficacy of BW crackers compared with rice crackers to modify glucose metabolism in both healthy and type 2 diabetic subjects was investigated. No changes were observed in glucose or insulin concentrations. However, a modulation of the gastrointestinal satiety hormones such as glucagon-like peptide-1 (potentiator of insulin secretion) and glucagon-dependent insulinotropic peptide (GIP) was documented after consumption (single dose) of BW cracker in healthy and type 2 diabetic volunteers.[92] Therefore, BW consumption may modulate satiety by altering the postprandial levels of satiety hormones.

Attempts to identify the bioactive compounds responsible for the observed effects and the mechanisms associated have led to several publications looking at the antidiabetic effects of different BWext or their individual compounds in vitro and in vivo. Previous studies by Larner et al. have highlighted the role of DCI mediating mechanisms associated with diabetes.[93−97] Kawa et al. investigated the effects of a BW concentrate (common BW), containing 10 and 20 mg DCI kg^{-1} of body weight, on serum glucose concentrations of streptozotonic (STZ) rats in comparison with normal rats, demonstrating that a single oral dose of BW concentrate reduced the serum glucose level by 12−19% in STZ rats after 90−120 min of treatment.[98] Using hyperinsulinemic KK-A^y mice, Yao et al. studied the effect of DCI-enriched tartary BW bran extract (equivalent to 40 mg kg^{-1} DCI) supplementation for 5 weeks on blood glucose, lipid profile, and other markers related to diabetes. The results showed that oral administration of 45−182 mg kg^{-1} of DCI-enriched tartary BW bran extract lowered plasma glucose, C-peptide level, glucagon, TG, and plasma urea and improved glucose tolerance and insulin immunoreactivity.[99] Diabetic rats administered 100−400 mg kg^{-1} day^{-1} of the overall flavonoids from BW flowers and leaves showed lower blood glucose (20.8−27.7%) and improvement in renal damage.[100] BW bran extract decreased the blood glucose level in nondiabetic Balb/c mice following sucrose administration, which was associated with the capacity of this extract to inhibit α-glucosidase activity, an enzyme that hydrolyzes carbohydrates in the gastrointestinal tract.[101] Lee et al. investigated the antihyperglycemic and anti-insulin resistance of an ethanol BWext (tartary BW), rutin, and quercetin in vitro and in vivo. These authors demonstrated that ethanol BWext (50 mg kg^{-1} body weight (bw)), rutin (11.5 mg kg^{-1} bw), and quercetin (3 mg kg^{-1} bw) improved hyperglucemia and hyperinsulinemia in C57BL6 mice fed a high-fructose diet for 8 weeks, suggesting that rutin was the major active compound of the extract. The in vitro assay revealed that the hypoglycemic effect may be due to an increase in the glucose uptake mediated by increasing levels of glucose transporter 2 (GLUT2) in FL83B cells, the major glucose transporter in hepatocytes. These hypoglycemic effects were accompanied by a reduction of oxidative stress, induction of antioxidant enzymes, and improvement of plasma and hepatic lipids.[102] Further evidence of the antidiabetic properties of BW has been reported recently by Lee et al., describing that ethanol BWext (200 mg mL^{-1}) and rutin (40 mg mL^{-1}) reduced oxidative stress, attenuated AGE formation, and inhibited α-amylase and α-glucosidase activity.[103]

Although the animal and in vitro studies support the antidiabetic effect of BW in humans after its consumption, some investigators have reported contradictory results. Schrader et al. described that BW (0.1 and 1 g kg^{-1} diet) had no blood glucose-lowering effect in db/db mice, but a dose-dependent PPAR-γ activity, a molecule involved in regulating insulin sensitivity and glucose homeostasis,[104] was shown in COS-1 cells.[105] Another study carried out by Curran et al. described that BW inhibited glucose uptake in rat H4IIE hepatoma cells. Furthermore, these authors reported that other compounds, such as DCI, rutin, or quercetin, were not the active components responsible for the observed effects.[106] These contradictory results point out the need for future studies to clarify the cellular and molecular mechanisms underlying the beneficial effects attributed to BW and its individual compounds and the compound(s) responsible for the observed effects.

Anticancer Activity. Cancer is the leading cause of death in economically developed countries and the second leading cause of death in developing countries.[107] Functional food for the prevention of chronic diseases such as cancer is one of the century's key global challenges. In the study carried out by Shen et al. (2008) in Xuanmei (China), the frequent consumption of different foods, including BW, was associated with a reduced risk of lung cancer.[108]

Because oxidative DNA damage is implied in cancer initiation and promotion,[109] the anticancer activity of BW has been associated with its antioxidant properties. It has been reported that ethanol BWext from tartary and common BW protected DNA from being damage by hydroxyl radical.[110] Methanolic extracts of common and tartary BWF, rutin, and quercetin showed high antioxidant capacity (DPPH scavenging activity) and reduced *tert*-butylhydroperoxide-induced DNA damage in the HepG2 cell line.[111] In addition to the antioxidant capacity, mechanisms of action such as alteration of gene expression, inhibition of proliferation, cell cycle arrest, and/or the induction of apoptosis have been documented in vivo and in vitro. Sprague−Dawley rats fed a BWPext showed a decreased development in mammary tumor by lowering serum estradiol[112] and a lower incidence of colon adenocarcinoma (Table 3).[113] In the latter study a decrease in the colonic cell proliferation and a down-regulation in the expression of *c-myc* and *c-fos*, genes involved in colon cancer development, were also described.[114] Different fractions of an ethanolic BWext decreased tumor formation in mice treated with sarcoma cells and inhibited the cell growth of different cancer cell lines.[115] BWHext rich in polyphenols exhibited antioxidant activity and growth inhibitory activity in HeLa cancer cells (up to 50% at 100 μg mL^{-1}, 72 h).[116]

Flavonoids,[39,117,118] polysaccharides,[119] lectins,[120] and phenylpropanoids[121,122] from BW have been shown to induce apoptotis, differentiation, and cytotoxicity against a wide range of cancer cell lines in vitro. In a recent study, Yuan et al. observed that a ribonuclease isolated from BW seeds inhibited the proliferative activity of HepG2 (IC_{50} = 79.2 μM) and MCF-7 (IC_{50} = 63.8 μM) cancer cells.[123] BW proteins have also been revealed to exert anticancer activity. As reviewed by de Mejia and Dia, isolated BWPs such as BW protease inhibitors (BWI-1 and BWI-2a) and the recombinant form of BWI-1 (rBWI-1) have anticancer activity, evidenced mainly by induction of apoptosis and growth inhibition against a wide range of cancer cell models.[124] Recent studies have reported new BWPs that show anticancer activity. Leung and Ng isolated a peptide from BW seeds that exhibited antiproliferative activity against HepG2 cells (IC_{50} = 33 μM), leukemia L1210 (IC_{50} = 4 μM), breast cancer MCF-7 (IC_{50} = 25 μM), and liver embryonic WRL68 (IC_{50} = 37 μM) cell lines.[125] TBWSP31 protein, isolated from tartary BW, has been identified as novel antitumor protein showing antiproliferative activity, causing cell cycle arrest in G_0/G_1

DOI: 10.1021/acs.jafc.5b02498
J. Agric. Food Chem. 2015, 63, 7896−7913

Table 3. Animal and in Vitro Studies Describing the Anticancer Activity Related to Buckwheat Consumption[a]

Animal Studies					
model	dose; duration	assayed product	parameters	effect	ref
♀ Sprague−Dawley rats	38.1% in diet; 61 days	BWPext	incidence mammary tumors	↓	112
			serum estradiol	↓	
♂ Sprague−Dawley rats	277 g kg^{-1}; 124 days	BWPext	incidence colon adenocarcinoma	↓	113
			incidence bloody stool	↓	
			cell proliferation	↓	
			mRNA *c-myc* and *c-fos*	↓	
♂ BALB/C mice (n = 78) infected with sarcoma-180 tumor growth cells	20 or 50 mg kg^{-1} day^{-1}; 20 days	ethanol BWHext	tumor growth	−	115
♀ BALB/C mice (n = 50) infected with H22 hepatic carcinoma cells	6.25−1 mg kg^{-1}; 8 days	rBWI (common BW)	ascites formation	↓	172
In Vitro Studies					
test model	dose; duration	assayed product	parameters	effect	ref
lymphoblastic leukemia (JURKAT and CCRF-CEM)	up to 50 μg mL^{-1}; 24−48 h	BWI-1 and BWI-2a (common BW)	cell growth	↓	173
			apoptosis	↑	
			DNA fragmentation	↑	
breast cancer (Bcap37)	5−200 μg mL^{-1}; 48−72 h	TBWSP31 (tartary BW)	cell growth	↓	127
myeloid leukemia K562	12.5−200 μg mL^{-1}; 24 h	rBWI	cell growth	↓	174
			apoptosis	↑	
			DNA fragmentation	↑	
hepatoma (Hep G2) leukemia (L1210) breast cancer (MCF-7) liver embryonic (WRL 68)	up to 50 μM; 48 h	isolated peptide (common BW)	cell growth	↓	125
human B lymphoblast IM-9	25−200 μg mL^{-1}; 24 h	rBWI (common BW)	apoptosis	↑	175
			cell growth	↓	
lung cancer (A594) breast cancer (MCF-7) gastric cancer (AGS) cervix cancer (HeLa) liver cancer (Hep3B)	0.25−1 mg mL^{-1}; 48 h	ethanol BWHext (common BW)	proliferation	−	115
esophageal carcinoma (EC9706) hepatoma (HepG2) cervix cancer (HeLa)	6.25−50 mg mL^{-1}; 6−60 h	rBWI (common BW)	cell growth	↓	176
			apoptosis	↑	
			DNA fragmentation	↑	
			expression: Bax	↑	
			expression: Bak	↑	
			expression: bcl-2	↓	
			expression: Bcl-xl	↓	
			release of Cyt *c*	↑	
			caspase-3 and -9	+	
			disruption of MMP		
breast cancer (Bcap37)	5−200 mg mL^{-1}; 24−96 h	TBWSP31 (tartary BW)	apoptosis	↑	126
			cell growth	↓	
			expression: bcl-2	↓	
			expression: FAS	↑	
			cell cycle arrest in G0/G1		
leukemic (THP-1) monocytes from peripheral blood	5−200 μg mL^{-1} 1−5 days	BW polysaccharides (tartary BW)	cell viability	↓	119
			cell differentiation	↑	
			TNF-α	↑	
			IL-1β	↑	

DOI: 10.1021/acs.jafc.5b02498
J. Agric. Food Chem. 2015, 63, 7896−7913

Table 3. continued

In Vitro Studies					
test model	dose; duration	assayed product	parameters	effect	ref
lung cancer (A594) colon cancer (HCT116) leukemia (HL-60) breast cancer (ZR-75−30)	0.001−100 μg mL^{-1}; 72 h	phenylpropanoids (tartary BW)	proliferation	−	121
cervix cancer (HeLa)	100 μg mL^{-1}; 72 h	BWHext (common and tartary BW)	cell death	↑	116
hepatoma (HepG2)	0.04−1% v/v (extBW) 4−100 μM (rutin) 2−50 μM (quercetin)	BWext (common and tartary BW) rutin quercetin	antioxidant activity *tert*-butylhydroperoxide-induced DNA damage	↑ ↓	111
hepatoma cells H22; normal liver cells 7702	6.25−50 μg mL^{-1}	rBWI (common BW)	apoptosis cell viability release of Cyt *c* caspase-3, -8, and -9 DNA fragmentation	↑ ↓ ↑ + ↑	172

[a]↑, increase; ↓, decrease; +, activation; −, inhibition. Abbreviations: BW, buckwheat; BWext, buckwheat extract; BWHext, buckwheat hull extract; BWI, buckwheat protease inhibitor; BWPext, buckwheat protein extract; Cyt *c*, cytochrome *c*; MMP, mitochondrial membrane potential; rBWI, recombinant buckwheat protease inhibitor.

phase, and inducing apoptosis in human mammary cancer cell Bcap37 at concentrations ranging from 5 to 200 μg mL^{-1}.[126,127]

Although these studies open a door to new therapies for the prevention and treatment of malignancies such as cancer, more in vitro and in vivo studies must be performed to substantiate the potential health-promoting functions of BW and its individual compounds.

Anti-inflammatory Activity. Inflammation is a normal biological process in response to tissue injury, microbial pathogens, and chemical irritation.[85] Because chronic inflammation is a well-documented risk for promoting cancer,[128] elimination or prevention of chronic inflammation has been proposed as a major way to prevent cancer.

Nuclear factor kappa B (NF-κB) plays a pivotal role in the regulation of the genes related to inflammation including tumor necrosis factor alpha (TNF-α), interleukin (IL)-1β, IL-8, and IL-6[129] and important mediators of the inflammatory response, such as inducible nitric oxide synthase (iNOS) and cyclooxygenase-2 (COX-2).[130] Hole et al. demonstrated that different phenolic BWext (30−50 mg mL^{-1}) and the phenolic acids present in BW 8,5-difeluric (10 mg mL^{-1}), feluric (70 mg mL^{-1}), and *p*-coumaric (70 mg mL^{-1}) reduced the lipopolisaccharide (LPS)-induced NF-κB activity in the U937 cell line.[131] Karki et al. reported that both tartary BWSext (100 and 500 μg mL^{-1}) and rutin (100 μg mL^{-1}) inhibited the NF-κB activation in LPS-stimulated macrophages (RAW264.7). This effect was accompanied by a decrease in the expression of COX-2 and iNOS, and a reduction of TNF-α and IL-6 levels.[132] Ishii et al. evaluated the anti-inflammatory activity of an BWSext in vitro and in vivo. BWSext was able to diminish the LPS-induced gene expression and serum concentration of several pro-inflammatory cytokines including IL-6, IL-8, or TNF-α in mice (100 μg mL^{-1}) and in different cancer cell models (1 mg mL^{-1}). However, the six flavonoids present in the BWext (orientin, isoorientin, vitexin, isovitexin, chlorogenic acid, and rutin) exerted no anti-inflammatory effect on LPS-stimulated CoLoTC cells, indicating that other compounds are responsible for the effects observed.[133] Similarly, Lee et al. found that the levels of IL-6, IL-1β, and TNF-α were significantly reduced by ethanol BWext (50 mg kg^{-1} bw) in the liver of mice and rats treated with ethanol and CCl_4. Rutin (11.5 mg kg^{-1} bw) and quercetin (3 mg kg^{-1} bw) could also reduce ethanol- and CCl_4-induced expression of the cytokines.[134]

These studies indicate that BW, through its phenolic acids and flavonoids, has potential anti-inflamatory properties. Nevertheless, it is difficult to draw conclusions due to the low number of studies performed so far. Therefore, further studies investigating the anti-inflammatory effects of BW are required.

Effects on the Vascular System. It was reported that >25% of the population worldwide (approximately 1 billion) were affected by hypertension in 2000, and this figure is predicted to increase to 1.56 billion by 2025.[135] The renin−angiotensin system regulates blood pressure. Plasma renin is responsible for the conversion of angiotensinogen into angiotensin I, which in the presence of angiotensin I-converting enzyme (ACE) is transformed into angiotensin II, a vasoconstrictor that increases blood pressure.[136] Therefore, the use of ACE inhibitors is believed to lower hypertension.

Although there is increasing interest in the identification of antihypertensive foods, the number of studies investigating the hypotensive effect of BW consumption is scarce. Li et al. cited a study performed by Kawasaki et al. in which a clinical examination made in the Mustang District of Nepal, where the inhabitants rely on BW as their principal food, demonstrated that the pathogenesis of hypertension was quite low (<25% in the Thakali Tribe) regardless of their salt tea intake.[137,138]

This hypotensive effect observed in humans consuming BW appears reflected in in vitro and in vivo studies. BW has been found to have high levels of ACE inhibitory activity.[139] A decrease in systolic blood pressure and a reduction of the oxidative damage in aortic endothelial cells was observed in spontaneously hypertensive rats (SHRs) and normotensive Wistar Kyoto rats after they had consumed raw and germinated BWext (300−600 mg kg^{-1}) for 5 weeks.[140] The administration of 0.01−10 mg kg^{-1} of lactic-fermented BWS to SHRs decreased systolic and diastolic blood pressure, and this effect was

DOI: 10.1021/acs.jafc.5b02498
J. Agric. Food Chem. 2015, 63, 7896−7913

Table 4. Human, Animal, and in Vitro Studies Describing Health Benefits Related to Buckwheat Consumption[a]

Human Studies

population of study	intake; duration	foodstuff	main outcome	parameters	effect	ref
diabetic patients (n = 60; 32 ♀ and 28 ♂)	2 tablets of pressed BW herb, 3 times a day; 3 months	BW herb	improvement of retinopathy parameters	serum: glucose	↓	177
				serum: fructosamine	↓	
				serum: hemoglobin[b]	↓	
				serum: TCh	↓	
				serum: TG	↓	
				serum: HDL	↑	
patients with chronic venous insufficiency (n = 77)	dose equivalent to ∼270 mg of rutin (3 times a day);12 weeks	BW tea	leg edema protection	increase in leg volume	↓	178
				diameter of the femoral veins[c]	↓	
				permeability[c]	imprv	
healthy (n = 3; 2 ♀ and 1 ♂)	BW dough; single-dose	BWF	stomach activity improvement	NO in the stomach	↑	179
healthy (n = 62 ♀)	four common or tartary BW cookies (daily); 4 weeks	BW cookies	antifatigue	fatigue	↓	180
				nasal irritation	↓	
				headache	↓	

Animal Studies

model	dose; duration	assayed product	main outcome	parameters	effect	ref
♀ Wistar Hannover rats (n = 20)	30 days	boiled BW	prebiotic	*Lactobacillus plantarum*	↓	181
				Bifidobacterium spp.	↑	
				Enterobacteria	↓	
				potential harmful bacteria	↓	
♂ Sprague−Dawley rats (n = 15)	38.1% in diet; 21 days	BWPext	ameliorate growth depression	amaranth-induced growth depression	imprv	182
♀ ICR (CD-1) mice	20% in the diet; 5 weeks	BWF and BWext	immunomodulation	chemotactic capacity	↑	183, 184
				lymphoproliferative response	↑	
				IL2	↑	
				CAT	↑	
				oxidized glutathione	↓	
				TNFα	↓	
				MDA	↓	
♂ Kunming mice (n = 96)	60−240 mg kg^{-1} day^{-1}; 28 days	BWext	antifatigue	TBUN	↓	185
				increase of blood lactic acid	−	
				tissue glycogen content	↑	
				exhausting swimming time	↑	
				antioxidant enzymes	↑	

In Vitro Studies

test model	dose; duration	assayed product	main outcome	parameters	effect	ref
human keratynocites (HaCaT)	0.1% v/v	BW honey	wound healing	cell migration	↑	186
human lymphocytes; leukemia (HL-60)	10 mg mL^{-1}; 48 h	BW peptide	immunomodulation	lymphoproliferative response	↑	187

[a]↑, increase; ↓, decrease; −, inhibition; imprv, improvement. Abbreviations: BW, buckwheat; BWext, buckwheat extract; BWF, buckwheat flour; CAT, catalase; HDL, high-density lipoprotein; MDA, malondialdehyde; NO, nitric oxide; TBUN, total blood urea nitrogen; TCh, total cholesterol; TG, triglycerides; TNF-α, tumor necrosis factor α. [b]Hemoglobin glycosylated. [c]Not significant.

associated with a decrease of the ACE activity and vasoralaxation effect on the blood vessel rings.[141,142] Recently, Merendino et al. evaluated the hypotensive and antioxidant responses of pasta containing tartary BWS by measuring the levels of some molecules involved in the regulation of blood pressure and the antioxidant status in normotensive Wistar Kyoto rats and SHRs. In this study, an increase in the expression of bradykinin (BK) and NO (vasodilators), a decrease in endothelin-1 (ET-1) (vasoconstrictor), and an improvement in the antioxidant status were reported.[143]

DOI: 10.1021/acs.jafc.5b02498
J. Agric. Food Chem. 2015, 63, 7896−7913

Several studies have tried to determine which compounds present in BW may be involved in the hypotensive effect observed. 2HN is a recently discovered compound that is present in BW flour, which has been reported to exhibit high inhibitory activity (IC_{50} = 0.08 μM) toward ACE.[47,144] Koyama et al. indicated that lactic fermentation in BWS increases the amount of blood pressure lowering compounds such as γ-aminobutyric acid (GABA) and tyrosine, which could contribute to the blood pressure lowering effect exerted by lactic-fermented BWS on SHRs rats.[141] BW flavonoids might be also implied in the hypotensive effects associated with BW consumption. Tsai et al. described that extracts of different portions of BW, as well as rutin and quercetin, presented a remarkable inhibitory ACE activity.[145] Ushida et al. exposed isolated rat thoracic aorta to rutin-free tartary BWext, observing vasorelaxant effects. In this study, it was suggested that these vasorelaxants effects may be mediated through NO.[146]

A series of reports by several researchers attest to the existence of several proteins capable of generating peptides that can contribute to the blood pressure lowering effect. Kawakami et al. reported that a hydrolysate of BW protein exerted a strong ACE interference.[147] Li et al. documented that tartary BW peptides generated after in vitro digestion exhibited ACE inhibitory activity both in vitro and in vivo.[137] A tripeptide isolated from common BW has also been reported to exert ACE inhibitory activity (IC_{50} = 6.25 μg protein mL^{-1}).[148] Recently, Koyama et al. found that different peptides isolated from lactic-fermented BWS inhibited ACE activity in thoracic aorta tissue and suppressed angiotensin II-mediated vasoconstriction.[149]

Neurodegenerative Diseases. Alzheimer's disease is associated with mental dysfunction and impairment in cognitive function.[150] Aggregation of amyloid β peptides, induction of reactive oxygen species (ROS), and induction of pro-inflammatory mediators such as NO, PGE_2, ILs, and TNF-α represent important neuropathological hallmarks of Alzheimer's disease.[151]

BW consumption has been reported to exhibit neuroprotective effects in animal models. The administration of 600 mg kg^{-1} for 21 days of common BW to rats subjected to repeated cerebral isquemia ameliorated spatial memory impairment by inhibiting glutamate release, reducing the generation of NO_x^- (NO_2^- + NO_3^-), and preventing hippocampal cell necrosis and apoptosis.[152] These effects were confirmed later by Pu et al., showing that common BW comsumption (600 mg kg^{-1}) by rats significantly improved the spatial memory impairment induced by scopolamine in an eight-arm radial maze. To determine the mechanism of BW protective action, the authors exposed primary cultures of rat hippocampal neurons to common BWext. This extract showed DPPH radical-scavenging activity and reduced cell damage induced by glutamate, kainite, and β-amyloid.[153] In an in vitro study, ethyl acetate and ethanol extracts of the seeds, stem, and aerial parts of common BW showed neuroprotective effects through acetylcholisterase, butylcolinesterase, and tyrosinase inhibitory and antioxidant activities.[154] These studies suggest that common BW exerts neuroprotective effects. However, it should be considered that cells of the nervous system do not contact the whole extract in vivo. Therefore, these in vitro studies do not represent a physiological situation.

The number of studies investigating the possible beneficial effects of tartary BW is small. Choi et al. compared the neuroprotective effect of common and tartary BW in an in vivo mouse model of Alzheimer's disease. Oral administration (100 mg kg^{-1} day^{-1}, 14 days) of methanol extracts of tartary and common BW improved cognition and memory function and reduced the NO levels and lipid peroxidation (MDA), tartary BW exerting a stronger protective activity than common BW.[155] Recent studies have suggested that rutin seems to be involved in the neuroprotective effects attributed to BW,[156] although the identity of the compound(s) responsible for the observed effects remains unknown.

Other Effects. Different BW-derived products have been investigated and have been shown to exert health benefits other than those reported above, including prebiotic, antifatigue, wound healing, immunomodulation, and leg edema protection effects and improvement of stomach activity (Table 4).

CONCLUSION

Overall, the animal studies and in vitro work carried out so far begin to define the mechanisms by which BW may help to prevent chronic diseases. The strong antioxidant activity exhibited by BW may help to prevent lipid and DNA oxidation, delaying the development of chronic diseases such as cancer, inflammation, hypercholesterolemia, and neurological diseases. Furthermore, newly discovered mechanisms of action, such as the ones described in this review, can help to explain the beneficial effects exerted by BW. BW protein and polyphenols, especially rutin and quercetin, have been considered partially responsible for the effects observed. Nevertheless, most animal studies described above were carried out with BW-derived extracts, which contain not only polyphenols but also fiber, sugars, and other compounds that may be responsible in whole or in part for the observed effects. Although most of the in vitro cell studies included in this review indicate that BW may prevent cancer, hypertension, or neurological disorders, some of them do not represent dietary/physiological conditions: (i) the concentrations of BW products used in some cases are higher than those described in vivo;[157] (ii) in vivo, lung cells, hepatocytes, cells of the vascular wall, or cells of the nervous system are not exposed to whole extracts or original compounds, but mainly to derived metabolites formed and absorbed after gastrointestinal digestion and metabolic conjugation, including glucuronides, methyls, and sulfates.[158,159] Therefore, future in vitro studies need to be carefully designed so that the results obtained can contribute to clarifying which compounds are responsible for the observed effects and the cellular and molecular mechanisms underlying the beneficial effects attributed to BW. In addition, future research should be directed to epidemiologic studies and toward consolidating the mechanisms of action, especially in humans. These studies will give a valuable approach for using this pseudocereal in the design of novel and healthy foods and enhance its consumption.

AUTHOR INFORMATION

Corresponding Author

*(H.Z.) Phone: +48 89 523 46 82. Fax: +48 89 524 01 24. E-mail: h.zielinski@pan.olsztyn.pl.

Funding

The study was supported by Project REFRESH (FP7-REGPOT-2010-1-264105) − Unlocking the potential of the Institute of Animal Reproduction and Food Research for strengthening integration with the European Research Area and region development. The project was financed in the area of "Research Potential" of the Seventh Framework Programme.

Notes

The authors declare no competing financial interest.

DOI: 10.1021/acs.jafc.5b02498
J. Agric. Food Chem. 2015, 63, 7896−7913

ABBREVIATIONS USED

2HN, 2″-hydroxynicotianamine
ACAT2, acyl-CoA:Ch acyltransferatse 2
ACC1 or 2, acetyl-coenzyme a carboxylase 1 or 2
ACE, angiotensin I converting enzyme
ApoA1, apolipoprotein A1
ApoB, apolipoprotein B
ApoE, apolipoprotein E
BK, bradykinin
BW, buckwheat
BWext, buckwheat extract
BWF, buckwheat flour
BWG, buckwheat groats
BWH, buckwheat hull
BWHext, buckwheat hull extract
BWI, buckwheat protease inhibitor
BWP, buckwheat protein
BWPext, buckwheat protein extract
BWS, buckwheat sprouts
BWSext, buckwheat sprouts extract
CAT, catalase
C/EBPα, CCAAT/enhancer-binding protein-α
Ch, cholesterol
ChREBP, carbohydrate responsive element-binding protein
COX-2, cyclooxygenase-2
CPT, carnitine palmitoyltransferase
Cyt *c*, cytochrome *c*
DCI, D-chiro-inositol
DPPH, 2,2-diphenyl-1-picrylhydrazyl
ET-1, endothelin-1
FA, fatty acid
FFA, free fatty acid
FLS, fluorescent substance
G6PDH, glucose-6-phosphate dehydrogenase
GABA, γ-aminobutyric acid
GIP, glucagon-dependent insulinotropic peptide
GLUT2, glucose transporter 2
GSH-Px, gluthatione peroxidase
HbA1c, glycated hemoglobin A1c
HDL, high-density lipoprotein
HMG-CoA, 3-hydroxy-3-methylglutaryl-coenzyme A
IC_{50}, inhibitory concentration 50
IL, interleukin
iNOS, inducible nitric oxide synthase
LDL, low-density lipoproteins
LPS, lipopolysaccharide
MDA, malondialdehyde
MMP, mitochondrial membrane potential
MPO, myeloperoxidase
N_2, nitrogen
NF-κB, nuclear factor kappa B
NO, nitric oxide
NPC1L1, Niemann−Pick C1-like 1
oxLDL, oxidized low-density lipoproteins
PGE_2, prostaglandin E_2
PPAR-γ, peroxisome proliferator-activated receptor-γ
PUFA, polyunsaturated fatty acids
rBWI, recombinant buckwheat protease inhibitor
ROS, reactive oxygen species
SCD1, stearoyl-coenzyme a oxidase
SCFA, short-chain fatty acids
SFA, saturated fatty acid
SHRs, spontaneously hypertensive rats
SOD, superoxide dismutase
SREBP-1c, sterol regulatory element-binding protein 1c
STZ, streptozotonic
TBARS, thiobarbituric acid reactive substances
TBUN, total blood urea nitrogen
TCh, total cholesterol
TG, triglycerides
TNF-α, tumor necrosis factor α

REFERENCES

(1) Sanchez, A.; Schuster, T.; Burke, J.; Kron, K. Taxonomy of *Polygonoideae* (*Polygonaceae*): a new tribal classification. *TAXON* **2011**, *60*, 151−160.
(2) Li, S. Q.; Zhang, Q. H. Advances in the development of functional foods from buckwheat. *Crit. Rev. Food Sci. Nutr.* **2001**, *41*, 451−464.
(3) Stember, R. H. Buckwheat allergy. *Allergy Asthma Proc.* **2006**, *27*, 393−395.
(4) Zhang, Z.; Zhou, M.; Tang, Y.; Li, F.; Tang, Y.; Shao, J.; Xue, W.; Wu, Y. Bioactive compounds in functional buckwheat food. *Food Res. Int.* **2012**, *49*, 389−395.
(5) Gimenez-Bastida, J.; Piskula, M.; Zielinski, H. Recent advances in processing and development of buckwheat derived bakery and non-bakery products − a review. *Pol. J. Food Nutr. Sci.* **2015**, *65*, 9−20.
(6) Saturni, L.; Ferretti, G.; Bacchetti, T. The gluten-free diet: safety and nutritional quality. *Nutrients* **2010**, *2*, 16−34.
(7) Krkoskova, B.; Mrazova, Z. Prophylactic components of buckwheat. *Food Res. Int.* **2005**, *38*, 561−568.
(8) González-Sarrías, A.; Larrosa, M.; García-Conesa, M. T.; Tomás-Barberán, F. A.; Espín, J. C. Nutraceuticals for older people: facts, fictions and gaps in knowledge. *Maturitas* **2013**, *75*, 313−334.
(9) Liu, R. H. Health benefits of fruit and vegetables are from additive and synergistic combinations of phytochemicals. *Am. J. Clin. Nutr.* **2003**, *78*, 517S−520S.
(10) D'Archivio, M.; Filesi, C.; Varì, R.; Scazzocchio, B.; Masella, R. Bioavailability of the polyphenols: *status* and controversies. *Int. J. Mol. Sci.* **2010**, *11*, 1321−1342.
(11) Steadman, K.; Burgoon, M.; Lewis, B.; Edwardson, S.; Obendorf, R. Buckwheat seed milling fractions: description, macronutrient composition and dietary fibre. *J. Cereal Sci.* **2001**, *33*, 271−278.
(12) Wijngaard, H.; Arendt, E. Buckwheat. *Cereal Chem.* **2006**, *83*, 391−401.
(13) Steadman, K. J.; Burgoon, M. S.; Schuster, R. L.; Lewis, B. A.; Edwardson, S. E.; Obendorf, R. L. Fagopyritols, D-chiro-inositol, and other soluble carbohydrates in buckwheat seed milling fractions. *J. Agric. Food Chem.* **2000**, *48*, 2843−2847.
(14) Lu, L.; Murphy, K.; Baik, B. K. Genotypic variation in nutritional composition of buckwheat groats and husks. *Cereal Chem.* **2013**, *90*, 132−137.
(15) Tahir, I.; Farooq, S. Grain composition in some buckwheat cultivars (*Fagopyrum* spp.) with particular reference to protein-fractions. *Qual. Plant.−Plant Foods Hum. Nutr.* **1985**, *35*, 153−158.
(16) Liu, C. L.; Chen, Y. S.; Yang, J. H.; Chiang, B. H. Antioxidant activity of tartary (*Fagopyrum tataricum* (L.) Gaertn.) and common (*Fagopyrum esculentum* Moench) buckwheat sprouts. *J. Agric. Food Chem.* **2008**, *56*, 173−178.
(17) Steadman, K. J.; Fuller, D. J.; Obendorf, R. L. Purification and molecular structure of two digalactosyl D-chiro-inositols and two trigalactosyl D-chiro-inositols from buckwheat seeds. *Carbohydr. Res.* **2001**, *331*, 19−25.
(18) Horbowicz, M.; Brenac, P.; Obendorf, R. L. Fagopyritol B1, *O*-α-D-galactopyranosyl-(1→2)-D-chiro-inositol, a galactosyl cyclitol in maturing buckwheat seeds associated with desiccation tolerance. *Planta* **1998**, *205*, 1−11.

DOI: 10.1021/acs.jafc.5b02498
J. Agric. Food Chem. 2015, 63, 7896−7913

(19) Obendorf, R. L.; Horbowicz, M.; Ueda, T.; Steadman, K. Fagopyritols: occurrence, biosynthesis, analyses, and possible role. *Eur. J. Plant Sci. Biotechnol.* **2012**, *6*, 27−36.
(20) Larner, J.; Huang, L. C.; Schwartz, C. F. W.; Oswald, A. S.; Shen, T. Y.; Kinter, M.; Tang, G.; Zeller, K. Rat-liver insulin mediator which stimulates pyruvate-dehydrogenase phosphatase contains galactosamine and D-chiro-inositol. *Biochem. Biophys. Res. Commun.* **1988**, *151*, 1416−1426.
(21) Ortmeyer, H. K.; Huang, L. C.; Lu, Z.; Hansen, B. C.; Larner, J. Chiroinositol deficiency and insulin resistance. II. Acute effects of D-chiroinositol administration in streptozotocin-diabetic rats, normal rats given a glucose-load, and spontaneously insulin-resistant rhesus-monkeys. *Endocrinology* **1993**, *132*, 646−651.
(22) Ortmeyer, H. K.; Larner, J.; Hansen, B. C. Effects of D-chiroinositol added to a meal on plasma glucose and insulin in hyperinsulinemic rhesus monkeys. *Obes. Res.* **1995**, *3*, S605−S608.
(23) Gómez, L.; Molinar-Toribio, E.; Calvo-Torras, M.; Adelantado, C.; Juan, M. E.; Planas, J. M.; Cañas, X.; Lozano, C.; Pumarola, S.; Clapés, P.; Torres, J. L. D-Fagomine lowers postprandial blood glucose and modulates bacterial adhesion. *Br. J. Nutr.* **2012**, *107*, 1739−1746.
(24) Amézqueta, S.; Galán, E.; Vila-Fernández, I.; Pumarola, S.; Carrascal, M.; Abian, J.; Ribas-Barba, L.; Serra-Majem, L.; Torres, J. L. The presence of D-fagomine in the human diet from buckwheat-based foodstuffs. *Food Chem.* **2013**, *136*, 1316−1321.
(25) Peng, L. X.; Wang, J. B.; Hu, L. X.; Zhao, J. L.; Xiang, D. B.; Zou, L.; Zhao, G. Rapid and simple method for the determination of emodin in tartary buckwheat (*Fagopyrum tataricum*) by high-performance liquid chromatography coupled to a diode array detector. *J. Agric. Food Chem.* **2013**, *61*, 854−857.
(26) Izhaki, I. Emodin − a secondary metabolite with multiple ecological functions in higher plants. *New Phytol.* **2002**, *155*, 205−217.
(27) Aubrecht, E.; Biacs, P. Characterization of buckwheat grain proteins and its products. *Acta Aliment.* **2001**, *30*, 71−80.
(28) Kato, N.; Iwami, K. Resistant protein; its existence and function beneficial to health. *J. Nutr. Sci. Vitaminol.* **2002**, *48*, 1−5.
(29) Zielinska, D.; Szawara-Nowak, D.; Zielinski, H. Comparison of spectrophotometric and electrochemical methods for the evaluation of the antioxidant capacity of buckwheat products after hydrothermal treatment. *J. Agric. Food Chem.* **2007**, *55*, 6124−6131.
(30) Zielinska, D.; Szawara-Nowak, D.; Zieliński, H. Determination of the antioxidant activity of rutin and its contribution to the antioxidant capacity of diversified buckwheat origin material by updated analytical strategies. *Pol. J. Food Nutr. Sci.* **2010**, *60*, 315−321.
(31) Fabjan, N.; Rode, J.; Kosir, I. J.; Wang, Z.; Zhang, Z.; Kreft, I. Tartary buckwheat (*Fagopyrum tataricum* Gaertn.) as a source of dietary rutin and quercitrin. *J. Agric. Food Chem.* **2003**, *51*, 6452−6455.
(32) Zielinska, D.; Zielinski, H. Low molecular weight antioxidants and other biologically active components of buckwheat seeds. *Eur. J. Plant Sci. Biotechnol.* **2009**, *3*, 29−38.
(33) Kim, S. J.; Maeda, T.; Sarker, M. Z.; Takigawa, S.; Matsuura-Endo, C.; Yamauchi, H.; Mukasa, Y.; Saito, K.; Hashimoto, N.; Noda, T.; Saito, T.; Suzuki, T. Identification of anthocyanins in the sprouts of buckwheat. *J. Agric. Food Chem.* **2007**, *55*, 6314−6318.
(34) Sharma, S.; Ali, A.; Ali, J.; Sahni, J. K.; Baboota, S. Rutin: therapeutic potential and recent advances in drug delivery. *Expert Opin. Invest. Drugs* **2013**, *22*, 1063−1079.
(35) Zielinska, D.; Turemko, M.; Kwiatkowski, J.; Zielinski, H. Evaluation of flavonoid contents and antioxidant capacity of the aerial parts of common and tartary buckwheat plants. *Molecules* **2012**, *17*, 9668−9682.
(36) Horbowicz, M.; Wiczkowski, W.; Koczkodaj, D.; Saniewski, M. Effects of methyl jasmonate on accumulation of flavonoids in seedlings of common buckwheat (*Fagopyrum esculentum* Moench). *Acta Biol. Hung.* **2011**, *62*, 265−278.
(37) Li, Y. Q.; Zhou, F. C.; Gao, F.; Bian, J. S.; Shan, F. Comparative evaluation of quercetin, isoquercetin and rutin as inhibitors of α-glucosidase. *J. Agric. Food Chem.* **2009**, *57*, 11463−11468.
(38) Zhang, R.; Yao, Y.; Wang, Y.; Ren, G. Antidiabetic activity of isoquercetin in diabetic KK-Ay mice. *Nutr. Metab.* **2011**, *8*, 85.
(39) Li, Y.; Duan, S.; Jia, H.; Bai, C.; Zhang, L.; Wang, Z. Flavonoids from tartary buckwheat induce G2/M cell cycle arrest and apoptosis in human hepatoma HepG2 cells. *Acta Biochim. Biophys. Sin.* **2014**, *46*, 460−470.
(40) Kalinova, J.; Triska, J.; Vrchotova, N. Distribution of vitamin E, squalene, epicatechin, and rutin in common buckwheat plants (*Fagopyrum esculentum* Moench). *J. Agric. Food Chem.* **2006**, *54*, 5330−5335.
(41) Guo, X. D.; Ma, Y. J.; Parry, J.; Gao, J. M.; Yu, L. L.; Wang, M. Phenolics content and antioxidant activity of tartary buckwheat from different locations. *Molecules* **2011**, *16*, 9850−9867.
(42) Sytar, O. Phenolic acids in the inflorescences of different varieties of buckwheat and their antioxidant activity. *J. King Saud Univ., Sci.* **2015**, *27*, 136−142.
(43) Normen, L.; Bryngelsson, S.; Johnsson, M.; Evheden, P.; Ellegard, L.; Brants, H.; Andersson, H.; Dutta, P. The phytosterol content of some cereal foods commonly consumed in Sweden and in the Netherlands. *J. Food Compos. Anal.* **2002**, *15*, 693−704.
(44) Zhang, Z. L.; Zhou, M. L.; Tang, Y.; Li, F. L.; Tang, Y. X.; Shao, J. R.; Xue, W. T.; Wu, Y. M. Bioactive compounds in functional buckwheat food. *Food Res. Int.* **2012**, *49*, 389−395.
(45) Gimenez-Bastida, J. A.; Piskula, M.; Zielinski, H. Recent advances in development of gluten-free buckwheat products. *Trends Food Sci. Technol.* **2015**, *44*, 58−65.
(46) Miyake, K.; Morita, R.; Handoyo, T.; Maeda, T.; Morita, N. Characterization of graded buckwheat flours and some properties of germinated 'Mancan' buckwheat grains. *Fagopyrum* **2004**, *21*, 91−97.
(47) Aoyagi, Y. An angiotensin-I converting enzyme inhibitor from buckwheat (*Fagopyrum esculentum* Moench) flour. *Phytochemistry* **2006**, *67*, 618−621.
(48) Maejima, Y.; Nakatsugawa, H.; Ichida, D.; Maejima, M.; Aoyagi, Y.; Maoka, T.; Etoh, H. Functional compounds in fermented buckwheat sprouts. *Biosci., Biotechnol., Biochem.* **2011**, *75*, 1708−1712.
(49) Schramm, D. D.; Karim, M.; Schrader, H. R.; Holt, R. R.; Cardetti, M.; Keen, C. L. Honey with high levels of antioxidants can provide protection to healthy human subjects. *J. Agric. Food Chem.* **2003**, *51*, 1732−1735.
(50) Gheldof, N.; Wang, X. H.; Engeseth, N. J. Buckwheat honey increases serum antioxidant capacity in humans. *J. Agric. Food Chem.* **2003**, *51*, 1500−1505.
(51) Bojňanská, T.; Frančáková, H.; Chlebo, P.; Vollmannová, A. Rutin content in buckwheat enriched bread and influence of its consumption on plasma total antioxidant status. *Czech J. Food Sci.* **2009**, *27*, S236−S240.
(52) Mukoda, T.; Sun, B.; Ishiguro, A. Antioxidant activities of buckwheat hull extract toward various oxidative stress *in vitro* and *in vivo*. *Biol. Pharm. Bull.* **2001**, *24*, 209−213.
(53) Zduńczyk, Z.; Flis, M.; Zieliński, H.; Wróblewska, M.; Antoszkiewicz, Z.; Juśkiewicz, J. In vitro antioxidant activities of barley, husked oat, naked oat, triticale, and buckwheat wastes and their influence on the growth and biomarkers of antioxidant status in rats. *J. Agric. Food Chem.* **2006**, *54*, 4168−4175.
(54) Yokozawa, T.; Fujii, H.; Kosuna, K.; Nonaka, G. Effects of buckwheat in a renal ischemia-reperfusion model. *Biosci., Biotechnol., Biochem.* **2001**, *65*, 396−400.
(55) Wroblewska, M.; Brzuzan, L.; Jaroslawska, J.; Zdunczyk, Z. Effect of buckwheat sprouts and groats on the antioxidant potential of blood and caecal parameters in rats. *Int. J. Vitam. Nutr. Res.* **2011**, *81*, 286−294.
(56) Quettier-Deleu, C.; Gressier, B.; Vasseur, J.; Dine, T.; Brunet, C.; Luyckx, M.; Cazin, M.; Cazin, J. C.; Bailleul, F.; Trotin, F. Phenolic compounds and antioxidant activities of buckwheat (*Fagopyrum esculentum* Moench) hulls and flour. *J. Ethnopharmacol.* **2000**, *72*, 35−42.
(57) Morishita, T.; Yamaguchi, H.; Degi, K. The contribution of polyphenols to antioxidative activity in common buckwheat and tartary buckwheat grain. *Plant Prod. Sci.* **2007**, *10*, 99−104.
(58) Kabir, F.; Tow, W.; Hamauzu, Y.; Katayama, S.; Tanaka, S.; Nakamura, S. Antioxidant and cytoprotective activities of extracts

DOI: 10.1021/acs.jafc.5b02498
J. Agric. Food Chem. 2015, 63, 7896−7913

prepared from fruit and vegetable wastes and by-products. *Food Chem.* **2015**, *167*, 358−362.
(59) Zhou, X.; Hao, T.; Zhou, Y.; Tang, W.; Xiao, Y.; Meng, X.; Fang, X. Relationships between antioxidant compounds and antioxidant activities of tartary buckwheat during germination. *J. Food Sci. Technol.* **2015**, *52*, 2458−2463.
(60) Gorinstein, S.; Vargas, O.; Jaramillo, N.; Salas, I.; Ayala, A.; Arancibia-Avila, P.; Toledo, F.; Katrich, E.; Trakhtenberg, S. The total polyphenols and the antioxidant potentials of some selected cereals and pseudocereals. *Eur. Food Res. Technol.* **2007**, *225*, 321−328.
(61) Gorinstein, S.; Lojek, A.; Ciz, M.; Pawelzik, E.; Delgado-Licon, E.; Medina, O.; Moreno, M.; Salas, I.; Goshev, I. Comparison of composition and antioxidant capacity of some cereals and pseudocereals. *Int. J. Food Sci. Technol.* **2008**, *43*, 629−637.
(62) Alvarez-Jubete, L.; Wijngaard, H.; Arendt, E.; Gallagher, E. Polyphenol composition and *in vitro* antioxidant activity of amaranth, quinoa buckwheat and wheat as affected by sprouting and baking. *Food Chem.* **2010**, *119*, 770−778.
(63) Vollmannova, A.; Margitanova, E.; Toth, T.; Timoracka, M.; Urminska, D.; Bojnanska, T.; Cicova, I. Cultivar influence on total polyphenol and rutin contents and total antioxidant capacity in buckwheat, amaranth, and quinoa seeds. *Czech J. Food Sci.* **2013**, *31*, 589−595.
(64) Zieliński, H.; Kozłowska, H. Antioxidant activity and total phenolics in selected cereal grains and their different morphological fractions. *J. Agric. Food Chem.* **2000**, *48*, 2008−2016.
(65) Kreft, I.; Fabjan, N.; Yasumoto, K. Rutin content in buckwheat (*Fagopyrum esculentum* Moench) food materials and products. *Food Chem.* **2006**, *98*, 508−512.
(66) Ghica, M. E.; Brett, A. M. O. Electrochemical oxidation of rutin. *Electroanalysis* **2005**, *17*, 313−318.
(67) Zhou, J.; Li, P.; Cheng, N.; Gao, H.; Wang, B.; Wei, Y.; Cao, W. Protective effects of buckwheat honey on DNA damage induced by hydroxyl radicals. *Food Chem. Toxicol.* **2012**, *50*, 2766−2773.
(68) Azorín-Ortuño, M.; Yáñez-Gascón, M. J.; González-Sarrías, A.; Larrosa, M.; Vallejo, F.; Pallarés, F. J.; Lucas, R.; Morales, J. C.; Tomás-Barberán, F. A.; García-Conesa, M. T.; Espín, J. C. Effects of long-term consumption of low doses of resveratrol on diet-induced mild hypercholesterolemia in pigs: a transcriptomic approach to disease prevention. *J. Nutr. Biochem.* **2012**, *23*, 829−837.
(69) Zhang, H. W.; Zhang, Y. H.; Lu, M. J.; Tong, W. J.; Cao, G. W. Comparison of hypertension, dyslipidaemia and hyperglycaemia between buckwheat seed-consuming and non-consuming Mongolian-Chinese populations in Inner Mongolia, China. *Clin. Exp. Pharmacol. Physiol.* **2007**, *34*, 838−844.
(70) Wieslander, G.; Fabjan, N.; Vogrincic, M.; Kreft, I.; Janson, C.; Spetz-Nyström, U.; Vombergar, B.; Tagesson, C.; Leanderson, P.; Norbäck, D. Eating buckwheat cookies is associated with the reduction in serum levels of myeloperoxidase and cholesterol: a double blind crossover study in day-care centre staffs. *Tohoku J. Exp. Med.* **2011**, *225*, 123−130.
(71) Kayashita, J.; Shimaoka, I.; Nakajoh, M.; Y, A.; Kato, N. Feeding of buckwheat protein extract reduces body fat content in rats. In *Current Advances in Buckwheat Research*, Proceedings of the 6th International Symposium on Buckwheat, Shinshu, August 24−29, 1995; Matano, T., Ujihara, A., Eds.; Shinshu University Press: Shinshu, China, 1995; pp 935−940.
(72) Kayashita, J.; Shimaoka, I.; Nakajoh, M.; Kato, N. Feeding of buckwheat protein extract reduces hepatic triglyceride concentration, adipose tissue weight, and hepatic lipogenesis in rats. *J. Nutr. Biochem.* **1996**, *7*, 555−559.
(73) Kayashita, J.; Shimaoka, I.; Nakajyoh, M. Hypocholesterolemic effect of buckwheat protein extract in rats fed cholesterol-enriched diets. *Nutr. Res. (N. Y.)* **1995**, *15*, 691−698.
(74) Tomotake, H.; Shimaoka, I.; Kayashita, J.; Yokoyama, F.; Nakajoh, M.; Kato, N. Stronger suppression of plasma cholesterol and enhancement of the fecal excretion of steroids by a buckwheat protein product than by a soy protein isolate in rats fed on a cholesterol-free diet. *Biosci., Biotechnol., Biochem.* **2001**, *65*, 1412−1414.
(75) Tomotake, H.; Shimaoka, I.; Kayashita, J.; Yokoyama, F.; Nakajoh, M.; Kato, N. A buckwheat protein product suppresses gallstone formation and plasma cholesterol more strongly than soy protein isolate in hamsters. *J. Nutr.* **2000**, *130*, 1670−1674.
(76) Tomotake, H.; Yamamoto, N.; Yanaka, N.; Ohinata, H.; Yamazaki, R.; Kayashita, J.; Kato, N. High protein buckwheat flour suppresses hypercholesterolemia in rats and gallstone formation in mice by hypercholesterolemic diet and body fat in rats because of its low protein digestibility. *Nutrition* **2006**, *22*, 166−173.
(77) Kayashita, J.; Shimaoka, I.; Nakajoh, M.; Yamazaki, M.; Kato, N. Consumption of buckwheat protein lowers plasma cholesterol and raises fecal neutral sterols in cholesterol-fed rats because of its low digestibility. *J. Nutr.* **1997**, *127*, 1395−1400.
(78) Metzger, B. T.; Barnes, D. M.; Reed, J. D. Insoluble fraction of buckwheat (*Fagopyrum esculentum* Moench) protein possessing cholesterol-binding properties that reduce micelle cholesterol solubility and uptake by Caco-2 cells. *J. Agric. Food Chem.* **2007**, *55*, 6032−6038.
(79) Son, B. K.; Kim, J. Y.; Lee, S. S. Effect of adlay, buckwheat and barley on lipid metabolism and aorta histopathology in rats fed an obesogenic diet. *Ann. Nutr. Metab.* **2008**, *52*, 181−187.
(80) Yang, N.; Li, Y.; Zhang, K.; Jiao, R.; Ma, K.; Zhang, R.; Ren, G.; Chen, Z. Hypocholesterolemic activity of buckwheat flour is mediated by increasing sterol excretion and down-regulation of intestinal NPC1L1 and ACAT2. *J. Funct. Foods* **2014**, *6*, 311−318.
(81) Xie, C.; Zhou, Z. S.; Li, N.; Bian, Y.; Wang, Y. J.; Wang, L. J.; Li, B. L.; Song, B. L. Ezetimibe blocks the internalization of NPC1L1 and cholesterol in mouse small intestine. *J. Lipid Res.* **2012**, *53*, 2092−2101.
(82) Choi, I.; Seog, H.; Park, Y.; Kim, Y.; Choi, H. Suppressive effects of germinated buckwheat on development of fatty liver in mice fed with high-fat diet. *Phytomedicine* **2007**, *14*, 563−567.
(83) Hosaka, T.; Sasaga, S.; Yamasaka, Y.; Nii, Y.; Edazawa, K.; Tsutsumi, R.; Shuto, E.; Okahisa, N.; Iwata, S.; Tomotake, H.; Sakai, T. Treatment with buckwheat bran extract prevents the elevation of serum triglyceride levels and fatty liver in KK-A(y) mice. *J. Med. Invest.* **2014**, *61*, 345−352.
(84) Kuwabara, T.; Han, K. H.; Hashimoto, N.; Yamauchi, H.; Shimada, K.; Sekikawa, M.; Fukushima, M. Tartary buckwheat sprout powder lowers plasma cholesterol level in rats. *J. Nutr. Sci. Vitaminol.* **2007**, *53*, 501−507.
(85) Pan, M. H.; Lai, C. S.; Ho, C. T. Anti-inflammatory activity of natural dietary flavonoids. *Food Funct.* **2010**, *1*, 15−31.
(86) Collares, C. V.; Evangelista, A. F.; Xavier, D. J.; Takahashi, P.; Almeida, R.; Macedo, C.; Manoel-Caetano, F.; Foss, M. C.; Foss-Freitas, M. C.; Rassi, D. M.; Sakamoto-Hojo, E. T.; Passos, G. A.; Donadi, E. A. Transcriptome meta-analysis of peripheral lymphomononuclear cells indicates that gestational diabetes is closer to type 1 diabetes than to type 2 diabetes mellitus. *Mol. Biol. Rep.* **2013**, *40*, 5351−5358.
(87) Ajala, O.; English, P.; Pinkney, J. Systematic review and meta-analysis of different dietary approaches to the management of type 2 diabetes. *Am. J. Clin. Nutr.* **2013**, *97*, 505−516.
(88) Zeng, Y.; Pu, X.; Du, J.; Yang, S.; Yang, T.; Jia, P. Use of functional foods for diabetes prevention in China. *Afr. J. Pharm. Pharmacol.* **2012**, *6*, 2570−2579.
(89) Skrabanja, V.; Liljeberg Elmståhl, H. G.; Kreft, I.; Björck, I. M. Nutritional properties of starch in buckwheat products: studies in vitro and in vivo. *J. Agric. Food Chem.* **2001**, *49*, 490−496.
(90) Su-Que, L.; Ya-Ning, M.; Xing-Pu, L.; Ye-Lun, Z.; Guang-Yao, S.; Hui-Juan, M. Effect of consumption of micronutrient enriched wheat steamed bread on postprandial plasma glucose in healthy and type 2 diabetic subjects. *Nutr. J.* **2013**, *12*, 64.
(91) Berti, C.; Riso, P.; Brusamolino, A.; Porrini, M. Effect on appetite control of minor cereal and pseudocereal products. *Br. J. Nutr.* **2005**, *94*, 850−858.
(92) Stringer, D. M.; Taylor, C. G.; Appah, P.; Blewett, H.; Zahradka, P. Consumption of buckwheat modulates the post-prandial response

DOI: 10.1021/acs.jafc.5b02498
J. Agric. Food Chem. 2015, 63, 7896−7913

of selected gastrointestinal satiety hormones in individuals with type 2 diabetes mellitus. *Metab., Clin. Exp.* **2013**, *62*, 1021−1031.
(93) Larner, J. D-Chiro-inositol in insulin action and insulin resistance − old-fashioned biochemistry still at work. *IUBMB Life* **2001**, *51*, 139−148.
(94) Larner, J. D-Chiro-inositol − its functional role in insulin action and its deficit in insulin resistance. *Int. J. Exp Diabetes Res.* **2002**, *3*, 47−60.
(95) Larner, J.; Brautigan, D. L.; Thorner, M. O. D-Chiro-inositol glycans in insulin signaling and insulin resistance. *Mol. Med.* **2010**, *16*, 543−551.
(96) Larner, J.; Craig, J. W. Urinary myo-inositol-to-chiro-inositol ratios and insulin resistance. *Diabetes Care* **1996**, *19*, 76−78.
(97) Larner, J.; Price, J. D.; Heimark, D.; Smith, L.; Rule, G.; Piccariello, T.; Fonteles, M. C.; Pontes, C.; Vale, D.; Huang, L. Isolation, structure, synthesis, and bioactivity of a novel putative insulin mediator. A galactosamine chiro-inositol pseudo-disaccharide Mn^{2+} chelate with insulin-like activity. *J. Med. Chem.* **2003**, *46*, 3283−3291.
(98) Kawa, J. M.; Taylor, C. G.; Przybylski, R. Buckwheat concentrate reduces serum glucose in streptozotocin-diabetic rats. *J. Agric. Food Chem.* **2003**, *51*, 7287−7291.
(99) Yao, Y.; Shan, F.; Bian, J.; Chen, F.; Wang, M.; Ren, G. D-Chiro-inositol-enriched tartary buckwheat bran extract lowers the blood glucose level in KK-Ay mice. *J. Agric. Food Chem.* **2008**, *56*, 10027−10031.
(100) Chu, J. X.; Wang, Z. L.; Han, S. Y. The effects of total flavonoids from buckwheat flowers and leaves on renal damage and PTP1B expression in type 2 diabetic rats. *Iran J. Pharm. Res.* **2011**, *10*, 511−517.
(101) Hosaka, T.; Nii, Y.; Tomotake, H.; Ito, T.; Tamanaha, A.; Yamasaka, Y.; Sasaga, S.; Edazawa, K.; Tsutsumi, R.; Shuto, E.; Okahisa, N.; Iwata, S.; Sakai, T. Extracts of common buckwheat bran prevent sucrose digestion. *J. Nutr. Sci. Vitaminol.* **2011**, *57*, 441−445.
(102) Lee, C.; Hsu, W.; Shen, S.; Cheng, Y.; Wu, S. *Fagopyrum tataricum* (buckwheat) improved high-glucose-induced insulin resistance in mouse hepatocytes and diabetes in fructose-rich diet-induced mice. *Exp. Diabetes Res.* **2012**, *2012*, 375673.
(103) Lee, C. C.; Lee, B. H.; Lai, Y. J. Antioxidation and antiglycation of *Fagopyrum tataricum* ethanol extract. *J. Food Sci. Technol.* **2015**, *52*, 1110−1116.
(104) Monsalve, F. A.; Pyarasani, R. D.; Delgado-Lopez, F.; Moore-Carrasco, R. Peroxisome proliferator-activated receptor targets for the treatment of metabolic diseases. *Mediators Inflammation* **2013**, *2013*, 549627.
(105) Schrader, E.; Wein, S.; Kristiansen, K.; Christensen, L. P.; Rimbach, G.; Wolffram, S. Plant extracts of winter savory, purple coneflower, buckwheat and black elder activate PPAR-γ in COS-1 cells but do not lower blood glucose in db/db mice *in vivo*. *Plant Foods Hum. Nutr.* **2012**, *67*, 377−383.
(106) Curran, J. M.; Stringer, D. M.; Wright, B.; Taylor, C. G.; Przybylski, R.; Zahradka, P. Biological response of hepatomas to an extract of *Fagopyrum esculentum* M. (buckwheat) is not mediated by inositols or rutin. *J. Agric. Food Chem.* **2010**, *58*, 3197−3204.
(107) Jemal, A.; Bray, F.; Center, M. M.; Ferlay, J.; Ward, E.; Forman, D. Global cancer statistics. *Ca-Cancer J. Clin.* **2011**, *61*, 69−90.
(108) Shen, M.; Chapman, R. S.; He, X.; Liu, L. Z.; Lai, H.; Chen, W.; Lan, Q. Dietary factors, food contamination and lung cancer risk in Xuanwei, China. *Lung Cancer* **2008**, *61*, 275−282.
(109) Poulsen, H. E.; Prieme, H.; Loft, S. Role of oxidative DNA damage in cancer initiation and promotion. *Eur. J. Cancer Prev.* **1998**, *7*, 9−16.
(110) Cao, W.; Chen, W.; Suo, Z.; Yao, Y. Protective effects of ethanolic extracts of buckwheat groats on DNA damage caused by hydroxyl radicals. *Food Res. Int.* **2008**, *41*, 924−929.
(111) Vogrinčič, M.; Kreft, I.; Filipič, M.; Zegura, B. Antigenotoxic effect of tartary (*Fagopyrum tataricum*) and common (*Fagopyrum esculentum*) buckwheat flour. *J. Med. Food* **2013**, *16*, 944−952.
(112) Kayashita, J.; Shimaoka, I.; Nakajoh, M.; Kishida, N.; Kato, N. Consumption of a buckwheat protein extract retards 7,12-dimethylbenz[α]anthracene-induced mammary carcinogenesis in rats. *Biosci., Biotechnol., Biochem.* **1999**, *63*, 1837−1839.
(113) Liu, Z.; Ishikawa, W.; Huang, X.; Tomotake, H.; Kayashita, J.; Watanabe, H.; Kato, N. A buckwheat protein product suppresses 1,2-dimethylhydrazine-induced colon carcinogenesis in rats by reducing cell proliferation. *J. Nutr.* **2001**, *131*, 1850−1853.
(114) Buzzi, N.; Colicheo, A.; Boland, R.; de Boland, A. R. MAP kinases in proliferating human colon cancer Caco-2 cells. *Mol. Cell. Biochem.* **2009**, *328*, 201−208.
(115) Kim, S. H.; Cui, C. B.; Kang, I. J.; Kim, S. Y.; Ham, S. S. Cytotoxic effect of buckwheat (*Fagopyrum esculentum* Moench) hull against cancer cells. *J. Med. Food* **2007**, *10*, 232−238.
(116) Danihelová, M.; Jantová, S.; Šturdík, E. Cytotoxic and antioxidant activity of buckwheat hull extracts. *J. Microbiol. Biotechnol. Food Sci.* **2013**, *2*, 1314−1323.
(117) Ren, W.; Qiao, Z.; Wang, H.; Zhu, L.; Zhang, L.; Lu, Y.; Cui, Y.; Zhang, Z.; Wang, Z. Tartary buckwheat flavonoid activates caspase 3 and induces HL-60 cell apoptosis. *Methods Find. Exp. Clin. Pharmacol.* **2001**, *23*, 427−432.
(118) Ren, W.; Qiao, Z.; Wang, H.; Zhu, L.; Zhang, L.; Lu, Y.; Zhang, Z.; Wang, Z. Molecular basis of Fas and cytochrome *c* pathways of apoptosis induced by tartary buckwheat flavonoid in HL-60 cells. *Methods Find. Exp. Clin. Pharmacol.* **2003**, *25*, 431−436.
(119) Wu, S. C.; Lee, B. H. Buckwheat polysaccharide exerts antiproliferative effects in THP-1 human leukemia cells by inducing differentiation. *J. Med. Food* **2011**, *14*, 26−33.
(120) Bai, C. Z.; Ji, H. J.; Feng, M. L.; Hao, X. L.; Zhong, Q. M.; Cui, X. D.; Wang, Z. H. Stimulation of dendritic cell maturation and induction of apoptosis in lymphoma cells by a stable lectin from buckwheat seeds. *GMR, Genet. Mol. Res.* **2015**, *14*, 2162−2175.
(121) Zheng, C.; Hu, C.; Ma, X.; Peng, C.; Zhang, H.; Qin, L. Cytotoxic phenylpropanoid glycosides from *Fagopyrum tataricum* (L.) Gaertn. *Food Chem.* **2012**, *132*, 433−438.
(122) Li, Y.; Wang, S.; Xia, W.; Rahman, K.; Zhang, Y.; Peng, H.; Zhang, H.; Qin, L. Effects of tatariside G isolated from *Fagopyrum tataricum* roots on apoptosis in human cervical cancer HeLa cells. *Molecules* **2014**, *19*, 11145−11159.
(123) Yuan, S.; Yan, J.; Ye, X.; Wu, Z.; Ng, T. Isolation of a ribonuclease with antiproliferative and HIV-1 reverse transcriptase inhibitory activities from Japanese large brown buckwheat seeds. *Appl. Biochem. Biotechnol.* **2015**, *175*, 2456−2467.
(124) de Mejia, E. G.; Dia, V. P. The role of nutraceutical proteins and peptides in apoptosis, angiogenesis, and metastasis of cancer cells. *Cancer Metastasis Rev.* **2010**, *29*, 511−528.
(125) Leung, E. H.; Ng, T. B. A relatively stable antifungal peptide from buckwheat seeds with antiproliferative activity toward cancer cells. *J. Pept. Sci.* **2007**, *13*, 762−767.
(126) Guo, X.; Zhu, K.; Zhang, H.; Yao, H. Anti-tumor activity of a novel protein obtained from tartary buckwheat. *Int. J. Mol. Sci.* **2010**, *11*, 5201−5211.
(127) Guo, X.; Zhu, K.; Zhang, H.; Yao, H. Purification and characterization of the antitumor protein from chinese tartary buckwheat (*Fagopyrum tataricum* Gaertn.) water-soluble extracts. *J. Agric. Food Chem.* **2007**, *55*, 6958−6961.
(128) Mantovani, A.; Allavena, P.; Sica, A.; Balkwill, F. Cancer-related inflammation. *Nature* **2008**, *454*, 436−444.
(129) Gosslau, A.; Li, S. M.; Ho, C. T.; Chen, K. Y.; Rawson, N. E. The importance of natural product characterization in studies of their anti-inflammatory activity. *Mol. Nutr. Food Res.* **2011**, *55*, 74−82.
(130) Hsieh, I. N.; Chang, A. S.; Teng, C. M.; Chen, C. C.; Yang, C. R. Aciculatin inhibits lipopolysaccharide-mediated inducible nitric oxide synthase and cyclooxygenase-2 expression via suppressing NF-κB and JNK/p38 MAPK activation pathways. *J. Biomed. Sci.* **2011**, *18*, 28.
(131) Hole, A.; Grimmer, S.; Naterstad, K.; Jensen, M.; Paur, I.; Johansen, S.; Balstad, T.; Blomhoff, R.; Sahlstrom, S. Activation and

DOI: 10.1021/acs.jafc.5b02498
J. Agric. Food Chem. 2015, 63, 7896−7913

inhibition of nuclear factor κB activity by cereal extracts: role of dietary phenolic acids. *J. Agric. Food Chem.* **2009**, *57*, 9481−9488.
(132) Karki, R.; Park, C. H.; Kim, D. W. Extract of buckwheat sprouts scavenges oxidation and inhibits pro-inflammatory mediators in lipopolysaccharide-stimulated macrophages (RAW264.7). *J. Integr. Med.* **2013**, *11*, 246−252.
(133) Ishii, S.; Katsumura, T.; Shiozuka, C.; Ooyauchi, K.; Kawasaki, K.; Takigawa, S.; Fukushima, T.; Tokuji, Y.; Kinoshita, M.; Ohnishi, M.; Kawahara, M.; Ohba, K. Anti-inflammatory effect of buckwheat sprouts in lipopolysaccharide-activated human colon cancer cells and mice. *Biosci., Biotechnol., Biochem.* **2008**, *72*, 3148−3157.
(134) Lee, C. C.; Shen, S. R.; Lai, Y. J.; Wu, S. C. Rutin and quercetin, bioactive compounds from tartary buckwheat, prevent liver inflammatory injury. *Food Funct.* **2013**, *4*, 794−802.
(135) Kearney, P.; Whelton, M.; Reynolds, K.; Muntner, P.; Whelton, P.; He, J. Global burden of hypertension: analysis of worldwide data. *Lancet* **2005**, *365*, 217−223.
(136) Jao, C.-L.; Huang, S.-L.; Hsu, K.-C. Angiotensin I-converting enzyme inhibitory peptides: Inhibition mode, bioavailability, and antihypertensive effects. *BioMedicine* **2012**, *2*, 130−136.
(137) Li, C. H.; Matsui, T.; Matsumoto, K.; Yamasaki, R.; Kawasaki, T. Latent production of angiotensin I-converting enzyme inhibitors from buckwheat protein. *J. Pept. Sci.* **2002**, *8*, 267−274.
(138) Kawasaki, T.; Itoh, K.; Ogaki, T.; Yoshimizu, Y.; Ghimire, P.; Regmi, P.; Acharya, G. A study on the genesis of hypertension in mountain people habitually taking Tibetan tea and buckwheat in Nepal. *J. Health Sci.* **1995**, *17*, 121−130.
(139) Lam, L. H.; Shimamura, T.; Sakaguchi, K.; Noguchi, K.; Ishiyama, M.; Fujimura, Y.; Ukeda, H. Assay of angiotensin I-converting enzyme-inhibiting activity based on the detection of 3-hydroxybutyric acid. *Anal. Biochem.* **2007**, *364*, 104−111.
(140) Kim, D. W.; Hwang, I. K.; Lim, S. S.; Yoo, K. Y.; Li, H.; Kim, Y. S.; Kwon, D. Y.; Moon, W. K.; Won, M. H. Germinated buckwheat extract decreases blood pressure and nitrotyrosine immunoreactivity in aortic endothelial cells in spontaneously hypertensive rats. *Phytother. Res.* **2009**, *23*, 993−998.
(141) Koyama, M.; Naramoto, K.; Nakajima, T.; Aoyama, T.; Watanabe, M.; Nakamura, K. Purification and identification of antihypertensive peptides from fermented buckwheat sprouts. *J. Agric. Food Chem.* **2013**, *61*, 3013−3021.
(142) Nakamura, K.; Naramoto, K.; Koyama, M. Blood-pressure-lowering effect of fermented buckwheat sprouts in spontaneously hypertensive rats. *J. Funct. Foods* **2013**, *5*, 406−415.
(143) Merendino, N.; Molinari, R.; Costantini, L.; Mazzucato, A.; Pucci, A.; Bonafaccia, F.; Esti, M.; Ceccantoni, B.; Papeschi, C.; Bonafaccia, G. A new "functional" pasta containing tartary buckwheat sprouts as an ingredient improves the oxidative status and normalizes some blood pressure parameters in spontaneously hypertensive rats. *Food Funct.* **2014**, *5*, 1017−1026.
(144) Higasa, S.; Fujihara, S.; Hayashi, A.; Kimoto, K.; Aoyagi, Y. Distribution of a novel angiotensin I-converting enzyme inhibitory substance (2″-hydroxynicotianamine) in the flour, plant parts, and processed products of buckwheat. *Food Chem.* **2011**, *125*, 607−613.
(145) Tsai, H.; Deng, H.; Tsai, S.; Hsu, Y., Bioactivity comparison of extracts from various parts of common and tartary buckwheats: evaluation of the antioxidant- and angiotensin-converting enzyme inhibitory activities. *Chem. Cent. J.* **2012**, *6*.7810.1186/1752-153X-6-78
(146) Ushida, Y.; Matsui, T.; Tanaka, M.; Matsumoto, K.; Hosoyama, H.; Mitomi, A.; Sagesaka, Y.; Kakuda, T. Endothelium-dependent vasorelaxation effect of rutin-free tartary buckwheat extract in isolated rat thoracic aorta. *J. Nutr. Biochem.* **2008**, *19*, 700−707.
(147) Kawakami, A.; Inbe, T.; Kayahara, H.; Horii, A. Preparations of enzymatic hydrolysates of buckwheat globulin and their angiotensin I converting enzyme inhibitory activities. In *Current Advances in Buckwheat Research*, Proceedings of the 6th International Symposium on Buckwheat in Shinshu, August 24−29, 1995; Toshiko, M., Akio, U., Eds.; Shinshu University Press: Shinshu, China, 1995; pp 927−934.
(148) Ma, M.; Bae, I.; Lee, H.; Yang, C. Purification and identification of angiotensin I-converting enzyme inhibitory peptide from buckwheat (*Fagopyrum esculentum* Moench). *Food Chem.* **2006**, *96*, 36−42.
(149) Koyama, M.; Hattori, S.; Amano, Y.; Watanabe, M.; Nakamura, K. Blood pressure-lowering peptides from neo-fermented buckwheat sprouts: a new approach to estimating ACE-inhibitory activity. *PLoS One* **2014**, *9*, e105802.
(150) Koppel, J.; Greenwald, B. Optimal treatment of Alzheimer's disease psychosis: challenges and solutions. *Neuropsychiatr. Dis. Treat.* **2014**, *10*, 2253−2262.
(151) Ma, T.; Tan, M.; Yu, J.; Tan, L. Resveratrol as a therapeutic agent for Alzheimer's disease. *BioMed Res. Int.* **2014**, *2014*, 350516.
(152) Pu, F.; Mishima, K.; Egashira, N.; Iwasaki, K.; Kaneko, T.; Uchida, T.; Irie, K.; Ishibashi, D.; Fujii, H.; Kosuna, K.; Fujiwara, M. Protective effect of buckwheat polyphenols against long-lasting impairment of spatial memory associated with hippocampal neuronal damage in rats subjected to repeated cerebral ischemia. *J. Pharmacol. Sci.* **2004**, *94*, 393−402.
(153) Pu, F.; Mishima, K.; Irie, K.; Egashira, N.; Ishibashi, D.; Matsumoto, Y.; Ikeda, T.; Iwasaki, K.; Fujii, H.; Kosuna, K.; Fujiwara, M. Differential effects of buckwheat and kudingcha extract on neuronal damage in cultured hippocampal neurons and spatial memory impairment induced by scopolamine in an eight-arm radial maze. *J. Health Sci.* **2005**, *51*, 636−644.
(154) Gulpinar, A.; Orhan, I.; Kan, A.; Senol, F.; Celik, S.; Kartal, M. Estimation of *in vitro* neuroprotective properties and quantification of rutin and fatty acids in buckwheat (*Fagopyrum esculentum* Moench) cultivated in Turkey. *Food Res. Int.* **2012**, *46*, 536−543.
(155) Choi, J. Y.; Cho, E. J.; Lee, H. S.; Lee, J. M.; Yoon, Y. H.; Lee, S. Tartary buckwheat improves cognition and memory function in an *in vivo* amyloid-β-induced Alzheimer model. *Food Chem. Toxicol.* **2013**, *53*, 105−111.
(156) Choi, J. Y.; Lee, J. M.; Lee, D. G.; Yoon, Y. H.; Cho, E. J.; Lee, S. The n-Butanol fraction and rutin from tartary buckwheat improve cognition and memory in an *in vivo* model of amyloid-β-induced Alzheimer's disease. *J. Med. Food* **2015**, *18*, 631−641.
(157) Manach, C.; Williamson, G.; Morand, C.; Scalbert, A.; Remesy, C. Bioavailability and bioefficacy of polyphenols in humans. I. Review of 97 bioavailability studies. *Am. J. Clin. Nutr.* **2005**, *81*, 230S−242S.
(158) Graefe, E.; Wittig, J.; Mueller, S.; Riethling, A.; Uehleke, B.; Drewelow, B.; Pforte, H.; Jacobasch, G.; Derendorf, H.; Veit, M. Pharmacokinetics and bioavailability of quercetin glycosides in humans. *J. Clin. Pharmacol.* **2001**, *41*, 492−499.
(159) Zhao, G.; Zou, L.; Wang, Z.; Hu, H.; Hu, Y.; Peng, L. Pharmacokinetic profile of total quercetin after single oral dose of tartary buckwheat extracts in rats. *J. Agric. Food Chem.* **2011**, *59*, 4435−4441.
(160) Bijlani, R. L.; Sud, S.; Sahi, A.; Gandhi, B. M.; Tandon, B. N. Effect of sieved buckwheat (*Fagopyrum esculentum*) flour supplementation on lipid profile and glucose tolerance. *Indian J. Physiol. Pharmacol.* **1985**, *29*, 69−74.
(161) Bijlani, R. L.; Gandhi, B. M.; Gupta, M. C.; Manocha, S.; Tandon, B. N. Effect of whole buckwheat (*Fagopyrum esculentum*) flour supplementation on lipid profile and glucose tolerance. *Indian J. Med. Res.* **1985**, *81*, 162−168.
(162) He, J.; Klag, M. J.; Whelton, P. K.; Mo, J. P.; Chen, J. Y.; Qian, M. C.; Mo, P. S.; He, G. Q. Oats and buckwheat intakes and cardiovascular disease risk factors in an ethnic minority of China. *Am. J. Clin. Nutr.* **1995**, *61*, 366−372.
(163) Ogawa, H.; Takatera, K.; Fukuta, Y.; Murakami, T. Effect of buckwheat protein extract on lipid metabolism in diet-induced hypercholesterolemic stroke-prone SHR (SHRSP). *Jpn. Heart J.* **1997**, *38*, 602−602.
(164) Wojcicki, J.; Samochowiec, L.; Gonet, B.; Juiwiak, S.; Dabrowska-Zamojcin, E.; Katdonska, M.; Tustanowski, S. Effect of buckwheat extract on free radical generation in rabbits administered high-fat diet. *Phytother. Res.* **1995**, *9*, 323−326.
(165) Lin, L. Y.; Peng, C. C.; Yang, Y. L.; Peng, R. Y. Optimization of bioactive compounds in buckwheat sprouts and their effect on blood cholesterol in hamsters. *J. Agric. Food Chem.* **2008**, *56*, 1216−1223.

DOI: 10.1021/acs.jafc.5b02498
J. Agric. Food Chem. 2015, 63, 7896−7913

(166) Tomotake, H.; Yamamoto, N.; Kitabayashi, H.; Kawakami, A.; Kayashita, J.; Ohinata, H.; Karasawa, H.; Kato, N. Preparation of tartary buckwheat protein product and its improving effect on cholesterol metabolism in rats and mice fed cholesterol-enriched diet. *J. Food Sci.* **2007**, *72*, S528−S533.
(167) Peng, C. C.; Chen, K. C.; Yang, Y. L.; Lin, L. Y.; Peng, R. Y. Aqua-culture improved buckwheat sprouts with more abundant precious nutrients and hypolipidemic activity. *Int. J. Food Sci. Nutr.* **2009**, *60*, 232−245.
(168) Wang, M.; Liu, J. R.; Gao, J. M.; Parry, J. W.; Wei, Y. M. Antioxidant activity of tartary buckwheat bran extract and its effect on the lipid profile of hyperlipidemic rats. *J. Agric. Food Chem.* **2009**, *57*, 5106−5112.
(169) Đurendić-Brenesel, M.; Popović, T.; Pilija, V.; Arsić, A.; Milić, M.; Kojić, D.; Jojić, N.; Milić, N. Hypolipidemic and antioxidant effects of buckwheat leaf and flower mixture in hyperlipidemic rats. *Bosn. J. Basic Med. Sci.* **2013**, *13*, 100−108.
(170) Watanabe, M.; Ayugase, J. Effects of buckwheat sprouts on plasma and hepatic parameters in type 2 diabetic db/db mice. *J. Food Sci.* **2010**, *75*, H294−H299.
(171) Lee, J.; Bok, S.; Jeon, S.; Kim, H.; Do, K.; Park, Y.; Choi, M. Antihyperlipidemic effects of buckwheat leaf and flower in rats fed a high-fat diet. *Food Chem.* **2010**, *119*, 235−240.
(172) Bai, C. Z.; Feng, M. L.; Hao, X. L.; Zhao, Z. J.; Li, Y. Y.; Wang, Z. H. Anti-tumoral effects of a trypsin inhibitor derived from buckwheat *in vitro* and *in vivo*. *Mol. Med. Rep.* **2015**, *12*, 1777−1782.
(173) Park, S. S.; Ohba, H. Suppressive activity of protease inhibitors from buckwheat seeds against human T-acute lymphoblastic leukemia cell lines. *Appl. Biochem. Biotechnol.* **2004**, *117*, 65−74.
(174) Wang, Z. H.; Gao, L.; Li, Y. Y.; Zhang, Z.; Yuan, J. M.; Wang, H. W.; Zhang, L.; Zhu, L. Induction of apoptosis by buckwheat trypsin inhibitor in chronic myeloid leukemia K562 cells. *Biol. Pharm. Bull.* **2007**, *30*, 783−786.
(175) Zhang, Z.; Li, Y.; Li, C.; Yuan, J.; Wang, Z. Expression of a buckwheat trypsin inhibitor gene in *Escherichia coli* and its effect on multiple myeloma IM-9 cell proliferation. *Acta Biochim. Biophys. Sin.* **2007**, *39*, 701−707.
(176) Li, Y. Y.; Zhang, Z.; Wang, Z. H.; Wang, H. W.; Zhang, L.; Zhu, L. rBTI induces apoptosis in human solid tumor cell lines by loss in mitochondrial transmembrane potential and caspase activation. *Toxicol. Lett.* **2009**, *189*, 166−175.
(177) AArchimowicz-Cyrylowska, B.; Adamek, B.; Drozdzik, M.; Samochowiec, L.; Wojcicki, J. Clinical effect of buckwheat herb, *Ruscus* extract and troxerutin on retinopathy and lipids in diabetic patients. *Phytother. Res.* **1996**, *10*, 659−662.
(178) Ihme, N.; Kiesewetter, H.; Jung, F.; Hoffmann, K.; Birk, A.; Muller, A.; Grutzner, K. Leg oedema protection from a buckwheat herb tea in patients with chronic venous insufficiency: a single centre, randomised, double blind, placebo controlled clinical trial. *Eur. J. Clin. Pharmacol.* **1996**, *50*, 443−447.
(179) Takahama, U.; Tanaka, M.; Hirota, S. Proanthocyanidins in buckwheat flour can reduce salivary nitrite to nitric oxide in the stomach. *Plant Foods Hum. Nutr.* **2010**, *65*, 1−7.
(180) Wieslander, G.; Fabjan, N.; Vogrincic, M.; Kreft, I.; Vombergar, B.; Norback, D. Effects of common and tartary buckwheat consumption on mucosal symptoms, headache and tiredness: a double-blind crossover intervention study. *J. Food Agric. Environ.* **2012**, *10*, 107−110.
(181) Prestamo, G.; Pedrazuela, A.; Penas, E.; Lasuncion, M.; Arroyo, G. Role of buckwheat diet on rats as prebiotic and healthy food. *Nutr. Res. (N. Y.)* **2003**, *23*, 803−814.
(182) Kayashita, J.; Nagai, H.; Kato, N. Buckwheat protein extract suppression of the growth depression in rats induced by feeding amaranth (Food Red No. 2). *Biosci., Biotechnol., Biochem.* **1996**, *60*, 1530−1531.
(183) Alvarez, P.; Alvarado, C.; Mathieu, F.; Jimenez, L.; De la Fuente, M. Diet supplementation for 5 weeks with polyphenol-rich cereals improves several functions and the redox state of mouse leucocytes. *Eur. J. Nutr.* **2006**, *45*, 428−438.
(184) Alvarez, P.; Alvarado, C.; Puerto, M.; Schlumberger, A.; Jimenez, L.; De la Fuente, M. Improvement of leukocyte functions in prematurely aging mice after five weeks of diet supplementation with polyphenol-rich cereals. *Nutrition* **2006**, *22*, 913−921.
(185) Jin, H. M.; Wei, P. Anti-fatigue properties of tartary buckwheat extracts in mice. *Int. J. Mol. Sci.* **2011**, *12*, 4770−4780.
(186) Ranzato, E.; Martinotti, S.; Burlando, B. Epithelial mesenchymal transition traits in honey-driven keratinocyte wound healing: comparison among different honeys. *Wound Repair Regen.* **2012**, *20*, 778−785.
(187) Liu, J.; Wang, S.; Qi, J.; Wang, X.; Song, Y. The immunostimulatory effect of bio-active peptide from pollen on murine and human lymphocytes. *Mech. Ageing Dev.* **1998**, *104*, 125−132.

DOI: 10.1021/acs.jafc.5b02498
J. Agric. Food Chem. 2015, 63, 7896−7913

the cytotoxicities of the enantiomers for the first time using the 3-(4,5-dimethylthiazol-2-yl)-2,5-diphenyltetrazolium (MTT) method and flow cytometry. Interactions between the propisochlor enantiomers in the cytotoxicity tests were also studied using an isobologram and a combination index (CI). The interaction studies improved our understanding of the cytotoxicities of each of the enantiomers and allowed for the toxic effects caused by interactions between the enantiomers to be identified.

MATERIALS AND METHODS

Reagents. Racemic propisochlor [98%, 2-chloro-*N*-(isopropylmethyl)-*N*-(2-ethylmethyl-6-methyl)phenylacetamide], MTT, dimethyl sulfoxide, culture medium RPMI-1640, penicillin, and streptomycin were purchased from Sigma (St. Louis, MO). Fetal bovine serum was purchased from Hangzhou Sijiqing Biological Engineering Materials Co. (Hangzhou, China). An Annexin V-fluorescein isothiocyanate (FITC)/propidium iodide (PI) apoptosis detection kit and a 4′,6-diamidino-2-phenylindole (DAPI) staining kit were purchased from the Nanjing Jiancheng Bioengineering Institute (Nanjing, China). A Chiralpak AD-H column [150 mm long, 4.6 mm inner diameter, with an amylose tris(3,5-dimethylphenylcarbamate) stationary phase] was obtained from Daicel (Tokyo, Japan). Other solvents and chemicals were of chromatographic or analytical grade.

Separating Propisochlor Enantiomers by HPLC. The propisochlor enantiomers were separated using a Shimadzu LC-20A series HPLC system equipped with a LC-20AT intelligent gradient pump, a SPD-20A ultraviolet−visible (UV−vis) light absorbance detector, a CTO-10AS vp temperature-controlled column compartment, a SIL-20A automatic sampler, and a CMB-20A data collector (Shimadzu, Kyoto, Japan). A Chiralpak AD-H column, kept at 35 °C, was used in the HPLC system. The mobile phase was a 99:1 (by volume) mixture of *n*-hexane and isopropanol. The fractions containing the separated propisochlor enantiomers were collected automatically at the outlet and then evaporated to dryness under vacuum. The separate enantiomers obtained in this way were used in the subsequent experiments.

Cell Culture. SP2/0 cells were cultured in RPMI-1640 medium containing 10% (v/v) fetal bovine serum. Cells were incubated with different concentrations of *rac*-propisochlor, *R*-(+) isomer, and *S*-(−) isomer for 12, 24, or 48 h. Interactions between *R*-(+) and *S*-(−) isomers were identified by exposing cells to mixtures of the enantiomers at different ratios for 24 h. The cells were analyzed at the end of each test using the MTT assay.

Assessing Cell Viability. The enantioselective effects of propisochlor on SP2/0 cell viability were examined by assessing the growth of cells exposed to propisochlor using the MTT assay. Aliquots of the cells were taken, and the medium in each was replaced with medium containing 0, 10, 50, 100, 200, 400, 600, or 800 μM *rac*-propisochlor, *R*-(+) isomer, or *S*-(−) isomer. The cultures were then incubated for 12, 24, or 48 h, and then 20 μL of MTT (1 mg/mL) was added to each well. The plate was incubated at 37 °C for another 4 h. The cultured cells were then collected and centrifuged. The supernatant was discarded, and then 150 μL of dimethyl sulfoxide were added to each well. The cells were then shaken for 10 min, and the absorbance at 490 nm was measured using a 1420 multilabel counter (PerkinElmer, Waltham, MA). The experiments were carried out using 96-well plates, and four replicates of each test were performed. Cell viability was calculated using the equation

$$\text{cell viability (\% of control)} = \frac{\text{OD}_{490\text{ nm}} \text{ of the test wells}}{\text{OD}_{490\text{ nm}} \text{ of the control wells}} \times 100$$

where $\text{OD}_{490\text{ nm}}$ is the optical density at 490 nm.

The half maximal effective concentration (EC_{50}) values were calculated using nonlinear statistical regressions, performed using GraphPad Prism 5.0.1 software.[20] The result for each test is later expressed as the mean ± standard deviation of the four independent replicates of the test.

Annexin V-FITC/PI Double Staining. The Annexin V-FITC/PI double staining assay was used to determine the effect of propisochlor on apoptosis in the SP2/0 cells. Aliquots of the SP2/0 cells were taken, and each was treated with a 0, 10, 50, 100, or 200 μM solution of *rac*-propisochlor, *R*-(+) isomer, or *S*-(−) isomer for 24 h. The cells were then centrifuged at 1000 rpm for 10 min, and the supernatant solutions were discarded. The precipitated cells were then washed twice with phosphate-buffered saline, resuspended in 500 μL of binding buffer, and then stained with 5 μL of Annexin V-FITC and 5 μL of PI. The cells were then stored in the dark for 5−15 min at room temperature. The stained cells were then analyzed by flow cytometry using a Cytomics TMFC500 instrument (Beckman Coulter, Brea, CA). Four replicates of each test were performed. The result for each test is later expressed as the mean ± standard deviation of the four independent replicates of the test. Statistical analyses of the apoptosis ratios of the SP2/0 cells exposed to propisochlor were performed using SPSS 19.0 software (IBM, Armonk, NY).

Observing Changes in Cellular Morphology Induced by Propisochlor. Growing SP2/0 cells were allowed to adhere to glass plates. The SP2/0 cells on the glass plates were exposed to different concentrations of *rac*-propisochlor, *R*-(+) isomer, and *S*-(−) isomer for 24 h, and then the cells were harvested and fixed with 4% polyformaldehyde for 10 min and then washed 3 times with phosphate-buffered saline (PBS). One drop of DAPI staining solution was placed on each glass plate, and the plates were stored in the dark. The morphologies of the cells on the plates were observed, and photographs were taken using a fluorescence microscope (Nikon, Tokyo, Japan).

Interactions between Propisochlor Enantiomers. A 100 μL aliquot of the RPMI-1640 medium containing SP2/0 cells (giving 3×10^5 cells/well) was added to each well of a 96-well culture plate. To each well was added a 5:1, 3:1, 1:1, 1:3, or 1:5 mixture of *R*-(+) and *S*-(−) isomers of propisochlor to give a final total propisochlor concentration of 0, 10, 50, 100, 200, 400, 600, or 800 μM. The cells were then incubated for 24 h, and then cell viability was assessed as described in the "Assessing Cell Viability" subsection above.

Interactions between *R*-(+) and *S*-(−) isomers were identified using an isobologram and using CI values.[21−23] A normalized isobologram for *R*-(+) and *S*-(−) isomers at their EC_{50} values was constructed using OriginPro 8.5.1 software (OriginLab, Northampton, MA). Interactions between the isomers were identified from the positions of the EC_{50} values for the five isomer mixture compositions that were used in the normalized isobologram. The normalized isobologram was divided into three areas, representing synergism (area A), additive effects (area B), and antagonism (area C), as shown in Figure 6. The CI values were calculated using the formula

$$\text{CI} = \frac{a}{A} + \frac{b}{B}$$

where *A* and *B* are the concentrations of the separate enantiomers required to produce the same effect as the combination tested and *a* and *b* are the proportions of the two enantiomers in the combination tested.

A CI value less than 0.9 was taken to indicate synergism; a CI value higher than 1.1 was taken to indicate antagonism; and a CI value between 0.9 and 1.1 was taken to indicate additivity.

RESULTS

Chiral Resolution of the Enantiomers. Baseline separation between the two enantiomers in the *rac*-propisochlor was achieved using the Chiralpak AD-H column at 35 °C with a 99:1 (by volume) mixture of *n*-hexane and isopropanol mobile phase at a flow rate of 1 mL/min. A resolution of 2.41 was achieved, and the results are shown in Figure 2. The retention mechanism and the enantiomer selection at the temperature used were the same as we have found previously. We concluded that the propisochlor enantiomers were separated and isolated successfully. We have previously demonstrated that *R*-(+)

DOI: 10.1021/acs.jafc.5b03027
J. Agric. Food Chem. 2015, 63, 7914−7920

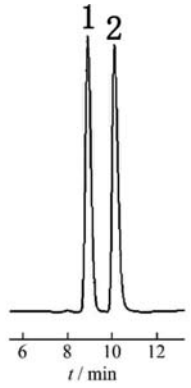

Figure 2. Chromatogram of propisochlor on the Chiralpak AD-H column with a mobile phase *n*-hexane/isopropanol (99:1, v/v), flow velocity of 1 mL/min, and column temperature at 35 °C. Peak 1 was *R*-(+) isomer enantiomer, and peak 2 was *S*-(−) isomer enantiomer.

isomer eluted first (peak 1) and *S*-(−) isomer eluted second (peak 2).

Enantioselective Cytotoxicity to SP2/0 Cells. SP2/0 cells were incubated with different concentrations of *rac*-propisochlor, *R*-(+) isomer, and *S*-(−) isomer for 12, 24, and 48 h. As shown in Figure 3 and Table 1, the cell viability decreased as the *rac*-propisochlor, *R*-(+) isomer, and *S*-(−) isomer concentrations increased. The EC_{50} values for *rac*-propisochlor, *R*-(+) isomer, and *S*-(−) isomer after 24 h of incubation were 111 ± 0.15, 68 ± 0.09, and 99 ± 0.21 μM, respectively. According to the EC_{50} values, the cytotoxicity to SP2/0 cells decreased in the order *R*-(+) isomer > *S*-(−) isomer > *rac*-propisochlor. The cells exposed to 200 μM propisochlor (as *rac*-propisochlor, *R*-(+) isomer, or *S*-(−) isomer) were 20% less viable than the control group cells after 24 h.

Apoptosis occurred in more than 70% of the cells treated with a propisochlor [as *rac*-propisochlor, *R*-(+) isomer, or *S*-(−) isomer] concentration higher than 50 μM, and apoptosis occurred in more cells treated with *R*-(+) isomer than with *rac*-propisochlor or *S*-(−) isomer, as shown in Figure 4. We concluded from the cell viability and apoptosis analyses that *R*-(+) isomer is more toxic than *rac*-propisochlor and *S*-(−) isomer to SP2/0 cells. The apoptosis ratios for the SP2/0 cells exposed to propisochlor were statistically analyzed using SPSS 19.0, and the results are shown in Figure 4, in which asterisks indicate significant differences ($p < 0.05$).

Changes in Cellular Morphology. Nuclear pyknosis is a reliable indicator of cell damage.[24] The nuclei of untreated SP2/0 cells were integrated and homogeneous, as seen in Figure 5D. The nuclei of cells exposed to 50 μM *rac*-propisochlor were similar to the nuclei of untreated cells, as seen in Figure 5A1. Pyknosis occurred in cells exposed to *rac*-propisochlor at concentrations higher than 50 μM (Figure 5A2). Pyknosis occurred in the nuclei of cells treated with *R*-(+) isomer at a concentration of 50 μM and cells treated with *S*-(−) isomer at a concentration of 200 μM, as seen in panels B and C of Figure 5. These results suggest that *rac*-propisochlor, *R*-(+) isomer, and *S*-(−) isomer may all affect the vitalities of and apoptosis in SP2/0 cells by affecting the cell nuclei.

Interactions between the Propisochlor Enantiomers. Interactions between the propisochlor enantiomers were investigated by analyzing the effects on the SP2/0 cells of combinations of *R*-(+) and *S*-(−) isomers at five different

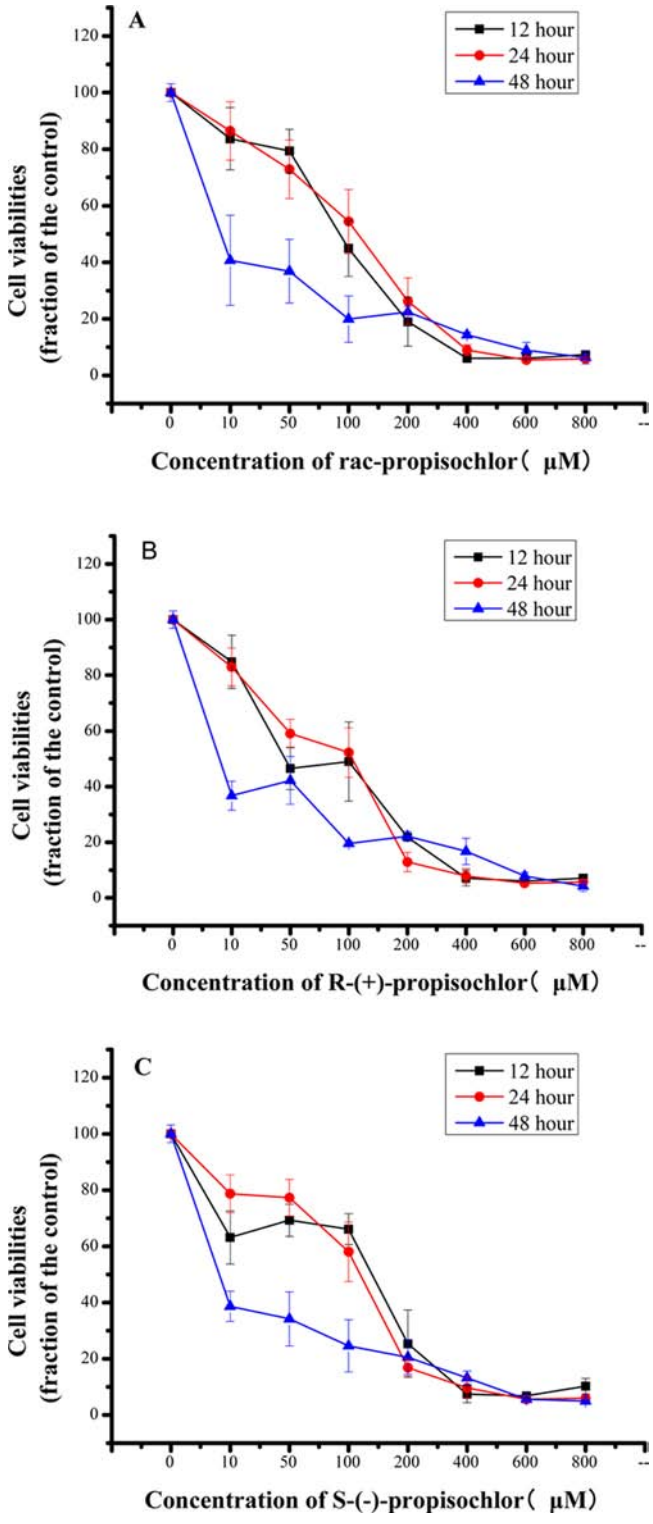

Figure 3. Effects of (A) *rac*-propisochlor, (B) *R*-(+) isomer, and (C) *S*-(−) isomer on the cell viabilities of SP2/0 were analyzed by the MTT assay after exposure to varying concentrations of propisochlor for 12, 24, or 48 h.

ratios. A dose−response curve and an EC_{50} value were produced for each combination. The results of the interaction analyses are shown in Figures 6 and 7, and the EC_{50} values are shown in Table 2. The CI values were less than 0.9 when the *R*-(+) to *S*-(−) isomer ratio was 5:1, 3:1, or 1:5, indicating that the enantiomers interacted synergistically. However, antago-

DOI: 10.1021/acs.jafc.5b03027
J. Agric. Food Chem. 2015, 63, 7914−7920

Table 1. EC_{50} Values of *rac*-Propisochlor, *R*-(+) Isomer, and *S*-(−) Isomer after Exposure to Varying Concentrations of Propisochlor for 24 h

propisochlor	EC_{50} (μM)	95% confidence intervals	coefficient of determination (R^2)
rac-propisochlor	111 ± 0.15	96.13−127.3	0.97
R-(+) isomer	68 ± 0.09	50.73−90.49	0.93
S-(−) isomer	99 ± 0.21	86.79−112.1	0.97

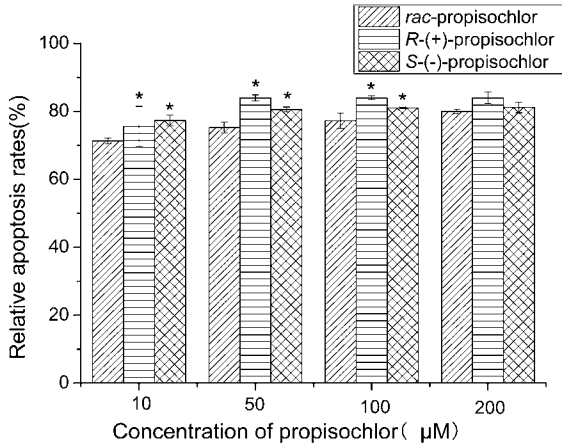

Figure 4. Apoptosis rates of SP2/0 after treated with propisochlor for 24 h. The apoptosis rates of SP2/0 cells were detected by flow cytometry after staining with Annexin V-FITC/PI. The apoptosis rates of SP2/0 after treating with *R*-(+) isomer were higher those of *rac*-propisochlor and *S*-(−) isomer. The asterisks represented significant difference ($p < 0.05$).

nistic interactions (CI > 1.1) were found when the *R*-(+) to *S*-(−) isomer ratio was 1:1 or 3:1. These results show that *R*-(+) and *S*-(−) isomers in *rac*-propisochlor could interact, resulting in less cytotoxicity occurring than if either was present alone.

DISCUSSION

We assessed the cytotoxicities of *rac*-propisochlor and both enantiomers. The EC_{50} values for *R*-(+) and *S*-(−) isomers, determined from the MTT analysis results, were 68 ± 0.09 and 99 ± 0.21 μM, respectively, as shown in Table 1. *R*-(+) isomer was found to be 1.46 times more cytotoxic than *S*-(−) isomer to the SP2/0 cells. As shown in Figure 3, the cytotoxicity increased more rapidly as the concentration of *R*-(+) isomer was increased from 0 to 400 μM than when the concentration of *S*-(−) isomer was increased from 0 to 400 μM. Less than 40% of the cells exposed to either enantiomer for 48 h remained viable, and as little as 20% of the cells remained viable at concentrations of 200 μM. Several studies focused on the enantioselective cytotoxicities of pesticides with asymmetric chiral centers have been performed, and these studies have shown that the enantiomers of chiral pesticides may have different biological activities both *in vitro* and *in vivo*.[25] Interestingly, our results showed that the cytotoxicity of the axial chiral herbicide propisochlor is also enantioselective, with *R*-(+) isomer being more toxic than *S*-(−) isomer to SP2/0 cells.

The differences between the cytotoxicities of the propisochlor enantiomers were investigated further by identifying differences between the abilities of the enantiomers to induce apoptosis in SP2/0 cells and changes in the cell nuclei. The relative amounts of apoptosis induced in SP2/0 cells by *rac*-

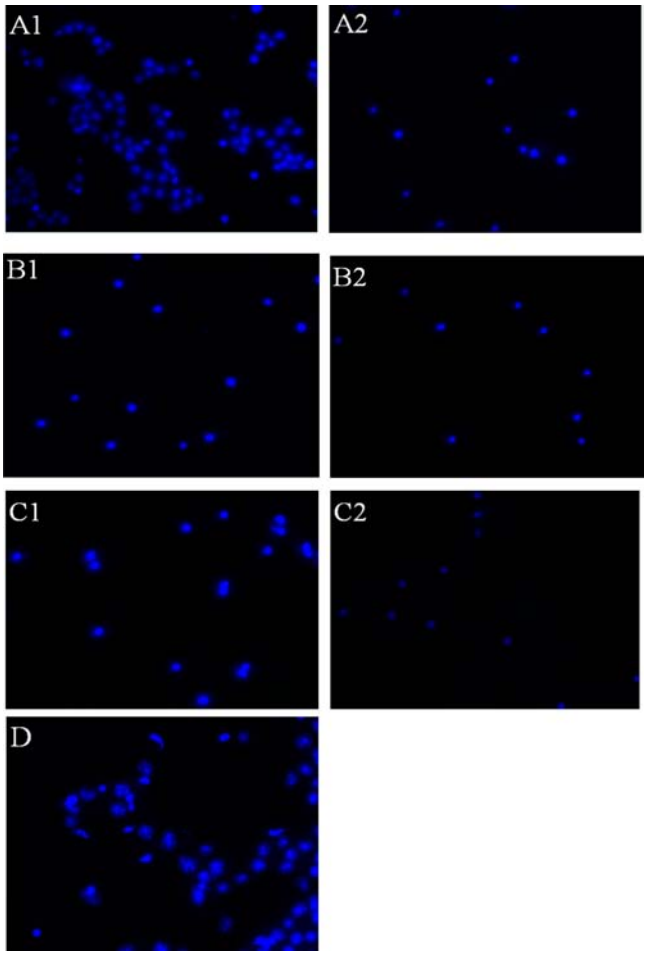

Figure 5. Cellular morphology change induced by different concentrations of propisochlor (400×): (A1 and A2) 50 and 200 μM *rac*-propisochlor, (B1 and B2) 50 and 200 μM *R*-(+) isomer, (C1 and C2) 50 and 200 μM *S*-(−) isomer, and (D) control group.

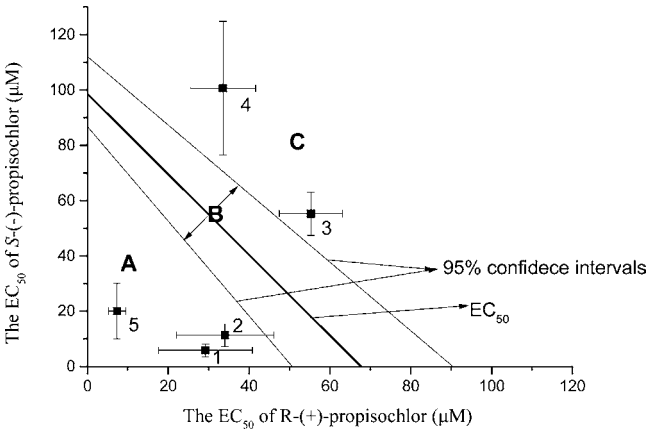

Figure 6. Normalized isobologram analyzes the interaction of the two propisochlor enantiomers. The numbers 1, 2, 3, 4, and 5 mean that the rates of *R*-(+) isomer and *S*-(−) isomer were 5:1, 3:1, 1:1, 1:3, and 1:5, respectively. The three areas of the normalized isobologram were, namely, A, B, and C, which represent synergism, additive, and antagonism, respectively. According to the positions of the five combinations, the positions of 1, 2, and 5 exhibit synergism, while the positions of 3 and 4 exhibit antagonism.

DOI: 10.1021/acs.jafc.5b03027
J. Agric. Food Chem. 2015, 63, 7914−7920

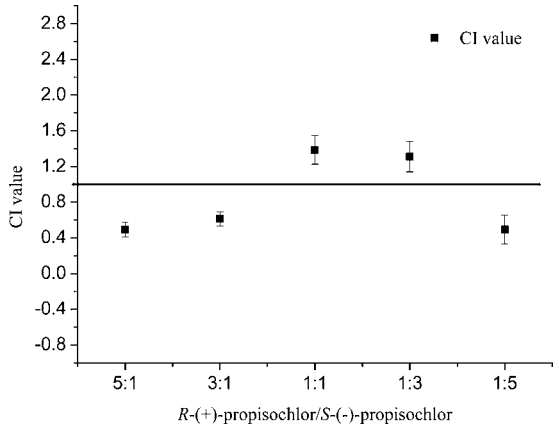

Figure 7. CI values of different rates of *R*-(+) isomer and *S*-(−) isomer. After exposure with different combinations of *R*-(+) isomer and *S*-(−) isomer (5:1, 3:1, 1:1, 1:3, and 1:5, respectively), the CI values were calculated by the formula showed as 2.7. CI values were less than 0.9, between 0.9 and 1.1, more than 1.1, which indicated synergy, additivity, and antagonism, respectively. When the ratio of *R*-(+) isomer and *S*-(−) isomer was 5:1, 3:1, and 1:5, the CI values indicated synergy. However, the CI values indicated antagonism when the ratio of *R*-(+) isomer and *S*-(−) isomer was 1:1 and 1:3.

Table 2. Interaction of Two Propisochlor Enantiomers

rates of *R*-(+) isomer and *S*-(−) isomer	EC_{50} (μM)	95% confidence intervals	coefficient of determination (R^2)	CI
1:0	67.75	50.73−90.49	0.93	
5:1	35.03	23.81−51.55	0.91	0.493 ± 0.08
3:1	45.40	32.04−64.31	0.91	0.614 ± 0.079
1:1	110.6	96.13−127.3	0.97	1.385 ± 0.16
1:3	134.2	105.7−170.3	0.92	1.31 ± 0.17
1:5	44.17	29.8−66.20	0.94	0.495 ± 0.16
0:1	98.64	86.79−112.1	0.97	

propisochlor and the separate enantiomers after 24 h of exposure are shown in Figure 4. The apoptosis rates were higher in the SP2/0 cells treated with *R*-(+) isomer than in the cells treated with *S*-(−) isomer. Changes in the cell nuclei were seen when the cells were exposed to *rac*-propisochlor, *R*-(+) isomer, and *S*-(−) isomer for 24 h. As seen in Figure 5A1, the amount of pyknosis that occurred in the cell nuclei increased as the concentration of *rac*-propisochlor or either isomer increased but similar amounts of pyknosis occurred in cells exposed to 50 μM *rac*-propisochlor and untreated cells. Various factors can influence cell vitality and apoptosis. In this study, *rac*-propisochlor and *R*-(+) and *S*-(−) isomers may have affected SP2/0 cell vitality and apoptosis by causing changes to occur in the cell nuclei.

The cytotoxic mechanisms of chiral pesticides have been described in previous publications.[26−32] Bifenthrin (BF) is a synthetic pyrethroid (SP). SPs are commonly used to control agricultural and indoor insect pests. It has been found that *cis*-BF can induce apoptosis through the enantioselective activation of the JNK/MAPK signaling pathway, causing changes in the control of intracellular reactive oxygen species (ROS) and allowing DNA damage to occur. SPs have also been found to be estrogenic endocrine-disrupting chemicals (EDCs). It has been shown that *S*-(+)-acetofenate (AF) is clearly more toxic than *R*-(−)-AF and *rac*-AF to macrophages and that *S*-(+)-AF induces the generation of intracellular ROS, causes DNA damage, and upregulates p53 gene expression.[6] Some chiral herbicides have been found to induce the generation of ROS, increase the malondialdehyde (MDA) concentration, increase superoxide dismutase (SOD) activity, and trigger toxin production.[28] Chiral pesticides and herbicides have been found to cause enantioselective ecotoxicological effects.[33−36] The effects of the chiral herbicide diclofop-methyl (DM) and its major metabolite diclofop acid (DA) on *Microcystis aeruginosa* have been studied, and *rac*-DA was found to be more toxic than DM, *R*-DA, and *S*-DA.[37] The results described above significantly improved our understanding of the cytotoxicities of pesticides with asymmetric chiral centers and the risks that they pose to ecological and human health. The enantioselective cytotoxicities of pesticides with asymmetric chiral axes have seldom been studied. We have shown here that the cytotoxicity of the axial chiral herbicide propisochlor is enantioselective, although we have not identified the specific toxic mechanisms involved.

The EC_{50} values showed that *rac*-propisochlor, *R*-(+) isomer, and *S*-(−) isomer had different cytotoxicities to SP2/0 cells; therefore, we supposed that a combination effect could have occurred when SP2/0 cells were exposed to both isomers simultaneously. We therefore used an isobologram and CI values to identify interactions between *R*-(+) and *S*-(−) isomers.[21,22] At least three types of interactions (synergism, additive, and antagonism) can occur between two different chemicals interacting with a cell line.[38] Analysis of our isobologram and our CI values showed that antagonism occurred when the *R*-(+) to *S*-(−) isomer ratio was 1:1 (Figures 6 and 7). To the best of our knowledge, this is the first time an interaction between *R*-(+) and *S*-(−) isomers of propisochlor has been found.

Propisochlor is an axial chiral herbicide with two enantiomers, *R*-(+) and *S*-(−) isomers. Propisochlor belongs to the chloroacetamide group of herbicides, which is the most widely used group of herbicides around the world. It has been shown in several studies that applying mixtures of different chloroacetamide herbicides markedly increases the effectiveness with which weeds are killed. Metolachlor is another chloroacetamide herbicide. Applying high doses of dimethenamid-p and *S*-metolachlor together has been found to cause transient injuries to but not to interfere with the maturities and yields of pinto and small red Mexican beans.[39] However, the effects of the co-exposure of non-target organisms to different herbicides and specific interactions between different herbicides have not previously been reported. In this study, we co-exposed SP2/0 cells to both propisochlor isomers and found that some *R*-(+) to *S*-(−) isomer ratios gave synergistic cytotoxic effects and other ratios gave antagonistic cytotoxic effects. A relatively environmentally benign herbicide must be a broad-spectrum herbicide, interfere little with the crops that it is applied to, and must have few toxic effects on non-target organisms. Mixtures of different herbicides, including with different isomer ratios, may prove to be useful treatments.

We investigated the cytotoxicities of *rac*-propisochlor and *R*-(+) and *S*-(−) isomers of propisochlor and the interactions between the two enantiomers for the first time. We found that *R*-(+) isomer is more toxic than *S*-(−) isomer and *rac*-propisochlor. The apoptosis rates that we found showed that *R*-(+) and *S*-(−) isomers may have different biological activities. More importantly, we found that *R*-(+) and *S*-(−) isomers can interact antagonistically, meaning that *rac*-propisochlor is less cytotoxic than either enantiomer. Our results suggest that interactions between enantiomers should be considered when

DOI: 10.1021/acs.jafc.5b03027
J. Agric. Food Chem. 2015, 63, 7914−7920

developing and using chiral pesticides and that this may result in a decrease in pesticide application rates and reduced harm to the environment.

AUTHOR INFORMATION

Corresponding Authors

*E-mail: hzzhoulj@126.com.
*E-mail: ymsun@scau.edu.cn.
*Telephone: +86-20-8528-3448. Fax: +86-20-8528-0270. E-mail: hongtao@scau.edu.cn.

Funding

This work was supported by Guangdong Natural Science Foundation (S2013030013338), Natural Science Foundation of China (U1301214), Guangdong Planed Program in Science and Technology (2013B051000072, 2014TX01N250, 2012A020100002), and National Basic Research Program of China (973 Program, 2012CB720803).

Notes

The authors declare no competing financial interest.

ABBREVIATIONS USED

HPLC, high-performance liquid chromatography; MTT, 3-(4,5-dimethylthiazol-2-yl)-2,5-diphenyltetrazolium; EC_{50}, half maximal effective concentration; CI, combination index; BF, bifenthrin; SP, synthetic pyrethroid; EDC, endocrine-disrupting chemical; AF, acetofenate; ROS, reactive oxygen species; MDA, malondialdehyde; SOD, superoxide dismutase; DM, diclofop-methyl; DA, diclofop acid

REFERENCES

(1) Nillos, M. G.; Gan, J.; Schlenk, D. Chirality of organophosphorus pesticides: analysis and toxicity. *J. Chromatogr. B: Anal. Technol. Biomed. Life Sci.* **2010**, *878*, 1277−1284.

(2) Ulrich, E. M.; Morrison, C. N.; Goldsmith, M. R.; Foreman, W. T. Chiral pesticides: identification, description, and environmental implications. *Rev. Environ. Contamt.* **2012**, *217*, 1−74.

(3) Leone, A. D.; Amato, S.; Falconer, R. L. Emission of chiral organochlorine pesticides from agricultural soils in the cornbelt region of the U.S. *Environ. Sci. Technol.* **2001**, *35*, 4592−4596.

(4) Kurt-Karakus, P. B.; Bidleman, T. F.; Jones, K. C. Chiral organochlorine pesticide signatures in global background soils. *Environ. Sci. Technol.* **2005**, *39*, 8671−8677.

(5) Zhao, M.; Wang, C.; Zhang, C.; Wen, Y.; Liu, W. Enantioselective cytotoxicity profile of o,p′-DDT in PC 12 cells. *PLoS One* **2012**, *7*, e43823.

(6) Zhao, M.; Liu, W. Enantioselectivity in the immunotoxicity of the insecticide acetofenate in an in vitro model. *Environ. Toxicol. Chem.* **2009**, *28*, 578−585.

(7) Mai, H.; Morin, B.; Pardon, P.; Gonzalez, P.; Budzinski, H.; Cachot, J. Environmental concentrations of irgarol, diuron and S-metolachlor induce deleterious effects on gametes and embryos of the Pacific oyster, Crassostrea gigas. *Mar. Environ. Res.* **2013**, *89*, 1−8.

(8) Hladik, M. L.; Bouwer, E. J.; Roberts, A. L. Neutral chloroacetamide herbicide degradates and related compounds in Midwestern United States drinking water sources. *Sci. Total Environ.* **2008**, *390*, 155−165.

(9) Zhang, J.; Zheng, J. W.; Liang, B.; Wang, C. H.; Cai, S.; Ni, Y. Y.; He, J.; Li, S. P. Biodegradation of chloroacetamide herbicides by Paracoccus sp. FLY-8 in vitro. *J. Agric. Food Chem.* **2011**, *59*, 4614−4621.

(10) Park, S. G.; Jin, H.; Thangadurai, D. T.; Yoo, Y. J.; Lee, Y. I. Detoxification of cytotoxic alachlor by glutathione: characterization of conjugated adducts by electrospray ionization tandem mass spectrometry. *J. Agric. Food Chem.* **2009**, *57*, 9838−9847.

(11) Bernasinska, J.; Duchnowicz, P.; Koter-Michalak, M.; Koceva-Chyla, A. Effect of safeners on damage of human erythrocytes treated with chloroacetamide herbicides. *Environ. Toxicol. Pharmacol.* **2013**, *36*, 368−377.

(12) Pereira, S. P.; Fernandes, M. A.; Martins, J. D.; Santos, M. S.; Moreno, A. J.; Vicente, J. A.; Videira, R. A.; Jurado, A. S. Toxicity assessment of the herbicide metolachlor comparative effects on bacterial and mitochondrial model systems. *Toxicol. In Vitro* **2009**, *23*, 1585−1590.

(13) Coleman, S.; Linderman, R.; Hodgson, E.; Rose, R. L. Comparative metabolism of chloroacetamide herbicides and selected metabolites in human and rat liver microsomes. *Environ. Health Perspect.* **2000**, *108*, 1151−1157.

(14) Souissi, Y.; Bouchonnet, S.; Bourcier, S.; Kusk, K. O.; Sablier, M.; Andersen, H. R. Identification and ecotoxicity of degradation products of chloroacetamide herbicides from UV-treatment of water. *Sci. Total Environ.* **2013**, *458*−*460*, 527−534.

(15) Rauch, R.; Foldenyi, R. The effect of alginite on the decomposition of the herbicide propisochlor. *J. Environ. Sci. Health, Part B* **2012**, *47*, 670−676.

(16) Hu, J. Y.; Zhen, Z. H.; Deng, Z. B. Simultaneous determination of acetochlor and propisochlor residues in corn and soil by solid phase extraction and gas chromatography with electron capture detection. *Bull. Environ. Contam. Toxicol.* **2011**, *86*, 95−100.

(17) Hu, X.; Dai, G.; Huang, J.; Ye, T.; Fan, H.; Youwen, T.; Yu, Y.; Liang, Y. Molecularly imprinted polymer coated on stainless steel fiber for solid-phase microextraction of chloroacetanilide herbicides in soybean and corn. *J. Chromatogr. A* **2010**, *1217*, 5875−5882.

(18) Huang, Q.; Li, F.; Wang, M.; Wang, Y.; Gu, Q.; Wang, Q. Photolysis behavior of herbicide propisochlor in water media and preliminary analysis of photoproducts under different light sources. *J. Environ. Sci. Health, Part B* **2006**, *41*, 253−267.

(19) Konda, L. N.; Pasztor, Z. Environmental distribution of acetochlor, atrazine, chlorpyrifos, and propisochlor under field conditions. *J. Agric. Food Chem.* **2001**, *49*, 3859−3863.

(20) Xu, X.; Jiang, J.; Wang, X.; Shen, Z.; Li, R.; Zhou, Z. Stereoselective metabolism and toxicity of the herbicide fluroxypyr methylheptyl ester in rat hepatocytes. *Chirality* **2011**, *23*, 860−866.

(21) Chou, T. C.; Talalay, P. Quantitative analysis of dose-effect relationships: the combined effects of multiple drugs or enzyme inhibitors. *Adv. Enzyme Regul.* **1984**, *22*, 27−55.

(22) Tsakalozou, E.; Eckman, A. M.; Bae, Y. Combination effects of docetaxel and Doxorubicin in hormone-refractory prostate cancer cells. *Biochem. Res. Int.* **2012**, *2012*, 1−10.

(23) Park, S. O.; Yoo, Y. B.; Kim, Y. H.; Baek, K. J.; Yang, J. H.; Choi, P. C.; Lee, J. H.; Lee, K. R.; Park, K. S. Effects of combination therapy of docetaxel with selenium on the human breast cancer cell lines MDA-MB-231 and MCF-7. *Ann. Surg. Treat. Res.* **2015**, *88*, 55−62.

(24) Wohlan, K.; Goy, S.; Olling, A.; Srivaratharajan, S.; Tatge, H.; Genth, H.; Gerhard, R. Pyknotic cell death induced by Clostridium difficile TcdB: chromatin condensation and nuclear blister are induced independently of the glucosyltransferase activity. *Cell. Microbiol.* **2014**, *16*, 1678−1692.

(25) Liu, H.; Zhao, M.; Zhang, C.; Ma, Y.; Liu, W. Enantioselective cytotoxicity of the insecticide bifenthrin on a human amnion epithelial (FL) cell line. *Toxicology* **2008**, *253*, 89−96.

(26) Hu, F.; Li, L.; Wang, C.; Zhang, Q.; Zhang, X.; Zhao, M. Enantioselective induction of oxidative stress by permethrin in rat adrenal pheochromocytoma (PC12) cells. *Environ. Toxicol. Chem.* **2010**, *29*, 683−690.

(27) Liu, H. J.; Cai, W. D.; Huang, R. N.; Xia, H. L.; Wen, Y. Z. Enantioselective toxicity of metolachlor to Scenedesmus obliquus in the presence of cyclodextrins. *Chirality* **2012**, *24*, 181−187.

(28) Wen, Y.; Li, C.; Fang, Z.; Zhuang, S.; Liu, W. Elucidation of the enantioselective enzymatic hydrolysis of chiral herbicide dichlorprop methyl by chemical modification. *J. Agric. Food Chem.* **2011**, *59*, 1924−1930.

(29) Ye, J.; Zhang, Y.; Chen, S.; Liu, C.; Zhu, Y.; Liu, W. Enantioselective changes in oxidative stress and toxin release in

DOI: 10.1021/acs.jafc.5b03027
J. Agric. Food Chem. 2015, 63, 7914−7920

Microcystis aeruginosa exposed to chiral herbicide diclofop acid. *Aquat. Toxicol.* **2014**, *146*, 12−19.
(30) Wang, C.; Li, Z.; Zhang, Q.; Zhao, M.; Liu, W. Enantioselective induction of cytotoxicity by o,p′-DDD in PC12 cells: implications of chirality in risk assessment of POPs metabolites. *Environ. Sci. Technol.* **2013**, *47*, 3909−3917.
(31) Boerth, D. W.; Eder, E.; Stanks, J. R.; Wanek, P.; Wacker, M.; Gaulitz, S.; Skypeck, D.; Pandolfo, D.; Yashin, M. DNA adducts as biomarkers for oxidative and genotoxic stress from pesticides in crop plants. *J. Agric. Food Chem.* **2008**, *56*, 6751−6760.
(32) de Oliveira, J. L.; Campos, E. V.; Goncalves da Silva, C. M.; Pasquoto, T.; Lima, R.; Fraceto, L. F. Solid lipid nanoparticles co-loaded with simazine and atrazine: preparation, characterization, and evaluation of herbicidal activity. *J. Agric. Food Chem.* **2015**, *63*, 422−432.
(33) Jarman, J. L.; Jones, W. J.; Howell, L. A.; Garrison, A. W. Application of capillary electrophoresis to study the enantioselective transformation of five chiral pesticides in aerobic soil slurries. *J. Agric. Food Chem.* **2005**, *53*, 6175−6182.
(34) Cai, X.; Liu, W.; Sheng, G. Enantioselective degradation and ecotoxicity of the chiral herbicide diclofop in three freshwater alga cultures. *J. Agric. Food Chem.* **2008**, *56*, 2139−2146.
(35) Bidleman, T. F.; Leone, A. D.; Falconer, R. L.; Harner, T.; Jantunen, L. M.; Wiberg, K.; Helm, P. A.; Diamond, M. L.; Loo, B. Chiral pesticides in soil and water and exchange with the atmosphere. *Sci. World J.* **2002**, *2*, 357−373.
(36) Celis, R.; Gamiz, B.; Adelino, M. A.; Hermosin, M. C.; Cornejo, J. Environmental behavior of the enantiomers of the chiral fungicide metalaxyl in Mediterranean agricultural soils. *Sci. Total Environ.* **2013**, *444*, 288−297.
(37) Ye, J.; Wang, L.; Zhang, Z.; Liu, W. Enantioselective physiological effects of the herbicide diclofop on cyanobacterium Microcystis aeruginosa. *Environ. Sci. Technol.* **2013**, *47*, 3893−3901.
(38) Wang, H. W.; Wang, J. Q.; Zheng, B. Q.; Li, S. L.; Zhang, Y. D.; Li, F. D.; Zheng, N. Cytotoxicity induced by ochratoxin A, zearalenone, and alpha-zearalenol: effects of individual and combined treatment. *Food Chem. Toxicol.* **2014**, *71*, 217−224.
(39) Sikkema, P. H.; Robinson, D. E.; Nurse, R. E.; Soltani, N. Pre-emergence herbicides for potential use in pinto and small red mexican bean (Phaseolus vulgaris) production. *Crop Prot.* **2008**, *27*, 124−129.

DOI: 10.1021/acs.jafc.5b03027
J. Agric. Food Chem. 2015, 63, 7914−7920

practical to use cancer chemopreventive agents such as D3T as feed additives. In addition to these limitations, bans by European countries on the use of synthetic antioxidants due to their side effects in livestock feed have made natural plant-derived antioxidant compounds increasingly attractive as feed additives. The use of abundant plant-derived antioxidants such as tea catechins (TCs) is feasible due to lower costs and strong antioxidant properties, provided their effectiveness can be demonstrated in these animals. TCs are known to positively regulate the expression of antioxidant enzymes and to scavenge reactive oxygen species.[8] Similar to D3T, TCs have been reported to exert antioxidant activity through the Nrf2−Keap1 signaling pathway in humans.[9] Several studies have reported that TCs have potent antioxidant properties against oxidative stress in vivo and in vitro[10] and that TCs improved meat quality by decreasing lipid oxidation, enhancing meat color stability, and changing fatty acid composition in goat meat.[11,12] The partial gene sequence of goat Keap1 has been cloned in our laboratory (GenBank KF038327.1), demonstrating the presence of this antioxidant system. However, functional studies are needed to reveal whether TCs can afford protection to goat muscle tissue against oxidative stress through modulation of Keap1 and induce phase 2 antioxidant enzyme expression, subsequently improving meat quality.

The objectives of this study were (1) to study the effectiveness of TCs against oxidative stress in goat skeletal muscle cells (SMCs) through modulation of Keap1-mediated phase 2 antioxidant enzyme expression compared with a known enzyme inducer in vitro and (2) to determine whether the above mechanisms function to improve oxidative health and meat quality in live goats when TCs are administered as a dietary supplement in vivo.

MATERIALS AND METHODS

Chemicals. All chemicals, cell culture reagents, and D3T were obtained from Sigma Chemical Co. (St. Louis, MO, USA) unless otherwise stated. Primary antibodies were purchased from Abcam Co. (San Francisco, CA, USA). Secondary antibodies and all Western blot reagents were ordered from KenGen Co. (Nanjing, China).

TC Preparement. The TCs (purity of 80.11%) were extracted from green tea leaves (*Camellia sinensis* L.) by high-pressure liquid chromatography (Waster 600, Waters Corp., Milford, MA, USA) and contained 57.67% (−)-epigallocatechin gallate, 1.61% (+)-catechin and (−)-catechin, 5.77% (−)-epicatechin, 0.47% (−)-epigallocatechin, 13.03% (−)-epicatechin gallate, and 1.56% (−)-gallocatechin gallate. In addition, the extracted mixture contained caffeine.

In Vitro Experimental Procedures. The use of the animals and the experimental procedures were approved by the Animal Care Committee, College of Animal Science and Technology, Jilin Agricultural University, Changchun, Jilin, China.

Isolation, Cell Culture, and Treatment. One male early weaned Boer goat at the age of 4 weeks was electrically stunned and slaughtered by exsanguination using commercial procedures conducted according to the recommendations of the animal ethics committee at the Jilin Agricultural University. The *longissimus dorsi* (LD) muscle was collected for cell culture. The procedures of LD muscle collection and the primary SMC isolation and culture were the same as described in Zhong et al.[8] Briefly, the isolated SMCs were seeded in 60 flasks (25 cm^2) at a density of 3×10^6 cells/mL and in two 96-well plates at a density of 2.5×10^5 cells/mL in Dulbecco's modified Eagle's medium (DMEM; Gibco BRL, Gaithersburg, MD, USA) supplemented with 10% heat-inactivated fetal calf serum, 100 U of penicillin−streptomycin/mL, and 5 μg/mL gentamicin. The cells were cultured at 37 °C in a humidified atmosphere of 5% CO_2.

After 24 h of culture, cells in flasks and plates were assigned to one of five treatments, and each treatment was replicated six times. The five treatments were defined as H_2O_2-induced as control (H_2O_2), H_2O_2-induced + D3T incubation (H_2O_2D3T), H_2O_2-induced + TC incubation (H_2O_2TC), D3T incubation (D3T), and TCs incubation (TC) groups, respectively. Briefly, cells in all H_2O_2-induced groups were preincubated with 1 mM H_2O_2 for 3 h. Then, cells in H_2O_2D3T, H_2O_2TC, D3T, and TC groups were subsequently treated with 50 μmol/L D3T, 2.5 μg/mL TC, 50 μmol/L D3T, and 2.5 μg/mL TCs, respectively, according to the concentrations recommended by Zhong et al. and Cao et al.[8,13] Cells were harvested at 45 h postincubation with D3T or TCs. Media from each treatment in two 96-well plates were collected to analyze cell membrane integrity. Cells in 30 flasks (6 flasks per treatment) were disrupted in media and centrifuged, and then the supernatant was used to analyze enzyme activities.[15] Cells in the other 30 flasks (6 flasks per treatment) were collected by centrifugation to analyze enzyme mRNA and protein expression levels.

Cell membrane integrity was determined by the presence of lactate dehydrogenase (LDH) in the growth media and was measured using an in vitro LDH activity assay kit (Jiancheng Biology Co., Nanjing, China). Catalase (CAT) activity in the SMC homogenates was assayed using the spectrophotometric method of Aebi,[14] in which the disappearance of H_2O_2 in a phosphate buffer is detected at 240 nm. The activity of CuZn-SOD in the SMC homogenates was assayed by monitoring the inhibition of the rate of xanthine oxidase-mediated reduction of cytochrome *c* as described by Spitz and Oberley.[15] The GPx activity in the SMC homogenates was measured spectrophotometrically according to the method of Levander et al.[16] The activity of NQO1 in cells was measured according to method of Prochaska and Santamaria[17] and expressed as nanomoles of 3-[4,5-dimethylthiazol-2-yl]-2,5-diphenyl tetrazolium bromide (MTT) reduced per minute per milligram of protein. The activity of total GST was measured using 1-chloro-2,4-dinitrobenzene as the substrate and expressed as milliunits of conjugate formed per milligram of protein (1 mU = 1 nmol of conjugate formed/min).[18]

RNA Isolation, cDNA Synthesis, and Real-Time Quantitative RT-PCR. Oligonucleotide primers of CAT, CuZn-SOD, GPx, GST, NQO1, Keap1, and β-actin genes were designed using Premier 5 software (Premier Co., Canada). The details of the oligonucleotide primer sequences, primer lengths, and predicted amplified product lengths are listed in Table 1. The procedures of total RNA isolation, cDNA synthesis, and real-time qRT-PCR for CAT, CuZn-SOD, GPx, NQO1, GST, and Keap1 expressions are performed according to methods of Zhong et al.[8] Changes in mRNA expression levels determined by real-time qRT-PCR were calculated according to the $2^{-\Delta\Delta CT}$ method.[19]

Western Blot Analysis. Total proteins in SMCs were extracted using a commercial kit (KEP210, KeyGEN Biotech, Nanjing, China), and total protein content was measured according to the method of Lowry et al.[20] The extracted proteins were denatured, separated by reducing 10% sodium dodecyl sulfate−polyacrylamide gel electrophoresis gel (Bio-Rad, Hercules, CA, USA), transferred onto polyvinylidene fluoride membranes (Millipore, Bedford, MA, USA), and incubated with CAT, CuZn-SOD, GPX, NQO1, GST, Keap1, and β-actin primary antibodies (Abcam Co., ab50434, ab62800, ab50434, ab166778, ab150000, ab166958, and ab15263) at concentrations of 3.0, 0.02, 2.0, 0.5, 1.0, 1.0, and 2 μg/mL. Subsequently, the protein affinity with primary antibodies was tested by horseradish peroxidase conjugated secondary antibodies for 2.5 h at 4 °C. The intensity of each protein was determined by enhanced chemiluminescence reagent (GE Healthcare, Waukesha, WI, USA) and visualized by exposure to Hyperfilm ECL (GE Healthcare). β-Actin served as an internal control. The relative expressions of proteins were expressed as the ratio of band intensities of proteins to β-actin.

In Vivo Experimental Procedures. *Animals and Treatment.* Thirty male early weaned Boer goats, aged 4 weeks and with initial body weights (BW) averaging 15.8 ± 0.7 kg, were randomly assigned to one of five groups (n = 6 goats/group) according to their BWs for a feeding period of 21 days. The five treatments consisted of (1) H_2O_2-infused group (H_2O_2), (2) H_2O_2-infused and fed 0.5 mmol/kg of BW D3T (H_2O_2D3T), (3) H_2O_2-infused and fed 0.5% of TCs (dry matter (DM) basis of feed) (H_2O_2TC), (4) fed 0.5 mmol/kg of BW D3T

DOI: 10.1021/acs.jafc.5b00816
J. Agric. Food Chem. 2015, 63, 7921−7928

Table 1. Sequences of Primers, Lengths of Primers, and Size of Quantitative RT-PCR Products

target gene[a]	primers (5′→ 3′)	primer size (bp)	product size (bp)
CAT, forward	TGGGACCCAACTATCTCCAG	20	178
CAT, reverse	AAGTGGGTCCTGTGTTCCAG	20	
CuZn-SOD, forward	TGCAGGCCCTCACTTTAATC	20	207
CuZn-SOD, reverse	CTGCCCAAGTCATCTGGTTT	20	
GPx, forward	ACATTGAAACCCTGCTGTCC	20	216
GPx, reverse	TCATGAGGAGCTGTGGTCTG	20	
GSTA2, forward	AAGAGGCGGAGTTAGTCG	18	290
GSTA2, reverse	GGCACTTGCTGGAACATC	18	
NQO1, forward	CAGGGCAACCAGCAGACCA	19	253
NQO1, reverse	AGATGACGGGATTGAAGT	18	
Keap1, forward	CATTGAGTTCGCCTACACCG	20	271
Keap1, reverse	GCAGTGGGACAGGTTGAAGAA	21	
β-actin, forward	CCAACCGTGAGAAGATGACC	20	201
β-actin, reverse	CGCTCCGTGAGAATCTTCAT	20	

[a]Keap1, Kelch-like ECH-associated protein 1; CuZn-SOD, CuZn superoxide dismutase; GPx, glutathione peroxidase; CAT, catalase; GSTA2, glutathione *S*-transferase A2; NQO1, NADPH:quinine oxidoreductase.

(D3T) without H_2O_2 infusion, and (5) fed 0.5% of TCs (TC) without H_2O_2 infusion. Goats in the stressed control were fed the basal diet (30% *Aneurolepidium chinense*, 47.5% ground corn grain, 15.0% solid soybean meal, 5.0% molasses, 1.0% dicalcium phosphate, 0.5% limestone, and 1.0% trace mineral salt and vitamins for ruminants) formulated according to the NRC.[21] Goats in the other experimental groups were fed the same basal diet and supplemented with D3T or TCs.

Each goat was assigned to a single metabolism cage in the same environmentally controlled bard barn at 25 °C, with free access to fresh water. The experimental diets were prepared every day by mixing D3T or TC powder with the basal diet before morning and afternoon feeding. Goats were fed twice daily at 6:00 a.m.and 6:00 p.m. The feed supply and orts for each goat were recorded daily. From days 0 to 21, goats in stressed groups were continuously infused a total amount of 50 μmol/g BW H_2O_2 into the jugular vein for 1 h at 5:00 a.m. to induce oxidative stress according to the procedure of Lee et al.[22] Goats in unstressed groups were subjected to the same infusion with saline as the goats in stressed groups. After 21 days of feeding period, all goats were humanely slaughtered and samples collected.

Sampling and Analytical Procedures. At days 0, 7, 14, and 21, blood samples (7 mL) were taken from the jugular vein of each goat before the morning feeding and H_2O_2 infusion and centrifuged at 2500*g* for 15 min at 4 °C to harvest plasma for biochemical indices and enzyme activity determination. The total protein, albumin, globulin, total cholesterol, high-density lipoprotein cholesterol (HDL-C), low-density lipoprotein cholesterol (LDL-C), triglyceride, and urea nitrogen (PUN) concentrations in plasma were measured using an automated biochemical analyzer (Hitachi, 7020, Beijing, China) and commercial kits (Jiancheng Biology Co., Nanjing, China). The activity of lipoprotein lipase (LPL) was determined according to method of Karpe et al.[23] The activities of CAT, CuZn-SOD, GPx, and GST in plasma were determined using the methods described above for cell lysates.

After 21 days, all goats were electrically stunned and slaughtered by exsanguination using procedures accepted by the animal ethics committee at the Jilin Agricultural University. After slaughter, the carcasses were allowed to bleed until they were drained, after which the left side of the carcass was kept under aseptic conditions at 4 °C for sampling. The left LD muscle (10 g) from the same region of each animal was removed and snap-frozen at −70 °C for determination of Keap1 protein expression according to the method of Kavitha et al.[24] Another 200 g of the left LD muscle from the same region of each animal was sampled at 24 h post-mortem for determination of meat quality parameters. Briefly, the pH value of the LD samples was

Table 2. Effects of Tea Catechins (TCs) and D3T Incubation on Enzyme Activities and mRNA Expression Levels in H_2O_2–Induced Skeletal Muscle Cells of Goats

parameter[b]	treatment[a]					*P* value
	H_2O_2	$H_2O_2D_3T$	H_2O_2TC	D3T	TC	
Activity of Phase 2 Enzymes						
CAT (U/mg protein)	6.68 ± 1.29b	8.10 ± 0.95a	7.46 ± 1.07ab	3.62 ± 1.13c	2.97 ± 0.37c	<0.001
CuZn-SOD (U/mg protein)	14.7 ± 0.91c	20.2 ± 1.24b	19.1 ± 1.91b	24.2 ± 2.39a	26.4 ± 2.21a	<0.001
GPx (U/mg protein)	2.62 ± 0.26c	5.03 ± 0.75b	4.24 ± 0.73b	12.4 ± 2.37a	2.56 ± 0.56c	<0.001
GST (mU/mg protein)	49.7 ± 1.79c	67.4 ± 2.01a	61.8 ± 2.26b	45.5 ± 8.80cd	42.1 ± 1.85d	<0.001
NQO1 (nmol MTT2 reduced/min/mg protein)	23.2 ± 2.18e	48.5 ± 1.14c	42.8 ± 2.63d	78.0 ± 6.15a	64.5 ± 1.09b	<0.001
LDH (U/L)	9.54 ± 0.65a	5.99 ± 0.47c	7.51 ± 0.39b	3.40 ± 0.44e	4.94 ± 0.26d	<0.001
Expression of Phase 2 Enzymes (mRNA)[c]						
CAT	1.00 ± 0.00d	2.03 ± 0.20a	1.47 ± 0.11b	1.02 ± 0.13d	1.20 ± 0.10c	<0.001
CuZn-SOD	1.00 ± 0.00d	4.85 ± 0.14a	3.63 ± 0.50b	2.28 ± 0.45c	1.12 ± 0.10d	<0.001
GPx	1.00 ± 0.00d	1.66 ± 0.19c	0.49 ± 0.09d	3.61 ± 1.03b	6.18 ± 0.14a	<0.001
GSTA2	1.00 ± 0.00c	5.93 ± 0.31b	9.07 ± 1.52a	5.46 ± 0.68b	5.45 ± 0.68b	<0.001
NQO1	1.00 ± 0.00d	10.8 ± 0.98b	14.8 ± 0.91a	0.69 ± 0.13d	3.79 ± 1.02c	<0.001
Keap1	1.00 ± 0.00b	1.02 ± 0.19b	1.06 ± 0.13b	1.28 ± 0.22a	1.30 ± 0.12a	0.002

[a]Mean values with different letters in the same row differ significantly ($P < 0.05$). [b]CAT, catalase; CuZn-SOD, CuZn superoxide dismutase; GPx, glutathione peroxidase; GST, glutathione *S*-transferase; NQO1, NADPH:quinine oxidoreductase; LDH, lactate dehydrogenase; Keap1, Kelch-like ECH-associated protein 1. [c]mRNA expression levels were calculated according to the $2^{-\Delta\Delta CT}$ method.[25]

DOI: 10.1021/acs.jafc.5b00816
J. Agric. Food Chem. 2015, 63, 7921−7928

measured using a portable pH-meter (Testo 205, Testo AG, Lenzkirch, Germany) with a plastic body, a spear-tipped probe coupled with a temperature probe. Shear force analysis was conducted using a Warner-Bratzler shear device (C-LM3B, Beijing, China). The lipid oxidation levels of the LD samples were measured using the 2-thiobarbituric acid reactive substance (TBARS) method modified as described by Olsvik et al.[25] The intramuscular fat content of the LD samples was determined using the methods of ether extraction on a Sohxtex.[26] The total heme pigment content was determined according to the methods of Zhong et al.[11] In addition, a Minolta color-meter (model CR410, Minolta Camera Co. Ltd., Osaka, Japan) was used to measure the meat color parameters of lightness (L^*), redness (a^*), and yellowness (b^*).

Statistical Analyses. Data from the analysis of gene and protein expression levels and enzyme activities in cells and meat quality parameters were analyzed using a General Linear Model followed by Duncan's multiple-range tests.[27] The data from the blood metabolite measurements were analyzed with SAS[27] using the MIXED model procedure described by Littell et al.,[28] with a model consisting of dietary treatment, sampling time, and treatment × time interaction as fixed effects and with the animal as the random effect. The measurements obtained from each goat at different sampling times were treated as repeated measures for each blood metabolite measurement. The means were separated using the least-squares mean and are presented with the standard error of the mean (SEM). The results were considered statistically significant at $P \leq 0.05$.

RESULTS

Treatment of goat SMCs with D3T or TCs affected phase 2 antioxidant enzyme activities (Table 2). However, effects were different between H_2O_2-induced and noninduced cells, and changes in enzyme activity were different among enzymes. Treatment with D3T or TCs increased CuZn-SOD and NQO1 activities regardless of oxidative stress induction ($P < 0.001$). In contrast, activities of CAT and GST in H_2O_2-induced cells increased but decreased in noninduced cells following D3T and TCs treatment ($P < 0.001$). Treatment with D3T or TCs decreased LDH activity in cells regardless of oxidative stress induction compared to treatment with H_2O_2 alone ($P < 0.001$).

Real-time qRT-PCR was performed to detect mRNA expression of the phase 2 antioxidant enzymes in treated SMCs (Table 2). The expression levels of all enzyme genes in the H_2O_2D3T group were up-regulated ($P < 0.001$) relative to the H_2O_2 group. Treatment of unstressed cells with D3T caused an increase in the expression of CuZn-SOD, GPx, and GSTA2, but not CAT and NQO1, relative to the H_2O_2 group. The expression levels of CAT, GSTA2, and NQO1 genes in both the H_2O_2TC and TC groups were up-regulated ($P < 0.001$) compared with the H_2O_2 group. However, the mRNA expression levels of CuZn-SOD in the TC group and GPx in the H_2O_2TC group did not change compared with the H_2O_2 group. The mRNA expression levels of Keap1 in the D3T and TC groups were up-regulated ($P = 0.002$) but did not change in the H_2O_2D3T and H_2O_2TC groups compared with the H_2O_2 group.

The protein expression levels of enzymes and Keap1 in SMCs are shown in Figure 1. The protein expression levels of all enzymes in the H_2O_2D3T and D3T groups, except for CuZn-SOD in the H_2O_2D3T and NQO1 in the D3T group, increased ($P < 0.001$) compared with the H_2O_2 group. The capacity of TCs to regulate protein expression of enzymes was different in stressed cells compared to unstressed cells. The protein expression levels of CAT and CuZn-SOD in the TC group were elevated approximately 3- and 2-fold, respectively ($P < 0.001$) but did not change in the H_2O_2TC group when

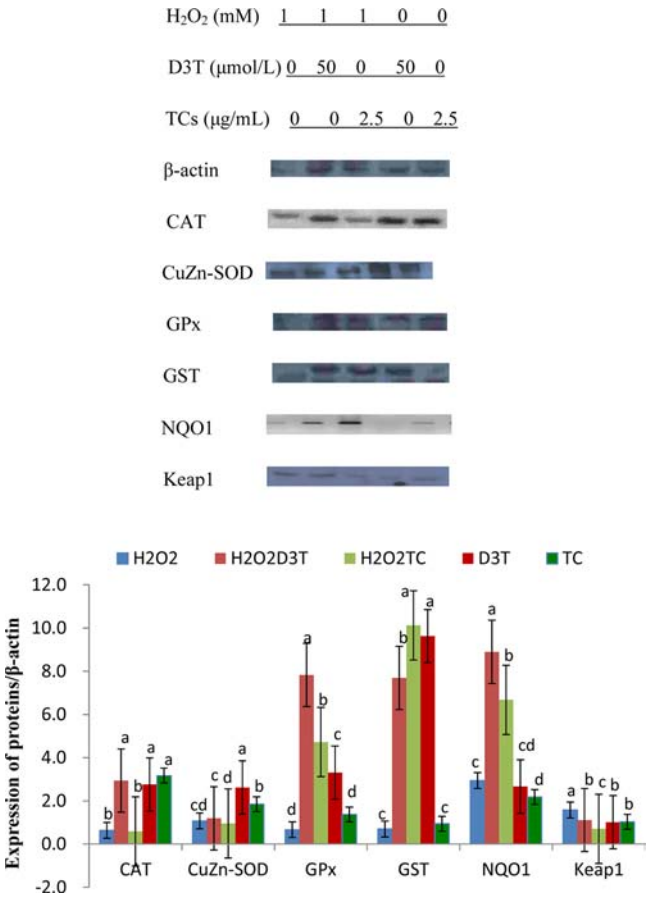

Figure 1. Effects of tea catechins (TCs) and D3T incubation on expression level of proteins in H_2O_2-induced skeletal muscle cells (SMCs).

compared with the H_2O_2 group. Treatment with D3T and TC decreased ($P < 0.001$) the protein expression level of Keap1 in stressed and unstressed SMCs compared with the H_2O_2 group.

In the vivo experiment, the dry matter intakes of goats from each group were 0.81, 0.94, 0.97, 0.85, and 0.88 kg/day, respectively (not shown in the tables). The average daily gain of goats from each group was 205, 232, 226, 265, and 234 g/day, respectively. The average amounts of TCs consumed in the H_2O_2TC and TC groups were 21.6 and 19.5 g/kg BW of animals. The blood biochemical parameters of goats are listed in Table 3. Results showed that an interaction effect on the contents of total protein ($P < 0.001$), albumin ($P = 0.001$), globulin ($P < 0.001$), triglyceride ($P < 0.001$), total cholesterol ($P < 0.001$), HDL-C ($P < 0.001$), and plasma urea nitrogen ($P < 0.001$) and the activities of CAT, CuZn-SOD, GPx, GST, and LPL in plasma ($P < 0.001$) was identified between treatment and sampling time. Overall, the values of triglyceride, cholesterol, and HDL-C and the activity of LPL in the H_2O_2D3T, H_2O_2TC, D3T, and TC groups were lower than those in the H_2O_2 group. However, these values increased as the duration of the feeding period increased. The activities of plasma CAT, CuZn-SOD, GPx, and GST increased as the duration of the feeding period increased ($P < 0.001$).

The values of L^* ($P = 0.001$) and a^* ($P < 0.001$) and the contents of total heme pigment and IMF ($P < 0.001$) in goats fed D3T or TCs increased regardless of whether goats were H_2O_2 infused or not (Table 4). The TBARS value in LD of D3T goats was significantly lower than those in other groups (P

DOI: 10.1021/acs.jafc.5b00816
J. Agric. Food Chem. 2015, 63, 7921−7928

Table 3. Effects of Tea Catechins (TCs) and D3T feeding on Blood Biochemical Variables of Goats under H_2O_2–Induced Oxidative Stress Conditions in the in Vivo Experiment

	treatment[a]					sampling time[a]				*P* value		
parameter[b]	H_2O_2	$H_2O_2D_3T$	H_2O_2TC	D3T	TC	day 0	day 7	day 14	day 21	treatment	time	interaction
Blood Biochemical Variables												
total protein (g/L)	52.7 ± 2.78	58.5 ± 5.42	57.0 ± 4.74	58.2 ± 6.57	58.3 ± 5.35	51.9 ± 4.86	56.4 ± 4.26	60.0 ± 4.43	59.5 ± 4.37	<0.001	<0.001	<0.001
albumin (g/L)	22.1 ± 3.48	23.2 ± 2.57	21.0 ± 2.01	22.1 ± 1.75	22.0 ± 2.06	23.2 ± 2.33	22.9 ± 2.42	21.9 ± 2.47	20.3 ± 1.79	0.038	<0.001	0.001
globumin (g/L)	30.6 ± 4.04	35.3 ± 6.09	36.0 ± 5.94	36.1 ± 7.20	36.3 ± 5.63	28.7 ± 5.04	33.5 ± 4.69	38.1 ± 4.87	39.2 ± 3.55	<0.001	<0.001	<0.001
triglyceride (mmol/L)	0.51 ± 0.20	0.34 ± 0.10	0.29 ± 0.07	0.25 ± 0.06	0.29 ± 0.07	0.29 ± 0.07	0.32 ± 0.09	0.31 ± 0.14	0.42 ± 0.21	<0.001	<0.001	<0.001
total cholesterol (mmol/L)	2.62 ± 0.86	1.87 ± 0.45	1.88 ± 0.49	1.42 ± 0.25	1.74 ± 0.31	1.55 ± 0.25	1.96 ± 0.46	2.06 ± 0.79	2.06 ± 0.79	<0.001	<0.001	<0.001
HDL-C (mmol/L)	1.89 ± 0.76	0.99 ± 0.30	0.96 ± 0.24	0.79 ± 0.25	0.98 ± 0.25	0.98 ± 0.22	1.13 ± 0.24	1.32 ± 0.65	1.06 ± 0.84	<0.001	<0.001	<0.001
LDL-C (mmol/L)	0.73 ± 0.45	0.89 ± 0.49	0.92 ± 0.61	0.63 ± 0.17	0.76 ± 0.32	0.57 ± 0.19	0.82 ± 0.43b	0.74 ± 0.43c	1.00 ± 0.54a	0.121	0.001	0.336
urea nitrogen (mg/dL)	5.19 ± 0.77	4.73 ± 0.78	7.62 ± 2.10	5.25 ± 1.03	6.69 ± 1.19	5.11 ± 0.72	6.14 ± 1.62	6.51 ± 1.87	5.84 ± 1.88	<0.001	<0.001	<0.001
Phase 2 Enzyme Activity												
CAT (U/mL)	32.6 ± 2.88	32.0 ± 5.38	37.8 ± 1.78	31.8 ± 5.02	24.9 ± 2.89	29.6 ± 5.62	29.4 ± 4.90	35.0 ± 4.40	33.2 ± 5.50	<0.001	<0.001	<0.001
CuZn-SOD (U/mL)	6.87 ± 2.95	11.8 ± 4.32	14.6 ± 4.66	14.1 ± 4.45	10.5 ± 1.71	9.58 ± 2.99	9.39 ± 2.62	17.0 ± 4.70	10.3 ± 3.22	<0.001	<0.001	<0.001
GPx (U/mL)	345 ± 54.7	332 ± 43.1	298 ± 36.6	345 ± 59.9	320 ± 54.6	289 ± 23.3	324 ± 42.6	381 ± 44.4	317 ± 49.9	<0.001	<0.001	<0.001
GST (U/mL)	6.34 ± 1.61	8.34 ± 2.65	10.9 ± 4.18	10.9 ± 3.74	12.1 ± 4.49	4.75 ± 0.75	11.3 ± 3.31	11.9 ± 3.40	10.9 ± 2.96	<0.001	<0.001	<0.001
LPL (nmol/min/mL)	34.0 ± 10.42	19.9 ± 4.94	21.7 ± 2.10	16.7 ± 3.53	19.4 ± 2.88	18.2 ± 2.16	26.0 ± 6.43	22.7 ± 10.11	22.3 ± 9.78	<0.001	<0.001	<0.001

[a]Mean values with different letters in the same row differ significantly ($P < 0.05$). [b]HDL-C, high-density lipoprotein cholesterol; LDL-C, low-density lipoprotein cholesterol; CAT, catalase; CuZn-SOD, CuZn superoxide dismutase; GPx, glutathione peroxidase; GST, glutathione *S*-transferase; LPL, lipoprotein lipase.

DOI: 10.1021/acs.jafc.5b00816
J. Agric. Food Chem. 2015, 63, 7921−7928

Table 4. Effects of Tea Catechins (TCs) and D3T Feeding on Meat Quality of Goats under H_2O_2−Induced Oxidative Stress Conditions

parameter[b]	treatment[a]					*P* value
	H_2O_2	$H_2O_2D_3T$	H_2O_2TC	D3T	TC	
meat quality						
pH 24 h post-mortem	5.47 ± 0.12	5.47 ± 0.20	5.48 ± 0.05	5.56 ± 0.08	5.49 ± 0.03	0.610
color						
*L**	31.0 ± 2.09b	35.3 ± 1.57a	34.1 ± 1.74a	34.8 ± 0.55a	33.8 ± 1.80a	0.001
*a**	10.5 ± 0.78d	12.5 ± 1.55c	13.7 ± 0.91b	15.1 ± 0.46a	13.9 ± 0.24b	<0.001
*b**	5.26 ± 0.37a	3.98 ± 0.14c	4.21 ± 0.25bc	4.50 ± 0.23b	3.35 ± 0.34d	<0.001
total heme pigment (μg/g meat)	141 ± 5.9c	182 ± 14.7b	183 ± 11.8b	170 ± 10.4b	200 ± 6.3a	<0.001
shear force, N	27.3 ± 1.43a	23.4 ± 2.25b	24.5 ± 2.36b	25.5 ± 2.05ab	20.2 ± 1.23c	<0.001
TBARS (μg MDA/g meat)	1.32 ± 0.15a	1.36 ± 0.32a	1.11 ± 0.13ab	0.96 ± 0.11b	1.20 ± 0.19ab	0.012
intramuscular fat (g/kg)	79.5 ± 1.54d	81.1 ± 1.75d	86.8 ± 1.47c	90.0 ± 0.99b	95.9 ± 2.38a	<0.001
protein expression levels in LD muscle						
Keap1	2.11 ± 0.37a	1.17 ± 0.11b	1.34 ± 0.13b	1.20 ± 0.15b	1.43 ± 0.23b	<0.001

[a]Mean values with different letters in the same row differ significantly ($P < 0.05$). [b]*L**, lightness; *a**, redness; *b**, yellowness; TBARS, thiobarbituric acid reactive substances; MDA, malondialdehyde; NQO1, NADPH:quinine oxidoreductase; Keap1, Kelch-like ECH-associated protein 1.

= 0.012). Shear force of LD in the H_2O_2D3T, H_2O_2TC, and TC groups, but not in the D3T group, decreased ($P < 0.001$) compared with that in the H_2O_2 group. There were no differences in pH values among all groups ($P = 0.610$). The protein expression levels of Keap1 decreased in D3T- and TC-fed goat meat no matter whether goats were H_2O_2 infused or not ($P < 0.001$).

DISCUSSION

Oxidative stress has been implicated in numerous disease processes in small ruminants. The use of in vitro cell culture models to study responses to oxidative stressors such as H_2O_2 is a recognized way to study the mechanisms of action of antioxidants. Multiple papers have described high (usually ≥50 μM) levels of H_2O_2 as being cytotoxic to a wide range of animal, plant, and bacterial cells in culture.[29,30] The administration of plant-derived polyphenolic antioxidants is effective in preventing skeletal muscle damage induced by oxidative stress in rats.[31] Here, we showed that direct exposure of goat SMCs to 1 mM H_2O_2 led to serious injury of cell membrane and that incubation with TCs or with D3T provided protection to cell membrane integrity based on reduced LDH activity in SMCs. Thus, our results suggest that the SMC model of oxidative/antioxidative status is effective in assessing the antioxidant properties of antioxidant compounds such as TCs and D3T.

Antioxidant enzymes function as the first line of defense against oxidative stress by detoxifying free radicals. Tea catechins affect the gene expression of phase 2 antioxidant enzymes through activating the Nrf2−Keap1 signaling pathway in numerous organs, including skin, liver, lung, muscle, and small intestines, and in cultured human and mouse cells.[32,9] D3T exerts its chemopreventive capacity by inducing cellular GST and NQO1 expression.[33] Our previous studies reported that TCs increase CAT and CuZn-SOD mRNA and protein expression levels and associated enzyme activities in goat SMCs induced by H_2O_2 in a dose-dependent manner.[8] Here, we further demonstrate that TCs promote the protein expression of all the enzymes we examined but that the effects on enzyme activities were slightly different, and sometimes even opposite, in stressed versus unstressed cells. The effect of D3T and TCs on CuZn-SOD and GPx was minimal. As expected, the overall changed tendencies of enzymes in D3T-treated cells are similar to those in TCs-treated cells, especially for stressed SMCs. Similar findings were reported in a recent study by Yang et al.[34]

Previous studies have confirmed that the protective effects of D3T on cancer have been associated with the induction of detoxifying phase 2 enzymes via Nrf2−Keap1 signaling.[35] Our results show that D3T increases the activities of phase 2 antioxidant enzymes and suppresses Keap1 protein expression, but does not change Keap1 mRNA expression levels in SMCs. This is consistent with previous studies showing that D3T directly covalently modifies the sensitive cysteine residues of Keap1 and thereby disrupts the Keap1−Nrf2 complex, releasing Nrf2 so that it can migrate to the nucleus.[13] Plant polyphenolic compounds such as TCs contain α,β-unsaturated ketone elements, which are believed to modify the cysteine and thiol groups in Keap1 and thereby activate the Nrf2−Keap1 pathway.[36] Kavitha et al.[24] also reported that TC inclusion inhibits Keap1 expression to activate the Nrf2−Keap1 pathway and downstream phase 2 and antioxidant enzyme expression. The results presented here imply that the pathway through which TCs regulate phase 2 antioxidant enzymes is mediated by Keap1 protein in goat SMCs and is highly similar to pathways employed by D3T.

To further verify the protective effects of TCs and D3T against oxidative stress in goat muscles, an in vivo experiment was conducted to compare the antioxidant activities of D3T and TCs in goats. Findings in our previous study have demonstrated that dietary TC (0.2−0.4% of feed) supplementation did not affect blood metabolites.[37] However, the differences between both experiments are that the amount of TCs in diets was increased to 0.5% of feed, the animals in the present study were subjected to early weaning stress, and different results were observed in the present study in which plasma total protein, globumin, and LDL-C contents increased and plasma triglyceride, total cholesterol, and HDL-C decreased after TCs or D3T treatment. Moreover, the changes were amplified by extending the length of the experiment in the current study. In addition, the animals in the previous studies were not maintained under stressful conditions, whereas the goats in this study were maintained under greater oxidative stress induced by a combination of daily H_2O_2 infusion and stress induced by early weaning. Results of increased plasma total protein content and decreased plasma triglyceride and cholesterol contents in both H_2O_2TC and TC treatments

DOI: 10.1021/acs.jafc.5b00816
J. Agric. Food Chem. 2015, 63, 7921−7928

compared with H_2O_2 treatment and our previous results[37] indicate that TCs exert potent positive effects on improving the health of goats exposed to oxidative stress, and a feeding 0.5% TCs for 21 days was sufficient for testing effects of TCs on blood metabolisms according to the review by Crespy and Williamson.[38] However, these protective effects are less pronounced when the animals are raised under normal physiological conditions. Similar trends were also observed in the activities of antioxidant enzymes in in vitro experiments. In addition, both D3T and TCs had a positive effect on plasma lipid metabolites; changes were observed in levels of triglyceride, TP, and HDL-C contents. This provides direct evidence for profound impacts of D3T on lipid metabolism reported by Kwak et al. and Huang et al.[7,39] The effects may be associated with the antioxidant properties of TCs on lipid peroxidation and activity of LPL, a key enzyme that transforms triglycerides of chylomicrons and LDL-C into free fatty acids, thus permitting their uptake by adipocytes.[40]

In in vivo experiments, the activities of CuZn-SOD and GST in the plasma of goats fed D3T and TCs increased, regardless of whether the goats were infused with H_2O_2. In contrast to the present in vitro results, in which the effect on the enzymes was dependent upon the presence of H_2O_2 stress, the changes in antioxidant enzymes induced by TCs or D3T in blood from stressed goats are consistent with those from unstressed goats (with the exception of CAT). This difference has a simple explanation: in vitro enzyme activities in cell cultures do not always correlate with in vivo activities and responses of in vitro experiments in a flask cannot accurately replicate the complex metabolic and regulatory interplay present in vivo due to transcript production and modification, translation, post-translational modification, and metabolic feedback.[41]

Higher meat quality is the ultimate aim of improving the antioxidant pathway activity of industrially raised goats. In the present study, D3T and TCs enhanced meat color stability, tenderness, and IMF contents of goats under H_2O_2 induction or noninduction conditions. The improvement might be associated with changes in plasma antioxidant enzymes.[10,11] The suppression protein levels of Keap1 in meat of D3T and TCs treatments are consistent with results in vitro, implying that TCs target Keap1 and therefore induce phase 2 and antioxidant enzyme expression to protect goats against oxidative stress.

In summary, results from the in vitro and in vivo experiments presented here provide the first evidence that TCs exert their antioxidant activity in goats through targeting the Keap1 protein and downstream pathways. We showed that TCs modulate the Keap1 protein and induce phase 2 antioxidant enzyme expression, protecting muscle tissue against oxidative stress in goats. Thus, we demonstrate that supplementation of goat feed with moderate levels of an affordable, accessible, natural supplement may significantly improve the quality of meat produced by goats raised under conditions that are typical in the small-ruminant industry.

AUTHOR INFORMATION

Corresponding Author

*(G.-X.Q.) Phone: +86-431-84513789. Fax: +86-431-84531264. E-mail: qgx@jlau.edu.cn.

Funding

This study was supported by the National Natural Science Foundation of China (31201820) and the China Postdoctoral Science Foundation (2013M530997). R.-Z.Z. received a postdoctoral fellowship granted by the National Science Foundation of China. Part of the work was supported by the Northeast Institute of Geography and Agroecology, Chinese Academy of Sciences.

Notes

The authors declare no competing financial interest.

ACKNOWLEDGMENTS

We thank all of the colleagues of the Key Laboratory of Animal Production, Product Quality and Security for their help and cooperation at every stage of this work. We greatly appreciate the critical and judicious comments of the anonymous reviewers that enabled considerable improvement in the presentation of the manuscript.

ABBREVIATIONS USED

*a**, redness; ARE, antioxidant response element; *b**, yellowness; CAT, catalase; CuZn-SOD, CuZn superoxide dismutase; D3T, 3*H*-1,2-dithiole-3-thione; GPx, glutathione peroxidase; GST, glutathione *S*-transferases; HDL-C, high-density lipoprotein cholesterol; IMF, intramuscular fat; Keap1, Kelch-like ECH-associated protein 1; *L**, lightness; LD, *longissimus dorsi*; LDH, lactate dehydrogenase; LDL-C, low-density lipoprotein cholesterol; MDA, malondialdehyde; MTT, 3-[4,5-dimethylthiazol-2-yl]-2,5-diphenyl tetrazolium bromide; Nrf2, nuclear factor E2-related factor 2; NQO1, NADPH:quinine oxidoreductase; NRC, National Research Council; PUN, plasma urea nitrogen; qRT-PCR, quantitative RT-PCR; TBARS, thiobarbituric acid reactive substances; TCs, tea catechins; SEM, standard error of the mean; SMC, skeletal muscle cell

REFERENCES

(1) Celi, P. Oxidative stress in ruminants. *Stud. Vet. Med.* **2011**, 191−231.

(2) Celi, P. The role of oxidative stress in small ruminants' health and production. *R. Bras. Zootec.* **2010**, *39*, 348−363.

(3) Devling, T. W. P.; Lindsay, C. D.; McLellan, L. I.; McMahon, M.; Hayes, J. D. Utility of siRNA against Keap1 as a strategy to stimulate a cancer chemopreventive phenotype. *Proc. Natl. Acad. Sci. U. S. A.* **2005**, *102*, 7280−7285.

(4) Cho, B. O.; Ryu, H. W.; Jin, C. H.; Choi, D. S.; Kang, S. Y.; Kim, D. S.; Byun, M. W.; Jeong, I. Y. Blackberry extract attenuates oxidative stress through up-regulation of N2f2-dependent antioxidant enzymes in carbon tetrachloride-treated rates. *J. Agric. Food Chem.* **2011**, *59*, 11442−11448.

(5) Lee, J. M.; Johnson, J. A. An important role of Nrf2-ARE pathway in the cellular defense mechanism. *J. Biochem. Mol. Biol.* **2004**, *37*, 139−143.

(6) Lam, S.; MacAulay, C.; LeRiche, J. C.; Dyachkova, Y.; Coldman, A.; Guillaud, M.; Hawk, E.; Christen, M. O.; Gazdar, A. F. A randomized phase IIb trail of anethole dithiolethione in smokers with bronchial dysplasia. *J. Natl. Cancer Inst.* **2002**, *94*, 1001−1009.

(7) Kwak, M. K.; Wakabayashi, N.; Itoh, K.; Motohashi, H.; Yamamoto, M.; Kensler, T. W. Modulation of gene expression by cancer chemopreventive dithiolethiones through the Keap1-Nrf2 pathway. *J. Biol. Chem.* **2003**, *278*, 8135−8145.

(8) Zhong, R. Z.; Zhou, D. W.; Tan, C. Y.; Tan, Z. L.; Han, X. F.; Zhou, C. S.; Tang, S. X. Effect of tea catechins on regulation of antioxidant enzyme expression in H_2O_2-indiced skeletal muscle cells of goat in vitro. *J. Agric. Food Chem.* **2011**, *59*, 11338−11343.

(9) Na, H. K.; Surh, Y. J. Modulation of Nrf2-mediated antioxidant and detoxifying enzyme induction by the green tea polyphenol EGCG. *Food Chem. Toxicol.* **2008**, *46*, 1271−1278.

DOI: 10.1021/acs.jafc.5b00816
J. Agric. Food Chem. 2015, 63, 7921−7928

(10) He, Y.; Shahidi, F. Antioxidant activity of green tea and its catechins in a fish meat model system. *J. Agric. Food Chem.* **1997**, *45*, 4262−4266.
(11) Zhong, R. Z.; Tan, Z. Y.; Han, X. F.; Tang, S. X.; Tan, Z. L.; Zeng, B. Effect of dietary tea catechins supplementation in goats on the quality of meat kept under refrigeration. *Small Rumin. Res.* **2009**, *87*, 122−125.
(12) Tan, C. Y.; Zhong, R. Z.; Tan, Z. L.; Han, X. F.; Tang, S. X.; Xiao, W. J.; Sun, Z. H.; Wang, M. Dietary inclusion of tea catechins changes fatty acid composition of muscle in goats. *Lipids* **2011**, *46*, 239−247.
(13) Cao, Z. X.; Li, Y. B. Protecting against peroxynitrite-mediated cytotoxicity in vascular smooth muscle cells via upregulating endogenous glutathione biosynthesis by 3H-1,2-dithiole-3-thione. *Cardiovasc. Toxicol.* **2004**, *4*, 339−353.
(14) Aebi, H. Catalase in vitro. *Methods Enzymol.* **1984**, *105*, 121−126.
(15) Spitz, D.; Oberley, L. An assay for superoxide dismutase activity in mammalian tissue homogenates. *Anal. Biochem.* **1989**, *179*, 8−18.
(16) Levander, O. A.; Deloach, D. P.; Morris, V. C.; Moser, P. B. Platelet glutathione peroxidase activity as an index of selenium 313 status in rats. *J. Nutr.* **1983**, *113*, 55−63.
(17) Prochaska, H. J.; Santamaria, A. B. Direct measurement of NAD(P)H: quinone reductase from cells cultured in microtiter wells: a screening assay for anticarcinogenic enzyme inducers. *Anal. Biochem.* **1988**, *169*, 328−336.
(18) Habig, W. H.; Pabst, M. J.; Jakoby, W. B. Glutathione S-transferases: the Trst enzymatic step in mercapturic acid formation. *J. Biol. Chem.* **1974**, *249*, 7130−7139.
(19) Livak, K. J.; Schmittgen, T. D. Analysis of relative gene expression data using real-time quantitative PCR and the 2−ΔΔCT method. *Methods* **2001**, *25*, 402−408.
(20) Lowry, O. H.; Rosebrough, N. J.; Farr, A. L.; Randall, R. J. Protein measurement with the Folin phenol reagent. *J. Biol. Chem.* **1951**, *193*, 265−275.
(21) NRC. *Nutrient Requirements of Small Ruminants, Sheep, Goats, Cervids, and New World Camelids*; National Research Council of the National Academies, The National Academy Press: Washington, DC, USA, 2007.
(22) Lee, J. M.; Chan, K.; Kan, Y. W.; Johnson, J. A. Targeted disruption of Nrf2 causes regenerative immune-mediated hemolytic anemia. *Proc. Natl. Acad. Sci. U. S. A.* **2004**, *101*, 9751−9756.
(23) Karpe, F.; Olivecrona, T.; Walldius, G.; Hamsten, A. Lipoprotein lipase in plasma after an oral fat load: relation to free fatty acids. *J. Lipid Res.* **1992**, *33*, 975−984.
(24) Kavitha, K.; Thiyagarajan, P.; Nandhini, J. R.; Mishra, R.; Nagini, S. Chemopreventive sffects of diverse dietary phytochemicals against DMBA-induced hamster buccal pouch carcinogenesis via the induction of Nrf2-mediated cytoprotective antioxidant, detoxification, and DNA repair enzymes. *Biochimie* **2013**, *93*, 1629−1639.
(25) Olsvik, P. A.; Kristensen, T.; Waagbø, R.; Rosseland, B. O.; Tollefsen, K. E.; Baeverfjord, G.; Berntssen, M. H. G. mRNA expression of antioxidant enzymes (SOD, Cat and GSH-Px) and lipid peroxidative stress in liver of Atlantic salmon (*Salmo salar*) exposed to hyperoxic water during smoltification. *Comp. Biochem. Physiol., Part C: Toxicol. Pharmacol.* **2005**, *141*, 314−323.
(26) AOAC (Association of Official Analytical Chemists). *Official Methods of Analysis*, 5th ed.; AOAC: Arlington, VA, USA, 1990; Vol. 2.
(27) SAS. *SAS/STAT User's Guide: Statistics*, version 9.1 ed.; SAS Institute: Cary, NC, USA, 2002.
(28) Littell, R. C.; Milliken, G. A.; Stroup, W. W.; Wolfinger, R. D. *SAS System for Mixed Models*; SAS Institute: Cary, NC, USA, 1996.
(29) Halliwell, B.; Clement, M. V.; Ramalingam, J.; Long, L. H. Hydrogen peroxide, ubiquitous in cell culture and in vivo. *IUBMB Life* **2000**, *50*, 251−257.
(30) Chen, Q.; Espey, M. G.; Sun, A. Y.; Lee, J. H.; Krishna, M. C.; Shacter, E.; Choyke, P. L.; Pooput, C.; Kirk, K. L.; Buettner, G. R.; Levine, M. Ascorbate in pharmacologic concentrations selectively generates ascorbate radical and hydrogen peroxide in extracellular fluid in vivo. *Proc. Natl. Acad. Sci. U. S. A.* **2007**, *104*, 8749−8754.
(31) Hurst, R. D.; Wells, R. W.; Hurst, S. M.; McGhie, T. K.; Cooney, J. M.; Jensne, D. J. Blueberry fruit polyphenolics suppress oxidative stress-induced skeletal muscle cell damage *in vitro*. *Mol. Nutr. Food Res.* **2010**, *54*, 353−363.
(32) Khan, S. G.; Katiyar, S. K.; Agarwal, R.; Mukhtar, H. Enhancement of antioxidant and phase II enzymes by oral feeding of green tea polyphenols in drinking water to SKH-1 hairless mice: possible role in cancer chemoprevention. *Cancer Res.* **1992**, *52*, 4050−4052.
(33) Jia, Z.; Zhu, H.; Misra, H. P.; Li, Y. Potent induction of total cellular GSH and NQO1 as well as mitochondrial GSH by 3H-1,2-dithiole-3-thione in SH-SY5Y neuroblastoma cells and primary human neurons: protection against nuerocytotoxicity elicited by dopamine, 6-hydroxydopamine, 4-hydroxy-2-nonenal, or hydrogen peroxide. *Brain Res.* **2008**, *1197*, 159−169.
(34) Yang, T.; Li, X. M.; Zhu, W.; Chen, C.; Sun, Z. H.; Tan, Z. L.; Kang, J. H. Alteration of antioxidant enzymes and associated genes induced by grape seed extracts in the primary muscle cells of goats in vitro. *PLoS One* **2014**, *9*, e107670.
(35) Dong, J.; Yan, D.; Chenm, S. Y. Stabilization of Nrf2 protein by D3T provides protection against ethanol-induced apoptosis in PC12 cells. *PLoS One* **2011**, *6*, e16845.
(36) Das, B. N.; Kim, Y. W.; Keum, Y. S. Mechanisms of Nrf2/Keap1-dependent phase II cytoprotective and detoxifying gene expression and potential cellular targets of chemopreventive isothiocyanates. *Oxid. Med. Cell. Longevity* **2013**, *2013*, 839409.
(37) Zhong, R. Z.; Xiao, W. J.; Ren, G. P.; Zhou, D. W.; Tan, C. Y.; Tan, Z. L.; Han, X. F.; Tang, S. X.; Zhou, C. S.; Wang, M. Dietary tea catechin inclusion changes plasma biochemical parameters, hormone concentrations and glutathione redox status in goats. *Asian-Australas. J. Anim. Sci.* **2011**, *24*, 1681−1689.
(38) Crespy, V.; Williamson, G. A review of the health effects of green tea catechins in in vivo animal models. *J. Nutr.* **2004**, *134*, 3432S−3440S.
(39) Huang, Y.; Yan, J.; Lubet, R.; Kensler, T. W.; Sutter, T. R. Identification of novel transcriptional networks in response to treatment with the anticarcinogen 3H-1,2-dithiole-3-thione. *Physiol. Genomics* **2006**, *24*, 144−153.
(40) Pak-Dek, M. S.; Abdul-Hamid, A.; Osman, A.; Soh, C. S. Inhibitory effect of *Morinda Citrifolia* L. on lipoprotein lipase activity. *J. Food Sci.* **2008**, *78*, 595−598.
(41) Grüning, N. M.; Lehrach, H.; Ralser, M. Regulatory crosstalk of the metabolic network. *Trends Biochem. Sci.* **2010**, *35*, 220−227.

DOI: 10.1021/acs.jafc.5b00816
J. Agric. Food Chem. 2015, 63, 7921−7928

plasma and liver, the hepatic expression of genes related to lipid metabolism, and the plasma metabolic profiles of the hamsters.

MATERIALS AND METHODS

Chemicals. GSN was purchased from Chengdu Must Biotechnology Co., Ltd. (Chengdu, China). Oil-Red O and 2-propanol were from Sigma-Aldrich (Shanghai, China). TRIzol Reagent was obtained from Invitrogen (Carlsbad, CA, USA). Moloney murine leukemia virus reverse transcriptase and dNTPs were purchased from TaKaRa Bio, Inc. (Dalian, China). EvaGreen reagents were provided by Biotium Inc. (Hayward, CA, USA). D_2O was obtained from Cambridge Isotope Laboratories, Inc. (Tewksbury, MA, USA), and sodium trimethylsilyl propionate was obtained from Merck KGaA (Darmstadt, Germany).

Animal Treatment and Management. A total of 45 male golden Syrian hamsters (9 weeks old) were purchased from Charles River Company (Vital River, Beijing, China). After acclimation for 1 week, the hamsters were randomly assigned to one of the following dietary groups (n = 15 each): normal-fat diet (NFD) group, HFD group, or HFD + 2 g/kg GSN group (equivalent to 76 mg/kg body weight). GSN (98%) was mixed in with the feed. The dose of GSN used in this study was based on that used in a former study in which the serum and hepatic lipids of mice fed a HFD were not affected until the level of dietary GSN supplementation reached 2 g/kg.[10] No adverse effects occurred at the dose used, on the basis of a 90-day feeding study that showed no toxicity in animals fed GSN at doses up to 63 mg/kg bodyweight/day or a GSN/daidzein isoflavone mixture (2:1) at 100 mg/kg bodyweight/day.[18] The present study was conducted over 6 weeks, and the hamsters were given access to feed and water ad libitum. Dietary consumption and bodyweight were measured every week and after 6 weeks. The NFD (protein 22 g %, fat 5 g %, carbohydrate 54 g %) was formulated on the basis of the hamsters' nutritional requirements and was produced by Beijing Keao Xieli Feed Co., Ltd. (Beijing, China). The HFD (protein 20 g %, fat 21 g %, carbohydrate 50 g %) was purchased from Research Diets, Inc. (New Brunswick, NJ, USA). The animals were housed in steel cages (five hamsters per cage) in an environmentally controlled room (20−24 °C, 12 h alternating light/dark cycle). The study protocol was approved by the Animal Care and Use Committee of the Chinese Academy of Agricultural Sciences.

Sample Collection. To meet the statistical requirements of metabonomics data ($n \geq 6$) and to reduce errors resulting from sampling time, six hamsters from each treatment group were sampled. (Were all the hamsters sampled, sampling would have taken a whole day.) After fasting for 12 h, six hamsters from each treatment group were killed under anesthesia induced with pentobarbital. Blood was obtained from the orbital vein with heparin-treated glass capillary tubes. Plasma was obtained after the blood was centrifuged (3000 rpm at 4 °C for 10 min) and stored at −80 °C until analysis. The liver, heart, kidney, and abdominal and epididymal fat were separated, weighed, and flash frozen in liquid nitrogen.

Plasma Parameters, Hepatic Lipid Determination, and Oil-Red O Staining. The plasma total cholesterol (TC), triglycerides (TG), high-density lipoprotein cholesterol (HDL-C), and LDL cholesterol (LDL-C) were determined with an autoanalyzer (Hitachi 7060, Hitachi, Chiyoda, Tokyo, Japan) with commercial kits (BioSino Biotechnology and Science Inc., Beijing, China). The superoxide dismutase (SOD), malondialdehyde (MDA), and free fatty acids (FFA) in the plasma and hepatic TC and TG were measured with commercial kits (Jiancheng Biotechnology, Nanjing, China). The same liver lobes were sampled from the hamsters in each group, immersed in liquid nitrogen, and stored at −80 °C until frozen sectioning. The sections were rinsed with distilled water, stained with 0.2% Oil-Red O and 60% 2-propanol for 10 min at 37 °C, and then rinsed again with distilled water. Lipid accumulation in the liver was then observed under a microscope (Leica DM4000B, Bensheim, Germany) and photographed.

Real-Time PCR. The expression of 13 genes involved in lipid metabolism in the liver was determined with real-time PCR. Total RNA was extracted from the liver with TRIzol Reagent, and quantified spectrophotometrically. Complementary DNA was synthesized with Moloney murine leukemia virus reverse transcriptase, random hexamers, deoxyribonucleosides, RNase inhibitor, and 4 μg of total RNA. The mRNA expression of the target genes was determined with real-time PCR using EvaGreen reagents in an MJ-Chromo 4 thermocycler (Bio-Rad, Hercules, CA, USA). Changes in fluorescence during the PCR were calculated according to the manufacturer's instructions. The amplification of glyceraldehyde phosphate dehydrogenase (GAPDH) mRNA was used as the internal control. The real-time PCR results were normalized as previously described.[19] The gene-specific primers are listed in Table 1.

Table 1. Oligonucleotide Primers[a]

primer	sequence (5′−3′)
GAPDH-F	TGGCAAGTTCAAAGGCACAG
GAPDH-R	AACATACTCGGCGCCAGCATC
LDL-R-F	CTCCACTCTATCTCCAGCATTG
LDL-R-R	TTTCAGCCACCAAATTAACATC
ERα-F	ACCAAAGCCTCGGGAATG
ERα-R	GCGGCGTTGAACTCGTAG
ERβ-F	GGTGAAGGAGCTGCTGCTGA
ERβ-R	GGCTGGGCCAAGAAAATCC
SREBP-2-F	GGCTGGTTTGACTGGATGG
SREBP-2-R	CGGATAAGCAGGTTTGTAGGTT
CYP7A1-F	AGCAACTAAACAACCTGCCAGTACTA
CYP7A1-R	GTCCGGATATTCAAGGATGCA
CYP27A1-F	GGAGCAGTGGAAGGATCACC
CYP27A1-R	TGTTCAAAGCCTGGCGC
ERK1-F	TTGTATCATCAACATGAAGGCTCG
ERK1-R	TGAAGGTCAACATCCGGTCC
ERK2-F	GCCTTGCCCGTGTTGC
ERK2-R	AATACCCAGGATGTGATTCAGC
ERK5-F	AGAGTCGCCTGATGTCAACCT
ERK5-R	CGATGTCAGCGGGGTTCA
p38-F	CGAAAATGTGATTGGTCT
p38-R	CACGATGTTGTTCAGGTC
JNK-F	TCCAGCACCCATACATCAACG
JNK-R	CGCTCCTCCAAGTCCATTACC
AR-F	TCCGCTGGCTCTGACCG
AR-R	CAGCTGCACTCCCTCCATG
PPARα-F	CCTGTCTGTTGGGATGTCAC
PPARα-R	AGGTAGGCCTCGTGGATTCT

[a]GAPDH, glyceraldehyde phosphate dehydrogenase; LDL-R, low-density lipoprotein receptor; ER, estrogen receptor; SREBP-2, sterol regulatory element binding protein 2; CYP7A1, cholesterol 7 α-hydroxylase; CYP27A1, sterol 27-hydroxylase; ERK, extracellular regulated protein kinase; JNK, c-Jun N-terminal kinase; AR, androgen receptor; PPARα, peroxisome proliferator-activated receptor alpha.

Plasma ^{1}H NMR Metabonomics. Before the measurements were made, the plasma samples (200 μL) were mixed with 300 μL of D_2O and 100 μL of sodium trimethylsilyl propionate D_2O solution (1 mg/mL) and then centrifuged (13 000 rpm at 4 °C for 10 min). The supernatant of each sample was transferred individually to a 5 mm NMR tube.

All NMR measurements were made on a Varian Inova 600 MHz spectrometer (Varian Inc., Palo Alto, CA, USA) equipped with a triple-resonance inverse probe. A total of 64 transients were collected into 32 K data points for each spectrum, with a spectral width of 8000 Hz and a recycle delay of 2 s. The plasma was analyzed using the Carr−Purcell−Meiboom−Gill (CPMG) pulse sequence to detect low-molecular-weight metabolites and with the bipolar-pair longitudinal-eddy-current (BPP-LED) pulse sequence to detect high-molecular-weight metabolites. Two ^{1}H NMR spectra were acquired for each sample. The CPMG spectra were acquired using the CPMG pulse

DOI: 10.1021/acs.jafc.5b01590
J. Agric. Food Chem. 2015, 63, 7929−7936

Table 2. Effects of 2 g/kg Dietary Genistein on Bodyweight, Feed Intake, Organ Weight, and Visceral Fat Weight in Hamsters Fed a High-Fat Diet[a]

	NFD		HFD		HFD + 2 g/kg GSN	
measures[c]	mean[b]	SE	mean	SE	mean[b]	SE
			ADFI and BW			
initial BW (g)	135	1.76	135	1.90	134	1.90
final BW (g)	149	2.67	154	2.54	156	1.74
ADFI (g/d)	6.74**	0.01	5.69	0.21	5.81	0.10
			Organ and Visceral Fat Weight (g/100 g BW)			
heart weight	0.32**	0.01	0.28	0.01	0.30	0.01
liver weight	2.94***	0.12	4.54	0.15	4.32	0.11
kidney weight	0.64	0.02	0.68	0.02	0.67	0.02
abdominal fat	1.78*	0.17	2.82	0.34	2.05*	0.12
epididymal fat	2.84*	0.16	3.45	0.19	3.19	0.13

[a]NFD, normal-fat diet; HFD, high-fat diet; HFD + 2 g/kg GSN, high-fat diet +2 g/kg genistein; ADFI, average daily feed intake; BW, bodyweight. [b]Mean values were significantly different from those of the HFD group: *, $P < 0.05$, **, $P < 0.01$, and ***, $P < 0.001$. [c]Fifteen replicates were used for BW, three for ADFI, and six for organ weight and visceral fat weight per group.

sequence $(-RD-90°-(\tau-180°-\tau)n-ACQ)$ with a total spin−spin relaxation delay $(2n\tau)$ of 320 ms and a delay T_e of 400 μs. Irradiation of the water resonance was used during recycle delay. The BPP-LED spectra were acquired using the BPP-LED pulse sequence (−RD−90°−G1−180°−G1−90°−T−90°−G1−180°−G1−90°−τ−90°−ACQ) with a diffusion delay of 100 ms and a delay T_e of 5 ms, with water peak irradiation during recycle delay. The free induction decay signal was zero-filled. Line-broadening factors of 0.5 Hz (CPMG) and 3 Hz (BPP-LED) were added and then Fourier transformed to the ^{1}H NMR spectra. The ^{1}H NMR spectra were manually corrected for phase and baseline, with reference to the lactate doublet signal at 1.33 ppm. The CPMG and BPP-LED spectra were binned into 0.01 and 0.04 ppm integral regions, respectively. To exclude the water signal, the region from 4.6−5.0 ppm was not included in the statistical analysis. The spectra were normalized to remove any concentration effects.

Statistical Analysis. Bodyweight, feed intake, organ weight, plasma parameters, hepatic lipid content, and the relative expression of mRNAs are shown as mean values and their standard errors (SE). Student's *t* test was used to compare differences (NFD vs HFD, HFD vs HFD + 2 g/kg GSN). Differences were considered significant at $P < 0.05$. The ^{1}H NMR metabonomic data were examined with multivariate analysis using the SIMCA-P+ software package (version 11; Umetrics, Umeå, Sweden), with the binned integral regions used as input. The plasma metabonomic data were analyzed after centering was applied. Principal components analysis (PCA), an unsupervised pattern-recognition technique, was used to analyze the data sets. The data sets were then explored further with a supervised multivariate data analytical tool, orthogonal signal correction partial least-squares (OSC-PLS). The quality of each model was judged by its R^2 and Q^2 values. Permutation testing was carried out on each OSC-PLS model to assess its validity (with 20 permutations).

RESULTS

Feed Intake, Bodyweight, and Organ Weight. The different dietary groups did not differ in their bodyweights at the end of the study (Table 2). The hamsters in the HFD group had lower average daily feed intake and heart weights ($P < 0.05$) and higher liver, abdominal, and epididymal fat weights ($P < 0.05$) than did the NFD group. Although the average daily feed intake and the liver and epididymal fat weights of the HFD and HFD + 2 g/kg GSN groups did not differ significantly ($P > 0.05$), the hamsters fed the GSN diet had a significantly lower abdominal fat weight than those fed the HFD ($P < 0.05$).

Plasma Parameters and Hepatic Lipids. Table 3 shows that the TC, TG, LDL-C, MDA, and FFA concentrations were all significantly higher in the plasma of the HFD group than in that of the NFD group ($P < 0.05$). The TC, TG, LDL-C, and MDA contents of the GSN-treated group were all significantly lower than those of the HFD group ($P < 0.05$). The plasma FFA levels of the GSN-treated group were 29% lower than those of the HFD group, although the difference was not significant.

Table 3. Effects of 2 g/kg Dietary Genistein on Plasma Biochemical Parameters in Hamsters Fed a High-Fat Diet[a]

	NFD		HFD		HFD + 2 g/kg GSN	
indices[c]	mean[b]	SE	mean	SE	mean[b]	SE
TC (mmol/L)	4.20***	0.16	12.4	0.37	9.11***	0.40
TG (mmol/L)	1.56***	0.17	14.7	1.18	8.07**	1.08
HDL-C (mmol/L)	0.26	0.01	0.26	0.01	0.29	0.02
LDL-C (mmol/L)	0.94***	0.10	4.48	0.27	2.69***	0.20
SOD (U/mL)	38.8	6.14	30.3	3.71	32.4	5.64
MDA (μmol/L)	7.94**	0.95	14.0	1.15	7.77*	1.64
FFA (μmol/L)	2767***	678	9337	843	6598	1255

[a]NFD, normal-fat diet; HFD, high-fat diet; HFD + 2 g/kg GSN, high-fat diet +2 g/kg genistein; TC, total cholesterol; TG, triglycerides; HDL-C, high-density lipoprotein cholesterol; LDL-C, low-density lipoprotein cholesterol; SOD, superoxide dismutase; MDA, malondialdehyde; FFA, free fatty acid. [b]Mean values were significantly different from those of the HFD group: *, $P < 0.05$, **, $P < 0.01$, ***, $P < 0.001$. [c]Six replicates were used per group.

The hepatic lipid contents in the HFD group were higher than those in the NFD group (29.9 vs 12.2 μmol/g for TC, respectively, and 37.1 vs 24.8 μmol/g for TG, respectively; $P < 0.05$). The HFD + 2 g/kg GSN group had significantly lower hepatic TC (20.9 μmol/g; $P < 0.05$) and 16.6% lower TG (31.0 μmol/g; $P = 0.223$) than did the HFD group (Figure 1a). Oil-Red O staining showed that the hepatic lipid droplets in the HFD + 2 g/kg GSN group were smaller than those in the HFD group (Figure 1b).

Hepatic mRNA Expression. The mRNA expression of the lipid metabolism genes in the liver is shown in Figure 2. Some genes related to LDL-C clearance, including those encoding the LDL-R and sterol regulatory element binding protein 2 (SREBP-2), were downregulated in the HFD group compared with their expression in the NFD group ($P < 0.05$). LDL-R

DOI: 10.1021/acs.jafc.5b01590
J. Agric. Food Chem. 2015, 63, 7929−7936

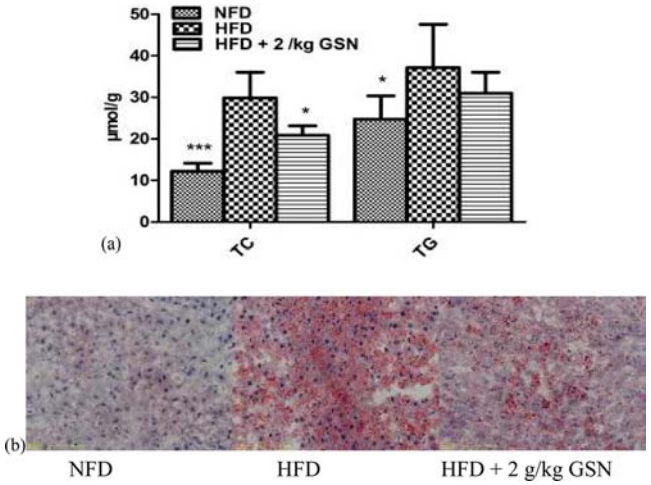

Figure 1. (a) Concentrations of total cholesterol (TC) and triglycerides (TG) in the liver. Values are presented as means (n = 6) and standard errors. Mean values were significantly different from those of the HFD group at *, $P < 0.05$ and ***, $P < 0.001$. (b) Histology (Oil-Red O staining, 400×) of a representative liver section from each group. NFD, normal-fat diet; HFD, high-fat diet; HFD + 2 g/kg GSN, high-fat diet +2 g/kg genistein.

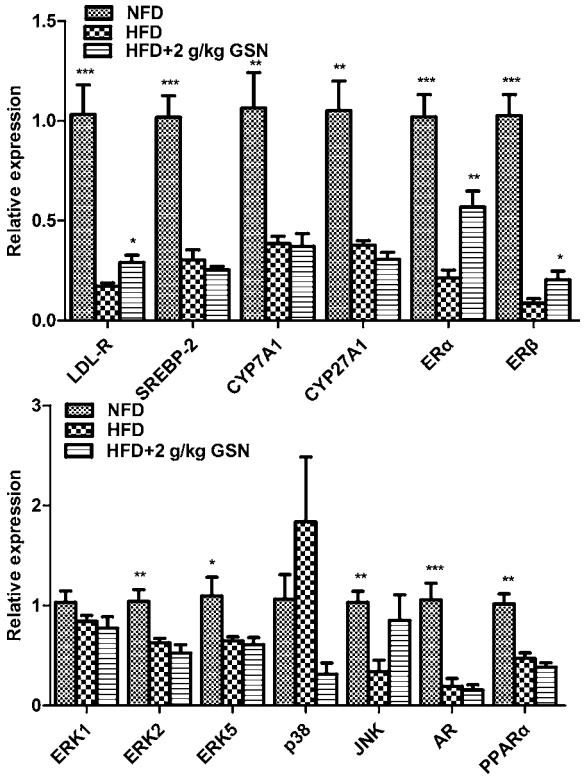

Figure 2. Relative mRNA expression of genes related to lipid metabolism in the livers of the normal-fat diet (NFD), high-fat diet (HFD), and high-fat diet +2 g/kg genistein (HFD + 2 g/kg GSN) groups. The genes analyzed encoded the low-density lipoprotein receptor (LDL-R), sterol regulatory element binding protein 2 (SREBP-2), cholesterol 7 α-hydroxylase (CYP7A1), sterol 27-hydroxylase (CYP27A1), estrogen receptor (ER), extracellular regulated protein kinase (ERK), c-Jun N-terminal kinase (JNK), androgen receptor (AR), and peroxisome proliferator-activated receptor α (PPARα). GAPDH mRNA was amplified as the internal control. Mean values were significantly different from those of the HFD group at *, $P < 0.05$, **, $P < 0.01$, and ***, $P < 0.001$.

expression was significantly higher in the HFD + 2 g/kg GSN group than in the HFD group ($P < 0.05$). The expression of cholesterol 7 α-hydroxylase (CYP7A1) and sterol 27-hydroxylase (CYP27A1) was lower in the HFD group than in the NFD group ($P < 0.05$) and were unaffected by GSN treatment. The different diets significantly affected the expression of the estrogen receptor (ER). The expression of both ERα and ERβ was downregulated in the HFD group compared with the NFD group ($P < 0.05$) but was upregulated in the HFD + 2 g/kg GSN group compared with the HFD group ($P < 0.05$).

The hepatic expression of ERK2, ERK5, and c-Jun N-terminal kinase (JNK), which are involved in the MAPK pathway, was downregulated in the HFD group as compared with their expression in the NFD group ($P < 0.05$). However, there were no significant differences between the HFD and HFD + 2 g/kg GSN groups in ERK1, ERK2, or ERK5 mRNA expression. The transcription of both p38 and JNK almost returned to normal in the HFD + 2 g/kg GSN group relative to that in the HFD group, but the change was not significant. The expression of the androgen receptor (AR) and PPARα was downregulated in the HFD group ($P < 0.05$), but it was unaffected by the GSN treatment.

Plasma ^{1}H NMR Metabonomics. As indicated by the CPMG score plots shown in Figures 3a,c, the plasma metabolic profiles of the NFD and HFD groups were clearly separated in both the PCA and OSC-PLS analyses. However, the HFD and HFD + 2 g/kg GSN groups could not be differentiated with PCA (Figure 3a) but were separated with OSC-PLS (Figure 3c). In the OSC-PLS analysis, the NFD group was on the right half of the ellipse, and the HFD group was on the left half of the ellipse. The samples in the HFD + 2 g/kg GSN group were differentiated from those in the HFD group and were shifted closer to those in the NFD group. Validation of the OSC-PLS model with permutation testing resulted in a Q_2 intercept of (0.0, − 0.27).

Figure 4 presents the results of BPP-LED analyzed with both PCA and OSC-PLS. In PCA, the HFD group was distributed between the lower ($^5/_6$) and upper ($^1/_6$) ellipse, the NFD group was in the left ellipse, and the HFD + 2 g/kg GSN group was distributed between the right ($^5/_6$) and left ($^1/_6$) ellipse (Figure 4a). The plasma BPP-LED results were also subjected to OSC-PLS, and three clusters were apparent: the NFD, HFD, and HFD + 2 g/kg GSN groups. This result indicates that metabolic changes occurred in the hamster plasma in response to the different dietary treatments (Figure 4c). The metabolic profiles of the HFD + 2 g/kg GSN group differed from those of the HFD group and were closer to those of the NFD group. The OSC-PLS model was validated with permutation testing, which had a Q_2 intercept of (0.0, − 0.27).

Table 4 shows the changes in the plasma metabolite concentrations according to CPMG and BPP-LED. The concentrations of lactate and lipoprotein in the HFD group were lower and higher, respectively, than those in the NFD group. Very low-density lipoprotein (VLDL; lipid, CH_3), LDL and VLDL (lipid, CH_2), VLDL (lipid, CH_2), lipid (CH_2CH_2CO), lipid ($CH_2C{=}C$), lipid (CH_2CO), and unsaturated fatty acids (UFA, $=CH$) levels were higher in the HFD group than they were in the NFD group. Most of the abnormal lipid metabolites, including VLDL (lipid, CH_3), VLDL (lipid, CH_2), lipid (CH_2CH_2CO), lipid ($CH_2C{=}C$), lipid (CH_2CO), phosphatidylcholine, and UFA ($=CH$), were reversed by GSN supplementation.

DOI: 10.1021/acs.jafc.5b01590
J. Agric. Food Chem. 2015, 63, 7929−7936

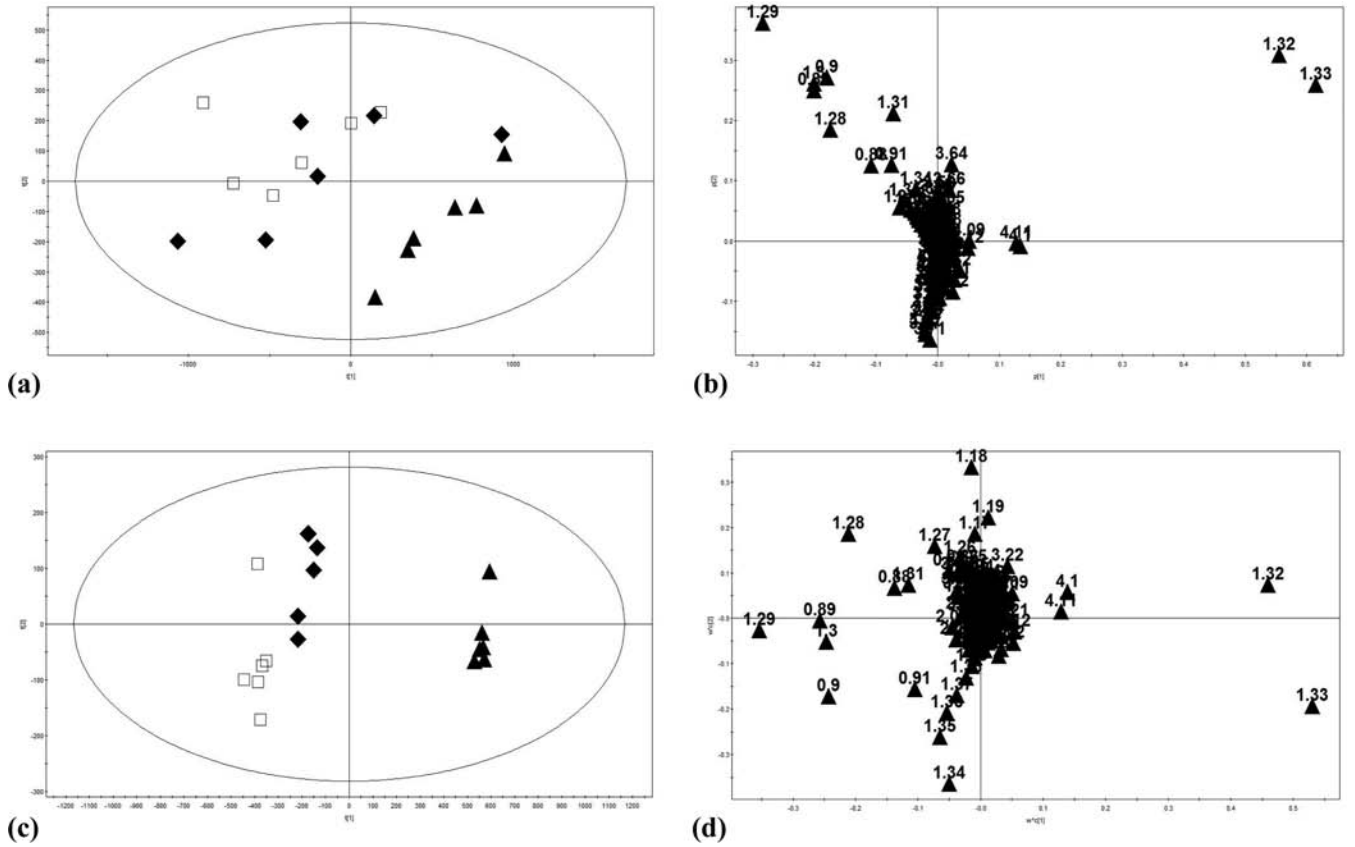

Figure 3. (a and b) Principal components analysis (PCA). R^2X = 0.945, Q^2 = 0.905. (c and d) Orthogonal signal correction partial least-squares (OSC-PLS). R^2X = 0.891, R^2Y = 0.728, Q^2 = 0.62. Scores plots and loading plots derived from the ^{1}H CPMG NMR spectra of the plasma metabolic profiles of the normal-fat diet (▲), high-fat diet (□), and high-fat diet +2 g/kg GSN (♦) groups.

DISCUSSION

Feed Intake, Bodyweight, Organ Weight, and Plasma and Hepatic Lipid Levels. There has been little agreement on the effects of GSN on the feed intake and bodyweights of animal models. Some researchers have reported that GSN reduces feed intake or bodyweight,[20,21] whereas others have shown no effect of dietary GSN on feed intake and bodyweight.[22] These discrepancies may be attributable to differences in the animal models used, HFD compositions, GSN doses, or the durations of the experiments. It is unclear whether the changes in feed intake caused by GSN influence the experimental results because this factor is not accounted for in many experiments. Feed intake was not affected by GSN in this study, so all the results were attributable to the biological effects of GSN rather than to different patterns of food intake. Although 2 g/kg of dietary GSN significantly reduced the liver weights of mice fed a HFD (18% fat),[10] liver weight was not significantly affected by the same concentration of GSN in the present study, which could be explained by the differences in the HFD composition (21% fat in this study) and the animal species used. GSN has previously been shown to affect adipose deposition,[21] and we also observed significantly less abdominal fat in the hamsters fed 2 g/kg GSN than in the HFD hamsters.

Plasma and hepatic lipid levels reflect the lipid metabolism in animals. At the end of 6 weeks, the plasma and liver lipids in the HFD group were all significantly higher than those in the NFD group, suggesting the induction of hyperlipidemia. This hyperlipidemia was alleviated in the 2 g/kg GSN group, which had lower lipid levels in both the plasma and liver than did the HFD group. Previous studies have shown that GSN reduces the plasma and hepatic lipids in animal models, although the lowest observable levels have varied in different studies.[10,11,23] One study found that 2 g/kg of dietary GSN reduced plasma TC and liver TG in mice fed a HFD.[21] Another study found that the serum and liver lipids of mice fed a HFD were not affected until GSN was increased to 2 g/kg.[10] In this study, the lipids in both the plasma and livers of the 2 g/kg GSN group were lower than those in the HFD group, which is consistent with previous studies.[10,21] We also found that GSN exerted an antioxidant effect by reducing plasma MDA production, which is consistent with a previous study in which lipid peroxidation was inhibited by GSN treatment.[24] The biochemical parameters of the plasma and liver demonstrated that 2 g/kg dietary GSN improved the lipid metabolism of hamsters with diet-induced hyperlipidemia by reducing lipid circulation and inhibiting lipid peroxidation.

Hepatic mRNA Expression. Several mechanisms have been proposed to explain the antihyperlipidemic effects of GSN. One study reported that of the 97 transcripts altered in the HFD-fed group, the expression of 84 were normalized with GSN supplementation.[21] Genes that are involved in cholesterol metabolism are regulated by GSN,[7] which was confirmed here by the observed increase in hepatic LDL receptor mRNA expression, indicating an improvement in LDL-C clearance. Isoflavones have previously been reported to increase the mature nuclear form of SREBP-2 in vitro.[25] However, hepatic SREBP-2 mRNA expression was not affected by GSN in the present study, consistent with another study.[11] CYP7A1 and

DOI: 10.1021/acs.jafc.5b01590
J. Agric. Food Chem. 2015, 63, 7929−7936

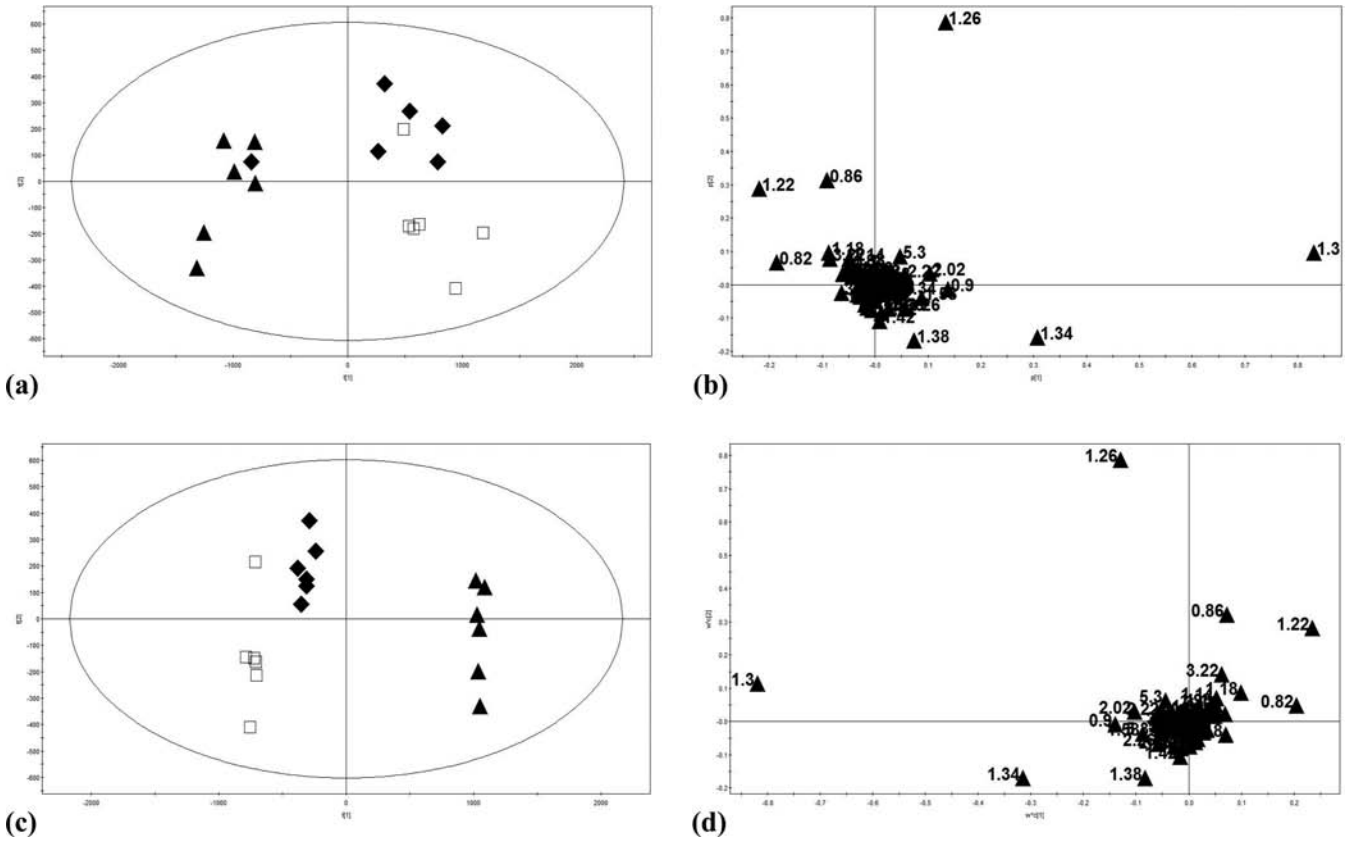

Figure 4. (a and b) Principal components analysis (PCA). R^2X = 0.983, Q^2 = 0.921. (c and d) Orthogonal signal correction partial least-squares (OSC-PLS). R^2X = 0.99, R^2Y = 0.724, Q^2 = 0.7. Scores plots and loading plots derived from the ^{1}H BPP-LED NMR spectra of the plasma metabolic profiles of the normal-fat diet (▲), high-fat diet (□), and high-fat diet +2 g/kg genistein (♦) groups.

CYP27A1 were upregulated in mice fed a soy protein diet plus 2% cholesterol.[26] We observed no effect of GSN on CYP7A1 or CYP27A1 expression in this study, which warrants further investigation. Because GSN has a structure similar to that of estradiol, it is reported to bind both ERα and ERβ,[27] the two nuclear ERs upon which estradiol acts. The binding of estradiol to the ERs inhibits lipogenesis primarily by reducing the activity of lipoprotein lipase, an enzyme that regulates lipid uptake by adipocytes.[6] Hepatic expression of ERα and ERβ mRNA was upregulated in the GSN group, indicating that the ERs were activated by GSN ingestion. This may explain the primary mechanism underlying the hypolipidemic effects of GSN in this study, although more evidence is required to demonstrate the molecular mechanism of GSN activity on hyperlipidemia.

Increasing evidence has established that GSN acts not only through the ERs but also via other pathways. PPARα is important in the β oxidation of fatty acids and is mainly expressed in tissues such as the liver, where lipoprotein metabolism is crucial. GSN binds directly to and activates PPARα in vitro, which may result in lipid catabolism and reduce blood lipids.[6,9] However, hepatic PPARα mRNA expression was not affected by GSN supplementation in vivo.[10,11] We also found no difference in hepatic PPARα mRNA expression in this study. Although GSN reportedly upregulates the expression of ERK1/2 in vitro,[12] we saw no significant effect of GSN treatment on any gene involved in the liver MAPK pathway. Therefore, the actions of GSN in vivo and in vitro may not be consistent, so further studies of this discrepancy are required.

Plasma ^{1}H NMR Metabonomics. The aim of the ^{1}H NMR metabonomic analysis was not to quantify absolutely the differences between the groups but rather to compare their relative differences. The distinct plasma metabolic profiles of the HFD and NFD groups indicate that ^{1}H NMR metabonomic data directly reflect the abnormal metabolic profiles induced by HFD in hamsters, which recapitulates the results of previous studies.[28,29] Although numerous studies have reported the beneficial effects of GSN on lipid metabolism, this is the first study to use an ^{1}H NMR metabonomic analysis of plasma metabolites profiles to identify the biological effects of GSN in hamsters fed an HFD. The restoration of the plasma metabolic profiles in the 2 g/kg GSN group indicates that GSN improved hamster hyperlipidemia. These results are consistent with the plasma and hepatic results that we obtained with traditional approaches.

A multivariate statistical analysis of the NMR spectra of the plasma samples revealed differences in the intensities of the different spectral regions, which could be ascribed to differences in lipoproteins, lactate, VLDL, LDL, phosphatidylcholine, UFA, or other lipids among the three groups, as listed in Table 4. Lactate, an important intermediate of glycometabolism, was lower in the HFD group than in the NFD group, consistent with a previous study,[29] and the change was reversed in the GSN group. A reduction in blood lactate implies that glycolysis is inhibited and that the energy consumption pattern may shifted to lipid oxidation in response to hyperlipidemia.[29] Therefore, the reversion of lactate levels by GSN might contribute to the restoration of normal energy consumption patterns. However, other NMR metabonomic studies have

DOI: 10.1021/acs.jafc.5b01590
J. Agric. Food Chem. 2015, 63, 7929−7936

Table 4. Metabolic Differences in Plasma among the Normal-Fat Diet, High-Fat Diet, and High-Fat Diet +2 g/kg Genistein Groups[a]

NMR spectral region (ppm)	assignment	HFD[b]	HFD + 2 g/kg GSN[b]
	CPMG Spectra		
0.84−0.90	lipoprotein	↑	↓
1.26−1.30	lipoprotein	↑	↓
1.32−1.34 4.09−4.10	lactate	↓	↑
	BPP-LED Spectra		
0.82, 0.86	VLDL/LDL (lipid, CH_3)	↓	↑
0.90	VLDL (lipid, CH_3)	↑	↓
1.22	LDL (lipid, CH_2)	↓	↑
1.26	LDL/VLDL (lipid, CH_2)	↑	↑
1.30, 1.34	VLDL (lipid, CH_2)	↑	↓
1.58	lipid (CH_2CH_2CO)	↑	↓
2.02, 2.06	lipid ($CH_2C{=}C$)	↑	↓
2.22, 2.26	lipid (CH_2CO)	↑	↓
3.22	PCho	↓	↑
5.3, 5.34	UFA (=CH)	↑	↓
		NFD	HFD

[a]NFD, normal-fat diet; HFD, high-fat diet; HFD + 2 g/kg GSN, high-fat diet +2 g/kg genistein; VLDL, very low-density lipoprotein; LDL, low-density lipoprotein; Pcho, phosphatidylcholine; UFA, unsaturated fatty acids; CPMG, Carr−Purcell−Meiboom−Gill pulse sequence; BPP-LED, bipolar-pair longitudinal-eddy current. [b]The symbols ↑ and ↓ indicate higher and lower concentrations in groups listed in the top compared with groups at the bottom of the table.

reported that blood lactate is higher in hamsters fed a HFD.[30,31] Therefore, further research is required. The BPP-LED spectra were dominated by the signals from lipids, and GSN treatment restored the signal intensities of VLDL, phosphorylcholine, UFA, and other lipids to those of the NFD group. VLDL and LDL, which are considered to be the major cholesterol-containing lipoproteins implicated in the development of atherosclerosis, were restored to normal levels in the GSN group. LDL-C is mainly cleared by the hepatic LDL-R pathway, in which ERs are critically involved.[32] Therefore, in this study, the reversion of VLDL and LDL in the GSN group observed with ^{1}H NMR metabonomics may be explained by the upregulated expression of hepatic ERα, ERβ, and the LDL receptor. Polyunsaturated fatty acids, which have a high degree of unsaturation in the *n*-6 and *n*-3 series, accelerate cell-mediated LDL peroxidation and therefore aggravate the atherosclerotic process.[33] The restoration of the plasma lipid profiles after GSN supplementation suggests that hyperlipidemia was globally ameliorated in these hamsters.

We have demonstrated that dietary 2 g/kg GSN ameliorated hyperlipidemia in hamsters by reducing the weight of abdominal fat and decreasing plasma and hepatic lipid contents. The improvement in lipid metabolism was associated with the upregulated expression of hepatic LDL receptor, ERα, and ERβ mRNAs. ^{1}H NMR and multivariate data analyses showed that both the abnormal small and macromolecular metabolic plasma profiles in the HFD group of hamsters were shifted toward normal profiles by GSN supplementation. Further research to quantify absolutely the plasma lipid profiles in relation to GSN ingestion would be of great value.

AUTHOR INFORMATION

Corresponding Author

*E-mail: zhjmxms@sina.com. Fax: 86-010-62815537. Tel.: 86-010-62815852.

Funding

This study was financially supported by the Agricultural Science and Technology Innovation Program (ASTIP-IAS12) and the Special Basic Research Fund for Central Public Research Institutes (2015ywf-zd-28).

Notes

The authors declare no competing financial interest.

ACKNOWLEDGMENTS

We thank Bo Sun for her technical support during sample analysis.

ABBREVIATIONS USED

GSN, genistein; NMR, nuclear magnetic resonance; NFD, normal-fat diet; HFD, high-fat diet; HFD + 2 g/kg GSN, high-fat diet +2 g/kg genistein; ADFI, average daily feed intake; BW, bodyweight; TC, total cholesterol; TG, triglyceride; HDL-C, high-density lipoprotein (HDL) cholesterol; LDL-C, low-density lipoprotein (LDL) cholesterol; SOD, superoxide dismutase; MDA, malondialdehyde; FFA, free fatty acids; GAPDH, glyceraldehyde phosphate dehydrogenase; LDL-R, low-density lipoprotein (LDL) receptor; SREBP-2, sterol regulatory element binding protein 2; CYP7A1, cholesterol 7 α-hydroxylase; CYP27A1, sterol 27-hydroxylase; ER, estrogen receptor; ERK, extracellular regulated protein kinase; JNK, c-Jun N-terminal kinase; AR, androgen receptor; PPARα, peroxisome proliferator-activated receptor α; MAPK, mitogen-activated protein kinase; CPMG, Carr−Purcell−Meiboom−Gill; BPP-LED, bipolar-pair longitudinal-eddy current; PCA, principal components analysis; OSC-PLS, orthogonal signal correction partial least-squares

REFERENCES

(1) World Health Organization. *Global atlas on cardiovascular disease prevention and control*; World Health Organization in collaboration with the World Heart Federation and the World Stroke Organization: Geneva, Switzerland, 2011.

(2) U.S. Food and Drug Administration. Food labeling health claims; soy protein and coronary heart disease. *Fed. Regist.* **1999**, *64*, 57699−57733.

(3) Anderson, J. W.; Johnstone, B. M.; Cook-Newell, M. E. Meta-analysis of the effects of soy protein intake on serum lipids. *N. Engl. J. Med.* **1995**, *333*, 276−282.

(4) Sagara, M.; Kanda, T.; NJelekera, M.; Teramoto, T.; Armitage, L.; Birt, N.; Birt, C.; Yamori, Y. Effects of dietary intake of soy protein and isoflavones on cardiovascular disease risk factors in high risk, middle-aged men in Scotland. *J. Am. Coll. Nutr.* **2004**, *23*, 85−91.

(5) Merz-Demlow, B. E.; Duncan, A. M.; Wangen, K. E.; Xu, X.; Carr, T. P.; Phipps, W. R.; Kurzer, M. S. Soy isoflavones improve plasma lipids in normocholesterolemic, premenopausal women. *Am. J. Clin. Nutr.* **2000**, *71*, 1462−1469.

(6) Ørgaard, A.; Jensen, L. The effects of soy isoflavones on obesity. *Exp. Biol. Med.* **2008**, *233*, 1066−1080.

(7) Borradaile, N.; De Dreu, L.; Wilcox, L.; Edwards, J.; Huff, M. Soya phytoestrogens, genistein and daidzein, decrease apolipoprotein B secretion from HepG2 cells through multiple mechanisms. *Biochem. J.* **2002**, *366*, 531−539.

(8) Kirk, E. A.; Sutherland, P.; Wang, S. A.; Chait, A.; LeBoeuf, R. C. Dietary Isoflavones Reduce Plasma Cholesterol and Atherosclerosis in

DOI: 10.1021/acs.jafc.5b01590
J. Agric. Food Chem. 2015, 63, 7929−7936

C57BL/6 Mice but not LDL Receptor−Deficient Mice. *J. Nutr.* **1998**, *128*, 954−959.
(9) Kim, S.; Shin, H.-J.; Kim, S. Y.; Kim, J. H.; Lee, Y. S.; Kim, D.-H.; Lee, M.-O. Genistein enhances expression of genes involved in fatty acid catabolism through activation of PPARα. *Mol. Cell. Endocrinol.* **2004**, *220*, 51−58.
(10) Lee, Y. M.; Choi, J. S.; Kim, M. H.; Jung, M. H.; Lee, Y. S.; Song, J. Effects of dietary genistein on hepatic lipid metabolism and mitochondrial function in mice fed high-fat diets. *Nutrition* **2006**, *22*, 956−964.
(11) Jeon, S.; Park, Y. J.; Kwon, Y. H. Genistein alleviates the development of nonalcoholic steatohepatitis in ApoE$^{-/-}$ mice fed a high-fat diet. *Mol. Nutr. Food Res.* **2014**, *58*, 830−841.
(12) Borrás, C.; Gambini, J.; Gómez-Cabrera, M. C.; Sastre, J.; Pallardó, F. V.; Mann, G. E.; Viña, J. Genistein, a soy isoflavone, up-regulates expression of antioxidant genes: involvement of estrogen receptors ERK1/2, and NFκB. *FASEB J.* **2006**, *20*, 2136−2138.
(13) Dixon, R. A.; Gang, D. R.; Charlton, A. J.; Fiehn, O.; Kuiper, H. A.; Reynolds, T. L.; Tjeerdema, R. S.; Jeffery, E. H.; German, J. B.; Ridley, W. P.; et al. Applications of metabolomics in agriculture. *J. Agric. Food Chem.* **2006**, *54*, 8984−8994.
(14) Wang, Y.; Tang, H.; Nicholson, J. K.; Hylands, P. J.; Sampson, J.; Holmes, E. A metabonomic strategy for the detection of the metabolic effects of chamomile (Matricaria recutita L.) ingestion. *J. Agric. Food Chem.* **2005**, *53*, 191−196.
(15) Solanky, K. S.; Bailey, N. J.; Holmes, E.; Lindon, J. C.; Davis, A. L.; Mulder, T. P.; Van Duynhoven, J. P.; Nicholson, J. K. NMR-based metabonomic studies on the biochemical effects of epicatechin in the rat. *J. Agric. Food Chem.* **2003**, *51*, 4139−4145.
(16) Solanky, K. S.; Bailey, N. J.; Beckwith-Hall, B. M.; Davis, A.; Bingham, S.; Holmes, E.; Nicholson, J. K.; Cassidy, A. Application of biofluid 1 H nuclear magnetic resonance-based metabonomic techniques for the analysis of the biochemical effects of dietary isoflavones on human plasma profile. *Anal. Biochem.* **2003**, *323*, 197−204.
(17) Sullivan, M. P.; Cerda, J. J.; Robbins, F. L.; Burgin, C. W.; Beatty, R. J. The gerbil, hamster, and guinea pig as rodent models for hyperlipidemia. *Lab. Anim. Sci.* **1993**, *43*, 575−578.
(18) The Archer Daniels Midland Company. GRAS Notification for Isoflavones Derived from Soybeans.http://www.fda.gov/downloads/food/ingredientspackaginglabeling/gras/noticeinventory/ucm264301.pdf.
(19) Livak, K. J.; Schmittgen, T. D. Analysis of Relative Gene Expression Data Using Real-Time Quantitative PCR and the $2^{-\Delta\Delta CT}$ Method. *Methods* **2001**, *25*, 402−408.
(20) Kim, H.-K.; Nelson-Dooley, C.; Della-Fera, M. A.; Yang, J.-Y.; Zhang, W.; Duan, J.; Hartzell, D. L.; Hamrick, M. W.; Baile, C. A. Genistein decreases food intake, body weight, and fat pad weight and causes adipose tissue apoptosis in ovariectomized female mice. *J. Nutr.* **2006**, *136*, 409−414.
(21) Kim, S.; Sohn, I.; Lee, Y. S.; Lee, Y. S. Hepatic gene expression profiles are altered by genistein supplementation in mice with diet-induced obesity. *J. Nutr.* **2005**, *135*, 33−41.
(22) Ae Park, S.; Choi, M.-S.; Cho, S.-Y.; Seo, J.-S.; Jung, U. J.; Kim, M.-J.; Sung, M.-K.; Park, Y. B.; Lee, M.-K. Genistein and daidzein modulate hepatic glucose and lipid regulating enzyme activities in C57BL/KsJ-db/db mice. *Life Sci.* **2006**, *79*, 1207−1213.
(23) Fang, Y.-C.; Chen, B.-H.; Huang, R.-F. S.; Lu, Y.-F. Effect of genistein supplementation on tissue genistein and lipid peroxidation of serum, liver and low-density lipoprotein in hamsters. *J. Nutr. Biochem.* **2004**, *15*, 142−148.
(24) Wijeratne, S. S.; Cuppett, S. L. Soy isoflavones protect the intestine from lipid hydroperoxide mediated oxidative damage. *J. Agric. Food Chem.* **2007**, *55*, 9811−9816.
(25) Mullen, E.; Brown, R. M.; Osborne, T. F.; Shay, N. F. Soy isoflavones affect sterol regulatory element binding proteins (SREBPs) and SREBP-regulated genes in HepG2 cells. *J. Nutr.* **2004**, *134*, 2942−2947.
(26) González-Granillo, M.; Steffensen, K.; Granados, O.; Torres, N.; Korach-André, M.; Ortíz, V.; Aguilar-Salinas, C.; Jakobsson, T.; Díaz-Villaseñor, A.; Loza-Valdes, A.; et al. Soy protein isoflavones differentially regulate liver X receptor isoforms to modulate lipid metabolism and cholesterol transport in the liver and intestine in mice. *Diabetologia* **2012**, *55*, 2469−2478.
(27) Kuiper, G. G.; Lemmen, J. G.; Carlsson, B.; Corton, J. C.; Safe, S. H.; van der Saag, P. T.; van der Burg, B.; Gustafsson, J. A. Interaction of estrogenic chemicals and phytoestrogens with estrogen receptor β. *Endocrinology* **1998**, *139*, 4252−4263.
(28) Jiang, C. Y.; Yang, K. M.; Yang, L.; Miao, Z. X.; Wang, Y. H.; Zhu, H. B. A ^{1}H NMR-Based Metabonomic Investigation of Time-Related Metabolic Trajectories of the Plasma, Urine and Liver Extracts of Hyperlipidemic Hamsters. *PLoS One* **2013**, *8*, e66786.
(29) Song, X.; Wang, J.; Wang, P.; Tian, N.; Yang, M.; Kong, L. ^{1}H NMR-based metabolomics approach to evaluate the effect of Xue-Fu-Zhu-Yu decoction on hyperlipidemia rats induced by high-fat diet. *J. Pharm. Biomed. Anal.* **2013**, *78-79*, 202−210.
(30) Sun, Y.; Lian, Z.; Jiang, C.; Wang, Y.; Zhu, H. Beneficial metabolic effects of 2′, 3′, 5′-tri-acetyl-N6-(3-hydroxylaniline) adenosine in the liver and plasma of hyperlipidemic hamsters. *PLoS One* **2012**, *7*, e32115.
(31) Sun, Y.; Wang, Y.-H.; Qu, K.; Zhu, H.-B. Beneficial effects of cordycepin on metabolic profiles of liver and plasma from hyperlipidemic hamsters. *J. Asian Nat. Prod. Res.* **2011**, *13*, 534−546.
(32) Parini, P.; Angelin, B.; Rudling, M. Importance of estrogen receptors in hepatic LDL receptor regulation. *Arterioscler., Thromb., Vasc. Biol.* **1997**, *17*, 1800−1805.
(33) Maziere, C.; Dantin, F.; Conte, M.; Degonville, J.; Ali, D.; Dubois, F.; MAZIERE, J. Polyunsaturated fatty acid enrichment enhances endothelial cell-induced low-density-lipoprotein peroxidation. *Biochem. J.* **1998**, *336*, 57−62.

DOI: 10.1021/acs.jafc.5b01590
J. Agric. Food Chem. 2015, 63, 7929−7936

was subsequently evaporated, and the residue was extracted with ethyl acetate three times. The combined organic layers were washed with brine, dried over anhydrous $MgSO_4$, filtered, and concentrated under reduced pressure to give h-MHES (37 g) as a yellow solid. The product was dissolved in dimethyl sulfoxide (DMSO) prior to use in cell experiments.

Analysis of h-MHES by Means of High-Performance Liquid Chromatography (HPLC). HPLC analysis was performed by using an Agilent 1220 Infinity LC (Agilent Technologies, Santa Clara, CA, USA) with UV detection (254 nm) and an InertSustain C18 column (⌀ 3.0 × 50 mm, GL Science, Tokyo, Japan). The temperature of the column oven was set at 40 °C. The mobile phase consisted of 0.1% formic acid in water (solution A) and acetonitrile (solution B); the run conditions were as follows: isocratic elution, 70% A/30% B, 0−1.5 min; linear gradient from 70% A/30% B to 30% A/70% B, 1.5−5.5 min; linear gradient from 30% A/70% B to 0% A/100% B, 5.5−6.0 min. The flow rate was 1.0 mL/min.

Isolation of Flavanones (AG1, AG2) and Chalcones (AG3, AG4). Thin-layer chromatography (TLC) was performed by using TLC silica gel 60 F_{254} (Merck, Darmstadt, Germany); spots were visualized by using UV light and treatment with phosphomolybdic acid stain followed by heating. Flash column chromatography was performed by using Hi-Flash column silica gel (Yamazen, Osaka, Japan). Nuclear magnetic resonance (NMR) spectra were recorded on a Bruker Avance 600 spectrometer with Cryoprobe (Bruker, Newark, DE, USA). Chemical shifts (δ) are reported in parts per million based on the resonance of tetramethylsilane (0 ppm for ^{1}H NMR in $CDCl_3$) or the respective solvent (^{1}H NMR, 2.49 ppm in DMSO-d_6; ^{13}C NMR, 77.0 ppm in $CDCl_3$ or 39.7 ppm in DMSO-d_6) as the internal standard.

The h-MHES (3.32 g) was fractionated by using flash column chromatography and eluted with hexane/ethyl acetate/methanol. Ten fractions (F1−F10) were collected.

5,7-Dihydroxy-3′,4′-dimethoxyflavanone (AG1) (865 mg) was obtained as a white solid by recrystallizing the F2 fraction from hexane/ethyl acetate: ^{1}H NMR (DMSO-d_6) δ 12.13 (1H, s), 10.80 (1H, s), 7.11 (1H, d, J = 1.9 Hz), 7.01 (1H, dd, J = 8.3, 1.9 Hz), 6.95 (1H, d, J = 8.3 Hz), 5.88 (1H, d, J = 2.2 Hz), 5.87 (1H, d, J = 2.2 Hz), 5.46 (1H, dd, J = 12.9, 3.0 Hz), 3.75 (3H, s), 3.74 (3H, s), 3.32 (1H, d, J = 17.1, 12.9 Hz), 2.68 (1H, dd, J = 17.1, 3.0 Hz); ^{13}C NMR (DMSO-d_6) δ 196.3, 166.6, 163.5, 162.8, 149.0, 148.7, 130.9, 119.3, 111.4, 110.5, 101.7, 95.8, 95.0, 78.5, 55.5, 42.1.

7-Hydroxy-5,3′,4′-trimethoxyflavanone (AG2) (609 mg) was obtained as a pale yellow solid from the F7 and F8 fractions: ^{1}H NMR (DMSO-d_6) δ 10.53 (1H, s), 7.07 (1H, d, J = 1.9 Hz), 6.98 (1H, dd, J = 8.4, 1.9 Hz), 6.94 (1H, d, J = 8.4 Hz), 6.04 (1H, d, J = 2.1 Hz), 5.95 (1H, d, J = 2.1 Hz), 5.35 (1H, dd, J = 12.7, 2.8 Hz), 3.75 (3H, s), 3.73 (3H, s), 3.71 (3H, s), 3.03 (1H, d, J = 16.5, 12.7 Hz), 2.52 (1H, dd, J = 16.5, 2.8 Hz); ^{13}C NMR (DMSO-d_6) δ 188.1, 164.7, 164.6, 162.6, 149.3, 149.1, 131.8, 119.4, 111.9, 110.8, 104.8, 96.0, 93.6, 78.6, 56.0, 55.9, 45.3.

4′-Hydroxy-3,4,2′,6′-tetramethoxychalcone (AG3) (156 mg) was obtained as a pale yellow solid from the F5 fraction: ^{1}H NMR (DMSO-d_6) δ 9.82 (1H, s), 7.25 (1H, d, J = 2.0 Hz), 7.15 (1H, dd, J = 8.4, 2.0 Hz), 7.10 (1H, d, J = 16.0 Hz), 6.93 (1H, d, J = 8.4 Hz), 6.84 (1H, d, J = 16.0 Hz), 6.10 (2H, s), 3.77 (3H, s), 3.76 (3H, s), 3.62 (6H, s); ^{13}C NMR (DMSO-d_6) δ 194.1, 160.4, 158.4, 151.3, 149.4, 144.4, 127.7, 127.6, 123.3, 111.9, 110.9, 110.2, 92.4, 55.99, 55.95, 55.89.

4′,6′-Dihydroxy-3,4,2′-trimethoxychalcone (AG4) (112 mg) was obtained as an orange solid from the F3 fraction: ^{1}H NMR (DMSO-d_6) δ 13.72 (1H, s), 10.58 (1H, s), 7.69 (1H, d, J = 15.6 Hz), 7.60 (1H, d, J = 15.6 Hz), 7.26 (2H, m), 7.00 (1H, d, J = 8.8 Hz), 5.99 (1H, d, J = 2.1 Hz), 5.89 (1H, s), 3.85 (3H, s), 3.81 (3H, s), 3.79 (3H, s); ^{13}C NMR (DMSO-d_6) δ 192.2, 166.4, 165.1, 162.9, 151.4, 149.3, 142.9, 128.1, 125.6, 123.1, 112.1, 111.1, 105.6, 96.2, 56.4, 56.0, 55.9.

Synthesis of 2′,4′,6′-Trihydroxy-3,4-dimethoxychalcone (AG5). To a stirred solution of 2′,4′,6′-trihydroxyacetophenone monohydrate (2.01 g) in tetrahydrofuran (50 mL), diisopropylethylamine (18.8 mL) and chloromethyl methyl ether (3.28 mL) were added at 0 °C; the mixture was then stirred at room temperature for 9.5 h. After the solution was cooled to 0 °C, water (10 mL) was added. Then the mixture was extracted with ethyl acetate. The organic layer was washed with 0.5 M HCl and brine, dried over anhydrous $MgSO_4$, filtered, and concentrated under reduced pressure. The residue was purified by using flash chromatography (hexane/ethyl acetate) to give 2′-hydroxy-4′,6′-bis-methoxymethoxyacetophenone (1.71 g, 62%) as a white solid: ^{1}H NMR ($CDCl_3$) δ 13.71 (1H, s), 6.24 (1H, d, J = 2.5 Hz), 6.22 (1H, d, J = 2.5 Hz), 5.23 (2H, s), 5.15 (2H, s), 3.50 (3H, s), 3.45 (3H, s), 2.64 (3H, s); ^{13}C NMR ($CDCl_3$) δ 203.2, 166.8, 163.4, 160.3, 106.9, 97.1, 94.4, 94.0, 56.7, 56.5, 33.1.

To a stirred solution of 2′-hydroxy-4′,6′-bis-methoxymethoxyacetophenone (1.12 g) in methanol (20 mL), veratraldehyde (728 mg) and potassium hydroxide (2.85 g) in water (2 mL) were added at 0°C, and the mixture was stirred at room temperature for 55 h. Then, the mixture was neutralized with 2 M sodium hydroxide (30 mL) and extracted twice with ethyl acetate. The combined organic layers were washed with brine, dried over anhydrous $MgSO_4$, filtered, and concentrated under reduced pressure. The residue was purified by using flash column chromatography (hexane/ethyl acetate) to give 6′-hydroxy-3,4-dimethoxy-2′,4′-bis-methoxymethoxychalcone (1.13 g, 64%) as a yellow solid: ^{1}H NMR (DMSO-d_6) δ 12.15 (1H, s), 7.49 (1H, d, J = 15.7 Hz), 7.45 (1H, d, J = 15.7 Hz), 7.28 (1H, d, J = 1.9 Hz), 7.24 (1H, dd, J = 8.4, 1.9 Hz), 6.99 (1H, d, J = 8.4 Hz), 6.26 (1H, d, J = 2.3 Hz), 6.23 (1H, d, J = 2.3 Hz), 5.24 (2H, s), 5.20 (2H, s), 3.785 (3H, s), 3.783 (3H, s), 3.375 (3H, s), 3.368 (3H, s); ^{13}C NMR (DMSO-d_6) δ 192.8, 162.0, 161.2, 157.8, 151.1, 148.9, 143.6, 127.4, 125.6, 123.1, 111.6, 110.3, 109.1, 96.6, 94.53, 94.45, 93.8, 56.2, 55.9, 55.6, 55.4.

To a stirred solution of 6′-hydroxy-3,4-dimethoxy-2′,4′-bis-methoxymethoxycalcone (1.13 g) in methanol (60 mL), 1M HCl (30 ml) was added at room temperature, and refluxed for 50 min. After the solution was cooled to room temperature, the mixture was diluted with water (60 mL), and extracted twice with ethyl acetate. The combined organic layers were washed with brine, dried over anhydrous $MgSO_4$, filtered, and concentrated under reduced pressure. The residue was purified by using flash chromatography (hexane/EtOAc) to give 2′,4′,6′-trihydroxy-3,4-dimethoxychalcone (AG5) (585 mg, 66%) as an orange solid: ^{1}H NMR (DMSO-d_6) δ 12.53 (2H, s), 10.40 (1H, s), 8.01 (1H, d, J = 15.6 Hz), 7.65 (1H, d, J = 15.6 Hz), 7.25−7.23 (2H, m), 7.01 (1H, d, J = 8.9 Hz), 5.82 (2H, s), 3.792 (3H, s), 3.788 (3H, s); ^{13}C NMR (DMSO-d_6) δ 191.6, 164.8, 164.4, 150.9, 148.9, 142.1, 127.8, 125.0, 122.6, 111.7, 110.6, 104.2, 94.8, 55.6, 55.4.

Cell Culture. Human epidermal keratinocytes (Cascade Biologics, Portland, OR, USA) were grown in EpiLife medium containing 0.06 mM Ca^{2+}, human keratinocyte growth supplement (0.4% bovine pituitary extract, 10 μg/mL insulin, 0.67 μg/mL hydrocortisone, and 0.1 ng/mL human epidermal growth factor), and an antibiotic mixture (50 μg/mL gentamicin and 50 ng/mL amphotericin B) (Cascade Biologics). HEK293 cells (American Type Culture Collection, Manassas, VA, USA) were grown in Dulbecco's modified Eagle medium (Gibco, Grand Island, NY, USA) with 10% fetal bovine serum (Gibco) and 1% penicillin/streptomycin (Invitrogen, Carlsbad, CA, USA). Both cell types were grown at 37 °C in a humidified atmosphere of 5% CO_2 and 95% air until 80% confluence and then used for experiments.

Microarray Analysis. Total RNA was extracted by using the RNeasy Mini Kit (Qiagen, Venlo, The Netherlands). cRNA synthesis and labeling reactions were performed using a Low Input Quick Amp Labeling Kit (Agilent Technology) according to the manufacturer's protocol. Array hybridization was performed using a Whole Human Genome microarray 4 × 44K ver.2 (Agilent Technology). The hybridized array slide was scanned with a SureScan Microarray Scanner (Agilent Technology).

The microarray data were normalized by using GeneSpring GX 11.5 software (Agilent Technology). The cutoff value was set at 0.5−2.0 for the ratio (>2.0, up-regulation; <0.5, down-regulation). Ingenuity Pathway Analysis (IPA) software (Ingenuity, Redwood City, CA, USA) was then used to identify the specific pathways involved in the response to treatment with h-MHES.

DOI: 10.1021/acs.jafc.5b01992
J. Agric. Food Chem. 2015, 63, 7937−7944

Real-Time PCR Analysis. Total RNA was extracted by using an RNeasy Mini Kit (Qiagen) according to the manufacturer's instructions. cDNA was generated by using a High Capacity RNA-to-cDNA Kit (Applied Biosystems, Foster City, CA, USA). mRNA expression levels were determined by use of the TaqMan gene expression assay with the 7500 Real Time PCR System (Applied Biosystems). The primer and probe sets for the target genes were as follows: G6PD, Hs00166169_m1; GCLC, Hs00155249_m1; GCLM, Hs00157694_m1; GPX2, Hs01591589_m1; GSR, Hs00167317_m1; HMOX1, Hs01110250_m1; NFE2L2, Hs00232352_m1; NQO1, Hs00168547_m1; PRDX1, Hs03044567_g1; SRXN1, Hs00607800_m1; TXN, Hs01555212_g1 and TXNRD1, Hs00917067_m1. Target gene expression was normalized to RPLP0 (Hs99999902_m1) gene expression.

Extraction of Nuclear Protein. Nuclear extracts were obtained from the keratinocytes by using a Nuclear Extract Kit (Active Motif, Carlsbad, CA, USA) according to the manufacturer's instructions.

SDS-PAGE and Western Blotting. Cells were washed with cold PBS and lysed in RIPA buffer (25 mM Tris-HCl, pH 7.6, 150 mM NaCl, 1% NP-40, 1% sodium deoxycholate, 0.1% SDS) (Pierce, Rockford, IL, USA) containing protease inhibitor cocktail (Sigma-Aldrich, St. Louis, MO, USA) and phosphatase I and II inhibitor cocktail (Sigma-Aldrich) by passing them through a 25G needle. After incubating on ice for 15 min, the lysates were centrifuged at 15000*g* for 15 min at 4 °C, and then supernatants were collected. Protein concentration was determined by using a BCA protein assay kit (Pierce). The supernatants normalized by protein concentration were mixed with SDS sample buffer (Novagen, Madison, WI, USA) and denatured by boiling at 95 °C for 5 min.

Ten micrograms of protein per sample was loaded onto 4−15% gradient polyacrylamide gels (Bio-Rad, Hercules, CA, USA), and the samples were separated electrophoretically in Tris−glycine−SDS buffer (25 mM Tris, 192 mM glycine, 0.1% SDS; pH 8.3) (Bio-Rad). The separated proteins were transferred to polyvinylidene fluoride membranes (Bio-Rad) in Tris−glycine buffer (25 mM Tris, 192 mM glycine; pH 8.2) (Bio-Rad) containing 20% methanol. After being blocked at room temperature for 1 h in Tris-buffered saline−Tween (TBS-T) buffer (200 mM Tris, 5 M NaCl, 0.1% Tween-20; pH 7.4) (Bio-Rad) with 5% skim milk (Wako Pure Chemical Industries, Osaka, Japan), the membranes were incubated at 4 °C overnight in immunoreaction enhancer solution (Can Get Signal Solution 1; Toyobo, Osaka, Japan) containing a 1:1000 dilution of antibodies against HO-1 (Santa Cruz Biotechnology, Santa Cruz, CA, USA; sc-10789), GCLC (Abcam, Cambridge, UK; ab40929), β-actin (Cell Signaling Technology, Beverly, MA; 4970), Nrf2 (Santa Cruz Biotechnology; sc-722), histone H1 (Santa Cruz Biotechnology; sc-10806), phosphorylated p38 (Thr180/Tyr182) MAPK (Cell Signaling Technology; 4511), p38 MAPK (Cell Signaling Technology; 8690), phosphorylated Akt (Ser473) (Cell Signaling Technology; 4058), Akt (Cell Signaling Technology; 4691), phosphorylated ERK1/2 (Thr202/Tyr204) (Cell Signaling Technology; 4370), ERK1/2 (Cell Signaling Technology; 4695), phosphorylated SAPK/JNK (Thr183/Tyr185) (Cell Signaling Technology; 4671), and SAPK/JNK (Cell Signaling Technology; 9252). The membranes were then washed three times in TBS-T and incubated for 1 h at room temperature in immunoreaction enhancer solution (Can Get Signal Solution 2; Toyobo) containing a 1:5000 dilution of anti-rabbit IgG, HRP-linked secondary antibody (GE Healthcare, Piscataway, NJ, USA). Protein-blot analysis was carried out using the ECL plus Western blotting detection reagent (GE Healthcare) with the luminescent image analyzer LAS-4000 (Fujifilm, Tokyo, Japan).

Determination of Intracellular Glutathione Levels. Cells were frozen at −80 °C and subsequently thawed at 37 °C in 5% metaphosphoric acid solution. Lysates were centrifuged at 1000*g* for 5 min, and supernatants were used for the glutathione (GSH) assay. Intracellular GSH was determined by using a commercial assay kit (Northwest Life Science Specialties, Vancouver, WA, USA) according to the manufacturer's protocol.

Luciferase Reporter Assay. ARE-luciferase reporter plasmids were generated by using the pGL3-promoter vector (Promega, Madison, WI, USA). The sense and antisense oligonucleotides containing three copies of the human GCLC ARE[16] (GCLC 3×ARE_F, CTAGCTCCCCGTGACTCAGCGCTTTGCCCTCCC-CGTGACTCAGCGCTTTGCCCTCCCCGTGACTCAGCGCTT-TGC; GCLC 3×ARE_R, TCGAGCAAAGCGCTGAGTCACGGG-GAGGGCAAAGCGCTGAGTCACGGGGAGGGCAAAGCGCTG-AGTCACGGGGAG) were annealed. The double-strand oligonucleotide was ligated to the *Nhe*I and *Xho*I sites of the pGL3-promoter vector.

HEK293 cells were grown at 37 °C in a humidified atmosphere of 5% CO_2 and 95% air until 80% confluence and then cultured in growth factor-free medium for 16 h. The cells were then cotransfected with the pARE-luc and pRL-TK (Promega) reporter plasmids by using the SuperFect transfection reagent (Qiagen). Cells were treated with h-MHES for 16 h, and then the luciferase assay was performed using the dual-luciferase reporter assay system (Promega). Firefly luciferase activities stemming from the pARE-luc plasmid were standardized to the corresponding Renilla luciferase activities from the pRL-TK control plasmid.

Transfection of Small Interfering RNA. Nrf2 siRNA and control siRNA were purchased from Santa Cruz Biotechnology. Keratinocytes were transfected with 5 nM Nrf2 or control siRNA by using the HiPerFect transfection reagent (Qiagen) according to the manufacturer's protocol. At 16 or 24 h after transfection, the cells were used for each experiment.

Treatment with Kinase Inhibitors. For kinase inhibitor experiments, keratinocytes were pretreated with growth factor-free medium containing 20 μM SB203580 (Sigma-Aldrich), LY294002 (Sigma-Aldrich), PD98059 (Sigma-Aldrich), or SP600125 (Sigma-Aldrich) for 1 h, and then h-MHES (final concentration = 16.5 μg/mL) was added. The cells were then incubated for a further 24 h. Treated cells were then washed twice with cold PBS and used for mRNA or protein analysis.

Determination of Intracellular Reactive Oxygen Species (ROS) Levels. The production of cellular ROS was detected by using 2′,7′-dichlorodihydrofluorescein diacetate (H_2DCFDA) (Invitrogen). Cells were pretreated with h-MHES (16.5 μg/mL) for 16 h. Then, the cells were incubated with Hank's balanced salt solution (HBSS) containing 10 μM H_2DCFDA at 37 °C for 20 min. After that, the cells were washed and incubated in HBSS buffer with 0, 100, or 200 μM H_2O_2 or irradiated with 0, 20, or 60 mJ/cm^2 UVB (1 mW/cm^2) by using GL20SE UVB lamps (emission peak, 306 nm; Sankyo denki, Tokyo, Japan). After 30 min of H_2O_2 treatment or 15 min of UVB irradiation, ROS generation was measured by the fluorescence intensity at 535 nm after excitation at 485 nm on an EnVision 2104 multilabel reader (PerkinElmer, Waltham, MA, USA) and imaged by means of confocal laser scanning microscopy (TCP-SP5; Leica, Mannheim, Germany).

Statistical Analysis. Data are expressed as the mean ± standard error (SEM). Analysis of variance and a two-tailed unpaired Student's *t* test were used for statistical analysis. Differences between groups were considered to be significant at $P < 0.05$.

RESULTS

Preparation of h-MHES. h-MHES was prepared by acid hydrolysis of MHES, as described under Materials and Methods. HPLC analysis of h-MHES showed that it consisted mainly of four compounds (Figure 1A). This hydrolyzed MHES was used in experiments in this study. In addition, we fractionated h-MHES, by means of flash column chromatography, and isolated two flavanones and two chalcones. Structure determination from NMR data revealed that peak a was 7-hydroxy-5,3′,4′-trimethoxyflavanone (AG2), peak b was 4′-hydroxy-3,4,2′,6′-tetramethoxychalcone (AG3), peak c was 5,7-dihydroxy-3′,4′-dimethoxyflavanone (AG1), and peak d was 4′,6′-dihydroxy-3,4,2′-trimethoxychalcone (AG4) (Figure 1). Sakieki et al. reported that MHES is a mixture of six methylated derivatives of hesperidin,[9,10] and we expected that five aglycons

DOI: 10.1021/acs.jafc.5b01992
J. Agric. Food Chem. 2015, 63, 7937−7944

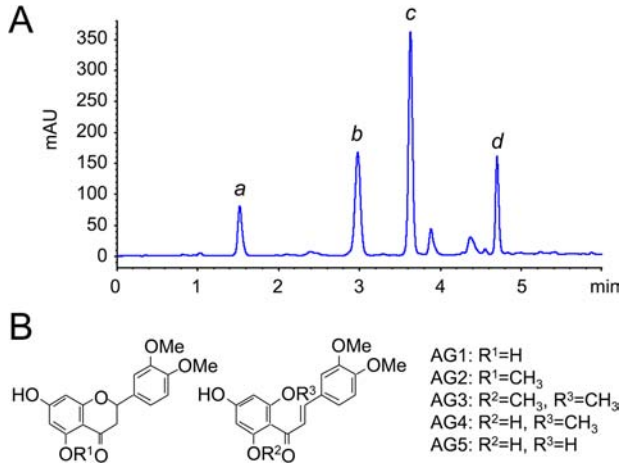

Figure 1. Chemical structures of h-MHES: (A) chromatogram for acid-hydrolyzed MHES; (B) chemical structures of flavanone and chalcone derivatives. AG1, 5,7-dihydroxy-3′,4′-dimethoxyflavanone (peak c); AG2, 7-hydroxy-5,3′,4′-trimethoxyflavanone (peak a); AG3, 4′-hydroxy-3,4,2′,6′-tetramethoxychalcone (peak b); AG4, 4′,6′-dihydroxy-3,4,2′-trimethoxychalcone (peak d); AG5, 2′,4′,6′-trihydroxy-3,4-dimethoxychalcone.

Table 1. h-MHES Up-regulates the mRNA of Antioxidant-Related Genes[a]

gene symbol	description	h-MHES (fold change) 2 h	8 h	24 h
G6PD	glucose-6-phosphate dehydrogenase	1.1	1.4	2.0
GCLC	glutamate-cysteine ligase, catalytic subunit	1.4	4.9	6.6
GCLM	glutamate-cysteine ligase, modifier subunit	1.2	3.2	2.4
GPX2	glutathione peroxidase 2	1.1	1.7	3.8
GSR	glutathione reductase	1.0	1.7	2.3
HMOX1	heme oxygenase 1	2.6	15.3	2.9
NQO1	NAD(P)H:quinone oxidoreductase 1	1.1	2.6	2.9
SRXN1	sulfiredoxin 1	1.4	4.6	5.1
TXN	thioredoxin	1.0	1.2	2.1
TXNRD1	thioredoxin reductase 1	1.7	6.7	4.1

[a]Keratinocytes were treated with h-MHES (16.5 μg/mL) for 2, 8, or 24 h. G6PD, GCLC, GCLM, GPX2, GSR, HMOX1 (HO-1), NQO1, SRXN1, TXN, and TXNRD1 expression levels were analyzed by using qRT-PCR. Fold changes in transcript levels relative to the control transcript level (untreated cells) are shown.

would be produced from the MHES by hydrolysis. As expected, AG1, AG2, AG3, and AG4 were produced, but there was no 2′,4′,6′-trihydroxy-3,4-dimethoxychalcone (AG5) in h-MHES. It may be that AG5 was completely converted to the corresponding flavanone (AG1) during acid hydrolysis. We, therefore, prepared AG5 by chemical synthesis (Figure 1B).

h-MHES Induces Antioxidant-Related Gene Expression. In a preliminary study to investigate the pharmacological effects of h-MHES, we treated keratinocytes and fibroblasts with h-MHES under conditions of UVB irradiation or cytokine stimulation. By using the Agilent Whole Human Genome Array, we found that h-MHES changed the gene expression as follows: In UVB-irradiated keratinocytes, 947 transcripts were either up-regulated or down-regulated (fold-change >2.0 or <0.5, respectively) by h-MHES. Similarly, 3346 transcripts were either up-regulated or down-regulated by h-MHES in IL-1β-stimulated fibroblasts. A total of 181 transcripts were common to both experiments. Of these 181 transcripts, 134 transcripts showed the same direction of change in both experiments. Transcriptomic analysis of these 134 transcripts suggested a highly significant association with the Nrf2-mediated oxidative stress response (data not shown). To validate the microarray data, we measured the mRNA levels of detoxication and antioxidant genes, including the rate-limiting enzyme for bilirubin biosynthesis (HO-1) and the enzymes associated with glutathione (GSH) synthesis and recycling (GCLC, GCLM, GSR) by using quantitative RT-PCR. Treatment of keratinocytes with h-MHES for 24 h increased mRNA expression levels of G6PD (2.0-fold), GCLC (6.6-fold), GCLM (2.4-fold), GPX2 (3.8-fold), GSR (2.3-fold), HO-1 (2.9-fold), NQO1 (2.9-fold), SRXN1 (5.1-fold), TXN (2.1-fold), and TXNRD1 (4.1-fold) (Table 1). The effect of h-MHES on HO-1 and GCLC induction was concentration dependent (Figure 2A,C), peaking at 8 h for HO-1 and at 24 h for GCLC (Figure 2B,D).

h-MHES Induces Glutathione Synthesis. h-MHES induced the expression of GCLC and GCLM, which are the rate-limiting enzymes in glutathione (GSH) biosynthesis. We therefore examined whether h-MHES could increase the level of GSH in keratinocytes. Total GSH levels of h-MHES-treated keratinocytes increased in a time-dependent manner, reaching a 2.8-fold high after 24 h of treatment (Figure 3A). To assess whether h-MHES affects GSH depletion, h-MHES-pretreated keratinocytes were irradiated with UVB, and total GSH levels were measured. At 3 and 6 h after UVB irradiation, the GSH levels in the h-MHES-pretreated keratinocytes were 1.7- and 1.9-fold higher, respectively, than in the control keratinocytes. h-MHES thus attenuated the depletion of the cellular GSH (Figure 3B).

h-MHES Promotes Nrf2 Nuclear Translocation and ARE Luciferase Activity. To determine whether the induction of antioxidant gene expression by h-MHES was mediated through the activation of Nrf2, we examined ARE luciferase activity and the nuclear translocation of Nrf2 in h-MHES-treated cells. Cells were transfected with pARE-luc vector, and the reporter luciferase activity was measured. h-MHES enhanced the ARE luciferase activity in a concentration-dependent manner (Figure 4A). Keratinocytes were treated with h-MHES for 16 h and assessed for nuclear accumulation of Nrf2 protein. We found that nuclear translocation of Nrf2 was enhanced 1.8-fold by h-MHES treatment (Figure 4B). To determine whether antioxidant gene induction by h-MHES is mediated via Nrf2 activation, we transfected cells with Nrf2 siRNA and assessed the expression of HO-1, GCLC, and NQO1 by using qRT-PCR. The h-MHES-induced up-regulation of HO-1, GCLC, and NQO1 was totally abolished by Nrf2 knockdown (Figure 4C). These findings indicate that h-MHES up-regulates antioxidant genes such as HO-1, GCLC, and NQO1 via the Nrf2−ARE pathway.

p38 MAPK Contributes to h-MHES-Induced Antioxidant-Related Gene Expression. To further elucidate the upstream pathway of antioxidant gene expression induced by h-MHES, we examined the phosphorylation level of several kinases in cells treated with h-MHES. After treatment with h-MHES, the level of phosphorylated p38 mitogen-activated protein kinase (MAPK) increased in a time-dependent manner (Figure 5A). In contrast, the levels of phosphorylated Akt, phosphorylated extracellular signal-regulated kinase (ERK), and

DOI: 10.1021/acs.jafc.5b01992
J. Agric. Food Chem. 2015, 63, 7937−7944

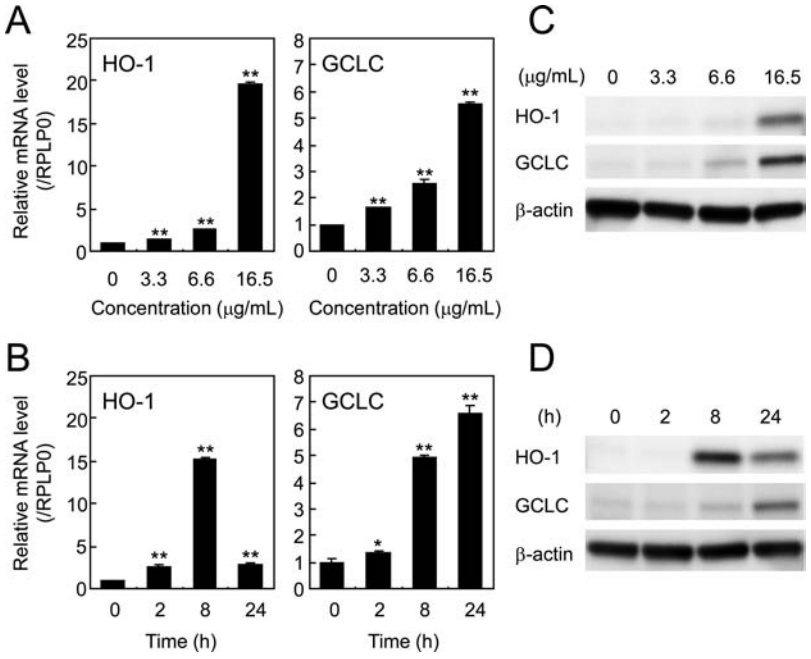

Figure 2. h-MHES induces HO-1 and GCLC. (A, B) Effect of h-MHES on mRNA levels. Keratinocytes were incubated with growth factor-free medium containing h-MHES (0, 3.3, 6.6, or 16.5 μg/mL) for 24 h (A) and with h-MHES (16.5 μg/mL) for the indicated period (B). HO-1 and GCLC expression levels were analyzed by use of qRT-PCR. Data are presented as the mean ± SEM (n = 3). (*) $P < 0.05$ and (**) $P < 0.01$ versus negative control (0 μg/mL or 0 h). (C, D) Effect of h-MHES on protein levels. Keratinocytes were incubated with growth factor-free medium containing h-MHES (0, 3.3, 6.6, or 16.5 μg/mL) for 24 h (C) and with h-MHES (16.5 μg/mL) for the indicated period (D). HO-1 and GCLC protein levels were determined by use of Western blotting with appropriate antibodies. β-Actin was used as an internal control.

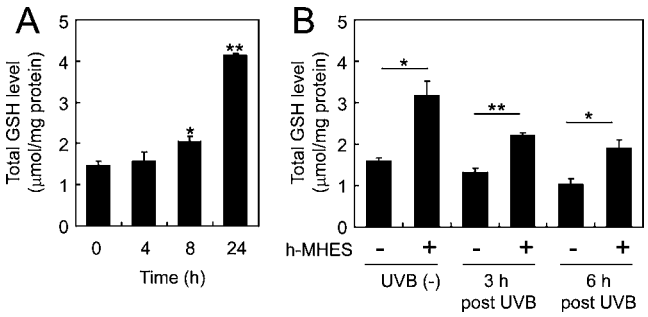

Figure 3. h-MHES enhances GSH production. (A) Effect of h-MHES on GSH content. Keratinocytes were incubated with growth factor-free medium containing h-MHES (16.5 μg/mL) for 0, 4, 8, or 24 h. Data are presented as the mean ± SEM (n = 3). (*) $P < 0.05$ and (**) $P < 0.01$ versus 0 h. (B) Effect of h-MHES on GSH depletion induced by UVB. Keratinocytes were pre-incubated with growth factor-free medium containing h-MHES (16.5 μg/mL) for 16 h and irradiated with UVB (20 mJ/cm^2) in PBS. Then, the cells were incubated with growth factor-free medium containing h-MHES (16.5 μg/mL) for 0, 3, or 6 h. Data are presented as the mean ± SEM (n = 3). (*) $P < 0.05$ and (**) $P < 0.01$.

phosphorylated c-jun N-terminal kinase (JNK) did not increase in h-MHES-treated keratinocytes. We also examined the effects of SB203580, LY294002, PD98059, and SP600125, which are specific inhibitors of p38 MAPK, phosphoinositide-3 kinase (PI3K), ERK, and JNK, respectively. h-MHES-induced HO-1 and GCLC expressions were suppressed by SB203580 and LY294002; however, inhibition of ERK and JNK had no effect (Figure 5B). These results suggest that p38 MAPK and PI3K participate in the regulation of h-MHES-induced HO-1 and GCLC expression.

h-MHES Decreases Intracellular ROS Levels. Intracellular ROS levels were determined by measuring the oxidative conversion of 2′,7′-dichlorodihydrofluorescein diacetate (H_2DCFDA) to the fluorescent compound 2′,7′-dichlorofluorescein (DCF). The intracellular ROS levels in UVB-irradiated keratinocytes were 2.4- and 4.5-fold higher at 20 and 60 mJ/cm^2, respectively, than those in non-irradiated keratinocytes (Figure 6A). h-MHES attenuated the increase in ROS production caused by UVB irradiation (Figure 6B). h-MHES also suppressed H_2O_2-induced ROS accumulation in keratinocytes, but it failed to suppress ROS production in Nrf2 siRNA-treated keratinocytes (Figure 6C,D). These findings indicate that h-MHES prevents UVB- and H_2O_2-induced ROS production via the Nrf2 pathway.

Isolation and Comparison of h-MHES Derivatives. A comparison of h-MHES derivatives showed that the methoxychalcones (AG3, AG4) induced highly enhanced ARE activity and significantly up-regulated the gene expression of HO-1 and GCLC (Figure 7A,B). Furthermore, these methoxychalcones had an inhibitory effect on ROS generation (Figure 7C). In contrast, the flavanones (AG1, AG2), including hesperetin, which is the aglycon form of hesperidin, barely activated the Nrf2−ARE pathway (Figure 7A).

DISCUSSION

In the present study, we investigated the pharmacological activity of h-MHES, the aglycon form of methylated derivatives of the citrus flavonoid hesperidin, and found that h-MHES attenuated oxidative stress through the Nrf2−ARE pathway. In addition, we identified the methoxychalcones AG3 and AG4 as active components of h-MHES.

Nrf2 functions as a master regulator of antioxidant systems that are involved in cytoprotection in response to oxidative and

DOI: 10.1021/acs.jafc.5b01992
J. Agric. Food Chem. 2015, 63, 7937−7944

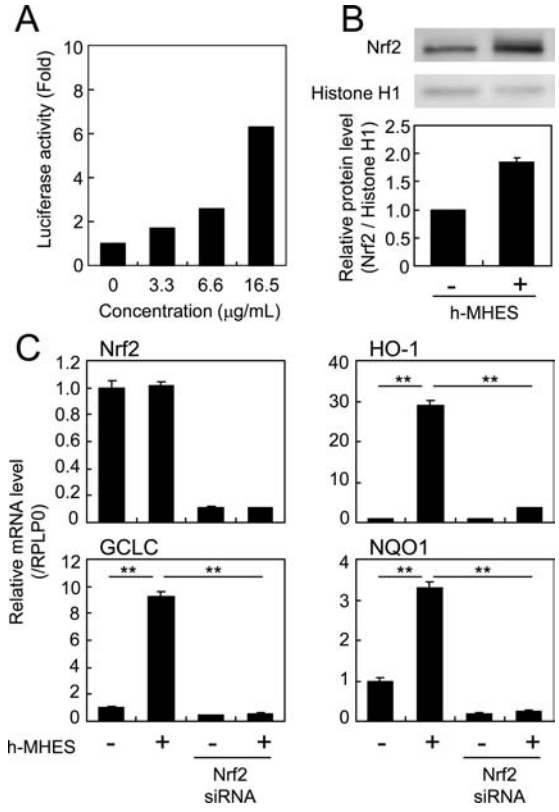

Figure 4. h-MHES activates the Nrf2−ARE pathway. (A) Effect of h-MHES on ARE activation. HEK293 cells were transfected with ARE-luciferase reporter plasmids and then incubated with growth factor-free medium containing h-MHES (0, 3.3, 6.6, or 16.5 μg/mL) for 16 h. Mean data are presented (n = 2). (B) Effect of h-MHES on Nrf2 nuclear translocation. Keratinocytes were incubated with growth factor-free medium containing h-MHES (16.5 μg/mL) for 16 h, after which their nuclei were extracted. The Nrf2 protein levels in the nuclei were determined by using Western blotting and appropriate specific antibodies. Histone H1 was used as an internal control. (C) Effect of Nrf2 siRNA on h-MHES-induced mRNA expression levels of HO-1, GCLC, and NQO1. Keratinocytes were transfected with 5 nM siRNA by using the HiPerFect transfection reagent. After transfection for 16 h, the cells were incubated with growth factor-free medium containing h-MHES (16.5 μg/mL) for a further 10 h. Data are presented as the mean ± SEM (n = 3). (**) $P < 0.01$.

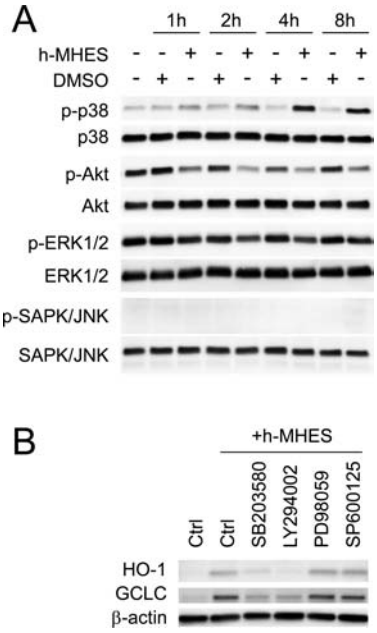

Figure 5. p38 and PI3K/Akt contribute to h-MHES-induced antioxidant-related gene expression. (A) Keratinocytes were incubated with growth factor-free medium containing h-MHES (16.5 μg/mL) for the indicated period. Protein levels were determined by use of Western blotting with appropriate antibodies. (B) Keratinocytes were pre-incubated with 20 μM kinase inhibitor for 1 h and then incubated with growth factor-free medium containing h-MHES (16.5 μg/mL) for 24 h. SB203580, a p38 inhibitor; LY294002, a PI3K inhibitor; PD98059, an ERK inhibitor; or SP600125, a JNK inhibitor.

electrophilic stresses.[17] We predicted that h-MHES may activate the Nrf2−Keap1 pathway, because h-MHES induced several antioxidant genes (Table 1). Nrf2 siRNA inhibited h-MHES-induced HO-1, GCLC, and NQO1 mRNA expression (Figure 4), indicating that h-MHES induced these antioxidant genes via Nrf2. Moreover, the nuclear translocation of Nrf2 was observed after h-MHES treatment, although h-MHES did not affect Nrf2 mRNA levels (Figure 4). This result suggests that h-MHES-induced antioxidant gene expression is mediated not by the induction of the Nrf2 transcript but by the activation of Nrf2 nuclear translocation. Previous studies have demonstrated that several kinase pathways are involved in Nrf2 activation.[18] We observed that h-MHES enhanced the phosphorylation of p38 MAPK and that an inhibitor of p38 MAPK (SB203580) abolished h-MHES-induced expression of HO-1 and GCLC. These results indicate that h-MHES induced antioxidant gene expression through the activation of p38 MAPK. An inhibitor of PI3K (LY294002) also attenuated HO-1 and GCLC expression induced by h-MHES, yet phosphorylated Akt was not increased by h-MHES. Therefore, h-MHES does not seem to induce phosphorylation of Akt directly, even though PI3K participates in the regulation of h-MHES-induced HO-1 and GCLC expression. Our study suggests that h-MHES stimulates the Nrf2−ARE pathway mainly via p38 MAPK activation, but further work is needed to elucidate the precise mechanism involved.

HPLC and NMR analysis revealed that h-MHES was a mixture of methoxyflavanones and methoxychalcones. We showed that two methoxychalcones, AG3 and AG4, activated the Nrf2−ARE pathway to a greater extent than did the methoxyflavanones. Chalcones bear an α,β-unsaturated ketone moiety and could therefore act as Michael acceptors that have the potential to change the cellular redox environment and direct cysteine modification in Keap1.[19] However, AG5, one of the methoxychalcones, did not activate the Nrf2−ARE pathway in the present study, and previous studies have shown that not all chalcones have the ability to activate Nrf2.[19,20] Therefore, further studies are needed to clearly determine whether h-MHES derivatives activate Nrf2 by direct thiol modification of Keap1, ROS production, or some other mechanism.

HO-1, GCLC, GSR, and GPX, which are h-MHES-induced genes, participate in antioxidant and cytoprotective systems.[21] HO-1 catalyzes the conversion of heme into biliverdin, free iron, and carbon monoxide (CO)[22] and provides cytoprotection against oxidative stress and inflammation.[23,24] GCLC is a component of glutamate cysteine ligase (GCL), which is the rate-limiting enzyme in glutathione (GSH) synthesis.[25] GSH is a ubiquitous intracellular peptide with diverse functions that include detoxification, antioxidant defense, and maintenance of thiol status.[25] The activity of GSH is dependent on not only a

DOI: 10.1021/acs.jafc.5b01992
J. Agric. Food Chem. 2015, 63, 7937−7944

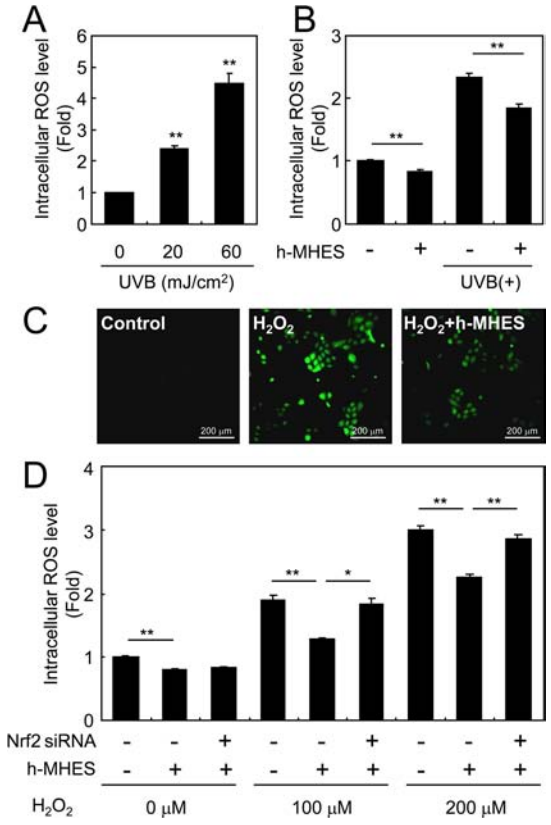

Figure 6. h-MHES decreases intracellular ROS levels. (A) Effect of UVB on intracellular ROS generation. Keratinocytes were incubated with H_2DCFDA in Hank's balanced salt solution (HBSS) for 20 min and then irradiated with UVB (0, 20, or 60 mJ/cm^2) for 15 min. ROS generation was then measured. Data are presented as the mean ± SEM (n = 6). (**) P < 0.01 versus 0 mJ/cm^2 UVB. (B) Effect of h-MHES on ROS generation induced by UVB irradiation. Keratinocytes were pretreated with h-MHES (16.5 μg/mL) for 16 h, incubated with H_2DCFDA in HBSS for 20 min, and then irradiated with UVB (0 or 20 mJ/cm^2) for 15 min. ROS generation was then measured. Data are presented as the mean ± SEM (n = 6). (C) Effect of h-MHES on ROS generation induced by H_2O_2 treatment. Keratinocytes were pretreated with h-MHES (16.5 μg/mL) for 16 h, incubated with H_2DCFDA for 20 min, and then treated with H_2O_2 (0 or 200 μM) for 30 min. (D) Effect of Nrf2 siRNA on ROS suppression by h-MHES. After siRNA transfection for 24 h, keratinocytes were pretreated with h-MHES (16.5 μg/mL) for 16 h, incubated with H_2DCFDA for 20 min, and then treated with H_2O_2 (0, 100, or 200 μM) for 30 min. Data are presented as the mean ± SEM (n = 3) (B, D). (*) P < 0.05 and (**) P < 0.01.

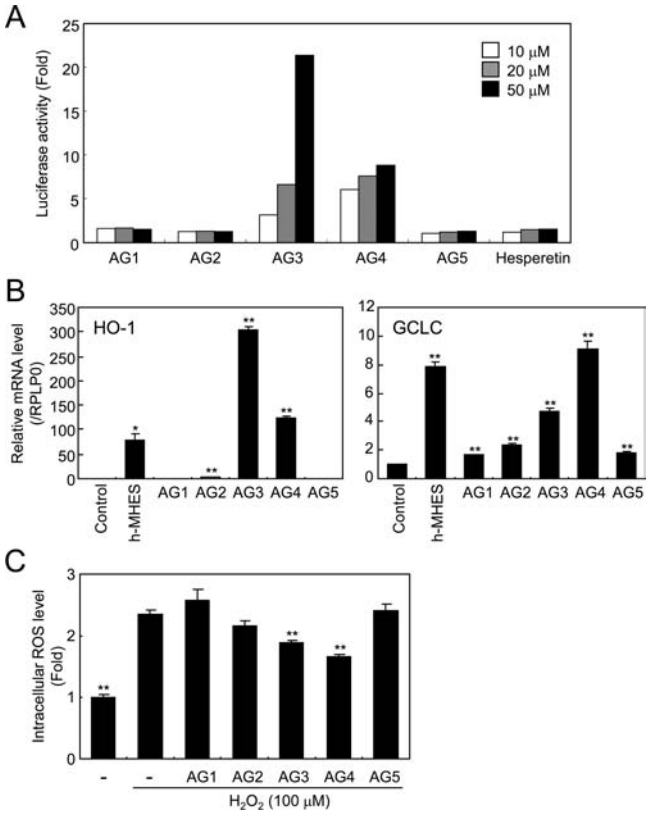

Figure 7. Comparison of h-MHES derivatives. (A) Effect of h-MHES on ARE activation. HEK293 cells were transfected with ARE-luciferase reporter plasmids and then incubated with growth factor-free medium containing AG1, AG2, AG3, AG4, AG5, or hesperetin (10, 20, or 50 μM) for 16 h. Mean data are presented (n = 2). (B) Comparison of h-MHES derivative induction of HO-1 and GCLC mRNA. Keratinocytes were incubated with growth factor-free medium containing h-MHES (16.5 μg/mL), AG1, AG2, AG3, AG4, or AG5 (50 μM) for 8 h. Data are presented as the mean ± SEM (n = 3). (*) P < 0.05 and (**) P < 0.01 versus control. (C) Comparison of h-MHES derivative suppression of ROS accumulation. Keratinocytes were pretreated with AG1, AG2, AG3, AG4, or AG5 (20 μM) for 16 h, incubated with H_2DCFDA for 20 min, and then treated with H_2O_2 (100 μM) for 30 min. Data are presented as the mean ± SEM (n = 3). (* P < 0.05 and (**) P < 0.01 versus control (100 μM H_2O_2).

steady supply of GSH but also the support of glutathione-cycle related enzymes such as GPX and GSR. GPX catalyzes the oxidation of GSH to oxidized GSH (GSSG), and the resulting GSSG is recycled back to reduced GSH by GSR using NADPH. h-MHES increased the expression of these antioxidant-related genes and the intracellular GSH content, suggesting that h-MHES could protect cells from oxidative stress. Accordingly, we assessed whether h-MHES could enhance cellular antioxidant capacity through the activation of biological antioxidant systems. h-MHES pretreatment of keratinocytes prevented UVB- and H_2O_2-induced intracellular ROS production (Figure 6), indicating that h-MHES provided the cells with resistance to oxidative stress.

MHES likely has unique pharmacological effects that are absent in hesperidin, because h-MHES activated the Nrf2 pathway to a much greater extent than did hesperetin (hesperidin aglycon). UVB-irradiated Nrf2−/− mice show a stronger sunburn reaction and accelerated photoaging, such as coarse wrinkle formation, loss of skin flexibility, and epidermal thickening.[26,27] However, Nrf2 activation strongly reduces UVB-induced apoptosis.[28] These reports suggest that the Nrf2−ARE pathway plays an important role in protection against UVB damage. Therefore, MHES, as an Nrf2 activator, may protect the skin from oxidative stress caused by UVB in vivo.

In conclusion, we found that h-MHES activates the Nrf2−ARE pathway, resulting in the induction of cytoprotective gene expression and attenuation of oxidative stress in keratinocytes. Our findings reveal MHES as a new agent for protecting cells against oxidative stress through its ability to enhance biological antioxidant capacity.

DOI: 10.1021/acs.jafc.5b01992
J. Agric. Food Chem. 2015, 63, 7937−7944

AUTHOR INFORMATION

Corresponding Author

*(T.M.) Phone: +81 285 68 7871. Fax: +81 285 68 7469. E-mail: murase.takatoshi@kao.co.jp.

Funding

This study was supported financially by Kao Corp.

Notes

The authors declare no competing financial interest.

ABBREVIATIONS USED

ARE, antioxidant response element; G6PD, glucose-6-phosphate dehydrogenase; GCLC, glutamate−cysteine ligase catalytic subunit; GCLM, glutamate−cysteine ligase modifier subunit; GPX2, glutathione peroxidase 2; GSR, glutathione reductase; h-MHES, hydrolyzed methylhesperidin; HO-1, heme oxygenase-1; MHES, methylhesperidin; NQO1, NAD(P)H:quinone oxidoreductase 1; Nrf2, nuclear factor erythroid 2-related factor 2; ROS, reactive oxygen species; SRXN1, sulfiredoxin 1; TXN, thioredoxin; TXNRD1, thioredoxin reductase 1; UV, ultraviolet

REFERENCES

(1) Durackova, Z. Some current insights into oxidative stress. *Physiol. Res.* **2010**, *59*, 459−469.

(2) Briganti, S.; Picardo, M. Antioxidant activity, lipid peroxidation and skin diseases. What's new. *J. Eur. Acad. Dermatol. Venereol.* **2003**, *17*, 663−669.

(3) Shindo, Y.; Witt, E.; Packer, L. Antioxidant defense mechanisms in murine epidermis and dermis and their responses to ultraviolet light. *J. Invest. Dermatol.* **1993**, *100*, 260−265.

(4) Marchitti, S. A.; Chen, Y.; Thompson, D. C.; Vasiliou, V. Ultraviolet radiation: cellular antioxidant response and the role of ocular aldehyde dehydrogenase enzymes. *Eye Contact Lens.* **2011**, *37*, 206−213.

(5) Taguchi, K.; Motohashi, H.; Yamamoto, M. Molecular mechanisms of the Keap1−Nrf2 pathway in stress response and cancer evolution. *Genes Cells* **2011**, *16*, 123−140.

(6) Bryan, H. K.; Olayanju, A.; Goldring, C. E.; Park, B. K. The Nrf2 cell defense pathway: Keap1-dependent and -independent mechanisms of regulation. *Biochem. Pharmacol.* **2013**, *85*, 705−717.

(7) Stefanson, A. L.; Bakovic, M. Dietary regulation of Keap1/Nrf2/ARE pathway: focus on plant-derived compounds and trace minerals. *Nutrients* **2014**, *6*, 3777−3801.

(8) Lee, J. M.; Li, J.; Johnson, D. A.; Stein, T. D.; Kraft, A. D.; Calkins, M. J.; Jakel, R. J.; Johnson, J. A. Nrf2, a multi-organ protector? *FASEB J.* **2005**, *19*, 1061−1066.

(9) Sakieki, I. Studies on methyl derivatives of hesperidin. I-II. II. Structure of methylated products of hesperidin. *Nippon Kagaku Zasshi* **1958**, *79*, 736−740.

(10) Sakieki, I. Studies on methyl derivatives of hesperidin. III-IV. III. Structure of methylated products of hesperidin. Part 2. *Nippon Kagaku Zasshi* **1958**, *79*, 1103−1107.

(11) Li, R.; Li, J.; Cai, L.; Hu, C. M.; Zhang, L. Suppression of adjuvant arthritis by hesperidin in rats and its mechanisms. *J. Pharm. Pharmacol.* **2008**, *60*, 221−228.

(12) Aranganathan, S.; Selvam, J. P.; Nalini, N. Effect of hesperetin, a citrus flavonoid, on bacterial enzymes and carcinogen-induced aberrant crypt foci in colon cancer rats: a dose-dependent study. *J. Pharm. Pharmacol.* **2008**, *60*, 1385−1392.

(13) Benavente-García, O.; Castillo, J. Update on uses and properties of citrus flavonoids: new findings in anticancer, cardiovascular, and anti-inflammatory activity. *J. Agric. Food Chem.* **2008**, *56*, 6185−6205.

(14) Nowakowska, Z. A review of anti-infective and anti-inflammatory chalcones. *Eur. J. Med. Chem.* **2007**, *42*, 125−137.

(15) Nielsen, I. L.; Chee, W. S.; Poulsen, L.; Offord-Cavin, E.; Rasmussen, S. E.; Frederiksen, H.; Enslen, M.; Barron, D.; Horcajada, M. N.; Williamson, G. Bioavailability is improved by enzymatic modification of the citrus flavonoid hesperidin in humans: a randomized, double-blind, crossover trial. *J. Nutr.* **2006**, *136*, 404−408.

(16) Wang, X.; Tomso, D. J.; Chorley, B. N.; Cho, H. Y.; Cheung, V. G.; Kleeberger, S. R.; Bell, D. A. Identification of polymorphic antioxidant response elements in the human genome. *Hum. Mol. Genet.* **2007**, *16*, 1188−1200.

(17) Taguchi, K.; Motohashi, H.; Yamamoto, M. Molecular mechanisms of the Keap1-Nrf2 pathway in stress response and cancer evolution. *Genes Cells* **2011**, *16*, 123−140.

(18) Son, T. G.; Camandola, S.; Mattson, M. P. Hormetic dietary phytochemicals. *NeuroMol. Med.* **2008**, *10*, 236−246.

(19) Kumar, V.; Kumar, S.; Hassan, M.; Wu, H.; Thimmulappa, R. K.; Kumar, A.; Sharma, S. K.; Parmar, V. S.; Biswal, S.; Malhotra, S. V. Novel chalcone derivatives as potent Nrf2 activators in mice and human lung epithelial cells. *J. Med. Chem.* **2011**, *54*, 4147−4159.

(20) Izumi, Y.; Matsumura, A.; Wakita, S.; Akagi, K.; Fukuda, H.; Kume, T.; Irie, K.; Takada-Takatori, Y.; Sugimoto, H.; Hashimoto, T.; Akaike, A. Isolation, identification, and biological evaluation of Nrf2-ARE activator from the leaves of green perilla (*Perilla frutescens* var. *crispa* f. *viridis*). *Free Radical Biol. Med.* **2012**, *53*, 669−679.

(21) Hine, C. M.; Mitchell, J. R. Nrf2 and the phase II response in acute stress resistance induced by dietary restriction. *J. Clin. Exp. Pathol.* **2012**, *S4*, 004.

(22) Tenhunen, R.; Marver, H. S.; Schmid, R. The enzymatic conversion of heme to bilirubin by microsomal heme oxygenase. *Proc. Natl. Acad. Sci. U. S. A.* **1968**, *61*, 748−755.

(23) Immenschuh, S.; Ramadori, G. Gene regulation of heme oxygenase-1 as a therapeutic target. *Biochem. Pharmacol.* **2000**, *60*, 1121−1128.

(24) Lundvig, D. M.; Immenschuh, S.; Wagener, F. A. Heme oxygenase, inflammation, and fibrosis: the good, the bad, and the ugly? *Front. Pharmacol.* **2012**, *3*, 81.

(25) Lu, S. C. Regulation of glutathione synthesis. *Mol. Aspects Med.* **2009**, *30*, 42−59.

(26) Kawachi, Y.; Xu, X.; Taguchi, S.; Sakurai, H.; Nakamura, Y.; Ishii, Y.; Fujisawa, Y.; Furuta, J.; Takahashi, T.; Itoh, K.; Yamamoto, M.; Yamazaki, F.; Otsuka, F. Attenuation of UVB-induced sunburn reaction and oxidative DNA damage with no alterations in UVB-induced skin carcinogenesis in Nrf2 gene-deficient mice. *J. Invest. Dermatol.* **2008**, *128*, 1773−1779.

(27) Hirota, A.; Kawachi, Y.; Yamamoto, M.; Koga, T.; Hamada, K.; Otsuka, F. Acceleration of UVB-induced photoageing in nrf2 gene-deficient mice. *Exp. Dermatol.* **2011**, *20*, 664−668.

(28) Schäfer, M.; Dütsch, S.; auf dem Keller, U.; Navid, F.; Schwarz, A.; Johnson, D. A.; Johnson, J. A.; Werner, S. Nrf2 establishes a glutathione-mediated gradient of UVB cytoprotection in the epidermis. *Genes Dev.* **2010**, *24*, 1045−1058.

DOI: 10.1021/acs.jafc.5b01992
J. Agric. Food Chem. 2015, 63, 7937−7944

again by molecular modeling, we investigated for comparison the interaction of peptide **1** with the catalytic site of HMGCoAR.

MATERIALS AND METHODS

Chemicals. Dulbecco's modified Eagle's medium (DMEM), L-glutamine, fetal bovine serum (FBS), phosphate-buffered saline (PBS), penicillin/streptomycin, chemiluminescent reagent, and 96-well plates were purchased from Euroclone (Milan, Italy). Bovine serum albumin (BSA), RIPA buffer, HMGCoAR assay kit, lovastatin, and the antibody against β-actin were bought from Sigma-Aldrich (St. Louis, MO, USA). The antibody against HMGCoAR was bought from Abcam (Cambridge, UK). The antibodies against SREBP-2, rabbit Ig-HRP, mouse Ig-HRP, phenylmethanesulfonylfluoride (PMSF), Na-orthovanadate inhibitors, and goat anti-rabbit Ig-HRP were purchased from Santa Cruz Biotechnology, Inc. (Santa Cruz, CA, USA). The antibodies against LDLR were bought from Pierce (Rockford, IL, USA); the inhibitor cocktail Complete Midi was purchased from Roche (Basel, Swiss). Mini protean TGX precast gel 7.5% and Mini nitrocellulose Transfer Packs were purchased from BioRad (Hercules, CA, USA). YVVNPDNDEN and YVVNPDNNEN were bought from PRIMM (Milan, Italy), which certified >95% purity by HPLC.

Computational Methods. The structures of peptides **1**−**3** were built by using two different strategies. The shortest derivatives (peptides **2** and **3**) were manually modeled in a canonical α-helix by using the Peptide Builder function of the VEGA suite of programs; then, their conformational profiles were explored by a MonteCarlo procedure, which produced 20 000 conformers by randomly rotating the backbone torsions only. The final geometries were then clustered according to their similarity to discard redundant ones; here, two conformations were considered as nonredundant when they differed by more than 60° in at least one backbone torsion angle. For each cluster, the lowest energy structure was collected and memorized. By contrast, the structure of the longest peptide (**1**) was generated by homology modeling, using the Fugue online program, on the basis of the resolved structure of phaseolin as the template (Protein Database (PDB) ID: 2PHL). This model was completed by adding side chains and hydrogen atoms and then minimized by keeping the backbone atoms fixed to preserve the predicted folding.

Among the resolved human HMG-CoA reductase structures, the study involved the complex between the enzyme and a statin (i.e., (3*R*,5*R*)-7-[2-(4-fluorophenyl)-4-{[(1S)-2-hydroxy-1-phenylethyl]-carbamoyl}-5-(1-methylethyl)-1H-imidazol-1-yl]-3,5-dihydroxyheptanoic acid, PDB ID: 3CCZ) because this showed the best resolution (1.70 Å).[21] Even though the resolved structure is a homotetramer, the simulations were focused on a functionally active homodimer, which completely encompasses the catalytic binding site. After deleting water molecules, ions, and crystallization additives, the selected dimer bound to the statin was completed by adding the hydrogen atoms and then optimized by keeping the backbone atoms fixed to preserve the resolved folding. The inhibitor was finally deleted, and the obtained protein structure underwent the following docking simulations.

Although requiring different strategies, all docking simulations were carried out by using the program Protein−Ligand ANT System (PLANTS, release 1.1),[23] which generates reliable ligand poses by using ant colony optimization algorithms (ACO).

For the shortest peptides (peptides **2** and **3**), docking simulations involved the 20 lowest energy conformations as derived by the previous MonteCarlo analysis in order to minimize the biasing effects of the starting conformation on the obtained results. In detail, the search was focused on a 15.0 Å radius sphere around the bound statin, thus including the entire binding cavity. PLANTS was used with default settings and without geometric constraints: Speed 1 was used, and 5 poses were generated and scored for each conformer by using the ChemPLP function. The obtained poses were evaluated by considering both the docking scores and the conformational energies of the docked conformers. The best poses were then minimized, keeping fixed all atoms inside a 15.0 Å radius sphere around the bound peptide. Although adopting the same computational procedures already described, the docking study for the longest peptide **1** was focused on the single conformation as derived by homology modeling.

The computed complexes for peptide **1** and **2** underwent 10 ns molecular dynamic (MD) study. It should be noted here that the MD simulations had the primary objective of assessing the stability of the generated complexes as well as of their key stabilizing contacts and were not aimed at investigating the conformational changes induced by the bound ligand on the protein structure because this would have clearly required longer simulations. First, the complexes were embedded in a cubic box of water (85 Å × 85 Å × 85 Å) containing 16 250 solvent molecules. The systems were then minimized to optimize the relative position of the solvent molecules and then were subjected to MD runs with the following characteristics: (a) Periodic boundary conditions (95 Å × 95 Å × 95 Å) were applied to stabilize the simulation space. (b) Newton's equation was integrated using the r-RESPA method (every 4 fs for long-range electrostatic forces, 2 fs for short-range non bonded forces, and 1 fs for bonded forces). (c) The long-range electrostatic potential was computed by the Particle Mesh Ewald summation method (80 × 80 × 80 grid points). (d) The temperature was maintained at 300 ± 10 K by Langevin's algorithm. (e) Lennard-Jones (L-J) interactions were calculated with a cutoff of 10 Å, and the pair list was updated every 20 iterations. (f) A frame was memorized every 10 ps, thus generating 1000 frames. (g) No constraints were imposed on the systems. The simulations were carried out in two phases: an initial period of heating from 0 to 300 K over 300 000 iterations (300 ps, i.e., 1 K/ps) and the monitored phase of 10 ns. The mentioned minimizations were carried out using the conjugate gradient algorithm until the rms gradient was smaller than 0.01 kcal mol^{-1} $Å^{-1}$. All calculations were carried out by Namd2.10,[24] with the force-field CHARMm v22 and Gasteiger's atomic charges.

HMGCoAR Activity Assay. HMGCoAR (catalytic domain), NADPH, assay buffer, and substrate solution were provided in the HMGCoAR assay kit (Sigma-Aldrich, St. Louis, MO, USA). The experiments were carried out at 37 °C following the manufacturer's instructions. In particular, each reaction (200 μL) was prepared by adding the reagents in the following order: 1X assay buffer; peptide **2** (at 100, 125, 150, and 250 μM), and peptide **3** (at 150, 175, 200, and 250 μM), or vehicle (C); NADPH (4 μL); substrate solution (12 μL); and finally HMGCoAR (2 μL). Subsequently, the samples were mixed, and the absorbance at 340 nm was read by a microplate reader (Synergy H1 from Biotek, Bad Friedrichshall, Germany) at 0 and 10 min. The HMGCoA-dependent oxidation of NADPH and the inhibition properties of soy peptides were measured by the absorbance reduction, which is directly proportional to enzyme activity.

Cell Line Culture. The HepG2 cell line was bought from ATCC (HB-8065, ATCC from LGC Standards, Milan, Italy). It was cultured in high-glucose DMEM with stable L-glutamine supplemented with 10% FBS, 100 U/mL penicillin, and 100 μg/mL streptomycin (complete growth medium) and incubated at 37 °C under 5% CO_2 atmosphere. HepG2 cells were used for no more than 20 passages after thawing because the increase of passage number may change cell characteristics and impair assay results.

Western Blot Analysis. HepG2 (1.5×10^5 cells/well of a 24-well plate) were treated with peptides **2** and **3** (each 350 and 500 μM) for 24 h. After each treatment, cells were scraped in 40 μL of ice-cold lysis buffer (RIPA buffer + inhibitor cocktail + 1:100 PMSF + 1:100 Na-orthovanadate) and transferred in an ice-cold microcentrifuge tube. After centrifugation at 16 060 g for 15 min at 4 °C, the supernatant was recovered and transferred to a new ice-cold tube. Total proteins were quantified by the Bradford method, and 50 μg of total proteins were loaded on a precast 7.5% sodium dodecyl sulfate−polyacrylamide (SDS-PAGE) gel at 130 V for 45 min. Subsequently, the gel was pre-equilibrated with 0.04% SDS in H_2O for 15 min at room temperature (RT) and transferred to a nitrocellulose membrane (Mini nitrocellulose Transfer Packs), using a Trans-blot Turbo at 1.3 A and 25 V for 7 min. Target proteins on the milk-blocked membrane were detected by primary antibodies as follows: rabbit anti-SREBP2, anti-LDLR, anti-HMGCoAR, and anti-β-actin. Secondary antibodies conjugated with HRP and a chemiluminescent reagent were used to visualize target proteins, and their signal was quantified using the

DOI: 10.1021/acs.jafc.5b03497
J. Agric. Food Chem. 2015, 63, 7945−7951

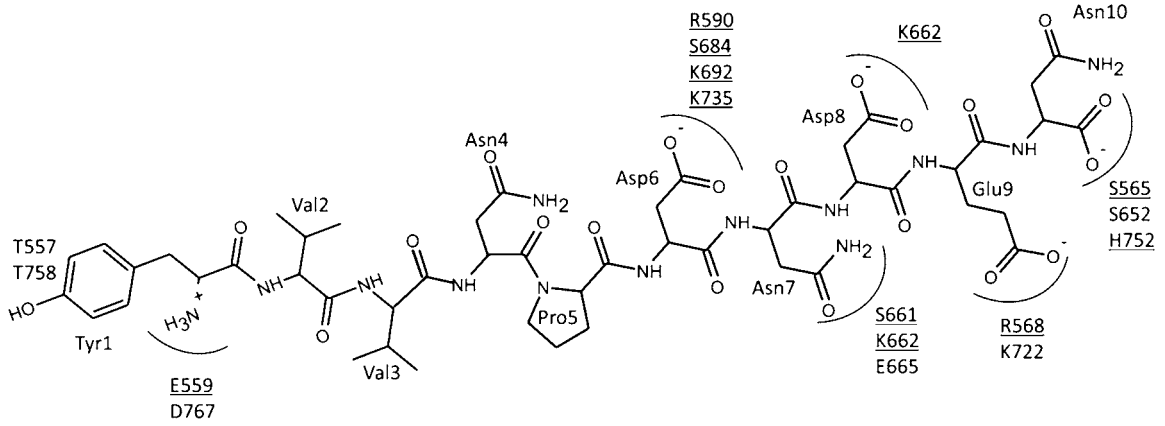

Figure 1. Bidimensional scheme reporting the key interactions stabilizing the putative complex for peptide **2**. The residues involved in the binding of the statin as found in the resolved crystal structure utilized here (PDB ID: 3CCZ) are underlined.

ImageJ Software. The internal control β-actin was used to normalize loading variations.

Fluorescent LDL Uptake Cell-Based Assay. A total of 3×10^4 HepG2 cells were seeded per well of 96-well plates and kept in complete growth medium for 2 days before treatment. On the third day, cells were treated with peptide **2** and **3** at the concentrations of 50 and 100 μM, respectively, or mock treatment (H_2O) for 24 h. At the end of the treatment period, the culture medium was replaced with 50 μL/well LDL-DyLight 550 working solution (Cayman Chemical Company, Ann Arbor, Michigan, USA). The cells were additionally incubated for 2 h at 37 °C; then, the culture medium was aspirated, washed, and replaced with PBS (100 μL/well). The degree of LDL uptake was measured using the Synergy H1 fluorescent plate reader from Biotek (excitation and emission wavelengths 540 and 570 nm, respectively).

Statistical Analysis. Statistical analyses were carried out by one-way ANOVA (Graphpad Prism 6) followed by Dunnett's test and/or *t* test. Values were expressed as means ± SEM; *P* values < 0.05 were considered to be significant.

RESULTS

Molecular Modeling Investigation. An in silico modeling study was undertaken to investigate the potential interaction of peptides **1**−**3** with the catalytic domain of HMGCoAR. Figure 1 shows a bidimensional scheme summarizing the key interactions stabilizing the putative complex between peptide **2** and the enzymatic cavity of HMGCoAR, whereas Figure S1A gives an overall view of the pose of peptide **2** within the HMGCoAR displayed by cartoon. Notably, most key polar interactions are elicited by the last five residues of the C terminus, whereas the first N-terminal residues are mostly involved in hydrophobic contact, with the exception of the N-terminal ammonium head, which is engaged in ionic interactions with Glu559 and Asp767, and the phenolic function of Tyr1, which stabilizes H bonds with Thr557 and Thr758. In detail, Asp6, Asp8, and Glu9 are engaged in an extended network of ion pairs involving the rich set of positively charged residues, which characterize the catalytic pocket of HMGCoAR and surround the C-terminal portion of the bound peptide, whereas the carboxyl terminus and Asn6 elicit only H bonds.

Figure 1 highlights (underlined) the residues stabilizing the key contacts with the peptide **2** that were also found to be involved in the stabilization of the experimentally resolved complex between HMGCoAR and a statin. Notably, the underlined residues mostly interact with the negatively charged C-terminal portion of peptide **2**, thus confirming that this segment is primarily involved in the inhibition of HMGCoAR by mimicking most of the polar interactions already seen for the binding of the statin polar moieties. In contrast, the hydrophobic N-terminal portion is inserted in a deeper and rather apolar subpocket that does not match that accommodating the statin hydrophobic moieties but rather roughly corresponds to that harboring the NADPH cofactor. Indeed, the statin polar groups interact with the residues contacting the HMG groups, whereas the statin apolar moieties are accommodated in the apolar subpocket interacting with the pantothenic acid moiety of CoA, and no region of the NADP(H) binding site is engaged by statins. Here, a different arrangement is observed because the hydrophobic portion of peptide **2** is partly accommodated in the elongated binding cavity of the cofactor, thus suggesting that it may also affect the NADPH binding. Similar docking simulations of peptide **3** revealed that the mutation Asp8 into Asn8 does not markedly affect the interaction pattern because Asn8 elicits H bonds with Lys662 (already seen for peptide **2**) and Glu665 (complex not shown).

Figure S1B shows the pose of peptide **1** and suggests the β-hairpin motif stabilized by several intramolecular polar contacts, among which the salt bridge between the two ionized termini has a key role in determining such a folded structure. Figure S1B also reveals that this longer peptide is accommodated within a more superficial region of the binding cavity compared to peptide **2**, and its inhibition can be due to a sort of lid mechanism involving additional regions adjacent to the rim of the catalytic pocket.

Figure S2 is a schematic representation of the key contacts stabilizing the putative complex as computed for the longer peptide **1**. Similar to what was seen for the shorter derivative, Figure S2 reveals that the conserved portion between Asp15 and Asn19 is involved in the key polar interactions with the ionizable residues lining the HMGCoAR binding cavity. Apart from Arg21, which stabilizes two ion pairs with Glu559 and Asp767, the remaining residues are generally engaged in an extended network of intramolecular and intermolecular hydrophobic contacts that contribute to the overall stabilization of the obtained complex. Remarkably, there are some residues (highlighted in green), especially in the N-terminal region, that are exclusively involved in intramolecular contacts. One may imagine that such intramolecular interactions can play a dual role because they stabilize the folded conformation and shield some unfit side chains, thus minimizing potential repulsing

DOI: 10.1021/acs.jafc.5b03497
J. Agric. Food Chem. 2015, 63, 7945−7951

contacts with surrounding enzyme residues (as in the case of Arg2).

A primary objective of the MD simulations thus carried out was to assess the stability of the computed complexes. Hence, Figure 2 compares the rmsd values of the two bound peptides

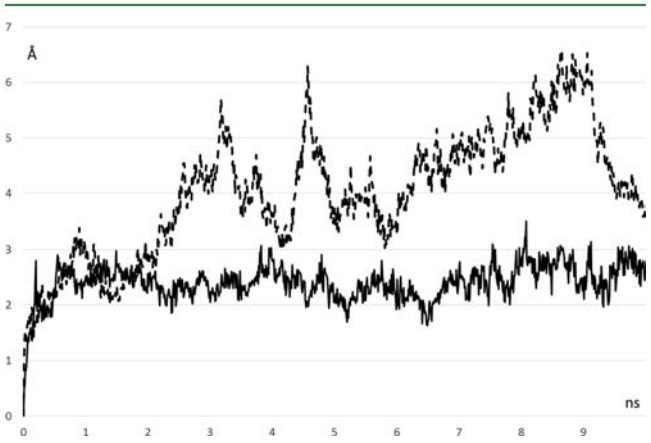

Figure 2. Rmsd profiles for the simulated peptides bound to the enzyme as derived by MD runs considering the backbone atoms only (solid black line = peptide **1**, dashed black line = peptide **2**).

as computed during the MD runs considering only the backbone atoms. It reveals two markedly different profiles because peptide **2** shows a low and rather constant profile, which is suggestive of a very stable complex in which most residues are tightly involved in key contacts. Figure S3A reports the rmsd values as dissected per residue and computed considering all atoms and confirms the key role of the ionized residues, which indeed remains nearly fixed during all the MD run.

In contrast, peptide **1** shows a higher and more variable profile, which may suggest that not all residues are equally involved in the key contacts and that some portions of peptide **1** conserve a notable mobility even within the HMGCoAR binding cavity. To better investigate this finding, Figure S3B shows the rmsd values as dissected per residue and reveals a significant variability between the thus-computed rmsd values in line with the number of polar contacts elicited by each residue. In detail, Figure S3 confirms that the region between Asn13 and Arg21 plays a key role in complex stabilization and indeed remains stably bound to the enzyme, whereas the segment between Ala5 and Val12 is engaged at most in apolar contacts and is arranged in a more superficial region of the HMGCoAR binding cavity, thus conserving a marked mobility during the MD simulation. The two terminal segments show an intermediate flexibility probably due to the ionic contact between the two terminal ionized groups. Overall, these results suggest that the computed pose of peptide **1** is stable even though a such an extended peptide cannot be completely stabilized within the enzyme catalytic site, thus explaining the observed residual flexibility.

The satisfactory stability of the two simulated complexes is further confirmed by the dynamic profile of some representative contacts as derived from MD runs and compiled in Table 1. Indeed, the reported distance values emphasize that most key ionic contacts are completely stable because the corresponding distances are comprised in very narrow ranges.

Peptides 2 and 3 Inhibit the HMGCoAR in Vitro. The experimental characterization of the molecular mechanism

Table 1. Dynamic profile of some representative contacts as derived from MD runs for the two simulated complexes[a]

interaction	distance mean	distance minimum	distance maximum
	Peptide **2**		
$NH_3^+ \rightarrow$ E559	2.94 ± 0.095	2.69	3.45
$NH_3^+ \rightarrow$ D767	2.89 ± 0.11	2.61	3.31
Tyr1 → T557	7.84 ± 2.97	2.99	13.76
Asp6 → R590	5.04 ± 0.59	3.49	6.55
Asp6 → K692	3.08 ± 0.29	2.63	4.16
Asp6 → K735	3.04 ± 0.13	2.71	3.71
Asp8 → K662	3.16 ± 0.33	2.62	4.05
	Peptide **1**		
Asp17 → R568	3.74 ± 0.14	3.37	4.31
Glu18 → R590	4.19 ± 0.26	3.42	4.89
Asn19 → R590	4.75 ± 1.29	2.67	8.06
Arg21 → E559	3.96 ± 0.14	3.53	4.59
Arg21 → D767	6.52 ± 0.49	4.69	7.77

[a]All distances are expressed in angstroms.

through which peptides **2** and **3** may potentially mediate a hypocholesterolemic effect was carried out in two steps: first, evaluating their capacity to inhibit the catalytic activity of HMGCoAR; second, investigating in HepG2 cells how they modulate cholesterol metabolism and modify the LDL uptake. To confirm that indeed peptides **2** and **3** inhibit the catalytic activity of HMGCoAR as their main molecular target, an in vitro assay was carried out using the purified catalytic domain of this enzyme. A concentration range from 100 and 250 μM was tested. Each peptide inhibited HMGCoAR activity in a dose-dependent manner, with an IC_{50} of about 150 and 200 μM for peptides **2** and **3**, respectively (Figure 3). On the basis of these results, we decided to treat HepG2 cells in the following experiments at slightly higher concentrations, i.e., 350 and 500 μM.

Peptides 2 and 3 Induce the LDLR-SREBP2 Pathway. To verify the consequences of the HMGCoAR inhibition activity exerted by peptides **2** and **3** on the modulation of the LDLR-SREBP2 pathway, HepG2 cells were treated with both peptides at the concentrations of 350 and 500 μM, and each sample was investigated with immunoblotting experiments. Figure 4A–D shows that the treatment with each peptide induced an up-regulation of the N-terminal fragment of the SREBP2 protein level (mature form with a molecular weight of 68 kDa). In particular, peptide **2** up-regulated the mature SREBP2 protein level by 134.0 ± 10.5 and 141.1 ± 18.0% at 350 and 500 μM, respectively, whereas peptide **3** up-regulated the mature SREBP2 protein level by 158.0 ± 9.2 and by 155.2 ± 14.6% at 350 and 500 μM, respectively, versus the untreated sample.

In the same experiments, the LDLR and HMGCoAR protein level variations were also measured by immunoblotting (Figure 4B,C). All peptides increased the LDLR and HMGCoAR protein levels, in agreement with their capacity to up-regulate the transcriptional active SREBP2 fragment (mature-SREBP2) protein level. In particular, peptide **2** increased the LDLR protein level by 152.0 ± 20.0 and 167.0 ± 31.7% and peptide **3** by 164.0 ± 17.9 and 182.2 ± 41.8% versus the untreated sample at 350 and 500 μM, respectively (Figure 4E). Peptide **2** enhanced the production of the HMGCoAR protein by 171 ± 29.9 and by 187 ± 34.6% versus the untreated sample at 350 and 500 μM, respectively, whereas peptide **3** induced an

DOI: 10.1021/acs.jafc.5b03497
J. Agric. Food Chem. 2015, 63, 7945−7951

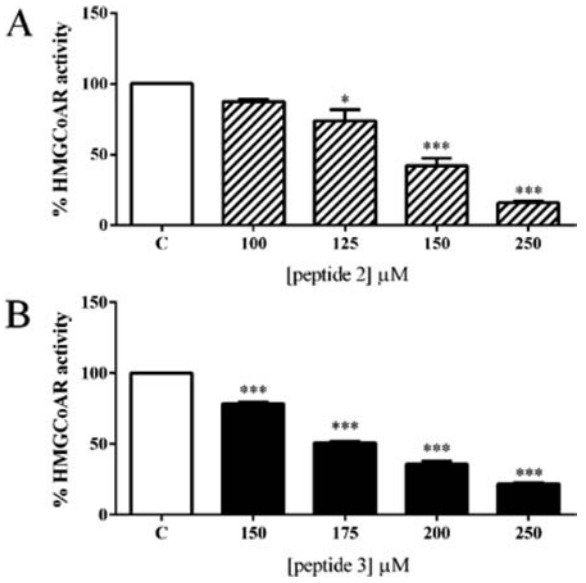

Figure 3. Effects of peptides **2** and **3** on the catalytic domain of HMGCoAR. Bars indicate the effects on the HMGCoAR activity of (A) peptide **2** (100, 125, 150, and 250 μM) and (B) peptide **3** (150, 175, 200, and 250 μM). The HMGCoAR physiologically catalyzes the four-electron reduction of HMGCoA to coenzyme A (CoA) and mevalonate (HMGCoA + 2NADPH + $2H^+$ → mevalonate +$2NADP^+$ + CoA-SH). In this assay, the absorbance decrease at 340 nm, which represents the oxidation of NADPH by the catalytic subunit of HMGCoAR in the presence of the substrate HMGCoA, was measured spectrophotometrically. The data points represent the averages ± SEM of three independent experiments in triplicate. *, $P < 0.05$, and ***, $P < 0.0001$ vs C. C = untreated samples.

increase of the HMGCoAR protein by 170 ± 50.0 and by 177.0 ± 40.5% versus the untreated sample at 350 and 500 μM, respectively (Figure 4F).

Peptides 2 and 3 Increase HepG2 Ability to Uptake Extracellular LDL. Fluorescent LDL uptake experiments permitted us to evaluate the change of the functional capability of HepG2 cells to uptake extracellular LDL after treatment with these peptides. As shown in Figure 5, each peptide is able to

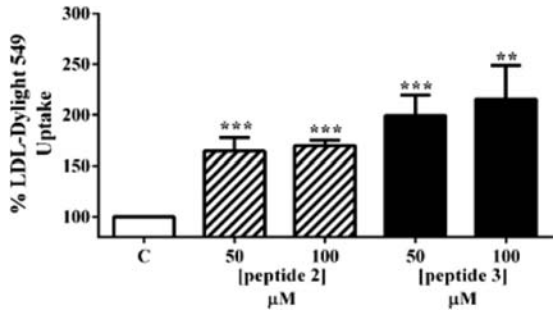

Figure 5. LDL uptake after peptide **2** and **3** treatments. HepG2 cells (3×10^4) were treated with 50 and 100 μM of each peptide for 24 h. LDL-Dylight 549 (10.0 μg/mL) was then incubated for additional 2 h. Excess of LDL-Dylight 549 was removed, cells washed twice with PBS, and specific fluorescent LDL-uptake analyzed by Synergy H1 (Biotek). The data points represent the averages ± SEM of three independent experiments in triplicate. **, $P < 0.001$, and ***, $P < 0.0001$, vs C. C = untreated sample.

increase the LDL uptake versus the untreated sample in a statistically significant way. In fact, the treatments with peptide **2** and **3**, at concentrations of 50 and 100 μM, led to an increase of the LDL uptake by 64 ± 29.9 and 70 ± 14.4% and 100 ± 53.1 and 215 ± 88.1%, respectively, versus the untreated sample.

DISCUSSION

Recently, our research group is dedicating much effort to investigate the potential bioactivity of plant food peptides[13,17,25] because this is a very promising area in functional foods.[26−28] In the framework of research aimed at investigating and characterizing the hypocholesterolemic effects of soy peptides, we have recently studied the mechanism of action through which three peptides from soy glycinin exert their hypocholesterolemic effects in HepG2 cells.[19] Unfortunately, the relevant

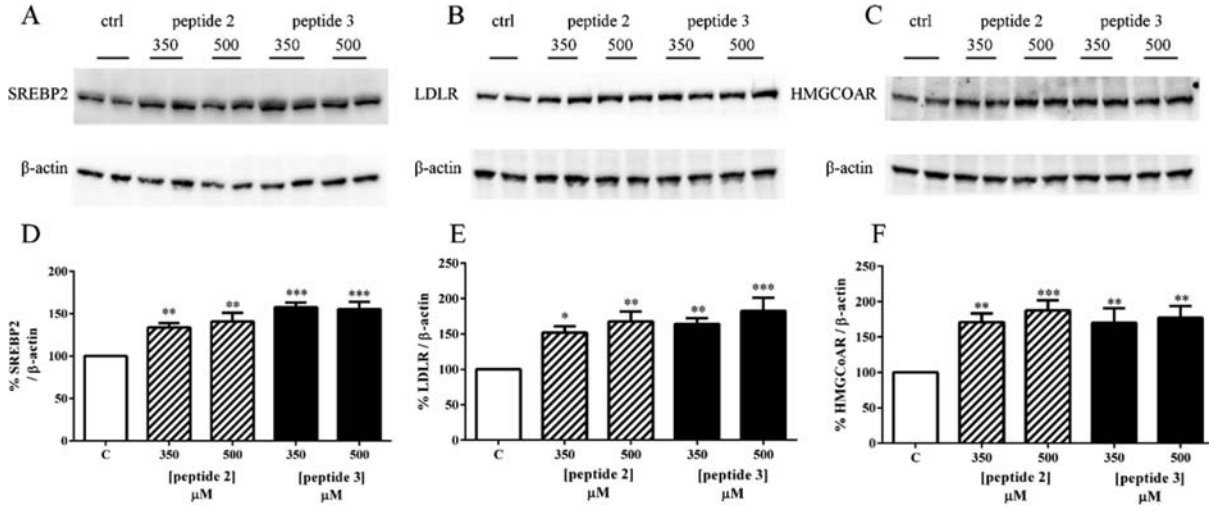

Figure 4. Effects of peptides **2** and **3** on the SREBP2, LDLR, and HMGCoAR protein levels. HepG2 cells (1.5×10^5) were treated with 350 and 500 μM of each peptide for 24 h, respectively. (A−C) SREBP2, LDLR, HMGCoAR, and β-actin immunoblotting signals were detected using specific anti-SREBP2, anti-LDLR, anti-HMGCoAR, and anti-β-actin primary antibodies, respectively. (D) SREBP2, (E) LDLR, and (F) HMGCoAR signals were quantified by ChemiDoc Image Lab (Biorad) and normalized with β-actin signals. Bars represent the averages of duplicate samples ± SEM of three independent experiments. *, $P < 0.05$, **, $P < 0.001$, and ***, $P < 0.0001$ vs C. C = mock treatments.

DOI: 10.1021/acs.jafc.5b03497
J. Agric. Food Chem. 2015, 63, 7945−7951

issue of the actual absorbability and bioavailability of those peptides in the gut remained unsolved.[16] The present research represents a main progress in respect to that paper because peptides **2** and **3** are very likely to be bioavailable.[22]

Another important aspect of this work is that it provides new information on peptide **1**, which has been shown to modulate LDL uptake and degradation in HepG2 cells about 15 years ago,[7] without any further verification of a direct interaction with HMGCoAR either in vitro or in silico. Our modeling study shows that the interaction of this peptide with HMGCoAR is partially impaired by its excessive length, whereas the interaction with the shorter peptide **2** encrypted in peptide **1** is much more favorable. Thus, it seems possible to hypothesize that peptide **2** may be the active part of peptide **1**.

The computational study emphasizes that a suitable HMGCoAR inhibitor should combine a negatively charged portion (residues DNDEN in peptide **2**) that mimics the HMGCoAR substrate with a more hydrophobic portion (residues YVVNP in peptide **2**). It is useful to underline that a similar situation is also observed in statins but with some differences because the statin apolar moieties mimic the pantothenic acid of coenzyme A, whereas the hydrophobic regions of these soy peptides appear to be inserted in the cofactor binding cavity.[20,21]

The in vitro experiments aimed at assessing whether peptides **2** and **3** are direct inhibitors of HMGCoAR have demonstrated for the first time that indeed these peptides, deriving either from the α or α' subunits of β-conglycinin, are able to act as competitive inhibitors of HMGCoAR with a statin-like behavior, in agreement with the in silico investigation.

The studies carried out on human hepatic cells have shown that either peptide **2** or **3** is able to modulate cholesterol metabolism. In particular, the functional results suggest that the improved capability of HepG2 cells to uptake the LDL is strictly correlated with the molecular increase of the intracellular LDLR protein levels induced by these peptides upon inhibition of the HMGCoAR activity. The outcomes of these experimentations, i.e., increase of LDLR protein levels through activation of SREBP2 and enhanced cell capacity to uptake LDL cholesterol, appear to be perfectly in line with the behavior of three soy glycinin peptides, i.e., IAVPGEVA, IAVPTGVA, and LPYP, recently investigated by us.[19] In practice, we have demonstrated that the hypocholesterolemic effects can be exerted by peptides deriving from hydrolysis of either β-conglycinin and glycinin, in contrast to what has been indicated in the past.[11]

To our knowledge, this is the first work showing the molecular mechanism through which two conglycinin peptides modulate the cholesterol pathway in HepG2 cells. It may indicate how these bioavailable peptides function in cholesterol homeostasis in the liver.

■ ASSOCIATED CONTENT

Supporting Information

The Supporting Information is available free of charge on the ACS Publications website at DOI: 10.1021/acs.jafc.5b03497.

Overall view of the computed pose for peptides **2** (S1A) and **1** (S1B). Bidimensional scheme reporting the key interactions stabilizing the putative complex for peptide **1**. Rmsd values dissected per residue for the peptide **2** (S3A) and peptide **1** (S3B) bound to the enzyme as derived by MD runs considering all atoms. (PDF)

■ AUTHOR INFORMATION

Corresponding Author

*Tel.: +390250319372. Fax: +390250319343. E-mail anna.arnoldi@unimi.it.

Author Contributions

Experiment ideation and design: C.L. and G.V. Experiments and data analysis: experiments in HepG2 cells, C.L. and C.Z.; molecular modeling, G.V. Figure preparation: G.V. and CZ. Grant retrieval: A.A. Manuscript writing: C.L., G.V., and A.A..

Funding

Research was funded in part by the European Union Seventh Framework Program (FP7/2007-2013), under grant agreement no. 285819. We are indebted to the Alpro Foundation for funding of a postdoc fellowship to C.Z., and to Carlo Sirtori Foundation (Milan, Italy) for having provided part of the equipment used in this study.

Notes

The authors declare no competing financial interest.

■ ABBREVIATIONS USED

Akt, protein kinase B; 3-hydroxy-3-methylglutaryl CoA reductase; GSK3, glycogen synthase kinase 3; LDL, low-density liproteins; LDLR, low-density lipoprotein receptors; SREBP-2, sterol regulatory-element-binding protein 2

■ REFERENCES

(1) Anderson, J. W.; Johnstone, B. M.; Cook-Newell, M. E. Meta-analysis of the effects of soy protein intake on serum lipids. *N. Engl. J. Med.* **1995**, *333*, 276−82.

(2) Sirtori, C. R.; Eberini, I.; Arnoldi, A. Hypocholesterolaemic effects of soya proteins: results of recent studies are predictable from the Anderson meta-analysis data. *Br. J. Nutr.* **2007**, *97*, 816−822.

(3) Harland, J.; Haffner, T. Systematic review, meta-analysis and regression of randomised controlled trials reporting an association between an intake of circa 25 g soya protein per day and blood cholesterol. *Atherosclerosis* **2008**, *200*, 13−27.

(4) Sirtori, C. R.; Galli, G.; Lovati, M. R.; Carrara, P.; Bosisio, E.; Kienle, M. G. Effects of dietary proteins on the regulation of liver lipoprotein receptors in rats. *J. Nutr.* **1984**, *114*, 1493−1500.

(5) Lovati, M. R.; Manzoni, C.; Canavesi, A.; Sirtori, M.; Vaccarino, V.; Marchi, M.; Gaddi, G.; Sirtori, C. R. Soybean protein diet increases low density lipoprotein receptor activity in mononuclear cells from hypercholesterolemic patients. *J. Clin. Invest.* **1987**, *80*, 1498−502.

(6) Baum, J. A.; Teng, H.; Erdman, J. W. J.; Weigel, R. M.; Klein, B. P.; Persky, V. W.; Freels, S.; Surya, P.; Bakhit, R. M.; Ramos, E.; Shay, N. F.; Potter, S. M. Long-term intake of soy protein improves blood lipid profiles and increases mononuclear cell low-density-lipoprotein receptor messenger RNA in hypercholesterolemic, postmenopausal women. *Am. J. Clin. Nutr.* **1998**, *68*, 545−551.

(7) Lovati, M. R.; Manzoni, C.; Gianazza, E.; Arnoldi, A.; Kurowska, E.; Carroll, K. K.; Sirtori, C. R. Soy protein peptides regulate cholesterol homeostasis in Hep G2 cells. *J. Nutr.* **2000**, *130*, 2543−2549.

(8) Gianazza, E.; Eberini, I.; Arnoldi, A.; Wait, R.; Sirtori, C. R. A proteomic investigation of isolated soy proteins with variable effects in experimental and clinical studies. *J. Nutr.* **2003**, *133*, 9−14.

(9) Consonni, A.; Lovati, M. R.; Manzoni, C.; Pizzagalli, A.; Morazzoni, P.; Duranti, M. Cloning, yeast expression, purification and biological activity of a truncated form of the soybean 7S globulin alpha' subunit involved in Hep G2 cell cholesterol homeostasis. *J. Nutr. Biochem.* **2010**, *21*, 887−91.

(10) Consonni, A.; Lovati, M. R.; Parolari, A.; Manzoni, C.; Morazzoni, P.; Magni, C.; Duranti, M. Heterologous expression and purification of the soybean 7S globulin α' subunit extension region: in

DOI: 10.1021/acs.jafc.5b03497
J. Agric. Food Chem. 2015, 63, 7945−7951

vitro evidence of its involvement in cell cholesterol homeostasis. *Protein Expression Purif.* **2011**, *80*, 125−9.
(11) Duranti, M.; Lovati, M. R.; Dani, V.; Barbiroli, A.; Scarafoni, A.; Castiglioni, S.; Ponzone, C.; Morazzoni, P. The alpha' subunit from soybean 7S globulin lowers plasma lipids and upregulates liver beta-VLDL receptors in rats fed a hypercholesterolemic diet. *J. Nutr.* **2004**, *134*, 1334−1339.
(12) Aluko, R. E. Determination of nutritional and bioactive properties of peptides in enzymatic pea, chickpea, and mung bean protein hydrolysates. *J. AOAC Int.* **2008**, *91*, 947−956.
(13) Boschin, G.; Scigliuolo, G. M.; Resta, D.; Arnoldi, A. Optimization of the enzymatic hydrolysis of lupin (*Lupinus*) proteins for producing ACE-inhibitory peptides. *J. Agric. Food Chem.* **2014**, *62*, 1846−51.
(14) Martinez-Villaluenga, C.; Bringe, N.; Berhow, M.; Gonzalez de Mejia, E. Beta-conglycinin embeds active peptides that inhibit lipid accumulation in 3T3-L1 adipocytes in vitro. *J. Agric. Food Chem.* **2008**, *56*, 10533−43.
(15) Cho, S.; Juillerat, M.; Lee, C. Cholesterol lowering mechanism of soybean protein hydrolysate. *J. Agric. Food Chem.* **2007**, *55*, 10599−604.
(16) Vermeirssen, V.; Van Camp, J.; Verstraete, W. Bioavailability of angiotensin I converting enzyme inhibitory peptides. *Br. J. Nutr.* **2004**, *92*, 357−366.
(17) Lammi, C.; Zanoni, C.; Scigliuolo, G. M.; D'Amato, A.; Arnoldi, A. Lupin peptides lower low-density lipoprotein (LDL) cholesterol through an up-regulation of the LDL receptor/sterol regulatory element binding protein 2 (SREBP2) pathway at HepG2 cell line. *J. Agric. Food Chem.* **2014**, *62*, 7151−9.
(18) Mochizuki, Y.; Maebuchi, M.; Kohno, M.; Hirotsuka, M.; Wadahama, H.; Moriyama, T.; Kawada, T.; Urade, R. Changes in lipid metabolism by soy beta-conglycinin-derived peptides in HepG2 cells. *J. Agric. Food Chem.* **2009**, *57*, 1473−80.
(19) Lammi, C.; Zanoni, C.; Arnoldi, A. IAVPGEVA, IAVPTGVA, and LPYP, three peptides from soy glycinin, modulate cholesterol metabolism in HepG2 cells. *J. Funct. Foods* **2015**, *14*, 469.
(20) Istvan, E. S.; Deisenhofer, J. Structural mechanism for statin inhibition of HMG-CoA reductase. *Science* **2001**, *292*, 1160−1164.
(21) Sarver, R. W.; Bills, E.; Bolton, G.; Bratton, L. D.; Caspers, N. L.; Dunbar, J. B.; Harris, M. S.; Hutchings, R. H.; Kennedy, R. M.; Larsen, S. D.; Pavlovsky, A.; Pfefferkorn, J. A.; Bainbridge, G. Thermodynamic and structure guided design of statin based inhibitors of 3-hydroxy-3-methylglutaryl coenzyme A reductase. *J. Med. Chem.* **2008**, *51*, 3804−13.
(22) Amigo-Benavent, M.; Clemente, A.; Caira, S.; Stiuso, P.; Ferranti, P.; del Castillo, M. D. Use of phytochemomics to evaluate the bioavailability and bioactivity of antioxidant peptides of soybean β-conglycinin. *Electrophoresis* **2014**, *35*, 1582−9.
(23) Korb, O.; Stützle, T.; Exner, T. E. Empirical scoring functions for advanced protein-ligand docking with PLANTS. *J. Chem. Inf. Model.* **2009**, *49*, 84−96.
(24) Phillips, J. C.; Braun, R.; Wang, W.; Gumbart, J.; Tajkhorshid, E.; Villa, E.; Chipot, C.; Skeel, R. D.; Kalé, L.; Schulten, K. Scalable molecular dynamics with NAMD. *J. Comput. Chem.* **2005**, *26*, 1781−802.
(25) Boschin, G.; Scigliuolo, G. M.; Resta, D.; Arnoldi, A. ACE-inhibitory activity of enzymatic protein hydrolysates from lupin and other legumes. *Food Chem.* **2014**, *145*, 34−40.
(26) Puchalska, P.; Marina Alegre, M. L.; García López, M. C. Isolation and characterization of peptides with antihypertensive activity in foodstuffs. *Crit. Rev. Food Sci. Nutr.* **2015**, *55*, 521−51.
(27) Singh, B. P.; Vij, S.; Hati, S. Functional significance of bioactive peptides derived from soybean. *Peptides* **2014**, *54*, 171−9.
(28) Cam, A.; de Mejia, E. G. Role of dietary proteins and peptides in cardiovascular disease. *Mol. Nutr. Food Res.* **2012**, *56*, 53−66.

DOI: 10.1021/acs.jafc.5b03497
J. Agric. Food Chem. 2015, 63, 7945−7951

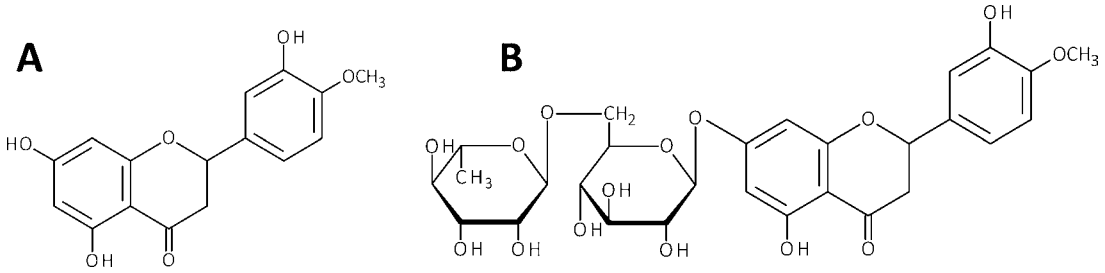

Figure 1. Chemical structures of (A) hesperetin and (B) hesperidin (hesperetin-7-*O*-rutinoside).

Table 1. Percentage Composition of Experimental Diets[a]

	control	0.5% hesperetin	1.0% hesperidin
casein	20	20	20
DL-methionine	0.3	0.3	0.3
corn starch	55	55	55
sucrose	10	10	10
corn oil	5.0	5.0	5.0
cellulose powder	5.0	4.5	4.0
mineral mix	3.5	3.5	3.5
vitamin mix	1.0	1.0	1.0
choline bitartrate	0.2	0.2	0.2
hesperetin	–	0.5	–
hesperidin	–	–	1.0

[a]Source of ingredients: casein, corn starch, sucrose, cellulose powder, mineral AIN-76 mix, and vitamin AIN-76 mix (Oriental Yeast Co., Ltd., Tokyo, Japan); DL-methionine and choline bitartrate (Wako Pure Chemical Industries, Ltd., Osaka, Japan).

(16.4 mmol/kg diet). The rats had free access to tap water and the experimental diets for 3 weeks. Food intake and body weight were determined three times weekly. All feces were collected during the third week of the feeding period and stored at −40 °C until further processing. At the end of the experiment, rats were sacrificed by drawing blood from the heart under diethyl ether anesthesia. Cecum and abdominal adipose tissues were immediately excised and weighed. The cecum content was stored at −40 °C until use. This study was approved by the Animal Research Committee of Tokyo Kasei Gakuin University, and all experimental procedures followed the guidelines for the care and use of experimental animals.

Determination of Fecal Bacterial 16S rRNA Gene Copy Number. Before analysis, all fecal samples collected for a week were freeze-dried and ground by a grinder mill (type TML161, Tescom Co., Ltd., Tokyo, Japan). DNA was extracted according to the method of Tanigawa et al.[14] The bacterial 16S copy number was calculated from the standard curve of known bacterial 16S copy number by quantitative real-time PCR of 16S rRNA gene using 341f (5′-CCTACGGGAGGCAGCAG-3′) and 534r (5′-ATTACCGCGGCT-GCTGG-3′) primers.[15] Amplification reactions were performed by a Rotor-Gene Q apparatus (Qiagen, Germany) using the SYBR Premix Ex *Taq*II (Tli RNaseH Plus, Takara Bio, Shiga, Japan).

Fecal Microbial Composition Analysis. Fecal samples of rats were analyzed by targeting the bacterial 16S rRNA genes using a terminal restriction fragment length polymorphism (T-RFLP) technique according to the procedure described by Nagashima et al.[16] The fluorescently labeled primers 516f (5′-TGCCAGCAGCCG-CGGTA-3′) and 1510r (5′-GGTTACCTTGTTACGACTT-3′) were used to amplify the 16S rRNA genes. The purified PCR products were digested with the restriction enzyme *Bsl*I (New England BioLabs Japan, Inc., Tokyo, Japan). The length of the terminal restriction fragments was determined using an automated sequence analyzer (ABI PRISM 3130xl DNA Sequencer, Applied Biosystems, Carlsbad, CA, USA). The abundance of each terminal restriction fragment was determined on the basis of fluorescence intensity using the software GeneMapper ver. 4 (Applied Biosystems). Fragment sizes were assigned to categories of operational taxonomic units (OTU). The OTU data were used to identify the phylotypes by matching to those predicted from various phylotypes in the literature.[16]

Analyses of SCFA in Cecum Content. The SCFA (acetic, propionic, and butyric acids) in the homogenate of cecum content were derivatized with 2-nitrophenylhydrazine hydrochloride in the presence of 1-ethyl-3-(3-(dimethylamino)propyl)carbodiimide hydrochloride and were measured by a high-performance liquid chromatography (HPLC) system.[17] The derivatives were separated using a reversed-phase column (type FA, 6.0 mm × 250 mm, YMC Co., Ltd., Kyoto, Japan) with an acetonitrile/methanol/water (30:16:54, v/v/v) mobile phase at the flow rate of 1.2 mL/min and were detected with a variable-wavelength monitor with the absorbance set at 400 nm.

Analyses of Starch and Proteins in Feces. The concentrations of undigested starch in the feces were determined after hydrolysis with thermostable α-amylase and amyloglucosidase, followed by a determination of the released glucose using an enzymatic colorimetric assay kit (Glucose CII-test, Wako Pure Chemical Industries, Ltd.).[18] Results were corrected to a starch basis by multiplying them by 0.9. Total fecal nitrogen was determined by Kjeldahl's method,[19] and results were multiplied by 6.25 to calculate the amount of protein in the feces.

Analyses of HP and HD in Feces. The flavonoids were extracted with the mixture of dimethyl sulfoxide and methanol (1:1, v/v).[3] One hundred milligrams of the ground fecal samples was sonicated three times with 3 mL of the extraction solvent for 1 min (Branson Ultrasonics, Ltd., Danbury, CT, USA). After centrifugation at 1000*g* for 10 min, the supernatants were combined, and the volume of combined extracts was adjusted to 10 mL. After a 10-fold dilution, the resulting extract was filtered with a 0.45 μm membrane filter and was injected into the HPLC system. The flavonoids were separated using a reversed-phase column (type Unison UK C_{18}, 4.6 mm × 150 mm, Imtakt Co., Kyoto, Japan) by a two-solvent linear gradient program from initially acetonitrile/water/phosphoric acid (10:90:0.05, v/v/v) to finally acetonitrile/water (80:20, v/v) in 20 min at the flow rate of 0.8 mL/min. The flavonoids were detected at UV 285 nm.

In Vitro Pancreatic α-Amylase Inhibition. Porcine pancreatic extract was suspended in 20 mM phosphate buffer (pH 6.9) containing 6 mM sodium chloride. The reaction mixture was composed of 0.1 mL of the various concentrations of test samples, 0.7 mL of 10 mg/mL soluble starch, and 0.1 mL of 0.1 mg/mL porcine pancreatic extract and was incubated at 37 °C for 30 min. The reaction was terminated by adding 1.0 mL of acetonitrile. After centrifugation at 2000*g* for 10 min, the supernatant was filtered with a 0.45 μm membrane filter. The liberated maltose levels in the filtrate were measured by the HPLC system with a refractive index detector. Separation was carried out by using an amino-bonded silica column (type Unison UK-amino, 4.6 mm × 150 mm, Imtakt Co.) with an acetonitrile/water (80:20, v/v) mobile phase.

Statistical Analysis. All data are shown as the mean ± standard deviation (SD). The bacterial 16S rRNA gene copy numbers were converted into logarithm values before the statistical analysis. Significant differences among the groups were determined by one-way ANOVA, followed by Tukey's test, using a commercial software package (GraphPad Prism 5 for Windows, GraphPad Software, Inc., San Diego, CA, USA). Differences were considered significant at $P < 0.05$.

DOI: 10.1021/acs.jafc.5b02649
J. Agric. Food Chem. 2015, 63, 7952−7957

RESULTS

Body Weight Gain and Organ Weights. There were no differences among the groups in food intake or body weight gain during the 3 week experiment (Table 2). Averaged daily intakes of HT and HD were 0.40 g (1.34 mmol) and 0.83 g (1.36 mmol) per kilogram of body weight. The rats fed the HT diet had a lower weight of abdominal adipose tissues (the mass of mesenteric, perirenal, and epididymal adipose tissues) compared with those fed the control diet. The HT diet led to a significant increase in the weight of cecum content, whereas the HD group showed no differences with the control group.

Table 2. Food Intake, Body Weight Gain, and Organ Weights in Rats Fed the Experimental Diet for 3 Weeks[a]

	control	0.5% hesperetin	1.0% hesperidin
food intake (g)	471 ± 3	459 ± 14	464 ± 11
initial body wt (g)	136 ± 8	136 ± 8	137 ± 8
final body wt (g)	291 ± 11	291 ± 7	289 ± 11
body wt gain (g)	155 ± 7	155 ± 3	152 ± 11
liver wt (g)	13.6 ± 3.5	12.5 ± 1.4	11.4 ± 0.7
abdominal adipose tissue[b] (g)	12.8 ± 2.1 b	10.4 ± 1.6 a	12.1 ± 1.5 ab
mesenteric	3.5 ± 0.7	3.1 ± 0.2	3.6 ± 0.4
perirenal	4.2 ± 0.9	3.5 ± 1.0	4.2 ± 0.7
epididymal	5.1 ± 1.1 b	3.8 ± 0.5 a	4.4 ± 0.7 ab
cecum content wt (g)	2.2 ± 0.6 a	3.4 ± 0.9 b	2.7 ± 0.5 ab

[a]Values are the mean ± SD (n = 7). Treatments with different letters are significantly different (P < 0.05). [b]Sum of the mass of mesenteric, perirenal, and epididymal adipose tissues.

Fecal Microbiota. The dry weight of feces collected during the third week of the feeding period did not show statistical significances among the groups (Table 3). Changes in the bacterial 16S rRNA gene copy number and composition in the feces of five randomly selected rats of each group are shown in Table 4. There was no significant difference in the copy numbers of 16S rRNA gene of all bacteria among the groups. After 3 weeks of feeding, the taxonomic composition of the fecal microbiota significantly differed among the groups. In the control rats, the T-RFLP analysis revealed that the order of *Clostridium* was the most predominant group, followed by *Lactobacillales*. The fecal microbiota of rats that received HT in their diet presented a remarkable alteration in the proportion of *Clostridium*. In particular, feeding the HT diet resulted in a significant decrease in the ratio of *Clostridium* subcluster XIVa in the fecal microbiota compared to other diets. In contrast, the feces of rats fed the control diet displayed very low proportions of *Clostridium* clusters IV and XVIII, but the HT diet significantly increased their ratios. Treatment with HT in the diet slightly affected the abundance of *Bifidobacterium* and *Lactobacillales*, although these results did not reach significance.

Table 3. Fecal Excretions of Starch, Protein, Hesperetin, and Hesperidin in Rats Fed the Experimental Diets[a]

	control	0.5% hesperetin	1.0% hesperidin
dry wt[b] (g/7 days)	14.4 ± 0.5	14.3 ± 1.1	13.5 ± 1.5
fecal nutrient			
starch (mg/7 days)	65 ± 2 a	91 ± 36 b	61 ± 5 a
protein (g/7 days)	1.4 ± 0.2	1.6 ± 0.2	1.5 ± 0.1
fecal flavonoid			
hesperetin (mmol/7 days)	–	0.9 ± 0.3	1.1 ± 0.6
hesperidin (mmol/7 days)	–	–	0.4 ± 0.1

[a]Values are the mean ± SD (n = 7). Treatments with different letters are significantly different (P < 0.05). [b]Collected during the third week of experimental diet feeding period.

Table 4. Effect of Dietary Hesperetin and Hesperidin on the Profile of Microbiota in Feces of Rats[a]

	control	0.5% hesperetin	1.0% hesperidin
16S rRNA Gene Copy Number (log_{10} Copies)			
all bacteria (per g dry feces)	12.0 ± 0.1	12.2 ± 0.1	12.1 ± 0.1
all bacteria (per 7-day dry feces)	13.2 ± 0.1	13.4 ± 0.1	13.3 ± 0.1
Ratio of Peak Area of Each OTU[b]			
Bifidobacterium	3.1 ± 3.6	7.1 ± 8.5	3.0 ± 3.5
Lactobacillales	25.0 ± 10.8	29.8 ± 11.3	31.1 ± 13.5
Bacteroides	7.9 ± 3.6	10.7 ± 4.3	11.1 ± 2.9
Prevotella	9.2 ± 7.0	5.0 ± 3.1	3.0 ± 3.2
Clostridium	32.7 ± 3.8 b	20.3 ± 8.7 a	31.5 ± 3.7 b
Clostridium cluster IV	0.1 ± 0.3 a	1.2 ± 0.9 b	0.1 ± 0.1 a
Clostridium subcluster XIVa	19.8 ± 4.3 b	5.3 ± 1.5 a	15.4 ± 5.8 b
Clostridium cluster XI	10.4 ± 1.9	9.1 ± 6.5	14.0 ± 7.1
Clostridium cluster XVIII	2.3 ± 0.7 a	4.7 ± 1.9 b	2.1 ± 0.9 a
other	22.1 ± 10.1	25.9 ± 7.2	20.4 ± 12.1

[a]Values are the mean ± SD (n = 5). Treatments with different letters are significantly different (P < 0.05). [b]Values are expressed as percentages of the peak area of a particular OTU to the total peak area of all OTUs.

Amount of Starch and Proteins in Feces. Little starch was excreted in the feces of rats fed the control diet, whereas the feces of rats fed the HT diet contained a significant amount of starch (Table 3). However, the HD diet had little impact on the fecal starch level. Both treatments with HT and HD did not lead to significant differences in protein excretions in the feces as compared with the control.

Cecal SCFA Pools. Figure 2 summarizes the cecal SCFA pools in rats fed the different experimental diets. Feeding the HT diet resulted in significant increases in the cecal pools of acetic and butyric acids as compared to the control, but treatment with the HD diet did not yield significantly different results compared with the control. The additions of these flavonoids to the diet had little influence on the cecal pool of propionic acid.

Fecal Excretions of HT and HD. Parts of dietary HT and HD were excreted in the feces in unchanged forms. Feces collected during the third week of feeding contained 0.9 mmol of HT in the 0.5% HT diet group and 0.4 mmol of HD in the 1.0% HD diet group (Table 3). Because the rats consumed 2.7 mmol of HT or HD from their respective diet, 33 and 15% were estimated to be excreted in the feces in the unchanged form, respectively. In addition, the feces collected from the rat fed the 1.0% HD diet also contained 1.1 mmol of HT.

Inhibition of Pancreatic α-Amylase in Vitro. HT inhibited the enzyme activity of porcine pancreatic α-amylase in a concentration-dependent manner (Figure 3), but HD lacked the inhibitory activity for α-amylase.

DOI: 10.1021/acs.jafc.5b02649
J. Agric. Food Chem. 2015, 63, 7952−7957

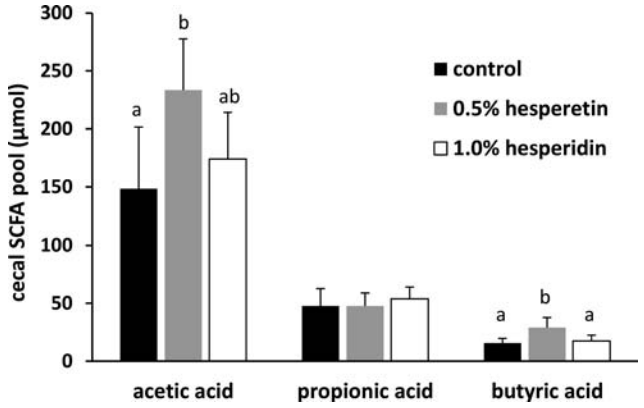

Figure 2. Effects of dietary supplementations of hesperetin and hesperidin on the cecal SCFA pool. The cecal SCFA pool (μmol) = SCFA concentration (μmol/g) × cecum content (g). Values are the mean ± SD (n = 7). Statistical comparisons were performed using one-way ANOVA with Tukey's post hoc test. Treatments with different letters are significantly different (P < 0.05).

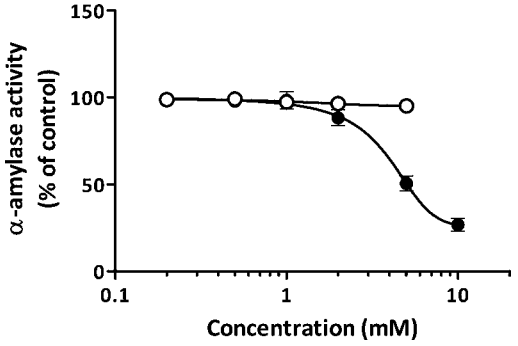

Figure 3. Dose-dependent inhibition of hesperetin against pancreatic α-amylase activity. Data are the mean ± SD from triplicate measurements. Open circles and solid circles indicate hesperidin and hesperetin, respectively.

DISCUSSION

It is well recognized that the structure and activity of microorganisms inhabiting our gut are influenced by dietary intake. Such diet-induced changes in gut microbial communities could be responsible for the development of metabolic disorders. It is of current interest that dietary polyphenols raise a possibility for modulating the composition of intestinal microorganisms and the formation of fermentation end products, which may be involved in their underlying mechanisms for beneficial health effects. Citrus flavonoids exhibit a range of biological activities and beneficial health effects.[20] In a type 2 diabetes animal model, dietary supplementation of 1% (w/w) HD resulted in decreases in blood glucose and serum triacylglycerols.[21] This study aimed to evaluate the impact of dietary supplementation with two types of citrus flavonoids on the structure and activity of gut microbiota in rats, in relative relation to the presence of sugar moiety to the flavonoid skeleton.

The rats consumed the respective experimental diets that were supplemented with equimolar concentrations of HT and HD. Compared to the control diet, feeding the 0.5% HT diet resulted in a significant increase in starch excretion in the feces. This finding let us understand that dietary HT could interfere with starch digestion in the small intestine, leading to the influx of undigested starch into the large intestine. Indeed, the result of in vitro experiments offers supporting evidence that HT had an inhibitory effect against pancreatic α-amylase in a concentration-dependent fashion. Parts of the starch undigested in the small intestine can then be microbially hydrolyzed to monosaccharides in the cecum (rodents) and colon (humans), where they are further degraded into biologically active metabolites represented by SCFA.[22] It is commonly understood that the growth of pathogenic microorganisms could be inhibited by reducing luminal pH with more SCFA productions, eventually increasing the growth and/or activity of beneficial bacteria.[23] Feeding the HT diet raised the proportion of *Bifidobacterium* and the *Lactobacillales* to a lesser extent, but there were no significant changes. In addition, it is worth noting that HT served to modulate the abundance of *Clostridium* spp. Particularly, the present study demonstrated that the proportion of *Clostridium* subcluster XIVa in the feces was significantly decreased by the HT diet as compared to the control diet. Similar results were observed in several previous studies in relation to polyphenols from red wine,[24] grape seed extracts,[25] and green tea.[26] Likewise, feeding a diet abundant in resistant starch can reduce the proportion of *Clostridium* cluster XIVa in the luminal contents of pig colon.[27] Resistant starch is a type of dietary fiber that is highly fermentable by colonic bacteria, resulting in the production of SCFA; an acidified condition for the lumen of the large intestine may be involved in reducing the proportion of *Clostridium* subcluster XIVa. In the light of increased levels of SCFA in rat cecum content by feeding the HT diet, it seems reasonable to suppose that dietary HT had some degree of influence in modulating the proportion of *Clostridium* subcluster XIVa through the stimulation of SCFA production.

The close associations among the energy harvest from foods, the development of obesity, and the microbial population inhabiting the intestinal tract are becoming clearer. Obese mice had an increased abundance of bacteria from the *Firmicutes* phylum,[28] the main constituents of which were *Clostridium* cluster IV (mainly *Clostridium* leptum group) and *Clostridium* cluster XIVa (mainly *Clostridium* coccoides group).[29] It is known that *Clostridium* cluster XIVa was substantially increased by high-fat diet feeding, but was reduced by antibiotic treatment.[30] There is evidence that an obesity treatment program comprising a calorie-restricted diet and physical activity over 3 months had an impact on the decreased abundance of the *Clostridium* cluster XIVa on the structure of the fecal microbiota of overweight and obese subjects.[31] Furthermore, vegetarians had a decreased relative abundance of *Clostridium* cluster XIVa bacteria compared with omnivores.[32] In this light, alteration of microbial ecology by HT may be of relevance to a significant reduction of abdominal adipose tissue weights of rats. In addition, it is interesting to note that SCFA themselves regulate the balance among fatty acid synthesis, fatty acid oxidation, and lipolysis in the body.[10] SCFA formed by colonic bacterial fermentation enter the blood circulation from the intestine and are taken up by tissues, where they function as signal molecules. GPR41 and GPR43 have been identified as SCFA receptors. SCFA activate the sympathetic nervous system by stimulating GPR41 in sympathetic ganglia, leading to an increase in energy expenditure.[33] SCFA-mediated activation of GPR43 suppresses insulin signaling in adipocytes and thereby inhibits fat accumulation in adipose tissues.[34] Regulation of the energy metabolism by SCFA may also contribute in a practical way to the loss of body fat in rats fed the HT diet. The present study

DOI: 10.1021/acs.jafc.5b02649
J. Agric. Food Chem. 2015, 63, 7952−7957

also demonstrated that a significant increase in the excretion of starch in the feces was promoted by the dietary addition of HT. Needless to say, an increased energy loss originating from starch in the feces may at least partially influence the body fat reduction by HT.

The present study exhibited considerably different results between HT and HD. The HT diet affected the excretion of starch in the feces and the pools of SCFA in the cecum content, but the HD diet did not. The inhibitory effect of HT on starch digestion was stronger than that of HD. That is to say, the attachment of the rutinose moiety to the flavanone structure can diminish the effectiveness. Limiting the pancreatic α-amylase activity in the small intestine must be the key to producing SCFA in the large intestine. Although certain types of bacterial strains produced amylolytic enzymes in the intestine,[35] it remains to be seen that HT may have an effect on the production and activity of microbial α-amylase. Furthermore, HT also affected the proportion of *Clostridium* subcluster XIVa in rat feces, but HD did not. Because the feces collected from the rat fed the HD diet contained a significant amount of HT, dietary HD reached the large intestine, where the glycosidic linkage of HD was hydrolyzed to generate HT. Given that both treatments yielded the same compound in the large intestine, it is likely that the modulation of gut microbiota only by the HT diet may be a consequential result of the stimulation of SCFA productions in the large intestine, as is the case with resistant starch. Besides, we must keep constantly in mind the fact that the large intestine is a very active site for the microbial catabolism of HT, leading to further degradation of the flavanone skeleton. Such transformations could be mainly due to the genera of *Clostridium* spp. in the colon.[36]

In conclusion, the present study provides detailed insights into the effects of dietary HT on the composition of gut microbiota and the cecal pools of SCFA in rats and may lead to design strategies for functional foods that aim to reduce the risk of obesity in humans. More research also is needed to further elucidate in more depth the underlying molecular mechanisms of dietary polyphenols as well as their microbial metabolites to modulate the composition and activity of gut microbiota and the link to the antiobesity effect.

AUTHOR INFORMATION

Corresponding Author

*(T.U.) Phone: +81 3 3262 2789. Fax: +81 3 3262 2174. E-mail: tunno@kasei-gakuin.ac.jp.

Funding

This work was supported by JSPS KAKENHI Grant 24500998.

Notes

The authors declare no competing financial interest.

ACKNOWLEDGMENTS

We acknowledge Nana Obara, Aki Tanegashima, and Minori Miyoshi for assistance with the animal experiments.

ABBREVIATIONS USED

HD, hesperidin; HT, hesperetin; SCFA, short-chain fatty acids; T-RFLP, terminal restriction fragment length polymorphism; OTU, operational taxonomic units

REFERENCES

(1) Bravo, L. Polyphenols: Chemistry, dietary sources, metabolism, and nutritional significance. *Nutr. Rev.* **1998**, *56*, 317−333.

(2) Chun, O. K.; Chung, S. J.; Song, W. O. Estimated dietary flavonoid intake and major food sources of U.S. adults. *J. Nutr.* **2007**, *137*, 1244−1252.

(3) Manthey, J. A.; Grohmann, K. Concentrations of hesperidin and other orange peel flavonoids in citrus processing byproducts. *J. Agric. Food Chem.* **1996**, *44*, 811−814.

(4) Pereira-Caro, G.; Borges, G.; van der Hooft, J.; Clifford, M. N.; Del Rio, D.; Lean, M. E. J.; Roberts, S. A.; Kellerhals, M. B.; Crozier, A. Orange juice (poly)phenols are highly bioavailable in humans. *Am. J. Clin. Nutr.* **2014**, *100*, 1378−1384.

(5) Schär, M. Y.; Curtis, P. J.; Hazim, S.; Ostertag, L. M.; Kay, C. D.; Potter, J. F.; Cassidy, A. Orange juice-derived flavanone and phenolic metabolites do not acutely affect cardiovascular risk biomarkers: a randomized, placebo-controlled, crossover trial in men at moderate risk of cardiovascular disease. *Am. J. Clin. Nutr.* **2015**, *101*, 931−938.

(6) Garg, A.; Garg, S.; Zaneveld, L. J. D.; Singla, A. K. Chemistry and pharmacology of the citrus bioflavonoid hesperidin. *Phytother. Res.* **2001**, *15*, 655−669.

(7) Nicholson, J. K.; Holmes, E.; Kinross, J.; Burcelin, R.; Gibson, G.; Jia, W.; Pettersson, S. Host-gut microbiota metabolic interactions. *Science* **2012**, *336*, 1262−1267.

(8) Tremaroli, V.; Bäckhed, F. Functional interactions between the gut microbiota and host metabolism. *Nature* **2012**, *489*, 242−249.

(9) Tagliabue, A.; Elli, M. The role of gut microbiota in human obesity: recent findings and future perspectives. *Nutr., Metab. Cardiovasc. Dis.* **2013**, *23*, 160−168.

(10) den Besten, G.; van Eunen, K.; Groen, A. K.; Venema, K.; Reijngoud, D. J.; Bakker, B. M. The role of short-chain fatty acids in the interplay between diet, gut microbiota, and host energy metabolism. *J. Lipid Res.* **2013**, *54*, 2325−2340.

(11) Etxeberria, U.; Fernández-Quintela, A.; Milagro, F. I.; Aguirre, L.; Martínez, J. A.; Portillo, M. P. Impact of polyphenols and polyphenol-rich dietary sources on gut microbiota composition. *J. Agric. Food Chem.* **2013**, *61*, 9517−9533.

(12) Cardona, F.; Andrés-Lacueva, C.; Tulipani, S.; Tinahones, F. J.; Queipo-Ortuño, M. I. Benefits of polyphenols on gut microbiota and implications in human health. *J. Nutr. Biochem.* **2013**, *24*, 1415−1422.

(13) Duda-Chodak, A. The inhibitory effect of polyphenols on human gut microbiota. *J. Physiol. Pharmacol.* **2012**, *63*, 497−503.

(14) Tanigawa, T.; Watanabe, T.; Otani, K.; Nadatani, Y.; Ohkawa, F.; Sogawa, M.; Yamagami, H.; Shiba, M.; Watanabe, K.; Tominaga, K.; Fujiwara, Y.; Takeuchi, K.; Arakawa, T. Rebamipide inhibits indomethacin-induced small intestinal injury: possible involvement of intestinal microbiota modulation by upregulation of α-defensin 5. *Eur. J. Pharmacol.* **2013**, *704*, 64−69.

(15) Muyzer, G.; de Waal, E. C.; Uitterlinden, A. G. Profiling of complex microbial populations by denaturing gradient gel electrophoresis analysis of polymerase chain reaction-amplified genes coding for 16S rRNA. *Appl. Environ. Microbiol.* **1993**, *59*, 695−700.

(16) Nagashima, K.; Mochizuki, J.; Hisada, T.; Suzuki, S.; Shimomura, K. Phylogenetic analysis of 16S ribosomal RNA gene sequences from human fecal microbiota and improved utility of terminal restriction fragment length polymorphism profiling. *Biosci. Microflora* **2006**, *25*, 99−107.

(17) Miwa, H.; Hiyama, C.; Yamamoto, M. High-performance liquid chromatography of short- and long-chain fatty acids as 2-nitrophenylhydrazides. *J. Chromatogr.* **1985**, *321*, 165−174.

(18) Unno, T.; Matsumoto, Y.; Yamamoto, Y. Gallated form of tea catechin, not nongallated form, increases fecal starch excretion in rats. *J. Nutr. Sci. Vitaminol.* **2012**, *58*, 45−49.

(19) Protein (crude) in animal feed. Copper catalyst Kjeldahl method. In *Official Method of Analysis*, 15th ed.; Helrich, K., Keys, F., Eds.; Association of Official Analytical Chemists, Inc.: Arlington, VA, USA, 1990.

(20) Assini, J. M.; Mulvihill, E. E.; Huff, M. W. Citrus flavonoids and lipid metabolism. *Curr. Opin. Lipidol.* **2013**, *24*, 34−40.

(21) Akiyama, S.; Katsumata, S.; Suzuki, K.; Nakaya, Y.; Ishimi, Y.; Uehara, M. Hypoglycemic and hypolipidemic effects of hesperidin and

DOI: 10.1021/acs.jafc.5b02649
J. Agric. Food Chem. 2015, 63, 7952−7957

cyclodextrin-clathrated hesperetin in Goto-Kakizaki rats with type 2 diabetes. *Biosci., Biotechnol., Biochem.* **2009**, *73*, 2779−2782.
(22) Gibson, G. R.; Roberfroid, M. B. Dietary modulation of the human colonic microbiota: introducing the concept of prebiotics. *J. Nutr.* **1995**, *125*, 1401−1412.
(23) Brownawell, A. M.; Caers, W.; Gibson, G. R.; Kendall, C. W.; Lewis, K. D.; Ringel, Y.; Slavin, J. L. Prebiotics and the health benefits of fiber: current regulatory status, future research, and goals. *J. Nutr.* **2012**, *142*, 962−974.
(24) Queipo-Ortuño, M. I.; Boto-Ordóñez, M.; Murri, M.; Gomez-Zumaquero, J. M.; Clemente-Postigo, M.; Estruch, R.; Cardona Diaz, F.; Andrés-Lacueva, C.; Tinahones, F. J. Influence of red wine polyphenols and ethanol on the gut microbiota ecology and biochemical biomarkers. *Am. J. Clin. Nutr.* **2012**, *95*, 1323−1334.
(25) Fiesel, A.; Gessner, D. K.; Most, E.; Edor, K. Effects of dietary polyphenol-rich plant products from grape or hop on pro-inflammatory gene expression in the intestine, nutrient digestibility and faecal microbiota of weaned pigs. *BMC Vet. Res.* **2014**, *10*, 196.
(26) Unno, T.; Sakuma, M.; Mitsuhashi, S. Effect of dietary supplementation of (−)-epigallocatechin gallate on gut microbiota and biomarkers of colonic fermentation in rats. *J. Nutr. Sci. Vitaminol.* **2014**, *60*, 213−219.
(27) Haenen, D.; Zhang, J.; Souza da Silva, C.; Bosch, G.; van der Meer, I. M.; van Arkel, J.; van den Borne, J. J.; Pérez Gutiérrez, O.; Smidt, H.; Kemp, B.; Müller, M.; Hooiveld, G. J. A diet high in resistant starch modulates microbiota composition, SCFA concentrations, and gene expression in pig intestine. *J. Nutr.* **2013**, *143*, 274−283.
(28) Ley, R. E.; Bäckhed, F.; Turnbaugh, P.; Lozupone, C. A.; Knight, R. D.; Gordon, J. I. Obesity alters gut microbial ecology. *Proc. Natl. Acad. Sci. U. S. A.* **2005**, *102*, 11070−1107.
(29) Hayashi, H.; Sakamoto, M.; Kitahara, M.; Benno, Y. Molecular analysis of fecal microbiota in elderly individuals using 16S rDNA library and T-RFLP. *Microbiol. Immunol.* **2003**, *47*, 557−570.
(30) Yoshimoto, S.; Loo, T. M.; Atarashi, K.; Kanda, H.; Sato, S.; Oyadomari, S.; Iwakura, Y.; Oshima, K.; Morita, H.; Hattori, M.; Honda, K.; Ishikawa, Y.; Hara, E.; Ohtani, N. Obesity-induced gut microbial metabolite promotes liver cancer through senescence secretome. *Nature* **2013**, *499*, 97−101.
(31) Remely, M.; Tesar, I.; Hippe, B.; Gnauer, S.; Rust, P.; Haslberger, A. G. Gut microbiota composition correlates with changes in body fat content due to weight loss. *Benefic. Microbes* **2015**, *6*, 431−439.
(32) Kabeerdossa, J.; Devia, S.; Marya, R.; Ramakrishna, B. S. Faecal microbiota composition in vegetarians: comparison with omnivores in a cohort of young women in southern India. *Br. J. Nutr.* **2012**, *108*, 953−957.
(33) Kimura, I.; Inoue, D.; Maeda, T.; Hara, T.; Ichimura, A.; Miyauchi, S.; Kobayashi, M.; Hirasawa, A.; Tsujimoto, G. Short-chain fatty acids and ketones directly regulate sympathetic nervous system via G protein-coupled receptor 41 (GPR41). *Proc. Natl. Acad. Sci. U. S. A.* **2011**, *108*, 8030−8035.
(34) Kimura, I.; Ozawa, K.; Inoue, D.; Imamura, T.; Kimura, K.; Maeda, T.; Terasawa, K.; Kashihara, D.; Hirano, K.; Tani, T.; Takahashi, T.; Miyauchi, S.; Shioi, G.; Inoue, H.; Tsujimoto, G. The gut microbiota suppresses insulin-mediated fat accumulation via the short-chain fatty acid receptor GPR43. *Nat. Commun.* **2013**, *4*, 1829.
(35) Huntington, G. B. Starch utilization of ruminants: from basics to the bunk. *J. Anim. Sci.* **1997**, *75*, 852−867.
(36) Schoefer, L.; Mohan, R.; Schwiertz, A.; Braune, A.; Blaut, M. Anaerobic degradation of flavonoids by *Clostridium orbiscindens*. *Appl. Environ. Microbiol.* **2003**, *69*, 5849−5854.

DOI: 10.1021/acs.jafc.5b02649
J. Agric. Food Chem. 2015, 63, 7952−7957

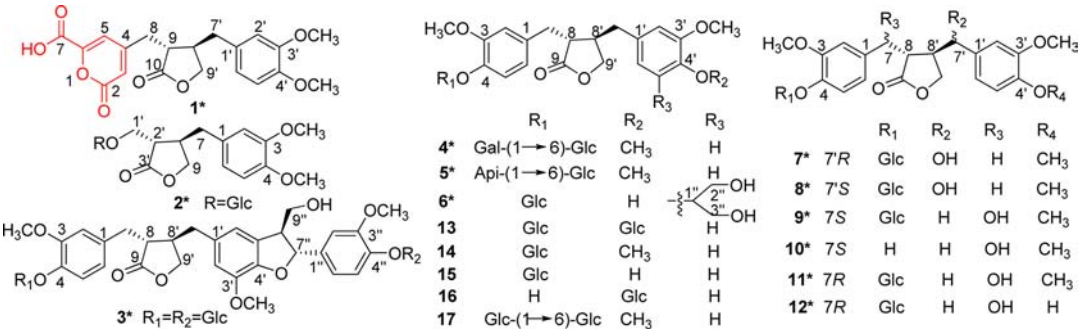

Figure 1. Structures of compounds **1**−**17**.

Extraction and Isolation. Air-dried mature fruits (100 kg) of *A. lappa* L. were extracted with 80% EtOH (3 × 600 L) under reflux three times. The solvent was evaporated under reduced pressure. Then, the residue (4.2 kg) was suspended in H_2O (10 L) and extracted with EtOAc (3 × 10 L). The aqueous layer (400 g) was subjected to an HP-20 macroporous adsorbent resin (4000 g) column and eluted with H_2O (20 L), 15% EtOH (20 L), 30% EtOH (20 L), 50% EtOH (20 L), and 95% EtOH (10 L), which yielded five corresponding fractions (fractions A−E).

Fraction C (86.4 g) was submitted to flash chromatography with a C_{18} column (55 × 8 cm, 20 μm), eluting with a 10-step gradient of MeOH/H_2O (2 L for one step, from 0:100 to 100:0) to provide 13 fractions (fractions C1−C13). Fraction C11 (301 mg) was separated on a Sephadex LH-20 (100 g) column, eluting with H_2O (1.2 L) to yield four fractions (fractions C11-1−C11-4). Then fraction C11-1 (25 mg) was further purified by reverse-phase preparative HPLC, eluting with MeOH/H_2O (25:75) at a flow rate of 5 mL/min to afford **1** (5 mg, 48 min). Fraction C12 (812 mg) was separated on a Sephadex LH-20 column (H_2O, 1.5 L) and then further purified by reverse-phase preparative HPLC, eluting with MeOH/H_2O (40:60) at a flow rate of 5 mL/min to afford **2** (27 mg, 45 min), **12** (5 mg, 51 min), and **13** (33 mg, 32 min). Fraction C13 (1.695 g) was subjected to a Sephadex LH-20 column and eluted with H_2O (2 L) to give eight fractions (fractions C13-1−C13-8). Purification of fraction C13-3 (97 mg) with MeOH/H_2O (30:70) on reverse-phase preparative HPLC at a flow rate of 5 mL/min afforded **6** (10 mg, 37 min) and **7** (13 mg, 49 min). Fraction C13-5 (255 mg) was applied successively to chromatography on Sephadex LH-20 (H_2O, 1.2 L) to yield six fractions (fractions C13-5-1−C13-5-6). Compound **14** (100 mg, 57 min) was obtained from fraction C13-5-3 (188 mg) on reverse-phase preparative HPLC using MeOH/H_2O (27:78) at a flow rate of 5 mL/min. Fraction C13-8 (127 mg) was applied successively to chromatography on Sephadex LH-20 (H_2O, 1 L) to yield five fractions (fractions C13-8-1−C13-8-5). Fraction C13-8-3 (157 mg) was performed on reverse-phase preparative HPLC with MeOH/H_2O (30:70) at a flow rate of 5 mL/min to afford **9** (80 mg, 47 min) and **11** (10 mg, 57 min).

Fraction D (210 g) was submitted to flash chromatography with a C_{18} column (55 × 8 cm, 20 μm), eluting with a 10-step gradient of MeOH/H_2O (4 L for one-step, from 0:100 to 100:0) to yield 40 fractions (fractions D1−D40). Fraction D27 (1.4 g) was separated on a Sephadex LH-20 column and eluted with H_2O (1.5 L) to give six fractions (fractions D27-1−D27-6). Fraction D27-3 (316 mg) was subjected to reverse-phase preparative HPLC, eluting with MeOH/H_2O (35:65) as the mobile phase at a flow rate of 5 mL/min, to afford **4** (7 mg, 23 min), **5** (6 mg, 31 min), **10** (5 mg, 44 min), and **17** (24 mg, 59 min). Fraction D13 (2.3 g) was separated into four fractions (fractions D13-1−D13-4) on Sephadex LH-20 eluted with H_2O (2 L). Fraction D13-1 (42 mg) gave **3** (10 mg, 35 min) after purification over a reverse-phase preparative HPLC column with MeOH/H_2O (40:60) at a flow rate of 5 mL/min. Fraction D13-2 (116 mg), with Sephadex LH-20 (H_2O, 1 L) and reverse-phase preparative HPLC with MeOH/H_2O (45:55) at a flow rate of 5 mL/min, yielded **15** (5 mg, 25 min) and **16** (82 mg, 42 min). Fraction D13-4 (29 mg) was purified via reverse-phase preparative HPLC with MeOH/H_2O (35:65) as the mobile phase at a flow rate of 5 mL/min to afford **8** (4 mg, 27 min). The structures of compounds **1**−**17** are shown in Figure 1.

*Spectral Data. Arctiidilactone (**1**):* white amorphous powder; $[\alpha]_{25}^{D}$ −28.9 (*c* 0.26, MeOH); CD (MeOH) λ_{max} ($\Delta\varepsilon$) 236 (−1.21), 279 (−0.34) nm; UV (MeOH) λ_{max} (log ε) 230 (3.51), 285 (3.29), 305 (3.22) nm; IR (KBr) ν_{max} 3364, 2922, 2851, 1765, 1712, 1640, 1515, 1465, 1391, 1263, 1238, 1157, 1077, 1024 cm^{-1}; (+)-HRESIMS *m*/*z* 389.1235 $[M + H]^+$ (calcd for $C_{20}H_{21}O_8$, 389.1236). For ^1H and ^{13}C NMR spectroscopic data, see Tables 1 and 2.

*Arctiiapolignan A (**2**):* white amorphous powder; $[\alpha]_{25}^{D}$ +6.97 (*c* 0.18, MeOH); CD (MeOH) λ_{max} ($\Delta\varepsilon$) 227 (−4.39) nm; UV (MeOH) λ_{max} (log ε) 230 (3.10), 280 (2.70) nm; IR (KBr) ν_{max} 3403, 2912, 1764, 1591, 1515, 1464, 1420, 1263, 1238, 1159, 1078, 1029 cm^{-1}; (+)-HRESIMS *m*/*z* 451.1584 $[M + Na]^+$ (calcd for $C_{20}H_{28}O_{10}Na$, 451.1580). For ^1H and ^{13}C NMR spectroscopic data, see Tables 1 and 2.

*Arctiisesquineolignan A (**3**):* white amorphous powder; $[\alpha]_{25}^{D}$ +18.54 (*c* 0.15, MeOH); CD (MeOH) λ_{max} ($\Delta\varepsilon$) 230 (−3.55), 248 (+1.2), 275 (−0.58), 295 (+0.39) nm; UV (MeOH) λ_{max} (log ε) 228 (3.87), 279 (3.42) nm; IR (KBr) ν_{max} 3413, 2921, 1760, 1598, 1514, 1454, 1421, 1266, 1226, 1141, 1075, 1030 cm^{-1}; (+)-HRESIMS *m*/*z* 883.2981 $[M + Na]^+$ (calcd for $C_{42}H_{52}O_{19}Na$, 883.3000). For ^1H and ^{13}C NMR spectroscopic data, see Tables 1 and 2.

*Arctigenin-4-O-α-D-galactopyranosyl-(1→6)-O-β-D-glucopyranoside (**4**):* white amorphous powder; $[\alpha]_{25}^{D}$ +6.3 (*c* 0.07, MeOH); CD (MeOH) λ_{max} ($\Delta\varepsilon$) 230 (−3.02), 272 (−0.34) nm; UV (MeOH) λ_{max} (log ε) 230 (3.12), 278 (2.69) nm; IR (KBr) ν_{max} 3382, 2926, 1761, 1593, 1515, 1454, 1421, 1265, 1235, 1155, 1081, 1029 cm^{-1}; (+)-HRESIMS *m*/*z* 719.2529 $[M + Na]^+$ (calcd for $C_{33}H_{44}O_{16}Na$, 719.2527). For ^1H and ^{13}C NMR spectroscopic data, see Tables 1 and 2.

*Arctigenin-4-O-β-D-apiofuranosyl-(1→6)-O-β-D-glucopyranoside (**5**):* white amorphous powder; $[\alpha]_{25}^{D}$ −52.6 (*c* 0.12, MeOH); CD (MeOH) λ_{max} ($\Delta\varepsilon$) 231 (−6.82), 274 (−0.78) nm; UV (MeOH) λ_{max} (log ε) 229 (3.58), 278 (3.19) nm; IR (KBr) ν_{max} 3418, 2929, 1760, 1592, 1515, 1454, 1421, 1265, 1235, 1158, 1068, 1025 cm^{-1}; (+)-HRESIMS *m*/*z* 689.2430 $[M + Na]^+$ (calcd for $C_{32}H_{42}O_{15}Na$, 689.2421). For ^1H and ^{13}C NMR spectroscopic data, see Tables 1 and 2.

*5′-Propanediolmatairesinoside (**6**):* white amorphous powder; $[\alpha]_{25}^{D}$ −53.4 (*c* 0.11, MeOH); CD (MeOH) λ_{max} ($\Delta\varepsilon$) 229 (−6.49), 278 (−1.19) nm; UV (MeOH) λ_{max} (log ε) 230 (3.48), 280 (3.10) nm; IR (KBr) ν_{max} 3426, 2928, 1758, 1597, 1513, 1461, 1422, 1267, 1228, 1157, 1072, 1030 cm^{-1}; (+)-HRESIMS *m*/*z* 617.2207 $[M + Na]^+$ (calcd for $C_{29}H_{38}O_{13}Na$, 617.2210). For ^1H and ^{13}C NMR spectroscopic data, see Tables 1 and 2.

*(7′R,8R,8′R)-Rafanotrachelogenin-4-O-β-D-glucopyranoside (**7**):* white amorphous powder; $[\alpha]_{25}^{D}$ −13.6 (*c* 0.12, MeOH); CD (MeOH) λ_{max} ($\Delta\varepsilon$) 230 (−2.00), 267 (−0.22) nm; UV (MeOH) λ_{max} (log ε) 230 (3.41), 277 (3.08) nm; IR (KBr) ν_{max} 3423, 2931, 1759, 1594, 1514, 1463, 1421, 1266, 1232, 1156, 1075, 1027 cm^{-1}; (+)-HRESIMS *m*/*z* 573.1954 $[M + Na]^+$ (calcd for $C_{27}H_{34}O_{12}Na$, 573.1948). For ^1H and ^{13}C NMR spectroscopic data, see Tables 2 and 3.

DOI: 10.1021/acs.jafc.5b02838
J. Agric. Food Chem. 2015, 63, 7958−7966

Table 1. ^{1}H NMR Data for 1 in Acetic Acid-d_4 and for 2−6 in DMSO-d_6 (500 MHz)

no.	1	2	3	4	5	6
2		6.81, brs	6.78, d (1.5)	6.77, d (2.0)	6.77, d (2.0)	6.79, d (1.5)
3	6.41, s					
5	7.01, s	6.84, d (8.0)	6.98, d (8.5)	7.04, d (8.5)	6.98, d (8.5)	6.97, d (8.5)
6		6.73, d (8.0)	6.68, dd (8.5, 1.5)	6.70, dd (8.5, 2.0)	6.70, dd (8.5, 2.0)	6.64, dd (8.5, 1.5)
7		2.82, dd (13.5, 6.5)	2.82, m	2.85, dd (13.5, 5.5)	2.83, dd (13.5, 5.5)	2.81, m
		2.65, dd (13.5, 8.5)		2.75, dd (13.5, 7.0)	2.76, dd (13.5, 7.0)	
8	2.83, m	3.03, m	2.74, m	2.69, m	2.69, m	2.72, m
	2.69, m					
9	2.89, brdd (8.0, 5.0)	4.22, dd (8.5, 8.5)				
		3.89, dd (8.5, 8.5)				
1′		4.04, dd (10.5, 3.0)				
		3.33, dd (10.5, 3.0)				
2′	6.73, d (1.5)	2.60, m	6.56, brs	6.62, d (1.5)	6.62, d (2.0)	6.48, brs
5′	6.82, d (8.0)			6.81, d (8.0)	6.81, d (8.0)	
6′	6.68, dd (8.0, 1.5)		6.60, brs	6.57, dd (8.0, 1.5)	6.58, dd (8.0, 2.0)	6.47, brs
7′	2.80, m		2.56, m	2.47, overlap	2.47, m	2.52, m
	2.71, m		2.46, m			2.42, overlap
8′	2.63, m		2.44, overlap	2.47, overlap	2.50, overlap	2.42, overlap
9′	4.46, dd (8.0, 9.0)		4.11, dd (8.5, 8.5)	4.10, dd (8.5, 8.5)	4.09, dd (8.5, 8.5)	4.07, dd (8.5, 8.5)
	4.08, dd (8.0, 9.5)		3.87, dd (8.5, 8.5)	3.88, dd (8.5, 8.5)	3.88, dd (8.5, 8.5)	3.84, dd (8.5, 8.5)
1″		3.95, d (7.5)		4.75, d (7.5)	4.79, d (7.5)	3.14, m
2″		2.93, m	6.94, d (2.0)	3.24, m	3.22, m	3.64, m
						3.57, m
3″		3.01, m		3.25, m	3.23, m	3.64, m
						3.57, m
4″		3.04, m		3.14, m	3.08, m	
5″		3.10, m	7.04, d (8.5)	3.48, m	3.43, m	
6″		3.63 dd (11.5, 5.5)	6.83, dd (8.5, 2.0)	3.62, overlap	3.82, dd (9.5, 4.5)	
		3.43, m		3.54, overlap	3.43, m	
7″			5.46, d (4.5)			
8″			3.42, m			
9″			3.68, m			
			3.59, m			
1‴			4.87, d (7.5)	4.64, d (3.0)	4.80, d (2.0)	4.82, d (7.5)
2‴			3.22, m	3.59, m	3.72, m	3.23, m
3‴			3.27, m	3.60, m		3.24, m
4‴			3.14, m	3.64, m	3.85, d (9.5)	3.14, m
					3.57, d (9.5)	
5‴			3.25, m	3.57, m	3.33, overlap	3.24, m
6‴			3.64, overlap	3.39, m		3.64, overlap
			3.42, overlap			3.43, m
1⁗			4.82, d (7.5)			
2⁗			3.22, m			
3⁗			3.27, m			
4⁗			3.14, m			
5⁗			3.25, m			
6⁗			3.64, overlap			
			3.43, m			
3-CH_3O	3.81, s	3.74, s	3.70, s	3.69, s	3.70, s	3.71, s
4-CH_3O	3.81, s	3.70, s				
3′-CH_3O			3.73, s	3.68, s	3.69, s	3.71, s
4′-CH_3O				3.70, s	3.68, s	
3″-CH_3O			3.72, s			

*(7′S,8R,8′R)-Rafanotrachelogenin-4-O-β-D-glucopyranoside (**8**):* white amorphous powder; $[\alpha]_{25}^{D}$ −19.2 (*c* 0.23, MeOH); CD (MeOH) λ_{max} ($\Delta\varepsilon$) 232 (−4.42), 283 (+1.15) nm; UV (MeOH) λ_{max} (log ε): 228 (3.04), 278 (2.68) nm; IR (KBr) ν_{max} 3423, 2931, 1759, 1514, 1463, 1421, 1266, 1232, 1156, 1075, 1027 cm^{-1}; (+)-HRESIMS *m*/*z* 573.1956 $[M + Na]^+$ (calcd for $C_{27}H_{34}O_{12}Na$, 573.1948). For ^{1}H and ^{13}C NMR spectroscopic data, see Tables 2 and 3.

*(7S,8S,8′R)-4,7-Dihydroxy-3,3′,4′-trimethoxyl-9-oxo dibenzylbutyrolactone lignan-4-O-β-D-glucopyranoside (**9**):* white amorphous powder; $[\alpha]_{25}^{D}$ −48.5 (*c* 0.21, MeOH); CD (MeOH) λ_{max} ($\Delta\varepsilon$) 230 (−55.97), 278 (−5.38) nm; UV (MeOH) λ_{max} (log ε) 230 (3.48), 278 (3.04) nm; IR (KBr) ν_{max} 3390, 2936, 1757, 1595, 1515, 1454, 1419,

DOI: 10.1021/acs.jafc.5b02838
J. Agric. Food Chem. 2015, 63, 7958−7966

Table 2. ^{13}C NMR Data for 1 in Acetic acid-d_4 and for 2−12 in DMSO-d_6 (125 MHz)

no.	1	2	3	4	5	6	7	8	9	10	11	12
1		131.7	132.3	132.5	132.4	132.3	132.0	131.9	137.1	134.2	136.6	136.6
2	161.5	112.9	114.3	114.2	114.2	114.3	114.3	114.2	110.3	110.1	111.2	111.2
3	118.7	149.2	149.1	149.2	149.1	149.0	149.0	148.9	149.0	147.8	148.8	148.8
4	155.8	147.8	145.8	145.7	145.7	145.7	145.7	145.7	145.9	145.8	146.1	146.0
5	112.5	112.3	115.6	116.4	115.8	115.5	115.5	115.3	115.3	115.4	115.1	115.1
6	148.2	121.9	121.7	121.8	121.9	121.8	121.8	121.8	117.9	118.1	118.7	118.7
7	161.9	37.3	33.9	34.3	34.2	33.8	34.2	34.8	70.5	70.4	71.0	71.8
8	34.4	38.0	46.0	46.0	46.0	45.9	43.2	42.8	52.8	52.8	52.5	52.5
9	44.0	71.5	178.9	178.9	178.9	179.0	179.1	179.3	178.1	178.0	176.6	176.6
10	179.2											
1′	130.5	66.9	132.2	131.5	131.5	128.8	136.4	135.9	131.4	131.6	131.8	130.1
2′	111.5	46.0	113.1	112.8	112.8	110.4	110.1	110.0	112.6	112.6	113.0	113.3
3′	149.0	177.7	144.0	149.1	149.1	147.7	149.0	149.0	149.2	149.0	149.1	148.0
4′	147.8		146.5	147.8	147.8	143.1	148.4	148.3	147.6	147.6	147.8	145.4
5′	112.2		129.5	112.3	112.4	128.5	112.0	111.8	112.2	112.1	112.7	115.9
6′	120.8		117.3	120.9	120.8	121.1	118.3	118.4	120.7	120.6	121.0	121.3
7′	37.9		37.5	37.4	37.4	37.5	72.4	72.8	38.9	38.8	38.1	38.2
8′	41.7		41.4	41.2	41.2	41.2	46.3	45.4	36.1	35.8	39.5	39.5
9′	72.0		71.2	71.2	71.2	71.1	68.0	68.9	72.1	71.8	71.8	71.0
1″		104.3	135.8	101.1	100.8	44.3	100.6	100.6	100.7		100.6	100.6
2″		73.9	110.9	73.7	73.7	62.2	73.7	73.7	73.8		73.7	73.7
3″		77.3	149.4	77.5	77.3	62.2	77.5	77.5	77.5		77.5	77.4
4″		70.4	146.6	70.5	70.4		70.1	70.2	70.2		70.1	70.1
5″		77.1	115.7	75.4	76.0		77.3	77.4	77.4		77.4	77.4
6″		61.4	118.4	66.8	68.1		61.1	61.2	61.2		61.1	61.0
7″			87.2									
8″			53.8									
9″			63.5									
1‴			100.7	99.1	109.8	100.7						
2‴			73.7	70.0	76.4	73.7						
3‴			77.5	69.4	79.2	77.4						
4‴			70.1	68.8	73.8	70.1						
5‴			77.3	71.3	63.7	77.3						
6‴			61.1	61.0		61.1						
1⁗			100.5									
2⁗			73.7									
3⁗			77.4									
4⁗			70.1									
5⁗			77.3									
6⁗			61.1									
3-CH_3O	55.0	55.9	56.2	55.9	56.1	56.2	55.9	55.8	55.8	55.9	55.9	56.0
4-CH_3O	54.9	56.0										
3′-CH_3O			56.1	55.8	55.9	56.1	56.1	55.9	56.1	55.7	55.9	56.1
4′-CH_3O				56.1	55.9		56.0	56.0	55.9	56.0	56.1	
3″-CH_3O			56.1									

1264, 1234, 1141, 1077, 1028 cm^{-1}; (+)-HRESIMS m/z 573.1949 [M + Na]$^+$ (calcd for $C_{27}H_{34}O_{12}Na$, 573.1948). For ^{1}H and ^{13}C NMR spectroscopic data, see Tables 2 and 3.

*(7S,8S,8′R)-4,7-Dihydroxy-3,3′,4′-trimethoxyl-9-oxo dibenzylbutyrolactone lignan (**10**):* white amorphous powder; $[\alpha]_{25}^{D}$ −44.3 (*c* 0.11, MeOH); CD (MeOH) λ_{max} ($\Delta\varepsilon$) 234 (−8.20), 285 (−0.37) nm; UV (MeOH) λ_{max} (log ε) 231 (2.98), 279 (2.97) nm; IR (KBr) ν_{max} 3387, 2921, 1760, 1595, 1516, 1464, 1423, 1265, 1237, 1154, 1026 cm^{-1}; (+)-HRESIMS m/z 411.1416 [M + Na]$^+$ (calcd for $C_{21}H_{24}O_7Na$, 411.1420). For ^{1}H and ^{13}C NMR spectroscopic data, see Tables 2 and 3.

*(7R,8S,8′R)-4,7-Dihydroxy-3,3′,4′-trimethoxyl-9-oxo dibenzylbutyrolactone lignan-4-O-β-D-glucopyranoside (**11**):* white amorphous powder; $[\alpha]_{25}^{D}$ −30.4 (*c* 0.13, MeOH); CD (MeOH) λ_{max} ($\Delta\varepsilon$) 227 (−3.11), 276 (−1.00) nm; UV (MeOH) λ_{max} (log ε) 229 (3.51), 279 (3.07) nm; IR (KBr) ν_{max} 3410, 2920, 1758, 1594, 1514, 1464, 1420, 1265, 1235, 1156, 1076, 1028 cm^{-1}; (+)-HRESIMS m/z 573.1950 [M + Na]$^+$ (calcd for $C_{27}H_{34}O_{12}Na$, 573.1948). For ^{1}H and ^{13}C NMR spectroscopic data, see Tables 2 and 3.

*(7R,8S,8′R)-4,7,4′-Trihydroxy-3,3′-dimethoxyl-9-oxo dibenzylbutyrolactone lignan-4-O-β-D-glucopyranoside (**12**):* white amorphous powder; $[\alpha]_{25}^{D}$ −37.5 (*c* 0.35, MeOH); CD (MeOH) λ_{max} ($\Delta\varepsilon$) 227 (−0.89), 275 (−0.36) nm; UV (MeOH) λ_{max} (log ε) 230 (3.27), 280 (2.90) nm; IR (KBr) ν_{max} 3392, 2917, 1755, 1601, 1514, 1454, 1426, 1270, 1226, 1156, 1075, 1031 cm^{-1}; (+)-HRESIMS m/z 559.1795 [M + Na]$^+$ (calcd for $C_{26}H_{32}O_{12}Na$, 559.1791). For ^{1}H and ^{13}C NMR spectroscopic data, see Tables 2 and 3.

*Enzymatic Hydrolysis of **2**−**9**, **11**, and **12**.* Compound **2** (3.0 mg) was dissolved in 0.1 M sodium citrate buffer (5.0 mL), and then cellulase (3.0 mg, Sigma-Aldrich, St. Louis, MO, USA) was added. The reaction mixture was maintained at 40 °C for 5 h. The solution was then transferred to a liquid−liquid extractor and extracted with EtOAc

DOI: 10.1021/acs.jafc.5b02838
J. Agric. Food Chem. 2015, 63, 7958−7966

Table 3. ^{1}H NMR Data for 7−12 in DMSO-d_6 (500 MHz)

no.	7	8	9	10	11	12
2	6.65, d (1.5)	6.60, d (2.0)	6.97, d (1.5)	6.90, d (1.5)	6.90, d (1.5)	6.89, d (1.5)
5	6.95, d (8.0)	6.89, d (8.0)	7.03, d (8.5)	6.73, d (8.5)	7.00, d (8.5)	7.01, d (8.0)
6	6.56, dd (8.0, 1.5)	6.48, dd (8.0, 2.0)	6.86, dd (8.5, 1.5)	6.79, dd (8.5, 1.5)	6.78, dd (8.5, 1.5)	6.77, dd (8.0, 1.5)
7	2.70, dd (13.5, 6.5)	2.82, overlap	5.10, t (4.0)	5.08, brs	4.83, t (4.0)	4.81, t (3.5)
	2.53, dd (13.5, 5.5)	2.63, dd (15.5, 7.5)				
8	2.83, m	2.82, overlap	2.66, dd (6.5, 2.5)	2.61, dd (7.0, 3.0)	2.75, dd (7.5, 4.0)	2.74, m
2′	6.78, d (1.5)	6.82, d (2.0)	6.45, d (2.0)	6.42, d (1.5)	6.73, d (2.0)	6.69, d (1.5)
5′	6.88, d (8.0)	6.86, d (8.0)	6.75, d (8.5)	6.71, d (8.5)	6.84, d (8.0)	6.66, d (8.0)
6′	6.74, dd (8.0, 1.5)	6.75, dd (8.0, 2.0)	6.39, dd (8.5, 2.0)	6.38, dd (8.5, 1.5)	6.66, dd (8.0, 2.0)	6.54, dd (8.0, 1.5)
7′	4.36, brs	4.60, d (5.0)	2.32, dd (13.5, 9.0)	2.28, dd (13.5, 9.5)	2.79, dd (11.5, 4.5)	2.74, m
			2.05, dd (13.5, 6.0)	1.98, dd (13.5, 5.5)	2.61, m	2.60, m
8′	2.47, overlap	2.50, overlap	2.78, m	2.78, m	2.61, m	2.60, m
9′	4.14, t (8.5)	4.00, d (7.5)	4.15, t (8.5)	4.12, t (8.5)	3.95, t (8.5)	3.95, t (8.5)
	4.00, t (8.5)		3.89, dd (8.5, 3.0)	3.87, dd (8.5, 6.5)	3.84, t (8.5)	3.82, dd (8.5, 6.5)
1″	4.83, d (7.5)	4.82, d (7.5)	4.87, d (7.5)		4.87, d (7.5)	4.85, d (7.5)
2″	3.23, m	3.23, m	3.24, m		3.23, m	3.23, m
3″	3.26, m	3.28, m	3.28, m		3.27, m	3.27, m
4″	3.14, m	3.14, m	3.16, m		3.15, m	3.15, m
5″	3.24, m	3.23, m	3.28, m		3.27, m	3.27, m
6″	3.65, overlap	3.65, overlap	3.65, overlap		3.64, dd (11.5, 4.5)	3.64, dd (11.5, 4.5)
	3.43, m	3.44, m	3.46, m		3.43, m	3.43, m
3-CH_3O	3.69, s	3.67, s	3.65, s	3.67, s	3.71, s	3.71, s
4-CH_3O						
3′-CH_3O	3.72, s	3.70, s	3.72, s	3.66, s	3.71, s	3.72, s
4′-CH_3O	3.71, s	3.73, s	3.68, s	3.72, s	3.70, s	

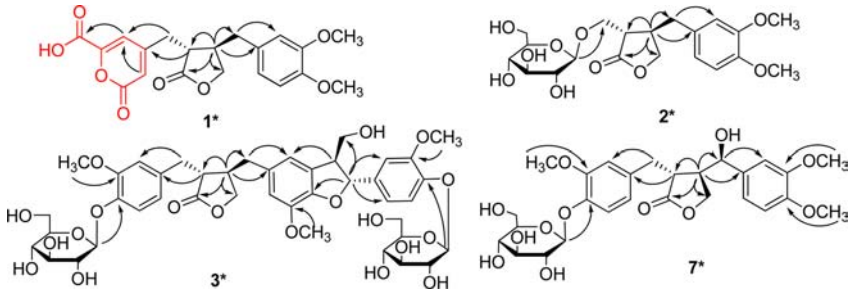

Figure 2. Key HMBC correlations in compounds 1−3 and 7.

(5.0 mL). The organic layer was evaporated under reduced pressure and purified using reversed-phase preparative HPLC with MeOH/H_2O (45:55) as the mobile phase to afford **2a** (1.1 mg, 43 min). The aqueous layer was evaporated and dried under reduced pressure to yield a monosaccharide residue. This residue was purified by preparative silica gel thin-layer chromatography (PTLC) [$CHCl_3$/MeOH/H_2O (7:3:1)] to afford glucose (R_f = 0.2) with positive optical rotation ($[\alpha]_{25}^{D}$ +36.5). Hydrolysis of **3**−**9**, **11**, and **12** and sugar identification were performed according to the procedure described for **2**. The D-galactose (R_f = 0.16, $[\alpha]_{25}^{D}$ + 62.8) and D-apiose (R_f = 0.5, $[\alpha]_{25}^{D}$ +8.7) were confirmed by TLC analysis [$CHCl_3$/MeOH/H_2O (7:3:1)] in comparison with standard samples.

*$Rh_2(OCOCF_3)_4$-Induced CD Experiments of Compounds **7a** and **8a**.* Compound **7a** (0.2 mg) was dissolved in dried chloroform (1 mL). The CD spectrum of **7a** in the 450−300 nm region was measured. Then, $Rh_2(OCOCF_3)_4$ (2 mg) was added in the solution, and the mixture was stirred at room temperature for 10 min. The CD spectrum of the reaction mixture in the 450−300 nm region was also measured. On the basis of the bulkiness rule for secondary alcohols,[11] a negative Cotton effect at 340 nm (the E band) in the $Rh_2(OCOCF_3)_4$-induced CD spectrum (Figure S49, Supporting Information) indicated the 7′*R* configuration of **7a**. Similarly, the 7′*S* configuration of **8a** was confirmed.

Anti-inflammatory Effects of Compounds. Compounds **1**−**17** were tested for anti-inflammatory activity on BV2 cells.[12,13] After the BV2 cells were pre-incubated for 24 h at 37 °C under a 5% CO_2 atmosphere in a 96-well plate, the cells were treated with various concentrations of the test compounds (1×10^{-5}, 1×10^{-6}, and 1×10^{-7} M), followed by stimulation with LPS for 24 h. The production of NO was determined by measuring the concentration of nitrite in the culture supernatant. $NaNO_2$ was used to generate a standard curve. The absorbances at 540 nm were measured. Curcumin was utilized as a positive control.

RESULTS AND DISCUSSION

Structure Elucidation of the New Compounds. Compound **1**, a white amorphous powder, had the molecular formula $C_{20}H_{20}O_8$ (*m*/*z* 389.1235 $[M + H]^+$ in HRESIMS), which indicated 11 degrees of unsaturation. The IR spectrum exhibited absorption bands attributable to hydroxyl groups (3364 cm^{-1}), carbonyl groups (1765, 1712, and 1640 cm^{-1}), and aromatic rings (1515 and 1465 cm^{-1}). In the ^{1}H NMR spectrum (Table 1), ABX-system aromatic proton signals [δ_H 6.73 (1H, d, *J* = 1.5 Hz, H-2), 6.82 (1H, d, *J* = 8.0 Hz, H-5), and 6.68 (1H, dd, *J* = 8.0, 1.5 Hz, H-6)] and two proton signals that displayed as a broad singlet [δ_H 6.41 (1H, s, H-3) and 7.01

DOI: 10.1021/acs.jafc.5b02838
J. Agric. Food Chem. 2015, 63, 7958−7966

(1H, s, H-5)] were observed in the downfield region. In addition, two oxygenated methylene protons at δ_H 4.46 (1H, dd, J = 8.0, 9.0 Hz, H-9′a) and 4.08 (1H, dd, J = 8.0, 9.5 Hz, H-9′b), four methylene protons at δ_H 2.83 (1H, m, H-8a), 2.69 (1H, m, H-8b), 2.80 (1H, m, H-7′a), and 2.71 (1H, m, H-7′b), two methine protons at δ_H 2.89 (1H, brdd, J = 8.0, 5.0 Hz, H-9) and 2.63 (1H, m, H-8′), and two methoxy groups at δ_H 3.81 (3H, s) and 3.81 (3H, s) were also observed. The ^{13}C NMR spectrum (Table 2) of **1** displayed 20 carbon signals, including two C6−C3 units and two methoxy groups. On the basis of the aforementioned data, compound **1** was determined as a butyrolactone lignan similar to arctigenin, except that NMR resonances for the 6-carboxyl-2-pyrone moiety in **1** were observed in place of the resonances for the 4-hydroxy-3-methoxyphenyl unit in arctigenin. This interpretation was verified by the HMBC and ^{13}C NMR spectra. The correlations from H-8′ to C-8, C-9, C-10, C-1′, C-7′, and C-9′ and from H-9 to C-4, C-8, C-10, C-7′, C-8′, and C-9′ indicated the presence of a benzylbutyrolactone moiety in **1**. Detailed analysis of the ^{13}C NMR spectrum, together with the remaining five degrees of unsaturation, implied the existence of a 6-carboxyl-2-pyrone moiety; this moiety was verified by the HMBC correlations (Figure 2) from H-3 to C-2 and C-5 and from H-5 to C-6 and C-7. The connection between C-8 and C-4 was also determined by the key correlations from H-8 to C-3, C-4, and C-5. The previous study indicated that the relative configuration of H-9 and H-8′ could be determined by the $\Delta\delta_{H9'a-H9'b}$ values ($\Delta\delta_{H9'a-H9'b} \geq 0.2$ for *trans*, $\Delta\delta_{H9'a-H9'b} \approx 0$ for *cis*).[14,15] Therefore, the *trans* configuration of H-9 and H-8′ was established by the H-9′a (δ_H 4.46) and H-9′b (δ_H 4.08) signals in the ^{1}H NMR spectrum. This result, combined with the negative Cotton effect at 230 nm in the CD spectrum, suggested that the absolute configurations of C-9 and C-8′ in **1** were 9*R* and 8′*R*, respectively.[16] Consequently, **1** was identified as in Figure 1 and named arctiidilactone.

Compound **2** was obtained as a white amorphous powder; its molecular formula was confirmed to be $C_{20}H_{28}O_{10}$ on the basis of the positive HRESIMS ion observed at m/z 451.1584 [M + Na]$^+$. The ^{1}H NMR spectrum (Table 1) of **2** showed three aromatic proton signals at δ_H 6.81 (1H, brs, H-2), 6.84 (1H, d, J = 8.0 Hz, H-5), and 6.73 (1H, d, J = 8.0 Hz, H-6), revealing the presence of an ABX-system aromatic ring. Additionally, two methoxy groups at δ_H 3.74 (3H, s) and 3.70 (3H, s) and a glucopyranosyl anomeric proton at δ_H 3.95 (1H, d, J = 7.5 Hz, H-1″) were also observed in the upfield region. In the ^{13}C NMR spectrum (Table 2), signals associated with a C3−C6−C3 unit, two methoxy groups, and a glucopyranosyl group were observed. All of the aforementioned spectroscopic data indicated that **2** was a butyrolactone-type lignan, but without an aromatic ring. The HMBC correlations (Figure 2) from H-7 to C-1, C-2, C-6, C-8, C-9, and C-2′ and from H-1′ to C-8, C-2′, and C-3′ confirmed the benzylbutyrolactone skeleton of **2**. The linkage point of the glucose was identified by the correlation between the anomeric proton H-1″ of glucose and C-1′ in the HMBC experiment. The 8*R*,2′*S* configurations of **2** were deduced from the chemical shifts of H-9 (δ_H 4.22, 3.89) in the ^{1}H NMR spectrum (Table 1) and from the negative Cotton effect at 227 nm in the CD spectrum. Thus, **2** was determined to be arctiiapolignan A.

The IR spectrum of compound **3** showed absorptions for a hydroxyl group (3413 cm^{-1}), methylene (2921 cm^{-1}), benzene ring (1598, 1514, and 1454 cm^{-1}), and carbonyl group (1760 cm^{-1}). The molecular formula of **3** was determined to be $C_{42}H_{52}O_{19}$ on the basis of the positive HRESIMS ion (m/z 883.2981 [M + Na]$^+$). The ^{1}H NMR spectroscopy data (Table 1) of **3** revealed two sets of ABX-system aromatic rings [δ_H 6.78 (1H, d, J = 1.5 Hz, H-2), 6.98 (1H, d, J = 8.5 Hz, H-5), 6.68 (1H, dd, J = 8.5, 1.5 Hz, H-6), 6.94 (1H, d, J = 2.0 Hz, H-2″), 7.04 (1H, d, J = 8.5 Hz, H-5″), 6.83 (1H, dd, J = 8.5, 2.0 Hz, H-6″)] and a 1,3,4,5-tetrasubstituted aromatic ring [δ_H 6.56 (1H, brs, H-2′), 6.60 (1H, brs, H-6′)]. Additionally, two oxymethylene protons [δ_H 4.11 (1H, dd, J = 8.5, 8.5 Hz, H-9′a), 3.87 (1H, dd, J = 8.5, 8.5 Hz, H-9′b), 3.68 (1H, m, H-9″a), 3.59 (1H, m, H-9″b)], an oxymethine proton [δ_H 5.46 (1H, d, J = 4.5 Hz, H-7″)], two methylene protons [δ_H 2.82 (2H, m, H-7), 2.56 (1H, m, H-7′a), 2.46 (1H, m, H-7′b)], three methine protons [δ_H 2.74 (1H, m, H-8), 2.44 (1H, overlap, H-8′), 3.42 (1H, m, H-8″)], three methoxyl protons [δ_H 3.70 (3H, s, 3-OCH$_3$), 3.73 (3H, s, 3′-OCH$_3$), 3.72 (3H, s, 3″-OCH$_3$)], and two glucopyranosyl anomeric protons [δ_H 4.87 (1H, d, J = 7.5 Hz, H-1‴), 4.82 (1H, d, J = 7.5 Hz, H-1⁗)] were observed in the upfield region. The ^{13}C NMR spectrum (Table 2) of **3** displayed 42 carbon signals, 12 of which were assigned to two glucose units; the remaining 30 carbons were assigned to three C6−C3 units and three methoxy groups. These data revealed that **3** was a sesquineolignan.[17] In the HMBC spectrum (Figure 2), the characteristic correlations from H-7 (δ_H 2.82) to C-1, C-2, C-9, and C-8′, from H-7′ (δ_H 2.56, 2.46) to C-1′, C-2′, C-9′, and C-8, and from H-7″ (δ_H 5.46) to C-4′, C-5′, C-1″, and C-9″ suggested the presence of a dihydrobenzofuran unit and a benzylbutyrolactone unit in compound **3**. The HMBC correlation peaks of three methoxy groups at δ_H 3.70, 3.73, and 3.72 with C-3, C-3′, and C-3″ confirmed the linkage positions of these methoxy groups. Two glucose units were determined to be located at C-4 and C-4″ on the basis of the correlations of H-1‴ with C-4 and H-1⁗ with C-4″ in the HMBC spectrum. The chemical shifts of H-9′ (δ_H 4.11 and 3.87) indicated the *trans* configuration of H-8/H-8′. Moreover, the correlation peaks of H-7″ with H-9″ and of H-8″ with H-2″ and H-6″ in the ROESY spectrum (Figure 3) indicated the

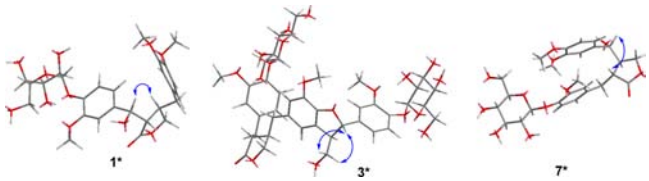

Figure 3. Key ROESY correlations in compounds **1**, **3**, and **7**.

trans configuration of H-7″/H-8″. In the CD spectrum, the negative Cotton effect at 230 revealed the 8*R*,8′*R* configurations of the benzylbutyrolactone unit,[16] and the negative Cotton effect at 290 nm revealed the 7″*R*,8″*S* configurations of the dihydrobenzofuran unit.[18] Therefore, compound **3** was confirmed to be arctiisesquineolignan A.

The spectroscopic data for compound **4** were similar to those of arctiin, except for an additional galactose unit.[19] The downfield shift of C-6″ (δ_C 66.8) of glucose in **4** suggested that the linkage point of the galactose was at C-6″ of glucose, which was further confirmed by the correlations between the anomeric proton H-1‴ of galactose and C-6″ of glucose in the HMBC experiment. The *trans* configuration of H-8 and H-8′ was established on the basis of the H-9′a (δ_H 4.10) and H-9′b (δ_H 3.88) signals in the ^{1}H NMR spectrum (Table 1). The

DOI: 10.1021/acs.jafc.5b02838
J. Agric. Food Chem. 2015, 63, 7958−7966

absolute configurations of C-8 and C-8′ in **4** were defined as 8*R*,8′*R* on the basis of the negative Cotton effect at 230 nm observed in the CD spectrum. Thus, **4** was identified as Figure 1 and named arctigenin-4-*O*-*α*-D-galactopyranosyl-(1→6)-*O*-*β*-D-glucopyranoside.

Compound **5** was demonstrated to have the molecular formula $C_{32}H_{42}O_{15}$ on the basis of HRESIMS with *m*/*z* 689.2430 $[M + Na]^+$. The IR spectrum exhibited signals for a hydroxyl group (3418 cm^{-1}), a methylene (2929 cm^{-1}), aromatic rings (1592, 1515, and 1454 cm^{-1}), and a carbonyl group (1760 cm^{-1}). Detailed analysis of the 1D NMR spectra (Table 1) suggested that the structure of **5** was similar to that of **4**. The difference between these two compounds was the presence of an apiofuranose group[20] at C″-6 in **5** instead of a galactose group at C″-6 in **4**, which was supported by the HMBC correlation between the apiofuranose anomeric proton H-1‴ (δ_H 4.80) and C-6″ (δ_C 68.1) in **5**. The absolute configurations of C-8 and C-8′ in **5** were also confirmed by the same method used to confirm those in **4**. The chemical shifts of H-9′a (δ_H 4.09) and H-9′b (δ_H 3.88) verified the *trans* configuration of H-8/8′. This result, combined with the negative Cotton effect at 230 nm in the CD spectrum, indicated the 8*R*,8′*R* configurations for **5**. Thus, compound **5** was determined to be arctigenin-4-*O*-*β*-D-apiofuranosyl-(1→6)-*O*-*β*-D-glucopyranoside.

Compound **6** had the molecular formula $C_{29}H_{38}O_{13}$, and its IR spectrum exhibited absorption bands that were attributed to a hydroxyl (3426 cm^{-1}), a methylene (2928 cm^{-1}), a carbonyl group (1758 cm^{-1}), and an aromatic ring (1597, 1513, and 1461 cm^{-1}). Comprehensive analysis of the NMR spectra indicated that compound **6** was a dibenzylbutyrolactone lignan glucoside with an additional C3 unit. In the HMBC spectrum, the correlation peaks from H-2″ (δ_H 3.57, 3.64) and H-3″ (δ_H 3.57, 3.64) to C-1″ (δ_C 44.3) and from H-1″ (δ_H 3.14) to C-2″ (δ_C 62.2) and C-3″ (δ_C 62.2), together with their chemical shifts, demonstrated the propanediol structure of the C3 unit. In addition, the HMBC correlations from H-1″ (δ_H 3.14) to C-4′ (δ_C 143.1), C-5′ (δ_C 128.5), and C-6′ (δ_C 121.1) indicated that C-1″ of the propanediol moiety was connected to C-5′ of the dibenzylbutyrolactone lignan by a C−C bond. The absolute configurations of C-8 and C-8′ were determined by the procedure described for **4** and **5**. A negative Cotton effect at 229 nm observed in the CD spectrum, in combination with the chemical shifts of H-9′ at δ_H 4.07 and 3.84, verified the 8*R*,8′*R* configurations for **6**. On the basis of the aforementioned information, compound **6** was confirmed to be 5′-propanediolmatairesinoside.

Compound **7** was obtained as a white amorphous powder with a molecular formula of $C_{27}H_{34}O_{12}$ on the basis of an ion peak at *m*/*z* 573.1954 $[M + Na]^+$ in the HRESIMS spectrum. The spectroscopic data (Tables 2 and 3) for **7** were almost identical to the data for rafanotrachelogenin-4-*O*-*β*-D-glucopyranoside,[21] which was isolated from *Trachelospermum lucidum*. However, the absolute configurations of rafanotrachelogenin-4-*O*-*β*-D-glucopyranoside had not yet been identified. To determine the absolute configuration of C-8, C-7′, and C-8′ in compound **7**, the ROESY spectrum, CD exciton chirality, and $Rh_2(OCOCF_3)_4$-induced CD spectrum were assayed. The relative configuration of H-8 and H-8′ in **7** was defined as *trans* on the basis of the characteristic correlation peaks of H-7′ with H-8 in the ROESY spectrum (Figure 3). In combination with the negative Cotton effect at 230 nm in the CD spectrum, the absolute configuration of C-8 and C-8′ was confirmed as 8*R*,8′*R*. Cellulase hydrolysis of **7** resulted in **7a** (the aglycone) and D-glucose. The 7′*R* configuration was supported by a negative Cotton effect at 340 nm in the $Rh_2(OCOCF_3)_4$-induced CD spectrum of **7a** (Figure S49, Supporting Information).[11] Consequently, **7** was identified as Figure 1 and named (7′*R*,8*R*,8′*R*)-rafanotrachelogenin-4-*O*-*β*-D-glucopyranoside.

Compound **8** was obtained as a white amorphous powder. Its molecular formula was determined to be $C_{27}H_{34}O_{12}$ on the basis of the positive HRESIMS ion observed at *m*/*z* 573.1956 $[M + Na]^+$. A comparison of the IR, UV, and NMR data (Table 2) of **8** with those of **7** revealed that these two compounds possessed the same planar structure. As previously described, the ROESY correlation of H-7′/H-8 indicated the *trans* configuration of H-8/H-8′ in **8**. In the CD spectrum, a negative Cotton effect at 227 nm helped confirm the 8*R*,8′*R* configurations for **8**. The 7′*S* configuration was determined by a positive Cotton effect at 340 nm in the $Rh_2(OCOCF_3)_4$-induced CD spectrum of **8a** (the aglycone) (Figure S57, Supporting Information), which was obtained by cellulase hydrolysis of **8**. Thus, compound **8** was deduced to be (7′*S*,8*R*,8′*R*)-rafanotrachelogenin-4-*O*-*β*-D-glucopyranoside.

Compound **9** had the same molecular formula as **8**: $C_{27}H_{34}O_{12}$. A comparison of the NMR spectra of **9** and **8** revealed that the differences between these two compounds were the linkage point of the alcoholic hydroxyl group. In the HMBC spectrum, the correlation peaks from H-7 (δ_H 5.10) to C-1, C-2, C-6, C-8, C-9, and C-8′ and from H-7′ (δ_H 2.32, 2.05) to C-1′, C-2′, C-6′, C-8′, C-9′, and C-8, together with the chemical shifts of H-7/7′ and C-7/7′, indicated that the hydroxyl was located at C-7. Thus, the planar structure of **9** was elucidated as 4,7-dihydroxy-3,3′,4′-trimethoxyl-9-oxo dibenzylbutyrolactone lignan-4-*O*-*β*-D-glucopyranoside. The relative configuration of H-8 and H-8′ in **9** was defined as *trans* on the basis of the characteristic correlation peak of H-8′ with H-7 in the ROESY spectrum. The 8*S*,8′*R* configuration for **9** was confirmed by the negative Cotton effects at 243 and 282 nm in the CD spectrum. Cellulase hydrolysis of **9** resulted in **9a** (the aglycone), which was purified by preparative HPLC. The 7,8-*erythro* configuration of **9a** was deduced on the basis of the coupling constant $J_{7,8}$ (4.0 Hz) in the ^1H NMR experiment (Figure S66, Supporting Information).[22] Thus, **9** was elucidated to be (7*S*,8*S*,8′*R*)-4,7-dihydroxy-3,3′,4′-trimethoxyl-9-oxo dibenzylbutyrolactone lignan-4-*O*-*β*-D-glucopyranoside.

A comparison of the molecular formula ($C_{21}H_{24}O_7$) and NMR data of **10** with those of **9** (Tables 2 and 3) indicated the absence of glucose unit resonances in **10**. Using the same methods as described for **9** (Figures S74−S76, Supporting Information), we elucidated the 7*S*,8*S*,8′*R* configurations of **10**. Thus, compound **10** was determined to be (7*S*,8*S*,8′*R*)-4,7-dihydroxy-3,3′,4′-trimethoxyl-9-oxo dibenzylbutyrolactone lignan.

Compound **11** had the same planar structure as **9**, as indicated by a comparison of their NMR spectra and molecular formulas. The absolute configurations of C-8 and C-8′ were established as 8*S*,8′*R* by the correlation of H-7/8′ in the ROESY spectrum and the negative Cotton effects at 243 and 282 nm in the CD spectrum. However, in the ^1H NMR spectrum of **11a** (the aglycone) (Figure S84, Supporting Information), which was obtained by hydrolysis of **11**, the coupling constant of H-7 ($J_{7,8}$ = 8.5 Hz) suggested that the relative configuration between C-7 and C-8 was *threo* instead of the *erythro* configuration in **9**.[21] Thus, the 7*R* configuration was

DOI: 10.1021/acs.jafc.5b02838
J. Agric. Food Chem. 2015, 63, 7958−7966

Scheme 1. Plausible Biogenetic Pathway of 1

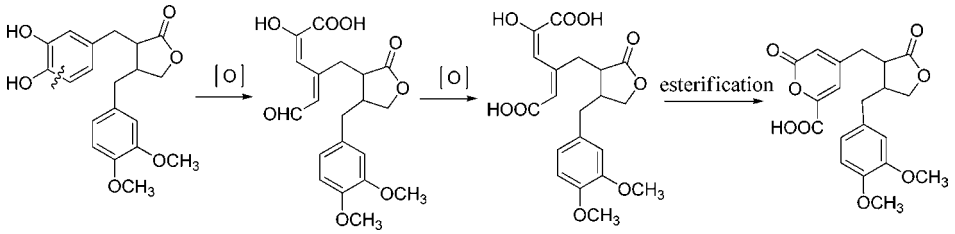

determined and the structure of **11** was characterized as Figure 1 and named (7*R*,8*S*,8′*R*)-4,7-dihydroxy-3,3′,4′-trimethoxyl-9-oxo dibenzylbutyrolactone lignan-4-*O*-*β*-D-glucopyranoside.

The molecular formula of compound **12** was determined to be $C_{26}H_{32}O_{12}$ on the basis of the positive HRESIMS ion observed at *m*/*z* 559.1795 $[M + Na]^+$. The UV, IR, and NMR spectra of **12** were almost identical to the corresponding spectra of **11**; the difference between the compounds was that **12** contained a 4′-OH group in place of the 4′-OCH_3 in **11**. The 7*R*,8*S*,8′*R* configuration of **12** was also confirmed by the ROESY correlation and CD spectrum and by the coupling constant of H-7 ($J_{7,8}$ = 8.0 Hz) in **12a** (the aglycone) (Figure S93, Supporting Information). On the basis of these results, **12** was determined to be (7*R*,8*S*,8′*R*)-4,7,4′-trihydroxy-3,3′-dimethoxyl-9-oxo dibenzylbutyrolactone lignan-4-*O*-*β*-D-glucopyranoside.

The known compounds matairesinol-4,4′-di-*O*-*β*-D-glucopyranoside (**13**),[23] arctiin (**14**),[24] styraxlignolide E (**15**),[25] styraxlignolide D (**16**),[25] and arctigenin-4-*O*-*β*-D-gentiobioside (**17**)[26] were identified by comparison of these physical and spectral data with literature values. In addition, their absolute configurations were established from NMR and CD data.

Cytotoxic Activity. All of the isolated compounds were tested for cytotoxic activity using an MTT assay in HCT-8, Bel-7402, BGC-823, A549, and A2780 cells.[27] Compounds **1**−**17** exhibited no significant cytotoxicity in the cell model systems at a concentration of 10 *μ*M.

Hepatoprotective Activity. Given our previous bioactivity screening results for the lignan glucosides, the hepatoprotective activities[10] of **1**−**17** were tested through in vitro assays. Unfortunately, all of the tested compounds exhibited weak hepatoprotective activities at a concentration of 10 *μ*M.

Anti-inflammatory Activity. Compounds **1**−**17** were tested for anti-inflammatory activity by suppressing the production of NO in lipopolysaccharide-induced BV2 cells. From the data obtained, compounds **1**, **6**, **8**, and **10** exhibited stronger anti-inflammatory effects than the positive control curcumin at a concentration of 10 *μ*M. Among them, compound **1** demonstrated 75.51, 70.72, and 61.17% inhibition at 10, 1, and 0.1 *μ*M, respectively, whereas the positive control curcumin showed 53.02, 36.74, and 0% inhibition at 10, 1, and 0.1 *μ*M. Furthermore, compound **6** exhibited 71.59, 38.64, and 2.27% inhibition at 10, 1, and 0.1 *μ*M, respectively. Compound **8** exhibited 87.77, 53.24, and 11.51% inhibition at 10, 1, and 0.1 *μ*M, respectively. Compound **10** exhibited 63.31, 40.29, and 37.41% inhibition at 10, 1, and 0.1 *μ*M, respectively.

In the continued search for bioactive natural products from Arctii Fructus, 17 butyrolactone type lignans (**1**−**17**) were isolated, including a novel rare butyrolactone lignan with a 6-carboxyl-2-pyrone moiety, named arctiidilactone (**1**); a new apolignan glucoside without an aromatic ring (**2**); a new sesquineolignan with a dihydrobenzofuran unit and a butyrolactone unit (**3**); three new dibenzylbutyrolactone lignans (**4**−**6**); six new dibenzylbutyrolactone lignans with an additional hydroxyl at C-7/7′ (**7**−**12**); and five known compounds (**13**−**17**). A literature search revealed that no butyrolactone lignan with a 6-carboxyl-2-pyrone moiety has been previously reported. A plausible biogenetic pathway of **1** is proposed in Scheme 1. The 6-carboxyl-2-pyrone might be formed from a 3,4-dihydroxy phenyl moiety through oxidative cleavage, oxidation, and esterification.

■ ASSOCIATED CONTENT

Supporting Information

The Supporting Information is available free of charge on the ACS Publications website at DOI: 10.1021/acs.jafc.5b02838.

NMR, IR, MS, and CD spectra of compounds **1**−**12** (PDF)

■ AUTHOR INFORMATION

Corresponding Author

*(P.-C.Z.) Phone: +86-10-63165231. E-mail: pczhang@imm.ac.cn. Fax: 86-10-63017757.

Author Contributions

‖Y.-N.Y. and X.-Y.H. contributed equally to this work.

Funding

This research was supported by the National Science and Technology Project of China (No. 2012ZX09301002-002) and the Fundamental Research Funds for the Central Institutes (No. 2014TD03).

Notes

The authors declare no competing financial interest.

■ ACKNOWLEDGMENTS

We thank Ying-hong Wang for NMR measurements.

■ REFERENCES

(1) Liu, J. Y.; Cai, Y. Z.; Wong, R. N. S.; Lee, C. K.; Tang, S. C. W.; Sze, S. C. W.; Tong, Y.; Zhang, Y. B. Comparative analysis of caffeoylquinic acids and lignans in roots and seeds among various burdock (*Arctium lappa*) genotypes with high antioxidant activity. *J. Agric. Food Chem.* **2012**, *60*, 4067−4075.

(2) Ming, D. S.; Guns, E.; Eberding, A.; Towers, N. G. H. Isolation and characterization of compounds with anti-prostate cancer activity from *Arctium lappa* L. using bioactivity-guided fractionation. *Pharm. Biol.* **2004**, *42*, 44−48.

(3) Matsumoto, T.; Hosono-Nishiyama, K.; Yamada, H. Antiproliferative and apoptotic effects of butyrolactone lignans from *Arctium lappa* on leukemic cells. *Planta Med.* **2006**, *72*, 276−278.

(4) Xu, Z. H.; Wang, X.; Zhou, M.; Ma, L.; Deng, Y.; Zhang, H.; Zhao, A.; Zhang, Y. Y.; Jia, W. The antidiabetic activity of total lignan from Fructus Arctii against alloxan-induced diabetes in mice and rats. *Phytother. Res.* **2008**, *22*, 97−101.

DOI: 10.1021/acs.jafc.5b02838
J. Agric. Food Chem. 2015, 63, 7958−7966

(5) Kim, J. H.; Bae, J. T.; Song, M. H.; Lee, G. S.; Choe, S. Y.; Pyo, H. B. Biological activities of Fructus Arctii fermented with the basidiomycete *Grifola frondosa*. *Arch. Pharmacal Res.* **2010**, *33*, 1943−1951.
(6) Dos Santos, A. C.; Baggio, C. H.; Freitas, C. S.; Lepieszynski, J.; Mayer, B. Gastroprotective activity of the chloroform extract of the roots from *Arctium lappa* L. *J. Pharm. Pharmacol.* **2008**, *60*, 795−801.
(7) Park, S. Y.; Hong, S. S.; Han, X. H.; Hwang, J. S.; Lee, D.; Ro, J. S.; Hwang, B. Y. Lignans from *Arctium lappa* and their inhibition of LPS-induced nitric oxide production. *Chem. Pharm. Bull.* **2007**, *55*, 150−152.
(8) Umehara, K.; Nakamura, M.; Miyase, T.; Kuroyanagi, M.; Ueno, A. Studies on differentiation inducers VI. Lignan derivatives from Arctium Fructus. *Chem. Pharm. Bull.* **1996**, *44*, 2300−2304.
(9) Kravtsova, S. S.; Khasanov, V. V. Lignans and fatty-acid composition of *Arctium lappa* seeds. *Chem. Nat. Compd.* **2011**, *47*, 800−801.
(10) Yang, Y. N.; Huang, X. Y.; Feng, Z. M.; Jiang, J. S.; Zhang, P. C. Hepatoprotective activity of twelve novel 7′-hydroxy lignan glucosides from Arctii Fructus. *J. Agric. Food Chem.* **2014**, *62*, 9095−9102.
(11) Frelek, J.; Szczepek, W. J. $[Rh_2(OCOCF_3)_4]$ as an auxiliary chromophore in chiroptical studies on steroidal alcohols. *Tetrahedron: Asymmetry* **1999**, *10*, 1507−1520.
(12) Yang, S.; Tamai, R.; Akashi, S.; Takeuchi, O.; Akira, S.; Sugawara, S.; Takada, H. Synergistic effect of muramyldipeptide with lipopolysaccharide or lipoteichoic acid to induce inflammatory cytokines in human monocytic cells in culture. *Infect. Immun.* **2001**, *69*, 2045−2053.
(13) Vidal, V.; Dewulf, J.; Bahr, G. M. Enhanced maturation and functional capacity of monocyte-derived immature dendritic cells by the synthetic immunomodulator Murabutide. *Immunology* **2001**, *103*, 479−487.
(14) Corrie, J. E. T.; Green, G. H.; Ritchie, E.; Taylor, W. C. The chemical constituents of Australian *Zanthoxylum* species. V. The constituents of *Z. pluviatile* Hartley; the structures of two new lignans. *Aust. J. Chem.* **1970**, *23*, 133−145.
(15) Lopes, L. M. X.; Yoshida, M.; Gottlieb, O. R. Dibenzylbutyrolactone lignans from *Virola sebifera*. *Phytochemistry* **1983**, *22*, 1516−1518.
(16) Ren, Y. L.; Yang, J. S. The spectroscopic features of dibenzylbutyrolactone lignans. *Chin. J. Magn. Reson.* **2002**, *19*, 15−24.
(17) Cutillo, F.; D'Abrosca, B.; DellaGreca, M.; Fiorentino, A.; Zarrelli, A. Lignans and neolignans from *Brassica fruticulosa*: effects on seed germination and plant growth. *J. Agric. Food Chem.* **2003**, *51*, 6165−6172.
(18) Yang, Y. N.; Liu, Z. Z.; Feng, Z. M.; Jiang, J. S.; Zhang, P. C. Lignans from the root of *Rhodiola crenulata*. *J. Agric. Food Chem.* **2012**, *60*, 964−972.
(19) Chakladar, S.; Cheng, L.; Choi, M.; Liu, J.; Bennet, A. J. Mechanistic evaluation of melA α-galactosidase from *Citrobacter freundii*: a family 4 glycosyl hydrolase in which oxidation is rate-limiting. *Biochemistry* **2011**, *50*, 4298−4308.
(20) Park, J. H.; Jung, Y. J.; Jung, J. W.; Shrestha, S.; Lim, D. W.; Han, D.; Baek, N. I. A new flavonoid glycoside from the root bark of *Morus alba* L. *Nat. Prod. Res.* **2014**, *28*, 1859−1863.
(21) Kousar, F.; Noomrio, M. H.; Talpur, M. M. A.; Ahmad, V. U.; Arfan, M. Two new lignan glycosides from *Trachelospermum lucidum* (D. Don) Schum. *J. Asian Nat. Prod. Res.* **2008**, *10*, 285−288.
(22) Neidigh, K. A.; Kingston, D. G. I.; Lewis, N. G. Synthesis of stereospecifically deuterated matairesinol, podorhizol, epipodorhizol, and yatein. *J. Nat. Prod.* **1994**, *57*, 791−800.
(23) Ekholm, F. S.; Eklund, P.; Leino, R. A short semi-synthesis and complete NMR-spectroscopic characterization of the naturally occurring lignan glycoside matairesinol 4,4′-di-*O*-β-D-diglucoside. *Carbohydr. Res.* **2010**, *345*, 1963−1967.
(24) Shi, Y.; Shi, R.; Liu, B.; Lu, Y.; Du, L. Isolation and elucidation of chemical constituents with antiviral action from Yinqiaosan on influenza virus. *Chin. J. Chin. Mater. Med.* **2003**, *28*, 47−51.
(25) Min, B. S.; Na, M. K.; Oh, S. R.; Ahn, K. S.; Jeong, G. S.; Li, G.; Lee, S. K.; Joung, Y.; Lee, H. K. New furofuran and butyrolactone lignans with antioxidant activity from the stem bark of *Styrax japonica*. *J. Nat. Prod.* **2004**, *67*, 1980−1984.
(26) Nishibe, S.; Hisada, S.; Inagaki, I. Lignans of *Trachelospermum liukiuense* and *T. foetidum*. *Chem. Pharm. Bull.* **1973**, *21*, 674−675.
(27) Li, C. L.; Zhang, D. M.; Luo, Y. M.; Yu, S. S.; Li, Y.; Lu, Y. Bis-sesquiterpenes and diterpenes from *Chloranthus henryi*. *Phytochemistry* **2008**, *69*, 2867−2874.

DOI: 10.1021/acs.jafc.5b02838
J. Agric. Food Chem. 2015, 63, 7958−7966

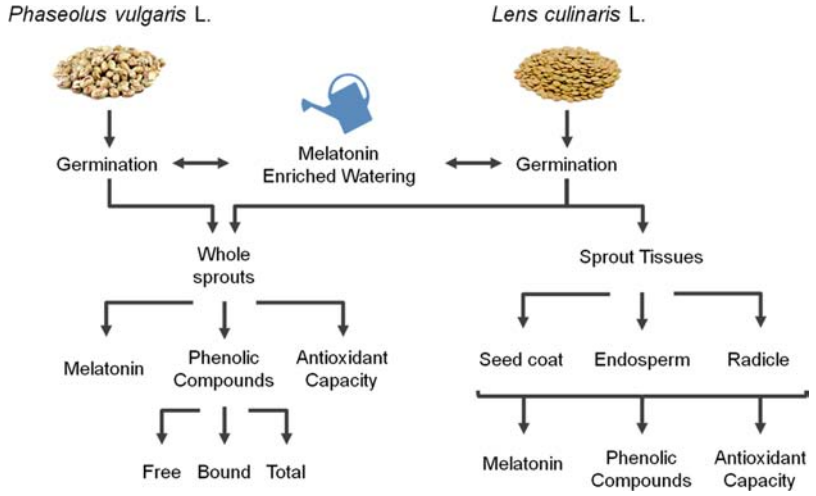

Figure 1. Illustrative diagram of the experimental design.

the effect on the antioxidant capacity in both sprouts. In addition, a sensory analysis was carried out on hummus of lentil sprouts to evaluate the influence of adding exogenous melatonin during their germination, in order to assess the potential legume sprout-based food for improving consumer's health.

MATERIALS AND METHODS

Plant Materials. Two varieties of common legumes, lentil (*Lens culinaris* L., var. *Salmantina*) and kidney bean (*Phaseolus vulgaris* L., var. *Pinta*), were provided by Institute of Food Science, Technology and Nutrition (CSIC, Spain) and stored under refrigeration conditions.

Processing Conditions. Three batches of seeds (20 g of lentils and 50 g of kidney beans) were sterilized in 1% NaClO solution for 30 min to reduce bacterial and fungal growth. Seeds were washed three times with distilled water until neutral pH and then soaked in a 20 μM melatonin solution for 5 h for seed hydration (ratio 1:20, m/v). Seeds were germinated for 3, 6, 8, and 10 days in an incubator (Construcciones Frigoríficas, Confri, S. L.) at 20 °C, 80% RH, and darkness. Seeds were maintained wet by capillarity using a 20 μM melatonin solution. Lentil and kidney bean samples were withdrawn, frozen in N_2, freeze-dried, and milled. Flours were passed through a 50 μm sieve and stored at 4−6 °C for further analysis. In addition, lentil sprouts were separated into different tissues as seed coat, endosperm, and radicle. These samples were also frozen in N_2, freeze-dried, and milled. Flours were passed through a 50 μm sieve and stored at 4−6 °C for further analysis. The experimental design is illustrated in Figure 1.

Melatonin Extraction and Quantification by HPLC-MS/MS. The extraction procedure was carried out according to Aguilera et al.[32] Briefly, lentil and kidney bean flours (2 g) were extracted with 10 mL of methanol (MeOH) for 16 h at 4 °C in darkness. After a brief centrifugation at 2000*g* for 15 min at room temperature, the supernatants were filtered under vacuum by a filter (11 μm, Whatman) and evaporated to dryness under N_2 (g). The residues were resuspended in 2 mL of water, after a mild ultrasonic treatment for 2 min at room temperature. The reconstituted extracts were filtered using solid phase extraction (SPE, cartridge C-18, Waters) as follows: first, a conditioning step was carried out with 1 mL of MeOH and 1 mL of water to activate the column, followed by sample application (1 mL of extract) and washing step with 2 mL of MeOH 10%; finally, 1 mL of MeOH was used for the elution step. The extracts obtained were evaporated to dryness by use of an evaporator centrifuge (Speed Vac SC 200, Savant, USA). The residues were dissolved in MeOH/H_2O (80:20, v/v) + 0.1% formic acid. Melatonin was determined by HPLC-ESI-MS/MS triple quadrupole (Varian 1200L with API-ES between 10 and 1500 Da range mass). The system consisted of two pumps, Varian Prostar 210 and an Intensity Trio C18 (150 mm × 2.0 mm ID, S-3 μm, 12 nm BRYTC18032150; Bruker) column, at a flow rate of 0.2 mL/min. Acetonitrile containing 0.1% formic acid (solvent A) and 0.1% formic acid in H_2O (solvent B) as mobile phase were pumped with the following gradient: 5% solvent A (0−4 min), 5−100% solvent A (4−15 min), 100% solvent A (15−18 min), and 100−5% solvent A (18−25 min) to recover initial conditions. The injection volume was 50 μL. Quantification was performed using the external standard method, using pure melatonin (Sigma-Aldrich Química, Spain) dissolved in MeOH/H_2O (80:20, v/v) containing 0.1% formic acid. Melatonin content was expressed as ng/g dry weight (DW).

Phenolic Compound Extraction and Determination. Extraction of phenolic compounds was carried out following the method of Gou et al.[20] with some modifications. Raw and germinated flours (2 g) were blended using 30 mL of 80% chilled acetone (1:2, w/v) for 5 min and vortex for 10 min. The homogenates were then centrifuged at 2000*g* for 5 min. Supernatants were collected, and the extraction was repeated three times. All the supernatants were pooled and evaporated until 10% of the supernatants remained. The soluble free phytochemical extracts were brought to 10 mL in water and were kept at −40 °C until analysis. For the extractions of bound phytochemicals, the residues from the above soluble free extraction were flushed with N_2 and hydrolyzed directly with 20 mL of 4 M NaOH at room temperature for 1 h with shaking. The mixture was acidified to pH 2 with concentrated HCl, centrifuged at 3000*g* for 5 min, and extracted three times with ethyl acetate. The ethyl acetate fractions were evaporated to dryness and were reconstituted into 1.5 mL of methanol and stored at −40 °C until analysis.

Phenolic compounds were determined by Folin−Ciocalteu colorimetric method according to Singleton et al.[36] using gallic acid as standard. Phenolic compounds were expressed as mg GAE/100 g DW.

Oxygen Radical Absorbing Capacity (ORAC) Assay. The above methanol extracts were used for determining the radical scavenging activity by the ORAC method using fluorescein as a fluorescence probe.[37] Briefly, the reaction was carried out at 37 °C in 75 mM phosphate buffer (pH 7.4), and the final assay mixture (200 μL) contained fluorescein (70 nM), 2,2-azobis(2-methyl-propionamidine)-dihydrochloride (12 mM), and antioxidant standard (Trolox [10−80 μM] or sample extracts). A Polarstar Galaxy plate reader (BMG Labtechnologies GmbH, Offenburg, Germany) was used to read fluorescence at wavelengths of 485 nm excitation and 520 nm emission. The equipment was controlled by the Fluostar Galaxy software version (4.31-0) for fluorescence measurement. Black 96-well untreated microplates (PS Balck, Porvair, Leatherhead, UK) were used. The plate was automatically shaken before preincubation, and the fluorescence was recorded every minute for 80 min. All reaction

DOI: 10.1021/acs.jafc.5b03128
J. Agric. Food Chem. 2015, 63, 7967−7974

mixtures were prepared in duplicate, and at least three independent runs were performed for each sample. Fluorescence measurements were normalized to the oxidation control (phosphate buffer) and stability control (no antioxidant). From the normalized curves, the area under the fluorescence decay curve (AUC) was calculated as

$$\mathrm{AUC} = 1 + \sum_{i=1}^{i=80} f_i/f_0$$

where f_0 is the initial fluorescence reading at 0 min and f_i is the fluorescence reading at time i. The net AUC corresponding to a sample was calculated as follows:

$$\text{net AUC} = \text{AUC antioxidant} - \text{AUC blank}$$

The net AUC was plotted against the antioxidant concentration, and the regression equation of the curve was calculated. The ORAC value was obtained by dividing the slope of the latter curve by the slopes of the Trolox curve obtained in the same assay. Final ORAC values were expressed as μmol of Trolox equivalents/g of dry seed (μmol TE/g DW).

Sensory Analysis. Two different hummuses were prepared using lentil sprouts germinated for 10 days with and without (control) melatonin in the watering. Sensory evaluation was carried out in two sessions involving in total 40 trained and 60 untrained panelists. Sensory analysis was performed using three different tests; a descriptive test and two affective tests. To assess the sensory profile, each evaluated character was scored in a 10-point intensity scale (1 (lowest) to 10 (highest)). Color, odor, fluidity, consistency, texture, astringency, aftertaste, and flavor of the selected hummus, A (hummus prepared with enriched melatonin lentil sprouts) and B (hummus prepared without enriched melatonin lentil sprouts), were tested by 40 trained judges. For each attribute, the average of the panelists' scores was calculated. Satisfaction tests consisted of a 9-point verbal scale showing the acceptance of the product (like extremely = +4; like very much = +3; like moderately = +2; like slightly = +1; neither like nor dislike = 0; dislike slightly = −1; dislike moderately = −2; dislike very much = −3; dislike extremely = −4). Hummus was considered acceptable if their mean value for overall quality scores was equal to or above 0 (neither like nor dislike). Sensory evaluation was completed by a paired preference test. Untrained judges should choose between both samples tested, in order to assessing the distribution of panelists' preferences.

Statistical Analysis. Each sample was analyzed in triplicate. Data were expressed as mean ± standard deviation (SD). The data were analyzed by one-way analysis of variance (ANOVA) and post hoc Duncan's test. Student's t test (independent samples, 2 groups) was used to analyze differences in satisfaction between both hummus samples. Differences in the preference between these hummuses were studied by a binomial test and were considered to be significant at $p < 0.05$. The statistical analysis was performed using SPSS 21.0.

RESULTS AND DISCUSSION

Melatonin. *Melatonin Content in Whole Lentil and Bean Sprouts.* Raw kidney beans exhibited higher melatonin content (1.0 ng/g DW) than lentils (0.5 ng/g DW). These contents can be considered as natural sources of melatonin if they are compared with other plant foods; in general, seeds, such as almond, sunflower, and mustard, exhibited higher melatonin content.[9,38−40] Earlier studies indicated that traditional germination increased melatonin levels of different seeds.[31−33] However, these contents might not be sufficient to be incorporated as dietary supplements to increase melatonin in blood plasma in humans and, consequently, their scavenging and antioxidant actions. Thus, adding exogenous melatonin during watering might be a strategy to increase their melatonin levels during germination processing.

Germination with exogenous melatonin watering (20 μM) showed significant increases of melatonin in both legumes (Figure 2). In lentil sprouts, melatonin concentration increased from 0.5 ng/g DW in raw seeds to 1089.8 ng/g DW at the seventh day. However, a sharp melatonin decrease (42% with respect to the seventh germination day) was observed, reaching to 630.4 ng/g DW on the tenth day. Kidney bean sprouts presented lower melatonin contents than lentil sprouts throughout the whole germination process, although initially raw kidney beans exhibited higher melatonin levels than lentils. At the sixth day of germination, melatonin reached the highest levels in kidney bean sprout (529.1 ng/g DW). Thereafter, its content decreased gradually to 124.9 ng/g DW (76% decrease with respect to sixth germination day).

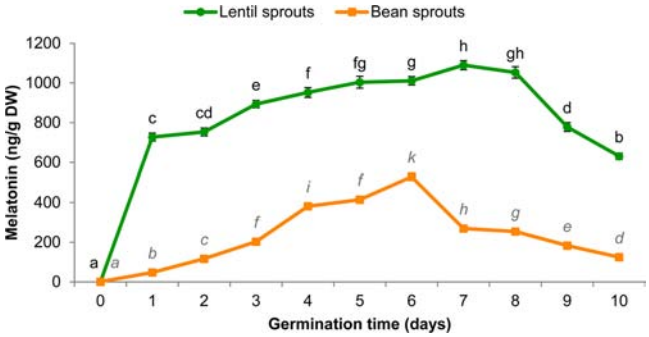

Figure 2. Melatonin contents in lentil (a) and kidney bean (b) sprouts grown with 20 μM melatonin in watering. Points with different letters significantly differ when subjected to Duncan's multiple range test ($p < 0.05$).

From these results, both lentil and kidney bean sprouts experienced a significant decrease of melatonin from the sixth or seventh germination day depending on the type of legumes; these reductions may be interpreted through melatonin metabolism.[33] The process of adding exogenous melatonin to the water increased the melatonin levels in these legumes, in contrast to those germinated by the traditional method (2.5 and 9.4 ng/g DW in lentil and kidney bean, respectively).[32]

It is worth emphasizing that sprouts germinated with exogenous melatonin watering absorbed up to 24% of added melatonin in the case of lentils and up to 11% in kidney beans. These differences were likely due to seed physiological factors such as thickness and surface area of the seed coats. Lentils exhibit seed coat thickness between 25 and 35 μm, depending on cultivar, being 8% of whole seed. However, kidney beans are associated with relatively thicker seed coats (40−60 μm), representing 12% of seeds.[41] Therefore, kidney bean seed coats might not allow melatonin diffusion as well as lentil ones.

Melatonin Content in Lentil Sprout Tissues. There is scarce information about melatonin content in sprouts after using an enriched watering. Because lentil exhibited higher melatonin levels than kidney bean sprouts, a detailed study was designed to measure this bioactive compound in the different tissues of lentil sprouts (seed coat, endosperm, and radicle). From the third day of germination, melatonin levels were higher in the seed coats than in the other tissues (endosperm and radicle) (Figure 3), increasing in all sprout tissues up to the eighth germination day. Afterward, melatonin decreased sharply (34%) in the seed coat from 897.2 ng/g DW to 589.6 ng/g DW, reaching lower levels than those found on the third day. In case of endosperm and radicle, they exhibited lower melatonin levels (92.1 ng/g DW and 26.4 ng/g DW, respectively), but significant increases were observed at the end of germination

DOI: 10.1021/acs.jafc.5b03128
J. Agric. Food Chem. 2015, 63, 7967−7974

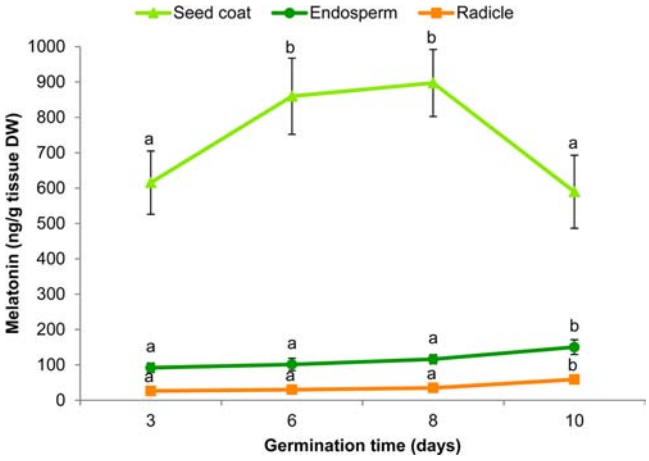

Figure 3. Melatonin contents in the different tissues (seed coat, endosperm, and radicle) of lentil sprout grown with 20 μM melatonin in watering. Points with different letters significantly differ when subjected to Duncan's multiple range test ($p < 0.05$).

period (tenth germination day), showing 150.3 ng/g DW and 58.9 ng/g DW in endosperm and radicle, respectively.

Melatonin Effects on Radicle Development. Melatonin exhibits auxin-like activity, promoting vegetative plant growth in a similar way to indole-3-acetic acid (IAA).[12] Indeed, significant enhancement ($p < 0.05$) of development of roots was observed as in lentil and in kidney bean sprouts (Figure 4).

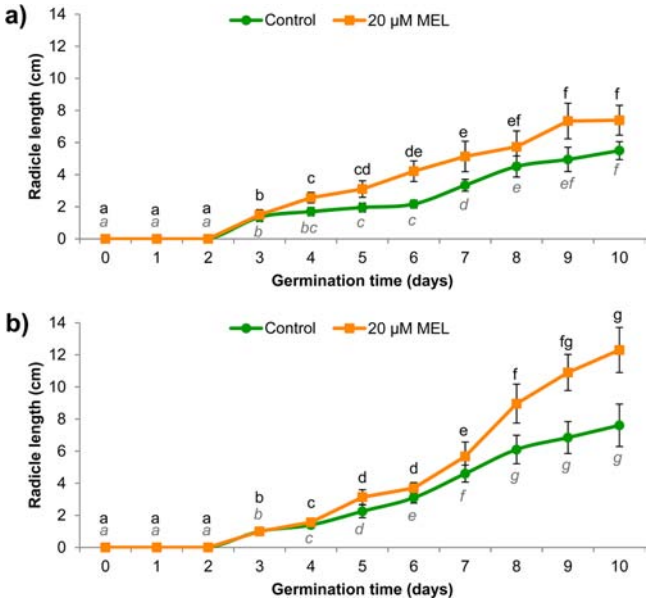

Figure 4. Radicle development in lentil (a) and kidney bean (b) sprouts grown with 20 μM melatonin in watering. Points with different letters significantly differ when subjected to Duncan's multiple range test ($p < 0.05$).

The radicles of lentils watered with 20 μM melatonin grew 1.4-fold more than those watered with H_2O (control); in the case of kidney beans, the increase was 1.6-fold. As described in the literature, the benefits of melatonin in plants vary with concentration. Germination rate and root development can be enhanced or inhibited.[12,15,17,42,43] From our results, 20 μM melatonin solution may suggest use as a correct concentration as biostimulator, as reported Janas and Posmyk.[16] Melatonin is likely to increase the final germination percentage besides the seed growth; therefore, sprout production becomes more economical and may increase sales and mark-up.

Furthermore, melatonin content in endosperms and radicles show positive correlations with the length of the sprouts (r = 0.877−0.879, $p < 0.01$) (Table 1). The increase of melatonin content could be explained not only by the growth stimulation of added melatonin but also by the influence of the germination.

Phenolic Compounds. The free (FPC), bound (cell wall-associated; BPC), and total phenolic compounds (TPC) of lentil and kidney bean sprouts are shown in Figure 5. Raw lentils and kidney beans exhibited lower TPC (487.5 mg GAE/100 g DW and 379.1 mg GAE/100 g DW, respectively) in comparison to TPC found in broad and red beans or in black beans by Amarowicz et al.[44] and Guajardo-Flores et al.[45] Nevertheless, TPC were higher compared with those found in mung bean by Guo et al.[20] and by Huang et al.[46] FPC and BPC in raw legumes were similar to those reported by Aguilera et al.,[32] FPC being the main fraction (95−98%).

Germination with exogenous melatonin watering induced changes in phenolic compound concentrations. Lentils showed slight decreases in a time-dependent manner in FPC from the first day (92% of TPC) to the tenth day (89% of TPC), and inversely, BPC increased 17%, reaching 44.3 mg GAE/100 g DW, attributable to the glycosylation of FPC. The highest decrease in TPC was found on the sixth day (21% of reduction from raw seed), and no more significant decreases were shown. On the tenth day of germination, lentil sprouts displayed 393.7 mg GAE/100 g DW (81% of the initial TPC content). Kidney beans exhibited no significant decrease in TPC nor in FPC. Nonetheless, a slight increase in BPC was shown from the eighth day. Kidney bean sprouts exhibited 36.5 mg GAE/100 g DW, 57% higher BPC compared with raw kidney beans.

Several authors have previously reported decreases in the phenolic content of legumes following germination.[47−49] A similar trend was found by Aguilera et al.,[32] where decreases in TPC in lentils were more accentuated after a traditional germination procedure. The activation of endogenous enzymes during germination could bring about changes in the phenolic composition of beans and lentils.[50] Thus, decreases in TPC could be attributed to the increases in activity of polyphenol oxidase and other catabolic enzymes, as observed by Khandelwal et al.[48] Furthermore, it has been reported that during germination procyanidins and catechins could condense to give more highly polymerized forms.[51] Oxidation could also be the cause of TPC decrease.[47] Melatonin, as antioxidant, could protect the sprout against oxidation, avoiding phenolic compound degradation. The results obtained compared with those obtained by Aguilera et al.[32] could corroborate the above hypothesis.

Antioxidant Activity. Both legumes revealed significant increases in the antioxidant capacity along the germination process (Figure 6), although lentils exhibited higher antioxidant capacity than beans. The antioxidant capacity of lentils increased 1.3 times (85.3 μmol TE/g tissue DW) during the germination process and the capacity of beans increased 1.7 times (55.8 μmol TE/g tissue DW). It is noticed that when melatonin content decreased during germination, the antioxidant capacity levels of these sprouts increased. This fact could be attributed to higher accumulation of compounds as melatonin metabolites from its catabolism. These compounds (AFMK, AMK, and cyclic 3-hydroxymelatonin) are more highly

DOI: 10.1021/acs.jafc.5b03128
J. Agric. Food Chem. 2015, 63, 7967−7974

Table 1. Correlation Coefficients between the Contents of Melatonin, Phenolic Compounds, and Antioxidant Capacity in Lentil and Bean Sprouts[a]

Correlations in Lentil Sprouts												
	MEL	MEL-SC	MEL-END	MEL-RDC	length	TPC	FPC	BPC	AC	AC-SC	AC-END	AC-RDC
MEL	1	0.792[c]	−0.572	−0.730[c]	0.497	0.349	0.199	−0.379	0.855[c]	0.129	−0.262	−0.041
MEL-SC		1	0.024	−0.182	0.096	0.503	0.476	0.497	0.204	−0.021	0.371	0.550
MEL-END			1	0.970[c]	0.877[c]	0.263	0.704[b]	0.217	0.849[c]	−0.198	0.902[c]	0.788[c]
MEL-RDC				1	0.879[c]	0.105	0.555	0.053	0.820[c]	−0.264	0.811[c]	0.649[b]
length					1	0.328	0.576[b]	−0.398	0.827[c]	−0.590[b]	0.820[c]	0.661[b]
TPC						1	0.390	0.994[c]	−0.441	0.538	0.385	0.506
FPC							1	0.320	0.353	−0.185	0.704[b]	0.698[b]
BPC								1	−0.490	0.625[b]	0.349	0.498
AC									1	−0.452	0.855[c]	0.721[c]
AC-SC										1	−0.157	−0.001
AC-END											1	0.900[c]
AC-RDC												1

Correlations in Kidney Bean Sprouts						
	MEL	length	TPC	FPC	BPC	AC
MEL	1	0.051	−0.257	0.237	−0.301	0.338
length		1	−0.130	0.789[c]	−0.249	0.942[c]
TPC			1	0.286	0.982[c]	−0.151
FPC				1	0.139	0.838[c]
BPC					1	−0.275
AC						1

[a]MEL, melatonin; SC, seed Coat; RDC, radicle; END, endosperm; TPC, total phenolic compounds; FPC, free phenolic compounds; BPC, bound phenolic compounds; AC, antioxidant capacity. [b]Significant correlation for $p < 0.05$. [c]Significant correlation for $p < 0.01$.

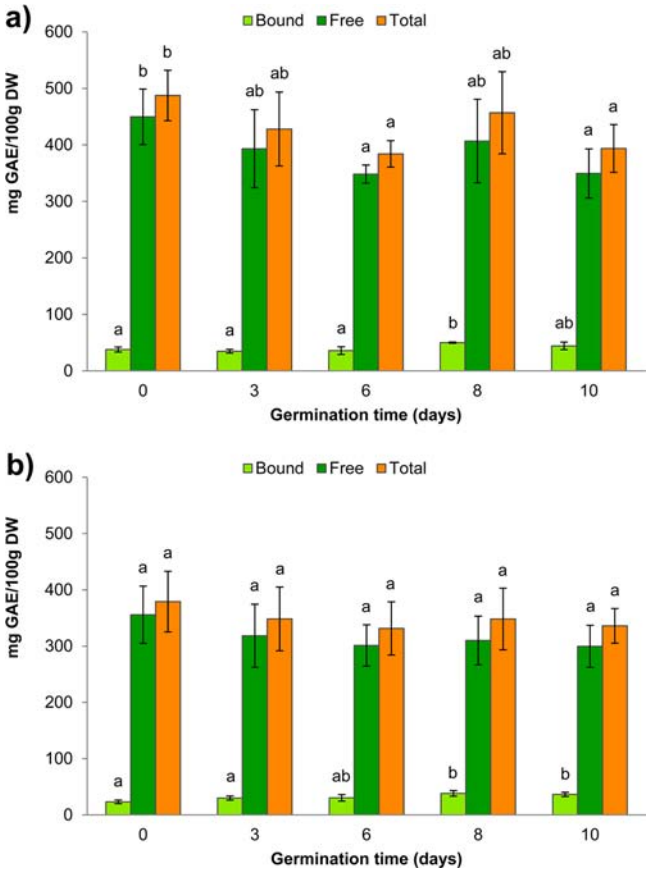

Figure 5. Phenolic compound contents in lentil (a) and kidney bean (b) sprouts grown with 20 μM melatonin in watering. Bars with different letters significantly differ when subjected to Duncan's multiple range test ($p < 0.05$).

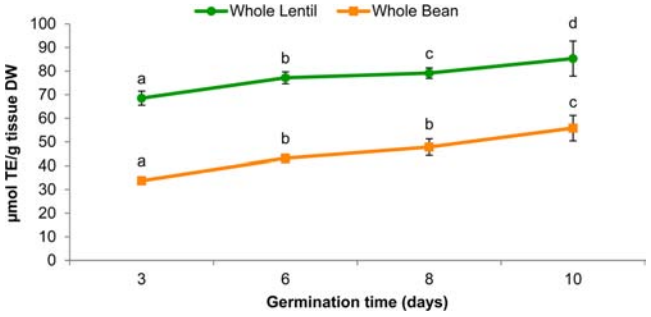

Figure 6. Antioxidant capacity (μmol TE/g DW) in lentil and kidney bean sprouts grown with 20 μM melatonin in watering. Points with different letters significantly differ when subjected to Duncan's multiple range test ($p < 0.05$).

effective scavengers than melatonin.[5,16,39,52] Melatonin showed a positive correlation with antioxidant capacity in lentil sprouts ($r = 0.855$, $p < 0.01$), but with bean sprouts the correlation was not significant (Table 1).

Because melatonin and phenolic compounds present relevant antioxidant properties, the study of antioxidant capacity was carried out in different tissues of the lentil sprouts; some of them had shown significant levels of these bioactive components (Table 2). Thus, seed coats were the tissues with the highest antioxidant capacity, 6-fold higher compared with endosperms, and they exhibited a significant decrease along germination. As was expected, endosperms showed the lowest antioxidant capacity during germination, although their levels increased to 24% on the tenth day of this process. Finally, radicles exhibited 3-fold higher antioxidant capacity than endosperms but did not show a significant enhancement during germination. Endosperm and radicle exhibited different behaviors compared with that reported by Guajardo-Flores et

DOI: 10.1021/acs.jafc.5b03128
J. Agric. Food Chem. 2015, 63, 7967−7974

Table 2. Antioxidant Activity (μmol TE/g DW) in Different Tissues (Seed Coat, Endosperm, and Radicle) Of Lentil Sprouts Germinated with 20 μM Melatonin in Watering

germination time (days)	lentil sprouts		
	seed coat	endosperm	radicle
3	278.3 ± 25.4 b	44.6 ± 5.6 a	135.4 ± 9.7 a
6	234.8 ± 14.6 a	50.4 ± 4.3 ab	154.5 ± 20.4 a
8	228.5 ± 14.2 a	51.2 ± 3.3 ab	155.9 ± 20.6 a
10	225.9 ± 18.5 a	55.2 ± 3.7 b	161.3 ± 21.3 a

Results are reported as mean ± SD (n = 3). Mean values of each tissue of the lentil sprout followed by different letters significantly differ when subjected to Duncan's multiple range test (p < 0.05).

al.;[45] these differences could be attributed to aspects related to the germination process and watering with melatonin.

Thus, melatonin concentration reveals strong correlations with antioxidant capacity in lentil endosperms and whole sprouts (r = 0.902 and r = 0.855, respectively, p < 0.01). Analogous correlation is established between melatonin and their antioxidant capacity in the radicles. The length of the radicles exhibits positive correlation with the antioxidant capacity in lentils (r= 0.827, p < 0.01) and in beans (r = 0.942, p < 0.01), showing the positive effect of the germination process with enriched melatonin watering on the final antioxidant status of the sprouts.

Sensory Analysis of the Hummus. Figure 7 shows a spider-web diagram comparing descriptive profile results. Most

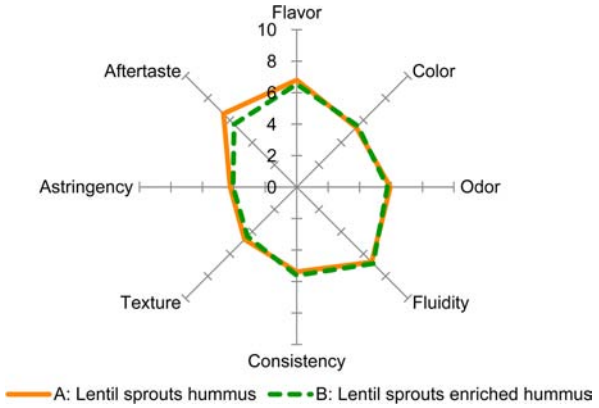

Figure 7. Spider-web diagram of sensorial attributes in lentil hummus. Mean scores (n = 40).

attributes such as flavor, color, aroma, fluidity, and consistency present similar scores, equal to or higher than five. Texture and astringency exhibit a score lower than five, but similar between A (nonenriched hummus) and B (enriched hummus). Only aftertaste brought about different points (7 in case of hummus A and 6 in hummus B). Therefore, melatonin enriched watering seems not to have any impact on the final product sensory quality, although radicle development is different in lentil sprouts germinated with enriched or nonenriched watering, which could increase green taste and grassy odor. Germination could have enhanced bitter taste and aftertaste, reducing sweet flavor and also showing more fibrousness.[40,42,49]

Satisfaction test results (n = 60) revealed a great acceptance of these hummuses; mean scores for the two samples exceeded the acceptance level (A = 1.1 and B = 1.3); t-test showed no significant differences between samples (p = 0.46). Regarding the preference test (n = 60), conclusions were reaffirmed; results do not show statistical significant difference (p = 0.37) (26 individuals preferred hummus A against 34 who preferred B). The panel found the lentil sprout hummus as flavorful products and indicate their probable product purchase if they could be found in the market. Thus, the melatonin-enriched hummus might be a good alternative to increase blood melatonin levels and, thereby, equilibrate the oxidative balance of the organism, as well as promote health, by increasing the dietary intake of plant-based foods.

This alternative method of germination with 20 μM melatonin in watering might be valid in sprout production, either lentils or beans. Adding exogenous melatonin into legume germination seems to increase its production and sprout healthiness, providing higher food quality. Lentil sprouts contained more melatonin than bean sprouts; but their concentration was considerably higher than other plant foods. Both sprouts showed good characteristics in order to be added to healthy diet. Therefore, these sprouts could be employed as functional ingredients by food industry, when developing melatonin-enriched novel foods. They might have an important nutritional impact because of melatonin's beneficial effects for human health.

AUTHOR INFORMATION

Corresponding Author

*E-mail: maria.martin@uam.es. Tel: 0034 91 497 8678. Fax: 0034 91 497 3826.

Funding

This research was financially supported by Second Call for Interuniversity Cooperation Projects University Autónoma de Madrid and Santander Bank with United States (2013−2014).

Notes

The authors declare no competing financial interest.

ABBREVIATIONS USED

AFMK, N(1)-acetyl-N(2)-formyl-5-methoxykynuramine; AMK, N(1)-acetyl-5-methoxykynuramine; BPC, bound phenolic compounds; DW, dry weight; FPC, free phenolic compounds; GAE, gallic acid equivalents; HPLC-MS/MS, high-performance liquid chromatography tandem mass spectrometry; MEL, melatonin; MRM, multiple reaction monitoring; TE, Trolox equivalents; TPC, total phenolic compounds; WW, wet weight

REFERENCES

(1) Posmyk, M. M.; Janas, K. M. Melatonin in plants. *Acta Physiol. Plant.* **2009**, *31*, 1−11.

(2) Reiter, R. J.; Tan, D. X.; Zhou, Z.; Cruz, M. H. C.; Fuentes-Broto, L.; Galano, A. Phytomelatonin: Assisting plants to survive and thrive. *Molecules* **2015**, *20*, 7396−7437.

(3) Hardeland, R.; Cardinali, D. P.; Srinivasan, V.; Spence, D. W.; Brown, G. M.; Pandi-Perumal, S. R. Melatonin − A pleiotropic, orchestrating regulator molecule. *Prog. Neurobiol.* **2011**, *93*, 350−384.

(4) Zhang, H. M.; Zhang, Y. Melatonin: A well-documented antioxidant with conditional pro-oxidant actions. *J. Pineal Res.* **2014**, *57*, 131−146.

(5) Reiter, R. J.; Tan, D. X.; Fuentes-Broto, L. Chapter 8 - Melatonin: A Multitasking Molecule. *Prog. Brain Res.* **2010**, *181*, 127−151.

(6) Rodriguez, C.; Mayo, J. C.; Sainz, R. M.; Antolín, I.; Herrera, F.; Martín, V.; Reiter, R. J. Regulation of antioxidant enzymes: a significant role for melatonin. *J. Pineal Res.* **2004**, *36*, 1−9.

(7) Tan, D. X.; Reiter, R. J.; Manchester, L. C.; Yan, M. T.; El-Sawi, M.; Sainz, R. M.; Mayo, J. C.; Kohen, R.; Allegra, M.; Hardeland, R. Chemical and physical properties and potential mechanisms:

DOI: 10.1021/acs.jafc.5b03128
J. Agric. Food Chem. 2015, 63, 7967−7974

melatonin as a broad spectrum antioxidant and free radical scavenger. *Curr. Top. Med. Chem.* **2002**, *2*, 181−197.
(8) Reiter, R. J.; Tan, D. X. Melatonin: An antioxidant in edible plants. *Ann. N. Y. Acad. Sci.* **2002**, *957*, 341−344.
(9) Manchester, L. C.; Tan, D. X.; Reiter, R. J.; Park, W.; Monis, K.; Qi, W. High levels of melatonin in the seeds of edible plants: Possible function in germ tissue protection. *Life Sci.* **2000**, *67*, 3023−3029.
(10) Liu, J.; Wang, W.; Wang, L.; Sun, Y. Exogenous melatonin improves seedling health index and drought tolerance in tomato. *Plant Growth Regul.* **2015**, DOI: 10.1007/s10725-015-0066-6.
(11) Paredes, S. D.; Korkmaz, A.; Manchester, L. C.; Tan, D. X.; Reiter, R. J. Phytomelatonin: A review. *J. Exp. Bot.* **2009**, *60*, 57−69.
(12) Park, W. J. Melatonin as an endogenous plant regulatory signal: Debates and perspectives. *J. Plant Biol.* **2011**, *54*, 143−149.
(13) Tan, D. X.; Hardeland, R.; Manchester, L. C.; Korkmaz, A.; Ma, S.; Rosales-Corral, S.; Reiter, R. J. Functional roles of melatonin in plants, and perspectives in nutritional and agricultural science. *J. Exp. Bot.* **2012**, *63*, 577−597.
(14) Wei, W.; Li, Q. T.; Chu, Y. N.; Reiter, R. J.; Yu, X. M.; Zhu, D. H.; Zhang, W. K.; Ma, B.; Lin, Q.; Zhang, J. S.; Chen, S. Y. Melatonin enhances plant growth and abiotic stress tolerance in soybean plants. *J. Exp. Bot.* **2015**, *66*, 695−707.
(15) Arnao, M. B.; Hernández-Ruiz, J. Growth conditions determine different melatonin levels in *Lupinus albus* L. *J. Pineal Res.* **2013**, *55*, 149−155.
(16) Janas, K. M.; Posmyk, M. M. Melatonin, an underestimated natural substance with great potential for agricultural application. *Acta Physiol. Plant.* **2013**, *35*, 3285−3292.
(17) Tiryaki, I.; Keles, H. Reversal of the inhibitory effect of light and high temperature on germination of *Phacelia tanacetifolia* seeds by melatonin. *J. Pineal Res.* **2012**, *52*, 332−339.
(18) Jati, I. R. A. P.; Vadivel, V.; Biesalski, H. K. Antioxidant Activity of Anthocyanins in Common Legume Grains, In *Bioactive Food as Dietary Interventions for Liver and Gastrointestinal Disease*; Watson, R. R., Preedy, V. R., Eds.; Academic Press: San Diego, CA, 2013; Chapter 31, pp 485−497.
(19) Paśko, P.; Bartoń, H.; Zagrodzki, P.; Gorinstein, S.; Fołta, M.; Zachwieja, Z. Anthocyanins, total polyphenols and antioxidant activity in amaranth and quinoa seeds and sprouts during their growth. *Food Chem.* **2009**, *115*, 994−998.
(20) Guo, X.; Li, T.; Tang, K.; Liu, R. H. Effect of germination on phytochemical profiles and antioxidant activity of mung bean sprouts (*Vigna radiata*). *J. Agric. Food Chem.* **2012**, *60*, 11050−11055.
(21) Nithiyanantham, S.; Selvakumar, S.; Siddhuraju, P. Total phenolic content and antioxidant activity of two different solvent extracts from raw and processed legumes, *Cicer arietinum* L. and *Pisum sativum* L. *J. Food Compos. Anal.* **2012**, *27*, 52−60.
(22) Mohd Esa, N.; Kadir, K. A.; Amom, Z.; Azlan, A. Antioxidant activity of white rice, brown rice and germinated brown rice *(in vivo* and *in vitro*) and the effects on lipid peroxidation and liver enzymes in hyperlipidaemic rabbits. *Food Chem.* **2013**, *141*, 1306−1312.
(23) Aguilera, Y.; Díaz, M. F.; Jiménez, T.; Benítez, V.; Herrera, T.; Cuadrado, C.; Martín-Pedrosa, M.; Martín-Cabrejas, M. A. Changes in nonnutritional factors and antioxidant activity during germination of nonconventional legumes. *J. Agric. Food Chem.* **2013**, *61*, 8120−8125.
(24) Chai, M. Y.; Azlan, A.; Al-Sheraji, S. H.; Hassan, F. A.; Nagendra Prasad, K. Antioxidant activities and total phenolic content in germinated and non-germinated legume extracts following alkaline-acid hydrolysis. *Pak. J. Nutr.* **2014**, *12*, 1036−1041.
(25) Benítez, V.; Cantera, S.; Aguilera, Y.; Mollá, E.; Esteban, R. M.; Díaz, M. F.; Martín-Cabrejas, M. A. Impact of germination on starch, dietary fiber and physicochemical properties in non-conventional legumes. *Food Res. Int.* **2013**, *50*, 64−69.
(26) Martín-Cabrejas, M. A.; Díaz, M. F.; Aguilera, Y.; Benítez, V.; Mollá, E.; Esteban, R. M. Influence of germination on the soluble carbohydrates and dietary fibre fractions in non-conventional legumes. *Food Chem.* **2008**, *107*, 1045−1052.
(27) Dueñas, M.; Hernández, T.; Estrella, I.; Fernández, D. Germination as a process to increase the polyphenol content and antioxidant activity of lupin seeds (*Lupinus angustifolius* L.). *Food Chem.* **2009**, *117*, 599−607.
(28) Cevallos-Casals, B. A.; Cisneros-Zevallos, L. Impact of germination on phenolic content and antioxidant activity of 13 edible seed species. *Food Chem.* **2010**, *119*, 1485−1490.
(29) Bonnefont-Rousselot, D.; Collin, F. Melatonin: Action as antioxidant and potential applications in human disease and aging. *Toxicology* **2010**, *278*, 55−67.
(30) Garrido, M.; Rodríguez, A. B.; Terrón, M. P. Tryptophan and Melatonin-Enriched Foodstuffs to Improve Antioxidant Status in Aging. In *Aging*; Preedy, V. R., Ed.; Academic Press: San Diego, CA, 2014; Chapter 13, pp 129−136.
(31) Zielinski, H.; Lewczuk, B.; Przybylska-Gornowicz, B.; Kozłowska, H. Melatonin in germinated legume seeds as a potentially significant agent for health. In *Biologically-active Phytochemicals in Food: Analysis, Metabolism, Bioavailability and Function*, Pfannhauser, W., Fenwick, G. R., Khokhar, S., Eds.; Royal Society of Chemistry: Cambridge, U.K., 2001; pp 110−117.
(32) Aguilera, Y.; Liébana, R.; Herrera, T.; Rebollo-Hernanz, M.; Sanchez-Puelles, C.; Benítez, V.; Martín-Cabrejas, M. A. Effect of illumination on the content of melatonin, phenolic compounds, and antioxidant activity during germination of lentils (*Lens culinaris* L.) and kidney beans (*Phaseolus vulgaris* L.). *J. Agric. Food Chem.* **2014**, *62*, 10736−10743.
(33) Aguilera, Y.; Herrera, T.; Benítez, V.; Arribas, S. M.; López de Pablo, A. L.; Esteban, R. M.; Martín-Cabrejas, M. A. Estimation of scavenging capacity of melatonin and other antioxidants: Contribution and evaluation in germinated seeds. *Food Chem.* **2015**, *170*, 203−211.
(34) Sae-Teaw, M.; Johns, J.; Johns, N. P.; Subongkot, S. Serum melatonin levels and antioxidant capacities after consumption of pineapple, orange, or banana by healthy male volunteers. *J. Pineal Res.* **2013**, *55*, 58−64.
(35) European Food Safety Authority Panel on Dietetic Products, Nutrition and Allergies. Scientific opinion on the substantiation of health claims related to melatonin and alleviation of subjective feelings of jet lag (ID 1953), and reduction of sleep onset latency, and improvement of sleep quality (ID 1953) pursuant to Article 13 (1) of Regulation (EC) No 1924/20061. *EFSA Journal* **2010**, *8*, 1467.
(36) Singleton, V. L.; Orthofer, R.; Lamuela-Raventós, R. M. Analysis of total phenols and other oxidation substrates and antioxidants by means of Folin-Ciocalteu reagent. *Methods Enzymol.* **1999**, *299*, 152−178.
(37) Dávalos, A.; Gómez-Cordovés, C.; Bartolomé, B. Extending applicability of the oxygen radical absorbance capacity (ORAC-Fluorescein) Assay. *J. Agric. Food Chem.* **2004**, *52*, 48−54.
(38) Garcia-Parrilla, M. C.; Cantos, E.; Troncoso, A. M. Analysis of melatonin in foods. *J. Food Compos. Anal.* **2009**, *22*, 177−183.
(39) Korkmaz, A.; Reiter, R. J.; Tan, D. X.; Manchester, L. C. Melatonin; from pineal gland to healthy foods. *Spatula DD* **2011**, *1*, 33−36.
(40) Sarrou, E.; Therios, I.; Dimassi-Theriou, K. Melatonin and other factors that promote rooting and sprouting of shoot cuttings in *Punica granatum* cv. Wonderful. *Turk. J. Bot.* **2014**, *38*, 293−301.
(41) Tiwari, B.; Singh, N. *Pulse Chemistry and Technology*; Royal Society of Chemistry: Cambridge, U.K., 2012; p 310.
(42) Chen, Q.; Qi, W.; Reiter, R. J.; Wei, W.; Wang, B. M. Exogenously applied melatonin stimulates root growth and raises endogenous indoleacetic acid in roots of etiolated seedlings of *Brassica juncea*. *J. Plant Physiol.* **2009**, *166*, 324−328.
(43) Park, S.; Back, K. Melatonin promotes seminal root elongation and root growth in transgenic rice after germination. *J. Pineal Res.* **2012**, *53*, 385−389.
(44) Amarowicz, R.; Troszyńska, R. A.; Baryłko-Pikielna, N.; Shahidi, F. Polyphenolic extracts from legume seeds: correlations between total antioxidant activity, total phenolics content, tannins content and astringency. *J. Food Lipids* **2004**, *11*, 278−286.
(45) Guajardo-Flores, D.; Serna-Saldívar, S. O.; Gutiérrez-Uribe, J. A. Evaluation of the antioxidant and antiproliferative activities of

DOI: 10.1021/acs.jafc.5b03128
J. Agric. Food Chem. 2015, 63, 7967−7974

extracted saponins and flavonols from germinated black beans (*Phaseolus vulgaris* L.). *Food Chem.* **2013**, *141*, 1497−1503.
(46) Huang, X.; Cai, W.; Xu, B. Kinetic changes of nutrients and antioxidant capacities of germinated soybean (*Glycine max* L.) and mung bean (*Vigna radiata* L.) with germination time. *Food Chem.* **2014**, *143*, 268−276.
(47) Dueñas, M.; Martínez-Villaluenga, C.; Limón, R. I.; Peñas, E.; Frias, J. Effect of germination and elicitation on phenolic composition and bioactivity of kidney beans. *Food Res. Int.* **2015**, *70*, 55−63.
(48) Khandelwal, S.; Udipi, S. A.; Ghugre, P. Polyphenols and tannins in Indian pulses: Effect of soaking, germination and pressure cooking. *Food Res. Int.* **2010**, *43*, 526−530.
(49) Troszyńska, A.; Estrella, I.; Lamparski, G.; Hernández, T.; Amarowicz, R.; Pegg, R. B. Relationship between the sensory quality of lentil (*Lens culinaris*) sprouts and their phenolic constituents. *Food Res. Int.* **2011**, *44*, 3195−3201.
(50) López-Amorós, M. L.; Hernández, T.; Estrella, I. Effect of germination on legume phenolic compounds and their antioxidant activity. *J. Food Compos. Anal.* **2006**, *19*, 277−283.
(51) Bartolomé, B.; Estrella, I.; Hernández, T. Changes in phenolic compounds in lentils (Lens culinaris) during germination and fermentation. *Z. Lebensm.-Unters. Forsch.* **1997**, *205*, 290−294.
(52) Hardeland, R. Melatonin, hormone of darkness and more - Occurrence, control mechanisms, actions and bioactive metabolites. *Cell. Mol. Life Sci.* **2008**, *65*, 2001−2018.

DOI: 10.1021/acs.jafc.5b03128
J. Agric. Food Chem. 2015, 63, 7967−7974

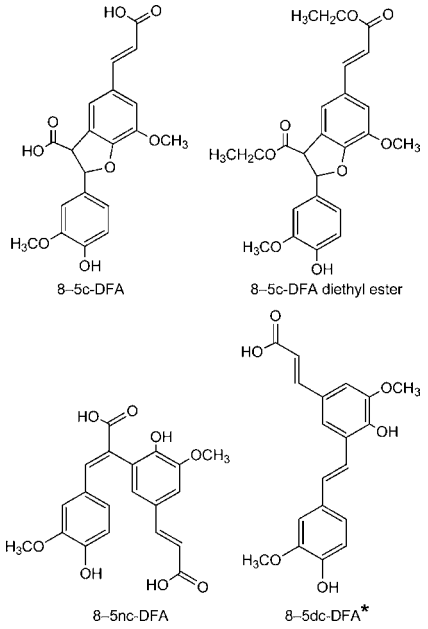

Figure 1. 8−5-Coupled dehydrodiferulate (DFA) compounds. 8−5c-DFA, 8−5c-DFA diethyl ester, and 8−5nc-DFA were synthesized as individual standard compounds for incubation with human fecal suspensions. *8−5dc-DFA was not synthesized as a standard compound, but was observed as a breakdown product of 8−5c-DFA during control (medium without feces) incubations. Abbreviations used: c, cyclic; dc, decarboxylated; nc, noncyclic.

LDL oxidation,[24] a relevant discussion of the physiological effects of DFAs must include their susceptibility to microbial metabolism and the physiological effects of these metabolites.

In vitro metabolism of the 8−*O*−4- and 5−5-DFA regioisomers by human intestinal microbiota, including structural characterization of the metabolites, has been described.[25,26] The 8−5-coupled regioisomer, the most abundant DFA in cereal grains,[27] is also susceptible to attack by human intestinal microbiota,[28] but its microbial metabolites have not been reported. In this study, we examine the structural transformations of free 8−5-DFAs (both the cyclic and the non-native open forms) and an esterified analogue, 8−5-DFA diethyl ester (cyclic), by human intestinal microbiota *in vitro* and structurally elucidate all major metabolites.

MATERIALS AND METHODS

Chemicals. Ferulic acid was from Aldrich (Seelze, Germany). Chromatography and NMR solvents were purchased from VWR (Bruchsal, Germany). Lyophilized peroxidase enzyme from horseradish (type II, 150−250 units/mg) was from Sigma-Aldrich (Munich, Germany). *N*,*O*-Bis(trimethylsilyl)trifluoracetamide (BSTFA) was obtained from Fluka (Buchs, Switzerland).

Synthesis of 8−5-Coupled Dehydrodiferulates. 8−5c-DFA diethyl ester was prepared by biomimetic peroxidase-H_2O_2-catalyzed radical coupling of ethyl ferulate followed by flash chromatography cleanup (Biotage Horizon flash chromatograph, Charlottesville, VA, USA) as described by Ralph et al.[29] Saponification of the diethyl ester (2 M NaOH, 12 h, stirring while protected from light) and subsequent extraction of released acids with diethyl ether following acidification to pH 2 with HCl led to 8−5c- and 8−5nc-DFA, in addition to other DFAs. 8−5c- and 8−5nc-DFAs were semipreparatively separated by HPLC with diode array detection (DAD) (monitored at 280 nm) using a Hitachi (Tokyo, Japan) L-7100 pump and L-7450A DAD detector, a Luna Phenyl-Hexyl column (Phenomenex, Aschaffenburg, Germany, 250 × 10 mm, 100 Å, 5 μm particle size), 3 mL/min flow rate, and the tertiary gradient described by Dobberstein et al.[30] Purity of the three synthesized standard compounds was verified by ^{1}H NMR using a Bruker (Rheinstetten, Germany) AV 250 MHz spectrometer (solvent: acetone-d_6).

Fermentation with Human Fecal Suspensions. A *preliminary* incubation trial was performed to determine appropriate sampling times and incubation length. A fecal sample was provided by a healthy human volunteer who had not taken antibiotics in the three months prior to the study and was consuming a mixed Western diet. The fresh sample was stored under anaerobic conditions using Anaerocult sachets (Merck, Darmstadt, Germany) and kept at room temperature for not longer than 2 h before usage. In an anaerobic workstation (A45, Don Whitley Scientific Limited, Shipley, West Yorkshire, UK; $N_2/CO_2/H_2$ (80/10/10, v/v/v)) feces (2.5 g) were put into a 16 mL Hungate tube containing 10 mL of anaerobic brain-heart medium (pH 7.6, Merck) and homogenized. After incubating for 10 min at 37 °C and centrifuging for 10 min at 300*g* to remove larger particles, equal volumes of the mixtures' supernatants were combined and homogenized. Aliquots (0.5 mL) of the resulting suspension were used to inoculate the samples (substituted with 0.5 mL of medium in the fecal-free controls). The Hungate tubes were supplemented with 8−5c-DFA, 8−5nc-DFA, or 8−5-DFA diethyl ester at a final concentration of 370 μM using 50 μL of the respective stock solution in DMSO. A parallel incubation of 8−5-DFA diethyl ester was also performed at 1/10 the concentration, or 37 μM. The fecal suspension was also incubated in the absence of any standard compounds using 50 μL of DMSO instead of stock solution (fecal control). The tubes were incubated at 37 °C in the dark with slow shaking (6 rpm). Sample aliquots were anaerobically withdrawn at defined incubation times (0, 6, 24, 48, and 120 h) with a syringe and stored at −20 °C until GC-MS analysis.

For the *scaled-up* incubation trial, fecal samples were provided by five healthy human volunteers who had not taken antibiotics in the three months prior to the study and were consuming mixed Western diets. Fresh fecal samples and fecal suspensions were prepared as described above, except that 10 g of feces was mixed with 30 g of medium. Schott flasks containing 200 mL of N_2-gassed medium were supplemented with 8−5c-DFA, 8−5nc-DFA, or 8−5c-DFA diethyl ester at a final concentration of 455, 370, and 340 μM using 1 mL of the respective stock solution in DMSO. A parallel incubation of 8−5nc-DFA was also performed at 1/10 the concentration, or 37 μM. Incubation started with the addition of 7.5 mL of pooled fecal suspension, whereas the fecal-free controls were supplemented with the same amount of medium. Additionally, a fecal control was prepared using 1 mL of DMSO instead of a standard compound stock solution. The flasks were incubated while stirring at 37 °C in the anaerobic workstation in the dark, and 1 mL aliquots were withdrawn at 0, 3, 5, 20, 28, 45, 69, and 117 h for LC-MS screening. On the basis of the results of the *preliminary* trial, additional 30−60 mL samples were taken at appropriate time points for metabolite isolation. All samples were stored at −20 °C until further preparation. The observed microbial metabolites were exclusively detected in the fecal suspensions incubated with 8−5-dimers. None of the metabolites were found in either the fecal-free or fecal controls.

pH Stability Test of 8−5c-DFA. Hungate tubes (16 mL) filled with 10 mL of brain-heart medium were adjusted to pH values of 6.0, 6.4, 6.8, 7.2, and 7.6 (two replicates per pH value). The tubes were gassed with N_2 and autoclaved, monitoring the pH values after each step. Each tube was supplemented with 8−5c-DFA at a final concentration of 370 μM using 50 μL of the respective stock solution in DMSO. The tubes were incubated at 37 °C in the dark on a shaker at 6 rpm without the addition of any fecal components. Sample aliquots were anaerobically withdrawn at defined incubation times (0, 6, 24, 48, and 72 h) with a syringe and stored at −20 °C until LC-MS analysis.

Sample Preparation for GC- and LC-MS Analyses. Aliquots (400 μL) from both the *preliminary* and *scaled-up* trials as well as the 8−5c-DFA pH stability test were acidified to pH ∼2 with 20 μL of 2 M HCl and extracted with ethyl acetate (2 × 800 μL). The organic layers were combined and dried under a nitrogen stream. Dried extracts from the *preliminary* fecal incubation trial were analyzed via GC-MS, and dried extracts from the *scaled-up* incubation trial and 8−5c-DFA pH stability test were analyzed with LC-MS.

DOI: 10.1021/acs.jafc.5b03234
J. Agric. Food Chem. 2015, 63, 7975−7985

GC-MS Analysis. The dried extracts were derivatized by trimethylsilylation with BSTFA (40 μL) and pyridine (10 μL) for 30 min at 60 °C in sealed glass vials. The trimethylsilylated samples were 1:10 diluted with acetonitrile and analyzed on a Shimadzu GC-MS system (Kyoto, Japan; GC-2010-Plus oven, QP 2010 Ultra mass spectrometer, and AOC-20i autosampler). Samples were injected (1 μL, injection port temperature: 275 °C) using a 10:1 split ratio and separated on an Rtx-5MS column (30 m, 0.25 mm diameter, 0.25 μm film thickness) using the following temperature gradient: initial temperature, 220 °C; hold for 1 min; heat to 270 °C at 3 °C/min; hold for 5 min; heat to 280 °C at 4 °C/min; hold for 20 min; heat to 300 °C at 10 °C/min; and hold for 10 min. Helium (40 cm/s) was used as the carrier gas. The transfer line and ion source temperatures were held at 290 and 180 °C, respectively. The ionization energy was 70 eV. Total ion chromatograms were recorded (m/z 50−800 scan range, 0.30 s scan time).

LC-MS Analysis. Dried sample extracts were dissolved in 80 μL of MeOH/H_2O (50/50, v/v). The solution was diluted 1:30 with MeOH/H_2O (50/50, v/v) and analyzed on a Waters LC-MS (Eschborn, Germany) system equipped with a 2690 Separations Module pump and autosampler, a Micromass Quattro Micro mass spectrometer, and a 996 PDA-DAD. Samples (20 μL injection volume) were separated at room temperature on a Phenomenex Kinetex Phenyl-Hexyl column (150 × 4.6 mm, 2.6 μm particle size) with a flow rate of 0.5 mL/min. The following gradient was applied: A = H_2O with 0.01% formic acid, B = acetonitrile with 0.01% formic acid; initially, 90% A, 10% B; B from 10% to 27% in 10 min; B from 27% to 45% in 20 min; B from 45% to 60% in 2 min; B from 60% to 100% in 5 min; hold for 1 min; B from 100% to 10% in 1 min; and re-equilibration for 6 min. The ion source temperature was 100 °C, and the desolvation temperature was 350 °C. Ionization was performed in the ESI negative ion mode with a capillary voltage of 4.00 kV. Ionized molecules were detected in the full scan mode, using a scan range from m/z 180 to 500 and a scan time of 1 s.

Isolation of Metabolites for NMR Spectroscopy. Frozen sample aliquots were thawed and mixed thoroughly before acidifying with 2 M HCl to pH ∼2. The acidified solutions were extracted with ethyl acetate: first with a solvent volume double the total acidified solution volume and then twice with solvent volumes equal to the acidified solution volume. The organic layers were combined and evaporated under reduced pressure using a rotary evaporator (30 °C). The residue was dissolved in 2 mL of MeOH/H_2O (50/50, v/v) and 1 mL of acetonitrile at 35 °C with sonication (15 min), followed by centrifugation (5 min, 4000g). An aliquot of the supernatant (1 mL) was mixed with 500 μL of MeOH/H_2O (50/50, v/v), and the mixture was centrifuged again (5 min, 18500g). The final supernatant was separated on a Knauer (Berlin, Germany) Azura semipreparative HPLC system equipped with a P2.1L pump and a UVD 2.1L UV detector. Samples were manually injected (injection loop volume, 2 mL) and separated at room temperature on a Luna Phenyl-Hexyl column (250 × 10 mm, 100 Å, 5 μm particle size) using a flow rate of 3.5 mL/min. For metabolites of 8−5c-DFA and 8−5nc-DFA the following gradient was used: A = 1 mM trifluoroacetic acid (TFA) in water, B = acetonitrile/1 mM TFA in water (90/10, v/v); initially, 90% A, 10% B; B from 10% to 27% in 10 min; B from 27% to 45% in 20 min; B from 45% to 60% in 2 min; B from 60% to 100% in 5 min; hold for 1 min; B from 100% to 10% in 1 min; re-equilibrate for 6 min. For separation of the 8−5c-DFA diethyl ester metabolites, the same eluents were used with different gradient steps: initial conditions, 85% A, 15% B; B from 15% to 32% in 10 min; B from 32% to 45% in 20 min; B from 45% to 80% in 20 min; B from 80% to 100% in 2 min; hold for 2 min; B from 100% to 15% in 1 min; followed by re-equilibration. Detection wavelength was 260 nm for 8−5nc-DFA metabolites, 238 nm for 8−5c-DFA diethyl ester metabolites, and either 238, 260, or 280 nm for 8−5c-DFA metabolites. Fractions were collected by hand and rotary-evaporated under reduced pressure (30 °C). The residues were frozen and lyophilized overnight to ensure complete dryness.

NMR Spectroscopy. The metabolites were dissolved in 500 μL of acetone-d_6 and analyzed at 298 K on a Bruker Ascend 500 MHz NMR spectrometer equipped with a Prodigy cryoprobe. ^{1}H, ^{1}H−^{1}H-COSY, phase-sensitive ^{1}H−^{13}C-HSQC, and ^{1}H−^{13}C-HMBC experiments (standard Bruker implementations) were performed. Data were analyzed using MestReNova software, and spectra were calibrated against the central acetone residual peak (methyl proton, 2.05 ppm; methyl carbon, 29.84 ppm).[31]

High-Resolution MS. Exact masses of the metabolites were determined by high-resolution MS experiments performed on an LC-ToF-MS/MS system consisting of a 1290 Infinity HPLC system (1290 Bin Pump G4220A with degasser, 1290 Sampler G4226A autosampler, and 1290 DAD G4212A DAD detector from Agilent Technologies, Santa Clara, CA, USA) coupled to a TripleTOF 5600 mass spectrometer (AB Sciex Instruments, Framingham, MA, USA). The same chromatographic conditions described in the LC-MS Analysis section above were used. The Duo Spray ion source was used in ESI negative mode at 650 °C with curtain gas, 45 psi; ion source gas-1, 70 psi; ion source gas-2, 60 psi; and declustering potential, −100 V. ToF-MS experiments were completed over a scan range of m/z 100−1000 using an accumulation time of 200 ms and a collision energy voltage of −10 V. ToF-MS/MS experiments (product ion scans of m/z 50−500 for m/z 317, 327, 331, 387, 389, 401, 427, and 429) were performed with the following parameters, using nitrogen as collision gas: collision energy voltage, −45 V; collision energy spread, 25 V; and accumulation time, 80 ms.

RESULTS

Incubation of 8−5nc-DFA, 8−5c-DFA, and 8−5c-DFA diethyl ester with pooled fecal samples from five donors produced a gradual disappearance of the parental diferulates, with the exception of the diethyl ester, whose concentration decreased for the first 5 h of incubation, increased sharply between 5 and 20 h, and then sank again (see Figure 2A). This pattern likely arose from the poor solubility of 8−5c-DFA diethyl ester in the medium, with only partial initial dissolution of this compound. Metabolism of this initially dissolved portion produced an early concentration decrease, but gradual dissolution of the remaining

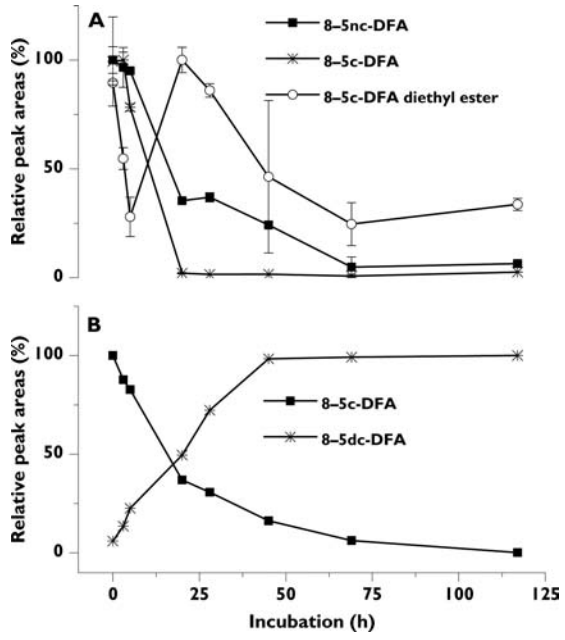

Figure 2. Time course of disappearance of substrate compounds during the *scaled-up* trial. Relative peak areas were calculated as (LC-PDA peak area at time point/maximum peak area of compound during incubation) × 100. When provided, error bars represent the range from two incubation replicates. Compound structures are provided in Figure 1. Abbreviations used: c, cyclic; dc, decarboxylated; DFA, dehydrodiferulate; nc, noncyclic. (A) Disappearance of substrate compounds during incubation with human fecal microbiota. (B) Disappearance of 8−5c-DFA and appearance of 8−5dc-DFA during control incubation (medium without human fecal microbiota).

DOI: 10.1021/acs.jafc.5b03234
J. Agric. Food Chem. 2015, 63, 7975−7985

standard compound resulted in an apparent rise in its concentration between 5 and 20 h. To confirm that the metabolism of 8−5c-DFA diethyl ester was not influenced by this behavior, we performed parallel incubations at two 8−5c-DFA diethyl ester concentrations, 370 and 37 μM, and observed no differences in the resulting metabolite profiles (data not shown).

No metabolites or artifacts were observed in the control incubations of 8−5nc-DFA and 8−5c-DFA diethyl ester. In contrast, a gradual, yet complete, disappearance of 8−5c-DFA and a corresponding appearance of 8−5dc-DFA were observed in the control incubation without fecal inoculum (see Figure 2B). Decarboxylation of 8−5c-dimers is a well-known reaction and has been described before under alkaline conditions.[32] However, Ralph and co-workers described ring-opening of the 8−5c-DFA diethyl ester, ester cleavage, and decarboxylation of the resulting 8−5nc-DFA as a competing reaction to the cleavage of the ester linkages of the 8−5c-DFA diethyl ester. They did not observe ring-opening or decarboxylation during alkaline treatment of the free (nonesterified) 8−5c-DFA. Nevertheless, to test whether the breakdown of 8−5c-DFA independent of bacterial metabolism was caused by the slightly alkaline pH (7.6) of our incubation trial, we incubated 8−5c-DFA again at pH values of 6.0, 6.4, 6.8, 7.2, and 7.6 without the addition of fecal samples. With longer incubation times the peak areas (UV detection) of 8−5c-DFA decreased to the same extent for all tested pH values and the amount of 8−5dc-DFA increased concurrently (see Figure 3). Interestingly, 8−5nc-DFA was not detected. The

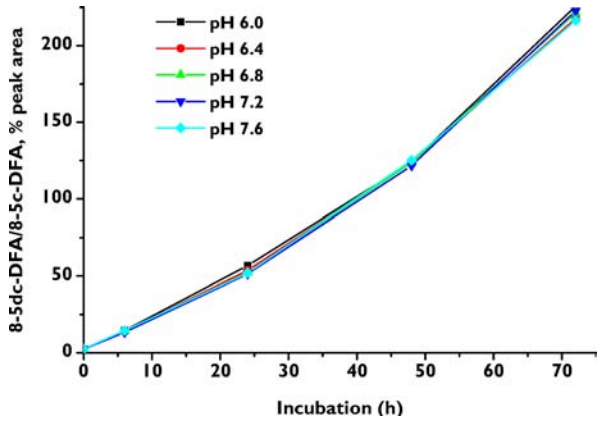

Figure 3. Disappearance of 8−5c-DFA and appearance of 8−5dc-DFA at different medium pH values during the pH stability test. Abbreviations used: c, cyclic; dc, decarboxylated.

extent of decarboxylation was influenced only by incubation length and not by the incubation pH. Reported pH values in the cecum of healthy individuals range from 5.7 to 6.8, with a gradual rise along the colon, leading to rectal pH values between 6.1 and 7.2.[33] Because decarboxylation of 8−5c-DFA was observed at all pH values between 6.0 and 7.6, we hypothesize that the reaction, although independent of microbial influence, is physiologically relevant, provided that none of the medium ingredients were responsible for this behavior.

Conversion of 8−5-Noncyclic Dehydrodiferulic Acid by Human Intestinal Microbiota. 8−5nc-DFA does not exist *in planta*, but is instead formed from 8−5c-DFA esters during exposure to alkaline conditions.[3] Alkaline pretreatment of cereal brans or flours to potentially enhance bioavailability of (di)ferulates[5] partially converts the native cyclic form to the open/noncyclic form. The *preliminary* incubation of 8−5nc-DFA with human fecal microbiota at a substrate concentration of 370 μM produced only a single metabolite structure. To test for a possible antimicrobial effect of 8−5nc-DFA at this concentration, two concentrations (370 and 37 μM) were incubated during the *scaled-up* trial. However, both substrate concentrations again produced the same single metabolite, **NCyc$_1$**. This compound was not detected in either control. LC-DAD/ESI-MS (LC retention time at 14.8 min) showed a UV absorption maximum at 325 nm and a molecular ion of m/z 387 $[M - H]^-$, indicating a gain of two mass units compared to the parent structure. The EI mass spectrum (Figure 4, molecular ion of the trimethylsilylated compound at m/z 676) also suggests a molecular mass of 388, indicating a simple reduction of the propenyl side chain on the B-unit (see structure in Figure 5). This hypothesis was confirmed by NMR data (see Tables 1 and 2) and by high-resolution MS, where the measured molecular ion (m/z 387.1083 $[M - H]^-$) matched the theoretical value for the sum formula $C_{20}H_{19}O_8$ ($[M - H]^-$) almost perfectly. In MS mode, the error was −1.4 ppm, while the intensity-weighted error calculated from 35 MS/MS fragments was 3.2 ppm. Major MS/MS fragments are presented in Table 3. Only a fraction of the parent 8−5nc-DFA compound remained at the end of incubation (see Figure 2A).

Conversion of 8−5-Cyclic Dehydrodiferulic Acid by Human Intestinal Microbiota. In comparison to 8−5nc-DFA, which produced only one microbial metabolite, the native 8−5c-DFA produced six metabolites in the *preliminary* trial, of which five compounds were isolated in semipreparative amounts from the *scaled-up* trial and fully characterized. The first metabolite, **Cyc$_1$**, was formed rapidly, with its peak concentration being found in the 6 h incubation aliquot, but then disappearing after 48 h of incubation (see Figure 6B). Eluting after 16.5 min in the LC system, its UV spectrum showed a maximum at 325 nm, and its ESI-MS (negative ionization) spectrum showed a quasimolecular ion of m/z 387 $[M - H]^-$, or a gain of two mass units compared to the original substrate. Following trimethylsilylation, **Cyc$_1$** produced the EI mass spectrum shown in Figure 4. Besides the molecular ion at m/z 676, a diagnostic fragment at m/z 209 was observed, which represents a resonance-stabilized A-ring carbocation formed via cleavage of the β-bond between C7 and C8 of the A-ring moiety. NMR data (see Tables 1 and 2) showed that the structure was formed by reductive opening of the substrate benzofuran ring (Figure 5). The two H7 protons on the A-ring were chemically distinct, resulting in two H7 signals at 3.32 and 3.04 ppm, respectively. Although the signal at 3.32 ppm lay under the residual water signal in the ^{1}H spectrum and could not be integrated, ^{1}H−^{1}H-COSY showed clear couplings from the proton at 3.32 ppm to both H8 (4.40 ppm) and the H7 proton, represented by the signal at 3.04 ppm, both of which produced integrals corresponding to one proton. Additionally, HSQC data showed that both signals assigned to H7 coupled to the same carbon nucleus. High-resolution MS data (see Table 3) further confirmed this structural characterization. The mass error of the measured molecular ion, m/z 387.1087 $[M - H]^-$, was 0.4 ppm relative to the theoretical value, while the intensity-weighted error determined from 10 MS/MS fragments was 2.8 ppm.

The second isolated metabolite, **Cyc$_2$**, was first detected in trace quantities in the 5 h sample aliquot, rising to its peak concentration at 20 h and then tapering off (see Figure 6B). The compound had an LC retention time of 16.30 min and a UV absorption maximum at 280 nm with no absorption above 300 nm, which indicated reduction of both propenyl side chains. The structure's molecular ion (LC-ESI-MS) was m/z 389 $[M - H]^-$,

DOI: 10.1021/acs.jafc.5b03234
J. Agric. Food Chem. 2015, 63, 7975−7985

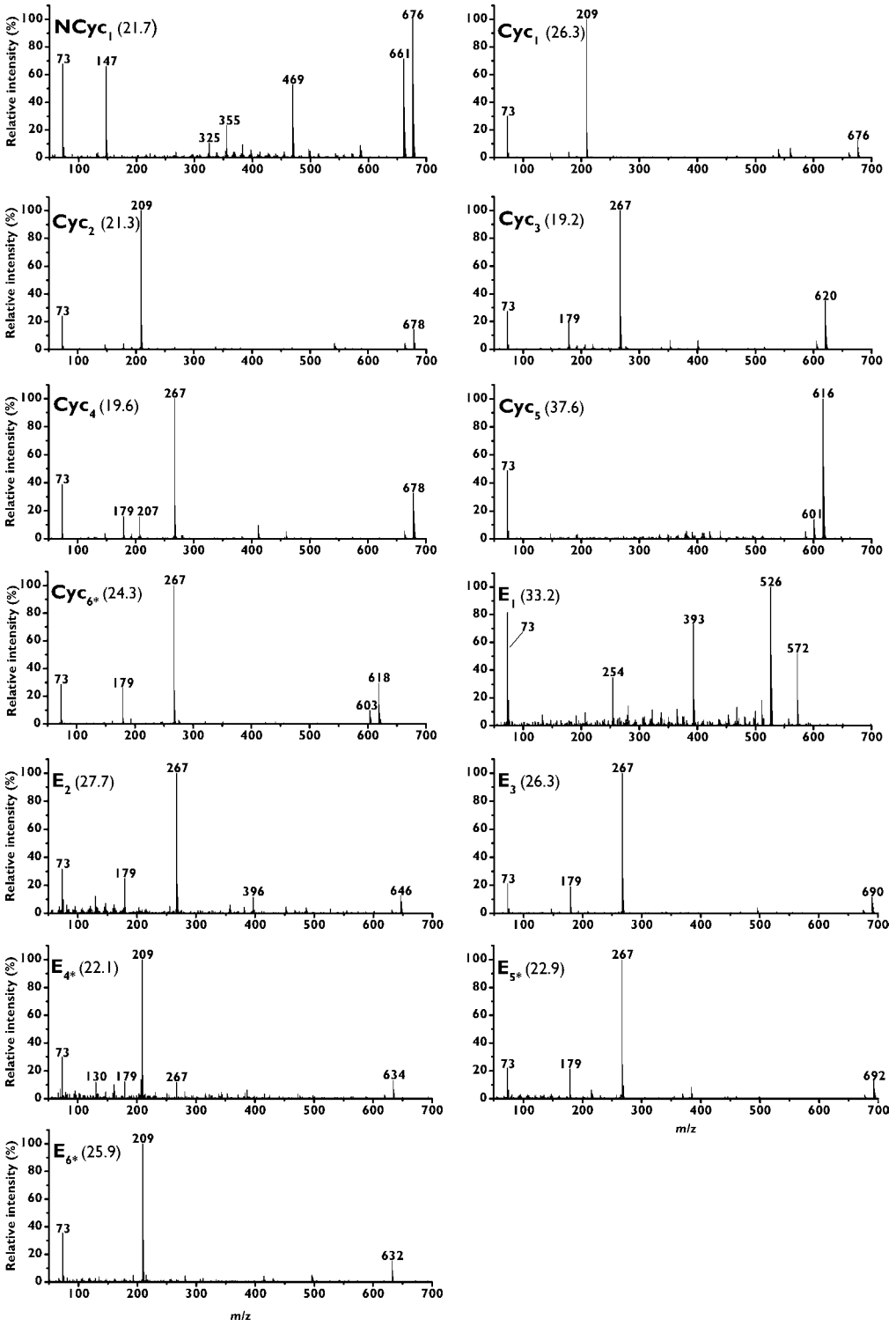

Figure 4. Electron impact mass spectra from trimethylsilylated metabolites of 8−5-coupled dehydrodiferulate (DFA) compounds following incubation with human fecal microbiota. Metabolite structures are provided in Figures 5 and 7. Title of each spectrum includes the abbreviated metabolite name and GC retention time (min) of the trimethylsilylated compound.

a gain of four mass units compared to 8−5c-DFA. The molecular ion of the trimethylsilylated compound, *m*/*z* 678, the same characteristic fragment as **Cyc$_1$**, *m*/*z* 209, and NMR data (see Tables 1 and 2) showed that the **Cyc$_2$** structure was similar to **Cyc$_1$**, except for reduction of the propenyl side chain on the B-unit (Figure 5). The H7 protons on the A-unit were again chemically distinct in the NMR spectrum, producing two ^{1}H signals both integrating to one proton. These data were in agreement with the high-resolution MS and MS/MS results (see Table 3), which produced an accurate mass of *m*/*z* 389.1238 [M − H]$^-$. Deviation from the theoretical exact mass for $C_{20}H_{21}O_8$ ([M − H]$^-$) was only −1.0 ppm in the MS mode and 5.7 ppm in the MS/MS mode (intensity-weighted error was calculated from 19 fragments).

DOI: 10.1021/acs.jafc.5b03234
J. Agric. Food Chem. 2015, 63, 7975−7985

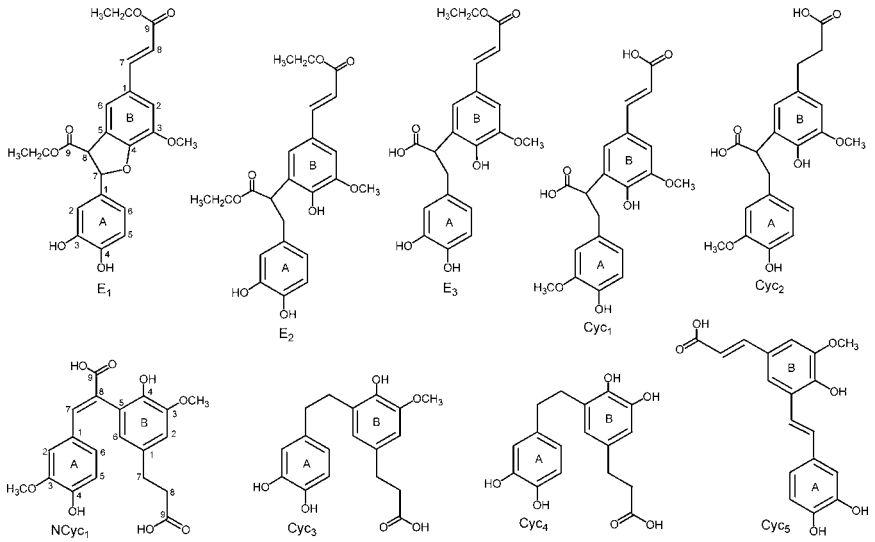

Figure 5. Metabolites of 8−5-coupled dehydrodiferulate (DFA) compounds following incubation with human fecal microbiota. All depicted compounds were fully characterized by 1D- and 2D-NMR spectroscopy. **E** compounds: metabolites of 8−5-cyclic DFA diethyl **e**ster; **Cyc** compounds: metabolites of 8−5-**cyc**lic DFA; **NCyc** compound: metabolite of 8−5-**n**on-**cyc**lic DFA.

Table 1. ^{1}H NMR Shifts of Isolated Metabolites (in Acetone-d_6)[a]

metabolite		H2	H5	H6	H7a	H7b	H8	OMe	OEt (CH_2)	OEt (CH_3)
NCyc$_1$	A-ring	6.73 (1H, d, 1.7)	6.76 (1H, d, 6.76)	6.89 (1H, dd, 8.1, 1.9)	7.78 (1H, s)			3.49 (3H, s)		
	B-ring	6.97 (1H, d, 1.7)		6.63 (1H, d, 1.7)	2.87[b]		2.61 (2H, t, 7.7)	3.90 (3H, s)		
Cyc$_1$	A-ring	6.83 (1H, s)	6.70[c]	6.70[c]	3.32[b]	3.04 (1H, dd, 13.8, 7.8)	4.40 (1H, t, 7.7)	3.78 (3H, s)		
	B-ring	7.27 (1H, s)		7.24 (1H, s)	7.61 (1H, d, 15.9)		6.40 (1H, d, 15.9)	3.95 (3H, s)		
Cyc$_2$	A-ring	6.70[c]	6.70[c]	6.78 (1H, s)	3.24 (1H, dd, 13.8, 8.3)	2.93 (1H, dd (13.8, 6.8)	4.35 (1H, dd, 8.2, 7.0)	3.77 (3H, s)		
	B-ring	6.82[c]		6.83[c]	2.84 (2H, t, 7.8)		2.58 (2H, t, 7.8)	3.85 (3H, s)		
Cyc$_3$	A-ring	6.78[c]	6.76[c]	6.60 (1H, dd, 8.0, 1.5)	2.76 (2H)		2.84[b]			
	B-ring	6.78[c]		6.65 (1H, s)	2.83 (2H)[b]		2.59 (2H, t, 7.8)	3.87 (3H, s)		
Cyc$_4$	A-ring	6.78 (1H, d, 1.7)	6.76 (1H, d, 8.0)	6.61 (1H, dd, 8.0, 1.7)	2.76 (2H)[c]		2.83 (2H)[c]			
	B-ring	6.64 (1H, d, 1.7)		6.55 (1H, d, 1.5)	2.76 (2H)[c]		2.54 (2H, t, 7.8)			
Cyc$_5$	A-ring	7.12 (1H, d, 1.9)	6.82 (1H, d, 8.1)	6.93 (1H, dd, 8.1, 1.9)	7.25 (1H)[c]		7.29 (1H)[c]			
	B-ring	7.24 (1H, d, 1.7)		7.55 (1H, d, 1.4)	7.63 (1H, d, 15.9)		6.44 (1H, d, 15.9)	3.95 (3H, s)		
E$_1$	A-ring	6.93 (1H, d, 1.9)	6.87 (1H, d, 8.1)	6.82 (1H, dd, 8.1, 1.8)	6.04 (1H, d, 7.4)		4.38 (1H, d, 7.2)		4.30	1.34 (3H)[c]
	B-ring	7.38 (1H, s)		7.33 (1H, s)	7.66 (1H, d, 16.0)		6.46 (1H, d, 15.9)	3.96 (3H, s)	4.23 (2H, q, 7.1)	1.31 (3H)[c]
E$_2$	A-ring	6.77 (1H)	6.71 (1H, d, 8.0)	6.58 (1H, dd, 8.0, 1.6)	3.16 (1H, dd, 13.8, 8.9)	2.85[b]	4.28 (1H, dd, 8.8, 6.4)		4.08	1.14 (3H, t, 7.1)
	B-ring	7.30 (1H, d, 1.5)		7.21 (1H, d, 1.6)	7.61 (1H, d, 15.9)		6.42 (1H, d, 15.9)	3.96 (3H, s)	4.22 (2H, q, 7.1)	1.31 (3H, t, 7.1)
E$_3$	A-ring	6.78 (1H, d, 1.8)	6.70 (1H, d, 8.0)	6.60 (1H, dd, 8.0, 1.9)	3.26 (1H, dd, 13.9, 8.7)	2.93[b]	4.39 (1H, dd, 8.2, 7.9)			
	B-ring	7.30 (1H, d, 1.6)		7.24 (1H, d, 1.6)	7.61 (1H, d, 15.9)		6.42 (1H, d, 15.9)	3.96 (3H, s)	4.22 (2H, q, 7.1)	1.31 (3H, t, 7.1)

[a]For numbering and A-ring/B-ring notation, see Figure 5. Abbreviations used: c, cyclic; d, doublet; DFA, dehydrodiferulate; q, quadruplet; nc, noncyclic; s, singlet; t, triplet. [b]Signal in the ^{1}H spectrum was under a residual water signal, so the proton shift was taken from HSQC. [c]Coupling constant(s) could not be determined because of signal overlap.

The third isolated 8−5c-DFA metabolite, **Cyc$_3$**, eluted after 19.6 min on the LC and displayed a UV absorption maximum at 280 nm with no absorption above 300 nm, again pointing toward reduction of both ferulate propenyl side chains. LC-ESI-MS

DOI: 10.1021/acs.jafc.5b03234
J. Agric. Food Chem. 2015, 63, 7975−7985

Table 2. ^{13}C NMR Shifts of Isolated Metabolites (in Acetone-d_6)[a]

		C1	C2	C3	C4	C5	C6	C7	C8	C9	OMe	OEt (CH_2)	OEt (CH_3)
NCyc$_1$	A-ring	128.99	113.76	148.73	149.53	116.06	127.18	141.68	128.00	170.03	56.06		
	B-ring	134.27	112.64	149.54	144.49	125.66	123.80	31.88	36.76	174.83	57.03		
Cyc$_1$	A-ring	132.54	113.83	148.54	146.49	115.92	122.65	39.98	47.07	175.41	56.44		
	B-ring	127.13	109.73	149.26	148.06	127.45	123.69	146.39	116.54	168.89	56.81		
Cyc$_2$	A-ring	132.83	113.88	148.38	146.28	116.10	122.62	39.42	47.28	175.62	56.56		
	B-ring	133.09	111.38	148.53	143.93	127.00	121.03	32.00	37.04	174.80	56.75		
Cyc$_3$	A-ring	135.85	116.86	146.11	144.82	116.47	120.99	36.67	34.11				
	B-ring	133.27	110.72	148.63	143.86	129.29	123.38	32.04	37.19	174.87	56.84		
Cyc$_4$	A-ring	135.57	116.84	146.42	144.59	116.40	120.89	36.93	34.05				
	B-ring	133.94	114.35	146.21	142.88	130.21	121.98	31.67	37.01	174.97			
Cyc$_5$	A-ring	131.15	113.49	146.01	146.46	116.04	119.68	130.30	119.99				
	B-ring	126.77	108.79	148.82	147.41	125.69	120.59	145.93	116.15	168.22	56.32		
E$_1$	A-ring	133.29	114.64	147.01	147.38	116.85	119.22	88.62	56.80	172.14		62.75	15.16
	B-ring	130.02	113.77	146.45	151.46	127.71	119.62	145.94	117.15	167.79	56.97	61.01	15.16
E$_2$	A-ring	132.25	117.31	145.88	144.72	116.42	121.59	39.11	47.51	174.42		61.36	15.05
	B-ring	126.90	109.87	148.97	147.38	127.40	123.45	146.05	116.66	167.76	57.01	60.91	15.06
E$_3$	A-ring	132.94	117.56	145.77	144.83	116.31	121.59	39.07	47.21	175.03			
	B-ring	127.53	110.94	149.07	147.72	127.34	123.75	146.31	116.60	167.90	57.00	61.03	15.29

[a]Chemical shifts δ_C in ppm. For numbering and A-ring/B-ring notation, see Figure 5. Data taken from HSQC and HMBC 2D-NMR experiments.

Table 3. High-Resolution MS Analysis of Isolated Metabolites

compound[a]	elemental composition	m/z $[M - H]^-$	major MS/MS ions
NCyc$_1$	$C_{20}H_{20}O_8$	387.1080	269.0800 (100)[b], 121.0297 (86), 283.0969 (78), 343.1177 (57), 268.0734 (55), 311.0914 (42), 284.1050 (38), 255.0671 (30), 328.0954 (30), 147.0455 (26), 241.0518 (15)
Cyc$_1$	$C_{20}H_{20}O_8$	387.1087	148.0527 (100), 147.0433 (24), 192.0408 (20), 191.0345 (15)
Cyc$_2$	$C_{20}H_{22}O_8$	389.1238	149.0596 (100), 150.0680 (78), 285.1124 (64), 135.0440 (64), 271.0962 (54), 122.0367 (51), 148.0528 (36), 59.0158 (35), 121.0296 (32), 313.1066 (25), 345.1316 (24), 134.0368 (23), 259.0966 (20), 208.0745 (19), 123.0448 (15)
Cyc$_3$	$C_{18}H_{20}O_6$	331.1187	149.0605 (100), 271.0952 (80), 150.0672 (65), 135.0448 (54), 122.0375 (49), 331.1163 (49), 121.0304 (42), 134.0376 (31), 123.0440 (25), 259.0979 (24), 313.1081 (24), 256.0749 (23)
Cyc$_4$	$C_{17}H_{18}O_6$	317.1028	135.0445 (100), 123.0453 (67), 121.0300 (44), 151.0752 (31), 107.0500 (29), 317.1004 (27), 149.0601 (27), 257.0810 (26), 122.0371 (24), 273.1119 (24), 177.0545 (18), 109.0298 (15)
Cyc$_5$	$C_{18}H_{16}O_6$	327.0875	268.0725 (100), 267.0655 (56), 312.0615 (54), 327.0862 (53), 121.0284 (47), 283.0956 (43), 211.0756 (25), 147.0442 (22), 251.0707 (20), 239.0716 (15)
E$_1$	$C_{23}H_{24}O_8$	427.1393	381.0959 (100), 366.0730 (82), 265.0508 (50), 237.0542 (37), 266.0586 (35), 353.0667 (31), 294.0525 (28), 427.1361 (23), 338.0775 (22), 322.0843 (21), 293.0497 (21), 221.0594 (21), 249.0546 (17)
E$_2$	$C_{23}H_{26}O_8$	429.1549	246.0516 (100), 261.0758 (73), 174.0310 (20), 307.1173 (18), 200.0116 (17)
E$_3$	$C_{21}H_{22}O_8$	401.1242	147.0442 (100), 220.0738 (94), 311.0910 (47), 296.0681 (42), 268.0730 (31), 119.0494 (23), 191.0345 (22), 174.0307 (19), 357.1324 (16)

[a]For compound structures, see Figure 5. [b]Values in parentheses indicate relative intensities.

(negative ionization mode) produced a quasimolecular ion with m/z 331 $[M - H]^-$ or a loss of 54 mass units compared to the parent structure. The molecular mass was once again confirmed by GC-MS of the trimethylsilylated compound (see Figure 4). In addition to the molecular ion, m/z 620, the fragment ion at m/z 267 stemming from the formation of a resonance-stabilized A-ring carbocation via cleavage of the β-bond between C7 and C8 of the A-ring moiety was diagnostic, as well as a following fragment reduced by 88 mass units (here m/z 179) often observed in trimethylsilylated phenolic compounds with two vicinal hydroxyl substituents.[34] NMR data (see Tables 1 and 2) confirmed that **Cyc$_3$** had been formed by O-demethylation and decarboxylation of the ferulate A-unit, in addition to reduction of the propenyl side chain on the B-unit. This structure (see Figure 5) was confirmed by high-resolution MS and MS/MS results (see Table 3), which produced an exact mass of m/z 331.1187 $[M - H]^-$, with no observable deviation from the theoretical result for $C_{18}H_{19}O_6$ ($[M - H]^-$) in MS mode and only 2.9 ppm intensity-weighted error (calculated from 16 fragments) in MS/MS mode. The time-course appearance of **Cyc$_3$** showed that, following its initial appearance between 6 and 20 h, its concentration continued to gradually rise throughout the incubation (see Figure 6B).

A similar kinetic pattern was observed for the metabolite **Cyc$_4$**. The LC retention time of **Cyc$_4$** was 15.4 min, and the compound produced a UV absorption maximum at 280 nm with no absorption above 300 nm. The LC-ESI-MS quasimolecular ion (m/z 317 $[M - H]^-$) and GC-MS analysis of the trimethylsilylated compound (molecular ion at m/z 678, see Figure 4) indicated a loss of 68 mass units compared to 8−5c-DFA. The same characteristic GC-MS fragment ions of the trimethylsilylated compound, m/z 267 and 179, were observed, pointing to an A-ring structure similar to **Cyc$_3$**. NMR analysis (see Tables 1 and 2) confirmed these results, showing that **Cyc$_4$** was formed by O-demethylation of both the A- and B-rings, decarboxylation of the A-unit, and reduction of the B-unit propenyl side chain (Figure 5). High-resolution MS results were also satisfactory (see Table 3), with the measured exact mass of m/z 317.1028 $[M - H]^-$ varying from the theoretical calculated

DOI: 10.1021/acs.jafc.5b03234
J. Agric. Food Chem. 2015, 63, 7975−7985

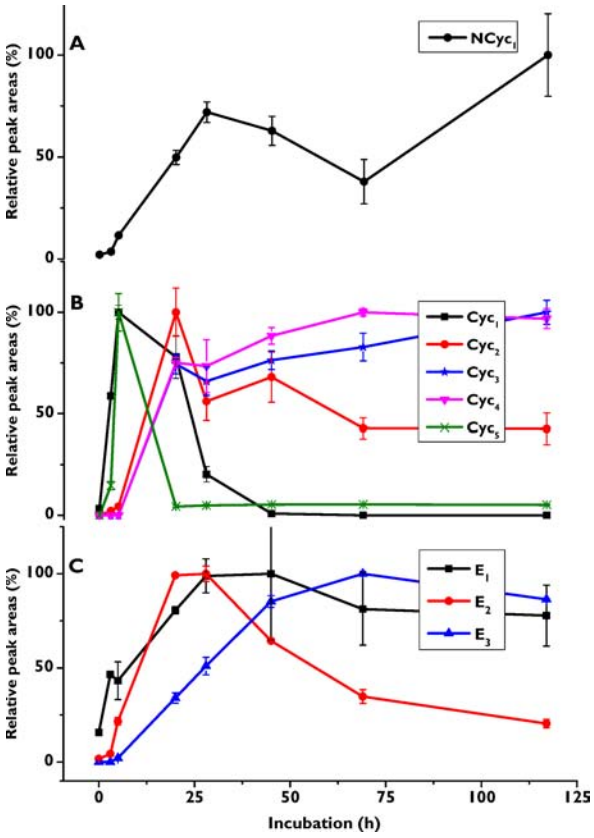

Figure 6. Time course of appearance of 8−5-coupled dehydrodiferulate (DFA) metabolites during the *scaled-up* trial. Relative peak areas were calculated as (LC-PDA peak area at time point/maximum peak area of compound during incubation) × 100. Error bars represent the range from two incubation replicates. Metabolite structures are provided in Figure 5. Abbreviations used: c, cyclic; nc, noncyclic. (A) Appearance of 8−5nc-DFA's metabolite, **NCyc$_1$**, during incubation with human fecal suspension. (B) Appearance of metabolites of 8−5c-DFA during incubation with human fecal suspension. (C) Appearance of metabolites of 8−5c-DFA diethyl ester during incubation with human fecal suspension.

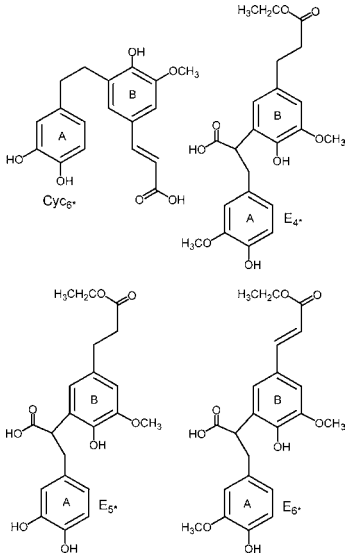

Figure 7. Tentative structures of four additional metabolites of 8−5-coupled dehydrodiferulate (DFA) compounds following incubation with human fecal microbiota. *Proposed structures are based only on GC-EI-MS fragmentation, and structures different from those shown are possible. **E** compounds: metabolites of 8−5-cyclic DFA diethyl ester; **Cyc** compounds: metabolites of 8−5-cyclic DFA.

mass for $C_{17}H_{17}O_6$ ($[M - H]^-$) by only −0.8 ppm in MS mode and 2.8 ppm in MS/MS mode (21 fragment ions).

The final fully characterized 8−5c-DFA metabolite, **Cyc$_5$** (LC retention time: 21.0 min), had a UV absorption maximum at 322 nm, an LC-ESI-MS (negative ionization mode) quasimolecular ion of *m/z* 327 $[M - H]^-$, and a GC-MS molecular ion of the trimethylsilylated compound of *m/z* 616. NMR analysis provided the exact structure, a singly demethylated metabolite of 8−5dc-DFA (see Figure 5 for metabolite structure). The exact mass of the isolated substance as determined by high-resolution MS was *m/z* 327.0875 $[M - H]^-$, which differed from the theoretical calculated mass for $C_{18}H_{15}O_6$ ($[M - H]^-$) by only 0.3 ppm. The intensity-weighted average error in MS/MS mode was 3.0 ppm (19 fragment ions).

A sixth metabolite of 8−5c-DFA, **Cyc$_{6*}$**, was observed in GC-MS analysis, but we were unable to preparatively isolate sufficient amounts of this compound for unambiguous NMR-based structure characterization. However, a *tentative* structure (see Figure 7, please note that the asterisk in the structure's name indicates that the structure must be treated as indefinite and that other structures are possible) can be proposed based on the EI mass spectrum of the trimethylsilylated compound (Figure 4). Because the compound showed the same base fragment as **Cyc$_3$** and **Cyc$_4$** (*m/z* 267, arising from cleavage of the *β*-alkyl bond linking the A- and B-rings to form a strongly resonance-stabilized carbocation on the A-ring moiety), a following fragment reduced by 88 mass units, here *m/z* 179, indicating two phenolic trimethylsilylated vicinal hydroxyl substituents,[34] and a molecular ion of *m/z* 618, two mass units less than **Cyc$_3$**, the compound is likely **Cyc$_3$**'s precursor with an unreduced propenyl side chain on the ferulate B-unit. The maximum GC-MS peak area for this compound was observed at the 6 h incubation point and then dropped off gradually (data not shown), further supporting the idea that this compound is a precursor to **Cyc$_3$**, which first appeared later, in the 20 h incubation samples.

Conversion of the Diethyl Ester of 8−5-Cyclic Dehydrodiferulic Acid by Human Intestinal Microbiota. Incubation of 8−5c-DFA diethyl ester with human fecal microbiota produced several metabolites, three of which were isolated and fully characterized: **E$_1$**, **E$_2$**, and **E$_3$** (see Figure 5 for structures and Figure 6C for the metabolites' time course of appearance). **E$_1$** was detected almost immediately following addition of fecal suspension to the sample (however, the formation required the presence of fecal suspension: no **E$_1$** was detected in the fecal-free control incubation), reaching maximum concentration at 28 h and remaining constant throughout the rest of the incubation. The structure had a UV absorption maximum at 328 nm, an LC-ESI-MS quasimolecular ion at *m/z* 427 $[M - H]^-$ (retention time: 35.6 min), and a GC-MS molecular ion of the trimethylsilylated compound at *m/z* 572 (Figure 4), indicating a loss of 14 mass units from the parent substrate. NMR experiments (see Tables 1 and 2) showed that, compared to the parent structure, **E$_1$** was demethylated on the A-ring. The structure (see Figure 5) was confirmed by high-resolution MS (see Table 3), displaying an exact mass of *m/z* 427.1393 $[M - H]^-$, with only −1.3 ppm difference in MS mode from the theoretical value for $C_{23}H_{23}O_8$ ($[M - H]^-$) and 2.4 ppm intensity-weighted error in MS/MS mode (calculated from 27 fragments).

DOI: 10.1021/acs.jafc.5b03234
J. Agric. Food Chem. 2015, 63, 7975−7985

$\mathbf{E}_2$ was also produced rapidly (although not to the extent of $\mathbf{E}_1$, compare Figure 6C), first appearing in substantial amounts at the 6 h time point, reaching maximum concentration at 24 h and steadily decreasing after 28 h. The compound eluted at 32.6 min on the LC system and had a UV absorption maximum at 329 nm and a quasimolecular ion of m/z 429 $[M - H]^-$, representing a difference of 12 mass units compared to the substrate. The molecular mass of 430 was consistent with the GC-MS results, which produced a molecular ion of the trimethylsilylated compound at m/z 646. As observed for other metabolites, the fragment ion at m/z 267 represents the formation of a resonance-stabilized A-ring carbocation via cleavage of the β-bond between C7 and C8 of the ferulate A-unit. NMR experiments (see Tables 1 and 2) showed that $\mathbf{E}_2$ had been formed from the parent compound by A-ring O-demethylation and reductive opening of the benzofuran ring (see Figure 5). High-resolution MS analysis was in accord with these results, producing an exact mass of m/z 429.1549 $[M - H]^-$, diverging from the theoretically calculated value for $C_{23}H_{25}O_8$ ($[M - H]^-$) by only −1.4 ppm in MS mode. MS/MS fragmentation (see Table 3) also produced only 3.5 ppm error (intensity-weighted, calculated from nine fragments).

$\mathbf{E}_3$ eluted at 23.2 min on the LC and produced a quasimolecular ion of m/z 401 $[M - H]^-$. GC-MS analysis of the trimethylsilylated compound resulted in a molecular ion of m/z 690 (see Figure 4), respectively. The compound absorbed UV energy at 326 nm, suggesting an intact propenyl side chain. On the other hand, the m/z 267 fragment ion in the GC-MS spectrum suggested a reduced ferulate A-ring unit, as observed for $\mathbf{E}_2$. Interpretation of the NMR data (see Tables 1 and 2) showed that, in comparison to $\mathbf{E}_2$, $\mathbf{E}_3$ had been de-esterified on the A-ring moiety (see Figure 5). Kinetic data (see Figure 6C) confirmed the hypothesis that $\mathbf{E}_3$ is formed from $\mathbf{E}_2$, with substantial detection of the compound first occurring after 24 h of incubation and maximum concentration levels at 72 h. The structure was confirmed by high-resolution MS experiments (see Table 3). The measured exact mass, m/z 401.1242 $[M - H]^-$, showed no measurable difference from the theoretical value for $C_{21}H_{21}O_8$ ($[M - H]^-$) in the MS mode and only 2.4 ppm intensity-weighted error in MS/MS mode (calculated from 12 fragments).

Three additional unique metabolites, $\mathbf{E}_{4*}$, $\mathbf{E}_{5*}$, and $\mathbf{E}_{6*}$, were detected in GC-MS analysis of the 8−5c-DFA diethyl ester incubation extracts, but were not isolated in sufficient quantities for NMR analysis. GC-MS fragmentation of the trimethylsilylated compounds (see Figure 4) enabled *tentative* structural proposals (see Figure 7). The first, $\mathbf{E}_{4*}$, which, like $\mathbf{E}_3$, was observed in the 24, 48, and 120 h incubation time points (data not shown), was, in contrast to $\mathbf{E}_3$, likely not demethylated on the A-ring, as indicated by the presence of the m/z 209 fragment, although a small amount of m/z 267 is also present in the spectrum. However, because the m/z 267 fragment was observed to be the dominant fragment in all confirmed structures displaying the necessary A-ring reduction and demethylation, it is more likely that the fragment represents a minor coelution. The molecular ion, m/z 634, would then represent single de-esterification, reductive ring-opening of the benzofuran moiety and reduction of the B-ring propenyl side chain. It was not possible to assign the position of single de-esterification, and it is possible that de-esterification occurred on the B-ring unit instead of the A-ring ferulate unit as depicted in Figure 7.

The EI spectrum of the trimethylsilylated $\mathbf{E}_{5*}$ indicates that the compound is likely identical to $\mathbf{E}_3$, except for reduction of the B-ring propenyl side chain (molecular ion m/z 692). Furthermore, the main fragment, m/z 267, and the following m/z 179 fragment are indicative of a reduced A-ring side chain and A-ring O-demethylation. The hypothesis that $\mathbf{E}_{5*}$ represents a further metabolism of $\mathbf{E}_3$ also corresponds to the observation that the structure was first observed at the 24 h incubation time point and then persisted throughout the rest of the incubation (data not shown). It is possible that de-esterification occurred on the B-ring unit instead of the A-ring ferulate unit as depicted in Figure 7.

$\mathbf{E}_{6*}$ was observed in small amounts at both the 48 and 117 h time points (data not shown). The EI spectrum of the trimethylsilylated compound (Figure 4) presented m/z 209 as the main fragment ion, pointing toward reductive opening of the benzofuran moiety and an intact methoxy substituent on the A-ring. The molecular ion, m/z 632, could correspond to the tentative structure depicted in Figure 7, with single de-esterification (de-esterification could also have occurred on the B-ring unit instead of the A-ring ferulate unit as depicted in Figure 7) and reductive opening of the benzofuran structural component. The emergence of this singly de-esterified, but otherwise relatively unmetabolized structure so late in the incubation time frame stands in contrast to the other 8−5c-DFA diethyl ester metabolites, where de-esterification was observed primarily after or concurrently with other metabolic transformations such as O-demethylation and reduction. Finally, in addition to the six metabolites of 8−5c-DFA diethyl ester described above, we were able to confirm the formation of trace amounts of $\mathbf{Cyc}_2$, $\mathbf{Cyc}_3$, and $\mathbf{Cyc}_4$ after 48 h of incubation of the esterified substrate. The presence of these fully de-esterified compounds establishes the ability of human gut microbiota to release 8−5-coupled diferulates from their ester linkages.

DISCUSSION

Numerous potential health benefits have been suggested for the hydroxycinnamate components of cereal grains,[19] of which DFAs form a substantial portion. Insoluble dietary fiber from maize grain, for example, contains over 12.5 mg DFAs/g fiber.[35] At 35% to 59% of the total DFAs, the 8−5-coupled DFA regioisomer is the most abundant DFA regioisomer in all major cereals.[27] Because the majority of 8−5-coupled DFAs are consumed esterified to cereal arabinoxylans, their bioavailability depends upon their release from the fiber matrix by the cooperative action of microbial xylanases and esterases in the large intestine. As previously demonstrated,[21,28] human intestinal microbiota can cleave ester linkages to DFAs, which we confirmed in this study by the isolation and complete structural characterization of a singly de-esterified metabolite, $\mathbf{E}_3$, the tentative identification of three additional singly esterified metabolites, $\mathbf{E}_{4*}$, $\mathbf{E}_{5*}$, and $\mathbf{E}_{6*}$, and the detection of several fully de-esterified compounds ($\mathbf{Cyc}_2$, $\mathbf{Cyc}_3$, and $\mathbf{Cyc}_4$) following incubation of a model DFA ester, 8−5c-DFA diethyl ester, with a human fecal inoculum. However, although these findings confirm that gut bacterial esterases can cleave ester bonds attached to 8−5coupled-DFAs, the physiochemical properties (especially solubility and steric considerations) of the model diethyl ester used in this study cannot be expected to induce metabolite formation as accurately as an authentic 8−5c-DFA diarabinose ester. O-Demethylation tended to occur faster than hydrogenation of the B-ring propenyl side chain in the esterified compound, as evidenced by $\mathbf{E}_1$, $\mathbf{E}_2$, $\mathbf{E}_3$, and $\mathbf{E}_{5*}$, which all display A-ring O-demethylation without hydrogenation of the B-ring. However, the tentative structure $\mathbf{E}_{4*}$ appeared to be an exception to this pattern, similar to nonesterified, monomeric ferulic acid and 5−5-DFA, where

DOI: 10.1021/acs.jafc.5b03234
J. Agric. Food Chem. 2015, 63, 7975−7985

side chain hydrogenation occurs faster than O-demethylation.[25,28] We also observed reductive opening of the benzofuran ring in several metabolites, although the unambiguous characterization of E_1, which displayed an intact benzofuran ring, showed that benzofuran ring-opening, although rapid, is not spontaneous.

The results from the free acid 8−5c-DFA, which was variously transformed by human gut microbiota via side chain hydrogenation, reductive opening of the benzofuran ring, and O-demethylation, showed no clear preference for the rate of O-demethylation compared to side chain hydrogenation. Several decarboxylated metabolites were characterized that likely arose from microbial metabolism of 8−5dc-DFA, whose decarboxylation occurred independently from microbial metabolism. However, because the 8−5dc-DFA originated under physiologically relevant temperature and pH conditions, these metabolites may be regarded as authentic end points of 8−5c-DFA's exposure to the colonic environment and microbiota, provided decarboxylation was not accelerated by ingredients in the brain-heart medium.

Incubation of 8−5nc-DFA, a non-native byproduct of 8−5c-DFA, produced only one metabolite, substantially fewer than the six metabolites from 8−5c-DFA. In particular, O-demethylation of 8−5nc-DFA was not observed. The reason for the lack of metabolite diversity for 8−5nc-DFA compared to 8−5c-DFA is unknown. These results underline the fine-tuned structure dependence of microbial metabolism and the danger of assuming that comparable structures will be similarly metabolized without laboratory confirmation.

Dehydroxylation was not observed in any metabolites from any of the three substrate compounds. In contrast, bacterial metabolism of ferulic acid monomers results in dehydroxylation of the phenyl ring, producing 3-phenylpropionic acid as an end product.[26] Dehydroxylation was also observed in the bacterial metabolism of 8−*O*−4-DFA, although this occurred only following cleavage of the dimeric DFAs to monomers. Similar to our results with 8−5-coupled DFAs, the 5−5-DFA regioisomer was not susceptible to dehydroxylation.[25] No cleavage to monomers was observed for any of the three 8−5-coupled standard compounds, in contrast to 8−*O*−4-DFA, which is completely converted to monomeric metabolites by human gut microbiota.[25]

Substantial metabolite formation was observed within 28 h from each of the 8−5-coupled DFA standard compounds investigated in this study. Importantly, de-esterification was not necessary for metabolism of the 8−5c-DFA diethyl ester compound (although de-esterification was observed to occur to a measurable extent within this time frame), indicating that the release of already-metabolized 8−5-coupled DFAs instead of only the free acids is theoretically possible. While colonic transit time is influenced by many factors, including age, physical activity level, and diet, with reported literature values ranging from approximately 23 to 30 h in healthy individuals consuming their routine diets,[36,37] these results indicate that 8−5-coupled DFAs are susceptible to microbial degradation within the colonic transit time span. Detection of the described microbial metabolites in urine or plasma (as conjugates) will be necessary to confirm the physiological relevance of these *in vitro* results.

AUTHOR INFORMATION

Corresponding Author

*Tel: (+49) 721 608 42936. Fax: (+49) 721 608 47255. E-mail: mirko.bunzel@kit.edu.

Notes

The authors declare no competing financial interest.

ACKNOWLEDGMENTS

The authors thank Luisa Martinez-Postigo for experimental support.

ABBREVIATIONS

BSTFA, *N*,*O*-bis(trimethylsilyl)trifluoracetamide; c, cyclic; DAD, diode array detection; dc, decarboxylated; DFA, dehydrodiferulate; MS, mass spectrometry; nc, noncyclic; TFA, trifluoroacetic acid; THF, tetrahydrofuran; ToF, time-of-flight

REFERENCES

(1) Ishii, T. Structure and functions of feruloylated polysaccharides. *Plant Sci.* **1997**, *127*, 111−127.

(2) Levigne, S. V.; Ralet, M.-C. J.; Quemener, B. C.; Pollet, B. N.-L.; Lapierre, C.; Thibault, J.-F. J. Isolation from sugar beet cell walls of arabinan oligosaccharides esterified by two ferulic acid monomers. *Plant Physiol.* **2004**, *134*, 1173−1180.

(3) Bunzel, M. Chemistry and occurrence of hydroxycinnamate oligomers. *Phytochem. Rev.* **2010**, *9*, 47−64.

(4) Allerdings, E.; Ralph, J.; Schatz, P. F.; Gniechwitz, D.; Steinhart, H.; Bunzel, M. Isolation and structural identification of diarabinosyl 8-O-4-dehydrodiferulate from maize bran insoluble fibre. *Phytochemistry* **2005**, *66*, 113−124.

(5) Guo, M.; Petrofsky, K.; Zhang, L.; Chen, P.; Hohn, A.; Youn, M.; Gallaher, D.; Liu, R.; Faubion, J.; Bunzel, M.; Marquart, L.; Ruan, R. Improving the functionality and bioactivity in wheat bran. *FASEB J.* **2011**, *25*, 581.5.

(6) Ralet, M.-C.; André-Reloux, G.; Quemener, B.; Thibault, J. F. Sugar beet (*Beta vulgaris*) pectins are covalently cross-linked through diferulic bridges in the cell wall. *Phytochemistry* **2005**, *66*, 2800−2814.

(7) Wefers, D.; Gmeiner, B. M.; Tyl, C. E.; Bunzel, M. Characterization of diferuloylated pectic polysaccharides from quinoa (Chenopodium quinoa WILLD.). *Phytochemistry* **2015**, *116*, 320−328.

(8) Saulnier, L.; Crepeau, M. J.; Lahaye, M.; Thibault, J. F.; Garcia-Conesa, M. T.; Kroon, P. A.; Williamson, G. Isolation and structural determination of two 5,5′-diferuloyl oligosaccharides indicate that maize heteroxylans are covalently cross-linked by oxidatively coupled ferulates. *Carbohydr. Res.* **1999**, *320*, 82−92.

(9) Bunzel, M.; Allerdings, E.; Ralph, J.; Steinhart, H. Cross-linking of arabinoxylans via 8−8-coupled diferulates as demonstrated by isolation and identification of diarabinosyl 8−8(cyclic)-dehydrodiferulate from maize bran. *J. Cereal Sci.* **2008**, *47*, 29−40.

(10) Buanafina, M. d. O. Feruloylation in grasses: Current and future perspectives. *Mol. Plant* **2009**, *2*, 861−872.

(11) Zamora-Ros, R.; Rothwell, J. A.; Scalbert, A.; Knaze, V.; Romieu, I.; Slimani, N.; Fagherazzi, G.; Perquier, F.; Touillaud, M.; Molina-Montes, E.; Huerta, J. M.; Barricarte, A.; Amiano, P.; Menendez, V.; Tumino, R.; de Magistris, M. S.; Palli, D.; Ricceri, F.; Sieri, S.; Crowe, F. L.; Khaw, K. T.; Wareham, N. J.; Grote, V.; Li, K.; Boeing, H.; Forster, J.; Trichopoulou, A.; Benetou, V.; Tsiotas, K.; Bueno-de-Mesquita, H. B.; Ros, M.; Peeters, P. H.; Tjonneland, A.; Halkjaer, J.; Overvad, K.; Ericson, U.; Wallstrom, P.; Johansson, I.; Landberg, R.; Weiderpass, E.; Engeset, D.; Skeie, G.; Wark, P.; Riboli, E.; Gonzalez, C. A. Dietary intakes and food sources of phenolic acids in the European Prospective Investigation into Cancer and Nutrition (EPIC) study. *Br. J. Nutr.* **2013**, *110*, 1500−1511.

(12) Mellen, P. B.; Walsh, T. F.; Herrington, D. M. Whole grain intake and cardiovascular disease: A meta-analysis. *Nutr. Metab. Cardiovasc. Dis.* **2008**, *18*, 283−290.

(13) Erkkilä, A. T.; Herrington, D. M.; Mozaffarian, D.; Lichtenstein, A. H. Cereal fiber and whole-grain intake are associated with reduced progression of coronary-artery atherosclerosis in postmenopausal women with coronary artery disease. *Am. Heart J.* **2005**, *150*, 94−101.

DOI: 10.1021/acs.jafc.5b03234
J. Agric. Food Chem. 2015, 63, 7975−7985

(14) de Munter, J. S. L.; Hu, F. B.; Spiegelman, D.; Franz, M.; van Dam, R. M. Whole grain, bran, and germ intake and risk of type 2 diabetes: a prospective cohort study and systematic review. *PLoS Med.* **2007**, *4*, e261.
(15) Ardisson Korat, A. V.; Willett, W. C.; Hu, F. B. Diet, lifestyle, and genetic risk factors for type 2 diabetes: a review from the Nurses' Health Study, Nurses' Health Study 2, and Health Professionals' Follow-up Study. *Curr. Nutr. Rep.* **2014**, *3*, 345−354.
(16) Schatzkin, A.; Mouw, T.; Park, Y.; Subar, A. F.; Kipnis, V.; Hollenbeck, A.; Leitzmann, M. F.; Thompson, F. E. Dietary fiber and whole-grain consumption in relation to colorectal cancer in the NIH-AARP Diet and Health Study. *Am. J. Clin. Nutr.* **2007**, *85*, 1353−1360.
(17) Egeberg, R.; Olsen, A.; Loft, S.; Christensen, J.; Johnsen, N. F.; Overvad, K.; Tjonneland, A. Intake of wholegrain products and risk of colorectal cancers in the Diet, Cancer and Health cohort study. *Br. J. Cancer* **2010**, *103*, 730−734.
(18) Jensen, M. K.; Koh-Banerjee, P.; Hu, F. B.; Franz, M.; Sampson, L.; Grønbæk, M.; Rimm, E. B. Intakes of whole grains, bran, and germ and the risk of coronary heart disease in men. *Am. J. Clin. Nutr.* **2004**, *80*, 1492−1499.
(19) Vitaglione, P.; Napolitano, A.; Fogliano, V. Cereal dietary fibre: a natural functional ingredient to deliver phenolic compounds into the gut. *Trends Food Sci. Technol.* **2008**, *19*, 451−463.
(20) Andreasen, M. F.; Kroon, P. A.; Williamson, G.; Garcia-Conesa, M. T. Esterase activity able to hydrolyze dietary antioxidant hydroxycinnamates is distributed along the intestine of mammals. *J. Agric. Food Chem.* **2001**, *49*, 5679−5684.
(21) Andreasen, M. F.; Kroon, P. A.; Williamson, G.; Garcia-Conesa, M. T. Intestinal release and uptake of phenolic antioxidant diferulic acids. *Free Radical Biol. Med.* **2001**, *31*, 304−314.
(22) Kern, S. M.; Bennett, R. N.; Mellon, F. A.; Kroon, P. A.; Garcia-Conesa, M. T. Absorption of hydroxycinnamates in humans after high-bran cereal consumption. *J. Agric. Food Chem.* **2003**, *51*, 6050−6055.
(23) Russell, W. R.; Scobbie, L.; Chesson, A. Structural modification of phenylpropanoid-derived compounds and the effects on their participation in redox processes. *Bioorg. Med. Chem.* **2005**, *13*, 2537−2546.
(24) Andreasen, M. F.; Landbo, A.-K.; Christensen, L. P.; Hansen, Å.; Meyer, A. S. Antioxidant effects of phenolic rye (*Secale cereale* L.) extracts, monomeric hydroxycinnamates, and ferulic acid dehydrodimers on human low-density lipoproteins. *J. Agric. Food Chem.* **2001**, *49*, 4090−4096.
(25) Braune, A.; Bunzel, M.; Yonekura, R.; Blaut, M. Conversion of dehydrodiferulic acids by human intestinal microbiota. *J. Agric. Food Chem.* **2009**, *57*, 3356−3362.
(26) Russell, W. R.; Scobbie, L.; Chesson, A.; Richardson, A. J.; Stewart, C. S.; Duncan, S. H.; Drew, J. E.; Duthie, G. G. Anti-inflammatory implications of the microbial transformation of dietary phenolic compounds. *Nutr. Cancer* **2008**, *60*, 636−642.
(27) Jilek, M. L.; Bunzel, M. Dehydrotriferulic and dehydrodiferulic acid profiles of cereal and pseudocereal flours. *Cereal Chem.* **2013**, *90*, 507−514.
(28) Chesson, A.; Provan, G. J.; Russell, W. R.; Scobbie, L.; Richardson, A. J.; Stewart, C. Hydroxycinnamic acids in the digestive tract of livestock and humans. *J. Sci. Food Agric.* **1999**, *79*, 373−378.
(29) Ralph, J.; Garcia-Conesa, M. T.; Williamson, G. Simple preparation of 8−5-coupled diferulate. *J. Agric. Food Chem.* **1998**, *46*, 2531−2532.
(30) Dobberstein, D.; Bunzel, M. Separation and detection of cell wall-bound ferulic acid dehydrodimers and dehydrotrimers in cereals and other plant materials by reversed phase high-performance liquid chromatography with ultraviolet detection. *J. Agric. Food Chem.* **2010**, *58*, 8927−8935.
(31) Gottlieb, H. E.; Kotlyar, V.; Nudelman, A. NMR chemical shifts of common laboratory solvents as trace impurities. *J. Org. Chem.* **1997**, *62*, 7512−7515.
(32) Ralph, J.; Quideau, S.; Grabber, J. H.; Hatfield, R. D. Identification and synthesis of new ferulic acid dehydrodimers present in grass cell walls. *J. Chem. Soc., Perkin Trans. 1* **1994**, 3485−3498.
(33) Nugent, S. G.; Kumar, D.; Ramption, D. S.; Evans, D. F. Intestinal luminal pH in inflammatory bowel disease: possible determinants and implications for therapy with aminosalicylates and other drugs. *Gut* **2001**, *48*, 571−577.
(34) Maul, R.; Schebb, N. H.; Kulling, S. E. Application of LC and GC hyphenated with mass spectrometry as tool for characterization of unknown derivatives of isoflavonoids. *Anal. Bioanal. Chem.* **2008**, *391*, 239−250.
(35) Bunzel, M.; Ralph, J.; Marita, J. M.; Hatfield, R. D.; Steinhart, H. Diferulates as structural components in soluble and insoluble cereal dietary fibre. *J. Sci. Food Agric.* **2001**, *81*, 653−660.
(36) Timm, D.; Willis, H.; Thomas, W.; Sanders, L.; Boileau, T.; Slavin, J. The use of a wireless motility device (SmartPill®) for the measurement of gastrointestinal transit time after a dietary fibre intervention. *Br. J. Nutr.* **2011**, *105*, 1337−1342.
(37) Farmer, A. D.; Mohammed, S. D.; Dukes, G. E.; Scott, S. M.; Hobson, A. R. Caecal pH is a biomarker of excessive colonic fermentation. *World J. Gastroenterol.* **2014**, *20*, 5000−5007.

DOI: 10.1021/acs.jafc.5b03234
J. Agric. Food Chem. 2015, 63, 7975−7985

tumor necrosis factor (TNF)-α, mouse interferon (IFN)-γ, and mouse interleukin (IL)-1β were purchased from Nanjing Jiancheng Bioengineering Institute (Nanjing, China). All other reagents used in this study were of analytical grade.

Preparation of SCP-1. *Extraction of SCP.* Briefly, fresh *S. constricta* was collected and washed carefully with water. After removal of the shells and impurities, the flesh was crushed by a high-speed disintegrator, and the homogenate was kept in 85% of ethanol (v/v) for 1 week to defat and remove pigments and small molecule substances. The collected flesh was then air-dried at 50 °C and used for the extraction. The dried powder of *S. constricta* was dissolved in deionized water (20 mL/g (v/w) for ratio of water/material) containing 2.0% papain. After incubation at 50 °C for 6 h, the mixture was boiled for 10 min and centrifuged at 3040*g* for 20 min. The supernatant was precipitated with 3 volumes of dehydrated ethanol (ethanol final concentration, 75%) at 4 °C for 12 h, and the resulting precipitates were obtained by centrifugation at 3040*g* for 15 min. The precipitates were dissolved in deionized water, the pH was adjusted with 1.0 M HCl to 2.5, and the mixtures were kept at 4 °C for 4 h and then centrifuged at 3040*g* for 15 min to remove acidic albumen.[24] The supernatant was adjusted to neutral and precipitated again with dehydrated ethanol. Finally, the precipitates were collected by centrifugation at 3040*g* for 15 min and vacuum freeze-dried, affording the crude SCP.

Purification of Crude SCP. The crude SCP was applied to a DEAE-52 cellulose column (2.6 × 50 cm) and eluted stepwise with NaCl solutions from low to high concentration (0, 0.1, and 0.3 M) at a flow rate of 1.0 mL/min. The fractions were collected (10 mL/tube) and checked by tracking the absorbance at 490 nm using the phenol−sulfuric acid method.[25] The major polysaccharide fraction (F-1) was collected, dialyzed, freeze-dried, and loaded onto a column (1.6 × 60 cm) of Sephadex G-100. The column was eluted with deionized water at a flow rate of 15 mL/h, and the elution was checked as described above. As a result, one purified fraction was collected and vacuum freeze-dried, affording SCP-1.

Determination of Contents of Carbohydrate, Protein, Uronic Acid, and Sulfuric Radical. The contents of carbohydrate, protein, uronic acid, and sulfuric radical in SCP-1 were determined according to the reported methods.[26]

Determination of Homogeneity and Molecular Weight. The homogeneity and molecular weight of SCP-1 were determined by high-performance gel permeation chromatography (HPGPC) with an Agilent 1200 series apparatus (Agilent Technologies, Santa Clara, CA, USA) equipped with a Shodex OHpak SB-804 HQ column (8 × 300 mm). The column was eluted with 0.1 M NaCl at a flow rate of 0.5 mL/min, and the column temperature was kept constant at 35 °C. The molecular weight and polydispersity index (M_w/M_n) were estimated by HPGPC, and the column was calibrated by standard D-series dextrans (D-2, D-3, D-4, D-5, D-6, D-7, and D-8) with known molecular weight.

Analysis of Monosaccharide Composition. The monosaccharide composition of SCP-1 was analyzed by HPLC as described previously.[27] The polysaccharide solution (100 μL, 5.0 mg/mL) was mixed with 100 μL of 4.0 M trifluoroacetic acid (TFA) and hydrolyzed at 120 °C for 2 h. The resulting solution was cooled to room temperature, and the excess TFA was removed by repeated codistillations with methanol. The residue was dissolved with deionized water (100 μL) and mixed with 100 μL of 0.6 M NaOH, and half of the mixture was derivatized with 0.5 M methanol solution of PMP (100 μL) for 100 min at 70 °C. After neutralization with 0.3 M HCl, the resultant solution was concentrated to dryness under reduced pressure. Deionized water and chloroform were added to the residue, followed by vortexing. The water phase was filtered through a 0.45 μm membrane and then analyzed by an Agilent HPLC using Eclipse Plus C18 column (4.6 × 250 mm, 5 μm, Agilent) and ultraviolet (UV) detector at a flow rate of 1.0 mL/min at 30 °C. The mobile phase contained 83% phosphate-buffered saline (PBS, 0.1 M, pH 6.7) and 17% acetonitrile (v/v). In a similar manner, the monosaccharide standards were PMP-labeled and analyzed by HPLC.

FT-IR Spectral Analysis. The polysaccharide sample was incorporated into potassium bromide (KBr, spectroscopic grade) and pressed into a 1 mm pellet. The IR spectrum of SCP-1 in a range of 400−4000 cm^{-1} was recorded with a Nicolet 6700 FT-IR spectrometer (Thermo Fisher Scientific Inc., Waltham, MA, USA).

Methylation and GC-MS Analysis. SCP-1 was methylated according to the reported method.[28,29] Briefly, SCP-1 (dried) was dissolved in dimethyl sulfoxide (DMSO), and NaOH was then added. The mixture was treated for 20 min under ultrasonic condition. Then, SCP-1 was methylated under darkness by the addition of methyl iodide with ultrasonic for 2 h, and the remaining methyl iodide was decomposed by the addition of deionized water. The methylated sample was extracted with trichloromethane and evaporated to dryness by a stream of nitrogen. Then, the dried methylated sample was hydrolyzed by 2 M TFA at 120 °C for 2 h, reduced with sodium borodeuteride at 50 °C for 2 h, and acetylated with pyridine and acetic anhydride at 100 °C for 1 h. Deionized water and dichloromethane were added to the acetylated derivatives, and the organic phase was dried under nitrogen, dissolved in dichloromethane, and analyzed by GC-MS. The GC-MS analysis was performed on a HP6890GC/5973MS system equipped with an ion trap MS detector and fitted with a HP-5MS quartz capillary column (30 mm × 0.25 mm, 0.25 μm film thickness, 150−200 °C at 2 °C/min and then 200−280 °C at 5 °C/min).

NMR Analysis. NMR analysis was performed at 298 K on a Bruker DRX Avance III 500 MHz spectrometer (Bruker Corp., Karlsruhe, Germany) equipped with a $^{13}C/^{1}H$ dual probe in FT mode. The freeze-dried SCP-1 was dissolved in deuterium (D_2O, 99.9% D) and lyophilized three times to replace exchangeable protons with D_2O. The lyophilized sample was then dissolved in D_2O at a concentration of 100 mg/mL and analyzed by NMR spectrometer. All chemical shifts are relative to internal sodium 2,2-dimethyl-isotope 2-silapentane-5-sulfonate (DSS).

Assay of Immunomodulatory Activity in Vitro of SCP-1. *Cell Culture.* The murine macrophage RAW264.7 cells were cultured in DMEM supplemented with 10% (v/v) new bovine calf serum and 1% (v/v) penicillin−streptomycin at 37 °C in a humidified atmosphere containing 5% CO_2. The cells were cultivated in sterile tissue culture flasks and subcultured for experimentation.

Assay of Cell Viability. The viability of RAW264.7 cells was assessed by using MTT-based colorimetric assay.[30] Briefly, 100 μL/well of RAW264.7 cell suspension was plated in a 96-well culture plate and incubated (37 °C, 5% CO_2) for 12 h. The adherent RAW264.7 cells were washed twice by PBS and then incubated with medium containing various concentrations of sample (12.5, 25.0, 50.0, 100.0, and 200.0 μg/mL) as well as complete medium alone (blank control) or LPS (10.0 μg/mL, positive control) for 48 h. The stimulated cells were washed twice by PBS, and 200 μL of MTT solution (0.5 mg/mL) was added to each well. After further incubation for 4 h, 150 μL of DMSO was added to each well to dissolve the formazen crystals. The absorbance (Abs) at 570 nm was determined by using a microplate reader. The cell viability was calculated by using the following equation:

$$\text{cell viability} = \text{Abs}_{\text{sample}}/\text{Abs}_{\text{blank control}}$$

Assay of Phagocytosis. The influence of SCP-1 on phagocytic activity was investigated by using the neutral red phagocytosis assay.[31] As described above, confluent cultures of RAW264.7 cells in 96-well plates were exposed to complete medium alone or different concentrations of sample or LPS solution and incubated for 48 h at 37 °C. After removal of supernatant, the nonadherent cells were removed by washing twice with PBS, and 100 μL of neutral red solution was added to each well. The plates were incubated for 1 h, followed by the removal of the supernatant. To remove the excess neutral red solution, the cells were washed with PBS twice. After that, 100 μL of cell lysate (1.0 M acetic acid/ethanol = 1:1, v/v) was then added to each well. After incubation overnight at room temperature, the Abs at 540 nm of each well was measured by a microplate reader. The phagocytosis index of macrophages was calculated by using the following equation:

$$\text{phagocytosis index} = \text{Abs}_{\text{sample}}/\text{Abs}_{\text{blank control}}$$

Assay of Acid Phosphatase. The effect of SCP-1 on acid phosphatase activity of RAW264.7 cells was investigated according to the reported method.[32] The cultured RAW264.7 cells were treated with complete

DOI: 10.1021/acs.jafc.5b03306
J. Agric. Food Chem. 2015, 63, 7986−7994

medium alone or SCP-1 solution (12.5, 25.0, 50.0, 100.0, and 200.0 μg/mL) or LPS (10.0 μg/mL). After incubation for 48 h at 37 °C, the supernatant was aspirated from the wells, 25 μL of 1% Triton X-100 and 150 μL of 1.0 mg/mL *p*-nitrophenyl phosphate (substrate of acid phosphatase) were added to each well, and the plate was incubated at 37 °C for 1 h. The reaction was terminated by the addition of 50 μL of 3.0 M NaOH solution, and the Abs of the culture well was measured at 405 nm by spectrophotometer. The index of acid phosphatase activity was calculated by using the following equation:

$$\text{index of acid phosphatase activity} = \text{Abs}_{\text{sample}}/\text{Abs}_{\text{blank control}}$$

Assay of Cytokine and NO. The levels of NO, TNF-α, IFN-γ, and IL-1β in the supernatants of the RAW264.7 cells from each group were determined by using ELISA kits according to the manufacturers' protocols.

Statistical Analysis. Data were expressed as means ± standard deviations (SD), and a one-way ANOVA was performed, followed by Duncan's multiple-range tests. *P* values of <0.05 were considered to be statistically significant. All statistical analyses were performed using SPSS software version 19.0 (Chicago, IL, USA).

RESULTS AND DISCUSSION

Preparation of SCP-1. The crude SCP was obtained in a yield of 18.4% from dried *S. constricta* through steps of extraction, deproteination, and ethanol precipitation. The crude SCP was first separated through anion-exchange chromatography of DEAE-52, affording two independent elution peaks as detected by the phenol−sulfuric acid assay (Figure 1A). Notably, F-1 (eluted by deionized water) was the main polysaccharide fraction of crude SCP. In the present study, the leading polysaccharide fraction (F-1) was further purified by Sephadex G-100 size exclusion chromatography. As shown in Figure 1B, it yielded a single elution peak, named SCP-1.

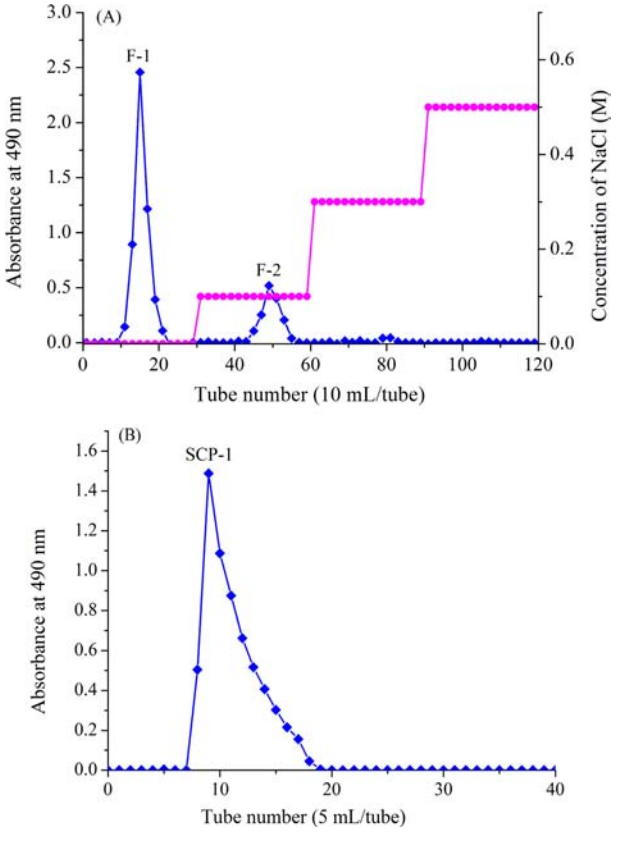

Figure 1. Stepwise elution curve of crude SCP on a DEAE-52 column (A) and elution profile of F-1 on a Sephadex G-100 column (B).

Characterization of SCP-1. *Contents of Carbohydrate, Protein, Uronic Acid, and Sulfuric Radical in SCP-1.* The contents of carbohydrate, uronic acid, and sulfuric radical in SCP-1 were 99.96, 0.13, and 0.20%, respectively. However, SCP-1 had a negative response to the Bradford test and showed no absorption at 280 or 260 nm in the UV spectrum, indicating the absence of protein or nucleic acid in SCP-1.

Molecular Weight and Monosaccharide Composition of SCP-1. As shown in Figure 2, SCP-1 was eluted as a single and symmetrical peak from HPGPC on a Shodex OHpak SB-804 HQ column, indicating that SCP-1 was a homogeneous polysaccharide. The average molecular weight of SCP-1 was estimated to be 15.63 kDa on the basis of calibration with standard D-series dextrans. M_w/M_n was used to determine the width of the molecular weight distribution, which represents the dispersibility and homogeneity of a polymer.[33] As a result, the M_w/M_n for SCP-1 was 1.695 estimated by GPC software version B01.01 (Agilent, USA). Furthermore, the monosaccharide composition of SCP-1 was analyzed by HPLC. Obviously, SCP-1 was composed of only glucose (Figure 3), indicating that it is a homopolysaccharide.

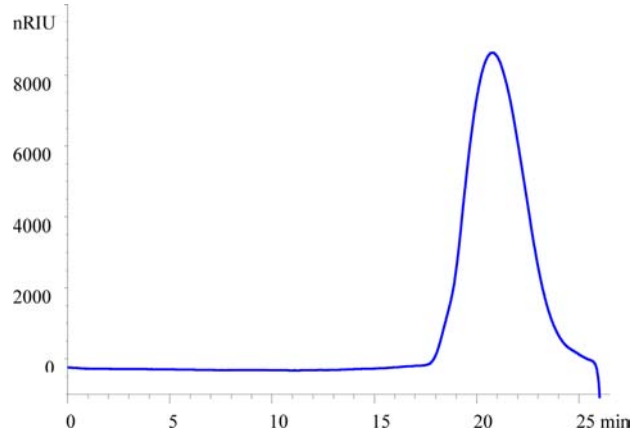

Figure 2. HPGPC profile of SCP-1.

FT-IR Spectrum of SCP-1. The FT-IR spectrum of SCP-1 is shown in Figure 4. The bands at 3359.26 and 2928.54 cm^{-1} were ascribed to the stretching vibrations of O−H and C−H, respectively.[34] The band in the region of 1641.02 cm^{-1} was due to the associated water. Absorption at 849.72 cm^{-1} indicated the presence of an α-type glycosidic linkage, which is consistent

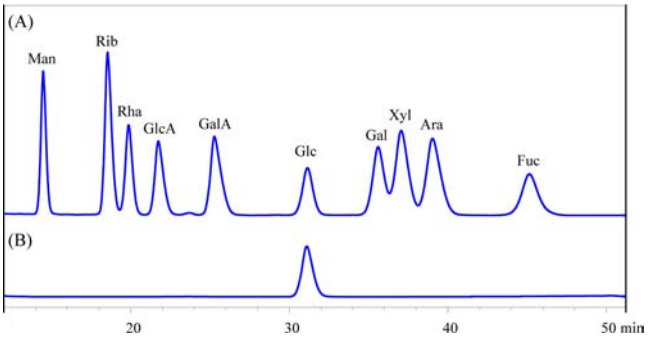

Figure 3. Chromatograms of PMP derivatives of mixed monosaccharide standards (A) and SCP-1 (B).

DOI: 10.1021/acs.jafc.5b03306
J. Agric. Food Chem. 2015, 63, 7986−7994

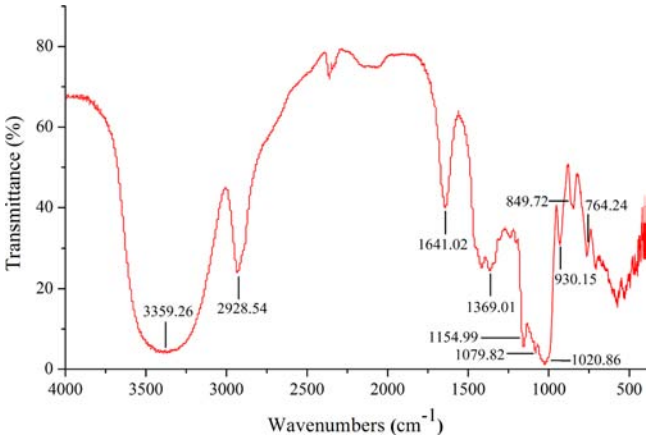

Figure 4. FT-IR spectrum of SCP-1.

with its high positive value of optical rotation ($[\alpha]_D^{25}$ = +172.27° (*c* 0.1, water)).[35] The absorptions at 1020.86, 1079.82, and 1154.99 cm^{-1} also indicated the presence of a pyranose form of sugars.[36,37] The absorption bands at 930.15, 849.72, and 764.24 cm^{-1} suggested that SCP-1 was a D-glucopyranose derivative.[38] Therefore, it can be concluded that SCP-1 belongs to the α-type glucans with a pyran group.

Methylation Analysis of SCP-1. The methylation of SCP-1 yielded *O*-methyl-D-glucans, and the hydrolysis of the methylated polysaccharide and the acetylation of the methyl-D-glucosides yielded residues of 2,3,4,6-tetra-, 2,3,6-tri-, and 2,3-di-*O*-methylglucose, based on GC-MS analysis. The molar ratio of main chain to branch was estimated as (3.87 + 0.74):1.00 from the peak areas (Table 1). These results indicated that SCP-1 had (1→4)-glucose linkage in the main chain and (1→6) glucose linkage in the branch.

NMR Analysis of SCP-1. The structural features of SCP-1 were further elucidated by NMR spectral analysis. The ^{1}H NMR spectrum of SCP-1 is shown in Figure 5A. The three anomeric protons at 5.36, 5.39, and 4.96 ppm were assigned to →4)-α-D-Glc*p*→1 (residue A), →4,6)-α-D-Glc*p*(1→ (residue B), and α-D-Glc*p*(1→ (residue C), respectively.[39] Consistent with the presence of the FT-IR band at 849.72 cm^{-1} and relatively high positive value of optical rotation ($[\alpha]_D^{25}$ = +172.27°(*c* 0.1, water)), the results demonstrated that the sugar residues were α-glycosidically linked.[38,40] Furthermore, the molar proportion of the residues ((A + B)/C) was appropriately 5:1 based on the ratio of peak area of the integration of the H-1 signal for A, B, and C residues. The result is in agreement with the overall substitution pattern observed by methylation analysis (appropriately 4.61:1). The chemical shifts of 3.3−4.0 ppm (in overlapping peaks) were assigned to the protons of carbons C-2−C-6 of the glycosidic rings.[41]

In the ^{13}C NMR spectrum of SCP-1 (Figure 5B), the anomeric carbon signals for the residues of →4)-α-D-Glc*p*→1, →4,6)-α-D-Glc*p*(1→, and α-D-Glc*p*(1→ were assigned at 102.43, 102.43, and 101.19 ppm, respectively.[42] The typical signal of O-substituted C-4 (79.52 ppm) supported the high proportion of α-D-(1→4) linkages in linear arrangement that was previously demonstrated by GC-MS analysis.[43] The branching of C-6 was shown by the signals of O-substituted C-6 and unsubstituted C-6 at 73.84 and 63.14 ppm, respectively.[44,45] All of the chemical shifts of SCP-1 in the ^{1}H and ^{13}C NMR spectra are summarized in Table 2, which are assigned on the data of COSY, ROESY, TOCSY, HMBC (data not shown), and HSQC (Figure 5C) spectra and with reference to previous studies.[45−49] As a result of all of the structural information described above, a possible structural scheme for SCP-1 is proposed as Figure 6.

Immunomodulatory Activity in Vitro of SCP-1. *Effect of SCP-1 on Macrophage Viability.* In contrast to β-glucan, research on the biological activity of α-glucan is scant. To date, it has been reported that α-glucan obtained from different sources has potent biological activities such as anticancer and immunostimulatory activities.[50,51] A growing body of research confirm that the immunostimulatory activity of polysaccharide may be one of the mechanisms in its antitumor, anticomplementary, and anti-inflammatory functions.[32,52] Accordingly, the immunostimulatory activity is considered to be one of the most important biological activities of polysaccharides. Therefore, in the present study, the action of SCP-1 on some parameters of immune activation was evaluated.

The immunological action of polysaccharides may begin with the activation of effector cells such as macrophages.[53] Macrophages play an important role in host defense as part of the nonspecific defense (innate immunity) as well as specific defense (adaptive immunity). Macrophages not only maintain homeostasis but also provide a defense against pathogens and invading cells, such as cancer cells.[54] The viability of macrophages in vitro can be served as an indicator of immunoactivation. In this study, activation of RAW264.7 cells by SCP-1 was investigated by MTT assay. As shown in Figure 7A, it was found that SCP-1 significantly increased the viability of RAW264.7 cells in a dose-dependent manner from 12.5 to 100.0 μg/mL. SCP-1 (≥25.0 μg/mL) significantly promoted the viability of RAW264.7 cells compared with the blank control ($P < 0.01$).

Effect of SCP-1 on Macrophages Phagocytosis. The phagocytosis of macrophages represents the first and imperative step in immune response,[55] and one of the most remarkable characteristics of activated macrophages is an increase in phagocytosis.[56] Thus, the phagocytic ability of RAW264.7 cells was measured via neutral red uptake. As shown in Figure 7B, SCP-1 showed a promoting effect on macrophage phagocytosis in the dose range of 12.5−200.0 μg/mL. The results indicated that SCP-1 might play an important role in the phagocytosis of macrophages in the immune response as other polysaccharides from mollusk (for example, *Glossaulax didyma*) do.[57,58]

Effect of SCP-1 on Acid Phosphatase Activity. As a marker enzyme of lysosome, acid phosphatase is a signal enzyme for macrophage activation.[59] Significant change in an acid

Table 1. Methylation Analysis and Mode of Linkage of SCP-1

methylated alditol acetate[a]	type of linkage	relative retention time[b]	molar ratio	mass fragments (*m*/*z*)
2,3,4,6-Me4-Glc	terminal Glc*p*	1.00	1.00	43, 58, 71, 101, 117, 129, 145, 161, 205
2,3,6-Me3-Glc	1,4-linked Glc*p*	1.31	3.87	43, 58, 71, 87, 101, 113, 117, 129, 131, 143, 161, 173, 233
2,3-Me2-Glc	1,4,6-linked Glc*p*	1.64	0.74	43, 58, 85, 101, 117, 127, 142, 159, 201, 261

[a]2,3,4,6-Me4-Glc = 1,5-di-*O*-acetyl-2,3,4,6-tetra-*O*-methylglucose, etc. [b]Retention times are given relative to that of 1,5-di-*O*-acetyl-2,3,4,6-tetra-*O*-methyl-D-glucitol on HP-5MS.

DOI: 10.1021/acs.jafc.5b03306
J. Agric. Food Chem. 2015, 63, 7986−7994

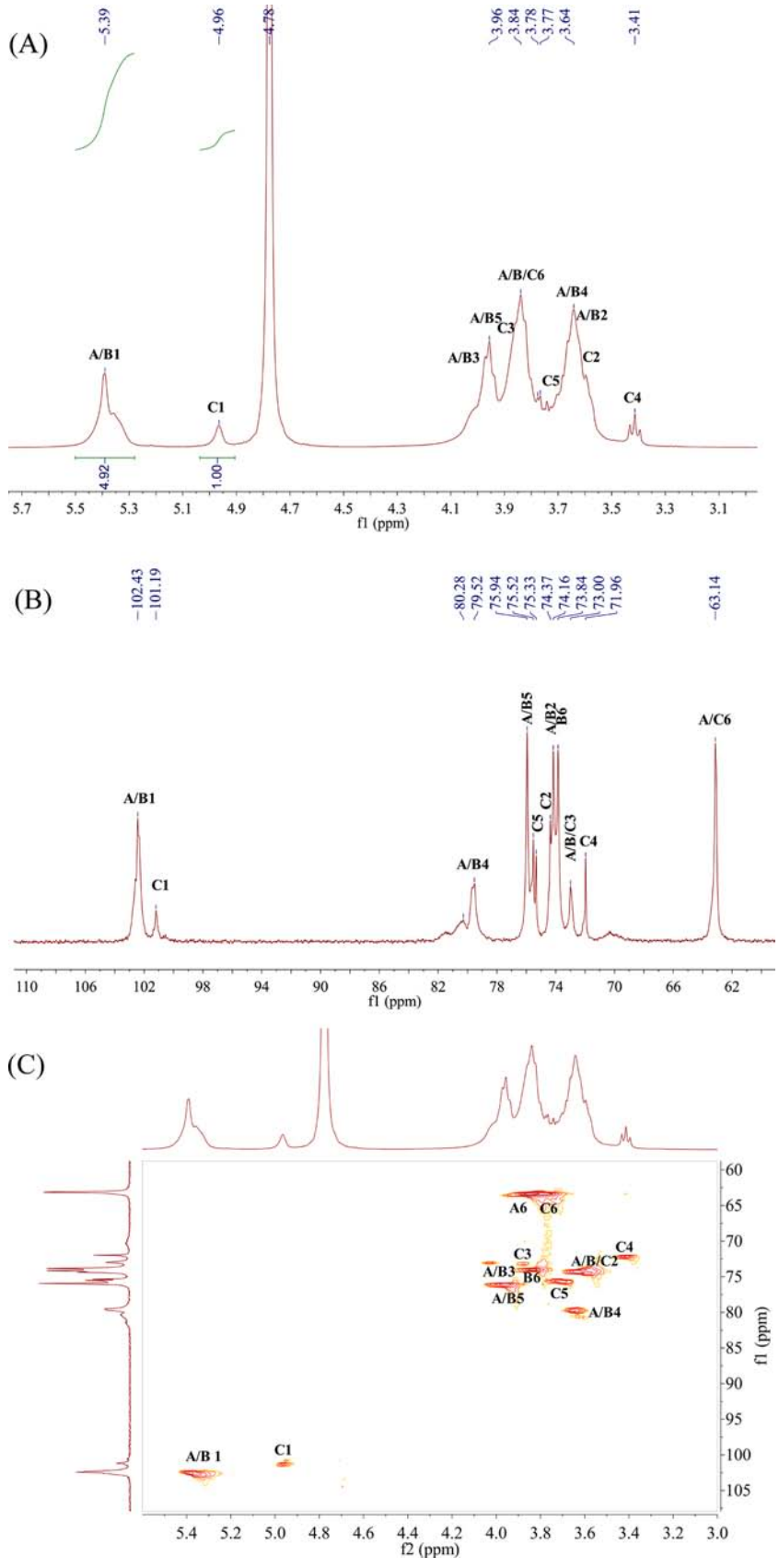

Figure 5. ^{1}H NMR (A), ^{13}C NMR (B), and HSQC (C) spectra of SCP-1. A, B, and C in the spectra represent →4)-*α*-D-Glc*p*→ 1, →4,6)-*α*-D-Glc*p*(1→, and *α*-D-Glc*p*(1→ , respectively.

phosphatase activity is associated with the activation or inhibition of macrophages.[60] The immunocompetence of macrophages can therefore be represented by the activity of acid phosphatase. In this study, the effect of SCP-1 on acid phosphatase activity of

DOI: 10.1021/acs.jafc.5b03306
J. Agric. Food Chem. 2015, 63, 7986−7994

Table 2. Summary of ^{1}H and ^{13}C NMR Chemical Shifts for SCP-1 in D_2O

		chemical shifts[a] (ppm)						
sugar residue		1	2	3	4	5	6a	6b
residue A, →4)-α-D-Glc*p*→1	H	5.36	3.61	4.02	3.64	3.96	3.85	3.72
	C	102.43	74.16	73.00	**79.52**	75.94	63.14	
residue B, →4,6)-α-D-Glc*p*(1→	H	5.39	3.61	4.02	3.64	3.96	3.85	
	C	102.43	74.16	73.00	**79.52**	75.94	**73.84**	
residue C, α-D-Glc*p*(1→	H	4.96	3.58	3.87	3.41	3.73	3.78	3.88
	C	101.19	74.37	72.96	71.96	75.33	63.14	

[a]The 500 MHz NMR spectra were recorded at 298 K. All chemical shifts are relative to internal sodium 2,2-dimethyl-isotope 2-silapentane-5-sulfonate (DSS) at 0 ppm. Values in boldface indicate positions bearing substitution by sugar residue.

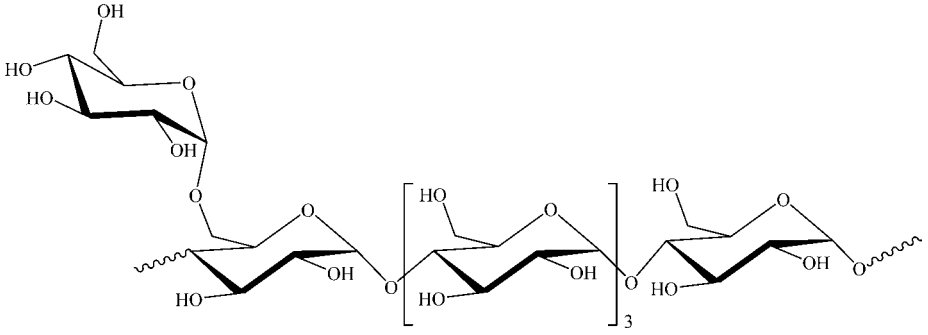

Figure 6. Predicted structure of SCP-1.

RAW264.7 cells is depicted in Figure 7C. The acid phosphatase activity of macrophages increased with the increase of concentration of SCP-1 from 12.5 to 100.0 μg/mL, whereas it tended to decline at a concentration of 200.0 μg/mL.

Effects of SCP-1 on Production of NO and Cytokines. Activated macrophages secrete NO and cytokines including TNF-α, IFN-γ, and IL-1β that are directly involved in removing pathogens and inhibiting cancer cells.[61−63] NO is a highly reactive free radical and plays a pivotal role in host defense.[64] It is also one important cytotoxic mediator contributing to the antimicrobial and tumoricidal activities of the macrophages.[65] It has been reported that various natural polysaccharides derived from animals, fungi, bacteria, and plants can stimulate NO production by macrophages.[66] TNF-α, produced chiefly by activated macrophages, is able to induce the expression of a number of other immunoregulatory and inflammatory mediators and to inhibit tumorigenesis.[67−69] The most important cytokine responsible for cell-mediated immunity is IFN-γ.[62] IL-1β is a pro-inflammatory cytokine responding to infection, injury, and immunological challenges.[70] Therefore, we further investigated the immunocompetence of SCP-1 in activating RAW264.7 cells by monitoring its effects on the production of NO and cytokines including TNF-α, IFN-γ, and IL-1β.

The stimulatory effect of SCP-1 on macrophage NO production is shown in Figure 7D. SCP-1 increased NO production in RAW264.7 cells in a dose-dependent manner. Compared with the untreated group, NO concentration was significantly increased due to the treatment of SCP-1 (12.5−200.0 μg/mL, $P < 0.05$). The concentration of NO reached 12.78 μmol/L after treatment by 100.0 μg/mL of SCP-1, and it is even higher than that for the positive control (LPS, 10.0 μg/mL). Therefore, SCP-1 can increase the NO production, which may play an important role in the host defense system.

The effects of SCP-1 on the production of TNF-α, IFN-γ, and IL-1β are shown in Table 3. Untreated RAW264.7 cells (control) secreted minimum levels of TNF-α, IFN-γ, and IL-1β, whereas the production of cytokines (TNF-α, IFN-γ, and IL-1β) in RAW264.7 cells was enhanced in a dose-dependent manner due to the treatment of SCP-1. Compared with the control, SCP-1 significantly increased the production of TNF-α from 50.0 to 200.0 μg/mL ($P < 0.01$) and the production of IFN-γ and IL-1β from 12.5 to 200.0 μg/mL ($P < 0.01$). These results indicate that SCP-1 can promote the secretion of cytokines in RAW264.7 cells. A report in the literature also provides evidence that α-D-glucan from *Strongylocentrotus nudus* eggs enhances the secretion of pro-inflammatory cytokines such as TNF-α and IL-1β.[71]

It is well-known that bioactivities of polysaccharides are related to their molecular weights, chemical components, branch degrees, type of monosaccharide, and glycosidic linkages.[26] In the present study, the α-glucan from *S. constricta*, SCP-1, had a linear backbone of (1→4)-linked α-D-Glc*p* residue with one branch, α-D-Glc*p*, attached to the main chain by a (1→6) glycosidic bond at every five α-D-Glc*p* units, which was characterized by methylation analysis and NMR spectroscopy. As mentioned above, the contents of carbohydrate, uronic acid, and sulfuric radical in SCP-1 were 99.96, 0.13, and 0.20%, respectively. Thus, the potent immunomodulatory activity of SCP-1 might not be related to the presence of uronic acid and sulfate in SCP-1 due to their low contents. In contrast, the potent immunomodulatory activity of SCP-1 should be caused and influenced by its fine structures such as (1→4)- and (1→6)-glycosidic linkages, molecular size, and the length of side chains, because increasing evidence has demonstrated that α-glucans with various structural features obtained from different organisms such as *Tricholoma matsutake*, *Ipomoea batatas*, and *Arca subcrenata* Lischke show different immunostimulatory potentials.[51,72,73] The structural and conformational features related to the immunostimulatory activity of SCP-1 need to be further studied.

In summary, for the first time, a purified neutral polysaccharide of SCP-1 was successfully obtained from *S. constricta* and characterized. SCP-1 is an α-glucan with a molecular weight of

DOI: 10.1021/acs.jafc.5b03306
J. Agric. Food Chem. 2015, 63, 7986−7994

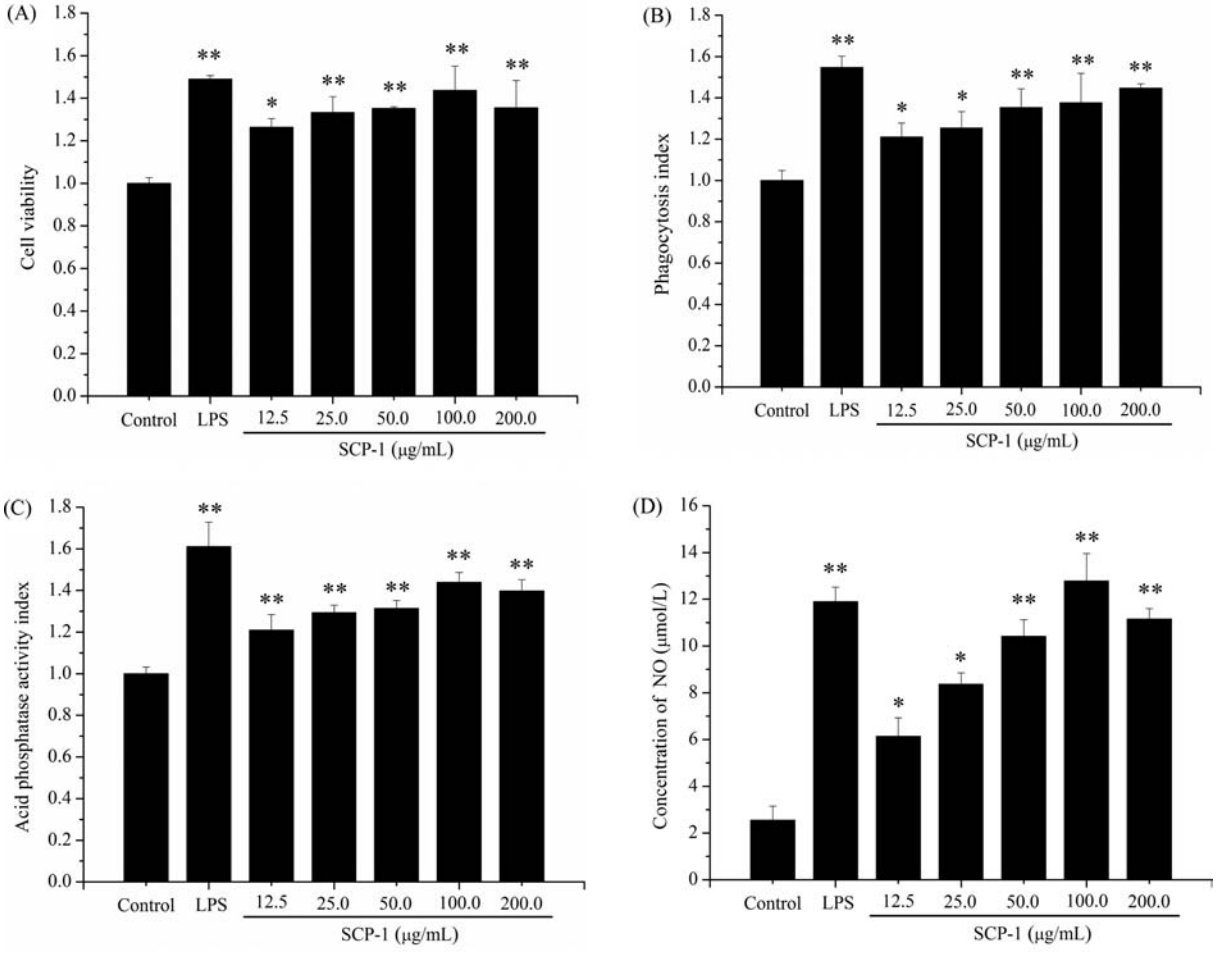

Figure 7. Effects of SCP-1 on cell viability (A), phagocytosis (B), acid phosphatase activity (C), and production of NO (D) of RAW264.7 macrophages in vitro. Values are presented as means ± SD (n = 6); * and ** represent $P < 0.05$ and $P < 0.01$ compared with control, respectively.

Table 3. Effects of SCP-1 on the Cytokine Secretion of RAW264.7 Macrophage Cells[a]

treatment	TNF-α (pg/mL)	IFN-γ (pg/mL)	IL-1β (pg/mL × 10^{-1})
control	1.86 ± 0.49	11.79 ± 0.98	1.97 ± 0.18
LPS	9.74 ± 0.64**	39.66 ± 0.41**	15.03 ± 0.85**
SCP-1			
12.5 μg/mL	3.51 ± 0.39	21.47 ± 1.22**	4.26 ± 0.40**
25.0 μg/mL	5.03 ± 0.44*	25.02 ± 1.13**	6.41 ± 0.23**
50.0 μg/mL	7.36 ± 0.66**	28.95 ± 1.62**	9.98 ± 0.03**
100.0 μg/mL	8.63 ± 0.86**	36.03 ± 0.93**	12.52 ± 0.37**
200.0 μg/mL	8.01 ± 0.12**	35.20 ± 0.90**	13.13 ± 0.53**

[a]Values are presented as means ± SD (n = 6), * and ** represent $P < 0.05$ and $P < 0.01$ compared with control, respectively.

15.63 kDa that is composed of a α-(1→4)-linked backbone with a side chain of α-(1→6)-linked residue. Moreover, SCP-1 was demonstrated to have a potent immunostimulating activity by enhancing the viability of macrophages, strengthening macrophages to devour neutral red, increasing the activity of acid phosphatase, and promoting the production of NO and cytokines in macrophages. All of these results suggested that SCP-1 had a beneficial effect on immunostimulating activity. The next studies will be focused on the immunomodulatory activity in vivo and the possible mechanisms of immunomodulatory action of SCP-1.

AUTHOR INFORMATION

Corresponding Author

*(X.Z.) Fax: +86 25 84396791. E-mail: zengxx@njau.edu.cn.

Funding

This work was supported by grants from the Specialized Research Fund for the Doctoral Program of Higher Education (20130097110021), the National Undergraduate Student Research Training (SRT) Program (201410307053), and a project funded by the Priority Academic Program Development of Jiangsu Higher Education Institutions.

Notes

The authors declare no competing financial interest.

DOI: 10.1021/acs.jafc.5b03306
J. Agric. Food Chem. 2015, 63, 7986−7994

REFERENCES

(1) Song, J. J.; Li, L.; Liu, Z. G.; Li, Q. Y.; Ran, P. X. Sequence analysis and expression of a cDNA clone encoding tropomysin in *Sinonovacula constricta*. *Mol. Biol. Rep.* **2009**, *36*, 315−321.

(2) Li, C. H.; Li, H.; Su, X. R.; Li, T. W. Identification and characterization of a clam ferritin from *Sinonovacula constricta*. *Fish Shellfish Immunol.* **2011**, *30*, 1147−1151.

(3) Niu, D. H.; Li, J. L.; Liu, D. B. Polymorphic microsatellite loci for population studies of the razor clam, *Sinonovacula constricta*. *Conserv. Genet.* **2008**, *9*, 1393−1394.

(4) Niu, D. H.; Feng, B. B.; Liu, D. B.; Zhong, Y. M.; Shen, H. D.; Li, J. L. Significant genetic differentiation among ten populations of the razor clam *Sinonovacula constricta* along the coast of China revealed by a microsatellite analysis. *Zool. Stud.* **2012**, *51*, 406−414.

(5) Feng, B. B.; Dong, L. L.; Niu, D. H.; Meng, S. S.; Zhang, B.; Liu, D. B.; Hu, S. N.; Li, J. L. Identification of immune genes of the Agamaki clam (*Sinonovacula constricta*) by sequencing and bioinformatic analysis of ESTs. *Mar. Biotechnol.* **2010**, *12*, 282−291.

(6) Yan, H. W.; Li, Q.; Liu, W. G.; Yu, R. H.; Kong, L. F. Seasonal changes in reproductive activity and biochemical composition of the razor clam *Sinonovacula constricta* (Lamarck 1818). *Mar. Biol. Res.* **2010**, *6*, 78−88.

(7) Fan, D. P.; Pan, L. Q.; Ma, S.; Dong, S. L. Effects of temperature on oxygen consumption rate and ammonia excretion rate of *Sinonovacula constricta*. *J. Ocean Univ. Qingdao* **2002**, *32*, 56−62.

(8) Yan, H. W.; Li, Q.; Liu, W. G.; Ke, Q. Z.; Yu, R. H.; Kong, L. F. Seasonal changes of oestradiol-17β and testosterone concentrations in the gonad of the razor clam *Sinonovacula constricta* (Lamarck, 1818). *J. Mollus. Stud.* **2011**, *77*, 116−122.

(9) Kong, Z. L.; Chiang, L. C.; Fang, F.; Shinohara, K.; Pan, P. Immune bioactivity in shellfish toward serum-free cultures human cell lines. *Biosci., Biotechnol., Biochem.* **1997**, *61*, 24−28.

(10) Niu, D. H.; Jin, K.; Wang, L.; Feng, B. B.; Li, J. L. Molecular characterization and expression analysis of four cathepsin L genes in the razor clam. *Fish Shellfish Immunol.* **2013**, *35*, 581−588.

(11) Niu, D. H.; Jin, K.; Wang, L.; Sun, F. Y.; Li, J. L. Identification of cathepsin B in the razor clam *Sinonovacula constricta* and its role in innate immune responses. *Dev. Comp. Immunol.* **2013**, *41*, 94−99.

(12) Woo, E. R.; Kim, W. S.; Kim, Y. S. Virus-cell fusion inhibitory activity for the polysaccharides from various Korea edible clams. *Arch. Pharmacal Res.* **2001**, *24*, 514−517.

(13) Tzianabos, A. O. Polysaccharide immunomodulators as therapeutic agents: structural aspects and biologic function. *Clin. Microbiol. Rev.* **2000**, *13*, 523−533.

(14) Bertozzi, C. R.; Kiessling, L. L. Chemical glycobiology. *Science* **2001**, *291*, 2357−2264.

(15) Schepetkin, I. A.; Quinn, M. T. Botanical polysaccharides: macrophage immunomodulation and therapeutic potential. *Int. Immunopharmacol.* **2006**, *6*, 317−333.

(16) Cunningham-Rundles, S.; Lin, H.; Ho-Lin, D.; Dnistrian, A.; Cassileth, B. R.; Perlman, J. M. Role of nutrients in the development of neonatal immune response. *Nutr. Rev.* **2009**, *67*, S152−S163.

(17) Wang, Y.; Fang, J. P.; Ni, X. Y.; Li, J.; Liu, Q.; Dong, Q.; Duan, J. Y.; Ding, K. Inducement of cytokine release by GFPBW2, a novel polysaccharide from fruit bodies of *Grifola frondosa*, through dectin-1 in macrophages. *J. Agric. Food Chem.* **2013**, *61*, 11400−11409.

(18) Ruthes, A. C.; Smiderle, F. R.; Iacomini, M. D-Glucans from edible mushrooms: a review on the extraction, purification and chemical characterization approaches. *Carbohydr. Polym.* **2015**, *117*, 753−761.

(19) Dai, Z. Y.; Zhang, H.; Zhang, Y. P.; Wang, H. H. Chemical properties and immunostimulatory activity of a water-soluble polysaccharide from the clam of *Hyriopsis cumingii* Lea. *Carbohydr. Polym.* **2009**, *77*, 365−369.

(20) Qiao, D. L.; Luo, J. G.; Ke, C. L.; Sun, Y.; Ye, H.; Zeng, X. X. Immunostimulatory activity of the polysaccharides from *Hyriopsis cumingii*. *Int. J. Biol. Macromol.* **2010**, *47*, 676−680.

(21) Qiao, D. L.; Wei, C. B.; Ke, C. L.; Zeng, X. X. Effects of *Hyriopsis cumingii* polysaccharides on angiogenesis, macrophage chemotaxis, proliferation and phagocytosis. *Food Funct.* **2015**, *6*, 869−877.

(22) Jing, Y. S.; Zhu, J. H.; Liu, T.; Bi, S. X.; Hu, X. J.; Chen, Z. Y.; Song, L. Y.; Lv, W. J.; Yu, R. M. Structural characterization and biological activities of a novel polysaccharide from cultured *Cordyceps militaris* and its sulfated derivative. *J. Agric. Food Chem.* **2015**, *63*, 535−544.

(23) Xiao, J. B.; Jiang, H. X. A review on the structure-function relationship aspect of polysaccharides from tea materials. *Crit. Rev. Food Sci. Nutr.* **2015**, *55*, 930−938.

(24) Wu, M. Y.; Xu, S. M.; Zhao, J. H.; Kang, H.; Ding, H. Physicochemical characteristics and anticoagulant activities of low molecular weight fractions by free-radical depolymerization of a fucosylated chondroitin sulphate from sea cucumber *Thelenata ananas*. *Food Chem.* **2010**, *122*, 716−723.

(25) Dubois, M.; Gilles, K. A.; Hamilton, J. K.; Rebers, P. A.; Smith, F. Colorimetric method for determination of sugars and related substances. *Anal. Chem.* **1956**, *28*, 350−356.

(26) Yuan, Q. X.; Xie, Y. F.; Wang, W.; Yan, Y. H.; Ye, H.; Jabbar, S.; Zeng, X. X. Extraction optimization, characterization and antioxidant activity *in vitro* of polysaccharides from mulberry (*Morus alba* L.) leaves. *Carbohydr. Polym.* **2015**, *128*, 52−62.

(27) Dai, J.; Wu, Y.; Chen, S. W.; Zhu, S.; Yin, H. P.; Wang, M.; Tang, J. Sugar compositional determination of polysaccharides from *Dunaliella salina* by modified RP-HPLC method of precolumn derivatization with 1-phenyl-3-methyl-5-pyrazolone. *Carbohydr. Polym.* **2010**, *82*, 629−635.

(28) Gong, L.; Zhang, H.; Niu, Y. G.; Chen, L.; Liu, J.; Alaxi, S.; Shang, P. P.; Yu, W. J.; Yu, L. L. A novel alkali extractable polysaccharide from *Plantago asiatic* L. seeds and its radical-scavenging and bile acid-binding activities. *J. Agric. Food Chem.* **2015**, *63*, 569−577.

(29) Ciucanu, I.; Costello, C. E. Elimination of oxidative degradation during the per-*O*-methylation of carbohydrates. *J. Am. Chem. Soc.* **2003**, *125*, 16213−16219.

(30) Li, J. E.; Nie, S. P.; Xie, M. Y.; Li, C. Isolation and partial characterization of a neutral polysaccharide from *Mosla chinensis* Maxim. cv. Jiangxiangru and its antioxidant and immunomodulatory activities. *J. Funct. Foods* **2014**, *6*, 410−418.

(31) Dai, Z. Q.; Su, D.; Zhang, Y.; Sun, Y.; Hu, B.; Ye, H.; Jabbar, S.; Zeng, X. X. Immunomodulatory activity in vitro and in vivo of verbascose from mung beans (*Phaseolus aureus*). *J. Agric. Food Chem.* **2014**, *62*, 10727−10735.

(32) Wang, M. C.; Jiang, C. X.; Ma, L. P.; Zhang, Z. J.; Cao, L.; Liu, J.; Zeng, X. X. Preparation, preliminary characterization and immunostimulatory activity of polysaccharide fractions from the peduncles of *Hovenia dulcis*. *Food Chem.* **2013**, *138*, 41−47.

(33) Tsukamoto, T.; Hattori, M.; Sakabe, M.; Haginaka, J. Determination of the molecular mass of new L-fucose-containing glycosaminoglycan and its distribution by high-performance gel-permeation chromatography with laser light-scattering detection. *Anal. Sci.* **2001**, *17*, 555−558.

(34) Zhu, Y.; Li, Q.; Mao, G. H.; Zou, Y.; Feng, W. W.; Zheng, D. H.; Wang, W.; Zhou, L. L.; Zhang, T. X.; Yang, J.; Yang, L. Q.; Wu, X. Y. Optimization of enzyme-assisted extraction and characterization of polysaccharides from *Hericium erinaceus*. *Carbohydr. Polym.* **2014**, *101*, 606−613.

(35) Tsumuraya, Y.; Misaki, A.; Takaya, S.; Torii, M. A new fungal α-D-glucan, elsinan, elaborated by *Elsinoe leucospila*. *Carbohydr. Res.* **1978**, *66*, 53−65.

(36) Wang, Z. F.; Liu, Y.; Sun, Y. J.; Mou, Q.; Wang, B.; Zhang, Y.; Huang, L. J. Structural characterization of LbGp1 from the fruits of *Lycium barbarum* L. *Food Chem.* **2014**, *159*, 137−142.

(37) Sun, X.; Gao, R. L.; Xiong, Y. K.; Huang, Q. C.; Xu, M. Antitumor and immunomodulatory effects of a water-soluble polysaccharide from *Lilii Bulbus* in mice. *Carbohydr. Polym.* **2014**, *102*, 543−549.

(38) Barker, S. A.; Bourne, E. J.; Stacey, M.; Whiffen, D. H. Infra-red spectra of carbohydrates. Part I. Some derivatives of D-glucopyranose. *J. Chem. Soc.* **1954**, 171−176.

(39) Reddy, G. P.; Chang, C. C.; Bush, C. A. Determination by heteronuclear NMR spectroscopy of the complete structure of the cell wall polysaccharide of *Streptococcus sanguis* strain K103. *Anal. Chem.* **1993**, *65*, 913−921.

DOI: 10.1021/acs.jafc.5b03306
J. Agric. Food Chem. 2015, 63, 7986−7994

(40) Perepelov, A. V.; Senchenkova, S. N.; Torzewska, A.; Bartodziejska, B.; Shashkov, A. S.; Rozalski, A.; Knirel, Y. A. Structure of an O-acetylated acidic O-specific polysaccharide of *Proteus vulgaris* O46. *Carbohydr. Res.* **2000**, *328*, 229−234.
(41) Chauveau, C.; Talaga, P.; Wieruszeski, J. M.; Strecker, G.; Chavant, L. A water-soluble *β*-D-glucan from *Boletus erythropus*. *Phytochemistry* **1996**, *43*, 413−415.
(42) Norrild, J. C.; Eggert, H. Evidence for mono- and bisdentate boronate complexes of glucose in the furanose form. Application of $^{1}J_{C\text{-}C}$ coupling constants as a structural probe. *J. Am. Chem. Soc.* **1995**, *117*, 1479−1484.
(43) Seymour, F. R.; Knapp, R. D.; Nelson, T. E.; Pfannemuller, B. Structural analysis of comb-like, amylose derivatives by ^{13}C-N.M.R. spectroscopy. *Carbohydr. Res.* **1979**, *70*, 125−133.
(44) Pang, X. B.; Yao, W. B.; Yang, X. B.; Xie, C.; Liu, D.; Zhang, J. Purification, characterization and biological activity on hepatocytes of a polysaccharide from *Flammulina velutipes* mycelium. *Carbohydr. Polym.* **2007**, *70*, 291−297.
(45) Wu, Y. L.; Sun, C. R.; Pan, Y. J. Studies on isolation and structural features of a polysaccharide from the mycelium of a Chinese edible fungus (*Cordyceps sinensis*). *Carbohydr. Polym.* **2006**, *63*, 251−256.
(46) Bittencourt, V. C.; Figueiredo, R. T.; da Silva, R. B.; Mourao-Sa, D. S.; Fernandez, P. L.; Sassaki, G. L.; Mulloy, B.; Bozza, M. T.; Barreto-Bergter, E. An *α*-glucan of *Pseudallescheria boydii* is involved in fungal phagocytosis and Toll-like receptor activation. *J. Biol. Chem.* **2006**, *281*, 22614−22623.
(47) Niu, Y. G.; Wang, H. Y.; Xie, Z. H.; Whent, M.; Gao, X. D.; Zhang, X.; Zou, S.; Yao, W. B.; Yu, L. L. Structural analysis and bioactivity of a polysaccharide from the roots of *Astragalus membranaceus* (Fisch) Bge. var. *mongolicus* (Bge.) Hsiao. *Food Chem.* **2011**, *128*, 620−626.
(48) Chakraborty, I.; Mondal, S.; Pramanik, M.; Rout, D.; Islam, S. S. Structural investigation of a water-soluble glucan from an edible mushroom, *Astraeus hygrometricus*. *Carbohydr. Res.* **2004**, *339*, 2249−2254.
(49) Wang, J. F.; Falke, J. J.; Chan, S. I. A proton NMR study of the mechanism of the erythrocyte glucose transporter. *Proc. Natl. Acad. Sci. U. S. A.* **1986**, *83*, 3277−3281.
(50) Zhu, Q. Q.; Jiang, Y. M.; Lin, S.; Wen, L. R.; Wu, D.; Zhao, M. M.; Chen, F.; Jia, Y. X.; Yang, B. Structural identification of (1→6)-*α*-D-glucan, a key responsible for the health benefits of longan, and evaluation of anticancer activity. *Biomacromolecules* **2013**, *14*, 1999−2003.
(51) Hoshi, H.; Iijima, H.; Ishihara, Y.; Yasuhara, T.; Matsunaga, K. Absorption and tissue distribution of an immunomodulatory *α*-D-glucan after oral administration of *Tricholoma matsutake*. *J. Agric. Food Chem.* **2008**, *56*, 7715−7720.
(52) Zhou, G. F.; Sun, Y. P.; Xin, H.; Zhang, Y. N.; Li, Z. E.; Xu, Z. H. In vivo antitumor and immunomodulation activities of different molecular weight lambda-carrageenans from *Chondrus ocellatus*. *Pharmacol. Res.* **2004**, *50*, 47−53.
(53) Liao, W. Z.; Luo, Z.; Liu, D.; Ning, Z. X.; Yang, J. G.; Ren, J. Y. Structure characterization of a novel polysaccharide from *Dictyophora indusiata* and its macrophage immunomodulatory activities. *J. Agric. Food Chem.* **2015**, *63*, 535−544.
(54) Gamal-Eldeen, A. M.; Amer, H.; Helmy, W. A.; Talaat, R. M.; Ragab, H. Chemically-modified polysaccharide extract derived from *Leucaena leucocephala* alters Raw 264.7 murine macrophage functions. *Int. Immunopharmacol.* **2007**, *7*, 871−878.
(55) Bai, Y. G.; Zhang, P. Y.; Chen, G. C.; Cao, J. F.; Huang, T. T.; Chen, K. S. Macrophage immunomodulatory activity of extracellular polysaccharide (PEP) of Antarctic bacterium *Pseudoaltermonas* sp.S-5. *Int. Immunopharmacol.* **2012**, *12*, 611−617.
(56) Cheng, A. W.; Wan, F. C.; Wang, J. Q.; Jin, Z. Y.; Xu, X. M. Macrophage immunomodulatory activity of polysaccharides isolated from *Glycyrrhiza uralensis* fish. *Int. Immunopharmacol.* **2008**, *8*, 43−50.
(57) Jiang, C. X.; Zhao, L.; Li, S. L.; Zhao, X.; Zhang, Q. H.; Xiong, Q. P. Preliminary characterization and immunostimulatory activity of polysaccharides from *Glossaulax didyma*. *Food Chem. Toxicol.* **2013**, *62*, 226−230.
(58) Li, X.; Zhao, L.; Zhang, Q. H.; Xiong, Q. P.; Jiang, C. X. Purification, characterization and bioactivity of polysaccharides from *Glossaulax didyma*. *Carbohydr. Polym.* **2014**, *102*, 912−919.
(59) Ke, C. L.; Qiao, D. L.; Luo, J. G.; Li, Z. M.; Sun, Y.; Ye, H.; Zeng, X. X. Immunostimulatory activity and structure of polysaccharide from *Streptococcus equi* subsp. *zooepidemicus*. *Int. J. Biol. Macromol.* **2013**, *57*, 218−225.
(60) Shin, K. H.; Lim, S. S.; Lee, S.; Lee, Y. S.; Jung, S. H.; Cho, S. Y. Anti-tumour and immuno-stimulating activities of the fruiting bodies of *Paecilomyces japonica*, a new type of *Cordyceps* spp. *Phytother. Res.* **2003**, *17*, 830−833.
(61) Lee, J. S.; Synytsya, A.; Kim, H. B.; Choi, D. J.; Lee, S.; Lee, J. S.; Kim, W. J.; Jang, S. J.; Park, Y. I. Purification, characterization and immunomodulating activity of a pectic polysaccharide isolated from Korean mulberry fruit Oddi (*Morus alba* L.). *Int. Immunopharmacol.* **2013**, *17*, 858−866.
(62) Commins, S. P.; Borish, L.; Steinke, J. W. Immunologic messenger molecules: cytokines, interferons, and chemokines. *J. Allergy Clin. Immunol.* **2010**, *125*, S53−S72.
(63) Galdiero, M. R.; Bonavita, E.; Barajon, I.; Garlanda, C.; Mantovani, A.; Jaillon, S. Tumor associated macrophages and neutrophils in cancer. *Immunobiology* **2013**, *218*, 1402−1410.
(64) Beckman, J. S.; Koppenol, W. H. Nitric oxide, superoxide, and peroxynitrite: the good, the bad, and the ugly. *Am. J. Physiol.* **1996**, *271*, C1424−C1437.
(65) Bogdan, C. Nitric oxide and the immune response. *Nat. Immunol.* **2001**, *2*, 907−916.
(66) Ohta, T.; Ido, A.; Kusano, K.; Miura, C.; Miura, T. A novel polysaccharide in insects activates the innate immune system in mouse macrophage RAW264 cells. *PLoS One* **2014**, *9*, e114823.
(67) Baugh, J. A.; Bucala, R. Mechanisms for modulating TNF*α* in immune and inflammatory disease. *Curr. Opin. Drug Discovery Dev.* **2001**, *4*, 635−650.
(68) Lejeune, F. J.; Liénard, D.; Matter, M.; Rüegg, C. Efficiency of recombinant human TNF in human cancer therapy. *Cancer Immun.* **2006**, *6*, 6−16.
(69) Boehm, U.; Klamp, T.; Groot, M.; Howard, J. C. Cellular responses to interferon-*γ*. *Annu. Rev. Immunol.* **1997**, *15*, 749−795.
(70) Dinarello, C. Interleukin-1*β*, interleukin-18, and the interleukin-1*β* converting enzyme. *Ann. N. Y. Acad. Sci.* **1998**, *856*, 1−11.
(71) Ma, Y. H.; Xing, Y. Y.; Mi, H. W.; Guo, Z. Q.; Lu, Y. Y.; Xi, T. Extraction, preliminary characterization and immunostimulatory activity *in vitro* of a polysaccharide isolated from *Strongylocentrotus nudus* eggs. *Carbohydr. Polym.* **2014**, *111*, 576−583.
(72) Zhao, G. H.; Kan, J. Q.; Li, Z. X.; Chen, Z. D. Characterization and immunostimulatory activity of an (1→6)-*α*-D-glucan from the root of *Ipomoea batatas*. *Int. Immunopharmacol.* **2005**, *5*, 1436−1445.
(73) He, Y. M.; Liu, C. H.; Chen, Y. X.; Ji, A. C.; Shen, Z. L.; Xi, T.; Yao, Q. S. Isolation and structural characterization of a novel polysaccharide prepared from *Arca subcrenata* Lischke. *J. Biosci. Bioeng.* **2007**, *104*, 111−116.

DOI: 10.1021/acs.jafc.5b03306
J. Agric. Food Chem. 2015, 63, 7986−7994

Sletr1-1 exhibits impaired petal abscission.[8] In the ripening process, heterozygous *Nr* mutants have a more pronounced impairment than *Sletr1-1* and *Sletr1-2*, so those mutants are more suitable than *Nr* for use in breeding programs for the development of a long-shelf life tomato. Additionally, *Sletr1-2* showed prolonged fruit shelf life without a reduction in carotenoid content.[8]

Crossing commercial tomato cultivars with ripening mutants that have prolonged fruit shelf life, *rin*, *Sletr1-1*, and *Sletr1-2*, may facilitate the development of an F1 hybrid line that has the desired characteristic. Several studies have shown that F1 hybrid lines of *rin* exhibited prolonged shelf life.[13] Hybrids of the *nor* mutant locus have an extended shelf life and intermediate fruit color but no differences in pH, soluble solids content, or fruit size.[12] However, not all ethylene-insensitive mutants can be used for improving the postharvest characteristics of tomato in breeding programs; for instance, *Nr* has an incomplete ripening phenotype, even in the heterozygous form (*Nr/nr*), and also has insufficient red coloration.[7]

High-quality tomato fruit, such as fruit with a long shelf life and high nutrient content, is attractive for consumers. Generating new F1 hybrid lines from *Sletr1-1* and *Sletr1-2* by crossing these mutants with large commercial tomato cultivars will improve tomato fruit quality by combining the prolonged shelf life of these mutants with other desired characteristics from commercial tomato cultivars. The objective of this study was to evaluate the effect of the *Sletr1-1* and *Sletr1-2* mutation on the plant development and fruit quality characteristics of F1 hybrid lines of *Sletr1-1* and *Sletr1-2* crossed with four commercial pure-line tomato cultivars, 'Aichi First', 'Ailsa Craig', 'Moneymaker', and 'M82'.

MATERIALS AND METHODS

Plant Materials and Cultivation. Two ethylene receptor (*SlETR1*) mutant alleles, *Sletr1-1* and *Sletr1-2*, and the wild-type Micro-Tom (WT-MT) were crossed with four pure-line cultivars ('Aichi First', 'Ailsa Craig', 'Moneymaker', and 'M82'). Tested plants were cultivated with four biological replications using the nutrient film technique (NFT) cultivation system in the greenhouse of the Agricultural and Forestry Research Center, University of Tsukuba, Japan, during the winter season from October 2013 to February 2014. At the beginning of the plants' cultivation, seeds were sown in paper pots 10 cm in diameter filled with commercial coir coco peat as a growing medium and were fertilized with a commercial nutrient solution (OAT house A, OAT Agrio Co., Ltd., Tokyo, Japan) that had an electrical conductivity (EC) level of 1−1.2 dS/m. After plants produced 5−6 true leaves, they were transplanted into the NFT cultivation system and irrigated with a commercial nutrient solution (OAT house A) with an EC level of 2−2.5 dS/m. Four trusses per plant were maintained for obtaining a test-fruit sample. When the fruits were showing a change of <10% in the surface fruit color from green to yellow, pink, or red, they were tagged as being at the breaker stage (Br). Some parameters were investigated during plant growth and development, for example, number of leaves under the first truss, time to Br, number of flowers per truss, and number of fruits per truss.

Ethylene Triple Response. To investigate the ethylene sensitivity of the seedlings, we investigated all of the F1 hybrid lines via the addition of exogenous ethylene at different concentrations (0, 0.1, 1, 2.5, and 5 ppm). Seeds were sterilized for 20 min by being soaked in 10% commercial bleach including a detergent (Kitchen Haiter, Kao, Tokyo, Japan) and then rinsed with sterilized water three times for 5 min. Three sterilized seeds were grown in a 50 mL glass bottle containing 10 mL of 1/2 Murashige and Skoog (MS) and sealed with rubber septum caps.[8,14] Using a syringe, exogenous ethylene at desired concentrations was injected into the sealed glass bottles containing seeds. The seeds were grown and kept in the dark at 25 °C for 7 days. The seedling triple response was investigated by measuring the hypocotyl and root lengths.

Fruit Characteristic Analysis. The harvested fruits were evaluated to elucidate fruit characterization. All of the tomato fruits were harvested at 6 days after the breaker stage (Br+6), which was characterized by >60% and <90% of the fruit surface having changed to a red color or when the fruit was at the light red stage. The harvesting time was initiated as 0 days post-storage (DPS) and was used as the initial time of fruit storage for the shelf life analysis. The evaluated characteristics were fruit diameter, length, weight, locule number, and pericarp thickness.

Evaluation of Fruit Shelf Life. The Br date was tagged to determine a fruit-harvesting time and the stage of fruit maturation. Investigated fruits were stored on the laboratory bench under the following conditions: temperature, 20 ± 2 °C; humidity, 80%. To evaluate shelf life, fruits were harvested at the same maturation stage (Br+6), which was initiated at 0 DPS when the harvested fruit was at the light red stage and its fruits would be acceptable to consumers in the market. The shelf life was determined by counting the days from the beginning of storage until the fruit quality was lost, which was indicated by the appearance of black spots or wrinkling of >10% of the fruit surface.

Determination of Ethylene Production and Respiration Rate. To elucidate the ethylene production and respiration rate in F1 hybrid lines of *Sletr1-2*, fruits at the same stage of maturation (Br +6) were analyzed. The analysis was repeated every 4 DPS for a total of 12 days. The harvested fruits were kept for 2−3 h before measurement to minimize the contamination of ethylene production from the wound caused by harvesting the fruit from the stalk. Two fruits were stored in a 440 mL sealed plastic chamber at 25 ± 2 °C for 60 min. A 1 mL gas sample was taken from the headspace of the chamber using a syringe to determine ethylene production and respiration rate. For ethylene production, the gas sample was analyzed using a gas chromatograph (GC-18A; Shimadzu, Kyoto, Japan) equipped with a Porapak Q (mesh 60/80) column and flame ionization detector, with helium (He) as the carrier gas and injector, cooling, and detector temperatures of 100, 130, and 100 °C, respectively. The respiration rate was analyzed using a gas chromatograph (GC-8A; Shimadzu, Kyoto, Japan) equipped with a photoionization detector, with He as the carrier gas and 180 and 70 °C detector/injector temperature and column temperature, respectively. Ethylene production and respiration rate were represented as micrograms per gram of fresh weight per hour (μg/g FW/h).

Fruit Color Analysis. Fruit color was evaluated to assess the effects of the mutations in the *SlETR1* gene of the *Sletr1-2* allele on color during the ripening process. Fruit color was evaluated during storage and every 10 days until fruit quality was lost, to a maximum of 30 DPS. The measurement of fruit color was performed according to the CIELAB color space analysis. Color measurements were taken from three points on the surface of individual fruits (the middle, base, and ends of the fruit) using a Minolta Color Reader CR-10 (Konica Minolta Sensing, Inc., Osaka, Japan). Three color parameters were represented as the lightness of the color/brightness (L^*), the red to green scale (a^*), and the yellow to blue scale (b^*). a^* and b^* were used to measure the hue ($h°$), which indicates the pure spectrum colors or the gradation of color, using the following equation:

$$h = \arctan\left(\frac{b}{a}\right)$$

An increased L^* value indicated that the fruit had more brightness, and a decreased $h°$ indicated that the fruit color had changed to red.

Carotenoid Analysis. Because tomato contains high levels of carotenoids, especially lycopene and β-carotene, it has become popular for human consumption. The lycopene and β-carotene contents were analyzed every 10 days from the beginning of storage until fruit quality was lost, to a maximum of 30 DPS. Frozen fruit was ground into a fine powder in liquid nitrogen, and 300 mg of tomato powder was extracted with 3 mL of acetone/hexane (4:6 v/v), resulting in a clear supernatant as described by Nagata and Yamashita.[15] Absorption was measured using a spectrophotometer (Beckman Coulter DU 640

DOI: 10.1021/acs.jafc.5b02742
J. Agric. Food Chem. 2015, 63, 7995−8007

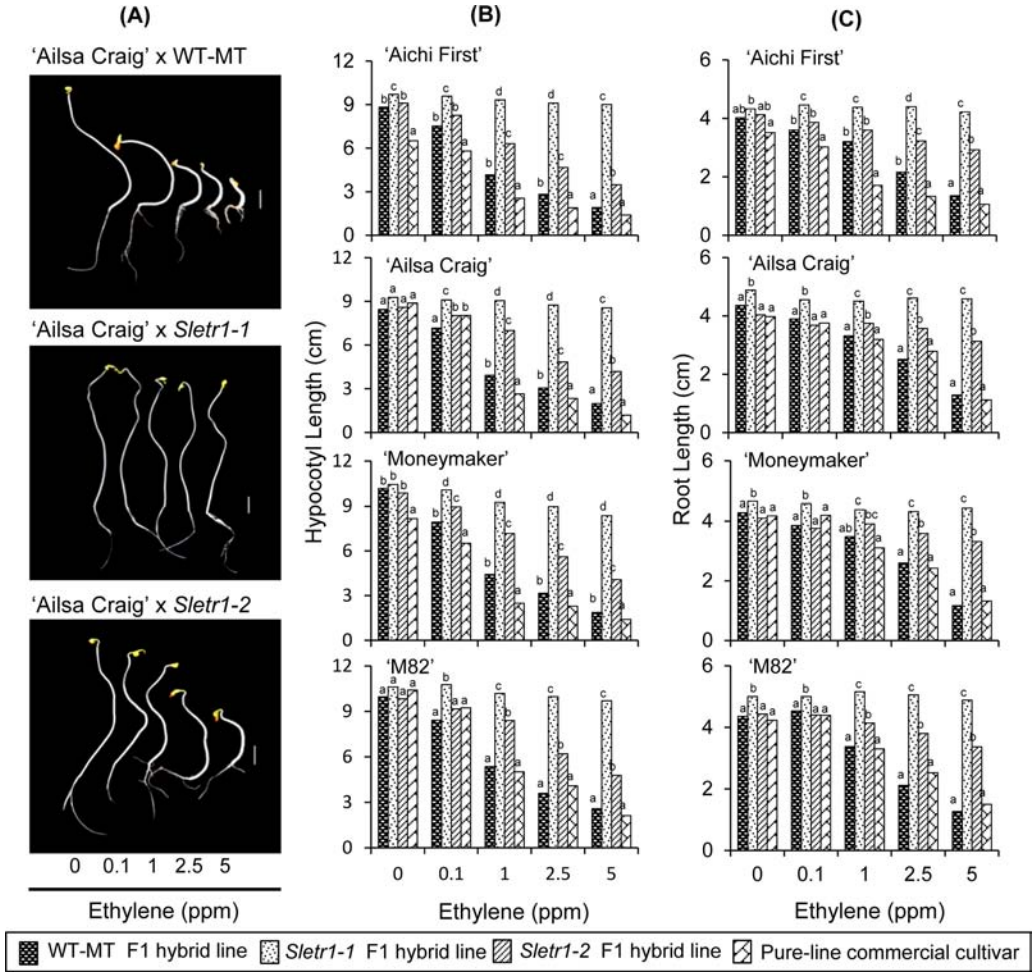

Figure 1. Seedling responses of WT-MT F1, *Sletr1-1* F1, and *Sletr1-2* F1 hybrid lines and pure-line commercial cultivars to exogenous ethylene exposure. (A) Seedling phenotypes of WT-MT, *Sletr1-1*, and *Sletr1-2* crossed with 'Ailsa Craig' as an ethylene response at different concentrations (0−5 ppm). Bar = 1 cm. The seedling quantifications are represented by (B) hypocotyl length and (C) root length of pure-line cultivar parents, WT-MT F1, *Sletr1-1* F1, and *Sletr1-2* F1, on each pure-line cultivar background, 'Aichi First', 'Ailsa Craig', 'Moneymaker', and 'M82'. Mean values with the same storage time tags followed by the same letters are not significantly different according to the Tukey−Kramer test at $p < 0.05$.

spectrophotometer, Fullerton, CA, USA) at absorbances of 663 (A_{663}), 645 (A_{645}), 505 (A_{505}), and 453 nm (A_{453}). Lycopene (C_{LYC}) and β-carotene (C_{CAR}) were measured using the following equations:

$$C_{LYC} = -0.04584(A_{663}) + 0.204(A_{645}) + 0.372(A_{505}) - 0.0806(A_{453})$$

$$C_{CAR} = 0.216(A_{663}) - 1.22(A_{645}) - 0.304(A_{505}) + 0.452(A_{453})$$

The lycopene and β-carotene contents were represented by micrograms per grams of fresh weight (μg/g FW).

Fruit Firmness Analysis. Firmness is an important characteristic for the marketability of tomato fruit. To analyze the effect of the *Sletr1-2* mutation, we tested the firmness of the fruits. Br+6 fruits were tested using an Ultrasonic Hardness Tester model FHR-5 (Nippon Optical Works Co., Ltd., Tokyo, Japan). The measurement was repeated every 10 days until 30 DPS.

Analysis of the Total Soluble Solids (TSS), pH, and Titratable Acidity (TA). To evaluate the effect of the *Sletr1-2* mutation on four *Sletr1-2* F1 hybrid lines, we measured the TSS, pH and TA. The TSS was used to estimate the sugar level, and TA was used to estimate the organic acid level. The TSS was measured using a refractometer PAL-J (Atago, Tokyo, Japan). The pH and TA was measured using a pH meter SevenCompact pH/Ion S220 (Mettler-Toledo AG, Schwerzenbach, Switzerland). The TA was measured using pH meter methods by titration of 0.1 N sodium hydroxide up to a pH of 8.1 as described by Dalal et al.[16]

Data Analysis. This experiment was conducted in a completely randomized design with four replicates. For statistical data analysis, to test the normality of the data we used the Kolmogorov−Smirnov test. On the basis of this test, we found the data to have normal distribution. Therefore, one factor analysis of variance (ANOVA) was conducted to analyze the data followed by the Tukey−Kramer test at $p < 0.05$ to compare differences among investigated lines.

RESULTS

Under Heterozygous Conditions, *Sletr1-1* and *Sletr1-2* Expressed Ethylene-Insensitive Phenotypes. All of the *Sletr1-1* F1 and *Sletr1-2* F1 hybrid lines showed a similar tendency with ethylene exogenous exposure, that is, reduced hypocotyl and root lengths. These measurements were significantly longer than in the WT-MT F1 hybrid lines and the commercial pure-line cultivars (Figure 1A). All of the *Sletr1-1* F1 hybrid lines resulted in a strong ethylene-insensitive phenotype. Exogenous ethylene exposure of 5 ppm was able to reduce the hypocotyl and root lengths of all of the investigated plants. However, the reductions in the *Sletr1-1* F1 hybrid lines were no more than 19.4% (*Sletr1-1* × 'Moneymaker') and 5.4% (*Sletr1-1* × 'Ailsa Craig'), respectively (Figure 1B,C).

DOI: 10.1021/acs.jafc.5b02742
J. Agric. Food Chem. 2015, 63, 7995−8007

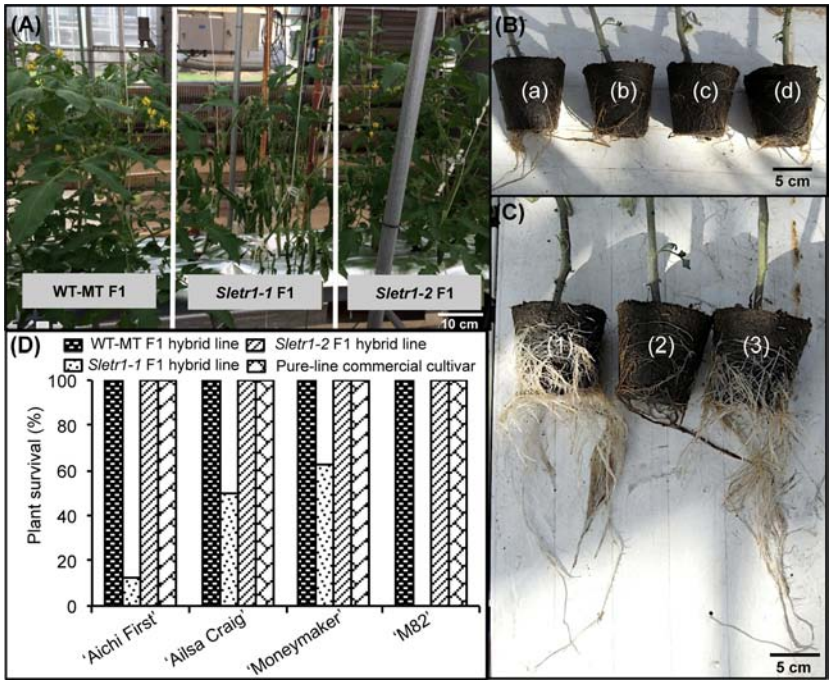

Figure 2. Vegetative growth of WT-MT F1, *Sletr1-1* F1, and *Sletr1-2* F1 hybrid lines and pure-line commercial cultivars. (A) The F1 hybrid line of *Sletr1-1* (crossed with 'Ailsa Craig') showed wilting as a response to the transplanting process to the NFT system; the photograph was taken 3 weeks after transplanting. (B) Injured roots of all of the *Sletr1-1* F1 hybrid lines from crosses with four different pure-line background cultivars: 'Aichi First' (a), "Ailsa Craig" (b), 'Moneymaker' (c), and 'M82' (d). (C) Representative photographs of the root systems of the hybrid lines of MT-WT F1 (1), *Sletr1-1* F1 (2), and *Sletr1-2* F1 (3) (crossed with 'Ailsa Craig'); the photographs were taken 2 weeks after transplanting to the NFT system. (D) Plant survival of two F1 hybrid mutant lines, *Sletr1-1* and *Sletr1*-2, compared with WT-MT F1. Data were taken 4 weeks after transplanting to the NFT system (n = 8).

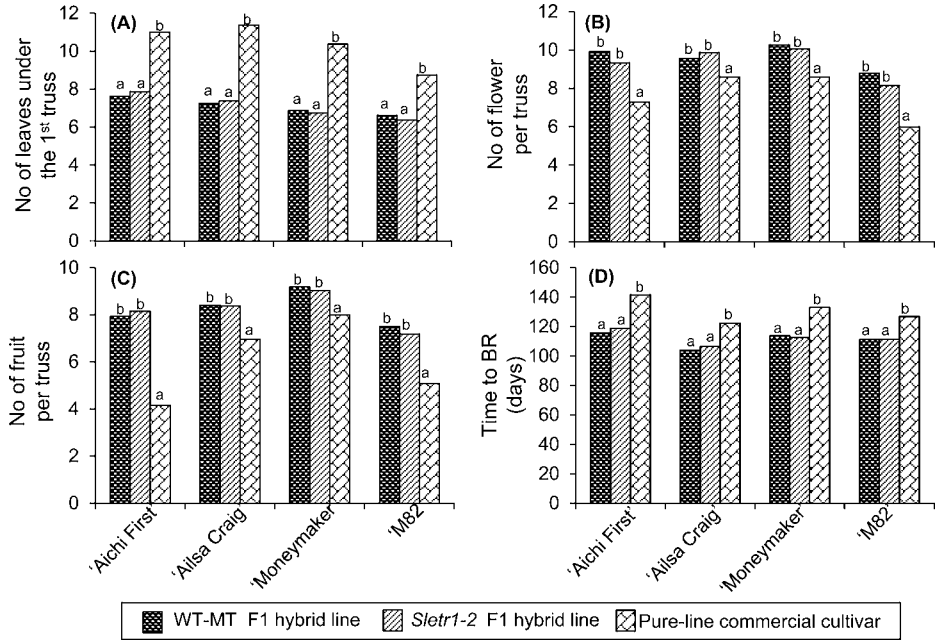

Figure 3. Vegetative characteristics of *Sletr1-2* F1 and WT-MT F1 hybrid lines and pure-line commercial cultivars. (A) The number of leaves under the first truss is the average number of leaves from eight plants. (B) The number of flowers per truss and (C) the number of fruits per truss are the average numbers of flowers and fruits from four trusses per plant. (D) The time to breaker stage for the investigated fruits was observed as the number of days from seed sowing until the first fruit of one plant reached the BR stage or the fruit color changed to pink or yellow. Mean values with the same storage time tags followed by the same letters are not significantly different according to the Tukey–Kramer test at $p < 0.05$.

Exogenous ethylene exposure in the *Sletr1-2* F1 hybrid lines resulted in an intermediate ethylene-insensitive phenotype. Those hybrid lines expressed weaker ethylene sensitivity phenotypes compared with the *Sletr1-1* F1 hybrid lines; however, these lines were more ethylene-sensitive than the WT-MT F1 hybrid lines and the pure-line commercial cultivar

DOI: 10.1021/acs.jafc.5b02742
J. Agric. Food Chem. 2015, 63, 7995–8007

parent (Figure 1A). Treatment with 5 ppm of exogenous ethylene reduced hypocotyl length by 61.7% (*Sletr1-2* × 'Aichi First') and root length by 29.5% (*Sletr1-2* × 'Aichi First') (Figure 1B,C).

***Sletr1-1* F1 Hybrid Line Shows Weak Phenotype Characteristics during Stress Conditions.** Two weeks after being transplanted to the NFT system, all of the *Sletr1-1* F1 hybrid lines showed stress response, which was characterized by leaf wilting and disease sensitivity. However, the *Sletr1-2* F1 hybrid lines did not show any stress responses (Figure 2A). Plant wilting in *Sletr1-1* F1 hybrid lines was caused by damage to the root system. All of the roots were browning, the root tips were injured, and some of the roots were rotting (Figure 2B). However, in all of the *Sletr1-2* F1 hybrid lines, the roots appeared healthy and were white in color, and no roots were rotting (Figure 2C), which was similar to the characteristics of the WT-MT F1 hybrid line and the pure-line commercial cultivars background. Furthermore, only a few new *Sletr1-1* F1 hybrid lines roots were formed for the 2 weeks after transplanting. At 4 weeks after transplantation, no *Sletr1-1* × 'M82' specimens survived; however, *Sletr1-1* × 'Aichi First', 'Ailsa Craig', and 'Moneymaker' survived at percentages of less than 13, 50, and 63%, respectively (Figure 2D). Because all of the *Sletr1-1* F1 hybrid lines had the lowest rates of plant survival, even *Sletr1-1* × 'M82' did not survive (Figure 2D). Thus, the *Sletr1-1* F1 hybrid lines were not used for further investigation in this study.

Mutation of the *SlETR1* Gene of the *Sletr1-2* Mutant Does Not Affect the Vegetative and Generative Characteristics of Its F1 Hybrid Lines. Crossing all of the pure-line cultivars with WT-MT and *Sletr1-2* resulted in similar tendencies in reducing the number of leaves under the first truss in the F1 hybrid lines, which were significantly different from those of the pure-line cultivar parent but did not show any differences between the *Sletr1-2* F1 and WT-MT F1 hybrid lines. The greatest number of leaves under the first truss was observed on *Sletr1-2* × 'Aichi First', whereas the fewest were observed on *Sletr1-2* × 'M82' (Figure 3A). Crossing *Sletr1-2* with 'Aichi First', 'Ailsa Craig', 'Moneymaker', and 'M82' reduced the average of the number of leaves under the first truss by approximately 3.13, 4.00, 3.63, and 2.38, respectively, compared with the pure-line cultivar parent (Figure 3A). The plant growth type in the hybrid lines was similar to that of the commercial pure-line cultivar parent, which included the indeterminate growth type for 'Aichi First', 'Ailsa Craig', and 'Moneymaker' and the determinate growth type for 'M82'. The data showed that all of the *Sletr1-2* F1 hybrid lines resulted in numbers of flowers and fruits per truss similar to those of the WT-MT F1 hybrid line; however, the numbers were significantly higher than those for the pure-line cultivar parents, for which the average numbers of flowers per truss were 9.34, 9.88, 10.06, and 8.16 and the numbers of fruits per truss were 8.16, 8.38, 9.03, and 7.19 for *Sletr1-2* crossed with 'Aichi First', 'Ailsa Craig', 'Moneymaker', and 'M82', respectively (Figure 3B,C).

The time to the breaker stage for all of the *Sletr1-2* F1 hybrid lines was similar to that for the WT-MT F1 hybrid lines; however, they were significantly faster than the pure-line cultivar parents. The first fruit to reach the breaker stage was *Sletr1-2* × 'Ailsa Craig', with an average time of 104 days after sowing, and the last to reach it was *Sletr1-2* × 'Aichi First', with an average time of 119 days after sowing, or 15 days later than *Sletr1-2* × 'Ailsa Craig' (Figure 3D). The early breaker stage of this F1 hybrid line is most likely correlated with its pure-line cultivar parent, 'Ailsa Craig', which reached the breaker stage earlier than the other three commercial pure-line cultivars at approximately 122 days after sowing (Figure 3D).

***Sletr1-2* F1 Hybrid Resulted in Fruit Characteristics Similar to Its WT-MT F1 Hybrids.** The appearance of the fruits from all of the *Sletr1-2* F1 hybrid lines was similar to that of fruit from the WT-MT F1 hybrid lines, which showed an intermediate fruit size (smaller than the pure-line cultivar parents and bigger than the *Sletr1-2* and WT-MT parents). Moreover, the fruit shapes were slightly similar to those of the Micro-Tom parents (Figure 4). Quantification analysis revealed

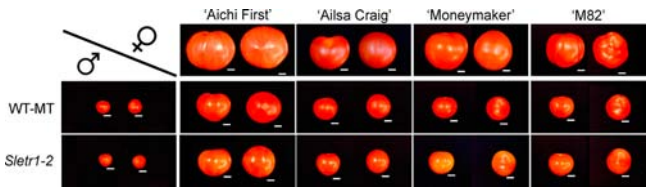

Figure 4. Fruit appearance of *Sletr1-2* F1 and WT-MT F1 hybrid lines and pure-line commercial cultivars. The photograph was taken at Br+6 of the fruit maturation stage. All of the F1 hybrid lines resulted in an intermediate fruit size. The *Sletr1-2* F1 and WT-MT F1 hybrid lines appear to have similar fruit sizes and an almost identical red fruit color. Bar = 1 cm.

that the fruit diameter, fruit length, fruit weight, and pericarp thickness of all of *Sletr1-2* F1 hybrid lines were significantly smaller than those of the pure-line cultivar parents. However, they did not show any significant differences compared with WT-MT F1 hybrid line (Figure 5). The *Sletr1-2* F1 hybrid line from 'Aichi First' resulted in a large fruit that had a greater diameter, length, and weight compared with the other three F1 hybrid lines with average values of 39.73 mm, 34.87 mm, and 32.81 g, respectively (Figure 5A–C). On the other hand, the diameter, length, and weight of the *Sletr1-2* F1 hybrid line from 'Ailsa Craig', 'Moneymaker', and 'M82' were similar to each other, with the length ranging from 29.87 mm (*Sletr1-2* × 'M82') to 30.85 mm (*Sletr1-2* × 'Ailsa Craig'), the diameter ranging from 32.53 mm (*Sletr1-2* × 'M82') to 34.01 mm (*Sletr1-2* × 'Ailsa Craig'), and the weight per fruit ranging from 20.67 g (*Sletr1-2* × 'M82') to 22.00 g (*Sletr1-2* × 'Moneymaker') (Figure 5A–C). The *Sletr1-2* mutant crossed with 'Moneymaker' resulted in the highest reduction in average pericarp thickness compared with the pure-line cultivar parents, with a reduction of approximately 36% (Figure 5E). The locule numbers of all of the *Sletr1-2* F1 hybrid lines from all of the different pure-line cultivar parents were not significantly different from those of the WT-MT F1 hybrid lines. However, the significance varied compared with the pure-line cultivar parent. Among all of the *Sletr1-2* F1 hybrid lines, *Sletr1-2* × 'Aichi First' resulted in the highest number of fruit locules (3.71); the lowest locule number was observed on *Sletr1-2* × 'Moneymaker' (2.46) (Figure 5D).

***Sletr1-2* Mutant Has the Potential To Be an F1 Hybrid Parent for Improving Fruit Shelf Life.** In all of the WT-MT F1 hybrid lines, wrinkles appeared on the fruit surface earlier than on the *Sletr1-2* F1 hybrid lines. At 30 DPS, >50% of the total fruit surface of the WT-MT F1 hybrid line was wrinkled, whereas in *Sletr1-2* F1 hybrid lines, only some of the fruit surface was wrinkled (Figure 6). Although the fruit shelf life of the three *Sletr1-2* F1 hybrid lines from 'Aichi First', 'Ailsa Craig',

DOI: 10.1021/acs.jafc.5b02742
J. Agric. Food Chem. 2015, 63, 7995−8007

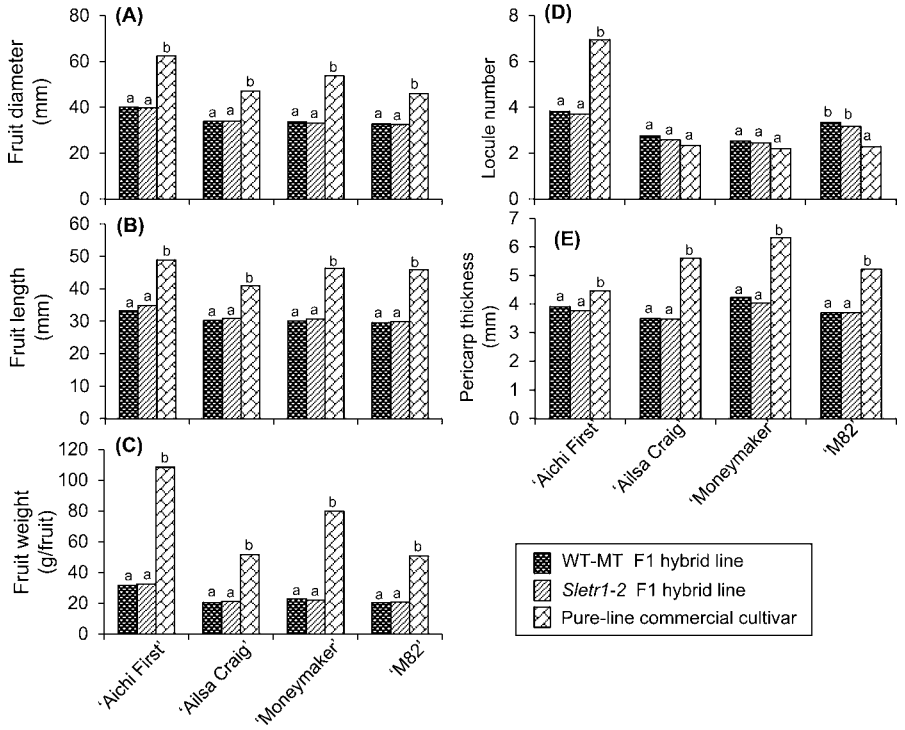

Figure 5. Fruit characterizations of the *Sletr1-2* F1 and WT-MT F1 hybrid lines and pure-line commercial cultivars. Fruit characteristics are represented by (A) diameter, (B) length, (C) weight, (D) locule number, and (E) pericarp thickness. These characteristics were measured from six fruits per replicate at the (Br+6) fruit maturation stage. Mean values with the same storage time tags followed by the same letters are not significantly different according to the Tukey–Kramer test at $p < 0.05$.

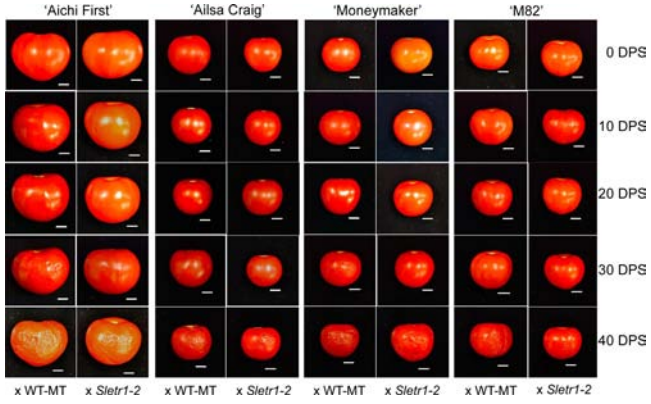

Figure 6. Representative photographs indicating tomato fruit shelf life during storage of *Sletr1-2* F1 and WT-MT F1 hybrid lines and pure-line commercial cultivars. The fruits were stored for 40 days under room conditions (20 + 2 °C) until wrinkling or black spots appeared on the fruit surface. Bar = 1 cm.

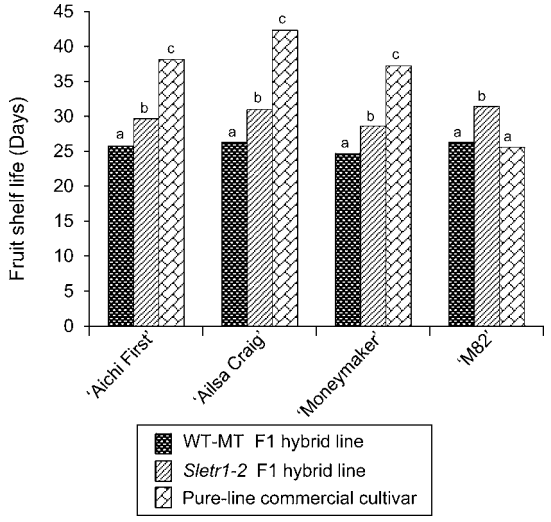

Figure 7. Fruit shelf life of *Sletr1-2* F1 and WT-MT F1 hybrid lines and pure-line commercial cultivars. Shelf life was evaluated under room conditions until wrinkling appeared on the fruit surface. Mean values with the same storage time tags followed by the same letters are not significantly different according to the Tukey–Kramer test at $p < 0.05$.

and 'Moneymaker' was significantly reduced compared with the pure-line cultivar parent (8.46, 11.33, and 8.63 days shorter than the shelf life for 'Aichi First', 'Ailsa Craig', and 'Moneymaker' fruits, respectively), all of the *Sletr1-2* F1 hybrid lines showed significant improvement in fruit shelf life compared with the WT-MT F1 hybrid lines (Figure 7). In the four genetic backgrounds of pure-line cultivars, the *Sletr1-2* mutation effectively extended the fruits' shelf life up to 3.96, 4.71, 3.92, and 5.13 days longer than the fruit shelf life of WT-MT F1 hybrid line for the *Sletr1-2* F1 hybrid lines from 'Aichi First', 'Ailsa Craig', 'Moneymaker', and 'M82' background, respectively (Figure 7).

Ethylene Production and Respiration Rate of the *Sletr1-2* F1 Hybrid Line Were Similar to Those of the WT-MT F1 Hybrid Line in All of the Pure-Line Cultivar Parents. Our data indicate that ethylene production and the respiration rate of the investigated fruits decreased during storage until 12 DPS. The mutation in the *SlETR1* gene of the *Sletr1-2* F1 hybrid lines did not affect either ethylene production (Figure 8A) or respiration rate (Figure 8B) until

DOI: 10.1021/acs.jafc.5b02742
J. Agric. Food Chem. 2015, 63, 7995–8007

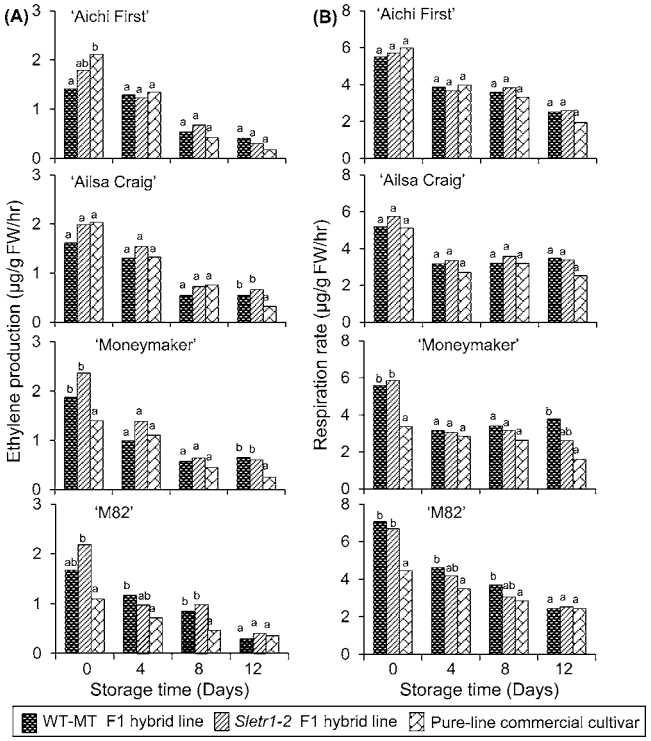

Figure 8. Ethylene production and respiration rate of *Sletr1-2* F1 and WT-MT F1 hybrid lines and pure-line commercial cultivars. Ethylene production (A) and respiration rate (B) were measured every 4 days for 12 DPS. Mean values with the same storage time tags followed by the same letters are not significantly different according to the Tukey–Kramer test at $p < 0.05$.

12 DPS, which was similar to the findings for WT-MT F1 hybrid lines. Although ethylene production in *Sletr1-2* crossed with all four pure-line cultivar parents was not significantly different from that of the WT-MT F1 hybrid lines, there was a tendency for the ethylene production and respiration rate of all the *Sletr1-2* F1 hybrid lines, except for the respiration rate of *Sletr1-2* crossed with 'M82', to be higher than those of the WT-MT F1 hybrid line (Figure 8A,B). At the beginning of storage, *Sletr1-2* × 'Moneymaker' had the highest ethylene production (2.36 μg/g FW/h) (Figure 8A), whereas the highest respiration rates were reached by both *Sletr1-2* and WT-MT crossed with 'M82,' with values of 6.69 and 7.07 μg/g FW/h, respectively. However, the other F1 hybrid lines showed almost the same values for ethylene production and respiration rate until 12 DPS, at which point the ethylene production of *Sletr1-2* F1 hybrid lines ranged between 0.31 μg/g FW/h (*Sletr1-2* × 'Aichi First') and 0.67 μg/g FW/h (*Sletr1-2* × 'Ailsa Craig') (Figure 8A) and the respiration rate ranged between 2.53 μg/g FW/h (*Sletr1-2* × 'M82') and 3.36 μg/g FW/h (*Sletr1-2* × 'Ailsa Craig') (Figure 8B). Compared with the pure-line commercial cultivars, the ethylene production and respiration rate of *Sletr1-2* F1 hybrid lines varied during 30 days of storage. At 0 DPS, *Sletr1-2* crossed with 'Moneymaker' and 'M82' had significant increases in both ethylene production of 0.96 and 1.09 μg/g FW/h and respiration rate of 2.47 and 2.23 μg/g FW/h, respectively, whereas, at 12 DPS, all of the *Sletr1-2* F1 hybrid lines except for *Sletr1-2* × 'M82' resulted in higher ethylene production than that for the pure-line cultivar; however, it had a similar respiration rate (Figure 8A,B).

Fruit Color Varied among All of the *Sletr1-2* F1 Hybrid Lines from Different Commercial Pure-Line Cultivar Parents. Generally, the L^* and h° values of all of the *Sletr1-2* F1 hybrid lines varied from those of the WT-MT F1 hybrid lines and the pure-line commercial cultivar parents. In all of the *Sletr1-2* F1 and WT-MT F1 hybrid lines, L^* and h° dramatically decreased at 10 DPS, and then their values were stable. However, in the pure-line cultivar, the values were similar during postharvest storage up to 30 DPS. Our statistical analysis of the data showed different significance during postharvest storage under different pure-line cultivar backgrounds. Compared with the WT-MT F1 hybrid lines, the *Sletr1-2* mutation significantly increased the L^* value only in *Sletr1-2* crossed with 'Aichi First' up to 20 DPS (42.13 at 0 DPS, 37.02 at 10 DPS, and 35.70 at 20 DPS) and in *Sletr1-2* crossed with 'Moneymaker' at 0 DPS with the value of 42.29 (Figure 9A). Of all the F1 hybrid lines, *Sletr1-2* crossed with

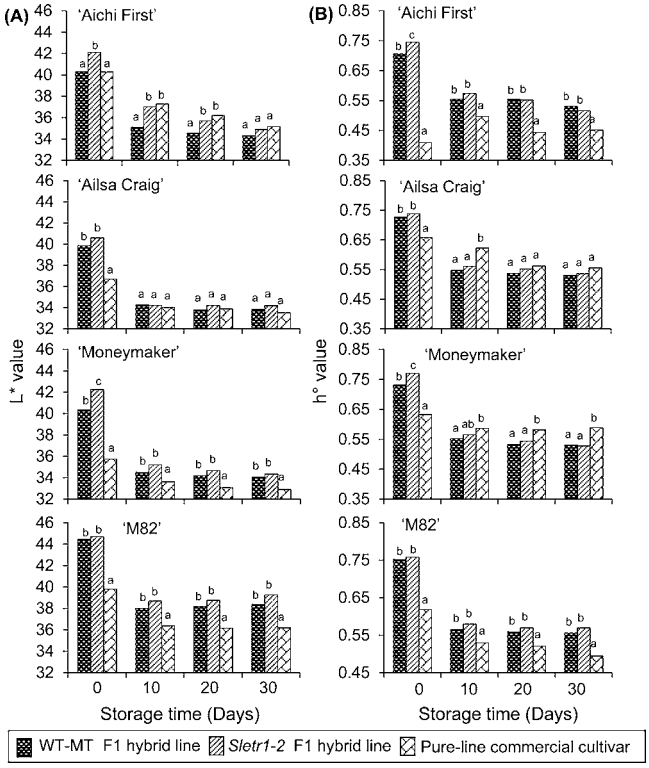

Figure 9. Fruit color of *Sletr1-2* F1 and WT-MT F1 hybrid lines and pure-line commercial cultivars. Color was represented by (A) the L^* value as the lightness of the color, where ($L^* = 0$ indicates black and $L^* = 100$ indicates white), and (B) the h° value, the pure spectrum or the gradation of color (e.g., red, purple, blue). Mean values with the same storage time tags followed by the same letters are not significantly different according to the Tukey–Kramer test at $p < 0.05$.

'M82' had the highest values of L^* (44.71 at 0 DPS and 39.7 at 30 DPS) (Figure 9A). Compared with the pure-line cultivar, the clear significance in increasing the L^* value of *Sletr1-2* F1 hybrid lines up to 30 DPS was observed from the *Sletr1-2* crossed with 'Moneymaker' and 'M82'. However, in crosses with 'Aichi First' and 'Ailsa Craig', it was observed only at 0 DPS, after which they were similar (Figure 9A).

The h° value was measured to refer to the pure color. The significant effect of the *Sletr1-2* mutation on the h° value was observed at 0 DPS only in *Sletr1-2* crossed with 'Aichi First' and 'Moneymaker', with values of 0.75 and 0.77, respectively, and

DOI: 10.1021/acs.jafc.5b02742
J. Agric. Food Chem. 2015, 63, 7995–8007

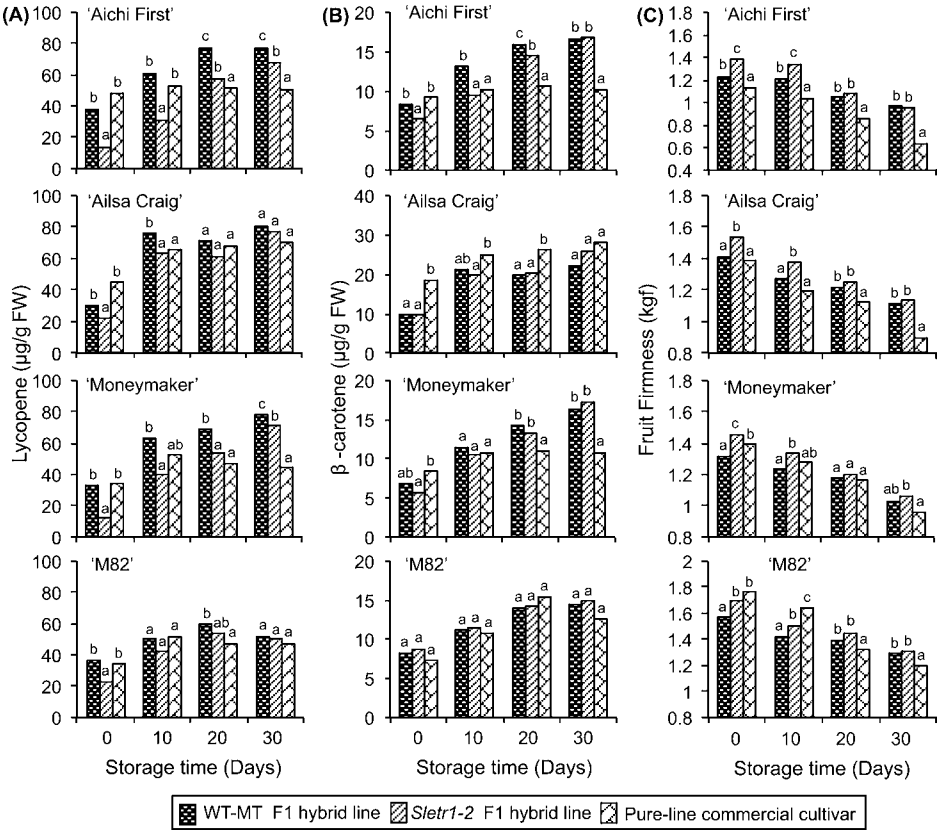

Figure 10. Carotenoid content and fruit firmness of *Sletr1-2* F1, WT-MT F1 hybrid lines, and pure-line commercial cultivars. (A) Lycopene content and (B) β-carotene content represent the carotenoid content of the fruits during postharvest storage. (C) Fruit firmness represents the fruit hardness during the 30 days of storage. Mean values with the same storage time tags followed by the same letters are not significantly different according to the Tukey–Kramer test at $p < 0.05$.

after 10 DPS, there were no significant differences from the WT-MT F1 hybrid lines. (Figure 9B). Although the $h°$ value of the *Sletr1-2* F1 hybrid lines generally was not significantly different from that of WT-MT F1 hybrid lines during storage time up to 30 DPS, it varied from its pure-line cultivar parent. In *Sletr1-2* crossed with 'Aichi First' and 'M82', the $h°$ value significantly increased up to 30 DPS. In *Sletr1-2* × 'Moneymaker', the $h°$ value was significantly lower during the storage time except at 0 DPS, whereas in *Sletr1-2* × 'Ailsa Craig', the $h°$ value was similar except at 0 and 10 DPS (Figure 9B).

Carotenoid Content of the *Sletr1-2* F1 Hybrid Line Is Slightly Affected by Mutation in the *SlETR1* Gene. All of the *Sletr1-2* F1 hybrid lines synthesized slightly less lycopene than the WT-MT F1 hybrid lines but varied from the pure-line cultivar parent. On the basis of the statistical analyses of the data, at 0 DPS, there was significantly lower lycopene content in all of the *Sletr1-2* F1 hybrid lines than in the WT-MT F1 hybrid lines and the pure-line cultivar parent, with the average value varying between 11.75 μg/g FW (*Sletr1-2* × 'Moneymaker') and 23.25 μg/g FW (*Sletr1-2* × 'M82') (Figure 10A). The lycopene content increased gradually during storage in all of the F1 hybrid lines up to 30 DPS; however, its amount in the pure-line cultivar remained stable after 10 DPS. At 30 DPS, >60 μg/g FW of lycopene was detected in the three *Sletr1-2* F1 hybrid lines (crossed with 'Aichi First', 'Ailsa Craig', and 'Moneymaker') but in *Sletr1-2* × 'M82', at only 50.05 μg/g FW (Figure 10A). Compared with the WT-MT F1 hybrid lines, both *Sletr1-2* × 'Aichi First' and *Sletr1-2* × 'Moneymaker' had significantly lower lycopene content up to 30 DPS, whereas in *Sletr1-2* × 'Ailsa Craig' and *Sletr1-2* × 'M82', no significant differences in lycopene content were detected after 20 and 10 DPS, respectively (Figure 10A). Compared to the pure-line cultivar parent, *Sletr1-2* F1 hybrid lines showed variations in the lycopene content depending on the pure-line cultivar background. At 0 DPS, both *Sletr1-2* × 'Aichi First' and *Sletr1-2* × 'Moneymaker' had significantly lower lycopene content; however, after 20 DPS, the value was significantly higher, whereas in *Sletr1-2* × 'Ailsa Craig' and *Sletr1-2* × 'M82', no significant differences in lycopene content were detected after 10 DPS (Figure 10A).

In addition to the lycopene content, the β-carotene content increased during 30 days of storage. In *Sletr1-2* × 'M82', the β-carotene content did not increase as much as in the three other *Sletr1-2* F1 hybrid lines; the value was only increased 6.05 μg/g FW, whereas in the other *Sletr1-2* F1 hybrid lines, it was increased >10 μg/g FW (Figure 10B). The significant effect of the *SlETR1* gene mutation of the *Sletr1-2* F1 hybrid lines on the β-carotene content was detected only in *Sletr1-2* × 'Aichi First' and *Sletr1-2* × 'Moneymaker' and occurred at 10 and 0 DPS, respectively, whereas at the end of storage, it was similar to that of the WT-MT F1 hybrid lines (Figure 10B). At the beginning of storage, *Sletr1-2* × 'Aichi First' and *Sletr1-2* × 'Moneymaker' had reductions of 21 and 16%, respectively, compared with the WT-MT F1 hybrid lines. The changes in β-carotene in all *Sletr1-2* F1 hybrid lines differed from those of the pure-line cultivar parent. Both *Sletr1-2* × 'Aichi First' and *Sletr1-2* × 'Moneymaker' had significantly lower β-carotene content at the beginning of storage; however, after 20 DPS, it was significantly

DOI: 10.1021/acs.jafc.5b02742
J. Agric. Food Chem. 2015, 63, 7995–8007

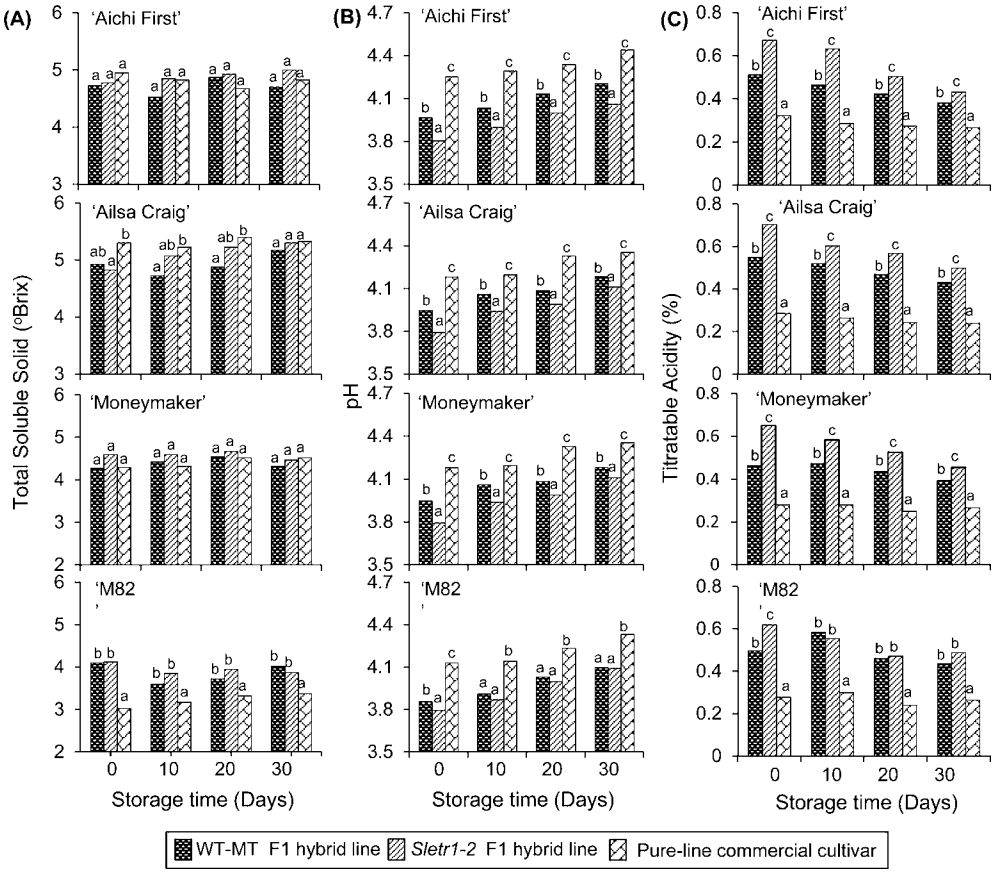

Figure 11. Effect of *Sletr1-2* mutation on fruit taste quality of its F1 hybrid line as represented by (A) total soluble solids, (B) pH, and (C) titratable acidity. Mean values with the same storage time tags followed by the same letters are not significantly different according to the Tukey–Kramer test at $p < 0.05$.

higher. In *Sletr1-2* × 'Ailsa Craig', it was significantly higher than that of the pure-line cultivar parent up to 20 DPS, whereas in *Sletr1-2* × 'M82', no significant differences in β-carotene content were detected (Figure 10B).

Fruit of the *Sletr1-2* F1 Hybrid Lines Is Harder than That of the F1 Hybrid Lines. The hardness of the fruit is indicated by a firmness value, which is an important characteristic for fresh tomato fruit. The firmness of all the investigated fruits decreased during storage up to 30 DPS. The statistical data analysis revealed that, from 0 until 10 DPS for *Sletr1-2* crossed with 'Aichi First', 'Ailsa Craig', and 'Moneymaker' and until 20 DPS for *Sletr1-2* × 'M82', the fruits were significantly harder compared with the WT-MT F1 hybrid lines, with firmness values 0.15, 0.12, 0.14, and 0.12 kgf higher than those for the WT-MT F1 hybrid lines, respectively, at 0 DPS. However, no significant differences were detected at the end of storage, with values of 0.95, 1.13, 1.06, and 1.31 kgf for *Sletr1-2* crossed with 'Aichi First', 'Ailsa Craig', 'Moneymaker', and 'M82', respectively (Figure 10C). Compared with the pure-line cultivar parent, significant improvements in the fruit hardness of the *Sletr1-2* F1 hybrid lines occurred up to 30 DPS, except for *Sletr1-2* × 'M82', which showed a lower fruit firmness at the beginning of storage and a similar one at 30 DPS (Figure 10C). A greater improvement in firmness compared with the pure-line cultivar parents was observed in *Sletr1-2* × 'Aichi First', with an improved firmness of 0.26 kgf (Figure 10C).

Mutation in the *Sletr1-2* Allele Affects the Fruit pH and Titratable Acidity (TA) but Does Not Affect the Total Soluble Solids (TSS). During 30 days of storage, all of the *Sletr1-2* F1 hybrid lines had TSS levels similar to those for the WT-MT F1 hybrid lines; however, these levels differed from those for the pure-line cultivar. At 0 DPS, the TSS from the four *Sletr1-2* F1 hybrid lines (*Sletr1-2* crossed with 'Aichi First', 'Ailsa Craig', 'Moneymaker', and 'M82') were 4.78, 4.83, 4.60, and 4.13 °Brix, respectively, whereas at 30 DPS, they were 5.00, 5.30, 4.48, and 3.88 °Brix (Figure 11A). Crossing both WT-MT and *Sletr1-2*, with 'M82' significantly increased the TSS values of their F1 hybrid lines and resulted in values of 1.10, 0.68, 0.63, and 0.50 °Brix higher than the 'M82' parent at 0, 10, 20, and 30 DPS, respectively (Figure 11A).

The analyzed data indicate that *Sletr1-2* affected the pH and TA of the fruit; however, the effect was dependent on the genetic background of the pure-line cultivar parent. All of the *Sletr1-2* F1 hybrid lines showed the lowest fruit pH and the highest fruit TA during the 30 days of storage compared with the WT-MT F1 hybrid line, except for the pH and TA of *Sletr1-2* crossed with 'M82' that showed similar level after 10 DPS (Figure 11). At 0 DPS, the pH from *Sletr1-2* crossed with 'Aichi First', 'Ailsa Craig', 'Moneymaker', and 'M82' was 3.81, 3.77, 3.79 and 3.80, respectively, whereas at 30 DPS it was 4.06, 4.08, 4.11, and 4.09 (Figure 11B). In all of the investigated fruits, the pH increased during the 30 days of storage; however, the TA decreased. This study showed that the fruits of the *Sletr1-2* F1 hybrid lines with the lowest pH contained the highest TA levels that were significantly different from the levels of the WT-MT F1 hybrid line and the pure-line cultivar parents during the 30 days of storage (Figure 11C). At 0 DPS, the TA from *Sletr1-2* crossed with 'Aichi First', 'Ailsa Craig', 'Moneymaker', and

DOI: 10.1021/acs.jafc.5b02742
J. Agric. Food Chem. 2015, 63, 7995–8007

'M82' was 0.67, 0.70, 0.65, and 0.62%, respectively, whereas at 30 DPS, it was 0.43, 0.50, 0.46, and 0.49% (Figure 11C).

DISCUSSION

Fruit shelf life is an important trait in fresh tomato. Generating new cultivars with longer fruit shelf life may be an interesting approach to improving the postharvest quality of tomato. Mutations in the *Sletr1* mutant alleles, *Sletr1-1* and *Sletr1-2*, resulted in ethylene-insensitive phenotypes in the F1 hybrid lines. However, these F1 hybrid lines showed different ethylene sensitivities at the seedling stage, with the *Sletr1-1* F1 hybrid lines exhibiting less ethylene sensitivity than the *Sletr1-2* F1 hybrid lines (Figure 1). The ethylene-insensitive phenotype of the *Sletr1-1* F1 hybrid line was inherited from the *Sletr1* mutant alleles, which exhibited dominant inheritance.[8] The effect of ethylene on seedling development is characterized by hypocotyl elongation inhibition, hypocotyl base expansion, and primary root elongation inhibition.[17,18] All of the *Sletr1-1* F1 hybrid lines responded slightly to the application of 5 ppm of exogenous ethylene, whereas the *Sletr1-2* F1 hybrid lines responded even at low concentrations (1 ppm) (Figure 1). On the basis of these data, the ethylene sensitivities of *Sletr1-1* and *Sletr1-2* were reduced in the heterozygous condition compared with the homozygous condition, whereas under homozygous condition, the *Sletr1-1* mutant did not show any response to ethylene exposure up to 10 ppm.[8] Reduction of ethylene sensitivity in *Sletr1-1* and *Sletr1-2* mutants and these F1 hybrid lines was due to the mutations in the first and second domains of transmembrane region of the ethylene receptor gene (*SlETR1*), which is an important region for ethylene binding. Amino acid substitution of P51L in the *Sletr1-1* mutant as a result of mutation in the first domain of the transmembrane region is similar to the amino acid substitution of P36L in *Nr* and *Arabidopsis etr2-1*, whereas in *Sletr1-2*, the amino acid substitution of V69D is located in the second domain of the transmembrane region (V69D).[8] In *Arabidopsis* and tomato, mutations in these regions of ethylene receptor genes affect ethylene binding activity and ethylene sensitivity.[9,10,19]

Improving agronomic characteristics in F1 hybrid lines is an important issue in a breeding program. Because favorable allelic interactions at heterozygous loci in F1 hybrid lines improve performance, crossing two homozygous lines that have the characteristics desired for making an F1 hybrid line is a tool used in breeding programs to obtain new and improved agronomic characteristics. *Sletr1* mutant alleles could make interesting contributions to a breeding program because these mutants exhibit dominant inheritance in improving tomato fruit shelf life.[8] However, undesirable characteristics most likely have been expressed in F1 hybrid lines. We detected several undesirable effects of *Sletr1-1* mutation in the *Sletr1-1* F1 hybrid lines; however, these effects were not detected in the *Sletr1-2* F1 hybrid lines (Figure 2). The low survival rate of the *Sletr1-1* F1 hybrid line is most likely due to the fact that this line does not have the capacity to develop and recover new roots when the old roots are injured. Prolonged root damage without recovery caused an inhibition of water uptake that was detrimental to all of the processes involved in plant growth and development. The inability of all of the *Sletr1-1* F1 hybrid lines to recover from root injuries and develop new roots quickly resulted in secondary diseases, such as fungi that attack the root system and the stem neck. The disease symptoms of the *Sletr1-1* F1 hybrid lines were similar to those of the *Sletr1-1* mutant parent, which showed an increased susceptibility to infestation by *Fusarium oxysporum*. An undesirable effect of *ETR1* mutation was also detected in *Arabidopsis Atetr1-1*, which exhibited an increase in disease infection by pathogens such as *Botrytis cinerea*, *Fusarium solani*, *Fusarium oxysporum* f. sp. *matthiolae*, *Xanthomonas campestris* pv. Campestris, and *Pythium* spp.[20−22] Our results are consistent with the *Nr* mutant, which does not have the capacity to produce adventitious roots under waterlogging stress conditions. Ethylene has an important role during flooding stress because it initiates and is involved in adventitious root development.[23,24] Therefore, it plays an important role in mediating plant responses, which may enable the plant to survive. Our data suggest that the *Sletr1-1* F1 hybrid lines exhibited a strong ethylene-insensitive phenotype and a strong sensitivity to biotic and abiotic stresses. Therefore, *Sletr1-1* is not appropriate for breeding. However, *Sletr1-2* may have potential for breeding because its F1 hybrid lines did not show any undesirable effects under those stresses. Other studies have reported that only the *rin* mutant is suitable for use in breeding programs, whereas *Nr* is not suitable because it increases susceptibility to some pathogens.[25−27] Moreover, it has insufficient red coloration.[3,14]

Through breeding programs, the desired characteristics can be obtained. Hence, to improve the growth and yield quality of tomato plants, hybrid breeding can be used efficiently.[28] The vegetative and generative characters of *Sletr1-2* F1 hybrid lines were comparable to those of WT-MT F1 hybrid lines even though these lines were the result of crosses with the four genetic backgrounds of pure-line cultivars (Figures 3−5). Vegetative and generative performance in the *Sletr1-2* F1 and WT-MT F1 hybrid lines was indicated mostly by the intermediate characteristics resulting from the *Sletr1-2* or WT-MT parent (initially from the Micro-Tom cultivar background having both a small plant size (15−20 cm) and a small fruit size)[29] and the commercial pure-line cultivar parents. A similar study on the intermediate characteristics of F1 hybrid line yielded the same findings for *rin* and *nor* F1 hybrid lines, although *rin* had a smaller effect than *nor*.[4] Another study found intermediate average mean values for fruit set, shape, weight, TSS content, and flowers per cluster in the F1 hybrid line.[30,31] On the basis of this study, we conclude that mutation in the *SlETR1* gene of the *Sletr1-2* mutant allele did not affect vegetative and generative performance, although mutation did improve fruit shelf life of its F1 hybrid lines (Figure 7). Similar results have been shown for fruits of the heterozygous *rin* and *nor* F1 hybrid lines that had improved shelf life.[30,32] These results suggest that the effect of the *Sletr1-2* allele on fruit shelf life is a dominant genetic action and is not dependent on genetic background, although the *nor* gene is dependent on genetic background.[33] In the present study, the shelf life of the *Sletr1-2* F1 hybrid line was 4−5 days longer than that of the WT-MT F1 hybrid lines (Figure 7), which was enough to maintain the freshness of the tomato fruit. Prolonged fruit shelf life is important for transportation to distant markets, fruit storage, and handling, especially at markets and for the consumer.

During the ripening process, increases in ethylene production and respiration rate occur, and the peaks are reached in the breaker stage when the first red coloration is visible. Ethylene production and respiration then decline when fruit senescence is reached.[34] In our study, no peaks of ethylene and CO_2 were detected for the investigated fruit during storage because red fruits were used. There were similar declines in ethylene production and respiration rate during storage time until the

DOI: 10.1021/acs.jafc.5b02742
J. Agric. Food Chem. 2015, 63, 7995−8007

fruits reached senescence at 30 DPS for all of the *Sletr1-2* F1, WT-MT F1 hybrid lines, and pure-line cultivar parent (Figure 8). Mutation in the *Sletr1-2* mutant allele did not have significant effects on ethylene production and respiration rate of its F1 hybrid line, even when this mutant was crossed with the different genetic background of the pure-line cultivar parents. The respiration rates of the *Sletr1-2* F1 hybrid lines were similar to those found in the F1 hybrid line of *rin* mutant which showed that the *rin* F1 mutant had no effect on respiration rate.[11] For ethylene biosynthesis, their result for the *rin* F1 mutant conflicted with ours. The *rin* F1 hybrid lines had significantly lower ethylene production, with the peak reduced by approximately 50% in single *rin* mutant hybrids and by 25% in double-mutant hybrids.[4,11,13] The reduction in ethylene production in the *rin* F1 hybrid lines is due to reductions in the *ACO* gene expression levels.[5,35] 1-Aminocyclopropane 1-carboxylate synthase (ACS) and 1-aminocyclopropane 1-carboxylate oxidase (ACO) are involved in and important for the ethylene biosynthesis pathway. Therefore, during the ripening process, the amount of ethylene produced increases. For ethylene biosynthesis, ACS activity is a key step, whereas ACO activity is constitutive.[36] The same level of ethylene production was measured for the *Sletr1-2* F1 and WT-MT F1 hybrid lines, indicating that no changes were caused by the *SlETR1* gene mutation in the ethylene biosynthesis pathway.

The fruit ripening process is associated with several processes, such as increases in respiration rate and ethylene biosynthesis and changes in metabolic properties, including changes in fruit color, softening, texture, aroma, volatiles, sugar content, and pathogen susceptibility.[37] Color performance is an important external characteristic in tomatoes as an indicator of fruit ripeness and postharvest life.[38] Color change is easily detected when the onset of the ripening process occurs due to chlorophyll degradation and the accumulation of carotenoids, which cause the fruit to change to a red color.[5] In our study, fruit color is represented by L^* and h°, which indicate fruit brightness and color purity, respectively. Both the L^* and h° values of the *Sletr1-2* F1 hybrid lines varied according to the different genetic backgrounds of the pure-line cultivar parent, and these values were mostly higher than those for the WT-MT F1 hybrid lines and the pure-line cultivar parents at the beginning of storage (Figure 9). We suggest that the high L^* and h° values indicate that the ripening process was delayed or inhibited. Moreover, we believe that the effect of the *Sletr1-2* mutation on the fruit color was dominant or negative over dominance, depending on the genetic background. Our results are consistent with other studies that have shown that the effect of the *nor* gene on the chroma and L^* indices of color was dependent on the analyzed cross or genetic background.[33] Although the L^* and h° values were significantly different between the *Sletr1-2* F1 hybrid lines and the WT-MT F1 hybrid lines, according to visual inspection, they had almost identical red fruit colors, indicating that the fruit was red-ripened (Figure 6). Similar results for *rin* F1 hybrid lines have also shown the development of red color.[39] Contrasting results have been reported for the *nor* F1 hybrid line, which is incapable of developing a red fruit during ripening.[12]

The color change of the fruit from green to red is due to the transformation of chlorophyll to chromoplasts as a result of the deposition of lycopene and β-carotene in the fruit during the ripening process.[40] Because *Sletr1-2* has a dominant inheritance pattern,[8] *Sletr1-2* F1 hybrid lines exhibited reductions in ethylene sensitivity phenotypes, such as a delay in the ripening process, that affect other physiological changes, such as lycopene biosynthesis. The synthesis of lycopene was seemingly intimately dependent on ethylene for initiation and continuance of the response.[41] In the present study, there was a relationship between fruit color and lycopene content. Fruit with higher L^* and h° values resulted in a lower lycopene content (Figures 9 and 10). Another study showed that the increase in color was related to increases in both β-carotene and lycopene.[42] Lycopene and β-carotene in the F1 hybrid line of the *Sletr1-2* mutant were lower than in the WT-MT F1 hybrid line; however, this effect was dependent on the genetic background of the parent (Figure 10A,B). Although the *Sletr1-2* F1 hybrid line had a lower lycopene content compared with the WT-MT F1 hybrid line, its fruit had the capacity to develop red-ripened fruit (Figures 4 and 6). We believe that *Sletr1-2* has potential for use in breeding for improved tomato fruit shelf life because the lycopene and β-carotene contents and the fruit color of the *Sletr1-2* F1 hybrid lines were nearly the same as those of the wild-type F1 hybrid lines.

Firmness is an important characteristic for both indicating and helping to enhance postharvest fruit quality and shelf life, in addition to water status and cuticle structure.[43,44] Our results showed that the *Sletr1-2* F1 hybrid lines had the highest firmness values (Figure 10C), which means that softening of those fruits was delayed compared with the WT-MT F1 hybrid line and the pure-line cultivar parent. The delayed softening observed in the *Sletr1-2* F1 fruits was characterized by increased firmness during the early fruit maturation stages when the fruits were harvested. Our results are consistent with findings for the *nor* × Ca F1 hybrid line and *alc* × 'Mospomorist', which both showed improved fruit firmness compared with their parents.[33,45] Other studies have reported that the F1 hybrid line of *rin* has a lower softening value and that the F1 *nor* line has delayed fruit ripening.[32,46] From these results, we conclude that the mutation effect of the *Sletr1-2* allele on fruit firmness is a dominant genetic action in different genetic backgrounds. Because the *Sletr1-2* F1 hybrid line exhibits delayed fruit softening, *Sletr1-2* may be an interesting contributor to plant breeding programs for improving the postharvest quality of tomatoes.

For consumers, both shelf life and flavor quality influence the acceptability of fruits. TSS and TA are used in tomato fruits primarily to estimate sugar and organic acids, respectively, which are commonly associated with fruit sweetness and sourness, respectively.[47] During 30 days of postharvest storage, mutation in *Sletr1-2* did not affect the TSS in the *Sletr1-2* F1 hybrid lines, and the TSS of the *Sletr1-2* F1 hybrid lines was comparable to those of the WT-MT F1 hybrid lines. Generally, the effect of the *Sletr1-2* mutation was similar to the effect of 1-MCP in inhibiting ethylene action at the receptor level. It can be seen from other authors who studied 1-MCP that it does not affect the TSS of treated tomato fruits.[48,49] Although the TSS in *Sletr1-2* F1 hybrid line was not affected by the *Sletr1-2* mutation, the TSS was significantly different from that of the commercial pure-line cultivar parent (Figure 11A). This result is consistent with the study on the F1 hybrid line of the *nor* mutant that had a different TSS value from that of the 'Caimanta' parent.[33]

There was detected a relationship between pH and TA in all investigated fruit during storage, when fruit with a lower pH contained higher TA (Figure 11B,C). Another study also found a close relationship between total acidity and pH in tomato.[50] The *Sletr1-2* mutation had a significant effect on the pH and TA

DOI: 10.1021/acs.jafc.5b02742
J. Agric. Food Chem. 2015, 63, 7995−8007

of all of the F1 hybrid lines. Inhibition of the ethylene action as a result of mutation in the *SLETR1* gene was effective at inhibiting the loss of fruit acidity in *Sletr1-2* F1 hybrid lines; however, the effect was dependent on the genetic background of the pure-line cultivar parent. Thus, all *Sletr1-2* F1 hybrid fruits had a higher TA content. Our results are consistent with other studies that showed that the inhibition of ethylene action by 1-MCP significantly increased the TA in tomato fruits.[49] On the basis of these results, pH and TA are ethylene-dependent effects. Many studies have stated that the reduction of organic acid degradation caused by the suppression of the ethylene biosynthesis and action correlated with the reduction of respiration rate because organic acids are substrates for respiration.[47] This result is in contrast to our study, which showed that even though the respiration rates of the *Sletr1-2* F1 hybrid lines were similar to those in the WT-MT F1 hybrid lines and the pure-line cultivar parent (Figure 8B), the TA and pH were different (Figure 11B,C).

In conclusion, all of the results show that *Sletr1-2* exhibited strong inheritance patterns that improved the fruit shelf life of hybrid lines when crossed with different genetic backgrounds. Moreover, the hybrids did not show many undesirable characteristics, such as negative responses to stress conditions and highly reduced lycopene content and red fruit color. The plants provided similar levels of β-carotene and TSS and higher levels of TA and fruit firmness. All of these characteristics are important for the tomato fruit quality traits that appeal to the consumer. We conclude that the *Sletr1-2* mutant has potential as a contributor to breeding programs for the development of new tomato cultivars with improved fruit shelf life.

AUTHOR INFORMATION

Corresponding Author

*(H.E.) Phone/fax: +81-29-853-7263. E-mail: ezura@gene.tsukuba.ac.jp.

Funding

This work was supported by a grant-in-aid for scientific research category A (No. 25252008) to H.E. from the Ministry of Education, Science, Sports, and Technology of Japan.

Notes

The authors declare no competing financial interest.

ACKNOWLEDGMENTS

We thank the National BioResearch Project (NBRP), MEXT, Japan for providing the seeds of *S. lycopersicum* cv. Micro-Tom, *Sletr1-1*, *Sletr1-2*, 'Aichi First', 'Ailsa Craig', 'Moneymaker', and 'M82'. We also thank all members of our laboratory for helpful discussions throughout the work.

REFERENCES

(1) Garg, N.; Cheema, D. S. Assessment of fruit quality attributes of tomato hybrids involving ripening mutants under high temperature conditions. *Sci. Hortic.* **2011**, *131*, 29−38.

(2) Kader, A. A. Quality and safety factor: definition and evaluation for fresh horticultural crops. In *Postharvest Technology of Horticultural Crops*, 3rd ed.; Kader, A. A., Ed.; University of California, Division of Agriculture and Natural Resources: Richmond, CA, USA, 2002; pp 279−287.

(3) Opiyo, A. M.; Ying, T. J. The effects of 1-methylcyclopropene treatment on the shelf life and quality of cherry tomato (*Lycopersicon esculentum* var. *cerasiforme*) fruit. *Int. J. Food Sci. Technol.* **2005**, *40*, 665−673.

(4) Kitagawa, M.; Ito, H.; Shiina, T.; Nakamura, N.; Inakuma, T.; Kasumi, T.; Ishiguro, Y.; Yabe, K.; Ito, Y. Characterization of tomato fruit ripening and analysis of gene expression in F1 hybrids of the ripening inhibitor (*rin*) mutant. *Physiol. Plant.* **2005**, *123*, 331−338.

(5) Alexander, L.; Grierson, D. Ethylene biosynthesis and action in tomato: a model for climacteric fruit ripening. *J. Exp. Bot.* **2002**, *53*, 2039−2055.

(6) Jones, J. B. *Tomato Plant Culture: in the Field, Greenhouse, And Home Garden*; CRC Press: Boca Raton, FL, USA, 2007; pp 101−128.

(7) Lanahan, M. B.; Yen, H. C.; Giovannoni, J. J.; Kleea, H. J. The *never ripe* mutation blocks ethylene perception in tomato. *Plant Cell* **1994**, *6*, 521−530.

(8) Okabe, Y.; Asamizu, E.; Saito, T.; Matsukura, C.; Ariizumi, T.; Bres, C.; Rothan, C.; Mizaguchi, T.; Ezura, H. Tomato TILLING technology: development of a reverse genetic tool for the efficient isolation of mutants from Micro-Tom mutant libraries. *Plant Cell Physiol.* **2011**, *52*, 1994−2005.

(9) Chang, C.; Kwok, S. F.; Bleecker, A. B.; Meyerowitz, E. M. Arabidopsis ethylene-response gene ETR1: similarity of product to two-component regulators. *Science* **1993**, *262*, 539−544.

(10) Wilkinson, J. Q.; Lanahan, M. B.; Yen, H. C.; Giovannoni, J. J.; Klee, H. J. An ethylene-inducible component of signal transduction encoded by never-ripe. *Science* **1995**, *270*, 1807−1809.

(11) Tigchelaar, E. C.; Mcglasson, W. B.; Franklin, M. J. Natural and ethephon-stimulated ripening of F_1 hybrids of the ripening inhibitor (*rin*) and non-ripening (*nor*) mutants of tomato (*Lycopersicon esculentum* Mill.). *Aust. J. Plant Physiol.* **1978**, *5*, 449−456.

(12) McGlasson, W. B.; Smueghy, J. B.; Morris, L. L.; McBride, R. L.; Best, D. J.; Tigchelaar, E. C. Yield and evaluation of F_1 tomato hybrids incorporating the non-ripening *nor* gene. *Aust. J. Exp. Agric.* **1983**, *23*, 106−112.

(13) Kitagawa, M.; Nakamura, N.; Usuda, H.; Shiina, T.; Ito, H.; Yasuda, J.; Inakuma, T.; Ishiguro, Y.; Kasumi, T.; Ito, Y. Ethylene biosynthesis regulation in tomato fruit from the F_1 hybrid of the *ripening inhibitor* (*rin*) mutant. *Biosci., Biotechnol., Biochem.* **2006**, *70*, 1769−1772.

(14) Murashige, T.; Skoog, F. A revised medium for rapid growth and bioassays with tobacco tissue cultures. *Physiol. Plant.* **1962**, *15*, 473−497.

(15) Nagata, M.; Yamashita, I. Simple method for simultaneous determination of chlorophyll and carotenoids in tomato fruit. *Nippon Shokuhin Kogyo Gakkaishi* **1992**, *39*, 925−928.

(16) Dalal, K. B.; Salunkhe, D. K.; Boe, A. A.; Olsen, L. E. Certain physiological and biochemical changes in the developing tomato fruit (*Lycopersicon esculentum* Mill.). *J. Food Sci.* **1965**, *30*, 504−508.

(17) Crocker, W.; Knight, L. I.; Rose, R. C. A delicate seedling test. *Science* **1913**, *37*, 380−381.

(18) Guzmán, P.; Ecker, J. R. Exploiting the triple response of *Arabidopsis* to identify ethylene-related mutants. *Plant Cell* **1990**, *2*, 513−524.

(19) O'Malley, R. C.; Rodriguez, F. I.; Esch, J. J.; Binder, B. M.; O'Donnell, P.; Klee, H. J.; Bleecker, A. B. Ethylene-binding activity, gene expression levels, and receptor system output for ethylene receptor family members from *Arabidopsis* and tomato. *Plant J.* **2005**, *41*, 651−659.

(20) Geraats, B. P. J.; Bakker, P. A. H. M.; van Loon, L. C. Ethylene insensitivity impairs resistance to soilborne pathogens in tobacco and *Arabidopsis thaliana*. *Mol. Plant−Microbe Interact.* **2002**, *15*, 1078−1085.

(21) Geraats, B. P. J.; Bakker, P. A. H. M.; Lawrence, C. B.; Achuo, E. A.; Höfte, M.; van Loon, L. C. Ethylene-insensitive tobacco shows differentially altered susceptibility to different pathogens. *Phytopathology* **2003**, *93*, 813−821.

(22) O'Donnell, P. J.; Schmelz, E. A.; Moussatche, P.; Lund, S. T.; Jones, J. B.; Klee, H. J. Susceptible to intolerance a range of hormonal actions in a susceptible *Arabidopsis* pathogen response. *Plant J.* **2003**, *33*, 245−257.

DOI: 10.1021/acs.jafc.5b02742
J. Agric. Food Chem. 2015, 63, 7995−8007

(23) Vidoz, M. L.; Loreti, E.; Mensuali, A.; Alpi, A.; Perata, P. Hormonal interplay during adventitious root formation in flooded tomato plants. *Plant J.* **2010**, *63*, 551−562.
(24) Visser, E. J. W.; Voesenek, L. A. C. J. Acclimation to soil flooding − sensing and signal-transduction. *Root Physiol.: Gene Funct.* **2004**, *254*, 197−214.
(25) Francia, D.; Demaria, D.; Calderini, O.; Ferraris, L.; Valentino, D.; Arcioni, S.; Tamietti, G.; Cardinale, F. Wounding induces resistance to pathogens with different lifestyles in tomato: role of ethylene in cross-protection. *Plant, Cell Environ.* **2007**, *30*, 1357−1365.
(26) Kavroulakis, N.; Ntougias, S.; Zervakis, G. I.; Ehaliotis, C.; Haralampidis, K.; Papadopoulou, K. K. Role of ethylene in the protection of tomato plants against soil-borne fungal pathogens conferred by an endophytic *Fusarium solani* strain. *J. Exp. Bot.* **2007**, *58*, 3853−3864.
(27) Cantu, D.; Blanco-Ulate, B.; Yang, L.; Labavitch, J. M. Ripening-regulated susceptibility of tomato fruit to *Botrytis cinerea* requires *NOR* but not *RIN* or ethylene. *Plant Physiol.* **2009**, *150*, 1434−1449.
(28) Hannan, M. M.; Biswas, M. K.; Ahmed, M. B.; Hossain, M.; Islam, R. Combining ability analysis of yield and yield components in tomato (*Lycopersicon esculentum* Mill.). *Turk. J. Bot.* **2007**, *31*, 559−563.
(29) Matsukura, C.; Aoki, K.; Fukuda, N.; Mizoguchi, T.; Asamizu, E.; Saito, T.; Shibata, D.; Ezura, H. Comprehensive resources for tomato functional genomics based on the miniature model tomato Micro-Tom. *Curr. Genomics* **2008**, *9*, 436−443.
(30) Pratta, G.; Zorzoli, R.; Picardi, L. A. Diallel analysis of production traits among domestic, exotic and mutant germplasms of *Lycopersicon*. *Genet. Mol. Res.* **2003**, *2*, 206−213.
(31) Shalaby, T. A. Mode of gene action, heterosis and inbreeding depression for yield and its components in tomato (*Solanum lycopersicum* L.). *Sci. Hortic.* **2013**, *164*, 540−543.
(32) Buescher, R. W.; Sistruck, W. A.; Tigchelaar, E. C.; Ng, T. J. Softening, pectolytic activity, and storage life of *rin* and *nor* tomato hybrids. *HortScience* **1976**, *11*, 603−604.
(33) Rodríguez, G. R.; Pratta, G. R.; Liberatti, D. R.; Zorzoli, R.; Picardi, L. A. Inheritance of shelf life and other quality traits of tomato fruit estimated from F1's, F2's and backcross generatios derived from standard cultivar, *nor* homozygote and wild cherry tomato. *Euphytica* **2010**, *176*, 137−147.
(34) Munns, R.; Schmidt, S.; Christine, B. *Plant in Action*, 2nd ed.; http://plantsinaction.science.uq.edu.au/ (Sept 10, 2014).
(35) Thompson, A. J.; Tor, M.; Barry, C. S.; Vrebalov, J.; Orfila, C.; Jarvis, M. C.; Giovannoni, J. J.; Grierson, D.; Seymour, G. B. Molecular and genetic characterization of a novel pleiotropic tomato-ripening mutant. *Plant Physiol.* **1999**, *120*, 383−389.
(36) Theologis, A.; Oeller, P. W.; Wong, L. M.; Rottmann, W. H.; Gantz, D. M. Use of a tomato mutant constructed with reverse genetics to study fruit ripening, a complex developmental process. *Dev. Genet.* **1993**, *14*, 282−295.
(37) Barry, C. S.; Giovannoni, J. J. Ethylene and fruit ripening. *J. Plant Growth Regul.* **2007**, *26*, 143−159.
(38) Shibli, R. A.; Kushad, M.; Yousef, G. G.; Lila, M. A. Physiological and biochemical responses of tomato microshoots to induced salinity stress with associated ethylene accumulation. *Plant Growth Regul.* **2007**, *51*, 159−169.
(39) Nguyen, V. Q.; Ashcroft, W. J.; Jones, K. J.; McGlasson, W. B. Evaluation of F1 hybrids incorporating the *rin* (ripening inhibitor) gene to improve the storage life and fruit quality of fresh market tomatoes (*Lycopersicon esculentum* Mill). *Aust. J. Exp. Agric.* **1991**, *31*, 407−413.
(40) Sies, H.; Stahl, W. Lycopene: antioxidant and biological effects and its bioavailability in the human. *Exp. Biol. Med.* **1998**, *218*, 121−124.
(41) Jeffery, D.; Smith, C.; Goodenough, P.; Prosser, I.; Grierson, D. Ethylene-independent and ethylene-dependent biochemical changes in ripening tomatoes. *Plant Physiol.* **1984**, *74*, 32−38.
(42) Boe, A. A.; Salunkhe, D. K. Ripening tomatoes: ethylene, oxygen and light treatments. *Econ. Bot.* **1967**, *21*, 312−319.
(43) Matas, A. J.; Gapper, N. E.; Chung, M. Y.; Giovannoni, J. J.; Rose, J. K. C. Biology and genetic engineering of fruit matura- tion for enhanced quality and shelf-life. *Curr. Opin. Biotechnol.* **2009**, *20*, 197−203.
(44) Saladie, M.; Matas, A. J.; Isaacson, T.; Jenks, M. A.; Goodwin, S. M.; Niklas, K. J.; Ren, X. L.; Labavitch, J. M.; Shackel, K. A.; Fernie, A. R.; Lytovchenko, A.; O'Neill, M. A.; Watkins, C. B.; Rose, J. K. C. A reevaluation of the key factors that influence tomato fruit softening and integrity. *Plant Physiol.* **2007**, *144*, 1012−1028.
(45) Dias, T. J. M.; Maluf, W. R.; Faria, M. V.; De Freitas, J. A. *Alcobaça allele* and genotypic backgrounds affect yield and fruit shelf life of tomato hybrids. *Sci. Agric.* **2003**, *60*, 269−275.
(46) Aly, M. A. A.; Beltagy, A. S.; Hobson, G. E. Comparison between three tomato lines (RIN RIN, RIN rin and rin rin) in ACC content loss in firmness and loss in weight. *Acta Hortic.* **1986**, *190*, 183−190.
(47) Defilippi, B. G.; Dandekar, A. M.; Kader, A. A. Impact of suppression of ethylene action and biosynthesis on flavor metabolites in apple (*Malus domestica* Borkh) fruits. *J. Agric. Food Chem.* **2004**, *52*, 5694−5701.
(48) Mir, N.; Canoles, M.; Beaudry, R.; Baldwin, E.; Pal Mehla, C. Inhibiting tomato ripening with 1-methylcyclopropene. *J. Am. Soc. Hortic. Sci.* **2004**, *129*, 112−120.
(49) Opiyo, A. M.; Ying, T. J. The effects of 1-methylcyclopropene treatment on the shelf life and quality of cherry tomato (*Lycopersicon esculentum* var. *cerasiforme*) fruit. *Int. J. Food Sci. Technol.* **2005**, *40*, 665−73.
(50) Paulson, K. N.; Stevens, M. A. Relationships among titratable acidity, pH and buffer composition of tomato fruits. *J. Food Sci.* **1974**, *39*, 354−357.

DOI: 10.1021/acs.jafc.5b02742
J. Agric. Food Chem. 2015, 63, 7995−8007

Table 1. Statistical Analysis of Grain Elemental Concentration Traits Generated at E1 and E2, Hangzhou, China, in 2012 among the USDA Rice Mini-Core Collection

trait	environment type	mean ± SE	minimum	maximum	heritability (%)	genotype[a] (G)	environment[a] (E)	genotype × environment[a] (G×E)
micronutrients (mg/kg)								
Zn	E1	32 ± 0.36	19	55	85.9			
	E2	26 ± 0.29	16	49	92.6	44.70**[b]	342.51**	39.71**
Fe	E1	17 ± 0.35	7	46	74.3	27.39**	362.52**	16.91**
	E2	11 ± 0.27	4	47	96.1			
Mn	E1	31 ± 0.44	13	59	84.6	24.25**	4.28**	14.41**
	E2	31 ± 0.46	14	56	86.8			
Cu	E1	6 ± 0.07	3	9	88.1			
	E2	3 ± 0.07	2	9	95.7	26.62**	2114.30**	17.97**
macronutrients (mg/kg)								
P	E1	3474 ± 27	2082	4862	72.3	28.39**	2.09**	21.95**
	E2	3296 ± 36	1775	5613	69.6			
Ca	E1	126 ± 1.5	18	274	63.6	22.77**	2007.60**	20.70**
	E2	129 ± 2.4	19	280	91.4			
K	E1	2919 ± 21	1744	3699	72.9	24.68**	5.55**	19.22**
	E2	2789 ± 29	1256	4361	61.2			
Mg	E1	1406 ± 12	848	2978	56.3	17.94**	0.96**	13.68**
	E2	1323 ± 17	674	2536	69.4			

[a]Depicts relevant effect (F value). [b]**, values are highly significant at Pr > F = <0.001.

MATERIALS AND METHODS

Plant Material. The USDA Rice Mini-Core Collection was introduced from the Genetic Stock *Orzya* collection (managed by the Dale Bumpers National Rice Research Center of the USDA ARS, Stuttgart, AR, USA), which consists of 211 *O. sativa*, 5 *O. glaberrima*, 2 *O. rufipogon*, and 1 *O. nivara* accession. In this study, 219 accessions were cultivated in two field locations: the Experimental Farm of Zhejiang University, Zijingang Campus in Hangzhou (environment 1, E1) and the Experimental Farm of Zhejiang Zhijiang Seed Co. in Yuhang (environment 2, E2) during the growing season of 2012. The samples were grown in triplicate in randomized complete block design in both locations. The two locations are not too distant from one another, but the soils in the two locations were quite different; the field in E1 was recently reclaimed and had low fertility made up of fluvo-aquic soils, whereas the field in E2 was a traditional rice-growing area with purplish clayey soils. Routine agronomic practice was adopted during the growth of rice plants. The wild relatives, *O. glaberrima*, *O. rufipogon*, and *O. nivara*, were excluded from association mapping analysis as they contain many rare alleles that may increase the risk of type I errors or spurious associations.[22] Of 219 accessions grown, only 175 flowered early enough to produce seeds. Those with late flowering could not set seeds and hence were excluded from our analysis (Table S1 in the Supporting Information).

Preparation, Extraction, and Measurement of Grain Mineral Elements. The harvested rice grains were dried, cleared, and dehusked in an electrical dehusker (model B-76, Huangyan, Zhejiang, China) and subsequently used for the detection of four microelements (Zn, Fe, Cu, and Mn) and four macroelements (P, Ca, K, and Mg), respectively.

The dehusked rice samples were ground to pass a 100-mesh screen with a cyclone grinder (model 3010-019, Fort Collins, CO, USA). About 0.15 g of powdered material was digested with 6 mL of nitric acid (HNO_3) and 0.2 mLof hydrogen peroxide (H_2O_2) using a microwave digestion system (Microwave 3000, Anton PAAR, Graz, Austria). The microwave digester was programmed to ramp in high temperature and pressure set at a final power of 1200 W for 20 min. The digested samples were adjusted to a volume of 25 mL with double-deionized water. Finally, multielement analysis on grain digests was carried out by inductively coupled plasma optical emission spectrometer or ICP-OES (Optima 8000DV, PerkinElmer, USA). To control the variation within samples, each sample was measured three times, and the mean of triplicate observations was used to represent the content of mineral elements in each sample. For error control among samples, all samples were measured in a set of 20 samples containing two blanks and two standard reference samples with known concentrations of mineral elements. Standard reference samples of rice grains were used to compensate for possible matrix interference variations during microwave digestion, whereas external standards were used to construct the standard curve for calibration of ICP.

Data Analysis. Correlation analysis was performed to characterize the relationships between the examined elements. The Pearson correlation coefficients between traits were calculated on the basis of the mean values over three replications using two significance levels (p < 0.001), via the Correlate Procedure in SPSS version 16.0 for Windows (SPSS Inc., Chicago, IL, USA).

The analysis of variance for eight essential elements was conducted by the MIXED Procedure in SAS version 9.2, where genotype was defined as a fixed factor and replication and interaction between replication and genotype were random factors. Broad-sense heritability was calculated as $H^2 = \sigma g^2/ (\sigma g^2 + \sigma e^2/n)$, where σg^2 is the genotypic variance, σe^2 is the environmental variance, and n is the number of replications.

Genotyping. A total of 155 molecular markers covering the entire rice genome, approximately one marker per 10 cM on average, were used for the genotyping of the 175 accessions in the USDA Mini-Core Collection. Among the markers, 149 SSRs were obtained from the Gramene database (http://www.gramene.org/) and 5 other SSRs, AP5652-1, AP5652-2, AL606682-1, con673, and LJSSR1, with the remaining marker an indel at the *Rc* locus, named Rid 12.[21] The genetic and physical positions of SSR markers were determined using the map of Gramene Annotated Nipponbare Sequence 2009 (http://www.gramene.org/) and Rice TOGO Browser (http://agri-trait.dna.affrc.go.jp/). The obtained information on these markers was thus used to align the SSR marker maps and is reported here on the basis of the markers' cM genetic locations.

Association Mapping. The association between molecular markers and grain elemental content was carried out by the General Linear Model (GLM) and Mixed Linear Model (MLM), implemented in Tassel version 3.0.167 software (http://www2.maizegenetics.net/). Aimed at GLM, the Q method was performed where population membership estimates served as covariates. In MLM analysis markers tested and subpopulation data (Q matrix) were considered as fixed-effect factors, whereas the kinship matrix was considered as a random-effect factor,[23] taking the gross level population structure (Q) and kinship (K) into account.[24,25] The P value (marker) determining

DOI: 10.1021/acs.jafc.5b01191
J. Agric. Food Chem. 2015, 63, 8008−8016

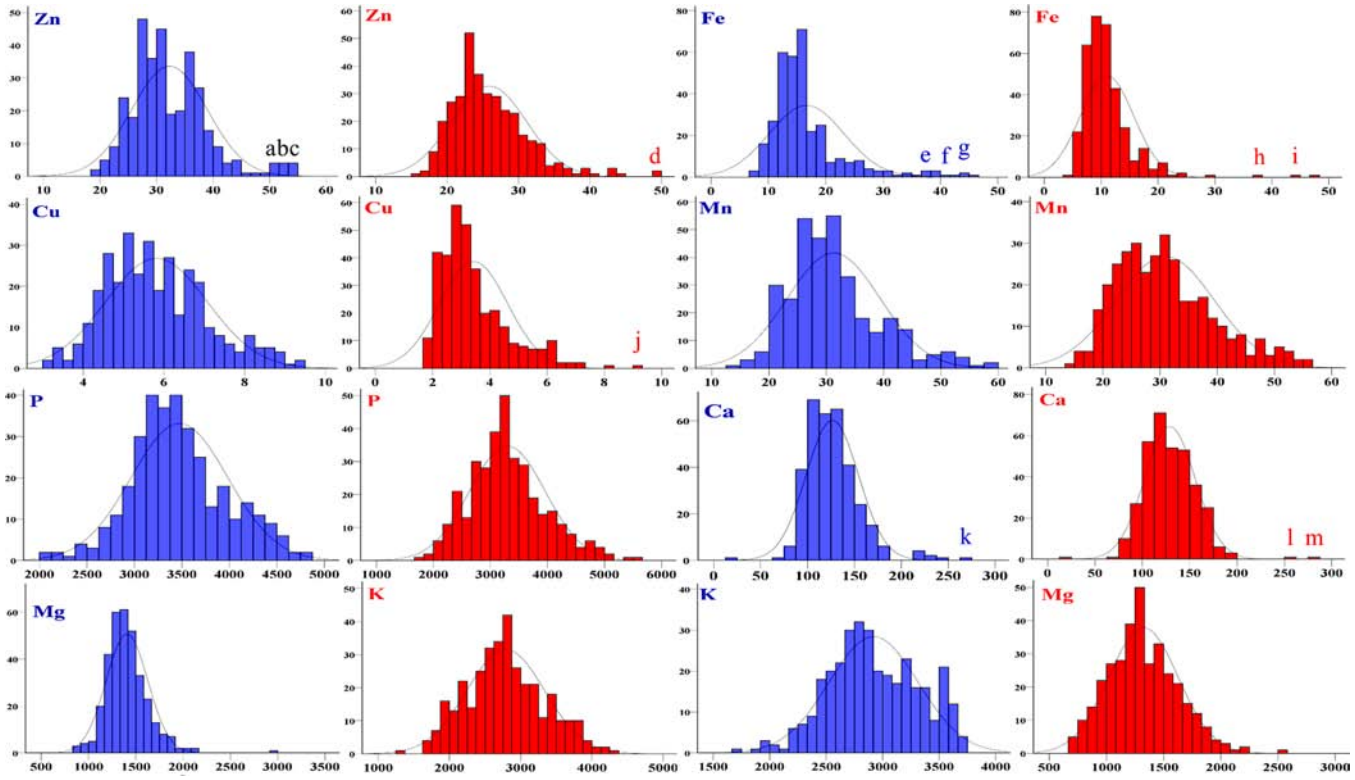

Figure 1. Histograms showing frequency distribution of micro- and macro-elements among USDA mini-core germplasm cultivated in E1 (shown in blue color) and E2 (shown in red), Hangzhou, in 2012. The values are shown in mg/kg for micro- and macro-elements. The *y*-axis denotes the value of frequency, whereas the *x*-axis shows resultant groups of accessions. *a*–*z* are the out groups, where *a* = 311180, *b* = 310724, *c* = 311206, *d* = 311689, *e* = 310598, *f* = 310131, *g* = 310998, *h* = 311635, *i* = 311643, *j* = 311269, *k* = 311236, *l* = 311689, *m* = 311140, *n* = 310102, and *o* = 311677 are the accessions of these outgroups as given in Supporting Information Table S1.

Table 2. Pearson Correlation for Micro- and Macroelements among the USDA Rice Mini-Core Collection, Evaluated in Replicated Tests at E1 (Upper Right) and E2 (Lower Left) in Hangzhou, China, in 2012

	Zn	Fe	Mn	Cu	P	Ca	K	Mg
Zn		**0.503**[a]	**0.40****	**0.398****	**0.427****	**0.364****	**0.463****	**0.424****
Fe	0.459**		**0.36****	**0.255****	**0.353****	**0.326****	**0.456****	**0.409****
Mn	0.456**	0.275**		**0.436****	**0.528****	**0.26****	**0.428****	**0.394****
Cu	0.525**	0.363**	0.46**		**0.50****	**0.489****	**0.439****	**0.449****
P	0.637**	0.609**	0.452**	0.460**		**0.353****	**0.728****	**0.80****
Ca	0.452**	0.459**	0.238**	0.536**	0.567**		**0.430****	**0.324****
K	0.59**	0.532**	0.427**	0.563**	0.882**	0.64**		**0.659****
Mg	0.572**	0.60**	0.379**	0.423**	0.963**	0.564**	0.825**	

[a]**, correlation is significant at the 0.01 level (two-tailed).

whether the SSR marker is associated with the trait and the R^2 (marker) indicating the fraction of the total variation explained by the marker were recorded. Markers with the adjusted *P* value >0.001 were regarded as significant. Genetic maps were constructed using MapDraw V2.1.[26]

RESULTS

Genotypic and Environmental Effects on Grain Elemental Concentration. The mean values, ranges, heritability and related data of seed mineral concentrations are presented in Table 1. Analysis of variance (ANOVA) demonstrated significant ($p < 0.05$) genotypic and environmental variations for all the elements. Nearly all fell into similar range of concentrations in both environments.

The effects of environment, genotype, and interaction of genotype × environment on concentrations of micro- and macroelements were all highly significant ($p < 0.00001$). The maximum genotypic and genotype × environment effect was observed for Zn and Mg. The greatest effect of environment was detected for Cu (2114.30) and the lowest for Mg (0.96) (Table 1).

The average concentrations of both micro- and macro-elements in grains of E1 were significantly higher than in grains of E2, except Ca and Mn, which were similar in both environments. P was found to be the most abundant grain element, with concentrations of 3474 and 3296 mg/kg in E1 and E2, respectively, followed by K, Mg, and Ca (Table 1). Among the micronutrients, Mn was the most abundant, with concentrations of 31 mg/kg in both E1 and E2, followed by Zn, Fe, and Cu (Table 1).

Frequency distributions of accessions' phenotype from both locations showed clear differences due to the strong environmental effect on the concentrations of micro- and macroele-

DOI: 10.1021/acs.jafc.5b01191
J. Agric. Food Chem. 2015, 63, 8008–8016

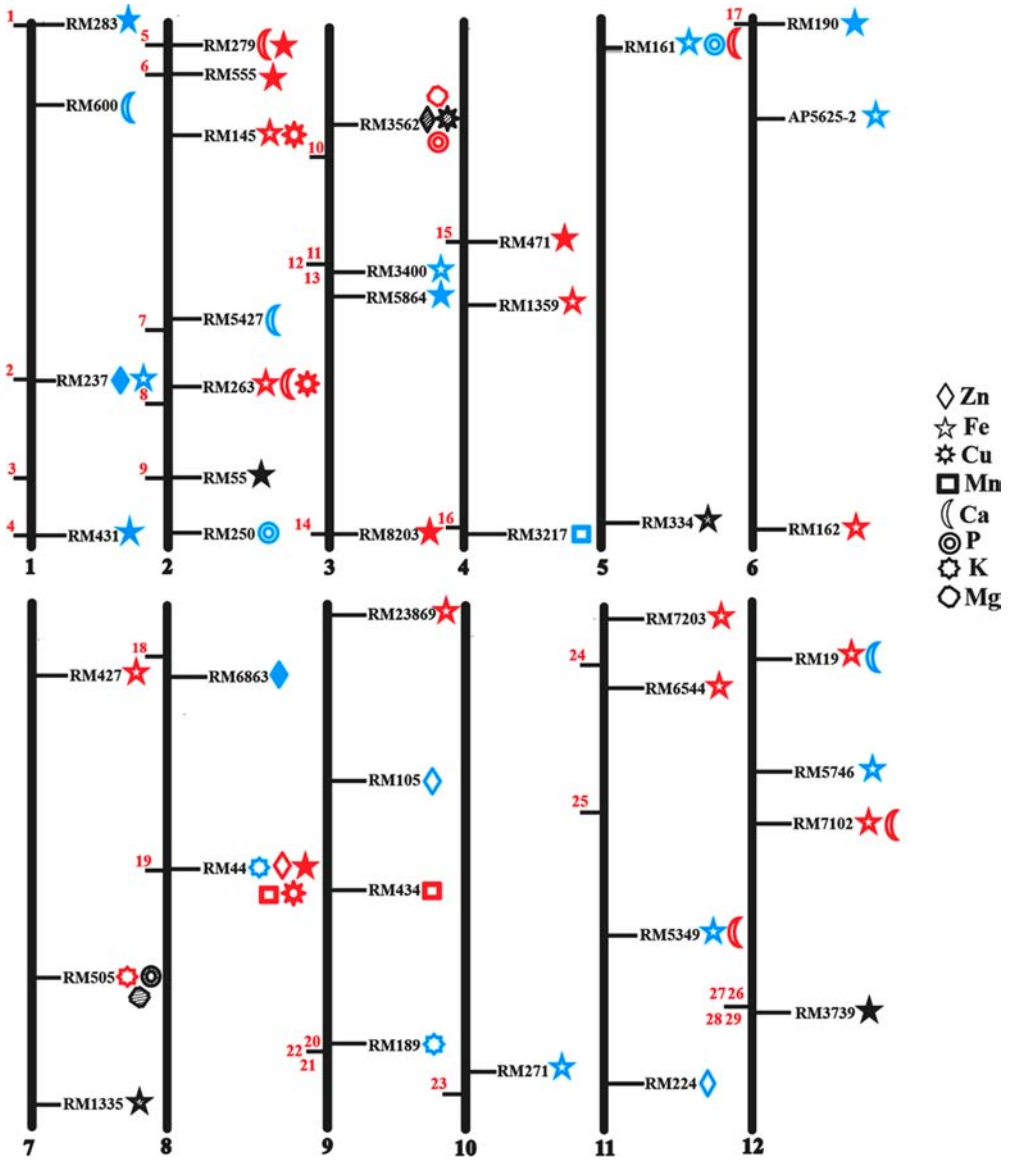

Figure 2. Sketch genetic maps of SSR markers associated with grain (brown rice) Zn, Fe, Cu, Mn, Ca, P, K, and Mg concentrations in different chromosomes. Chromosome numbers are indicated below; horizontal bars represent loci with associated marker name labeled to the right. The location information on these markers was downloaded from Gramene (http://gramene.org/) and Rice Togo Browser (http://agri-trait.dna.affrc.go.jp/). The genetic maps were drawn by Map Draw v 2.1xls. Every element is represented by a specific symbol; solid fill represents association similar to a reference at the same location; striated for consistency of marker across two locations; blue color indicates marker association with data from E1 (Zijingang), red for E2 (Yuhang), and black for both locations. The numbers on the left of each chromosome show the co-located reference from the literature: 1, 3, 14 = Norton et al.;[38] 2 = Stangoulis et al.;[32] 4, 8, 15, 16, 28 = Ishikawa et al.;[30] 5, 6, 10, 11, 12, 18, 18, 20, 21, 22, 23, 25, 26, 27 = Gracia-Oliveira et al.;[37] 7, 13, 24 = Lu et al.;[45] 9, 17, 19, 29 = Zhang et al.[8]].

ments (Figure 1). This variation existed among individual elements in the same environment as well as the same element in different environments. Among the micro and macroelements, highest variation was observed in Cu and K, respectively, in E1. The lowest variation was shown by Fe in both environments, whereas Mg showed greater variation in E2.

Correlations of Grain Elemental Concentrations and Heritability. Correlation analyses revealed a strong positive correlation between the concentrations of macro- and microelements. Overall greater correlations were found among macroelements than among microelements, where stronger correlations were present among the macroelements than among microelements. Element P strongly correlated with other macro- and microelements. The strongest correlation was exhibited among P and Mg, followed by P−K and P−Ca, across E1 and E2. Similarly, Mg and K were strongly correlated from E1 and E2, respectively. Among microelements, P strongly correlated with Fe and Zn (Table 2).

Microelements showed strong to medium correlations that were more or less consistent in the two locations. It was observed that microelements were more strongly correlated with macroelements, as compared to the microelements. The correlation among Zn and Fe was strongly positive in E1 and E2, respectively, followed by Mn and Cu. Among macroelements, Zn showed higher correlations following the descending order K < Mg < Ca.

The proportion of phenotypic variance explained by genotype is also known as broad sense heritability (H^2). The

DOI: 10.1021/acs.jafc.5b01191
J. Agric. Food Chem. 2015, 63, 8008−8016

heritability of each of the eight elements in the two environments was >60%, indicating that these traits were suitable for association mapping (Table 1). Generally high heritability was observed for Fe followed by Cu, Zn, and Ca, which had H^2 > 90% from E2. Microelements exhibited high levels of heritability as well, whereas medium to high levels of heritability were observed for macroelements. Among the macroelements, high heritability was observed for K, followed by P, Ca, and Mg from E1. Although the heritability of Mg was <60% from E1, it was considered for association mapping as it exhibited 69.39% heritability from E2. Similar variation was observed in values of H^2 among microelements across two environments (Table 1).

QTLs/Markers Associated with Grain Elemental Concentrations. A total of 60 QTLs, that is, 30 each in E1 and E2, were identified to have significant association with grain elemental concentrations. Among the eight elements, Fe concentration was associated with the highest number of markers (16/E1 in 13/E2), followed by Zn (5/E1, 2/E2) and Ca (3/E1, 4/E2). Mg was associated only with one marker in each environment. In E1, 16 of the 30 markers were associated with grain Fe, 5 with Zn, 3 with Ca, 2 each with K and P, and 1 each with Cu, Mg, and Mn. Likewise, 13 of the 30 markers in E2 were associated with grain Fe, 5 with Cu, 4 with Ca, 2 each with Zn, Mn, and P, and 1 each with K and Mg (Figure 2).

The 60 element marker associations were often found linked or grouped into multielement clusters, where this clustering was especially common in E2. Three such synchronous associations were detected in E1, for example, RM 237 co-associated with Fe and Zn and RM3562 with Zn and Cu, whereas RM161 co-associated with Fe and P. Similarly, 5 co-associations were identified in E2, for example, RM3562 with Zn, Cu, P, and Mg; RM44 with Zn, Cu, and Mn; RM263 with Fe, Cu, and Ca; RM279 with Fe and Ca, Cu; RM7102 with Fe and Ca; and RM145 with Fe and Cu, respectively (Figure 1 and Figure S2 in the Supporting Information). Markers RM3562, RM3739, RM55, RM1335, RM334, and RM505 were consistently true among both locations. For example, RM3562 associated with Zn and Cu, RM505 with Mg, and the rest with Fe. In addition, the same marker also associated with different traits across two locations. RM44 proved to be a unique marker associating with K (E1), Zn, Fe, Cu, and Mn (E2) (Tables S2 and S3 in the Supporting Information).

DISCUSSION

In this study, we identified 60 QTLs/marker loci associated with rice grain elemental concentrations by using GWA mapping approaches. We also identified co-located markers for different elemental concentrations. Moreover, adequate genetic variations in concentrations of zinc, iron, and other essential elements were also observed among USDA Mini-Core accessions. The USDA Mini-Core Rice Collection has a unique genetic diversity and has been characterized for identification of genes and QTLs for a number of traits. These traits include grain yield, harvest index, sheath blight resistance, hull silica concentration, and protein concentration.[10,27,28] About 20 new marker-grain elemental concentration associations are observed in the present study. These new associations are concerned with important grain elements such as Zn, Fe, and P along with Mn, Cu, Ca, and K. Zn, Fe, and P are considered important as their deficiency is causing hazards for the human race.

A wide range of variation was observed in contents of micro and macroelements of rice grains. These results are in accordance with the values reported by other researchers in different rice populations.[8,29−32] We found that a few accessions performed consistently across the two environments, indicating that these rice varieties can be grown and developed for biofortification programs from a grain elemental concentration perspective, especially zinc and iron. The genotypes with high grain Zn content can be a genetic source for breeding high-Zn varieties (data not shown).

Correlation analysis of different characteristics is considered very useful in exploring interrelationships.[33] In our case, numerous significant correlations were found between the different grain nutrient concentrations. Particularly, close associations existed among all four macronutrients and micronutrients or with each other. These correlations may be due to the impact of a single gene on multiple grain elemental concentrations or co-association of physically close located genes. Our observations are in agreement with previous studies.[8,31−33] The pattern of the frequency distribution in the USDA Mini-Core Collection revealed a continuous variation in all elements analyzed, suggesting that elemental uptake and subsequent accumulation in rice may be controlled by multiple genes.

It is reported that rice accessions derived from different geographic regions react to environmental signals differently.[34] Our data showed that grain concentration traits for all elements were significantly affected by environment and environment × genotype interaction, suggesting genotypic sensitivities to differences in environmental conditions in the two locations. The USDA Mini-Core represents a wide geographical and ecological diversity of rice. Therefore, the prevailing genotype × environment interaction for the accumulation of elements may be the reason for having different association results across the two locations.[35] Further elucidation of genotype × environment interaction for grain elements and related traits is required.

To comprehend the underlying genetics for the accumulation of grain elemental concentration, many researchers used different populations of rice as experimental material such as double haploids, introgression lines, recombinant inbred lines (RILs), and backcross introgression lines (BILs). RILs and BILs maintain more or less different environmental conditions.[8,19,30,32,34,36,37] The lines derived from a biparent cross shared a relatively simple genetic background. The present study is the first report of its kind about GWA mapping of grain elemental concentration in rice. Table S4 in the Supporting Information shows a comparison of a few previous works. Some of the regions associating with markers identified in this study are confirmatory, as they have been previously identified as regions controlling elemental concentration in other rice mapping populations (Table S5 in the Supporting Information).[34,38] For example, in our study zinc was associated with RM237, RM224, RM105, RM6863, RM3562, and RM44 across the two locations. Previously, a number of QTLs/SSR markers linked with zinc were reported around the same regions.[32,37]

Micro- and macroelements were positively correlated, which is reflected in the co-location of associated makers in the current study. The co-locations of markers associated with grain elemental concentration suggest the importance of these regions for mineral accumulation in rice grain and may be due to physiological coupling of the accumulation of certain minerals or tight linkage of different genes.[37] Co-locations of QTLs/markers linked with grain concentration of Zn and Fe have been described by earlier workers.[8,32,37−39] RM505 co-

DOI: 10.1021/acs.jafc.5b01191
J. Agric. Food Chem. 2015, 63, 8008−8016

Table 3. Co-location of Molecular Markers Associated with Grain Element Concentration and Genes for Metal Transport

						physical distance (Mbp)		genetic distance (cM)	
no.	marker	element	chr	gene and locus	gene function	marker	gene	marker	gene
1	RM237	Zn	1	vacuolar ATP synthase subunit E, vacuolar proton pump E subunit Os01g0659200	proton-transport, ATP hydrolysis coupled proton transport	28.57	28.57	113	113
2	RM431	Fe	1	*OSZIP1* Os01g0972200	metal ion transport, iron, zinc ion transport	40.08−40.21	44.8	149.1−150.7	180
3	RM145, RM555, and RM279	Fe	2	1. *OsHMA4* Os02g0196600 2. aspartate aminotransferase	metal transporter, metal efflux, transferase activity	7.74/4.04/2.67	5.26/7.74	36.8/18.4/12.8	25.8/36.8
4	RM279 and RM555	Ca, Fe	2	*OsACA2* Os02g0176700	Ca transport, cation transport	2.67/4.04	3.83	12.8/18.4	17.6
5	RM3562	Cu, Mg, P, Zn	3	1. *OsNAS1* Os03g0307300 2. *OsNAS2* Os03g0307200 3. *OsDMAS1* Os03g0237100 4. similar to 14 kDa zinc-binding protein (protein kinase C inhibitor) Os03g0322500 5. cytidine and deoxycytidylate deaminase zinc-binding region family protein Os03g0321900	Zn, iron, and other metal transport, zinc binding	11.58	11.29−11.58/ 11.29−11.58/ 6.71−6.78/ 11.29−11.58/ 11.29−11.58	50.8	49.3−50.8/ 49.3−50.8/ 31−31.3/ 49.3−50.8/ 49.3−50.8/
6	MRG4864/ RM5864 and RM3400	Fe	3	*OsZIP2* Os03g0411800	metal ion transporter, zinc ion transport, transmembrane transport	23.10− 23.14/ 17.6	17.59	88.7/83.3	83.3
7	RM8203	Fe	3	*OsCNGC14* Os03g0758300	Ca transport	32.36	32.36	140.1	140.1
8	RM3217	Mn, Fe	4	*OsZIP3* Os04g0613000	metal ion transport	30.72	31.2	100.7	102.7
9	RM161	Fe	5	1. *OsZIP5* Os05g0472700 2. *OsZIP9* Os05g0472400	metal ion transport, zinc ion transport/cation transport, zinc ion transport, transmembrane transport	20.88	22.97	80.7	95.8
10	RM162	Fe	6	1. *OsHMA2* Os06g0700700 2. ABC transporter domain containing protein Os06g0607700	metal ion transport, metal ion binding, ATP binding	24.92	30.28/24.9	87.5	115.9/88.5
11	RM1335	Fe	7	1. *OsNAS3* Os07g0689600 2. peroxidase Os07g0677300 3. potassium transporter 7 *OsHAK7* Os07g0669700 4. heavy metal transporter Os07g0671400	metal ion transport, metal ion binding, K ion transporter,	29.34−29.39	30.25/29.67/ 29.34−29.39/ 29.34−29.39	115.5− 115.8	118.6/116.6/ 115.5−115.8/ 115.5−115.8
12	RM6863 and RM44	Zn	8	*OsZIP4* Os08g0207500 lies between rm6863 and rm44	zinc ion transport, metal ion transport	2.06/11.67	6−7.4	16.4/54	44.6−45.6

J. Agric. Food Chem. 2015, 63, 8008−8016
DOI:10.1021/acs.jafc.5b01191

Table 3. continued

no.	marker	element	chr	gene and locus	gene function	physical distance (Mbp)		genetic distance (cM)	
						marker	gene	marker	gene
13	RM105	Zn	9	outer mitochondrial membrane protein porin -boltage-dependent anion- selective channel protein Os09g0361400	anion transport, regulation of anion transport, zinc ion transmembrane transporter activity	12.41	12.41	36	36
14	RM189	K	9	*OsCNGC9*, Os09g0558300	conducting Ca^{2+} through the plant cell plasma membrane	23.12	23	91.8	91.5
15	RM271	Fe	10	Os10g0456800 CHY zinc finger family protein	zinc ion binding, metal ion binding	17.04	17.04	41.9	41.9
16	RM19	Ca, Fe	12	*OsACA9* Os12g0136900	Ca transport	2.25	1.61−1.87	12.2	10.3−11.5

associated with K, P, and Mg at chromosome 7, making a cluster of all macroelements except Ca, whereas all microelements shared the same loci at chromosome 8 with the exception of K. Zhang et al.[29] reported two loci associated with elements, P, Mg, and K, one each on chromosomes 5 and 7. This co-location of markers is also in congruence with correlation existing among respective elements. The co-locations of multiple traits for element concentration at different loci may be due to underlying genes involved in maintaining elemental/metal homeostasis. We can infer that the co-locations observed in the current study may have resulted from close linkage of genes.

The results of various earlier and recent studies point toward the existence and connection of a complex coordinated system involving many genes associated with the regulation, uptake, sequestration, distribution, mobilization, and localization of minerals in rice.[8,34] We found 16 genetic regions where genes responsible for metal ion binding and transport lie at the same locus or close to the molecular markers associated with element grain concentration (Table 3 and Figure S2 in the Supporting Information). This can be a very important finding for unraveling the mechanism of acquisition and transport of metal/element in rice seeds. Of these, RM3562, which co-associated with Cu, Mg, P, and Zn, has seven genes around this region, including *OsNAS1*, *OsNAS2*, *OsDMAS1*, 14 kDa zinc-binding protein, and cytidine and deoxycytidylate deaminase zinc-binding region family protein. Members of the NAS family have been shown to be involved in enhancing Fe and Zn in rice endosperm.[40,41] Likewise, the role of *OsDMAS1* in iron acquisition was demonstrated by Bashir et al.[42] Five ZIP transporters were also located in the regions associated with Fe and Zn. This information can be useful for future analysis of these genetic regions, linked genes, and traits. We analyzed the *OsZIP4* (Os08g0207500) gene lying in the region of RM6863 and RM44 and found many polymorphic regions (data under process). Future elucidation may result in some novel findings relating to these transporters. The current study presents a novel method of exploiting data and information provided by bioinformatics for exploring genes/factors associated with certain phenotypes.

Another important feature of the current study is the consistency of 6/60 markers across the two environmental locations. This reflects a large environmental effect on the traits under study. Zhao et al.[20] and Norton et al.[35] have previously reported a similar environmental influence on flowering time and grain elemental contents. It has also been demonstrated that the environment greatly affects the accumulation of elements in rice grains.[8,13,29,35,38,43,44]

■ ASSOCIATED CONTENT

Supporting Information

The Supporting Information is available free of charge on the ACS Publications website at DOI: 10.1021/acs.jafc.5b01191.

Tables S1−S5 and Figures S1 and S2 (PDF)

■ AUTHOR INFORMATION

Corresponding Author

*(Q.S.) Phone: +86571 86971405. Fax: +86571 86971421. E-mail: qyshu@zju.edu.cn.

Author Contributions

‖Z.N. and K.U.K. contributed equally.

DOI: 10.1021/acs.jafc.5b01191
J. Agric. Food Chem. 2015, 63, 8008−8016

Funding

The research was financially supported by the Special Funds for Agro-scientific Research in the Public Interest (201103007), Harvestplus-China Program 2014H8320.ZHE.

Notes

The authors declare no competing financial interest.

■ ACKNOWLEDGMENTS

We thank Dr. Zhongchang Wu of Zhejiang University for assistance in measuring element concentrations for all samples.

■ REFERENCES

(1) White, P. J.; Bradshaw, J. E.; Finlay, M.; Dale, B.; Ramsay, G.; Hammond, J. P.; Broadley, M. R. Relationships between yield and mineral concentrations in potato tubers. *HortScience* **2009**, *44*, 6−11.

(2) Gibson, R. S. Zinc: the missing link in combating micronutrient malnutrition in developing countries. *Proc. Nutr. Soc.* **2006**, *65*, 51−60.

(3) Graham, R. D.; Welch, R. M.; Saunders, D. A.; Ortiz-Monasterio, I.; Bouis, H. E.; Bonierbale, M.; De Haan, S.; Burgos, G.; Thiele, G.; Liria, R. Nutritious subsistence food systems. *Adv. Agron.* **2007**, *92*, 1−74.

(4) Bouis, H. E. Plant breeding: a new tool for fighting micronutrient malnutrition. *J. Nutr.* **2002**, *132*, 491S−494S.

(5) Genc, Y.; Humphries, J. M.; Lyons, G. H.; Graham, R. D. Exploiting genotypic variation in plant nutrient accumulation to alleviate micronutrient deficiency in populations. *J. Trace Elem. Med. Biol.* **2005**, *18*, 319−324.

(6) Pfeiffer, W. H.; McClafferty, B. HarvestPlus: breeding crops for better nutrition. *Crop Sci.* **2007**, *47*, S-88−S-105.

(7) Parengam, M.; Judprasong, K.; Srianujata, S.; Jittinandana, S.; Laoharojanaphand, S.; Busamongko, A. Study of nutrients and toxic minerals in rice and legumes by instrumental neutron activation analysis and graphite furnace atomic absorption spectrophotometry. *J. Food Compos. Anal.* **2010**, *23*, 340−345.

(8) Zhang, M.; Pinson, S. R.; Tarpley, L.; Huang, X.-Y.; Lahner, B.; Yakubova, E.; Baxter, I.; Guerinot, M. L.; Salt, D. E. Mapping and validation of quantitative trait loci associated with concentrations of 16 elements in unmilled rice grain. *Theor. Appl. Genet.* **2014**, *127*, 137−165.

(9) Abdurakhmonov, I. Y.; Abdukarimov, A. Application of association mapping to understanding the genetic diversity of plant germplasm resources. *Int. J. Plant Genomics* **2008**, *2008*, 1−18.

(10) Li, X.; Yan, W.; Agrama, H.; Jia, L.; Jackson, A.; Moldenhauer, K.; Yeater, K.; McClung, A.; Wu, D. Unraveling the complex trait of harvest index with association mapping in rice (*Oryza sativa* L.). *PLoS One* **2012**, *7*, e29350.

(11) Flint-Garcia, S. A.; Thornsberry, J. M., IV B. Structure of linkage disequilibrium in plants. *Annu. Rev. Plant Biol.* **2003**, *54*, 357−374.

(12) Jannink, J.-L.; Walsh, B. Association mapping in plant populations. *Quantitative Genetics, Genomics and Plant Breeding* **2001**, 59−68.

(13) Zhang, Y.-M.; Mao, Y.; Xie, C.; Smith, H.; Luo, L.; Xu, S. Mapping quantitative trait loci using naturally occurring genetic variance among commercial inbred lines of maize (*Zea mays* L.). *Genetics* **2005**, *169*, 2267−2275.

(14) Baxter, I.; Brazelton, J. N.; Yu, D.; Huang, Y. S.; Lahner, B.; Yakubova, E.; Li, Y.; Bergelson, J.; Borevitz, J. O.; Nordborg, M. A coastal cline in sodium accumulation in *Arabidopsis thaliana* is driven by natural variation of the sodium transporter *AtHKT1*; 1. *PLoS Genet.* **2010**, *6*, e1001193.

(15) Todesco, M.; Balasubramanian, S.; Hu, T. T.; Traw, M. B.; Horton, M.; Epple, P.; Kuhns, C.; Sureshkumar, S.; Schwartz, C.; Lanz, C. Natural allelic variation underlying a major fitness trade-off in *Arabidopsis thaliana*. *Nature* **2010**, *465*, 632−636.

(16) Kump, K. L.; Bradbury, P. J.; Wisser, R. J.; Buckler, E. S.; Belcher, A. R.; Oropeza-Rosas, M. A.; Zwonitzer, J. C.; Kresovich, S.; McMullen, M. D.; Ware, D. Genome-wide association study of quantitative resistance to southern leaf blight in the maize nested association mapping population. *Nat. Genet.* **2011**, *43*, 163−168.

(17) Tian, F.; Bradbury, P. J.; Brown, P. J.; Hung, H.; Sun, Q.; Flint-Garcia, S.; Rocheford, T. R.; McMullen, M. D.; Holland, J. B.; Buckler, E. S. Genome-wide association study of leaf architecture in the maize nested association mapping population. *Nat. Genet.* **2011**, *43*, 159−162.

(18) Huang, X.; Wei, X.; Sang, T.; Zhao, Q.; Feng, Q.; Zhao, Y.; Li, C.; Zhu, C.; Lu, T.; Zhang, Z.; Li, M.; Fan, D.; Guo, Y.; Wang, A.; Wang, L.; Deng, L.; Li, W.; Lu, Y.; Weng, Q.; Liu, K.; Huang, T.; Zhou, T.; Jing, Y.; Li, W.; Lin, Z.; Buckler, E. S.; Qian, Q.; Zhang, Q. F.; Li, J.; Han, B. Genome-wide association studies of 14 agronomic traits in rice landraces. *Nat. Genet.* **2010**, *42*, 961−967.

(19) Famoso, A. N.; Zhao, K.; Clark, R. T.; Tung, C.-W.; Wright, M. H.; Bustamante, C.; Kochian, L. V.; McCouch, S. R. Genetic architecture of aluminum tolerance in rice (*Oryza sativa*) determined through genome-wide association analysis and QTL mapping. *PLoS Genet.* **2011**, *7*, e1002221.

(20) Zhao, K.; Tung, C.-W.; Eizenga, G. C.; Wright, M. H.; Ali, M. L.; Price, A. H.; Norton, G. J.; Islam, M. R.; Reynolds, A.; Mezey, J. Genome-wide association mapping reveals a rich genetic architecture of complex traits in *Oryza sativa*. *Nat. Commun.* **2011**, *2*, 467.

(21) Li, X.; Yan, W.; Agrama, H.; Jia, L.; Shen, X.; Jackson, A.; Moldenhauer, K.; Yeater, K.; McClung, A.; Wu, D. Mapping QTLs for improving grain yield using the USDA Rice Mini-Core Collection. *Planta* **2011**, *234*, 347−361.

(22) Breseghello, F.; Sorrells, M. E. Association mapping of kernel size and milling quality in wheat (*Triticum aestivum* L.) cultivars. *Genetics* **2006**, *172*, 1165−1177.

(23) Pritchard, J. K.; Stephens, M.; Rosenberg, N. A.; Donnelly, P. Association mapping in structured populations. *Am. J. Hum. Genet.* **2000**, *67*, 170−181.

(24) Bradbury, P. J.; Zhang, Z.; Kroon, D. E.; Casstevens, T. M.; Ramdoss, Y.; Buckler, E. S. TASSEL: software for association mapping of complex traits in diverse samples. *Bioinformatics* **2007**, *23*, 2633−2635.

(25) Yu, J.; Pressoir, G.; Briggs, W. H.; Bi, I. V.; Yamasaki, M.; Doebley, J. F.; McMullen, M. D.; Gaut, B. S.; Nielsen, D. M.; Holland, J. B. A unified mixed-model method for association mapping that accounts for multiple levels of relatedness. *Nat. Genet.* **2006**, *38*, 203−208.

(26) Liu, R.; Meng, J. [MapDraw: a microsoft excel macro for drawing genetic linkage maps based on given genetic linkage data]. *Yi chuan = Hereditas/Zhongguo yi chuan xue hui Bian ji* **2003**, *25*, 317−321.

(27) Bryant, R. J.; Jackson, A. K.; Yeater, K. M.; Yan, W. G.; McClung, A. M.; Fjellstrom, R. G. Genetic variation and association mapping of protein concentration in brown rice using a diverse rice germplasm collection. *Cereal Chem.* **2013**, *90*, 445−452.

(28) Yan, W.; Jackson, A.; Jia, M.; Zhou, W.; Xiong, H.; Bryant, R. Association mapping of four important traits using the USDA rice mini-core collection. *Rice − Germplasm, Genetics and Improvement*; InTech: Rijeka, Croatia, 2014

(29) Gregorio, G. B.; Senadhira, D.; Htut, H.; Graham, R. D. Breeding for trace mineral density in rice. *Food Nutr. Bull.* **2000**, *21*, 382−386.

(30) Ishikawa, S.; Abe, T.; Kuramata, M.; Yamaguchi, M.; Ando, T.; Yamamoto, T.; Yano, M. A major quantitative trait locus for increasing cadmium-specific concentration in rice grain is located on the short arm of chromosome 7. *J. Exp. Bot.* **2010**, *61*, 923−934.

(31) Moraes, M. F.; Abreu, C. H., Jr.; Hart, J. J.; Welch, R. M.; Kochian, L. V. Genotypic variation in micronutrient and cadmium concentrations in grains of 35 upland rice cultivars. In *19th World Congress of Soil Science*; Soil Science Australia: Warragul, VIC, Australia, 2010.

(32) Stangoulis, J. C.; Huynh, B.-L.; Welch, R. M.; Choi, E.-Y.; Graham, R. D. Quantitative trait loci for phytate in rice grain and their relationship with grain micronutrient content. *Euphytica* **2007**, *154*, 289−294.

DOI: 10.1021/acs.jafc.5b01191
J. Agric. Food Chem. 2015, 63, 8008−8016

(33) Agarwal, S.; Batchu, A. K.; Babu, A. P.; BP Mallikarjuna Swamy, B.; Longvah, T.; Sarla, N. Evaluating rice germplasm for iron and zinc concentration in brown rice and seed dimensions. *J. Phytol.* **2012**, *4*.1925
(34) Vaughan, D. A.; Lu, B.-R.; Tomooka, N. The evolving story of rice evolution. *Plant Sci.* **2008**, *174*, 394−408.
(35) Norton, G. J.; Douglas, A.; Lahner, B.; Yakubova, E.; Guerinot, M. L.; Pinson, S. R.; Tarpley, L.; Eizenga, G. C.; McGrath, S. P.; Zhao, F.-J. Genome wide association mapping of grain arsenic, copper, molybdenum and zinc in rice (*Oryza sativa* L.) grown at four international field sites. *PLoS One* **2014**, *9*, e89685.
(36) Zhang, X.; Zhang, G.; Guo, L.; Wang, H.; Zeng, D.; Dong, G.; Qian, Q.; Xue, D. Identification of quantitative trait loci for Cd and Zn concentrations of brown rice grown in Cd-polluted soils. *Euphytica* **2011**, *180*, 173−179.
(37) Garcia-Oliveira, A. L.; Tan, L.; Fu, Y.; Sun, C. Genetic identification of quantitative trait loci for contents of mineral nutrients in rice grain. *J. Integr. Plant Biol.* **2009**, *51*, 84−92.
(38) Norton, G. J.; Deacon, C. M.; Xiong, L.; Huang, S.; Meharg, A. A.; Price, A. H. Genetic mapping of the rice ionome in leaves and grain: identification of QTLs for 17 elements including arsenic, cadmium, iron and selenium. *Plant Soil* **2010**, *329*, 139−153.
(39) Ghandilyan, A.; Ilk, N.; Hanhart, C.; Mbengue, M.; Barboza, L.; Schat, H.; Koornneef, M.; El-Lithy, M.; Vreugdenhil, D.; Reymond, M. A strong effect of growth medium and organ type on the identification of QTLs for phytate and mineral concentrations in three *Arabidopsis thaliana* RIL populations. *J. Exp. Bot.* **2009**, *60*, 1409−1425.
(40) Johnson, A. A.; Kyriacou, B.; Callahan, D. L.; Carruthers, L.; Stangoulis, J.; Lombi, E.; Tester, M. Constitutive overexpression of the OsNAS gene family reveals single-gene strategies for effective iron-and zinc-biofortification of rice endosperm. *PLoS One* **2011**, *6*, e24476.
(41) Lee, S.; Persson, D. P.; Hansen, T. H.; Husted, S.; Schjoerring, J. K.; Kim, Y. S.; Jeon, U. S.; Kim, Y. K.; Kakei, Y.; Masuda, H. Bio-available zinc in rice seeds is increased by activation tagging of nicotianamine synthase. *Plant Biotechnol. J.* **2011**, *9*, 865−873.
(42) Bashir, K.; Nishizawa, N. K. Deoxymugineic acid synthase: a gene important for Fe-acquisition and homeostasis. *Plant Signaling Behav.* **2006**, *1*, 290−292.
(43) Gregorio, G. B. Progress in breeding for trace minerals in staple crops. *J. Nutr.* **2002**, *132*, 500S−502S.
(44) Wissuwa, M.; Ismail, A. M.; Yanagihara, S. Effects of zinc deficiency on rice growth and genetic factors contributing to tolerance. *Plant Physiol.* **2006**, *142*, 731−741.
(45) Lu, K.; Li, L.; Zheng, X.; Zhang, Z.; Mou, T.; Hu, Z. Quantitative trait loci controlling Cu, Ca, Zn, Mn and Fe content in rice grains. *J. Genet.* **2008**, *87*, 305−310.

DOI: 10.1021/acs.jafc.5b01191
J. Agric. Food Chem. 2015, 63, 8008−8016

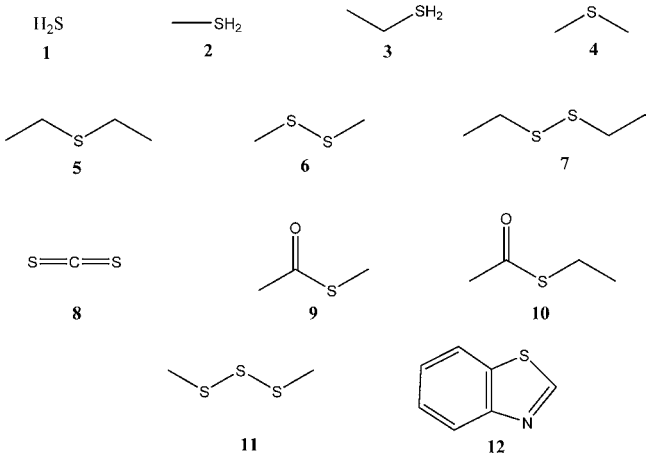

Figure 1. Chemical structures of the VSCs analyzed in this work: hydrogen sulfide (**1**), methanethiol (**2**), ethanethiol (**3**), dimethyl sulfide (**4**), diethyl sulfide (**5**), dimethyl disulfide (**6**), diethyl disulfide (**7**), carbon disulfide (**8**), methyl thioacetate (**9**), *S*-ethyl thioacetate (**10**), dimethyl trisulfide (**11**), and benzothiazole (**12**).

Table 1. SGM Composition As Adapted from Henschke and Jiranek (*Wine Microbiology and Biotechnology* 1993, 77−164 (Table 4.4, p 92))[a]

carbon source, salts, minerals, lipids, and vitamins	amount	nitrogen source	amount (mg/L)
glucose	105 g/L	L-alanine	100
fructose	105 g/L	L-arginine-HCl	484
potassium tartrate	5 g/L	L-aspartic acid	50
malic acid	3 g/L	L-cysteine	5
citric acid	0.2 g/L	L-glutamic acid	100
K_2HPO_4	1.14 g/L	L-glutamine	125
$MgSO_4{\cdot}7H_2O$	1.23 g/L	L-glycine	5
$CaCl_2{\cdot}2\ H_2O$	0.44 g/L	L-histidine	20
$MnCl_2{\cdot}4\ H_2O$	198.2 mg/L	L-isoleucine	25
$ZnSO_4{\cdot}7\ H_2O$	287.5 mg/L	L-leucine	25
$FeSO_4{\cdot}7\ H_2O$	70.1 mg/L	L-lysine-HCl	6
$CuSO_4$	25.3 mg/L	L-methionine	10
H_3BO_3	5.7 mg/L	L-phenylalanine	40
$CoCl_2{\cdot}6H_2O$	23.8 mg/L	L-proline	300
$NaMoO_4{\cdot}2H_2O$	24.2 mg/L	L-serine	60
KIO_3	10.8 mg/L	L-threonine	75
myo-inositol	100 mg/L	L-tryptophan	10
pyridoxine hydrochloride	2 mg/L	L-tyrosine	10
nicotinic acid	2 mg/L	L-valine	30
sodium panthothenate	1 mg/L	$(NH_4)_2HPO_4$	363
thiamin hydrochloride	0.5 mg/L	glutathione	50 mg/L
p-aminobenzoic acid	0.2 mg/L		
riboflavin	0.2 mg/L		
biotin	0.125 mg/L		
folic acid	0.2 mg/L		
ergosterol	15 mg/L		
Tween 80	0.5 mL/L		

[a]The amino acids and diammonium phosphate ($(NH_4)_2HPO_4$), i.e., the nitrogen sources, were modified to reflect Marlborough Sauvignon Blanc (2004, 2005, and 2006) juice and winemaking practice. Amt, amount.

synthetic grape medium (SGM) (pH 3.2, total YAN = 300 mg N/L) (Table 1) or Sauvignon Blanc grape juice (SB juice) from the Rapaura region of Marlborough in New Zealand [21. °Brix (measured at 22 °C), pH 3.14, total YAN = 206 mg N/L] (kindly supplied by Andy Frost of Pernod Ricard NZ Ltd.).

Fermentation and H_2S Quantitation. Fermentations were carried out in triplicate in 250 mL conical flasks containing 100 mL of SGM or SB juice. Flasks were sealed with rubber stoppers fitted with H_2S-detecting, silver nitrate tubes (25−2000 ppm; Komyo Kitagawa, Tokyo, Japan). Fermentation was performed at 28 °C, with rotary shaking at 100 rpm, and was monitored by daily weighing. The concentrations of **1** were recorded by visual reading from the tubes daily. Ferments were considered finished when weight loss was ≤ 0.1 g per 24 h. Wine was separated from yeast cells and solids by centrifugation at 6000 *g* for 10 min and was stored frozen at −20 °C. Dimethyldicarbonate (DMDC), 0.2 μL/L, was used to sterilize the SB juice prior to inoculation and both media after the wine was collected.

Cultures were harvested at time zero and at five different stages of fermentation completion, as estimated by percentage of weight loss: 2, 25, 50, 70, and 100%.

Control ferments of both media with no cells were also analyzed, as well as media harvested immediately after inoculation with yeast.

Samples were kept in 50 mL containers with limited head space and frozen before analysis, remaining frozen for no longer than 14 days as this has been observed to minimize VSC loss.[18]

Quantitation of VSCs. All of the HS-SPME/GC-MS analyses were performed in triplicate. The sample preparation procedure and the analytical method used for quantitation of the sulfur compounds have been described elsewhere.[19,20]

Either the wine samples or serial dilutions in model wine (12% ethanol, 5 g/L tartaric acid, pH 3.2) containing the pure analytes that would make up the calibration curves were separately prepared to a final volume of 10 mL and placed in amber screw-top 20 mL vials. Fifty microliters of the IS mix (30 μg/L d_6-DMS, 2 μg/L DPDS, and 547 μg/L MTH), magnesium sulfate salt, and magnetic stir bars were introduced as described before.[19] To prevent degradation/oxidation reactions from taking place, each sample was purged with argon gas before analysis.

In the cases of **1** and **2**, which are gaseous at room temperature, standards were prepared fresh using sodium sulfide nonahydrate (Sigma) or sodium thiomethoxide (Sigma) in a solution with model wine.

Analysis was carried out on an Agilent Technologies 7890 GC system coupled with a 5975C inert XL MSD (Agilent, USA). The fiber composition was divinylbenzene/carboxen-polydimethylsiloxane (DVB/CAR-PDMS; 50/30 μm × 2 cm) (product 57298U, Supelco, Bellefonte, PA, USA). The separating column was composed of a 30 m × 0.320 mm × 0.25 μm HP-1MS coupled with a 30 m × 0.320 mm × 0.25 μm HP-Innowax fused silica capillary column (Agilent, J&W Scientific, New Zealand). Agitation time and intensity was automated using magnetic stirrer bars in a Gerstel agitator/stirrer controlled by MAESTRO software (version 1.2.0) (Gerstel, Mülheim an der Ruhr, Germany).

Analysis of the samples was performed using the MassHunter workstation software (Agilent Technologies, USA). The ions used for the identification and quantitation of each compound were chosen according to the literature and NIST library. The statistical software used was SPSS (version 22, IBM) using one-way ANOVA ($p < 0.05$) and post hoc Tukey's HSD test ($p < 0.05$).

d_6-DMS was used to quantify **1**−**5**, **9**, and **10**. Isopropyl disulfide was used for **6**−**8** and **11**. **12** was quantified using 3-(methylthio)-1-hexanol as the internal standard.

In the cases for **1** and **12**, the R^2 values of the calibration curves are not ideal. **1** and **12** are the two extremes of the volatility/chromatographic space studied; the chromatography for **1** is not ideal due to its high volatility, which we have overcome by using a second method of detection (Kitagawa columns). In the case of **12**, its absorption on the fiber does not show high reproducibility for reasons that are unclear. Given the broad and novel scope of this paper and the attempt to measure such a wide range of sulfur species, these measurements were nevertheless included to complement the overall screening for VSCs.

RESULTS AND DISCUSSION

The experiments used two yeast strains: BY4743, a diploid auxotrophic version of the widely used laboratory strain S288c; and

DOI: 10.1021/acs.jafc.5b02984
J. Agric. Food Chem. 2015, 63, 8017−8024

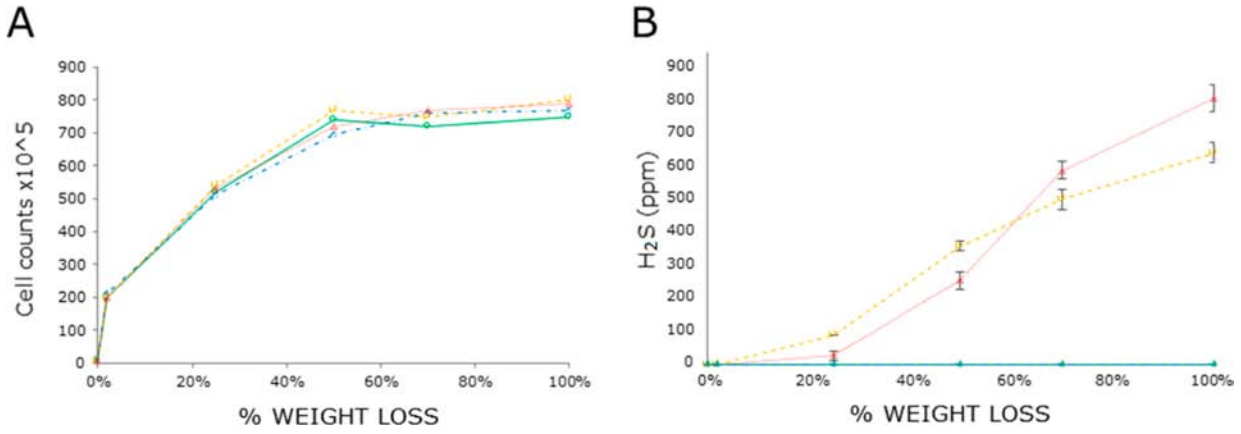

Figure 2. Fermentation progress assessed by (A) growth curves as estimated by colony counts plated and (B) production of **1** measured using detection columns. The data are shown for BY4743 in SGM (solid line green), BY4743 in SB juice (dash-dotted line blue), F15 in SGM (dashed line, orange), and F15 in SB Juice (dotted line, red). Error bars show standard deviation between replicates (n = 3).

F15, a homozygous diploid, prototrophic, commercial wine yeast strain with a known sequence.[21] The strains were grown both in synthetic medium resembling grape juice (SGM) and in Sauvignon Blanc (SB) grape juice. Ferments were sampled in triplicate for HS-SPME/GC-MS analysis of VSCs.

Both strains grew normally in the media provided (Figure 2A). To assess metabolite production, five stages of fermentation were compared with the time zero stage (as well as uninoculated media, see Materials and Methods). The five stages correlate with times during fermentation during which groups of known fermentation genes are activated.[22,23] The stages of 2 and 25% weight loss correlate to early and late stages of exponential growth. By 50% weight loss, most cell growth was completed, with the number of total cells reaching a plateau at around 7.5×10^7 cells for both strains (Figure 2A). From 50 to 100% weight loss, the cells fermented the remaining sugars, producing increased levels of alcohol, but the total number of cells in the culture did not change (Figure 2A).

In this work, of the 12 compounds detected by HS-SPME/GC-MS, only 7 (those for which results are shown in Figure 3) were found at concentrations above the background level, which is defined as the concentration found at time zero, which for all compounds was indistinguishable from the concentration found in media without cells. Of the five compounds that were not detected, the "background level" for three of them was low (**7**, 0.52 ± 0.01 ng/mL; **11**, 2.4 ± 0.2 ng/mL; **6**, 16 ± 1 ng/mL). There was, however, significant background detected for both **8** (0.164 ± 0.001 μg/mL) and **4** (1.341 ± 0.002 μg/mL). These high backgrounds possibly originated as contaminants of these compounds in the internal standard mix injected into the sample.

Arguably the most studied and the most common VSC to arise during winemaking is **1**. It is also the best understood VSC in terms of yeast genetics, with a number of known mutations in the sulfate assimilation pathway that can influence its production during wine making.[21,24,26] Its rotten egg aroma also makes it most undesirable. Low production of **1** is therefore one of the most sought after traits in a winemaking yeast strain.[24,25] In this study, production of **1** was measured daily using detection tubes[16] (Figure 2B), as well as by HS-SPME/GC-MS (Figure 3A). By both measurements, the laboratory strain BY4743 did not produce detectable **1** during fermentation in either media. Both methods, however, did detect **1** from both F15 ferments, and both indicated that the majority of production of **1** by F15 occurred close to the time cell growth was completed (around 50% weight loss, see Figure 2A), although some production was initially detected at 25% weight loss in some samples. By HS-SPME/GC-MS, the final concentrations of **1** by F15 in both media stabilized well above the 1 ng/L sensory threshold,[27] with production in SB juice being higher than in SGM for this strain (Table 2).

The actual concentrations of **1** measured by the two approaches used here differed by 2 orders of magnitude. This difference is perhaps not surprising because the methods measured very different parameters: the tubes measured total accumulated production of **1** from a 100 mL sample over the course of the fermentation, whereas the HS-SPME/GC-MS detection approach measured the steady state concentration of **1** that can be removed from the solution into the head space at each time point. In addition to differences in the sensitivity of both detection methods, the volatility of **1** could have played a role in the different concentrations seen; there may also be effects associated with sample handling when the anaerobic confinement of the culture is broken and the wine is harvested. Recently, it has been revealed that the partition coefficients of VSCs, specifically those of **1** in grape juice media, are dependent on the temperature of the fermentation and the composition of the media, especially its sugar content.[28] The same was observed for the partitioning of higher alcohols and esters[29] and may well be the case for heavier VSCs.**1** is known to be highly reactive and can combine with other compounds to form more complex VSCs.[30] For example, **3** can be formed in vitro by the reaction of **1** with ethanol or acetaldehyde[31] and can combine to form **5**.[32] Interestingly, in this study **3** presented steady state patterns that were generally similar to those of **1**. It was not detected in either ferment of strain BY4743, and yet appeared high in F15, generally rising throughout the course of fermentation (Figure 3B). However, the kinetics were different because the concentration rose early with clear production even at 2% weight loss and achieved its peak of accumulation at 70% weight loss. In the case of SB juice this was followed by a drop at the end of fermentation, indicating that the compound may either be consumed by yeast or act as the substrate for a chemical reaction near the end of fermentation (Table 2).

Following a similar trend, **9** was also not produced by BY4743 in either media, but was produced by F15. In SGM, production had started by 25% weight loss and increased steadily until the end of fermentation; in SB juice, however, it was found only at the final stages of fermentation (Figure 3C).

DOI: 10.1021/acs.jafc.5b02984
J. Agric. Food Chem. 2015, 63, 8017−8024

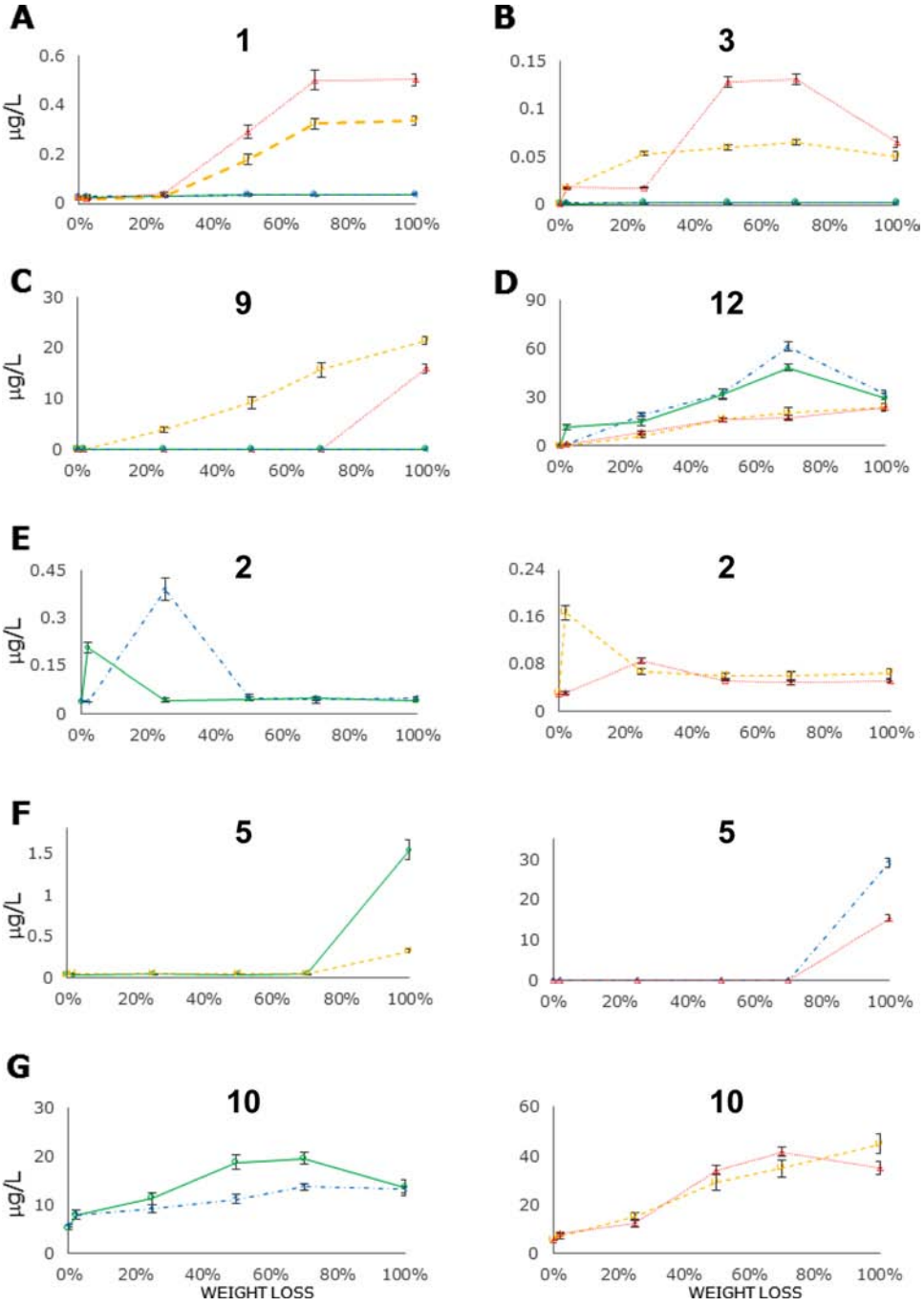

Figure 3. Cumulative concentrations of VSCs produced at 0, 2, 25, 50, 70, and 100% of fermentation for BY4743 in SGM (solid line, green), BY4743 in SB juice (dash-dotted line, blue), F15 in SGM (dashed line, orange), and F15 in SB juice (dotted line, red). Error bars show standard deviation between replicates (n = 3).

Previously, the biosynthesis of **9** has been linked to the availability of a **2** donor in yeast;[33] however, this correlation in the timing of production could not be observed in this study. Previous findings, however, are consistent with genetic strain differences playing a key role in affecting the composition of volatiles in wine.[34,35] Given that the formation of **2** has been linked to **1**,[31] it may be that the biosyntheses of **1**, **3**, and **9** are associated with each other and the latter two derive from high production of **1** by F15. To date, genetic differences in four genes have been related to differential production of **1** by yeast strains: *SKP2, MET5, MET10* and *MET2*.[21,26,36a,b] Of these, the $R_{310}G$ amino acid difference in *MET2* stands out in a comparison of F15 and BY4743, because the same genetic difference has already been shown to be responsible for productivity of **1** in a cross between F15 and another wine yeast, M2.[21] The F15 *MET2* R_{310} allele is less efficient at producing *O*-acetylhomoserine, the nitrogen−carbon skeleton into which **1** is incorporated to form homocysteine. Further experiments are needed to confirm this role for *MET2* in the production of **1** by F15 and to determine whether or how this difference in the production of **1** also affects **3** and **9** concentrations.

The production of **2** had the most distinct kinetics, as shown in Figure 3E. This compound was found as a discrete pulse early during fermentation, with the pulse occurring earlier in

DOI: 10.1021/acs.jafc.5b02984
J. Agric. Food Chem. 2015, 63, 8017−8024

Table 2. Statistical Analysis of VSC Concentrations (μg/L) Using One-Way ANOVA ($p < 0.05$) and Post Hoc Tukey's HSD Test ($p < 0.05$)[a]

		% of Fermentation																						
		0%				2%				25%				50%				70%				100%			
VSC	Strain and media	Aver.	ST Dev.	Sig. 1	Sig. 2	Aver.	ST Dev.	Sig. 1	Sig. 2	Aver.	ST Dev.	Sig. 1	Sig. 2	Aver.	ST Dev.	Sig. 1	Sig. 2	Aver.	ST Dev.	Sig. 1	Sig. 2	Aver.	ST Dev.	Sig. 1	Sig. 2
1	F15 SGM	0.020	0.001	a	A	0.018	0.004	a	A	0.028	0.006	a	A	0.177	0.021	b	A	0.326	0.021	c	A	0.337	0.017	c	A
	F15 SB Juice	0.024	0.003	a	AB	0.021	0.004	a	AB	0.041	0.006	b	A	0.292	0.029	c	B	0.502	0.041	d	B	0.504	0.025	d	B
	BY4743 SGM	0.026	0.001	a	BC	0.026	0.005	a	BC	0.030	0.004	ab	A	0.033	0.005	ab	C	0.033	0.003	ab	C	0.037	0.002	b	C
	BY4743 SB Juice	0.030	0.001	a	C	0.030	0.004	a	C	0.032	0.003	a	A	0.036	0.004	a	C	0.034	0.002	a	C	0.036	0.002	a	C
2	F15 SGM	0.033	0.002	a	AB	0.167	0.012	b	A	0.068	0.004	c	A	0.062	0.004	c	A	0.061	0.006	c	A	0.064	0.008	c	A
	F15 SB Juice	0.030	0.001	a	A	0.033	0.003	a	B	0.085	0.004	b	B	0.053	0.002	c	A	0.050	0.003	c	A	0.052	0.002	c	AB
	BY4743 SGM	0.036	0.002	a	BC	0.207	0.016	b	C	0.042	0.005	a	C	0.045	0.007	a	A	0.047	0.005	a	A	0.041	0.004	a	B
	BY4743 SB Juice	0.040	0.001	a	C	0.036	0.001	a	B	0.389	0.035	b	D	0.050	0.010	a	A	0.043	0.011	a	A	0.047	0.007	a	B
3	F15 SGM	0.0015	0.0001	a	A	0.0176	0.0011	b	A	0.0534	0.0023	cd	A	0.0596	0.0028	de	A	0.0648	0.0028	e	A	0.0507	0.0047	c	A
	F15 SB Juice	0.0014	0.0001	a	A	0.0182	0.0009	b	A	0.0178	0.0009	b	B	0.1285	0.0055	c	B	0.1315	0.0057	c	B	0.0657	0.0052	d	B
	BY4743 SGM	0.0014	0.0001	a	A	0.0015	0.0002	a	B	0.0016	0.0002	a	C	0.0016	0.0001	a	C	0.0016	0.0002	a	C	0.0016	0.0001	a	C
	BY4743 SB Juice	0.0015	0.0001	a	A	0.0017	0.0001	a	B	0.0017	0.0001	a	C	0.0018	0.0002	a	C	0.0018	0.0001	a	C	0.0017	0.0001	a	C
5	F15 SGM	0.034	0.003	a	A	0.036	0.004	a	A	0.038	0.003	a	A	0.036	0.003	a	A	0.036	0.002	a	A	0.321	0.020	b	A
	F15 SB Juice	0.033	0.002	a	A	0.039	0.004	a	A	0.036	0.002	a	A	0.034	0.003	a	A	0.040	0.003	a	A	15.338	0.850	b	B
	BY4743 SGM	0.036	0.003	a	A	0.035	0.003	a	A	0.035	0.004	a	A	0.035	0.003	a	A	0.038	0.004	a	A	1.541	0.115	b	C
	BY4743 SB Juice	0.037	0.001	a	A	0.040	0.001	a	A	0.038	0.008	a	A	0.036	0.004	a	A	0.033	0.003	a	A	29.213	1.183	b	D
9	F15 SGM	0.0063	0.0010	a	A	0.0052	0.0005	a	A	3.7141	0.5151	b	A	9.2268	1.1548	c	A	15.6670	1.4832	d	A	21.4962	0.6965	e	A
	F15 SB Juice	0.0048	0.0006	a	A	0.0055	0.0003	a	A	0.0061	0.0004	a	B	0.0060	0.0006	a	B	0.0050	0.0005	a	B	15.9310	0.9447	b	B
	BY4743 SGM	0.0053	0.0005	a	A	0.0055	0.0004	a	A	0.0056	0.0009	a	B	0.0059	0.0002	a	B	0.0053	0.0008	a	B	0.0055	0.0008	a	C
	BY4743 SB Juice	0.0061	0.0006	a	A	0.0061	0.0005	a	A	0.0065	0.0007	a	B	0.0065	0.0008	a	B	0.0062	0.0006	a	B	0.0061	0.0003	a	C
10	F15 SGM	5.42	0.46	a	A	6.77	1.04	a	A	14.68	1.63	b	A	28.97	3.05	c	A	34.75	3.55	c	A	44.79	3.87	d	A
	F15 SB Juice	5.40	0.47	a	A	8.02	0.20	ab	A	12.16	1.42	b	AB	33.90	1.84	c	A	41.61	1.82	d	A	34.83	2.77	c	B
	BY4743 SGM	5.12	0.29	a	A	8.03	0.90	a	A	11.35	1.15	b	AB	18.79	1.45	c	B	19.63	1.19	c	B	13.52	1.66	b	C
	BY4743 SB Juice	5.73	0.17	a	A	8.05	0.94	b	A	9.14	0.81	b	B	11.29	1.04	c	C	13.76	0.63	c	C	13.28	0.69	c	C
12	F15 SGM	0.61	0.04	a	A	0.31	0.27	a	A	6.05	1.09	b	A	16.20	1.11	c	A	20.14	3.66	cd	A	24.08	2.01	d	A
	F15 SB Juice	0.61	0.05	a	A	0.85	0.15	a	A	7.97	1.19	b	A	16.14	1.19	c	A	16.93	1.67	c	A	23.88	2.52	d	A
	BY4743 SGM	0.59	0.04	a	A	0.85	0.13	a	A	19.15	1.24	b	B	32.30	2.96	c	B	61.14	2.87	d	B	31.50	2.87	c	B
	BY4743 SB Juice	0.60	0.03	a	A	11.74	1.56	b	B	14.52	1.83	b	B	31.73	3.51	c	B	48.22	2.21	d	C	29.68	3.24	c	AB

[a]Statistically similar data points are grouped with similar characters. Lower case letters (sig 1): comparison of VSC concentrations at six different time points (0, 2, 25, 50, 70, and 100% weight loss) for each strain and media combination. Capital letters (sig 2): comparison of VSC concentrations within the four treatments of strain and media for each given time point. Av, average concentration of VSC (n = 3 for each data point; SD, standard deviation; sig, significance group. All values are shown in μg/L of wine.

J. Agric. Food Chem. 2015, 63, 8017−8024
DOI: 10.1021/acs.jafc.5b02984

SGM than in grape juice. In SGM, **2** increased dramatically at 2% weight loss, an early exponential stage of growth at which transcription is particularly active.[23] It then dropped just as dramatically by 25% during fermentation in SGM and remained at background levels throughout the remainder of the fermentation. This early peak in the biosynthesis of **2** was conserved for both strains and in both media. Interestingly, there was a delay for this peak in SB juice as opposed to synthetic media for both yeast strains. There was also a strain-specific medium response, with F15 more productive in SGM than in SB juice for this metabolite, whereas the opposite was true for BY4743 (Table 2).

2 was found recently to be formed by a methionine gamma lyase in *Brevibacterium linens*,[37] hinting that a possible enzymatic origin could be found also in yeast. Together with our finding, this could be interpreted if **2** is the product of early, rapid catalysis/assimilation of sulfur-containing nutrients during the first stages of cellular growth. Such sources may be more readily available in SGM (containing methionine, cysteine, glutathione, sulfate, biotin, and thiamine) than those found in SB juice, the sulfur sources of which include peptides and sulfurylated organic molecules as well as those in SGM. Alternative explanations for the difference might include an unknown competitive inhibitor suppressing production of **2** that is present in SB juice but missing in SGM. The subsequent disappearance of **2** during the latter stages of yeast growth could be explained by its being utilized as a substrate for the biosynthesis of more complex sulfur-containing compounds, either via chemical reactions or by a yeast biosynthetic pathway. A detailed experimental procedure will be needed to further test these hypotheses.

Heavier VSCs such as **5**, **10**, and **12** have also been detected in wine,[10] yet to date their origin remains unknown. First, the evolution of **12** production followed a steady increase throughout most of the fermentation (Figure 3D). In the case of BY4743, production in both media was very similar, peaking at 70% weight loss. In both media this strain produced **12** at slightly above the perception threshold (50 μg/L), but concentrations decreased by the end of fermentation. In F15 both media presented similar production curves, but at generally lower concentrations than BY4743. At the end of fermentation, F15 in both media and BY4743 in SB juice attained similar final concentrations, with BY4743 in SGM showing slight, but significant, differences ($p < 0.05$).

Second, **5** was not detected until the end of fermentation, when a marked rise in production was observed. For both strains, this late burst was more pronounced in SB juice than in SGM, achieving values for this metabolite an order of magnitude greater than the sensory threshold of 0.93 μg/L.[27] Significant strain differences were seen, with BY4743 showing higher concentrations than F15 (Figure 3F) (Table 2), which would translate to a large difference in taste for these wines.

Interestingly, together with **1**, both **12** and **5** were produced at concentrations above their perception thresholds. This result does not necessarily associate this set of compounds to the overall off-flavors detected in these wines, because the interaction with other compounds produced during fermentation is known to produce a synergistic effect that lowers the perception limits for some VSCs.[38] Conversely, some compounds that are present well below threshold values are known to influence overall aroma perception (e.g., β-damascenone).[38]

Finally, **10** followed a steadily increasing concentration pattern that was generally similar for both strains and media. This metabolite's biosynthesis was detected early in the fermentation, rising steadily and plateauing at 70% weight loss. Strain differences were evident, with F15 producing twice as much as BY4743 (Figure 3G). For BY4743, production in SGM was higher than in juice (Table 2).

In fact, overall we observed most compounds increased slowly during fermentation, with some plateauing and some peaking at 70% weight loss. None of the compounds clearly followed the cell growth curve (Figure 2A); this is perhaps surprising, because during fermentation of wine yeast in synthetic media, transcription of genes in the sulfur assimilation pathway was induced during the cell growth period and down-regulated subsequently.[22] However, it has been observed that there is sustained induction of the Met4p transcription factor late in the fermentation of Riesling grape juice,[39] and this, in turn, has been confirmed by our own previous data in SB juice,[40,41] which show induced transcription of many genes in the sulfur assimilation pathway late in fermentation (at 70% weight loss).

In summary, we have observed strain differences in either final concentration or production during growth in the biosynthesis of **1**−**3**, **5**, **9**, **10**, and **12**. Progeny studies using these strains or a detailed screening of candidate gene deletions with possible involvement in sulfur−carbon chemical reactions seem to be the best approach to shed light on the origin of these compounds.

Different media also affected the production of some VSCs. In particular, the production of **5** was up to 17 times higher in SB juice fermentation compared to that in SGM, whereas for **2**, SB juice produced a delay in this gas's biosynthetic peak. Although there may be unidentified compounds in juice that are important for these differences, it may also be possible to identify constituents of defined media that affect these parameters.[42]

Within this context, yeast assimilable nitrogen (YAN) supply in grape juice has been well documented to influence yeast growth and metabolism during winemaking.[43] Often observed, a low YAN can lead to stuck or sluggish fermentations. This deficiency, however, can be overcome by supplementation with diammonium phosphate (DAP), an ammonium source. In addition, high nitrogen (e.g., 480 mg N/L) can result in undesirable aromas being produced,[44] including, but not limited to, the accumulation of **1**. In our study, however, F15 produced significantly more of **1** fermenting SB juice (YAN, 206 mg N/L) than SGM (300 mg N/L) (Table 2). The complexity and diversity of nitrogen-containing metabolites within SB juice as compared to that of SGM make it difficult to predict if this difference in YAN is solely responsible for the difference in VSC production in our study. A more thorough and comprehensive study is needed.

Because we measured steady state levels, we cannot distinguish between several alternative explanations for the temporal changes: they may result from differences in production of the compounds or differences in their degradation or their use in subsequent pathways or chemical reactions, or they may even occur as the result of changes in the rate of their transport outside the cell. However, the knowledge of the approximate timing of their peak concentration detailed here will allow these options to be evaluated more fully. The use of precursors with labeling on different atoms and positions will be critical in such work, along with careful selection of optimal sampling times.[45]

Wine quality can be affected dramatically by the production of VSCs, and understanding the parameters and conditions in which they are produced could have profound applications in the wine industry. The differences in the timing of production

DOI: 10.1021/acs.jafc.5b02984
J. Agric. Food Chem. 2015, 63, 8017−8024

by yeast, for the seven VSCs presented here, will facilitate detailed analysis of the biochemical pathways involved, about which very little is currently known. The strain and medium differences noted here should also provide an initial basis for determining some of the genetic and physiological influences on this class of wine aroma molecules.

■ ASSOCIATED CONTENT

Supporting Information

The Supporting Information is available free of charge on the ACS Publications website at DOI: 10.1021/acs.jafc.5b02984.

Time zero control graphs, calibration curves used, composition of SGM, and ion list used for identification and quantitation of VSCs (PDF)

■ AUTHOR INFORMATION

Corresponding Authors

*(M.I.K.) Phone: + 64 9 9238473. Fax: + 64 9 3737422. E-mail: mkin586@aucklanduni.ac.nz.

*(B.F.) E-mail: b.fedrizzi@auckland.ac.nz.

Funding

We thank New Zealand Winegrowers and the Romeo Bragato Trust (Grant NZW 13-102) for funding to make this research possible.

Notes

The authors declare no competing financial interest.

■ ACKNOWLEDGMENTS

We thank Andy Frost (Pernod Ricard NZ Ltd.) for supplying grape juice.

■ REFERENCES

(1) Boelens, M. H.; van Gemert, L. Volatile character-impact sulfur compounds and their sensory properties. *Perfum. Flavor.* **1993**, *18*, 29.

(2) Mestres, M.; Busto, O.; Guasch, J. Analysis of organic sulfur compounds in wine aroma. *J. Chromatogr. A* **2000**, *881*, 569−581.

(3) Dittrich, H. H. *Mikrobiologie des Weines*; Ulmer GmbH Verlag: Stuttgart, Germany, 1987.

(4) Maga, J. A. The role of sulfur compounds in food flavour. *CRC Crit. Rev. Food Sci.* **1976**, *7*, 147−192.

(5) Shankaranarayana, M. L.; Raghavan, B.; Abraham, K. O.; Natarajan, C. P.; Brodnitz, H. H. Volatile sulfur compounds in food flavors. *CRC Crit. Rev. Food Technol.* **1974**, *4*, 395−435.

(6) Landaud, S.; Helinck, S.; Bonnarme, P. Formation of volatile sulfur compounds and metabolism of methionine and other sulfur compounds in fermented food. *Appl. Microbiol. Biotechnol.* **2008**, *77*, 1191−1205.

(7) Darriet, P.; Lavigne-Cruege, V.; Tominaga, T. A paradox: the volatile sulphur compounds responsibles for both defects and qualities in wines. *J. Int. Sci. Vigne Vin* **1999**, *33*, 127.

(8) Segurel, M. A.; Razungles, A. J.; Riou, C.; Salles, M.; Baumes, R. L. Contribution of dimethyl sulfide to the aroma of Syrah and Grenache Noir wines and estimation of its potential in grapes of these varieties. *J. Agric. Food Chem.* **2004**, *52*, 7084−7093.

(9) Segurel, M. A.; Razungles, A. J.; Riou, C.; Trigueiro, M. G. L.; Baumes, R. L. Ability of possible DMS precursors to release DMS during wine aging and in the conditions of heat-alkaline treatment. *J. Agric. Food Chem.* **2005**, *53*, 2637−2645.

(10) Fedrizzi, B.; Magno, F.; Badocco, D.; Nicolini, G.; Versini, G. Aging effects and grape variety dependence on the content of sulfur volatiles in wine. *J. Agric. Food Chem.* **2007**, *55*, 10880−10887.

(11) Fedrizzi, B.; Magno, F.; Finato, F.; Versini, G. Variation of some fermentative sulfur compounds in Italian "Millesimè" classic sparkling wines during aging and storage on lees. *J. Agric. Food Chem.* **2010**, *58*, 9716−9722.

(12) Fedrizzi, B.; Zapparoli, G.; Finato, F.; Tosi, E.; Turri, A.; Azzolini, M.; Versini, G. Model aging and oxidation effects on varietal, fermentative, and sulfur compounds in a dry botrytized red wine. *J. Agric. Food Chem.* **2011**, *59*, 1804−1813.

(13) Franco-Luesma, E.; Ferreira, V. Quantitative analysis of free and bonded forms of volatile sulfur compouds in wine. Basic methodologies and evidences showing the existence of reversible cation-complexed forms. *J. Chromatogr. A* **2014**, *1359*, 8−15.

(14) Winter, G.; Curtin, C. In situ high throughput method for H_2S detection during micro-scale wine fermentation. *J. Microbiol. Methods* **2012**, *91*, 165−170.

(15) Thomas, D.; Surdin-Kerjan, Y. Metabolism of sulfur amino acids in *Saccharomyces cerevisiae*. *Microbiol. Mol. Biol. Rev.* **1997**, *61*, 503−532.

(16) Park, S. K. Development of a method to measure hydrogen sulfide in wine fermentation. *J. Microbiol. Biotechnol.* **2008**, *18*, 1550−1554.

(17) Harsch, M. J.; Gardner, R. C. Yeast genes involved in sulfur and nitrogen metabolism affect the production of volatile thiols from Sauvignon Blanc musts. *Appl. Microbiol. Biotechnol.* **2013**, *97*, 223−235.

(18) Gonda, I.; Lev, S.; Bar, E.; Sikron, N.; Portnoy, V.; Davidovich-Rikanati, R.; Burger, J.; Schaffer, A. A.; Tadmor, Y. a.; Giovannonni, J. J.; Huang, M.; Fei, Z.; Katzir, N.; Fait, A.; Lewinsohn, E. Catabolism of l−methionine in the formation of sulfur and other volatiles in melon (*Cucumis melo L.*) fruit. *Plant J.* **2013**, *74*, 458−472.

(19) Nguyen, D.-D.; Nicolau, L.; Dykes, S. I.; Kilmartin, P. A. Influence of microoxygenation on reductive sulfur off-odors and color development in a Cabernet Sauvignon wine. *Am. J. Enol. Vitic.* **2010**, *61*, 457−464.

(20) Nguyen, D. D. N. L.; Kilmartin, P. A. Application of an automated headspace solid phase micro-extraction for the GC-MS detection and quantification of reductive sulfur compounds in wines. *Gas Chromatography in Plant Science, Wine Technology, Toxicology and Some Specific Applications*; Salih, B., Ed.; INTECH: Rijeka, Croatia, 2012; Chapter 9.

(21) Huang, C.; Roncoroni, M.; Gardner, R. MET2 affects production of hydrogen sulfide during wine fermentation. *Appl. Microbiol. Biotechnol.* **2014**, *98*, 7125−7135.

(22) Rossignol, T.; Dulau, L.; Julien, A.; Blondin, B. Genome-wide monitoring of wine yeast gene expression during alcoholic fermentation. *Yeast* **2003**, *20*, 1369−1385.

(23) Mendes-Ferreira, A.; del Olmo, M.; García-Martínez, J.; Jiménez-Martí, E.; Mendes-Faia, A.; Pérez-Ortín, J. E.; Leão, C. Transcriptional response of *Saccharomyces cerevisiae* to different nitrogen concentrations during alcoholic fermentation. *Appl. Environ. Microbiol.* **2007**, *73*, 3049−3060.

(24) Linderholm, A. L.; Findleton, C. L.; Kumar, G.; Hong, Y.; Bisson, L. F. Identification of genes affecting hydrogen sulfide formation in *Saccharomyces cerevisiae*. *Appl. Environ. Microbiol.* **2008**, *74*, 1418−1427.

(25) Spiropoulos, A.; Tanaka, J.; Flerianos, I.; Bisson, L. F. Characterization of hydrogen sulfide formation in commercial and natural wine isolates of *Saccharomyces*. *Am. J. Enol. Vitic.* **2000**, *51*, 233−248.

(26) Cordente, A. G.; Heinrich, A.; Pretorius, I. S.; Swiegers, J. H. Isolation of sulfite reductase variants of a commercial wine yeast with significantly reduced hydrogen sulfide production. *FEMS Yeast Res.* **2009**, *9*, 446−459.

(27) Roland, A.; Schneider, R.; Razungles, A.; Cavelier, F. Varietal thiols in wine: discovery, analysis and applications. *Chem. Rev.* **2011**, *111*, 7355−7376.

(28) Mouret, J.-R.; Sablayrolles, J.-M.; Farines, V. Study and modeling of the evolution of gas−liquid partitioning of hydrogen sulfide in model solutions simulating winemaking fermentations. *J. Agric. Food Chem.* **2015**, *63* (12), 3271−3278.

(29) Morakul, S.; Athes, V.; Mouret, J.-R.; Sablayrolles, J.-M. Comprehensive study of the evolution of gas−liquid partitioning of aroma compounds during wine alcoholic fermentation. *J. Agric. Food Chem.* **2010**, *58*, 10219−10225.
(30) Vermeulen, C.; Gijs, L.; Collin, S. Sensorial contribution and formation pathways of thiols in foods: a review. *Food Rev. Int.* **2005**, *21*, 69−137.
(31) Rauhut, D. Yeast production of sulfur compounds. In *Wine Microbiology and Biotechnology*; Fleet, G. H., Ed.; Harwood Academic Publishers: Chur, Switzerland, 1993; pp 77−164.
(32) Bobet, R. A.; Noble, A. C.; Boulton, R. B. Kinetics of the ethanethiol and diethyl disulfide interconversion in wine-like solutions. *J. Agric. Food Chem.* **1990**, *38*, 449−452.
(33) Matsui, S.; Yabuuchi, S.; Amaha, M. Production of *S*-methyl thioacetate from methyl mercaptan by *Saccharomyces cerevisiae*. *Agric. Agric. Biol. Chem.* **1981**, *45*, 771−772.
(34) Ugliano, M.; Fedrizzi, B.; Siebert, T.; Travis, B.; Magno, F.; Versini, G.; Henschke, P. A. Effect of nitrogen supplementation and *Saccharomyces* species on hydrogen sulfide and other volatile sulfur compounds in Shiraz fermentation and wine. *J. Agric. Food Chem.* **2009**, *57*, 4948−4955.
(35) Ugliano, M.; Travis, B.; Francis, I. L.; Henschke, P. A. Volatile composition and sensory properties of Shiraz wines as affected by nitrogen supplementation and yeast species: rationalizing nitrogen modulation of wine aroma. *J. Agric. Food Chem.* **2010**, *58*, 12417−12425.
(36) (a) Linderholm, A.; Dietzel, K.; Hirst, M.; Bisson, L. F. Identification of MET10-932 and Characterization as an Allele Reducing Hydrogen Sulfide Formation in Wine Strains of *Saccharomyces cerevisiae*. *Appl. Environ. Microbiol.* **2010**, *76*, 7699−7707. (b) Noble, J.; Sanchez, I.; Blondin, B. Identification of new *Saccharomyces cerevisiae* variants of the MET2 and SKP2 genes controlling the sulfur assimilation pathway and the productions of undesirable sulfur compounds during alcoholic fermentation. *Microb Cell Fact.* **2015**, *14*, 68, DOI: 10.1186/s12934-015-0245-1.
(37) Amarita, F.; Yvon, M.; Nardi, M.; Chambellon, E.; Delettre, J.; Bonnarme, P. Identification and functional analysis of the gene encoding methionine-γ-lyase in *Brevibacterium linens*. *Appl. Environ. Microbiol.* **2004**, *70*, 7348−7354.
(38) Álvarez-Pérez, J. M.; Campo, E.; San-Juan, F.; Coque, J. J. R.; Ferreira, V.; Hernández-Orte, P. Sensory and chemical characterisation of the aroma of Prieto Picudo rosé wines: the differential role of autochthonous yeast strains on aroma profiles. *Food Chem.* **2012**, *133*, 284−292.
(39) Marks, V. D.; Ho Sui, S. J.; Erasmus, D.; van der Merwe, G. K.; Brumm, J.; Wasserman, W. W.; Bryan, J.; van Vuuren, H. J. J. Dynamics of the yeast transcriptome during wine fermentation reveals a novel fermentation stress response. *FEMS Yeast Res.* **2008**, *8*, 35−52.
(40) Deed, N. K.; van Vuuren, H. J. J.; Gardner, R. C. Effects of nitrogen catabolite repression and di-ammonium phosphate addition during wine fermentation by a commercial strain of *S. cerevisiae*. *Appl. Microbiol. Biotechnol.* **2011**, *89*, 1537−1549.
(41) Deed, R. C.; Deed, N. K.; Gardner, R. C. Transcriptional response of *Saccharomyces cerevisiae* to low temperature during wine fermentation. *Antonie van Leeuwenhoek* **2015**, *107*, 1029−1048.
(42) Moreira, N.; Mendes, F.; Hogg, T.; Vasconcelos, I. Alcohols, esters and heavy sulphur compounds production by pure and mixed cultures of apiculate wine yeasts. *Int. J. Food Microbiol.* **2005**, *103*, 285−294.
(43) Beltran, G.; Novo, M.; Rozès, N.; Mas, A.; Guillamón, J. M. Nitrogen catabolite repression in *Saccharomyces cerevisiae* during wine fermentations. *FEMS Yeast Res.* **2004**, *4*, 625−632.
(44) Bell, S.-J.; Henschke, P. A. Implications of nitrogen nutrition for grapes, fermentation and wine. *Aust. J. Grape Wine Res.* **2005**, *11*, 242−295.
(45) Eschenbruch, R.; Haasbroek, F. J.; de Viliers, J. F. On the metabolism of sulphate and sulphite during the fermentation of grape must by *Saccharomyces cerevisiae*. *Arch. Microbiol.* **1973**, *93*, 259−266.

DOI: 10.1021/acs.jafc.5b02984
J. Agric. Food Chem. 2015, 63, 8017−8024

Table 1. Description of Training Sessions[a]

training session	method	instructions	concentrations of stimuli (% w/w)	replicates
training 1	150 mm VAS (not sweet at all−extremely sweet)	taste the sample (as many sips as needed)	3, 4, 5	duplicate
	duo-trio	choose the sample that is most similar to the reference sample	reference, 4; other samples, 3.5, 4.5	duplicate
training 2	150 mm VAS (not sweet at all−extremely sweet)	taste the sample (as many sips as needed) in comparison to the 3, 4 and 5%	2.5, 3.5, 4, 4.5, 5.5	duplicate
	paired comparison	choose the sample that is sweetest	3.6, 4 and 4, 4.4	duplicate
training 3	150 mm VAS (little sweet−very sweet)	taste the sample (only once) in comparison to the reference sample (4%)	3.6, 4, 4.4	duplicate
			3.7, 4, 4.3	duplicate
	paired comparison	choose the sample that is sweetest	3.8, 4 and 4, 4.2	duplicate
training 4	150 mm VAS (little sweet−very sweet)	taste the sample (only once) in comparison to the reference (4%)	3.7, 4, 4.3	triplicate
			3.8, 4, 4.2	duplicate
training 5	150 mm VAS (little sweet−very sweet)	taste the reference (4%) before, take a sip of water, taste the sample (only once)	3.7, 4, 4.3	triplicate
		taste the reference (4%) before, take a sip of water, process the o/w emulsion (t = 30 s),, expectorate, taste blind 4% sucrose, and score sweetness relative to the reference	4	
			o/w emulsions: 1, 10, and 20	
training 6	150 mm VAS (little sweet−very sweet)	taste the reference (4%) before, take a sip of water, process the o/w emulsion (t = 3, 6, 9, 15 s), expectorate, taste blind 4% sucrose, and score sweetness relative to the reference	4	
			o/w emulsions: 1, 10, and 20	
extra session 1	150 mm VAS (little sweet−very sweet)	taste the reference (4%) before, take a sip of water, taste the sample (only once)	3.8, 4, 4.2	triplicate
extra session 2	150 mm VAS (little sweet−very sweet)	taste the reference (4%) before, take a sip of water, taste the sample (only once)	3.9, 4, 4.1	triplicate

[a]Concentrations are sucrose concentrations, unless specified.

buds to trigger a taste response and consequently leading to a decline in taste intensity. The hypothesis might hold true when oil coatings form a sufficiently thick film covering the tongue surface, which might be the case after orally processing bulk fats and oils. Perceptual effects such as taste−taste, flavor−taste, or texture−taste interactions between the food used to coat the tongue and the subsequently provided tastant stimulus might have an impact when complex, multicomponent commercial products are consumed. To better understand the mechanisms underlying taste suppression due to oil deposition on the tongue surface, it is important to study oral coatings formed by foods with low taste and flavor intensity at realistic oil contents as they occur in foods. Besides the effect of oral coatings on subsequent taste perception, several studies focused on the factors affecting the dynamics of physical clearance of oral coatings after stimulus expectoration.[4−8] Little is known about the dynamics of the formation of oil deposits on the tongue while drinking.

The first aim of this study was to quantitate the dynamic formation of oil deposits on the tongue surface formed by o/w emulsion differing in oil content from 1 to 20% (w/w). For this purpose one sip (20 mL) of o/w emulsion containing 1, 10, and 20% (w/w) oil and 3.2% (w/w) sodium caseinate was processed in the mouth for different times ranging from natural consumption time (3 s) to times that were hypothesized to create maximum oil deposition on the tongue (15 s). In vivo fluorescence measurements were used to quantitate the oil fraction deposited on the tongue at each time point. The second aim of this study was to investigate the effect of oil deposits on the tongue surface formed by o/w emulsions on subsequent sweetness perception of sucrose solutions. A trained panel was used to evaluate the sweetness intensity of 4% (w/w) sucrose solutions after oral processing of the o/w emulsions for different times.

We hypothesize that the oil fraction deposited on the tongue increases with increasing oral processing time until, at longer oral processing times, the amount of oil deposited on the tongue reaches a plateau. We hypothesize that oral processing of o/w emulsions with relatively low oil content does not lead to the formation of a hydrophobic barrier that is sufficient to reduce the accessibility of hydrophilic tastants to the taste buds and, consequently, does not influence subsequent taste perception.

MATERIALS AND METHODS

Materials. Sunflower oil (Albert Heijn, purchased from local retailer), sodium caseinate (Excellion sodium caseinate S, DMV International, The Netherlands, protein content = 91%), and tap water were used for the preparation of the emulsions. Curcumin (7% w/w curcumin dissolved in propylene glycol and polysorbate; L-WS; Sensient, Elburg, The Netherlands) was added to the o/w emulsions as a hydrophobic fluorescent dye. Sucrose (Van Gilse Kristalsuiker, purchased from a local retailer) and bottled mineral water (C1000, purchased from a local retailer) were used for the preparation of the aqueous sucrose solutions. All ingredients were of food grade.

Preparation and Characterization of o/w Emulsions and Sucrose Solutions. All o/w emulsions were prepared in a food grade environment. The aqueous phase of the o/w emulsions consisted of 3.2% (w/w) sodium caseinate solution. The aqueous phase was prepared by dissolving sodium caseinate in tap water at room temperature. The aqueous phase was then prehomogenized with the

DOI: 10.1021/acs.jafc.5b02562
J. Agric. Food Chem. 2015, 63, 8025−8030

sunflower oil (1, 10, and 20% w/w) using an Ultra Turrax (IKA RW 20 Digital) at 4000 min^{-1} for 2 min and homogenized with a two-stage homogenizer (Niro-Soavi S.p.A. NS1001L2K) at pressures between 200 and 350 bar. All o/w emulsions had a neutral pH. The emulsion droplet size distribution was measured by light scattering (Mastersizer 2000, Malvern Instruments) in duplicate using the refractive index of sunflower oil (1.469). The average Sauter diameter of the emulsion droplets, $d_{3,2}$, was determined for each o/w emulsion (average $d_{3,2}$ = 0.70 μm) accounting for differences in batches (one batch of each o/w emulsion was made per week). Emulsions were stored after preparation in a refrigerator at 4 °C and used for further studies no later than 3 days after preparation. Curcumin solutions were added to the o/w emulsions under magnetic stirring before consumption.[5]

Sucrose solutions varying in concentration were prepared by dissolving sucrose in water under stirring at room temperature. For the screening sessions (to find suitable subjects for the experiments), a range of 2−8% (w/w) sucrose solutions was prepared. For the training sessions of selected subjects, 2.5, 3.0, 3.5, 3.6, 3.7, 3.8, 3.9, 4.0, 4.1, 4.2, 4.3, 4.4, 4.5, 5.0, and 5.5% (w/w) sucrose solutions were prepared. For the experiment addressing the second objective of this study, a 4% (w/w) sucrose solution was prepared.

Panel Selection. Twenty-eight subjects (21 females, 7 males; age 25.5 ± 5.2 years) were invited for a screening session of 1 h. The screening session started with a ranking test in which subjects were asked to taste four sucrose solutions (2, 4, 6, and 8% (w/w) sucrose) and rank them in order of increasing sweetness. This was followed by a second ranking test in which subjects were asked to taste five sucrose solutions (2, 3, 4, 5, and 6% (w/w) sucrose) and rank them in order of increasing sweetness. The presentation order of stimuli in the screening session was randomized in both ranking tests. All subjects performed both ranking tests in duplicate. The third test of the screening session was a duo-trio test in which the subjects were asked to first taste the reference stimulus (4% (w/w) sucrose solution) and then choose of two stimuli the one that was most similar to the reference stimulus. The sucrose concentrations of the two stimuli were either 3 and 4% (w/w) or 4 and 5% (w/w). The test was performed in duplicate by all subjects. Presentation order and position were randomized over subjects in the duo-trio test. The performance of each subject on the screening session was determined. The correct answers given were weighted for the difficulty of the task, that is, one-fold for the first ranking test, two-fold for the second ranking test and the duo-trio test. This resulted in an individual performance score for each subject. On the basis of the performance score 15 subjects (12 females and 3 males; age 23.6 ± 3.5 years) with the highest performance scores were selected to participate in the study from the 28 subjects participating in the screening session.

The screening session ended with a consumption time measurement. All 28 subjects were asked to measure the drinking time between ingesting and swallowing a sip (20 mL) of full-fat milk (FrieslandCampina, The Netherlands). A stopwatch was used by each subject. This test was performed in triplicate. The average oral processing time of 20 mL of full-fat milk was found to be 3.3 ± 0.2 s.

All subjects signed a consent form and received financial compensation for their efforts.

Panel Training. The panel (n = 15) was trained on sweetness intensity evaluation of sucrose solutions to ensure that the panel was able to discriminate sweetness intensity of stimuli varying in sucrose concentration by <0.4% (w/w) sucrose relative to a reference stimulus (4.0% (w/w) sucrose). The panel was trained in six sessions of 1 h twice a week for 3 weeks. Each training session started with individual feedback on the performance during the previous training session to improve panel performance. The panel used a 150 mm visual analogue scale (VAS) during all training sessions. The training sessions involved group discussions during which the panel was first introduced to the 150 mm VAS, tasting instructions, reference stimuli, and stimuli with different sweetness intensities. The use of the scale and its suitability were discussed for different sucrose solutions. These group discussions were followed by individual tasting tests.

An overview of the training sessions is given in Table 1. During the first training session, samples representing concentration differences of 1% (w/w) sucrose were presented to the subjects. Because the effects of a coating on sweetness intensity were expected to be small, the sucrose concentration differences between stimuli were lowered during the following training sessions ending with a concentration difference of 0.1% (w/w) (Table 1). During the second training session, samples were assessed in comparison to 3, 4, and 5% (w/w) sucrose. In the first two sessions subjects were allowed to take as many sips as they wanted of the reference and the test stimulus in order to score the sweetness. From the third training session onward, the reference stimuli were presented to the panel. The end points of the 150 mm VAS were defined as the sweetness of 2.5 and 5.5% (w/w) sucrose solutions to demonstrate the limits of the scale and to prevent end-use avoidance. Furthermore, the 4% (w/w) sucrose solution was termed as "reference". The panel was instructed to score this reference in the middle of the scale. The panel was trained to evaluate the samples with respect to how different the sweetness intensity of each sample was compared to the reference. From the third session onward, the panel was instructed to first taste the reference, clean the palate with water, then taste the test sample only once and rate the sweetness perception on the scale. During the fifth and sixth training sessions, the subjects were introduced to and familiarized with the procedure of the final experiments (oral-processing protocol, different o/w emulsions, and different oral-processing times). The panel was instructed to taste the reference (4% (w/w) sucrose), take a sip of water, ingest the o/w emulsion, spit it out after a specified time period, taste the sweet sample (only once), and rate the sweetness of this stimulus. The panel was trained and instructed to focus on the sweetness perception of the sample.

In Vivo Fluorescence Measurements To Determine Oil Fraction Deposited on the Tongue. The method used in the present study has been previously described in detail.[5] Fluorescence measurements were made with a single-point measurement (Flouorolog Instruments SA Inc., HORIBA Jobin Yvon, Longjumeau, France) at an excitation wavelength of 440 nm, an emission wavelength of 495 nm with a slit width of 0.95 mm, and a measurement time of 0.1 s. A fluorescence remote read fiber optic probe was used to measure on tongue surfaces (in vivo for determination of oil fraction and ex vivo for calibration curves). The probe was put perpendicularly to the anterior back part of the tongue surface and with slight pressure to avoid deformation of the papillae and the coating. To convert the fluorescence intensity measured on the subject's tongue surface to the oil fraction deposited on the tongue surface, that is, the mass of oil per area of tongue (mg/cm^2), calibration lines (data not shown) were made following the procedure described previously.[5]

Oral-Processing Protocol. To study the formation of the oil oral coating, 20 mL o/w emulsions (1, 10, and 20% (w/w) o/w emulsion) were processed in the mouth for different time periods (t = 3, 4.5, 6, 9, and 15 s) and then expectorated. The different oral-processing times were chosen to range from the natural drinking time of one sip of 20 mL of full-fat milk (3.3 ± 0.2 s) to a consumption time that hypothetically creates maximum oil deposition on the tongue. To verify whether the oral-processing protocol would influence the perception of the 4.0% (w/w) sucrose solution (reference), that is, to verify whether the panel is able to score the 4.0% (w/w) sucrose solution in the middle of the VAS as in the training sessions, a blank coating stimulus was added to the design. The blank coating stimulus consisted of water with curcumin (to have a similar color as the o/w emulsions) and was processed in the mouth for 9 s. The oral-processing time of 9 s was chosen as it was approximately in the middle of the range of the oral-processing times of the measured o/w emulsions.

To assess the effect of oil deposition on the tongue on subsequent sweetness perception, the trained panel processed in-mouth the three o/w emulsions for different times or the blank stimulus at room temperature. The emulsions or the blank coating were then expectorated and the in vivo fluorescence measurement was performed. Immediately after the fluorescence measurement, which typically took around 1−2 s, the 4.0% (w/w) sucrose solution was tasted and sweetness intensity assessed on a continuous 150 mm VAS (anchored with little sweet on the left end and very sweet on the right

DOI: 10.1021/acs.jafc.5b02562
J. Agric. Food Chem. 2015, 63, 8025−8030

end of the scale). Only one sip of the sucrose solution was tasted with a maximum sip size of 20 mL. The middle point of the scale (75 mm) was marked with an anchor. Sensory data were collected using EyeQuestion (version 3.11.1).

Sixteen conditions ((3 o/w emulsions × 5 oral-processing times) + 1 blank) were tested by the $n = 15$ subjects in triplicate, resulting in 48 measurements per subject. Subjects participated in eight evaluation sessions of 1 h. During each session eight stimuli were assessed by each subject. A completely randomized design was used randomizing the 48 measurements over subjects and sessions.

The panel was not allowed to drink or eat 1 h before the start of a session. Prior to the first measurement, the subjects cleaned their tongue with cold water. Before the consumption of each o/w emulsion or blank coating, the subjects were asked to taste the reference (4.0% w/w sucrose) to refamiliarize themselves with the reference, after which they cleaned the tongue with water. This was followed by a background fluorescence measurement of the tongue. Between the fluorescent measurements the tongue was cleaned extensively to remove the oil deposited at the tongue for which crackers, a tongue scraper, and both room temperature (20 °C) and warm (40 °C) water were used.

Statistical Data Analysis. SPSS Statistics version 21 (IBM Software, Armonk, NY, USA) was used for the statistical analysis. Descriptive statistics were used to obtain the mean and standard error (SE). Outliers ($z > 2$) were removed from the data. The data obtained during the training sessions were used to verify panel performance. The discriminative ability of the panel and the influence of the protocol on perception were tested by an one-way analysis of variance (ANOVA). Subject and replicate effects were verified for both the fluorescence and the sensory data by a one-way ANOVA. Fluorescence intensity data were normalized with a square root transformation. The effects of oil content (within-subject factor: 1, 10, and 20% w/w), oral-processing time (within subject factor: 3, 4.5, 6, 9, and 15 s), and the interaction on the formation of the coating were tested with a repeated-measures ANOVA. The assumption of sphericity was verified by Mauchly's test, being violated for oil content and the interaction effect. Therefore, the Greenhouse−Geisser correction was applied. The effects of oil content (within subject factor: 1, 10, and 20% w/w), oral-processing time (within subject factor: 3, 4.5, 6, 9, and 15 s), and the interaction on sweetness were tested with a repeated-measures ANOVA. The assumption of sphericity was violated, and the Greenhouse−Geisser correction was applied. When significant main effects were found, Bonferroni pairwise tests were performed. A significance level of $p < 0.05$ was chosen.

RESULTS AND DISCUSSION

The aims of this study were to investigate (a) the dynamic formation of oral oil coatings formed by o/w emulsions on the tongue surface and (b) the effect of oil coatings formed by o/w emulsions on subsequent sweetness perception of sucrose solutions.

Panel Training. The results from the training sessions are shown in Figure 1. The panel scored the sweetness intensity of a blind 4.0% (w/w) sucrose solution close to the middle of the 150 mm line scale (75.4 ± 2.1 mm). The discriminative ability of the panel, that is, the minimum difference of sucrose concentration relative to the reference (4% (w/w) sucrose solution) leading to a significant difference of sweetness, was determined (Figure 1). The panel assessed the sweetness of the 3.7% sucrose solution as significantly less sweet ($p < 0.001$) than the 4.0% (w/w) sucrose solution. The sweetness intensity of the 4.3% (w/w) sucrose solution ($p < 0.01$) was significantly higher than the sweetness of the 4.0% (w/w) sucrose solution. The panel did not perceive the sweetness of the 3.8% ($p = 0.118$) and the 4.2% (w/w) solution ($p = 0.168$) as significantly different from the 4.0% (w/w) sucrose solution (Figure 1). The minimum difference in sucrose concentration between stimulus

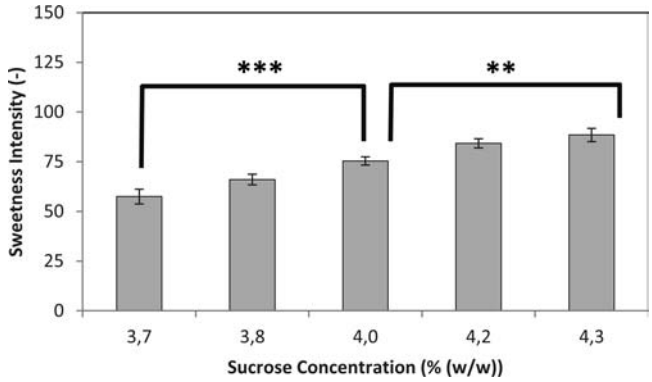

Figure 1. Sweetness intensity of sucrose stimuli varying in concentration rated on a 150 mm VAS scale. Each bar represents the average intensity of $n = 15$ subjects assessing the stimuli in triplicate. Significance level is represented by ** for $p < 0.01$ and *** for $p < 0.001$. Error bars represent the standard error.

and 4.0% (w/w) sucrose solution that led to a significant difference in sweetness intensity was 0.3% (w/w).

Dynamic Formation of Oral Oil Coatings of o/w Emulsions. Figure 2 depicts the oil fraction deposited on the anterior back part of the tongue for 1, 10, and 20% (w/w) o/w emulsions after oral processing of the emulsion for different times. A significant main effect of oil content on the oil fraction deposited on the tongue ($F[1.4, 63.4] = 323.7$ $p < 0.001$) was found with a higher oil content of the o/w emulsions resulting in a higher oil fraction deposited on the tongue surface. All of the o/w emulsions differed significantly from each other at every oral-processing time point ($p < 0.001$).

It was hypothesized that the oil fraction deposited on the tongue increases with increasing oral processing time until, at longer oral-processing times, the amount of oil deposited on the tongue reaches a plateau. The oil fraction deposited on the tongue tended (not significant) to be influenced by oral processing time ($p = 0.057$) (Figure 2). No significant differences in oil fraction deposited on the tongue were observed between o/w emulsions orally processed for $t = 3$ s and longer oral-processing times ($t = 4.5$, 6, 9, and 15 s). This demonstrates that a saturation with oil deposited on the tongue was reached already after an oral-processing time of $t = 3$ s for all emulsions tested. The dynamics of the oil coating formation is similar for the three emulsions studied. This fast saturation of oil deposited on the tongue surface suggests that the o/w emulsions contain oil droplets that can easily adhere to the tongue surface. This suggests that within the natural drinking time of one sip of 20 mL of a liquid stimulus (3.3 ± 0.2 s for full-fat milk), the tongue surface is already coated with the drink's oil, which can adhere to the tongue. We speculate that the observations of previous studies of, for instance, Pivk et al. (study used samples of 0.5−16 mL of bulk MCT oil) and Camacho et al. (study used samples of 20 mL, as is the case of this study), which used an oral-processing time of 30 s to investigate oil deposition on the tongue, are likely to be similar to results that would have been obtained with shorter oral-processing times of <5 s.

Influence of Oil Coatings on Subsequent Sweetness Perception. The influence of the oral-processing protocol during the fluorescence measurements on the evaluation of sweetness intensity of the sucrose samples was verified by adding a blank coating sample (water with curcumin) to the experiment. The sweetness intensity of the 4.0% sucrose sample

DOI: 10.1021/acs.jafc.5b02562
J. Agric. Food Chem. 2015, 63, 8025−8030

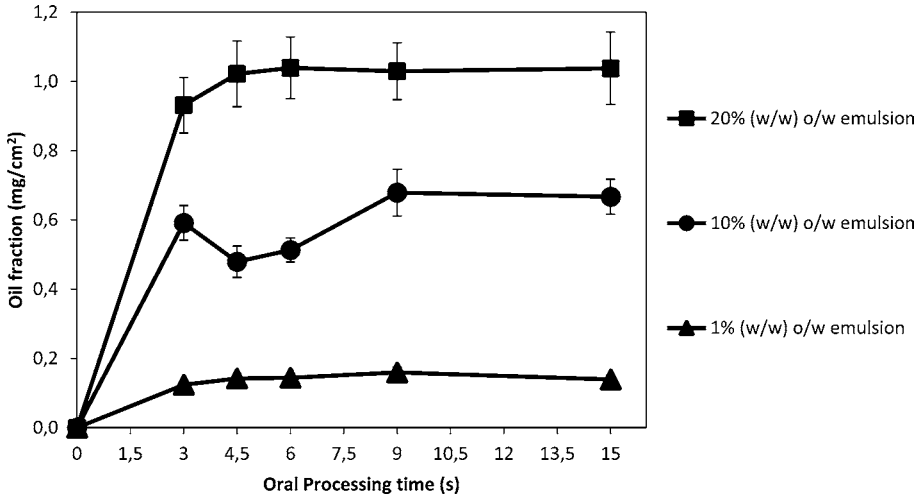

Figure 2. Oil fraction deposited on the back part of the anterior tongue of 1, 10, and 20% (w/w) o/w emulsions processed orally for different time periods. Each point represents the average of n = 15 subjects assessing the stimuli in triplicate. The error bars represent the standard error.

after consumption of the blank (76.7 ± 2.5 mm) did not differ significantly from the sweetness intensity of the 4% sucrose solution without consumption of the blank (75.4 ± 2.1 mm) (p = 0.696). This indicates that the oral-processing protocol did not affect the panel performance and, furthermore, the addition of curcumin did not affect sweetness.

Different oil fractions deposited on the tongue (Figure 2) after different oral-processing times did not significantly affect subsequent sweetness intensity (p = 0.294) (Figure 3).

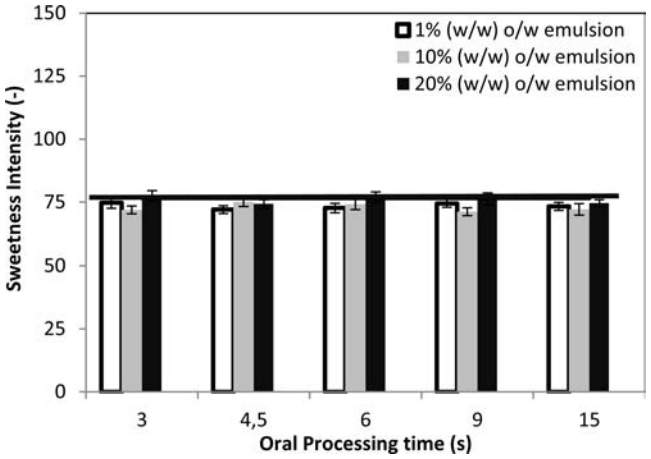

Figure 3. Sweetness intensity after consumption of 1, 10, and 20% (w/w) o/w emulsions for different oral processing times (t = 3, 4.5, 6, 9, and 15 s). Each bar represents the average value of n = 15 subjects assessing the stimuli in triplicate. The error bars represent the standard error. The line represents the average sweetness intensity of the blank sample (i.e., water).

Sweetness intensities of the 4.0% (w/w) sucrose stimulus, after oral processing of the different o/w emulsions for different times, ranged from 71.1 ± 2.1 to 77.4 ± 2.2 mm. Sweetness intensity was not correlated with the oil fraction deposited on the back part of the anterior tongue (Figure 4). We suggest that by orally processing o/w emulsions ranging in oil content from 1 to 20% (w/w), the oil fraction adhering to the tongue surface is not sufficient to form a homogeneous film of oil covering the tongue. We suggest that the oil droplets deposited on the tongue do not form a hydrophobic barrier that is sufficient to

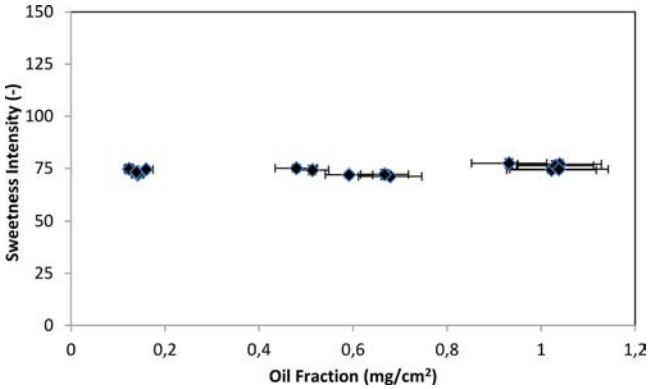

Figure 4. Oil fraction deposited on the back part of the anterior tongue as a function of sweetness intensity for 1, 10, and 20% (w/w) o/w emulsions orally processed for different times (t = 3, 4.5, 6, 9, and 15 s). Each point represents the average of n = 15 subjects assessing the stimuli in triplicate. The error bars represent the standard error.

reduce the accessibility of sucrose to the taste buds. This proposes that the migration of sucrose molecules to the taste buds is not sufficiently reduced and, consequently, sweetness perception is not altered. An additional explanation might be due to the morphology of the tongue. Fungiform papillae, which contain taste buds with taste receptor cells (TRCs), are mainly found in the front part of the anterior tongue. The front part of the anterior tongue has consequently been demonstrated to be more sensitive for taste perception.[9] In previous studies, it was found that less oil deposits at the front part of the anterior tongue compared to the back part.[4−6] Taking the uneven distribution of oil deposition on the tongue into account, tastants could likely migrate to the taste buds and bind to the TRCs present at the tip of the tongue because the amount of oil deposited there is even smaller than on the back part of the tongue. Consequently, no effect of oral oil deposition on sweetness intensity is observed.

The results of this study did not confirm previous findings in the literature,[1-3] which reported that sweetness intensity was suppressed by preceding consumption of bulk oil or dispersed oil. Lynch et al. found that the consumption of either coconut oil or sunflower oil reduced subsequent sweetness intensity of sweet gelatin gels compared to preceding consumption of

DOI: 10.1021/acs.jafc.5b02562
J. Agric. Food Chem. 2015, 63, 8025−8030

water. Valentová and Pokorný found that the consumption of bulk sunflower oil reduced subsequent sweetness intensity of sucrose solutions. Both studies used oils to coat the tongue, whereas this study used o/w emulsions with a maximum oil content of 20% (w/w). The difference in oil content between stimuli used in the literature and our study led to differences in the amount of oil fraction deposited on the tongue. It is likely that the oil coatings formed with bulk oil form a hydrophobic layer and might have created a thicker physical barrier and thus suppress the migration of hydrophilic tastants to the taste buds, leading to a suppression of sweetness perception. Furthermore, coconut oil seemed to have a higher effect in the suppression of sweetness intensity compared to sunflower oil.[1] Coconut oil has a higher viscosity compared to sunflower oil.[10] Viscosity was found to affect taste intensity, indicating a taste−texture interaction.[11] Taste−taste interactions could have also contributed to the sweetness suppression, as coconut oil has an inherent coconut taste, which could have caused sensory adaptation. Therefore, texture−taste or taste−taste interactions might have contributed to the suppression of sweetness intensity due to preceding coconut oil consumption found by Lynch et al. Next to this, the sunflower oil used by Valentová and Pokorný was refined with oily and buttery flavors, which might also have partly suppressed the subsequent perceived sweetness by flavor−taste interactions. Furthermore, although these studies used panels experienced with time−intensity and sensory profiling, it is not explicit whether and how the panels were trained specifically on sweetness perception. The training of subjects to assess taste intensity and the resulting discrimination sensitivity of the subjects used is likely to differ between the different studies. Highly trained subjects should be used because the effects of oil coatings on subsequent taste perception are expected to be small.

Ahn et al. and Valentová and Pokorný both observed sweetness intensity suppression after consumption of bulk oils or foods with high oil content. Those studies used sucrose solutions with concentrationa of 0.12 and 15.5% (w/w), respectively. In our study we did not observe sweetness intensity suppression. We used a sucrose concentration of 4.0% (w/w) and o/w emulsions with up to 20% (w/w) oil. This suggests that the fraction of oil deposited on the tongue is the main factor that determines whether suppression of taste intensity due to oral oil coatings occurs.

Valentová and Pokorný found that consumption of commercial emulsions, that is, yogurt dressing, flavored emulsion, and mayonnaise, resulted in a decrease in subsequent sweetness intensity. However, these products have a complex food matrix and contain not only fat but also tastants and aromas. The ingredients and flavor might have contributed to the suppression of the sweetness by various mechanisms, for example, texture−taste, taste−taste, or flavor−taste interactions.

Milk is known to form a mouth coating.[12] This coating effect was thought to alter perception, because the consumption of milk was found to reduce subsequent perception of sweetness.[3] The suppression of sweetness intensity by milk might be better explained by taste interactions. The sweetness of milk[12] might have resulted in adaptation leading to a suppression in sweetness intensity of the tastant solution. Another reason might be that tastants or aroma molecules present in the oral cavity after the consumption of milk might have masked the succeeding sweetness of the tastant solution.

In conclusion, the dynamics of oral oil deposition is fast with the maximum oil fraction adhering to the tongue surface occurring within the natural drinking time of one sip of a beverage. Longer oral processing does not increase the oil fraction deposited on the tongue. The oil fraction deposited on the tongue after oral processing of o/w emulsion with up to 20% (w/w) oil did not affect subsequent sweetness perception of sucrose solutions. We suggest that this is caused by a limited fraction of oil being deposited on the tip of the tongue where humans have a high density of taste papillae and consequently are most sensitive to taste perception. We suggest that the oil droplets deposited on the tongue did not form a hydrophobic barrier that is sufficient to reduce the accessibility of sucrose to the taste buds and consequently does not suppress taste perception.

AUTHOR INFORMATION

Corresponding Author

*(M.S.) Mail: Agrotechnology and Food Sciences Group, Division of Human Nutrition, Wageningen University, P.O. Box 8129, 6700 EV Wageningen, The Netherlands. Phone: +31 317 481694. E-mail: markus.stieger@wur.nl.

Notes

The authors declare no competing financial interest.

ABBREVIATIONS USED

o/w, oil-in-water; VAS, visual analogue scale

REFERENCES

(1) Lynch, J.; Liu, Y. H.; Mela, D. J.; MacFie, H. J. H. A time-intensity study of the effect of oil mouthcoatings on taste perception. *Chem. Senses* **1993**, *18*, 121−129.

(2) Valentova, H.; Pokorny, J. Effect of edible oils and oil emulsions on the perception of basic tastes. *Nahrung* **1998**, *42*, 406−408.

(3) Ahn, N.; Frost, M. B.; Frandsen, L. W.; Dijksterhuis, G.; Martens, M. The effect of some beverages on the perception of succeeding basic tastes. *J. Sens. Stud.* **2002**, *17*, 571−581.

(4) Pivk, U.; Godinot, N.; Keller, C.; Antille, N.; Juillerat, M. A.; Raspor, P. Lipid deposition on the tongue after oral processing of medium-chain triglycerides and impact on the perception of mouthfeel. *J. Agric. Food Chem.* **2008**, *56*, 1058−1064.

(5) Camacho, S.; van Riel, V.; de Graaf, C.; van de Velde, F.; Stieger, M. Physical and sensory characterizations of oral coatings of oil/water emulsions. *J. Agric. Food Chem.* **2014**, *62*, 5789−5795.

(6) Camacho, S.; den Hollander, E.; de Graaf, C.; van de Velde, F. Properties of oil/water emulsions affecting the deposition, clearance, and after-feel sensory perception of oral coatings. *J. Agric. Food Chem.* **2015**, *63*, 2145−2153.

(7) Prinz, J. F.; Huntjens, L.; de Wijk, R. A. Instrumental and sensory quantitation of oral coatings retained after swallowing semi-solid foods. *Arch. Oral Biol.* **2006**, *51*, 1071−1079.

(8) De Jongh, H. H. J.; Janssen, A. M. Differential clearance kinetics of adhered layer constituents from the oral cavity as modulator for afterfeel of dressings: ATR FT-IR measurements of localized oral coatings. *J. Texture Stud.* **2007**, *38*, 70−86.

(9) Chandrashekar, J.; Hoon, M. A.; Ryba, N. J.; Zuker, C. S. The receptors and cells for mammalian taste. *Nature* **2006**, *444*, 288−294.

(10) De Dios, A. J. Mechanical properties of vegetable oils and fats. *Grasas Aceites* **1995**, *46*, 264−269.

(11) Kokini, J. L. The physical basis of liquid food texture and texture-taste interactions. *J. Food Eng.* **1987**, *6*, 51−81.

(12) Frost, M. B.; Dijksterhuis, G.; Martens, M. Sensory perception of fat in milk. *Food Qual. Prefer.* **2001**, *12*, 327−336.

DOI: 10.1021/acs.jafc.5b02562
J. Agric. Food Chem. 2015, 63, 8025−8030

proposing the effect of glucosamine degradation on 4-MeI formation.

MATERIALS AND METHODS

Chemicals and Reagents. 4-MeI, sodium hydroxide (50%), and methanesulfonic acid (MSA, 99%) were purchased from Sigma-Aldrich Chemical Co. (St. Louis, MO, USA). Methanol, NH_4Cl, and hydrochloric acid (HCl, 35−37%) were of analytic grade and purchased from Merck (Damstadt, Germany). Phosphate buffer solutions (PBS, 0.2 mol/L) of pH 7.4 and Na_2HPO_4−citric acid buffer solutions (0.2 mol/L Na_2HPO_4 stock solution, 0.1 mol/L citric acid stock solution) of pH 5.0, 7.0, and 8.0 were also used. The mixed standard stock solution of 4-MeI (10 mg/L) was prepared by dissolving the analytes into deionized water.

Sample Preparation. In glucose−NH_4^+ Maillard reaction, glucose (40 mmol/L) was mixed with NH_4Cl (free ammonium, 40 mmol/L) in 10 mL of Na_2HPO_4−citric acid buffer solutions (0.2 mol/L) with or without sulfite sodium (40 mmol/L) at various pH values (5, 7, and 8, respectively). In bound amino compound Maillard reaction, glucosamine (40 mmol/L) and *N*-acetylglucosamine (40 mmol/L) were each dissolved in 10 mL of Na_2HPO_4−citric acid buffer solutions (0.2 mol/L) with or without sulfite sodium (40 mmol/L) at various pH values (5, 7, and 8, respectively). Four milliliter mixtures were incubated at 120 °C for up to 120 min in a swing-top bottle. After a defined reaction time, the reaction mixtures were cooled to room temperature by iced water immediately to stop the reaction. One milliliter of reaction mixture was incubated with *o*-phenylenediamine (1 mL, 0.5 mg/mL in 0.2 mol/L PBS of pH 7.4) for 12 h at room temperature, and the rest of the reaction mixture was stored at 4 °C for further analyses.

Absorbance Measurements of Reaction Mixtures. The UV absorbance and browning intensity of the Maillard reaction products were measured according to the literature with a slight modification.[3] A 150-fold dilution of the treated solution was detected at 420 nm using a UV-1901 spectrophotometer (Puxi, Beijing, China).

Analyses of Dicarbonyls by HPLC-UV. Interception of α-dicarbonyls as quinoxalines was carried out according to the method of Gobert et al.[11] with slight modifications. The analyses were performed in an HPLC-DAD system, which consisted of a 5 μm Waters Atlantis T3 150 × 4.6 mm column (Waters Co., Milford, MA, USA), a Waters 600 pump, and a Waters 2998 diode array detector. One milliliter of reaction solution was mixed with 1 mL of OPD solution (0.5 mg/mL) and reacted at 25 °C for 12 h in the dark. The injection volume was 20 μL (sterilized through 0.45 μm filters), and the mobile phases were methanol and water and set as 5% v/v methanol, 0−5 min, then a linear gradient from 5% v/v methanol to 30% v/v methanol, 5−10 min, subsequently changed to 40% v/v methanol, 10−45 min, and, finally, 100% v/v methanol was used for elution from 45 to 65 min at a flow rate of l mL/min. Column temperature was set at 25 °C. Spectral data from all peaks were accumulated in the range of 200−600 nm, and chromatograms were recorded at 315 nm.

The regression equation for 2-methylquinoxaline standard was $a^* = 10^7 \times C_1$ (R^2 = 0.9999), where C_1 = 2-methylquinoxaline concentration (mmol/L) and a^* = peak area of 2-methylquinoxaline. The retention time of 2-methylquinoxaline was about 27.6 min, and the experimental range of MGO was 0.500−50.000 mg/L in this test.

Analyses of 4-MeI by HPCEC-APCI-MS. According to the literature[12] with slight modification, an Ansys SPEC SCX Disc 15 mg/3 mL cartridge (Varian, Walnut Creek, CA, USA) was conditioned with 1 mL of methanol and 1 mL of water. Then 3 mL of Maillard reaction mixtures acidified with 20 μL of HCl (0.1 mol/L) was loaded and passed through the cartridge. The retained 4-MeI was eluted with 6 mL of methanol/ammonia (5%, v/v). The collected extract was evaporated by vacuum concentration at 39 °C, and the residues were dissolved by 3 mL of deionized water for HPCEC-APCI-MS analyses.

HPCEC-APCI-MS was used for the determination and quantitation of 4-MeI. The samples were filtered through a Millex-HN nylon clarification kit of 0.45 μm pore size (Millipore, Bedford, MA, USA) and analyzed on a DX 5000 Dionex system (Dionex Corp., Sunnyvale, CA, USA) with a gradient pump (model EG40) with online degassing. Separation was accomplished on a CS12A cation exchange column (250 × 4 mm, Dionex) and a CS12A guard column (50 × 4 mm, Dionex) using the isocratic elution (10 mmol/L MSA) for 50 min. All tests used a constant flow rate of 0.7 mL/min. The injection volume was 25 μL.

Atmospheric pressure chemical ionization (APCI) (positive ionization mode) (ThermoFisher Co., San Jose, CA, USA) was coupled with the HPCEC system. The desalter was a 4 mm CSRS-300 (PN: 064556) with a constant current of 30 mA on the autosuppression external water mode (regenerant flow rate of approximately 3 mL/min). The spray current was set at 5 μA, capillary voltage was 0.50 kV, and capillary temperature and source temperature were both 300 °C. Nitrogen source was used as sheath and auxiliary gas. Argon was used as the collision gas, and the multiplier was set to 570 V. The m/z 83 parent ion was used to obtain the daughter ions m/z 56 and 42 at a collision energy of 23 eV. Selected ion monitoring (SIM) mode was used to monitor the m/z 83 ion.

The regression equation for 4-MeI standard was $y = 859.9x - 198$ (R^2 = 0.9999), where x is 4-MeI concentration (mg/L) and y is the peak area of 4-MeI. The retention time of 4-MeI was about 15 min, and the detection range was 0.003−0.2 mg/L in this test. The recovery of 4-MeI in reaction mixtures was about 96% (w/w).

Analyses of Pyrazines by Gas Chromatography−Mass Spectrometry (GC-MS). According to the literature,[13] a gas chromatograph HP 5890 series with a mass spectrometric detector 5972 from Hewlett-Packard (Palo Alto, CA, USA) was used to analyze the chemical composition of the brown solution dichloromethane extract. The column employed was an Agilent HP-5MS, 30 m × 0.25 mm (i.d.), film thickness = 0.25 μm. The injector temperature of the GC was 300 °C. The GC oven temperature was programmed as follows: (1) The initial temperature was 60 °C and kept for 2 min. (2) The temperature was then increased from 60 to 140 °C at a rate of 3 °C/min and kept for 1 min. Thereafter, the temperature was increased from 140 to 320 °C at a rate of 8 °C/min and kept for 1 min. (3) The injection volume was 1 μL. (4) The carrier gas was He at a flow rate of 1 mL/min. The MS conditions were as follows: electron impact mode, total ion current recorded. The mass spectra of the compounds were compared to the spectra from the NIST02 spectral library. The mass scan ranged from 50 to 650 Da.

Statistical Analysis. Means and standard deviations of the data were calculated for each treatment. Analysis of variance (ANOVA) was carried out to determine any significant differences ($p < 0.05$) among the applied treatments by the SPSS software package (SPSS 10.0 for windows).

RESULTS

Formation of 4-MeI in Class III Caramel Color. During class III caramel color manufacture, the formation of 4-MeI was influenced by the amino source. The chromatograms from HPCEC-APCI-MS of 4-MeI in model systems are shown in Figure 1. 4-MeI was detected in the glucose−NH_4^+ and glucosamine model systems, but nearly no 4-MeI was detected in the acetylglucosamine model system. Moreover, the level of 4-MeI in the glucose−NH_4^+ model system was higher than that in the glucosamine model system under different pH conditions (pH 5, 7, and 8, respectively.). In addition, the formation of 4-MeI was promoted in the alkaline solution. The detailed data are listed in Table 1.

Formation of 4-MeI in Class IV Caramel Color. Sulfite was an important adduct during the manufacture of class IV caramel color. The effect of sulfite (40 mmol/L) on 4-MeI formation was studied in glucose−NH_4^+, glucosamine or acetylglucosamine model systems, respectively. As shown in Figure 2, sulfite significantly promoted the formation of 4-MeI in the glucose−NH_4^+ model system (pH 7). However, sulfite

DOI: 10.1021/acs.jafc.5b02616
J. Agric. Food Chem. 2015, 63, 8031−8036

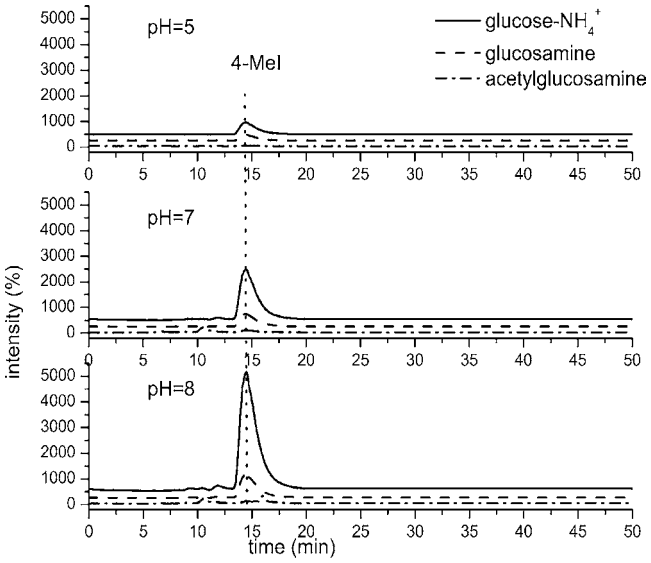

Figure 1. HPCEC-APCI-MS chromatograms of 4-MeI obtained from caramel color model systems under various pH conditions (5, 7, 8).

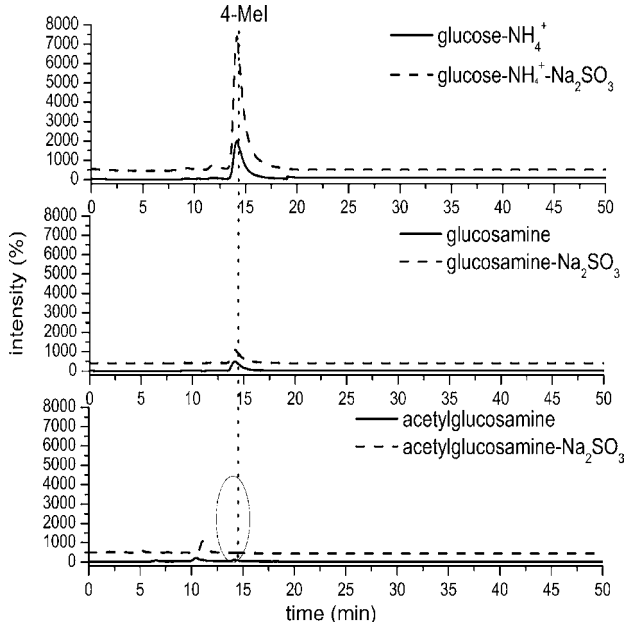

Figure 2. HPCEC-APCI-MS chromatograms of 4-MeI obtained from caramel color model systems with or without sodium sulfite (40 mmol/L).

slightly promoted 4-MeI formation in the glucosamine or acetylglucosamine model system (Table 1).

Change of Brown Intensity. Browning intensity (A_{420}) is the easiest measurable consequence of the advanced stage of the Maillard reaction. A_{420} intensity is often used as an indication of the extent to which the Maillard reaction takes place in foods.[15] In this study, the amino source in model caramel systems showed a great influence on the change of A_{420} (Figure 3). The value of A_{420} in the acetylglucosamine model system was higher than that in the glucose−NH_4^+ and glucosamine model systems under pH 7 condition. In addition, the value of A_{420} decreased in all three model systems containing sulfite (40 mmol/L).

Formation of MGO in Caramel Model System. MGO was confirmed as the precursor of 4-MeI.[1] In the class III model caramel system, pH was a great factor of MGO formation. As shown in Figure 4, the content of MGO in the alkaline model reaction system (pH 8) was higher than that in the acid model reaction system (pH 5). In addition, the amino source also influenced MGO formation. For example, the level of MGO formed in the glucose−NH_4^+ model reaction system was significantly higher than that in glucosamine or acetylglucosamine model reaction system (Table 1). In the class IV model caramel system, sulfite was the important factor of MGO formation. However, the increased level of MGO was dependent on the amino source. As shown in Figure 5, the

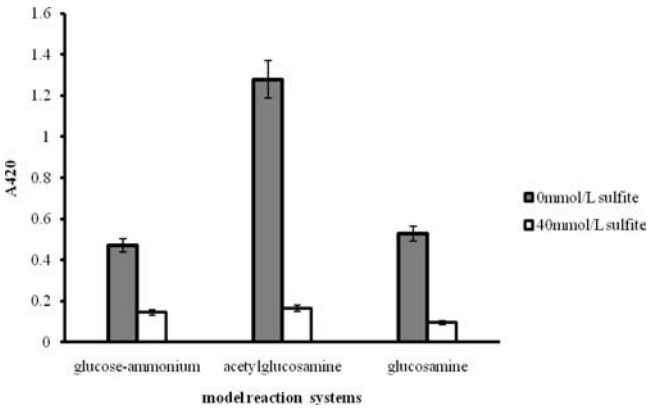

Figure 3. Changes of brown intensity (420 nm) obtained from caramel color model systems with or without sodium sulfite (40 mmol/L).

MGO content in the glucosamine or glucose−NH_4^+ model reaction system was significantly promoted by sulfite (40 mmol/L) under pH 7 condition. However, the MGO content was slightly increased by sulfite (40 mmol/L) in acetylglucosamine model reaction system.

Table 1. Contents of 4-MeI and MGO in Maillard Reaction Model System with or without Sulfite[a]

					sodium sulfite (40 mmol/L)		
compound	pH	model 1	model 2	model 3	model 1	model 2	model 3
4-MeI (mg/L)	5	0.067 ± 0.012	0.027 ± 0.008	ND[b]	0.513 ± 0.028	0.067 ± 0.012	ND
	7	0.312 ± 0.017	0.056 ± 0.012	ND	0.777 ± 0.052	0.092 ± 0.020	ND
	8	0.549 ± 0.020	0.063 ± 0.019	0.014 ± 0.006	0.779 ± 0.047	0.064 ± 0.011	ND
MGO (mg/L)	5	0.792 ± 0.032	ND	ND	26.64 ± 0.110	17.928 ± 0.058	1.944 ± 0.014
	7	2.016 ± 0.027	1.368 ± 0.030	1.080 ± 0.021	7.992 ± 0.081	7.200 ± 0.042	0.864 ± 0.047
	8	3.744 ± 0.016	2.016 ± 0.029	1.656 ± 0.028	4.248 ± 0.093	3.168 ± 0.051	0.720 ± 0.022

[a]Models 1, 2, and 3 were the model systems of glucose−NH_4^+, glucosamine, and acetylglucosamine, resepectively. [b]ND, not detected.

DOI: 10.1021/acs.jafc.5b02616
J. Agric. Food Chem. 2015, 63, 8031−8036

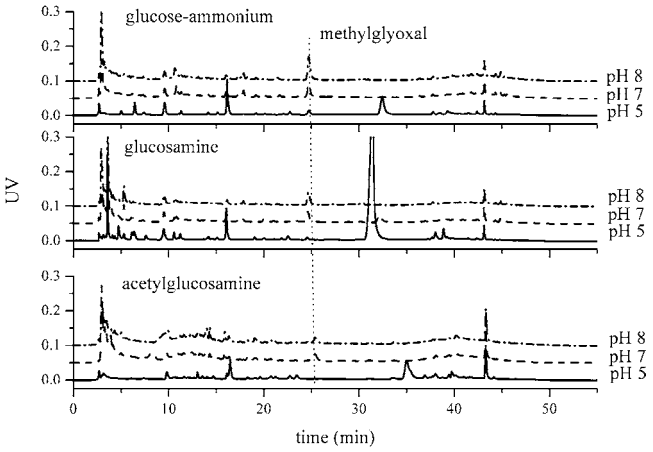

Figure 4. HPLC chromatograms of methylglyoxal obtained from caramel color model systems under various pH conditions (5, 7, 8).

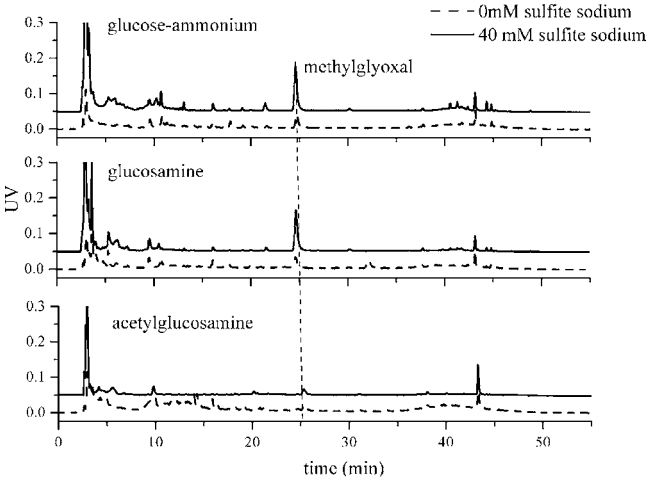

Figure 5. HPLC chromatograms of methylglyoxal obtained from caramel color model systems with (dash line) or without 40 mmol/L sodium sulfite (solid line).

Formation of Pyrazines. Table 2 lists the four types of pyrazines mainly detected in the study of the caramel model system solutions. When sulfite was not spiked into the caramel color model system, the majority of the pyrazines detected were 2-methylpyrazine (**3**), followed by 2,6-dimethylpyrazine (**2**), pyrazine (**4**), and 2-methyl-6-ethylpyrazine (**1**). Moreover, the contents of the four pyrazines in the glucose−NH_4^+ model reaction system were higher than that in the glucosamine or acetylglucosamine model reaction system. In addition, 2-methyl-6-ethylpyrazine (**1**) and 2,6-dimethylpyrazine (**2**) were not observed in the acetylglucosamine model reaction system.

By comparison, sulfite had a great influence on the formation of four pyrazines in the class IV caramel color model system. The formation of 2-methylpyrazine (**3**) and 2,6-dimethylpyrazine (**2**) was promoted by sulfite in glucosamine and glucose−NH_4^+ except for the acetylglucosamine model reaction system. Besides, the formation of pyrazine and 2-methyl-6-ethylpyrazine was significantly inhibited by sulfite in the caramel color model system. Similarly, the content of the four pyrazines in the glucose−NH_4^+ model reaction system was higher than that in the glucosamine or acetylglucosamine model reaction system when sulfite was added.

Table 2. Effect of Sulfite on the Formation of Pyrazines in Maillard Reaction

pyrazines	m/z	Model reaction systems	Ratio of peak area (%)	
			0 mmol/L sodium sulfite	40 mmol/L sodium sulfite
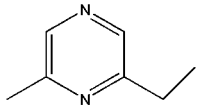 1	122	Glucose-NH_4^+	2.7±0.5	0.5±0.1
		Glucosamine	1.7±0.2	0.4±0.1
		Acetylglucosamine	ND.	ND.[a]
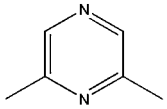 2	108	Glucose-NH_4^+	16.5±1.5	19.9±0.8
		Glucosamine	11.1±0.5	11.7±0.7
		Acetylglucosamine	ND.	ND.
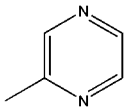 3	94	Glucose-NH_4^+	130.2±1.3	132.6±1.1
		Glucosamine	80.7±0.7	88.3±2.9
		Acetylglucosamine	4.1±0.9	1.1±0.1
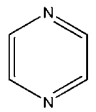 4	80	Glucose-NH_4^+	9.6±1.5	3.2±0.4
		Glucosamine	6.0±2.1	2.9±0.3
		Acetylglucosamine	3.5±0.3	1.3±0.8

[a]ND, not detected.

DISCUSSION

Using model reaction systems to investigate the formation of 4-MeI had been reported in some studies.[1,3,7,14] In this study, the effect of amino source including free ammonium, glucosamine, and acetylglucosamine on the formation of 4-MeI was detailed using a model reaction system. Obviously, the formation of 4-MeI was significantly promoted by free ammonium with respect to glucosamine and acetylglucosamine. Interesting, nearly no 4-MeI was formed in the acetylglucosamine model system. On the basis of the previous studies, the formation of 4-MeI was correlated to the amino aldehyde intermediates formed from methylglyoxal with ammonia, which could produce either 4-MeI by interacting with formaldehyde[15] or pyrazines via condensation reaction with dicarbonyls.[16] In this study, the result of 4-MeI formation was consistent with the result from MGO formation in the model reaction (Figure 4). Thus, the low level of 4-MeI formation in glucosamine analogue model systems was related to the low level of MGO formed from glucosamine analogue model systems with respect to the free ammonium−glucose model reaction system.

On the basis of the early research, MGO formation via the Maillard reaction or caramelization reaction was briefly defined as follows:

Maillard reaction route: glucose + ammonium → ARPs or HRPs →3-DG → MGO.[17]

Caramelization reaction route: glucose → 3-DG → MGO.[11,18]

First, the Maillard reaction route rather than the caramelization reaction route in glucosamine or acetylglucosamine (HRPs analogs) model system was mainly carried out to form a low level of MGO.[19,20] The explanation of this phenomenon was that ARPs or HRPs could mainly form dimerization products via intermolecular reaction[10] or further polymerize into melanoidins (confirmed by brown intensity from Figure 3); these formed products were hardly degraded into MGO. However, in the glucose−ammonium model system, the

DOI: 10.1021/acs.jafc.5b02616
J. Agric. Food Chem. 2015, 63, 8031−8036

caramelization reaction and Maillard reaction were simultaneously carried out, which induced a high level of MGO. Therefore, promotion of the polymerization reaction of HRPs or ARPs was important to induce a low level of MGO and subsequently inhibit 4-MeI formation. The main reason was that the low level of MGO formation inhibited the condensation reaction between dicarbonyls and ammonium, which induced the low level of 4-MeI formed in glucosamine analogue model systems with respect to the glucose−NH_4^+ model system. In addition, the effects of condensation reaction between dicarbonyls and ammonium on 4-MeI formation could be confirmed by the results of pyrazines.

Meanwhile, it was worthwhile to note that the formation of MGO and 4-MeI was affected by the pH value. Obviously, the formation of MGO and 4-MeI under alkaline condition was promoted with respect to the reaction under acid condition. However, the increased ratio of MGO and 4-MeI in the glucosamine analogue model reaction system was lower than that in the glucose−NH_4^+ model system. Therefore, the manufacture of caramel color with a low level of 4-MeI using glucosamine analogues as amino source was slightly affected by the value of pH. Especially, using acetyl to protect the amino group of glucosamine, the formation of MGO and 4-MeI was significantly inhibited. Some studies had indicated that the formation of MGO was degraded from 1- or 3- deoxyglucosone (DG) via enolization and retroaldolization reaction.[21,22] In theory, the acetyl-protected amino group of glucosamine would block the enamine product formation and subsequently inhibit the formation of 1- or 3-DG. Consequently, MGO formation was inhibited in the acetylglucosamine model system, which induced a low level of 4-MeI.

In the class IV caramel color model system, sulfite was usually added as ammonium sulfite, inducing the formation of negative melanoidins, which are mainly applied for coloring beverages.[23] In this study, sodium sulfite as sulfite additive significantly promoted the formation of MGO and 4-MeI in the class IV caramel reaction system but inhibited the melanoidin formation. In our previous study, the addition of sulfite significantly reduced the levels of osones (such as glucosone and pentosone) except for deoxyosones (3-deoxyglucosone and MGO). The effect of sulfite on dicarbonyl formation was comfirmed by H/D exchange experiments, which indicated that the promotion of aldo-eneol transition by sulfite accelerated the 3-C-elimination reaction of 1,2-enediol to form 3-DG, subsequently degraded into the increased MGO. Besides, the inhibition of oxidative dicarbonyl (glucosone, glyoxal, and so on) formation was attributed to the reductive sulfite inhibiting the oxidation of enediol products. Because sulfite inhibited a majority of oxidative dicarbonyl formation except for deoxyosones (3-deoxyglucosone and MGO), the total levels of dicarbonyls in the reaction systems were reduced, which induced the inhibition of brown products formation.

In this study, under pH 7 condition, the promotion effect of sulfite on 4-MeI formation was slight in the glucosamine analogue model system with respect to the glucose−NH_4^+ model system (Figure 2). Meanwhile, the formation of MGO (the precursor of 4-MeI) was slightly affected by sulfite in the acetylglucosamine model reaction system. In contrast, the content of MGO in the glucosamine model system was significantly increased by sulfite. Therefore, the protected amino group on glucosamine inhibited the promotion effect of sulfite on MGO formation.

In the caramel color model reaction system, pyrazines were recognized as the main flavor compounds from the Maillard reaction. Some literature has reported that pyrazines were formed from the condensation reaction between dicarbonyls and ammonium.[14] To some extent, the content of pyrazines in the model reaction marked the development of condensation reaction between dicarbonyls and free ammonium to form 2-aminopropanal analogues, which were the potential precursors of pyrazines or 4-MeI formation.[15] For example, MGO reacted with free ammonia to form 2-aminopropanal, which interacted with formaldehyde to form 4-MeI or reacted with ethylglyoxal to form 2-ethyl-6-methylpyrazine (**1**).[14] In this study, the levels of pyrazines in the glucose−NH_4^+ model system were significantly higher than that in the glucosamine analogue model reaction system. Because the levels of MGO and free ammonium in the glucose−NH_4^+ model system were higher than that in the glucosamine analogue model reaction system, the formation of 2-aminopropanal was promoted in the glucose−NH_4^+ model system with respect to the glucosamine analogue model reaction system. As a result, the formations of pyrazines and 4-MeI derived from 2-aminopropanal were promoted in the glucose−NH_4^+ model system. In contrast, the glucosamine analogues could mainly produce melanoidins via intra-intermolecular polymerization rather than degrade into dicarbonyls and free ammonium. The guessed result could be confirmed by the fact that the brown intensity in the glucosamine analogue model reaction systems was higher than that in the glucose−NH_4^+ model system.

In the class IV caramel color model reaction system, sulfite promoted 2-methylpyrazine (**3**) and 2,6-dimethylpyrazine (**2**) formation but inhibited pyrazine (**4**) and 2-methyl-6-ethylpyrazine (**1**) formation. In our previous studies, sulfite inhibited oxysone (including glyoxal and acetylglyoxal) formation but promoted MGO formation. Therefore, the formation of 2-methylpyrazine (**3**) and 2,6-dimethylpyrazine (**2**) was dependent on the formation of MGO, whereas the formation of pyrazine (**4**) and 2-methyl-6-ethylpyrazine (**1**) was dependent on the formation of oxysones. Similar results could be observed from the data reported by Seo et al.[14]

In summary, high levels of MGO and free ammonium in the caramel glucose−NH_4^+ model resulted in a high level of 4-MeI formation. In addition, the protected amino group on glucosamine analogues as caramel color amino source could reduce the levels of MGO and free ammonium; thus, the manufacture of caramel color with a low level of 4-MeI could be implemented on glucosamine analogues.

AUTHOR INFORMATION

Corresponding Author

*(S.-J.Y.) E-mail: shujuanyu8@gmail.com. Phone: +86 20 87113668. Fax: +86 20 87113668.

Funding

All of the authors acknowledge financial support from the National Science Foundation of China (Grant 31271889), the Science and Technology Planning Project of Guangdong Province, China (No. 2014B020205001), and the Science and Technology Planning Project of Guang Zhou, China (No. 2013J4500036).

Notes

The authors declare no competing financial interest.

DOI: 10.1021/acs.jafc.5b02616
J. Agric. Food Chem. 2015, 63, 8031−8036

REFERENCES

(1) Hengel, M.; Shibamoto, T. Carcinogenic 4(5)-methylimidazole found in beverages, sauces, and caramel colors: chemical properties, analysis, and biological activities. *J. Agric. Food Chem.* **2013**, *61*, 780−789.

(2) Chappel, C. I.; Howell, J. C. Caramel colours—a historical introduction. *Food Chem. Toxicol.* **1992**, *30*, 351−357.

(3) Lee, K.-G.; Jang, H.; Shibamoto, T. Formation of carcinogenic 4(5)-methylimidazole in caramel model systems: a role of sulfite. *Food Chem.* **2013**, *136*, 1165−1168.

(4) Petruci, J. F. d. S.; Pereira, E. A.; Cardoso, A. A. Determination of 2-methylimidazole and 4-methylimidazole in caramel colors by capillary electrophoresis. *J. Agric. Food Chem.* **2013**, *61*, 2263−2267.

(5) Brusick, D. J.; Jagannath, D. R.; Galloway, S. M.; Nestmann, E. R. Genotoxicity hazard assessment of caramel colours III and IV. *Food Chem. Toxicol.* **1992**, *30*, 403−410.

(6) Sengar, G.; Sharma, H. Food caramels: a review. *J. Food Sci. Technol.* **2014**, *51*, 1686−1696.

(7) Jang, H. W.; Jiang, Y.; Hengel, M.; Shibamoto, T. Formation of 4(5)-methylimidazole and its precursors, α-dicarbonyl compounds in Maillard model systems. *J. Agric. Food Chem.* **2013**, *61*, 6865−6872.

(8) Martins, S. I. F. S.; Jongen, W. M. F.; van Boekel, M. A. J. S. A review of Maillard reaction in food and implications to kinetic modelling. *Trends Food Sci. Technol.* **2000**, *11*, 364−373.

(9) Fang, C.; Peng, M.; Li, G.; Tian, J.; Yin, D. New functions of glucosamine as a scavenger of the lipid peroxidation product malondialdehyde. *Chem. Res. Toxicol.* **2007**, *20*, 947−953.

(10) Jun, M.; Shao, Y.; Ho, C.-T.; Koetter, U.; Lech, S. Structural identification of nonvolatile dimerization products of glucosamine by gas chromatography−mass spectrometry, liquid chromatography−mass spectrometry, and nuclear magnetic resonance analysis. *J. Agric. Food Chem.* **2003**, *51*, 6340−6346.

(11) Gobert, J.; Glomb, M. A. Degradation of glucose: reinvestigation of reactive α-dicarbonyl compounds. *J. Agric. Food Chem.* **2009**, *57*, 8591−8597.

(12) Xu, X. B.; Liu, D. B.; Zhao, Y.; Yu, S. J.; Zhao, Z. G. Simultaneous analysis of 2-and 4-methylimidazole in caramel color and soft drinks using IC-PAD with post-column addition of hydroxide. *Food Anal. Methods* **2015**, *8*, 467−473.

(13) Guan, Y.-G.; Zhang, B.-S.; Yu, S.-J.; Wang, X.-R.; Xu, X.-B.; Wang, J.; Han, Z.; Zhang, P.-J.; Lin, H. Effects of ultrasound on a glycin−glucose model system—a means of promoting Maillard reaction. *Food Bioprocess Technol.* **2011**, *4*, 1391−1398.

(14) Seo, S.; Ka, M.-H.; Lee, K.-G. Reduction of carcinogenic 4(5)-methylimidazole in a caramel model system: influence of food additives. *J. Agric. Food Chem.* **2014**, *62*, 6481−6486.

(15) Moon, J.-K.; Shibamoto, T. Formation of carcinogenic 4(5)-methylimidazole in Maillard reaction systems. *J. Agric. Food Chem.* **2011**, *59*, 615−618.

(16) Wong, J. M.; Bernhard, R. A. Effect of nitrogen source on pyrazine formation. *J. Agric. Food Chem.* **1988**, *36*, 123−129.

(17) van Boekel, M. A. J. S. Kinetic aspects of the Maillard reaction: a critical review. *Nahrung* **2001**, *45*, 150−159.

(18) Hollnagel, A.; Kroh, L. W. Formation of α-dicarbonyl fragments from mono- and disaccharides under caramelization and Maillard reaction conditions. *Z. Lebensm.-Unters. -Forsch. A (Food Res. Technol.)* **1998**, *207*, 50−54.

(19) Shu, C.-K. Degradation products formed from glucosamine in water. *J. Agric. Food Chem.* **1998**, *46*, 1129−1131.

(20) Chen, J.; Wang, M.; Ho, C.-T. Volatile compounds generated from thermal degradation of *N*-acetylglucosamine. *J. Agric. Food Chem.* **1998**, *46*, 3207−3209.

(21) Usui, T.; Yanagisawa, S.; Ohguchi, M.; Yoshino, M.; Kawabata, R.; Kishimoto, J.; Arai, Y.; Aida, K.; Watanabe, H.; Hayase, F. Identification and determination of α-dicarbonyl compounds formed in the degradation of sugars. *Biosci., Biotechnol., Biochem.* **2007**, *71*, 2465−2472.

(22) Smuda, M.; Glomb, M. A. Fragmentation pathways during Maillard-induced carbohydrate degradation. *J. Agric. Food Chem.* **2013**, *61*, 10198−10208.

(23) Kamuf, W.; Nixon, A.; Parker, O.; Barnum, G. Overview of caramel colors. *Cereal Foods World* **2003**, *48*, 64−69.

DOI: 10.1021/acs.jafc.5b02616
J. Agric. Food Chem. 2015, 63, 8031−8036

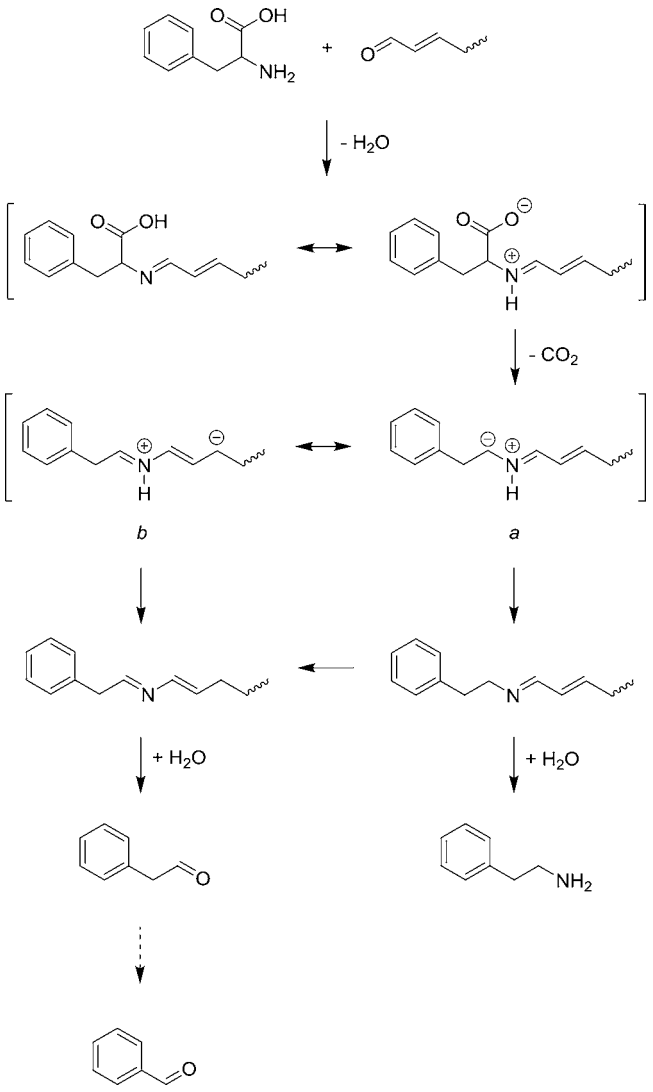

Figure 1. Reaction pathway for the formation of 2-phenylethylamine and phenylacetaldehyde by phenylalanine degradation in the presence of lipid-derived reactive carbonyls. Benzaldehyde is also produced, mostly by phenylacetaldehyde degradation under oxidative conditions.

conditions. Furthermore, the produced changes in the Strecker aldehyde/amine ratio can be mostly understood on the basis of their formation pathway.

MATERIALS AND METHODS

Chemicals. Different hydroperoxides and lipid-derived reactive carbonyls from ω-3 and ω-6 fatty acids were employed in these studies. 13-Hydroperoxyoctadeca-9,11-dienoic acid (LOOH), methyl 13-hydroperoxyoctadeca-9,11-dienoate (LOOMe), and methyl 13-hydroperoxyoctadeca-9,11,15-trienoate (LnOOMe) were prepared by oxidation of the corresponding fatty acids with lipoxygenase and later esterification with diazomethane following a previously described procedure.[16,17] 2-Octenal (OC) and 2,4-alkadienals [2,4-heptadienal (HD) and 2,4-decadienal (DD)] were purchased from Aldrich (Milwaukee, WI). 4,5-Epoxy-2-alkenals [4,5-epoxy-2-heptenal (EH) and 4,5-epoxy-2-decenal (ED)] were prepared by epoxidation of 2,4-alkadienals (2,4-heptadienal and 2,4-decadienal, respectively) with 3-chloroperoxybenzoic acid.[18,19] 4-Oxo-2-alkenals [4-oxo-2-hexenal (OH) and 4-oxo-2-nonenal (ON)] were synthesized from 2-alkylfurans (2-ethylfuran and 2-pentylfuran, respectively) with *N*-bromosuccinimide.[20,21] 4-Hydroxy-2-nonenal was prepared according to the procedure of Gardner et al.[22] All other chemicals were purchased from Sigma-Aldrich (St. Louis, MO), Fluka (Buchs, Switzerland), or Merck (Darmstadt, Germany) and were analytical-grade.

Phenylalanine/Oxidized Lipid Reaction Mixtures. Model reactions were carried out according to the procedure of Zamora and Hidalgo,[23] which was modified. Briefly, mixtures of phenylalanine and the lipid derivative (10 μmol of each) were singly homogenized with 50−70-mesh sand (600 mg) (Aldrich), 30 μL of 0.3 M buffer, and 80 μL of water. Samples were heated under a controlled atmosphere in closed test tubes at the indicated times and temperatures, usually 1 h at 140 °C. After cooling (5 min at room temperature and 15 min at −30 °C), 20 μL of internal standard (24.09 mg of ethylpyridine in 50 mL of methanol) and 1 mL of methanol/water (80:20) were added. The mixture was stirred for 1 min and centrifuged for 10 min at 2000*g*. A total of 700 μL of the obtained supernatant were transferred to a new test tube and reduced with 1 mg of sodium borohydride for 30 min. After this time, 500 μL of acetone was added and the test tube was stirred and centrifuged for 10 min at 2000*g*. The produced compounds were determined by gas chromatography−mass spectrometry (GC−MS). The ions monitored for the quantitation of the different analytes were $[C_7H_8N]^+$ = 106 for the internal standard, $[C_7H_7]^+$ = 91 for 2-phenylethylamine, $[C_8H_{10}O]^+$ = 122 for phenylacetaldehyde (determined as 2-phenylethanol), and $[C_7H_8O]^+$ = 108 for benzaldehyde (determined as benzyl alcohol).

GC−MS Analyses. GC−MS analyses were conducted with a Hewlett-Packard 6890 GC Plus coupled with an Agilent 5973 mass selective detector (MSD, quadrupole type). A fused-silica CAM capillary column (30 m × 0.25 mm inner diameter, with a coating thickness of 0.25 μm) was used, and 1 μL of sample was injected in the pulsed splitless mode. Working conditions were as follows: carrier gas, helium (1 mL/min at constant flow); injector, 250 °C; oven temperature program, from 80 °C (4 min) to 120 °C at 2 °C/min and then to 220 °C at 15 °C/min; transfer line to MSD, 280 °C; electron ionization (EI), 70 eV; ion source temperature, 230 °C; and mass range, 28−550 amu.

Determination of 2-Phenylethylamine, Phenylacetaldehyde, and Benzaldehyde Contents. Quantitation of 2-phenylethylamine, phenylacetaldehyde (as 2-phenylethanol), and benzaldehyde (as benzyl alcohol) was carried out by preparing standard curves of these compounds in the 600 mg of sand containing 80 μL of water and 30 μL of sodium phosphate buffer at pH 6 and following the whole procedure described above (without heating). A total of 10 different concentration levels of the determined compounds were used (0, 0.25, 0.5, 1, 2, 3, 4, 5, 7.5, and 10 μmol). 2-Phenylethylamine, phenylacetaldehyde, and benzaldehyde contents were directly proportional to the analyte/internal standard area ratio (r = 0.998; p < 0.0001). The coefficients of variation were less than 8%.

Statistical Analysis. All data given are mean ± standard deviation (SD) values of, at least, three independent experiments. Statistical comparisons among different groups were made using analysis of variance. When significant F values were obtained, group differences were evaluated by the Tukey test.[24] Statistical comparisons were carried out using Origin, version 7.0 (OriginLab Corporation, Northampton, MA). The significance level is p < 0.05, unless otherwise indicated.

RESULTS AND DISCUSSION

Formation of 2-Phenylethylamine, Phenylacetaldehyde, and Benzaldehyde in Phenylalanine/Lipid Oxidation Product Reaction Mixtures. When mixtures of phenylalanine and lipid oxidation products were heated together, the formation of 2-phenylethylamine, phenylacetaldehyde, and benzaldehyde was observed. The amount of the formed compounds depended upon the reaction conditions and the lipid oxidation product involved. Table 1 shows the formation of these three compounds in the presence of different lipid oxidation products at two pH values (3 and 6) and in the presence of either nitrogen or air.

DOI: 10.1021/acs.jafc.5b02619
J. Agric. Food Chem. 2015, 63, 8037−8043

Table 1. 2-Phenylethylamine, Phenylacetaldehyde, and Benzaldehyde Produced in Mixtures of Phenylalanine with Lipid Oxidation Products[a]

	2-phenylethylamine				phenylacetaldehyde				benzaldehyde			
	pH 3		pH 6		pH 3		pH 6		pH 3		pH 6	
lipid	nitrogen	air	nitrogen	air	nitrogen	air	nitrogen	air	nitrogen	air	nitrogen	air
Phe	0.00 ± 0.00 f	4.83 ± 1.22 e	5.71 ± 1.01 b,c	0.83 ± 0.31 d	0.45 ± 0.19 e	3.87 ± 0.46 g	0.00 ± 0.00 e	21.08 ± 3.72 d,e,f	2.27 ± 0.18 a	6.02 ± 0.92 f	0.00 ± 0.00 e	3.43 ± 1.33 f
LOOH	25.95 ± 2.18 a,b	25.89 ± 3.00 a	11.56 ± 1.12 b	7.55 ± 1.22 a	20.75 ± 5.50 c,d	104.52 ± 6.85 b,c	5.55 ± 0.83 c,d	31.71 ± 7.35 d,e	6.37 ± 1.32 a,b	60.57 ± 4.71 a,b	1.69 ± 0.51a,b,c,d	18.99 ± 3.92 c,d
LOOMe	20.99 ± 2.88 b,c	13.77 ± 2.90 b,c	10.60 ± 0.87 b	3.58 ± 1.18 b	33.30 ± 3.46 a,b	160.54 ± 32.76 a	14.26 ± 0.80 b	52.79 ± 6.60 a	6.33 ± 1.43 a,b	69.87 ± 8.70 a	3.14 ± 0.41 a	34.62 ± 0.49 a
LnOOMe	16.05 ± 3.62 c,d	14.67 ± 3.34 b,c	11.25 ± 2.07 b	2.15 ± 0.40 b,c,d	42.17 ± 9.83 a	118.08 ± 7.43 b,c	14.72 ± 3.36 b	49.04 ± 5.73 a,b,c	5.49 ± 0.59 a,b,c	51.40 ± 4.52 b,c	2.94 ± 0.78 a,d	27.90 ± 5.15 a,b
OC	8.87 ± 0.83 d,e	15.00 ± 2.80 b	23.98 ± 4.53 a	2.74 ± 0.22 b,c	3.34 ± 0.26 e	30.96 ± 5.03 f,g	2.69 ± 0.16 d,e	15.52 ± 2.58 e,f	5.52 ± 0.43 a,b,c	20.54 ± 5.62 d,e	0.54 ± 0.21 b,e	10.89 ± 1.81 d,e,f
HD	25.30 ± 5.77 a,b	7.95 ± 0.55 d,e	27.63 ± 4.59 a	3.18 ± 0.71 b,c	18.80 ± 4.01 c,d	81.96 ± 9.88 c,d,e	2.49 ± 0.74 d,e	14.07 ± 2.60 f	6.88 ± 1.61 a,b	19.48 ± 1.11 d,e,f	1.60 ± 0.43 b,c,d	12.42 ± 0.19 c,d,e
DD	30.99 ± 3.37 a	11.23 ± 2.03b,c,d,e	27.22 ± 5.02 a	3.95 ± 0.56 b	21.07 ± 6.37 c,d	126.82 ± 13.58 a,b	3.93 ± 0.95 d,e	36.88 ± 6.00 b,c,d	7.79 ± 1.64 a	47.55 ± 6.60 c	2.23 ± 0.38 a,c,d	19.71 ± 1.79 b,c
EH	4.24 ± 1.42 e,f	8.50 ± 0.69b,c,d,e	8.12 ± 0.84 b,c	3.78 ± 0.70 b	28.10 ± 5.33 b,c	102.81 ± 9.91 b,c,d	6.37 ± 2.03 c,d	34.29 ± 4.37 c,d,e	5.52 ± 1.10 a,b,c	24.53 ± 4.03 d,e	1.14 ± 0.24 b,c,e	11.23 ± 2.23 e
ED	6.56 ± 1.78 e,f	12.36 ± 1.31 b,c,d	13.63 ± 1.69 b	3.57 ± 0.65 b	28.12 ± 1.19 a,b,c	122.60 ± 5.20 b	24.21 ± 2.20 a	27.18 ± 6.11 d,e	5.56 ± 0.74 a,b,c	30.27 ± 0.43 d	2.67 ± 0.75 a,d	15.31 ± 3.45 c,d,e
OH	0.20 ± 0.10 f	8.18 ± 1.05 c,d,e	1.76 ± 0.56 c	3.35 ± 0.33 b	29.18 ± 1.81 a,b,c	43.46 ± 3.48 e,f	12.74 ± 3.02 b	52.27 ± 12.16 a,b	6.92 ± 0.83 a,b	13.41 ± 1.52 e,f	2.87 ± 0.85 a	16.89 ± 1.78 c,d,e
ON	0.10 ± 0.04 f	7.07 ± 1.70 d,e	0.83 ± 0.23 c	1.18 ± 0.20 c,d	11.25 ± 2.12 d,e	66.02 ± 2.09 d,e	7.72 ± 1.15 c	33.59 ± 3.82 d,e	5.51 ± 1.34 a,b,c	16.46 ± 1.52 d,e,f	1.93 ± 0.62 a,c,d	14.08 ± 2.15 c,d,e
HN	5.46 ± 1.39 e,f	5.48 ± 1.48 e	8.58 ± 0.61 b,c	0.64 ± 0.12 d	0.00 ± 0.00 e	11.46 ± 2.04 f,g	0.24 ± 0.06 e	22.45 ± 0.58 d,e,f	4.56 ± 0.50 b,c	14.56 ± 3.51 e,f	0.00 ± 0.00 e	11.99 ± 2.73 d,e

[a]Values are mean ± SD values (in nmol/μmol of phenylalanine) of, at least, three independent experiments. Means with the same letters (a−g) in the same column are not significantly different ($p < 0.05$). Abbreviations: DD, 2,4-decadienal; ED, 4,5-epoxy-2-decenal; EH, 4,5-epoxy-2-heptenal; HD, 2,4-heptadienal; HN, 4-hydroxy-2-nonenal; LnOOMe, methyl 13-hydroperoxyoctadeca-9,11,15-trienoate; LOOH, 13-hydroperoxyoctadeca-9,11-dienoic acid; LOOMe, methyl 13-hydroperoxyoctadeca-9,11-dienoate; OC, 2-octenal; OH, 4-oxo-2-hexenal; ON, 4-oxo-2-nonenal; and Phe, phenylalanine.

As observed, phenylalanine was converted into 2-phenylethylamine with a reaction yield of 0−3%, which depended upon the lipid involved, the pH of the reaction, and the presence or not of oxygen. The highest yields were observed when the reaction was carried out in the presence of alkadienals. These compounds produced about 3% of amine when the reaction was carried out under nitrogen, and this yield was reduced to 1% or less when the reaction was carried out under air. Other good producers of 2-phenylethylamine were the assayed hydroperoxides. These compounds produced amine with a yield of 1.4−2.6% at pH 3, and this yield was independent of the presence or not of oxygen. The yield decreased to about 1% at pH 6 in the presence of nitrogen and to about 0.2−0.8% in the presence of air at this pH. Other assayed lipids were worse producers of amine, and the obtained yields were usually lower than 1%, with the exception of 2-octenal (1.5% at pH 3 under air and 2.4% at pH 6 under nitrogen) and 4,5-epoxy-2-decenal (1.2% at pH 3 under air and 1.3% at pH 6 under nitrogen).

Different from 2-phenylethylamine, phenylacetaldehyde was produced to a higher extent under air than under nitrogen. At pH 3, under air, many lipids produced more than 10% phenylacetaldehyde, including hydroperoxides (11−16%), alkadienals (8−13%), and epoxyalkenals (10−12%) but not oxoalkenals (4−7%) or 4-hydroxynonenal (1%). These yields decreased to less than 4% when the reaction was carried out under nitrogen. Phenylacetaldehyde was produced with a reaction yield of 2−5% at pH 6 under air, and this yield decreased to <2.5% when the reaction was carried out under nitrogen at this pH.

A behavior similar to that of phenylacetaldehyde was also observed for benzaldehyde, which is in agreement with the production of benzaldehyde from phenylacetaldehyde as its main formation pathway.[15] Nevertheless, benzaldehyde was produced to a lower extent than phenylacetaldehyde, and there were not too many differences among the different lipid oxidation products. Thus, benzaldehyde was produced with a yield of 1−7% at pH 3 under air, and this yield decreased to 0.5−0.8% when the reaction was carried out under nitrogen at this pH. Analogously, benzaldehyde was produced with a yield of 1−4% at pH 6 under air, and this yield decreased to 0−0.3% when the reaction was carried out under nitrogen at this pH.

All these changes and mainly the changes in the produced 2-phenylethylamine/phenylacetaldehyde ratios can be understood on the basis of the reaction pathway schematized in Figure 1. The obtained results showed that alkenals, alkadienals, hydroxyalkenals, and linoleic acid hydroperoxide but not hydroperoxide methyl esters were the compounds that produced the highest 2-phenylethylamine/phenylacetaldehyde ratios at both pH 3 and 6 under nitrogen. However, there was not a clear difference among the different lipid oxidation products when the reaction was carried out under air. This behavior is likely related to the role of the chain in the charge distribution of azomethine ylide shown in Figure 1. Thus, under nitrogen, the presence of electron-withdrawing groups in the chain, such as oxoalkenals or epoxyalkenals, favored a charge distribution closer to mesomer *b* and, therefore, the formation of aldehyde. On the contrary, the presence of electron-donating groups in the chain, such as alkoxyl or carbon−carbon double bonds, favored a charge distribution closer to mesomer *a* and, therefore, the formation of amine. In the presence of oxygen, double bonds are expected to be oxidized and converted into electron-withdrawing groups. Therefore, under air, there was not so

DOI: 10.1021/acs.jafc.5b02619
J. Agric. Food Chem. 2015, 63, 8037−8043

clear of a difference among the different assayed carbonyl compounds.

To carry out a detailed study of the effect of reaction conditions on the formation of these amino acid degradation products, 2,4-decadienal was selected as the lipid oxidation product because it is a good producer of both 2-phenylethylamine and phenylacetaldehyde and the mechanism by which these two compounds are produced has been previously studied.[9,25]

Effect of the Percentage of Oxygen in the Atmosphere on the Formation of 2-Phenylethylamine, Phenylacetaldehyde, and Benzaldehyde in Phenylalanine/2,4-Decadienal Reaction Mixtures. As expected according to the data shown in Table 1, 2-phenylethylamine on one hand and phenylacetaldehyde and benzaldehyde on the other exhibited oppositing effects in relation to the presence of oxygen at both pH 3 and 6 (Figures S1A and S1B, respectively, of the Supporting Information). 2-Phenylethylamine formation was very sensitive to the presence of oxygen, and, at pH 6, >20% of oxygen completely inhibited its formation. At pH 3, although oxygen inhibited its formation, small amounts of 2-phenylethylamine were also produced in a 100% atmosphere of oxygen. On the contrary, the amount of both phenylacetaldehyde and benzaldehyde usually increased as a function of the oxygen content in the atmosphere. Thus, at pH 3, the amount of both phenylacetaldehyde and benzaldehyde increased rapidly from 0 to 20% oxygen, then the amount of phenylacetaldehyde remained more or less stable, but the amount of benzaldehyde continued to increase but to a lower extent. Something similar occurred at pH 6. The concentration of both phenylacetaldehyde and benzaldehyde increased rapidly from 0 to 20% oxygen and then increased to a lower extent at a higher oxygen content. Therefore, the presence of oxygen rapidly shifted the 2-phenylethylamine/phenylacetaldehyde ratio toward the formation of aldehyde (Figure 2A).

As discussed above, in the presence of oxygen, double bonds should be oxidized and converted into electron-withdrawing groups, consequently favoring a charge distribution closer to mesomer *b* and, then, the formation of aldehyde. This effect was so important that the amount of phenylacetaldehyde increased by 4−5 times in relation to the amount of this compound produced in the absence of air (Table 1). This effect was also observed in the formation of benzaldehyde, although this compound was more dependent upon oxygen and increased about 5−6 times in relation to the amount of this compound produced in the absence of air at pH 3 and about 9−10 times in relation to the amount of this compound produced in the absence of air at pH 6. This higher dependence of benzaldehyde in the presence of air suggests an oxidative formation pathway for this last compound.

Effect of Reaction pH on the Formation of 2-Phenylethylamine, Phenylacetaldehyde, and Benzaldehyde in Phenylalanine/2,4-Decadienal Reaction Mixtures. 2-Phenylethylamine formation did not exhibit big changes as a function of reaction pH (Figure S2A of the Supporting Information), although it seemed to increase linearly (r = 0.85; p = 0.0017) as a function of pH from 2.3% at pH 2.15 to 2.8% at pH 9. On the contrary, the phenylacetaldehyde concentration decreased linearly (r −0.998; p < 0.0001) between pH 2.15 and 6.5 (from 1.6 to 0.4%) and remained unchanged afterward. The benzaldehyde concentration also decreased linearly (r = −0.79; p = 0.0066) as a function of pH from 0.28% at pH 2.15 to 0.06% at pH 9. When the 2-phenylethylamine/phenylacetaldehyde ratio

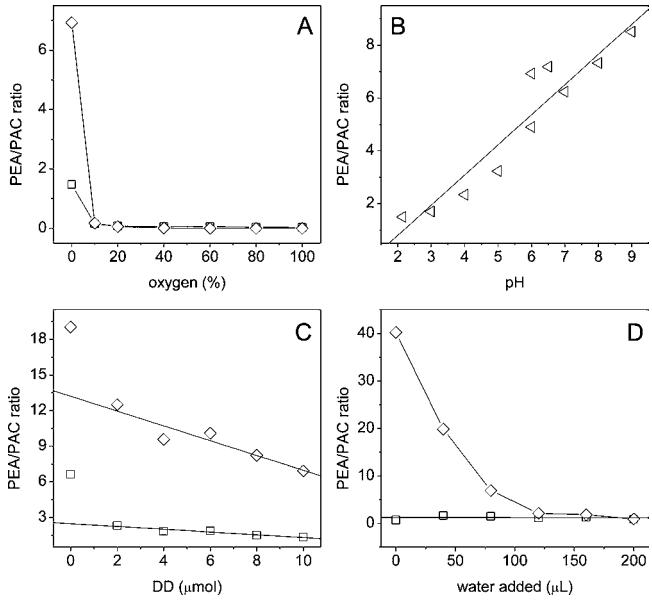

Figure 2. Effect of the (A) oxygen content in the reaction atmosphere, (B) pH, (C) aldehyde concentration, and (D) water on the 2-phenylethylamine/phenylacetaldehyde (PEA/PAC) ratio produced by phenylalanine degradation in the presence of 2,4-decadienal in sodium citrate buffer at pH 3 (□) and sodium phosphate buffer at pH 6 (◇). Samples were heated for 1 h at 140 °C.

was considered (Figure 2B), this ratio increased linearly (r = 0.94; p < 0.0001) as a function of reaction pH along the whole pH range studied (from pH 2.15 to 9). This behavior might be a consequence of either a preference of the electronic distribution of mesomer *a* in Figure 1 at higher pH values or an inhibition of the conversion of amine into aldehyde, which is known to occur a pH ≥ 6.[14]

Effect of the Lipid Concentration on the Formation of 2-Phenylethylamine, Phenylacetaldehyde, and Benzaldehyde in Phenylalanine/2,4-Decadienal Reaction Mixtures. The formation of 2-phenylethylamine, phenylacetaldehyde, and benzaldehyde depended upon the concentration of 2,4-decadienal. At pH 3 (Figure S3A of the Supporting Information), a small concentration of alkadienal (2 μmol) produced a big increase in the concentration of 2-phenylethylamine, which also continued to increase but to a lower extent when higher concentrations of alkadienal were present. On the contrary, phenylacetaldehyde and benzaldehyde produced increased linearly (r > 0.98; p < 0.0004) as a function of the amount of 2,4-decadienal added between 0 and 10 μmol. Something similar occurred at pH 6 (Figure S3B of the Supporting Information). The 2-phenylethylamine concentration increased rapidly from 0 to 4 μmol of 2,4-decadienal and later remained unchanged. On the contrary, phenylacetaldehyde and benzaldehyde concentrations increased linearly (r > 0.94; p < 0.006) as a function of the amount of 2,4-decadienal added between 0 and 10 μmol. An explanation for this different behavior of amine and aldehydes as a function of the concentration of the carbonyl compound can be explained on the basis of the pathway shown in Figure 1. The formation of the amine is accompanied by the recovery of initial reactive carbonyl. Therefore, small amounts of reactive carbonyl will produce amine, and reactive carbonyl will be recovered for producing more amine (the process is catalytic in nature). On the other hand, the formation of Strecker aldehyde and benzaldehyde is

DOI: 10.1021/acs.jafc.5b02619
J. Agric. Food Chem. 2015, 63, 8037−8043

accompanied by the destruction of reactive carbonyl. Therefore, higher amounts of reactive carbonyls will increase the formation of Strecker aldehyde.

Considering the 2-phenylethylamine/phenylacetaldehyde ratio (Figure 2C), an increase in the amount of the carbonyl compound reduced this ratio linearly ($r < -0.94$; $p < 0.015$) at the two pH values studied. This is likely a consequence of both the catalytic nature of the formation of amine from reactive carbonyls described above and the conversion of amine into aldehyde shown in Figure 1, a conversion favored at higher concentrations of lipid-derived carbonyl.[14]

Effect of the Amount of Water Added on the Formation of 2-Phenylethylamine, Phenylacetaldehyde, and Benzaldehyde in Phenylalanine/2,4-Decadienal Reaction Mixtures. The effect of water added was different at pH 3 and 6. At pH 3 (Figure S4A of the Supporting Information), both 2-phenylethylamine and phenylacetaldehyde were produced to a higher extent when 70−80 μL of water was added. An increase in the amount of water decreased the amount of both compounds, and 2-phenylethylamine formation seemed to be more sensitive to the presence of large amounts of water than phenylacetaldehyde. Benzaldehyde formation also decreased when the amount of water increased, and there was not a maximum like the maximum observed for 2-phenylethylamine or phenylacetaldehyde. At pH 6 (Figure S4B of the Supporting Information), 2-phenylethylamine was produced to a higher extent with 0−50 μL of water and decreased afterward. On the contrary, the amount of phenylacetaldehyde produced increased with the addition of water from 0 to 120 μL and remained stable afterward. Finally, the amount of benzaldehyde seemed to increase slightly when the amount of water increased.

Therefore and different from the other analyzed factors, the amount of water added did not always have the same consequences on the 2-phenylethylamine/phenylacetaldehyde ratio (Figure 2D). Thus, this ratio remained more or less unchanged at pH 3 but decreased exponentially at pH 6, a behavior that cannot seem to be easily understood only on the basis of the reaction pathway shown in Figure 1.

Effect of the Reaction Time and Temperature on the Formation of 2-Phenylethylamine and Phenylacetaldehyde in Phenylalanine/2,4-Decadienal Reaction Mixtures. The amount of 2-phenylethylamine formed increased linearly ($r > 0.98$; $p < 0.01$) as a function of time at the different assayed temperatures when phenylalanine was heated in the presence of 2,4-decadienal at both pH 3 (Figure S5A of the Supporting Information) and pH 6 (Figure S6A of the Supporting Information). Reaction rates at the different assayed temperatures were calculated using the following equation:

$$[\text{2-phenylethylamine}] = [\text{2-phenylethylamine}]_0 + kt$$

where $[\text{2-phenylethylamine}]_0$ represents the intercept, k is the rate constant, and t is the time. These rate constants were used in an Arrhenius plot for calculation of the activation energy (E_a) of 2-phenylethylamine formation from phenylalanine in the presence of 2,4-decadienal at pH 3 (Figure 3A) and pH 6 (Figure 3B). The values obtained for E_a were 51 kJ/mol at pH 3 and 65 kJ/mol at pH 6.

Analogously, the amount of phenylacetaldehyde formed also increased linearly ($r > 0.98$; $p < 0.01$) as a function of the time at the different assayed temperatures when phenylalanine was heated in the presence of 2,4-decadienal at both pH 3 (Figure S5B of the Supporting Information) and pH 6 (Figure S6B of the Supporting Information). Reaction rates at the different assayed temperatures were also calculated using

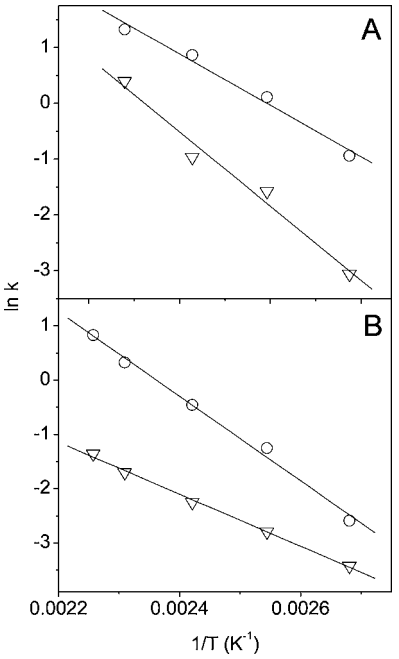

Figure 3. Arrhenius plot for 2-phenylethylamine (○) and phenylacetaldehyde (▽) formation by phenylalanine (Phe) degradation in the presence of 2,4-decadienal. Equimolecular mixtures of both compounds (10 μmol of each) were heated under nitrogen for 1 h in (A) sodium citrate buffer at pH 3 and (B) sodium phosphate buffer at pH 6.

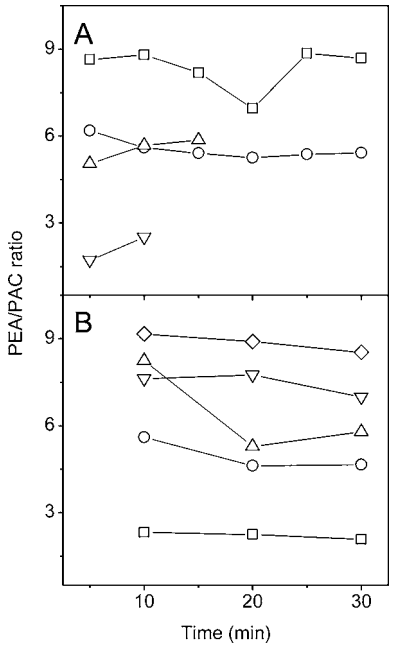

Figure 4. Effect of the time and temperature on the 2-phenylethylamine/phenylacetaldehyde (PEA/PAC) ratio produced by phenylalanine degradation in the presence of 2,4-decadienal in (A) sodium citrate buffer at pH 3 and (B) sodium phosphate buffer at pH 6. Equimolecular mixtures of both compounds (10 μmol of each) were heated under nitrogen at the indicated times and temperatures. The temperatures assayed were 100 °C (□), 120 °C (○), 140 °C (△), 160 °C (▽), and 170 °C (◇).

DOI: 10.1021/acs.jafc.5b02619
J. Agric. Food Chem. 2015, 63, 8037−8043

an equation similar to that described above for 2-phenylethylamine. The obtained rate constants were used in an Arrhenius plot for calculation of E_a of phenylacetaldehyde formation from phenylalanine in the presence of 2,4-decadienal at pH 3 (Figure 3A) and pH 6 (Figure 3B). The values obtained for E_a were 74 kJ/mol at pH 3 and 40 kJ/mol at pH 6.

Different from 2-phenylethylamine and phenylacetaldehyde, benzaldehyde was produced to a very low extent under the assayed conditions and it was not possible to determine its formation E_a.

2-Phenylethylamine/phenylacetaldehyde ratios were more or less constant at each temperature but decreased with the temperature at pH 3 (Figure 4A) and increased with the temperature at pH 6 (Figure 4B), which might be related to the easiness of conversion of amine into aldehyde at the different pH values and temperatures.

All of these data as well as all other data obtained in this study suggest that the 2-phenylethylamine/phenylacetaldehyde ratio can be modified as a function of reaction conditions. Thus, it can be increased using electron-donating groups in the chain of the carbonyl compound, small amounts of carbonyl compound, low oxygen content, increasing the pH, or increasing temperature at pH 6. Contrary conditions (use of electron-withdrawing groups in the chain of the carbonyl compound, large amounts of carbonyl compound, high oxygen contents, low pH values, and increasing temperatures at low pH values) would decrease the 2-phenylethylamine/phenylacetaldehyde ratio and the formation of aldehydes over amines in amino acid degradations would be favored.

■ ASSOCIATED CONTENT

Supporting Information

The Supporting Information is available free of charge on the ACS Publications website at DOI: 10.1021/acs.jafc.5b02619.

Effect of oxygen (Figure S1), reaction pH (Figure S2), aldehyde concentration (Figure S3), and water (Figure S4) in the formation of 2-phenylethylamine, phenylacetaldehyde, and benzaldehyde by phenylalanine degradation in the presence of 2,4-decadienal and effect of time and temperature in the formation of 2-phenylethylamine and phenylacetaldehyde by phenylalanine degradation in the presence of 2,4-decadienal (Figures S5 and S6) (PDF)

■ AUTHOR INFORMATION

Corresponding Author

*Telephone: +34-954-611-550. Fax: +34-954-616-790. E-mail: fhidalgo@ig.csic.es.

Funding

This study was supported in part by the European Union (FEDER funds) and the Plan Nacional de I + D of the Ministerio de Economía y Competitividad of Spain (Project AGL2012-35627).

Notes

The authors declare no competing financial interest.

■ ACKNOWLEDGMENTS

The authors are indebted to José L. Navarro for technical assistance.

■ REFERENCES

(1) Muttucumaru, N.; Powers, S. J.; Elmore, J. S.; Mottram, D. S.; Halford, N. G. Effects of water availability on free amino acids, sugars, and acrylamide-forming potential in potato. *J. Agric. Food Chem.* **2015**, *63*, 2566−2575.

(2) Jansson, T.; Jensen, H. B.; Sundekilde, U. K.; Clausen, M. R.; Eggers, N.; Larsen, L. B.; Ray, C.; Andersen, H. J.; Bertram, H. C. Chemical and proteolysis-derived changes during long-term storage of lactose-hydrolyzed ultrahigh-temperature (UHT) milk. *J. Agric. Food Chem.* **2014**, *62*, 11270−11278.

(3) Rakete, S.; Klaus, A.; Glomb, M. A. Investigations on the Maillard reaction of dextrins during aging of pilsner type beer. *J. Agric. Food Chem.* **2014**, *62*, 9876−9884.

(4) Van Rooijen, C.; Bosch, G.; van der Poel, A. F. B.; Wierenga, P. A.; Alexander, L.; Hendriks, W. H. Quantitation of Maillard reaction products in commercially available pet foods. *J. Agric. Food Chem.* **2014**, *62*, 8883−8891.

(5) Zhang, L. Y.; Xia, Y. L.; Peterson, D. G. Identification of bitter modulating Maillard-catechin reaction products. *J. Agric. Food Chem.* **2014**, *62*, 8470−8477.

(6) Nashalian, O.; Yaylayan, V. A. Thermally induced oxidative decarboxylation of copper complexes of amino acids and formation of Strecker aldehyde. *J. Agric. Food Chem.* **2014**, *62*, 8518−8523.

(7) Rizzi, G. P. The Strecker degradation of amino acids: Newer avenues for flavor formation. *Food Rev. Int.* **2008**, *24*, 416.

(8) Granvogl, M.; Bugan, S.; Schieberle, P. Formation of amines and aldehydes from parent amino acids during thermal processing of cocoa and model systems: new insights into pathways of the Strecker reaction. *J. Agric. Food Chem.* **2006**, *54*, 1730−1739.

(9) Zamora, R.; Delgado, R. M.; Hidalgo, F. J. Formation of β-phenylethylamine as a consequence of lipid oxidation. *Food Res. Int.* **2012**, *46*, 321−325.

(10) Hidalgo, F. J.; Navarro, J. L.; Delgado, R. M.; Zamora, R. Histamine formation by lipid oxidation products. *Food Res. Int.* **2013**, *52*, 206−213.

(11) Schieberle, P.; Köhler, P.; Granvogl, M. New aspects on the formation and analysis of acrylamide. In *Advances in Experimental Medicine and Biology*; Friedman, M., Mottram, D., Eds.; Springer-Verlag: Berlin, Germany, 2005; Vol. *561*, pp 205−222.

(12) Zamora, R.; Delgado, R. M.; Hidalgo, F. J. Conversion of 3-aminopropionamide and 3-alkylaminopropionamide into acrylamide in model systems. *Mol. Nutr. Food Res.* **2009**, *53*, 1512−1520.

(13) Hidalgo, F. J.; Zamora, R. Amino acid degradations produced by lipid oxidation products. *Crit. Rev. Food Sci. Nutr.* in press. DOI: 10.1080/10408398.2012.761173.

(14) Zamora, R.; Delgado, R. M.; Hidalgo, F. J. Chemical conversion of phenylethylamine into phenylacetaldehyde by carbonyl−amine reactions in model systems. *J. Agric. Food Chem.* **2012**, *60*, 5491−5496.

(15) Chu, F. L.; Yaylayan, V. A. Model studies on the oxygen-induced formation of benzaldehyde from phenylacetaldehyde using pyrolysis GC-MS and FTIR. *J. Agric. Food Chem.* **2008**, *56*, 10697−10704.

(16) Hidalgo, F. J.; Zamora, R.; Vioque, E. Syntheses and reactions of methyl (*Z*)-9,10-epoxy-13-oxo-(*E*)-11-octadecenoate and methyl (*E*)-9,10-epoxy-13-oxo-(*E*)-11-octadecenoate. *Chem. Phys. Lipids* **1992**, *60*, 225−233.

(17) Zamora, R.; Gallardo, E.; Hidalgo, F. J. Model studies on the degradation of phenylalanine initiated by lipid hydroperoxides and their secondary and tertiary oxidation products. *J. Agric. Food Chem.* **2008**, *56*, 7970−7975.

(18) Hidalgo, F. J.; Zamora, R. Modification of bovine serum albumin structure following reaction with 4,5(*E*)-epoxy-2(*E*)-heptenal. *Chem. Res. Toxicol.* **2000**, *13*, 501−508.

(19) Zamora, R.; Navarro, J. L.; Gallardo, E.; Hidalgo, F. J. Chemical conversion of α-amino acids into α-keto acids by 4,5-epoxy-2-decenal. *J. Agric. Food Chem.* **2006**, *54*, 2398−2404.

(20) Shimozu, Y.; Shibata, T.; Ojika, M.; Uchida, K. Identification of advanced reaction products originating from the initial 4-oxo-2-nonenal-cysteine Michael adducts. *Chem. Res. Toxicol.* **2009**, *22*, 957−964.

(21) Zamora, R.; Alcon, E.; Hidalgo, F. J. Effect of lipid oxidation products on the formation of 2-amino-1-methyl-6-phenylimidazo[4,5-*b*]-pyridine (PhIP) in model systems. *Food Chem.* **2012**, *135*, 2569−2574.

DOI: 10.1021/acs.jafc.5b02619
J. Agric. Food Chem. 2015, 63, 8037−8043

(22) Gardner, H. W.; Bartelt, R. J.; Weisleder, D. A facile synthesis of 4-hydroxy-2(*E*)-nonenal. *Lipids* **1992**, *27*, 686−689.
(23) Zamora, R.; Hidalgo, F. J. Contribution of lipid oxidation products to acrylamide formation in model systems. *J. Agric. Food Chem.* **2008**, *56*, 6075−6080.
(24) Snedecor, G. W.; Cochran, W. G. *Statistical Methods*, 7th ed.; Iowa State University Press: Ames, IA, 1980.
(25) Zamora, R.; Gallardo, E.; Hidalgo, F. J. Strecker degradation of phenylalanine initiated by 2,4-decadienal or methyl 13-oxooctadeca-9,11-dienoate in model systems. *J. Agric. Food Chem.* **2007**, *55*, 1308−1314.

DOI: 10.1021/acs.jafc.5b02619
J. Agric. Food Chem. 2015, 63, 8037−8043

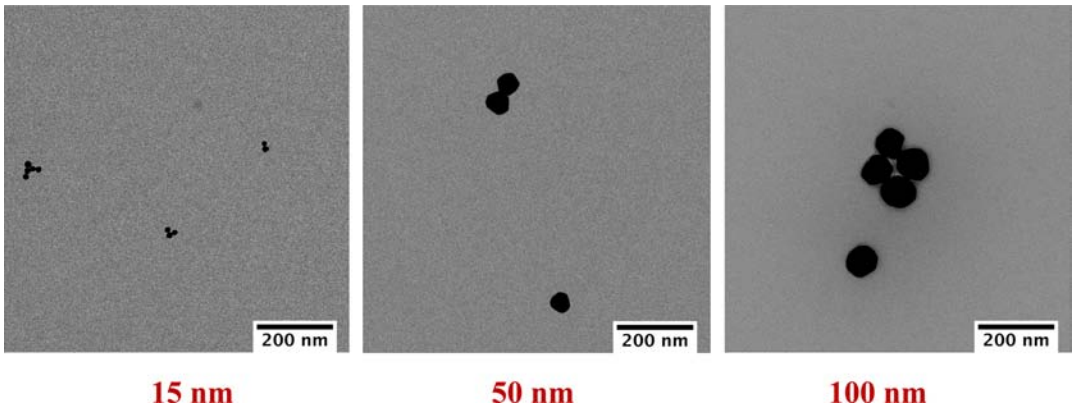

Figure 1. Morphology of the initial gold nanoparticle suspensions (nominal diameters of 15, 50, and 100 nm) used in this study. All images were taken under transmission electron microscopy as described under Materials and Methods.

important for understanding the gastrointestinal fate of inorganic nanoparticles that may be ingested.

MATERIALS AND METHODS

Materials. The following products were purchased from Sigma-Aldrich Chemicals (St. Louis, MO, USA): 4% osmium tetroxide (OsO_4), phosphotungstic acid (PTA), nitric acid, and hydrochloric acid. AuNPs with different diameters (15, 50, and 100 nm) were purchased from Nanopartz (Loveland, CO, USA). A mitochondrial membrane potential probe (JC-1 dye) was purchased from Life Technologies (Thermo Fisher Scientific, Agawam, MA, USA). Hank's balanced salt solution (HBSS), glutaraldehyde, cacodylate, Formvar/carbon Cu grids 200 mesh, and epoxy resin were purchased from EM Sciences (Hatfield, PA, USA).

Cell Culture. Caco-2 cells (passage 55−65) were cultured in complete Dulbecco's modified essential medium (DMEM) containing high glucose, 10% fetal bovine serum (FBS), 1% antibiotic, and 1% amino acids as we described previously.[19] Cells were seeded at 3×10^5 cells/mL on transwells (Corning Inc., Tewksbury, MA, USA) containing polyester filters (3 mm pore size and 4.7 cm^2 surface area) and grown for 21 days. The transepithelial electrical resistance (TEER) was monitored using a Millicell ERS-2 epithelial voltammeter (World Precision Instruments, Sarasota, FL, USA). The TEER data are presented as resistance per unit surface area, $\Omega \times cm^2$.

Transmission Electron Microscopy (TEM) Analysis. To visualize the AuNPs, a drop of liquid sample was allowed to air-dry onto a carbon-coated 200 mesh copper grid, and then the sample was stained with 2% PTA. Samples were visualized with a transmission electron microscope (Tecani 12 TEM, FEI Co., Hillsboro, OR, USA). To visualize the uptake of AuNPs in intestinal epithelial cells, suspensions of AuNPs (5 μg/mL; 15, 50, or 100 nm) were applied on Caco-2 cell monolayers. After treatment for 0.5, 1, 2, 4, 8, and 24 h, the media in both the apical and basolateral sides were removed and the monolayers were rinsed with HBSS that had been warmed to 37 °C. The monolayers were immediately fixed in 2.5% glutaraldehyde and 2% paraformaldehyde (0.1 M sodium cacodylate buffer, pH 7.4) for 2 h at 37 °C. They were then postfixed in 1% aqueous osmium tetroxide solution and then embedded in epoxy resin. Thin sections were obtained using an ultramicrotome with a diamond knife (DDK, Wilmington, DE, USA). The sections were stained with uranyl acetate followed by lead citrate. The image samples were then viewed with the transmission electron microscope (Tecani 12, FEI Co.).

ICP-MS Analysis. After treatment with AuNPs, the cell monolayers and medium samples were collected at the specific time period from the apical and basolateral sides of the transwell as described above. A bicinchoninic acid (BCA) kit was used to quantify the protein concentration of the monolayers in each well. Each sample was mixed with 0.5 mL of aqua regia and then the sample was diluted to 10 mL with deionized water. A series of standard solutions of Au were prepared under the same conditions. Inductively coupled plasma (ICP) mass spectrometry (MS) measurements were performed on a mass spectrometer (NexION 300X ICP, PerkinElmer, Cambridge, MA, USA).

Calculation of the Number of Gold Nanoparticles. The number of gold nanoparticles in a given sample was calculated from the Au concentration measured by ICP-MS. The number of gold atoms per gold nanoparticle (n) can be estimated from the expression[20]

$$n = \frac{D^3}{d^3}$$

where D is the diameter of a gold nanoparticle and d is the diameter of a single gold atom, which is approximately 0.28 nm.[21] Hence, the number of AuNPs can be calculated from the measured Au concentration as

$$C_n = \frac{C_m}{N_A \times n}$$

where C_n is the number of AuNPs per unit volume, C_m is the measured mass of Au per unit volume, and N_A is Avogadro's constant.

Determination of Mitochondrial Membrane Potential. Aqueous suspensions of AuNPs (5 μg/mL; 15, 50, or 100 nm) were applied onto a well-differentiated Caco-2 monolayer (TEER > 200 Ω). Four hours after the treatment, the apical and basolateral media were removed and the monolayers were rinsed three times with warmed HBSS. A medium containing 10 μg/mL of JC-1 (mitochondrial membrane potential probe) in warmed DMEM solution was added to the Caco-2 cell monolayers. After the incubation for 15 min (37 °C, 5% carbon dioxide, and 100% humidity), the monolayers were washed twice with HBSS and placed onto a microscope slide. After adding a fluorescent dye (DAPI) to the samples, the slides were rapidly sealed and stored overnight at 4 °C. The microstructure of the samples was observed using a confocal fluorescent microscope (Olympus FV-1000, Waltham, MA, USA). The JC-1 treated coverslips were excited at 488 nm, and the emission was recorded simultaneously at 527 and 590 nm by independent detectors.[22] Two-photon excitation of JC-1-labeled Caco-2 cell monolayers allowed for the real-time analysis of mitochondria membrane potential. The data were analyzed using the following expression as described previously:[23]

$$\text{ratio} = 5 \times I_{red}/I_{green}$$

Here I_{red} and I_{green} are the intensities of the signals in the red and green regions of the spectra. The factor "5" is used to transform the ratiometric results into an 8-bit scale of 256 levels.

Statistical Analysis. All values are expressed as means ± standard deviations (SD) unless stated otherwise. The differences among samples were analyzed by ANOVA with a significance level of $p < 0.05$.

DOI: 10.1021/acs.jafc.5b03242
J. Agric. Food Chem. 2015, 63, 8044−8049

RESULTS AND DISCUSSION

Properties of Gold Nanoparticles. The AuNPs used in this study have been reported to be monodispersed spheres in an aqueous sodium citrate buffer that acted as a stabilizer to prevent particle aggregation.[24] The manufacturer reported that the droplet diameters of the three AuNPs samples used were 15, 50, and 100 nm, respectively, and that all of the particles had a negative charge (around −40 mV). The initial gold concentration was given as 50 ppm for all of the AuNPs suspensions when they were adjusted to an optical density of 1 cm^{-1}. The morphology of the AuNPs was confirmed using TEM (Figure 1). All of the samples contained fairly uniform spheres with dimensions that conformed to those stated by the manufacturer. Nevertheless, the TEM images suggested that some of the particles clustered together and formed aggregates. These aggregates may have been present within the initial samples, or they may have been introduced as a result of the method used to prepare the samples for TEM analysis. Previous studies have shown that inorganic nanoparticles (1−100 nm) might affect normal cellular functions, including inducing cell death, in a manner that depended on their particle size.[25,26] We therefore hypothesized that the initial size of the AuNPs used in this study can influence their absorption, accumulation, and cytotoxicity in the intestinal epithelial cells.

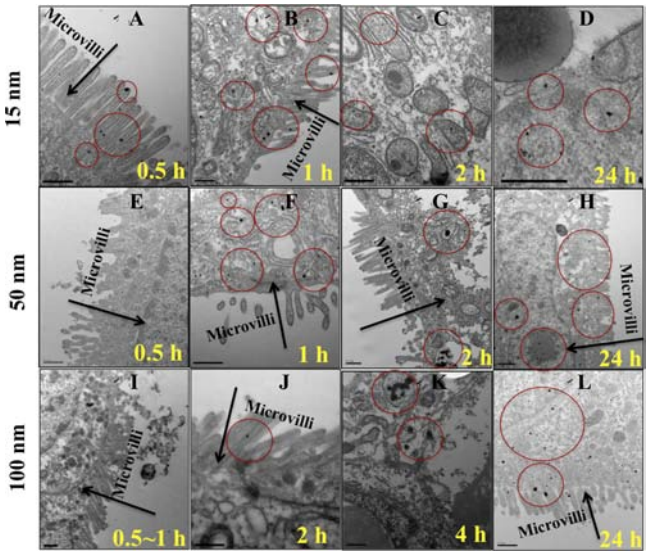

Figure 2. Absorption of AuNPs by intestinal epithelial cells. Caco-2 cell monolayers were incubated with AuNPs (15, 50, or 100 nm) for various time periods (up to 24 h). After a thorough wash, Caco-2 cell monolayers were processed for TEM analysis to visualize AuNPs absorbed by the cells. AuNPs are highlighted by circles. Arrows indicate the direction from apical to basolateral side across microvilli. Different magnifications were used in different images. The scale bar represents 500 nm. Representative images were selected from replicates of at least three.

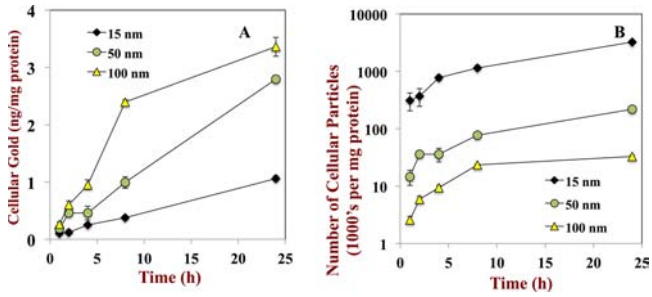

Figure 4. Accumulation of AuNPs within the intestinal epithelium: change in the amount of gold measured in the Caco-2 monolayers after incubation of Caco-2 cell monolayers with 5 μg/mL of AuNPs in the apical compartment of the transwells. The amount of gold was expressed as either particle mass (A) or particle number (B) in the Caco-2 cell monolayer.

Migration of Gold Nanoparticles within Intestinal Epithelium. It is well-known that particle characteristics (such as size, shape, and surface chemistry) play an important role in determining the interactions of inorganic nanoparticles with biological membranes.[27] In this study we focused on the role of particle size on cellular uptake by using AuNPs with the same shape (spherical) and surface chemistry (bare gold), but different diameters (15, 50, and 100 nm).

Caco-2 cells were cultured in the transwells to form well-differentiated and polarized monolayers. The monolayers were used to mimic absorptive functions of intestinal epithelium. Aqueous suspensions of AuNPs (15, 50, or 100 nm) were then placed on the apical side of the polarized monolayers for different incubation periods. The migration of AuNPs across the model intestinal cells was visualized by TEM. The results are shown in Figure 2 (the most apparent AuNPs are highlighted by circles, and arrows indicate the direction from apical to basolateral side across microvilli). It is clear that the migration of AuNPs across the intestinal epithelial cells showed a distinct size-dependent pattern: the smaller the particle size, the faster the migration (Figure 2). At 0.5 h, 15 nm AuNPs

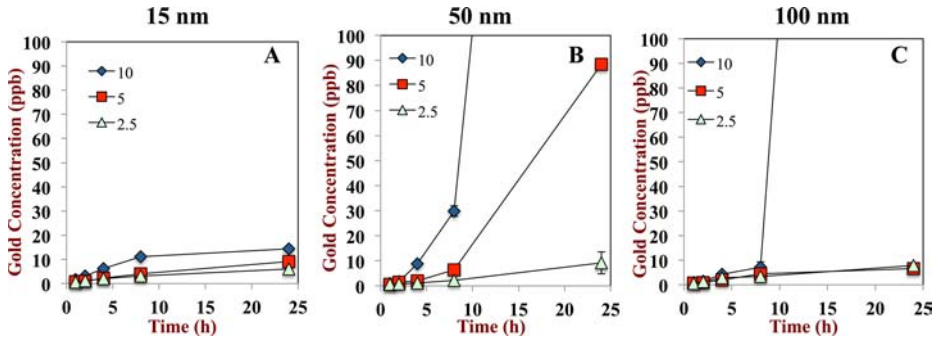

Figure 3. Transport of AuNPs across the intestinal epithelium: change in the concentration of gold measured in the basolateral compartment after incubation of Caco-2 cell monolayers with AuNPs in the apical compartment of the transwells. Suspensions containing different concentrations of gold nanoparticles were used (shown in the figure): 2.5, 5, and 10 μg/mL in the apical medium.

DOI: 10.1021/acs.jafc.5b03242
J. Agric. Food Chem. 2015, 63, 8044−8049

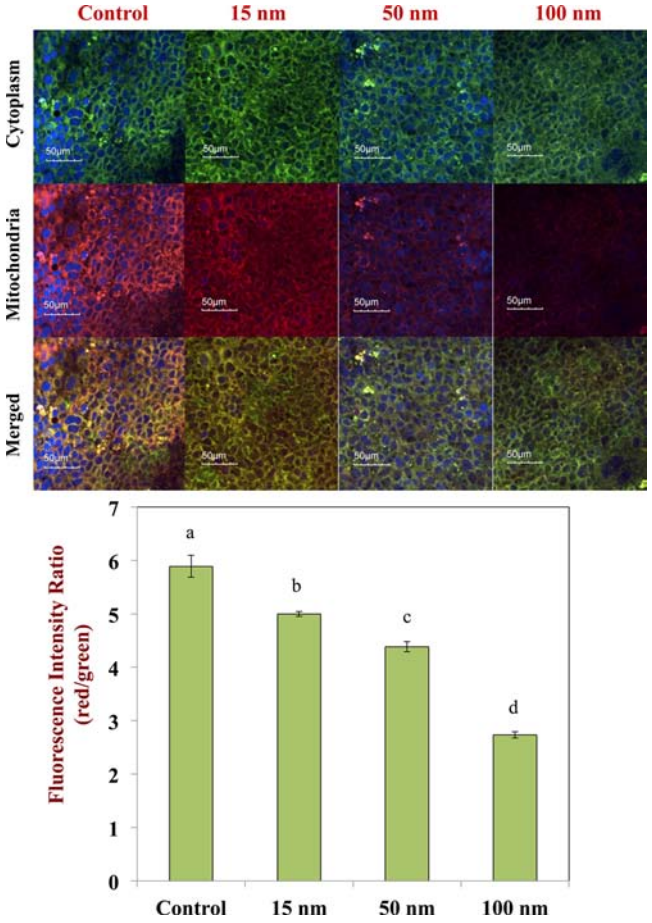

Figure 5. Effects of AuNPs on the mitochondrial membrane potentials of intestinal epithelial cells. Caco-2 cell monolayers were incubated with AuNPs (15, 50, or 100 nm) for 4 h separately. Mitochondria toxicity of AuNPs was visualized by confocal microscope using the red fluorescent dye JC-1 (A). JC-1 exhibits potential-dependent accumulation in mitochondria, indicated by a fluorescence emission shift from green to red. Cells with high mitochondria membrane potential (healthy) promote the formation of dye aggregates that fluoresce red, whereas cells with low mitochondria membrane potential (damaged) remain monomeric JC-1 that fluoresce green. The red/green ratio was quantified using image J (B). Representative images were selected from replicates of three. Different letters indicate statistical difference among the three groups at the given time point ($P < 0.05$).

have already been observed within the microvilli (Figure 2A), whereas no 50 or 100 nm AuNPs were found anywhere in the cells (Figure 2E,II). After 1 h of incubation, an appreciable number of 15 and 50 nm AuNPs could be observed in the cytoplasm (Figure 2B,F). In contrast, only a few 100 nm AuNPs had entered the microvilli after 2 h of incubation (Figure 2J). At 1−2 h, the 15 and 50 nm AuNPs have migrated into various cellular organelles, such as the mitochondria and lysosome (Figure 2B,C,G). In contrast, not until 4 h of incubation were 100 nm AuNPs found in the mitochondria and lysosome (Figure 2K). Some of AuNPs appeared as aggregates in lysosomes (Figure 2G,K), After 24 h of incubation, all AuNPs (15, 50, and 100 nm) were found throughout the entire cell monolayer (Figure 2D,H,L). It is noteworthy that some of the nanoparticles were observed in the cell nuclei (Figure 2H,L), which suggested that AuNPs may have the potential to induce genotoxicity. In general, the smallest gold nanoparticles (15 nm) were internalized at a faster rate than the large ones (50 or 100 nm).

Transport of Gold Nanoparticles across the Intestinal Epithelium. Microscopic analysis is useful for obtaining direct visualization of the migration and location of AuNPs in epithelial cells, but it is less useful for providing quantitative information about the amount of AuNPs that has been transported across the intestinal epithelial monolayer and that has been accumulated inside the epithelial cells. For this reason, quantitative analysis of the gold concentration was carried out using a highly sensitive ICP-MS method.[13] This method utilized acid digestion to dissolve the gold nanoparticles, and then the gold concentration was determined by mass spectrometry.

We established the influence of initial particle size of AuNPs on the transport of the AuNPs across the epithelial monolayers into the basolateral compartment of the transwells. After incubation of the Caco-2 monolayers with AuNPs in the apical compartment of the transwells, a fixed volume of medium was collected from the basolateral compartment of the transwells at different times and then the amount of gold was quantified by ICP-MS (Figure 3). The concentrations of gold in the basolateral compartment increased with increasing incubation time for all three types of AuNPs studied. For 15 and 50 nm nanoparticles (Figure 3A,B), the higher the initial level of AuNPs in the apical compartment, the higher the basolateral concentration of gold that was detected at the same time point, particularly at 8 and 24 h of incubation. This effect can be attributed to the fact that there were more gold nanoparticles per unit surface area in contact with the apical cell membrane (microvilli) at the higher concentration of AuNPs, and so endocytosis occurred more frequently. Interestingly, a much higher concentration of intermediate-sized nanoparticles (50 nm) was transported across the epithelial cell monolayer into the basolateral compartment than small (15 nm) or large (100 nm) ones (Figure 3B). A possible explanation of this phenomenon is the size-dependent nature of the receptor-mediated endocytosis according to previous research.[28,29] The endocytosis of nanoparticles depends on two competitive processes that require two different energies: (i) the binding energy between ligands and receptors and (ii) the free energy for particle envelopment. When nanoparticles have diameters below about 40 nm, they do not produce a sufficiently large free energy change to become completely enveloped by the surface of the membrane. Conversely, when the nanoparticles have diameters greater than about 80 nm, the lack of free receptors limits the ligand−receptor binding energy. This much higher transport rate of 50 nm AuNPs across the intestinal epithelium may lead to higher levels of AuNPs in the systemic circulation, which may have a profound impact on the tissue/organ distribution and potential toxicity of these AuNPs in human body.

In contrast to 15 and 50 nm AuNPs, the transport of 100 nm AuNPs across the epithelial monolayer into the basolateral compartment of the transwells was found to be concentration independent (Figure 3C). At 2.5 and 5 μg/mL, the basolateral concentration of AuNPs remained relatively low after 24 h of incubation, but at 10 μg/mL there was a steep increase (Figure 3C). Correspondingly, the TEER of the monolayers decreased drastically to values below 100 $\Omega \cdot cm^2$, which suggests the monolayers had become leaky, hence the drastic increase in transport of AuNPs across the epithelium. Standard TEER values of healthy cells are around 260 ± 65 Ω.[18] The 10 μg/mL

DOI: 10.1021/acs.jafc.5b03242
J. Agric. Food Chem. 2015, 63, 8044−8049

of AuNPs suspension caused the same problem after 24 h of incubation (Figure 3B). These results suggested that AuNPs (50 and 100 nm) at the concentration of 10 μg/mL damaged the integrity of the epithelial monolayers.

Accumulation of Gold Nanoparticles within the Intestinal Epithelium. On the basis of the above results, we used the nanoparticle suspensions with intermediate gold concentration (5 μg/mL that is not detrimental to the integrity of the epithelial monolayer) to further quantify the cellular accumulation of AuNPs within the Caco-2 cell monolayers. The data on the gold concentration were analyzed in two different but complementary ways (Figure 3B). First, the mass of gold was normalized by the amount of cellular protein in each sample, so the results are presented as mass of gold per unit mass of protein (Figure 4A). Because the diameter of the AuNPs was known, it was also possible to calculate the number of nanoparticles per unit mass of protein (Figure 4B). The incubation of Caco-2 monolayers with AuNPs was stopped after different incubation times, and the amount of gold that had accumulated in the monolayer was quantified by ICP-MS as described under Materials and Methods. The cellular accumulation of AuNPs clearly showed a size-dependent pattern, which depend on the way that the particle concentration was represented. In terms of total particle mass, the smaller the particle size, the lower the total amount of gold accumulated in the epithelial cells: 15 nm < 50 nm < 100 nm. Conversely, in terms of total particle number, the smaller the particle size, the greater the total accumulation of gold within the epithelial cells: 100 nm < 50 nm < 15 nm. This latter trend is similar to that reported previously for in vivo permeation of AuNPs through rat intestine.[30] A similar trend was also reported when Caco-2 cells were exposed to AuNPs of 5 and 30 nm sizes.[31]

The results suggest that smaller gold nanoparticles can more easily penetrate into cells, which leads to a greater number of small particles inside the cells. However, the total mass of gold that accumulates in the cells is greater for the larger AuNPs (even though they penetrate into the cells more slowly) because the number of gold atoms per particle is proportional to the cube of the particle size. These results also indicated that larger AuNPs had a slower excretion rate from inside epithelial cells to the basolateral compartment. This highly size-dependent pattern of cellular accumulation of AuNPs may have a profound impact on the potential toxicity of these AuNPs in epithelial cells.

Effects of Gold Nanoparticles on Mitochondria Potential. The ICP-MS results provided valuable quantitative information about endocytosis, accumulation, and excretion of the AuNPs by the Caco-2 intestinal epithelial cell monolayers. The TEM images indicated that the gold nanoparticles progressively spread throughout the model epithelium cells after absorption and were eventually accumulated within different cellular organelles such as endosomes, lysosomes, Golgi apparatus, mitochondria, and nucleus (Figure 2). The accumulation of AuNPs within these cellular substructures may promote cytotoxicity, because previous studies have shown that AuNPs can depolarize the membranes of the mitochondria in mammalian cells.[17] A decrease in mitochondrial membrane potential is an early indicator of cell death.[12] In addition, impaired mitochondrial function has been shown to result in elevated levels of DNA damage.[32] Hence, we determined the mitochondria potential using a mitochondrion-specific dye (JC-1) after the Caco-2 cell monolayers had been incubated with AuNPs (5 μg/mL in apical medium) for 4 h. At this incubation time, the TEM images showed that the nanoparticles had accumulated within the mitochondria (Figure 2). Cells with high mitochondria membrane potential (healthy) promote the formation of dye aggregates that fluoresce red, whereas cells with low mitochondria membrane potential (damaged) remain monomeric JC-1 that fluoresce green.[33] As a result, the decrease of the red/green intensity ratio provides an indication of the damage of the mitochondria membrane function.

Our results showed a distinct size-dependent trend in the mitochondria toxicity caused by the gold nanoparticles: the larger the nanoparticles, the higher the toxicity, as evidenced by a decrease in the intensity of red florescence when the particle diameter increased (Figure 5A). Quantification of the ratio of red/green florescence further confirmed that the larger the AuNPs, the lower the relative red florescence (Figure 5B) This finding is consistent with our results by ICP-MS that showed the cellular accumulation of total mass of gold follows the trend 100 nm > 50 nm > 15 nm (Figure 4A).

In summary, the absorption, accumulation, and transfer of AuNPs in the intestinal epithelial cells were highly dependent on their particle diameter (15, 50, or 100 nm). AuNPs with intermediate sizes (50 nm) were the most efficiently transported across the intestinal epithelium: taken up from the apical side and excreted into the basolateral side. The smaller AuNPs (15 nm) were more rapidly absorbed by the intestinal epithelial cells and more quickly spread throughout the interior of the cells. Conversely, the larger AuNPs (100 nm) tended to accumulate within the intestinal epithelial cells because their rate of excretion into the basolateral side was slow. The increasing accumulation of the total mass of gold caused by AuNPs resulted in increasing mitochondria toxicity to the intestinal epithelial cells. Overall, this study provided detailed information on the impact of particle size on the absorption, accumulation, and cytotoxicity of AuNPs in the intestinal epithelium.

AUTHOR INFORMATION

Corresponding Author

*(H.X.) E-mail: hangxiao@foodsci.umass.edu. Phone: (413) 545-2281. Fax (413) 545-1262.

Funding

This study was partially supported by grants from U.S. Department of Agriculture.

Notes

The authors declare no competing financial interest.

REFERENCES

(1) Yun, Y.; Cho, Y. W.; Park, K. Nanoparticles for oral delivery: targeted nanoparticles with peptidic ligands for oral protein delivery. *Adv. Drug Delivery Rev.* **2013**, *65*, 822−832.

(2) Fisichella, M.; Berenguer, F.; Steinmetz, G.; Auffan, M.; Rose, J.; Prat, O. Intestinal toxicity evaluation of TiO_2 degraded surface-treated nanoparticles: a combined physico-chemical and toxicogenomics approach in Caco-2 cells. *Part. Fibre Toxicol.* **2012**, *9*, 18 .

(3) Chaudhry, Q.; Scotter, M.; Blackburn, J.; Ross, B.; Boxall, A.; Castle, L.; Aitken, R.; Watkins, R. Applications and implications of nanotechnologies for the food sector. *Food Addit. Contam., Part A* **2008**, *25*, 241−258.

(4) Duncan, T. V. Applications of nanotechnology in food packaging and food safety: barrier materials, antimicrobials and sensors. *J. Colloid Interface Sci.* **2011**, *363*, 1−24.

(5) Weiss, J.; McClements, D. J.; Takhistov, P. Functional materials in food nanotechnology. *Food Aust.* **2007**, *59*, 274−275.

DOI: 10.1021/acs.jafc.5b03242
J. Agric. Food Chem. 2015, 63, 8044−8049

(6) Wang, H. F.; Du, L. J.; Song, Z. M.; Chen, X. X. Progress in the characterization and safety evaluation of engineered inorganic nanomaterials in food. *Nanomedicine* **2013**, *8*, 2007−2025.
(7) Abbott, L. C.; Maynard, A. D. Exposure assessment approaches for engineered nanomaterials. *Risk Anal.* **2010**, *30*, 1634−1644.
(8) Weber, C. R.; Nalle, S. C.; Tretiakova, M.; Rubin, D. T.; Turner, J. R. Claudin-1 and claudin-2 expression is elevated in inflammatory bowel disease and may contribute to early neoplastic transformation. *Lab. Invest.* **2008**, *88*, 1110−1120.
(9) Yamashita, K.; Yoshioka, Y.; Higashisaka, K.; Mimura, K.; Morishita, Y.; Nozaki, M.; Yoshida, T.; Ogura, T.; Nabeshi, H.; Nagano, K.; Abe, Y.; Kamada, H.; Monobe, Y.; Imazawa, T.; Aoshima, H.; Shishido, K.; Kawai, Y.; Mayumi, T.; Tsunoda, S.; Itoh, N.; Yoshikawa, T.; Yanagihara, I.; Saito, S.; Tsutsumi, Y. Silica and titanium dioxide nanoparticles cause pregnancy complications in mice. *Nat. Nanotechnol.* **2011**, *6*, 321−328.
(10) Lagopati, N.; Tsilibary, E. P.; Falaras, P.; Papazafiri, P.; Pavlatou, E. A.; Kotsopoulou, E.; Kitsiou, P. Effect of nanostructured TiO_2 crystal phase on photoinduced apoptosis of breast cancer epithelial cells. *Int. J. Nanomed.* **2014**, *9*, 3219−3230.
(11) Wang, J.; Zhou, G.; Chen, C.; Yu, H.; Wang, T.; Ma, Y.; Jia, G.; Gao, Y.; Li, B.; Sun, J.; Li, Y.; Jiao, F.; Zhao, Y.; Chai, Z. Acute toxicity and biodistribution of different sized titanium dioxide particles in mice after oral administration. *Toxicol. Lett.* **2007**, *168*, 176−185.
(12) Thubagere, A.; Reinhard, B. M. Nanoparticle-induced apoptosis propagates through hydrogen-peroxide-mediated bystander killing: insights from a human intestinal epithelium in vitro model. *ACS Nano* **2010**, *4*, 3611−3622.
(13) Liang, M.; Lin, I. C.; Whittaker, M. R.; Minchin, R. F.; Monteiro, M. J.; Toth, I. Cellular uptake of densely packed polymer coatings on gold nanoparticles. *ACS Nano* **2010**, *4*, 403−413.
(14) Ghosh, P.; Han, G.; De, M.; Kim, C. K.; Rotello, V. M. Gold nanoparticles in delivery applications. *Adv. Drug Delivery Rev.* **2008**, *60*, 1307−1315.
(15) Frohlich, E.; Roblegg, E. Models for oral uptake of nanoparticles in consumer products. *Toxicology* **2012**, *291*, 10−17.
(16) El-Sayed, I. H.; Huang, X.; El-Sayed, M. A. Surface plasmon resonance scattering and absorption of anti-EGFR antibody conjugated gold nanoparticles in cancer diagnostics: applications in oral cancer. *Nano Lett.* **2005**, *5*, 829−834.
(17) Dykman, L. A.; Khlebtsov, N. G. Uptake of engineered gold nanoparticles into mammalian cells. *Chem. Rev.* **2014**, *114*, 1258−1288.
(18) Hubatsch, I.; Ragnarsson, E. G. E.; Artursson, P. Determination of drug permeability and prediction of drug absorption in Caco-2 monolayers. *Nat. Protoc.* **2007**, *2*, 2111−2119.
(19) Yao, M. F.; Chen, J. J.; Zheng, J. K.; Song, M. Y.; McClements, D. J.; Xiao, H. Enhanced lymphatic transport of bioactive lipids: cell culture study of polymethoxyflavone incorporation into chylomicrons. *Food Funct.* **2013**, *4*, 1662−1667.
(20) Gu, Y. J.; Cheng, J. P.; Lin, C. C.; Lam, Y. W.; Cheng, S. H.; Wong, W. T. Nuclear penetration of surface functionalized gold nanoparticles. *Toxicol. Appl. Pharmacol.* **2009**, *237*, 196−204.
(21) Coulter, J. A.; Jain, S.; Butterworth, K. T.; Taggart, L. E.; Dickson, G. R.; McMahon, S. J.; Hyland, W. B.; Muir, M. F.; Trainor, C.; Hounsell, A. R.; O'Sullivan, J. M.; Schettino, G.; Currell, F. J.; Hirst, D. G.; Prise, K. M. Cell type-dependent uptake, localization, and cytotoxicity of 1.9 nm gold nanoparticles. *Int. J. Nanomed.* **2012**, *7*, 2673−2685.
(22) Wadia, J. S.; Chalmers-Redman, R. M. E.; Ju, W. J. H.; Carlile, G. W.; Phillips, J. L.; Fraser, A. D.; Tatton, W. G. Mitochondrial membrane potential and nuclear changes in apoptosis caused by serum and nerve growth factor withdrawal: time course and modification by (−)-deprenyl. *J. Neurosci.* **1998**, *18*, 932−947.
(23) Keil, V. C.; Funke, F.; Zeug, A.; Schild, D.; Muller, M. Ratiometric high-resolution imaging of JC-1 fluorescence reveals the subcellular heterogeneity of astrocytic mitochondria. *Pfluegers Arch.* **2011**, *462*, 693−708.
(24) Polte, J.; Ahner, T. T.; Delissen, F.; Sokolov, S.; Emmerling, F.; Thunemann, A. F.; Kraehnert, R. Mechanism of gold nanoparticle formation in the classical citrate synthesis method derived from coupled in situ XANES and SAXS evaluation. *J. Am. Chem. Soc.* **2010**, *132*, 1296−1301.
(25) Datta, S. R.; Brunet, A.; Greenberg, M. E. Cellular survival: a play in three Akts. *Genes Dev.* **1999**, *13*, 2905−2927.
(26) Jiang, W.; Kim, B. Y. S.; Rutka, J. T.; Chan, W. C. W. Nanoparticle-mediated cellular response is size-dependent. *Nat. Nanotechnol.* **2008**, *3*, 145−150.
(27) Nel, A. E.; Madler, L.; Velegol, D.; Xia, T.; Hoek, E. M. V.; Somasundaran, P.; Klaessig, F.; Castranova, V.; Thompson, M. Understanding biophysicochemical interactions at the nano-bio interface. *Nat. Mater.* **2009**, *8*, 543−557.
(28) Yang, P. H.; Sun, X. S.; Chiu, J. F.; Sun, H. Z.; He, Q. Y. Transferrin-mediated gold nanoparticle cellular uptake. *Bioconjugate Chem.* **2005**, *16*, 494−496.
(29) Wang, S. H.; Lee, C. W.; Chiou, A.; Wei, P. K. Size-dependent endocytosis of gold nanoparticles studied by three-dimensional mapping of plasmonic scattering images. *J. Nanobiotechnol.* **2010**, *8*, 33.
(30) Sonavane, G.; Tomoda, K.; Sano, A.; Ohshima, H.; Terada, H.; Makino, K. In vitro permeation of gold nanoparticles through rat skin and rat intestine: effect of particle size. *Colloids Surf., B* **2008**, *65*, 1−10.
(31) Bajak, E.; Fabbri, M.; Ponti, J.; Gioria, S.; Ojea-Jimenez, I.; Collotta, A.; Mariani, V.; Gilliland, D.; Rossi, F.; Gribaldo, L. Changes in Caco-2 cells transcriptome profiles upon exposure to gold nanoparticles. *Toxicol. Lett.* **2015**, *233*, 187−199.
(32) Taggart, L. E.; McMahon, S. J.; Currell, F. J.; Prise, K. M.; Butterworth, K. T. The role of mitochondrial function in gold nanoparticle mediated radiosensitisation. *Cancer Nanotechnol.* **2014**, *5*, 5.
(33) Wang, L. M.; Liu, Y.; Li, W.; Jiang, X. M.; Ji, Y. L.; Wu, X. C.; Xu, L. G.; Qiu, Y.; Zhao, K.; Wei, T. T.; Li, Y. F.; Zhao, Y. L.; Chen, C. Y. Selective targeting of gold nanorods at the mitochondria of cancer cells: implications for cancer therapy. *Nano Lett.* **2011**, *11*, 772−780.

DOI: 10.1021/acs.jafc.5b03242
J. Agric. Food Chem. 2015, 63, 8044−8049

Table 1. Sequences of the Used Aptamers and Calculated Dissociation Constants for *B. cereus* Spores[a]

aptamer	aptamer sequence (5′-3′)	K_D [nM]
BacApt1	*CATCCGTCACACCTGCTC*GGTGCAGACCCATAGGGGGGGCGTGCGGATGTGCGGAGTAG*GGTGTTGGCTCCCGTATC*	5.7
BacApt2	*CATCCGTCACACCTGCTC*CCCCAATGAAGCGAGATGGACGCCTAGCACCCCCCGCGTCC*GGTGTTGGCTCCCGTATC*	6.8
BacApt3	*CATCCGTCACACCTGCTC*GGTGCAGACCCATAGGGGGGGCGTGCGGATGTAGGAGTAG*GGTGTTGGCTCCCGTATC*	35.5
BacApt4	*CATCCGTCACACCTGCTC*CCAGCGTGCGTCGACCCGGACCCCTGTCAGCCCCCTCGCG*GGTGTTGGCTCCCGTATC*	44.6
BacApt5	*CATCCGTCACACCTGCTC*CAGGTGGGGGGGCGTATTACTGAGGCAGAGTAGTTGGCCG*GGTGTTGGCTCCCGTATC*	19.1
BacApt6	*CATCCGTCACACCTGCTC*CATTGACGTTGTCAGGTAATGGTTTGGGAGGTCGTGGTGT*GGTGTTGGCTCCCGTATC*	22.2
BacApt7	*CATCCGTCACACCTGCTC*GCCGGGAGAACGGTACTGGTGGGGGATGACAGCTCGGGGGGGTGTTGGCTCCCGTATC	23.5
BacApt8	*CATCCGTCACACCTGCTC*CCCGCCAGGCAATGCCTGCCGCGTCTCGAACACGTACGGTC*GGTGTTGGCTCCCGTATC*	31.6
BacApt9	*CATCCGTCACACCTGCTC*GCACGGGTGGTTGGTCACGCCTAGTCTCCAATTGCGTTGC*GGTGTTGGCTCCCGTATC*	52.6

[a]Primer regions of aptamers are italicized.

cereus was applied.[35] The trapping was realized in milk simulating buffer and in sterilized milk (containing 0.3, 1.5, and 3.5% fat) for verification of the suitability of the technique under real conditions. The aptamer-based trapping technique was developed to replace the necessary time-consuming microbiological enrichment of *B. cereus* spores in routine analysis.

The novelty of the presented work is given by the application of aptamers for spore enrichment in different milk samples. The combination of an aptamer-based enrichment by magnetic separation and a specific real-time PCR represents a new and rapid spore detection system. Additionally, due to the fact that spore forming germs are important for many industrial food processes this enrichment technique is easily adaptable to further investigations. In particular the presented system could be adapted for aptamer-based enrichment of, e.g., *Bacillus* spp. from soups, spices, and fruits or *Clostridium* spp. in chilled foods, cheese, and meat products.[36,37]

MATERIALS AND METHODS

Aptamers with an Affinity to *B. cereus* Spores. The aptamers used in this study have been generated via the SELEX process (systematic evolution of ligands by exponential enrichment) (unpublished data). Aptamer sequences (Table 1) were purchased from Invitrogen Life Technologies GmbH (Darmstadt, Germany) for further characterization.

Determination of Dissociation Constants (K_D) of Aptamers Using SPR. *Spore Lysis.* To generate a spore lysate of 10^6 CFU/mL, different *B. cereus* strains (Table 2) were diluted in 400 μL of 10 mM sodium acetate (pH 5.0), and 250 mg of glass beads (⌀ = 0.5 mm) were added. The spore solution was lysed by mechanical treatment (5 min at 30 Hz, twice) using a TissueLyser (Qiagen GmbH, Hilden, Germany). The supernatant with fragmented spores was subsequently used for immobilization on an SPR sensor chip.

Table 2. *Bacillus* Spp. Strains Used in This Study for Determination of Aptamer Selectivity

Bacillus spp.	strain
B. cereus	MHI M1[a]
B. cereus	AH 187
4× *B. cereus*	wild types
B. weihenstephanensis	wild type
B. thuringiensis	ATCC 10792
B. subtilis	DSM2109
B. subtilis	ATCC 6633
B. licheniformis	DSM 13
B. coagulans	ATCC 7050
B. circulans	ATCC9966
B. sphaericus	ATCC 245
Paenibacillus polymixa	ATCC10401

[a]This strain was used for aptamer selection.

SPR Chip Preparation. An SPR-2 biosensor system (Sierra Sensors GmbH, Hamburg, Germany) was used for SPR spectroscopy. One channel of this two-channel system was used as active spot and contained the immobilized spore lysate, and the other channel with immobilized bovine serum albumin (BSA) was used as a reference to detect unspecific binders. The temperature control together with an integrated autosampler allowed automated measurements at a temperature of 25 °C. All SPR experiments were carried out with a flow rate of 25 μL/min using degassed PBS buffer containing 0.05% Tween 20 as running buffer.

SPR-AS-AM sensor chips (Sierra Sensors GmbH, Hamburg, Germany) with carboxylated surface were used for immobilization of fragmented spores. Each sensor chip was initially activated for 7 min by injecting a mixture (1/1, v/v) of 100 mM *N*-hydroxysuccinimide (NHS) and 400 mM 1-ethyl-3-(3-dimethylaminopropyl)carbodiimide hydrochloride (EDC). Subsequently, fragmented spores diluted in 10 mM sodium acetate (pH 5.0) were injected for 7 min, followed by an injection of 3 min using 50 μg/mL bovine serum albumine (BSA) diluted in 10 mM sodium acetate (pH 5.0). The remaining surface areas were blocked by injecting 1 M ethanolamine (pH 8.5) for 7 min.

SPR Assay Design. The aptamers were diluted (2.5 mM, 5.0 mM, 7.5 mM, and 10.0 mM) in milk simulating buffer (55 mM NaCl, 20 mM $MgCl_2$, 67 mM $CaCl_2$, 80 mM KCl, 40 mM Tris-HCl, pH 6.6). For each assay, aptamers were injected onto the chip surface for 6 min in increasing concentrations. A dissociation time of 3 min was set to observe the binding behavior after completed injection. Bound aptamers were removed by injecting a mixture (1/1, v/v) of 10 mM sodium hydroxide and 1 M sodium chloride for 30 s. Four different concentrations of each aptamer were measured. Response units (RU) of the spot containing spore fragments were subtracted by RU of the reference spot containing BSA and RU of milk simulating buffer injections for 6 min to obtain double-referenced SPR data. The evaluation was performed using AnalyserR2 (Sierra Sensors GmbH, Hamburg, Germany) and Scrubber (BioLogic Software Pty Ltd., Campbell, Australia) software. The mean values of resulting dissociation constants were calculated and presented in nM (Table 1).

Determination of Aptamer Selectivity via SPR. *SPR Chip Preparation.* SPR chips were prepared essentially as previously described with the following modifications: An SPR-4 four-channel biosensor system (Sierra Sensors GmbH, Hamburg, Germany) was used for SPR spectroscopy. Three spots were used as active spots and contained immobilized streptavidin and the three biotinylated aptamers that were used for subsequent aptamer-based trapping of *B. cereus* spores. The fourth spot was used as a reference with immobilized streptavidin without aptamer. The sensor chips SPR-AS-AM were used for immobilization of streptavidin to bind biotinylated aptamers on the sensor chip surface. Initially, the sensor chip was activated as mentioned and streptavidin, diluted in 10 mM sodium acetate (pH 5.0) to a concentration of 0.9 μM, was injected for 7 min, followed by blocking of the remaining surface areas as mentioned. Afterward, biotinylated aptamers were diluted in milk simulating buffer

DOI: 10.1021/acs.jafc.5b03738
J. Agric. Food Chem. 2015, 63, 8050−8057

(10 μM) and injected for 6 min, each on one channel to determine the selectivity of each aptamer individually.

SPR Assay Design. For determination of aptamer selectivity, various *Bacillus* spp. spores (Table 2) were diluted in milk simulating buffer (final concentration 10^7 CFU/mL) and lysed as mentioned above. *B. cereus* strain MHI M1, which was used among other *B. cereus* strains as a selection target, was measured as a reference. For the assay, the spore lysates were injected for 1 min onto the prepared sensor chip surface. A dissociation time of 5 min was set, and afterward the bound spores were removed by injecting a mixture (1/1, v/v) of 10 mM sodium hydroxide and 1 mM sodium chloride for 30 s. The resulting RU signals were put into relation to the obtained RU signal for the reference strain MHI M1 in order to classify the aptamer selectivity of each strain. Data analysis was performed using the AnalyserR2 (Sierra Sensors GmbH, Hamburg, Germany) software.

Fluorescence Microscopy. Fluorescence microscopy was carried out using a fluorescence correlation spectroscope ConfoCor2 (Carl Zeiss GmbH, Jena, Germany) to visualize the aptamer target interactions. Therefore, aptamers were labeled at the 5′-terminus by PCR with fluorescein modified primers as described as follows: After an initial denaturation at 95 °C for 5 min, 25 cycles (95 °C for 30 s, 56 °C for 30 s, and 72 °C for 30 s each) were carried out. For a final elongation, reaction mixtures were incubated for 7 min at 72 °C. The PCR mix consisted of the following: 1× DreamTaq buffer (10×, Fisher Scientific-Germany GmbH, Schwerte, Germany), 0.8 mM dNTPs (10 mM, Bioline GmbH, Luckenwalde, Germany), 0.05 unit of DreamTaq polymerase (5.0 U/μL, Fisher Scientific-Germany GmbH, Schwerte, Germany), 1.0 μM of each primer (Invitrogen Life Technologies GmbH, Darmstadt, Germany), 25 μL of the DNA solution, and ddH2O filled up to 50 μL. For subsequent strand separation 5′-biotinylated aptamer was used. Strand separation was based on binding of biotin to streptavidin-coated magnetic beads (DynaBeads M-280 Streptavidin, Invitrogen Life Technologies GmbH, Darmstadt, Germany) to separate ssDNA for fluorescence microscopy. 5 nM fluorescent labeled aptamers were incubated with *B. cereus* spores (10^6 CFU/mL) in 350 μL of milk simulating buffer for 1 h at 25 °C. After incubation, spore suspensions were washed by centrifugation (5 min at 10500*g*) and spore pellets were resuspended in 350 μL of milk simulating buffer for fluorescence microscopy. The analyses were carried out under the following conditions: argon laser (5 mW), 25% output, transmission 15%, wavelength 488 nm, 40× and 100× lens.

Aptamer-Based Trapping of *B. cereus* Spores in Milk Simulating Buffer and Milk. *Preparation of Aptamer-Linked Magnetic Beads.* Before the aptamers could be used for trapping, they had to be linked to magnetic SiMAG-Carboxyl Beads (chemicell GmbH, Berlin, Germany). Therefore, 200 μL of SiMAG beads were washed twice with 1 mL of MES-buffer (0.1 M 2-(*N*-morpholino)-ethanesulfonic acid, pH 5.0), suspended in 250 μL of MES-buffer containing 10 mg of EDC (1-ethyl-3-(3-dimethylaminopropyl)-carbodiimide hydrochloride) and incubated under agitation for 10 min. Afterward, 50 μL of aminated aptamers was added and the mix was incubated for 2 h. After incubation, magnetic beads were washed three times with 1 mL of PBS buffer and finally redissolved in 1 mL of blocking/storage-buffer (PBS buffer containing 0.1% BSA, 0.05% sodium azide). Before each trapping experiment the required volume of magnetic beads was transferred to a new reaction tube, washed, and taken up in the initial volume of ddH_2O. For the subsequent aptamer-based trapping a mixture of aptamer-linked magnetic beads (BacApt3, BacApt4, and BacApt5) was used to cover a wide range of potential binding sites.

Aptamer-Based Trapping Using Magnetic Separation. Before each experiment, the mixture of aptamer-linked magnetic beads was washed once with the same volume of milk simulating buffer and refolded for 5 min at 95 °C with subsequent cooling to 4 °C to ensure correct aptamer folding. Then 10 μL of aptamer-linked magnetic bead mixture was diluted with 940 μL of (i) milk simulating buffer, (ii) milk with 0.3% fat, (iii) milk with 1.5% fat, and (iv) milk with 3.5% fat. These solutions were spiked each with 50 μL of *B. cereus* spores (10^7 CFU/mL, used strains MHI M1 and two wild types) and incubated for 30 min under agitation. Thereafter, the solution was centrifuged (2 min, 10000*g*) and the supernatant was removed. The resulting bead pellets were washed three times with 1 mL of ddH_2O and finally taken up into 100 μL of ddH_2O. Aptamer-bound spores were then heat eluted for 5 min at 96 °C, and the hot supernatant containing enriched spores was transferred to a new reaction tube. The samples were stored at −20 °C until further use.

Real Time PCR Detection of B. cereus Spores. Real time PCR was performed to demonstrate the success of aptamer-based trapping. Therefore, the solutions containing enriched spores were diluted 1:10 with ddH_2O and lysed as mentioned above, and real time PCR assay was performed using a iCycler iQ5 (BioRad Laboratories, Inc.; Hercules, CA). The used real time assay and conditions have been described in detail elsewhere.[35] The primers used in this assay target the hbID gene of *B. cereus*. Each reaction mix consisted of following components: 1× DreamTaq buffer (10×, Fisher Scientific-Germany GmbH, Schwerte, Germany), 0.8 mM dNTPs (10 mM, Bioline GmbH, Luckenwalde, Germany) 0.25 unit of DreamTaq polymerase (5.0 U/μL, Fisher Scientific-Germany GmbH, Schwerte, Germany), 0.25 μM of each primer (mp3L1R1for and mp3L1R1rev, Invitrogen Life Technologies GmbH, Darmstadt, Germany), 0.3125× SYBR Green I nucleic acid gel stain (10000×, Invitrogen GmbH, Karlsruhe, Germany), 3 μL of enriched and lysed spore solution, and ddH_2O filled up to 20 μL. After an initial denaturation at 95 °C for 10 min, 35 cycles (95 °C for 15 s, 60 °C for 10 s, and 72 °C for 10 s each) were carried out. For final elongation, the reaction mixtures were incubated for 10 min at 72 °C. For quantitation and comparison, an external calibration with *B. cereus* (wild type, 10^3 to 10^7 CFU/mL) was applied. A milk simulating buffer/milk sample spiked at a concentration equal to pre-enrichment was used as control. The assay was additionally performed using *B. subtilis* and *B. thuringiensis* spores as template to demonstrate the specificity of the protocol.

RESULTS AND DISCUSSION

The presented work includes the characterization of aptamers with an affinity to *B. cereus* spores by SPR and fluorescence microscopy and subsequent development of an aptamer-based trapping technique in milk. The trapping was performed in both milk simulating buffer and milk containing different fat contents. Moreover its effectiveness was demonstrated by real time PCR.[35]

Determination of Dissociation Constants (K_D) of Aptamers Using SPR. Suitable SPR sensor chips were prepared to determine the dissociation constants (K_D) of the aptamers to *B. cereus* spores. Immobilization of spores fragmented using glass beads and a TissueLyser enabled the preparation of suitable sensor chips for the determination of dissociation constants.

Spore Lysis. The degree of spore fragmentation proved to be a crucial parameter for successful sensor chip preparation. Thus, several treatments (e.g., ultrasonic disruption), pH values, and spore fragmentation methods were investigated and assessed (data not shown). The developed mechanical treatment with glass beads is applicable for fragmentation of spores and supplies the ideal degree of spore fragmentation for subsequent immobilization on carboxylated SPR sensor chips.

SPR Chip Preparation. During immobilization of fragmented spores on activated SPR sensor chip surfaces approximately 400−800 RU could be observed. According to Karlsson one RU corresponds to approximately 1 pg of immobilized fragmented compounds per mm^2.[38] Thus, on a sensor chip surface of approximately 1.2 mm^2, 440−960 pg of fragmented spores can be immobilized. The high amount of immobilized fragments allows the conclusion that a sufficient amount of spore coat fragments were immobilized and therefore the developed SPR immobilization method is suitable

DOI: 10.1021/acs.jafc.5b03738
J. Agric. Food Chem. 2015, 63, 8050−8057

for investigations concerning interaction of the aptamers and spore surfaces.

SPR Assay. Regeneration conditions were obtained using sodium hydroxide (10 mM) and sodium chloride (1 M) (1/1, v/v) and a contact time of 30 s. The stability and the activity of the chip surface were further monitored by multiple injections of an aptamer solution (10 mM) and subsequent regeneration. Due to the obtained response signals of 214 RU (first aptamer injection) and 191 RU (50th aptamer injection) a decrease of approximately 10.75% in surface activity was determined, which is less than the recommended cutoff value of 20%.[39,40] Therefore, the developed SPR chip surface regeneration procedure fulfilled the compulsory requirements.

SPR analyses were carried out using milk simulating buffer, because the selected aptamers will be used for applications in milk. Milk itself was not suitable for SPR measurements because of its fat content and the included milk sugar. Therefore, the selection conditions were chosen as far as possible similar to the conditions of milk by using a simulating buffer. Dissociation constants of aptamer were measured by immobilization of fragmented spores on chip surface and injection of several aptamer concentrations (2.5 mM, 5.0 mM, 7.5 mM, and 10.0 mM). Exemplary overlays of aptamer injections are shown in Figure 1 and Figure S1. RU of spore

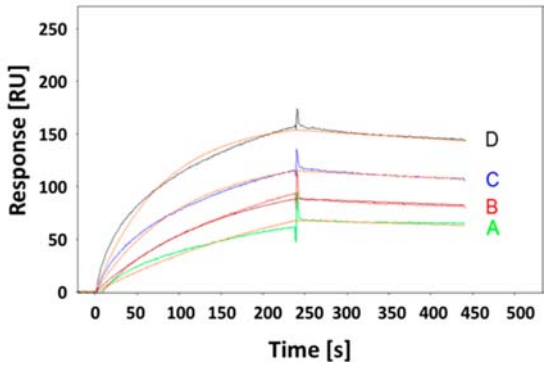

Figure 1. Exemplary overlay of fitted raw data (BacApt2) for evaluation of dissociation constants (K_D). The raw data were fitted using the Langmuir 1:1 model including mass transport limitation. The data was analyzed using AnalyserR2 (Sierra Sensors GmbH, Hamburg, Germany) and Scrubber (BioLogic Software Pty Ltd., Campbell, Australia) software.

fragment containing spots were subtracted by RU of reference spots containing BSA and injections of milk simulating buffer for 6 min to obtain double referenced SPR data. The obtained curves were fitted in accordance with the Langmuir 1:1 model including a mass transport limitation factor to determine the dissociation constants (Figure 1). Although an appropriate multivalent binding kinetic could be more precise for performed experiments, it is not yet available, so that the Langmuir binding model was chosen. SPR data were normally distributed according to David (confidence intervals of 90%) regarding the calculation of dissociation constants.[41] Furthermore, no outlier according to Dixon (confidence intervals of 95%) was identified.[42] A summary of calculated K_D values is shown in Table 1.

In summary, the dissociation constants of aptamers with an affinity to *B. cereus* spores could be detected in a low-nanomolar range. Hence, the selected aptamers were considered suitable for the subsequent development of an aptamer-based trapping technique.

Determination of Aptamer Selectivity via SPR. Aptamer selectivity was determined to investigate the specificity of our trapping protocol and the aptamers used in this study. For that, the three aptamers applied for capturing were immobilized onto an SPR chip surface and binding interaction differences were observed between aptamers and *B. cereus* spores as well as various other *Bacillus* spp. spores (Figure S2). The spores were chosen for their degree of relationship to *B. cereus* and included both closely related (*B. thuringiensis* and *B. subtilis*) and more distant spores (e.g., *B. weihenstephanensis* and *B. coagulans*). The selectivity results were calculated in relation to the strain *B. cereus* MHI M1, which had been one of the targets for aptamer selection. MHI M1 was chosen as a reference because it was expected that aptamers have the highest affinity to their selection target.

Principally, all aptamers exhibited a higher affinity to *B. cereus* spores in comparison to other *Bacillus* spores (Figure S2). However, the selectivity was not equal for all *B. cereus* strains used in this assay. This could be due to small differences in surface composition and spore lysates preparation. For instance, the affinity of BacApt3 to *B. cereus* AH 187 is much higher than to the reference strain MHI M1.

Figure 2 graphically describes the affinity of the three used aptamers to all *Bacillus* spores in comparison. It can be clearly seen that, unsurprisingly, the selectivity toward *B. cereus* spores is highest, followed by closely related spores, i.e., *B. subtilis* and *B. thuringiensis* spores. Considerably lower interactions between the selected aptamers and more distantly related spores could be observed. In conclusion, the use of the selected aptamers for highly selective trapping of targets is limited due to structural similarities of *Bacillus* spp. spores. However, high selectivity can be achieved by performing a highly selective real time PCR following trapping which excludes closely related spores.[43] Real time PCR results will be discussed later.

Fluorescence Microscopy. Fluorescence microscopy was carried out to visualize the interactions of aptamers with *B. cereus* spores and therefore to verify the aptamer affinities. Spores without prior incubation were used as a blank sample to define the optimal settings for fluorescence microscopy. Adjustment of the blank sample settings was necessary to obtain low intrinsic fluorescence of spores (shown in Figure 3, 1A to 1C). The aptamer spore complexes were investigated by microscopy after incubation of fluorescent-labeled aptamers with spores and corresponding washing steps. Furthermore, to generate representative fluorescence images, a mixture of all nine aptamers was used for fluorescence microscopy (shown in Figure 3, 2A to 2C, 3A to 3C).

The visualization of aptamer spore interactions by fluorescence microscopy confirmed the affinity of selected aptamers to *B. cereus* spores and underlined the obtained SPR results, respectively.

Aptamer-Based Trapping of *B. cereus* Spores in Milk. *Aptamer-Based Trapping of B. cereus Spores Using Real Time PCR Detection.* To verify the suitability and specificity of the used real time PCR assay, the PCR was performed using *B. cereus*, *B. subtilis*, and *B. thuringiensis* spores (each 10^3 CFU/mL). An external calibration was used (Figure 4A,B), for which a regression coefficient of 0.99 was obtained. The results demonstrate that *B. cereus* spores were amplified while *B. subtilis* and *B. thuringiensis* spores show no amplification in obtained threshold cycle number (data not shown). The real time PCR

DOI: 10.1021/acs.jafc.5b03738
J. Agric. Food Chem. 2015, 63, 8050−8057

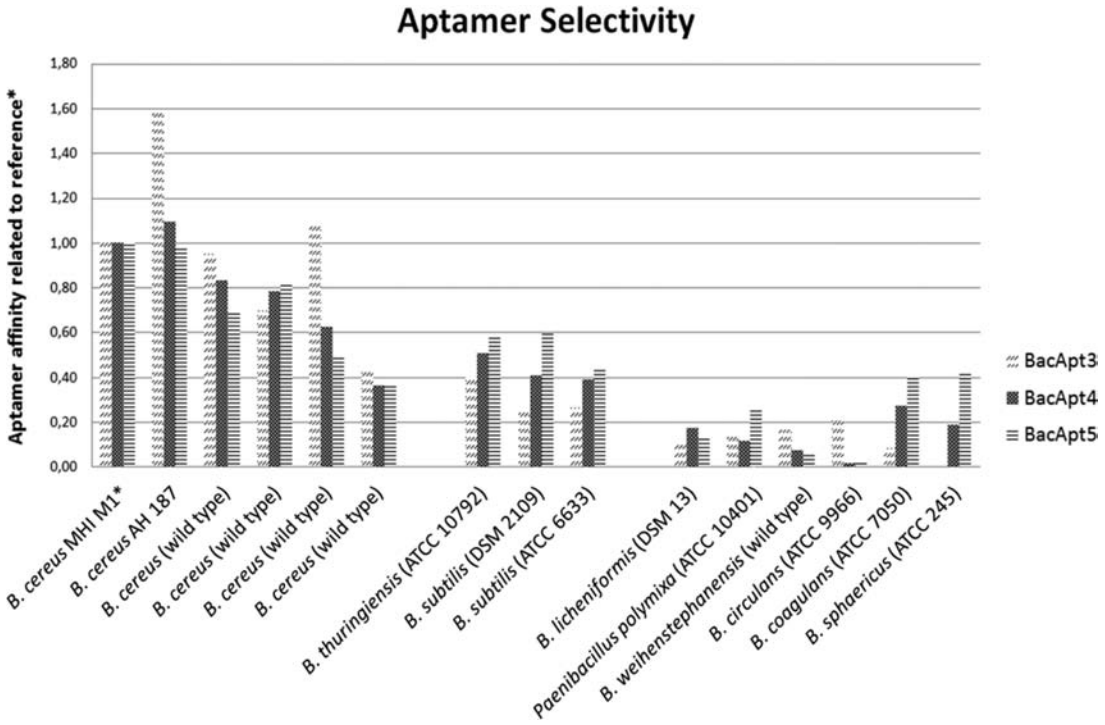

Figure 2. Aptamer selectivity of BacApt3, BacApt4 and BacApt5 determined by SPR measurements with spores of different *Bacillus* strains. As a reference, the affinity of *B. cereus* MHI M1 was set to 1. The selectivity of other spores is assigned as relative affinity compared to the reference.

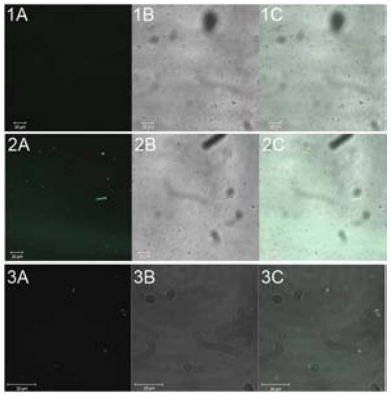

Figure 3. Fluorescence microscopy recordings of *B. cereus* spores in milk simulating buffer as blank sample (1A to 1C with 40× lens). Exemplary images of spores after incubation with a fluorescently labeled mix of obtained aptamers (2A to 2C with 40× lens and 3A to 3C with 100× lens). (A) Fluorescence images; (B) visual images; (C) overlays of the fluorescence and visual images.

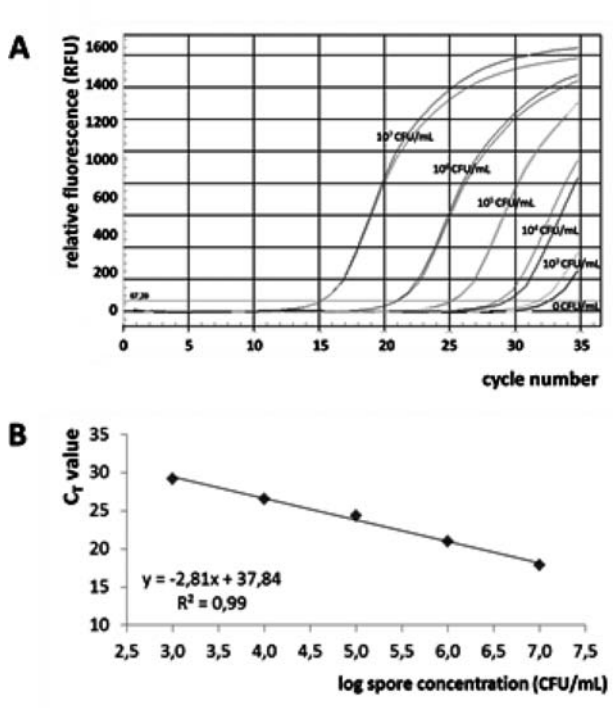

Figure 4. (A) Example of amplification curves during real time PCR with different *B. cereus* MHI M1 spore concentrations (from left to right): 10^7 CFU/mL, 10^6 CFU/mL, 10^5 CFU/mL, 10^4 CFU/mL, 10^3 CFU/mL, and 0 CFU/mL. (B) Resulting calibration line during real time PCR with $R^2 = 0.99$. Spore concentration (from left to right): 10^3 CFU/mL, 10^4 CFU/mL, 10^5 CFU/mL, 10^6 CFU/mL, 10^7 CFU/mL.

assay thus proved to be a highly specific tool for detection and quantitation of *B. cereus* spores after trapping.

Trapping was performed in three different matrices and milk simulating buffer. Milk simulating buffer was included as a trapping matrix since aptamers are expected to achieve highest target affinities in their selection buffer. This is due to conformational changes caused by, e.g., ion concentration and pH value of the medium. Milk simulating buffer was chosen for aptamer selection as it on one hand simulates milk in ion concentration and pH value and on the other hand does not contain substances like sugars and fat which could disturb the SELEX process. Milk with three different fat contents was selected to demonstrate the applicability of the trapping technique under real conditions. This was done to evaluate a possible interference of fat and sugar with aptamer confirmation.

DOI: 10.1021/acs.jafc.5b03738
J. Agric. Food Chem. 2015, 63, 8050−8057

Overall enrichment factors between 3.1 and 7.5 (Table 3) could be achieved. As expected, the highest enrichment factor was observed in milk simulating buffer (6.0 ± 1.0 on average). Trapping was also successful in milk, however at a lower efficiency in comparison to milk simulating buffer (on average 3.5 ± 1.0 to 5.4 ± 1.9). No significant differences were observed between different fat contents. Thus, it can be assumed that fat content is not a relevant parameter for trapping. The successful enrichment in milk also allows the assumption that milk sugar does not influence the aptamer–target interaction because aptamers show high affinity despite milk samples containing milk sugar.

Table 3. Obtained Enrichment Factors for Aptamer-Based Trapping in Milk Simulating Buffer and Milk with Different Fat Contents[a]

strain	milk simulating buffer	milk 0.3% fat	milk 1.5% fat	milk 3.5% fat
B. cereus wild type	5.2	3.5	4.3	4.0
B. cereus wild type	5.7	3.1	6.7	4.8
B. cereus MHI M1	7.1	3.9	3.2	7.5
mean value	6.0 ± 1.0	3.5 ± 0.4	4.7 ± 1.8	5.4 ± 1.9
mean value 2	4.91 ± 1.07			

[a]The maximal trapping factor was determined mathematically to 10.

The ion strength of milk (or milk simulating buffer) has been shown to be a disruptive factor for subsequent detection and quantitation via real time PCR. Therefore, it was necessary to include several washing steps of aptamer-linked magnetic beads with ddH_2O following trapping in order to achieve successful real time PCR quantitation. Furthermore, PCR results were improved by diluting the samples prior to measurement to minimize the effect of residual ions (data not shown).

In this study, we demonstrate the successful aptamer-based entrapment of *B. cereus* spores in milk simulating buffer as well as in milk with different fat contents. The presented work includes an extensive characterization of DNA aptamers with an affinity to *B. cereus* spores. The detection of vegetative cells was not considered relevant for the presented study because pasteurization, which is typically performed during the production of milk, inactivates vegetative *B. cereus* cells and only spores survive heat treatment. The aptamers were characterized by SPR and fluorescence microscopy to gain dissociation constants and to determine the selectivity of the aptamers used for trapping. Aptamer affinities in a low-nanomolar range could be obtained. However, more detailed binding properties in terms of kinetics and binding sites are to be determined by further research. Thus, selecting only one aptamer for developed detection methods seems not advisible. Due to the presumption of multivalent binding kinetics, utilization of an aptamer mix for aptamer-based trapping was chosen. It was shown that trapping was successful in buffer and different milk samples, whereby as expected the best enrichment factor was achieved by using milk simulating buffer. Moreover, it was shown that the usage of aptamers to perform a high selective trapping is limited. We recommend to perform a *B. cereus* specific real time PCR following trapping to ensure a reliable detection.[44]

In general, it was shown that aptamers are suitable for applications in trapping and detection tools. Further research could amplify the range of aptamer-based application, e.g., in Apta-PCR, which allows an indirect detection of targets at low concentrations.[45,46] Moreover the development of aptamer-based lateral flow dipsticks/devices (LFDs) could fulfill many expectations for manufacturing industry, because they enable a specific, rapid, and simple optical target detection with less expenditure of instrumentation due to interactions with specific aptamers.[47,48]

■ ASSOCIATED CONTENT

Supporting Information

The Supporting Information is available free of charge on the ACS Publications website at DOI: 10.1021/acs.jafc.5b03738.

Overlays of several BacApt injection sensorgrams for the K_D determination and selectivity measurements (PDF)

■ AUTHOR INFORMATION

Corresponding Author

*Tel: +49-40-428384357. Fax: +49-40-428384342. E-mail: markus.fischer@chemie.uni-hamburg.de.

Author Contributions

‡C.F., T.H., and J.-H.J. contributed equally

Funding

This research project was supported by the German Ministry of Economics and Technology (via AiF) and the FEI (Forschungskreis der Ernaehrungsindustrie e. V., Bonn, Germany); Project AiF 331 ZN.

Notes

The authors declare no competing financial interest.

■ ACKNOWLEDGMENTS

We acknowledge Sven Malik from Sierra Sensors GmbH, Hamburg, for the support with the SPR evaluations, and Hauke Wessels from the HAMBURG SCHOOL OF FOOD SCIENCE; Institute of Food Chemistry, University of Hamburg for proof reading. Furthermore, we acknowledge our project partners at the Ludwig-Maximilians-Universitaet Muenchen, Lehrstuhl fuer Hygiene und Technologie der Milch (Oberschleißheim, Germany) for support.

■ ABBREVIATIONS USED

SELEX, systematic evolution of ligands by exponential enrichment; ssDNA, single stranded DNA; PCR, polymerase chain reaction; ATP, adenosine triphosphate; SPR, surface plasmon resonance; NHS, *N*-hydroxysuccinimide; EDC, 1-ethyl-3-(3-dimethylaminopropyl)carbodiimide hydrochloride; BSA, bovine serum albumin; LFD, lateral flow dipstick

■ REFERENCES

(1) Tuerk, C.; Gold, L. Systematic evolution of ligands by exponential enrichment: RNA ligands to bacteriophage T4 DNA polymerase. *Science* **1990**, *249*, 505−510.

(2) Ellington, A. D.; Szostak, J. W. In vitro selection of RNA molecules that bind specific ligands. *Nature* **1990**, *346*, 818−822.

(3) Ellington, A. D.; Szostak, J. W. Selection in vitro of single-stranded DNA molecules that fold into specific ligand-binding structures. *Nature* **1992**, *355*, 850−852.

(4) Nimjee, S. M.; Rusconi, C. P.; Sullenger, B. A. Aptamers: an emerging class of therapeutics. *Annu. Rev. Med.* **2005**, *56*, 555−583.

(5) Duan, N.; Wu, S.; Chen, X.; Huang, Y.; Xia, Y.; Ma, X.; Wang, Z. Selection and characterization of aptamers against *Salmonella typhimurium* using whole-bacterium systemic evolution of ligands by

DOI: 10.1021/acs.jafc.5b03738
J. Agric. Food Chem. 2015, 63, 8050−8057

exponential enrichment (SELEX). *J. Agric. Food Chem.* **2013**, *61*, 3229−3234.
(6) Tuleuova, N.; Jones, C. N.; Yan, J.; Ramanculov, E.; Yokobayashi, Y.; Revzin, A. Development of an aptamer beacon for detection of interferon-gamma. *Anal. Chem.* **2010**, *82*, 1851−1857.
(7) Brody, E. N.; Gold, L. Aptamers as therapeutic and diagnostic agents. *Rev. Mol. Biotechnol.* **2000**, *74*, 5−13.
(8) Proske, D.; Blank, M.; Buhmann, R.; Resch, A. Aptamers—basic research, drug development, and clinical applications. *Appl. Microbiol. Biotechnol.* **2005**, *69*, 367−374.
(9) Rimmele, M. Nucleic acid aptamers as tools and drugs: recent developments. *ChemBioChem* **2003**, *4*, 963−971.
(10) Dwarakanath, S.; Bruno, J. G.; Shastry, A.; Phillips, T.; John, A.; Kumar, A.; Stephenson, L. D. Quantum dot-antibody and aptamer conjugates shift fluorescence upon binding bacteria. *Biochem. Biophys. Res. Commun.* **2004**, *325*, 739−743.
(11) Kloepfer, J.; Mielke, R.; Wong, M.; Nealson, K.; Stucky, G.; Nadeau, J. Quantum dots as strain-and metabolism-specific microbiological labels. *Appl. Environ. Microbiol.* **2003**, *69*, 4205−4213.
(12) Hünniger, T.; Wessels, H.; Fischer, C.; Paschke-Kratzin, A.; Fischer, M. Just in Time-Selection: A Rapid Semiautomated SELEX of DNA Aptamers Using Magnetic Separation and BEAMing. *Anal. Chem.* **2014**, *86*, 10940−10947.
(13) Kong, L.; Xu, J.; Xu, Y.; Xiang, Y.; Yuan, R.; Chai, Y. A universal and label-free aptasensor for fluorescent detection of ATP and thrombin based on SYBR Green I dye. *Biosens. Bioelectron.* **2013**, *42*, 193−197.
(14) Bruno, J. G.; Kiel, J. L. In vitro selection of DNA aptamers to anthrax spores with electrochemiluminescence detection. *Biosens. Bioelectron.* **1999**, *14*, 457−464.
(15) Vater, A.; Klussmann, S. Toward Third-generation aptamers: Spiegelmers and their therapeutic prospects. *Curr. Opin. Drug Discovery Dev.* **2003**, *6*, 253−261.
(16) Helgason, E.; Økstad, O. A.; Caugant, D. A.; Johansen, H. A.; Fouet, A.; Mock, M.; Hegna, I.; Kolstø, A.-B. *Bacillus anthracis, Bacillus cereus*, and *Bacillus thuringiensis*—one species on the basis of genetic evidence. *Appl. Environ. Microbiol.* **2000**, *66*, 2627−2630.
(17) Drobniewski, F. The safety of *Bacillus* species as insect vector control agents. *J. Appl. Bacteriol.* **1994**, *76*, 101−109.
(18) Bruno, J. G.; Ulvick, S. J.; Uzzell, G. L.; Tabb, J. S.; Valdes, E. R.; Batt, C. A. Novel immuno-FRET assay method for *Bacillus* spores and *Escherichia coli* O157: H7. *Biochem. Biophys. Res. Commun.* **2001**, *287*, 875−880.
(19) Bennet, R. W.; Harmon, S. M. *Bacillus cereus* food poisoning. Laboratory diagnosis of infectious disesases: principles and practice. *Bacterial, mycotic and parasitic diseases*; Springer-Verlag: New York, 1990.
(20) Lambert, B.; Peferoen, M. Insecticidal promise of *Bacillus thuringiensis*. *BioScience* **1992**, *42*, 112−122.
(21) de Maagd, R. A.; Bravo, A.; Crickmore, N. How *Bacillus thuringiensis* has evolved specific toxins to colonize the insect world. *Trends Genet.* **2001**, *17*, 193−199.
(22) Setlow, P. Mechanisms which contribute to the long-term survival of spores of *Bacillus* species. *J. Appl. Bacteriol.* **1994**, *76*, 49S−60S.
(23) Beutling, D.; Böttcher, C. *Bacillus cereus:* ein Risikofaktor in Lebensmitteln. *Arch. Lebensmittelhyg.* **1998**, *49*, 90−96.
(24) Collins, E. Heat resistant psychrotrophic microorganisms. *J. Dairy Sci.* **1981**, *64*, 157−160.
(25) Dufrenne, J.; Bijwaard, M.; Te Giffel, M.; Beumer, R.; Notermans, S. Characteristics of some psychrotrophic *Bacillus cereus* isolates. *Int. J. Food Microbiol.* **1995**, *27*, 175−183.
(26) Gibson, T.; Gordon, R. E. *Bacillus* Cohn 1872. In *Bergey's Manual of Determinative Bacteriology*; Buchanan, R. E., Gibbons, N. E., Eds.; The Williams & Wilkins Co.: Baltimore, 1974; pp 529−550.
(27) Kramer, J. M.; Gilbert, R. J. *Bacillus cereus* and other *Bacillus* species. *Foodborne bacterial pathogens*; Doyle, M. P., Ed.; Marcel Dekker, Inc.: New York, 1989; Chapter 2, pp 21−70.
(28) Sutherland, A. D.; Limond, A. M. Influence of pH and sugars on the growth and production of diarrhoeagenic toxin by *Bacillus cereus*. *J. Dairy Res.* **1993**, *60*, 575−580.
(29) Te Giffel, M.; Beumer, R.; Van Dam, W.; Slaghuis, B.; Rombouts, F. Sporicidal effect of disinfectants on *Bacillus cereus* isolated from the milk processing environment. *Int. Biodeterior. Biodegrad.* **1995**, *36*, 421−430.
(30) Dierick, K.; Van Coillie, E.; Swiecicka, I.; Meyfroidt, G.; Devlieger, H.; Meulemans, A.; Hoedemaekers, G.; Fourie, L.; Heyndrickx, M.; Mahillon, J. Fatal family outbreak of *Bacillus cereus*-associated food poisoning. *J. Clin. Microbiol.* **2005**, *43*, 4277−4279.
(31) Mahler, H.; Pasi, A.; Kramer, J. M.; Schulte, P.; Scoging, A. C.; Bar, W.; Krahenbuhl, S. Fulminant liver failure in association with the emetic toxin of *Bacillus cereus*. *N. Engl. J. Med.* **1997**, *336*, 1142−1148.
(32) Lund, T.; Granum, P. E. Characterisation of a non-haemolytic enterotoxin complex from *Bacillus cereus* isolated after a foodborne outbreak. *FEMS Microbiol. Lett.* **1996**, *141*, 151−156.
(33) Lund, T.; De Buyser, M. L.; Granum, P. E. A new cytotoxin from *Bacillus cereus* that may cause necrotic enteritis. *Mol. Microbiol.* **2000**, *38*, 254−261.
(34) Regulation, C. No. 2073/2005 of 15 November 2005 on microbiological criteria for foodstuffs. *Off. J. Eur. Union L.* **2005**, *338*, 1−26.
(35) Wehrle, E.; Didier, A.; Moravek, M.; Dietrich, R.; Märtlbauer, E. Detection of *Bacillus cereus* with enteropathogenic potential by multiplex real-time PCR based on SYBR green I. *Mol. Cell. Probes* **2010**, *24*, 124−130.
(36) Andersson, A.; Rönner, U.; Granum, P. E. What problems does the food industry have with the spore-forming pathogens *Bacillus cereus* and *Clostridium perfringens*? *Int. J. Food Microbiol.* **1995**, *28*, 145−155.
(37) Heyndrickx, M. The Importance of Endospore-Forming Bacteria Originating from Soil for Contamination of Industrial Food Processing. *Appl. Environ. Soil Sci.* **2011**, *2011*, 561975.
(38) Karlsson, R. SPR for molecular interaction analysis: a review of emerging application areas. *J. Mol. Recognit.* **2004**, *17*, 151−161.
(39) Skottrup, P.; Hearty, S.; Frøkiær, H.; Leonard, P.; Hejgaard, J.; O'Kennedy, R.; Nicolaisen, M.; Justesen, A. F. Detection of fungal spores using a generic surface plasmon resonance immunoassay. *Biosens. Bioelectron.* **2007**, *22*, 2724−2729.
(40) Wong, R. L.; Mytych, D.; Jacobs, S.; Bordens, R.; Swanson, S. J. Validation parameters for a novel biosensor assay which simultaneously measures serum concentrations of a humanized monoclonal antibody and detects induced antibodies. *J. Immunol. Methods* **1997**, *209*, 1−15.
(41) Gumbel, E.; Greenwood, J. A.; Durand, D. The circular normal distribution: Theory and tables. *J. Am. Stat. Assoc.* **1953**, *48*, 131−152.
(42) Dixon, W. J.; Massey, F. J. *Introduction to statistical analysis*; McGraw-Hill: New York, 1969; Vol. *344*.
(43) Hünniger, T.; Fischer, C.; Wessels, H.; Hoffmann, A.; Paschke-Kratzin, A.; Haase, I.; Fischer, M. Food Sensing: Selection and Characterization of DNA Aptamers to *Alicyclobacillus* Spores for Trapping and Detection from Orange Juice. *J. Agric. Food Chem.* **2015**, *63*, 2189−2197.
(44) Hünniger, T.; Felbinger, C.; Wessels, H.; Mast, S.; Hoffmann, A.; Schefer, A.; Martlbauer, E.; Paschke-Kratzin, A.; Fischer, M. Food Targeting: A Real-Time PCR Assay Targeting 16S rDNA for Direct Quantification of Alicyclobacillus spp. Spores after Aptamer-Based Enrichment. *J. Agric. Food Chem.* **2015**, *63*, 4291−4296.
(45) Pinto, A.; Redondo, M. C. B.; Ozalp, V. C.; O'Sullivan, C. K. Real-time apta-PCR for 20000-fold improvement in detection limit. *Mol. BioSyst.* **2009**, *5*, 548−553.
(46) Pinto, A.; Polo, P. N.; Henry, O.; Redondo, M. C.; Svobodova, M.; O'Sullivan, C. K. Label-free detection of gliadin food allergen mediated by real-time apta-PCR. *Anal. Bioanal. Chem.* **2014**, *406*, 515−524.
(47) McKeague, M.; Giamberardino, A.; DeRosa, M. C. Advances in aptamer-based biosensors for food safety. *Environ. Biosens* **2011**, 17−42.

DOI: 10.1021/acs.jafc.5b03738
J. Agric. Food Chem. 2015, 63, 8050−8057

(48) Tombelli, S.; Minunni, M.; Mascini, M. Aptamers-based assays for diagnostics, environmental and food analysis. *Biomol. Eng.* **2007**, *24*, 191−200.

DOI: 10.1021/acs.jafc.5b03738
J. Agric. Food Chem. 2015, 63, 8050−8057

PGRs with multiple operations. In addition, to both the experimenter and the environment, tedious operation with high reagent consumption was always unsatisfactory. Consequently, although a few works have been done, there are still challenges in the sensitive, accurate, efficient, and convenient determination of endogenous PGRs in complex samples.

A precolumn derivatization technique is usually applied to overcome the above difficulties by improving sensitivity and selectivity as well as accuracy.[36,37] Practically, derivatization might also contribute to the stabilization of labile PGRs via molecular modification. To the best of our knowledge, no derivatization was found for the simultaneous determination of PGRs involved in a signal transduction system to date. A recently synthesized fluorescent probe, 2-(12,13-dihydro-7*H*-dibenzo[*a*,*g*]carbazol-7-yl)ethyl4-methylbenzenesulfonate (DDCETS), was selected for this study,[42] which, however, provided unsatisfactory derivatization yield and low efficiency in tentative experiments. Microwave proved to be an efficient technique for complex samples.[43] Thus, the combination of microwave-assisted extraction with derivatization will be beneficial to establishing the desired method.

In this study, a method with microwave-assisted extraction−derivatization (MAED) followed by high-performance liquid chromatography (HPLC)−fluorescence detection (FLD) coupled with mass spectra (MS/MS) (MAED-HPLC-FLD-MS/MS) has been developed for the quantification of six acidic PGRs (IAA, IPA, IBA, 1-NAA, 2-NAA, and GA_3) in transgenic and nontransgenic edible oils including soybean oil, sunflower oil, and rapeseed oil. The MAED technique allows for an efficient pretreatment for oil samples, with DDCETS used as fluorescent reagent to improve sensitivity as well as stability. Experimental conditions are optimized by single- and multivariable methods to maximize response of analytes.[44] Instead of gas chromatography (GC), HPLC is selected to avoid the potential decomposition or isomerization caused by high temperature. The combination of FLD with tandem MS/MS enables both the sensitive quantification and the real-time monitoring of labile analyte and interference. This is the first time that the MAED technique has been applied to acidic PGR analysis. Sensitivity, accuracy, precision, recovery, and repeatability are significantly improved, especially for labile PGRs. Correlations between PGRs and components/genes are explored, providing a promising approach to establish an objective evaluation for transgenic foods.

MATERIALS AND METHODS

Materials and Chemicals. Standards of IAA, IPA, IBA, 1-NAA, 2-NAA, and GA_3 were purchased from Shanghai Chemical Reagent Co. (≥98%). HPLC grade methanol, formic acid, and acetonitrile (ACN) were purchased from Sigma-Aldrich Co. (St. Louis, MO, USA). Water was purified on a Milli-Q system (Millipore, Bedford, MA, USA). DDCETS was prepared following a literature method.[42] Transgenic soybean oil, nontransgenic soybean oil, transgenic sunflower oil, nontransgenic sunflower oil, transgenic rapeseed oil, and nontransgenic rapeseed oil were all purchased from a supermarket in Qufu (Shandong province, China).

Preparation of Solutions. Solutions for PGRs (GA_3, 5.46×10^{-3} mol L^{-1}; IAA, 5.65×10^{-3} mol L^{-1}; IPA, 5.18×10^{-3} mol L^{-1}; IBA, 5.62×10^{-3} mol L^{-1}; 1-NAA, 8.22×10^{-3} mol L^{-1}; 2-NAA, 8.27×10^{-3} mol L^{-1}) were prepared by dissolving an appropriate amount of corresponding standard in ACN, respectively. The stock solution (5×10^{-4} mol L^{-1}) was prepared by diluting the mixed solution with ACN. Then, in a similar way, the working solutions for calibration curves and validation (30, 50, 100, 200, 1000, 1500, and 3500 ng mL^{-1}) were prepared. Derivatizing reagent solution (1.04×10^{-2} mol L^{-1}) was prepared by dissolving 120.5 mg of DDCETS in 25 mL of anhydrous ACN. When not in use, all solutions were stored at 4 °C in a refrigerator.

Microwave-Assisted Extraction−Derivatization (MAED). A sample of 3 g was weighed and transferred to a Teflon vessel, to which 6 mL of methanol, 5 mL of *N*,*N*-dimethylformamide (DMF), 1 mL of DDCETS (1.04×10^{-2} mol L^{-1}), and 40 mg of K_2CO_3 were added successively. The screwed vessel was placed into a microwave oven, which was then set at 130 °C (power set as 1000 W) for 35 min with magnetic stirring. The resulting mixture was transferred into a tube for centrifugation (2500*g* for 5 min). The supernatant was concentrated by nitrogen stream (55 kPa) until a final volume of 4 mL, which was then filtered through a 0.22 μm nylon film and injected to HPLC-FLD-MS/MS system. Chemical structures of PGRs and derivatization scheme are shown in Figure 1.

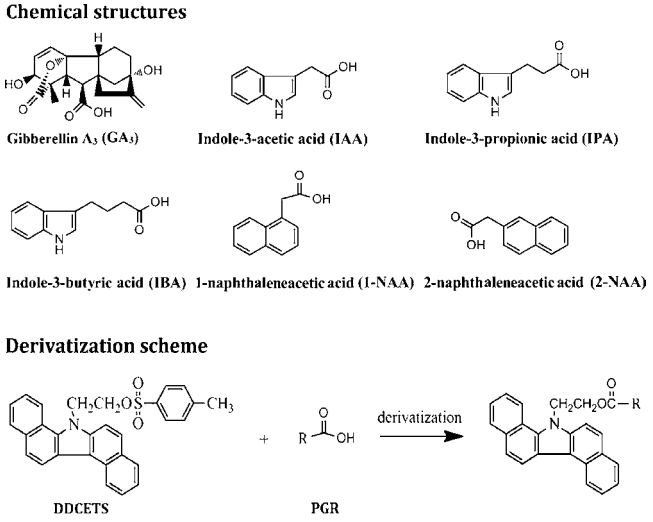

Figure 1. Chemical structures of PGRs (gibberellin A_3 (GA_3), indole-3-acetic acid (IAA), indole-3-propionic acid (IPA), indole-3-butyric acid (IBA), 1-naphthaleneacetic acid (1-NAA), and 2-naphthaleneacetic acid (2-NAA)) and derivatization scheme of DDCETS with PGRs.

Optimization of MAED. First, single-variable experiments were carried out to evaluate factors including extraction solvents (methanol; ACN; chloroform; ethanol; DMF), cosolvents (DMF; ethyl acetate; acetone; dimethyl sulfoxide (DMSO); chloroform), 40 mg of basic catalysts (pyridine; 2-methylpyridine; K_2CO_3; Na_2CO_3; $K_2C_2O_4$), derivatization reagent (concentration = 1.04×10^{-2} mol L^{-1}; volume = 0.6, 0.8, 1.0, 1.2, or 1.4 mL), temperature (80, 100, 130, 135, or 140 °C), and microwave time (15, 25, 35, 45, or 55 min). All experiments were performed at three sample levels (weight = 1.0, 3.0, and 5.0 g). Considering the interaction of factors with each other, Box−Behnken designs[45] with five variables, microwave exposition time (X_1, min), temperature (X_2, °C), DMF volume (X_3, mL), DDCETS volume (X_4, mL), and methanol volume (X_5, mL) were applied to optimize conditions for MAED, which were statistically analyzed by software Design-Expert 7.1.3 Trial.

Instrumental Analysis. An XH-100A microwave synthesis apparatus (Beijing Xiang Hu Science and Technology Development Co. Ltd.) was used to perform MAED operation. HPLC analysis was performed using an Agilent 1100 system equipped with online vacuum degasser (G1322A), quaternary pump (G1311A), autosampler (G1329A), and thermostated column compartment (G1316A). Chromatographic separation was achieved on an Aglient ZORBAX SB-C18 column (150 mm × 4.6 mm, 5 μm i.d., USA). Elution conditions were as follows: 0 min, 35% A and 65% B; 20 min, 20% A and 80% B; 25 min, 0% A and 100% B (stop time, 5 min), where A and B were 5% ACN solution (ACN/H_2O: 5/95, v/v) and 100% ACN, respectively. Flow rate was constant at 1 mL/min, and column

DOI: 10.1021/acs.jafc.5b02489
J. Agric. Food Chem. 2015, 63, 8058−8067

Table 1. Box–Behnken Design (BBD), Validation by Multicriteria, Nonparametric Tests, and Optima

	independent variable[a]					response[b]			
run[c]	X_1	X_2	X_3	X_4	X_5	exptl	BBD	validation[d]	
1	20	130	7	1.0	6	477.82	319.33	multicriteria	
2	35	140	3	1.0	6	170.51	163.23	AME	7.7200
3	20	140	5	1.0	6	169.30	163.58	CE	0.9996
4	50	140	5	1.0	6	295.94	301.03	MAE	−3.4378
5	20	130	5	1.4	6	332.91	339.22	RMSE	23.7900
6	35	130	3	0.6	6	396.90	404.62	MRE	−0.8800
7	50	130	5	1.0	4	382.31	387.39	R^2	0.9875
8	20	120	5	1.0	6	115.50	107.84		
9	20	130	3	1.0	6	327.31	333.84	nonparametric tests	
10	35	130	5	1.0	6	798.90	803.45	p value	0.1177
11	35	130	5	1.0	6	800.50	803.45		
12	50	130	5	1.4	6	722.20	719.40	optima	
13	35	130	5	0.6	8	513.90	510.99	X_1	34.87
14	20	130	5	1.0	8	370.22	363.23	X_2	130.05
15	35	130	5	1.4	4	459.17	459.53	X_3	4.69
16	35	130	3	1.0	8	411.90	413.74	X_4	1.07
17	50	120	5	1.0	6	419.06	422.20	X_5	6.24
18	35	130	5	0.6	4	380.10	380.30	BBD	803.45
19	50	130	5	0.6	6	420.80	414.83	exptl	809.51
20	35	120	7	1.0	6	390.64	393.81		
21	35	140	7	1.0	6	401.90	404.39		
22	50	130	5	1.0	8	754.14	747.85		
23	35	130	5	1.0	6	805.80	803.45		
24	35	130	3	1.0	4	405.42	400.73		
25	50	130	7	1.0	6	760.00	757.61		
26	35	130	7	0.6	6	454.46	456.42		
27	35	130	3	1.4	6	410.51	408.85		
28	35	130	5	1.0	6	803.10	803.45		
29	35	140	5	0.6	6	202.58	199.89		
30	50	130	3	1.0	6	343.22	347.37		
31	35	130	7	1.0	4	412.00	409.85		
32	35	130	7	1.0	8	795.98	800.35		
33	35	130	7	1.4	6	760.20	752.77		
34	35	140	5	1.4	6	393.60	396.97		
35	35	130	5	1.0	6	200.22	202.75		
36	35	120	5	0.6	6	280.85	279.39		
37	35	120	5	1.0	8	477.82	484.21		
38	35	130	5	1.0	6	809.51	803.45		
39	20	130	5	0.6	6	340.05	343.20		
40	35	140	5	1.0	8	341.78	348.13		
41	35	120	5	1.0	4	180.68	179.10		
42	35	140	5	1.0	4	251.35	249.74		
43	35	130	5	1.4	8	735.10	732.35		
44	35	120	3	1.0	6	245.84	239.24		
45	20	130	5	1.0	4	315.80	320.19		
46	35	120	5	1.4	6	800.50	803.45		

[a]Independent variables were X_1, derivatization time (min); X_2, derivatization temperature (°C); X_3, DMF volume; X_4, DDCETS volume; X_5, methanol volume. [b]Average experimental and predicted total peak areas of derivatives (n = 6). [c]The 46 runs from the BBD were given by the software Design-Expert 7.1.3 trial. [d]Validation: multicriteria (AME, absolute maximum error; CE, coefficient of efficiency; MAE, mean absolute error; RMSE, root mean squared error; MRE, mean relative error; R^2, correlation of determination and nonparametric tests (p value with Wilcoxon rank sum method)).

temperature was kept at 30 °C. The HPLC system was followed in sequence by a fluorescence detector (FLD, G1321A, λ_{ex}= 292 nm and λ_{em}= 402 nm) and an online mass spectrometer 1100 series LC-MSD Trap-SL (ion trap) with an atmospheric pressure chemical ionization (APCI) source (Bruker Daltonik, Bremen, Germany). The auto-MS operation parameters were as follows: APCI in positive ion detection mode; nebulizer pressure, 60 psi; dry gas temperature, 350 °C; dry gas flow, 5.0 L/min; APCI Vap temperature, 350 °C; corona current, 4000 nA; capillary voltage, 3500 V. The injection volume was 10 μL.

Validation of the Proposed Method. Linearity was measured from 30 to 3500 ng mL^{-1} for each PGR. Limit of detection (LOD) and limit of quantification (LOQ) were defined as the minimum detectable amount of analyte with a signal-to-noise ratio (S/N) of 3 and 10, respectively. FLD repeatability was investigated by measuring the relative standard deviations (RSD) for peak area and retention

DOI: 10.1021/acs.jafc.5b02489
J. Agric. Food Chem. 2015, 63, 8058–8067

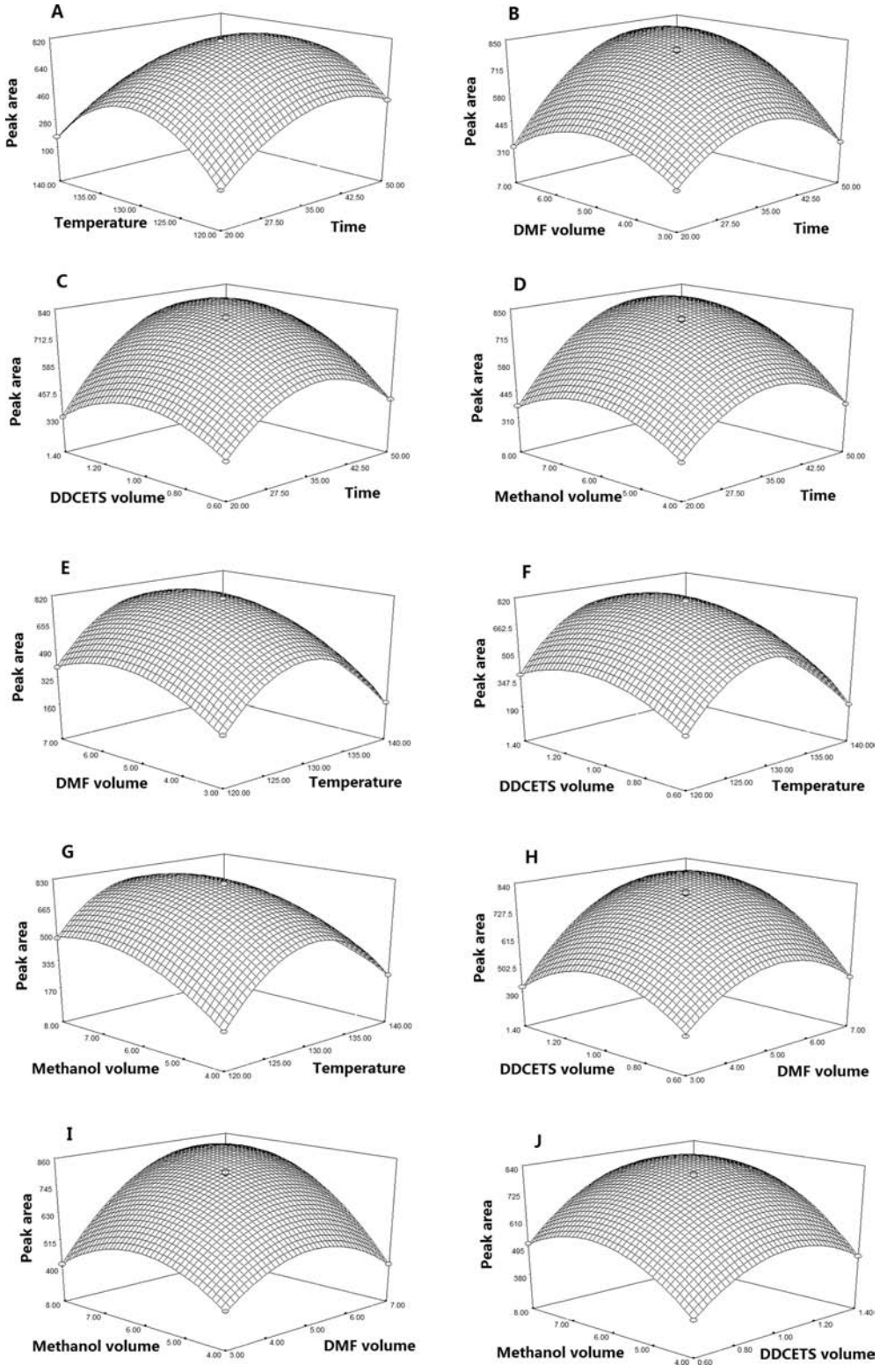

Figure 2. Response surface of the extraction−derivatization yield (expressed as peak area) affected by time and temperature (A), time and DMF volume (B), time and DDCETS volume (C), time and methanol volume (D), temperature and DMF volume (E), temperature and DDCETS volume (F), temperature and methanol volume (G), DMF volume and DDCETS volume (H), DMF volume and methanol volume (I), and DDCETS volume and methanol volume (J).

time with 10 μL of standard sample (0.5 ng of PGR injected; six replicates ($n = 6$)). Recovery was investigated with the equation $(S_2 - S_1)/S_0 \times 100\%$, where S_0, S_1, and S_2 are the peak areas of quality control (QC) solution (20, 50, 100 ng mL^{-1} of standard solutions), samples, and samples spiked with QC solution, respectively. The matrix effect was evaluated as follows: matrix effect (%) = $S_p/S_s \times 100\%$, where S_s and S_p are the peak areas of QC solution and postextraction sample spiked with QC solution, respectively. Intraday and interday precisions were determined by running samples spiked with QC solutions at three levels (50, 200, and 1000 ng mL^{-1}) ($n = 6$).

DOI: 10.1021/acs.jafc.5b02489
J. Agric. Food Chem. 2015, 63, 8058−8067

Table 2. Linear Regression Equation, Coefficient of Determination (r^2), Repeatability of Retention Time and Peak Area, Limit of Detection (LOD), Limit of Quantification (LOQ) with Fluorescence Detection, and Intra- and Interday Accuracy (RE%) and Precision (RSD%) for Giberellin A_3 (GA_3), Indole-3-acetic Acid (IAA), Indole-3-propionic Acid (IPA), Indole-3-butyric acid (IBA), 1-Naphthaleneacetic Acid (1-NAA), and 2-Naphthaleneacetic Acid (2-NAA) (n = 6)

				repeatability (RSD%)		fluorescence detection (ng mL^{-1})			intraday			interday		
analyte	linear regression eq[a] $Y = (a \pm SD)X + (b \pm SD)$	r^2	linear range (ng mL^{-1})	retention time	peak area	LOD[b]	LOQ[b]	spike (ng mL^{-1})	mean[c] ± SD[d]	RE%[e]	RSD %[f]	mean[c] ± SD[d]	RE%[e]	RSD %[f]
GA_3	$Y = (0.7142 \pm 0.03953)X + (-0.1157 \pm 0.11786)$	0.9998	50−3500	0.26	1.11	1.36	4.22	50	48.6 ± 0.32	−2.72	0.66	48.1 ± 0.89	−3.84	1.85
								200	197.8 ± 1.28	−1.11	0.65	193.9 ± 3.25	−3.05	1.68
								1000	993.5 ± 5.21	−0.65	0.52	988.6 ± 7.47	−1.14	0.76
IAA	$Y = (1.3064 \pm 0.02688)X + (-0.1713 \pm 0.4812)$	0.9999	30−1500	0.17	1.51	1.05	3.16	50	51.5 ± 1.52	2.20	2.97	48.5 ± 2.30	−3.00	4.74
								200	195.6 ± 5.65	−2.21	2.89	192.9 ± 9.30	−3.55	4.82
								1000	997.4 ± 8.26	2.27	0.83	968.0 ± 8.54	−3.20	0.88
IPA	$Y = (1.3309 \pm 0.01885)X + (-0.2052 \pm 0.2563)$	0.9999	30−1500	0.17	1.31	1.01	3.54	50	51.0 ± 1.29	2.00	2.53	48.1 ± 2.32	−3.80	4.82
								200	196.8 ± 6.92	−1.60	3.52	194.4 ± 10.70	−2.80	5.50
								1000	1003.4 ± 7.55	0.34	0.75	989.0 ± 10.43	−1.10	1.05
IBA	$Y = (1.6114 \pm 0.02852)X + (-0.4006 \pm 0.3804)$	0.9998	30−3500	0.14	1.21	1.13	3.59	50	50.7 ± 1.21	1.40	2.39	48.0 ± 0.95	−3.96	1.99
								200	203.2 ± 4.92	1.60	2.42	195.2 ± 6.11	−2.40	3.13
								1000	1007.7 ± 4.92	0.77	0.49	978.0 ± 26.45	−2.20	2.70
1-NAA	$Y = (1.0484 \pm 0.01536)X + (-0.1427 \pm 0.1942)$	0.9998	30−1500	0.08	1.28	0.37	1.20	50	48.9 ± 2.19	−2.16	4.48	48.2 ± 3.18	−3.60	6.60
								200	202.4 ± 4.19	1.20	2.07	193.4 ± 10.36	−3.30	5.36
								1000	970.4 ± 25.6	−2.96	2.64	957.0 ± 45.35	−4.30	4.74
2-NAA	$Y = (1.1675 \pm 0.02929)X + (0.2053 \pm 0.7177)$	0.9996	30−1500	0.07	1.13	0.37	1.11	50	48.9 ± 2.19	−2.22	4.48	48.2 ± 2.21	−3.60	4.59
								200	205.2 ± 7.28	2.60	3.55	194.2 ± 10.96	−2.90	5.64
								1000	978.9 ± 18.90	−2.11	1.93	1036.8 ± 32.22	3.68	3.11

[a] Y, peak area; X, injected mole (pmol); SD, standard deviations of six duplicates (n = 6). [b] LODs and LOQs were obtained on the basis of signal-to-noise ratios of 3 and 10, respectively. [c] The mean value obtained from all of the spiked blank samples. [d] Standard deviation (n = 6). [e] The relative errors percentage for accuracy. [f] The relative standard deviation percentage for precision (n = 6).

J. Agric. Food Chem. 2015, 63, 8058−8067
DOI: 10.1021/acs.jafc.5b02489

In view of the potential instability of GA_3, NAA, and IAA,[24,38,39] all PGRs and their DDCETS-labeled derivatives were investigated for short-term (12 h) and long-term stability (7 days). Storage stability was evaluated at 4 °C for 7 days. Freeze−thaw stability was evaluated after two cycles of freeze (−20 °C for 7 days)−thaw (room temperature, spontaneously) performance. Six duplicates spiked at each of three concentration levels (100, 500, and 1000 ng mL^{-1}) were analyzed, and the mean ± standard deviation (SD) with percent relative error (RE%) was calculated.

RESULTS AND DISCUSSION

Optimization of MAED. *Single-Variable Optimization.* On the basis of solvent investigation, absolute methanol was found to be the best medium for high response (Figure S1, 1a−1e). Due to the large structure of derivatized analyte, cosolvent is necessary to improve the solubility. As shown in Figure S1, 2a−2e, DMF proved to be the most suitable cosolvent. Moreover, addition of DMF effectively avoided the precipitation of hydrophobic derivative found in ethyl acetate. Catalyst investigation showed the enhanced response when 40 mg of K_2CO_3 was added, owing to its specifically strong basicity in DMF (Figure S1, 3a−3e). Temperature investigation (Figure S1, 5a−5e) from 80 to 140 °C revealed that, for the efficient extraction−derivatization of PGRs, the system should be heated to a temperature lower than 135 °C, otherwise decomposition might occur. In addition, 35 min of MAED was sufficient for the complete extraction−derivatization of PGRs, which can be seen from Figure S1, 6a−6e, for time investigation.

Multivariate Optimization. For efficient pretreatment, a thorough optimization with 46 runs of experiments for interactive variables is listed in Table 1, and response surfaces are plotted in Figure 2. Results for correlation (R^2 = 0.9875) and coefficient of efficiency (CE = 0.9996 (approximate to 1)) indicated the multivariate model was satisfactorily established. A nonparametric test gave a p value of 0.1177 (>0.05), showing that the differences between experimental and predicted values were statistically insignificant (at the 95% confidence level).[46] Together, these results demonstrated that values correlating well with experimental data can be predicted by regression of the multivariate model. Accordingly, the optimal variables combination (X_1, 34.87; X_2, 130.05; X_3, 4.69; X_4, 1.07; and X_5, 6.24) was achieved, which was confirmed by being applied to three independent replicates of MAED operations, giving a peak area of 809.51, an experimental value quite approximate to the predicted 803.45.

Thus, the optimal conditions for MAED are established: to a 50 mL vessel were added successively 3 g of edible oil, 6 mL of methanol, 5 mL of DMF, 40 mg of K_2CO_3, and 1 mL of DDCETS (1.04×10^{-2} mol L^{-1}); then the vessel was placed in the microwave apparatus at 130 °C with shaking for 35 min.

Method Validation. It can be seen from Table 2 that linear equations with excellent correlation coefficients of ≥0.9996 were developed over the wide ranges. As expected, quite low LODs (0.37−1.36 ng mL^{-1}) and LOQs (1.11−4.22 ng mL^{-1}) were obtained with higher analytical sensitivity than most of those reported,[17,19−22,26−28,35,36] which should be attributed to the strong fluorescence responses and low interferences of this method. The satisfactory repeatability for retention times (0.07−0.26%) and peak areas (1.11−1.51%) demonstrated that FLD quantification was reliable, whereas no obvious analyte loss was observed. Benefiting from the high efficiency, the sensitivity and accuracy (RE%, intraday, −2.96 to 2.60%; interday −4.30 to 3.68%) and precision (RSD%, intraday, 0.49−4.48%; interday, 0.76−6.60%) for these PGRs (Table 2) were improved.[18,31,32] Especially, GA_3 was usually determined with rather unsatisfactory results: accuracy (RE%, intraday, −22 to −2%; interday, −21 to −9%) and precision (RSD%, intraday, 3.5−6.8%, 2.66−10.9%; interday, 4.4−10.8%, 1.73−11.95%),[18,31] whereas with this method, obvious improvements of accuracy (RE%, intraday −2.72 to −0.65%; interday −3.84 to −1.14%) and precision (RSD%, intraday, 0.52−0.66%; interday, 0.76−1.85%) for GA_3 were achieved.

To assess the effect of matrix in blank and real samples, corresponding investigations were performed (Table S1). Results for matrix effects (95.5−103.9%) showed that no obvious interference was caused by blank matrices. Meanwhile, satisfactory recovery (96.1−104.4%) indicated an insignificant effect of real sample matrix on analytes. Therefore, this method was almost not affected by coexistent components, revealing its high selectivity for PGRs.

In addition, stability was studied. From Table S2 it can be found that the loss of PGRs (particularly for GA_3) caused by light or temperature seems to be unavoidable. Meanwhile, a short-term experiment showed the obviously low RE% relative to long term. In view of these facts, it was reasonable to have extraction and quantification finished as soon as possible with analyte being protected. In practice, the rapid experimental process of MAED saved much time, thereby reducing the susceptibility of analytes. Moreover, when PGRs were derivatized, the RE% values were improved, particularly for GA_3, with a significant improvement from −9.91 to −2.70%, indicating the protective effect of MAED pretreatment on labile analyte. Besides, comparing RE% values in 4 °C with those in −20 °C, the storage temperature of 4 °C should be beneficial for all stock solutions and samples.

Method Development and Comparison. Comparisons between previous and present methods are listed in Table S3. GC-MS was usually applied for PGR detection,[21,22] but the elevated temperature was disadvantageous to labile GA_3.[38,39] SPE, LLME, ultrasonic-assisted extraction (UAE), and MAE integrated with LC-MS[17,18,23,27,30−35] were widely used, providing low detection limits but meanwhile needing multiple operations with rather long time (2.5 h−1.5 days). Complicated operations tended to cause high system errors, as poor recoveries for labile GA_3 were usually observed.[18,27,31,33] Among the reported methods, HPLC-FLD with derivatization technique provided more accurate determination with excellent recoveries,[24,36,37] probably because of the stabilizing effect of derivatization (see Table S2). In the present work, instead of using conventional SPE or LLME, this method is improved by integrating the extraction and derivatization in a closed Teflon vessel, thus allowing the pretreatment to be finished with a facile operation in 1.5 h. Moreover, the microwave oven can contain 10 Teflon vessels at least, which makes this method more suitable for batch analysis than conventional 10 sets of instruments equipped with an oil bath or a sand bath, demonstrating the remarkable capacity, efficiency, and convenience relative to conventional methods.[17−37] With the derivatization technique, the detection limits are improved and, more importantly, labile analytes can be stabilized via the molecular modification. Nevertheless, in view of the susceptibility of GA_3, further identification by online MS/MS was followed. As shown in Figure S2, a molecular ion peak (m/z 641.0) and specific fragment ion peaks (m/z 295.7, 346.3, and 374.1) identified the DDCETS-derivatized GA_3. No impurity but excessive probe was observed, showing the good selectivity

DOI: 10.1021/acs.jafc.5b02489
J. Agric. Food Chem. 2015, 63, 8058−8067

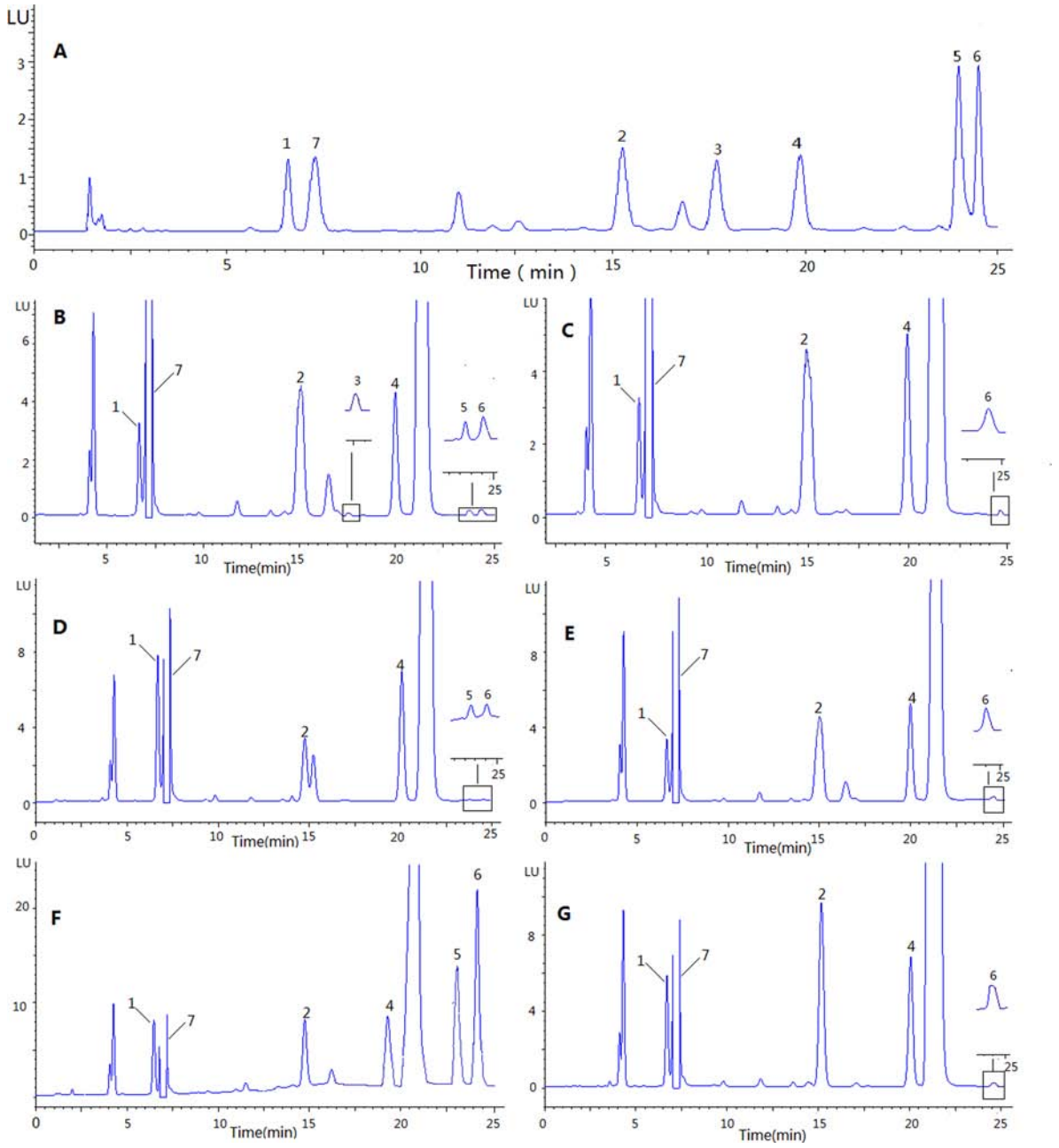

Figure 3. Typical chromatograms for PGR standards (A), nontransgenic soybean oil (B), transgenic soybean oil (C), nontransgenic sunflower oil (D), transgenic sunflower oil (E), nontransgenic rapeseed oil (F), and transgenic rapeseed oil (G). Peaks: 1, gibberellin A_3 (GA_3); 2, indole-3-acetic acid (IAA); 3, indole-3-propionic acid (IPA); 4, indole-3-butyric acid (IBA); 5, 1-naphthaleneacetic acid (1-NAA); 6, 2-naphthaleneacetic acid (2-NAA); 7, excessive DDCETS.

of this method. Thus, the proposed MAED-HPLC-FLD-MS method proved to be more powerful for the accurate, rapid, and convenient determination of PGRs.

Sample Analysis. The developed method was applied to the simultaneous determination of six PGRs in edible oil samples including transgenic and nontransgenic soybean oil, sunflower oil, and rapeseed oil. Chromatography is shown in Figure 3, and PGRs contents are summarized in Table 3. Overall, remarkable differences were observed between transgenic and nontransgenic samples: 1-NAA was detected only in nontransgenic samples; IPA was detected only in transgenic rapeseed oil and nontransgenic soybean oil samples; GA_3, IAA, IBA, and 2-NAA were found in all of the samples at different contents. In the signal transduction system, release of component depends on the PGRs in biosynthesis. GA_3 promoted production of α-amylase, thereby regulating the content of sugar; thus, its higher level in nontransgenic samples (rapeseed oil, 8.86 μg g^{-1}; sunflower oil, 7.66 μg g^{-1}) should be consistent with the fact that nontransgenic foods contained higher levels of sugar than transgenic foods.[47,48] Serine was adjusted by IAA; thus, its contents in transgenic rapeseed oil, nontransgenic soybean oil, and transgenic sunflower oil would be higher.[11] NAA was much higher in nontransgenic rapeseed oil than in the other samples, probably indicating the higher content of fatty acid in the nontransgenic rapeseed.[49] Transgenic food has been criticized and unrecognized, but

DOI: 10.1021/acs.jafc.5b02489
J. Agric. Food Chem. 2015, 63, 8058−8067

Table 3. Contents of Gibberellin A_3 (GA_3), Indole-3-acetic Acid (IAA), Indole-3-propionic Acid (IPA), Indole-3-butyric acid (IBA), 1-Naphthaleneacetic Acid (1-NAA), and 2-Naphthaleneacetic Acid (2-NAA) in Six Oil Samples (n = 6)

		rapeseed oil						soybean oil						sunflower oil					
		nontransgenic			transgenic			nontransgenic			transgenic			nontransgenic			transgenic		
PGRs	weighed content[a] g	mean (μg)	av[b] (μg/g)	RSD[c] (%)	mean (μg)	av[b] (μg/g)	RSD[c] (%)	mean (μg)	av[b] (μg/g)	RSD[c] (%)	mean (μg)	av[b] (μg/g)	RSD[c] (%)	mean (μg)	av[b] (μg/g)	RSD[c] (%)	mean (μg)	av[b] (μg/g)	RSD[c] (%)
GA_3	1	8.71	8.860	1.9	5.61	5.900	1.1	3.23	3.300	1.8	3.24	3.340	2.0	7.56	7.660	2.1	3.35	3.530	0.7
	3	26.98		0.9	18.21		1.8	9.85		2.5	10.05		1.4	23.16		3.6	10.97		1.3
	5	44.46		2.5	30.01		2.9	16.99		3.1	17.10		1.9	38.51		2.4	17.99		1.9
IAA	1	2.87	2.930	2.4	4.48	4.830	1.5	3.03	3.150	0.6	1.31	1.360	2.3	2.05	2.160	0.9	2.93	3.060	1.1
	3	8.98		2.8	15.01		1.7	9.77		0.7	4.13		2.7	6.71		1.3	9.22		1.9
	5	14.68		1.4	25.10		2.1	15.82		1.1	6.99		2.6	11.01		1.8	15.93		3.1
IPA	1	–[d]	–	–	0.03	0.030	0.7	0.02	0.018	1.3	–	–	–	–	–	–	–	–	–
	3	–		–	0.09		0.9	0.06		1.8	–		–	–		–	–		–
	5	–		–	0.15		1.5	0.09		2.6	–		–	–		–	–		–
IBA	1	3.67	3.790	3.4	2.79	2.870	2.1	1.78	1.910	0.8	2.05	2.160	1.8	2.79	2.880	0.9	2.10	2.270	1.6
	3	11.65		2.1	8.68		3.0	5.99		1.2	6.67		1.2	8.59		0.7	7.00		0.6
	5	19.12		1.8	14.57		1.3	9.76		0.7	11.01		1.2	14.99		1.5	11.90		2.4
1-NAA	1	8.15	8.290	1.6	–	–	–	0.03	0.042	1.1	–	–	–	0.03	0.037	0.9	–	–	–
	3	24.88		1.9	–		–	0.13		1.4	–		–	0.11		1.6	–		–
	5	42.10		1.0	–		–	0.26		1.8	–		–	0.19		1.2	–		–
2-NAA	1	10.67	10.850	3.8	0.03	0.034	1.5	0.04	0.039	3.1	0.02	0.017	1.8	0.04	0.040	1.9	0.03	0.026	3.2
	3	32.73		2.5	0.10		1.7	0.12		2.7	0.06		0.7	0.12		2.0	0.08		1.3
	5	54.79		2.3	0.19		1.2	0.19		2.6	0.08		1.3	0.21		1.5	0.14		1.9

[a]Weighed three amount levels of samples. [b]The average contents of GA_3, IAA, IPA, IBA, 1-NAA, and 2-NAA in oil samples. [c]The relative standard deviation (n = 6). [d]–, not found.

DOI: 10.1021/acs.jafc.5b02489
J. Agric. Food Chem. 2015, 63, 8058−8067

this study reflects the advantages of nontransgenic food as well as transgenic foods in terms of some nutrients. Consequently, PGR-induced nutrient variation is promising to be an important index for the objective evaluation of transgenic foods.

On the other hand, for transgenic foods, what should be explored is which and how many genes are directly or indirectly modified. As the ending point of the signal transduction system, variations of genetic trait and composition are reflected by PGRs.[3−5] GA_3 was biosynthesized with the aid of two essential genes (copalyl pyrophosphate synthase and ent-kaurene synthase); thus, its higher levels in nontransgenic samples (rapeseed oil, 8.86 $\mu g\ g^{-1}$; sunflower oil, 7.66 $\mu g\ g^{-1}$) indicated these two genes would decrease after the plant was gene-modified.[10] Similarly, tryptophan monooxygenase and indoleacetamide hydrolase were higher in transgenic rapeseed oil.[12,50] IPA was found in transgenic rapeseed oil (0.03 $\mu g\ g^{-1}$) and nontransgenic soybean oil (0.018 $\mu g\ g^{-1}$), implying that the tryptophan aminotransferase genes in transgenic rapeseed and nontransgenic soybean were relatively higher.[14] The higher IBA level in nontransgenic rapeseed oil (3.79 $\mu g\ g^{-1}$), transgenic soybean oils (2.16 $\mu g\ g^{-1}$), and nontransgenic sunflower oils (2.88 $\mu g\ g^{-1}$) might indicate the higher content of glutamate-γ-semialdehyde participating in the biosynthesis of IBA via the tryptophan pathway.[13] Therefore, the results might reflect the PGR-induced genetic variation in addition to artificial gene modification, which is an added benefit of PGRs determination.

■ ASSOCIATED CONTENT

Supporting Information

The Supporting Information is available free of charge on the ACS Publications website at DOI: 10.1021/acs.jafc.5b02489.

Figures of single-variable experiments and mass spectrum and tables of recovery, matrix effect, stability, method comparison, and content (PDF)

■ AUTHOR INFORMATION

Corresponding Authors

*(G.C.) Mail: Key Laboratory of Pharmaceutical Intermediates and Analysis of Natural Medicine, Qufu Normal University, Qufu, China. Phone: +86 537 4456305. Fax: +86 537 4456305. E-mail: chenandguang@163.com.

*(J.Y.) E-mail: jmyou6304@163.com.

Author Contributions

‖M.L. and G.C. contributed equally to this work.

Funding

This work was supported by the Natural Science Foundation of Shandong Province, China (ZR2013BQ019) and the National Natural Science Foundation of China (General Program) (21475074). This research work was supported by the Open Funds of the Shandong Province Key Laboratory of Detection Technology for Tumor Markers (KLDTTM2015-6), the Undergraduate Technology Innovation Project (201410446021), the National Natural Science Foundation of China (General Program) (21475075), the 100 Talents Program of The Chinese Academy of Sciences (328), the National Natural Science Foundation of China (General Program) (21275089), the National Natural Science Foundation of China (21405093, 21405094, 81303179, 31301595, 21305076, 21302110, 21402106), the Natural Science Foundation of Shandong Province, China (ZR2014BM029), the Key Laboratory of Bioorganic Analysis Shandong Province, and the Key Laboratory of Pharmaceutical Intermediates and Analysis of Natural Medicine Shandong Province.

Notes

The authors declare no competing financial interest.

■ REFERENCES

(1) Giannakoula, A. E.; Ilias, I. F.; Dragišić Maksimović, J. J.; Maksimović, V. M.; Živanović, B. D. The effects of plant growth regulators on growth, yield, and phenolic profile of lentil plants. *J. Food Compos. Anal.* **2012**, *28*, 46−53.

(2) Lee, J. J.; Woodward, A. W.; Chen, Z. J. Gene expression changes and early events in cotton fibre development. *Ann. Bot.* **2007**, *100*, 1391−1401.

(3) Davies, P. J. Regulatory factors in hormone action: level, location and signal transduction. In *Plant Hormones: Biosynthesis, Signal Transduction, Action!*, 3rd ed.; Davies, P. J., Ed.; Kluwer Academic: Dordrecht, The Netherlands, 2004; pp 16−35.

(4) Chapman, E. J.; Estelle, M. Mechanism of auxin-regulated gene expression in plants. *Annu. Rev. Genet.* **2009**, *43*, 265−285.

(5) Hagen, G.; Guilfoyle, T. Auxin-responsive gene expression: genes, promoters and regulatory factors. *Plant Mol. Biol.* **2002**, *49*, 373−385.

(6) Wilkinson, J. Q.; Lanahan, M. B.; Yen, H. C.; Giovannoni, J. J.; Klee, H. J. An ethylene-inducible component of signal transduction encoded by Never-ripe. *Science* **1995**, *270*, 1807−1809.

(7) Santner, A.; Estelle, M. Recent advances and emerging trends in plant hormone signalling. *Nature* **2009**, *459*, 1071−1078.

(8) Groat, J.; Briggs, D. Gibberellins and α-amylase formation in germinating barley. *Phytochemistry* **1969**, *8*, 1615−1627.

(9) Kaneko, M.; Itoh, H.; Ueguchi-Tanaka, M.; Ashikari, M.; Matsuoka, M. The α-amylase induction in endosperm during rice seed germination is caused by gibberellin synthesized in epithelium. *Plant Physiol.* **2002**, *128*, 1264−1270.

(10) Hedden, P.; Phillips, A. L. Gibberellin metabolism: new insights revealed by the genes. *Trends Plant Sci.* **2000**, *5*, 523−530.

(11) Patten, C. L.; Glick, B. R. Bacterial biosynthesis of indole-3-acetic acid. *Can. J. Microbiol.* **1996**, *42*, 207−220.

(12) Schröder, G.; Waffenschmidt, S.; Weiler, E. W.; Schröder, J. The T-region of Ti plasmids codes for an enzyme synthesizing indole-3-acetic acid. *Eur. J. Biochem.* **1984**, *138*, 387−391.

(13) Epstein, E.; Ludwig-Müller, J. Indole-3-butyric acid in plants: occurrence, synthesis, metabolism and transport. *Physiol. Plant.* **1993**, *88*, 382−389.

(14) Bartel, B. Auxin biosynthesis. *Annu. Rev. Plant Physiol. Plant Mol. Biol.* **1997**, *48*, 51−66.

(15) Ewen, S. W.; Pusztai, A. Effect of diets containing genetically modified potatoes expressing *Galanthus nivalis* lectin on rat small intestine. *Lancet* **1999**, *354*, 1353−1354.

(16) Losey, J. E.; Rayor, L. S.; Carter, M. E. Transgenic pollen harms monarch larvae. *Nature* **1999**, *399*, 214−214.

(17) Durgbanshi, A.; Arbona, V.; Pozo, O.; Miersch, O.; Sancho, J. V.; Gomez-Cadenas, A. Simultaneous determination of multiple phytohormones in plant extracts by liquid chromatography-electrospray tandem mass spectrometry. *J. Agric. Food Chem.* **2005**, *53*, 8437−8442.

(18) Han, Z.; Liu, G.; Rao, Q.; Bai, B.; Zhao, Z.; Liu, H.; Wu, A. A liquid chromatography tandem mass spectrometry method for simultaneous determination of acid/alkaline phytohormones in grapes. *J. Chromatogr. B: Anal. Technol. Biomed. Life Sci.* **2012**, *881*, 83−89.

(19) Segura Carretero, A.; Cruces-Blanco, C.; Soriano Peña, M.; Cortacero Ramírez, S.; Fernández Gutiérrez, A. Determination of phytohormones of environmental impact by capillary zone electrophoresis. *J. Agric. Food Chem.* **2004**, *52*, 1419−1422.

(20) Chen, H.; Guo, X. F.; Zhang, H. S.; Wang, H. Simultaneous determination of phytohormones containing carboxyl in crude extracts of fruit samples based on chemical derivatization by capillary electrophoresis with laser-induced fluorescence detection. *J. Chromatogr. B: Anal. Technol. Biomed. Life Sci.* **2011**, *879*, 1802−1808.

(21) Birkemeyer, C.; Kolasa, A.; Kopka, J. Comprehensive chemical derivatization for gas chromatography−mass spectrometry-based multi-targeted profiling of the major phytohormones. *J. Chromatogr. A* **2003**, *993*, 89−102.
(22) Giannarelli, S.; Muscatello, B.; Bogani, P.; Spiriti, M.; Buiatti, M.; Fuoco, R. Comparative determination of some phytohormones in wild-type and genetically modified plants by gas chromatography−mass spectrometry and high-performance liquid chromatography−tandem mass spectrometry. *Anal. Biochem.* **2010**, *398*, 60−68.
(23) Pan, X.; Welti, R.; Wang, X. Quantitative analysis of major plant hormones in crude plant extracts by high-performance liquid chromatography−mass spectrometry. *Nat. Protoc.* **2010**, *5*, 986−992.
(24) Li, G.; Liu, S.; Sun, Z.; Xia, L.; Chen, G.; You, J. A simple and sensitive HPLC method based on pre-column fluorescence labelling for multiple classes of plant growth regulator determination in food samples. *Food Chem.* **2015**, *170*, 123−130.
(25) Liu, X.; Ma, L.; Lin, Y.; Lu, Y. Determination of abscisic acid by capillary electrophoresis with laser-induced fluorescence detection. *J. Chromatogr. A* **2003**, *1021*, 209−213.
(26) De Toledo, R.; Vaz, C. Use of a graphite−polyurethane composite electrode for electroanalytical determination of indole-3-acetic acid in soil samples. *Microchem. J.* **2007**, *86*, 161−165.
(27) Liu, S.; Chen, W.; Qu, L.; Gai, Y.; Jiang, X. Simultaneous determination of 24 or more acidic and alkaline phytohormones in femtomole quantities of plant tissues by high-performance liquid chromatography−electrospray ionization−ion trap mass spectrometry. *Anal. Bioanal. Chem.* **2013**, *405*, 1257−1266.
(28) Wu, Y.; Hu, B. Simultaneous determination of several phytohormones in natural coconut juice by hollow fiber-based liquid−liquid−liquid microextraction-high performance liquid chromatography. *J. Chromatogr. A* **2009**, *1216*, 7657−7663.
(29) Kristl, J.; Krajnčič, B.; Brodnjak-Vončina, D.; Veber, M. Evaluation of measurement uncertainty in the determination of jasmonic acid in Lemna minor L. by liquid chromatography with fluorescence detection. *Accredit. Qual. Assur.* **2007**, *12*, 303−310.
(30) Ross, A. R.; Ambrose, S. J.; Cutler, A. J.; Allan Feurtado, J.; Kermode, A. R.; Nelson, K.; Zhou, R.; Abrams, S. R. Determination of endogenous and supplied deuterated abscisic acid in plant tissues by high-performance liquid chromatography-electrospray ionization tandem mass spectrometry with multiple reaction monitoring. *Anal. Biochem.* **2004**, *329*, 324−333.
(31) Chen, M.; Fu, X.; Liu, J.; Ye, T.; Hou, S.; Huang, Y.; Yuan, B.; Wu, Y.; Feng, Y. Highly sensitive and quantitative profiling of acidic phytohormones using derivatization approach coupled with nano-LC-ESI-Q-TOF-MS analysis. *J. Chromatogr. B: Anal. Technol. Biomed. Life Sci.* **2012**, *905*, 67−74.
(32) Xue, J.; Wang, S.; You, X.; Dong, J.; Han, L.; Liu, F. Multi-residue determination of plant growth regulators in apples and tomatoes by liquid chromatography/tandem mass spectrometry. *Rapid Commun. Mass Spectrom.* **2011**, *25*, 3289−3297.
(33) Li, Y.; Wei, F.; Dong, X.; Peng, J.; Liu, S.; Chen, H. Simultaneous analysis of multiple endogenous plant hormones in leaf tissue of oilseed rape by solid-phase extraction coupled with high-performance liquid chromatography−electrospray ionisation tandem mass spectrometry. *Phytochem. Anal.* **2011**, *22*, 442−449.
(34) Pan, X.; Welti, R.; Wang, X. Simultaneous quantification of major phytohormones and related compounds in crude plant extracts by liquid chromatography−electrospray tandem mass spectrometry. *Phytochemistry* **2008**, *69*, 1773−1781.
(35) Mao, X.; Tang, L.; Tan, T.; Wan, Y. Determination of plant growth regulators in pears by microwave-assisted extraction and liquid chromatography with electrospray ionization mass spectrometry. *J. Sep. Sci.* **2014**, *37*, 1352−1358.
(36) Chen, H.; Zhang, Z.; Zhang, G.; Guo, X.; Zhang, H.; Wang, H. Liquid chromatographic determination of endogenous phytohormones in vegetable samples based on chemical derivatization with 6-oxy (acetylpiperazine) fluorescein. *J. Agric. Food Chem.* **2010**, *58*, 4560−4564.
(37) Xiong, X.; Rao, W.; Guo, X.; Wang, H.; Zhang, H. Ultrasensitive determination of jasmonic acid in plant tissues using high-performance liquid chromatography with fluorescence detection. *J. Agric. Food Chem.* **2012**, *60*, 5107−5111.
(38) Grigor'eva, N. Y.; Kucherov, V. Gibberellins. *Russ. Chem. Rev.* **1966**, *35*, 850−863.
(39) Powell, L. E.; Tautvydas, K. J. Chromatography of gibberellins on silica gel partition columns. *Nature* **1967**, *213*, 292−293.
(40) Chatfield, S. P.; Stirnberg, P.; Forde, B. G.; Leyser, O. The hormonal regulation of axillary bud growth in *Arabidopsis*. *Plant J.* **2000**, *24*, 159−169.
(41) Coggins, C. W., Jr; Jolliffe, V. A.; Shindy, W. W.; Knapp, J. C. Naphthaleneacetic acid disappearance and residue studies in citrus. *J. Agric. Food Chem.* **1972**, *20*, 76−79.
(42) Wu, H.; Li, G.; Liu, S.; Liu, D.; Chen, G.; Hu, N.; Suo, Y.; You, J. Simultaneous determination of six triterpenic acids in some Chinese medicinal herbs using ultrasound-assisted dispersive liquid−liquid microextraction and high-performance liquid chromatography with fluorescence detection. *J. Pharm. Biomed. Anal.* **2015**, *107*, 98−107.
(43) Sparr Eskilsson, C.; Björklund, E. Analytical-scale microwave-assisted extraction. *J. Chromatogr. A* **2000**, *902*, 227−250.
(44) Liu, J.; Liu, M.; Li, X.; Lu, X.; Chen, G.; Sun, Z.; Li, G.; Zhao, X.; Zhang, S.; Song, C. Development of ultrasonic-assisted closed in-syringe extraction and derivatization for the determination of labile abietic acid and dehydroabietic acid in cosmetics. *J. Chromatogr. A* **2014**, *1371*, 20−29.
(45) Li, G.; Zhang, X.; You, J.; Song, C.; Sun, Z.; Xia, L.; Suo, Y. Highly sensitive and selective pre-column derivatization high-performance liquid chromatography approach for rapid determination of triterpenes oleanolic and ursolic acids and application to *Swertia* species: optimization of triterpenic acids extraction and pre-column derivatization using response surface methodology. *Anal. Chim. Acta* **2011**, *688*, 208−218.
(46) Modarres, R. Multi-criteria validation of artificial neural network rainfall-runoff modeling. *Hydrol. Earth Syst. Sci.* **2009**, *13*, 411−421.
(47) Gibson, S. I. Sugar and phytohormone response pathways: navigating a signalling network. *J. Exp. Bot.* **2004**, *55*, 253−264.
(48) Jacobsen, J.; Beach, L. Control of transcription of α-amylase and rRNA genes in barley aleurone protoplasts by gibberellin and abscisic acid. *Nature* **1985**, *316*, 275−277.
(49) Wang, Y.; Yang, X.; Zhang, X. Effects of growth regulators on the main characters and fatty acid composition of perilla. *J. Southwest Univ. (Nat. Sci.)* **2014**, *36*, 88−92 (in Chinese).
(50) Endo, S.; Kasahara, T.; Sugita, K.; Ebinuma, H. A new GST-MAT vector containing both ipt and iaaM/H genes can produce marker-free transgenic tobacco plants with high frequency. *Plant Cell Rep.* **2002**, *20*, 923−928.

DOI: 10.1021/acs.jafc.5b02489
J. Agric. Food Chem. 2015, 63, 8058−8067

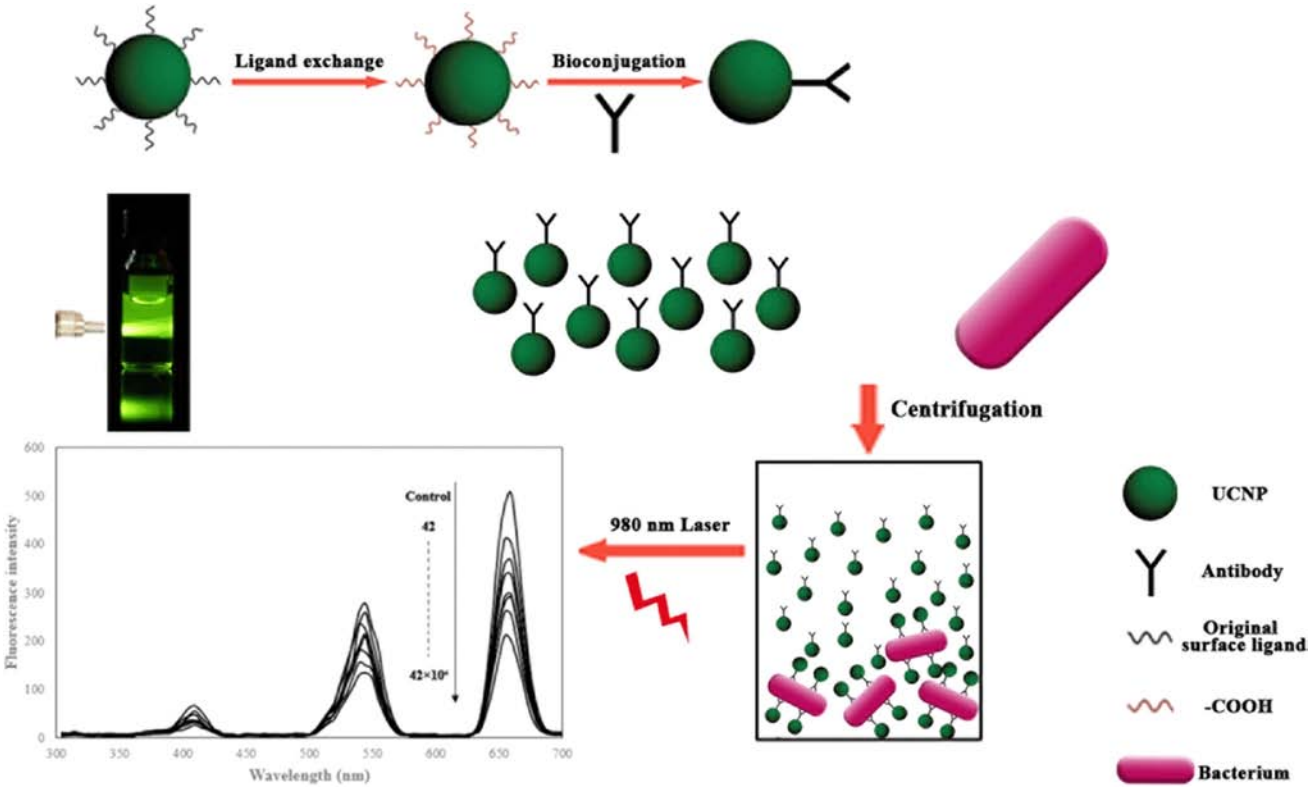

Figure 1. Scheme of this proposed fluorescence bioassay platform.

UCNPs have low toxicities in vitro and in vivo, which are therefore suitable for biological applications.[30,31]

The main objective of this study was to develop a photostable and selective fluorescent probe for rapidly sensing pathogens in food. Figure 1 presents the scheme of this proposed fluorescence bioassay platform. Specific procedures are outlined as follows. (1) Upconversion nanoparticles (UCNPs) were synthesized and functionalized. (2) The resultant water-soluble UCNPs were conjugated with anti-*E. coli* antibodies to produce biological fluorescent probes. (3) A fluorescence standard curve was prepared with different concentrations of *E. coli*. (4) Independent food samples were tested. As an efficient, specific, and technically simple biological probe, these selective sensors can be used for rapidly detecting pathogens in food.

MATERIALS AND METHODS

Reagents. The rare earth salts used in this work, including YCl_3, $YbCl_3$, and $ErCl_3$, were of 99.99% purity and were purchased from Aladdin Industrial, Inc. (Shanghai, China). Methanol, ethanol, oleic acid, 1-octadecene, cyclohexane, toluene, sodium citrate, diethylene glycol, 1-ethyl 3-[3-(dimethylamino)propyl]carbodiimide hydrochloride (EDC), tryptone, beef extract, NaCl, agar, NH_4F, and NaOH were of analytical grade and were purchased from Sinopharm Chemical Reagent Co., Ltd. (Shanghai, China). *N*-Hydroxysuccinimide (NHS) was obtained from Adamas Reagent Co., Ltd. (Shanghai, China). *E. coli* strain O157:H7 (NCTC 12900-2) was purchased from American Type Culture Collection (Manassas, VA), and the corresponding anti-*E. coli* antibody (ab75244) was purchased from Abcam Co., Ltd.

Instruments. X-ray diffraction (XRD) measurements were performed using a D8-advance instrument (Bruker AXS, Ltd.). The size and morphology of UCNPs, UCNP antibodies, and UCNP antibody−*E. coli* complexes were determined using a JEM-2100HR transmission electron microscope (TEM, JEOL, Ltd.) operated at 200 kV. Upconversion fluorescence spectra were measured using a Cary Eclipse fluorescence spectrophotometer (Varian Inc.) modified with an external 0−1300 mW adjustable continuous wave 980 nm laser (Beijing Hi-Tech Optoelectronic Co., Beijing, China). Fourier transform infrared (FT-IR) spectra were obtained using a Nicolet Nexus 470 Fourier transform infrared spectrophotometer (Thermo Electron Co.) with the KBr method.

Synthesis of Water-Soluble Upconversion Nanoparticles (UCNPs). Oleic acid-capped $NaYF_4$:Yb,Er UCNPs were synthesized according to the method reported in refs 32−34 with a few modifications. In a typical experiment, 2 mL of $RECl_3$ [0.2 M; RE = Y (78%), Yb (20%), or Er (2%)] in methanol was added to a 50 mL flask containing 3 mL of oleic acid and 7 mL of 1-octadecene. The prepared solution was heated to 160 °C for 30 min and cooled to room temperature. Thereafter, 5 mL of a methanol solution of NH_4F (1.6 mmol) and NaOH (1 mmol) was added, and the solution was stirred for 30 min. After the methanol evaporated, the solution was heated to 300 °C under argon for 1.5 h and cooled to room temperature. The resulting nanoparticles were precipitated by the addition of ethanol, collected by centrifugation, washed with methanol and ethanol several times, and finally dried in an oven at 60 °C.

The obtained oleic acid-capped UCNPs dispersed well in nonpolar solvents. However, for biological applications, hydrophilic UCNPs are required for compatibility with biomolecules,[35] such as antibodies. Hydrophobic UCNPs were surface-modified via a ligand exchange process as described in ref 20. Briefly, a mixture of 2 mmol of sodium citrate in 15 mL of diethylene glycol was first heated to 110 °C under argon for 30 min. Oleic acid-capped UCNPs (10 mg) were dispersed in cyclohexane. Toluene was added to the mixture, and the reaction mixture was heated to 160 °C to evaporate the cyclohexane and toluene. After the evaporation, the reaction mixture was further maintained at 160 °C for 3 h. Subsequently, water-soluble UCNPs were collected by centrifugation, washed with ethanol and ultrapure water several times, and finally dispersed in ultrapure water.

Bioconjugation of UCNPs with Anti-*E. coli* Antibodies. The bioconjugation of UCNPs with anti-*E. coli* antibodies was performed by EDC/NHS linking chemistry. Here, UCNPs (5 mg/mL in water) were activated with EDC (25 μL, 2 mg/mL) and NHS (12.5 μL, 2

DOI: 10.1021/acs.jafc.5b02331
J. Agric. Food Chem. 2015, 63, 8068−8074

mg/mL) for approximately 3 h at room temperature. The activated UCNPs were purified by centrifugation at 9350*g* for 15 min and redispersed in ultrapure water. Subsequently, 50 μg of anti-*E. coli* antibody was incubated with 1 mg of activated UCNPs. After being shaken overnight at 4 °C, unbound UCNPs were removed by centrifugation at 6000*g* for 5 min at 4 °C. The bioconjugated particles were washed once with ultrapure water and then redispersed in ultrapure water. The centrifugation parameters, i.e., 6000*g* for 5 min, were optimized in preliminary tests with purely water-soluble UCNPs. The obtained UCNP antibody precipitates were validated by FTIR spectra measurements.

Immunoassay Procedure. *Bacterial Culture and Preparation.* Stock cultures of *E. coli* (NCTC 12900-2) were inoculated and grown in Luria-Bertani (LB) medium for 24 h at 37 °C. The cultures were pelleted by centrifugation at 5000*g* for 5 min, washed twice with ultrapure water, and redispersed in ultrapure water. Thereafter, serial 10-fold dilutions were prepared in ultrapure water to produce various concentrations [$1-10^8$ colony-forming units (cfu)/mL] of bacteria. Bacterial counts were determined using the colony counting method.

Capturing Bacteria with UCNP Antibody Probes. The UCNP–antibody (100 μL, 1 mg/mL) probes were mixed with various concentrations ($1-10^8$ cfu/mL) of bacteria and incubated for 2 h at 37 °C with agitation. As a control, 500 μL of ultrapure water was also treated. Thereafter, the reaction suspensions were pelleted by centrifugation at 5000*g* for 5 min to separate redundant UCNP–antibody probes. The resulting supernatants were used to monitor changes in emission fluorescence intensity.

Fluorescence Spectral Measurement. The fluorescence spectra of the obtained supernatants (from 400 to 700 nm) were measured with a fluorescence spectrophotometer equipped with a 980 nm excitation laser at 1.3 W. The intensity differences ($\Delta I = I_0 - I$) between the supernatants and the control (I_0) were used to generate a standard curve against the bacterial concentration (log cfu/mL). Here, the 657 nm peak intensity emission wavelength was used.

RESULTS AND DISCUSSION

Characterization. In this work, bacterium-specific antibodies with high selectivity and sensitivity were conjugated onto the surface of UCNPs to yield UCNP–antibody probes, as illustrated in Figure 1. Prior to the conjugation, the precursor UCNPs were first characterized by X-ray diffraction (XRD), as shown in Figure 2. Here, the diffraction peaks of the XRD pattern were identified as pure hexagonal β-phase $NaYF_4$ crystals (JCPDS Standard Card No. 16-0334); no diffraction peaks corresponding to cubic phase crystals or other impurities were observed. Furthermore, successful bioconjugation, selectivities, sizes, and luminance and spectral properties of UCNPs before and after surface modification were validated by transmission electron microscopy (TEM) and by fluorescence spectral measurements, as presented in Figure 3. The TEM images confirmed the hexagonal UCNP structures and revealed that the particles were uniform with an average diameter of approximately 50 nm before and after surface modification and bioconjugation. The fluorescence spectra of the UCNPs showed the expected characteristic emission peaks at approximately 407, 542, and 657 nm upon NIR (980 nm) excitation, corresponding to blue, green, and red light, respectively (the naked-eye images in the inset show the visible intensity of the UCNPs). The peaks are ascribed to the transitions from the $^2H_{9/2}$, $^4S_{3/2}$, and $^4F_{9/2}$ levels to the $^4I_{15/2}$ ground state of the Er^{3+} ion.[36−38] Additionally, the fluorescence properties were also retained, as both the UCNP antibodies and the UCNPs showed the same characteristic emission peaks upon NIR excitation. When mixed with bacteria, the fluorescence intensity of the supernatant decreased, as shown in Figure 3D. The inset TEM image shows electron-dense dark spheres with diameters of approximately 50 nm, which correspond to the sizes of the UCNPs; these spheres decorated the outer surface of the bacterial cells. Negligible intensity signals were observed within the cytoplasm of the UCNP-labeled bacteria, indicating that the UCNPs were not internalized.

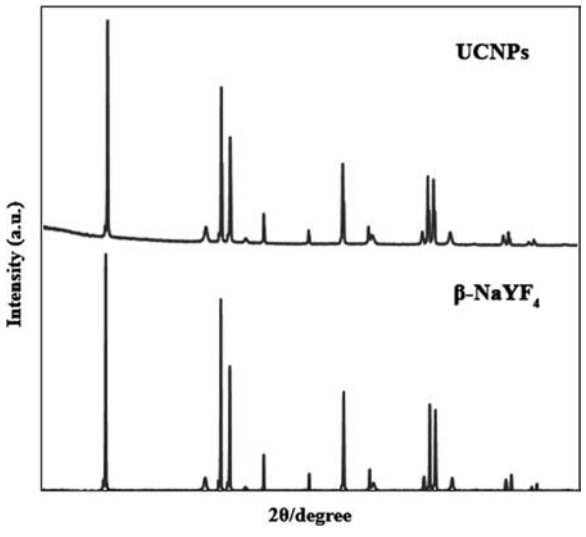

Figure 2. X-ray diffraction (XRD) pattern of oleic acid-capped UCNPs.

Figure 4 displays the Fourier transform infrared (FT-IR) spectra of UCNPs (A), UCNP–antibody probes (B), and UCNP–antibody–bacterium complexes (C), confirming the presence of antibodies on the UCNPs and the presence of UCNP–antibody probes on the bacteria. The water-soluble UCNPs presented with a single broad peak at 3427 cm^{-1}, corresponding to the stretching vibration of hydroxide radicals (-OH). The characteristic peak at 1629 cm^{-1} is related to the asymmetric stretching vibration of carboxyl groups (-COOH) of the citrate ligands on the surface of the UCNPs. These two peaks indicated that the carboxyl groups from the ligand exchange were successfully modified on the surface of UCNPs to produce water-soluble UCNPs. When the EDC/NHS-prepared antibodies were introduced, three characteristic peaks at 2360, 2335, and 1396 cm^{-1} appeared. The peaks at 2360 and 2335 cm^{-1} corresponded to methylene stretching vibrations ($-CH_2-$). The peak at 1396 cm^{-1} corresponded to carboxyl stretching vibrations (COO-) due to the linking reaction between the water-soluble UCNPs and the antibodies. Furthermore, a new peak was observed at 1540 cm^{-1} upon comparison of the spectra of the UCNP–antibody–bacterium complex and the UCNP–antibody probe; this peak is attributed to the distinct amide I and amide II vibration modes characteristic of bacterial proteins and peptides.

On the basis of these characterizations, the proposed UCNP-based method is suitable for sensing bacteria.

Evaluation of Specificity. To evaluate the specificity of the fluorescent probe for *E. coli*, two commonly encountered foodborne pathogens, *Staphylococcus aureus* (ATCC 25923) and *Salmonella typhimurium* (ATCC 14028), were tested. The results are shown in Figure 5 (the concentrations of these bacteria were 10^2 cfu/mL, and the figure was plotted with a peak intensity at 657 nm). Both *S. aureus* and *Sa. typhimurium* induced negligible changes in the fluorescence intensity,

DOI: 10.1021/acs.jafc.5b02331
J. Agric. Food Chem. 2015, 63, 8068−8074

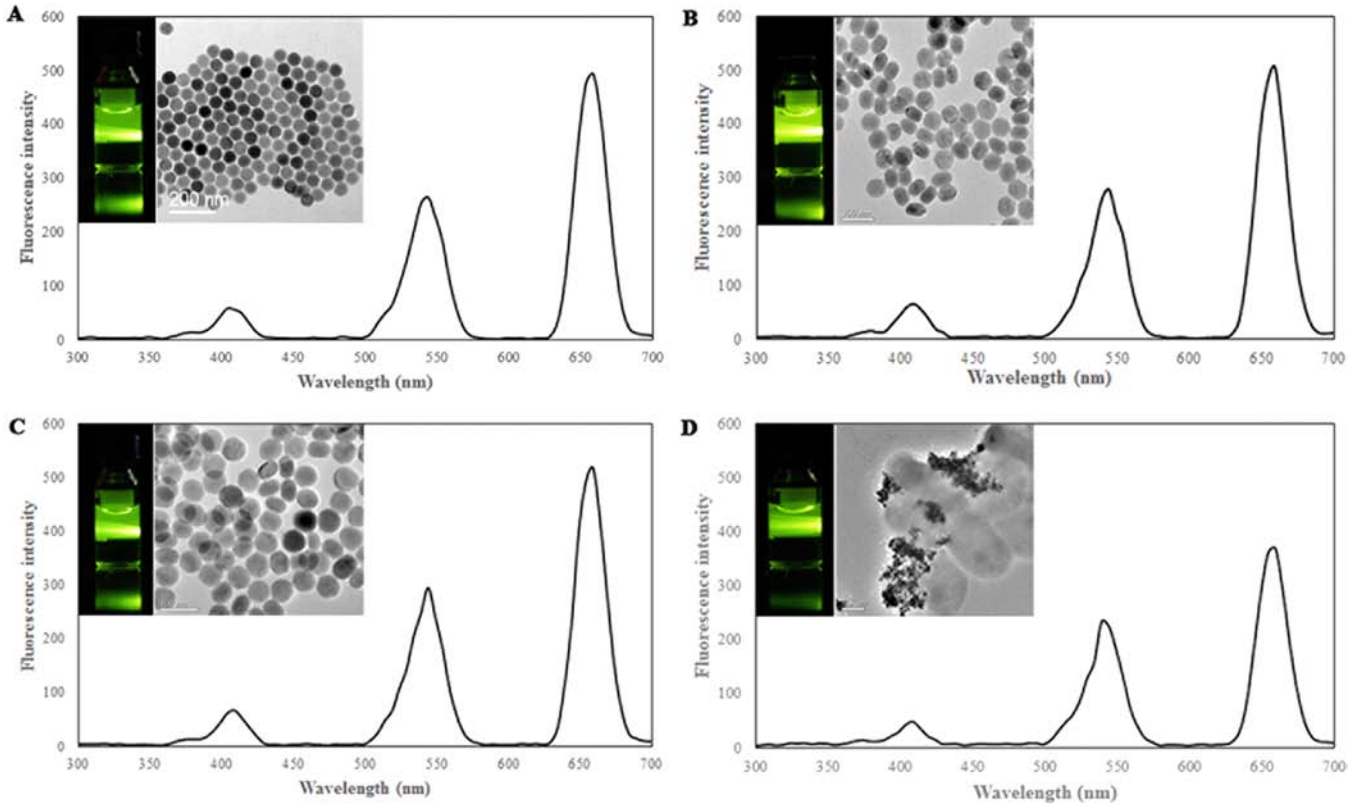

Figure 3. Fluorescence properties of oleic acid-capped UCNPs (A), water-soluble UCNPs (B), bioconjugated UCNPs (C), and UCNP−antibody−bacterium complexes (D). Insets show naked-eye photographs and TEM images of particles.

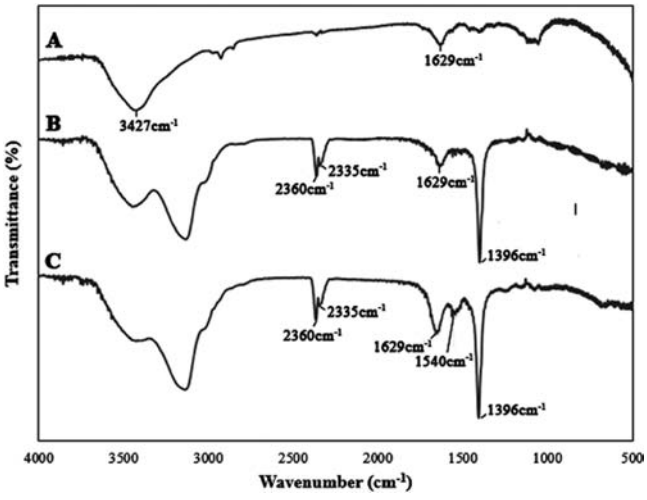

Figure 4. Fourier transform infrared (FT-IR) spectra of UCNPs (A), UCNP−antibody probes (B), and UCNP−antibody−bacterium complexes (C).

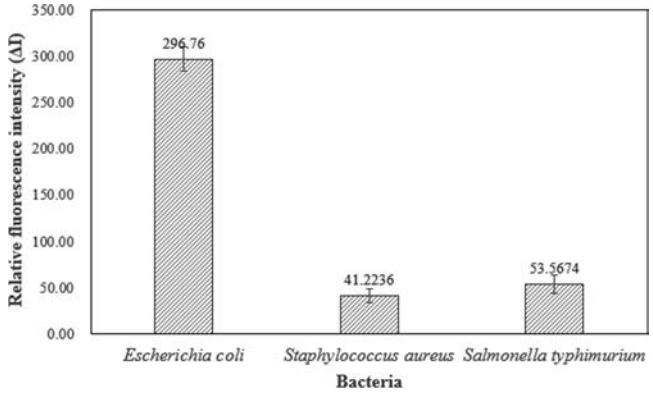

Figure 5. Specific selectivity evaluation of the proposed method for *E. coli* (10^2 cfu/mL) against other bacteria (10^2 cfu/mL).

whereas a significant change was observed for *E. coli*. These results show the specificity of the designed fluorescent probe for *E. coli*.

Bacterial Detection. In a typical experiment, different concentrations of *E. coli* were incubated under agitation with the UCNP−antibody probes for 2 h at 37 °C. On the basis of the specificity of the antibody for the bacteria, UCNP−antibody−bacterium complexes were formed. The samples were subsequently concentrated and separated by centrifugation at 5000*g* for 5 min to separate the unbound UCNP−antibody probes. The centrifugation parameters were previously optimized to maximize the separation of the complex without disrupting the UCNP−antibody probes.

Thereafter, serial dilutions of the supernatants were prepared to examine the fluorescence spectra of the complexes. The 657 nm emission peak was used to monitor the *E. coli* concentration. In the absence of bacteria (i.e., the control), the fluorescence intensity of the supernatant was at a maximum. In the presence of bacteria, the decrease in the fluorescence intensities (ΔI) of the supernatants varied proportionally with the concentration of bacteria. Selections of fluorescence spectra of bacterium-containing supernatants (log cfu/mL) are shown in Figure 6; the fluorescence intensity rapidly decreased as the *E. coli* concentration increased from 42 to 42 × 10^6 cfu/mL. A strong linear correlation (R^2 = 0.9802) was obtained between

DOI: 10.1021/acs.jafc.5b02331
J. Agric. Food Chem. 2015, 63, 8068−8074

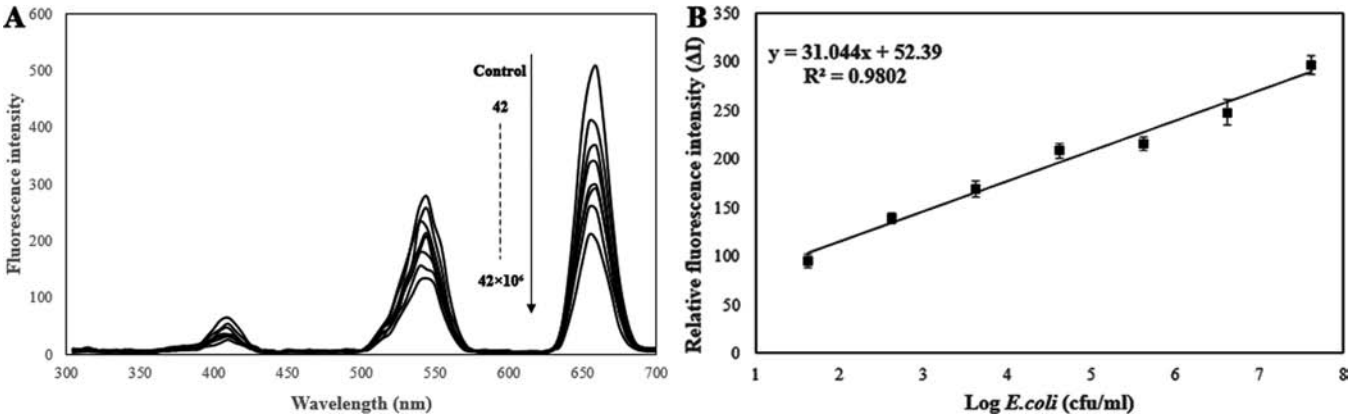

Figure 6. (A) Typical recording output for detecting different concentrations of *E. coli* using the proposed method. (B) Standard curve of the decreased upconversion fluorescence intensity ($\Delta I = I_0 - I$) vs the concentration of *E. coli*.

Table 1. Comparison of the Linear Ranges and LODs of Several Selected Fluorescence-Capturing Methods for Bacterial Detection

material	linear range (cfu/mL)	LOD (cfu/mL)	ref
organic dye	10^4–10^7	10^4	39
organic dye coated with antibody	10–10^4	5	40
lysozyme AuNCs	2.4×10^4 to 6.0×10^6	2×10^4	41
quantum dots (QDs) coated with streptavidin	10^3–10^7	10^3	42
CdTe QDs coated with antibody	3×10^2 to 3×10^7	1×10^2	43
CdSe/ZnS QDs coated with antibody	not mentioned	10	44
UCNPs	42–42×10^6	10	this work

the relative intensity of the upconversion fluorescence and the concentration of *E. coli*: $\Delta I = 31.044c + 52.39$ (c = log cfu/mL). The sensitivity of the developed immunoassay was also investigated. The limit of detection (LOD) is defined as LOD = $3S_0/K$, where S_0 is the standard deviation of n control measurements (n = 10) and K is the slope of the calibration graph. In this work, the LOD of the proposed *E. coli*-sensing method was 10 cfu/mL. The total detection time from the addition of the fluorescent probes to the detection solution to obtaining the final result was <3 h (the water-soluble UCNPs can be produced on a large scale because of their high photostability and stored under appropriate conditions).

Analytical Performance. For comparative purposes, the linear ranges and LODs of several fluorescence-based capturing methods for detecting pathogens are summarized in Table 1. The proposed UCNP-based method has a relatively low LOD compared with those of conventional fluorescence-based capturing methods. Conventional fluorescent dyes are subject to photobleaching, photodamage, and autofluorescence issues; QDs also generate background autofluorescence because a shorter excitation wavelength is used to excite the nanoparticles. The proposed method has overcome these problems and provides a wider detection range and higher sensitivity. Additionally, fluorescent dyes based on antibody–antigen interactions typically achieve better selectivity but cannot be prepared on large scales because of photobleaching and photodamage.[44] The prepared UCNPs had reduced photodamage and prolonged photostability, i.e., properties suitable for industrial processing.

Analytical Applications. To further evaluate the feasibility and reliability of the proposed UCNP-based method for practical applications, the designed fluorescent probes were used to detect *E. coli* in solid (pork) and liquid (milk) samples adulterated with specific amounts of *E. coli*. Prior to probing, a series of pretreatment procedures were performed. For the milk samples, 5 mL of each sample was centrifuged at 7000*g* for 10 min at 10 °C. The upper layer of cream was removed, and the milk was diluted with distilled water at a 1:20 ratio. Finally, the

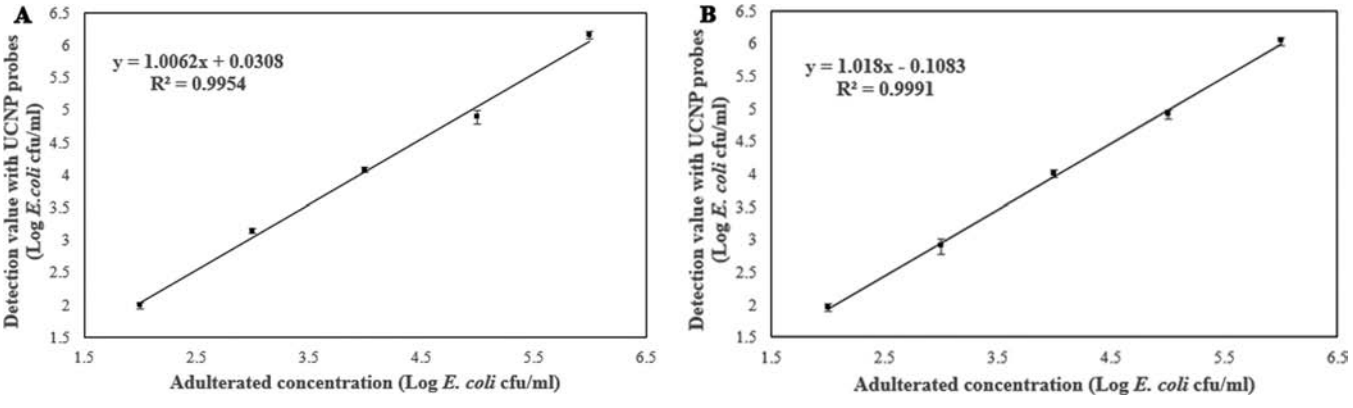

Figure 7. Standard graphs for detecting *E. coli* in milk (A) and pork (B) samples using the proposed UCNP-based method.

DOI: 10.1021/acs.jafc.5b02331
J. Agric. Food Chem. 2015, 63, 8068–8074

supernatant was filtered with a disposable syringe filter holder. For the pork samples, 25 g of pork was aseptically dipped in 225 mL of alkaline peptone with 3% (w/v) NaCl, homogenized for 5 min, and allowed to stand for 30 min to precipitate macroaggregates and seston. Finally, the supernatant was filtered through a 0.45 μm filtration membrane. After these pretreatment steps, both the pretreated and raw adulterated samples were probed using the UCNP-based probes. As shown in Figure 7, the results were similar and highly correlated. This confirmed that the proposed detection method using fluorescent probes can be applied to the detection of bacteria in real samples.

In this study, sensitive fluorescent probes consisting of upconversion nanoparticles conjugated with antibodies were prepared for the rapid detection of bacterial contaminants in food. The fluorescence intensity decreased as the concentration of *E. coli* increased. A linear relationship was established with a correlation coefficient (R^2) of 0.9802 and a LOD of 10 cfu/mL, which significantly expanded the detection range compared with those of other biological labeling methods. The proposed biosensing method can be easily adopted for the detection of other bacterial pathogens by substituting specific antibodies for those pathogens. This novel fluorescent probe, as an efficient, specific, and technically simple biological probe, provides a convenient, sensitive, and stable platform for biological applications.

■ ASSOCIATED CONTENT

Supporting Information

The Supporting Information is available free of charge on the ACS Publications website at DOI: 10.1021/acs.jafc.5b02331.

Data regarding the binding efficiency of the antigen−antibody interaction (PDF)

■ AUTHOR INFORMATION

Corresponding Author

*Phone: +86-511-88790318. Fax: +86-511-88780201. E-mail: q.s.chen@hotmail.com.

Funding

This work was financially supported by the National Natural Science Foundation of China (31271875) and a Project Funded by the Priority Academic Program Development of Jiangsu Higher Education Institutions (PAPD).

Notes

The authors declare no competing financial interest.

■ ACKNOWLEDGMENTS

We are grateful to many of our colleagues for stimulating discussions in this field.

■ REFERENCES

(1) Velusamy, V.; Arshak, K.; Korostynska, O.; Oliwa, K.; Adley, C. An overview of foodborne pathogen detection: in the perspective of biosensors. *Biotechnol. Adv.* **2010**, *28*, 232−254.

(2) Van Boxstael, S.; Habib, I.; Jacxsens, L.; De Vocht, M.; Baert, L.; Van De Perre, E.; Rajkovic, A.; Lopez-Galvez, F.; Sampers, I.; Spanoghe, P.; De Meulenaer, B.; Uyttendaele, M. Food safety issues in fresh produce: Bacterial pathogens, viruses and pesticide residues indicated as major concerns by stakeholders in the fresh produce chain. *Food Control* **2013**, *32*, 190−197.

(3) Roy Chowdhury, P. R.; McKinnon, J.; Wyrsch, E.; Hammond, J. M.; Charles, I. G.; Djordjevic, S. P. Genomic interplay in bacterial communities: implications for growth promoting practices in animal husbandry. *Front. Microbiol.* **2014**, *5*, 394 DOI: 10.3389/fmicb.2014.00394.

(4) Mandal, P.; Biswas, A.; Choi, K.; Pal, U. Methods for rapid detection of foodborne pathogens: an overview. *Am. J. Food Technol.* **2011**, *6*, 87−102.

(5) Biswas, A.; Kondaiah, N.; Bheilegaonkar, K.; Anjaneyulu, A.; Mendiratta, S.; Jana, C.; Singh, H.; Kumar, R. Microbial profiles of frozen trimmings and silver sides prepared at Indian buffalo meat packing plants. *Meat Sci.* **2008**, *80*, 418−422.

(6) Shan, S.; Lai, W. H.; Xiong, Y. H.; Wei, H.; Xu, H. Y. Novel Strategies To Enhance Lateral Flow Immunoassay Sensitivity for Detecting Foodborne Pathogens. *J. Agric. Food Chem.* **2015**, *63*, 745.

(7) Pan, W. X.; Zhao, J. W.; Chen, Q. S. Classification of foodborne pathogens using near infrared (NIR) laser scatter imaging system with multivariate calibration. *Sci. Rep.* **2015**, *5*, 9524.

(8) Allen, M. J.; Edberg, S. C.; Reasoner, D. J. Heterotrophic plate count bacteria—what is their significance in drinking water? *Int. J. Food Microbiol.* **2004**, *92*, 265−274.

(9) Salinas, F.; Garrido, D.; Ganga, A.; Veliz, G.; Martínez, C. Taqman real-time PCR for the detection and enumeration of Saccharomyces cerevisiae in wine. *Food Microbiol.* **2009**, *26*, 328−332.

(10) Van Dyck, E.; Ieven, M.; Pattyn, S.; Van Damme, L.; Laga, M. Detection of Chlamydia trachomatis andNeisseria gonorrhoeae by Enzyme Immunoassay, Culture, and Three Nucleic Acid Amplification Tests. *J. Clin Microbiol.* **2001**, *39*, 1751−1756.

(11) Yan, J.; Estévez, M. C.; Smith, J. E.; Wang, K.; He, X.; Wang, L.; Tan, W. Dye-doped nanoparticles for bioanalysis. *Nano Today* **2007**, *2*, 44−50.

(12) Yang, L.; Li, Y. Simultaneous detection of Escherichia coli O157:H7 and Salmonella Typhimurium using quantum dots as fluorescence labels. *Analyst* **2006**, *131*, 394−401.

(13) Bae, P. K.; So, H.-M.; Kim, K. N.; You, H. S.; Choi, K. S.; Kim, C. H.; Park, J.-K.; Lee, J.-O. Simple route for the detection of Escherichia coli using quantum dots. *BioChip J.* **2010**, *4*, 129−133.

(14) Shukla, S.; Leem, H.; Lee, J.-S.; Kim, M. Immunochromatographic strip assay for the rapid and sensitive detection of Salmonella Typhimurium in artificially contaminated tomato samples. *Can. J. Microbiol.* **2014**, *60*, 399−406.

(15) Li, B.; Yu, Q.; Duan, Y. Fluorescent labels in biosensors for pathogen detection. *Crit. Rev. Biotechnol.* **2015**, *35*, 82.

(16) Papillard-Marechal, S.; Enouf, V.; Schnuriger, A.; Vabret, A.; Macheras, E.; Rameix-Welti, M. A.; Page, B.; Freymuth, F.; Van Der Werf, S.; Garbarg-Chenon, A.; et al. Monitoring epidemic viral respiratory infections using one-step real-Time Triplex RT-PCR targeting influenza A and B viruses and respiratory syncytial virus. *J. Med. Virol.* **2011**, *83*, 695−701.

(17) Luo, J.; Liu, X.; Tian, Q.; Yue, W.; Zeng, J.; Chen, G.; Cai, X. Disposable bioluminescence-based biosensor for detection of bacterial count in food. *Anal. Biochem.* **2009**, *394*, 1−6.

(18) Hoebe, R.; Van Oven, C.; Gadella, T. W.; Dhonukshe, P.; Van Noorden, C.; Manders, E. Controlled light-exposure microscopy reduces photobleaching and phototoxicity in fluorescence live-cell imaging. *Nat. Biotechnol.* **2007**, *25*, 249−253.

(19) Tsoi, K. M.; Dai, Q.; Alman, B. A.; Chan, W. C. Are quantum dots toxic? Exploring the discrepancy between cell culture and animal studies. *Acc. Chem. Res.* **2013**, *46*, 662−671.

(20) Ong, L. C.; Ang, L. Y.; Alonso, S.; Zhang, Y. Bacterial imaging with photostable upconversion fluorescent nanoparticles. *Biomaterials* **2014**, *35*, 2987−2998.

(21) Yan, B.; Boyer, J.-C.; Branda, N. R.; Zhao, Y. Near-infrared light-triggered dissociation of block copolymer micelles using upconverting nanoparticles. *J. Am. Chem. Soc.* **2011**, *133*, 19714−19717.

(22) Cheng, L.; Wang, C.; Liu, Z. Upconversion nanoparticles and their composite nanostructures for biomedical imaging and cancer therapy. *Nanoscale* **2013**, *5*, 23−37.

(23) Xu, Y. L.; Niu, X. Y.; Zhang, H. J.; Xu, L. F.; Zhao, S. G.; Chen, H. L.; Chen, X. G. Switch-on Fluorescence Sensing of Glutathione in Food Samples Based on a Graphitic Carbon Nitride Quantum Dot (g-

CNQD)-Hg2+ Chemosensor. *J. Agric. Food Chem.* **2015**, *63*, 1747−1755.
(24) Smith, A. M.; Mancini, M. C.; Nie, S. Bioimaging: second window for in vivo imaging. *Nat. Nanotechnol.* **2009**, *4*, 710−711.
(25) Xu, S. Y.; Huang, S.; He, Q.; Wang, L. Y. Upconversion nanophosphores for bioimaging. *TrAC, Trends Anal. Chem.* **2015**, *66*, 72−79.
(26) Liu, J. L.; Lu, L. L.; Li, A. Q.; Tang, J.; Wang, S. G.; Xu, S. Y.; Wang, L. Y. Simultaneous detection of hydrogen peroxide and glucose in human serum with upconversion luminescence. *Biosens. Bioelectron.* **2015**, *68*, 204−209.
(27) Wang, L. Y.; Li, Y. D. Green upconversion nanocrystals for DNA detection. *Chem. Commun.* **2006**, 2557−2559.
(28) Wang, L. Y.; Yan, R. X.; Huo, Z. Y.; Wang, L.; Zeng, J. H.; Bao, J.; Wang, X.; Peng, Q.; Li, Y. D. Fluorescence resonant energy transfer biosensor based on upconversion-luminescent nanoparticles. *Angew. Chem., Int. Ed.* **2005**, *44*, 6054−6057.
(29) Wu, S. J.; Duan, N.; Shi, Z.; Fang, C. C.; Wang, Z. P. Simultaneous aptasensor for multiplex pathogenic bacteria detection based on multicolor upconversion nanoparticles labels. *Anal. Chem.* **2014**, *86*, 3100−3107.
(30) Wang, F.; Banerjee, D.; Liu, Y.; Chen, X.; Liu, X. Upconversion nanoparticles in biological labeling, imaging, and therapy. *Analyst* **2010**, *135*, 1839−1854.
(31) Zhou, J.; Liu, Z.; Li, F. Upconversion nanophosphors for small-animal imaging. *Chem. Soc. Rev.* **2012**, *41*, 1323−1349.
(32) Wang, F.; Han, Y.; Lim, C. S.; Lu, Y.; Wang, J.; Xu, J.; Chen, H.; Zhang, C.; Hong, M.; Liu, X. Simultaneous phase and size control of upconversion nanocrystals through lanthanide doping. *Nature* **2010**, *463*, 1061−1065.
(33) Wang, L. Y.; Li, Y. D. Controlled synthesis and luminescence of lanthanide doped $NaYF_4$ nanocrystals. *Chem. Mater.* **2007**, *19*, 727−734.
(34) Deng, M. L.; Wang, L. Y. Unexpected luminescence enhancement of upconverting nanocrystals by cation exchange with well retained small particle size. *Nano Res.* **2014**, *7*, 782−793.
(35) Huang, S.; Bai, M.; Wang, L. Y. General and facile surface functionalization of hydrophobic nanocrystals with poly(amino acid) for cell luminescence imaging. *Sci. Rep.* **2013**, *3*, 2023−2028.
(36) Wang, L. Y.; Li, P.; Li, Y. D. Down- and up-conversion luminescent nanorods. *Adv. Mater.* **2007**, *19*, 3304−3307.
(37) Wang, L. Y.; Li, Y. D. $Na(Y_{1.5}Na_{0.5})F_6$ Single-crystal nanorods as multicolor luminescent materials. *Nano Lett.* **2006**, *6*, 1645−1649.
(38) Disney, M. D.; Zheng, J.; Swager, T. M.; Seeberger, P. H. Detection of bacteria with carbohydrate-functionalized fluorescent polymers. *J. Am. Chem. Soc.* **2004**, *126*, 13343−13346.
(39) Deng, M. L.; Ma, Y. X.; Huang, S.; Hu, G. F.; Wang, L. Y. Monodisperse upconversion $NaYF_4$ nanocrystals: syntheses and bioapplications. *Nano Res.* **2011**, *4*, 685−694.
(40) Cho, I. H.; Mauer, L.; Irudayaraj, J. In-situ fluorescent immunomagnetic multiplex detection of foodborne pathogens in very low numbers. *Biosens. Bioelectron.* **2014**, *57*, 143−148.
(41) Liu, J. L.; Lu, L. L.; Xu, S. Y.; Wang, L. Y. One-pot synthesis of gold nanoclusters with bright red fluorescence and good biorecognition abilities for visualization fluorescence enhancement detection of *E. coli*. *Talanta* **2015**, *134*, 54−59.
(42) Yang, L.; Li, Y. Quantum dots as fluorescent labels for quantitative detection of Salmonella typhimurium in chicken carcass wash water. *J. Food Protect.* **2005**, *68*, 1241−1245.
(43) Wang, B.; Huang, X.; Ma, M.; Shi, Q.; Cai, Z. A simple quantum dot-based fluoroimmunoassay method for selective capturing and rapid detection of Salmonella Enteritidis on eggs. *Food Control* **2014**, *35*, 26−32.
(44) Wang, L. X.; Wu, C. S.; Fan, X. D.; Mustapha, A. Detection of Escherichia coli O157:H7 and Salmonella in ground beef by a bead-free quantum dot facilitated isolation method. *Int. J. Food Microbiol.* **2012**, *156*, 83−87.

DOI: 10.1021/acs.jafc.5b02331
J. Agric. Food Chem. 2015, 63, 8068−8074

1−40 mg/kg in horticultural crops in Japan. Thus, a new strategy was examined to develop an adequate sensitive immunoassay for the analysis of boscalid residues in horticultural crops.

In this study, the synthesis of a new hapten, preparation of monoclonal antibodies (MoAb's) to boscalid, methodologies of the direct competitive enzyme-linked immunosorbent assay (dc-ELISA) and SPR-sensor, and comparison of the dc-ELISA and SPR-sensor (using the same MoAb) for determination of boscalid in horticultural crops are described.

MATERIALS AND METHODS

Materials. Boscalid, benalaxyl, fenhexamid, pencycuron, and tecloftalam, which were of analytical grade for pesticide residue analysis, *N*-hydroxysuccinimide, and keyhole limpet hemocyanin (KLH) were purchased from Wako Pure Chemical Industries, Ltd. (Osaka, Japan). Bovine serum albumin (BSA; product no. A7888), hypoxanthine−aminopterin−thymidine (HAT) medium supplement, and polyethylene glycol (molecular weight 1450) solution were purchased from Sigma-Aldrich Co. (St. Louis, MO). 1-Ethyl-3-(3-(dimethylamino)propyl)carbodiimide hydrochloride (EDC) was purchased from Dojindo Molecular Technologies, Inc. (Kumamoto, Japan). Dichloromethane (CH_2Cl_2) was purchased from Kanto Chemical Co., Inc. (Tokyo, Japan). Sodium dodecyl sulfate (SDS), guanidine hydrochloride (GdnHCl), and RPMI 1640 medium were purchased from Nacalai Tesque, Inc. (Kyoto, Japan). Fetal bovine serum (FBS) was purchased from PAA Laboratories, GmbH (Pasching, Austria). Ninety-six-well microplates for cell culture (Nunc), 96-well microtiter plates for ELISA (Nunc MaxiSorp), and horseradish peroxidase (HRP)-labeled antimouse IgG (H+L) antibody from rabbit (Invitrogen) and antimouse IgG (H+L) antibody from goat (Pierce) were purchased from Thermo Fisher Scientific K.K. (New York). HRP was purchased from Toyobo Co. Ltd. (Osaka, Japan). Freund's complete adjuvant and incomplete adjuvant (Difco) were purchased from Becton, Dickinson and Co. (Franklin Lakes, NJ). All other chemicals and reagents used were of analytical grade and were purchased from Wako Pure Chemical Industries, Ltd. or Nacalai Tesque, Inc.

Hapten Synthesis. *General Procedure.* Unless otherwise noted, all reactions were performed under an atmosphere of argon. All reactions were monitored by thin-layer chromatography (TLC) on glass plates precoated with silica gel in a layer thickness of 0.2 mm (60 F_{254}) from Merck KGaA (Darmstadt, Deutschland). The products were visualized by irradiation with UV light, by treatment with a solution of phosphomolybdic acid, or by treatment with a solution of *p*-anisaldehyde. Flash column chromatography was performed using silica gel (art. no. 7734) from Merck KGaA. ^{1}H NMR (500 and 400 MHz) and ^{13}C NMR (125 and 100 MHz) spectra were recorded on JEOL JNM-ECX500 and JEOL JNM-ECS400 spectrometers. Chemical shifts are reported as δ values (ppm) relative to $CDCl_3$ (7.26 ppm). Elemental analyses were performed on a Yanaco CHN CORDER MT-6 analyzer. Optical rotations were performed with a JASCO P-1030 polarimeter at the sodium D line (1.0 mL sample cell). DART (direct analysis in real time) mass (positive mode) analyses were performed on an LC-TOF JMS-T100LP spectrometer.

*Synthesis of 2-Chloro-N-(2-iodophenyl)pyridine-3-carboxyamide (**3**).* A solution of chloronicotinoyl chloride (**1**) (704.0 mg, 4.0 mmol) in CH_2Cl_2 (20 mL) was stirred into a mixture of 2-iodoaniline (**2**) (876.1 mg, 4.0 mmol) and Et_3N (836 μL, 6.0 mmol, d = 0.73) in CH_2Cl_2 (4 mL) for over 15 min at 0 °C. The resulting mixture was stirred at room temperature for an additional 2 h. Then the solvent was removed under reduced pressure. The residue was purified by column chromatography on a silica gel that was eluted with a hexane and ethyl acetate mixture (2:1, v/v) to give the desired product **3** (603.4 mg) in 42% yield: ^{1}H NMR (400 MHz, $CDCl_3$) δ 8.56 (dd, 1H, J = 4.88, 1.83 Hz, H-6 Py), 8.43 (br s, 1H, NH), 8.38 (d, 1H, J = 8.24 Hz, H-4 Py), 8.23 (dd, 1H, J = 7.63, 1.83 Hz, H-6 Ph), 7.86 (dd, 1H, J = 8.10, 1.34 Hz, H-3 Ph), 7.41−7.45 (m, 2H, H-5 Py, H-5 Ph), and 6.94 (dt, 1H, J = 7.63, 7.63, 1.53 Hz, H-4 Ph) ppm.

*Synthesis of the Boscalid Hapten Precursor Methyl 2′-(2-Chloronicotinamido)biphenyl-4-carboxylate (**5**).* A mixture of product **3** (179.3 mg, 0.5 mmol), 4-(methoxycarbonyl)phenylboronic acid (**4**) (90.0 mg, 0.5 mmol), $(Ph_3P)_4Pd$ (28.9 mg, 0.0025 mmol), and K_2CO_3 (207.3 mg, 1.5 mmol) in anhydrous *i*-PrOH (6.3 mL) was degassed and exchanged with Ar.[42] The resulting mixture was heated to 50 °C for 2 h and 100 °C for 21 h with stirring. The suspension was then cooled to room temperature and filtered. The solvent was removed under reduced pressure, and the residue was purified by column chromatography on silica gel that was eluted with a hexane and ethyl acetate mixture (2:1 to 1:1, v:v). At this stage, the isopropyl ester produced as a side reaction product was a contaminant, and therefore, the mixture of methyl ester and isopropyl ester was repurified and eluted with a chloroform and acetone solution (30:1, v/v) to give the desired precursor **5** (27.5 mg) in 15% yield: ^{1}H NMR (500 MHz, $CDCl_3$) δ 8.41 (dd, 1H, J = 4.59, 1.91 Hz, H-6 Py), 8.38 (d, 1H, J = 8.03, H-3′ Ph), 8.19 (br s, 1H, NH), 8.09−8.11 (m, 3H, H-4 Py, H-3 and H-5 Ph), 7.47−7.51, 7.29−7.34 (m, 6H, H-5 Py, H-2 and H-6 Ph, H-4′ and H-5′ and H-6′ Ph), and 3.93 (s, 3H) ppm. ^{13}C NMR (125 MHz, $CDCl_3$) δ 166.5, 162.5, 151.2, 146.6, 142.6, 140.0, 134.1, 132.5, 131.0, 130.2, 130.0, 129.8, 129.5, 129.1, 125.4, 122.8, 122.3, and 52.3 ppm; IR (neat) ν 3279, 3045, 1714, and 1676 cm^{-1}; HRMS (DART) m/z calcd for $C_{20}H_{16}ClN_2O_3$ (M + 1$^+$) 367.0849, found 367.0850.

*Boscalid Hapten, 2′-(2-Chloronicotinamido)biphenyl-4-carboxylic acid (**6**).* To a solution of boscalid hapten precursor **5** (36.8 mg, 0.1 mmol) in CH_3OH (1.3 mL) was added a solution of NaOH (40.0 mg, 1.0 mmol) in H_2O (0.5 mL) at 0 °C. The mixture was stirred for 3 h at room temperature and then acidified with a 1 N HCl solution to pH 2.0. The solvent was removed, and the residue was washed with tetrahydrofuran. The tetrahydrofuran mixture was concentrated to give the desired hapten **6** (23.7 mg) in 67% yield: ^{1}H NMR (500 MHz, CD_3OD) δ 8.41 (dd, 1H, J = 4.97, 1.91 Hz, H-6 Py), 8.07−8.10 (m, 2H, H-3 and H-5 Ph), 7.77 (dd, 1H, J = 7.64, 1.91 Hz, H-4 Py), 7.64 (d, 1H, J = 7.64 Hz, H-6′ Ph), 7.55−7.57 (m, 2H, H-2 and H-6 Ph), 7.47−7.51 (m, 1H, H-5′ Ph), and 7.42−7.44 (m, 3H, H-5 Py, H-3′ and H-4′ Ph) ppm; ^{13}C NMR (125 MHz, $CDCl_3$) δ 174.0, 167.1, 151.5, 148.4, 143.0, 139.5, 139.2, 136.5, 134.6, 133.9, 131.5, 130.5, 129.8, 129.5, 128.6, 128.4, and 124.1 ppm; HRMS (DART) m/z calcd for $C_{19}H_{14}ClN_2O_3$ (M + 1$^+$) 353.0693, found 353.0657; IR (neat) ν 3417 and 1644−1660 cm^{-1}.

Preparation of the Hapten−Protein Conjugate. The synthesized hapten was conjugated with proteins (KLH, BSA, or HRP) by the activated ester method as described previously.[23] In brief, 100 μL of the hapten (5 μmol) in anhydrous dimethyl sulfoxide was mixed with 5 μL of *N*-hydroxysuccinimide (6 μmol) and 10 μL of EDC (6 μmol) in anhydrous dimethyl sulfoxide, and the mixture was allowed to stand at room temperature for 1.5 h. Then 1 mL of each of the proteins (10 mg) dissolved in 10 mmol/L PBS (10 mmol/L phosphate buffer and 150 mmol/L NaCl, pH 7.0) was added to the mixture, which was then gently stirred for 1.5 h. The hapten−KLH conjugate and the hapten−BSA conjugate were respectively dialyzed in 10 mmol/L PBS, whereas the hapten−HRP conjugate was purified through gel filtration chromatography. The hapten−KLH conjugate was emulsified with an equal volume of Freund's complete adjuvant or incomplete adjuvant for use in mouse immunization and booster immunization, respectively. The hapten−BSA conjugate was used for the indirect ELISA (i-ELISA), indirect competitive ELISA (ic-ELISA), and SPR-sensor experiments. The hapten−HRP conjugate was used for the dc-ELISA.

Preparation of Monoclonal Antibodies. MoAb's were prepared as described previously.[23] In brief, Balb/c mice (7 week old females) purchased from Japan SLC, Inc. (Shizuoka, Japan) were immunized with 100 μL of the hapten−KLH conjugate (100 μg/mouse) in Freund's complete adjuvant. After 1 month, the booster immunization was performed twice at 2 week intervals using 100 μL of the hapten−KLH conjugate (25 μg/mouse) in Freund's incomplete adjuvant. After 3 days from the last immunization, spleen cells of the mice were

DOI: 10.1021/acs.jafc.5b03637
J. Agric. Food Chem. 2015, 63, 8075−8082

collected and prepared for cell fusion with P3-X63-AG8.653 myeloma cells (5.5×10^7 cells) using polyethylene glycol solution. The fused cells were suspended at 8×10^5 cells/mL in HAT medium (RPMI 1640 medium, 10% FBS, and HAT medium supplement) and transferred to 96-well microplates. After incubation at 37 °C for 7−10 days, colonies secreting antiboscalid MoAb's were identified by i-ELISA and ic-ELISA and picked up. The selected hybridoma cells were cloned by the limiting dilution method. Two MoAb's, BSC7 and BSC72, were purified from the ascite fluid by ammonium sulfate fractionation and anion-exchange chromatography. BSC7 showed the highest reactivity upon the ELISA screenings, whereas BSC72 was the representative MoAb among various MoAb's showing similar reactivity.

The mouse experiments were performed under the guidelines of the Animal Experiment Committee of Kyoto Women's University following bulletin no. 71 (2006) of the Ministry of Education, Culture, Sports, Science and Technology of Japan.

i-ELISA and ic-ELISA. The i-ELISA and ic-ELISA methods were conducted as described previously.[23] The specific conditions were that the hapten−BSA concentration was 1.0 μg/mL and the boscalid standard solution was prepared at concentrations from 0.6 to 2500 ng/mL in 10% methanol.

dc-ELISA. The dc-ELISA method was conducted as described previously.[23] Each well of a 96-well microtiter plate was coated overnight with 100 μL of antimouse IgG goat antibody (5 μg/mL) in 10 mmol/L PBS at 4 °C and then blocked for 1 h with 300 μL of 10 mmol/L PBS containing 0.4% BSA at 25 °C. One hundred microliters of purified MoAb BSC7 (500 ng/mL) or culture fluid containing MoAb BSC72 in 10 mmol/L PBS containing 0.2% BSA was added to the appropriate wells, and incubation was carried out at 25 °C for 1 h. The plate was washed once with washing buffer (10 mmol/L PBS containing 0.02% Tween 20). Each solution (150 μL) of boscalid (0.038−156 ng/mL), boscalid-related pesticides (10 μg/mL) used in a cross-reactivity test, and vegetable samples prepared in 10% methanol was mixed with an equal volume of the hapten−HRP conjugate (250 ng/mL) in 10 mmol/L PBS containing 0.2% BSA. The mixture (100 μL) was added to the wells of the plate for competitive reaction and incubated at 25 °C for 1 h. After the plate was washed three times with the washing buffer, 100 μL of the color development solution (100 μg/mL 3,3′,5,5′-tetramethylbenzidine, 0.006% H_2O_2, and 0.1 mol/L acetate buffer, pH 5.5) was added. After 10 min at 25 °C, 100 μL of 0.5 mol/L sulfuric acid was added to stop the color development reaction. The absorbance was measured at 450 nm with an xMark microplate reader (Bio-Rad Laboratories, Hercules, CA), so that the maximum absorbance reading was around 1.3.

SPR-Sensor. The SPR-sensors consisted of commercially available instruments of microflow type (Biacore T200; GE Healthcare Europe, Munich, Germany), and the sensor chips were coated with carboxymethyl dextran (CM5; GE Healthcare Europe). The sensor chips were functionalized via the following steps, based on the instruction manual.

Step 1: Preparation of the Sensor Chip for Boscalid. The sensor chip was placed in the instrument, and the surface was initially rinsed with 10 mmol/L PBS containing 0.005% Tween 20 at a rate of 5 μL/min for 600 s. It was activated by flushing with a mixture of 80 μL of EDC (400 mmol/L) and 80 μL of *N*-hydroxysuccinimide (100 mmol/L) in distilled water for 350 s. The hapten−BSA (40 μg/mL) solution dissolved in acetic acid buffer (10 mmol/L, pH 5.0) was then flowed through the system for 120 s to bind the chip's activated carboxyl groups to the amino group residues of hapten−BSA. This was followed by flowing ethanolamine (1 mol/L, pH 8.5) through the system for 350 s to block residual carboxy groups. After being rinsed with the running buffer (50 mmol/L phosphate buffer and 75 mmol/L NaCl, pH 7.0, containing 5% methanol and 0.1% BSA), the sensor chip was ready to be used.

Step 2: Preparation of the Samples. The boscalid solutions were serially diluted at final concentrations in the range of 2.4−3100 ng/mL in 10% methanol with distilled water. The other structurally related pesticides were prepared at 10 μg/mL. MoAb BSC7 was diluted to 15 μg/mL with 100 mmol/L PBS (100 mmol/L phosphate buffer and 150 mmol/L NaCl, pH 7.0) containing 0.2% BSA. The boscalid or other pesticide solution (75 μL) was mixed with an equal volume of MoAb BSC7 solution (75 μL) to form the pesticide−MoAb BSC7 complex. This mixture (final 5% methanol solution) was used for pesticide determination by the SPR-sensor.

Step 3: Determination of the Pesticides. The mixed solutions were flushed through the sensor system at 20 μL/min for 180 s to allow free MoAb BSC7 to bind with the hapten−BSA immobilized on the sensor surface. The solution was then changed to the running buffer, which was allowed to flow continuously at 20 μL/min for 180 s.

Step 4: Regeneration of the Sensor Surface. After the pesticide determination had been completed, the MoAb BSC7 was removed from the immobilized hapten−BSA in the following way. The sensor surface was initially washed with GdnHCl (3.0 mol/L) in acetic acid (1.0 mol/L, pH 1.9) at 20 μL/min for 60 s. After being rinsed with distilled water at 20 μL/min for 60 s, the sensor surface was washed with 0.2% SDS at 20 μL/min for 120 s, as described previously.[39] After the regeneration had been completed, the sensor chip was used again, repeating steps 2−4 described above.

Step5: Data Processing. Raw data were output as a resonance unit (RU), where 1000 RU was defined as a 0.1° refractive index shift by the SPR phenomenon. The actual response curve was drawn, where the *x*-axis represented the boscalid concentration and the *y*-axis represented the Δ(RU) between the starting point of the reaction and a time point of 180 s.

Treatment of Vegetable Samples. Cucumber, tomato, green sweet pepper, cabbage, spinach, and orange, purchased from a market in Kyoto city, were used at 100 g each for the recovery examinations. Boscalid-treated tomato (200 g) was harvested from an experimental farm at the Aichi Agricultural Research Center. Real tomato samples were used to examine for correlations between the dc-ELISA or the SPR-sensor and high-performance liquid chromatography (HPLC). The vegetable samples were homogenized in a blender. For the recovery examinations, boscalid was added to the homogenized samples at final concentrations in the range from 1 to 15 mg/kg.

For the dc-ELISA and the SPR-sensor, 25 mL of methanol was added to the homogenized samples (5.0 g) in a 50 mL screw-cap tube. The mixture was first vigorously shaken (Shaker SA320; Yamato Scientific Co., Ltd., Tokyo, Japan) for 30 min to extract the boscalid and then was centrifuged at 3000 rpm at room temperature for 10 min. The supernatant was diluted 8.5-fold with distilled water to prepare a 10% methanol equivalent solution. The diluted sample was applied to the dc-ELISA and the SPR-sensor. Further dilution using 10% methanol with distilled water was carried out to adjust the concentrations of boscalid for most of the samples in the dc-ELISA and a part of the samples in the SPR-sensor.

For HPLC, 100 mL of acetone was added to the homogenized sample (20 g), and the boscalid was extracted for 30 min using a shaker (Recipro Shaker SR-II; Taiyo Chemical Industry, Gunma, Japan). The mixture was filtered through a filter-paper-lined funnel by suction. The residue was then retreated with 60 mL of acetone. Both filtered extracts were mixed, and the acetone was distilled away by evaporation at <40 °C in a flask. The concentrated solution was applied to 20 mL of a porous kieselguhr column (Inert Sep k-solute; GL Science, Tokyo, Japan) and held at room temperature for 10 min. The fraction containing boscalid was eluted with 100 mL of hexane. The eluted sample was evaporated to dryness by evaporation and N_2 purge. The dried sample was dissolved in 5 mL of acetonitrile and then applied to 6 mL of a bilayer column with activated charcoal and aminopropyl silica gel (GL-Pak GC/NH2; GL Sciences). The column was washed three times with 5 mL of acetonitrile, and the boscalid was then eluted with a mixture of acetonitrile and toluene (3:1, v/v; 15 mL). The eluted sample was dried by evaporation and N_2 purge and redissolved with a mixture of acetonitrile and distilled water (50:50, v/v; 2 mL). A portion of the solution (4 μL) was applied to HPLC.

HPLC Analysis. The HPLC system consisted of the Waters Acquity UPLC-PDA detector, equipped with a Waters BEH C18 reversed-phase column (1.7 μm, 2.1 i.d. × 50 mm; Waters, Milford, MA). The mobile phase was a methanol and water mixture (45:55, v/v) running at a flow rate of 0.5 mL/min. The column oven

DOI: 10.1021/acs.jafc.5b03637
J. Agric. Food Chem. 2015, 63, 8075−8082

temperature was 40 °C, and the injection volume of the sample was 4 μL. Boscalid was detected at a wavelength of 230 nm.

RESULTS AND DISCUSSION

Hapten Design. Boscalid is one of the carboxamide fungicides that have two chlorine atoms, as shown in Figure 1. In designing the hapten, the chlorine residues are potent

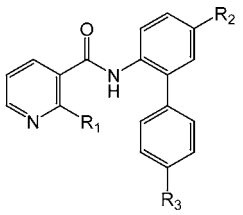

compound	R_1	R_2	R_3	reference
boscalid	Cl	H	Cl	1
hapten 1	$S(CH_2)_4COOH$	H	Cl	40
hapten 2	Cl	$(CH_2)_5COOH$	Cl	41
hapten 3	Cl	H	$S(CH_2)_4COOH$	41
new hapten	Cl	H	COOH	

Figure 1. Structure of boscalid and the haptens.

candidates for introducing the hapten linker. Abad-Fuentes et al. actually used the chlorine (R_1) for the linker site, and prepared a highly reactive PoAb to boscalid from hapten 1.[40] Esteve-Turrillas et al. (of the same research group) subsequently synthesized the other haptens by introducing an alkanecarboxylic acid to the position of R_2 (hapten 2), as well as introducing a carboxy group to the position of R_3 (hapten 3) using a thiol group.[41] In the dc-ELISAs, the IC_{50} values of the prepared PoAb's were 0.4−1.6 ng/mL for hapten 1, 0.6−1.2 ng/mL for hapten 2, and 0.8−1.6 ng/mL for hapten 3. The reactivity values, however, seemed too sensitive to determine boscalid at the MRLs for horticultural crops (1−40 mg/kg), because the concentration was more than 1000-fold. It seemed that the PoAb with hapten 3 had the lowest reactivity. In our study, therefore, the R_3 position was chosen as the linker site of the newly synthesized hapten. Furthermore, the linker was directly introduced without a thiol group, because the structure is more stable in the mouse abdominal cavity. The key step of the synthesis of the boscalid hapten was achieved by using the Suzuki−Miyaura coupling reaction in the presence of a Pd catalyst, as shown in Figure 2.[42]

Preparation of MoAb's Reacting with Boscalid. The MoAb preparation was carried out by using the conjugate of the new hapten and KLH as the immunogen. MoAb's reacting with the boscalid hapten conjugate were screened, via i-ELISA and ic-ELISA, from 2000 wells in which the colony had formed, and the reactivity of each MoAb was compared with that of the PoAb prepared from the same mouse. Of the two MoAb's finally prepared, MoAb BSC7 had the highest reactivity of all the MoAb's upon screening, whereas MoAb BSC72 was the representative one among various MoAb's showing similar reactivity. As shown in Figure 3, with the ic-ELISA, the IC_{50} values of the PoAb, MoAb BSC7, and MoAb BSC72 were 90, 3.3, and 43 ng/mL, respectively, indicating that the reactivity of MoAb BSC72 was much closer to that of the PoAb. The reactivity of the ic-ELISA seemed adequate when compared with the boscalid MRLs. On the other hand, MoAb BSC7 had a 30 times higher reactivity than PoAb, which was too high for determining the boscalid residue by ic-ELISA. Hence, the test samples would have to be diluted to adequate boscalid concentrations to adjust to the working MRL range.

Reactivity of MoAb's with Boscalid in the dc-ELISA. The dc-ELISA is the most widely used method for pesticide residue analysis among the various immunoassays, and many of the test kits based on the dc-ELISA are commercially available for pesticide determination. The kits have been validated for agricultural products.[24−26] The effectiveness of the dc-ELISA for determining boscalid using MoAb BSC7 and MoAb BSC72 was therefore examined, and the results are shown in Figure 4.

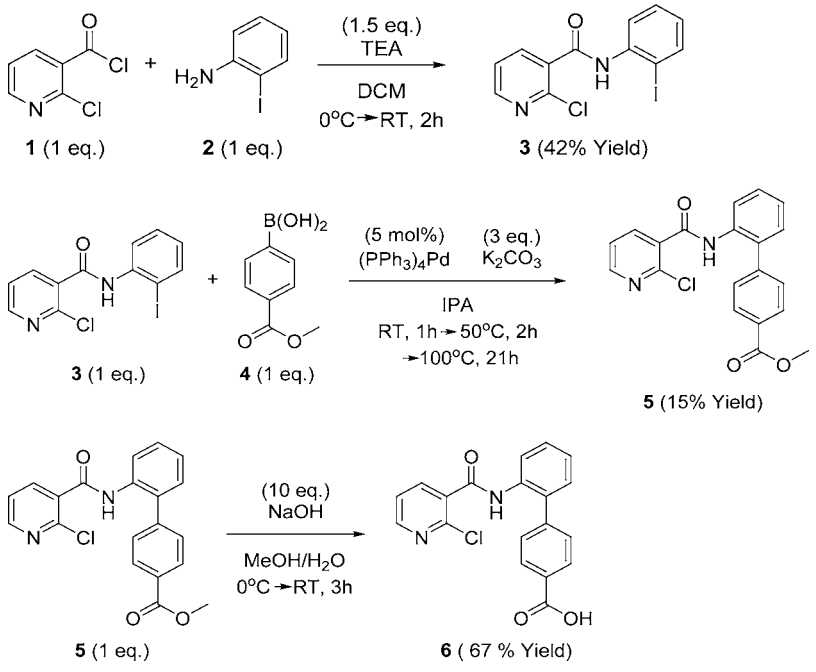

Figure 2. Scheme of the hapten synthesis.

DOI: 10.1021/acs.jafc.5b03637
J. Agric. Food Chem. 2015, 63, 8075−8082

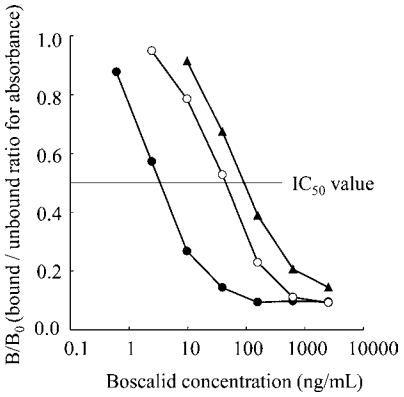

Figure 3. Reactivity of the prepared antibodies with boscalid in ic-ELISA: (●) MoAb BSC7; (○) MoAb BSC72; (▲) PoAb. Each data point is the mean of duplicates in independent examinations.

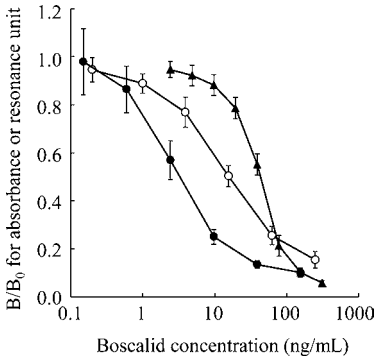

Figure 4. Reactivity of MoAb's with boscalid in the dc-ELISA and in the SPR-sensor: (●) MoAb BSC7 in the dc-ELISA; (○) MoAb BSC72 in the dc-ELISA; (▲) MoAb BSC7 in the SPR-sensor. Each data point is the mean of four replicates in independent examinations; error bars indicate ±SD.

The working range was defined as concentrations between the IC_{20} and IC_{80} values. The IC_{20}, IC_{50}, and IC_{80} values with MoAb BSC7 were 0.8, 3.3, and 16 ng/mL, respectively, similar to the results obtained with the ic-ELISA. These results suggest that it would be possible to use the dc-ELISA with MoAb BSC7 for boscalid residue analysis in horticultural crops, although most of the test samples would have to be diluted to adequate concentrations prior to analysis. On the other hand, the IC_{20}, IC_{50}, and IC_{80} values with MoAb BSC72 were 2.5, 15, and 120 ng/mL, respectively, in the dc-ELISA. The degree of slope on the standard curve for the dc-ELISA was more gradual than that for the ic-ELISA, indicating dc-ELISA's higher sensitivity and hence adequacy for residue analysis around the MRLs of horticultural crops.

Reactivity of MoAb BSC7 in the SPR-Sensor. SPR-sensors are rarely used for pesticide residue analysis in horticultural crops, although various electrochemical sensors have been applied.[28,39] There may be several reasons for this. First, the organic solvent containing high concentrations of the sample matrixes may gum the microflow channel in the sensor chip by precipitation. To resolve the precipitation problem, the test samples were solubilized in 5% methanol as well as the condition of competitive reaction for the above-described dc-ELISA, and the running buffer was also mixed with 5% methanol to maintain the solubility of the sample. Second, the antibody bound to the immobilized antigen may be unable to dissociate from the sensor chip. A combination of GdnHCl (3.0 mol/L) in acetic acid (1.0 mol/L, pH 1.9) and 0.2% SDS was therefore recently applied to dissociate the bound antibody, as described previously.[39]

The reactivity of MoAb BSC7 with boscalid was examined in the SPR-sensor, as shown in Figure 4. The working range was defined as concentrations between the IC_{20} and IC_{80} values as well as the dc-ELISA. The IC_{20}, IC_{50}, and IC_{80} values were 17, 42, and 80 ng/mL, respectively. MoAb BSC7 showed a 15-fold lower reactivity in the SPR-sensor than in the dc-ELISA. The reactivity of MoAb BSC72 in the SPR-sensor was too low to determine boscalid residues in horticultural crops (data not shown). The lower reactivity may be because much more MoAb and hapten−BSA were necessary for the SPR-sensor compared with the dc-ELISA.

The SPR-sensor with MoAb BSC7 seemed to show adequate sensitivity for determination of boscalid residues in horticultural crops, with higher reproducibility for the standard curve than the dc-ELISA, as shown in Figure 4. The advantages of the SPR-sensor with MoAb BSC7 are its ability to make both quantitative and rapid determinations of boscalid residues in horticultural crops. Further comparisons of the SPR-sensor and the dc-ELISA, using MoAb BSC7 only, were therefore carried out.

Cross-Reactivity of MoAb BSC7. Cross-reactivity of MoAb BSC7 in the dc-ELISA and the SPR-sensor was examined using other structurally related pesticides: benalaxyl, fenhexamid, pencycuron, and tecloftalam. MoAb BSC7 was highly specific to boscalid, as shown in Table 1. MoAb's generally recognize slight differences in the immunogen, such as the position and molecular size of the functional group, and even the optical isomerism of the molecules. Since the boscalid structure has many differences from the other carboxamide fungicides of the same group, the high assay specificity would be due to its structural uniqueness.

Table 1. Cross-Reactivity of MoAb BSC7 with Boscalid and the Other Structurally Related Pesticides in the dc-ELISA and SPR-Sensor[b]

Pesticide	CR (%)[a]		Pesticide	CR (%)	
	ELISA	SPR		ELISA	SPR
boscalid	100	100	benalaxyl	<0.03	<0.4
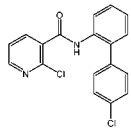			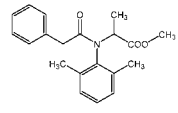		
fenhexamid	<0.03	<0.4	pencycuron	<0.03	<0.4
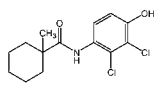			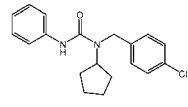		
tecloftalam	<0.03	<0.4			
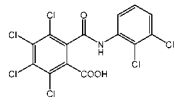					

[a]CR = cross-reactivity (%) compared to the IC_{50} value of boscalid. [b]Each data point is the mean of three replicates in independent examinations.

DOI: 10.1021/acs.jafc.5b03637
J. Agric. Food Chem. 2015, 63, 8075−8082

Table 2. Recovery of Boscalid Spiked in Horticultural Crops by the dc-ELISA and SPR-Sensor[a]

cucumber					tomato				
	ELISA		SPR			ELISA		SPR	
spiked concn[b]	rec[c]	RSD[d]	rec	RSD	spiked concn	rec	RSD	rec	RSD
3	116	5.6	101	4.3	3	109	13.3	104	5.5
5	114	12.4	85	3.1	5	122	16.1	90	7.4
7	124	12.1	94	8.8	7	124	8.9	93	5.8
green sweet pepper					cabbage				
	ELISA		SPR			ELISA		SPR	
spiked concn	rec	RSD	rec	RSD	spiked concn	rec	RSD	rec	RSD
5	120	13.2	89	6.3	1	109	9.8	104	10.6
10	114	2.6	95	9.0	3	116	9.6	109	5.2
15	122	7.4	94	14.5	5	113	7.4	105	9.2
spinach					orange				
	ELISA		SPR			ELISA		SPR	
spiked concn	rec	RSD	rec	RSD	spiked concn	rec	RSD	rec	RSD
1	100	9.7	95	2.9	1	103	5.4	102	10.2
3	104	13.4	107	3.5	2	120	4.2	97	11.1

[a]Each data point is the mean of three replicates in independent examinations. [b]The units for concentration are milligrams per kilogram. [c]The abbreviation "rec" is short for recovery (%). [d]RSD = relative standard deviation (%).

Boscalid Recovery in Pesticide-Spiked Horticultural Crops. The applicability of the dc-ELISA and the SPR-sensor, using MoAb BSC7, to boscalid residue analysis in horticultural crops was examined by recovery examinations. The limit of quantity values of boscalid for horticultural crops were 0.04 mg/kg in the dc-ELISA and 0.87 mg/kg in the SPR-sensor. The fruit vegetables cucumber (*Cucumis sativus* L.), tomato (*Solanum lycopersicum* L.), and green sweet pepper (*Capsicum annuum* L. var. *grossum*), the leaf vegetables cabbage (*Brassica oleracea* L. var. *capitata*) and spinach (*Spinacia oleracea* L.), and the fruit orange (*Citrus unshiu*) were chosen as the representative horticultural crops. As shown in Table 2, the recovery values were 100−124% in the dc-ELISA and 85.0−109% in the SPR-sensor, indicating that both immunoassays could be applied to boscalid residue analysis in horticultural crops. The SPR-sensor especially showed a higher quantitative performance than the dc-ELISA, since each of the recovery results was closer to the trueness value (100%), except for the results of spinach. The RSD values for the SPR-sensor were also lower than those for the dc-ELISA, although some exceptions were found for green sweet pepper, cabbage, and orange.

The dc-ELISA performance for determination of boscalid residues was as good as that of previously reported dc-ELISAs for other pesticides.[24−26] The SPR-sensor also showed performance equal to or greater than that of the dc-ELISA except for the sensitivity. The reasons would be that for the SPR-sensor (1) sample dilution was not necessary for most of the samples, (2) bound/free separation of the MoAb was not necessary, and (3) labeling of the MoAb, such as with HRP in the dc-ELISA, was not necessary.

Correlation between HPLC and the dc-ELISA or SPR-Sensor. The applicability of the dc-ELISA and the SPR-sensor was also examined by comparing them with HPLC, using real tomato samples to which a boscalid formulation had been applied before harvesting. As shown in Figure 5, the correlation values for HPLC with both immunoassays were high (R^2 = 0.97 with the dc-ELISA; R^2 = 0.95 with the SPR-sensor), suggesting that both of the newly developed immunoassays had high applicability to boscalid residue analysis in horticultural crops. The SPR-sensor had a lower bias (slope 1.14) than the dc-ELISA (slope 1.26), and did not show a visible *y*-intercept difference, whereas the *y*-intercept difference from the dc-ELISA was considerable (0.53 mg/kg). The result suggested that the SPR-sensor has high accuracy even near the lowest determination limit. Therefore, this SPR-sensor would be useful as a rapid, simple, and accurate method for the determination of boscalid residues in horticultural crops. On the other hand, the dc-ELISA has sufficient applicability for on-site analysis. In conclusion, each of the two immunoassays developed for boscalid determination should be used according to the required purpose.

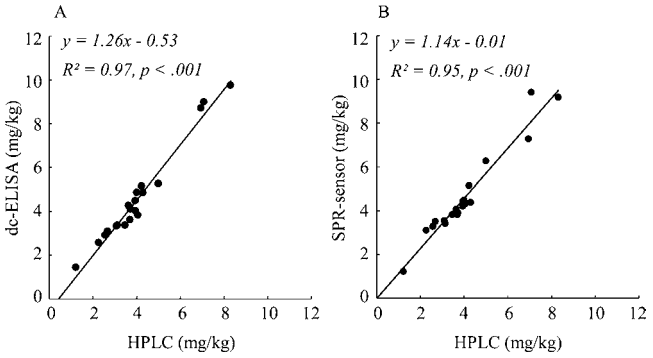

Figure 5. Correlation of the determined boscalid residue in real tomato samples between (A) the dc-ELISA and HPLC or (B) the SPR-sensor and HPLC. Each data point is the mean of duplicates in independent examinations.

AUTHOR INFORMATION

Corresponding Author

*Phone: +81 75-366-5265. Fax: +81-75-925-5491. E-mail: miyake@astem.or.jp.

DOI: 10.1021/acs.jafc.5b03637
J. Agric. Food Chem. 2015, 63, 8075−8082

Funding

This study was supported by the Aichi Science and Technology Foundation and by the Kyoto Integrated Science & Technology Bio-Analysis Center (KIST-BIC).

Notes

The authors declare no competing financial interest.

■ ACKNOWLEDGMENTS

We thank Yuka Horio and Asako Yamaguchi for their assistance.

■ REFERENCES

(1) Boscalid. In *The Pesticide Manual*, 16th ed.; MacBean, C., Ed.; British Crop Protection Council: Hampshire, U.K., 2012; pp 122−123.

(2) Hanafi, A.; Garau, V. L.; Caboni, P.; Sarais, G.; Cabras, P. Minor crops for export: a case study of boscalid, pyraclostrobin, lufenuron and lambda-cyhalothrin residue levels on green beans and spring onions in Egypt. *J. Environ. Sci. Health, Part B* **2010**, *45*, 493−500.

(3) Chen, L.; Zhang, S. Dissipation and residues of boscalid in strawberries and soils. *Bull. Environ. Contam. Toxicol.* **2010**, *84*, 301−304.

(4) Angioni, A.; Dedola, F.; Garau, V. L.; Schirra, M.; Caboni, P. Fate of iprovalicarb, indoxacarb, and boscalid residues in grapes and wine by GC-ITMS analysis. *J. Agric. Food Chem.* **2011**, *59*, 6806−6812.

(5) Munitz, M. S.; Resnik, S. L.; Montti, M. I. Method development and validation for boscalid in blueberries by solid-phase microextraction gas chromatography, and their degradation kinetics. *Food Chem.* **2013**, *136*, 1399−1404.

(6) Dedola, F.; Cabizza, M.; Satta, M. Determination of 28 pesticides applied on two tomato cultivars with a different surface/weight ratio of the berries, using a multiresidue GC-MS/MS method. *J. Environ. Sci. Health, Part B* **2014**, *49*, 671−678.

(7) Sadło, S.; Szpyrka, E.; Stawarczyk, M.; Piechowicz, B. Behavior of Pyrimethanil, pyraclostrobin, boscalid, cypermethrin and chlorpyrifos residues on raspberry fruit and leaves of Laszka variety. *J. Environ. Sci. Health, Part B* **2014**, *49*, 159−168.

(8) Sadło, S.; Szpyrka, E.; Piechowicz, B.; Grodzicki, P. A case study on toxicological aspects of the pest and disease control in the production of the high-quality raspberry (*Rubus idaeus* L.). *J. Environ. Sci. Health, Part B* **2015**, *50*, 8−14.

(9) Akiyama, Y.; Matsuoka, T.; Yoshioka, N.; Akamatsu, S.; Mitsuhashi, T. Pesticide residues in domestic agricultural products monitored in Hyogo Prefecture, Japan, FY 1995−2009. *J. Pestic. Sci.* **2011**, *36*, 66−72.

(10) Otsuka, K.; Kobayashi, M.; Tamura, Y.; Tomizawa, S.; Kinoshita, T.; Kamijo, K.; Iwakoshi, K.; Sato, C.; Takano, T. Survey of pesticide residues in domestic vegetables and fruits (April 2010−March 2011). *Annu. Rep. Tokyo Metrop. Inst. Public Health* **2011**, *62*, 177−182.

(11) Reilly, T. J.; Smalling, K. L.; Orlando, J. L.; Kuivila, K. M. Occurrence of boscalid and other selected fungicides in surface water and groundwater in three targeted use areas in the United States. *Chemosphere* **2012**, *89*, 228−234.

(12) Smalling, K. L.; Reilly, T. J.; Sandstrom, M. W.; Kuivila, K. M. Occurrence and persistence of fungicides in bed sediments and suspended solids from three targeted use areas in the United States. *Sci. Total Environ.* **2013**, *447*, 179−185.

(13) Smalling, K. L.; Kuivila, K. M.; Orlando, J. L.; Phillips, B. M.; Anderson, B. S.; Siegler, K.; Hunt, J. W.; Hamilton, M. Environmental fate of fungicides and other current-use pesticides in a central California estuary. *Mar. Pollut. Bull.* **2013**, *73*, 144−153.

(14) Gulkowska, A.; Buerge, I. J.; Poiger, T. Online solid phase extraction LC-MS/MS method for the analysis of succinate dehydrogenase inhibitor fungicides and its applicability to surface water samples. *Anal. Bioanal. Chem.* **2014**, *406*, 6419−6427.

(15) Liu, X.; Dong, F.; Qin, D.; Zheng, Y. Residue analysis of kresoxim-methyl and boscalid in fruits, vegetables and soil using liquid-liquid extraction and gas chromatography-mass spectrometry. *Biomed. Chromatogr.* **2010**, *24*, 367−373.

(16) Lagunas-Allue, L.; Sanz-Asensio, J.; Martinez-Soria, M. T. Comparison of four extraction methods for the determination of fungicide residues in grapes through gas chromatography-mass spectrometry. *J. Chromatogr. A* **2012**, *1270*, 62−71.

(17) Tran, K.; Eide, D.; Nickols, S. M.; Cromer, M. R.; Sabaa-Srur, A.; Smith, R. E. Finding of pesticides in fashionable fruit juices by LC-MS/MS and GC-MS/MS. *Food Chem.* **2012**, *134*, 2398−2405.

(18) Abad-Fuentes, A.; Ceballos-Alcantarilla, E.; Mercader, J. V.; Agullo, C.; Abad-Somovilla, A.; Esteve-Turrillas, F. A. Determination of succinate-dehydrogenase-inhibitor fungicide residues in fruits and vegetables by liquid chromatography-tandem mass spectrometry. *Anal. Bioanal. Chem.* **2015**, *407*, 4207−4211.

(19) Kondo, M.; Yamashita, H.; Uchigashima, M.; Kono, T.; Takemoto, T.; Fujita, M.; Saka, M.; Iwasa, S.; Ito, S.; Miyake, S. Development of an enzyme-linked immunosorbent assay for residue analysis of the insecticide emamectin benzoate in agricultural products. *J. Agric. Food Chem.* **2009**, *57*, 359−364.

(20) Kondo, M.; Tsuzuki, K.; Hamada, H.; Yamaguchi Murakami, Y.; Uchigashima, M.; Saka, M.; Watanabe, E.; Iwasa, S.; Narita, H.; Miyake, S. Development of an enzyme-linked immunosorbent assay (ELISA) for residue analysis of the fungicide azoxystrobin in agricultural products. *J. Agric. Food Chem.* **2012**, *60*, 904−911.

(21) Uchigashima, M.; Watanabe, E.; Ito, S.; Iwasa, S.; Miyake, S. Development of immunoassay based on monoclonal antibody reacted with the neonicotinoid insecticides clothianidin and dinotefuran. *Sensors* **2012**, *12*, 15858−15872.

(22) Watanabe, E.; Miyake, S.; Yogo, Y. Review of enzyme-linked immunosorbent assays (ELISAs) for analyses of neonicotinoid insecticides in agro-environments. *J. Agric. Food Chem.* **2013**, *61*, 12459−12472.

(23) Okazaki, F.; Hirakawa, Y.; Yamaguchi-Murakami, Y.; Harada, A.; Watanabe, E.; Iwasa, S.; Narita, H.; Miyake, S. Development of direct competitive ELISA for residue analysis of fungicide chlorothalonil in vegetables. *Shokuhin Eiseigaku Zasshi* **2014**, *55*, 65−72.

(24) Watanabe, E.; Kobara, Y.; Miyake, S. Validation of a commercial ELISA for the analysis of the insecticide dinotefuran in a variety of analytically challenging vegetables. *Food Addit. Contam., Part A* **2012**, *29*, 1067−1073.

(25) Watanabe, E.; Kobara, Y.; Miyake, S. Rapid and simple immunochemical screening combined with hand-shaking extraction for thiamethoxam residue in agricultural products. *J. Sci. Food Agric.* **2013**, *93*, 1839−1844.

(26) Watanabe, E.; Miyake, S. Quantitative analysis of fungicide azoxystrobin in agricultural samples with rapid, simple and reliable monoclonal immunoassay. *Food Chem.* **2013**, *136*, 695−702.

(27) Tomassetti, M.; Martini, E.; Campanella, L. New immunosensors operating in organic phase (OPIEs) for analysis of triazinic pesticides in olive oil. *Electroanalysis* **2012**, *24*, 842−856.

(28) Garcia-Febrero, R.; Valera, E.; Muriano, A.; Pividori, M.; Sanchez-Baeza, F.; Marco, M. An electrochemical magneto immunosensor (EMIS) for the determination of paraquat residues in potato samples. *Anal. Bioanal. Chem.* **2013**, *405*, 7841−7849.

(29) March, C.; Manclús, J.; Jiménez, Y.; Arnau, A.; Montoya, A. A piezoelectric immunosensor for the determination of pesticide residues and metabolites in fruit juices. *Talanta* **2009**, *78*, 827−833.

(30) Harris, R. D.; Luff, B. J.; Wilkinson, J. S.; Piehler, J.; Brecht, A.; Gauglitz, G.; Abuknesha, R. A. Integrated optical surface plasmon resonance immunoprobe for simazine detection. *Biosens. Bioelectron.* **1999**, *14*, 377−386.

(31) Svitel, J.; Dzgoev, A.; Ramanathan, K.; Danielsson, B. Surface plasmon resonance based pesticide assay on a renewable biosensing surface using the reversible concanavalin A monosaccharide interaction. *Biosens. Bioelectron.* **2000**, *15*, 411−415.

(32) Kim, S. J.; Gobi, K. V.; Iwasaka, H.; Tanaka, H.; Miura, N. Novel miniature SPR immunosensor equipped with all-in-one multi-microchannel sensor chip for detecting low-molecular-weight analytes. *Biosens. Bioelectron.* **2007**, *23*, 701−707.

DOI: 10.1021/acs.jafc.5b03637
J. Agric. Food Chem. 2015, 63, 8075−8082

(33) Mauriz, E.; Calle, A.; Manclus, J. J.; Montoya, A.; Lechuga, L. M. Multi-analyte SPR immunoassays for environmental biosensing of pesticides. *Anal. Bioanal. Chem.* **2007**, *387*, 1449−1458.
(34) Gouzy, M.-F.; Keß, M.; Krämer, P. M. A SPR-based immunosensor for the detection of isoproturon. *Biosens. Bioelectron.* **2009**, *24*, 1563−1568.
(35) Mauriz, E.; Calle, A.; Abad, A.; Montoya, A.; Hildebrandt, A.; Barcelo, D.; Lechuga, L. M. Determination of carbaryl in natural water samples by a surface plasmon resonance flow-through immunosensor. *Biosens. Bioelectron.* **2006**, *21*, 2129−2136.
(36) Farré, M.; Martínez, E.; Ramón, J.; Navarro, A.; Radjenovic, J.; Mauriz, E.; Lechuga, L.; Marco, M. P.; Barceló, D. Part per trillion determination of atrazine in natural water samples by a surface plasmon resonance immunosensor. *Anal. Bioanal. Chem.* **2007**, *388*, 207−214.
(37) Mauriz, E.; García-Fernández, C.; Mercader, J.; Abad-Fuentes, A.; Escuela, A.; Lechuga, L. Direct surface plasmon resonance immunosensing of pyraclostrobin residues in untreated fruit juices. *Anal. Bioanal. Chem.* **2012**, *404*, 2877−2886.
(38) Tomassetti, M.; Martini, E.; Campanella, L.; Favero, G.; Sanzó, G.; Mazzei, F. A new surface plasmon resonance immunosensor for triazine pesticide determination in bovine milk: a comparison with conventional amperometric and screen-printed immunodevices. *Sensors* **2015**, *15*, 10255−10270.
(39) Hirakawa, Y.; Yamasaki, T.; Watanabe, E.; Okazaki, F.; Murakami-Yamaguchi, Y.; Oda, M.; Iwasa, S.; Narita, H.; Miyake, S. Development of an immunosensor for determination of the fungicide chlorothalonil in vegetables, using surface plasmon resonance. *J. Agric. Food Chem.* **2015**, *63*, 6325−6330.
(40) Abad-Fuentes, A.; Esteve-Turrillas, F. A.; Agulló, C.; Abad-Somovilla, A.; Mercader, J. V. Development of competitive enzyme-linked immunosorbent assays for boscalid determination in fruit juices. *Food Chem.* **2012**, *135*, 276−284.
(41) Esteve-Turrillas, F. A.; Mercader, J. V.; Agullo, C.; Marzo, J.; Abad-Somovilla, A.; Abad-Fuentes, A. Design and development of heterologous competitive immunoassays for the determination of boscalid residues. *Analyst* **2014**, *139*, 3636−3644.
(42) For reviews on Suzuki−Miyaura coupling reactions, see: (a) Miyaura, N.; Suzuki, A. Palladium-catalyzed cross-coupling reactions of organoboron compounds. *Chem. Rev.* **1995**, *95*, 2457−2483. (b) Bräse, S.; de Meijere, A. In *Metal-Catalyzed Cross-Coupling Reactions*; Diederich, F., Stang, P. J., Eds.; Wiley-VCH: Weinheim, Germany, 1998; Chapters 2, 3, and 5. (c) Chemler, S. R.; Trauner, D.; Danishefsky, S. The B-alkyl Suzuki-Miyaura cross-coupling reaction: Development, mechanistic study, and applications in natural product synthesis. *Angew. Chem., Int. Ed.* **2001**, *40*, 4545−4568. (d) Miura, M. Rational ligand design in constructing efficient catalyst systems for Suzuki−Miyaura coupling. *Angew. Chem., Int. Ed.* **2004**, *43*, 2201−2203.

DOI: 10.1021/acs.jafc.5b03637
J. Agric. Food Chem. 2015, 63, 8075−8082

Table 2. Metabolites Identified in Watermelon Rootstocks and Scions[a]

	metabolite	^{1}H chemical shifts (ppm) (functional group or specific H, multiplicity of peak)	^{13}C chemical shifts (ppm) (functional group or specific C)
1	2-hydroxybutyrate	**0.86** (CH_3, t); 1.6 (CH_2, m); 1.7 (CH_2, m); 3.9 (CH, m)	**10.0** (CH_3); 33 (CH_2); 29 (CH_2); 72 (CH)
2	leucine	**0.96**, 1.0 (H^{δ}, d); 1.7 (H^{γ}, m); 1.7 (H^{β}, m); 3.7 (H^{α}, m)	**24.0**, 25 (C^{δ}); 27 (C^{γ}); 43 (C^{β}); 56 (C^{α})
3	valine	**1.00**, **1.05** (H^{γ}, d); 2.3 (H^{β}, m); 3.6 (H^{α}, d)	**19.0**, **21.0** (C^{γ}); 32 (C^{β}); 63 (C^{α})
4	isoleucine	**0.92** (H^{δ}, t), **0.99** (H^{γ}, d); 1.2, 1.5 (H^{γ}, m); 2.0 (H^{β}, m); 3.7 (H^{α}, d)	**14.0** (C^{δ}); 18, **27.0** (C^{γ}); 39 (C^{β}); 62 (C^{α})
5	methylmalonate	**1.22** (CH_3, d); 3.1 (CH, q)	**18.0** (CH_3); 56 (CH, q)
6	alanine	**1.47** (H^{β}, d); **3.78** (H^{α}, q)	**19.2** (C^{β}); **53.3** (C^{α})
7	**melatonin**	**7.4** (^{4}CH, d); 7.2 (^{1}CH, d); **1.91**($^{8}CH_3$, s)	133 (^{4}CH); 120 (^{1}CH); **22.0** ($^{8}CH_3$)
8	methionine	**2.12** (H^{δ}, q)	**31.0** (C^{δ})
9	levulinate	**2.20** (CH_3, s); 2.4 (CH_2, t)	**32.0**(CH_3); 33 (CH_2)
10	4-aminobutyrate	**2.28** (CH_2, t); 1.9 (CH_2, m)	**43.0** (CH_2); 37 (CH_2)
11	malate	**2.36**, **2.66** (CH_2, dd); **4.29** (CH, dd)	**46.0** (CH_2); 73 (CH)
12	succinate	**2.40** (CH_2, s)	**36.9** (CH_2)
13	aspartate	**2.80**, **2.66** (H^{β}, dd); 3.9 (H^{α}, q)	**40.0** (C^{β}); 55 (C^{α})
14	asparagine	**2.83**, **2.92** (H^{β}, dd); 3.9 (H^{α}, q)	**38.0** (C^{β}); 54 (C^{α})
15	malonate	**3.10** (CH_2, s)	**50.0** (CH_2)
16	**choline**	**3.19** (CH_3, s); 3.5, 4.0 (CH_2, m)	**57.0** (CH_3); 70 (CH_2)
17	**glucose**	**5.22** ($^{1\beta}$CH, d); **4.64** ($^{1\alpha}$CH, d); **3.23** ($^{2\beta}$CH, dd); **3.52** ($^{2\alpha}$CH, dd); **3.48** ($^{3\beta}$CH, t); **3.70** ($^{3\alpha}$CH, t); **3.41** (^{4}CH, dd); **3.47** ($^{5\beta}$CH, m); **3.84** ($^{5\alpha}$CH, m); **3.71** ($^{6\beta}CH_2$, dd); **3.89** ($^{6\alpha}CH_2$, dd)	**95.0** ($^{1\beta}$CH); **99.0** ($^{1\alpha}$CH); **77.1** ($^{2\beta}$CH); **74.4** ($^{2\alpha}$CH); **78.6** ($^{3\beta}$CH); **75.6** ($^{3\alpha}$CH); **72.5** (^{4}CH); **78.8** ($^{5\beta}$CH); **74.4** ($^{5\alpha}$CH); **63.6** ($^{6}CH_2$)
18	maltose	5.2 (^{1}CH, d); **3.60** (^{2}CH, m); **3.65** (^{3}CH, t); **3.41** (^{4}CH, t); 3.7 (^{5}CH, m); 3.8 ($^{6}CH_2$, m); **5.41** ($^{1'}$CH, dd); **3.27** ($^{2'}$CH, t); **3.97** ($^{3'}$CH, m); 3.7 ($^{4'}$CH, t); **3.68**, **3.90** ($^{5\alpha\beta'}$CH, m); 3.8 ($^{6'}CH_2$, m)	95 (^{1}CH); **74.6** (^{2}CH); **75.4** (^{3}CH); **78.8** (^{4}CH); 75 (^{5}CH); 63 ($^{6}CH_2$); **102.5** ($^{1'}$CH); **77.0** ($^{2'}$CH); **76.2** ($^{3'}$CH); 72 ($^{4'}$CH); **79.7**, **72.4** ($^{5\alpha\beta'}$CH); 63 ($^{6'}CH_2$)
19	**fructose**	**3.56**, **3.70** ($^{1}CH_2$, dd); **3.80** (^{3}CH, d); **4.12** (^{4}CH, d); **3.81** (^{5}CH, d); **3.56**, **3.69** ($^{6}CH_2$, dd)	**66.8** ($^{1}CH_2$); **70.4** (^{3}CH); **77.3** (^{4}CH); **70.5** (^{5}CH); **65.3** ($^{6}CH_2$)
20	galactose	**3.48** (^{2}CH, q); **3.64** (^{3}CH, dd); **3.74** (^{3}CH, m); 3.9, **3.98** (^{4}CH, q); **4.58**, **5.25** (^{1}CH, d)	**75.0** (^{2}CH); **71.0** (^{3}CH); **65**.0 (^{3}CH); 70 (^{4}CH); **99.0** (^{1}CH)
21	**IAA**	**7.38** (^{4}CH, d); **3.58** ($^{1}CH_2$,S); 6.8 (^{6}CH, d)	**133.5** (^{4}CH); **62.0**($^{1}CH_2$); (^{6}CH, d); 118(^{6}CH)
22	myo-inositol	3.2 (^{1}CH, t); **3.52**, (^{3}CH, dd); 3.6 (^{2}CH, t); 4.0(^{4}CH, t)	77 (^{1}CH); **74.0** (^{3}CH); 75 (^{2}CH, t); 75 (^{4}CH)
23	guanosine	**5.93** (^{1}CH, d); 7.9 (^{2}CH, s)	**92.0** (^{1}CH); 140 (^{2}CH)
24	adenosine	**6.06** (^{1}CH, d); 8.2, 8.3 (^{2}CH, s)	**91.0** (^{1}CH); 143 (^{2}CH)
25	**fumarate**	**6.50** (CH, s)	**138.2** (CH)
26	glycerate	3.6 ($^{2}CH_2$, q); 3.8 ($^{2}CH_2$, dd); **4.07** (^{1}CH, q)	66.9 ($^{2}CH_2$); **76.0** (^{1}CH)
27	glycine	**3.57** (H^{α}, s)	**44.3** (C^{α})

[a] ^{1}H chemical shifts (ppm) and their corresponding ^{13}C chemical shifts (ppm) are listed. Bold chemical shifts indicate an identified peak in the spectra. Bold metabolite names indicate metabolites that were found to be statistically significant (in concentration change) in the comparison between resistant and susceptible watermelon tissues.

DOI: 10.1021/acs.jafc.5b02108
J. Agric. Food Chem. 2015, 63, 8083−8091

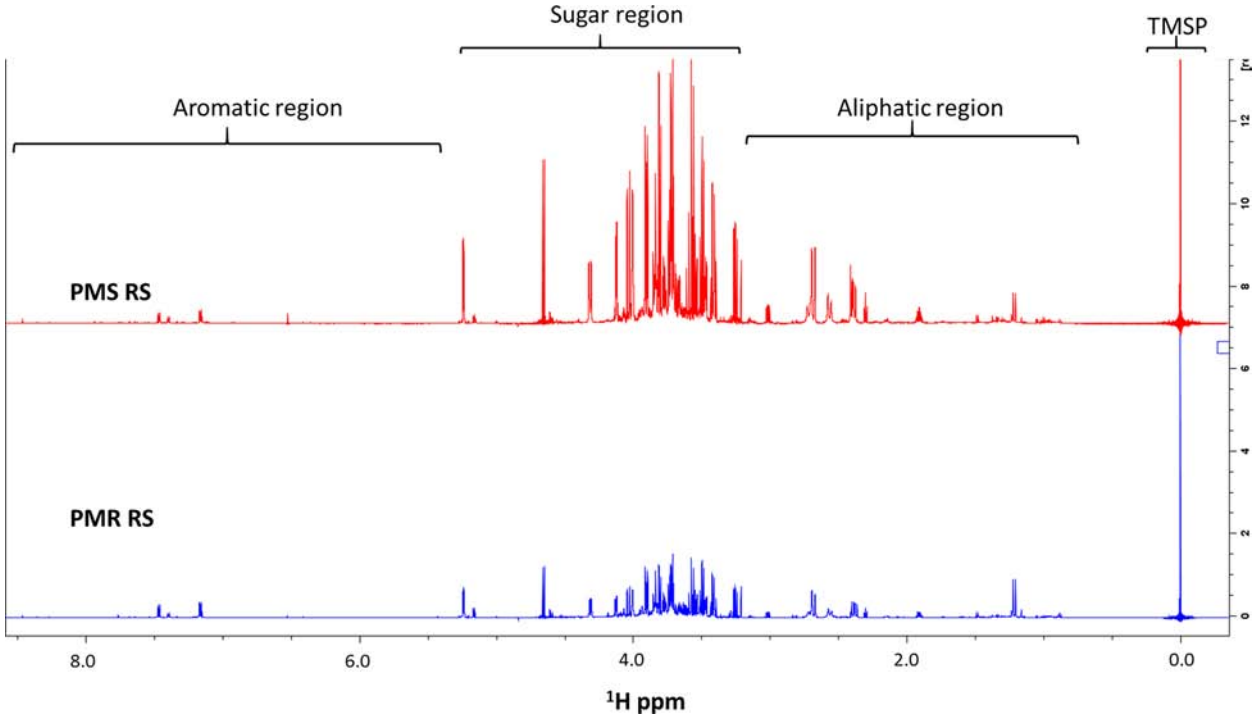

Figure 1. Proton spectral comparisons. Higher intensity of ^{1}H signals were observed for sugar compounds in powdery mildew susceptible rootstocks (PMS RS) compared to powdery mildew resistant rootstocks (PMR RS). The spectra were scaled with the internal reference and standard TMSP (1 mM).

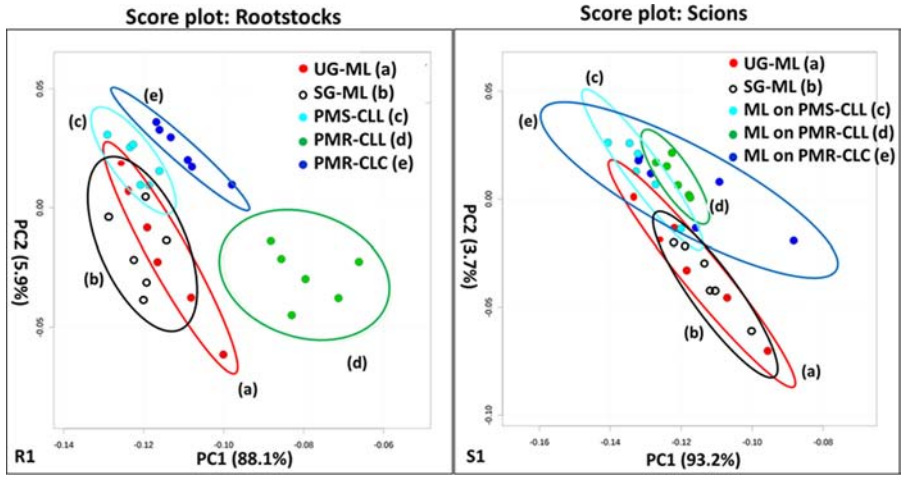

Figure 2. PCA score plots. PC1 versus PC2 score plots are shown for each. The total explained variance is >90%. The ovals represent 95% confidence intervals. Each oval represents a sample group, and each point in the oval represents a single sample/spectrum. R1 represents all of the rootstock samples: UG-ML, ungrafted Mickey Lee (a); SG-ML, self-grafted Mickey Lee (b); powdery mildew susceptible (PMS) rootstock PMS-CLL; (c) powdery mildew resistant (PMR) rootstocks PMR-CLL (d); PMR rootstocks PMR-CLC (e). S1 represents all of the corresponding grafted scions (PMS Mickey Lee) on all rootstocks.

Europe for managing soilborne diseases.[8,9] Watermelon scions are grafted on various rootstocks including bottle gourds, intraspecific squash hybrids, and watermelons.[10,11] Grafting is generally done using various methods such as approach graft, hole insertion graft, or single-cotyledon graft.[10] The U.S. Vegetable Laboratory (USVL), USDA-ARS, in Charleston, SC, USA, has developed a watermelon with resistance to PM as a part of their prebreeding program using grafting techniques. In preliminary experiments, moderate but significant levels of resistance to PM and fruit rot were reported in grafted watermelon (commercial PM susceptible scion grafted on wild PM resistant rootstock). To understand what specific resistance components translocate from resistant rootstocks to the susceptible scion Mickey Lee through grafting, we utilized NMR-based metabolomics, a novel analytical chemical approach for biomarker discovery. This is rapidly being applied to the development of diagnostic tools for a variety of environmental conditions as well as diseases in animals and humans.[12]

In food science, various analytical techniques including NMR, UPLC-MS, and GC-MS are widely used in targeted as well as untargeted metabolomics studies.[13] Among these, NMR-based metabolomics is a burgeoning analytical tool to investigate metabolism due to its nondestructive and unbiased nature, robustness, reproducibility, and simultaneous wide-ranging detection patterns.[12,14] Recently in the plant biotechnology field, the NMR-based metabolomics approach has been extensively applied to develop protocols for plant metabolomics research,[14−20] plant

DOI: 10.1021/acs.jafc.5b02108
J. Agric. Food Chem. 2015, 63, 8083−8091

disease research,[21,22] and plant metabolic profiling[23,24] and also in plant tissue culture research.[25−27]

In this study, we compared metabolic profiles of powdery mildew susceptible (PMS) and resistant (PMR) watermelon rootstocks to identify differences in their metabolic profiles using NMR spectroscopy. We also verified translocation of metabolites from resistant rootstocks to susceptible scions in grafted watermelon plants.

MATERIALS AND METHODS

Experimental Design. Mickey Lee (PM susceptible watermelon cultivar) scions individually were grafted using the one cotyledon grafting method[10] to two varieties of watermelon rootstocks, *C. lanatus* var. *lanatus* (CLL) and *C. lanatus* var. *citroides* (CLC), and two lines for each variety (Table 1) for a total of four PMR lines. Each combination of grafting was performed six times (six replications) and planted in trays in a greenhouse. Two independent experiments were conducted for each variety (CLL or CLC) of grafted plant. Additionally, six replicates of ungrafted Mickey Lee (ML-UG) were used as negative controls for both the PMS comparisons and self-grafted Mickey Lee (ML-SG) comparisons. All plants were of the same age and were grown in the same experimental conditions.

Sample Harvesting and Metabolism Quenching. To harvest each sample from 8-week-old grafted plants, 1 cm of rootstock (stem) directly below the grafting site and 1 cm of scion (stem) directly above the grafting site were collected. At the same time, 1 cm leaf tissues as well as cotyledon tissue were collected separately from rootstocks and their corresponding scion. The samples were immediately submerged into liquid nitrogen to quench all metabolic processes and to prevent any stress responses from the cutting process. Frozen samples were then lyophilized for 48 h, at −40 °C and 0.05 mPa, to remove all water and permanently quench metabolism. Once the samples were dried, they were manually homogenized prior to extraction.

Metabolite Extraction. Methanol−chloroform−water extractions of the dried rootstocks were performed as described in ref 15. Briefly, 20 mg of dried and homogenized plant material was used for each sample/replicate, and the solvent volumes were calculated using the dry mass to achieve a constant ratio of 2:2:1.8 of chloroform/methanol/water according to the Bligh and Dyer method.[28,29] The dried plant material was rehydrated with the appropriate ice-cold methanol/water solution. After vortex-mixing, the mixture was transferred into the ice-cold chloroform/water solution in glass tubes. The sample was incubated on ice for 10 min and centrifuged for 10 min at 2000*g* at 4 °C. The top layer, that is, the hydrophilic extract, was transferred into new microcentrifuge tubes. The hydrophilic extracts were dried using a Centrivap centrifuge for ∼15 h and stored at −20 °C until further preparation for NMR analysis.

NMR Sample Preparation and Spectroscopy. The dried hydrophilic extracts from each sample were resuspended in 620 μL of NMR buffer (100 mM sodium phosphate buffer (pH 7.3), 1 mM 3-(trimethylsilyl)propionic-2,2,3,3-d_4 acid (internal standard, TMSP; CAS Registry No. 24493-21-8), and 0.1% sodium azide, in 99.9 atom % D_2O) and then vortex-mixed and centrifuged to remove any remaining undissolved material. The experiments were conducted at 298 K using 600 μL of sample in 5 mm NMR tubes (Norell). All NMR spectra were recorded on a Bruker Avance III spectrometer operating at 700 MHz. The first increment of a presat-noesy experiment was acquired using the standard Bruker noesypr1d pulse sequence. This resulted in a one-dimensional ^{1}H spectrum (metabolic profile) for each sample. All data were collected using a spectral width of 16.0 ppm and 64K points resulting in an acquisition time of 2.9 s. The spectra were collected with 120 scans, 4 dummy scans, 3 s relaxation delay, and presaturation at the residual water frequency. The 90° pulse widths were measured for each sample using the automatic pulse calculation experiment (pulsecal) in TopSpin 2.1.1 (BrukerBioSpin, Billerica, MA, USA). Two-dimensional ^{1}H−^{13}C HSQC data were collected for a representative rootstock and scion sample using the Bruker hsqcedetgpsisp2.2 pulse sequence. The ^{1}H was observed in the F2 channel with a spectral width of 11 ppm,

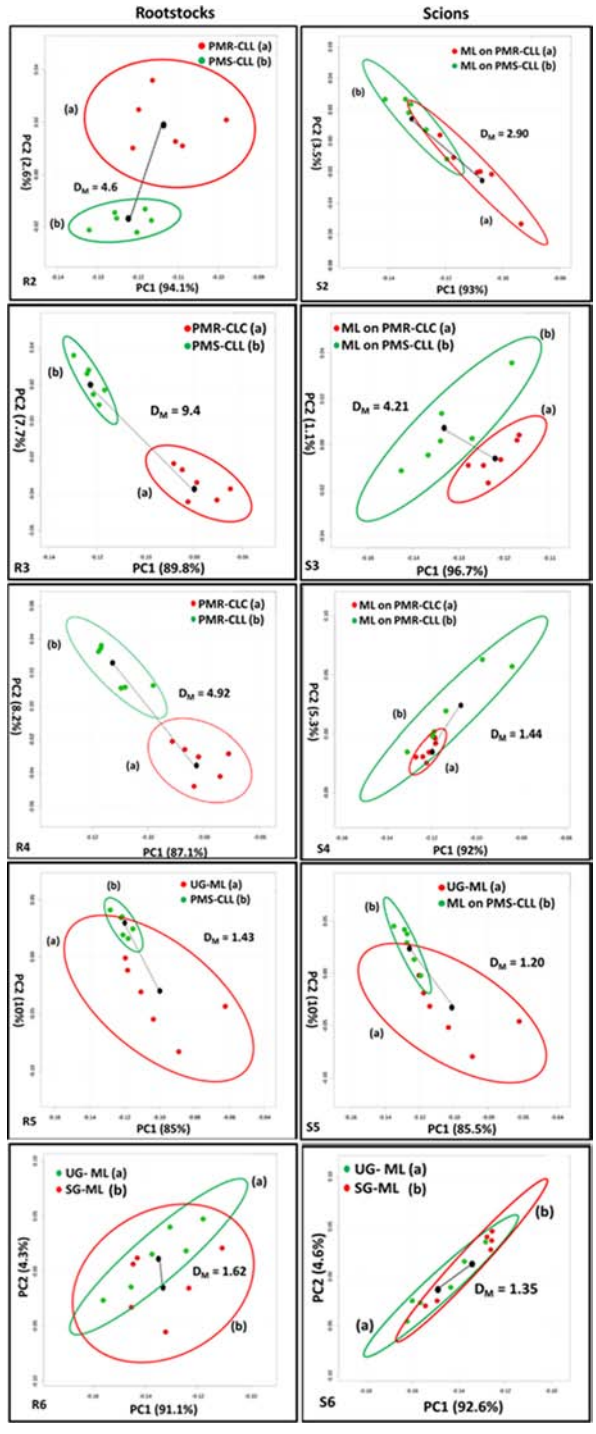

Figure 3. Pairwise PCA score plots. PC1 versus PC2 score plots are shown for each pairwise comparison. In each, the total explained variance is >90%. The ovals represent 95% confidence intervals. R2, R3, R4, R5, and R6 are pairwise comparisons of rootstocks: R2, PMR-CLL (a) versus PMS-CLL (b); R3, PMR-CLC (a) versus PMS-CLL (b); R4, PMR-CLC (a) versus PMR-CLL (b); R5, UG-ML (a) versus PMS-CLL (b); R6, UG-ML(a) versus SG-ML (b). S2, S3, S4, S5, and S6 are pairwise comparisons of the corresponding scions: S2, ML grafted on PMR-CLL (a) versus ML grafted on PMS-CLL (b); S3, ML grafted on PMR-CLC (a) versus ML grafted on PMS-CLL (b); S4, ML grafted on PMR-CLC (a) versus ML grafted on PMR-CLL (b); S5, UG-ML (a) versus ML grafted on PMS-CLL (b); S6, UG-ML (a) versus SG-ML (b). The Mahalanobis distances (D_M) are listed for each.

DOI: 10.1021/acs.jafc.5b02108
J. Agric. Food Chem. 2015, 63, 8083−8091

Table 3. Statistical Significance Analysis[a]

statistical parameter	R2	S2	R3	S3	R4	S4	R5	S5	R6	S6
D_M	4.6	2.90	9.4	4.21	4.92	1.44	1.43	1.20	1.62	1.35
T^2	70	25.33	265.4	52.91	72.72	6.21	6.09	4.56	7.16	5.72
F_c	4.96	4.96	4.96	4.96	4.96	4.96	4.96	4.96	4.96	4.96
F_t	**31.9**	**11.40**	**119.4**	**23.81**	**32.73**	2.84	2.74	2.10	3.25	2.45
significance status	**yes**	**yes**	**yes**	**yes**	**yes**	no	no	no	no	no

[a]Mahalanobis distance (D_M), two-sample Hotellings' T^2 test, and F test values shown, where F-true > F-critical indicates a statistically significant separation between the groups. R2, R3, R4, S2, and S3 have statistically significant separations, whereas R5, R6, S4, S5, and S6 do not.

whereas the ^{13}C was observed in the F1 channel with a spectral width of 180 ppm.

NMR Data Analysis. *Multivariate Statistical Analysis.* Prior to principal component analyses (PCA), bucket tables were generated by using AMIX software (version 3.9.7, BrukerBioSpin). Once data were normalized to total intensities, spectra were binned into 0.01 ppm wide buckets over the region of 0.5−10.0 ppm using advanced bucketing in AMIX. Other bucket widths (either larger or smaller) resulted in similar results. The water region (4.75−4.90 ppm) of the spectra was eliminated for all analyses. No scaling method was found necessary. PCA was performed on the bucket tables generated from AMIX using MetaboAnalyst 2.0 (MetaboAnalyst 2.0, a comprehensive server for metabolomic data analysis).[30] For each score plot generated during the analysis, the Mahalanobis distance (D_M), two-sample Hotelling's T^2 statistic (T^2), F values (F_t) and critical F values (F_c) were calculated using MatLabR2010b.[31]

Spectral Analysis and Metabolite Identification. To identify the metabolites that are different in concentration when resistant and susceptible rootstocks and scions were compared, fold changes and related p values were determined for each bucket. The calculations of fold changes and t tests were performed with MetaboAnalyst 2.0 to determine whether or not the changes in bucket intensities were statistically significant. Buckets with corresponding p values <0.05 were considered statistically significant. The metabolites corresponding to these peaks in the buckets were identified using the Biological Magnetic Resonance Data Bank (BMRB) (http://www.bmrb.wisc.edu/metabolomics/), Madison Metabolomics Consortium Database (MMCD) (http://mmcd.nmrfam.wisc.edu/), ChenomX NMR Suite (ChenomX Inc., Edmonton, AB, Canada), and published studies.[32,33] Metabolic data interpretation was facilitated with the Metabolic Pathway Analysis (MetPA) component of MetaboAnalyst 2.0.[30]

RESULTS AND DISCUSSION

NMR-based metabolomics was used to idenitfy and study PMR-related metabolites in resistant wild rootstocks of watermelon as well as metabolite translocation to the corresponding susceptible watermelon commercial cultivar scion, Mickey Lee (ML).

Metabolic Profile Comparisons. Metabolic profile comparisons were made between PMR rootstocks and PMS rootstocks as well as their corresponding susceptible ML scions. Two independent experiments were conducted for each variety of rootstock shown in Table 1. Similar results were observed for repetitive experiments as well as for both varieties of PMR-CLL (USVL531 and USVL516) and PMR-CLC (USVL225 and USVL331); therefore, only the results from one of each experiment are described here.

By 1D ^1H NMR spectroscopy, we identified 27 metabolites from rootstocks as well as their corresponding scions as shown in Table 2 and Supplemental Figure 1. The 1D proton spectral comparison between powdery mildew resistant rootstock and its corresponding PMS ML scion showed distinct differences in signal intensities, specifically in the sugar zone, which is higher in intensity in the case of susceptible cultivar than wild resistant variety due to the presence of high sugar compounds (Figure 1). Similar metabolic profile comparison trends were also investigated for both leaf and cotyledon tissues from resistant and susceptible groups (data not shown). We verified the assignments of the metabolites identified from rootstocks as well as their corresponding scions using 2D $^1H-^{13}C$ NMR spectral data (Supplemental Figure 2).

Multivariate Statistical Analysis. *Rootstock Comparisons.* PCA score plots showed clear separations between the metabolic profiles of susceptible and resistant rootstocks (Figures 2R1 and 3R2,R3), indicating distinct differences in the metabolism of the two types (PMR and PMS) of rootstocks. Pairwise metabolic profile comparisons were made between PMR CLL rootstocks and PMS CLL rootstocks (R2), between PMR CLC rootstocks and PMS-CLL rootstocks (R3), between PMR-CLL rootstocks and PMR-CLC rootstocks (R4), between PMS-CLL rootstocks and ungrafted ML (UG-ML) rootstocks (R5), and between PMS-CLL rootstocks and self-grafted ML (SG-ML) rootstocks (R6). Significant separations between the susceptible and resistant metabolic profiles were observed in R2 and R3 rootstock comparisons (Figure 3 and Table 3). These significant separations indicate distinct differences in the metabolism between the susceptible and resistant rootstocks. In the R4 comparison between two resistant rootstocks (PMR-CLL and PMR-CLC), a significant separation was also observed. This result may be attributed to the fact that these two watermelon varieties have distinct genetic differences.[34,35] Moreover, the R5 comparison did not show significant separations, most likely because both of these varieties are susceptible to powdery mildew. A nonsignificant separation in R6 comparison where SG-ML rootstock was compared with UG-ML rootstock indicates that the stress of the grafting process did not contribute to the metabolic difference between the resistant and susceptible rootstocks.

Scion (Grafted on PMR and PMS Rootstock) Comparisons. PCA score plots also showed separations between the metabolic profiles of ML scions grafted on susceptible and resistant rootstock sources (Figures 2S1 and 3S2,S3), indicating possible translocation of metabolites related to PM resistance from PMR rootstocks to the susceptible scion after grafting. Similar to rootstock comparisons, pairwise metabolic profile comparisons were made between susceptible ML scions grafted on rootstocks of PMR CLL and PMS CLL (S2), between susceptible ML scion grafted on rootstocks of PMR CLC and PMS-CLL (S3), between susceptible ML scion grafted on rootstocks of PMR-CLL and PMR-CLC (S4), between susceptible ML scion grafted on rootstocks of PMS-CLL and UG-ML (S5), and between self-grafted ML scion grafted on rootstocks of ML and UG-ML (S6). Significant separations were observed in S2 and S3 comparisons (Figure 3 and Table 3). S4 comparisons did not show a significant metabolic profile separation, which is most likely because translocation of metabolites from both resistant rootstocks (PMR-CLL and PMR-CLC) could be quantitatively similar, excluding glucose and fructose. Similarly, in the S5 comparison, no significant metabolic profile separations were observed,

DOI: 10.1021/acs.jafc.5b02108
J. Agric. Food Chem. 2015, 63, 8083−8091

probably because both the rootstock and scion sources were susceptible (PMS-CLL and UG-ML). Moreover, in the S6 self-grafted comparison, no significant metabolic profile separations were observed, which indicates minor stress contributions from grafting.

Mahalanobis Distance (D_M). For each pairwise comparison described above and shown in Figure 3, a calculated D_M indicates the magnitude of the metabolic profile separation. This distance was considered significant on the basis of the other calculated values given in Table 3 and described in ref 31. If the F_t value is higher than the F_c value, then D_M represents a statistically significant separation in the comparison, which is the case for R2, R3, R4, S2, and S3.

Identification of Metabolites and Determination of Fold Changes. Each data point in a score plot represents all metabolites present in one sample; therefore, the separations between the grouped metabolic profiles can be based on individual metabolites. Metabolite differences (qualitative or quantitative) that contribute to score plot separations were identified using loading plots (Supplemental Figure 3), and their fold changes were determined using volcano plots (Supplemental Figure 4). On the basis of the fold changes of aligned and normalized bucket intensities, choline, 5-hydroxyindole-3-acetate (IAA), melatonin, fumarate, glucose, and fructose were identified from PMR rootstocks as well as their corresponding PMS scions as significantly different in concentration (Table 4) in the spectra of R2, R3, R4, S2, and S3 comparisons, whereas in spectra used for R5, R6, S4, S5, and S6 comparisons, only glucose and fructose showed significant concentration differences. Choline, IAA, and melatonin have higher concentrations, whereas fumarate, glucose, and fructose have lower concentrations, in PMR rootstocks as well as their corresponding PMS scions (Figure 4 and Supplemental Figure 5). Sugars (glucose and fructose) have decreased concentrations in both the PMR-CLL and PMR-CLC rootstocks. To find out the potential role of these metabolites in disease resistance, we conducted metabolic pathway analysis.

Metabolic Pathway Analysis. Metabolic pathway analysis was performed using MetPA[30] for grafted watermelon metabolites that were affected by powdery mildew disease. Pathway analysis suggested the involvement of 11 statistically significant metabolic pathways based on p values <0.05 and an impact factor threshold >0. Metabolic profile analysis of ML scion 2 months after grafting on PMR and PMS rootstocks revealed that the PM disease regulates an array of metabolites involved in pathways. Levels of choline, IAA, melatonin, fumarate, glucose, and fructose changed significantly in response to grafting on PMR rootstocks and are labeled in the various pathways shown in Figure 5.

This study identified and verified the metabolites choline, IAA, melatonin, fumarate, glucose, and fructose in PMR rootstocks and their corresponding ML scions as significantly different in concentration. Investigation showed significantly increased levels of choline, melatonin, and IAA (1.5, 3.21, and 2.51 FC, respectively) in PMR rootstocks and their corresponding scions and significantly decreased levels (0.62, 0.35, and 0.45 FC, respectively) in PMS watermelon rootstocks and their corresponding scions (Figure 4) and also significantly decreased levels of fumarate, glucose, and fructose (0.62, 0.28, and 0.15 FC, respectively) in PMR rootstocks and their corresponding scions and significantly increased levels (1.45, 2.35, and 3.12 FC, respectively) in PMS watermelon rootstocks and their corresponding scions (Figure 4). Biochemical pathway analysis suggested that significantly higher levels of choline, melatonin, and IAA and lower levels of fumarate, glucose, and fructose are

Table 4. Commonly Identified PMR-Related Significant Metabolites[a]

	fold change = ratio of average bucket intensities ((a) and (b) labels correspond to those in Figure 3)											
significantly different metabolite	R2 PMR-CLL(a) PMS-CLL(b)	S2 ML on PMR-CLL(a) ML on PMS-CLL(b)	R3 PMR-CLC (a) PMS-CLL(b)	S3 ML on PMR-CLC(a) ML on PMS-CLL(b)	R4 PMR-CLC(a) PMR-CLL(b)	S4 ML on PMR-CLC(a) ML on PMR-CLL(b)	R5 UG-ML(a) PMS-CLL(b)	S5 UG-ML(a) ML on PMS-CLL(b)	R6 UG-ML(a) SG-ML(b)	S6 UG-ML(a) SG-ML(b)
choline	**1.48**	**1.35**	**1.53**	**1.65**	**1.50**	–	–	–	–	–
melatonin	**3.19**	**2.28**	**3.24**	**2.41**	**3.20**	–	–	–	–	–
IAA	**2.47**	**1.87**	**2.55**	**1.98**	**2.52**	–	–	–	–	–
fumarate	0.58	0.53	0.61	–	0.66	–	–	–	–	–
glucose	0.32	0.25	0.34	0.30	0.39	0.81	2.35	2.21	0.56	0.21
fructose	0.41	0.39	0.46	0.49	0.46	0.72	3.12	2.97	0.41	0.18

[a]Choline, melatonin, 5-hydroxyindole-3-acetate, fumarate, glucose, and fructose have significant concentration differences in the spectra of R2, R3, R4, S2, and S3 comparisons. In spectra used for R5, R6, S4, S5, and S6 comparisons, all metabolites are present, but only glucose and fructose showed significant concentration differences. Each numerical value indicates the average fold change of the metabolite and was calculated by taking a ratio of the average bucket intensities: the specific ratio for each comparison is indicated. A fold change >1 indicates metabolites are up-regulated for the sample in the numerator. A fold change <1 indicates metabolites are down-regulated for the sample in the numerator. A dash indicates that the metabolite is present but not significantly different.

DOI: 10.1021/acs.jafc.5b02108
J. Agric. Food Chem. 2015, 63, 8083−8091

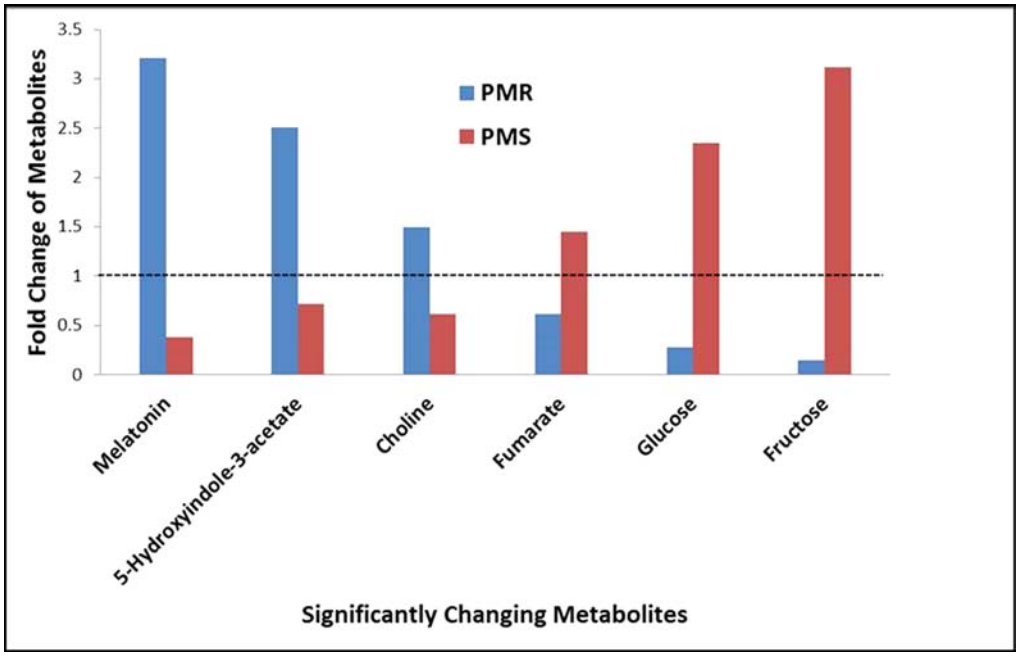

Figure 4. Fold-change analysis. Metabolites were determined to be significant on the basis of volcano plots in PMR of watermelon. Fold changes >1.00 indicate a net increase and fold changes <1.00 indicate a net decrease in the levels of metabolites. Choline, IAA, and melatonin have increased concentrations and glucose, fructose, and fumarate have decreased concentrations in PMR rootstocks as well as their corresponding scions when compared with PMS watermelon.

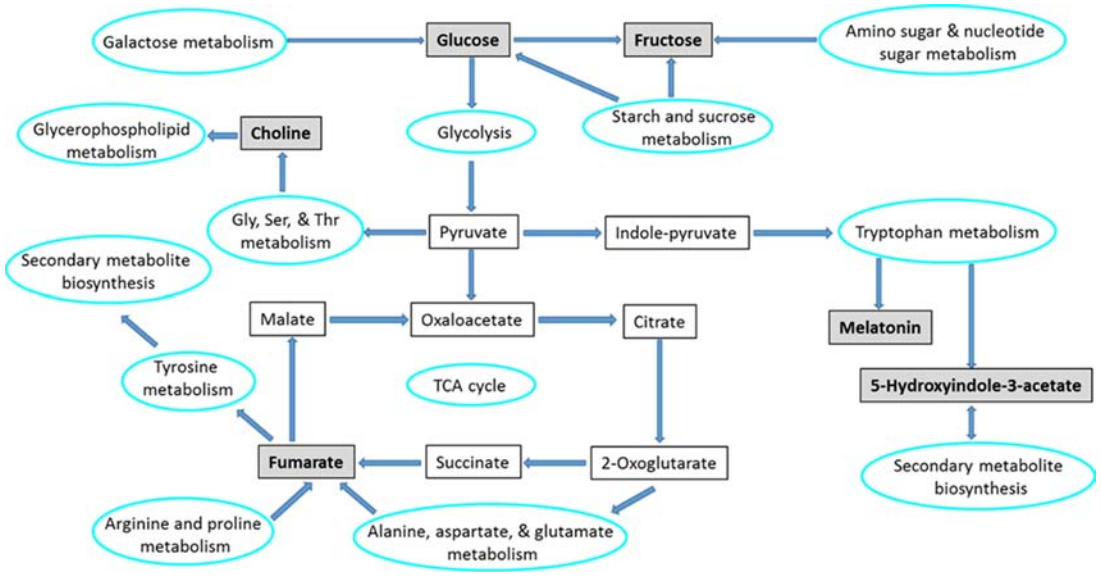

Figure 5. Biochemical pathway analysis. These metabolic pathways contain the metabolites that were determined to be significantly different in concentration when the resistant and susceptible watermelon tissues were compared and could lead to the synthesis of metabolites by response of powdery mildew disease in watermelon. The KEGG database and MetaboAnalyst were used to elucidate metabolic networks. The metabolites that accumulated and were identified as significantly different in concentration by NMR are shown in bold.

related to various amino acid metabolism pathways and may have a link with different secondary metabolite biosynthesis pathways.

Melatonin, an important tryptophan metabolism pathway derivative, has been shown to play a significant role in maintaining cellular stability, which may provide an important mechanism for the survival of many plant species.[36] Also, exogenously applied melatonin improved the resistance capacity to Marssonina apple blotch (*Diplocarpon mali*) and enhanced the activities of plant defense-related enzymes, possibly improving disease resistance.[37] Interestingly, the powdery mildew pathogen (*P. xanthii*) also belongs to the same division as apple blotch (*D. mali*): Ascomycotaas. Melatonin also acts as an effective free radical scavenger and natural antioxidant and even has protective mechanisms in mitochondria and chloroplasts.[38] Additionally, it acts as a plant protector against environmental insults, and high levels of melatonin have been identified in a pollutant-resistant plant: the water hyacinth *Eichhornia crassipes*.[39] Another important metabolite in tryptophan metabolism, IAA, has also been shown to play a significant role in plant defense. For example, in tomato, IAA reduced the tomato wilt pathogen

DOI: 10.1021/acs.jafc.5b02108
J. Agric. Food Chem. 2015, 63, 8083−8091

Fusarium oxysporum lycopersici spore germination, mycelial dry weight, and protein content.[40] IAA and abscisic acid (ABA) are involved in the *Pseudomonas fluorescens*-mediated control of *Fusarium* head blight disease of barley.[41] Resistance to necrotrophic fungi is reduced in IAA signaling mutants.[42] Moreover, plant−pathogen interactions identify IAA as a key character in pathogenesis and plant defense.[43] Some of the phenylpropanoids (caffeoyl and 5-hydroxyferuloyl malate) together with IAA decreased significantly after fungal infection in *Brassica rapa*.[44]

Additionally, choline was found to be involved with glycine, serine, and threonine metabolism and also interacted with fatty acid and secondary metabolite biosynthesis pathways (Figure 5). It is reported that *P. syringae* pv tomato strain DC3000 derived greater osmoprotection from exogenous choline, which is distinct from most bacterial species.[45] Choline and phosphorylcholine are ubiquitous in plants, whereas glycine betaine is produced in detectable amounts by some plant species but not others, and betaine and choline levels have a relationship with NaCl stress.[46] The control plants of *Brassica rapa* were characterized by high levels of choline but their fungal infected counterpart has a lower level of choline.[44] *Brassica rapa* plants infected with *Fusarium oxysporum* fungi produced higher concentrations of glucose and fumaric acids.[44]

We also speculate that the increased concentrations of choline, IAA, and melatonin indicate involvement of these naturally occurring metabolites in powdery mildew or other types of disease resistance in watermelon. From the corresponding PMS Mickey Lee scion metabolic profiles, we also identified the same PMR-related metabolites as significantly increased in concentration, therefore validating our hypothesis that melatonin, IAA, and choline were translocated from PMR rootstocks to the PMS commercial Mickey Lee (watermelon) scion through grafting. Further studies to confirm this hypothesis by applying these chemicals or their analogues on a PMS line are warranted.

In summary, we identified choline, IAA, melatonin, fumarate, glucose, and fructose to be significantly different in concentration in PMR lines compared to the PMS lines. PCA showed significant metabolic profile separations between the susceptible and resistant groups, indicating distinct differences in the metabolisms of the two types of rootstocks as well as their corresponding PMS scion. Pairwise comparisons of each variety of PMR rootstock with the PMS rootstock as well as their corresponding scions showed significant separations, and calculated Mahalanobis distances (D_M) indicated that both PMR-CLL and PMR-CLC varieties have a statistically significant difference in metabolic profiles when compared to the susceptible varieties. Choline, IAA, and melatonin have higher concentrations, whereas fumarate, glucose, and fructose have lower concentrations, in PMR rootstocks and their corresponding scions.

The present study revealed that NMR-based metabolomics is a useful technique to identify potential metabolites that may play a role in powdery mildew resistance in watermelon. Our results stem from the observance of PM resistance on susceptible grafted scions in greenhouse studies.

■ ASSOCIATED CONTENT

Supporting Information

The Supporting Information is available free of charge on the ACS Publications website at DOI: 10.1021/acs.jafc.5b02108

Supplemental Figures 1−5 (1D ^{1}H NMR spectral comparison; corresponding 2D ^{1}H−^{13}C NMR spectrum; loading plots corresponding to PCA score plots; volcano plots corresponding to PCA loading plots; box plots and whisker plots (PDF)

■ AUTHOR INFORMATION

Corresponding Author

*(A.F.B.) E-mail: aboroujerdi@claflin.edu.

Notes

The authors declare no competing financial interest.

■ ACKNOWLEDGMENTS

A.F.B. is supported by SC-INBRE (2 P20 GM103499). Miki Watanabe is thanked for her methods development work. Jennifer Ikerd and Mark Schaffer of USDA are thanked for their assistance. No trademark names or proprietary products constitute a guarantee of the product by USDA, ARS, Clemson University or Claflin University, nor do they imply exclusion of other suitable products.

■ REFERENCES

(1) McGrath, M. T.; Thomas, C. E. Powdery mildew. In *Compendium of Cucurbit Diseases*; APS Press: St. Paul, MN, USA, 1996; pp 29−30.

(2) McGrath, M. *Managing cucurbit powdery mildew organically*; http://www.extension.org/pages/30604/managing-cucurbit-powdery-mildew-organically#.Uv6OTWJdXni (accessed Aug 10, 2015).

(3) Keinath, A. P. Effect of protectant fungicide application schedules on gummy stem blight epidemics and marketable yield of watermelon. *Plant Dis.* **2000**, *84*, 254−260.

(4) Cohen, R.; Burger, Y.; Katzir, N. Monitoring physiological races of *Podosphaera xanthii* (syn. *Sphaerotheca fuliginea*), the causal agent of powdery mildew in cucurbits: factors affecting race identification and the importance for research and commerce. *Phytoparasitica* **2004**, *32*, 174−183.

(5) Keinath, A. P.; DuBose, V. B. Evaluation of fungicides for prevention and management of powdery mildew on watermelon. *Crop Prot.* **2004**, *23*, 35−42.

(6) Kousik, C. S.; Donahoo, R. S.; Webster, C. G.; Turechek, W. W.; Adkins, S. T.; Roberts, P. D. Outbreak of cucurbit powdery mildew on watermelon fruit caused by *Podosphaera xanthii* in southwest Florida. *Plant Dis.* **2011**, *95*, 1586.

(7) Hammett, K. R. W. Taxonomy of Erysiphaceae in New Zealand. *N. Z. J. Bot.* **1977**, *15*, 687−711.

(8) Bruton, B. D.; Fish, W. W.; Roberts, W.; Popham, W. The influence of rootstock selection on fruit quality attributes of watermelon. *Open Food Sci. J.* **2009**, *3*, 15−34.

(9) Davis, A. R.; Perkins-Veazie, P.; Sakata, Y.; Lopez-Galarza, S.; Maroto, J. V.; Lee, S. G.; Huh, Y. C.; Sun, Z.; Miguel, A.; King, S. R.; Cohen, R.; Lee, J. M. Cucurbit grafting. *Crit. Rev. Plant Sci.* **2008**, *27*, 50−74.

(10) Hassell, R.; Memmott, F.; Liere, D. Grafting methods for watermelon production. *HortScience* **2008**, *43*, 1677−1679.

(11) Kousik, C. S.; Donahoo, R. S.; Hassell, R. Resistance in watermelon rootstocks to crown rot caused by *Phytophthora capsici*. *Crop Prot.* **2012**, *39*, 18−25.

(12) Nicholson, J. K.; Lindon, J. C. Systems biology: metabonomics. *Nature* **2008**, *455*, 1054−1056.

(13) Cevallos-Cevallos, J. M.; Reyes-De-Corcuera, J. I.; Etxeberria, E.; Danyluk, M. D.; Rodrick, G. E. Metabolomic analysis in food science: a review. *Trends Food Sci. Technol.* **2009**, *20*, 557−566.

(14) Ward, J. L.; Beale, M. H. NMR spectroscopy in plant metabolomics. *Biotechnol. Agric. For.* **2006**, *57*, 81−91.

(15) Kim, H. K.; Choi, Y. H.; Verpoorte, R. NMR-based metabolomic analysis of plants. *Nat. Protoc.* **2010**, *5*, 536−549.

(16) Schripsema, J. Application of NMR in plant metabolomics: techniques, problems and prospects. *Phytochem. Anal.* **2010**, *21*, 14−21.

DOI: 10.1021/acs.jafc.5b02108
J. Agric. Food Chem. 2015, 63, 8083−8091

(17) Tarachiwin, L.; Masako, O.; Fukusaki, E. Quality evaluation and prediction of *Citrullus lanatus* by ^{1}H NMR-based metabolomics and multivariate analysis. *J. Agric. Food Chem.* **2008**, *56*, 5827−5835.
(18) Dixon, R.; Gang, D.; Charlton, A.; Fiehn, O.; Kuiper, H.; Reynolds, T.; Tjeerdema, R.; Jeffery, E.; German, J.; Ridley, W.; Seiber, J. Applications of metabolomics in agriculture. *J. Agric. Food Chem.* **2006**, *54* (24), 8984−8994.
(19) Pacifico, D.; Casciani, L.; Ritota, M.; Mandolino, G.; Onofri, C.; Moschella, A.; Parisi, B.; Cafiero, C.; Valentin, M. NMR-based metabolomics for organic farming traceability of early potatoes. *J. Agric. Food Chem.* **2013**, *61*, 11201−11211.
(20) Harrigan, G. G.; Skogerson, K.; MacIsaac, S.; Bickel, A.; Perez, T.; Li, X. Application of H-1 NMR profiling to assess seed metabolomic diversity. A case study on a soybean era population. *J. Agric. Food Chem.* **2015**, *63*, 4690−4697.
(21) Choi, Y. H.; Tapias, E. C.; Kim, H. K.; Lefeber, A. W. M.; Erkelens, C.; Verhoeven, J. T. J.; Brzin, J.; Zel, J.; Verpoorte, R. Metabolic discrimination of *Catharanthus roseus* leaves infected by phytoplasma using ^{1}H-NMR spectroscopy and multivariate data analysis. *Plant Physiol.* **2004**, *135*, 2398−2410.
(22) Lima, M. R. M.; Felgueiras, M. L.; Gracxa, G. NMR metabolomics of esca disease-affected *Vitis vinifera* cv. Alvarinho leaves. *J. Exp. Bot.* **2010**, *61*, 4033−4042.
(23) Kim, S. W.; Ban, S. H.; Jeong, S. C. Genetic discrimination between *Catharanthus roseus* cultivars by metabolic fingerprinting using ^{1}H NMR spectra of aromatic compounds. *Biotechnol. Bioprocess Eng.* **2007**, *12*, 646−652.
(24) Mahmud, I.; Chowdhury, A.; Boroujerdi, A. Tissue-specific metabolic profile study of *Moringa oleifera* L. using nuclear magnetic resonance spectroscopy. *Plant Tissue Cult. Biotechnol.* **2014**, *24*, 77−86.
(25) Mahmud, I.; Shrestha, B.; Boroujerdi, A.; Chowdhury, A. NMR-based metabolomics profile comparisons to distinguish between embryogenic and non-embryogenic callus tissue of sugarcane at the biochemical level. *In Vitro Cell. Dev. Biol.: Plant* **2015**, *51*, 340−349.
(26) Mahmud, I.; Thapaliya, M.; Boroujerdi, A.; Chowdhury, A. NMR-based metabolomics study of the biochemical relationship between sugarcane callus tissues and their respective nutrient culture media. *Anal. Bioanal. Chem.* **2014**, *406*, 5997−6005.
(27) Palama, T. L.; Menard, P.; Fock, I.; Choi, Y. H.; Bourdon, E.; Soulange, J. G.; Bahut, M.; Payet, B.; Verpoorte, R.; Kodja, H. Shoot differentiation from protocorm callus cultures of *Vanilla planifolia* (Orchidaceae): proteomic and metabolic responses at early stage. *BMC Plant Biol.* **2010**, *10*, 82.
(28) Bligh, E. G.; Dyer, W. J. A rapid method of total lipid extraction and purification. *Can. J. Biochem. Physiol.* **1959**, *37* (8), 911−917.
(29) Wu, H.; Southam, A. D.; Hines, A.; Viant, M. R. High-throughput tissue extraction protocol for NMR- and MS-based metabolomics. *Anal. Biochem.* **2008**, *372*, 204−212.
(30) Xia, J.; Mandal, R.; Sinelnikov, I. V.; Broadhurst, D.; Wishart, D. S. MetaboAnalyst 2.0 − a comprehensive server for metabolomic data analysis. *Nucleic Acids Res.* **2012**, *40* (Web Server issue), W127−W133.
(31) Goodpaster, A. M.; Kennedy, M. A. Quantification and statistical significance analysis of group separation in NMR-based metabonomics studies. *Chemom. Intell. Lab. Syst.* **2011**, *109*, 162−170.
(32) Beckonert, O.; Keun, H. C.; Ebbels, T. M.; Bundy, J.; Holmes, E.; Lindon, J. C.; Nicholson, J. K. Metabolic profiling, metabolomic and metabonomic procedures for NMR spectroscopy of urine, plasma, serum and tissue extracts. *Nat. Protoc.* **2007**, *2* (11), 2692−2703.
(33) MacIntyre, D. A.; Jimenez, B.; Lewintre, E. J.; Martin, C. R.; Schafer, H.; Ballesteros, C. G.; Mayans, J. R.; Spraul, M.; Garcia-Conde, J.; Pineda-Lucena, A. Serum metabolome analysis by ^{1}H-NMR reveals differences between chronic lymphocytic leukaemia molecular subgroups. *Leukemia* **2010**, *24* (4), 788−797.
(34) Hwang, J.; Kang, J.; Son, B.; Kim, K.; Park, Y. Genetic diversity in watermelon cultivars and related species based on AFLPs and EST-SSRs. *Not. Bot. Hortic. Agrobo.* **2011**, *39* (2), 285−292.
(35) Levi, A.; Thies, J. A.; Wechter, W. P.; Kousik, C. S.; Ling, K.; Harrison, H. F., Jr; Simmons, A. M.; Reddy, U. K.; Nimmakayala, P.; Fei, Z. Exploiting genetic diversity in *Citrullus* spp. to enhance watermelon cultivars. *Acta Hortic.* **2012**, 41−48.
(36) Murch, S. J.; Saxena, P. K. Melatonin: a potential regulator of plant growth and development? *In Vitro Cell. Dev. Biol.: Plant* **2002**, *38*, 531−536.
(37) Yin, L.; Wang, P.; Li, M.; et al. Exogenous melatonin improves *Malus* resistance to Marssonina apple blotch. *J. Pineal Res.* **2013**, *54*, 426−434.
(38) Tan, D. X.; Manchester, L. C.; Liu, X.; Corral, S. A. R.; Castroviejo, D. A.; Reiter, R. J. Mitochondria and chloroplasts as the original sites of melatonin synthesis: a hypothesis related to melatonin's primary function and evolution in eukaryotes. *J. Pineal Res.* **2013**, *54*, 127−138.
(39) Tan, D. X.; Manchester, L. C.; Di Mascio, P.; Martinez, G. R.; Prado, F. M.; Reiter, R. J. Novel rhythms of N1-acetyl-N2-formyl-5-methoxy-kynuramine and its precursor melatonin in water hyacinth: importancefor phytoremediation. *FASEB J.* **2007**, *21*, 1724−1729.
(40) Sharaf, E. F.; Farrag, A. A. Induced resistance in tomato plants by IAA against *Fusarium oxysporum lycopersici*. *Polym. J. Microbiol.* **2004**, *53*, 111−116.
(41) Petti, C.; Reiber, K.; Ali, S. S.; Berney, M.; Doohan, F. M. Auxin as a player in the biocontrol of *Fusarium* head blight disease of barley and its potential as a disease control agent. *BMC Plant Biol.* **2012**, *12*, 224.
(42) Llorente, F.; Muskett, P.; Sánchez-Vallet, A.; et al. Repression of the auxin response pathway increases *Arabidopsis* susceptibility to necrotrophic fungi. *Mol. Plant* **2008**, *1*, 496−509.
(43) Fu, J.; Liu, H.; Li, Y.; Yu, H.; Li, X.; Xiao, J.; Wang, S. Manipulating broad-spectrum disease resistance by suppressing pathogen-induced auxin accumulation in rice. *Plant Physiol.* **2011**, *155*, 589−602.
(44) Abdel-Farid, I. B.; Jahangir, M.; van den Hondel, C. A. M. J. J.; Kim, H. K.; Choi, Y. H.; Verpoorte, R. Fungal infection-induced metabolites in *Brassica rapa* cultivars. *Plant Sci.* **2009**, *176*, 608.
(45) Chen, C. L.; Beattie, G. A. Characterization of the osmoprotectant transporter OpuC from *Pseudomonas syringae* and demonstration that cystathionine-beta-synthase domains are required for its osmoregulatory function. *J. Bacteriol.* **2007**, *189*, 6901−6912.
(46) Storey, R.; Wyn Jones, R. G. Betaine and choline levels in plants and their relationship to NaCl stress. *Plant Sci. Lett.* **1975**, *4*, 161−168.

DOI: 10.1021/acs.jafc.5b02108
J. Agric. Food Chem. 2015, 63, 8083−8091

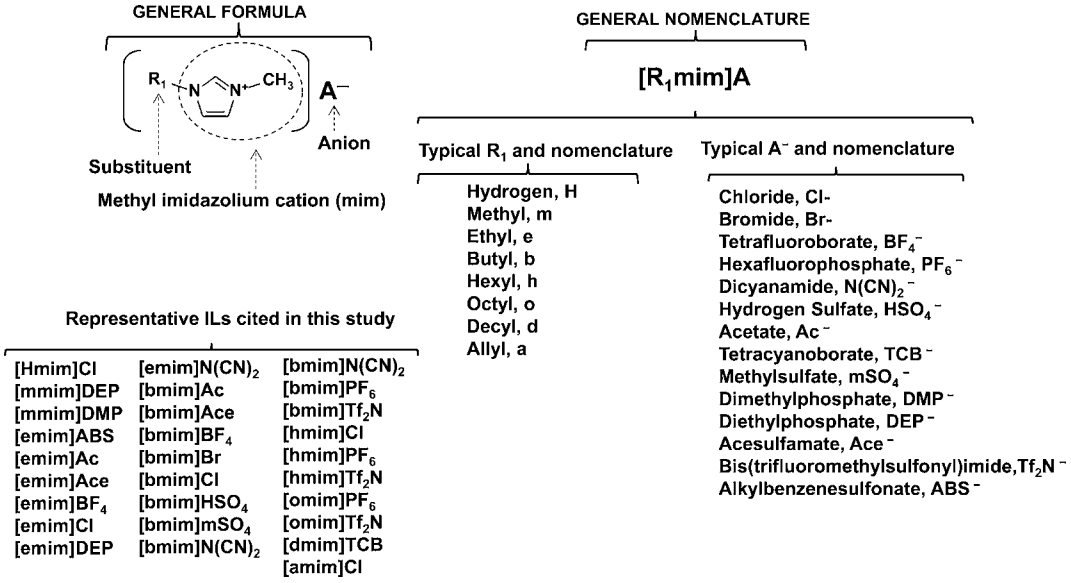

Figure 1. General nomenclature employed for imidazolium-based ILs and representative examples of ILs employed for biomass processing.

STRATEGIES FOR THE UTILIZATION OF LIGNOCELLULOSIC MATERIALS: BIOREFINERIES

In general terms, the benefit of LCM can be accomplished according to two different philosophies:

- direct utilization as a whole (for example, by combustion, pyrolysis, liquefaction, or gasification) or
- LCM "fractionation" (in which the major components of the feedstock are separated into "fractions" made up of compounds with related properties) followed by separate processing of each fraction for specific purposes.

LCM fractionation is the conceptual basis of the "lignocellulose biorefinery", which has been defined by the National Renewable Energy Laboratory (NREL) as "a facility that integrates conversion processes and equipment to produce fuels, power and chemicals from biomass". According to this definition, biorefineries are expected to work under a general idea analogous to today's petroleum refineries.[13] The IEA Bioenergy Task 42 broadened the biorefinery concept, proposing that biorefinery stands for "the sustainable processing of biomass into a spectrum of bio-based products (food, feed, chemicals and/or materials) and bioenergy (biofuels, power and/or heat)", so that a biorefinery can be a concept, a facility, a process, a plant, or even a cluster of facilities.[14] Integrated biorefineries, characterized by a reduced carbon footprint of the final products, can provide a sustainable approach to valuable products that can also improve biomass processing economics as well as environmental issues[14] and have been considered crucial for extracting the maximum value from biomass.[15] In the medium term, relatively small-scale biorefineries making use of local or regional resources have been considered as the most favored method to introduce more advanced (green, whole-crop, and lignocellulosic) biorefinery processes into the market.[14]

The main issue in LCM processing lies within its complex structure and chemical composition, an important issue when envisioning new processes.[16]

Usually, LCM fractionation intends the selective separation of the structural components (lignin, cellulose, and hemicelluloses), which have to be recovered and further processed to yield an array of tailored commercial products. A recent analysis of the potential demand, biomass availability, and energy efficiency led to the conclusion that the production of chemicals from biomass is more beneficial than the production of transportation fuels or electricity.[17]

It is desirable that operation in biorefineries should follow the basic principles of green chemistry, for example, regarding an efficient utilization of raw materials and avoiding the utilization of wastes instead of performing end-of-pipe waste remediation,[3] enabling the production of end-products fulfilling societal needs, and shortening the dependence on fossil resources.[18] In this way, a sustainable industrial and societal development can be achieved by meeting the needs of the present generation without compromising the needs of future generations to meet their own needs.[19]

On the other hand, the implementation of biorefineries has been identified as the most promising route to the creation of a new domestic biobased industry (NREL, 2014), paving the way for a future low-carbon bioeconomy,[20,21] which would be driven by clean, sustainable environmental development, economic growth, and green politics,[22] and result in a highly efficient and cost-effective processing of biological feedstocks to a range of biobased products.[23] On this basis, the implementation of biorefineries could also contribute to the revitalization of rural areas.[24] There is a long way to go: only about 5% of the European economy was biobased in 2010, whereas in the United States, about 12% of all products (excluding energy use) in 2010 was originated from biomass.[25]

IONIC LIQUIDS IN LIGNOCELLULOSE BIOREFINERIES

Increasing attention is being paid to the utilization of ionic liquids (ILs) in a variety of fields. ILs are salts composed of large organic cations and inorganic or organic anions, with melting points below 100 °C, which can be designed to be liquid at room temperature.[26] Their low volatility (many ILs can be distilled at 200−300 °C just under significantly reduced pressure and at very low distillation rate)[27] limits the losses in vapor phase. This is an important advantage over the conventional solvents employed in industries, which can be responsible for emissions of volatile organic compounds

DOI: 10.1021/acs.jafc.5b03461
J. Agric. Food Chem. 2015, 63, 8093−8102

(VOC), identified as a major source of waste,[28,29] and show hazards related to inhalation and explosion.[30] Additionally, some ILs present catalytic activity. In this case, they show many of the advantages of both homogeneous and heterogeneous catalysts, such as high acid density, uniform catalytic active centers, easy separation, and recyclability.[31]

The most common ILs can be classified in four groups according to their cations: quaternary ammonium ILs, *N*-alkylpyridinium ILs, *N*-alkyl-isoquinolinium ILs, and imidazolium-based ILs.[32] Among them, the latter group has received special attention and is the focus of this study. Figure 1 presents the general formula of 3-methylimidazolium-based ILs ([mim]) employed for biomass processing, as well as the nomenclature employed in this work for the various ILs.

ILs are considered green chemicals[33,34] and offer a unique environment for chemistry, biocatalysts, separation, material synthesis, and electrochemistry.[35] However, ILs can be used as more than just alternative green solvents, because they differ from molecular solvents by their unique ionic character and their structure and organization, which can lead to specific effects.[27] Nonflammability, lack of toxicity, and thermal and chemical stability are usual ILs properties of special importance for application in biorefineries. An ideal ionic liquid should be inexpensive, nontoxic, biodegradable, and recyclable.[3]

Thermally stable ILs can be employed as reaction media or catalysts to carry out reactions at high temperatures using conventional equipment, in a way that their negligible vapor pressure would facilitate the recovery of volatile reaction products. Due to the unique solvent properties of ILs, these solvents promise advantages with regard to conversion and selectivity, leading to energy savings when compared to conventional solvents.[26] Additionally, their properties can be tuned for specific chemical tasks[36] by selecting the type of constituent cation and anion:[37] for example, a number of ILs show unique solvating properties.[38] Increasing knowledge on the chemical, physical, and technical properties of ILs is expected to allow a wider and more efficient utilization.

POTENTIAL APPLICATIONS OF ILS IN BIOREFINERIES

On the basis of the above information on the nature of LCM and properties of ILs, a number of potential applications of ILs in lignocellulose biorefineries have been identified, including their utilization as agents for separation, cellulose dissolution, and derivatization, LCM fractionation, or LCM pretreatment (see the following sections). The utilization of ILs as reaction media and/or catalyst for the hydrolysis−dehydration of polysaccharides into furans is also an interesting research subject, but it falls outside the scope of this paper.

ILs as Separation Agents for Compounds Present in Biorefinery Streams. ILs find a number of applications in biorefineries, for example, in processes dealing with the production of second-generation biofuels (such as bioethanol or biobutanol) or short-chain organic acids. In these kinds of technologies, LCM are processed to hydrolyze polysaccharides (cellulose and/or hemicelluloses) into sugars, which are fermented to yield the target products.

One of the major techno-economic challenges in biorefineries manufacturing second-generation ethanol from LCM is the comparatively low ethanol content of the fermentation broth. The ethanol concentration can be increased by ordinary distillation up to concentrations near the azeotrope (95.5 wt % ethanol), but the separation becomes increasingly difficult as this threshold is approached. On the other hand, fuel applications require almost anhydrous ethanol, making the utilization of alternative separation technologies (typically, azeotropic or extractive distillation) necessary. Both azeotropic and extractive distillations involve the addition of a third component (entrainer) able to break the azeotrope. Imidazolium-based ionic liquids have been successfully employed as separation agents for the dehydration of ethanol−water mixtures,[26,39,40] as they can greatly enhance the relative volatility of ethanol over water, showing advantages derived from low viscosity, thermal stability, good solubility, and lower corrosiveness with respect to the high melting salts suitable for the same purpose.[40] In a comparative evaluation of [bmim]BF_4, [emim]BF_4, and [bmim]Cl (see Figure 1 for nomenclature), the ability to improve the separation was found to follow the order [bmim]Cl > [emim][BF_4] > [bmim][BF_4], in a way that the two best ILs performed better than the reference compound.[39,41] Figueroa et al.[41] simulated the ethanol recovery using a number of ILs ([bmim]Cl, [emim]Cl, [emim]BF_4, [bmim]Ac, [bmim]BF_4, [bmim]$N(CN)_2$, [hmim]Cl, and [bmim]mSO_4) and concluded that, in the best cases, high-purity ethanol could be obtained at 96 wt % recovery. In a related study, Meinsderma et al.[42] proposed an energy-efficient process for ethanol dehydration based on extractive distillation with [emim]$N(CN)_2$ enabling the production of 99.91% ethanol in facilities at pilot scale. Other reported advantages of ILs as separation agents include:[40]

- ILs do not pollute the distillate due to their nonvolatile character;
- reduced heat duties are required because of their nonvolatility, high selectivities, and heat capacities;
- ILs properties such as solubility, capacity, selectivity, viscosity, and thermal stability can be tailored;
- only one distillation column is required.

Alternatively, ILs can be used for ethanol extraction from aqueous solutions. Arlt et al.[43] proposed a number of ILs (including imidazolium- and phosphonium-based ones) as potential solvents for the extractive separation of close-boiling or azeotropic mixtures, including water−ethanol. This approach was claimed to be superior to conventional extractive rectification in terms of cost-effectiveness and exergetic aspects, as a result of the selectivity and the unusual characteristic profile of the ionic liquids. Solubility data for ternary mixtures of ethanol, water, and a hydrophobic IL ([bmim]PF_6, [hmim]PF_6, or [omim]PF_6) were reported by Swatloski et al.,[44] whereas [hmim]Tf_2N was found to be suitable for separating ethanol from water, but acceptable recovery rates could be achieved only by using unreasonably high solvent/feed ratios.[45] On the basis of ternary liquid−liquid equilibrium studies, a number of tetradecyltrihexylphosphonium-based ILs obtained by combination with seven different anions have been recently proposed as candidates for ethanol recovery from aqueous solutions by liquid−liquid extraction.[46] On the basis of equilibrium calculations, the authors suggested the use of a single liquid−liquid extraction stage coupled to extractive fermentation as a favorable solution to recover ethanol from dilute aqueous solutions, a possibility favored by the comparatively low toxicity of some of the ILs assayed.

Biobutanol (*n*-butanol of biological origin) is an attractive biofuel[47,48] with higher energy density and lower volatility as compared to ethanol. Biobutanol production from LCM presents a number of challenging technological problems,

DOI: 10.1021/acs.jafc.5b03461
J. Agric. Food Chem. 2015, 63, 8093−8102

some of them related to the complex composition of culture media, which contain large amounts of water, microbial cells (usually, bacteria belonging to the *Clostridium* genus), non-polysaccharide byproducts resulting from LCM hydrolysis, residual sugars, and volatile fermentation coproducts (such as acetone and ethanol). Additionally, the fermentation products are toxic to cells, a fact limiting the maximum achievable butanol concentration (which is typically within the 1−2 wt % range). In a screening study, Knoshaug and Zhang[49] found just two *Lactobacillus* strains able to tolerate and grow in up to 3 wt % butanol, the same level achieved by a mutant *Clostridium biejerinckii* strain.[30] Distillation, the technology traditionally employed to separate the volatile components present in this type of fermentation broth,[50] involves high steam consumption.[51] Alternative, energy-efficient separation methods have been proposed, including adsorption−desorption, extraction, and membrane-based technologies. ILs may find application in these two latter technologies.

Very high boiling extractants have been recommended as extraction solvents for butanol fermentation products, a purpose for which ILs are suitable,[30] either by direct contact with the broth inside the fermenter[52] or by downstream processing. ILs containing anions such as PF_6^- or Tf_2N^- are water immiscible and enable the formation of biphasic systems suitable for extraction applications.[53] In particular, ILs such as [hmim]PF_6 or [bmim]Tf_2N, together with others bearing a tetracyanoborate anion (such as [dmim]TCB), have been considered for *n*-butanol extraction,[30,51,54] whereas the same purpose has been achieved using imidazolium-based ILs with alkyl chains of various lengths in combination with tetrafluoroborate or trifluoromethanesulfonate anions.[30] The hydrophobicity was correlated to the butanol distribution coefficient between ILs and water, whereas the extraction efficiency and selectivity were directly related to the polarity.[30] Ha et al.[55] studied 11 imidazolium-based ionic liquids as extraction agents to recover butanol from aqueous media and also found an interrelationship between extraction efficiency, selectivity, and polarity. The best results were achieved with [omim]Tf_2N, which showed high extraction efficiency and allowed >74% butanol recovery in a single extraction stage. Fadeev and Meagher[56] employed [bmim]PF_6 and [omim]PF_6 to extract butanol from aqueous solutions and subjected the ionic liquid-rich phase (simulating the composition in equilibrium with 1 wt % butanol−water solution) to pervaporation through a commercial polydimethylsiloxane membrane, obtaining an IL-free permeate. Pervaporation with IL-supported membranes[51,57] has been employed to reduce the IL demand and to avoid its direct contact with the production organisms, avoiding possible toxic effects.[58]

Imidazolium-based ILs have also been proposed as separation agents for short-chain organic acids, including lactic acid.[59−62] The biotechnological production of lactic acid in biorefineries by hydrolysis−fermentation of LCM is an interesting possibility, because this compound is an important commodity chemical for the production of specialty chemicals such as 2,3-pentanedione, acrylic acid, propionic acid, pyruvic acid, and polylactic acid. Lactic acid can be obtained at high yield by fermentation of LCM-derived pentoses or hexoses.[63] Depending on the operational conditions, the lactic fermentation can be stereospecific, or it may lead mixtures of the two isomers. Interestingly, polylactic acid stereocomplexes with improved properties can be produced from pure optical isomers. Several 1-alkyl-3-methylimidazolium hexafluorophosphates (including [bmim]PF_6, [hmim]PF_6, and [omim]PF_6) have been employed for the extractive fermentation of lactic acid, acting as a water-immiscible phase (instead of conventional organic solvents) to which lactic acid can be transferred in situ from the fermentation broth, avoiding cell inhibition.[59,60] Although the extractability of the organic acid in the pure ILs was poor, the addition of tri-*n*-butylphosphate increased the extraction ability to a level similar to those of conventional organic solvents. The relatively low toxicity of the considered ILs allowed the growth of the fermenting cells (*Lactobacillus*), which were able to consume glucose and to produce lactate. A comparative evaluation of the various ILs showed that the length of the alkyl substituent in the imidazolium cation had little influence on cell survival.[60]

In biorefineries, ILs can play a number of general roles common to other industries, for example, in the removal of VOC and hazardous pollutants from effluents.[64−66] ILs such as [bmim]PF_6, [bmim]Tf_2N, or [bmim]BF_4 can be directly employed in bioreactors, either for performing enzyme-mediated biocatalytic reactions[67] or in the presence of whole cells, for example, in VOC absorption−biodegradation systems,[67,68] enabling the biotransformation of toxic substrates in the presence of an immiscible liquid phase acting as a substrate reservoir.

The ability of ILs to selectively dissolve gases, together with their nonvolatility, makes them potentially useful for gas separations[69] (for example, CO_2), acting as conventional liquid phases in absorbers or as components of supported liquid membranes.[53,70,71] CO_2 has relatively high solubility in a number of imidazolium ILs, particularly in those containing the bis(trifluoromethylsulfonyl)imide anion, whereas there is little difference in CO_2 solubility between ionic liquids possessing the tetrafluoroborate or hexafluorophosphate anion.[69] Amine-functionalized imidazolium ionic liquids have been specifically designed for CO_2 capture.[72]

ILs as Agents for Cellulose Dissolution−Regeneration and Homogeneous Derivatization. Cellulose is hardly soluble in many conventional solvents because of its strong intermolecular hydrogen bonding. Traditional cellulose solvents, such as carbon disulfide, *N*-methylmorpholine-*N*-oxide (NMMO), and mixtures of *N*,*N*-dimethylacetamide and lithium chloride (DMAC/LiCl), show a number of practical drawbacks, including limited dissolving capability, toxicity, high cost, difficult solvent recovery, uncontrollable side reaction, instability during cellulose processing,[73] and/or the need for multistep pretreatments followed by prolonged stirring.[74]

The ability of some molten ILs (*N*-alkylpyridinium or *N*-arylpyridinium chloride salts) to dissolve cellulose (in the presence of a nitrogen-containing base) has been known since the mid-1930s,[75] but interest in this topic was renewed when Swatloski et al.[76] claimed the ability of ILs made of a number cations (including alkyl-imidazolium-based ones) and anions (including Cl^-, I^-, PF_6^-, BF_4^-, acetate, and trifluoroacetate) to achieve cellulose dissolution. Cellulose dissolution in ILs involves the interaction of hydroxyl groups in cellulose with both the cation and anion in IL.[77] The oxygen atoms of OH groups and IL anions act as electron donors during the dissolution process, in a way that anions acting as strong electron donors (for example, halogen and pseudohalogen ions) gave good cellulose dissolution results, whereas hydrogen atoms of hydroxyl groups and IL cations act as electron acceptors. The review by Wang et al.[78] summarizes extensive literature information on ILs able to dissolve cellulose, the

DOI: 10.1021/acs.jafc.5b03461
J. Agric. Food Chem. 2015, 63, 8093−8102

respective cellulose solubilities, and the suitable operational conditions.

After dissolution, cellulose can be regenerated by adding a miscible antisolvent such as water, alcohols, ethers, or ketones. When an antisolvent such as water is added to the homogeneous IL−cellulose system, the IL ions form hydrogen bonds with water molecules and are displaced into the aqueous phase, whereas cellulose (which previously interacted with IL) is expelled and rebuilds its intra- and intermolecular hydrogen bonds and is then precipitated.[79]

Cellulose dissolution/regeneration in ILs is affected by many factors, including the type of anion and cation, the basicity and H-bonding capability of the anion, and the position and length of the side chain in the cation.[80] As representative examples, [bmim]Cl,[76] [amim]Cl,[73,81] and [emim]Ac[82] can dissolve cellulose at comparatively high concentrations. On the basis of their physicochemical properties, ILs with strongly basic anions (such as formate, acetate, or phosphate) have been cited as favorable candidates for cellulose dissolution under mild operational conditions.[73,74,83] The dissolved cellulose could be readily regenerated by antisolvent addition: for example, water, ethanol, or acetone have been employed to regenerate cellulose from [bmim]Cl,[84] whereas Zhang et al.[81] employed water to regenerate cellulose from [amim]Cl.

The regenerated cellulose can be different from the native cellulose in terms of macro- and microstructure, crystallinity, and even degree of polymerization, depending on the processing conditions.[79,85] In fact, cellulose regenerated from ILs was found to be essentially amorphous and porous.[38] Additionally, it can be noted that complete cellulose dissolution in ILs provides the opportunity of working with new functional groups, opening new ways for product design or enabling a better control of the reaction (for example, regarding the degree of substitution).[86] The manufacture of cellulose derivatives in homogeneous systems by esterification, etherification,[73,86] acylation, carbanilation,[87] carboxymethylation, succination, phthalation,[88] alkylation, silylation, and halogenation[86] has been reported. Other interesting examples of cellulose derivatization in ILs have been reported in related studies.[89−94] On the other hand, cellulose dissolution−regeneration enables the recovery of cellulose nanofibers or its utilization as film, powder, gel, or capsule.[95]

ILs as Agents for LCM Fractionation. The complicated chemical composition and morphology of native LCM, characterized by the presence of both nonstructural components and a cross-linked, tridimensional matrix of polysaccharides and lignin, together with the crystalline nature of cellulose, are major hindrances for processing. Considered as feedstocks for chemical and/or biotechnological processess, LCM are recalcitrant substrates that must be deconstructed (or fractionated) to achieve separation of their major components. This is a key step in the conversion of lignocellulosic biomass into fuels and valuable chemicals and materials.[96] LCM dissolution may imply the hydrolysis of carbohydrate polymers or the chemical disruption of the lignocellulose composite.[97] ILs or IL mixtures (eventually in the presence of catalysts, water, and/or other components) have demonstrated great promise as efficient solvents for biomass fractionation, via total or partial dissolution.[98] The interaction of ILs with lignocellulose may involve ionic, $\pi-\pi$, and hydrogen-bonding interactions. LCM dissolution in ILs depends on a number of factors, including the type of constituent cation and anion, the nature and previous processing of biomass (for example, milling or drying), the characteristics of the substrate (including composition, particle size distribution, moisture), the relative amount of LCM, other operational conditions (including temperature heating profile, maximum temperature, and processing time), and the possible presence of additional components in the medium (for example, water, catalysts, or cosolvents). For example, DMSO has been used in combination with [bmim]Cl or [amim]Cl to achieve the partial dissolution of lignified raw materials,[96,99] whereas the utilization of two ILs ([emim]Ac in combination with [amim]Cl or [bmim]Cl) has been proposed for the same purpose.[100]

Complete dissolution has been reported for LCM of low lignin content (such as bagasse, straws, grasses, or husks) but also for recalcitrant substrates such as hardwoods or softwoods. With regard to wood dissolution, [bmim]Cl and [emim]Ac have been identified as the two most promising ionic liquids.[101] Representative studies and reviews on LCM dissolution using a number of imidazolium-based ionic liquids have been reported in the past few years.[37,38,88,96,97,99,102−112] Once biomass is dissolved, the various structural components can be recovered using a number of operational strategies, many of them based on the precipitation of cellulose (or cellulose-enriched solids) upon antisolvent addition.[97]

An alternative to completely dissolving biomass is to selectively dissolve just a single biomass component.[12] This approach may involve hemicellulose hydrolysis or lignin extraction. Delignification-based processes usually enable the recovery of polysaccharides (at least, cellulose) as insoluble solids.[26,113,114] Representative information on the delignification of multiple LCM in media containing imidazolium-based ionic liquids (including [emim]Ac, [emim]Ace, [emim]ABS, [emim][Cl], [bmim]Ac, [bmim]Ace, [bmim]mSO_4, [bmim]Br, [bmim]BF_4, [bmim]PF_6, [amim]Cl, and [hmim]Cl) has been summarized in recent studies.[37,97,100,113,115−118]

The ideal technology for LCM biorefineries would be one in which the three major components of the biomass were obtained at high yields and purities.[119] However, the recovery of hemicelluloses (the most easily hydrolyzable of the three main lignocellulosic polymers) is challenging,[37] as this fraction can be considerably depolymerized and dissolved in ILs and, eventually, decomposed (as has been found in the processing of pine wood with [hmim]Cl),[113] resulting in losses that increase the cost of downstream separation.[110] Although delignification increases with high temperatures, such conditions promote hemicellulose losses.[120] On the other hand, treatments allowing delignification and hemicellulose solubilization simultaneously may entail losses of cellulose as soluble hydrolysis products.[114] In some dissolution−regeneration approaches, hemicellulose and cellulose can be obtained as separated fractions from the regenerated material, using specific solvents to maximize the fractionation process.[37,121] The selective dissolution of hemicelluloses (up to 39% of the total) from extracted or native spruce wood has been addressed in the literature using switchable ionic liquids.[101] Starting from bleached paper grade pulps, separate fractions of hemicelluloses and cellulose (both of high purity) were recovered upon processing with [emim]Ac containing 15−20% water.[122] Under severe conditions (for example, in high-temperature treatments with strongly acidic ILs), the formation of carbohydrate degradation products able to react with lignin (leading to the formation of pseudolignin) has been reported.[114] Oppositely, in treatments with ILs possessing strongly basic anions, hemicelluloses are converted into oligosaccharides, generating only trace amounts

DOI: 10.1021/acs.jafc.5b03461
J. Agric. Food Chem. 2015, 63, 8093−8102

of monomeric sugars (xylose and glucose).[123] In some operational schemes, cellulose and lignin are precipitated sequentially, and the hemicellulose-derived saccharides left in the IL phase are subjected to further chemical modification.[124]

The integral benefit of the various LCM components can be achieved by coupling conventional separation treatments with IL processing. Following this idea, dissolution in [bmim]Cl followed by NaOH extraction has been reported for bagasse utilization,[121] whereas the implementation of a first stage of hemicellulose removal (for example, hydrothermolysis or prehydrolysis) before treatment with ILs (aiming at the separation of cellulose and lignin) has also been proposed.[97] This latter approach follows the philosophy underlying the commercial prehydrolysis−kraft process and is being studied as an alternative to increase the added value from hemicelluloses in conventional kraft pulping technology.

ILs as Pretreatment Agents for the Enzymatic Hydrolysis of Cellulose. The enzymatic hydrolysis of cellulose leads to glucose solutions suitable as fermentation media for manufacturing a wide range of biofuels, solvents, polymers, and other marketable compounds. However, native LCM is recalcitrant to the action of cellulases, a fact attributed to a number of factors, such as substrate accessibility, cellulose degree of polymerization, crystallinity, particle size, and porosity, as well as to the presence of hemicellulose and lignin.[111] In particular, cellulose is embedded in a matrix of lignin and hemicelluloses, which are cross-linked by ester and ether linkages in the plant cell wall, hindering the access of enzymes to the cellulose glycosidic bonds. To disrupt the cell wall structure, some type of processing (by mechanical, biological, physical, and/or chemical methods, individually or in combination) is necessary. This type of processing is referred to in the literature as "pretreatment" and has been extensively reviewed owing to its economic and technological importance. Chemical pretreatments modify the composition of substrates, and some of them can be considered as true fractionation treatments. This dual behavior (as pretreatment and/or fractionation agents) defines well the potential of ILs in the field: in fact, a number of references included in this work (particularly, some of the ones employed to discuss the LCM fractionation by ILs) are directly oriented to the production of substrates suitable for enzymatic hydrolysis, because ILs show ability for removing lignin, disrupting the crystalline structure of cellulose, and increasing the accessibility of enzymes to cellulose.[32] The ILs most frequently utilized for LCM pretreatment are the ones suitable for cellulose dissolution, including [emim]Ac, [amim]Cl, [bmim]Cl, and dialkylimidazolium dialkylphosphates, which have been applied to a number of substrates.[104,112,125−129] Depending on the IL employed, the effects caused by processing may resemble those of aqueous stages performed under alkaline or acidic conditions, as happens for acetate- and chloride-based ILs, respectively.[130] Data on the comparative saccharification efficiency achievable with selected ILs have been reported recently.[129]

In typical processing schemes, LCM are treated with ILs to cause dissolution−regeneration or delignification, yielding cellulose-enriched substrates of decreased crystallinity and improved enzyme accessibility, which are extensively washed to remove the residual IL and further hydrolyzed with enzymes at high yield with fast kinetics. It can be noted that ILs are comparatively expensive and that efficient and cost-effective recovery methods have to be implemented for economic feasibility. The best IL depends on the substrate considered;[112] for a given IL, the optimal processing conditions must be optimized for different substrates.[109] In terms of saccharification yields, material recovery, and delignification, [emim]Ac ranks as the most suitable IL for biomass pretreatment,[130] but [bmim]Cl performed very well for simple cellulosic substrates, and [bmim]HSO_4 has been recommended for processing hybrid aspen.[112] Acetate-based ILs present advantages over chloride-based ILs derived from their lower melting point, lower viscosity, lower corrosive character, and ability to work with higher loadings.[131] Strongly acidic ionic liquids may cause partial polysaccharide depolymerization, hydrolysis, and dehydration, leading to the formation of furans as reaction byproducts.

It must be considered that, in integrated processes, ILs may be present in the aqueous hydrolysis media as a result of recycling streams from IL recovery stages. This is important because the presence of ILs in the hydrolysis media (even in trace amounts) can inhibit or denature enzymes, depending on the type and concentration of the considered IL. According to Turner et al.,[132] *Trichoderma reesei* cellulases are subjected to ionic strength-induced inactivation and unfolding in media containing as little as 22 mM [bmim]Cl. Refolding of denatured cellulase was possible only when the enzyme was contacted with solutions containing 0−5% [bmim]Cl. The Cl^- ion was, in part, responsible for the inactivation of the cellulase, because the IL produces a dehydrating and denaturing environment.

In most cases, the enzyme activity drops quickly when the ionic liquid concentration is increased, but no general conclusions on this subject can be drawn owing to the diversity of conditions assayed. In integrated biorefinery processes, keeping a very low IL concentration in the hydrolysis media would require extensive processing and cleanup of the cellulosic substrates. Because of this, the cellulases should be preferably able to perform optimally in solutions containing up to 15 wt % IL, which corresponds to the amount retained by the hydrolysis substrates upon processing.[133] To deal with this problem, two possible approaches can be followed (individually or simultaneously): utilization of ILs causing minimal inhibition and/or using cellulases with increased tolerance to the IL.

The IL [emim]Ac shows minimal inhibitory effects on enzymes compared to ionic liquids containing Cl^- or Br^- anions,[96,133,134] whereas favorable compatibility has been also reported for [emim]DEP,[135] [mmim]DEP, and [mmim]-DMP.[136] With regard to the role of enzymes, Wahlström and Suurnäkki[125] summarized literature on the action of cellulases and other glycosyl hydrolases in IL solutions. Interesting possibilities lay in the utilization of enzymes from extremophilic strains able to perform at high temperature and salt concentration, as the utilization of enzymes capable of withstanding higher concentrations of salt and ionic liquids and higher pH would make the washing steps less cumbersome, facilitating the industrial biomass conversion process.[133,137] Datta et al.[133] investigated the stability of recombinant, extremophilic enzymes, as a function of IL concentration, and reported that (unlike the reference *Trichoderma viride* cellulase), the tested enzymes retained between 44 and 79% of their activity in the presence of 15% [emim]Ac. In this field, a GH5 family cellulase able to keep activity in the presence of 30% (v/v) IL has been identified,[138] whereas a hyperthermostable archaeal endoglucanase was reported to retain considerable activity (30−50%) in the presence of 25% (v/v) [mmim]DMP.[139]

DOI: 10.1021/acs.jafc.5b03461
J. Agric. Food Chem. 2015, 63, 8093−8102

In conclusion, ILs are potentially suitable for a number of duties in LCM biorefineries. Considered as agents for physicochemical processing of liquid process streams, ILs are suitable as entrainers for the dehydration of ethanol−water mixtures, as well as agents for the in situ separation of microbial metabolites (including selected alcohols and acids) from the fermentation media. ILs are also suitable for preventing pollution from gaseous waste streams, for example, by removing VOC or carbon dioxide from them. With regard to the chemical modification of native LCM, operational schemes based on dissolution−regeneration or delignification provide interesting alternatives for developing alternative processing technologies. One of the most suited schemes for LCM biorefineries (pretreatment/fractionation followed by enzymatic hydrolysis and fermentation) could be conveniently perfomed by using selected ILs (causing limited losses of enzymatic activity and/or showing enhanced compatibility with microorganisms), as well as by using tolerant enzymes produced by extremophilic microorganisms.

AUTHOR INFORMATION

Corresponding Author

*(J.C.P.) Phone: +34988387033. Fax: +34988387001. E-mail: jcparajo@uvigo.es.

Funding

We are grateful to the Spanish Ministry of Economy and Competitivity for supporting this study within the framework of the research project "Advanced processing technonologies for biorefineries" (reference CTQ2014-53461-R), partially funded by the FEDER program of the European Union. S.R. thanks the Ministry for her predoctoral grant.

Notes

The authors declare no competing financial interest.

REFERENCES

(1) Yu, W.; Tang, Y.; Mo, L.; Chen, P.; Lou, H.; Zheng, X. One-step hydrogenation-esterification of furfural and acetic acid over bifunctional Pd catalysts for bio-oil upgrading. *Bioresour. Technol.* **2011**, *102*, 8241−8246.

(2) Blanco-Rosete, S.; Webb, C. Emerging biorefinery markets: global context and prospects for Latin America. *Biofuels, Bioprod. Biorefin.* **2008**, *2*, 331−342.

(3) Sheldon, R. Green and sustainable manufacture of chemicals from biomass: state of the art. *Green Chem.* **2014**, *16*, 950−963.

(4) Clark, J. H.; Deswarte, F. E. I.; Farmer, T. J. The integration of green chemistry into future biorefineries. *Biofuels, Bioprod. Biorefin.* **2009**, *3*, 72−90.

(5) Mittal, A.; Chatterjee, S. G.; Scott, G. M.; Amidon, T. E. Modeling xylan solubilization during autohydrolysis of sugar maple and aspen wood chips: reaction kinetics and mass transfer. *Chem. Eng. Sci.* **2009**, *64*, 3031−3041.

(6) Marcuschamer, D. K.; Simmons, B. A.; Blanch, H. W. Techno-economic analysis of a lignocellulosic ethanol biorefinery with ionic liquid pre-treatment. *Biofuels, Bioprod. Biorefin.* **2011**, *5*, 562−569.

(7) Sen, S. M.; Binder, J. B.; Raines, R. T.; Maravelias, C. T. Conversion of biomass to sugars via ionic liquid hydrolysis: process synthesis and economic evaluation. *Biofuels, Bioprod. Biorefin.* **2012**, *6*, 444−452.

(8) Shao, X.; Lynd, L. Kinetic modeling of xylan hydrolysis in co- and countercurrent liquid hot water flow-through pretreatments. *Bioresour. Technol.* **2013**, *130*, 117−124.

(9) Corma, A.; Iborra, S.; Velty, A. Chemical routes for the transformation of biomass into chemicals. *Chem. Rev.* **2007**, *107*, 2411−2502.

(10) Binder, J. B.; Raines, R. T. Fermentable sugars by chemical hydrolysis of biomass. *Proc. Natl. Acad. Sci. U. S. A.* **2010**, *107*, 4516−4521.

(11) Vargas-Hernández, D.; Rubio-Caballero, J. M.; Santamaría-González, J.; Moreno-Tost, R.; Mérida-Robles, J. M.; Pérez-Cruz, M.; Jiménez-López, A.; Hernández-Huesca, R.; Maireles-Torres, P. Furfuryl alcohol from furfural hydrogenation over copper supported on SBA-15 silica catalysts. *J. Mol. Catal. A: Chem.* **2014**, *383*−*384*, 106−113.

(12) Rackemann, D. W.; Doherty, W. O. The conversion of lignocellulosics to levulinic acid. *Biofuels, Bioprod. Biorefin.* **2011**, *5*, 198−214.

(13) Budarin, V. L.; Shuttleworth, P. S.; Dodson, J. R.; Hunt, A. J.; Lanigan, B.; Marriott, R.; Milkowski, K. J.; Wilson, A. J.; Breeden, S. W.; Fan, J.; Sin, E. H. K.; Clark, J. H. Use of green chemical technologies in an integrated biorefinery. *Energy Environ. Sci.* **2011**, *4*, 471−479.

(14) Clark, J. H.; Luque, R.; Matharu, A. S. Green chemistry, biofuels, and biorefinery. *Annu. Rev. Chem. Biomol. Eng.* **2012**, *3*, 183−207.

(15) Beach, E. S.; Cui, Z.; Anastas, P. T. Green chemistry: a design framework for sustainability. *Energy Environ. Sci.* **2009**, *2*, 1038−1049.

(16) Luque, R. Catalytic biomass processing: prospects in future biorefineries. *Curr. Green Chem.* **2015**, *2*, 90−95.

(17) Bos, H. L.; Sanders, J. P. M. Raw material demand and sourcing options for the development of a bio-based chemical industry in Europe. *Biofuels, Bioprod. Biorefin.* **2013**, *7*, 246−259.

(18) Rosatella, A.; Simeonov, S. P.; Frade, R. F. M.; Afonso, C. A. M. 5-Hydroxymethylfurfural (HMF) as a building block platform: biological properties, synthesis and synthetic applications. *Green Chem.* **2011**, *13*, 754−793.

(19) World Commission on Environment and Development. Report: Our Common Future (The Brundtland Report). *Med. War* **1988**, *4*, 17−25.

(20) German Federal Government. Biorefineries Roadmap. Retrieved from http://www.bmbf.de/pub/BMBF_Roadmap-Bioraffinerien_en_bf.pdf (last accessed July 2015).

(21) Höltinger, S.; Schmidt, J.; Schönhart, M.; Schmid, E. A spatially explicit techno-economic assessment of green biorefinery concepts. *Biofuels, Bioprod. Biorefin.* **2014**, *8*, 325−341.

(22) De Jong, W.; Marcotullio, G. Overview of biorefineries based on bo-production of furfural, existing concepts and novel developments. *Int. J. Chem. React. Eng.* **2010**, *8*, 1−27.

(23) De Jong, E.; Higson, A.; Walsh, P.; Wellisch, M. Product developments in the bio-based chemicals arena. *Biofuels, Bioprod. Biorefin.* **2012**, *6*, 606−624.

(24) Cherubini, F. The biorefinery concept: using biomass instead of oil for producing energy and chemicals. *Energy Convers. Manage.* **2010**, *51*, 1412−1421.

(25) Vandermeulen, V.; Van der Steen, M.; Stevens, C. V.; Van Huylenbroeck, G. Industry expectations regarding the transition toward a biobased economy. *Biofuels, Bioprod. Biorefin.* **2012**, *6*, 453−464.

(26) Stark, A. Ionic liquids in the biorefinery: a critical assessment of their potential. *Energy Environ. Sci.* **2011**, *4*, 19−32.

(27) Olivier-Bourbigou, H.; Magna, L.; Morvan, D. Ionic liquids and catalysis: recent progress from knowledge to applications. *Appl. Catal., A* **2010**, *373*, 1−56.

(28) Sheldon, R. A. Green solvents for sustainable organic synthesis: state of the art. *Green Chem.* **2005**, *7* (5), 267−278.

(29) Sheldon, R. A. Fundamentals of green chemistry: efficiency in reaction design. *Chem. Soc. Rev.* **2012**, *41* (4), 1437−1451.

(30) Simoni, L. D.; Chapeaux, A.; Brennecke, J. F.; Stadtherr, M. A. Extraction of biofuels and biofeedstocks from aqueous solutions using ionic liquids. *Comput. Chem. Eng.* **2010**, *34*, 1406−1412.

(31) Long, J.; Guo, B.; Teng, J.; Yu, Y.; Wang, L.; Li, X. SO_3H-functionalized ionic liquid: efficient catalyst for bagasse liquefaction. *Bioresour. Technol.* **2011**, *102*, 10114−10123.

DOI: 10.1021/acs.jafc.5b03461
J. Agric. Food Chem. 2015, 63, 8093−8102

(32) Liu, C.-Z.; Wang, F.; Stiles, A. R.; Guo, C. Ionic liquids for biofuel production: opportunities and challenges. *Appl. Energy* **2012**, *92*, 406−414.
(33) Earle, M. J.; Seddon, K. R. Ionic liquids. Green solvents for the future. *Pure Appl. Chem.* **2000**, *72* (7), 1391−1398.
(34) Huddleston, J. G.; Visser, A. E.; Reichert, W. M.; Willauer, H. D.; Broker, G. A.; Rogers, R. D. Characterization and comparison of hydrophilic and hydrophobic room temperature ionic liquids incorporating the imidazolium cation. *Green Chem.* **2001**, *3*, 156−164.
(35) Niknam, K.; Damya, M. 1-Butyl-3-methylimidazolium hydrogen sulfate [bmim] HSO_4: an efficient reusable acidic ionic liquid for the synthesis of 1,8-dioxo-octahydroxanthenes. *J. Chin. Chem. Soc.* **2009**, *56*, 659−665.
(36) Fraga-Dubreuil, J.; Bourahla, K.; Rahmouni, M.; Bazureau, J. P.; Hamelin, J. Catalysed esterifications in room temperature ionic liquids with acidic counteranion as recyclable reaction media. *Catal. Commun.* **2002**, *3* (5), 185−190.
(37) Mäki-Arvela, P.; Anugwom, I.; Virtanen, P.; Sjöholm, R.; Mikkola, J. P. Dissolution of lignocellulosic materials and its constituents using ionic liquids−a review. *Ind. Crops Prod.* **2010**, *32*, 175−201.
(38) Vancov, T.; Alston, A. S.; Brown, T.; McIntosh, S. Use of ionic liquids in converting lignocellulosic material to biofuels. *Renewable Energy* **2012**, *45*, 1−6.
(39) Seiler, M.; Jork, C.; Kavarnou, A.; Arlt, W.; Hirsch, R. Separation of azeotropic mixtures using hyperbranched polymers or ionic liquids. *AIChE J.* **2004**, *50*, 2439−2454.
(40) Huang, H. J.; Ramaswamy, S.; Tschirner, U. W.; Ramarao, B. V. A review of separation technologies in current and future biorefineries. *Sep. Purif. Technol.* **2008**, *62*, 1−21.
(41) Figueroa, J. J.; Hoss Lunelli, B.; Maciel Filho, R.; Wolf Maciel, M. R. Improvements on anhydrous ethanol production by extractive distillation using ionic liquid as solvent. *Procedia Eng.* **2012**, *42*, 1016−1026.
(42) Meindersma, G. W.; Quijada-Maldonado, E.; Aelmans, T. A. M.; Gutiérrez Hernéndez, J. P.; de Haan, A. B. Ionic liquids in extractive distillation of ethanol/water: from laboratory to pilot plant. *ACS Symp. Ser.* **2012**, *No. 1117*, 239−257.
(43) Arlt, W.; Seiler, M.; Jork, C.; Schneider, T. Ionic liquids as selective additives for separation of close-boiling or azeotropic mixtures. U.S. Patent 20040133058 A1, 2004.
(44) Swatloski, R. P.; Visser, A. E.; Reichert, W. M.; Broker, G. A.; Farina, L. M.; Holbrey, J. D.; Rogers, R. D. On the solubilization of water with ethanol in hydrophobic hexafluorophosphate ionic liquids. *Green Chem.* **2002**, *4* (2), 81−87.
(45) Chapeaux, A.; Simoni, L. D.; Ronan, T. S.; Stadtherr, M. A.; Brennecke, J. F. Extraction of alcohols from water with 1-hexyl-3-methylimidazolium bis(trifluoromethylsulfonyl)imide. *Green Chem.* **2008**, *10*, 1301−1306.
(46) Neves, C. M. S. S.; Granjo, J. F. O.; Freire, M. G.; Robertson, A.; Oliveira, N. M. C.; Coutinho, J. A. P. Separation of ethanol−water mixtures by liquid−liquid extraction using phosphonium-based ionic liquids. *Green Chem.* **2011**, *13*, 1517−1526.
(47) Dürre, P. Biobutanol: an attractive biofuel. *Biotechnol. J.* **2007**, *2* (12), 1525−1534.
(48) Bankar, S. B.; Survase, S. A.; Ojamo, H.; Granström, T. Biobutanol: the outlook of an academic and industrialist. *RSC Adv.* **2013**, *3*, 24734−24757.
(49) Knoshaug, E. P.; Zhang, M. Butanol tolerance in a selection of microorganisms. *Appl. Biochem. Biotechnol.* **2009**, *153*, 13−20.
(50) Green, E. M. Fermentative production of butanol-the industrial perspective. *Curr. Opin. Biotechnol.* **2011**, *22*, 337−343.
(51) Heitmann, S.; Krings, J.; Kreis, P.; Lennert, A.; Pitner, W. R.; Górak, A.; Schulte, M. M. Recovery of n-butanol using ionic liquid-based pervaporation membranes. *Sep. Purif. Technol.* **2012**, *97*, 108−114.
(52) Kaminski, W.; Tomczak, E.; Gorak, A. Biobutanol − production and purifciaton methods. *Ecol. Chem. Eng. S−Chemia I Inz. Ekol. S* **2011**, *18*, 31−37.
(53) Zhao, H.; Xia, S.; Ma, P. Use of ionic liquids as "green" solvents for extractions. *J. Chem. Technol. Biotechnol.* **2005**, *80*, 1089−1096.
(54) Kubiczek, A.; Jonowe, C. Ionic liquids for the extraction of n-butanol from aqueous solutions. *Proc. ECOPole* **2013**, *7*, 125−131.
(55) Ha, S. H.; Mai, N. L.; Koo, Y. M. Butanol recovery from aqueous solution into ionic liquids by liquid-liquid extraction. *Process Biochem.* **2010**, *45*, 1899−1903.
(56) Fadeev, A. G.; Meagher, M. M. Opportunities for ionic liquids in recovery of biofuels. *Chem. Commun.* **2001**, *3*, 295−296.
(57) Plaza, A.; Merlet, G.; Hasanoglu, A.; Isaacs, M.; Sánchez, J.; Romero, J. Separation of butanol from ABE mixtures by sweep gas pervaporation using a supported gelled ionic liquid membrane: analysis of transport phenomena and selectivity. *J. Membr. Sci.* **2013**, *444*, 201−212.
(58) Cascon, H. R.; Choudhari, S. K.; Nisola, G. M.; Vivas, E. L.; Lee, D. J.; Chung, W. J. Partitioning of butanol and other fermentation broth components in phosphonium and ammonium-based ionic liquids and their toxicity to solventogenic clostridia. *Sep. Purif. Technol.* **2011**, *78*, 164−174.
(59) Matsumoto, M.; Mochiduki, K.; Fukunishi, K.; Kondo, K. Extraction of organic acids using imidazolium-based ionic liquids and their toxicity to *Lactobacillus rhamnosus*. *Sep. Purif. Technol.* **2004**, *40*, 97−101.
(60) Matsumoto, M.; Mochiduki, K.; Kondo, K. Toxicity of ionic liquids and organic solvents to lactic acid-producing bacteria. *J. Biosci. Bioeng.* **2004**, *98*, 344−347.
(61) Li, Q.; Jiang, X.; Zou, H.; Cao, Z.; Zhang, H.; Xian, M. Extraction of short-chain organic acids using imidazolium-based ionic liquids from aqueous media. *J. Chem. Pharm. Res.* **2014**, *6*, 374−381.
(62) Tonova, K.; Svinyarov, I.; Bogdanov, M. G. Biocompatible ionic liquids in liquid−liquid extraction of lactic acid: a comparative study. *Int. J. Chem. Mol. Nuclear Mater. Metallurgical Eng.* **2015**, *9*, 554−558.
(63) Gullón, P.; Romaní, A.; Vila, C.; Garrote, G.; Parajó, J. C. Potential of hydrothermal treatments in lignocellulose biorefineries. *Biofuels, Bioprod. Biorefin.* **2012**, *6*, 219−232.
(64) Zhu, S. Use of ionic liquids for the efficient utilization of lignocellulosic materials. *J. Chem. Technol. Biotechnol.* **2008**, *83*, 777−779.
(65) Milota, M. R.; Li, K. *VOC and HAP recovery using ionic liquids*. Retrieved from http://www.osti.gov/scitech/servlets/purl/909870 (last accessed July 2015).
(66) Quijano, G.; Couvert, A.; Amrane, A.; Darracq, G.; Couriol, C.; Le Cloirec, P.; Paquin, L.; Carrié, D. Absorption and biodegradation of hydrophobic volatile organic compounds in ionic liquids. *Water, Air, Soil Pollut.* **2013**, *224*, 1−9.
(67) Quijano, G.; Couvert, A.; Amrane, A. Ionic liquids: applications and future trends in bioreactor technology. *Bioresour. Technol.* **2010**, *101*, 8923−8930.
(68) Quijano, G.; Couvert, A.; Amrane, A.; Darracq, G.; Couriol, C.; Le Cloirec, P.; Paquin, L.; Carrié, D. Potential of ionic liquids for VOC absorption and biodegradation in multiphase systems. *Chem. Eng. Sci.* **2011**, *66*, 2707−2712.
(69) Cadena, C.; Anthony, J. L.; Shah, J. K.; Morrow, T. I.; Brennecke, J. F.; Maginn, E. J. Why is CO_2 so soluble in imidazolium-based ionic liquids? *J. Am. Chem. Soc.* **2004**, *126*, 5300−5308.
(70) Galán Sánchez, L. M.; Meindersma, G. W.; de Haan, A. B. Solvent properties of functionalized ionic liquids for CO_2 absorption. *Chem. Eng. Res. Des.* **2007**, *85*, 31−39.
(71) Hasib-ur-Rahman, M.; Siaj, M.; Larachi, F. Ionic liquids for CO_2 capture − development and progress. *Chem. Eng. Process.* **2010**, *49*, 313−322.
(72) Bates, E. D.; Mayton, R. D.; Ntai, I.; Davis, J. H., Jr. CO_2 capture by a task specific ionic liquid. *J. Am. Chem. Soc.* **2002**, *124*, 926−927.
(73) Cao, Y.; Wu, J.; Zhang, J.; Li, H.; Zhang, Y.; He, J. Room temperature ionic liquids (RTILs): a new and versatile platform for cellulose processing and derivatization. *Chem. Eng. J.* **2009**, *147*, 13−21.

DOI: 10.1021/acs.jafc.5b03461
J. Agric. Food Chem. 2015, 63, 8093−8102

(74) Fukaya, Y.; Hayashi, K.; Wada, M.; Ohno, H. Cellulose dissolution with polar ionic liquids under mild conditions: required factors for anions. *Green Chem.* **2008**, *10*, 44−46.
(75) Graenacher, C. Cellulose solution. U.S. Patent 1943176 A, 1934.
(76) Swatloski, R. P.; Rogers, R. D.; Holbrey, J. D. Dissolution and processing of cellulose using ionic liquids. Patent WO 2003029329 A2, 2003.
(77) Feng, L.; Chen, Z. L. Research progress on dissolution and functional modification of cellulose in ionic liquids. *J. Mol. Liq.* **2008**, *142*, 1−5.
(78) Wang, H.; Gurau, G.; Rogers, R. D. Ionic liquid processing of cellulose. *Chem. Soc. Rev.* **2012**, *41*, 1519−1537.
(79) Tan, H. T.; Lee, K. T. Understanding the impact of ionic liquid pretreatment on biomass and enzymatic hydrolysis. *Chem. Eng. J.* **2012**, *183*, 448−458.
(80) Gupta, K. M.; Jiang, J. Cellulose dissolution and regeneration in ionic liquids: a computational perspective. *Chem. Eng. Sci.* **2015**, *121*, 180−189.
(81) Zhang, H.; Wu, J.; Zhang, J.; He, J. 1-allyl-3-methylimidazolium chloride room temperature ionic liquid: a new and powerful nonderivatizing solvent for cellulose. *Macromolecules* **2005**, *38*, 8272−8277.
(82) Ignatyev, I.; Van Doorslaer, C.; Mertens, P. G. N.; Binnemans, K.; de Vos, D. E. Synthesis of glucose esters from cellulose in ionic liquids. *Holzforschung* **2011**, *66*, 417−425.
(83) Fukaya, Y.; Sugimoto, A.; Ohno, H. Superior solubility of polysaccharides in low viscosity, polar and halogen-free 1,3-dialkylimidazolium formates. *Biomacromolecules* **2006**, *7*, 3295−3297.
(84) Swatloski, R. P.; Spear, S. K.; Holbrey, J. D.; Rogers, R. D. Dissolution of cellulose with ionic liquids. *J. Am. Chem. Soc.* **2002**, *124*, 4974−4975.
(85) Zhao, H.; Jones, C. L.; Baker, G. A.; Xia, S.; Olubajo, O.; Person, V. N. Regenerating cellulose from ionic liquids for an accelerated enzymatic hydrolysis. *J. Biotechnol.* **2009**, *139*, 47−54.
(86) Wu, J.; Zhang, J.; Zhang, H.; He, J.; Ren, Q.; Guo, M. Homogeneous acetylation of cellulose in a new ionic liquid. *Biomacromolecules* **2004**, *5*, 266−268.
(87) Barthel, S.; Heinze, T. Acylation and carbanilation of cellulose in ionic liquids. *Green Chem.* **2006**, *8*, 301−306.
(88) Ogawa, S.; Miyafuji, H. Reaction behavior of milled wood lignin in an ionic liquid, 1-ethyl-3-methylimidazolium chloride. *J. Wood Sci.* **2015**, *61*, 285−291.
(89) Gericke, M.; Liebert, T.; Heinze, T. Interaction of ionic liquids with polysaccharides, 8-synthesis of cellulose sulfates suitable for polyelectrolyte complex formation. *Macromol. Biosci.* **2009**, *9*, 343−353.
(90) Mormann, W.; Wezstein, M. Trimethylsilylation of cellulose in ionic liquids. *Macromol. Biosci.* **2009**, *9*, 369−375.
(91) Köhler, S.; Liebert, T.; Schöbitz, M.; Schaller, J.; Meister, F.; Günther, W.; Heinze, T. Interactions of ionic liquids with polysaccharides 1. Unexpected acetylation of cellulose with 1-ethyl-3-methylimidazolium acetate. *Macromol. Rapid Commun.* **2007**, *28*, 2311−2317.
(92) Köhler, S.; Liebert, T.; Heinze, T. Ammonium-based cellulose solvents suitable for homogeneous etherification. *Macromol. Biosci.* **2009**, *9*, 836−841.
(93) Crépy, L.; Chaveriat, L.; Banoub, J.; Martin, P.; Joly, N. Synthesis of cellulose fatty esters as plastics-influence of the degree of substitution and the fatty chain length on mechanical properties. *ChemSusChem* **2009**, *2*, 165−170.
(94) Li, W. Y.; Jin, A. X.; Liu, C. F.; Sun, R. C.; Zhang, A. P.; Kennedy, J. F. Homogeneous modification of cellulose with succinic anhydride in ionic liquid using 4-dimethylaminopyridine as a catalyst. *Carbohydr. Polym.* **2009**, *78*, 389−395.
(95) Ohno, H.; Fukaya, Y. Task specific ionic liquids for cellulose technology. *Chem. Lett.* **2009**, *38*, 2−7.
(96) Wang, X.; Li, H.; Cao, Y.; Tang, Q. Cellulose extraction from wood chip in an ionic liquid 1-allyl-3-methylimidazolium chloride (AmimCl). *Bioresour. Technol.* **2011**, *102*, 7959−7965.
(97) Brandt, A.; Gräsvik, J.; Hallett, J. P.; Welton, T. Deconstruction of lignocellulosic biomass with ionic liquids. *Green Chem.* **2013**, *15*, 550−583.
(98) Zhu, S.; Yu, P.; Wang, Q.; Cheng, B.; Chen, J.; Wu, Y. Breaking the barriers of lignocellulosic ethanol production using ionic liquid technology. *BioResources* **2013**, *8*, 1510−1512.
(99) Fort, D. A.; Remsing, R. C.; Swatloski, R. P.; Moyna, P.; Moyna, G.; Rogers, R. D. Can ionic liquids dissolve wood? Processing and analysis of lignocellulosic materials with 1-n-butyl-3-methylimidazolium chloride. *Green Chem.* **2007**, *9*, 63−69.
(100) Espinoza-Acosta, J. L.; Torres-Chávez, P. I.; Carvajal-Millán, E.; Ramírez-Wong, B.; Bello-Pérez, L. A.; Montaño-Leyva, B. Ionic liquids and organic solvents for recovering lignin from lignocellulosic miomass. *BioResources* **2014**, *9*, 3660−3687.
(101) Anugwom, I.; Mäki-Arvela, P.; Virtanen, P.; Willför, S.; Sjöholm, R.; Mikkola, J. P. Selective extraction of hemicelluloses from spruce using switchable ionic liquids. *Carbohydr. Polym.* **2012**, *87*, 2005−2011.
(102) Kilpelainen, I.; Xie, H.; King, A.; Granstrom, M.; Heikkinen, S.; Argyropoulos, D. S. Dissolution of wood in ionic liquids. *J. Agric. Food Chem.* **2007**, *55*, 9142−9148.
(103) Li, C.; Knierim, B.; Manisseri, C.; Arora, R.; Scheller, H. V.; Auer, M.; Vogel, K. P.; Simmons, B. A.; Singh, S. Comparison of dilute acid and ionic liquid pretreatment of switchgrass: biomass recalcitrance, delignification and enzymatic saccharification. *Bioresour. Technol.* **2010**, *101*, 4900−4906.
(104) Singh, S.; Simmons, B. A.; Vogel, K. P. Visualization of biomass solubilization and cellulose regeneration during ionic liquid pretreatment of switchgrass. *Biotechnol. Bioeng.* **2009**, *104*, 68−75.
(105) Samayam, I. P.; Schall, C. A. Saccharification of ionic liquid pretreated biomass with commercial enzyme mixtures. *Bioresour. Technol.* **2010**, *101*, 3561−3566.
(106) Sun, N.; Rahman, M.; Qin, Y.; Maxim, M. L.; Rodríguez, H.; Rogers, R. D. Complete dissolution and partial delignification of wood in the ionic liquid 1-ethyl-3-methylimidazolium acetate. *Green Chem.* **2009**, *11*, 646.
(107) Lee, S. H.; Doherty, T. V.; Linhardt, R. J.; Dordick, J. S. Ionic liquid-mediated selective extraction of lignin from wood leading to enhanced enzymatic cellulose hydrolysis. *Biotechnol. Bioeng.* **2009**, *102*, 1368−1376.
(108) Da Costa Lopes, A. M.; João, K. G.; Morais, A. R. C.; Bogel-Łukasik, E.; Bogel-Łukasik, R. Ionic liquids as a tool for lignocellulosic biomass fractionation. *Sustainable Chem. Processes* **2013**, *1*, 1−31.
(109) Shill, K.; Padmanabhan, S.; Xin, Q.; Prausnitz, J. M.; Clark, D. S.; Blanch, H. W. Ionic liquid pretreatment of cellulosic biomass: enzymatic hydrolysis and ionic liquid recycle. *Biotechnol. Bioeng.* **2011**, *108*, 511−520.
(110) Xu, F.; Shi, Y. C.; Wang, D. Enhanced production of glucose and xylose with partial dissolution of corn stover in ionic liquid, 1-ethyl-3-methylimidazolium acetate. *Bioresour. Technol.* **2012**, *114*, 720−724.
(111) Sathitsuksanoh, N.; George, A.; Zhang, Y. H. P. New lignocellulose pretreatments using cellulose solvents: a review. *J. Chem. Technol. Biotechnol.* **2013**, *88*, 169−180.
(112) Gräsvik, J.; Winestrand, S.; Normark, M.; Jönsson, L. J.; Mikkola, J. P. Evaluation of four ionic liquids for pretreatment of lignocellulosic biomass. *BMC Biotechnol.* **2014**, *14*, 1−11.
(113) Cox, B. J.; Ekerdt, J. G. Pretreatment of yellow pine in an acidic ionic liquid: Extraction of hemicellulose and lignin to facilitate enzymatic digestion. *Bioresour. Technol.* **2013**, *134*, 59−65.
(114) Brandt, A.; Hallett, J. P.; Leak, D. J.; Murphy, R. J.; Welton, T. Ionic liquid pretreatment of lignocellulosic biomass with ionic liquid-water mixtures. *Green Chem.* **2011**, *13*, 2489−2499.
(115) Tan, S. S. Y.; MacFarlane, D. R.; Upfal, J.; Edye, L. A.; Doherty, W. O. S.; Patti, A. F.; Pringle, J. M.; Scott, J. L. Extraction of lignin from lignocellulose at atmospheric pressure using alkylbenzenesulfonate ionic liquid. *Green Chem.* **2009**, *11*, 339−345.

DOI: 10.1021/acs.jafc.5b03461
J. Agric. Food Chem. 2015, 63, 8093−8102

(116) Fu, D.; Mazza, G.; Tamaki, Y. Lignin extraction from straw by ionic liquids and enzymatic hydrolysis of the cellulosic residues. *J. Agric. Food Chem.* **2010**, *58*, 2915−2922.
(117) Fu, D.; Mazza, G. Optimization of processing conditions for the pretreatment of wheat straw using aqueous ionic liquid. *Bioresour. Technol.* **2011**, *102*, 8003−8010.
(118) Pinkert, A.; Goeke, D. F.; Marsh, K. N.; Pang, S. Extracting wood lignin without dissolving or degrading cellulose: investigations on the use of food additive-derived ionic liquids. *Green Chem.* **2011**, *13*, 3124−3136.
(119) Eerhart, A. J. J. E.; Huijgen, W. J. J.; Grisel, R. J. H.; van der Waal, J. C.; de Jong, E.; de Sousa Dias, A.; Faaij, A. P. C.; Patel, M. K. Fuels and plastics from lignocellulosic biomass via the furan pathway; a technical analysis. *RSC Adv.* **2014**, *4*, 3536−3549.
(120) Bensah, E. C.; Mensah, M. Chemical pretreatment methods for the production of cellulosic ethanol: technologies and innovations. *Int. J. Chem. Eng.* **2013**, *1*, 1−21.
(121) Lan, W.; Liu, C. F.; Sun, R. C. Fractionation of bagasse into cellulose, hemicelluloses, and lignin with ionic liquid treatment followed by alkaline extraction. *J. Agric. Food Chem.* **2011**, *59*, 8691−8701.
(122) Froschauer, C.; Hummel, M.; Iakovlev, M.; Roselli, A.; Schottenberger, H.; Sixta, H. Separation of hemicellulose and cellulose from wood pulp by means of ionic liquid/cosolvent systems. *Biomacromolecules* **2013**, *14*, 1741−1750.
(123) Arora, R.; Manisseri, C.; Li, C.; Ong, M. D.; Scheller, H. V.; Vogel, K.; Simmons, B. A.; Singh, S. Monitoring and analyzing process streams towards understanding ionic liquid pretreatment of switchgrass (*Panicum virgatum* L.). *BioEnergy Res.* **2010**, *3*, 134−145.
(124) Van Spronsen, J.; Cardoso, M. A. T.; Witkamp, G. J.; de Jong, W.; Kroon, M. C. Separation and recovery of the constituents from lignocellulosic biomass by using ionic liquids and acetic acid as co-solvents for mild hydrolysis. *Chem. Eng. Process.* **2011**, *50*, 196−199.
(125) Wahlström, R. M.; Suurnäkki, A. Enzymatic hydrolysis of lignocellulosic polysaccharides in the presence of ionic liquids. *Green Chem.* **2015**, *17*, 694−714.
(126) Bose, S.; Armstrong, D. W.; Petrich, J. W. Enzyme-catalyzed hydrolysis of cellulose in ionic liquids: a green approach toward the production of biofuels. *J. Phys. Chem. B* **2010**, *114*, 8221−8227.
(127) Yáñez, R.; Gómez, B.; Martínez, M.; Gullón, B.; Alonso, J. L. Valorization of an invasive woody species, *Acacia dealbata*, by means of ionic liquid pretreatment and enzymatic hydrolysis. *J. Chem. Technol. Biotechnol.* **2014**, *89*, 1337−1343.
(128) Kamiya, N.; Matsushita, Y.; Hanaki, M.; Nakashima, K.; Narita, M.; Goto, M.; Takahashi, H. Enzymatic *in situ* saccharification of cellulose in aqueous-ionic liquid media. *Biotechnol. Lett.* **2008**, *30*, 1037−1040.
(129) Khare, S. K.; Pandey, A.; Larroche, C. Current perspectives in enzymatic saccharification of lignocellulosic biomass. *Biochem. Eng. J.* **2015**, *102*, 38−44.
(130) Karatzos, S. K.; Edye, L. A.; Doherty, W. O. Sugarcane bagasse pretreatment using three imidazolium-based ionic liquids; mass balances and enzyme kinetics. *Biotechnol. Biofuels* **2012**, *5*, 62.
(131) Francisco, M.; Mlinar, A. N.; Yoo, B.; Bell, A. T.; Prausnitz, J. M. Recovery of glucose from an aqueous ionic liquid by adsorption onto a zeolite-based solid. *Chem. Eng. J.* **2011**, *172*, 184−190.
(132) Turner, M. B.; Spear, S. K.; Huddleston, J. G.; Holbrey, J. D.; Rogers, R. D. Ionic liquid salt-induced inactivation and unfolding of cellulase from *Trichoderma reesei*. *Green Chem.* **2003**, *5*, 443−447.
(133) Datta, S.; Holmes, B.; Park, J. I.; Chen, Z.; Dibble, D. C.; Hadi, M.; Blanch, H. W.; Simmons, B. A.; Sapra, R. Ionic liquid tolerant hyperthermophilic cellulases for biomass pretreatment and hydrolysis. *Green Chem.* **2010**, *12*, 338−345.
(134) Li, L.; Yu, S. T.; Liu, F. S.; Xie, C. X.; Xu, C. Z. Efficient enzymatic in situ saccharification of cellulose in aqueous-ionic liquid media by microwave pretreatment. *BioResources* **2011**, *6*, 4494−4504.
(135) Li, Q.; He, Y. C.; Xian, M.; Jun, G.; Xu, X.; Yang, J. M.; Li, L. Z. Improving enzymatic hydrolysis of wheat straw using ionic liquid 1-ethyl-3-methyl imidazolium diethyl phosphate pretreatment. *Bioresour. Technol.* **2009**, *100*, 3570−3575.
(136) Engel, P.; Mladenov, R.; Wulfhorst, H.; Jäger, G.; Spiess, A. C. Point by point analysis: how ionic liquid affects the enzymatic hydrolysis of native and modified cellulose. *Green Chem.* **2010**, *12*, 1959−1966.
(137) Guerriero, G.; Hausman, J.-F.; Strauss, J.; Ertan, H.; Siddiqui, K. S. Destructuring plant biomass: focus on fungal and extremophilic cell wall hydrolases. *Plant Sci.* **2015**, *234*, 180−193.
(138) Pöttkamper, J.; Barthen, P.; Limberger, N.; Schwaneberg, U.; Schenk, A.; Schulte, M.; Ignatiev, N.; Streit, W. Applying metagenomics for the identification of bacterial cellulases that are stable in ionic liquids. *Green Chem.* **2009**, *11*, 957−965.
(139) Graham, J. E.; Clark, M. E.; Nadler, D. C.; Huffer, S.; Chokhawala, H. A.; Rowland, S. E.; Blanch, H. W.; Clark, D. S.; Robb, F. T. Identification and characterization of a multidomain hyperthermophilic cellulase from an archaeal enrichment. *Nat. Commun.* **2011**, *2*, 1−10.

DOI: 10.1021/acs.jafc.5b03461
J. Agric. Food Chem. 2015, 63, 8093−8102

activity relationships of the constituent in the target organism. Proteomic and metabolomic tools may be used to gain deeper insight into complex biological processes but also require a structure-targeted approach.[4−6]

Manuscripts can encompass cell-based or other in vitro assays, animal models, human intervention studies, clinical trials, or a combination thereof as the fundamental component; however, target compounds need to be tested at relevant dose levels and test systems applied must be validated, should allow the quantitation of time and dose response effects, and need to be appropriate for in vivo conditions. Antioxidants need to be considered as a prominent example of the sometimes misleading prediction of a bioactive constituent's relationship to human health. Neither have less appropriate in vitro "antioxidant" test assays (ORAC, FRAP, TEAC, etc.) shown that they are able to predict protection against DNA damage or lipid and protein oxidation in vivo, nor has it been established that plasma antioxidant status predicts a physiological benefit. Rather, molecules that stimulate endogenous antioxidant and anti-inflammatory cell signaling cascades in ways that promote health seem to be more relevant to establishing bioactivity.[7]

To demonstrate bioefficacy as an overall aim of the "bioactives research" theme, the bioavailability of the target food constituent has to be substantial and may, in some cases, not be sufficient to exert the desired effect after dietary intake. Therefore, the discussion on nutritional relevance and conclusions on human health aspects need to be carefully formulated considering the experimental design used (appropriate cell-based or other in vitro assays, animal models, clinical human trials, significance of test/trial, relevant dose levels, etc.) and the robustness of the data set obtained and addressing the underlying mechanism of action. If, for example the bioactivity of a given compound is tested in a postabsorptive cell system, the compound's bioavailability characteristics, particularly the chemical structures of the metabolites formed, the metabolite and the parent compound concentrations after dietary intake, and the relevance of the cell line have to be considered. This can be illustrated by the general class of polyphenols, such as the flavonoids, most of which are metabolized by phase II enzymes in the intestinal tissues during the absorption process to render methylated, sulfated, or glucuronidated derivatives[8] or, if present in the food as glycosides, hydrolyzed or directly absorbed, or in the case of rhamnosides or rutinosides cannot be hydrolyzed without the help of gut microbiota to release the aglycones that would be then absorbed.

Overall, the manuscripts submitted to the "Bioactives" section of the *Journal of Agricultural and Food Chemistry* should consider the following five focus areas in increasing our integrated understanding of bioactive compound functions:

- identification of bioactive molecules in agricultural and food products by applying an activity-guided fractionation approach using relevant in vitro assays or any other appropriate target compound directed discovery technologies, followed by an unequivocal structure determination using state-of-the-art spectrometric and spectroscopic techniques;[9]
- accurate quantitation of bioactive target compound(s) using validated biochemical, molecular−biological, and/or chemical analytical tools;[10]
- demonstration of the bioavailability of bioactive constituents in a relevant in vitro model or in/ex vivo;
- unequivocal identification and quantitation of metabolites generated upon ingestion of bioactive target compounds;
- mechanistic studies, using relevant compounds at a demonstrated level of purity in appropriate cell-based models, animal trials, or human intervention studies.

Given the complexity of this approach, at least two of these criteria should be met for considering the described work as relevant to the field. In any case, chemical, biochemical, and molecular−biological methods and reproducibility of the work should be the fundamental principle behind the experimental design and should be combined with a biological and/or toxicological evaluation of structure−activity relationsships of the matrix constituents in living organisms related to agriculture and/or food. If the experimental approach is mainly based on individual test systems, the work is likely to remain only observational and descriptive. As a general rule, manuscripts dealing with traditional medicines and herbal remedies or those testing commercially available reference compounds, selected without any convincing rationale, in cell-based in vitro assays to draw conclusions on their impact on disease states (e.g., "anticancer" activity) will generally not be accepted for review. Moreover, it is mandatory that manuscripts reporting on biological properties of individual constituents include information on the purity of the test components and on how it has been determined (e.g., ^{1}H NMR, GC-FID, HPLC-ELSD). Similarly, investigations performed with crude extracts need to present detailed information on the chemical composition of the extracts responsible for the described properties. This means that key representatives of the chemical class investigated (e.g., polyphenols, terpenoids, alkaloids, peptides) should be quantitatively fingerprinted. In general, lack of the unequivocal chemical characterization of the bioactive target components may limit the reproducibility of the results and, as a consequence, such work might not be considered suitable for review.

JAFC has already published a number of good examples of bioactivity research on plants,[5,6,11] pathogens,[12,13] and food/nutrition aspects[14−22] that illustrate the breadth and depth of this field. With the boundaries defined in this perspective, we invite future authors to conform to the highest standards of chemical/biological research on bioactives spanning the range from whole foods to drug-like isolated compounds that are required to best serve the needs of our society.

AUTHOR INFORMATION

Corresponding Author

*(T.H.) Phone: +49-8161/71-2902. Fax: +49-8161/71-2949. E-mail: thomas.hofmann@tum.de.

Notes

The authors declare no competing financial interest.

REFERENCES

(1) Patil, B. S.; Jayaprakasha, G. K.; Chidambara Murthy, K. N.; Vikram, A. Bioactive compounds: historical perspectives, opportunities, and challenges. *J. Agric. Food Chem.* **2009**, *57*, 8142−8160.

(2) Zhang, L.; Hou, D.; Chen, X.; Li, D.; Zhu, L.; Zang, Y.; Li, J.; Bian, Z.; Liang, X.; Cai, X.; Yin, Y.; Wang, Ch.; Zhang, T.; Zhu, D.; Zhang, D.; Xu, J.; Chen, Q.; Ba, Y.; Liu, J.; Wang, Q.; Chen, J.; Wang, J.; Wang, M.; Zhang, Q.; Zhang, J.; Zen, K.; Zhang, Ch.-Y. Exogenous plant MIR168a specifically targets mammalian LDLRAP1: evidence of cross-kingdom regulation by microRNA. *Cell Res.* **2012**, *22*, 107−126.

DOI: 10.1021/acs.jafc.5b04312
J. Agric. Food Chem. 2015, 63, 8103−8105

(3) Espìn, J. C.; Garcìa-Conesa, M. T.; Tomàs-Barberàn, F. A. Nutraceuticals: facts and fiction. *Phytochemistry* **2007**, *68*, 2986−3008.
(4) Seiber, J. N.; Molyneux, R. J.; Schieberle, P. Targeted metabolomics: a new section in the *Journal of Agricultural and Food Chemistry*. *J. Agric. Food Chem.* **2014**, *62*, 22−23.
(5) Paudel, L.; Wyzgoski, F. J.; Giusti, M. M.; Johnson, J. L.; Rinaldi, P. L.; Scheerens, J. C.; Chanon, A. M.; Bomser, J. A.; Miller, A. R.; Hardy, J. K.; Reese, R. N. NMR-based metabolomic investigation of bioactivity of chemical constituents in black raspberry (*Rubus occidentalis* L.) fruit extracts. *J. Agric. Food Chem.* **2014**, *62*, 1989−1998.
(6) Macherius, A.; Seiwert, B.; Schröder, P.; Huber, C.; Lorenz, W.; Reemtsma, T. Identification of plant metabolites of environmental contaminants by UPLC-QToF-MS: the in vitro metabolism of triclosan in horseradish. *J. Agric. Food Chem.* **2014**, *62*, 1001−1009.
(7) Finley, J. W.; Kong, A.-N.; Hintze, K. J.; Jeffery, E. H.; Ji, L. L.; Lei, X. G. Antioxidants in foods: state of the science important to the food industry. *J. Agric. Food Chem.* **2011**, *59*, 6837−46.
(8) Blount, J. W.; Redan, B. W.; Ferruzzi, M. G.; Reuhs, B. L.; Cooper, B. R.; Harwood, J. S.; Shulaev, V.; Pasinetti, G.; Dixon, R. A. Synthesis and quantitative analysis of plasma-targeted metabolites of catechin and epicatechin. *J. Agric. Food Chem.* **2015**, *63*, 2233−2240.
(9) Molyneux, R. J.; Schieberle, P. Compound identification: a *Journal of Agricultural and Food Chemistry* perspective. *J. Agric. Food Chem.* **2007**, *55*, 4625−4629.
(10) Schieberle, P.; Molyneux, R. J. Quantitation of sensory-active and bioactive constituents of food: a *Journal of Agricultural and Food Chemistry* perspective. *J. Agric. Food Chem.* **2012**, *60*, 2404−2408.
(11) Ku, K.-M.; Jeffery, E. H.; Juvik, J. A.; Kushad, M. M. Correlation of quinone reductase activity and allyl isothiocyanate formation among different genotypes and grades of horseradish roots. *J. Agric. Food Chem.* **2015**, *63*, 2947−2955.
(12) Lu, S.; Sun, W.; Meng, J.; Wang, A.; Wang, X.; Tian, J.; Fu, X.; Dai, J.; Liu, Y.; Lai, D.; Zhou, L. Bioactive bis-naphtho-γ-pyrones from rice false smut pathogen *Ustilaginoidea virens*. *J. Agric. Food Chem.* **2015**, *63*, 3501−3508.
(13) Nakano, H.; Schrader, K. K.; Mamonov, L. K.; Kustova, T. S.; Mursaliyeva, V. K.; Cantrell, C. L. Isolation and identification of *Flavobacterium columnare* and *Streptococcus iniae* antibacterial compounds from the terrestrial plant *Atraphaxis laetevirens*. *J. Agric. Food Chem.* **2012**, *60*, 10415−10419.
(14) Grienke, U.; Mair, C. E.; Saxena, P.; Baburin, I.; Scheel, O.; Ganzera, M.; Schuster, D.; Hering, S.; Rollinger, J. M. Human ether-à-go-go related gene (hERG) channel blocking aporphine alkaloids from lotus leaves and their quantitative analysis in dietary weight loss supplements. *J. Agric. Food Chem.* **2015**, *63*, 5634−5639.
(15) Somoza, V.; Lindenmeier, M.; Wenzel, E.; Frank, O.; Erbersdobler, H. F.; Hofmann, T. Activity-guided identification of a chemopreventive compound in coffee beverage using in vitro and in vivo techniques. *J. Agric. Food Chem.* **2003**, *51*, 6861−6869.
(16) Tedesco, I.; Carbone, V.; Spagnuolo, C.; Minasi, P.; Russo, G. L. Identification and quantification of flavonoids from two southern Italian cultivars of *Allium cepa* L., Tropea (red onion) and Montoro (copper onion), and their capacity to protect human erythrocytes from oxidative stress. *J. Agric. Food Chem.* **2015**, *63*, 5229−5238.
(17) Walker, J.; Hell, J.; Liszt, K. I.; Dresel, M.; Pignitter, M.; Hofmann, T.; Somoza, V. Identification of beer bitter acids regulating mechanisms of gastric acid secretion. *J. Agric. Food Chem.* **2012**, *60*, 1405−1412.
(18) Wang, Y.; Dawid, C.; Kottra, G.; Daniel, H.; Hofmann, T. Gymnemic acids inhibit the sodium-dependent glucose transporter 1. *J. Agric. Food Chem.* **2014**, *62*, 5925−5931.
(19) Macke, S.; Jerz, G.; Empl, T. L.; Steinberg, P.; Winterhalter, P. Activity-guided isolation of resveratrol oligomers from a grapevine-shoot extract using countercurrent chromatography. *J. Agric. Food Chem.* **2012**, *60*, 11919−11927.
(20) Rubach, M.; Lang, R.; Skupin, C.; Hofmann, T.; Somoza, V. Activity-guided fractionation to characterize a coffee beverage that effectively down-regulates mechanisms of gastric acid secretion as compared to regular coffee. *J. Agric. Food Chem.* **2010**, *58*, 4153−4161.
(21) Schueller, K.; Pignitter, M.; Somoza, V. Sulfated and glucuronated *trans*-resveratrol metabolites regulate chemokines and sirtuin-1 expression in U-937 macrophages. *J. Agric. Food Chem.* **2015**, *63*, 6535−6545.
(22) Murotomi, K.; Umeno, A.; Yasunaga, M.; Shichiri, M.; Ishida, N.; Koike, T.; Matsuo, T.; Abe, H.; Yoshida, Y.; Nakajima, Y. Oleuropein-rich diet attenuates hyperglycemia and impaired glucose tolerance in type 2 diabetes model mouse. *J. Agric. Food Chem.* **2015**, *63*, 6715−6722.

DOI: 10.1021/acs.jafc.5b04312
J. Agric. Food Chem. 2015, 63, 8103−8105

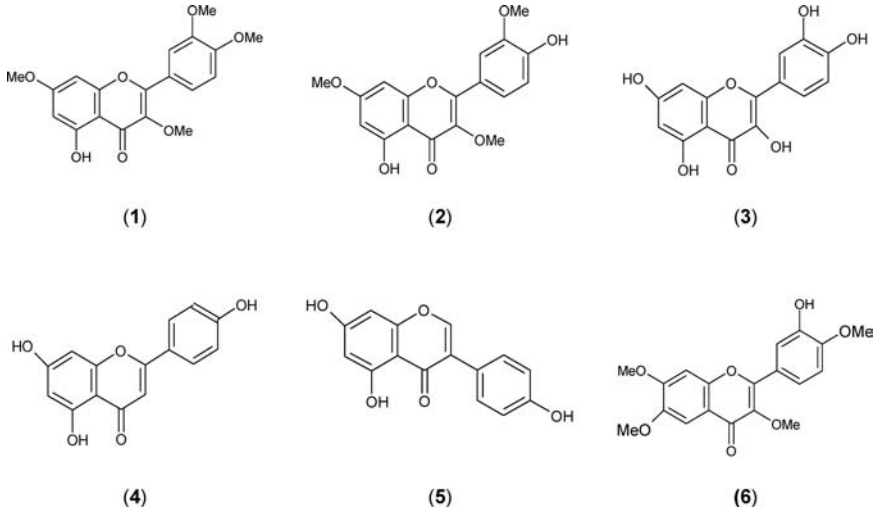

Figure 1. Structures of the evaluated flavonoids: Retusin (**1**), pachypodol (**2**), quercetin (**3**), apigenin (**4**), genistein (**5**), and eupatorin (**6**).

ciliatoglanduliferus Ort. by column chromatography (CC) separation and then were purified by preparative thin-layer chromatography (PTLC) as previously reported.[15] Open column chromatography (silica gel 60, 70−230 mesh, Merck) and PTLC (silica gel 60 F_{254}, 1 mm plates) were used. The identity of compounds **1** and **2** were corroborated by spectroscopic methods and compared with previously reported data.[15] ^{1}H NMR and ^{13}C experiments were recorded on a Varian Unity INOVA at 300 MHz, and EI mass spectra were obtained on a JEOL SX 102A mass spectrometer. Quercetin (**3**), apigenin (**4**), genistein (**5**), and eupatorin (**6**) were purchased from Sigma-Aldrich and used as received (Figure 1).

Chloroplasts Isolation and Chlorophyll Determination. Intact chloroplasts were isolated from market spinach leaves (*Spinacia oleracea* L.) as previously reported.[17,18] Chloroplasts were suspended in a small volume of a solution containing 400 mM sucrose, 5 mM $MgCl_2$, 10 mM KCl, and 30 mM tricine−KOH (pH 8.0), and they were stored as a concentrated suspension in the dark at 4 °C. The chlorophyll (Chl) concentration was measured according to Strain.[19]

Noncyclic Electron Transport Determination. Light-induced noncyclic electron transport determination was performed in the presence of 50 μM methylviologen (MV) as an electron acceptor using a Clark type electrode.[20] Basal electron transport was polarographically determined by illuminating chloroplasts (20 μg chlorophyll/mL) during 1 min in a medium containing 100 mM sorbitol, 10 mM KCl, 5 mM $MgCl_2$, 0.5 mM KCN, 50 μM MV, and 15 mM tricine−KOH (pH 8.0) as previously published.[18,20] Phosphorylating noncyclic electron transport was measured with the basal medium plus 1 mM adenosine diphosphate (ADP) and 3 mM KH_2PO_4.[18,20] Uncoupled electron transport was tested in the basal medium, and 6 mM NH_4Cl was added as an uncoupler.[18,20]

Uncoupled Photosystem II (PSII), Photosystem I (PSI), and Their Partial Electron Flow Determination. These electron flow activities were monitored with an oxygen monitor YSI (Yellow Spring Instruments) model 5300A using a Clark type electrode. The uncoupled electron transport rate was measured from water to 2,5-dichloro-1,4-benzoquinone (DCBQ)[21] using the medium for PSII reactions. This medium is the same for basal measurements without MV but with 100 μM DCBQ, 1 μM 2,5-dibromo-6-isopropyl-3-methyl-1,4-benzoquinone (DBMIB) and 6 mM NH_4Cl. Chloroplasts (20 μg Chl/mL) were then added and illuminated during 1 min.

Uncoupled partial reaction of PSII was measured from water to sodium silicomolybdate (SiMo), determined in the reaction medium for PSII (3 mL), plus 200 μM SiMo[22,23] and 10 μM 3-(3,4-dichlorophenyl)-1,1-dimethylurea (DCMU) before the addition of chloroplasts (20 μg Chl/mL), and then illuminated for 1 min.

The uncoupled PSII partial electron transport rate was measured from DPC (diphenylcarbazide), which is an efficient electron donor to the inactive oxygen-evolving complex of PSII in Mn-depleted thylakoids (thylakoids previously treated with 0.8 M hydroxymethyl aminomethane (Tris) at pH 8.0).[24,25] DPC donates electrons at Z,[26] and the reduction of DCPIP was measured using a Beckman DU 650 spectrophotometer.

The uncoupled PSI electron transport was determined using the basal electron transport medium, plus 10 μM DCMU (to inhibit PSII at Q_B level) and 100 μM dichlorophenol indophenol (DCPIP) reduced with 300 μM ascorbate, and uncoupled with 6 mM NH_4Cl.[27]

All reaction mixtures were illuminated with filtered light (filtered through 5 cm of 1% $CuSO_4$ solution) from a projector lamp (GAF 2660) at room temperature. For each reaction, a blank experiment was performed with the chloroplasts in the reaction medium. The I_{50} value is the concentration producing 50% inhibition of activity and was determined from the plots of activity versus different concentrations of each compound calculated by linear regression analysis by probit.[28]

Chlorophyll *a* (Chl *a*) Fluorescence Determination. Chl *a* fluorescence was measured at room temperature with a Hansatech Fluorescence Handy PEA (plant efficiency analyzer).[29,30] The maximum fluorescence yield from the sample was generated using three red intensity light-emitting diodes (broadband 650 nm) of 3000 μmol m^{-2} s^{-1}. The pulse duration was 2 s. To monitor transients of Chl *a* fluorescence, aliquots of dark-adapted thylakoids containing 20 μg of Chl were transferred to filter paper by gravity and immediately dipped in 3 mL of basal noncyclic electron transport medium at different concentrations of the compounds. Photosynthetic parameters associated with PSII were obtained according to the equations of the O-J-I-P test using the program Biolyzer.[31]

Sample Preparation. Each compound was dissolved in dimethyl sulfoxide (DMSO) to prepare a 20 mM stock solution. For the chlorophyll *a* fluorescence determination, dry biomass, and leaf chlorophyll determination assays, an aliquot of each stock solution was taken to obtain the desired concentration in a deionized aqueous solution (25 mL) containing Tween 20 (0.02% v/v, to avoid the surface tension). The negative control group was sprayed with a solution of deionized water (containing 0.02% v/v of Tween) and DMSO in the same proportion as that used to prepare the one with the major concentration of flavonoid (300 μM). For the positive control, an aliquot of a solution 3 mM DCMU in EtOH was taken to prepare 50 μM DCMU in an aqueous solution containing Tween 20 at 0.02% v/v.

For the germination and seedling growth bioassays, an aliquot of each flavonoid solution was taken to prepare the desired concentration (50 and 100 μM) in an aqueous solution where *T. alexandrinum*, *P. ixocarpa*, and *L. perenne* seeds were grown. To measure the *T. alexandrinum* seedling respiration, test solutions were diluted employing Hoagland medium which consists of 6 mM KNO_3, 4 mM $Ca(NO_3)_2 \cdot 4H_2O$, 1 mM $NH_4H_2PO_4$, 2 mM $MgSO_4 \cdot 7H_2O$, 46 μM H_3BO_3, 13.6 μM Fe−EDTA, 9 μM $MnCl_2 \cdot 4H_2O$, 0.8 μM $ZnSO_4 \cdot 7H_2O$, 0.3 μM $CuSO_4 \cdot 5H_2O$, and 0.1 μM $H_2MoO_4 \cdot H_2O$ (pH = 5.2−5.5).[32]

DOI: 10.1021/acs.jafc.5b02842
J. Agric. Food Chem. 2015, 63, 8106−8115

Table 1. I_{50} Values (μM) from Electron Transport Rates of Spinach Thylakoids Treated with the Tested Flavonoids

compound	basal I_{50}	phosphorylating I_{50}	uncoupled I_{50}	log P
1	n/c[a]	n/c	n/c	2.74
2	n/c	30	74	2.62
3	n/c	200	114	1.37
4	72	112	n/c	2.63
5	n/c	n/c	200	2.74
6	n/c	173	130	2.84

[a]n/c means not calculated.

Plant Material. The seeds of three plant species, green tomato (*Physalis ixocarpa*), clover (*Trifolium alexandrinum*), and grass (*Lolium perenne*), were washed with a 10% sodium hypochlorite solution for 15 min in an orbital shaker (VWR minishaker). After this time, the hypochlorite solution was removed and the seeds were rinsed three times with deionized water. One hundred seeds were placed in 12 cm diameter pots containing a mixture of 50:25:25 v/v soil/peat-moss/agrolita. All pots were watered every third day and maintained in a greenhouse at room temperature (25−30 °C) with a normal day/night (12/12 h) illumination. After 15 days of emergence for *P. ixocarpa* and *L. perenne*, and 20 days for *T. alexandrinum*, the plants were selected by uniformity and similar size and were divided into three groups: (a) the control; (b) the experimental, which was sprayed manually with 25 mL of flavonoid solutions at different concentrations (25, 50, 100, 200, and 300 μM); (c) the positive control (sprayed with 25 mL of 50 μM DCMU).

Chlorophyll *a* Fluorescence Determination in Intact Leaves in Vivo. The chlorophyll *a* (Chl *a*) fluorescence determination was performed at 24, 48 72 and 168 h after treatment of plants and dark adapted for 30 min. The leaves were excited with saturating light as above-mentioned for chloroplasts and processed according to the concept of the JIP-test[29] with the program Biolyzer which executes the JIP test equations for the analysis of the fluorescence transient O-J-I-P.[30]

Leaf Chlorophyll Determination. Leaves of treated species (100 mg) harvested randomly from plants were placed into test tubes and incubated with 5 mL of *N*,*N*-dimethylformamide (DMF) at 4 °C for 24 h in the dark for chlorophyll extraction. The absorbance of each 3.0 mL sample was determined at 664.5 nm for chlorophyll *a* and at 647 nm for chlorophyll *b* using a spectrophotometer (Thermo model G-10S). The extinction coefficients assigned by Inskeep were used to estimate the chlorophyll concentration.[33]

Dry Biomass. After 15 days of treatment with the test compounds, all plants were harvested at ground level and dried in an oven at 65 °C to reach constant weight. Then the dry mass was determined employing an analytical balance.[34]

Germination and Seedling Growth Bioassays. Forty seeds of *P. ixocarpa*, *T. alexandrinum*, and *L. perenne* selected for uniformity (undersized or damaged materials were discarded) were washed and placed in 10 cm Petri dishes using Whatman no. 1 filter paper as support. In each Petri dish 10 mL of deionized water and the aliquot of the stock solution (20 mM) of flavonoid were added; for the negative control, 10 mL of deionized water and the aliquot with the major concentration of solvent used to prepare the test solution were employed. The Petri dishes were incubated at 28 °C in the dark. After 7 days, the values of root and stem lengths as well as the number of germinated seeds were obtained (the number of germinated seeds was determined according to the criteria of 1 mm extrusion of the root). Each assay was conducted in triplicate, and the statistical differences between the treatments were evaluated by Student's *t* test for assessing the statistical significance. Data were presented as the percentage of differences from control in bar graphics. The negative control represents 0%, positive values represent stimulation of the studied parameter, and negative values represent inhibition.

Measurement of the Effect of Flavonoids on the Respiration of *T. alexandrinum* Seedlings. Two hundred seeds of *T. alexandrinum* were placed in 15 cm Petri dishes, 20 mL of a 50% v/v Hoagland medium was added,[32] and flavonoids were added at different concentrations (50, 100, 150, and 200 μM). Then the Petri dishes were incubated in darkness for 7 days at 28 °C. Etiolated seedlings (200 mg) were placed

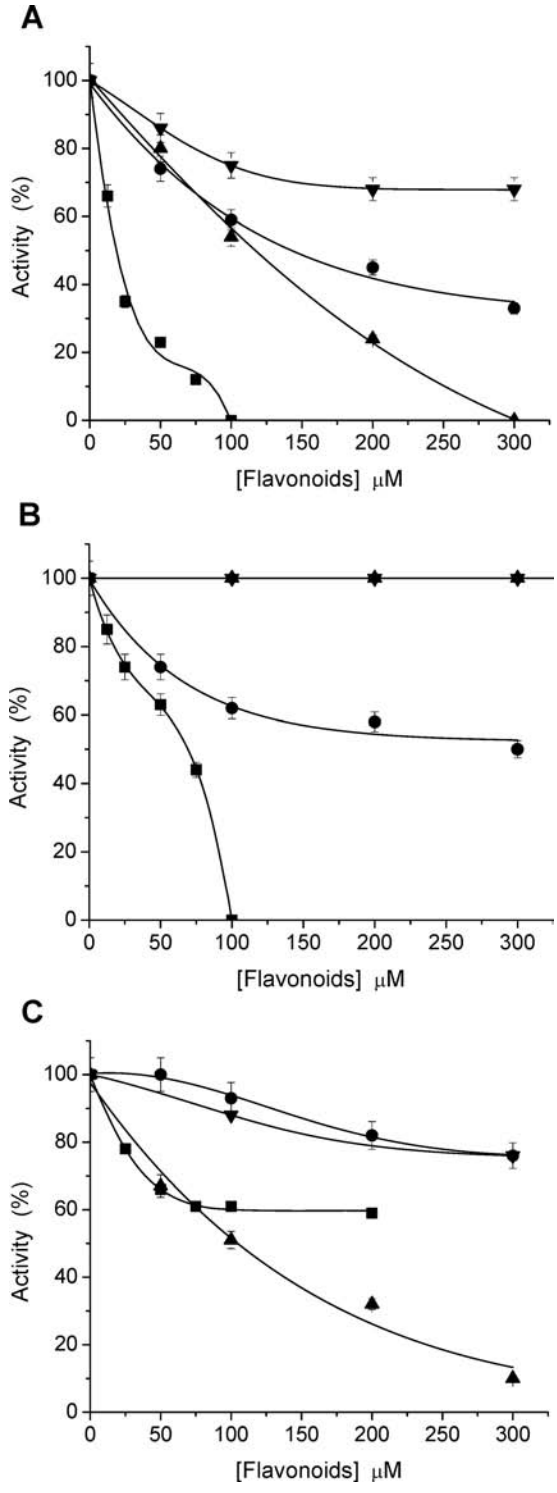

Figure 2. Effect of flavonoids **3** (■), **4** (●), **5** (▲), and **6** (▼) on partial reactions in PSII from H_2O to DCBQ (panel A), from H_2O to SiMo (panel B), and from DPC to DCPIP (panel C). Control value rates for photosystem II from H_2O to DCBQ and from H_2O to SiMo were 520 ± 52 and 110 ± 5 μequiv e^- mg^{-1} Chl h^{-1}, respectively. For the PS II partial reaction measured from DPC to DCPIP, controls for flavonoid **3** and **4** were 80 ± 4 μM DCPIPred mg^{-1} Chl h^{-1}; for **5** and **6**, controls were 96 ± 4.8 μM DCPIPred mg^{-1}. Data are means of three replicates.

DOI: 10.1021/acs.jafc.5b02842
J. Agric. Food Chem. 2015, 63, 8106−8115

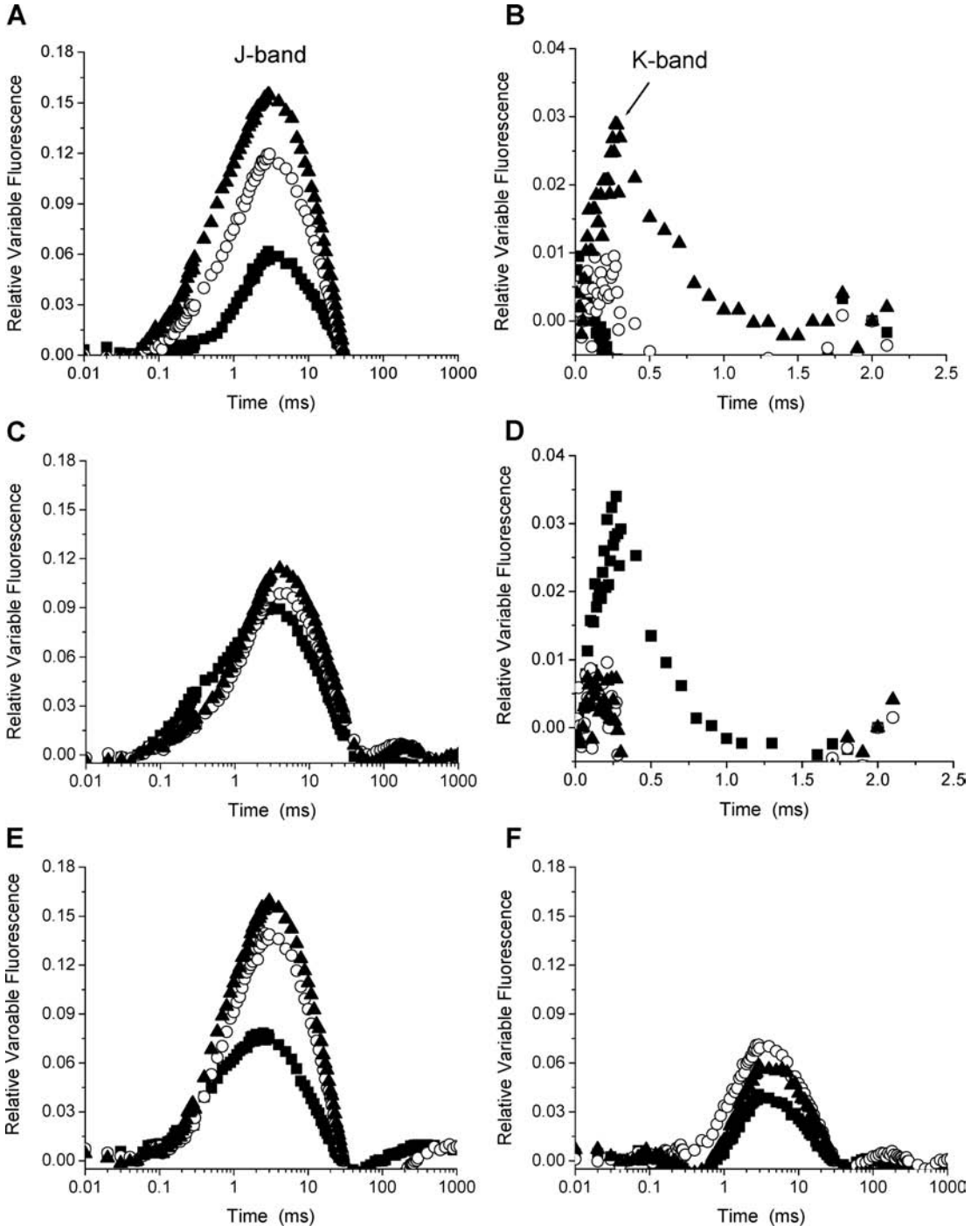

Figure 3. Appearance of a J-band in the normalized relative variable fluorescence of chlorophyll *a* of thylakoids infiltrated with 25 μM (■), 150 μM (○), and 300 μM (▲) of the following: Panel A, **3**; panel C, **4**; panel E, **5**; panel F, **6**. Appearance of a K-band with 300 μM (▲) of **3**, panel B, and 25 μM (■) of **4**, panel D. Each curve is an average of three replicates.

in a reaction vessel, and 3 mL of 50% v/v Hoagland medium was added. The seedling respiration was measured as O_2 uptake using a Clark type electrode attached to a Yellow Spring Instruments (YSI) model 5300A oxymeter. The current generated during the O_2 reduction to water was converted to voltage, and the signal was recorded on a Kipp and Zonen chart recorder. The current was stoichiometrically related to the oxygen consumed at the cathode. The consumption rate was calculated with the following equation:

$$\left(\frac{1200\ \text{nmol O}_2}{20\ \text{cm}}\right)\left(\frac{60\ \text{min}}{1\ \text{h}}\right)\left(\frac{y}{1\ \text{min}}\right)\left(\frac{1}{\text{mg seedlings}}\right) = \text{nmol O}_2\ \text{h}^{-1}\ \text{mg}^{-1}$$

The results were reported as nmol O_2 h^{-1} mg^{-1} of seedlings.[35] In the equation, 20 cm on the recorder paper corresponds to 1200 nmol O_2 and y corresponds to the recorded distance in cm when the O_2 uptake of seedlings in aqueous medium occurred.

RESULTS AND DISCUSSION

Isolation of Retusin (1) and Pachypodol (2). The natural flavonoids **1** and **2** were isolated from the hexane extract of the aerial parts of *Croton ciliatoglanduliferus* in approximate 0.5% yield for both compounds, as previously published.[15]

DOI: 10.1021/acs.jafc.5b02842
J. Agric. Food Chem. 2015, 63, 8106−8115

Table 2. Experimental Average Values ± Standard Deviation of Chlorophyll *a* Fluorescence Obtained in *P. ixocarpa* Leaves Plant at Different Times after Treatment with Compound 1

time (h)		F_0	F_M	$F_{(0.3\ ms)}$	$F_{(2\ ms)}$	F_V/F_M	TR_0/RC	area
24	control	284 ± 18	1449 ± 63	528 ± 34	779 ± 46	0.804 ± 0.16	1.754 ± 0.104	27333 ± 2386
	25	277 ± 23	1424 ± 60	522 ± 45	795 ± 46	0.805 ± 0.016	1.692 ± 0.124	28746 ± 2403
	50	269 ± 20	1436 ± 71	510 ± 39	778 ± 47	0.811 ± 0.018	1.669 ± 0.115	27940 ± 2120
	100	295 ± 34	1308 ± 60	550 ± 47	786 ± 52	0.771 ± 0.037	1.853 ± 0.2	22753 ± 2832
	200	276 ± 25	1429 ± 62	520 ± 40	779 ± 37	0.806 ± 0.022	1.735 ± 0.121	28161 ± 2884
	300	297 ± 29	1338 ± 82	550 ± 53	796 ± 65	0.776 ± 0.034	1.814 ± 0.116	24500 ± 2483
	DCMU	503 ± 42	1028 ± 61	804 ± 63	1004 ± 62	0.51 ± 0.043	2.187 ± 0.159	2383 ± 789
48	control	268 ± 16	1359 ± 114	528 ± 34	789 ± 45	0.801 ± 0.023	1.633 ± 0.197	21282 ± 2943
	25	274 ± 20	1336 ± 104	513 ± 46	771 ± 51	0.790 ± 0.042	2.113 ± 0.414	24000 ± 2392
	50	293 ± 29	1260 ± 94	560 ± 52	799 ± 48	0.760 ± 0.06	1.677 ± 0.652	18680 ± 2860
	100	325 ± 32	989 ± 78	543 ± 71	726 ± 58	0.639 ± 0.14	1.713 ± 0.117	1283 6 ± 2475
	200	266 ± 29	1148 ± 94	470 ± 68	680 ± 59	0.77 ± 0.049	2.136 ± 0.226	18965 ± 2736
	300	353 ± 32	1029 ± 74	600 ± 48	783 ± 41	0.657 ± 0.011	1.726 ± 0.25	12525 ± 2536
	DCMU	461 ± 53	962 ± 86	746 ± 56	931 ± 67	0.516 ± 0.079	2.151 ± 0.162	3189 ± 1917
72	control	278 ± 23	1469 ± 86	536 ± 54	810 ± 54	0.816 ± 0.02	1.633 ± 0.197	25626 ± 2515
	25	270 ± 31	1464 ± 64	534 ± 30	832 ± 27	0.679 ± 0.04	2.113 ± 0.414	29543 ± 2242
	50	264 ± 19	1365 ± 81	509 ± 35	773 ± 54	0.815 ± 0.016	1.677 ± 0.065	24808 ± 2638
	100	349 ± 31	1241 ± 75	671 ± 62	895 ± 43	0.806 ± 0.02	1.713 ± 0.117	16836 ± 2082
	200	264 ± 27	1373 ± 57	499 ± 33	757 ± 35	0.708 ± 0.049	2.136 ± 0.22	26195 ± 2134
	300	363 ± 22	1090 ± 66	634 ± 43	817 ± 29	0.777 ± 0.067	1.873 ± 0.341	15379 ± 1714
	DCMU	468 ± 31	1076 ± 51	803 ± 39	1039 ± 31	0.554 ± 0.077	2.151 ± 0.167	3408 ± 1749
168	control	260 ± 22	1378 ± 69	504 ± 51	764 ± 64	0.814 ± 0.008	1.711 ± 0.125	24042 ± 2592
	25	258 ± 22	1349 ± 53	483 ± 44	728 ± 52	0.808 ± 0.013	1.705 ± 0.150	26387 ± 2237
	50	272 ± 27	1236 ± 87	541 ± 39	760 ± 55	0.784 ± 0.011	1.848 ± 0.136	20102 ± 2092
	100	304 ± 37	1256 ± 57	572 ± 66	778 ± 55	0.760 ± 0.04	2.05 ± 0.257	21119 ± 3137
	200	257 ± 22	1267 ± 48	500 ± 54	729 ± 58	0.800 ± 0.027	2.069 ± 0.831	22729 ± 2643
	300	268 ± 38	1272 ± 68	494 ± 50	719 ± 52	0.800 ± 0.027	1.747 ± 0.106	23487 ± 2790
	DCMU	266 ± 90	1450 ± 76	564 ± 131	930 ± 118	0.780 ± 0.06	1.679 ± 0.118	27619 ± 2340

Effect of Flavonoids on the Photosynthetic Electron Transport Chain. Previously, results showed that compound **2** inhibited the photosynthetic electron flow from water to MV on freshly lysed intact spinach chloroplasts.[15] To know the effect of the flavonoids **3**–**6** on the electron transport flow (basal, phosphorylating, and uncoupled), they were assayed under the same conditions as that for **2**. Table 1 shows the I_{50} values for the tested compounds and for each transport. It was found that flavonoid **1** inhibited 20% the electron flow for the three conditions (basal, phosphorylating, and uncoupled) at 300 μM.[15] The most active compound to inhibit the uncoupled electron transport was **2** with an I_{50} value of 74 μM, followed by **3**, **5**, and **6**, with I_{50} values of 114, 200, and 130 μM, respectively. **4** inhibited basal and phosphorylating electron flow; however, at the concentrations evaluated, the I_{50} value for the uncoupled electron flow was not reached (Table 1). Thus, **2**, **5**, and **6** behave as Hill reaction inhibitors and **3** as uncoupler and electron transport inhibitor (Table 1). The most active compounds as uncoupled electron transport inhibitors were **2** and **3**, with I_{50} values of 74 and 114 μM with lower log *P* values of 2.62 and 1.37, respectively.

Localization of Interaction Sites of Flavonoids on PSII, PSI, and Partial Reactions. To localize the inhibition site of flavonoids on the thylakoid electron transport chain, the effects of increasing concentrations of **3**, **4**, **5**, and **6** on PSII, PSI, and the partial reactions were assayed using artificial electron donors and electron acceptors, as well as appropriate inhibitors.[27] Figure 2A shows that flavonoids **3**, **4**, **5**, and **6** inhibit uncoupled PSII from water to $DCBQ_2$ with **3** being the most active followed by **5**. Compound **3** inhibited 100% at 100 μM the electron flow measured from water to SiMo (Figure 2B) and partially (40% at 200 μM) the span from DPC to DCPIP (Figure 2C). Compound **4** also inhibited to a minor degree these partial reactions. Flavonoids **5** and **6** did not affect the electron flow from water to SiMo; however, compound **5** inhibited almost 100% at 300 μM the span from DPC to DCPIP and **6** only did partially. On the other hand, neither one showed inhibitory activity on PSI measured from DCPIP reduced to MV (data not shown).

Chl *a* Fluorescence Determination in Chloroplasts. To corroborate findings by polarography on the interaction site of **3**, **4**, **5**, and **6** at PSII, chlorophyll *a* fluorescence kinetics were determined in freshly lysed spinach chloroplasts incubated for 5 min in the dark at room temperature. The treated chloroplasts contained various concentrations of the flavonoids (25, 150, and 300 μM), and each concentration was measured three times. Control chloroplasts contained the corresponding amount of DMSO used for each treatment. The fluorescence of chlorophyll *a* transients obtained from the treated and control chloroplasts was normalized, and the differences between them revealed an increase in intensity between 2 and 4 ms appearing as a J-band (Figure 3, panels A, C, E, and F). Moreover, experiments with **3** and **4** exhibited lower K-bands (Figure 3, panels B and D).

In samples treated with increasing concentrations of DCMU a single induction phase is observed and the F_M is reached after about 2 ms (J-step).[36] DCMU displaces the secondary quinone acceptor, Q_B, from its binding site at the D1 protein of photosystem II (PSII)[37] and prevents the reoxidation of Q_A^- by forward electron transport. The fluorescence rise is mainly determined by the redox state of Q_A^-.[36]

On the other hand, the appearance of the K-band results from an imbalance in the electron flow between the donor and

DOI: 10.1021/acs.jafc.5b02842
J. Agric. Food Chem. 2015, 63, 8106−8115

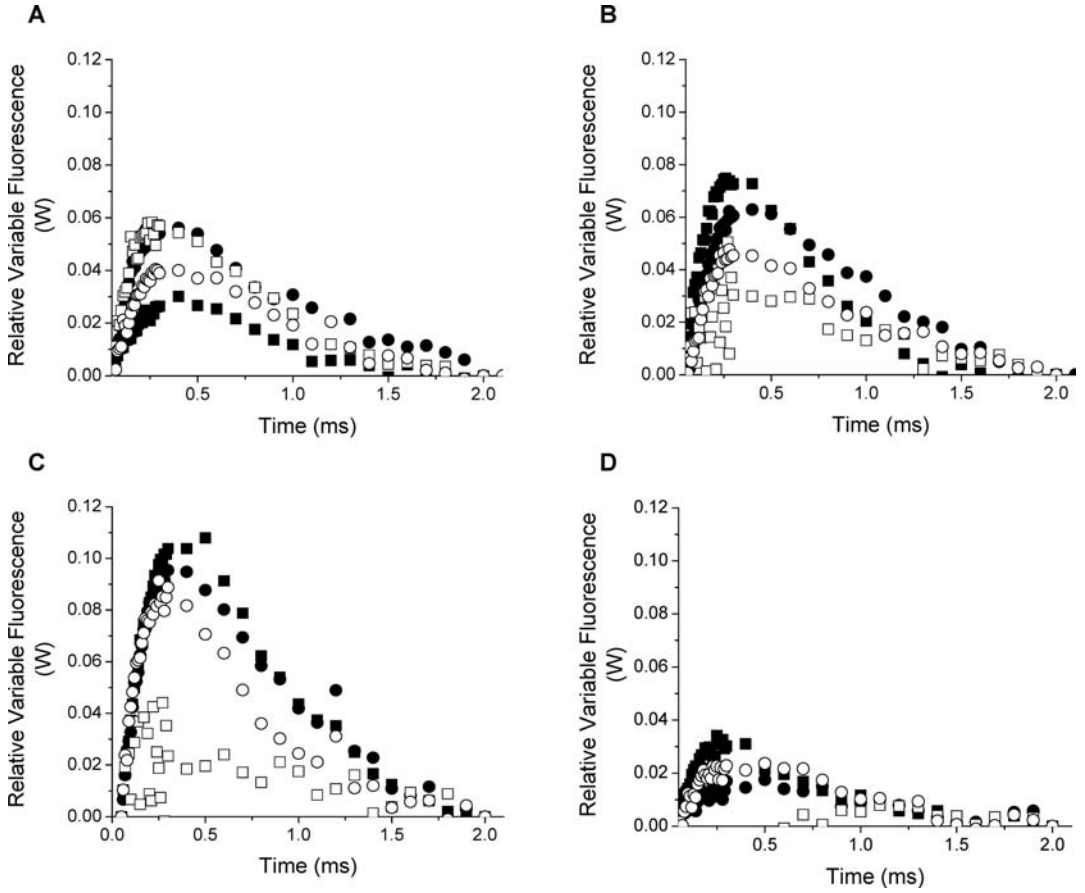

Figure 4. Appearance of the K-band at about 300 μs with the fluorescence of chlorophyll *a* measured in *P. ixocarpa* leaves. The ordinate is the difference between the *W* of the sample minus the *W* of the control, where *W* is the relative variable fluorescence between F_0 and F_J. Therefore, $Wt = V_{0J}(t) = FV_t/(F_J - F_0) = (F_t - F_0)/(F_J - F_0)$. (■) **1**, (●) **2**, (□) **3**, and (○) **5** at 300 μM at 24 (A), 48 (B), 72 (C) h, and 7 days (D).

the acceptor side of PSII. Under this condition, the electron flow from OEC to Z is slower than the electron flow from P_{680} to Q_A. The fast initial fluorescence rise is due to the reduction of Q_A to Q_A^- followed by the reduction of P_{680}^+ by Tyr_Z (a tyrosine residue) without the direct participation of OEC.[37]

Thus, the flavonoids assayed, pachypodol (**2**), quercetin (**3**), genistein (**5**), and eupatorin (**6**), inhibited the electron flow, behaving as Hill reaction inhibitors. The polarographic technique and Chl *a* fluorescence measurements suggested that flavonoids **3** and **4** inhibited the donor side of PSII and partially the acceptor site from P_{680} to Q_A and that **5** and **6** inhibit the acceptor site of PSII probably from P_{680} to Q_B. The potency of these flavonoids is similar to that of other natural products such as siderin[38] and lasiodiplodin[39] among others.

Chl *a* Fluorescence Determination in Leaves. To know if the flavonoids act as postemergent herbicides, plants of *P. ixocarpa* and *L. perenne* were grown for 15 days and 20 days for *T. alexandrinum*, they were treated with the flavonoids, and 24, 48, 72, and 168 h later the chlorophyll *a* fluorescence was measured. The fluorescence curves obtained from these assays showed that compounds **1**, **2**, **3**, and **5** affected *P. ixocarpa* leaves, while **4** and **6** did not show effects. From the chlorophyll *a* transients, the following parameters were obtained: (a) Fluorescence intensity level (F_0) when the electron acceptor (Q_A) is fully oxidized. (b) Fluorescence intensity level (F_M) when Q_A is fully reduced. (c) Fluorescence intensity level at time 0.05 ms (F_1), at 0.1 ms (F_2), at 0.3 ms (F_3), at 2 ms (F_4 or F_J), and at 30 ms (F_5).[40] (d) Area: the area over the curve between F_0 and F_M. It is composed of the area over the OJ-phase, which represents the reduction of the acceptor side of PSII, the area above the transients J-I that is caused by a partial reoxidation of the PQ-pool and electron transfer toward PSI, and the area above the IP-phase, which represents the reduction of the acceptor side of PSI; thus, the total area is a measure of the quantity of electron acceptors between the acceptor side of PSII and the acceptor side of PSI.[41] The values obtained for *P. ixocarpa* leaves treated with **1** are shown in Table 2. The data for the treatments with **2**, **3**, and **5** were similar to that for **1** and are not shown. The transients of fluorescence of chlorophyll *a* obtained with the *P. ixocarpa* leaves control and for the treatments with **1**, **2**, **3**, and **5** were normalized from F_0 to F_4, and the difference between the treated and control normalized transients revealed a band near 0.3 ms (K-band) (Figure 4). As time passed, the K-band intensity was increased; the major K-bands were found at 72 h of treatment (Figure 4C), indicating that the flavonoids **1**, **2**, **3**, and **5** needed time to penetrate the leaves to reach their target. After 7 days of treatment, the bands decreased, indicating that probably the plant metabolized these flavonoids. When the transients were normalized from F_0 and F_5, the difference between the treated and control normalized transients revealed an increase in intensity between 2 and 4 ms, appearing as a J-band (Figure 5). Flavonoids **1**, **2**, **3**, and **5** interact at this site, and the unused energy is dissipated as heat.[30] Besides the appearance of K- and J-bands, F_V/F_M values of the samples treated with **1**, **2**, **3**, and **5** decreased with respect to the control, and TR_0/RC [trapped energy flux per RC (at t = 0)

DOI: 10.1021/acs.jafc.5b02842
J. Agric. Food Chem. 2015, 63, 8106−8115

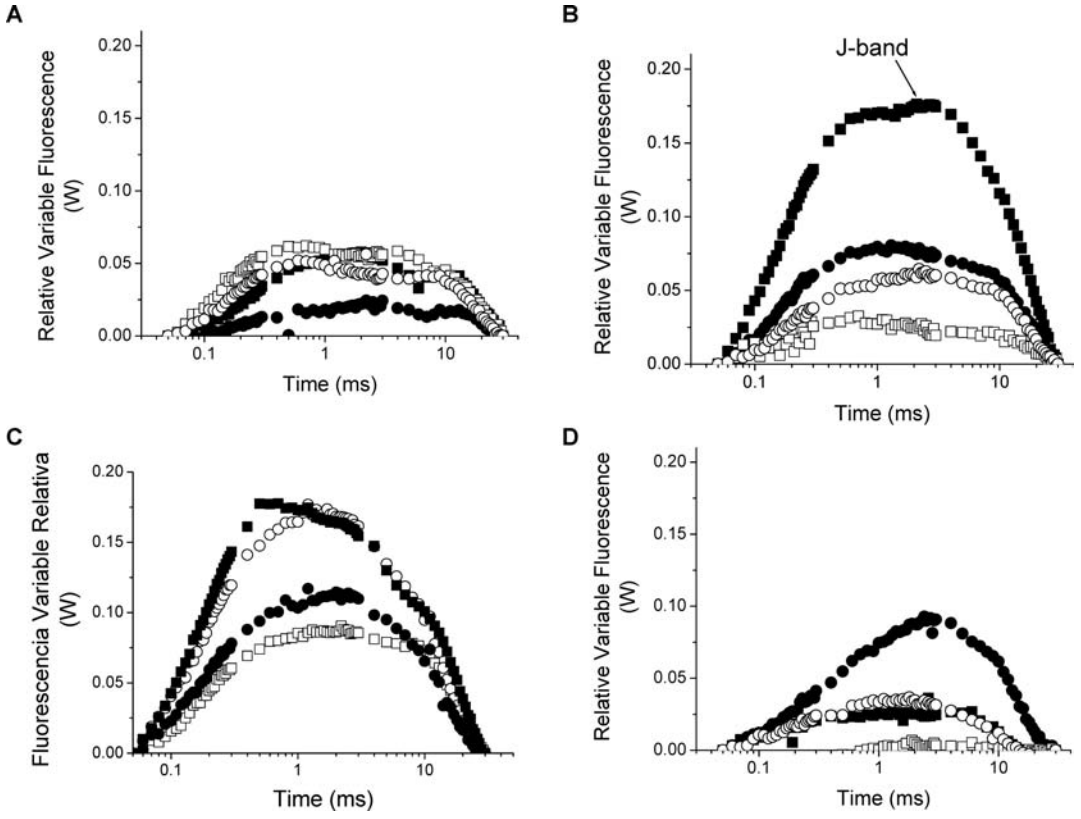

Figure 5. Appearance of the J-band occurs at about 2 ms. The ordinate is the difference between the W of the sample minus the W of the control, where W is the relative variable fluorescence between F_0 and F_I. Therefore, $Wt = V_{0I}(t) = FV_t/(F_I - F_0) = (F_t - F_0)/(F_I - F_0)$. (■) **1**, (●) **2**, (□) **3**, and (○) **5** at 300 μM at 24 (A), 48 (B), 72 (C) h, and 7 days (D).

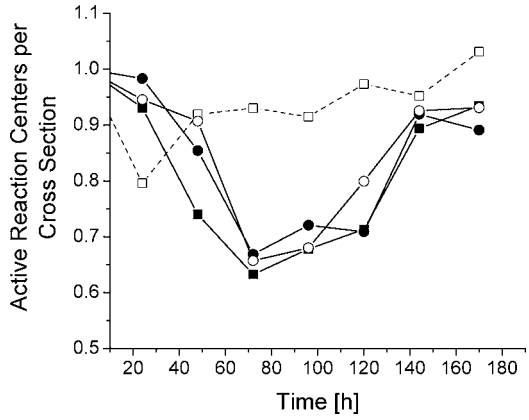

Figure 6. Active reaction centers per cross section of (■) **1**, (●) **2**, (□) **3**, and (○) **5** at 300 μM.

is equal to $M_0(1/V_J)$ where $M_0 = 4(F_{300\,\mu s} - F_0)/(F_M - F_0)$ and $V_J = (F_J - F_0)/(F_M - F_0)$] values were almost stable (Table 2 only shows these values for *P. ixocarpa* leaves treated with compound **1**); these observations suggested[30] that some PSII RCs were transformed to heat sinks or silent reaction centers. These centers cannot reduce Q_A, and their excitation energy is dissipated as heat.[30] The mechanism of action of **1** on *P. ixocarpa* leaves is similar to that observed for other natural products such as robustaflavone on chloroplasts[42] or β-caryophyllene in plants.[35]

Figure 6 shows how the active reaction centers (calculated as $[(ABS/RC)_C/(ABS/RC)_T \times 100]$ for each treatment, where $(ABS/RC)_C$ means the control value and $(ABS/RC)_T$ means the treatment values), decreased as a function of time when plants are treated with 300 μM **1**, **2**, and **5**. After 72 h of treatment, 63% of the reaction centers remained active, indicating that 37% of active reaction centers were transformed to silent reaction centers (RC^{Si}). Treatment with **3** only produced 20% of RC^{Si}; these centers cannot reduce Q_A nor transfer back their excitation energy to the antenna. Hence, the corresponding PSII units do not contribute to the variable fluorescence, whose yield remains constantly low and equal to the units with open RCs.[30] After the 72 h, the RC^{Si} are reactivated (Figure 6), probably as soon as the plant metabolized the flavonoids or these reaction centers are quickly taken apart and repaired.[43] It was observed that **3** only transformed 20% of the active reaction centers to RC^{Si}, and it is known that **3** inhibits electron transport under phosphorylation conditions (ADP + Pi), but it did not inhibit the basal electron transport. This behavior corresponds to an energy transfer inhibition in competition with

Table 3. Dry Biomass of Plants of *P. ixocarpa* (green tomato) Treated with the Flavonoids[a]

	inhibition (%)			
concn, μM	**1**	**2**	**3**	**5**
0	0	0	0	0
25	10	9	7	4
50	14	12	3.5	7
100	8	20	10	33
200	23	25	14	28
300	24	26	24	20
DCMU, 50	30	30	40	40

[a]Control value for flavonoids **1** and **2** was 1.15 ± 0.07 and 1.22 ± 0.07 g for flavonoids **3** and **5**.

DOI: 10.1021/acs.jafc.5b02842
J. Agric. Food Chem. 2015, 63, 8106−8115

Table 4. Dry Biomass of Plants of *Trifolium alexandrinum* (clover) Treated with the Flavonoids[a]

	inhibition (%)					
concn, μM	1	2	3	4	5	6
0	0	0	0	0	0	0
25	33	27	35	8	22	22
50	31	47	38	18	40	38
100	32	44	56	31	59	25
200	34	42	49	12	22	33
300	37	39	39	40	60	36
DCMU, 50	46	46	38	38	42	42

[a]Control value for flavonoids **1** and **2** was 0.712 ± 0.06, 0.663 ± 0.04 for **3** and **4** and 0.775 ± 0.05 g for **5** and **6**.

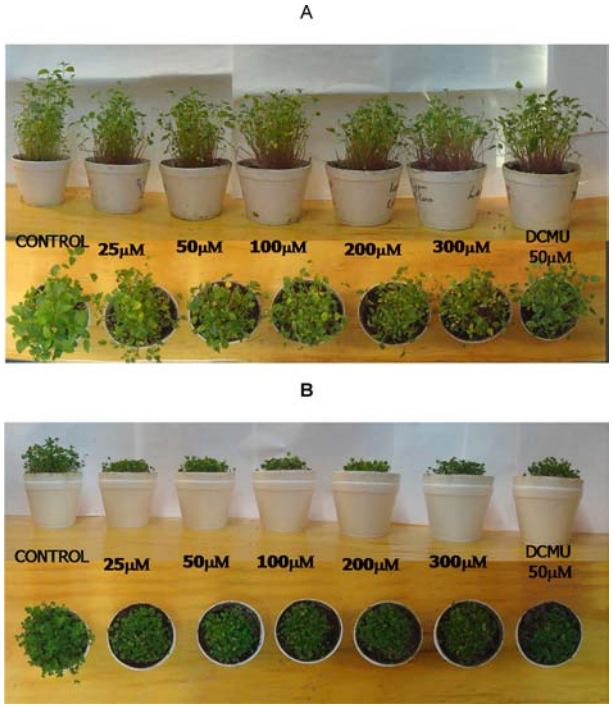

Figure 7. *P. ixocarpa* (A) and *T. alexandrinum* (B) plants treated with different concentrations of compound **1** and compared with 50 μM DCMU (positive control). Control (negative control) plants were sprayed with Tween 0.02% and the major concentration of DMSO used to prepare the flavonoid solutions. The assays were performed in three replicates. For clarity, only one is presented.

the substrate nucleotide, inhibiting the photophosphorylation. Two quercetin molecules cooperatively bind to sites on the β-subunits of CF1 in situ.[44]

Dry Biomass. Flavonoids **1**, **2**, **3**, and **5** decreased the *P. ixocarpa* dry biomass by more than 30% for **1** and **2** and by more than 40% for **3** and **5** (Table 3). Compounds **4** and **6** did not have this effect nor did they affect the chlorophyll *a* fluorescence of this plant. These results suggest that the reduction on dry biomass could be produced because **1**, **2**, **3**, and **5** affected the electron photosynthetic flow in PS II, when transforming the active reaction centers to RC^{Si}. Even if the flavonoids were metabolized 7 days later, the results suggest that their effects in the first 72 h of application are enough to reduce the dry biomass. However, the visual effects on the growth of *P. ixocarpa* and *T. alexandrinum* were observed after 15 days of treatment (Tables 3 and 4). *L. perenne* plants were not affected (data not shown). Figure 7A shows the dramatic effects after 15 days of application of different concentrations of **1** on *P. ixocarpa* plant elongation, compared to DCMU treatment. Table 4 shows the inhibition of the dry biomass in *T. alexandrinum*; in this plant, the six assayed flavonoids decreased the dry biomass by 46% (**1** and **2**), 38% (**3** and **4**), and 42% (**5** and **6**). Figure 7B shows the effect of increasing concentrations of **1** on *T. alexandrinum* after 15 days of treatment; however, the flavonoids did not affect the chlorophyll *a* fluorescence in *T. alexandrinum* plants. Thus, the dry biomass inhibition is not due to their effect on the photosynthetic electron flow.

To know the mechanism of action of flavonoids on dry biomass of *T. alexandrinum* plants, their effects on seedling respiration at different concentrations were assayed. The results (Table 5) showed that compounds **1**−**6** increased the respiration in a concentration-dependent manner, with **3** being the most active; these increments are in agreement with data previously obtained by Takahashi et al.[45] who found that **3** affects the respiratory activity of isolated soybean hypocotyl mitochondria by uncoupling oxidative phosphorylation among other mechanisms.

Chlorophyll Concentration. To know if flavonoids **1**−**6** affect the contents of chlorophyll *a* (Chl *a*) and chlorophyll *b* (Chl *b*), the chlorophyll concentration was measured on treated plants after 15 days. Evaluated flavonoids did not affect the total chlorophyll contents of any plant (data not shown).

Pre-emergence Bioassay Effect on Seed Germination and Seedling Growth. Flavonoids were evaluated to investigate their potential as pre-emergent herbicides, and they were assayed for seed germination and growth (root and shoot lengths) of dicot (*P. ixocarpa* and *T. alexandrinum*) and in monocot (*L. perenne*) seedlings. Figure 8A and 8B shows the effects of **1**−**6** on *P. ixocarpa* and *T. alexandrinum* seeds, respectively. Flavonoids **1**, **3**, and **5** partially inhibited the root elongation of *P. ixocarpa* with significance values ($p < 0.05$), **1** exhibited 39% and 58% inhibition of the roots at 50 and 100 μM respectively; shoot elongation and germination of seeds were not affected by this compound because the p values for the two populations were ≥0.5. *P. ixocarpa* roots decreased 44% and 42% at 50 and 100 μM **3**; **5** decreased the roots 60% and 50% at these same concentrations, and finally **4** and **5** increased slightly the germination (Figure 8A).

Almost all compounds inhibited the root elongation of *T. alexandrinum* seeds at both concentrations (50 and 100 μM)

Table 5. Effect of Increasing Concentrations of Flavonoids 1−6 on *T. alexandrinum* Seed Respiration[a]

concn, μM	1	2	3	4	5	6
0	1720 ± 96	1720 ± 96	1720 ± 96	1720 ± 96	1720 ± 96	1720 ± 96
50	3174 ± 190	2655 ± 185	3173 ± 206	1886 ± 122	3144 ± 251	2167 ± 104
100	3695 ± 192	4701 ± 305	4235 ± 211	2752 ± 137	3860 ± 162	3202 ± 231
200	4590 ± 239	6307 ± 315	6388 ± 311	4776 ± 235	4817 ± 253	3176 ± 207
300	4700 ± 225	6285 ± 383	6500 ± 455	4500 ± 270	4800 ± 259	3300 ± 240

[a]Experiments were conducted in three replicates, and data are expressed as the mean (nmol O_2 h^{-1} $seed^{-1}$) ± SD (standard deviation).

DOI: 10.1021/acs.jafc.5b02842
J. Agric. Food Chem. 2015, 63, 8106−8115

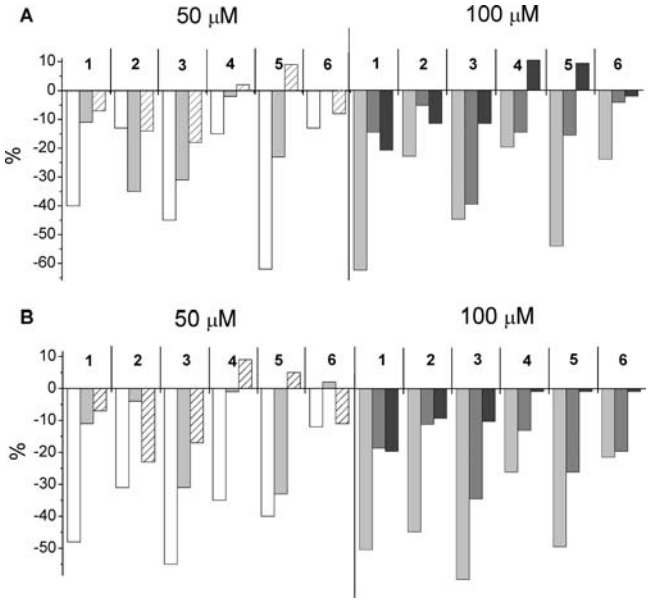

Figure 8. Effect of flavonoids **1**–**6** at 50 μM on root length (white bars) and shoot length (light gray) of seedlings and on germination (diagonal lines), and effect at 100 μM on root length (light gray bars) and shoot length (gray) of seedlings and on germination (dark gray) of *P. ixocarpa* (panel A) and *T. alexandrinum* seeds (panel B). Results are the average of three replicates.

(Figure 8B); the exception was compound **6** with a p value $\geq$0.05. The most active root inhibitor was compound **3** with 55% and 65% inhibition at 50 and 100 μM, respectively. All compounds inhibited shoot elongation, with **1** and **3** being more active as inhibitors of this activity. Figure 9 illustrates the

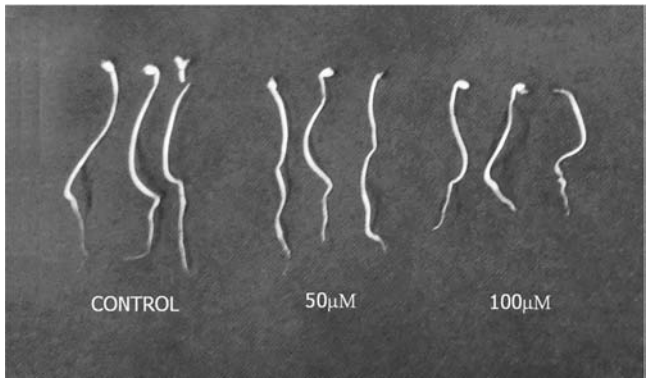

Figure 9. Effect of compound **1** on root and shoot length of *T. alexandrinum* seedlings. The seedlings for this picture were randomly taken from the assays of germination and root and shoot elongation.

inhibition of root and shoot length on *T. alexandrinum* seedlings produced by 50 and 100 μM **3**. *L. perenne* was not affected by any flavonoid (data not shown).

Finally, the flavonoids **1**, **2**, **3**, and **5** behaved as pre- and postemergent herbicides, with **3** and **5** being the most active (an isoflavonoid where the ring B is linked to C-3).

■ ASSOCIATED CONTENT

Ⓢ Supporting Information

The Supporting Information is available free of charge on the ACS Publications website at DOI: 10.1021/acs.jafc.5b02842.

Full data of chlorophyll *a* fluorescence measured on thylakoids (XLSX)

Full data of chlorophyll *a* fluorescence measured on *Physalis ixocarpa* plants at 24 h after spraying with the compounds (XLSX)

Full data of chlorophyll *a* fluorescence measured on *Physalis ixocarpa* plants at 48 h after spraying with the compounds (XLSX)

Full data of chlorophyll *a* fluorescence measured on *Physalis ixocarpa* plants at 72 h after spraying with the compounds (XLSX)

Full data of chlorophyll *a* fluorescence measured on *Physalis ixocarpa* plants at 168 h after spraying with the compounds (XLSX)

■ AUTHOR INFORMATION

Corresponding Author

*E-mail: kingbeat@unam.mx. Tel: +55-5622-5294.

Funding

The authors acknowledge financial support from DGAPA-UNAM IT102012-3, and F. Morales-Flores acknowledges the fellowship awarded by CONACyT México.

Notes

The authors declare no competing financial interest.

■ ACKNOWLEDGMENTS

We acknowledge the technical suggestions from I. Romero-Álvarez and S. Sánchez-Nieto and the spectroscopic assistance from A. Acosta, G. Duarte, M. Guzmán, and M. Gutiérrez.

■ REFERENCES

(1) Ollila, F.; Halling, K.; Vuorela, P.; Vuorela, H.; Slotte, J. P. Characterization of flavonoid–biomembrane interactions. *Arch. Biochem. Biophys.* **2002**, *399*, 103–108.

(2) Havsteen, B. H. The biochemistry and medical significance of the flavonoids. *Pharmacol. Ther.* **2002**, *96*, 67–202.

(3) Hollman, P. C.; Katan, M. B. Dietary flavonoids: Intake, health effects and bioavailability. *Food Chem. Toxicol.* **1999**, *37*, 937–42.

(4) Huang, H.; Xiao, Xi.; Ghadouani, A.; Wu, J.; Nie, Z.; Peng, C.; Xu, X.; Shi, J. Effects of natural flavonoids on photosynthetic activity and cell integrity in *Microcystis aeruginosa*. *Toxins* **2015**, *7*, 66–80.

(5) Heim, K. E.; Tagliaferro, A. R.; Bobilya, D. J. Flavonoid antioxidants: Chemistry, metabolism and structure-activity relationships. *J. Nutr. Biochem.* **2002**, *13*, 572–584.

(6) Poklar, U. N.; Ota, A.; Sentjurc, M.; Kure, S.; Abram, V. Flavonoids and cell membrane fluidity. *Food Chem.* **2010**, *121*, 78–84.

(7) Oteiza, P. I.; Erlejman, A. G.; Verstraeten, S. V.; Keen, C. L.; Fraga, C. G. Flavonoid- membrane interactions: A protective role of flavonoids at the membrane surface? *Clin. Dev. Immunol.* **2005**, *12*, 19–25.

(8) Van Hoorn, D. E. C.; Nijveldt, R. J.; Van Leeuwen, P. A. M.; Hofman, Z.; M'Rabet, L.; De Bont, D. B. A.; Van Norren, K. Accurate prediction of xanthine oxidase inhibition based on the structure of flavonoids. *Eur. J. Pharmacol.* **2002**, *451*, 111–118.

(9) Yang, G.-F.; Wei, D.-G.; Wan, J.; Zhan, C.-G. Binding model construction of antifungal 2-aryl-4-chromanones using CoMFA, CoMSIA, and QSAR analyses. *J. Agric. Food Chem.* **2005**, *53*, 1604–1611.

(10) Tsuchiya, H. Structure-dependent membrane interaction of flavonoids associated with their bioactivity. *Food Chem.* **2010**, *120*, 1089–1096.

(11) Wu, T.; He, M.; Zang, X. A structure-activity relationship study of flavonoids as inhibitors of *E. coli* by membrane interaction effect. *Biochim. Biophys. Acta, Biomembr.* **2013**, *1828*, 2751–2756.

DOI: 10.1021/acs.jafc.5b02842
J. Agric. Food Chem. 2015, 63, 8106–8115

(12) Kumar, S.; Pandey, A. K. Chemistry and biological activities of flavonoids: An overview. *Sci. World J.* **2013**. Article ID 162750. http://dx.doi.org/10.1155/2013/162750.10.1155/2013/962185
(13) Levin, V. A. Relationship of octanol/water partition coefficient and molecular weight to rat brain capillary permeability. *J. Med. Chem.* **1980**, *23*, 682−684.
(14) Céspedes, C. L.; Achnine, L.; Lotina-Hennsen, B.; Salazar, J. R.; Gómez-Garibay, F.; Calderón, J. S. Inhibition of photophosphorylation and electron transport by flavonoids and biflavonoids from endemic *Tephrosia* spp. of Mexico. *Pestic. Biochem. Physiol.* **2001**, *69*, 63−76.
(15) González-Vázquez, R.; King-Díaz, B.; Aguilar, M. I.; Diego, N.; Lotina-Hennsen, B. Pachypodol from *Croton Ciliatoglanduliferus* Ort. as water-splitting enzyme inhibitor on thylakoids. *J. Agric. Food Chem.* **2006**, *54*, 1217−1221.
(16) Macías, F. A.; Castellano, D.; Molinillo, J. M. G. Search for a standard phytotoxic bioassay for allelochemicals. Selection of standard target species. *J. Agric. Food Chem.* **2000**, *48*, 2512−2521.
(17) Mills, J. D.; Mitchell, P.; Schurrmann, P. Modulation of coupling ATPase activity in intact chloroplasts. *FEBS Lett.* **1980**, *112*, 173−177.
(18) Veiga, T. A. M.; King-Díaz, B.; Marques, A. S. F.; Sampaio, O. M.; Vieira, P. C.; Silva, M. F. G. F.; Lotina-Hennsen, B. Furoquinoline alkaloids isolated from *Balfourodendron riedelianum* as photosynthetic inhibitors in spinach chloroplasts. *J. Photochem. Photobiol., B* **2013**, *120*, 36−43.
(19) Strain, H. H.; Cope, T.; Svec, M. A. Analytical procedures for the isolation, identification, estimation and investigation of the chlorophylls. *Methods Enzymol.* **1971**, *23*, 452−466.
(20) Saha, S.; Ouitrakul, R.; Izawa, S.; Good, N. Electron transport and photophosphorylation in chloroplasts as a function of the electron acceptor. *J. Biol. Chem.* **1971**, *246*, 3204−3209.
(21) Yruela, I.; Montoya, G.; Alonso, P. J.; Picorel, R. Identification of the pheophytin-Q_A-Fe domain of the reducing side of the photosystem II as the Cu(II)-inhibitory binding site. *J. Biol. Chem.* **1991**, *266*, 22847−22850.
(22) Giaquinta, R. T.; Dilley, R. A. A partial reaction in photosystem II: Reduction of silicomolybdate prior to the site of dichlorophenyldimethyl-urea inhibition. *Biochim. Biophys. Acta, Bioenerg.* **1975**, *387*, 288−305.
(23) Schansker, G.; van Rensen, J. J. S. Characterization of the complex interaction between the electron acceptor silicomolybdate and photosystem II. *Photosynth. Res.* **1993**, *37*, 165−175.
(24) Vernon, L. P.; Shaw, E. R. Photoreduction of 2,6-dichlorophenol by diphenylcarbazide: A photosystem 2 reaction catalyzed by Tris-washed chloroplasts and subchloroplasts fragments. *Plant Physiol.* **1969**, *44*, 1645−1649.
(25) Rashid, A.; Popovic, R. Electron donation to photosystem II by diphenylcarbazide is inhibited both by the endogenous manganese complex and by exogenous manganese ions. *Biochem. Cell Biol.* **1995**, *73*, 241−245.
(26) Yerkes, C. T.; Babcock, G. T. Photosystem II oxidation of charged electron donors: Surface charge effects. *Biochim. Biophys. Acta, Bioenerg.* **1980**, *590*, 360−372.
(27) Allen, J. F.; Holmes, N. G. In *Photosynthesis, Energy Transduction. A Practical Approach*; Hipkinns, M. F., Baker, N. R., Eds.; IRL Press: Oxford, U. K., 1986; pp 103−141.
(28) Lieberman, H. R. Estimating LD_{50} using the probit technique: A basic computer program. *Drug Chem. Toxicol.* **1983**, *6*, 111−116.
(29) Strasser, R. J.; Srivastava, A.; Govindjee. Polyphasic chlorophyll *a* fluorescence transients in plants and cyanobacteria. *Photochem. Photobiol.* **1995**, *61*, 32−42.
(30) Strasser, R. J.; Srivastava, A.; Tsimilli-Michael, M. In *Advances in Photosynthesis and Respiration. Chlorophyll Fluorescence a Signature of Photosynthesis*, Papageorgiou, G. C., Govindjee, Eds.; Kluwer Academic Publishers: The Netherlands, 2004; pp 321−362.
(31) Panda, D.; Rao, D. N.; Sharma, S. G.; Strasser, R. J.; Sarkar, R. K. Subemergence effects on rice genotypes during seedling stage: Probing of subemergence driven changes of photosystem 2 by chlorophyll *a* fluorescence induction O-J-I-P transients. *Photosynthetica* **2006**, *44*, 69−75.
(32) Hoagland, D. R.; Arnon, D. I. The water-culture method for growing plants without soil. *Circ. - Calif. Agric. Exp. Stn.* **1950**, *347*, 1−32.
(33) Inskeep, W. P.; Bloom, P. R. Extinction Coefficients of Chlorophyll *a* and *b* in *N*,*N*-dimethylformamide and 80% acetone. *Plant Physiol.* **1985**, *77*, 483−485.
(34) González-Ibarra, M.; Farfán, N.; Trejo, C.; Uribe, S.; Lotina-Hennsen, B. Selective herbicide activity of 2,5-di(benzylamine)-*p*-benzoquinone against the monocot weed *Echinochloa crusgalli*. An in vivo analysis of photosynthesis and growth. *J. Agric. Food Chem.* **2005**, *53*, 3415−3420.
(35) Sánchez-Muñoz, B. A.; Aguilar, M. I.; King-Díaz, B.; Rivero, J. F.; Lotina-Hennsen, B. The sesquiterpenes *β*-caryophyllene and caryophyllene oxide isolated from *Senecio salignus* act as phytogrowth and photosynthesis inhibitors. *Molecules* **2012**, *17*, 1437−1447.
(36) Tóth, S. Z.; Schansker, G.; Strasser, R. J. In intact leaves, the maximum fluorescence level (FM) is independent of the redox state of the plastoquinone pool: A DCMU-inhibition study. *Biochim. Biophys. Acta, Bioenerg.* **2005**, *1708*, 275−282.
(37) Strasser, B. J. Donor side capacity of photosystem probed by chlorophyll *a* fluorescence transients. *Photosynth. Res.* **1997**, *52*, 147−155.
(38) Veiga, T. A. M.; González-Vázquez, R.; Neto, J. O.; Silva, M. F. G. F.; King-Díaz, B.; Lotina-Hennsen, B. Siderin from *Toona ciliata* (Meliaceae) as photosystem II inhibitor on spinach thylakoids. *Arch. Biochem. Biophys.* **2007**, *465*, 38−43.
(39) Veiga, T. A. M.; Silva, S.-C.; Francisco, A.-C.; Filho, E. R.; Vieira, P. C.; Fernandes, J. B.; Silva, M. F. G. F.; Müller, M. W.; Lotina-Hennsen, B. Inhibition of photophosphorylation and electron transport chain in thylakoids by lasiodiplodin, a natural product from *Botryosphaeria rhodina*. *J. Agric. Food Chem.* **2007**, *55*, 4217−4221.
(40) Jiang, H. X.; Chen, L. S.; Zheng, J. G.; Han, S.; Tang, N.; Smith, B. R. Aluminium induced effects of photosystem II photochemistry in Citrus leaves assessed by the chlorophyll *a* fluorescence transient. *Tree Physiol.* **2008**, *28*, 1863−1871.
(41) Toth, S. Z.; Schansker, G.; Strasser, R. J. A non-invasive assay of the plastoquinone pool redox state based on the OJIP-transient. *Photosynth. Res.* **2007**, *93*, 193−203.
(42) Aguilar, M. I.; Romero, M. G.; Chávez, M. I.; King-Díaz, B.; Lotina-Hennsen, B. Biflavonoids isolated from *Selaginella lepidophylla* inhibit photosynthesis in spinach chloroplasts. *J. Agric. Food Chem.* **2008**, *56*, 6994−7000.
(43) Aro, E.-M.; Virgin, I.; Andersson, B. Photoinhibition of PSII. Inactivation, protein damage and turnover. *Biochim. Biophys. Acta, Bioenerg.* **1993**, *1143*, 113−134.
(44) Mukohata, Y.; Nakabayashi, S.; Higashida, M. Quercetin, an energy transfer inhibitor in photophosphorylation. *FEBS Lett.* **1978**, *85*, 215−218.
(45) Takahashi, L.; Sert, M. A.; Kelmer-Bracht, A. M.; Bracht, A.; Ishii-Iwamoto, E. L. Effects of rutin and quercetin on mitochondrial metabolism and on ATP levels in germinating tissues of Glycine max. *Plant Physiol. Biochem.* **1998**, *36*, 495−501.

DOI: 10.1021/acs.jafc.5b02842
J. Agric. Food Chem. 2015, 63, 8106−8115

Table 1. Pesticide Tolerances (ppm = mg/kg) in the U.S. for Tea[a]

CFR code	pesticide	commodity	tolerance (ppm = mg/kg)
180.578	acetamiprid	tea, dried	50
180.442	bifenthrin	tea, dried	30
180.511	buprofezin	tea	20
180.515	carfentrazone-ethyl	tea, dried	0.1
180.628	chlorantraniliprole	tea, dried	50
180.586	clothianidin	tea, dried	70
180.418	cypermethrin and isomer, zeta-cypermethrin	tea oil plant, refined oil	0.4
180.418	cypermethrin and isomer, zeta-cypermethrin	tea oil plant, seed	0.2
180.163	dicofol	tea, dried	50
180.603	dinotefuran	tea, dried	50
180.652	ethiprole	tea, dried	30
180.593	etoxazole	tea, dried	15
180.466	fenpropathrin	tea, dried	2
180.566	fenproximate	tea, dried	20
180.364	glyphosate	tea, instant	7
180.364	glyphosate	tea, dried	1
180.582	pyraclostrobin	tea oil plant, seed	0.45
180.51	pyriproxyfen	tea	0.02
180.607	spiromesifen	tea, dried	40
180.565	thiamethoxam	tea, dried	20

[a]Source: electronic Code of Federal Regulations (eCFR) 180 as of December 12, 2013.

into GC-MS.[3,6,12] Cleanup methods have included using dispersive SPE (as used in QuEChERS with the addition of GCB[4] or with $CaCl_2$ instead of $MgSO_4$[6,12]), using dispersive multiwalled carbon nanotubes,[15] using liquid:liquid extraction (LLE),[5] or using an SPE column containing PSA and GCB.[3,10] Recently, comparisons of three[9,16] or four[6] different extraction and cleanup procedures have been published, although some with mixed conclusions. One suggested that hydration was essential for good recoveries,[6] while another concluded the opposite.[9] A third study concluded that QuEChERS, or a commonly used ethyl acetate extraction, was more effective than a "mini-Luke" procedure based on the older Luke method.[16] In 2008, Lee et al.[17] also compared three extraction and cleanup procedures for 49 pesticides and concluded that QuEChERS[11] gave superior recovery for some pesticides when compared to LLE after hydration or pressurized liquid extraction with acetone for tobacco leaves.

In a prior study in our laboratory with 310 pesticides,[3] a dual-phase GCB/PSA SPE cleanup was shown to provide good results with green tea. In this study, we determined whether two alternative brands of SPE dual-phase cleanup columns (carbon/PSA) could be used in our method without modification.[3] We then employed the method[3] with an alternative SPE brand for measuring 170 pesticides in 62 teas collected from 18 different vendors.

MATERIALS AND METHODS

Materials and Standards Preparation. Pesticide standard mixes (custom-made solutions in acetone at 100 mg/L) were obtained from AccuStandard (New Haven, CT) and prepared at the US FDA pesticide monitoring laboratories for GC-MS analysis. The following 12 custom mixes were used: S-10954-R2, S-10236-R4, S-10238-R4, S-10237A-R3, S-10693B-R1, S-10237B-R2, S-10696B-R1, S-10956-R1, S-10953, S-10952-R1, S-10694-R6, and S-10692A-R3. These custom mixes contained a combined total of 227 pesticides, synergists, isomers, metabolites, flame retardants, and plastizers. The internal standards were hexachlorocyclohexane-D6 (α), methoxychlor-p,p′-D6, and tributyl phosphate-D27 (C/D/N Isotopes Inc., Pointe-Claire, Quebec, Canada), and the mass spectrometry quality standards were acenaphthene-D10, phenanthrene-D10, and chrysene-D12 (Sigma-Aldrich, Milwaukee, WI). The internal standard, tris(1,3-dichloroisopropyl) phosphate, was purchased from TCI America (Portland, OR). Pesticide-grade acetonitrile and toluene, HPLC-grade water, and certified-grade anhydrous sodium sulfate and sodium chloride were purchased from Thermo Fisher Scientific (Pittsburgh, PA). The SPE columns consisted of a dual phase of 250 mg of GCB (top layer) and 500 mg of PSA (bottom layer) with a Teflon frit (p/n ECPSACB256) ("ECPSA" in the tables herein), purchased from United Chemical Technologies (UCT, Bristol, PA). Two alternative SPE columns were the dual-phase Agela "Cleanert" (p/n TPT0006) ("TPT" in the tables herein), consisting of 500 mg of PSA (top layer) and 500 mg of GCB (bottom layer), purchased from Bonna-Agela Technologies Inc. (Wilmington, DE), and dual-phase QuECHERS SPE tubes (p/n 1605349139) from United Sciences (Center City, MN), consisting of columns with 500 mg of carbon X Plus carbon coated on alumina (COA in tables) with 6% synthetic carbon coated to it (top layer) and 500 mg of PSA (bottom layer).

The following types of black, green, Oolong, or white teas (*Camellia sinensis*) were collected: "black", "Ceylon orange pekoe", "decaffeinated green", "decaffeinated Earl Grey", "decaffeinated Lady Grey" "Darjeeling", "English Breakfast", "Earl Grey", "green", "Irish Breakfast", "Jasmine green", "Lady Grey", "Lapsang Souchong", "Oolong", "Organic Green Mint", "Organic Jasmine", "Rose Oolong", "Dao Ren", "Pu-erh", "Rooibos", and "Rooibos red". These tea products were purchased or obtained from retail commercial outlets, including tea marketed as "organic" sources believed to be free of pesticide residues. All products were accepted as being the product indicated by the label, and our selection of products was not intended to be a representative sampling any particular tea product sold in the U.S. nor to represent all tea products sold in the U.S. The black and green teas used for fortification were teas marketed as "organic" and therefore represented to be free of pesticides. Analysis of the unfortified teas did not detect the pesticides monitored in this study.

Twelve AccuStandard custom mixes were combined in a 10 mL volumetric flask by transferring 0.5 mL from each of the 12 mixes. The remaining volume was made up with toluene to produce a stock at 5 mg/L for calibration and fortification standards. The working standards used for quantification were prepared by dilution of this 5 mg/L mixture to give 50 mL of each in a volumetric flask for 0.5, 0.2, 0.1, and 0.05 mg/L in toluene. The resulting standards were then used to prepare lower concentration calibration standards at 0.020, 0.010, 0.005, 0.002, and 0.001 mg/L of the pesticides in toluene. The internal and quality control standards were prepared by dissolving hexachlorocyclohexane-D6, methoxychlor-D6, tris(1,3-dichloroisopropyl) phosphate, and tributyl phosphate-D27 each to a 0.060 mg/L working solution in acetonitrile, and the deuterated polycyclic hydrocarbons to a 0.50 mg/L working solution in toluene.

Tea Leaf Extraction. Tea leaves were ground and homogenized to a fine powder that would pass through an 18-mesh sieve. Dried homogenized tea powder (1.00 ± 0.02 g), 10 mL of water, and 10 mL of extraction solvent (0.060 mg/L of the internal standard, hexachlorocyclohexane-D6 (α), methoxychlor-D6, tris(1,3-dichloroisopropyl) phosphate, or tributyl phosphate-D27, in acetonitrile) were added to a disposable 50 mL centrifuge tube. To ensure complete wetting of the botanical samples, tubes were shaken and allowed to stand for 15 min after the water and the extraction solvent were added. All tea test portions were extracted as previously described.[3]

Solid-Phase Extraction Cleanup. The SPE system consisted of a manifold fitted with 24 conditioned SPE columns, with a rack containing 15 mL glass centrifuge tubes. These SPE cartridges were conditioned with 3 column volumes of acetone and remained wetted with acetone. The collection rack holding the 15 mL disposable centrifuge tubes was inserted in the vacuum manifold. An aliquot (1.25 mL) of the mostly acetonitrile-containing upper layer of the

DOI: 10.1021/acs.jafc.5b02860
J. Agric. Food Chem. 2015, 63, 8116−8124

Table 2. Mean Recoveries, Mean Relative Standard Deviations, Number with Recoveries between 70% and 120%, and Total Number of Pesticides at 10, 25, 100, and 500 μg/kg Fortifications Using One of Three Carbon/PSA Dual-Phase SPE Columns for Green Tea (Top) and Black Tea (Bottom)[a]

	Green Tea											
	SPE column and solvent[b]											
	ECPSA, 3:1 ace/tol				TPT, 3:1 ace/tol				COA, EA			
eluent (μg/kg)	rec (%)	RSD	70−120% (*N*)	total (*N*)	rec (%)	RSD	70−120% (*N*)	total (*N*)	rec (%)	RSD	70−120% (*N*)	total (*N*)
10	95	13	80	102	102	10	88	103	93	12	85	110
25	88	10	106	131	98	12	130	137	81	8	100	134
100	76	8	119	163	85	8	145	159	76	6	111	163
500	73	7	106	164	86	11	141	166	84	6	143	167
	Black Tea											
	SPE column and solvent[b]											
	ECPSA, 3:1 ace/tol				TPT, 3:1 ace/tol				COA, ace			
eluent (μg/kg)	rec (%)	RSD	70−120% (*N*)	total (*N*)	rec (%)	RSD	70−120% (*N*)	total (*N*)	rec (%)	RSD	70−120% (*N*)	total (*N*)
10	91	15	59	78	83	14	91	111	83	11	73	105
25	95	13	90	113	86	10	121	141	83	9	107	141
100	90	8	146	160	77	8	122	162	90	6	134	160
500	94	9	152	168	80	10	138	169	80	6	118	168

[a]Mean recoveries (rec) and mean relative standard deviations (RSD) calculated from only the pesticides measured in common to all three SPEs during fortification at any given fortifying concentration. [b]ECPSA = 0.25 g GCB/0.5 g PSA, TPT = 0.5 g PSA/0.5 g GCB, COA = ∼6% carbon-coated alumina (Carbon X)/0.5 g PSA and elution solvent (EA = ethyl acetate, ace = acetone, 3:1 ace/tol =3:1 acetone/toluene).

centrifuged tea leaves/salt/water/acetonitrile mixture was loaded and allowed to percolate onto a tandem SPE column, "ECPSA" topped with anhydrous sodium sulfate. The columns were rinsed with 1 mL of acetone, and eluted and collected with 12 mL of 3:1 acetone/toluene. The cleaned extract was reduced to approximately 100 μL with a gentle nitrogen stream and a water bath (50 °C) using a nitrogen evaporator (N-Evap, Organomation, Associates, Berlin, MA). Toluene (0.5 mL), QC standards (50 μL of deuterated polycyclic aromatic hydrocarbons mixture, 0.5 mg/L), and 25 mg of magnesium sulfate were added, and the extracts were centrifuged[3] at 3000 rpm × 5 min. The toluene extracts were divided between two GC vials with 250 μL vial inserts (Restek Corp., Bellefonte, PA) in order to create a duplicate reserve set of vials.

The TPT SPE columns were operated exactly as the ECPSA columns. The COA SPE columns were operated exactly as described for the ECPSA columns, except the COA columns were eluted with 12 mL of either acetone or ethyl acetate in place of 12 mL of 3:1 acetone/toluene. Incurred teas were cleaned up using the COA column with acetone elution.

Fortification Studies. Black tea and green tea test portions were fortified at 10, 25, 100, and 500 μg/kg. Test portions (1.0 g) were fortified by adding 100 μL of the appropriate fortification solution (0.10, 1.0, and 5.0 mg/L standards prepared in toluene) to the dry test portion, producing a final concentration of 10, 100, and 500 μg/kg, respectively. For the 25 μg/kg fortification, 50 μL of a 0.5 mg/L solution was added. Each centrifuge tube with fortified tea test portion was vigorously vortexed to distribute the pesticides and then allowed to rest for 10 min.

In addition, the entire fortification study for black and green teas was repeated three times from the beginning (i.e., samples were spiked, extracted, and cleaned). The first replication used cleanup on the Agela "Cleanert" (TPT) SPE columns. The second replication used cleanup on the United Science dual-phase QuEChERS Carbon X Plus (COA) column, eluting with acetone. The third replication was identical to the second, but eluting the COA columns with ethyl acetate instead of acetone. Fortification results for COA with black tea and ethyl acetate were not reportable because of laboratory quality assurance issues. Each fortification required two types of tea with five replicates at each of the four concentrations from extraction to cleanup with 20 SPE columns for each tea type, so that in total the fortifications included 160 final fortified extracts, 135 of which were reportable. Blanks are not included in this number. Four blank tea portions were processed with each batch of 20.

Quantification was performed by using the peak area ratio of the responses of analyte to that of the internal standard, tris(1,3-dichloroisopropyl) phosphate or tributyl phosphate-D27, and calculating the concentration by preparing a calibration curve using the peak area ratios of matrix-matched calibration standards to that of the same internal standard. Matrix-matched standards were prepared by extracting tea blanks and fortifying all tea extracts after extraction and cleanup with standards in toluene. Tea standards were prepared at 0.001, 0.002, 0.005, 0.010, 0.02, 0.05, 0.1, 0.2, 0.5, and 1.0 mg/L for use in constructing matrix-matched calibration standards.

GC-QQQ Analysis. A TRACE gas chromatograph coupled with a TSQ Quantum triple-quadrupole mass spectrometer and a TriPlus autosampler (ThermoFisher, San Jose, CA) were employed for sample analysis. Analytes were separated with a 30 m × 0.25 mm i.d. TG-5MS fused silica capillary column (ThermoFisher, San Jose, CA) preceded by a deactivated guard column (5 m × 0.25 mm i.d., Restek Corp., Bellefonte, PA). The column flow rate was 1.4 mL/min, with pressure ramps to maintain a constant flow of helium. Temperature programming, source, transfer-line temperatures, spiltless injection, and multiple reaction monitoring (MRM) optimization were done as previously described.[3] Identifying pesticide residues required the measurement of two precursor/product ion transitions with the correct ion ratio and retention time during the time-dependent MRM window, as previously described.[3] We restricted our screen to the 170 pesticides we had previously optimized[3] that were available in the 12 custom AccuStandard mixtures used in this study. Anthraquinone was weighed out separately, optimized, and added to the mixed standards for the GC-QQQ method. A complete list of pesticide common names, CAS Registry Numbers, structures, molecular weights, retention times, dynamic range, MS/MS transitions, and collision energies is provided in Supporting Table 1.[3]

Statistical Analysis and Calculations. Means and standard deviations from fortification-incurred studies and matrix-dependent instrument quantitation limits (MDIQLs) were determined using Microsoft Excel 2007. Pesticide concentrations were determined by using Thermo Fisher Quanlab Forms 3.0 software to build calibration curves. MDIQLs were estimated for all pesticides through eight measurements, each from one of a series matrix-matched calibration standards for both black tea and green tea (2, 5, 10, and 20 μg/L or 8, 20, 40, and 80 μg/kg in the tea) and from using the standard deviation

DOI: 10.1021/acs.jafc.5b02860
J. Agric. Food Chem. 2015, 63, 8116−8124

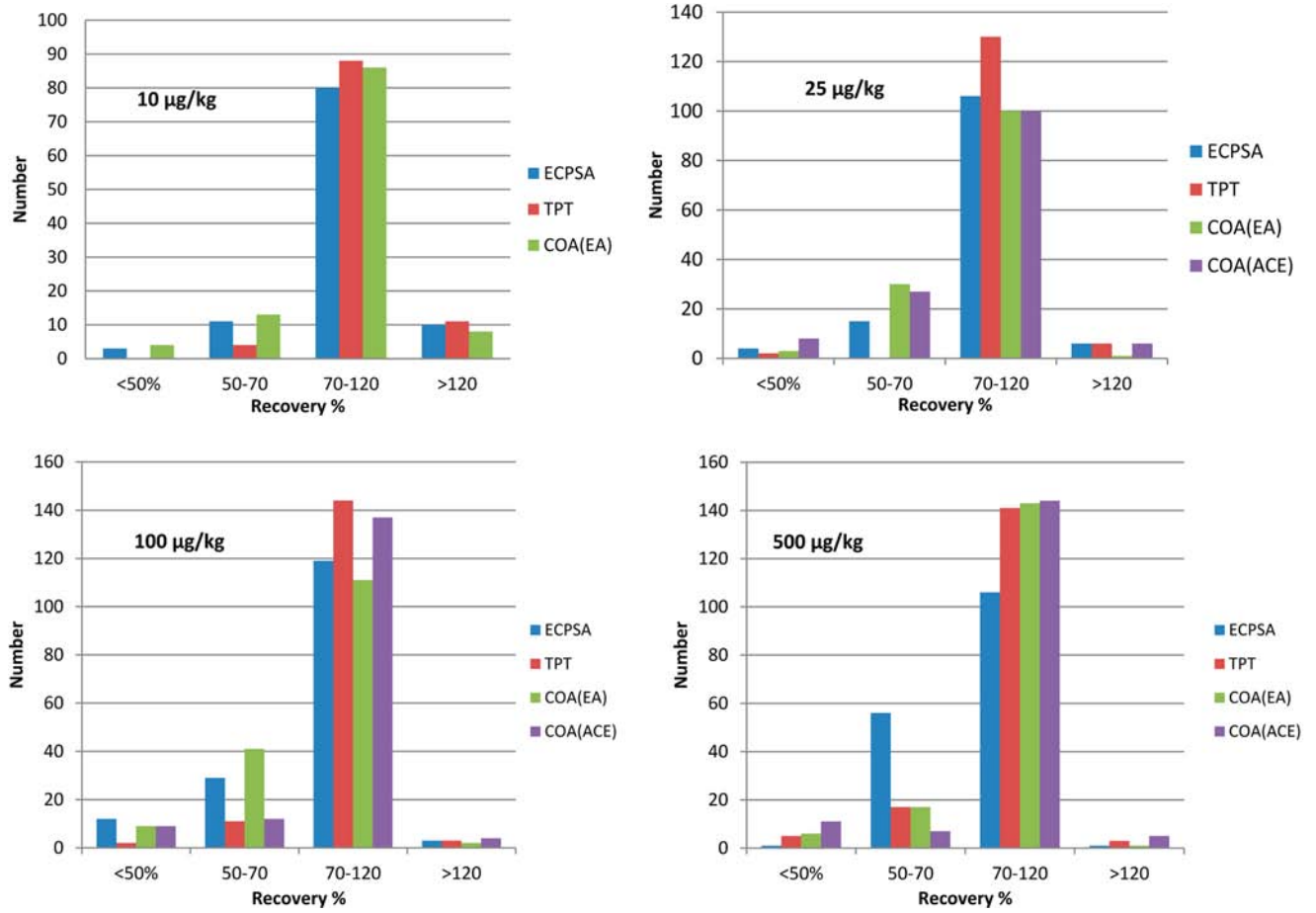

Figure 1. Green tea pesticide recovery profiles at 10, 25, 100, and 500 µg/kg for different SPE carbon/PSA dual-phase SPE columns: ECPSA, TPT, COA(EA), and COA(ACE); EA = ethyl acetate elution and ACE = acetone elution. *Y*-axis is number recovered, and *X*-axis is recovery range.

obtained from 8 quantifications multiplied by 2.998 (*t* test, 1% critical value, degrees of freedom = 7). MDIQLs calculations for each pesticide in both black tea and green tea were verified by manual inspection to ensure sufficient signal-to-noise, repeatability, and the presence of both transitions with the correct ion ratio and retention time. Ion ratios were required to be ±20%, or ±25% for ions <50% of the base peak and >20% of the base peak, or ±30% between 10% and 20% of the base peak, or ±50% for ions <10% of the base peak.[3]

RESULTS AND DISCUSSION

Fortification of Black and Green Teas. Both black and green teas were fortified with the same mixture of standards containing most of the pesticides previously reported on tea by GC-MS, but not dicofol.[3,5,6,11,12,18] Table 2 summarizes the mean recoveries and the mean of their relative standard deviations (RSDs) of the pesticides at each concentration for both green and black teas by SPE column brand. Note the mean recoveries and RSDs in Table 2 reflect the values for only the recoveries of pesticides measured in common across all three columns. Supporting Tables 2 and 3 contain means generated from all measured pesticides fortified on the ECPSA and COA SPE columns. Of the 24 overall mean recoveries reported in Table 2, 13 did not change when only pesticides in common to all SPEs were used for the mean rounded to the nearest 1%. Nine others changed less than 2%, and only two at 10 ppb for black tea went down by 4% or 5% (COA and TPT, respectively). The corresponding RSDs were unchanged, except four at 10 ppb, lower by 1 or 2 percentage points.

Table 2 also reports the total number of pesticides reported at each concentration by SPE column brand and the number with recoveries between 70% and 120%. The fraction of pesticides with recoveries within the desired recovery limits varied from 65% to 95% of the total reported and demonstrated no relationship to SPE column or tea type or the fortifying concentration. Recovery profiles for both green tea and black tea are provided in Figures 1 and 2, respectively, for all three SPE brands. The profiles are quite similar by concentration and SPE brand.

The recovery distributions and RSDs are in general agreement with findings of Pang et al.,[10] except we did not find improved performance with the TPT column with respect to RSDs. Table 3 gives the percentage of the pesticides with RSDs <20% or <10% at 100 or 500 µg/kg spiking concentrations for both green and black teas. The ECPSA and COA columns both demonstrate 97−99% of the pesticide RSDs <20% and 69−85% of the RSDs <10%, while the TPT brand reports 90−95% of the RSDs <20% and 49−81% of the RSDs <10% variously from different spike concentrations or tea type (Table 3).

In 2013, Pang et al.[9,10] established a method using the TPT brand SPE for tea that utilizes twice the volume of toluene for elution as the method used in this study.[10] Sufficient amounts of toluene are reported to be essential for eluting planar pesticides such as hexachlorobenzene completely from GCB.[19] For example, in our study, hexachlorobenzene mean recoveries using TPT were 45% and 34% for the means of all four

DOI: 10.1021/acs.jafc.5b02860
J. Agric. Food Chem. 2015, 63, 8116−8124

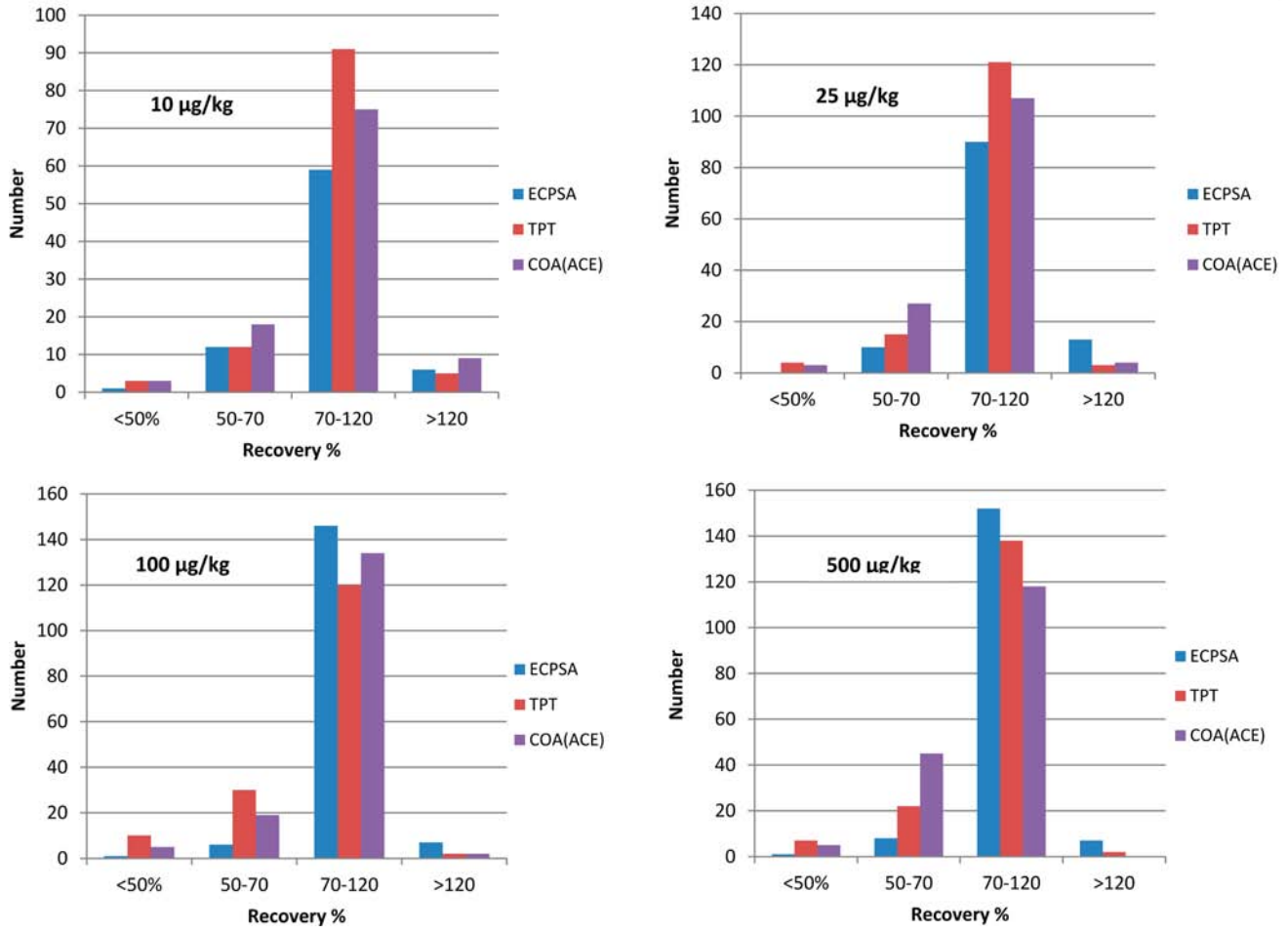

Figure 2. Black tea pesticide recovery profiles at 10, 25, 100, and 500 μg/kg for different SPE carbon/PSA dual-phase SPE columns: ECPSA, TPT, and COA(ACE); ACE = acetone elution. *Y*-axis is number recovered, and *X*-axis is recovery range.

Table 3. Percentage Amounts of Pesticides at 100 or 500 μg/kg with RSDs <20% or <10% for Green and Black Tea by SPE Column Brand (Percent ± 95% Confidence Interval)

	SPE column		
	ECPSA	TPT	COA
Green Tea			
100 μg/kg pesticide			
RSDs <10%	84 ± 5.6	79 ± 6.3	85 ± 5.5
RSDs <20%	98 ± 2.1	92 ± 4.2	98 ± 2.1
500 μg/kg pesticide			
RSDs <10%	78 ± 6.3	58 ± 7.5	77 ± 6.4
RSDs <20%	98 ± 2.1	90 ± 4.6	97 ± 2.6
Black Tea			
100 μg/kg pesticide			
RSDs <10%	69 ± 7.2	81 ± 6.0	84 ± 5.7
RSDs <20%	97 ± 2.6	93 ± 3.9	99 ± 1.5
500 μg/kg pesticide			
RSDs <10%	69 ± 7.0	49 ± 7.5	85 ± 5.4
RSDs <20%	98 ± 2.1	95 ± 3.3	97 ± 2.6

fortifications in green and black teas, respectively, with mean RSDs of 15% and 17% for green tea and black tea, respectively. The other two brands of SPE had mean recoveries between 50% and 63%, with mean RSDs ranging between 4% and 9%.

The mean recoveries of pesticides at the different fortifying concentrations and SPE brands varied between 73% and 102% (Table 2). Some tea extracts inadvertently reached complete dryness or nearly dry after elution through a specific SPE, which is known to affect recoveries of semivolatile compounds.[9] Lower mean recoveries will result in a smaller fraction of pesticides falling in the desired recovery limits (70−120%), as observed for some fortified concentrations and all SPE brands (Table 2, Figures 1 and 2, and Supporting Tables 2 and 3). The presence in the extracts of four internal standards with differing boiling points from the start of the procedure did not completely compensate for such losses.

No important differences in the mean recoveries or recovery profiles that can be attributed to the use of a specific SPE brand were observed at any concentration or tea type (Table 2, Figures 1 and 2). The accuracy and precision results for all the individual pesticides at each concentration, utilizing either ECPSA or COA SPE columns, can be found in Supporting Table 2 for green tea (COA eluting with ethyl acetate) and Supporting Table 3 for black tea (COA eluting with acetone).

Two examples supporting SPE equivalence were the mean recoveries and mean RSDs for green and black teas fortified at 10 μg/kg. The mean recoveries for green tea were 95%, 102%, and 93%, with mean RSDs of 13%, 10%, and 12% for ECPSA, TPT, and COA (EA), respectively (Table 2). The black tea mean recoveries were also quite similar, at 91%, 83%, and 83%,

DOI: 10.1021/acs.jafc.5b02860
J. Agric. Food Chem. 2015, 63, 8116−8124

Table 4. Concentration Ranges of Pesticides on Green, Black, White, and Oolong Teas by Tea Type (n), in μg/kg Dry Tea Leaves for Each Pesticide or Mean (n = 3) ± Standard Deviation When the Number of Pesticides Measured (Shown in Parentheses) Is 2 or Less[a]

	tea type (number of products)			
pesticide	green (18)	black (39)	oolong (2)	white (3)
anthraquinone	42 ± 3, 490	41 ± 2		
azoxystrobin	27 ± 2			
HCH, α-		41 ± 2		
HCH, β-		32 ± 2		
HCH, δ-		26 ± 1		
bifenthrin	12–230 (11)	14–3200 (17)	95 ± 8	14 ± 2, 120 ± 7 (2)
buprofesin	31–50 (3)	72 ± 21 (1)		
chlorpyrifos	3–36 (5)	3–14 (6)	3 ± 1	
cyhalothrin	39–81(4)	28–390 (3)		
cypermethrin	84–200 (4)	58–260 (4)		
DDE, o,p′-	DNQ (1)			
DDE, p,p′-	27 ± 4	1–18 (3)		
DDT, o,p′-		2–12 (6)		
DDT, p,p′-		1–87 (9)		
deltamethrin		19, 19, 28 (3)		1100 ± 40
dicrotophos		42 ± 6		
endosulfan, α-	19 ± 2, 208 ± 20	57 ± 9		
endosulfan, β-	78 ± 19, 530 ± 34	33 ± 8, 180 ± 22 (2)		
fenvalerate	470			
heptachlor		12 ± 4		
lindane (BHC, γ-)		36 ± 4		
phenyl phenol	21 ± 2	48 ± 4		
pyridaben	150 ± 0.5	16 ± 0.2, 17 ± 2 (2)		
tebuconazole	1400 ± 280			
tebufenpyrad	20 ± 2			
triazophos	22–190(4)	12–47 (3)		8 ± 1

[a]Anthraquinone values are estimates due to low and variable recovery. DNQ = detected but not quantified.

with mean RSDs of 15%, 14%, and 11% for ECPSA, TPT, and COA (acetone) SPEs, respectively (Table 2). Mean recovery and mean RSD for green tea using the ECPSA SPE fortified at 10 μg/kg (95% and 13%) were nearly identical to the values previously reported for this method during the validation study that included green tea (91% and 13%).[3]

Other examples supporting SPE equivalency were the fortifications of both black and green teas at 100 μg/kg (Table 2). The mean recoveries pesticides were 90% in black tea for the ECPSA and COA SPEs (Table 2) and 76% in green tea for both brands (Table 2 and Supporting Table 2). The mean RSDs for both black and green tea were 6% and 8% for COA and ECPSA, respectively (Table 2). In addition, >97% of the RSDs were <20%, while 85% were 10% or less for both ECPSA and COA SPE in either green tea or black tea. The total number of pesticides reported at 100 μg/kg fortification for green tea and black tea was identical at 163 and 160, respectively, using ECPSA and COA SPE (Table 2). Matrix-dependent instrument quantitation limits (MDIQLs) resulted in a geometric mean MDIQL of 10 μg/kg for black tea using either ECPSA or COA SPE and 7 μg/kg for green tea (Supporting Tables 2 and 3).

TPT SPE columns showed similar mean recoveries at a 100 μg/kg fortification only with the mean recoveries of 85% for green tea and 77% for black tea, with mean RSDs of 8% for both green and black teas (Table 2). We concluded that no important differences in the accuracy and precision should be anticipated using either the ECPSA or COA brands of SPE column or either elution solvents, and these SPEs are "fit for purpose" with this method.[3] Recovery variability was more related to variability in test portion handling or to a specific pesticide's behavior in GC-MS than their performance on specific SPE brand.

While overall recoveries using the three SPE columns were similar, some differences were observed, as was the case with anthraquinone. Anthraquinone was never validated for this method,[3] but was reported to be on tea.[2] Anthraquinone was almost always not recovered during the fortifications (Supporting Tables 2 and 3) or if measured the recoveries were low (<30%) and reported using the COA SPE. In addition, chlorothalonil, one of the few pesticides known to be quite sensitive to basic character of PSA,[19] was usually not measured at any concentration or recoveries were quite low (<30%). However, chlorothalonil was determined close to the desired recovery range (70–120%) at all four fortifying concentrations in green tea using the TPT SPE (57–71%), at the two highest concentrations using the COA SPE (44% and 55%), and at the higher concentrations in black tea using TPT SPE (66% and 70%).

Incurred Black, Green, Oolong, and White Teas. Pesticides were measured on 41 of the 62 tea leaf products. Before 2007, only one pesticide, glyphosate, had a US EPA tolerance on tea; however, as of December 2013, 18 pesticides have been registered with tolerances on tea (Table 1). Three pesticides (bifenthrin, buprofesin, and cypermethrin) determined on teas in this study are registered for use on tea leaves, tea seeds, or tea oil by US EPA; all samples with these pesticides were below tolerance (Table 1 and Supporting Table

DOI: 10.1021/acs.jafc.5b02860
J. Agric. Food Chem. 2015, 63, 8116–8124

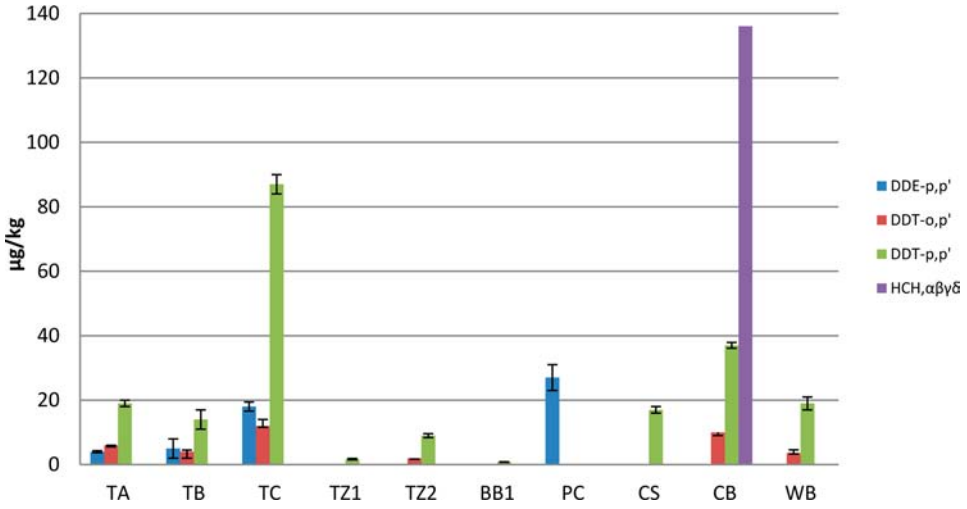

Figure 3. DDT isomer distributions in 10 teas with DDT-p,p′, DDE-p,p′, and isomers along with HCHs found in one sample. Concentrations are in μg/kg dry tea leaves $n = 3$ with error bar = ±SD (HCH is a sum of $\alpha,\beta,\gamma,\delta$). TA, TB, TC, and PC are different Chinese teas, WB is India tea, and the remaining teas are commercial teas purchased in the USA in 2013 (except CB, purchased in 1990) of unknown origins.

4). However, a total of 31 products had pesticide residues having no established tolerance on tea leaves. Those pesticides were anthraquinone, azoxystrobin, chlorpyrifos, cyhalothrin, DDE, DDT, deltamethrin, dicrotophos, fenvalerate, heptachlor, HCH ($\alpha,\beta,\gamma,\delta$), phenylphenol, pyridaben, tebuconazole, tefubenpyrad, and triazophos. Ranges for pesticides and the numbers detected in black, green, white, and Oolong teas are presented in Table 4. Of all pesticides detected in this study, the highest concentrations were for bifenthrin (3200 μg/kg), tebuconazole (1400 μg/kg), deltamethrin (1100 μg/kg), and endosulfans α and β (750 μg/kg) in black, green, white, and black teas, respectively. Although bifenthrin is a pesticide registered for use on tea with a tolerance of 30 000 μg/kg on tea leaves, tebuconazole and deltamethrin have no registered uses on tea. The tolerance for endosulfan has been revoked and will expire in 2016.[18] Endosulfan concentrations did not exceed the revoked tolerance.

Bifenthrin was the most frequently detected pesticide, with residues found on 31 teas (50% of the 62 teas), followed by chlorpyrifos on 12, DDTs on 10, cypermethrin on 9, triazophos on 8, cyhalothrin on 7, endosulfan on 4, deltamethrin on 4, and pyridaben on 3. Seven pesticides were found only on one tea each: azoxystrobin, dicrotophos, fenvalerate, hexachlorocyclohexanes (HCHs), heptachlor, tebuconazole, and tebufenpyrad. In 2012, Lozano et al.[12] reported the highest frequencies for detected pesticides on 75 teas using both GC-MS and LC-MS were acetamiprid (48%) bifenthrin (40%), biphenyl (49%), carbendazim (48%), chloropyrifos (45%), endosulfan (32%), and imidiacloprid (41%).[12] In a 2014 study, Zhu et al.,[18] screening 101 teas using GC-MS, also found high frequencies of detection for bifenthrin (63%), cyhalothrin (55%), cypermethrin (46%), and fenvalerate (25%) and also found higher frequencies of detection for endosulfan (63%), DDTs (56%, ND-400 μg/kg), HCHs (25%), and heptachlor (16%).[18] The concentrations and standard deviations of all identified pesticides on all 62 tea products can be found in Supporting Table 4.

Pesticide usage on tea has increased during the past decade in response to increasing resistance developed by the more than 300 arthropod pests that feed on the tea leaves in northeast India.[20] As a consequence, residue concentrations on tea products increase, resulting in higher frequencies of positive findings for DDT, endosulfan, and synthetic pyrethroids. Although DDT has been banned from use in pest management, increased use in tea growing regions of northeast India results in DDT concentrations as high as 0.2 ppm or more.[20] A large-scale study of selected pesticides used on tea in southern India was conducted in 2006−2008, in which 915 samples were collected.[21] The study using GC and HPLC reported concentrations for dicofol, DDT, ethion, quinalophos, hexaconazole, fenpropathrin, fenvalerate, and propargite and found mainly 0.5−6% of the teas with detectable residues of any pesticide over a three year period above 0.1 mg/kg.[21] Ethion was found in 23% of teas in 2007, but always below the European Union (EU) maximum residue limit of 3 mg/kg. DDTs were screened and not found above a quantitation limit of 0.1 mg/kg in any year.

Ten tea products in this study had measurable amounts of DDT-p,p′, DDT-o,p′ and/or DDE-p,p′, and HCHs (Figure 3) measured on one of the ten. Both DDT and HCHs are listed by the Stockholm Convention as persistent organic pollutants (POPs).[21] The HCHs (α,β,γ) are found in Annex A of ref 22 (designated for elimination), while DDT is listed in Annex B of ref 22 (use restricted to vector control for malaria and as an intermediate for manufacture of dicofol). Nonetheless, we found concentrations for DDTs and HCHs in teas ranging from 1 to 136 μg/kg for DDTs and the sum of the HCHs (Figure 3). The MDIQLs for DDT-p,p′ were between 0.82 and 0.96 μg/kg for green tea and between 0.93 and 1.4 μg/kg for black tea (Supporting Tables 2 and 3). In nine products, DDT-p,p′ dominated the isomer/metabolite pattern, with one tea containing only DDE-p,p′. DDT-o,p′ isomer was measured in 6 of 10 teas always at lower concentration than DDT-p,p′. The ratio between DDT-p,p′ and DDT-o,p′ (3.2−7.3) is in the approximate range found for technical DDT.[23]

DDT has been measured on teas beginning at least in 1969, when it was reported on green tea from Japan with an average of 3.5 mg/kg and concentrations as high as 17 mg/kg.[24] DDT concentrations in green tea fell 10-fold by 1970 when Japan established a 0.5 ppm tolerance for DDT.[24] As early as 1986, a Danish study of 99 black teas from several major tea producing countries found DDT expressed as a sum of DDT-p,p′ + DDE-

DOI: 10.1021/acs.jafc.5b02860
J. Agric. Food Chem. 2015, 63, 8116−8124

p,p′ + DDT-o,p′ + DDD-p, with a range from 20 to 300 μg/kg.[25] DDT detection frequencies varied with the country of origin ranging from 0% (Sri Lanka) to 100% from China.[25] A study of 3 dozen teas sampled in Poland found low μg/kg concentrations of DDTs, HCHs in most teas.[26] In 2002, DDE-p,p′ was reported on four Chinese teas as well as PAHs and PCDD/Fs,[7] but no DDT-p,p′ or DDT-o,p′. In 2004, eight herbal Indian teas (not *Camellia sinensis*) were found with detectable levels of HCHs (20−250 μg/kg) while on one herbal tea had detectable DDT at 6 μg/kg.[27]

One possible source for the DDT currently found on teas is application of dicofol to tea (Table 1).[20,28] Dicofol used on tea leaves typically breaks down or dissipates 95% within about 10 days.[8] Dichlorobenzophenone, a breakdown product of dicofol, could not be found on most teas with DDT measured in this study. However, technical grade dicofol is contaminated with DDT (p,p and o,p), Cl-DDT-p,p′, and DDE-o,p.[28] Directives from US EPA and EU mandate the sum of DDTs must be less than 0.1% in dicofol formulations. The amounts of DDTs and related contaminants were found to vary in dicofol formulations.[28] Dicofol formulations used in China show a trend with DDT-o,p′ ≥ Cl-DDT-p,p′ > DDE,o,p′ > DDT-p′,p, and these products exceeded US EPA and EU mandates.[28] The teas shown in Figure 3 have measurable DDT-p,p′, but do not demonstrate this trend. As we did not include dichlorobenzophenone or Cl-DDT-p,p′ in our tea method; therefore, dicofol as a source of the DDT-p,p′ on teas cannot be excluded. The relatively low amounts of DDT-o,p′ argue against dicofol as the main source.[28]

It has been suggested that higher DDE/DDT ratios found on some teas might originate from GC-MS analysis converting DDT to DDE.[28] Our recovery studies with DDE and DDT did not exhibit evidence for significant conversion in our GC-MS method,[3] yet the teas in our study contain higher DDT concentration in almost all samples (Figure 3). Four of the teas with DDTs originated from China, one was from India, while the rest are of unknown origin. DDT uses on tea have been banned in China since 1983.[28] World-wide contamination in the environment by DDT use over many decades could perhaps be responsible for some contamination.[29]

Pesticides with no US EPA registered tolerance were found on 31 of 62 teas using only GC-QQQ for determinations and a targeted list of only 170 pesticide isomers and metabolites. Additional registered and nonregistered pesticide residues were found on 30 of these teas using LC-MS techniques (manuscript in preparation), similar to reports by other researchers.[4,30] One concern with these residues is that the pesticides may transfer to the brewed tea during the brewing process. DDT, at least by one report, does not show much transfer.[24] A recent study for pesticides in brewed and leaf tea using LC-MS/MS revealed that substantial (>50%) amounts of the 11 pesticides found on incurred teas will transfer during the brewing process.[30] Two recent reports studied transfer of deltamethrin[31] or difenaconazole and azoxystrobin incurred on dry tea leaves by infusion to brewed tea.[32] Both studies suggested transfer would occur to a greater extent if the pesticides were more soluble in water, with lower amounts transferred for the more insoluble pryethroids.[31]

■ ASSOCIATED CONTENT

Supporting Information

The Supporting Information is available free of charge on the ACS Publications website at DOI: 10.1021/acs.jafc.5b02860.

Supporting Table 1, complete list of all pesticide names and transitions used (PDF)

Supporting Table 2, pesticide recoveries from green tea (PDF)

Supporting Table 3, pesticide recoveries from green and black tea, respectively. (PDF)

Supporting Table 4, list of all 62 incurred teas with their pesticide findings (PDF)

■ AUTHOR INFORMATION

Corresponding Authors

*Tel.: (240) 402-1654. Fax: (240) 402-2332. E-mail: douglas.hayward@fda.hhs.gov.

*Tel.: (240) 402-2172. Fax: (301) 436-2332. E-mail: jon.wong@fda.hhs.gov.

Present Address

†(For H.Y.P.) Joint Institute for Food Safety and Applied Nutrition, University of Maryland, College Park, MD 20742-6730

Notes

The authors declare no competing financial interest.

■ REFERENCES

(1) Khan, N.; Mukhtar, H. Teas and health: studies in humans. *Curr. Pharm. Des.* **2013**, *19* (34), 6141−6147.

(2) https://glaucusresearch.com/consumer-watchdog-reports/

(3) Hayward, D. G.; Wong, J. W.; Shi, F.; Zhang, K.; Lee, N. S.; DiBenedetto, A. L.; Hengel, M. J. Multiresidue pesticide analysis of botanical dietary supplements using salt-out acetonitrile extraction, solid-phase extraction cleanup column and gas chromatography-triple quadrupole mass spectrometry. *Anal. Chem.* **2013**, *85*, 4686−4693.

(4) Wang, J.; Chow, W.; Leung, D. Applications of LC/ESI-MS/MS and UHPLC/Qq-TOF-MS for the determination of 141 pesticides in tea. *J. AOAC Int.* **2011**, *94* (6), 1685−1714.

(5) Amirahmadi, M.; Shoeibi, S.; Abdollahi, M.; Rastegar, H.; Khosrokhavar, R.; Hamedani, M. P. Monitoring of some pesticides residue in consumed tea in Tehran market. *Iran. J. Environ. Health Sci. Eng.* **2013**, *10* (1), 9.

(6) Cajka, T.; Sandy, C.; Bachanova, V.; Drabova, L.; Kalachova, K.; Pulkrabova, J.; Hajslova, J. Streamling sample preparation and gas chromatography-tandem mass spectrometry analysis of multiple pesticide residues in tea. *Anal. Chim. Acta* **2012**, *743*, 51−60.

(7) Fiedler, H.; Cheung, C. K.; Wong, M. H. PCDD/PCDF, chlorinated pesticides and PAH in Chinese teas. *Chemosphere* **2002**, *46* (9−10), 1429−1433.

(8) Saha, K.; Saha, T.; Banerjee, H.; Bhattacharyya, A.; Chowdhury, A.; Somchoudhury, A. K. Persistence of Dicofol Residue on tea under Northeast Indian Climatic Conditions. *Bull. Environ. Contam. Toxicol.* **2004**, *73*, 347−350.

(9) Fan, C. L.; Chang, Q. Y.; Pang, G. F.; Li, A. Y.; Kang, J.; Pan, G. Q.; Zheng, S. Z.; Wang, W. W.; Yao, C. C.; Ji, X. X. High-throughput analytical techniques for determination of residues of 653 multiclass pesticides and chemical pollutants in tea. Part II: Comparative study of extraction efficiencies of three sample preparation techniques. *J. AOAC Int.* **2013**, *96* (2), 432−440.

(10) Pang, G. F.; Fan, C. L.; Chang, Q. Y.; Li, Y.; Kang, J.; Wang, W. W.; Cao, J.; Zhao, Y. B.; Li, N.; Li, Z. Y.; Chen, Z. M.; Luo, F. J.; Lou, Z. Y. High-throughput analytical techniques for multiresidue determination of 653 pesticides and chemical pollutants in tea-Part III: Evaluation of the cleanup efficiency of an SPE cartridge newly developed for multiresidues in tea. *J. AOAC Int.* **2013**, *96* (4), 887−896.

(11) Anastassiades, M.; Lehotay, S. J.; Štajnbaher, D.; Schenck, F. J. Fast and easy multi-residue method employing acetonitrile extraction/partitioning and "dispersive solid-phase extraction" for the determi-

DOI: 10.1021/acs.jafc.5b02860
J. Agric. Food Chem. 2015, 63, 8116−8124

nation of pesticide residues in Produce. *J. AOAC Int.* **2003**, *86* (2), 412−431.
(12) Lozano, A.; Rajski, L.; Belmonte-Valles, N.; Uclés, A.; Uclés, S.; Mezcua, M.; Fernández-Alba, A. R. Pesticide analysis in teas and chamomile by liquid chromatography and gas chromatography tandem mass spectrometry using a modified QuEChERS method: Validation and pilot survey in real samples. *J. Chromatogr. A* **2012**, *1268*, 109−122.
(13) Xu, D.; Lu, S.; Chen, D.; Lang, J.; Zhang, Z.; Yang, F.; Zhou, Y. Determination of ten pesticides of pyrazoles and pyrroles in tea by accelerated solvent extraction coupled with gas chromatography-tandem mass spectrometry. *Sepu* **2013**, *31*, 218−222.
(14) Pan, Y.; Yi, X.; Deng, X.; Zhao, S.; Chen, S.; Yang, H.; Han, L.; Zhu, J. Determination of multi-pesticides in black tea by subcritical water extraction and gas chromatography-tandem mass spectrometry. *Sepu* **2013**, *30* (11), 1159−1165.
(15) Hou, X.; Lei, S.; Qui, S.; Guo, L.; Yi, S.; Liu, W. A Multi-residue method for the determination of pesticides in tea using multi-walled carbon nanotubes as a dispersive solid phase extraction adsorbent. *Food Chem.* **2014**, *153*, 121−129.
(16) Rajski, L.; Lozano, A.; Belmonte-Valles, N.; Uclés, A.; Uclés, S.; Mezcua, M.; Fernandez-Alba, A. R. Comparison of three multiresidue methods to analyze pesticides in green tea with liquid and gas chromatography/tandem mass spectrometry. *Analyst* **2013**, *138* (3), 921−931.
(17) Lee, J.-M.; Park, J.-W.; Jang, G.-C.; Hwang, K.-J. Comparative study of pesticide multi-residue extraction in tobacco for gas chromatography-triple quadrupole mass spectrometry. *J. Chromtogr. A* **2008**, *1187*, 25−33.
(18) Zhu, P.; Miao, H.; Du, J.; Zou, J. H.; Zhang, G. W.; Zhao, Y. F.; Wu, Y. N. Organochlorine pesticide and pyrethroids in Chinese tea by screening and confirmatory detection using GC-NCI-MS and GC-MS/MS. *J. Agric. Food Chem.* **2014**, *62* (29), 7092−7100.
(19) Lehotay, S. J.; Maštovská, K.; Lightfield, A. R. Use of buffering and other means to improve results of problematic pesticides in a fast and easy method for residue analysis of fruits and vegetables. *J. AOAC Int.* **2005**, *88* (2), 615−629.
(20) Gurusubramanian, G.; Rahman, A.; Sarmah, M.; Ray, S.; Bora, S. Pesticide usage pattern in tea ecosystem, their retrospects and alternative measures. *J. Environ. Biol.* **2008**, *29* (6), 813−826.
(21) Seenivasan, S.; Muraleedharan, N. Survey on the pesticide residues in tea in south India. *Environ. Monit. Assess.* **2011**, *176* (1−4), 365−371.
(22) http://chm.pops.int/TheConvention/Overview/TextoftheConvention/tabid/2232/Default.aspx
(23) World Health Organization. DDT in Indoor Residual Spraying: Human Health Aspects. *Environmental Health Criteria 241*; WHO Press: Geneva, Switzerland, 2011.
(24) Bevenue, A.; Kwano, Y. Green tea and DDT residues. *Bull. Environ. Contam. Toxicol.* **1971**, *6* (2), 136−141.
(25) Petersen, J. H.; Jensen, K. G. Pesticide residues in black tea. *Z. Lebensm.-Unters. Forsch.* **1986**, *182* (6), 489−491.
(26) Góralczyk, K.; Wawrzyńczak, D.; Ludwicki, J. K. Organochlorine pesticide residues in tea. *Rocz. Panstw. Zakl. Hig.* **2000**, *51* (2), 129−134.
(27) Naithani, V.; Kakkar, P. An evaluation of residual organochlorine pesticides in popular Indian herbal teas. *Arch. Environ. Health* **2004**, *59* (8), 426−430.
(28) Qiu, X.; Zhu, T.; Yao, B.; Hu, J.; Hu, S. Contribution of dicofol to the current DDT pollution in China. *Environ. Sci. Technol.* **2005**, *39*, 4385−4390.
(29) Wania, F.; Mackay, D. Tracking the distribution of persistent organic pollutants. *Environ. Sci. Technol.* **1996**, *30* (9), 390A−396A.
(30) Wang, J.; Cheung, W.; Leung, D. Determination of pesticide residue transfer rates (percent) from dried tea leaves to brewed tea. *J. Agric. Food Chem.* **2014**, *62*, 966−983.
(31) Paramasivam, M.; Chandrasekaran, S. Persistence behaviour of deltamethrin on its transfer from processed tea to infusion. *Chemosphere* **2014**, *111*, 291−295.
(32) Xue, J.; Li, H.; Liu, F.; Xue, J.; Chen, X.; Zhan, J. Transfer of difenoconazole and azoxystrobin residues from chrysanthemum flower tea to its infusion. *Food Addit. Contam., Part A* **2014**, *31* (4), 666−675.

DOI: 10.1021/acs.jafc.5b02860
J. Agric. Food Chem. 2015, 63, 8116−8124

contains only a single chitinase and up to 17 endoglucanase entries.

Despite the intensive research, the study focused on the drought still needs attention.[13,14] We therefore analyzed growth and physiological responses (biomass formation, photosynthetic pigments, mineral nutrients), metabolite profile (amino acids, phenolics), and the isoforms/activity/gene expression of glucanases and chitinases in a new Slovak wheat line after prolonged drought stress.

MATERIAL AND METHODS

Plant Material, Cultivation, and Experimental Design. Wheat (*Triticum aestivum*) plants, line SK-196 that is currently under varietal testing in Slovakia, were sown in plastic pots (32.8 cm diameter and 25.8 cm depth) with commercial substrate BORA (BORA s.r.o., Slovakia) (measured pH of 7.4, 0.17% total N, 25 ppm P and 2.1 ppm Zn). Experiment in randomized complete block design with three replications, 6 pots per condition, was conducted at Faculty of Natural Sciences, University of Constantine the Philosopher in Nitra, Slovakia. A total of 20 seeds were planted per pot. One week after emergence, seedlings were thinned to ten per pot. The plants were grown in a temperature-controlled chamber at 18 °C between 6 p.m. and 6 a.m. and 22 °C between 6 a.m. and 6 p.m., relative humidity of 60% with a 16/8 h photoperiod with light intensity ranging from 300 to 400 μE/m^2/s. When tillering began, the plants were vernalized at 5 °C for 3 weeks in dim light. The pots were regularly irrigated twice a week with 750 mL of distilled water and once in 2 weeks fertilized using standard liquid fertilizer with micronutrients (Akrokompakt NPK 15-10-10, Agrona, Slovakia). The plants were treated preventively with insecticide Karate Zeon 5 CS (in May 2013). Water stress was applied at stage 5 on Feekes growth scale (leaf sheaths strongly erect[15]) by limiting the water supply to 250 mL of water each 48 h, while the control plants were kept well watered. Volumetric soil moisture content was measured for each pot at three different positions using a Theta Probe ML2 (Delta-T Device Ltd.) connected with an Infield 7 Data Logger (UMS GmbH München). The conductivity values measured for stressed plants dropped up to 13% (Figure 1A). Samples were taken 20 days after the start of the experiment. Roots were washed, dried using paper towels, and frozen immediately in liquid nitrogen. Samples were stored at −80 °C until analysis.

Assay of Basic Physiology, Lipid Peroxidation, and Mineral Nutrients. Content of assimilation pigments (chlorophylls and total carotenoids) was determined according to Lichtenthaler and Wellburn[16] on 8−10 leaves that were taken from 5 plants per replicate per treatment. The amount of reducing sugars was determined using the Anthron method.[17] The level of malondialdehyde (MDA) was estimated using the thiobarbituric acid assay.[18]

For the quantification of mineral nutrients, dry samples were mineralized in the mixture of concentrated HNO_3 and water (3 + 3 mL) using microwave decomposition (Ethos Sel Microwave Extraction Labstation, Milestone Inc.) at 200 °C over 1 h. Resulting clear solution was quantitatively placed in glass flasks and diluted to a final volume of 20 mL. All measurements were carried out using an atomic absorption spectrometer AA30 (Varian Ltd.; Mulgrave, Australia) and the air-acetylene flame.[19]

Assay of Chitinase and Glucanase Proteins. Total proteins were extracted from roots and leaves.[20] Aliquots (20 μg)[21] were separated in 12.5% polyacrylamide gels with 0.01% (w/v) glycol chitin as an enzyme substrate. Profiles of total chitinases as well as profiles of acidic/neutral and basic/neutral chitinase isoforms after separation were stained for enzyme activity with 0.01% (w/v) Fluorescent Brightener 28 (Sigma) and subsequent illumination under UV light as described previously.[8] The gels were photographed (BioDoc-It 210 Imaging System, UVP, California, USA) and stained with Coomassie Brilliant Blue R250. The sizes of individual chitinase isoforms were determined based on a co-separated molecular standard (Page Ruler Plus Prestained Protein Ladder, Thermo Scientific) by measuring migration distances of protein bands. Gel images were processed using

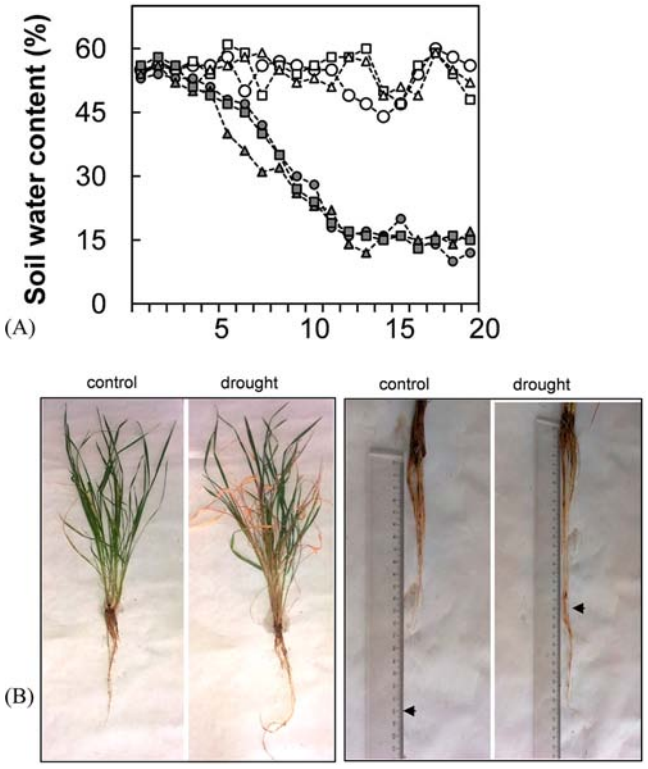

Figure 1. (A) Soil moisture content of the substrate in the pots of control plants (empty symbols) and drought-stressed plants (filled symbols) measured in the period of 20 days (axis x). Three replicates are represented by different symbols, while each symbol indicates average value taken at 3 distinct positions in a pot (respectively). (B) Phenotype of experimental wheat plants watered regularly (controls) and after drought stress (drought) applied by withholding water for the period of 20 days. Lengths of roots were significantly affected; arrows indicate 20 cm on the ruler.

Scion Image software (http://www.scioncorp.com). Background-corrected integrated density (ID) of chitinase bands was calculated in areas of constant size: ID = N*(mean-background) where N is the number of pixels in the selected area and background is the modal gray value (pixels).

Total chitinase activity in samples was measured fluorimetrically using 4-methylumbelliferyl-β-D-N,N',N''-triacetylchitotrioside [4-MU-(GlcNAc)3] as substrate, as described previously.[22]

For the analyses of glucanase enzymes, protein samples were separated in 12.5% polyacrylamide gels containing 0.01% (w/v) laminarin (Sigma), as described above. Activities of individual isoforms in profiles of all active glucanases in samples were detected by boiling of the gels for 10 min in 1 M NaOH containing 0.1% (w/v) 2,3,5-triphenyltetrazolium chloride.[8] The sizes of individual isoforms were determined directly based on a coseparated molecular standard (Page Ruler Plus Prestained Protein Ladder, Thermo Scientific). The gels were scanned; intensity of the bands was taken as a measure of the glucanase activity and determined as described above.

The activity of total β-(1,3)-glucanases in protein samples was measured with DNS method by measuring total reducing sugar content.[23]

Analyses of Gene Expression by qRT-PCR. Total RNA was isolated using the RNease Plant Mini Kit (Quiagen), quantified spectrophotometrically (BioSpec-nano, Shimadzu Biotech), and stored at −80 °C until use. cDNA was made from 1 μg RNA using the Maxima H Minus First Strand cDNA Synthesis Kit and OligodT primers (Thermo Scientific) as per manufacturer's instructions and stored at −20 °C until use. Among the wheat chitinase (6) and glucanase (7) genes available in the NCBI gene bank (to the July 2013), PCR conditions were optimized for those listed in Table S1.

DOI: 10.1021/acs.jafc.5b02951
J. Agric. Food Chem. 2015, 63, 8125−8133

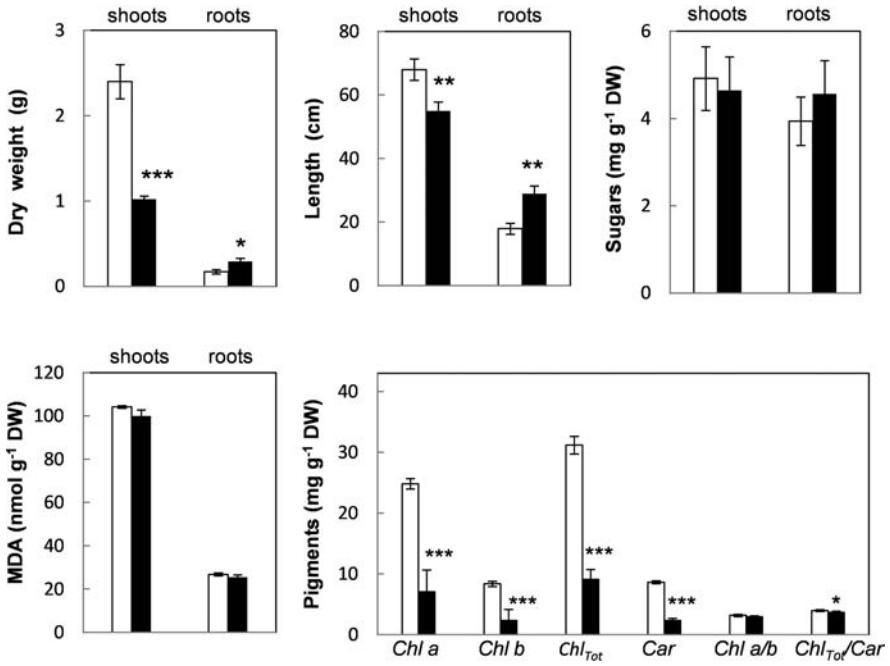

Figure 2. Growth and physiological parameters in wheat control (watered) plants (white columns) or exposed to drought (black columns) over 20 days. Data are means ± SEM (n = 10 for dry mass and length, n = 5 for the content of total reducing sugars, n = 4 for the content of malondialdehyde). Assimilation pigments were quantified in the apical parts of leaves (chlorophyll a (Chl a), chlorophyll b (Chl b), total chlorophyll (Chl a + Chl b = Chl_{Tot}), content of total carotenoids (Car), ratio of chlorophylls Chl a/b, and ratio of total Chl to Car content, n = 7). The significance of difference between control and drought-stressed plants is indicated with * at $p < 0.05$, ** at $p < 0.01$ and *** at $p < 0.001$.

Table 1. Accumulation of Free Amino Acids (μmol g^{-1} DW) in Wheat Control (Watered) Plants or Exposed to Drought Over 20 Days[a]

	shoots		roots	
	control	drought	control	drought
aspartic acid	7.30 ± 1.79	8.96 ± 1.07	7.01 ± 1.05	6.53 ± 0.79
glutamic acid	5.79 ± 0.62	4.40 ± 0.13*	0.74 ± 0.063	0.85 ± 0.13
serine	33.8 ± 1.02	12.3 ± 1.47***	3.06 ± 0.17	2.80 ± 0.21
histidine	24.6 ± 1.46	14.8 ± 1.77**	2.68 ± 0.20	4.06 ± 0.30**
glycine	1.51 ± 0.076	1.66 ± 0.12	0.51 ± 0.034	0.56 ± 0.040
threonine	14.7 ± 0.80	6.30 ± 1.24***	1.30 ± 0.15	1.23 ± 0.17
arginine	4.92 ± 0.37	3.51 ± 0.33**	1.07 ± 0.12	1.37 ± 0.11
alanine	26.3 ± 1.02	14.9 ± 0.76***	2.78 ± 0.077	2.52 ± 0.20
tyrosine	7.38 ± 1.33	2.80 ± 0.30**	0.22 ± 0.013	0.34 ± 0.050*
cysteine	13.4 ± 0.95	5.48 ± 0.57***	0.66 ± 0.14	0.53 ± 0.087
valine	28.5 ± 1.55	11.9 ± 0.65***	1.50 ± 0.087	1.55 ± 0.19
methionine	0.24 ± 0.019	0.19 ± 0.023	0.065 ± 0.013	0.073 ± 0.008
phenylalanine	13.3 ± 0.64	6.11 ± 1.18***	0.29 ± 0.013	0.48 ± 0.060**
isoleucine	16.6 ± 1.37	6.23 ± 1.22***	0.89 ± 0.050	0.78 ± 0.086
leucine	12.3 ± 0.97	3.36 ± 0.30***	0.75 ± 0.19	0.69 ± 0.17
lysine	0.78 ± 0.081	0.61 ± 0.12	0.18 ± 0.015	0.22 ± 0.031
proline	20.1 ± 3.14	52.3 ± 6.49**	1.30 ± 0.10	1.24 ± 0.19
sum	232.7 ± 8.65	156.0 ± 7.94***	25.0 ± 1.93	25.8 ± 1.05

[a]Data are means ± SEMs (n = 4). The significance of difference between control and drought-stressed plants is indicated with * at $p < 0.05$, ** at $p < 0.01$, and *** at $p < 0.001$.

Primers were from the literature or were designed using IDT-PrimerQuest Input (http://eu.idtdna.com/PrimerQuest/Home/Index). Actin (GenBank accession AB181991) and β-tubulin (U76895[24]) were used as internal standards. Reaction mixtures contained 5 μL of 2X SYBR Green PCR Master Mix (Life Technologies), 0.3 μL of 10 μM of both forward and reverse gene specific primers, nuclease-free water, and 1 μL of 1:3 diluted cDNA. The qPCR was carried out in LightCycler Nano (Roche) real-time PCR system in duplicate in 8 well PCR strips. The PCR program started with initial incubation at 50 °C for 2 min, followed by denaturation at 95 °C for 10 min. Forty-five cycles of amplification were performed using a thermal cycling profile of 95 °C for 10 s and 60 °C for 30 s. Subsequently, a melting curve was recorded by holding at 95 °C for 10 s, cooling to 60 °C, and then heating at 0.1 °C/s up to 95 °C. The amplification and melting curve data were collected and analyzed using the LightCycler Nano software 1.0.

Quantification of Metabolites. Soluble phenols were extracted with 80% methanol and quantified using Folin-Ciocalteu method with

DOI: 10.1021/acs.jafc.5b02951
J. Agric. Food Chem. 2015, 63, 8125−8133

gallic acid as standard with detection at 750 nm.[18] In these extracts, selected cinnamic and benzoic acid derivatives were also measured by liquid chromatography with mass spectrometry detection (LC-MS/MS) using device Agilent 1200 Series Rapid Resolution LC system coupled online to Agilent 6460 Triple quadrupole detector with Agilent Jet Stream Technologies: compounds were identified based on the specific m/z values and retention time and quantified using commercially available standards.[25] Flavonoid glycoside isoorientin was also quantified.[26] Thereafter, pellet was 5 times resuspended in 80% methanol followed by centrifugation to remove soluble phenols, dried, and dissolved in 2 M NaOH to release cell wall-bound phenols as reported earlier.[19] Quantifications of the sum of phenols with the Folin-Ciocalteu method and individual metabolites with LC-MS/MS were the same as above.

Free amino acids were extracted with 80% aqueous ethanol and analyses were performed on an HP 1100 liquid chromatograph (Hewlett-Packard, Waldbronn, Germany) with fluorometric detector FLD HP 1100 and using precolumn derivatization with *o*-phtalaldehyde and 9-fluorenylmethyl chloroformate.[25]

Statistical Analyses. Differences between control and drought-stressed plants were evaluated by Student's *t*-test (Microsoft Excel 2003); homogeneity of variance was checked by Levene's test. Number of repetitions in table/figure legends indicates individual plants analyzed for the given parameter.

RESULTS AND DISCUSSION

Drought Affected Wheat Growth and Physiology More Negatively in the Shoots than Roots. The drought evoked in the experimental soil (Figure 1A) suppressed shoot biomass at the level of length and dry weight (Figure 1B and Figure 2). In contrast, a more developed root system was retained in the stressed wheat plants (Figure 1B) due to well-controlled cell expansion for reaching deeper water resources.[27] Leaf necroses were observed and the amount of chlorophylls decreased (Figure 2) as observed by others.[28] The relatively low levels of MDA appeared unaffected by water shortage (Figure 2), contrasting to earlier study.[29] Previously, wheat genotypes with lower MDA content (such as our Slovak wheat line) have been indicated as more tolerant to drought,[30] and it seems that our present wheat line is also tolerant considering duration and intensity of the water deficiency.

The profile of free amino acids revealed a decrease in the majority of detected compounds in the shoot biomass, while the amount of proline increased considerably in response to drought (+160%, Table 1). This is in line with the above-mentioned decrease in assimilation pigments and overall growth. On the other hand, elevated proline accumulation may serve as a protective mechanism aimed at maintaining protein structures and ROS balance. A similar increase in proline has been found in four wheat cultivars under soil drought stress,[29] while application of PEG did not affect it significantly.[31] At the root level, only negligible changes of individual amino acids were observed (significant increase of three compounds, Table 1). The amount of proline was not affected which contradicts data from PEG-treated wheat.[31] Based on the significant increase in root dry biomass (Figure 2) we assume shoot-to-root amino acids translocation aimed at maintaining root growth allowing "search" for water in the soil. On the contrary to previous study with barley exposed to nitrogen deficiency,[26] not only root length but also root dry biomass increased in the present study (Figure 2), indicating investment of metabolites into the growth. Further research focused on phloem exudates is needed to verify this aspect and its regulation by drought.

Mineral nutrients in drought-stressed plants have not been extensively studied yet. Analyses of changes at the level of various macro- and micronutrients showed significant depletion of Ca in the shoots and Na in the roots only (Figure 3). It is evident that despite severe soil water deficiency, tissues retain mineral nutrients effectively.

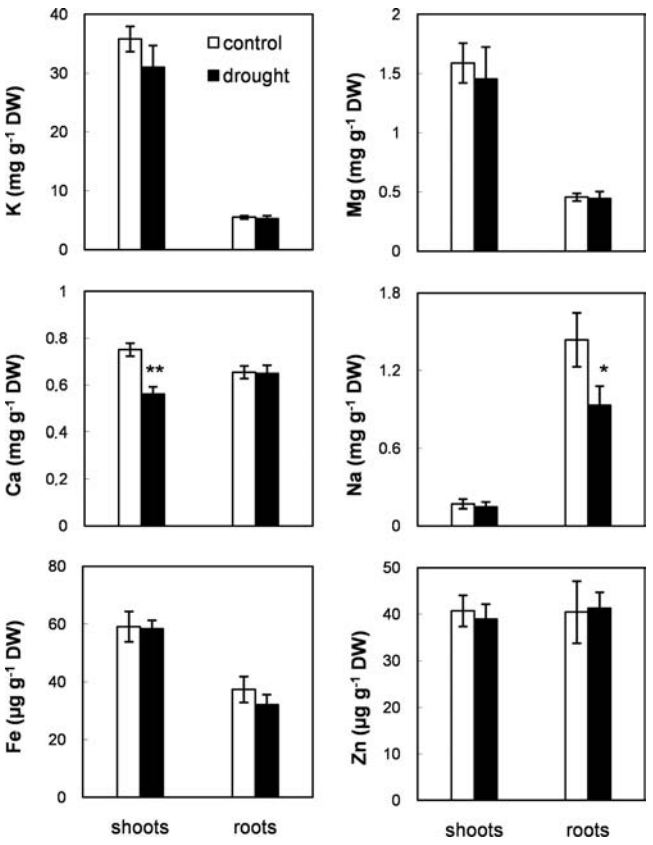

Figure 3. Quantitative changes of selected mineral nutrients in wheat control (watered) plants (white columns) or exposed to drought (black columns) over 20 days. Data are means ± SEM (n = 4). Explanation of statistics is the same as in Figure 2.

Drought Variably Influenced PR Protein Profile. Only a few studies reported the activity of chitinases under abiotic stress.[7,8] Our experiment revealed the presence of at least 7 active chitinase isoforms in wheat (5 acidic and 2 basic ones) in shoots and 10 (6 acidic and 4 basic) isoforms in roots (Figure 4). Previously, up to six different chitinase activity peaks were separated by polyacrylamide gel electrophoresis in wheat plants.[32] In our Slovak wheat line, drought conditions induced chitinases mainly in roots, mainly at the level of acidic isoforms of ~40 kDa (isoforms D and F, Figure 4A). In shoots, small (but significant) induction of a single basic isoform "b" was not reflected into a change of total enzyme activity (Figure 5). No chitinase was newly induced by water shortage in either shoots or roots. These data are in agreement with transcript levels that were elevated for 3 of 4 tested chitinase genes in roots but mostly repressed in shoots (except for a single gene *CD490414*) (Figure 7). In the literature, chitinases are rarely explicitly mentioned in high-throughput drought research. An acidic chitinase has been identified as drought responsive in a proteomic study.[33] Our observations fit well with transcriptomic data of Ergen et al.,[14] who identified 18 chitinase gene representatives differentially expressed in wild emmer

DOI: 10.1021/acs.jafc.5b02951
J. Agric. Food Chem. 2015, 63, 8125−8133

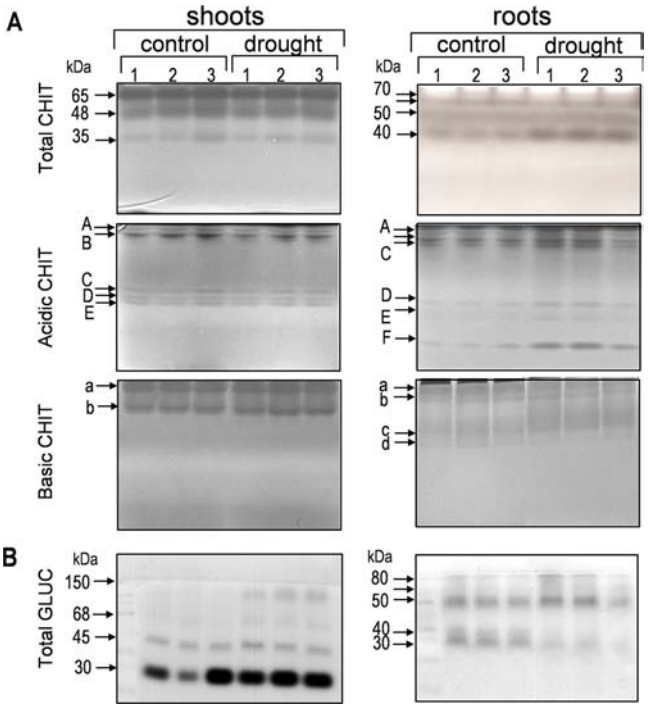

Figure 4. Representative photographs of in-gel detection of the activities of the studied PR proteins in wheat plants grown under normal (control) or drought conditions. Protein extracts from roots and shoots were separated in SDS-PAGE and subsequently renatured for detection of total chitinases (A) and glucanases (B) enzymes profiles (size of isoforms in kDa). Chitinases were also separated for more detailed analysis of acidic- (upper case letters) as well as basic (lower case letters) isoforms, respectively (A). Detected isoforms are indicated with arrows. Size of individual glucanase isoforms was determined by coseparation of a molecular weight standard (Page Ruler Plus Prestained Protein Ladder, Thermo Scientific). Molecular sizes of chitinase isoforms were determined based on Coomassie-stained protein profiles.

wheat upon quick dehydration, mostly in roots. However, the published transcriptomic data on chitinase activity under drought are inconsistent: induction[34,35] or unaffected expression[36] are known. Regulation of individual chitinase genes may depend on genotype, tissue type, and time point.[13,14] Enhanced chitinase activity has been suggested to coincide with drought tolerance of durum wheat[13] and Tibetan wild barley genotypes.[35]

Similarly to chitinases, the profile and activity of glucanases in wheat, especially under abiotic stress, is poorly known.[7,35] Our analyses identified up to 4 different enzyme fractions in wheat tissue. In shoots, each isoform fraction (~30, 45, 68, and 150 kDa) showed an enhanced accumulation by drought (Figure 4B) that resulted in increased overall glucanase activity (Figure 6). Such induction by drought has been reported previously.[14] Only one of the 3 glucanase genes we studied was activated in shoots by drought (*AF112967*), the other was repressed (*DQ090946*), while the third was unaffected (Figure 7). In contrast, in root samples the overall activities of glucanases did not alter markedly (Figure 6), possibly due to differential effect of drought on individual isoforms (Figures 4B and 6) as reported previously.[14,37] Suppression of the activity of some of the glucanase isoforms has been associated with abscisic acid-mediated callose deposition leading to increased water holding capacity.[35]

Comparing the Defense Strategy of Tissues/Organs. The activity of glucanases and chitinases differed in shoot and root tissue (Figures 5 and 6). Furthermore, their often synergistic action described during biotic stress[10] does not seem to be applicable under drought. Roots responded by an activation of chitinases at both enzyme- and gene activity levels and by repression of two glucanase isoforms (Figures 4A and 5). In shoots the glucanase enzyme isoforms were significantly induced, while the examined genes behaved adversely (Figure 4B). Here we note that data can depend not only on organ type or experimental conditions but also might be influenced by the presence of highly similar homologues in the allohexaploid wheat. Genome-specific primers would be very helpful for exploring the gene families of PRs in wheat. At the same time, PR proteins can be constitutively expressed in tissue at very low levels;[10] therefore, their research might be hampered by detection limit of the approach applied, too.

The opposing expression of studied drought-responsive genes in the two organ types might imply specific role of chitinases and glucanases in drought adaptation. It is proposed that chitinases alter the flexibility-elasticity of the cell wall[38] enabling it to withstand the shrinking of cells during dehydration. They also may reduce the risk of plant infection by pathogenic microbes naturally persisting in the soil. On the contrary, the action of glycoside-hydrolyzing, cell wall polysaccharide modifying enzymes like glucanases is suggested to affect accumulation of soluble sugars under water stress.[38] Wheat genotypes with higher concentrations of small organic osmolytes (including sugars released by glucanases) revealed better tolerance to drought.[30] Besides, accumulated PRs can serve as storage proteins under conditions of growth limitations such as reduction of photoperiod, low temperatures, or nutritional/water deficiency.[6,39]

Intriguingly, altered activities of defense proteins in drought-stressed plants are supposed to be associated with overlapping defense responses to water limitation and pathogen attack.[40] Correlation between the isoform banding pattern and activity of chitinases and the genetic resistance of plants to biotic[32] or abiotic[8] stress has been suggested but is not clearly established. Furthermore, kinetics and amplitude of their action has been suggested to contribute to overall susceptibility/resistance of plants.[8] However, though PRs can help plants to endure and recover from mild- or short-term stress, at terminal drought their accumulation can have negative influence on growth,[6] possibly due to additional costs for their synthesis in damaged plants.

Responses of Phenolics to Drought Differed in Shoots and Roots. Phenolic metabolites are abundant plant compounds induced by various stress stimuli.[19,26] In our study, total phenols (Folin-Ciocalteu assay) were affected only in the shoots in the free fraction (Table 2) that is in accordance e.g. with no or slight changes reported in various barley cultivars:[35] we note a strong quantitative discrepancy with our values (10 mg/g DW = ~ 1 mg/g FW) which is physically impossible (ca. 500 mg/g FW, cf. ref 35). In rice grains, prolonged drought even depleted the amount of total phenols,[41] indicating tissue and/or species-specific differences.

Surprisingly, detailed quantification of individual metabolites under drought has only rarely been reported.[42−44] Infusion prepared from peppermint grown at various levels of soil moisture revealed that strong drought (12%) depleted phenolics more than moderate stress.[43] This could be a reason why we observed a relatively slight increase in phenolic acids

DOI: 10.1021/acs.jafc.5b02951
J. Agric. Food Chem. 2015, 63, 8125−8133

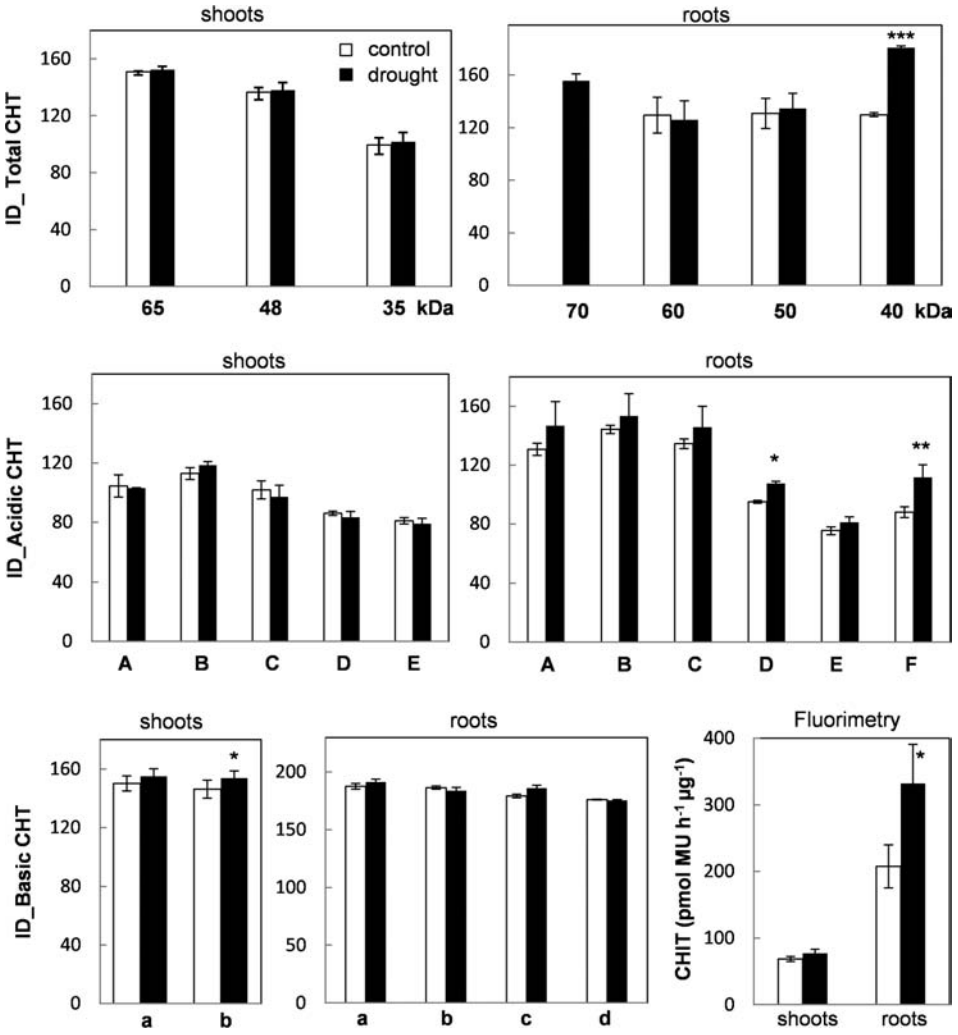

Figure 5. Quantification of the activities of individual chitinase isoforms (total, acidic and basic) in protein extracts from roots and shoots of wheat plants grown under normal and drought conditions. Values are expressed as average raw integrated densities of pixels (ID) ± SE for $n \geq 3$. Total chitinase enzyme activity of samples measured fluorimetrically is also given. Explanation of statistics is the same as in Figure 2 (n.q. − isoform was nonquantifiable due to high background).

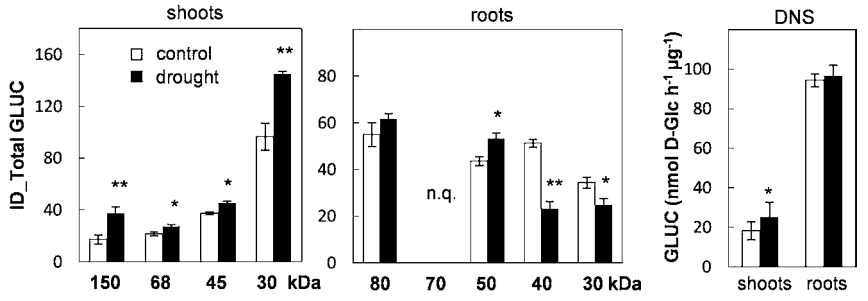

Figure 6. Quantification of activities of individual glucanase isoforms in extracts from roots and shoots of wheat plants grown under normal and drought conditions. Values are expressed as average raw integrated densities of pixels (ID) ± SE for $n \geq 3$. Enzyme activity values in samples measured with DNS method are also shown. Explanation of statistics is the same as in Figure 2 (n.q. − isoform that was nonquantifiable due to high background).

(Table 2) at an ca. 15% soil moisture (Figure 1A). However, stimulation of acids was clearly significant at the level of sum (+44%) and individual metabolites in the shoots but only occasional in the roots. These data fit well with the increase in proline and support, at least partially, a metabolic connection between proline and phenolics: biosynthesis of proline depletes the amount of NADPH, leading to stimulation of pentose phosphate pathway forming not only NADPH but also precursors for phenolics such as erythrose 4-phosphate.[45] This fact was even more visible at the level of isoorientin, a flavonoid glycoside from the luteolin family, which increased 3 times in the shoots but not in the roots (Table 2).

Unlike free phenolic acids serving as a storage pool (for more complex compounds) or as antioxidants, cell wall-bound

DOI: 10.1021/acs.jafc.5b02951
J. Agric. Food Chem. 2015, 63, 8125−8133

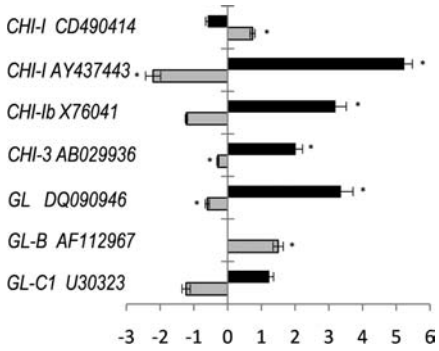

Figure 7. Relative gene expression data by means of the fold change values on a vertical scale for the set of studied PR genes under drought conditions in roots (black columns) and shoots (gray columns). Significant changes ($p \leq 0.05$) are indicated with asterisks. Sequences of primers are shown in Supplementary Table S1.

compounds contribute to fortification by forming bridges with carbohydrates.[4] In agreement with data from drought-stressed triticale,[4] cell wall-bound acids (revealed by alkaline hydrolysis) were quantitatively typically more abundant than respective free counterparts (Table 2). This was mainly visible at the level of lignin precursors including ferulic, *p*-coumaric, and sinapic acids. Overall, our data clearly confirm that synthesis of free and wall-bound phenols in the above-ground biomass of wheat may contribute to protection of photosynthetic organs against oxidative stress and dehydration of the leaves.

In conclusions, prolonged soil drought stress depleted shoot growth and assimilation pigments in wheat, but stimulated root growth and biomass that was also visible at the level of amino acids changes and shoot-to-root translocation is expected. At the same time, mineral nutrients were not affected extensively. Chitinases and glucanases were activated in wheat under drought. Directly as components of defense mechanisms and/or in morphophysiological adjustments of cells during water shortage they contribute to plant capability to survive. Though individual glucanases and chitinases were identified here as drought-responsive, their numbers even under slightly different conditions, another growth stage, and/or using other approaches is likely much larger and requires further research at both genome and proteome levels. Detailed quantification of phenolic metabolites revealed their increase in the free and bound fraction almost exclusively in the shoots, indicating protective action under water deficiency.

■ ASSOCIATED CONTENT

Supporting Information

The Supporting Information is available free of charge on the ACS Publications website at DOI: 10.1021/acs.jafc.5b02951.

Supplementary Table S1 (PDF)

■ AUTHOR INFORMATION

Corresponding Author

*Phone: 420 545 133281. Fax: 420 545 212044. E-mail: jozkovacik@yahoo.com. Corresponding author address: Institute of Chemistry and Biochemistry, Faculty of Agronomy, Mendel University in Brno, Zemědělská 1, 613 00 Brno, Czech Republic.

Table 2. Accumulation of Phenolic Acids (μg g^{-1} DW), Flavonoid Isoorientin (μg g^{-1} DW), and Total Phenols (Assay by Folin-Ciocalteu, mg g^{-1} DW) in Wheat Control (Watered) Plants or Exposed to Drought over 20 Days[a]

	shoots		roots	
free compounds	control	drought	control	drought
gallic acid	0.16 ± 0.025	0.15 ± 0.028	0.15 ± 0.023	0.27 ± 0.019**
p-hydroxybenzoic acid	5.84 ± 0.14	8.48 ± 0.72**	4.47 ± 0.22	4.61 ± 0.34
p-hydroxybenzoic aldehyde	3.49 ± 0.26	2.93 ± 0.30	10.7 ± 0.46	10.0 ± 0.51
protocatechuic acid	1.25 ± 0.10	1.46 ± 0.15	0.55 ± 0.04	0.69 ± 0.028*
salicylic acid	4.99 ± 0.31	5.14 ± 0.63	0.62 ± 0.027	0.68 ± 0.021
syringic acid	11.2 ± 0.91	16.8 ± 0.86**	0.35 ± 0.040	0.31 ± 0.024
vanillic acid	6.19 ± 0.50	13.1 ± 1.81**	9.64 ± 0.65	10.1 ± 0.24
vanillin	4.73 ± 0.49	3.85 ± 0.25*	14.3 ± 1.90	13.2 ± 1.55
ferulic acid	5.26 ± 0.48	8.98 ± 0.86**	2.96 ± 0.15	3.66 ± 0.18**
p-coumaric acid	2.91 ± 0.37	6.82 ± 0.53***	31.3 ± 2.77	32.4 ± 2.20
sinapic acid	1.54 ± 0.33	1.37 ± 0.19	0.48 ± 0.034	0.56 ± 0.039
sum of phenolic acids	47.5 ± 1.21	68.8 ± 2.67***	75.7 ± 4.02	76.2 ± 1.99
isoorientin	158.4 ± 12.6	477.3 ± 26.2***	15.1 ± 1.04	16.4 ± 1.85
total phenols	10.3 ± 0.59	12.0 ± 0.56*	4.72 ± 0.28	5.67 ± 0.80
alkaline hydrolysis				
gallic acid	0.13 ± 0.011	0.14 ± 0.020	0.26 ± 0.04	0.25 ± 0.03
syringic acid	22.9 ± 2.25	33.5 ± 2.64**	32.5 ± 2.23	26.5 ± 4.40
salicylic acid	2.28 ± 0.22	2.16 ± 0.19	1.49 ± 0.03	1.26 ± 0.21
ferulic acid	390.0 ± 24.3	481.4 ± 31.8*	395.3 ± 12.1	372.1 ± 15.0
p-coumaric acid	556.1 ± 34.9	676.2 ± 35.9*	2882.7 ± 151.8	2704.1 ± 329.4
sinapic acid	5.10 ± 0.22	9.44 ± 1.03**	26.1 ± 2.85	21.5 ± 2.94
caffeic acid	5.91 ± 0.37	8.96 ± 0.68**	18.3 ± 1.37	20.4 ± 2.09
sum of phenolic acids	982.6 ± 18.8	1211.8 ± 61.3**	3356.8 ± 137.6	3144.2 ± 328.9
total phenols	2.57 ± 0.12	2.63 ± 0.11	13.0 ± 1.12	12.3 ± 0.54

[a]Data are means ± SEMs (n = 4). Free compounds means 80% methanolic extracts and alkaline hydrolysis means cell wall-bound compounds. The significance of difference between control and drought-stressed plants is indicated with * at $p < 0.05$, ** at $p < 0.01$, and *** at $p < 0.001$.

DOI: 10.1021/acs.jafc.5b02951
J. Agric. Food Chem. 2015, 63, 8125−8133

Funding

Gregorová and Kuna received funding for equipment from European Community under project no 26220220180: Building Research Centre "AgroBioTech". The work of Maglovski, Hauptvogel, and Matušíková was supported by the Slovak Research and Development Agency under the contract no. APVV-0197-10. Kováčik received funding from OP Education for Competitiveness (European Social Fund and the state budget of the Czech Republic) CZ.1.07/2.3.00/30.0017 Postdocs in Biological Sciences at MENDELU. Klejdus and Kováčik received funding for metabolic analyses with research infrastructure supported by the CEITEC − Central European Institute of Technology (project CZ.1.05/1.1.00/02.0068 financed from European Regional Development Fund). Sponsors had no involvement in the present study.

Notes

The authors declare no competing financial interest.

■ ACKNOWLEDGMENTS

The authors thank Silvia Mihaličová, Ph.D. for proofreading the manuscript.

■ REFERENCES

(1) Fleury, D.; Jefferies, S.; Kuchel, H.; Langridge, P. Genetic and genomic tools to improve drought tolerance in wheat. *J. Exp. Bot.* **2010**, *61*, 3211−3222.

(2) Pinheiro, C.; Chaves, M. M.; Ricardo, C. P. Alterations in carbon and nitrogen metabolism induced by water deficit in the stems and leaves of *Lupinus albus* L. *J. Exp. Bot.* **2001**, *52*, 1063−1070.

(3) Chakraborty, U.; Pradhan, B. Drought stress-induced oxidative stress and antioxidative responses in four wheat (*Triticum aestivum* L.) varieties. *Arch. Agron. Soil Sci.* **2012**, *58*, 617−630.

(4) Hura, T.; Hura, K.; Dziurka, K.; Ostrowska, A.; Baczek-Kwinta, R.; Grzesiak, M. An increase in the content of cell wall-bound phenolics correlates with the productivity of triticale under soil drought. *J. Plant Physiol.* **2012**, *169*, 1728−1736.

(5) Wu, S.-w.; Wang, H.-w.; Yang, Z.-d.; Kong, L.-r. Expression comparisons of pathogenesis-related (PR) genes in wheat in response to infection/infestation by *Fusarium*, yellow dwarf virus (YDV) aphid-transmitted and hessian fly. *J. Integr. Agric.* **2014**, *13*, 926−936.

(6) Lee, B. R.; Jung, W. J.; Lee, B. H.; Avice, J. C.; Ourry, A.; Kim, T. H. Kinetics of drought-induced pathogenesis-related proteins and its physiological significance in white clover leaves. *Physiol. Plant.* **2008**, *132*, 329−337.

(7) Zur, I.; Gołebiowska, G.; Dubas, E.; Golemiec, E.; Matušíková, I.; Libantová, J.; Moravčíková, J. β-1,3-glucanase and Chitinase activities in winter triticales during cold hardening and subsequent infection by Microdochium nivale. *Biologia (Warsaw, Pol.)* **2013**, *68*, 241−248.

(8) Mészáros, P.; Rybanský, A.; Hauptvogel, P.; Kuna, R.; Libantová, J.; Moravčíková, J.; Piršelová, B.; Tirpáková, A.; Matušíková, I. Cultivar-specific kinetics of Chitinase induction in soybean roots during exposure to arsenic. *Mol. Biol. Rep.* **2013**, *40*, 2127−2138.

(9) Kwon, Y.; Kim, S. H.; Jung, M. S.; Kim, M. S.; Oh, J. E.; Ju, H. W.; Kim, K. I.; Vierling, E.; Lee, H.; Hong, S. W. *Arabidopsis* hot2 encodes an endochitinase-like protein that is essential for tolerance to heat, salt and drought stresses. *Plant J.* **2007**, *49*, 184−193.

(10) Jongedijk, E.; Tigelaar, H.; van Roekel, J. S. C.; Bres-Vloemans, S. A.; Dekker, I.; van den Elzen, P. J. M.; Cornelissen, B. J. C.; Melchers, L. S. Synergistic activity of chitinases and β-1,3-glucanases enhances fungal resistance in transgenic tomato plants. *Euphytica* **1995**, *85*, 173−180.

(11) Yokoyama, R.; Nishitani, K. Genomic basis for cell-wall diversity in plants. A comparative approach to gene families in rice and *Arabidopsis*. *Plant Cell Physiol.* **2004**, *45*, 1111−1121.

(12) The International Wheat Genome Sequencing Consortium (IWGSC). A chromosome-based draft sequence of the hexaploid bread wheat (*Triticum aestivum*) genome. *Science* **2014**, *345*, no. 6194.

(13) Aprile, A.; Mastrangelo, A. M.; De Leonardis, A. M.; Galiba, G.; Roncaglia, E.; Ferrari, F.; De Bellis, L.; Turchi, L.; Giuliano, G.; Cattivelli, L. Transcriptional profiling in response to terminal drought stress reveals differential responses along the wheat genome. *BMC Genomics* **2009**, *10*, 279.

(14) Ergen, N. Z.; Thimmapuram, J.; Bohnert, H. J.; Budak, H. Transcriptome pathways unique to dehydration tolerant relatives of modern wheat. *Funct. Integr. Genomics* **2009**, *9*, 377−396.

(15) Miller, T. D. Growth stages of wheat: Identification and understanding improve crop management. Texas Agricultural Extension Service, SCS-1999-16, 1999.

(16) Lichtenthaler, H.; Wellburn, A. Determinations of total carotenoids and chlorophylls a and b of leaf extracts in different solvents. *Biochem. Soc. Trans.* **1983**, *11*, 591−592.

(17) Yemm, E. W.; Willis, A. J. The estimation of carbohydrates in plant extracts by anthrone. *Biochem. J.* **1954**, *57*, 508−514.

(18) Kováčik, J.; Bačkor, M. Phenylalanine ammonia-lyase and phenolic compounds in chamomile tolerance to cadmium and copper excess. *Water, Air, Soil Pollut.* **2007**, *185*, 185−193.

(19) Kováčik, J.; Klejdus, B.; Hedbavny, J.; Zoń, J. Significance of phenols in cadmium and nickel uptake. *J. Plant Physiol.* **2011**, *168*, 576−584.

(20) Hurkman, W. J.; Tanaka, C. K. Solubilization of plant membrane proteins for analysis by two-dimensional gel electrophoresis. *Plant Physiol.* **1986**, *81*, 802−806.

(21) Bradford, M. M. A rapid and sensitive method for the quantitation of microgram quantities of protein utilizing the principle of protein-dye binding. *Anal. Biochem.* **1976**, *72*, 248−254.

(22) Libantová, J.; Kämäräinen, T.; Moravčíková, J.; Matušíková, I.; Salaj, J. Detection of chitinolytic enzymes with different substrate specificity in tissues of intact sundew (*Drosera rotundifolia* L.): Chitinases in sundew tissues. *Mol. Biol. Rep.* **2009**, *36*, 851−856.

(23) Miller, G. Use of dinitrosalicylic acid reagent for determination of reducing sugar. *Anal. Chem.* **1959**, *31*, 426−428.

(24) Desmond, O. J.; Edgar, C. I.; Manners, J. M.; Maclean, D. J.; Schenk, P. M.; Kazan, K. Methyl jasmonate induced gene expression in wheat delays symptom development by the crown rot pathogen *Fusarium pseudograminearum*. *Physiol. Mol. Plant Pathol.* **2005**, *67*, 171−179.

(25) Klejdus, B.; Kováčik, J.; Babula, P. PAL inhibitor evokes different responses in two *Hypericum* species. *Plant Physiol. Biochem.* **2013**, *63*, 82−88.

(26) Kováčik, J.; Klejdus, B.; Babula, P.; Jarošová, M. Variation of antioxidants and secondary metabolites in nitrogen-deficient barley plants. *J. Plant Physiol.* **2014**, *171*, 260−268.

(27) Sharp, R. E.; Poroyko, V.; Hejlek, L. G.; Spollen, W. G.; Springer, G. K.; Bohnert, H. J.; Nguyen, H. T. Root growth maintenance during water deficits: Physiology to functional genomics. *J. Exp. Bot.* **2004**, *55*, 2343−2351.

(28) Nikolaeva, M. K.; Maevskaya, S. N.; Shugaev, A. G.; Bukhov, N. G. Effect of drought on chlorophyll content and antioxidant enzyme activities in leaves of three wheat cultivars varying in productivity. *Russ. J. Plant Physiol.* **2010**, *57*, 87−95.

(29) Chakraborty, U.; Pradhan, B. Oxidative stress in five wheat varieties (*Triticum aestivum* L.) exposed to water stress and study of their antioxidant enzyme defense system, water stress responsive metabolites and H_2O_2 accumulation. *Braz. J. Plant Physiol.* **2012**, *24*, 117−130.

(30) Nezhadahmadi, A.; Prodhan, Z. H.; Faruq, G. Drought tolerance in wheat. *Sci. World J.* **2013**, *2013*, 610721.

(31) Kovács, V.; Gondor, O. K.; Szalai, G.; Majláth, I.; Janda, T.; Pál, M. UV-B radiation modifies the acclimation processes to drought or cadmium in wheat. *Environ. Exp. Bot.* **2014**, *100*, 122−131.

(32) Botha, A. M.; Nagel, M. A. C.; Van Der Westhuizen, A. J.; Botha, F. C. Chitinase isoenzymes in near-isogenic wheat lines

DOI: 10.1021/acs.jafc.5b02951
J. Agric. Food Chem. 2015, 63, 8125−8133

challenged with Russian wheat aphid, exogenous ethylene, and mechanical wounding. *Bot. Bull. Acad. Sin.* **1998**, *39*, 99−106.
(33) Habash, D. Z.; Baudo, M.; Hindle, M.; Powers, S. J.; Defoin-Platel, M.; Mitchell, R.; Saqi, M.; Rawlings, C.; Latiri, K.; Araus, J. L.; Abdulkader, A.; Tuberosa, R.; Lawlor, D. W.; Nachit, M. M. Systems responses to progressive water stress in durum wheat. *PLoS One* **2014**, *9* (9), e108431.
(34) Li, W. L.; Faris, J. D.; Muthukrishnan, S.; Liu, D. J.; Chen, P. D.; Gill, B. S. Isolation and characterization of novel cDNA clones of acidic chitinases and β-1,3-glucanases from wheat spikes infected by *Fusarium graminearum*. *Theor. Appl. Genet.* **2001**, *102*, 353−362.
(35) Ahmed, I. M.; Nadira, U. A.; Bibi, N.; Cao, F.; He, X.; Zhang, G.; Wu, F. Secondary metabolism and antioxidants are involved in the tolerance to drought and salinity, separately and combined, in Tibetian wild barley. *Environ. Exp. Bot.* **2015**, *111*, 1−12.
(36) Krugman, T.; Chague, V.; Peleg, Z.; Balzergue, S.; Just, J.; Korol, A. B.; Nevo, E.; Saranga, Y.; Chalhoub, B.; Fahima, T. Multilevel regulation and signalling processes associated with adaptation to terminal drought in wild emmer wheat. *Funct. Integr. Genomics* **2010**, *10*, 167−186.
(37) Faghani, E.; Gharechahi, J.; Komatsu, S.; Mirzaei, M.; Khavarinejad, R. A.; Najafi, F.; Farsad, L. K.; Salekdeh, G. H. Comparative physiology and proteomic analysis of two wheat genotypes contrasting in drought tolerance. *J. Proteomics* **2015**, *114*, 1−15.
(38) Konno, H.; Yamasaki, Y.; Sugimoto, M.; Takeda, K. Differential changes in cell wall matrix polysaccharides and glycoside-hydrolyzing enzymes in developing wheat seedlings differing in drought tolerance. *J. Plant Physiol.* **2008**, *165*, 745−754.
(39) Avice, J. C.; Le Dily, F.; Goulas, E.; Noquet, C.; Meuriot, F.; Volenec, J. J.; Cunningham, S. M.; Sors, T. G.; Dhont, C.; Castonguay, Y.; Nadeau, P.; Bélanger, G.; Chalifour, F. P.; Ourry, A. Vegetative storage proteins in overwintering storage organs of forage legumes: Roles and regulation. *Can. J. Bot.* **2003**, *81*, 1198−1212.
(40) Enright, S.; Cipollini, D. Overlapping defense responses to water limitation and pathogen attack and their consequences for resistance to powdery mildew disease in garlic mustard, *Alliaria petiolata*. *Chemoecology* **2011**, *21*, 89−98.
(41) Emam, M. M.; Khattab, H. E.; Helal, N. M.; Deraz, A. E. Effect of selenium and silicon on yield quality of rice plant grown under drought stress. *Austr. J. Crop Sci.* **2014**, *8*, 596−605.
(42) Collado-González, J.; Cruz, Z. N.; Rodríguez, P.; Galindo, A.; Díaz-Banos, F. G.; García; De La Torre, J.; Ferreres, F.; Medina, S.; Torrecillas, A.; Gil-Izquierdo, A. Effect of water deficit and domestic storage on the procyanidin profile, size, and aggregation process in pear-jujube (*Z. jujuba*) fruits. *J. Agric. Food Chem.* **2013**, *61*, 6187−6197.
(43) Figueroa-Pérez, M. G.; Rocha-Guzmán, N. E.; Pérez-Ramírez, I. F.; Mercado-Silva, E.; Reynoso-Camacho, R. Metabolite profile, antioxidant capacity, and inhibition of digestive enzymes in infusions of peppermint (*Mentha piperita*) grown under drought stress. *J. Agric. Food Chem.* **2014**, *62*, 12027−12033.
(44) Xu, Y.; Goodacre, R.; Harrigan, G. G. Compositional equivalence of grain from multi-trait drought-tolerant maize hybrids to a conventional comparator: Univariate and multivariate assessments. *J. Agric. Food Chem.* **2014**, *62*, 9597−9608.
(45) Hare, P. D.; Cress, W. A. Metabolic implications of stress-induced proline accumulation in plants. *Plant Growth Regul.* **1997**, *21*, 79−102.

DOI: 10.1021/acs.jafc.5b02951
J. Agric. Food Chem. 2015, 63, 8125−8133

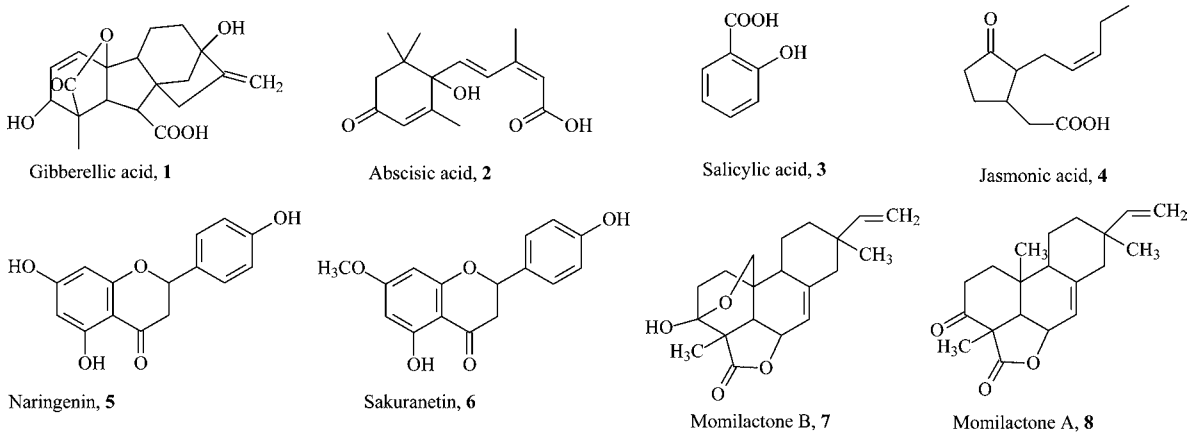

Figure 1. Chemical structures of the analytes: (**1**) gibberellic acid; (**2**) abscisic acid; (**3**) salicylic acid; (**4**) jasmonic acid; (**5**) naringenin; (**6**) sakuranetin; (**7**) momilactone B; (**8**) momilactone A.

response to the pathogen, a molecular method based on a TaqMan quantitative polymerase chain reaction (PCR), was developed to quantitate the fungal presence in the plant tissues.

MATERIALS AND METHODS

Plant Material and Fungal Cultures. Two rice (*O. sativa* L.) cultivars, Selenio and Dorella, were used throughout the experiments. Seed lots of the rice cultivars were provided by the Rice Research Unit of Consiglio per la Ricerca e la Sperimentazione in Agricoltura.

The monoconidial strain VE13 of *F. fujikuroi*,[13] used for artificial inoculation of rice seeds, was stored in potato dextrose agar (PDA) (Merck, Darmstadt, Germany) with 27 mg/L streptomycin (Merck). A small plug was transferred into 500 mL of potato dextrose broth (PDB) (Liofilchem, Roseto degli Abruzzi, Italy) and grown under stirring at 90 rpm and 23 °C for 10 days. The fungal culture was filtered through a sterile gauze to get a conidial suspension at 10^6 conidia/mL. Rice seeds were surface-disinfected in 1% sodium hypochlorite for 2 min and rinsed in sterile distilled water. For each group, 40 seeds per replicate and 3 replicates per experiment were tested. Seeds were soaked in 100 mL of spore suspension and shaken for 30 min at room temperature, while uninoculated seeds for each genotype were soaked in sterile distilled water. The seeds were placed in a sterilized soil in a greenhouse and grown at 24−26 °C during the day and 16−18 °C during the night. Leaves and culms were collected every week for 4 weeks after seed germination (around 7 days after pathogen inoculation). The phenological rice stages at 1, 2, 3, and 4 weeks postgermination (wpg) were V1, V2, V3, and V4, corresponding to the number of leaves with collars on the main stem during vegetative development.[14]

Disease Index. The germination rate and disease index, for three biological replications, were evaluated 28 days after germination using a scale of five distinct classes of symptoms. Each symptom corresponds to a reference number: 0, asymptomatic plants; 25, plants with yellow leaves; 50, plants with long internodes; 75, necrotic plants; 100, dead plants.[15]

Phytohormone and Phytoalexin Extraction and Analysis. *Reagents and Standards.* LC−MS-grade acetonitrile and formic acid used as the mobile phase were purchased from Sigma-Aldrich (St Louis, MO). Methanol, acetonitrile, acetone, ethyl acetate, dichloromethane, and formic acid (HPLC-grade) used for extraction procedures were purchased from Merck (Darmstadt, Germany).

Salicylic acid (purity ≥99%), jasmonic acid (purity ≥95%), abscisic acid (purity ≥98.5%), gibberellic acid (purity ≥95%), naringenin (purity ≥95%), and sakuranetin (purity ≥95%) were purchased from Sigma-Aldrich. Momilactone A and momilactone B were prepared by Prof. Morifumi Hasegawa (College of Agriculture, Ibaraki University, Japan).

Preparation of Standard Solutions. Stock solutions of each analyte were prepared at 1 mg/mL in CH_3OH. Working solutions were prepared by diluting stock solutions in CH_3OH/H_2O (8:2) at different concentrations depending on the range of the calibration curve. A stock solution mixture, made from these individual stock solutions, was prepared in the LC mobile phase and matrixes to obtain calibration curves and to determine the ion suppression, recovery, limit of detection (LOD), and limit of quantitation (LOQ) for each analyte.

Extraction Procedure. Acetone, ethyl acetate, dichloromethane, methanol, acetonitrile, water, and two different mixtures of water/methanol (1:1 and 2:8 pure or containing 0.1% CH_3COOH) were tested. In a second set of analyses, the influence of three extraction times (1 h, 2 h, overnight) and two methods (ultrasonic bath or rotary shaker) on the recovery was evaluated. An analyte-free rice matrix was not available, so for each test two sets of samples, with or without standard additions, were prepared, and each extraction was performed twice for each sample.

A few plants of rice were ground, and 0.2 g of fresh plant material was transferred in 2 mL centrifuge tubes with 1 mL of extraction solution (80% CH_3OH acidified with 0.1% CH_3COOH). The samples were frozen in liquid nitrogen, homogenized by using TissueLyser (Qiagen, Venlo, The Netherlands), and then shaken at 4 °C in the dark overnight. Finally, the samples were centrifuged at 15 000 rpm and 4 °C for 2 min, and the supernatant was analyzed by HPLC−MS/MS.

HPLC−MS/MS Analysis. All analyses were carried out by using a 1260 Agilent Technologies (Santa Clara, CA) system consisting of a binary pump and a vacuum degasser, connected to a Varian model 410 Prostar autosampler (Palo Alto, CA) equipped with a 20 μL loop coupled with a Varian 310-MS TQ mass spectrometer.

HPLC separation of the analytes was performed using a 150 × 2 mm i.d., 3 μm Luna phenyl-hexyl column (Phenomenex, Torrance, CA) under a flow of 200 μL/min. The column temperature was set at 25 °C. Solvent A was H_2O with 0.1% HCOOH, and solvent B was CH_3CN. HPLC analysis was programmed as follows: 40% solvent B for 7 min, followed by a linear gradient from 40% to 100% B in 5 min, and finally holding at 100% B for 4 min.

Samples were ionized using an electrospray (ESI) ion source operating in negative ion mode for salicylic acid, jasmonic acid, abscisic acid, gibberellic acid, naringenin, and sakuranetin and in positive ion mode for momilactone A and momilactone B. For the multiple-reaction monitoring (MRM) experiments, the quantification transitions for each compound were (1) m/z 345 → 239, CE = 14 V, (2) m/z 263 → 153, CE = 12 V, (3) m/z 137 → 93, CE = 16 V, (4) m/z 209 → 59, CE = 14 V, (5) m/z 271 → 151, CE = 18 V, (6) m/z 285 → 119, CE = 30 V, (7) m/z 331 → 269, CE = 25 V, and (8) m/z 315 → 271, CE = 14 V. The collision gas (Ar) pressure was set at 2 mbar for all experiments.

Method Validation. The HPLC−MS/MS method was validated in terms of accuracy, linearity, LOD, and LOQ. The validation was performed on both matrixes using noninoculated samples collected 1 week after germination.

DOI: 10.1021/acs.jafc.5b03018
J. Agric. Food Chem. 2015, 63, 8134−8142

Linearity and Range. The linearity of measurement was evaluated by analyzing different concentrations of the standard solutions of the analytes. Calibration standards were prepared by diluting the stock solutions to obtain specific concentrations.

LOD and LOQ. Usually the LOD and LOQ were established using matrix samples spiked after the extraction procedure with a low amount of standards. An analyte-free matrix was not available, so LOD and LOQ were determined in solvent. The detection and quantification limits were determined on the basis of the standard deviation of the response (σ) and slope of the calibration curve (S) ratio in accordance with the ICH Harmonised Tripartite Guideline[16] expressed as LOD = $3.3\sigma/S$ and LOQ = $10\sigma/S$.

Accuracy. Recovery studies were performed with rice samples spiked at 50%, 100%, and 150% levels with all stock solutions prepared. The accuracy of the method was expressed by [(mean observed concentration)/(spiked concentration)] × 100.

Besides validation, the influence of the components of both rice cultivars on the quantification of every analyte was evaluated. The matrix effect was calculated using the formula ($\text{slope}_{\text{matrix}}/\text{slope}_{\text{solvent}}$) × 100.

Statistical Analysis. Rice samples were harvested at 1, 2, 3, and 4 wpg in three biological replicates. The biological replicates were extracted separately in two technical replicates, and every technical replicate was analyzed twice. The data reported are the average of 12 data points, and the standard deviation is reported as an error bar. Statistical analysis among data of the same analyte was performed using Student's t test at 99% confidence.

Molecular Identification of *F. fujikuroi*. *DNA Extraction.* DNA extraction was performed on 0.1 g of fresh plant material using the commercial EZNA plant DNA kit (Omega Bio-Tek, Norcross, GA), according to the instructions of the manufacturer. For the final elution of DNA, 25 μL of elution buffer was used.

Design of the Real-Time PCR Primers and Probe. The purpose of this work was to identify regions of variability able to discriminate *F. fujikuroi* from other species associated with bakanae disease on rice[5] (*Fusarium proliferatum* and *Fusarium verticilloides*). A part of the elongation factor 1α (TEF) gene was sequenced for different strains. Multiple sequence alignment showed a deletion of six nucleotides in all the strains of *F. fujikuroi* but not in other species.[17] The deletion of *F. fujikuroi* was used as the basis for design of the following primers and probe with the Primer Express 3.0.1 software (Applied Biosystems, Foster City, CA): forward primer FujiF (5′-ATGGGCGCGTTTTGCCCTTT-3′), reverse primer FujiR (5′-GGCGTACTTGAAGGAACCCT-3′), and TaqMan FfujiPq (5′-[FAM]-TTGTCACGTGTCAAACTAAACATTCGAC-[TAMRA]-3′) labeled with the fluorescent reporter dye FAM at the 5′-end and the TAMRA quencher at the 3′-end. The primers and the probe were purchased from Applied Biosystems.

TaqMan Real-Time PCR Assay. The real-time TaqMan PCR assays were conducted using an Applied Biosystems Plus detection system. Twenty microliter reactions containing 12.5 μL of Taqman Master Mix (2×) (Applied Biosystems), PCR primers at a concentration of 10 μM, the TaqMan FfujiPq at 5 μM, and 5 μL of DNA at a concentration of about 30 ng/μL were prepared in triplicate. Amplification and detection were performed in 96-well optical reaction plates (Applied Biosystems) sealed with MicroAmp optical adhesive film (Applied Biosystems) on an ABI Prism 7900HT sequence detection system real-time thermal cycler. The amplification conditions were 2 min at 50 °C and 10 min at 95 °C followed by 15 s at 95 °C and 40 s at 62 °C for 40 cycles.

A standard curve was prepared by serial dilution of known quantities of *F. fujikuroi* DNA to quantitate the fungus inside the rice tissues. In the preparation of the standard curve, the initial concentration of DNA was 386 ng/μL.

Primer and Probe Design, Specificity, and Sensitivity. The primer pair FujiF and FujiR was designed to amplify a 117 bp unique sequence found in the TEF gene of *F. fujikuroi*. For confirmation of the specificity of the amplified product, the TaqMan FfujiPq probe was designed for inclusion in the real-time PCR assay.

The combination of primers FujiF and FujiR with the dual-labeled probe FfujiPq was then tested in real-time PCR with a series of DNA extracts from pure cultures of three species of *Fusarium*. Real-time reactions using this primer−probe combination proved to be specific, and low C_t values were obtained for all *F. fujikuroi* strains and not for isolates of any other *Fusarium* spp.

The sensitivity of the FujiF/FujiR and FfujiPq combination was measured with a six-dilution series of *F. fujikuroi* DNA in deionized DNA-free water, in a range of concentrations from 386 ng/μL down to 0.3 fg/μL. A standard curve was built, and the corresponding amplification efficiency was 96.18%. The results showed a linear relationship between C_t values and concentration, and the correlation coefficient (R^2) was 0.999.

The optimized sequences FujiF/FujiR and FfujiPq permitted the real-time PCR to be run under high-stringency conditions (annealing or elongation at 62 °C), providing maximum specificity without any significant effect on the performance of amplification.

The quantity of the fungus in the plants was measured in nanograms per 100 mg by extraction of DNA from the culm and from the leaves of the cultivars Selenio and Dorella.

RESULTS

Rice Germination and Disease Index. In plants of rice cv. Selenio, symptoms of bakanae were not observed, while typical bakanae-diseased symptoms were observed in plants of cv. Dorella. The disease index calculated for cv. Selenio was 5.0%, while for cv. Dorella it was 72.4%. Also the percentage of germination was different, 72.5% for cv. Dorella and 93.0% for cv. Selenio.

Phytohormone and Phytoalexin Extraction and Analysis. In the first step, authentic standard mixtures were used to evaluate the retention times, m/z values of the corresponding ions, and characteristic MS/MS fragmentation patterns. Each analyte was characterized by two specific precursor−fragment ion combinations and a characteristic retention time. For each analyte, quantification relied on the most intense transition, while the less intense one was used to confirm the assignment.

The choice of the appropriate chromatographic system is the most important factor that influences the sensitivity of HPLC−MS analysis. Samples were analyzed using a phenyl-hexyl column, which allows a good separation of all the analytes in a short time (Figure 2). It was possible to separate the analytes to perform a change of polarity and to detect all the analytes in a single analysis.

Plant hormones and phytoalexins are structurally diverse with different physiochemical properties. The choice of extraction solvent is very important, so during the method optimization, the composition of the extraction solution was first evaluated. Different organic solvents/mixtures and the influence of acidification were tested. A nonpolar extraction solvent extracted a large amount of chlorophyll, and purification was necessary. A mixture of methanol and water provided a high extraction efficiency for all the analytes and did not require purification because a low chlorophyll amount was extracted using an 8:2 ratio.

Validation of the Analytical Method. A validation procedure was carried out to evaluate the applicability of this method. The range of calibration curves was defined for each compound on the basis of the amount in both rice matrixes. The calibration curves showed a good linearity of correlation coefficient ($R^2 > 0.9999$) for all analytes. The LOD for different analytes ranged from 0.87 ng/g for abscisic acid to 20.7 ng/g for salicylic acid, and the LOQ ranged from 2.90 ng/g for abscisic acid to 69.1 ng/g for salicylic acid calculated on the

DOI: 10.1021/acs.jafc.5b03018
J. Agric. Food Chem. 2015, 63, 8134−8142

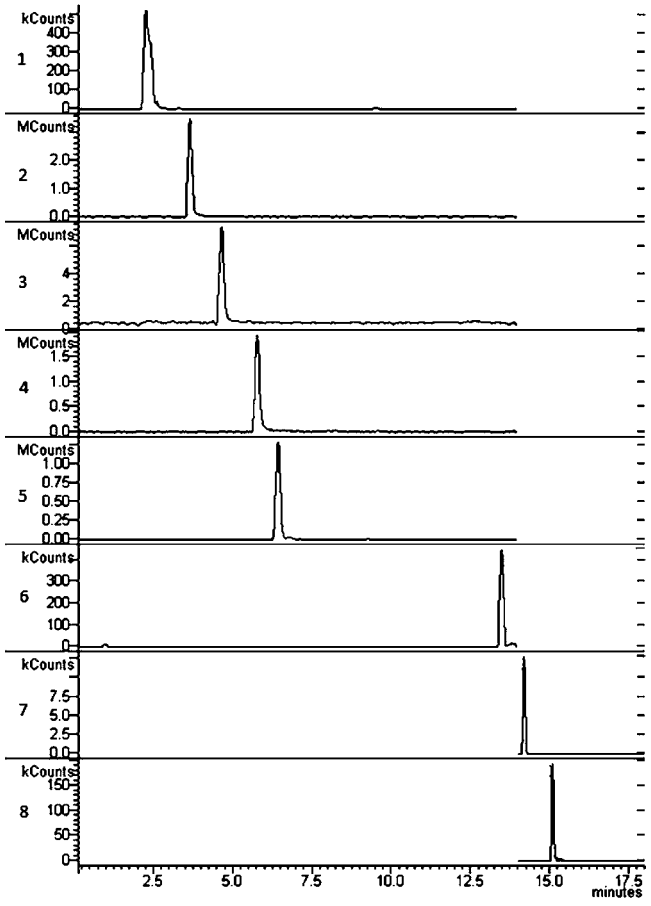

Figure 2. Chromatograms of a standard solution containing a 200 ng/mL concentration of the analytes under MRM conditions.

basis of the fresh weight. For sakuranetin in cv. Selenio and abscisic acid in cv. Dorella, the recovery was very high (around 98%). For the other analytes, recoveries in both cultivars were always higher than 70%. The matrix components can affect the analyte stability, extraction, and ionization. For both cultivars, positive and negative trends were similar; only for naringenin the matrix effect did not affect ionization. The matrixes mostly influenced salicylic acid and momilactone A. The components of the matrix affected the response of each analyte with different intensities. To consider all the effects of the matrix on the quantitative results, a quantitation method developed in the presence of the matrix was used.

Accumulation of Phytohormones. Abscisic acid and gibberellic acid (Figure 3) showed a very different trend in the susceptible cultivar Dorella (D) compared to the resistant one Selenio (S). In the susceptible cultivar, for both phytohormones, it is possible to observe, after *F. fujikuroi* inoculation (D+), an increased concentration in the third (347 ng/g for gibberellic acid and 63.7 ng/g for abscisic acid) and fourth (607 ng/g for gibberellic acid and 82.5 ng/g for abscisic acid) wpg. In the resistant cultivar, abscisic acid was statistically higher in inoculated plants (S+) compared to the uninoculated control (S−) at the four time points. In Selenio, gibberellic acid was not statistically different after pathogen inoculation for the first three wpgs, while it showed a slight increase at 4 wpg.

The trends of jasmonic acid and salicylic acid in the resistant cultivar and in the susceptible cultivar are shown in Figure 4. The trend and the amount of jasmonic acid accumulated in both cultivars were similar during the 4 weeks. For cv. Dorella, the quantity of jasmonic acid in inoculated plants significantly decreased at 3 and 4 wpg compared to that in the uninoculated control (64.8 ng/g for D− and 39.4 ng/g for D+ at 3 wpg, 44.8 ng/g for D− and 23.1 ng/g for D+ at 4 wpg). The accumulation of salicylic acid in both cultivars was quite similar (from 4480 to 7910 ng/g for cv. Selenio and from 5440 to 10700 ng/g for cv. Dorella). Infested rice had a similar trend compared to the control, and the difference of salicylic acid accumulation between them gradually increased with increasing infestation time. In the susceptible cultivar, the concentration of salicylic acid was always higher compared to that in the uninoculated control.

Accumulation of Phytoalexins. An increase of all the phytoalexins in the resistant cultivar was observed. The major

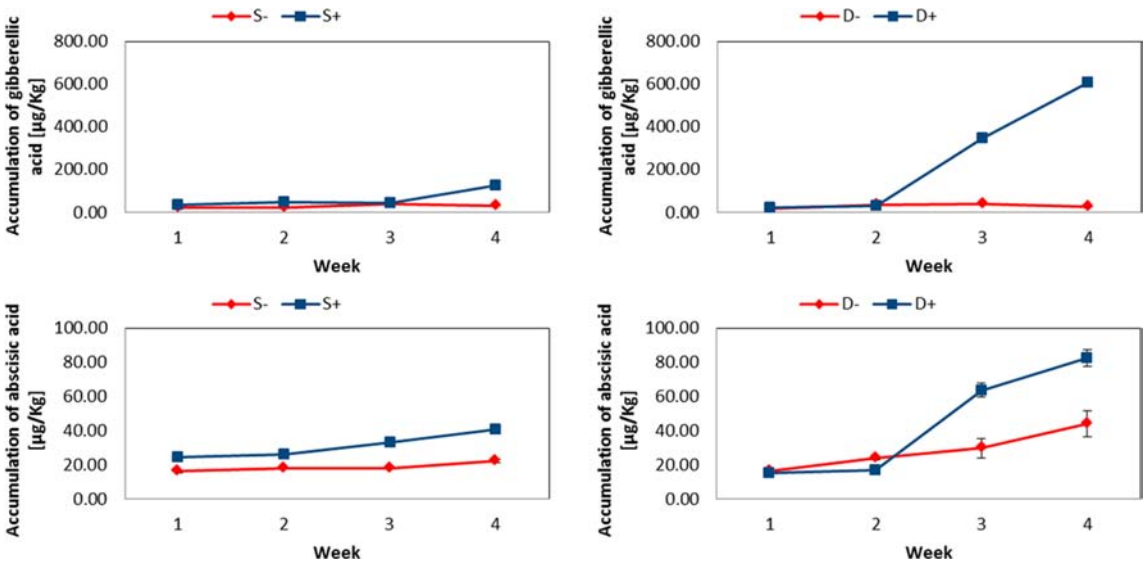

Figure 3. Changes in phytohormone gibberellic acid and abscisic acid accumulation during 4 weeks after germination in resistant (Selenio, S) and susceptible (Dorella, D) rice cultivars, inoculated (+) or not (−) with *F. fujikuroi*. Values are means ± SD (n = 12 independent analyses) in fresh plant tissues (ng/g of fresh weight, FW).

DOI: 10.1021/acs.jafc.5b03018
J. Agric. Food Chem. 2015, 63, 8134−8142

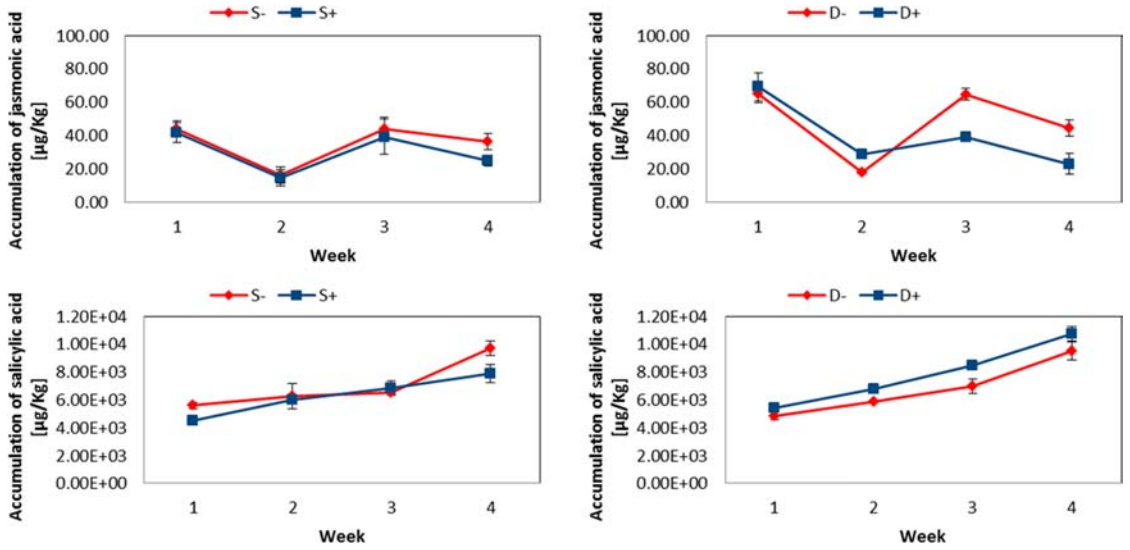

Figure 4. Changes in phytohormone jasmonic acid and salicylic acid accumulation during 4 weeks after germination in resistant (Selenio, S) and susceptible (Dorella, D) rice cultivars, inoculated (+) or not (−) with *F. fujikuroi*. Values are means ± SD (n = 12 independent analyses) in fresh plant tissues (ng/g of fresh weight, FW).

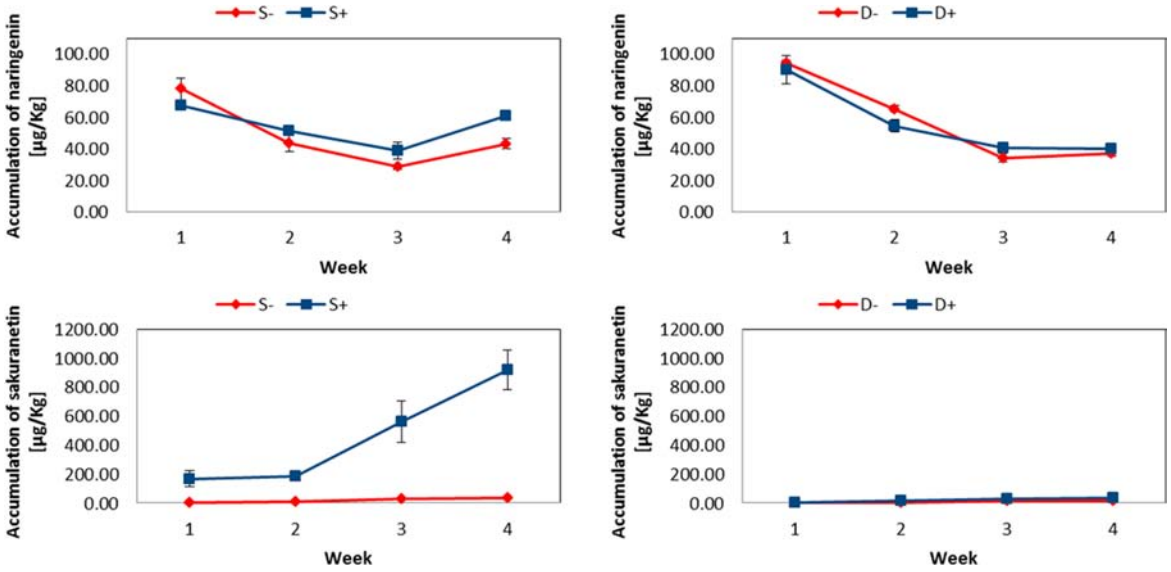

Figure 5. Changes in phytoalexin naringenin and sakuranetin accumulation during 4 weeks after germination in resistant (Selenio, S) and susceptible (Dorella, D) rice cultivars, inoculated (+) or not (−) with *F. fujikuroi*. Values are means ± SD (n = 12 independent analyses) in fresh plant tissues (ng/g of fresh weight, FW).

difference between the two cultivars was found in the accumulation of sakuranetin, which greatly increased (24 times) from the third week in cv. Selenio (Figure 5), while it increased slightly (twice) in the susceptible cultivar. The accumulation of momilactone A (from 1170 to 1960 ng/g for cv. Selenio and from 183 to 1020 ng/g from cv. Dorella) was also higher in the resistant cultivar compared to the susceptible one from 1 wpg (Figure 6). For the other two PAs, differences between the two cultivars are lower: naringenin ranged from 68 to 61 ng/g in cv. Selenio and from 90 to 40 ng/g in cv. Dorella (Figure 5); momilactone B ranged from 115 to 168 ng/g in cv. Selenio and from 66 to 176 ng/g in cv. Dorella (Figure 6).

Quantification of *F. fujikuroi*. The results obtained from real-time PCR allowed the quantification of the fungal DNA and were used to calculate the concentration of *F. fujikuroi* in plants during their growth.

The results showed different trends between the resistant and susceptible cultivars (Figure 7). Inoculated plants of cv. Dorella showed typical bakanae symptoms expressed by abnormal and excessive growth compared to healthy plants. The quantity of *F. fujikuroi* increased during plant growth. At 3 wpg the amount (ng) of fungus was maximum; afterward the quantity of *F. fujikuroi* started to decrease (Figure 7). Conversely, in the inoculated plants of cv. Selenio, symptoms of bakanae were not observed and the quantity of *F. fujikuroi* was steadily lower during 4 weeks (Figure 7). In the uninoculated control of both cultivars, the amount of *F. fujikuroi* was lower throughout the 4 wpg.

DISCUSSION

In this study the differences between the responses of two rice cultivars (Selenio and Dorella) to *F. fujikuroi* were investigated;

DOI: 10.1021/acs.jafc.5b03018
J. Agric. Food Chem. 2015, 63, 8134−8142

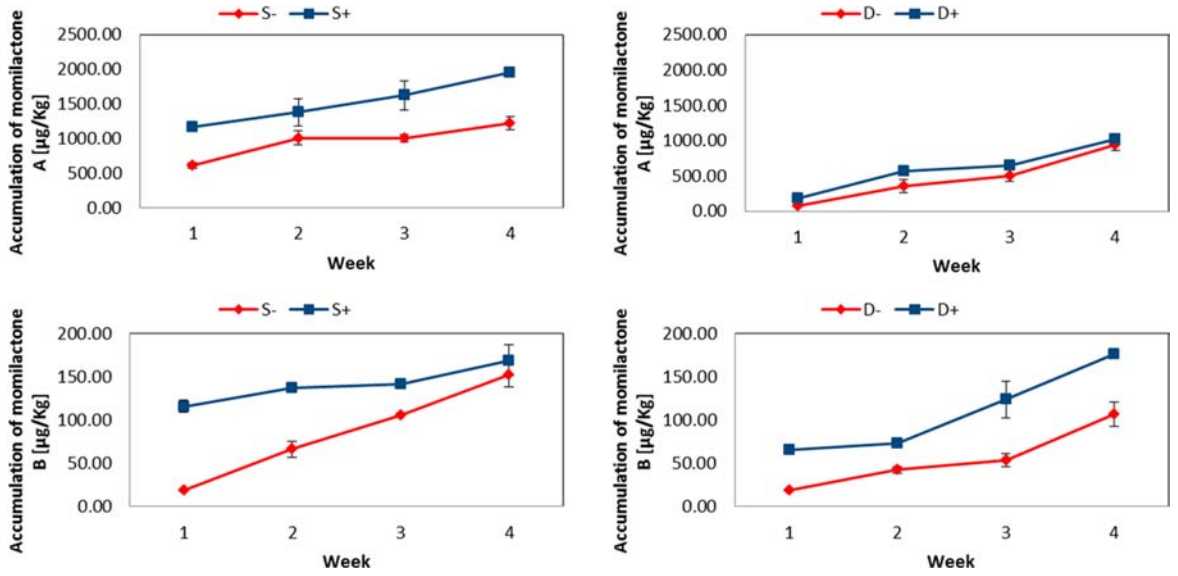

Figure 6. Changes in phytoalexin momilactone A and momilactone B accumulation during 4 weeks after germination in resistant (Selenio, S) and susceptible (Dorella, D) rice cultivars, inoculated (+) or not (−) with *F. fujikuroi*. Values are means ± SD (n = 12 independent analyses) in fresh plant tissues (ng/g of fresh weight, FW).

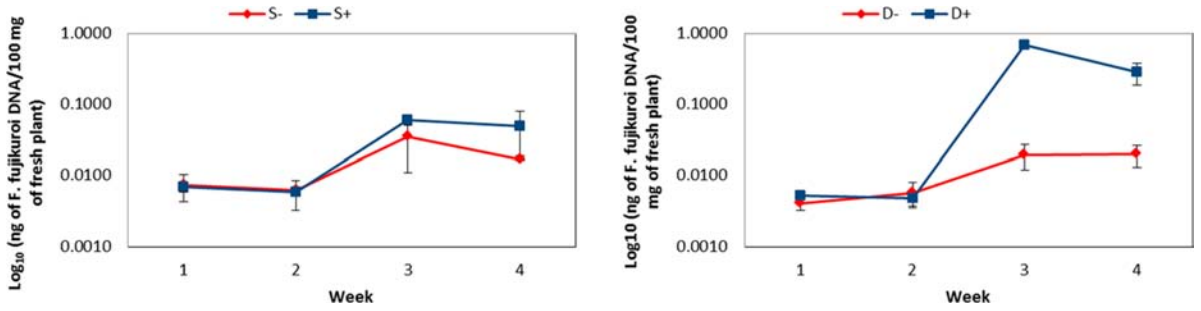

Figure 7. Quantification of pathogen with TaqMan real-time PCR growth during 4 weeks after germination in resistant (Selenio, S) and susceptible (Dorella, D) rice cultivars, inoculated (+) or not (−) with *F. fujikuroi*. Values are means ± SD (n = 9 independent analyses) in fresh plant tissues [log(ng of DNA of *F. fujikuroi*/100 mg of plant tissue)].

different types of analyses, in vivo tests and chemical and molecular analyses, were performed to elucidate the rice resistance mechanism involved.

Several HPLC−MS/MS methods for separation and analysis of free and conjugated phytohormones were developed in plants.[17,18] Liu et al.[19] developed a method for the simultaneous determination of some hormones and phytoalexins to study rice−bacterium interactions. With the same method, Duan et al.[20] studied rice metabolites involved in disease resistance to *M. oryzae*, an agent of rice blast. In this work, a simple and specific method for simultaneous extraction and quantification of metabolites involved in the interaction between rice and *F. fujikuroi* was developed and validated. All the analytes were extracted with a good recovery using a minimal amount of sample.

After pathogen infection or abiotic stress, phytoalexins are produced and accumulated by plants. Changes in phytoalexin concentrations over time may be important in the disease resistance of rice plants.[21] In general, flavonoids in plants have a protective function against stress. Naringenin 7-*O*-methyltransferase (NOMT) catalyzes naringenin methylation to sakuranetin when rice leaves are UV-irradiated[22] or in the presence of an increase of jasmonic acid or a jasmonic acid-related compound.[23] Sakuranetin biosynthesis is rapidly induced by biotic and abiotic stresses and was not found in healthy rice leaves.[24] In this work an increased concentration of sakuranetin was found only in cv. Selenio inoculated plants, not in the uninoculated control or in any sample of susceptible cultivar. It was demonstrated that sakuranetin, during rice−pathogen interaction, was induced in higher quantities in cultivars resistant to blast than in the susceptible ones.[25] Hasegawa et al.[26] established that sakuranetin has a stronger antifungal activity against *M. oryzae* compared with momilactone A, which is the major rice diterpenoid phytoalexin. The main difference observed between the two cultivars is the increase of sakuranetin in resistant inoculated plants. In the interaction of rice with *F. fujikuroi*, sakuranetin is the most important phytoalexin, induced at all the time points.

Momilactones are naturally present in rice plants and are spread in all plant tissues;[27] generally, the content of momilactone A is higher than that of momilactone B. Momilactone A was first isolated from the seed husk of rice and identified as a growth inhibitor,[28] and then it was isolated from rice leaves and characterized as a phytoalexin.[29] The phytoalexin momilactone A was detected in higher levels in cv. Selenio compared to cv. Dorella, from the first week of growth, either in inoculated plants or in uninoculated controls. In inoculated plants the level of momilactone A was always higher

DOI: 10.1021/acs.jafc.5b03018
J. Agric. Food Chem. 2015, 63, 8134−8142

than that in uninoculated controls. MomilactoneA showed a high basal level of production, also without *F. fujikuroi* inoculation, in the resistant rice genotype.

Momilactone B is a potent growth inhibitor and is secreted from the roots throughout the life cycle of the plant,[30] produced in different concentrations depending on the rice cultivars.[31] Generally, stress could induce an increase of the production of allelochemicals, which play an important role in the defense mechanism.[32] In rice, the increased allelopathy with elevated secretion of momilactone B was recorded in different stress conditions.[33] The increase in momilactone B in both cultivars inoculated with *F. fujikuroi* was probably due to a response to stress, but since it also acts as a phytoalexin, momilactone B may play an important role in defense against biotic and abiotic stress. Plant−pathogen interactions produce variations in the level of various phytohormones simultaneously, but each hormone has a characteristic biological effect.[34]

Various plant hormones are often involved in the same biological process with additive, synergistic, or antagonistic action.[35] The rice pathogen *F. fujikuroi* is able to produce large amounts of giberellins, especially the bioactive compound gibberellic acid.[36] Gibberellic acid was significantly detected in cv. Dorella infected with *F. fujikuroi.* At 3 and 4 wpg, increased levels of gibberellic acid were observed and the plants showed typical bakanae symptoms: infected seedlings were elongated, more slender, and slightly chlorotic when compared to healthy seedlings. The increased level of gibberellic acid could be attributed to the presence of the pathogen, which was confirmed by quantitative PCR, only in the susceptible cultivar starting at 2 wpg. Gibberellin A3 production contributes to an increase in the pathogenicity of *F. fujikuroi* on rice.[37] The resistant cultivar Selenio did not show the typical symptoms of bakanae, despite a slight increase of *F. fujikuroi* being observed in inoculated plants at 3 and 4 wpg. Gibberellic acid was observed at low levels in inoculated plants of the resistant cultivar only at 4 wpg.

Jasmonic acid levels had a different trend between infected plants and the uninoculated control for cv. Dorella. At 3 wpg, a decrease of jasmonic acid was observed in inoculated plants of the susceptible cultivar in correspondence with an increase of gibberellic acid, as previously described by Yang et al.[38] Gene expression studies and pathobiological assays suggested that gibberellic acid controls jasmonic acid-responsive gene expression and jasmonic acid-mediated plant immune responses.[39] Gibberellic acid promotes plant growth by regulating the degradation of a class of nuclear growth-repressing proteins called DELLAs. Slender rice 1 (SR1), the only DELLA protein in rice, inhibits JAZ1, the key repressor of jasmonic acid signaling.[40] The increase of gibberellic acid, produced by the fungus, restricts jasmonic acid signaling that is strongly activated during necrotroph infections.[41]

The free salicylic acid level in rice leaves usually ranges from 5 to 30 μg/g of fresh weight.[42,43] A large amount of salicylic acid was accumulated in many plant species (*Arabidopsis*, tobacco) after pathogen inoculation; on the contrary, in rice no significant induction was reported after bacterial or fungal infection.[44] In both uninoculated cultivars, the salicylic acid level was similar, but in cv. Dorella after inoculation the amount of salicylic acid was higher compared to that in cv. Selenio. This is probably due to the role that salicylic acid plays in the modulation of redox balance to protect the plant from oxidative stress and in the defense against pathogen attacks.[45]

Abscisic acid probably compromises rice defense against pathogens. Jiang et al.[46] demonstrated that abscisic acid suppresses the basal resistance of rice when it interacts with the pathogen *M. oryzae* at 3 and 4 wpg. An increased concentration of this phytohormone was observed only in diseased plants of cv. Dorella. A high level of abscisic acid in the susceptible cultivar could be related to the response to biotic stress, as it could antagonize gibberellic acid.[47] Conversely, the concentration of abscisic acid remained constant in the resistant cultivar Selenio; however, the levels of this phytohormone were higher in the inoculated plants compared to the uninoculated control. The role of abscisic acid in disease resistance remains unclear due to its multifaceted function in different tissues and the development stage of the plant. Abscisic acid plays an ambiguous role in the rice immune signaling network; a general pattern suggests that abscisic acid plays a stimulatory role in plant defense during the earlier stages of the pathogen invasion, and vice versa, at later colonization stages, it could have a suppressive role.[48]

The analytical method developed in this paper could be used to study the response of rice to other biotic or abiotic stresses, besides *F. fujikuroi.* The pathogen considered in this work is a seedborne pathogen, and the chemical responses of plants have rarely been studied in relationship to seedborne pathogen infection. Some responses are similar to those activated in response to other rice pathogens, such as *M. oryzae*, which is a foliar fungal pathogen, with the main difference that gibberelins are typically produced by *F. fujikuroi*. The levels of phytohormones and phytoalexins in rice showed that *F. fujikuroi* may behave differently with respect to the cultivar. In the susceptible cultivar, the pathogen could systemically act as a necrotroph destroying the plant cells. On the contrary, in the resistant cultivar, the pathogen is present on rice, though at lower concentration, without damaging the plants, and it triggers salicylic acid and, presumably, a hypersensitive response. Collectively, this information provides important information to elucidate the rice responses occurring during *F. fujikuroi* infection.

■ ASSOCIATED CONTENT

Supporting Information

The Supporting Information is available free of charge on the ACS Publications website at DOI: 10.1021/acs.jafc.5b03018.

Tables listing the parameters of calibration for each analyte and the regression, matrix effect, and recovery for both matrixes (PDF)

■ AUTHOR INFORMATION

Corresponding Author

*Phone: +39-0116708942. Fax: +39-0112368942. E-mail: davide.spadaro@unito.it.

Funding

This work was carried out with grants from the project RISINNOVA "Integrated genetic and genomic approaches for new Italian rice breeding strategies", funded by the AGER Foundation (Grant 2010-2369), and from the project TESTA "Seed health: development of seed treatment methods, evidence for seed transmission and assessment of seed health", funded by the European Union (Grant Agreement 311875).

Notes

The authors declare no competing financial interest.

DOI: 10.1021/acs.jafc.5b03018
J. Agric. Food Chem. 2015, 63, 8134−8142

■ ACKNOWLEDGMENTS

We acknowledge Prof. Morifumi Hasegawa (College of Agriculture, Ibaraki University, Japan) for providing the chemical standards of momilactones A and B and Dr. Giampiero Vale (Rice Research Unit of Consiglio per la Ricerca e la Sperimentazione in Agricoltura, Italy) for providing the rice seeds.

■ ABBREVIATIONS USED

D−, cv. Dorella not inoculated; D+, cv. Dorella inoculated; MRM, multiple-reaction monitoring; S−, cv. Selenio not inoculated; S+, cv. Selenio inoculated

■ REFERENCES

(1) O'Donnell, K.; Cigelnik, E.; Nirenberg, H. I. Molecular systematics and phylogeography of the *Gibberella fujikuroi* species complex. *Mycologia* **1998**, *90*, 465−493.

(2) Hwang, I. S.; Kang, W. R.; Hwang, D. J.; Bae, S. C.; Yun, S. H.; Ahn, I. P. Evaluation of bakanae disease progression caused by *Fusarium fujikuroi* in *Oryza sativa* L. *J. Microbiol.* **2013**, *51*, 858−865.

(3) Wiemann, P.; Brown, D. W.; Kleigrewe, K.; Bok, J. W.; Keller, N. P.; Humpf, H. U.; Tudzynski, B. FfVel1 and FfLae1, components of a velvet-like complex in *Fusarium fujikuroi*, affect differentiation, secondary metabolism and virulence. *Mol. Microbiol.* **2010**, *77*, 972−994.

(4) Jang, S. W.; Hamayun, M.; Sohn, E. Y.; Shin, D. H.; Kim, K. U.; Lee, B. H.; Lee, I. J. Effect of elevated nitrogen levels on endogenous gibberellin and jasmonic acid contents of three rice (*Oryza sativa* L.) cultivars. *J. Plant Nutr. Soil Sci.* **2008**, *171*, 181−186.

(5) Wulff, E. G.; Sørensen, J. L.; Lübeck, M.; Nielsen, K. F.; Thrane, U.; Torp, J. *Fusarium* spp. associated with rice Bakanae: ecology, genetic diversity, pathogenicity and toxigenicity. *Environ. Microbiol.* **2010**, *12*, 649−657.

(6) Hasegawa, M.; Mitsuhara, I.; Seo, S.; Imai, T.; Koga, J.; Okada, K.; Yamane, H.; Ohashi, Y. Phytoalexin accumulation in the interaction between rice and blast fungus. *Mol. Plant-Microbe Interact.* **2010**, *23*, 1000−1011.

(7) Kanno, H.; Hasegawa, M.; Kodama, O. Accumulation of salicylic acid, jasmonic acid and phytoalexins in rice, *Oryza sativa*, infested by the white-backed planthopper, *Sogatella furcifera* (Hemiptera: Delphacidae). *Appl. Entomol. Zool.* **2012**, *47*, 27−34.

(8) Grayer, R. J.; Kokubun, T. Plant-fungal interaction: the search for phytoalexins and other antifungal compounds from higher plants. *Phytochemistry* **2001**, *56*, 253−263.

(9) Dillon, V. M.; Overton, J.; Grayer, R. J.; Harborne, J. B. Differences in phytoalexin response among rice cultivars of different resistance to blast. *Phytochemistry* **1997**, *44*, 599−603.

(10) Weiss, D.; Ori, N. Mechanisms of cross talk between gibberellin and other hormones. *Plant Physiol.* **2007**, *144*, 1240−1246.

(11) Kende, H.; Knaap, E. V.; Cho, H. T. Deepwater Rice: A model plant to study stem elongation. *Plant Physiol.* **1998**, *118*, 1105−1110.

(12) Matic, S.; Bagnaresi, P.; Biselli, C.; Valé, G.; Garibaldi, A.; Gullino, M. L.; Spadaro, D. Transcriptome analysis of two rice genotypes in response to *Fusarium fujikuroi*. *J. Plant Pathol.* **2014**, *96*, S4.34−S4.35.

(13) Amatulli, M. T.; Spadaro, D.; Gullino, M. L.; Garibaldi, A. Molecular identification of *Fusarium* spp. associated with bakanae disease of rice in Italy and assessment of their pathogenicity. *Plant Pathol.* **2010**, *59*, 839−844.

(14) Counce, P. A.; Keisling, T. C.; Mitchell, A. J. A Uniform, Objective, and Adaptive System for Expressing Rice Development. *Crop Sci.* **2000**, *40*, 436−443.

(15) Matic, S.; Spadaro, D.; Garibaldi, A.; Gullino, M. L. Antagonistic yeasts and thermotherapy as seed treatments to control *Fusarium fujikuroi* on rice. *Biol. Control* **2014**, *73*, 59−67.

(16) International Conference on Harmonisation of Technical Requirements for Registration of Pharmaceuticals for Human Use (ICH). *Validation of Analytical Procedures: Text and Methodology Q2(R1)*; ICH Harmonised Tripartite Guideline; ICH: Geneva, Switzerland, 1994; p 17.

(17) Amatulli, M. T.; Spadaro, D.; Gullino, M. L.; Garibaldi, A. Conventional and real-time PCR for identification of *Fusarium fujikuroi* and *Fusarium proliferatum* from diseased rice tissues and seeds. *Eur. J. Plant Pathol.* **2012**, *134*, 401−408.

(18) Almeida Trapp, M.; De Souza, G. D.; Rodrigues-Filho, E.; Boland, W.; Mithöfer, A. Validated method for phytohormone quantification in plants. *Front. Plant Sci.* **2014**, *5*, 1−11.

(19) Liu, H.; Li, X.; Xiao, J.; Wang, S. A convenient method for simultaneous quantification of multiple phytohormones and metabolites: application in study of rice-bacterium interaction. *Plant Methods* **2012**, *8*, 2.

(20) Duan, L.; Liu, H.; Li, X.; Xiao, J.; Wang, S. Multiple phytohormones and phyoalexins are involved in disease resistance to *Magnaporthe oryzae* invaded from roots in rice. *Physiol. Plant.* **2014**, *152*, 486−500.

(21) Nakazato, Y.; Tamogami, S.; Kawai, H.; Hasegawa, M.; Kodama, O. Methionine-induced phytoalexin production in rice leaves. *Biosci., Biotechnol., Biochem.* **2000**, *64*, 577−583.

(22) Rakwal, R.; Agrawal, G. K.; Yonekura, M.; Kodama, O. Naringenin 7-O-methyltransferase involved in the biosynthesis of the flavanone phytoalexin sakuranetin from rice (*Oryza sativa* L.). *Plant Sci.* **2000**, *155*, 213−221.

(23) Tamogami, S.; Rakwal, R.; Kodama, O. Phytoalexin production by amino acid conjugates of jasmonic acid through induction of naringenin-7-O-methyltransferase, a key enzyme on phytoalexin biosynthesis in rice (*Oryza sativa* L.). *FEBS Lett.* **1997**, *401*, 239−242.

(24) Shimizu, T.; Lin, F.; Hasegawa, M.; Okada, K.; Nojiri, H.; Yamane, H. Purification and identification of naringenin 7-O-methyltransferase, a key enzyme in biosynthesis of flavonoid phytoalexin sakuranetin in rice. *J. Biol. Chem.* **2012**, *287*, 19315−19325.

(25) Kodama, O.; Miyakawa, J.; Akatsuka, T.; Kiyosawa, S. Sakuranetin, a flavanone phytoalexin from ultraviolet-irradiated rice leaves. *Phytochemistry* **1992**, *31*, 3807−3809.

(26) Hasegawa, M.; Mitsuhara, I.; Seo, S.; Okada, K.; Yamane, H.; Iwai, T.; Ohashi, Y. Analysis on blast fungus-responsive characters of a flavonoid phytoalexin sakuranetin; accumulation in infected rice leaves, antifungal activity and detoxification by fungus. *Molecules* **2014**, *19*, 11404−11418.

(27) Fukuta, M.; Dang Xuan, T.; Deba, F.; Tawata, S.; Dang Khanh, T.; Min Chung, I. Comparative efficacies in vitro of antibacterial, fungicidal, antioxidant, and herbicidal activities of momilatones A and B. *J. Plant Interact.* **2007**, *2*, 245−251.

(28) Kato, T.; Kabuto, C.; Sasaki, N.; Tsunagawa, M.; Aizawa, H.; Fujita, K.; Kato, Y.; Kitahara, Y.; Takahashi, N. Momilactones, growth inhibitors from rice, *Oryza sativa* L. *Tetrahedron Lett.* **1973**, *14*, 3861−3864.

(29) Cartwright, D. W.; Langcake, P.; Pryce, R. J.; Leworthy, D. P.; Ride, J. P. Isolation and characterization of two phytoalexins from rice as momilactones A and B. *Phytochemistry* **1981**, *20*, 535−537.

(30) Kato-Noguchi, H.; Ino, T.; Ichii, M. Changes in release of momilactone B into the environment from rice throughout its life cycle. *Funct. Plant Biol.* **2003**, *30*, 995−997.

(31) Kato-Noguchi, H.; Ino, T. Concentration and release level of momilactone B in the seedlings of eight rice cultivars. *J. Plant Physiol.* **2005**, *162*, 965−969.

(32) Belz, R. G. Allelopathy in crop/weed interactions-an update. *Pest Manage. Sci.* **2007**, *63*, 308−326.

(33) Kato-Noguchi, H. Stress-induced allelopathic activity and momilactone B in rice. *Plant Growth Regul.* **2009**, *59*, 153−158.

(34) Santner, A.; Estelle, M. Recent advances and emerging trends in plant hormone signalling. *Nature* **2009**, *459*, 1071−1078.

(35) Robert-Seilaniantz, A.; Navarro, L.; Bari, R.; Jones, J. D. G. Pathological hormone imbalances. *Curr. Opin. Plant Biol.* **2007**, *10*, 372−379.

DOI: 10.1021/acs.jafc.5b03018
J. Agric. Food Chem. 2015, 63, 8134−8142

(36) Tudzynski, B. Biosynthesis of gibberellins in *Gibberella fujikuroi*: biomolecular aspects. *Appl. Microbiol. Biotechnol.* **1999**, *52*, 298−310.
(37) Wiemann, P.; Sieber, C. M. K.; von Bargen, K. W.; Studt, L.; Niehaus, E. M.; Espino, J. J.; Huß, K.; Michielse, C. B.; Albermann, S.; Wagner, D.; Bergner, S. V.; Connolly, L. R.; Fischer, A.; Reuter, G.; Kleigrewe, K.; Bald, T.; Wingfield, B. D.; Ophir, R.; Freeman, S.; Hippler, M.; Smith, K. M.; Brown, D. W.; Proctor, R. H.; Münsterkötter, M.; Freitag, M.; Humpf, H. U.; Güldener, U.; Tudzynski, B. Deciphering the cryptic genome: genome-wide analyses of the rice pathogen *Fusarium fujikuroi* reveal complex regulation of secondary metabolism and novel metabolites. *PLoS Pathog.* **2013**, *9*, e1003475.
(38) Yang, D. L.; Yao, J.; Mei, C. S.; Tong, X. H.; Zeng, L. J.; Li, Q.; Xiao, L. T.; Sun, T.; Li, J.; Deng, X. W.; Lee, C. M.; Thomashow, M. F.; Yang, Y.; He, Z.; He, S. Y. Plant hormone jasmonate prioritizes defense over growth by interfering with gibberellin signaling cascade. *Proc. Natl. Acad. Sci. U. S. A.* **2012**, *109*, E1192−E1200.
(39) Schwechheimer, C. Gibberellin signaling in plants - the extended version. *Front. Plant Sci.* **2012**, *2*, 1−7.
(40) Sun, T.-P. The Molecular mechanism and evolution of the review GA−GID1−DELLA signaling module in plants. *Curr. Biol.* **2011**, *21*, R338−R345.
(41) Navarro, L.; Bari, R.; Achard, P.; Lisón, P.; Nemri, A.; Harberd, N. P.; Jones, J. D. DELLAs control plant immune responses by modulating the balance of jasmonic acid and salicylic acid signaling. *Curr. Biol.* **2008**, *18*, 650−655.
(42) Wang, D. H.; Li, X. X.; Su, Z. K.; Ren, H. X. The role of salicylic acid in response of two rice cultivars to chilling stress. *Biol. Plant.* **2009**, *53*, 545−552.
(43) Pál, M.; Kovács, V.; Szalai, G.; Soós, V.; Ma, X.; Liu, H.; Mei, H.; Janda, T. Salicylic acid and abiotic stress responses in rice. *J. Agron. Crop Sci.* **2014**, *200*, 1−11.
(44) Silverman, P.; Seskar, M.; Kanter, D.; Schweizer, P.; Métraux, J. P.; Raskin, I. Salicylic acid in rice. *Plant Physiol.* **1995**, *108*, 633−639.
(45) Yang, Y.; Qi, M.; Mei, C. Endogenous salicylic acid protects rice plants from oxidative damage caused by aging as well as biotic and abiotic stress. *Plant J.* **2004**, *40*, 909−919.
(46) Jiang, C. J.; Shimono, M.; Sugano, S.; Kojima, M.; Yazawa, K.; Yoshida, R.; Inoue, H.; Hayashi, N.; Sakakibara, H.; Takatsuji, H. Abscisic acid interacts antagonistically with salicylic acid signaling pathway in rice-*Magnaporthe grisea* interaction. *Mol. Plant-Microbe Interact.* **2010**, *23*, 791−798.
(47) Ko, J. H.; Yang, S. H.; Han, K. H. Upregulation of an Arabidopsis RING-H2 gene, XERICO, confers drought tolerance through increased abscisic acid biosynthesis. *Plant J.* **2006**, *47*, 343−355.
(48) Koga, H.; Dohi, K.; Mori, M. Abscisic acid and low temperatures suppress the whole plant-specific resistance reaction of rice plants to the infection of *Magnaporthe grisea*. *Physiol. Physiol. Mol. Plant Pathol.* **2004**, *65*, 3−9.

DOI: 10.1021/acs.jafc.5b03018
J. Agric. Food Chem. 2015, 63, 8134−8142

of oligopeptides.[15] For example, the antihypertensive oligopeptides VLPVP and HLPLP have been shown to be transported through Caco-2 cell monolayers mainly via the paracellular pathway.[17,18] Additionally, it has been reported that the antihypertensive tripeptide VPP, derived from milk β-casein, is also transported across Caco-2 cell monolayers via the paracellular pathway rather than the PepT1-mediated pathway.[18] However, the molecular mechanism behind the regulation of paracellular transport has not been clearly identified. As such, further studies are needed to assess the transepithelial transport of bioactive peptides, especially oligopeptides, through the human intestine.

As a good protein source for bioactive peptides, chicken egg white, which is composed predominantly of ovalbumin, ovotransferrin, ovomucoid, globulins, and lysozyme, is widely used to prepare antihypertensive peptides.[19] In our previous study, egg-white-derived peptide RVPSL (ovotransferrin 328−332) was identified with in vitro ACE-inhibitory and in vivo antihypertensive activities, making it a prospective functional food candidate and providing an approach for the therapy of hypertension.[20−22] Before studying the bioavailability and pharmacokinetics of the antihypertensive peptide RVPSL in vivo, it is necessary to evaluate its permeability through the intestinal epithelium. Therefore, the objective of this paper was to investigate the resistance to brush border membrane peptidases and the transepithelial transport of RVPSL in the human intestinal Caco-2 cell monolayers. In addition, the structure−transport relationship of RVPSL across Caco-2 cell monolayers was also studied.

MATERIALS AND METHODS

Chemicals. Caco-2 cell lines were purchased from American Type Culture Collection. The antihypertensive peptide RVPSL and other peptides with purity over 95% were synthesized by solid-phase procedures using Fmoc-protected amino acid synthetic methods by ChinaPeptide Co., Ltd. (Shanghai, China). Diprotin A and glycyl-sarcosine (Gly-Sar) were purchased from ChinaPeptide Co., Ltd. (Shanghai, China). Dulbecco's modified Eagle's medium (DMEM), fetal bovine serum, penicillin−streptomycin, and Hanks' balanced salt solution (HBSS) were purchased from Gibco BRL Life Technology (Carlsbad, CA). Nonessential amino acid solution, trypsin, L-glutamine, dimethyl sulfoxide (DMSO), ethylenediaminetetraacetic acid (EDTA), collagen type I, cytochalasin D, wortmannin, and sodium azide were all purchased from Sigma−Aldrich (St. Louis, MO). Acetonitrile (ACN), trifluoroacetic acid (TFA), and methanol were purchased from Fisher Scientific (Waltham, MA). All other reagents were analytical-grade.

Cell Culture. The Caco-2 cells were grown in DMEM containing 10% fetal bovine serum, 1% nonessential amino acid solution, 100 units/mL penicillin, 100 μg/mL streptomycin, and 4 mM L-glutamine at 37 °C in an atmosphere of 5% CO_2 and 90% relative humidity. Stock cultures were grown in 75 cm^2 tissue culture flasks and were split at 80−90% confluency with 0.25% trypsin and 0.02% EDTA solution. The cells from passage numbers 30−40 were used and seeded on collagen type I-coated permeable polycarbonate inserts (12 mm diameter, 0.4 μm pore size, 1.12 cm^2 grown surface area; Costar, Corning, NY) in 12 transwell plates at a density of 1×10^5 cells/insert. The culture medium (0.5 mL in the apical side and 1.5 mL in the basolateral side) was replaced every 2 days for the first week and then daily until they were used for experiments 21 days after seeding. The integrity of the cell monolayers was evaluated by measuring transepithelial electrical resistance (TEER) values with an EVOM epithelial volt/ohmmeter (Millicell-ERS, Millipore, Billerica, MA). Only cell monolayers with TEER values higher than 300 $\Omega \cdot cm^2$ were used for transport studies.

Transport Experiments. The bidirectional transepithelial transport of antihypertensive peptide RVPSL in human intestinal Caco-2 cell monolayers was conducted as previously described.[23] Caco-2 cell monolayers were rinsed with HBSS twice and then incubated with HBSS for 30 min at 37 °C in 5% CO_2 prior to transport experiments. Then the HBSS was removed and replaced with 0.5 mL of 5 mM RVPSL (dissolved in HBSS, pH 6.0) on the apical side and 1.5 mL of fresh HBSS on the basolateral side (pH 7.4). Alternatively, to research the efflux of RVPSL, 0.5 mL of fresh HBSS on the apical side (pH 6.0) and 1.5 mL of 5 mM RVPSL (dissolved in HBSS, pH 7.4) on the basolateral side were used. All of the plates were incubated at 37 °C in 5% CO_2 for 2 h. Then the RVPSL concentrations on both the apical and basolateral sides were determined by HPLC analysis.

The resistance of RVPSL to brush border membrane peptidases was studied as described previously by use of diprotin A, an inhibitor of membrane peptidase dipeptidyl peptidase IV (DPPIV, EC 3.4.14.5), which is a major brush border membrane peptidase.[24] Briefly, Caco-2 cell monolayers were preincubated with 1 mM diprotin A at 37 °C in 5% CO_2 for 30 min before transport experiments. Then 0.5 mL of 5 mM RVPSL was added on the apical side. After 2 h of incubation, samples were collected both from apical and basolateral sides and detected by HPLC analysis.

The transepithelial transport mechanism of RVPSL across Caco-2 cell monolayers was investigated by use of transport inhibitors as described previously.[25] Namely, the Caco-2 cell monolayer was preincubated with cytochalasin D (a TJ disruptor, 0.5 μg/mL), wortmannin (a transcytosis inhibitor, 500 nM), sodium azide (an ATP synthesis inhibitor, 10 mM), or Gly-Sar (a peptide transport PepT 1 substrate, 25 mM) for 30 min, followed by addition of 0.5 mL of 5 mM RVPSL to the apical side. Cytochalasin D, wortmannin, and sodium azide were dissolved in DMSO (the final concentration of DMSO in HBSS was 0.044%), and Gly-Sar was dissolved in HBSS. As a control, DMSO was used. After 2 h of incubation, the RVPSL on the basolateral side was detected by HPLC analysis.

The relationship between the structure of RVPSL and transport across Caco-2 cell monolayers was investigated by analyzing the intact transport of a number of peptides, which were re-formed and synthesized based on the structure of RVPSL. These peptides contained two parts: 10 pentapeptides derived from RVPSL by amino acid replacement with Pro residue, and six terminal fragment smaller peptides of RVPSL, including two tetrapeptides, two tripeptides, and two dipeptides. In the transport experiments, peptides (5 mM, pH 6.0) were added on the apical side. After 2 h of incubation, peptide concentrations on the basolateral side were detected by HPLC analysis.

The apparent permeability coefficient (P_{app}, centimeters per second) was calculated as follows:

$$P_{app} = \frac{dC}{dt}\frac{1}{A}\frac{1}{C_0}V$$

where dC/dt is the change of RVPSL concentration in the receiving chamber (micromoles per liter per minute); A is the area of membrane (square centimeters), C_0 iss the initial peptide concentration in donor chamber (millimoles per liter), and V is the volume of the receiving chamber.

Reverse-Phase High-Performance Liquid Chromatography. The peptide was quantified on a Shimadzu HPLC system equipped with LC solution software, a LC-20AD binary gradient pump, a SIL-20AC autosampler, a CTO-20AC column oven, and SPD-20AV UV detector (Shimadzu, Kyoto, Japan). The analytical column was a C18 reverse-phase column (Symmetry C18 column, 250 × 4.6 mm, particle size 5 μm; Waters, Milford, MA). The mobile phases were solvent A (0.1% TFA in water) and solvent B (0.1% TFA in ACN). Samples were eluted with a gradient of solvent B from 10% to 55% in 15 min and held at 55% for 5 min at a flow rate of 0.5 mL/min. The injection volume was 20 μL, and the absorbance detector wavelength was set at 220 nm. The peptide concentration was calculated by a linear regression analysis of the peak area by the method of Lei et al.[16] A calibration curve was constructed over a RVPSL concentration range

DOI: 10.1021/acs.jafc.5b01824
J. Agric. Food Chem. 2015, 63, 8143−8150

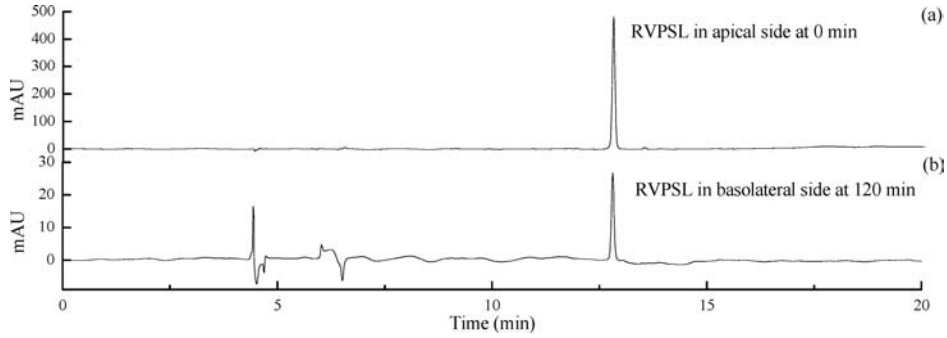

Figure 1. Representative chromatograph of RVPSL with retention time of 12.78 min and total RP-HPLC run time of 20.00 min. (a) RVPSL on the apical side at 0 min (approximately 5 mM); (b) RVPSL on the basolateral side at 120 min (approximately 187 μM) in apical to basolateral transport experiment.

of 10 μM to 5 mM. The HPLC analysis condition was the same as for samples. The peak area of RVPSL was measured, and the calibration curves of peak area versus concentration and the coefficient were then analyzed.

Assay of ACE-Inhibitory Activity. The ACE-inhibitory activity of peptides was determined as described previously.[26] Namely, an aliquot of 30 μL of 4 mM HHL was mixed with 10 μL of sample solutions and then incubated at 37 °C for 5 min. Then, 20 μL of 0.25 unit of ACE was added and the reaction mixture was incubated at 37 °C for an additional 30 min, followed by the addition of 60 μL of 1 M HCl to stop the reaction. The whole assay was conducted in borate buffer (100 mM, pH 8.3) containing 300 mM NaCl. The same buffer was used for solution preparation of the HHL, hippuric acid, peptides, and enzyme dilutions. HPLC analysis was used to quantify the hippuric acid produced by the enzymatic hydrolysis of the substrate hippuryl-L-histidyl-L-leucine (HHL). The analytical column was a C18 reverse-phase column (Symmetry C18 column, 250 × 4.6 mm, particle size 5 μm; Waters, Milford, MA). The isocratic mobile phase consisted of 25% acetonitrile in deionized water (v/v) with 0.5% TFA. The injection volume was 10 μL, and HHL and hippuric acid were detected at 228 nm when the mobile phase was controlled at 0.5 mL/min.

ACE inhibitory activity, as a percentage, was calculated as follows:

$$\text{ACE inhibitory activity} = \frac{(A - B)}{B} \times 100$$

where A is the peak area of the reaction blank, containing the same volume of buffer solution instead of the sample; B is the peak area of the reaction in the presence of both ACE and enzymatic peptide sample; and the IC_{50} value is defined as the concentration of inhibitor inhibiting 50% of the ACE activity under the assayed conditions.

Statistical Analysis. All data were expressed as the mean ± SD (n = 3). The difference between groups was carried out by one-way analysis of variance (ANOVA) followed by least significant difference (LSD) test with the significance level at $P < 0.05$ by use of SPSS 19.0 software.

RESULTS

Validation of RVPSL by RP-HPLC Analysis. As shown in Figure 1, the retention time for RVPSL was 12.78 min out of a total running time of 20.00 min. On both the apical side (Figure 1 a) and basolateral side (Figure 1 b), no matrix-specific interfering peaks were observed. To quantify the RVPSL in the sample, a calibration curve was established over a concentration range of 10 μM to 5 mM. Linear regression analysis of the peak area and concentration of RVPSL revealed a typical equation $y = 446.75x + 31821$ with a mean correlation coefficient $r^2 = 0.9994$, indicating good linearity in this calibration curve and that the equation could be used to determine the concentration of RVPSL in this work. The other peptides used in this study were all previously validated by HPLC analysis.

Transepithelial Flux of RVPSL across Caco-2 Cell Monolayers. In the transepithelial flux experiment, the synthetic peptide RVPSL at a concentration of 5 mM was added to the apical side of Caco-2 cell monolayers and incubated at 37 °C in 5% CO_2 for 2 h. The levels of RVPSL on both the apical and basolateral sides were then determined. As shown in Figure 2, after 2 h of incubation, the accumulated

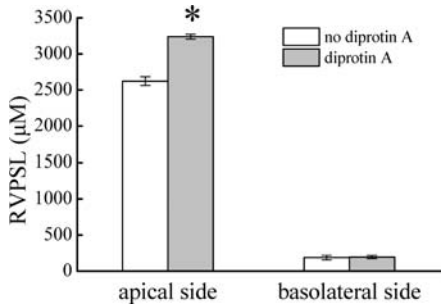

Figure 2. Effect of diprotin A on accumulated amount of RVPSL on the apical and basolateral sides of Caco-2 cell monolayers. In the presence of diprotin A, the RVPSL remaining on the apical side was significantly higher than that without diprotin A ($P < 0.001$). However, no significant increase in the transport of RVPSL to the basolateral side was observed ($P > 0.05$). All values are means ± SD (n = 3). (*) $P < 0.001$ as compared to RVPSL level on the apical side without diprotin A.

concentration of RVPSL on the basolateral side reached 187.46 ± 29.84 μM, and the P_{app} value was found to be (6.97 ± 1.11) × 10^{-6} cm/s, suggesting that the antihypertensive peptide RVPSL could be absorbed intact through the Caco-2 cell monolayers. However, only 2622.20 ± 61.22 μM RVPSL remained on the apical side, indicating that 47.56% ± 1.22% of the initial RVPSL added to the apical side had disappeared. Except for the portion that had been transported, there was 36.31% ± 1.22% of the initial RVPSL that may have been hydrolyzed to shorter fragments or free amino acids by brush border membrane peptidases. However, no other fragments in addition to RVPSL were detected on the basolateral side and in Caco-2 cells under the HPLC conditions used in the present study.

To verify the low resistance of RVPSL to brush border membrane peptidases, the Caco-2 cell monolayer was preincubated with diprotin A, a protease inhibitor, prior to the transport experiment. As a result, the activity of DPPIV, the

DOI: 10.1021/acs.jafc.5b01824
J. Agric. Food Chem. 2015, 63, 8143−8150

main group of brush border membrane peptidases, was restricted. As shown in Figure 2, the amount of intact RVPSL on the basolateral side in the presence and absence of diprotin A was not significantly increased ($P > 0.05$). However, the accumulated RVPSL on the apical side increased to 3238.04 ± 34.11 μM, which was 1.23-fold higher than in the absence of diprotin A ($P < 0.001$), and only 35.24% ± 0.68% of the initial RVPSL had disappeared. Consequently, except for the portion that was transported, degradation of the initial RVPSL by brush border membrane peptidases decreased to 23.49% ± 0.68% ($P < 0.001$).

A bidirectional transport experiment was also designed to determine whether the transepithelial transport of RVPSL was passive or polarized. The permeability coefficient P_{app} for both directions, transport from apical side to basolateral side (AP-BL) and transport from basolateral side to apical side (BL-AP), was tested. As shown in Figure 3, in the absence of diprotin A,

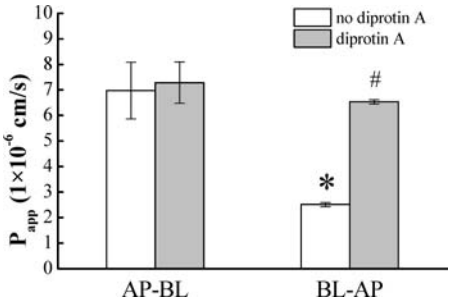

Figure 3. Effects of diprotin A on bidirectional transport of RVPSL across Caco-2 cell monolayers. In the presence of diprotin A, P_{app} for BL-AP increased significantly ($P < 0.001$). However, this was still slightly lower than P_{app} for AP-BL, although the difference was not significant ($P > 0.05$). All values are means ± SD ($n = 3$). (*) $P < 0.001$ as compared to P_{app} for AP-BL in the absence of diprotin A; (#) $P < 0.001$ as compared to P_{app} for BL-AP in the absence of diprotin A.

P_{app} for AP-BL, $(6.97 \pm 1.11) \times 10^{-6}$ cm/s, was approximately 3-fold higher than P_{app} for BL-AP, $(2.52 \pm 0.08) \times 10^{-6}$ cm/s ($P < 0.001$). However, P_{app} for BL-AP increased significantly to $(6.53 \pm 0.08) \times 10^{-6}$ cm/s in the presence of 1 mM diprotin A ($P < 0.001$). It was still slightly lower than P_{app} for AP-BL of $(7.29 \pm 0.81) \times 10^{-6}$ cm/s in the presence of diprotin A; however, no significant difference was observed ($P > 0.05$). These results suggested that the transepithelial transport of RVPSL across Caco-2 cell monolayers was passive and nonpolarized. In addition, the susceptibility of peptides to brush border membrane peptidases might lead to an underestimate of P_{app} for BL-AP.

Effects of Various Compounds on RVPSL Transport. To determine which transport pathways were involved in the transepithelial transport of RVPSL through the intestinal epithelium, Caco-2 cell monolayers were preincubated for 30 min before transport experiment with a range of inhibitors. As shown in Figure 4, in the presence of Gly-Sar, a good substrate for PepT1, the permeability coefficient P_{app} of RVPSL decreased slightly but not significantly ($P > 0.05$), suggesting that the transport of RVPSL across the Caco-2 cell monolayers was not mediated by PepT1. Sodium azide, an ATP synthesis inhibitor, also had little effect on the P_{app} of RVPSL ($P > 0.05$), indicating that transepithelial transport of RVPSL was energy-independent. In addition, the effect of transcytosis, initiated by endocytosis at the apical cell membrane, on RVPSL transport was examined by wortmannin, a transcytosis inhibitor.

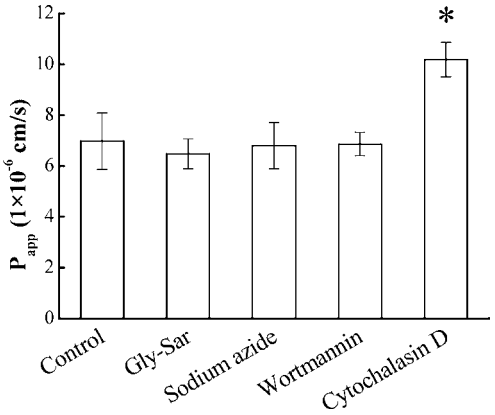

Figure 4. Effects of various compounds on transport of RVPSL across Caco-2 cell monolayers. Gly-Sar, sodium azide, and wortmannin all had little effect on P_{app} of RVPSL ($P > 0.05$). In contrast, cytochalasin D increased the transport of RVPSL significantly ($P < 0.001$), suggesting that RVPSL mainly transported across Caco-2 cell monolayers via the paracellular pathway mediated by TJs. All values are means ± SD ($n = 3$). (*) $P < 0.001$ as compared to the control group.

However, RVPSL transport did not decrease significantly in the presence of wortmannin ($P > 0.05$), indicating that the transcytosis was not involved in RVPSL transport. In contrast, in the presence of cytochalasin D, a TJ disruptor, the permeability coefficient P_{app} of RVPSL across the Caco-2 cell monolayers increased by 46.03%. It was significantly higher than that of the control group ($P < 0.001$), suggesting that RVPSL was transported across the Caco-2 cell monolayers via the paracellular pathway mediated by TJs.

Structure–Transport Relationship of RVPSL Caco-2 Cell Monolayers. To investigate the relationship between RVPSL structure and transport across Caco-2 cell monolayers, Pro was used to replace one or two of the amino acid residues of RVPSL. The P_{app} values of 11 pentapeptides (RVPSL, PVPSL, RPPSL, RVPPL, RVPSP, PVPPL, PVPSP, RPPPL, RPPSP, PPPSL, and RVPPP) varied from $(4.13 \pm 0.62) \times 10^{-6}$ to $(2.08 \pm 2.76) \times 10^{-5}$ cm/s, as shown in Figure 5. The modified pentapeptide RVPSP had the highest P_{app} value at $(2.08 \pm 2.76) \times 10^{-5}$ cm/s. Interestingly, P_{app} values of the other 10 pentapeptides were in the order PPP-X-X > RPP-X-X > PVP-X-X > RVP-X-X (where X represents Pro/P, Leu/L, or Ser/S), suggesting that the N-terminal Pro residue was more beneficial for intact transport of the pentapeptide than Val and Arg residues. Moreover, replacement of N-terminal amino acids was most informative and a high P_{app} arose when the N-terminal Arg residue and Val residue were both replaced by Pro, followed by replacement of Val alone, and then replacement of Arg alone. However, no similar results or other structure–transport relationships were observed at the C-terminus. Furthermore, there was no significant statistical relationship between P_{app} and molecular properties such as molecular weight, log D, molecular volume, molecular surface area, or polar surface area of the 11 pentapeptides. On the other hand, transport of terminal fragments resulting from cleavage of RVPSL was detected as shown in Figure 6. Except for the tetrapeptide VPSL, whose low transport rate might due to a Val residue at the N-terminal first position, all other fragment peptides had higher P_{app} values than the pentapeptide RVPSL, suggesting that the antihypertensive peptide RVPSL could be absorbed more easily through the Caco-2 cell monolayers in

DOI: 10.1021/acs.jafc.5b01824
J. Agric. Food Chem. 2015, 63, 8143–8150

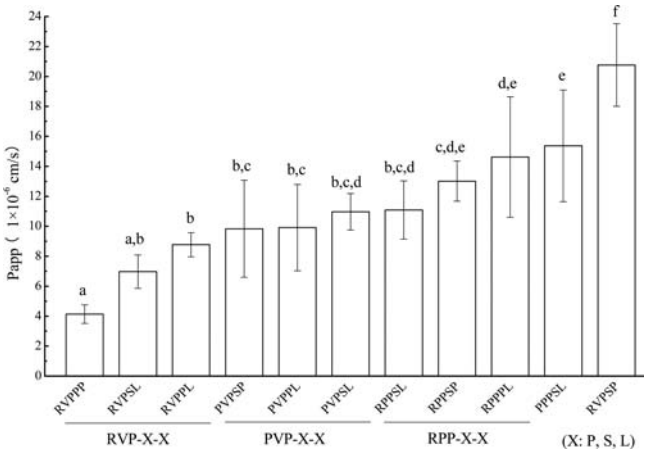

Figure 5. Effects of Pro residue replacement on transport of RVPSL across Caco-2 cell monolayers. Except for RVPSP, with the highest P_{app} value, P_{app} values of the other peptides were in the order PPP-X-X > RPP-X-X > PVP-X-X > RVP-X-X, suggesting that N-terminal Pro residues were more beneficial for intact transport of pentapeptides than Val or Arg residues. However, similar results were not observed at the C-terminus. All values are means ± SD (n = 3). For each measurement, the data marked by different letters are significantly different (P < 0.05).

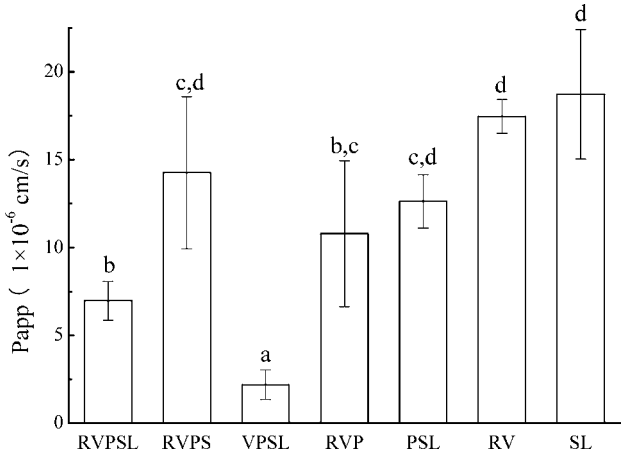

Figure 6. Transport of terminal fragment peptides derived from RVPSL across Caco-2 cell monolayers. Most of the peptide fragments had higher P_{app} values than the pentapeptide RVPSL, suggesting that antihypertensive peptide RVPSL could be more easily absorbed across Caco-2 cell monolayers in smaller fragments, especially in the form of dipeptides and tripeptides. All values are means ± SD (n = 3). For each measurement, the data marked by different letters are significantly different (P < 0.05).

smaller fragments, especially in the form of dipeptides and tripeptides.

Additionally, the ACE-inhibitory activities of the synthetic peptides are shown in Table 1. Besides the precursor peptide sequence RVPSL, which had an ACE-inhibitory IC_{50} value of 20.00 μM, peptides with the sequences PVPSL, RVPPL, RVPSP, PVPSP, RPPPL, RPPSP, and RVP all also exhibited ACE-inhibitory activity. Among these peptides, PVPSL showed the highest ACE-inhibitory activity with an IC_{50} value of 5.51 μM. RVPSP and RPPPL showed ACE-inhibitory activity with IC_{50} values of 51.43 and 47.25 μM, respectively. The remaining peptides all had very low ACE-inhibitory activities with IC_{50} values over 500 μM. However, the peptides PVPSL, RPPPL, and RVPSP all exhibited high permeability through the Caco-2 cell monolayers and genuine ACE-inhibitory activity, suggesting their potential in functional food.

Table 1. ACE-Inhibitory Activities of Synthetic Peptides

no.	peptide sequence	IC_{50} (μM)
1	RVPSL	20.00
2	PVPSL	5.51
3	RPPSL	>500
4	RVPPL	117.43
5	RVPSP	51.43
6	PVPPL	>500
7	PVPSP	152.97
8	RPPPL	47.25
9	RPPSP	357.18
10	PPPSL	>500
11	RVPPP	>500
12	RVPS	>500
13	VPSL	>500
14	RVP	152.39
15	PSL	>500
16	RV	>500
17	SL	>500

DISCUSSION

Food-derived antihypertensive peptides meet the desired properties of modulating physiological health and reducing hypertension through food. However, many of these peptides have limited practical applications due to their instability and low bioavailability in vivo.[27] Thus, it is critical for bioactive peptides to overcome two physiological barriers: extensive enzymatic degradation in the gastrointestinal tract and poor permeability through the intestinal epithelium. In our previous work, the peptide RVPSL, identified from egg white ovotransferrin, had been shown to have ACE-inhibitory activity in vitro and antihypertensive activity in vivo in SHR. In addition, in a simulated gastrointestinal digestion experiment with pepsin and trypsin, 94.42% ± 0.41% of the initial RVPSL remained. From these positive results, in the present study, we investigated the transepithelial transport of RVPSL and its resistance to brush border membrane peptidases using Caco-2 cell monolayers.

It has been demonstrated that Caco-2 cells express at least eight membrane peptidases in their apical surface, and these peptidases exhibit different activities at different growth stages. Among these peptidases, DPPIV has the highest activity, especially when Caco-2 cells are completely differentiated.[28] DPPIV is a member of the prolyl oligopeptidase family of serine proteases and is highly expressed on endothelial cells, differentiated epithelial cells, and lymphocytes. It predominantly cleaves N-terminal dipeptides from proteins containing proline or alanine in the penultimate position.[29] The activity of DPPIV can be specifically inhibited by diprotin A, which transitorily binds to the catalytic site of the enzyme and blocks the degradation of substrates.[30] In the present study, we found that the antihypertensive peptide RVPSL was susceptible to brush border membrane peptidases. Approximately 36.31% ± 1.22% of the initial RVPSL (5 mM) added to the apical chamber was degraded, and this degradation significantly decreased to 23.49% ± 0.68% in the presence of diprotin A. On one hand, although diprotin A is a well-known inhibitor of DPPIV with an IC_{50} value of 1.1 μg/mL (3.22 μM)[31,32] and is

DOI: 10.1021/acs.jafc.5b01824
J. Agric. Food Chem. 2015, 63, 8143−8150

widely used to verify the action of DPPIV, 1 mM diprotin A may be insufficient to fully inhibit the protease. On the other hand, degradation of RVPSL may also be due to the action of other brush border membrane peptidases on the apical surface. The susceptibility of peptides to the membrane peptidases depends on their structural and chemical properties.[33] Some human or bovine milk β-casomorphin-derived peptides have been reported to be very susceptible to DPPIV.[34,35] In general, the N-terminal dipeptide (Xaa-Pro or Xaa-Ala) was regarded as easily cleaved by DPPIV specifically.[29] In addition, N-terminal bulky hydrophobic or basic amino acid residues with an obligate free amino group are good substrates for cleavage by DPPIV.[36] In terms of RVPSL, as the N-terminal Arg is a basic amino acid and contains a free amino group and Val is also a small molecular weight hydrophobic amino acid, these factors may contribute to its degradation by DPPIV. Although Pro residues in the third position are resistant to DPPIV hydrolysis,[36] many natural peptides containing Xaa-Xaa-Pro at the N-terminus have been shown to have high binding affinity for DPPIV without being cleaved.[37] This may also have an influence on the decrease of RVPSL on the apical side, as determined by HPLC.

Caco-2 serves as an in vitro model of the human intestinal epithelium, so the expression of various brush border membrane peptidases in Caco-2 cells is essential. However, it is difficult to evaluate the real transport rate when the tested peptides are susceptible to these membrane peptidases.[24] It has been found that the transport rate of some bioactive peptides increased significantly when membrane peptidases were inhibited by diprotin A.[34,35] In the present study, we also determined the bidirectional transepithelial flux of RVPSL in the presence and absence of diprotin A. The results showed that the P_{app} value for AP-BL was 2.8-fold higher than that for BL-AP in the absence of diprotin A. However, when membrane peptidases were inhibited by diprotin A, there was a significant increase in the amount of RVPSL in the apical chamber in BL-AP transport, leading to a significant increase in P_{app} for BL-AP transport but not AP-BL. As a consequence, no significant difference in the transport rate between AP-BL and BL-AP flux was observed in the presence of diprotin A, suggesting that the permeability of RVPSL across Caco-2 cell monolayers might be nonpolarized and passive. This result was consistent with transport of RVPSL by the paracellular pathway.

Bioactive peptides, especially oligopeptides, are generally thought not to be absorbed intact through the human intestinal epithelium. Previous publications that have focused on the transport of bioactive peptides through in vivo intestine models and in vitro Caco-2 cell monolayers have shown low permeability for these peptides, with permeability coefficients P_{app} ranging from 1×10^{-8} to 1×10^{-6} cm/s. In this work, the antihypertensive pentapeptide RVPSL had good permeability across Caco-2 cell monolayers with a P_{app} value of $(6.97 \pm 1.11) \times 10^{-6}$ cm/s, which is similar to that of human β-casomorphin-7, slightly higher than those of lactoferroxin A,[34] VLPVP[16] and QIGLF,[25] and higher than the values of many other bioactive peptides reported elsewhere, such as KVLPVP,[38] HLPLP,[17] Gly-Ala-Hyp-Gly-Leu-Hyp-Gly-Pro,[39] bovine β-casomorphin-5 and -7, casoxin-6,[35] VYIHPF,[40] and α_{s1}-casein-(f91−97).[41] Moreover, RVPSL even had a higher transport rate than the well-studied tripeptides VPP[18] and YPI.[10] The high permeability of RVPSL across Caco-2 cell monolayers may be due to its structural characteristics and molecular properties. On the other hand, differences in the integrity and tightness of TJs of Caco-2 cell monolayers used in different laboratories may also have important influences on peptide transport. In addition, since Caco-2 cell monolayers have tighter TJs than human intestinal epithelial cells, the paracellular permeability of RVPSL in vivo in human intestinal epithelium is likely to be higher.[42]

There are three possible mechanisms for transport of oligopeptides: transcytosis, paracellular transport and PepT1-mediated transport. There are two types of transcytosis, specific receptor-mediated transport and nonspecific pinocytotic transport, which are mainly responsible for the transport of some proteins and large molecular peptides,[43] such as β-casein (193−209), a 17-residue peptide, which may be absorbed intact through transcytosis via internalized vesicles.[44] In contrast, PepT1 can transport small peptides, including a range of dipeptides and tripeptides, though not all.[13] It is known that PepT1 is a low-affinity, high-capacity transporter and can be inhibited by its substrate glycyl dipeptide.[45] The affinity of peptides for PepT1 depends on the structural characteristics and molecular properties of the peptides, such as charge, hydrophobicity, and side-chain flexibility.[46] However, in the present study, the above two transport pathways were not involved in intact transport of antihypertensive peptide RVPSL across Caco-2 cell monolayers. Another transport mechanism is the paracellular pathway, which is mediated by TJs. The paracellular pathway involves the passive diffusion of water-soluble low molecular mass substances, including oligopeptides.[47] Although TJs, which consist of several proteins such as zonula occludens 1 (ZO-1), occludins, and claudins, form a tight biological barrier against the permeation of exogenous macromolecules or cytotoxic substances, a great number of pores still exist in TJs.[48] The pores usually have a radius no more than 15 Å and selectively allow some minerals and molecules to pass through.[49] Studies have shown that the paracellular pathway is also involved in the transepithelial transport of many bioactive peptides. Again, the properties of peptides such as their molecular size, hydrophilicity, and some molecular surface properties all have important influences on their paracellular flux.[15] In the present study, cytochalasin D, a disruptor of TJs, caused an approximately 1.5-fold increase of the permeability coefficient P_{app} of RVPSL compared to controls, suggesting that the paracellular pathway mediated by TJs might be the major transport route of RVPSL through the intestinal epithelium. This result is similar to that of other previously reported peptides, such as VLPVP,[16] HLPLP,[17] QIGLF,[25] Gly-Ala-Hyp-Gly-Leu-Hyp-Gly-Pro,[39] GGYR,[24] and VPP.[18]

Proline is a key amino acid residue in ACE-inhibitory peptides and is usually found at the C-terminus of a large number of these peptides.[1] In the present study on the relationship between RVPSL structure and transport, Pro was used to replace individual amino acids in RVPSL due to its structure, hydrophobicity, and relatively low molecular weight, which may play important roles in the transport of peptides.[11,12,15] For instance, it had been previously demonstrated that dipeptides with C-terminal Pro residues but not N-terminal Pro residues exhibit high affinity for PepT1.[50,51] However, it was also found that N-terminal, but not C-terminal, Pro residues had important roles on the transport of peptides across Caco-2 cell monolayers in this study. This finding has not been reported elsewhere and will need to be investigated further.

DOI: 10.1021/acs.jafc.5b01824
J. Agric. Food Chem. 2015, 63, 8143−8150

AUTHOR INFORMATION

Corresponding Author

*Telephone +86 431 87836351; fax +86 431 87836391; e-mail ljb168@sohu.com.

Notes

The authors declare no competing financial interest.

ACKNOWLEDGMENTS

This work was funded by the National Natural Science Foundation of China (31271907, 31471597), Specialized Research Fund for the Doctoral Program of Higher Education (20130061110088), and Project of National Key Technology Research and Development Program (2012BAD33B03).

ABBREVIATIONS

RVPSL, Arg-Val-Pro-Ser-Leu; ACE, angiotensin-converting enzyme; SHR, spontaneously hypertensive rat; CVD, cardiovascular disease; PepT1, peptide transporter 1; TJs, tight junctions; Gly-Sar, glycyl-sarcosine; RP-HPLC, reverse-phase high-performance liquid chromatography; DMEM, Dulbecco's modified Eagle's medium; HBSS, Hanks' balanced salt solution; DMSO, dimethyl sulfoxide; EDTA, ethylenediaminetetraacetic acid; ACN, acetonitrile; TFA, trifluoroacetic acid; TEER, transepithelial electrical resistance; DPPIV, dipeptidyl peptidase IV; P_{app}, apparent permeability coefficient

REFERENCES

(1) Iwaniak, A.; Minkiewicz, P.; Darewicz, M. Food-Originating ACE Inhibitors, Including Antihypertensive Peptides, as Preventive Food Components in Blood Pressure Reduction. *Compr. Rev. Food Sci. Food Saf.* **2014**, *13*, 114−134.

(2) Erdmann, K.; Cheung, B. W. Y.; Schroeder, H. The possible roles of food-derived bioactive peptides in reducing the risk of cardiovascular disease. *J. Nutr. Biochem.* **2008**, *19*, 643−654.

(3) Martinez-Maqueda, D.; Miralles, B.; Recio, I.; Hernandez-Ledesma, B. Antihypertensive peptides from food proteins: a review. *Food Funct.* **2012**, *3*, 350−361.

(4) Nakamura, Y.; Yamamoto, N.; Sakai, K.; Takano, T. Antihypertensive effect of sour milk and peptides isolated from it that are inhibitors to angiotensin I-converting enzyme. *J. Dairy Sci.* **1995**, *78*, 1253−7.

(5) Miguel, M.; Gomez-Ruiz, J. A.; Recio, I.; Aleixandre, A. Changes in arterial blood pressure after single oral administration of milk-casein-derived peptides in spontaneously hypertensive rats. *Mol. Nutr. Food Res.* **2010**, *54*, 1422−1427.

(6) Fujita, H.; Usui, H.; Kurahashi, K.; Yoshikawa, M. Isolation and characterization of ovokinin, a bradykinin B1 agonist peptide derived from ovalbumin. *Peptides* **1995**, *16*, 785−90.

(7) Hidalgo, I. J.; Raub, T. J.; Borchardt, R. T. Characterization of the human colon carcinoma cell line (Caco-2) as a model system for intestinal epithelial permeability. *Gastroenterology* **1989**, *96*, 736−749.

(8) Artursson, P.; Karlsson, J. Correlation between oral drug absorption in humans and apparent drug permeability coefficients in human intestinal epithelial (Caco-2) cells. *Biochem. Biophys. Res. Commun.* **1991**, *175*, 880−885.

(9) Shimizu, M.; Son, D. O. Food-derived peptides and intestinal functions. *Curr. Pharm. Des.* **2007**, *13*, 885−895.

(10) Miguel, M.; Davalos, A.; Manso, M. A.; de la Pena, G.; Lasuncion, M. A.; Lopez-Fandino, R. Transepithelial transport across Caco-2 cell monolayers of antihypertensive egg-derived peptides. PepT1-mediated flux of Tyr-Pro-Ile. *Mol. Nutr. Food Res.* **2008**, *52*, 1507−1513.

(11) Artursson, P.; Palm, K.; Luthman, K. Caco-2 monolayers in experimental and theoretical predictions of drug transport. *Adv. Drug Delivery Rev.* **2001**, *46*, 27−43.

(12) Shimizu, K.; Sato, M.; Zhang, Y.; Kouguchi, T.; Takahata, Y.; Morimatsu, F.; Shimizu, M. Molecular Size of Collagen Peptide Reverses the Permeability of Caco-2 Cells. *Biosci., Biotechnol., Biochem.* **2010**, *74*, 1123−1125.

(13) Vig, B. S.; Stouch, T. R.; Timoszyk, J. K.; Quan, Y.; Wall, D. A.; Smith, R. L.; Faria, T. N. Human PEPT1 pharmacophore distinguishes between dipeptide transport and binding. *J. Med. Chem.* **2006**, *49*, 3636−3644.

(14) Fei, Y. J.; Kanai, Y.; Nussberger, S.; Ganapathy, V.; Leibach, F. H.; Romero, M. F.; Singh, S. K.; Boron, W. F.; Hediger, M. A. Expression cloning of a mammalian proton-coupled oligopeptide transporter. *Nature* **1994**, *368*, 563−566.

(15) Pauletti, G. M.; Okumu, F. W.; Borchardt, R. T. Effect of size and charge on the passive diffusion of peptides across Caco-2 cell monolayers via the paracellular pathway. *Pharm. Res.* **1997**, *14*, 164−168.

(16) Lei, L.; Sun, H.; Liu, D.; Liu, L.; Li, S. Transport of Val-Leu-Pro-Val-Pro in human intestinal epithelial (Caco-2) cell monolayers. *J. Agric. Food Chem.* **2008**, *56*, 3582−3586.

(17) Quiros, A.; Davalos, A.; Lasuncion, M. A.; Ramos, M.; Recio, I. Bioavailability of the antihypertensive peptide LHLPLP: Trans-epithelial flux of HLPLP. *Int. Dairy J.* **2008**, *18*, 279−286.

(18) Satake, M.; Enjoh, M.; Nakamura, Y.; Takano, T.; Kawamura, Y.; Arai, S.; Shimizu, M. Transepithelial transport of the bioactive tripeptide, Val-Pro-Pro, in human intestinal Caco-2 cell monolayers. *Biosci., Biotechnol., Biochem.* **2002**, *66*, 378−384.

(19) Kovacs-Nolan, J.; Phillips, M.; Mine, Y. Advances in the value of eggs and egg components for human health. *J. Agric. Food Chem.* **2005**, *53*, 8421−8431.

(20) Liu, J.; Yu, Z.; Zhao, W.; Lin, S.; Wang, E.; Zhang, Y.; Hao, H.; Wang, Z.; Chen, F. Isolation and identification of angiotensin-converting enzyme inhibitory peptides from egg white protein hydrolysates. *Food Chem.* **2010**, *122*, 1159−1163.

(21) Yu, Z.; Yin, Y.; Zhao, W.; Wang, F.; Yu, Y.; Liu, B.; Liu, J.; Chen, F. Characterization of ACE-Inhibitory Peptide Associated with Antioxidant and Anticoagulation Properties. *J. Food Sci.* **2011**, *76*, C1149−C1155.

(22) Yu, Z.; Yin, Y.; Zhao, W.; Chen, F.; Liu, J. Antihypertensive Effect of Angiotensin-Converting Enzyme Inhibitory Peptide RVPSL on Spontaneously Hypertensive Rats by Regulating Gene Expression of the Renin-Angiotensin System. *J. Agric. Food Chem.* **2014**, *62*, 912−917.

(23) Hubatsch, I.; Ragnarsson, E. G. E.; Artursson, P. Determination of drug permeability and prediction of drug absorption in Caco-2 monolayers. *Nat. Protoc.* **2007**, *2*, 2111−2119.

(24) Shimizu, M.; Tsunogai, M.; Arai, S. Transepithelial transport of oligopeptides in the human intestinal cell, Caco-2. *Peptides* **1997**, *18*, 681−687.

(25) Ding, L.; Zhang, Y.; Jiang, Y.; Wang, L.; Liu, B.; Liu, J. Transport of Egg White ACE-Inhibitory Peptide, Gln-Ile-Gly-Leu-Phe, in Human Intestinal Caco-2 Cell Monolayers with Cytoprotective Effect. *J. Agric. Food Chem.* **2014**, *62*, 3177−3182.

(26) Liu, J.; Yu, Z.; Zhao, W.; Lu, J.; Chen, F.; Lin, S. Liquid Chromatographic Assay of Peptides Activity with Inhibiting Angiotensin Converting Enzyme. *Chem. Res. Chin. Univ.* **2010**, *26*, 712−716.

(27) Vermeirssen, V.; Van Camp, J.; Verstraete, W. Bioavailability of angiotensin I converting enzyme inhibitory peptides. *Br. J. Nutr.* **2004**, *92*, 357−366.

(28) Howell, S.; Kenny, A. J.; Turner, A. J. A survey of membrane peptidases in two human colonic cell lines, Caco-2 and HT-29. *Biochem. J.* **1992**, *284*, 595−601.

(29) Aertgeerts, K.; Ye, S.; Tennant, M. G.; Kraus, M. L.; Rogers, J.; Sang, B.-C.; Skene, R. J.; Webb, D. R.; Prasad, G. S. Crystal structure of human dipeptidyl peptidase IV in complex with a decapeptide reveals details on substrate specificity and tetrahedral intermediate formation. *Protein Sci.* **2004**, *13*, 412−421.

DOI: 10.1021/acs.jafc.5b01824
J. Agric. Food Chem. 2015, 63, 8143−8150

(30) Wiedeman, P. E.; Trevillyan, J. M. Dipeptidyl peptidase IV inhibitors for the treatment of impaired glucose tolerance and type 2 diabetes. *Curr. Opin. Invest. Drugs* **2003**, *4*, 412−420.
(31) Umezawa, H.; Aoyagi, T.; Ogawa, K.; Naganawa, H.; Hamada, M.; Takeuchi, T. Diprotins A and B, inhibitors of dipeptidyl aminopeptidase IV, produced by bacteria. *J. Antibiot.* **1984**, *37*, 422−425.
(32) Rahfeld, J.; Schierborn, M.; Hartrodt, B.; Neubert, K.; Heins, J. Are diprotin A (Ile-Pro-Ile) and diprotin B (Val-Pro-Leu) inhibitors or substrates of dipeptidyl peptidase IV? *Biochim. Biophys. Acta, Protein Struct. Mol. Enzymol.* **1991**, *1076*, 314−316.
(33) Fernandez-Musoles, R.; Salom, J. B.; Castello-Ruiz, M.; Contreras, M. d. M.; Recio, I.; Manzanares, P. Bioavailability of antihypertensive lactoferricin B-derived peptides: Transepithelial transport and resistance to intestinal and plasma peptidases. *Int. Dairy J.* **2013**, *32*, 169−174.
(34) Iwan, M.; Jarmolowska, B.; Bielikowicz, K.; Kostyra, E.; Kostyra, H.; Kaczmarski, M. Transport of mu-opioid receptor agonists and antagonist peptides across Caco-2 monolayer. *Peptides* **2008**, *29*, 1042−1047.
(35) Sienkiewicz-Szlapka, E.; Jarmolowska, B.; Krawczuk, S.; Kostyra, E.; Kostyra, H.; Bielikowicz, K. Transport of bovine milk-derived opioid peptides across a Caco-2 monolayer. *Int. Dairy J.* **2009**, *19*, 252−257.
(36) Mentlein, R. Dipeptidyl-peptidase IV (CD26)-role in the inactivation of regulatory peptides. *Regul. Pept.* **1999**, *85*, 9−24.
(37) Hoffmann, T.; Reinhold, D.; Kahne, T.; Faust, J.; Neubert, K.; Frank, R.; Ansorge, S. Inhibition of dipeptidyl peptidase IV (DP IV) by anti-DP IV antibodies and non-substrate X-X-Pro- oligopeptides ascertained by capillary electrophoresis. *J. Chromatogr. A* **1995**, *716*, 355−362.
(38) Sun, H.; Liu, D.; Li, S.; Qin, Z. Transepithelial Transport Characteristics of the Antihypertensive Peptide, Lys-Val-Leu-Pro-Val-Pro, in Human Intestinal Caco-2 Cell Monolayers. *Biosci., Biotechnol., Biochem.* **2009**, *73*, 293−298.
(39) Shimizu, K.; Sato, M.; Zhang, Y.; Kouguchi, T.; Takahata, Y.; Morimatsu, F.; Shimizu, M. The Bioavailable Octapeptide Gly-Ala-Hyp-Gly-Leu-Hyp-Gly-Pro Stimulates Nitric Oxide Synthesis in Vascular Endothelial Cells. *J. Agric. Food Chem.* **2010**, *58*, 6960−6965.
(40) Chua, H. L.; Jois, S.; Sim, M. K.; Go, M. L. Transport of angiotensin peptides across the Caco-2 monolayer. *Peptides* **2004**, *25*, 1327−1338.
(41) Cakir-Kiefer, C.; Miclo, L.; Balandras, F.; Dary, A.; Soligot, C.; Le Roux, Y. Transport Across Caco-2 Cell Monolayer and Sensitivity to Hydrolysis of Two Anxiolytic Peptides from alpha(s1)-Casein, alpha-Casozepine, and alpha(s1)-Casein-(f91−97): Effect of Bile Salts. *J. Agric. Food Chem.* **2011**, *59*, 11956−11965.
(42) Antunes, F.; Andrade, F.; Ferreira, D.; Nielsen, H. M.; Sarmento, B. Models to Predict Intestinal Absorption of Therapeutic Peptides and Proteins. *Curr. Drug Metab.* **2013**, *14*, 4−20.
(43) Shimizu, M. Modulation of intestinal functions by food substances. *Nahrung* **1999**, *43*, 154−158.
(44) Regazzo, D.; Molle, D.; Gabai, G.; Tome, D.; Dupont, D.; Leonil, J.; Boutrou, R. The (193−209) 17-residues peptide of bovine beta-casein is transported through Caco-2 monolayer. *Mol. Nutr. Food Res.* **2010**, *54*, 1428−1435.
(45) Daniel, H. Molecular and integrative physiology of intestinal peptide transport. *Annu. Rev. Physiol.* **2004**, *66*, 361−384.
(46) Brandsch, M. Drug transport via the intestinal peptide transporter PepT1. *Curr. Opin. Pharmacol.* **2013**, *13*, 881−887.
(47) Salamat-Miller, N.; Johnston, T. P. Current strategies used to enhance the paracellular transport of therapeutic polypeptides across the intestinal epithelium. *Int. J. Pharm.* **2005**, *294*, 201−216.
(48) Marchiando, A. M.; Graham, W. V.; Turner, J. R. Epithelial Barriers in Homeostasis and Disease. *Annu. Rev. Pathol.: Mech. Dis.* **2010**, *5*, 119−144.
(49) Linnankoski, J.; Makela, J.; Palmgren, J.; Mauriala, T.; Vedin, C.; Ungell, A.-L.; Lazorova, L.; Artursson, P.; Urtti, A.; Yliperttula, M. Paracellular Porosity and Pore Size of the Human Intestinal Epithelium in Tissue and Cell Culture Models. *J. Pharm. Sci.* **2010**, *99*, 2166−2175.
(50) Brandsch, M.; Knutter, I.; Thunecke, F.; Hartrodt, B.; Born, I.; Borner, V.; Hirche, F.; Fischer, G.; Neubert, K. Decisive structural determinants for the interaction of proline derivatives with the intestinal H+/peptide symporter. *Eur. J. Biochem.* **1999**, *266*, 502−508.
(51) Brandsch, M.; Knuetter, I.; Bosse-Doenecke, E. Pharmaceutical and pharmacological importance of peptide transporters. *J. Pharm. Pharmacol.* **2008**, *60*, 543−585.

DOI: 10.1021/acs.jafc.5b01824
J. Agric. Food Chem. 2015, 63, 8143−8150

400 spectrometer (^{1}H at 300 MHz), on an Avance III HD 500 MHz Bruker spectrometer (Bruker BioSpin, Rheinstetten, Germany), and/or on a Mercury plus 300 MHz Varian spectrometer (Varian Inc., Palo Alto, CA, USA). $CDCl_3$ was used as solvent, and the chemical shifts are given in parts per million referring to the residual nondeuterated solvent signal ($CDCl_3$ 7.27 and 77.0 ppm for ^{1}H and ^{13}C, respectively). Column chromatography was performed with Si gel (70−230 mesh) from Merck (Darmstadt, Germany). TLC analysis was carried out using Si gel GF-254, 0.2 mm precoated plates (Merck): the spots were visualized either using a UV lamp at 254 nm or by spraying with 2% sulfuric acid in ethanol.

Plant Material. The unripe fruits of *E. umbelliflora* were collected in June 2008 in Itapema, Santa Catarina, Brazil, and identified by Prof. Msc. Oscar Benigno Iza (Universidade do Vale do Itajaí, Itajaí-SC). A voucher specimen (VC Filho 50) was deposited at the Barbosa Rodrigues Herbarium, Itajaí, Santa Catarina, Brazil.

Extraction and Isolation. The unripe fruits, air-dried and cut into small pieces (310.45 g), were extracted twice with methanol (MeOH) at room temperature over a period of 7 days. The combined MeOH extracts were evaporated under reduced pressure with a rotary evaporator at 40 °C to obtain a brown gummy residue, which was suspended in a solution of MeOH/H_2O (4:1) and successively partitioned with *n*-hexane (300 mL), CH_2Cl_2 (300 mL), and ethyl acetate (300 mL) to give three different nonpolar extracts. The residue that remained after partitioning was dried under reduced pressure to give the residual extract. Part of the CH_2Cl_2 extract (8.7 g) was subjected to silica gel 60 (Merck) open column chromatography (4 × 50 cm) and eluted with 400 mL each of a gradient of *n*-hexane/CH_2Cl_2 in ratios to 100:0, 90:10, 80:20, 70:30, 60:40, and 50:50, respectively. On the basis of similar R_f values on TLC developed with the eluent *n*-hexane/CH_2Cl_2 (3:7) and sprayed with 10% sulfuric acid, six fractions (C1−C6) were grouped.

Fraction C3 (0.8 g) was further purified by silica gel 60 open column chromatography (1.5 × 25 cm) and eluted with 200 mL each of mixtures of *n*-hexane/CH_2Cl_2 in ratios 100:0, 90:10, and 80:20 and finally purified by centrifugally accelerated preparative TLC on a Chromatotron (Harrison Research, Palo Alto, CA, USA) on 1 mm plates with hexane/CH_2Cl_2 (9:1), yielding 42 mg of compound **1** and 82 mg of compound **2**.[8]

Fraction C4 (1.2 g) was further purified by silica gel 60 open column chromatography (2 × 30 cm) and eluted with 300 mL each of a mixture of *n*-hexane/CH_2Cl_2 in ratios of 80:20, 70:30, and 60:40, respectively, yielding 125 mg of a white precipitate, which was eugenial C (**3**). Fraction C5 (1.6 g) was purified by centrifugally accelerated preparative TLC and eluted with 500 mL of a gradient of *n*-hexane/CH_2Cl_2 (70:30) to give 45 mg of eugenial D (**4**).

*Eugenial C (**3**):* amorphous white solid; mp 136−138 °C; $[\alpha]_D$ −7 (*c* 0.13, $CHCl_3$); IR (KBr) 3503, 2960, 2884, 1621, 1458, 1380 cm^{-1}; NMR data, see Table 1; EIMS (%) 440 (2), M$^{\bullet+}$ 237 (60) $C_{12}H_{13}O_5$, phloroglucinol, 219 (18), 203 (100) $C_{15}H_{23}$, sesquiterpene; 161 (12), 149 (7), 147 (40), 129 (20), 105 (35). HRESIMS, found 440.2781 (calcd 440.2793 for $C_{27}H_{36}O_5$).

*Eugenial D (**4**):* amorphous white solid; mp 162−165 °C; $[\alpha]_D$ −22 (*c* 0.22, $CHCl_3$); IR (KBr) 3505, 2960, 2875, 1625, 1437, 1380 cm^{-1}; NMR data, see Table 2; EIMS *m*/*z* (%) 440 (30), M$^{\bullet+}$ 237 (100) $C_{12}H_{13}O_5$, phloroglucinol, 219 (21), 203 (95) $C_{15}H_{23}$, sesquiterpene, 161 (25), 149 (24), 147 (55), 129 (30), 105 (40); HRESIMS, found 440.2793 (calcd 440.2787 for $C_{27}H_{36}O_5$).

Microorganisms, Media, and Inocula. For the antimicrobial evaluation, strains of the American Type Culture Collection (ATCC), Rockville, MD, USA, were used, as follows: bacteria, *Bacillus subtilis* ATCC 23858, *Escherichia coli* ATCC 25922, and *Staphylococcus aureus* ATCC 6538P; and yeast *Candida albicans* ATCC 10231. The methicillin-resistant *Staphylococcus aureus* (MRSA) strains (Sa3, Sa4, Sa5, Sa6, Sa8) were obtained from clinical material collected at the Hospital and Maternity Marieta Konder Bornhausen in Itajaí, Santa Catarina, Brazil. The strains were deposited at the Laboratory of Research in Microbiology Univali in Itajaí, Santa Catarina, Brazil.

Quantitative Antimicrobial Evaluation. The minimum inhibitory concentration (MIC) of each compound was determined using broth microdilution techniques, following the guidelines of CLSI[13] M07-A8 for bacteria and CLSI (formerly NCCLS) M27-A2 for yeasts.[14] Stock solutions of compounds diluted in DMSO were added to each medium to give serial 2-fold dilutions, resulting in concentrations ranging from 1000 to 62.5 μg/mL and also from 100 to 0.19 μg/mL. Inocula of 100 μL (5 × 10^5 CFU/mL for bacteria and 10^3−10^4 CFU/mL for yeasts) were added to Mueller−Hinton broth medium (Merck) for bacteria and RPMI-1640 broth medium (Gibco, Grand Island, NY, USA) for yeast. Vancomycin hydrochloride (Sigma, St. Louis, MO, USA) and amphotericin B (Sigma) were used as positive controls. Plates were incubated for 24 h at 35 °C for bacteria and at 30 °C for yeasts. MIC was defined as the lowest concentration of compound capable of causing total inhibition of the growth of microorganism compared with control. All of the antimicrobial assays were tested in duplicate.

Statistical Analysis. The data are reported as mean ± standard error of the mean (SEM) and were compared using one-way analysis of variance (ANOVA), followed by Dunnett's pairwise test, and *p* values <0.05 were considered significant.

Table 1. NMR Data of Eugenial A (1),[11] Eugenial C (3), and Macrocarpal C/G (5)[16]

	1[a]	5[b]	3[c]	
position	δ_C	δ_C	δ_C	δ_H (*J* in Hz)
1	100.5	106.77	104.4 s	
2	161.8	171.70	162.1 s	
2-OH				5.77 brs
3	103.9	106.77	103.3 s	
4	168.3	171.17	168.0 s	
4-OH				14.42 s
5	103.8	106.77	104.1 s	
6	171.9	170.05	172.7 s	
6-OH				15.49 s
7	20.6	39.16	32.9 t	2.28 d (14.8)
				2.72 d (14.8)
8	191.8	193.45	192.1 d	10.10 s
9	206.7	193.29	206.9 s	
10	45.9	36.48	46.1 t	3.12 t (7.5)
11	17.9	28.71	17.8 t	1.74 sex (7.5)
12	14.0	24.47	13.8 q	1.02 t (7.5)
13	23.0			
1′	78.3	52.92	50.8 d	2.45 m
2′	130.1	29.17	26.0 t	1.76 m
				1.92 m
3′	133.1	37.91	40.1 t	1.46 m
				1.64 m
4′	38.7	50.33	47.0 s	
5′	27.4	52.15	53.7 d	1.22 dd (10.5, 10.5)
6′	33.3	28.89	27.7 d	0.62 dd (10.5, 10.5)
7′	27.6	29.96	27.5 d	0.79 ddd (10.5, 10.5, 6.5)
8′	33.1	27.34	25.5 t	1.01 m
				2.06 m
9′	19.8	41.06	39.3 t	2.03 dd (12.5, 12.5)
				2.45 m
10′	19.6	156.89	154.8 s	
11′		21.51	20.1 s	
12′		18.04	16.6 q	1.03 s
13′		29.96	28.9 q	1.12 s
14′		106.77	105.5 t	4.76 brs
				4.70 brs
15′		25.48	20.4 q	0.92 s

[a]In $CDCl_3$ at 75.5 MHz (^{13}C). [b]In CD_3OD at 67.5 MHz (^{13}C). [c]In $CDCl_3$ at 500 MHz (^{1}H) and 75.5 MHz (^{13}C). Multiplicity for ^{13}C assigned by DEPT method: s = C, d = CH, t = CH_2, and q = CH_3.

DOI: 10.1021/acs.jafc.5b03562
J. Agric. Food Chem. 2015, 63, 8151−8155

Table 2. NMR Data of Eugenial D (4)[a]

position	δ_C	δ_H (J in Hz)
1	105.3 s	
2	161.5 s	
2-OH		5.73 brs
3	104.1 s	
4	168.0 s	
4-OH		14.35 s
5	103.3 s	
6	171.9 s	
6-OH		15.35 s
7	22.2 t	2.65 m
		2.29 dd (14.3, 12.0)
8	192.0 d	10.10 s
9	206.9 s	
10	46.1 t	3.10 t (7.3)
11	17.8 t	1.73 sex (7.3)
12	13.9 q	1.01 t (7.3)
1′	38.0 s	
2′	49.3 d	1.25 m
3′	22.9 t	1.32 m
		1.59 m
4′	32.8 t	1.45 m
		1.53 m
5′	38.8 d	2.49 m
6′	148.0 s	
7′	123.9 d	5.28 d (4.1)
8′	41.3 d	2.64 t (5.3)[b]
9′	22.4 t	1.64 m
		1.87 m
10′	34.4 t	1.44 m
		1.78 m
11′	147.9 s	
12′	22.3 q	1.79 s
13′	111.6 t	4.85 brs
		4.64 brs
14′	21.3 q	1.19 s
15′	22.3 q	1.15 d (7.6)

[a]In $CDCl_3$ at 500 MHz (^1H) and 75.5 MHz (^{13}C). Multiplicity for ^{13}C assigned by DEPT method: s = C, d = CH, t = CH_2, and q = CH_3. [b]Coupling constant measured from selective TOCSY experiment.

RESULTS AND DISCUSSION

Phytochemical analyses of the CH_2Cl_2 fraction of *E. umbelliflora* fruits led to the isolation of four phloroglucinols: **1**, **2**,[11,15] and two new meroterpenoids, **3** and **4** (Figure 1), which were identified (^1H,^{13}C NMR, 1D and 2D-COSY, NOESY, HMQC/HSQC, HMBC experiments, FTIR, and HRESIMS) and compared with those previously reported in the literature for model compounds (Tables 1 and 2).[11,16]

Compound **3** was obtained in the form of a white amorphous solid, mp 136−138 °C; its IR spectrum exhibited a strong carbonyl band at 1621 cm^{-1}. A molecular formula $C_{27}H_{36}O_5$ was inferred from the HRESIMS. The ^1H and ^{13}C NMR data are summarized in Table 1, all of the protons being assigned to the appropriate carbon by HMQC and quaternary carbons by HMBC spectroscopy. The data suggested that the compound consists of two parts: a fully substituted phoroglucinol and a sesquiterpene. The ^{13}C and DEPT spectra of **3** showed 27 carbon signals, including 4 methyls, 8 methylenes, 5 methines, and 10 quaternary carbons. Of these, seven carbons [δ_C 192.1 (d, C-8), 172.7 (s, C-6), 168.0 (s, C-4), 162.1 (s, C-2), 104.4 (s, C-1), 104.1 (s, C-5), and 103.3 (s, C-3)] arose from a typical formylphloroglucinol unit, and signals for a typical linear butyroyl substituent [δ_C 206.9 (s, C-9), 46.1 (t, C-10), 17.8 (t, C-11), and 13.8 (q, C-12)] were observed. In the ^1H NMR spectrum, the phloroglucinol substituents were established by the signal for an aldehyde (δ_H10.10), two hydrogen-bonded hydroxyls (δ_H15.49 and 14.42), a phenolic hydroxyl (δ_H 5.77), and a linear butyroyl group at δ_H 3.12 (t, J = 7.5 Hz), 1.74 (dt, J = 7.5 Hz), and 1.02 (t, J = 7.5 Hz). The relative position of these substituents was proposed on the basis of HMBC connectivities (Figure 2) and showed a close similarity with the phloroglucinol portion of compound **1** (Table 1). The hydroxyl proton 6-OH (δ_H 15.49) showed HMBC correlations with C-1 and C-6 and the hydroxyl proton 4-OH (δ_H 14.42) with C-4 and C-5, whereas the hydroxyl proton 2-OH (δ_H 5.77) was correlated with C-2 and C-3. The HMBC correlations of H-8 (δ_H 10.10) with C-3 and C-4 confirmed that the formyl group was located at carbon C-3.

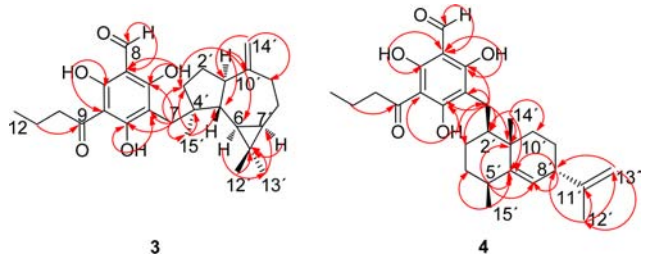

Figure 2. Key HMBC correlations for compounds **3** and **4**.

With respect to the sesquiterpene moiety, it was established as aromadendrene, as shown in structure **3**, from the remaining ^1H and ^{13}C NMR signals and by comparison (Table 1) with the NMR data of model compound macrocarpal C/G (**5**) (Figure 1) isolated from *Eucalyptus macrocarpa*.[16] The aromadendrene skeleton is further supported by HMBC connectivities (Figure 2). The correlations of protons Me-15′ with C-3′, C-4′, and C-5′ allowed the connections of C-3′ and C-5′ to the quaternary carbon C-4′, whereas the correlations of H-1′ with C-5′, C-6′, C-10′, and C-14′, as well as the correlations of H-14′ with C-9′ and C-1′, indicated that the exomethylene group is located at the $\Delta^{10(14)}$ position. The HMBC correlations of protons Me-12′ and Me-13′ to C-11′ and of Me-13′ to C-7′, together with the correlations of H-6′ to C-13′ and H-7′ to C-11′, indicated the connectivity of quaternary carbon C-11′ of the cyclopropane ring to the methine carbons C-6′ and C-7′.

In addition, the HMBC correlations revealed that the two parts of eugenial C are linked by a methylene bridge; the methylene protons in position 7 (δ_H 2.72 and 2.28 d) showed correlations with the carbons C-1, C-2, and C-6 of the phloroglucinol derivative and with C-3′, C-4′, and C-15′ of the aromadendrene skeleton.

The relative configuration of **3** was established on the basis of the NOESY experiments (Figure 3). The NOE correlations of Me-15′ with H-6′ and H-1′ and of H-5′ with H-7 and Me-12′ indicated that H-1′, H-6′, and Me-15′ adopted an α-configuration, whereas H-5′ and Me-12′ adopted a β-configuration, as shown in the previously reported macrocarpals.[17] In addition, the Me-13′ correlated with H-6′ and H-7′. The *trans* relationship among H-5′ and H-1′ was also deduced from the large coupling constants values of the H-5′

DOI: 10.1021/acs.jafc.5b03562
J. Agric. Food Chem. 2015, 63, 8151−8155

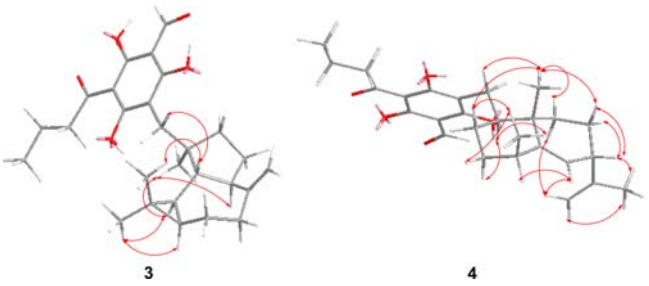

Figure 3. Selected NOESY correlations for compounds **3** and **4**.

(δ_H 1.22, dd, J = 10.5, 10.5 Hz), observed in the ^{1}H NMR spectrum. Therefore, eugenial C was assigned structure **3**.

Compound **4** was obtained in the form of a white amorphous solid (mp 162−165 °C) and exhibited a strong carbonyl bond at 1625 cm^{-1} in the IR spectrum. The molecular formula $C_{27}H_{36}O_5$ was established by HRESIMS and was found to be an isomer of **3**. Structure **4** for eugenial D was assigned on the basis of the following considerations. The EIMS spectrum showed two main fragments at m/z 237 (base peak) and at m/z 203 (95%), which may be attributed, respectively, to the phloroglucinol part ($C_{12}H_{13}O_5$) and to the sesquiterpene moiety ($C_{15}H_{23}$) by C-7/C-2′ cleavage. NMR data enriched by HMBC long-range correlations (Figure 2) are reported in Table 2, and it is evident that eugenial D maintains all of the features exhibited by eugenial C (**3**) (Table 1) for the phloroglucinol moiety, in particular, the ^{1}H NMR signals for the butyroyl chain (δ_H 1.01, 1.73, and 3.10), the aldehyde (δ_H 10.10), and chelated hydroxyls (δ_H 15.35 and 14.35). The correlations observed in HMBC spectra indicated the position of these substituents. The hydroxyl proton 6-OH (δ_H 15.35) showed HMBC correlations with C-5 and C-6 and the hydroxyl proton 4-OH (δ_H 14.35) with C-3 and C-4, whereas the hydroxyl proton 2-OH (δ_H 5.73) was correlated with C-2 and C-3. The H-8 (δ_H 10.10) showed HMBC correlations with C-3 and C-4.

With respect to the sesquiterpene part, the remaining ^{13}C NMR signals of Table 2 were attributed by DEPT and HMQC experiments to two methyls (δ_C 21.3 and 22.3), four methylenes (δ_C 22.4, 22.9, 32.8, and 34.4), three methines (δ_C 38.8, 41.3, and 49.3), and a quartenary carbon (δ_C 38.0). Signals were also present for a trisubstituted double bond (δ_C148.0 and 123.9) and an isopropylene group (δ_C 22.2, 111.6, and 147.9). On the basis of long-range connectives observed in the HMBC spectra (Figure 2) these signals may be collectively assembled in the sesquiterpene with the eudesmane skeleton depicted in structure **4**. The correlations of protons Me-15′ with C-6′ and H-5′ with C-1′, C-6′, and C-7′, as well as of H-8′ to C-6′ and C-7′, linked a trisubstituted double bond $\Delta_{6',7'}$ to C-8′. The correlations of protons Me-14′ with C-1′, C-2′, C-6′, and C-10′ allowed the connections of C-2′, C-6′, and C-10′ to the quaternary carbon C-1′. The correlations of protons Me-12′ with C-8′, C-11′, and C-13′ and of protons Me-13′ with C-12′ and C-8′ established the isopropylene group at C-8′.

Finally, the HMBC correlations of the methylene protons at position 7 (δ_H 2.65 and 2.29) with C-1, C-2, and C-6, as well as with C-1′, C-2′, and C-3′ established the two parts (sesquiterpene and phloroglucinol) of compound **4** are linked.

The relative stereochemistry for **4** was proposed from the NOESY analysis (Figure 3). The NOE correlations of Me-14′ with H-7, H-3′, H-9′, and H-10′ indicated these protons were cofacially oriented, which established Me-14′ as β-oriented. The H-2′ showed correlation with H-4′α and/or H-10′α, indicating that H-2′ was α-oriented. The NOE observed among Me-15′ and H-3′ pointed out Me-15′ as a β-configuration. The H-8′ showed NOE correlations with H-7′, Me-12′, and both H-9′α and H-9′β, which indicated that the isopropylene group at C-8′ adopted the α-axial orientation. In addition, the chemical shifts of C-8′ at δ 41.3 and H-8′ at δ 2.64 (t, J = 5.3 Hz) were in agreement with those reported for the sesquiterpene, which has an isopropylene group at C-8′ with α-axial orientation.[18] The coupling constant of H-8′ (t, J = 5.2 Hz) also was consistent with their equatorial position. Therefore, eugenial D was assigned structure **4**.

It should be emphasized that the meroterpenoids (**1**−**4**) found in *E. umbelliflora* contain, in the phloroglucinol part, both an aldehyde and a butyroyl chain, whereas the analogous compounds widely occurring in the species *Eucalyptus* contain two aldehyde substituents.

Compounds **3** and **4** isolated in the present research were tested against bacteria and yeast. The results showed that both compounds exhibited significant activity against Gram-positive bacteria, including strains of MRSA, which constitute a significant healthcare problem (Table 3).

S. aureus is a versatile and dangerous bacterial pathogen that quickly develops resistance to early antibiotics. Because methicillin is rarely used today, the term "MRSA" is now used to describe strains of *S. aureus* resistant to all β-lactam antibiotics. Therefore, the results against the staphylococci strains were very promising, with MIC values similar to that of vancomycin, which is recognized as the most effective agent for MRSA. However, the compounds were inactive when tested against Gram-negative bacteria and yeasts. This can be explained by the fact that the secondary metabolites from plants often show considerable activity against Gram-positive bacteria, but not against Gram-negative species or yeasts.[19] Both yeasts and Gram-negative bacteria have evolved significant permeability barriers.[20]

The results of antimicrobial activity corroborate the findings of Yamakoshi et al.,[16] who reported that macrocarpals B−G

Table 3. Antimicrobial Activity of Compounds Isolated from Fruits of *Eugenia umbelliflora* against Bacteria and Yeast[a]

	minimal inhibitory concentration (μg/mL)								
compound	Bs	Sa	Sa3	Sa4	Sa5	Sa6	Sa8	Ec	Ca
3	0.78	3.12	1.56	0.39	0.78	1.56	0.39	>1000	>1000
4	0.78	1.56	0.78	0.78	0.39	0.78	3.12	>1000	>1000
vancomycin		0.5	1	1	1	0.5	1		
amphotericin B									0.78

[a]Bs, *Bacillus subtilis*; Sa, *Staphylococcus aureus*; Sa3, Sa4, Sa5, Sa6, and Sa8, different strains of methicillin-resistant *S. aureus*; Ec, *Escherichia coli*; Ca, *Candida albicans*.

DOI: 10.1021/acs.jafc.5b03562
J. Agric. Food Chem. 2015, 63, 8151−8155

presented antibacterial activity. The new compound, **3**, also presented a similar antimicrobial profile.

With regard to compounds **3** and **4**, equivalent activity to the antibiotics commonly used in anti-infection therapy was found. Due to their superior activity against *S. aureus* (MIC 3.12 μg/mL), **3** and **4** were also submitted to the test against different strains of MRSA. The results showed that the antibacterial activities of these compounds were similar to that of the standard strain of the bacteria, demonstrating their potential against MRSA (MIC = 0.39−3.12 μg/mL).

Given that nowadays MRSA is a major cause of nosocomial infections worldwide and may be related to exposure to broad-spectrum antibiotics, the discovery of a compound that can be specific to a single bacterium, as described in this study, can contribute to treatment,[21] as it minimizes interference with the host microbial flora.[22]

In conclusion, this study allowed the isolation of two previously unknown phloroglucinols from the fruits of *E. umbelliflora* that showed high antibacterial activity mainly against MRSA standardized and clinical strains, similar to that of antibiotics in clinical use.

AUTHOR INFORMATION

Corresponding Author

*(C.M.-S.) Phone: +55 47 33417664. Fax: +55 47 33417744. E-mail: cmeyre@univali.br.

Funding

We are grateful to CNPq, FAPESC-SC, and ProPPEC/UNIVALI for providing financial support.

Notes

The authors declare no competing financial interest.

ACKNOWLEDGMENTS

We are grateful to Prof. Msc Oscar Benigno Iza (UNIVALI) for the classification and collection of plant material, Dr. Luis M. Peña-Rodríguez and Fabiola Escalante-Erosa (Centro de Investigación Científca de Yucatán-México) for the HRESIMS analysis, and Dr. Luiz Carlos Dias and Emílio Júnior (UNICAMP) for the optical rotations.

REFERENCES

(1) Lorenzi, H.; Matos, F. J. A. *Plantas Medicinais no Brasil Nativas e Exóticas [Medicinal Plants in Native and Exotic Brazil]*; São Paulo, Instituto Plantarum de Estudos da Flora Ltda: Nova Odessa, Brazil, 2002.

(2) Mosimann, R. M. S.; Reis, A. Frutos nativos da Ilha de Santa Catarina, Florianópolis [Frutis natives from Santa Catarina island, Florianópolis]. *Insula* **1975**, *8*, 30−46.

(3) Coelho de Souza, G.; Haas, A. P.S.; Von Poser, G. L.; Schapoval, E. E. S.; Elisabetsky, E. Ethnopharmacological studies of antimicrobial remedies in the south of Brazil. *J. Ethnopharmacol.* **2004**, *90*, 135−143.

(4) Hussein, S. A. M.; Hashem, A. N. M.; Seliem, M. A.; Lindequist, U.; Nawwar, M. A. M. Polyoxygenated flavonoids from *Eugenia edulis*. *Phytochemistry* **2003**, *64*, 883−889.

(5) Oliveira, R. N.; Camara, C. A. G. Estudo comparativo do óleo essencial de *Eugenia punicifolia* (HBK) DC. de diferentes localidades de Pernambuco [Comparative study of the essential oil of *Eugenia punicifolia* (HBK) DC. from different locations of Pernambuco]. *Rev. Bras. Farmacogn.* **2005**, *15*, 39−43.

(6) Romagnolo, M. R.; Souza, M. C. O gênero *Eugenia* L. (Myrtaceae) na planície de alagável do Alto Rio Paraná, Estados de Mato Grosso do Sul e Paraná, Brasil [The genus *Eugenia* L. (Myrtaceae) on the Upper Paraná River floodplain, Mato Grosso do Sul and Paraná States, Brazil]. *Acta Bot. Bras.* **2006**, *20*, 529−548.

(7) Auricchio, M.; Bacchi, E. M. Folhas de *Eugenia uniflora* L. (pitanga): propriedades farmacobotânicas, químicas e farmacológicas [*Eugenia uniflora* L. "Brazilian cherry" leaves: pharmacobotanical, chemical and pharmacological properties]. *Rev. Inst. Adolfo Lutz* **2003**, *62*, 55−61.

(8) Oussalah, M.; Caillet, S.; Saucier, L.; Lacroix, M. Inhibitory effects of selected plant essential oils on the growth of four pathogenic bacteria: *E. coli* O157:H7, *Salmonella typhimurium*, *Staphylococcus aureus* and *Listeria monocytogenes*. *Food Control* **2007**, *18*, 414−420.

(9) Machado, K. E.; Cechinel Filho, V.; Tessarolo, M. L.; Meyre-Silva, C.; Bella Cruz, A. Potent antibacterial activity of *Eugenia umbelliflora*. *Pharm. Biol.* **2005**, *43*, 636−639.

(10) Kuskoski, E. M.; Vega, J. M.; Rios, J. J.; Fett, R.; Troncoso, A. M.; Asuero, A. G. Characterization of anthocyanins from the fruits of baguaçu (*Eugenia umbelliflora* Berg). *J. Agric. Food Chem.* **2003**, *51*, 5450−5454.

(11) Faqueti, L. G.; Maes Petri, C.; Meyre-Silva, C.; Machado, K. E.; Bella Cruz, A.; Garcia, P. A.; Cechinel Filho, V.; San Feliciano, A.; Delle Monache, F. Euglobal-like compounds from the genus *Eugenia*. *Nat. Prod. Res.* **2013**, *27*, 28−31.

(12) Machado, K. E.; Cechinel-Filho, V.; Bella Cruz, R. C.; Meyre-Silva, C.; Bella Cruz, A. Antifungal activity of *Eugenia umbelliflora* against dermatophytes. *Nat. Prod. Commun.* **2009**, *4*, 1181−1184.

(13) CLSI − Clinical and Laboratory Standards Institute. Methods for dilution antimicrobial susceptibility tests for bacteria that grow aerobically. *Approved Standard M07-A8*; CLSI: Wayne, PA, USA, 2009.

(14) NCCLS. Reference method for broth dilution antifungal susceptibility testing of yeasts. *Approved Standard*, 2nd ed.; NCCLS document M27-A2; NCCLS: Wayne, PA, USA, 2002.

(15) Singh, I. P.; Bharate, S. B. Phloroglucinol compounds of natural origin: synthetic aspects. *Nat. Prod. Rep.* **2006**, *23*, 558−591.

(16) Yamakoshi, Y.; Murata, M.; Shimizu, A.; Homma, S. Isolation and characterization of macrocarpals B−G antibacterial compounds from *Eucalyptus macrocarpa*. *Biosci., Biotechnol., Biochem.* **1992**, *56*, 1570−1576.

(17) Nishizawa, M.; Emura, M.; Kan, Y.; Yamada, H.; Ogawa, K.; Hamanaka, N. HIV-RTase inhibitors of *Eucalyptus globulus*. *Tetrahedron Lett.* **1992**, *33*, 2983−2986.

(18) Adio, A. M.; Paul, C.; Tesso, H.; Kloth, P.; König, W. A. Absolute configuration of helminthogermacrene. *Tetrahedron: Asymmetry* **2004**, *15*, 1631−1635.

(19) Lewis, K. In search of natural substrates and inhibitors of MDR pumps. *J. Mol. Microbiol. Biotechnol.* **2001**, *3*, 247−254.

(20) Tegos, G.; Stermitz, F. R.; Lomovskaya, O.; Lewis, K. Multidrug pump inhibitors uncover remarkable activity of plant antimicrobials. *Antimicrob. Agents Chemother.* **2002**, *46*, 3133−3141.

(21) Rudkin, J. K.; Edwards, A. M.; Bowden, M. G.; Brown, E. L.; Pozzi, C.; Waters, E. M.; Chan, W. C.; Williams, P.; O'Gara, J. P.; Massey, R. C. Methicillin resistance reduces the virulence of healthcare-associated methicillin-resistant *Staphylococcus aureus* by interfering with the agar quorum sensing system MRSA. *J. Infect. Dis.* **2012**, *205*, 798−806.

(22) Rafii, F.; Sutherland, J. B.; Cerniglia, C. E. Effects of treatment with antimicrobial agents on the human colonic microflora. *Ther. Clin. Risk. Manage.* **2008**, *4*, 1343−1357.

DOI: 10.1021/acs.jafc.5b03562
J. Agric. Food Chem. 2015, 63, 8151−8155

m above sea level) were measured by use of a spectroradiometer system (DTM300, Bentham Ltd., Reading, UK) The system is operated by the German Federal Environment Agency as a member of the German Solar UV Monitoring Network, lead-managed by the German Federal Office for Radiation Protection. The duration of each single scan was 6 min,and time was given in Universal Time Coordinated (UTC) defined as Central European Summer Time (CEST) minus 2 h. Time data in the present work are all presented in UTC. The experiments were performed on July 3, 2014, soon after summer solstice with highest natural UV-B irradiance. Sky conditions were cloudless at an outdoor temperature and relative air humidity of 18.0 ± 0.9 °C and 54 ± 3%, respectively.

Experimental Design. The mushroom slices were completely separated from each other on horizontally positioned food trays. The beginning and end pieces of the sliced mushrooms were all placed with their slice plane facing the solar radiation. A temperature sensor was inserted into a representative mushroom slice to monitor the internal temperature. Immediately after their exposure period, the samples were double-sealed in polyethylene zipper bags, labeled, and repacked into EPS boxes with dry ice, which were shipped back to the University Medical Centre Freiburg. Upon receipt at the center, the boxes were stored at −26 °C until replenishment with dry ice and shipment via overnight express delivery to the Danish Technical University, Copenhagen, for the determination of dry matter and vitamin D_2 content.

Different UV-B Doses. To investigate the response of vitamin D_2 content to different UV-B doses, eight different sun exposure times were employed as follows: 0, 15, 30, 45, 60, 120, 240, and 360 min. For logistical reasons and with the aim of exposing the samples to high UV-B doses and attaining a reasonably linear increase in UV-B dose hitting the different dose−response samples (Table 1), all other exposure measurements started at 10:15 a.m. except for the 6 h samples, which started at 8:00 a.m.

Increase in Exposure Surface Area. In a further experiment, both slice sides were exposed successively for 60 min starting at 10:15 a.m., then turned over manually between 11:15 and 11:17 a.m. and exposed for another hour until 12:15 p.m.

Different Slice Thicknesses. In addition to the standard 9 mm thick slices used in the present study, the effect of the ratio of surface area exposed to the solar radiation to mass by two further slice thicknesses (6 and 9 mm) at a sun exposure time of 1 h (10:15−11:15 a.m.) was also assessed.

Table 1. Calculated UV-B Doses for Each Exposure Time and Final Vitamin D_2 Content of Four 9 mm Sliced Mushroom Samples[a]

sun exposure time (min)	start of sun exposure (UTC)	UV-B dose (J/cm²)	vitamin D_2 (μg/g DW)[b] (μg/100 g FW)[c]	P[d]
0		0	0.03 ± 0.01	
			0.2 ± 0.1	
15	10:15 a.m.	0.13	2.2 ± 0.5	<0.001
			17.5 ± 3.6	
30	10:15 a.m.	0.26	2.5 ± 0.3	0.38
			21.6 ± 2.7	
45	10:15 a.m.	0.39	3.3 ± 0.4	0.02
			28.0 ± 3.7	
60	10:15 a.m.	0.53	3.9 ± 0.8	0.12
			32.5 ± 6.8	
120	10:15 a.m.	1.08	3.3 ± 0.4	0.09
			27.8 ± 3.0	
240	10:15 a.m.	2.01	3.7 ± 0.7	0.20
			30.5 ± 5.4	
360	8:00 a.m.	2.80	2.2 ± 0.2	<0.001
			17.8 ± 1.7	

[a]Abbreviations: DW, dry weight; FW, fresh weight; UV-B, ultraviolet B. [b]Represents mean ± SD values (n = 4). [c]Using moisture content of each sample in the range of 91.5−92.1%. [d]Results of consecutive measurements from ANOVA with LSD post hoc test.

Vitamin D_2 Analysis of Mushroom Slices. The content of vitamin D_2 in mushrooms was quantified in freeze-dried materials by a LC-MS/MS method modified to include vitamin D_2.[17] The standards used were vitamin D_2 (ergocalciferol) (Sigma-Aldrich, Steinheim, Germany) and as internal 26,26,26,27,27,27-d_6-vitamin D_2 (d_6-vitamin D_2) (Chemaphor Inc., Ottawa, ON, Canada). In short, 0.1−0.5 g of freeze-dried mushrooms was saponified using 0.2 g of sodium ascorbate, 9 mL of ethanol, and 3 mL of potassium hydroxide at room temperature for 18 h. The cleanup procedure included liquid−liquid extraction with 10 mL of ethyl acetate in heptane and silica solid phase extraction (Isolute, IST, Hengoed, UK). For detection, vitamin D_2 was derivatized with 4-phenyl-1,2,4-triazoline-3,5-dione (PTAD). The mass spectrometer was operated in positive MRM mode using the following transitions for vitamin D_2 (m/z 603.4 → 298.0) and d_6-vitamin D_2 (m/z 609.4 → 298.0). The validation of the LC-MS/MS method included comparison with the standardized method for vitamin D (HPLC-UV/DAD) performed accredited according to ISO17025.[16,18] For house-reference materials, freeze-dried vitamin D-enriched mushrooms, no differences were found between the LC-MS/MS (n = 5) and the standardized HPLC-UV method (n = 10), 17.0 ± 1.0 and 15.8 ± 1.0 μg vitamin D_2/g DW, respectively.

Statistical Analysis. The study was analyzed using SPSS statistics version 22 (IBM Corp., Armonk, NY, USA). Graphs were created either with SPSS or Microsoft Excel 2010 (Microsoft Corp., Redmond, WA, USA). For descriptive data analyses, values are presented as means ± standard deviations. Group comparisons were analyzed by analysis of variance (ANOVA), and the means were compared using least significant difference (LSD) post hoc test with $P < 0.05$.

RESULTS AND DISCUSSION

Mushroom Samples. In the first hour of sun exposure the internal temperature dramatically increased by 17.8 °C, starting at 10:15 a.m. from a base of 10.4 °C. Thereafter, the temperature increased almost linearly by 2.0 ± 0.7 °C per hour, with the highest temperature of 34.0 °C measured at study end for the 360 min samples.

Solar UV-B Irradiation and Effect of UV-B Doses on Vitamin D_2 Content. The daily dose of solar UV-B measured at the meteorological station Schauinsland and the window in which the various sun exposure times were employed in the present work are shown in Figure 1. The intensity of UV-B wavelengths hitting the mushrooms peaked between 11:00 a.m. and 12:00 p.m., with mean UV-B doses of 0.055 J/cm² during

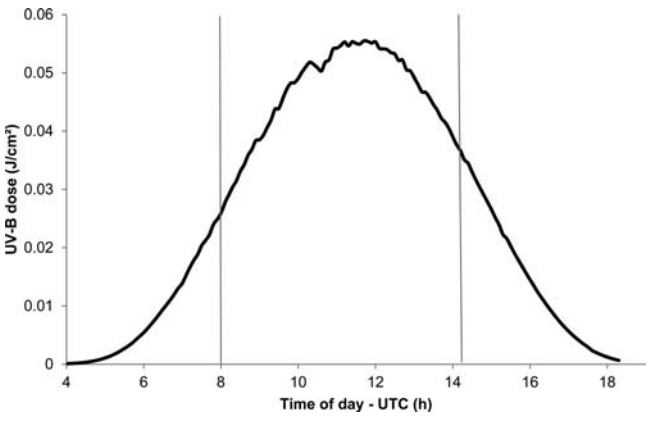

Figure 1. Daily dose of UV-B (280−315 nm), expressed in J/cm², for the 6 min duration of each scan at the meteorological station Schauinsland. The two vertical lines indicate the experimental period, starting at 8:00 a.m. and ending at 4:15 p.m. UTC.

DOI: 10.1021/acs.jafc.5b02945
J. Agric. Food Chem. 2015, 63, 8156−8161

each 6 min scan. At the time with the highest UV-B dose, the sun was nearest its zenith: sun rays penetrate the shortest distance through the atmosphere, and the radiant flux on a horizontal surface is at its densest. The doses of UV-B for each exposure time are shown in Table 1.

Cumulative doses of UV-B for the different sun exposure times ranged from 0.13 to 2.80 J/cm^2 (Table 1). As expected, the vitamin D_2 content of the unexposed control mushrooms was negligible (0.03 ± 0.01 μg/g DW). As little as 15 min of sun exposure leading to a UV-B dose of 0.13 J/cm^2 increased significantly the vitamin D_2 content of the mushroom slices (2.2 ± 0.5 μg/g DW; $P < 0.001$). This is equivalent to 17.6 μg of vitamin D_2 per 100 g of fresh mushroom slices exposed to solar radiation for one-fourth of an hour and could contribute 110% of the North American RDA for vitamin D (15 μg/day).[19]

With longer sun exposure times, the vitamin D_2 content increased linearly with the UV-B dose, to 0.53 J/cm^2 after 60 min when the maximum vitamin D_2 content (3.9 ± 0.8 μg/g DW) was attained. Continuing the exposure for >60 min showed no increase but rather a decrease in vitamin D_2 compared to 60 min for 9 mm mushroom slices (Figure 2).

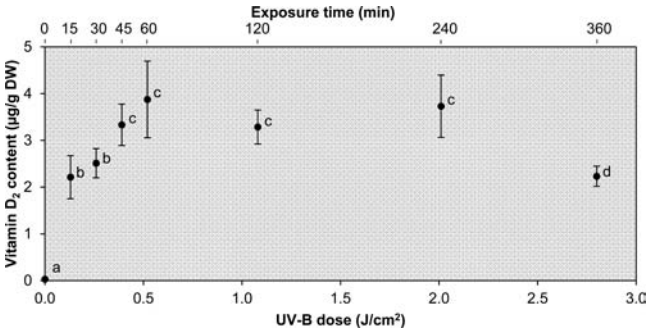

Figure 2. Relationship between vitamin D_2 content in 9 mm sliced white button mushrooms and different sun exposure times, expressed directly in measured UV-B doses. Mean values ($n = 4$) with different lower case letters are significantly different ($P < 0.05$). Error bars represent 2 standard errors. DW, dry weight.

Table 2 summarizes published data from research studies investigating the effect of sun exposure on vitamin D_2 content in harvested mushrooms. The present findings are consistent with the magnitude of vitamin D_2 yields after sun exposure in mushrooms published in two recent papers, however, without data on UV-B doses.[14,15] Simon et al. compared the compositional changes in whole button mushrooms exposed to solar radiation randomly spread on a tarp with those occurring after artificial UV exposure.[14] Sun exposure of 150 min led to a vitamin D_2 content of 27.4 μg/100 g FW, which is almost identical to the contents in the present study after 120 min (24.8 μg/100 g FW).

Phillips and Rasor evaluated the reliability of a consumer-friendly protocol to increase vitamin D_2 in sliced mushrooms by solar radiation at different durations, times of day, and seasons.[15] By choosing results from conditions comparable to those in the present study, they noted a vitamin D_2 content of 36.6 μg/100 g FW attained after 30 min of sun exposure, which was about twice the yield observed in the present study. It should be noted that their study was performed at a lower altitude (633 m), a lower latitude, 37.1° N vs 47.9° N, and hence with more natural UV-B irradiance.

Table 2. Summary of Data from Published Results from Research Studies Investigating the Effect of Sun Exposure on Vitamin D_2 Content in Harvested Mushrooms[a]

mushroom	region/time of year and day/weather conditions	sun exposure time (min)	UV-B dose (J/cm^2)	vitamin D_2 content		refs
				μg/g DW	μg/100 g FW	
whole button mushrooms	Watsonville, CA, USA (36.55° N)/late summer/mid-day (11:30 a.m.–12:45 p.m.)/clear sky	150	–[b]	3.7 ± 0.9[c]	27.4 ± 6.4[d,e]	Simon et al., 2011
whole button mushrooms	Copenhagen, Denmark (55.40° N)/–, mid-day/–	20	0.2	0.1 (0.09–0.12)[f,g]	0.9 (0.8–1.1)[f]	Kristensen et al., 2012
sliced button mushrooms[h]	Blacksburg, VA, USA (37.13° N)/sample A, 29.06, 2:45 p.m.; samples B + C, 30.08, 2:17 p.m./clear sky	A 15	–[i]	–	21.8	Phillips et al., 2013
		B 15	–[j]	–	27.0	
		C 30	–[j]	–	36.6	

[a]Abbreviations: DW, dry weight; FW, fresh weight. [b]No data due to limitations in the sensitivity of the UV-monitoring device. [c]Control: 0.05 ± 0.05 μg/g DW. [d]Calculated on the basis of published moisture content of 92.7%. [e]Control: 0.4 ± 0.2 μg/100 g FW. [f]Median (min–max). [g]Calculated on the basis of published moisture content of 90.6%. [h]No data on slice thickness and moisture content of mushrooms. [i]UV index 4–10. [j]UV index 8–9.

DOI: 10.1021/acs.jafc.5b02945
J. Agric. Food Chem. 2015, 63, 8156–8161

Discrepant results were reported in a further study investigating the effects of solar radiation on the vitamin D_2 content of whole button mushrooms.[16] An UV-B dose of 0.2 J/cm^2 after 20 min of mid-day sun exposure produced a median vitamin D_2 content of only 1.0 μg/100 g FW. Although our study was carried out at seven degrees of lower latitude (47.9 vs 55.4° N) and at almost 1000 m higher altitude, both major factors for more natural UV-B irradiance, the UV-B dose measured by the high-performance spectroradiometer operated by a member of the German Solar UV Monitoring Network in the present study was 0.18 J/cm^2 in 20 min at noon. This may raise some doubt about the accuracy of the portable UV-B photometer used in the study by Kristensen et al.[16] Furthermore, the divergent results between the two studies might be explained by their mushrooms having been exposed to a significantly lower UV-B dose than that measured.

As mentioned above, sun exposure times within the range of 60−240 min produced a plateau in vitamin D_2 content of the mushroom slices, whereas 360 min of UV-B exposure (equivalent to 2.8 J/cm^2) triggered a significant decline in vitamin D_2 content (2.2 ± 0.2 μg/g DW; P = 0.005). These long sun exposure samples, having captured the highest UV-B dose and reached the highest internal temperature of 34.0 °C, had vitamin D_2 contents similar to those in the 15 min samples. In previous dose−response studies with artificial UV exposure of different mushroom species on vitamin D_2 content and various experimental designs, some researchers did find a plateau,[10,13,16,20,21] whereas others described continuous increases in vitamin D_2 with exposure time.[1,8,11,22,23] The sole significant decrease in vitamin D_2 after intensive UV irradiation was found after the artificial irradiation of mushroom powder.[13] All took place under laboratory conditions; moreover, the durations of artificial UV exposure were much shorter than ours, lasting seconds or from several minutes to a maximum of 2 h. It is worth mentioning that the vitamin D_2 contents achieved with artificial UV light were often >10 times higher than in the present study using solar radiation during the drying process.[10,22−25]

Several possible explanatory models are described in the literature for the significant decline of vitamin D_2 after an extended sun exposure period observed in the present study (Figure 2). Provitamin D_2 (ergosterol), its main photoisomer previtamin D_2, and the two major photoisomers of previtamin D_2, lumisterol$_2$ (ring closure) and tachysterol$_2$ (E/Z-isomerization), absorb in the same UV region and, once excited, they can all interconvert by photoisomerizations. Previtamin D_2 can also be isomerized to vitamin D_2 via a thermal reaction.[2,3,26] The ratio of photoisomers at the stationary state is influenced by the irradiation wavelength, with longer wavelengths (>305 nm) favoring the formation of the ring-closed isomers provitamin D and lumisterol.[27] Additionally, prolonged irradiation periods produce irreversible "over-irradiation products" by dimerization and ring cleavage of previtamin D_2 and tachysterol.[28] Furthermore, longer wavelengths of UV-A are able to break down vitamin D.[29] A relevant difference from the studies with artificial UV exposure is the high ratio of UV-A to UV-B in the solar spectrum. During all measurements the energy hitting the mushroom slices in the form of UV-A (315−400 nm) was 41 ± 4 times higher than that of UV-B. UV-B is only a very small part of the total solar UV irradiance on the Earth's surface. A limitation of the present study consists of not having analyzed the samples for ergosterol and some further photoisomerization byproducts.

Sun exposure for only 15 min, which is similar to an UV-B dose of 0.13 J/cm^2, produced a content of vitamin D_2 in sliced button mushrooms at a comparable level to vitamin D_3 levels found in fatty fish suc as Atlantic salmon−the often quoted richest food source of vitamin D.[30]

Effects of Modifying the Exposure Surface Area. By exposing either both slice sides of the mushrooms or slices with different thicknesses to the solar radiation, we investigated the effect of the ratio of the mushrooms' exposed surface area to its mass on vitamin D_2 content (Figures 3 and 4).

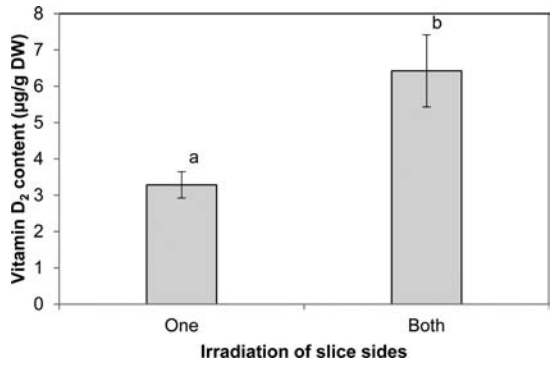

Figure 3. UV-B dose during sun exposure was 1.08 J/cm^2 after 120 min. Samples exposed on both sides were irradiated in the two 60 min periods with 0.53 and 0.55 J/cm^2, respectively. Mean values (n = 4) with different lower case letters are significantly different (P < 0.01). Error bars represent 2 standard errors. Vitamin D_2 content in μg/g DW: one side, 3.3 ± 0.4; both sides, 6.4 ± 1.0.

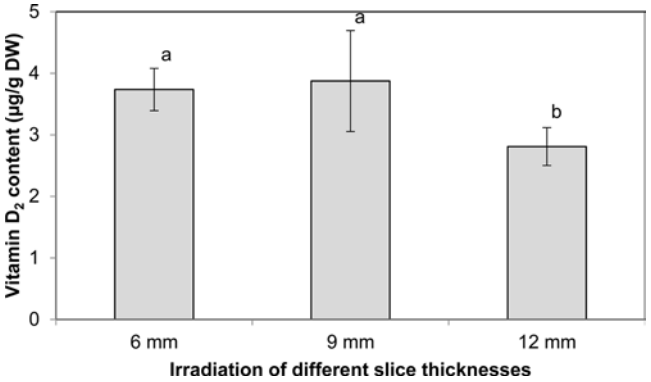

Figure 4. Vitamin D_2 content of different mushroom slice thicknesses after solar irradiation for 60 min with an UV-B dose of 0.53 J/cm^2. Mean values (n = 4) with different lower case letters are significantly different (P < 0.05). Error bars represent 2 standard errors. Vitamin D_2 content in μg/g DW: 6 mm, 3.5 ± 0.3; 9 mm, 3.9 ± 0.8; 12 mm, 2.8 ± 0.3.

After 120 min of sun exposure, the sliced mushroom samples that were turned around and exposed from both sides contained the highest vitamin D_2 of the present study and virtually twice as much as the samples exposed to the total UV-B dose of 1.08 J/cm^2 on only one side (6.4 ± 1.0 vs 3.3 ± 0.4 μg/g DW; P = 0.005).

The highest ratio of exposure area to mass did not lead to higher vitamin D_2 contents than the 9 mm slices. However, the thickest samples (12 mm) contained significantly less vitamin D_2 compared to the 9 mm slices (2.8 ± 0.3 vs 3.9 ± 0.8 μg/g DW; P = 0.05).

DOI: 10.1021/acs.jafc.5b02945
J. Agric. Food Chem. 2015, 63, 8156−8161

The present findings are consistent with data from studies that demonstrated a significantly higher yield of vitamin D_2 in sliced compared to whole mushrooms[20] and data on artificial UV-B exposure of mushroom powder with extremely high yields in vitamin D_2 content (498 μg/g DW),[13] showing the essentiality of the ratio of exposure area to mass.

Sun-Drying. Although the sun-drying process was already well advanced with a water loss of 84% relative to the initial total water content during the longest exposure period (360 min), still the drying process was not completed. The sun-triggered dehydration in the 360 min samples reached a mean water loss of 14% per hour relative to the initial weight. Approximately a minimum of an extra hour of sun exposure would have produced a final moisture content at the recommended level of 4−8% for safe storage.[31]

We found a substantial linear increase up to 1 h of exposure, showing the highest content of 31 μg/100 g FW produced by a UV-B dose of 0.53 J/cm^2. After sun exposure for only 15 min, similar to an UV-B dose of 0.13 J/cm^2, the vitamin D_2 content of sliced button mushrooms was comparable to vitamin D_3 levels found in salmon. This is particularly interesting for vegetarians, because all other dietary sources of vitamin D are of animal origin. In conclusion, the traditional and still practiced method of mushroom dehydration consisting of slicing, sun-drying, and, if needed, final indoor drying, can lead to an underappreciated, unexploited vitamin D-rich food source.

AUTHOR INFORMATION

Corresponding Author

*(P.U.) Phone: +49-761-2703360. Fax: +49-761-2703334. E-mail: paul.urbain@uniklinik-freiburg.de.

Author Contributions

P.U., study concept, study performance, and statistical analysis; J.J., analytics, critical review; all authors interpreted the data, drafted the manuscript, and saw and approved the final version of the manuscript.

Funding

This project has received funding from the European Union's Seventh Framework Programme (FP7/2007−2013) under Grant Agreement 613977 (ODIN).

Notes

The authors declare no competing financial interest.

ACKNOWLEDGMENTS

We are grateful to K. Cashman for his critical review, to C. Cuerten for editorial assistance, to J. Valverde from Monaghan Mushrooms Ireland for providing the button mushrooms, to I. Mayer and F. Meinhardt form the German Federal Office for Radiation Protection for receiving real-time UV-B data, to E. Maier, F. Jaeger, and F. Lorenz from University Medical Center's central kitchen for providing material for the experiments and storage of samples, and to K. Saliger and H. Urbain for helping out with sample preparation and experiments.

ABBREVIATIONS USED

EPS, expanded polystyrene; FW, fresh weight; DW, dry weight; LC-MS/MS, liquid chromatography−tandem mass spectrometry; RDA, recommended daily allowance; SEP, solid phase extraction; UTC, Universal Time Coordinated; UV, ultraviolet; UV/DAD, ultraviolet diode array detection

REFERENCES

(1) Teichmann, A.; Dutta, P. C.; Staffas, A.; Jägerstad, M. Sterol and vitamin D2 concentrations in cultivated and wild grown mushrooms: effects of UV irradiation. *LWT − Food Sci. Technol.* **2007**, *40* (5), 815−822.

(2) Havinga, E.; de Kock, R. J.; Rappoldt, M. P. The photochemical interconversions of provitamin D, lumisterol, previtamin D and tachysterol. *Tetrahedron* **1960**, *11* (4), 276−284.

(3) Dmitrenko, O.; Frederick, J. H.; Reischl, W. Previtamin D conformations and the wavelength-dependent photoconversions of previtamin D. *J. Photochem. Photobiol., A* **2001**, *139* (2−3), 125−131.

(4) Holick, M. F. The cutaneous photosynthesis of previtamin D3: a unique photoendocrine system. *J. Invest. Dermatol.* **1981**, *77* (1), 51−58.

(5) Mattila, P. H.; Piironen, V. I.; Uusi-Rauva, E. J.; Koivistoinen, P. E. Vitamin D contents in edible mushrooms. *J. Agric. Food Chem.* **1994**, *42* (11), 2449−2453.

(6) Phillips, K. M.; Ruggio, D. M.; Horst, R. L.; Minor, B.; Simon, R. R.; Feeney, M. J.; Byrdwell, W. C.; Haytowitz, D. B. Vitamin D and sterol composition of 10 types of mushrooms from retail suppliers in the United States. *J. Agric. Food Chem.* **2011**, *59* (14), 7841−7853.

(7) Mattila, P.; Könkö, K.; Eurola, M.; Pihlava, J. M.; Astola, J.; Vahteristo, L.; Hietaniemi, V.; Kumpulainen, J.; Valtonen, M.; Piironen, V. Contents of vitamins, mineral elements, and some phenolic compounds in cultivated mushrooms. *J. Agric. Food Chem.* **2001**, *49* (5), 2343−2348.

(8) Mau, J.-L.; Chen, P.-R.; Yang, J.-H. Ultraviolet irradiation increased vitamin D2 content in edible mushrooms. *J. Agric. Food Chem.* **1998**, *46* (12), 5269−5272.

(9) Jasinghe, V. J.; Perera, C. O. Distribution of ergosterol in different tissues of mushrooms and its effect on the conversion of ergosterol to vitamin D2 by UV irradiation. *Food Chem.* **2005**, *92* (3), 541−546.

(10) Jasinghe, V. J.; Perera, C. O. Ultraviolet irradiation: the generator of vitamin D2 in edible mushrooms. *Food Chem.* **2006**, *95* (4), 638−643.

(11) Ko, J. A.; Lee, B. H.; Lee, J. S.; Park, H. J. Effect of UV-B exposure on the concentration of vitamin D2 in sliced shiitake mushroom (*Lentinus edodes*) and white button mushroom (*Agaricus bisporus*). *J. Agric. Food Chem.* **2008**, *56* (10), 3671−3674.

(12) Roberts, J. S.; Teichert, A.; McHugh, T. H. Vitamin D2 formation from post-harvest UV-B treatment of mushrooms (*Agaricus bisporus*) and retention during storage. *J. Agric. Food Chem.* **2008**, *56* (12), 4541−4544.

(13) Wu, W.-J.; Ahn, B.-Y. Statistical optimization of ultraviolet irradiate conditions for vitamin D2 synthesis in oyster mushrooms (*Pleurotus ostreatus*) using response surface methodology. *PLoS One* **2014**, *9* (4), e95359.

(14) Simon, R. R.; Phillips, K. M.; Horst, R. L.; Munro, I. C. Vitamin D mushrooms: comparison of the composition of button mushrooms (*Agaricus bisporus*) treated postharvest with UVB light or sunlight. *J. Agric. Food Chem.* **2011**, *59* (16), 8724−8732.

(15) Phillips, K. M.; Rasor, A. S. A nutritionally meaningful increase in vitamin D in retail mushrooms is attainable by exposure to sunlight prior to consumption. *J. Nutr. Food Sci.* **2013**, *03* (06)10.4172/2155-9600.1000236.

(16) Kristensen, H. L.; Rosenqvist, E.; Jakobsen, J. Increase of vitamin D2 by UV-B exposure during the growth phase of white button mushroom (*Agaricus bisporus*). *Food Nutr. Res.* **2012**, *56*, 7114.

(17) Burild, A.; Frandsen, H. L.; Jakobsen, J. Simultaneous quantification of vitamin D3, 25-hydroxyvitamin D3 and 24,25-dihydroxyvitamin D3 in human serum by LC-MS/MS. *Scand. J. Clin. Lab. Invest.* **2014**, *74* (5), 418−423.

(18) CEN. *EN12821 Foodstuffs − determination of vitamin D by high performane liquid chromatography − measurement of cholecalciferol (D3) and ergocalciferol (D2)*; 36; European Committee for Standardization, 2008.

(19) Institute of Medicine. *Dietary Reference Intakes for Calcium and Vitamin D*; Ross, A. C., Taylor, C. L., Yaktine, A. L., Del Valle, H. B., Eds.; The National Academies Collection: Reports funded by National

DOI: 10.1021/acs.jafc.5b02945
J. Agric. Food Chem. 2015, 63, 8156−8161

Institutes of Health; National Academies Press: Washington, DC, USA, 2011.
(20) Kalaras, M. D.; Beelman, R. B.; Elias, R. J. Effects of postharvest pulsed UV light treatment of white button mushrooms (*Agaricus bisporus*) on vitamin D2 content and quality attributes. *J. Agric. Food Chem.* **2012**, *60* (1), 220−225.
(21) Keegan, R.-J. H.; Lu, Z.; Bogusz, J. M.; Williams, J. E.; Holick, M. F. Photobiology of vitamin D in mushrooms and its bioavailability in humans. *Derm.−Endocrinol.* **2013**, *5* (1), 165−176.
(22) Koyyalamudi, S. R.; Jeong, S.-C.; Song, C.-H.; Cho, K. Y.; Pang, G. Vitamin D2 formation and bioavailability from *Agaricus bisporus* button mushrooms treated with ultraviolet irradiation. *J. Agric. Food Chem.* **2009**, *57* (8), 3351−3355.
(23) Krings, U.; Berger, R. G. Dynamics of sterols and fatty acids during UV-B treatment of oyster mushroom. *Food Chem.* **2014**, *149*, 10−14.
(24) Jasinghe, V. J.; Perera, C. O.; Barlow, P. J. Vitamin D2 from irradiated mushrooms significantly increases femur bone mineral density in rats. *J. Toxicol. Environ. Health, Part A* **2006**, *69* (21), 1979−1985.
(25) Urbain, P.; Singler, F.; Ihorst, G.; Biesalski, H.-K.; Bertz, H. Bioavailability of vitamin D_2 from UV-B-irradiated button mushrooms in healthy adults deficient in serum 25-hydroxyvitamin D: a randomized controlled trial. *Eur. J. Clin. Nutr.* **2011**, *65* (8), 965−971.
(26) Kalaras, M. D.; Beelman, R. B.; Holick, M. F.; Elias, R. J. Generation of potentially bioactive ergosterol-derived products following pulsed ultraviolet light exposure of mushrooms (*Agaricus bisporus*). *Food Chem.* **2012**, *135* (2), 396−401.
(27) Braun, M.; Fuß, W.; Kompa, K. L.; Wolfrum, J. Improved photosynthesis of previtamin D by wavelengths of 280−300 nm. *J. Photochem. Photobiol., A* **1991**, *61* (1), 15−26.
(28) Boomsma, F.; Jacobs, H. J. C.; Havinga, E.; van der Gen, A. The "overirradiation products" of previtamin D and tachysterol: Toxisterols. *Recl. Trav. Chim. Pays-Bas* **1977**, *96* (4), 104−112.
(29) Webb, A. R.; Decosta, B. R.; Holick, M. F. Sunlight regulates the cutaneous production of vitamin D3 by causing its photodegradation. *J. Clin. Endocrinol. Metab.* **1989**, *68* (5), 882−887.
(30) Souci, S. W.; Fachmann, W.; Kraut, H. *Food Composition and Nutrition Tables*; CRC Press: Boca Raton, FL, USA, 2008.
(31) Komanowsky, M.; Talley, F. B.; Eskew, R. K. Air drying of cultivated mushrooms. *Food Technol.* **1970**, *24* (9).

DOI: 10.1021/acs.jafc.5b02945
J. Agric. Food Chem. 2015, 63, 8156−8161

Table 1. ^{1}H and ^{13}C NMR Data for Compound 1 in Methanol-d_4 and DMSO-d_6

	methanol-d_4		DMSO-d_6	
position	δ_C	δ_H mult (J in Hz)	δ_C	δ_H mult (J in Hz)
2	162.7, C		159.7, C	
3	112.3, CH	6.19, d (9.6)	111.7, CH	6.18, d (9.6)
4	146.1, CH	7.88, d (9.6)	144.7, CH	7.94, d (9.6)
4a	114.1, C		112.2, C	
5	126.2, CH	7.37, d (8.8)	125.3, CH	7.40, d (8.8)
6	115.0, CH	6.95, d (8.8)	113.6, CH	6.93, d (8.8)
7	156.0, C		154.2, C	
8	130.4, C		128.2, C	
8a	149.9, C		148.3, C	
1′	158.8, C		156.8, C	
2′	103.2, CH	6.35, d (2.4)	101.5, CH	6.24, d (2.4)
3′	157.3, C		155.9, C	
4′	122.1, C		120.2, C	
5′	131.3, CH	6.93, d (8.4)	130.1, CH	6.89, d (8.4)
6′	106.8, CH	6.27, dd (8.4, 2.4)	105.3, CH	6.19, dd (8.4, 2.4)
7′	26.5, CH_2	a (2.80, m), b (2.80, m)	24.8, CH_2	a (2.66, m), b (2.66, m)
8′	35.1, CH_2	a (2.56, m), b (2.56, m)	33.5, CH_2	a (2.46, m), b (2.46, m)
9′	175.8, C		172.9, C	
9′-C−OMe	51.9, CH_3	3.62, s	51.1, CH_3	3.52, s
7-OH				10.63, s
3′-OH				9.37, s

(Lifescan, Inc., Milpitas, CA). Mice with fasting blood glucose levels of ≥16.0 mmol/L were classified as diabetic mice.

General Experimental Procedures. Melting points were determined on an X-4 digital display micromelting point apparatus and are uncorrected. Optical rotations ($[\alpha]_D^{25}$) were measured on a PerkinElmer 341 polarimeter. Infrared (IR) spectra were obtained using a Thermo Nicolet 6700 FTIR spectrometer. Ultraviolet (UV) spectra were recorded on a PerkinElmer Lambda 25 Shimadzu 160 UV/vis spectrometer. The high-resolution electrospray ionization mass spectrometry (HRESIMS) spectra were recorded on an Agilent 6210 series LC/MSD TOF from Agilent Technologies. Nuclear magnetic resonance (NMR) spectra were acquired on a Bruker AVANCE HD III-400 using tetramethylsilane (TMS) as an internal standard. The X-ray diffraction data were collected on a SuperNova, Dual, Eos diffractometer. The structure was solved with the Superflip program using charge flipping and refined with the ShelXL program (using graphite-monochromated Mo Kα radiation). Silica gel (200−300 mesh, Qingdao Marine Chemical Factory, China), macroreticular resin (D-101, Sinopharm Chemical Reagent Co., Ltd., Shanghai, China), Sephadex LH-20 gel (GE Healthcare, Uppsala, Sweden), and MCI gel (CHP20P, 75−150 μm, Mitsubishi Chemical Industries, Ltd., Tokyo, Japan) were used for column chromatography (CC). Preparative high-performance liquid chromatography (HPLC) was carried out on a Shimadzu LC-6AD instrument with a SPD-20A detector, using a YMC-Pack ODS-A column (250 × 20 mm, 5 μm). Thin-layer chromatography (TLC) was performed using Merck precoated plates (Si gel 60 F254, Germany) of 0.25 mm thickness. The spots on TLC were detected with 254 and 365 nm UV light and visualized by spraying with 98% H_2SO_4/C_2H_5OH (5:95, v/v), followed by heating. The absorbances in the enzymatic assay were determined at 405 nm using a Bio-Rad model 680 microplate reader.

Extraction and Isolation. The dried powder of the flower of *E. gardneri* (12.0 kg) was extracted 3 times with MeOH (40 L) for 7 days each at room temperature. The combined extracts were concentrated under reduced pressure, and the residue (862 g) was partitioned into H_2O and extracted with petroleum ether, EtOAc, and *n*-BuOH, successively.

The EtOAc fraction (118 g) was subjected to CC over silica gel (petroleum ether/EtOAc, 40:1, 30:1, 20:1, 15:1, 10:1, 8:1, 5:1, 3:1, 1.5:1, 1:1, and 0:1, v/v) to give nine major fractions (A−I). Fraction A (1.2 g) was chromatographed over MCI (MeOH/H_2O, 9:1) to yield two fractions, A1 and A2. Fraction A2 (231 mg) was subjected to Sephadex LH-20 ($CHCl_3$/MeOH, 1:1) to yield compound **6** (22 mg). Fraction B (2 g) was purified by CC over MCI (MeOH/H_2O, 9:1) to yield two major fractions, B1 and B2. Fraction B1 (506 mg) was run again by CC over Sephadex LH-20 ($CHCl_3$/MeOH, 1:1) to obtain compounds **7** (16 mg), **8** (31 mg), and **9** (27 mg). Fraction B2 (700 mg) was also run again by CC over Sephadex LH-20 ($CHCl_3$/MeOH, 1:1) to obtain compound **10** (123 mg). Fraction C (1.1 g) was purified by CC over MCI (MeOH/H_2O, 9:1) to yield one fraction C1, and fraction C1 (638 mg) was separated by CC over Sephadex LH-20 ($CHCl_3$/MeOH, 1:1) to obtain compounds **1** (14 mg), **11** (56 mg), and **12** (21 mg). Fraction E (1.1 g) was purified by CC over MCI (MeOH/H_2O, 9:1) to yield one fraction E1, and fraction E1 was recrystallized from methanol to yield compound **3** (34 mg). Fraction G (1.6 g) was applied to MCI (MeOH/H_2O, 9:1) to give three major fractions (G1−G3). Fraction G1 (300 mg) was subjected to CC over Sephadex LH-20, eluted with MeOH/H_2O (1:1), and finally purified by prep-HPLC (MeOH/H_2O, 4:6) to yield compound **13** (11 mg). Fraction H (1.8 g) was subjected to CC over MCI (MeOH/H_2O, 9:1) to yield three fractions, H1−H3. Fraction H1 (1.5 g) was subjected to CC over Sephadex LH-20, eluted with MeOH/H_2O (1:1) and then purified by prep-HPLC (MeOH/H_2O, 4:6) to yield compound **14** (30 mg). Fraction I (82 g) was chromatographed over MCI (MeOH/H_2O, 9:1) to yield three fractions, I1−I3. Fraction I1 (61 g) was recrystallized from methanol to yield compound **5** (53 g) and a mother liquor (3.6 g). The mother liquor was subjected to CC over silica gel ($CHCl_3$/MeOH, 10:1, 5:1, 3:1, and 0:1) to yield two subfractions, I1.1 and I1.2. Fraction I1.2 (1.4 g) was purified by CC over Sephadex LH-20 ($CHCl_3$/MeOH, 1:1) to yield compound **15** (18 mg). Fraction I2 (2.3 g) was subjected to CC over Sephadex LH-20 (MeOH/H_2O, 1:1) to yield two subfractions, I2.1 and I2.2. Fraction I2.2 (1.4 g) was purified by CC over Sephadex LH-20 ($CHCl_3$/MeOH, 1:1) to yield compound **16** (45 mg).

The *n*-BuOH fraction (118 g) was subjected to CC over D-101 macroreticular resin with a H_2O/EtOH gradient (1:0, 8:1, 5:1, 3:1, 1.5:1, 1:1, and 0:1) to yield four major fractions (1−4). Fraction 2 was subjected to CC over silica gel ($CHCl_3$/MeOH, 4:1, 3:1, 2:1, and 0:1) to yield two fractions, 2.1 and 2.2. Fraction 2.2 (2.6 g) was purified by CC over Sephadex LH-20 ($CHCl_3$/MeOH, 1:1) to obtain compounds **17** (19 mg) and **18** (31 mg). Fraction 3 (42 g) was evaluated by TLC and compared to flavonoid standards, including standards for compounds **5**, **10**, **11**, **15**, and **16**, and the spots were visualized by spraying them with a

DOI: 10.1021/acs.jafc.5b03081
J. Agric. Food Chem. 2015, 63, 8162−8169

Table 2. ^{1}H and ^{13}C NMR Data for Compound 2 in Methanol-d_4 and DMSO-d_6

	methanol-d_4		DMSO-d_6	
position	δ_C	δ_H mult (J in Hz)	δ_C	δ_H mult (J in Hz)
2	162.2, C		159.5, C	
3	114.7, CH	6.28, d (9.6)	113.5, CH	6.34, d (9.6)
4	145.6, CH	7.90, d (9.6)	144.4, CH	8.05, d (9.6)
4a	116.3, C		114.3, C	
5	126.0, CH	7.46, d (8.8)	125.1, CH	7.40, d (8.8)
6	114.1, CH	7.29, d (8.8)	112.5, CH	6.93, d (8.8)
7	154.7, C		153.4, C	
8	132.4, C		130.2, C	
8a	149.3, C		148.3, C	
1′	158.7, C		156.9, C	
2′	103.8, CH	6.39, d (2.4)	102.4, CH	6.33, d (2.4)
3′	157.1, C		155.8, C	
4′	122.9, C		121.0, C	
5′	131.4, CH	6.96, d (8.4)	130.0, CH	6.94, d (8.4)
6′	107.3, CH	6.31, dd (8.4, 2.4)	105.7, CH	6.27, dd (8.4, 2.4)
7′	26.5, CH_2	a (2.79, m), b (2.79, m)	25.1, CH_2	a (2.65, m), b (2.65, m)
8′	35.8, CH_2	a (2.53, m), b (2.53, m)	34.6, CH_2	a (2.40, m), b (2.40, m)
9′	178.7, C		175.1, C	
1″	101.8, CH	5.09, d (7.6)	100.2, CH	5.07, d (7.6)
2″	74.6, CH	3.37, overlap	73.0, CH	3.16, overlap
3″	77.8, CH	3.45, overlap	76.7, CH	3.25, m
4″	70.9, CH	3.37, overlap	69.4, CH	3.13, overlap
5″	78.2, CH	3.45, overlap	77.2, CH	3.36, m
6″	62.2, CH_2	a (3.86, m), b [3.69, dd (12.0, 5.2)]	60.5, CH_2	a (3.67, m), b [3.45, dd (12.0, 5.2)]

5% H_2SO_4/EtOH solution, followed by heating. The TLC results showed that the spots displayed by fraction 3 were similar to those of flavonoids (compounds **5**, **15**, and **16**). Moreover, the content of compound **5** was the highest in this fraction. Fraction 3 (14 g) was subjected to CC over silica gel ($CHCl_3$/MeOH, 4:1, 3:1, 2:1, and 0:1) to yield three fractions, 3.1−3.3. Fraction 3.1 (2.6 g) was purified by CC over Sephadex LH-20 ($CHCl_3$/MeOH, 1:1) to obtain two subfractions, 3.1.1 and 3.1.2. Fraction 3.1.2 (827 mg) was run again by CC over Sephadex LH-20 ($CHCl_3$/MeOH, 1:1) to obtain compounds **17** (19 mg) and **18** (31 mg). Fraction 3.2 (3.1 g) was applied to CC over Sephadex LH-20 ($CHCl_3$/MeOH, 1:1) to yield two subfractions, 3.2.1 and 3.2.2. Fraction 3.2.1 (216 mg) was purified by prep-HPLC (MeOH/H_2O, 3:7) to yield compound **4** (22 mg). Fraction 3.2.2 (3.1 g) was chromatographed over Sephadex LH-20 ($CHCl_3$/MeOH, 1:1) to yield crude **19** (34 mg) and **20** (11 mg), and then they were separately recrystallized from MeOH. Fraction 3.3 (2.9 g) was subjected to CC over Sephadex LH-20 ($CHCl_3$/MeOH, 1:1) to obtain crude **2** (41 mg) and compound **21** (8 mg), and then compound **2** was recrystallized from MeOH.

Structural Elucidation of New Products. Gardnerol A (**1**): colorless crystals (MeOH); melting point (mp), 191−192 °C; IR (KBr) ν_{max}, 3228, 1693, 1589, 1513, 1433, 1031, 836, 792, 456 cm^{-1}; UV (MeOH) λ_{max} (log ε), 208 (4.40), 212 (4.41), 285 (3.90), 322 (4.12) nm; ^{1}H (DMSO-d_6 and methanol-d_4, 400 MHz) and ^{13}C NMR (DMSO-d_6 and methanol-d_4, 100 MHz) data, see Table 1; HRESIMS m/z, 357.0970 $[M + H]^+$ (calcd for $C_{19}H_{17}O_7$, 357.0969).

Gardnerol B (**2**): with powder ($CHCl_3$−MeOH); $[\alpha]_D^{25}$, −10.5 (c 0.38, MeOH); IR (KBr) ν_{max}, 3407, 3078, 2923, 1743, 1721, 1611, 839, 723 cm^{-1}; UV (MeOH) λ_{max} (log ε), 214 (4.26), 252 (3.62), 286 (3.93), 308 (3.98) nm; ^{1}H (DMSO-d_6 and methanol-d_4, 400 MHz) and ^{13}C NMR (DMSO-d_6 and methanol-d_4, 100 MHz) data, see Table 2; HRESIMS m/z, 343.0811 $[M + H]^+$ (calcd for $C_{18}H_{15}O_7$, 343.0812).

X-ray Analysis. The measurement was collected on a SuperNova, Dual, Eos diffractometer with graphite-monochromated Mo Kα radiation (λ = 0.710 73 Å). The structure of compound **1** was solved by direct method (SHELXS-2008).

Crystal Data for Compound 1. Gardnerol A (**1**) was crystallized from $CHCl_3$/ CH_3OH (1:1) to give colorless crystals. A single crystal of dimensions 0.35 × 0.31 × 0.24 mm^3 was used for X-ray measurements. Crystal data: $C_{19}H_{16}O_7$, space group P 1 $2_1/c$ 1, a = 14.7352(17) Å, b = 8.7127(9) Å, c = 14.2158(12) Å, α = 90.00°, β = 114.431(12)°, γ = 90.00°, V = 1661.6(3) $Å^3$, Z = 4, D_{calc} = 1.424 g/cm^3, R_1 = 0.0713, and wR_2 = 0.2056.

The supplementary crystallographic data for compound **1** reported in this paper has been deposited at the Cambridge Crystallographic Data Centre, under the reference number CCDC 1403668. Copies of the data can be obtained, free of charge, on application to the Director, CCDC, 12 Union Road, Cambridge CB2 1EZ, U.K., fax: +44-1223-336033 or e-mail: data_request@ccdc.cam.ac.uk.

α-Glucosidase Inhibition. The α-glucosidase inhibition was assessed according to the slightly modified method of Jeon et al.[19] The α-glucosidase (0.1 unit/mL) and substrate (*p*-NPG, 1.0 mM) were dissolved in potassium phosphate buffer (0.1 M, pH 6.7), and all samples were dissolved in DMSO. The inhibitor (10 μL) was preincubated with α-glucosidase (40 μL) at 37 °C for 10 min, and then the substrate (50 μL) was added to the reaction mixture. The enzymatic reaction was performed at 37 °C for 30 min. The reaction was then terminated by the addition of Na_2CO_3 (1 M, 100 μL). All samples were analyzed in triplicate with five different concentrations near the IC_{50} values, and the absorbance at 405 nm was determined using a microplate reader. The inhibition percentage (%) was calculated by the following equation:

$$\text{inhibition (\%)} = [(OD_{control} - OD_{control\ blank}) - (OD_{sample} - OD_{sample\ blank}) / (OD_{control} - OD_{control\ blank})] \times 100$$

Type of α-Glucosidase Inhibition. The mode of inhibition of α-glucosidase was investigated with increasing concentrations of substrate (4-nitrophenyl α-D-glucopyranoside) and compound **5**. Then, the inhibition type was determined by a Lineweaver−Burk plot according to Michaelis−Menten kinetics. Origin (version 8.0) software was used for plotting the results.

Oral Sucrose Tolerance Test (OSTT). The fasting normal and STZ-induced diabetic mice were orally administered with compound **5** (150 and 300 mg/kg of body weight), acarbose (5 mg/kg), or the

DOI: 10.1021/acs.jafc.5b03081
J. Agric. Food Chem. 2015, 63, 8162−8169

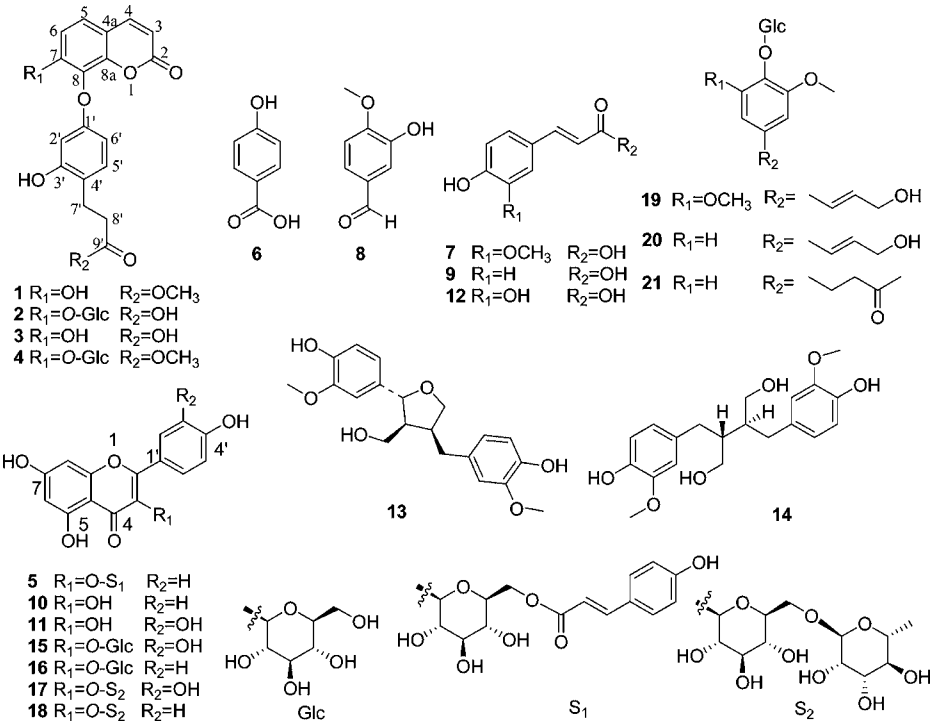

Figure 1. Structures of compounds **1**−**21**.

control and, after 30 min, were given a sucrose solution (3 g/kg of body weight). Each group has six mice. Compound **5** and acarbose were suspended in 0.5% sodium carboxymethyl cellulose (CMC−Na). The control mice were administered with the same volume of 0.5% CMC−Na solution. The tail vein glucose concentrations were measured with a glucometer at 0, 0.5, 1.0, 1.5, 2.0, and 3.0 h after the sucrose load.

Hypoglycemic Activity Assay. The fasting normal and STZ-induced diabetic mice (n = 6 for each group) were orally administered with compound **5** (150 and 300 mg/kg of body weight), glibenclamide (10 mg/kg), or the control (0.5% CMC−Na). The tail vein glucose concentrations were measured with a glucometer at 0, 1.5, 3, 5, 7, and 9 h after administration.

Statistical Analysis. The data were expressed as the mean ± standard error of the mean (SEM) and were analyzed using SPSS (version 19.0) statistical software (SPSS, Chicago, IL). The statistical significance of the differences ($p < 0.05$) between the mean values of the treatment and control groups were obtained from a one-way analysis of variance (ANOVA) followed by Tukey's or Dunnett's test.

RESULTS AND DISCUSSION

Isolation of Compounds from the Flower of *E. gardneri*. The extract was subjected to repeated CC over silica gel, Sephadex LH-20, and octadecyl silica (ODS) to yield 21 compounds (Figure 1). Compounds **1** and **2** were identified as new compounds. The 19 known compounds were identified as edgeworic acid (**3**),[20] 8-(3-(2,4-benzenediol)-propionic acid methyl ester)-coumarin-7-β-D-glucoside (**4**), tiliroside (**5**), 4-hydroxybenzoic acid (**6**), ferulic acid (**7**), 4-hydroxybenzaldehyde (**8**), *trans-p*-hydroxycinnamic acid (**9**), kaempferol (**10**), quercetin (**11**), caffeic acid (**12**), (+)-lariciresinol (**13**), (−)-secoisolariciresinol (**14**), isoquercetin (**15**), kaempferol-3-*O*-β-D-glucoside (**16**), rutin (**17**), kaempferol-3-rutinoside (**18**), syringin (**19**), coniferin (**20**), and zingerone 4-*O*-β-D-glucopyranoside (**21**).

Structure Elucidation of the Two New Compounds. Gardnerol A (**1**) was obtained as colorless crystals after crystallization from $CHCl_3$−CH_3OH. The molecular formula of compound **1** was established as $C_{19}H_{16}O_7$ from the $[M + H]^+$ ion at m/z 357.0907 (calcd. for $C_{19}H_{17}O_7$, 357.0967) in the HRESIMS. The IR spectrum exhibited strong absorption bands at 3228 cm^{-1} (OH), 1693 cm^{-1} (conjugated ester C═O), and 1619, 1582, and 1513 cm^{-1} (aromatic, C═C). The UV spectrum of compound **1** showed the characteristic maxima of a coumarin structure at 231, 252, and 325 nm. The ^1H NMR spectrum exhibited the typical signals in the aromatic region associated with H-3 at δ_H 6.18 (d, J = 9.6 Hz), H-4 at δ_H 7.88 (d, J = 9.6 Hz), H-5 at 7.37 (d, J = 8.8 Hz), and H-6 at δ_H 6.95 (d, J = 8.8 Hz, H-6) of a 7,8-disubstituted coumarin. The heteronuclear multiple-bond correlation (HMBC) correlations from the hydroxy proton at δ_H 10.63 to C-6, C-7, and C-8 confirmed that the hydroxy group was connected to C-7 (Figure 2). Additionally, the aromatic region of the ^1H NMR spectrum clearly showed the presence of an ABX spin system [δ_H 6.35 (d, J = 2.0 Hz, H-2′), δ_H 6.93 (d, J = 8.4 Hz, H-5′), and δ_H 6.27 (dd, J = 8.4, 2.0 Hz, H-6′)], indicative of a tri-substituted aromatic ring, which was confirmed by proton-coupling patterns and ^1H−^1H correlation spectros-

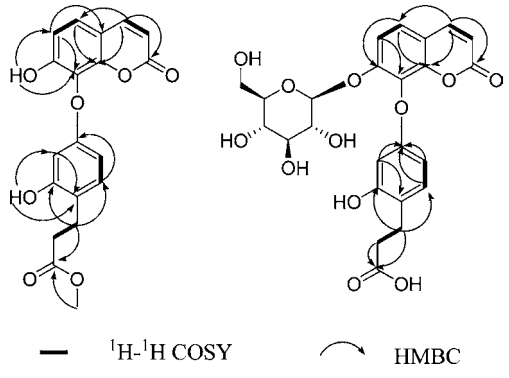

Figure 2. Key ^1H−^1H COSY and HMBC correlations for compounds **1** and **2**.

DOI: 10.1021/acs.jafc.5b03081
J. Agric. Food Chem. 2015, 63, 8162−8169

copy (COSY) correlations (Figure 2). The HMBC correlations of the hydroxy proton at δ_H 9.37 with C-2′, C-3′, and C-4′ supported the assignment that the hydroxy was attached to C-3′. In addition, one singlet at δ_H 3.52 (3H, s, $-COOCH_3$) and two mutually coupled triplets at δ_H 2.66 (2H, t, J = 8.0 Hz, H-7′) and δ_H 2.46 (2H, t, J = 8.0 Hz, H-8′) evidenced the presence of a methyl propionate side chain. The location of this side chain at C-4′ was determined on the basis of cross-peaks from H-7′ to C-3′, C-4′, and C-5′ and from H-4′ to C-7′ in the HMBC spectrum. The linkage of C-1′ to C-8 by one atom of oxygen was deduced from the above-mentioned reasoning and the molecular weight. Thus, the structure of compound **1** was defined as methyl 3-(2-hydroxy-4-*O*-(7-hydroxycoumarinyl)phenyl)propanoate. An X-ray diffraction analysis corroborated this proposed structure (Figure 3).

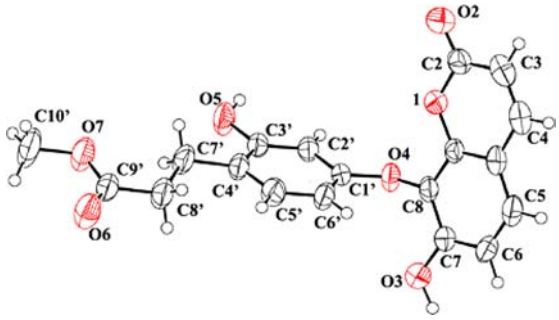

Figure 3. X-ray structure of compound **1**.

Gardnerol B (**2**) was obtained as a white powder. The HRMS data of compound **2** showed a molecular ion at m/z 527.1173 $[M + Na]^+$ (calcd. 527.1160), which was 162 mass units (i.e., $C_6H_{10}O_5$) more than that of compound **3** (m/z 343.0811, $[M + H]^+$). Correspondingly, the ^1H and ^{13}C NMR data of compound **2** were similar to those of compound **3**, except for the presence of an additional glucopyranosyl moiety.[20] The observation of the anomeric proton signal at δ_H 5.09 as a doublet with a coupling constant of 7.6 Hz indicated the presence of the β-glucopyranosyl moiety. The HMBC correlation between the anomeric proton (H-1‴, δ_H 5.09) and C-7 (δ_C 154.7) indicated that the β-glucopyranosyl moiety was attached to C-7 (Figure 2). Furthermore, to confirm the structure of compound **2**, compound **2** was hydrolyzed under acidic conditions. The sugar residue of compound **2** was identified as D-(+)-glucose by TLC comparison to an authentic sample and by its optical rotation value (see the Supporting Information). On the basis of the above analyses, the structure of compound **2** was identified as edgeworic acid-7-*O*-β-D-glucoside.

α-Glucosidase Inhibition. The IC_{50} values of compounds **1**−**21** and extracts from the flower of *E. gardneri* are shown in Table 3. In accordance with the previous report, the flower extract exhibited a significant inhibitory activity with an IC_{50} value of 267 μg/mL. Among these compounds, compound **11** was the most active, with an IC_{50} value of 5.1 μg/mL. Additionally, compound **10** showed a potent inhibitory activity with an IC_{50} value of 56.2 μg/mL. Compound **5**, the most abundant compound in the extract, showed a moderate activity, with an IC_{50} value of 202 μg/mL. Compounds **8**, **12**−**13**, and **16**−**18** also showed moderate activities with IC_{50} values of 486, 957, 279, 179, 272, and 253 μg/mL, respectively. Unfortunately, compounds **2**, **3**, **7**, **14**, and **19**−**21** showed no activities at the maximum concentration tested (3000 μg/mL). Previous

Table 3. α-Glucosidase Inhibition by Extract and Compounds 1−21[a]

	IC_{50} (μg/mL)		IC_{50} (μg/mL)
extract	267 ± 19	**12**	957 ± 36
1	517 ± 24	**13**	279 ± 14
2	>2000[b]	**14**	>2000
3	>2000	**15**	1233 ± 87
4	897 ± 59	**16**	179 ± 9.2
5	202 ± 12	**17**	272 ± 15
6	1200 ± 134	**18**	253 ± 19
7	>2000	**19**	>2000
8	486 ± 45	**20**	>2000
9	541 ± 32	**21**	>2000
10	56.2 ± 4.1	acarbose	465 ± 37
11	5.1 ± 0.3		

[a]Values are the means ± SEM from at least three independent experiments. [b]Exceeds the maximum concentration tested.

literature reported that flavonoids with 7, 3, 3′, and 4′ hydroxy groups showed significant α-glucosidase inhibitory activity.[21] Our results revealed that the 3′ hydroxy groups are responsible for increased activity because compounds **10** and **11**, with a 3′ hydroxy group, were more active than compounds **5** and **15**−**18**, without a 3′ hydroxy group. Compounds **2** and **3** showed significantly less activity than compounds **1** and **4**. This result suggests that the methyl ester group has an impact on the inhibitory activity. When compound **4** was compared to compound **1**, the inhibitory activity was reduced because of the absence of the hydroxy groups at the C-5 position.

Types of α-Glucosidase Inhibition. To clarify the α-glucosidase inhibition mode of compound **5**, which was the most abundant compound in the extract, Lineweaver−Burk plots were generated (Figure 4).[22] As shown in Figure 4, the value of the vertical axis intercept ($1/V_{max}$) remained unchanged with the increase of the concentrations of compound **5**, indicating that compound **5** was a competitive inhibitor. According to Michaelis−Menten kinetics, the value of the inhibition constant (K_i) is 0.473 mM.

Antihyperglycemic Effects of Compound 5 on Oral Sucrose Tolerance in Normal and STZ-Induced Diabetic Mice. The OSTT is usually performed to evaluate the efficacy of a drug in inhibiting intestinal α-glucosidase *in vivo*.[23] Compound **5** was a major constituent of the extract of *E. gardneri*, and 53 g of compound **5** were obtained from the extract. In addition, compound **5** showed significant α-glucosidase inhibitory activity *in vitro*. Thus, compound **5** was evaluated for its antihyperglycemic effects using an OSTT in both normal and STZ-induced diabetic mice. In comparison to the vehicle, the oral administration of compound **5** at a dose of 300 mg/kg significantly ($p < 0.05$) reduced the postprandial blood glucose level of normal mice (Figure 5A). The antihyperglycemic effect was observed at 30, 60, and 90 min after sucrose loading and was compared to that of acarbose (5 mg/kg). In contrast, the 150 mg/kg dose did not show a significant decrease in glycemia throughout the experiment. The OSTT was repeated in STZ-induced diabetic mice. These results were similar to those for normal mice (Figure 5B). According to the results of the OSTT, compound **5** inhibited the activity of intestinal α-glucosidase.

Hypoglycemic Effect of Compound 5 on Normal and STZ-Induced Diabetic Mice. According to previous methods,[24,25] the hypoglycemic activity of compound **5** was evaluated in both normal and STZ-induced diabetic mice. As shown in

DOI: 10.1021/acs.jafc.5b03081
J. Agric. Food Chem. 2015, 63, 8162−8169

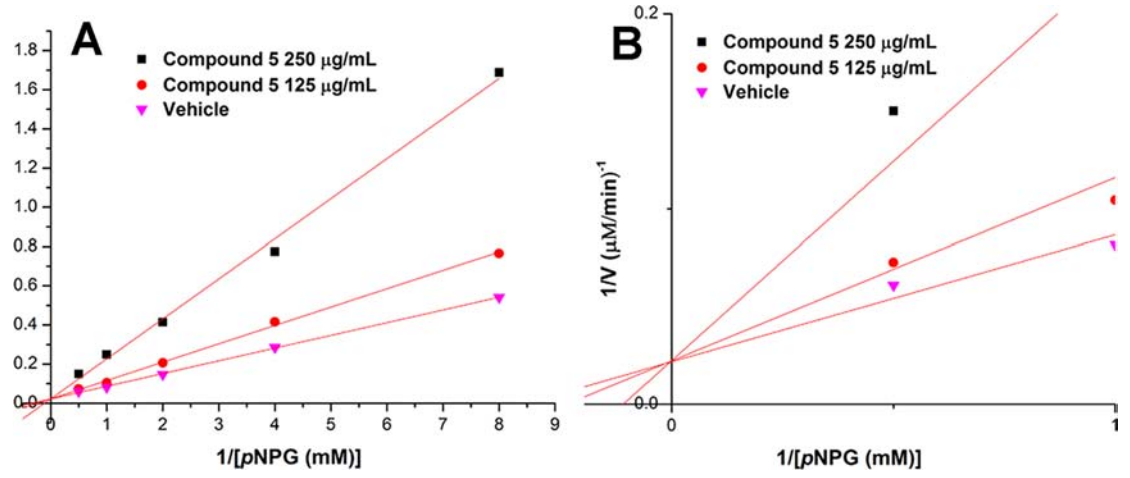

Figure 4. (A) Lineweaver−Burk plots of the reaction of α-glucosidase at different concentrations of substrate and compound **5**. (B) Partially enlarged view of panel A.

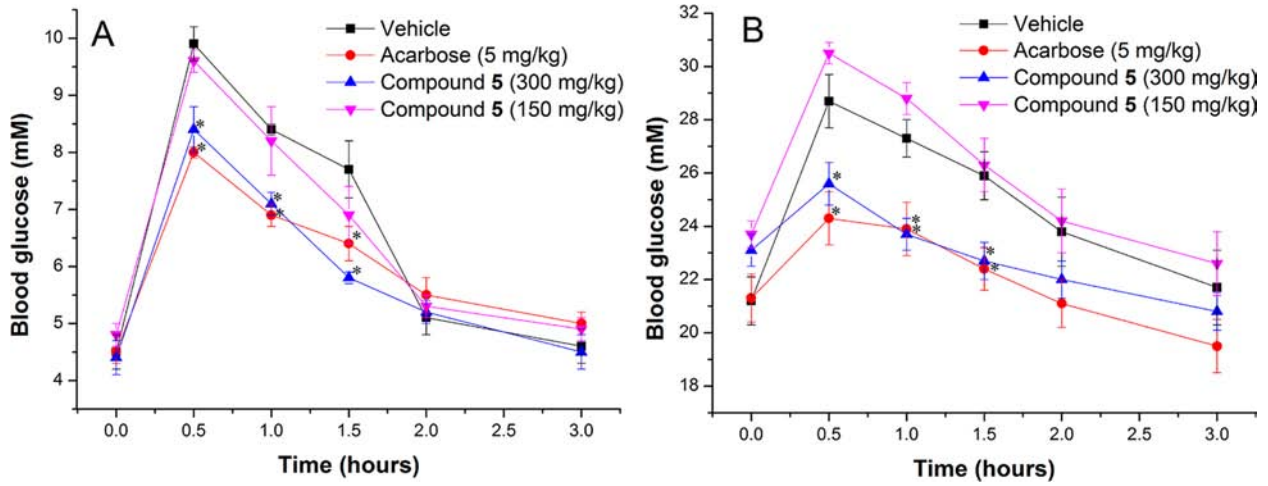

Figure 5. Effects of compound **5** on blood glucose levels in (A) normal and (B) STZ-induced diabetic mice using the OSTT. Data are the means ± SEM for six mice in each group. (∗) $p < 0.05$ by one-way ANOVA with a post-hoc test compared to the control.

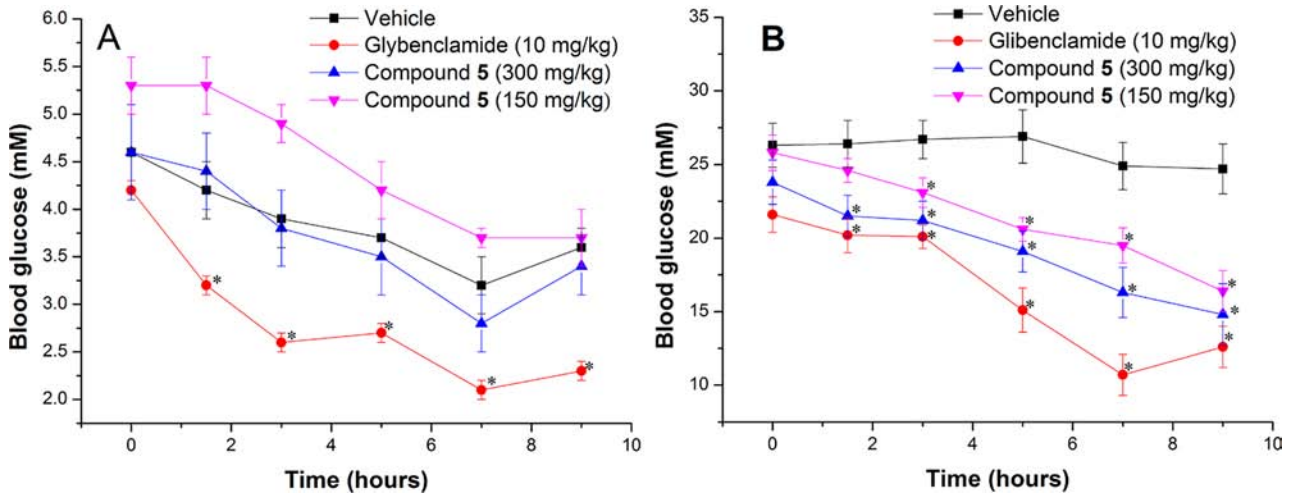

Figure 6. Hypoglycemic effect of compound **5** on (A) normal and (B) STZ-induced diabetic mice. Data are the means ± SEM for six mice in each group. (∗) $p < 0.05$ by one-way ANOVA with a post-hoc test compared to the control.

Figure 6, compound **5**, which had decreased fasting glucose levels in STZ-induced diabetic mice, did not lower the fasting glucose levels in normal mice. In diabetic mice, the oral administration of compound **5** at 150 and 300 mg/kg at both doses significantly decreased the fasting glucose levels when compared to the vehicle-treated groups ($p < 0.05$). The dose at 300 mg/kg

DOI: 10.1021/acs.jafc.5b03081
J. Agric. Food Chem. 2015, 63, 8162−8169

resulted in a significant decrease in the glucose level at 1.5 h (−9.7%), 3 h (−10.9%), 5 h (−18.5%), 7 h (−31.5%), and 9 h (−37.8%). After an administration of 150 mg/kg of compound **5**, the glucose level decreased by 4.7% at 1.5 h, 10.5% at 3 h, 20.2% at 5 h, 24.4% at 7 h, and 36.4% at 9 h. Because compound **5** displayed a hypoglycemic effect in diabetic mice but not in normal mice, in contrast with glibenclamide, these results indicate that compound **5** may not act directly via insulin liberation. Previous studies suggested that kaempferol, the hydrolysis products of compound **5**, improved the chronic hyperglycemia-impaired pancreatic β-cell viability and insulin-secretory function.[26] Therefore, the hypoglycemic action of compound **5** probably involves the protection of pancreatic β-cell survival and function. Further studies are necessary to demonstrate the mechanisms by which compound **5** decreased the fasting glucose levels in STZ-induced diabetic mice.

In summary, two new phenolics, along with 19 known phenolics, were isolated from the flower of *E. gardneri*. Their inhibitory activity against α-glucosidase from *S. cerevisiae* was evaluated, and the data showed that the flower of *E. gardneri* is a rich source of natural α-glucosidase inhibitors. Compound **5**, the most abundant compound in the extract, showed a significant α-glucosidase inhibitory activity and acted as a competitive inhibitor of α-glucosidase. Furthermore, compound **5** is effective *in vivo* for reducing the fasting and postprandial blood glucose levels in STZ-induced diabetic mice. In conclusion, the present study complements the current knowledge about the chemical composition and antihyperglycemic activity of the flower of *E. gardneri*, and it provides scientific evidence to substantiate the use of this flower for traditional therapeutic and dietary uses.

■ ASSOCIATED CONTENT

Supporting Information

The Supporting Information is available free of charge on the ACS Publications website at DOI: 10.1021/acs.jafc.5b03081.

Structure of gardnerol A (**1**) (CIF)

Acid hydrolysis procedure and HRESIMS, IR, and ^{1}H, ^{13}C, and 2D NMR spectra of compounds **1** and **2** (PDF)

■ AUTHOR INFORMATION

Corresponding Authors

*Telephone/Fax: +86-20-39323363. E-mail: zhiyundu@gdut.edu.cn.

*Telephone/Fax: +86-20-39323363. E-mail: kzhang@gdut.edu.cn.

Author Contributions

†Yan-Yan Ma and Deng-Gao Zhao contributed equally to this work and should be considered co-first authors.

Funding

This work was supported by the National Natural Science Foundation of China (21402030, 21402031, and 21272043).

Notes

The authors declare no competing financial interest.

■ REFERENCES

(1) Wild, S.; Roglic, G.; Green, A.; Sicree, R.; King, H. Global Prevalence of Diabetes: Estimates for the year 2000 and projections for 2030. *Diabetes Care* **2004**, *27*, 1047−1053.

(2) Blonde, L. Benefits and risks for intensive glycemic control in patients with diabetes mellitus. *Am. J. Med. Sci.* **2012**, *343*, 17−20.

(3) Bolen, S.; Feldman, L.; Vassy, J.; Wilson, L.; Yeh, H. C.; Marinopoulos, S.; Wiley, C.; Selvin, E.; Wilson, R.; Bass, E. B.; Brancati, F. L. Systematic review: comparative effectiveness and safety of oral medications for type 2 diabetes mellitus. *Ann. Intern. Med.* **2007**, *147*, 386−399.

(4) Lebovitz, H. E. α-Glucosidase inhibitors. *Endocrinol. Metab. Clin. North Am.* **1997**, *26*, 539−551.

(5) Fujisawa, T.; Ikegami, H.; Inoue, K.; Kawabata, Y.; Ogihara, T. Effect of two α-glucosidase inhibitors, voglibose and acarbose, on postprandial hyperglycemia correlates with subjective abdominal symptoms. *Metab., Clin. Exp.* **2005**, *54*, 387−390.

(6) Bhat, M.; Zinjarde, S. S.; Bhargava, S. Y.; Kumar, A. R.; Joshi, B. N. Antidiabetic Indian plants: a good source of potent amylase inhibitors. *Evidence-Based Complementary Altern. Med.* **2011**, *2011*, 810207.

(7) Benalla, W.; Bellahcen, S.; Bnouham, M. Antidiabetic medicinal plants as a source of α-glucosidase inhibitors. *Curr. Diabetes Rev.* **2010**, *6*, 247−254.

(8) Yilmazer-Musa, M.; Griffith, A. M.; Michels, A. J.; Schneider, E.; Frei, B. Grape seed and tea extracts and catechin 3-gallates are potent inhibitors of α-amylase and α-glucosidase activity. *J. Agric. Food Chem.* **2012**, *60*, 8924−8929.

(9) Li, Y. Q.; Zhou, F. C.; Gao, F.; Bian, J. S.; Shan, F. Comparative evaluation of quercetin, isoquercetin and rutin as inhibitors of α-glucosidase. *J. Agric. Food Chem.* **2009**, *57*, 11463−11468.

(10) McDougall, G. J.; Shpiro, F.; Dobson, P.; Smith, P.; Blake, A.; Stewart, D. Different polyphenolic components of soft fruits inhibit α-amylase and α-glucosidase. *J. Agric. Food Chem.* **2005**, *53*, 2760−2766.

(11) da Silva Pinto, M.; Kwon, Y.-I.; Apostolidis, E.; Lajolo, F. M.; Genovese, M. I.; Shetty, K. Functionality of bioactive compounds in Brazilian strawberry (Fragaria × ananassa Duch.) cultivars: evaluation of hyperglycemia and hypertension potential using in vitro models. *J. Agric. Food Chem.* **2008**, *56*, 4386−4392.

(12) Gonçalves, R.; Mateus, N.; de Freitas, V. Inhibition of α-amylase activity by condensed tannins. *Food Chem.* **2011**, *125*, 665−672.

(13) Liu, M.; Yin, H.; Liu, G.; Dong, J. J.; Qian, Zh.H.; Miao, J. L. Xanthohumol, a Prenylated Chalcone from Beer Hops, Acts as an α-Glucosidase Inhibitor in Vitro. *J. Agric. Food Chem.* **2014**, *62*, 5548−5554.

(14) Xu, P.; Xia, Z.; Lin, Y. Chemical constituents from *Edgeworthia gardneri* (Thymelaeaceae). *Biochem. Syst. Ecol.* **2012**, *45*, 148−150.

(15) Wang, Q.-Y.; Xu, H.-Y.; Xu, Z.-H.; Lu, Z.-M.; Liu, M.; Shi, J.-S. Hypoglycemic effect of water extracts from *Edgeworthia gardneri* (Wall.) Meissn on type 2 diabetic mice. *Nat. Prod. Res. Dev.* **2014**, *26*, 1385−1388.

(16) Geng, Y.; Yang, H.-M.; Xu, H.-Y.; Shi, J.-S. α-Glucosidase inhibitory activity of the alabastrum of *Edgeworthia gardneri* (Wall.) Meissn. *J. Food Sci. Biotechnol.* **2013**, *32* (9), 967−971.

(17) Gao, D.; Zhang, Y.-L.; Xu, P.; Lin, Y.-X.; Yang, F.-Q.; Liu, J.-H.; Zhu, H.-W.; Xia, Z.-N. In vitro evaluation of dual agonists for PPARγ/β from the flower of *Edgeworthia gardneri* (wall.)Meisn. *J. Ethnopharmacol.* **2015**, *162*, 14−19.

(18) Li, S.-S.; Gao, Z.; Feng, X.; Hecht, S. M. Biscoumarin derivatives from *Edgeworthia gardneri* that inhibit the lyase activity of DNA polymerase β. *J. Nat. Prod.* **2004**, *67*, 1608−1610.

(19) Jeon, S. Y.; Oh, S.; Kim, E.; Imm, J. Y. α-Glucosidase Inhibiton and Antiglycation Activity of Laccase-Catalyzed Catechin Polymers. *J. Agric. Food Chem.* **2013**, *61*, 4577−4584.

(20) Li, X. N.; Tong, S. Q.; Cheng, D. P.; Li, Q. Y.; Yan, J. Z. Coumarins from *Edgeworthia chrysantha*. *Molecules* **2014**, *19*, 2042−2048.

(21) Escandón-Rivera, S.; González-Andrade, M.; Bye, R.; Linares, E.; Navarrete, A.; Mata, R. α-Glucosidase Inhibitors from Brickellia cavanillesii. *J. Nat. Prod.* **2012**, *75*, 968−974.

(22) Yan, J.; Zhang, G.; Pan, J.; Wang, Y. α-Glucosidase inhibition by luteolin: Kinetics, interaction and molecular docking. *Int. J. Biol. Macromol.* **2014**, *64*, 213−223.

(23) Brindis, F.; Rodríguez, R.; Bye, R.; Gonzalez-Andrade, M.; Mata, R. Z)-3-Butylidenephthalide from Ligusticum porteri, an α-Glucosidase Inhibitor. *J. Nat. Prod.* **2011**, *74*, 314−320.

(24) Nuñez-López, A. M.; Paredes-López, O.; Reynoso-Camacho, R. Functional and Hypoglycemic Properties of Nopal Cladodes (*O.*

DOI: 10.1021/acs.jafc.5b03081
J. Agric. Food Chem. 2015, 63, 8162−8169

ficusindica) at Different Maturity Stages Using in Vitro and in Vivo Tests. *J. Agric. Food Chem.* **2013**, *61*, 10981−10986.
(25) Narváez-Mastache, M. J.; Garduño-Ramírez, L. M.; Alvarez, L.; Delgado, G. Antihyperglycemic Activity and Chemical Constituents of *Eysenhardtia platycarpa*. *J. Nat. Prod.* **2006**, *69*, 1687−1691.
(26) Zhang, Y.; Liu, D. Flavonol kaempferol improves chronic hyperglycemia-impaired pancreatic beta-cell viability and insulin secretory function. *Eur. J. Pharmacol.* **2011**, *670*, 325−332.

DOI: 10.1021/acs.jafc.5b03081
J. Agric. Food Chem. 2015, 63, 8162−8169

F-127 were purchased from Biotium Inc. (Hayward, CA, USA). HPLC-grade acetonitrile was purchased from Fisher Chemical (Bridgewater, NJ, USA), and HPLC-grade water was prepared using a Milli-Q system (Millipore Ibérica, Madrid, Spain). Trifluoroacetic acid (TFA) of HPLC grade was purchased from Sigma Chemical Co. (St. Louis, MO, USA). All other chemicals employed were of analytical reagent grade, and the water used was double-deionized.

Preparation of Desalted Duck Egg White Peptides (DPs). DPs with molecular weight of <5 kDa were prepared from salted duck egg white as described in our previous work.[13] Salted duck egg white was desalted by electrodialysis equipment, and then the desalted duck egg white was denatured for 30 min in boiling water and cooled to 50 °C. The pH was adjusted to 6.5 prior to the addition of protamex (E:S = 1:25) and maintained at 6.5. After 3.5 h, the hydrolyzed solution was bathed in boiling water for 10 min to inactivate the enzyme. Finally, the mixture was centrifuged at 3000*g* for 10 min, and the supernatant was filtered through a hollow fiber membrane with a molecular weight cutoff of 5 kDa (PLCC, Millipore, Billerica, MA, USA). The filtrate was lyophilized and thereafter referred to as DPs.

Establishment of Caco-2 Cell Monolayers. The Caco-2 cells were used as a model of the intestinal epithelium, and this cell line was purchased from the Cell Bank of Chinese Academy of Sciences (Shanghai, China). The cells were routinely grown in 75 cm^2 plastic flasks (Greiner Bio-One GmbH, Germany) in MEM medium (GIBCO) with 15% fetal bovine serum, supplemented with 1% nonessential amino acids (GIBCO) in the presence of 100 u/mL streptomycin and 100 u/mL penicillin. The cells were then incubated at 37 °C with 5% CO_2. Cell passage numbers of 30−50 were used in this experiment. The culture medium was changed every 2 days until the flasks reached 90% confluence. Cell viability was assessed by the MTT test, and cell morphology was examined through an optical microscope.

At 90% confluence, the Caco-2 cells were detached with trypsin−EDTA treatment (final concentration of 0.005 g/L), followed by seeding of the cells on 12-well millicell cell culture inserts (0.4 μm pore size, 12 mm diameter, Millipore Corp., Billerica, MA, USA) with a cell density of 1.2×10^5 cells/mL and 21 days of incubation. The volume of culture medium was 1.95 mL in the basolateral side and 0.4 mL in the apical side. Transepithelial electric resistance (TEER) values were checked every 2 days by using a Millicell-ERS system (Millipore) to evaluate the tight junction permeability of the Caco-2 cell monolayers.

Calcium Transport Studies. Caco-2 cell monolayers with TEERs exceeding 500 $\Omega \cdot cm^{-2}$ were used for the calcium transport experiments. The monolayers were set in a 12-well plate and washed twice with warm (37 °C) balanced salt solution without calcium and magnesium (HBS) (125 mM NaCl, 4 mM KCl, 4 mM L-Glu, 10 mM glucose, 30 mM HEPES, adjusted to pH 7.4) and incubated at 37 °C for 20 min. The wells were then transferred to a new cluster plate containing 1.95 mL of HBS buffer. Different concentrations of calcium solution (0−20 mM, 0.4 mL) were added to the apical side of the inset, and the calcium transport rates across Caco-2 cell monolayers were measured every hour for 3 h. After the optimum conditions were determined, DPs of different concentrations (0−8 mg/mL) were added to the apical side with the optimum calcium solution. After incubation, samples were collected from the basolateral side for further analysis. The TEERs were monitored before and after the addition of the calcium and DP samples. The calcium contents were measured with an atomic absorption spectrophotometer (AA6300C, Shimadzu, Kyoto, Japan).

Measurement of Ca^{2+} in Caco-2 Cell Population Model. At 90% confluence, the Caco-2 cells were detached with trypsin−EDTA treatment and then washed several times with HBS. About 4×10^6 cells were loaded in HBS with 5 μmol/L Fluo-3/AM and 2.5 μmol/L Pluronic F-127 for 30 min at 37 °C. The loaded cell suspension was rinsed thoroughly two times with calcium-free HBS and then divided into eight portions, each containing 0.5×10^6 cells. Each aliquot was suspended in 1 mL of HBS containing different calcium concentrations (2−6 mM) and then transferred to a cuvette and placed in a Hitachi F-4600 spectrofluorometer (Hitachi, Japan). The cells were stirred continuously during the experiment, and fluorescence excitation/emission wavelengths were set at 488/525 nm for Fluo-3-loaded cells. Then different concentrations of DPs were added into the cuvette through the injection port. To maintain cell viability, the duration of the whole experiment never exceeded 20 min. The results in each case were expressed as Ca^{2+} peak of fluorescence intensity units from baseline.

Everted Rat Intestine Permeation. Wistar male rats in the weight range of 250−300 g were obtained from Hubei Laboratory Animal Research Center and kept under standard environmental conditions. The animals were handled in accordance with the Declaration of Helsinki and the Guiding Principles in the Care and Use of Animals and the Chinese standards (GB 14925-2001). Food was removed about 18 h prior to trial, but water was allowed ad libitum before sacrifice. The entire small intestine was immediately collected via a midline incision of the abdomen and placed into the buffer solution (136 mM NaCl, 8.17 mM KCl, 1.0 mM $MgCl_2$, 11.1 mM glucose, 20 mM HEPES, adjusted to pH 7.4) at 4 °C. The first 15 cm of duodenum was discarded, and the intestine was washed thoroughly with the buffer. The surface liquid was sopped up by the filter paper, and then the intestine was everted. Each everted intestinal segment was about 6 cm in length, and 4 mL of buffer solution (drug free) was then placed into the serosal compartment. The two distal ends were ligatured, and the entire everted intestine segment was placed into the flasks containing 100 mL of buffer with various concentrations of DPs and calcium at 37 °C. Meanwhile, 95% O_2 was constantly bubbled through the buffer. After 120 min of incubation, the serosal solution was collected and the transported calcium was measured with an atomic absorption spectrophotometer (AA6300C, Shimadzu, Kyoto, Japan).

HPLC Analysis Instrumentation. The HPLC analysis was performed on a Waters e2695 HPLC-DAD system (Waters, Milford, MA, USA), equipped with a diode array detector, a vacuum degasser, an autosampler, a binary pump, and a column compartment. DPs (<5 kDa) at a concentration of 10 mg/mL were analyzed on a ZORBAX SB-C18 column (250 mm × 4.6 mm, 5 μm, Agilent Co., Santa Clara, CA, USA) at a flow rate of 1 mL/min, with the temperature of the column maintained at 30 °C. A binary gradient elution system, comprising water (with 0.1% TFA, A) and acetonitrile (with 0.1% TFA, B), was applied as follows: 0.0−20.0 min, 5−15% B; 20.0−35.0 min, 15−20% B; 35.0−40.0 min, 20−30% B; 40.0−50.0 min, 30−40% B. The volume of injection was 10 μL, and the DAD detector was set at 220 nm for analysis.

HPLC-ESI-MS/MS Analysis Instrumentation. For HPLC-ESI-MS/MS analysis, the HPLC system described above was replaced by an Agilent1100 series HPLC-ESI-MS system (Agilent Technologies) but with the same column and gradient elution as in the HPLC analysis. Mass spectrometry conditions were set as follows: ESI^+ ion source; drying gas temperature, 325 °C; nebulizer, 40.00 psi; dry gas flow rate, 10.0 L/min; capillary voltage, 3500 V; scan spectra from m/z 100 to 1000.

The sequences were identified using LCMSD-Trap Data Analysis software and confirmed by searching the online MS database on the UCSF Mass Spectrometry Facility (http://prospector.ucsf.edu/prospector/cgi-bin/msform.cgi?form=mspattern).

Isothermal Titration Calorimetry (ITC). ITC was undertaken with an ITC200 calorimeter (MicroCal, Northampton, MA, USA). The titrant was 10 mM $CaCl_2$, and the sample cell contained 0.5 mM peptides or 0.4 mM EDTA dissolved in double-distilled water (pH 7.8). The titration comprised 20 × 2 μL injections at 25 °C. Data were analyzed with the Origin 5.0 software package (ITC Data Analysis in Origin, MAU130010 REV F-4, MicroCal). The binding constants K, ΔH, and ΔS were calculated.

Statistical Analysis. The sample treatments described in this experiment were conducted in triplicate, and the data were presented as mean values ± SD. Data were calculated using one-way ANOVA of SPSS 18.0 followed by Duncan's multiple-range test. Differences were considered significant at P values <0.05.

RESULTS AND DISCUSSION

Permeability of Caco-2 Cell Monolayers. Native epithelial tissues are traditional subjects for the research of transport processes, but these tissues are complex and contain many different cell types. Caco-2 cells are human intestinal

DOI: 10.1021/acs.jafc.5b03097
J. Agric. Food Chem. 2015, 63, 8170−8176

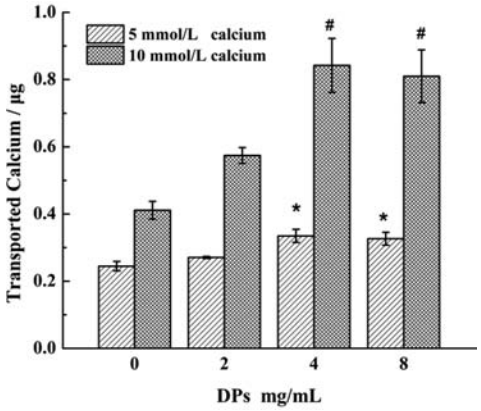

Figure 1. Effects of DPs on calcium transport across Caco-2 monolayers. DPs (0−8 mg/mL) were added to the apical side with calcium solution (5 or 10 mM, 0.4 mL) and then incubated for 120 min. Mean values with different letters are significantly different at $P < 0.05$.

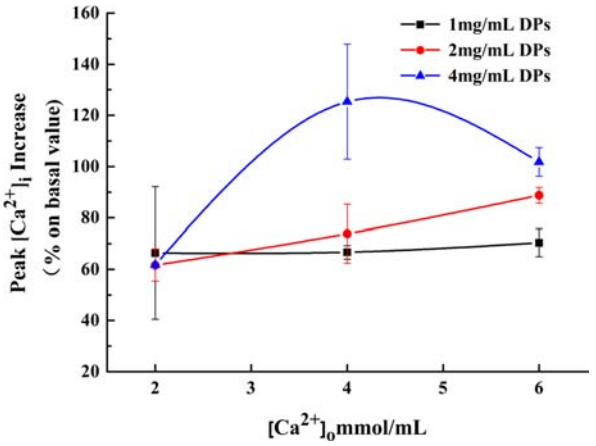

Figure 2. Calcium uptake by Caco-2 cells as influenced by different concentrations of DPs (1−4 mg/mL) and extracellular Ca^{2+} (0−4 mM). Intracellular calcium concentrations are expressed as an increase in fluorescence intensity compared to baseline, which is the original fluorescence intensity before the addition of DPs to the aliquot containing 0.5×10^6 cells.

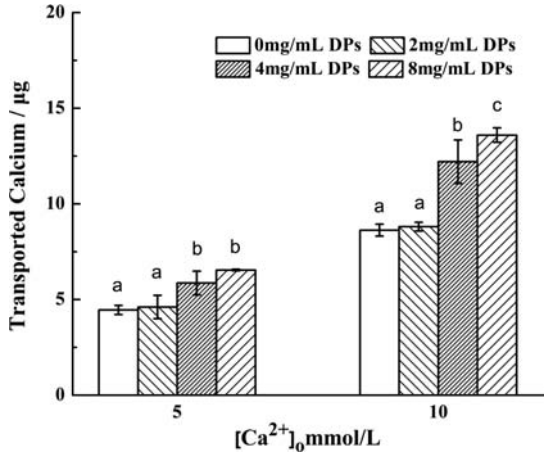

Figure 3. Effects of DPs on calcium transport across everted intestinal sac. DPs (0−8 mg/mL) were added to the mucosal solutions containing 5 or 10 mM Ca^{2+} and then incubated for 120 min. Mean values with different letters are significantly different at $P < 0.05$.

Table 1. Amino Acid Composition (g/100 g Peptides) of DPs (M_w < 5 kDa)

amino acid	DPs (<5 kDa)	amino acid	DPs (<5 kDa)
Asx[a] (D + N)	7.14	Ile (I)	3.3
Thr (T)	5.19	Leu (L)	7.17
Ser (S)	7.44	Tyr (Y)	3
Glx[b] (E + Q)	12.14	Phe (F)	6.17
Gly (G)	2.84	Lys (K)	4.5
Ala (A)	3.95	His (H)	1.54
Cys (C)	1.16	Arg (R)	3.52
Val (V)	4.97	Pro (P)	2.11
Met (M)	5.1	total amino acid	81.24

[a]Asx = Asp + Asn (D + N). [b]Glx = Glu + Gln (E + Q).

adenocarcinoma cells exhibiting enterocyte-like biochemical and morphological characteristics, and they have been reported to be an excellent in vitro model of human enterocytes for absorption studies involving minerals,[14] polyphenols,[15] proteins, and peptides.[16] In the present study, Caco-2 monolayers were used to evaluate the effect of DPs on calcium transport.

After cells had been seeded on 12-well millicell cell culture inserts, different concentrations of calcium were added to the apical compartment and the calcium on the basolateral side was measured. When 5 or 10 mM Ca^{2+} was added, no significant change in calcium transport was observed. When the concentration was increased to 20 mM, the calcium transport showed a 2-fold increase compared to control. As the total Ca^{2+} concentrations in the intestinal lumen may reach 3−4 mM in rats and 7−8 mM in humans after a proper meal,[17] 5 and 10 mM were chosen as suitable Ca^{2+} concentrations for further experiments. The effect of incubation time on calcium transport was then evaluated and found to increase with the extension of incubation time. On the basis of the retention time of food in the intestine (about 120−180 min) and cell viability, an incubation time of 120 min was determined to be the optimum duration for further experiments (data not shown).

Effect of DPs on Calcium Transport in Caco-2 Monolayers. Cell viability was evaluated to be >90% after treatment with different DPs concentrations (0−8 mg/mL). Figure 1 shows the effect of 0−8 mg/mL DPs on calcium transport with 5 and 10 mM Ca^{2+} in Caco-2 cell monolayers. In the presence of 4 and 8 mg/mL DPs, the calcium transport showed increases of 36.77 and 33.33% over that of the control group at the concentration of 5 mM Ca^{2+}. Increasing the concentration of Ca^{2+} to 10 mM increased the calcium transport by 104.88% (4 mg/mL DPs) and 97.01% (8 mg/mL DPs) versus the control group. For a given calcium concentration, the increase in Ca^{2+} transport was roughly equal whether 4 or 8 mg/mL DPs were used, implying that the influence of DPs on the transport process was saturable.

Drugs may be transported across the intestinal epithelium by one or more of four different routes: passive transcellular and paracellular routes, carrier-mediated route, and transcytosis.[18] Because the surface area of the brush border membranes is about 1000-fold larger than the paracellular surface area,[19] drugs can be assumed to be transported mainly by the transcellular route. The TEER value is a highly sensitive measure of membrane permeability, and its variation largely reflects the function of tight junctions that gate the entrance to the paracellular pathway. TEER values showed no significant difference after 120 min of incubation with different concentrations of DPs and calcium. Thus, our results from the Caco-2 cell monolayer experiment

DOI: 10.1021/acs.jafc.5b03097
J. Agric. Food Chem. 2015, 63, 8170−8176

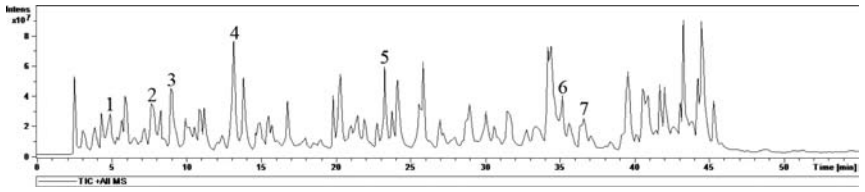

Figure 4. Total ion current (TIC) chromatogram of DPs (<5 kDa). Seven peaks of DPs with M_w < 5 kDa in the TIC chromatogram are numbered.

Table 2. Structure Summary of DPs (<5 kDa) Using HPLC-ESI-MS, MS/MS[a]

peak	retention time (min)	peptide $[M + H]^+$	sequence	protein name
1	5.0	383.2037	VHQ	ovostatin
2	7.7	463.2035	VSEE	ovalbumin
3	8.8	375.1874	INE	ovalbumin
4	13.2	487.3239	ILKN	lysozyme precursor
5	23.3	624.2875	LYAEE	ovalbumin
6	35.1	519.2562	INSW	ovalbumin
				ovalbumin-related protein Y
7	36.4	495.2813	LSYL	ovoglobulin

[a]The primary structures of the DPs (<5 kDa) were determined and validated by searching three mass spectrometry databases of SwissProt.2013.6.27, NCBInr.2013.6.17, and UniProtKB.2013.6.17 with the Protein Prospector engine.

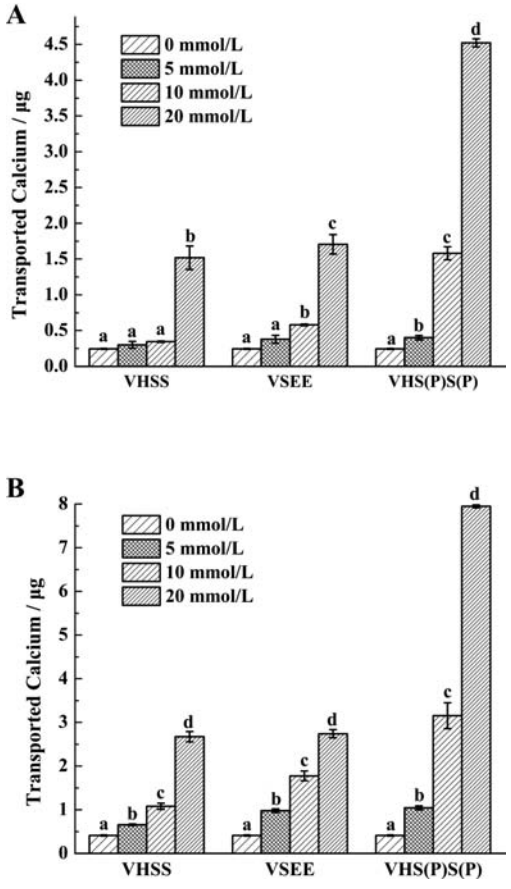

Figure 5. Effects of three pivotal peptides (VHS(p)S(p), VSEE, and VHSS) on calcium transport across Caco-2 monolayers. Peptides (0−20 mM) were added to the apical side with calcium solution (5 mM (A) and 10 mM (B), 0.4 mL) and then incubated for 120 min. Mean values with different letters are significantly different at $P < 0.05$.

confirmed the hypothesis that the paracellular pathway was a minor contributor to calcium transport by DPs. This conclusion is in contrast to the traditional theory holding the paracellular pathway as the major route of calcium transport across Caco-2 cell monolayers.[20] Various mechanisms have been reported to contribute to the absorption of calcium from the intestine, and the paracellular way has been confirmed for many bioactive substances such as vitamin D[21] and CPP.[22] However, the challenge to clearly describe calcium transport at the cellular level remains. Now, our current results provide a new insight into the DPs-mediated calcium transport pathway.

Effect of DPs on Calcium Uptake in Caco-2 Population Model. The effect of DPs (1−4 mg/mL) on the intracellular free calcium concentration, $[Ca^{2+}]_i$, was found to be concentration-dependent in the cell population model with 4 and 6 mM Ca^{2+} (Figure 2). This result is consistent with published studies of CPPs[8] and soluble soybean protein hydrolysate−calcium complex,[2] which may act as calcium carriers and interact with the plasma membrane to transport calcium to the cytosol. This function has been reported to be related to the β-pleated sheet structure of the peptides, which can interact with the plasma membrane to form unregulated Ca^{2+} channels.[23] The β-pleated sheet structure was also found in calreticulin, which is involved in calcium binding in the lumen of the endoplasmic reticulum.[24]

In addition, the optimal DPs/Ca^{2+} ratio for the enhancement of Ca^{2+} uptake was observed to be 4 mM Ca^{2+}/4 mg/mL DPs, indicating the importance of a suitable DPs/Ca^{2+} ratio for promoting calcium absorption. A similar finding was also reported for CPPs in both in vitro cell model[17] and animal models.[25]

Effect of DPs on Calcium Transport in Everted Intestinal Sac Model. Figure 3 shows the amount (μg) of Ca^{2+} absorbed across the everted intestinal sac (6 cm) with mucosal solutions containing 5 or 10 mM Ca^{2+} and 0−8 mg/mL DPs. Using 5 mM Ca^{2+}, calcium transport increased by 31.71% over control with 4 mg/mL DPs and by 46.95% with 8 mg/mL DPs. Similar to the findings in the Caco-2 cell monolayers, the extent of Ca^{2+} transport increase was similar whether 8 or 4 mg/mL DPs was used. At the 10 mM Ca^{2+} concentration, calcium transport exhibited a significant increase over control in the presence of 4 mg/mL DPs (41.45%, $P < 0.05$) and 8 mg/mL DPs (57.59%), but not 2 mg/mL DPs. These results indicate the various Ca^{2+} concentrations are a main driver behind the increase in calcium transport and thus may influence the involvement of the paracellular pathway. Thus, we conclude the paracellular pathway may not be the main transport route in the presence of 5 mM Ca^{2+} concentration. However, when the external concentration of Ca^{2+} was increased to 10 mM, the entrance of the paracellular pathway was opened.

Despite being an in vitro model, the everted intestinal sac model has the advantage of being similar to in vivo intestinal absorption, which has been used in the study of calcium absorption by CPPs.[26] A CPP/Ca ratio of 15 was found to have a significant effect on mineral absorption, and the positive effect of

DOI: 10.1021/acs.jafc.5b03097
J. Agric. Food Chem. 2015, 63, 8170−8176

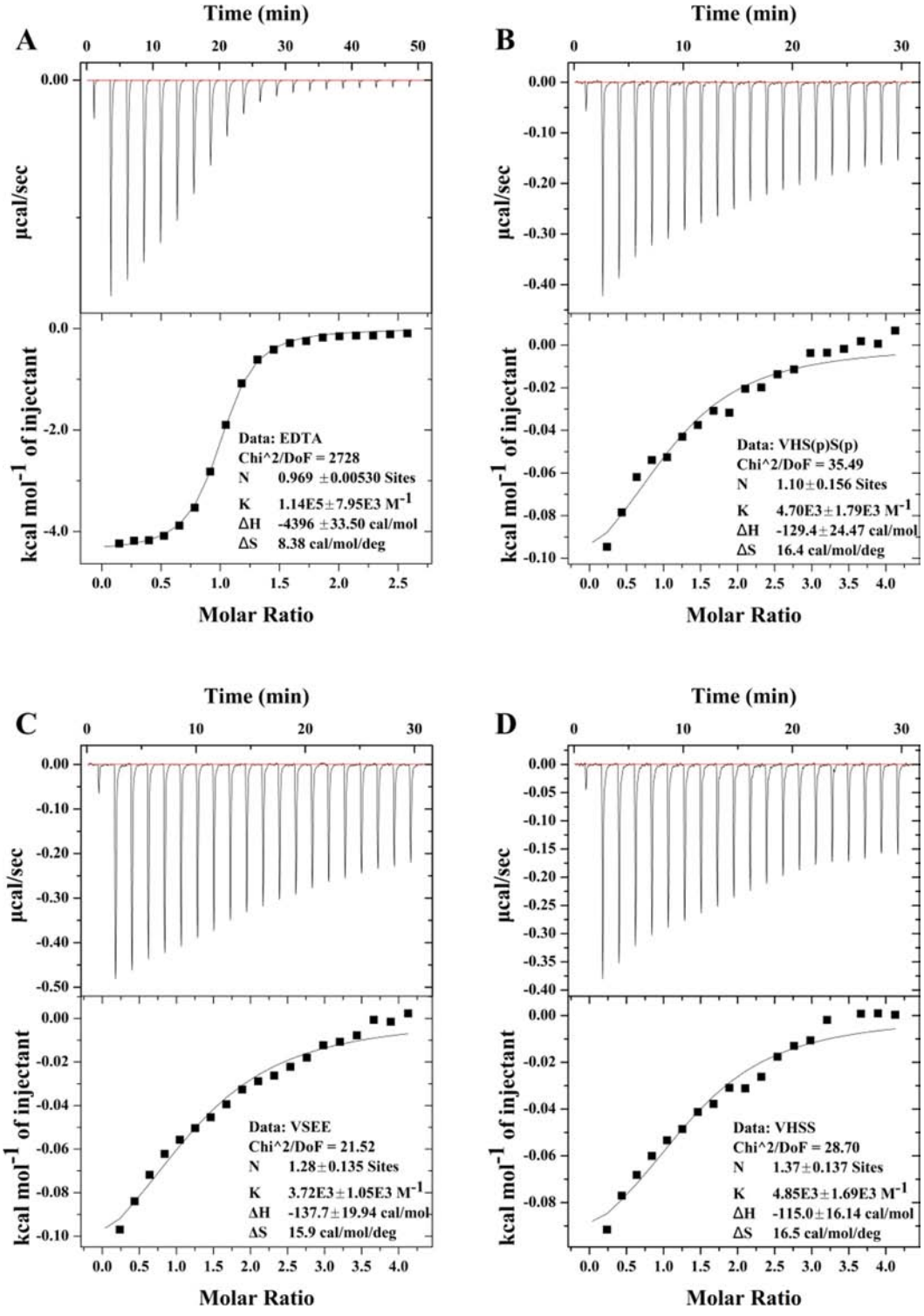

Figure 6. Thermograms and binding isotherms from ITC analysis of the interactions between (A) EDTA and (B) VHS(p)S(p), (C) VSEE, and (D) VHSS at 30 °C.

CPPs on passive Ca absorption seems to depend on the relative amounts of both species in the intestinal lumen. In this study, from both the Caco-2 cell monolayer and everted intestinal sac models, the same conclusion can be drawn: in the presence of DPs, the paracellular pathway is not the main route of calcium absorption.

Identification of High Bioactivity of DPs. The ability of DPs to promote calcium absorption was affected greatly by the amino acid composition of the peptides. The most abundant amino acids in the DPs (<5 kDa) were Glx (Glu + Gln) and Asx (Asp + Asn), accounting for 12.14 and 7.14% of the mass of the peptide, respectively. The contents of Ser, Leu, Phe, Thr, and Met were each also >5% (Table 1). Glu and Ser amino acid residues were also present in the calcium-binding peptides derived from cheese whey protein hydrolysates,[27] porcine blood plasma protein hydrolysates,[28] and Hoki protein hydrolysates.[29]

DOI: 10.1021/acs.jafc.5b03097
J. Agric. Food Chem. 2015, 63, 8170−8176

The carboxyl in some acidic amino acids, the δ-N of the imidazole ring of histidine (His), and N in amidogen of the side chain were the optimal binding sites of Ca^{2+}, and these three amino acids accounted for 35.50% of the total amino acids, which was close to the 37.64% found in soybean peptides.[30]

According to the retention time, seven peaks from DPs with M_w < 5 kDa in the total ion current (TIC) chromatogram were numbered (Figure 4), and the amino acid sequences of the seven peaks were identified as Val-Ser-Glu-Glu (VSEE), Leu-Tyr-Ala-Glu-Glu (LYAEE), Ile-Asn-Glu (INE), Leu-Ser-Tyr-Leu (LSYL), Leu-Asn-Ser-Trp (LNSW), Val-His-Gln (VHQ), and Ile-Leu-Lys-Asn (ILKN) (Table 2). The peptides possess the characteristics of high contents of E, L, N, and S, which is consistent with the result of amino acid composition of DPs. In our previous work, we described a DPs−calcium chelate found using Fourier transform infrared spectroscopy and fluorescence spectroscopy of DPs.[31] The results indicated that the carboxyl groups in some acidic amino acids were the optimal binding sites for Ca^{2+}. The calcium ions caused peptide folding and led to the formation of a DP−calcium chelate. Interestingly, a repeating Glu sequence was found in the C-terminal of VSEE and LYAEE, providing many potential binding sites (the carboxyl groups) for calcium. "Glu-Glu" was also found in the characteristic "acidic motif" Ser(P)-Ser(P)-Ser(P)-Glu-Glu in CPPs.[32] Ser was also found to exist in the peptides LSYL and LNSW, the phosphorylation of which may improve calcium binding, as it has been reported that the phosphorylation of peptides derived from isolated soybean protein could enhance the absorption of calcium in Caco-2 cells.[33] The existence of His in VHQ may contribute considerably to binding calcium due to the δ-N of the imidazole ring. One calcium-binding peptide, Thr-Cys-His, has been identified from a shrimp-processing byproduct hydrolysate, and its high calcium-binding activity may be due to the presence of a His residue.[34] N in amidogen of a side chain of Lys in ILKN was a binding site with calcium, and Lys occupied 4.5% of the mass in DPs (<5 kDa). Lys also been identified in some calcium-binding peptides from tilapia scale protein hydrolysate and bovine serum protein hydrolysates.[4] From the results of those studies, it can be deduced that Glu, Asp, His, and Ser residues may play a crucial role in the chelating of DPs with calcium.

Effect of Three Pivotal Peptides on Calcium Transport in Caco-2 Monolayers. VSEE and VHSS (which had been identified in our laboratory) and phosphorylated VHSS (VHS(p)S(p)) were synthesized by HeFei GuoTai Biology Co., Ltd. (Hefei, China). Figure 5 shows the effect of these three peptides (0−20 mM) on calcium transport, using 5 and 10 mM Ca^{2+}, in Caco-2 cell monolayers. In the presence of 5 mM Ca^{2+}, groups treated with the lower dosage of VHSS and VSEE did not show any significant increase in calcium transport over the control group. As the concentration of peptides was increased to the highest dose (20 mM), the calcium transport increased by >200%. At all doses tested, calcium transport facilitated by VHS(p)S(p) was always higher than that of the other two peptides. In the presence of 10 mM Ca^{2+}, each of the doses tested of VHSS, VSEE, and VHS(p)S(p) stimulated calcium transport.

Figure 6 shows the ITC curves of Ca^{2+} titrated into peptide solutions, as well as the thermodynamic parameters for interaction of peptides with calcium including the stoichiometry (n), association constant (K), change in enthalpy (H), and change in entropy (S). The binding association constants were similar for all peptides, but significantly lower than those for EDTA, which indicates that these three peptides could release calcium easily. The stoichiometry (n) demonstrated a significant difference in how the calcium is bound to peptides. VHS(p)S(p) provides seven binding sites, including an oxygen atom from a hydroxyl in the C-terminal carboxyl, a δ-N atom in the imidazole ring of histidine (His), a N atom of amidogen in the N-terminal, and four oxygen atoms in the phosphate group. Therefore, a small amount of VHS(p)S(p) can bind many calcium ions, which supports the results seen in the Caco-2 monolayers, indicating that the binding activity of peptides is necessary in the process of calcium transport in this cell model. VHSS and VSEE contained three and four functional chelating sites, respectively, so they also could act as calcium-binding peptides. In addition, the three peptides were all detected by HPLC in the basolateral samples, indicating that all three peptides participated in calcium transport, most likely as carriers (data not shown).

On the basis of the mechanisms of calcium uptake in the three models, the amino acid composition, and the sequences of the peptides, the contribution of DPs to calcium absorption may be attributed to two factors: (1) the structure of DPs can ensure high bioactivity is maintained, in order for calcium to interact with the membrane and open the specific calcium channels; and (2) the most suitable DPs structures will not only bind calcium for transport but also release the ion easily.

In summary, the present study provides evidence from three experimental models that DPs (<5 kDa) have a significant effect on calcium absorption. Our results suggest that rather than relying on the paracellular pathway, DPs may facilitate calcium transport by acting as calcium carriers and interacting with the cell membrane to open a special Ca^{2+} channel. Furthermore, our findings shed light on the relationship between amino acid composition and bioactivity. Glu, His, Lys, and Ser in DPs may play crucial roles in the chelation of DPs with calcium, and some peptides containing pivotal amino acid sequences, such as VSEE, have high calcium-binding capability. Future work should focus on the relationship between the bioactivity and structure of DPs to help identify a peptide with the capability of not only binding desired quantities of calcium but also interacting with the plasma membrane to enhance the entrance of Ca^{2+} into cells.

AUTHOR INFORMATION

Corresponding Author

*(H.H.) Mail: College of Food Science and Technology, Huazhong Agricultural University, Wuhan 430070, People's Republic of China. Phone: 011-86-27-87280346. Fax: 011-86-27-87282966. E-mail: hehui@mail.hzau.edu.cn.

Funding

This work was financially supported by the Fundamental Research Funds for the Central Universities (Program 52902-0900205185).

Notes

The authors declare no competing financial interest.

REFERENCES

(1) Daengprok, W.; Garnjanagoonchorn, W.; Naivikul, O.; Pornsinlpatip, P.; Issigonis, K.; Mine, Y. Chicken eggshell matrix proteins enhance calcium transport in the human intestinal epithelial cells, Caco-2. *J. Agric. Food Chem.* **2003**, *51*, 6056−6061.

(2) Lv, Y.; Bao, X. L.; Yang, B. C.; Ren, C. G.; Guo, S. T. Effect of soluble soybean protein hydrolysate-calcium complexes on calcium uptake by Caco-2 cells. *J. Food Sci.* **2008**, *73*, H168−H173.

(3) Pan, D.; Lu, H.; Zeng, X. A newly isolated Ca binding peptide from whey protein. *Int. J. Food Prop.* **2013**, *16*, 1127−1134.

DOI: 10.1021/acs.jafc.5b03097
J. Agric. Food Chem. 2015, 63, 8170−8176

(4) Choi, D.-W.; Lee, J.-H.; Chun, H.-H.; Bin Song, K. Isolation of a calcium-binding peptide from bovine serum protein hydrolysates. *Food Sci. Biotechnol.* **2012**, *21*, 1663−1667.
(5) Bennett, T.; Desmond, A.; Harrington, M.; McDonagh, D.; FitzGerald, R.; Flynn, A.; Cashman, K. D. The effect of high intakes of casein and casein phosphopeptide on calcium absorption in the rat. *Br. J. Nutr.* **2000**, *83*, 673−680.
(6) Cosentino, S.; Donida, B. M.; Marasco, E.; Del Favero, E.; Cantu, L.; Lombardi; Ferraretto, A. Calcium ions enclosed in casein phosphopeptide aggregates are directly involved in the mineral uptake by differentiated HT-29 cells. *Int. Dairy J.* **2010**, *20* (11), 770−776.
(7) Jiang, B.; Mine, Y. Phosphopeptides derived from hen egg yolk phosvitin: effect of molecular size on the calcium-binding properties. *Biosci., Biotechnol., Biochem.* **2001**, *65*, 1187−1190.
(8) Lv, Y.; Bao, X.; Liu, H.; Ren, J.; Guo, S. Purification and characterization of caclium-binding soybean protein hydrolysates by Ca^{2+}/Fe^{3+} immobilized metal affinity chromatography (IMAC). *Food Chem.* **2013**, *141*, 1645−1650.
(9) Lv, Y.; Liu, Q.; Bao, X.; Tang, W.; Yang, B.; Guo, S. Identification and characteristics of iron-chelating peptides from soybean protein hydrolysates using IMAC-Fe^{3+}. *J. Agric. Food Chem.* **2009**, *57*, 4593−4597.
(10) Ferraretto, A.; Signorile, A.; Gravaghi, C.; Fiorilli, A.; Tettamanti, G. Casein phosphopeptides influence calcium uptake by cultured human intestinal HT-29 tumor cells. *J. Nutr.* **2001**, *131*, 1655−1661.
(11) Perego, S.; Cosentino, S.; Fiorilli, A.; Tettamanti, G.; Ferraretto, A. Casein phosphopeptides modulate proliferation and apoptosis in HT-29 cell line through their interaction with voltage-operated L-type calcium channels. *J. Nutr. Biochem.* **2012**, *23* (7), 808−816.
(12) Perego, S.; Zabeo, A.; Marasco, E.; Giussani, P.; Fiorilli, A.; Tettamanti, G.; Ferraretto, A. Casein phosphopeptides modulate calcium uptake and apoptosis in Caco2 cells through their interaction with the TRPV6 calcium channel. *J. Funct. Foods* **2013**, *5* (2), 847−857.
(13) Zhao, N.; Hu, J.; Hou, T.; Ma, Z.; Wang, C.; He, H. Effects of desalted duck egg white peptides and their products on calcium absorption in rats. *J. Funct. Foods* **2014**, *8*, 234−242.
(14) Camara, F.; Barbera, R.; Amaro, M. A.; Farre, R. Calcium, iron, zinc and copper transport and uptake by Caco-2 cells in school meals: influence of protein and mineral interactions. *Food Chem.* **2007**, *100*, 1085−1092.
(15) Willenberg, I.; Michael, M.; Wonik, J.; Bartel, L. C.; Empl, M. T.; Schebb, N. H. Investigation of the absorption of resveratrol oligomers in the Caco-2 cellular model of intestinal absorption. *Food Chem.* **2015**, *167*, 245−250.
(16) Rubio, L. A.; Seiquer, I. Transport of amino acids from in vitro digested legume proteins or casein in Caco-2 cell cultures. *J. Agric. Food Chem.* **2002**, *50*, 5202−5206.
(17) Gravaghi, C.; Del Favero, E.; Cantu, L.; Donetti, E.; Bedoni, M.; Fiorilli, A.; Tettamanti, G.; Ferraretto, A. Casein phosphopeptide promotion of calcium uptake in HT-29 cells − relationship between biological activity and supramolecular structure. *FEBS J.* **2007**, *274*, 4999−5011.
(18) Artursson, P.; Palm, K.; Luthman, K. Caco-2 monolayers in experimental and theoretical predictions of drug transport. *Adv. Drug Delivery Rev.* **2012**, *64*, 280−289.
(19) Pappenheimer, J. R.; Reiss, K. Z. Contribution of solvent drag through intercellular junctions to absorption of nutrients by the small intestine of the rat. *J. Membr. Biol.* **1987**, *100*, 123−136.
(20) Blais, A.; Aymard, P.; Lacour, B. Paracellular calcium transport across Caco-2 and HT29 cell monolayers. *Pfluegers Arch.* **1997**, *434*, 300−305.
(21) Chirayath, M. V.; Gajdzik, L.; Hulla, W.; Graf, J.; Cross, H. S.; Peterlik, M. Vitamin D increases tight-junction conductance and paracellular Ca^{2+} transport in Caco-2 cell cultures. *Am. J. Physiol.* **1998**, *274*, G389−G396.
(22) Sato, R.; Noguchi, T.; Naito, H. Casein phosphopeptide (CPP) enhances calcium absorption from the ligated segment of rat small intestine. *J. Nutr. Sci. Vitaminol.* **1986**, *32*, 67−76.
(23) Kawahara, M.; Kuroda, Y.; Arispe, N.; Rojas, E. Alzheimer's beta-amyloid, human islet amylin, and prion protein fragment evoke intracellular free calcium elevations by a common mechanism in a hypothalamic GnRH neuronal cell line. *J. Biol. Chem.* **2000**, *275*, 14077−14083.
(24) Dar, M. A.; Wahiduzzaman; Islam, A.; Hassan, M. I.; Ahmad, F. Purification and characterization of calreticulin: a Ca^{2+}-binding chaperone from sheep kidney. *Appl. Biochem. Biotechnol.* **2014**, *174*, 1771−1783.
(25) Tsuchita, H.; Suzuki, T.; Kuwata, T. The effect of casein phosphopeptides on calcium absorption from calcium-fortified milk in growing rats. *Br. J. Nutr.* **2001**, *85*, 5−10.
(26) Erba, D.; Ciappellano, S.; Testolin, G. Effect of the ratio of casein phosphopeptides to calcium (w/w) on passive calcium transport in the distal small intestine of rats. *Nutrition* **2002**, *18*, 743−746.
(27) Kim, S. B.; Lim, J. W. Calcium-binding peptides derived from tryptic hydrolysates of cheese whey protein. *Asian−Australas. J. Anim. Sci.* **2004**, *17*, 1459−1464.
(28) Lee, S. H.; Song, K. B. Isolation of a calcium-binding peptide from enzymatic hydrolysates of porcine blood plasma protein. *Han'guk Eungyong Sangmyong Hwahakhoeji* **2009**, *52*, 290−294.
(29) Jung, W.-K.; Kim, S.-K. Calcium-binding peptide derived from pepsinolytic hydrolysates of hoki (*Johnius belengerii*) frame. *Eur. Food Res. Technol.* **2007**, *224*, 763−767.
(30) Bao, X. L. *The Forming Mechanism and Stability of the Soluble Complexes during Calcium Binding by Soybean Peptides*; China Agricultural University, Beijing, 2007.
(31) Zhao, N.. *Study on Preparation and Modification of Calcium-Binding Desalted Duck Egg White Peptides and Their Effects on Enhancing Bone Mineral Density in Rats*; Huazhong Agricultural University, Wuhan, 2014.
(32) Ferraretto, A.; Gravaghi, C.; Fiorilli, A.; Tettamanti, G. Casein-derived bioactive phosphopeptides: role of phosphorylation and primary structure in promoting calcium uptake by HT-29 tumor cells (FEBS 27468) (Vol. 551, p 92, 2003). *FEBS Lett.* **2003**, *553*, 218−218.
(33) Lee, S. H.; Yang, J. I.; Hong, S. M.; Hahm, D. H.; Lee, S. Y.; Kim, I. H.; Choi, S. Y. Phosphorylation of peptides derived from isolated soybean protein: effects on calcium binding, solubility and influx into Caco-2 cells. *BioFactors* **2005**, *23*, 121−128.
(34) Huang, G.; Ren, L.; Jiang, J. Purification of a histidine-containing peptide with calcium binding activity from shrimp processing byproducts hydrolysate. *Eur. Food Res. Technol.* **2011**, *232*, 281−287.

DOI: 10.1021/acs.jafc.5b03097
J. Agric. Food Chem. 2015, 63, 8170−8176

ice. Plasma was separated from blood by centrifugation at 2300×*g* for 10 min at 4 °C, and then frozen at −80 °C until analysis. Plasma acetaminophen concentrations were measured using acetaminophen detection kit (Kanto Chemical Co., Inc., Tokyo, Japan).

In a separate experiment, the effects of various aliphatic compounds having the same carbon chain length as 2,4-decadienal were investigated. 2,4-Decadienal, decanal (saturated aldehyde, Tokyo Chemical Industry Co., Ltd.), decanol (saturated alcohol, Kanto Chemical Co., Inc., Tokyo, Japan), decanoic acid (saturated fatty acid, Tokyo Chemical Industry Co., Ltd.), or vehicle (2% ethanol in saline) was orally administered at a dose of 100 mg/kg body weight; all these solutions contained acetaminophen (100 mg/kg body weight). Tail vein blood samples (60 μL) were collected, and plasma acetaminophen concentrations were measured as described above.

Phenol Red Test. 2,4-Decadienal (100 mg/kg body weight) or its vehicle (1.5% carboxymethyl cellulose and 2% ethanol in saline) was orally administered (10 mL/kg body weight) through a feeding tube (6 Fr, Atom Medical Co., Tokyo, Japan). The suspensions contained phenol red (5 mg/kg body weight), as a nonabsorbable marker, in addition to acetaminophen (100 mg/kg body weight) to assess gastric emptying rate.[10,11] Portal blood was collected into a syringe containing heparin (final concentration 50 IU/mL), aprotinin (final concentration 500 KIU/mL), and dipeptidyl peptidase-IV inhibitor (final concentration 50 μM, Millipore, MA, U.S.A.) 15 min after oral administration from animals under isoflurane anesthesia (MSD K.K., Tokyo, Japan). Plasma was separated and stored as described above. Rats were euthanized by exsanguination immediately after the procedure, and the luminal contents of the stomach, as well as that of the proximal and distal small intestine were collected. The interiors of these tissues were flushed twice with cold saline, and the washout solution was collected. The debris was removed by centrifugation at 8400×*g* for 10 min at 4 °C. After adding 1 N NaOH to the supernatant (1/30 volume of the supernatant), concentration of phenol red was measured spectrophotometrically at 560 nm. The gastric emptying rate was calculated as follows.

Gastric emptying rate (%) = [{the amount of phenol red administrated (mg) − the amount of phenol red remained in the stomach (mg)}/the amount of phenol red administrated (mg)] × 100

Effect of Intraperitoneal Administration of 2,4-Decadienal on Gastric Emptying Rate. We examined the effect of intraperitoneal administration of 2,4-decadienal on gastric emptying. Rats were divided into control, intraperitoneal 2,4-decadienal, and oral 2,4-decadienal groups. Control rats were intraperitoneally administered sterilized saline (10 mL/kg) immediately after oral pretreatment with 10 mL/kg phenol red (5 mg/kg) dissolved in saline containing 1.5% carboxymethyl cellulose. The intraperitoneal 2,4-decadienal group was administered 2,4-decadienal intraperitoneally (100 mg/kg) suspended in sterilized saline immediately after oral pretreatment with phenol red solution. An oral 2,4-decadienal group was administered saline intraperitoneally immediately after oral administration of 2,4-decadienal (100 mg/kg) suspended in the phenol red solution. The gastric content was collected 15 min after intraperitoneal or oral administration, and the gastric emptying rate was determined as described above.

Effect of Duodenal Administration of 2,4-Decadienal on Gastric Emptying Rate. To administer 2,4-decadienal directly into the small intestinal lumen, a catheter was implanted into the duodenum in rats fed with reduced amount of the diet (10 g) on the day before the surgical operation. A middle incision was made under pentobarbital anesthesia (40 mg/kg body weight; Nembutal Injection, Dainippon Sumitomo Pharma, Osaka, Japan or Somnopentyl Injection, Kyoritsu Seiyaku Co., Tokyo, Japan). A silicone catheter (Silascon no. 00; internal diameter 0.5 mm; outer diameter 1.0 mm; Dow Corning Co., Kanagawa, Japan), the tip of which housed a small segment (2−3 mm) of a polyethylene tube (Hibiki Fr No. 4; Kunii Co., Tokyo, Japan), was inserted into the duodenum (2 cm distal to the pyloric part of the stomach) and fixed with a thread. The free end of the catheter was dorsally exteriorized, which allowed the experiment to be carried out in conscious and unrestrained rats. Rats were used for subsequent experiments after a recovery period of 3−4 days. After overnight fasting, 2,4-decadienal (0−25 mg/kg) was administered into the duodenal lumen through the catheter, followed by oral administration of acetaminophen or phenol red solution, as described above.

Statistical Analysis. All results are expressed as mean ± SEM. Significant differences among the groups were determined using Student's *t* test ($P < 0.05$) for two-group comparison or Dunnett's posthoc test ($P < 0.05$) for multiple group comparison as described in the figure legends.

RESULTS AND DISCUSSION

Plasma acetaminophen concentrations in the tail vein blood increased immediately after oral administration of acetaminophen at 100 mg/kg, and then gradually decreased after 45 min (Figure 1A and B). Appearance of acetaminophen in peripheral

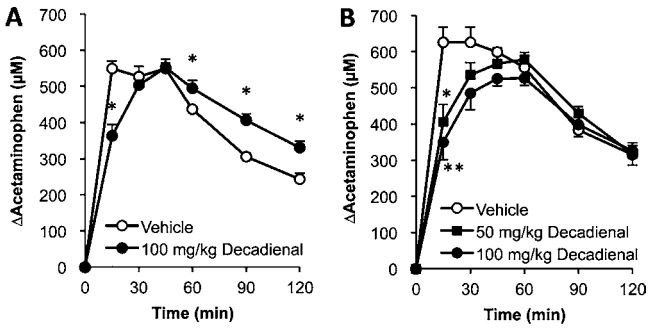

Figure 1. Effects of oral administration of 2,4-decadienal on gastric emptying rate (acetaminophen absorption test). 2,4-Decadienal (decadienal) at 100 mg/kg (A, $n = 6$ in each treatment), or 50 and 100 mg/kg (B, $n = 4$ in each treatment) were orally administered to fasted rats together with acetaminophen. Tail vein blood was collected and acetaminophen concentrations were measured in the plasma. Values are expressed as means ± SEM of changes in acetaminophen concentration from the basal level (0 min). Plots with asterisks (*) have significant difference compared to the value of control group at the same time point ($p < 0.05$, A: Student's *t* test, B: Dunnett's test).

blood was delayed by oral coadministration of 2,4-decadienal (50 and 100 mg/kg), suggesting delayed gastric emptying in the presence of 2,4-decadienal. We used 100 mg/kg dose of 2,4-decadienal in further experiments because of its apparent effect on plasma acetaminophen levels.

To further investigate the inhibitory effect of 2,4-decadienal on gastric emptying rate, we used an unabsorbable marker such as phenol red. In this experiment, luminal contents 15 min after the oral administration were collected, not only from the stomach, but also from the proximal and the distal small intestine, and the remaining amounts of phenol red in the lumen were determined (Figure 2A). The remaining amount of phenol red in the stomach lumen was much higher in the 2,4-decadienal group than the amount in the control group. The gastric emptying rate calculated using the amount of remaining phenol red was significantly lower in the 2,4-decadienal group than the gastric emptying rate of the control group (Figure 2B). Indeed, amounts of luminal phenol red in the proximal and the distal small intestine were lower in the 2,4-decadienal group than that in the control group (Figure 2A). These results confirm the inhibitory effect of orally administered 2,4-decadienal on gastric emptying. Plasma acetaminophen levels in the portal vein were lower in rats treated with oral 2,4-decadienal (Figure 2C), further supporting the gastric inhibitory effect of 2,4-decadienal.

DOI: 10.1021/acs.jafc.5b03126
J. Agric. Food Chem. 2015, 63, 8177−8181

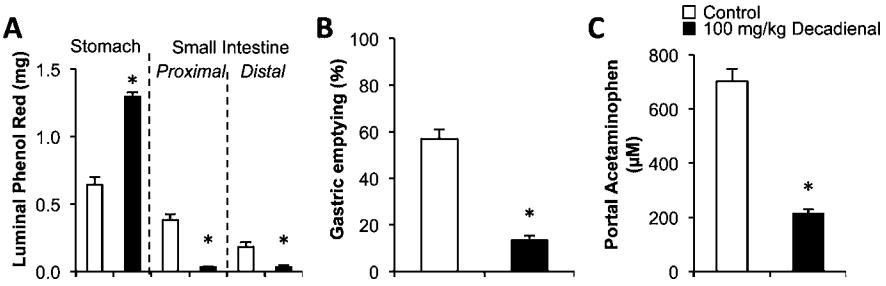

Figure 2. Effects of oral administration of 2,4-decadienal on gastric emptying rate (phenol red recovery method). 2,4-Decadienal (decadienal) at 100 mg/kg was orally administered to fasted rats together with phenol red and acetaminophen (n = 6 in each treatment). Portal blood and luminal contents (stomach and proximal and distal small intestine) were collected 15 min after oral administration. The gastric emptying rate (B) was calculated by using the amount of luminal phenol red in the stomach (A). Portal acetaminophen (C) levels were measured in the plasma. Values are expressed as means ± SEM. Bars with asterisks (*) have significant difference compared to the value of control group (p < 0.05, Student's t test).

In our previous in vitro study, 2,4-decadienal (diunsaturated aldehyde), but not decanal (saturated aldehyde), decanol (saturated alcohol), and decanoic acid (saturated fatty acid), stimulated CCK secretion from enteroendocrine STC-1 cells.[7] In the present study, the effect of the structure−activity relationship on gastric emptying was examined in vivo. As shown in Figure 3, oral administration of 2,4-decadienal

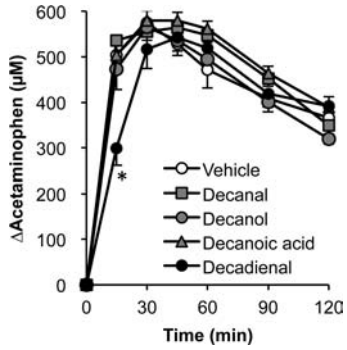

Figure 3. Effects of oral administration of various aliphatic compounds on gastric emptying rate. Aliphatic compounds (decanal, decanol, or decanoic acid) having the same carbon chain length as 2,4-decadienal (decadienal) were orally administered (100 mg/kg) to fasted rats in the acetaminophen absorption test (n = 6 in each treatment). Values are expressed as means ± SEM. Asterisks (*) indicate significant difference compared to the value of control group (p < 0.05, Dunnett's test).

attenuated the elevated plasma acetaminophen levels, but decanal, decanol, or decanoic acid had no effects on plasma acetaminophen levels. The structure−activity relationship consistent with that in our previous in vitro study suggests that 2,4-decadienal acts directly on enteroendocrine cells, rather than after absorption from the intestine.

To determine whether 2,4-decadienal acts in the gastrointestinal lumen or after absorption, gastric emptying rate was measured after oral or intraperitoneal administration of 2,4-decadienal. Gastric emptying rate significantly reduced after oral administration 2,4-decadienal, but not after intraperitoneal administration of 2,4-decadienal, compared to that after control treatment (Figure 4). The result indicates that 2,4-decadienal exerted its inhibitory effects on gastric emptying in the gastrointestinal lumen, and led us to investigate whether the effect was triggered in the small intestinal lumen, by using rats equipped with the duodenal catheter.

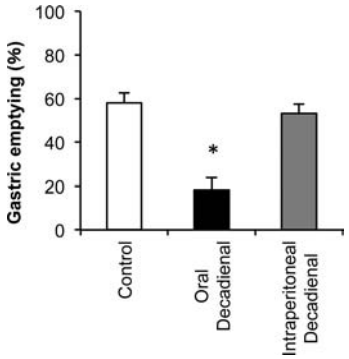

Figure 4. Effect of intraperitoneal administration of 2,4-decadienal, on gastric emptying rate. 2,4-Decadienal solution (decadienal) was orally or intraperitoneally coadministered to fasted rats together with oral phenol red. Gastric emptying rate was determined by measuring luminal phenol red collected from the stomach 15 min after the administration (n = 7−8 in each treatment). Values are expressed as means ± SEM. Asterisks (*) indicate significant difference compared to the value of control group (p < 0.05, Dunnett's test).

Duodenal administration of 2,4-decadienal reduced acetaminophen appearance in plasma of the tail vein in a dose-dependent manner (Figure 5). Compared to control treatment, 10 mg/kg dose of 2,4-decadienal had significantly lower acetaminophen concentration at 15 min, similar to the

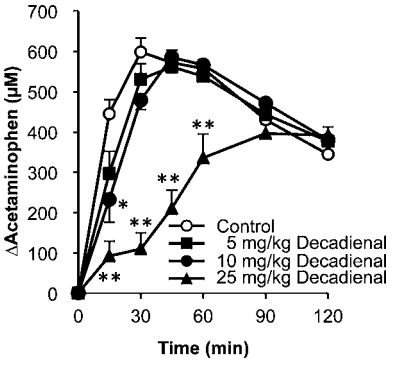

Figure 5. Effect of duodenal administration of 2,4-decadienal on gastric emptying rate. 2,4-Decadienal (decadienal: 0, 5, 10, and 25 mg/kg) was administered into the duodenal lumen through the duodenal catheter followed by oral administration of acetaminophen in fasted rats (n = 6 in each treatment). Values are expressed as means ± SEM. Asterisks (*) indicate significant difference compared to the value of control group at the same time point (p < 0.05, Dunnett's test).

DOI: 10.1021/acs.jafc.5b03126
J. Agric. Food Chem. 2015, 63, 8177−8181

reduction caused by 100 mg/kg dose of oral administration. Duodenal administration of 25 mg/kg dose led to a much greater and sustained (~60 min) reduction in acetaminophen levels. Because the effective duodenal dose (10 mg/kg) is lower than the oral dose (50−100 mg/kg), the result indicates that 2,4-decadienal exerts its gastric inhibitory effect in the small intestinal lumen, rather than in the gastric lumen.

Gut hormones such as CCK, serotonin, and GLP-1 inhibit gastric emptying,[1−5] and 2,4-decadienal potently stimulates CCK secretion in the enteroendocrine STC-1 cells.[7] Because 2,4-decadienal exerts its effects rapidly (~15 min) after oral and duodenal administration, we investigated the involvement of CCK and serotonin that are produced in the proximal small intestine, rather than GLP-1 that is released from the distal small intestine and the large intestine. When a CCK-A receptor antagonist, devazepide was intraperitoneally injected, gastric inhibitory effect of orally administered 2,4-decadienal decreased, but single administration of devazepide accelerated gastric emptying (Figure 6A). Therefore, involvement of CCK signaling has not been clarified in the present study. In contrast, a serotonin type 3 receptor ($5HT_3R$) antagonist, tropisetron, treatment reversed the gastric inhibitory effect of duodenal 2,4-decadienal in the acetaminophen test (Figure 6B). Although a single administration of tropisetron led to significantly higher acetaminophen levels at 15 min compared to control/vehicle treatment, the effect was limited to that time point, and it was smaller than the reversible effect on 2,4-decadienal-reduced gastric emptying. Phenol red test (Figure 6C) confirmed the involvement of serotonin signal, since reduced gastric emptying rate caused by duodenal 2,4-decadienal was clearly attenuated by tropisetron treatment. These results further support the notion that 2,4-decadienal acts directly on serotonin-producing enteroendocrine cells, namely, enterochromaffin cells. We previously demonstrated that 2−4-decadienal stimulated CCK secretion via transient-receptor potential ankyrin 1 (TRPA1).[7] TRPA1 functions in serotonin-producing enteroendocrine cells, not only in CCK-producing cells.[12,13] A recent study in mice demonstrated TRPA1 is expressed in enteoroendocrine cells expressing serotonin and the cells coexpressing serotonin and CCK, but not in the cells only expressing CCK.[14] Thus, compared to CCK secretion, serotonin secretion may be more responsive to TRPA1 activation in the upper small intestine. However, the gastric inhibitory effect of 2,4-decadienal was not completely canceled by the tropisetron treatment (Figure 6B and C), suggesting partial involvement of the TRPA1-CCK signaling pathway. Treatment with the combination of the CCK-A receptor antagonist and the serotonin receptor antagonist may demonstrate the role of CCK secretion in 2,4-decadienal-delayed gastric emptying in the future study. In addition, further studies will be necessary in the future to elucidate the cellular mechanisms that stimulate serotonin secretion from the serotonin-producing enteroendocrine cells.

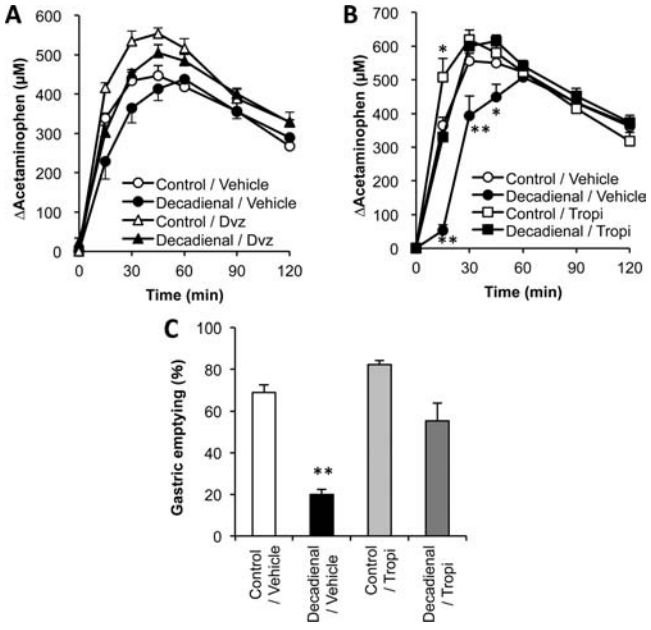

Figure 6. Effect of CCK-A receptor antagonist (devazepide) and 5-HT_3 receptor antagonist (tropisetron) on luminal 2,4-decadienal-induced reduction in gastric emptying rate. (A) Devazepide (Dvz) at 0.5 mg/kg or its vehicle (10% TWEEN80 + 10% DMSO in saline) was intraperitoneally injected 10 min before the oral administration of 2,4-decadienal (decadienal: 100 mg/kg), followed by oral administration of acetaminophen in fasted rats (n = 5−6 in each treatment). (B) Tropisetron (Tropi) at 0.5 mg/kg or its vehicle (saline) was intraperitoneally injected just before the duodenal administration of 2,4-decadienal (decadienal: 0, 10 mg/kg), followed by oral administration of acetaminophen in fasted rats (n = 6−7 in each treatment). Tail vein blood was collected, and acetaminophen concentrations were measured in the plasma. (C) Tropisetron (Tropi) at 0.5 mg/kg or its vehicle (saline) was intraperitoneally injected just before the duodenal administration of 2,4-decadienal (decadienal: 0, 10 mg/kg), followed by oral administration of phenol red in fasted rats (n = 6−7 in each treatment). Gastric emptying rate was determined by measuring luminal phenol red collected from the stomach 15 min after the administration (n = 4−5 in each treatment). Values are expressed as means ± SEM. Asterisks (*) indicate significant difference compared to the value of control/vehicle group (p < 0.05, Dunnett's test).

Gastric emptying decreases in the presence of luminal lipids, proteins, and glucose. In previous studies, duodenal (not oral) administration of lipid (50−100 mg/250−300 g body weight) or glucose (50−100 mg/250−300 g body weight) reduced gastric emptying in rats.[11,15,16] Another study[17] demonstrated that oral administration of peptone or lipid (250−1250 mg/250−300 g body weight) reduced gastric emptying in rats. Although the experimental conditions were different from that employed in the present study, our findings suggest that 2,4-decadienal has more potent inhibitory effect on gastric emptying than these macronutrients.

2,4-Decadienal is one of the flavoring compounds in chicken meat,[18] and is used as a flavoring agent and fragrance, but the physiological effects of orally administered 2,4-decadienal have not been studied. A recent study demonstrated that orally administered 2,4-decadienal was metabolized to 2,4-decadienoic acid and a cysteine-conjugated compound.[19] Unsaturated aldehydes are generated during lipid peroxidation and play critical roles in oxidative stress.[20,21] The structure activity relationship demonstrated in the present study suggests that serotonin-producing enteroendocrine cells sense luminal unsaturated aldehydes to prevent the excess absorption and ingestion of potent peroxides such as unsaturated aldehydes through delaying gastric emptying followed by suppression of appetite. 2,4-Decadienal might be involved in deteriorated lipid-induced appetite suppression or nausea through potent inhibition of gastric emptying. In a previous study investigating the chronic effect of 2,4-decadienal, the no-observed-adverse-effect level was determined to be 100 mg/kg in rats and mice.[22] Although the dose of 100 mg/kg used in the present study was

DOI: 10.1021/acs.jafc.5b03126
J. Agric. Food Chem. 2015, 63, 8177−8181

not found to be very toxic, it is not possible to ingest this dose in a single meal. However, a small amount of 2,4-decadienal ingested together with other macronutrients could potentiate its inhibitory effects on gastric emptying. Because rapid gastric emptying contributes to postprandial hyperglycemia and lipidemia, suppressing gastric emptying is a promising target for preventing or reducing glucose intolerance and dyslipidemia. Although the physiological relevance of structure−activity relationships observed in the present study is still unclear, potent activation of enteroendocrine cells by 2,4-decadienal[7] could explain the potent effect in vivo. Further studies are needed to elucidate the molecular and signaling mechanisms involved in the gastric inhibitory effect of orally administered 2,4-decadienal.

In summary, oral administration of 2,4-decadienal reduced gastric emptying in rats, as assessed by the acetaminophen absorption test and the phenol red recovery method. Structure−activity relationship study revealed the specific potential of 2,4-decadienal to reduce gastric emptying in vivo. Furthermore, duodenal but not intraperitoneal 2,4-decadienal reduced gastric emptying, and the gastric inhibitory effect was mediated via serotonin signaling. These results demonstrate that orally administered 2,4-decadienal has potent inhibitory effect on gastric emptying by acting directly on serotonin-producing enteroendocrine cells.

AUTHOR INFORMATION

Corresponding Author

*Tel/Fax: +81-11-706-2811. E-mail: hira@chem.agr.hokudai.ac.jp (T.H.).

Author Contributions

All authors are involved in research design; A.Y. and T.H. conducted research and analyzed data; and T.H. and A.Y. wrote the paper. T.H. had primary responsibility for final content. All authors read and approved the final manuscript.

Notes

The authors declare no competing financial interest.

ABBREVIATIONS USED

2,4-decadienal,*trans*,*trans*-2,4-decadienal; $5HT_3R$,serotonin type 3 receptor; CCK,cholecystokinin

REFERENCES

(1) Hellström, P. M.; Grybäck, P.; Jacobsson, H. The physiology of gastric emptying. *Bailliere's Best Pract. Res., Clin. Anaesthesiol.* **2006**, *20*, 397−407.

(2) Luttikhold, J.; de Ruijter, F. M.; van Norren, K.; Diamant, M.; Witkamp, R. F.; van Leeuwen, P. A.; Vermeulen, M. A. Review article: the role of gastrointestinal hormones in the treatment of delayed gastric emptying in critically ill patients. *Aliment. Pharmacol. Ther.* **2013**, *38*, 573−83.

(3) Phillips, L. K.; Deane, A. M.; Jones, K. L.; Rayner, C. K.; Horowitz, M. Gastric emptying and glycaemia in health and diabetes mellitus. *Nat. Rev. Endocrinol.* **2015**, *11*, 112−28.

(4) Muramatsu, M.; Hira, T.; Mitsunaga, A.; Sato, E.; Nakajima, S.; Kitahara, Y.; Eto, Y.; Hara, H. Activation of the gut calcium-sensing receptor by peptide agonists reduces rapid elevation of plasma glucose in response to oral glucose load in rats. *American Journal of Physiology-Gastrointestinal and Liver Physiology* **2014**, *306*, C1099−C1107.

(5) Westphal, S.; Kästner, S.; Taneva, E.; Leodolter, A.; Dierkes, J.; Luley, C. Postprandial lipid and carbohydrate responses after the ingestion of a casein-enriched mixed meal. *Am. J. Clin. Nutr.* **2004**, *80*, 284−90.

(6) Endo, Y.; Hayashi, C.; Yamanaka, T.; Takayose, K.; Yamaoka, M.; Tsuno, T.; Nakajima, S. Linolenic Acid as the Main Source of Acrolein Formed During Heating of Vegetable Oils. *J. Am. Oil Chem. Soc.* **2013**, *90*, 959−964.

(7) Nakajima, S.; Hira, T.; Yahagi, A.; Nishiyama, C.; Yamashita, T.; Imagi, J.; Hara, H. Unsaturated aldehydes induce CCK secretion via TRPA1 in STC-1 cells. *Mol. Nutr. Food Res.* **2014**, *58*, 1042−1051.

(8) Heading, R. C.; Nimmo, J.; Prescott, L. F.; Tothill, P. The dependence of paracetamol absorption on the rate of gastric emptying. *Br. J. Pharmacol.* **1973**, *47*, 415−21.

(9) Maida, A.; Lovshin, J. A.; Baggio, L. L.; Drucker, D. J. The glucagon-like peptide-1 receptor agonist oxyntomodulin enhances beta-cell function but does not inhibit gastric emptying in mice. *Endocrinology* **2008**, *149*, 5670−8.

(10) Feldman, S.; Gibaldi, M. Effect of bile salts on gastric emptying and intestinal transit in the rat. *Gastroenterology* **1968**, *54*, 918−21.

(11) Nishimukai, M.; Hara, H.; Aoyama, Y. The addition of soybean phosphatidylcholine to triglyceride increases suppressive effects on food intake and gastric emptying in rats. *J. Nutr.* **2003**, *133*, 1255−8.

(12) Doihara, H.; Nozawa, K.; Kawabata-Shoda, E.; Kojima, R.; Yokoyama, T.; Ito, H. TRPA1 agonists delay gastric emptying in rats through serotonergic pathways. *Naunyn-Schmiedeberg's Arch. Pharmacol.* **2009**, *380*, 353−7.

(13) Nozawa, K.; Kawabata-Shoda, E.; Doihara, H.; Kojima, R.; Okada, H.; Mochizuki, S.; Sano, Y.; Inamura, K.; Matsushime, H.; Koizumi, T.; Yokoyama, T.; Ito, H. TRPA1 regulates gastrointestinal motility through serotonin release from enterochromaffin cells. *Proc. Natl. Acad. Sci. U. S. A.* **2009**, *106*, 3408−13.

(14) Cho, H. J.; Callaghan, B.; Bron, R.; Bravo, D. M.; Furness, J. B. Identification of enteroendocrine cells that express TRPA1 channels in the mouse intestine. *Cell Tissue Res.* **2014**, *356*, 77−82.

(15) Hölzer, H. H.; Turkelson, C. M.; Solomon, T. E.; Raybould, H. E. Intestinal lipid inhibits gastric emptying via CCK and a vagal capsaicin-sensitive afferent pathway in rats. *Am. J. Physiol.* **1994**, *267*, G625−9.

(16) Raybould, H. E.; Glatzle, J.; Robin, C.; Meyer, J. H.; Phan, T.; Wong, H.; Sternini, C. Expression of 5-HT3 receptors by extrinsic duodenal afferents contribute to intestinal inhibition of gastric emptying. *Am. J. Physiol Gastrointest Liver Physiol* **2003**, *284*, G367−72.

(17) White, W. O.; Schwartz, G. J.; Moran, T. H. Role of endogenous CCK in the inhibition of gastric emptying by peptone and Intralipid in rats. *Regul. Pept.* **2000**, *88*, 47−53.

(18) Jayasena, D. D.; Ahn, D. U.; Nam, K. C.; Jo, C. Flavour chemistry of chicken meat: a review. *Asian-Australas. J. Anim. Sci.* **2013**, *26*, 732−42.

(19) Pan, K. L.; Huang, W. J.; Hsu, M. H.; Lee, H. L.; Liu, H. J.; Cheng, C. W.; Tsai, M. H.; Shen, M. Y.; Lin, P. Identification of trans,trans-2,4-decadienal metabolites in mouse and human cells using liquid chromatography-mass spectrometry. *Chem. Res. Toxicol.* **2014**, *27*, 1707−19.

(20) Quiles, J. L.; Huertas, J. R.; Battino, M.; Ramírez-Tortosa, M. C.; Cassinello, M.; Mataix, J.; Lopez-Frias, M.; Mañas, M. The intake of fried virgin olive or sunflower oils differentially induces oxidative stress in rat liver microsomes. *Br. J. Nutr.* **2002**, *88*, 57−65.

(21) Grimsrud, P. A.; Xie, H.; Griffin, T. J.; Bernlohr, D. A. Oxidative stress and covalent modification of protein with bioactive aldehydes. *J. Biol. Chem.* **2008**, *283*, 21837−41.

(22) Chan, P. C. NTP toxicity studies of toxicity studies of 2,4-decadienal (CAS No. 25152−84−5) administered by gavage to F344/N Rats and B6C3F1 mice. *Toxic Rep. Ser.* **2011**, 1−94.

DOI: 10.1021/acs.jafc.5b03126
J. Agric. Food Chem. 2015, 63, 8177−8181

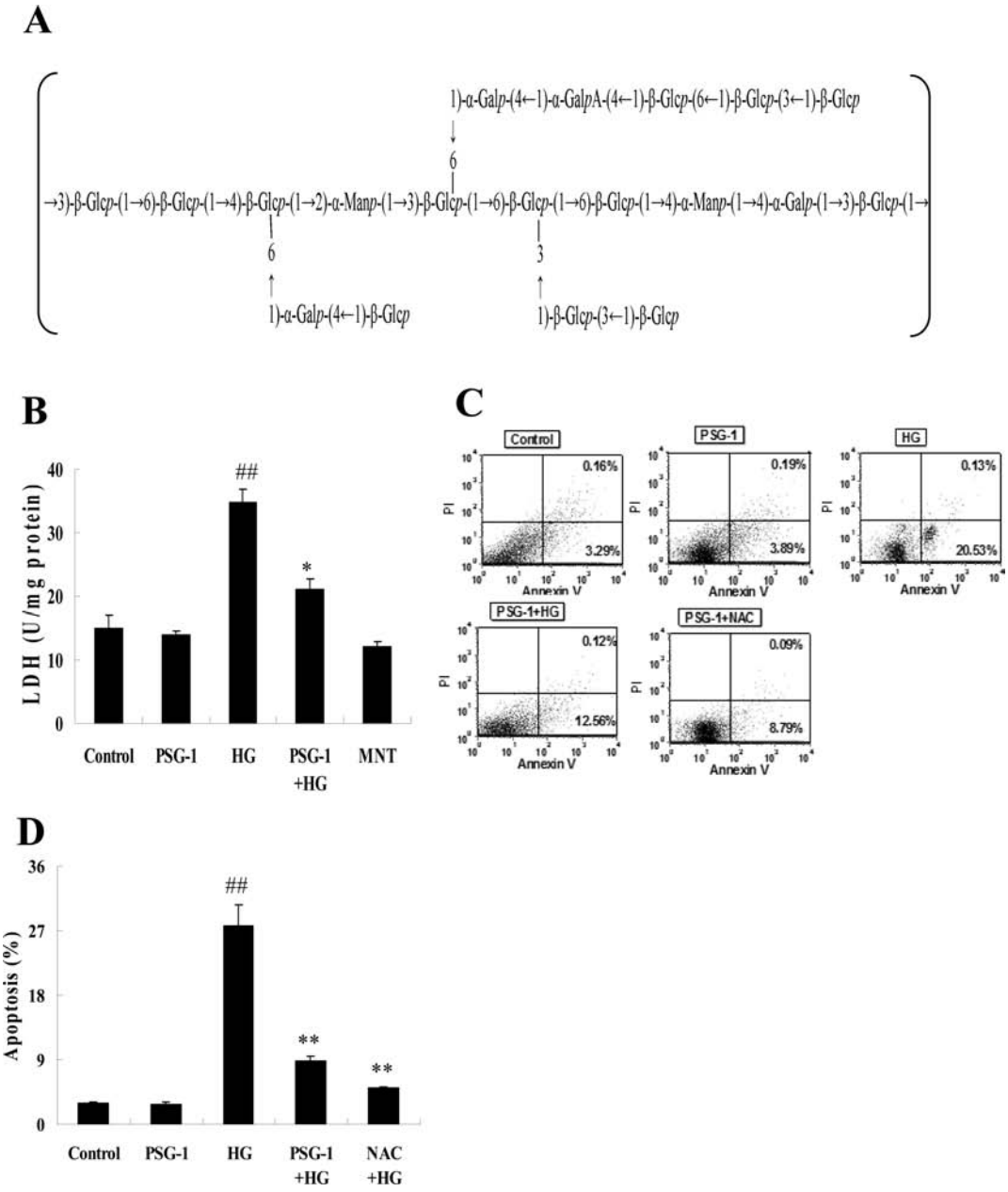

Figure 1. Effects of PSG-1 on high glucose (HG)-induced LDH release and apoptosis in HUVECs. (A) The structure of PSG-1. PSG-1 was proved as a hyteropolysaccharide comprising a backbone of 1,3-linked and 1,6-linked β-Glcp residues substituted at O-3 and O-6 positions as the branch points. The residues of α-1,4-Galp, α-1,2-Manp, and α-1,4-Manp were also found in the backbone. Side chains were terminated by β-Glcp, with the composition of α-1,4-Galp, α-1,4-GalpA, β-1,3-Glcp, and β-1,6-Glcp. (B) Effects of PSG-1 on LDH activity in HUVECs exposed to HG. (C and D) Effects of PSG-1 on the apoptosis in HUVECs exposed to HG. (C) Determination of apoptosis by AnnexinV and PI double staining. (D) Column bar graph of apoptosis. ##$P < 0.01$ vs the control group; *$P < 0.05$, **$P < 0.01$ vs HG group.

Disruption of mitochondria changes the permeability of the mitochondrial membrane and leads to apoptosis in endothelial cells, which indicates that mitochondria play a critical role in vascular complications of diabetes.[16] Attention has been focused recently on the role of the mitochondrial permeability transition pore (mPTP) in the regulation of the permeability of the mitochondrial membrane and as a trigger for apoptosis.[17] Opening mPTP increases ROS generation, so mPTP might have an important role in ROS signaling. Hence, mitochondrial targeting of ROS generation or mPTP in mitochondria is emerging as a novel approach in the treatment of diabetic angiopathy.[18,19]

In the present study, we have used an experimental model in which human umbilical vein cells (HUVECs) are exposed to high concentrations of glucose, which partly mimics what happens *in vivo* in diabetic patients.[20] To elucidate the role of PSG-1 in ROS generation and mitochondrial function during hyperglycemia-induced angiopathy, we investigated whether PSG-1 can promote the survival of HUVECs by preventing the overproduction of ROS and mitochondrial dysfunction using the ROS scavengers, the oxidizing agent *tert*-butyl hydroperoxide (tBH), mPTP blockers, and caspase inhibition.

DOI: 10.1021/acs.jafc.5b03462
J. Agric. Food Chem. 2015, 63, 8182−8191

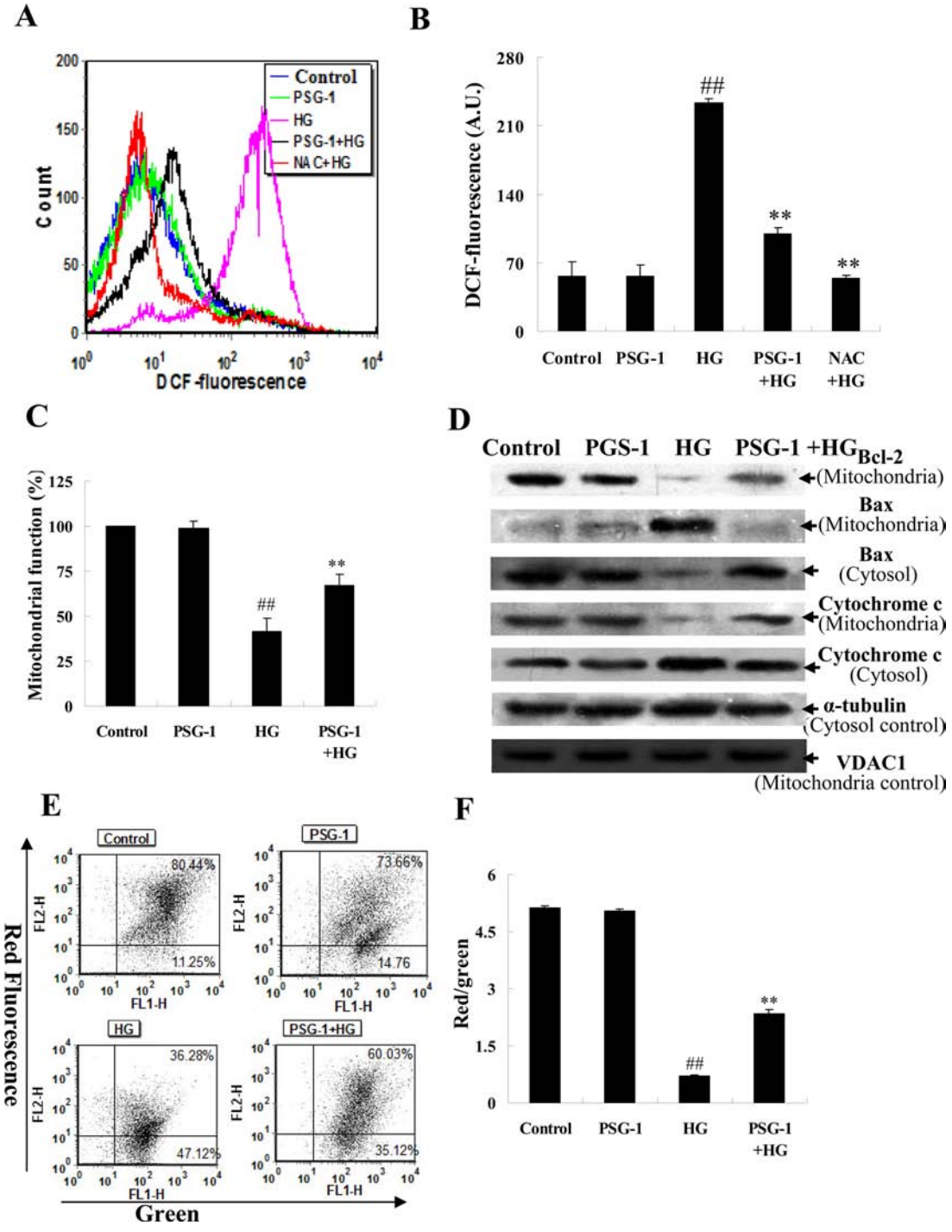

Figure 2. Effects of PSG-1 on high glucose (HG)-induced ROS production and mitochondrial pathology in HUVECs. (A and B) Flow cytometric analysis of ROS generation. A significant decrease of DCF fluorescence was observed in the PSG-1 pretreatment group. (C) Effect of PSG-1 on mitochondrial function by the MTT assay. (D) Effect of PSG-1 on cytochrome *c* release and the expression of Bcl-2 and Bax by Western blotting analysis. Expressions of the cytosolic and mitochondrial proteins were determined by Western blotting with anti-α-tubulin, anti-VDAC1, anticytochrome *c*, anti-Bax, and anti-Bcl-2 antibodies. (E and F) Effect of PSG-1 on the loss of $\Delta\Psi$m subjected to HG. (E) Flow cytometric analysis of $\Delta\Psi$m as determined by JC-1staining. FL1-H, green; FL2-H, red. (F) The quantitation of $\Delta\Psi$m was expressed as the ratio of red fluorescence over green fluorescence. $^{**}P < 0.01$ vs the HG group.

MATERIALS AND METHODS

Reagents. PSG-1 was prepared as previously described.[12] MTT, cyclosporine A (CsA), and *N*-acetyl cysteine (NAC) were purchased from Sigma (St. Louis, MO, USA). Cell culture products were obtained from Life Technologies (Paisley, Scotland, USA). The 5,5′,6,6′-tetrachloro-1,1′,3,3′-tetraethylbenzimidazolcarbocyanine iodide (JC-1) assay kit was purchased from Beyotime Institute of Biotechnology (Shanghai, China). Annexin V-FITC apoptosis detection kits were from BD Biosciences (San Jose, SD, USA); anti-Bcl-2, anti-Bax, anticytochrome *c*, anti-β-actin, and anti-α-tubulin primary antibodies, as well as the HRP-linked secondary antibody, were from Santa Cruz Biotechnology (Santa Cruz, CA, USA). 2′,7′-Dichlorofluorescein diacetate (DCFH-DA) was purchased from Molecular Probes Inc. (Eugene, OR, USA). Anti-VDAC1 rabbit

DOI: 10.1021/acs.jafc.5b03462
J. Agric. Food Chem. 2015, 63, 8182−8191

polyclonal antibody was purchased from Abcam Biotechnology (Abcam, Cambridge, UK). Mitochondria/cytosol fractionation kit and Z-VAD-FMK were obtained from Biovision (Mountain View, CA, USA).

Cells and Cell Culture. HUVECs were purchased from the American Type Culture Collection (ATCC, Catalog No: CRL-1730, US). The cells were seeded in 60 mm Petri dishes and cultured in DMEM supplemented with 10% fetal bovine serum, penicillin (100 U/mL), and streptomycin (100 μg/mL) in a humidified incubator (5% CO2, 37 °C). HUVECs, at 80−90% confluence, were treated with a high concentration of glucose (35.5 mmol/L) for the required time of pretreatment with PSG-1 for 1 h before the high glucose treatment. At the indicated time points, the cells were collected for further evaluation.

Determination of Cell and Mitochondrial Viability. Cell and mitochondrial viability were determined by modification of a previously published protocol.[21] HUVECs were seeded in 96-cell plates at 1×10^4/well for 24 h. The cells were then incubated with high glucose alone or in the presence of PSG-1 for specified times. Cell viability was determined by measuring lactate dehydrogenase (LDH) released from the cells using LDH assay kits (Nanjing Jiancheng Bioengineering Institute, Nanjing, China). Mitochondrial function was determined by measuring NADPH dehydrogenase activity using the MTT assay.

Analysis of Apoptosis. HUVECs were treated with PSG-1 and incubated for prescribed periods. After incubation, HUVECs were harvested and washed with ice-cold PBS, and stained with Annexin V and PI in buffer. Stained cells were analyzed by flow cytometry with a FACSort cell sorter (Becton Dickinson, San Jose, CA, USA).

Determination of ROS Generation. After the incubation period, HUVECs were harvested and washed with ice-cold PBS. Washed cells were further incubated with10 μM DCFH-DA at 37 °C for 20 min in dark. Cells were washed in PBS and analyzed by flow cytometry with a FACSort cell sorter.

Measurement of Mitochondrial Membrane Potential ($\Delta\Psi$m). Flow cytometry with a JC-1 fluorescent probe was used to determine the change of $\Delta\Psi$m in HUVECs. The HUVECs were harvested and washed with 500 μL of culture medium, and then 500 μL of JC-1staining fluids was added to the cells according to the manufacturer's instructions. $\Delta\Psi$m was expressed as a ratio of red fluorescence intensity over green fluorescence intensity.

SDS−PAGE and Western Blot Analyses. SDS−PAGE and Western blot analyses of Bcl-2, Bax, or cytochrome *c* were performed as previously described.[8,22] Anti-α-tubulin and anti-VDAC1 antibodies were used as total control, cytosolic loading control, and mitochondrial loading control, respectively.

Determination of mPTP Opening. The opening of mPTP was determined using the mPTP fluorescence detection kit (Genmed Scientific Inc., USA). After the indicated treatment, the fluorescence intensity of samples was determined by using a Varioskan Flash Multimode Reader (Thermo Electron Corporation, USA).

Assay of Caspase Activities. Caspase activities were measured by a colorimetric assay kit (Biovision, CA, USA). The absorbance at 405 nm of the released ρNA was monitored spectrophotometerically. The protein contents were measured by a BCA kit (Beyotime Company, Nanjing, China).

Statistical Analyses. All data are expressed as the mean ± SEM. Statistical significance was tested by one-way analysis of variance. A value of $P < 0.05$ was considered to be statistically significant.

RESULTS

Effects of PSG-1 on High Glucose-Induced Cytotoxicity in HUVECs. Increase of LDH release is widely used as an index of cellular necrosis.[21] To investigate the effect of PSG-1 on high glucose-induced cell damage, we treated HUVECs for 48 h with a high concentration of glucose (35.5 mmol/L) alone or after pretreatment with PSG-1 (50 μg/mL) for 1 h.[11] HUVECs subjected to high glucose insults induced a significant increase of LDH release. Simultaneous treatment of cells with PSG-1 significantly decreased the amount of LDH released. Such PSG-1 pretreatment caused no significant cytotoxicity in normal cells. To avoid the effect of osmotic pressure on cell injury, mannitol (5.5 mmol/L glucose + 30.0 mmol/L mannitol) was used as a control (Figure 1B). The data showed that mannitol did not protect against high glucose-induced cytotoxicity in HUVECs. These results indicated that PSG-1 was a protective agent against high glucose-induced injury in HUVECs.

Effects of PSG-1 on High Glucose-Induced Apoptosis in HUVECs. Apoptosis was determined by Annexin V and PI double staining. Figure 1C and D showed a significant increase of apoptosis in endothelial cells exposed to high glucose. However, when cells had been pretreated with PSG-1 for 1 h before being subjected to high glucose, a decrease in the number of apoptotic cells was observed. These data suggested that PSG-1 could protect endothelial cells against apoptosis induced by high glucose.

Effects of PSG-1 on High Glucose-Induced ROS Production in HUVECs. Our recent studies have suggested that overproduction of ROS could be attenuated by PSG-1 both *in vivo* and *in vitro*.[9,23] To further analyze the effects of PSG-1 on ROS production, HUVECs were incubated with PSG-1 prior to being exposed to high glucose. It was found that PSG-1 significantly reduced 2′,7′-dichlorofluorescein (DCF) fluorescence, suggesting a significant decrease of ROS production (Figure 2A and B). We considered that this showed a link between the attenuation of intracellular oxidative stress by PSG-1 and its protective effect against hyperglycemia toxicity. To find the relationship between the overproduction of ROS and apoptosis, we used NAC, a ROS scavenger, to investigate the role of ROS in apoptosis after HUVECs had been cultured under elevated glucose concentration conditions. Confirming that glucotoxicity is related to oxidative stress resulting from ROS generation, pretreatment of endothelial cells with 15 mmol/L NAC for 1 h, significantly ameliorates high glucose-induced apoptosis (Figure 1C and D) and ROS generation (Figure 2A and B).

Effects of PSG-1 on High Glucose-Induced Mitochondrial Dysfunction in HUVECs. Mitochondria are believed to play a crucial role in controlling ROS generation, and its dysfunction is one of the prominent phenomenons of ROS-induced cell damage.[24] We further examined the effects of PSG-1 on mitochondrial dysfunction induced by high glucose in HUVECs. As shown in Figure 2C, treatment with high glucose for 48 h induced a significant loss of the activity of mitochondrial dehydrogenase, this points to mitochondrial impairment, which could be significantly attenuated by the addition of PSG-1. The maintenance of the $\Delta\Psi$m is also crucial for mitochondrial functions such as ATP generation and electron transport. Previously, we showed that the bioactivity of PSG-1 is a factor in maintaining $\Delta\Psi$m in cardiomyocytes exposed to anoxia/reoxygenation.[9] In this work, high glucose led to a significant decrease in the red (JC-1 aggregates FL2-H+/FL1-H+)/green (JC-1 monomers FL2-H−/FL2-H+) ratio, suggesting the loss of $\Delta\Psi$m in endothelial cells (Figure 2E and F). Significantly, the loss of $\Delta\Psi$m was blocked by PSG-1 pretreatment, indicating that PSG-1 could alleviate hyperglycemia-promoted mitochondrial dysfunction by both increasing the activity of mitochondrial dehydrogenase and maintaining $\Delta\Psi$m in HUVECs.

Effects of PSG-1 on the Mitochondrial Apoptotic Pathway in HUVECs Subjected to High Glucose. Over-

DOI: 10.1021/acs.jafc.5b03462
J. Agric. Food Chem. 2015, 63, 8182−8191

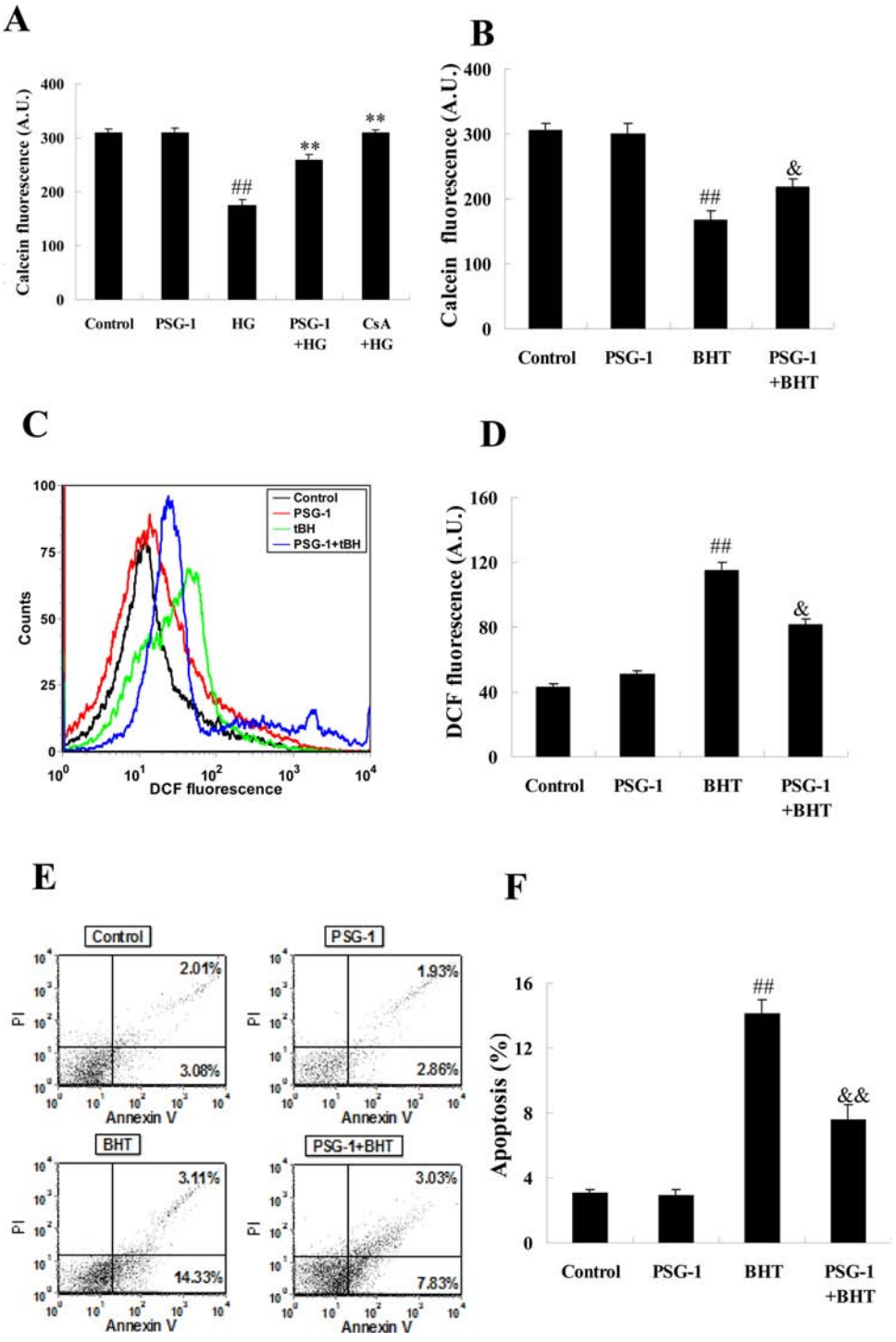

Figure 3. Effects of PSG-1 on mPTP opening, ROS generation, and apoptosis in HUVECs subjected to high glucose (HG) or BHT. (A) Effects of PSG-1 on mPTP opening in HUVECs subjected to HG. The opening of mPTP was analyzed by calcein fluorescence. The decrease of calcein fluorescence suggested the opening of mPTP. (B) Effects of PSG-1 on mPTP opening in HUVECs subjected to BHT. (C and D) Effects of PSG-1 on ROS generation in HUVECs subjected to BHT. (E and F) Effects of PSG-1 on apoptosis in HUVECs subjected to BHT. ##P < 0.01 vs the control group; *P < 0.05, **P < 0.01 vs the HG group; and P < 0.05 and P < 0.01 vs the BHT group.

production of ROS particularly affects the mitochondria, which causes the collapse of the $\Delta\Psi$), triggering the release of mitochondrial cytochrome *c* to activate the mitochondrial apoptotic pathway.[25,26] The data showed that cytochrome *c* in control mitochondrial cells was highly expressed, with very low expression in cytosol, but cytochrome *c* diffused out of the mitochondria and was significantly accumulated in the cytosol after 48 h of treatment with high glucose. However, cytochrome *c* release from mitochondria into cytosol was significantly reduced when HUVECs were incubated with PSG-1 before high glucose treatment (Figure 2D).

Bax and Bcl-2, the two main members of the Bcl-2 family, act as an upstream checkpoint of mitochondrial dysfunction associated with cytochrome *c* release.[27] Western blotting

DOI: 10.1021/acs.jafc.5b03462
J. Agric. Food Chem. 2015, 63, 8182−8191

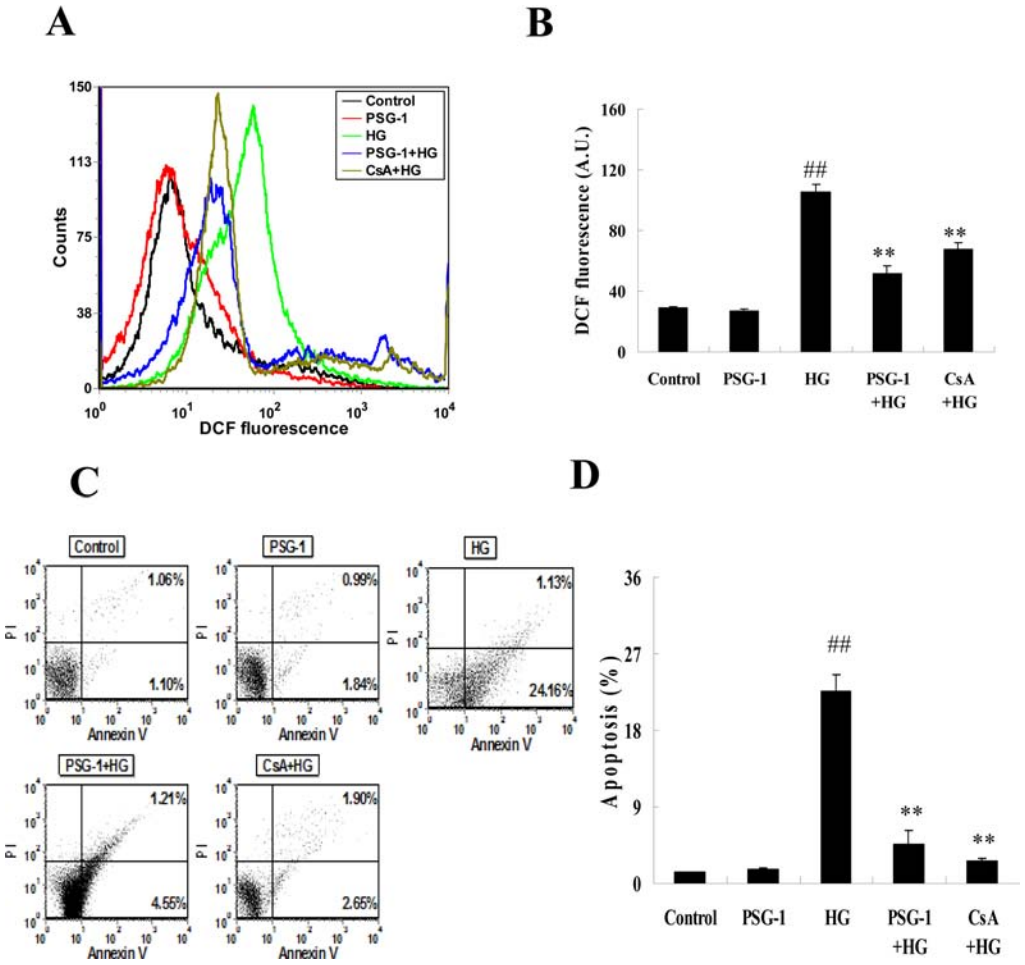

Figure 4. Effects of PSG-1 or CsA on ROS generation and apoptosis in HUVECs subjected to high glucose (HG). (A) and (B) Effects of PSG-1 or CsA on ROS generation in HUVECs subjected to HG. (C and D) Effects of PSG-1 or CsA on apoptosis in HUVECs subjected to HG. ##P < 0.01 vs the control group; *P < 0.05, **P < 0.01 vs the HG group.

analysis showed that Bcl-2 expression was significantly reduced from the mitochondria after high glucose treatment (Figure 2D), but after treatment with high glucose for 48 h, an increased amount of Bax was found in the mitochondrial fraction of HUVECs, whereas the protein of cytosolic Bax was decreased with this treatment. In contrast, PSG-1 alleviated the changes of antiapoptotic Bcl-2 and proapoptotic Bax in HUVECs under high glucose conditions. Meanwhile, PSG-1 inhibited the release of cytochrome *c* into the cytosol and alteration of Bcl-2 paralleled with the increase of $\Delta\Psi$m and the attenuation of apoptosis. The results indicated that high glucose triggered the mitochondrial apoptotic pathway, which was suppressed by PSG-1 in HUVECs.

Effects of PSG-1 on mPTP Opening in HUVECs Subjected to High Glucose. Opening of the mPTP is a mechanism which releases apoptotic factors (such as cytochrome *c*) and mitochondrial membrane permeabilization as occurs during apoptosis.[28] Induction of mPTP opening results in a decrease of calcein fluorescence, and the decrease of fluorescence intensity corresponds to such opening. The results showed that high glucose markedly enhanced the opening of mPTP (Figure 3A). Significantly, PSG-1 inhibited the opening of mPTP, indicating that its effect against apoptosis may be associated with inhibiting the opening of mPTP in HUVECs when exposed to high glucose.

An oxidizing agent, tBH, which is known to cause mPTP opening in living cells,[29] was also used to investigate the opening of mPTP in HUVECs. There was a remarkable increase in apoptosis accompanying the opening of mPTP in HUVECs treated with 500 μmol/L tBH for 45 min. This result confirms that mPTP is an oxidative stress-sensitive channel related to apoptosis (Figure 3B). When HUVECs were subjected to PSG-1 for 1 h, the tBH-induced opening of mPTP decreased significantly in parallel with the attenuation of ROS generation (Figure 3C and D) and apoptosis (Figure 3E and F). These results suggested that PSG-1 may ameliorate oxidative stress-related mPTP opening in HUVECs.

Next, we examined whether manipulation of mPTP opening may alter ROS production. Treatment of the reference mPTP inhibitor CsA resulted in the inhibition of ROS generation (Figure 4Aand B) and also alleviated apoptosis (Figure 4C and D) in HUVECs exposed to high glucose. This would suggest that manipulation of mPTP opening could influence ROS production. Similar results were observed with PSG-1, which was also found to inhibit ROS generation and apoptosis. These findings suggested that mPTP opening was a necessary factor for apoptosis and was closely related to ROS generation. Inhibition of mPTP opening may, therefore, be a means of protecting PSG-1 against hyperglycemia toxicity-induced apoptosis in HUVECs.

DOI: 10.1021/acs.jafc.5b03462
J. Agric. Food Chem. 2015, 63, 8182−8191

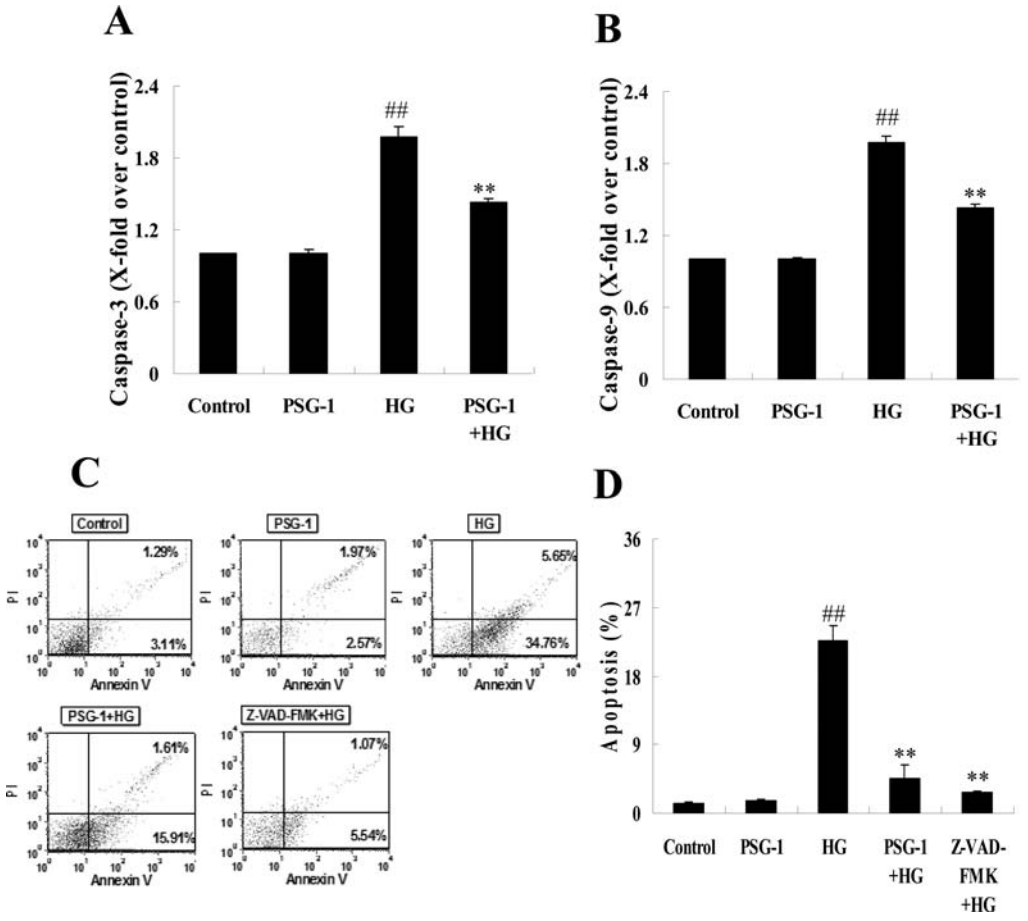

Figure 5. Effects of PSG-1 on caspase activity in HUVECs subjected to high glucose (HG). (A and B) Effects of PSG-1 on the activities of caspase-3 and caspase-9. (C and D) Effects of caspase inhibitor "Z-VAD-FMK" or PSG-1 on apoptosis in HUVECs subjected to HG. ##P < 0.01 vs the control group; *P < 0.05, **P < 0.01 vs the HG group.

Effects of PSG-1 on Caspase Activity in Endothelial Cells. Caspase activation is believed to play an important role in the execution of apoptosis.[30] We found that the activities of caspase-3 and caspase-9 were significantly increased by the high glucose treatment (Figure 5A and B). PSG-1 was found to attenuate the activation of both caspases produced by high glucose. PSG-1 therefore may protect endothelial cells against apoptosis by attenuation of caspase activation. Meanwhile, high glucose-induced apoptosis (Figure 5C and D) was alleviated by treatment with caspase inhibitor "Z-VAD-FMK" (20 μmol/L). These results suggested that high glucose-stimulated apoptosis was caspase-dependent and that PSG-1 could reduce caspase activation.

DISCUSSION

Diabetic angiopathy has been defined as endothelial dysfunction and is recognized as the main complication of diabetes.[31] The present study was designed to investigate the role of a novel *Ganoderma atrum* polysaccharide, PSG-1, in the cell damage of hyperglycemic endothelial cells. We have shown, for the first time, that PSG-1 inhibits endothelial dysfunction by ameliorating mitochondrial damage and apoptosis in high glucose-stimulated endothelial cells.

There is also mounting evidence that hyperglycemia-induced oxidative stress resulting from the overproduction of ROS is a major factor contributing to the development and progression of diabetic angiopathy. Overproduction of ROS is a factor in hyperglycemia-induced angiopathy, but its role in the apoptotic process has not been elucidated. Our results have demonstrated a rapid increase of the ROS levels is associated with a significant increase of apoptosis. This would indicate that enhancement of ROS production is an essential factor for hyperglycemia-induced apoptosis in endothelial cells. Because enhancement of ROS generation can cause apoptosis in high glucose conditions, we have, therefore, examined whether inhibiting ROS production with the potent antioxidant and free radical scavenger NAC can prevent apoptosis in sustained high glucose systems.[32,33] Our results showed that addition of NAC did inhibit apoptosis and added to the evidence that oxidative stress resulting from overproduction of ROS plays a crucial role in hyperglycemia-induced apoptosis. Having demonstrated that PSG-1 did alleviate oxidative stress by the attenuation of ROS generation both *in vitro* and *in vivo*,[9,10] we have therefore further investigated whether endothelial cells are similarly influenced in the context of hyperglycemia. We found that decreased levels of ROS generation led to a reduction in apoptosis and cell injury, indicating that attenuation of ROS generation could enable PSG-1 to be effective against diabetic angiopathy.

The mitochondria generate a steady stream of ROS, which is particularly susceptible to oxidative stress.[34] In the present study, we found that high glucose-treated endothelial cells showed marked changes in several parameters of the mitochondrial function. Interestingly, these changes were

DOI: 10.1021/acs.jafc.5b03462
J. Agric. Food Chem. 2015, 63, 8182−8191

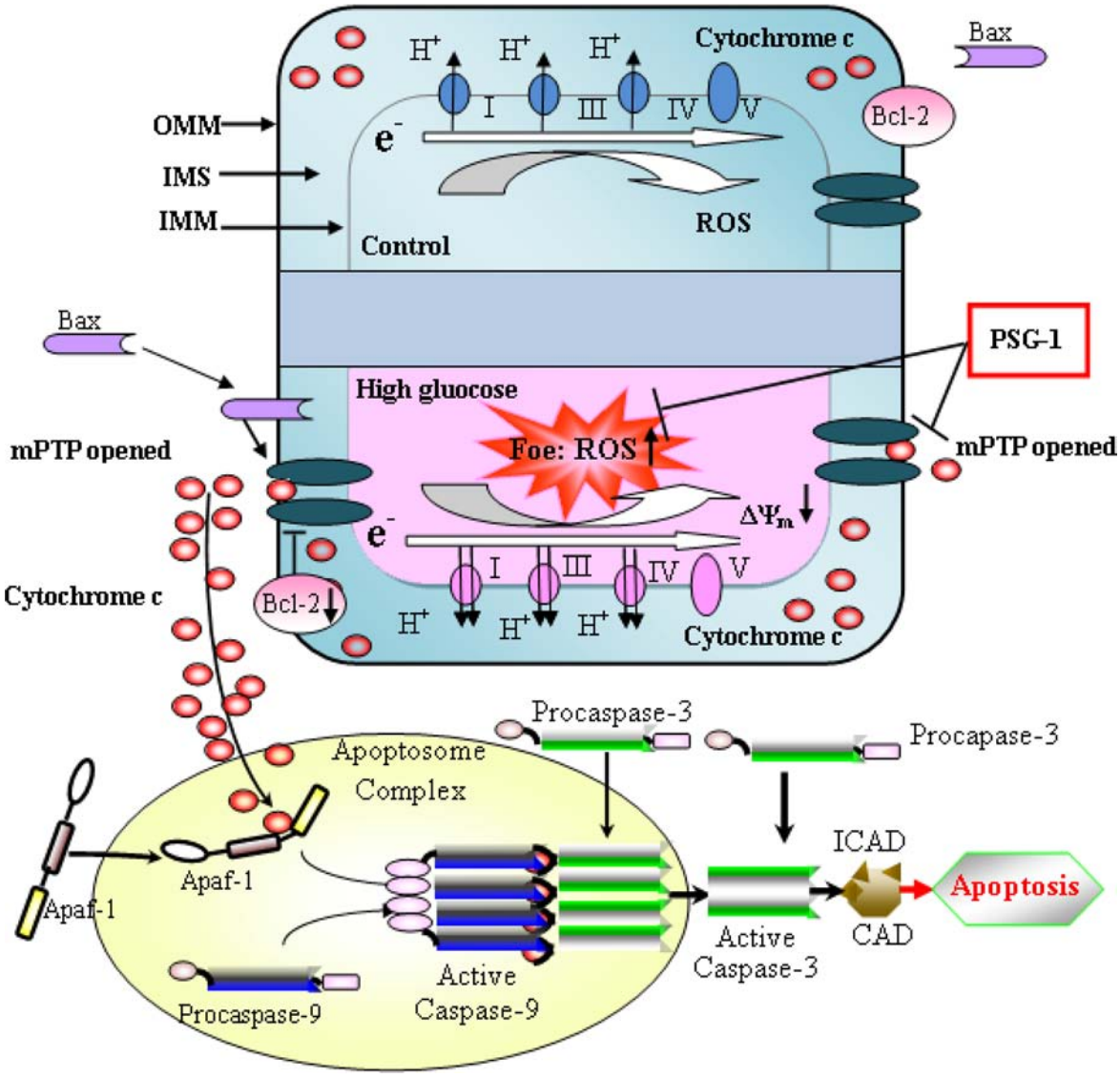

Figure 6. Schematic model for the cellular mechanisms of PSG-1 on the amelioration of apoptosis induced by high glucose in HUVECs. Mitochondria are the primary source of ROS, which are produced by the mitochondrial electron transport chain (ETC). A low level of ROS was generated by the mitochondrial electron transport chain (ETC), and mPTP remains closed under normal conditions. However, under high glucose conditions, ROS are generated in excess and raised to a level that leads to the opening of mPTP. Moreover, the opening of mPTP could trigger the enhancement of ROS generation. These changes coincide with the alteration of Bcl-2 family and the loss of ΔΨm, resulting in cytochrome *c* release and caspase-9 activation. Caspase-9 activation in turn triggers the caspase-3 activation, which subsequently executed apoptosis. Accordingly, PSG-1 could ameliorate endothelial cell damage in response to high glucose via preventing the overproduction of ROS and opening of mPTP. Red circle, cytochrome *c*; IMS, intermembrane space; OMM, outer mitochondrial membrane; IMM, inner mitochondrial membrane; ICAD, inhibitor of caspase-activated deoxyribonuclease; CAD, Caspase-activated deoxyribonuclease.

significantly ameliorated by PSG-1, as evidenced by enhancing the activity of mitochondrial dehydrogenase and maintaining ΔΨm, indicating that PSG-1 may improve mitochondrial function in endothelial cells under high glucose conditions.

In response to overproduction of ROS, the outer mitochondrial membrane becomes permeable, which leads to the loss of ΔΨm, triggers the release of cytochrome *c* from mitochondria to the cytoplasm, and activates the mitochondrial apoptotic pathway.[35] It was consistent therefore that there was a significant decrease in ΔΨm in high glucose conditions in endothelial cells. We also found that release of cytochrome *c* from mitochondria to the cytoplasm was significantly increased. Incubation of endothelial cells with PSG-1 for 1 h significantly attenuated the effect of high glucose on the loss of ΔΨm and release of mitochondrial cytochrome *c*. The Bcl-2 family, which includes both antiapoptotic and proapoptotic proteins, acts as a checkpoint upstream for mitochondrial apoptosis. Antiapoptotic proteins promote cell survival, whereas proapoptotic proteins mediate mitochondria-dependent apoptosis. Bax and Bcl-2, the two main members of this family, influence the permeability of the mitochondrial membrane. Upon apoptotic stimulation, Bax, a pore-forming cytoplasmic protein, translocates to the outer mitochondrial membrane, changes its permeability, and induces cytochrome *c* release from the mitochondria to the cytosol. The antiapoptotic Bcl-2 is associated with the outer mitochondrial membrane where it stabilizes the membrane permeability and thus suppresses the release of cytochrome *c*.[26,35,36] During high glucose-induced apoptosis, a decrease of mitochondrial Bcl-2 expression and distribution of Bax from the cytosol to mitochondria were

DOI: 10.1021/acs.jafc.5b03462
J. Agric. Food Chem. 2015, 63, 8182−8191

observed in endothelial cells. Significantly, the PSG-1 treatment decreased the alteration of Bcl-2 family protein expression in the endothelial cells stimulated by high glucose.

The Bcl-2 family dependent changes in the permeability of the mitochondrial membrane that resulted in the loss of $\Delta\Psi$m and the release of cytochrome *c* are mediated by a high-conductance channel, mPTP. Although Hunter and Haworth in the late 1970s first observed and described mPTP, its function in the vascular complication of diabetes has still not been clarified.[18,37−39] The present study was designed to further explore the role of mPTP in high glucose-induced apoptotic cell death. Our results not only supported the idea of an increase in the opening of mPTP as one of the key events during apoptotic cell death in high glucose but also suggested that mPTP may be an oxidative stress-sensitive channel opened by increased ROS production. Therefore, we have investigated whether inhibition of the opening of mPTP may prevent apoptotic cell death under high glucose conditions. Treatment with CsA significantly inhibited cell death under high glucose conditions, which supported the view that opening of mPTP may play a critical role in high glucose inducing cell death. PSG-1 also inhibited the opening of mPTP with an efficacy similar to that of CsA. PSG-1 can thus influence the oxidative stress-related opening of mPTP, which points to novel insight into the potential therapeutic targets for PSG-1 intervention.

During transduction of an apoptotic signal into the mitochondria, the apoptotic protein of cytochrome *c* is translocated into the cytoplasm, which leads to the activation of caspase-9. Active caspase-9 then activates caspase-3, which contributes to the execution of apoptosis.[40−42] In keeping with these observations, our results showed that high glucose-induced apoptosis was accompanied by a significant increase of caspase-9 and caspase-3 activities, compared with cells under control conditions. Likewise, PSG-1 treatment significantly decreased the high glucose-induced activation of both caspases. Since the final pathway that contributes to the execution of cell death signal is caspase activation, we used a caspase inhibitor Z-VAD-FMK to treat the endothelial cells under high glucose conditions. We found that the caspase inhibitor significantly decreases high glucose-stimulated apoptosis, which suggested that high glucose-induced apoptosis in the endothelial cells might be caspase-dependent, which could be alleviated by PSG-1.

Overall, we have provided *in vitro* evidence about the effects of the *Ganoderma atrum* polysaccharide, PSG-1, on diabetic angiopathy. These interesting findings suggested that PSG-1 alleviated HG-associated cell dysfunction by its effect on the modification of the redox system and implied that antioxidant effects of PSG-1 might be related to its protective effect against vascular dysfunction. On the basis of these results, we have drawn up a schematic model (Figure 6) for the effects of PSG-1 on endothelial cells under high glucose conditions, which describe how ROS production and the opening of mPTP are centrally involved in apoptosis and diabetic angiopathy. Accordingly, PSG-1 could ameliorate endothelial cell damage in response to high glucose via a mitochondria-reactive oxygen species pathway. Meanwhile, factors affecting the permeability of the mitochondrial membrane have a profound influence on cell survival and cell death. Future work is necessary to investigate the molecular basis of the relationship between mPTP and the health benefits of PSG-1 against diabetic angiopathy. Together, these findings make PSG-1 an attractive candidate as a new interventional approach for diabetic angiopathy.

AUTHOR INFORMATION

Corresponding Author

*(M.-Y.X.) Tel: +86 791-3969009. Fax: +86 791-3969009. E-mail: myxie@ncu.edu.cn/xmync@163.com.

Funding

The financial support for the present study by the National Natural Science Foundation of China (Nos: 31130041, 31471702, and 31201326), Natural Science Foundation of Jiangxi Province (20132BAB214001 and 20151BAB204038), and Key Science and Technique Project of Department of Science, Jiangxi Province, is gratefully acknowledged.

Notes

The authors declare no competing financial interest.

ABBREVIATIONS USED

CAD, caspase-activated deoxyribonuclease; CsA, cyclosporine A; DCF, 2′,7′-dichlorofluorescein; DCFH-DA, 2′,7′-dichlorodihydrofluorescein diacetate; HUVECs, human umbilical vein cells; ICAD, inhibitor of caspase-activated deoxyribonuclease; IMS, intermembrane space; IMM, inner mitochondrial membrane; JC-1, 5,5′,6,6′-tetrachloro-1,1′,3,3′-tetraethylbenzimidazolcarbocyanine iodide; LDH, lactate dehydrogenase; $\Delta\Psi$m, mitochondrial membrane potential; mPTP, mitochondrial permeability transition pore; MTT, 3-(4,5-dimethylthiazol-2-yl)-2,5-diphenyltetrazolim bromide; NAC, *N*-acetyl cysteine; OMM, outer mitochondrial membrane; PSG-1, *Ganoderma atrum* polysaccharide; ROS, reactive oxygen species; tBH, *tert*-butyl hydroperoxide

REFERENCES

(1) Chan, K. C.; Lin, M. C.; Huang, C. N.; Chang, W. C.; Wang, C. J. Mulberry 1-deoxynojirimycin pleiotropically inhibits glucose-stimulated vascular smooth muscle cell migration by activation of AMPK/RhoB and down-regulation of FAK. *J. Agric. Food Chem.* **2013**, *61*, 9867−9875.

(2) Silvestre, J. S.; Lévy, B. I. Molecular basis of angiopathy in diabetes mellitus. *Circ. Res.* **2006**, *98*, 4−6.

(3) Rochette, L.; Zeller, M.; Cottin, Y.; Vergely, C. Diabetes, oxidative stress and therapeutic strategies. *Biochim. Biophys. Acta, Gen. Subj.* **2014**, *1840*, 2709−2729.

(4) Wang, W.; Fang, H.; Groom, L.; Cheng, A.; Zhang, W.; Liu, J.; Wang, X.; Li, K.; Han, P.; Zheng, M.; Yin, J.; Wang, W.; Mattson, M. P.; Kao, J. P.; Lakatta, E. G.; Sheu, S. S.; Ouyang, K.; Chen, J.; Dirksen, R. T.; Cheng, H. Superoxide flashes in single mitochondria. *Cell* **2008**, *134*, 279−290.

(5) Busik, J. V.; Mohr, S.; Grant, M. B. Hyperglycemia-induced reactive oxygen species toxicity to endothelial cells is dependent on paracrine mediators. *Diabetes* **2008**, *57*, 1952−1965.

(6) Dorenkott, M. R.; Griffin, L. E.; Goodrich, K. M.; Thompson-Witrick, K. A.; Fundaro, G. Y. L.; Stevens, J. R.; Ali, M.; O'Keefe, S. F.; Hulver, M. W.; Neilson, A. P. Oligomeric cocoa procyanidins possess enhanced bioactivity compared to monomeric and polymeric cocoa procyanidins for preventing the development of obesity, insulin resistance, and impaired glucose tolerance during high-fat feeding. *J. Agric. Food Chem.* **2014**, *62*, 2216−2227.

(7) Aruoma, O. I. Methodological considerations for characterizing potential antioxidant actions of bioactive components in plant foods. *Mutat. Res., Fundam. Mol. Mech. Mutagen.* **2003**, *523*−*524*, 9−20.

(8) Li, W. J.; Nie, S. P.; Peng, X. P.; Liu, X. Z.; Li, C.; Chen, Y.; Li, J. E.; Song, W. R.; Xie, M. Y. *Ganoderma atrum* polysaccharide improves age-related oxidative stress and immune impairment in mice. *J. Agric. Food Chem.* **2012**, *60*, 1413−1418.

DOI: 10.1021/acs.jafc.5b03462
J. Agric. Food Chem. 2015, 63, 8182−8191

(9) Li, W. J.; Nie, S. P.; Chen, Y.; Xie, M. Y.; He, M.; Yu, Q.; Yan, Y. *Ganoderma atrum* polysaccharide protects cardiomyocytes against anoxia/reoxygenation-induced oxidative stress by mitochondrial pathway. *J. Cell. Biochem.* **2010**, *110*, 191−200.
(10) Li, W. J.; Nie, S. P.; Xie, M. Y.; Yu, Q.; Chen, Y.; He, M. *Ganoderma atrum* polysaccharide attenuates oxidative stress induced by d-galactose in mouse brain. *Life Sci.* **2011**, *88*, 713−718.
(11) Li, W. J.; Nie, S. P.; Yu, Q.; Yan, Y.; Wang, Y. X.; Xie, M. Y. *Ganoderma atrum* polysaccharide protects human umbilical vein cells against injury by high glucose. *Acta Nutrimenta Sin.* **2010**, *32*, 264−267.
(12) Zhang, H.; Li, W. J.; Nie, S. P.; Chen, Y.; Xie, M. Y. Structural characterisation of a novel bioactive polysaccharide from *Ganoderma atrum*. *Carbohydr. Polym.* **2012**, *88*, 1047−1054.
(13) Yokozawa, T.; Kim, H. J.; Cho, E. J. Gravinol ameliorates high-fructose-induced metabolic syndrome through regulation of lipid metabolism and proinflammatory state in rats. *J. Agric. Food Chem.* **2008**, *56*, 5026−5032.
(14) Song, J.; Li, J.; Hou, F.; Wang, X.; Liu, B. Mangiferin inhibits endoplasmic reticulum stress-associated thioredoxin-interacting protein/NLRP3 inflammasome activation with regulation of AMPK in endothelial cells. *Metab., Clin. Exp.* **2015**, *64*, 428−437.
(15) Hoye, A. T.; Davoren, J. E.; Wipf, P.; Fink, M. P.; Kagan, V. E. Targeting mitochondria. *Acc. Chem. Res.* **2008**, *41*, 87−97.
(16) Eirin, A.; Ebrahimi, B.; Zhang, X.; Zhu, X. Y.; Woollard, J. R.; He, Q.; Textor, S. C.; Lerman, A.; Lerman, L. O. Mitochondrial protection restores renal function in swine atherosclerotic renovascular disease. *Cardiovasc. Res.* **2014**, *103*, 461−472.
(17) Kokoszka, J. E.; Waymire, K. G.; Levy, S. E.; Sligh, J. E.; Cai, J.; Jones, D. P.; MacGregor, G. R.; Wallace, D. C. The ADP/ATP translocator is not essential for the mitochondrial permeability transition pore. *Nature* **2004**, *427*, 461−465.
(18) Kinnally, K. W.; Peixoto, P. M.; Ryu, S. Y.; Dejean, L. M. Is mPTP the gatekeeper for necrosis, apoptosis, or both? *Biochim. Biophys. Acta, Mol. Cell Res.* **2011**, *1813*, 616−622.
(19) Li, C.; Ding, Q.; Nie, S. P.; Zhang, Y. S.; Xiong, T.; Xie, M. Y. Carrot juice fermented with Lactobacillus plantarum NCU116 ameliorates type 2 diabetes in rats. *J. Agric. Food Chem.* **2014**, *62*, 11884−11891.
(20) Quagliaro, L.; Piconi, L.; Assaloni, R.; Martinelli, L.; Motz, E.; Ceriello, A. Intermittent high glucose enhances apoptosis related to oxidative stress in human umbilical vein endothelial cells. *Diabetes* **2003**, *52*, 2795−2804.
(21) Zhao, K.; Luo, G.; Giannelli, S.; Szeto, H. H. Mitochondria-targeted peptide prevents mitochondrial depolarization and apoptosis induced by tert-butyl hydroperoxide in neuronal cell lines. *Biochem. Pharmacol.* **2005**, *70*, 1796−1806.
(22) Zhang, G.; Parkin, K. L.S-alk(en)ylmercaptocysteine: chemical synthesis, biological activities, and redox-related mechanism. *J. Agric. Food Chem.* **2013**, *61*, 1896−1903.
(23) Li, W. J.; Nie, S. P.; Chen, Y.; Wang, Y. X.; Li, C.; Xie, M. Y. Enhancement of cyclophosphamide-induced antitumor effect by a novel polysaccharide from *Ganoderma atrum* in sarcoma 180-bearing mice. *J. Agric. Food Chem.* **2011**, *59*, 3707−3716.
(24) Raimundo, N.; Song, L.; Shutt, T. E.; McKay, S. E.; Cotney, J.; Guan, M. X.; Gilliland, T. C.; Hohuan, D.; Santos-Sacchi, J.; Shadel, G. S. Mitochondrial Stress Engages E2F1 Apoptotic Signaling to Cause Deafness. *Cell* **2012**, *148*, 716−726.
(25) Qiao, A.; Wang, Y.; Xiang, L.; Wang, C.; He, X. A novel triterpenoid isolated from apple functions as an anti-mammary tumor agent via a mitochondrial and caspase-independent apoptosis pathway. *J. Agric. Food Chem.* **2015**, *63*, 185−191.
(26) Thangam, R.; Senthilkumar, D.; Suresh, V.; Sathuvan, M.; Sivasubramanian, S.; Pazhanichamy, K.; Gorlagunta, P.; Kannan, S.; Gunasekaran, P.; Rengasamy, R.; Sivaraman, J. Induction of ROS-dependent mitochondria-mediated intrinsic apoptosis in MDA-MB-231 cells by glycoprotein from Codium decorticatum. *J. Agric. Food Chem.* **2014**, *62*, 3410−3421.
(27) Li, X.; Gao, L.; Zheng, L.; Kou, J.; Zhu, X.; Jiang, Y.; Zhong, Z.; Dan, J.; Xu, H.; Yang, Y.; Li, H.; Shi, S.; Cao, W.; Zhao, Y.; Tian, Y.; Yang, L. The efficacy and mechanism of apoptosis induction by hypericin-mediated sonodynamic therapy in THP-1 macrophages. *Int. J. Nanomed.* **2015**, *10*, 821−838.
(28) Zhang, Y.; Han, L.; Qi, W.; Cheng, D.; Ma, X.; Hou, L.; Cao, X.; Wang, C. Eicosapentaenoic acid (EPA) induced apoptosis in HepG2 cells through ROS-Ca(2+)-JNK mitochondrial pathways. *Biochem. Biophys. Res. Commun.* **2015**, *456*, 926−932.
(29) Detaille, D.; Guigas, B.; Chauvin, C.; Batandier, C.; Fontaine, E.; Wiernsperger, N.; Leverve, X. Metformin prevents high-glucose−induced endothelial cell death through a mitochondrial permeability transition-dependent process. *Diabetes* **2005**, *54*, 2179−2187.
(30) Weiss, J. N.; Korge, P.; Honda, H. M.; Ping, P. Role of the mitochondrial permeability transition in myocardial disease. *Circ. Res.* **2003**, *93*, 292−301.
(31) Vlassara, H.; Cai, W.; Crandall, J.; Goldberg, T.; Oberstein, R.; Dardaine, V.; Peppa, M.; Rayfield, E. J. Inflammatory mediators are induced by dietary glycotoxins, a major risk factor for diabetic angiopathy. *Proc. Natl. Acad. Sci. U. S. A.* **2002**, *99*, 15596−15601.
(32) Yuan, L.; Wei, S.; Wang, J.; Liu, X. Isoorientin induces apoptosis and autophagy simultaneously by reactive oxygen species (ROS)-related p53, PI3K/Akt, JNK, and p38 signaling pathways in HepG2 cancer cells. *J. Agric. Food Chem.* **2014**, *62*, 5390−5400.
(33) Khazim, K.; Gorin, Y.; Cavaglieri, R. C.; Abboud, H. E.; Fanti, P. The antioxidant silybin prevents high glucose-induced oxidative stress and podocyte injury *in vitro* and *in vivo*. *Am. J. Physiol. Renal. Physiol.* **2013**, *305*, F691−700.
(34) Kowaltowski, A. J.; Vercesi, A. E. Mitochondrial damage induced by conditions of oxidative stress. *Free Radical Biol. Med.* **1999**, *26*, 463−471.
(35) Shimizu, S.; Narita, M.; Tsujimoto, Y. Bcl-2 family proteins regulate the release of apoptogenic cytochrome c by the mitochondrial channel VDAC. *Nature* **1999**, *399*, 483−487.
(36) Czabotar, P. E.; Westphal, D.; Dewson, G.; Ma, S.; Hockings, C.; Fairlie, W. D.; Lee, E. F.; Yao, S.; Robin, A. Y.; Smith, B. J.; Huang, D. C.; Kluck, R. M.; Adams, J. M.; Colman, P. M. Bax crystal structures reveal how BH3 domains activate Bax and nucleate its oligomerization to induce apoptosis. *Cell* **2013**, *152*, 519−531.
(37) Naga, K. K.; Sullivan, P. G.; Geddes, J. W. High cyclophilin D content of synaptic mitochondria results in increased vulnerability to permeability transition. *J. Neurosci.* **2007**, *27*, 7469−7475.
(38) Don, A. S.; Kisker, O.; Dilda, P.; Donoghue, N.; Zhao, X.; Decollogne, S.; Creighton, B.; Flynn, E.; Folkman, J.; Hogg, P. J. A peptide trivalent arsenical inhibits tumor angiogenesis by perturbing mitochondrial function in angiogenic endothelial cells. *Cancer Cell* **2003**, *3*, 497−509.
(39) Qin, C. Z.; Zhang, X.; Wu, L. X.; Wen, C.; Hu, L.; Lv, Q. L.; Shen, D. Y.; Zhou, H. H. Advances in molecular signaling mechanisms of β-phenethyl isothiocyanate antitumor effects. *J. Agric. Food Chem.* **2015**, *63*, 3311−3322.
(40) White, M. J.; McArthur, K.; Metcalf, D.; Lane, R. M.; Cambier, J. C.; Herold, M. J.; van Delft, M. F.; Bedoui, S.; Lessene, G.; Ritchie, M. E.; Huang, D. C.; Kile, B. T. Apoptotic caspases suppress mtDNA-induced STING-mediated type I IFN production. *Cell* **2014**, *159*, 1549−1562.
(41) Rongvaux, A.; Jackson, R.; Harman, C. C.; Li, T.; West, A. P.; de Zoete, M. R.; Wu, Y.; Yordy, B.; Lakhani, S. A.; Kuan, C. Y.; Taniguchi, T.; Shadel, G. S.; Chen, Z. J.; Iwasaki, A.; Flavell, R. A. Apoptotic caspases prevent the induction of type I interferons by mitochondrial DNA. *Cell* **2014**, *159*, 1563−1577.
(42) Kim, S. P.; Nam, S. H.; Friedman, M. The Tomato Glycoalkaloid α-Tomatine Induces Caspase-Independent Cell Death in Mouse Colon Cancer CT-26 Cells and Transplanted Tumors in Mice. *J. Agric. Food Chem.* **2015**, *63*, 1142−115.

DOI: 10.1021/acs.jafc.5b03462
J. Agric. Food Chem. 2015, 63, 8182−8191

the Iwate University Animal Research Committee and conformed to the Guidelines for Animal Experiments of Iwate University.

Experimental Design and Experimental Diets. *Experiment 1.* A total of 20 rats were allowed free access to tap water and were provided with a 20% (w/w) casein diet based on AIN-93G[11] for 12 days. On day 13, the rats were fasted for 18 h and then fed a control diet (Table 1; 20C, 20% casein diet; 10C, 10% casein diet) or experimental diet (Table 1; 20CK, Lys-rich 20% casein diet; 10CK, Lys-rich 10% casein diet) for 1 h (9:00−10:00). After 3 h of fasting (10:00−13:00), each rat was anesthetized with pentobarbital, then its abdomen was opened, and blood was collected from the inferior vena cava. Each rat was euthanized after the collection of blood. The blood was centrifuged at 3500*g* for 15 min to obtain plasma, which was frozen in liquid nitrogen and stored at −80 °C until analysis. The soleus muscle, extensor digitorum longus (EDL) muscle, and gastrocnemius muscle were removed from the hind leg and weighed.

Table 1. Compositions of the Control and Experimental Diets

	control and experimental diets			
	20C	20CK	10C	10CK
	Ingredient (g/kg of diet)			
milk casein[a]	200	200	100	100
L-lysine[b]	0	6.5	0	6.5
L-cystine[b]	3.0	3.0	3.0	3.0
sucrose[c]	100	100	100	100
α-cornstarch[a]	529.5	523.0	629.5	623.0
soybean oil[c]	70	70	70	70
mineral mixture[a]	35	35	35	35
vitamin mixture[a]	10	10	10	10
choline bitartrate[a]	2.5	2.5	2.5	2.5
cellulose[a]	50	50	50	50
	Composition (%)			
protein	20	20	10	10
total Lys[d]	1.30	1.95	0.65	1.30

[a]Obtained from the Oriental Yeast Co., Tokyo, Japan. [b]Obtained from the Ajinomoto Co., Tokyo, Japan. [c]Obtained from the Toyo Sugar Refining Co., Tokyo, Japan. [d]Total Lys was calculated from the sum of Lys contained in casein[11] and the amounts of supplemented Lys with diet.

Experiment 2. A total of 10 rats were allowed free access to tap water and were provided a control (Table 1; 10C, 10% casein diet) or experimental (Table 1; 10CK, Lys-rich 10% casein diet) diet for 15 days. During this period, the food consumption of rats fed the Lys-rich diet was adjusted to that of rats fed the standard 10% casein diet. Excreted urine was collected for 24 h from the morning of the 13th day to the morning of the 14th day; thereafter, the experimental design was the same as for experiment 1. On the 15th day, the rats were fasted for 18 h and then provided a 10% casein diet or Lys-rich 10% casein diet for 1 h and skeletal muscles and blood were collected 3 h later.

Measurement of Myofibrillar Proteolysis. 3-Methylhistidine (MeHis) released from the isolated muscles was measured as described previously[8] by incubating the isolated EDL muscle or soleus muscle in Krebs-Ringer bicarbonate buffer containing 10 mM glucose under 95% O_2/5% CO_2 at 37 °C for 2 h after a 30 min preincubation at 37 °C. The amount of MeHis in the incubation buffer solution was measured using a high-performance liquid chromatography (HPLC) method.[12]

The plasma concentration of MeHis provides an index of myofibrillar proteolysis[13] and was measured by HPLC after derivatization with *o*-phthalaldehyde using the method of Nagasawa et al.,[14] with a slight modification.

The amount of MeHis in urine, commonly used as an index of myofibrillar proteolysis,[15] was measured by HPLC as described by Nagasawa et al.[13,16] It has been proposed that skeletal muscle accounts for 40% of the entire body mass of rats and that 700 nmol of MeHis is present in 1 g of skeletal muscle.[15] Therefore, we expressed our results as a fractional degradation rate (K_d) calculated using the following formula:

$$K_d\ (\%) = 100E/[0.4(W + W_0)700/2]$$

where E (nmol) is the amount of MeHis excretion over 24 h, W_0 (g) is the whole body weight when urine collection started, and W (g) is the whole body weight when urine collection finished.

Measurement of Plasma Amino Acid Concentrations. Plasma was mixed with an equal volume of 3% sulfosalicylic acid during overnight at 4 °C, and then the mixture was centrifuged at 18000*g* for 15 min. Plasma amino acid concentrations in the supernatant were measured using an amino acid autoanalyzer (JLC-500/V, JEOL, Tokyo, Japan).

Measurement of the Plasma Insulin Concentration. The plasma insulin concentration was measured using an enzyme-linked immunosorbent assay (ELISA) according to the protocol (Morinaga Institute of Biological Science, Yokohama, Japan).

Western Blot Analysis. Western blot analysis was performed as reported previously.[8] Gastrocnemius muscle was homogenized in 10 volumes of buffer solution followed by centrifugation at 3800*g*. The supernatant was used as the sodium dodecyl sulfate−polyacrylamide gel electrophoresis (SDS−PAGE) sample and was separated on a 10% polyacrylamide gel, followed by transfer to a polyvinylidene fluoride (PVDF) membrane (Millipore Corporation, Billerica, MA). The membrane was blocked for 1 h with 5% skim milk in Tris-buffered saline (TBS) containing 0.1% Tween 20 (TBS-T) at room temperature. The membrane was incubated overnight at 4 °C with primary antibodies, and then the membrane was incubated with HRP-conjugated goat anti-rabbit IgG or HRP-conjugated goat anti-mouse IgG in TBS-T. After detection, the membrane was stained with Coomassie Brilliant Blue (CBB) to verify that equal quantities of each protein had been transferred.

Gene Expression of E3 Ubiquitin Ligases. mRNA expression of E3 ubiquitin ligases was assessed by northern blotting as described previously.[8] A total of 10 μg of total RNA extracted from the gastrocnemius muscle were separated on a 1.2% agarose−formaldehyde gel and transferred to a positively charged nylon membrane (Pall Corporation, Port Washington, NY). After ultraviolet (UV) cross-linking, the membranes were hybridized with a digoxigenin-labeled cDNA probe specific to MuRF1, atrogin-1, or glyceraldehyde-3-phosphate dehydrogenase (GAPDH) for 16 h at 50 °C in hybridization solution. Specific hybridization was detected with an anti-digoxigenin antibody conjugated with alkaline phosphatase, and blots were developed with CDP-star reagent (Tropix, Bedford, MA).

Statistical Analysis. Data are expressed as the mean with standard error of the mean (SEM). Data analysis was performed using GraphPad InStat software, version 3.0a (2001, GraphPad Software, Inc., San Diego, CA). Data were analyzed by analysis of variance (ANOVA) and Tukey's post-test in multi-group (more than three groups) comparisons to determine whether there were significant differences ($p < 0.05$) among the groups. Comparisons of two groups were performed using unpaired *t* tests, and the two-tailed *p* value was calculated.

RESULTS

Experiment 1. *Lys-Rich 10% Casein Diet Suppressed the Rate of Proteolysis and Autophagy Activity.* The average food intake for 1 h after 18 h of fasting on the final day did not differ between the groups [20C, 4.4 ± 0.6 g (average ± SE); 20CK, 4.5 ± 0.1 g; 10C, 4.4 ± 0.1 g; and 10CK, 4.3 ± 0.2 g]. The rates of MeHis released from isolated muscles (EDL and soleus muscles) and the plasma MeHis concentration significantly increased in rats fed the standard 10C diet compared to rats fed the 20C diet (panels A and B of Figure 1). However, the values of MeHis in rats fed the 10CK diet were lower than those in the 10C group (panels A and B of Figure 1), whereas

DOI: 10.1021/acs.jafc.5b03811
J. Agric. Food Chem. 2015, 63, 8192−8198

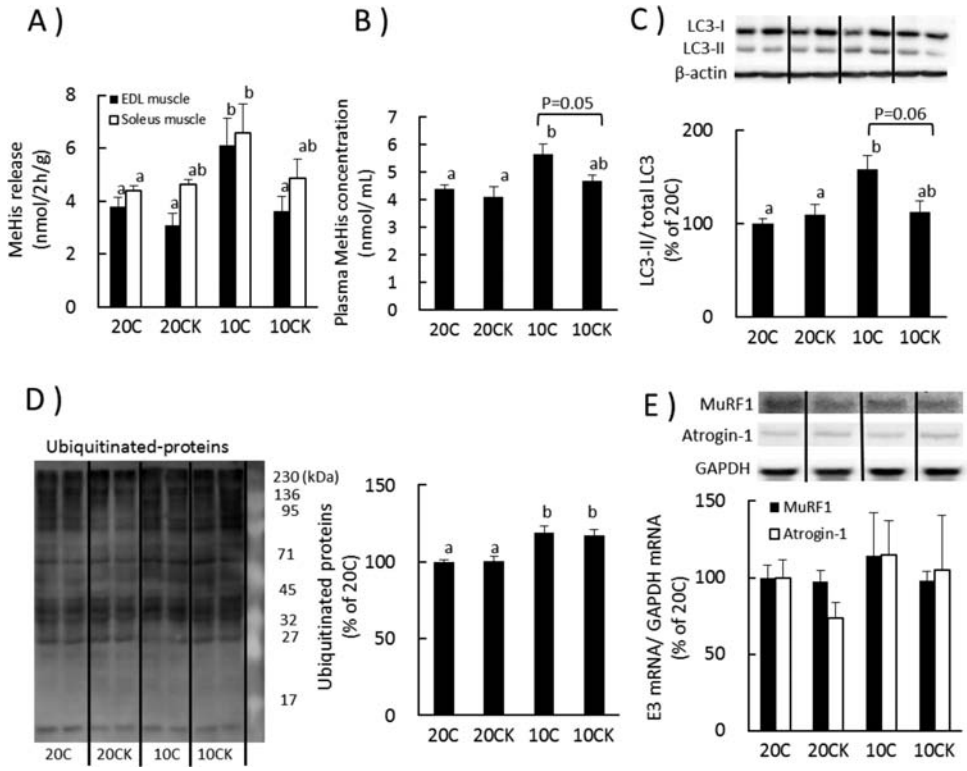

Figure 1. Bolus intake of a Lys-rich 10% casein diet suppresses proteolysis and autophagy. Rats were fed a standard 20% casein diet (20C), Lys-rich 20% casein diet (20CK), standard 10% casein diet (10C), or Lys-rich 10% casein diet (10CK) for 1 h and then fasted for 3 h. (A) Rate of myofibrillar proteolysis was evaluated from the amount of MeHis released from isolated EDL muscle (black bars) or soleus muscle (white bars). (B) Plasma concentration of MeHis was also used as an index of proteolysis. (C) Autophagy activity was evaluated from LC3-II/total LC3 by western blotting. Activity of the ubiquitin−proteasomal system was evaluated from (D) levels of ubiquitinated proteins determined by western blotting and (E) mRNA levels of the E3 ubiquitin ligases, MuRF1 (black bars) and atrogin-1 (white bars), determined by northern blotting. Values are means with SE (n = 5). Different letters indicate significant differences among the groups ($p < 0.05$).

supplementation of Lys to the 20% casein diet did not affect the rate of proteolysis (panels A and B of Figure 1).

We evaluated autophagy activity from the light chain 3 (LC3)-II/total LC3 ratio,[17] and ubiquitin−proteasomal system activity was assessed from the levels of ubiquitinated proteins and the mRNA expression of the E3 ubiquitin ligases, muscle RING-finger protein 1 (MuRF1) and atrogin-1. Consistent with the rate of proteolysis (panels A and B of Figure 1), autophagy activity was suppressed by 45% in rats fed the 10CK diet compared to those fed the standard 10C diet (Figure 1C). The levels of ubiquitinated proteins significantly increased in rats fed the low-protein diets (Figure 1D), despite the same amount of protein being transferred to the membrane for all groups (evaluated by CBB staining; data not shown). Lys supplementation did not suppress ubiquitin−proteasomal activity (panels D and E of Figure 1). These results indicated that supplementing Lys with the 10% casein diet suppresses autophagic proteolysis.

Lys-Rich 10% Casein Diet Stimulated Akt Phosphorylation and Recovered mTOR Signaling Activity. The phosphorylation level of Akt Thr308 increased by 32% in rats fed the 10CK diet compared to rats fed the 10C diet (Figure 2B). A similar increase was observed for Ser473 phosphorylation in Akt (Figure 2B). The mTOR signaling activity was evaluated from the phosphorylation levels of eIF4E-binding protein 1 (4E-BP1) and p70 ribosomal protein S6 kinase 1 (S6K1), which are downstream targets of mTOR. mTOR signaling activity (both of 4E-BP1 and S6K1) in rats fed the 10C diet decreased by 30% compared to rats fed the 20C diet, but supplementation of the 10C diet with Lys restored mTOR signaling activity (panels C and D of Figure 2). This activation effect of Lys on Akt/mTOR signaling was not observed in rats fed the 20CK diet (panels B−D of Figure 2). The phosphorylation level of eukaryotic initiation factor 2 α (eIF2α), which increases in amino-acid-limited conditions and regulates translation and autophagy,[18,19] did not differ among the groups (Figure 2E). These results indicated that supplementing Lys with 10% casein suppressed autophagy through Akt/mTOR signaling activation. On the other hand, the phosphorylation level of eIF2α tended to decrease in 20CK (Figure 2E). Therefore, supplementing Lys with a high-casein diet may stimulate protein synthesis through a mTOR-independent pathway.

Lys-Rich 10% Casein Diet Did Not Affect the Plasma Concentrations of Insulin and Basic Amino Acids Other than Lys. The plasma Lys concentration was significantly higher in rats fed Lys-rich diets (10CK and 20CK) compared to those fed the standard diets (10C and 20C) (Figure 3A). However, the plasma concentrations of two basic amino acids, histidine (His) and arginine (Arg), were unaffected by Lys supplementation of the diet (panels B and C of Figure 3) nor was the plasma insulin concentration affected (Figure 3D). The plasma concentration of amino acids other than Lys did not differ between the standard diet group and the Lys-rich diet group (20C versus 20CK and 10C versus 10CK), whereas the plasma threonine, asparagine, valine, isoleucine, leucine, phenylalanine, and tryptophan concentrations in rats fed the 10C diet were significantly lower than those fed the 20C diet

DOI: 10.1021/acs.jafc.5b03811
J. Agric. Food Chem. 2015, 63, 8192−8198

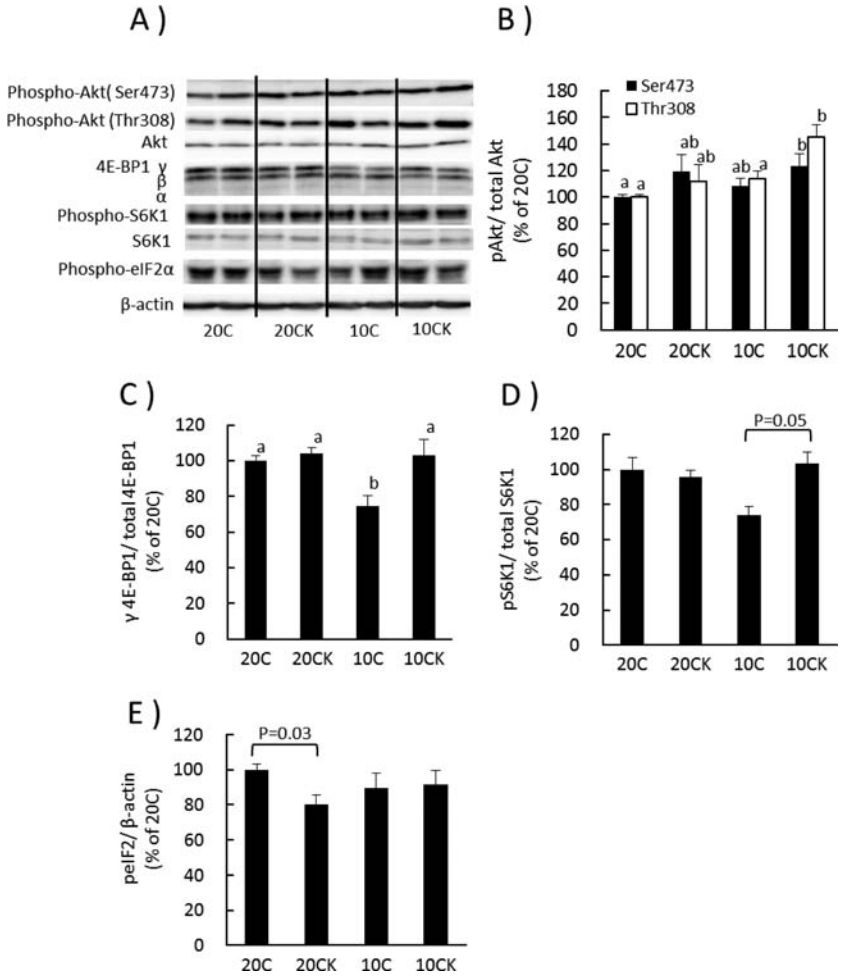

Figure 2. Supplementation of Lys into a 10% casein diet increases Akt phosphorylation and improves the activity of mTOR signaling. Rats were fed a standard 20% casein diet (20C), Lys-rich 20% casein diet (20CK), standard 10% casein diet (10C), or Lys-rich 10% casein diet (10CK) for 1 h and then fasted for 3 h. (A) Representative blots of the detected proteins are shown. Phosphorylation of Akt Ser473(B, black bars), Akt Thr308(B, white bars), (C) 4E-BP1, (D) S6K1, and (E) eIF2α were analyzed by western blotting. Results are expressed as the level relative to the control group. Values are means with SE (n = 5). Different letters indicate significant differences among the groups ($p < 0.05$).

(20C or 20CK versus 10C or 10CK) (panels B and C of Figure 3 and data not shown). These results indicated that the suppressive effect of Lys on autophagy did not depend upon the increase of insulin or other amino acids than Lys.

Experiment 2. *Continuous Intake of the Lys-Rich 10% Casein Diet Increased Skeletal Muscle Mass.* We investigated whether the continuous intake of a Lys-rich diet results in increased skeletal muscle mass in experiment 2, given that bolus intake of a Lys-rich diet suppressed proteolysis (panels A–C of Figure 1) and restored Akt/mTOR signaling activity (panels A–D of Figure 2) in experiment 1. The average food intake per day by rats fed the 10C diet was 9.6 ± 0.6 g (SE) (62 mg of total Lys/day), and those fed the 10CK diet was 9.9 ± 0.6 g (SE) (129 mg of total Lys/day). As expected, 15 days of Lys-rich diet intake significantly increased the masses of the soleus and gastrocnemius muscles, whereas the final body weight and mass of the EDL muscle did not increase (panels A–C of Figure 4). The weights of the soleus and gastrocnemius muscles adjusted for body weight in rats fed the Lys-rich diets also tended to be higher than those of rats fed the corresponding control diet (p = 0.07 and 0.09, respectively). The rate of proteolysis was calculated from the amount of MeHis excreted in the urine and was suppressed by 33% in rats fed Lys-rich diets (Figure 4D). Similarly, autophagy was reduced by 30% in rats fed Lys-rich diets (Figure 4E). These results indicated that continuous intake of the Lys-rich 10% casein diet increased skeletal muscle mass through inhibition of autophagy.

DISCUSSION

A low-protein diet causes loss of skeletal muscle, and Leu has attracted attention as a dietary supplement, which preserves muscle mass in mammals fed a low-protein diet. Yin et al.[20] showed that supplementation of Leu to a low-protein diet (10% whey protein-based diet, 1.88% total Leu) improved protein synthesis in pigs. Similar results have been reported in rats[21] and humans.[22] In addition, it was reported that intake of a 10% whey diet supplemented with Leu (6% total Leu) resulted in increased skeletal muscle mass,[23] although supplementation of Leu to a 20% whey protein diet did not result in increased muscle mass in mice.[24] To our knowledge, there has been no previous study investigating supplementation of a single amino acid other than Leu that diminishes muscle mass loss caused by a low-protein diet.

We previously showed that oral administration of Lys by gavage (114 mg/100 g of body weight) markedly suppressed the rate of proteolysis in fasted rats,[8] and therefore, we

DOI: 10.1021/acs.jafc.5b03811
J. Agric. Food Chem. 2015, 63, 8192–8198

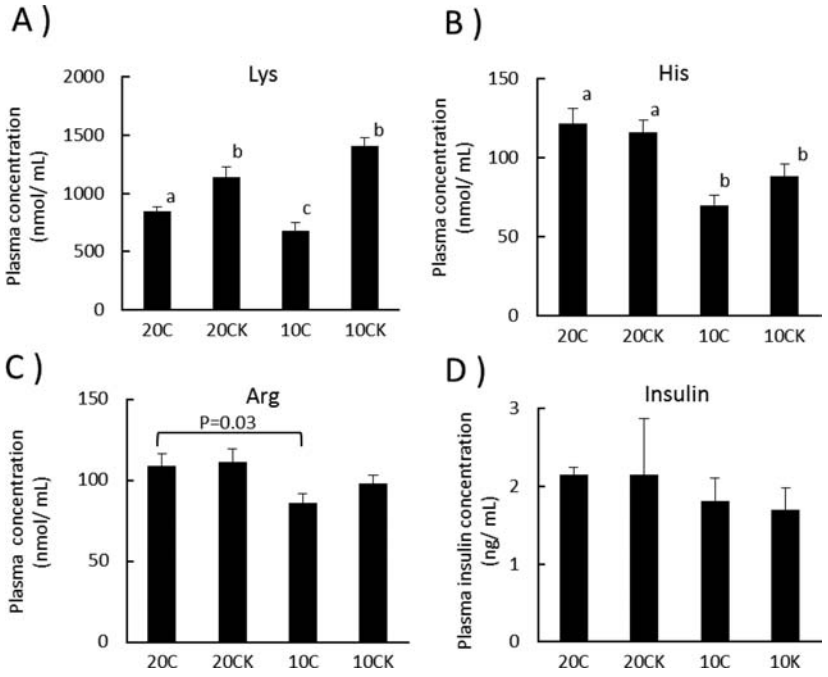

Figure 3. Supplementation of Lys into a 10% casein diet increases the plasma concentration of Lys, but the concentrations of histidine, arginine, and insulin remain unchanged. Rats were fed a standard 20% casein diet (20C), Lys-rich 20% casein diet (20CK), standard 10% casein diet (10C), or Lys-rich 10% casein diet (10CK) for 1 h and then fasted for 3 h. Plasma concentrations of (A) Lys, (B) His, and (C) Arg were measured using an amino acid autoanalyzer, and (D) insulin concentration was measured by ELISA. Values are means with SE (n = 5). Different letters indicate significant differences among the groups ($p < 0.05$).

anticipated that Lys may be a useful dietary supplement for decreasing muscle mass loss. In this study, we supplemented Lys with a low-protein diet and investigated the suppressive effect of dietary Lys on proteolysis, autophagy, and the loss of muscle mass induced by intake of a low-protein diet in rats.

The effect of dietary Lys on proteolysis was evaluated from the rate of proteolysis by measuring MeHis released from isolated muscles (EDL and soleus muscles), the plasma concentration of MeHis, and the amount of MeHis excreted in the urine. In addition, the activity of autophagy, a major proteolytic system,[25] was evaluated from LC3-II/total LC3 (because LC3-II localizes at the autophagosome membrane[17]). First, we investigated the suppressive effect of a bolus intake of a Lys-rich diet on proteolysis and on proteolytic systems (autophagy and the ubiquitin−proteasomal system) after fasting. Supplementation of Lys with the 10% casein diet clearly suppressed the rate of proteolysis and autophagy activity stimulated by the intake of a low-protein diet (Figure 1), whereas the activity of the ubiquitin−proteasomal system[25] was not suppressed by a Lys-rich diet (panels D and E of Figure 1). Therefore, the present results indicate that supplementing Lys with the 10% casein diet would suppress autophagy but not the ubiquitin−proteasomal system, consistent with our previous studies.[8−10] This is the first demonstration that supplementation of Lys to a low-protein diet suppresses proteolysis and autophagy. On the other hand, the supplementation of Lys to the 20% casein diet did not affect the rate of proteolysis or autophagy (panels A−C of Figure 1). The rates of proteolysis and autophagy in rats fed the 20% casein diet were likely suppressed sufficiently, regardless of amino acid supplementation.

We continuously provided a Lys-rich low-protein diet to rats for 15 days and investigated the effect of Lys supplementation into the diet on muscle mass. The continuous feeding of a Lys-rich diet significantly increased the masses of the soleus and gastrocnemius muscles (panels B and C of Figure 4); furthermore, the rate of proteolysis, evaluated from MeHis excreted in the urine, was significantly suppressed by intake of a Lys-rich diet (Figure 4D), as was autophagy (Figure 4E). These results indicate that continuous feeding of a Lys-rich low-protein diet can preserve the mass of skeletal muscle.

Akt is an important regulator of autophagy. Zhao et al.[26] showed that Akt and not mTOR is the central regulator of autophagic proteolysis in skeletal muscle cells. It has been reported that Leu stimulates Akt[9,10,27−31] and that Leu supplementation increased muscle mass and Akt/mTOR signaling activity in rats suffering from malnutrition.[32] We previously demonstrated that Lys suppresses autophagy and activates mTOR signaling, which regulates autophagy through Akt in C2C12 myotubes.[10] In this study, we observed significant phosphorylation of Akt Thr308, which regulates Akt activity,[33−35] in rats fed a Lys-rich diet (Figure 2B). In addition, the activity of mTOR signaling was recovered in rats fed a Lys-rich 10% casein diet, although the activity of mTOR signaling activity decreased in rats fed a standard 10% casein diet (panels C and D of Figure 2). Therefore, a Lys-supplemented diet likely regulates autophagy through the Akt/mTOR signaling pathway in rats fed a low-protein diet.

Akt is phosphorylated through the insulin signaling pathway,[36] and Lys activates the secretion of insulin.[37−39] However, the plasma insulin concentrations of rats fed a Lys-rich diet did not increase (Figure 3D). We previously showed that Lys markedly phosphorylated Akt in the absence of insulin.[9,10] Hence, Akt would be stimulated by an insulin-independent pathway in rats fed a Lys-rich diet.

We previously showed that oral administration of glycine, which is the same nitrogen level of Lys, did not suppress the rate of protein degradation in fasted rats.[8] In addition, we

DOI: 10.1021/acs.jafc.5b03811
J. Agric. Food Chem. 2015, 63, 8192−8198

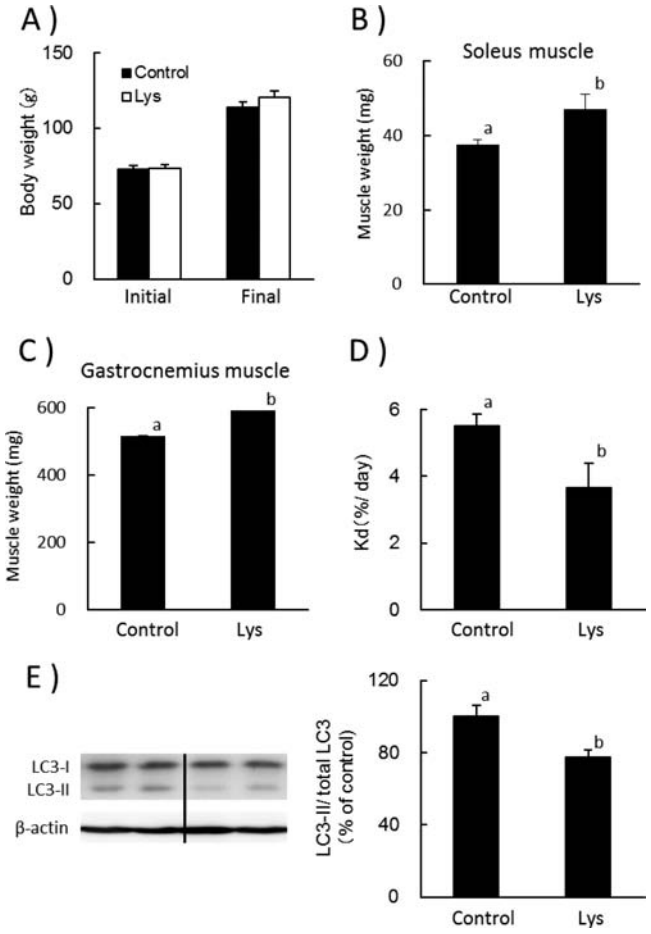

Figure 4. Continuous feeding of a Lys-rich 10% casein diet results in increased muscle mass and suppresses proteolysis and autophagy. Rats were fed a standard 10% casein diet or a Lys-rich 10% casein diet for 15 days. Urine was collected for 24 h, from the morning of the 13th day to the morning of the 14th day. (A) Initial body weight was measured at the start of feeding the control (black bars) or experimental (white bars) diets, and final body weight was measured prior to dissection. The weights of the (B) soleus and (C) gastrocnemius muscles were measured following dissection. (D) Amount of MeHis excreted in urine was measured by HPLC. (E) Autophagy activity evaluated from LC3-II/total LC3 was analyzed by western blotting. Values are means with SE (n = 5). Different letters indicate significant differences among the groups (p < 0.05).

demonstrated that the same molar dose of glycine could not regulate proteolysis, autophagy, and mTOR signaling activity in the C2C12 myotube.[9,10] Therefore, the effect of Lys on proteolysis and autophagy may not depend upon nitrogen uptake.

In conclusion, we demonstrated that supplementation of Lys to a 10% casein diet regulates autophagic proteolysis and Akt/mTOR signaling and continuous feeding of a Lys-rich diet may suppresses muscle mass loss caused by the intake of a low-protein diet. Tesseraud et al. indicated that a Lys-deficient diet induced stimulation of protein degradation in the muscle of chicks.[40] However, they did not show whether supplementing Lys with a diet suppresses proteolysis in skeletal muscle, and the effects of Lys on autophagy and the ubiquitin−proteasomal system were not demonstrated. Therefore, this is the first study that reported supplementing Lys with a low-protein diet suppresses autophagic proteolysis in mammals. Furthermore, we observed recovery of the mTOR signaling activity, which regulates translation in rats fed a Lys-rich low-protein diet compared to rats fed a standard low-protein diet (panels C and D of Figure 2). Therefore, the stimulation of protein synthesis might contribute to the increase of muscle in rats fed a Lys-rich low-protein diet. Supplementing Lys with a low-protein diet might be a beneficial strategy for preventing skeletal muscle loss in chronic kidney disease patients advised to adhere to a low-protein diet. Moreover, the present results may help overcome stunting caused by low-quality dietary protein.

AUTHOR INFORMATION

Corresponding Author

*Fax: +81-19-621-6262. E-mail: address:tnaga@iwate-u.ac.jp.

Funding

This study was supported in part by JSPS KAKENHI Grant 21580134.

Notes

The authors declare no competing financial interest.

ABBREVIATIONS USED

Akt, protein kinase B; Arg, arginine; CBB, Coomassie Brilliant Blue; eIF2α, eukaryotic initiation factor 2 α; GAPDH, glyceraldehyde-3-phosphate dehydrogenase; His, histidine; LC3, light chain 3; Leu, leucine; Lys, lysine; MeHis, 3-methylhistidine; MuRF1, muscle RING-finger protein 1; mTOR, mammalian target of rapamycin; S6K1, p70 ribosomal protein S6 kinase 1; 4E-BP1, eukaryotic initiation factor 4E binding protein 1

REFERENCES

(1) Oumi, M.; Miyoshi, M.; Yamamoto, T. The ultrastructure of skeletal and smooth muscle in experimental protein malnutrition in rats fed a low protein diet. *Arch. Histol. Cytol.* **2000**, *63*, 451−457.

(2) Mukai, R.; Horikawa, H.; Fujikura, Y.; Kawamura, T.; Nemoto, H.; Nikawa, T.; Terao, J. Prevention of disuse muscle atrophy by dietary ingestion of 8-prenylnaringenin in denervated mice. *PLoS One* **2012**, *7*, e45048.

(3) Wang, X. H.; Mitch, W. E. Mechanisms of muscle wasting in chronic kidney disease. *Nat. Rev. Nephrol.* **2014**, *10*, 504−516.

(4) Cruz-Jentoft, A. J.; Baeyens, J. P.; Bauer, J. M.; Boirie, Y.; Cederholm, T.; Landi, F.; Martin, F. C.; Michel, J. P.; Rolland, Y.; Schneider, S. M.; Topinková, E.; Vandewoude, M.; Zamboni, M. Sarcopenia: European consensus on definition and diagnosis: Report of the European Working Group on Sarcopenia in Older People. *Age Ageing* **2010**, *39*, 412−423.

(5) Dodd, K. M.; Tee, A. R. Leucine and mTORC1: a complex relationship. *Am. J. Physiol Endocrinol Metab.* **2012**, *302*, E1329−E1342.

(6) Anthony, J. C.; Yoshizawa, F.; Anthony, T. G.; Vary, T. C.; Jefferson, L. S.; Kimball, S. R. Leucine stimulates translation initiation in skeletal muscle of postabsorptive rats via a rapamycin-sensitive pathway. *J. Nutr.* **2000**, *130*, 2413−2419.

(7) Sugawara, T.; Ito, Y.; Nishizawa, N.; Nagasawa, T. Regulation of muscle protein degradation, not synthesis, by dietary leucine in rats fed a protein-deficient diet. *Amino Acids* **2009**, *37*, 609−616.

(8) Sato, T.; Ito, Y.; Nagasawa, T. Regulation of skeletal muscle protein degradation and synthesis by oral administration of lysine in rats. *J. Nutr. Sci. Vitaminol.* **2013**, *59*, 412−419.

(9) Sato, T.; Ito, Y.; Nedachi, T.; Nagasawa, T. Lysine suppresses protein degradation through autophagic-lysosomal system in C2C12 myotubes. *Mol. Cell. Biochem.* **2014**, *391*, 37−46.

(10) Sato, T.; Ito, Y.; Nagasawa, T. Lysine suppresses myofibrillar protein degradation by regulating the autophagic-lysosomal system through phosphorylation of Akt in C2C12 cells. *SpringerPlus* **2014**, *3*, 584.

DOI: 10.1021/acs.jafc.5b03811
J. Agric. Food Chem. 2015, 63, 8192−8198

(11) Reeves, P. G.; Nielsen, F. H.; Fahey, G. C., Jr. AIN-93 purified diets for laboratory rodents: Final report of the American Institute of Nutrition ad hoc writing committee on the reformulation of the AIN-76A rodent diet. *J. Nutr.* **1993**, *123*, 1939−1951.
(12) Wassner, S. J.; Schlitzer, J. L.; Li, J. B. A rapid, sensitive method for the determination of 3-methylhistidine levels in urine and plasma using high-pressure liquid chromatography. *Anal. Biochem.* **1980**, *104*, 284−289.
(13) Nagasawa, T.; Yoshizawa, F.; Nishizawa, N. Plasma N^{τ}-methylhistidine concentration is a sensitive index of myofibrillar protein degradation during starvation in rats. *Biosci., Biotechnol., Biochem.* **1996**, *60*, 501−502.
(14) Nagasawa, T.; Sakai, T.; Onodera, R. Simple and sensitive determination of plasma N^{τ}-methylhistidine by high-performance liquid chromatography using pre-column derivative formation with o-phthalaldehyde-2-mercaptoethanol. *J. Chromatogr., Biomed. Appl.* **1991**, *566*, 223−227.
(15) Funabiki, R.; Watanabe, Y.; Nishizawz, N.; Hareyama, S. Quantitative aspect of the myofibrillar protein turnover in transient state on dietary protein depletion and repletion revealed by urinary excretion of N^{τ}-methylhistidine. *Biochim. Biophys. Acta, Gen. Subj.* **1976**, *451*, 143−150.
(16) Nagasawa, T.; Kido, T.; Yoshizawa, F.; Ito, Y.; Nishizawa, N. Rapid suppression of protein degradation in skeletal muscle after oral feeding of leucine in rats. *J. Nutr. Biochem.* **2002**, *13*, 121−127.
(17) Naito, T.; Kuma, A.; Mizushima, N. Differential contribution of insulin and amino acids to the mTORC1-autophagy pathway in the liver and muscle. *J. Biol. Chem.* **2013**, *288*, 21074−21081.
(18) Harding, H. P.; Novoa, I.; Zhang, Y.; Zeng, H.; Wek, R.; Schapira, M.; Ron, D. Regulated translation initiation controls stress-induced gene expression in mammalian cells. *Mol. Cell* **2000**, *6*, 1099−1108.
(19) B'chir, W.; Maurin, A. C.; Carraro, V.; Averous, J.; Jousse, C.; Muranishi, Y.; Parry, L.; Stepien, G.; Fafournoux, P.; Bruhat, A. The eIF2α/ATF4 pathway is essential for stress-induced autophagy gene expression. *Nucleic Acids Res.* **2013**, *41*, 7683−7699.
(20) Yin, Y.; Yao, K.; Liu, Z.; Gong, M.; Ruan, Z.; Deng, D.; Tan, B.; Liu, Z.; Wu, G. Supplementing L-leucine to a low-protein diet increases tissue protein synthesis in weanling pigs. *Amino Acids* **2010**, *39*, 1477−1486.
(21) Rieu, I.; Balage, M.; Sornet, C.; Debras, E.; Ripes, S.; Rochon-Bonhomme, C.; Pouyet, C.; Grizard, J.; Dardevet, D. Increased availability of leucine with leucine-rich whey proteins improves postprandial muscle protein synthesis in aging rats. *Nutrition* **2007**, *23*, 323−331.
(22) Churchward-Venne, T. A.; Breen, L.; Di Donato, D. M.; Hector, A. J.; Mitchell, C. J.; Moore, D. R.; Stellingwerff, T.; Breuille, D.; Offord, E. A.; Baker, S. K.; Phillips, S. M. Leucine supplementation of a low-protein mixed macronutrient beverage enhances myofibrillar protein synthesis in young men: a double-blind, randomized trial. *Am. J. Clin. Nutr.* **2014**, *99*, 276−286.
(23) Freudenberg, A.; Petzke, K. J.; Klaus, S. Comparison of high-protein diets and leucine supplementation in the prevention of metabolic syndrome and related disorders in mice. *J. Nutr. Biochem.* **2012**, *23*, 1524−1530.
(24) Noatsch, A.; Petzke, K. J.; Millrose, M. K.; Klaus, S. Body weight and energy homeostasis was not affected in C57BL/6 mice fed high whey protein or leucine-supplemented low-fat diets. *Eur. J. Nutr.* **2011**, *50*, 479−488.
(25) Sandri, M. Protein breakdown in muscle wasting: role of autophagy-lysosome and ubiquitin-proteasome. *Int. J. Biochem. Cell Biol.* **2013**, *45*, 2121−2129.
(26) Zhao, J.; Brault, J. J.; Schild, A.; Cao, P.; Sandri, M.; Schiaffino, S.; Lecker, S. H.; Goldberg, A. L. FoxO3 coordinately activates protein degradation by the autophagic/lysosomal and proteasomal pathways in atrophying muscle cells. *Cell Metab.* **2007**, *6*, 472−483.
(27) Lee, M. Y.; Jo, S. D.; Lee, J. H.; Han, H. J. L-leucine increases [^{3}H]-thymidine incorporation in chicken hepatocytes: involvement of the PKC, PI3K/Akt, ERK1/2, and mTOR signaling pathways. *J. Cell. Biochem.* **2008**, *105*, 1410−1419.
(28) Coëffier, M.; Claeyssens, S.; Bensifi, M.; Lecleire, S.; Boukhettala, N.; Maurer, B.; Donnadieu, N.; Lavoinne, A.; Cailleux, A. F.; Déchelotte, P. Influence of leucine on protein metabolism, phosphokinase expression, and cell proliferation in human duodenum1,3. *Am. J. Clin. Nutr.* **2011**, *93*, 1255−1262.
(29) Zeanandin, G.; Balage, M.; Schneider, S. M.; Dupont, J.; Hébuterne, X.; Mothe-Satney, I.; Dardevet, D. Differential effect of long-term leucine supplementation on skeletal muscle and adipose tissue in old rats: an insulin signaling pathway approach. *Age (Dordr).* **2012**, *34*, 371−387.
(30) Ribeiro, C. B.; Christofoletti, D. C.; Pezolato, V. A.; de Cássia Marqueti Durigan, R.; Prestes, J.; Tibana, R. A.; Pereira, E. C.; de Sousa Neto, I. V.; Durigan, J. L.; da Silva, C. A. Leucine minimizes denervation-induced skeletal muscle atrophy of rats through akt/mtor signaling pathways. *Front. Physiol.* **2015**, *6*, 73.
(31) Gil, J. H.; Kim, C. K. Effects of different doses of leucine ingestion following eight weeks of resistance exercise on protein synthesis and hypertrophy of skeletal muscle in rats. *J. Exerc Nutrition Biochem.* **2015**, *6*, 31−38.
(32) Gao, X.; Tian, F.; Wang, X.; Zhao, J.; Wan, X.; Zhang, L.; Wu, C.; Li, N.; Li, J. Leucine supplementation improves acquired growth hormone resistance in rats with protein-energy malnutrition. *PLoS One* **2015**, *10*, e0125023.
(33) Alessi, D. R.; James, S. R.; Downes, C. P.; Holmes, A. B.; Gaffney, P. R.; Reese, C. B.; Cohen, P. Characterization of a 3-phosphoinositide-dependent protein kinase which phosphorylates and activates protein kinase Bα. *Curr. Biol.* **1997**, *7*, 261−269.
(34) Stephens, L.; Anderson, K.; Stokoe, D.; Erdjument-Bromage, H.; Painter, G. F.; Holmes, A. B.; Gaffney, P. R.; Reese, C. B.; McCormick, F.; Tempst, P.; Coadwell, J.; Hawkins, P. T. Protein kinase B kinases that mediate phosphatidylinositol 3,4,5-trisphosphate-dependent activation of protein kinase B. *Science* **1998**, *279*, 710−714.
(35) Pillai, V. B.; Sundaresan, N. R.; Gupta, M. P. Regulation of Akt signaling by sirtuins: its implication in cardiac hypertrophy and aging. *Circ. Res.* **2014**, *114*, 368−378.
(36) Valentine, R. J.; Coughlan, K. A.; Ruderman, N. B.; Saha, A. K. Insulin inhibits AMPK activity and phosphorylates AMPK Ser485/491 through Akt in hepatocytes, myotubes and incubated rat skeletal muscle. *Arch. Biochem. Biophys.* **2014**, *562*, 62−69.
(37) Floyd, J. C., Jr.; Fajans, S. S.; Conn, J. W.; Knopf, R. F.; Rull, J. Stimulation of insulin secretion by amino acids. *J. Clin. Invest.* **1966**, *45*, 1487−1502.
(38) Rozance, P. J.; Limesand, S. W.; Hay, W. W., Jr. Decreased nutrient-stimulated insulin secretion in chronically hypoglycemic late-gestation fetal sheep is due to an intrinsic islet defect. *Am. J. Physiol.: Endocrinol. Metab.* **2006**, *291*, E404−E411.
(39) Liu, Z.; Jeppesen, P. B.; Gregersen, S.; Chen, X.; Hermansen, K. Dose- and glucose-dependent effects of amino acids on insulin secretion from isolated mouse islets and clonal INS-1E beta-cells. *Rev. Diabet Stud.* **2008**, *5*, 232−244.
(40) Tesseraud, S.; Maaa, N.; Peresson, R.; Chagneau, A. M. Relative responses of protein turnover in three different skeletal muscles to dietary lysine deficiency in chicks. *Br. Poult. Sci.* **1996**, *37*, 641−650.

DOI: 10.1021/acs.jafc.5b03811
J. Agric. Food Chem. 2015, 63, 8192−8198

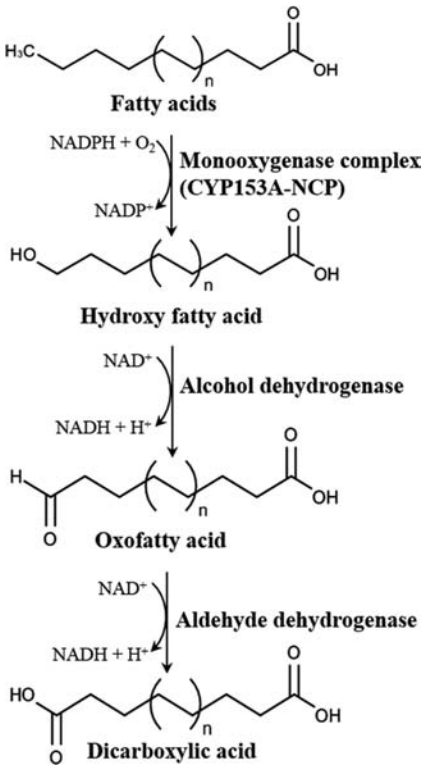

Figure 1. ω-Oxidation pathway. Biotransformation of fatty acids by the sequential oxidation of the terminal methyl group yields the dicarboxylic acid product. Protein ID (Genbank): CYP153A (ABM17701.01); NADPH:cytochrome P450 oxidoreductase (ACZ37122.1); alcohol dehydrogenase (AAA344101.1); and aldehyde dehydrogenase (U.S. Patent no. WO 2013006730 A2).

improve the fatty acid uptake, resulting in high productivity.[18,19] In addition to this, to obtain the maximum yield, the toxicity of accumulated H_2O_2 has to be reduced.[6,16] To the best of our knowledge, to date there are no reports of the production of α,ω-DCAs directly from fatty acid substrates, through utilization of a CYP450-dependent ω-oxidation pathway in *Escherichia coli*, a highly versatile organism that has been widely used for heterologous protein production and for genetic recombination studies because of its rapid growth and potential for high-density cultivation on inexpensive substrates. Additionally, its well-characterized genetics and the availability of an increasingly large number of cloning vectors and mutant host strains make *E. coli* an attractive model for genetic studies.[20] *E. coli* has been demonstrated as a suitable host for heterologous monooxygenase related reactions, including CYP153A, and exhibited higher catalytic activities and product yields when compared to other hosts, such as *Pseudomonas*.[16,21,22] Moreover, using *E. coli* as a host for heterologous expression of CYP450s is advantageous, as *E. coli* lacks endogenous CYP450s that could interfere with heterologous P450 expression. The present study exploits the advantages of the *E. coli* model system to demonstrate a novel biotechnology system that efficiently produces long-chain α,ω-dicarboxylic acids (C12 and C14) from fatty acids by introduction of the ω-oxidation pathway into *E. coli*.

MATERIALS AND METHODS

Microbial Strains and Plasmids. The wild-type *E. coli* MG1655 strain (laboratory stock) was used as the parental strain for all genetic modifications, including gene knockouts and introduction of expression constructs. The *E. coli* DH10B strain (laboratory stock) was used for cloning. *Marinobacter aquaeolei* (DSMZ, DSM 11845), *B. megaterium* (Korean Culture Center of Microorganisms, KCCM 11745), *Saccharomyces cerevisiae* (Korean Collection for Type Cultures, KCTC 7296), and *C. tropicalis* (American Type Culture Collection, ATCC 20336) were procured from the indicated cell culture collection centers. The Biobrick plasmids, pBbA6C and pBbE6K (A = p15A replicon; E = colE1 replicon; 6 = PLlacO promoter; C = chloramphenicol resistance; and K = kanamycin resistance), were used for expression constructs.[23]

Chemicals, Enzymes, and Culture Conditions. All chemicals, including fatty acids and DCAs, were purchased from Sigma-Aldrich (St. Louis, MO). Restriction enzymes (New England Biolabs, Ipswich, MA), DNA ligase (New England Biolabs, Ipswich, MA), and Phusion high-Fidelity DNA polymerase (Thermo Fischer Scientific, Waltham, MA) were used for cloning and plasmid construction. Oligonucleotides were synthesized by Macrogen (Korea). Microbial cells were grown at 37 °C (30 °C for strains carrying temperature-sensitive plasmids) in Luria−Bertani (LB) broth supplemented with suitable antibiotics (kanamycin at 50 μg/mL, ampicillin at 100 μg/mL, or chloramphenicol at 30 μg/mL).

Table 1. Primers Used for PCR and Cloning[a]

primer name	primer sequence
FadR_del_F	TCTGGTATGATGAGTCCAACTTTGTTTTGCTGTGTTATGGAAATCTCACTGTGTAGGCTGGAGCTGCTTC
FadR_del_R	AACAACAAAAAACCCCTCGTTTGAGGGGTTTGCTCTTTAAACGGAAGGGAATTCCGGGGATCCGTCGACC
FadE_del_F	CCATATCATCACAAGTGGTCAGACCTCCTACAAGTAAGGGGCTTTTCGTTGTGTAGGCTGGAGCTGCTTC
FadE_del_R	TTACGCGGCTTCAACTTTCCGCACTTTCTCCGGCAACTTTACCGGCTTCGATTCCGGGGATCCGTCGACC
Maq_F	ATAGATCTTTTAAGAAGGAGATATACATATGCCAACACTGCCCAGAAC
Maq_R	CTGTTCAGTGCTAGGTGAAGGAATGCTGCCGCCGCTGCCGCCGCTGCCGCC ACTGTTCGGTGTCAGTTTGACCATCAACCTGGAA
NCP_F	GCGGCAGCATTCCTTCACCTAGCACTGAACAGTCTGCTAAAAAAGTACGCA AAAAGGCAGAAAACGCTATAATACGCCGCTGC
NCP_R	ATTCTCGAGCGATATCGATCGTTATTACCCAGCCCACACGTCTTTTG
AlkL_F	GGTCGATCGTTTAAGAAGGAGATATACAT ATGAGTTTTTCTAATTATAAAGTAATCGCGATGCCG
AlkL_R	ATCTCGAGTTATTAGAAAACATATGACGCACCAA
ADH1_F	TTTAAGAAGGAGATATACACATGTCTATCCCAGAAACTCA
ADH1_R	CTTACTCGAGTTATTTAGAAGTGTCAACAACGT
ALD5_F	ATACATATGTCTTTGCCAGTCGTCACCAA
ALD5_R	GTGTATATCTCCTTCTTAAAAGATCCTTAAGTGAGCTTAATTCTAACAG
ALD_F	AGGCCTCGAGAATTGTGAGCGGATAACAATTGAC

[a]Underline formatting indicates restriction sites.

DOI: 10.1021/acs.jafc.5b03833
J. Agric. Food Chem. 2015, 63, 8199−8208

Strain Construction. Knockout of *fadR* and *fadE* in MG 1655 was performed using the lambda Red and FLP-mediated site-specific recombination system as described previously.[24] Primers used for gene deletion and cloning are shown in Table 1. The monooxygenase (CYP153A), NADPH:cytochrome P450 oxidoreductase (NCP), alcohol dehydrogenase, and aldehyde dehydrogenase were amplified using Phusion high-Fidelity DNA polymerase from the genomic DNA of *M. aquaeolei* (DSM 11845), *B. megaterium* (KCCM 11745), *S. cerevisiae* (KCTC 7296), and *C. tropicalis* (ATCC 20336).

First, the fusion construct components of CYP153A from *M. aquaeolei* and NCP from *B. megaterium* were amplified using the primers Maq_F and Maq_R and NCP_F and NCP_R, respectively, and these two genes were linked by overlap extension PCR with a 3xGGS tandem region in the linker between CYP and NCP.[16] The pBbA6C-FP plasmid was constructed by cloning of the fusion construct (CYP-NCP) into the *Bgl*II and *Xho*I site of the pBbA6C plasmid. The *Pseudomonas putida*-alkane transporter gene (*alkL*) was synthesized and cloned into pGEM-B1 by Bioneer (Korea). *AlkL* was then amplified using primers AlkL_F and AlkL_R from the pGEM-B1 plasmid. Subsequently, *Pvu*I- and *Xho*I-digested pBbA6C-FP and *alkL* were ligated to generate the pBbA6C-FP/AlkL plasmid. Alcohol dehydrogenase (*ADH1*) was amplified from *S. cerevisiae* (KCTC 7296) using primers ADH1_F and ADH1_R, and aldehyde dehydrogenase (*ALD5*) was amplified from *C. tropicalis* (ATCC 20336) using primers ALD5_F and ALD5_R. These two genes were linked by overlap extension PCR and cloned into the *Nde*I/*Xho*I site of the pBbE6K plasmid to study the activities of ADH and ALD on the first intermediate of ω-oxidation pathway, ω-hydroxy fatty acid. Subsequently, primers ALD_F and ADH1_R were used to amplify *ADH1* and *ALD5* from the pBbE6K plasmid; these products were then digested with *Xho*I. Finally, the *Xho*I digested pBbA6C-FP/AlkL plasmid and the ALD-ADH PCR product were ligated to yield the final construct, the pBbA6C-ω plasmid. For biotransformation studies, pBbA6C-ω was transformed into MG1655:Δ*fadE* or MG1655:Δ*fadR*:Δ*fadE*, which were designated as Eω and REω, respectively.

Protein Expression and SDS-PAGE Analysis. Protein expression in recombinant cells, grown until OD_{600} reached 0.5, was induced with 0.1 mM of isopropyl β-D-1-thiogalactopyranoside (IPTG). After incubation at 25 °C for 16 h, the cells were collected, sample loading buffer was added, and the mixture was heated at 95 °C for 20 min. The whole cell lysate samples were run on 10% sodium dodecyl sulfate-polyacrylamide gels. Protein bands were visualized by staining with Coomassie Brilliant Blue R-250.

Whole Cell Biotransformation. A single colony of recombinant *E. coli* cells (Eω and REω strains) was selected and grown overnight in 5 mL of Luria−Bertani (LB) medium at 37 °C with rotation at 200 rpm. Five hundred microliters of the culture was inoculated into 50 mL of LB medium and grown overnight at 37 °C with rotation at 200 rpm. Subsequently, this culture was inoculated (1:100) into 1 L of Luria−Bertani (LB) medium, and expression of target genes was induced with 0.1 mM IPTG in addition to 0.25 mM of 5-aminolevulinic acid (ALA) at an OD_{600} of 0.5−0.6. Following the addition of IPTG and ALA, temperature was reduced to 25 °C to facilitate soluble expression of the target genes, with rotation at 200 rpm for 20 h. The recombinant cells were harvested by centrifugation at 12 000*g* for 15 min at 4 °C, washed twice with potassium phosphate buffer (0.1 M, pH 7.4), and used as biocatalysts in the biotransformation studies. The biotransformation was conducted in 250 mL shake flasks by adding a fatty acid (C12 or C14) substrate stock solution containing 20% of FA in DMSO to a final concentration of 1g/L into 0.1 M potassium phosphate buffer (pH 7.4) containing the following: 50 g_{cww}/L of the induced resting cells, 0.5% Tween 80, 1X filter sterilized trace element solution[25] (g/L: 2.4 g of $FeCl_3 \cdot 6H_2O$, 0.3 g of $CoCl_2 \cdot H_2O$, 0.15 g of $CuCl_2 \cdot 2H_2O$, 0.3 g of $ZnCl_2$, 0.3 g of $Na_2MO_4 \cdot 2H_2O$, 0.075 g of H_3BO_3, and 0.495 g of $MnCl_2 \cdot 4H_2O$), and 30 μg/mL of chloramphenicol. The biotransformation was carried out in the presence and absence of cosubstrates (1% (w/v) glycerol and 0.4% (w/v) D-glucose). The biotransformations were conducted in a shaking incubator (30 °C and 200 rpm), and samples were collected at different time points for product quantification and identification by (gas chromatography) GC.

Effects of Temperature on DCA Production. To examine the effect of temperature on DCA production, the biotransformation was conducted at 25, 30, and 37 °C using the engineered *E. coli* strain, REω. Biotransformations were conducted in a shaking incubator (200 rpm), samples were collected at different time points, and products were quantified using GC.

Biotransformations in Mini-Bioreactor. Because REω performed better in shake flask conditions than did Eω, REω was used for further biotransformation studies that were carried out in a homemade, mini-bioreactor (250 mL capacity) that had precise monitoring and control systems for pH, temperature, and agitation speed. The biotransformation medium and conditions were maintained as for the shake flask experiments. Agitation speed was set at 1200 rpm. The biotransformations were conducted at 30 °C, and samples were collected every 2 h for product quantification by GC.

Effects of 5-Aminolevulinic Acid and Thiourea on DCA Production. To determine the effect of heme precursors, such as 5-aminolevulinic acid (ALA), on the production of DCA, 0.25 mM ALA and 0.1 mM IPTG were added at the time of heterologous gene induction in REω. For analyzing the effects of thiourea, thiourea was added to the biotransformation reaction for a final concentration of 1 mM.[6] The biotransformations were conducted in a shaking incubator (30 °C and 200 rpm), and samples were collected at different time points for product quantification by GC.

Production of LDCAs from Coconut Oil Hydrolysate. Coconut oil was hydrolyzed according to the method described by Chua et al.[26] with slight modifications. Briefly, the reaction mixture contained 10 mL of coconut oil (Samchun, Korea), 1.75 mL of distilled water, 13.25 mL of hexane, and 0.25 g of lipase lipozyme from *Mucor miehei* (Sigma-Aldrich, St. Louis, MO). The mixture was incubated at 40 °C with rotation at 200 rpm for 12 h. After hydrolysis, water and hexane were removed by rotary evaporation at 60 °C. The resulting residue was used for biotransformation studies with REω. The biotransformation medium and conditions were maintained as described in a previous section. The biotransformations were conducted in a shaking incubator (30 °C and 200 rpm), and samples were collected for product identification by GC.

Product and Data Analysis. For the quantification and identification of α,ω-DCAs, the cell-free supernatant from the culture media of recombinant *E. coli* was acidified with HCl. DCAs produced through biotransformation were extracted twice with an equal volume of ethyl acetate containing 1 g/L methyl nonadecanoate (C19 FA) as an internal standard and then subjected to derivatization with (trimethylsilyl) diazomethane solution (TMS). The silylated derivatives were analyzed and quantified by a gas chromatograph (GC) (Agilent 7890A, U.S.) equipped with a flame ionization detector (FID) and an Agilent capillary column-DB WAX (30 m length, 0.320 mm internal diameter, 0.50 μm film thickness). The temperature program employed was 120 °C for 2 min, followed by a linear temperature gradient, increasing 10 °C/min to 220 °C. The concentration of biotransformation products was determined using calibration curves (R^2 > 0.99). Identification was performed on GC (Agilent 7890A) equipped with a mass selective detector (MSD, Agilent 5975C). Samples were prepared as for GC/FID. Mass spectra were obtained by electron impact ionization at 70 eV. The expected reaction products were identified by their characteristic mass fragmentation pattern and compared to authentic standards. All of the experimental data were subjected to one-way analysis of variance (ANOVA) or multivariate analysis of variance (MANOVA) followed by Tukey's test using SPSS (Version 11) software to determine levels of significance. Probability (P) values of <0.01 or <0.05 were considered significant.

RESULTS AND DISCUSSION

Strain Engineering. Two molecular modifications may increase DCA product yield by the ω-oxidation pathway: (1) increasing fatty acid uptake efficiency and (2) inhibition of substrate degradation by alternative pathways. Fatty acid

DOI: 10.1021/acs.jafc.5b03833
J. Agric. Food Chem. 2015, 63, 8199−8208

degradation (β-oxidation) in *E. coli* is catalyzed by enzymes encoded by the *fad* regulon, which are responsible for the transport and activation of long-chain fatty acids and their β-oxidative cleavage into acetyl-CoAs. Genes in the regulon encode for the outer-membrane-bound fatty acid transport protein FadL[27] and inner-membrane-associated protein FadD,[28] which are responsible for transport of exogenous long-chain fatty acids into the cell by a specific transport process. Genes in the *fad* regulon are repressed by *fadR*.[29] Cho et al.[30] found that the expression levels of fadL and fadD were elevated 4- and 3-fold, respectively, in the ΔfadR mutant. The degradation of imported fatty acids is avoided by deleting the critical conversion step carried out by acyl-CoA dehydrogenase (*fadE*), thus preventing the β-oxidation pathway. For this study, in the parental strain, MG1655, *fadR*, and/or *fadE* were successfully knocked out.

Additionally, the pBbA6C-ω construct was made by fusion of genes responsible for the direct conversion of fatty acids into the corresponding DCAs. The highly ω-regioselective (>95%) and catalytically active fusion construct that consists of CYP of *M. aquaeolei* and NCP of *B. megaterium*, generated by Scheps et al.,[16] was used in the present study. The linker region between CYP and NCP domains contained a native linker, found between the heme and NCP domains in self-sufficient CYP450 of *B. megaterium*. A 3xGGS region preceded the native linker, as this sequence was found to be conducive for linkage of different protein domains.[16,31] The AlkL gene of *P. putida* was engineered into the final construct to improve the fatty acid uptake efficiency.[18,19] Alcohol dehydrogenase (ADH) of *S. cerevisiae* and aldehyde dehydrogenase (ALD) of *C. tropicalis* were employed to oxidize the product of the fusion construct (ω-hydroxy fatty acids) into DCA. The activities of both ADH and ALD on the pBbE6K plasmid were analyzed by expressing them in the Δ*fadE* strain when the strain was fed with 12-hydroxydodecanoic acid (ω-hydroxy fatty acid); the product was confirmed to be 1,12-dodecanedioic acid (C12 DCA) by GC−MS (data not shown). The various genes inserted into the final construct, pBbA6C-ω, were PCR amplified and confirmed by gene sequencing (Macrogen, Korea). All of the inserted genes were expressed well and visualized as clear bands by SDS-PAGE analysis (Figure 2).

Production of Dodecanedioic Acid (C12 DCA) and Tetradecanedioic Acid (C14 DCA). Both Eω and REω *E. coli* strains were used for the production of dodecanedioic acid (C12 DCA) and tetradecanedioic acid (C14 DCA), with the supplementation of cosubstrates (glycerol or glucose), from C12 FA and C14 FA (Figure 3a). In REω, in the presence of cosubstrates, a maximum of 76 mg/L C12 DCA and 157 mg/L C14 DCA was produced in 48 h of biotransformation. REω produced 142% more C12 DCA and 204% more C14 DCA than Eω during 48 h of biotransformation. This result suggests that *fadR* deletion facilitates the transport of fatty acids into the cell via increased expression of *fadL* and *fadD*, which are responsible for FA import. REω began producing DCAs earlier in the course of biotransformation as compared to Eω. Additionally, REω produced a higher concentration of C14 DCA when compared to C12 DCA concentration ($P < 0.5$). Glycerol and glucose had inhibitory effects on the induction of alkane-degrading and DCA-producing enzymes in yeasts.[32,33] Expression of the fad regulon genes is strongly repressed by glucose via Crp, in both the presence and the absence of oleate.[30] In contrast, ω-hydroxy fatty acid (C12) was synthesized in engineered *E. coli* containing engineered CYP153A/AlkL with cosubstrates (glycerol−glucose) in biotransformation.[16]

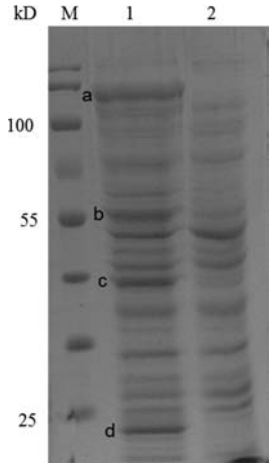

Figure 2. Expression of ω-oxidation genes. Lane M, marker; lanes 1 and 2, total fractions of REω and wild type, respectively; a, fusion protein (CYP-NCP, 120 kD); b, aldehyde dehydrogenase (ALD1, 54 kD); c, alcohol dehydrogenase (ADH5, 37 kD); and d, alkane transporter (AlkL, 25 kD). The molecular mass of each enzyme was calculated on the basis of their sequence by the online ExPasy tool.

Because REω performed better than Eω in terms of DCA production, subsequent biotransformations were carried out in REω strains without cosubstrates. REω synthesized a maximum of 150 mg/L C12 DCA and 308 mg/L C14 DCA (Figure 3b). The conversion efficiency of REω was 15% and 31% for C12 DCA and C14 DCA respectively. Notably, the final amount of DCA was about 2-fold higher than that of cosubstrate fed REω. Moreover, this concentration was already reached after just 12 h as compared to 48 h in cosubstrates fed biotransformations. This strategy is consistent with that of Song et al.,[34] wherein no cosubstrates were added for the synthesis of DCA by Baeyer−Villiger monooxygenase/esterase-based whole cell biotransformation. Jeon et al.[5] observed that the maximum product formation rate and final product concentration were greater when glucose was excluded from the biotransformation, indicating that glucose did not help convert oleic acid into 10-hydroxystearic acid. Therefore, further experiments were conducted employing REω strains without any cosubstrates.

Fasan et al.[35] previously listed the following factors as impacting the final yield in whole-cell biotransformations using P450-containing resting cells: accessibility of substrate and oxygen; toxicity of substrate, oxygen, and product; and ability of the cells to regenerate NAD(P)H. In the present study, no glucose or glycerol was used; however, these molecules are considered important for the regeneration of cofactors.[21,36] Therefore, further investigations are underway to construct a cofactor regeneration system that will circumvent the redox balance issue. In the future, this system could be effectively used along with the system presented here to achieve higher product yield.

Effects of Temperature on DCA Production. After the addition of IPTG, the temperature was reduced from 37 to 25 °C, as lower temperatures serve to control metabolic fluctuations and improve both protein solubility and activity; this therefore reduces the formation of insoluble fractions of proteins (inclusion bodies).[37] Heterologous gene expression can influence the biotransformation performance of the *E. coli*-based biocatalyst.[5] This study used three different temperatures

DOI: 10.1021/acs.jafc.5b03833
J. Agric. Food Chem. 2015, 63, 8199−8208

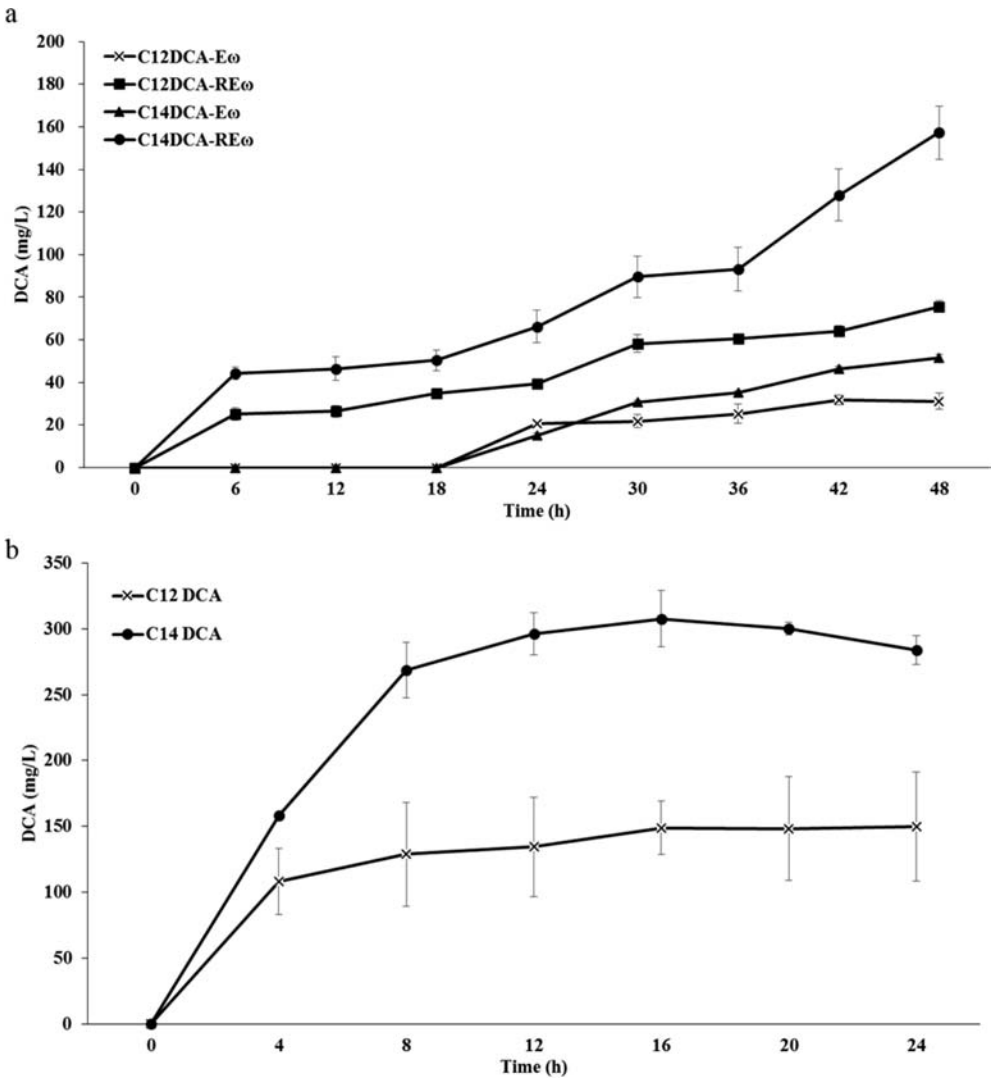

Figure 3. Production of DCAs by Eω and REω. (a) Production of C12 and C14 DCA by Eω and REω supplemented with cosubstrates. Cosubstrate mixture contains 0.4% (w/v) glucose and 1% (w/v) glycerol. (b) Production of C12 and C14 DCA by REω without cosubstrates. No product was formed in the wild-type strain. Data represent the means of three different experiments, and error bars represent standard deviation.

for biotransformations: preparation of starter cultures was performed at 37 °C, enzyme expression after induction was at 25 °C, and biotransformation occurred at 30 °C. The effect of temperature on DCA production during biotransformation was evaluated at 25, 30, and 37 °C using the engineered strain, REω. The results presented in Figure 4 show that 30 °C was the optimum temperature for biotransformation, producing the maximum titer. It was found that a maximum of 3.99- and 3.54-fold increased C12 DCA and 2.11- and 2.70-fold increased C14 DCA was obtained at 30 °C when compared to that of 25 and 37 °C, respectively. Many studies involving *E. coli* whole cell biotransformation by CYP450s are performed at 30 °C, to achieve the maximum yield.[16,38] In the present study, REω ($P < 0.05$) produced significantly more C12 DCA and C14 DCA at 30 °C than at 25 or 37 °C, confirming that 30 °C was the optimum temperature for catalytic action of ω-pathway enzymes.

Biotransformations in Mini-Bioreactor. To increase productivity, transformations were carried out in a mini-bioreactor, providing efficient mixing with an impeller at high speed. The formation of fatty acid droplets is speculated to cause inefficient transportation of the fatty acids inside the cells.[5] Efficient mixing allows improved fatty acid transport and dispersal of fatty acid droplets. The data suggest that the bioconversion rate was rapid and the level of DCA production stabilized after 8−10 h (Figure 3b). Therefore, samples were withdrawn every 2 h for 10 h. Bioreactor efficiency in regard to DCA production was compared to that in the shake flask condition (Figure 5). DCA production was improved in bioreactor when compared to the shake flask. A maximum increase of 2.61-fold C12 DCA and 1.70-fold C14 DCA production was observed in the mini-bioreactor when compared to the shake flask. The maximum titer was achieved in the bioreactor in a shorter period of time (6 h), when compared to the shake flask condition (8−10 h).

Effects of 5-Aminolevulinic Acid and Thiourea on DCA Production. In addition to the productive catalytic cycle in the monooxygenase enzyme complex, some unproductive reactions occur, as P450 inefficiency and oxidative stress yield H_2O_2 as a side-product.[17,39] In *E. coli*, accumulation of H_2O_2 is toxic and causes growth defects.[40] It has been reported that exposing *E. coli* to reactive oxygen species (ROS) such as H_2O_2 causes damage to all macromolecules, potentially damaging enzymes by oxidizing sulfhydryl and iron−sulfur moieties.

DOI: 10.1021/acs.jafc.5b03833
J. Agric. Food Chem. 2015, 63, 8199−8208

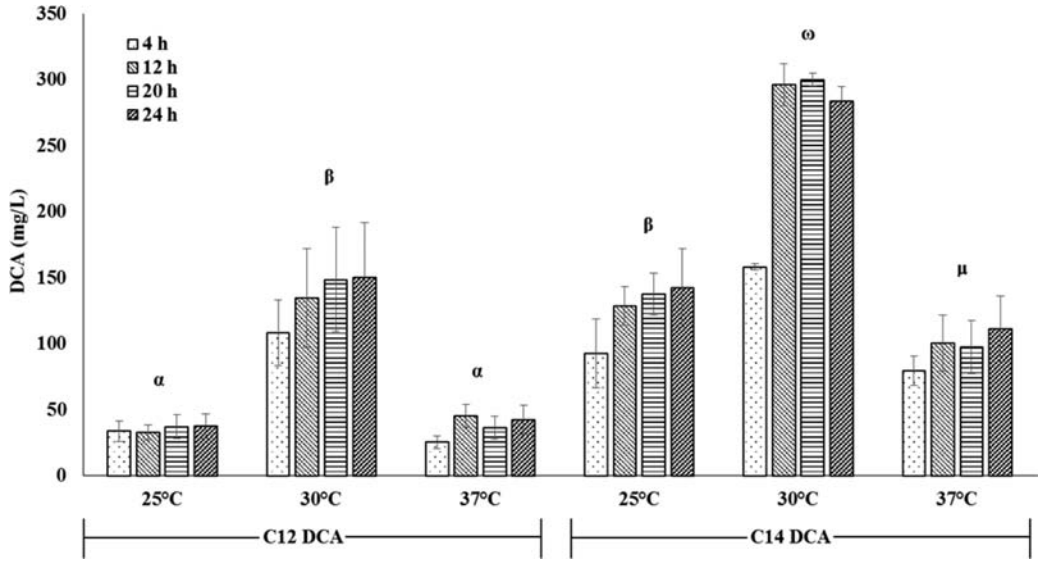

Figure 4. Effects of temperature on biotransformation of C12 and C14 FA to corresponding DCAs by REω. Temperature of 30 °C was determined to be the optimum for this biotransformation. Data represent the means of two different experiments. and error bars represent standard deviation. Different symbols above each set of bars indicate significant difference ($P < 0.05$) according to Tukey's test.

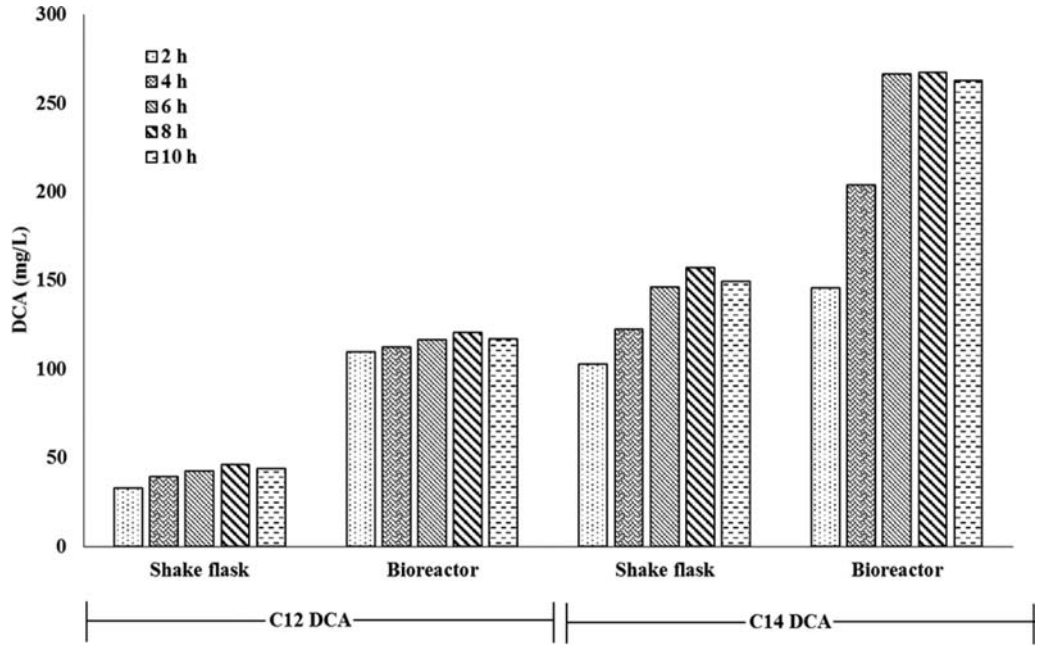

Figure 5. Production of DCAs in a mini-bioreactor by REω. C12 and C14 DCA product concentrations were increased by performing the biotransformation in the mini-bioreactor. Temperature was maintained at 30 °C and agitation speed was maintained at 1200 rpm throughout the biotransformation process.

Conversion of H_2O_2 to a hydroxyl radical can produce mutagenic and lethal lesions.[41] Scheps et al.[16] observed that a concentration of 274 μM of H_2O_2 was produced by CYP153A during production of 12-hydroxy fatty acid after 20 h of biotransformation. They also claimed that reduction in the final DCA concentration could be due to the toxicity of accumulated H_2O_2, as well as acetate. Therefore, to obtain the maximum production, the process can be equipped with a scavenging system for H_2O_2. We investigated the effect of the antioxidant reagent thiourea, which has been shown to decrease intracellular H_2O_2 concentrations, reduce the damage caused by free radicals generated from H_2O_2, and promote fatty acid utilization.[6,42] Figure 6a depicts the effect of addition of thiourea on the production of C12 and C14 DCAs. Addition of 1 mM thiourea showed an at least 7% increased C12 DCA and 33% increased C14 DCA production as compared to that of respective controls. Our results are consistent with the findings of Doi et al.,[6] wherein the authors obtained an 8.3% increase in product formation from fatty acid substrates on supplementation with thiourea.

Because the constructed CYP153A is a heme-dependent monooxygenase, the effect of heme precursors was investigated. *E. coli* does not tend to accumulate heme beyond its metabolic requirement, as free heme is toxic.[43] The effect of the heme precursor 5-aminolevulinic acid (ALA) on product concentration was evaluated by inducing the REω cells with 0.25 mM

DOI: 10.1021/acs.jafc.5b03833
J. Agric. Food Chem. 2015, 63, 8199−8208

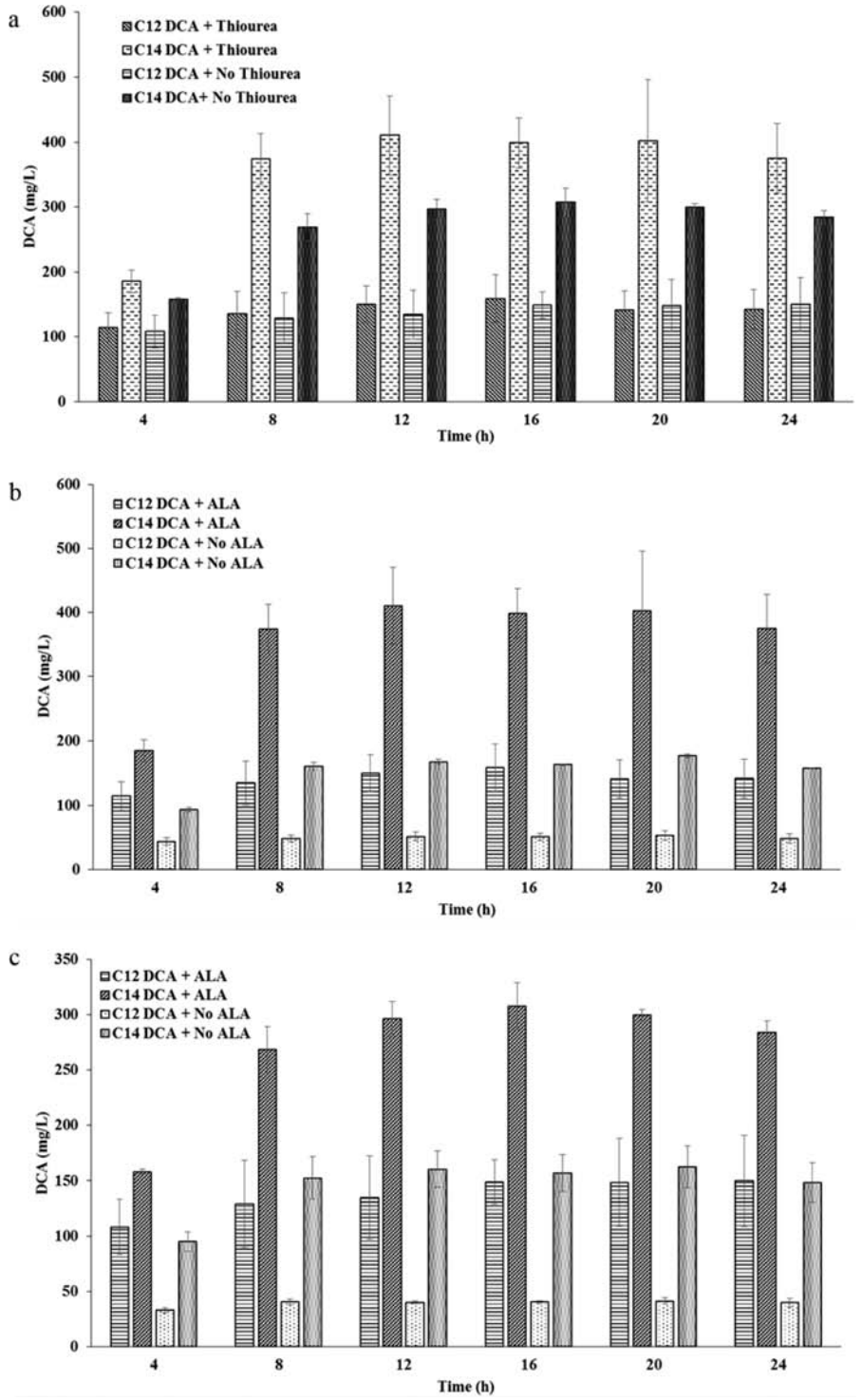

Figure 6. Effects of thiourea and 5-aminolevulinic acid (ALA) supplement on DCA production. (a) Thiourea was added to a final concentration of 1 mM during the biotransformation. Thiourea significantly ($P < 0.01$) increased the concentration of C14 DCA by REω but not C12 DCA. ALA supplementation increased product concentration in the presence (b) and absence (c) of thiourea. REω cells were induced with 0.25 mM of ALA and 0.1 mM of IPTG to induce expression of ω-oxidation pathway genes. Addition of ALA resulted in a significant difference ($P < 0.01$) in the concentration of C12 and C14 DCA when compared to the non-ALA supplemented REω. Data represent the means of three different experiments, and error bars represent standard deviation.

of ALA alongside 0.1 mM of IPTG. Figure 6b and c shows that, regardless of thiourea supplementation, addition of ALA resulted in a significant difference ($P < 0.01$) in the concentration of C12 DCA and C14 DCA when compared to the non-ALA supplemented REω. C12 DCA and C14 DCA increased by 2.98- and 2.44-fold, respectively, following addition of ALA.

Under the optimized condition, engineered *E. coli* produced a maximum of 159 mg/L C12 DCA and 410 mg/L C14 DCA, respectively, in 4−8 h shorter than corresponding controls by

DOI: 10.1021/acs.jafc.5b03833
J. Agric. Food Chem. 2015, 63, 8199−8208

whole cell biotransformation from fatty acids. Table 2 consolidates all of the data on the production of C12 DCA and C14 DCA under different growth conditions. We suggest that, by employing our direct synthesis of DCA system, it is possible to produce DCAs with various chain-lengths in a single reactor simply by changing the substrates. Even when increased monooxygenase expression and activity occurred following supplementation of ALA and thiourea, the amount of C12 DCA was comparatively less than that of C14 DCA. This may be due to limitation in substrate conversion efficiency during C12 DCA formation. CYP153A possessed higher substrate conversion efficiency for C14 fatty acids (80−85%) than C12 fatty acids (60−65%).[15] Apparently, high CYP450 content in biomass does not necessitate higher product yield.[36] To increase CYP450 monooxygenase-based whole cell biotransformation cost-effectiveness and feasibility for industrial production, methods for circumventing H_2O_2-dependent issues [such as overexpression of oxidative-stress regulator (OxyS)][6] and combinatorial overexpression of heme biosynthesis genes (such as *hemALDF*)[44] should be explored.

Table 2. Consolidated Data on the Production of Dodecanedioic Acid (C12 DCA) and Tetradecanedioic Acid (C14 DCA) under Different Growth Conditions[a]

	growth condition			maximum concentration of the product (mg/L)			
strain	cosubstrates	ALA	thiourea	C_{12} DCA	time (h)	C_{14} DCA	time (h)
Eω	+	+	−	32	48	52	48
REω	+	+	−	77	48	157	48
	−	−	−	41	20	163	20
	−	−	+	53	20	177	20
	−	+	−	150	24	308	16
	−	+	+	159	16	410	12
	−	−	+	121	8	267	6

[a]REω strain was selected for its efficiency over Eω strain. All of the experiments were carried out in a shake flask except the last row that was performed in a mini-bioreactor. Values are rounded off to the nearest one. Cosubstrates, 1% (w/v) glycerol and 0.4% (w/v) D-glucose; ALA, 5-aminolevulinic acid (0.25 mM); thiourea, 1 mM.

Production of LDCAs from a Fatty Acid-Rich Feedstock-Coconut Oil Hydrolysate. Plant oils are available from various oilseeds in large quantities. Various vegetable oil feedstock, including corn oil, palm oil, coconut oil, sunflower oil, olive oil, and palm kernel oil, have been evaluated for the production of one of the Bioplastic monomers, polyhydroxyalkanoate (PHA).[45] Conversion of fatty acids from renewable feedstock to specialty chemicals is an attractive commercial opportunity.[4,11] Notably, oils from nonedible crops could be used for DCA production. In the present study, the constructed synthetic biocatalytic system (REω) in *E. coli* was evaluated for production of DCAs of various chain lengths, using coconut oil as a substrate. The main purpose of using this oil was simply to demonstrate the capability and applicability of our engineered system to produce DCAs from a fatty acid-rich renewable biomass source. The routine usage of coconut oil in terms of culinary and medicinal properties likely precludes large-scale usage in DCA production; however, other plant-based oils could easily be employed using the system presented here. It was found that the coconut oil hydrolysate contained the following FAs (% w/w): C8 (5.4%), C10 (5.1%), C12 (47.68%), C14 (15.18%), C16 (7.02%), C18 (5.62%), C18.1 (7.74%). The remaining lysate portions may contain other saturated FAs and unsaturated FAs or be accounted for by incomplete enzyme digestion of oil. Subsequently, the hydrolysate was subjected to the constructed ω-oxidation pathway system (REω). The data show that the system can synthesize decanedioic acid (C10 DCA), dodecanedioic acid (C12 DCA), tetradecanedioic acid (C14 DCA), and hexadecanedioic acid (C16 DCA) from the coconut oil hydrolysate (Figure 7). Therefore, our system could be used for the production of DCAs from any plant oils high in fatty acids, including the nonedible vegetable oils.

To conclude, we engineered an *E. coli* strain capable of producing α,ω-dicarboxylic acids directly from fatty acid substrates. The constructed system could be extended to produce high value LDCAs from cost-effective renewable plant oils. Further improvements in construction of self-sufficient

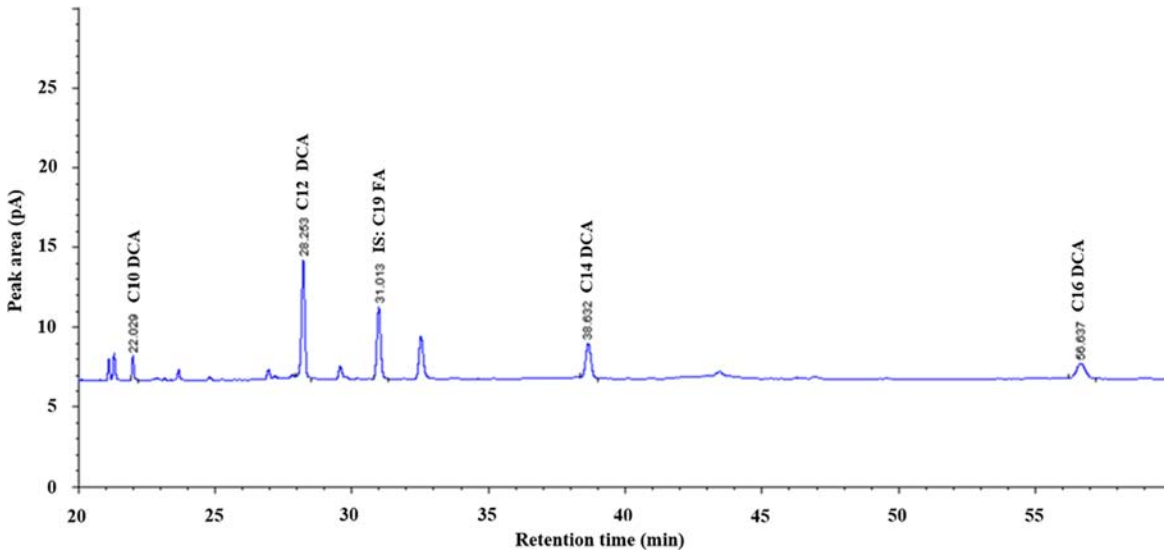

Figure 7. Gas chromatographic analysis patterns of different chain length of DCAs produced from coconut oil using the engineered *E. coli* strain REω.

DOI: 10.1021/acs.jafc.5b03833
J. Agric. Food Chem. 2015, 63, 8199−8208

strains could make the process more economically feasible. Although the utilization of fats and oils for the production of industrial chemicals/monomers is an emerging field, the process has to be industrialized and scaled up to cope with product cost, environmental concerns, available feedstock, and sustainable industrial processes. We suggest that the engineered microbial system presented here could serve as an efficient platform for the industrial production of α,ω-dicarboxylic acids.

AUTHOR INFORMATION

Corresponding Author

*Tel.: +82 52 217 2514. Fax: +82 52 217 2509. E-mail: sklee@unist.ac.kr.

Funding

This work was supported by the National Research Foundation of Korea (NRF) through grants funded by the Ministry of Science, ICT & Future Planning (MSIP) (NRF-2009-C1AAA001-2009-0093491), and by a grant from the Next-Generation Bio Green 21 Program (SSAC, PJ011181), Rural Development Administration, Republic of Korea.

Notes

The authors declare no competing financial interest.

REFERENCES

(1) Huf, S.; Krugener, S.; Hirth, T.; Rupp, S.; Zibek, S. Biotechnological synthesis of long-chain dicarboxylic acids as building blocks for polymers. *Eur. J. Lipid Sci. Technol.* **2011**, *113*, 548−561.

(2) Liu, S.; Li, C.; Fang, X.; Cao, Z. Optimal pH control strategy for high-level production of long-chain α,ω-dicarboxylic acid by *Candida tropicalis*. *Enzyme Microb. Technol.* **2004**, *34*, 73−77.

(3) Mobley, D. P. Biosynthesis of long-chain dicarboxylic acid monomers from renewable resources. Final Technical Report, 1999; Prepared for the United States Department of Energy Under Cooperative Agreement no. DE-FC36-95G01 0099.

(4) Dellomonaco, C.; Rivera, C.; Campbell, P.; Gonzalez, R. Engineered respiro-fermentative metabolism for the production of biofuels and biochemicals from fatty acid-rich feedstocks. *Appl. Environ. Microbiol.* **2010**, *76*, 5067−5078.

(5) Jeon, E. Y.; Lee, J. H.; Yang, K. M.; Joo, Y. C.; Oh, D. K.; Park, J. B. Bioprocess engineering to produce 10-hydroxystearic acid from oleic acid by recombinant *Escherichia coli* expressing the oleate hydratase gene of *Stenotrophomonas maltophilia*. *Process Biochem.* **2012**, *47*, 941−947.

(6) Doi, H.; Hoshino, Y.; Nakase, K.; Usuda, Y. Reduction of hydrogen peroxide stress derived from fatty acid beta-oxidation improves fatty acid utilization in *Escherichia coli*. *Appl. Microbiol. Biotechnol.* **2014**, *98*, 629−639.

(7) Isin, E. M.; Guengerich, F. P. Complex reactions catalyzed by cytochrome P450 enzymes. *Biochim. Biophys. Acta, Gen. Subj.* **2007**, *1770*, 314−329.

(8) Munro, A. W.; Girvan, H. M.; McLean, K. J. Variations on a (t)heme—novel mechanisms, redox partners and catalytic functions in the cytochrome P450 superfamily. *Nat. Prod. Rep.* **2007**, *24*, 585−609.

(9) Van Bogaert, I. N. A.; Groeneboer, S.; Saerens, K.; Soetaert, W. The role of cytochrome P450 monooxygenases in microbial fatty acid metabolism. *FEBS J.* **2011**, *278*, 206−221.

(10) Yun, C. H.; Kim, K. H.; Kim, D. H.; Jung, H. C.; Pan, J. G. The bacterial P450 BM3: A prototype for a biocatalyst with human P450 activities. *Trends Biotechnol.* **2007**, *25*, 289−297.

(11) Eschenfeldt, W. H.; Zhang, Y.; Samaha, H.; Stols, L.; Eirich, L. D.; Wilson, C. R.; Donnelly, M. I. Transformation of fatty acids catalyzed by cytochrome P450 monooxygenase enzymes of *Candida tropicalis*. *Appl. Environ. Microbiol.* **2003**, *69*, 5992−5999.

(12) Picataggio, S.; Rohrer, T.; Deanda, K.; Lanning, D.; Reynolds, R.; Mielenz, J.; Eirich, D. L. Metabolic engineering of *Candida tropicalis* for the production production of long-chain dicarboxylic acids. *Bio/Technology* **1992**, *10*, 894−898.

(13) Sumita, T.; Iida, T.; Hirata, A.; Horiuchi, H.; Takagi, M.; Ohta, A. Peroxisome deficiency represses the expression of n-alkaneinducible YlALK1 encoding cytochrome P450ALK1 in *Yarrowia lipolytica*. *FEMS Microbiol. Lett.* **2002**, *214*, 31−38.

(14) Nicaud, J. M.; Chardot, T.; Beopoulos, A. Mutant yeast strains capable of accumulating a large quantity of lipids. U.S. patent no. US008597931B2, 2013.

(15) Malca, S. H.; Scheps, D.; Kuhnel, L.; Venegas, V. E.; Seifert, A.; Nestl, B. M.; Hauer, B. Bacterial CYP153A monooxygenases for the synthesis of omega-hydroxylated fatty acids. *Chem. Commun.* **2012**, *48*, 5115−5117.

(16) Scheps, D.; Malca, S. H.; Richter, S. M.; Marisch, K.; Nestl, B. M.; Hauer, B. Synthesis of ω-hydroxy dodecanoic acid based on an engineered CYP153A fusion construct. *Microb. Biotechnol.* **2013**, *6*, 694−707.

(17) Pazmino, D. E. T.; Winkler, M.; Glieder, A.; Fraaije, M. W. Monooxygenases as biocatalysts: Classification, mechanistic aspects and biotechnological applications. *J. Biotechnol.* **2010**, *146*, 9−24.

(18) Grant, C.; Deszcz, D.; Wei, Y. C.; Martinez-Torres, R. J.; Morris, P.; Folliard, T.; Sreenivasan, R.; Ward, J.; Dalby, P.; Woodley, J. M.; Baganz, F. Identification and use of an alkane transporter plug-in for applications in biocatalysis and whole-cell biosensing of alkanes. *Sci. Rep.* **2014**, *284*, 5844.

(19) Julsing, M. K.; Schrewe, M.; Cornelissen, S.; Hermann, I.; Schmid, A.; Bühler, B. Outermembrane protein AlkL boosts biocatalytic oxyfunctionalization of hydrophobic substrates in *Escherichia coli*. *Appl. Environ. Microbiol.* **2012**, *78*, 5724−5733.

(20) Baneyx, F. Recombinant protein expression in *Escherichia coli*. *Curr. Opin. Biotechnol.* **1999**, *10*, 411−421.

(21) Fujita, N.; Sumisa, F.; Shindo, K.; Kabumoto, H.; Arisawa, A.; Ikenaga, H.; Misawa, N. Comparison of two vectors for functional expression of a bacterial cytochrome P450 gene in *Escherichia coli* using CYP153 genes. *Biosci., Biotechnol., Biochem.* **2009**, *73*, 1825−1830.

(22) Kuhn, D.; Bühler, B.; Schmid, A. Production host selection for asymmetric styrene epoxidation: *Escherichia coli* vs. solvent-tolerant *Pseudomonas*. *J. Ind. Microbiol. Biotechnol.* **2012**, *39*, 1125−1133.

(23) Lee, T. S.; Krupa, R. A.; Zhang, F.; Hajimorad, M.; Holtz, W. J.; Prasad, N.; Lee, S. K.; Keasling, J. D. BglBrick vectors and datasheets: A synthetic biology platform for gene expression. *J. Biol. Eng.* **2011**, *5*, 12.

(24) Datsenko, K. A.; Wanner, B. L. One-step inactivation of chromosomal genes in *Escherichia coli* K-12 using PCR products. *Proc. Natl. Acad. Sci. U. S. A.* **2000**, *97*, 6640−6645.

(25) Zhou, L.; Zuo, Z. R.; Chen, X. Z.; Niu, D. D.; Tian, K. M.; Prior, B. A.; Shen, W.; Shi, G. Y.; Singh, S.; Wang, Z. X. Evaluation of genetic manipulation strategies on D-lactate production by *Escherichia coli*. *Curr. Microbiol.* **2011**, *62*, 981−989.

(26) Chua, L. S.; Alitabarimansor, M.; Lee, C. T.; Mat, R. Hydrolysis of virgin coconut oil using immobilized lipase in a batch reactor. *Enzyme Res.* **2012**, *2012*, 1.

(27) Black, P. N. Primary sequence of the *Escherichia coli fadL* gene encoding an outer membrane protein required for long-chain fatty acid transport. *J. Bacteriol.* **1991**, *173*, 435−442.

(28) Black, P. N.; DiRusso, C. C.; Metzger, A. K.; Heimert, T. L. Cloning, sequencing, and expression of the *fadD* gene of *Escherichia coli* encoding acyl coenzyme A synthetase. *J. Biol. Chem.* **1992**, *267*, 25513−25520.

(29) Campbell, J. W.; Morgan-Kiss, R. M.; Cronan, J. E. A new *Escherichia coli* metabolic competency: growth on fatty acids by a novel anaerobic b-oxidation pathway. *Mol. Microbiol.* **2003**, *47*, 793−805.

(30) Cho, B. K.; Knight, E. M.; Palsson, B. O. Transcriptional regulation of the *fad* regulon genes of *Escherichia coli* by ArcA. *Microbiology* **2006**, *152*, 2207−2219.

(31) Robinson, C. R.; Sauer, R. T. Optimizing the stability of single-chain proteins by linker length and composition mutagenesis. *Proc. Natl. Acad. Sci. U. S. A.* **1998**, *95*, 5929−5934.

DOI: 10.1021/acs.jafc.5b03833
J. Agric. Food Chem. 2015, 63, 8199−8208

(32) Nazarko, T.; Mala, M.; Nicaud, J. M.; Sibirny, A. Mutants of the yeast *Yarrowia lipolytica* deficient in the inactivation of peroxisomal enzymes. *Proc. Lviv. Univ.* **2004**, *35*, 128−136.
(33) Seghezzi, W.; Meili, C.; Ruffiner, R.; Kuenzi, R.; Sanglard, D.; Fiechter, A. Identification and characterization of additional members of the cytochrome P450 multigene family CYP52 of *Candida tropicalis*. *DNA Cell Biol.* **1992**, *11*, 767−780.
(34) Song, J. W.; Lee, J. H.; Bornscheuer, U. T.; Park, J. B. Microbial synthesis of medium-chain α, ω-dicarboxylic acids and ω-amino-carboxylic acids from renewable long-chain fatty acids. *Adv. Synth. Catal.* **2014**, *356*, 1782−1788.
(35) Fasan, R.; Chen, M. M.; Crook, N. C.; Arnold, F. H. Engineered alkane-hydroxylating cytochrome P450 (BM3) exhibiting native like catalytic properties. *Angew. Chem., Int. Ed.* **2007**, *46*, 8414−8418.
(36) Gudiminchi, R. K.; Randall, C.; Opperman, D. J.; Olaofe, O. A.; Harrison, S. T. L.; Albertyn, J.; Smit, M. S. Whole-cell hydroxylation of n-octane by *Escherichia coli* strains expressing the CYP153A6 operon. *Appl. Microbiol. Biotechnol.* **2012**, *96*, 1507−1516.
(37) Sahdev, S.; Khattar, S. K.; Saini, K. S. Production of active eukaryotic proteins through bacterial expression systems: A review of the existing biotechnology strategies. *Mol. Cell. Biochem.* **2007**, *307*, 249−264.
(38) Clomburg, J. M.; Blankschien, M. D.; Vick, J. E.; Chou, A.; Kim, S. H.; Gonzalez, R. Integrated engineering of β-oxidation reversal and ω-oxidation pathways for the synthesis of medium chain ω-functionalized carboxylic acids. *Metab. Eng.* **2015**, *28*, 202−212.
(39) Cabiscol, E.; Tamarit, J.; Ros, J. Oxidative stress in bacteria and protein damage by reactive oxygen species. *Int. Microbiol.* **2000**, *3*, 3−8.
(40) Jang, S.; Imlay, J. A. Micromolar intracellular hydrogen peroxide disrupts metabolism by damaging iron-sulfur enzymes. *J. Biol. Chem.* **2007**, *282*, 929−937.
(41) Storz, G.; Imlay, J. A. Oxidative stress. *Curr. Opin. Microbiol.* **1999**, *2*, 188−194.
(42) Brandi, G.; Cattabeni, F.; Albano, A.; Cantoni, C. Role of hydroxyl radicals in *Escherichia coli* killing induced by hydrogen peroxide. *Free Radical Res.* **1989**, *6*, 47−55.
(43) Harnastai, I. N.; Gilep, A. A.; Usanov, S. A. The development of an efficient system for heterologous expression of cytochrome P450s in *Escherichia coli* using hemA gene co-expression. *Protein Expression Purif.* **2006**, *46*, 47−55.
(44) Zhang, L.; Kang, Z.; Chen, J.; Du, G. Optimization of the heme biosynthesis pathway for the production of 5-aminolevulinic acid in *Escherichia coli*. *Sci. Rep.* **2015**, *5*, 8584.
(45) Lee, W. H.; Loo, C. Y.; Nomura, C. T.; Sudesh, K. Biosynthesis of polyhydroxyalkanoate copolymers from mixtures of plant oils and 3-hydroxyvalerate precursors. *Bioresour. Technol.* **2008**, *99*, 6844−6851.

DOI: 10.1021/acs.jafc.5b03833
J. Agric. Food Chem. 2015, 63, 8199−8208

According to sequence analysis, OVMG contains 13 potential N-glycosylation sites,[17,20] but this has not been confirmed experimentally yet. The present study explored the glycosylation of OVMG using mass spectrometry and two-dimensional electrophoresis (2-DE). OVMG was purified from fresh egg white, and the molecular weight of the OVMG subunit was measured by MALDI-TOF MS; thus, the mass of carbohydrate moieties was calculated. Then, OVMG was deglycosylated by PNGase F and subsequently digested by proteases, and the N-glycosylation sites were identified using HPLC-ESI-MS/MS. Finally, 2-DE analysis of OVMG was performed to display the heterogeneity of glycosylation of OVMG.

MATERIALS AND METHODS

Preparation of OVMG. Fresh hen eggs laid within 24 h from White Leghorns were used for the purification of OVMG. The operation was performed as previously described.[21] Briefly, fresh hen egg white (100 mL) was diluted with an equal volume of distilled water, followed by two-step PEG (polyethylene glycol 8000) precipitation (5−9%, w/v) to obtain OVMG-rich precipitate (P_{5-9}). Then the precipitate was dissolved in PBS and further purified by gel filtration chromatography (Sephacryl S-200 HR, GE Healthcare Biosciences AB, Uppsala, Sweden) at a flow rate of 0.75 mL/min with an automatic liquid chromatography system (JiaPeng Technology, Shanghai, China). The first peak of eluent was collected and desalted with distilled water using an Amicon Ultra-15 centrifugal filter device (100 kDa NMWL, Millipore, Bedford, MA, USA) and then stored at 4 °C. The purity of OVMG was tested by HPLC using a TSK gel G2000SWXL column (7.8 × 300 mm; TOSOH, Tokyo, Japan) with a Waters 2695 separations module (Waters, Milford, MA, USA) as previously described,[21] and the result is shown in Figure S1.

Measurement of the Molecular Weight of OVMG Subunit by MALDI-TOF MS. The molecular weight of the OVMG subunit was measured by a Bruker Reflex III MALDI-TOF mass spectrometer (Bruker Daltonik GmbH, Bremen, Germany) working in positive ion mode. A saturated solution of α-cyano-4-hydroxycinnamic acid in acetonitrile and 0.1% TFA was used for the matrix.[22,23] Purified OVMG (about 2 μM) was reduced with 10 mmol/L DTT, and then 1 μL of sample solution was mixed with 1 μL of matrix solution. The mixed solution was deposited on the stainless steel target plate and dried at room temperature. The ions were ionized under a laser intensity of 80% and accelerated with an acceleration voltage of 20 kV, then measured in a linear mode and m/z range of 40000−220000.[22]

PNGase F Deglycosylation and Protease Digestion. PNGase F digestion was performed following the instructions of the manufacturer. OVMG was dissolved in distilled water to 1.5 mg/mL and the pH adjusted to 8.0 by 100 mM NH_4HCO_3. Denatured OVMG was prepared by adding 30 μL of 0.15% SDS with 80 mM 2-mercaptoethanol to 255 μL of OVMG solution and incubating for 20 min at 95 °C. After that, the solution was kept at room temperature to cool, 15 μL of PNGase F enzyme solution (500 U/mL, Sigma-Aldrich) was then added and incubated at 37 °C overnight to release asparagine-linked oligosaccharides.[11]

Deglycosylated OVMG solution (300 μL) was alkylated with 50 mM iodoacetamide for 30 min at room temperature. Then the solution was equally divided into three parts and separately digested with trypsin, chymotrypsin, and endoproteinase Glu-C (Sigma-Aldrich) at an enzyme-to-substrate ratio of 1:50 w/w overnight at 37 °C; the reaction was then stopped by heating to 100 °C for 5 min. The samples were then lyophilized for subsequent LC-MS/MS analysis.

Identification of the N-Glycosylation Sites of OVMG Using HPLC-ESI-MS/MS. The digests (by trypsin, chymotrypsin, and Glu-C) of deglycosylated OVMG were analyzed separately to identify the N-glycosylation sites. Mass spectrometric measurements were performed by HPLC-ESI-MS/MS using an LTQ mass spectrometer (Thermo-Fisher Science, Bremen, Germany) equipped with a nanospray source and Eksigent RP-HPLC (Eksigent Technologies, Dublin, CA, USA). Ten microliters of the digests was loaded onto a PepMap C18 analytical column (75 μm × 15 cm, Dionex), and separation was carried out at a flow rate of 300 nL/min using a gradient constructed from solution A (2% ACN, 0.1% formic acid) and solution B (80% ACN, 0.1% formic acid): 2−40% B for 90 min; 40−100% B for 15 min; 100% B for 15 min. The spray voltage was set as 2.2 kV, and the temperature of the ion transfer capillary was 200 °C. The mass rangesfor the MS scan was set to m/z 200−2000. For MS/MS analysis, peptides were subjected to fragmentation by collision-induced decomposition (CID), and normalized collision energy was 35%.

For the identification of N-glycosylation sites, a matching search was performed against a local database containing the OVMG FASTA file (P20740-OVOS_CHICK) using the MASCOT search engine (Matrix Science). Types of searches were MS/MS ion search, with either trypsin, chymotrypsin, or Glu-C as the enzyme allowing up to two missed cleavages. Carbamidomethylation (C) was set as a fixed modification; deamidation (NQ) and oxidation (M) were specified as variable modifications. The data were searched with a peptide ion mass tolerance and a fragment ion mass tolerance of ±0.25 Da. Only peptides with Mascot ion score >23 ($p < 0.005$) and containing the PNGase consensus sequence (N-X-S/T, X ≠ P) were considered for further analysis.[24]

Two-Dimensional Electrophoresis and Protein Identification. 2-DE analysis was carried out with the Ettan IPGphor 3 System for the first-dimension isoelectric focusing (IEF) and the Ettan DALTSix System (GE Healthcare) for the second-dimension SDS-PAGE. Sample (100 μL, 80 μg of protein) was loaded onto DryStrip IPG strips (24 cm; pH 4−7) and isoelectrically focused for a total of 64000 Vh per gel using the same conditions previously described (20 °C; 300 V for 0.5 h, 700 V for 0.5 h, 1500 V for 1.5 h, 9000 V for 3 h, and 9000 V for 5 h).[25] After equilibration to resolubilize proteins and reduce disulfide bonds, the second-dimension electrophoresis was performed using a 10% SDS-PAGE. The gels were run at 2 W per gel for 40 min and followed by 17 W per gel for approximately 4 h. Protein spots on 2-DE gels were visualized by Coomassie Brilliant Blue staining. Gel evaluation and data analysis were carried out using the Image Master V 7.0 program (GE Healthcare).[25] For identification, the candidate protein spots were excised manually from the stained gels and digested with trypsin (Promega, Madison, WI, USA). The digested peptides were extracted and then identified using a MALDI-TOF MS/MS (Bruker, Karlsruhe, Germany). Data were searched against the protein database (NCBInr, *Gallus gallus*) via the MASCOT program (http://www.matrixscience.com).[26]

Bioinformatics Analysis. To compare the N-glycosylation sites of chicken OVMG (UniProtKB accession P20740) with its homologous proteins, another nine egg macroglobulins (OVMGs) from *Aves* were selected: common turkey (G1NMI3, *Meleagris gallopavo*), duck (R0J9X6, *Anas platyrhynchos*), emperor penguin (A0A087R4G8, *Aptenodytes forsteri*), adelie penguin (A0A093NQZ9, *Pygoscelis adeliae*), dalmatian pelican (A0A091SNW1, *Pelecanus crispus*), flamingo (A0A091V5J9, *Phoenicopterus ruber*), red-legged seriema (A0A091M0T0, *Cariama cristata*), white-tailed sea-eagle (A0A091P9X7, *Haliaeetus albicilla*), and hoatzin (A0A091VDK9, *Opisthocomus hoazin*). The sequences of OVMGs were obtained from the UniProt database, and N-glycosylation sites were predicted by NetNGlyc 1.0 Server (http://www.cbs.dtu.dk/services/NetNGlyc/). Alignment of the 10 sequences was performed online (http://www.uniprot.org/align). Finally, the comparison of three representative OVMGs (chicken, P20740; turkey, G1NMI3; duck, R0J9X6) was visualized and presented by Illustrator for Biological Sequences (IBS, version 1.0).[27]

RESULTS AND DISCUSSION

Molecular Mass of Glycan Moiety in OVMG. OVMG includes a 36-residue signal peptide and a 1437-residue main chain.[17] The molecular weight (MW) of the main chain is 162.2 kDa,[20] but the measured MW of the subunit was reported from

DOI: 10.1021/acs.jafc.5b02618
J. Agric. Food Chem. 2015, 63, 8209−8215

165 to 195 kDa by different methods.[28−30] In the present study, the MW of OVMG subunit was measured by MALDI-TOF MS. As shown in Figure 1, four ion signal peaks were observed at m/z 44791, 62154, 92203, and 183297, which respectively correspond to ($[M + 4H]^{4+}$), ($[M + 3H]^{3+}$), ($[M + 2H]^{2+}$), and ($[M + H]^{+}$). Thereby, the MW of OVMG subunit is 183.3 kDa, and the MW of the glycan moiety was calculated as 21.1 kDa, accounting for 11.5% of the whole OVMG molecular.

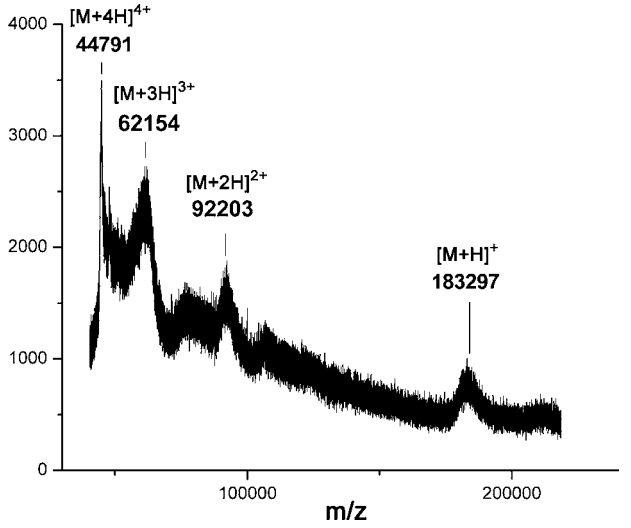

Figure 1. MALDI-TOF-MS analysis of OVMG subunit. OVMG was reduced by DTT and mixed with matrix solution, then ionized under a laser and measured by TOF MS in a linear mode. Four ion signals peaks were observed at m/z 44791, 62154, 92203, and 183297, which respectively correspond to ($[M + 4H]^{4+}$), ($[M + 3H]^{3+}$), ($[M + 2H]^{2+}$), and ($[M + H]^{+}$) of OVMG; thereby, the MW of OVMG subunit is 183.3 kDa.

This result provided a more accurate MW of OVMG and was consistent with those of sequence speculation[17] and experimental analysis.[31,32] Additionally, the full width at half-maximum (fwhm) of the molecular ion peak of OVMG subunit ($[M + H]^{+}$) was approximately 6000 (m/z), indicating the glycosylation of OVMG is not homogeneous.

By comparison with other egg white glycoproteins, the proportion of OVMG glycan is higher than those of ovalbumin, ovotransferrin, and lysozyme, but lower than those of ovomucin and ovomucoid.[10,33] Because glycans play an important role in the recognition of allergens by the immune system,[34] such a high proportion of glycans in OVMG strongly suggests that OVMG should be considered as a suspected allergen, and its potential allergenicity needs to be confirmed in future studies.

N-Glycosylation Sites of OVMG. To identify the N-glycosylation sites, OVMG was deglycosylated by PNGase F and subsequently digested by proteinase, and then the digests were analyzed by HPLC-ESI MS/MS. PNGase F cleaves N-linked oligosaccharides from glycoproteins and results in a transfer of the originally glycosylated asparagine to aspartic acid with a 0.98 Da increase in molecular weight. The mass change of peptide fragments in which the glycosylated asparagine is converted to aspartic acid can be exploited to identify N-glycosylation sites.

Table 1. N-Glycosylation Sites of OVMG Identified by HPLC-ESI MS/MS

site	sequence	peptide position	M_r (calcd)	m/z (obsd)	glycosylation[d]
N^{67}	NLNQTISVRVVL (CT[a])	65−76	1355.78	678.90^{2+}	+
N^{82}	VVLEYDTINTTIFEK (T[b])	74−88	1784.91	893.46^{2+}	+
	EYDTINTTIF (CT)	77−86	1216.55	609.28^{2+}	+
	YDTINTTIFE (G-C[c])	78−87	1216.55	609.28^{2+}	+
N^{89}	EKNTTTSNGLQCL (CT)	87−99	1465.67	733.85^{2+}	+
N^{191}	MYPLIAVQDPQNNRIFQWQNVTSE (G-C)	172−195	2891.39	964.81^{3+}	+
	IFQWQNVTSEINIVQIEFPLTEEPILGNYK (T)	186−215	3562.82	1188.63^{3+}	+
N^{403}	VNNKNTHNFTTDINGIAPF (CT)	395−414	2117.02	1059.52^{2+}	+
	NTHNFTTDINGIAPFSIDTSK (T)	400−420	2293.09	1147.56^{2+}	+
N^{527}	TGEIKVNIQADQNGTF (CT)	515−530	1734.84	868.43^{2+}	+
N^{588}	QMLTTSNVSLVIEAAANSFCAVR (T)	582−604	2482.22	828.42^{3+}	+
N^{757}	EFFPETWIWDIILINSTGK (T)	743−761	2309.16	1155.59^{2+}	+
	IWDIILINSTGKASVSY (CT)	750−766	1879.99	941.01^{2+}	+
	DIILINSTGKASVSY (CT)	752−766	1580.83	791.43^{2+}	+
	IILINSTGKASVSYTIPDTITE (G-C)	753−774	2336.24	1169.13^{2+}	+
	INSTGKASVSY(CT)	756−766	1126.55	564.28^{2+}	+
N^{1141}	CLETASEKNITDIY (CT)	1133−1146	1656.76	829.39^{2+}	+
N^{1221}	ITSYVLLALLYKPNRSQE (G-C)	1208−1225	2107.17	703.40^{3+}	/
	KPNRSQEDLTKASAIVQW (CT)	1219−1236	2070.09	1036.06^{2+}	/
	KPNRSQEDLTKASAIVQW (CT)	1219−1236	2071.07	1036.54^{2+}	+
N^{1315}	YSLTVNGTGCVLIQTALR (T)	1310−1327	1966.02	984.02^{2+}	+
	SLTVNGTGCVL (CT)	1311−1321	1120.54	561.26^{2+}	+
N^{1347}	YNIHLPEGAFGFSLSVQTSNASCPR (T)	1328−1352	2752.29	918.44^{3+}	+
	GAFGFSLSVQTSNASCPRDQPGKFD (G-C)	1335−1359	2673.21	892.08^{3+}	+
	SLSVQTSNASCPRDQPGKF (CT)	1340−1358	2078.97	1040.50^{2+}	+
	SVQTSNASCPRDQPGKF (CT)	1342−1358	1878.86	940.44^{2+}	+

[a]Peptides identified from chymotrypsin digestion of OVMG. [b]Peptides identified from trypsin digestion of OVMG. [c]Peptides identified from Glu-C digestion of OVMG. [d]+, glycosylated; /, non-glycosylated.

DOI: 10.1021/acs.jafc.5b02618
J. Agric. Food Chem. 2015, 63, 8209−8215

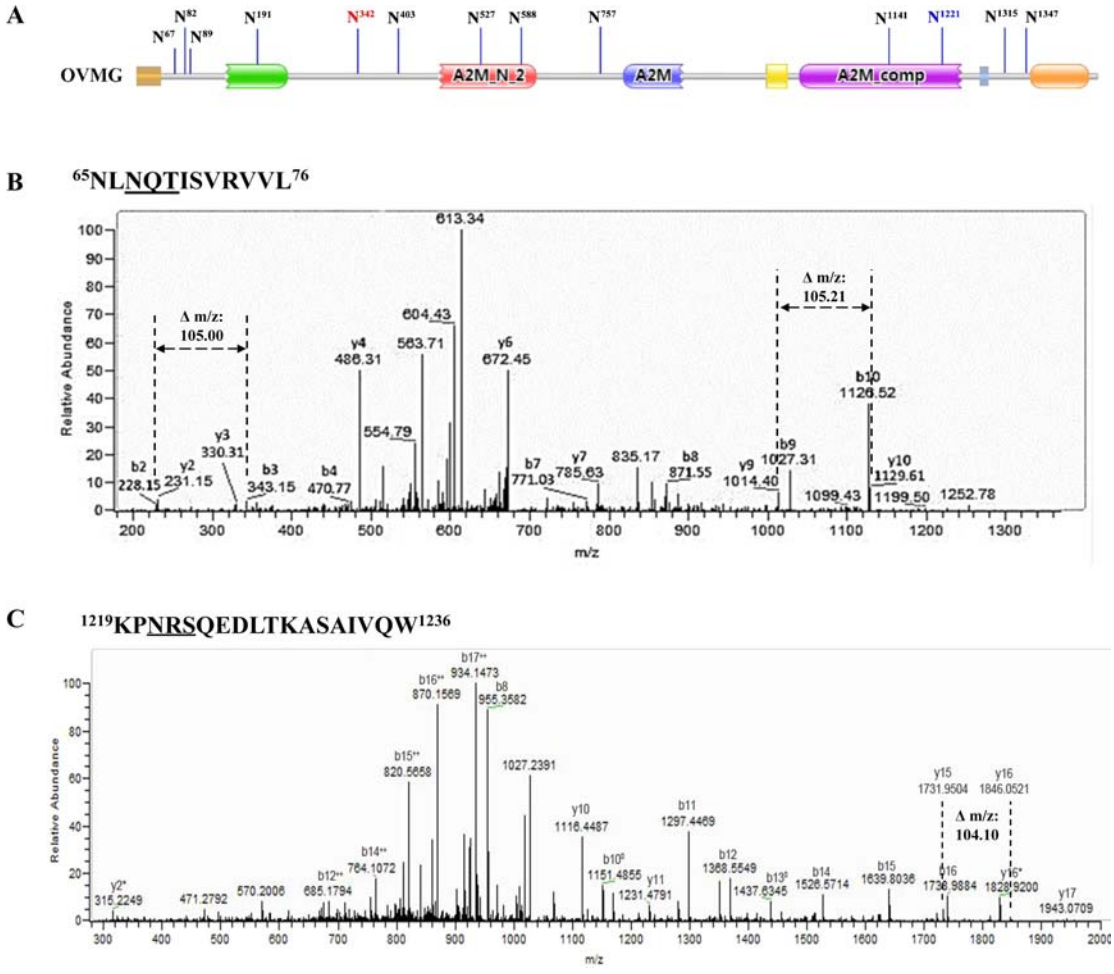

Figure 2. Location of N-glycosylation sites on OVMG and two representative MS/MS spectrums of peptides that contain the PNGase consensus sequence. (A) Location of identified N-glycosylation sites on the sequence of OVMG. Domains of OVMG were assigned by Pfam (http://pfam.xfam.org/); N^{1221} was partly glycosylated, and N^{342} was not covered in the analysis. (B) MS/MS spectrum of peptide ^{65}NLNQTISVRVVL^{76}, in which the glycosylated asparagine (Asn, N^{67}) is converted to aspartic acid (Asp); the mass difference between y10 and y9 (or b3 and b2) is 115 Da. (C) MS/MS spectrum of peptide ^{1219}KPNRSQEDLTKASAIVQW^{1236}, which does not glycosylate on its potential site (N^{1221}); the mass difference between y15 and y16 is 114 Da.

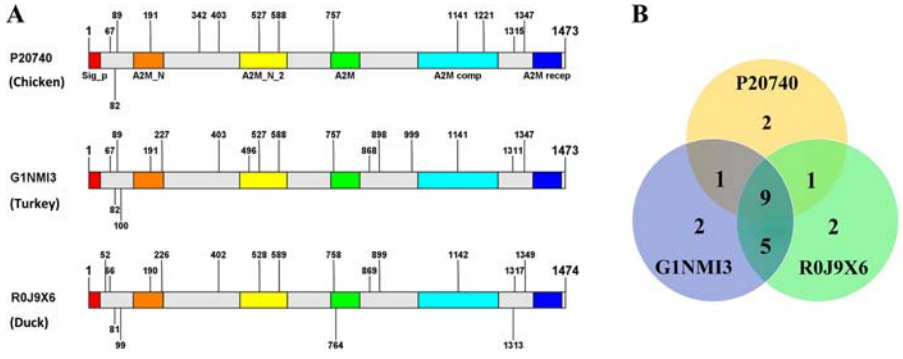

Figure 3. Comparison of OVMG N-glycosylation sites with its homologous proteins: (A) location of N-glycosylation sites on the sequence of OVMGs from chicken (P20740, *Gallus gallus*), turkey (G1NMI3, *Meleagris gallopavo*), and duck (R0J9X6, *Anas platyrhynchos*); (B) Venn diagram illustrating the number of conserved N-glycosylation sites in the three proteins.

For getting higher sequence coverage, deglycosylated OVMG was digested by three different proteases (trypsin, chymotrypsin, and Glu-C), and then digests were subjected to HPLC-ESI MS/MS. The MS/MS data were searched against a local database containing the OVMG FASTA file by the Mascot engine to identify peptides containing deglycosylated asparagines. A total of 439 peptides (Table S1) were found by the following conditions: Mascot ion score >23 ($p < 0.005$) and including PNGase consensus sequence. These peptides contain 12 N-glycosylation sites, among them, only 1 site (N^{1221}) existed in both glycosylated and not glycosylated forms, whereas all other 11 sites were glycosylated (Table 1 and

DOI: 10.1021/acs.jafc.5b02618
J. Agric. Food Chem. 2015, 63, 8209−8215

Figure 2A). Another potential glycosylation site (N^{342}) was not covered in the MS/MS analysis. Two representative MS/MS spectra of the N-glycosylation sites, N^{67} and N^{1221}, are presented in Figure 2, and other spectra of N-glycosylation sites are shown in Figure S2.

Alignment of OVMG N-Glycosylation Sites with Their Homologous Proteins. Glycosylation has an important impact on the folding, structure, and function of protein and results in the diversity of glycoproteins. To understand well the role of glycosylation in the function of a protein, glycosylated sites are indispensable information. The macroglobulin family is ancient and conservative; the BLAST protein sequence of OVMG against the UniProtKB database (http://www.uniprot.org/blast/) showed that the sequence identity between OVMGs from different species of *Aves* is >80%. Two representative bird OVMGs (G1NMI3, from common turkey; and R0J9X6, from duck) were selected, and their sequence, structural domain, and N-glycosylation sites were compared with chicken OVMG (P20740). The results were visualized and are shown in Figure 3. It was observed that the domains of these three proteins are highly conserved (Figure 3A), suggesting that they possess structural similarities. The numbers of predicted N-glycosylation sites of these three proteins are 13 (P20740), 17 (G1NMI3), and 17 (R0J9X6), respectively, and the alignment results revealed that a total of 9 predicted N-glycosylation sites were located at identical positions among all three proteins.

Interestingly, G1NMI3 has a higher sequence identity with P20740, but shares more predicted N-glycosylation sites with R0J9X6 (Figure 3B). To further explore this finding, another seven sequences of OVMGs from birds (*Aves*) were selected, and their predicted N-glycosylation sites were compared with the above three OVMGs. Results showed that total numbers of predicted N-glycosylation sites of the ten OVMGs are between 13 and 17, and chicken OVMG possesses the fewest sites (Table S2). For further analysis, we define a "conserved site" to be the N-glycosylation site that exists in more than six sequences. The alignment results revealed that the total number of conserved N-glycosylation sites of the ten OVMGs is 15. Chicken OVMG (P20740) has 10, common turkey OVMG (G1NMI3) and mallard OVMG (R0J9X6) have 13, and the other seven OVMGs have 14−15 conserved N-glycosylation sites.

The above results showed that chicken OVMG has some differences with other OVMGs with respect to N-glycosylation sites. The fewest total and conserved N-glycosylation sites indicated that chicken OVMG loses some of them, but the reason is not clear yet. Because the sequence identity of the ten OVMGs is >83%, there should be some other reasons besides the genetic factors. Among these ten species, only chicken, turkey, and duck are domesticated. The domestication of chicken began approximately 5400 BCE,[35] much earlier than that of duck (500 BCE) and turkey (300 BCE−100 CE).[36,37] Therefore, the domestication processes might play a certain role in the loss of OVMG N-glycosylation sites. Because most food allergens are glycoproteins, the loss of glycosylation sites may result in reduced food allergenicity. Recently, transcriptome analyses of carrot also suggested the human selection to reduce allergy: compared with wild carrot roots, putative allergen-related protein genes were silenced in cultivated carrot roots.[38] A systematic bioinformatics analysis is needed to confirm whether the loss of N-glycosylation sites is widespread in other domesticated animals and plants. The study of this phenomenon will provide important information for the research of food allergenicity.

The sequence identity between OVMG and mammalian macroglobulin is 39−44%.[17] Comparison of OVMG and human A2MG showed that the cysteine residues are highly conserved between these two proteins. Twenty-four of the total 27 cysteine residues of OVMG are placed at identical positions in the sequence compared with A2MG, suggesting these two proteins share a similar folding pattern and tertiary structure. In contrast, the alignment results revealed that OVMG and A2MG share only three N-glycosylation sites at positions N^{67}, N^{82}, and N^{403}. The few conserved sites implied that the differences between OVMG and A2MG, as reported in the previous research,[28,29,39] might be partly due to their difference in glycosylation sites.

Heterogeneity of OVMG Glycosylation. Glycoproteins usually exist in multiple glycoforms, and the heterogeneity is considered to affect the physical and chemical properties of the protein, immunogenicity, and biology functions. Results of MW of glycan moiety and N-glycosylation sites had revealed the heterogeneity of OVMG glycosylation. Moreover, an intuitive demonstration of the heterogeneity of OVMG was also achieved by 2-DE assay.

After expanding in 2-DE gel, OVMG showed two series of spots around the molecular weight of 170 kDa (Figure 4).

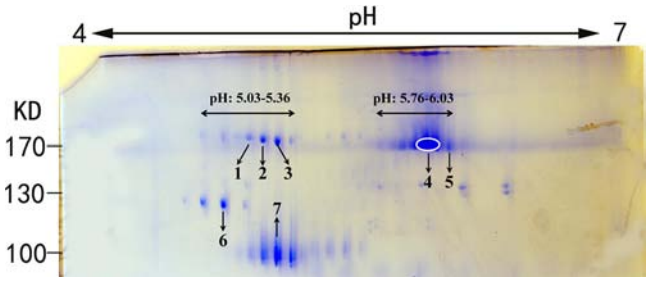

Figure 4. Visual illustration of the heterogeneity of OVMG glycosylation using 2-DE. OVMG was separated by 2-DE using 24 cm (pH 4−7) IEF strips and 10% SDS-PAGE gels. Spots were identified using MALDI-TOF MS/MS. Spots 1−5 and 7 were identified as OVMG; spot 6 was identified as ovalbumin.

Spots 1, 2, and 3 were relatively separate with p*I* values ranging from 5.18 to 5.30; spots 4 and 5 were undivided spots with a train of vertical streaks and p*I* values ranging from 5.90 to 6.05. All five spots were identified as OVMG (gil45382565, ovostatin [*Gallus gallus*]; Table 2). Spot 7, which has a molecular weight of about 100 kDa and a p*I* value range of 5.30, also was identified as OVMG, corresponding to the degradation fragment of OVMG.[28,39] The wide range of p*I* and vertical streaks could be considered as evidence of the heterogeneity of OVMG glycosylation.

The heterogeneity of glycoprotein occurs at glycosylation sites (macroheterogeneity) with variable occupancy of glycosylation sites, and the glycan profile (microheterogeneity) on each site occupied more than one kind of glycan. Combined with the N-glycosylation site results, it was initially speculated that OVMG has a low heterogeneity in N-glycan sites, but a high heterogeneity in glycan profiles.

Interestingly, spot 6, which has a MW of 123.2 kDa and a p*I* of 5.07, was identified as ovalbumin. The MW is approximately 3 times that of normal ovalbumin, indicating that ovalbumin might self-cross-link by non-disulfide covalent bonds. This kind

DOI: 10.1021/acs.jafc.5b02618
J. Agric. Food Chem. 2015, 63, 8209−8215

Table 2. Identification of Protein Spots in 2-DE by MALDI-TOF MS/MS

spot	gi no.	protein name	score	matched peptides/sequence coverage	pI/M_r (kDa) exptl	pI/M_r (kDa) theor
1	gil45382565	ovostatin [*Gallus gallus*][a]	367	10/6%	5.18/178.7	5.64/165.5
2	gil45382565	ovostatin [*Gallus gallus*]	342	15/12%	5.24/176.4	5.64/165.5
3	gil45382565	ovostatin [*Gallus gallus*]	346	13/10%	5.30/174.5	5.64/165.5
4	gil45382565	ovostatin [*Gallus gallus*]	358	9/7%	5.95/175.3	5.64/165.5
5	gil45382565	ovostatin [*Gallus gallus*]	364	16/11%	6.03/170.0	5.64/165.5
6	gil223299	ovalbumin [*Gallus gallus*]	462	11/42%	5.07/123.2	5.20/43.1
7	gil45382565	ovostatin [*Gallus gallus*]	342	18/14%	5.30/100.0	5.64/165.5

[a]Ovomacroglobulin also named "ovostatin".

of ovalbumin covalent aggregate also appeared in the previous comparative proteomic research of egg white proteins,[26] but how they are formed has not been studied yet. A hypothesis is that ovalbumin is oxidized during the purification process or storage, resulting in the covalent cross-linking of ovalbumin.

This study experimentally confirmed the glycosylation of chicken OVMG and reported the N-glycosylation sites for the first time. The data also demonstrated the heterogeneity of OVMG glycosylation. These results will provide valuable information to understand the bioactivity function and identify potential allergenic sites of OVMG. However, to fully characterize the glycosylation of OVMG, the glycan profile and glycopeptide structure should be investigated in the future.

■ ASSOCIATED CONTENT

Supporting Information

The Supporting Information is available free of charge on the ACS Publications website at DOI: 10.1021/acs.jafc.5b02618.

Purity of OVMG and MS/MS spectrum of peptides containing deglycosylated asparagine (PDF)

Mascot results of peptides containing PNGase consensus sequence (XLSX)

Comparison of OVMGs' N-glycosylation sites (XLSX)

■ AUTHOR INFORMATION

Corresponding Author

*(M.M.) Phone: +86-27-87283177. Fax: +86-27-87283177. E-mail: mameihuhn@163.com.

Funding

This research was supported by the Special Fund for Agro-scientific Research in the Public Interest (201303084), the Earmarked Fund for Modern Agro-industry Technology Research System (CARS-41-K23), and the Fundamental Research Funds for the Central Universities (2014PY050).

Notes

The authors declare no competing financial interest.

■ ABBREVIATIONS USED

2-DE, two-dimensional electrophoresis; A2MG, α2-macroglobulin; ACN, acetonitrile; CID, collision-induced decomposition; fwhm, full width at half-maximum; IEF, isoelectric focusing; MW, molecular weight; NMWL, nominal molecular weight limit; PEG, polyethylene glycol; OVMG, ovomacroglobulin

■ REFERENCES

(1) Robinson, D.; Monsey, J. Changes in the composition of ovomucin during liquefaction of thick egg white. *J. Sci. Food Agric.* **1972**, *23*, 29−38.

(2) Kato, A.; Ogino, K.; Kuramoto, Y.; Kobayashi, K. Degradation of the O-glycosidically linked carbohydrate units of ovomucin during egg white thinning. *J. Food Sci.* **1979**, *44*, 1341−1344.

(3) Kato, A.; Sato, Y. The release of carbohydrate rich component from ovomucin gel during storage. *Agric. Biol. Chem.* **1972**, *36*, 831−836.

(4) Kato, A.; Imoto, T.; Yagishita, K. The binding groups in ovomucin-lysozyme interaction. *Agric. Biol. Chem.* **1975**, *39*, 541−544.

(5) Mine, Y.; Yang, M. Recent advances in the understanding of egg allergens: basic, industrial, and clinical perspectives. *J. Agric. Food Chem.* **2008**, *56*, 4874−4900.

(6) Matsuda, T.; Nakamura, R.; Nakashima, I.; Hasegawa, Y.; Shimokata, K. Human IgE antibody to the carbohydrate-containing third domain of chicken ovomucoid. *Biochem. Biophys. Res. Commun.* **1985**, *129*, 505−510.

(7) Rupa, P.; Nakamura, S.; Katayama, S.; Mine, Y. Effects of ovalbumin glycoconjugates on alleviation of orally induced egg allergy in mice via dendritic-cell maturation and T-cell activation. *Mol. Nutr. Food Res.* **2014**, *58*, 405−417.

(8) Rupa, P.; Nakamura, S.; Katayama, S.; Mine, Y. Attenuation of allergic immune response phenotype by mannosylated egg white in orally induced allergy in Balb/c mice. *J. Agric. Food Chem.* **2014**, *62*, 9479−9487.

(9) Shan, Y.; Xu, Q.; Ma, M. Mg^{2+} binding affects the structure and activity of ovomucin. *Int. J. Biol. Macromol.* **2014**, *70*, 230−235.

(10) Robinson, D.; Monsey, J. Studies on the composition of egg-white ovomucin. *Biochem. J.* **1971**, *121*, 537−547.

(11) Offengenden, M.; Fentabil, M. A.; Wu, J. N-glycosylation of ovomucin from hen egg white. *Glycoconjugate J.* **2011**, *28*, 113−123.

(12) Yamashita, K.; Kamerling, J.; Kobata, A. Structural study of the carbohydrate moiety of hen ovomucoid. Occurrence of a series of pentaantennary complex-type asparagine-linked sugar chains. *J. Biol. Chem.* **1982**, *257*, 12809−12814.

(13) Kato, I.; Schrode, J.; Kohr, W. J.; Laskowski, M., Jr Chicken ovomucoid: determination of its amino acid sequence, determination of the trypsin reactive site, and preparation of all three of its domains. *Biochemistry* **1987**, *26*, 193−201.

(14) http://www.uniprot.org/uniprot/P01005.

(15) Stein, P. E.; Leslie, A. G.; Finch, J. T.; Carrell, R. W. Crystal structure of uncleaved ovalbumin at 1· 95 Å resolution. *J. Mol. Biol.* **1991**, *221*, 941−959.

(16) Harvey, D.; Wing, D.; Küster, B.; Wilson, I. Composition of N-linked carbohydrates from ovalbumin and co-purified glycoproteins. *J. Am. Soc. Mass Spectrom.* **2000**, *11*, 564−571.

(17) Nielsen, K. L.; Sottrup-Jensen, L.; Nagase, H.; Thøgersen, H. C.; Etzerodt, M. Amino acid sequence of hen ovomacroglobulin (ovostatin) deduced from cloned cDNA. *Mitochondrial DNA* **1994**, *5*, 111−119.

(18) Mann, K.; Gautron, J.; Nys, Y.; McKee, M. D.; Bajari, T.; Schneider, W. J.; Hincke, M. T. Disulfide-linked heterodimeric clusterin is a component of the chicken eggshell matrix and egg white. *Matrix Biol.* **2003**, *22*, 397−407.

(19) Craig-Barnes, H. A.; Doumouras, B. S.; Palaniyar, N. Surfactant protein D interacts with α2-macroglobulin and increases its innate immune potential. *J. Biol. Chem.* **2010**, *285*, 13461−13470.

DOI: 10.1021/acs.jafc.5b02618
J. Agric. Food Chem. 2015, 63, 8209−8215

(20) http://www.uniprot.org/uniprot/P20740.
(21) Geng, F.; Huang, X.; Yan, N.; Jia, L.; Ma, M. Purification of hen egg white ovomacroglobulin using one-step chromatography. *J. Sep. Sci.* **2013**, *36*, 3717−3722.
(22) Signor, L.; Erba, E. B. Matrix-assisted laser desorption/ionization time of flight (MALDI-TOF) mass spectrometric analysis of intact proteins larger than 100 kDa. *J. Visualized Exp.* **2013**, *79*, 50635.
(23) Jiang, K.; Wang, C. J.; Sun, Y. J.; Liu, Y.; Zhang, Y.; Huang, L. J.; Wang, Z. F. Comparison of chicken and pheasant ovotransferrin N-glycoforms via electrospray ionization mass spectrometry and liquid chromatography coupled with mass spectrometry. *J. Agric. Food Chem.* **2014**, *62*, 7245−7254.
(24) Melo-Braga, M. N.; Verano-Braga, T.; León, I. R.; Antonacci, D.; Nogueira, F. C.; Thelen, J. J.; Larsen, M. R.; Palmisano, G. Modulation of protein phosphorylation, N-glycosylation and Lys-acetylation in grape (*Vitis vinifera*) mesocarp and exocarp owing to *Lobesia botrana* infection. *Mol. Cell. Proteomics* **2012**, *11*, 945−956.
(25) Qiu, N.; Ma, M.; Cai, Z.; Jin, Y.; Huang, X.; Huang, Q.; Sun, S. Proteomic analysis of egg white proteins during the early phase of embryonic development. *J. Proteomics* **2012**, *75*, 1895−1905.
(26) Qiu, N.; Ma, M.; Zhao, L.; Liu, W.; Li, Y.; Mine, Y. Comparative proteomic analysis of egg white proteins under various storage temperatures. *J. Agric. Food Chem.* **2012**, *60*, 7746−7753.
(27) Liu, W.; Xie, Y.; Ma, J.; Luo, X.; Nie, P.; Zuo, Z.; Lahrmann, U.; Zhao, Q.; Zheng, Y.; Zhao, Y. IBS: an illustrator for the presentation and visualization of biological sequences. *Bioinformatics* **2015**, btv362.
(28) Kitamoto, T.; Nakashima, M.; Atsushi, I. Hen egg white ovomacroglobulin has a protease inhibitory activity. *J. Biochem.* **1982**, *92*, 1679−1682.
(29) Nagase, H.; Harris, E.; Woessner, J.; Brew, K. Ovostatin: a novel proteinase inhibitor from chicken egg white. I. Purification, physicochemical properties, and tissue distribution of ovostatin. *J. Biol. Chem.* **1983**, *258*, 7481−7489.
(30) Saxena, I.; Tayyab, S. Protein proteinase inhibitors from avian egg whites. *Cell. Mol. Life Sci.* **1997**, *53*, 13−23.
(31) Kitamoto, T.; Nakashima, M.; Ikai, A. Hen egg-white ovomacroglobulin has a protease inhibitory activity. *J. Biochem.* **1982**, *92*, 1679−1682.
(32) Nagase, H.; Harris, E. D.; Woessner, J. F.; Brew, K. Ovostatin − a novel proteinase-inhibitor from chicken egg-white. 1. Purification, physicochemical properties, and tissue distribution of ovostatin. *J. Biol. Chem.* **1983**, *258*, 7481−7489.
(33) Mine, Y.; D'Silva, I. Bioactive components in egg white. In *Egg Bioscience and Biotechnology*; Mine, Y. Ed.; Wiley: Hoboken, NJ, USA, 2008; pp 141−184.
(34) Al-Ghouleh, A.; Johal, R.; Sharquie, I. K.; Emara, M.; Harrington, H.; Shakib, F.; Ghaemmaghami, A. M. The glycosylation pattern of common allergens: the recognition and uptake of Der p 1 by epithelial and dendritic cells is carbohydrate dependent. *PLoS One* **2012**, *7*, e33929.
(35) Underhill, A. P. Current issues in Chinese neolithic archaeology. *J. World Prehistory* **1997**, *11*, 103−160.
(36) Larson, G.; Fuller, D. Q. The evolution of animal domestication. *Annu. Rev. Ecol., Evol., Systematics* **2014**, *45*, 115−136.
(37) Thornton, E. K.; Emery, K. F.; Steadman, D. W.; Speller, C.; Matheny, R.; Yang, D. Earliest Mexican turkeys (*Meleagris gallopavo*) in the Maya region: implications for pre-hispanic animal trade and the timing of Turkey domestication. *PLoS One* **2012**, *7*, e42630.
(38) Rong, J.; Lammers, Y.; Strasburg, J. L.; Schidlo, N. S.; Ariyurek, Y.; de Jong, T. J.; Klinkhamer, P. G.; Smulders, M. J.; Vrieling, K. New insights into domestication of carrot from root transcriptome analyses. *BMC Genomics* **2014**, *15*, 895.
(39) Nagase, H.; Harris, E. Ovostatin: a novel proteinase inhibitor from chicken egg white. II. Mechanism of inhibition studied with collagenase and thermolysin. *J. Biol. Chem.* **1983**, *258*, 7490−7498.

DOI: 10.1021/acs.jafc.5b02618
J. Agric. Food Chem. 2015, 63, 8209−8215

emerging elicitation technology has been applied to generate fruits, vegetables, and herbs enriched with valuable phytochemicals either for fresh consumption or as a source for functional foods and nutraceuticals, causing the increased ingestion of these health-beneficial substances.[22−26] Additionally, UV radiation is a promising and clean elicitation approach that does not taint the production system and that, moreover, can be easily manipulated. Therefore, an interesting possibility is to exploit UV radiation for enhancing isoflavonoid accumulation in AMHRCs. This can satisfy consumer demand for these naturally derived health-promoting products.

The main objective of this work was to improve isoflavonoid production in AMHRCs through UV (UV-A, UV-B, and UV-C) elicitation and to obtain extracts with higher antioxidant activity for possible use in ther food, nutraceutical, pharmaceutic, and cosmetic industries. Moreover, the transcriptional expressions of genes involved in isoflavonoid biosynthetic pathway were examined to shed light on the molecular changes that took place in the elicited AMHRCs and the possible bottlenecks that controlled isoflavonoid biosynthesis. To the best of our knowledge, no information about the effect of UV elicitation on isoflavonoid accumulation, biosynthetic gene expression, and antioxidant activity in AMHRCs is currently available.

MATERIALS AND METHODS

Plant Materials and Reagents. All experiments were conducted with a highly productive *A. membranaceus* hairy root line II (AMHRL II) established previously by our laboratory.[4] Stock cultures of AMHRL II were maintained on Murashige and Skoog (MS)-based solid medium supplemented with 30 g/L sucrose and 1 g/L casein hydrolysate but without NH_4NO_3, at 25 ± 1 °C in the dark. Standard compounds including CAG, ON, ASG, CA, and FO were purchased from Weikeqi Biological Technology Co. Ltd. (Sichuan province, China). MiniBEST Plant RNA Extraction Kit, PrimeScript RT Reagent Kit, and SYBR Premix Ex *Taq*II Kit were provided by TaKaRa (Dalian, China). Ascorbic acid (VC), 2,2-diphenyl-1-picrylhydrazyl-hydrate (DPPH), linoleic acid, butylated hydroxytoluene (BHT), and β-carotene were obtained from Sigma-Aldrich Co. (Steinheim, Germany). Lamps (40 W) of UV-A, UV-B, and UV-C were bought from Beijing Institute of Electric Light Source (Beijing, China). Other reagents of either analytical or optical grade were purchased from Beijing Chemical Reagents Co. (Beijing, China).

UV Elicitation Treatments to AMHRCs. After AMHRCs were cultured under the optimal conditions described previously,[4] the spent media were then renewed. The distance of UV lamps from AMHRCs was adjusted to obtain a low intensity (3 W/m^2) monitored by a DRC-100X photometer (Spectronics, Westbury, NY, USA). The UV elicitation dose (typically in kJ/m^2) was calculated as 3 W/m^2 multiplied by the irradiation time. During elicitation experiments, cultures were divided into four groups: one being used as control at 28 ± 1 °C in the dark and the others being irradiated by UV-A (λ_{max} = 365 nm), UV-B (λ_{max} = 313 nm), and UV-C (λ_{max} = 254 nm) at 28 ± 1 °C for 4 h, that is, 43.2 kJ/m^2, respectively. Moreover, AMHRCs were harvested under a series of UV-B doses (0, 5.4, 10.8, 21.6, 43.2, 64.8, 75.6, 86.4, 97.2, 129.6, and 172.8, kJ/m^2) that were calculated as 3 W/m^2 multiplied by different exposure durations (0, 0.5, 1, 2, 4, 6, 7, 8, 9, 12, and 16, h). After elicitation treatments, parts of UV-elicited and control root samples were placed into aluminum foil packets, frozen immediately with liquid nitrogen, and stored at −80 °C for further RNA isolation. The remaining root samples were rinsed with tap and distilled water, dry-blotted on filter paper, and dried in a vacuum oven at 50 °C to a constant dry weight (DW) for liquid−solid extraction of isoflavonoids. Meanwhile, the medium samples were also collected for liquid−liquid extraction of isoflavonoids.

RNA Isolation and cDNA Preparation. Total RNA was isolated from frozen hairy roots (250 mg, fresh weight) using a MiniBEST Plant RNA Extraction Kit (TaKaRa) in accordance with the manufacturer's protocols. The quality and quantity of RNA were assessed by agarose gel electrophoresis and determined by a GeneQuant II RNA/DNA calculator (Pharmacia Biotech, Cambridge, UK), respectively. Subsequently, total RNA (500 ng) was reverse-transcribed to cDNA using a PrimeScript RT reagent Kit (TaKaRa) following the manufacturer's instructions. Finally, the synthesized cDNA (20 μL) was diluted to 200 μL with sterile water and used as the template for the subsequent molecular experiments.

Quantitative Real-Time PCR Analysis. Quantitative real-time PCR (qRT-PCR) was performed with a Stratagene Mx3000P Real-Time PCR system (Agilent Technologies, Santa Clara, CA, USA). Specific primers for genes (Table 1) involved in isoflavonoid biosynthetic pathway were designed as suggested previously.[27] The reaction solution (20 μL) for qRT-PCR assay contained 10 μL of SYBR Premix Ex *Taq*II (TaKaRa), 0.8 μL of each specific primer (10 μM), 2 μL of the above cDNA template, and 6.4 μL of sterile water. The amplification procedure for all investigated genes was set as follows: initial denaturation at 95 °C for 3 min, followed by 40 cycles of denaturation at 95 °C for 15 s, annealing at 55 °C for 30 s, and extension at 72 °C for 20 s. The relative expression level of each gene

Table 1. Primers for Associated Genes Involved in Isoflavonoid Biosynthetic Pathway

gene name	primer sequence (5′ to 3′)	product size (bp)
PAL	forward: CATCAAATCTCTCTGGCAGTAGGAA reverse: AGTTCACATCTTGGTTATGCTGCTC	147
C4H	forward: AACAAAGTGAGGGATGAAATTGACA reverse: GGATTGCCATTCTTAGCCTTAGTGT	127
4CL	forward: TGTCCCTCCTATTGTTTTGGCTATT reverse: CTTTGGGGAATTTAGCTCTGACAGT	140
CHS	forward: CCTTCTTTGGATGCTAGACAAGACA reverse: CGAAGACCCAAGAGTTTGGTTAGTT	188
CHR	forward: AAACAAGGTTACAGGCATTTTGACA reverse: GGAAGAACGAGATGAGGATGATTTT	164
CHI	forward: ATCGAGTTTTTCCACCAGGATCTAC reverse: ATCATAGTCTCCAACACAGCCTCAG	154
IFS	forward: CCTTCACCTATTGGACAAACCTCTT reverse: CCTGGTATTAAAGGAAGAAGCCTCA	172
I3′H	forward: GGATGTTAAAGAAGCGAAGCAATTT reverse: ATCAAACAATCTCAACAAAGGCAAA	106
18S	forward: TGCAGAATCCCGTGAACCATC reverse: AGGCATCGGGCAACGATATG	104

DOI: 10.1021/acs.jafc.5b03138
J. Agric. Food Chem. 2015, 63, 8216−8224

was calculated using the *18S* gene as the internal reference. Results were analyzed by Mxpro-Mx3000P software according to the delta CT method.[28]

Isoflavonoid Extraction and LC-MS/MS Analysis. The complete extraction of isoflavonoids from root samples was performed as described previously.[4] To extract isoflavonoids from liquid media, samples were partitioned twice with ethyl acetate in a separatory funnel. The organic phases were combined and then evaporated to dryness at 45 °C using a rotary evaporator. All extracts obtained from both root and medium samples were redissolved in 25 mL of methanol (HPLC grade) and then filtered through a 0.45 μm membrane for LC-MS/MS analysis.

An Agilent 1100 series HPLC (Agilent Technologies, San Jose, CA, USA) coupled to an API 3000 triple tandem quadrupole MS (Applied Biosystems, Concord, ON, Canada) with a Phenomenex Gemini C18 110A reversed-phase column (250 mm × 4.6 mm i.d., 5 μm) was used for the determination of five target isoflavonoids. According to our previous research,[4] the mass spectra of selected reaction monitoring at m/z 445.2 → 283.0, 428.8 → 266.9, 463.2 → 301.1, 283.0 → 268.0, and 267.0 → 252.0 were chosen for the identification and quantification of CAG, ON, ASG, CA, and FO, respectively. The content of each target compound was calculated by the calibration curve and reported as micrograms per gram based on the DW of roots.

Determination of Antioxidant Activities. Antiradical activities and antilipid peroxidation capacities of extracts from AMHRCs were respectively determined by DPPH radical-scavenging assay and β-carotene/linoleic acid bleaching test.[4] Antioxidant properties of samples were expressed as IC_{50} values, which were calculated through the logarithmic regression curves for DPPH radical scavenging ratio (%) or β-carotene bleaching inhibition percentages (%) versus sample concentration (mg/mL). The higher antioxidant activity was corresponding to the lower IC_{50} value. Activities of antioxidant enzymes including superoxide dismutases (SOD, EC 1.15.1.1), catalase (CAT, EC 1.11.1.6), ascorbate peroxidase (APX, EC 1.11.1.11), and glutathione reductase (GR, EC 1.6.4.2) were determined according to the previously reported methods.[29]

Statistical Analysis. All experiments were conducted three times. Results were expressed as means ± standard deviations. The data were statistically analyzed using the SPSS statistical software (version 17.0, SPSS Inc., Chicago, IL, USA). Differences between means were determined by analysis of variance with Tukey's test on the level of significance declared at $P < 0.05$.

RESULTS

Effect of Different Types of UV radiation on Isoflavonoid Accumulation. Under the optimal culture conditions described previously,[4] 34-day-old AMHRCs are capable of achieving the maximum isoflavonoid accumulation and biomass production. Therefore, 34-day-old AMHRCs adopted in this work were elicited by UV radiation for further enhancing isoflavonoid biosynthesis without affecting biomass productivity. Nevertheless, whether UV elicitation can promote isoflavonoid biosynthesis in AMHRCs was still unknown. Accordingly, 34-day-old AMHRCs were individually exposed to UV-A, UV-B, and UV-C at a fixed radiation dose (43.2 kJ/m^2) to assess their effects on the yield of total target isoflavonoids (sum amount of CAG, ON, ASG, CA, and FO). As shown in Figure 1, the elicitation treatment regardless of UV type increased isoflavonoid yields in the range of 362.15−443.04 μg/g DW relative to the control (231.88 μg/g DW). The results demonstrated that UV elicitation was indeed beneficial for promoting isoflavonoid (usually acting as phytoalexins/phytoanticipins) accumulation in AMHRCs as a consequence of countering unfavorable environmental stresses. Moreover, the isoflavonoid yield decreased in the order UV-B (443.04 ± 15.38 μg/g DW) > UV-C (417.66 ± 8.16 μg/g DW) > UV-A

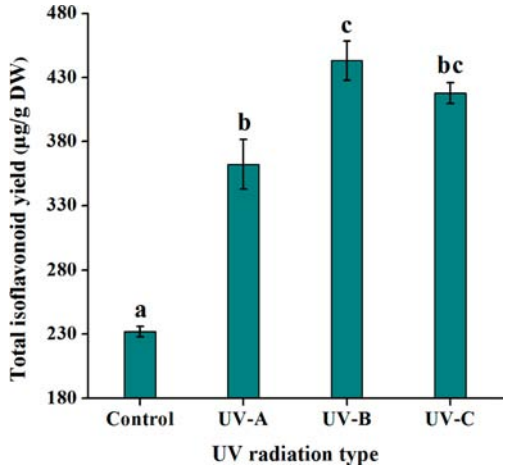

Figure 1. Effects of UV-A, UV-B, and UV-C treatments (43.2 kJ/m^2, i.e., 4 h) on the yield of total target isoflavonoids in 34-day-old AMHRCs. Control: nontreated AMHRCs. Mean ± SD values not sharing the same lower case letters are significantly different ($P < 0.05$).

(362.15 ± 19.42 μg/g DW). Overall, UV-B was screened as the best elicitor that was adopted for the subsequent experiments.

Effect of Elicitation Dose of UV-B on Isoflavonoid Accumulation. The effect of an elicitor on the yield of secondary metabolites for a specific plant in vitro culture primarily depends on the elicitation dose.[9,14−16] Thus, it is of great necessity to investigate the effects of different UV-B radiation doses on the yield of total target isoflavonoids in 34-day-old AMHRCs. As exhibited in Figure 2A, it is obviously demonstrated that the mild-dose UV-B radiation (86.4 kJ/m^2) was the most favorable for isoflavonoid accumulation. The decrease of isoflavonoid amount under high-dose UV-B treatments (97.2−129.8 kJ/m^2) might be associated with the irreversible damage of cellular macromolecules such as proteins, nucleic acids, and lipids due to the absorption of the energy-rich radiation.[20,30] Additionally, it is worth mentioning that UV-B-elicited AMHRCs (Figure 2C) showed a significant indication of stress (browning color in root tissues) in comparison with the corresponding control cultures (Figure 2B).

Isoflavonoid Profiles in Response to UV-B Elicitation. Isoflavonoid profiles in AMHRCs treated by different UV-B radiation doses are presented in Table 2. Under the optimal elicitation dose (86.4 kJ/m^2), UV-B-treated AMHRCs were capable of yielding 533.54 ± 13.61 μg/g DW of total isoflavonoids, which was 2.29-fold higher as against that of control (232.93 ± 3.08 μg/g DW). In detail, the contents of CAG, ON, ASG, CA, and FO in the elicited AMHRCs were 14.57 ± 0.87, 5.83 ± 0.46, 119.59 ± 6.72, 225.01 ± 8.28, and 168.54 ± 5.36 μg/g DW, respectively, which were correspondingly 1.61-, 1.42-, 1.87-, 2.35-, and 2.90-fold higher as compared to those in the control (9.06 ± 0.13 μg/g DW CAG, 4.12 ± 0.19 μg/g DW ON, 64.95 ± 3.77 μg/g ASG, 95.64 ± 2.80 μg/g CA, and 59.16 ± 1.65 μg/g DW FO). These differences could be appreciated by comparing the LC-MS/MS chromatograms of extracts from different treated AMHRCs (Figure 3).

Putative Isoflavonoid Biosynthetic Pathway. To elucidate the transcriptional regulation of isoflavonoid biosynthesis upon UV-B elicitation, a better understanding of the isoflavonoid biosynthetic pathway is essential. On the basis of current ideas,[17,27,31,32] a putative biosynthetic scheme of target

DOI: 10.1021/acs.jafc.5b03138
J. Agric. Food Chem. 2015, 63, 8216−8224

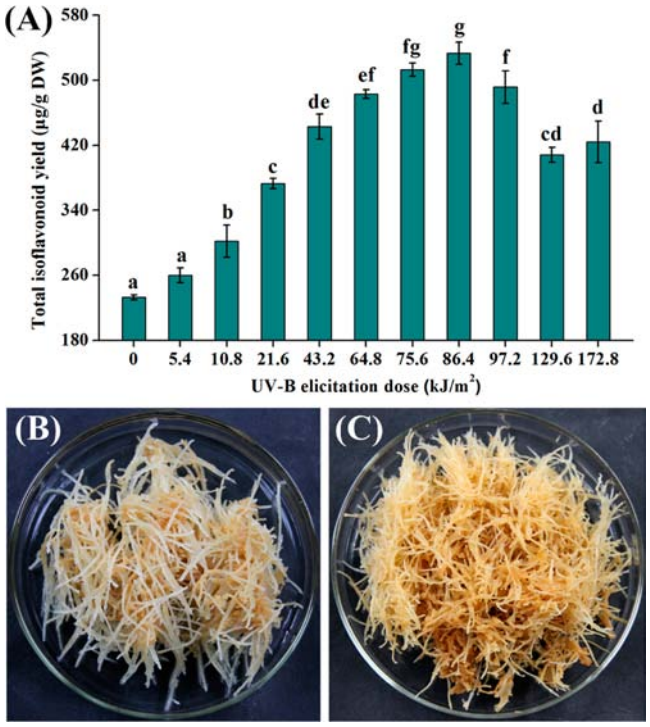

Figure 2. (A) Effects of different UV-B elicitation doses (0, 5.4, 10.8, 21.6, 43.2, 64.8, 75.6, 86.4, 97.2, 129.6, and 172.8 kJ/m^2, i.e., 0, 0.5, 1, 2, 4, 6, 7, 8, 9, 12, and 16, h) on the yield of total target isoflavonoids in 34-day-old AMHRCs. Phenotypes of (B) control and (C) UV-B-treated AMHRCs. Control, nontreated AMHRCs. Mean ± SD values not sharing the same lower case letters are significantly different (P < 0.05).

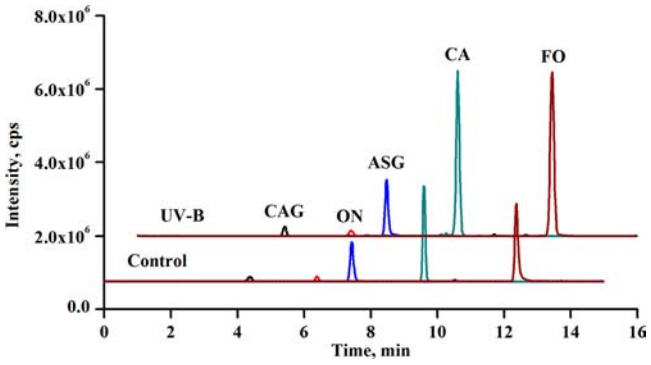

Figure 3. Representative LC-MS/MS with SRM total ion chromatograms of extracts form control and UV-B-treated AMHRCs. Control, nontreated AMHRCs.

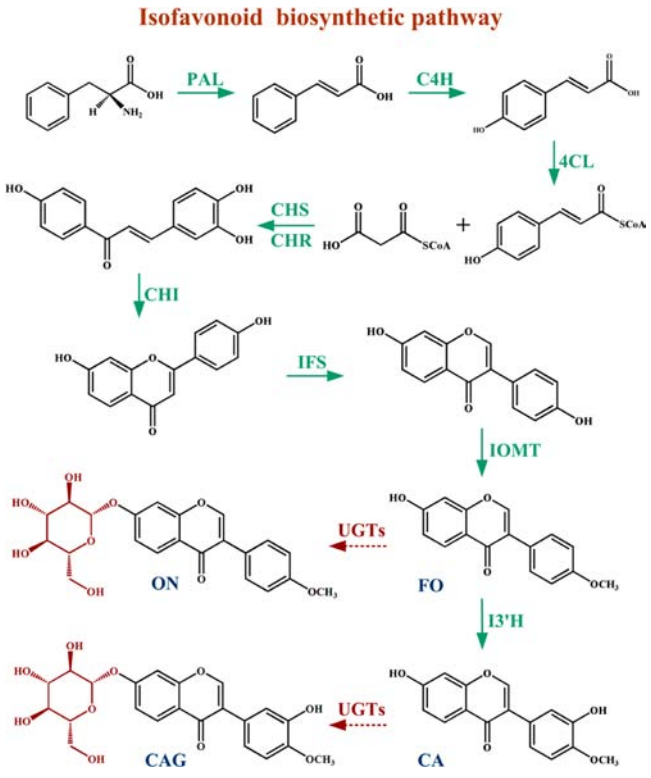

Figure 4. Putative isoflavonoid biosynthetic pathway in *A. membranaceus*.

isoflavonoids is proposed in this study (Figure 4). Overall, the pathway consists of 10 metabolic steps, beginning with phenylalanine ammonia-lyase (PAL) that catalyzes the deamination of phenylalanine into cinnamic acid. Consecutively, cinnamate-4-hydroxylase (C4H) catalyzes the hydroxylation of cinnamic acid into *p*-coumaric acid. Afterward, 4-coumarate coenzyme A ligase (4CL) catalyzes the conversion of *p*-coumarate into its CoA ester. Subsequently, chalcone synthase (CHS) and chalcone reductase (CHR) co-catalyze the condensation of *p*-coumaryl CoA with three malonyl-CoA molecules toward the formation of an isoflavonoid skeleton, isoliquritigenin, which can be further converted into liquiritigenin with the catalysis of chalcone isomerase (CHI). After

Table 2. Isoflavonoid Profiles in AMHRCs Treated by Different UV-B Radiation Doses

	contents of five target isoflavonoids in UV-B-treated AMHRCs (μg/g DW)				
dose (kJ/m^2)	CAG	ON	ASG	CA	FO
0	9.06 ± 0.13	4.12 ± 0.19	64.95 ± 3.77	95.64 ± 2.80	59.16 ± 1.65
5.4	9.38 ± 0.22	4.07 ± 0.09	70.99 ± 4.15	107.28 ± 6.96	68.16 ± 3.74
10.8	9.55 ± 0.08	4.16 ± 0.11	74.03 ± 6.81	134.90 ± 12.31	79.57 ± 9.05
21.6	10.82 ± 0.18	4.86 ± 0.15	85.25 ± 3.47	168.39 ± 5.76	103.57 ± 4.82
43.2	12.54 ± 0.59	5.20 ± 0.37	97.91 ± 5.55	194.42 ± 15.08	132.97 ± 8.69
64.8	13.39 ± 0.62	5.14 ± 0.12	105.77 ± 7.40	201.70 ± 6.49	157.28 ± 3.46
75.6	14.11 ± 0.75	5.55 ± 0.39	112.75 ± 8.18	214.27 ± 6.05	166.39 ± 6.25
86.4	14.57 ± 0.87	5.83 ± 0.46	119.59 ± 6.72	225.01 ± 8.28	168.54 ± 5.36
97.2	14.61 ± 0.49	5.64 ± 0.28	109.51 ± 9.33	207.36 ± 14.56	154.73 ± 8.28
129.6	10.33 ± 0.69	4.90 ± 0.35	88.63 ± 6.54	178.79 ± 8.73	125.61 ± 6.33
172.8	9.65 ± 0.43	4.25 ± 0.12	84.45 ± 8.45	186.53 ± 17.62	139.24 ± 15.70

DOI: 10.1021/acs.jafc.5b03138
J. Agric. Food Chem. 2015, 63, 8216−8224

that, liquiritigenin is catalyzed by isoflavone synthase (IFS) to form daidzein, which is then converted into FO under the catalytic action of isoflavone *O*-methyltransferase (IOMT). The subsequent hydroxylation at the 3′-position of the B-ring in FO leads to the formation of CA through the catalysis of isoflavone 3′-hydroxylase (I3′H). Eventually, FO and CA are transformed into their glycosides (ON and CAG) via the catalysis of uridine diphosphate-dependent glycosyltransferases (UGTs). Due to the large enzyme families with significant functional diversity, the last glycosylation steps remain to be identified.

Biosynthetic Gene Expressions in Response to UV-B Elicitation. With the aim of clarifying the molecular mechanism underlying isoflavonoid enhancement in the presence of UV-B elicitation, the transcriptional profiles of isoflavonoid biosynthetic genes (*PAL*, *C4H*, *4CL*, *CHS*, *CHR*, *CHI*, *IFS*, and *I3′H*; Figure 4) were determined by qRT-PCR. In this study, samples from UV-B-treated AMHRCs were taken for analysis at three different elicitation doses (43.2, 86.4, and 129.6, kJ/m^2). Gene expression levels were normalized using the reference *18S* gene as internal standard, and the transcripts of all related genes in control were set as 1.

As presented in Figure 5, the expression levels of all investigated genes were significantly promoted following UV-B elicitation, which suggested that the enhanced isoflavonoid accumulation was a result of the improved expressions of these

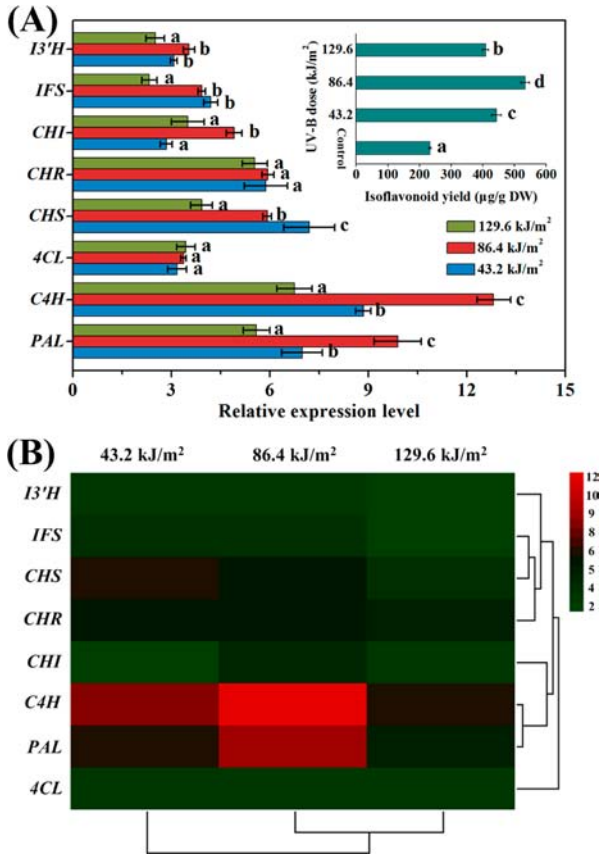

Figure 5. (A) Total isoflavonoid yields and transcriptional levels of isoflavonoid biosynthetic genes in 34-day-old AMHRCs exposed to three different UV-B elicitation doses (43.2, 86.4, and 129.6, kJ/m^2, i.e., 4, 8, and 12 h). (B) Hierarchical analyses of gene expressions in samples. Control, nontreated AMHRCs. Mean ± SD values not sharing the same lower case letters are significantly different (P < 0.05).

biosynthetic genes. Interestingly, not all genes displayed the highest expression levels at the optimal elicitation dose (86.4 kJ/m^2) where isoflavonoid amount was the maximum. The transcriptional levels of *PAL*, *C4H*, *CHI*, and *I3′H* genes were observed to be gradually stimulated and reached their individual peak values at 86.4 kJ/m^2, with expression levels of 9.90-, 12.83-, 4.92-, and 3.54-fold higher as against control, respectively. However, the maximum transcriptional levels of *4CL*, *CHS*, *CHR*, and *IFS* genes were not observed at the optimal elicitation dose necessary for the highest isoflavonoid yield. The expression levels of *CHS* and *IFS* genes were highest at 43.2 kJ/m^2, where they were 7.20- and 4.25-fold higher as compared to control, respectively, but decreased gradually afterward. Moreover, the transcriptional profiles of *4CL* and *CHR* genes had no significant changes during the elicitation period and remained approximately 3- and 6-fold higher relative to control, respectively.

Antioxidant Activities in Response to UV-B Elicitation. As shown in Figure 6, activities of antioxidant enzymes

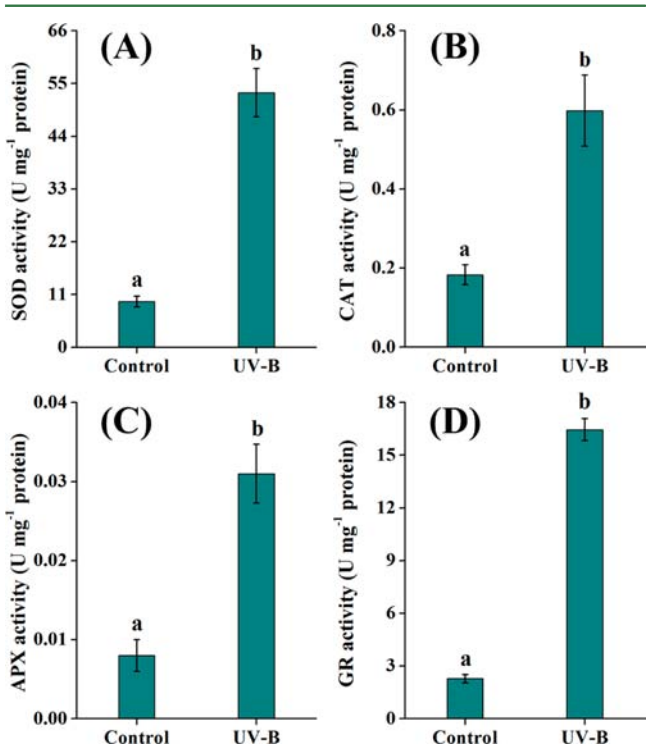

Figure 6. Activities of antioxidant enzymes including (A) SOD, (B) CAT, (C) APX, and (D) GR in control and UV-B-treated AMHRCs. Control, nontreated AMHRCs.

including SOD, CAT, APX, and GR in UV-B-treated AMHRCs were significantly higher than those in control, indicating that antioxidant enzymes were indeed activated to protect AMHRCs from UV-B damage. With the purpose of studying the antioxidant response of AMHRCs to UV-B elicitation and investigating if a correlation exists with the levels of isoflavonoids in extracts, DPPH radical-scavenging assay and *β*-carotene/linoleic acid bleaching test were respectively applied to determine antiradical activities and antilipid peroxidation capacities of extracts from differently treated AMHRCs. Obviously, the observations with extracts from both control and UV-B-elicited AMHRCs exhibited dose-dependent relationships in antioxidant properties (Figure 7). As expected from the quantified levels of isoflavonoids, the UV-B-treated samples

DOI: 10.1021/acs.jafc.5b03138
J. Agric. Food Chem. 2015, 63, 8216−8224

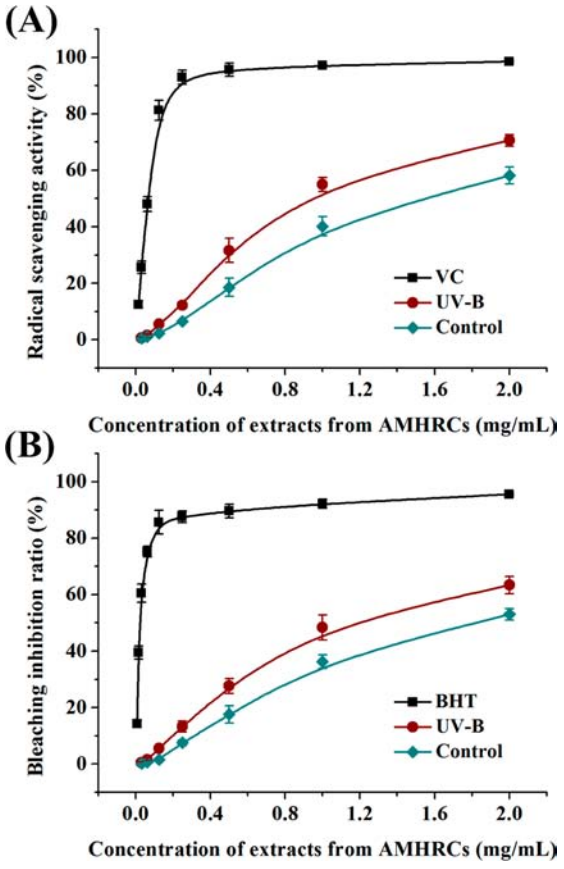

Figure 7. Antioxidant activities of extracts from control and UV-B-treated AMHRCs as assessed by (A) DPPH radical scavenging assay and (B) β-carotene/linoleic acid bleaching test. Control, nontreated AMHRCs. *X* axis, concentration of extracts from AMHRCs (mg/mL); *Y* axis, antioxidant activities (inhibition percentage/ratio, %) in DPPH radical scavenging assay and β-carotene/linoleic acid bleaching test.

showed much higher antioxidant efficacies in terms of antiradical (IC_{50} value of 0.85 mg/mL) and lipid peroxidation inhibition (IC_{50} value of 1.08 mg/mL), as compared to the corresponding values of control samples (1.38 and 1.71 mg/mL).

DISCUSSION

It is well documented that three classes of UV radiation (UV-A, UV-B, and UV-C) are important regulators of plant's secondary metabolism, triggering the biosynthesis of various phytochemicals (e.g., phenolic compounds, alkaloids, terpenes, carotenoids, and glucosinolates) that can play an important role in a plant's defense systems.[19−21] Obviously, the three types of UV radiation exhibited distinct influences on isoflavonoid yield in AMHRCs (Figure 1). Due to the various wavelengths of UV-A, UV-B, and UV-C, the perceptions of diverse UV photons and the subsequent signal transductions in plant cells are different.[33,34] The consequence of a given radiation dose of UV-A, UV-B, and UV-C can result in different damaging effects on DNA, proteins, lipids, and membranes and/or physiological processes of plant cells, which can induce diverse influences on a plant's secondary metabolism,[23,24,35,36] thus promoting the synthesis of distinct levels of isofavonoids to protect AMHRCs from UV damage. In this work, UV-B offering the highest isoflavonoid yield was adopted as the appropriate elicitor.

Generally, plant tissues exposed to an elicitor (or stressor) can cause reversible and elastic "eustress" (an activating, temporal, and constructive elicitation/stress through predisposing plant cells/organs to a state of low alert via stimuli-specific signaling pathways that leads to the activation of defense secondary metabolisms), and once the exposure exceeds a tolerance-limit dose, an irreversible and plastic "distress" (a strong elicitation/stress event under severely unfavorable environment conditions that results in metabolic damage or, in extreme cases, the death of plant cells/organs) takes place.[30,37] In this work, the appropriate UV-B exposure dose (86.4 kJ/m^2) could realize the balance between "eustress" and "distress" for maximally inducing isoflavonoid accumulation in AMHRCs (Figure 2A).

UV-B radiation has been extensively demonstrated to cause multiple cellular injuries in plants than can activate various signaling pathways involving nonspecific DNA damage, reactive oxygen species (ROS), wound/defense signaling, and specific photomorphogenic signaling.[20,38] It is evident that the existence of these signaling pathways can contribute to stimulating the expression of genes involved in the biosynthesis of various secondary metabolites.[19−24,26] Molecular studies were able to clarify the transcriptional expressions of genes involved in isoflavonoid biosynthetic pathway in response to UV-B elicitation. This could be helpful in discovering and exploring those genes which were the possible bottlenecks that controlled isoflavonoid biosynthesis and provide useful information for isoflavonoid production via engineering manipulation in the future.

It is reported that the promoters of a series of genes involved in flavonoid biosynthetic pathway contain a specially recognized domain that can interact with MYB family transcriptional factors with light-responsive elements.[23,24,39,40] As inferred, these transcriptional factors could be activated by UV-B radiation, thus leading to the transcriptional activation of all investigated isoflavonoid biosynthetic genes in this work (Figure 5). Additionally, a positive correlation was observed between the expression profiles of *PAL*, *C4H*, *CHI*, and *I3′H* genes and the accumulation patterns of isoflavonoids (Figure 5A), which indicated that the boosted isoflavonoid biosynthesis in AMHRCs might be activated by the simultaneous up-regulation of these genes following UV-B elicitation. Moreover, *PAL* and *C4H* genes exhibited significantly higher expression levels than those of other genes (Figure 5B). These results suggested that *PAL* and *C4H* genes might be more sensitive and critical than other genes for isoflavonoid biosynthesis in UV-B-elicited AMHRCs. Factually, the promoter of *PAL* gene contains similar light-responsive elements with G-box sequence, which can significantly up-regulate the expression of *PAL* gene in response to UV induction.[23,24] Generally, *PAL* and *C4H* genes have been proposed as two dominant control points of phenylpropanoid, flavonoid, and isoflavonoid biosynthesis in response to various biotic and abiotic stresses, inclusive of pathogen attack, UV radiation, and mechanical wounding.[22,31,41−44] Moreover, *PAL* and *C4H* encoding enzymes are thought to be physically associated with each other in organized multienzyme complexes exhibiting coordinated expression.[41] Similarly, *PAL* (a smart gene switch) and *C4H* genes play a key role in controlling the accumulation of CAG and CA in *A. membranaceus* plants during low-temperature treatment.[32] Cumulatively, the results of this study confirmed that *PAL* and *C4H* genes were crucial regulatory points controlling

DOI: 10.1021/acs.jafc.5b03138
J. Agric. Food Chem. 2015, 63, 8216−8224

isoflavonoid biosynthesis in AMHRCs responsive to UV-B elicitation.

Factually, plants exposed to UV-B stress can greatly enhance the generation of ROS, resulting in an oxidative disturbance (i.e., imbalances between ROS production and antioxidant scavenging capacity).[20,30] Generally, plants utilize antioxidant enzymes as representing the first line of defense against ROS overproduction, preventing oxidative damage of cell membrane systems, nucleic acids, lipids, and proteins, and maintaining the stability of their functions.[45,46] In the present study, the activities of antioxidant enzymes (SOD, CAT, APX, and GR) in AMHRCs were significantly stimulated by UV-B radiation (Figure 6). However, the action of antioxidant enzymes needs to be complemented by that of nonenzymatic ROS scavenging systems in plants suffering from stress conditions.[45] Flavonoids have been proposed as constituting a secondary antioxidant system that is activated as a consequence of the depletion of antioxidant enzyme activity.[45−47] Moreover, there is a growing body of evidence that flavonoids can screen harmful UV-B radiation and especially scavenge ROS formed under stressful conditions, thus protecting plant cells from oxidative damages.[48,49]

In this study, the significantly induced isoflavonoids (2.29-fold higher than control) might actively balance the cell redox status of AMHRCs under UV-B-mediated oxidative stress through their antioxidant and free radical scavenging abilities. In addition, the intake of isoflavonoids is vitally important for human health (e.g., prevention of cancer, inflammation, and cardiovascular and age-related diseases), which is believed to be related to their antioxidant activities.[2,4,50] Currently, natural products containing isoflavonoids are of great interest in the food, cosmetic, and pharmaceutical fields for their possible use as antioxidant additives to replace toxic synthetic ones.[51,52] From this point of view, the isoflavonoid enhancement driven by UV-B possesses benefits for both ends of the biobased food chain, that is, for plants themselves as well as for human health.

Previously, several in vitro antioxidant assays have shown that CAG, ASG, CA, and FO were the primary antioxidant contributors acting as hydrogen/electron donors to neutralize peroxyl free radicals.[4−6,53] The better antioxidant activities of the UV-B-treated samples as against control (Figure 7) might be partly ascribed to the higher levels of these antioxidant compounds. However, antioxidant capacities of plant extracts are not dependent on some single molecules, due to the synergistic and redox interactions among multiple components that are present. Factually, UV-B radiation can induce the accumulation of many cellular antioxidants, such as ascorbic acid, glutathione, proline, tocopherol, flavonols, phenolics, and carotenoids.[19−21,45] Herein, it was inferred that the possible synergistic effects of these antioxidant constituents contributed to the tremendous increase in antioxidant activity of UV-B-treated samples. Anyway, the results of this study confirmed that UV-B-elicited AMHRCs could offer health-promoting extracts with higher antioxidant activity as natural additives in functional foods and nutraceuticals.

Overall, the present study established an effective, convenient, and feasible UV-B elicitation approach to enhance isoflavonoid biosynthesis in AMHRCs. We found that UV-B radiation as elicitor possessed the potential to induce the transcriptional activation of biosynthetic genes that ultimately boosted isoflavonoid accumulation in AMHRCs. This investigation also opened a gate to clarify the crucial regulatory points (*PAL* and *C4H* genes) in the isoflavonoid biosynthetic pathway of *A. membranaceus*.

AUTHOR INFORMATION

Corresponding Authors

*(Y.-J.F.) Phone/fax: +86-451-82190535. E-mail: yujie_fu2011@yahoo.com.

*(W.M.) Phone/fax: +86-451-82193430. E-mail: mawei@hljucm.net

Author Contributions

∥J.J. and Q.-Y.G. contributed equally to this work.

Funding

We gratefully acknowledge financial support from the Special Fund of Forestry Industrial Research for Public Welfare of China (201004079), the Application Technology Research and Development Program of Harbin (2013AA3BS014), the Fundamental Research Funds for the Central Universities (2572014AA06, and 2572015AA14), the Special Fund of the National Natural Science Foundation of China (31270618), the Key Program of the National Natural Science Foundation of China (81274010), and the Heilongjiang Province Outstanding Youth Fund (JC201101).

Notes

The authors declare no competing financial interest.

ABBREVIATIONS USED

AMHRCs, *A. membranaceus* hairy root cultures; AMHRL II, *A. membranaceus* hairy root line II; ASG, astraisoflavan-7-*O*-*β*-D-glucoside; BHT, butylated hydroxytoluene; CA, calycosin; CAG, calycosin-7-*O*-*β*-D-glucoside; C4H, cinnamate-4-hydroxylase; CHI, chalcone isomerase; CHR, chalcone reductase; CHS, chalcone synthase; 4CL, 4-coumarate coenzyme A ligase; DPPH, 2,2-diphenyl-1-picrylhydrazyl-hydrate; DW, dry weight; FO, formononetin; HRCs, hairy root cultures; IFS, isoflavone synthase; I3′H, isoflavone 3′-hydroxylase; IOMT, isoflavone *O*-methyltransferase; ON, ononin; PAL, phenylalanine ammonia-lyase; qRT-PCR, quantitative real-time PCR; ROS, reactive oxygen species; UGTs, uridine diphosphate-dependent glycosyltransferases; UV, ultraviolet; VC, ascorbic acid

REFERENCES

(1) Napolitano, A.; Akay, S.; Mari, A.; Bedir, E.; Pizza, C.; Piacente, S. An analytical approach based on ESI-MS, LC-MS and PCA for the quail-quantitative analysis of cycloartane derivatives in *Astragalus* spp. *J. Pharm. Biomed. Anal.* **2013**, *85*, 46−54.

(2) Zhang, L. J.; Liu, H. K.; Hsiao, P. C.; Kuo, L. M. Y.; Lee, I. J.; Wu, T. S.; Chiou, W. F.; Kuo, Y. H. New isoflavonoid glycosides and related constituents from astragali radix (*Astragalus membranaceus*) and their inhibitory activity on nitric oxide production. *J. Agric. Food Chem.* **2011**, *59*, 1131−1137.

(3) Zheng, K. Y. Z.; Choi, R. C. Y.; Cheung, A. W. H.; Guo, A. J. Y.; Bi, C. W. C.; Zhu, K. Y.; Fu, Q.; Du, Y.; Zhang, W. L.; Zhan, J. Y. X.; Duan, R.; Lau, D. T. W.; Dong, T. T. X.; Tsim, K. W. K. Flavonoids from Radix Astragali induce the expression of erythropoietin in cultured cells: a signaling mediated via the accumulation of hypoxia-inducible factor-1*α*. *J. Agric. Food Chem.* **2011**, *59*, 1697−1704.

(4) Jiao, J.; Gai, Q. Y.; Fu, Y. J.; Ma, W.; Peng, X.; Tan, S. N.; Efferth, T. Efficient production of isoflavonoids by *Astragalus membranaceus* hairy root cultures and evaluation of antioxidant activities of extracts. *J. Agric. Food Chem.* **2014**, *62*, 12649−12658.

(5) Chen, C. Y.; Zu, Y. G.; Fu, Y. J.; Luo, M.; Zhao, C. J.; Wang, W.; Zhao, B. S.; Li, J.; Efferth, T. Preparation and antioxidant activity of Radix Astragali residues extracts rich in calycosin and formononetin. *Biochem. Eng. J.* **2011**, *56*, 84−93.

DOI: 10.1021/acs.jafc.5b03138
J. Agric. Food Chem. 2015, 63, 8216−8224

(6) Zhao, B. S.; Fu, Y. J.; Wang, W.; Zu, Y. G.; Gu, C. B.; Luo, M.; Efferth, T. Enhanced extraction of isoflavonoids from Radix Astragali by incubation pretreatment combined with negative pressure cavitation and its antioxidant activity. *Innovative Food Sci. Emerging Technol.* **2011**, *12*, 577−585.
(7) Ma, X. Q.; Shi, Q.; Duan, J. A.; Dong, T. T.; Tsim, K. W. Chemical analysis of Radix Astragali (Huangqi) in China: a comparison with its adulterants and seasonal variations. *J. Agric. Food Chem.* **2002**, *50*, 4861−4866.
(8) Fu, J.; Wang, Z.; Huang, L.; Zheng, S.; Wang, D.; Chen, S.; Zhang, H.; Yang, S. Review of the botanical characteristics, phytochemistry, and pharmacology of *Astragalus membranaceus* (Huangqi). *Phytother. Res.* **2014**, *28*, 1275−1283.
(9) Wang, J. W.; Wu, J. Y. Effective elicitors and process strategies for enhancement of secondary metabolite production in hairy root cultures. In *Biotechnology of Hairy Root Systems*; Doran, P. M., Ed.; Springer-Verlag: Berlin, Germany, 2013; pp 55−89.
(10) Sharma, P.; Padh, H.; Shrivastava, N. Hairy root cultures: a suitable biological system for studying secondary metabolic pathways in plants. *Eng. Life Sci.* **2013**, *13*, 62−75.
(11) Ludwig-Müller, J.; Jahn, L.; Lippert, A.; Püschel, J.; Walter, A. Improvement of hairy root cultures and plants by changing biosynthetic pathways leading to pharmaceutical metabolites: strategies and applications. *Biotechnol. Adv.* **2014**, *32*, 1168−1179.
(12) Mehrotra, S.; Srivastava, V.; Rahman, L. U.; Kukreja, A. K. Hairy root biotechnology—indicative timeline to understand missing links and future outlook. *Protoplasma* **2015**, *252*, 1189.
(13) Tian, L. Using hairy roots for production of valuable plant secondary metabolites. *Adv. Biochem. Eng./Biotechnol.* **2015**, *149*, 275.
(14) Namdeo, A. G. Plant cell elicitation for production of secondary metabolites: a review. *Pharmacogn. Rev.* **2007**, *1*, 69−79.
(15) Gorelick, J.; Bernstein, N. Elicitation: an underutilized tool for the development of medicinal plants as a source for therapeutic secondary metabolites. *Adv. Agron.* **2014**, *124*, 201−230.
(16) Murthy, H. N.; Lee, E. J.; Paek, K. Y. Production of secondary metabolites from cell and organ cultures: strategies and approaches for biomass improvement and metabolite accumulation. *Plant Cell, Tissue Organ Cult.* **2014**, *118*, 1−16.
(17) Yi, J.; Derynck, M. R.; Li, X.; Telmer, P.; Marsolais, F.; Dhaubhadel, S. A single-repeat MYB transcription factor, GmMYB176, regulates *CHS8* gene expression and affects isoflavonoid biosynthesis in soybean. *Plant J.* **2010**, *62*, 1019−1034.
(18) Dixon, R. A. Natural products and plant disease resistance. *Nature* **2001**, *411*, 843−847.
(19) Schreiner, M.; Mewis, I.; Huyskens-Keil, S.; Jansen, M. A. K.; Zrenner, R.; Winkler, J. B.; O'Brien, N.; Krumbein, A. UV-B-induced secondary plant metabolites-potential benefits for plant and human health. *Crit. Rev. Plant Sci.* **2012**, *31*, 229−240.
(20) Matsuura, H. N.; de Costa, F.; Yendo, A. C. A.; Fett-Neto, A. G. Photoelicitation of bioactive secondary metabolites by ultraviolet radiation: Mechanisms, strategies, and applications. In *Biotechnology for Medicinal Plants*; Chandra, S., Lata, H., Varma, A., Eds.; Springer-Verlag: Berlin, Germany, 2013; pp 171−190.
(21) Kumari, R.; Prasad, M. N. V. Medicinal plant active compounds produced by UV-B exposure. In *Sustainable Agriculture Reviews*; Lichtfouse, E., Ed.; Springer: Dordrecht, The Netherlands, 2013; pp 225−254.
(22) Kanazawa, K.; Hashimoto, T.; Yoshida, S.; Sungwon, P.; Fukuda, S. Short photoirradiation induces flavonoid synthesis and increases its production in postharvest vegetables. *J. Agric. Food Chem.* **2012**, *60*, 4359−4368.
(23) Zhang, Z. Z.; Li, X. X.; Chu, Y. N.; Zhang, M. X.; Wen, Y. Q.; Duan, C. Q.; Pan, Q. H. Three types of ultraviolet irradiation differentially promote expression of shikimate pathway genes and production of anthocyanins in grape berries. *Plant Physiol. Biochem.* **2012**, *57*, 74−83.
(24) Zhang, Z. Z.; Che, X. N.; Pan, Q. H.; Li, X. X.; Duan, C. Q. Transcriptional activation of flavan-3-ols biosynthesis in grape berries by UV irradiation depending on developmental stage. *Plant Sci.* **2013**, *208*, 64−74.
(25) Nguyen, C. T.; Kim, J.; Yoo, K. S.; Lim, S.; Lee, E. J. Effect of prestorage UV-A, -B, and-C radiation on fruit quality and qnthocyanin of 'Duke' blueberries during cold storage. *J. Agric. Food Chem.* **2014**, *62*, 12144−12151.
(26) Pandey, N.; Pandey-Rai, S. Short term UV-B radiation-mediated transcriptional responses and altered secondary metabolism of in vitro propagated plantlets of *Artemisia annua* L. *Plant Cell, Tissue Organ Cult.* **2014**, *116*, 371−385.
(27) Kim, Y. B.; Thwe, A. A.; Li, X.; Tuan, P. A.; Zhao, S.; Park, C. G.; Lee, L. W.; Park, S. U. Accumulation of flavonoids and related gene expressions in different organs of *Astragalus membranaceus* Bge. *Appl. Biochem. Biotechnol.* **2014**, *173*, 2076−2085.
(28) Livak, K. J.; Schmittgen, T. D. Analysis of relative gene expression data using real-time quantitative PCR and the $2^{-\Delta\Delta C}$T method. *Methods* **2001**, *25*, 402−408.
(29) Arbona, V.; Flors, V.; Jacas, J.; García-Agustín, P.; Gómez-Cadenas, A. Enzymatic and non-enzymatic antioxidant responses of Carrizo citrange, a salt-sensitive citrus rootstock, to different levels of salinity. *Plant Cell Physiol.* **2003**, *44*, 388−394.
(30) Hideg, É.; Jansen, M. A.; Strid, Å. UV-B exposure, ROS, and stress: inseparable companions or loosely linked associates? *Trends Plant Sci.* **2013**, *18*, 107−115.
(31) Xu, R. Y.; Nan, P.; Yang, Y.; Pan, H.; Zhou, T.; Chen, J. Ultraviolet irradiation induces accumulation of isoflavonoids and transcription of genes of enzymes involved in the calycosin-7-*O*-*β*-D-glucoside pathway in *Astragalus membranaceus* Bge. var. *mongholicus* (Bge.) Hsiao. *Physiol. Plant.* **2011**, *142*, 265−273.
(32) Pan, H.; Fang, C.; Zhou, T.; Wang, Q.; Chen, J. Accumulation of calycosin and its 7-*O*-*β*-D-glucoside and related gene expression in seedlings of *Astragalus membranaceus* Bge. var. *mongholicus* (Bge.) Hsiao induced by low temperature stress. *Plant Cell Rep.* **2007**, *26*, 1111−1120.
(33) Kovacs, E.; Keresztes, A. Effect of gamma and UV-B/C radiation on plant cells. *Micron* **2002**, *33*, 199−210.
(34) Hollósy, F. Effects of ultraviolet radiation on plant cells. *Micron* **2002**, *33*, 179−197.
(35) Barta, C.; Kálai, T.; Hideg, K.; Vass, I.; Hideg, É. Differences in the ROS-generating efficacy of various ultraviolet wavelengths in detached spinach leaves. *Funct. Plant Biol.* **2004**, *31*, 23−28.
(36) Mahdavian, K.; Ghorbanli, M.; Kalantari, K. M. The effects of ultraviolet radiation on the contents of chlorophyll, flavonoid, anthocyanin and proline in *Capsicum annuum* L. *Turk. J. Bot.* **2008**, *32*, 25−33.
(37) Kranner, I.; Minibayeva, F. V.; Beckett, R. P.; Seal, C. E. What is stress? Concepts, definitions and applications in seed science. *New Phytol.* **2010**, *188*, 655−673.
(38) Jenkins, G. I. Signal transduction in responses to UV-B radiation. *Annu. Rev. Plant Biol.* **2009**, *60*, 407−431.
(39) Takos, A. M.; Jaffé, F. W.; Jacob, S. R.; Bogs, J.; Robinson, S. P.; Walker, A. R. Light-induced expression of a MYB gene regulates anthocyanin biosynthesis in red apples. *Plant Physiol.* **2006**, *142*, 1216−1232.
(40) Cominelli, E.; Gusmaroli, G.; Allegra, D.; Galbiati, M.; Wade, H. K.; Jenkins, G. I.; Tonelli, C. Expression analysis of anthocyanin regulatory genes in response to different light qualities in *Arabidopsis thaliana*. *J. Plant Physiol.* **2008**, *165*, 886−894.
(41) Singh, K.; Kumar, S.; Rani, A.; Gulati, A.; Ahuja, P. S. *Phenylalanine ammonia-lyase* (*PAL*) and *cinnamate 4-hydroxylase* (*C4H*) and catechins (flavan-3-ols) accumulation in tea. *Funct. Integr. Genomics* **2009**, *9*, 125−134.
(42) Xu, H.; Park, N. I.; Li, X.; Kim, Y. K.; Lee, S. Y.; Park, S. U. Molecular cloning and characterization of phenylalanine ammonia-lyase, cinnamate 4-hydroxylase and genes involved in flavone biosynthesis in *Scutellaria baicalensis*. *Bioresour. Technol.* **2010**, *101*, 9715−9722.
(43) Tuan, P. A.; Park, N. I.; Li, X.; Xu, H.; Kim, H. H.; Park, S. U. Molecular cloning and characterization of phenylalanine ammonia-

DOI: 10.1021/acs.jafc.5b03138
J. Agric. Food Chem. 2015, 63, 8216−8224

lyase and cinnamate 4-hydroxylase in the phenylpropanoid biosynthesis pathway in garlic (*Allium sativum*). *J. Agric. Food Chem.* **2010**, *58*, 10911−10917.
(44) Park, J. H.; Park, N. I.; Xu, H.; Park, S. U. Cloning and characterization of phenylalanine ammonia-lyase and cinnamate 4-hydroxylase and pyranocoumarin biosynthesis in *Angelica gigas*. *J. Nat. Prod.* **2010**, *73*, 1394−1397.
(45) Gill, S. S.; Tuteja, N. Reactive oxygen species and antioxidant machinery in abiotic stress tolerance in crop plants. *Plant Physiol. Biochem.* **2010**, *48*, 909−930.
(46) Fini, A.; Brunetti, C.; Di Ferdinando, M.; Ferrini, F.; Tattini, M. Stress-induced flavonoid biosynthesis and the antioxidant machinery of plants. *Plant Signaling Behav.* **2011**, *6*, 709−711.
(47) Agati, G.; Azzarello, E.; Pollastri, S.; Tattini, M. Flavonoids as antioxidants in plants: location and functional significance. *Plant Sci.* **2012**, *196*, 67−76.
(48) Agati, G.; Tattini, M. Multiple functional roles of flavonoids in photoprotection. *New Phytol.* **2010**, *186*, 786−793.
(49) Agati, G.; Biricolti, S.; Guidi, L.; Ferrini, F.; Fini, A.; Tattini, M. The biosynthesis of flavonoids is enhanced similarly by UV radiation and root zone salinity in *L. vulgare* leaves. *J. Plant Physiol.* **2011**, *168*, 204−212.
(50) Rüfer, C. E.; Kulling, S. E. Antioxidant activity of isoflavones and their major metabolites using different in vitro assays. *J. Agric. Food Chem.* **2006**, *54*, 2926−2931.
(51) Wuttke, W.; Jarry, H.; Seidlová-Wuttke, D. Isoflavones — safe food additives or dangerous drugs? *Ageing Res. Rev.* **2007**, *6*, 150−188.
(52) Carocho, M.; Ferreira, I. C. A review on antioxidants, prooxidants and related controversy: natural and synthetic compounds, screening and analysis methodologies and future perspectives. *Food Chem. Toxicol.* **2013**, *51*, 15−25.
(53) Huang, X.; Liu, Y.; Song, F.; Liu, Z.; Liu, S. Studies on principal components and antioxidant activity of different Radix Astragali samples using high-performance liquid chromatography/electrospray ionization multiple-stage tandem mass spectrometry. *Talanta* **2009**, *78*, 1090−1101.

DOI: 10.1021/acs.jafc.5b03138
J. Agric. Food Chem. 2015, 63, 8216−8224

crystallography. The crystal of the WT was obtained from a solution containing PEG 8000. The unit cell was relatively large, and 10 protein subunits were likely to be present in the asymmetric unit.[32] Molecular replacement using various available structures was not successful. Consequently, we solved the structure of M6 using experimental phasing with CsCl as the anomalous scatterer. The aim of this study was to improve the thermostability of EstF27 by directed evolution and also provide useful information about the structure−function relationship.

MATERIALS AND METHODS

Materials. *E. coli* DH5α and pUC19 (TaKaRa, Dalian, China) were used for the construction of the random mutagenesis libraries. The *E. coli* strain BL21(DE3) and the pET-28a (+) plasmid (Novagen, Madison, WI) were used for protein expression. Restriction endonucleases, DNA polymerase, and T4 DNA ligase were purchased from Thermo Fisher Scientific (Hudson, NH). FA was purchased from Sigma-Aldrich (St. Louis, MO). 4-Nitrophenyl ferulate (pNPF) was procured from the Slovak Academy of Sciences (Bratislava, Slovakia). All other chemicals and reagents were of analytical grade and were purchased from commercial sources, unless indicated otherwise.

Construction and Screening of a Random Mutagenesis Library. The plasmid pUC19-*estF27* (GenBank accession number HQ241478) was used as the template for the first round of mutagenesis and gave rise to a stable mutant with four mutations (named M4, T27I/S84L/V161I/G243C). Then the plasmid pUC19-*M4* was further used as the template for the second round of mutagenesis. The random mutagenesis was performed with the GeneMorph II random mutagenesis kit (Stratagene, La Jolla, CA) following the manufacture's protocol with the primers 5′-TATAACAGCTATGACCATGATTACGCCAAGCTTATG-3′ (forward) and 5′-GAATTCGAGCTCGGTACCCGGGGATCC-3′ (reverse). The error-prone polymerase chain reaction (epPCR) product was recovered and digested with *Bam*HI and *Hin*dIII and then ligated into pUC19, which had been previously digested with the same restriction enzymes. The ligation product was transformed into *E. coli* DH5α via electroporation, and the transformants were cultured on LB-agar plates containing 100 μg/mL ampicillin, 0.1% (v/v) tributyrin, 0.3% (w/v) poly(vinyl alcohol), 80 μg/mL rhodamine B, and 0.1 mM isopropyl β-D-1-thiogalactopyranoside (IPTG) at 37 °C overnight. Single colonies that formed a transparent zone were picked, transferred on duplicate LB-agar plates containing 100 μg/mL ampicillin and 0.02 mM IPTG, and cultivated at 37 °C for 48 h. One plate was incubated for 50 min at 60 °C for the first round of mutagenesis or 25 min at 85 °C for the second round of mutagenesis. After the plate was cooled to room temperature, about 5 mL of a mixture containing 0.3 mg/mL 1-naphthyl acetate and 1.3 mg/mL Fast Blue B salt was added to it. Positive colonies were confirmed by the brown halos formed around the colonies. The plasmid of the transformants expressing the mutants with improved thermostability was subsequently extracted for sequence analysis.

Site-Directed Mutagenesis. In vitro site-directed mutagenesis was performed with the TaKaRa MutanBEST kit (TaKaRa, Dalian, China) following the instructions of the manufacturer by using the plasmid pET-28a(+) as the template. The primers used are listed in Table S1. The correctness of the mutants was confirmed by sequencing.

Overexpression and Purification of the Target Proteins. The full-length EstF27 gene was PCR-amplified using the primers 5′-GATAGGGCCATATGACCCCCGAATTGCGCGCCAA-3′ and 5′-TTGCACTTCTCGAGTCACCGCGTACCCTGCGCAC-3′. After double digestion by the *Xho*I and *Nde*I restriction enzymes, the digested PCR product was ligated into a modified pET28a(+) vector in which the thrombin site (recognition peptide LVPRGS) was replaced by a Tobacco etch virus (TEV) protease cleavage site (recognition peptide ENLYFQG). The plasmids encoding the target proteins contain a 6× histidine tag at the N-terminus, and were transformed into *E. coli* BL21(DE3) for overexpression.

The cells carrying pET28a/EstF27 plasmids were grown at 37 °C and 190 rpm overnight in LB medium containing 30 μg/mL kanamycin. A 500 mL volume of fresh culture medium was then inoculated with 5 mL of the overnight culture. When the absorbance at 600 nm (OD_{600}) reached 0.6−0.8, 1 mM IPTG was added to the culture and the cells were subsequently induced overnight at 37 °C. Then the cells were harvested by centrifugation at 5000*g* for 15 min and resuspended in prechilled nickel−nitrilotriacetic acid (Ni−NTA) buffer A containing 40 mM Tris−HCl (pH 8.0), 250 mM NaCl, 10 mM imidazole, 1 mM phenylmethanesulfonyl fluoride (PMSF), and 1 mM β-mercaptoethanol. After sonication, the cell lysate was cleared by centrifugation at 14000*g* for 1 h at 4 °C. The resulting supernatant was mixed with Ni−NTA (Qiagen) resin at 4 °C for 1 h. The bound protein was washed with 10 column volumes of buffer A. The target protein was then eluted with Ni−NTA buffer B containing 40 mM Tris−HCl (pH 8.0), 250 mM NaCl, 250 mM imidazole, 1 mM PMSF, and 1 mM β-mercaptoethanol. The protein was pooled, concentrated, loaded onto a Superdex 200 column (GE Healthcare), and eluted with a buffer containing 20 mM Tris−HCl (pH 8.0), 150 mM NaCl, and 1 mM DTT. The eluted protein displayed a symmetric peak on the Superdex 200 column and was concentrated to 15 mg/mL before being flash frozen and stored at −80 °C for further crystallization experiments.

The recombinant proteins used for activity analysis were purified according to the same method without the addition of PMSF in Ni−NTA buffers. The enzymes in buffer B were further dialyzed three times in phosphate buffer (100 mM, pH 7.0) and then stored at 4 °C for further study.

The molecular mass of the recombinant protein was determined by using sodium dodecyl sulfate−polyacrylamide gel electrophoresis (SDS−PAGE) with suitably sized protein markers (Thermo Fisher Scientific, Waltham, MA) as standards. The protein concentration was determined by using the CoomassiePlus (Bradford) assay kit (Thermo Fisher Scientific) according to the product manual.

Determination of the Thermostability and Kinetic Parameters. The optimal pH values and optimal temperatures of EstF27 and the mutants were determined by using pNPF as the substrate. The concentration of pNP released was determined by measuring the absorbance of the solution at 405 nm. The reaction mixture contained 10 μL of the diluted enzyme solution and 490 μL of the substrate solution. The substrate solution was prepared according to Mastihuba et al.[33] The pH buffers included 100 mM citric acid−sodium citrate buffer (pH 5.0−6.0), phosphate buffer (pH 6.0−8.0), Tris−HCl buffer (pH 8.0−9.0), and glycine−NaOH buffer (pH 9.0−10.0). The optimal temperature was determined by measuring the initial reaction rates in the temperature range of 30−70 °C in phosphate buffer (100 mM, pH 7.0).

Two parameters were measured to evaluate the thermostability of EstF27 and the mutants. One is the half-life ($t_{1/2}$), which is defined as the incubation time needed to inactivate 50% of the initial enzyme activity. The purified enzymes (0.1 mg/mL) were incubated at 55, 65, or 70 °C in 100 mM phosphate buffer (pH 7.0). Samples were collected at various time intervals, cooled in ice, and assayed at 40 °C using pNPF as the substrate. The other one is the average size of the protein particles (*z*-average), measured by dynamic light scattering. The measurements were carried out with a photogoniometer as the plate reader (Wyatt Technology, Goleta, CA).[34] The WT protein and different mutants (1 mg/mL, 100 mM phosphate buffer, pH 7.0) were centrifuged at 14000*g* for 10 min, and the supernatant was transferred to the 384-well plates. Mineral oil was added on top to prevent evaporation during the heating process. The plate was subjected to a 2000*g* centrifugation for 2 min to remove air bubbles before readout in the temperature-controlled DynaPro plate reader. The temperature range was set to 25−75 °C, and the temperature increase rate was 0.35 °C/min. Each sample was run in triplicate, and each well was measured five times, with a 5 s acquisition time.

The storage stability of EstF27 and the mutant M6 was determined at 25 °C in 100 mM phosphate buffer (pH 7.0). After different storage times (0−150 days), the residual activities were tested. The initial activity of the enzymes was defined as 100%.

The kinetic parameters (K_{cat} and K_m) of EstF27 and the mutant M6 were determined by assaying the activity in 100 mM phosphate buffer (pH 7.0) at 40 and 65 °C with seven different concentrations (0.5K_m to 5.0K_m) of pNPF as the substrate. The kinetic data were fitted to a

DOI: 10.1021/acs.jafc.5b03424
J. Agric. Food Chem. 2015, 63, 8225−8233

Lineweaver−Burk curve using the SigmaPlot software (Systat Software, Chicago, IL).

Release of FA from DSWB. The wild-type EstF27 and the thermostable mutant M6 were each applied to degrade DSWB synergistically with xylanase from *Thermomyces lanuginosus* (Sigma-Aldrich, St. Louis, MO). The reactions were performed at 40 and 65 °C in 1 mL of phosphate buffer (100 mM, pH 7.0) containing 50 mg of DSWB. The enzyme loads were 10 U/mL for xylanase and 0.5 mg/mL for EstF27 and M6. Samples were collected at different time intervals, boiled for 5 min, and filtered. The concentration of FA released was determined by high-performance liquid chromatography (HPLC). A C18 reversed-phase column (8.0 × 300 mm, 5 μm, ODS, Japan) was used for the HPLC analysis. A mixture of methanol/HPLC-grade water containing 1% (w/v) acetic acid (30:70, v/v) was used as the mobile phase at a flow rate of 1.0 mL/min at 30 °C. The injection volume was 10 μL, and the absorbance at 280 and 320 nm was recorded. The wheat bran was destarched on the basis of the method described by Topakas et al.[35] The total FA content in the DSWB was determined according to the method of Garcia et al.[36]

Crystallization and Data Collection. The mutant M6 was crystallized using the sitting-drop vapor-diffusion method in 96-well plates. The commercial screens Index and Crystal Screen and a home-made PEG/ammonium sulfate-based screen were used for initial crystallization screening. Crystals of M6 grew to optimal sizes in 5−7 days at 25 °C in 1.2 M ammonium sulfate and 100 mM HEPES (pH 7.5). A single crystal was flash-frozen in liquid nitrogen using 20% glycerol (v/v) plus the crystallization solution as a cryoprotectant.

A native X-ray diffraction data set (a total of 214 frames) was collected at 100 K using an in-house Oxford Diffraction Xcalibur Nova diffractometer operating at 50 kV and 0.8 mA. The rotation was 0.75° per frame, and the crystal-to-detector distance was 60 mm. The exposure time was 30 s, and the data were recorded with a 165 mm Onyx CCD detector. To determine the phase, derivative crystals were obtained by soaking the native crystals in the above cryoprotectant with 1 M CsCl for 15 min. The soaked crystals had no apparent decay, and a data set of 180 frames was collected afterward, with a rotation of 1° per frame. The crystal-to-detector distance was 65 mm, and the exposure time was 90 s.

Accession Numbers. The atomic coordinates and structure factors have been deposited in the Protein Data Bank with the accession code 4ZRS.

RESULTS AND DISCUSSION

Screening for Mutants with Improved Thermostability. Two epPCR libraries were successfully constructed for screening mutants with improved thermostability, which contained about 30000 and 25000 clones, respectively. Twenty clones of each library were randomly picked and sequenced to estimate the diversity of the library. The results showed that the error rates of the libraries were 0.95 and 1.2 nucleotide changes/kb, respectively. About 45% of the clones were identified to be active by the transparent zone formed around the colonies. Then they were transformed to duplicate LB-agar plates for further screening the mutants with enhanced thermostability.

To avoid significant changes of the protein expression on the transformed plates, a low induction concentration of IPTG (0.02 mM) was applied (Figure S1). After a heat treatment for 50 min at 60 °C, the WT completely lost activity (Figure S2A). Four positive clones were identified out of nearly 13,500 clones after the first library was screened. Sequence analysis identified that the mutations were T27I, S84L, G243C, and V161I/G243C, respectively. The individual contribution of each mutation to the thermostabilization was subsequently determined (Table 1). The combination of four such mutations resulted in the mutant M4 with a half-life of 4 h at 65 °C. To further improve the thermostability, a second random library was constructed on the basis of M4. The screening was performed after the heat treatment for 25 min at 85 °C (Figure S2B). Two more mutants, H195L and A259V, were identified. Combination of all the beneficial mutations gave rise to the mutant M6.

Table 1. Half-Lives of EstF27 and the Mutants

enzyme	$T_{1/2}$ at 55 °C (h)	$T_{1/2}$ at 65 °C (h)	$T_{1/2}$ at 70 °C (h)
EstF27	0.5[a]	ND[b]	ND
EstF27-T27I	30	ND	ND
EstF27-S84L	6	ND	ND
EstF27-V161I	1.5	ND	ND
EstF27-G243C	45	ND	ND
M4	70	4	ND
M4-H195L	430	30	ND
M4-A259V	330	20	ND
M4-H195L/A259V (M6)	1680	140	3

[a]Different from that in the previous report[31] because the fusion tag was different. [b]ND = not determined.

Enzymatic Characterization. The optimal temperature (T_{opt}) of EstF27 is 40 °C (Figure 1A). The mutations increase the optimal temperatures to 60 °C (M4) and 65 °C (M6), which are 20 and 25 °C higher than that of the WT, respectively (Figure 1A). Meanwhile, the optimal pH values of the recombinant protein shift 0.5−1.0 unit toward the alkaline direction by the mutations (Figure 1B). The half-life of EstF27 at 55 °C is 0.5 h (Table 1), different from that in the previous report, in which EstF27 remained at only 25% activity after incubation for 10 min at 55 °C.[31] The discrepancy may be due to the effects of the fusion tags present in the different expression vectors. Four mutations (T27I, S84L, V161I, and G243C) were identified after the first round of screening, resulting in 3−30-fold improvement of the half-life (Table 1). Combination of the four thermostabilizing mutations results in the mutant M4 with a half-life of 70 h at 55 °C, which is an about 140-fold improvement over that of the WT. The combination of another two mutations (H195L and A259V) obtained from the second random library further extends the half-life from 70 h (M4) to 1680 h (M6).

Dynamic light scattering (DLS) is a useful method for monitoring the presence of aggregated protein as has been used to monitor the change in the dimensions of the protein during denaturation and renaturation.[37,38] The effects of temperature on the protein particle sizes measured by DLS are shown in Figure 2. The temperatures that significantly changed the protein particle size of M4 and M6 are 63 and 68 °C, which are 7 and 12 °C higher than that of the WT (56 °C), respectively. These critical temperatures at which the protein particle sizes change dramatically are an indication of formation of aggregates in solution, which may lead to further denaturation.[39] The increase in these temperatures suggests improvement in enzymatic thermostability, consistent with the trend observed by the half-life measurements.

The storage stability of EstF27 and the mutant M6 was also determined. After storage at 25 °C for 150 days, the activity of M6 was almost constant (100.5 ± 2.1%), whereas that of the WT was only 21.2 ± 2.7% (Table 2). This result again showed the better thermostability of mutant M6 than that of the WT.

The measured kinetic parameters of EstF27 and the mutant M6 are listed in Table 3. The catalytic efficiency of the protein was increased by the mutations. The K_{cat}/K_m value of M6 at its T_{opt} of 65 °C is about 1.9-fold higher that of WT at its T_{opt} of 40 °C. Previous studies on directed evolution of enzymes have suggested that increased thermostability of enzymes may come at the cost of their activities at low temperature.[40,41] However, the

DOI: 10.1021/acs.jafc.5b03424
J. Agric. Food Chem. 2015, 63, 8225−8233

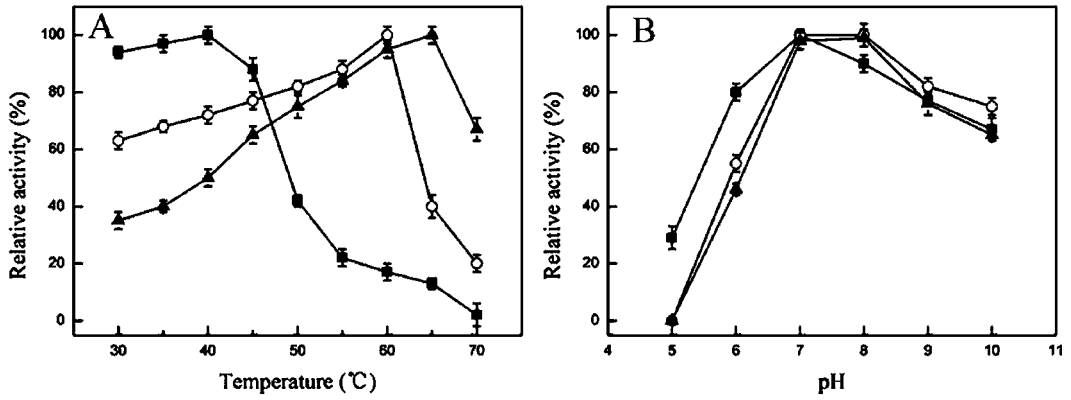

Figure 1. Effects of the temperature (A) and pH (B) on the initial reaction rates of EstF27 (■), M4 (○), and M6 (▲). The data points are the average of triplicate measurements, and the error bars represent the standard deviation.

mutations identified in this work significantly enhanced the thermostability of EstF27 while maintaining its activity at 40 °C. A reasonable explanation is that only the clones that showed transparent zones at 37 °C were picked for further screening, and the positive clones were identified at room temperature after heat treatment. Thus, both properties of thermostability and activity at low temperature were constrained during the directed evolution process.[24]

Releasing FA from DSWB. Wheat bran is one of the major byproducts of the milling industries and a good source of FA.[4,42] FAEs usually work synergistically with xylanases to degrade such natural substrates. To investigate the effects of enhanced thermostability on the hydrolysis of DSWB, such reactions were performed at both 40 and 65 °C. The total FA present in DSWB was determined to be 0.49% (w/w). No FA was detected when only xylanase was added (Figure 3, Figure S4). During a hydrolysis of 10 h at 40 °C, the concentrations of FA released by EstF27 and M6 were 223.2 ± 6.8 and 273.3 ± 8.1 μM, representing 17.7% and 21.6% of the total FA. At 65 °C, the concentration of FA released by M6 in 10 h was 464.8 ± 11.9 μM, representing 36.8% of the total FA, whereas EstF27 appeared to have completely lost its activity quickly as little FA was detected (Figure 3). M6 released 2-fold more ferulic acid at its T_{opt} of 65 °C than EstF27 at its T_{opt} of 40 °C. These results show the advantage of the thermostable mutant M6 over EstF27 in releasing ferulic acid at high temperature.

Structure of the Mutant M6 and Comparison to Other Structural Homologues. To further understand the structural basis of the enhanced thermostability, we seek to solve the crystal structure of the thermostable mutant M6. EstF27 belongs to a distant family of carboxylesterase, and its closest orthologue in sequence is a phenmedipham hydrolase from *Altererythrobacter atlanticus* (AKH43926), which shares 72% sequence identity with EstF27. The molecular replacement with several homologous structures as the search probes using the native data did not yield a plausible solution. To solve the structure, experimental phasing was pursued using CsCl as the anomalous scatterer. Cesium has an f'' of 7.9 e^- at 1.54 Å (the Cu Kα wavelength), which is higher than that of iodine (6.8 e^-). The crystals did not show apparent morphology changes after 15 min of CsCl soaking, and a complete SAD data set was collected at this wavelength to a resolution of 2.4 Å at the home X-ray source. Surprisingly, cell content analyses indicated that the asymmetric unit contains only one molecule, in contrast to the original two in the native data set. Therefore, the quick-soaking procedure still induced significant changes in the unit cells. Experimental phasing by Phaser generated a high-quality map, in which seven cesium sites were found. Of these, one cesium ion is bound to the dimer interface and most likely disrupts the association of the two monomers (data not shown). The Cs-bound derivative structure was built using the autobuild option of Phenix followed by manual rebuilding. The structure of the mutant M6 was subsequently solved at a resolution of 2.0 Å using molecular replacement with the SAD solution as the search probe.

The crystals of the mutant M6 belong to an orthorhombic system with the space group $P2_1$, and each asymmetric unit contains two monomers with 54.6% solvent content. Both chains are completely intact from G-1 to R290 with no internal disorders and of excellent electron density (Table S2). The spherical protein displays the α/β hydrolase fold, featuring a central eight-stranded mixed β-sheet sandwiched by five helices on each side (Figure 4A). Among these, only the β2 strand is antiparallel to the other strands, while the remainder of the strands are all parallel to each other.

A DALI search shows that the closest structural homologues for this protein are a putative carboxylesterase from *Lactobacillus plantarum* (PDB code 3BJR) and a cloned carboxylesterase, EstE1, from a metagenomic library (PDB code 2C7B).[43] The basic α/β hydrolase fold is conserved as indicated by structure overlay. The rms deviation values are 2.6 Å over 223 Cα atoms and 3.2 Å over 248 Cα atoms between the M6 structure and the above two structures, respectively (Figure 4B). While the central eight-stranded sheet structures align well, noticeable local structural differences are also observed. For example, as shown in Figure S5, when compared to that of EstE1, the N-terminus of EstF27 resolves more residues and forms two helices instead of a single helix; in addition, regions between β6 and β7 display substantial rearrangements: the β6−α6 loop is shorter and forms only one helix (α6), as compared to the two helices in EstE1, and the Cα trace of the α6−α7 helices in EstF27 also has significant shifts. These structural changes may be related to the substrate specificity that each enzyme catalyzes.

Additionally, most of the essential residues are conserved as demonstrated by the multiple sequence alignment (Figure S6). A catalytic triad formed by Ser, His, and Asp/Glu residues has been reported to be critical to the activity of α/β hydrolases.[44,45] At the active site, the catalytic triad Ser151−His263−Asp230 is well conserved, suggesting that these proteins share a common catalytic mechanism. The OD1 atom of the carboxylate group in Asp230 forms a hydrogen bond with the ND1 atom of the His263 imidazole ring and constitutes part of the proton-shuffling network. Interestingly, we found that extra density was

DOI: 10.1021/acs.jafc.5b03424
J. Agric. Food Chem. 2015, 63, 8225−8233

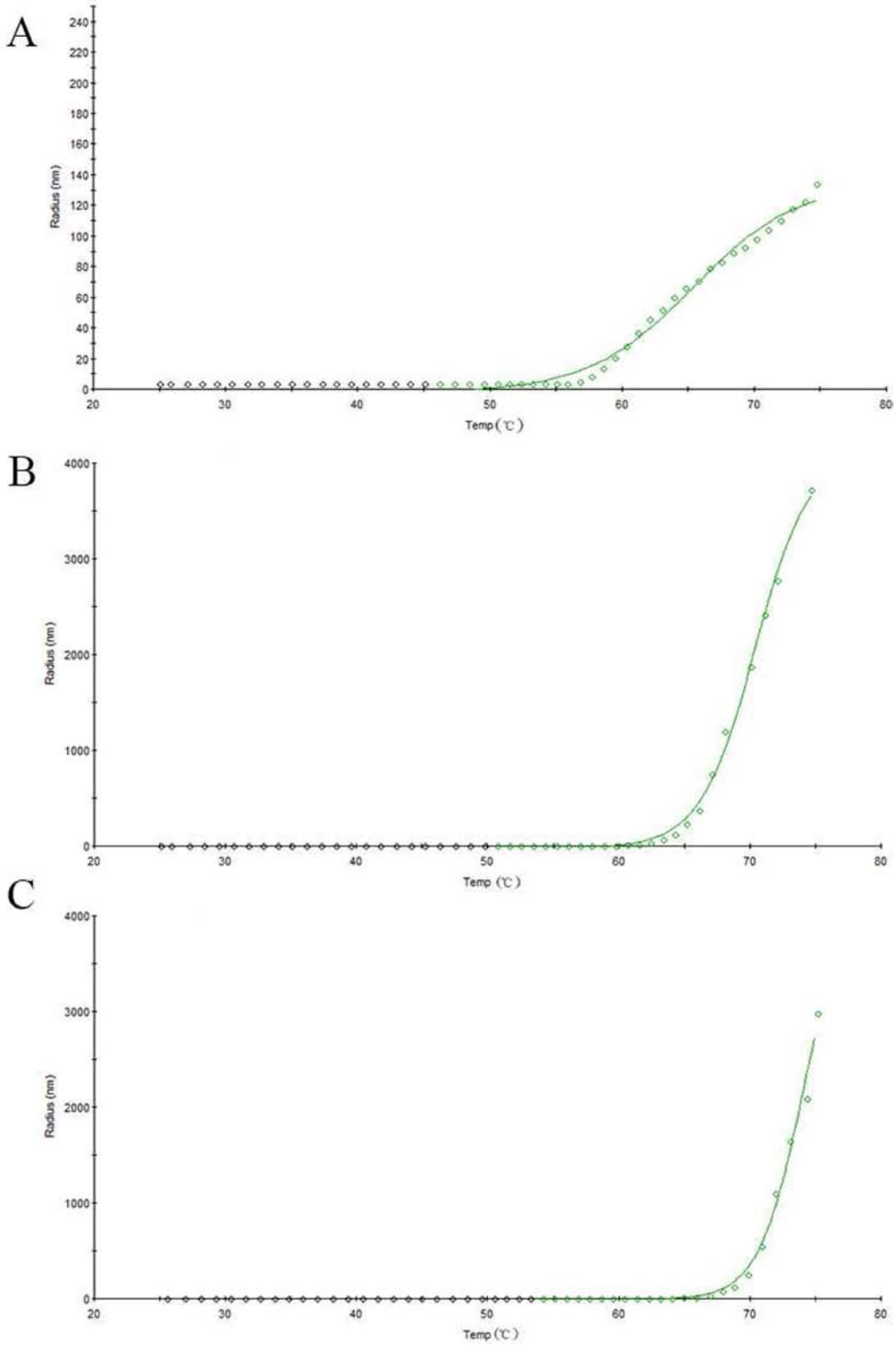

Figure 2. Effects of the temperature on the protein particle sizes of EstF27 (A) and mutants M4 (B) and M6 (C).

connected to the side chain of S151. After careful inspection, a sulfamoyl moiety was built into the density successfully (Figure S7). The most possible scenario was that S151 acts as a nucleophile and attacks PMSF (intended for protease inhibition) during the course of protein purification, leading to the covalent linkage. Additionally, the four-residue motif 73HGGG76, a signature of the hormone-sensitive esterase/lipase (HSL) family,[46,47] is located in a loop, flanking the other side of the S151 nucleophile.

EstF27 exists as a dimer in solution as indicated by size-exclusion chromatography studies, and this observation is

DOI: 10.1021/acs.jafc.5b03424
J. Agric. Food Chem. 2015, 63, 8225−8233

Table 2. Storage Stability of EstF27 and the Mutant M6 at 25 °C

storage time (days)	residual activity (%)	
	EstF27	M6
0	100.0 ± 1.1	100.0 ± 2.3
10	92.5 ± 1.6	100.0 ± 0.3
20	87.6 ± 3.5	99.8 ± 1.1
50	78.5 ± 2.8	102.2 ± 1.6
80	56.2 ± 2.4	100.8 ± 2.5
100	40.6 ± 1.1	99.5 ± 1.7
150	21.2 ± 2.7	100.5 ± 2.1

Table 3. Kinetic Parameters of EstF27 and the Mutant M6

temp (°C)	enzyme	K_m (mM)	K_{cat} (s^{-1})	K_{cat}/K_m ($s^{-1}mM^{-1}$)	ref
40	EstF27	0.5 ± 0.04	19.7 ± 3	39.4	31
	M6	0.36 ± 0.06	18.85 ± 0.94	52.36	this study
65	EstF27	ND[a]	ND	ND	this study
	M6	0.42 ± 0.07	32.16 ± 1.62	76.56	this study

[a]ND = not determined.

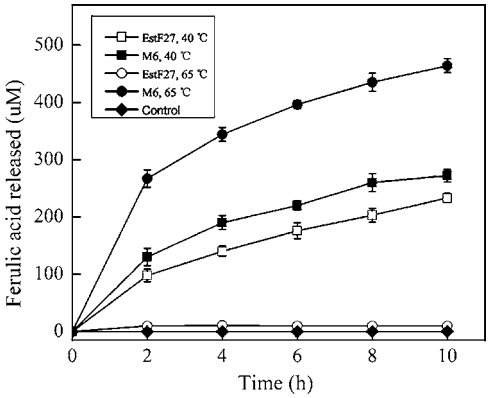

Figure 3. Time course of ferulic acid production from DSWB at 40 and 65 °C. Xylanase (◆) was used alone as a control. The data points are the average of triplicate measurements, and the error bars represent the standard deviation.

consistent with two monomers being in the asymmetric unit. However, we have encountered problems in assigning the dimer interface. In the current structure, the two subunits dimerize through a C-terminal helix, α8 (dimer type I). Alternatively, they could provide intermolecular contacts and result in another type of dimer via interactions using α2 and α6 (dimer type II) (Figure S8). Interestingly, both types of dimers are reasonable in terms of dimer interface as well as free energy according to the PISA server: the buried surface area is 2570 and 2380 Å^2, and ΔG^{int} is −16.8 and −19.7 kcal/mol, respectively. To find the physiological dimer interface, we examined the structure and discovered that C243, a residue at the dimer interface, forms a disulfide bond with its counterpart from the other subunit in the electron density map (Figure 5A). The S−S bond formation is supported by the extra band at ∼70 kDa on an SDS−PAGE gel under a nonreducing environment. Upon reduction, this band disappears and the monomeric-form band appears (Figure 5B), indicating the interface as shown in the crystal structure is the genuine biological dimerization mode. We also tested the mutant

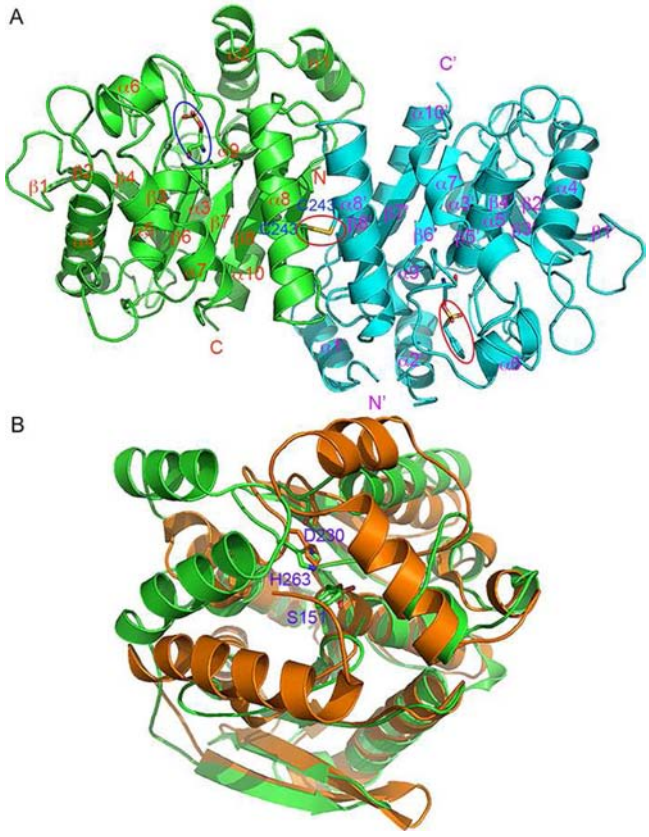

Figure 4. Overall structure of EstF27 and comparison with the orthologues. (A) The two subunits are colored in cyan and in green. The major secondary elements and the N- and C-termini are labeled. The intersubunit C243−C243′ disulfide bond is shown as a ball-and-stick model and circled. The modified S151 on each subunit is also circled. (B) Structure overlay of Cα traces of EstF27 (green) and a cloned carboxylesterase from a metagenomic library (PDB code 2C7B). The catalytic triad is shown as a ball-and-stick model.

C243G, which reverts the cysteine residue back to the original glycine, and the extra band was not observed, further strengthening our argument (Figure 5B). Coincidentally, C243 is also one of the resulting mutants obtained from our first-round mutagenesis screen, and the disulfide bridge enhances the stability of the dimer.

Another interesting discovery is that K164−G172, a fragment connecting α5 and β6, adopts different paths in each subunit (Figure S9). This region is at least 16 Å from the nucleophile S151, and the cause of different conformations and their biological significance are unclear.

Rationalization of the Mutations. We generated a series of mutants through random mutagenesis that greatly promote the thermostability of EstF27. We subsequently determined the crystal structure of the most stable mutant M6 at high resolution, and the crystal structure reveals that G243C, a mutant at the dimer interface, forms a disulfide bridge with C243′ and presumably stabilizes the dimer through the S−S covalent bond. Examination of the other mutant sites on the structure suggests that most of the mutations tend to increase the hydrophobicity of the protein, and several of them besides C243 are located at the dimer interface. For an example, the mutations T27I, H195L, and S84L all change polar residues to hydrophobic residues, while the mutations V161I and A259V tend to increase the hydrophobicity of EstF27. Hydrophobic interactions may play a very important

DOI: 10.1021/acs.jafc.5b03424
J. Agric. Food Chem. 2015, 63, 8225−8233

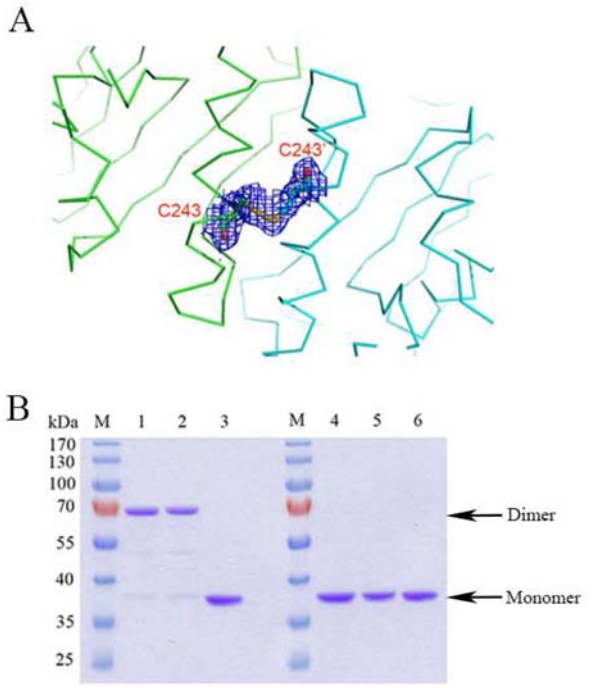

Figure 5. Structural and biochemical characterization of the G243 mutation. (A) Electron map around the C243−C243′ disulfide bond. The map is contoured at 1σ, and the Cα trace of each subunit is shown. (B) SDS−PAGE analysis of the molecular weight of mutant M6 and mutant M6-C243G: lane M, standard protein molecular mass marker (Thermo Fisher Scientific, sizes in kilodaltons are indicated on the left); lines 1−3, purified recombinant protein of M6 which was untreated (line 1) and treated by 2 mM oxidized glutathione (GSSG) (line 2) or 5 mM DTT (line 3); lines 4−6, purified recombinant protein of M6-C243G which was untreated (line 4) and treated by 2 mM oxidized glutathione (GSSG) (line 5) or 5 mM DTT (line 6).

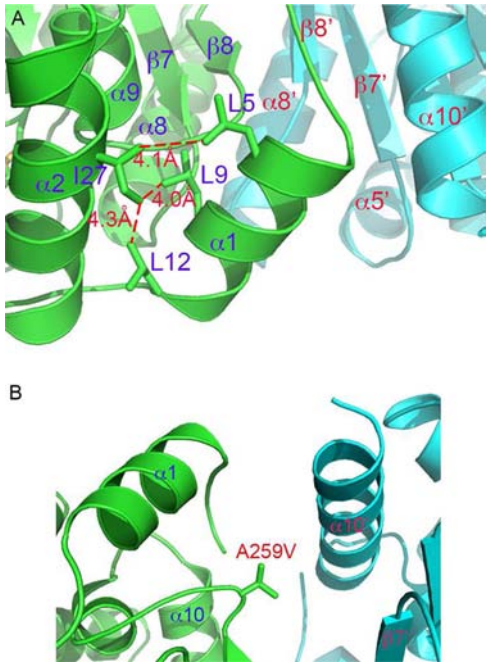

Figure 6. Details of the hydrophobic interaction. (A) Local environment of I27, which could possibly form hydrophobic interactions with L5, L9, and L12 residues from α1 (close to the interface). (B) Local environment of V259, which could possibly form hydrophobic interactions with α10′ from the other subunit. The residues of interest are shown as a ball-and-stick model, and the major secondary elements are labeled.

role in forming the inner core of the enzyme, and these mutations turn out to boost the thermostability. Specifically, T27I may form hydrophobic interactions with L5 (the closest distance between the two residues is 4.94 Å), L9 (4.0 Å), and L12 (4.3 Å) of α1, which is close to the dimer interface (Figure 6A). Similarly A259V may promote the stability of the dimer interface by increasing the hydrophobic interactions with α10′ from the other monomer (Figure 6B). Byun et al.[43] discovered that the thermostability of EstE1, an EstF27 homologue, correlates with its ability to form a dimer. In contrast, disruption of the hydrophobic interactions between the two monomers destabilizes its stability, which supports our current data. Furthermore, after mutation, L195 is in a hydrophobic environment formed by Y199, F77, W206, and I183. The closest distances between the δC atoms of L195 and the aromatic rings of the former three residues are 3.7−3.9 Å. Similarly, L84 is in close range to F89 and Y90. I161 is also in a hydrophobic pocket, and within 5.0 Å, it is surrounded by residues L222, L215, I220, I157, I179, and I174 (Figure S10). These findings provide an explanation for the contribution of the P195L, S84L, and V161I mutations. One must realize that the crystal structure could not provide a perfect explanation for the role of every mutant, because the crystal structure only reflects a static state of the mutant M6 in the crystal lattice. The thermostability evaluation, performed at a temperature as high as 70 °C (Table 1), is a combined result of both thermodynamic and dynamic properties of each mutant. Ideally, the crystal structure of each mutant and detailed solution studies using NMR etc. will greatly help to elucidate the structural basis of the thermostability and enzymatic behavior.

In conclusion, the thermostability of EstF27 was significantly enhanced by the substitutions of six amino acids. The mutations also enhanced the storage stability and improved the catalysis efficiency. The thermostable mutant M6 released 2-fold more ferulic acid at its T_{opt} of 65 °C than the wild type at its T_{opt} of 40 °C in a 10 h hydrolysis of destarched wheat bran. The crystal structure of M6 was determined at 2.0 Å, and structural analysis showed that a new disulfide bond, as well as hydrophobic interactions formed by the mutations, may play an important role in stabilizing the protein. These results may provide useful information for the further engineering of EstF27 in a subsequent study.

■ ASSOCIATED CONTENT

Supporting Information

The Supporting Information is available free of charge on the ACS Publications website at DOI: 10.1021/acs.jafc.5b03424.

Optimization of the IPTG concentration used in the epPCR library screening, determination of the heat treatment condition of library screening for mutants with enhanced thermostability, SDS−PAGE analysis of the recombinant EstF27 and the mutants; HPLC analysis of the concentration of the ferulic acid released from DSWB, comparison of the structures of EstF27 and EstE1, multiple sequence alignment of EstF27, carboxylesterase from *L. plantarum* (PDB code 3BJR), and carboxylesterase from a metagenomic library (PDB code 2C7B), electron map around the modified active-site residue S151, two possible dimerization modes in the asymmetric unit, structure overlay of the two monomers of the EstF27 homodimer, local environment of mutated residues L195,

DOI: 10.1021/acs.jafc.5b03424
J. Agric. Food Chem. 2015, 63, 8225−8233

L84, and I161, primers used to construct the mutants of EstF27, and data collection and refinement statistics (PDF)

AUTHOR INFORMATION

Corresponding Authors

*E-mail: xiewei6@mail.sysu.edu.cn. Phone: 86-20-39332943. Fax: 86-20-39332847

*E-mail: lsslyh@mail.sysu.edu.cn. Phone: 86-20-84113712. Fax: 86-20-84036215

Author Contributions

W.X. and Y.-h.L. designed the research and wrote the paper, and L.-C.C. and R.C. performed the experiments and contributed equally to this work.

Funding

This research was supported by the National Natural Science Foundation of China (Grants 31100579 and 31170117), Guangdong Innovative Research Team Program (Grant 2011Y038), Science & Technology Projects of Guangdong Provincial Oceanic and Fishery Bureau (Grant A201301C04), National Marine Research Special Funds for Public Welfare Projects of China (Grant 201205020), and Major Science and Technology Projects of Guangdong Province, China (Grant 2011A080403006).

Notes

The authors declare no competing financial interest.

ABBREVIATIONS USED

E. coli, *Escherichia coli*; CIAP, calf intestine alkaline phosphatase; IPTG, isopropyl β-D-1-thiogalactopyranoside; DSWB, de-starched wheat bran; SDS−PAGE, sodium dodecyl sulfate−polyacrylamide gel electrophoresis; pNPF, 4-nitrophenyl ferulate; PMSF, phenylmethanesulfonyl fluoride; HPLC, high-performance liquid chromatography

REFERENCES

(1) Kroon, P. A.; Williamson, G. Hydroxycinnamates in plants and food: current and future perspectives. *J. Sci. Food Agric.* **1999**, *79*, 355−361.

(2) Ou, S.; Kwok, K.-C. Ferulic acid: pharmaceutical functions, preparation and applications in foods. *J. Sci. Food Agric.* **2004**, *84*, 1261−1269.

(3) Mancuso, C.; Santangelo, R. Ferulic acid: pharmacological and toxicological aspects. *Food Chem. Toxicol.* **2014**, *65*, 185−95.

(4) Lequart, C.; Nuzillard, J.-M.; Kurek, B.; Debeire, P. Hydrolysis of wheat bran and straw by an endoxylanase: production and structural characterization of cinnamoyl-oligosaccharides. *Carbohydr. Res.* **1999**, *319*, 102−111.

(5) Micard, V.; Renard, C. M. G. C.; Colquhoun, I. J.; Thibault, J.-F. End-products of enzymic saccharification of beet pulp, with a special attention to feruloylated oligosaccharides. *Carbohydr. Polym.* **1997**, *32*, 283−292.

(6) Saulnier, L.; Thibault, J. F. Ferulic acid and diferulic acids as components of sugar-beet pectins and maize bran heteroxylans. *J. Sci. Food Agric.* **1999**, *79*, 396−402.

(7) Williamson, G.; Kroon, P. A.; Faulds, C. B. Hairy plant polysaccharides: a close shave with microbial esterases. *Microbiology* **1998**, *144*, 2011−2023.

(8) Topakas, E.; Vafiadi, C.; Christakopoulos, P. Microbial production, characterization and applications of feruloyl esterases. *Process Biochem.* **2007**, *42*, 497−509.

(9) Koseki, T.; Fushinobu, S.; Ardiansyah; Shirakawa, H.; Komai, M. Occurrence, properties, and applications of feruloyl esterases. *Appl. Microbiol. Biotechnol.* **2009**, *84*, 803−10.

(10) Crepin, V. F.; Faulds, C. B.; Connerton, I. F. Functional classification of the microbial feruloyl esterases. *Appl. Microbiol. Biotechnol.* **2004**, *63*, 647−52.

(11) Benoit, I.; Navarro, D.; Marnet, N.; Rakotomanomana, N.; Lesage-Meessen, L.; Sigoillot, J. C.; Asther, M.; Asther, M. Feruloyl esterases as a tool for the release of phenolic compounds from agro-industrial by-products. *Carbohydr. Res.* **2006**, *341*, 1820−7.

(12) Rakotoarivonina, H.; Hermant, B.; Chabbert, B.; Touzel, J. P.; Remond, C. A thermostable feruloyl-esterase from the hemicellulolytic bacterium *Thermobacillus xylanilyticus* releases phenolic acids from non-pretreated plant cell walls. *Appl. Microbiol. Biotechnol.* **2011**, *90*, 541−52.

(13) Abokitse, K.; Wu, M.; Bergeron, H.; Grosse, S.; Lau, P. C. Thermostable feruloyl esterase for the bioproduction of ferulic acid from triticale bran. *Appl. Microbiol. Biotechnol.* **2010**, *87*, 195−203.

(14) Record, E.; Asther, M.; Sigoillot, C.; Pages, S.; Punt, P. J.; Delattre, M.; Haon, M.; van den Hondel, C. A. M.J. J.; Sigoillot, J. C.; Lesage-Meessen, L.; Asther, M. Overproduction of the *Aspergillus niger* feruloyl esterase for pulp bleaching application. *Appl. Microbiol. Biotechnol.* **2003**, *62*, 349−55.

(15) Tapin, S.; Sigoillot, J.-C.; Asther, M.; Petit-Conil, M. Feruloyl Esterase Utilization for Simultaneous Processing of Nonwood Plants into Phenolic Compounds and Pulp Fibers. *J. Agric. Food Chem.* **2006**, *54*, 3697−3703.

(16) Tabka, M. G.; Herpoël-Gimbert, I.; Monod, F.; Asther, M.; Sigoillot, J. C. Enzymatic saccharification of wheat straw for bioethanol production by a combined cellulase xylanase and feruloyl esterase treatment. *Enzyme Microb. Technol.* **2006**, *39*, 897−902.

(17) Yu, P.-Q.; Mckinnon, J. J.; Maenz, D. D.; Olkowski, A. A.; Racz, V. J.; Christensen, D. A. Enzymic Release of Reducing Sugars from Oat Hulls by as Influenced by *Aspergillus* Ferulic Acid Esterase and *Trichoderma* Xylanase. *J. Agric. Food Chem.* **2003**, *51*, 218−223.

(18) Yu, P.; McKinnon, J.; Christensen, D. Improving the nutritional value of oat hulls for ruminant animals with pretreatment of a multienzyme cocktail: in vitro studies. *J. Anim. Sci.* **2005**, *83*, 1133−1141.

(19) Chen, J.; Fales, S. L.; Varga, G. A.; Royse, D. J. Biodegradation of cell wall components of maize stover colonized by white-rot fungi and resulting impact on in-vitro digestibility. *J. Sci. Food Agric.* **1995**, *68*, 91−98.

(20) Topakas, E.; Vafiadi, C.; Stamatis, H.; Christakopoulos, P. *Sporotrichum thermophile* type C feruloyl esterase (StFaeC): purification, characterization, and its use for phenolic acid (sugar) ester synthesis. *Enzyme Microb. Technol.* **2005**, *36*, 729−736.

(21) Mastihubová, M.; Mastihuba, V.; Bilaničová, D.; Boreková, M. Commercial enzyme preparations catalyse feruloylation of glycosides. *J. Mol. Catal. B: Enzym.* **2006**, *38*, 54−57.

(22) Kikugawa, M.; Tsuchiyama, M.; Kai, K.; Sakamoto, T. Synthesis of highly water-soluble feruloyl diglycerols by esterification of an *Aspergillus niger* feruloyl esterase. *Appl. Microbiol. Biotechnol.* **2012**, *95*, 615−22.

(23) Haki, G. Developments in industrially important thermostable enzymes: a review. *Bioresour. Technol.* **2003**, *89*, 17−34.

(24) Giver, L.; Gershenson, A.; Freskgard, P.-O.; Arnold, F. H. Directed evolution of a thermostable esterase. *Proc. Natl. Acad. Sci. U. S. A.* **1998**, *95*, 12809−12813.

(25) Hecky, J.; Müller, K. M. Structural perturbation and compensation by directed evolution at physiological temperature leads to thermostabilization of β-lactamase. *Biochemistry* **2005**, *44*, 12640−12654.

(26) Kim, M. S.; Lei, X. G. Enhancing thermostability of *Escherichia coli* phytase AppA2 by error-prone PCR. *Appl. Microbiol. Biotechnol.* **2008**, *79*, 69−75.

(27) Ruller, R.; Deliberto, L.; Ferreira, T. L.; Ward, R. J. Thermostable variants of the recombinant xylanase A from *Bacillus subtilis* produced by directed evolution show reduced heat capacity changes. *Proteins: Struct., Funct., Genet.* **2008**, *70*, 1280−1293.

(28) Zhang, S. B.; Pei, X. Q.; Wu, Z. L. Multiple amino acid substitutions significantly improve the thermostability of feruloyl esterase A from *Aspergillus niger*. *Bioresour. Technol.* **2012**, *117*, 140−147.

DOI: 10.1021/acs.jafc.5b03424
J. Agric. Food Chem. 2015, 63, 8225−8233

(29) Wong, D. W. S. Feruloyl Esterase. *Appl. Biochem. Biotechnol.* **2006**, *133*, 87−112.
(30) Fazary, A. E.; Ju, Y.- H. Feruloyl Esterases as Biotechnological Tools: Current and Future Perspectives. *Acta Biochim. Biophys. Sin.* **2007**, *39*, 811−828.
(31) Sang, S. L.; Li, G.; Hu, X. P.; Liu, Y. H. Molecular cloning, overexpression and characterization of a novel feruloyl esterase from a soil metagenomic library. *J. Mol. Microbiol. Biotechnol.* **2011**, *20*, 196−203.
(32) Chen, S. K.; Wang, K.; Liu, Y. H.; Hu, X. P. Crystallization and preliminary X-ray analysis of a novel halotolerant feruloyl esterase identified from a soil metagenomic library. *Acta Crystallogr., Sect. F: Struct. Biol. Cryst. Commun.* **2012**, *68*, 767−70.
(33) Mastihuba, V. r.; Kremnický, L. r.; Mastihubová, M.; Willett, J.; Côté, G. L. A spectrophotometric assay for feruloyl esterases. *Anal. Biochem.* **2002**, *309*, 96−101.
(34) Leiros, H. K.; Flydal, M. I.; Martinez, A. Structural and thermodynamic insight into phenylalanine hydroxylase from the human pathogen *Legionella pneumophila*. *FEBS Open Bio* **2013**, *3*, 370−8.
(35) Topakas, E.; Stamatis, H.; Biely, P.; Kekos, D.; Macris, B. J.; Christakopoulos, P. Purification and characterization of a feruloyl esterase from *Fusarium oxysporum* catalyzing esterification of phenolic acids in ternary water−organic solvent mixtures. *J. Biotechnol.* **2003**, *102*, 33−44.
(36) Mukherjee, G.; Singh, R. K.; Mitra, A.; Sen, S. K. Ferulic acid esterase production by *Streptomyces* sp. *Bioresour. Technol.* **2007**, *98*, 211−213.
(37) Nicoli, D.; Benedek, G. Study of thermal denaturation of lysozyme and other globular proteins by light-scattering spectroscopy. *Biopolymers* **1976**, *15*, 2421−2437.
(38) Gast, K.; Damaschun, H.; Misselwitz, R.; Müller-Frohne, M.; Zirwer, D.; Damaschun, G. Compactness of protein molten globules: temperature-induced structural changes of the apomyoglobin folding intermediate. *Eur. Biophys. J.* **1994**, *23*, 297−305.
(39) Morris, A. M.; Watzky, M. A.; Finke, R. G. Protein aggregation kinetics, mechanism, and curve-fitting: a review of the literature. *Biochim. Biophys. Acta, Proteins Proteomics* **2009**, *1794*, 375−97.
(40) Shoichet, B. K.; Baase, W. A.; Kuroki, R.; Matthews, B. W. A relationship between protein stability and protein function. *Proc. Natl. Acad. Sci. U. S. A.* **1995**, *92*, 452−456.
(41) Cherry, J. R.; Lamsa, M. H.; Schneider, P.; Vind, J.; Svendsen, A.; Jones, A.; Pedersen, A. H. Directed evolution of a fungal peroxidase. *Nat. Biotechnol.* **1999**, *17*, 379−384.
(42) Hegde, S.; Muralikrishna, G. Isolation and partial characterization of alkaline feruloyl esterases from *Aspergillus niger* CFR 1105 grown on wheat bran. *World J. Microbiol. Biotechnol.* **2009**, *25*, 1963−1969.
(43) Byun, J. S.; Rhee, J. K.; Kim, N. D.; Yoon, J.; Kim, D. U.; Koh, E.; Oh, J. W.; Cho, H. S. Crystal structure of hyperthermophilic esterase EstE1 and the relationship between its dimerization and thermostability properties. *BMC Struct. Biol.* **2007**, *7*, 47.
(44) Heikinheimo, P.; Goldman, A.; Jeffries, C.; Ollis, D. L. Of barn owls and bankers: a lush variety of α/β hydrolases. *Structure* **1999**, *7*, R141−R146.
(45) Wei, Y.; Contreras, J. A.; Sheffield, P.; Osterlund, T.; Derewenda, U.; Kneusel, R. E.; Matern, U.; Holm, C.; Derewenda, Z. S. Crystal structure of brefeldin A esterase, a bacterial homolog of the mammalian hormone-sensitive lipase. *Nat. Struct. Biol.* **1999**, *6*, 340−345.
(46) De Simone, G.; Menchise, V.; Manco, G.; Mandrich, L.; Sorrentino, N.; Lang, D.; Rossi, M.; Pedone, C. The Crystal Structure of a Hyper-thermophilic Carboxylesterase from the Archaeon *Archaeoglobus fulgidus*. *J. Mol. Biol.* **2001**, *314*, 507−518.
(47) Lenfant, N.; Hotelier, T.; Velluet, E.; Bourne, Y.; Marchot, P.; Chatonnet, A. ESTHER, the database of the α/β-hydrolase fold superfamily of proteins: tools to explore diversity of functions. *Nucleic Acids Res.* **2013**, *41*, D423−D429.

DOI: 10.1021/acs.jafc.5b03424
J. Agric. Food Chem. 2015, 63, 8225−8233

Figure 1. Effect of moisture on color development before and after roasting at 120 °C for 90 min in (a) raw and roasted almonds exposed to 5% moisture (control) and (b) raw and roasted almonds exposed to 11% moisture.

Little information is available regarding the chemical changes that occur in raw almonds with CD as most experimental data are derived on roasted nuts where the defect can be seen. However, information on the chemical changes that occur in the raw almonds is critical for developing screening methods and for optimizing drying, roasting, and storage conditions to decrease product loss related to CD. The specific objectives of this study were to (1) develop a colorimetric method based upon CIE *LCh* color values to identify CD in raw almonds; (2) evaluate the influence of temperature and moisture on the development of CD in raw almonds; and (3) evaluate the volatile profiles of raw almonds with CD to further identify the chemical changes that occur with the development of CD.

MATERIALS AND METHODS

Chemicals and Reagents. Reagents were purchased from either Sigma-Aldrich (St. Louis, MO, USA) or Fisher Scientific (Pittsburgh, PA, USA) and included C_7−C_{40} saturated alkanes standard (1000 μg/mL in hexane), ethanol (HPLC/spectrophotometric grade), and 2-methyl-1-propanol, 1-butanol, 3-methyl-1-butanol, 1-pentanol, 1-hexanol, heptanol, 1-octanol, 1-nonanol, benzyl alcohol, phenylethyl alcohol, hexanal, nonanal, and benzaldehyde. Octanal-d_{16}, 2-methylpyrazine-d_6, and *n*-hexyl-d_{13} alcohol were used as stable isotope internal standards for three major categories of identified compounds (i.e., aldehydes, pyrazines, and alcohols). Stable isotopes were purchased from C/D/N Isotopes Inc. (Quebec, Canada).

Experimental Design. Dehulled raw kernels (100 lb, var. Nonpareil) were supplied by the Nickels Soil Laboratory (Arbuckle, CA, USA) in September 2012. Twenty-seven vessels each containing 100 almond kernels were exposed to conditions that produced an internal kernel moisture content of 5% (actual 4.75 ± 0.4%), 8% (actual 8.4 ± 0.35%), or 11% (actual 11.55 ± 0.35%) moisture in a controlled-atmosphere incubator (Thermo Scientific, Marietta, OH, USA) at 35 ± 2 °C. Three individual vessels were removed every other day, and samples were evaluated for moisture, CIE *LCh* color, and volatile analysis by HS-SPME-GC/MS. Almonds treated at 5 and 8% moisture were monitored for 18 days. Almonds treated with 11% moisture were monitored for 7 days. The same procedure was repeated at 45 ± 2 °C.

Moisture Determination. The moisture content of the almonds was determined gravimetrically by drying homogenized samples (~1 g) at 95−105 °C under vacuum for 48 h. Moisture was determined in triplicate, and the results were averaged.

Colorimetric Measurements. Raw almond kernels (420) were split in half along the natural seam, and each half was placed into one of two identical racks with individual identifying slots. One rack of the split kernels was roasted at 120 °C for 90 min, whereas the other rack was not roasted. Almonds with visual apparent darkening after roasting (i.e., those with CD) were grouped separately from the nondarkened kernels (i.e., those without CD), and the surface color of each individual kernel was measured using a LabScan XE spectrophotometer (HunterLab, Reston, VA, USA). The color values *L** (lightness), *C* (chroma), and *h* (hue), according to the CIE *LCh* color scale, were recorded using a port size of 0.4 in. with a D65 optical sensor, 0° geometry, and 10° angle of vision.

As CD is apparent only after heat treatment, raw almond half-kernels with CD were identified by matching the half-kernels that developed CD upon roasting with the corresponding raw half-kernels. Color measurement of raw kernels was made as described above. Evaluations were performed in triplicate and the results averaged.

HS-SPME-GC/MS Analysis. Volatiles were analyzed using a previously reported method, with a smaller sample size (200 mg versus 5 g).[16] Briefly, ground almonds (200 mg) were added to a 2 mL crimp-top vial with 5 μL of mixture of internal standard (10 μg/mL, octanal-d_6, 2-methylpyrazine-d_6, and *n*-hexyl-d_{13} alcohol) and sealed with an aluminum seal (PTFE/silicone liner, Fisherbrand, Fisher Scientific, USA). The samples were incubated for 60 min at room temperature. Samples were exposed to a previously conditioned 1 cm 50/30 μm DVB/CAR/PDMS solid phase microextraction (SPME) fiber (Supelco, Inc., Bellefonte, PA, USA) over the headspace (HS) of the sample for 60 min at ambient temperature. The SPME fiber was immediately injected for 10 min into a Hewlett-Packard 6890 series gas chromatography (GC) system coupled with a HP 5973 mass selective detector (MS; Agilent Technologies, Palo Alto, CA, USA). An Agilent DB-Wax column (30 m length, 0.25 mm i.d., 0.25 μm film) was used to separate compounds. The oven temperature program started with an initial setting of 40 °C for 1 min, followed by a ramp of 5 °C/min to 180 °C, then 10 °C/min to 210 °C with a hold time of 3 min. The injector temperature was set at 240 °C. Helium was used as the carrier gas at a flow at 0.7 mL/min. MS transfer line temperature was set at 250 °C. The temperatures of MS quadrupole and MS source were 150 and 230 °C, respectively. Total ion chromatograms (TICs) were collected by scanning from *m*/*z* 30 to 180 at a rate of 2.48 scans/s.

Identification and Relative Quantitation. Volatile compounds were identified by comparison of their MS spectra and retention times with those of authentic standards. Volatile compounds without authentic standards were tentatively identified by comparing the Kovats' retention indices (KI) and/or mass spectrum with those reported in the NIST Mass Spectral Search Program (version 2.0 a) with >80% as a cutoff to match compounds. The KIs were calculated from the retention times of C_7−C_{40} *n*-alkanes.

Relative quantitation of each volatile compound was performed by comparing the total peak area at of each compound to the total peak area of one of three internal standards (IS) (i.e., octanal-d_{16}, 2-methylpyrazine-d_6, and *n*-hexyl-d_{13} alcohol, for aldehydes, pyrazines, and alcohols, respectively). Relative concentration was determined using eq 1 according to Baek et al.[17] and Hopfer et al.:[18]

$$\text{rel concn}\left(\frac{\text{ng}}{\text{g}}\right) = \frac{\left(\frac{\text{peak area}}{\text{IS peak area}}\right)}{\text{sample wt}} \times \text{IS added} \quad (1)$$

Statistical Analysis. All statistical analyses were performed using Graphpad Pism version 6.01 (GraphPad Software, Inc.). All data sets were tested for significance (p value < 0.05) using a t test for

DOI: 10.1021/acs.jafc.5b03121
J. Agric. Food Chem. 2015, 63, 8234−8240

Table 1. CIE *LCh* (Lightness, Chroma, and Hue) Color Values for Raw and Roasted Almonds with Concealed Damage (CD) and without Concealed Damage (NCD)[a]

	raw almonds		roasted almonds	
	NCD	CD	NCD	CD
lightness (L)	79.46 ± 2.97	70.62 ± 6.40	78.71 ± 3.69	58.82 ± 8.22
chroma (C)	16.65 ± 2.26	20.69 ± 2.32	20.55 ± 3.32	31.82 ± 4.48
hue (h)	87.24 ± 1.15	86.24 ± 1.52	82.73 ± 12.45	71.20 ± 4.11

[a]All values are significant at the $p < 0.05$ level.

comparing temperature (35 and 45 °C), moisture content (5, 8, and 11%), and group (NCD and CD).

Values given in Table 3 were calculated as follows. The mean (18 day average) was calculated for each volatile at 5 and 8% moisture, in each group (i.e., CD and NCD) at 35 °C (data not shown). The difference between the means was determined (CD − NCD) and is given in column (a) (5% moisture) or column (b) (8% moisture). A positive value indicates that the volatile is higher in the CD group as compared to the NCD group. The value reported in column (c) (% relative change) was obtained using eq 2.

$$\text{rel \% change} = \frac{(\text{mean at 8\%} - \text{mean at 5\%})}{\text{mean at 5\%}} \times 100 \quad (2)$$

A positive value indicates that there was an increase in this volatile in the 8% moisture group relative to the 5% moisture group. Values for Table 4 were calculated as above but using data obtained at 45 °C.

Values given in Table 5 were calculated as follows. The mean (18 day average) was calculated for each volatile at 35 and 45 °C, at 5 or 8% moisture (data not shown). The difference between the group means (45 − 35 °C) for each volatile was calculated, and data are given in column (a) for 5% moisture or in column (b) for 8% moisture. A positive value indicates that there was an increase in the volatile at 45 °C relative to that at 35 °C. The value reported in column (c) (% relative change) was obtained using eq 3.

$$\text{rel \% change} = \frac{(\text{mean at 45 °C} - \text{mean at 35 °C})}{\text{mean at 35 °C}} \times 100 \quad (3)$$

RESULTS AND DISCUSSION

Although CD is defined by the almond industry as a "dark" brown color covering ~50% of the kernel after heat treatment, this definition varies among processors and identification relies on a subjective visual inspection of the roasted kernels.[19] To date, processors have tried several methods to identify the extent of CD before roasting, including blanching raw almonds and splitting open the kernels and visually determining the number of kernels with CD. Currently, there are no reliable methods for measuring CD in raw almonds, and a lack of screening methods can result in considerable production losses. Herein the CIE lightness (L), chroma (C), and hue (h) color values were measured in raw and roasted almonds with the goal of identifying a numerical color value corresponding to CD in both raw and roasted almonds. As CD is not visible in raw almonds, kernels were first split in half along the natural seam, and half of the kernel was roasted at 120 °C for 90 min, whereas the other half was not. CIE color values were measured in the roasted kernel halves with visual discoloration over ≥50% of the kernel (i.e., those with visible CD; Figure 1b) and in roasted kernels without visual discoloration (those with no visible CD (NCD); Figure 1a), and the results are given in Table 1. The means of the lightness (L) color value had the greatest difference (78.71 ± 3.69 for NCD and 58.82 ± 8.22 for CD) as compared to hue (h) and chroma (C) and allowed for the separation of CD and NCD almonds using an L color value cutoff of 70.00 (Table 1). More than 400 almonds were evaluated in this way to establish this relationship. Therefore, for the purpose of this study, roasted almonds with CD are defined as those with an L color value of ≤70.0, whereas those with an L color value of ≥70.0 are defined as having no concealed damage (NCD).

Using this definition, the roasted kernel halves were matched to their corresponding raw kernel halves, and the CIE *LCh* color values were measured in the raw kernels. In the raw kernels, the mean L color value was significantly lower in almonds with CD (70.62 ± 6.40) as compared to almonds with NCD (79.46 ± 2.97). The mean C color value was significantly higher in almonds with CD (20.69 ± 2.32) as compared to the NCD almonds (16.65 ± 2.26), and the mean h color value was significantly higher in NCD almonds (87.24 ± 1.15) as compared to the almonds with CD (86.98 ± 1.52). Although color values were significantly different at the $p < 0.05$ level in the raw almonds, there is not enough difference (±2 SD) for these values to be used as a robust screening tool for detecting CD in raw almonds by colorimetry. Therefore, all studies investigating the influence of moisture and temperature on volatiles relied on splitting almond kernels in half, roasting half, and identifying the roasted half kernels with CD using an L color value of ≤70.0. These were then matched with the corresponding raw kernel half to identify the raw kernels with CD.

In raw almonds exposed to 5% moisture and 45 °C, only 2–3% of the kernels formed CD over the 18 days of the study (Figure 2). These almonds were considered the control group for all comparisons. An approximately 20% increase in CD was observed in almonds exposed to 8% moisture at 35 °C. These levels remained consistent at ~25% over the 18 days. At 45 °C, the trend was similar and approximately 20% of the almonds

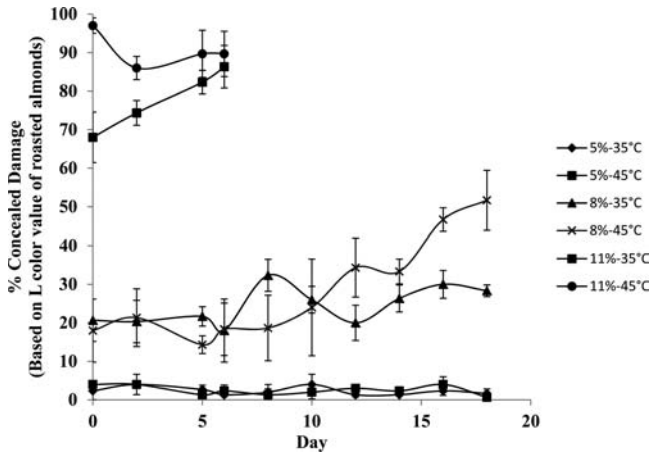

Figure 2. Percent concealed damage (CD) as measured by the CIE L color value in raw almonds held at 5, 8, and 11% moisture and stored at 35 and 45 °C for 18 days.

DOI: 10.1021/acs.jafc.5b03121
J. Agric. Food Chem. 2015, 63, 8234–8240

had CD until day 10. After the 10th day, CD increased, reaching 52% on the 18th day of the study. In comparison, almonds exposed to 11% moisture displayed a significant level of CD beginning the first day of the experiment. For example, 68 ± 7% of the almonds stored at 35 °C displayed CD on the first day of this study and levels increased to ∼100% by day 5, whereas 97 ± 2% of the almonds stored at 45 °C displayed CD on the first day of the study (Figure 2). As so many of the almond kernels exposed to 11% moisture developed CD immediately, we were unable to make reliable comparisons between the CD and NCD almonds in this group. Walton et al.[8] demonstrated a similar result in raw macadamia nuts exposed to a moisture content >20% for 5 days at temperatures ≥30 °C; after 5 days, discoloration affected 90% of the kernels.

The profile of volatile compounds was measured in raw almond kernels using HS-SPME-GC/MS.[16] The main volatiles identified include 19 alcohols, 3 aldehydes, 3 lactones, and 3 organic acids (Table 2). Volatiles identified herein were similar to volatiles reported in Monterey and a Greek variety of almond (name not provided)[20−22] and include 3-methyl-butanol, 3-methyl-3-buten-1-ol, 1-pentanol, 1-hexanol, benzyl alcohol, phenylethyl alcohol, hexanal, nonanal, benzaldehyde, butyrolactone, γ-hexalactone, and acetic acid. Herein, 1-nonanol was identified in almonds for the first time, whereas the following compounds were tentatively identified: 1-propanol, 2-methyl-2,3-pentanediol, 3-methyl-2-butanol, 2-methyl-3-pentanol, 2-methyl-2-buten-1-ol, γ-pentalactone, pentanoic acid, and hexanoic acid.

Almonds exposed to 5% moisture and stored at 35 °C showed little significant difference in the volatile composition between the CD and NCD groups (Table 3, column a). More significant differences were observed when CD and NCD almonds from the 8% moisture group (Table 3, column (b)) were compared. In general, increasing the moisture content from 5 to 8% significantly increased levels of most volatiles (Table 3, column (c)) with the exceptions of hexanal and 3-methyl-1-butanol, which decreased. A decrease in hexanal could be due to increased dehydrogenase activity at the higher moisture level.

In contrast, at 45 °C and either 5 or 8% moisture, significant differences were observed for numerous volatile compounds (Table 4, columns (a) and (b)). Significant increases ($p < 0.05$) were observed in the aldehydes (i.e., hexanal, nonanal, and benzaldehyde) and lactones (i.e., γ-pentalactone, butyrolactone, and γ-hexalactone) at 45 °C as compared to 35 °C. In general, increases in temperature enhance the rate at which many reactions (chemical, enzymatic, and metabolic) occur,[23] which could explain the higher levels of volatile found in both the 5 and 8% moisture groups at 45 °C as compared to 35 °C. Increasing moisture from 5 to 8% at 45 °C also produced a significant increase in the relative concentrations of almost all volatiles (Table 4, column (c)). Volatiles that increased can be broadly categorized as byproducts of lipid oxidation (3−9 carbon alcohols, aldehydes, and organic acids), lipid metabolism (lactones), and compounds resulting from increases in enzymatic activities (benzaldehyde, phenylethyl alcohol, benzyl alcohol). These findings agree with results reported by Mira et al.,[24] who characterized the volatiles in lettuce seeds stored at 35 °C with water contents ranging from 3 to 9% moisture. Seeds stored at a water content >6% moisture showed an increase in volatiles related with lipid peroxidation (4−7 carbon alkanes, alcohols, aldehydes, and ketones). When the effect of just temperature (Table 5) is considered, it is apparent that increases in temperature enhanced the levels of most volatiles measured. Greater than 90% increases were observed with compounds primarily related with lipid oxidation and include hexanal, nonanal, acetic acid, 2-ethyl-1-hexanol, γ-pentalactone, and pentanoic and hexanoic acid.

Although benzaldehyde and benzyl alcohol are important flavor components in bitter almonds, the levels appear to be

Table 2. HS-SPME-GC/MS Identification of Volatiles in Raw Almonds (var. Nonpareil)

volatile compound	KI	standard KI	literature KI[a]	internal standard[b]
1-propanol[c]	1037		1037/1038	hexyl-d_{13} alcohol
hexanal[d]	1078	1070	1084/1067	octanal-d_{16}
2-methyl-1-propanol[d]	1098	1093	−/1085	hexyl-d_{13} alcohol
2-methyl-2,3-pentanediol[c]	1114			hexyl-d_{13} alcohol
3-methyl-2-butanol[c]	1125			hexyl-d_{13} alcohol
1-butanol[d]	1149	1147	1145/1138	hexyl-d_{13} alcohol
2-methyl-3-pentanol[c]	1161			hexyl-d_{13} alcohol
3-methyl-1-butanol[d]	1214	1207	1205/1206	hexyl-d_{13} alcohol
3-methyl-3-buten-1-ol[c]	1254		−/1240	hexyl-d_{13} alcohol
1-pentanol[d]	1257	1251	1255/1244	hexyl-d_{13} alcohol
2-methyl-2-buten-1-ol[c]	1329		−/1315	hexyl-d_{13} alcohol
1-hexanol[d]	1362	1354	1360/1360	hexyl-d_{13} alcohol
nonanal[c]	1399	1393	1385/1402	octanal-d_{16}
acetic acid[c]	1454		1450/1452	hexyl-d_{13} alcohol
heptanol[d]	1464	1456	1467/−	hexyl-d_{13} alcohol
2-ethyl-1-hexanol[c]	1498		−/1492	hexyl-d_{13} alcohol
benzaldehyde[d]	1527	1519	1495/1525	octanal-d_{16}
1-octanol[d]	1567	1559	1553/1566	hexyl-d_{13} alcohol
1,2-propanediol[c]	1599		−/1603	hexyl-d_{13} alcohol
γ-pentalactone[c]	1614		−/1600	octanal-d_{16}
butyrolactone[c]	1631		1647/1640	octanal-d_{16}
1-nonanol[d]	1670	1661		hexyl-d_{13} alcohol
γ-hexalactone[c]	1707		−/1694	octanal-d_{16}
pentanoic acid[c]	1746			hexyl-d_{13} alcohol
hexanoic acid[c]	1855		−/1847	hexyl-d_{13} alcohol
benzyl alcohol[d]	1882	1872	1865/−	hexyl-d_{13} alcohol
phenylethyl alcohol[d]	1919	1908		hexyl-d_{13} alcohol
total 2,3-butanediol[c,e]				hexyl-d_{13} alcohol

[a]KI, Kovats' indices. Values were obtained from Flavornet, http://www.flavornet.org/f_kovats.html/Pherobase, http://www.pherobase.com/database/kovats/kovats-index.php [b]Internal standard used for relative quantitation. [c]Compounds "tentatively identified" on the basis of their MS spectra and MS fragmentation pattern. [d]Compounds verified with authentic standards. [e]Corresponds to the sum of the two isomers.

DOI: 10.1021/acs.jafc.5b03121
J. Agric. Food Chem. 2015, 63, 8234−8240

Table 3. Effect of Increasing Moisture from 5 to 8% at 35 °C on the Relative Concentrations of Volatiles in Raw Almonds[a]

	(a) 5% moisture, difference between means (CD − NCD) (μg/kg ± SEM)	(b) 8% moisture, difference between means (CD − NCD) (μg/kg ± SEM)	(c) rel % change
1-propanol	−1.04 ± 2.24	−4.07 ± 2.69	5
hexanal	6.19 ± 4.26	ND	−100*
2-methyl-1-propanol	−2.06 ± 3.62	−3.31 ± 6.83	70*
2-methyl-2,3-pentanediol	ND	−0.13 ± 0.36	1267*
3-methyl-2-butanol	−0.08 ± 0.60	0.13 ± 2.16	169*
1-butanol	−1.75 ± 0.97*	0.03 ± 0.77	−15*
2-methyl-3-pentanol	0.07 ± 0.89	−0.50 ± 0.53	42*
3-methyl-1-butanol	15.10 ± 8.98	24.30 ± 47.90	139*
3-methyl-3-buten-1-ol	−0.80 ± 1.35	1.56 ± 0.74*	−7
1-pentanol	−6.99 ± 5.31	40.60 ± 15.20*	9
2-methyl-2-buten-1-ol	−0.61 ± 0.89	−1.09 ± 1.14	47*
1-hexanol	5.11 ± 11.90	181 ± 100*	152*
nonanal	0.95 ± 2.11	16.10 ± 2.52*	51*
acetic acid	12.50 ± 7.56	12.20 ± 20.90	153*
1-heptanol	−0.17 ± 1.27	7.15 ± 11.20	108*
2-ethyl-1-hexanol	−0.24 ± 0.59	−2.43 ± 5.52	609*
benzaldehyde	−0.17 ± 0.51	3.96 ± 1.28*	40*
1-octanol	−1.02 ± 1.09	3.84 ± 7.12	168*
1,2-propanediol	0.17 ± 0.48	−0.60 ± 0.51	18*
γ-pentalactone	ND	3.62 ± 0.78*	100*
butyrolactone	4.05 ± 3.11	19.50 ± 2.24*	87*
1-nonanol	1.32 ± 0.76*	−1.55 ± 1.24	215*
γ-hexalactone	ND	2.90 ± 0.51*	100*
pentanoic acid	0.42 ± 0.42	−0.34 ± 0.96	8
hexanoic acid	−0.26 ± 1.78	−9.17 ± 3.60*	125*
benzyl alcohol	−0.84 ± 0.59	−3.66 ± 1.33*	235*
phenylethyl alcohol	−0.19 ± 0.49	−2.40 ± 0.66*	678*
total 2,3-butanediol	0.60 ± 3.72	12.10 ± 12.00	240*

[a]Columns (a) and (b) represent the difference between CD and NCD group means at 5 and 8% moisture, respectively. Column (c) represents the relative % change induced by increasing moisture from 5 to 8%. *, values significant at $p < 0.05$. ND, not detected; SEM, standard error of the mean.

Table 4. Effect of Increasing Moisture from 5 to 8% at 45 °C on the Relative Concentrations (μg/kg) of Volatiles in Raw Almonds[a]

	(a) 5% moisture, difference between means (CD − NCD) (μg/kg ± SEM)	(b) 8% moisture, difference between means (CD − NCD) (μg/kg ± SEM)	(c) rel % change
1-propanol	−12.00 ± 1.40*	−14.40 ± 6.71*	90*
hexanal	26.40 ± 5.87*	15.60 ± 1.62*	−74*
2-methyl-1-propanol	−14.60 ± 3.62*	−26.20 ± 10.50*	87*
2-methyl-2,3-pentanediol	ND	−2.32 ± 0.55*	100*
3-methyl-2-butanol	−2.87 ± 0.47*	−7.90 ± 3.28*	224*
1-butanol	−16.00 ± 2.58*	−15.70 ± 3.73*	40*
2-methyl-3-pentanol	−6.16 ± 0.64*	7.20 ± 2.21*	61*
3-methyl-1-butanol	−22.70 ± 16.40	−207 ± 103*	264*
3-methyl-3-buten-1-ol	−2.94 ± 0.67*	−1.93 ± 0.74*	−17*
1-pentanol	−57.60 ± 22.00*	18.70 ± 23.30	−8
2-methyl-2-buten-1-ol	−2.87 ± 0.59*	1.43 ± 1.90	31*
1-hexanol	−55.40 ± 39.00	287 ± 113*	120*
nonanal	20.60 ± 4.90*	30.70 ± 3.17*	−10
acetic acid	−15.70 ± 3.84*	−66.20 ± 100.00	733*
1-heptanol	−6.97 ± 3.43*	28.90 ± 15.80*	188*
2-ethyl-1-hexanol	−0.33 ± 1.89	−0.96 ± 3.48	151*
benzaldehyde	2.76 ± 0.69*	10.10 ± 1.62*	−18
1-octanol	−3.78 ± 2.63	19.20 ± 9.45*	213*
1,2-propanediol	−2.75 ± 0.23*	−2.63 ± 1.89	165*
γ-pentalactone	2.25 ± 0.34*	10.50 ± 2.31*	945*
butyrolactone	−3.91 ± 0.92*	32.77 ± 7.15*	102*
1-nonanol	1.95 ± 1.14	−0.13 ± 2.53	117*
γ-hexalactone	1.42 ± 0.25*	7.54 ± 1.55*	1000*
pentanoic acid	0.45 ± 0.79	0.81 ± 1.72	92*
hexanoic acid	−0.41 ± 3.53	−1.17 ± 16.50	217*
benzyl alcohol	−0.64 ± 1.17	−1.33 ± 1.39	50*
phenylethyl alcohol	−0.59 ± 0.52	−1.94 ± 2.41	386*
total 2,3-butanediol	3.67 ± 4.84	−13.1 ± 11.15	78*

[a]Columns (a) and (b) represent the difference between CD and NCD group means at 5 and 8% moisture, respectively. Column (c) represents the relative % change induced by increasing moisture from 5 to 8%. *, values significant at $p < 0.05$. ND, not detected; SEM, standard error of the mean.

relatively low in sweet almond varities.[16,18] The opposite appears to be true with 2,3-butanediol, for which levels are relatively higher in some sweet varieties as compared to bitter varieties.[25] To date, little information is available with respect to the content and relationships of these compounds in different varieties of sweet almonds. Herein, we show that benzyl alcohol and 2,3-butanediol are influenced by moisture but not temperature and that levels of benzaldehyde are influenced by temperature at low moisture levels (<5%).

In conclusion, we demonstrate that CIE *LCh* colorimetric measurement of raw almond kernels, for routine screening for CD, is not possible using the conditions described herein. However, CIE *LCh* colorimetric measurements of roasted almonds can be used to identify CD in roasted almonds and have potential as a post-roasting screening tool. Studies of volatiles indicate that although the profiles are similar between CD and NCD almonds, the levels of volatiles related to lipid peroxidation and amino acid degradation are higher in the CD group. These studies suggest that postharvest moisture exposure resulting in a kernel moisture content ≥8% is a key factor in the development of CD in almonds and that increases in temperature will accelerate this process. Future studies should focus on investigating if CD can be reduced by drying almonds with moisture levels ≥8% to <6% prior to roasting, evaluating the impact of CD on storage and shelf life of almonds, and alternative screening methods (e.g., near infrared reflectance spectroscopy, NIR) for detecting CD in raw almonds.

DOI: 10.1021/acs.jafc.5b03121
J. Agric. Food Chem. 2015, 63, 8234−8240

Table 5. Effect of Temperature at a Moisture Content of either 5 or 8% on the Relative Concentration of Volatiles in Raw Almonds[a]

	(a) 5% moisture, difference between means (45 − 35 °C) (μg/kg ± SEM)	(b) 8% moisture, difference between means (45 − 35 °C) (μg/kg ± SEM)	(c) rel % change
1-propanol	−3.45 ± 1.88*	12.10 ± 3.92*	19*
hexanal	17.70 ± 4.70*	12.20 ± 1.95*	103*
2-methyl-1-propanol	1.94 ± 3.01	9.61 ± 6.80	12
2-methyl-2,3-pentanediol	ND	−1.21 ± 0.42*	−16
3-methyl-2-butanol	−0.08 ± 0.50	3.42 ± 2.12	13
1-butanol	3.31 ± 2.28	11.60 ± 2.58*	61*
2-methyl-3-pentanol	1.72 ± 0.91*	4.38 ± 1.38*	37*
3-methyl-1-butanol	28.50 ± 9.62*	280.00 ± 60.10*	65*
3-methyl-3-buten-1-ol	−1.90 ± 0.81*	−3.04 ± 0.58*	19*
1-pentanol	40.00 ± 13.1*	33.50 ± 13.80*	48*
2-methyl-2-buten-1-ol	1.61 ± 0.62*	0.26 ± 1.10*	7
1-hexanol	60.80 ± 20.80*	91.10 ± 83.00	32
nonanal	23.30 ± 3.51*	11.7 ± 4.44*	90*
acetic acid	1.12 ± 4.72	208.00 ± 50.50*	173*
1-heptanol	−2.07 ± 1.95	7.47 ± 10.00	11
2-ethyl-1-hexanol	1.73 ± 0.96*	−4.74 ± 3.19	310*
benzaldehyde	3.44 ± 0.52*	−1.83 ± 1.60	8
1-octanol	0.72 ± 1.45	5.81 ± 6.18	23
1,2-propanediol	−1.42 ± 0.41*	3.44 ± 1.00*	19
γ-pentalactone	1.13 ± 0.31*	5.11 ± 1.74*	94*
butyrolactone	2.37 ± 1.71	7.22 ± 5.70	21
1-nonanol	1.45 ± 0.72*	−1.16 ± 1.3*8	2
γ-hexalactone	0.71 ± 0.20*	2.46 ± 1.22*	59*
pentanoic acid	2.35 ± 0.44	6.68 ± 0.96*	168*
hexanoic acid	5.49 ± 1.92*	27.0 ± 8.36*	103*
benzyl alcohol	2.53 ± 0.65*	−2.58 ± 1.04*	−0.3
phenylethyl alcohol	1.36 ± 0.35*	3.57 ± 1.27*	54*
total 2,3-butanediol	17.8 ± 3.00*	−20.4 ± 8.24*	−2

[a]Columns (a) and (b) represent the difference between means at 35 and 45°C. Column (c) represents the relative % change due to increasing temperature from 35 to 45 °C. *, values significant at $p < 0.05$. ND, not detected; SEM, standard error of the mean.

AUTHOR INFORMATION

Corresponding Author

*(A.E.M.) Phone: (530) 304-6618. Fax: (530) 752-4759. E-mail: aemitchell@ucdavis.edu.

Present Address

#(J.L.) Department of Food Science and Technology, Chung-Ang University, Anseong 456-756, South Korea. E-mail: jihlee@cau.ac.kr.

Funding

The Almond Board of California provided financial support for this study. We also acknowledge the support of the John Kinsella Endowed Chair in food, nutrition, and health.

Notes

The authors declare no competing financial interest.

ACKNOWLEDGMENTS

We thank Dr. Thomas Gradziel (Plant Science, UC Davis) and Franz Niederholzer (UC Farm Advisor Colusa/Sutter/Yuba Counties) for many thoughtful conversations on almond flavor and breeding and for providing almond samples. Additionally, we thank Dr. Susan Ebeler and Anna Hjelmeland from the UC Davis Food Safety and Measurement Facility.

ABBREVIATIONS USED

CD, concealed damage; NCD, no concealed damage; HS-SPME-GC/MS, headspace solid phase microextraction gas chromatography/mass spectrometry

REFERENCES

(1) USDA, N. A. S. S., and C. F. Office California Agricultural Statistics 2011 Crop Year; http://www.nass.usda.gov/Statistics_by_State/California/Publications/California_Ag_Statistics/Reports/2011cas-all.pdf.

(2) King, A. D., Jr.; Halbrook, W. U.; Fuller, G.; Whitehand, L. C. Almond nutmeat moisture and water activity and its influence on fungal flora and seed composition. *J. Food Sci.* **1983**, *48*, 615−617.

(3) Reil, W., Labavitch, J. M.; Holmberg, D. Harvesting. In *Almond Production Manual*; Micke, W. C., Ed.; Publication 3364; University of California, Division of Agriculture and Natural Resources: Oakland, CA, USA, 1996; pp 260−264.

(4) Kader, A. A.; Thompson, J. F. Postharvest handling systems: tree nuts. In *Postharvest Technology of Horticultural Crops*; Kader, A. A., Ed.; Publication 3311; University of California, Division of Agriculture and Natural Resources: Oakland, CA, USA, 1992; pp 254.

(5) California, A. B. o. Field Quality: Stockpile Management + Concealed Damage; http://www.almonds.com/sites/default/files/content/attachments/12._field_quality_stockpile_management_and_concealed_damage_2013.pdf.

(6) Almond Board of California. HARVEST OVERVIEW: The California Almond Harvest; http://www.almonds.com/growers/in-the-orchard.

(7) Lampinen, B.; Michailides, T. *Almond Stockpile Monitoring for Aflatoxin Potential. Final research report 08-AFLA2-Lampinen*; Almond Board of California: 1150 9th St., Suite 1500 Modesto, CA 95354 USA, 2008−2009.

(8) Walton, D. A.; Randall, B. W.; Le Lagadec, M. D.; Wallace, H. M. Maintaining high moisture content of macadamia nuts-in-shell during storage induces brown centres in raw kernels. *J. Sci. Food Agric.* **2013**, *93*, 2953−2958.

(9) Özdemir, M.; Seyhan, F. G.; Bakan, A. K.; Ílter, S.; Özay, G.; Devres, O. Analysis of internal browning of roasted hazelnuts. *Food Chem.* **2001**, *73*, 191−196.

(10) Prichavudhi, K.; Yamamoto, H. Y. Effect of drying temperature on chemical composition and quality of macadamia nuts. *Food Technol.* **1965**, *1153*, 129−132.

(11) Zamora, R.; Hidalgo, F. J. The Maillard reaction and lipid oxidation. *Lipid Technol.* **2011**, *23*, 59−62.

(12) Sathe, S.; Seeram, N.; Kshirsagar, H.; Heber, D.; Lapsley, K. Fatty acid composition of California grown almonds. *J. Food Sci.* **2008**, *73*, C607−C614.

(13) Venkatachalam, M.; Sathe, S. K. Chemical composition of selected edible nut seeds. *J. Agric. Food Chem.* **2006**, *54*, 4705−4714.

(14) Eskin, N. M.; Shahidi, F. *Biochemistry of Foods*; Academic Press: San Diego, CA, USA, 2012.

(15) Zamora, R.; Hidalgo, F. J. Coordinate contribution of lipid oxidation and Maillard reaction to the nonenzymatic food browning. *Crit. Rev. Food Sci. Nutr.* **2005**, *45*, 49−59.

(16) Xiao, L.; Lee, J.; Zhang, G.; Ebeler, S. E.; Wickramasinghe, N.; Seiber, J.; Mitchell, A. E. HS-SPME GC/MS characterization of volatiles in raw and dry-roasted almonds (*Prunus dulcis*). *Food Chem.* **2014**, *151*, 31−39.

DOI: 10.1021/acs.jafc.5b03121
J. Agric. Food Chem. 2015, 63, 8234−8240

(17) Baek, H. H.; Cadwallader, K. R. Volatile compounds in flavor concentrates produced from crayfish-processing byproducts with and without protease treatment. *J. Agric. Food Chem.* **1996**, *44*, 3262−3267.
(18) Hopfer, H.; Ebeler, S. E.; Heymann, H. The combined effects of storage temperature and packaging type on the sensory and chemical properties of Chardonnay. *J. Agric. Food Chem.* **2012**, *60*, 10743−10754.
(19) Pearson, T. C. Spectral properties and effect of drying temperature on almonds with concealed damage. *LWT−Food Sci. Technol.* **1999**, *32*, 67−72.
(20) Beck, J. J.; Higbee, B. S.; Merrill, G. B.; Roitman, J. N. Comparison of volatile emissions from undamaged and mechanically damaged almonds. *J. Sci. Food Agric.* **2008**, *88*, 1363−1368.
(21) Beck, J. J.; Mahoney, N. E.; Cook, D.; Gee, W. S. Volatile analysis of ground almonds contaminated with naturally occurring fungi. *J. Agric. Food Chem.* **2011**, *59*, 6180−6187.
(22) Mexis, S.; Badeka, A.; Chouliara, E.; Riganakos, K.; Kontominas, M. Effect of γ-irradiation on the physicochemical and sensory properties of raw unpeeled almond kernels (*Prunus dulcis*). *Innovative Food Sci. Emerging Technol.* **2009**, *10*, 87−92.
(23) Copeland, L. O. *Principles of Seed Science and Technology*; Springer: Berlin, Germany, 1995.
(24) Mira, S.; González-Benito, M. E.; Hill, L. M.; Walters, C. Characterization of volatile production during storage of lettuce (*Lactuca sativa*) seed. *J. Exp. Bot.* **2010**, *61*, 3915−3924.
(25) Wirthensohn, M. G.; Chin, W. L.; Franks, T. K.; Baldock, G.; Ford, C. M.; Sedgley, M. Characterising the flavour phenotypes of almond (*Prunus dulcis* Mill.) kernels. *J. Hortic. Sci. Biotechnol.* **2008**, *83*, 462−468.

NOTE ADDED AFTER ASAP PUBLICATION

This article published September 8, 2015 with a mistake in the spelling of an author name. Guangwei Huang's name was amended, and the article reposted September 14, 2015.

DOI: 10.1021/acs.jafc.5b03121
J. Agric. Food Chem. 2015, 63, 8234−8240

method to the quantitative and enantioselective analysis of **2a** in young and old white and red wines as well as some juice samples. Studies of the fate of glucose ester **2b** during fermentation were also conducted to determine whether menthiafolic acid (**2a**) could be formed from **2b** during vinification. Finally, the chirality of wine lactone (**1**) and menthiafolic acid (**2a**) in an older wine was also investigated to see whether the isomeric distribution of **1a** and **1b** in the wine was that expected if **1** was formed primarily from **2a**.

MATERIALS AND METHODS

General. All reagents used were purchased from Sigma-Aldrich (Australia). Solvents for GC/MS were CHROMASOLV Plus (Sigma-Aldrich, Australia) or Pest-grade, purchased from Asis Scientific (Hindmarsh, South Australia), and dispensed using a Puresolv solvent purification system (Innovative Technologies, Massachusetts, USA). Other solvents used were OmniSolv HPLC-grade from VWR (Murrarie, QLD, Australia), with the exception of ethanol that was fractionally distilled food-grade ethanol. The water used was purified by a Milli-Q system. Racemic and (6*R*)-(*E*)-2,6-dimethyl-6-hydroxyocta-2,7-dienoic acid (menthiafolic acid, **2a**), menthiafolic acid glucose ester **2b**, racemic d_5-menthiafolic acid, racemic and (3*S*,3a*S*,7a*R*)-3a,4,5,7a-tetrahydro-3,6-dimethylbenzofuran-2-one (wine lactone) were synthesized as described previously.[8,14,17] Commercial wine samples were bottled products obtained from local retail outlets. Juice samples were prepared by homogenizing grape samples (ca. 500 g), centrifuging them at 4 °C at 10 000 rpm (17 666 g) for 30 min, and taking the supernatant to be used for further analyses. The pH of Maggie Beer verjuice (a commercial juice product) was adjusted to 3.2 with potassium hydroxide (aqueous, 1 M). Model wine was redistilled ethanol in Milli-Q water (10 + 90, v/v), saturated with potassium hydrogen tartrate and pH-adjusted to pH 3.2 with L-(+)-tartaric acid (10% w/v in water). Chemically defined grape juice medium (CDGJM) was prepared as described by Ugliano et al.[18] The prepared CDGJM was sterilized by filtration with a 0.22 μm membrane. Synthetic wine was produced by fermentation of CDGJM (3 L) which was inoculated with 4 × 10^6 cells/mL of *Saccharomyces cerevisiae* AWRI 838 cells preadapted in 50:50 YM/CDGJM (60 mL) as described below and incubated at 22.5 °C for 14 days. Progress of fermentations was assessed by weight, and completion was confirmed when residual glucose and fructose concentration was <2g/L. The wine was cold-settled for 5 days at 4 °C and was sterilized by filtration with a 0.22 μm Stericap (Millipore, MA, USA) bottle-top filter device. For gas chromatography−mass spectrometry (GC-MS), positive-ion electron impact (EI) mass spectra were recorded on an Agilent 6890 gas chromatograph (GC) coupled to an Agilent 5973N mass spectrometer (MS) with a GERSTEL MPS2Multi Purpose Sampler. Details of GC-MS operating parameters for quantitative and enantioselective analysis of menthiafolic acid and for enantioselective and nonenantioselective analysis of wine lactone have been given previously.[14,17]

Sample Preparation. For analysis of menthiafolic acid in white wines and grape juices, samples were prepared as described in Giaccio et al.[17] for white wines. Red wine samples (100 mL) were spiked with a solution of d_5-2,6-dimethyl-6-hydroxyocta-2,7-dienoic acid (250 μL, 0.10 mg/mL in ethanol) and then stirred with PVPP (ca. 5 g) under nitrogen for 16 h. The wines were then centrifuged at 10 000 rpm (17 666 g) at 4 °C for 25 min and the supernatant then treated in the same way as the white wine and grape juice samples. For enantioselective analysis of wine lactone in Chardonnay E, the wine (250 mL) containing added sodium chloride (25 g) was continuously extracted with dichloromethane (150 mL) over 24 h. The organic layer was washed with brine (2 × 100 mL), dried ($MgSO_4$), and concentrated to 100 mL through a Vigreux column. The concentrate was then washed with aqueous sodium bicarbonate solution (0.5 M, 2 × 200 mL), dried ($MgSO_4$), and further concentrated to 5 mL. The concentrated extract was then purified by column chromatography on silica gel 60 (30 × 2 cm^2 column, filled to 20 cm). Elution was carried out using pentane/ether (95:5, 200 mL, collected as fraction 1; 90:10, 200 mL, fraction 2; 70:30, 100 mL, fraction 3; 70:30 100 mL, fraction 4; 60:40, 200 mL, fraction 5; and 0:100, 200 mL, fraction 6). All fractions were concentrated to 5 mL as above and further concentrated to 200 μL under a stream of nitrogen. Samples were then transferred into a 2 mL GC/MS vial fitted with a 250 μL insert ready for analysis by GC-MS. Wine lactone was detected in fractions 3 and 4.

Method Validation for Quantitative Analysis of Menthiafolic Acid in Wine and Grape Juice. Calibration curves for menthiafolic acid (**2a**) were obtained with spiked standard additions to model wine (pH 3.3), white wine, and grape juice. The analyte (**2a**) was added to afford the following concentrations: in model wine, 0, 5, 10, 50, 100, 250, 500, and 2000 μg/L; in white wine, 0, 5, 10, 50, 100, 150, 250, 500, 1000, and 2000 μg/L; and in grape juice, 0, 5, 10, 150, 250, 500, and 2000 μg/L. All spiked samples were prepared, extracted, and analyzed in duplicate as previously described.[17] For the white wine, six replicates of the 10 and 500 μg/L spiked wine samples were prepared, extracted, and analyzed to test the repeatability of the method. The calibration curves were linear throughout the concentration range, with correlation coefficients (r^2) for **2a** of 0.9998, 0.9987, and 0.9993 for the model wine, white wine, and grape juice, respectively. For the white wine, the standard deviations were 6.5 and 3.5% at 10 and 500 μg/L, respectively. The slopes of the calibration curves were virtually identical. The LOD was 5 μg/L, and LOQ was 15 μg/L on the basis of visual evaluation. On the day of each set of analyses of the commercial wine and juice samples and of the various ferments described below, a minicurve was prepared in model wine. Three concentration points were prepared in duplicate at 5, 500, and 2000 μg/L and extracted simultaneously with the wine samples. QC's with additions of 10 and 500 μg/L were also prepared in duplicate and analyzed along with the wine, juice, and fermentation samples, each of which were also analyzed in duplicate.

Fermentation Studies with Menthiafolic Acid Glucose Ester (2b). All fermentation treatments were conducted in triplicate with either CDGJM (150 mL) or synthetic wine (150 mL) containing glucose ester **2b** at a concentration of 1.32 mg/L. Triplicate control experiments were carried out (a) with inoculated medium (150 mL) containing no glucose ester **2b** and (b) with noninoculated medium (150 mL) spiked with glucose ester **2b** and stored for the same time and temperature as the ferments. Starter cultures were prepared as follows: *S. cerevisiae* strain AWRI 838 and *Dekkera bruxellensis* strain AWRI 1499 were both obtained from the Australian Wine Research Institute culture collection maintained on yeast malt (YM) medium (Amyl Media, Dandenong Australia) supplemented with 1.5% agar and stored at 5 °C. Starter cultures were prepared by adding a loopful of yeast cells to YM (10 mL) and incubating at 28 °C with shaking for 48 h (*Saccharomyces*) or 72 h (*Dekkera*). Preadaptation of the cells to the fermentation medium was carried out by inoculating 600 μL (*Saccharomyces*) or 1 mL (*Dekkera*) of the starter culture into a 50:50 solution of CDGJM/YM (30 mL) and incubating at 28 °C overnight (*Saccharomyces*) or for 48 h (*Dekkera*). *Oenococcus oeni* (Lallemand VP-41) was reconstituted from a commercial preparation according to manufacturers instructions by addition of the freeze-dried bacteria (0.15 g) to sterilized water (30 mL) at 20 °C, which was then allowed to stand for 15 min with occasional stirring.

Alcoholic Fermentations. *S. cerevisiae* strain AWRI 838 (300 μL of a ca. 2 × 10^8 cell count culture) in 1:1 YM/CDGJM was inoculated into CDGJM (150 mL) containing glucose ester **2b**. Fermentations were incubated at 22 °C for 9 days and were shaken constantly at 120 rpm. Fermentation progress was monitored by weight, and ferments were deemed complete when no further weight loss was recorded. This was verified by analysis of residual glucose and fructose, which showed an average final total sugar content of 6.4 g/L.

Malolactic Fermentations. *O. oeni* (Lallemand VP-41) in sterile water (300 μL) was inoculated into synthetic wine (150 mL), containing the glucose ester **2b**, that had previously been stored in an anaerobic chamber to remove all oxygen. The fermentations were incubated under anaerobic conditions for 13 days at 22 °C. Fermentation progress was monitored by malic acid content, which was an average of 0.48 g/L at the end of fermentation.

DOI: 10.1021/acs.jafc.5b03147
J. Agric. Food Chem. 2015, 63, 8241−8246

***Dekkera* Fermentations.** *D. bruxellensis* AWRI 1499 was inoculated at 2×10^6 cfu/mL into synthetic wine (150 mL, adjusted to 5 g/L fructose) containing the glucose ester **2b** that had previously been stored in an anaerobic chamber to remove all oxygen. Fermentations were incubated under anaerobic conditions at 22 °C for 13 days before analysis for **2a**. Ferments were monitored by glucose plus fructose content. The fermentation did not go to completion and had average sugar levels of 13.1 g/L after 14 days.

RESULTS

Quantitative Analysis of Grape and Wine Samples for Menthiafolic Acid (2a). A total of 28 white wines, 4 Shiraz wines, and 6 white grape juice samples were analyzed for menthiafolic acid (**2a**) using a previously described stable isotope dilution assay that determines **2a** as the corresponding methyl ester.[17] The results of these analyses are shown in Tables 1 and 2. Menthiafolic acid was detected in all but one of the wine samples at concentrations ranging from 26 to 342 μg/L. The highest concentrations were found in a Chardonnay (234 μg/L), Gewürztraminer (272 μg/L), and Lexia (342 μg/L) wine. On the basis of the hydrolysis kinetics we reported earlier,[14] these quantities of **2a** would be sufficient to generate wine lactone at a concentration above its reported odor detection threshold after one to two years of aging, provided that the wine lactone (**1**) formed is predominantly the same enantiomer (**1a**) as that reported by Guth.[6] Lexia, a monoterpene-dependent variety, showed the highest concentration of **2a** of all the wines analyzed. Lexia is produced from Muscat grapes and can be aged from 5 to 8 years. Chardonnay wines can also sometimes undergo aging, albeit for shorter periods. The Shiraz wines, which are most often aged for a few years prior to drinking, also had significant quantities of **2a**.

Table 1. Concentration of Menthiafolic Acid (2a) in Various Wine Samples Analyzed in 2011

	vintage	conc. (μg/L)	% SD
	White Wines		
Chardonnay A	2011	146	9.2
Chardonnay B	2010	75	0.2
Chardonnay C	2011	194	0.7
Chardonnay D	2011	165	0.4
Chardonnay E	2007	234	1.4
Chardonnay F	2010	160	12
Chardonnay G	2010	138	1.2
Riesling A	2010	83	2.1
Riesling B	2010	95	5.0
Semillon Sauvignon Blanc A	2010	118	0.4
Semillon Sauvignon Blanc B	2010	121	3.9
Semillon	2010	128	2.3
Viognier A	2011	148	4.7
Viognier B	2009	<10	n.d.
Moscato A	2011	143	4.8
Moscato B	2011	116	7.3.
Lexia	2011	342	3.4
Sauvignon Blanc	2011	98	3.0
Marsanne	2010	115	4.7
Gewürztraminer	2009	272	2.6
Pinot Gris A	2011	26	19
Pinot Gris B	2010	41	0.3
Verdelho	2011	45	3.1
Blended dry white A	2011	79	1.1
Blended dry white B	2010	45	3.3
Blended dry white C	2011	60	0.2
Blended dry white D	2010	66	2.0
Blended dry white E	2010	41	0.02
	Red Wines		
Shiraz A	2010	140	1.5
Shiraz B	2010	140	1.3
Shiraz C	2010	113	0.7
Shiraz D	2009	107	1.8

Table 2. Concentration of Menthiafolic Acid (2a) in Six Grape Juice Samples

variety	sugar (brix)	conc. (μg/L)	% SD
Chardonnay	17.2	44	0.9
Gewürztraminer	20.2	236	0.7
Riesling	18.8	28	10
Sauvignon Blanc	17.8	105	0.5
Semillon	13.6	16	1.8
Viognier	13.8	27	2.6

The grape juice samples analyzed contained **2a** at variable concentrations (Table 2). To our knowledge, this is the first report of the occurrence of menthiafolic acid (**2a**) in grape juice. The Gewürztraminer had the highest concentration of **2a** (235 μg/L), whereas the other juices contained significantly less. Although the concentration of **2a** in half of the juice samples was lower than in most of the wines, we note that the sample numbers were relatively small, the variation in concentration is large, and the wines were not made from these juices so a direct comparison of the two sets of data ought not to be made.

Formation of Menthiafolic Acid (2a) from the Corresponding Glucose Ester 2b during Fermentation with *Saccharomyces*, *Oenococcus*, and *Dekkera* spp. The analyses demonstrate that menthiafolic acid (**2a**) is a component of at least some grape juices, but it is possible that additional quantities of **2a** could be produced from other precursors such as glucose ester **2b** by microbiological processes occurring during various winemaking steps such as fermentation and barrel aging. This possibility was therefore investigated by conducting a series of replicated model fermentations in which the media were spiked with synthetic **2b**. CDGJM was inoculated with *S. cerevisiae* (strain AWRI 838) for alcoholic fermentation, whereas secondary ferments were conducted with model wines (produced from fermented CDGJM) inoculated with either *O. oeni* commercial preparation VP-41 from Lallemand or *D. bruxellensis* strain AWRI 1499. These strains are among the most commonly used for or (for *D. bruxellensis*) encountered during winemaking in Australia.

In all fermentation treatments to which glucose ester **2b** was added, menthiafolic acid (**2a**) was detected at the end of fermentation, although the amounts found in the *D. bruxellensis* treatments were below the limit of quantification (15 μg/L, equivalent to 2% conversion). No menthiafolic acid was detected in the control ferments to which no glucose ester had been added or in uninoculated control samples containing the glucose ester. This suggests that the menthiafolic acid was formed by biological transformation of **2b**. The proportion of ester converted to acid is shown in Table 3.

In these experiments, the greatest degree of release of **2a** by wine microorganisms was during alcoholic fermentation, whereas a smaller amount was also released during subsequent malolactic fermentation. Together, these fermentations were

DOI: 10.1021/acs.jafc.5b03147
J. Agric. Food Chem. 2015, 63, 8241−8246

Table 3. Percent Conversion of Glucose Ester (2b) to Menthiafolic Acid (2a)

inoculating organism	% conversion	% sd
Saccharomyces cerevisiae AWRI 978	14.7	1.7
Oenococcus oeni VP-41	4.7	2.8
Dekkera bruxellensis AWRI 1499	<2	

able to convert around 20% of the added glucose ester **2b** to menthiafolic acid **2a**. Of course, commercial wine production encompasses a whole range of winemaking conditions and practices, including addition of exogenous enzymes, and the extent to which menthiafolic acid can be formed from its glucose ester is likely to be highly variable. Whether this formation is important to the final concentration of menthiafolic acid in wine will also depend on the proportions of this acid and its glucose ester in the corresponding must. There is not yet, however, a method for quantifying ester **2b** in juice or wine. In addition, it is possible that juice contains other, as yet unidentified, conjugates of menthiafolic acid that can also be converted to **2b** during vinification.[9]

Enantioselective Analysis of Menthiafolic Acid and Wine Lactone. Although grape juices can contain menthiafolic acid (**2a**) in significant concentration and this concentration can be augmented through the action of some wine microorganisms with esterase activity, an assessment of the importance of **2a** as a precursor to the odor-active form of wine lactone **1a** requires a determination of the chirality of **2a**. Several of the wine and juice samples listed in Tables 1 and 2 were therefore reanalyzed by enantioselective chromatography. The results are shown in Table 4.

Table 4. Percentage of (*R*)- and (*S*)-Menthiafolic Acid 2a in Various Samples

	% (*R*)[a]	% (*S*)[a]	SD (%)
	Wine Sample		
Chardonnay E	11	89	1.1
Gewürztraminer	23	77	0.5
Shiraz A	17.5	82.5	0.2
Shiraz B	19.5	80.5	2.8
	Grape Juice Sample		
Gewürztraminer	15	85	0.8

[a]Percentage of total menthiafolic acid **2** present. Samples are the same as those for Tables 1 and 2.

Each sample contained **2a** in both *R*- and *S*-forms. When samples were spiked with synthetic *R*-menthiafolic acid, only the peak assigned as the *R*-methyl ester of **2a** on gas chromatography was symmetrically enhanced, confirming the assignments. The *S*-isomer predominated in all samples. This result was earlier suggested by Luan et al. because both linalool and its oxidation products were found to have mainly *S*-configuration.[15] On the basis of the observed stereochemistry of wine lactone formation,[14,15] if wine lactone in wine is formed primarily from acid-catalyzed rearrangement of menthiafolic acid, then wine lactone in the wines studied here would be expected to comprise mostly the relatively odorless enantiomer **1b** not the potent odorant **1a** reported by Guth.[1,6]

The method reported by Guth for measuring wine lactone in wine was a time-consuming process involving salting, continuous liquid–liquid extraction, concentration, washing, and column chromatography.[1,2] We therefore trialed various other methods for enantioselective analysis of wine lactone in wine. Although ethyl acetate extraction of model wine solutions of wine lactone in relatively high concentration was satisfactory for the model studies described previously,[14] a more sensitive method was required for real wines. Initially, we examined extraction methods for model wine solutions of wine lactone at a concentration of 5 μg/L. Recoveries by organic solvent extraction were poor, and solid-phase microextraction with a variety of fibers failed to detect any wine lactone at all. Salting out solutions did not improve these results. When a dichloromethane solution of wine lactone was back-washed with a single volume of model wine equivalent to the volume used for the extraction experiments, some 85% of the wine lactone was lost from the organic phase in a single extraction, indicating the hydrophilic nature of the analyte and that partitioning of wine lactone between organic and aqueous ethanolic solutions would only favor solution in the former when used in a relatively high volume. Partial dealcoholization of model wine solutions of wine lactone under alkaline conditions (in which the wine lactone was converted to the open-chain salt form), followed by reacidification and extraction with organic solvents, gave no improvement of extraction efficiency, and freeze-drying of solutions resulted in total loss of wine lactone.

The use of solid-phase extraction (SPE) sorbents gave variable results with model wine solutions of wine lactone. Optimal recovery of wine lactone, as indicated by GC peak intensity, was achieved with LiChrolutEN sorbent. The model wine solutions were first salted out, then percolated through the sorbent, and eluted with dichloromethane giving a recovery of 54%. However, when this technique was applied to a commercial white wine spiked with 10 μg/L of wine lactone, the recovered analyte was barely detectable by GC-MS. It appears that wine lactone was not efficiently adsorbed onto the solid phase when other wine components were present.

Isolation of wine lactone from white wine following a method similar to that used by Guth was ultimately successful.[1,2] A white wine (250 mL) spiked with **1** (5 μg/L) was extracted continuously with dichloromethane over 16 h. The extract was concentrated and analyzed by GC-MS showing wine lactone **1** as a significant peak. However, other peaks coeluting with **1** were also present, and these could not be resolved on a range of available GC-MS columns. When the dichloromethane extract was washed with base, evaporated, and subjected to column chromatography on silica, a much cleaner extract was obtained, with wine lactone (**1**) being easily observed free of coeluters by GC-MS. Although this method was not practical for large sample numbers because of its cumbersome and time-consuming steps, it was adequate to examine the chirality of wine lactone in a wine (Chardonnay E from Table 1) containing a high concentration of menthiafolic acid (**2a**). This wine was four years old at the time of analysis.

Chardonnay E contained both enantiomers of wine lactone **1a** and **1b**. To our knowledge, this is the first reported occurrence of the relatively odorless form **1b** as a wine constituent. Furthermore, and in contrast to the report of Guth who studied young white wines, **1b** was the dominant enantiomer, with a ratio of **1a**/**1b** = 31:69. On the basis of the enantioselectivity of the hydrolytic conversion of menthiafolic acid (**2a**) to wine lactone at pH 3.0 determined previously[14] and the relative proportions (Table 4) of (*R*)- and (*S*)-menthiafolic acid in Chardonnay E (which had a pH of 3.06), the predicted ratio of **1a**/**1b** that would be formed from

DOI: 10.1021/acs.jafc.5b03147
J. Agric. Food Chem. 2015, 63, 8241−8246

hydrolysis, at ambient temperature, of **2a** present in this wine would be 38:62, a result close to the ratio measured.

DISCUSSION

Ever since wine lactone was observed as a wine component, researchers have sought to understand the origin of this powerful and pleasant odorant that is present in young wine but can increase in concentration during bottle aging.[7] Bonnländer et al. proposed the monoterpene acid **2a**, commonly known as menthiafolic acid and found in numerous conjugated forms in a variety of plants,[9] as one possible precursor to wine lactone.[8] However, three separate studies have shown that enantiomerically pure menthiafolic acid gives two enantiomers of wine lactone on mild acid hydrolysis and not just the single enantiomer observed by Guth in his study of young white wines.

On the basis of our observations that menthiafolic acid (**2a**) in five grape and wine samples was always present mainly as the (*S*)-form and that the wine lactone in an aged Chardonnay wine was mainly the relatively odorless **1b** enantiomer, it seems unlikely that the **1a** enantiomer of wine lactone observed by Guth in young wines was formed from **2a**. It is possible that the additional wine lactone that Guth observed to be formed during bottle aging was indeed formed by hydrolysis of **2a** but was in fact partially, or even mostly, **1b**. If this was the case, then the enantiomerically pure **1a** in the younger wines must have had a biogenetic origin different from that formed from **2a** in older wine.

The ratio of **1a**/**1b** in wine probably varies from one sample to another, but wines that are more than a year old presumably contain at least some of the weakly odorous **1b** enantiomer. This being the case, simple nonenantioselective analysis of wine samples for wine lactone could lead to an overestimation of the impact of wine lactone on the aroma and flavor of wine. Such an assessment requires quantitative enantioselective analysis of samples. However, since the original studies by Guth, quantitative data for wine lactone in any form in wine samples has been lacking, presumably because of the difficulty in obtaining reference standards and because wine lactone is not easily extracted from wine using the most commonly employed techniques such as SPME. This poor extractability could also explain why wine lactone does not normally feature in lists of important wine odorants as determined by aroma extract dilution analyses.

The laborious method used by Guth to quantify wine lactone in his wine samples was adopted by us for enantioselective analysis of wine lactone in Chardonnay E after a variety of ultimately futile attempts to develop a streamlined analytical method. This more laborious procedure was adequate for individual samples but not for screening larger sample numbers. A more rapid procedure, suitable for larger sample numbers will probably require the sensitivity and resolving power of, for example, GC/GC/MS, to overcome problems of poor analyte recovery and coelution with other wine components.

AUTHOR INFORMATION

Corresponding Author

*E-mail: dennis.taylor@adelaide.edu.au. Phone: +61 8 8313-7239. Fax: +61 8 8313 4711.

Funding

This project was supported by the School of Agriculture, Food & Wine of The University of Adelaide, and by Australia's grapegrowers and winemakers through their investment body, the Australian Grape and Wine Authority (AGWA), formally known as the Grape and Wine Research and Development Corporation (GWRDC), with matching funds from the Australian Government. Additional support came from the Australian Wine Research Institute (AWRI). The University of Adelaide and AWRI are part of the Wine Innovation Cluster. (www.wineinnovationcluster.com). J.G is indebted to the University of Adelaide, School of Agriculture, Food & Wine, for a Ph.D. scholarship and a C. J. Everard Award.

Notes

The authors declare no competing financial interest.

ACKNOWLEDGMENTS

We thank Mariola Kwiatsowski for providing grape samples.

ABBREVIATIONS USED

CDGJM, chemically defined grape juice medium; YM, yeast malt; SPME, solid-phase microextraction; GC-MS, gas chromatography/mass spectrometry; EI, electron impact; SPE, solid-phase extraction

REFERENCES

(1) Guth, H. Identification of character impact odorants of different white wine varieties. *J. Agric. Food Chem.* **1997**, *45*, 3022−3026.

(2) Guth, H. Quantification and sensory studies of character impact odorants of different white wine varieties. *J. Agric. Food Chem.* **1997**, *45*, 3027−3032.

(3) Lopez, R.; Ferreira, V.; Hernandez, P.; Cacho, J. F. Identification of impact odorants of young red wines made with Merlot, Cabernet Sauvignon and Grenache grape varieties: A comparative study. *J. Sci. Food Agric.* **1999**, *79*, 1461−1467.

(4) Jagella, T.; Grosch, W. Flavour and off-flavour compounds of black and white pepper (*Piper Nigrum* L.) 1. Evaluation of potent odorants of black pepper by dilution and concentration techniques. *Eur. Food Res. Technol.* **1999**, *209*, 16−21.

(5) Buettner, A.; Schieberle, P. Characterization of the most odor-active volatiles in fresh hand-squeezed juice of grapefruit (*Citrus paradisi* Macfayden). *J. Agric. Food Chem.* **1999**, *47*, 5189−5193.

(6) Guth, H. Determination of the configuration of wine lactone. *Helv. Chim. Acta* **1996**, *79*, 1559−1571.

(7) Guth, H. Comparison of different white wine varieties in odor profiles by instrumental analysis and sensory studies. In *Chemistry of Wine Flavor*; Waterhouse, A.L., Ebeler, S. E., Eds.; ACS Symposium Series 714; American Chemical Society: Washington, DC, 1998; pp 39−54.

(8) Bonnländer, B.; Baderschneider, B.; Messerer, M.; Winterhalter, P. Isolation of two novel terpenoid glucose esters from Riesling wine. *J. Agric. Food Chem.* **1998**, *46*, 1474−1478.

(9) Goodger, J. Q.; Woodrow, I. E. α,β-Unsaturated monoterpene acid glucose esters: structural diversity, bioactivities and functional roles. *Phytochemistry* **2011**, *72*, 2259−2266.

(10) Winterhalter, P.; Messerer, M.; Bonnländer, B. Isolation of the glucose ester of (E)-2,6-dimethyl-6-hydroxyocta-2,7-dienoic acid from Riesling wine. *Vitis* **1997**, *36*, 55−56.

(11) Winterhalter, P.; Bonnländer, B. Aroma-active benzofuran derivatives: analysis, sensory properties, and pathways of formation. In *Aroma Active Compounds in Foods*; Takeoka, G.R.; M. Güntert, Engel, K.-H., Eds.; ACS Symposium Series 794; American Chemical Society: Washington, DC, 2001; pp 21−32.

(12) Sefton, M. A.; Francis, I. L.; Williams, P. J. The free and bound volatile secondary metabolites of Vitis vinifera grape cv Semillon. *Aust. J. Grape Wine Res.* **1996**, *2*, 179−183.

(13) Sefton, M. A. Hydrolytically-released volatile secondary metabolites from a juice sample of *Vitis vinifera* grape cvs Merlot and Cabernet Sauvignon. *Aust. J. Grape Wine Res.* **1998**, *4*, 30−38.

DOI: 10.1021/acs.jafc.5b03147
J. Agric. Food Chem. 2015, 63, 8241−8246

(14) Giaccio, J.; Capone, D. L.; Håkansson, A. E.; Smyth, H. E.; Elsey, G. M.; Sefton, M. A.; Taylor, D. K. The formation of wine lactone from grape-derived secondary metabolites. *J. Agric. Food Chem.* **2011**, *59*, 660−664.
(15) Luan, F.; Degenhardt, A.; Mosandl, A.; Wüst, M. Mechanism of wine lactone formation: demonstration of stereoselective cyclization and 1,3-hydride shift. *J. Agric. Food Chem.* **2006**, *54*, 10245−10252.
(16) Bonnländer, B. Isolierung, Charakterisierung und Synthese von Aromavorläufern aus Wein, Dillkraut und Lindenblüten. Ph.D. Thesis, Technische Universität Braunschweig, Braunschweig, Germany, 2003.
(17) Giaccio, J.; Sefton, M. A.; Taylor, D. K. Quantitative analysis of a wine lactone precursor in wine. In *Flavour Science*; Proceedings from XIII Weurman Flavour Research Symposium; Ferreira, V., Lopez, R., Eds.; Academic Press: San Diego, CA, 2014; pp 137−140.
(18) Ugliano, M.; Bartowsky, E. J.; McCarthy, J.; Moio, L.; Henschke, P. A. Hydrolysis and transformation of grape glycosidically bound volatile compounds during fermentation with three *Saccharomyces* yeast strains. *J. Agric. Food Chem.* **2006**, *54*, 6322−6331.

DOI: 10.1021/acs.jafc.5b03147
J. Agric. Food Chem. 2015, 63, 8241−8246

Table 1. Free Fraction (Values in Parentheses) of Theaspirane and Derived Compounds in Hop and Amounts Released by β-Glucosidase Hydrolysis (Milligrams per Kilogram, Theaspirane Equivalents for Compounds 3−7)[a]

				Amarillo	Citra	Mosaic	Hallertau Blanc	Warrior	Saaz
		substance		*alpha*-acid content (% w/w)					
				8−11	11−13	11.5−13.5	9−12	16−18	3−4.5
no.	RI (CPSil 5 CB)	name	odor (GC-O)	amount (mg/kg)					
1	1305	theaspirane A	camphor	1429.2[a] (nd)	70.7[b] (nd)	22.4[c] (7.3)	15.6[d] (nd)	nd (nd)	0.64e (nd)
2	1305	theaspirane B	blackcurrant	861.1[a] (nd)	40.7[b] (nd)	14.1[c] (6.3)	10.7[d] (nd)	nd (nd)	0.5e (nd)
3	1373	4-hydroxy-7,8-dihydro-β-ionone	grenadine	9.8[a] (nd)	0.3[b] (nd)	nd (0.1)	0.8[c] (nd)	nd (nd)	tr (nd)
4	1394	6-hydroxy-7,8-dihydro-α-ionone	–	0.3[a] (nd)	0.1[b] (nd)	nd[b] (0.1)	0.1 (nd)	nd (nd)	nd (nd)
5	1419	dihydrodehydro-β-ionone	dried fruit/ sauterne	1.8[a] (nd)	0.2[b] (nd)	nd (0.2)	4.0[c] (nd)	nd (nd)	nd (nd)
6	1560	3,4-epoxy-5,6-dehydro-7,8-dihydro-β-ionone	–	nd (nd)	nd (nd)	nd (0.1)	nd (nd)	nd (nd)	nd (nd)
7	1570	3,4-dehydro-5,6-epoxy-7,8-dihydro-β-ionone	–	nd (nd)	nd (nd)	nd (0.2)	nd (nd)	nd (nd)	nd (nd)

[a]Assays in duplicate. All samples that do not share a common letter are significantly different ($p < 0.05$) according to Tukey's test. tr.: detected below the quantitation limit (0.01 μg/kg). nd: not detected.

Samples. Four hop samples were kindly supplied by Yakima Chief (Louvain-la-Neuve, Belgium): Amarillo, Citra, Mosaic, and Warrior (harvest 2013). Saaz hop (harvest 2013) and Hallertau Blanc were provided by Hopsteiner (Mainburg, Hallertau, Germany). A brown beer, bought at a local supermarket and stored for two years in a dark room at 20 °C for natural aging, was used for beer investigation.

Theaspirane Chemical Oxidation. A 0.485 g sample of commercial theaspirane (85% purity, final concentration 0.05 M), 50 mL of Milli-Q water, and 1 mL of hydrogen peroxide solution were mixed in the presence of 60 mg of iron chloride, used as catalyst. The reaction medium was heated at 100 °C for 3 h. After three diethyl ether extractions (3 × 20 mL), the extract was dried with anhydrous sodium sulfate. Dodecane was added as external standard, and the mixture was concentrated to 10 mL in a Kuderna-Danish apparatus at 39 °C (total concentration factor, 5; final EST concentration, 7 mg/L). The final extract was stored at −80 °C and analyzed by gas chromatography−mass spectrometry (GC-MS), gas chromatography−high-resolution mass spectrometry (GC-HRMS), and gas chromatography−olfactometric detection (GC-O).

Hop and Beer XAD 2 Extraction Procedure with or without Glucoside Enzymatic Release. For hop extraction, 20 g of finely ground hop and 1000 μL of internal standard (IST, 1 g/L octyl-glucopyranoside) were added to 250 mL of water/methanol (80:20 v/v) and mixed thoroughly with an Omni Mixer (Omni international, Kennesaw, GA) for ten 30 s periods interrupted by ten 30 s resting periods. The mixture was then centrifuged for 10 min at 10000 rpm; the upper phase was recovered, whereas the lower one was re-extracted in the same way. Both fractions were filtered with a Büchner funnel, and methanol was removed with a Rotavapor to a final volume of 300 mL. Polyphenols were eliminated by treatment for 1 h under agitation with 6 g of polyvinylpolypyrrolidone (AEB, Brescia, Italy). After a second Büchner filtration, the hop extract was divided into two 250 mL Schott flasks.

In the case of beer extraction, 150 mL of degassed beer and 500 μL of internal standard (IST, 1 g/L octyl-glucopyranoside) were poured into a Schott flask.

Six grams of Amberlite XAD 2 resin thoroughly rinsed with Milli-Q water (approximately 400 mL) were poured into each hop or beer flask. After being shaken in a dark room for 2 h, the mixtures were poured into a glass column for separation. After natural elution from the XAD 2 resin, 50 mL of water and 25 mL of diethyl ether were consecutively poured for resin washing. Glucosides were finally eluted with 25 mL of methanol. The extract was evaporated to dryness and resuspended in 25 mL of acetate buffer (pH 5). Enzymatically treated samples and controls (giving also free amounts of theaspirane analogs) were incubated at 35 °C for 2 h, with or without β-glucosidase (14 mg). Both were extracted three times with 15 mL of diethyl ether

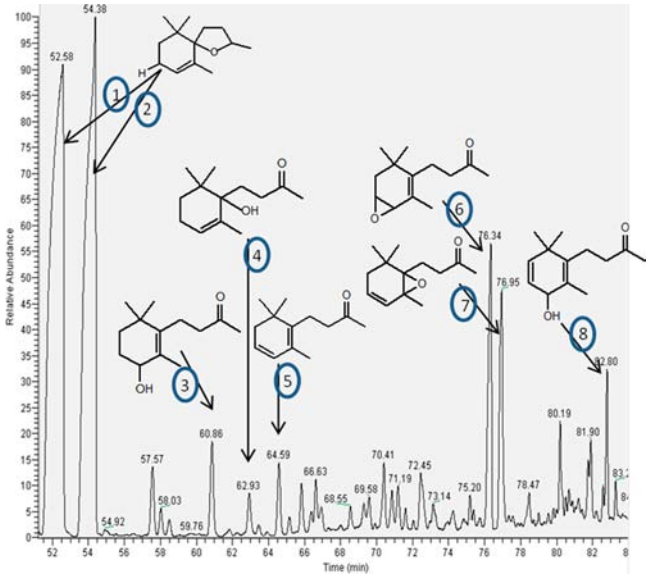

Figure 1. Total ion MS chromatogram of the theaspirane chemical oxidation media. (**1**) Theaspirane A, (**2**) theaspirane B, (**3**) 4-hydroxy-7,8-dihydro-β-ionone, (**4**) 6-hydroxy-7,8-dihydro-α-ionone, (**5**) dihydro-dehydro-β-ionone, (**6**) 3,4-epoxy-5,6-dehydro-7,8-dihydro-β-ionone, (**7**) 3,4-dehydro-5,6-epoxy-7,8-dihydro-β-ionone, and (**8**) 4-hydroxy-2,3-dehydro-7,8-dihydro-β-ionone.

(10 min, 1000 rpm). The combined organic phase was dried with anhydrous sodium sulfate, and 0.5 mL of EST (20 mg/L dodecane; final EST concentration, 20 mg/L) was added to the extract before concentration to 0.5 mL in a Danish-Kuderna apparatus at 39 °C. The final extracts were stored at −80 °C and analyzed by GC-MS.

Gas Chromatography−Mass Spectrometry. A 1 μL sample of hop, beer, or model extract was analyzed with a ThermoFinnigan Trace GC 2000 gas chromatograph equipped with a low-bleed MS capillary column (CP-Sil5-CB, 50 m × 0.32 mm i.d., 1.2 μm film thickness) and a splitless injector (250 °C). The split vent was opened 0.5 min postinjection. The oven temperature was programmed to rise from 36 to 85 °C at 20 °C/min, then to 145 °C at 1 °C/min, and finally to 250 °C at 3 °C/min. The carrier gas was helium, and the pressure was set at 100 kPa. Electronic impact (EI) mass spectra were recorded at 70 eV (full scan with a mass range from 40 to 380 m/z, or SIM mode on m/z = 70/84 for octanol; 57/71 for dodecane; 82/138 for theaspirane; 126/158 for 4-hydroxy-7,8-dihydro-β-ionone and

DOI: 10.1021/acs.jafc.5b03195
J. Agric. Food Chem. 2015, 63, 8247−8253

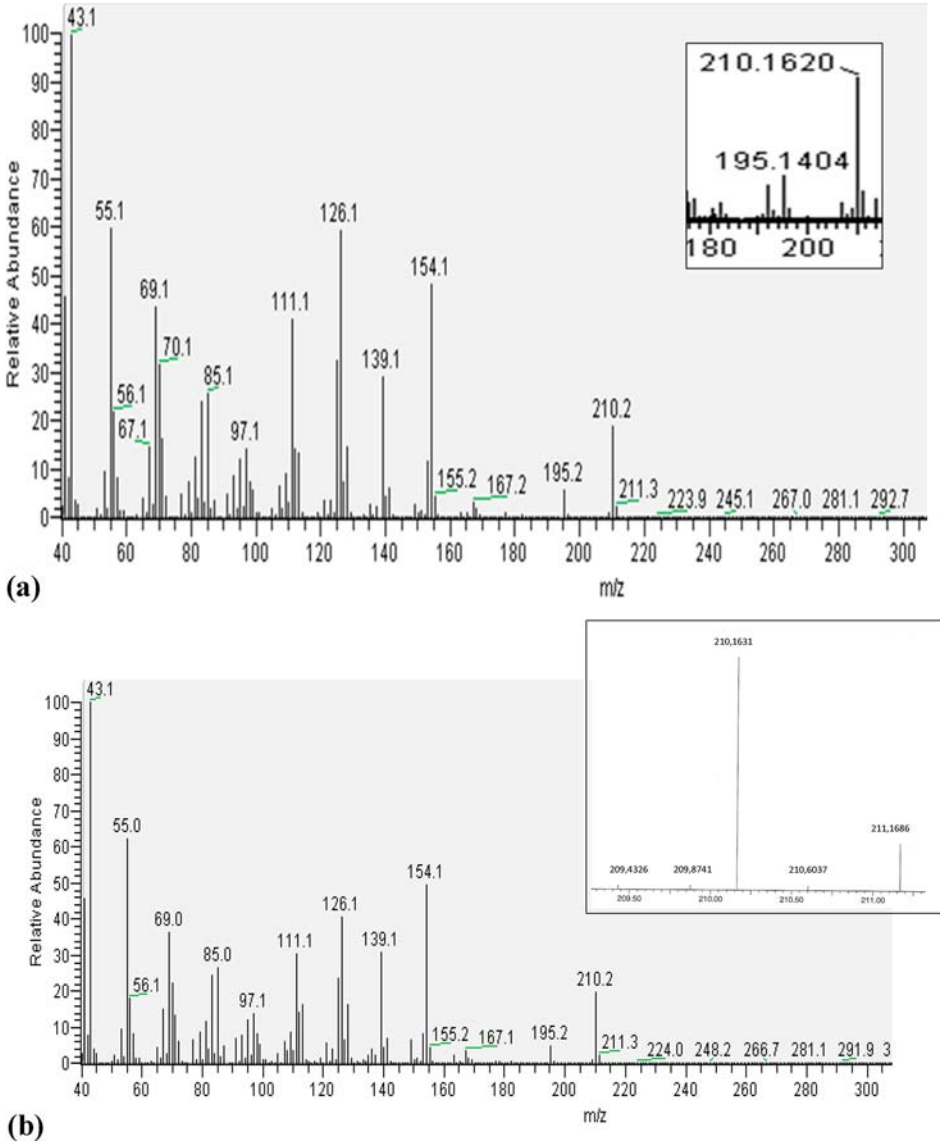

Figure 2. MS and HRMS spectra of 4-hydroxy-7,8-dihydro-β-ionone (a) and 6- hydroxy-7,8-dihydro-α-ionone (b).

6-hydroxy-7,8-dihydro-α−ionone; 119/134 for dihydrodehydro-β-ionone; 110/152 for 3,4-epoxy-5,6-dehydro-7,8-dihydro-β-ionone; 191/209 for 3,4-dehydro-5,6-epoxy-7,8-dihydro-β-ionone; and 165/137 for 4-hydroxy-2,3-dehydro-7,8-dihydro-β-ionone) on a ThermoFinnigan Trace MS simple quadrupole mass spectrometer. Spectral recording was automatic throughout separation (Xcalibur software was used, NIST databank).

Gas Chromatography−High-Resolution Mass Spectrometry. The apolar column described above for GC-MS was connected to a GC-HR mass spectrometer from Waters (HRMS, GCT Premier, ToF). Perfluorotributylamine was injected on line as MS standard (the ions 69 and 131 were found in all spectra). Electron ionization (EI) mass spectra were recorded at 70 eV (trap current, 200 IA; emission current, 400 IA). Spectral recording was automatic throughout separation (Xcalibur software was used, NIST databank).

Gas Chromatography−Olfactometric Detection. A 1 μL sample of hop, beer, or model extract was analyzed with a Chrompack CP9001 gas chromatograph equipped with a splitless injector maintained at 250 °C; the split vent was opened 0.5 min postinjection. Compounds were analyzed with the wall-coated open tubular (WCOT) apolar CP-Sil5-CB column (50 m × 0.32 mm i.d., 1.2 μm film thickness). The carrier gas was nitrogen, and the pressure was set at 60 kPa (CP-Sil5-CB). The oven temperature was programmed to rise from 36 to 85 °C at 20 °C/min, then to 145 °C at 1 °C/min, and finally to 250 °C at 3 °C/min. In order to assess the olfactory potential of the extracts, the column was connected to a GC-O port (Chrompack) maintained at 250 °C. The effluent was diluted with a large volume of air (20 mL/min) prehumidified with an aqueous copper(II) sulfate solution.

Statistical Analyses. All analyses were carried out in duplicate. Multiple comparisons of means were performed by means of Tukey's test, with SAS software version 9.2 (SAS Institute, Inc., Cary, NC). Values in Table 1 that do not share a common letter are significantly different ($p < 0.05$).

RESULTS AND DISCUSSION

Investigation of Theaspirane Degradation Media. In order to study theaspirane oxidation products, theaspirane degradation medium was analyzed by GC-HRMS. Besides 4-hydroxy-7,8-dihydro-β-ionone ($RI_{CPSil5CB}$ = 1373, peak 3, Figure 1), having a nice grenadine-like flavor, and dihydrodehydro-β-ionone ($RI_{CPSil5CB}$ = 1419, peak 5, Figure 1), exhaling a dried fruit/Sauternes aroma, already identified by Collin et al. (2012)[6] in the same oxidation medium, four major compounds (**4** ($RI_{CPSil5CB}$ = 1493), **6** ($RI_{CPSil5CB}$ = 1657), **7** ($RI_{CPSil5CB}$ = 1667), and **8** ($RI_{CPSil5CB}$ = 1774)) were evidenced (Figure 1). As depicted

DOI: 10.1021/acs.jafc.5b03195
J. Agric. Food Chem. 2015, 63, 8247−8253

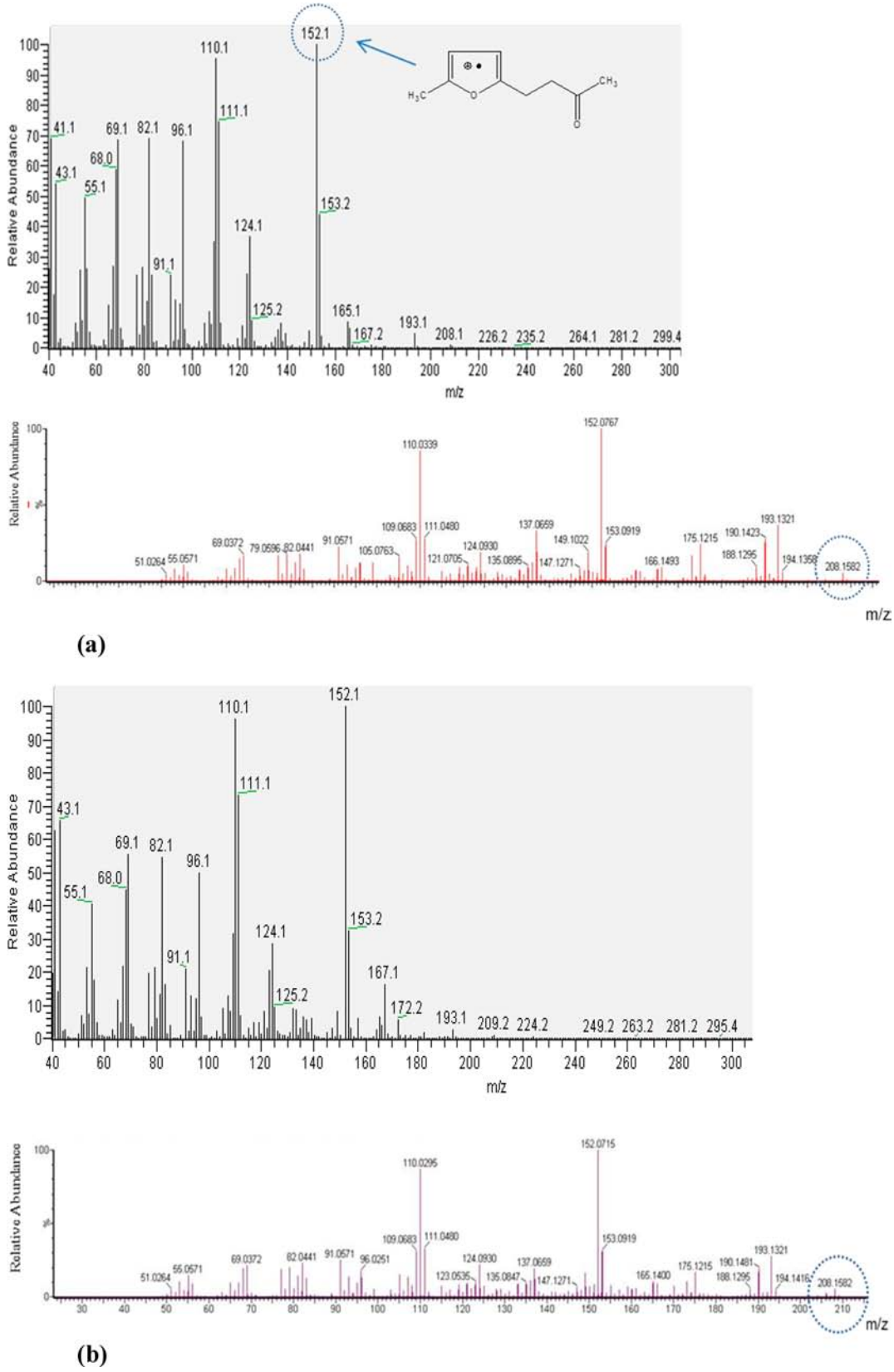

Figure 3. MS and HRMS spectra of (**6**) 3,4-epoxy-5,6-dehydro-7,8 dihydro-β-ionone (a) and (**7**) 3,4-dehydro-5,6-epoxy-7,8-dihydro-β-ionone (b).

in Figure 2, compound **4** exhibits the same mass spectrum as 4-hydroxy-7,8-dihydro-β-ionone (compound **3**), but no odor was detected at the GC-O sniffing port in the theaspirane degradation medium. Compound **4** is here tentatively identified as 6-hydroxy-7,8-dihydro-α-ionone by GC-HRMS (Figure 2 b) (experimental m/z = 210.1631; calculated m/z = 210.1620; δ = 5.2 ppm). Upon fragmentation, peaks 6 and 7 yielded the same mass spectrum, as illustrated in Figure 3a,b. These compounds appeared to be the

DOI: 10.1021/acs.jafc.5b03195
J. Agric. Food Chem. 2015, 63, 8247−8253

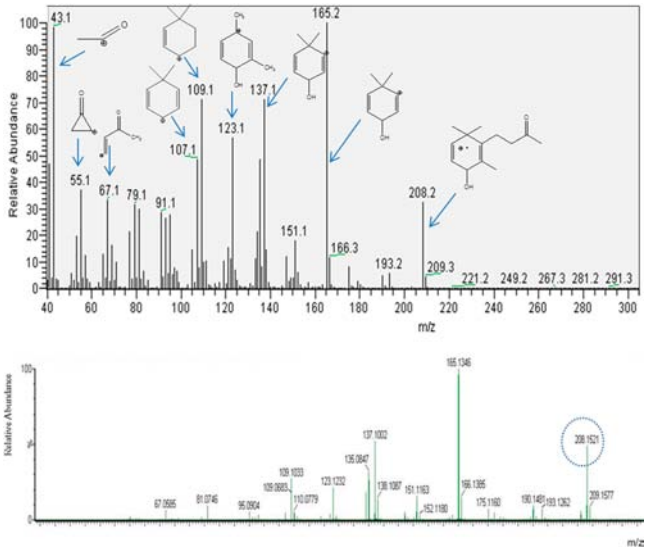

Figure 4. MS and HRMS spectra of compound **8**.

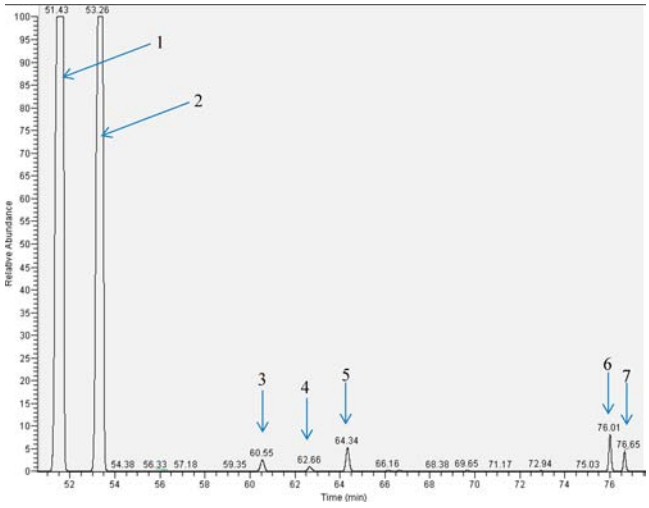

Figure 6. SIM chromatogram of Mosaic hop: (**1**) theaspirane A, (**2**) theaspirane B, (**3**) 4-hydroxy-7,8-dihydro-β-ionone, (**4**) 6-hydroxy-7,8-dihydro-α-ionone, (**5**) dihydrodehydro-β-ionone, (**6**) 3,4-epoxy-5,6-dehydro-7,8-dihydro-β-ionone, and (**7**) 3,4-dehydro-5,6-epoxy-7,8-dihydro-β-ionone.

most abundant degradation products of theaspirane after harsh oxidative treatment. GC-HRMS analysis and the existence of fragment m/z = 152.0715, corresponding to isobutene loss and creation of a furan, led us to suspect that compounds **6** and **7** were epoxides (experimental m/z = 208.1582), both potentially

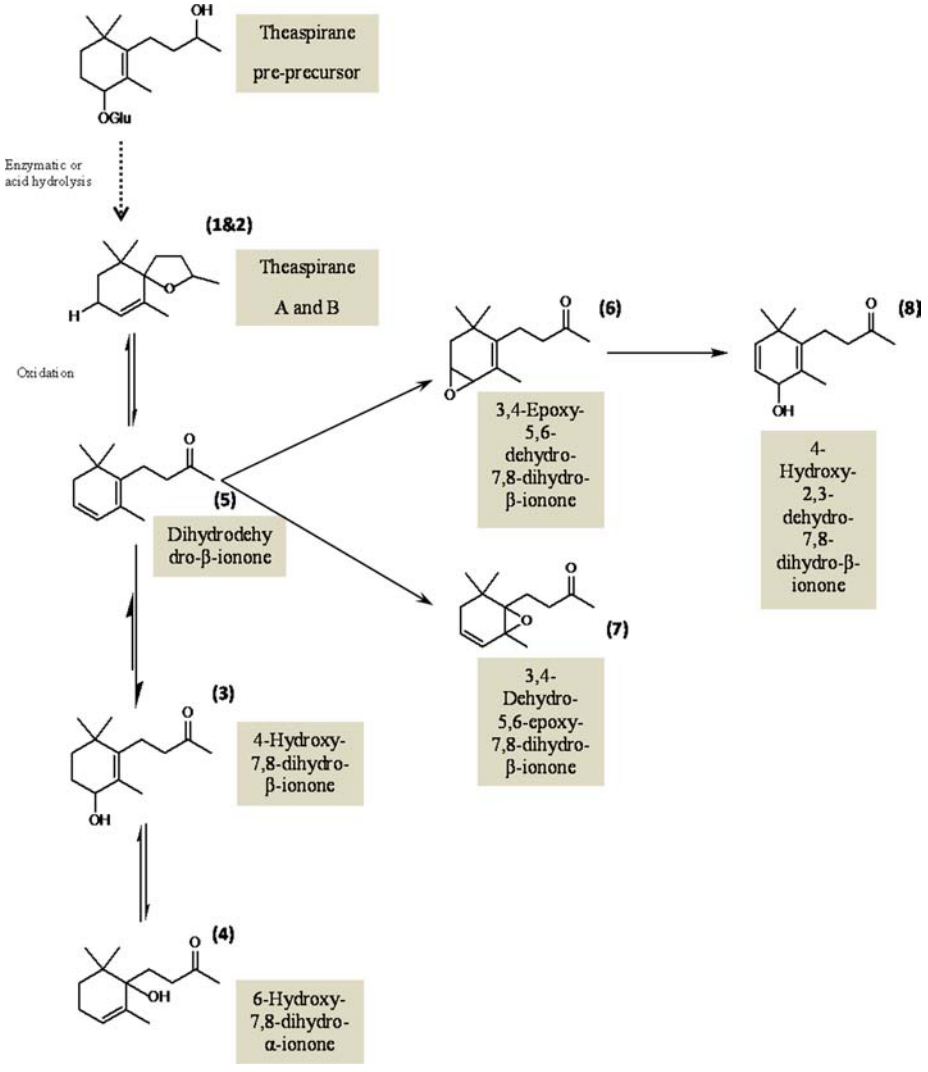

Figure 5. Hypothetical theaspirane degradation pathways.

DOI: 10.1021/acs.jafc.5b03195
J. Agric. Food Chem. 2015, 63, 8247−8253

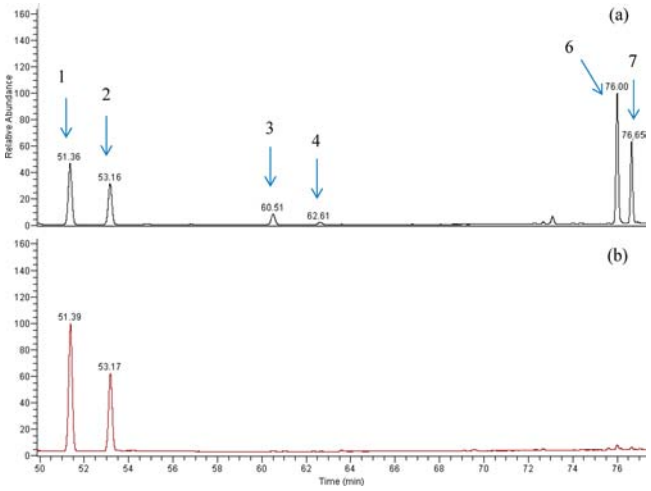

Figure 7. SIM chromatograms of a fresh beer (a) and a 2-year-aged beer (b). (**1**) Theaspirane A, (**2**) theaspirane B, (**3**) 4-hydroxy-7,8-dihydro-β-ionone, (**4**) 6-hydroxy-7,8-dihydro-α-ionone, (**6**) 3,4-epoxy-5,6-dehydro-7,8-dihydro-β-ionone, and (**7**) 3,4-dehydro-5,6-epoxy-7,8-dihydro-β-ionone.

issued from degradation of compound **5**. Another compound (**8**), with an experimental m/z of 208.1521 but without any 152 fragment, was most probably issued from epoxide opening in compound **6**, leading to 4-hydroxy-2,3-dehydro-7,8-dihydro-β-ionone (fragmentation pattern proposed in Figure 4). Figure 5 gives a hypothetical succession of degradations (including oxidation, hydration, epoxidation, epoxide opening), starting from theaspirane or its preprecursor and giving rise to compounds **3**–**8**.

Investigation of Free and Bound Precursors of Theaspirane and Derived Compounds in Hop. The existence of a theaspirane glucosidic precursor has been mentioned by Daenen et al. (2008)[4] for the Saaz hop variety. Therefore, theaspirane and its degradation products were here investigated in six hop varieties before and after enzymatic treatment. The GC-MS chromatogram of Mosaic XAD-2 extract (Figure 6) revealed, for the first time, the existence of huge quantities of free theaspirane (**1** and **2**) in hop (7.3 and 6.3 mg/kg,respectively), together with 4-hydroxy-7,8-dihydro-β-ionone (**3**), 6-hydroxy-7,8-dihydro-α-ionone (**4**), dihydrodehydro-β-ionone (**5**), and both monoepoxides (**6** and **7**). Yet Mosaic emerged as the only variety among those investigated here to contain these compounds mainly in free form. Citra and Amarillo proved to be much more interesting sources of the theaspirane preprecursor (111 and 2290 mg/kg enzymatically released, respectively; Table 1). Together with theaspirane, 4-hydroxy-7,8-dihydro-β-ionone was also found in hop extracts subjected to β-glucosidase treatment, especially for the hop Amarillo (10 mg/kg). Although containing only 26 mg/kg theaspirane, the dual hop variety Hallertau Blanc emerged as the best source of the nice dried-fruit-like dihydrodehydro-β-ionone (4 mg/kg from bound form, Table 1). From the brewer's standpoint, we can suspect free compounds to be massively lost through volatilization during boiling, while glucosides should be able to release an unexpected range of flavors through enzymatic or chemical hydrolysis during fermentation or beer aging. The enzymatic treatment applied to conventional hops (the aromatic Saaz and the bitter Warrior) yielded much less interesting profiles (<2 mg/kg theaspirane and no derived compounds detected). The four dual hops investigated here have also been described, recently, to be of particular interest for their citrus-like potential, brought by very delicate polyfunctional thiols and terpenols.[13]

Investigation of Theaspirane Degradation Products in Fresh and Aged Beer. Scholtes et al. (2012)[5] have recently shown that glucosides, partially hydrolyzed and oxidized during hop or beer aging, can release theaspirane analogs in Gueuze beers. This mechanism, although less favored in usual unoxidized lager and special beers, could also be a source of interesting flavors.Theaspirane and its oxidation-derived compounds were next investigated in a Belgian top-fermentation beer, both fresh and allowed to age for two years. For the first time in a top-fermentation beer, theaspirane A (**1**), theaspirane B (**2**), 4-hydroxy-7,8-dihydro-β-ionone (**3**), 6-hydroxy-7,8-dihydro-α-ionone (**4**), and both monoepoxides (**6** and **7**) were all evidenced by GC-MS in the fresh beer samples (Figure 7).

Despite unavoidable oxidation in the bottle, analysis of the 2-year-aged beer samples revealed the presence of theaspiranes A and B in the same concentration range as found in the fresh samples (3.6 μg/L theaspirane A in fresh beer and 4.4 μg/L after 2 years; 2.4 μg/L theaspirane B in fresh beer and 2.7 μg/L after 2 years). This supports the hypothesis of a balance due to glucoside hydrolysis. Of course, complementary data are still needed to confirm the occurrence of glucosidic forms in fresh beer, and their ability to be enzymatically or chemically hydrolyzed through aging. On the other hand, 4-hydroxy-7,8-dihydro-β-ionone (**3**), 6-hydroxy-7,8-dihydro-α-ionone, and both monoepoxides (**6** and **7**), present in fresh samples (0.7, 0.2, 4.7, and 2.8 μg/L, respectively), proved to be degraded to unquantifiable levels after 2 years.

AUTHOR INFORMATION

Corresponding Author

*E-mail: sonia.collin@uclouvain.be. Fax: +32 10 47 21 78. Tel: +32 10 47 29 13.

Notes

The authors declare no competing financial interest.

REFERENCES

(1) Winterhalter, P.; Schreier, P. 4-Hydroxy-7, 8-dihydro-beta-ionol natural precursor of theaspirane in quince fruit (*Cydonia-Oblonga*, Mill). *J. Agric. Food Chem.* **1988**, *36*, 560−562.

(2) Schmidt, G.; Full, G.; Winterhalter, P.; Schreier, P. Synthesis and enantiodifferentiation of isomeric theaspiranes. *J. Agric. Food Chem.* **1992**, *40*, 1188−1191.

(3) Pons, A.; Lavigne, V.; Landais, Y.; Darriet, P.; Dubourdieu, D. Identification of a sotolon pathway in dry white wines. *J. Agric. Food Chem.* **2010**, *58*, 7273−7279.

(4) Daenen, L.; Saison, D.; De Schutter, D. P.; De Cooman, L.; Verstrepen, K. J.; Delvaux, F. R.; Derdelinckx, G.; Verachtert, H. Bioflavouring of beer through fermentation, refermentation and plant parts addition. In *Beer in Health and Disease Prevention*; Preedy, V. R., Ed.: Elsevier, Amsterdam. 2008, 33−48.

(5) Scholtes, C.; Nizet, S.; Collin, S. Occurrence of sotolon, abhexon and theaspirane-derived molecules in gueuze beers. Chemical similarities with "Yellow wines. *J. Inst. Brew.* **2012**, *118*, 223−229.

(6) Collin, S.; Nizet, S.; Claeys Bouuaert, T.; Despatures, P.-M. Main odorant in Jura flor-sherry wines. Relative contributions of sotolon, abhexon, and theaspirane-derived compounds. *J. Agric. Food Chem.* **2012**, *60*, 380−387.

(7) Liégeois, C.; Meurens, N.; Badot, C.; Collin, S. Release of deuterated (E)-2-nonenal during beer aging from labeled precursors synthesized before boiling. *J. Agric. Food Chem.* **2002**, *50*, 7634−7638.

(8) Scholtes, C.; Nizet, S.; Collin, S. Guaiacol and 4-methylphenol as specific markers of torrefied malts. Fate of volatile phenols in special beers through aging. *J. Agric. Food Chem.* **2014**, *62*, 9522−9528.

DOI: 10.1021/acs.jafc.5b03195
J. Agric. Food Chem. 2015, 63, 8247−8253

(9) Callemien, D.; Dasnoy, S.; Collin, S. Identification of a stale-beer-like odorant in extracts of naturally aged beer. *J. Agric. Food Chem.* **2006**, *54*, 1409−1413.
(10) Gijs, L.; Chevance, F.; Jerkovic, V.; Collin, S. How low pH can intensify beta-damascenone and dimethyl trisulfide production through beer aging. *J. Agric. Food Chem.* **2002**, *50*, 5612−5616.
(11) Chevance, F.; Guyot-Declerck, C.; Dupont, J.; Collin, S. Investigation of the beta-damascenone level in fresh and aged commercial beers. *J. Agric. Food Chem.* **2002**, *50*, 3818−3821.
(12) Scholtes, C.; Nizet, S.; Collin, S. How sotolon can impart a Madeira off-flavor to aged beers. *J. Agric. Food Chem.* **2015**, *63*, 2886−2892.
(13) Kankolongo Cibaka, M.-L.; Gros, J.; Nizet, S.; Collin, S. Quantitation of selected terpenoids and mercaptans in the dual-purpose hop varieties Amarillo, Citra, Hallertau Blanc, Mosaic, and Sorachi Ace. *J. Agric. Food Chem.* **2015**, *63*, 3022−3030.

DOI: 10.1021/acs.jafc.5b03195
J. Agric. Food Chem. 2015, 63, 8247−8253

place in beer based mainly on following the rate of oxygen consumption. Oxygen is a central reactant in oxidative reactions, and the amount of consumed oxygen is therefore an excellent measure of the overall extent of oxidation. However, this technique has so far not been used for mechanistic studies of oxidative reactions in beer, despite its successful use in mechanistic studies of oxidation mechanisms in wine.[17] The focus of this study has been characterization of the interactions between compounds that are important for the formation of radicals by metal-catalyzed oxidation reactions. This has included studies of intermediary radicals detected by ESR and characterization of the antioxidant properties of sulfite and thiols in beer.

MATERIALS AND METHODS

Chemicals. ThioGlo 1 fluorescent thiol reagent was obtained from Berry & Associates, Inc. (Dexter, MI, U.S.A.). Acetonitrile, glutathione (GSH), $FeSO_4{\cdot}7H_2O$, H_2O_2, N-*tert*-butyl-α-nitrone (PBN), 1-octanol, hydrochloric acid (37%), and 2,2,6,6-tetramethylpiperidine-1-oxy (TEMPO) were purchased from Sigma-Aldrich (St. Louis, MO, U.S.A.). Tris(hydroxymethyl)amino methane (tris), $Fe_2(SO_4)_3{\cdot}H_2O$, trifluoroacetic acid (TFA, > 99.8%), and sodium ascorbate were obtained from Merck (Darmstadt, Germany). Sodium sulfite was obtained from J.T. Baker, Deventer, The Netherlands. All chemicals were of analytical grade or highest possible purity. Water was purified through a Milli-Q water purification system (Millipore, Billerica, U.S.A.).

An all-malt pilsner beer (bottled with crown corks, 4.6% vol. alcohol) was obtained from a local supermarket and stored at 4 °C in the dark. All bottles were from one production batch and replicate analyses were performed by using different bottles. Before experiments, 150 mL beer was degassed by stirring 5 min in a Blue Cap bottle. Excessive foaming was prevented by addition of 15 μL 1-octanol.

Forced Aging of Beer. Forced aging was conducted by incubating the beer at elevated temperatures or by addition of Fenton reagents (Fe(II) or Fe(III) and H_2O_2 either alone or in combination) at different concentrations. All reagents were prepared fresh every day. The specific conditions and concentrations are given in the figure texts of each figure.

Measurement of Oxygen Consumption. Experiments studying the effects of addition of Fenton reagents were carried out using a 150 mL two-necked, round-bottomed flask equipped with a magnetic stirring bar placed in a water bath at 26 °C. One neck was closed with a rubber septum, and a HQ 30d Luminescent Dissolved Oxygen (LDO) sensor (Hach Lange, Düsseldorf, Germany) was placed in the other neck. The flask was completely filled with degassed beer, which had been freshly saturated with atmospheric air by bubbling for 2 min. The oxygen measurements were started immediately after the flask was filled. The oxygen concentration was recorded every 10 s, and the sensor had initially been calibrated against air saturated water at 26 °C. The oxygen consumptions were typically measured during 8 h. Solutions of Fenton reagents (Fe(II), Fe(III), or H_2O_2) were added during the experiments through the rubber septa using syringes and needles.

In experiments where effects of temperature were studied, a set up using a Clark electrode (Unisense NR-sensor, Aarhus, Denmark) was used. Aliquots of 50 mL of degassed beer were air saturated by flushing with atmospheric air for 2 min in a preheated water bath adjusted to the desired temperature (26 °C, 40 °C, and 60 °C). Subsequently, the sample was quickly transferred to a 2 mL chamber (MR-chamber, Unisense, Aarhus, Denmark) leaving no headspace of air. Aliquots of 20 μL of 0.36 mM Fe solution was added immediately before closing the chamber in experiments testing the effects of iron. The filled chamber was placed in a thermostated water bath adjusted to the same temperature as that for the air saturation and equipped with a Clark electrode. The measurement was started immediately. The oxygen concentration was recorded every 10 s using an oxygen analyzer (Picoammeter PA 2000, Unisense, Aarhus, Denmark). The electrode and oxygen analyzer were calibrated by a two-point calibration using air saturated water and oxygen-free solutions of 0.1 M sodium ascorbate in 0.1 M NaOH at the same temperatures as those in the experiments. The calibrations were performed before each analysis. The molar concentrations of oxygen in air saturated beer at the different temperatures were calculated from Ostwald coefficients for oxygen solubility in alcohol−water solutions at 4, 12, 25, and 50 °C, as reported by Shchukarev and Tolmacheva.[18] The Ostwald coefficient (I) describes the solubility of a gas in a liquid and is defined according to eq 1, where V_G is the volume of absorbed gas, and V_L is the volume of absorbed liquid:[19]

$$I = \frac{V_G}{V_L} \tag{1}$$

The Ostwald coefficients are reported by Shchukarev and Tolmacheva as a function of the alcohol concentration as mass %. The beer used in this study had a density of 1.01 g/mL, resulting in an alcohol content equal to 3.6 mass %. The Ostwald coefficients for water and 3.6% ethanol in water at 26 and 40 °C were obtained from interpolation of second order polynomial fits of Van't Hoff plots of Shchukarev and Tolmacheva's data, whereas the coefficients for water and 3.6% ethanol in water at 60 °C were obtained by equivalent second order polynomial extrapolation (Table 1). The Ostwald coefficients were converted to molar concentrations using the ideal gas law, eq 2.

Table 1. Ostwald Coefficients and Oxygen Concentrations in Water and in 3.6%(w/w) Ethanol in Water in Contact with Atmospheric Air[a]

	Ostwald coefficient		oxygen concentration (μM)	
T (°C)	in water	in 3.6% (w/w) ethanol	in water	in 3.6% (w/w) ethanol
4	0.0451[b]	0.0468	416	432
12	0.0381[b]	0.0387	342	347
25	0.0310[b]	0.0322	266	277
26	0.0305	0.0314	261	268
40	0.0259	0.0264	212	215
50	0.0238[b]	0.0239	189	189
60	0.0223	0.0222	172	170

[a]The values are calculated from data reported by Shchukarev & Tolmacheva (1968) as described in Materials and Methods. [b]Data from Shchukarev & Tolmacheva (1968).

$$n = \frac{p{\cdot}V_G}{R{\cdot}T} \tag{2}$$

where p is the atmospheric pressure of gas, R the universal gas constant, and T is the temperature.

From the loss of oxygen concentration over time, the rate constants of oxygen consumption were calculated at 26 °C, 40 °C, and 60 °C and plotted in order to determine the temperature dependency according to the Arrhenius eq 3, where k is the rate constant, E_a is the activation energy, A is the preexponential factor, R the universal gas constant, and T is the temperature:

$$\ln k = \ln A - \frac{E_a}{R}{\cdot}\frac{1}{T} \tag{3}$$

The slope of the Arrhenius plot (E_a/R) is used for the calculation of the temperature coefficient (Q_{10}) by eq 4:

$$\log Q_{10} = \frac{10{\cdot}E_a}{2.3{\cdot}R{\cdot}T^2} \tag{4}$$

where the Q_{10} value indicates the increase in reaction rates when the temperature is increased by 10 °C.

DOI: 10.1021/acs.jafc.5b02617
J. Agric. Food Chem. 2015, 63, 8254−8261

ESR Lag Phase Measurements during Forced Aging. Measurements of lag phases for radical formation were performed by ESR according to Uchida et al.[9] Beer was degassed by stirring on a magnetic stirrer for 5 min. Degassed beer containing 30 mM PBN was heated at 60 °C in closed Blue Cap bottles with a headspace of atmospheric air. Samples were analyzed at given time intervals. ESR spectra were recorded at room temperature with a JES-FR30 ESR spectrometer (Jeol, Tachikawa, Japan) using a quartz capillary (ID 0.75 mm) sample cell (Wilmad Glass, Buena, NJ). The settings were as follows: Microwave power, 4 mW; sweep width, 50.0 G; sweep time, 2 min; modulation amplitude 1.25 G; time constant 0.3 s. Intensities of the ESR signals were calculated relative to an internal Mn(II) standard attached to the ESR cavity. All ESR measurements were performed in duplicate as a minimum.

Sulfite and Thiol Analysis. Quantification of sulfite and thiols was performed according to Abrahamsson et al.[20] and Hoff et al.[21] based on derivatization of sulfite and thiols with ThioGlo 1 fluorescent reagent followed by separation with Reversed Phase High Performance Liquid Chromatography (RP-HPLC) and fluorescence detection. Sulfite and thiol determinations were performed in duplicate as a minimum.

Data Analysis. Statistical analysis was performed using SAS 9.2 package, SAS Institute, Inc., U.S.A. Data were analyzed by analysis of variance using proc glm. Means were used to compare differences and LSD was applied to compare the mean values. The significance level was $p < 0.05$.

RESULTS

Effects of Iron and Hydrogen Peroxide on Oxygen Consumption. Oxygen is a central reactant in various oxidative reactions, and the rate of oxygen consumption is therefore expected to provide quantitative information about the overall rate of oxidation reactions in the tested beer. Experiments were carried out at temperatures from 25 to 60 °C using degassed beer that had been quickly saturated with atmospheric air immediately before the oxygen measurements were initiated. The oxygen concentration in 3.6% (w/w) ethanol in water, which is equivalent to the alcohol concentration of the applied lager beer, was calculated at different temperatures as described in the Materials and Methods section from Ostwald coefficients reported by Shchukarev and Tolmacheva for oxygen solubility in ethanol–water mixtures (Table 1).[18] The results showed that ethanol concentration of 3.6% (w/w) only had a minor influence on the oxygen solubility as compared to pure water.

Oxygen consumption in the lager beer that was saturated by atmospheric air was measured at 26 °C, and within the first 10 min of the measurements, the oxygen concentration decreased quickly, followed by a slower linear decrease during the following 8 h (Figure 1). Only about 25% of the initial amount of oxygen was consumed during the experiment. The addition of Fe(II) or Fe(III) after 2 h was found to have a major effect on the rate and extent of oxygen consumption at high concentrations (36 μM). The subsequent addition of H_2O_2 after 4 h significantly increased the rate of oxygen consumption, and the rate increase was larger when 36 μM Fe had been added in advance as compared to addition of only 3.6 μM Fe. Surprisingly, the additions of Fe(II) or Fe(III) had very similar effects. This may be due to the rapid conversion of Fe(III) to Fe(II) by reducing compounds in beer, in agreement with the findings of Kunz et al.[21] Further addition of H_2O_2 after 6 h did not affect the rate of oxygen consumption, which suggests the system had already been saturated after the first addition of H_2O_2. The addition of H_2O_2 alone did not result in any significant increase in the rate of oxygen consumption as compared to the control (data not shown). This demonstrates that the combination of Fe and H_2O_2 increases the rate of oxygen consumption in beer to a greater extent than the individual compounds alone.

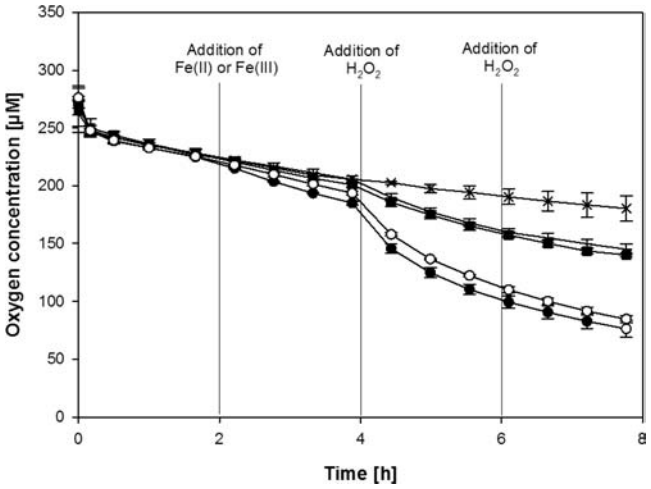

Figure 1. Oxygen consumption in beer, in which 3.6 μM Fe(II) (−), 3.6 μM Fe(III) (■), 36 μM Fe(II) (●), or 36 μM Fe(III) (○) were added after 2 h, and 180 μM H_2O_2 was added after 4 and 6 h at 26 °C. The control beer (x) was studied without addition of the Fenton reagents. Means are presented, and standard deviations are shown as error bars, $n = 2$.

The rates of oxygen consumption in air saturated lager beer were determined at 26 °C, 40 °C, and 60 °C, with and without the addition of 3.6 μM Fe(II), in order to establish the temperature dependency of the oxidation processes. The oxygen consumption was found to be linear with time and with slightly increasing rates for increasing temperatures both with and without added Fe(II). An Arrhenius plot of the rates of oxygen consumption gave linear correlations with activation energies equal to 26.6 and 22.4 kJ/mol with added Fe(II) (Figure 2). The temperature coefficient (Q_{10}), which describes the ratio by which reaction rates are increased when the temperature is increased 10 °C, was determined from the

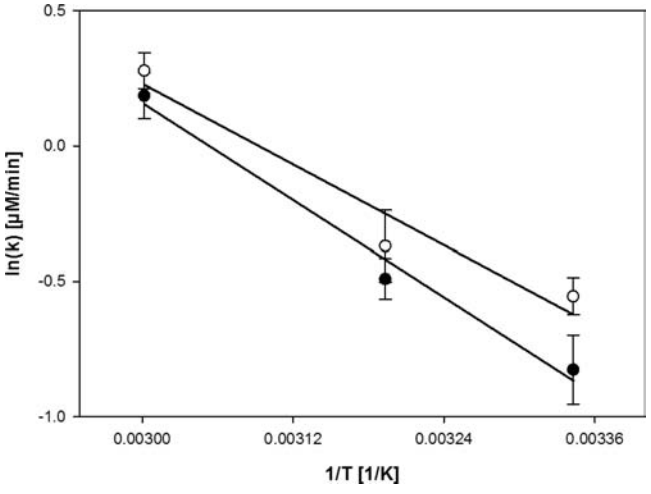

Figure 2. Arrhenius plot of the rate constants for oxygen consumption obtained at 26 °C, 40 °C, and 60 °C for fresh beer (●) and beer mixed with 3.6 μM Fe(II) (○). Means are presented and standard deviations are shown as error bars, $n = 3$.

DOI: 10.1021/acs.jafc.5b02617
J. Agric. Food Chem. 2015, 63, 8254–8261

activation energies by eq 4. Q_{10} was 1.4 ± 0.1 for beer and 1.3 ± 0.1 for beer with added of Fe(II). The addition of Fe(II) had no significant influence on the temperature dependency of the oxygen consumption. For most biological reactions, the Q_{10} is between 2 and 3.[22] Thus, the temperature dependency of oxygen consumption in beer is low, which may be due to a low enthalpy of reaction for the initial binding of dioxygen.

Formation of Radicals in Beer Determined by ESR Spectroscopy. The effects of the oxygen consumption on the formation of radicals were investigated by measuring the ESR lag phase. Beers were heated for different periods of time at 50 or 60 °C in the presence of atmospheric air. Subsequently, the spin trap PBN was added, and the lag phase measurements were initiated. Preincubation of the beer for up to 120 min at 50 °C was found to have no significant effect on the length of the lag phase (Figure 3). Increasing the preincubation

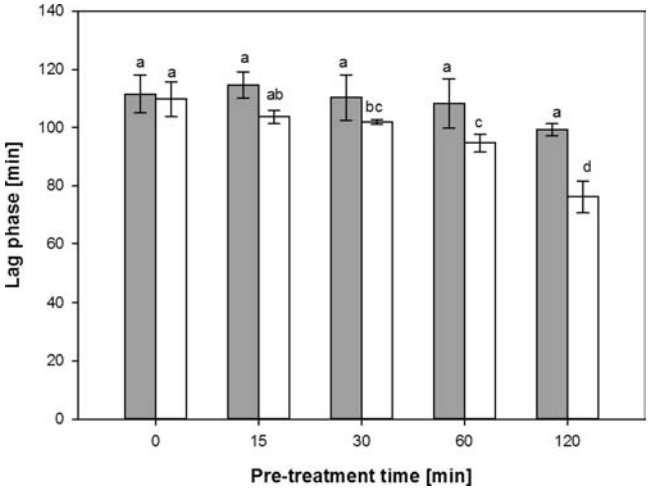

Figure 3. Lag phases determined by ESR spectroscopy of fresh beer and of beer preincubated at 50 °C (gray bars) and 60 °C (white bars) for 15 min, 30 min, 60 and 120 min. Means are presented and standard deviations are shown as error bars, n = 3. Different letters above bars indicate significantly different values (p < 0.05).

temperature to 60 °C decreased the lag phase slightly, and significantly more after 30 min preincubation, and the effects were more pronounced after 60 and 120 min of preincubation time. It is noteworthy that the lag phase of the fresh beer was 110 min, whereas incubation of the beer without the presence of the spin trap PBN at 60 °C for 120 min only reduced the lag phase by about 30 min. This suggests that the spin trap plays a more active role in the radical generating mechanisms in beer than by only trapping radicals. The moderate effect of preincubation on the length of the lag phase is in good agreement with the oxygen consumption measurements. Clearly, the beer still contained active antioxidants even after 120 min at 60 °C in the presence of atmospheric air. Addition of 3.6 μM of Fe(II) or Fe(III) to the beer and incubating for 15 min at room temperature decreased the ESR lag phase by about 30 min. Incubating the beer with added iron for longer times did not further shorten the lag phase (data not shown). Also, in these experiments, the addition of Fe(II) and Fe (III) had similar effects on the length of the lag phases.

The combined addition of Fe(II) and increasing concentrations of H_2O_2 15 min before the ESR lag phase measurements had two effects: (1) The length of the lag phase decreased, and (2) at the same time the initial level of trapped radicals increased (Figure 4A). Adding H_2O_2 in increasing concentrations (50−130 μM) without addition of

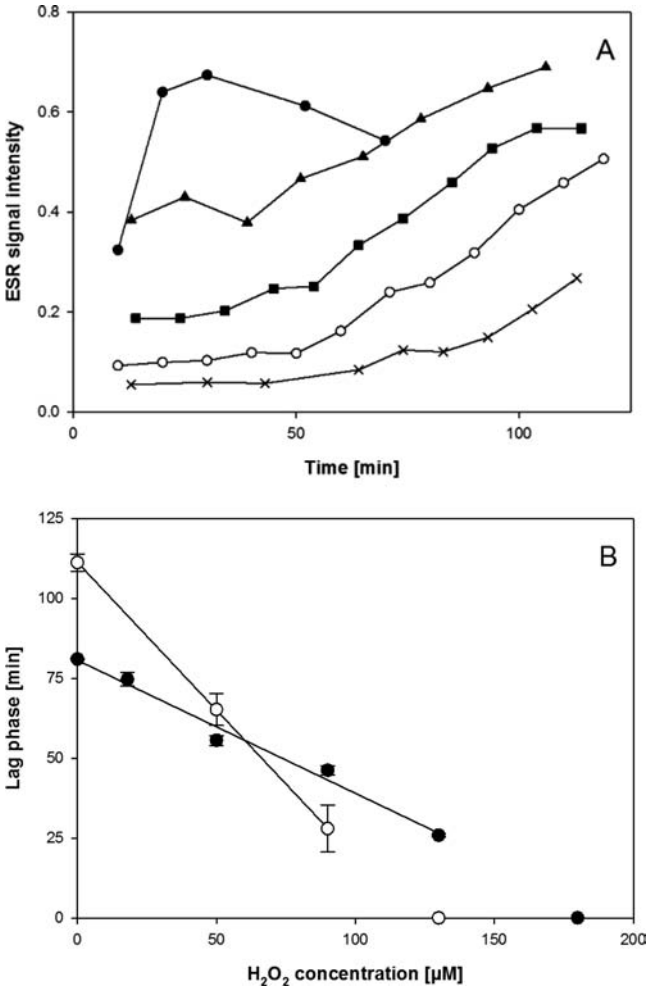

Figure 4. (A) Radical formation measured by ESR in beer at 60 °C with added 3.6 μM Fe(II) and H_2O_2 in the concentrations 18 μM (x), 50 μM (○), 90 μM (■), 130 μM (▲), and 180 μM (●) 15 min prior to analysis. Samples were run in duplicates and representative single measurements are presented. (B) Plot of ESR lag phases of beer with 3.6 μM Fe(II) added (●) and without 3.6 μM Fe(II) added (○) as a function of H_2O_2 concentration. Means are presented, and standard deviations are shown as error bars, n = 2.

Fe(II) only decreased the lag phases and did not influence the initial level of detected radicals (data not shown). Similar experiments have been performed by Uchida & Ono,[10] who observed a complete loss of lag phase by adding H_2O_2, which is likely due to the fact that they used much higher H_2O_2 concentrations (300−900 μM). According to Uchida & Ono,[23] H_2O_2 can accumulate in concentrations up to 15 μM at 60 °C in beer. The lag phase was found to decrease linearly with increasing H_2O_2 concentration, and the addition of Fe(II) decreased the slope of the linear dependence (Figure 4B).

Consumption of Sulfite and Thiols in Beer during Forced Aging. Sulfite is known to be an important antioxidant in beer and the concentration of sulfite is often found to correlate with the ESR lag phase.[10,12] Thus, the sulfite concentration was also quantified in beer during forced aging. Incubation of the beer with 50 μM H_2O_2 for 15 min at 26 °C caused a decrease in sulfite concentration of ca. 40 μM

DOI: 10.1021/acs.jafc.5b02617
J. Agric. Food Chem. 2015, 63, 8254−8261

independent of the addition of 3.6 μM Fe(II) (Figure 5). This suggests that sulfite mainly reacts with H_2O_2 in beer. Increasing

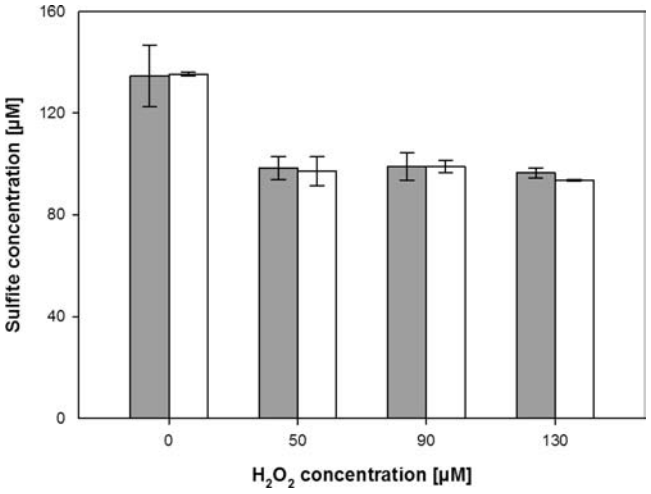

Figure 5. Sulfite concentrations in beer treated with different concentrations of H_2O_2. The beer either contained no additional Fe(II) (gray bars), or was added 3.6 μM Fe(II) (white bars). The beers were kept for 15 min at 26 °C before sulfite concentrations were determined. Means are presented, and standard deviations are shown as error bars, n = 2.

the H_2O_2 concentration did not result in further consumption of sulfite (Figure 5). Incubating the beer at 26 °C with only 3.6 μM Fe(II) did not affect the sulfite concentration. Similarly, the sulfite concentration was unaffected by addition of 36 μM Fe(II) or Fe(III) (3.6 μM and 36 μM) in the absence of of H_2O_2 (data not shown), which indicates that sulfite alone cannot protect the beer from oxidative processes during forced aging.

The consumption of sulfite was further investigated by incubating the beer at 26 °C for 8 h and at 60 °C for 1 and 8 h. Sulfite consumption was found to be highly temperature dependent; incubation at 26 °C for 8 h without addition of either Fe(II) or H_2O_2 resulted in a loss of about 40%, while incubation at 60 °C for 8 h caused a complete depletion of sulfite (Figure 6A). By incubation at 26 °C, the addition of 36 μM Fe(II) did not influence the sulfite concentration, whereas addition of 180 μM H_2O_2 caused an almost complete depletion of sulfite, proving the direct reaction between H_2O_2 and sulfite. Addition of 3.6 μM Fe(II) in combination with 180 μM H_2O_2 resulted in a similar sulfite consumption as without addition of Fe(II). Again, this observation confirms the ability of sulfite to remove H_2O_2 in beer. Surprisingly, addition of 36 μM Fe(II) in combination with 180 μM H_2O_2 resulted in a higher final sulfite concentration as compared with the addition of 3.6 μM Fe(II).

To clarify the role and reaction mechanism of protein thiols as antioxidants in beer, thiols were also quantified in the same samples as described above. Consumption of thiols was clearly not as temperature dependent as that of sulfite, as the consumption patterns were very similar at 26 and 60 °C (Figure 6B). When incubating the beer for 8 h at 60 °C, only approximately 50% of the thiols were consumed, whereas sulfite was depleted (Figure 6, parts A and B). In beer without additives, all incubation conditions caused a loss of thiols, whereas addition of Fe(II) and/or H_2O_2 caused an additional loss of thiols. Addition of a combination of Fe(II) and H_2O_2 caused the greatest loss of thiols, indicating that thiols primarily

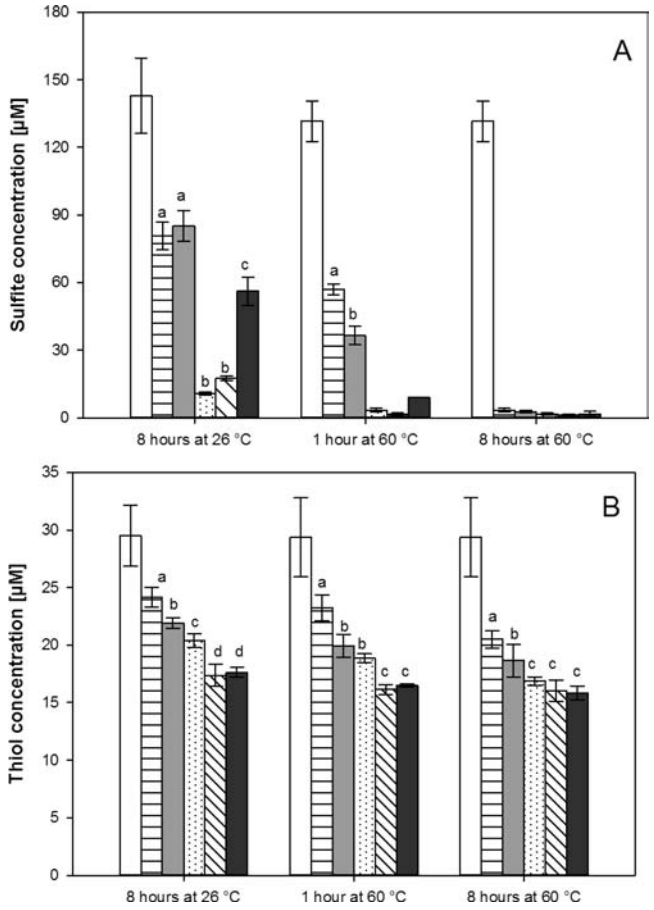

Figure 6. Sulfite (A) and thiol (B) concentrations in fresh beer (white bars) and incubated beers with no additives (horizontal striped bars) and with addition of 36 μm Fe(II) (gray bars), 180 μM H_2O_2 (dotted bars), 3.6 μM Fe(II) + 180 μM H_2O_2 (slanting striped bars), and 36 μM Fe(II) + 180 μM H_2O_2 (black bars) as determined by RP-HPLC with ThioGlo 1 after incubation for the specified periods and temperatures. Means are presented, and standard deviations are shown as error bars, n = 3. The different letters above the bars indicate significantly different values ($p < 0.05$).

react with 1-hydroxyethyl radicals formed via the Fenton reaction. Considering the observed preservation of sulfite in beer with added 36 μM Fe(II) and 180 μM H_2O_2 compared to addition of 3.6 μM Fe(II) and 180 μM H_2O_2 (Figure 6A), it can be ruled out that thiols protect sulfite from consumption, as no additional loss of thiols happened by addition of the high concentration of Fe(II) in combination with H_2O_2.

DISCUSSION

The early oxidative reactions in beer can be described by the mechanism shown in Scheme 1, which is based on iron catalyzed trapping of oxygen leading to the initial formation of hydrogen peroxide, which then initiates ethanol oxidation driven by the Fenton reaction. In this study, the focus has been on iron as the prooxidative catalyst; however, trace levels of copper are expected to play a similar role as that of iron. Similar mechanisms have been suggested for metal catalyzed oxidations in wine based on model studies, and they may therefore be of general relevance for a broad range of alcoholic beverages.[17,24] Oxygen is consumed both by the initial formation of hydrogen peroxide and also during the ethanol oxidation cycle, and the rates of oxygen consumption are therefore a combined measure

DOI: 10.1021/acs.jafc.5b02617
J. Agric. Food Chem. 2015, 63, 8254−8261

Scheme 1. Early Stages of Oxidative Reactions in Beer

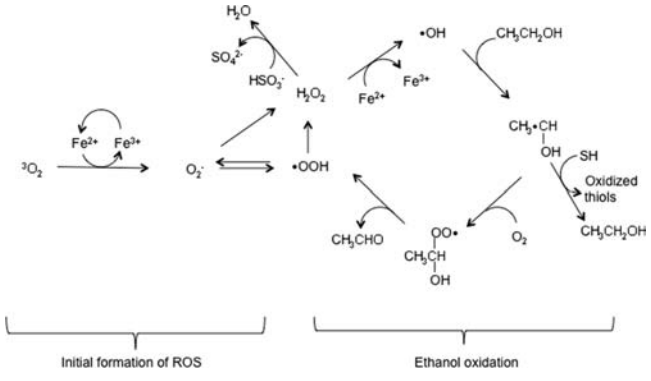

of both parts of the oxidation scheme. The ESR lag phase measurements are based on trapping the 1-hydroxyethyl radical, which is a central intermediate in ethanol oxidation.

The ethanol oxidation involves the formation of hydroperoxyl radicals, $HOO^{\bullet}$, which disproportionate and generate oxygen and hydrogen peroxide reaction 4. The overall stoichiometry of the ethanol oxidation is therefore equivalent to reaction 5, which emphasizes that hydrogen peroxide and Fe(II) are consumed together with oxygen.

$$2HOO^{\bullet} \rightarrow H_2O_2 + O_2 \quad (4)$$

$$2CH_3CH_2OH + O_2 + H_2O_2 + 2Fe^{2+} + 2H^+ \rightarrow 2CH_3CHO + 4H_2O + 2Fe^{3+} \quad (5)$$

$$H_2O_2 + HSO_3^- \rightarrow H_2O + SO_4^{2-} + H^+ \quad (6)$$

Hydrogen peroxide is a central intermediate in Scheme 1 linking the initial trapping of oxygen to the ethanol oxidation. However, hydrogen peroxide may also react with sulfite reaction 6, and the competition between this reaction and the Fenton reaction, reaction 1, determines the amount of ethanol being oxidized. In wine, a similar competition between the Fenton reaction and the direct reaction of H_2O_2 with sulfite has been demonstrated.[25] The beer in this study contained 140 μM sulfite. Keeping the beer for 8 h under atmospheric air resulted in a linear consumption of 92 μM oxygen (Figure 1). Under the same conditions, only approximately 60 μM sulfite was consumed (Figure 6), which indicates that ethanol oxidation occurred to some extent together with the reaction with sulfite, resulting in extra oxygen being consumed according to reaction 5. Consumption of sulfite was found to depend mainly on the addition of H_2O_2 and not on the addition of Fe (Figure 5), which supports a direct reaction between sulfite and hydrogen peroxide. In the beer used in the present study, this competition was also observed, as shorter ESR lag phases were seen when increasing H_2O_2 concentrations were added, whereas in the presence of Fe(II), the initial level of radicals formed in the beer also increased with increasing H_2O_2 concentrations (Figure 4A).

The competition of H_2O_2 reacting in the Fenton reaction, resulting in ethanol oxidation, or reacting with sulfite depends on the kinetics of the two reaction routes. The rate constant for the reaction between H_2O_2 and sulfite is around 10^3 M^{-1} s^{-1},[8] whereas rate constants for the Fenton reaction vary from 60 M^{-1} s^{-1} to 10^5 M^{-1} s^{-1} depending on the Fe(II) ligands.[26−28] Consequently, the ratio of the concentrations sulfite and with Fe(II) determine which reaction route that will dominate, and hydrogen peroxide is consumed by the Fenton reaction when a high level of Fe is present, while the reaction with sulfite is the major route at low iron concentrations. The depletion of sulfite and its efficiency as antioxidant will therefore be directly linked to the relative amounts of iron and copper ions that are present.

The addition of iron alone had only minor effects on the rates of oxygen consumption and the consumption of sulfite, indicating a negligible effect on the initial trapping of oxygen. However, the iron addition had an effect when hydrogen peroxide was also added, which according to Scheme 1 will directly initiate the oxidation of ethanol. Interestingly, additions of either Fe(III) or Fe(II) had the same effects on the oxygen consumption, the radical formation and lag phases as determined by ESR spectroscopy, and the decrease of sulfite concentrations during forced aging of beer. Uchida & Ono[10] have demonstrated that Fe(II) has prooxidative activity in beer by decreasing the ESR lag phase, but in their study Fe(III) was not included. Recently, it was shown by Kunz et al.[21] that intermediate Maillard reaction products with an enediol structure are capable of reducing Fe(III) to Fe(II) in beer. Assuming fast redox equilibria between Fe(II) and Fe(III) species in beer may explain the similar effects of adding the two species. Polyphenols and sulfite have been shown to efficiently reduce Fe(III) to Fe(II) in wine.[17,25] However, a similar role of polyphenols in beer is less likely as they neither inhibit nor increase radical formation.[29] In this study, we observed that addition of Fe(III) did not affect the sulfite concentrations, suggesting that sulfite is not able to reduce Fe(III) in beer in contrast to wine. This may be due to the differences in pH as well as the different types of ligands that are present in beer and wine. In wine, Fe ions are coordinated to tartaric and malic acid.[30] In beer, iron is found as a mixture of negatively charged, positively charged, and neutral species, suggesting coordination to a variety of ligands.[31]

The concentrations of thiols in beer decreased during incubation at different conditions (Figure 6B), but not to the same extent as that observed for sulfite. This suggests that thiols play a secondary role as antioxidants in beer. Thiols are not expected to efficiently react with H_2O_2 due to the low rate constant of 10^{-2} to 10^{-3} M^{-1} s^{-1} as observed for cysteine.[32] Accordingly, the addition of 180 μM H_2O_2 had a smaller effect on the thiol concentrations than on the sulfite concentrations (Figure 6). It is hypothesized that once sulfite is depleted in beer, thiols act as secondary antioxidants by removing 1-hydroxyethyl radicals (Scheme 1). This is supported by the high rate constant of 10^9 M^{-1} s^{-1} for this reaction.[16] However, the thiols will be competing with hop-derived bitter acids which also react with 1-hydroxyethyl radicals with similar high rate constants.[33] Recently, it has been suggested that sulfite and thiols in beer may reversibly bind staling aldehydes as adducts, and that these aldehydes may be released during beer aging.[34] On the basis of the present results, the aldehydes bound to sulfite would be the first to be released, followed by the thiol adducts at later stages of beer oxidation. Furthermore, a major fraction of the thiols seemed to be resistant to oxidation, suggesting that beer thiols have widely different redox properties. Interestingly, thiol consumption was not observed to be as temperature dependent as sulfite consumption. This observation is in agreement with a previous storage experiment of beers performed at 22 and 35 °C, where sulfite was depleted more rapidly at 35 °C, while thiol depletion was less temperature dependent.[35] This may suggest that beers exposed to heat, e.g., during long distance shipment will be depleted in

DOI: 10.1021/acs.jafc.5b02617
J. Agric. Food Chem. 2015, 63, 8254−8261

their content of sulfite (the primary antioxidant), but may still contain thiols as secondary antioxidants.

A remarkably low temperature dependency of oxygen consumption in beer was found with a Q_{10} of 1.3, which is most likely due to a low enthalpy of reaction for the initial reactions trapping oxygen. Addition of a combination of iron and H_2O_2 to beer caused an increased rate of oxidation as determined by oxygen consumption and increased radical formation as determined by ESR spectroscopy in comparison to addition of either iron or H_2O_2 alone, which is consistent with Fenton-mediated oxidation in beer leading to ethanol oxidation and the formation of 1-hydroxyethyl radicals. Sulfite was found to compete with the Fenton reaction for H_2O_2, and the primary antioxidative mechanism of sulfite was found to be through the direct reaction with H_2O_2, while protein thiols are suggested to play a secondary role as antioxidants in beer by removing 1-hydroxyethyl radicals. On the basis of these results, it will be possible to develop quantitative kinetic models that can potentially be used for predicting the shelf life of beer as well as the effect of various combinations of intrinsic and extrinsic factors.

AUTHOR INFORMATION

Corresponding Author

*Phone: +45 3533 3262. E-mail: mola@food.ku.dk (M.L.A.).

Notes

The authors declare no competing financial interest.

ACKNOWLEDGMENTS

The authors thank The Danish Council for Independent Research/Technology and Production within The Danish Agency for Science Technology and Innovation for granting the project entitled: "New defence systems against beer oxidation" (DFF-1335-00337).

REFERENCES

(1) Vanderhaegen, B.; Neven, H.; Verachtert, H.; Derdelinckx, G. The chemistry of beer aging - a critical review. *Food Chem.* **2006**, *95*, 357−381.

(2) Intelmann, D.; Haseleu, G.; Dunkel, A.; Lagemann, A.; Stephan, A.; Hofmann, T. Comprehensive sensomics analysis of hop-derived bitter compounds in beer during storage. *J. Agric. Food Chem.* **2011**, *59*, 1939−1953.

(3) Karabín, M.; Rýparová, A.; Jelínek, L.; Kunz, T.; Wietstock, P.; Methner, F.-J.; Dostálek, P. Relationship of iso-a-acid content and endogenous antioxidative potential during storage of lager beer. *J. Inst. Brew.* **2014**, *120*, 212−219.

(4) Kaneda, H.; Kano, Y.; Koshino, S.; Ohya-Nishiguchi, H. Behavior and role of iron ions in beer deterioration. *J. Agric. Food Chem.* **1992**, *40*, 2102−2107.

(5) Andersen, M. L.; Skibsted, L. H. Electron spin resonance spin trapping identification of radicals formed during aerobic forced aging of beer. *J. Agric. Food Chem.* **1998**, *46*, 1272−1275.

(6) De Cooman, L.; Aerts, G.; Overmeire, H.; De Keukeleire, D. Alterations of the profiles of iso-a-acids during beer ageing, marked instability of trans-iso-a-acids and implications for beer bitterness consistency in relation to tetrahydroiso-a-acids. *J. Inst. Brew.* **2000**, *106*, 169−178.

(7) Bamforth, C. W. 125th Anniversary Review: The non-biological instability of beer. *J. Inst. Brew.* **2011**, *117*, 488−497.

(8) Drexler, C.; Elias, H.; Fecher, B.; Wannowius, K. J. Kinetic investigation of sulfur(IV) oxidation by peroxo compounds R-OOH in aqueous solution. *Fresenius' J. Anal. Chem.* **1991**, *340*, 605−615.

(9) Uchida, M.; Suga, S.; Ono, M. Improvement for oxidative flavor stability of beer - rapid prediction method for beer flavor stability by electron spin resonance spectroscopy. *J. Am. Soc. Brew. Chem.* **1996**, *54*, 205−211.

(10) Uchida, M.; Ono, M. Improvement for oxidative flavor stability of beer - role of OH-radical in beer oxidation. *J. Am. Soc. Brew. Chem.* **1996**, *54*, 198−204.

(11) Andersen, M. L.; Outtrup, H.; Skibsted, L. H. Potential Antioxidants in Beer Assessed by ESR Spin Trapping. *J. Agric. Food Chem.* **2000**, *48*, 3106−3111.

(12) Lund, M. N.; Andersen, M. L. Detection of thiol groups in beer and their correlation with oxidative stability. *J. Am. Soc. Brew. Chem.* **2011**, *69*, 163−169.

(13) Rogers, P.; Clarke, F. M. *Sustainable Redox Power from Beer Proteins*; 31st International Congress of the European Brewery Convention: Venice, Italy, 2007.

(14) Wu, M. J.; Rogers, P. J.; Clarke, F. M. 125th Anniversary Review: The role of proteins in beer redox stability. *J. Inst. Brew.* **2012**, *118*, 1−11.

(15) Wu, M. J.; Clarke, F. M.; Rogers, P. J.; Young, P.; Sales, N.; O'Doherty, P. J.; Higgins, V. J. Identification of a protein with antioxidant activity that is important for the protection against beer ageing. *Int. J. Mol. Sci.* **2011**, *12*, 6089−6103.

(16) de Almeida, N. E. C.; Lund, M. N.; Andersen, M. L.; Cardoso, D. R. Beer redox stability conferred by thiol-containing compounds: a kinetic study of 1-hydroxyethyl radical scavenging ability. *J. Agric. Food Chem.* **2013**, *61*, 9444−9452.

(17) Danilewicz, J. C. Reactions involving iron in mediating catechol oxidation in model wine. *Am. J. Enol. Vitic.* **2013**, *64*, 316−324.

(18) Shchukarev, S. A.; Tolmacheva, T. A. Solubility of oxygen in ethanol-water mixtures. *J. Struct. Chem.* **1968**, *9*, 21−28.

(19) Battino, R.; Rettich, T. R.; Tominaga, T. The solubility of nitrogen and air in liquids. *J. Phys. Chem. Ref. Data* **1984**, *13*, 563−600.

(20) Abrahamsson, V.; Hoff, S.; Nielsen, N. J.; Lund, M. N.; Andersen, M. L. Determination of sulfite in beer based on fluorescent derivatives and liquid chromatographic separation. *J. Am. Soc. Brew. Chem.* **2012**, *70*, 296−302.

(21) Kunz, T.; Strähmel, A.; Cortés, N.; Kroh, L. W.; Methner, F.-J. Influence of intermediate Maillard reaction products with enediol structure on the oxidative stability of beverages. *J. Am. Soc. Brew. Chem.* **2013**, *71*, 114−123.

(22) Reyes, B. A.; Pendergast, J. S.; Yamazaki, S. Mammalian peripheral circadian oscillators are temperature compensated. *J. Biol. Rhythms* **2008**, *23*, 95−98.

(23) Uchida, M.; Ono, M. Determination of hydrogen peroxide in beer and its role in beer oxidation. *J. Am. Soc. Brew. Chem.* **1999**, *57*, 145−150.

(24) Kreitman, G. Y.; Laurie, V. F.; Elias, R. J. Investigation of ethyl radical quenching by phenolics and thiols in model wine. *J. Agric. Food Chem.* **2013**, *61*, 685−692.

(25) Elias, R. J.; Waterhouse, A. L. Controlling the Fenton reaction in wine. *J. Agric. Food Chem.* **2010**, *58*, 1699−1707.

(26) de Laat, J.; Gallard, H. Catalytic decomposition of hydrogen peroxide by Fe(III) in homogenous aqueous solution: Mechanism and kinetic modelling. *Environ. Sci. Technol.* **1999**, *33*, 2726−2732.

(27) Kremer, M. L. Mechanism of the Fenton reaction. Evidence for a new intermediate. *Phys. Chem. Chem. Phys.* **1999**, *1*, 3595−3605.

(28) Rush, J. D.; Maskos, Z.; Koppenol, W. H. Reactions of iron(II) nucleotide complexes with hydrogen peroxide. *FEBS Lett.* **1990**, *261*, 121−123.

(29) Andersen, M. L.; Skibsted, L. H. Modification of the levels of polyphenols in wort and beer by addition of hexamethylenetetramine or sulfite during mashing. *J. Agric. Food Chem.* **2001**, *49*, 5232−5237.

(30) Danilewicz, J. C. Role of tartaric and malic acids in wine oxidation. *J. Agric. Food Chem.* **2014**, *62*, 5149−5155.

(31) Pohl, O.; Prusisz, B. Chemical fractionation of Cu. *J. Food Compos. Anal.* **2010**, *23*, 86−94.

(32) Luo, D.; Smith, S. W.; Anderson, B. D. Kinetics and mechanism of the reaction of cysteine and hydrogen peroxide in aqueous solution. *J. Pharm. Sci.* **2005**, *94*, 304−316.

DOI: 10.1021/acs.jafc.5b02617
J. Agric. Food Chem. 2015, 63, 8254−8261

(33) de Almeida, N. E. C.; Homem-de-Mello, P.; De Keukeleire, D.; Cardoso, D. R. Reactivity of beer bitter acids toward the 1-hydroxyethyl radical as probed by spin-trapping electron paramagnetic resonance (EPR) and electrospray ionization-tandem mass spectrometry (ESI-MS/MS). *J. Agric. Food Chem.* **2011**, *59*, 4183−4191.
(34) Baert, J. J.; De Clippeleer, J.; De Cooman, L.; Aerts, G. Exploring the Binding Behavior of Beer Staling Aldehydes in Model Systems. *J. Am. Soc. Brew. Chem.* **2015**, *73*, 100−108.
(35) Lund, M. N.; Petersen, M. A.; Andersen, M. L.; Lunde, C. Effect of protease treatment during mashing on protein-derived thiol content and flavor stability of beer during storage. *J. Am. Soc. Brew. Chem.* **2015**, *73*, 287−295.

DOI: 10.1021/acs.jafc.5b02617
J. Agric. Food Chem. 2015, 63, 8254−8261

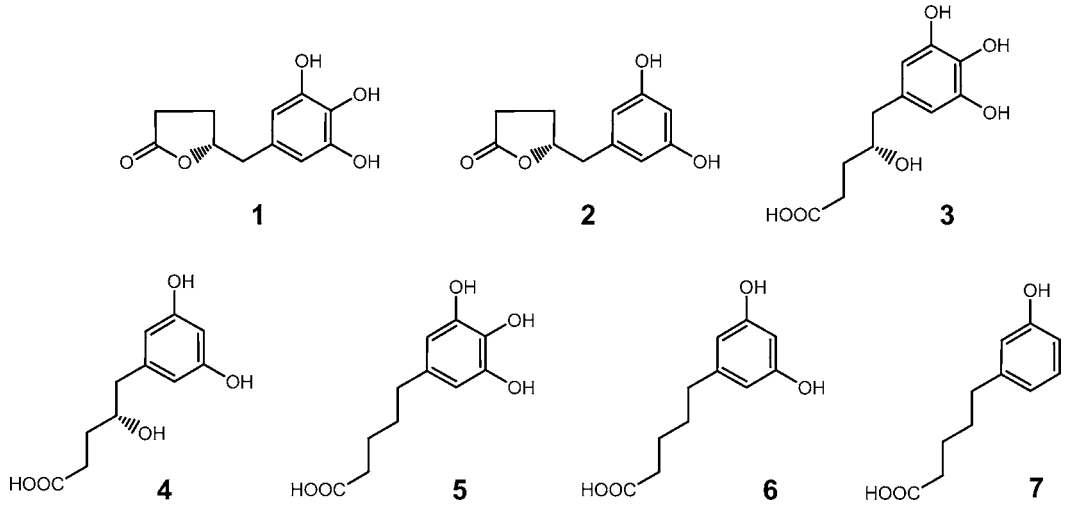

Figure 1. Chemical structures of EGCG metabolites.

Furthermore, two intestinal bacteria (*Adlercreutzia equolifaciens* MT4s-5 and *Flavonifractor plautii* MT42) capable of degrading EGC were isolated and identified.[25] In this study, we found that *A. equolifaciens* MT4s-5 catalyzed the conversion of EGC into 1-(3,4,5-trihydroxyphenyl)-3-(2,4,6-trihydroxyphenyl)propan-2-ol and then *F. plautii* MT42 converted the propan-2-ol into 5-(3,4,5-trihydroxyphenyl)-γ-valerolactone (**1**) and 4-hydroxy-5-(3,4,5-trihydroxyphenyl)valeric acid simultaneously. In a similar way, 5-(3,5-dihydroxyphenyl)-γ-valerolactone (**2**) was produced from 1-(3,5-dihydroxyphenyl)-3-(2,4,6-trihydroxyphenyl)propan-2-ol, which was formed from EGC by *A. equolifaciens* MT4s-5 in the presence of hydrogen. These developments made it possible to prepare enough intestinal EGCG or EGC metabolites to be able to examine their physiological activity in vivo.

Thus, in the context as described above, we attempted to investigate the hypotensive activity of intestinal metabolites derived from EGCG or EGC. The metabolites were first screened for their ACE inhibitory activities, and major metabolites **1** and **2** excreted in human and rat urine were then examined for their blood pressure lowering activity in SHR.

MATERIALS AND METHODS

Materials. EC, EGC, EGCG, and (−)-epicatechin gallate (ECG) were purchased from Sigma-Aldrich Japan (Tokyo). (−)-Catechin (C), (−)-gallocatechin gallate (GCG), and (−)-catechin gallate (CG) were prepared according to the method previously described.[26] EGCG metabolites, 5-(3,4,5-trihydroxyphenyl)-γ-valerolactone (**1**), 5-(3,5-dihydroxyphenyl)-γ-valerolactone (**2**), 4-hydroxy-5-(3,4,5-trihydroxyphenyl)valeric acid (**3**), 4-hydroxy-5-(3,5-dihydroxyphenyl)-valeric acid (**4**), 5-(3,4,5-trihydroxyphenyl)valeric acid (**5**), 5-(3,5-dihydroxyphenyl)valeric acid (**6**), and 5-(3-hydroxyphenyl)valeric acid (**7**), were prepared according to our previous papers.[18,24,26] The chemical structures of EGCG metabolites (**1**−**7**) are illustrated in Figure 1. ACE from rabbit lung, hippuryl-His-Leu (HHL), and hippuric acid were obtained from Sigma-Aldrich Japan (Tokyo). All other reagents were available products of analytical or HPLC grade.

Assay of ACE Inhibitory Activity. EGCG metabolites (**1**−**7**) and catechins (C, EC, EGC, ECG, CG, EGCG, and GCG) were individually dissolved in 10 mM citrate−phosphate buffer (pH 4.0) containing 5% methanol, and each solution was adequately diluted with distilled water to give final concentrations of 100 mM for metabolites **2** and **4**, C, and EC, 75 mM for EGC, 50 mM for metabolites **1** and **3**, 25 mM for metabolites **5**−**7**, and 10 mM for ECG, CG, EGCG, and GCG. The sample solution prepared above was used as stock solution. To measure ACE inhibitory activity, an adequate volume of distilled water was added to each stock solution, ranging from 10 to 70 μL, to make a total volume of 70 μL. To the solution (70 μL) was added 200 μL of 150 mM HEPES (4-(2-hydroxyethyl)-1-piperazineethanesulfonic acid) buffer (pH 8.3) containing 450 mM NaCl and 6 mM hippuryl-His-Leu (HHL) and 30 μL of ACE solution (0.1 U/mL). The mixture was incubated for 30 min at 37 °C. The reaction was stopped by the addition of 200 μL of 1 M acetate buffer (pH 4.0). After centrifugation, hippuric acid in the supernatant was analyzed by an LC-MS system. The LC-MS analysis was performed by a Surveyor HPLC and an LCQ Deca XPplus system (Thermo Fisher Scientific K.K., Yokohama, Japan). HPLC was carried out with a 100 mm × 2 mm i.d., 5 mm, CAPCELL PAK C18 MG column (Shiseido Co. Ltd., Tokyo, Japan) at a flow rate of 0.2 mL/min and 40 °C. The column was eluted with solvent A (10% (v/v) acetonitrile aqueous solution containing 0.2% (v/v) formic acid) for 3 min, followed by a linear gradient in solvent B (40% acetonitrile aqueous solution containing 0.2% formic acid) from 0 to 50% for 3−15 min and then a linear gradient from 50% B to 100% A for 15−20 min. Quantification of hippuric acid liberated from HHL by ACE was performed with the selected ion monitoring (SIM) mode. The separated $[M + H]^+$ ion chromatogram was selected at m/z 180 for the specific parent ion of hippuric acid. The concentration of the hippuric acid was determined on the basis of the standard calibration curve of authentic sample. ACE inhibitory activities were calculated as follows: ACE inhibitory activity (%) = 100 × (ACE activity of the control − ACE activity of the sample)/ACE activity of the control. Then, concentrations of the sample versus ACE inhibitory activities were plotted, and IC_{50} was calculated from the resulting curves.

Animals. Male SHR (14 weeks of age) were purchased from Charles Liver Laboratories Japan, Inc. (Yokohama) and housed in a room at 23 ± 3 °C and 60 ± 5% relative humidity, with a 12 h light−dark cycle. The rats were fed a pelleted diet (Rodent Labo Diet EQ, Japan SLC) for a week. All experimental procedures were in accordance with the guidelines for animal experiments of Food Research Laboratories, Mitsui Norin Co., Ltd.

Measurement of Systolic Blood Pressure (SBP) after Oral Administration of Metabolites 1 and 2 to SHR. Male SHR at 15 weeks of age were divided into two groups (n = 6−8) with almost the same average values of SBP. After a 16 h fast, 100 or 150 mg/kg of 5-(3,4,5-trihydroxyphenyl)-γ-valerolactone (**1**) dissolved in saline (1 mL) was administered orally to SHR with a gastric metal probe. Only saline (1 mL) was administered to the control group. In the same way, 150 or 200 mg/kg of 5-(3,5-dihydroxyphenyl)-γ-valerolactone (**2**) was orally administered. SBP was measured before and 2 and 4 h after dosage by the tail cuff method using a pneumatic pulse transducer (BP-98A; Softron, Tokyo, Japan).

DOI: 10.1021/acs.jafc.5b03676
J. Agric. Food Chem. 2015, 63, 8262−8266

Statistical Analysis. All values of SBP are expressed as means ± SEM. Statistical comparisons of the SBP values 2 and 4 h after the single administration between control and test substance-treated groups were performed by using Student's *t* test with the Bonferroni correction. The statistical differences between SBP before (basal SBP) and after administration of the metabolites were analyzed by using Dunnett's *t* test. The statistical calculations were done with IBM SPSS Statistics 19 computer software (IBM Japan, Tokyo). Differences are considered significant at $p < 0.05$.

RESULTS AND DISCUSSION

ACE Inhibitory Activity of EGCG Metabolites. ACE inhibitory activities of EGCG metabolites (**1**−**7**) produced by intestinal bacteria were evaluated. In addition, the inhibitory activities of catechins (C, EC, EGC, ECG, CG, EGCG, and GCG) were also measured for the purpose of reference. IC_{50} values of the compounds tested are indicated in Table 1. All of the EGCG metabolites showed ACE inhibitory activities and the order of IC_{50} was hydroxyphenyl valeric acids (**5** ≥ **6** > **7**) > trihydroxyphenyl-γ-valerolactone (**1**) > trihydroxyphenyl 4-hydroxyvaleric acid (**3**) ≫ dihydroxyphenyl 4-hydroxyvaleric acid (**4**) ≫ dihydroxyphenyl-γ-valerolactone (**2**). With regard to ACE inhibitory activities of the catechins, galloylated catechins (EGCG, GCG, CG, and ECG) showed stronger inhibitory activities than nongalloylated catechins (EGC, EC, and C).

Table 1. ACE Inhibitory Activity (IC_{50}) of EGCG Metabolites and Catechins

metabolite	IC_{50} (mM)	catechin	IC_{50} (mM)
1	2.89	EC	4.96
2	19.59	C	5.29
3	5.41	EGC	5.05
4	12.12	ECG	0.70
5	1.51	CG	0.35
6	2.38	EGCG	0.38
7	3.00	GCG	0.55

Hypotensive Activities of Metabolites 1 and 2 after a Single Oral Dosage to SHR. All of the EGCG metabolites tested showed ACE inhibitory activity, although their activity was of varying degrees. To examine the hypotensive activity of these metabolites after a single oral administration to SHR, we selected 5-(3,4,5-trihydroxyphenyl)-γ-valerolactone (**1**) and 5-(3,5-dihydroxyphenyl)-γ-valerolactone (**2**) because they are reported to be not only the dominant metabolites in the gut tract[18] but also the major urinary metabolites in humans and rats,[16,17,19,27] whereas the other metabolites were scarcely found in urine, if at all.

Metabolite **1** was orally administered to SHR at a dosage of 100 or 150 mg/kg. Basal SBP values (mm of Hg) were 189.0 ± 4.7 for the control group versus 192.1 ± 3.7 for the 100 mg/kg dosage group and 193.9 ± 4.7 for the control group versus 193.4 ± 2.4 for the 150 mg/kg dosage group. The administration of 100 mg/kg of **1** brought about no significant decrease in SBP as compared with the control group. However, a significant decrease in SBP was observed between basal SBP (SBP before administration) and SBP 4 h after administration (−14.9 ± 5.6 mm of Hg, $p = 0.029$, Dunnett's *t* test) in the 100 mg/kg dose group, but no significant change was observed in the control group as shown in Table 2. On the other hand, as shown in Figure 2A SBP significantly reduced 2 h after oral dosage of 150 mg/kg of **1** as compared with the control group ($p = 0.002$, Student's *t* test with the Bonferroni correction), although no significant decrease in SBP was observed 4 h after administration. Significant decrease in SBP of the 150 mg/kg dose group was also observed between basal SBP and SBP 2 h after dosage (−13.7 ± 5.0 mm of Hg, $p = 0.024$, Dunnett's *t*-test) but not between basal SBP and SBP 4 h after dosage. There was no significant change in SBP in the control group.

Table 2. Change in Systolic Blood Pressure after Oral Administration of Metabolites 1 and 2 to SHR[a]

	metabolite **1**		metabolite **2**	
	control	100 mg/kg dosage	control	150 mg/kg dosage
0 h	189.0 ± 4.7	192.1 ± 3.7	195.9 ± 6.7	197.7 ± 3.5
2 h	186.0 ± 4.6	186.1 ± 3.9	180.0 ± 4.2[a]	179.3 ± 2.8*[2]
4 h	184.4 ± 3.5	177.3 ± 4.3*[1]	180.4 ± 4.0[b]	181.7 ± 6.7*[3]

[a]Each SBP value (mm of Hg) represents the mean ± SEM. Statistical differences within each group were conducted using Dunnett's *t* test. Differences from basal SBP value (0 h) within each group are considered significant at $p < 0.05$: *[1], $p = 0.029$; *[2], $p = 0.023$; *[3], $p = 0.049$; [a], $p = 0.076$; [b], $p = 0.085$. Statistical differences between the control and the dosage groups were performed with Student's *t* test. There were no significant differences ($p < 0.05$) between the two groups.

In the case of metabolite **2**, 150 or 200 mg/kg was administered and changes in SBP were measured. No significant reduction in SBP at the 150 mg dose of **2** was observed as compared with the control group. A significant reduction of SBP was detected both between basal SBP and SBP 2 h after the administration of the 150 mg/kg dosage (−18.4 ± 6.6 mm of Hg, $p = 0.023$, Dunnett's *t* test) and between basal SBP and SBP 4 h after the same dosage (−16.0 ± 6.6 mm of Hg, $p = 0.049$, Dunnett's *t* test) as indicated in Table 2. While there was found to be a decreasing trend but no significant reduction of SBP was observed either between basal SBP and SBP after 2 h (−15.9 ± 7.3 mm of Hg, $p = 0.076$, Dunnett's *t* test) or between basal SBP and SBP after 4 h (−15.4 ± 7.3 mm of Hg, $p = 0.085$, Dunnett's *t* test) in the control group (Table 2). Accordingly, SBP-decreasing effects of the 150 mg/kg dosage of metabolite **2** were unclear. Figure 2B shows the time course changes in SBP after a 200 mg/kg administration of **2** and saline (control group). Basal SBP was 197.0 ± 5.2 for the control group and 198.7 ± 5.6 for the 200 mg/kg of dose. Metabolite **2** (200 mg/kg) showed hypotensive effects 4 h after oral intake ($p = 0.044$, Student's *t* test with the Bonferroni correction) as compared with the control group (after 4 h). A significant decrease in SBP change of the 200 mg/kg dose group was also observed between basal SBP and SBP 4 h after dosage (−30.3 ± 11.4 mm of Hg, $p = 0.033$, Dunnett's *t* test).

There are some reports on the physiological activities of intestinal catechin metabolites including 5-(3,4,5-trihydroxyphenyl)-γ-valerolactone (**1**) and 5-(3,5-dihydroxyphenyl)-γ-valerolactone (**2**), which are the major metabolites detected in rat and human urine.[20−23] However, no information is available on their blood pressure lowering effects. In this study, we revealed that intestinal EGCG metabolites possessed ACE inhibitory activity in vitro, although their activities were estimated to be about $^1/_4$ to $^1/_{50}$ of those of EGCG. As far as metabolites **1** and **2** are concerned, the ACE inhibitory activities were about $^1/_8$ for **1** and $^1/_{50}$ for **2** as compared with those of EGCG (Table 1), whereas the absorptivity of metabolites **1** and **2** is calculated to be about 10−85 times

DOI: 10.1021/acs.jafc.5b03676
J. Agric. Food Chem. 2015, 63, 8262−8266

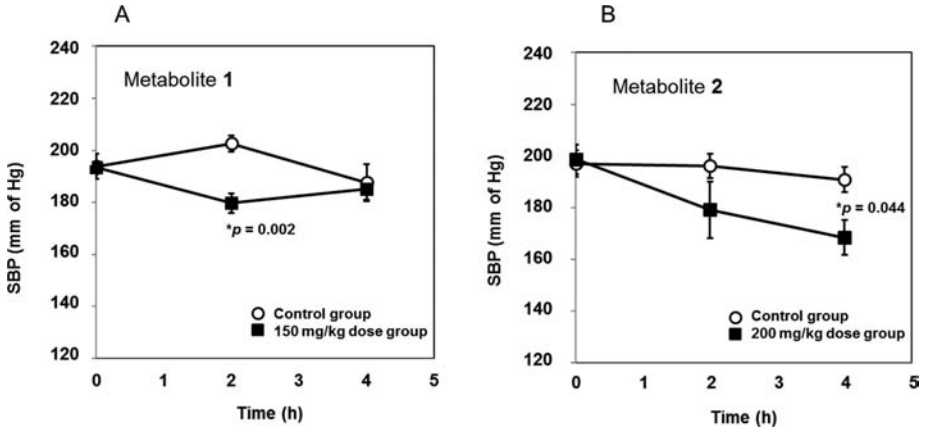

Figure 2. Effects of a single oral administration of metabolites **1** and **2** on systolic blood pressure in SHR. SBP values are expressed as means ± SEM. Statistical analysis was performed using Student's *t* test with the Bonferroni correction. Significant difference (*p* value) from the control group is shown.

higher than that of EGCG based on their urinary excretion amounts.[15−17,19] From the above observations, it was expected that these metabolites could show hypotensive effects in vivo. Accordingly, we examined hypotensive effects of metabolites **1** and **2** in in vivo experiments with SHR. The experiments clearly demonstrated hypotensive effects were observed after a single oral administration of the metabolites to SHR. In addition, our preliminary study on the metabolism of compound **1** showed that after a single oral administration of 5 mg/rat to SHR the compound peaked at 1 h, then decreased gradually, and at >4 h after dosage had almost disappeared from the rat plasma. During this period of time only a slight amount of degraded products derived from **1** was detected in plasma (data not shown). In the case of metabolite **2**, we did not examine its metabolism, but it is presumed that results similar to those for metabolite **1** would be obtained, judging from the similarity of their chemical structures and results of our previous study.[16] Therefore, it is likely that the two metabolites do actually possess hypotensive effects in vivo.

With respect to the mechanism for hypotensive activity of metabolites **1** and **2** in vivo, we found that these metabolites possessed ACE inhibitory activity. Although a direct relationship between the ACE inhibitory activity and hypotensive effects of the metabolites has not yet been proven and the mechanism remains unclear, the possibility cannot be denied that ACE inhibitory activities may be associated with their hypotensive effects. Apart from the mechanism proposed above, nitric oxide (NO) released from endothelium is considered to function as an important factor for vasodilation and consequently to reduce blood pressure.[13,14] Hence, the reduction of NO bioavailability by active oxygen species would cause endothelial dysfunction and, in the worst case, cardiovascular complications. Accordingly, antioxidants are thought to play an important role in the suppression of hypertension by preventing the reduction of NO bioavailability in arteries.[11,14] Our previous study revealed that intestinal catechin metabolites including metabolites **1** and **2** possessed antioxidative activities and their activities were stronger than or nearly equal to those of Trolox, a vitamin E derivative.[20] It is therefore possible that the metabolites may contribute as antioxidants, at least in part, to suppress the increase in blood pressure through the prevention of NO reduction by active oxygen species. As discussed above, the question of how mechanisms responsible for the hypotensive effects of metabolites **1** and **2** are at work remains unanswered. Further study is needed to clarify the mechanism of their hypotensive activity in vivo.

It is well recognized that EGCG has a variety of physiological activities including suppression of cholesterol and triglyceride in the blood,[5] suppression of glucose level in the blood,[6] antihypertensive activity,[8−10] antioxidant activity,[1−4] and chemopreventive activity.[7] Among the physiological activities, it is explainable to some extent that suppression of cholesterol in blood may be due to the prevention of cholesterol absorption through the small intestine by intact EGCG[28] and that suppression of glucose levels in the blood may be due to the inhibition of α-amylase and sucrase by intact EGCG in the small intestine.[29,30] However, it is doubtful in some cases whether intact EGCG actually acts as a major bioactive substance, because it has been reported to be poorly absorbed in the body.[15−17] On the other hand, intestinal metabolites such as 5-(3,4,5-trihydroxyphenyl)-γ-valerolactone (**1**) and 5-(3,5-dihydroxyphenyl)-γ-valerolactone (**2**) have been reported to be absorbed in large amounts in the body,[16,17,19] leading us to suppose that the metabolites may act as in vivo bioactive substances. In this context, we previously examined the antioxidative activity of EGCG metabolites and demonstrated they possessed antioxidative activity at least equivalent to that of Trolox, although their activities were weaker than those of their original catechins.[20] Among them, metabolites **1** and **2** may be the main antioxidant contributors in the body due to their good absorptivity. In this study, we observed that the EGCG metabolites had ACE inhibitory activity in vitro and that two major metabolites **1** and **2** had hypotensive effects in in vivo experiments. However, the relationship between ACE inhibitory activity and hypotensive effects remains to be investigated. Therefore, it seems reasonable to surmise that blood pressure lowering effects by catechin intake may be due, in part, to the hypotensive effects of metabolites **1** and **2**. Thus, study on the biological activity of intestinal metabolites such as **1** and **2** likely makes it possible to explain some of the health beneficial effects of tea catechins in the body. Accordingly, further in vivo studies on the physiological activity of the metabolites will be required.

DOI: 10.1021/acs.jafc.5b03676
J. Agric. Food Chem. 2015, 63, 8262−8266

AUTHOR INFORMATION

Corresponding Author

*(F.N.) E-mail: fnanjo@mitsui-norin.co.jp. Phone: +81-54-639-0080. Fax: +81-54-648-2001.

Notes

The authors declare no competing financial interest.

ACKNOWLEDGMENTS

We acknowledge the assistance of Andrea K. Suzuki (Mitsui Norin Co., Ltd.) in the review of the manuscript.

ABBREVIATIONS USED

ACE, angiotensin I-converting enzyme; SHR, spontaneously hypertensive rats; SBP, systolic blood pressure; EGCG, (−)-epigallocatechin gallate; EC, (−)-epicatechin; EGC, (−)-epigallocatechin; ECG, (−)-epicatechin gallate; C, (−)-catechin; GCG, (−)-gallocatechin gallate; CG, (−)-catechin gallate

REFERENCES

(1) Nanjo, F.; Honda, M.; Okushio, K.; Matsumoto, N.; Ishigaki, F.; Ishigami, T.; Hara, Y. Effects of dietary tea catechins on α-tocopherol levels, lipid peroxidation, and erythrocyte deformability in rats fed on high palm oil and perilla oil diets. *Biol. Pharm. Bull.* **1993**, *16*, 1156−1159.

(2) Nanjo, F.; Goto, K.; Seto, R.; Suzuki, M.; Sakai, M.; Hara, Y. Scavenging effects of tea catechins and their derivatives on 1,1-diphenyl-2- picrylhydrazyl radical. *Free Radical Biol. Med.* **1996**, *21*, 895−902.

(3) Nanjo, F.; Mori, M.; Goto, K.; Hara, Y. Radical scavenging activity of tea catechins and their related compounds. *Biosci., Biotechnol., Biochem.* **1999**, *63*, 1621−1623.

(4) Higdon, J. V.; Frei, B. Tea catechins and polyphenols: health effects, metabolism, and antioxidant functions. *Crit. Rev. Food Sci. Nutr.* **2003**, *43*, 89−143.

(5) Muramatsu, K.; Fukuyo, M.; Hara, Y. Effect of green tea catechins on plasma cholesterol level in cholesterol-fed rats. *J. Nutr. Sci. Vitaminol.* **1986**, *32*, 613−622.

(6) Matsumoto, N.; Ishigaki, F.; Ishigaki, A.; Iwashina, H.; Hara, Y. Reduction of blood glucose levels by tea catechin. *Biosci., Biotechnol., Biochem.* **1993**, *57*, 525−527.

(7) Yang, C. S.; Lambert, J. D.; Hou, Z.; Ju, J.; Lu, G.; Hao, X. Molecular targets for the cancer preventive activity of tea polyphenols. *Mol. Carcinog.* **2006**, *45*, 431−435.

(8) Hara, Y. Hypotensive action of tea polyphenols. In *Green Tea: Health Benefits and Applications*; CRC Press, Taylor & Francis Group: Boca Raton, FL, USA, 2001; pp 139−148.

(9) Negishi, H.; Xu, J.-W.; Ikeda, K.; Njelekela, M.; Nara, Y.; Yamori, Y. Black and green tea polyphenols attenuate blood pressure increases in stroke-prone spontaneously hypertensive rats. *J. Nutr.* **2004**, *134*, 38−42.

(10) Hodgson, J. M.; Devine, A.; Puddey, I. B.; Chan, S. Y.; Beilin, L. J.; Prince, R. L. Tea intake is inversely related to blood pressure in older women. *J. Nutr.* **2003**, *133*, 2883−2886.

(11) Galleano, M.; Pechanova, O.; Fraga, C. G. Hypertension, nitric oxide, oxidants, and dietary plant polyphenols. *Curr. Pharm. Biotechnol.* **2010**, *11*, 837−848.

(12) Medina-Remón, A.; Estruch, R.; Tresserra-Rimbau, A.; Vallverdú-Queralt, A.; Lamuela-Raventos, R. M. The effect of polyphenol consumption on blood pressure. *Mini-Rev. Med. Chem.* **2013**, *13*, 1137−1149.

(13) Potenza, M.; Marasciulo, F. L.; Tarquinio, M.; Tiravanti, E.; Colantuono, G.; Federici, A.; Kim, J.; Quon, M. J.; Montagnani, M. EGCG, a green tea polyphenol, improves endothelial function and insulin sensitivity, reduces blood pressure, and protects against myocardial I/R injury in SHR. *Am. J. Physiol. Endocrinol. Metab.* **2007**, *292*, E1378−E1387.

(14) Grassi, D.; Desideri, G.; Di Giosia, P.; De Feo, M.; Fellini, E.; Cheli, P.; Ferri, L.; Ferri, C. Tea, flavonoids, and cardiovascular health: endothelial protection. *Am. J. Clin. Nutr.* **2013**, *98* (Suppl.), 1660S−1666S.

(15) Chen, L.; Lee, M.-J.; Li, H.; Yang, C. S. Absorption, distribution, and elimination of tea polyphenols in rats. *Drug Metab. Dispos.* **1997**, *25*, 1045−1050.

(16) Kohri, T.; Matsumoto, N.; Yamakawa, M.; Suzuki, M.; Nanjo, F.; Hara, Y.; Oku, N. Metabolic fate of (−)-[4-^{3}H]epigallocatechin gallate in rats after oral administration. *J. Agric. Food Chem.* **2001**, *49*, 4102−4112.

(17) Del Rio, D.; Calani, L.; Cordero, C.; Salvantore, S.; Pellegrini, N.; Brighenti, F. Bioavailability and catabolism of green tea flavan-3-ols in humans. *Nutrition* **2010**, *26*, 1110−1116.

(18) Takagaki, A.; Nanjo, F. Metabolism of (−)-epigallocatechin gallate by rat intestinal flora. *J. Agric. Food Chem.* **2010**, *58*, 1313−1321.

(19) Li, C.; Lee, M.-J.; Sheng, S.; Meng, X.; Prabhu, S.; Winnik, B.; Huang, B.; Chung, J. Y.; Yan, S.; Ho, C.-T.; Yang, C. S. Structural identification of two metabolites of catechins and their kinetics in human urine and blood after tea ingestion. *Chem. Res. Toxicol.* **2000**, *13*, 177−184.

(20) Takagaki, A.; Otani, S.; Nanjo, F. Antioxidative activity of microbial metabolites of (−)-epigallocatechin gallate produced in rat intestines. *Biosci., Biotechnol., Biochem.* **2011**, *75*, 582−585.

(21) Lambert, J. D.; Rice, J. E.; Hong, J.; Hou, Z.; Yang, C. S. Synthesis and biological activity of the tea catechin metabolites, M4 and M6 and their methoxy-derivatives. *Bioorg. Med. Chem. Lett.* **2005**, *15*, 873−876.

(22) Unno, T.; Tamemoto, K.; Yayabe, F.; Kakuda, T. Urinary excretion of 5-(3′,4′-dihydroxyphenyl)-γ-valerolactone, a ring-fission metabolite of (−)-epicatechin, in rats and its in vitro antioxidant activity. *J. Agric. Food Chem.* **2003**, *51*, 6893−6898.

(23) Uhlenhut, K.; Högger, P. Facilitated cellular uptake and suppression of inducible nitric oxide synthase by a metabolite of maritime pine bark extract (pycnogenol). *Free Radical Biol. Med.* **2012**, *53*, 305−313.

(24) Takagaki, A.; Nanjo, F. Catabolism of (+)-catechin and (−)-epicatechin by rat intestinal microbiota. *J. Agric. Food Chem.* **2013**, *61*, 4927−4935.

(25) Takagaki, A.; Kato, Y.; Nanjo, F. Isolation and characterization of rat intestinal bacteria involved in biotransformation of (−)-epigallocatechin. *Arch. Microbiol.* **2014**, *196*, 681−695.

(26) Seto, R.; Nakamura, H.; Nanjo, F.; Hara, Y. Preparation of epimers of tea catechins by heat treatment. *Biosci., Biotechnol., Biochem.* **1997**, *61*, 1434−1439.

(27) Sang, S.; Lee, M.-J.; Yang, I.; Buckley, B.; Yang, C. S. Human urinary metabolite profile of tea polyphenols analyzed by liquid chromatography/electrospray ionization tandem mass spectrometry with data-dependent acquisition. *Rapid Commun. Mass Spectrom.* **2008**, *22*, 1567−1578.

(28) Ikeda, I.; Imasato, Y.; Sasaki, E.; Nakayama, M.; Nagao, H.; Takeo, T.; Yayabe, F.; Sugano, M. Tea catechins decrease micellar solubility and intestinal absorption of cholesterol in rats. *Biochim. Biophys. Acta.* **1992**, *1127*, 141−146.

(29) Hara, Y.; Honda, M. The inhibition of α-amylase by tea polyphenols. *Agric. Biol. Chem.* **1990**, *54*, 1939−1945.

(30) Honda, M.; Hara, Y. Inhibition of rat small intestinal sucrase and α-glucosidase activities by tea polyphenols. *Biosci., Biotechnol., Biochem.* **1993**, *57*, 123−124.

DOI: 10.1021/acs.jafc.5b03676
J. Agric. Food Chem. 2015, 63, 8262−8266

Table 1. Purified Enzymes Used in This Study

name	supplier	catalogue name	description	declared activity
Pect	Sigma-Aldrich	Pectinase	Pectolytic enzyme preparation: contains mainly pectintranseliminase, polygalacturonase, pectin esterase, and small amounts of hemicellulases and cellulases.	19 U/mg
EPG	Megazyme	E-PGALS	Endopolygalacturonase from *A. niger*, contains minor levels of endogalactanase, endoarabinase, pectin transeliminase, arabinofuranosidase, and β-galactosidase activity.	280 U/mg protein, polygalacturonic acid as substrate
EG	Megazyme	E-CELTR	Endo-1,4-β-glucanase with minor levels of endo-1,4-β-xylanase, endo-1,4-β-mannanase, α-glucosidase, β-glucosidase, β-xylosidase, α- and β-galactosidase, β-mannosidase, and α-L-arabinofuranosidase activities.	19−71[a] U/mg, assumed 40 U/mg for this study
XG	Megazyme	E-XEGP	Xyloglucan-specific endo-1,4-β-glucanase, recombinant enzyme.	104 U/mg
EA	Megazyme	E-EARAB	Endoarabinase with α-L-arabinofuranosidase <0.01% (on beet arabinan); endogalactanase <0.01%.	15 U/mg

[a]Depending on substrate.

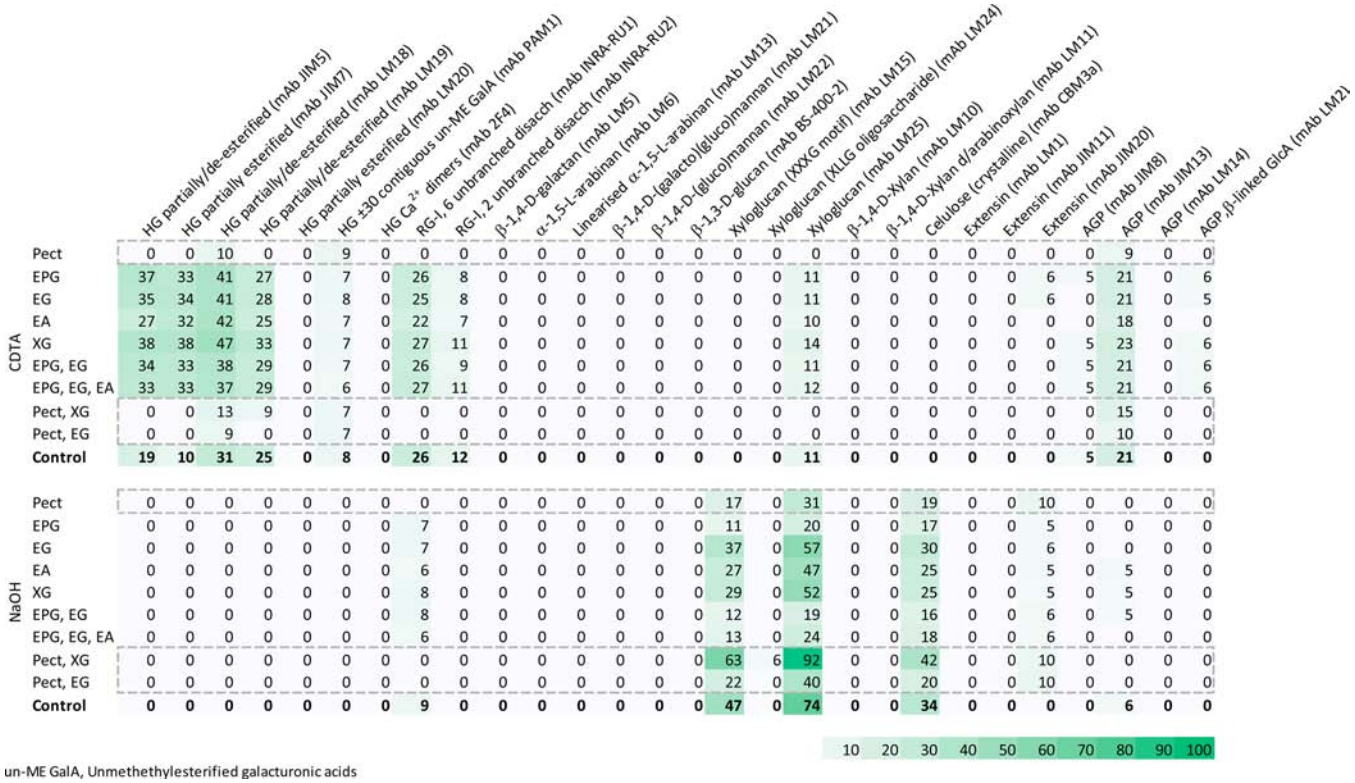

Figure 1. CoMPP analysis of the CDTA (pectin) and NaOH (hemicellulose) fractions extracted from Pinotage skin AIR hydrolyzed with pure enzymes. The values in the heat map are the average of three biological samples and show the relative abundance of the different epitopes normalized to the highest signal in the data set, which was set to 100. The boxed sections indicate enzymes that caused extensive enzymatic hydrolysis. The enzymes that were used are described in Table 1, and the monoclonal antibodies are listed in the Supporting Information (Table S1).

MATERIALS AND METHODS

Pinotage Skin Cell Wall Preparation. *Vitis vinifera* cv Pinotage grapes were harvested in 2012 in the Boland wine-producing area of South Africa. The sugar concentration of the grapes was established from three random juice samples (50 mL each) to be 22.7 °B by using Fourier transform infrared (FT-IR) spectroscopy with a WineScan FT120 Basic (FOSS Analytical, Hillerød, Denmark) instrument. The scans were done in duplicate. Berries were sampled from bunches randomly selected from different harvest crates, and the berries were picked from the top, middle, and bottom of a bunch. The grapes were frozen at −20 °C before the skins were manually peeled with a scalpel and flash frozen with liquid nitrogen in 20 10 g (wet weight) batches. The frozen skins were kept at −80 °C and then freeze-dried. The freeze-dried skins were dry milled and homogenized with a Retsch MM400 mixer mill (Retsch, Haan, Germany) at 30 Hz for 30 s, and from the resulting powder, the cell wall or alcohol insoluble residue (AIR) was extracted. The AIR extraction method described by Ortega-Regules et al.[17] was followed except that the first acetone step after the buffered phenol extraction was omitted and after the third acetone wash, the AIR was air-dried, mixed with an equal volume of Milli-Q water, frozen at −80 °C, and then freeze-dried and stored for further analysis.

Enzymatic Hydrolysis of Pinotage AIR Using Purified Enzymes. A representative sample of AIR was obtained by mixing together 200 mg from each of the 20 AIR samples. From this pooled sample, 50 mg were used per reaction or biological repeat. The AIR was suspended in citrate phosphate buffer, pH 5 to form a 7.5% (w/v) suspension, and sodium azide was added at a final concentration of 0.02% (w/v) to prevent bacterial growth. The enzymes used in the experiment (Pect, EPG, EG, EA, and XG) are described in Table 1. A Thermo Scientific Pierce BCA Protein Assay (Thermo Fisher Scientific Inc., Waltham, MA) kit was used to determine the protein concentration of each enzyme. Enzymes were added in excess to ensure a potentially complete hydrolysis. Therefore, a dosage of 180 U/g dry matter of pectinase-containing enzymes (Pect and EPG) and 40 U/g of all other enzymes (EG, EA, and XG) were added individually or in combinations (EPG−EG; EPG−EG−EA; Pect−XG; Pect−EG). The reactions, performed in triplicate, were incubated at 40 °C for 48 h; after the

DOI: 10.1021/acs.jafc.5b02847
J. Agric. Food Chem. 2015, 63, 8267−8274

Table 2. Monosaccharide Composition of Pinotage AIR Treated with Different Enzymes and Enzyme Combinations[a]

	(pM/mg AIR)							
	Ara	Rha	Fuc	Xyl	GalA	Man	Gal	Glc
Pect	52 ± 9	25 ± 3	31 ± 3	77 ± 17	**123** ± 22	36 ± 5	39 ± 6	39 ± 6
EPG	78 ± 28	37 ± 4	28 ± 3	64 ± 8	**381** ± 44	28 ± 2	39 ± 5	32 ± 2
EG	103 ± 10	42 ± 3	32 ± 2	80 ± 5	**440** ± 43	34 ± 2	48 ± 3	40 ± 2
EA	71 ± 17	40 ± 6	30 ± 5	66 ± 7	**366** ± 35	29 ± 2	40 ± 7	33 ± 3
XG	102 ± 7	42 ± 3	31 ± 3	79 ± 5	**452** ± 33	33 ± 2	46 ± 2	38 ± 0
EPG+EG	89 ± 25	38 ± 6	29 ± 5	65 ± 20	**435** ± 62	29 ± 6	40 ± 8	33 ± 7
EPG+EG+EA	56 ± 25	35 ± 6	28 ± 5	51 ± 20	**294** ± 9	25 ± 6	33 ± 8	27 ± 7
Pect+XG	**36** ± 10	**21** ± 3	26 ± 6	52 ± 20	**72** ± 22	28 ± 8	30 ± 11	31 ± 9
Pect+EG	48 ± 6	**23** ± 2	29 ± 3	74 ± 15	**100** ± 29	34 ± 5	34 ± 11	37 ± 4
control	73 ± 5	35 ± 3	32 ± 2	74 ± 6	226 ± 10	34 ± 1	45 ± 2	39 ± 2

[a]The values are the averages of three samples. Samples that are statistically different (95% confidence level) from the control are bold. Ara, arabinose; Rha, rhamnose; Fuc, fucose; Xyl, xylose; GalA, galacturonic acid; Man, mannose; Gal, galactose; Glc, glucose.

residual solids were washed with sterile distilled water, they were finally freeze-dried.

Cell Wall Profiling of AIR Samples. The monosaccharide composition of the AIR collected before and after enzyme hydrolysis was analyzed as described in ref 8. The acid hydrolysis was performed with 2 M TFA at 110 °C for 2 h. The monosaccharide composition was expressed as pM/mg AIR, and each biological repeat was analyzed twice with standard deviations in the tables representing the average of three biological samples.

One sample for each biological repeat (enzyme hydrolysis reaction) was analyzed with the CoMPP technique and entailed the sequential extracted of the pectin- and hemicellulose-rich fractions from 10 mg of AIR per sample, using the solvents diamino-cyclo-hexane-tetra-acetic acid (CDTA) and NaOH respectively.[13,18] The different fractions were printed on nitrocellulose membranes and probed individually with 26 different monoclonal antibodies (mAbs) and carbohydrate binding modules (CBMs) as previously described[18] and listed in Table S1 in the Supporting Information. A mean spot signal was calculated after it was normalized to the highest signal (set as 100) in the data set, and a cutoff value of 5 was used.

Univariate and Multivariate Data Analysis. Statistical significant differences in the results were determined with the unpaired *t*-test (95% confidence level). The patterns and main trends within the data were investigated with principal component analysis (PCA)[19] and partial least-squares projections to latent structures (PLS)[20] using SIMCA 13 software (Umetrics, Umeå, Sweden).

RESULTS AND DISCUSSION

The cell walls or AIR isolated from fresh, ripe Pinotage grape berry skins were incubated with a collection of purified enzymes (Table 1) under buffered conditions favoring the enzymes (pH 5, 40 °C) to evaluate the (maximum) potential and impact of hydrolysis on this matrix. By using isolated cell walls as substrate, the aim was to eliminate any potential interfering substances (e.g., high sugar concentrations, phenolics, tannins and organic acids present in grape juice) and improve the accessibility of enzymes to the target polysaccharides. The enzymes were chosen to degrade different polysaccharide targets, namely pectins, celluloses, and hemicelluloses, and the purified enzyme preparations exhibited these main activities, although most (except the xyloglucanase) also contained some lesser side activities (Table 1).

The AIR was analyzed using CoMPP analysis, and the results are presented as a heat map in Figure 1. The relative abundance of specific cell wall polysaccharides, extracted with either CDTA or NaOH, is presented as a percentage of the whole data set. The CDTA fraction of the control samples (no enzyme added) contained an abundance of pectin-type polymers (Figure 1), but as expected,[8] some xyloglucan (mAb LM25), arabinogalactan proteins (AGPs), and extensins were also present. The NaOH extraction of the control samples mainly dissolved hemicelluloses, with some cellulose (mAb CBM3a) and some unbranched rhamnogalacturonan-I (RG-I) also present. The monosaccharide composition (Table 2) of the control samples confirmed the abundance of galacturonic acid (GalA) followed by arabinose, a profile previously also shown in other grape cultivars.[9]

It was hypothesized that all the enzymes that were used would be able to depolymerize and/or fragment the grape cell wall polymers, leading to fragments diffusing out into the incubation buffer and therefore an overall reduction in levels of polymers and monosaccharides recorded by the different methods. However, such a universal reduction was not seen; some of the enzyme-treated samples showed an increase and others a decrease in relative abundance of polymers (evaluated with CoMPP analysis). Strikingly, in all the reactions in which the Pect enzyme was involved (CDTA fraction) there was a drastic decrease in the values for homogalacturonan (HG) epitopes (mAbs JIM5 and JIM7, LM19, and to a lesser degree LM18) compared to the control samples. The HG with very low methylesterification, recognized by mAb PAM1, was an exception with the values staying more or less stable with or without enzyme addition. On the other hand, enzyme treatments lead to a complete removal of RG-I (mAbs INRA-RU1 and INRA-RU2) and xyloglucan (mAb LM25). In contrast, all the other enzymes (EPG, EG, EA, XG, and combinations of these) nearly doubled the levels of HG (specifically mAbs JIM5 and JIM7) that could be extracted with CDTA from the AIR (Figure 1, CDTA fraction). The XG treatment delivered the highest values in HG (mAbs JIM5, JIM7, LM18, and LM19) compared to the control samples, possibly indicating that the hydrolysis of the xyloglucan that cross-links the cellulose microfibrils has an influence on the release of polymers from within the cell wall. The levels of unbranched RG-I (mAbs INRA-RU1 and INRA-RU2), xyloglucan (mAb LM25), and AGPs (mAb JIM13) were not altered by these enzymes (in contrast with Pect). The major epitopes recognized in the NaOH fraction were xyloglucan (mAbs LM15 and mAbs LM25), cellulose (mAb CBM3a), and extensins (mAb JIM20). Although all of the mAb INRA-RU2 labeled RG-I were removed, either by enzyme hydrolysis or during CDTA extraction, low quantities of mAb INRA-RU1 labeled RG-I could be extracted with NaOH (Figure 1, NaOH fraction). This was seen in the control as well as the EPG-, EG-, EA-, and XG-treated samples. Moreover, all enzyme treatments

DOI: 10.1021/acs.jafc.5b02847
J. Agric. Food Chem. 2015, 63, 8267−8274

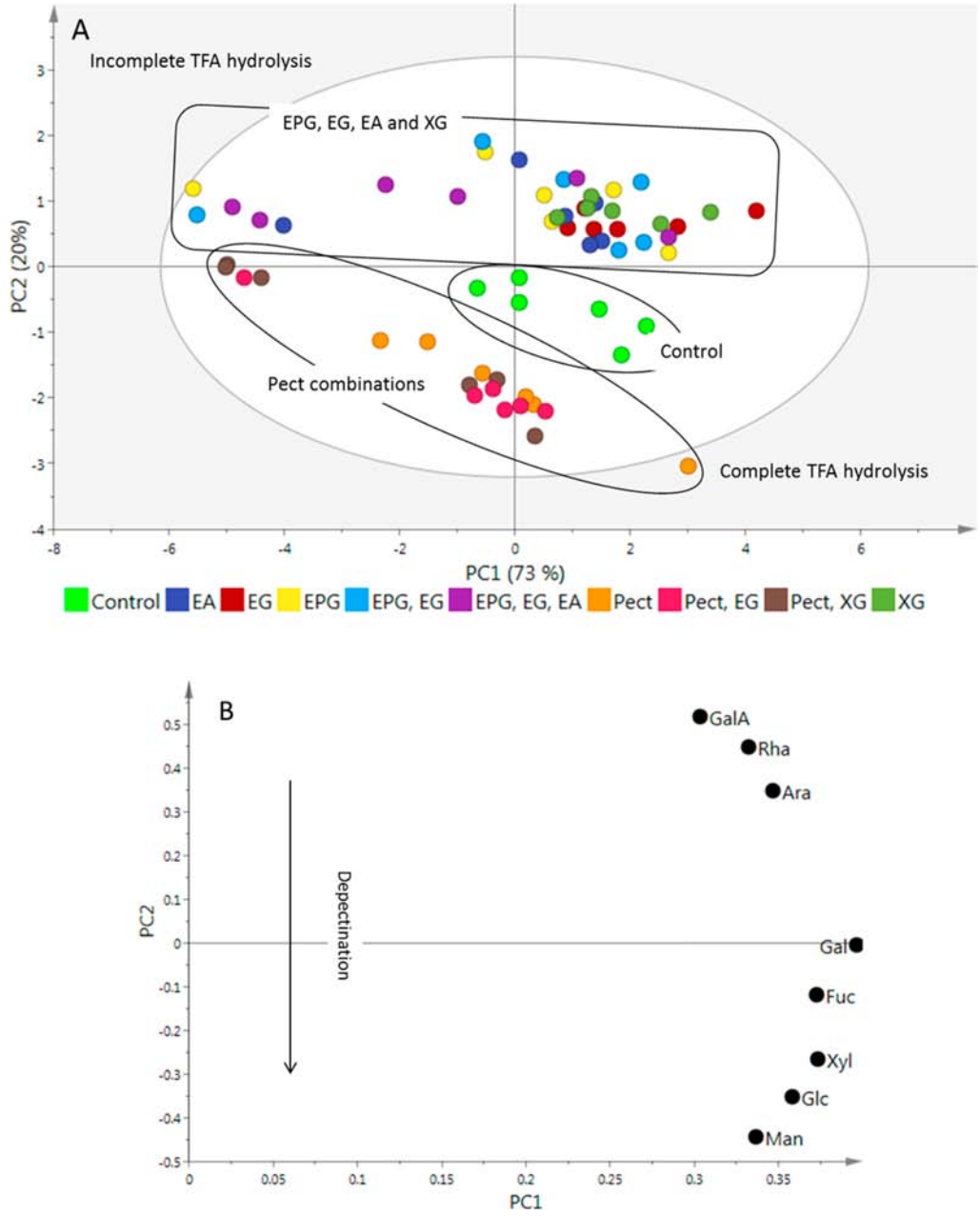

Figure 2. Principal component analysis (PCA) of the monosaccharide analysis on Pinotage AIR treated with pure enzymes. The score (A) and loading (B) plots show the variability in the efficiency of the TFA hydrolysis. The enzymes are described in Table 1.

increased the signal for extensins (mAb JIM20) compared to the control. These observations lead to two main conclusions (contextualized and discussed below): certain enzymes cause more complete hydrolysis than others, and some of the enzyme combinations have synergistic effects.

Synergistic Actions and Associations between Cell Wall Polymers, As Shown by the CoMPP Technique. Almost all the enzymes decreased the xyloglucan signals, presumably by removing some surface-exposed, pectin-associated xyloglucan due to pectin hydrolysis (EPG, Pect, and Pect–EG) or by direct xyloglucan hydrolysis (XG). The Pect–XG combination was the only treatment that increased both mAbs LM15 and LM25 labeling in the NaOH fraction compared to the control (Figure 1). Neither the XG nor the Pect enzymes on their own could show the same effect, confirming a synergism between the two enzymes under these conditions. Depectination by Pect probably facilitated better access for the XG enzyme to its target, leading to xyloglucan hydrolysis and an increased extraction (with NaOH) of partially degraded xyloglucan from within the hemicellulose–cellulose structure. We know plant cell wall xyloglucan is shielded by pectin,[21] but this synergistic effect between pectinases and xylanases has not been shown previously (to our knowledge) in grape tissues, and it is the first time that CoMPP was used to demonstrate such synergism. This interesting aspect could benefit from further investigation because according to a study by Hu et al.[22] synergistic effects are highly substrate-specific and also depend on the substrate preparation.

The enzyme hydrolysis in combination with the sequential extraction steps, as used in CoMPP analysis, provided the ability to identify possible associations between the cell wall polymers of the grape berry skins. For example, AGPs recognized by mAb

DOI: 10.1021/acs.jafc.5b02847
J. Agric. Food Chem. 2015, 63, 8267–8274

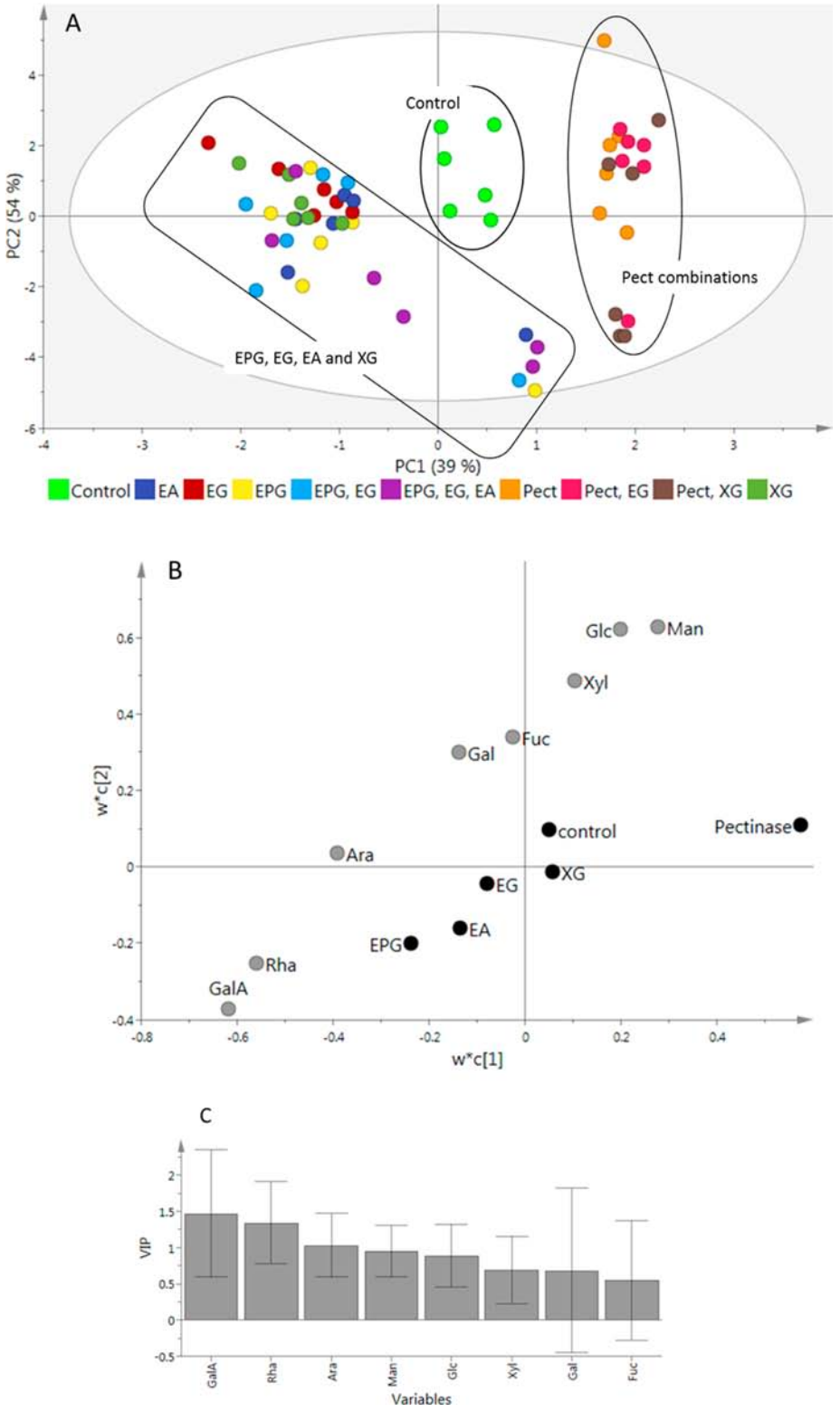

Figure 3. PLS (partial least-squares projections to latent structures) score (A) and loading plot (B) of the monosaccharide analysis of Pinotage AIR treated with pure enzymes show the Pect-treated samples separating from the other samples because of an abundance of Man and Glc and a scarcity of GalA, Rha, and GlcA. (C) VIP plot (variable importance for the projection) is an interpretation tool that summarizes the importance of variables in a PLS model, and a VIP value grater than 1 indicates that a variable has an above average influence on the model. The VIP plot indicated that GalA, followed by Rha and Ara were the most important contributors toward the configuration of the samples in the PLS plot.

JIM13 were reduced by Pect action (Figure 1), and the labeling pattern was similar to mAb INRA-RU1. This can indicate that these AGPs are bound to pectin polymers (as previously reported in other plants[23−25]) and subsequently removed during pectin hydrolysis. It might also just confirm the hydrolysis of RG-I because it should be noted that mAb JIM13 showed cross reactivity with RG-I of sycamore maple.[26] Another example is the association between the RG-I (specifically mAb INRA-RU1) and

DOI: 10.1021/acs.jafc.5b02847
J. Agric. Food Chem. 2015, 63, 8267−8274

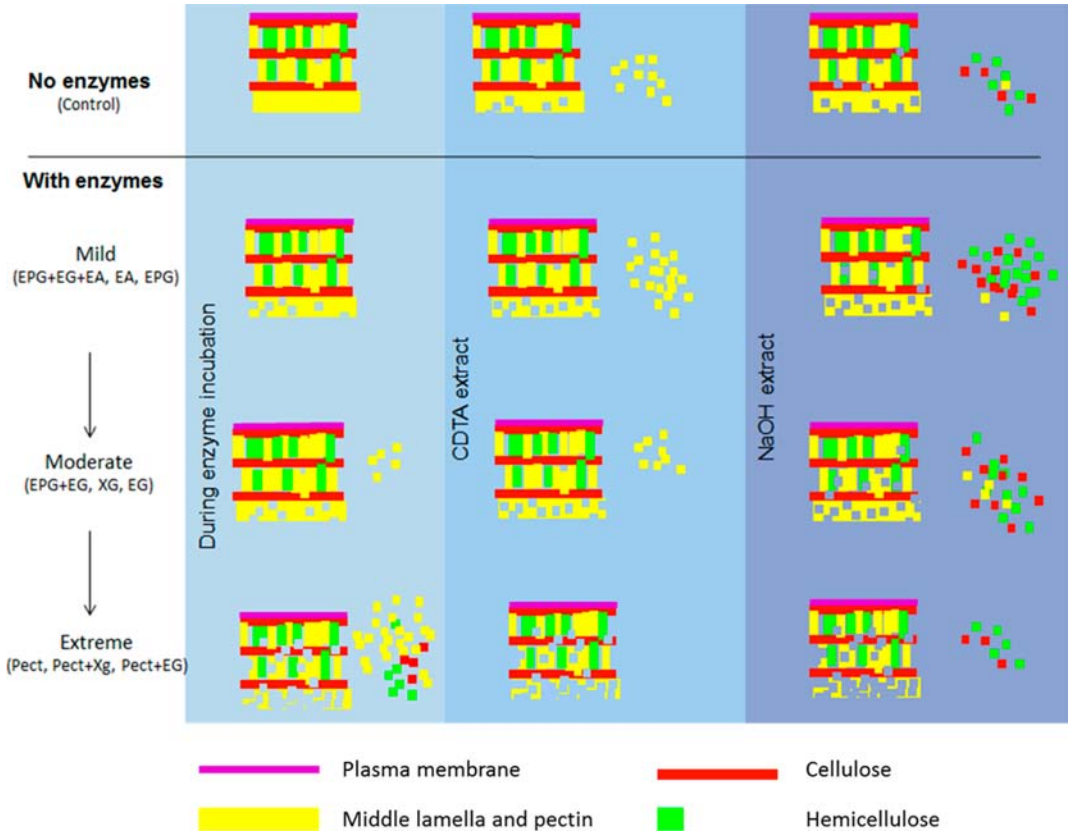

Figure 4. Schematic presentation (not to scale) of a section of the grape skin cell wall showing the presumed changes to the cell wall composition during enzyme hydrolysis and extraction with CDTA and NaOH. The colored blocks represent the polymers removed by enzymes and/or extraction solutions. Mild degradation is typified by pore formation and is seen with CoMPP analysis as an enhancement in the CDTA extract. As the degradation advances (longer incubation or more effective enzymes), smaller degradation products were removed during the enzyme hydrolysis step, resulting in a decrease in polymers that could be extracted. With moderate degradation, the pores presumably became large enough for the enzymes to penetrate the cell wall and break up hemicellulose polymers. At first those partially degraded polymers could only be removed from within the cell wall framework by extraction with NaOH. If the degradation proceeds far enough (pores are large enough and/or polymer size reduction went far enough), those partially degraded polymers will diffuse out unassisted during the enzymatic hydrolysis step.

xyloglucan; xyloglucan (specifically mAb LM25) is found in the pectin fraction, and similarly a signal for mAb INRA-RU1 was detectable in the NaOH fraction (even after enzyme hydrolysis and extraction with CDTA) which was probably a confirmation of the xyloglucan−pectin association found in grape[27] and other plant cell walls.[28,29] Similar results were also obtained in a profiling and fractionation study on berry cell wall extracts from pomace of Cabernet Sauvignon under wine-fermentation conditions.[30] Interestingly, the RG-I labeled by mAb INRA-RU2 (that has more galactosyl side chains than INRA-RU1 labeled RG-I) were absent in the NaOH fraction. Furthermore, the relative abundance of xyloglucan (mAb LM25) and RG-I (mAbs INRA-RU1 and INRA-RU2) was similarly influenced by the different enzyme treatments and concomitantly removed, but there was no resemblance between mAb LM25 and HG labeling patterns, which is an additional indication of a xyloglucan−RG-I specific association in grape berry tissue.

The Degree or Extent of Enzymatic Hydrolysis Influences the Cell Wall Composition. The monosaccharide compositional analysis of the AIR samples after enzyme hydrolysis revealed some interesting results (Table 2). Compared to the control samples, Pect−XG hydrolysis led to a decrease (statistically significant, 95% confidence interval) in Ara (arabinose) while Pect−XG and Pect−EG decreased the Rha (rhamnose) values. This corresponded well with the decrease in unbranched RG-I and AGPs (CoMPP analysis, Figure 1) of the Pect enzyme-treated samples. In addition, the Pect and Pect combination treatments caused a decrease in GalA (galacturonic acid) which could be attributed to depectination, and this was confirmed by the decrease in the signal for all the HG polymers (except mAb PAM1). In contrast, all the other enzymes caused an increase in GalA monosaccharides. An increase (compared to the control samples) in the monosaccharide concentration is only possible if it is accepted that incomplete TFA hydrolysis took place during the preparation steps prior to gas chromatography−mass spectrometry (GC-MS) monosaccharide analysis. Acid hydrolysis conditions for pectin-rich samples present a compromise between GalA and neutral sugar yields because of the difference in the susceptibility to acids demonstrated by different glycoside bonds.[31]

This incomplete acid hydrolysis took place in the control samples, but in contrast, the AIR samples treated with EPG, EG, EA, and XG were already partially hydrolyzed or unravelled. This led to a more complete acid hydrolysis by allowing better access for the TFA to penetrate the AIR particles, delivering quantities of monosaccharides that were higher than those of the control samples. This unravelling and rendering of access to the inner cell wall spaces by the action of the EPG, EG, EA, and XG enzymes were also demonstrated with the CoMPP results (Figure 1). In the case of the Pect-treated samples, the enzymatic hydrolysis

DOI: 10.1021/acs.jafc.5b02847
J. Agric. Food Chem. 2015, 63, 8267−8274

already removed a large fraction of the pectin cell wall polymers (HG and RG-I), which was probably enhanced by the presence of pectin esterase activity in the Pect preparation (Table 1). The residue remaining after enzyme hydrolysis thus contained less GalA. We therefore presume that complete acid hydrolysis could take place in the Pect samples by virtue of extensive enzymatic degradation and unravelling. Our findings are supported by the results of Wikiera et al.[32] who compared the GalA yields from apple pomace when using acid hydrolysis (2 M TFA, 100 °C, 2 h) against an enzyme and acid hydrolysis combination (0.2 M TFA, 80 °C, 72 h) and found that the latter resulted in higher yields of GalA.

Multivariate data analysis of monosaccharide composition of the samples revealed (PCA plot, Figure 2) the Pect-treated samples loosely grouped in the bottom half of the plot. The control samples formed a second group in the middle, and the rest of the samples were spread out along the top half of the plot. The spread of all the samples along the first component axis (PC1, 73%) illustrates the variation in the efficiency of the TFA hydrolysis which led to differences in the monosaccharide values (pM/mg AIR) recorded. Further analyses were done using a partial least squares (PLS)[20] (Figure 3) plot, which is a regression technique for modeling the association between two sets of variables and has the ability to analyze noisy, collinear, and incomplete sets of variables. The PLS analysis confirms the depectination that took place because of the influence of the Pect enzyme preparation with the latter being on opposite sides of the loading plot (Figure 3B) from GalA and Rha. This is supported by variable importance for the projection (VIP) plot (Figure 3C) that identified GalA followed by Rha as the principal influence for the configuration of the variables in the PLS plot.

The CoMPP results in combination with the monosaccharide analysis allowed "a view" of the cell walls (AIR) of Pinotage grape skins in which there were some HG, unbranched RG-I, xyloglucan (mAb LM25-binding motifs only), AGPs, and extensins exposed on the surface of the AIR particles (as confirmed with the results of the no enzyme treatment). During the CDTA extraction, the pectins and associated compounds were removed from the surface area of the AIR particles. When the extraction was preceded by enzymatic hydrolysis, the composition of the extracted fraction depended on the extent of the hydrolysis that took place (Figure 4). Extensive hydrolysis (as seen with Pect-treated samples), removed some AGPs and more or less all pectin polymers except some HG (labeled by mAbs PAM1, LM18, and LM19), which correlates with the low levels of GalA and Rha measured in these samples. This implies that the polymers were enzymatically reduced in size to the extent that the fragments could diffuse out from within the AIR particles and were subsequently removed at the end of the enzyme hydrolysis period. With less extensive enzyme hydrolysis (EPG, EG, EA, XG, and combinations of these enzymes), some of the bonds between the cell wall polysaccharides were broken but not enough to allow the removal of polymers into the hydrolysis buffer, as was seen with the Pect enzymes. Instead, it is better described as an "opening up" action, or unravelling and partial degradation of the AIR structure to allow better access for the CDTA in the subsequent extraction step to dissolve the pectins (HG extraction is enhanced) from the surface and subsurface layers of the particle leading to an increase in the abundance of these polymers in the CDTA extract. This is in contrast with the control samples in which only the outer pectin-rich layers were dissolved. This unravelling action is similar to our previous results[8] in the cell walls from Pinotage skins retrieved from fermentations supplemented with commercial maceration enzymes. The results indicate (Table 2, Figure 1) that depectination by both extreme and mild enzymatic hydrolysis unmasked the core hemicellulose−cellulose framework, and this presumably enabled cellulases and hemicellulases to remove some of the xyloglucan and cellulose (lower values than the control samples in the NaOH fraction (Figure 1) (except Pect−XG as discussed previously). This demonstration (Figure 4) of the different levels of enzymatic hydrolysis on grape skin cell walls provides a unique perspective, also confirming CoMPP as an effective method to evaluate different enzyme combinations and enzyme types for grape tissue degradation.

In summary, The CoMPP analyses proved to be a valuable, sensitive, and high-throughput method to trace modifications in the polymers of grape berries' cell walls. It highlighted synergism between different enzymes and gave indications of polymer associations. Furthermore, we could distinguish different levels of enzymatic hydrolysis and provide a "view" of how the skin cell walls are impacted by these hydrolyses. For future work it might be informative to use different enzyme-to-AIR ratios to study the effect of enzyme loading and improve the observation of subtle differences. It would also be valuable to repeat this study under winemaking conditions (pH 3−4, 18−25 °C) to determine the extent and influence of enzyme inhibition on the results. This study provided us with a new method for evaluating different enzymes or enzyme combinations as well as tests the effect of enzymes on different substrates or different incubation conditions. It could be a valuable tool to use not only in the development of enzyme preparations for the wine industry but also in industries in which enzymes are used for the degradation of plant tissues.

■ ASSOCIATED CONTENT

Supporting Information

The Supporting Information is available free of charge on the ACS Publications website at DOI: 10.1021/acs.jafc.5b02847.

List of the monoclonal antibodies used in this study (PDF)

■ AUTHOR INFORMATION

Corresponding Author

*Tel.: +27 21 808 3773. Fax: +27 21 808 3771. E-mail: mav@sun.ac.za.

Author Contributions

A.J.J.Z. collected the data, interpreted the results, and drafted the manuscript. J.P.M. and M.A.V. designed the study and helped with data interpretation and preparation of the final document. J.U.F. and W.G.T.W. did the CoMPP analysis.

Funding

Funding for this study for A.J.J.Z. was provided by National Research Council (South Africa), Grant 92290; Wine Industry Network of Expertise and Technology (South Africa), Grants IWBT P14/03 and IWBT P14/04; Technology and Human Resources for Industry Programme (South Africa), Grant TP13081327560. Funding for J.U.F. was provided by The Danish Research Council - (Denmark).

Notes

The authors declare no competing financial interest.

■ ABBREVIATIONS USED

AGP, arabinogalactan protein; AIR, alcohol insoluble residue; CBM, carbohydrate binding module; CDTA, diamino-cyclo-

DOI: 10.1021/acs.jafc.5b02847
J. Agric. Food Chem. 2015, 63, 8267−8274

hexane-tetra-acetic acid; CoMPP, comprehensive microarray polymer profiling; EA, endoarabinase; EG, endo-1,4-β-glucanase; EPG, endopolygalacturonase; FT-IR, Fourier transform-infrared spectroscopy; HG, homogalacturonan; mAb, monoclonal antibody; PCA, principal component analysis; Pect, pectolytic enzyme preparation; PLS, projections to latent structures; RG-I and -II, rhamnogalacturonan-I and -II; TFA, trifluoroacetic acid; VIP, variable importance for the projection; XG, xyloglucanase

REFERENCES

(1) Romero-Cascales, I.; Ros-García, J. M.; López-Roca, J. M.; Gómez-Plaza, E. The effect of a commercial pectolytic enzyme on grape skin cell wall degradation and colour evolution during the maceration process. *Food Chem.* **2012**, *130*, 626−631.

(2) Romero-Cascales, I.; Fernández-Fernández, J. I.; Ros-García, J. M.; López-Roca, J. M.; Gómez-Plaza, E. Characterisation of the main enzymatic activities present in six commercial macerating enzymes and their effects on extracting colour during winemaking of Monastrell grapes. *Int. J. Food Sci. Technol.* **2008**, *43*, 1295−1305.

(3) Fia, G.; Canuti, V.; Rosi, I. Evaluation of potential side activities of commercial enzyme preparations used in winemaking. *Int. J. Food Sci. Technol.* **2014**, *49*, 1902−1911.

(4) Kennedy, J. Grape and wine phenolics: Observations and recent findings. *Cienc. e Investig. Agrar.* **2008**, *35*, 107−120.

(5) Sieiro, C.; García-Fraga, B.; López-Seijas, J.; Da Silva, A. F.; Villa, T. G. Microbial pectic enzymes in the food and wine industry. In *Food industrial processes - Methods and Equipment*; Valdez, B., Ed.; InTech: Rijeka, 2010; pp 201−218.

(6) Van Rensburg, P.; Pretorius, I. S. Enzymes in winemaking: Harnessing natural catalysts for efficient biotransformations - A review. *South African J. Enol. Vitic.* **2000**, *21*, 52−73.

(7) Arnous, A.; Meyer, A. S. Quantitative prediction of cell wall polysaccharide composition in grape (*Vitis vinifera* L.) and apple (*Malus domestica*) skins from acid hydrolysis monosaccharide profiles. *J. Agric. Food Chem.* **2009**, *57*, 3611−3619.

(8) Zietsman, A. J. J.; Moore, J. P.; Fangel, J. U.; Willats, W. G. T.; Trygg, J.; Vivier, M. A. Following the compositional changes of fresh grape skin cell walls during the fermentation process in the presence and absence of maceration enzymes. *J. Agric. Food Chem.* **2015**, *63*, 2798−2810.

(9) Ortega-Regules, A.; Ros-García, J. M.; Bautista-Ortín, A. B.; Lopez-Roca, J. M.; Gomez-Plaza, E. Changes in skin cell wall composition during the maturation of four premium wine grape varieties. *J. Sci. Food Agric.* **2008**, *88*, 420−428.

(10) Vicens, A.; Fournand, D.; Williams, P.; Sidhoum, L.; Moutounet, M.; Doco, T. Changes in polysaccharide and protein composition of cell walls in grape berry skin (Cv. Shiraz) during ripening and over-ripening. *J. Agric. Food Chem.* **2009**, *57*, 2955−2960.

(11) Yakushiji, H.; Sakurai, N.; Morinaga, K. Changes in cell-wall polysaccharides from the mesocarp of grape berries during veraison. *Physiol. Plant.* **2001**, *111*, 188−195.

(12) Huang, X.-M.; Huang, H.-B.; Wang, H.-C. Cell walls of loosening skin in post-veraison grape berries lose structural polysaccharides and calcium while accumulate structural proteins. *Sci. Hortic. (Amsterdam, Neth.)* **2005**, *104*, 249−263.

(13) Moore, J. P.; Fangel, J. U.; Willats, W. G. T.; Vivier, M. A. Pectic-β(1,4)-galactan, extensin and arabinogalactan-protein epitopes differentiate ripening stages in wine and table grape cell walls. *Ann. Bot.* **2014**, *114*, 1279−1294.

(14) Nguema-Ona, E.; Moore, J. P.; Fagerström, A.; Fangel, J. U.; Willats, W. G. T.; Hugo, A.; Vivier, M. A. Profiling the main cell wall polysaccharides of tobacco leaves using high-throughput and fractionation techniques. *Carbohydr. Polym.* **2012**, *88*, 939−949.

(15) Fangel, J. U. Advanced technologies for plant cell wall evolution and diversity. Advanced technologies for plant cell wall evolution and diversity, Ph.D. Thesis, University of Copenhagen, 2013.

(16) Pedersen, H. L.; Fangel, J. U.; McCleary, B.; Ruzanski, C.; Rydahl, M. G.; Ralet, M.-C.; Farkas, V.; von Schantz, L.; Marcus, S. E.; Andersen, M. C. F.; Field, R.; Ohlin, M.; Knox, J. P.; Clausen, M. H.; Willats, W. G. T. Versatile high resolution oligosaccharide microarrays for plant glycobiology and cell wall research. *J. Biol. Chem.* **2012**, *287*, 39429−39438.

(17) Ortega-Regules, A.; Ros-García, J. M.; Bautista-Ortín, A. B.; López-Roca, J. M.; Gómez-Plaza, E. Differences in morphology and composition of skin and pulp cell walls from grapes (*Vitis vinifera* L.): technological implications. *Eur. Food Res. Technol.* **2008**, *227*, 223−231.

(18) Moller, I.; Sørensen, I.; Bernal, A. J.; Blaukopf, C.; Lee, K.; Øbro, J.; Pettolino, F.; Roberts, A.; Mikkelsen, J. D.; Knox, J. P.; Bacic, A.; Willats, W. G. T. High-throughput mapping of cell-wall polymers within and between plants using novel microarrays. *Plant J.* **2007**, *50*, 1118−1128.

(19) Jackson, J. E. *A User's Guide to Principal Components*; Wiley Series in Probability and Statistics; John Wiley & Sons, Inc.: Hoboken, NJ, 1991.

(20) Eriksson, L.; Byrne, T.; Johansson, E.; Trygg, J.; Vikström, C. *Multi- and megavariate data analysis. Basic principles and applications*, 3rd ed.; MKS Umetrics AB: Malmo, Sweden, 2013.

(21) Marcus, S. E.; Verhertbruggen, Y.; Hervé, C.; Ordaz-Ortiz, J. J.; Farkas, V.; Pedersen, H. L.; Willats, W. G. T.; Knox, J. P. Pectic homogalacturonan masks abundant sets of xyloglucan epitopes in plant cell walls. *BMC Plant Biol.* **2008**, *8*, 60.

(22) Hu, J.; Arantes, V.; Pribowo, A.; Saddler, J. N. The synergistic action of accessory enzymes enhances the hydrolytic potential of a "cellulase mixture" but is highly substrate specific. *Biotechnol. Biofuels* **2013**, *6*, 112.

(23) Keegstra, K.; Talmadge, K. W.; Bauer, W. D.; Albersheim, P. The Structure of Plant Cell Walls. *Plant Physiol.* **1973**, *51*, 188−196.

(24) Tan, L.; Eberhard, S.; Pattathil, S.; Warder, C.; Glushka, J.; Yuan, C.; Hao, Z.; Zhu, X.; Avci, U.; Miller, J. S.; Baldwin, D.; Pham, C.; Orlando, R.; Darvill, A.; Hahn, M. G.; Kieliszewski, M. J.; Mohnen, D. An *Arabidopsis* cell wall proteoglycan consists of pectin and arabinoxylan covalently linked to an arabinogalactan protein. *Plant Cell* **2013**, *25*, 270−287.

(25) Hijazi, M.; Roujol, D.; Nguyen-Kim, H.; Del Rocio Cisneros Castillo, L.; Saland, E.; Jamet, E.; Albenne, C. Arabinogalactan protein 31 (AGP31), a putative network-forming protein in Arabidopsis thaliana cell walls? *Ann. Bot.* **2014**, *114*, 1087−1097.

(26) Pattathil, S.; Avci, U.; Baldwin, D.; Swennes, A. G.; McGill, J. a; Popper, Z.; Bootten, T.; Albert, A.; Davis, R. H.; Chennareddy, C.; Dong, R.; O'Shea, B.; Rossi, R.; Leoff, C.; Freshour, G.; Narra, R.; O'Neil, M.; York, W. S.; Hahn, M. G. A comprehensive toolkit of plant cell wall glycan-directed monoclonal antibodies. *Plant Physiol.* **2010**, *153*, 514−525.

(27) Vidal, S.; Williams, P.; Doco, T.; Moutounet, M.; Pellerin, P. The polysaccharides of red wine: total fractionation and characterization. *Carbohydr. Polym.* **2003**, *54*, 439−447.

(28) Popper, Z. A.; Fry, S. C. Xyloglucan-pectin linkages are formed intra-protoplasmically, contribute to wall-assembly, and remain stable in the cell wall. *Planta* **2008**, *227*, 781−794.

(29) Cornuault, V.; Manfield, I. W.; Ralet, M.-C.; Knox, J. P. Epitope detection chromatography: a method to dissect the structural heterogeneity and inter-connections of plant cell-wall matrix glycans. *Plant J.* **2014**, *78*, 715−722.

(30) Gao, Y.; Fangel, J. U.; Willats, W. G. T.; Vivier, M. A.; Moore, J. P. Dissecting the polysaccharide-rich grape cell wall matrix during the red winemaking process, using high-throughput and fractionation methods. *Carbohydr. Polym.* **2015**, *133*, 567−577.

(31) Voragen, A. G. J.; Coenen, G. J.; Verhoef, R. P.; Schols, H. a. Pectin, a versatile polysaccharide present in plant cell walls. *Struct. Chem.* **2009**, *20*, 263−275.

(32) Wikiera, A.; Mika, M.; Starzyńska-Janiszewska, A.; Stodolak, B. Development of complete hydrolysis of pectins from apple pomace. *Food Chem.* **2015**, *172*, 675−680.

DOI: 10.1021/acs.jafc.5b02847
J. Agric. Food Chem. 2015, 63, 8267−8274

bonds of their substrates, thus being capable of giving rise to a variety of analogous volatile norisoprenoids.[13,22,30] Plant CCDs can be classified into six subfamilies according to the cleavage position and/or their substrate preferences: CCD1, CCD2, CCD4, CCD7, CCD8, and 9-cis-epoxy-carotenoid dioxygenases (NCEDs).[13,14,22,31] Plant CCD1 and CCD4 appear to be primarily functioning in the biosynthesis of norisoprenoid components of flavor, aroma, and pigmentation of fruits and flowers.[32] Recently, a novel CCD2 was identified and characterized from *Crocus sativus* that catalyzes the first dedicated step in crocin biosynthesis.[22] Conversely, CCD7 and CCD8 appear to be dedicated to the biosynthesis of strigolactones, plant growth regulators impacting several important physiological processes such as shoot branching and development of arbuscular mycorrhizae.[18−20] Finally, all NCEDs, which are only distantly related to CCDs, play a role in the biosynthesis of abscisic acid by producing its C15-precursor xanthotoxin from the 9-*cis* isomers of epoxy-carotenoids.[33]

The present study describes the carotenoid accumulation, norisoprenoid content, transcript level, and the isolation of a *CCD1* gene from fruits of *L. nobilis* (*LnCCD1*). To characterize the catalytic activity of *LnCCD1*, the gene was isolated and functionally expressed in *Escherichia coli*. The recombinant protein was assayed for cleavage activity with a variety of carotenoid substrates. To study the possible involvement of LnCCD1 in the synthesis of norisoprenoids flavor compounds, the expression pattern of this gene was determined in the fruit of *L. nobilis* by real-time-PCR.

MATERIALS AND METHODS

Chemicals. HPLC-grade acetonitrile, methanol, acetone, α-ionone, β-ionone, lycopene, lutein, and α- and β-carotenes were purchased from Sigma-Aldrich.

Plant Material. *Laurus nobilis* plants were grown in the "Newe Yaar" Research Center in northern Israel, under standard field irrigation and fertigation conditions. Pericarps of freshly harvested green and black fruits were crushed in liquid nitrogen and stored at −80 °C for analysis of carotenoids, norisoprenoid volatiles, and transcripts.

Carotenoid Extraction. Carotenoids were extracted by grinding fresh *L. nobilis* pericarp of green and black fruits (100 mg) in acetone. The solvent was collected and filtered and the grinding and collecting of solvent repeated until the solvent was colorless. Acetone was dried under a stream of N_2 and then redissolved in 1 mL of acetone. 100 μL of the sample in acetone was diluted 10 times and spared for spectroscopic quantification. The rest of the sample was again dried under a stream of N_2 and redissolved in acetone for further analysis by HPLC.

HPLC Analyses and Carotenoid Quantification. HPLC analysis was performed on a Waters HPLC system equipped with a Waters 600 pump, a Waters PDA detector 996, and a Waters 717 plus autosampler. A Spherisorb ODS2 C18 column (Waters, 5 μm, 4.6 × 250 mm) coupled to a guard cartridge system SecurityGuard (Phenomenex) was used. Gradient was applied at a constant flow of 1.6 mL/min with acetonitrile:water (9:1; A) and ethyl acetate (B) as described in Isaacson et al. (2004).[34] Data were collected in the range of 250−600 nm, and analyzed using the Empower software. Quantification of carotenoids was done spectroscopically on the diluted carotenoid sample in acetone.[35] Phytoene quantification was done by normalizing its integrated peak at 286 nm to correct for its specific mass extinction coefficient relative to β-carotene (factor of 2.074).

Extraction of Volatile Compounds from Fruits of *L. nobilis*. Three replicates of fresh *L. nobilis* pericarp of green and black fruits (1 g) were ground into a homogeneous powder under liquid nitrogen using mortar and pestle. The fine powders were placed in a 20 mL DuPont autosampler vial (DuPont Performance Elastomers, http://www.dupontelastomers.com) with a white solid-top polypropylene cap (Alltech, http://www.alltech.com). Samples were overlaid with 5 mL of NaCl (25%) solution and 1 g of NaCl (for inhibition of enzyme activity). To each sample, the internal standard 2-heptenone was added to produce a final concentration of 1 mg/kg (1 ppm). After incubation at room temperature (25 °C) for 1 h, the volatile compounds were collected with a solid phase micro extraction (SPME) device PDMS-100 with a polydimethylsiloxane fiber (Sigma-Aldrich) by inserting the fiber into the tube and leaving it in place for 20 min at room temperature. After this incubation step, the SPME fiber was injected directly into the GC−MS.

Auto-HS-SPME-GC−MS Analysis of Volatile Compounds. Volatile compounds were analyzed on a GC−MS apparatus (Agilent Technologies, CA) equipped with an Rtx-5SIL MS (30 m × 0.25 mm × 0.25 μm) fused-silica capillary column essentially as described by Yahyaa et al. (2015).[36] Briefly, He_2 (1 mL min^{-1}) was used as a carrier gas. The injector temperature was 250 °C, set for splitless injection. The oven was set to 50 °C for 1 min, and then the temperature was increased to 220 °C at a rate of 5 °C min^{-1}. For SPME analysis, thermal desorption was allowed for 40 min. The detector temperature was 280 °C. The mass range was recorded from 41 to 450 m/z, with electron energy of 70 eV. Identification of the main components was done by comparison of mass spectra and retention times with those of authentic standards and supplemented with a Wiley GC−MS library.

Isolation and Characterization of *L. nobilis* Fruit Carotenoid Cleavage Dioxygenase-1. Putative *L. nobilis* CCD encoding genes were searched for using a homology-based algorithm in the transcriptome database of *L. nobilis*, which has been assembled on the basis of available GenBank sequence data entries. A single full-length gene was tentatively identified as *L. nobilis* carotenoid cleavage dioxygenase-1 (*Ln*CCD1). Two specific primers corresponding to the *LnCCD1* protein-coding sequence 5′-end (5′-ATG GAG AAG GAA AAT GGA A-3′) and 3′-end (5′-CTT TCC CTG TTG TTG AAG TTG TTC C-3′) were designed. RNA from *L. nobilis* pericarp of the green and black fruits was isolated using the Spectrum Plant Total RNA Kit (Sigma-Adlich). For producing a cDNA clone, 5 μg of total RNA from fruits of *L. nobilis* was reverse transcribed using the SuperScript One-Step RT-PCR with Platinum *Taq* DNA polymerase (Invitrogen) used for amplification, yielding a 1650 bp specific fragment. The cDNA was inserted into the pEXP5-CT/TOPO TA expression vector (Invitrogen Corporation, Carlsbad, CA), yielding pEXP-*LnCCD1* in which the LnCCD1 coding sequence was fused with a His tag-coding extension at the C-terminus. The construct was introduced into *E. coli* Top10 cells. The constructs' fidelity and orientation of the inset in the vector were verified by DNA sequencing.

Functional Expression Experiments and Determination of Volatiles from Bacterial Headspace. *E. coli* strains engineered to accumulate phytoene (pBCAR-EB), lycopene (pBCAR-EBI), β-carotene (pBCAR-EBIY), δ-carotene (pDCAR), and zeaxanthin (pZEAX) were transformed with the expression construct pEXP-*LnCCD1*.[37,38]

Production of the recombinant protein was induced by IPTG, and the volatiles were collected by SPME and analyzed by GC−MS, respectively, as described by Yahyaa et al., 2013.[39]

***LnCCD1* Transcript Analysis.** For real-time RT-PCR analysis of *LnCCD1*, total RNA (5 μg) from *L. nobilis* pericarp of green and black fruits was extracted (Spectrum Plant Total RNA Kit, Sigma-Aldrich) and reverse transcribed using an oligo$(dT)_{12-18}$ primer and the SuperScript II first-strand system (Invitrogen). RNA quality and quantity were determined by using agarose gel electrophoresis, and the concentrations were measured using the NanoDrop ND-1000 spectrophotometer (Bargal Analytical Instruments). To remove the trace amounts of genomic DNA during RNA purification from RNA preparations, On-Column DNase I Digest Set was applied (Sigma-Aldrich).

Real-time RT-PCR was performed on an Applied Biosystem StepOnePlus Real-Time PCR System (Life technology) using ABsolute Blue qPCR SYBR Green ROX Mix (Tamar Laboratory

DOI: 10.1021/acs.jafc.5b02941
J. Agric. Food Chem. 2015, 63, 8275−8282

Supplies Ltd., Israel), using 5 ng of reverse-translated total RNA and 100 ng of primers.

Primers for *LnCCD1* were LnCCD1_F_qPCR (5′-AGT CTT ACA CAG GCA GGA AAC-3′) and LnCCD1_R_qPCR (5′-CAA ACT TGA TGA TGC CCT TCA C-3′). A relative quantification of gene expression was performed using actin from *L. nobilis* as a reference gene. The following actin primers were used as positive controls: Actin-F-qPCR (5′- GTG AGC TGA GGC TTG ATT GA-3′) and Actin-R-qPCR (5′- TCG ACC CAA GTA CAC AGA CTA-3′). Differences in relative expression levels of LnCCD1 were calculated from 2-ΔΔCt value after normalization of LnCCD1 data to actin. All analyses were performed using three biological replicates.

RESULTS AND DISCUSSION

Carotenoid Pigmentation Patterns of *L. nobilis* Influence Fruit Norisoprenoid Volatile Composition. We previously demonstrated that variation in terpenoid volatiles accumulation in different *L. nobilis* tissues is organ and gender dependent.[9] Also, variation in total content of *L. nobilis* green and black fruits terpenes has been reported.[8,9] However, to the best of our knowledge, the influence of carotenoid composition on volatile norisoprenoid accumulation in fresh *L. nobilis* pericarp of green and black fruits has never been shown. Therefore, it was of interest to analyze the carotenoid content of fresh *L. nobilis* pericarp of green and black fruits and the norisoprenoid volatiles using HPLC and GC−MS, respectively. The main carotenoid found in *L. nobilis* pericarp of the green and black fruits is lutein (Table 1). The content of β-carotene, zeaxanthin, antherexanthin, violaxanthin, and neoxanthin was different in pericarp of the green and black bay laurel fruits. The total carotenoid level in green fruits of *L. nobilis* was 2-fold higher than that found in the black fruits (Table 1). A drastic and marked decrease of the β-carotene and lutein contents was found during fruit development (in the black fruit). In accordance, our analyses showed that norisoprenoid volatiles such as 6-methyl-5-hepten-2-one (MHO), pseudoionone, and β-ionone are present only in the fresh pericarp of the black *L. nobilis* fruits (Table 1). Of particular interest is the fact that the levels of MHO, pseudoionone, and β-ionone, which could be derived from the breakdown of lycopene, α-carotene, and β-carotene, were correlated with the β-carotene content in the black fruits (Table 1).

Table 1. Carotenoids and Norisoprenoid Volatiles in *Laurus nobilis* Fruits

	green fruits	black fruits
Carotenoid[a] Content (μg g^{-1} of FW)		
β-carotene	38.51 ± 0.54	13.70 ± 1.4
zeaxanthin	0.42 ± 0.09	0.20 ± 0.05
lutein	83.25 ± 0.95	33.07 ± 3.67
antheraxanthin	8.88 ± 1.45	9.59 ± 2.47
violaxanthin	6.65 ± 0.50	4.92 ± 0.34
neoxanthin	7.58 ± 0.28	7.36 ± 1.05
total	145.29 ± 0.63	68.84 ± 1.49
Norisoprenoid[b] Compounds (ng g^{-1} of FW)		
6-methyl-5-hepten-2-one	nd	51.2 ± 5.1
pseudoionone	nd	48.7 ± 14.9
β-ionone	nd	31.6 ± 0.9

[a]Carotenoid standards were identified by HPLC on the basis of commercial standards. [b]Norisoprenoid compounds were identified by GC−MS on the basis of reference volatiles. The results shown are an average and standard errors of at least three biological replicates. nd = not detected.

Many volatiles are produced in plant tissues at specific developmental stages, for example, during flowering, ripening, or maturation. Although a single fruit synthesizes several hundred volatiles, only a small subset generates the "flavor fingerprint" that helps animals and humans recognize appropriate foods and avoid poor or dangerous food choices.[40]

β-Ionone is widely distributed in plants and is considered an important and potent flavor contributor in many fruits and fruit-based foods, due to its extremely low odor thresholds (0.007 ppb).[28,39,41] MHO is also an important flavor and aroma volatile found in a number of fruits such as tomato.[42] MHO is present as a component of the floral scent of numerous plants, occurring in over 50% of 991 species of flowering plants that had their floral scent analyzed.[43]

Our data presented above indicate that norisoprenoid volatiles found in the fresh *L. nobilis* pericarp black fruits indeed originate from the oxidative degradation of carotenoids as the main route, as it also is in many other plants, for example, in carrots and melon,[28,39] in watermelon and tomato,[29,44] in strawberry,[45] in *Rosa damascena*,[46] in pepper,[27] and in *Crocus sativus*.[22] Also, the function of fruit volatiles as a signal of ripeness and as an attractant for seed-dispersing organisms is supported by the fact that some substances are specifically formed by ripe fruits but are absent in vegetative tissues and nonripe fruit (Table 1). Unlike ripe fruits and flowers, vegetative tissues often produce and release many of the volatiles sensed as flavors only after their cells are disrupted.

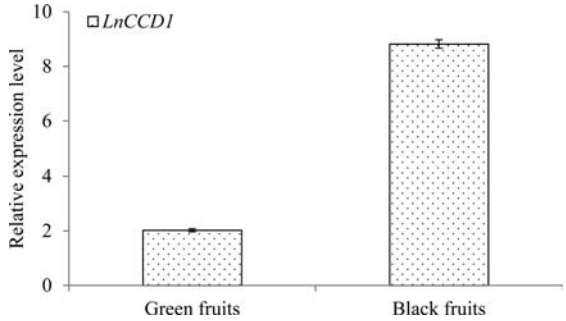

Figure 1. Expression patterns of *LnCCD1* in green and black fruits of *L. nobilis*. Quantification of *LnCCD1* transcript levels by real-time RT-PCR analysis normalized to actin transcripts. All analyses were performed using three biological replicates.

Expression Patterns of *LnCCD1* in Fruits of *L. nobilis*. The expression pattern of the *LnCCD1* gene along fruit development (green and black fruits) was examined by real-time RT-PCR (Figure 1). The expression level of the *LnCCD1* gene in black fruits was 6-fold higher than that found in the green fruits (Figure 1). Moreover, a significant correlation was observed between increase of the expression level of *LnCCD1* and the accumulation of norisoprenoids during fruits development and the decrease of β-carotene content (Table 1 and Figure 1).

In our analysis of norisoprenoid volatiles in *L. nobilis* green and black fruits, we were not able to detect volatile norisoprenoids in the green fruits (Table 1). Thus, we cannot conclude that the *LnCCD1* gene expression in *L. nobilis* green fruits is related to the production of norisoprenoids. However, a lag between CCD1 gene expression and norisoprenoid volatiles

DOI: 10.1021/acs.jafc.5b02941
J. Agric. Food Chem. 2015, 63, 8275−8282

production has been reported,[47,48] which could be explained by the different cellular localization of carotenoids and CCD1 enzymes.[21,47,49] Although there is a temporal delay in volatile emission in relation to gene expression, in tomato the silencing of both *LeCCD1A* and *LeCCD1B* genes generates a reduction in β-ionone and geranylacetone. This provides a cause-and-effect relationship between *LeCCD1* gene expression and the formation of those important flavor volatiles in vivo.[47]

Identification of LnDcCCD1. The role of CCDs in the formation of norisoprenoids and their flavor properties in *L. nobilis* fruits has not been reported. In attempts to identify a gene responsible for norisoprenoid formation in *L. nobilis* fruits, we examined the recently created *L. nobilis* transcriptome database[9] for genes exhibiting similarity to known CCD sequences from other plants.

Data mining of the *L. nobilis* database resulted in identification of one full length cDNA clone (Figure S1), displaying high sequence similarity to other plant carotenoid cleavage dioxygenases. The clone, designated *LnCCD1*, originated from a leaves expressed sequence tagged (EST) library of *L. nobilis*. The predicted LnCCD1 protein sequence consists of 550 amino acids, with a calculated molecular mass of 61.9 kDa. The deduced amino acid sequence of LnCCD1 contains two conserved domains, which are typically found in enzymes involved in the biosynthesis of norisoprenoids.[50]

LnCCD1 protein displays a high sequence similarity (86%) to the CCD from *Phoenix dactylifera* (date plum), and (84%) to CCD1 from *Nelumbo nucifera* (sacred lotus). LnCCD1 is also similar to the *Vitis vinifera* VvCCD1 (84%) that cleaves zeaxanthin symmetrically yielding 3-hydroxy-β-ionone, a C13-norisoprenoidic compound, and a C14-dialdehyde.[51] LnCCD1 is also similar to CCD1 from *Prunus mume* (chinese plum) (82%), to CCD1 from *Cucumis melo* (melon) (82%),[28] to *Malus* × *domestica* (apple) (81%), to CCD1 from *Osmanthus fragrans* (fragrant olive) (80%), and to DcCCD1 from *Daucus carota* (carrot) (80% identity), which encodes enzyme that cleaves only cyclic carotenoids to generate α- and β-ionone.[39] Phylogenetic analyses show that the protein encoded by this cDNA clusters with other plant CCD1 enzymes (Figure 2).

LnCCD1 Cleaves Multiple Carotenoids To Generate Norisoprenoids Volatiles Derived from 9,10 and 5,6 Double Bond Cleavage. To determine the substrate specificities and bond cleavage position preferences of the *LnCCD1*, the cDNA was cloned into bacterial expression vector pEXP5-CT/Topo, and the recombinant LnCCD1 protein was expressed in *E. coli* strains that accumulate various carotenoids biosynthesis enzymes.[37,38] Except for phytoene that is colorless, the carotenoids that accumulate in these strains provide a specific color to the cells depending on the carotenoid accumulated, and a loss of color indicates that the carotenoids could be metabolized to colorless compounds. Cultures expressing LnCCD1 and accumulating various carotenoids were grown in darkness, induced with IPTG, and grown for a further 12 h at room temperature. The norisoprenoid volatiles were collected by auto-HS-SPME and analyzed by GC−MS.

No isoprenoid-derived volatiles were identified in the culture synthesizing the acyclic carotenoids phytoene by GC−MS headspace analyses (Figure 3 and Table 2). To ensure that LnCCD1 did not cleave these acyclic carotenoids and generate nonvolatile products, the phytoene-accumulating *E. coli* cultures expressing the LnCCD1 were extracted and analyzed by HPLC. The phytoene carotenoid levels of the LnCCD1-expressing cultures were identical to controls harboring empty vectors and

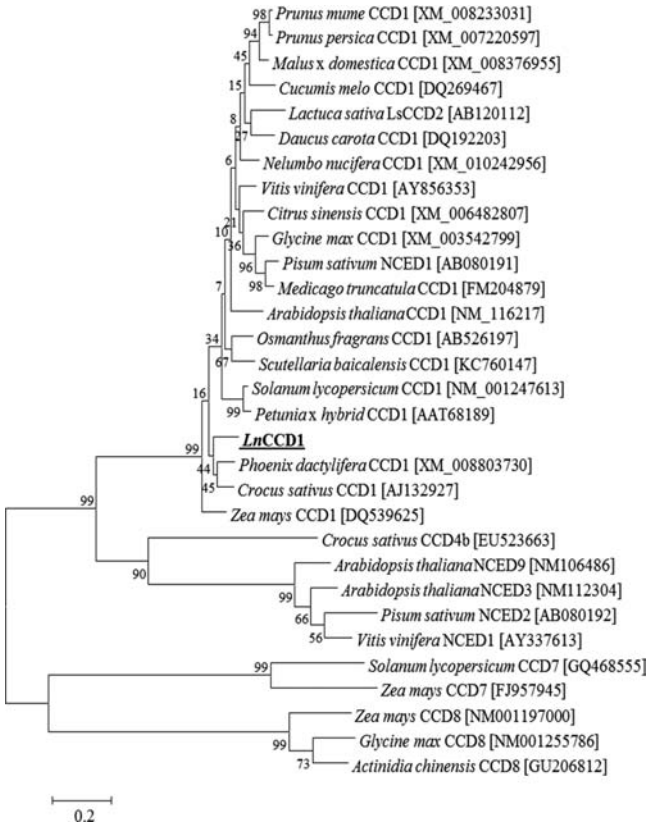

Figure 2. Phylogenetic tree of deduced amino acid sequences of carotenoid cleavage oxygenases from *L. nobilis* and other plant species. The tree was generated using Phylogeny Analysis MEGA6.1 program.[54] The resulting tree was bootstrap analyzed with 1000 replicates. The black bold underline indicates the *L. nobilis LnCCD1* gene identified in this study. Accession numbers are indicated in parentheses.

not overexpressing LnCCD1 (data not shown). Moreover, no new nonvolatile products were found, as compared to the control (data not shown), confirming that LnCCD1 did not cleave phytoene at a detectable rate. Similarly, Yahyaa et al. (2013)[39] reported that DcCCD1, a CCD isolated from *Daucus carota* roots, did not cleave the acyclic carotenoids phytoene. Also, similar results were reported by Vogel et al. (2008)[52] that ZmCCD1, a CCD isolated from maize, did not cleave phytoene.

Norisoprenoid volatiles were identified in vitro during coexpression of *LnCCD1* in different carotenoid producing *E. coli* strains (Table 2 and Figure 3). Pseudoionone and MHO were detected in lycopene-accumulating *E. coli* strain (Table 2 and Figure 4A). Pseudoionone is generated by 9,10 or 9′,10′ bond cleavage of lycopene, whereas MHO is generated by 5,6 or 5′,6′ bond cleavage. The presence of MHO and pseudoionone was unequivocally confirmed by a comparison of their retention indices (RI) and a mass spectra to that of authentic MHO and pseudoionone. Both pseudoionone and MHO were not detected in *E. coli* cells transformed with control plasmids devoid of the *LnCCD1* gene (Table 2 and Figure 4B). These results indicate that the *L. nobilis* CCD1 enzyme, like the *Arabidopsis*, maize, tomato, and *Rosa damascena* CCD1, cleaves lycopene at 9,10 (9′,10′) and 5,6 (5′,6′) bonds to generate pseudoionone and MHO.[46,52]

The norisoprenoid volatiles derived from δ- and β-carotene-accumulating *E. coli* strains revealed a similar pattern (Table 2,

DOI: 10.1021/acs.jafc.5b02941
J. Agric. Food Chem. 2015, 63, 8275−8282

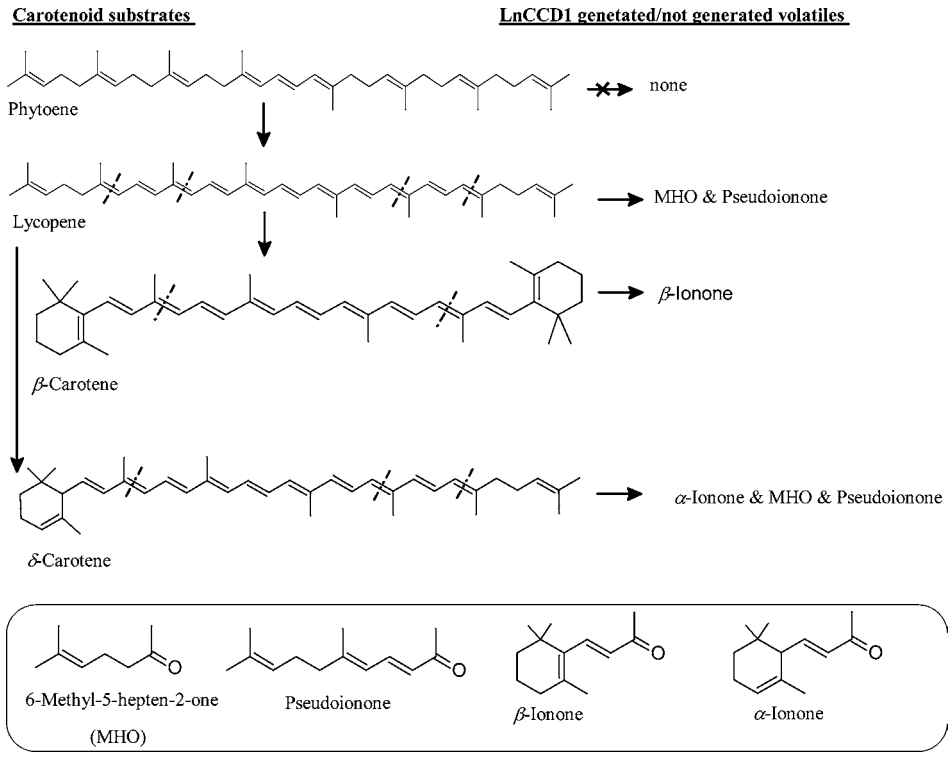

Figure 3. Proposed sites of LnCCD1 bond cleavage and the volatiles generated. An abbreviated version of the carotenoid biosynthetic pathway in higher plants is shown. Carotenoid substrates (left) are oxidatively cleaved by LnCCD1 to yield the norisoprenoid derivatives (right).

Table 2. Norisoprenoids Formed in Vitro during Coexpression of *LnCCD1* in Carotenoid Producing *E. coli* Strains

		norisoprenoids[a] present in headspaces of bacterial cultures (ng/mL)			
plasmid	carotenoid	6-methyl-5-hepten-2-one	pseudoionone	β-ionone	α-ionone
pBCAR-EB	phytoene				
pBCAR-EB + *LnCCD1*					
pBCAR-EBI	lycopene				
pBCAR-EBI + *LnCCD1*		36.05 ± 3.17	26.57 ± 1.08		
pBCAR-EBIY	β-carotene				
pBCAR-EBIY + *LnCCD1*		16.08 ± 0.91	1.36 ± 0.33	22.51 ± 4.61	
pZEAX	zeaxanthin				
pZEAX + *LnCCD1*		21.04 ± 2.12	4.92 ± 0.29	5.46 ± 0.86	
pDCAR	δ-carotene				
pDCAR + *LnCCD1*		38.07 ± 1.50	11.88 ± 0.64		1.56 ± 0.12

[a]Norisoprenoid compounds were identified by GC−MS on the basis of mass spectra matching with the standard NIST-98.L and Wiley 7N.I library (ms), comparison of retention index (RI) with literature data (RI), comparison with standard. The results shown are an average and standard errors of at least three biological replicates.

Figure 5A, and Figure S2). β-Ionone was detected from β-carotene-accumulating culture, and α-ionone was detected in the δ-carotene-accumulating culture, as evidenced by their retention index (RI) and a mass spectrum identical to that of authentic α- and β-ionone (Table 2, Figure 5A, and Figure S2). Both α- and β-ionone are indicative of 9,10 (9′10′) bond cleavage. Additionally, pseudoionone and MHO also were detected in both cultures expressing LnCCD1 enzyme, indicating cleavage of δ- and β-carotene precursor carotenoids at 9,10 (9′,10′) and 5,6 (5′,6′) bonds. Pseudoionone, MHO, and α- and β-ionone were absent in *E. coli* cells transformed with control plasmids devoid of the *LnCCD1* gene (Table 2, Figure 5B, and Figure S2).

LnCCD1 was also overexpressed in an *E. coli* strain accumulating the yellow-orange colored xanthophyll zeaxanthin, resulting in colorless colonies. The putative volatile enzymatic reaction products of the cleavage of zeaxanthin were further analyzed by auto-HS-SPME-GC−MS. MHO, pseudoionone, and β-ionone were identified in the head space of the *E. coli* strain accumulating zeaxanthin and expressing *LnCCD1* (Table 2 and Figure S3). 3-Hydroxy-β-ionone, the expected oxidative cleavage product of zeaxanthin, could not be detected in the headspace of these cultures (Table 2). MHO, pseudoionone, and β-ionone are breakdown products of lycopene and β-carotene, respectively, which are intermediate in zeaxanthin biosynthesis, suggesting that LnCCD1 may compete for the lycopene and β-carotenoid substrate with the β-carotene cyclase and the β-carotene hydroxylases (respectively) that are expressed in the zeaxanthin accumulating *E. coli* strain carrying that gene, the hydroxylase that catalyzes the formation of zeaxanthin in these cultures.[37,38] Similar observations (presence of β-ionone and not 3-hydroxy β-

DOI: 10.1021/acs.jafc.5b02941
J. Agric. Food Chem. 2015, 63, 8275−8282

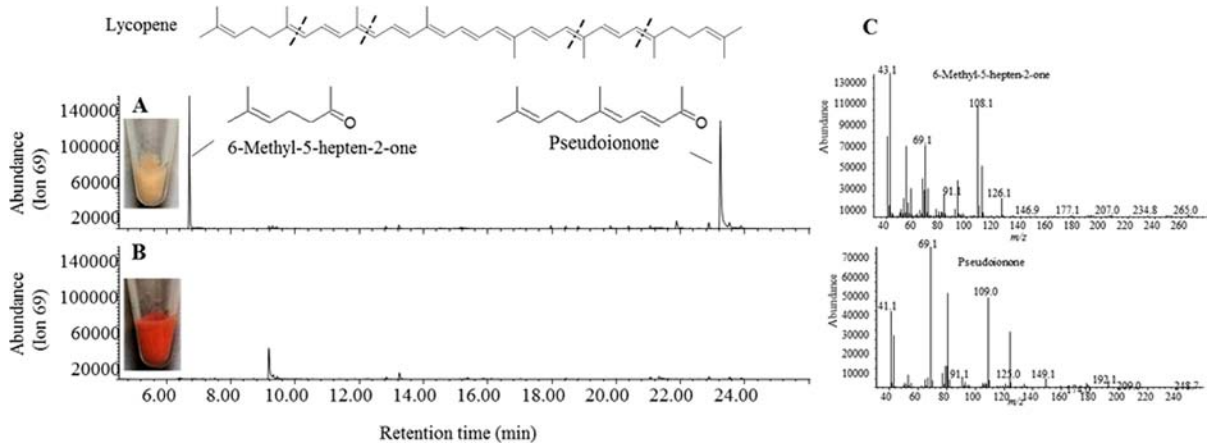

Figure 4. Functional expression of *LnCCD1* in *E. coli* cells previously engineered to accumulate lycopene. Dashed lines indicate sites of LnCCD1 cleavage. (A) GC−MS analysis of LnCCD1 activity after transformation in *E. coli* cells previously engineered to accumulate lycopene. (B) GC−MS analysis of bacterial pellets of *E. coli* cells engineered to accumulate lycopene. (C) The inset shows the structure and the mass spectrum of the enzymatic reaction products identified as MHO and pseudoionone by comparison of the retention index and the MS pattern with an authentic standard.

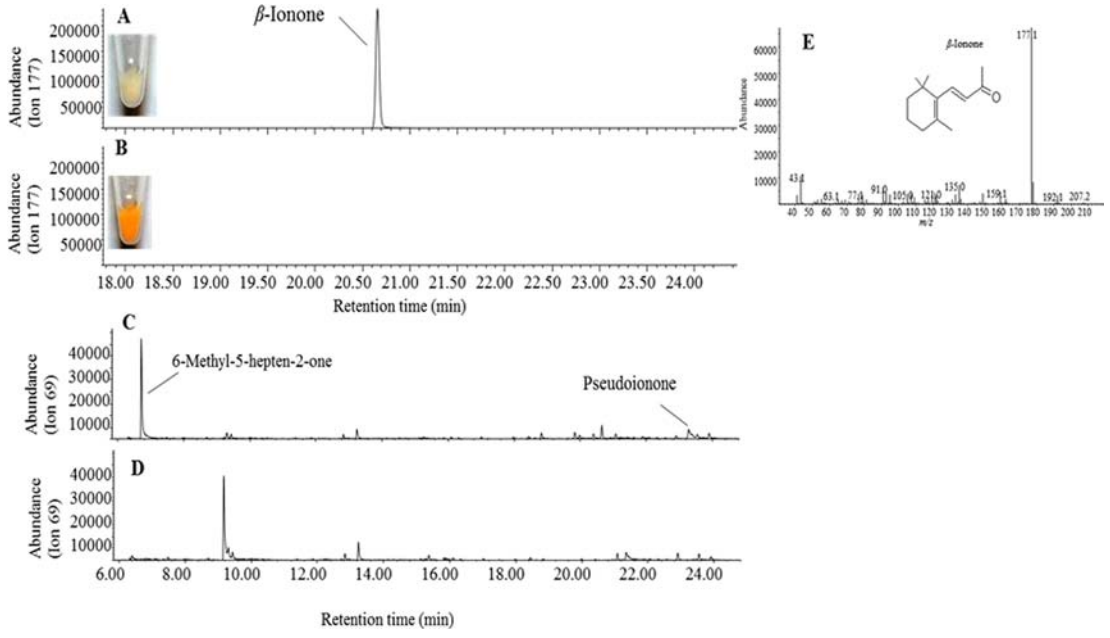

Figure 5. Functional expression of *LnCCD1* in *E. coli* cells previously engineered to accumulate *β*-carotene. (A and C) GC−MS analysis of LnCCD1 activity after transformation in *E. coli* cells previously engineered to accumulate *β*-carotene. (B and D) GC−MS analysis of bacterial pellets of *E. coli* cells engineered to accumulate *β*-carotene. 6-Methyl-5-hepten-2-one and pseudoionone are breakdown products of lycopene, which is intermediate in *β*-carotene biosynthesis. (E) The inset shows the structure and the mass spectrum of the enzymatic reaction product identified as *β*-ionone by matching the retention time and the MS pattern with an authentic standard. The identity of the cleavage products (peaks marked) was confirmed using authentic standards.

ionone) have been noted in previous studies of expression of the *DcCCD1* gene from carrot roots,[39] *RdCCD1* and *RdCCD4* genes from *Rosa damascena*, *MdCCD4* gene from *Malus* × *domestica*, *CmCCD4a* gene from *Chrysanthemum* × *morifolium*, and *OfCCD4* gene from *Osmanthus fragrans*.[46,53]

In each carotenoid accumulating *E. coli* strain tested in this study, additional norisoprenoid volatiles consistent with the cleavage of precursor carotenoids were observed, indicating that LnCCD1 cleaves precursor carotenoids before they can be converted into the final product. Similar results were reported by Vogel et al. (2008) and Huang et al. (2009),[46,52] who reported that ZmCCD1 and RdCCD1, CCDs isolated from maize and *Rosa damascena*, respectively, have a broad substrate specificity and cleaved multiple carotenoids at two different double bond positions (9,10, 9′10′, 5,6, and 5′6′).

One of the most significant findings of this work is that LnCCD1 can cleave lycopene at 9,10 (9′,10′) and 5,6 (5′,6′) double bonds to produce pseudoionone and MHO. Cleaving lycopene by LnCCD1 provides a biological route to synthesize MHO, an important flavor and aroma volatile found in a number of fruits such as tomato.[42] Accordingly, the bulk of the volatile norisoprenoid products detected in the recombinant *E. coli* overexpressing the *LnCCD1* gene apparently result from the 9,10 (9′,10′) and 5,6 (5′,6′) cleavage of different carotenoids. We therefore conclude that *LnCCD1* encodes a protein that displays 9,10 and 5,6-carotenoid cleavage

DOI: 10.1021/acs.jafc.5b02941
J. Agric. Food Chem. 2015, 63, 8275−8282

dioxygenase activity and can accept a wide range of carotenoids as a substrates. LnCCD1 is able to release MHO, pseudoionone, β-ionone, and α-ionone depending on the carotenoid substrate offered.

In conclusion, several carotenoids and norisoprenoid volatile compounds, for example, MHO, pseudoionone, and β-ionone, were detected in the *L. nobilis* pericarp of the black fruit. LnCCD1 was found to have a broad substrate specificity and to cleave multiple carotenoids at two different double bond positions (9,10, 9′10′, 5,6, and 5′6′). On the basis of the pattern of norisoprenoid volatiles detected by auto-HS-SPME-GC−MS analysis, and their odor thresholds, we suggest that LnCCD1 cleavage products may contribute to *L. nobilis* fruit flavor and aroma.

■ ASSOCIATED CONTENT

Supporting Information

The Supporting Information is available free of charge on the ACS Publications website at DOI: 10.1021/acs.jafc.5b02941.

Figure S1: Sequences of open reading frames and encoded protein of LnCCD1 from *Laurus nobilis*. Figure S2: Functional expression of LnCCD1 in *E. coli* cells previously engineered to accumulate δ-carotene. A and C: GC−MS analysis of LnCCD1 activity after transformation in *E. coli* cells previously engineered to accumulate δ-carotene. B and D: GC−MS analysis of bacterial pellets of *E. coli* cells engineered to accumulate δ-carotene. The identity of the cleavage products (peaks marked) was confirmed using authentic standards. Figure S3: Functional expression of LnCCD1 in *E. coli* cells previously engineered to accumulate zeaxanthin. A and C: GC−MS analysis of LnCCD1 activity after transformation in *E. coli* cells previously engineered to accumulate zeaxanthin. B and D: GC−MS analysis of bacterial pellets of *E. coli* cells engineered to accumulate zeaxanthin. 6-Methyl-5-hepten-2-one, pseudoionone, and β-ionone are breakdown products of lycopene and β-carotene, respectively, which are intermediate in zeaxanthin biosynthesis. The identity of the cleavage products (peaks marked) was confirmed using authentic standards (PDF)

■ AUTHOR INFORMATION

Corresponding Author

*Tel.: 00972-4-9539509. E-mail: mwafaq@volcani.agri.gov.il.

Notes

The authors declare no competing financial interest.

■ ACKNOWLEDGMENTS

We are grateful to Professor Eran Pichersky for critical reading of the manuscript and many discussions during the preparation of this work. We are grateful to Professor Nativ Dudai and Doya Sa'adi for taking care of the *Laurus nobilis* plants. We also thank Professor Joseph Hirschberg for providing the following plasmids: pBCAR-EB, pBCAR-EBI, pBCAR-EBIY, pDCAR, and pZEAX.

■ ABBREVIATIONS USED

CCD, carotenoid cleavage dioxygenase; LnCCD, *Laurus nobilis* carotenoid cleavage dioxygenase; FW, fresh weight; GC−MS, gas chromatography mass spectrometry; HPLC, high performance liquid chromatography; IPTG, isopropyl-1-thio-β-D-galactopyranoside; MHO, 6-methyl-5-hepten-2-one; HS-SPME, head-space-solid phase micro extraction

■ REFERENCES

(1) Dall'Acqua, S.; Viola, G.; Giorgetti, M.; Loi, M. C.; Innocenti, G. Two new sesquiterpene lactones from the Leaves of *Laurus nobilis*. *Chem. Pharm. Bull.* **2006**, *54*, 1187−1189.

(2) Julianti, E.; Jang, K. H.; Lee, S.; Lee, D.; Mar, W.; Oh, K.-B.; Shin, J. Sesquiterpenes from the leaves of *Laurus nobilis* L. *Phytochemistry* **2012**, *80*, 70−76.

(3) Cherrat, L.; Espina, L.; Bakkali, M.; Garcia-Gonzalo, D.; Pagan, R.; Laglaoui, A. Chemical composition and antioxidant properties of *Laurus nobilis* L. and *Myrtus communis* L. essential oils from Morocco and evaluation of their antimicrobial activity acting alone or in combined processes for food preservation. *J. Sci. Food Agric.* **2014**, *94*, 1197−1204.

(4) da Silveira, S. M.; Luciano, F. B.; Fronza, N.; Cunha, A.; Scheuermann, G. N.; Werneck Vieira, C. R. Chemical composition and antibacterial activity of *Laurus nobilis* essential oil towards foodborne pathogens and its application in fresh Tuscan sausage stored at 7 degrees C. *Food Sci. Technol.* **2014**, *59*, 86−93.

(5) Yilmaz, E. S.; Timur, M.; Aslim, B. Antimicrobial, antioxidant activity of the essential oil of Bay Laurel from Hatay, Turkey. *J. Essent. Oil-Bear. Plants* **2013**, *16*, 108−116.

(6) Patrakar, R.; Mansuriya, M.; Patil, P. Phytochemical and pharmacological review on *Laurus nobilis*. *Int. J. Pharm. Chem. Sci.* **2012**, *1*, 595−602.

(7) Bozan, B.; Karakaplan, U. Antioxidants from laurel (*Laurus nobilis* L.) berries: Influence of extraction procedure on yield and antioxidant activity of extracts. *Acta Aliment.* **2007**, *36*, 321−328.

(8) Kilic, A.; Hafizoglu, H.; Kollmannsberger, H.; Nitz, S. Volatile constituents and key odorants in leaves, buds, flowers, and fruits of *Laurus nobilis* L. *J. Agric. Food Chem.* **2004**, *52*, 1601−1606.

(9) Yahyaa, M.; Matsuba, Y.; Faigenboim, A.; Bar, E.; McCain, A.; Davidovitz Rikanati, R.; Lewinsohn, E.; Pichersky, E.; Ibdah, M. Identification, functional characterization, and evolution of terpene synthases from a basal dicot. *Plant Physiol.* **2015**, pp.00930.2015.

(10) Marzouki, H.; Piras, A.; Salah, K. B. H.; Medini, H.; Pivetta, T.; Bouzid, S.; Marongiu, B.; Falconieri, D. Essential oil composition and variability of *Laurus nobilis* L. growing in Tunisia, comparison and chemometric investigation of different plant organs. *Nat. Prod. Res.* **2009**, *23*, 343−354.

(11) Derwich, E.; Benziane, Z.; Boukir, A. Chemical composition and antibacterial activity of leaves essential oil of *Laurus nobilis* from Morocco. *Aust. J. Basic Appl. Sci.* **2009**, *3*, 3818−3824.

(12) Kaurinovic, B.; Popovic, M.; Vlaisavljevic, S. In vitro and in vivo effects of *Laurus nobilis* L. leaf extracts. *Molecules* **2010**, *15*, 3378.

(13) Walter, M. H.; Strack, D. Carotenoids and their cleavage products: Biosynthesis and functions. *Nat. Prod. Rep.* **2011**, *28*, 663−692.

(14) Auldridge, M. E.; McCarty, D. R.; Klee, H. J. Plant carotenoid cleavage oxygenases and their apocarotenoid products. *Curr. Opin. Plant Biol.* **2006**, *9*, 315−321.

(15) Walter, M.; Floss, D.; Strack, D. Apocarotenoids: hormones, mycorrhizal metabolites and aroma volatiles. *Planta* **2010**, *232*, 1−17.

(16) Zeevaart, J. A. D.; Creelman, R. A. Metabolism and physiology of abscisic acid. *Annu. Rev. Plant Physiol. Plant Mol. Biol.* **1988**, *39*, 439−473.

(17) Gomez-Roldan, V.; Fermas, S.; Brewer, P. B.; Puech-Pages, V.; Dun, E. A.; Pillot, J.-P.; Letisse, F.; Matusova, R.; Danoun, S.; Portais, J.-C.; Bouwmeester, H.; Becard, G.; Beveridge, C. A.; Rameau, C.; Rochange, S. F. Strigolactone inhibition of shoot branching. *Nature* **2008**, *455*, 189−194.

(18) Alder, A.; Jamil, M.; Marzorati, M.; Bruno, M.; Vermathen, M.; Bigler, P.; Ghisla, S.; Bouwmeester, H. J.; Beyer, P.; Al-Babili, S. The path from β-carotene to carlactone, a strigolactone-like plant hormone. *Science* **2012**, *335*, 1348−1351.

(19) Kohlen, W.; Charnikhova, T.; Lammers, M.; Pollina, T.; Toth, P.; Haider, I.; Pozo, M. J.; de Maagd, R. A.; Ruyter-Spira, C.;

DOI: 10.1021/acs.jafc.5b02941
J. Agric. Food Chem. 2015, 63, 8275−8282

Bouwmeester, H. J.; Lopez-Raez, J. A. The tomato carotenoid cleavage dioxygenase 8 (SlCCD8) regulates rhizosphere signaling, plant architecture and affects reproductive development through strigolactone biosynthesis. *New Phytol.* **2012**, *196*, 535−547.
(20) Rameau, C. Strigolactones, a novel class of plant hormone controlling shoot branching. *C. R. Biol.* **2010**, *333*, 344−349.
(21) Bouvier, F.; Suire, C.; Mutterer, J.; Camara, B. Oxidative remodeling of chromoplast carotenoids: Identification of the carotenoid dioxygenase *CsCCD* and *CsZCD* genes involved in crocus secondary metabolite biogenesis. *Plant Cell* **2003**, *15*, 47−62.
(22) Frusciante, S.; Diretto, G.; Bruno, M.; Ferrante, P.; Pietrella, M.; Prado-Cabrero, A.; Rubio-Moraga, A.; Beyer, P.; Gomez-Gomez, L.; Al-Babili, S.; Giuliano, G. Novel carotenoid cleavage dioxygenase catalyzes the first dedicated step in saffron crocin biosynthesis. *Proc. Natl. Acad. Sci. U. S. A.* **2014**, *111*, 12246−12251.
(23) Rubio, A.; Rambla, J. L.; Santaella, M.; Gomez, M. D.; Orzaez, D.; Granell, A.; Gomez-Gomez, L. Cytosolic and plastoglobule-targeted carotenoid dioxygenases from *Crocus sativus* are both involved in beta-ionone release. *J. Biol. Chem.* **2008**, *283*, 24816−24825.
(24) Plotto, A.; Barnes, K.; Goodner, K. Specific Anosmia Observed for β-Ionone, but not for α-Ionone: Significance for Flavor Research. *J. Food Sci.* **2006**, *71*, S401−S406.
(25) Teranishi, R.; RG, B. The significance of low threshold odor compounds in aroma research. In *Flavor Science and Technology*; Martens, M., Dalen, G. A., Russwurm, H., Eds.; John Wiley and Sons Inc.: Weinheim, 1987; pp 513−527.
(26) Goff, S. A.; Klee, H. J. Plant Volatile Compounds: Sensory Cues for Health and Nutritional Value? *Science* **2006**, *311*, 815−819.
(27) Borovsky, Y.; Tadmor, Y.; Bar, E.; Meir, A.; Lewinsohn, E.; Paran, I. Induced mutation in β-carotene hydroxylase results in accumulation of β-carotene and conversion of red to orange color in pepper fruit. *Theor. Appl. Genet.* **2013**, *126*, 557−565.
(28) Ibdah, M.; Azulay, Y.; Portnoy, V.; Wasserman, B.; Bar, E.; Meir, A.; Burger, Y.; Hirschberg, J.; Schaffer, A. A.; Katzir, N.; Tadmor, Y.; Lewinsohn, E. Functional characterization of CmCCD1, a carotenoid cleavage dioxygenase from melon. *Phytochemistry* **2006**, *67*, 1579−1589.
(29) Lewinsohn, E.; Sitrit, Y.; Bar, E.; Azulay, Y.; Meir, A.; Zamir, D.; Tadmor, Y. Carotenoid pigmentation affects the volatile composition of tomato and watermelon fruits, as revealed by comparative genetic analyses. *J. Agric. Food Chem.* **2005**, *53*, 3142−3148.
(30) Harrison, P. J.; Bugg, T. D. H. Enzymology of the carotenoid cleavage dioxygenases: Reaction mechanisms, inhibition and biochemical roles. *Arch. Biochem. Biophys.* **2014**, *544*, 105−111.
(31) Kloer, D. P.; Schulz, G. E. Structural and biological aspects of carotenoid cleavage. *Cell. Mol. Life Sci.* **2006**, *63*, 2291−2303.
(32) Ohmiya, A. Carotenoid cleavage dioxygenases and their apocarotenoid products in plants. *Plant Biotechnol.* **2009**, *26*, 351−358.
(33) Schwartz, S. H.; Tan, B. C.; Gage, D. A.; Zeevaart, J. A. D.; McCarty, D. R. Specific oxidative cleavage of carotenoids by VP14 of Maize. *Science* **1997**, *276*, 1872−1874.
(34) Isaacson, T.; Ohad, I.; Beyer, P.; Hirschberg, J. Analysis in vitro of the enzyme CRTISO establishes a poly-cis-carotenoid biosynthesis pathway in plants. *Plant Physiol.* **2004**, *136*, 4246−4255.
(35) Lichtenthaler, H. K. Chlorophylls and carotenoids - pigments of photosynthetic biomembranes. *Methods Enzymol.* **1987**, *148*, 350−382.
(36) Yahyaa, M.; Tholl, D.; Cormier, G.; Jensen, R.; Simon, P. W.; Ibdah, M. Identification and Characterization of Terpene Synthases Potentially Involved in the Formation of Volatile Terpenes in Carrot (Daucus carota L.) Roots. *J. Agric. Food Chem.* **2015**, *63*, 4870−4878.
(37) Misawa, N.; Nakagawa, M.; Kobayashi, K.; Yamano, S.; Izawa, Y.; Nakamura, K.; K, H. Elucidation of the *Erwinia uredovora* carotenoid biosynthetic pathway by functional analysis of gene products expressed in *Escherichia coli*. *J. Bacteriol.* **1990**, *172*, 6704−6712.
(38) Ronen, G.; Cohen, M.; Zamir, D.; Hirschberg, J. Regulation of carotenoid biosynthesis during tomato fruit development: expression of the gene for lycopene epsilon-cyclase is down-regulated during ripening and is elevated in the mutant Delta. *Plant J.* **1999**, *17*, 341−351.
(39) Yahyaa, M.; Bar, E.; Dubey, N. K.; Meir, A.; Davidovich-Rikanati, R.; Hirschberg, J.; Aly, R.; Tholl, D.; Simon, P. W.; Tadmor, Y.; Lewinsohn, E.; Ibdah, M. Formation of norisoprenoid flavor compounds in carrot (*Ddaucus carota* L.) roots: characterization of a cyclic-specific carotenoid cleavage dioxygenase 1 gene. *J. Agric. Food Chem.* **2013**, *61*, 12244−12252.
(40) Pichersky, E.; Noel, J. P.; Dudareva, N. Biosynthesis of plant volatiles: Nature's diversity and ingenuity. *Science* **2006**, *311*, 808−811.
(41) Plotto, A.; Barnes, K. W.; Goodner, K. L. Specific anosmia observed for β-ionone, but not for α-ionone: Significance for flavor research. *J. Food Sci.* **2006**, *71*, 401−406.
(42) Buttery, R. G. Quantitative and sensory aspects of flavor of tomato and other vegetable and fruits. In *Flavor Science: Sensible Principles and Techniques*; Acree, T.E., Teranishi, R., Eds.; American Chemical Society: Washington, DC, 1993; pp 259−286.
(43) Knudsen, J.; Eriksson, R.; Gershenzon, J.; Ståhl, B. Diversity and distribution of floral scent. *Bot. Rev.* **2006**, *72*, 1−120.
(44) Lewinsohn, E.; Sitrit, Y.; Bar, E.; Azulay, Y.; Ibdah, M.; Meir, A.; Yosef, E.; Zamir, D.; Tadmor, Y. Not just colors - carotenoid degradation as a link between pigmentation and aroma in tomato and watermelon fruit. *Trends Food Sci. Technol.* **2005**, *16*, 407−415.
(45) Garcia-Limones, C.; Schnaebele, K.; Blanco-Portales, R.; Luz Bellido, M.; Luis Caballero, J.; Schwab, W.; Munoz-Blanco, J. Functional characterization of FaCCD1: A carotenoid cleavage dioxygenase from strawberry involved in lutein degradation during fruit ripening. *J. Agric. Food Chem.* **2008**, *56*, 9277−9285.
(46) Huang, F.-C.; Horváth, G.; Molnár, P.; Turcsi, E.; Deli, J.; Schrader, J.; Sandmann, G.; Schmidt, H.; Schwab, W. Substrate promiscuity of RdCCD1, a carotenoid cleavage oxygenase from *Rosa damascena*. *Phytochemistry* **2009**, *70*, 457−464.
(47) Simkin, A. J.; Schwartz, S. H.; Auldridge, M.; Taylor, M. G.; Klee, H. J. The tomato carotenoid cleavage dioxygenase 1 genes contribute to the formation of the flavor volatiles beta-ionone, pseudoionone, and geranylacetone. *Plant J.* **2004**, *40*, 882−892.
(48) Fleischmann, P.; Watanabe, N.; Winterhalter, P. Enzymatic carotenoid cleavage in star fruit (*Averrhoa carambola*). *Phytochemistry* **2003**, *63*, 131−137.
(49) Auldridge, M. E.; Block, A.; Vogel, J. T.; Dabney-Smith, C.; Mila, I.; Bouzayen, M.; Magallanes-Lundback, M.; DellaPenna, D.; McCarty, D. R.; Klee, H. J. Characterization of three members of the Arabidopsis carotenoid cleavage dioxygenase family demonstrates the divergent roles of this multifunctional enzyme family. *Plant J.* **2006**, *45*, 982−993.
(50) Messing, S. A. J.; Gabelli, S. B.; Echeverria, I.; Vogel, J. T.; Guan, J. C.; Tan, B. C.; Klee, H. J.; McCarty, D. R.; Amzel, L. M. Structural insights into Maize viviparous14, a key enzyme in the biosynthesis of the phytohormone abscisic acid. *Plant Cell* **2010**, *22*, 2970−2980.
(51) Mathieu, S.; Terrier, N.; Procureur, J.; Bigey, F.; Gunata, Z. A carotenoid cleavage dioxygenase from *Vitis vinifera* L.: functional characterization and expression during grape berry development in relation to C-13-norisoprenoid accumulation. *J. Exp. Bot.* **2005**, *56*, 2721−2731.
(52) Vogel, J.; Tan, B. C.; McCarty, D. R.; Klee, H. The carotenoid clevage dioxygenase 1 enzyme has broad substarte specificity, cleaving ultiple carotenoids at two different bond positions. *J. Biol. Chem.* **2008**, *283*, 11364−11373.
(53) Huang, F.-C.; Molnár, P.; Schwab, W. Cloning and functional characterization of carotenoid cleavage dioxygenase 4 genes. *J. Exp. Bot.* **2009**, *60*, 3011−3022.
(54) Tamura, K.; Stecher, G.; Peterson, D.; Filipski, A.; Kumar, S. MEGA6: Molecular Evolutionary Genetics Analysis Version 6.0. *Mol. Biol. Evol.* **2013**, *30*, 2725−2729.

DOI: 10.1021/acs.jafc.5b02941
J. Agric. Food Chem. 2015, 63, 8275−8282

mostly composed of salts, proteins, lipids, and carbohydrates.[18] Despite the low content of lipids, they remain an indispensable component in jellyfish. For example, phosphonolipid (PnL), commonly present in the jellyfish, is a structural element of cell membranes and plays a special role in stabilizing cell membranes and protecting membrane lipids from hydrolytic enzymes.[19]

Sphingophosphonolipid (SPnL) and phospholipid (PL) from jellyfish *Aurelia Aurelia* and *Pelagia noctiluca* have been analyzed.[20,21] However, no assignment of fatty acids (FAs) to the *sn*-1 and *sn*-2 positions of the glycerol backbone has been achieved. Furthermore, traditional lipid analytical methods are complex and time-consuming. For instance, the confirmation of FA compositions in each lipid class needs the separation by thin layer chromatography (TLC), fraction collection, hydrolysis by lipase, derivatization, and identification of derivatized FAs by gas chromatography (GC) or gas chromatography coupled with mass spectrometry (GC-MS). Nuclear magnetic resonance (NMR) and electrospray ionization mass spectroscopy (ESI-MS) have been also used to characterize glycolipids and SPnL in *Phyllorhiza punctata*.[22] Even though detailed structural information on monogalactosyldiacylglycerol (MGDG), sulfoquinovosyldiacylglycerol (SQDG), and ceramide 2-aminoethylphosphonate (CAEP) has been obtained, a series of complex steps are still required to separate lipids by TLC. In addition, the infusion of crude lipid extracts into ESI-MS could result in a significant loss of ion signals from those low-abundance components.[23] Fortunately, this problem can be avoided by the separation of crude lipids using chromatography. Recently, the comprehensive characterization of a variety of lipids in marine organisms has been achieved by using UPLC coupled with Q-TOF MS in a MS^E data collection mode[24,25] without the requirement of preseparation. In the present study, the comprehensive characterization and semiquantification of lipid profile in different parts of jellyfish *R. esculentum* were conducted by ultraperformance liquid chromatography−electrospray ionization−quadrupole time-of-flight mass spectrometry (UPLC-ESI-Q-TOF-MS), which will facilitate the evaluation of the nutritional value of *R. esculentum* as a healthy food for humans or as a diet supplement for commercial fish.

MATERIALS AND METHODS

Sampling Method. Jellyfish *R. esculentum* were randomly caught from the coast of Ningbo by using a fishnet and dissected into three distinct body parts including umbrella, oral arms, and mouth stalk. These body parts of *R. esculentum* were freeze-dried, ground to fine powder in the presence of liquid nitrogen, and individually stored at −20 °C for future use.

Total Lipid (TL) Extraction and Lipid Standards. Briefly, 50 mg of different freeze-dried body parts of *R. esculentum* was extracted with chloroform/methanol (1:1, v/v) containing 0.05% butylated hydroxytoluene (BHT). The combined lipid extracts were evaporated on a rotary evaporator (IKA, Germany), and the residue was stored at −20 °C. Lipid standards including phosphatidylethanolamine (PE; 16:0−18:1), phosphatidylcholine (PC; 18:1−14:0), phosphatidylinositol (PI; 16:0−18:1), phosphatidylserine (PS; 16:0−18:1), ceramide (Cer; d18:1−16:0), and sphingosyl phosphoethanolamine (Cer-PE; d17:1−12:0) were purchased from Avanti Polar Lipids (Alabaster, AL, USA). triacylglycerol (TAG) (18:3−18:3−18:3) was purchased from Larodan (Limhamn, Sweden). All extraction procedures were performed in triplicate, and the data were expressed as the mean ± SD.

UPLC Analysis. Reversed-phase analysis was carried out on a Waters ACQUITY Ultra Performance LC system (UPLC) using an ACQUITY UPLC BEH C_8 analytical column (2.1 × 100 mm, 1.7 μm). The flow rate was 0.5 mL/min with mobile phase A composed of acetonitrile/isopropanol/tetrahydrofuran (1:1:1, v/v/v) and mobile phase B composed of water/acetonitrile (1:2, v/v), both containing 0.1% formic acid as well as 0.01% lithium acetate. Efficient separation of lipids was achieved with a gradient elution: 0−3 min, 2% A; 3.0−5.0 min, 2−30% A; 5−12 min, 30−50% A; 12−22 min, 50−80% A; 22−25 min, 80% A; 25−27 min, returning to initial 2% A; 27−30 min, 2% A. The temperature of the sample chamber was set at 6 °C, the column temperature was set at 40 °C, and the injection volume was 3 μL for each analysis. Before injection, samples were filtered with a 0.22 μm ultrafiltration membrane (Millipore, Bedford, MA, USA).

Mass Spectrometric Analysis. Mass spectrometric analysis was performed on a Waters Q-TOF Premier mass spectrometer in both positive and negative ion modes. The mass range was from 150 to 1200 with a scanning duration of 0.3 s. The nebulization gas was set at a constant flow rate of 600 L/h at 400 °C, and the source temperature was set at 120 °C. Compositions and contents of TLs were detected in both positive and negative modes. For positive mode, the capillary voltage was set at 3.0 kV; the sampling cone voltage was set at a ramp of 25−40 V, whereas for negative mode, the capillary voltage was set at 2.6 kV and the sampling cone voltage was set at a ramp of 25−40 V. MS^E analysis was performed on the mass spectrometer with the setting at 6 kV for low collision energy and a ramp of 25−50 kV for high collision energy. The time-of-flight analyzer was used in V mode and tuned for maximum resolution (>10000 resolving power at m/z 1000). The instrument was previously calibrated with sodium formate, and the lock mass spray for precise mass determination was set by leucine enkephalin ($[M + H]^+$ at m/z 556.2771 and $[M - H]^-$ at m/z 554.2615) at a concentration 0.2 ng/mL, which makes the maximum relative error up to 5 ppm.

Identification of Lipids by ESI-MS. The exact masses (the mass difference was <5 ppm) of lipids were determined on the Q-TOF MS system, which allowed for the possible elemental composition calculation of empirical chemical formula. The freely accessible databases of HMDB (http://www.hmdb.ca), MAPS (http://www.lipidmaps.org), and METLINE (http://metlin.Scripps.edu) were further used to elucidate the putative structures of lipids. The structural identification of each lipid species was carried out by UPLC-MS/MS analysis through comparison of the molecular compositions, retention times (RT), and specific fragmentation behaviors with lipid standards that are biologically relevant and commercially available. The fragmentation patterns of PC, PE, PI, PS, Cer, and TAG have been previously described.[26−29] Furthermore, the fragmentation pattern of PE (18:0/22:4) is shown in the Supporting Information for better illustrating the structural elucidation process of these lipids in *R. esculentum*. ESI-MS/MS information for the determination and structural elucidation of CAEP is also available.[22]

Semiquantitative Analysis of Lipids. Internal standards were spiked into samples for semiquantitative analysis of lipids in *R. esculentum*. It is noted that these internal standards were not detected in *R. esculentum* during pre-experiments. The TLs extracted from 50 mg of dried *R. esculentum* were dissolved in 1000 μL of methanol, ensuring a final concerntration of 5 nmol/mL for each lipid standard. An extracted ion chromatogram (EIC) of each lipid class was obtained from the low collision energy scan (6 V), and the peak area was integrated, respectively. After the variable ionization efficiencies in different proportions of mobile phase were calibrated, the semiquantitative analysis was carried out according to the area ratio of each lipid to that of the corresponding internal standard. Because CAEP standard is not commercially available,[20] the semiquantitative analysis of CAEP was performed according to the area ratio of CAEP to that of the Cer-PE internal standard, which has a structure remarkably similar to that of CAEP.

Meanwhile, semiquantitative analysis of FAs was also performed from liquid chromatography coupled with mass spectrometry (LC-MS) data by a normalization method. To obtain the contents of total FAs, a calculation factor was applied to each lipid species: 1 for Lysophophatidylcholine (LPC), lysophophatidylethanolamine (LPE), and lysophosphatidylinositol (LPI), CAEP, and Cer; 2 for PC, PE, PS and PI; and 3 for TAG.

DOI: 10.1021/acs.jafc.5b03145
J. Agric. Food Chem. 2015, 63, 8283−8291

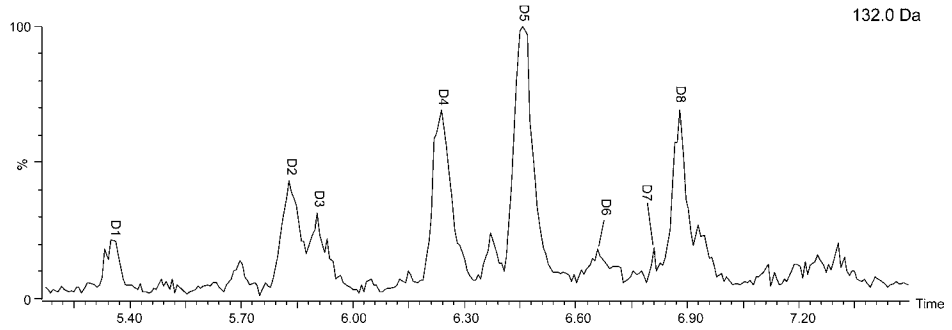

Figure 1. EIC for the characteristic ion of CAEP at m/z 132.0 from the high collsion energy scans. The marked peaks are consistent with the identified CAEP shown in Supporting Information Tables 1, 2, and 3.

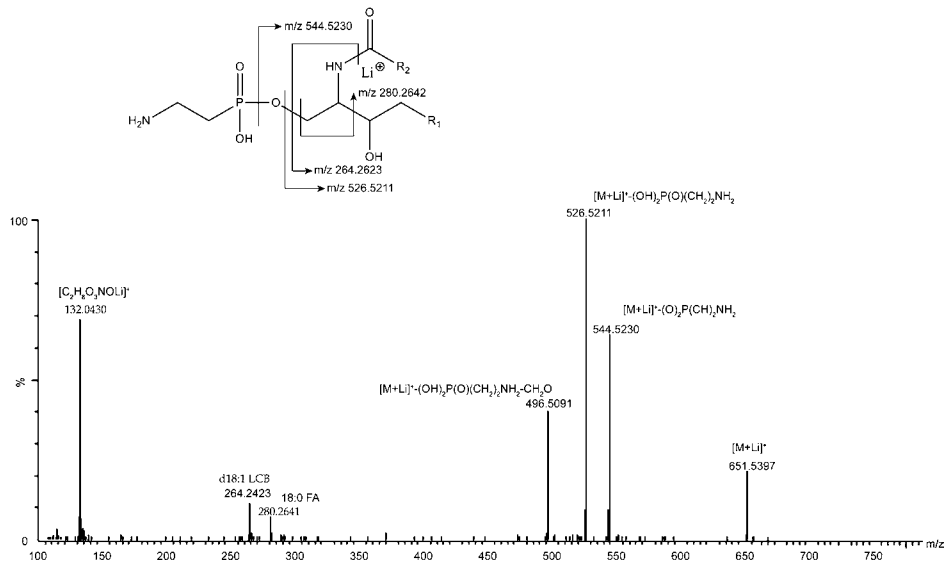

Figure 2. MS/MS spectrum and fragmentation pathways of the $[M + Li]^+$ at m/z 651.5397 of CAEP (d18:1/16:0).

Data Processing. The raw LC-MS data from both ESI^+ and ESI^- were acquired in the centroid mode by the UPLC-Q-TOF-MS system and analyzed using MassLynx (v4.1) software (Waters, Milford, MA, USA).

Phospholipase A2 (PLA2) Activity Assay. For PLA2 activity assay, 50 mg freeze-dried samples were homogenized with 1 mL of chilled 0.9% sodium chloride, and thereafter the samples were centrifuged at 12000 rpm for 10 min at 4 °C; finally, the supernatants were stored at −20 °C until assay. After thawing, the PLA2 catalytic activity of the extracts was assayed by a photometric method.[30] Briefly, bovine pancreatic PLA2 (Sigma-Aldrich, Madison, WI, USA) was used as the standard, and 7.9 mM 18:0−20:4 PC (Avanti) was used as the substrate in buffer containing 125 mM Tris-HCL, 4 mM calcium chloride, 1 mM deoxycholate, and 2.5 g/L Triton X-100 at pH 8.0. In total, 10 μL of PLA2 standard solution or sample was incubated with 50 μL of substrate mixture in a 96-well microplate at 37 °C for 20 min. Color reagents of the NEFA C Kit (Wako Chemical, Osaka, Japan) were added and incubated according to the manufacturer's instructions. Absorbance was measured at 550 nm (Microplate reader, Thermo Fisher, USA). The unit of PLA2 activity is defined as the activity for the release of 1 μmol of FA per minute. The protein concentration of the extract was measured as previously described[31] by using bovine serum albumin (Sigma-Aldrich) as the standard. The results were expressed as units per liter (u/L) and units per gram of protein (u/g) for the extract.

RESULTS AND DISCUSSION

In the negative mode, LPE, PE, LPI, PI, and PS were detected as the $[M - H]^-$ ion, and LPC and PC as $[M + HCOO]^-$.[27,28] The precursor ion $[M - H]^-$ of PE formed the characteristic fragment ions $[C_2H_7O_4NP]^-$ at m/z 140 and $[C_5H_{11}O_5NP]^-$ at m/z 196. The parent ion $[M - H]^-$ of PI produced the fragment ion $[C_6H_{10}O_8P]^-$ at m/z 241 that was unique to PI. The precursor ion $[M - H]^-$ of PS formed the ion $[M - H - 87]^-$ due to neutral loss of its headgroup $C_3H_5O_2N$. In addition, the parent ion $[M + HCOO]^-$ of PC produced the fragment ion $[M - CH_3]^-$ as the result of the loss of $C_2H_4O_2$, along with the unique ion $[C_4H_{11}O_4NP]^-$ at m/z 168. In addition, the compositions and positions of fatty acyl residues in those glycerophospholipids (GPLs) were identified by ESI-MS/MS in a negative mode.[28,32]

TAG and Cer were detected as $[M + Li]^+$ in positive mode.[22,26,29] For TAG, the MS/MS spectra of $[M + Li]^+$ produced fragment ions such as $[R_nCO\text{-}18]^+$, $[R_nCO]^+$, $[R_2CH{=}CHCOOH + Li]^+$, $[RnCOOH + Li]^+$, $[M + Li - R_nCOOH{-}R_2CH{=}CHCOOH]^+$, $[M + Li - R_nCOOLi]^+$, and $[M + Li - R_nCOOH]^+$ that were used for analysis of TAG, whereas for Cer, the precursor ion of $[M + Li]^+$ produced an abundant fragment ion that is the representative of long-chain base (LCB), *N*-acyl, and polar headgroup from the ESI-MS/MS spectrum, which allowed for the unequivocal identification of the structures for these lipids.

Identification of CAEP was performed on the basis of the MS fragmentation pattern provided by de Souza[22] with some modification. As has been reported, the MS/MS spectra of $[M + H]^+$ yielded fragment ion representing LCB. Ion reflecting

DOI: 10.1021/acs.jafc.5b03145
J. Agric. Food Chem. 2015, 63, 8283−8291

the FA constituents was not observed. In contrast, the product ion of $[M + Li]^+$ produced structurally informative fragment ions representing both LCB and FA in our work. Furthermore, abundant fragment ion $[C_2H_8O_3NPLi]^+$ at m/z 132.0, representing lithiated aminoethylphosphonate(AEP) headgroup, was generated in the MS/MS spectra of $[M + Li]^+$ rather than in the MS/MS spectra of $[M + H]^+$, which could be used as the characteristic fragment ion of CAEP.

From the EIC of the characteristic fragment ion at m/z 132.0 referred to above, a series of signal peaks representing CAEP were obtained at retention times between 5.0 and 7.0 min (Figure 1). The peak (D8) at the retention time of 6.9 min (Figure 1) was used as an example to illustrate the structural elucidation process in detail. A group of ions at m/z 645.5353 and 651.5397 were obtained in the mass spectra at the retention time of 6.9 min in the total ion chromatogram (TIC) of the low collision energy scan. Thus, the $[M + Li]^+$ ion of the CAEP was at m/z 651.5397 and the elemental composition was $C_{36}H_{73}O_5N_2PLi$. The MS/MS spectrum of the precursor ion $[M + Li]^+$ at m/z 651.5397 (Figure 2) produced a fragment ion at m/z 526.5211, corresponding to neutral loss of the headgroup-AEP $[(OH)_2P(O)-(CH_2)_2NH_2]$, along with the ion at m/z 544.5230, by eliminating $[(O)_2P-(CH_2)_2NH_2]$. Further elimination of CH_2O from m/z 526.5211 via charge-remote fragmentation produced an ion at m/z 496.5091, followed by neutral loss of LCB as the terminal conjugated diene or neutral loss of the FA as the ketene to produce ions at m/z 280.2642 and 264.2423 that reflect the 16:0 FA and d18:1 LCB in the molecule. Thus, the structure of CAEP at the retention time of 6.9 min could be easily determined as d18:1−16:0.

Compositions of Each Lipid Species from Different Parts of *R. esculentum*. Utilizing the method described above in both positive and negative modes, more than 87 species from 10 major lipid classes including LPC, PC, LPE, PE, LPI, PI, PS, Cer, CAEP, and TAG were identified (Supporting Information Tables 1, 2, and 3). Concerning the compositions and locations of FAs in these lipid species, several interesting observations were achieved in all parts of *R. esculentum*. First, longer and more unsaturated fatty acids (UFAs), such as 22:6ω-3 (docosahexenoic acid, DHA), 20:5ω-3 (eicosapentaenoic acid, EPA), and 20:4ω-6 (arachidonic acid, AA), were mainly located in the *sn*-2 position of GPLs, whereas relatively short saturated fatty acids (SFAs) and monounsaturated fatty acids (MUFAs) were primarily located at the *sn*-1 position of GPLs. For example, PCs were mainly composed of 20:4, 20:5, and 22:6 FA at the *sn*-2 position and SFAs with 13C−18C at the *sn*-1 position. PEs were composed of 20:4 and 20:5 FA at the *sn*-2 position and MUFAs of 15C−17C at the *sn*-1 position. PS and PI were composed of 18:0 at the *sn*-1 position and of 22:4, 22:5, 22:6, 24:5 and 24:6 FA at the *sn*-2 position. Second, the compositions of LCB and *N*-acyl chain in Cer were consistent with those in CAEP. Both contained d18:1 (sphingosine) and d18:2 (sphingadienine) LCB, along with *N*-acyl chains composed of SFAs with 14C−16C and MUFAs with 16C−18C. The compositions of CAEP in jellyfish *R. esculentum* were partly comparable to those obtained previously from jellyfish *Aurelia aurita*, which consisted primarily of dihydroxyl LCB with 16C−18C and trihydroxyl LCB, combined with SFAs with 14C−18C.[20] Previous studies have reported that the compositions of major CAEP from different jellyfish species do not reveal the specificity, whereas the compositions of minor CAEP reveal specificity to each jellyfish species.[21] Thus, one possible explanation for such a difference in CAEP compositions between jellyfish *R. esculentum* and *Aurelia aurita* could be associated with the species. Third, TAGs identified in all parts of *R. esculentum* were mainly composed of 22:6 FA at the *sn*-1/*sn*-3 position and 16:0 FA at the *sn*-2 position.

A total of 6 Cer species were identified from *R. esculentum*, with the predominant species composed of d18:2−16:0. LCB portions of Cer were composed of d18:1 and d18:2. The *N*-acyl chains of Cer were composed of SFAs with 15C and 16C and MUFAs with 17C and 18C. According to our current knowledge, the presence of Cer is first observed in jellyfish. Cer consisting of LCB linked to the FA via an amide bond was particularly important in triggering apoptosis and the activation of a variety of protein kinase cascades.[33] It is well-known that many diseases including cancer, atherosclerosis, neuropathies, diabetes, Parkinson's disease, and Alzheimer's disease could be induced when the organism failed to regulate apoptosis.[34] They were rarely found as such at greater than trace levels in tissues. Thus, one probable reason could be that the concentration of Cer in jellyfish was too low to be detected by using traditional methods such as TLC, which requires a large amount of lipids and gains poor separation. In contrast, UPLC-ESI-Q-TOF-MS could result in rapid separation and precise characterization of complex lipids with only a very small amount of samples. However, neither MGDG nor SQDG, previously detected from jellyfish *Phyllorhiza punctata*,[22] is detected in *R. esculentum* by using the method established by Xu.[35] The presence of MGDG and SQDG in jellyfish *Phyllorhiza punctata* seems to be the result of an endosymbiotic association with microalgae, because these glycerolipids are commonly detected in thylakoid membranes of photosynthetic tissues. Therefore, the absence of these glycerolipids in *R. esculentum* is probably due to the absence of endosymbiotic microalgae.

Contents of Each Lipid Species from Different Parts of *R. esculentum*. It is reported that the ion response is linear in a biologically relevant range for a great amount of different lipids on ESI-Q-TOF-MS, and internal lipid standards are spiked into the samples for the semiquantitative analysis.[36] In the present study, the dynamic range/linearity of total lipids is determined on the basis of concentration of mixed standard lipids up to 5 nmol/mL and reveals good linearity. Therefore, the lipid profile is semiquantified in comparison with the internal lipid standards.

On the basis of the method discussed above, the contents of each lipid species from different parts of *R. esculentum* were obtained and are partly shown in Tables 1, 2, and 3 (see Supporting Information Tables 1, 2, and 3 for the contents of all lipid species present in different parts of *R. esculentum*). Results showed that GPLs and sphingolipids (SPLs) were the major lipid classes in all parts of *R. esculentum*, accounting for 54−63 and 23−28% of TLs, respectively (Figure 3). Furthermore, GPLs were dominantly composed of PC and PE, accounting for 44.6−86.9% of GPLs (Figure 3). It is well-known that PC and PE are the essential constituents of the bilayer membrane, which plays an important role in the growth and metabolism of organisms. For example, PC, once named "lecithin", could significantly improve the performance of the brain and accelerate signal transfer among neurons.[37] Previous studies have confirmed that foods containing PC are critical for brain development in infants and children.[38] PE, once named "cephalin", is the second most abundant PL in animals and is particularly enriched in the brain. PE plays an important role in

DOI: 10.1021/acs.jafc.5b03145
J. Agric. Food Chem. 2015, 63, 8283−8291

Table 1. Lipid Compositions and Contents in Oral Arms of Jellyfish *Rhopilema esculentum* (nmol/mg Dry Weight *R. esculentum*)[a]

RT (min)	adduct ion	*m/z*	compound name	content (±SD)
1.25	$[M + Li]^+$	488.3	15:0-LPC	0.402 ± 0.020
1.66	$[M + Li]^+$	530.3	18:0-LPC	0.341 ± 0.020
6.41	$[M + Li]^+$	649.5	d18:2−16:0-CAEP	0.976 ± 0.020
6.86	$[M + Li]^+$	663.5	d18:1−17:1-CAEP	0.294 ± 0.020
8.57	$[M + Li]^+$	542.5	d18:2−16:0-Cer	0.067 ± 0.004
9.07	$[M + Li]^+$	556.5	d18:1−17:1-Cer	0.030 ± 0.004
8.29	$[M + Li]^+$	798.5	15:0−22:6-PC	0.348 ± 0.070
9.05	$[M + Li]^+$	800.5	17:0−20:5-PC	0.103 ± 0.010
16.04	$[M + Li]^+$	931.7	22:6/16:0/20:5-TAG	0.020 ± 0.001
16.3	$[M + Li]^+$	957.7	22:6/16:0/22:6-TAG	0.018 ± 0.003
1.4	$[M - H]^-$	462.3	17:2-LPE	0.094 ± 0.010
1.88	$[M - H]^-$	464.3	17:1-LPE	0.270 ± 0.020
2.15	$[M - H]^-$	599.3	18:0-LPI	0.075 ± 0.001
9.01	$[M - H]^-$	748.5	17:2−20:4-PE	0.042 ± 0.005
9.25	$[M - H]^-$	748.5	17:1−20:5-PE	0.131 ± 0.010
10.43	$[M - H]^-$	862.5	18:0−24:6-PS	0.076 ± 0.006
11.41	$[M - H]^-$	864.5	18:0−24:5-PS	0.044 ± 0.004
11.5	$[M - H]^-$	913.5	18:0−22:4-PI	0.069 ± 0.004
12.04	$[M - H]^-$	939.5	18:0−24:5-PI	0.014 ± 0.002

[a]$X \pm$ SD, $N = 3$. RT, retention time.

Table 2. Lipid Compositions and Contents in Umbrella of Jellyfish *Rhopilema esculentum* (nmol/mg Dry Weight *R. esculentum*)[a]

RT (min)	adduct ion	*m/z*	compound name	content (±SD)
1.23	$[M + Li]^+$	488.3	15:0-LPC	0.041 ± 0.009
1.66	$[M + Li]^+$	530.3	18:0-LPC	0.045 ± 0.006
6.43	$[M + Li]^+$	649.5	1d8:2−16:0-CAEP	0.525 ± 0.030
6.89	$[M + Li]^+$	663.5	d18:1−17:1-CAEP	0.152 ± 0.010
8.62	$[M + Li]^+$	542.5	d18:2−16:0-Cer	0.048 ± 0.010
9.07	$[M + Li]^+$	556.5	d18:1−17:1-Cer	0.020 ± 0.004
8.31	$[M + Li]^+$	798.5	15:0−22:6-PC	0.272 ± 0.016
9.01	$[M + Li]^+$	800.5	17:0−20:5-PC	0.128 ± 0.017
16.04	$[M + Li]^+$	931.7	22:6/16:0/20:5-TAG	0.071 ± 0.009
16.28	$[M + Li]^+$	957.7	22:6/16:0/22:6-TAG	0.071 ± 0.004
1.4	$[M - H]^-$	462.3	17:2-LPE	0.011 ± 0.002
1.88	$[M - H]^-$	464.3	17:1-LPE	0.058 ± 0.005
2.17	$[M - H]^-$	599.5	18:0-LPI	0.005 ± 0.001
8.99	$[M - H]^-$	748.5	17:2−20:4-PE	0.050 ± 0.010
9.25	$[M - H]^-$	748.5	17:1−20:5-PE	0.189 ± 0.017
10.4	$[M - H]^-$	862.5	18:0−24:6-PS	0.057 ± 0.010
11.37	$[M - H]^-$	864.5	18:0−24:5-PS	0.041 ± 0.003
11.52	$[M - H]^-$	913.5	18:0−22:4-PI	0.041 ± 0.003
12.04	$[M - H]^-$	939.5	18:0−24:5-PI	0.008 ± 0.000

[a]$X \pm$ SD, $N = 3$). RT, retention time.

heart and contractile ring disassembly at the cleavage furrow during cytokinesis of mammalian cells.[39]

PC and PE in *R. esculentum* are characteristics of high levels of AA, EPA, and DHA. The sum of these acids in PC reveals the variation from 46 to 49%. AA and EPA are predominant FAs in PE, accounting for 52−64 and 33−47% of total FAs in PE, respectively. The benefits of diets containing ω-3 and ω-6 FAs for humans are well proven.[40,41] These essential FAs can be incorporated into cell membranes when they are available, and the deficiency of these essential FAs is associated with

Table 3. Lipid Compositions and Contents in Mouth Stalk of Jellyfish *Rhopilema esculentum* (nmol/mg Dry Weight *R. esculentum*)[a]

RT (min)	adduct ion	*m/z*	compound name	content (±SD)
1.23	$[M + Li]^+$	488.3	15:0-LPC	0.012 ± 0.002
1.66	$[M + Li]^+$	530.3	18:0-LPC	0.013 ± 0.001
6.41	$[M + Li]^+$	649.5	d18:2−16:0-CAEP	0.258 ± 0.012
6.87	$[M + Li]^+$	663.5	d18:1−17:1-CAEP	0.057 ± 0.010
8.59	$[M + Li]^+$	542.5	d18:2−16:0-Cer	0.032 ± 0.002
9.09	$[M + Li]^+$	556.5	d18:1−17:1-Cer	0.007 ± 0.001
8.29	$[M + Li]^+$	798.5	15:0−22:6-PC	0.126 ± 0.017
9.01	$[M + Li]^+$	800.5	17:0−20:5-PC	0.079 ± 0.008
16.04	$[M + Li]^+$	931.7	22:6/16:0/20:5-TAG	0.027 ± 0.004
16.3	$[M + Li]^+$	957.7	22:6/16:0/22:6-TAG	0.019 ± 0.003
1.4	$[M - H]^-$	462.3	17:2-LPE	0.004 ± 0.000
1.88	$[M - H]^-$	464.3	17:1-LPE	0.022 ± 0.004
8.96	$[M - H]^-$	748.5	17:2−20:4-PE	0.021 ± 0.003
9.2	$[M - H]^-$	748.5	17:1−20:5-PE	0.117 ± 0.010
11.56	$[M - H]^-$	913.5	18:0−22:4-PI	0.016 ± 0.003
12.04	$[M - H]^-$	939.5	18:0−24:5-PI	0.003 ± 0.000

[a]$X \pm$ SD, $N = 3$). RT, retention time.

impaired brain function;[42] ω-3 and ω-6 FAs are available only from dietary sources in humans.[43] Besides, extensive studies have demonstrated that ω-3 FAs, especially EPA and AA, are highly required for optimum growth and survival of some commercial fish and crustaceans, because these species have a limited capability to elongate shorter chain precursors such as 18:3 and 18:2 FAs to longer ω-3 highly unsaturated fatty acids (HUFAs) such as EPA and DHA. Therefore, these essential FAs must be obtained from feed.[44−46]

Low levels of PS and PI were also detected in *R. esculentum*, accounting for 3.5−4.3 and 3% of GPLs (Figure 3). Although PS and PI are minor portions of GPLs, they are vitally important signing molecules. For instance, PI can regulate the functions of innumerable proteins integral to membranes by binding to cytosolic proteins or cytosolic domains of membrane proteins.[47] PS is not only a component of membranes for the precursor of other PLs but also an essential cofactor for binding to and activating a large number of proteins, especially proteins with signaling activities.[48] As described above, the FA located at the *sn*-1 position of PS and PI is 18:0 FA. PS and PI have longer and more UFAs at the *sn*-2 position. These unusual FAs include docosatetraenoic acid (22:4), docosapentenoic acid (22:5), tetracosapentaenoic acid (24:5), and tetracosahexaenoic acid (24:6). Despite the low concentrations of these FAs, they have many important functions, such as reducing blood lipid and enhancing memory.[49]

SPLs, the second most abundant lipid in *R. esculentum*, are composed of CAEP and Cer. The former PnL is relatively abundant in some invertebrates, and it has been reported in jellyfish *Aurelia aurita* and *Phyllorhiza punctata*.[20,22] High levels of CAEP have also been detected in jellyfish *R. esculentum* with variation from 20 to 25.6% of TLs (Figure 3). CAEP, composed of an ethanolamine headgroup linked to ceramide via a phosphono group (O−P−C), is different from the commonly encountered sphingomyelin (SM) that is composed of a choline polar head linked to a ceramide via a phosphate group (O−P−O). Previous studies suggest that the C−P bond could provide the molecule with a relative resistance to chemical hydrolysis and thermal decomposition when

DOI: 10.1021/acs.jafc.5b03145
J. Agric. Food Chem. 2015, 63, 8283−8291

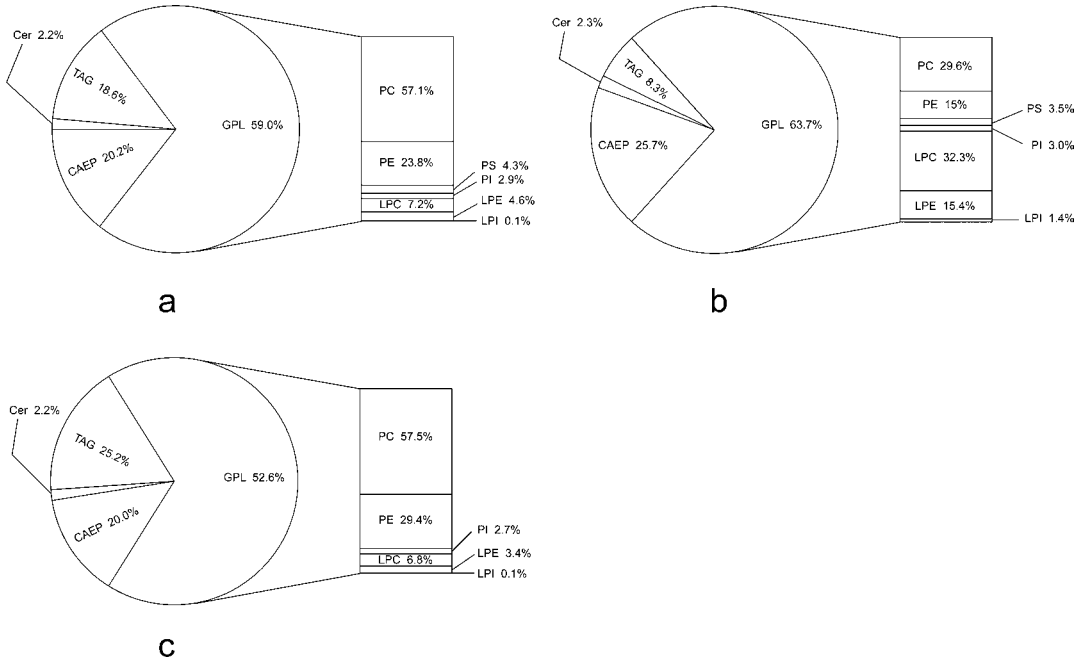

Figure 3. Relative contents of GPLs, CAEP, Cer, and TAG to TLs and the relative contents of PC, PE, PS, PI, LPC, LPE, and LPI to GPLs in oral arms (a), umbrella (b), and mouth stalk (c) of jellyfish *Rhopilema esculentum*.

compared with the common O−P bond.[50] Thus, CAEP could contribute to membrane stabilization, thus protecting membrane lipids from hydrolytic enzymes. Similarly, previous studies have demonstrated that cnidaria contains many hydrolytic enzymes. Therefore, the cell membrane of jellyfish *R. esculentum* may be benefit from the presence of CAEP. High CAEP proportions may also play an important role in the survival of jellyfish in an eutrophic environment where other organisms cannot survive.[51] Because "invertebrate" CAEP is thought to replace the "vertebrate" SM, the potential functions of CAEP may be similar to those of SM in vertebrates, such as endocytosis, virus budding, or immune cell signaling.[52] In addition, extensive studies have been conducted to evaluate the safety of CAEP to cell lines for applications in health foods and supplements. The results suggest that CAEP can effectively protect the liver from the damage caused by microcystin-LR, a cyclic peptide released by several bloom-forming toxic cyanobacteria, and complete the maintenance and promotion of human health.[53]

The contents of Cer were 3.8% in umbrella, 3.9% in oral arms, and 4.1% in mouth stalk (Figure 3). Despite the low concentration of Cer in membrane, it could exert important biological functions including cell differentiation, transformation, and proliferation as well as the regulation of apoptosis.[33] Cer is generally regarded as the precursor of SPLs in vertebrates and can be converted rapidly to more SPLs including SM and various glycosylceramides.[54] As mentioned above, LCB and *N*-acyl chain compositions of Cer were in agreement with those of CAEP. Thus, a hypothesis that Cer may also be the precursor of CAEP in invertebrates has been proposed. Further investigations are highly required for confirming this hypothesis.

Difference in Lipid Contents from Different Parts of Jellyfish *R. esculentum*. When the content of each lipid species in different parts of *R. esculentum* was analyzed, it was obvious that Lysophospholipid (LPL) contents in oral arms (LPC, 1.682 ± 0.010 nmol/mg; LPE, 0.801 ± 0.030 nmol/mg; LPI, 0.075 ± 0.005 nmol/mg) were much higher than those in umbrella (LPC, 0.270 ± 0.019 nmol/mg; LPE, 0.169 ± 0.009 nmol/mg; LPI, 0.005 ± 0.001 nmol/mg) and those in mouth stalk (LPC, 0.101 ± 0.007 nmol/mg; LPE, 0.052 ± 0.003 nmol/mg; LPI, 0.002 ± 0.001 nmol/mg) (Figure 4). Because

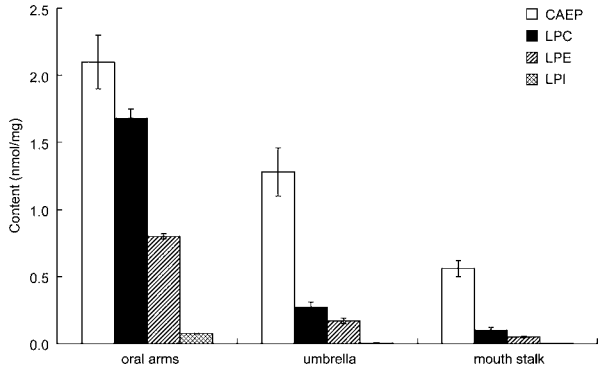

Figure 4. CAEP, LPC, LPE, and LPI contents in oral arms, umbrella, and mouth stalk of jellyfish *Rhopilema esculentum*.

these LPLs are commonly produced by the hydrolysis of GPLs in the presence of hydrolytic enzymes, PLA2[55] with the release of *sn*-2 FA and LPL, a high content of LPL may reflect the presence of PLA2 in large amounts. Therefore, the catalytic activity of PLA2 in different parts of *R. esculentum* was further measured, and a higher PLA2 level was determined in oral arms (149.5 ± 4.2 u/g protein) when compared that in umbrella (81.6 ± 2.7 u/g protein) and mouth stalk (21.3 ± 1.2 u/g protein) (Figure 5), which is in good agreement with the high proportion of LPL in oral arms.

Similar to LPC, LPE, and LPI, abundant CAEP (2.101 ± 0.031 nmol/mg) detected in oral arms was higher than that in umbrella (1.280 ± 0.020 nmol/mg) and mouth stalk (0.563 ± 0.009 nmol/mg) (Figure 4). According to the discussion above, CAEP can provide cell membranes relative resistance to

DOI: 10.1021/acs.jafc.5b03145
J. Agric. Food Chem. 2015, 63, 8283−8291

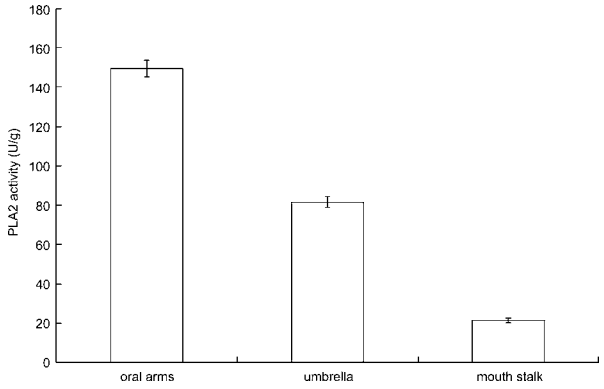

Figure 5. PLA2 activity in oral arms, umbrella, and mouth stalk of jellyfish *Rhopilema esculentum*.

chemical hydrolysis and thermal decomposition in the presence of hydrolytic enzymes such as PLA2. Therefore, cell membranes of oral arms containing high PLA2 may be benefit from the presence of CAEP.

Despite the high contents of LPC, LPE, LPI, and CAEP, oral arms contained a relatively lower proportion of TAG (8.3% of TLs) when compared with umbrella (18.6% of TLs) and mouth stalk (25.2% of TLs) (Figure 3). TAG containing three FAs with glycerol is usually regarded as an energy store. Previous studies have demonstrated that exercise will lead to the consumption of TAG.[56] Because the major functions of oral arms are food intake and movement with high requirement of large amount of energy, the relatively low TAG content detected in oral arms can be associated with the specific functions of oral arms.

In conclusion, considering the high level of GPLs and FA compositions in GPLs, the edible jellyfish *R. esculentum* has extensive potential as a health-promoting food for humans or as a supplemental feed for some commercial fish and crustaceans. Meanwhile, higher LPC, LPE, LPI, and CAEP in oral arms can be well explained due to the abundant PLA2 in oral arms. On the other hand, food intake and movement will lead to the consumption of TAG in oral arms.

■ ASSOCIATED CONTENT

Supporting Information

The Supporting Information is available free of charge on the ACS Publications website at DOI: 10.1021/acs.jafc.5b03145.

Text presenting the fragmentation patterns of PE (18:0/22:4) (PDF)

Tables 1−3 present overviews of the compositions and contents of all lipid species from oral arms, umbrella and mouth stalk, respectively (PDF)

Figure 1 depicting total ion current chromatograms (TICs) obtained from ESI^- (A) and ESI^+ (B) (PDF)

Figure 2 depicting the mass spectra of PE (18:0/22:4) at the low collision energy of 6 V in negative mode (A) and positive mode (B), as well as the MS/MS spectrum of $[M - H]^-$ (m/z 794.5618) in negative mode (C) (PDF)

■ AUTHOR INFORMATION

Corresponding Authors

*(J.X.) Phone: +86-574-87609570. Fax: +86-574-87609570. E-mail: xujilin@nbu.edu.cn.

*(X.Y.) Phone: +86-574-87600738. Fax: +86-574-87600458. E-mail: yanxiaojun@nbu.edu.cn.

Funding

This study was supported by the National Natural Science Foundation of China (31172448); Zhejiang Natural Science Foundation (LY15C190003), Ningbo Science and Technology Research Projects (2014C10005); and Zhejiang Natural Science Foundation (LY5C190003), Ningbo Science and Technology Research Projects (2015C110003); and partly sponsored by the K. C. Wong Magna Fund of Ningbo University.

Notes

The authors declare no competing financial interest.

■ ABBREVIATIONS USED

UPLC-ESI-Q-TOF-MS, ultraperformance liquid chromatography−electrospray ionization−quadrupole time-of-flight mass spectrometry; TLC, thin layer chromatography; GC, gas chromatography; GC-MS, gas chromatography coupled with mass spectrometry; LC-MS, liquid chromatography coupled with mass spectrometry; NMR, nuclear magnetic resonance; ESI-MS, electrospray ionization mass spectroscopy; TIC, total ion chromatogram; EIC, extracted ion chromatogram; BHT, butylated hydroxytoluene; PLA2, phospholipase A2; PC, phosphatidylcholine; PE, phosphatidylethanolamine; PI, phosphatidylinositol; PS, phosphatidylserine; LPL, lysophospholipid; LPC, lysophosphatidylcholine; LPE, lysophosphatidylethanolamine; LPI, lysophosphatidylinositol; Cer, ceramide; CAEP, ceramide 2-aminoethylphosphonate; TAG, triacylglycerol; SM, sphingomyelin; Cer-PE, sphingomyelin phosphoethanolamine; MGDG, monogalactosyldiacylglycerol; SQDG, sulfoquinovosyldiacylglycerol; TL, total lipid; PL, phospholipid; GPL, glycerophospholipid; SPL, sphingolipid; PnL, phosphonolipid; SPnL, sphingophosphonolipid; FA, fatty acid; SFA, saturated fatty acid; UFA, unsaturated fatty acid; MUFA, monounsaturated fatty acid; HUFA, highly unsaturated fatty acid; AA, arachidonic acid; EPA, eicosapentaenoic acid; DHA, docosahexenoic acid; LCB, long-chain base

■ REFERENCES

(1) Purcell, J. E.; Uye, S.-i.; Lo, W.-T. Anthropogenic causes of jellyfish blooms and their direct consequences for humans: a review. *Mar. Ecol.: Prog. Ser.* **2007**, *350*, 153.

(2) Uye, S.-i. Blooms of the giant jellyfish Nemopilema nomurai: a threat to the fisheries sustainability of the East Asian Marginal Seas. *Plankton Benthos. Res.* **2008**, *3*, 125−131.

(3) Richardson, A. J.; Bakun, A.; Hays, G. C.; Gibbons, M. J. The jellyfish joyride: causes, consequences and management responses to a more gelatinous future. *Trends Ecol. Evol.* **2009**, *24*, 312−322.

(4) Dong, Z.; Liu, D.; Keesing, J. K. Jellyfish blooms in China: dominant species, causes and consequences. *Mar. Pollut. Bull.* **2010**, *60*, 954−963.

(5) Pitt, K. A.; Lucas, C. H. *Jellyfish Blooms*; Springer: Berlin, Germany, 2014.

(6) Holland, D.; Davenport, J.; East, J. The fatty acid composition of the leatherback turtle Dermochelys coriacea and its jellyfish prey. *J. Mar. Biol. Assoc. U. K.* **1990**, *70*, 761−770.

(7) Hooper, S.; Paradis, M.; Ackman, R. G. Distribution oftrans-6-hexadecenoic acid, 7-methyl-7-hexadecenoic acid and common fatty acids in lipids of the ocean sunfish *Mola mola*. *Lipids* **1973**, *8*, 509−516.

(8) Dadzie, B. S.; Abou-Seedo, F.; Al-Qattan, E. The food and feeding habits of the silver pomfret, *Pampus argenteus* (Euphrasen), in Kuwait waters. *J. Appl. Ichthyol.* **2000**, *16*, 61−67.

(9) Miyajima, Y.; Masuda, R.; Kurihara, A.; Kamata, R.; Yamashita, Y.; Takeuchi, T. Juveniles of threadsail filefish, *Stephanolepis cirrhifer*,

DOI: 10.1021/acs.jafc.5b03145
J. Agric. Food Chem. 2015, 63, 8283−8291

can survive and grow by feeding on moon jellyfish *Aurelia aurita*. *Fish. Sci.* **2011**, *77*, 41−48.
(10) Wakabayashi, K.; Sato, R.; Ishii, H.; Akiba, T.; Nogata, Y.; Tanaka, Y. Culture of phyllosomas of *Ibacus novemdentatus* (Decapoda: Scyllaridae) in a closed recirculating system using jellyfish as food. *Aquaculture* **2012**, *330*, 162−166.
(11) Wu, B. Hai-tsue (*Rhopilema esculentum*). *Sheng Fu Xie Tong Bao [Biol. Newsl.]* **1955**, *4*, 35−40.
(12) Ma, Y.-q.; Yu, X.; Huang, X.-h. Research status on medicinal and edible value of jellyfish. *Guangdong Agric. Sci.* **2009**, *9*, 052.
(13) Hsieh, Y. P.; Rudloe, J. Potential of utilizing jellyfish as food in Western countries. *Trends Food Sci. Technol.* **1994**, *5*, 225−229.
(14) Dong, J.; Jiang, L.-x.; Tan, K.-f.; Liu, H.-y.; Purcell, J. E.; Li, P.-j.; Ye, C.-c. Stock enhancement of the edible jellyfish (*Rhopilema esculentum* Kishinouye) in Liaodong Bay, China: a review. *Hydrobiologia* **2009**, *616*, 113−118.
(15) Liu, C.-s.; Chen, S.-q.; Zhuang, Z.-m.; Yan, J.-p.; Liu, C.-l.; Cui, H.-t. Potential of utilizing jellyfish as food in culturing *Pampus argenteus* juveniles. *Hydrobiologia* **2015**, *754*, 189−200.
(16) Dowhan, W.; Bogdanov, M. Functional roles of lipids in membranes. *New Compr. Biochem.* **2002**, *36*, 1−35.
(17) Eyster, K. M. The membrane and lipids as integral participants in signal transduction: lipid signal transduction for the non-lipid biochemist. *Adv. Phys. Educ.* **2007**, *31*, 5−16.
(18) Lucas, C. Biochemical composition of *Aurelia aurita* in relation to age and sexual maturity. *J. Exp. Mar. Biol. Ecol.* **1994**, *183*, 179−192.
(19) Mukhamedova, K. S.; Glushenkova, A. Natural phosphonolipids. *Chem. Nat. Compd.* **2000**, *36*, 329−341.
(20) Kariotoglou, D. M.; Mastronicolis, S. K. Sphingophosphonolipids, phospholipids, and fatty acids from Aegean jellyfish *Aurelia aurita*. *Lipids* **2001**, *36*, 1255−1264.
(21) Kariotoglou, D. M.; Mastronicolis, S. K. Sphingophosphonolipid molecular species from edible mollusks and a jellyfish. *Comp. Biochem. Physiol., Part B: Biochem. Mol. Biol.* **2003**, *136*, 27−44.
(22) de Souza, L. M.; Iacomini, M.; Gorin, P. A.; Sari, R. S.; Haddad, M. A.; Sassaki, G. L. Glyco-and sphingophosphonolipids from the medusa *Phyllorhiza punctata*: NMR and ESI-MS/MS fingerprints. *Chem. Phys. Lipids* **2007**, *145*, 85−96.
(23) Jessome, L. L.; Volmer, D. A. Ion suppression: a major concern in mass spectrometry. *LC−GC N. Am.* **2006**, *24*, 498.
(24) Yan, X.; Xu, J.; Chen, J.; Chen, D.; Xu, S.; Luo, Q.; Wang, Y. Lipidomics focusing on serum polar lipids reveals species dependent stress resistance of fish under tropical storm. *Metabolomics* **2012**, *8*, 299−309.
(25) Li, S.; Xu, J.; Chen, J.; Chen, J.; Zhou, C.; Yan, X. The major lipid changes of some important diet microalgae during the entire growth phase. *Aquaculture* **2014**, *428*, 104−110.
(26) Liebisch, G.; Drobnik, W.; Reil, M.; Trümbach, B.; Arnecke, R.; Olgemöller, B.; Roscher, A.; Schmitz, G. Quantitative measurement of different ceramide species from crude cellular extracts by electrospray ionization tandem mass spectrometry (ESI-MS/MS). *J. Lipid Res.* **1999**, *40*, 1539−1546.
(27) Rainville, P. D.; Stumpf, C. L.; Shockcor, J. P.; Plumb, R. S.; Nicholson, J. K. Novel application of reversed-phase UPLC-oaTOF-MS for lipid analysis in complex biological mixtures: a new tool for lipidomics. *J. Proteome Res.* **2007**, *6*, 552−558.
(28) Yan, X.; Li, H.; Xu, J.; Zhou, C. Analysis of phospholipids in microalga *Nitzschia closterium* by UPLC-Q-TOF-MS. *Chin. J. Oceanol. Limnol.* **2010**, *28*, 106−112.
(29) Li, S.; Xu, J.; Chen, J.; Chen, J.; Zhou, C.; Yan, X. Structural elucidation of co-eluted triglycerides in the marine diatom model organism *Thalassiosira pseudonana* by ultra-performance liquid chromatography/quadrupole time-of-flight mass spectrometry. *Rapid Commun. Mass Spectrom.* **2014**, *28*, 245−255.
(30) Hoffmann, G.; Schmidt, D.; Bastian, B.; Guder, W. Photometric determination of phospholipase A. *Clin. Chem. Lab. Med.* **1986**, *24*, 871−876.
(31) Bradford, M. M. A rapid and sensitive method for the quantitation of microgram quantities of protein utilizing the principle of protein-dye binding. *Anal. Biochem.* **1976**, *72*, 248−254.
(32) Hvattum, E.; Hagelin, G.; Larsen, Å. Study of mechanisms involved in the collision-induced dissociation of carboxylate anions from glycerophospholipids using negative ion electrospray tandem quadrupole mass spectrometry. *Rapid Commun. Mass Spectrom.* **1998**, *12*, 1405−1409.
(33) Hannun, Y. A.; Obeid, L. M. Many ceramides. *J. Biol. Chem.* **2011**, *286*, 27855−27862.
(34) Young, M. M.; Kester, M.; Wang, H.-G. Sphingolipids: regulators of crosstalk between apoptosis and autophagy. *J. Lipid Res.* **2013**, *54*, 5−19.
(35) Xu, J.; Chen, D.; Yan, X.; Chen, J.; Zhou, C. Global characterization of the photosynthetic glycerolipids from a marine diatom *Stephanodiscus* sp. by ultra performance liquid chromatography coupled with electrospray ionization-quadrupole-time of flight mass spectrometry. *Anal. Chim. Acta* **2010**, *663*, 60−68.
(36) Sommer, U.; Herscovitz, H.; Welty, F. K.; Costello, C. E. LC-MS-based method for the qualitative and quantitative analysis of complex lipid mixtures. *J. Lipid Res.* **2006**, *47*, 804−814.
(37) Cole, L. K.; Vance, J. E.; Vance, D. E. Phosphatidylcholine biosynthesis and lipoprotein metabolism. *Biochim. Biophys. Acta, Mol. Cell Biol. Lipids* **2012**, *1821*, 754−761.
(38) Zeisel, S. H.; Char, D.; Sheard, N. F. Choline, phosphatidylcholine and sphingomyelin in human and bovine milk and infant formulas. *J. Nutr.* **1986**, *116*, 50−58.
(39) Vance, J. E.; Tasseva, G. Formation and function of phosphatidylserine and phosphatidylethanolamine in mammalian cells. *Biochim. Biophys. Acta, Mol. Cell Biol. Lipids* **2013**, *1831*, 543−554.
(40) Tapiero, H.; Ba, G. N.; Couvreur, P.; Tew, K. Polyunsaturated fatty acids (PUFA) and eicosanoids in human health and pathologies. *Biomed. Pharmacother.* **2002**, *56*, 215−222.
(41) Fleith, M.; Clandinin, M. Dietary PUFA for preterm and term infants: review of clinical studies. *Crit. Rev. Food Sci. Nutr.* **2005**, *45*, 205−229.
(42) Little, S.; Lynch, M.; Manku, M.; Nicolaou, A. Docosahexaenoic acid-induced changes in phospholipids in cortex of young and aged rats: a lipidomic analysis. *Prostaglandins, Leukotrienes Essent. Fatty Acids* **2007**, *77*, 155−162.
(43) Bezard, J.; Blond, J.; Bernard, A.; Clouet, P. The metabolism and availability of essential fatty acids in animal and human tissues. *Reprod., Nutr., Dev.* **1994**, *34*, 539−568.
(44) Suprayudi, M. A.; Takeuchi, T.; Hamasaki, K. Effects of *Artemia* enriched with eicosapentaenoic and docosahexaenoic acid on survival and occurrence of molting failure in megalop larvae of the mud crab *Scylla serrata*. *Fish. Sci.* **2004**, *70*, 650−658.
(45) Xu, X.; Ji, W.; Castell, J. D.; O'Dor, R. The nutritional value of dietary n-3 and n-6 fatty acids for the Chinese prawn (*Penaeus chinensis*). *Aquaculture* **1993**, *118*, 277−285.
(46) Hossain, M. A.; Almatar, S. M.; James, C. M. Effects of varying dietary docosahexaenoic acid levels on growth, proximate composition and tissue fatty acid profile of juvenile silver pomfrets, *Pampus argenteus* (Euphrasen, 1788). *Aquacult. Res.* **2012**, *43*, 1599−1610.
(47) Corda, D.; Zizza, P.; Varone, A.; Bruzik, K.; Mariggi, S. The glycerophosphoinositols and their cellular functions. *Biochem. Soc. Trans.* **2012**, *40*, 101−107.
(48) Leventis, P. A.; Grinstein, S. The distribution and function of phosphatidylserine in cellular membranes. *Annu. Rev. Biophys.* **2010**, *39*, 407−427.
(49) Heinrichs, S. C. Dietary ω-3 fatty acid supplementation for optimizing neuronal structure and function. *Mol. Nutr. Food Res.* **2010**, *54*, 447−456.
(50) Hori, T.; Sugita, M. Chemistry of phosphonolipids. *Biochem. Nat. CP Compd.* **1984**, 124−144.
(51) Nakhel, I. C.; Mastronicolis, S. K.; Miniadis-Meimaroglou, S. Phospho-and phosphonolipids of the Aegean pelagic scyphomedusa

DOI: 10.1021/acs.jafc.5b03145
J. Agric. Food Chem. 2015, 63, 8283−8291

Pelagia noctiluca. *Biochim. Biophys. Acta, Lipids Lipid Metab.* **1988**, *958*, 300−307.
(52) Slotte, J. P. Biological functions of sphingomyelins. *Prog. Lipid Res.* **2013**, *52*, 424−437.
(53) Komatsu, M.; Ichiyama, N.; Kurimoto, T.; Takumi, S.; Shiozaki, K.; Sugiyama, Y.; Furukawa, T.; Ando, S.; Itonori, S.; Saito, H. Ceramide aminoethylphosphonate from jumbo flying squid *Dosidicus gigas* attenuates the toxicity of cyanotoxin microcystin-LR. *Fish. Sci.* **2013**, *79*, 313−320.
(54) Merrill, A. H., Jr. Cell regulation by sphingosine and more complex sphingolipids. *J. Bioenerg. Biomembr.* **1991**, *23*, 83−104.
(55) Burke, J. E.; Dennis, E. A. Phospholipase A2 biochemistry. *Cardiovasc. Drugs Ther.* **2009**, *23*, 49−59.
(56) Hardman, A. E. The influence of exercise on postprandial triacylglycerol metabolism. *Atherosclerosis* **1998**, *141*, S93−S100.

DOI: 10.1021/acs.jafc.5b03145
J. Agric. Food Chem. 2015, 63, 8283−8291

and DM were suspended in aqueous 0.15 M NaCl before administration in mice.

Animals and Treatment. Male mice (21 ± 1 g, 7 weeks old) were obtained from Kunming Institute of Zoology. The mice were treated as described previously.[30] All animal experiments were done in compliance with Animal Ethical Committee of University of Science and Technology of China. Sixty male mice were divided randomly into six groups: one control group (0.15 M NaCl) and five experimental groups (50 mg/kg BW nano ZnO, 50 mg/kg BW bulk ZnO, 15 mg/kg BW DM, 50 mg/kg BW nano ZnO + 15 mg/kg BW DM, and 50 mg/kg BW bulk ZnO + 15 mg/kg BW DM). The animals were intragastrically administered with chemicals at a dose of 0.1 mL/10 g BW, respectively, for 14 consecutive days. After 2 weeks, the samples of blood were collected from the tail vein after the mice were anaesthetized by ether. The brain, heart, lung, liver, kidney, and spleen were excised, washed with 0.15 M NaCl, and weighed for determination of the coefficients of organs.

Serum Biochemical Parameters Assay. Liver function was determined by the serum levels of lactate dehydrogenase (LDH), alanine aminotransferase (ALT), aspartate aminotransferase (AST), total bilirubin (TBIL), alkaline phosphatase (ALP), total protein (TP), albumin protein (ALB), and albumin/globulin (A/G). Nephrotoxicity was evaluated with creatinine (CRE) and blood urea nitrogen (BUN). All of the biochemical parameters were determined by an automatic biochemical analyzer (Roche Modular DPP System) using commercial kits (Roche Diagnostics, Mannheim, Germany).

Histopathological Examination. Tissues of the kidney, liver, heart, lung, brain, and spleen were recovered from the necropsy. Their histological examinations were performed using an optical microscope as described previously.[30]

Measurement of Oxidative Stress Makers. The kidney and liver tissues were assayed for the malondialdehyde (MDA) level and the activities of superoxide dismutase (SOD), catalase (CAT), and glutathione peroxide (GPx) using the commercial kits (Nanjing Jiancheng Bioeng Inst.) as described previously.[30]

Measurement of ChE Activity. ChE activity was determined in liver tissue by the hydroxylamine–ferric chloride method using acetylcholine as a substrate.[31] The rate of acetylcholine hydrolysis was determined through the measurement of the remaining acetylcholine after hydrolysis catalyzed by ChE. The remaining acetylcholine reacted with NH_2OH to form acethydroximic acid, which reacted with Fe^{3+} to produce the purple-brown color of the ferric–acethydroximic acid compound. This compound could be spectrophotometrically determined at 520 nm. One unit of ChE activity is the amount of protein that decomposes 60 μmol of acetylcholine per hour at 37 °C.

Analysis of Biodistributions of Zn and DM. The liver, kidney, heart, lung, brain, or spleen tissue (~0.2 g) was digested with ultrapure HNO_3 solution for 12 h. The solutions were then mixed with 0.5 mL of H_2O_2 and heated at 130 °C to remove the remaining HNO_3. The remaining solutions were diluted to 5 mL with 2% (v/v) HNO_3. The Zn contents in the solutions were measured by inductively coupled plasma-atomic emission spectrometry (ICP-AES) (Optima 7300 DV, PerkinElmer Corp.). The DM contents in the organs were measured by gas chromatography–mass spectrometry (GC–MS).[32] The liver, kidney, heart, lung, brain, or spleen tissue (0.1–0.2 g) was homogenized and centrifuged at 4500 rpm for 25 min at 4 °C. The supernatant was added to a CNWBOND C18 SPE column. The column was washed with 10 mL of 5% CH_3OH and then eluted with 10 mL of CH_3OH. The eluate was evaporated to dryness by a nitrogen stream at 25 °C. The dry extract was dissolved in 50 μL of CH_3OH, and 1 μL of the solution was injected into a Thermo Trace GC-ISQ MS system (Thermo Fisher Scientific).

Assays for Stability of Nanoparticles. To evaluate the stability of nanoparticles in the stomach of mice, 5–40 mg of nano ZnO or bulk ZnO was incubated with 5 mL of artificial gastric fluid (AGF) (0.32% pepsin, 0.2% NaCl, pH 1.5) with gentle shaking for up to 4 h at 37 °C. Supernatants were collected after centrifugation at 12 000*g* for 20 min. The Zn concentration in supernatants was determined by ICP-AES.

Statistical Analysis. Data were analyzed by one-way analysis of variance (ANOVA) test by using SPSS 18.0 software (SPSS Inc.). The statistical significance was set at $p < 0.05$ for all tests.

RESULTS AND DISCUSSION

Coefficients of Organs. No abnormal daily behaviors were seen in the control, nano ZnO, and bulk ZnO groups during the entire experimental period. A few signs of acute organophosphate poisoning, including anorexia and reduced activity, were observed in the DM group. The mice coadministrated with DM and nano or bulk ZnO showed varying degrees of signs such as loss of appetite, mild tremor, and piloerection. As shown in Figure 1, the body weights of the mice in the nano and bulk ZnO groups increased a little more slowly than those in the control group, whereas the body weight of mice administrated with DM increased much more slowly, as compared with the control. Co-administration of DM with nano or bulk ZnO had a significantly enhanced adverse effect on the weight gain. As shown in Table 1, compared with the control, the coefficients of the liver of the nano and bulk ZnO groups did not change significantly, but a significantly higher coefficient of the liver was observed in the DM group ($p < 0.05$). In the nano ZnO + DM group, a significant increase was seen in the coefficient ($p < 0.05$) of the liver compared with either the nano ZnO or the DM group, revealing that nano ZnO and DM enhanced each other in affecting the coefficient of the liver. Similarly, co-administration of DM with bulk ZnO also had an enhanced influence on the coefficient of the liver. Compared with the control, the coefficients of the brain, kidney, heart, lung, and spleen of all exposure groups did not change significantly.

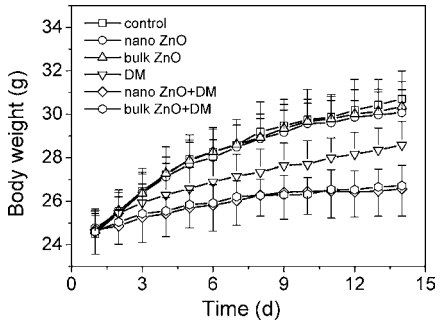

Figure 1. Changes of the body weight in mice ($n = 10$) during the administration period.

Combined Effects on Biodistributions of Zn and DM. Figure 2A shows the biodistribution of Zn in the mice after administration with nano or bulk ZnO and/or DM. A major percentage of Zn accumulated in the liver, lung, and spleen of mice after oral administration with nano or bulk ZnO. The biodistribution of Zn in the DM group was similar to that in the control group. Co-administration with nano ZnO and DM significantly increased the biodistribution densities of Zn in the liver and lung ($p < 0.05$) compared to the nano ZnO group. Similarly, co-administration with bulk ZnO and DM also significantly increased the biodistribution densities of Zn in the liver and lung compared to the bulk ZnO group. DM is lipophilic in nature and prone to interacting with the cell membrane, which results in a disturbance in the phospholipids bilayer structure,[33] allowing Zn^{2+} to easily pass through the membrane and distribute into the tissues. As a result, DM

DOI: 10.1021/acs.jafc.5b01979
J. Agric. Food Chem. 2015, 63, 8292–8298

Table 1. Coefficients of the Major Organs in Mice[a]

index	control	nano ZnO	bulk ZnO	DM	nano ZnO + DM	bulk ZnO + DM
liver/BW (mg/g)	54.8 ± 1.9	55.8 ± 1.8	55.3 ± 1.5	60.1 ± 1.7[b]	64.3 ± 3.3[b,c,d]	63.9 ± 2.2[b,e,d]
kidney/BW (mg/g)	14.2 ± 0.5	14.5 ± 0.6	14.2 ± 0.3	14.5 ± 0.5	14.8 ± 0.5	14.6 ± 0.4
heart/BW (mg/g)	4.53 ± 0.35	4.45 ± 0.28	4.49 ± 0.32	4.46 ± 0.29	4.52 ± 0.27	4.55 ± 0.24
lung/BW (mg/g)	7.96 ± 0.24	8.56 ± 0.56	8.90 ± 0.41	8.64 ± 0.36	9.02 ± 0.56	9.21 ± 0.51
spleen/BW (mg/g)	4.42 ± 0.68	4.38 ± 0.35	4.54 ± 0.38	4.38 ± 0.46	4.50 ± 0.39	4.49 ± 0.52
brain/BW (mg/g)	18.3 ± 1.6	18.6 ± 1.1	17.9 ± 0.7	18.3 ± 0.6	18.7 ± 0.5	18.1 ± 0.8

[a]The mice were intragastrically administered with nano or bulk ZnO and/or DM for 14 days. Data shown are means ± SD (n = 10). [b]$p < 0.05$ vs the control. [c]$p < 0.05$ vs the nano ZnO group. [d]$p < 0.05$ vs the DM group. [e]$p < 0.05$ vs the bulk ZnO.

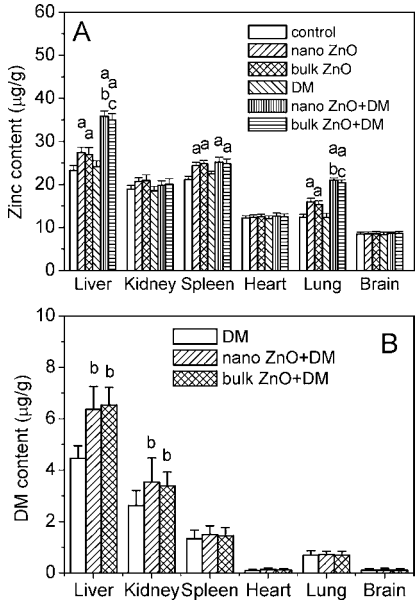

Figure 2. Biodistributions of DM and Zn in the mice tissues determined by GC−MS and ICP-AES. The male mice were intragastrically administered with nano or bulk ZnO and/or DM for 14 days. (A) The Zn contents in the different tissues of the mice. (B) The DM contents in different tissues of mice. Statistical significance: a, $p < 0.05$ vs the control; b, $p < 0.05$ vs the nano ZnO (A) or DM (B) group. Values represent means ± SD, n = 10.

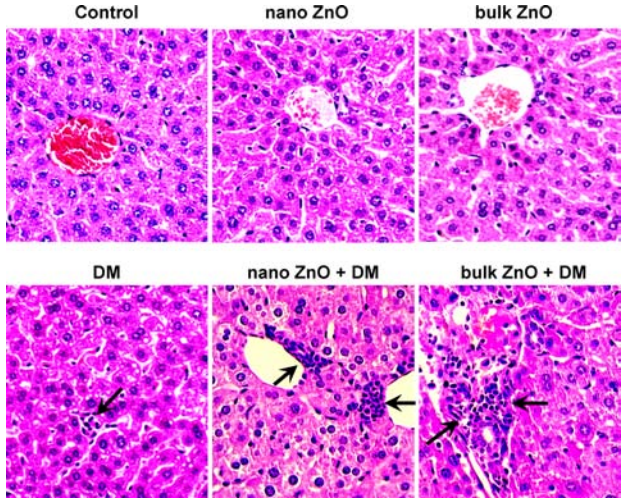

Figure 3. Pathological images of the mice liver tissue following daily intragastrical administrations of nano or bulk ZnO and/or DM for 14 days. No abnormalities were seen in the control, bulk ZnO, and nano ZnO groups. In the DM group, the infiltration of inflammatory cells (arrow) was seen around the central vein. In the nano ZnO + DM and bulk ZnO + DM groups, multiple areas of spotty necrosis (arrows) were induced around the central vein.

significantly increases the biodistribution density of Zn in mice liver.

As shown in Figure 2B, the majority of DM was accumulated in the liver, kidney, and spleen after administration with DM. Interestingly, co-administration with nano ZnO and DM significantly increased DM accumulation in the liver and kidney compared to the DM group. Similarly, coexposure to bulk ZnO and DM also significantly increased DM accumulation in the liver and kidney compared to the DM group. These results together indicate that co-administration of DM and nano or bulk ZnO results in the enhanced accumulation of Zn and DM in the liver.

Effects of Co-Administration on Pathological Changes in Tissues. As shown in Figure 3, in the nano and bulk ZnO groups, no abnormalities were observed in the liver. In the DM group, the infiltration of inflammatory cells around the central vein was observed in the liver. In the nano ZnO + DM group, multiple areas of spotty necrosis were found in the liver. These results indicate that co-administration with nano ZnO and DM induces more pathological damage in the liver than administration of either nano ZnO or DM alone, which is attributed to the co-administration-induced increases in the accumulation of DM and Zn in the liver. Similarly, multiple areas of spotty necrosis were also found in the liver in the bulk ZnO + DM group, indicating that co-administration with bulk ZnO and DM also increased DM-induced pathological damages in the liver. Compared with the control, no apparent abnormal changes were found in the cellular structures of heart, spleen, kidney, brain, and lung tissues in all administrated mice (Figure S2, SI).

Effects of Co-Administration on Liver and Kidney Functions. The combined toxicity of nano ZnO and DM in mice was analyzed by a blood biochemical assay. As shown in Table 2, administration with nano or bulk ZnO did not significantly effect the serum biochemical parameters of mice, except that their LDH that significantly increased ($p < 0.05$) compared with the control value, revealing that nano or bulk ZnO did not influence the kidney function but slightly influenced the liver function. On the contrary, administration with DM significantly increased the AST, ALP, LDH, and TBIL levels compared with the control ($p < 0.05$), indicating DM-induced liver dysfunction. Co-administration with nano ZnO and DM significantly increased the AST, ALT, ALP, LDH, and TBIL levels ($p < 0.05$), compared with either the nano ZnO or the DM group, suggesting that co-administration with nano ZnO and DM had an enhanced influence on the liver dysfunction, which is attributed to the co-administration-induced synergistic accumulation of DM and Zn in the liver.

DOI: 10.1021/acs.jafc.5b01979
J. Agric. Food Chem. 2015, 63, 8292−8298

Table 2. Changes in Biochemical Parameters in Mice Serum[a]

index	control	nano ZnO	bulk ZnO	DM	nano ZnO + DM	bulk ZnO + DM
AST (U/L)	93 ± 10	112 ± 9	109 ± 9	135 ± 14[b]	158 ± 16[b,c,e]	153 ± 12[b,d,e]
ALT (U/L)	31.2 ± 2.8	33.2 ± 4.8	31.9 ± 5.6	34.9 ± 7.1	62.0 ± 11.9[b,c,e]	60.3 ± 10.2[b,d,e]
ALP (U/L)	136 ± 15	139 ± 11	133 ± 17	174 ± 23[b]	218 ± 28[b,c,e]	226 ± 12[b,d,e]
LDH (U/L)	613 ± 23	809 ± 27[b]	797 ± 33[b]	838 ± 36[b]	987 ± 52[b,c,e]	973 ± 37[b,d,e]
TBIL (μmol/L)	0.98 ± 0.13	1.08 ± 0.11	1.03 ± 0.09	1.39 ± 0.12[b]	1.61 ± 0.08[b,c,e]	1.58 ± 0.16[b,d,e]
ALB (g/L)	36.4 ± 2.5	37.8 ± 1.9	36.9 ± 2.6	40.4 ± 2.3	39.5 ± 3.5	38.8 ± 3.4
TP (g/L)	52.4 ± 3.5	51.6 ± 2.9	52.8 ± 2.8	54.5 ± 3.9	52.6 ± 4.4	53.8 ± 3.1
CRE (μmol/L)	51.2 ± 3.2	50.8 ± 3.0	50.2 ± 2.2	49.5 ± 4.7	49.1 ± 2.8	50.7 ± 4.0
BUN (mmol/L)	8.63 ± 0.58	8.26 ± 0.36	8.94 ± 0.44	8.57 ± 0.39	8.73 ± 0.66	8.51 ± 0.45

[a]The mice were intragastrically administered with nano or bulk ZnO and/or DM for 14 days. Data shown are means ± SD (n = 10). [b]$p < 0.05$ vs the control. [c]$p < 0.05$ vs the nano ZnO group. [d]$p < 0.05$ vs the bulk ZnO group. [e]$p < 0.05$ vs the DM group.

Similarly, co-administration with bulk ZnO and DM also had an enhanced influence on the liver dysfunction. The significant increase in the LDH level was caused by hepatocellular necrosis after co-administration of nano or bulk ZnO with DM. The kidney function markers CRE and BUN did not change obviously in all administrated mice, suggesting that co-administration with nano or bulk ZnO and/or DM did not significantly influence the renal function.

Effects of Co-Administration on ChE Activity. The combined toxicity of nano ZnO and DM in mice was investigated by ChE assay. As reported previously, DM is a ChE inhibitor.[26,34] Figure 4 shows the ChE activities in the liver

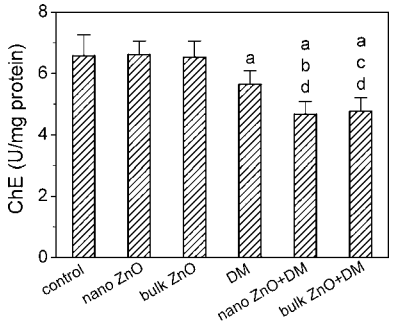

Figure 4. ChE activity of mice liver following daily intragastrical administrations of nano or bulk ZnO and/or DM for 14 days. Statistical significance: a, $p < 0.05$ vs the control; b, $p < 0.05$ vs the nano ZnO group; c, $p < 0.05$ vs the bulk ZnO; d, $p < 0.05$ vs the DM group. Values represent means ± SD, n = 10.

of the mice after administration with nano or bulk ZnO and/or DM. In the nano and bulk ZnO groups, the ChE activity did not significantly change compared with the control value. Administration with DM resulted in marked inhibition in the ChE activity in the liver. In the nano ZnO + DM group, ChE activity in the liver was significantly inhibited compared to either the nano ZnO or the DM group, revealing that nano ZnO significantly enhances the inhibition of the ChE activity by DM, which is attributed to an increase in DM and/or nano ZnO accumulation in the liver after co-administration with nano ZnO and DM. Similarly, co-administration with bulk ZnO and DM also significantly enhanced the inhibition of the ChE activity by DM.

Effects of Co-Administration on Oxidative Stress in Liver. The combined effect of co-administration of nano ZnO with DM on the oxidative damage in mice liver was investigated by analysis of the endogenous antioxidative enzymes, GPx, SOD, and CAT. Previous studies revealed that a decreased level of antioxidative enzyme is related to increased oxidative stress.[35] Figure 5 shows that administration with nano or bulk ZnO did not induce apparent oxidative stress in mice liver. On the contrary, administration with DM caused significant decreases in GPx and CAT activities in mice liver, indicating that DM induced significant oxidative stress in the liver. The oxidative stress is owing to a high accumulation of DM in the liver after administration with DM. It is worthwhile to note that administration with DM caused an increase of SOD activity in mice liver. The increased SOD activity is accounted for by a DM-activated compensatory mechanism.[36] Co-administration with nano ZnO and DM led to significant decreases ($p < 0.05$) in GPx, CAT, and SOD activities in mice liver compared to that in either nano ZnO or DM group, revealing that co-administration with nano ZnO and DM causes more severe oxidative stress in mice liver than administration with either nano ZnO or DM alone, which is attributed to the co-administration-induced enhanced accumulation of DM and Zn in the liver. Similarly, co-administration with bulk ZnO and DM also significantly enhanced the DM-caused oxidative stress in mice liver.

MDA is the final product of lipid peroxidation, and the MDA level indicates the level of oxidative damage in organs. Figure 5D shows that administration with nano or bulk ZnO did not significantly effect on the level of MDA in mice liver, compared to that in the control. By contrast, administration with DM induced a significant increase of the MDA level in mice liver ($p < 0.05$) than that in control group, indicating that the lipid peroxidation of the liver was induced by DM. The oxidative damage in mice liver resulted in its pathological change (Figure 3) and dysfunction (Table 2). Co-treatment with nano ZnO and DM resulted in a significantly higher concentration of MDA ($p < 0.05$) in mice liver compared to that in either the nano ZnO or the DM group, indicating an enhanced influence of nano ZnO and DM on lipid peroxidation in mice liver, which may be explained by the fact that DM and nano ZnO significantly enhanced the accumulation of each other in the liver. Similarly, co-administration with bulk ZnO and DM also significantly enhanced the DM-induced lipid peroxidation in the liver.

Stability of Nano or Bulk ZnO in Artificial Gastric Fluid. When nanoparticles are administrated orally to animals, the dissolution behaviors in gastric fluid should be checked. However, there are several conflicting results on the dissolution of nano ZnO in AGF. Seok et al. reported that around 98% of nano ZnO (40 nm) had dissolved in AGF (pH 1.7).[4] Cho et al. showed that all nano ZnO (89.3 nm) dissolved in AGF (pH 1.5) within 5 min.[8] However, Wang et al. found that only 3.3%

DOI: 10.1021/acs.jafc.5b01979
J. Agric. Food Chem. 2015, 63, 8292−8298

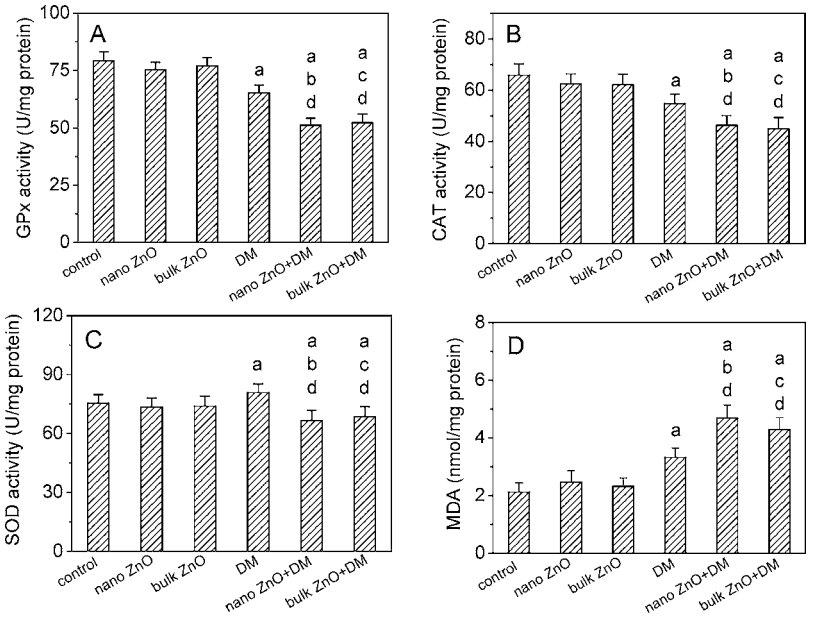

Figure 5. Activities of GPx, CAT, and SOD and the MDA level in the mice liver after daily intragastrical administrations with nano or bulk ZnO and/or DM for 14 days. Statistical significance: a, $p < 0.05$ vs the control; b, $p < 0.05$ vs the nano ZnO group; c, $p < 0.05$ vs the DM group; d, $p < 0.05$ vs the bulk ZnO. Data were shown as means ± SD ($n = 10$).

of nano ZnO (20 nm) had dissolved in AGF (pH 1.2).[37] Paek et al. demonstrated that about 13−14% of zinc ions in nano ZnO (20 and 70 nm) was released into the AGF (pH 1.5), and the release level was not influenced by size.[38] To analyze the stability of nano or bulk ZnO in gastric fluid, different amounts of bulk ZnO or nano ZnO were incubated with acidic AGF. When the concentration of bulk or nano ZnO was less than or equal to 5 mg/mL, the milk-white nano or bulk ZnO solution became clear within a few minutes after incubation with the AGF, indicating that all of nano or bulk ZnO mass had dissolved in the AGF. The ICP-AES data show that 98.4% of Zn^{2+} ions in nano ZnO and 97.8% of Zn^{2+} ions in bulk ZnO were released into supernatant after incubation of nano or bulk ZnO (5 mg/mL) with the AGF for 4 h (Figure 6B), further confirming that almost all of the nano or bulk ZnO dissolved in the AGF. However, when the concentration of nano or bulk ZnO exceeded 5 mg/mL, the milk-white nano or bulk ZnO solutions were still unclear after incubation with the AGF for 4 h, suggesting that only part of nano or bulk ZnO dissolved in the AGF. As shown in Figure 6A, the concentration of Zn^{2+} in AGF was almost constant with the increases of the concentrations of nano or bulk ZnO from 5 to 8 mg/mL, indicating that the dissolved Zn^{2+} concentration tended to equilibrium. These results reveal that the dissolution of bulk ZnO in AGF was similar to that of nano ZnO. Nano or bulk ZnO at low concentration (≤5 mg/mL) almost completely dissolved in the AGF. However, nano or bulk ZnO at high concentration (>5 mg/mL) partly dissolved in the AGF. The previous conflicting results on the dissolution of nano ZnO in AGF should be due to the concentrations of nano ZnO used in each experiment being different.[4,8,37,38]

In the present study, the concentration of administered nano or bulk ZnO was 0.5 mg/mL, which was much less than 5 mg/mL. After administration, the solution of nano or bulk ZnO was diluted with the gastric fluid and its concentration should further decrease. It appears that both bulk and nano ZnO administered by the oral route must dissolve completely in the

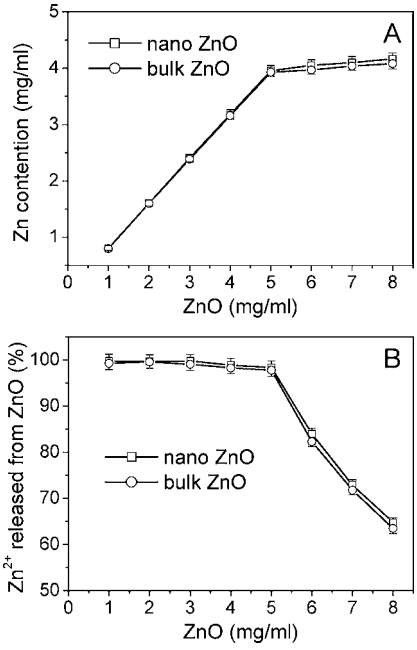

Figure 6. Zn^{2+} ions released from nano or bulk ZnO in AGF. The content of Zn^{2+} in AGF (A) and the percentage of dissolution of Zn^{2+} ion (B) were measured using ICP-AES after incubation of nano or bulk ZnO with the artificial gastric fluid (0.32% pepsin, 0.2% NaCl, pH 1.5) for 4 h. Data shown are means ± SD ($n = 3$).

stomach of mice. The dissolved Zn^{2+} ions will be absorbed through the small intestine and then enter into the systemic circulation.[39] The fast dissolution of both bulk and nano ZnO in acidic gastric fluid results in that bulk ZnO and nano ZnO have the nearly identical, slight effects on the liver function in the mice after oral administration, regardless of particle size. In addition, the results of the function and histopathology of mice liver show that both nano and bulk ZnO have nearly identical enhancement effects on the DM toxicity in the liver after oral

DOI: 10.1021/acs.jafc.5b01979
J. Agric. Food Chem. 2015, 63, 8292−8298

co-administration with DM. The data from the oxidative stress measurement and ChE activity assay also confirm that both nano and bulk ZnO have the nearly identical enhanced effects on DM-induced toxicity in mice liver.

Nano ZnO represents an important class of toxicant, because nano ZnO is unstable in aqueous solutions and releases Zn^{2+} and the high level of Zn^{2+} can induce oxidative stress inside cells.[40,41] It is well-known that free Zn^{2+} is highly reactive and toxic.[4] Our results demonstrated that oral administration of nano ZnO (30.1 nm) at a dose of 50 mg/kg BW for 14 days did not cause observable injury in mice, suggesting that most Zn^{2+} ions released from nano ZnO may form compounds with biomolecules and the amount of free Zn^{2+} is insufficient to cause injury in mice. However, Sharma et al. showed that oral administration of nano ZnO (30 nm) at a dose of 300 mg/kg BW for 14 consecutive days caused significant injury in mice liver.[27] Similarly, Esmaeillou et al. reported that exposure of nano ZnO (20−30 nm) through oral gavage at a single dose (333.33 mg/kg BW) had severe toxicological effects on the liver, kidney, and lung of mice.[42] These findings together with present results indicate that the low amount of nano ZnO is biocompatible; however, nano ZnO at high doses displays hazardous effects. Therefore, the content of nano ZnO in food and food supplements is the critical matter for its safe application.

Nano ZnO at low dose is safe for application in food and food supplements. However, in the case of coexposure with DM, our findings demonstrate that nano ZnO significantly enhances DM-induced damage in mice liver, which is attributed to the enhanced accumulation of Zn and DM in the liver. People may be exposed to nano ZnO and/or DM at different doses in different situations. The dose of nano ZnO or DM used in our experiments do not necessarily reflect the actual concentration of nano ZnO or DM found in real situations; however, the data can be used to assess the health risks from coexposure to nano ZnO and DM. In the present study, we have made the first attempt to evaluate the effect of nano ZnO on DM-induced toxicity in mice. Further evaluation of the combined toxicity of nano ZnO and DM in animals at various doses is needed.

In summary, although nano ZnO at a dose of 50 mg/kg BW is of low toxicity to male mice, co-administration with nano ZnO and DM significantly enhances DM-induced injury in mice liver, which is due to the enhanced accumulation of Zn and DM in mice liver. The increased accumulation of Zn and DM causes marked oxidative stress in mice liver, which results in severe liver damage. These findings suggest that close attention should be paid to the combined toxicity of nanoparticles and pesticides with the increasing use of nanomaterials in the world.

■ ASSOCIATED CONTENT

Supporting Information

The Supporting Information is available free of charge on the ACS Publications website at DOI: 10.1021/acs.jafc.5b01979.

TEM images of nano or bulk ZnO (Figure S1) and histopathological examination (Figure S2) (PDF)

■ AUTHOR INFORMATION

Corresponding Author

*Phone: + 8655163606082. Fax: + 8655163603388. E-mail: xuxl@ustc.edu.cn.

Author Contributions

X.Y. and R.R. contributed equally to this work.

Funding

This study was supported by grants from the National Natural Science Foundation of China (Grant Nos. 20571069, 20871111, 21171157).

Notes

The authors declare no competing financial interest.

■ ABBREVIATIONS USED

BW, body weight; DM, dimethoate; nano ZnO, ZnO nanoparticle; ALT, alanine aminotransferase; LDH, lactate dehydrogenase; AST, aspartate aminotransferase; TP, total protein; ALP, alkaline phosphatase; TBIL, total bilirubin; ALB, albumin protein; BUN, blood urea nitrogen; A/G, albumin/globulin; CRE, creatinine; MDA, malondialdehyde; ChE, cholinesterase; SOD, superoxide dismutase; GPx, glutathione peroxidase; CAT, catalase; BSA, bovine serum albumin; TEM, transmission electron microscopy; ICP-AES, inductive coupled plasma atomic emission spectrometer; ROS, reactive oxygen species; GC−MS, gas chromatography−mass spectrometry; AGF, artificial gastric fluid

■ REFERENCES

(1) Ng, K. W.; Khoo, S. P.; Heng, B. C.; Setyawati, M. I.; Tan, E. C.; Zhao, X.; Xiong, S.; Fang, W.; Leong, D. T.; Loo, J. S. The role of the tumor suppressor p53 pathway in the cellular DNA damage response to zinc oxide nanoparticles. *Biomaterials* **2011**, *32*, 8218−25.

(2) Zhang, P.; Liu, W. ZnO QD@PMAA-co-PDMAEMA nonviral vector for plasmid DNA delivery and bioimaging. *Biomaterials* **2010**, *31*, 3087−94.

(3) Liu, Y.; Ai, K.; Yuan, Q.; Lu, L. Fluorescence-enhanced gadolinium-doped zinc oxide quantum dots for magnetic resonance and fluorescence imaging. *Biomaterials* **2011**, *32*, 1185−92.

(4) Seok, S. H.; Cho, W. S.; Park, J. S.; Na, Y.; Jang, A.; Kim, H.; Cho, Y.; Kim, T.; You, J. R.; Ko, S.; Kang, B. C.; Lee, J. K.; Jeong, J.; Che, J. H. Rat pancreatitis produced by 13-week administration of zinc oxide nanoparticles: biopersistence of nanoparticles and possible solutions. *J. Appl. Toxicol.* **2013**, *33*, 1089−96.

(5) Sharma, V.; Anderson, D.; Dhawan, A. Zinc oxide nanoparticles induce oxidative DNA damage and ROS-triggered mitochondria mediated apoptosis in human liver cells (HepG2). *Apoptosis* **2012**, *17*, 852−70.

(6) Rashidi, L.; Khosravi-Darani, K. The applications of nanotechnology in food industry. *Crit. Rev. Food Sci. Nutr.* **2011**, *51*, 723−30.

(7) He, L.; Liu, Y.; Mustapha, A.; Lin, M. Antifungal activity of zinc oxide nanoparticles against Botrytis cinerea and Penicillium expansum. *Microbiol. Res.* **2011**, *166*, 207−15.

(8) Cho, W. S.; Kang, B. C.; Lee, J. K.; Jeong, J.; Che, J. H.; Seok, S. H. Comparative absorption, distribution, and excretion of titanium dioxide and zinc oxide nanoparticles after repeated oral administration. *Part. Fibre Toxicol.* **2013**, *10*, 9.

(9) Zhao, L.; Sun, Y.; Hernandez-Viezcas, J. A.; Servin, A. D.; Hong, J.; Niu, G.; Peralta-Videa, J. R.; Duarte-Gardea, M.; Gardea-Torresdey, J. L. Influence of CeO2 and ZnO nanoparticles on cucumber physiological markers and bioaccumulation of Ce and Zn: a life cycle study. *J. Agric. Food Chem.* **2013**, *61*, 11945−51.

(10) Gottschalk, F.; Sonderer, T.; Scholz, R. W.; Nowack, B. Modeled environmental concentrations of engineered nanomaterials (TiO(2), ZnO, Ag, CNT, Fullerenes) for different regions. *Environ. Sci. Technol.* **2009**, *43*, 9216−22.

(11) De Angelis, I.; Barone, F.; Zijno, A.; Bizzarri, L.; Russo, M. T.; Pozzi, R.; Franchini, F.; Giudetti, G.; Uboldi, C.; Ponti, J.; Rossi, F.; De Berardis, B. Comparative study of ZnO and TiO(2) nanoparticles:

DOI: 10.1021/acs.jafc.5b01979
J. Agric. Food Chem. 2015, 63, 8292−8298

physicochemical characterisation and toxicological effects on human colon carcinoma cells. *Nanotoxicology* **2013**, *7*, 1361−72.
(12) Fernandez-Cruz, M. L.; Lammel, T.; Connolly, M.; Conde, E.; Barrado, A. I.; Derick, S.; Perez, Y.; Fernandez, M.; Furger, C.; Navas, J. M. Comparative cytotoxicity induced by bulk and nanoparticulated ZnO in the fish and human hepatoma cell lines PLHC-1 and Hep G2. *Nanotoxicology* **2013**, *7*, 935−52.
(13) Shaymurat, T.; Gu, J.; Xu, C.; Yang, Z.; Zhao, Q.; Liu, Y. Phytotoxic and genotoxic effects of ZnO nanoparticles on garlic (Allium sativum L.): a morphological study. *Nanotoxicology* **2012**, *6*, 241−8.
(14) Croteau, M. N.; Dybowska, A. D.; Luoma, S. N.; Valsami-Jones, E. A novel approach reveals that zinc oxide nanoparticles are bioavailable and toxic after dietary exposures. *Nanotoxicology* **2011**, *5*, 79−90.
(15) Zhao, L. J.; Peralta-Videa, J. R.; Rico, C. M.; Hernandez-Viezcas, J. A.; Sun, Y. P.; Niu, G. H.; Servin, A.; Nunez, J. E.; Duarte-Gardea, M.; Gardea-Torresdey, J. L. CeO2 and ZnO Nanoparticles Change the Nutritional Qualities of Cucumber (Cucumis sativus). *J. Agric. Food Chem.* **2014**, *62*, 2752−2759.
(16) Priya, D. N.; Modak, J. M.; Trebse, P.; Zabar, R.; Raichur, A. M. Photocatalytic degradation of dimethoate using LbL fabricated TiO2/polymer hybrid films. *J. Hazard. Mater.* **2011**, *195*, 214−222.
(17) Ayed-Boussema, I.; Rjiba, K.; Moussa, A.; Mnasri, N.; Bacha, H. Genotoxicity associated with oxidative damage in the liver and kidney of mice exposed to dimethoate subchronic intoxication. *Environ. Sci. Pollut. Res.* **2012**, *19*, 458−66.
(18) Guo, R.; Ren, X.; Ren, H. A new method for analysis of the toxicity of organophosphorus pesticide, dimethoate on rotifer based on response surface methodology. *J. Hazard. Mater.* **2012**, *237*−*238*, 270−6.
(19) Ben Amara, I.; Soudani, N.; Troudi, A.; Bouaziz, H.; Boudawara, T.; Zeghal, N. Antioxidant effect of vitamin E and selenium on hepatotoxicity induced by dimethoate in female adult rats. *Ecotoxicol. Environ. Saf.* **2011**, *74*, 811−9.
(20) Feng, Z.; Sun, X.; Yang, J.; Hao, D.; Du, L.; Wang, H.; Xu, W.; Zhao, X.; Sun, C. Metabonomics analysis of urine and plasma from rats given long-term and low-dose dimethoate by ultra-performance liquid chromatography-mass spectrometry. *Chem.-Biol. Interact.* **2012**, *199*, 143−53.
(21) Soler, J.; Santos-Juanes, L.; Miro, P.; Vicente, R.; Arques, A.; Amat, A. M. Effect of organic species on the solar detoxification of water polluted with pesticides. *J. Hazard. Mater.* **2011**, *188*, 181−7.
(22) Athanasopoulos, P.; Kyriakidis, N. B.; Georgitsanakou, I. Effect of storage temperature on the degradation of dimethoate in fortified orange and peach juices. *J. Agric. Food Chem.* **2000**, *48*, 4896−9.
(23) Karanasios, E.; Tsiropoulos, N. G.; Karpouzas, D. G.; Ehaliotis, C. Degradation and adsorption of pesticides in compost-based biomixtures as potential substrates for biobeds in southern Europe. *J. Agric. Food Chem.* **2010**, *58*, 9147−56.
(24) Zhao, Q.; Lu, Q.; Yu, Q. W.; Feng, Y. Q. Dispersive microextraction based on ″magnetic water″ coupled to gas chromatography/mass spectrometry for the fast determination of organophosphorus pesticides in cold-pressed vegetable oils. *J. Agric. Food Chem.* **2013**, *61*, 5397−403.
(25) Wang, X.; Qiao, X.; Ma, Y.; Zhao, T.; Xu, Z. Simultaneous determination of nine trace organophosphorous pesticide residues in fruit samples using molecularly imprinted matrix solid-phase dispersion followed by gas chromatography. *J. Agric. Food Chem.* **2013**, *61*, 3821−7.
(26) Karalliedde, L. Organophosphorus poisoning and anaesthesia. *Anaesthesia* **1999**, *54*, 1073−88.
(27) Sharma, V.; Singh, P.; Pandey, A. K.; Dhawan, A. Induction of oxidative stress, DNA damage and apoptosis in mouse liver after sub-acute oral exposure to zinc oxide nanoparticles. *Mutat. Res., Genet. Toxicol. Environ. Mutagen.* **2012**, *745*, 84−91.
(28) Tezvergil-Mutluay, A.; Carvalho, R. M.; Pashley, D. H. Hyperzincemia from ingestion of denture adhesives. *J. Prosthet. Dent.* **2010**, *103*, 380−3.
(29) Sharma, Y.; Bashir, S.; Irshad, M.; Nag, T. C.; Dogra, T. D. Dimethoate-induced effects on antioxidant status of liver and brain of rats following subchronic exposure. *Toxicology* **2005**, *215*, 173−81.
(30) Guo, M.; Xu, X.; Yan, X.; Wang, S.; Gao, S.; Zhu, S. In vivo biodistribution and synergistic toxicity of silica nanoparticles and cadmium chloride in mice. *J. Hazard. Mater.* **2013**, *260*, 780−788.
(31) Hestrin, S. The reaction of acetylcholine and other carboxylic acid derivatives with hydroxylamine, and its analytical application. *J. Biol. Chem.* **1949**, *180*, 249−61.
(32) Raposo, R.; Barroso, M.; Fonseca, S.; Costa, S.; Queiroz, J. A.; Gallardo, E.; Dias, M. Determination of eight selected organophosphorus insecticides in postmortem blood samples using solid-phase extraction and gas chromatography/mass spectrometry. *Rapid Commun. Mass Spectrom.* **2010**, *24*, 3187−3194.
(33) Amara, I. B.; Soudani, N.; Troudi, A.; Hakim, A.; Zeghal, K. M.; Boudawara, T.; Zeghal, N. Dimethoate induced oxidative damage and histopathological changes in lung of adult rats: modulatory effects of selenium and/or vitamin E. *Biomed Environ. Sci.* **2012**, *25*, 340−51.
(34) Sayim, F. Dimethoate-induced biochemical and histopathological changes in the liver of rats. *Exp. Toxicol. Pathol.* **2007**, *59*, 237−243.
(35) Xu, B.; Xu, Z. F.; Deng, Y.; Yang, J. H. Protective effects of Chlorpromazine and Verapamil against cadmium-induced kidney damage in vivo. *Exp. Toxicol. Pathol.* **2010**, *62*, 27−34.
(36) Prakasam, A.; Sethupathy, S.; Lalitha, S. Plasma and RBCs antioxidant status in occupational male pesticide sprayers. *Clin. Chim. Acta* **2001**, *310*, 107−112.
(37) Wang, B.; Feng, W. Y.; Wang, M.; Wang, T. C.; Gu, Y. Q.; Zhu, M. T.; Ouyang, H.; Shi, J. W.; Zhang, F.; Zhao, Y. L.; Chai, Z. F.; Wang, H. F.; Wang, J. Acute toxicological impact of nano- and submicro-scaled zinc oxide powder on healthy adult mice. *J. Nanopart. Res.* **2008**, *10*, 263−276.
(38) Paek, H. J.; Lee, Y. J.; Chung, H. E.; Yoo, N. H.; Lee, J. A.; Kim, M. K.; Lee, J. K.; Jeong, J.; Choi, S. J. Modulation of the pharmacokinetics of zinc oxide nanoparticles and their fates in vivo. *Nanoscale* **2013**, *5*, 11416−27.
(39) Wang, J.; Chen, Y.; Chen, B.; Ding, J.; Xia, G.; Gao, C.; Cheng, J.; Jin, N.; Zhou, Y.; Li, X.; Tang, M.; Wang, X. M. Pharmacokinetic parameters and tissue distribution of magnetic Fe(3)O(4) nanoparticles in mice. *Int. J. Nanomed.* **2010**, *5*, 861−6.
(40) Chang, Y. N.; Zhang, M. Y.; Xia, L.; Zhang, J.; Xing, G. M. The Toxic Effects and Mechanisms of CuO and ZnO Nanoparticles. *Materials* **2012**, *5*, 2850−2871.
(41) Gilbert, B.; Fakra, S. C.; Xia, T.; Pokhrel, S.; Madler, L.; Nel, A. E. The fate of ZnO nanoparticles administered to human bronchial epithelial cells. *ACS Nano* **2012**, *6*, 4921−30.
(42) Esmaeillou, M.; Moharamnejad, M.; Hsankhani, R.; Tehrani, A. A.; Maadi, H. Toxicity of ZnO nanoparticles in healthy adult mice. *Environ. Toxicol. Pharmacol.* **2013**, *35*, 67−71.

DOI: 10.1021/acs.jafc.5b01979
J. Agric. Food Chem. 2015, 63, 8292−8298

an important task to ameliorate the condition of allergic patients.

The selection of wheat varieties expressing low or no concentrations of allergens is presently underway.[8] This is favored by the wide biodiversity of the genus *Triticum*. Indeed, differences in the IgE-binding capacity of certain wheat varieties have been observed in patients affected by baker's asthma[9−11] and food allergy,[10,12−14] including WDEIA. Although a certain degree of variability in the allergenic potency of the various cultivars was shown, previous works failed to find reliable hypoallergenic candidates. With regard to baker's asthma, the polysensitization profile of patients is one of the limiting factors.[15] Although sensitization is usually limited to ω-5 gliadins,[16] as far as food allergy is concerned, no wheat varieties expressing this allergen have been identified thus far, except for a translocated wheat, in which part of the short arm of the 1B chromosome was replaced with a portion of the short arm of the 1R chromosome of rye.[12] Finally, no study has specifically evaluated the immunoreactivity of different wheat varieties *in vivo* [i.e., by skin prick test (SPT)].

ω-5 gliadins, which are encoded at the Gli-B1 locus present in the B chromosome, are inevitably associated with durum and bread wheats. For this reason, the diploid wheat *Triticum monococcum* (*T.m.*), known also as "einkorn", might represent a potential alternative to conventionally used wheat. Indeed, the genome of *T.m.* is A^mA^m, very close to the A^uA^u present in modern wheat; thus, the only ω gliadins expressed are those associated with the locus Gli-A1, never related to WDEIA thus far.[12] Corbellini et al.[17] demonstrated that some einkorn accessions possessing good bread-making characteristics do not present the typical electrophoretic bands of *T.a.* ω gliadins, which would support the possible use of this cereal as a hypoallergenic option for WDEIA patients. The aim of this study was to assess the immunoreactivity of *T.m.* proteins among patients suffering from WDEIA, by immunochemical techniques and SPT, and to evaluate the suitability of this cereal in the future development of hypoallergenic flours.

MATERIALS AND METHODS

Wheat Extraction. Four einkorn wheat accessions cultivated at the Istituto Sperimentale della Cerealicoltura in Sant'Angelo Lodigiano, Lodi, Italy (ID109, ID358, ID1331, and Monlis) were selected. These accessions are characterized by good bread-making characteristics.[17,19,20] *T.a.* cv. Bologna was used as a wheat reference. A total of 1 g of seeds of each sample was milled in a mortar and extracted in phosphate-buffered saline (PBS, pH 7.2, 1:10, w/v) as previously described[21] for 2 h at room temperature (RT). After centrifugation at 12000*g*, the supernatants were collected and stored at −20 °C and the pellets were subsequently washed with PBS and distilled water. The supernatants obtained after these washing steps were discarded. The pellets were finally extracted with 40% ethanol (1:5) for 2 h and centrifuged. The supernatants containing the PBS-insoluble gliadins (mainly) and glutenins (to a lesser extent) were collected and stored at −20 °C.

Preparation of Prick Test Diagnostic Solutions. Diagnostic solutions were produced by diluting the protein extracts (accessions ID109, ID358, ID1331, and Bologna) in a storage solution containing 40% glycerol and 0.4% phenol for commercial preparations. The protein concentrations were 1.5 mg/mL for the PBS-soluble proteins and 0.5 mg/mL for the PBS-insoluble proteins. The concentration of ω-5 gliadin was 0.1 mg/mL. Diagnostic solutions were filtered at 0.20 μm in sterile conditions.

Sodium Dodecyl Sulfate−Polyacrylamide Gel Electrophoresis (SDS−PAGE) and IgE Immunoblotting. The protein extracts from the different wheat samples were mixed with 2× loading buffer (62.5 mM Tris−HCl at pH 6.8, 1.3% (w/v) SDS, 10% (w/v) glycerol, and 4% β-mercaptoethanol) and heated at 100 °C for 5 min. Proteins (50 μg/cm of lane width) were separated in 16% SDS−PAGE at 20 mA current by means of a Mini Protean III apparatus (Bio-Rad, Hercules, CA) in 25 mM Tris−192 mM glycine and 0.1% SDS (pH 8.4). The gels were stained with Coomassie R250.

Alternatively, proteins were electroblotted onto nitrocellulose (Millipore, Schwalbach, Germany) at 50 V for 150 min. The membrane was blocked with 1% BSA and 0.05% Tween 20 in PBS (PTB) and probed with the sera of patients at 1:10 dilution. Bound IgE was detected by a monoclonal horseradish peroxidase (HRP)-conjugated anti-IgE antibody (Southern Biotech, Birmingham, AL) at 1:1500 dilution, followed by chemiluminescence reaction with Immobilon Western Chemiluminescent HRP Substrate (Millipore) and image acquisition by a Chemidoc XRS apparatus (Bio-Rad).

Purification of ω-5 Gliadin. A *T.a.* extract from 20 g of seeds was used to purify ω-5 gliadin. The ethanol-soluble protein fraction was concentrated by adding 2 volumes of 1.5 M NaCl and leaving the solution overnight at 4 °C. After the centrifugation at 10000*g* for 15 min, the supernatant was discarded and the gluten proteins in the pellet were solubilized in 6 M guanidine HCl, adjusted to pH 8 with Tris−HCl + 50 mM dithiothreitol (DTT). Purification was carried out by reversed-phase high-performance liquid chromatography (RP-HPLC) on a Vydac 218TP C18 semi-preparative column (10 × 250 mm, 5 μm particle size) and separated at a 5 mL/min flow rate in 0.05% trifluoroacetic acid with a 10−70% acetonitrile gradient in 65 min and 70−90% acetonitrile gradient in 10 min as described previously.[22] Peaks were collected, lyophilized, and analyzed by immunoblotting with the sera of patients to identify the immunoreactive ω-5 gliadin.

HPLC−Tandem Mass Spectrometry (MS/MS) Analysis of the Purified ω-5 Gliadin. A protein amount of 3 μg of putative ω-5 gliadin isolated by HPLC was lyophilized and diluted in 50 μL of 0.084 N HCl. Pepsin from porcine pancreas (Sigma-Aldrich, St. Louis, MO) was added in a 1:60 enzyme/protein ratio. After 2 h, the digest underwent ZipTip cleaning (Millipore) following the procedure of the manufacturer and then lyophilized.

Peptides were separated by reversed-phase nano-HPLC-Chip technology (Agilent Technologies, Palo Alto, CA) online coupled with a three-dimensional (3D) ion trap mass spectrometer (model Esquire 6000, Bruker Daltonics, Bremen, Germany). The chip was composed of a Zorbax 300SB-C18 (150 mm × 75 μm, with a 5 μm particle size) analytical column and a Zorbax 300SB-C18 (40 nL, 5 μm) enrichment column. The complete system was fully controlled by ChemStation (Agilent Technologies) and EsquireControl (Bruker Daltonics) softwares. The scan range used was from m/z 300 to 1800. For MS/MS experiments, the system was operated with automatic switching between MS and MS/MS modes. The three most abundant peptides of each m/z were selected to be further isolated and fragmented. The MS/MS scanning was performed in the normal-resolution mode at a scan rate of m/z 13.000 per second. A total of five scans were averaged to obtain a MS/MS spectrum. Database searches were conducted using the MS/MS ion search of Mascot against all entries of the non-redundant National Center for Biotechnology Information (NCBI) database with the following parameters: specific pepsin digestion, up to two missed cleavage; fixed and variable modifications, carbamidomethyl-Cys and oxidated Met, respectively; peptide and fragment tolerances, ±0.9 and ±0.9 Da, respectively; and peptide charges, +1, +2, and +3. For positive identification, the score of the result of $[-10 \log(P)]$ had to be over the significance threshold level ($p < 0.05$).

Patients and Diagnosis. A total of 14 patients [mean age of 42 years, with a standard deviation (SD) of 12.2; 10 male] attending the Verona Allergy Unit between January 2012 and January 2014 with an unequivocal clinical history of WDEIA (allergic symptoms after exercise within 4 h of ingestion of wheat-based products) and positive serum ω-5 gliadin-specific IgE were studied in the standard diagnostic setting. All of the participants were informed about the study by the medical team and signed an informed consent approved by the ethics

DOI: 10.1021/acs.jafc.5b02648
J. Agric. Food Chem. 2015, 63, 8299−8306

Table 1. Clinical Characteristics of Patients and Results of Skin Tests

							in-house SPT[a]								
							soluble				insoluble				
patients	clinical symptoms	other co-factors	CAP wheat	CAP gluten	CAP ω-5 gliadin	SPT[a] wheat (Lofarma)	*T.a.*	ID109	ID358	ID1331	*T.a.*	ID109	ID358	ID1331	purified ω-5 gliadin
BT07	anaphylaxis	none	0.73	5.47	9.67	4/6	7/26	–[b]	–	–	10/40	–	–	–	15/27
BT09	urticaria	NSAIDs[c]	<0.35	<0.35	1.33	–	3/10	–	–	np[d]	4/13	3/15	–	np	np
BT14	anaphylaxis	none	<0.35	np	3.35	–	np	np	np	np	np	np	np	np	np
BT16	urticaria	NSAIDs	<0.35	1.31	6.67	–	4/21	–	–	–	4/22	–	–	–	7/41
BT19	anaphylaxis	none	1.37	5.11	37.6	–	2/29	–	–	–	4/21	–	–	–	7/29
BT24	anaphylaxis	none	3.09	5.19	9.31	–	5/29	–	–	–	9/25	–	–	–	9/26
BT25	anaphylaxis	NSAIDs and alcohol	<0.35	0.88	5.24	–	4/9	–	–	–	5/25	–	–	–	15/27
BT26	anaphylaxis	NSAIDs	4.09	13.5	49.5	3/5	9/21	–	–	–	11/22	–	–	–	9/39
BT27	urticaria	none	<0.35	<0.35	1.00	–	6/14	–	–	–	8/11	–	–	–	10/17
BT28	anaphylaxis	none	1.39	8.95	37.6	4/6	5/12	–	–	–	10/20	–	–	–	16/40
BT30	anaphylaxis	none	<0.35	<0.35	4.87	–	4/10	–	–	–	9/22	–	–	–	8/26
BT31	anaphylaxis	alcohol	2.21	4.52	7.12	3/6	4/16	–	–	–	7/20	–	–	–	8/30
BT33	anaphylaxis	alcohol	3.46	4.95	19.1	6/46	4/28	–	–	–	8/38	–	–	–	8/43
BT34	anaphylaxis	alcohol	1.15	1.91	4.48	3/8	–	–	–	–	17/40	–	–	–	12/40

[a]Wheal and flare diameters are in millimeters. [b]– = negative result. [c]NSAIDs = non-steroidal anti-inflammatory drugs. [d]np = not performed.

committee. The clinical characteristics of patients and the results of diagnostic workup are summarized in Table 1.

A total of 11 patients had a history of severe systemic reactions (urticaria angioedema, dyspnea, and/or hypotension), while 3 patients experienced only urticaria after exercise within 4 h of wheat product ingestion.

A total of 7 patients reported symptoms also in the case of exposure to co-factors other than exercise: 3 after NSAIDs intake, 3 with concomitant alcohol ingestion, and 1 with both.

The allergic patients underwent SPTs with a commercial wheat extract (Lofarma, Milano, Italy), solutions of PBS-soluble and -insoluble protein fractions of *T.a.*, three different accessions of *T.m.* (ID109, ID358, and ID1331), and purified ω-5 gliadin following standard procedures.[18] Results were considered positive if the mean wheal diameter was 3 mm or larger after 15 min. Histamine dihydrochloride (10 mg/mL, Alk-Abellò, Copenhagen, Denmark) and physiological saline were used for positive and negative controls.

Serum-specific IgE to wheat, gluten, and recombinant ω-5 gliadin were assayed with ImmunoCAP (Thermo Fisher Diagnostics, Uppsala, Sweden). Concentrations of ≥0.35 kU/L were considered positive.

Enzyme-Linked Immunosorbent Assay (ELISA) for Wheat-Specific IgE Detection. ELISA was performed on Maxisorp 96 well microplates (Nunc A/S, Roskilde, Denmark). Purified ω-5 gliadin (50 ng per well) or the ethanol extract from the different wheat accessions (0.1 mg/mL) was diluted in PBS and non-covalently coated for 30 min at RT. After washing with PBS and 0.05% Tween 20, the wells were blocked with PTB for 30 min at RT. The sera of patients were incubated at 1:10 dilution in PTB overnight. For ELISA inhibition performed on ω-5 gliadin-coated wells, sera were co-incubated with ethanol extracts from *T.a.* and *T.m.* accessions diluted in PTB (100 μg/mL final concentration). A buffer control was considered (no serum incubation), while the 100% signal was given by the omission of the inhibitor. Bound IgE was detected by incubation with an unlabeled mouse monoclonal anti-human IgE antibody (1:500, Southern Biotech, Birmingham, AL) for 1 h, followed by a HRP-conjugated anti-mouse immunoglobulin G (IgG) antibody (1:2000, Sigma-Aldrich) for 1 h, both diluted in PTB. Tetramethylbenzidine (TMB, Sigma-Aldrich) was used as the chromogenic substrate. Optical density (OD) was monitored at 450 nm by a Power Wave microplate reader (Bio-Tek, Winnoski, VT).

Statistics. Statistical analysis was performed by one-way, within subject, analysis of variation (ANOVA) test, followed by a post-hoc pairwise *t* test, with adjusted *p* values using the Holm method. Calculations were carried out using the R statistical computing platform. The Pearson coefficient was computed to test the correlations between the same data. All immunochemical analyses were performed in triplicate.

RESULTS

Purification of ω-5 Gliadin. The elution from HPLC revealed two main peaks in the region of the chromatogram, where ω gliadin was expected to elute as previously described.[22] MS/MS analysis identified the first peak as ω-5 gliadin, and SDS–PAGE confirmed the purity of the protein. The results are reported in Figure S1 and Table S1 of the Supporting Information.

***T.m.* Extracts Showed No Immunoreactivity by SPTs.** SPTs with the commercial wheat extract were positive only in six patients (42.8%), while 100% of tested patients were positive to the insoluble fraction of *T.a.* and purified ω-5 gliadin. Wheal diameters observed for the *T.a.*-insoluble fraction (8.1 ± 3.6 mm, with a range of 4–17 mm) and purified ω-5 gliadin (10.3 ± 3.3 mm, with a range of 7–16 mm) were larger than those obtained with the commercial wheat extract (1.6 ± 2.1 mm, with a range of 3–6 mm). These results are in agreement with previous data, showing a low sensitivity of commercial wheat SPTs[4,23] for patients affected by WDEIA. These findings might be a consequence of a low concentration of the responsible allergens (insoluble fraction) in wheat commercial extracts. Interestingly, 12 of 13 tested patients were also positive to *T.a.* salt-soluble extract (4.38 ± 2.2 mm, with a range of 2–9 mm).

A completely different pattern was observed for *T.m.* extracts. Both soluble and insoluble protein extracts of each *T.m.* accession failed to induce reactivity in almost all tested patients (Table 1). Only patient BT09 showed a positive signal with the insoluble fraction of ID109.

IgE of Patients React Mainly to Gluten Proteins. Specific IgE to wheat, gluten, and recombinant ω-5 gliadin measured by CAP were present in 8 (57.1%), 10 (71%), and 14 (100%) of the tested patients with a mean of 1.25, 3.98, and 14.06 kU_A/L, respectively. No significant correlations where found among the CAP values and SPT wheal diameters.

DOI: 10.1021/acs.jafc.5b02648
J. Agric. Food Chem. 2015, 63, 8299–8306

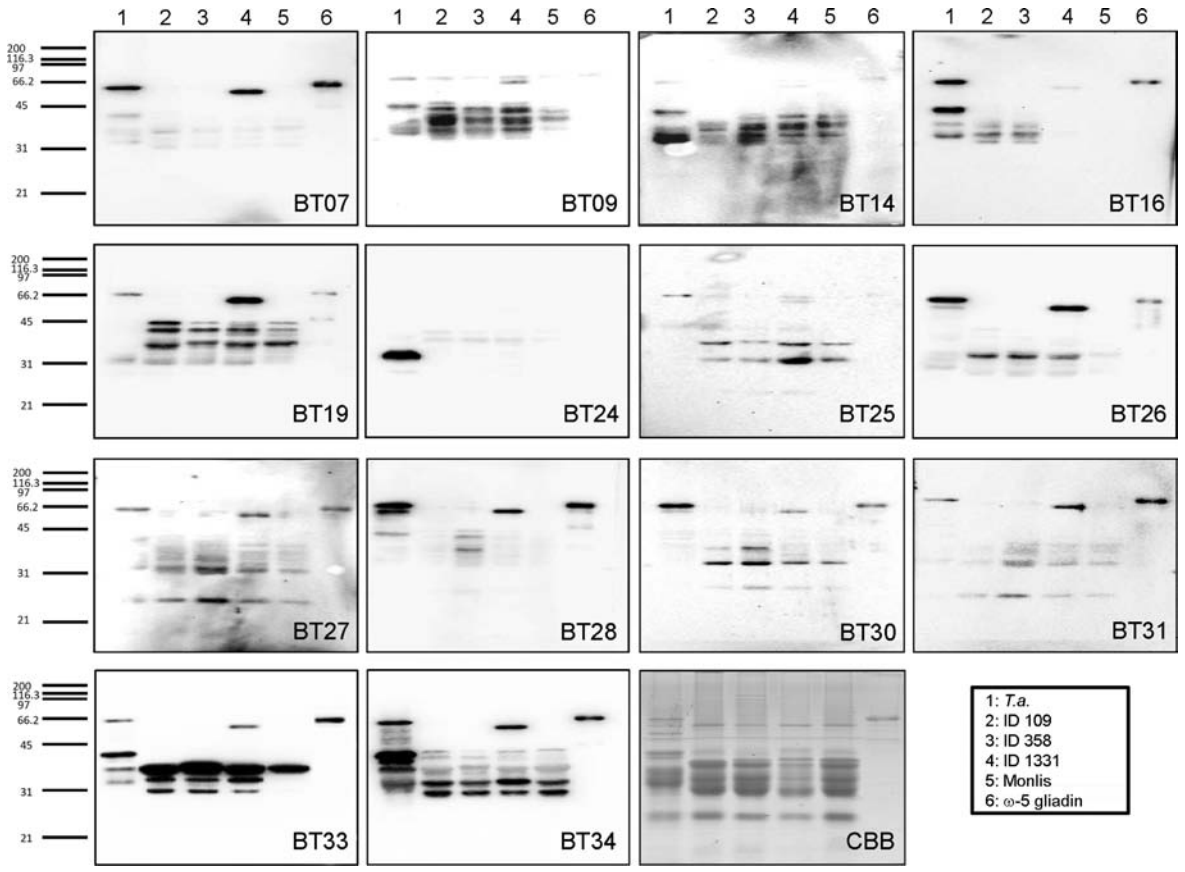

Figure 1. IgE immunoblotting of *T.a.* and *T.m.* PBS-insoluble extracts. Each panel corresponds with an immunoblotting developed with the serum of a specific patient. CBB = Coomassie Brilliant Blue staining.

Protein extracts from *T.a.*, ID109, ID358, ID1331, and Monlis were assayed with the sera of patients by immunoblotting to evaluate their IgE-binding capacity. In these experiments, we included *T.m.* Monlis, which, different from the other accessions, is registered as a marketable variety. Immunoblotting showed positive signals mainly for PBS-insoluble proteins (Figure 1), while the PBS-soluble proteins generated often faint signals and, in some cases, tested negative. This suggests that soluble proteins are scarcely involved in the pathogenesis of this disease. The results obtained for the PBS-soluble fraction are presented in Figure S2 of the Supporting Information. No significant correlations where found among the signals detected by immunoblotting and SPT wheal diameters. Concerning the immunoblotting carried out with the PBS-insoluble fraction (Figure 1), IgE-binding proteins were detected at 65 kDa in *T.a.* samples for 92% of the recruited patients, confirming that they possess IgE antibodies specific to ω-5 gliadin. The patient serum BT24 did not recognize ω-5 gliadin, despite a high CAP value to the same allergen. No patient resulted sensitized to HMW glutenins.

As far as *T.m.* accessions are concerned, in almost all patients, IgE bound proteins with lower molecular mass if compared to *T.a.*, and they are, therefore, reminiscent of α/β gliadins and LMW glutenins. In addition, ID1331 presents a protein band comigrating to ω-5 gliadin. This is in agreement with previous findings showing that ID1331, different from other *T.m.* accessions, possesses ω gliadins compatible with those of *T.a.*[17]

No IgE-binding protein was detected by immunoblotting with the sera of healthy volunteers (data not shown).

Einkorn Storage Proteins Show Partial Cross-Reactivity with ω-5 Gliadin Epitopes. A first set of direct ELISA experiments with the sera of patients was performed using insoluble protein extracts as coating (Figure 2). This demonstrated a general lower immunoreactivity of *T.m.* extracts in comparison to *T.a.*, except for the sera of four patients, i.e., BT14, BT24, BT27, and BT33, which showed rather similar immunoreactivity to all of the samples. ELISA experiments carried out with the sera of healthy volunteers showed negligible signals (data not shown). Measurements obtained by direct ELISA with the sera of individual patients on extracts from each wheat sample were grouped (Figure 3A), and differences between groups were analyzed statistically. *T.a.* extracts provided data significantly different from those obtained with the other wheats (Figure 3B; $p < 0.01$), whereas no differences were observed between the three *T.m.* accessions. Data from all samples were correlated (Figure 3C; Pearson coefficient > 0.90).

Because all patients are sensitized to ω-5 gliadin and given its role as a major allergen, we carried out ELISA inhibition experiments with purified ω-5 gliadin as coating. The results showed a limited cross-reactivity among *T.a.*- and *T.m.*-insoluble proteins (Figure 4). Indeed, the inhibition levels of *T.m.* accessions were generally lower than the *T.a.* auto-inhibition values, and for some patients (e.g., BT30 and BT31), no cross-reactivity was appreciable at all. Figure 5 summarizes the whole set of data. The percent inhibition values of *T.m.* accessions distributed differently (Figure 5A), with median values of 16% for ID109, 16% for ID358, and 23% for ID1331, with respect to 68% of *T.a.* Values measured for *T.a.* were

DOI: 10.1021/acs.jafc.5b02648
J. Agric. Food Chem. 2015, 63, 8299−8306

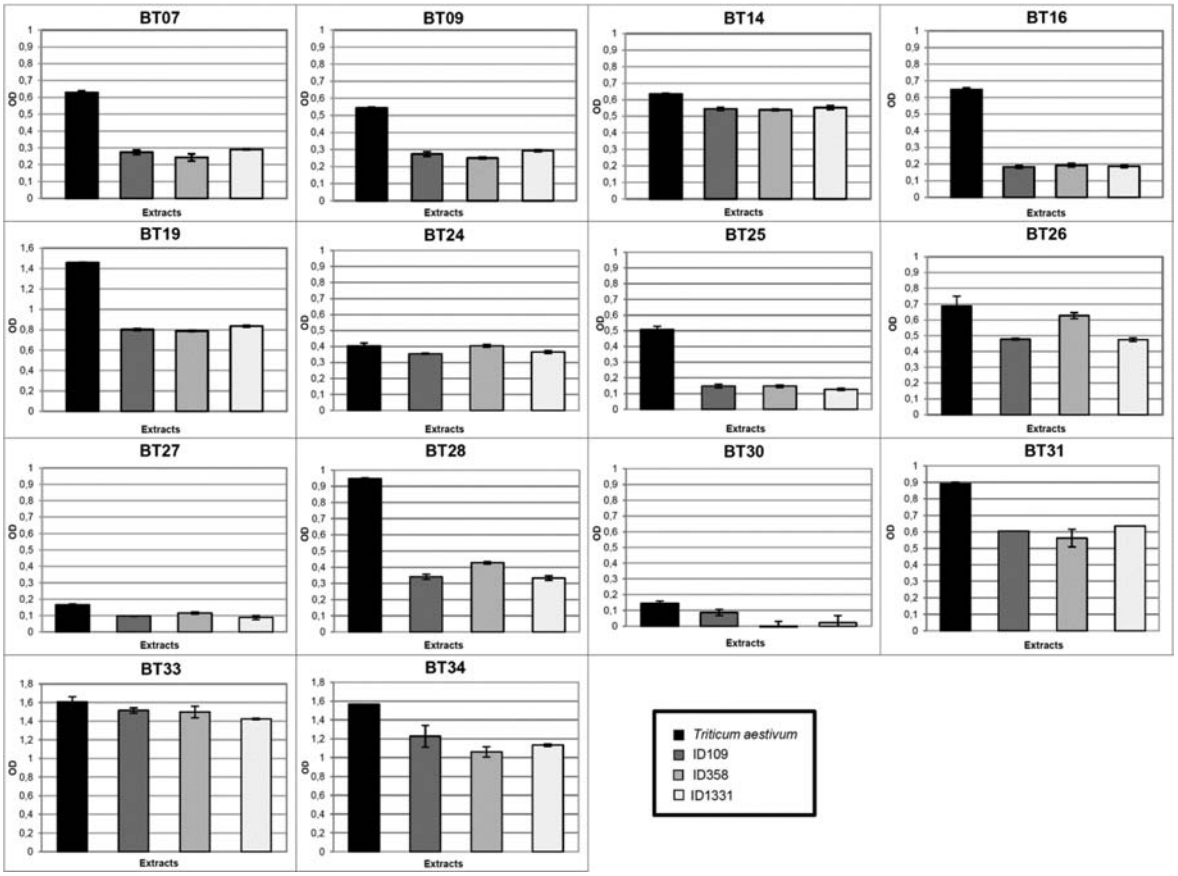

Figure 2. ELISA of the insoluble protein extracts of *T.a.* and *T.m.* (ID109, ID358, and ID1331) developed with the sera of patients for wheat-specific IgE detection.

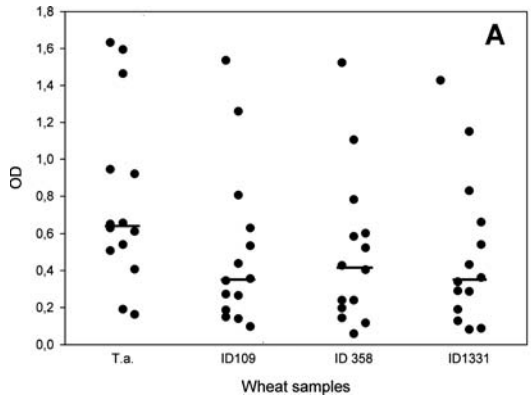

B

	ID109	ID358	ID1331
T.a.	7,40E-04	7,80E-04	3,70E-04
ID109		1,00	0,76
ID358			1,00

C

	ID109	ID358	ID1331
T.a.	0,91	0,90	0,92
ID109		0,99	1,00
ID358			0,99

Figure 3. (A) IgE-binding capacity (expressed as OD) of *T.a.* and *T.m.* (ID109, ID358, and ID1331) insoluble protein extracts obtained by direct ELISA with the sera of patients. (B) Matrix of *p* values calculated with ANOVA post-hoc pairwise *t* test with the Holm method. Values obtained for *T.a.* are significantly different from those obtained for all of the other accessions. (C) Matrix of Pearson correlation coefficients.

significantly different from those of *T.m.* accessions ($p < 0.01$; Figure 5B). Among the *T.m.* accessions, ID109 and ID358 showed the highest correlation level (Pearson coefficient = 0.92; Figure 5C), in agreement with the identical percent inhibition value calculated by ELISA. The higher percent inhibition value calculated for ID1331 correlates with the presence of the 65 kDa *ω*-5 gliadin-like band detected by IgE immunoblotting (Figure 1). The reason for the lack of total (i.e., 100%) autoinhibition of the IgE binding of *T.a.* proteins to the coated *ω*-5 gliadin is probably due to the low concentration of *ω*-5 gliadin in the *T.a.* protein extract. Notably, the sera of patients BT14 and BT33, despite a high immunoreactivity to *T.m.* accessions (Figure 2), showed low cross-reactivity with *ω*-5 gliadin. Patient BT24 showed higher cross-reactivity for all *T.m.* accessions.

DISCUSSION

The rationale of our work was to evaluate the immunoreactivity of wheat accessions whose genotype lacks B genome but, at the same time, possess good bread-making characteristics. A previous paper by Corbellini et al.[17] showed that some accessions of *T.m.* (A^mA^m) did not present typical *ω* gliadin electrophoretic bands. In addition, the accessions with this specific pattern showed good rheological traits, comparable to

DOI: 10.1021/acs.jafc.5b02648
J. Agric. Food Chem. 2015, 63, 8299−8306

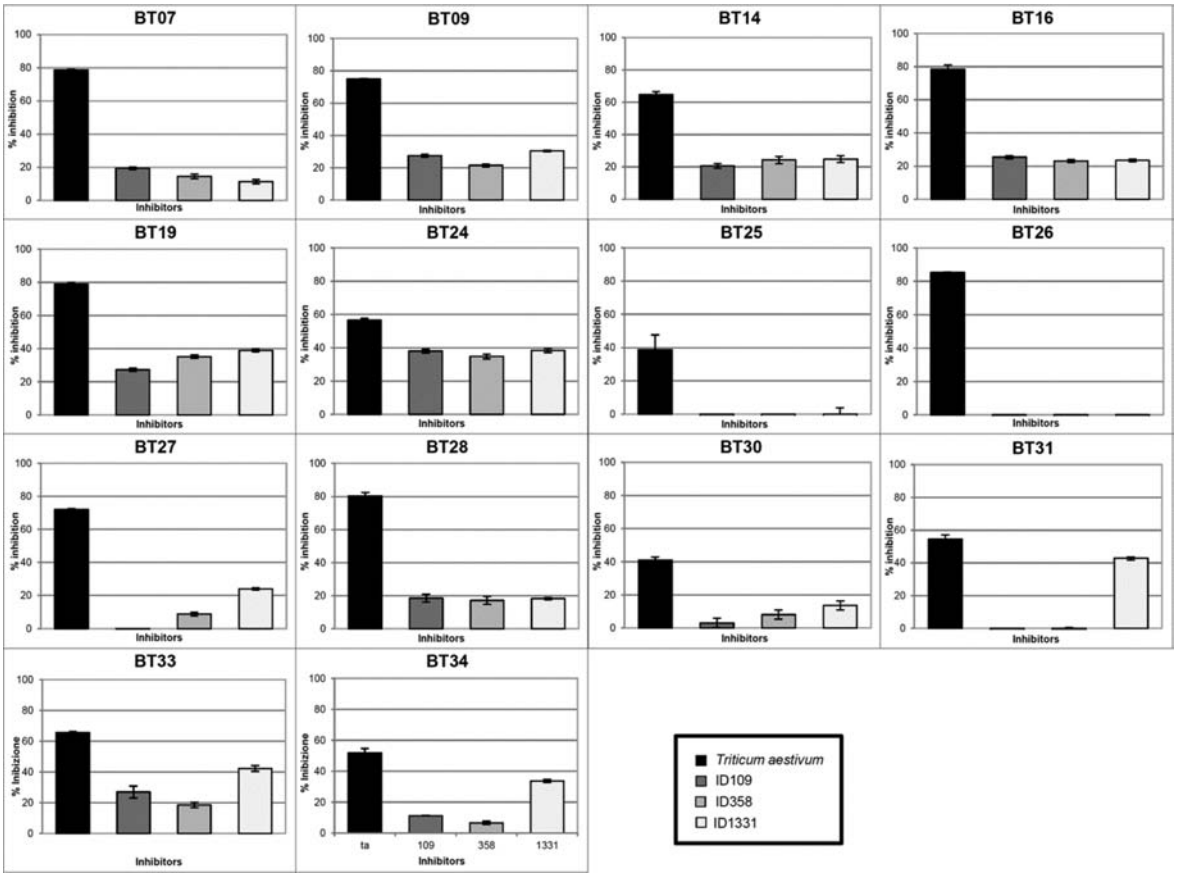

Figure 4. ELISA inhibition on purified ω-5 gliadin coating. The sera of allergic patients were incubated with *T.a.* and *T.m.* (ID109, ID358, and ID1331) PBS-insoluble protein extracts as IgE-binding inhibitors.

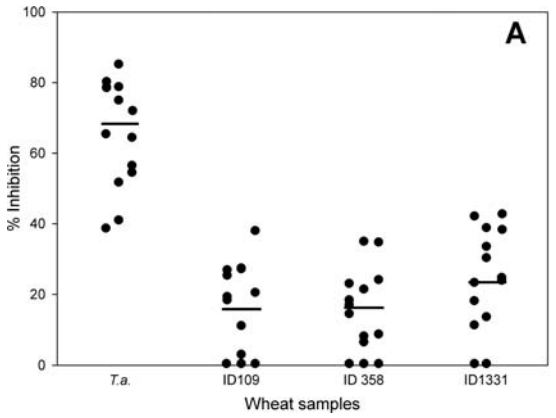

B

	ID109	ID358	ID1331
T.a.	1,80E-07	1,20E-05	2,20E-05
ID109		0,76	0,07
ID358			0,07

C

	ID109	ID358	ID1331
T.a.	0,33	0,34	-0,02
ID109		0,92	0,52
ID358			0,50

Figure 5. (A) IgE-binding inhibition levels (%) obtained by ELISA experiments on purified ω-5 gliadin coating. (B) Matrix of p values calculated with ANOVA post-hoc pairwise t test with the Holm method. Values obtained for *T.a.* are significantly different from those obtained for all of the other accessions. (C) Matrix of Pearson correlation coefficients. The p value and correlation coefficient for the comparison between ID109 and ID358 are highlighted in gray.

T.a., giving better results in the SDS-sedimentation test than *T.m.* accessions with ω gliadin-like bands. This represents an important point because the main reason for the low exploitation of einkorn with respect to modern wheat, besides the lower production yield, is its poor dough quality.[24]

In a previous publication,[21] we evaluated different quality traits of several einkorn accessions that could make this wheat suitable for the production of functional foods. In particular, we found that *T.m.* lacks α-amylase inhibition activity, which, together with its high content in nutraceutical molecules, such as carotenoids, represents an interesting and attractive characteristic. The patients recruited for the present study were selected on the basis of clinical history and presence of ω-5 gliadin-specific IgE. Western blotting results confirmed immunoCAP results; the sera of all patients but one (BT24) contained IgE specific for a 65 kDa band identified as ω-5 gliadin by MS.

SPTs performed with in-house gluten-containing extracts (*T.a.*-insoluble protein extract) appeared definitely more sensitive than SPTs performed with the commercial wheat

DOI: 10.1021/acs.jafc.5b02648
J. Agric. Food Chem. 2015, 63, 8299−8306

extract. Moreover, positive SPT responses to gluten solution agreed with positive specific IgE to ω-5 gliadin in 100% of patients, while only 76.9% of patients positive to gluten SPTs displayed gluten-specific IgE, as measured by ImmunoCAP. This means that, for SPTs with *T.a.*, the insoluble protein fraction appears to be an excellent screening test for the disease. SPT with PBS-soluble proteins tested positive in 92.3% of the patients, but the immunoblotting carried out with this protein fraction failed to detect any IgE binding proteins in several patients (Figure. S2); the denaturing conditions of SDS−PAGE possibly affected the epitopes present in the PBS-soluble protein fraction. If so, this would lead us to question the real contribution of such epitopes in allergic manifestations after ingestion of transformed foods, such as bread, where proteins normally undergo strong thermal denaturation. The same line of reasoning could help in interpreting the results obtained with the serum of the patient BT24 that showed reactivity toward ω-5 gliadin by ImmunoCAP, ELISA, and SPT but not by immunoblotting.

Once the sera were used to probe the storage proteins of the three *T.m.* accessions, different IgE-binding patterns were obtained in comparison to *T.a.* The 65 kDa band was not recognized in accessions ID109, ID358, and Monlis, confirming the initial hypothesis, namely, that these wheats do not possess ω-5 gliadin; instead, lower molecular mass proteins were detected suggesting that either certain epitopes harbored in these proteins could cross-react with ω-5 gliadins or recognition could be mediated by different epitopes.

To quantify the immunoreactivity of *T.m.*-insoluble proteins and to evaluate their possible cross-reactivity with ω-5 gliadin expressed in modern *T.a.*, we followed an ELISA approach based on the detection of IgE-binding epitopes (1) in the insoluble protein extracts and (2) after the co-incubation of the sera of patients with the insoluble protein extracts from the three *T.m.* accessions on a coating of ω-5 gliadin. While the first results showed a certain degree of reduction in the IgE-binding capacity toward the insoluble proteins of *T.m.* accessions in comparison to *T.a.*, the inhibition approach showed that, for the majority of the patients, the cross-reactivity level between *T.m.*-insoluble proteins and ω-5 gliadin is rather low, less than 20%. It is of note that, despite this cross-reactivity, SPT performed with extracts of the three *T.m.* accessions was negative for almost all of the tested patients. Because it is acknowledged that the negative predictive value (NPV) for SPT is relatively high,[25] our results indicate that, despite a limited cross-reactivity to modern ω-5 gliadin, there is a reasonable possibility that the recruited patients might tolerate *T.m.*-based foods.

Taken together, these results suggest that *T.m.* accessions might represent a potential candidate for the production of hypoallergenic bakery goods for patients sensitized to ω-5 gliadin. Further analyses, such as oral provocation with *T.m.*-based products, should be carried out to investigate their safety.

■ ASSOCIATED CONTENT

Supporting Information

The Supporting Information is available free of charge on the ACS Publications website at DOI: 10.1021/acs.jafc.5b02648.

MS analysis of the ω-5 gliadin peak collected by RP-HPLC (Table S1), HPLC chromatogram of ω-5 gliadin purification, with SDS−PAGE analysis of the purified peak (S, molecular mass standards; 1, ω-5 gliadin) as the inset (Figure S1), and IgE immunoblotting of *T.a.* and *T.m.* PBS-soluble extracts (Figure S2) (PDF)

■ AUTHOR INFORMATION

Corresponding Author

*Telephone: +39-045-8027952. Fax: +39-045-8027929. E-mail: gianni.zoccatelli@univr.it.

Author Contributions

†Carla Lombardo and Michela Bolla contributed equally to this work.

Notes

The authors declare no competing financial interest.

■ ACKNOWLEDGMENTS

The authors are grateful to Prof. Giovanni Passalacqua for the critical evaluation of the manuscript. Gianni Zoccatelli is member of the COST Action ImpARAS FA1402.

■ ABBREVIATIONS USED

T.a., *Triticum aestivum*; *T.m.*, *Triticum monococcum*

■ REFERENCES

(1) Sapone, A.; Bai, J. C.; Ciacci, C.; Dolinsek, J.; Green, P. H.; Hadjivassiliou, M.; Kaukinen, K.; Rostami, K.; Sanders, D. S.; Schumann, M.; Ullrich, R.; Villalta, D.; Volta, U.; Catassi, C.; Fasano, A. Spectrum of gluten-related disorders: consensus on new nomenclature and classification. *BMC Med.* **2012**, *10*, 13.

(2) Palosuo, K.; Alenius, H.; Varjonen, E.; Koivuluhta, M.; Mikkola, J.; Keskinen, H.; Kalkkinen, N.; Reunala, T. A novel wheat gliadin as a cause of exercise-induced anaphylaxis. *J. Allergy Clin. Immunol.* **1999**, *103*, 912−917.

(3) Morita, E.; Matsuo, H.; Mihara, S.; Morimoto, K.; Savage, A. W.; Tatham, A. S. Fast omega-gliadin is a major allergen in wheat-dependent exercise-induced anaphylaxis. *J. Dermatol. Sci.* **2003**, *33*, 99−104.

(4) Bouchez-Mahiout, I.; Snegaroff, J.; Tylichova, M.; Pecquet, C.; Branlard, G.; Lauriere, M. Low Molecular Weight Glutenins in Wheat-Dependant, Exercise-Induced Anaphylaxis: Allergenicity and Antigenic Relationships with Omega 5-Gliadins. *Int. Arch. Allergy Immunol.* **2010**, *153*, 35−45.

(5) Morita, E.; Matsuo, H.; Chinuki, Y.; Takahashi, H.; Dahlstrom, J.; Tanaka, A. Food-dependent exercise-induced anaphylaxis -importance of omega-5 gliadin and HMW-glutenin as causative antigens for wheat-dependent exercise-induced anaphylaxis. *Allergol. Int.* **2009**, *58*, 493−498.

(6) Matsuo, H.; Kohno, K.; Niihara, H.; Morita, E. Specific IgE determination to epitope peptides of omega-5 gliadin and high molecular weight glutenin subunit is a useful tool for diagnosis of wheat-dependent exercise-induced anaphylaxis. *J. Immunol.* **2005**, *175*, 8116−8122.

(7) Lamacchia, C.; Camarca, A.; Picascia, S.; Di Luccia, A.; Gianfrani, C. Cereal-Based Gluten-Free Food: How to Reconcile Nutritional and Technological Properties of Wheat Proteins with Safety for Celiac Disease Patients. *Nutrients* **2014**, *6*, 575−590.

(8) Altenbach, S. B.; Allen, P. V. Transformation of the US bread wheat 'Butte 86' and silencing of omega-5 gliadin genes. *GM. Crops.* **2011**, *2*, 66−73.

(9) Weiss, W.; Vogelmeier, C.; Gorg, A. Electrophoretic characterization of wheat grain allergens from different cultivars involved in bakers' asthma. *Electrophoresis* **1993**, *14*, 805−816.

(10) Constantin, C.; Touraev, A.; Heberle-Bors, E.; Quirce, S.; Huber, W. D.; Valenta, R. Detection of Antigens Reactive to IgE and IgA during Wheat Seed Maturation and in Different Wheat Cultivars. *Int. Arch. Allergy Immunol.* **2009**, *149*, 181−187.

(11) Sanchez-Monge, R.; Garcia-Casado, G.; Malpica, J. M.; Salcedo, G. Inhibitory activities against heterologous alpha-amylases and in

DOI: 10.1021/acs.jafc.5b02648
J. Agric. Food Chem. 2015, 63, 8299−8306

vitro allergenic reactivity of Einkorn wheats. *Theor. Appl. Genet.* **1996**, *93*, 745−750.
(12) Denery-Papini, S.; Lauriere, M.; Branlard, G.; Morisset, M.; Pecquet, C.; Choudat, D.; Merlino, M.; Pineau, F.; Popineau, Y.; Boulenc, E.; Bouchez-Mahiout, I.; Bodinier, M.; Moneret-Vautrin, D. A. Influence of the allelic variants encoded at the Gli-B1 locus, responsible for a major allergen of wheat, on IgE reactivity for patients suffering from food allergy to wheat. *J. Agric. Food Chem.* **2007**, *55*, 799−805.
(13) Nakamura, A.; Tanabe, S.; Watanabe, J.; Makino, T. Primary screening of relatively less allergenic wheat varieties. *J. Nutr. Sci. Vitaminol.* **2005**, *51*, 204−206.
(14) Constantin, C.; Huber, W. D.; Granditsch, G.; Weghofer, M.; Valenta, R. Different profiles of wheat antigens are recognised by patients suffering from coeliac disease and IgE-mediated food allergy. *Int. Arch. Allergy Immunol.* **2005**, *138*, 257−266.
(15) Sander, I.; Flagge, A.; Merget, R.; Halder, T. M.; Meyer, H. E.; Baur, X. Identification of wheat flour allergens by means of 2-dimensional immunoblotting. *J. Allergy Clin. Immunol.* **2001**, *107*, 907−913.
(16) Lehto, M.; Palosuo, K.; Varjonen, E.; Majuri, M. L.; Andersson, U.; Reunala, T.; Alenius, H. Humoral and cellular responses to gliadin in wheat-dependent, exercise-induced anaphylaxis. *Clin. Exp. Allergy* **2003**, *33*, 90−95.
(17) Corbellini, M.; Empilli, S.; Vaccino, P.; Brandolini, A.; Borghi, B.; Heun, M.; Salamini, F. Einkorn characterization for bread and cookie production in relation to protein subunit composition. *Cereal Chem.* **1999**, *76*, 727−733.
(18) Dreborg, S.; Frew, A. EAACI Position Paper - Allergen Standardization and Skin Tests. *Allergy* **1993**, *48*, 49−54.
(19) Taenzler, B.; Esposti, R. F.; Vaccino, P.; Brandolini, A.; Effgen, S.; Heun, M.; Schafer-Pregl, R.; Borghi, B.; Salamini, F. Molecular linkage map of Einkorn wheat: mapping of storage-protein and soft-glume genes and bread-making quality QTLs. *Genet. Res.* **2002**, *80*, 131−143.
(20) Brandolini, A.; Hidalgo, A.; Moscaritolo, S. Chemical composition and pasting properties of einkorn (*Triticum monococcum L. subsp monococcum*) whole meal flour. *J. Cereal Sci.* **2008**, *47*, 599−609.
(21) Zoccatelli, G.; Sega, M.; Bolla, M.; Cecconi, D.; Vaccino, P.; Rizzi, C.; Chignola, R.; Brandolini, A. Expression of alpha-amylase inhibitors in diploid Triticum species. *Food Chem.* **2012**, *135*, 2643−2649.
(22) Dupont, F. M.; Vensel, W. H.; Chan, R.; Kasarda, D. D. Characterization of the 1B-type omega-gliadins from Triticum aestivum cultivar Butte. *Cereal Chem.* **2000**, *77*, 607−614.
(23) Brockow, K.; Kneissl, D.; Valentini, L.; Zelger, O.; Grosber, M.; Kugler, C.; Werich, M.; Darsow, U.; Matsuo, H.; Morita, E.; Ring, J. Using a gluten oral food challenge protocol to improve diagnosis of wheat-dependent exercise-induced anaphylaxis. *J. Allergy Clin. Immunol.* **2015**, *135*, 977−984.
(24) Abdel-Aal, E. S. M.; Hucl, P.; Sosulski, F. W.; Bhirud, P. R. Kernel, milling and baking properties of spring-type spelt and einkorn wheats. *J. Cereal Sci.* **1997**, *26*, 363−370.
(25) Sampson, H. A. Food allergy. Part 2: diagnosis and management. *J. Allergy Clin. Immunol.* **1999**, *103*, 981−989.

DOI: 10.1021/acs.jafc.5b02648
J. Agric. Food Chem. 2015, 63, 8299−8306

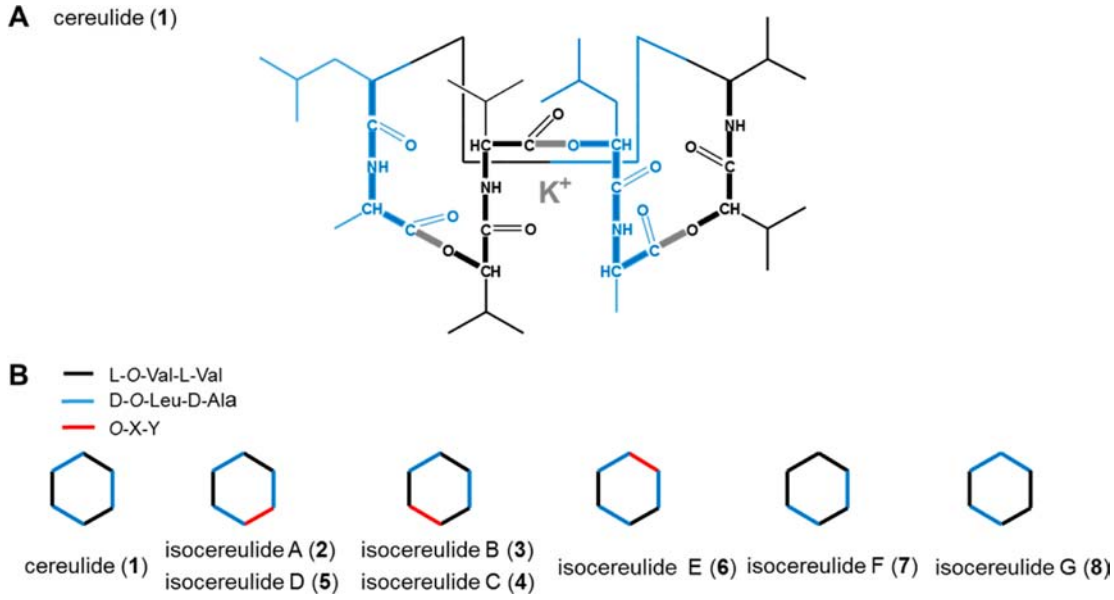

Figure 1. (A) Chemical structure of the cyclic dodecadepsipeptide cereulide (**1**), [D-*O*-Leu-D-Ala-L-*O*-Val-L-Val]$_3$; (B) chemical structure of isocereulides A (**2**) to G (**8**); *O*-X-Y indicates the position of the dipeptides L-*O*-Leu-L-Val (isocereulide A, **2**), D-*O*-Val-D-Ala (isocereulide B, **3**), D-*O*-Leu-D-Ser (isocereulide C, **4**), L-*O*-Val-L-Ala (isocereulide D, **5**), and D-*O*-Ile-D-Ala (isocereulide E, **6**).

A–G (**2**–**8**, Figure 1) were unequivocally determined in their chemical structure.[29,30] Most intriguingly, the isocereulides were found to differ widely in their cell toxicity correlating with their ionophoric properties; for example, purified isocereulide A showed about an 8-fold higher cytotoxicity than purified cereulide in the HEp-2 assay and induced an immediate breakdown of bilayer membranes.[30] As differences in the bioactivity of these dodecadepsipeptides and various concentrations might be correlated to gastrointestinal diseases ranging from acute and limited periods of vomiting to deadly intoxications, the knowledge-based risk assessment of *B. cereus* toxins in food and feed products requires more comprehensive quantitative tools to accurately analyze the major isocereulides along with cereulide. The objective of the present investigation was, therefore, to develop a rapid, sensitive, and robust stable isotope dilution assay for the combined quantitation of cereulide (**1**) and isocereulides A–G (**2**–**8**) by means of ultraperformance liquid chromatography–mass spectrometry (UPLC-MS/MS).

MATERIALS AND METHODS

Chemicals. Water for chromatographic separations was purified with an integral 5 system (Millipore, Schwalbach, Germany), and solvents used were of HPLC or LC-MS grade, respectively (J. T. Baker, Deventer, The Netherlands). For cultivation of bacteria strains, the following compounds were obtained commercially: MeOH and EtOH (Mallinckrodt Baker B.V., Deventer, The Netherlands); pepton tryptone, yeast extract (Oxoid, Hamphsire, UK); NaCl (Carl Roth, Karlsruhe, Germany); D-glucose monohydrate (Fluka, Sigma-Aldrich, Steinheim, Germany); and $^{13}C_1$-L-valine (Cambridge Isotope Laboratories, Inc., Andover, MA, USA). Eleven dairy-based desserts, five rice puddings, three cereals, two rice samples, two baby foods, and two animal feed products were purchased from a local supermarket (Freising, Germany). In addition, two suspicious noodle samples, each causing intoxications in child daycare facilities, were obtained from the German Health and Food Safety Authority.

UPLC-TOF-MS Profiling of Bacterial Strain Panel. A total of 78 representative *B. cereus* strains were collected on the basis of the following criteria as recently reported:[29] (i) source, clinical isolates from patients (associated with food poisoning/associated with other clinical infections), isolates from food (associated with food poisoning/not associated with food poisoning), environmental isolates; (ii) diversity in geographical origins; and (iii) diverse toxin gene profiles representing different subtypes. Strains were grown on Luria–Bertani (LB) agar plates or in LB broth (5 g/L NaCl, 5 g/L yeast extract, 10 g/L tryptone) at 24 °C for 24 h and were labeled with a designation number (1–78).

For UPLC-TOF-MS strain profiling, LB broth (100 mL) supplemented with D-glucose (0.2%) and NaCl (0.5%) was inoculated with an overnight preculture (10^3 cfu/mL) and incubated (24 h, 24 °C) in baffled flasks (500 mL) while rotary shaking (120 rpm). The optical density of the cell cultures was measured at 600 nm (OD_{600}) against LB medium (reference) using a GeneQuant pro spectrophotometer (Biochrom, UK). Cell cultures were diluted 1:20 in LB if the OD_{600} was >1.0. The cultures were autoclaved (15 min, 121 °C) and centrifuged (7800*g*, 20 °C, 12 min, Sigma 3-18 K), and the pellet obtained was extracted with ethanol (10 mL) by shaking for 15 h. After centrifugation (7800*g*, 12 min), the supernatant was centrifuged (18600*g*, 5 min) again and membrane filtered (0.2 μm; Phenomenex, Aschaffenburg, Germany), and aliquots (3 μL) were analyzed by UPLC-TOF MS.

Biosynthetic Production of Cereulide, Isocereulides, and $^{13}C_6$-Cereulide. For production of reference materials of cereulide (**1**), isocereulides A–G (**2**–**8**), and $^{13}C_6$-cereulide ($^{13}C_6$-**1**), the *B. cereus* strains F4810/72 and WSBC 10925 were cultivated for 24 h at 24 °C in LB broth supplemented with D-glucose (0.2%) and MOD medium,[31] modified by adding sucrose (20 mM) and adjusting the final concentration of L-valine or $^{13}C_1$-L-valine (for $^{13}C_6$-**1**) to 20 mM while omitting L-isoleucine as reported previously.[28–30,32] After EtOH extraction, the target compounds were purified by C18 SPE cleanup, followed by preparative RP-HPLC, and their chemical structures were verified by means of UPLC-TOF MS and NMR experiments.[28,30]

UPLC-MS/MS-SIDA Quantitation of Cereulide (1) and Isocereulides A–G (2–8). For the preparation of an ethanolic stock solution of the target analytes, purified cereulide (**1**) and isocereulides A–G (**2**–**8**) were solubilized in ethanol and the exact individual concentrations determined by UPLC-MS/MS quantitation of **1**–**8** using $^{13}C_6$-cereulide as internal standard (triplicate analysis): cereulide (**1**; 89.35 ng/mL); isocereulide A (**2**; 99.35 ng/mL); isocereulide B (**3**; 90.66 ng/mL); isocereulide C (**4**; 14.51 ng/mL); isocereulide D (**5**; 67.19 ng/mL); isocereulide E (**6**; 78.01 ng/mL); isocereulide F (**7**; 67.37 ng/mL); and isocereulide G (**8**; 161.20 ng/

DOI: 10.1021/acs.jafc.5b03705
J. Agric. Food Chem. 2015, 63, 8307–8313

Table 1. Validation Criteria for the Quantitation of Cereulide (1) and Isocereulides A–G (2–8) Using $^{13}C_6$-Cereulide as an Internal Standard and Boiled Rice as Matrix

	amount added (ng/g)	amount recovered[a] (ng/g)	recovery rate[a] (%)	reproducibility[b] (ng/g; %)	repeatability[c] (%)	LOD/LOQ[d] (ng/g)
cereulide (**1**)	36	37.25 (±0.80)	107.2 (±1.8)	37.25 (±1.4); 4	2	0.16/0.45
	107	113.51 (±1.51)	107.4 (±1.4)		1	
isocereulide A (**2**)	40	43.72 (±0.96)	113.3 (±1.8)	43.52 (±1.2); 3	2	0.14/0.57
	119	134.72 (±2.38)	114.7 (±1.1)		2	
isocereulide B (**3**)	36	40.34 (±1.01)	114.4 (±2.4)	40.28 (±1.0); 2	3	0.12/0.56
	109	121.61 (±2.26)	113.5 (±1.9)		2	
isocereulide C (**4**)	6	7.04 (±0.21)	125.0 (±4.0)	6.78 (±0.4); 5	3	0.09/0.62
	17	20.52 (±0.68)	119.7 (±3.6)		3	
isocereulide D (**5**)	27	28.66 (±0.55)	109.7 (±1.7)	26.78 (±2.2); 8	2	0.11/0.41
	81	84.24 (±1.04)	106.1 (±1.1)		1	
isocereulide E (**6**)	31	33.73 (±0.48)	111.3 (±1.2)	32.85 (±1.4); 4	1	0.13/0.58
	94	101.86 (±1.68)	110.5 (±1.3)		2	
isocereulide F (**7**)	27	29.91 (±0.82)	114.2 (±2.5)	30.14 (±0.9); 3	3	0.14/0.67
	81	93.56 (±1.55)	117.5 (±1.0)		2	
isocereulide G (**8**)	64	67.27 (±1.06)	107.4 (±1.4)	67.95 (±2.2); 3	2	0.18/0.50
	193	204.18 (±4.15)	107.2 (±1.2)		2	
			112.5% (±1.8)	4	2	0.1/0.5

[a]Concentrations are given as the mean of three independent sample preparations with triple injection. [b]Reproducibility (interday precision as RSD in % and amount in ng/g) of three independent sample preparations analyzed at three different days (triple injection, each). [c]Repeatability (intraday precision as RSD in %) was determined using three replicates for each concentration in 1 day. [d]Limits of detection (LOD) and quantitation (LOQ) were calculated by analyzing spiked rice blank samples and were determined as the lowest concentrations of analyte for which signal-to-noise ratios were 3 and 10.

mL). Homogenized food samples (0.25 g) were weighed into a centrifuge tube (15 mL, Sigma-Aldrich, Germany) and spiked with a solution of $^{13}C_6$-cereulide (1.72 ng/mL in EtOH) as internal standard. For validation experiments, aliquots of the ethanolic stock solution of analytes **1–8** were spiked at different concentrations to a rice sample. After vortexing for 30 s and equilibration for 30 min at room temperature, extraction with MeCN (3 mL) was performed by shaking tubes for 1 h horizontally on a rocking table (250 rpm; Gesellschaft für Labortechnik mbH, Germany). The mixture was then centrifuged for 10 min (4.4 rpm, Eppendorf AG, Germany), and the supernatant was membrane filtered (0.45 μm; Schleicher & Schuell, Germany) and then directly analyzed by means of UPLC-MS/MS. Quantitation of the analytes was performed by means of a calibration curve using cereulide as analyte and $^{13}C_6$-cereulide as internal standard. Standard solutions of cereulide (0.04, 0.08, 0.41, 0.83, 1.65, 4.13, 8.25, 10.32, 12.38, 16.51, and 20.63 ng/mL in MeCN) and $^{13}C_6$-cereulide (1.72 ng/mL) were mixed and analyzed in triplicates by means of UPLC-MS/MS. A calibration curve was prepared by plotting peak area ratios of analyte to internal standard against concentration ratios of each analyte to the internal standard using linear regression (origin excluded). The equation for the quantifier mass transition (m/z 1170.7 → 357.2) obtained was $y = 1.4017x - 0.0475$ (cereulide/[$^{13}C_6$]-cereulide, $R^2 = 0.9998$).

Method Validation. The trueness and accuracy of the method were studied by recovery experiments by spiking a cooked rice sample with cereulide (**1**) and isocereulides A–G (**2–8**) at two concentration levels, each in three replicates, and triple UPLC-MS/MS injection (Table 1). Reproducibility and repeatability were determined to evaluate the robustness of the method. To study reproducibility, the rice sample was spiked with analytes **1–8** (Table 1), two replicates each, and analyzed in triplicates on three different days. Technical repeatability was studied by evaluation of results from triplicates received through quantitation of three independent sample replicates prepared with two different concentrations of analytes **1–8** (Table 1). To determine the limit of detection (LOD) and the limit of quantitation (LOQ), blank rice samples were spiked with different concentrations of cereulide and isocereulides A–G (Table 1) and equilibrated for 24 h at room temperature, and, after addition of the internal standard $^{13}C_6$-cereulide, quantitation was performed by UPLC-MS/MS as detailed above. LOD and LOQ were calculated as the concentrations equaling signal-to-noise ratios of 3 and 10, respectively.

Ultraperformance Liquid Chromatography–Mass Spectrometry. Mass spectrometric analyses were performed on a Waters Xevo TQ-S mass spectrometer (Waters, Manchester, UK) coupled to an Acquity UPLC i-class core system (Waters, Milford, MA, USA) consisting of a binary solvent manager, sample manager, and column oven. Aliquots (2 μL) of prepared samples were injected into the UPLC/MS-MS system equipped with a 2.1 × 150 mm, 1.7 μm, UPLC CSH C18 column (Waters, Manchester, UK). Operated with a flow rate of 0.7 mL/min at a temperature of 55 °C, the following gradient was used for chromatography: starting with a mixture (85:15, v/v) of MeCN (0.25% HCOOH) as solvent A and $HCOONH_4$ (10 mmol, 0.1% HCOOH) as solvent B, solvent A was increased to 95% within 8.0 min, increased to 99% within 0.1 min, kept constant for 0.9 min, decreased within 0.1 min to 85%, and followed by re-equilibration on starting conditions for 0.9 min. Measurements were performed using positive electrospray ionization (ESI) and the quantitative calibration mode consisting of the following ion source parameters: capillary voltage, +3.6 kV; sampling cone, 50 V; source offset, 35 V; source temperature, 150 °C; desolvation temperature, 650 °C; cone gas, 250 L/h; desolvation gas, 1100 L/h; collision gas flow, 0.15 mL/min; and nebulizer gas flow, 7.0 bar. Calibration of the mass spectrometer in the range from m/z 40 to 1963 was performed using a solution of

DOI: 10.1021/acs.jafc.5b03705
J. Agric. Food Chem. 2015, 63, 8307–8313

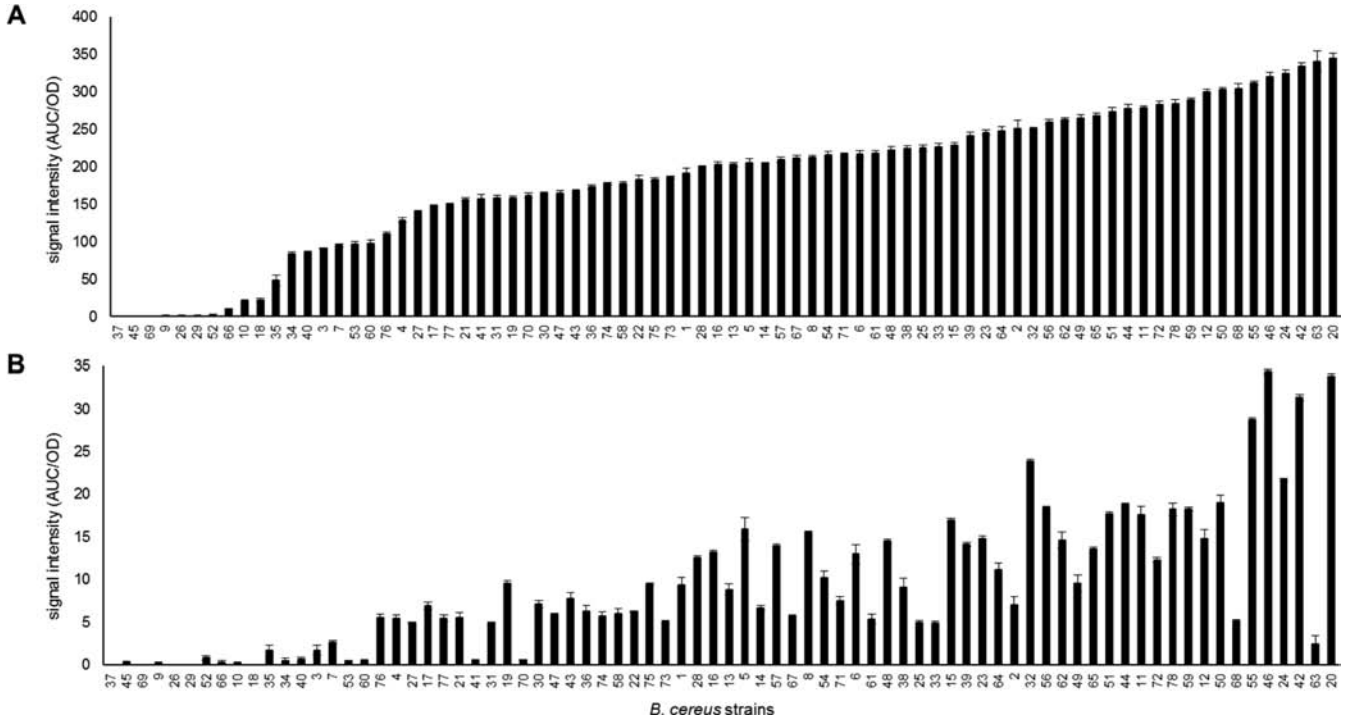

Figure 2. UPLC-ESI-TOF MS analysis of (A) cereulide and (B) isocereulides A–G (**2**–**8**) in 78 *B. cereus* strains.

phosphoric acid (0.1% in MeCN). The UPLC Xevo TQ-S system was operated with MassLynx 4.1 SCN 813 (Waters), and data processing and analysis were performed using TargetLynx (Waters). By means of the multiple reaction monitoring (MRM) mode, the ammonium adducts of cereulide and isocereulide G (m/z 1170.7 → qualifier, m/z 172.2, 314.2; quantifier, m/z 357.2), isocereulides A and F (m/z 1184.7 → qualifier, m/z 172.2, 314.2; quantifier, m/z 357.2), isocereulides B and E (m/z 1156.6 → qualifier, m/z 172.2, 314.2; quantifier, m/z 357.2), isocereulide C (m/z 1186.6 → qualifier, m/z 172.2, 314.2; quantifier, m/z 357.2), isocereulide D (m/z 1142.6 → qualifier, m/z 172.2, 314.2; quantifier, m/z 357.2) and $^{13}C_6$-cereulide (m/z 1176.7 → m/z qualifier, 173.2, 316.2; quantifier, m/z 358.2) were analyzed using the mass transitions (given in parentheses) monitored for a duration of 25 ms. ESI^+ mass and product ion spectra were acquired with direct flow infusion using IntelliStart. The MS/MS parameters were tuned for each individual compound, detecting the fragmentation of the $[M + NH_4]^+$ molecular ions into specific product ions after collision with argon.

High-Resolution Mass Spectrometry. UPLC-ESI-TOF-MS analyses were performed on a Waters Synapt G2 HDMS spectrometer that was coupled to an Acquity UPLC core system (Waters) equipped with a 2 × 150 mm, 1.8 μm, HSS T3 C18 column (Waters, Manchester, UK). Chromatographic and mass spectrometric parameters were identical with those reported recently.[29] The raw data obtained from UPLC-TOF-MS analysis were processed with MarkerLynx XS using ApexTrack peak integration to detect chromatographic peaks. Marker intensity threshold was set to 2000 cps, mass window was 0.02 Da, retention time window was 0.1 s, and data were deisotoped.

RESULTS AND DISCUSSION

Recent mass spectrometric screening demonstrated a high chemodiversity of the emetic toxin cereulide (**1**) and indicated a series of at least 18 cereulide variants, among which the major isocereulides A–G (**2**–**8**) were determined in their chemical structures (Figure 1).[29,30]

***B. cereus* Strain Profiling.** To answer the question of whether cereulide production by *B. cereus* strains is coupled to the generation of isocereulides A–G, 78 *B. cereus* strains representative for different sources (clinic, food intoxications, food, environment) and derived from diverse geographical origins were grown under defined conditions for 24 h at 24 °C in LB broth supplemented with 0.2% glucose (10^3 cfu/mL), extracted with ethanol and, then, analyzed by means of UPLC-TOF-MS.[29] To consider possible variations of the cereulide content due to different growth behaviors of *B. cereus* strains, the optical density of the cultures was determined after 24 h of incubation. The optical density (OD_{600}) of the various *B. cereus* cultures, each incubated under identical conditions, was in a rather narrow range between 14 and 19 (16.5 ± 1.8 relative standard deviation, RSD). The frequency of the $[M + Na]^+$ ion (area under the curve, AUC) recorded for cereulide (Figure 2A) and isocereulides A–G (Figure 2B) was then normalized for the optical density measured for each strain. No/low cereulide-producing *B. cereus* strains with AUC/OD ratios below 50 produced no or only low amounts of isocereulides A–G (Figure 2A). Most of the medium (AUC/OD ratios of 50–250) and high cereulide producers (AUC/OD > 250) generated also medium to high amounts of isocereulides (Figure 2B). Exceptions such as *B. cereus* strains 63, 68, and 70 might be due to variations in the strains' genetic backgrounds because isocereulide biosynthesis involves the relaxed substrate specificity of the A domains, an inefficient proofreading by Ces T, and a different peptide assembly compared to cereulide.[30,33] Although isocereulides A–G seem to be produced in about 10 times lower amounts when compared to cereulide, the ∼8 times increased cytotoxic activity found for isocereulide A requires an accurate quantitation of all these depsipeptides to enable a profound knowledge-based risk assessment of *B. cereus* toxins in foods.[30]

Development of a Stable Isotope Dilution Analysis. To develop a fast and robust SIDA for the combined quantitation of cereulide (**1**) and isocereulides A–G (**2**–**8**) by means of UPLC-MS/MS, first, reference material of the analytes **1**–**8** and $^{13}C_6$-cereulide to be used as the internal

DOI: 10.1021/acs.jafc.5b03705
J. Agric. Food Chem. 2015, 63, 8307–8313

standard were biosynthetically produced by cultivating *B. cereus* under optimized conditions in the presence of L-valine and $^{13}C_6$-L-valine, respectively, followed by straightforward downstream purification as reported recently.[28,30]

To evaluate the suitability of $^{13}C_6$-cereulide as internal standard for quantitation of analytes **1**–**8**, $^{13}C_6$-cereulide and the analytes were individually infused into the mass spectrometer using a syringe pump. Optimum intensities of pseudomolecular ions and respective fragments were obtained by software-assisted ramping of the declustering potential, the cell entrance potential, and the collision energy, as well as the cell exit potential, respectively. As the ion $[M + NH_4]^+$ of cereulide and isocereulides A–G was the most predominant pseudomolecular ion, these were selected for the optimization. Tuning of the ammonium adducts and the pseudomolecular ions $[M + H]^+$ revealed similar fragment patterns and fragment intensities.

Fast chromatographic baseline separation of the analytes **1**–**8** was achieved within 10 min using a RP-UPLC CSH C18 column (Figure 3A). For analysis of cereulide (**1**; *m/z* 1170.7),

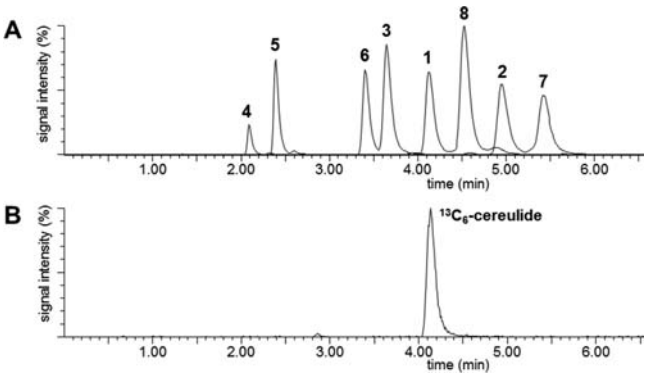

Figure 3. UPLC-ESI-MS/MS mass chromatogram of (A) cereulide (**1**) and isocereulides A–G (**2**–**8**) and (B) the internal standard $^{13}C_6$-cereulide.

isocereulide G (**8**; *m/z* 1170.7), isocereulides A (**2**) and F (**7**) (*m/z* 1184.7), isocereulides B (**3**) and E (**6**) (*m/z* 1156.6), isocereulide C (**4**; *m/z* 1186.6), and isocereulide D (**5**; *m/z* 1142.6), the same fragment ions were selected as qualifier (*m/z* 172.2, 314.2) and quantifier (*m/z* 357.2). For the internal standard $^{13}C_6$-cereulide (*m/z* 1176.7), the qualifier fragments *m/z* 173.2 and 316.2 and the quantifier ion *m/z* 358.2 were selected (Figure 3B).

Performance of the developed UPLC-MS/MS SIDA method was checked by using boiled rice as matrix and a mixture containing defined amounts of the analytes cereulide (**1**) and isocereulides A–G (**2**–**8**) in a range of 14.51–161.20 ng/mL for spiking experiments. Calibration over 2.5 order of magnitudes revealed good linearity for the analysis of cereulide using $^{13}C_6$-cereulide as internal standard with a correlation coefficient >0.999. The obtained calibration curve was used to check the performance of the developed UPLC-MS/MS method for a combined quantitation of cereulide and isocereulides A–G.

The trueness of the analytical method was studied by recovery experiments. To achieve this, a blank rice sample was spiked with analytes **1**–**8** at two different concentration levels and, then, analyzed by UPLC-MS/MS SIDA. The determined recovery rates ranged between 107% (**1**, **8**) and 125% (**4**) with RSD ranging from 1 to 4%, thus demonstrating appropriate trueness and precision of the developed UPLC-MS/MS method.

To evaluate the robustness of the SIDA method, repeatability and reproducibility were determined. Technical repeatability (intraday precision) of the analytical method was evaluated by considering the quantitative data obtained from triple injections of three sample replicates prepared with two concentrations of cereulide and isocereulides A–G (Table 1). For all analytes, the relative standard deviation was <3%. To study the reproducibility (interday precision) of the analytical method, three independent sample preparations with one concentration of cereulide and isocereulides A–G (Table 1), two replicates each, were analyzed in triplicates at three different days. Relative standard deviation of the analytes ranged from 3% (**2**) to 8% (**5**).

LOD and LOQ were determined in boiled rice as the concentration at which the peak height of cereulide and isocereulides A–G was at least 3 and 10 times, respectively, above the noise level. To achieve this, different concentrations of **1**–**8** were spiked to boiled rice and UPLC-MS/MS quantitation was performed using $^{13}C_6$-cereulide as internal standard. On average, LOD and LOQ were found to be 0.1 and 0.5 ng/g for cereulide and isocereulides A–G, respectively, thus indicating high sensitivity for the developed UPLC-MS/MS method.

To apply the UPLC-MS/MS SIDA quantitation of **1**–**8** to real food samples, a total of 25 randomly selected commercial food and feed samples (rice, puddings, desserts, cereals, baby foods, animal feeds) and two suspicious noodle samples, which were assumed to have caused intoxications in five child daycare facilities and were obtained from the German Health and Food Safety Authority, were analyzed. Whereas cereulide (**1**) and isocereulides A–G (**2**–**8**) could not be detected in amounts >0.1 ng/g (LOD) in any of the 25 commercial food and feed samples, both suspicious noodle samples showed elevated levels of cereulide (**1**) and isocereulides A–G (**2**–**8**) ranging from 0.59 ng/g (**7**) to 189.08 ng/g (**1**) in noodle sample 1 and from 5.77 ng/g (**7**) to 6198.17 ng/g (**1**) in sample 2 (Table 2).

Table 2. Concentrations of Cereulide (1) and Isocereulides A–G (2–8) in Suspicious Cooked Noodles

	concn[a] (ng/g) in	
analyte	sample 1	sample 2
cereulide (**1**)	189.08 (±28.88)	6198.17 (±162.09)
isocereulide A (**2**)	11.81 (±1.82)	268.28 (±9.56)
isocereulide B (**3**)	1.12 (±0.09)	15.40 (±0.79)
isocereulide C (**4**)	1.02 (±0.06)	10.13 (±0.33)
isocereulide D (**5**)	0.77 (±0.04)	9.34 (±0.31)
isocereulide E (**6**)	0.95 (±0.05)	9.61 (±0.45)
isocereulide F (**7**)	0.59 (±0.01)	5.77 (±0.09)
isocereulide G (**8**)	3.40 (±0.39)	84.56 (±3.48)

[a]Results are given as the mean of two independent cleanups with triple injection.

Because symptoms of intoxication caused by cereulide (**1**) are reported to be observable at concentrations of ≥10 μg/kg body weight, the detected cereulide concentration in both noodle samples indicates the potential to cause food poisoning in 2–6-year-old children, which have about 10–30 kg body weight.[5,34] Interestingly, isocereulide A (**2**) was detected in both noodle samples as the most predominant variant among the isocereulides. Although isocereulide A was found in both

DOI: 10.1021/acs.jafc.5b03705
J. Agric. Food Chem. 2015, 63, 8307–8313

noodle samples in 16 and 23 times lower concentrations when compared to cereulide (**1**), the ~8-fold increased cytotoxicity of **2** indicates isocereulide A as a potential key toxic component in *B. cereus*-contaminated food.[30]

In summary, a rapid, sensitive, and robust SIDA for the combined quantification of cereulide (**1**) and isocereulides A–G (**2**–**8**) by means of UPLC-MS/MS was developed. On average, trueness and precision of the method were 112.5% (±1.8 RSD), repeatability and reproducibility were 2 and 4% for cereulide and isocereulides A–G, and the LOD and LOQ of 0.1 and 0.5 ng/g demonstrated a high sensitivity for the developed SIDA method in the range or even better than the LOQ of 4.1 and 1.0 ng/g reported recently for cereulide,[26,35] thus supporting a knowledge-based risk assessment of the entire set of *B. cereus* toxins in foods. The observation that isocereulide A (**2**), showing an ~8-fold increased cytotoxicity when compared to cereulide (**1**), was present in *B. cereus*-contaminated noodle samples as the major isocereulide indicates isocereulide A as a potential key toxic component in *B. cereus*-contaminated food. These findings urge further studies to explore potential synergistic cocktail effects of cereulide and isocereulides on the biological function of these depsipeptides.

AUTHOR INFORMATION

Corresponding Author

*(T.H.) Phone: +49-8161-71-2902. Fax: +49-8161-71-2949 E-mail: thomas.hofmann@tum.de.

Author Contributions

‖S.M. and T.D.S. contributed equally to this work.

Funding

This research project (AiF 16845 N) was supported by the German Ministry of Economics and Technology (via AiF) and the FEI (Forschungskreis der Ernährungsindustrie e.V., Bonn).

Notes

The authors declare no competing financial interest.

REFERENCES

(1) Ehling-Schulz, M.; Fricker, M.; Scherer, S. *Bacillus cereus*, the causative agent of an emetic type of food-borne illness. *Mol. Nutr. Food Res.* **2004**, *48*, 479–487.

(2) Stenfors, A. L. P.; Fagerlund, A.; Einar, G. P. From soil to gut: *Bacillus cereus* and its food poisoning toxins. *FEMS Microbiol. Rev.* **2008**, *32*, 579–606.

(3) Agata, N.; Mori, M.; Ohta, M.; Suwan, S.; Ohtani, I.; Isobe, M. A novel dodecadepsipeptide, cereulide, isolated from *Bacillus cereus* causes vacuole formation in HEp-2 cells. *FEMS Microbiol. Lett.* **1994**, *121*, 31–34.

(4) Suwan, S.; Isobe, M.; Ohtani, I.; Agata, N.; Mori, M.; Ohta, M. Structure of cereulide, a cyclic dodecadepsipeptide toxin from *Bacillus cereus* and studies on NMR characteristics of its alkali metal complexes including a conformational structure of the K^+ complex. *J. Chem. Soc., Perkin Trans. 1* **1995**, 765–775.

(5) Agata, N.; Ohta, M.; Mori, M.; Isobe, M. A novel dodecadepsipeptide, cereulide, is an emetic toxin of *Bacillus cereus*. *FEMS Microbiol. Lett.* **1995**, *129*, 17–20.

(6) Mahler, H.; Pasi, A.; Kramer, J. M.; Schulte, P.; Scoging, A. C.; Bär, W.; Krähenbühl, S. Fulminant liver failure in association with the emetic toxin of *Bacillus cereus*. *N. Engl. J. Med.* **1997**, *336*, 1142–1148.

(7) Dierick, K.; Coillie, E. V.; Swiecicka, I.; Meyfroidt, G.; Devlieger, H.; Meulemans, A.; Hoedemaekers, G.; Fourie, L.; Heyndrickx, M.; Mahillon, J. Fatal family outbreak of *Bacillus cereus*-associated food poisoning. *J. Clin. Microbiol.* **2005**, *43*, 4277–4279.

(8) Ichikawa, K.; Gakumazawa, M.; Inaba, A.; Shiga, K.; Takeshita, S.; Mori, M.; Kikuchi, N. Acute encephalopathy of *Bacillus cereus* mimicking Reye syndrome. *Brain Dev.* **2009**, *32*, 688–690.

(9) Shiota, M.; Saitou, K.; Mizumoto, H.; Matsusaka, M.; Agata, N.; Nakayama, M.; Kage, M.; Tatsumi, S.; Okamoto, A.; Yamaguchi, S.; Ohta, M.; Hata, D. Rapid detoxification of cereulide in *Bacillus cereus* food poisoning. *Pediatrics* **2010**, *125*, 951–955.

(10) Naranjo, M.; Denayer, S.; Botteldoorn, N.; Delbrassinne, L.; Veys, J.; Waegenaere, J.; Sirtaine, N.; Driesen, R. B.; Sipido, K. R.; Mahillon, J.; Dierick, K. Sudden death of a young adult associated with *Bacillus cereus* food poisoning. *J. Clin. Microbiol.* **2011**, *49*, 4379–4381.

(11) Saleh, M.; Al Nakib, M.; Doloy, A.; Jacqmin, S.; Ghiglione, S.; Verroust, N.; Poyart, C.; Ozier, Y. *Bacillus cereus*, an unusual cause of fulminant liver failure: diagnosis may prevent liver transplantation. *J. Med. Microbiol.* **2012**, *61*, 743–745.

(12) Tschiedel, E.; Rath, P. M.; Steinmann, J.; Becker, H.; Dietrich, R.; Paul, A.; Felderhoff-Muser, U.; Dohna-Schwake, C. Lifesaving liver transplantation for multi-organ failure caused by *Bacillus cereus* food poisoning. *Pediatr. Transplant.* **2015**, *19*, E11–E14.

(13) Mikkola, R.; Saris, N. E. L.; Grigoriev, P. A.; Andersson, M. A.; Salkinoja-Salonen, M. S. Ionophoretic properties and mitochondrial effects of cereulide: the emetic toxin of *B. cereus*. *Eur. J. Biochem.* **1999**, *263*, 112–117.

(14) Hughes, S.; Bartholomew, B.; Hardy, J. C.; Kramer, J. M. Potential application of a HEp-2 cell assay in the investigation of *Bacillus cereus* emetic-syndrom food poisoning. *FEMS Microbiol. Lett.* **1988**, *52*, 7–12.

(15) Andersson, M. A.; Mikkola, R.; Helin, J.; Andersson, M. C.; Salkinoja-Salonen, M. A novel sensitive bioassay for detection of *Bacillus cereus* emetic toxin and related depsipeptide ionophores. *Appl. Environ. Microbiol.* **1998**, *64*, 1338–1343.

(16) Andersson, M. A.; Jääskeläinen, E. L.; Shaheen, R.; Pirhonen, T.; Wijnands, L. M.; Salkinoja-Salonen, M. S. Sperm bioassay for rapid detetion of cereulide-producing *Bacillus cereus* in food and related environments. *Int. J. Food Microbiol.* **2004**, *94*, 175–183.

(17) Rajkovic, A.; Uyttendaele, M.; Deley, W.; Van Soom, A.; Rijsselaere, T.; Debevere, J. Dynamics of boar semen motility inhibition as a semi-quantitative measurement of *Bacillus cereus* emetic toxin (cereulide). *J. Microbiol. Methods* **2006**, *65*, 525–534.

(18) Finlay, W. J. J.; Logan, N. A.; Sutherland, A. D. Semiautomated metabolic staining assay for *Bacillus cereus* emetic toxin. *Appl. Environ. Microbiol.* **1999**, *65*, 1811–1812.

(19) Kawamura-Sato, K.; Hirama, Y.; Agata, N.; Ito, H.; Torii, K.; Takeno, A.; Hasegawa, T.; Shimomura, Y.; Ohta, M. Quantitative analysis of cereulide, an emetic toxin of *Bacillus cereus*, by using rat liver mitochondria. *Microbiol. Immunol.* **2005**, *49*, 25–30.

(20) Fricker, M.; Messelhäußer, U.; Busch, U.; Scherer, S.; Ehling-Schulz, M. Diagnostic real-time PCR assays for the detection of emetic *Bacillus cereus* strains in foods and recent foodborne outbreaks. *Appl. Environ. Microbiol.* **2007**, *73*, 1892–1898.

(21) Oh, M. H.; Cox, J. M. Quantitative analysis of the Bacillus cereus emetic toxin, cereulide, using micellar electrokinetic chromatography-capillary electrophoresis. *J. Food Saf.* **2010**, *30*, 652–665.

(22) Häggblom, M. M.; Apetroaie, C.; Andersson, M. A.; Salkinoja-Salonen, M. S. Quantitative analysis of cereulide, the emetic toxin of *Bacillus cereus*, produced under various conditions. *Appl. Environ. Microbiol.* **2002**, *68*, 2479–2483.

(23) Jääskeläinen, E. L.; Häggblom, M. M.; Andersson, M. M.; Vanne, L.; Salkinoja-Salonen, M. S. Potential of *Bacillus cereus* for producing an emetic toxin, cereulide, in bakery products: quantitative analysis by chemical and biological methods. *J. Food Prot.* **2002**, *66*, 1047–1054.

(24) Delbrassinne, L.; Andjelkovic, M.; Rajkovic, A.; Bottledoorn, N.; Mahillon, J.; Van Loco, J. Follow-up of the *Bacillus cereus* emetic toxin production in penne pasta under household conditions using liquid chromatography coupled with mass spectrometry. *Food Microbiol.* **2011**, *28*, 1105–1109.

(25) Hormazabal, V.; Ostensvik, O.; O'Sullivan, K.; Granum, P. E. Quantification of *Bacillus cereus* emetic toxin (cereulide) in figs using LC/MS. *J. Liq. Chromatogr. Relat. Technol.* **2004**, *27*, 2531–2538.

(26) Biesta-Peters, E. G.; Reij, M. W.; Blaauw, R. H.; in't Veld, R. H.; Rajkovic, A.; Ehling-Schulz, M.; Abee, T. Quantification of the emetic

DOI: 10.1021/acs.jafc.5b03705
J. Agric. Food Chem. 2015, 63, 8307–8313

toxin cereulide in food products by liquid chromatography-mass spectrometry using synthetic cereulide as a standard. *Appl. Environ. Microbiol.* **2010**, *76*, 7466−7472.
(27) Ueda, S.; Nakajima, H.; Iwase, M.; Shinagawa, K.; Kuwabara, Y. LC-MS analysis of the emetic toxin, cereulide, produced by *Bacillus cereus*. *Biocontrol Sci.* **2012**, *17*, 191−195.
(28) Bauer, T.; Stark, T. D.; Hofmann, T.; Ehling-Schulz, M. Development of a stable isotope dilution analysis for the quantification of the *Bacillus cereus* toxin cereulide in foods. *J. Agric. Food Chem.* **2010**, *58*, 1420−1428.
(29) Stark, T.; Marxen, S.; Rütschle, A.; Lücking, G.; Scherer, S.; Ehling-Schulz, M.; Hofmann, T. Mass spectrometric profiling of *Bacillus cereus* strains and quantitation of the emetic toxin cereulide by means of stable isotope analysis and HEp-2 bioassay. *Anal. Bioanal. Chem.* **2013**, *405*, 191−201.
(30) Marxen, S.; Stark, T. D.; Frenzel, E.; Rütschle, A.; Lücking, G.; Pürstinger, G.; Pohl, E. E.; Scherer, S.; Ehling-Schulz, M.; Hofmann, T. Chemodiversity of cereulide, the emetic toxin of *Bacillus cereus*. *Anal. Bioanal. Chem.* **2015**, *407*, 2439−2453.
(31) Rosenfeld, E.; Duport, C.; Zigha, A.; Schmitt, P. Characterization of aerobic and anaerobic vegetative growth of the food-borne pathogen *Bacillus cereus* F4430/73 strain. *Can. J. Microbiol.* **2005**, *51*, 149−158.
(32) Ehling-Schulz, M.; Svensson, B.; Guinebretiere, M. H.; Lindbäck, T.; Andersson, M.; Schulz, A.; Fricker, M.; Christiansson, A.; Granum, P. E.; Märtlbauer, E.; Nguyen-The, C.; Salkinoja-Salonen, M.; Scherer, S. Emetic toxin formation of *Bacillus cereus* is restricted to a single evolutionary lineage of closely related strains. *Microbiology* **2005**, *151*, 183−197.
(33) Marxen, S.; Stark, T. D.; Rütschle, A.; Lücking, G.; Frenzel, E.; Scherer, S.; Ehling-Schulz, M.; Hofmann, T. Depsipeptide intermediates interrogate proposed biosynthesis of cereulide, the emetic toxin of *Bacillus cereus*. *Sci. Rep.* **2015**, *5*, 10637.
(34) Jääskeläinen, E. L.; Teplova, V.; Andersson, M. A.; Andersson, L. C.; Tammela, P.; Andersson, M. C.; Pirhonen, T. I.; Saris, N. E. L.; Vuorela, P.; Salkinoja-Salonen, M. S. In vitro assay for human toxicity of cereulide, the emetic mitochondrial toxin produced by food poisoning *Bacillus cereus*. *Toxicol. In Vitro* **2003**, *17*, 737−744.
(35) Muratovic, A. Z.; Tröger, R.; Granelli, K.; Hellenäs, K.-E. Quantitative analysis of cereulide toxin from *Bacillus cereus* in rice and pasta using synthetic cereulide standard and $^{13}C_6$-cereulide standard - a short validation study. *Toxins* **2014**, *6*, 3326−3335.

DOI: 10.1021/acs.jafc.5b03705
J. Agric. Food Chem. 2015, 63, 8307−8313

(QTOF) and ion trap or quadrupole orbital ion trap (Q-orbital trap) MS, can be used for screening for chemical contaminants in full-scan mode and aid in the structural elucidation, identification, and characterization of the chemical on the basis of high-resolution and -accuracy mass results in MS/MS mode with improved method performance and precision and accuracy of analytical data.[11−16]

This study reports the development and testing of a UHPLC/Q-orbital trap MS method for the simultaneous determination of common mycotoxins, including the major classes such as aflatoxins, ergot alkaloids, fumonisins, ochratoxins, and trichothecenes. The performance and practical applicability of UHPLC/Q-orbital trap MS will be assessed by evaluating a validated procedure used to analyze, quantitate, and identify 26 mycotoxins in commercially available finished grain and nut products and reference grain materials by LC-MS/MS.[17] This hybrid technology has already been applied to screening mycotoxins in dairy products in full-scan mode.[18] Finished samples will be screened using full-scan MS, and identification of mycotoxins is achieved by data-dependent MS/MS experiment (DDMS^2) using the hybrid Q-orbital trap MS technology. The high-resolution and -accuracy mass results generated will also be evaluated with results generated in previous work using LC-MS/MS. High mass accuracy results of the product ions generated from MS/MS fragmentation can be used to propose structural information on the products and will provide further confidence in the identification of mycotoxins in finished grain and nut samples.

MATERIALS AND METHODS

Safety. Mycotoxins are toxic chemical compounds that may be fatal if inhaled, absorbed through the skin, or swallowed and must be treated with extreme caution and care. All laboratory safety rules including wearing of safety goggles and gloves must be strictly followed at all times. All mycotoxin waste should be properly disposed of in a designated waste container to prevent the possible spread of these chemicals. All sample vials, vial caps, and other glassware used to prepare, contain, or make contact with the mycotoxin standards were soaked in a 1% minimum bleach solution for at least 72 h before proper disposal.

Chemicals and Materials. Aflatoxin B_1, aflatoxin B_2, aflatoxin G_1, aflatoxin G_2, beauvericin, deoxynivalenol, diacetoxyscirpenol, 15-acetyldeoxynivalenol, fumonisin B_1, fumonisin B_2, fusarenon-X, HT-2 toxin, neosolaniol, ochratoxin A, ochratoxin B, T-2 toxin, and zearalenone standards were purchased in neat form from Romer Laboratories, Inc. (Union, MO). Ergot alkaloids (ergocornine, ercocristine, ergocryptine, ergometrine, ergosine, ergotamine) were provided as a mixture, also purchased from Romer Laboratories. Citrinin, sterigmatocystin, and verrucarin A standards were purchased from Sigma-Aldrich (St. Louis, MO).

Stable isotope-labeled internal standards, $^{13}C_{17}$-aflatoxin B_1 (0.5 μg/mL), $^{13}C_{20}$-ochratoxin A (10 μg/mL), $^{13}C_{18}$-zearalenone (25 μg/mL), $^{13}C_{34}$-fumonisin B_1 (25 μg/mL), and $^{13}C_{24}$-T-2 toxin (25 μg/mL), and two reference materials, aflatoxin in maize and zearalenone in maize, were purchased from Romer Laboratories, Inc. (Union, MO). Native and isotope-labeled mycotoxins, CAS numbers, molecular formulas, molecular weight, and other relevant UHPLC and MS information are provided in the Supporting Information, Table S1. Nine reference materials (aflatoxin, deoxynivalenol, and zearalenone in corn and wheat) were generously provided by the United States Department of Agriculture, Grain Inspection, Packers and Stockyards Administration, Technology and Science Division (USDA-GIPSA-TSD, Kansas City, MO). Rice, wheat, corn, peanut, pistachio, and almond samples and finished grain (i.e., pasta) and nut (i.e., peanut butter) products were purchased from commercially available sources.

LC-grade acetonitrile, methanol, and water and MS-grade formic acid and ammonium formate were purchased from Fisher Scientific (Pittsburgh, PA). Plastic syringes (3 mL) and 13 mm × 0.2 μm PTFE syringe filters were purchased from Pall Life Sciences (Ann Arbor, MI). Positive- and negative-ion solutions used to calibrate the Q-orbital trap MS were purchased through ThermoFisher Scientific Inc. (San Jose, CA).

Standards Preparation. Stock standard solutions (200 μg/mL) of each of the 26 mycotoxin standards were prepared by dissolving 5.0 mg of the mycotoxin in 25 mL of acetonitrile. As previously described, two working standard solutions were used: groups A and B. Group A consisted of aflatoxin B_1, aflatoxin B_2, aflatoxin G_1, aflatoxin G_2, beauvericin, diacetoxyscirpenol, ergot alkaloids, HT-2 toxin, neosolaniol, ochratoxin A, ochratoxin B, sterigmatocystin, T-2 toxin, and verrucarin A, prepared to a concentration of 1.0 μg/mL by transferring 0.5 mL of the diluted individual stock standard solution (20 μg/mL) to a 10 mL volumetric flask, and then bringing the mixture up to volume with acetonitrile/water (50:50, v/v). Group B consisted of citrinin, deoxynivalenol, 15-acetyldeoxynivalenol, fumonisin B_1, fumonisin B_2, fusarenon-X, and zearalenone, prepared to a concentration of 10 μg/mL by delivering 0.5 mL of each individual stock standard (200 μg/mL) to a 10 mL volumetric flask and then bringing the mixture up to volume with acetonitrile/water (50:50, v/v). Stock solutions and working standard solutions used in the preparation of solvent-only calibration standards, matrix-matched calibration standards, and method recovery studies were stored at −20 °C.

Solvent-only calibration standards (SOCS) were prepared from the working standard solutions by diluting the group A and B working standard solutions to 500 and 5000 ng/mL, respectively. Eight SOCSs (0.5, 1.0, 2.5, 5.0, 10, 25, 50, and 100 ng/mL for group A; 5.0, 10, 25, 50, 100, 250, 500, and 1000 ng/mL for group B) were prepared by successive dilution of the group A and group B mixed working standard solutions with acetonitrile/water (50:50, v/v). The mixed isotope labeled internal standards solution was prepared by mixing 0.1 mL each of $^{13}C_{17}$-aflatoxin B_1 (0.5 μg/mL), $^{13}C_{20}$-ochratoxin A (2.5 μg/mL), $^{13}C_{18}$-zearalenone (5 μg/mL), $^{13}C_{34}$-fumonisin B_1 (25 μg/mL), and $^{13}C_{24}$-T-2 toxin (5 μg/mL) with 0.5 mL acetonitrile/water (50:50, v/v). These mixed isotope labeled internal standards solution was added (20 μL) to the SOCS and brought to volume at 1.0 mL, resulting in concentration levels of 1.0, 5.0, 10, 50, and 10 ng/mL, respectively.

Sample Preparation. As previously described, packaged grains and nuts (shells removed) were homogenized with dry ice in a RobotCoupe blender (Ridgeland, MS) until powdery consistencies were obtained.[11] The homogenized samples were transferred to polypropylene freezer bags stored in a −20 °C freezer, and the bags were left open to allow the carbon dioxide to sublime before being sealed until further use.

A volume of 5 mL of extraction solvent (acetonitrile/water, 85/15, v/v) was added to 1.00 ± 0.02 g of ground sample in 15 mL disposable screw capped polypropylene centrifuge tubes (Corning Inc., Corning, NY).[17] Samples were extracted for 30 min using a high-speed shaker with pulsation (Glas-Col, Terre Haute, IN) using a motor speed setting of 75 (1540−1560 rpm as measured by a DPM5 digital photo tachometer (Universal Enterprises, Inc. Beaverton, OR) and pulser frequency set at the middle mark of the dial (∼30−35 pulsations/min), followed by centrifugation for 5 min at 4500 rpm (4200*g*) (ThermoElectro Corp., Milford, MA). A 500 μL portion of the extract was transferred to a clean test tube, followed by the addition of 20 μL of the internal standard solution and 480 μL of 20 mM ammonium formate, and then the tube was vortexed for 15 s. Samples were filtered through 13 mm × 0.2 μm PTFE syringe filters (Pall Life Sciences, Ann Arbor, MI) and added via a 3 mL disposable syringe directly into an autosampler vial (National Scientific, Rockwood, TN).

Recovery Studies. Method recovery samples were prepared in quadruplicates from the homogenized sample matrices at three spiking concentrations (10, 50, and 100 μg/kg for group A; 100, 500, and 1000 μg/kg for group B). Method blank samples were also prepared in each sample batch as quality control samples, and also for matrix effect studies. For group A recovery studies, the spiking solution volumes of 100 μL (0.1 μg/mL), 50 μL (1 μg/mL) or 100 μL (1 μg/mL) was added to the sample tubes containing 1.00 ± 0.02 g of ground samples

DOI: 10.1021/jf505049a
J. Agric. Food Chem. 2015, 63, 8314−8332

to achieve fortification levels of 10, 50, or 100 μg/kg, respectively. For group B recovery studies, spiking solution volumes of 100 μL (1 μg/mL), 50 μL (10 μg/mL) or 100 μL (10 μg/mL) were added into sample tubes containing 1.00 ± 0.02 g of ground samples to achieve fortification levels of 100, 500, or 1000 μg/kg, respectively. After addition of 5 mL of extraction solvent (acetonitrile/water, 85/15, v/v), the sample tubes were placed on the high-speed shaker and extracted as described in the previous section.

Quantitation was performed by matching the peak area ratio responses of the analyte and calibration standards to that of the internal standard. For those native compounds without labeled internal standards, quantitation was performed by the external standard method; the concentration of the analyte was determined using the curve based on the peak areas of matrix-matched calibration standards. Matrix-matched standards were prepared by extracting rice, wheat, corn, peanut, pistachio, and almond blanks (matrices were determined blanks by analysis) and then fortifying the extracts with calibration standards to the appropriate concentrations. Calibration curves consisted of the eight calibration standards from the two mycotoxin groups (A and B) and were constructed using least-squares regression.

Analysis of Reference Materials and Commercial Products. Reference materials obtained from Romer Laboratories and USDA-GIPSA-TSD, and commercial finished grain and nut products were prepared in triplicates using procedures described in the Sample Preparation section. Whole samples were homogenized, while finished commercial products that were already in homogeneous form were used as provided. The samples were quantitated using matrix-matched standards prepared from matrices that were screened and determined to be free of the mycotoxins of interest using the internal standard calibration method.

Limits of Detection and Quantitation Studies. The matrix-dependent instrument limits of detection and quantitation (MD-ILD and MD-ILQ) for each analyte were obtained using procedures similar to those described by the U.S. Environmental Protection Agency's (EPA) protocol.[19] Matrix-matched LOD/Q can provide an estimate of the method LOD/Q as well as assess the sensitivity of the instrument and allow comparisons to other platforms in the presence of the matrix. The MD-ILD was determined from replicate (n = 8) analyses of the estimated detection limit using the lowest (or fortifying with a lower) concentration of a matrix-matched calibration standard (MMCS) that is statistically different from the matrix-matched blank and multiplying the standard deviation (SD) by 2.998 (critical $t_{0.010}$ = 2.998 for degrees of freedom (d_f) of 7). The MD-ILQ was calculated by multiplying the MD-IDL by a factor of 3.3.

UHPLC/Q-orbital Trap MS Analysis. An Accela ultrahigh-performance chromatograph coupled with a quadrupole orbital trap mass spectrometer (Q-orbital trap, QExactive, ThermoFisher Scientific, San Jose, CA) equipped with an electrospray ionization (ESI) interface source and controlled by Xcalibur software 2.2 was employed for all method validations. The UHPLC method validation was performed on a Hypersil GOLD aQ polar end-capped C18 column of dimensions 2.1 × 100 mm and a 2.1 × 10 mm guard column of the same stationary phase (ThermoFisher Scientific, San Jose, CA) using a flow rate of 0.3 mL/min. The mobile phases used were HPLC-grade water containing 0.1% formic acid and 5 mM ammonium formate (A) and HPLC-grade methanol containing 0.1% formic acid and 5 mM ammonium formate (B). After an initial time of 1 min at 100% A, the proportion of B was increased linearly to 100% in the following 8 min, followed by a hold time of 4 min at 100% B. The mobile phase was returned to the initial conditions in 0.5 min, and the column was equilibrated for 5.5 min. The total chromatographic run time was 18 min. The column was at room temperature (typically 27 °C), and the injection volume was set at 5 μL.

The Q-orbital trap MS was equipped with a heated electrospray ionization (HESI) probe and a collision cell to carry out higher-energy collision dissociation (HCD)-based tandem MS (MS/MS or MS^2) experiments. The Q-orbital trap MS was operated in either full-scan MS or full-scan $DDMS^2$ mode. The $DDMS^2$ mode uses the quadrupole to select target molecular ions from an inclusion list and then carries out HCD experiments using normalized collision energies (NCEs) in the collision cell to generate high-resolution, accurate mass spectra of precursor and/or product ions. In-house nitrogen gas was used for the shealth, auxiliary, and sweep gases with flow rates set at 30, 15, and 0 L/min, respectively, while the HESI spray voltage (positive), capillary temperature, S-lens level, and heater temperature were set at +4.0 kV, 350 °C, 50 kV, and 350 °C, respectively. Samples were analyzed in batches of about 50 and consisted of quality control samples (i.e., glassware rinses, blanks, calibration standards, and fortified samples) and field incurred samples. The commercially available calibration solutions were used to tune and calibrate the instrument in both positive and negative electrospray modes.

In full-scan MS mode, the Q-orbital trap performed without the HCD fragmentation, and the scan range was set from 100 to 900 m/z from 0 to 12 min during LC analysis. Optimized mass resolution (full width at half maximum, R_{FWHM}) of 70 000 at m/z = 200 was used along with one microscan. Automated gain control (AGC), the maximal number of ions allowed in the C-trap and consequent orbital trap MS analysis, was set at 1×10^6 with a maximum inject time of 250 ms to enhance the linearity of the orbital trap MS system. For $DDMS^2$ scan, the Q-orbital trap MS used prescan R_{FWHM}, AGC, maximum inject time, and isolation window settings of 17 500, 2×10^5, 50 ms, and 4.0 m/z, respectively. Based on previous NCE experiments, where the NCE ranged from 10 to 100 an overall NCE setting of 35 was selected. The masses of the precursor ions ($[M + H]^+$ or $[M + NH_4]^+$) for the 26 native mycotoxins and the 5 isotopically labeled mycotoxins listed the Supporting Information, Table S1 were provided in the inclusion list. Other $DDMS^2$ settings include an underfill ratio of 5.0%, an intensity threshold of 8.3×10^4, apex trigger of 3−6 s, and dynamic exclusion of 10.0 s, while the charge exclusion and peptide match options were not used.

Data Analysis. Mycotoxins were initially identified by their retention time (t_R) from the extraction ion chromatogram (XIC) of target ion m/z for each mycotoxin using full-scan accurate mass data collected in $DDMS^2$ mode. Calculations of the theoretical mono-isotopic m/z of precursor and product ions and A, A+1, and A+2 isotopes, as well as prediction of molecular composition using experimental m/z, were performed using the Xcalibur Qual Browser (V. 2.2 SP1.48) with a mass accuracy (δ_M) tolerance of 5 ppm and mass precision set to five decimal places. The mass accuracy δ_M for a measured ion is calculated by dividing the difference between the theoretical and measured m/z by the theoretical m/z and expressed as part-per-million (ppm):

$$\delta_M \text{ (ppm)} = 1 \times 10^6 \times \frac{(m/z_{measured} - m/z_{theoretical})}{m/z_{theoretical}}$$

Qualitative analyses to determine the mycotoxin and corresponding accurate m/z were based on molecular formula using TOXID 2.1.2, while Mass Frontier (V. 7.01 SR1) software was used to propose molecular structures from the $DDMS^2$ fragmentation studies. Quantitative determination of mycotoxins for recovery and incurred samples experiments, as well as detection and quantitation limits, were determined by LC Quan 2.7 software. All software packages were obtained from ThermoFisher Scientific (San Jose, CA). Results from the analysis were exported to Microsoft Excel 2007 (Microsoft Co., Redmond, WA), to process averages, standard deviations (SD), and relative standard deviations (RSD).

RESULTS AND DISCUSSION

Optimization of UHPLC/Q-Orbital Trap MS in Full-Scan Mode. The "dilute-and-shoot" procedure used for the UHPLC/Q-orbital trap MS multianalysis of mycotoxins had been previously applied to and validated using HPLC-MS/MS.[17] To determine the optimal resolution setting, native mycotoxins were fortified in solvent (acetonitrile/water) and extracts obtained from acetonitrile/water extracts of mycotoxin-free peanut and wheat samples at 1, 10, and 100 ng/mL. Replicate measurements (n = 9) of these solutions were performed by operating the UHPLC/Q-orbital trap MS in full-scan mode and using R_{FWHM} settings of 17 500, 35,000, 70 000, and 140 000.

DOI: 10.1021/jf505049a
J. Agric. Food Chem. 2015, 63, 8314−8332

Table 1. Average δ_M (Standard Deviations), in ppm, at Four Resolution Settings of the 26 Mycotoxins in Solvent (Acetonitrile/Water) and in Acetonitrile/Water Extracts of Peanut and Wheat Matrices at Concentration Levels of 1, 10, and 100 ng/mL[a]

	solvent			peanut extract			wheat extract		
resolution	1 ng/mL	10 ng/mL	100 ng/mL	1 ng/mL	10 ng/mL	100 ng/mL	1 ng/mL	10 ng/mL	100 ng/mL
17 500	−1.4 (1.1)	−1.8 (0.5)	−2.4 (0.2)	−0.5 (1.8)	−0.3 (0.8)	−0.9 (0.3)	−1.4 (1.7)	−2.0 (0.7)	−2.2 (0.3)
35 000	−2.2 (0.6)	−2.3 (0.3)	−2.4 (0.3)	−0.3 (1.1)	−0.1 (0.5)	−0.4 (0.2)	−1.5 (0.8)	−0.6 (0.4)	−0.6 (0.3)
70 000	0.5 (0.5)	0.4 (0.3)	−0.3 (0.3)	0.1 (0.7)	0.0 (0.6)	−0.3 (0.3)	0.2 (0.4)	0.2 (0.3)	0.8 (0.4)
140 000	0.4 (0.3)	−0.2 (0.3)	−0.8 (0.3)	0.5 (0.7)	0.4 (0.5)	0.5 (0.3)	−0.4 (0.3)	−0.8 (0.4)	−1.0 (0.3)

[a]Complete data and additional information on individual mycotoxins are provided in Supporting Information, Tables S2−S4.

Table 2. Mass Accuracy for A, A+1, and A+2 among the 26 Mycotoxins Studied[a]

	solvent			peanut extract			wheat extract		
	1 ng/mL	10 ng/mL	100 ng/mL	1 ng/mL	10 ng/mL	100 ng/mL	1 ng/mL	10 ng/mL	100 ng/mL
A									
0 to ±1 ppm	23	26	26	24	22	25	19	26	26
±1 to ±2 ppm	2	0	0	0	4	1	4	0	0
>+2 or <−2 ppm	0	0	0	1	0	0	0	0	0
not found	1	0	0	1	0	0	3	0	0
A+1									
0 to ±1 ppm	23	23	25	22	22	25	19	24	26
±1 to ±2 ppm	1	3	1	2	4	1	2	2	0
>+2 or <−2 ppm	0	0	0	0	0	0	1	0	0
not found	2	0	0	2	0	0	4	0	0
A+2									
0 to ±1 ppm	11	12	9	10	13	10	7	9	9
±1 to ±2 ppm	2	3	5	4	4	7	3	6	6
>+2 or <−2 ppm	8	11	12	7	8	9	11	11	11
not found	5	0	0	5	1	0	5	0	0

[a]Additional information on the specific mycotoxin is provided in Supporting Information, Table S5.

The experimental m/z values of the precursor ion ($[M+H]^+$ or $[M+NH_4]^+$) extracted from full-scan MS spectra, the theoretical m/z values, and the δ_M values for each mycotoxin are summarized in the Supporting Information, Tables S2−S4, for solvent, peanut, and wheat matrices. The average and standard deviation of δ_M values of the mycotoxins at each resolution in the three matrices were determined from the results in the Supporting Information tables and summarized in Table 1.

The resolution studies reveal the averages and standard deviations of δ_M values to be within a desirable range[20] of ±2.5 ppm and <2 ppm at R_{FWHM} = 17 500 and 35 000, respectively. At R_{FWHM} = 70 000 and 140 000, the average δ_M and SD improved to ±1.0 ppm and <1 ppm, respectively. These results are consistent with other studies using single-stage or hybrid (quadrupole and ion trap) orbital trap MS analyzers at various R_{FWHM} settings, ranging 10 000−100 000 for analyzing drugs in dried blood spots[21] and pesticides in fresh produce[22] as well as mycotoxins and other chemical contaminants in food commodities[23] and baby food.[24] The δ_M values from the solvent and wheat matrix at 1.0 ng/mL decrease, with increasing R_{FWHM}, but no significant trend was observed with the peanut matrix. Although neosolaniol could not be detected at 1.0 ng/mL at R_{FWHM} = 17 500 in the solvent or matrices, it was detected at the three higher R_{FWHM} settings. While the two lower and two higher R_{FWHM} settings provided δ_M < 2.5 and 1 ppm, respectively, and would meet the criterion for positive identification (i.e., <5 ppm with mass tolerance setting at 5 ppm),[20] the ability to analyze neosolaniol becomes a determining factor in selecting an optimal R_{FWHM} for routine analysis of mycotoxins. R_{FWHM} = 70 000 was selected for data acquisition because this setting can provide more data points from R_{FWHM} = 140 000 due to scan speeds (3 versus 1.5 Hz/s), allowing for better definition of extracted ion chromatogram (XIC) for quantitation.

Studies using R_{FWHM} 70 000 were conducted to evaluate δ_M and the measured % relative abundances ($\%_{RA}$) of the carbon-based A peak[25] (where A is a carbon-based organic compound which include $[M+H]^+$ and $[M+NH_4]^+$) and the A+1 and A+2 (and A+3 for Cl-containing ochratoxin A) isotope peaks for identification of the mycotoxins. Table 2 presents the number of mycotoxins identified with different ranges of δ_M of these three peaks; Supporting Information, Table S5 provides the measured $\%_{RA}$ of A+1 and A+2 to the A peak in solvent, peanut, and wheat matrices fortified at 1, 10, and 100 ng/mL. The δ_M values of the A base peak for each mycotoxin were within ±1 ppm and could be detected at 1 ng/mL or higher in the solvent and sample matrices. The RSD and $\%_{RA}$ of the A base peak and A+1 measured were generally <20%, allowing the use of the A+1 with δ_M = ±2 ppm, retention time window of ±30 s, and $\%_{RA}$ of ±20% as reliable criterion for identifying the targeted compounds.[26] The A+1 isotopes of the five trichlothecene mycotoxins could not be detected due to inferior ionization of neosolaniol and interferences from co-extractives present in the wheat matrix for 15-acetyl deoxynivalenol, deoxynivalenol, fusarenon-X, and HT-2.

The measured values of the A+2 isotopes generated higher RSD, lower $\%_{RA}$, and higher δ_M values when compared to their theoretically available values. It appears that the A+2 isotope, along with the use of retention time window and δ_M < 5 ppm

DOI: 10.1021/jf505049a
J. Agric. Food Chem. 2015, 63, 8314−8332

Table 3. Matrix-Dependent Instrument Limits of Detection and Limits of Quantitation (MD-ILD, MD-IQL), Reported as μg/kg of Mycotoxins Fortified in Six Matrices (Corn, Rice, Wheat, Almond, Peanut, and Pistachio)

		corn			rice			wheat			almond			peanut			pistachio		
mycotoxins	concn range (ng/mL)	r^2	MD-IDL	MD-IQL	r^2	MD-IDL	MD-IQL	r^2	MD-IDL	MD-IQL	r^2	MD-IDL	MD-IQL	r^2	MD-IDL	MD-IQL	r^2	MD-IDL	MD-IQL
15-acetyl deoxynivalenol	50−1000	0.9942	1.4	4.6	0.9962	2.0	6.0	0.9992	2.4	7.8	0.9919	1.8	5.4	0.9996	2.4	7.2	0.9967	2.8	8.6
aflatoxin B_1	0.5−100	0.9954	0.03	0.1	0.9998	0.01	0.03	0.9994	0.03	0.1	0.9929	0.03	0.1	0.9997	0.01	0.03	0.9986	0.01	0.02
aflatoxin B_2	0.5−100	0.9969	0.06	0.2	0.9986	0.01	0.03	0.9982	0.03	0.1	0.9914	0.03	0.1	0.9985	0.1	0.2	0.9966	0.02	0.04
aflatoxin G_1	0.5−100	0.9963	0.06	0.2	0.9983	0.01	0.02	0.9974	0.03	0.1	0.9915	0.03	0.1	0.9978	0.02	0.04	0.9960	0.02	0.04
aflatoxin G_2	0.5−100	0.9955	0.06	0.2	0.9981	0.01	0.03	0.9962	0.1	0.2	0.9934	0.03	0.1	0.9977	0.1	0.2	0.9952	0.02	0.04
beauvreicin	0.5−100	0.9950	0.1	0.2	0.9990	0.03	0.1	0.9962	0.1	0.3	0.9932	0.1	0.4	0.9979	0.2	0.4	0.9952	0.1	0.2
citrinin	5−1000	0.9925	1.1	3.5	0.9977	2.1	6.9	0.9936	1.1	3.7	0.9912	1.0	3.2	0.9911	1.1	3.5	0.9918	0.6	1.9
deoxynivalenol	50−1000	0.9929	1.1	3.7	0.9955	2.0	6.0	0.9933	2.9	8.9	0.9964	2.4	7.5	0.9918	3.0	9.6	0.9925	2.7	8.1
diacetoxyscirpenol	0.5−100	0.9979	0.1	0.3	0.9982	0.03	0.1	0.9984	0.1	0.2	0.9935	0.1	0.2	0.9985	0.1	0.2	0.9965	0.03	0.1
ergocornine	0.5−100	0.9978	0.1	0.2	0.9995	0.03	0.1	0.9992	0.03	0.1	0.9937	0.1	0.2	0.9994	0.1	0.2	0.9991	0.1	0.2
ergocristine	0.5−100	0.9951	0.1	0.3	0.9976	0.03	0.1	0.9979	0.03	0.1	0.9906	0.1	0.2	0.9971	0.1	0.3	0.9939	0.1	0.2
ergocryptine	0.5−100	0.9955	0.03	0.1	0.9973	0.03	0.1	0.9971	0.03	0.1	0.9912	0.1	0.3	0.9975	0.1	0.3	0.9935	0.03	0.1
ergometrine	0.5−100	0.9967	0.1	0.4	0.9986	0.03	0.1	0.9970	0.1	0.4	0.9955	0.2	0.6	0.9981	0.2	0.7	0.9940	0.1	0.3
ergosine	0.5−100	0.9953	0.1	0.3	0.9961	0.03	0.1	0.9957	0.1	0.3	0.9926	0.1	0.3	0.9941	0.1	0.2	0.9908	0.03	0.1
ergotamine	0.5−100	0.9934	0.1	0.2	0.9946	0.10	0.2	0.9929	0.03	0.1	0.9927	0.1	0.4	0.9985	0.2	0.6	0.9986	0.2	0.4
fumonisin B_1	5−1000	0.9986	0.7	2.1	0.9999	0.7	2.2	0.9961	0.8	2.5	0.9996	0.7	2.2	0.9980	1.0	3.2	0.9994	0.8	2.4
fumonisin B_2	5−1000	0.9996	0.6	1.7	0.9995	0.6	1.8	0.9984	0.5	1.5	0.9997	0.9	2.8	0.9979	1.9	5.9	0.9990	1.0	2.9
fusarenon-X	50−1000	0.9977	2.7	8.8	0.9992	2.3	6.9	0.9974	3	9.1	0.9904	3.5	11.5	0.9996	3.5	10.7	0.9961	3.7	11.6
HT-2	5−100	0.9976	0.2	0.6	0.9995	0.1	0.3	0.9994	0.2	0.7	0.9970	0.2	0.4	0.9998	0.1	0.3	0.9990	0.2	0.6
neosolaniol	0.5−100	0.9934	0.2	0.7	0.9916	0.2	0.7	0.9945	0.2	0.7	0.9939	0.2	0.7	0.9912	0.3	0.8	0.9919	0.3	0.8
ochratoxin A	0.5−100	0.9988	0.1	0.2	0.9997	0.1	0.2	0.9994	0.1	0.2	0.9989	0.1	0.3	0.9996	0.2	0.4	0.9998	0.1	0.2
ochratoxin B	0.5−100	0.9955	0.03	0.1	0.9950	0.1	0.2	0.9968	0.1	0.3	0.9924	0.03	0.1	0.9990	0.1	0.2	0.9971	0.03	0.1
sterigmatocystin	0.5−100	0.9939	0.03	0.1	0.9930	0.03	0.1	0.9964	0.03	0.1	0.9932	0.1	0.2	0.9997	0.03	0.1	0.9944	0.03	0.1
T-2	0.5−100	0.9998	0.1	0.2	0.9998	0.1	0.2	0.9997	0.1	0.2	0.9995	0.1	0.2	0.9998	0.1	0.2	0.9997	0.1	0.2
verrucarin A	50−1000	0.9977	0.5	1.5	0.9998	0.9	2.8	0.9955	0.4	1.3	0.9923	1.4	4.4	0.9975	0.4	1.3	0.9963	1.2	3.8
zearalenone	5−1000	0.9982	0.5	1.5	0.9999	0.4	1.2	0.9999	0.4	1.4	0.9993	0.03	1	0.9999	0.5	1.5	0.9998	0.6	1.8

J. Agric. Food Chem. 2015, 63, 8314−8332
DOI: 10.1021/jf505049a

Table 4. Average Recoveries (n = 4) and Relative Standard Deviations (RSDs) of 26 Mycotoxins Extracted from Three Grain and Three Nut Product Matrices at Three Fortification Levels Each[a]

	average recovery, % (RSD, %)																	
	corn			rice			wheat			almond			peanut			pistachio		
	10	50	100	10	50	100	10	50	100	10	50	100	10	50	100	10	50	100
Group A Mycotoxins																		
aflatoxin B_1	96 (3)	103 (2)	100 (2)	100 (2)	105 (1)	104 (3)	98 (5)	107 (2)	103 (1)	99 (3)	103 (2)	103 (12)	96 (6)	107 (2)	103 (1)	103 (2)	110 (2)	106 (2)
aflatoxin B_2	86 (8)	103 (2)	102 (3)	103 (1)	103 (2)	105 (4)	98 (4)	92 (6)	104 (2)	99 (2)	97 (7)	97 (7)	88 (5)	109 (2)	104 (2)	94 (9)	110 (2)	106 (2)
aflatoxin G_1	89 (7)	100 (4)	100 (4)	87 (5)	104 (2)	104 (5)	102 (4)	110 (2)	104 (2)	98 (3)	86 (9)	106 (3)	102 (4)	110 (2)	104 (2)	105 (2)	111 (4)	106 (3)
aflatoxin G_2	85 (6)	101 (4)	101 (4)	103 (2)	106 (2)	104 (3)	98 (5)	112 (7)	105 (1)	101 (2)	93 (9)	106 (3)	88 (7)	112 (7)	105 (1)	83 (6)	109 (2)	104 (3)
beauvericin	88 (2)	103 (3)	97 (3)	99 (6)	105 (2)	105 (8)	104 (2)	115 (2)	105 (2)	86 (8)	96 (3)	101 (3)	104 (2)	115 (2)	105 (2)	78 (5)	94 (10)	103 (4)
diacetoxyscirpenol	91 (8)	82 (11)	107 (7)	95 (07)	108 (2)	104 (4)	95 (5)	109 (4)	104 (2)	101 (4)	105 (3)	107 (3)	88 (6)	109 (4)	104 (2)	95 (11)	110 (9)	108 (3)
ergocornine	101 (5)	98 (2)	96 (3)	96 (2)	108 (1)	90 (8)	92 (3)	104 (2)	96 (3)	74 (5)	77 (14)	95 (10)	92 (3)	104 (2)	96 (3)	87 (5)	105 (9)	108 (2)
ergocristine	92 (6)	99 (4)	95 (4)	91 (1)	94 (9)	105 (4)	89 (1)	105 (4)	98 (3)	96 (4)	88 (15)	89 (7)	100 (9)	105 (4)	105 (8)	77 (9)	90 (22)	104 (3)
ergocryptine	88 (4)	91 (3)	90 (4)	94 (4)	104 (2)	105 (4)	95 (4)	84 (6)	101 (1)	77 (5)	84 (16)	81 (6)	95 (4)	107 (3)	103 (4)	85 (11)	110 (3)	89 (5)
ergometrine	82 (9)	94 (10)	99 (4)	102 (2)	94 (3)	109 (4)	101 (9)	105 (9)	111 (2)	87 (7)	88 (5)	88 (5)	101 (9)	105 (10)	111 (12)	78 (8)	94 (4)	95 (11)
ergosine	96 (9)	87 (7)	85 (4)	88 (7)	92 (10)	86 (13)	90 (9)	102 (6)	100 (3)	91 (8)	100 (16)	102 (13)	101 (6)	102 (6)	110 (11)	84 (7)	102 (6)	100 (3)
ergotamine	92 (7)	102 (2)	86 (9)	96 (6)	86 (10)	89 (11)	86 (5)	116 (3)	105 (6)	89 (13)	109 (7)	109 (5)	103 (5)	116 (3)	105 (6)	76 (6)	97 (13)	109 (6)
HT-2	103 (8)	102 (5)	105 (3)	97 (6)	97 (3)	95 (3)	99 (3)	101 (3)	97 (3)	100 (5)	83 (18)	79 (4)	104 (12)	78 (7)	97 (2)	91 (10)	74 (9)	77 (8)
neosolaniol	81 (6)	76 (8)	87 (14)	97 (6)	83 (9)	84 (5)	89 (4)	129 (3)	119 (5)	89 (9)	88 (19)	86 (13)	104 (9)	129 (3)	119 (5)	81 (5)	90 (7)	79 (6)
ochratoxin A	86 (7)	95 (4)	93 (2)	95 (5)	96 (3)	96 (4)	91 (5)	101 (2)	98 (3)	85 (10)	86 (9)	95 (2)	91 (5)	86 (9)	101 (2)	111 (6)	102 (9)	96 (5)
ochratoxin B	90 (3)	93 (3)	96 (3)	91 (5)	87 (4)	88 (4)	95 (6)	108 (7)	97 (10)	91 (9)	74 (8)	91 (11)	102 (11)	102 (11)	109 (12)	93 (6)	88 (7)	93 (8)
sterigmatocystin	98 (6)	90 (8)	90 (4)	94 (4)	108 (11)	102 (14)	94 (5)	110 (3)	102 (10)	88 (12)	90 (3)	90 (3)	94 (5)	110 (3)	117 (9)	74 (5)	85 (11)	96 (5)
T-2	89 (5)	102 (2)	93 (11)	96 (3)	88 (6)	102 (2)	101 (6)	109 (1)	107 (1)	102 (3)	96 (11)	98 (8)	102 (6)	109 (1)	116 (10)	84 (7)	88 (4)	106 (3)

	average recovery, % (RSD, %)																	
	corn			rice			wheat			almond			peanut			pistachio		
	100	500	1000	100	500	1000	100	500	1000	100	500	1000	100	500	1000	100	500	1000
Group B Mycotoxins																		
15-acetyldeoxynivalenol	95 (9)	86 (3)	80 (6)	106 (7)	89 (4)	84 (5)	107 (6)	114 (7)	90 (6)	87 (6)	82 (6)	75 (4)	91 (8)	122 (9)	104 (10)	112 (11)	128 (5)	104 (10)
citrinin	74 (7)	71 (10)	72 (4)	99 (3)	83 (2)	81 (3)	73 (9)	92 (3)	74 (6)	104 (5)	92 (2)	91 (3)	75 (14)	113 (6)	94 (6)	105 (12)	74 (13)	79 (6)
deoxynivalenol	91 (8)	89 (6)	84 (12)	93 (6)	77 (15)	83 (5)	95 (9)	110 (12)	102 (4)	105 (9)	88 (15)	94 (6)	93 (14)	110 (12)	102 (4)	113 (8)	101 (5)	113 (13)
fumonisin B_1	69 (9)	68 (3)	72 (6)	68 (5)	70 (9)	72 (5)	71 (7)	73 (9)	73 (6)	52 (5)	52 (4)	54 (8)	57 (9)	61 (8)	56 (8)	49 (7)	51 (5)	49 (5)
fumonisin B_2	67 (13)	63 (3)	64 (7)	71 (3)	73 (3)	74 (6)	67 (8)	72 (11)	71 (5)	68 (3)	69 (4)	61 (7)	53 (6)	57 (9)	62 (7)	54 (4)	52 (8)	57 (7)
fusarenon-X	102 (10)	87 (5)	102 (6)	83 (8)	84 (9)	112 (6)	72 (9)	108 (10)	108 (7)	119 (14)	109 (11)	106 (11)	112 (13)	100 (11)	87 (5)	118 (16)	121 (10)	105 (11)
verrucarin A	92 (5)	97 (4)	97 (4)	87 (9)	109 (2)	88 (9)	85 (7)	110 (3)	99 (4)	86 (5)	103 (4)	76 (15)	88 (11)	75 (8)	99 (4)	78 (5)	88 (19)	105 (3)
zearalenone	93 (4)	93 (9)	98 (1)	95 (2)	98 (5)	98 (2)	103 (2)	109 (1)	102 (1)	98 (3)	82 (5)	93 (7)	103 (2)	109 (1)	102 (1)	101 (2)	109 (9)	101 (3)

[a]The recoveries were the average of three spiking levels (10, 50, and 100 μg/kg for group A mycotoxins; 100, 500, and 1000 μg/kg for group B mycotoxins). Quantification was performed by using matrix-matched calibration.

J. Agric. Food Chem. 2015, 63, 8314−8332

DOI: 10.1021/jf505049a

Table 5. Analysis of Reference Materials and Comparison between Assigned and Measured Concentrations[a]

reference material	analyte	matrix	concentration, μg/kg certified n = 21	concentration, μg/kg measured (Q-orbital trap), n = 3	% diff
GIPSA-MRM2010-004A	aflatoxins	corn	10.2 ± 1.1	9.0 ± 1.3	−11.8
GIPSA-MRM2010-006	aflatoxins	corn	78.2 ± 5.7	70.4 ± 9.5	−10.0
GIPSA-MRM2010-010A	deoxynivalenol	wheat	1010 ± 60	1030 ± 90	1.9
GIPSA-MRM2010-016B	deoxynivalenol	corn	1100 ± 50	1050 ± 80	−4.5
GIPSA-MRM2010-017	deoxynivalenol	corn	2030 ± 90	1960 ± 120	−3.4
GIPSA-MRM2010-021	fumonisins	corn	2310 ± 110	1970 ± 170	−14.7
GIPSA-MRM2010-023	ochratoxin A	wheat	6.31 ± 0.31	5.10 ± 0.60	−19.2
GIPSA-MRM2010-025	zearalenone	corn	98.3 ± 9.9	97.0 ± 7.7	−1.3
GIPSA-MRM2011-004	deoxynivalenol	wheat	2060 ± 60	2030 ± 140	−1.4
Romer Laboratories 003010	aflatoxin B1	corn	15.47 ± 3.93	14.82 ± 1.81	−4.2
Romer Laboratories 003019	zearalenone	corn	177.3 ± 64.8	166.0 ± 32.1	−6.4

[a]Detailed procedures and materials are described in the Materials and Methods section. Percent difference is calculated as the difference between the measured and certified concentration (measured − certified) divided by the certified concentration, and the result multiplied by 100%. N = 21 for GIPSA reference materials. Total aflatoxins ($B_1 + B_2 + G_1 + G_2$) and total fumonisins ($B_1 + B_2$) are given; n is not provided for these sets of reference materials.

identification criteria, at best can be used as a reference rather than a reliable identification parameter. In some cases, chromatography could probably be refined to separate the interfering matrix components from the isotope masses of the mycotoxin analytes of interest. Five A+2 isotopes, including ergometrine, the ergot alkaloid in this study with the lowest molecular weight, could not be detected at 1 ng/mL. In contrast, ochratoxin A, the only mycotoxin in this study consisting of ^{35}Cl and ^{37}Cl isotopes, produced a fourth molecular isotope that could be reliably identified at all three concentration levels.

Results of Method Validation. *Matrix-Dependent Instrument Limits of Detection and Quantitation (MD-ILD and MD-ILQ).* The MD-ILDs for each mycotoxin in each of the six matrices, calculated using the procedures of the U.S. Environmental Protection Agency's protocol[19] based on the quantitative results obtained from the precursor ion of the mycotoxin obtained in full-scan mode, along with the MD-ILQ (3 × MD-ILD), are provided in Table 3. The EPA protocol provides a consistent and reliable metric other laboratories can use to carry out follow-up experiments for comparison purposes because statistical calculations rather than the subjective estimation of signal-to-noise ratios are used to determine the detection limits. The MD-ILDs and MD-ILQs were compound-dependent and independent of matrix type, as fusarenon-X, deoxynvalenol, and 15-acetyldeoxynivalenol were consistently higher than the other mycotoxins in the six matrices. The MD-ILQs of aflatoxins, sterigmatocystin, ochratoxins, diacetoxyscirpenol, neosolaniol, beauvericin, and ergot alkaloids were less than 0.3 μg/kg for all six matrices evaluated, whereas citrinin, deoxynivalenol, fusarenon-X, 15-acetyldeoxynivalenol, verrucarin A, HT-2, zearalenone, and fumonisins were determined to have MD-ILQs in the range of 1.4−9.8 μg/kg. These results indicate that the orbital trap in full-scan MS mode is sensitive enough to analyze grain and nut products in low (<10 μg/kg) to sub-μg/kg levels. Electrospray ionization in positive mode was used to ionize the mycotoxins and is the determining factor for detection since the orbital trap MS results were comparable to previous HPLC-MS/MS results using the same mycotoxins, matrices, and method.[17] Regulatory limits of deoxynivalenol and fumonisins determined by most countries and the European Union are in the 500−1000 μg/kg range, whereas aflatoxins and ochratoxin A limits are set at 20 and 50 μg/kg, respectively, in most grains and nut products.[28] As shown in Table 3, the method can achieve MD-ILQs a factor of at least 50 times lower than the MRLs required by the published regulatory requirements, which can be applied for screening purposes.

Recovery Studies. Method validation was performed using three grain (rice, wheat, and corn) and three nut matrices (peanut, pistachio, and almond). These recovery studies were performed by adding fortification standards to blank grain, and nut samples at three concentration levels, 10, 50, and 100 μg/kg and 100, 500, and 1000 μg/kg for groups A and B mycotoxin mixes (n = 4 at each fortification level), respectively, as listed in Table 4. The identification was achieved using criteria discussed above while the quantitation was performed using matrix-matched calibration curves (r^2 > 0.99 and calibration ranges provided in Table 3) and the precursor molecular ion, i.e., $[M+H]^+$ or $[M+NH_4]^+$. The linearity criterion using r^2 > 0.99 was achieved for all of the mycotoxins in all six sample matrix as the r^2 values of the mycotoxin calibration range are provided in Table 3, indicating that the Q-orbital trap MS in full-scan mode can be used for quantitative determination. The mean recoveries (n = 12, ± RSD) of all mycotoxins at the three fortification levels were 91 ± 10, 94 ± 10, 98 ± 12, 91 ± 13, 99 ± 15, and 93 ± 17% for corn, rice, wheat, almond, peanut, and pistachio, respectively. Most of the mycotoxins were recovered in the 70−120% recovery range in all six matrices, with the notable exception of fumonisin B_1 and B_2 in the nut matrices. The lower recoveries of the more polar fumonisins (49−73%) compared to the other mycotoxins (72−129%) in multimycotoxin procedures are attributed to the higher organic content of the extraction solvent, resulting in lower extraction efficiencies, which had been observed in previous studies.[27] In general, the multimycotoxin procedure is applicable to screening and determining the mycotoxin levels in a variety of cereal and nut products.

Method Accuracy in the Analysis of Reference Materials. The ability of this method to provide accurate analytical results is demonstrated by triplicate (n = 3) analysis of 11 corn and wheat reference materials obtained from USDA-GIPSA and Romer Laboratories. Results of the reference materials provided in Table 5 list concentration levels from 6.31 ± 0.31 μg/kg (n = 21) of ochratoxin A to as high as 2310 ± 110 μg/kg (n = 21) of fumonisins in corn. There was no statistical difference

DOI: 10.1021/jf505049a
J. Agric. Food Chem. 2015, 63, 8314−8332

Table 6. Survey Results of Mycotoxins in Different Grain and Nut Commercial Samples[a]

	no. of positive samples (concn range, μg/kg)					
	rice, 6 samples	wheat, 16 samples	corn, 18 samples	peanut, 11 samples	pistachio, 10 samples	almond, 9 samples
aflatoxin B_1				5 (0.3−0.6)	2 (0.5, 1.2)	1 (0.3)
aflatoxin B_2					1 (0.9)	
aflatoxin G_1					1 (0.5)	
beauvericin		1 (1.6)	14 (0.8−108)	2 (0.8−4.5)	1 (1.9)	
deoxynivalenol		2 (50, 90)	3 (61−115)			
ergocornine		2 (1.8, 3.7)				
ergocristine		2 (5.3, 7.3)				
ergocryptine		2 (7.4, 8.9)				
ergometrine		1 (3.4)				
ergosine		2 (1.1, 1.5)				
ergotamine		2 (9.0, 12.8)				
fumonisin B_1			11 (50−1175)			
fumonisin B_2			8 (27−750)			
neosolaniol					1 (46)	
ochratoxin A	1 (2.6)	5 (1.2−2.6)			3 (1.0−6.6)	
ochratoxin B					2 (0.5, 2.3)	
sterigmatosin	1 (0.8)	1 (1.4)				
T-2		1 (1.1)				
zearalenone			4 (102−279)			

[a]The range of contamination levels of each mycotoxin and each concentration listed is an average of three replicates (n = 3).

between the certified and measured values of these reference materials, with the exception of ochratoxin A in wheat, consistent with LC-MS/MS results.[17] The % difference ranged from +1.9% (zearalone in wheat) to −19.2% (ochratoxin A in wheat) with eight of the 11 reference materials ≤10% (absolute % difference) even though the reference values of the certified materials had been analyzed by a different combination of mycotoxin procedures for extraction and different analytical instrumentation, such as HPLC equipped with fluororescence or ultraviolet and mass spectrometric detection. The experimentally determined concentrations of target analytes were within the satisfactory range for the tested mycotoxins (aflatoxins, DON, fumonisins, ochratoxin A, zearalenone), indicating this validated method can accurately provide quantitative results.

Sample Analysis. The method was used to analyze finished cereal and nut products purchased from local markets and online stores in the United States in August 2011 to January 2012. A total of 70 commercial products were analyzed, which included six rice, 16 wheat, 18 corn, 11 peanut, ten pistachio and nine almond-based finished samples. Table 6 summarizes the frequency of mycotoxins present and the range of their concentrations in these finished products (Supporting Information, Table S6 provides additional and detailed information about these products and their mycotoxin concentrations). Of the grain products, rice contained the least number of mycotoxins, as only one rice flour sample contained sterigmatocystin and ochratoxin A at levels of 0.8 ± 0.2 and 2.6 ± 0.5 μg/kg (n = 3), respectively. Wheat products (wheat flour and dried pasta) were found to contain mycotoxins (deoxynivalenol, sterigmatocystin, ochratoxin A, T-2 toxin, ergometrine, ergosine, ergocornine, ergocryptin, ergotamine, ergocristine, and beauvericin) at concentration levels ranging from 1.1 (1.1 ± 0.3 μg/kg for ergosine, 1.1 ± 0.4 μg/kg for T2 toxin), to 90 ± 15 μg/kg (deoxynivalenol) (n = 3). Ochratoxin A was present in five wheat samples at concentrations <3 μg/kg, below the 3−50 μg/kg maximum tolerance levels set by most governments. Among the 18 corn meal, and flour samples, 16 were shown to be contaminated with various mycotoxins, such as beauvericin (14/18), ochratoxin A (1/18), T-2 toxin (1/18), fumonisin B_1 (11/18), fumonisin B_2 (8/18), zearalenone (4/18), and deoxynivalenol (3/18), at concentrations levels ranging from 0.8 ± 0.2 (beauvericin) to 1175 ± 182 (fumonisin B_1) μg/kg (n = 3). All levels of fumonisins analyzed were below the maximum levels of 2000−4000 μg/kg for degermed or partially degermed dry-milled corn products established by the U.S. Food and Drug Administration.[28]

Fewer mycotoxins were detected and at lower concentrations in finished nut products than grains. Five of the 11 peanut products (peanut flour, peanut butter, and raw peanut) surveyed were contaminated with aflatoxin B_1 at concentrations less than 0.6 μg/kg; two of those peanut products also contained beauvericin at concentrations of 4.5 ± 1.1 and 0.8 ± 0.2 μg/kg (n = 3, each). Pistachio products (roasted pistachio, pistachio butter, and pistachio flour) were found to contain a total of seven mycotoxins distributed among four of the ten samples studied. One pistachio product was cocontaminated with five mycotoxins, aflatoxin B_1, aflatoxin B_2, aflatoxin G_1, ochratoxin A, and ochratoxin B at levels <7 μg/kg. Of the nine almond samples studied, only one almond flour sample was found to contain aflatoxin B_1 at 0.3 ± 0.1 μg/kg. These results compared well with those obtained in a previous study in which the same 70 grain and nut samples were analyzed using HPLC-MS/MS[17] (both UHPLC-Orbitrap MS and HPLC-MS/MS are shown and compared in Supporting Information, Table S6) demonstrating that UHPLC/Q-Orbitrap MS in full-scan results can be used in routine quantitative analysis, providing enhanced data quality via accurate mass measurement of the precursor ions.

Identification of Mycotoxins by UHPLC/Q-Orbital Trap MS Using Data-Dependent Tandem Mass Spectrometry (DDMS²). LC-MS/MS, based on triple-quadrupole mass spectrometry, has been a reliable, proven procedure providing acceptable quantitative and qualitative results based on the retention time of the analyte and two precursor-to-product ion transitions based on nominal masses. The dominant primary

DOI: 10.1021/jf505049a
J. Agric. Food Chem. 2015, 63, 8314−8332

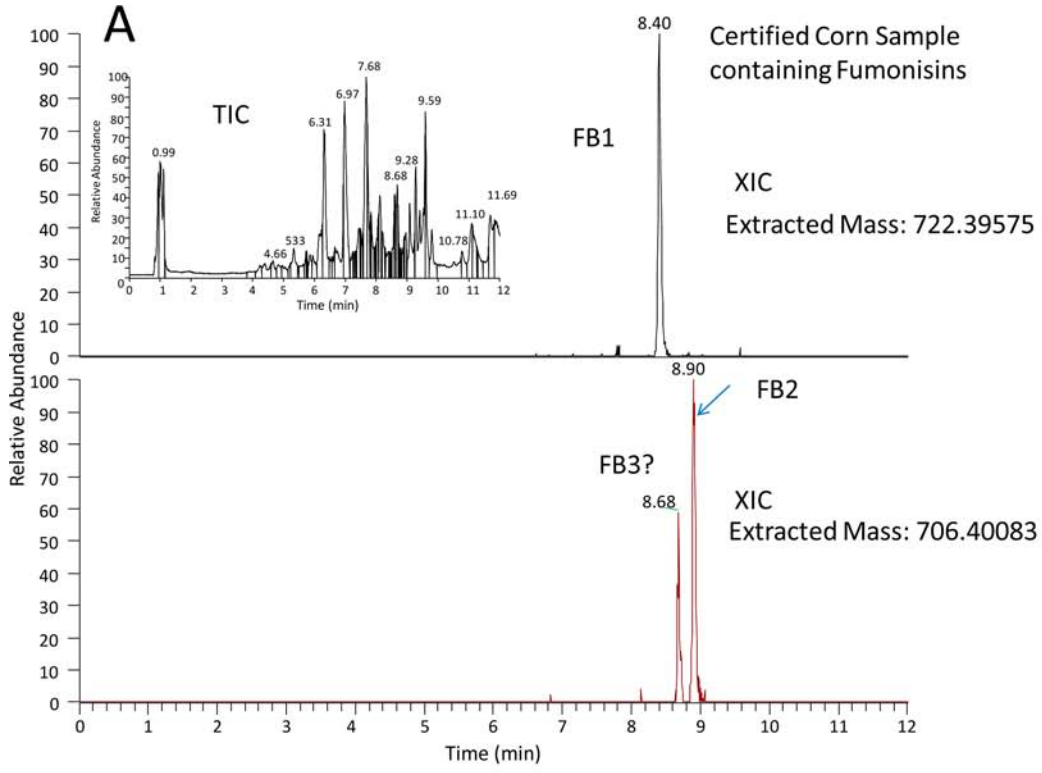

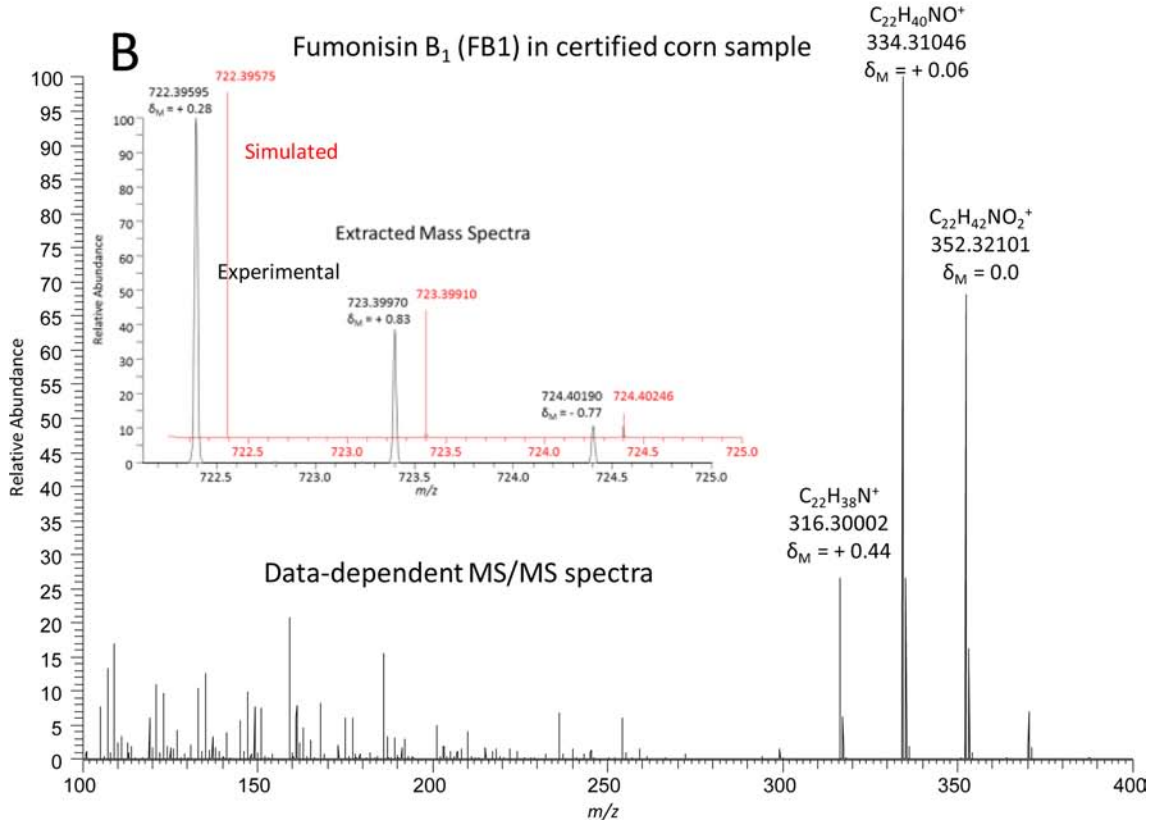

Figure 1. continued

DOI: 10.1021/jf505049a
J. Agric. Food Chem. 2015, 63, 8314−8332

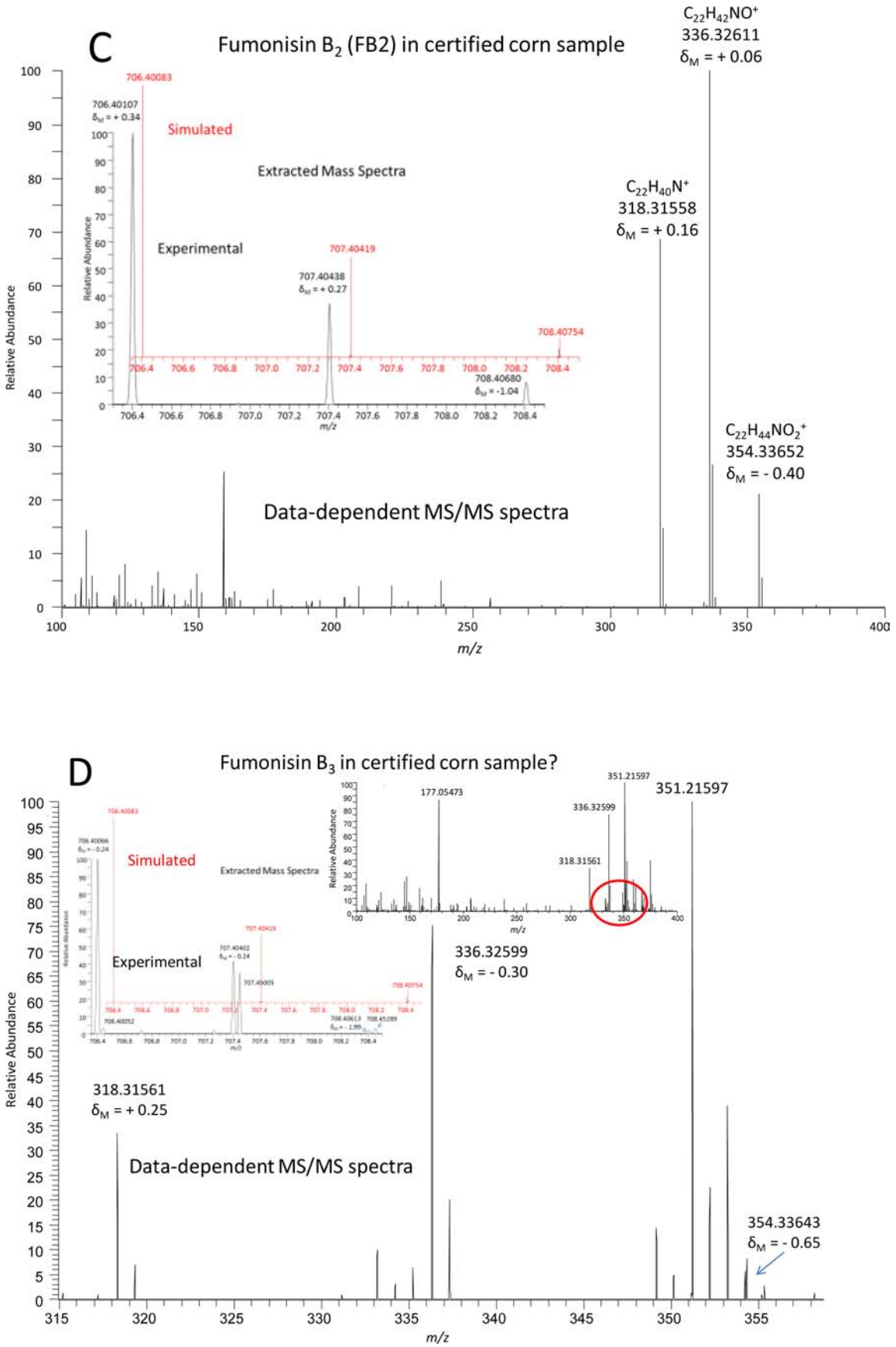

Figure 1. continued

DOI: 10.1021/jf505049a
J. Agric. Food Chem. 2015, 63, 8314−8332

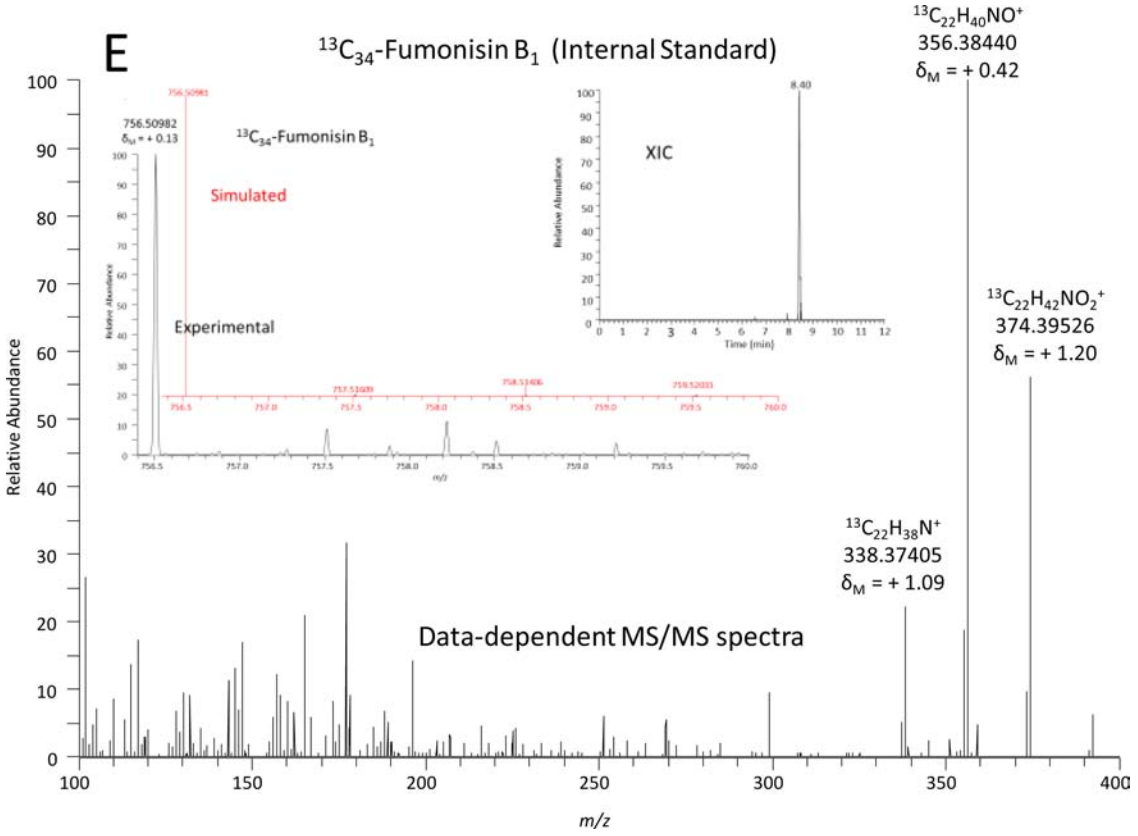

Figure 1. UHPLC-quadrupole orbital trap mass spectrometry analysis of a corn reference material (GIPSA-MRM2010-021) used for the analysis of fumonisins (FB1, FB2, FB3). (A) Total ion chromatogram (TIC) of a corn extract and resulting extracted ion chromatograms (XIC) of fumonisins using *m/z* 722.39575 (fumonisin B_1) and 706.40083 (fumonisins B_2 and B_3). The reason for the question mark for FB3 was that no reference standard was used for identifying fumonisin B_3. (B–D) Experimental and simulated mass spectra for $[M + H]^+$, $[M+1+H]^+$, and $[M+2+H]^+$ isotope peaks extracted from the TICs in full-scan mode (inset) and data-dependent MS/MS (DD-MS^2) spectra of FB1, FB2, and FB3, respectively, revealing fragments generated from collision experiments (NCE = 35). Only FB1 and FB2 were confirmed with reference standards in acetonitrile/water. (E) XIC, isotope mass spectra, and DD-MS^2 spectra of labeled $^{13}C_{34}$–FB1 used as an internal standard in the corn extract.

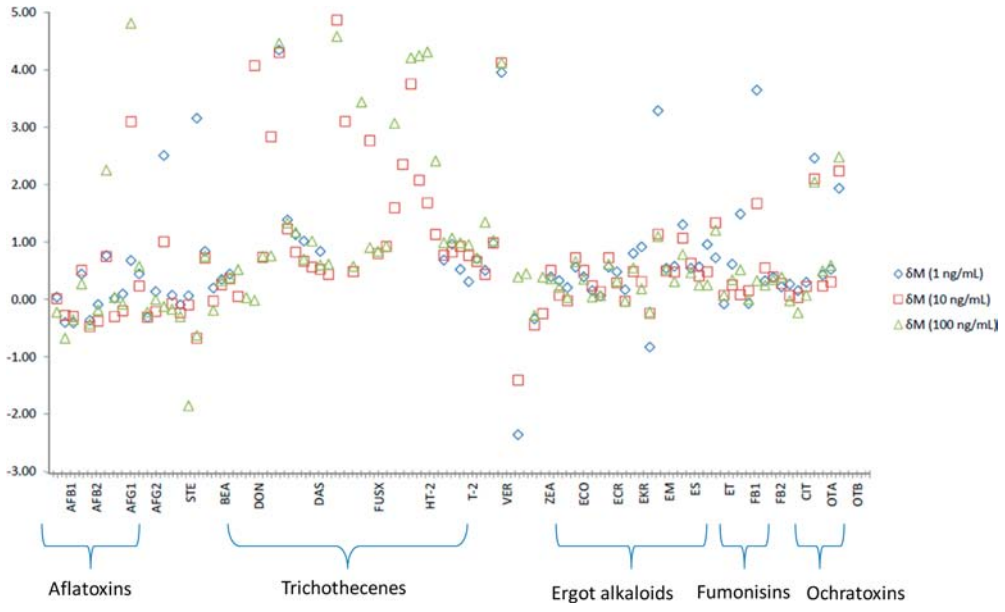

Figure 2. Mass accuracy distributions, δ_M (1 ng/mL), δ_M (10 ng/mL), and δ_M (100 ng/mL) of mycotoxin fragments extract from solvent (acetonitrile/water) and acetonitrile/water extracts of peanut and wheat matrices at concentration levels of 1, 10, and 100 ng/mL. Refer to Table 7 for a complete listing of mass ion fragments for each mycotoxin.

DOI: 10.1021/jf505049a
J. Agric. Food Chem. 2015, 63, 8314–8332

Table 7. Molecular Ions and Ion Ratios (%) Used To Identify Mycotoxins, Including Proposed Molecular Formulas and Theoretical Masses[a]

			1 ng/mL		10 ng/mL		100 ng/mL	
	molecular formula of ions	theoretical mass (m/z)	% avg	RSD	% avg	RSD	% avg	RSD
aflatoxin B_1	$[C_{17}H_{12}O_6 + H]^+$	**313.07066**	100		100		100	
	$C_{16}H_{13}O_5^+$	285.07575	29	0.7	29	1.9	30	2.6
	$C_{15}H_{10}O_5^+$	270.05227	6	6.0	6	3.2	6	2.1
	$C_{15}H_{13}O_4^+$	257.08084	4	5.1	4	2.2	4	9.7
aflatoxin B_2	$[C_{17}H_{14}O_6 + H]^+$	**315.08631**	100		100		100	
	$C_{16}H_{15}O_5^+$	287.09140	10	3.3	10	0.9	10	0.1
	$C_{14}H_{11}O_5^+$	259.06000	5	3.5	4	0.6	5	2.8
aflatoxin G_1	$[C_{17}H_{12}O_7 + H]^+$	**329.06558**	100		100		100	
	$C_{17}H_{11}O_6^+$	311.05501	31	3.3	30	6.3	34	10.8
	$C_{16}H_{11}O_5^+$	283.06001	12	1.9	11	33.6	11	15.1
	$C_{14}H_{11}O_4^+$	243.06519	20	1.3	19	5.2	20	5.0
aflatoxin G_2	$[C_{17}H_{14}O_7 + H]^+$	**331.08123**	100		100		100	
	$C_{17}H_{13}O_6^+$	313.07066	13	24.8	14	14.8	16	0.1
	$C_{16}H_{13}O_5^+$	285.07575	3	13.5	3	9.4	3	0.4
beauvreicin	$C_9H_{12}N^+$	**134.09643**	100		100		100	
	$C_{20}H_{28}NO_5^+$	362.19620	8	4.4	8	2.9	8	0.1
	$C_{15}H_{20}NO_3^+$	262.14377	25	0.6	26	1.3	27	1.6
	$C_{15}H_{18}NO_2^+$	244.13321	65	1.4	65	1.1	67	1.5
citrinin	$C_{13}H_{13}O_4^+$	**233.08084**	100		100		100	
	$[C_{13}H_{14}O_5 + H]^+$	251.09140	207	15.2	119	71.7	41	13.5
deoxynivalenol	$C_{13}H_{15}O_2^+$	**203.10666**			100		100	
	$C_{14}H_{17}O_4^+$	249.11214			32	0.5	35	1.3
	$C_{14}H_{15}O_3^+$	231.10157			52	13.0	56	4.4
	$C_{11}H_{11}O_2^+$	175.07536			79	8.5	78	4.2
	$C_8H_9O_2^+$	137.05971			56	13.1	52	4.1
diacetoxyscirpenol	$C_8H_9^+$	**105.06988**	100		100		100	
	$C_{12}H_{13}^+$	157.10118	53	5.8	51	2.5	52	2.9
	$C_{14}H_{15}^+$	183.11683	42	4.5	44	5.4	44	4.9
	$C_{14}H_{15}O^+$	199.11174	64	6.1	68	4.4	70	1.0
	$C_{15}H_{15}O^+$	211.11174	24	15.0	25	3.0	26	5.6
	$C_{15}H_{17}O_2^+$	229.12231	40	3.9	43	3.8	43	3.8
	$C_{15}H_{19}O_3^+$	247.13287	25	5.9	27	3.3	29	4.5
	$C_{15}H_{21}O_4^+$	265.14344			7	14.2	7	8.0
	$C_{17}H_{23}O_5^+$	307.15400	6	40.4	7	10.2	7	12.6
ergocornine	$C_{15}H_{15}N_2^+$	**223.12298**	100		100		100	
	$C_{19}H_{17}O_2N_2^+$	305.12845	25	3.4	24	2.2	22	21.5
	$C_{16}H_{18}N_3O^+$	268.14444	62	2.9	61	7.5	56	4.3
	$C_{14}H_{10}NO^+$	208.07569	64	3.2	62	5.6	59	3.8
ergocristine	$C_{15}H_{15}N_2^+$	**223.12298**	100		100		100	
	$C_{19}H_{17}O_2N_2^+$	305.12845	27	1.7	26	2.0	27	1.5
	$C_{16}H_{18}N_3O^+$	268.14444	34	7.9	36	3.2	35	7.3
	$C_{14}H_{10}NO^+$	208.07569	58	4.6	58	2.5	58	2.5
ergocryptine	$C_{15}H_{15}N_2^+$	**223.12298**	100		100		100	
	$C_{16}H_{18}N_3O^+$	268.14444	52	7.1	51	5.1	51	2.2
	$C_{14}H_{10}NO^+$	208.07569	64	3.4	65	3.0	65	2.8
ergometrine	$C_{15}H_{15}N_2^+$	**223.12298**	100		100		100	
	$C_{19}H_{24}N_3O_2^+$	326.18630	60	3.1	58	0.3	58	0.2

DOI: 10.1021/jf505049a
J. Agric. Food Chem. 2015, 63, 8314−8332

Table 7. continued

			1 ng/mL		10 ng/mL		100 ng/mL	
	molecular formula of ions	theoretical mass (m/z)	% avg	RSD	% avg	RSD	% avg	RSD
	$C_{14}H_{10}NO^+$	208.07569	40	2.9	43	4.3	41	0.6
ergosine	$C_{15}H_{15}N_2^+$	**223.12298**	100		100		100	
	$C_{14}H_{19}N_2O_3^+$	263.13902	18	3.2	18	0.6	10	0.6
	$C_{14}H_{10}NO^+$	208.07569	14	5.6	13	2.4	63	1.8
ergotamine	$C_{15}H_{15}N_2^+$	**223.12298**	100		100		100	
	$C_{17}H_{17}N_2O_3^+$	297.12337	21	2.2	21	0.3	21	1.0
	$C_{17}H_{13}N_2O_2^+$	277.09715	15	2.7	15	0.6	14	0.8
	$C_{14}H_{10}NO^+$	208.07569	13	7.0	13	2.5	12	3.7
fumonisin B_1	$C_{22}H_{40}NO^+$	**334.31044**	100		100		100	
	$C_{22}H_{42}NO_2^+$	352.32101	60	5.4	60	2.0	62	1.5
	$C_{22}H_{38}N^+$	316.29988	26	5.9	25	3.1	27	2.1
fumonisin B_2	$C_{22}H_{42}NO^+$	**336.32609**	100		100		100	
	$C_{22}H_{44}NO_2^+$	354.33666	18	15.7	21	6.5	20	7.2
	$C_{22}H_{40}N^+$	318.31553	65	2.4	70	0.0	69	4.1
fusarenon-X	$C_{14}H_{13}O_3^+$	**229.08592**			100		100	
	$C_{14}H_{15}O_4^+$	247.09649			44	9.0	45	3.5
	$C_{13}H_{13}O_2^+$	201.09101			72	9.1	76	3.3
	$C_{11}H_{11}O_2^+$	175.07536			121	5.4	125	3.3
	$C_8H_9O_2^+$	137.05971			132	12.4	132	1.7
HT-2	$C_{14}H_{15}O_4^+$	**169.10118**			100		100	
	$C_{15}H_{19}O_4^+$	263.12779			28	57.9	33	17.8
	$C_{14}H_{15}O_4^+$	215.10666			47	19.8	39	34.4
	$C_{14}H_{13}O^+$	197.09609			66	11.1	69	9.7
	$C_{13}H_{13}O^+$	185.09609			57	5.8	45	39.5
	$C_{12}H_{13}^+$	157.10118			101	20.6	104	19.0
	$C_{11}H_{13}^+$	145.10118			105	31.4	114	33.0
ochratoxin A	$C_{11}H_{10}ClO_5^+$	**257.02111**	100		100		100	
	$C_{19}H_{14}ClO_4^+$	341.05751	5	5.7	7	3.6	8	4.2
	$C_{11}H_8ClO_4^+$	239.01056	24	4.7	46	6.0	91	11.7
	$C_8H_{10}N^+$	120.08078	5	3.2	6	1.1	8	3.7
ochratoxin B	$C_{11}H_{11}O_5^+$	**223.06010**	100		100		100	
	$C_{11}H_9O_4^+$	205.04954	38	4.1	116	8.7	195	4.0
	$C_8H_{10}N^+$	120.08078	2	5.4	4	6.0	5	4.2
sterigmatocystin	$[C_{18}H_{12}O_6 + H]^+$	**325.07066**	100		100		100	
	$C_{17}H_{10}O_6^+$	310.04719	72	1.0	73	4.2	73	0.4
	$C_{17}H_{13}O_5^+$	297.07575	6	22.5	7	1.5	7	2.4
	$C_{16}H_9O_6^+$	281.04445	8	18.1	9	9.2	9	4.8
T-2	$C_{13}H_{13}O^+$	**185.09609**	100		100		100	
	$C_{14}H_{15}O_2^+$	215.10666	78	7.1	77	0.8	76	0.4
	$C_{14}H_{13}O^+$	197.09609	47	2.1	47	1.4	47	2.6
	$C_{13}H_{13}^+$	169.10118	67	6.7	62	1.2	61	2.0
verrucarin A	$C_{15}H_{19}O_2^+$	**231.13796**	100		100		100	
	$C_{15}H_{21}O_3^+$	249.14852	43	5.7	45	9.3	41	10.6
	$C_{12}H_{17}O_2^+$	193.12231	54	1.9	58	2.0	52	19.6
	$C_{10}H_{13}^+$	133.10118	53	11.3	62	3.4	57	9.1
	$C_8H_9^+$	105.06988	66	1.9	69	0.8	70	8.7
	$C_5H_9O^+$	85.06479	125	3.3	129	2.4	124	2.8

DOI: 10.1021/jf505049a
J. Agric. Food Chem. 2015, 63, 8314−8332

Table 7. continued

			1 ng/mL		10 ng/mL		100 ng/mL	
	molecular formula of ions	theoretical mass (m/z)	% avg	RSD	% avg	RSD	% avg	RSD
zearalenone	$C_{12}H_{11}O_2^+$	**187.07536**	100		100		100	
	$C_{18}H_{19}O_3^+$	283.13287	59	3.1	50	2.1	48	2.6
	$C_{12}H_{11}O_3^+$	203.07027	78	6.6	66	2.7	65	1.3
	$C_{13}H_{11}O_4^+$	231.06546	48	8.1	40	14.7	37	1.4

[a]Average ion ratios (% avg) and relative standard deviations (RSD) based on triplicate results each of the mycotoxins fortified in solvent (acetonitrile/water) and acetonitrile/water extracts from peanut and wheat matrices at 1, 10, and 100 ng/mL. The % ion ratio was determined by the ratio of the ion signal responses extracted of the ion to the response with the signal of the molecular ion (indicated in bold) of the highest signal intensity.

and the lesser abundant secondary transitions are typically used for quantitation and identification, respectively, of the analyte.[29,30] The Q-orbital trap operating in DDMS^2 mode provides accurate masses (δ_M < 5 ppm) of the precursor and product ions and offers a higher level of confidence in analyte identification than a triple-quadrupole mass analyzer in MS/MS mode. The DDMS^2 spectra of native mycotoxins can provide accurate masses, resulting in the probable molecular formulas of product ions (DDMS^2 spectra of native mycotoxins are provided in Supporting Information, Figure S1). Figure 1 reveals a wealth of information gained from UHPLC/Q-orbital trap MS in full and DDMS^2 scan modes of fumonisins from a corn reference sample. Extracted ion masses of 722.39575 and 706.40083 and retention times were able to determine the presence of fumonisin B_1 and B_2 (FB1 and FB2), respectively, as well as an additional peak consistent with the presence of fumonisin B_3 (FB3, Figure 1), though identification was incomplete without a reference standard. The three native fumonisin species could be identified by characteristic products (Figure 1B−E) that were resolved chromatographically or by mass (Figure 1E), such in the case of the isotope-labeled internal standard (Figure 1E) using DDMS^2. The DDMS^2 spectra were also used to identify aflatoxins, fumonisins, ochratoxins, and ergot alkaloids for the grain and nut samples in the survey because spectra could be triggered at levels of >10 ng/mL (>50 μg/kg) for these mycotoxin classes. Identification could not be achieved for most of the trichlothecene mycotoxins because the concentrations measured did not trigger the DDMS^2 response but the concentrations reported were significantly below the tolerance or regulatory levels. The available information provided by DDMS^2 spectra was used for identification by providing the characteristic product ions of the mycotoxin in the incurred or fortified food samples as well as additional product information that allows for advanced data interpretation to enhance the confidence of analysis and to carry out retrospective nontargeted analysis.

Figure 2 summarizes the δ_M values of products obtained from individual mycotoxins in the presence of solvent, wheat, and peanut matrices at 1, 10, and 100 ng/mL using a generalized NCE setting of 35 (the numerical δ_M results shown in Figure 2 at each level in solvent, peanut, and wheat matrices are provided in Supporting Information, Tables S7−S10, respectively). The products were selected and consistent with various MS/MS studies of aflatoxins,[31−33] ergot alkaloids,[34−37] fumonisins,[38] ochratoxins,[39,40] trichothecenes,[41,42] and others[43,44] produced by *Fusarium* species. Average δ_M values of products were typically within ±1 ppm, independent of the matrix and dependent on the relative abundances of the precursors and products. DDMS^2 spectra were not generated for 15-acetyl deoxynivalenol (15-acetyl DON), HT-2, T2, DON, DAS, fusarenon-X, and neosolaniol at 1 ng/mL and for 15-acetyl DON and neosolaniol at 10 and 100 ng/mL because either spectra could not be triggered at the lowest concentration level or the experimental m/z values could not be confidently matched with structures using a mass tolerance δ_M < 5 ppm. Further improvements in identification can be achieved by optimizing the intensity threshold and/or individual or step NCEs for individual mycotoxins rather than using the generalized NCE = 35 value used in this study. However, the ionization of trichlothecene mycotoxins generates excessive products, and the lack of any prominent products can result in lower abundances and signal intensities.

Ion ratios of the primary and secondary transitions are typically used in targeted MS/MS analysis for confirmation purposes and are evaluated for their reliability in the orbital trap MS analysis of mycotoxins. To provide additional guidelines, account for differences in the % ion ratios, and improve the confidence in identification, fortification studies of mycotoxins in various matrices at different concentrations were conducted. As shown in Table 7 (with additional information available in Supporting Information, Table S11), the ion ratios for most of the mycotoxins (aflatoxins, beauvreicin, ergot alkaloids, fumonisins, ochratoxins, trichothecenes, verrucarin, and zearalenone) were not influenced by either analyte concentration or sample matrix. The mass ion ratio for citrinin based on m/z 251.09140 (quasi molecular ion) and 233.08084 (resulting from the loss of the hydroxyl group from the molecular ion) listed in Table 7 (and Supporting Information, Table S11) were shown to be influenced by the matrix and its concentration in the matrix. The ion ratios were significantly different in nut and grain matrices and the solvent standard at each fortification level. The products generated from DDMS^2 Q-orbital trap MS signify an important distinction from triple-quadrupole MS/MS results because the high mass accuracy results obtained from the DDMS^2 Q-orbital trap provide the confidence that the products generated can be easily extracted or distinguished from artifacts of the same nominal masses. For example, the theoretical m/z ions of 283.13827 and 203.07027 from zearalenone were found at 10 and 100 ng/mL levels in solvent and matrix with δ_M < 2.5 ppm and were clearly distinguishable from the experimental artifact masses of 283.13722 (δ_M = 15.36) and 203.06904 (δ_M = −6.08) that are present at 1 ng/mL (results of δ_M > 5 ppm were not shown because the mass tolerance of 5 ppm was exceeded). These results in Table 7 also show that the differences of the % ion ratio responses of zearalenone and the other mycotoxins are concentration-dependent and well behaved and consistent within the presence of the matrix. However, differences in the average and standard deviation of ion responses are observed due to variability

DOI: 10.1021/jf505049a
J. Agric. Food Chem. 2015, 63, 8314−8332

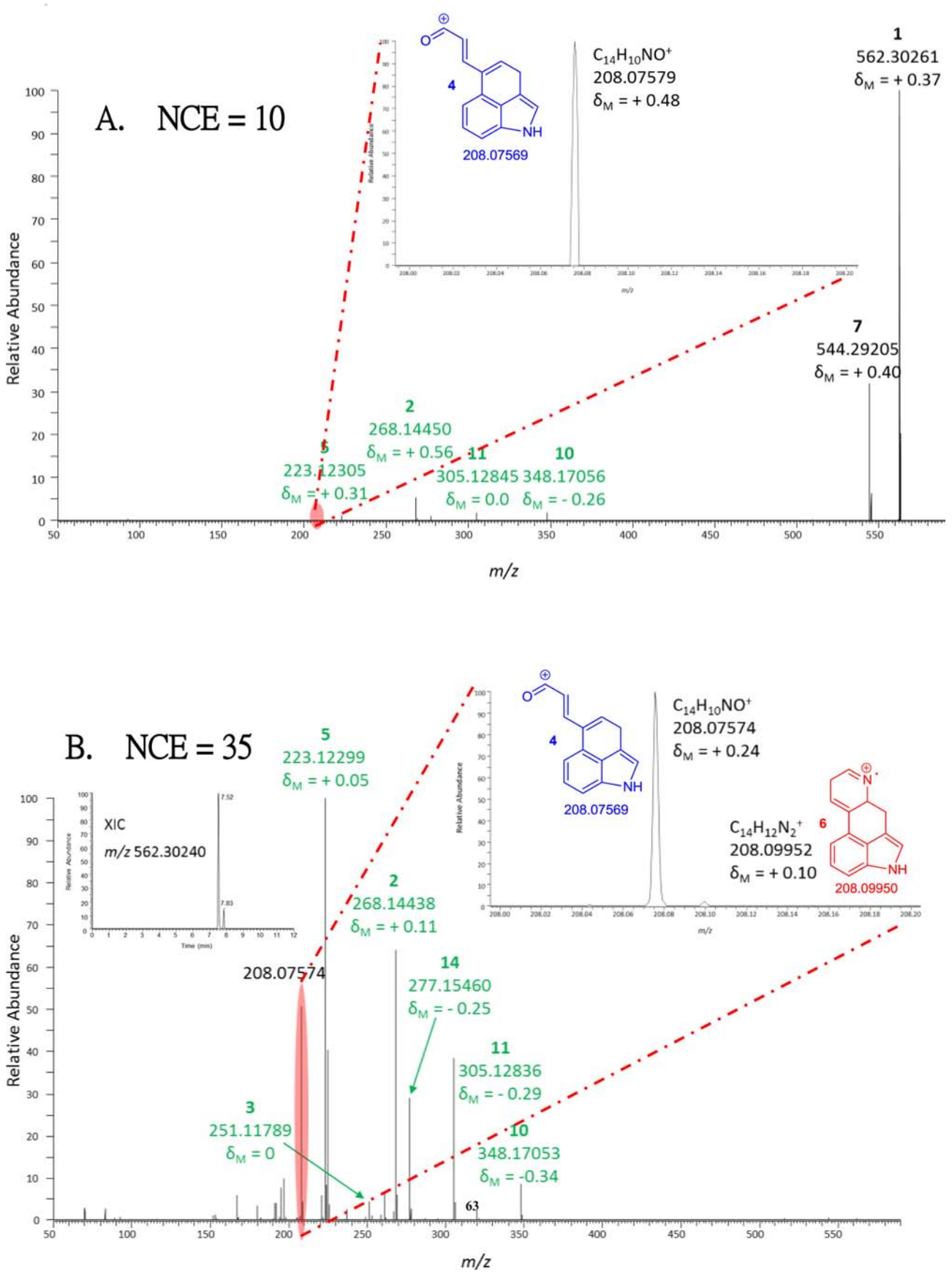

Figure 3. continued

DOI: 10.1021/jf505049a
J. Agric. Food Chem. 2015, 63, 8314−8332

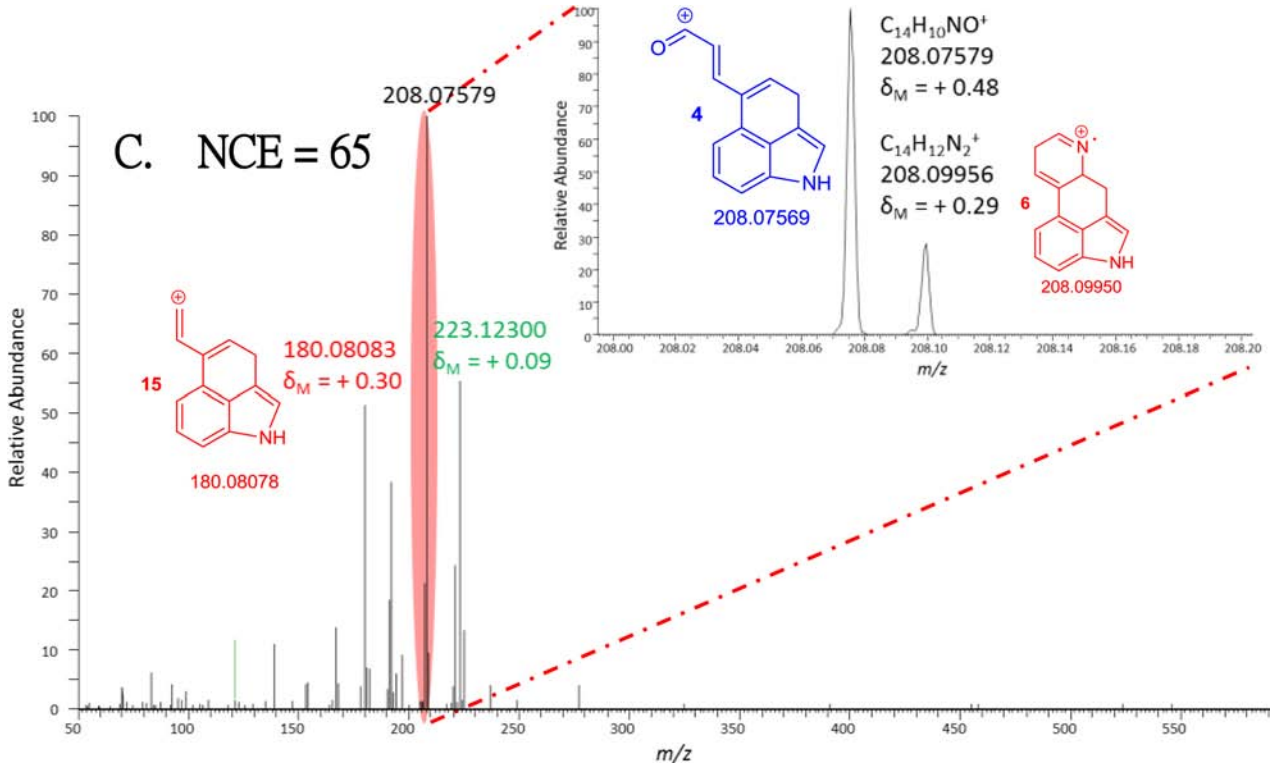

Figure 3. Data-data MS/MS (DDMS^2) spectra of the ergot alkaloid mycotoxin, ergocornine, generated using UHPLC-quadrupole orbital trap mass spectrometry at different normalized collision energies (NCEs): (A) 10, (B) 35 (inset: ion chromatogram of ergocornine (major peak) and −inine (minor peak) epimer extracted using its protonated adduct m/z 562.30240), and (C) 65. DDMS^2 spectra of ergocornine were determined at half peak height and refer to Figure 4 for product structures and numerical assignments.

between matrices (as indicated by peanut and wheat results provided in Supporting Information, Table S11).

High-Resolution Accurate Mass DDMS^2 Fragmentation Studies of Mycotoxins. The benefits of full-scan, high-resolution, accurate mass measurements are further demonstrated by comparing m/z of product ions obtained from LC-MS/MS and UHPLC/Q-orbital trap MS in DDMS^2 mode for the analysis of ergot alkaloid mycotoxins. DDMS^2 spectra are illustrated in Figure 3, revealing the accurate masses (δ_M < 5 ppm) of product ions obtained from HCD experiment of the dominant epimer (Figure 4B, inset) of ergocornine at three NCE levels of 10, 35, and 65. Previous LC-MS/MS studies have provided detailed fragmentation schemes of these peptide-like indole alkaloids, resulting in the formation of two characteristic lysergic acid moiety products (m/z 223 and 208), typically used for quantitation and identification. A possible fragmentation pathway from the precursor ion, ergocornine, to its various products is illustrated in Figure 4, based on previous LC-MS/MS studies[34,35] and supported by high-resolution/high-mass-accuracy DDMS^2 analysis. Fragmentation begins by protonation of the amide bond in **1A** (m/z 562.30240), leading to two possible pathways involving α- and β-cleavage of the amide bond, and then the formation of the ergoline products **2** (m/z 268.14435) and **12**, and **3A** (m/z 251.11789), respectively. Product **2** can also be fragmented directly to **3A** from the loss of $-NH_3$. Product **3A** can be further fragmented and either lose −CO via rearrangement to **3B** to form a lysergic acid derivative cation **5** (m/z 223.12298) or undergo further rearrangement to lose $-C_2H_3N$ to form cation **4** (m/z 208.07569). The current study supports the presence of lysergic acid derivative product ions, **5** $[C_{15}H_{15}N_2]^+$ (m/z 223.12298) and **4** $[C_{14}H_{10}NO]^+$ (m/z 208.07569), but not the formation of the radical **6** $[C_{14}H_{12}N_2^{\bullet}]^+$ ion (m/z 208.09950) due to the loss of the $-CH_3^{\bullet}$ group, as suggested by LC-MS/MS results.[34,35] Low (10) and medium (35) NCEs resulted in no and little product formation of the radical ion **6** (Figure 3A,B), indicating the loss of a methyl cation from the stable **5** product is highly unlikely. A higher NCE (65) (Figure 3C) is required to form the radical product ion **6**, but its signal intensity is still approximately one-third of that of product **5**. The formation of a product ion at m/z 180.08083 (and δ_M = 0.30 Figure 3**C**) indicating loss of −CO further supports the presence of product ion **4** (m/z 180.08078). The presence of one or both of these product masses observed by DDMS^2 results was also determined experimentally using HPLC coupled to a high-resolution mass analyzer consisting of an ion trap/orbital trap hybrid or single-stage orbital trap mass analyzers.[36,37] Other products based on results obtained from LC-MS/MS and UHPLC/Q-orbital trap DDMS^2 can be postulated by protonation of the hydroxide moiety in **1B** resulting in the loss of $-H_2O$ (**7**, m/z = 544.29183), followed by a number of rearrangement and fragmentation steps of the peptide moiety that forms the lysergic acid or the substituted indole cation products **10** (m/z 348.17065) and **11** (m/z 305.12845), respectively. The formation of products **14** (m/z 277.15467) is believed to be a result of a rearrangement and loss of $-H_2O$ of the peptide moiety **12**, formed as a fragmentation result of β-cleavage of the amide bond in **1A**.

Due to the full-scan capability of orbital trap MS, one can carry out MS/MS experiments using DDMS^2 mode, in which the quadrupole will select those coeluting precursor ions, and then carry out the HCD using an optimized or three-step NCE, such that targeted product ions can be measured in a single

DOI: 10.1021/jf505049a
J. Agric. Food Chem. 2015, 63, 8314−8332

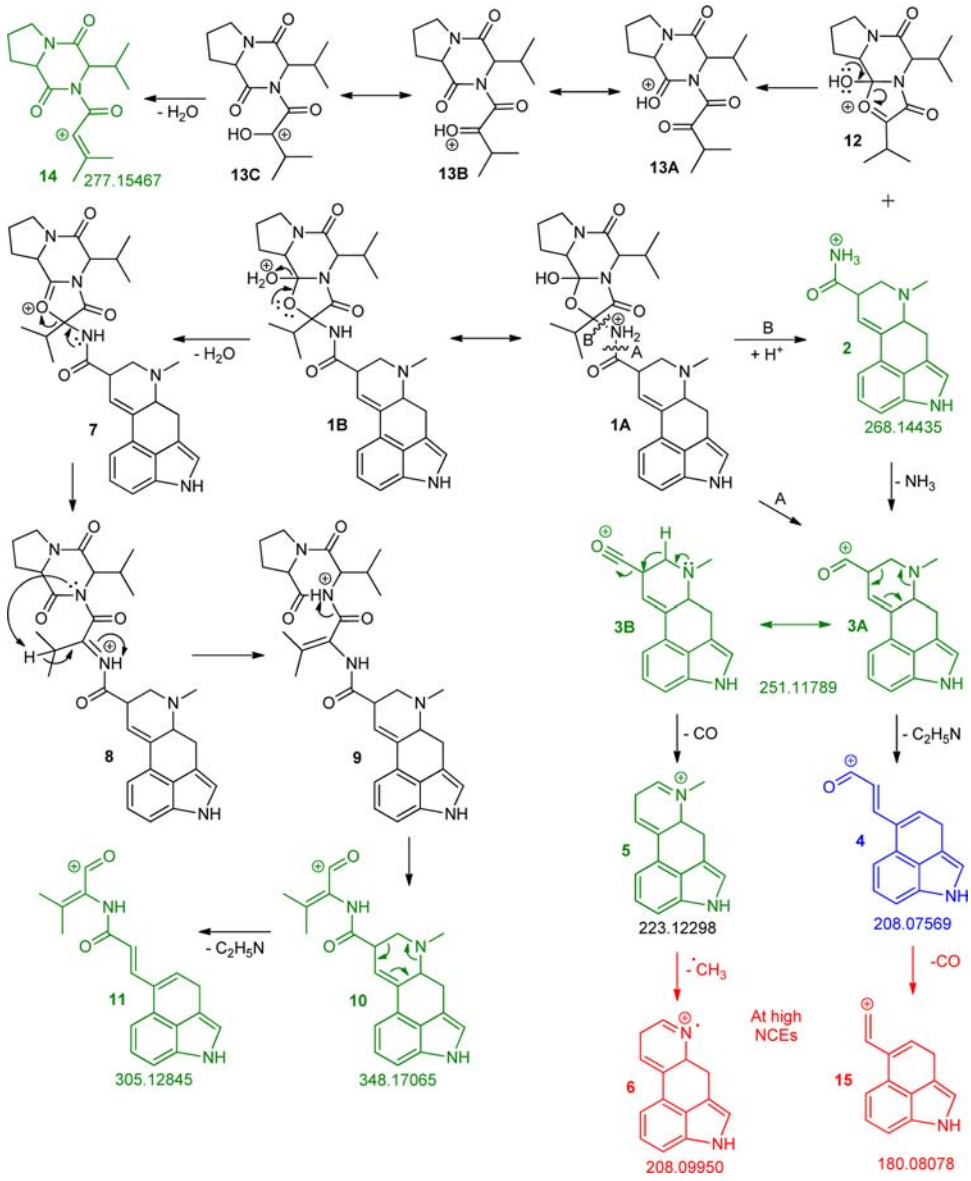

Figure 4. Possible fragmentation mechanism of ergocornine, as provided by LC-MS/MS studies of Lehner et al.[30] and Mohammed et al.[31] with experimental agreement and some modifications by studies performed in this work as well as by Mulac et al.[32] and Arroyo-Manzanares et al.[35] If protonation occurs at the amide bond **1A**, two fragmentation pathways (A,B) are possible: (A) α-cleavage of the amide bond to form **3A**, **3B**, or (B) β-cleavage of the amide bond in **2**, which can lose NH_3 to form **3A**, **3B**. Structures **3A**, **3B** can either lose CO to **5** or undergo rearrangement to **4**. The LC-MS/MS prediction of **6** (as indicated in red) is not consistent with the experimental result obtained from UHPLC-Quadrupole/orbital trap in data-dependent MS/MS experiments unless a higher NCE is used. High-resolution and high-accuracy studies indicate the formation of **4** is the more likely structure present (as indicated in blue and subsequent formation of **15** at a higher NCE) in the MS/MS spectrum in Figure 3. Protonation at the hydroxide moiety **1B** would result in the loss of H_2O followed by a number of steps to promote the formation of **10**, which can undergo rearrangement to **11**. Structure **14** is a result of the fragmentation of the peptide moiety **12** resulting from β-cleavage of the amide linkage in **1A**.

composite MS spectrum. The data acquisition duty cycle will increase when additional mycotoxins are added to the inclusion list to perform $DDMS^2$ analysis. This will limit the number of data points required to accurately define an extracted ion chromatogram peak for consistent quantitative analysis. Therefore, to ensure the data acquisition duty cycle would not adversely affect the use of both full MS and $DDMS^2$ scanning modes, UHPLC separation and intensity thresholds will need to be further evaluated and optimized for quantitative and qualitative analysis. Studies will be required to extract both quantitative and qualitative information from a single $DDMS^2$ analysis to determine whether the quality of such quantitative results will be acceptable for multianalyte procedures that are becoming popular due to cost and time effectiveness and efficiency.[22]

This validated method for analyzing finished and nut products was shown to be easy, efficient, and rugged for routine multi-mycotoxin sample analyses and could be modified and expanded to include other mycotoxins and fungal metabolites, if certified standards become available. The use of Q-orbital trap MS technology has been evaluated thoroughly by applying a validation for mycotoxins in grain and nut products comparable to a previous LC-MS/MS study, evaluating reference and actual food samples, and providing high-accuracy mass fragmentation information that was useful for mycotoxin identification. Future research will include

DOI: 10.1021/jf505049a
J. Agric. Food Chem. 2015, 63, 8314−8332

expanding and modifying this method to analyze additional chemical contaminants, optimize $DDMS^2$ conditions, evaluate other types of full-scan collision experiments such as data-independent acquisition,[45−47] and perform analyses using other food and agricultural matrices.

■ ASSOCIATED CONTENT

Supporting Information

Supporting Tables S1−S11, showing mycotoxin information and UHPLC-HRMS data, mass accuracies for mycotoxins, isotope analyses, Q-Orbitrap and LC-MS/MS data, experimental masses and mass accuracies of ions, and molecular ions and % ion ratios used to identify mycotoxins; Figure S1, showing ion extracted chromatograms and $DDMS^2$ spectra of native mycotoxins from standards prepared in 50:50 acetonitrile/water. This material is available free of charge via the Internet at http://pubs.acs.org.

■ AUTHOR INFORMATION

Corresponding Authors

*E-mail: cdliao@fda.gov.tw. Tel.: 866-2-26531461. Fax: 866-2-26531256.

*E-mail: jon.wong@fda.hhs.gov. Tel.: 240-402-2172. Fax: 301-436-2332.

Author Contributions

#C.-D.L. and J.W.W. contributed equally to this work.

Notes

The authors declare no competing financial interest.

■ ACKNOWLEDGMENTS

We thank Drs. Timothy D. Norden, Thomas A. Weber, and Jason Vanfossan of the United States Department of Agriculture, Grain Inspection, Packers and Stockyards Administration, Technology and Science Division (Kansas City, MO) for providing reference materials, suggestions and technical expertise. We also thank Dr. Dipankar Ghosh and Mr. Charles Yang of ThermoFisher Scientific (San Jose, CA) for providing available software to process and analyze the data. C.-D.L. and J.B.W. acknowledge the support of the FDA/CFSAN postdoctoral positions administered through the Oak Ridge Institute for Science and Education (ORISE) program.

■ REFERENCES

(1) Bennett, J. W.; Klich, M. Mycotoxins. *Clin. Microbiol. Rev.* **2003**, *16*, 497−516.

(2) Marin, S.; Ramos, A. J.; Cano-Sancho, G.; Sanchis, V. Mycotoxins: Occurrence, toxicity, and exposure assessment. *Food Chem. Toxicol.* **2013**, *60*, 218−237.

(3) Edite Bezerra da Rocha, M.; da Chagas Oliveira Freire, F.; Erlan Feitosa Maia, F.; Izabel Florindo Guedes, M.; Rondina, D. Mycotoxins and their effects on human and animal health. *Food Control.* **2014**, *36*, 159−165.

(4) Trucksess, M. W.; Page, S. W. Analytical aspects of mycotoxins. In *Mycotoxins in food safety*; DeVries, J. W., Trucksess, M. W., Jackson, L. S., Eds.; Kluwer Academic/Plenum Publishers: New York, 2002; pp 71−72.

(5) Turner, N. W.; Subrahmanyam, S.; Piletsky, S. A. Analytical methods for determination of mycotoxins: A review. *Anal. Chim. Acta* **2009**, *632*, 168−180.

(6) Zheng, M. Z.; Richard, J. L.; Binder, J. A review of rapid methods for the analysis of mycotoxins. *Mycopathologia* **2006**, *161*, 261−273.

(7) Berthiller, F.; Sulyok, M.; Krska, R.; Schuhmacher, R. Chromatographic methods for the simultaneous determination of mycotoxins and their conjugates in cereals. *Int. J. Food Microbiol.* **2007**, *119*, 33−37.

(8) Capriotti, A. L.; Caruso, G.; Cavaliere, C.; Foglia, P.; Samperi, R.; Laganà, A. Multiclass mycotoxin analysis in food, environmental and biological matrices with chromatography/mass spectrometry. *Mass Spectrom. Rev.* **2012**, *31*, 466−503.

(9) Shephard, G. S.; Berthiller, E.; Burdaspal, P. A.; Crews, C.; Jonker, M. A.; Krska, R.; MacDonald, S.; Malone, R. J.; Maragos, C.; Sabino, M.; Solfrizzo, M.; Van Egmond, H. P.; Whitaker, T. B. Developments in mycotoxin analysis: an update for 2010−2011. *World Mycot. J.* **2012**, *5*, 3−30.

(10) Mochizuki, N. Problems in LC-MS/MS analysis to ensure food safety. *Yakugaku Zasshi* **2011**, *131*, 1019−1025.

(11) Nácher-Mestre, J.; Ibáñez, M.; Serrano, R.; Pérez-Sánchez, J.; Hernández, F. Qualitative screening of undesirable compounds from feeds to fish by liquid chromatography coupled to mass spectrometry. *J. Agric. Food Chem.* **2013**, *61*, 2077−2087.

(12) Diaz, R.; Ibáñez, M.; Sancho, J. V.; Hernández, F. Qualitative validation of a liquid chromatography-quadrupole-time of flight mass spectrometry screening method for organic pollutants in waters. *J. Chromatogr. A* **2013**, *1276*, 47−57.

(13) Fedorova, G.; Randak, T.; Lindberg, R. H.; Grabic, R. Comparison of the quantitative performance of a Q-Exactive high resolution mass spectrometer with that of a triple quadrupole tandem mass spectrometer for the analysis of illicit drugs in wastewater. *Rapid Commun. Mass Spectrom.* **2013**, *27*, 1751−1762.

(14) Kumar, P.; Rúbies, A.; Centrich, F.; Granados, M.; Cortés-Francisco, N.; Caixach, J.; Companyó, R. Targeted analysis with benchtop quadrupole-orbitrap hybrid mass spectrometer: Application to determination of synthetic hormones in animal urine. *Anal. Chim. Acta* **2013**, *780*, 65−73.

(15) Wang, J.; Chow, W.; Leung, D.; Chang, J. Application of ultrahigh-performance liquid chromatography and electrospray ionization quadrupole orbitrap high-resolution mass spectrometry for determination of 166 pesticides in fruits and vegetables. *J. Agric. Food Chem.* **2012**, *60*, 12088−12104.

(16) Turnipseed, S. B.; Storey, J. M.; Clark, S. B.; Miller, K. E. Analysis of veterinary drugs and metabolites in milk using quadrupole time-of-flight liquid chromatography-mass spectrometry. *J. Agric. Food Chem.* **2011**, *59*, 7569−7581.

(17) Liao, C.-D.; Wong, J. W.; Zhang, K.; Hayward, D. G.; Lee, N. S.; Trucksess, M. W. Multi-mycotoxin analysis of finished grain and nut products using high-performance liquid chromatography-triple quadrupole mass spectrometry. *J. Agric. Food Chem.* **2013**, *61*, 4771−4782.

(18) Jia, W.; Chu, X.; Ling, Y.; Huang, J.; Chang, J. Multi-mycotoxin analysis in dairy products by liquid chromatography coupled to quadrupole orbitrap mass spectrometry. *J. Chromatogr. A* **2014**, *1345*, 107−114.

(19) Title 40. Protection of the Environment. Part 136: Guidlines establishing test procedures for the analysis of pollutants. Appendix B: Definition and Procedure for the Determination of the Method Detection Limit—Revision 1.11. *Code of Federal Regulations*; United States Government Printing Office: Washington, DC, 2010; http://ecfr.gpoaccess.gov/cgi/t/text/text-idx?c=ecfr&tpl=/ecfrbrowse/Title40/40cfr136_main_02.tpl.

(20) Nielen, M. W. F.; van Engelen, M. C.; Zuiderent, R.; Ramaker, R. Screening and confirmation criteria for hormone residue analysis using liquid chromatography accurate mass time-of-flight, Fourier transform ion cyclotron resonance and orbitrap mass spectrometry techniques. *Anal. Chim. Acta* **2007**, *586*, 122−129.

(21) Thomas, A.; Geyer, H.; Schänzer, W.; Crone, C.; Kellmann, M.; Moehring, T.; Thevis, M. Sensitive determination of prohibited drugs in dried blood spots (DBS) for doping controls by means of a benchtop quadrupole/Orbitrap mass spectrometer. *Anal. Bioanal. Chem.* **2012**, *403*, 1279−1289.

(22) Wang, J.; Chow, W.; Chang, J.; Wong, J. W. Ultra-high performance liquid chromatography electrospray ionization Q-orbitrap mass spectrometry for analysis of 451 pesticide residues in fruits and

DOI: 10.1021/jf505049a
J. Agric. Food Chem. 2015, 63, 8314−8332

vegetables: Method development and validation. *J. Agric. Food Chem.* **2014**, *62*, 10375−10391.
(23) Monaci, L.; De Angelis, E.; Visconti, A. Determination of deoxynivalenol, T-2 and HT-2 toxins in a bread model food by liquid chromatography-high resolution-Orbitrap-mass spectrometry equipped with a high-energy collision dissociation cell. *J. Chromatogr. A* **2011**, *1218*, 8646−8654.
(24) Gottfried, S.; Herebian, D. Determination of mycotoxins in food matrices using LC-MS/MS compared with high-resolution orbitrap MS technology. *Curr. Anal. Chem.* **2013**, *9*, 99−107.
(25) Wang, Y.; Gu, M. The concept of spectral accuracy for MS. *Anal. Chem.* **2010**, *82*, 7055−7062.
(26) Mol, H. G. J.; Zomer, P.; de Koning, M. Qualitative aspects and validation of a screening method for pesticides in vegetables and fruits based on liquid chromatography coupled to full scan high resolution (Orbitrap) mass spectrometry. *Anal. Bioanal. Chem.* **2012**, *403*, 2891−2908.
(27) Sulyok, M.; Krska, R.; Schuhmacher, R. A liquid chromatography/tandem mass spectrometric multi-mycotoxin method for the quantification of 87 analytes and its application to semi-quantitative screening of moldy food samples. *Anal. Bioanal. Chem.* **2007**, *389*, 1504−1523.
(28) FAO Food and Nutrition Paper 81. *Worldwide regulations for mycotoxins in food and feed in 2003*; Food and Agricultural Organization of the United Nations: Rome, Italy, 2004.
(29) Stolker, A. A. M.; Stephany, R. W.; van Ginkel, L. A. Identification of residues by LC-MS. The application of new EU guidelines. *Analusis* **2000**, *28*, 947−951.
(30) Method validation and quality control procedures for pesticide residues analysis in food and feed. Document No. SANCO/12495/2011 supersedes Document No. SANCO/10684/2009 implemented by 01/01/2012; http://www.crl-pesticides.eu/library/docs/fv/SANCO12495-2011.pdf.
(31) Liau, B.-C.; Jong, T.-T.; Lee, M.-R; Chang, C.-M. J. Supercritical fluid extraction and quantification of aflatoxins in Zizyphi Fructus by liquid chromatography/atmospheric pressure chemical ionization tandem mass spectrometry. *Rapid Commun. Mass Spectrom.* **2007**, *21*, 667−673.
(32) Liu, R.; Jin, Q.; Tao, G.; Shan, L.; Huang, J.; Liu, Y.; Wang, X.; Mao, W.; Wang, S. Photodegradation kinetics and byproducts identification of the Aflatoxin B_1 in aqueous medium by ultra-performance liquid chromatography-quadrupole time-of-flight mass spectrometry. *J. Mass Spectrom.* **2010**, *45*, 553−559.
(33) Tóth, K.; Nagy, L.; Mándi, A.; Kuki, Á.; Mézes, M.; Zsuga, M.; Kéki, S. Collision-induced dissociation of aflatoxins. *Rapid Commun. Mass Spectrom.* **2013**, *27*, 553−559.
(34) Lehner, A. F.; Craig, M.; Fannin, N.; Bush, L.; Tobin, T. Fragmentation patterns of selected ergot alkaloids by electrospray ionization tandem quadrupole mass spectrometry. *J. Mass Spectrom.* **2004**, *39*, 1275−1286.
(35) Mohamed, R.; Gremaud, E.; Tabet, J.-C.; Guy, P. A. Mass spectral characterization of ergot alkaloids by electrospray ionization, hydrogen/deuterium exchang, and multiple stage mass spectrometry: usefulness of precursor ion scan experiments. *Rapid Commun. Mass Spectrom.* **2006**, *20*, 2787−2799.
(36) Mulac; Grote, A.-K.; Kleigrewe, K.; Humpf, H.-U. Investigation of the metabolism of ergot alkaloids in cell culture by Fourier transformation mass spectrometry. *J. Agric. Food Chem.* **2011**, *59*, 7798−7807.
(37) Arroyo-Manzanares, N.; Malysheva, S. V.; Vanden Bussche, J.; Vanhaecke, L.; Di Mavungu, J. D.; De Saeger, S. Holistic approach based on high resolution and multiple stage mass spectrometry to investigate ergot alkaloids in cereals. *Talanta* **2014**, *118*, 359−367.
(38) Bartók, T.; Szécsi, A.; Szekeres, A.; Mesterházy, A.; Bartók, M. Detection of new fumonisin mycotoxins and fumonisin-like compounds by reversed-phase high-performance liquid chromatography/electrospray ionization ion trap mass spectrometry. *Rapid Commun. Mass Spectrom.* **2006**, *20*, 2447−2462.
(39) Tabata, S.; Iida, K.; Kimura, K.; Iwasaki, Y.; Nakazato, M.; Kamata, K.; Hirokado, M. Simultaneous determination of ochratoxin A, B and citrinin in foods by HPLC-FL and LC/MS/MS. *Shokuhin Eiseigaku Zasshi* **2008**, *49*, 100−105.
(40) Lau, B. P.-Y.; Scott, P. M.; Lewis, D. A.; Kanhere, S. R. Quantitative determination of ochratoxin A by liquid chromatography/electrospray tandem mass spectrometry. *J. Mass Spectrom.* **2000**, *35*, 23−32.
(41) Razzazi-Fazeli, E.; Rabus, B.; Cecon, B.; Böhm, J. Simultaneous quantification of A-trichothecene mycotoxins in grains using liquid chromatography-atmospheric pressure chemical ionization mass spectrometry. *J. Chromatogr. A* **2002**, *968*, 129−142.
(42) Liu, Z.-Y.; Yu, C.-H.; Wan, L.; Sun, Z.-L. Fragmentation study of five trichothecenes using electrospray hybrid ion trap/time-of-flight mass spectrometry with accurate mass measurements. *Int. J. Mass Spectrom.* **2012**, *309*, 133−140.
(43) Song, H.-H.; Lee, H.-S.; Lee, G.-P.; Ha, S.-D.; Lee, C. Structural analysis of enniatin H, I, and MK1688 and beauvericin by liquid chromatography-tandem mass spectrometry (LC-MS/MS) and their production by Fusarium oxysporum KFCC 11363P. *Food Add. Contamin.* **2009**, *26*, 518−526.
(44) Lattanzio, V. M. T.; Della Gatta, S.; Godula, M.; Visconti, A. Quantitative analysis of mycotoxins in cereal foods by collision cell fragmentation-high resolution mass spectrometry: performance and comparison with triple-stage quadrupole detection. *Food Add. Contam.* **2011**, *28*, 1424−1437.
(45) Hopfgartner, G.; Tonoli, D.; Varesio, E. High-resolution mass spectrometry for integrated qualitative and quantitative analysis of pharmaceuticals in biological matrices. *Anal. Bioanal. Chem.* **2012**, *402*, 2587−2596.
(46) Zhu, X.; Chen, Y.; Subramanian, R. Comparison of information-dependent acquisition, SWATH and MS (All) techniques in metabolite identification study employing ultrahigh-performance liquid chromatography-quadrupole time-of-flight mass spectrometry. *Anal. Chem.* **2014**, *86*, 1202−1209.
(47) Ma, S.; Chowdhury, S. K. Data acquisition and data mining techniques for metabolite identification using LC coupled to high-resolution MS. *Bioanalysis* **2013**, *5*, 1285−1297.

DOI: 10.1021/jf505049a
J. Agric. Food Chem. 2015, 63, 8314−8332

loading, sample cross-contamination, and the requirement for solvent washing between samples.

Because of these issues, indirect stoichiometric FTIR methods are generally a better approach to quantitation,[10−15] with a variety of bases having been used to convert FFAs to their salts. In these methods, the COO^-X^+ salts formed can be measured spectroscopically or, alternatively, the conjugate acid (X^-H^+) if it is infrared active and measurable. In all cases, solvents are used to reduce viscosity and facilitate sample handling. A complicating factor in the indirect stoichiometric procedures is how the samples are handled spectroscopically, in terms of being either split-sample or single-sample analyses. The distinction here is that in the split-sample approach, paired spectroscopic analyses are required, one of the oil samples with the reagent added (S_R) and the other the oil sample with only the solvent (S_S) added. By spectroscopically subtracting S_S from S_R, the differential spectrum ($\Delta S = S_R - S_S$) contains only the spectroscopic contributions related to the chemical changes taking place, the other spectroscopic contributions having been ratioed out. Although this is the more ideal approach from the standpoint of quantification, it also requires the analysis of two samples to obtain a single result. This requirement is generally considered impractical from a sample preparation and handling perspective by commercial laboratories when considering an automated method.[15] Most of these issues have been overcome by using sodium phenolate in 1-propanol (phenolate/1-PrOH) as the reagent in the single-sample mode, providing for oil−solvent miscibility as well as suitably located conjugated acid (phenol) absorption. By measuring the phenol formed at ∼1569 cm^{-1}, an accurate, single-sample, automated turnkey method has been implemented to deliver ASTM-identical AN (AV) results for the mineral-based lubricants.[15] To date, the $FTIR_{phenolate}$ procedure has only been applied to mineral-based oils with the objective of producing ASTM-identical AN results for lubricants.[11] As such, turnkey, autosampler-based FTIR instrumentation equipped with custom ancillary software designed for commercial lubricant laboratory use is required rather than a conventional, standard benchtop FTIR spectrometer.

This work was designed to develop and validate a generic, semiautomatable FTIR method capable of rapidly determining the acidity of ester-based oils using any basic FTIR spectrometer to produce results as, or more than, accurate as standard titration procedures.

MATERIALS AND METHODS

Materials. All reagents were of analytical grade, with sodium phenolate (phenolate), oleic acid, and *p*-toluenesulfonic acid (*p*-TSA) obtained from Aladdin Inc. (Shanghai, China) and 1-propanol (1-PrOH) obtained from Ling Feng Inc. (Shanghai, China). Vegetable oils, including soy, sunflower seed, peanut, palm, were obtained from local Chinese retailers. Freshly prepared phenolate/1-PrOH was stored in and delivered from a bottle dispenser; inlet air passed through a solution of $Ca(OH)_2$ (Sinopharm Chemical Reagent Co., Shanghai, China) to prevent atmospheric CO_2 ingression, which leads to carbonic acid formation and consumption of the phenolate. Any oil used for calibration or as reference oil (O_R) was passed through activated silica gel to remove any FFA, the silica gel (60−100 mesh) being preactivated at 280 °C for 4 h before use.

Instrumentation. The instrument used was a Tensor 27 FTIR spectrometer (Bruker Inc., Bremen, Germany) controlled by OPUS software (Bruker Inc.), with all spectra collected at a resolution of 4 cm^{-1} using 16 scans (∼30 s scanning) over a spectroscopic range of 400−4000 cm^{-1}. General spectroscopic processing, including spectroscopic subtraction, obtaining second-derivative spectra, region selection, and baselines for calibration and validation, was carried out using Omnic (Nicolet, Madison, WI, USA) software. Analyses were carried out using a 100 μm CaF_2 transmission flow cell equipped with Luer lock fittings, with the cell loaded by aspiration using a long stainless steel Leur-Lock needle connected via Tygon tubing to the cell and a three-way control valve, sample trap, and then vacuum.

Sample Preparation. For spectroscopic analysis, a standardized sample preparation protocol was used, requiring the dispensing of 10 mL of 1% phenolate dissolved in 1-PrOH from a calibrated bottle-topped dispenser into a 25 mL glass vial containing 5 g (±0.01) of oil. After reagent addition, the vial was capped and shaken until the solution was clear, after which it was ready for spectroscopic analysis. The sample can be taken either by opening the vial and aspirating the sample into the cell via the needle while using the valve or, if a septum cap is used, puncturing the septum with the needle and loading the cell.

Calibration. Acid-free oil is required for calibration, with any refined oil serving this purpose if treated with activated silica gel to ensure that all polar constituents have been removed. Using this acid-free oil, oleic acid-spiked calibration standards ($C_{0\rightarrow n}$) were prepared, the base oil to which no oleic acid had been added serving as the calibration reference oil (C_0). Using calibration samples prepared as above, a single-beam air spectrum was first taken, the cell loaded by aspiration, followed by a single-beam spectrum of the C_0 solution to produce its absorption spectrum (AC_0) and stored. The cell was then emptied by aspirating air through the cell, flushed with 1-PrOH, emptied again, and loaded with the next standard, the cell flushing step depending on whether any significant sample carry-over is encountered. Using the same air background, the single-beam spectrum of each of the subsequent spiked calibration standards was collected to produce the absorption spectrum of each standard ($AC_{1\rightarrow n}$). Differential spectra were then produced by subtracting AC_0 from each spectrum of the standards and its 5-5 gap-segment second-derivative taken ($\Delta^2AC_{1\rightarrow n}$) and multiplied by 100 to magnify the small absolute peak height obtained to more workable values. For calibration, the peak height of the $\nu_{phenolate^-}$ absorption (∼1588 cm^{-1}) and the ν_{COO^-} of the FFA salt (∼1569 cm^{-1}) in the $\Delta^2AC_{1\rightarrow n}$ spectra were measured relative to a zero baseline. These responses are related by linear regression to AV and %FFA, respectively, calculated from the oleic added standard to produce the calibrations.

Sample Analysis. The analysis of unknowns requires that a representative acid-free reference oil (O_R), which is analogous to CA_0 of the calibration set, be available, which is readily prepared by passing an oil through an activated silica gel column. Sample analysis parallels the calibration procedure by collecting the spectrum of the reagent-reacted reference oil, O_R, to produce AO_R, which was stored. The cell was then loaded with the first reagent-reacted oil sample to obtain its absorption spectrum (AO_{S1}); its differential spectrum was calculated ($\Delta AS_1 = AO_{S1} - AO_R$) and its 5-5 gap-segment second-derivative taken (Δ^2AS_1) and multiplied by 100; the second-derivative calibration equations derived for FFA and/or AV were used to predict the respective values.

Analytical Spectroscopy. A set of 11 calibration standards (C_0−C_{11}) were prepared covering a range 0−4% FFA_{oleic} (0−7.96 mg KOH/g as AV) by the gravimetric addition of pure oleic acid (±0.1 mg) to a refined, silica gel-treated peanut oil (acid-free). Using the second-derivative calibrations, a set of representative oils (soy, peanut, and sunflower), spiked with known amounts of oleic acid, were prepared and analyzed by FTIR in duplicate for their AV/FFA content. These samples were also analyzed in duplicate according to AOCS Cd 3d-63/Cd 5a-40. Both the AOCS and FTIR results were compared to the gravimetrically added AV/FFA oleic acid values in terms of accuracy and reproducibility; the gravimetric data were considered to reflect the true acidity of the samples. Three additional sets of samples were prepared in another acid-free oil, one gravimetrically spiked with *p*-TSA, a second with oleic acid, individually, and a third with mixtures of two acids to determine whether carboxylic and noncarboxylic acid contributions could be differentiated and quantified properly. Subsequently, FTIR and AOCS predictions were compared by analyzing used oils of unknown

DOI: 10.1021/acs.jafc.5b02738
J. Agric. Food Chem. 2015, 63, 8333−8338

provenance obtained from local vendors to validate the overall performance of the FTIR method. For these analyses, two spectroscopically divergent oils were used as O_R to determine if oil-type and/or other matrix effects affect the FTIR predictions relative to the AOCS results.

Validation Analysis. The spectra obtained were analyzed using TurboQuant (version 7.2.0) (Thermo-Electron Corp., Madison, WI, USA), a spectral analytical and chemometrics package providing for region selection, spectroscopic transformations, calibration development, and concurrent prediction of validation samples relative to known or chemically determined values as well as facilitating statistical analysis of the results.

RESULTS AND DISCUSSION

Calibration. As noted, the indirect phenolate-based FTIR method ($FTIR_{phenolate}$) has been applied only to mineral-based oils as a single-sample, automated procedure to determine AN with the objective of obtaining ASTM-identical results. In this work, the objective was to simplify and assess the performance of the $FTIR_{phenolate}$ procedure for its ability to analyze non-phosphate ester-based oils so as to make the FTIR procedure more generic and utilitarian. The phenolate stoichiometric reaction used for the analysis for AV in hydrophobic matrices can be generalized as

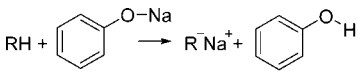

(1)

In the case of ester-based oils, carboxylic acids are effectively the only source of acidity:

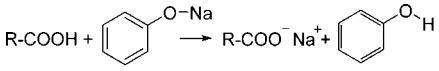

(2)

In eqs 1 and 2, all acidity with a pK_a value 1 order greater than that of phenolate should be readily measurable via the spectroscopic loss of the $\nu_{phenolate}$ absorption, whereas in eq 2, one may have the option of measuring acidity using either the $\nu_{phenolate}$, ν_{COO^-}, or both as a measure of FFAs. By using acid-free oil to calibrate and pure oleic acid as the acid source, a calibration devised in this manner should produce an identical response regardless of the mode of measurement. However, when acidity other than FFAs is present, AV and %FFA results will differ and a conversion ratio of FFA to AV (1.99 as oleic) will produce a lower result.

Figure 1 illustrates the simple differential and 5-5 gap-segment second-derivative spectra obtained for phenolate-reacted, oleic acid-spiked peanut oil calibration standards after subtraction of the spectrum of acid-free AC_0. The changes in the differential spectra reflect the loss of phenolate and the formation of COO^-Na^+, but are spectroscopically difficult to interpret due to spectroscopic overlap. However, after taking the gap-segment second-derivative, these absorption changes are more clearly parsed out, with the negative phenolate band at ~1588 cm^{-1} becoming smaller with acid concentration, whereas the positive oleate band at ~1569 cm^{-1} grows proportionately, thus providing means of differentiating between carboxylate (FFA) acidity and total acidity contributions (AV). Figure 2 presents calibration plots devised on the basis of the second-derivative spectra by measuring the minimum and maximum, respectively, of the COO^- and phenolate bands in each spectrum and relating the peak height to the %FFA and AV, respectively.

The calibration equations obtained for the $\Delta^2AC_{1\rightarrow n}$ spectra in terms of AV and FFA based solely on oleic acid being present are

$$FTIR_{AV} = 13.636 \times Abs_{(1588cm^{-1})} + 0.230 \quad (3)$$

$$R^2 = 0.9975, SD = 0.1441$$

$$FTIR_{FFA} = -5.454 \times Abs_{(1569cm^{-1})} + 0.047 \quad (4)$$

$$R^2 = 0.9989, SD = 0.0469$$

Both of these calibrations are highly linear and their respective SD values reflect a coefficient of variation (CV) of ~2.0 and 3.5%, respectively.

Validation. With these calibration relationships in hand, one can theoretically differentiate between carboxylate and other forms of acidity using the carboxyl (%FFA) and phenolate (AV) response at 1569 and 1588 cm^{-1}, respectively. To test this as well as the overall reproducibility and accuracy of FTIR method in determining acidity relative to the AOCS titrimetric method, soybean oil was gravimetrically spiked with oleic acid as well as with *p*-TSA, one set of each acid spiked into the oil alone, with another set where the two acids were present

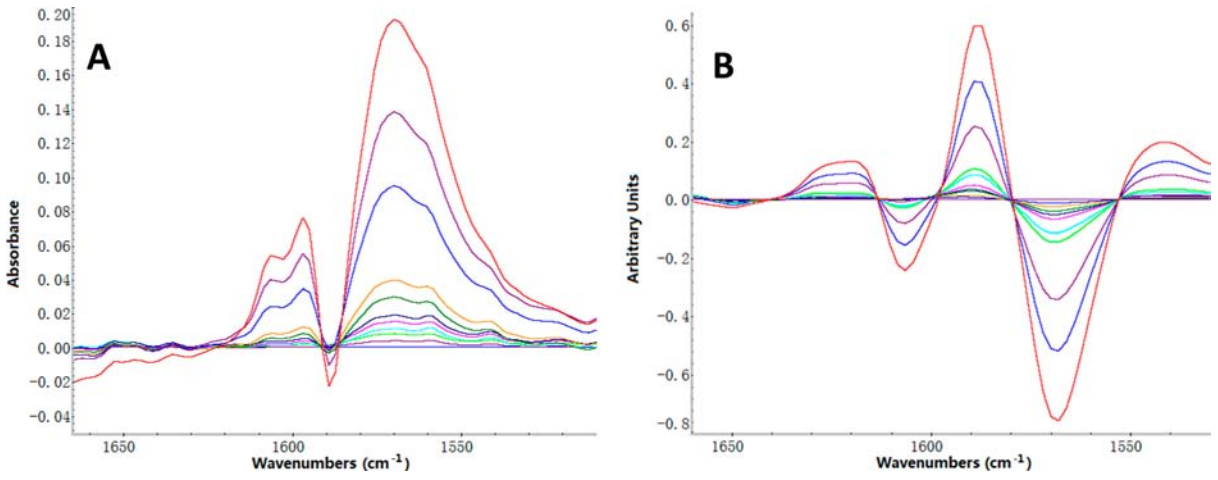

Figure 1. (A) Differential and (B) 5-5 gap segment second-derivative spectra for acid-free peanut oil spiked with oleic acid using sodium phenolate in 1-PrOH as the reagent to carry out the acid/base reaction. Spectra were recorded in a 103 μm cell at 4 cm^{-1} resolution.

DOI: 10.1021/acs.jafc.5b02738
J. Agric. Food Chem. 2015, 63, 8333−8338

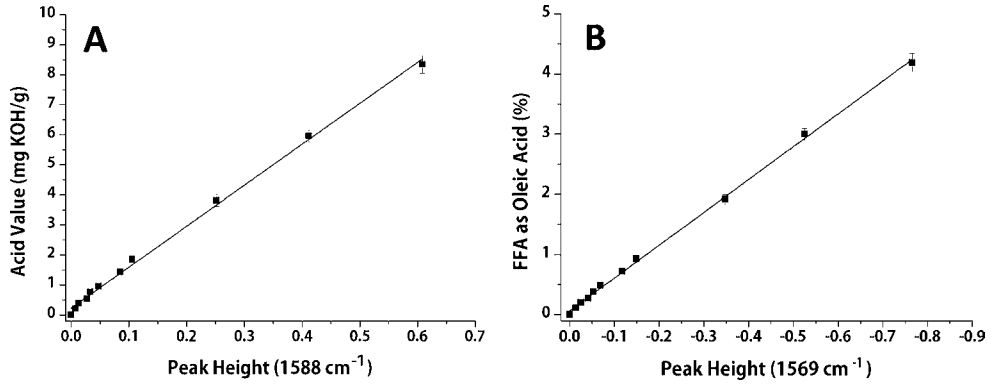

Figure 2. Calibration plots of acid-free oil spiked with oleic acid and reacted with phenolate obtained using TurboQuant: (A) AV versus peak height at ~1588 cm^{-1}; (B) FFA% versus peak height at 1569 cm^{-1}.

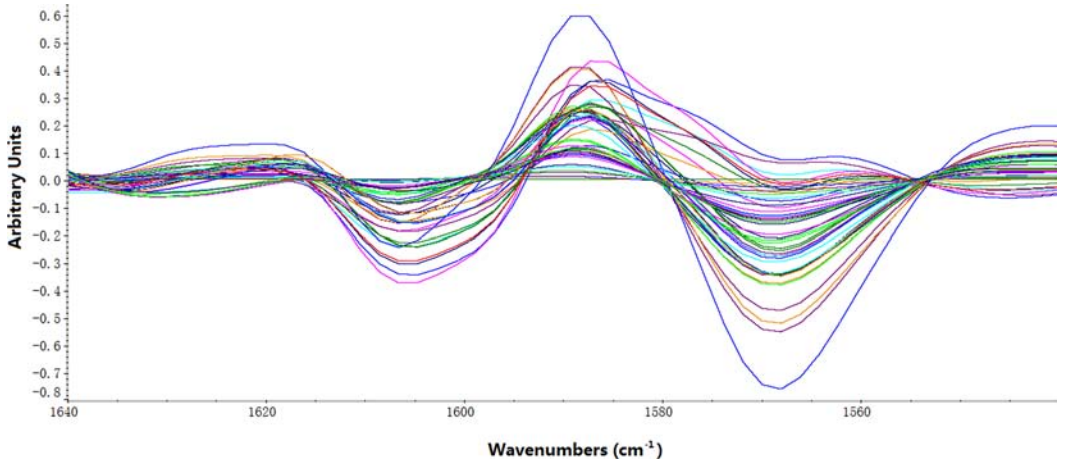

Figure 3. Collation of all second-derivative validation spectra illustrating the region over which the phenolate and $COO^{-}Na^{+}$ absorptions occur.

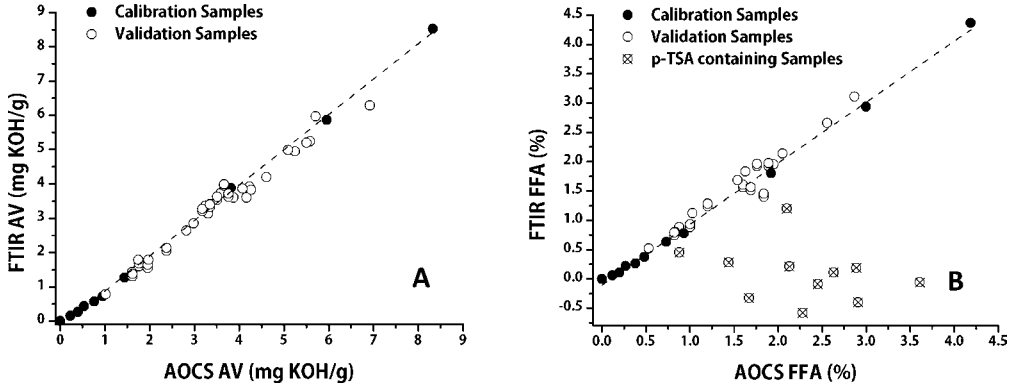

Figure 4. (A) Plot of AV calibration data points (●) and validation predictions (○). (B) Similar plot for %FFA, with the *p*-TSA containing samples (⊗) not being predictable.

together; all were also analyzed according to the AOCS method. In addition, a series of used oils of unknown provenance were analyzed according to the AOCS method and FTIR to compare their performance to gravimetric addition. The second-derivative spectra obtained for the calibration and validation samples were combined, a new calibration was derived, and the validation samples were predicted and compared to the known added acid amounts and/or chemically determined values using TurboQuant. All analyses were carried out in duplicate, including the reference titrimetric procedure, so as to obtain a comparative baseline in terms of accuracy (a) and reproducibility (r). On the basis of these duplicate analyses the mean difference (MD_r) and standard deviation of the difference (SDD_r) for reproducibility were determined to be 0.032 and 0.077 mg KOH/g for AV and 0.008 and 0.022% for FFA, respectively. Both the gravimetrically prepared calibration standards and the oleic/*p*-TSA samples can serve as a measure of the accuracy (a) of the titration procedure, with the MD_a and SDD_a obtained being 0.071 and 0.122 mg KOH/g oil, respectively, for AV, using the mean value of the duplicate analyses. Figure 3 presents a

DOI: 10.1021/acs.jafc.5b02738
J. Agric. Food Chem. 2015, 63, 8333−8338

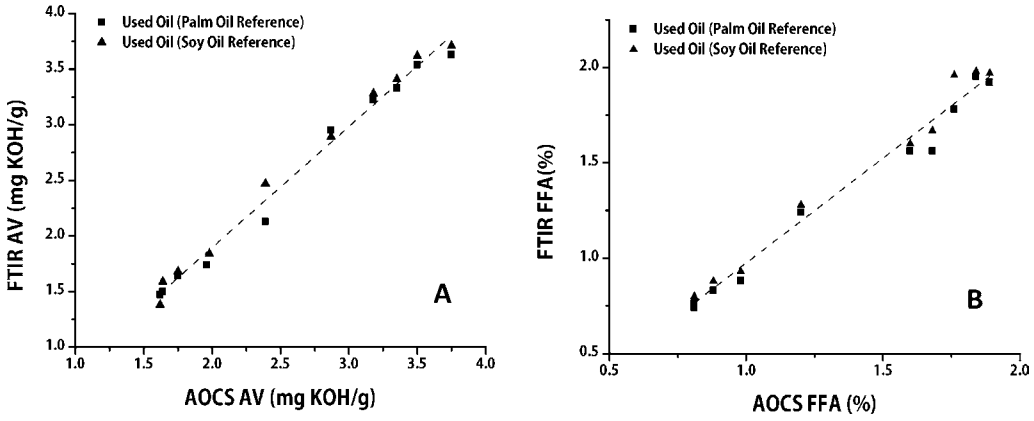

Figure 5. (A) Comparison plot of AV results obtained by AOCS and FTIR methods for used oil. (B) Similar plot for %FFA results.

composite grouping of all the validation second-derivative spectra collected.

These spectra are somewhat similar to the calibration spectra presented in Figure 1 but demonstrate substantially more variability in the phenolate band maxima. The COO^- band is more uniform, but confounded to some extent as some oils contain only *p*-TSA, which lacks the COO^- absorption. Even so, AV, defined as a measure of all acid contributions, carboxylic acids as well as noncarboxylic acids, can still be accurately measured via the loss of the phenolate band as seen in Figure 4A, which compares the FTIR predictions against the mean of the AOCS titration results for the same samples.

The ability to predict acids other than carboxylic acids correctly using the COO^- absorbance is by definition not possible and is confirmed in Figure 4B, where ⊗ represents only *p*-TSA-containing oils. Although this is an extreme example and unlikely to occur in reality, it demonstrates that, should acids other than carboxylic acids exist, the %FFA prediction will be erroneous relative to the titrimetrically determined value in such circumstances. Included in both of these assessments are used oils of unknown provenance in terms of oil type, requiring the use of an arbitrarily selected, acid-free reference oil (O_R). To assess whether the oil used as O_R affects the FTIR results significantly relative to the AOCS data, two chemically and spectroscopically divergent oils (soybean and palm oils), differing significantly in their saponification number (SN) and iodine values (IV) were used as O_R so as to generate their respective differential spectra. The FTIR AV and %FFA predictions of these used oils are compared to their mean AOCS AV and FFA results and illustrated in Figure 5, panels A and B, respectively, linear regression producing the following relationships:

$$AV_{FTIR} = 1.088 \times AV_{AOCS} - 0.280 \quad (5)$$

$$SD = 0.097, R^2 = 0.989$$

$$\%\,FFA_{FTIR} = 1.099 \times \%FFA_{AOCS} - 0.124 \quad (6)$$

$$SD = 0.070, R^2 = 0.980$$

On the basis of these results, there is minor oil-dependent bias introduced depending on which oil is used as O_R; however, as long as one consistently uses a particular oil as O_R, the results will track consistently.

Table 1 presents the overall performance of the methods relative to Figure 4 in terms of mean differences (MD_r) and standard deviation of the difference (SDD_r) between duplicates as well as in terms of accuracy (MD_a and SDD_a) of the AOCS and FTIR results relative to the amounts of acid added.

Table 1. MD and SDD for Reproducibility (r) and Accuracy (a) for Acidity of Oleic Acid and *p*-Toluenesulfonic Acid-Spiked Oils

	AV_{AOCS}	$AV_{FTIR\ C18:1}$	$AV_{FTIR p\text{-}TSA}$	$FFA_{FTIR\ C18:1}$	$FFA_{FTIR p\text{-}TSA}$
MD_r	0.032[a]	0.012[a]	0.018	0.008	NA[b]
SDD_r	0.077	0.028	0.041	0.022	NA
MD_a	0.071	0.025	0.088	0.056	NA
SDD_a	0.122	0.107	0.166	0.032	NA

[a]Absolute AV and COOH measurements from which these statistics are derived differ by a factor of ∼2, which affects their relative magnitudes. [b]NA, not applicable by definition to FTIR quantitation of FFA.

Comparison of both the AV and FFA results illustrates that the $FTIR_{phenolate}$ procedure consistently produces results statistically closer to the gravimetrically added acidity for COOH from the standpoint of either accuracy or reproducibility relative to the AOCS reference method. This confirms that the method is on firm ground in being considered a primary method in its own right. In the case of the *p*-TSA measurement, the accuracy is slightly lower, but of similar magnitude. Although one gains the impression that the COOH measure is significantly superior to that of the AV measurement on the basis of these comparative statistics, these differences are to a large degree a result of the relative magnitude of the measurements when the conversion ratio of FFA to AV is 1.99 rather than analytical differences.

As structured, the $FTIR_{phenolate}$ method performs well in determining the acidity of ester-based oils, expressed either as %FFA or as AV. Like the standard AOCS methods, this FTIR method is a primary, rather than a secondary, method. Calibration simply requires the standard addition of oleic acid to any refined, activated silica gel treated ester-based oil to ensure no residual inherent acidity exists to bias the calibration. For the analysis of unknown samples, any reasonably representative, acid-free oil can serve as reference oil, again, readily prepared by treating it with activated silica gel. Oil-type effects on quantification are minimal and consistent, with optimal results achieved using second 5-5 gap-segment derivative differential spectra. As configured, sample handling is facile, and accurate results can be obtained for all ester-based oils, other than phosphate esters, making the method of general utility even if the oil type or provenance is undefined. Because

DOI: 10.1021/acs.jafc.5b02738
J. Agric. Food Chem. 2015, 63, 8333−8338

the method uses an oil-miscible solvent as the phenolate carrier, sample handling issues associated with the high viscosity oils are minimized, facilitating rapid, even semiautomated, analysis. To the extent that a spectrometer and its attendant software allow one to program the spectroscopic data processing steps, it is possible to provide results directly in terms of %FFA or AV.

As configured, the $FTIR_{phenolate}$ method differs significantly from its specialized automated counterpart used to determine AN in mineral-based lubricants, which requires more sophisticated chemometrics to ensure delivery of ASTM-identical results. As such, this method is a hybrid procedure, combining elements of both the split-sample and the single-sample approaches, capable of ratioing out (subtracting) the oil spectrum, on the one hand, while avoiding the need for paired analysis, on the other. The sensitivity of the method can be increased or decreased simply by varying the path length proportionately. Although the method as developed here is based on a fixed oil-reagent ratio, one can develop a more generalized procedure by including an oil concentration calibration using the CH overtone region in the near IR portion of the spectrum (4500−4000 cm^{-1}). Using this approach one can spectroscopically determine the oil content of the sample prepared and dynamically normalize the differential spectra to vary the sensitivity. As designed, this simple FTIR procedure uses minimal amounts of solvent and sample, handles multiple samples readily, and provides accurate acidity results for ester-based oils, making it a utilitarian alternative to titrimetric procedures if a basic FTIR spectrometer is available.

AUTHOR INFORMATION

Corresponding Author

*(F.v.d.V.) Phone: (514) 632-7091. Fax: (514) 398-8124. E-mail: frederik.vandevoort@mcgill.ca.

Funding

We gratefully acknowledge the financial support provided by the National Natural Science Foundation of China (No. 31271887).

Notes

The authors declare no competing financial interest.

ABBREVIATIONS USED

FFA, free fatty acid; AV, acid value; *p*-TSA, *p*-toluenesulfonic acid; 1-PrOH, 1-propanol; O_R, acid-free reference oil; MD, mean difference; SDD, standard deviation of the difference; SN, saponification number; IV, iodine values

REFERENCES

(1) AOCS. *Official Methods and Recommended Practices of the American Oil Chemists' Society*; AOCS Press: Champaign, IL, USA, 1997; Method Cd 3d-63.

(2) AOCS. *Official Methods and Recommended Practices of the American Oil Chemists' Society*; AOCS Press: Champaign, IL, USA, 2009; Method Cd 5a-40.

(3) Winterfield, C.; van de Voort, F. R. Automated acid and base number determination of mineral-based lubricants by Fourier transform infrared spectroscopy: commercial laboratory evaluation. *J. Lab. Autom.* **2014**, *19*, 577−586.

(4) Lanser, A. C.; List, G. R.; Holloway, R. K.; Mounts, T. L. FTIR estimation of free fatty acid content in crude oils extracted from damaged soybeans. *J. Am. Oil Chem. Soc.* **1991**, *68*, 448−449.

(5) Man, Y. B. C.; Moh, M. H.; van de Voort, F. R. Determination of free fatty acids in crude palm oil and refined-bleached-deodorized palm olein using Fourier transform infrared spectroscopy. *J. Am. Oil Chem. Soc.* **1999**, *76*, 485−490.

(6) Bertran, E.; Blanco, M.; Coello, J.; Iturriaga, H.; Maspoch, S.; Montoliu, I. Determination of olive oil free fatty acid by Fourier transform infrared spectroscopy. *J. Am. Oil Chem. Soc.* **1999**, *76*, 611−616.

(7) Verleyen, T.; Verhe, R.; Cano, A.; Huyghebaert, A.; De Greyt, W. Influence of triacylglycerol characteristics on the determination of free fatty acids by Fourier transform infrared spectroscopy. *J. Am. Oil Chem. Soc.* **2001**, *78*, 981−984.

(8) Sherazi, S. T. H.; Mahesar, S. A.; Bhanger, M. I.; van de Voort, F. R.; Sedman, J. Rapid determination of free fatty acids in poultry feed lipid extracts by SB-ATR FTIR spectroscopy. *J. Agric. Food Chem.* **2007**, *55*, 4928−4932.

(9) Yu, X. Z.; van de Voort, F. R.; Sedman, J.; Gao, J. M. A new direct Fourier transform infrared analysis of free fatty acids in edible oils using spectral reconstitution. *Anal. Bioanal. Chem.* **2011**, *401*, 315−324.

(10) Ismail, A. A.; van de Voort, F. R.; Emo, G.; Sedman, J. Rapid quantitative determination of free fatty acids in fats and oils by Fourier transform infrared spectroscopy. *J. Am. Oil Chem. Soc.* **1993**, *70*, 335−341.

(11) van de Voort, F. R.; Sedman, J.; Yaylayan, V.; Saint-Laurent, C. The determination of acid and base number in lubricants by FTIR spectroscopy. *Appl. Spectrosc.* **2003**, *57*, 1425−1431.

(12) Al-Alawi, A.; van de Voort, F. R.; Sedman, J. New FTIR method for the determination of FFA in oils. *J. Am. Oil Chem. Soc.* **2004**, *81*, 441−446.

(13) Al-Alawi, A.; van de Voort, F. R.; Sedman, J. A new FTIR method for the analysis of low levels of FFA in refined edible oils. *Spectrosc. Lett.* **2005**, *38*, 389−403.

(14) Aryee, A. N. A.; van de Voort, F. R.; Simpson, B. K. FTIR determination of free fatty acids in fish oils intended for biodiesel production. *Process Biochem.* **2009**, *44*, 401−405.

(15) van de Voort, F. R.; Ghetler, A.; García-González, D. L.; Li, Y. D. Perspectives on quantitative Mid-FTIR spectroscopy in relation to edible oil and lubricant analysis: evolution and integration of analytical methodologies. *Food Anal. Method.* **2008**, *1*, 153−163.

DOI: 10.1021/acs.jafc.5b02738
J. Agric. Food Chem. 2015, 63, 8333−8338

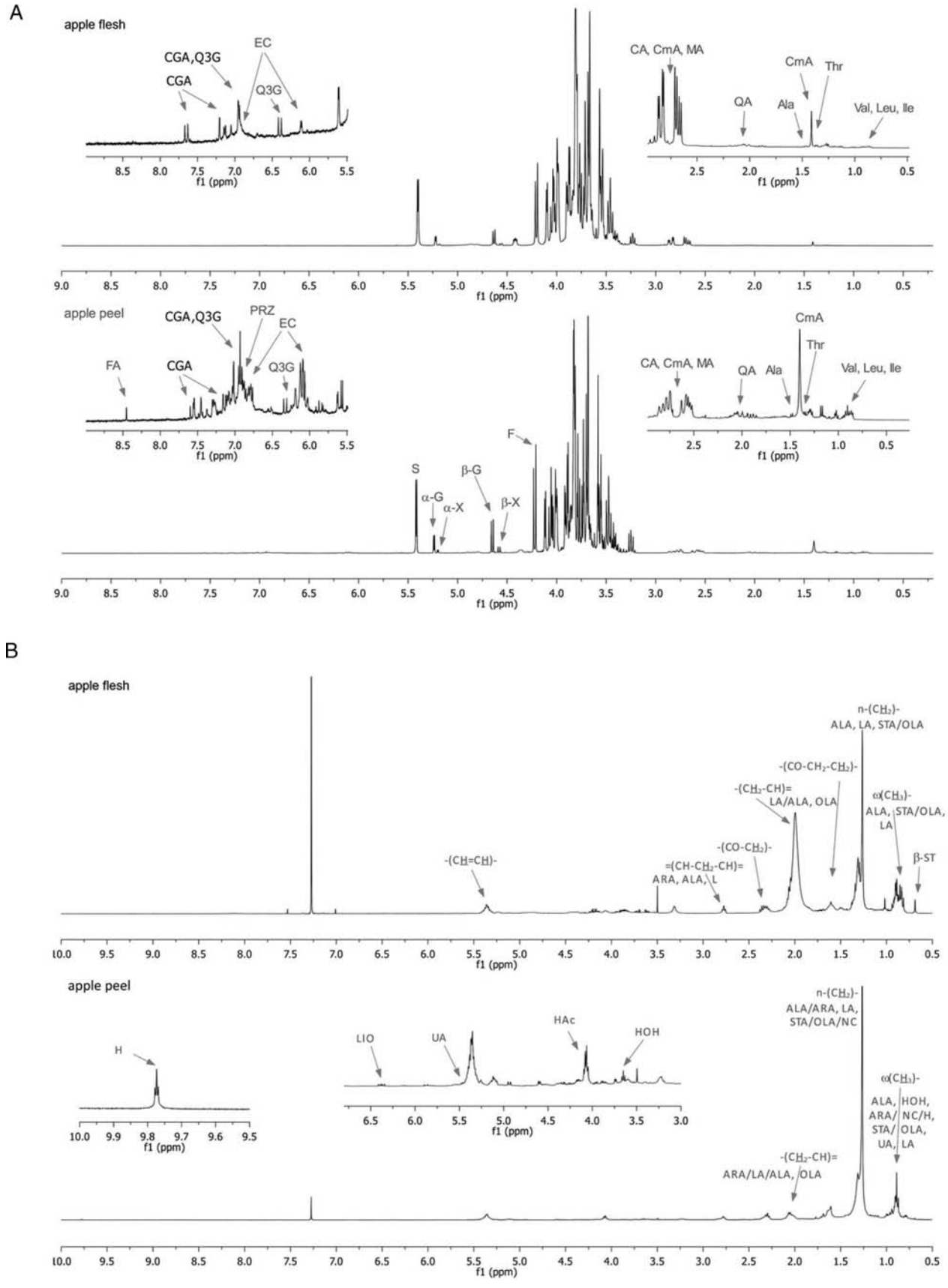

Figure 1. ^{1}H NMR spectrum of Almagold apple flesh (upper) and skin (lower) (A) hydroalcoholic and (B) chloroformic extracts at 298 K. The assignment of some resonances is reported.

DOI: 10.1021/acs.jafc.5b03311
J. Agric. Food Chem. 2015, 63, 8339−8347

antifungal activity by nuclear magnetic resonance (NMR) spectroscopy.

At present, an increasing importance is given to this technique[10] because it is able to point out different classes of chemical compounds, both endogenous and exogenous, at the same time, in a single spectrum, and it was successfully applied to several complex food matrices.[11−16] In particular, the comparison by NMR spectroscopy of cultivars of the same species with different degrees of resistance toward external attacks has already proven to be a reliable tool to detect molecules involved in fruit defense as well as their precursors.[12]

Because metabolites of flesh are closely related to fruit quality while those of peel are important in plant defense against fungal attacks, with the skin being a barrier between the fruit and the environment, hydroalcoholic and chloroformic extracts of both flesh and peel of the two apple cultivars were characterized by NMR spectroscopy.

MATERIALS AND METHODS

Sampling. Eight fruits of the Almagold cultivar (scab-resistant apple) and eight of the Golden Delicious cultivar (scab-susceptible apple) were hand-harvested in an organic farm orchard, located in Scurelle (Trento) in the northern Italian region Trentino-Alto Adige/Südtirol. The climate is temperate with significant rainfall during the year (annual average of 850 mm). The trees were 9 years old, grafted on M26 roostock, planted at a distance of 2.5 × 4.5 m, trained as "spindle", and irrigated with a drip irrigation system. The soil is classified sandy loam, sub-acid with a normal content of macro- and microelements. The harvest of fruits was made in the third decade of September at the stage of commercial maturity for both cultivars, which was assessed according to the following parameters: firmness of 6.4−6.9 kg/cm^2, soluble solid of 12.4−12.8 °Brix, and starch index of 2.5−3.0. These measurements were carried out following the official guidance on objective tests to determinate the quality of fruits.[17] The fruits, having a diameter of 70−75 mm, were taken from a single plant, in parts of the canopy well exposed to light to ensure higher and uniform quality characteristics. The yield has been regulated by manual thinning, leaving 70−80 fruits per tree. All apples were sampled in arbitrary order within a total time of 7 days, which were stored at 277 K before use. The selected fruits were without any apparent injury.

Sample Preparation. Slices of fresh cut flesh (about 1.2 g of fresh weight) were frozen in liquid nitrogen, finely powdered, and extracted according to the modified Bligh−Dyer methodology,[18] with a 2:2:1 methanol/chloroform/water final volumetric ratio. The sample was kept at 277 K for 1 h and then centrifuged for 20 min at 10000*g* at the same temperature. The upper hydroalcoholic phase and the lower organic phase were carefully separated and dried. The dried phases were stored at 193 K until the NMR analysis.

The peel was carefully separated from the flesh with the aid of a scalpel, pooled to acquire about 1.5 g of fresh material, and then underwent to the same extraction and drying procedures as the flesh.

Dry Matter Measurement. Dry matter was determined[17] by drying the apple sample in a oven at 70 °C until consecutive weightings made at 2 h intervals vary by less than 3 mg.

NMR Experiments. Each dry extract of the hydroalcoholic phase was dissolved in 0.6 mL of D_2O containing 2 mM 3-(trimethylsilyl)-propionic-2,2,3,3-d_4 acid sodium salt as the chemical shift and concentration reference.

Each chloroformic phase sample was resuspended in 0.6 mL of $CDCl_3$ containing 2 mM cyclohexamethyltrisiloxane as the chemical shift and concentration reference.

All solvents and standards were purchased from Sigma-Aldrich (St. Louis, MO).

All spectra were recorded at 298 K on a Bruker AVANCE III spectrometer operating at the proton frequency of 400.13 MHz and equipped with a Bruker multinuclear *z*-gradient inverse probehead.

Aqueous extract ^{1}H spectra were acquired employing the standard presat pulse sequence for solvent suppression with 64 transients, a spectral width of 6000 Hz, and 64 000 data points for an acquisition time of 5.5 s. The recycle delay was set to achieve a 15 s total acquisition time to avoid relaxation effects.

^{1}H spectra of the chloroformic phase samples were acquired with 64 transients with a spectral width of 6000 Hz and 32 000 data points for an acquisition time of 2.62 s. The recycle delay was set to achieve a 13 s total acquisition time to avoid relaxation effects.

Total correlation spectroscopy (TOCSY), heteronuclear single-quantum coherence (HSQC), and heteronuclear multiple-bond correlation (HMBC) two-dimensional spectra were acquired on a selection of samples to univocally assign ^{1}H and ^{13}C resonances. TOCSY experiments were acquired with a spectral width of 6000 Hz in both dimensions, a data matrix of 4000 × 256 points, a mixing time of 110 ms, and a relaxation delay of 2 s.

HSQC experiments were performed with a spectral width of 6000 and 25 500 Hz for the proton and carbon, respectively, a data matrix of 4000 × 256 points, an average $^1J_{C-H}$ of 145 Hz, and a recycle delay of 2 s.

Several HMBC spectra were acquired with a spectral width of 6000 and 25 500 Hz for the proton and carbon, respectively, a data matrix of 4000 × 256 points, long-range constants $^nJ_{C-H}$ of 4, 8, and 12 Hz, and a recycle delay of 2 s.

Quantification of the metabolites was performed by comparison of the signal integral to the reference integral, and quantities were expressed in milligrams per gram of fresh weight.

Statistical Analysis. The signals that could be clearly identified and had no overlap with neighboring signals were integrated for each sample. The resulting data set was submitted to analysis of variance (ANOVA) for the evaluation of statistical differences between the cultivars to point out the molecules responsible for the separation.

Data are presented as the mean ± standard deviation (SD). Univariate ANOVA was performed with Sigmaplot 11.0 software (Systat Software, Inc., San Jose, CA). A Shapiro−Wilk test was performed on each variable to assess their normality prior one-way ANOVA analysis. On the variables positive to ANOVA, a Holm−Sidak test, an all pairwise multiple comparison test, was applied to determinate which categories were discriminated by these metabolites ($p < 0.05$). Pearson correlation (Pearson product moment correlation) was carried out using Sigma stat software to observe the correlation between the quantified metabolites. The threshold value for correlation significance was $r = 0.765$. This value was chosen according to the sample population ($n = 8$) and α level = 0.05. Therefore, in this work, only the correlations with $r < -0.765$ and $r > 0.765$ were considered.

RESULTS AND DISCUSSION

Metabolic Profile. The comprehensive metabolic profile analysis of the two apple cultivars was carried out by ^{1}H NMR spectroscopy of hydroalcoholic and chloroformic extracts of both skin and flesh. Panels A and B of Figure 1 show representative ^{1}H NMR spectra (of aqueous and organic flesh and skin apple extracts) used for this purpose and the major NMR peaks that have contributed to the discrimination between the two cultivars. A total of 26 and 34 metabolites in flesh and skin, respectively, were identified. Their ^{1}H chemical shifts, multiplicity, and ^{13}C chemical shifts are reported in the Supporting Information.

Several NMR signals were identified by ^{1}H and ^{13}C NMR characteristic and cross-correlated signals in two-dimensional (2D) spectra as well as a comparison to literature data.[19,20] The assignment of the ^{1}H spectrum will be discussed for a class of compounds.

Hydroalcoholic Phase. Organic Acids. In the ^{1}H spectrum of aqueous flesh and skin apple extracts, acetic acid (AA), citric acid (CA), malic acid (MA), citramalic acid (CmA), succinic acid (SA), and quinic acid (QA) were identified by means of their diagnostic peaks and, with the exception of AA and SA,

DOI: 10.1021/acs.jafc.5b03311
J. Agric. Food Chem. 2015, 63, 8339−8347

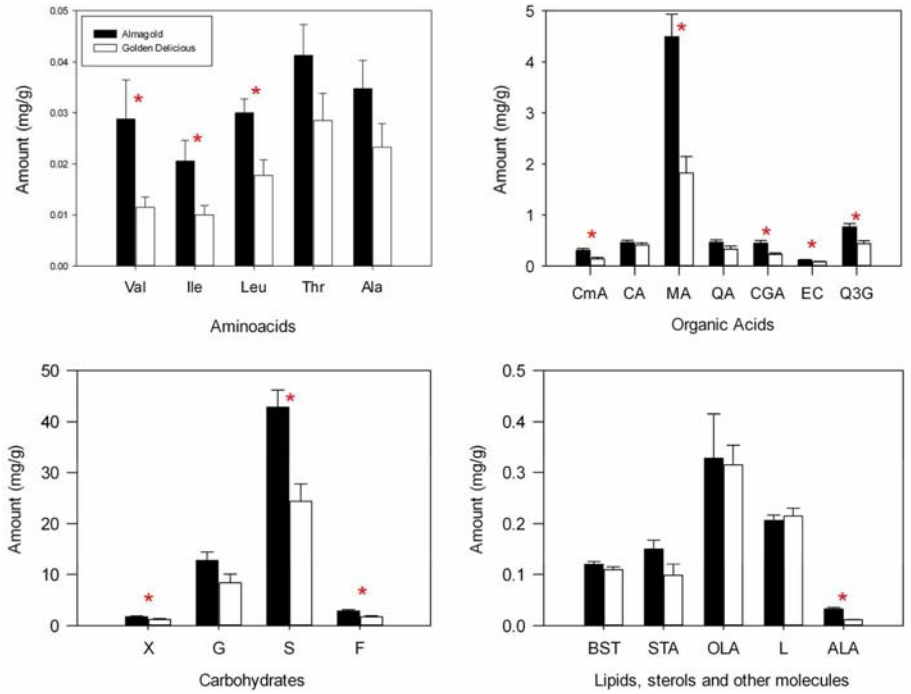

Figure 2. Amount of metabolites quantified by ^{1}H NMR in the flesh of Almagold (black bars) and Golden Delicious (white bars) apples. The metabolites positive to ANOVA ($p < 0.05$) are evidenced by an asterisk.

their TOCSY correlation patterns. CmA was univocally identified on the basis of its diagnostic singlet at 1.41 ppm (CH_3) and its doublets at 2.42 and 2.72 ppm (CH_2). The QA TOCSY spectrum showed scalar correlation among the signals at 1.89 and 2.09 ppm (CH_2-1), 2.00 and 2.06 ppm (CH_2-5), 3.55 (CH-3), 4.02 ppm (CH-2), and 4.15 ppm (CH-4).

Carbohydrates. The main carbohydrates detected in the ^{1}H spectrum of aqueous flesh and skin apple extracts were α- and β-glucose (G), α- and β-xylose (X), fructose (F), and sucrose (S). These molecules were identified on the basis of their diagnostic proton CH-1 anomeric doublets: α- and β-G at 5.25 and 4.69 ppm, respectively, α- and β-X at 5.18 and 4.57 ppm, S at 5.42 ppm, and CH-3 of F at 4.22 ppm. The remaining protons of the aforementioned spin systems were confirmed by means of 2D TOCSY experiments.

Free Amino Acids. The free amino acids leucine (Leu), isoleucine (Ile), valine (Val), threonine (Thr), and alanine (Ala) were identified by 2D TOCSY experiments of aqueous flesh and skin apple extracts. Their characteristic resonances are a multiplet at 0.97 ppm for Leu (δ,δ'-CH_3), a doublet at 1.02 ppm for Ile (γ-CH_3), a doublet at 1.05 ppm for Val (γ'-CH_3), a doublet at 1.33 ppm for Thr (γ-CH_3), and another doublet at 1.49 ppm for Ala (β-CH_3).

Phenolic Compounds. In the ^{1}H NMR spectrum of aqueous apple extracts, epicatechin (EC), chlorogenic acid (CGA), quercetin-3-*O*-galactoside (Q3G), and phloridzin (PRZ) were identified on the basis of their diagnostic spin systems. EC was identified through the TOCSY correlations between the resonances at 6.12 ppm (CH-6) and 6.14 ppm (CH-8), among the signals at 6.68 ppm (CH-6′), 6.75 ppm (CH-5′), and 6.95 ppm (CH-2′), and among the signals at 2.49 and 2.82 ppm (CH_2-4″), 3.97 ppm (CH-3″), and 4.56 ppm (CH-2″).

The caffeoyl moiety of CGA was univocally assigned as a result of the diagnostic doublets at 6.41 ppm (=CH−CO_2−) and 7.62 ppm (−CH=), while the QA moiety was assigned thanks to the TOCSY correlation pattern among the resonances at 2.07 and 2.22 ppm (CH_2-1′), 2.09 and 2.24 ppm (CH_2-5′), 3.88 ppm (CH-3′), 4.24 ppm (CH-4′), and 5.32 ppm (CH-2′).

Q3G aglycone was identified by TOCSY cross-peaks between the aromatic resonances at 6.20 ppm (CH-6) and 6.41 ppm (CH-8) and among the resonances at 7.69 ppm (CH-5′), 7.55 ppm (CH-6′), and 6.91 ppm (CH-2′) and its glycone was identified by the diagnostic doublet at 5.48 ppm (CH-1″).

PRZ was identified by TOCSY correlations between the resonances at 6.88 ppm (CH-3,5) and 7.15 ppm (CH-2,6) and the singlets at 6.05 ppm (CH-5′) and 6.21 ppm (CH-3′).

Organic Phase. Lipids. In the ^{1}H NMR spectrum of flesh and skin chloroformic phase, several lipid species were identified on the basis of TOCSY correlation patterns among the broad resonances at about 0.9 ppm (CH_3), 1.2 ppm (*n*-CH_2), 1.6 ppm (CO−CH_2−$C\underline{H}_2$), 2.0 ppm ($C\underline{H}_2$-CH=), 2.3 ppm (CO−$C\underline{H}_2$), 2.8 ppm (=CH−$C\underline{H}_2$−CH=), and 5.2 ppm (CH=CH). In comparison of the signals rising from CH_2 in α to the carboxyl group (2.3 ppm) to the signal from CH_2 in α to the unsaturations (2.0 ppm), it was possible to evaluate both the saturated and total unsaturated fatty acid contents. The amount of polyunsaturated fatty acids (PUFAs) was determined on the basis of linoleic (L) and linolenic (ALA) lipid diagnostic resonances at 2.77 and 2.82 ppm, respectively.

On the basis of the integrals of the aliphatic chain CH_2 and their ratio with the other fatty acid chain resonances, it was possible to assess that the average length of the chains is 18 carbon atoms. Therefore, the fatty acids were quantified in equivalents of stearic acid (STA), oleic acid (OLA), linoleic acid (L), and linolenic acid (ALA).

Arachidonic acid (ARA) was detected and quantified as a result of its diagnostic resonance at 2.92 ppm.

Sterols. β-Sitosterol (β-ST) was univocally assigned on the basis of the HSQCs between hydrogen at 0.68 ppm (CH_3-18) and carbon at 12.2 ppm and between the resonances at 1.01

DOI: 10.1021/acs.jafc.5b03311
J. Agric. Food Chem. 2015, 63, 8339−8347

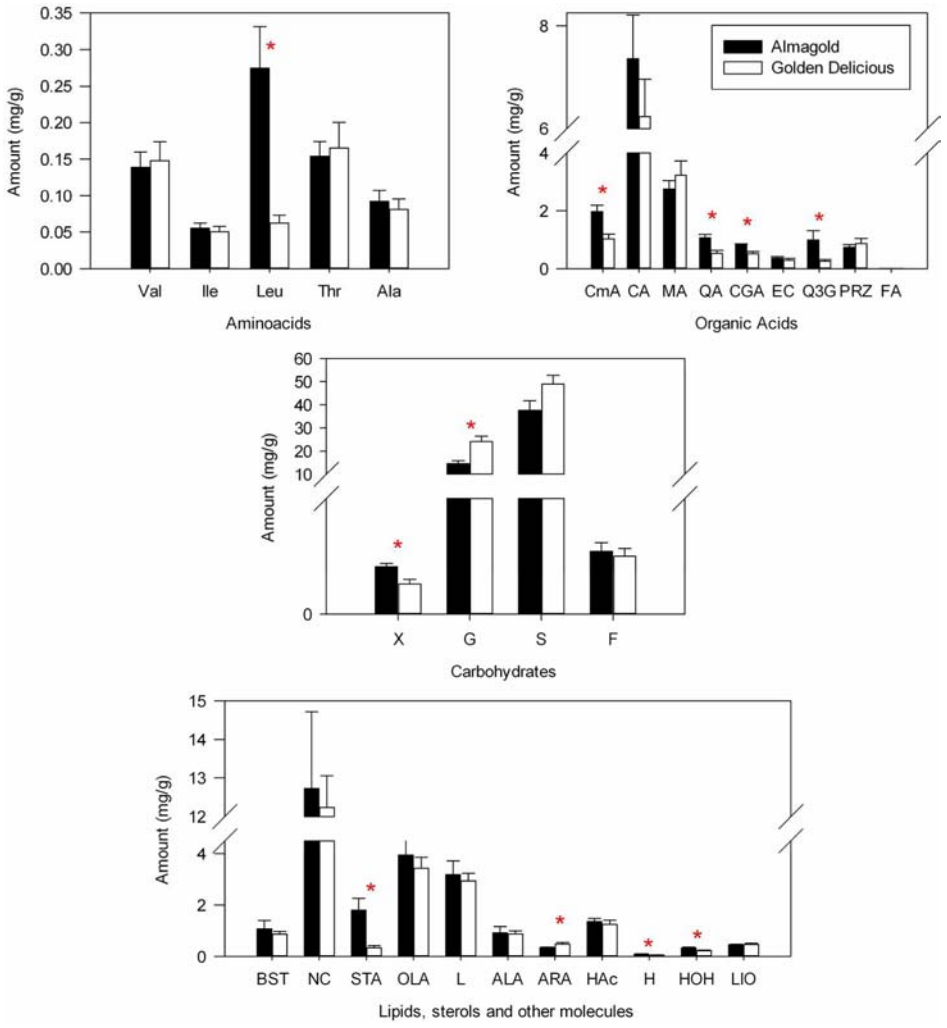

Figure 3. Amount of metabolites quantified by ^{1}H NMR in the skin of Almagold (black bars) and Golden Delicious (white bars) apples. The metabolites positive to ANOVA ($p < 0.05$) are evidenced by an asterisk.

ppm (CH_3-25) and 19.1 ppm. Other molecule resonances were identified on the basis of the TOCSY correlation pattern among the resonances at 5.34 ppm (CH-6), 1.98 and 1.52 ppm (CH_2-7), 1.46 ppm (CH-8), 0.99 ppm (CH-14), 1.57 ppm (CH_2-15), and 1.85 and 1.26 ppm (CH_2-16). Another TOCSY pattern that was attributed to the A ring of this sterol was formed by the proton signals at 3.52 ppm (CH−OH-3), 2.28 ppm (CH_2-4), 1.84 and 1.51 ppm (CH_2-2), and 1.85 and 1.08 ppm (CH_2-1).

Ursolic acid (UA) was univocally identified by HSQC and HMBC experiments. Some of the most diagnostic correlations were detected between the singlet at 5.49 ppm and the carbon signal at 125.7 ppm (CH-12), between hydrogen at 1.97 ppm and carbon at 37.4 ppm (CH_2-22), and between the protons at 1.61 ppm and carbon at 31.1 ppm (CH_2-21). Moreover, long-range correlations were observed between the protons 21 and 15 and carbon at 179.7 ppm (C-28).

Miscellaneous. Along with the aforementioned lipid species, several long-chain aliphatic molecules, such as nonadecane (NC), were observed in the ^{1}H NMR spectrum of the apple skin chloroformic phase. Their resonances were observed at 0.89 ppm (ω-CH_3) and 1.27 ppm (n-CH_2) and were distinguished from the similar lipid signals by their HSQCs as well as the absence of TOCSY correlations with the proton resonances of CH_2 in α and β positions with respect to the carboxyl group. These molecules are one of the main constituents of the waxy cuticle coating the apple skin and, along with other analogue linear olefins, are responsible for the relative adhesion of water, pesticides, fungal spores, and other airborne deposits on the fruit surface.

Linalool (LIO), hexanol (HOH), hexyl acetate (HAc), and hexanal (H) were detected only in the skin. LIO was identified on the basis of its diagnostic vinyl moiety resonance at 6.33 ppm (dd, =CH-2) and TOCSY correlation pattern with the resonances at 5.10 and 5.35 ppm (CH_2= 1a and 1b, respectively). Their complete assignment was performed by HSQC and HMBC experiments. Long-range HMBCs were observed between the H-2 and carbon in position 3 at 72.1 ppm, between this carbon and hydrogen at 0.96 and 1.21 ppm (CH_3-9 and CH_2-4, respectively), and between the quaternary carbon at 130.9 ppm (C-7) and the protons at 1.61, 1.68, and 5.08 ppm (CH_3-8, CH_3-10, and =CH-6, respectively). The resonance of proton in position 5 was univocally assigned on the basis of HSQC between its signal at 2.08 ppm and the carbon signal at 39.5 ppm and by HMBC between the aforementioned proton resonance and the carbon at 124 ppm (C-6).

DOI: 10.1021/acs.jafc.5b03311
J. Agric. Food Chem. 2015, 63, 8339−8347

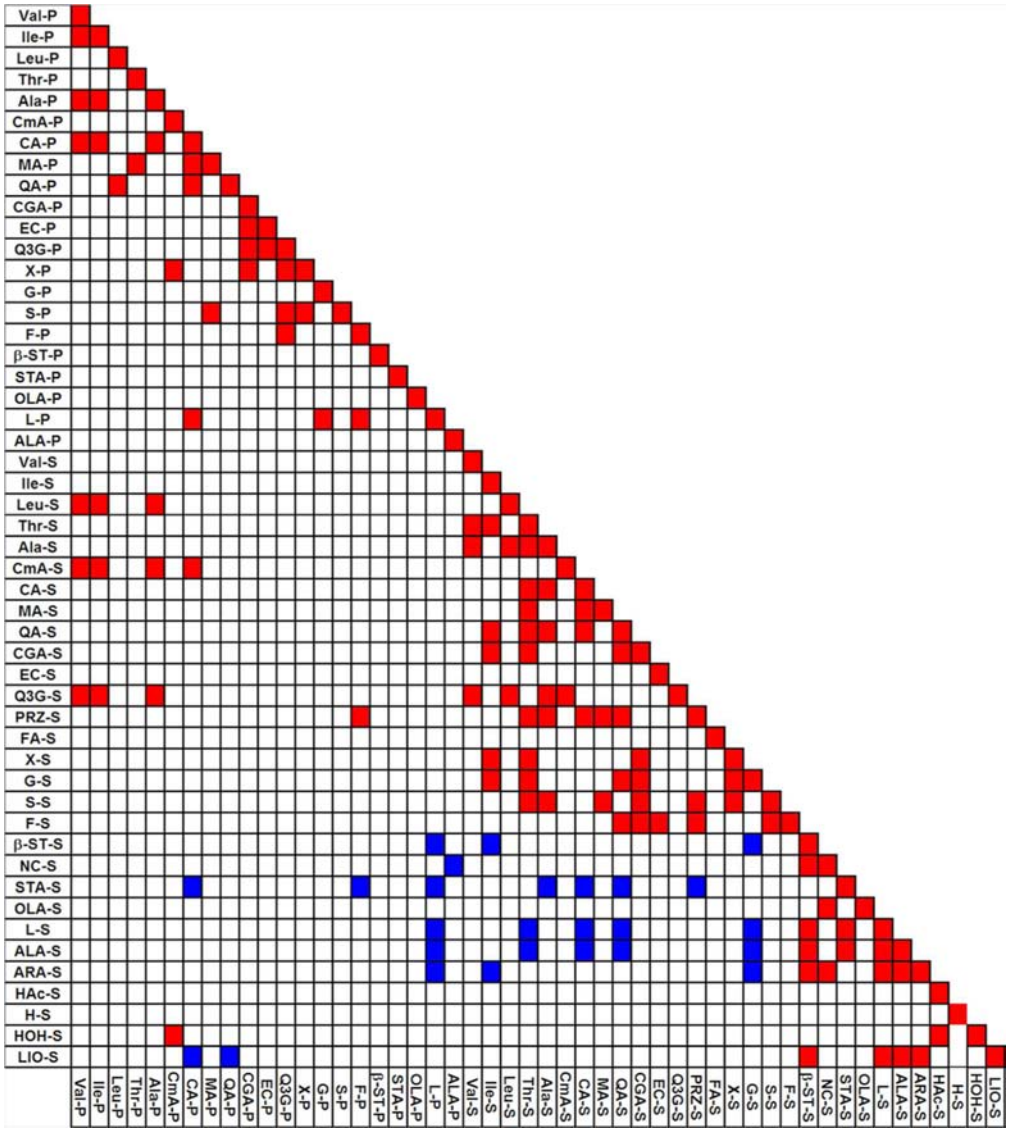

Figure 4. Pearson's correlation map of Almagold metabolites. Positive correlations are in red, while negative correlations are in blue. The correlation threshold is ±0.765.

The quantitative analysis is reported in Figures 2 and 3 for the flesh and peel metabolites, respectively.

Dry Matter Measurement. The measured dry matter content for Almagold samples was 16.7 ± 0.2%, while for Golden Delicious samples, it was 14.8 ± 0.3%. These data are in good agreement with NMR measurements for the apple flesh (Figure 2), because the metabolites present in Almagold are generally more abundant than those in the other cultivar.

Statistical Analysis. With regard to flesh analysis, the Almagold showed statistically ($p \leq 0.05$) larger amounts of Val, Ile, Leu, CmA, MA, CGA, Q3G, X, S, F, and ALA. With regard to peel analysis, the Almagold showed statistically ($p \leq 0.05$) larger amounts of Leu, CmA, QA, CGA, Q3G, X, and STA, while Golden Delicious contained larger amounts of G and ARA (Figures 2 and 3).

Because ANOVA is an univariate statistical analysis tool, this technique is unable to evidence correlations between the variables. These correlations are an important source of information because the ratios between the metabolites in a vegetal or animal sample are influenced by the metabolic network that is characteristic of each species or cultivar.

To quantify these correlations, Pearson coefficients were calculated and reported in Figures 4 and 5 for Almagold and Golden Delicious, respectively.

Comparison between Almagold and Golden Delicious. The metabolic profile comparison between the two apple varieties showed only quantitative differences (Figures 2 and 3) between metabolites, while both qualitative and quantitative differences were clearly highlighted between flesh and skin.

Most fruits and plants react to external attacks and pathogens producing several secondary metabolites to repel infections only after the first contact.[21] Nevertheless, it was observed that some fruits are able to resist against fungal attacks during quiescence not only on the basis of the synthesis of these defense metabolites after the infection but also because of the presence of preformed antifungal compounds.[22] Moreover, another benefit of pre-existent antimycotic metabolites is that, even in the case of a successful infection, those molecules were observed to reduce the secretion of fungal pathogenicity factors occurring during quiescent infections.[23]

DOI: 10.1021/acs.jafc.5b03311
J. Agric. Food Chem. 2015, 63, 8339−8347

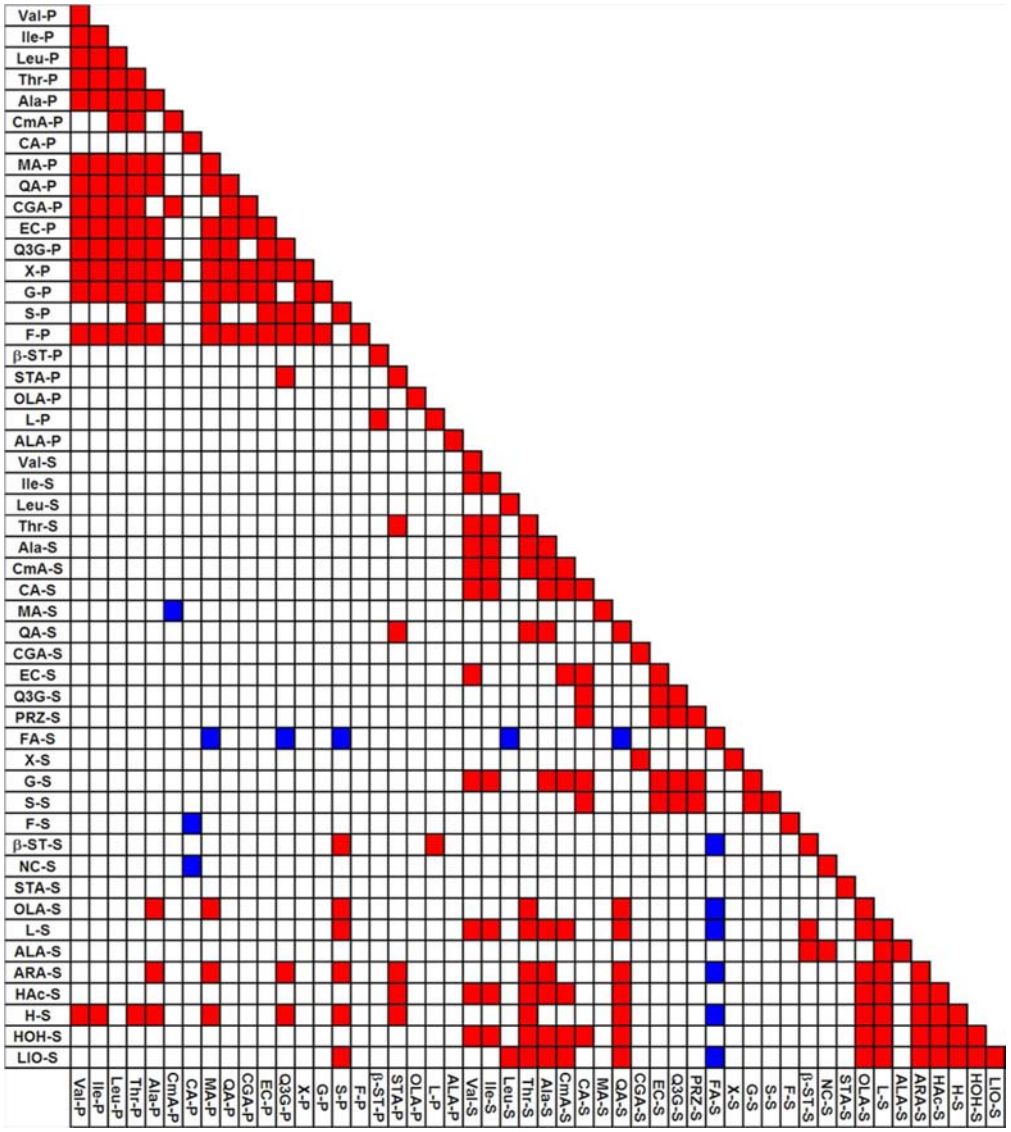

Figure 5. Pearson's correlation map of Golden Delicious metabolites. Positive correlations are in red, while negative correlations are in blue. The correlation threshold is ±0.765.

Skin Hydroalcoholic Phase. As stated before, statistical analysis performed on the skin metabolites shows that the Almagold cultivar, which is resistant to *V. inaequalis*, has a higher amount of Leu, CmA, QA, CGA, Q3G, and X and a lower amount of G (Figure 3), while metabolites such as EC and PRZ are not discriminant between the two cultivars. Among these molecules, QA, Q3G, and CGA play an important role in fruit defense against external threats, such as fungi attacks. In particular, QA is an intermediate of the phenylpropanoid pathway,[24] and it could be transformed into several different secondary metabolites according to external stimuli.

Q3G, the most abundant aromatic compound in both cultivars, is a flavonoid with a potent and non-specific antifungal activity found in many fruits and leaves,[24] was shown to be able to reduce the growth of several fungal species up to 99%, yet was never tested on *Venturia* strains specifically.

CGA is a powerful antioxidant, and high concentrations of this molecule in immature fruits were reported to aid the plant in repelling brown rot infection by interfering with fungal melanin production.[25] The same defense mechanism could be effective against other types of fungal attacks.

PRZ, detected only in the skin, is a glycosylated flavonoid that is involved in defense against herbivores and fungi attacks.[26] Nevertheless, this metabolite is present in almost the same amount in both cultivars (Figure 3), suggesting that this molecule is not directly involved in the protection against *V. inaequalis*.

In comparison of the skin metabolites of the two cultivars, it is also possible to observe that the total carbohydrate amount of Almagold is statistically lower than the total carbohydrate amount present in the Golden Delicious skin and that the sensible variety is especially rich in glucose. Fungi are unable to photosynthesize carbohydrates as a result of the lack of chloroplasts, and they need to absorb nutrients from other plants. Because the cultivar more vulnerable to *V. inaequalis* attacks, the Golden Delicious, is the cultivar with more carbohydrates in the skin, it is possible that the presence of readily available nutrients for the fungi could increase the infection diffusion in the fruit.

Skin Organic Phase. Several molecules, in particular, UA, LIO, NC, ARA, HOH, HAc, and H, were observed to be present only in the fruit skin.

DOI: 10.1021/acs.jafc.5b03311
J. Agric. Food Chem. 2015, 63, 8339−8347

Quantitative differences were detected between the two cultivars, in particular, the Almagold is richer in H, HOH, and STA, while the Golden Delicious has greater amounts of ARA.

UA is a pentacyclic triterpene whose biological role is the protection against microbial and fungi attacks.[27] LIO is a monoterpene found in many flowers and greatly contributes to the pleasant scent.[28] NC, other analogue linear olefins, and to a lesser extent, ARA are some of the main constituents of the waxy cuticle coating the apple skin, and they are responsible for the adhesion of water, pesticides, fungal spores, and other airborne deposits on the fruit surface. Moreover, PUFAs are also known to act as antimycotic agents because they fluidize the fungi cell membrane[29] and sensitize them against other antifungal agents. Because ARA is more abundant in the more sensible cultivar, it is possible that this defense mechanism is not viable against the *V. inaequalis* strain or that its antifungal efficiency is lower that the efficiency observed for L and ALA fatty acids.

Among the observed *n*-hexane derivatives, H possesses antifungal activity,[30] and its presence in the fruit skin can lead to a faster response toward detected fungi attacks.

Flesh Hydroalcoholic Phase. With regard to the flesh hydroalcoholic phase, the more resistant cultivar possesses a higher amount of CmA, MA, CGA, and Q3G, but only the last two molecules are known to be involved in the protection against fungal attacks. Their presence in the flesh of Almagold could be important because some defense compounds are produced in flesh,[31] with the purpose of a "last ditch defense" against damages, such as the damages produced by a successful *V. inaequalis* infection.

With regard to other molecules with known antifungal activity, it is interesting to observe that the amount of QA is statistically higher in the skin than in the flesh of both cultivars, but while, in the skin, it was more abundant in Almagold apples, in the flesh, there were no statistical differences between the two species.

Flesh Organic Phase. In comparison of the composition of flesh organic phases, the main difference between the two cultivars is that Almagold has a higher amount of ALA fatty acids. In addition to their aforementioned direct antifungal activity, it is worth noting that PUFAs are the precursors for the biosynthesis of volatile linear chain molecules and the main type of volatiles in apples are C_6 linear and branched alcohols, aldehydes, and acids.[32]

Pearson Correlations. The comparison of the Pearson's correlation maps of the two cultivars highlights several interesting differences regarding the metabolic correlations of the molecules with defensive roles. First of all, correlations of the same metabolite between the two locations (i.e., Ala in the flesh and Ala in the skin) were not observed in either cultivar. The absence of a direct correlation between the concentration of a metabolite in the flesh with the same in the skin suggests that no exchange occurs between the two molecule pools. This hypothesis implies that the metabolites involved in the defense from external attacks, which are those found in the skin, are synthesized *in loco*.

Moreover, it can also be observed that, in the peel of Golden Delicious (Figure 5) variety, PRZ, CGA, Q3G, and EC correlate only with molecules located in the skin and not with the molecules of the flesh, whereas in the Almagold (Figure 4) variety, PRZ, Q3G, and EC correlate with molecules located in both flesh and peel. These metabolites are involved in several defense mechanisms and, as reported before, are synthesized both prior and after an external stimulus.[21,22] Other molecules, in the peel, that show different correlations between the two cultivars are QA and CGA. This is important because variations in Pearson's correlation patterns could suggest that the metabolic pathways involved in their synthesis and their following reactions are different between the two cultivars.

This study, given its general approach, shows how the NMR-based characterization of the metabolic profile is a promising tool for the rational choice of cultivars for selective cross-breeding aimed to the development of disease-resisting fruit varieties. In particular, it is possible to attribute the resistance toward *V. inaequalis* to higher contents of QA, CGA, and Q3G and a minor amount of free carbohydrates in the peel of the fruit. Nevertheless, it is important to highlight that another major difference between the resistant and vulnerable cultivars lies in the correlation patterns among the levels of the molecules responsible for defense; this indicates that their biosynthetic pathways are different between the two cultivars, and this difference could also contribute to the different degrees of reaction to fungi attacks.

■ ASSOCIATED CONTENT

Supporting Information

The Supporting Information is available free of charge on the ACS Publications website at DOI: 10.1021/acs.jafc.5b03311.

Table of the metabolites identified in the ^{1}H NMR spectrum of the aqueous and chloroformic extracts of apples (PDF)

■ AUTHOR INFORMATION

Corresponding Author

*Telephone/Fax: 39-06-49913124. E-mail: fabio.sciubba@uniroma1.it.

Funding

The present work has been carried out under the project "Research for the Improvements of the Fruit Trees Protected Cultivation in Southern Italy" funded by the Italian Ministry of Agriculture and Forestry Policy.

Notes

The authors declare no competing financial interest.

■ ABBREVIATIONS USED

AA, acetic acid; Ala, alanine; ALA, linolenic acid; ARA, arachidonic acid; β-ST, β-sitosterol; CA, citric acid; CGA, chlorogenic acid; CmA, citramalic acid; EC, epicatechin; F, fructose; FA, formic acid; G, glucose; H, hexanal; HAc, hexyl acetate; HOH, hexanol; Ile, isoleucine; L, linoleic acid; Leu, leucine; LIO, linalool; MA, malic acid; NC, nonadecane; OLA, oleic acid; PRZ, phloridzin; PUFA, polyunsaturated fatty acid; QA, quinic acid; Q3G, quercetin-3-*O*-galactoside; SA, succinic acid; S, sucrose; STA, stearic acid; Thr, threonine; UA, ursolic acid; Val, valine; X, xylose

■ REFERENCES

(1) Bowen, J. K.; Mesarich, C. H.; Bus, V. G.; Beresford, R. M.; Plummer, K. M.; Templeton, M. D. *Venturia inaequalis*: the causal agent of apple scab. *Mol. Plant Pathol.* **2011**, *12*, 105−122.

(2) Carisse, O.; Dewdney, M. A review of non-fungicidal approaches for the control of apple scab. *Phytoprotection* **2002**, *83*, 1−29.

(3) Kühn, B. F.; Thybo, A. K. Sensory quality of scab-resistant apple cultivars. *Postharvest Biol. Technol.* **2001**, *23*, 41−50.

DOI: 10.1021/acs.jafc.5b03311
J. Agric. Food Chem. 2015, 63, 8339−8347

(4) Patocchi, A.; Bigler, B.; Koller, B.; Kellerhals, M.; Gessler, C. Vr $_2$: a new apple scab resistance gene. *Theor. Appl. Genet.* **2004**, *109*, 1087−1092.
(5) Belfanti, E.; Silfverberg-Dilworth, E.; Tartarini, S.; Patocchi, A.; Barbieri, M.; Zhu, J.; Vinatzer, B. A.; Gianfranceschi, L.; Gessler, C.; Sansavini, S. The HcrVf2 gene from a wild apple confers scab resistance to a transgenic cultivated variety. *Proc. Natl. Acad. Sci. U. S. A.* **2004**, *101*, 886−890.
(6) Pilo, V. Research pursuits in horticulture of the Italian Ministry for Agricultural Policy. *Acta Hortic.* **1998**, *495*, 531−534.
(7) Fideghelli, C. The activity on apple scab resistance within the National Research Programs´Fruit growing´ and Recommended fruit varieties´ supported by the Ministry for Agricultural and Forestry Policy. *Acta Hortic.* **2000**, *595*, 49−53.
(8) Sansavini, S.; Tartarini, S.; Gennari, F.; Barbieri, M. Scab (*Venturia inaequalis*) resistance in apple: the *Vf*-gene and polygenic resistance in the breeding strategy at DCA - Bologna. *Acta Hortic.* **2000**, *595*, 29−32.
(9) De Salvador, F. R.; Montanari, M. A New Scab-Resistant Apple: Almagold. EU Patent 38335, Gazzetta CPVO, 2014; 4.
(10) Gallo, V.; Intini, N.; Mastrorilli, P.; Latronico, M.; Scapicchio, P.; Triggiani, M.; Bevilacqua, V.; Fanizzi, P.; Acquotti, D.; Airoldi, C.; Arnesano, F.; Assfalg, M.; Benevelli, F.; Bertelli, D.; Cagliani, L. R.; Casadei, L.; Cesare Marincola, F.; Colafemmina, G.; Consonni, R.; Cosentino, C.; Davalli, S.; De Pascali, S. A.; D'Aiuto, V.; Faccini, A.; Gobetto, R.; Lamanna, R.; Liguori, F.; Longobardi, F.; Mallamace, D.; Mazzei, P.; Menegazzo, I.; Milone, S.; Mucci, A.; Napoli, C.; Pertinhez, T. A.; Rizzuti, A.; Rocchigiani, L.; Schievano, E.; Sciubba, F.; Sobolev, A. P.; Tenori, L.; Valerio, M. Performance assessment in fingerprinting and multi component quantitative NMR analyses. *Anal. Chem.* **2015**, *87*, 6709−6717.
(11) Mannina, L.; Sobolev, A. P.; Viel, S. Liquid state ^{1}H high field NMR in food analysis. *Prog. Nucl. Magn. Reson. Spectrosc.* **2012**, *66*, 1−39.
(12) Capitani, D.; Sobolev, A. P.; Tomassini, A.; Sciubba, F.; De Salvador, F. R.; Mannina, L.; Delfini, M. Peach fruit: metabolic comparative analysis of two varieties with different resistances to insect attacks by NMR spectroscopy. *J. Agric. Food Chem.* **2013**, *61*, 1718−1726.
(13) Capitani, D.; Mannina, L.; Proietti, N.; Sobolev, A. P.; Tomassini, A.; Miccheli, A.; Di Cocco, M. E.; Capuani, G.; De Salvador, F. R.; Delfini, M. Metabolic profiling and outer pericarp water state in Zespri, CI.GI, and Hayward kiwifruits. *J. Agric. Food Chem.* **2013**, *61*, 1727−1740.
(14) Praticò, G.; Capuani, G.; Tomassini, A.; Baldassarre, M. E.; Delfini, M.; Miccheli, A. Exploring human breast milk composition by NMR-based metabolomics. *Nat. Prod. Res.* **2014**, *28*, 95−101.
(15) Sciubba, F.; Di Cocco, M. E.; Gianferri, R.; Impellizzeri, D.; Mannina, L.; De Salvador, F. R.; Venditti, A.; Delfini, M. Metabolic profile of different Italian cultivars of hazelnut (Corylus avellana) by nuclear magnetic resonance spectroscopy. *Nat. Prod. Res.* **2014**, *28*, 1075−1081.
(16) Wyzgoski, F. J.; Paudel, L.; Rinaldi, P. L.; Reese, R. N.; Ozgen, M.; Tulio, A. Z.; Miller, A. R., Jr.; Scheerens, J. C.; Hardy, J. K. Modeling Relationships among Active Components in Black Raspberry (*Rubus occidentalis L.*) Fruit Extracts Using High-Resolution ^{1}H Nuclear Magnetic Resonance (NMR) Spectroscopy and Multivariate Statistical Analysis. *J. Agric. Food Chem.* **2010**, *58*, 3407−3414.
(17) Organisation for Economic Co-operation and Development (OECD). *Orientation pour la Réalisation des Tests Objectifs Visant à Déterminer la Qualité Interne des Fruits et Légumes Frais et Secs et Séchés*; OECD: Paris, France, 2005.
(18) Miccheli, A.; Ricciolini, R.; Piccolella, E.; Delfini, M.; Conti, F. Modulation of human lymphoblastoid B cell line by phorbol ester and sphingosine. A phosphorus-31 NMR study. *Biochim. Biophys. Acta, Mol. Cell Res.* **1991**, *1093*, 29−35.
(19) Fan, T. M. W. Metabolite profiling by one- and two-dimensional NMR analysis of complex mixtures. *Prog. Nucl. Magn. Reson. Spectrosc.* **1996**, *28*, 161−219.
(20) Wishart, D. S.; Tzur, D.; Knox, C.; et al. HMDB: the Human Metabolome Database. *Nucleic Acids Res.* **2007**, *35*, D521−6.
(21) Prusky, D.; Keen, N. T.; Sims, J. J.; Midland, S. L. Possible involvement of an antifungal diene in the latency of Colletotrichum gloeosporioides on unripe avocado fruits. *Phytopathology* **1982**, *72*, 1578−1582.
(22) Yakoby, N.; Kobiler, I.; Dinoor, A.; Prusky, D. pH regulation of pectate lyase secretion modulates the attack of *Colletotrichum gloeosporioides* on avocado fruits. *Appl. Environ. Microb.* **2000**, *66*, 1026−1030.
(23) Michalek, S.; Klebel, C.; Treutter, D. Stimulation of phenylpropanoid biosynthesis in apple (*Malus domestica* Borkh.) by abiotic elicitors. *Eur. J. Hortic. Sci.* **2005**, *70*, 116−120.
(24) Kanwal, Q.; Hussain, I.; Latif Siddiqui, H.; Javaid, A. Antifungal activity of flavonoids isolated from mango (*Mangifera indica* L.) leaves. *Nat. Prod. Res.* **2010**, *24*, 1907−1914.
(25) Villarino, M.; Sandín-España, P.; Melgarejo, P.; De Cal, A. High chlorogenic and neochlorogenic acid levels in immature peaches reduce Monilinia laxa infection by interfering with fungal melanin biosynthesis. *J. Agric. Food Chem.* **2011**, *59*, 3205−3213.
(26) Gosch, C.; Halbwirth, H.; Stich, K. Phloridzin: Biosynthesis, distribution and physiological relevance in plants. *Phytochemistry* **2010**, *71*, 838−843.
(27) Wolska, K. I.; Grudniak, A. M.; Fiecek, B.; Kraczkiewicz-Dowjat, A.; Kurek, A. Antibacterial activity of oleanolic and ursolic acids and their derivatives. *Cent. Eur. J. Biol.* **2010**, *5*, 543−553.
(28) Kessler, A.; Baldwin, I. T. Defensive function of herbivore-induced plant volatile emissions in nature. *Science* **2001**, *291*, 2141−2144.
(29) Walters, D.; Raynor, L.; Mitchell, A.; Walker, R.; Walker, K. Antifungal activities of four fatty acids against plant pathogenic fungi. *Mycopathologia* **2004**, *157*, 87−90.
(30) Song, J.; Leepipattwit, R.; Deng, W.; Beaudry, R. M. Hexanal vapor is a natural, metabolizable fungicide: Inhibition of fungal activity and enhancement of aroma biosynthesis in apple slices. *J. Am. Soc. Hortic. Sci.* **1996**, *121*, 937−942.
(31) Lalel, H. J. D.; Singh, Z.; Tan, S. C. Glycosidically-bound aroma volatile compounds in the skin and flesh of 'Kensington Pride' mango fruit at different stages of maturity. *Postharvest Biol. Technol.* **2003**, *29*, 205−218.
(32) Matich, A.; Rowan, D. Pathway Analysis of Branched-Chain Ester Biosynthesis in Apple Using Deuterium Labeling and Enantioselective Gas Chromatography − Mass Spectroscopy. *J. Agric. Food Chem.* **2007**, *55*, 2727−2735.

DOI: 10.1021/acs.jafc.5b03311
J. Agric. Food Chem. 2015, 63, 8339−8347

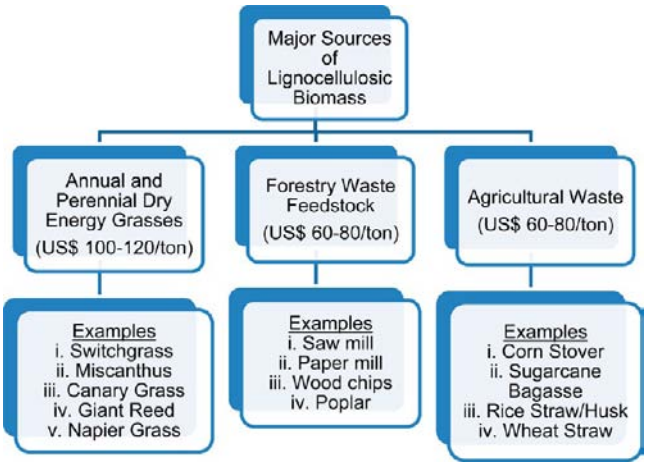

Figure 1. Major sources of lignocellulosic biomass.

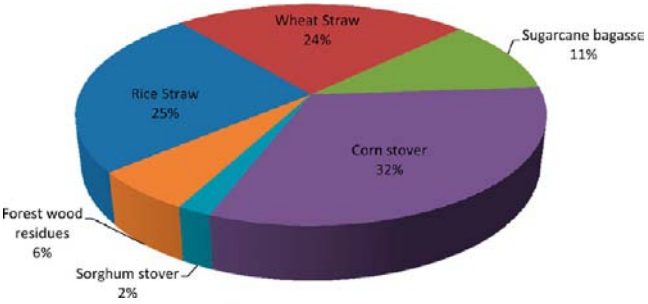

Figure 2. Global production of potentially available lignocellulosic biomass.

agricultural wastes contribute to the yearly global yield of lignocellulosic biomass.[46] For example, approximately 400 million tons of rice and wheat straw along with corn stalks are harvested in the United States each year. In mainland China, 700−800 million tons of agricultural residues are produced annually, and half of that amount is used as bioresources in the production of fuels and chemicals.[1,47,48] Brazil, which is the largest producer of sugar cane globally, generates 185 million tons of sugar cane bagasse per harvest.[49] Agricultural residues such as rice husks are used to produce electricity in gasification units and have been scrutinized intensely for use in silica production.[47] Additionally, rice husks were reported to be a potential source of biofertilizer after undergoing a biodegradation process.[50,51] Moreover, agricultural residues could be reprocessed into animal feed and used for farm cultivation.[48] However, agricultural residues are still underutilized because a large portion of this biomass is discarded as waste.[46] For instance, 10% of the corn straw in United States is collected for reuse purposes such as mulching, but most of the rice straw is disposed of by burning, which results in air pollution.[2,49,52,53] Rocha et al. also highlighted that certain components of agricultural residues such as sugar cane bagasse are still underutilized, although these residue components could potentially serve 40 different applications.[49]

Annual and Perennial Dry Energy Grasses. Annual and perennial energy crops are produced mainly to serve as raw materials in the production of biofuel due to their prominent characteristic of being low-cost and low-maintenance, which leads to economic and environmental advantages over other various forms of biomass.[40] For instance, these crops, which are normally densely planted, have the distinctive trait of high yields

Table 1. Breakdown of Worldwide Major Crops[44,45]

crop	world production (tonnes)	major producing country (tonnes) (% of world total production)	other countries (tonnes)
cassava	2.77×10^8	Nigeria: 5.3×10^7 (19.1%)	Thailand: 3.02×10^7 Indonesia: 2.39×10^7 Brazil: 2.15×10^7
hemp	1.24×10^5	France: 4.93×10^4 (39.8%)	China: 1.6×10^4 Korea: 1.4×10^4 Netherlands: 1.03×10^4
maize	1.02×10^9	United States: 3.54×10^8 (34.7%)	China: 2.19×10^8 Brazil: 8.03×10^7 Argentina: 3.21×10^7
oil palm	2.66×10^8	Indonesia: 1.2×10^8 (45.1%)	Malaysia: 9.57×10^7 Thailand: 1.28×10^7 Nigeria: 8.00×10^6
rapeseed	7.27×10^7	Canada: 1.79×10^7 (24.6%)	China: 1.45×10^7 India: 7.82×10^6 Germany: 5.78×10^6
soybean	2.76×10^8	United States: 8.95×10^7 (32.4%)	Brazil: 8.17×10^7 Argentina: 4.93×10^7 China: 1.20×10^7
sugar beet	2.46×10^8	Russia: 3.93×10^7 (16.0%)	France: 3.36×10^7 United States: 2.98×10^7 Germany: 2.28×10^7
sugar cane	1.91×10^9	Brazil: 7.68×10^8 (40.2%)	India: 3.41×10^8 China: 1.29×10^8 Thailand: 1.00×10^8
sorghum	6.23×10^7	United States: 9.88×10^6 (15.9%)	Nigeria: 6.7×10^6 Mexico: 6.31×10^6 India: 5.28×10^6

DOI: 10.1021/acs.jafc.5b01813
J. Agric. Food Chem. 2015, 63, 8349−8363

and do not require annual reseeding once established.[54] Some of the common forms of energy crop biomass are illustrated in Table 2, where switchgrass and *Miscanthus* straw are among the

Table 2. Biomass Yields of Different Energy Crops[42]

energy crop	establishment time (years)	dry matter biomass yield (tons/ha/year)
willow	3+	5−11
poplar	3+	2−10
eucalyptus	4+	10−12
Miscanthus	3+	5−43
switchgrass	2−3	5−19
reed canary grass	1−2	2−10
alfalfa	1−2	1−17
fiber sorghum	1−2	16−43

main contributors annually, at 5−19 and 5−43 tons/ha/year, respectively.[42] Similarly, the cost of both maintenance and investment are low for these perennial grasses because they require less harvesting and fertilizers, which account for the major portion of the total cost.[43] Energy crops are able to grow under poor soil conditions without compromising the energy yield. A steady supply flow of these perennial crops could be obtained, thus avoiding the concern of requirement for costly storage for large biomass volumes.[42] In both the United States and Canada, switchgrass serves as a major crop due to its abundant availability and its ability to resist both disease and harsh environments.[42] The effective growth of *Miscanthus* is well-known in Asia, whereas in European regions, *Miscanthus* is grown as a source of combustible energy.[19] In African grasslands, minimal amounts of nutrients are required for growing Napier grasses, which can swiftly be harvested and yield high amounts of lignocellulosic biomass.

Forestry Waste. Woody raw materials such as sawmill residues and wood chips are more flexible in terms of harvesting times. Thus, long latency periods for forestry waste storage can also be avoided.[43] Conventionally, the lignin content in woody feedstock is greater and contains less ash,[40] and woody raw materials are thus used in the manufacture of paper and pulp.[43] Because of these characteristics, high densities of woody biomass are considered to be more attractive for cost-effective transportation. In China, approximately 900 million tons of forestry wastes and products are produced annually, and one-third of the entire amount of waste could be converted into renewable energy sources.[1] Correspondingly, short-rotation forest crops are cultivated for the production of wood chips to serve as a substitute for fossil fuels and other products such as geotextiles and building materials in Europe.[55]

COMPOSITIONAL AND STRUCTURAL CHARACTERISTICS OF LIGNOCELLULOSIC BIOMASS

Lignocellulosic biomass is basically composed of different layers of plant cell wall (Figure 3).[56] First, the primary wall is formed, followed by the secondary wall layers, through the deposition of wall substances into the primary wall, where most cells are elongated and stretched during differentiation. The chemical composition of the cell walls is dependent on the species of the plants. Some cells contain only nonlignified primary cell wall, whereas others possess a thickened secondary cell wall that is normally lignified. This lignified secondary cell wall consists of a multilayered structure. As shown in Figure 4,[57] the outer part of a softwood bleached kraft pulp (SBKP) is the highly lignified compound that consists of middle lamellae and primary wall, followed by a thin S1 layer; a thick, less lignified middle S2 layer; a thin inner S3 later; and, finally, a warty layer formed by lignin precursors.[58] This lignified secondary wall accounts for the majority of the plant biomass and usually comprises 40−50, 15−25, 20−25, and 5−10% of cellulose, hemicellulose, lignin, and other components, respectively.[57,59] Other minor nonstructural components, such as proteins, ash, extractives, and pectin, are

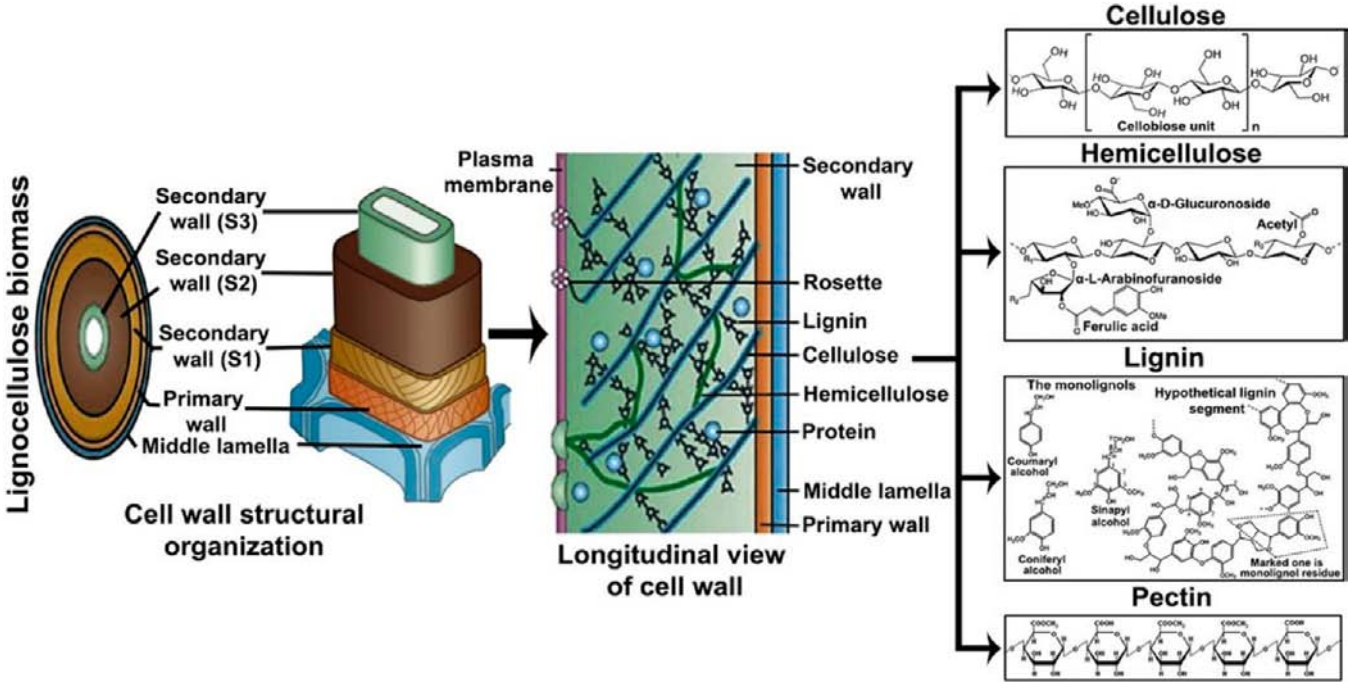

Figure 3. Structure and chemical composition of lignocellulose residues. Reprinted with permission from ref 56. Copyright 2015 Springer.

DOI: 10.1021/acs.jafc.5b01813
J. Agric. Food Chem. 2015, 63, 8349−8363

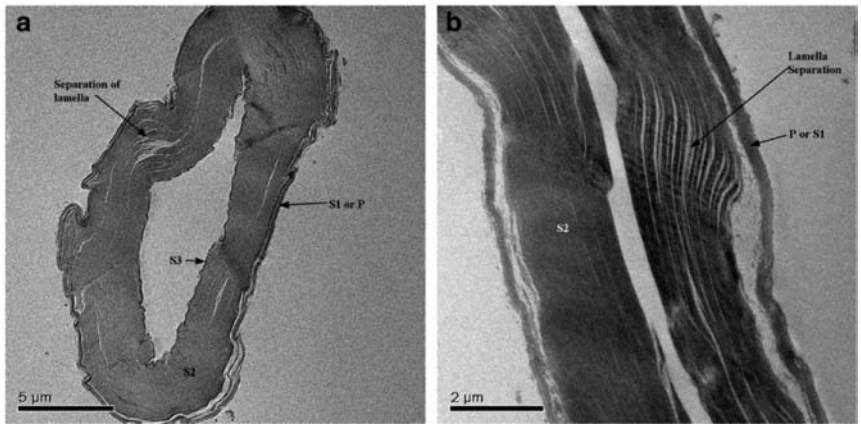

Figure 4. TEM images for SBKP (a) show the thin primary cell wall (P) and outermost layer (S1), middle layer (S2), and innermost layer (S3) of the thick secondary cell wall (S); (b) lamella separation, S1/P and S2. Reprinted with permission from ref 57. Copyright 2012 Wiley.

Table 3. Typical Components and Particle Size of Various Lignocellulosic Biomass, Mainly Agricultural Residues

		components of lignocellulose (%)			
lignocellulosic material	particle size (diameter)	cellulose	hemicellulose	lignin	ref
corn stover	0.279 mm	37.99	22.45	18.39	59
corn stover	N/A	36.4	22.6	16.6	60
wheat straw	N/A	38.2	24.7	23.4	
rice straw	N/A	34.2	24.5	11.9	
switchgrass	N/A	31.0	24.4	17.6	
poplar	N/A	49.9	25.1	18.1	
wood	500−1000 μm	13.9	57.9	28.1	61
	212−300 μm	9.1	65.2	25.7	
Miscanthus	500−1000 μm	31.2	42.1	26.7	
	212−300 μm	27.8	45.8	26.4	
straw	500−1000 μm	41.6	30.0	28.4	
	212−300 μm	37.4	37.0	25.6	
distiller dried grains	500−1000 μm	72.7	5.6	21.7	
	212−300 μm	77.7	1.8	20.5	
wheat shorts	500−1000 μm	66.8	11.5	21.7	
	212−300 μm	74.6	6.8	18.6	
sugar cane bagasse	N/A	42.19	27.60	21.56	62
sugar cane bagasse	N/A	37.74	27.23	20.57	63
straw	N/A	33.77	27.38	21.28	

dependent on factors such as the different species, tissues, plant maturity, harvest times, and method of storage and environmental factors. Extractives are usually complex mixtures that consist of sugars, terpenoid compounds, and monolignols.[60] Every plant has its own floral cell walls with different amounts of specific compounds.[59] Some of the components of lignocellulosic biomass that consist primarily of agricultural residues are summarized in Table 3.[59−63]

Cellulose. Normally, cellulose accounted for 30−40% of floral cell walls. Cellulose is a β-1,4-linked glucose polysaccharide that comprises the larger portion of the cell wall that is common to all plants. Cellulose is long, consists of oriented microfibrils, and has the ability to coalesce into larger and longer fibrils. These fibrils are hydrophobic and highly crystalline, which enhances the recalcitrance of biomass.[60] The field emission scanning electron microscopy (FE-SEM) image of microfibrils (Figure 5) can be seen clearly from the untreated SBKP.[57] Therefore, the fibril is difficult to be decomposed hydrolytically because of its connected area of crystalline and amorphous structures.[59] Generally, cellulose can withstand higher decomposition temperatures than hemicellulose and lignin, with decomposition occurring at a temperature of approximately 320−356 °C.[61]

Hemicellulose. Hemicellulose is known as the second most abundant polymer on earth, with an estimated production of 60 billion tons annually, and it comprises 30−35% of floral cell walls.[59,62] Hemicellulose chains usually interact with one or more cellulose fibrils to form noncovalent cross-links between cellulose bundles. As an example, hardwood species are composed mainly of glucuronoarabinoxylans, which are formed by the complex pentose sugar chain. Conversely, softwood species are the combination of galactoglucomannans with a backbone of β-1,4-linked D-mannopyranose and D-glucopyranose units.[60] Furthermore, hemicellulose consists of different branches of complex carbohydrate structures (xylose, arabinose, mannose, glucose, and galactose) that are not recalcitrant to conversion to monomeric sugars because of their amorphous, branched, and single-chain polysaccharides. Therefore, hemicellulose is more favored for the hydrolysis process than cellulose is.[59,60] The processing step of extraction of the hemicellulose from biomass can produce or liberate compounds such as acetic acid, which eventually will help in autohydrolysis pretreatment.

DOI: 10.1021/acs.jafc.5b01813
J. Agric. Food Chem. 2015, 63, 8349−8363

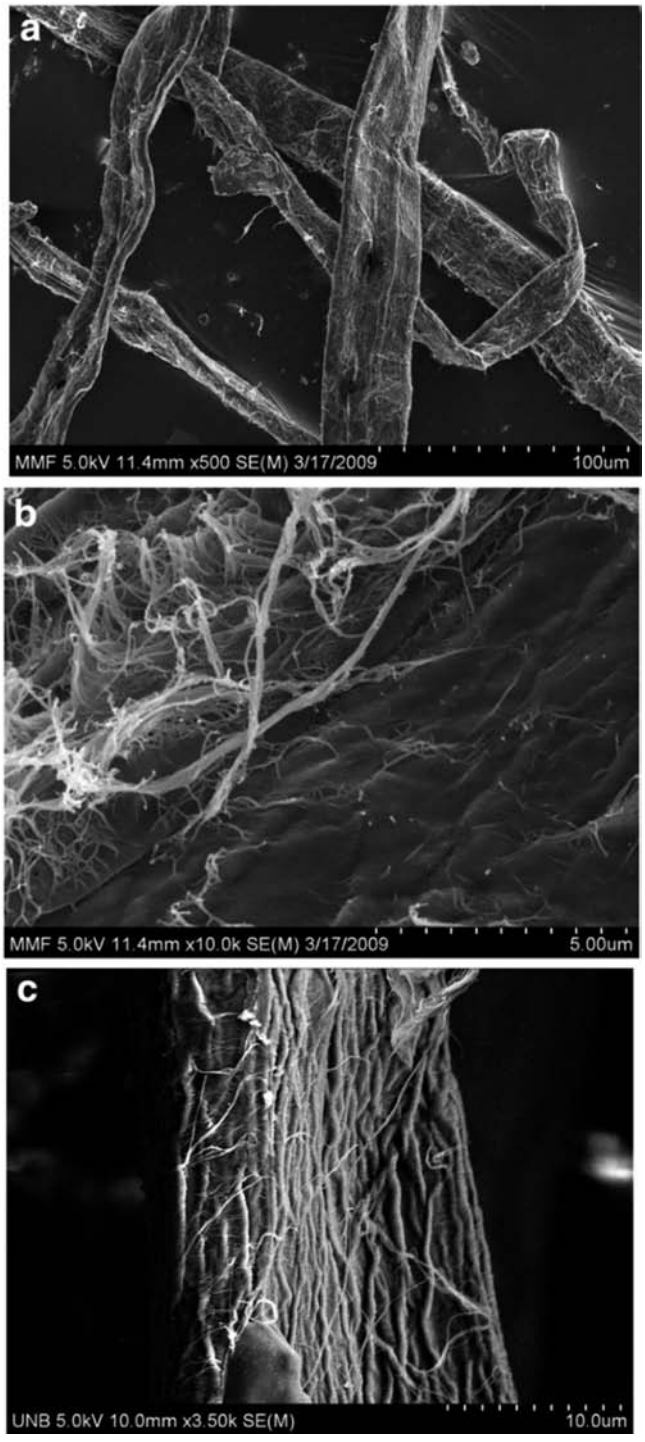

Figure 5. FE-SEM image of untreated SKBP (a) shows the microfibrils on the cell wall; (b) exposed P wall layer; (c) exposed secondary cell wall layer (S). Reprinted with permission from ref 57. Copyright 2012 Wiley.

However, acetic acid may inhibit subsequent fermentation steps, thereby lowering the production of ethanol and other compounds.[62]

Lignin. Lignin accounted for 11−25% of floral cell walls. Lignin is known as an amorphous phenolic macromolecule that can be found only in the secondary cell wall. Three primary units, namely, guaiacyl (G), sinapyl (S), and *p*-hydroxyphenyl (H), are linked by aryl ether or C−C bonds to form lignin.[58] The high level of heterogeneity of lignin is synthesized through the oxidative coupling of 4-hydrophenylpropanoids during secondary cell wall deposition, which results in layers of lignin in different monomers. Lignin acts as a protective barrier with impermeability and immunity to prevent an attack from microorganisms and chemical degradation by restricting the accessibility of efficient saccharification of cellulosic microfibils.[56,59,60] Additionally, lignin provides mechanical support and water transport for the cell.[61]

Overall, cellulose provides strength over the cell walls, whereas hemicellulose acts as a wire mesh that circulates around the cellulose and provides enhancement to the strength and linkage. Lignin fills the remaining space and sets everything in place and excludes water from the polysaccharide environment. This unique combination results in the high resistance of lignocellulosic biomass to mechanical and biological degradation.[60]

ROLE AND GOAL OF LIGNOCELLULOSIC BIOMASS PRETREATMENTS

Pretreatment is necessary in the bioconversion process to overcome the complex recalcitrant biomass structure. Pretreatment provides higher accessibility for the enzymes to convert cellulose and hemicellulose into useful fermentable sugars during the enzymatic hydrolysis process. When biomass is exposed to pretreatment, several operations, such as the increase in the surface area and porosity, modification of the lignin structure, removal of lignin, partial depolymerization of hemicellulose, and reduction of cellulose crystallinity, can be accomplished. These operations result in the improvement of the hydrolysis process such that a higher percentage of fermentable sugars can be recovered.[64,65] According to Singhvi et al.,[66] only 20% of the sugar can be recovered without introducing pretreatment, but 80−83% of the fermentable sugar can be recovered with introduction of a pretreatment process.[67] Generally, pretreatment can be categorized into three areas: mechanical, chemical, and biological pretreatments. Mechanical pretreatment such as milling, grinding, and chipping reduces the size of the biomass and therefore provides higher surface area and porosity.[64] Another important example of mechanical pretreatment is ultrasound pretreatment. Ultrasound pretreatment applies the principle of cavitation that forms millions of microscopic vapor bubbles. The explosion of these bubbles will create high temperature (1700−4700 °C) and pressure (1800 bar) in a microsecond, thus producing shockwaves that induce mechanical effects such as breaking larger molecules into smaller fractions with particle size reduction.[68,69] Chemical pretreatment involves the disruption of biomass recalcitrance by means of chemical reactions. Some of the conventional methods are liquid hot water, dilute and concentrated acid hydrolysis, alkaline hydrolysis, organosolv, oxidative delignification, and room temperature ionic liquids.[70] Moreover, certain methods are termed "physicochemical" pretreatments because they involve the integration of both mechanical and chemical pretreatments, such as steam explosion and CO_2 explosion.[64] Biological pretreatment involves the use of environmentally friendly enzymes such as cellulase and hemicellulase to break down complex carbohydrates into simple sugars.[70] However, enzymatic hydrolysis is usually inefficient if it is applied directly to biomass, unless the biomass has already undergone the aforementioned mechanical or chemical pretreatments. The advantages/disadvantages of some common biomass pretreatments are provided in Table 4.[3−18,20,21,35,38,70−75]

DOI: 10.1021/acs.jafc.5b01813
J. Agric. Food Chem. 2015, 63, 8349−8363

Table 4. Comparison of Different Biomass Pretreatments

pretreatment	advantages	disadvantages	refs
dilute acid hydrolysis	obtain high yields of fermentable sugars	produces inhibitory byproducts, corrosive, requires acid neutralization	3−7, 72
concentrated acid hydrolysis	obtain high yields of fermentable sugars	sugar recovery rate is slow, highly corrosive, requires acid recovery system for feasibility	71, 73
autohydrolysis (liquid hot water)	produces less inhibitors, simple operation	high-temperature operation, high energy and water input; dissolved pentose appeared mainly in oligomeric form, which required further post-hydrolysis step to obtain monomeric sugar	13−15, 20, 21
sodium hydroxide (NaOH)	effectively removes lignin, low temperature and pressure operation, low inhibitor production	long pretreatment time, expensive chemical, complex recovery process	8, 9
ammonia fiber expansion (AFEX)	low enzyme demands during enzymatic hydrolysis, low inhibitor production	produces high amounts of oligomers which cannot be fermented by microorganism, safety and environmental issues of ammonia	10, 21, 70
ammonia recycle percolation (ARP)	effectively removes lignin, low inhibitor production	can handle only low solid loadings	11, 12, 20
ionic liquid	effectively dissolves cellulose, minimal environmental impacts	high costs of reagents, regeneration requirements, lack of knowledge regarding toxicity and causticity of reagent	18, 20, 71, 74, 75
inorganic salt	less corrosive, low enzyme demands	little understanding of salt residues effect on downstream processing	35, 38, 71
steam explosion	low enzyme dosages demand, low energy demand.	formation of degradation product that inhibits subsequent hydrolysis and fermentation	16, 17
enzymatic hydrolysis	environmentally friendly, low energy demand	inefficient without other pretreatment beforehand, slow process	70

USE OF INORGANIC SALTS FOR BIOMASS PRETREATMENT

One of the most novel pretreatment technologies that has attracted interest is the use of inorganic salts either as aqueous solutions in an acid-free environment or as catalysts in an acid pretreatment system.[22] The integration of inorganic salts has also been implemented with organosolv[23,24] and microwave irradiation.[25] This inorganic salt pretreatment method has been used to pretreat various types of lignocellulosic biomass, as shown in Table 5.[22−24,26−38] Some examples of inorganic salts are NaCl, KCl, $CaCl_2$, $MgCl_2$, $Fe_2(SO_4)_3$, $FeCl_2$, $FeSO_4$, and $FeCl_3$, which have been proven to increase the hydrolysis rate and yield of cellulose or hemicelluloses.[27,30,31] Among all of the inorganic salts, $FeCl_3$ has been proven to be the most effective inorganic salt and could be used to replace acid for biomass hydrolysis.[70] $FeCl_3$ has the capability of solubilizing hemicelluloses into monomeric and oligomeric sugars in liquid hydrolysate with large amounts of xylose while producing a cellulose-rich solid substrate that is highly useful in enzymatic hydrolysis for producing glucose at a later stage.[28,32] Therefore, inorganic salts possess potential for the production of both cellulosic bioethanol and value-added chemicals from hemicellulose-derived sugars.

Hemicellulosic Sugar Recoveries. Pretreatment of biomass is carried out mostly to produce cellulosic bioethanol via fermentation. However, only limited studies have shown a remarkable recovery of hemicellulosic sugars from the biomass. One of the pretreatments that has been extensively studied is dilute acid hydrolysis, where Fields and Wilson[76] found that temperatures between 100 and 150 °C were usually preferred in xylose production. To compare the performance of inorganic salts with dilute acid in the aforementioned temperature range, Marcotullio et al.[38] investigated the selective production of hemicellulose-derived carbohydrates using $FeCl_3$. At 120 °C and 120 min, $FeCl_3$ achieved a performance comparable to that of HCl, with a total monomeric xylose yield of 20.6 wt % of the initial wheat straw in the hydrolysate. Dilute acid hydrolysis of hemicelluloses and cellulose also produced higher amounts of fermentable sugar yields when the biomass was first impregnated with $FeSO_4$, again proving the positive effect of an inorganic salt in the pretreatment of lignocellulosic biomass.[39] Nevertheless, the optimal operating conditions reported for hemicellulosic sugar recovery by using inorganic salt pretreatment have been somewhat contradictory. According to Linares et al.,[33] the use of 0.26 mol/L of $FeCl_3$ at 153 °C and 30 min produced a maximum of 63.2% total hemicellulosic sugar recovery from olive tree biomass. Liu et al.[27] reported 89.0% xylose recovery when corn stover was pretreated with 0.1 mol/L of $FeCl_3$ under conditions almost similar (140 °C, 20 min) to those of Linares et al.[33] Thus, it can be concluded that the optimal operating conditions for inorganic salt pretreatment vary depending on the biomass and the inorganic salt used. Generally, more severe operating conditions are not suggested for sugar recovery from the biomass because the conditions may cause sugar degradation to furfurals and/or other degradation products. Nevertheless, it is important to achieve a balance between pretreatment severity and reducing sugar production by using eq 1.[29,77]

$$\mathrm{CS} = \log R - \mathrm{pH}$$

$$\mathrm{CS} = \log\left[t \times \exp\left\{\frac{(T_H - T_R)}{14.75}\right\}\right] - \mathrm{pH} \quad (1)$$

CS (unitless) is the combined severity parameter, R (unitless) is the severity factor, t (min) is the pretreatment time, T_H (°C) is the reaction temperature, T_R (100 °C) is the reference temperature, and pH is the acidity of the aqueous solution after the pretreatment process of biomass.

At low severity, hemicelluloses could not be degraded, whereas at high severity, the yield of xylose was minimal due to the degradation of xylose into inhibitors, although up to 100% of hemicellulose degradation was achieved.[29,71] As a case in point, a high $FeCl_3$ concentration >0.10 mol/L accelerated the dissolution of oligomeric xylose to monomeric xylose and then monomeric xylose to degradation products, but not the transformation from xylan into oligomeric xylose.[27] At a temperature of 180 °C, the degradation of xylose and xylotriose was increased by 6- and 49-fold, respectively, when the xylose monomer and oligomer mixture were pretreated with 0.8% of $FeCl_3$ compared with using pressurized hot water.[78] However,

DOI: 10.1021/acs.jafc.5b01813
J. Agric. Food Chem. 2015, 63, 8349−8363

Table 5. Performance of Inorganic Salts Pretreatment for Various Biomass

biomass	initial pretreatment	subsequent pretreatment	key findings	ref
corn stover	$FeSO_4$ T = 180 °C time = 20 min 10% (w/v) $FeSO_4$	enzymatic hydrolysis cellulase (Celluclast 1.5L) 20 FPU/g substrate T = 50 °C, time = 72 h	(1) liquid fraction: 60.3% xylose recovery (2) solid fraction: ∼79% glucose recovery, ∼86% enzymatic hydrolysis yield	22
barley straw	Organosolv + $FeCl_3$ T = 170 °C time = 60 min L/S ratio = 7:1 (v/w) 0.1 mol/L $FeCl_3$, 50% (w/w) ethanol	enzymatic hydrolysis cellulase (Celluclast 1.5L) 20 FPU/g cellulose, β-glucosidase (Novozyme 188) 40 CBU/g cellulose T = 45 °C, time = 72 h	(1) solid fraction: 90% cellulose recovery, 89% enzymatic digestibility (2) liquid fraction: 0.011 g/L HMF, 0.148 g/L furfural	23
pitch pine	Organosolv + $MgCl_2$ T = 210 °C time = 10 min 0.1% (w/v) $MgCl_2$, 50% (v/v) ethanol	enzymatic hydrolysis cellulase (Celluclast 1.5L) 700 EGU/g WIS, β-glucosidase (Novozymes NS-50010) 250 CBU/g cellulose T = 50 °C, time = 72 h	(1) solid fraction: 75.8% glucose yield, 61.2% enzymatic digestibility	24
corn stover	$CuCl_2$ T = 160 °C time = 10 min 0.125 mol/L $CuCl_2$	enzymatic hydrolysis cellulase (Accelerase 1500) T = 50 °C, time = 72 h	(1) liquid fraction: 93% monomeric xylose yield (2) liquid fraction: 3.45 ± 0.34 g/L acetic acid, 0.42 ± 0.09 g/L HMF, 1.50 ± 0.33 g/L furfural	26
	$FeCl_3$ T = 160 °C time = 10 min 0.125 mol/L $FeCl_3$	enzymatic hydrolysis cellulase (Accelerase 1500) T = 50 °C, time = 72 h	(1) liquid fraction: 94% monomeric xylose yield (2) liquid fraction: 3.30 ± 0.61 g/L acetic acid, 0.52 ± 0.08 g/L HMF, 1.19 ± 0.15 g/L furfural	
corn stover	$FeCl_3$ T = 140 °C time = 20 min 0.1 mol/L $FeCl_3$	none	(1) liquid fraction: 89.0% xylose recover (2) solid fraction: ∼90% glucose recovery	27
corn stover	$FeCl_3$ T = 160 °C time = 20 min 0.1 mol/L $FeCl_3$	enzymatic hydrolysis cellulase (Celluclast 1.5L) 60 FPU/g glucan, β-glucosidase (Novozyme 188) T = 50 °C, time = 72 h	(1) solid fraction: 93.0% glucose recovery, 98.0% enzymatic hydrolysis yield	28
corn stover silage	$Fe(NO_3)_3$ T = 150 °C time = 10 min L/S ratio = 9:1 (w/w) 0.05 mol/L $Fe(NO_3)_3$	none	(1) liquid fraction: 91.80% xylose recovery, 19.09% glucose recovery, 96.74% arabinose recovery (2) liquid fraction: 0.03g/L total inhibitor concentration	29

J. Agric. Food Chem. 2015, 63, 8349−8363
DOI: 10.1021/acs.jafc.5b01813

Table 5. continued

biomass	initial pretreatment	subsequent pretreatment	key findings	ref
corn stover silage	$Fe(NO_3)_3$ T = 150 °C time = 21.2 min L/S ratio = 9:1 (w/w) 0.05 mol/L $Fe(NO_3)_3$	none	(1) liquid fraction: 81.66% xylose recovery (2) liquid fraction: 0.5 g/L furfural concentration	30
Miscanthus straw	NH_4Cl T = 185 °C time = 15 min L/S ratio = 10:1 2% NH_4Cl	enzymatic hydrolysis cellulase (Celluclast 1.5L) 30 FPU/g cellulose, β-glucosidase (Novozyme 188) 30 CBU/g cellulose T = 50 °C, time = 72 h	(1) liquid fraction: 90.2% xylan recovery (2) solid fraction: 94.4% glucan recovery, 39.7% enzymatic digestibility	31
	$MgCl_2$ T = 185 °C time = 15 min L/S ratio = 10:1 2% $MgCl_2$	enzymatic hydrolysis cellulase (Celluclast 1.5L) 30 FPU/g cellulose, β-glucosidase (Novozyme 188) 30 CBU/g cellulose T = 50 °C, time = 72 h	(1) liquid fraction: 94.6% xylan recovery (2) solid fraction: 95.0% glucan recovery, 29.9% enzymatic digestibility	
Miscanthus straw	$FeCl_3$ T = 200 °C time = 15 min L/S ratio = 10:1 0.5% $FeCl_3$	enzymatic hydrolysis cellulase (Celluclast 1.5L) 30 FPU/g cellulose, β-glucosidase (Novozyme 188) 30 CBU/g cellulose T = 50 °C, time = 72 h	(1) solid fraction: 60.1% glucan recovery, 71.6% enzymatic digestibility	32
olive tree biomass (OTB)	$FeCl_3$ T = 153 °C time = 30 min L/S ratio = 5:1 (v/w) 0.26 mol/L $FeCl_3$	enzymatic hydrolysis cellulase (Celluclast 1.5L) 45 FPU/g WIS, β-glucosidase (Novozyme 188) 15 CBU/g cellulose T = 50 °C, time = 48 h	(1) liquid fraction: 63.2% total hemicellulosic sugars recovery (2) solid fraction: 36.6% enzymatic hydrolysis yield	33
softwood chips	SO_2 + $FeSO_4$ T = 200 °C time = 5 min 0.5 mmol/L $FeSO_4$	enzymatic hydrolysis cellulase 15 FPU/g WIS, β-glucosidase 18 IU/g WIS T = 40 °C, time = 96 h	(1) solid fraction: 69.1% overall sugar yield	34
	H_2SO_3 + $FeSO_4$ T = 200 °C time = 5 min 0.5 mmol/L $FeSO_4$	enzymatic hydrolysis cellulase 15 FPU/g WIS, β-glucosidase 18 IU/g WIS; T = 40 °C, Ttime = 96 h	(1) solid fraction: 67.7% overall sugar yield	
sugar cane bagasse	$FeCl_3$ T = 170 °C time = 30 min L/S ratio = 10:1 (v/w) 0.1 mol/L $FeCl_3$	none	(1) liquid fraction: ~52% xylose recovery, ~16% glucose recovery (2) liquid fraction: 5.11 ± 0.15 g/L furfural, 0.752 ± 0.030 g/L HMF	35

J. Agric. Food Chem. 2015, 63, 8349−8363
DOI: 10.1021/acs.jafc.5b01813

Table 5. continued

biomass	initial pretreatment	subsequent pretreatment	key findings	ref
	$CrCl_3$ T = 170 °C time = 30 min L/S ratio =10:1 (v/w) 0.1 mol/L $CrCl_3$	none	(1) liquid fraction: ∼60% xylose recovery, ∼20% glucose recovery (2) liquid fraction: 1.88 ± 0.47 g/L furfural, 0.667 ± 0.003 g/L HMF	
	$AlCl_3$ T = 170 °C time = 30 min L/S ratio = 10:1 (v/w) 0.1 mol/L $AlCl_3$	none	(1) liquid fraction: ∼46% xylose recovery, ∼2% glucose recovery (2) liquid fraction: 1.70 ± 0.10 g/L furfural, 0.816 ± 0.058 g/L HMF	
	$FeCl_2$ T = 170 °C time = 30 min L/S ratio = 10:1 (v/w) 0.1 mol/L $FeCl_2$	none	(1) liquid fraction: ∼35% xylose recovery (2) liquid fraction: 3.72 ± 0.10 g/L furfural, 0.268 ± 0.007 g/L HMF	
	$ZnCl_2$ T = 170 °C time = 30 min L/S ratio = 10:1 (v/w) 0.1 mol/L $ZnCl_2$	none	(1) liquid fraction: ∼15% xylose recovery (2) liquid fraction: 0.870 ± 0.002 g/L furfural, 0.069 ± 0.022 g/L HMF	
sweet sorghum bagasse	$CuCl_2$ T = 184 °C time = 8 min (20 mL/min), 10 min (10 mL/min) 0.1% $CuCl_2$	enzymatic hydrolysis cellulase (Imperial Jade Biotechnology) 40 FPU/g dry solid T = 50 °C, time = 48 h	(1) liquid fraction: 2.5% glucan recovery, 19.7% xylan recovery (2) solid fraction: 42.0% glucan recovery, 2.7% xylan recovery, ∼86.0% enzymatic digestibility	36
Typha latifolia cattails	$MgCl_2$ T = 180 °C time = 15 min 0.4 mol/L $MgCl_2$	enzymatic hydrolysis cellulase 15 FPU/g glucan T = 37 °C, time = 48 h	(1) liquid fraction: 90% xylose recovery (2) solid fraction: 61.7% glucose recovery	37
wheat straw	$FeCl_3$ T = 120 °C time = 120 min L/S ratio = 5:1 (v/w) 0.2 mol/L $FeCl_3$	none	(1) liquid fraction: 22.9% xylose (20.6% monomeric), 2.6% glucose, 3.1% arabinose (d.b. initial wheat straw), 96.8% total pentose yield	38

J. Agric. Food Chem. 2015, 63, 8349−8363
DOI: 10.1021/acs.jafc.5b01813

the hemicellulose structure generally forms chemical bonds with cellulose and lignin that are more complicated than the pure monomer and oligomer interactions in the synthetic mixture.[32] Less severe parameters may be incapable of breaking down the hemicellulose structure, despite degrading the monomer and oligomer into inhibitors. Sun et al.[29] obtained the highest sugar content and a low inhibitor concentration at a moderate combined severity of 0.32, but when the combined severity was increased from 1.22 to 1.81, the concentration of total sugars dropped swiftly. The efficient solubilization of hemicellulose by using inorganic salts could be attributed to the reduced activation energy requirements for biomass hydrolysis.[39] Hence, in the case of pentose-oriented pretreatment, operating at mild temperatures and nearly atmospheric pressure could be a realistic option.[38]

Cellulosic Sugar Recoveries. In the context of glucose recovery, the removal of hemicelluloses and lignin fractions of the lignocellulosic biomass is essential during the pretreatment process. $FeSO_4$ was able to selectively hydrolyze up to 95.0% of the hemicelluloses into a liquid fraction, with the cellulose remaining in the biomass residue.[22] As a result of removing hemicellulose from the solid fraction, the subsequent enzymatic hydrolysis was enhanced by promoting cellulose exposure and enzymatic activity of cellulase.[22] Liu et al.[28] achieved a high enzymatic hydrolysis of 98.0% for the solid residue after undergoing a pretreatment process using 0.1 mol/L of $FeCl_3$, which contributed to 93.0% of the glucose recovery. In another notable study, Zhang et al.[37] achieved a satisfactory glucose yield of 61.7% via the enzymatic hydrolysis of pretreated cattail solid residue. Remarkably, the addition of 0.1 mol/L of $FeCl_3$ during the organosolv pretreatment also removed all hemicelluloses while conserving approximately 90% of the initial cellulose in the residue for subsequent enzymatic saccharification.[23]

The improvement of enzymatic digestibility and the subsequent increase in the cellulosic sugar recoveries from the biomass residue was attributed to the effects of the inorganic salt pretreatment on the biomass structure. Specifically, the smooth continuous surface of the cellulose was damaged for better enzyme access, and the amorphous hemicelluloses existing as irregular clumps were almost completely removed from the solid residue after the introduction of $Fe(NO_3)_3$ pretreatment, as shown in Figure 6.[29] Similar changes to the surface morphology of the biomass were also observed when NH_4Cl or $MgCl_2$ was used to pretreat *Miscanthus* straw, as shown in Figure 7.[31] According to Kang et al.,[31] both NH_4Cl and $MgCl_2$ caused damage to the compact structure of *Miscanthus* straw, but further studies to determine the cause of the different morphology were apparently inconclusive. An application of $FeCl_3$ also exhibited a disruption of the recalcitrant structures of the crystalline cellulose that are normally observed in the biomass. According to Liu et al.,[27] the exposure of the cell internal structure and an improved surface area and porosity made the material softer and more readily able to be digested. Hence, the enzymatic digestibility of the solid residue pretreated with 0.1 mol/L of $FeCl_3$ and 50% (w/w) ethanol was observed to reach as high as 89%.[23] Moreover, Yu et al.[36] managed to enhance the enzymatic digestibility to approximately 86.0% by applying $CuCl_2$ in the flow-through mode. The increase in the crystallinity index could possibly be explained by the fact that high amounts of hemicelluloses were removed without much alteration to the cellulosic structure due to the milder pretreatment conditions.[38] Thus, the crystalline structure of the cellulose core was exposed.

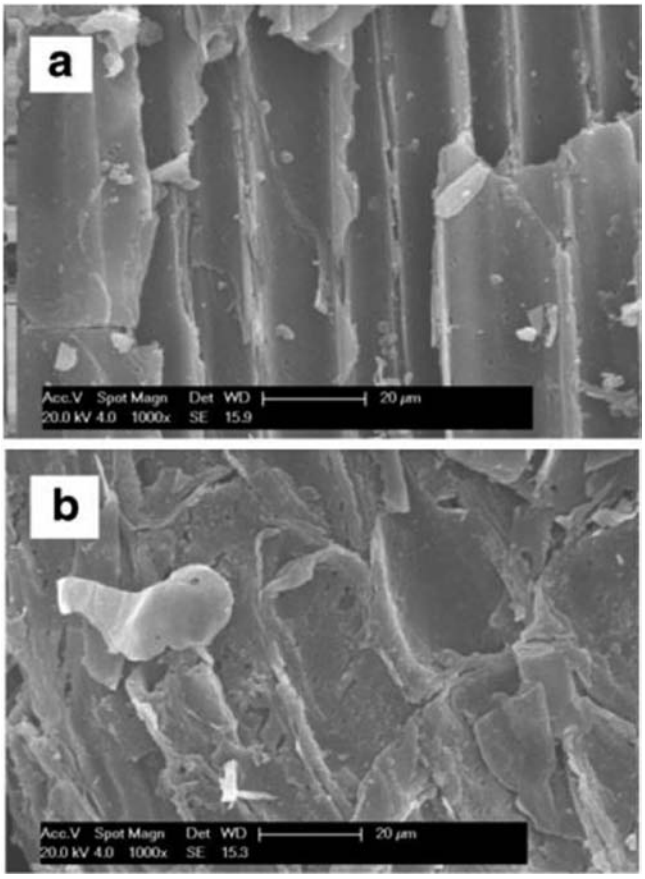

Figure 6. Scanning electron micrograph of (a) untreated and (b) $Fe(NO_3)_3$-pretreated corn stover silage at ×1000 magnification. Reprinted with permission from ref 29. Copyright 2011 Springer.

Production of Inhibitors. When lignocellulosic biomass is pretreated with inorganic salts, low generation of fermentation inhibitors might occur due to pentose dehydration.[23,24] Some studies have suggested that inorganic salts might generate fewer inhibitory coproducts compared with the acid hydrolysis pretreatments that are well-known to produce high amounts of toxic degradation compounds, primarily acetic acid, furfural, and 5-hydroxymethylfurfural (HMF).[20] For instance, low concentrations of furfural (0.011 g/L) and HMF (0.148 g/L) were achieved when organosolv was used together with $FeCl_3$.[23] The results were in agreement with the results of Kamireddy et al.,[26] who found that corn stover produced lower amounts of inhibitors when it was pretreated with $CuCl_2$ or $FeCl_3$ compared with H_2SO_4 using the same conditions (160 °C, 10 min). Specifically, $CuCl_2$ obtained approximately 0.42 g/L HMF and 1.50 g/L furfural, and $FeCl_3$ produced 0.52 g/L HMF and 1.19 g/L furfural. The HMF and furfural produced during H_2SO_4 hydrolysis were 1.10 and 2.40 g/L, respectively. Nonetheless, the production of inhibitors is heavily dependent on inorganic salt characteristics and pretreatment harshness. Increases in the $Fe(NO_3)_3$ concentration and pretreatment time were proven to intensify furfural production.[30] The trend of xylose monomer degradation was observed to accelerate significantly when the $FeCl_3$ concentration was increased from 0.1 to 0.4%.[27] When the concentration of $FeCl_3$ was increased from 100 to 200 mmol/L, Marcotullio et al.[38] observed a growth in acetic acid formation from 1.6 to 2.6 wt % during the pretreatment of wheat straw at 100 °C. Furthermore, temperature had a profound effect on

DOI: 10.1021/acs.jafc.5b01813
J. Agric. Food Chem. 2015, 63, 8349−8363

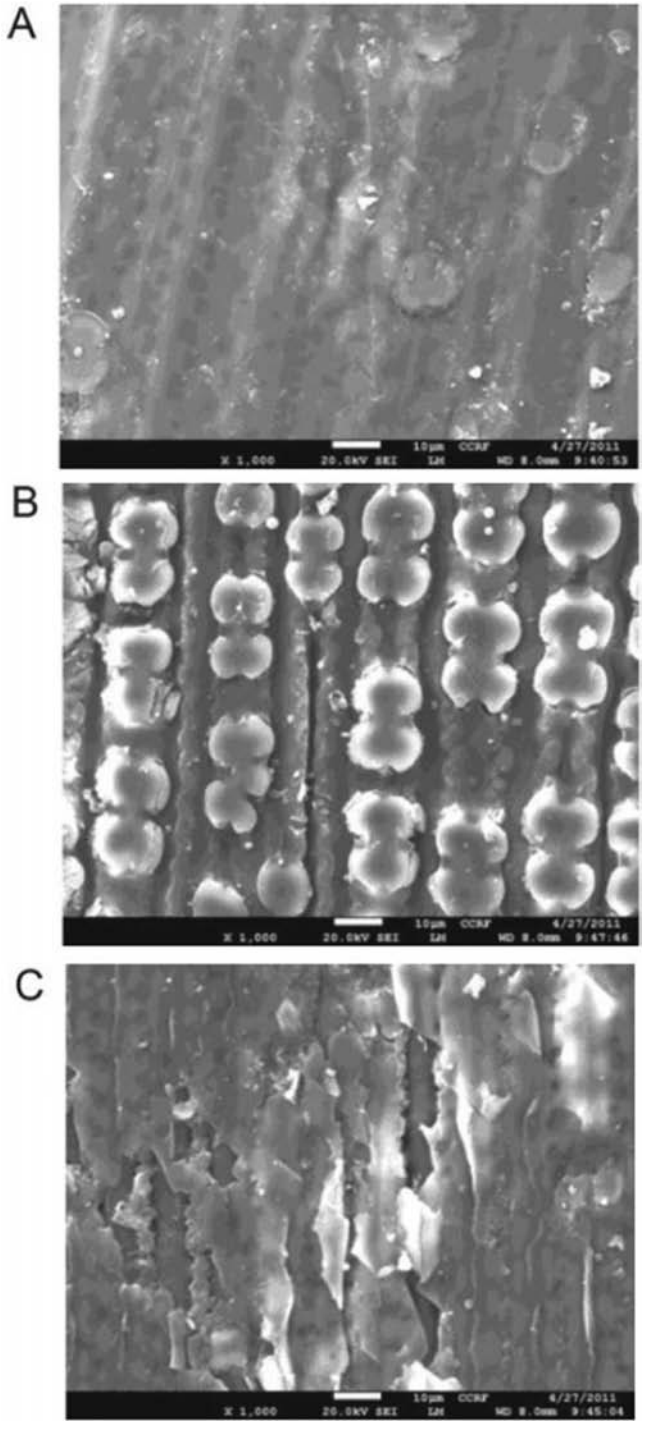

Figure 7. Scanning electron micrograph of (A) untreated, (B) NH_4Cl-pretreated, and (C) $MgCl_2$-pretreated *Miscanthus* straw at ×1000 magnification. Reprinted with permission from ref 31. Copyright 2013 Elsevier.

inhibitor production,[29,30] in which temperature >160 °C favored the conversion of xylose to furfural.[23] The increase in pretreatment temperature from 100 to 120 °C also caused the concentration of acetic acid to rise from 1.6 to 3.2 wt %, although the $FeCl_3$ concentration was maintained.[38]

Nonetheless, some previous studies were also done to test whether inorganic salts could be used for intentional conversion of sugars to furfural.[78−80] $FeCl_3$ was found to have a peculiar catalytic effect on xylose and xylotriose degradation, with the rate constants being 3- and 7-fold greater than those of dilute H_2SO_4 at the same pH.[78] Zhang et al.[80] noted that an isomerization of xylose for accelerating sugar dehydration and furfural production was promoted by metal chlorides at 185 °C and 100 min. The degradation rates of carbohydrates using inorganic salts were faster than those using dilute H_2SO_4 at the same pH.[78] Thus, this phenomenon suggests that the inorganic salts contributed to more efficient carbohydrate dehydration into the furfural compound, which is desirable in the context of using the furfural compound in the fields of chemical industry and liquid fuel production.

REACTION MECHANISM FOR INORGANIC SALT PRETREATMENT

Although some studies have reported the effects of inorganic salts on lignocellulosic biomass pretreatment, little is known about the reaction mechanism involved. To date, several mechanisms have been proposed to explain the behavior of inorganic salts. First, metal salts act as Lewis acid by dissolving in aqueous solvents to produce complex cations. A Lewis acid can be defined as a molecular body that serves as an electron pair acceptor that can react with a Lewis base to form a Lewis adduct.[71] Accordingly, coordinate covalent bonds with six water molecules as monodentate ligands are formed around the central metal cation. Leshkov and Davis[81] proposed the general expression of these metal ion ligand complexes as $[M(H_2O)_n]^{z+}$ (where M is the metal ion, z is the cation oxidation state, and n is the solvation number, typically ranging between 4 and 9). Hence, metal chlorides such as Al^{3+} and Fe^{3+} are presumed to follow this reaction mechanism to form six coordinate covalent bonds with water molecules, whereas Cu^{2+} achieves a stable complex ion by coordinating as a tetradentate ligand.[26,36]

The formation of the metal cations ultimately acting as Lewis acids would then aid in the cleavage of the glycosidic linkages. The coordinated water molecules from the hydrated cation play a pivotal role in xylose formation by participating as nucleophiles.[82,83] Similarly, the conversion of cellulose to glucose mediated by $ZnCl_2$ has also been examined to understand the mechanism of formation of inorganic salts as Lewis acids. First, the zinc was found to coordinate to the glycosidic oxygen to help break down the glycosidic linkage, resulting in the reduction of reaction energy. Then, in the second step of the mechanism, the coordinated water molecules of the metal cation complex participated as nucleophiles to yield D-glucose, as shown in Figure 8.[84] The same Lewis acid mechanism pathway can be observed for $AlCl_3$[83] and $FeCl_3$ salts.[85]

Second, metal ions can undergo hydrolysis when they are mixed with water to produce the H_3O^+ ion. The hydrolysis reactions are represented by eqs 2 and 3[86]

$$[M(H_2O)_6]^{2+} + H_2O \rightleftharpoons [M(H_2O)_5OH]^{+} + H_3O^{+} \quad (2)$$

$$[M(H_2O)_6]^{3+} + H_2O \rightleftharpoons [M(H_2O)_5OH]^{2+} + H_3O^{+} \quad (3)$$

where M is the metal ion.

Therefore, the aqueous metal salt solutions present a Brønsted acid character similar to that of HCl to depolymerize hemicelluloses into monosaccharides,[38,85] as shown in Figure 9.[26] Interestingly, $FeSO_4$ was proposed to facilitate the breakdown of the glycosidic linkage due to the adsorption of Fe^{2+} to the hydroxyl oxygen atoms and the oxygen of the cellulose pyran ring to form a carbohydrate complex.[22] In the dilute acid pretreatment, each proton pairs with one electron to

DOI: 10.1021/acs.jafc.5b01813
J. Agric. Food Chem. 2015, 63, 8349−8363

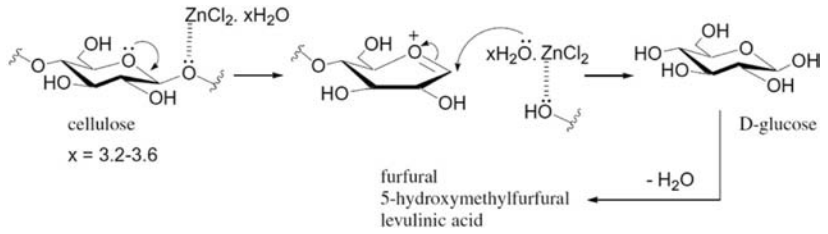

Figure 8. Conversion of cellulose into glucose via the Lewis acid mechanism. Reprinted with permission from ref 84. Copyright 2009 Elsevier.

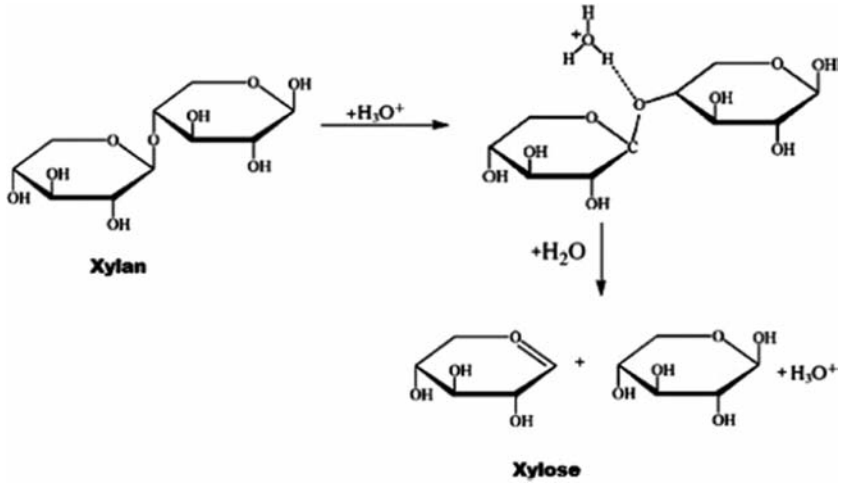

Figure 9. Conversion of xylan into xylose via the Brønsted acid mechanism. Reprinted from ref 26. Copyright 2013 American Chemical Society.

weaken the bond energy for easier bond rupture. Thus, Zhao et al.[22] suggested that metal ions could be playing the same role and may possibly be even more effective in assisting bond rupture because they have more positive charges to pair with more electrons.

However, the capability of metal salts to accept electrons and the different ionic radii of metal ions contribute to the various stabilities of the carbohydrate complexes.[32] The effect of the inorganic salts on the decomposition of hemicellulose seems to follow this particular order: transition metal chlorides ($FeCl_2$, $FeCl_3$, $CuCl_2$, $ZnCl_2$) > alkaline earth metal chlorides ($MgCl_2$, $CaCl_2$) > alkaline metal chlorides (KCl, NaCl). Transition metal ions such as Fe^{3+} and Fe^{2+} make good electron acceptors compared with the alkaline metal ions, namely K^+ and Na^+,[32] because transition metal ions are able to coordinate with the oxygen donor atoms of carbohydrates and their derivatives without losing the protons that make up the hydroxyl groups of the ligand.[36] Alkaline metal cations are weak electron acceptors and are unable to coordinate with carbohydrates, thus providing an explanation for the relatively low sugar recovery compared with the sugar recovery observed for transition and alkaline earth metals. Hence, the dissimilar arrangements of extranuclear electrons in the metal elements and the saccharide−metal cation intermediate complex between inorganic salts result in contrasting performance in hemicellulose hydrolysis.[36] According to Marcotullio et al.,[38] $FeCl_3$ produced filtrates with the pH lower than the HCl pretreatment (1.73−1.81 and 2.25−2.46, respectively). The results concur with those of Liu et al.,[27] where the pH after $FeCl_3$ pretreatment reached as low as 1.68. Pretreatment with other inorganic salts, namely NaCl, KCl, $CaCl_2$, and $MgCl_2$, produced filtrates with pH close to 7. When the pH approached neutral, hemicelluloses were mainly solubilized as oligomers, despite the lesser degradation of the hemicelluloses into toxic inhibitors.[22] With respect to the findings of Kang et al., the effect of a trivalent salt was reported to be greater than the effect of a di- or monovalent salt during biomass hydrolysis.[31] For example, $FeCl_3$ generated 71.6% enzymatic digestibility and almost 100% xylan removal from biomass, which were at least 26.7 and 31.8% higher than those of di- and monovalent metal salts, respectively.[31] Hence, Fe^{3+} apparently formed a stronger acid in aqueous solution than did other cations because of its pK_a (acid dissociation constant) value of 2.46, which was significantly lower than those of Al^{3+} (4.85), Cu^{2+} (6.50), Fe^{2+} (9.49), Mg^{2+} (11.4), Ca^{2+} (12.7), and Na^+ (14.1).[26]

PROSPECTS AND CHALLENGES OF THE INORGANIC SALT PRETREATMENT

Reduction in Operational Cost. Generally, inorganic salts have several advantages over the "current technology" of lignocellulosic biomass pretreatment, such as dilute acid hydrolysis. The dilute acid hydrolysis pretreatment method has been known to cause corrosion issues and requires expensive materials for equipment construction.[22] Corrosion occurs easily because inorganic acids such as H_2SO_4, which is commonly used in dilute acid hydrolysis, produces a strong electrolyte during the pretreatment process. An inorganic salt is less corrosive than an inorganic acid[35] because the former undergoes hydrolysis to release hydrogen ions as a weak electrolyte to provide a steadier reactive environment.[32] Moreover, Liu et al.[27] discovered that certain inorganic salts (NaCl, KCl, $MgCl_2$, $CaCl_2$) generated a hydrolysate with a pH that was more suitable for downstream fermentation. The need for high neutralization requirements may therefore be eliminated. However, stronger inorganic salts such as $FeCl_3$ and $Fe_2(SO_4)_3$ demonstrated higher xylose recovery, despite a low pH of ∼2.0 that may require additional

DOI: 10.1021/acs.jafc.5b01813
J. Agric. Food Chem. 2015, 63, 8349−8363

neutralization.[27] The inorganic salts can be recovered in the form of metal hydroxides via ultrafiltration, and the treatment with conjugated acids is able to convert the metal hydroxides back to metal chlorides, which could be recycled and reused in the later part of the biomass pretreatment process.[26]

Associated Limitations. However, some concerns arise regarding the use of inorganic salts for lignocellulosic biomass pretreatment. In particular, the effect of different inorganic salts on the cellulase hydrolysis is not well understood.[71] For instance, excessive Fe and Cl proportions left in the solid fraction might affect the microorganisms or enzymes during bioconversion at the later stage.[38] In a study to identify the inhibitory effects of metal ions, Fe^{3+} and Fe^{2+} were thought to target cellulose and cause undesirable impacts on cellulolysis.[87] Heavy metal elements such as chromium even caused the denaturing and inactivation of cellulase, which led to the unsatisfactory enzymatic hydrolysis of Cr^{3+}-pretreated sugar cane bagasse.[35] Kamireddy et al.[26] reported contradictory results, in which the enzymatic hydrolysis was improved due to the presence of metal complexes that formed lignin−metal complexes. This occurrence eliminated lignin inhibition and granted access to more cellulose sites. This result may explain the huge fluctuation of enzymatic hydrolysis yield, which ranged from 36.6 to 98.0%,[28,33] as well as other factors such as biomass characteristics, pretreatment severity, and enzymatic loadings. Kim et al.[23] argued that $FeCl_3$ could be removed via a washing/filtration process to a point where it was undetected. A novel approach has been developed to generate electricity while removing Fe^{2+} from the liquid fraction by using a fuel cell system.[88] Nevertheless, further investigations are required to analyze the mechanism of inorganic salt pretreatments and the effects on downstream applications caused by metal ions in the biomass residues and liquid hydrolysate.

Economic Feasibility. At present, the development of second-generation fuels and chemicals from lignocellulosic biomass via a biochemical route may present greater cost reduction potential than the thermochemical route because the latter involves extremely energy-intensive processes. The biotechnological conversion of biomass to second-generation products has not been intensively commercialized, although the subject has been studied for decades, mainly due to the uncertainty of the techno-economic feasibility of large-scale production.[46,66] Pretreatment of lignocellulosic biomass, which is necessary to achieve high sugar yields in biotechnological operation, has been singled out as the most expensive step, as it represents approximately 20% of the total cost of the whole process.[65] Among the available pretreatment technologies, those that employ chemicals currently offer better yields at lower costs, which are essential for economic viability. As part of an initiative of the U.S. Department of Agriculture, Eggeman and Elander performed a comprehensive economic analysis to evaluate various biomass pretreatment methods (dilute acid, hot water, ARP, AFEX, and lime).[89] They concluded that low-cost pretreatment reactors were often counterbalanced by the higher costs associated with catalysts/solvents and product recovery, which resulted in little difference in economic performance among the pretreatments investigated. To date, no literature is available regarding the economics of biomass pretreatment using inorganic salts. Generally, inorganic salts such as $FeCl_3$ and $AlCl_3$ are expensive.[90] Nonetheless, the application of inorganic salt has showed promising opportunities for reduced costs because of its less corrosive nature, which allow for the use of cheaper construction materials.[35] Furthermore, a recent study conducted by Liu et al.[27] proved that inorganic salts could be used directly as an aqueous solution for biomass pretreatment without an addition of acid, which reduced neutralization requirements. Additionally, Marcotullio et al.[38] successfully carried out pretreatment of biomass at mild temperatures and at approximately atmospheric pressure using an inorganic salt. Hence, scale-up issues concerning continuous biomass feeding at high pressures and material resistance could be avoided. Silva and Chandel[70] also stated that inorganic salts allowed simple process conditions that would reduce operational costs and energy consumption.

In conclusion, further research is necessary to investigate the physicochemical changes and mechanisms involved during not only inorganic salt pretreatment but also other lignocellulose pretreatment methods in general on a cellular scale. With an advancement in the field of analytical chemistry, better optimization studies could be performed to develop more cost-effective pretreatment technologies in the future.

AUTHOR INFORMATION

Corresponding Author

*(T.Y.W.) Phone: +60 3 55146258. Fax: +60 3 55146207. E-mail: wu.ta.yeong@.monash.edu, tayeong@hotmail.com.

Funding

The funding of this research is supported by the Ministry of Higher Education, Malaysia, under Long-term Research Grant Scheme (LRGS/2013/UKM-UKM/PT/01). In addition, we thank Monash University Malaysia for providing Yu-Loong Loow with a postgraduate scholarship.

Notes

The authors declare no competing financial interest.

REFERENCES

(1) Zhang, K.; Chang, J.; Guan, Y.; Chen, H.; Yang, Y.; Jiang, J. Lignocellulosic biomass gasification technology in China. *Renewable Energy* **2013**, *49*, 175−184.

(2) Sarkar, N.; Ghosh, S. K.; Bannerjee, S.; Aikat, K. Bioethanol production from agricultural wastes: an overview. *Renewable Energy* **2012**, *37*, 19−27.

(3) Kristiani, A.; Abimanyu, H.; Setiawan, A. H.; Sudiyarmanto; Aulia, F. Effect of pretreatment process by using diluted acid to characteristic of oil palm's frond. *Energy Procedia* **2013**, *32*, 183−189.

(4) Nguyen, Q. A.; Tucker, M. P.; Keller, F. A.; Eddy, F. P. Two-stage dilute-acid pretreatment of softwoods. *Appl. Biochem. Biotechnol.* **2000**, *84−86*, 561−576.

(5) Saha, B. C.; Iten, L. B.; Cotta, M. A.; Wu, Y. V. Dilute acid pretreatment, enzymatic saccharification, and fermentation of rice hulls to ethanol. *Biotechnol. Prog.* **2005**, *21* (3), 816−822.

(6) Sassner, P.; Martensson, C. G.; Galbe, M.; Zacchi, G. Steam pretreatment of H_2SO_4-impregnated Salix for the production of bioethanol. *Bioresour. Technol.* **2008**, *99* (1), 137−145.

(7) Sun, Y. E.; Cheng, J. J. Dilute acid pretreatment of rye straw and bermudagrass for ethanol production. *Bioresour. Technol.* **2005**, *96* (14), 1599−1606.

(8) Chiesa, S.; Gnansounou, E. Use of empty fruit bunches from the oil palm for bioethanol production: a thorough comparison between dilute acid and dilute alkali pretreatment. *Bioresour. Technol.* **2014**, *159*, 355−364.

(9) Ishiguro, M.; Endo, T. Addition of alkali to the hydrothermal-mechanochemical treatment of eucalyptus enhances its enzymatic saccharification. *Bioresour. Technol.* **2014**, *153*, 322−326.

(10) Holtzapple, M. T.; Lundeen, J. E.; Sturgis, R.; Lewis, J. E.; Dale, B. E. Pretreatment of lignocellulosic municipal solid-waste by ammonia fiber explosion (AFEX). *Appl. Biochem. Biotechnol.* **1992**, *34* (5), 5−21.

DOI: 10.1021/acs.jafc.5b01813
J. Agric. Food Chem. 2015, 63, 8349−8363

(11) Kim, T. H.; Lee, Y. Y. Pretreatment and fractionation of corn stover by ammonia recycle percolation process. *Bioresour. Technol.* **2005**, *96* (18), 2007−2013.
(12) Mes-Hartree, M.; Dale, B. E.; Craig, W. K. Comparison of steam and ammonia pretreatment for enzymatic hydrolysis of cellulose. *Appl. Microbiol. Biotechnol.* **1988**, *29* (5), 462−468.
(13) Boussarsar, H.; Roge, B.; Mathlouthi, M. Optimization of sugarcane bagasse conversion by hydrothermal treatment for the recovery of xylose. *Bioresour. Technol.* **2009**, *100*, 6537−6542.
(14) Carvalheiro, F.; Silva-Fernandes, T.; Duarte, L. C.; Girio, F. M. Wheat straw autohydrolysis: process optimization and products characterization. *Appl. Biochem. Biotechnol.* **2009**, *153*, 84−93.
(15) Cara, C.; Ruiz, E.; Carvalheiro, F.; Moura, P.; Ballesteros, I.; Castro, E.; Girio, F. Production, purification and characterization of oligosaccharides from olive tree pruning autohydrolysis. *Ind. Crops Prod.* **2012**, *40*, 225−231.
(16) Singh, J.; Suhag, M.; Dhaka, A. Augmented digestion of lignocellulose by steam explosion, acid and alkaline pretreatment methods: a review. *Carbohydr. Polym.* **2015**, *117*, 624−631.
(17) Theuretzbacher, F.; Lizasoain, J.; Lefever, C.; Saylor, M. K.; Enguidanos, R.; Weran, N.; Gronauer, A.; Bauer, A. Steam explosion pretreatment of wheat straw to improve methane yields: investigation of the degradation kinetics of structural compounds during anaerobic digestion. *Bioresour. Technol.* **2015**, *179*, 299−305.
(18) Tan, H. T.; Lee, K. T. Understanding the impact of ionic liquid pretreatment on biomass and enzymatic hydrolysis. *Chem. Eng. J.* **2012**, *183*, 448−458.
(19) Limayem, A.; Ricke, S. C. Lignocellulosic biomass for bioethanol production: current perspectives, potential issues and future prospects. *Prog. Energy Combust. Sci.* **2012**, *38*, 449−467.
(20) Brodeur, G.; Yau, E.; Badal, K.; Collier, J.; Ramachandran, K. B.; Ramakrishnan, S. Chemical and physicochemical pretreatment of lignocellulosic biomass: a review. *Enzyme Res.* **2011**, *2011*, 1−17.
(21) Mosier, N.; Wyman, C.; Dale, B.; Elander, R.; Lee, Y. Y.; Holtzapple, M.; Ladisch, M. Features of promising technologies for pretreatment of lignocellulosic biomass. *Bioresour. Technol.* **2005**, *96*, 673−686.
(22) Zhao, J.; Zhang, H.; Zheng, R.; Lin, Z.; Huang, H. The enhancement of pretreatment and enzymatic hydrolysis of corn stover by $FeSO_4$ pretreatment. *Biochem. Eng. J.* **2011**, *56*, 158−164.
(23) Kim, Y.; Yu, A.; Han, M.; Choi, G. W.; Chung, B. Ethanosolv pretreatment of barley straw with iron(III) chloride for enzymatic saccharification. *J. Chem. Technol. Biotechnol.* **2010**, *85*, 1494−1498.
(24) Park, N.; Kim, H. Y.; Koo, B. W.; Yeo, H.; Choi, I. G. Organosolv pretreatment with various catalysts for enhancing enzymatic hydrolysis of pitch pine (*Pinus rigida*). *Bioresour. Technol.* **2010**, *101*, 7046−7053.
(25) Lu, J.; Zhou, P. Optimization of microwave-assisted $FeCl_3$ pretreatment conditions of rice straw and utilization of *Trichoderma viride* and *Bacillus pumilus* for production of reducing sugars. *Bioresour. Technol.* **2011**, *102*, 6966−6971.
(26) Kamireddy, S. R.; Li, J.; Tucker, M.; Degenstein, J.; Ji, Y. Effects and mechanism of metal chlorides on pretreatment and enzymatic digestibility of corn stover. *Ind. Eng. Chem. Res.* **2013**, *52*, 1775−1782.
(27) Liu, L.; Sun, J.; Cai, C.; Wang, S.; Pei, H.; Zhang, J. Corn stover pretreatment by inorganic salts and its effects on hemicellulose and cellulose degradation. *Bioresour. Technol.* **2009**, *100*, 5865−5871.
(28) Liu, L.; Sun, J.; Li, M.; Wang, S.; Pei, H.; Zhang, J. Enhanced enzymatic hydrolysis and structural features of corn stover by $FeCl_3$ pretreatment. *Bioresour. Technol.* **2009**, *100*, 5853−5858.
(29) Sun, Y.; Lu, X.; Zhang, R.; Wang, X. Pretreatment of corn stover silage with $Fe(NO_3)_3$ for fermentable sugar production. *Appl. Biochem. Biotechnol.* **2011**, *164*, 918−928.
(30) Sun, Y.; Lu, X.; Zhang, S.; Zhang, R.; Wang, X. Kinetic study for $Fe(NO_3)_3$ catalyzed hemicellulose hydrolysis of different corn stover silages. *Bioresour. Technol.* **2011**, *102*, 2936−2942.
(31) Kang, K. E.; Park, D. H.; Jeong, G. T. Effects of NH_4Cl and $MgCl_2$ on pretreatment and xylan hydrolysis of Miscanthus straw. *Carbohydr. Polym.* **2013**, *92*, 1321−1326.
(32) Kang, K. E.; Park, D. H.; Jeong, G. T. Effects of inorganic salts on pretreatment of Miscanthus straw. *Bioresour. Technol.* **2013**, *132*, 160−165.
(33) Linares, J. C. L.; Romero, I.; Moya, M.; Cara, C.; Ruis, E. Pretreatment of olive tree biomass with $FeCl_3$ prior enzymatic hydrolysis. *Bioresour. Technol.* **2013**, *128*, 180−187.
(34) Monavari, S.; Galbe, M.; Zacchi, G. The influence of ferrous sulfate utilization on the sugar yields from dilute-acid pretreatment of softwood for bioethanol production. *Bioresour. Technol.* **2011**, *102*, 1103−1108.
(35) Chen, L.; Chen, R.; Fu, S. Preliminary exploration on pretreatment with metal chlorides and enzymatic hydrolysis of bagasse. *Biomass Bioenergy* **2014**, *71*, 311−317.
(36) Yu, Q.; Zhaung, X.; Yuan, Z.; Qi, W.; Wang, Q.; Tan, X. The effect of metal salts on the decomposition of sweet sorghum bagasse in flow-through liquid hot water. *Bioresour. Technol.* **2011**, *102*, 3445−3450.
(37) Zhang, B.; Shahbaz, A.; Wang, L.; Whitmore, A.; Riddick, B. A. Fermentation of glucose and xylose in cattail processed by different pretreatment technologies. *BioResources* **2012**, *7* (3), 2848−2859.
(38) Marcotullio, G.; Krisanti, E.; Giuntoli, J.; Jong, W. D. Selective production of hemicellulose-derived carbohydrates from wheat straw using dilute HCl or $FeCl_3$ solutions under mild conditions. X-ray and thermo-gravimetric analysis of the solid residues. *Bioresour. Technol.* **2011**, *102*, 5917−5923.
(39) Nguyen, Q. A.; Tucker, M. P. Dilute acid/metal salt hydrolysis of lignocellulosics. U.S. Patent 6,423,145 B1, 2002; 1−12.
(40) Hadar, Y. Sources For lignocellulosic raw materials for the production of ethanol. In *Lignocellulose Conversion*; Faraco, V., Ed.; Springer: Berlin, Germany, 2013; pp 21−38.
(41) Kurian, J. K.; Nair, G. R.; Hussain, A.; Raghavan, G. S. V. Feedstocks, logistics and pre-treatment processes for sustainable lignocellulosic biorefineries: a comprehensive review. *Renewable Sustainable Energy Rev.* **2013**, *25*, 205−219.
(42) Ho, D. P.; Ngo, H. H.; Guo, W. A mini review on renewable sources for biofuel. *Bioresour. Technol.* **2014**, *169*, 742−749.
(43) Maity, S. K. Opportunities, recent trends and challenges of integrated biorefinery: part I. *Renewable Sustainable Energy Rev.* **2015**, *43*, 1427−1445.
(44) Muller, A.; Schmidhuber, J.; Hoogeveen, J.; Steduto, P. Some insights in the effect of growing bio energy demand on global food security and natural resources. *Water Policy.* **2008**, *10*, 83−94.
(45) Food and Agriculture Organization of the United Nations (FAO). FAOSTAT. Production: Crops; http://faostat.fao.org/site/567/desktopdefault.aspx#ancor (accessed April 8, 2015).
(46) Menon, V.; Rao, M. Trends in bioconversion of lignocellulose: biofuels, platform chemicals and biorefinery concept. *Prog. Energy Combust. Sci.* **2012**, *38*, 522−550.
(47) Bazargan, A.; Bazargan, M.; Mckay, G. Optimization of rice husk pretreatment for energy production. *Renewable Energy* **2015**, *77*, 512−520.
(48) Ji, L. An assessment of agricultural residue resources for liquid biofuel production in China. *Renewable Sustainable Energy Rev.* **2015**, *44*, 561−575.
(49) Rocha, G. J. M.; Nascimento, V. M.; Goncalves, A. R.; Silva, V. F. N.; Martin, C. Influence of mixed sugarcane bagasse samples evaluated by elemental and physical-chemical composition. *Ind. Crops Prod.* **2015**, *64*, 52−58.
(50) Lim, S. L.; Wu, T. Y.; Sim, E. Y. S.; Lim, P. N.; Clarke, C. Biotransformation of rice husk into organic fertilizer through vermicomposting. *Ecol. Eng.* **2012**, *41*, 60−64.
(51) Shak, K. P. Y.; Wu, T. Y.; Lim, S. L.; Lee, C. A. Sustainable reuse of rice residues as feedstocks in vermicomposting for organic fertilizer production. *Environ. Sci. Pollut. Res.* **2014**, *21* (2), 1349−1359.
(52) Puri, M.; Abraham, R. E.; Barrow, C. J. Biofuel production: prospects, challenges and feedstock in Australia. *Renewable Sustainable Energy Rev.* **2012**, *16*, 6022−6031.
(53) Mushtaq, Z.; Imran, M.; Rehman, S.; Zahoor, T.; Ahmad, R. S.; Arshad, U. Biochemical perspectives of xylitol extracted from indigenous

DOI: 10.1021/acs.jafc.5b01813
J. Agric. Food Chem. 2015, 63, 8349−8363

agricultural by-product mung bean (*Vigna radiata*) hulls in a rat model. *J. Sci. Food Agric.* **2014**, *94*, 969−974.
(54) Gupta, V. K.; Potumarthi, R.; O'Donovan, A.; Kubicek, C. P.; Sharma, G. D.; Tuohy, M. G. Chapter 2 − Bioenergy research: an overview on technological developments and bioresources. In *Bioenergy Research: Advances and Applications*; Gupta, V. K., Tuohy, M. G., Kubicek, C. P., Saddler, J., Xu, F., Eds.; Elsevier: Amsterdam, The Netherlands, 2014; pp 23−47.
(55) Garcia, S. G.; Yudego, B. M.; Murphy, R. J. Life cycle assessment of potential energy uses for short rotation willow biomass in Sweden. *Int. J. Life Cycle Assess.* **2013**, *18*, 783−795.
(56) Manavalan, T.; Manavalan, A.; Heese, K. Characterization of lignocellulolytic enzymes from white-rot fungi. *Curr. Microbiol.* **2015**, *70*, 485.
(57) Li, X. P.; Clarke, K.; Li, K. C.; Chen, A. C. The pattern of cell wall deterioration in lignocellulose fibres throughout enzymatic cellulose hydrolysis. *Biotechnol. Prog.* **2012**, *28* (6), 1389−1399.
(58) Zeng, Y.; Zhao, S.; Yang, S.; Ding, S. Lignin plays a negative role in the biochemical process for producing lignocellulosic biofuels. *Curr. Opin. Biotechnol.* **2014**, *27*, 38−45.
(59) Kotarska, K.; Swierczynska, A.; Dziemianowicz, W. Study on the decomposition of lignocellulosic biomass and subjecting it to alcoholic fermentation: study on the decomposition of lignocellulosic biomass. *Renewable Energy* **2015**, *75*, 389−394.
(60) Davison, B. H.; Parks, J.; Davis, M. F.; Donohoe, B. S. Plant cell walls: basics of structure, chemistry, accessibility and the influence on conversion. In *Aqueous Pretreatment of Plant Biomass for Biological and Chemical Conversion to Fuels and Chemicals, 1*; Wyman, C. E., Ed.; Wiley: Hoboken, NJ, USA, 2013; pp 23−38.
(61) Pang, C. H.; Gaddipatti, S.; Tucker, G.; Lester, E.; Wu, T. Relationship between thermal behaviour of lignocellulosic components and properties of biomass. *Bioresour. Technol.* **2014**, *172*, 312−320.
(62) Rocha, G. J.; Nascimento, V. M.; Goncalves, A. R.; Silva, V. F. N.; Martin, C. Influence of mixed sugarcane bagasse samples evaluated by elemental and physical−chemical composition. *Ind. Crops Prod.* **2014**, *64*, 52−58.
(63) Szczerbowski, D.; Pitarelo, A. P.; Filho, A. Z.; Ramos, L. P. Sugarcane biomass for biorefineries: comparative composition of carbohydrate and non-carbohydrate components of bagasse and straw. *Carbohydr. Polym.* **2014**, *114*, 95−101.
(64) Harmsen, P. F. H.; Hujigen, W. J. J.; Lopez, L. M. B.; Bakker, R. R. C. *Literature Review of Physical and Chemical Pretreatment Processes for Lignocellulosic Biomass*; Energy Research Centre of the Netherlands: Wageningen, The Netherlands, 2010; 10-013.
(65) Yang, B.; Wyman, C. E. Pretreatment: the key to unlocking low-cost cellulosic ethanol. *Biofuels, Bioprod. Biorefin.* **2008**, *2*, 26−40.
(66) Singhvi, M. S.; Chaudhari, S.; Gokhale, D. V. Lignocellulose processing: a current challenge. *RSC Adv.* **2014**, *4*, 8271−8277.
(67) He, Y.; Zhang, J.; Bao, J. Dry dilute acid pretreatment by co-currently feeding of corn stover feedstock and dilute acid solution without impregnation. *Bioresour. Technol.* **2014**, *158*, 360−364.
(68) Tabasso, S.; Carnaroglio, D.; Gaudino, E. C.; Cravotto, G. Microwave, ultrasound and ball mill procedures for bio-waste valorisation. *Green Chem.* **2015**, *17*, 684−693.
(69) Wu, T. Y.; Guo, N.; Teh, C. Y.; Hay, J. X. W. *Advances in Ultrasound Technology for Environmental Remediation*; Springer: Dordrecht, The Netherlands, 2013; DOI: 10.1007/978-94-007-5533-8.
(70) Silva, S. S.; Chandel, A. K. Part I: Biomass hydrolysis for xylose recovery and detoxification. In *D-Xylitol: Fermentative Production, Application and Commercialization*; Silva, S. S., Chandel, A. K., Eds.; Springer: Heidelberg, Germany, 2012; pp 3−37.
(71) Zhang, B.; Shahbazi, A. Recent developments in pretreatment technologies for production of lignocellulosic biofuels. *J. Pet. Environ. Biotechnol.* **2011**, *2* (2), 1−8.
(72) Morikawa, Y.; Zhao, X.; Liu, D. Biological co-production of ethanol and biodiesel from wheat straw: a case of dilute acid pretreatment. *RSC Adv.* **2014**, *4*, 37878−37888.
(73) Goldstein, I. S. Acid processes for cellulose hydrolysis and their mechanisms wood and agricultural residues. In *Wood Agricultural Residues: Research on Use for Feed, Fuels, and Chemicals*; Soltes, E. J., Ed.; Academic Press: New York, 1983; pp 315−328.
(74) Agbor, V. B.; Cicek, N.; Sparling, R.; Berlin, A.; Levin, D. B. Biomass pretreatment: fundamentals toward application, biotechnology toward application. *Biotechnol. Adv.* **2011**, *29*, 675−685.
(75) Zheng, Y.; Pan, Z.; Zhang, R. Overview of biomass pretreatment for cellulosic ethanol production. *Int. J. Agric. Biol. Eng.* **2009**, *2* (3), 51−68.
(76) Fields, P.; Wilson, R. Process for the production of xylose. U.S. Patent 5340403A, 1994, 340−403.
(77) Pappas, I. A.; Koukoura, Z.; Tananaki, C.; Goulas, C. Effect of dilute acid pretreatment severity on the bioconversion efficiency of *Phalaris aquatica* L. lignocellulosic biomass into fermentable sugars. *Bioresour. Technol.* **2014**, *166*, 395−402.
(78) Liu, C.; Wyman, C. E. The enhancement of xylose monomer and xylotriose degradation by inorganic salts in aqueous solutions at 180 °C. *Carbohydr. Res.* **2006**, *341*, 2550−2556.
(79) Marcotullio, G.; De Jong, W. Chloride ions enhance furfural formation from D-xylose in dilute aqueous acidic solutions. *Green Chem.* **2010**, *12*, 1739−1746.
(80) Zhang, L.; Yu, H.; Wang, P.; Dong, H.; Peng, X. Conversion of xylan, D-xylose and lignocellulosic biomass into furfural using $AlCl_3$ as catalyst in ionic liquid. *Bioresour. Technol.* **2013**, *130*, 110−116.
(81) Leshkov, Y. R.; Davis, M. E. Activation of carbonyl containing molecules with solid Lewis acids in aqueous media. *ACS Catal.* **2011**, *1* (11), 1566−1580.
(82) Cotton, F.; Wilkinson, G. In *Advanced Inorganic Chemistry*, 5th ed.; Wiley: Hoboken, NJ, USA, 1988.
(83) Peng, L.; Lin, L.; Zhang, J.; Zhuang, J.; Zhang, B.; Gong, Y. Catalytic conversion of cellulose to levulinic acid by metal chlorides. *Molecules* **2010**, *15*, 5258−5272.
(84) Amarasekara, A. S.; Ebede, C. C. Zinc chloride mediated degradation of cellulose at 200 °C and identification of the products. *Bioresour. Technol.* **2009**, *100*, 5301−5304.
(85) Zhang, L.; Yu, H.; Wang, P.; Li, Y. Production of furfural from xylose, xylan and corncob in γ-valerolactone using $FeCl_3{\cdot}6H_2O$ as catalyst. *Bioresour. Technol.* **2014**, *151*, 355−360.
(86) Scienceaid.co.uk. Lewis acids and bases; http://scienceaid.co.uk/chemistry/inorganic/lewis.html (accessed Dec 24, 2014).
(87) Tejirian, A.; Xu, F. Inhibition of cellulase-catalyzed lignocellulosic hydrolysis by iron and oxidative metal ions and complexes. *Appl. Environ. Microbiol.* **2010**, *76* (23), 7673−7682.
(88) Kim, I.; Rehman, M. S. U.; Kim, K. H.; Han, J. I. Generation of electricity from $FeCl_3$ pretreatment of rice straw using a fuel cell system. *Bioresour. Technol.* **2013**, *135*, 635−639.
(89) Eggeman, T.; Elander, R. T. Process and economic analysis of pretreatment technologies. *Bioresour. Technol.* **2005**, *96*, 2019−2025.
(90) Degenstein, J.; Kamireddy, S. R.; Tucker, M. P.; Ji, Y. Oligomer saccharide reduction during dilute acid pretreatment co-catalyzed with Lewis acids on corn stover biomass. *Int. J. Agric. Biol. Eng.* **2013**, *6* (2), 54−62.

DOI: 10.1021/acs.jafc.5b01813
J. Agric. Food Chem. 2015, 63, 8349−8363

Table 1. Retention Times, Detection Limits, and Optimized MS/MS Parameters for Target PFCs and Internal Isotope PFC Standards

compounds	precursor ion (m/z)	qualifier ion (m/z)	DP (V)	CE (V)	CXP (V)	t_R (min)	IDLs ($\mu g\ kg^{-1}$)	MDLs ($\mu g\ kg^{-1}$)
PFOS	499.20	80[a]	−178	−94	−8	6.05	0.02	0.2
		99.10	−178	−60	−11			
PFDoA	613.0	569.80[a]	−58	−17	−15	8.51	0.04	0.04
		269.40	−58	−29	−15			
PFDS	599	80[a]	−220	−105	−108	7.89	0.004	0.1
		99.2	−220	−79	−108			
PFUdA	563.0	519.60[a]	−59	−17	−50	7.91	0.004	0.02
		269.40	−59	−29	−50			
PFNA	463.20	419.50[a]	−50	−14	−25	6.77	0.02	0.02
		219.40	−50	−26	−25			
PFHxA	313.10	269.40[a]	−38	−12	−28	3.96	0.04	0.04
		119.40	−38	−31	−13			
PFHxDA	813.3	769.8[a]	−79	−19	−40	10.46	0.004	0.2
		169.6	−79	−47	−20			
PFTeDA	713.20	669.60[a]	−79	−17	−44	9.43	0.004	0.08
		319.60	−79	−33	−20			
PFTrDA	663.24	319.8[a]	−62	−30	−18	9.13	0.4	0.4
		369.8	−62	−28	−24			
PFHpA	363.10	319.50[a]	−38	−14	−28	5.24	0.04	0.04
		169.30	−38	−27	−15			
PFHxS	399.10	80.0[a]	−85	−76	−29	5.30	0.004	0.004
		99.10	−85	−53	−10			
PFDA	513	469.6[a]	−51	−16	−36	7.29	0.004	0.004
		269.5	−51	−27	−25			
PFOA	413.2	369.8[a]	−41	−12	−25	6.16	0.04	0.04
		169.2	−41	−25	−21			
PFHpS	449.1	80[a]	−121	−82	−30	6.15	0.02	0.02
		99	−121	−56	−17			
PFBA	213.2	169.2[a]	−46	−11	−21	2.31	0.04	0.04
		97	−46	−24	−11			
PFBuS	299.0	80.0[a]	−167	−71	−13	2.97	0.04	0.04
		99.2	−167	−51	−14			
PFOSA	498.4	78.2[a]	−303	−72	−13	8.18	0.04	0.04
		169.4	−303	−40	−15			
TFMSA	113.2	69.0[a]	−37	−15	−7	2.15	0.04	0.04
		82.2	−37	−29	−5			
$^{13}C_4$-PFOS	503.4	79.7[a]	−88	−15	−40	6.78		
		99.3	−88	−24	−11			
$^{13}C_4$-PFBA	217.4	172.3[a]	−85	−14	−39	2.17		
		59.1	−85	−25	−20			
$^{13}C_2$-PFHxA	315.3	271.0[a]	−99	−48	−15	3.90		
		120.3	−99	−26	−21			
$^{18}O_2$-PFHxS	403.5	84.3[a]	−105	−15	−22	5.20		
		102.8	−105	−29	−11			
$^{13}C_4$-PFOA	417.5	373.1[a]	−68	−19	−24	6.13		
		169.6	−68	−28	−17			

[a]Quantifier ion.

MATERIALS AND METHODS

Chemicals and Instruments. Oil samples were purchased from local markets in Beijing in October−November 2013 and stored at normal atmospheric temperature. LC-MS grade acetonitrile and methanol were obtained from the Merck (Darmstadt, Germany), and HPLC grade formic acid (99.7%) and ammonium acetate (99.5%) were obtained from Dikma Technology Inc. (Richmond, VA, USA). Primary secondary amine (PSA), octadecyl (C_{18}), and graphitized carbon black (GCB) sorbents were obtained from Agela Technologies (Tianjin, China). Ultrapure water was produced using a Milli-Q RC apparatus (Millipore, Bedford, MA, USA).

The purities of most standard PFCs were ≥98%, with a minority of purity ≥92%. PFOS, PFOA, perfluoro-*n*-dodecanoic (PFDoA), perfluoruodecanesulfonic acid (PFDS), perfluoro-*n*-undecanoic acid (PFUdA), perfluoro-*n*-nonanoic acid (PFNA), perfluoro-*n*-hexanoic acid (PFHxA), perfluoro-*n*-hexadecanoic acid (PFHxDA), perfluoro-*n*-tetradecanoic acid (PFTeDA), perfluoro-*n*-tridecanoic acid (PFTrDA), perfluoro-*n*-heptanoic acid (PFHpA), perfluorohexanesulfonic acid (PFHxS), perfluoro-*n*-decanoic acid (PFDA), perfluoro-*n*-heptanesulfonate (PFHpS), perfluoro-*n*-butanoic acid (PFBA), perfluorooctanesulfonamide (PFOSA), sodium perfluoro-1-butanesulfonate (PFBuS), and trifluoromethanesulfonic acid (TFMSA), and isotopically labeled standards, namely, sodium perfluoro-1-[1,2,3,4-$^{13}C_4$]-octanesulfonate ($^{13}C_4$-PFOS), perfluoro-*n*-[1,2,3,4-$^{13}C_4$]-butanoic acid ($^{13}C_4$-PFBA), perfluoro-*n*-[1,2-$^{13}C_2$]-hexanoic acid ($^{13}C_2$-PFHxA), sodium perfluoro-1-hexane-[$^{18}O_2$]-sulfonate

DOI: 10.1021/acs.jafc.5b03903
J. Agric. Food Chem. 2015, 63, 8364−8371

($^{18}O_2$-PFHxS), and perfluoro-*n*-[1,2,3,4-$^{13}C_4$]-octanoic acid ($^{13}C_4$-PFOA), were purchased from Wellington Laboratory (Ontario, Canada). A cocktail solvent containing all 18 PFCs with respective concentrations of 10 μg/mL was prepared by diluting the standards with methanol. Working standard solvents for calibration were freshly prepared with methanol. Isotopic standard working solutions containing $^{13}C_4$-PFOA, $^{13}C_4$-PFOS, $^{13}C_4$-PFBA, $^{13}C_2$-PFHxA, and $^{18}O_2$-PFHxS with respective concentrations of 200 μg/mL were prepared by diluting the ISs with methanol. All solutions were stored at −20 °C.

HPLC Conditions. Chromatographic analyses were conducted using an Agilent series 1200 HPLC system (Agilent, Santa Clara, CA, USA) equipped with a binary pump, column oven, and autosampler. PFCs were separated using an XBridge C_{18} column (150 mm × 2.1 mm × 3.5 μm; Waters, Ireland) at 40 °C, with an injection volume of 5 μL. Mobile phases A (aqueous buffer with 5 mM ammonium acetate and 0.1% formic acid) and B (methanol with 5 mM ammonium acetate and 0.1% formic acid) were used, with a gradient elution of A:B = 40:60 (0−0.5 min), 20:80 (0.5−4 min), 5:95 (4−8 min, held 2 min), and 40:60 (10−13 min, held 7 min) at flow rates of 0.20 (0−0.5 min), 0.30 (0.5−8 min), 0.25 (8−10 min), and 0.20 (10−20 min) mL/min (see Table S1).

Tandem Mass Spectrometer Conditions. Mass spectrometric detection was performed using an API 5000 tandem quadrupole mass spectrometer (Applied Biosystems, Foster City, CA, USA) in negative electrospray ionization mode with multiple-reaction monitoring (MRM). Typical parameters of the electrospray ionization source were as follows: ion spray voltage, − 4500 V; curtain gas pressure (CUR), 35 psi; collision gas (CAD), 4 V; atomization air pressure (GS1), 60 psi; auxiliary gas pressure (GS2), 70 psi; dwell time, 200 ms; resolution Q1, low; resolution Q2, unit. The MRM transitions and collision energy (CE), declustering potential (DP), entrance potential (EP), and collision cell exit potential (CXP) used are summarized in Table 1. All system control, data acquisition, and data analysis were performed using AB Sciex Analyst 1.4.2 software (Applied Bioscience).

Sample Preparation. A homogenized edible oil sample (5 g) was weighed and placed into a 50 mL polypropylene (PP) centrifuge tube. Internal standards (ISs) containing $^{13}C_4$-PFOA, $^{13}C_4$-PFOS, $^{13}C_4$-PFBA, $^{13}C_2$-PFHxA, and $^{18}O_2$-PFHxS (100 μL, 20 μg/L) were spiked to the sample. After equilibrium for 20 min, acetonitrile (10 mL) was added and the tube was shaken vigorously for 3 min and centrifuged for 6 min (6000 rpm and 4 °C). The supernatant was transferred to a 50 mL bottle, and these procedures were performed twice. The combined supernatants were rotoevaporated (15 kPa, 110 rpm, and 30 °C), and the residues were reconstituted with cyclohexane:ethyl acetate (1:1 v/v, 10 mL) solvent for purification by an Accuprep MPS-GPC System (J2 Scientific, Columbia, MO, USA). This system comprised an autosampler, a solvent delivery module, an ultraviolet (UV) detector, a fraction collector, and a GPC column (400 mm × 30 mm) containing 50 g of polymer resin styrene−divinylbenzene Biobead SX-3 (Bio-Rad, Irvine, CA, USA). Ethyl acetate−cyclohexane (1:1, v/v) was used as the mobile phase at a flow rate of 4.7 mL/min. The fraction containing target compounds was collected over 20−60 min in a 250 mL tube. After GPC, the eluate was evaporated to dryness using a rotary evaporator (Heidolph, Schwabach, Germany) at 150 rpm and 30 °C. The residue was reconstituted in methanol (1 mL) and then transferred to a centrifuge tube containing

Table 2. Recoveries of Target PFCs (1 μg/kg) Using Different Extraction Solvents (n = 3)

	acetonitrile		methanol		acetonitrile + 0.1% formic acid	
compounds	average recovery (%)	RSD (%)	average recovery (%)	RSD (%)	average recovery (%)	RSD (%)
PFOS	100	13	44	4	117	30
PFDoA	74	17	40	16	207	42
PFDS	103	17	29	8	145	7
PFUdA	753	17	53	20	186	2
PFNA	98	14	93	23	217	1
PFHxA	121	15	85	48	347	23
PFHxDA	130	14	23	3	51	1
PFTeDA	85	3	46	20	104	23
PFTrDA	87	3	43	12	104	5
PFHpA	112	1	70	32	320	4
PFHxS	107	6	113	19	144	2
PFDA	78	14	39	15	217	18
PFOA	84	6	56	13	303	11
PFHpS	129	9	166	26	183	6
PFBA	112	10	85	13	214	14
PFBuS	103	15	53	3	122	24
PFOSA	103	12	37	8	139	10
TFMSA	103	13	37	6	116	21

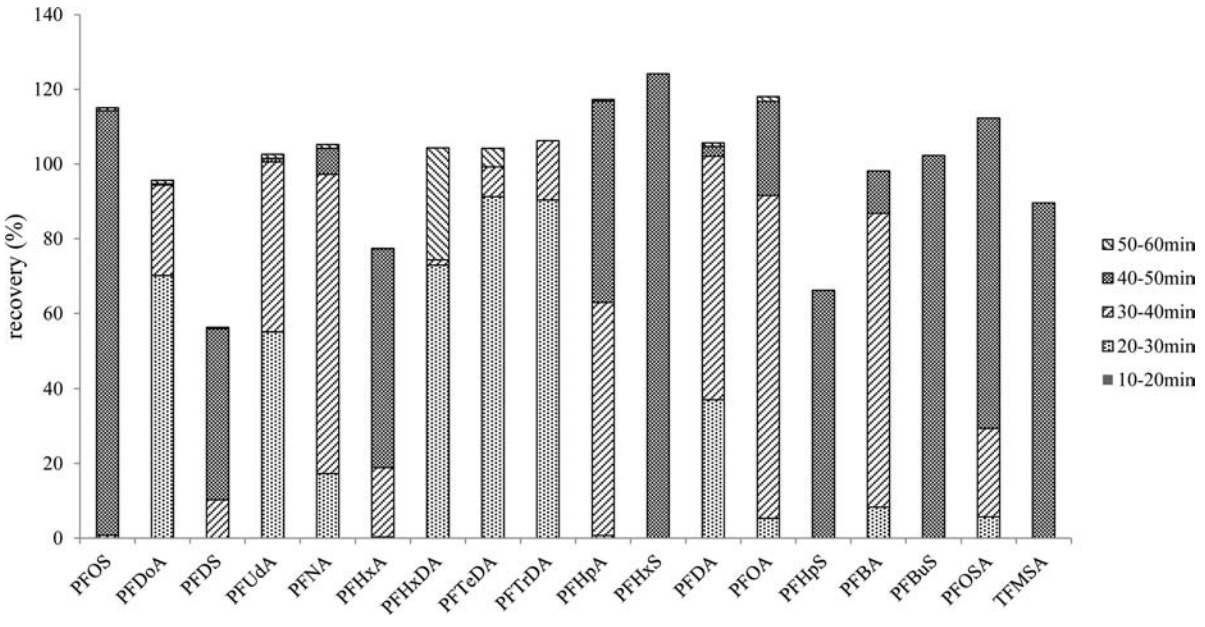

Figure 1. Recoveries of target PFCs at different time periods using GPC with cyclohexane:ethyl acetate (v/v, 1:1) as the mobile phase, at a flow rate of 4.7 mL/min.

DOI: 10.1021/acs.jafc.5b03903
J. Agric. Food Chem. 2015, 63, 8364−8371

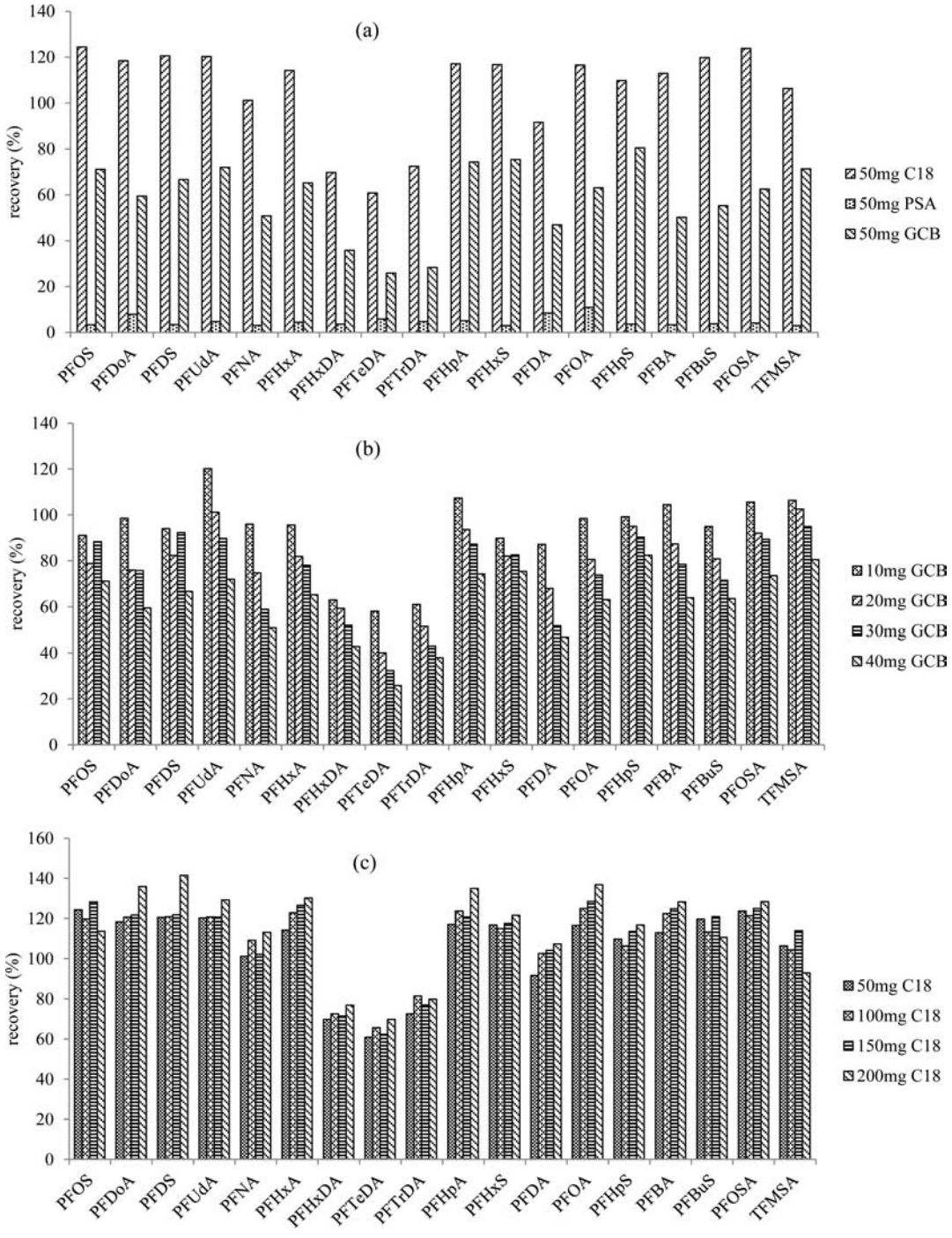

Figure 2. Recoveries of target PFCs spiked at 5 μg/kg in blank edible oil samples using (a) various DSPE sorbents, (b) different amounts of GCB, and (c) different amounts of C_{18}.

C_{18} (150 mg) and GCB (10 mg) as DSPE sorbents. The mixture was shaken for 2 min, centrifuged for 6 min (3000 rpm and 4 °C), and filtered through a 0.22 μm membrane prior to LC-MS/MS analysis.

Quality Assurance and Quality Control. The identification was based on retention time, the transitions, and their ion ratio by using SRMs of PFCs.[30,31] Concentrations of all target PFCs were quantified by the internal standard isotope method. Concentrations of PFOS, PFDS, and PFOSA in edible oil samples were quantified relative to $^{13}C_4$-PFOS; PFDoA, PFUdA, PFNA, PFHxDA, PFTeDA, PFTrDA, PFHpA, PFDA, and PFOA relative to $^{13}C_4$-PFOA; PFHxA relative to $^{13}C_2$-PFHxA; PFHxS, PFHpS, PFBuS, and TFMSA relative to $^{18}O_2$-PFHxS; and PFBA relative to $^{13}C_4$-PFBA. All equipment rinses were carried out with LC-MS grade methanol and pure water before use to avoid sample contamination. Procedural blanks were measured throughout the study, and low levels of PFOS, PFDS, PFHxDA, and PFTeDA (<0.004–0.027 μg/kg) were detected in the procedural blanks (see Table S2). During the sample analysis, a procedural blank and matrix spike were incorporated in the analytical procedures for every batch of 6 samples. The recoveries were evaluated using olive oil samples spiked with target compounds at three concentration levels including 0.1, 1, and 10 μg/kg. Trace amounts of PFOS, PFDS, PFUdA, PFHxDA, and PFTeDA in method blank were controlled at 0.03, 0.01, 0.004, 0.02, and 0.005 μg/kg with an acceptable RSD lower than 7% (n = 5) (see Figure S1), whereas other PFC background contamination was much lower. According to the regulation of ISO 25101 and EPA Method 573, a sample concentration that was 10-fold

DOI: 10.1021/acs.jafc.5b03903
J. Agric. Food Chem. 2015, 63, 8364–8371

Table 3. Matrix Effects (Slope Matrix/Slope Solvent) of Target PFCs in Seven Types of Edible Oil, Calibrated with Corresponding Internal Standards

compounds	blend oil	r^2	soybean oil	r^2	peanut oil	r^2	sunflower seed oil	r^2	corn oil	r^2	sesame oil	r^2	olive oil	r^2
PFOS	1.05	0.983	0.99	0.984	0.86	0.992	0.90	0.985	0.74	0.990	0.85	0.995	0.73	0.992
PFDoA	1.23	0.995	1.01	0.981	0.70	0.984	0.73	0.995	0.91	0.985	0.78	0.997	0.71	0.997
PFDS	0.99	0.992	0.93	0.995	0.70	0.982	0.67	0.984	0.72	0.992	0.72	0.991	0.73	0.993
PFUdA	1.39	0.988	0.98	0.991	0.58	0.987	0.80	0.997	1.86	0.997	0.76	0.995	0.66	0.999
PFNA	1.29	0.983	0.98	0.995	0.59	0.982	0.76	0.994	0.96	0.984	0.9	0.996	0.63	0.994
PFHxA	1.07	0.995	0.88	0.999	0.65	0.988	0.85	0.997	0.91	0.999	0.99	0.997	0.91	0.999
PFHxDA	1.02	0.998	1.09	0.999	0.61	0.985	0.78	0.994	1.24	0.998	0.82	0.995	0.73	0.998
PFTeDA	1.18	0.988	1.00	0.987	0.63	0.988	0.75	0.996	0.76	0.993	0.69	0.991	0.82	0.996
PFTrDA	1.24	1.000	1.26	0.997	1.18	0.986	0.72	0.995	0.85	0.998	0.7	0.999	0.64	0.998
PFHpA	0.97	0.996	0.76	0.997	0.68	0.989	0.71	0.996	1.11	0.986	0.93	0.995	0.72	0.998
PFHxS	1.05	0.999	0.90	0.995	0.76	0.983	0.85	0.992	0.77	0.998	0.98	0.995	0.87	0.996
PFDA	1.16	0.993	0.88	0.994	0.53	0.987	0.77	0.994	0.72	0.996	0.75	0.994	0.71	0.997
PFOA	1.13	0.982	0.74	0.994	0.54	0.989	0.79	0.994	0.86	0.998	0.72	0.993	0.71	0.998
PFHpS	1.05	0.999	0.90	0.996	0.93	0.992	0.85	0.992	0.78	0.998	0.98	0.995	0.87	0.996
PFBA	1.03	0.992	0.89	0.998	0.72	0.989	0.85	0.993	0.91	0.995	0.97	0.994	0.91	0.994
PFBuS	1.08	0.998	0.96	0.990	0.82	0.985	0.87	0.991	0.8	0.994	0.84	0.996	0.72	0.995
PFOSA	1.03	0.995	0.98	0.992	0.63	0.988	0.87	0.993	0.84	0.993	0.86	0.991	0.85	0.996
TFMSA	1.13	0.997	0.98	0.995	0.70	0.982	0.94	0.996	0.86	0.991	0.82	0.992	0.81	0.996

higher than the blank value would be considered to be validated and reported.[32,33] All results were blank corrected by subtracting the mean concentrations of the corresponding compounds in the procedural blanks of the batch. The instrument detection limits (IDLs) were defined as the concentration at a peak with a signal/noise (S/N) ratio of 3. The method detection limits (MDLs) were set to be the mean of the concentration plus three times the standard deviation in the blank samples, in which PFOS, PFDS, PFUdA, PFHxDA, and PFTeDA were detected. The MDLs for the other compounds, which were not detected in blank samples, were set to be the instrumental minimum detectable amounts.[34,35]

RESULTS AND DISCUSSION

Optimization of Extraction Solvent. The most commonly used solvents (acetonitrile and methanol) have been applied with regard to the extraction of PFCs in lipid matrices.[16−18,23] The extraction efficiencies of PFCs from edible oils were evaluated for the solvents. As shown in Table 2, the recoveries of PFCs ranged from 74% to 129% by using acetonitrile as the extraction solvent. However, relatively low extraction efficiencies with high deviation were observed (23−166%) when methanol was used for extraction. Considering that PFCAs contain acidic groups, it is expected that strongly acidic extraction solvents may exhibit relatively high extraction efficiencies.[36−38] Therefore, we also assessed the recoveries of PFCs extracted with acetonitrile containing 0.1% formic acid. The recoveries of PFCs by acidified acetonitrile ranged from 103 to 347% (except for a PFHxDA, 51%), which were much higher than those of extraction by acetonitrile. A similar phenomenon was also observed by Young et al. and Yeung et al. in analysis of PFCs in blood and milk samples.[36,39] The possible reason could be that formic acid extraction would introduce more interference, resulting in high recoveries.[36,39] Therefore, acetonitrile was chosen as the extraction solvent in this study.

Optimization of GPC. GPC is an effective procedure for removing high-molecular-weight interference on the basis of different molecular size from the target compounds, and it is appropriate for both polar and nonpolar compounds. In this study, the purification effect and recoveries of all target PFCs using GPC were evaluated by collecting the eluate at different time periods, and calculated by olive oil matrix-matched standards with ISs used for correction. In the first 10 min, all target PFCs were not detected in the eluate. Only less than 0.3% of PFCs was obtained in the eluates collected between 10 and 20 min; meanwhile, most of the large molecule interference such as fat and proteins eluted out (Figure 1). In the time period between 20 and 50 min, large amounts of PFCs were eluted out with recoveries ranging from 56% to 124%. Finally, the remaining 30% of PFHxDA was collected in eluates between 50 and 60 min. Therefore, about 180 μL of eluates, which discarded most of the lipids and gave satisfactory recoveries, was collected between 20 and 60 min for analysis of PFCs in the present study.

Optimization of DSPE. After purification by GPC, small amounts of pigment and free fatty acids in some oil samples with similar molecular masses as target compounds coeluted with the analytes. DSPE was further conducted after GPC to solve this problem. The cleanup effects of various DSPE sorbents, i.e., PSA, GCB, and C_{18}, were evaluated in a blank olive oil matrix extract, respectively.

As shown in Figure 2a, the recoveries of all target PFCs were only 3−11% when 50 mg of PSA DSPE sorbent was used, suggesting strong electrostatic interactions between PSA and PFCs, although PSA is a common sorbent for removing various polar impurities.[40,41] In comparison, the recoveries of samples using GCB (50 mg) and C_{18} (50 mg) DSPE sorbents were improved to 26−75% and 61−124%, respectively. While relatively low recoveries were found for samples using GCB DSPE sorbents, the extract solution became much clearer in GCB treated samples compared with samples treated with C_{18} DSPE sorbents. The observation is consistent with the fact that GCB sorbents are known to remove hydrophobic interaction-based compounds such as pigments which the C_{18} and PSA cannot completely remove.[42−45]

The amount of DSPE sorbents was further optimized for GCB and C_{18} sorbents, respectively. As shown in Figure 2b, the recoveries of PFCs decreased with the increase of the amount of GCB sorbent from 10 to 50 mg, which probably originated from the absorption enhancing by adding increasing amount of

DOI: 10.1021/acs.jafc.5b03903
J. Agric. Food Chem. 2015, 63, 8364−8371

GCB sorbent with special configuration of hexatomic ring. Thus, only a small amount of GCB sorbent could be applied to the cleanup of oil extracts to get sufficient recoveries of target PFCs. As for C_{18} sorbents, the recoveries of all target PFCs were 61−124%, 66−125%, 62−129%, and 70−142% when 50, 100, 150, and 200 mg of C_{18} sorbent were used, respectively (Figure 2c), thus no obvious variation was found for recoveries of PFCs at different amounts of C_{18}. Although a large amount of C_{18} DSPE sorbents could be applied to the cleanup, the sorbents might not as good as GCB sorbent in removing the pigments in oil samples. As shown in Figure S3, the extract solution became clearer and shallower by using a mixture of GCB and C18 DSPE sorbent compared with that only using C18 DSPE sorbent. To remove most interference in the sample extracts, we used a combination of 150 mg of C_{18} and 10 mg of GCB as the DSPE sorbent in this study, which greatly helped to remove the pigments and other interference in the elutes after GPC fractionations.

Matrix Effects. Matrix effects were determined by comparing slopes of calibration curves (n = 6) constructed by equal concentrations of standard solution and isotopic internal PFCs in pure methanol and different blank matrix extracts (seven kinds of oil). As shown in Table 3, significant suppression matrix effects for all 18 target PFCs were observed in sunflower seed oil, sesame oil, and olive oil samples. The slopes of calibration curves in the matrix extracts relative to those in the solvent ranged from 0.63 to 0.99. Both suppression and enhancement matrix effects were observed for various PFC isomers in the four other types of plant oil, namely, blend oil, soybean oil, peanut oil, and corn oil. The slope ratios of calibration curves between matrix and blank samples ranged from 1.02 to 1.39 for most target PFCs in blend oil except for PFDS and PFHpA, whose slope ratios were 0.99 and 0.97 respectively. In soybean oil matrix samples, most PFCs were suppressed as their slope ratio ranged from 0.74 to 1.0, except for PFDoA (1.01), PFHxDA (1.09), and PFTrDA (1.26). The same phenomenon was also observed in peanut oil: most PFCs were suppressed as their slope ratio ranged from 0.53 to 0.93 except for PFTrDA (1.18). Similarly, most PFCs were also suppressed in corn oil matrix samples as their slope ratio ranged from 0.72 to 0.96 except for PFUdA (1.86), PFHxDA (1.24), and PFHpA (1.11). Therefore, calibration curves were built by spiking blank extracts of the corresponding matrix with ISs to reduce the influence of the matrix for the quantification of samples.

Method Validation. The compound-specific matrix spiking recoveries were determined by spiking high level (1 μg/kg and 10 μg/kg) and lower level (0.1 μg/kg and 0.01 μg/kg) near to those limits of quantitation of the olive oil samples (n = 3). All recoveries for the entire method are shown in Table S3. Mean recoveries of each compound ranged from 60% to 129% with the RSDs no more than 20% at each fortification level for each compound in olive oil, demonstrating good extraction efficiency of the method. As shown in Table 1, the IDLs ranged from 0.004 to 0.4 μg/kg for all target PFCs on the basis of the peak-to-peak S/N (>3). The MDLs of all target PFCs were in the range from 0.004 to 0.4 μg/kg. It should be noted that the MDLs were almost 10 times lower than that obtained for milk by Young et al.,[39] and the results indicate that the method had relatively high sensitivities to the determination of trace concentrations of PFCs in edible oils.

Application to Edible Oils. Six types of edible plant oils with different manufacturing processes and brands purchased

Table 4. Concentrations of PFCs in Six Types of Edible Oil Samples from Markets in Beijing, China, in 2013

	blend oil (n = 9)		soybean oil (n = 6)		peanut oil (n = 3)		sesame oil (n = 6)		corn oil (n = 9)		sunflower seed oil (n = 3)	
compounds	concn range (μg/kg)	detection rate (%)	concn range (μg/kg)	detection rate (%)	concn range (μg/kg)	detection rate (%)	concn range (μg/kg)	detection rate (%)	concn range (μg/kg)	detection rate (%)	concn range (μg/kg)	detection rate (%)
PFNA	ND−4.64	66.7	0.02−0.47	100	ND[a]	0	0.03−1.06	100	ND−0.02	33.3	ND	0
PFHxA	ND−0.06	66.7	ND−0.44	50	0.08−0.10	100	ND−0.49	50	ND−0.45	66.7	0.4−0.5	100
PFHpA	ND	0	ND−0.04	50	ND	0	0.05−0.08	100	ND	0	ND	0
PFDA	ND	0	ND−0.04	50	ND	0	0.16−0.51	100	ND−0.04	66.7	0.4−0.6	100
PFOA	ND−0.43	66.7	0.13−0.16	100	0.18−0.24	100	0.15−0.50	100	0.15−0.17	100	0.40−0.5	100
PFHpS	ND	0	ND−0.02	50	ND	0	0.02−0.03	100	ND	0	ND	0

[a]ND: not detected.

DOI: 10.1021/acs.jafc.5b03903
J. Agric. Food Chem. 2015, 63, 8364−8371

from supermarkets in Beijing were analyzed with the developed method in 2013. As shown in Table 4, the detected PFC concentrations in the oils ranged from below the MDL to 4.64 μg/kg with acceptable RSDs less than 25% (n = 3), and these values are lower than those detected in fish[6,46−48] and eggs[15] and similar to those in milk.[21,49] The PFOA detection rate was the highest (92%) among the 18 PFCs with concentrations from below the MDL to 0.50 μg/kg, and the possible reason could be its widespread use as a processing agent in industrial products; 1.8 μg/kg of PFOA was also detected by Schecter et al. in olive oil.[50] Second to PFOA, the detection rates of PFHxA, PFNA, and PFDA were 67%, 58%, and 50%, respectively. It should be noted that the highest concentration detected was 4.64 μg/kg of PFNA in blend oil, and this is probably due to PFNA not being globally regulated. A similar result was reported by Van et al. in polar-bear liver.[51] PFHpA and PFHpS were detected at rates of 25%, with concentrations below the MDL to 0.50 μg/kg in all six types of edible oils. In general, C_6−C_{10} PFCAs and PFSAs were found extensively in the edible oils, which is similar to the findings reported by Chung et al. for fatty food.[52]

Lili Yang
Fen Jin*
Peng Zhang
Yanxin Zhang
Jian Wang
Hua Shao
Maojun Jin
Shanshan Wang
Lufei Zheng
Jing Wang
Key Laboratory of Agro-product Quality and Safety, Institute of Quality Standards & Testing Technology for Agro-products, Chinese Academy of Agricultural Sciences, Beijing 100081, China

■ ASSOCIATED CONTENT

Supporting Information

The Supporting Information is available free of charge on the ACS Publications website at DOI: 10.1021/acs.jafc.5b03903.

Procedure of gradient elution, procedure blank, recovery, purification efficiency by different DSPE sorbents, graphs of PFCs with remarkable blank value, and PFCs under different gradients (PDF)

■ AUTHOR INFORMATION

Corresponding Author

*Institute of Quality Standards & Testing Technology for Agro-products, Chinese Academy of Agricultural Sciences, Beijing 100081, China. Tel: 010-82106570. E-mail: jinfenbj@163.com.

Funding

Financial support from the National Key Technology R&D Program of China (2012BAD29B03) is gratefully acknowledged.

Notes

The authors declare no competing financial interest.

■ ACKNOWLEDGMENTS

We are grateful to the four anonymous reviewers whose comments and suggestion were very helpful to improve this paper. We also thank Yi Wan from Peking University, China.

■ REFERENCES

(1) Schultz, M. M.; Barofsky, D. F.; Field, J. A. Quantitative determination of fluorinated alkyl substances by large-volume-injection liquid chromatography tandem mass spectrometry-Characterization of municipal wastewaters. *Environ. Sci. Technol.* **2006**, *40*, 289−295.
(2) Yamashita, N.; Kannan, K.; Taniyasu, S.; Horii, Y.; Okazawa, T.; Petrick, G.; Gamo, T. Analysis of perfluorinated acids at parts-per-quadrillion levels in seawater using liquid chromatography-tandem mass spectrometry. *Environ. Sci. Technol.* **2004**, *38*, 5522−5528.
(3) Higgins, C. P.; Field, J. A.; Criddle, C. S.; Luthy, R. G. Quantitative determination of perfluorochemicals in sediments and domestic sludge. *Environ. Sci. Technol.* **2005**, *39*, 3946−3956.
(4) Stock, N. L.; Furdui, V. I.; Muir, D. C.; Mabury, S. A. Perfluoroalkyl contaminants in the Canadian arctic: Evidence of atmospheric transport and local contamination. *Environ. Sci. Technol.* **2007**, *41*, 3529−3536.
(5) Houde, M.; De Silva, A. O.; Muir, D. C. G.; Letcher, R. J. Monitoring of perfluorinated compounds in aquatic biota: An updated review. *Environ. Sci. Technol.* **2011**, *45*, 7962−7973.
(6) Peng, H.; Wei, Q. W.; Wan, Y.; Giesy, J. P.; Li, L. X.; Hu, J. Y. Tissue distribution and maternal transfer of poly- and perfluorinated compounds in Chinese sturgeon (acipenser sinensis): implications for reproductive risk. *Environ. Sci. Technol.* **2010**, *44*, 1868−1874.
(7) Kennedy, G. L.; Butenhoff, J. L.; Olsen, G. W.; O'Connor, J. C.; Seacat, A. M.; Perkins, R. G.; Biegel, L. B.; Murphy, S. R.; Farrar, D. G. The toxicology of perfluorooctanoate. *Crit. Rev. Toxicol.* **2004**, *34*, 351−384.
(8) Andersen, M. E.; Butenhoff, J. L.; Chang, S. C.; Farrar, D. G.; Kennedy, G. L., Jr.; Lau, C.; Olsen, G. W.; Seed, J.; Wallace, K. B. Perfluoroalkyl acids and related chemistries-toxicokinetics and modes of action. *Toxicol. Sci.* **2008**, *102*, 3−14.
(9) Harada, K.; Nakanishi, S.; Sasaki, K.; Furuyama, K.; Nakayama, S.; Saito, N.; Yamakawa, K.; Koizumi, A. Particle size distribution and respiratory deposition estimates of airborne perfluorooctanoate and perfluorooctanesulfonate in Kyoto area, Japan. *Bull. Environ. Contam. Toxicol.* **2006**, *76*, 306−310.
(10) Lau, C.; Anitole, K.; Hodes, C.; Lai, D.; Pfahles-Hutchens, A.; Seed, J. Perfluoroalkyl acids: A review of monitoring and toxicological findings. *Toxicol. Sci.* **2007**, *99*, 366−394.
(11) Berger, U.; Haukas, M. Validation of a screening method based on liquid chromatography coupled to high-resolution mass spectrometry for analysis of perfluoroalkylated substances in biota. *J. Chromatogr. A* **2005**, *1081*, 210−217.
(12) The third unregulated contaminant monitoring rule (UCMR 3): data summary. From http://water.epa.gov/lawsregs/rulesregs/sdwa/ucmr/upload/UCMR3_Data-Summary_June-2015_508.pdf.
(13) Quinones, O.; Snyder, S. A. Occurrence of perfluoroalkyl carboxylates and sulfonates in drinking water utilities and related waters from the United States. *Environ. Sci. Technol.* **2009**, *43*, 9089−9095.
(14) Gellrich, V.; Brunn, H.; Stahl, T. Perfluoroalkyl and polyfluoroalkyl substances (PFASs) in mineral water and tap water. *J. Environ. Sci. Health, Part A: Toxic/Hazard. Subst. Environ. Eng.* **2013**, *48*, 129−135.
(15) Wang, Y.; Yeung, L. W. Y.; Yamashita, N.; Taniyasu, S.; So, M. K.; Murphy, M. B.; Lam, P. K. S. Perfluorooctane sulfonate(PFOS) and related fluorochemicals in chicken egg in China. *Chin. Sci. Bull.* **2008**, *53*, 501−507.
(16) Wang, J. M.; Shi, Y. L.; Pan, Y. Y.; Cai, Y. Q. Perfluorooctane sulfonate (PFOS) and other fluorochemicals in viscera and muscle of farmed pigs and chickens in Beijing, China. *Chin. Sci. Bull.* **2010**, *55*, 3550−3555.
(17) Sinclair, E.; Mayack, D. T.; Roblee, K.; Yamashita, N.; Kannan, K. Occurrence of perfluoroalkyl surfactants in water, fish, and birds from New York State. *Arch. Environ. Contam. Toxicol.* **2006**, *50*, 398−410.
(18) Schuetze, A.; Heberer, T.; Effkemann, S.; Juergensen, S. Occurrence and assessment of perfluorinated chemicals in wild fish from Northern Germany. *Chemosphere* **2010**, *78*, 647−652.
(19) Chen, C. L.; Wang, T. Y.; Naile, J. E.; Li, J.; Geng, J.; Bi, C. C.; Hu, W. Y.; Zhang, X.; Khim, J. S.; Feng, Y.; Giesy, J. P.; Lu, Y.

DOI: 10.1021/acs.jafc.5b03903
J. Agric. Food Chem. 2015, 63, 8364−8371

Perfluorinated compounds in aquatic products from Bohai Bay, Tianjin, China. *Hum. Ecol. Risk Assess.* **2011**, *17*, 1279−1291.
(20) Tittlemier, S. A.; Pepper, K.; Edwards, L. Concentrations of perfluorooctanesulfonamides in Canadian total diet study composite food samples collected between 1992 and 2004. *J. Agric. Food Chem.* **2006**, *54*, 8385−8389.
(21) Still, M.; Schlummer, M.; Gruber, L.; Fiedler, D.; Wolz, G. Impact of industrial production and packaging processes on the concentration of per- and polyfluorinated compounds in milk and dairy products. *J. Agric. Food Chem.* **2013**, *61*, 9052−9062.
(22) Begley, T. H.; White, K.; Honigfort, P.; Twaroski, M. L.; Neches, R.; Walker, R. A. Perfluorochemicals: Potential sources of and migration from food packaging. *Food Addit. Contam.* **2005**, *22*, 1023−1031.
(23) Tang, C. M.; Tan, J. H.; Wang, C. W.; Peng, X. Z. Determination of perfluorooctanoic acid and perfluorooctane sulfonate in cooking oil and pig adipose tissue using reversed-phase liquid-liquid extraction followed by high performance liquid chromatography tandem mass spectrometry. *J. Chromatogr A* **2014**, *1341*, 50−56.
(24) Ballesteros-Gomez, A.; Rubio, S.; van Leeuwen, S. Tetrahydrofuran-water extraction, in-line clean-up and selective liquid chromatography/tandem mass spectrometry for the quantitation of perfluorinated compounds in food at the low pictogram per gram level. *J. Chromatogr. A* **2010**, *1217*, 5913−5921.
(25) Noorlander, C. W.; van Leeuwen, S. P. J.; te Biesebeek, J. D.; Mengelers, M. J. B.; Zeilmaker, M. J. Levels of perfluorinated compounds in food and dietary intake of PFOS and PFOA in the Netherland. *J. Agric. Food Chem.* **2011**, *59*, 7496−7505.
(26) Norli, H. R.; Christiansen, A.; Deribe, E. Application of QuEChERS method for extraction of selected persistent organic pollutants in fish tissues and analysis by gas chromatography mass spectrometry. *J. Chromatogr. A* **2011**, *1218*, 7234−7241.
(27) He, Z. Y.; Wang, L.; Peng, Y.; Luo, M.; Wang, W. W.; Liu, X. W. Multiresidue analysis of over 200 pesticides in cereals using a QuEChERS and gas chromatography-tandem mass spectrometry-based method. *Food Chem.* **2015**, *169*, 372−380.
(28) Kang, J.; Fan, C. L.; Chang, Q. Y.; Bu, M. N.; Zhao, Z. Y.; Wang, W.; Pang, G. F. Simultaneous determination of multi-class veterinary drug residues in different muscle tissues by modified QuEChERS combined with HPLC-MS/MS. *Anal. Methods* **2014**, *6*, 6285−6293.
(29) Abdallah, H.; Arnaudguilhem, C.; Jaber, F.; Lobinski, R. Multiresidue analysis of 22 sulfonamides and their metabolites in animal tissues using quick, easy, cheap, effective, rugged, and safe extraction and high resolution mass spectrometry (hybrid linear ion trap-Orbitrap). *J. Chromatogr. A* **2014**, *1355*, 61−72.
(30) Stephanson, N.; Sandqvist, S.; Lambert, M. S.; Beck, O. Method Validation and application of a liquid chromatography-tandem mass spectrometry method for drugs of abuse testing in exhaled breath. *J. Chromatogr. B: Anal. Technol. Biomed. Life Sci.* **2015**, *985*, 189−196.
(31) Niu, Y. M.; Zhang, J.; Wu, Y. N.; Shao, B. Simultaneous determination of bisphenol A and alkylphenol in plant oil by gel permeation chromatography and isotopic dilution liquid chromatography-tandem mass spectrometry. *J. Agric. Food Chem.* **2011**, *1218*, 5248−5253.
(32) *ISO 25101: Water quality—determination of perfluorooctanesulfonate (PFOS) and perfluorooctanoate (PFOA)—method for unfiltered samples using solid phase extraction and liquid chromatography/mass spectrometry*; International Standard Organization, 2009.
(33) *US EPA Method 573: Determination of selected perfuorinated alkyl acids in chromatography/tandem mass spectrometry (LC/MS/MS)*; United States Environmental Protection Agency, 2009.
(34) Zhang, K.; Wan, Y.; Giesy, J. P.; Lam, M. H. W.; Wiseman, S.; Jones, P. D.; Hu, J. Y. Tissue concentration of polybrominated compounds in Chinese sturgeon (Acipenser sinensis): origin, hepatic sequestration, and maternal transfer. *Environ. Sci. Technol.* **2010**, *44*, 5781−5786.
(35) Wan, Y.; Hu, J. Y.; Zhang, K.; An, L. H. Trophodynamics of polybrominated diphenyl ethers in the -arine food web of Bohai bay, North China. *Environ. Sci. Technol.* **2008**, *42*, 1078−1083.
(36) Yeung, L. W. Y.; Taniyasu, S.; Kannan, K.; Xu, D. Z. Y.; Guruge, K. S.; Lam, P. K. S.; Yamashita, N. An analytical method for the determination of perfluorinated compounds in whole blood using acetonitrile and solid phase extraction methods. *J. Chromatogr. A* **2009**, *1216*, 4950−4956.
(37) Tao, L.; Kannan, K.; Wong, C. M.; Arcaro, K. F.; Butenhoff, J. L. Perflourinated compounds in human milk from Massachusetts, U. S. A. *Environ. Sci. Technol.* **2008**, *42* (8), 3096−3101.
(38) Tao, L.; Ma, J.; Kunisue, T.; Libelo, E. L.; Tanabe, S.; Kannan, K. Perfluorinated compounds in human breast milk from several Asian countries and in infant formula and dairy milk from the United States. *Environ. Sci. Technol.* **2008**, *42* (22), 8597−8602.
(39) Young, W. M.; South, P.; Begley, T. H.; Diachenko, G. W.; Noonan, G. O. Determination of perfluorochemicals in cow's milk using liquid chromatography-tandem mass spectrometry. *J. Agric. Food Chem.* **2012**, *60*, 1652−1658.
(40) Wilkowska, A.; Biziuk, M. Determination of pesticide residues in food matrices using the QuEChERS methodology. *Food Chem.* **2011**, *125*, 803−812.
(41) Lehotay, S. J.; Mastovska, K.; Yun, S. J. Evaluation of two fast and easy methods for pesticide residue analysis in fatty food matrixes. *J. AOAC Int.* **2005**, *88*, 630−638.
(42) Li, C. M.; Jin, F.; Yu, Z. Y.; Qi, Y. M.; Shi, X. M.; Wang, M.; Shao, H.; Jin, M. J.; Wang, J.; Yang, M. Q. Rapid determination of chlormequat in meat by dispersive solid-phase extraction and hydrophilic interaction liquid chromatography (HILIC)-electrospray tandem mass spectrometry. *J. Agric. Food Chem.* **2012**, *60*, 6816−6822.
(43) Paz, M.; Correia-Sá, L.; Becker, H.; Longhinotti, E.; Domingues, V. F.; Delerue-Matos, C. Validation of QuECHERS method for organochlorine pesticides analysis in tamarined (Tamarindus indica) products: Peel, fruit and commercial pulp. *Food Control* **2015**, *54*, 374−382.
(44) Molina-Ruiz, J. M.; Cieslik, E.; Walkowska, I. Optimization of the QuEChERS method for determination of pesticide residues in chicken liver samples by gas chromatography-mass spectrometry. *Food Anal. Method* **2015**, *8*, 898−906.
(45) Walorczyk, S. Validation and use of a QuEChERS-based gas chromatographic-tandem mass spectrometric method for multiresidue pesticide analysis in blackcurrants including studies of matrix effects and estimation of measurement uncertainty. *Talanta* **2014**, *120*, 106−113.
(46) Stahl, L. L.; Snyder, B. D.; Olsen, A. R.; Kincaid, T. M.; Wathen, J. B.; McCarty, H. B. Perfluorinated compounds in fish from US urban rivers and the Great Lakes. *Sci. Total Environ.* **2014**, *499*, 185−195.
(47) Squadrone, S.; Ciccotelli, V.; Favaro, L.; Scanzio, T.; Prearo, M.; Abete, M. C. Fish consumption as a source of human exposure to perfluorinated alkyl substances in Italy: Analysis of two edible fish from Lake Maggiore. *Chemosphere* **2014**, *114*, 181−186.
(48) Shi, Y. L.; Wang, J. M.; Pan, Y. Y.; Cai, Y. Q. Tissue distribution of perfluorinated compounds in farmed freshwater fish and human exposure by consumption. *Environ. Toxicol. Chem.* **2012**, *31*, 717−723.
(49) Capriotti, A. L.; Cavaliere, C.; Cavazzini, A.; Foglia, P.; Lagana, A.; Piovesana, S.; Samperi, R. High performance liquid chromatography tandem mass spectrometry determination of perfluorinated acids in cow milk. *J. Chromatogr. A* **2013**, *1319*, 72−79.
(50) Schecter, A.; Colacino, J.; Haffner, D.; Patel, K.; Opel, M.; Papke, O.; Birnbaum, L. Perfluorinated compounds, polychlorinated biphenyls, and organochlorine pesticide contamination in composite food samples from Dallas, Texas, USA. *Environ. Health. Persp.* **2010**, *118*, 796−802.
(51) Van de Vijver, K. I.; Hoff, P.; Das, K.; Brasseur, S.; Van Dongen, W.; Esmans, E.; Reijnders, P.; Blust, R.; De Coen, W. Tissue distribution of perfluorinated chemicals in harbor seals (Phoca vimtina) from the Dutch Wadden seap. *Environ. Sci. Technol.* **2005**, *39*, 6978−6984.
(52) Chung, S. W. C.; Lam, C. H. Development of an ultra-performance liquid chromatography−tandem mass spectrometry method for the analysis of perfluorinated compounds in fish and fatty food. *J. Agric. Food Chem.* **2014**, *62*, 5805−5811.

DOI: 10.1021/acs.jafc.5b03903
J. Agric. Food Chem. 2015, 63, 8364−8371

δ^{15}N values of egg albumen as hens can roam and forage freely in pasture and soils, picking up insects, seeds, and grass. These dietary components also take on higher δ^{15}N values due to the ongoing deposition of poultry manure and the use of these nutrients for pasture growth over time. When analyzed for stable isotopes, these higher protein dietary inputs and nutrient transfers from poultry manure may confound eggs sampled from conventional free range farming systems with eggs from organic farming systems by increasing the overall δ^{15}N values, giving δ^{15}N values similar to those of organic eggs. However, when the δ^{15}N values of organic eggs are lower than expected, it is usually due to a nonorganic diet, unless the hen's diet is composed mainly of N-fixing plants (i.e., lucerne, alfalfa, or peas) or plants grown on green composts used to fertilize feed crops.

New Zealand organic eggs sampled in a previous study[7] showed a wide range of δ^{15}N values suggesting the likelihood of fraudulently labeled eggs. Several organic egg producers were found to be supplying organic eggs with much lower δ^{15}N values than other organic farms. Their isotope values were similar to those of eggs from conventional farming regimens, suggesting that the hens were not receiving an organic diet and/or they were not free ranging or had very limited outdoor access.

Organic farming practices worldwide aim to enhance biodiversity, biological cycles, and soil biological activity to achieve economically and ecologically sustainable systems. As yet there are no recognized scientific testing standards to distinguish free range and organic laid eggs (with outdoor access) from caged or barn laid eggs (indoor access only).[11] Evaluation frameworks by organic bodies use compliance and auditing systems to ensure eggs and commercial feed comply with regulations.[9] However, with the high price of compliance systems, some producers and distributors self-regulate and do not adopt any national certification standards, leaving the opportunity for misinterpretation of regulations or mislabeling to arise. Although past verification of egg products using stable isotopes[7] or carotenoid profiling[8,10] has been shown to identify cases that do not entirely fit within normal data sets, these can be more rigorously evaluated if they meet certain specifications. This screening potential holds great promise for the egg industry, especially if it can be shown to be applicable on an international, country, or regional scale.[8−10,12]

We investigate for the first time a large training set of poultry feed and corresponding egg albumen from barn, free range, and organic hens collected in The Netherlands in 2009 to understand isotopic feed variation, trophic transfer to egg albumen and provide guidelines for egg verification specific to Dutch farming systems. Data from a previous study of New Zealand eggs[7] and critical feed ingredients[4] are compared to new isotope data of eggs acquired in 2010 and 2014 to investigate if any significant feeding changes have occurred during this time. Finally, stable isotope egg profiles from barn, free range, and organic farmed egg albumen from both countries are compared to determine if isotope ranges used to verify and authenticate country-specific farming regimens are internationally applicable.

MATERIALS AND METHODS

Dutch Training Set. A training set of eggs and corresponding feed were collected from 49 Dutch layer hen farms in May 2009. Organic (24), free range (12), and barn (13) farms were selected with the help of the Dutch poultry and egg product board and the Dutch organic produce certification body SKAL. The selection was balanced with regard to sampling a range of geographical locations (north, east, south, west) and farm size per production system. Organic farm groups consisted of farm sizes of <5000, 5000−10000, and 10000−20000 hens; the conventional farm groups consisted of farm sizes of 10000−20000, 20000−50000, and >50000 hens. The differences in categories between organic and conventional productions reflect the particular farm populations; organic farms are usually smaller sized than conventional farms. Information on the breed and age of the laying hen flock, as well feed samples (type and supplier), was collected along with eggs. Fresh eggs and feed were stored at 4 °C until analysis.

New Zealand Test Set. Thirty different brands of (7 caged, 7 barn, 12 free range, and 4 organic) eggs were purchased from local poultry farmers and several grocery stores in Lower Hutt, New Zealand, in 2010. They were integrated with published results from 18 brands of eggs (5 caged, 3 barn, 6 free range, and 4 organic) sampled in 2008[7] to monitor changes within the egg industry during this time. A further 4 brands of organic eggs were sampled in 2014 to provide a final check on organic labeling practices. The eggs represented a range of producers from small cottage industries with 20−30 hens to large industrial operations with 20000−50000 hens.

Sample Preparation and Analyses. Nine eggs from each farm or egg brand were sampled for isotope analyses. Albumen from three eggs was separated from yolks, pooled in triplicate to avoid single anomalous results (i.e., if a particular hen was less free ranging than others), and freeze-dried. Egg albumen and feed samples were homogenized, ground, and weighed in duplicate. Approximately 1.5 mg of albumen and 3−10 mg of feed were transferred into 6 × 4 mm tin capsules. Carbon and nitrogen content and isotopic composition of Dutch and New Zealand egg albumen and feed samples were analyzed at the GNS Science Stable Isotope Laboratory, Lower Hutt, New Zealand, using a Europa Geo 20/20 (PDZ Europa Ltd. U.K.) isotope ratio mass spectrometer, interfaced to an ANCA-SL elemental analyzer (PDZ Europa Ltd. U.K.) in continuous flow mode (EA-IRMS). The carbon dioxide gas was resolved from nitrogen gas using gas chromatographic separation on a column at 65 °C and analyzed simultaneously for isotopic abundance as well as total organic carbon and nitrogen. International and working reference standards (NIST-N1, IAEA-CH_6, leucine, wheat flour, and beet sugar) and blanks were included during each run for calibration.

Isotopic ratios ($^{13}C/^{12}C$ and $^{15}N/^{14}N$) are expressed as isotopic deviations δ defined as

$$\delta\ (‰) = \frac{R_S - R_{Ref}}{R_{Ref}} \times 1000$$

where R_s is the isotopic ratio measured for the sample and R_{ref} that of the international standards. The δ^{13}C value is relative to the international Vienna Pee Dee Belemnite (VPDB) standard, and the δ^{15}N value is relative to atmospheric air. Results are expressed in δ (‰) versus the specific reference. Analytical precision (standard deviation, SD) of standards and samples are within ±0.1‰ for carbon and ±0.2‰ for nitrogen (1σ).

Statistical Analysis. Nitrogen and carbon isotopic data of Dutch and New Zealand eggs were subjected to multifactor analysis of variance (MANOVA; including country, farming regimen, farm, replicate analyses, year factors) to investigate the effects of two or more independent variables for significant effects on two or more metric dependents (in this case, nitrogen and carbon isotope ratio values). It allows a joint analysis of each dependent rather than requiring several univariate tests to be performed, thus avoiding multiple testing risks. Fisher's least significant difference (LSD) tests were carried out to determine significant differences among groups using XLSTAT 2014.3.02 (Addinsoft, Paris, France). A significance level of $p < 0.05$ was used throughout the study.

RESULTS

Dutch Poultry Feed. Feeds from 49 poultry farms were investigated using carbon and nitrogen isotopes. Values ranged

DOI: 10.1021/acs.jafc.5b01975
J. Agric. Food Chem. 2015, 63, 8372−8380

from −16.3 to −22.3‰ for δ^{13}C and from 1.5 to 4.0‰ for δ^{15}N. The 24 organic poultry feeds were completely distinguishable from 13 barn (conventional) feeds on the basis of δ^{15}N values (Figure 1). Organic poultry feeds had δ^{15}N values ranging between 2.8 and 4.0‰, whereas barn feeds (including omega-3-enriched feed) had δ^{15}N values ranging from 1.5 to 2.7‰. Free range feeds are expected to be similar to barn feeds as they are also grown conventionally. However, the free range feeds in this study had δ^{15}N values that spanned the range of both barn and organic farm feeds, ranging from 1.8 to 3.8‰, with 5 of 12 free range poultry feeds (FR2, FR 3, FR4, FR5, FR7) having δ^{15}N values >2.7‰. Poor isotopic separation between some free range and organic feeds suggested that some free range farms may be using organic feeds, even though their farming system is not labeled organic, and/or there was some other significant source of ^{15}N-enriched protein (plant, animal, or inorganic supplement) component included in feeds.[5,13−18]

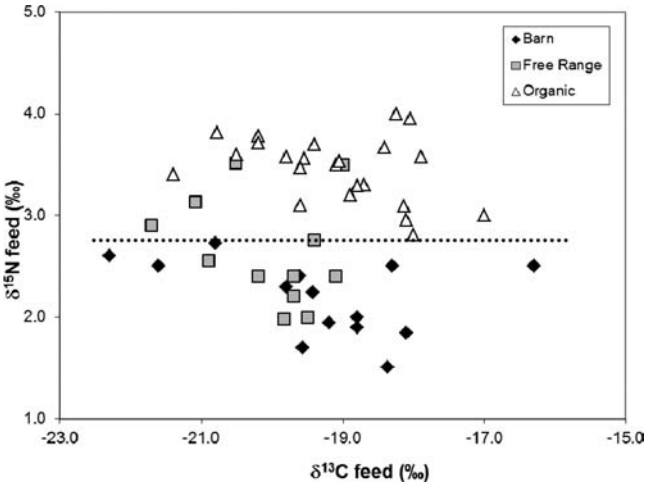

Figure 1. Distribution of carbon and nitrogen isotopes of feeds across different Dutch farming regimens.

Carbon isotopes gave an indication of the level of C_3 and C_4 feed components,[18] with more positive δ^{13}C values (< −18‰) suggesting a higher proportion of C_4 plants (i.e., maize) in the feed, where

$$\delta^{13}\text{C feed} = X(\delta^{13}\text{C } C_3 \text{ plants} + \text{additives}) + Y(\delta^{13}\text{C } C_4 \text{ plants})$$

$X + Y = 1$, δ^{13}C C_3 plants varies from −25 to −28‰, and δ^{13}C C_4 plants varies from −10 to −12‰. The feeds all showed a wide range of δ^{13}C values from −16.3 to −22.3‰, and using the above mixing model suggests feeds comprise between 20 and 70% C_4 plants (i.e., maize). Although barn feeds had the widest range of values of the three groups of feed, barn and free range feeds are farmed conventionally, suggesting the δ^{13}C isotopic feed differences are mostly determined by different combinations of feed. When feeds had more positive δ^{13}C values, it is likely that there was a higher C_4 plant component (i.e., maize) contained in the feed and a lower reliance on C_3 plant components (i.e., wheat and soy),[18,19] although the most positive feed δ^{13}C value was an omega-3-enriched barn feed at −16.3‰. Given that another omega-3-enriched feed had a δ^{13}C value of −20.2‰, the variation in δ^{13}C values is most likely due to a variation in C3 and C4 plant feed components than the dominance of specific omega-3-enriched additives. The δ^{13}C value of conventional and organic feeds will most likely vary seasonally as the use of C_3 and C_4 plants in poultry feed is usually indexed to the price of these feed components in any one year. Barn and free range eggs sell for lower prices than organic eggs and are likely to be produced usung the cheapest ingredients obtainable at the time while retaining a balanced diet.

Dutch Egg Albumen. The carbon and nitrogen isotope values of egg whites from 49 farms (13 barn, including 2 omega-3-enriched egg farms, 12 free range, and 24 organic farms) were investigated. Values ranged from −22.5 to −17.3‰ for δ^{13}C and from 3.4 to 6.2‰ for δ^{15}N (Figure 2; Table 1). Isotopic discrimination between organic and barn egg whites was feasible using δ^{15}N values, although discrimination between all three groups (organic, barn, and free range egg whites) or between free range and organic eggs was not clear (Table 1).

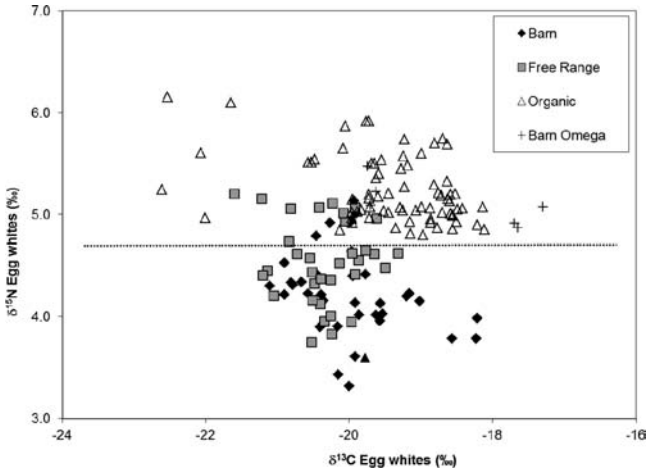

Figure 2. Distribution of carbon and nitrogen isotopes of egg whites across different Dutch farming regimens (including three composite samples measured from 49 different farms).

Table 1. Comparison of δ^{15}N and δ^{13}C Values of Dutch Poultry Feed and Egg Whites from 49 Farms Including 3 Farming Regimens (Mean ± SD)[a]

	farm type		
	barn (n = 13)	free range (n = 12)	organic (n = 24)
δ^{15}N feed	2.2 ± 0.4	2.7 ± 0.7	3.4 ± 0.4
δ^{13}C feed	−19.4 ± 1.6	−20.0 ± 1.0	−19.1 ± 1.1
δ^{15}N egg whites	4.3 ± 0.5^{B}	4.5 ± 0.4^{B}	5.3 ± 0.3^{A}
δ^{13}C egg whites	−19.8 ± 0.9^{A}	−20.3 ± 0.4^{B}	−19.5 ± 0.9^{A}

[a]Values with different letters in a row are significantly different (MANOVA, Fisher LSD test P < 0.05).

A histogram was constructed to demonstrate the frequency distribution of Dutch egg white δ^{15}N values from different farming regimens (Figure 3). All Dutch organic egg whites tested in this study had δ^{15}N values >4.8‰. This contrasted with barn and free range egg whites, for which the majority had δ^{15}N values below 4.8‰, apart from four barn and three free range farms, which had slightly higher values ranging between 4.8 and 5.2‰. Higher δ^{15}N values in egg whites from the three

DOI: 10.1021/acs.jafc.5b01975
J. Agric. Food Chem. 2015, 63, 8372−8380

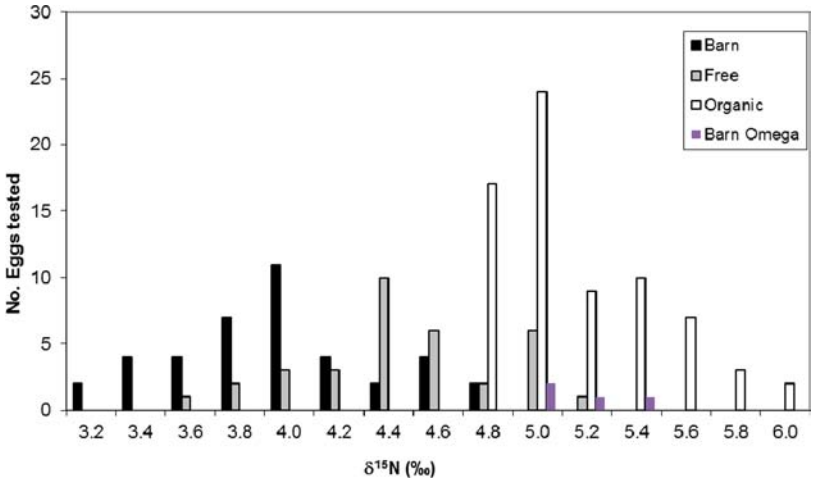

Figure 3. Frequency distribution of nitrogen isotopes of egg whites across different Dutch farming regimens.

free range farms may be due to use of organic feeds, increased ^{15}N from foraging in manured fields, or some other higher protein feed supplement not usually included in conventional feeds. The wide range of free range egg $\delta^{15}N$ values (from 3.6 to 5.2 ‰) may indicate poultry feed composition differences, but, on the basis of feedback from farmers, would more likely indicate that some hens are experiencing more opportunity to range freely than others.

Two barn farms supplemented their feed with omega-3 products to produce omega-3-enriched eggs. These egg whites also had a tight range of $\delta^{15}N$ values (ca. 5.1‰), although in this training set, only two farms (six composites of three eggs) were sampled. These values are above the usual range for barn-raised eggs possibly due to the added omega-3 supplement, which is usually derived from flaxseed or fish oil (increased ^{15}N from protein). However, their corresponding feeds do not indicate any noticeable enrichment in ^{15}N ($\delta^{15}N$ values of feeds for hens laying omega-3 eggs were 2.5 and 2.4‰, respectively) values expected with fish oil, so either there is a further omega-3 supplement included in their diet that was not tested or these hens are acquiring enriched dietary nitrogen from an unknown source, not typically used in conventional feeds.[7] The inclusion of barn omega-3 eggs in the data set (Table 1) skews the barn egg white $\delta^{15}N$ values from 4‰ (without omega-3 eggs) to 4.3‰ (with omega-3 eggs), also providing a higher SD than the other farming regimens.

It was not possible to discriminate between farming regimens on the basis of $\delta^{13}C$ values alone. Barn and free range egg whites had a narrower range of $\delta^{13}C$ values than organic egg whites. A large majority of organic egg whites had more positive $\delta^{13}C$ values than barn and free range egg whites due to a larger maize (C4) component in the feeds. Maize is a commonly grown organic crop and is frequently diverted into animal feeds. Two organic farms had egg whites with significantly more negative $\delta^{13}C$ values than all other samples. The hens that laid these eggs may have had a higher proportion of C3 components in their feed (i.e., wheat or soybeans) or significant access to fresh vegetation (grass or other green crops).[5,7]

Trophic effects (TE) or $\Delta^{15}N$ (egg−feed) values were examined across different Dutch farming regimens (Figures 4 and 5) to investigate differences between feeds and feeding regimens on the resultant egg products from each farm. Barn, free range, and organic raised eggs have an average TE of 2.1, 1.9, and 1.8‰, respectively (Table 1), consistent with strict

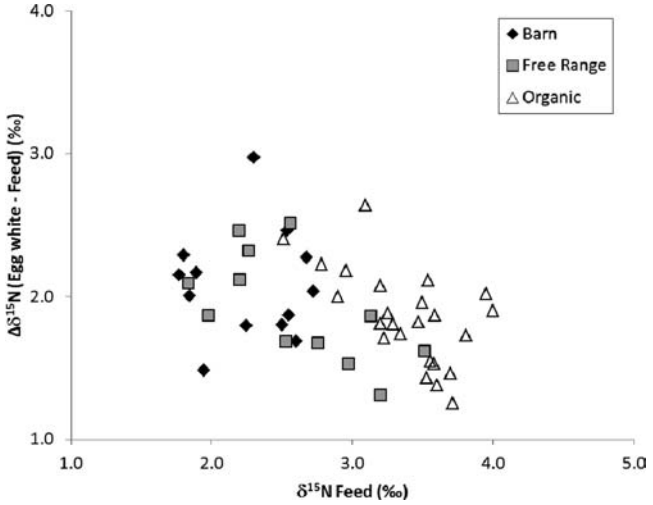

Figure 4. Trophic effect between Dutch poultry feeds and egg whites across different farming regimens.

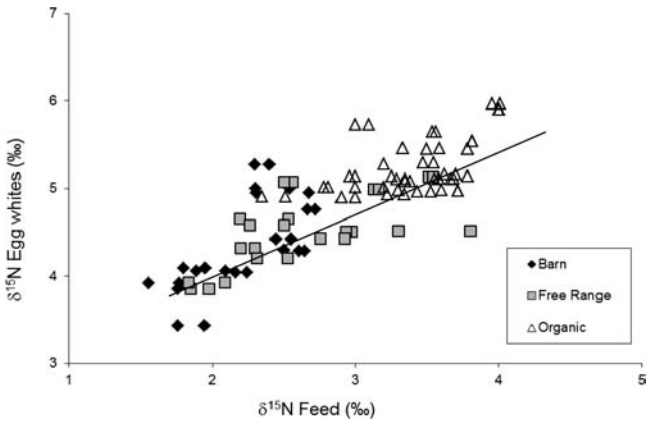

Figure 5. Isotopic correlation between $\delta^{15}N$ values feeding regimen (excluding omega-3 eggs) of Dutch egg whites where $y = 0.71x + 2.77$, $r^2 = 0.66$.

herbivores, which have TE values <2‰.[20−22] The slightly elevated TE in barn-raised eggs (from farm size E, Table 2) is due to the skew from the two barn omega-3 egg farms, which have TEs of 2.5 and 2.8‰, respectively. When the omega-3 egg data are removed, barn eggs have an average TE of 2.0‰.

DOI: 10.1021/acs.jafc.5b01975
J. Agric. Food Chem. 2015, 63, 8372−8380

Table 2. Trophic Effect Δ^{15}N(Egg−Feed) of Barn, Free Range, and Organic Farms from The Netherlands[a]

	farm size[a]					
farm type	A	B	C	D	E	farm type av (SD)
barn			2.3	1.6	2.1	
			1.8	2.6	1.8	
			1.5	2.1	2.1	
			2.6	2.2	2.5[b]	
				1.7	2.8[b]	
av			2.1	2.0	2.3	2.1 (0.4)
free range			1.6	1.3	1.6	
			1.6	1.9	1.4	
			2.6	2	2.3	
			2	2.2	1.9	
av			2.0	1.9	1.8	1.9 (0.4)
organic	1.5	1.3	1.5			
	1.5	1.6	1.8			
	1.7	2	2.7			
		1.9	1.8			
		1.9	1.8			
		2	2.1			
		1.7	2			
		1.9	1.8			
		2.4	1.5			
		1.6	1.9			
		2.2				
av	1.6	1.9	1.9			1.8 (0.3)

[a]Farm size: A, <5000 hens; B, 5000−10000 hens; C, 10000−20000 hens; D, 20000−50000 hens; E >50000 hens. [b]Omega-3 eggs.

Higher TE values (TE > 2‰) in omega-3 eggs may be due to added dietary omega-3-derived protein (such as algae or flax oil), rather than foraged worms and insects, which would contribute only a fraction of the daily protein intake.

Elevated TE values occur in all farming regimens (Table 2), although 60% of farms producing barn-raised eggs had a TE > 2‰, whereas free range and organic farms only had 25 and 17%, respectively. Higher TE may be caused by cannibalism, which can occur more frequently in barn-raised poultry due to their enclosed habitat, lack of outside foraging opportunities, and the obvious lack of animal protein in their diet. In this study, cannibalism is a more plausible explanation for higher TEs than the inclusion of added animal protein in feed due to strict regulations around MBM in European (EU) animal feeds. A meat product ban in EU poultry feed was instigated in the mid-1990s due to the bovine spongiform encephalopathy (BSE) or "mad cow disease" crisis in Europe, when more than 200 people (mainly in the UK) died of Creutzfeldt−Jacob disease.

It is also interesting to note that the dietary feed difference of 1.2‰ between average δ^{15}N (organic-barn feed) is almost fully retained in the egg whites, as the average δ^{15}N (organic-barn egg whites) is 1.0‰. On the basis of these similarities between TEs, it is possible to confirm δ^{15}N values of egg whites from its corresponding feed (excluding omega-3 feeds, Figure 5).

New Zealand Eggs. Egg whites from four egg farming regimens studied in New Zealand in 2008[7] were compared with a new suite of eggs collected in New Zealand in 2010 and 2014 to monitor changes of egg white δ^{15}N values. The previous 2008 study suggested that some hens producing free range and organic eggs had diets that were no different from those of cage or barn hens on the basis of δ^{15}N values, and the consumer was being misled. These conclusions were based on the small (1.4‰) difference between δ^{15}N (average cage-average organic) egg values, although cage and organic egg farming regimens had much bigger SDs (Table 3).

An evaluation of eggs from 2010 showed the difference between mean cage and organic eggs δ^{15}N values had increased only slightly from 1.4‰ (in 2008) to 1.6‰ (in 2010, Table 3). However, a stepwise change in feed composition had occurred over this time, and each farming regimen was more enriched relative to their 2008 mean values (up to 1.2‰ for caged eggs, 1.7‰ for barn eggs, 0.1‰ for free range eggs, and 1.3‰ for organic eggs; Table 3; Figure 6), reflecting a significant dietary composition shift of New Zealand poultry feeds.

In 2008, New Zealand poultry feeds would have consisted of mostly plant-derived products (similar to The Netherlands), yet by 2010 this study shows the isotopic composition of New Zealand eggs from cage, barn, and organic hens had both higher δ^{15}N and δ^{13}C values than those from 2008 due to a trophic level increase from leguminous proteins[23] to animal protein[18] (where estimated δ^{15}N and δ^{13}C values of grass-fed beef are ca. 8‰[22] and ca. −20‰,[24] respectively). Feed manufacturers have confirmed that up to 15% MBM (from conventionally raised animal origin) has been included in New Zealand organic poultry feeds since 2010. The addition of MBM can be attributed to economic and practical changes affecting New Zealand poultry farmers and feed growers over this time. Anecdotally, cannibalism frequently occurs in flocks that suffer protein deficiency, and personal accounts from several New Zealand farmers indicated the need for poultry feed manufacturers to include more animal protein in feeds to counteract this unwanted trait in noncaged farming systems.

Table 3. Comparison of δ^{15}N and δ^{13}C Values of New Zealand Egg Whites According to Farming Regimen and Year Sampled in 2008 (Rogers, 2009), 2010, and 2014 (Mean ± SD)[a]

	farm type			
	cage	barn	free range	organic
δ^{15}N whites 2008	4.3 ± 1.5^{D}	4.4 ± 0.9^{E}	5.7 ± 1.2^{BC}	5.8 ± 1.7^{BC}
δ^{15}N whites 2010	5.5 ± 0.6^{C}	6.1 ± 0.8^{B}	5.8 ± 0.9^{BC}	7.1 ± 1.0^{A}
δ^{15}N whites 2014	NA	NA	NA	6.9 ± 1.2^{A}
δ^{13}C whites 2008	−21.6 ± 2.9^{III,IV}	−22.6 ± 0.8^{III,IV}	−22.2 ± 2.3^{IV}	−21.3 ± 3^{III,IV}
δ^{13}C whites 2010	−20.1 ± 3.2^{II}	−19.2 ± 1.1^{I}	−20.1 ± 2.5^{II}	−21.2 ± 2.9^{III}
δ^{13}C whites 2014	NA	NA	NA	−19.6 ± 1.2^{I,II}

[a]Values with different superscript letters for δ^{15}N (A−E) and δ^{13}C (I−IV) are significantly different (MANOVA, Fisher LSD test $P < 0.05$).

DOI: 10.1021/acs.jafc.5b01975
J. Agric. Food Chem. 2015, 63, 8372−8380

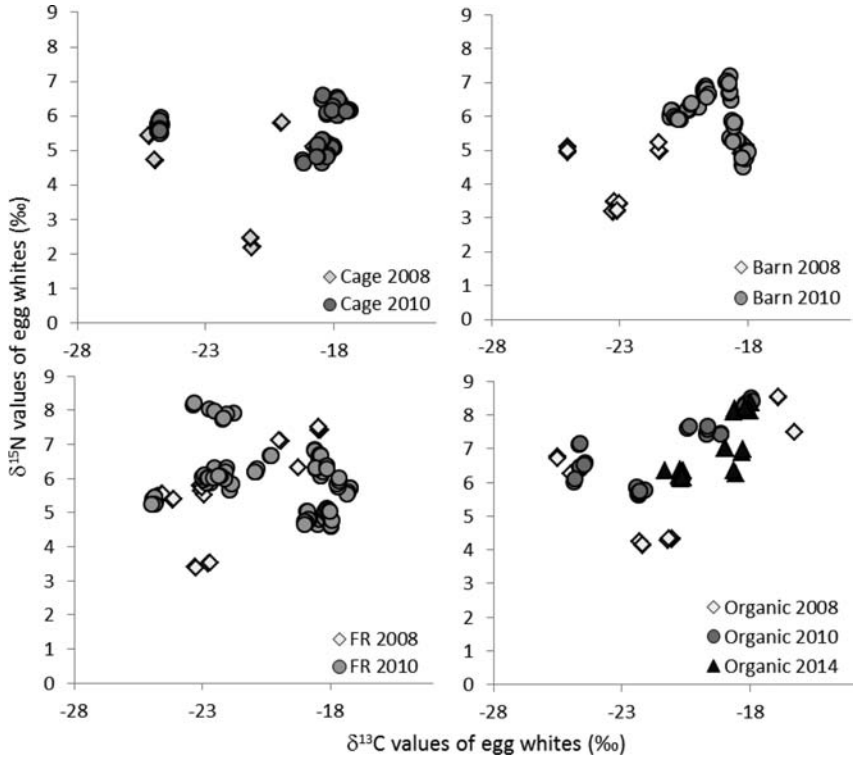

Figure 6. Comparison of carbon and nitrogen values of cage, barn, free range (FR), and organic egg whites from New Zealand sampled in 2008,[7] 2010, and 2014.

Table 4. Comparison of All δ^{15}N and δ^{13}C Values of New Zealand Egg Whites According to Farming Regimen Sampled from 2008 to 2014 (Rogers, 2009) (Mean ± SD)[a]

	farm type			
	cage	barn	free range	organic
all δ^{15}N whites 2008–2014	5.3^{C}	5.7^{B}	5.8^{B}	6.7^{A}
all δ^{13}C whites 2008–2014	-20.5^{A}	-19.8^{A}	-20.5^{A}	-20.7^{A}

[a]Values with different superscript letters in a row are significantly different (MANOVA, Fisher LSD test $P < 0.05$).

A further four brands of organic eggs were rechecked in 2014 to confirm the ^{15}N increase found in 2010. The δ^{15}N values of organic eggs sampled in 2014 were found to be very similar to those from 2010, although the δ^{13}C values were found to be slightly more positive (−19.6‰) than both the 2008 and 2010 values (−21.3 and −21.2‰ respectively). The variance (SD) of all δ^{13}C organic egg values decreased from 3.0 and 2.9‰ (in 2008 and 2010, $n = 4$ for each year) to 1.2‰ (in 2014, $n = 4$), suggesting a more uniform feed is now being used by egg producers. Nonetheless, as organic plant-only poultry feeds are significantly more expensive than conventional feed, the use of nonorganic dietary MBM included in New Zealand organic feeds conveniently lowers feed costs for organic poultry farmers, although the undisclosed use of MBM in organic poultry feed may be of interest to organic vegetarian egg consumers.

When the three New Zealand sampling events between 2008 and 2014 were taken into account (Table 4), key trends between farming regimens were observed for the δ^{15}N values but not for the δ^{13}C values. Organic eggs presented highest δ^{15}N values, followed by barn and free range eggs, which did not differ significantly, and finally cage eggs.

In 2008, organic egg whites had a δ^{15}N value of 5.8‰. and an SD of 1.7‰. Even though only four organic brands were sampled at this time, it was noted that two organic egg farms had considerably lower δ^{15}N values than the others. We compare these values with the average δ^{15}N value and SD of organic egg whites sampled in 2010 and 2014: 7.1‰ in 2010 and 6.9‰ in 2014, compared to 5.7‰ in 2008; and 1.0‰ in 2010 and 1.2‰ in 2014, compared to 1.7‰ in 2008. Organic eggs sampled in 2010 and 2014 have δ^{15}N values that are consistently higher and their SDs are smaller than 2008 values, confirming discrepancies in the integrity of some organic eggs sampled in 2008 and indicating potentially fraudulent labeling of organic eggs.

This observation was further supported by a MANOVA test of the organic egg white data (Table 3) with conventional (cage, barn, and free range) egg whites. The Fisher LSD test showed only small differences between δ^{15}N values of conventional (cage, barn, and free range) egg whites from 2008 compared to 2010. The Fisher LSD test results also showed a complete overlap between δ^{15}N values of organic and free range egg whites sampled in 2008 (Table 3).

Comparison between δ^{15}N Values of Dutch and New Zealand Egg Whites. A comparison between the δ^{13}C and δ^{15}N isotopic compositions of Dutch and New Zealand eggs under different farming systems was undertaken using MANOVA. Statistical analyses focused on the data per country.

DOI: 10.1021/acs.jafc.5b01975
J. Agric. Food Chem. 2015, 63, 8372−8380

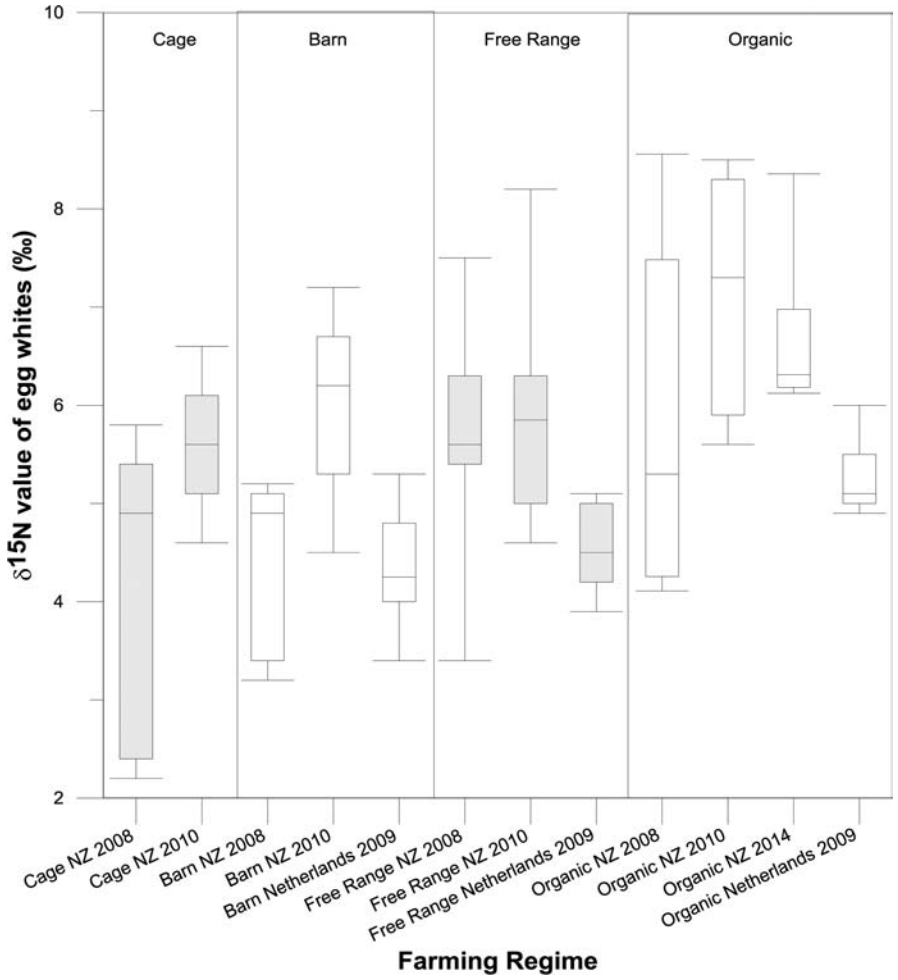

Figure 7. Box and whisker plot of δ^{15}N values of New Zealand and Dutch egg whites. The end whiskers represent the minimum and maximum range of δ^{15}N values, and the box indicates the first and third quartiles, with the whisker inside the box indicating the median value.

Table 5. *t* Test (Independence) and *p* Variance of Dutch Egg Whites Compared to New Zealand Egg Whites

	Dutch barn	Dutch free range	Dutch organic
barn 2008	0.12 (0.90)		
barn 2010	10.91 ($p < 0.001$)		
free range 2008		4.51 ($p < 0.001$)	
free range 2010		6.71 ($p < 0.001$)	
organic 2008			1.92 (0.06)
organic 2010			11.11 ($p < 0.001$)
organic 2014			11.05 ($p < 0.001$)

For the Dutch egg whites a significant difference in δ^{15}N values was observed between organic eggs and barn/free range eggs (Table 1). The δ^{13}C values of the Dutch egg whites showed significant differences between free range eggs and organic/barn eggs (Table 1).

A comparison between δ^{15}N values of egg whites from The Netherlands and New Zealand was made, including the three sets of New Zealand eggs sampled in 2008, 2010, and 2014 (Figure 7). Dutch egg whites (sampled in 2009) corresponded more closely with New Zealand egg whites sampled from 2008 (Figure 7; Table 5) rather than those from 2010 and 2014. Dutch barn and organic egg whites did not differ significantly from their respective New Zealand counterparts sampled in 2008 ($P < 0.05$), but Dutch free range egg whites differed significantly from the New Zealand free range egg whites sampled in 2008 ($P < 0.05$). New Zealand egg whites analyzed in 2010 and 2014 showed a significant increase in δ^{15}N values compared to New Zealand egg whites from 2008. Dutch eggs sampled in 2009 and New Zealand egg whites sampled in 2010 and 2014 demonstrated significant differences ($P < 0.05$) between their respective groups. The differences observed between the New Zealand egg whites (sampled in 2010 and 2014) and Dutch egg whites suggested that poultry feeds from these two countries comprised different components. From this study, δ^{15}N values showed that New Zealand hens from barn, free range, and organic farming systems in 2010 and from organic farming systems in 2014 were receiving a diet that was ^{15}N-enriched compared to hens from The Netherlands. Comparison of δ^{15}N values of New Zealand egg whites sampled in 2010 and 2014 to the initial data set of New

DOI: 10.1021/acs.jafc.5b01975
J. Agric. Food Chem. 2015, 63, 8372−8380

Zealand eggs sampled in 2008[7] also suggested an increase in δ^{15}N values of poultry feeds over this time, consistent with a higher level of dietary protein consumption by New Zealand hens. New Zealand egg whites analyzed in 2010 and 2014 also had more negative δ^{13}C values than the Dutch eggs (Tables 2 and 3), due to a preferential use of C3 plants (due to lower cost and a more suitable growing climate) in poultry feeds rather than the common usage of C4 plants (corn) in Dutch feeds.

The isotopic range and SD range of conventional and organic poultry egg whites sampled from the Dutch farms were smaller than corresponding isotopic and SD ranges of conventional and organic egg whites from New Zealand (2008−2014) and suggested that Dutch conventional and organic poultry feeds are more homogeneous, with similar dietary components, than those from New Zealand.

This study provides an isotopic comparison of δ^{15}N and δ^{13}C values of egg whites from The Netherlands and New Zealand to investigate whether it is possible to use isotopes as an internationally applicable verification and authentication tool for egg farming regimens across countries, continents, or hemispheres. Although the results showed there were significant isotopic differences in feeding regimens between Dutch egg whites and New Zealand egg whites sampled in 2010 and 2014, within a country or regional basis, δ^{15}N values of egg whites are shown to be a promising tool to authenticate and monitor truthfulness of labeling within markets using similar feeding systems and to identify instances when feeding practices may not be consistent with a specified farming regimen. This study found several key differences between New Zealand and Dutch eggs. New Zealand barn, free range, and organic eggs tend to be more enriched in ^{15}N and more depleted in ^{13}C than Dutch eggs, particularly for barn and organic farmed systems. Dutch egg whites had lower δ^{15}N values (<6‰) than New Zealand egg whites (up to 8.4‰) and confirmed an entirely plant based diet rather than one that contains supplementary MBM (commonly used in New Zealand but not permitted in EU countries).

Dutch organic eggs were easily discriminated from barn eggs using isotope analysis, but showed overlap with free range eggs. New Zealand free range and organic eggs showed considerable overlap for the eggs sampled in 2008, and some minor overlap was seen in 2010, but New Zealand organic eggs sampled in 2014 are generally distinguishable from cage, barn, and free range eggs sampled in 2010 and 2008. The shift in lowest New Zealand organic egg δ^{15}N value from 4.2‰ in 2008 to 6.1‰ in 2014 indicates that there was a significant change in feed composition. A smaller stepwise shift was also seen in cage, barn, and free range eggs between 2008 and 2010.

Feed manufacturers confirmed that up to 15% MBM can be found in organic feeds, although MBM is less frequently used in conventional feeds (personal communication). For countries that import eggs, a multi-isotope approach (C, S, H) might also be useful not only to verify farming regimen but also as a traceability tool, where country of origin labeling may an issue. Uptake of this research by verification authorities should be directed at auditing egg whites from organic and free range farms to assess and compare their ^{15}N variability and isotopic range. Given the range of egg white δ^{15}N values reported in this study, each farming regimen has a range of expected δ^{15}N values. On the basis of this study, Dutch organic egg whites presented a minimum δ^{15}N value of 4.8‰. New Zealand organic eggs derived from authentic organic feeds that incorporate up to 15% MBM, but are primarily from organic plant feeds, have a minimum δ^{15}N value of 6.0‰. In instances when this value is lower, further investigation into feeding practices of the specific farms is recommended.

AUTHOR INFORMATION

Corresponding Author

*(K.M.R.) Phone: +6445704636. Fax: +64 4 5704656. E-mail: k.rogers@gns.cri.nz.

Funding

We thank the Ministry of Economic Affairs of The Netherlands for financial support of the Dutch egg study. This research was funded by the New Zealand Government through the GNS Science Global Change through Time Programme (540GCT83).

Notes

The authors declare no competing financial interest.

ACKNOWLEDGMENTS

We thank the Stable Isotope Laboratory staff of GNS Science for their contribution to the analytical component of this research and Mike Sim, GNS Science, for helpful reviews and comments on the manuscript.

REFERENCES

(1) http://www.brisbanetimes.com.au/national/scramble-to-verify-freerange-eggs-20090906-fcu6.html (accessed Aug 16, 2014).

(2) http://www.theguardian.com/uk/2010/mar/11/egg-fraudster-supermarkets-free-range (accessed Aug 16, 2014).

(3) http://www.telegraph.co.uk/news/worldnews/europe/germany/9895504/German-farms-in-egg-fraud.html (accessed Aug 16, 2014).

(4) Rossmann, A. Determination of stable isotope ratios in food analysis. *Food Rev. Int.* **2001**, *17*, 347−381.

(5) Rogers, K. M. Nitrogen isotopes as a screening tool to determine the growing regimen of some organic and nonorganic supermarket produce from New Zealand. *J. Agric. Food Chem.* **2008**, *56*, 4078−4083.

(6) Woese, K.; Lange, D.; Boess, C.; Bogl, K. W. A comparison of organically and conventionally grown foods. Results of a review of the relevant literature. *J. Sci. Food Agric.* **1997**, *74*, 281−293.

(7) Rogers, K. M. Stable isotopes as a tool to differentiate eggs laid by caged, barn, free range, and organic hens. *J. Agric. Food Chem.* **2009**, *57*, 4236−4242.

(8) Van Ruth, S.; Alewijn, M.; Rogers, K.; Newton-Smith, E.; Tena, N.; Bollen, M.; Koot, A. Authentication of organic and conventional eggs by carotenoid profiling. *Food Chem.* **2011**, *126*, 1299−1305.

(9) Malec-Czechowska, K.; Wierzchnicki, R. A study of stable isotope composition of chosen foodstuffs from the Polish market. *Nukleonika* **2013**, *58*, 323−327.

(10) Van Ruth, S. M.; Koot, A. H.; Brouwer, S. E.; Boivin, N.; Carcea, M.; Zerva, C. N.; Haugen, J.-E.; Höhl, A.; Köroglu, D.; Mafra, I.; Rom, S. Eggspectation: organic egg authentication method challenged with produce from ten different countries. *Qual. Assur. Saf. Crops Foods* **2013**, *5*, 7−14.

(11) Siderer, Y.; Maquet, A.; Anklam, E. Need for research to support consumer confidence in the growing organic food market. *Trends Food Sci. Technol.* **2005**, *16*, 332−343.

(12) Rock, L.; Rowe, S.; Czerwiec, A.; Richmond, H. Isotopic analysis of eggs: evaluating sample collection and preparation. *Food Chem.* **2013**, *136*, 1551−1556.

(13) Minagawa, M.; Wada, E. Stepwise enrichment of ^{15}N along food chains: further evidence and the relation between δ^{15}N and animal age. *Geochim. Cosmochim. Acta* **1984**, *48*, 1135−1140.

(14) Hildalgo, A.; Rossi, M.; Clerici, S. R. A market study on the quality characteristics of eggs from different housing systems. *Food Chem.* **2008**, *106*, 1031−1038.

DOI: 10.1021/acs.jafc.5b01975
J. Agric. Food Chem. 2015, 63, 8372−8380

(15) Bateman, A. S.; Kelly, S. D.; Woolfe, M. Nitrogen isotope composition of organically and conventionally grown crops. *J. Agric. Food Chem.* **2007**, *55*, 2664−2670.
(16) De Niro, M. J.; Epstein, S. Influence of diet on the distribution of nitrogen isotopes in animals. *Geochim. Cosmochim. Acta* **1981**, *45*, 341−351.
(17) Nardoto, G. B.; Barboza de Godoy, P.; Sansigolo de Barros Ferrez, E.; Ometto, J. P. H.; Matinelli, L. A. Stable carbon and nitrogen isotopic fractionation between diet and swine tissues. *Sci. Agric. (Piracicaba, Braz.)* **2006**, *63*, 579−582.
(18) Ehleringer, J. R.; Epstein, S. C_3 and C_4 photosynthesis. In *Encyclopaedia of Global Environmental Change*; Mooney, H. A., Canadell, J., Eds.; Wiley: New York, 2001; Vol. II, pp 186−190.
(19) Schmidt, H.; Rossmann, A.; Voerkelius, S.; Schnitzler, W. H.; Georgi, M.; Grabmann, J.; Zimmermann, G.; Winkler, R. Isotope characteristics of vegetables and wheat from conventional and organic production. *Isot. Environ. Health Stud.* **2005**, *41*, 223−228.
(20) McCutchan, J. H.; Lewis, W. M.; Kendall, C.; McGrath, C. C. Variation in trophic shift for stable isotope ratios of carbon, nitrogen and sulfur. *Oikos* **2003**, *102*, 378−390.
(21) Carrijo, A. S.; Pezzato, A. C.; Ducatti, C.; Sartori, J. R.; Trinca, L.; Silva, E. T. Traceability of bovine meat and bone meal in poultry by stable isotope analysis. *Braz. J. Poult. Sci.* **2006**, *8*, 63−68.
(22) Denadai, J. C.; Ducatti, C.; Sartori, J. R.; Pezzato, A. C.; Gottmann, R. Traceability of bovine meat and bone meal in eggs of commercial laying hens through carbon and nitrogen stable isotopes technique. *Rev. Bras. Zootec.* **2011**, *40*, 2760−2766.
(23) Szpak, P.; Longstaffe, F. J.; Millaire, J.-F.; White, C. D. Large variation in nitrogen isotopic composition of a fertilised legume. *J. Arch. Sci.* **2014**, *45*, 72−79.
(24) Boner, M.; Forstel, H. Stable isotope variation as a tool to trace the authenticity of beef. *Anal. Bioanal. Chem.* **2004**, *378*, 301−310.

DOI: 10.1021/acs.jafc.5b01975
J. Agric. Food Chem. 2015, 63, 8372−8380

MATERIALS AND METHODS

Chemicals, Media, Strains, and Plasmids. Alachlor (≥99.4%), metolachlor (≥98.0%), acetochlor (≥98.2%), pretilachlor (≥95.6%), and butachlor (≥99.6%) were purchased from Beijing Qinchengyixin Technolog Co., Ltd. (China). All other chemicals used in this study were of analytical grade and obtained from Sinopharm Chemical Reagent Co., Ltd. (Shanghai, China). Inorganic salt medium (ISM, pH 7.0) contained (g/L) KH_2PO_4, 3.0; K_2HPO_4, 1.5; NH_4NO_3, 2.0; $MgSO_4{\cdot}7H_2O$, 0.1; $CaCl_2$, 0.01; and EDTA-2Na, 0.01. Luria−Bertani (LB, pH 7.0) medium contained (g/L) yeast extract, 5.0; tryptone, 10.0; and NaCl, 10.0. For solid medium, 20.0 g/L agar was added. Media were sterilized at 121 °C for 30 min. ISM and LB, which were purchased from Qingdao Hope Bio-Technology Co., Ltd., were used to isolate and culture the strains.

The primers and enzymes used for DNA amplification were purchased from the supplier (Shanghai SANGON Biological Engineering Co., Ltd., China). *E. coli* DH5α and *E. coli* BL21 (DE3) were used as hosts for constructing heterologous expression of protein. The plasmid pET-29a (+) was used for gene cloning and expression. *E. coli* strains were cultured in LB medium with the appropriate antibiotics at 37 °C.

Enrichment, Isolation, and Identification of Butachlor-Degrading Strain. The activated sludge used for the isolation of butachlor-degrading strain was obtained from Hangzhou Qingfeng Agro-chemical Co., Ltd., a pesticide manufacturer in Zhejiang province, China. Ten grams of activated sludge was added into a 250 mL Erlenmeyer flask containing 100 mL of ISM with 20 mg/L butachlor as the sole carbon source. The medium was incubated in a rotary shaker at 30 °C and 150 rpm for 7 days. Ten milliliters of the enrichment culture was transferred into another 100 mL of fresh ISM medium containing 50 mg/L butachlor and incubated at 30 °C and 150 rpm for another 7 days. The transfer was conducted weekly until the butachlor concentration gradually increased to 100 mg/L. Dilutions of the enrichment were spread onto LB agar plates containing 100 mg/L butachlor. After incubation at 30 °C for 7 days, the colonies were selected and purified to verify their degrading capabilities. The ability of isolates to degrade butachlor was determined by HPLC.

The isolate with high butachlor degradation rate was selected for further analysis. The physiological and biochemical characteristics of the strain were studied by using BioMerieux API 50 CHB/E reagent, which was purchased from Hangzhou Yidan Bio-Technology Co., Ltd. The 16S rRNA gene was amplified by PCR using the following primers: 27F (5′-AGAGTTTGATCCTGGCTCAG-3′) as the forward and 1492R (5′-TACGGTTACCTTGTTACGACTT-3′) as the reverse.[17] The PCR product was purified and cloned. The cloned insert was sequenced by Shanghai SANGON Biological Engineering Co., Ltd. The sequencing result was submitted to GenBank and compared with known 16S rRNA gene sequences in the GenBank database by BLAST.[18] Phylogenetic analysis was conducted using the neighbor-joining method with Clustal X[19] and MEGA 4.0 software.[20] Finally, this isolate was identified on the basis of its morphological and biochemical properties as well as phylogenetic analysis.

Biodegradation Experiment of Butachlor by Strain. The isolate was precultured in LB medium and incubated at 30 °C and 150 rpm for 24 h. Cells were harvested by centrifugation (5000*g*, 5 min) at 4 °C and washed twice with fresh ISM. Finally, cells were resuspended in fresh ISM at a concentration equivalent to an OD_{600} of 1.0. An inoculum (2%, v/v) was inoculated into a 250 mL Erlenmeyer flask containing 100 mL of ISM with 100 mg/L butachlor as the sole carbon source. Under optimal conditions (30 °C, pH 7.0), the medium was incubated on a rotary shaker at 150 rpm. Control experiment, which was incubated with inactivated cells, was carried out under the same condition. Each treatment was performed in three replicates. At 24 h intervals, sample aliquots were collected from the cultures. The residual concentration of butachlor was determined by HPLC, and the growth of cells was recorded by measuring the absorbance at 600 nm using a UV−vis spectrophotometer. The degradation rate was calculated according to the equation

$$\rho = \frac{X_0 - X_1}{X_0} \times 100\%$$

in which X_1 is the concentration of butachlor with cells inoculation and X_0 is the concentration of butachlor with inactivated cells inoculation.

Assays for Enzymatic Activitiy with Crude Cell Extracts. To prepare the crude cell extracts, strain hys-1 was cultured in LB medium with 100 mg/L butachlor to exponential phase in a rotary shaker at 30 °C and 150 rpm. The cells were harvested by centrifugation at 5000*g* for 10 min (Eppendorf centrifuge 5810R, Germany) at 4 °C. Precipitates were washed twice and resuspended with 20 mM sodium phosphate buffer solution (PBS, pH 7.0). Finally, the cell concentration was adjusted to the density of 5.0 (OD_{600}). The cells were then disrupted by sonication (Scientz-IID, Ningbo, China) for 30 min, and cell suspensions were centrifuged at 12000*g* for 20 min at 4 °C to remove cell debris. After being passed through a cellulose acetate filter with a pore size of 0.2 mm, the clear supernatants were referred to as crude cell extracts. Protein concentrations of the supernatants were determined by using the Bradford method[21] with bovine serum albumin (Sigma) as standard.

Enzyme activity of crude cell extracts against butachlor and other tested chloroacetamide herbicides was investigated in this study. Assays were performed by adding 0.5 mL of crude cell extracts to 4.5 mL of 50 mM PBS buffer (pH 7.0) containing 1.0 mM NADH and 0.5 mM substrates. The mixtures were incubated at 30 °C for 15 min. The reactions were terminated by adding 0.1 mL of 30% HNO_3. Then, the mixtures were centrifuged at 12000*g* for 15 min at 4 °C. The supernatants were then freeze-dried and redissolved in 1.0 mL of acetonitrile. The samples were filtered through a 0.22 μm Millipore membrane filter and subjected to HPLC analysis, which was used to determine the substrate concentration. One unit (U) of enzyme activity was defined as the amount of enzyme that consumed 1 μmol of substrate per minute. The specific activity (U/mg) of enzyme was defined as the consumption of 1 μmol of substrate per minute per milligram of protein. Control experiments without enzyme were also analyzed in parallel, and no spontaneous activity was detected. All experiments were repeated in triplicate.

Cloning, Expression, and Sequence Analysis of the Debutoxylase Gene. The Dbo gene was cloned from genomic DNA of strain hys-1 by PCR. Nucleotide sequences of esterase genes reported in the literature[22−24] were retrieved from NCBI (http://www.ncbi.nlm.nih.gov), and multiple pairs of primers were designed. Through final screening, the primer sequences 5′-ggtcgacatgatgaaattagcatct-3′ and 5′-gtcgacttaccaatctagttgctcc-3′ (the underlining indicates the *Sal*I restriction site) were designed for the PCR amplification. The PCR product was cloned into the *pEASY*-T1 (cloning vector). Plasmids were checked for inclusion of the desired insert and subsequently purified with a UNIQ-10 Gel Extraction Kit. The positive plasmid was subjected to DNA sequencing by SANGON Biotech Co. Ltd. (Shanghai, China). BlastN and BlastP were used for searching related nucleotide sequences and deducing amino acids (www.ncbi.nlm.nih.gov/Blast), respectively.

To remove the phosphate group to obtain a neutral sugar chain, pET-29a (+) undigested vector was digested with *Sal*I and was treated with calf intestinal alkaline phosphatase. Then the target fragment was cloned into the *Sal*I site by using the treated pET-29a (+) to obtain the plasmid pET-29a harboring genes and transformed into *E. coli* DH5α. The transformants were grown in LB medium at 37 °C until the OD_{600} of 0.5 and then spread onto LB selection plates supplemented with 100 mg/L kanamycin. The primer sequences, 5′-taatacgactcactataggg-3′ (T7 primer sequences) and 5′-gtcgacttaccaatctagttgctcc-3′ were used to identify the recombinant plasmid.

Then the positive plasmid was transformed into *E. coli* BL21 (DE3). The transformants were grown in LB medium at 37 °C until the OD_{600} of 0.5 and then were induced in the addition of isopropyl-β-D-thiogalactopyranoside (IPTG) to a final concentration of 1 mM. After growing for 18 h, cells were spread onto LB selection plates supplemented with 100 mg/L kanamycin and 200 mg/L butachlor. Kanamycin-resistant transformants were selected, and colonies with a clear transparent halo could be taken as the positive transformants. Such colonies were screened and further tested for the ability to degrade butachlor by HPLC analysis.

The phylogenetic analysis of Dbo with the closely related enzyme was performed using MEGA 4.0 software.[20] The Kimura two-parameter

DOI: 10.1021/acs.jafc.5b03326
J. Agric. Food Chem. 2015, 63, 8381−8390

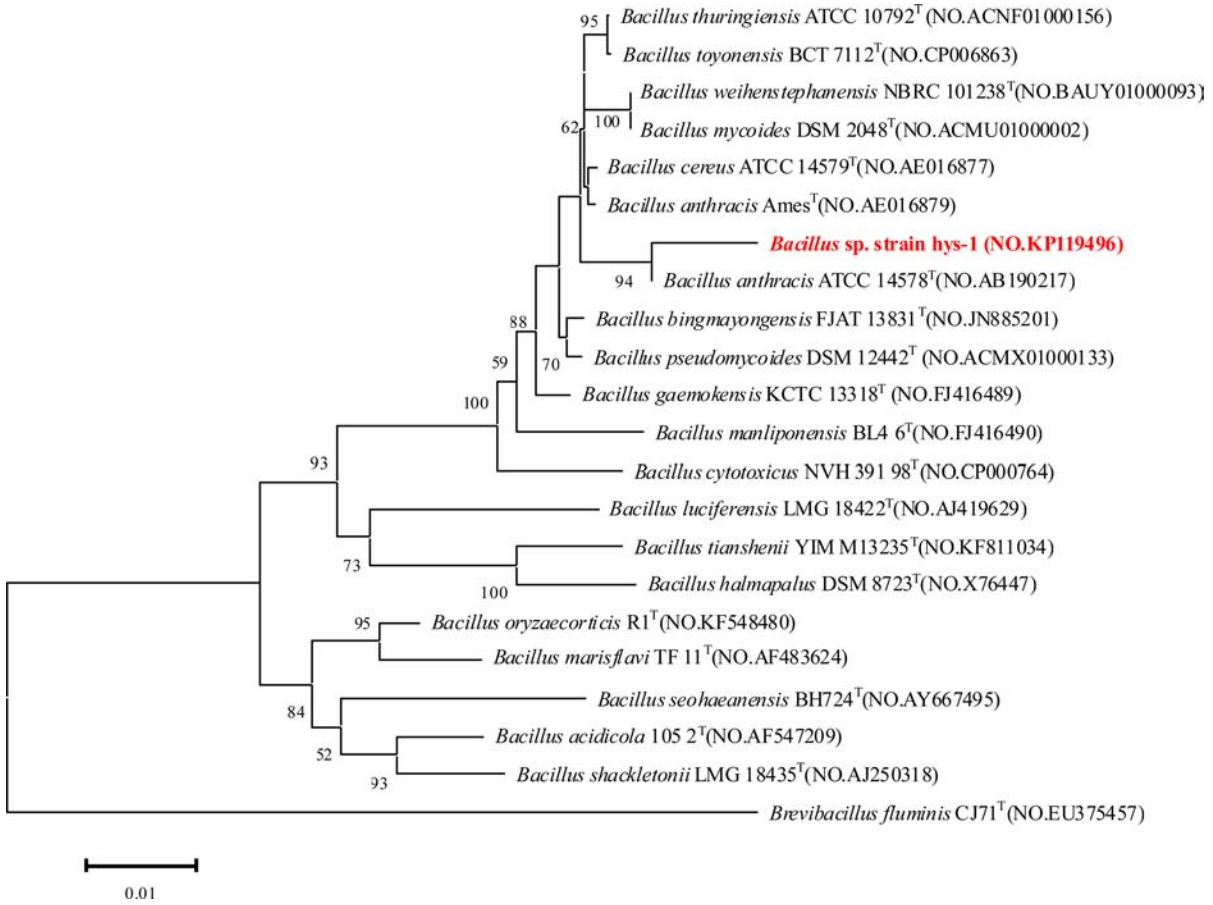

Figure 1. Neighbor-joining phylogenetic tree of 16S rRNA genes of strain hys-1. Bootstrap values above 50% (based on 1000 replications) are represented at the branch points. Bar = 0.01 substitution per nucleotide position.

distance model was used to calculate the distances, and the tree topology was evaluated on the basis of bootstrap analysis of 1000 times.

Purification and Characteristics of the Recombinant Enzymes. The positive recombinants of *E. coli* BL21 were incubated in LB medium containing 50 mg/L kanamycin until the OD_{600} of 0.5 at 37 °C and then were induced by adding 1 mM IPTG. After incubation at 18 °C for 10 h, the cells were harvested by centrifugation at 5000*g* for 10 min at 4 °C, washed twice, and resuspended with 50 mM PBS (pH 7.0). Cell suspensions were disrupted by sonication for 15 min and then centrifuged at 12000*g* for 15 min at 4 °C to remove the cell debris. The supernatant was used for further enzyme purification. The purification of the recombinant enzyme was carried out according to the methods described by Nguyen et al.[25] Protein concentrations were quantified via the Bradford method[21] using bovine serum albumin as the standard.

To determine the optimal pH, enzyme reaction was performed in various buffers at 30 °C. The following buffers were used: 20 mM citrate buffer (pH 3.0, 4.0, 5.0, 6.0); 20 mM PBS (pH 6.0, 6.5, 7.0, 7.5, 8.0, 8.5); and 0.1 M sodium bicarbonate buffer (pH 8.5, 9.0, 9.5, 10.0). To determine optimal temperature, enzyme reaction was conducted in 20 mM PBS (pH 7.0) at various temperatures from 20 to 50 °C. The effects of different metal ions on the enzymatic activity were determined by incubating 1 mM of various metal salts in 20 mM PBS buffer (pH 7.0) at 30 °C. PBS without additional metal salts was used as the control (100%). Enzyme activity was measured using the enzyme assay conditions described above, and butachlor was used as the substrate for the enzyme reaction assay. Three replicates were used for each sample.

Analytical Methods. To analyze butachlor and other chloroacetamide herbicides, the culture sample was centrifuged at 12000*g* for 20 min at room temperature. Then, the supernatants were freeze-dried, redissolved in 1.0 mL of acetonitrile, and filtered through a 0.22 μm Millipore membrane filter. Residual chloroacetamide herbicides were analyzed with HPLC (Waters e2695) equipped with a UV−vis detector (Waters 2489) and an XBridge C_{18} column (inner diameter, 4.6 mm; length, 25 cm; particle size, 5.0 μm). The temperature of the separation column was 35 °C. Mobile phase was acetonitrile/water (80:20, v/v), and the flow rate was 0.8 mL/min. The injection volume was 20 μL, and the column elution was monitored by measuring at 230 and 215 nm. The concentration was calculated on the basis of a peak area from calibration curve.

The reaction products were analyzed by LC-MS. The analyses were performed by a time-of-flight mass spectrometry (Waters Xevo G2 Q-TOF, USA) equipped with an electrospray ionization (ESI). The positive mode was set at a source temperature of 110 °C, a desolvation temperature of 450 °C, and a capillary voltage of 2.5 kV. The cone gas flow and desolvation gas flow were 50 and 1000 L/h, respectively. Nitrogen was used as the desolvation gas, and argon was used as the collision gas. The compounds were ionized in the positive electrospray ionization (ESI^+) ion source and were detected in high-resolution mode. Full scan signals were recorded from m/z 50 to 600. Finally, the data were collected and analyzed by Masslynx V 4.1 (Waters, USA). Structures of products were analyzed with formula weight matching software (*MassFragment*).

GenBank Accession Numbers. The GenBank accession numbers of the Dbo gene and the 16S rRNA gene sequence of strain hys-1 were KT121406 and KP119496, respectively.

RESULTS AND DISCUSSION

Isolation and Identification of hys-1. After 2 months of enrichment and screening, a single strain was isolated from the active sludge and designated hys-1. The strain was selected on the basis of its ability to use butachlor as the sole carbon source.

DOI: 10.1021/acs.jafc.5b03326
J. Agric. Food Chem. 2015, 63, 8381−8390

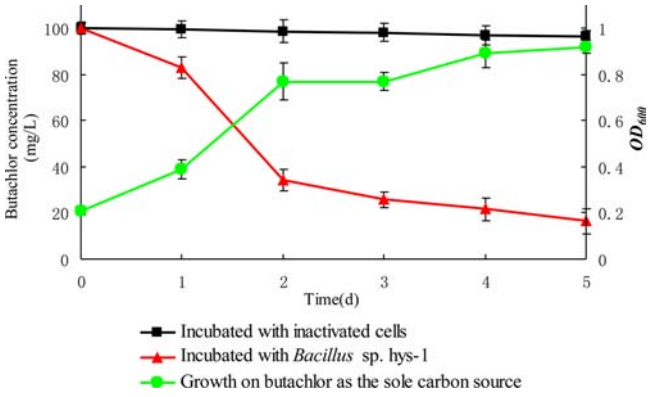

Figure 2. Utilization of butachlor during growth of hys-1. Error bars represent the standard error of three replicates.

Strain hys-1 degraded approximately 84% of butachlor within 5 days and >90% after 7 days if used at concentration of 100 mg/L in ISM. Strain hys-1 was an aerobic and Gram-positive bacterium. The electron micrograph of hys-1 cells showed that the bacterium was rod shaped (4.4−4.5 μm × 1.2−1.3 μm), spore-bearing, and atrichosis. Colonies grown on LB agar plates at 30 °C for 36 h were white, circular, and 2.0−3.0 mm in diameter. Strain hys-1 was able to grow within a temperature range of 25−40 °C, the optimal temperature being 30−37 °C. Growth occurred at pH 6.0−9.0, with optimal growth at pH 7.0−8.0. Growth of strain hys-1 was observed at NaCl concentrations between 5 and 12%, with an optimum of 8%. BioMerieux API 50 CHB/E reagent was used to determine the activities of constitutive enzymes and other physiological properties according to the manufacturer's instructions (data not shown). The 16S rRNA gene (1458) of strain hys-1 was sequenced and deposited in the GenBank database with the accession no. KP119496. Analysis of 16S rRNA gene sequences revealed the

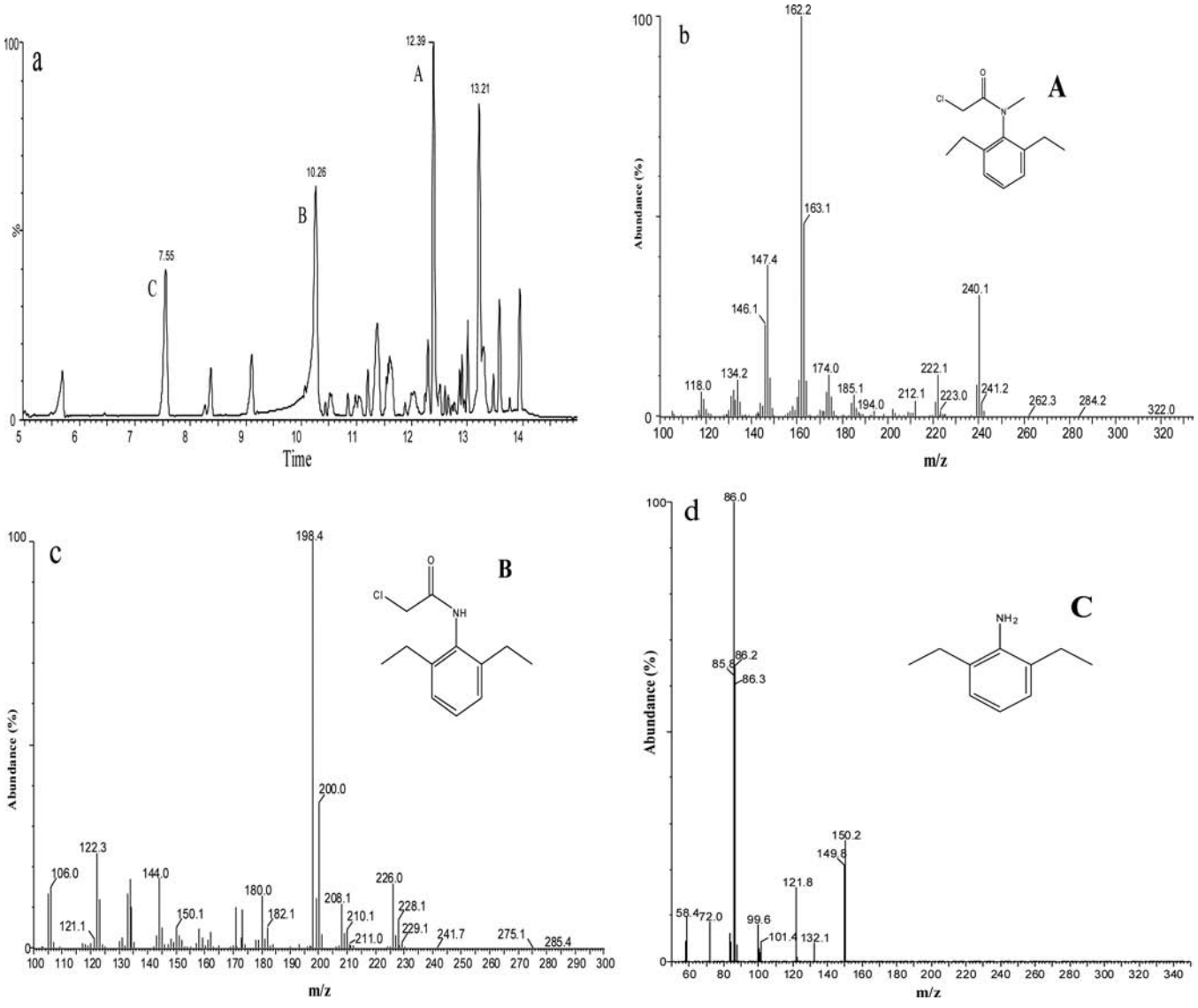

Figure 3. Mass spectrum analysis of the butachlor intermediates degraded by hys-1: (a) Total ion chromatogram (TIC) for intermediates A, B, and C. The retention time of each compounds was 12.39, 10.26, and 7.55 min, respectively. (b−d) The mass spectrum of characteristic ions for compounds A, B, and C. They were identified as 2-chloro-*N*-(2,6-diethylphenyl)-*N*-methylacetamide, 2-chloro-*N*-(2,6-diethylphenyl)-acetamide, and 2,6-diethylaniline, respectively.

DOI: 10.1021/acs.jafc.5b03326
J. Agric. Food Chem. 2015, 63, 8381−8390

Table 1. Retention Time, Mass, and Structure of the Identified Products (A, B, and C) by LC-MS and *MassFragment* Software Analysis[a]

Products	Retention time (min)	Mass (m/z)	Fragment(s) m/z	Score & H-deficit	Structure(s)	Results
A	12.39	240.1	174.0	S:1.5 B:2 H:-1		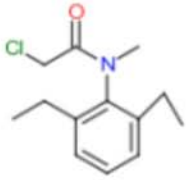
			162.2	S:0.5 B:1 H:0		
			147.4	S:1.5 B:2 H:0		
			134.2	S:2.5 B:3 H:+2		
B	10.26	226.0	208.1	S:2.0 B:1 H:-1	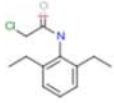	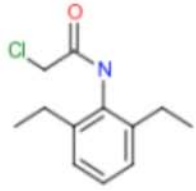
			198.4	S:2.0 B:2 H:+3	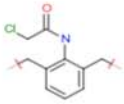	
			180.0	S:4.0 B:3 H:+1	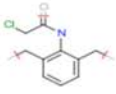	
			122.3	S:2.5 B:3 H:+4	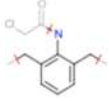	
			132.1	S:1.0 B:1 H:0	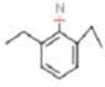	
C	7.55	150.2	121.8	S:2.0 B:2 H:+3	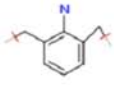	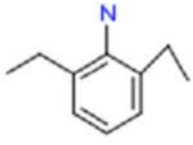
			105.1	S:2.0 B:3 H:+3	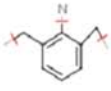	

[a]S, score; B, bond; H, deficit. In the *MassFragment* software, the lower the score (≤5), the better the matching results.

highest sequence identity (99%) with the 16S rRNA gene of *Bacillus anthracis* ATCC 14578^T (no. AB190217), and phylogenetic analysis showed that the two strains share the closest relationship (Figure 1). Thus, on the basis of the results of phenotypic and physiological characteristics and genotypic and phylogenetic analyses, strain hys-1 was considered as a *Bacillus* sp.

So far, various studies showed that many bacteria were able to degrade butachlor, including *Sphingomonas* sp.,[26] *Paracoccus* sp.,[13] *Pseudomonas* sp.,[27] *Catellibacterium caeni* sp.,[9] *Rhodococcus*

DOI: 10.1021/acs.jafc.5b03326
J. Agric. Food Chem. 2015, 63, 8381−8390

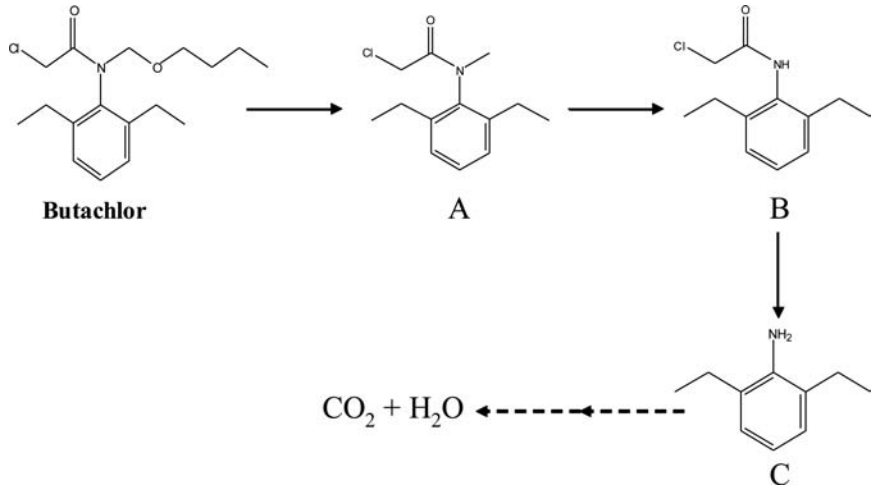

Figure 4. Complete biodegradation pathway of butachlor by strain hys-1.

Table 2. Specific Activities of Crude Cell Extracts[a]

substrate	specific activity (μmol min^{-1} mg^{-1})
alachlor	38.46 ± 1.27*
acetochlor	32.81 ± 1.04*
butachlor	27.35 ± 1.31*
metolachlor	−
pretilachlor	−

[a]Data in the table are shown as means ± SE. −, no activity was detected. The asterisk (*) indicates significant difference ($p < 0.05$, ANOVA test).

sp.,[15] *Acinetobacter* sp.,[28] *Mycobacterium* sp.,[14] and *Sphingobium* sp.[14,29] Members of *Bacillus* are widespread in nature and play an important role in the ecosystem. Tuo et al.[30] isolated a *Bacillus* sp. Q2 that could degrade 500 mg/L quinoline completely within 30 h under optimal conditions. Li et al.[31] obtained a *Bacillus* sp. GZB capable of effectively degrading bisphenol A (BPA) under anaerobic and aerobic conditions. Lu et al.[32] found that *Bacillus cereus* JP12 could use decabromodiphenyl ether (BDE-209) as the sole carbon and energy source for growth in mineral salt medium. Moreover, Zu et al.[33] isolated a *Bacillus* sp. GZT that had an excellent ability to simultaneously debrominate and mineralize 2,4,6-tribromophenol (TBP). All of this suggested that the *Bacillus* sp. strains could have a great potential application value in biodegradation of organic contaminants and remediation of water and soil. This study obtained a *Bacillus* sp. hys-1 from activated sludge, which was capable of degrading butachlor as the sole carbon, nitrogen, and energy source. The results expanded the application range of *Bacillus* sp. in the field of environmental pollution remediation.

Biodegradation Experiment of Butachlor by Strain hys-1. The butachlor degradation and growth patterns of strain hys-1 were studied in ISM with butachlor as the sole carbon source. Under optimal conditions (temperature, 30 °C; pH 7.0; butachlor concentration, 100 mg/L), hys-1 degraded butachlor rapidly, with 83.6% of the initial dose degraded within 5 days (Figure 2). At the beginning of the incubation period, strain hys-1 did not adapt to the environment quickly and the most efficient degradation was obtained the next day. No significant change of butachlor concentration was observed in the cultures incubated with inactivated cells. Butachlor degradation was associated with a concomitant increase in cell density from 0.21 to 0.92 (OD_{600}). These results indicated that butachlor served as the carbon source for strain hys-1 growth.

Identification of Metabolites and Butachlor Biodegradation Pathway. To elucidate the butachlor biodegradation pathway and the interaction with cell metabolism, the intermediates of butachlor degradation by strain hys-1 were identified with HPLC-ESI-MS/MS. Three metabolites, designated metabolites A, B, and C, were obtained with different retention times (Figure 3). For the first 3 days of butachlor degradation, metabolites A and B were determined with high concentration levels by HPLC. In positive-ion chemical ionization, metabolite A showed a protonated molecular ion peak at m/z 240.1 $[M + H]^+$ and characteristic fragment ion peaks at m/z 174.0, 162.2, 147.4, and 134.2. With the formula weight matching software (*MassFragment*), structures of characteristic fragments were matched and are shown in Table 1. On the basis of these results, product A was identified as 2-chloro-*N*-(2,6-diethylphenyl)-*N*-methylacetamide. The positive-ion chemical ionization of metabolite B showed a molecular ion peak m/z 226.0 $[M + H]^+$, and its characteristic fragment ion peaks were m/z 208.1, 198.4, 180.0, and 122.3. Furthermore, the matching results of characteristic fragments are shown in Table 1. According to these data, product B was identified as 2-chloro-*N*-(2,6-diethylphenyl)acetamide. In addition, the concentration of metabolite C increased after incubation for 5 days, and the mass spectrum gave a base peak at m/z 150.2 $[M + H]^+$ with the characteristic fragment ion peaks at m/z 132.1, 121.8, and 105.1. On the basis of these data, product C was identified as 2,6-diethylaniline. It should be noted that although the sample gave a peak at RT = 13.21 min, its molecular ion peak showed a higher molecular weight compared with butachlor, and its characteristic fragment ion peaks could not be detected by MS/MS. Therefore, we inferred it was an impurity peak. Moreover, these metabolites (A, B, and C) could hardly be detected after butachlor degradation for 10 days. Thus, we deduced that butachlor was completely degraded by strain hys-1.

Until now, few studies[9,13,14,34] have reported the possible aerobic and anaerobic degradation pathways of butachlor by microorganisms. In general, the major methods for butachlor degradation include dechlorination, hydroxylation, dehydrogenation, debutoxylation, debutoxymethylation, N-dealkylation, O-dealkylation, cyclization, etc.[35−37] Liu et al.[15] reported that butachlor was only hydrolyzed by strain B1 through N-dealkylation, which resulted in the production of butoxymetha-

DOI: 10.1021/acs.jafc.5b03326
J. Agric. Food Chem. 2015, 63, 8381−8390

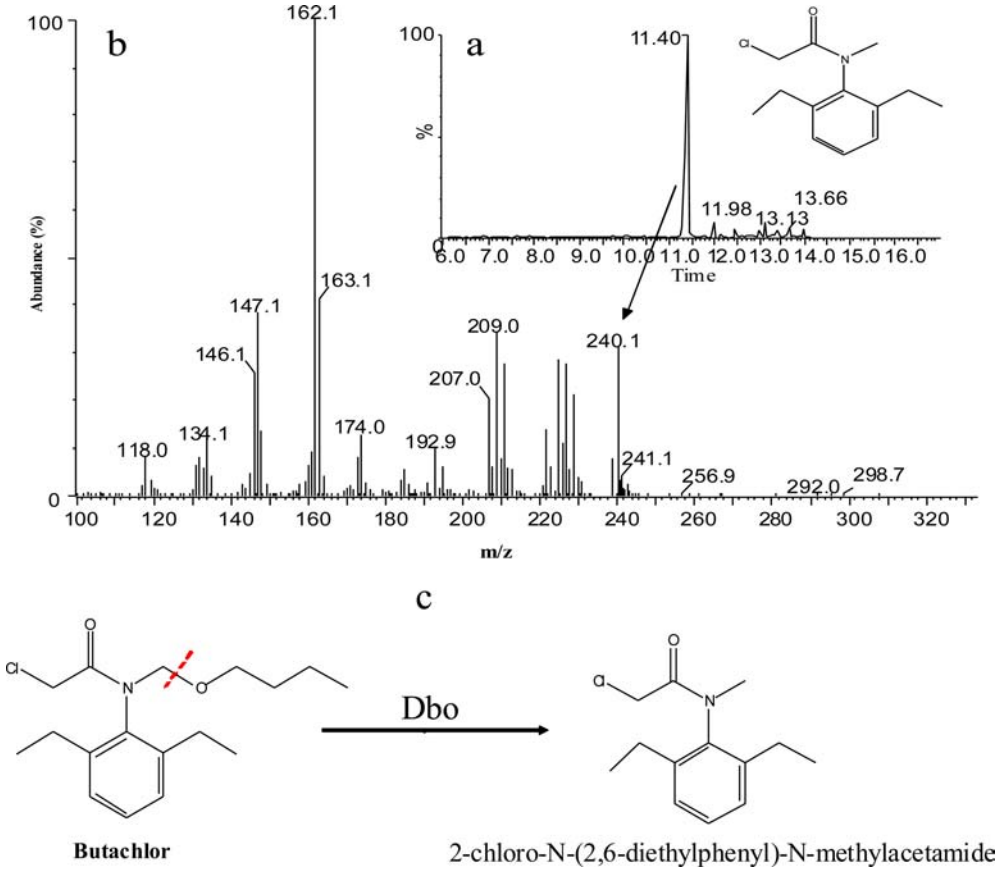

Figure 5. Mass spectrum of metabolite and proposed metabolic pathway: (a) Total ion chromatogram (TIC) for metabolite. The retention time was 11.40 min. (b) Mass spectrum of characteristic ions for the metabolite (RT = 11.40 min) identified as 2-chloro-*N*-(2,6-diethylphenyl)-*N*-methylacetamide. (c) Proposed metabolic pathway of butachlor by the positive clone. Butachlor was transformed into 2-chloro-*N*-(2,6-diethylphenyl)-*N*-methylacetamide by debutoxylation.

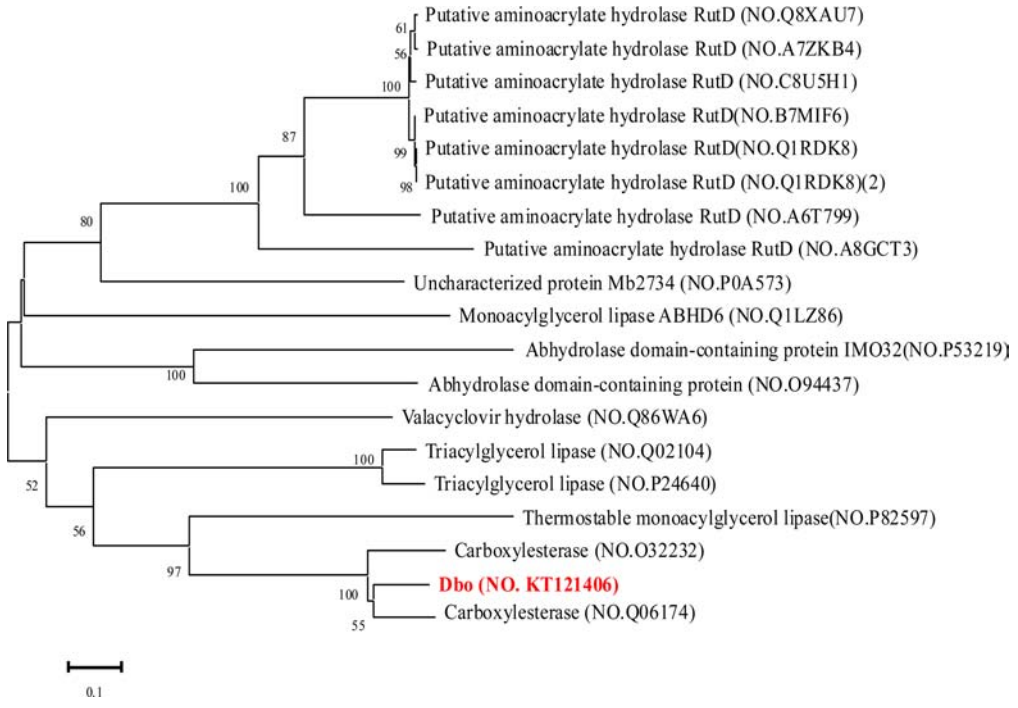

Figure 6. Phylogenetic relationships of butachlor debutoxylase amino acid sequences (Dbo).

nol and 2-chloro-*N*-(2,6-dimethylphenyl)acetamide. Analogously, a study by Chen et al.[16] also showed that sphingomonads DC-6 and DC-2 degraded butachlor via N-dealkylation. Otherwise, Zheng et al.[9] found that five metabolites were

DOI: 10.1021/acs.jafc.5b03326
J. Agric. Food Chem. 2015, 63, 8381−8390

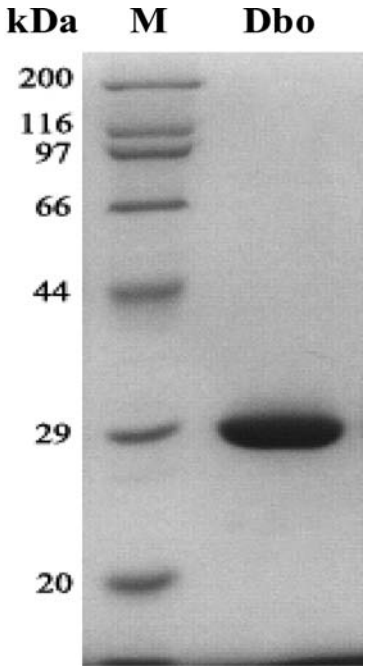

Figure 7. SDS-PAGE analysis of the purified enzymes. Lanes: M, protein marker; Dbo, purified recombinant Dbo.

produced during butachlor degradation by strain DCA-1^T, but three macromolecular degradation products remained in the culture medium, while not being further degraded. In addition, Kim et al.[14] reported that butachlor was completely degraded by the two isolates (*Mycobacterium* sp. J7A and *Sphingobium* sp. J7B) by syntrophic metabolism, whereas each isolate alone was not able to completely degrade butachlor. In a recent study, Zhang et al.[13] observed a plausible complete mineralization pathway of butachlor by *Paracoccus* sp. FLY-8. First, butachlor was degraded to alachlor by partial C-dealkylation and then through N-dealkylation to form 2-chloro-*N*-(2,6-dimethylphenyl)acetamide, which was further cleaved to 2,6-diethylaniline. 2,6-Diethylaniline was subsequently degraded via the metabolites aniline and catechol. In the end, catechol was oxidized through an ortho-cleavage pathway.

On the basis of all of the above results, the complete degradation pathway of butachlor by strain hys-1 is also proposed in Figure 4. Butachlor was initially metabolized to 2-chloro-*N*-(2,6-diethylphenyl)-*N*-methylacetamide by debutoxylation and then transformed to form 2-chloro-*N*-(2,6-diethylphenyl)-acetamide by N-demethylation. Subsequently, it was converted to 2,6-diethylaniline and further mineralized into CO_2 and H_2O. Butachlor was completely degraded by strain hys-1 finally, which was different from the reported butachlor mineralization pathway.[13] Thus, a new mineralization pathway by strain hys-1 was found as a novel metabolic mechanism of butachlor

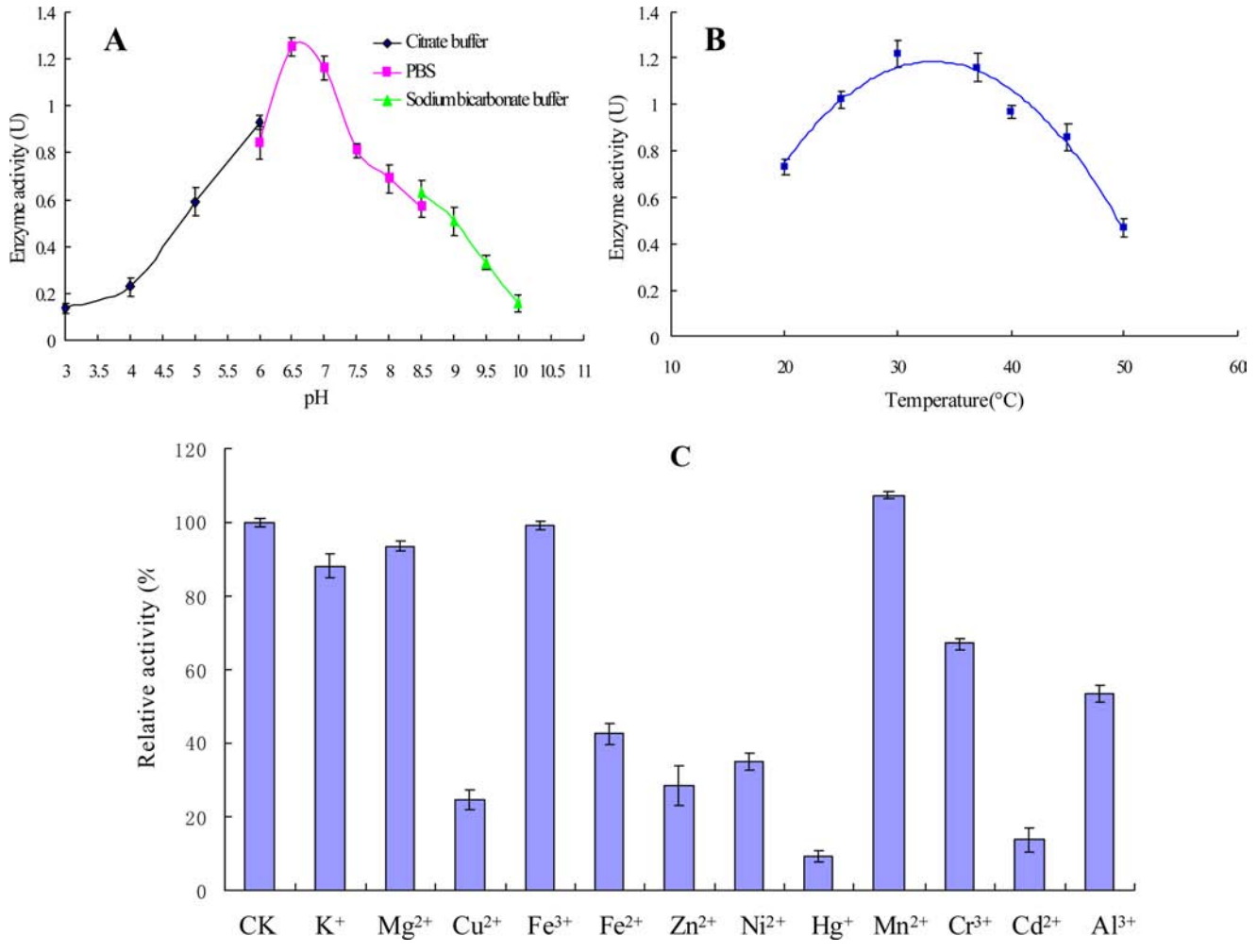

Figure 8. Effects of pH (A), temperature (B), and different metal ions (C) on Dbo activity. Error bars represent the standard error of three replicates.

DOI: 10.1021/acs.jafc.5b03326
J. Agric. Food Chem. 2015, 63, 8381−8390

biodegradation. In conclusion, strain hys-1 could degrade butachlor completely, which effectively reduce the secondary contamination caused by butachlor metabolites. Furthermore, the efficiency of butachlor degradation by strain hys-1 is much higher than that by *Paracoccus* sp. FLY-8.[13]

Substrate Specificity of the Enzyme. The substrate specificity of crude cell extracts was investigated using five chloroacetamide herbicides (Table 2). The results revealed that the crude cell extracts were able to catalyze alachlor, acetochlor, and butachlor degradation, with specific activities of 38.46, 32.81, 27.35 μmol min^{-1} mg^{-1} protein, respectively. No activity was detectable in the case of metolachlor and pretilachlor. This difference of reactivity may be related to the enzyme selectivity. Moreover, it was shown that the hydrolysis efficiency descended as alachlor > acetochlor > butachlor, which indicated that the hydrolysis activities decreased with the increase of the alkoxy chain length.

Dbo Gene Cloning, Expression, and Sequence Analysis. To clone the Dbo gene from strain hys-1, the gene was amplified by the primers as described previously. Next, the recombination genes were constructed and then transformed into *E. coli* BL21 (DE3). After growth on LB selection plates at 37 °C for 18 h, a positive clone was screened and the ability to degrade butachlor was confirmed by HPLC. In addition, the metabolites were further identified by LC-MS. The results indicated that the positive clone could transform butachlor into 2-chloro-*N*-(2,6-diethylphenyl)-*N*-methylacetamide by debutoxylation (Figure 5). Thus, it was subjected to gene sequencing. Finally, a continuous gene (744 bp in length) was obtained and deposited in the GenBank database with the accession no. KT121406. The gene encoding butachlor debutoxylase was designated Dbo.

Sequence analysis indicated that the GC content of Dbo was 38.31 mol % and a protein of 247 amino acids was encoded. Proteomic predictions showed that the molecular weight of Dbo is 28282.43 Da. The phylogenetic relationship of amino acid sequences is shown in Figure 6. The results showed the highest protein sequence identity (99%) with carboxylesterase (no. Q06174) and 97% identity with thermostable monoacylglycerol lipase (no. P82597). Both carboxylesterase and lipase are members of the esterase family. Thus, we speculated that Dbo could be a *Bacillus* esterase homologue that had the capability of realizing butachlor debutoxylation.

Purification and Characteristics of Dbo. To study the enzymatic properties, Dbo was expressed in *E. coli* BL21 and purified using Ni−nitrilotriacetic acid affinity chromatography. The purified enzyme was analyzed by SDS-PAGE and gave a single band (Figure 7). The molecular mass of the denatured enzyme was approximately 28 kDa, which is consistent with the molecular mass predicted from the amino acid sequence (28282.43 Da). Dbo could catalyze the debutoxylation of butachlor into 2-chloro-*N*-(2,6-diethylphenyl)-*N*-methylacetamide. Above all, Dbo involved in the degradation of butachlor was reported for the first time.

The effects of pH, temperature, and metal ions on Dbo activity were assayed with the purified enzyme. Dbo showed high activity at pH 6.5−7.0, with an optimum pH of 6.5, and the activity was inhibited under acidic (<5.0) or alkaline (>8.0) condition (Figure 8A). The enzyme showed relatively high activity at temperatures ranging from 25 to 40 °C, retaining >50% activity at 20 and 45 °C, yet 38% activity at 50 °C. The highest activity appeared at 30 °C (Figure 8B). Metal ions play an important role in Dbo activity (Figure 8C). Cu^{2+}, Fe^{2+}, Zn^{2+}, Ni^{2+}, Hg^{+}, and Cd^{2+} significantly inhibited the Dbo activity, whereas K^{+}, Mg^{2+}, and Fe^{3+} influenced enzyme activity indistinctively. Approximately 30−50% of Dbo activity was inhibited by Cr^{3+} and Al^{3+} ions. Furthermore, Mn^{2+} slightly activated Dbo activity at the tested concentration. The present study showed that Dbo could carry out the debutoxylation of butachlor and may possess potential to be used in bioremediation of butachlor-contaminated environments.

■ ASSOCIATED CONTENT

Supporting Information

The Supporting Information is available free of charge on the ACS Publications website at DOI: 10.1021/acs.jafc.5b03326.

Electron micrographs of *Bacillus* sp. hys-1 (PDF)

■ AUTHOR INFORMATION

Corresponding Author

*(Z.C.) E-mail: czj0501@sina.com. Phone: +86-580-2299884. Fax: +86-580-2299882.

Funding

This work was supported by the Natural Science Foundation of Zhejiang Province, China (LQ14B070002), and Science and Technology Plan Projects of Zhejiang Province, China (2014F30024).

Notes

The authors declare no competing financial interest.

■ REFERENCES

(1) Tomlin, C. D. S. *The Pesticide Manual: A World Compendium*, 14th ed.; British Crop Protection Council: Farnham, Surrey, UK, 2006.

(2) Couderchet, M.; Schmalfuß, J.; Böger, P. A specific and sensitive assay to quantify the herbicidal activity of chloroacetamides. *Pestic. Sci.* **1998**, *52*, 381−387.

(3) Hildebrandt, A.; Guillamón, M.; Lacort, S.; Tauler, R.; Barceló, D. Impact of pesticides used in agriculture and vineyards to surface and groundwater quality (north Spain). *Water Res.* **2008**, *42*, 3315−3326.

(4) Chiang, H. C.; Duh, J. R.; Wang, Y. S. Butachlor, thiobencarb, and chlomethoxyfen movement in subtropical soils. *Bull. Environ. Contam. Toxicol.* **2001**, *66*, 1−8.

(5) Dearfield, K. L.; McCarroll, N. E.; Protzel, A.; Stack, H. F.; Jackson, M. A.; Waters, M. D. A survey of EPA/OPP and open literature on selected pesticide chemicals. II. Mutagenicity and carcinogenicity of selected chloroacetanilides and related compounds. *Mutat. Res., Genet. Toxicol. Environ. Mutagen.* **1999**, *443*, 183−221.

(6) Coleman, S.; Linderman, R.; Hodgson, E.; Rose, R. L. Comparative metabolism of chloroacetamide herbicides and selected metabolites in human and rat liver microsomes. *Environ. Health Perspect.* **2000**, *108*, 1151−1157.

(7) Dwivedi, S.; Saquib, Q.; Al-Khedhairy, A. A.; Musarrat, J. Butachlor induced dissipation of mitochondrial membrane potential, oxidative DNA damage and necrosis in human peripheral blood mononuclear cells. *Toxicology* **2012**, *302*, 77−87.

(8) Yu, Y. L.; Chen, Y. X.; Luo, Y. M.; Pan, X. D.; He, Y. F.; Wong, M. H. Rapid degradation of butachlor in wheat rhizosphere soil. *Chemosphere* **2003**, *50*, 771−774.

(9) Zheng, J. W.; Li, R.; Zhu, J. C.; Zhang, J.; He, J.; Li, S. P.; Jiang, J. D. Degradation of the chloroacetamide herbicide butachlor by *Catellibacterium caeni* sp. nov DCA-1^{T}. *Int. Biodeterior. Biodegrad.* **2012**, *73*, 16−22.

(10) Tian, Q.; Zhou, Z. Q.; Jiang, S. R.; Ren, L. P.; Qiu, J. Research progress in butachlor degradation in the environment. *Chin. J. Pestic.* **2004**, *43*, 205−208.

(11) Lin, Y. J.; Lin, C.; Yeh, K. J.; Lee, A. Photodegradation of the herbicides butachlor and ronstar using natural sunlight and diethylamine. *Bull. Environ. Contam. Toxicol.* **2000**, *64*, 780−785.

DOI: 10.1021/acs.jafc.5b03326
J. Agric. Food Chem. 2015, 63, 8381−8390

(12) Pal, R.; Das, P.; Chakrabarti, K.; Chakraborty, A.; Chowdhury, A. Butachlor degradation in tropical soils: effect of application rate, biotic-abiotic interactions and soil conditions. *J. Environ. Sci. Health, Part B* **2006**, *41*, 1103−1113.
(13) Zhang, J.; Zheng, J. W.; Liang, B.; Wang, C. H.; Cai, S.; Ni, Y. Y.; Li, S. P. Biodegradation of chloroacetamide herbicides by *Paracoccus* sp. FLY-8 in vitro. *J. Agric. Food Chem.* **2011**, *59*, 4614−4621.
(14) Kim, N. H.; Kim, D. U.; Kim, I.; Ka, J. O. Syntrophic biodegradation of butachlor by *Mycobacterium* sp. J7A and *Sphingobium* sp. J7B isolated from rice paddy soil. *FEMS Microbiol. Lett.* **2013**, *344*, 114−120.
(15) Liu, H. M.; Cao, L.; Lu, P.; Ni, H. Y.; Li, Y. X.; Yan, X.; Hong, Q.; Li, S. P. Biodegradation of butachlor by *Rhodococcus* sp. strain B1 and purification of its hydrolase (ChlH) responsible for N-dealkylation of chloroacetamide herbicides. *J. Agric. Food Chem.* **2012**, *60*, 12238−12244.
(16) Chen, Q.; Wang, C. H.; Deng, S. K.; Wu, Y. D.; Li, Y.; Yao, L.; Jiang, J. D.; Yan, X.; He, J.; Li, S. P. Novel three-component rieske non-heme iron oxygenase system catalyzing the N-dealkylation of chloroacetanilide herbicides in sphingomonads DC-6 and DC-2. *Appl. Environ. Microbiol.* **2014**, *80*, 5078−5085.
(17) Weisburg, W. G.; Barns, S. M.; Pelletier, D. A.; Lane, D. J. 16S ribosomal DNA amplification for phylogenetic study. *J. Bacteriol.* **1991**, *173*, 697−703.
(18) Altschul, S. F.; Gish, W.; Miller, W.; Myers, E. W.; Lipman, D. J. Basic local alignment search tool. *J. Mol. Biol.* **1990**, *215*, 403−410.
(19) Larkin, M. A.; Blackshields, G.; Brown, N. P.; Chenna, R.; McGettigan, P. A.; Valentin, F. Clustal W and clustal X version 2.0. *Bioinformatics* **2007**, *23*, 2947−2948.
(20) Tamura, K.; Dudley, J.; Nei, M.; Kumar, S. MEGA 4: molecular evolutionary genetics analysis (MEGA) software version 4.0. *Mol. Biol. Evol.* **2007**, *24*, 1596−1599.
(21) Bradford, M. M. A rapid and sensitive method for the quantitation of microgram quantities of protein utilizing the principle of protein-dye binding. *Anal. Biochem.* **1976**, *72*, 248−254.
(22) Kambiranda, D. M.; Asraful-Islam, S. M.; Cho, K. M.; Math, R. K.; Lee, Y. H.; Kim, H.; Yun, H. D. Expression of esterase gene in yeast for organophosphates biodegradation. *Pestic. Biochem. Physiol.* **2009**, *94*, 15−20.
(23) Park, Y. J.; Chu, Y. J.; Shin, Y. H.; Lee, E. Y.; Kim, H. S. Molecular cloning and characterization of a novel acetylalginate esterase gene in *alg* operon from *Sphingomonas* sp. MJ-3. *Appl. Microbiol. Biotechnol.* **2014**, *98*, 2145−2154.
(24) Nam, J. K.; Park, Y. J.; Lee, H. B. Cloning, expression, purification, and characterization of a thermostable esterase from the archaeon *Sulfolobus solfataricus* P1. *J. Mol. Catal. B: Enzym.* **2013**, *94*, 95−103.
(25) Nguyen, H. D.; Studenik, S.; Diekert, G. Corrinoid activation by a RACE protein: studies on the interaction of the proteins involved. *FEMS Microbiol. Lett.* **2013**, *345*, 31−38.
(26) Chen, Q.; Yao, L.; Wang, C. H.; Deng, S. K.; Chu, C. W.; He, J. Isolation and characterization of acetochlor-degrading strain *Sphingomonas* sp. DC-6 and preliminary studies on its metabolic pathway. *J. Agric. Sci. Technol.* **2013**, *15*, 67−74.
(27) Wang, J. H.; Lu, Y. T.; Chen, Y. Y. Comparative proteome analysis of butachlor-degrading bacteria. *Environ. Geol.* **2008**, *53*, 1339−1344.
(28) Feng, L. P.; Xiong, M. H.; Cheng, X. S.; Hou, N.; Li, C. Y. Construction and analysis of an intergeneric fusant able to degrade bensulfuron-methyl and butachlor. *Biodegradation* **2013**, *24*, 47−56.
(29) Li, Y.; Chen, Q.; Wang, C. H.; Cai, S.; He, J.; Huang, X.; Li, S. P. Degradation of acetochlor by consortium of two bacterial strains and cloning of a novel amidase gene involved in acetochlor-degrading pathway. *Bioresour. Technol.* **2013**, *148*, 628−631.
(30) Tuo, B. H.; Yan, J. B.; Fan, B. A.; Yang, Z. H.; Liu, J. Z. Biodegradation characteristics and bioaugmentation potential of a novel quinoline-degrading strain of *Bacillus* sp. isolated from petroleum-contaminated soil. *Bioresour. Technol.* **2012**, *107*, 55−60.
(31) Li, G. Y.; Zu, L.; Wong, P. K.; Hui, X. P.; Lu, Y.; Xiong, J. K.; An, T. C. Biodegradation and detoxification of bisphenol A with one newly-isolated strain *Bacillus* sp. GZB: kinetics, mechanism and estrogenic transition. *Bioresour. Technol.* **2012**, *114*, 224−230.
(32) Lu, M.; Zhang, Z. Z.; Wu, X. J.; Xu, Y. X.; Su, X. L.; Zhang, M.; Wang, J. X. Biodegradation of decabromodiphenyl ether (BDE-209) by a metal resistant strain, *Bacillus cereus* JP12. *Bioresour. Technol.* **2013**, *149*, 8−15.
(33) Zu, L.; Li, G. Y.; An, T. C.; Wong, P. K. Biodegradation kinetics and mechanism of 2,4,6-tribromophenol by *Bacillus* sp. GZT: a phenomenon of xenobiotic methylation during debromination. *Bioresour. Technol.* **2012**, *110*, 153−159.
(34) Chu, X. Q.; Pang, G. H.; Fang, H.; Wang, X. G.; Gao, C. M.; Yu, Y. L. Isolation, identification and characteristics of a butachlor-degrading bacterium. *Chin. J. Agro-Environ. Sci.* **2009**, *28*, 145−150.
(35) Chen, Y. L.; Wu, T. C. Degradation of herbicide butachlor by soil microbes. *J. Pestic. Sci.* **1978**, *3*, 411−417.
(36) Chakraborty, S. K.; Bhattacharyya, A. Degradation of butachlor by two soil fungi. *Chemosphere* **1991**, *23*, 99−105.
(37) Chu, X. Q. *A Butachlor-Degrading Bacterium and Its Application in Wastewater Treatment and Soil Pollution Remediation*. Doctoral dissertation, Zhejiang University, Hangzhou, China, 2009.

DOI: 10.1021/acs.jafc.5b03326
J. Agric. Food Chem. 2015, 63, 8381−8390

water treatment to removal organic pollutants and heavy metals have been extensively tested,[17,18] studies on the use of biosorbents in the preparation of CRFs have emerged in recent years.[19,20]

The main objective of this research was the development of azadirachtin alginate-based CRFs using biosorbents as modifying agents not only to control the release rate of azadirachtin but also to stabilize this botanical insecticide against degradation.

To achieve this objective, the following tasks were performed: (i) preparation of azadirachtin alginate-based formulations using biosorbents like kraft lignin, olive pomace, and humic acid, (ii) characterization of prepared formulations, and (iii) evaluation of azadirachtin formulations through kinetic and photodegradation studies.

MATERIALS AND METHODS

Materials. Azadirachtin from a neem tree (17.7%) was provided from The Indian Neem Tree Company, Mumbai, India. The chemical structure of azadirachtin is shown in Figure 1.

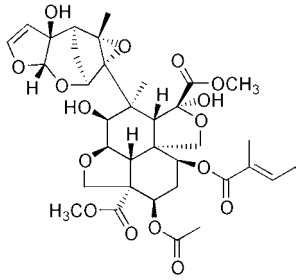

Figure 1. Chemical structure of azadirachtin.

Alginic acid was used as sodium salt obtained from *Macrocystis pyrifera*, and calcium chloride (97%) and sodium tripolyphospate (90%) were provided by Sigma-Aldrich Co LLC.

The lignin used in this study was a commercially available pine kraft lignin, Indulin AT (Westvaco Corp., Charleston, SC, USA). The olive pomace used in this study was obtained from a three phases extraction procedure on olive oil by the company Almazara de Felix S.C.A. The humic acid was provided by the company Sigma-Aldrich Co., LLC.

Chemical Analysis of Modifying Agents. The elemental analyses of lignin, humic acid, and olive pomace were performed for C, H, N, O, and S in an elemental analyzer from Elementar, model Vario Micro CHNS-O.

All of these characteristics of the modifying agents are shown in Table 1.

The total surface acidity (R-COOH, Ar-COOH, and Ar-OH groups) of humic acid and olive pomace was determined using the Schnitzer and Gupta method.[21] The total amount of carboxylic groups was determined using the method proposed by Schnitzer and Wright.[21,22] The total amount of phenolic hydroxyl groups was determined following the method proposed by Schnitzer,[22] that is

$$(\text{total surface acidity}) - (\text{carboxylic groups}) = \text{phenolic hydroxyl groups (meq g}^{-1})$$

These data are given in Table 1. The organic matter content of lignin, humic acid, and olive pomace was determined by the Walkley-Black method.[23] These data are given in Table 1.

Preparation of the Azadirachtin CRFs. The prepared CRFs were based on the gelling properties of the alginate in the presence of divalent cations. It was made up of formulations in water containing different percentages of technical grade azadirachtin (Az), sodium alginate (A), lignin (L), humic acid (H), and olive pomace (O) (shown in Table 2). These mixtures were vigorously stirred for 1 h.

Table 2. Percentage (by Weight) of the Components of CR Formulations Containing Azadirachtin

formulation[a]	azadirachtin	alginate	lignin	humic acid	olive pomace	water
AAz	0.28	1.47				98.25
AOAz	1.17	1.40			4.75	92.69
AHAz	1.17	1.40		4.75		92.69
ALAz	1.17	1.40	4.75			92.69

[a]AAz: alginate-azadirachtin. AOAz: alginate-olive pomace-azadirachtin. AHAz: alginate-humic acid-azadirachtin. ALAz: alginate-lignin-azadirachtin.

The alginate mixtures (100 g) were dropwise added to a 250 mL gellant bath of 0.25 M $CaCl_2$, as was described previously.[14] The resulting beads were allowed to gel in the 0.25 M $CaCl_2$ solution for a total of 20 min, then they were filtered and dried first at room temperature and then in an oven (40 °C) to constant weight. CRF granules were maintained in an oven at controlled environment (40 °C) before experiments were carried out. The resulting products are labeled in the text as AAz, ALAz, AHAz, and AOAz.

Azadirachtin CRFs Characterization. *Determination of Azadirachtin Content in CRFs.* The concentration of azadirachtin in the CRFs was determined by dissolving 20 mg of the dry granules in a 0.03 M tripolyphosphate solution (5 mL). This solution was placed in stoppered conical flasks and shaken in a thermostatic bath at 25 °C ± 0.1 °C for 2 h. After that, 80 mL of a methanol/water mixture (80:20 v/v) was added, and the solutions were left in the thermostatic bath at the same conditions for 24 h. The resulting extract was made up to 100 mL with methanol/water mixture (80:20 v/v) and filtered using 0.20 μm syringe nylon filters (Millex GN, Millipore Co., Billerica, MA USA). The insecticide concentration was determined by HPLC, using a Beckman Coulter Inc., System Gold HPLC (Fullerton, CA, USA) equipped with a diode-array detector and 32 Karat data station. HPLC operating conditions to analyze azadirachtin were described previously by other authors.[24−26] The mobile phase was an acetonitrile−water mixture 40:60, the flow rate was 1 mL/min, and the column used was a Nova-Pak C18 4 μm 3.9 × 150 mm supplied by Waters Assoc. (Massachusetts, USA). The analysis was performed at the wavelength of 217 nm by injecting a volume of 50 μL. External standard calibration was used, and three replicates were carried out for each formulation.

Mean Granule Size and Average Granule Mass. The average diameter of CR granules was determined using a Stereoscopic Zoom Microscope from Nikon, model SMZ1000, provided with a camera

Table 1. Physicochemical Characteristics of Modifying Agents

	elemental analysis (%)					total surface acidity (meq g^{-1})			organic matter content (%)	
modifying agent	C	S	H	N	O	total acidity	−COOH groups	−OH groups	O.C.	O.M
olive pomace	53.91	<1	7.32	1.18	36.59	8.51	0.70	7.81	40.12	69.01
humic acid	45.28	1.77	4.09	<1	47.86	5.36	1.07	4.29	32.61	56.09
lignin	62.54	1.67	5.75	<1	29.04				50.44	86.76

DOI: 10.1021/acs.jafc.5b03255
J. Agric. Food Chem. 2015, 63, 8391−8398

PixelLINK (Megapixel FireWire Camera) model PL-A662. Each measure was taken through the analysis of a basis of 20 particles using the software Image Pro-Plus 6.0.

To determine the average mass of the granules, an analytical balance Mettler Toledo model AG245 was used. Different populations of 10 granules were weighed 5 times to calculate the average mass per granule.

Morphological Study. The morphological and structural surface of the formulations was examined using a Hitachi S-3500-N scanning electron microscope (SEM) at the required magnification at room temperature. The granules were deposited on brass holds and sputtered with a thin coat of gold under vacuum. The acceleration voltage used was 10 kV with secondary electron image as a detector. To examine the internal morphology, the granules were carefully cut with the aid of a chisel, and their cross-sections were photomicrographed.

Water Uptake Tests. The water uptake was measured for granules using the method of Franson and Peppas.[27] Granules were immersed in water using stoppered conical flasks and shaken in a thermostatic bath at 25 °C ± 0.1 °C. Then, they were removed periodically (see Results and Discussion for intervals). The excess water was blotted from the surface of the granules using filter paper, and after that, granules were weighed. Three replicates (10 granules in each replicate) were carried out. The granules were then dried, first at room temperature and then in an oven (40 °C), to constant weight. The water uptake (g g^{-1} dry granule) was calculated.

Water Release Kinetics. For each formulation and technical azadirachtin (two replicates), an accurately weighed quantity of granules containing 8 mg of azadirachtin was added to 500 mL of distilled water and placed into stoppered conical flasks. Flasks were kept in a thermostatic bath at 25 (±0.1) °C. At different time intervals, aliquots of 0.5 mL were removed to determine azadirachtin concentration, and 0.5 mL of fresh water was added to the flasks to maintain sinking conditions.

Photodegradation Study. Photodegradation studies were carried out at 25 °C using a solar simulator Xenoterm model 1500RA from SECCI (Barcelona, Spain) provided with a xenon lamp (1500 W). An accurately weighed quantity of the different formulations (AAz and ALAz) and technical grade azadirachtin, containing about 1.5 mg of azadirachtin, were placed in Pyrex glass Petri dishes. The samples were placed in the solar simulator and were taken off the apparatus at different time intervals. These samples were extracted by the method described Azadirachtin CRFs Characterization section to determine the remaining amount of azadirachtin in each formulation. Dark controls of all experiments were conducted keeping Pyrex glass Petri dishes containing the different formulations at 25 °C. All experiments were carried out in duplicate.

RESULTS AND DISCUSSION

Azadirachtin CRF Characterization. Characteristics of alginate-based CR granules (dry products) containing azadirachtin are shown in Table 3. The results of practical azadirachtin loading and entrapment efficiency (EE) were calculated using eqs 1 and 2.

Table 3. Characteristics of Controlled Release Granules Containing Azadirachtin

formulation	theoretical azadirachtin loading (%)[a]	practical azadirachtin loading (%)	EE (%)	mean granule size (mm)	average granule mass (mg)
AAz	2.83	1.17	41.34	1.06	0.456
AOAz	2.83	2.55	90.10	1.93	4.234
AHAz	2.83	2.31	81.62	1.59	1.552
ALAz	2.83	2.81	99.50	1.96	1.379

[a]Theoretical azadirachtin loading (%) = (total amount of azadirachtin used to prepare the formulation/total amount of solid components used in the formulation process) × 100.

$$\text{practical azadirachtin loading (\%)} = \left(\frac{\text{amount of azadirachtin in CR granules}}{\text{amount of CR granules}}\right) \times 100 \quad (1)$$

$$\text{entrapment efficiency (\%)} = \left(\frac{\text{practical azadirachtin loading}}{\text{theoretical azadirachtin loading}}\right) \times 100 \quad (2)$$

The practical azadirachtin loadings ranged between 1.17% for AAz formulation and 2.81% for ALAz formulation. This insecticide content is suitable for a practical agricultural application.[28] The granules were generally spherically shaped, and the technical grade azadirachtin was readily incorporated in the alginate matrix, obtaining granules of size between 1.06 for AAz formulation mm and 1.96 mm for ALAz formulation. The addition of lignin, humic acid, and olive pomace to the alginate formulations led to larger and heavier granules that were spherical and dried with less aggregation. The addition of lignin to the alginate formulation led to the largest granules. The average mass of these granules oscillated between 0.456 mg/granule for the formulation AAz and 4.234 mg/granule for the formulation AOAz. The values of entrapment efficiency ranged between 41.43% for the formulation AAz and 99.50% for the formulation ALAz. In the granules containing modifying agents, the entrapment efficiency was higher than 81.62%, the highest value corresponding to the formulation prepared with lignin as modifying agent (99.50%), which may be attributed to the difference of the molecular structure among lignin, olive pomace, and humic acid. These data show the validity of the used method for the encapsulation of azadirachtin, mainly in the presence of modifying agents. Previous studies of encapsulation of synthetic pesticides with alginate and sorbents like bentonite, activated carbon and anthracite used as modifying agents showed higher entrapment efficiency values using these sorbents.[12−14]

Morphological Study. SEM pictures from the external morphology of the different azadirachtin controlled release formulations prepared are shown in Figure 2. A spherical shape for all the formulations that contain a modifying agent can be observed. From these formulations, the one that obtains a higher homogeneity is that modified with lignin (Figure 2b). An irregular morphology is shown by the formulation prepared without a modifying agent (Figure 2a).

SEM pictures with a higher resolution (×500) were also taken (Figure 3). The above-mentioned observations were confirmed, showing that the formulation AAz had some cracks (Figure 3a) that will affect the release of azadirachtin from the granules.

Water Uptake Test. The amount of water uptake by the different alginate-modifying sorbent granules is presented in Figure 4. Water uptake curves were characterized by a fast initial uptake of water followed by an apparent equilibrium or a slow water uptake. The plot of the water uptake versus time showed that the granules containing humic acid or olive pomace reached the water uptake equilibrium in approximately 2 h, with at least 24 h being necessary for lignin-based granules. The highest water absorption quantity is reached by the formulation modified by lignin, followed by the one modified with humic acid, showing the one modified with olive pomace had the lowest water uptake. Moreover, the granules retained their spherical morphology throughout the study without any disruptions.

The addition of olive pomace to the alginate formulation generated a greater density of the granules which can be due to

DOI: 10.1021/acs.jafc.5b03255
J. Agric. Food Chem. 2015, 63, 8391−8398

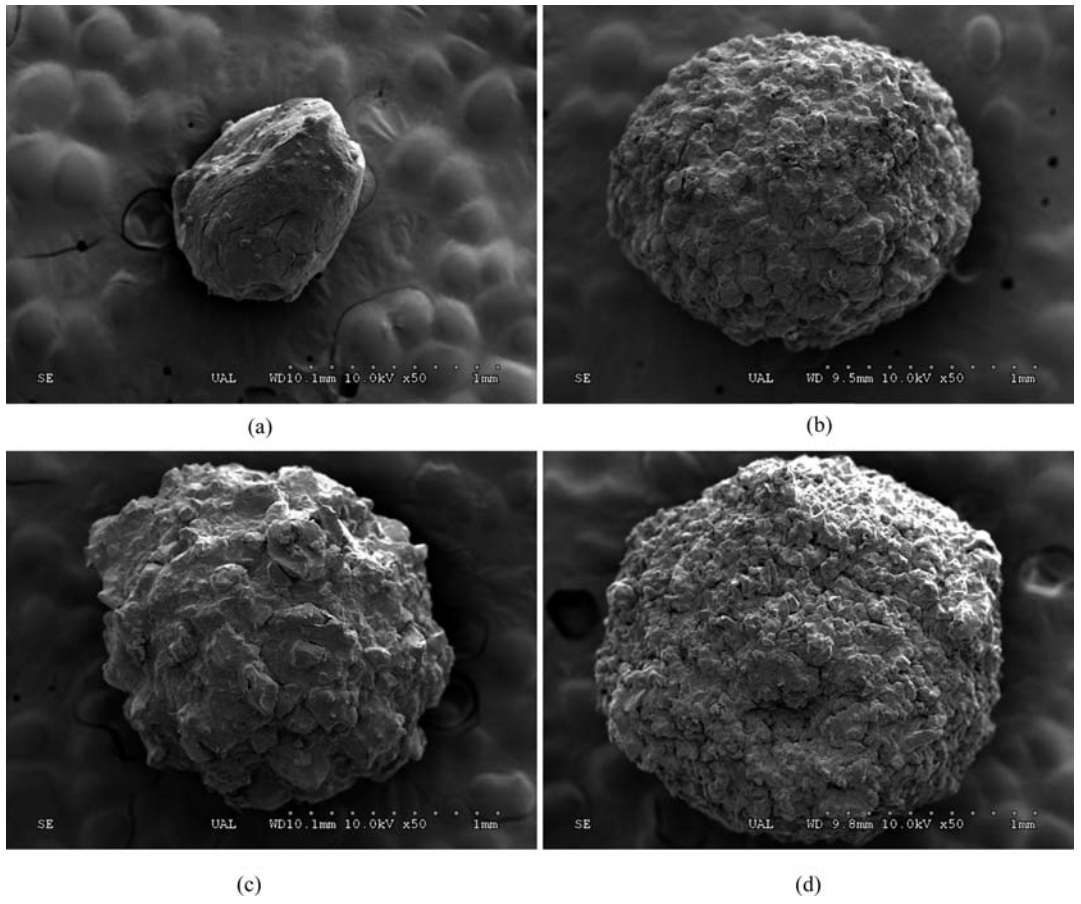

Figure 2. SEM of the shape and external morphology (×50 magnification): AAz (a), ALAz (b), AHAz (c), and AOAz (d).

the higher cross-linking between this sorbent and the hydrophilic groups of alginate chains. Consequently, the water uptake for olive pomace granules was lower than that obtained for granules prepared with lignin or humic acid as sorbents.[29] Thus, water uptake and intensity of interactions of the azadirachtin with lignin, humic acid, and olive pomace could affect the diffusion through the granules and hence the release of the active ingredient.

Water Release Kinetics. The effect of modifying agents on the release of azadirachtin from alginate granules was investigated. When the polymer matrix was placed in water, the granules swelled because of the absorption of water, and then, azadirachtin in the swollen part diffused out of the polymer matrix. In vitro release profiles of alginate CRFs and technical grade azadirachtin are shown in Figure 5.

From this figure, we can deduce that the granules made with alginate and azadirachtin (AAz) produced a slower release rate than the technical grade azadirachtin. It can be appreciated that 80% of technical grade azadirachtin was dissolved in less than 6 h but that it was necessary to have at least 192 h to release the same percentage of azadirachtin from the alginate-based CR formulation AAz.

The influence of the modifying agents such as lignin, humic acid, and olive pomace, appeared clearly defined for all CR formulations prepared. In this sense, the presence of the modifiers produced a slower release rate in comparison to the CRFs prepared without these modifiers (AAz) as is shown in Figure 4. It is observed that the addition of modifying sorbents produced a decrease in the release rate of active ingredient, which was higher for lignin than those prepared with humic acid and olive pomace, according to the difference observed between the release profiles. From Figure 5, it can be seen that approximately 58%, 78%, and 99% of azadirachtin is released in 550 h for the formulations ALAz, AHAz, and AOAz, respectively.

For all formulations, a decrease in the release rate of insecticide over time was observed. This result is probably due to an increase in the distance where dissolved molecules have to diffuse as the depleted zone advances to the center of the matrix. In diffusion-controlled matrix systems, this usually means that the release is proportional to the square root of time.[30] The formulations of this research are described as systems containing finely divided solute particles, which are uniformly dispersed within the matrix phase. Higuchi[31] originally analyzed analogous systems, such as drugs dispersed in a stationary matrix. In these spherical monoliths systems, Higuchi suggested the following equation assuming Fickian diffusion ($y = kt^{1/2}$):[31]

$$\left[\frac{1-\left(1-\frac{M_t}{M_0}\right)^{2/3}-\frac{2}{3}\frac{M_t}{M_0}}{2}\right]^{1/2} = K_H t^{1/2};$$

$$K_H = \left(\frac{1}{C_0 r^2}P\right)^{1/2} \quad (3)$$

where M_t/M_0 is the fraction of active ingredient released at time t, and K_H is a constant that depends on the radius of the sphere (r), the initial concentration of the active ingredient (C_0), and the permeability of the matrix (P). The K_H values and correlation

DOI: 10.1021/acs.jafc.5b03255
J. Agric. Food Chem. 2015, 63, 8391−8398

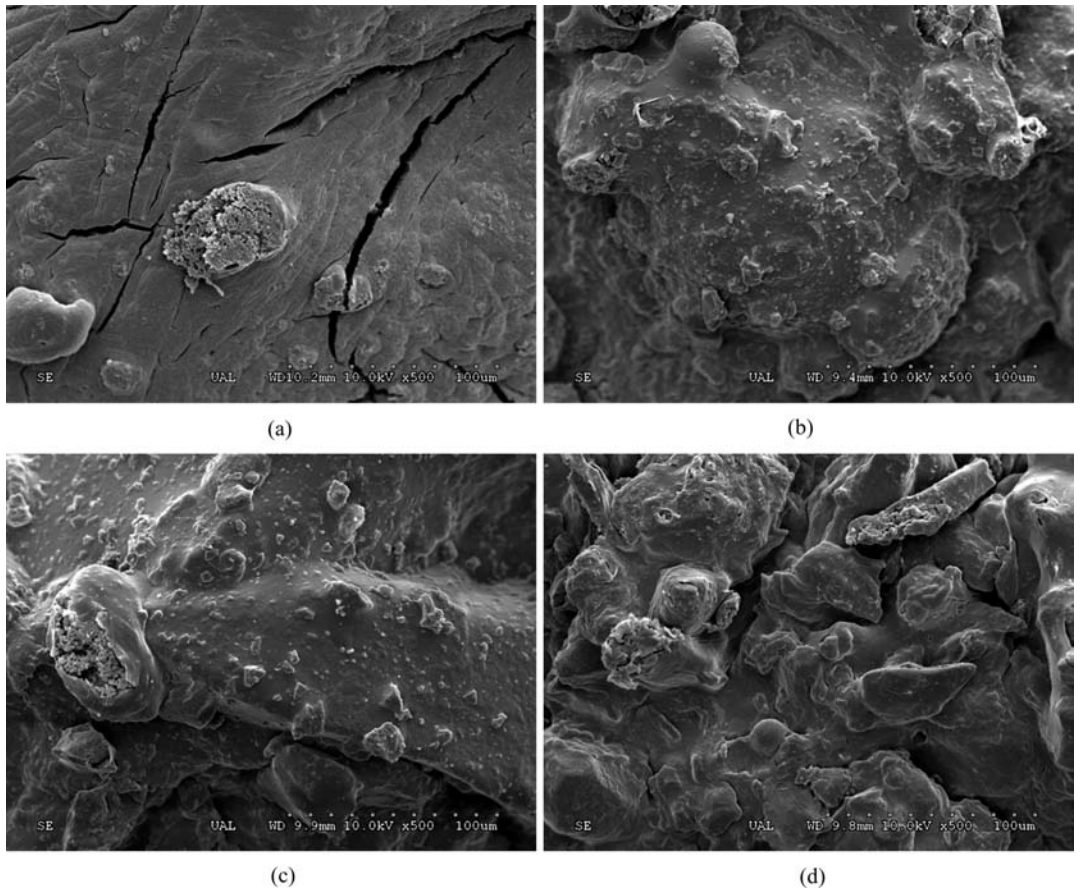

Figure 3. Detail of the surface morphology (×500 magnification): AAz (a), ALAz (b), AHAz (c), and AOAz (d).

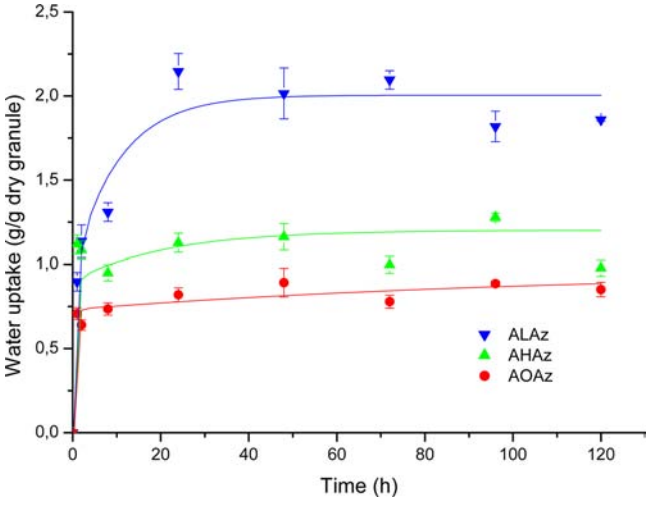

Figure 4. Water uptake of azadirachtin controlled release granules over time.

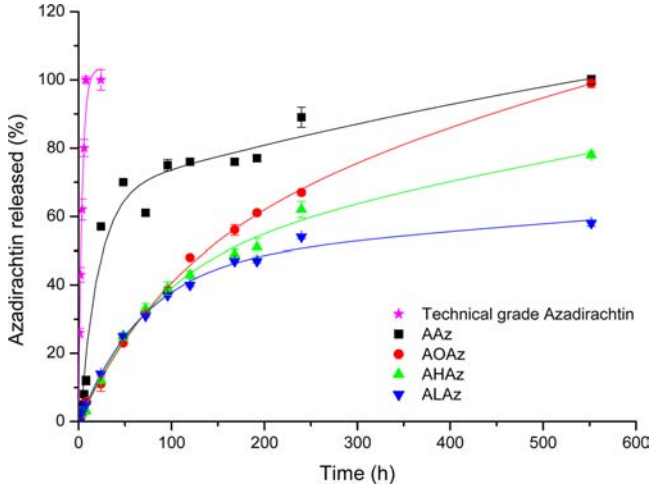

Figure 5. Cumulative release of azadirachtin from technical grade product and controlled release granules in water.

coefficients were obtained by applying the model proposed by Higuchi to release data, using the nonlinear curve-fitting utility of SigmaPlot software (version 9.0, Systat Software, Inc.). These values are presented in Table 4 together with values of *P*. The Higuchi model gave values of r^2 higher than 0.91, indicating that this model was suitable to describe the release of the azadirachtin from CRFs. For all formulations, the values of K_H were in the order of 10^{-2} $h^{-1/2}$.

Table 4. Constants from Fitting the Higuchi Equation to Release Data of Azadirachtin in Water and the Matrix Permeability Parameter

formulation	$K_H \times 10^2$ ($h^{-1/2}$)	R^2	$P \times 10^7$ (g $h^{-1}cm^{-1}$)
AAz	1.89	0.918	0.0977
AOAz	1.31	0.919	0.5222
AHAz	1.02	0.975	0.1277
ALAz	0.84	0.934	7.599

DOI: 10.1021/acs.jafc.5b03255
J. Agric. Food Chem. 2015, 63, 8391−8398

The variation order for K_H values was ALAz < AHAz < AOAz < AAz.

This variation order suggests that the factors which affect the K_H parameter and the release of active ingredient from the different granules studied should be the same and therefore produced by the presence of modifying agents as lignin, humic acid, and olive pomace. The variation observed for P values can be explained according to the different masses and sizes of the prepared granules that affect the C_0 values.

To simplify the analysis of curves from three-dimensional devices, the release data were analyzed by applying the empirical equation proposed by Ritger and Peppas:[32]

$$\frac{M_t}{M_0} = Kt^n \quad (4)$$

where M_t/M_0 is the percentage of active ingredient released at time t, K is a constant that incorporates characteristics of the macromolecular network system and the active ingredient, and n is a diffusional parameter, which is indicative of the transport mechanism.

The values of K and n obtained from 90% of maximum azadirachtin released, in each curve (Figure 4), were obtained using the nonlinear curve-fitting utility of SigmaPlot software. These values and the correlations coefficients are presented in Table 5. According to correlation coefficients, we can deduce that

Table 5. Constants from Fitting the Empirical Equation $M_t/M_o = Kt^n$ to Release Data of Azadirachtin in Water

formulation	$K \times 10^2$	n	r^2	T_{50} (h)
AAz	10.11	0.408	0.89	50.29
AOAz	1.55	0.697	0.99	146.25
AHAz	2.02	0.626	0.99	168.35
ALAz	2.49	0.569	0.99	194.79

the release profiles of insecticide azadirachtin fit well to the empirical equation. The n values ranged from 0.408 for AAz formulation up to 0.697 for AOAz formulation. Values of n close to 0.43 are indicative of Fickian diffusion in spherical monolithic matrixes.[32] The fact is that slightly different values of n equal to 0.43 could be explained by the complexity of the heterogeneous system involved together with the capacity of the modifying agents, olive pomace, humic acid, and lignin, to interact with the active ingredient. That is the reason why in these special cases, diffusion is not the only factor to consider in the release process.

The K values range between 10.11×10^{-2} h^{-n} for AAz and 1.55×10^{-2} h^{-n} for AOAz. After the analysis of these data, it was found that the use of modifying agents leads to lower K parameter values.

In general, the monolith systems in this study consist of a hydrophilic network of alginate and calcium ions with the active ingredient azadirachtin dispersed in it, which makes up water quickly as indicated in the water uptake section. These systems were changed in some cases by the addition of olive pomace, humic acid, and lignin. All of them made an alginate hydrogel with a continuous membrane around the insecticide and modifying agents. In this situation, the solid active ingredient was dissolved, spread through the macromolecular network, and released to the environment. Considering the molecular weight of azadirachtin (720.7 g mol^{-1}), it was not probably that steric impediments were produced by the alginate hydrogel. However, the crossing areas of alginate could make the movement of the active ingredient difficult.[33] In fact, the presence of modifying agents such as olive pomace, humic acid, and lignin increased the centers of interaction with azadirachtin. Additionally, the time taken for 50% of the insecticide to be released (T_{50}) was calculated from K and n constants and also presented in Table 5. The order of variation if this was the parameter for the prepared CRFs was AAz ≪ AOAz < AHAz < ALAz.

The lowest value of T_{50} means that this CRF produced the fastest azadirachtin release in water. The addition of biosorbents, olive pomace, humic acid, and lignin to the basic alginate formulation reduced the release rate. The formulation prepared with lignin as modifying agent produced the slowest release rate. So, the T_{50} values obtained could be explained if we take into account the different O. M. content and aromaticity of the biosorbent used in each case and the extent of the interactions between insecticide and biosorbents. These interactions will affect the diffusing process and thus the release rate of azadirachtin from the alginate-based granules.

Photodegradation Study. The aim of this experiment was to compare the efficiency of CRFs to improve the stability of azadirachtin against to photodegradation. For that, AAz, ALAz, and technical grade azadirachtin were tested under simulated sunlight.

In Figure 6, the stability of azadirachtin-loaded alginate granules and technical grade azadirachtin subjected to sunlight

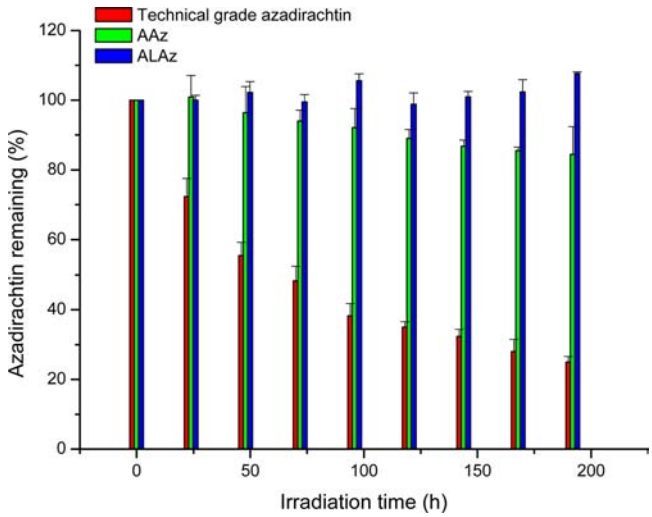

Figure 6. Percentage of remaining azadirachtin after simulated sunlight exposure.

irradiation is reported in terms of the percentage of azadirachtin remaining versus irradiation time. As shown in Figure 6, the azadirachtin remaining for AAz granules was 84.4% and 100% for ALAz granules after irradiating by sunlight for 192 h. In the case of technical grade azadirachtin, the azadirachtin remaining was 27.7% after 192 h irradiation time.

According to these values, the order of photostability of the formulations investigated under the experimental conditions was

technical grade azadirachtin < AAz < ALAz

These results showed that AAz formulation provided a moderate degree of azadirachtin photoprotection while the lignin-based formulation provided complete protection against simulated sunlight over the whole experiment. This can be explained if we consider that lignin is a biopolymer with different functional groups able to absorb UV radiation due to the presence of aromatic rings and "π" bonds in their structure.[34]

DOI: 10.1021/acs.jafc.5b03255
J. Agric. Food Chem. 2015, 63, 8391−8398

Thus, lignin was suitable to stabilize azadirachtin against photodegradation by absorption of UV radiation by the chromophores. Besides, the alginate-derived oligosaccharides have been used as potential UV protector in the areas of functional foods[35,36] and biological control.[37]

Some natural ultraviolet light absorbers such as ferulic acid, gallic acid, aloin, and rutin have been researched as photostabilizers of azadirachtin. These natural products showed a moderate degree of azadirachtin photostabilization with dissipation half-life ranging between 14.41 and 20.21 h.[5]

This study demonstrates that the use of natural polymers such as lignin and alginate to encapsulate azadirachtin improve its stability against photodegradation. These biosorbents can be selected and matched to stabilize UV-labile biopesticides. Therefore, this encapsulation method could be used to enhance the storage period of azadirachtin under conditions that cause photodegradation.

In conclusion, alginate and biosorbents have been used to optimize hybrid hydrogel-based CRFs for the botanical insecticide azadirachtin. High EE values for azadirachtin have been obtained using biosorbents as modifying agents, reaching a value of 99.5% for the lignin alginate-based formulation. SEM studies demonstrated that the use of modifying agents improves the formulation's homogeneity. The kinetic experiments of release in water have shown that the use of lignin, olive pomace, and humic acid as modifying agents of the alginate formulations reduces the release rate of the azadirachtin in comparison with that of the technical product and with alginate formulations without modifying agents and shows the highest decrease in release rate corresponding to the formulation prepared with lignin. The data obtained from photodegradation experiments indicated that natural polymers such as kraft lignin and alginate can be used to protect azadirachtin against photodegradation.

Therefore, these new formulations could be used to improve the delivery of the azadirachtin to its site of action and also to improve its photostability, developing new procedures to encapsulate botanical pesticides.

AUTHOR INFORMATION

Corresponding Author

*Tel: +34950015961. Fax: +34950015008. E-mail: mfernand@ual.es.

Funding

This research has been financially supported by the Ministerio de Ciencia e Innovación, Spain, Project AGL2010-18286 cofinanced by FEDER.

Notes

The authors declare no competing financial interest.

REFERENCES

(1) Copping, L. G.; Menn, J. J. Biopesticides: A review of their action, applications and efficacy. *Pest Manage. Sci.* **2000**, *56*, 651−676.

(2) Luiz de Oliveira, J.; Ramos Campos, E. V.; Bakshi, M.; Abhilash, P. C.; Fernandes Fraceto, L. Application of nanotechnology for the encapsulation of botanical insecticides for sustainable agriculture: Prospects and promises. *Biotechnol. Adv.* **2014**, *32*, 1550−1561.

(3) Devi, N.; Maji, T. K. Neem Seed Oil: Encapsulation and Controlled Release-Search for a Greener Alternative for Pest Control. In *Pesticides in the Modern World: Pesticides Use and Management*; Stoytcheva, M., Ed; InTech: Rijeka, Croatia, 2011; pp 191−232.

(4) Dureja, P.; Johnson, S. Photodegradation of azadirachtin-A: A neen-based pesticide. *Curr. Sci.* **2000**, *79*, 1700−1703.

(5) Tan, W.-H.; Song, Z.-Q. Research on effect of four natural ultraviolet light absorbers on photostabilization of azadirachtin. *Agric. Sci. China* **2006**, *5* (11), 855−858.

(6) Martins, I. M.; Barreiro, M. F.; Coelho, M.; Rodrigues, A. E. Microencapsulation of essential oils with biodegradable polymeric carriers for cosmetic applications. *Chem. Eng. J.* **2014**, *245*, 191−200.

(7) Kulkarni, A. R.; Soppimath, K. S.; Aminabhavi, T. M.; Mehta, M. H.; Dave, A. M. Urea−formaldehyde crosslinked starch and guar gum matrices for encapsulation of natural liquid pesticide [Azadirachta Indica A. Juss. (neem) seed oil]: swelling and release kinetics. *J. Appl. Polym. Sci.* **1999**, *73*, 2437−2446.

(8) Kumbar, S. G.; Kulkarni, A. R.; Dave, A. M.; Aminabhavi, T. M. Encapsulation efficiency and release kinetics of solid and liquid pesticides through urea formaldehyde crosslinked starch, guar gum, and starch + guar gum matrices. *J. Appl. Polym. Sci.* **2001**, *82*, 2863−2866.

(9) Forim, M. R.; Soares Costa, E.; das Graças Fernandes da Silva, M. F.; Batista Fernandes, J.; Marques Mondego, J.; Boiça Junior, A. L. Development of a new method to prepare nano-/microparticles loaded with extracts of *azadirachta indica*, their characterization and use in controlling *plutella xylostella*. *J. Agric. Food Chem.* **2013**, *61*, 9131−9139.

(10) Kulkarni, R.; Soppimath, K. S.; Aminabbavi, T. M.; Dave, A. M.; Mehta, M. H Glutaraldehyde crosslinked sodium alginate beads containing liquid pesticide for soil application. *J. Controlled Release* **2000**, *63*, 97−105.

(11) Riyajan, S.; Sakdapipanich, J. T. Encapsulated neem extract containing Azadiractin-A *within* hydrolyzed poly(vinyl acetate) for controlling its release and photodegradation stability. *Chem. Eng. J.* **2009**, *152*, 591−597.

(12) Fernández Pérez, M.; Flores Céspedes, F.; González Pradas, E.; Villafranca Sánchez, M.; Pérez García, S.; Garrido Herrera, F. J. Use of activated bentonites in controlled release formulations of atrazine. *J. Agric. Food Chem.* **2004**, *52*, 3888−3893.

(13) Fernández Pérez, M.; Villafranca Sánchez, M.; Flores Céspedes, F.; Garrido-Herrera, F. J.; Pérez-García, S. Use of bentonite and activated carbon in controlled release formulations of carbofuran. *J. Agric. Food Chem.* **2005**, *53*, 6697−6703.

(14) Flores Céspedes, F.; Villafranca Sánchez, M.; Pérez García, S.; Fernández Pérez, M. Modifying sorbents in controlled release formulations to prevent herbicides pollution. *Chemosphere* **2007**, *69*, 785−794.

(15) Gadd, G. M. Biosorption: critical review of scientific rationale, environmental importance and significance for pollution treatment. *J. Chem. Technol. Biotechnol.* **2009**, *84*, 13−28.

(16) Arthurs, S. P.; Lacey, L. A.; Behle, R. W. Evaluation of spray dried lignin-based formulations and adjuvants as solar protectants for the granulovirus of the codling moth, *Cydia pomonella* (L). *J. Invertebr. Pathol.* **2006**, *93*, 88−95.

(17) Tran, V. S.; Ngo, H. H.; Guo, W.; Zhang, J.; Liang, S.; Ton-That, C.; Zhang, X. Typical low cost biosorbents for adsorptive removal of specific organic pollutants from water. *Bioresour. Technol.* **2015**, *182*, 353−363.

(18) Gupta, V. K.; Nayak, A.; Agarwal, S. Bioadsorbents for remediation of heavy metals: Current status and their future prospects. *Environ. Eng. Res.* **2015**, *20*, 1−18.

(19) Shakeel, F.; Haq, N.; Alanazi, F. K.; Alsarra, I. A. Polymeric solid self-nanoemulsifying drug delivery system of glibenclamide using coffee husk as a low cost biosorbent. *Powder Technol.* **2014**, *256*, 352−360.

(20) Cui, L.; Jia, J.; Guo, Y.; Liu, Y.; Zhu, P. Preparation and characterization of IPN hydrogels composed of chitosan and gelatin cross-linked by genipin. *Carbohydr. Polym.* **2014**, *99*, 31−38.

(21) Schnitzer, M.; Gupta, U. C. Determination of acidity in soil organic matter. *Soil Sci. Soc. Am. Proc.* **1965**, *29*, 274−277.

(22) Schnitzer, M. Organic Matter Characterization. In *Methods of Soil Analysis. Part 2.*; Page, A. L., Miller, R. H., Keeney, D. B., Eds.; Agron. Monogr. 9 ASA-SSSA, American Society of Agronomy and Soil Science Society of America (ASA-SSSA):Madison, WI, 1982; pp 581−594.

(23) Walkley, A.; Black, I. A. An examination of the Degtjareff method for determining organic carbon in soils: Effect of variations in digestion

DOI: 10.1021/acs.jafc.5b03255
J. Agric. Food Chem. 2015, 63, 8391−8398

conditions and of inorganic soil constituents. *Soil Sci.* **1934**, *63*, 251−263.
(24) Thejavathi, R.; Yakkundi, S. R.; Ravindranath, B. Determination of azadirachtin by reversed-phase high performance liquid chromatography using anisole as internal standard. *J. Chromatogr. A* **1995**, *705*, 374−379.
(25) Kaushik, N. Determination of azadirachtin and fatty acid methyl esters of *Azadiractha indica* seeds by HPLC and GLC. *Anal. Bioanal. Chem.* **2002**, *374*, 1199−1204.
(26) Saxena, M.; Ravikanth, K.; Kumar, A.; Gupta, A.; Singh, B.; Sharma, A. Purification of *Azadirachta indica* seed cake and its impact on nutritional and antinutritional factors. *J. Agric. Food Chem.* **2010**, *58*, 4939−4944.
(27) Franson, N. M.; Peppas, N. A. Influence of copolymer composition on non fickian transport through glassy copolymers. *J. Appl. Polym. Sci.* **1983**, *28*, 1299−1310.
(28) MAGRAMA. Registro de productos fitosanitarios. URL: http://www.magrama.gob.es/es/agricultura/temas/sanidad-vegetal/productos-fitosanitarios/registro/productos/forexi.asp?e=0&susActiva=70 (06/29/2015).
(29) Straccia, M. C.; Gomez d'Ayala, G.; Romano, I.; Laurienzo, P. Novel zinc alginate hydrogels prepared by internal setting method with intrinsic antibacterial activity. *Carbohydr. Polym.* **2015**, *125*, 103−112.
(30) Baker, R. *Controlled Release of Biologically Active Agents*; Wiley: New York, 1987.
(31) Higuchi, T. Mechanism of sustained-action medication. Theoretical analysis of rate of release of solid drugs dispersed in solid matrices. *J. Pharm. Sci.* **1963**, *52*, 1145−1149.
(32) Ritger, P. L.; Peppas, N. A. A simple equation for description of solute release I. Fickian and non-Fickian release from non-swellable devices in the form of slabs, spheres, cylinders or discs. *J. Controlled Release* **1987**, *5*, 23−36.
(33) Oracesca, B.; Nixon, J. R.; Salomon, M. C. Factors affecting the permeation of drugs through alginate rate controlling membrane. *Proc. Int. Symp. Control. Rel. Bioact. Mater.* **1994**, *21*, 479−480.
(34) Adjalle, K. D.; Brar, S. K.; Tyagi, R. D.; Valéro, J. R.; Surampalli, R. Y. Photostabilization of *Bacillus thuringiensis* fermented wastewater and wastewater sludge based biopesticides using additives. *Acta Trop.* **2009**, *111*, 7−14.
(35) He, X.; Li, R.; Huang, G.; Hwang, H.; Jiang, X. Influence of marine oligosaccharides on the response of various biological systems to UV irradiation. *J. Funct. Foods* **2013**, *5*, 858−868.
(36) Tomida, H.; Yasufuku, T.; Fujii, T.; Kondo, Y.; Kai, T.; Anraku, M. Polysaccharides as potential antioxidative compounds for extended-release matrix tablets. *Carbohydr. Res.* **2010**, *345*, 82−86.
(37) Gifani, A.; Marzban, R.; Safekordi, A.; Ardjmand, M.; Dezianian, A. Ultraviolet protection of nucleopolyhedrovirus through micro-encapsulation with different polymers. *Biocontrol Sci. Techn.* **2015**, *25*, 814−827.

DOI: 10.1021/acs.jafc.5b03255
J. Agric. Food Chem. 2015, 63, 8391−8398

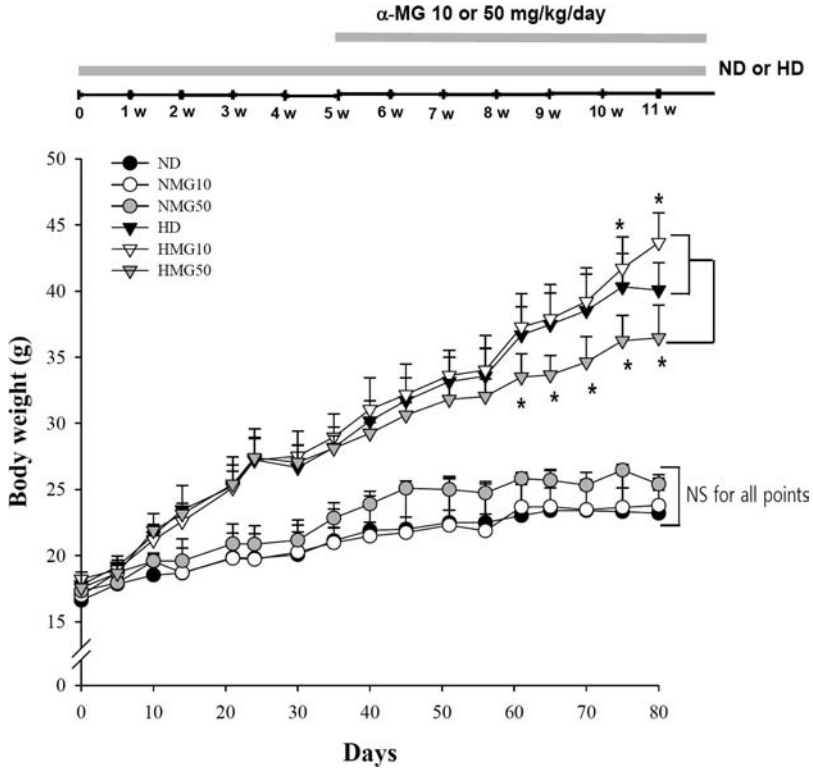

Figure 1. Effects of α-MG on body weight gain in ND, NMG10, NMG50, HD, HMG10, and HMG50 groups. (∗) Significantly different from ND group; (#) significantly different from HD group; (†) significantly different between MG10 and MG50 groups.

the previously reported protocol.[14] Polyethylene glycol 400 (PEG 400) was from Showa Chemical Co. (Tokyo, Japan). Antibodies against β-actin, SirT1, p-AMPK, AMPK, PPARγ, and RXRα were purchased from Cell Signaling Technology, Inc. (Danvers, MA, USA).

Animals. The protocols for the animal studies were approved by the Institute of Laboratory Animal Resources of Dongguk University, Seoul, South Korea (2012-0673; July 25, 2012). Male C57BL/6 mice were obtained from Charles River Orient (Seoul, South Korea) and acclimated for 1 week before the study was begun. Upon arrival, animals were randomized and housed at three per cage under strictly controlled environmental conditions (20−25 °C and 48−52% relative humidity). A 12 h light/dark cycle was used at an intensity of 150−300 Lux. C57BL/6 mice were started on either a normal diet (ND, 10% of kilocalories as fat; Pproduct N12450B) or a high-fat diet (HD, 60% of kilocalories as fat; product D12592, Research Diets, New Brunswick, NJ, USA) for 80 days. After 5 weeks (at day 35) of ND or HD, the mice were distributed into six treatment groups. α-MG (10 or 50 mg/kg/day) dissolved in PEG 400 and distilled water (6:4, v/v) was orally administered to mice with ND (NMG10 and NMG50 groups, respectively; n = 8 for each) or HD (HMG10 and HMG50 groups, respectively; n = 8 for each) every day during the last 6 weeks of diet feeding. ND and HD groups (n = 8 for each) were orally administered a vehicle instead of α-MG.

Measurement of Liver, Fats, and Kidney Weights and Triglyceride (TG) Levels in the Liver. At the end of the experimental period, the liver, fats, and kidney were extracted and the weights were measured. In the case of fats, the weights of total, epididymal, and retroperitoneal fats were measured separately. For the measurement of hepatic TG, 0.3 g of liver was homogenized in 0.1 M Tris-acetate buffer (pH 7.4), and 6 volumes of chloroform/methanol (2:1) was added. After vigorous stirring, the mixtures were incubated on ice for 1 h and centrifuged at 800g for 3 min. The resulting lower phase was aspirated. The hepatic TG content was determined using an Enzychrom TG assay kit.

Blood Chemistry. At the end of the experimental period, plasma samples were collected and total protein, albumin, aspartate aminotransferase (AST), alanine aminotransaminase (ALT), creatinine, total cholesterol (TC), high-density lipoprotein cholesterol (HDL-C), low-density lipoprotein cholesterol (LDL-C), TG, free fatty acid (FFA), glucose, blood urea nitrogen (BUN), and creatinine levels were analyzed (analyzed by Green Cross Reference Laboratory, Seoul, South Korea).

Hematoxylin and Eosin Staining in the Liver and Various Sites of Fat. The left lateral lobe of the liver and epididymal and retroperitoneal fats were excised,[19] fixed in 10% formalin, and embedded in paraffin. Four micrometer thick sections of liver and epididymal and retroperitoneal fats were obtained and stained with hematoxylin and eosin (H&E) for the histological examination of adipocytes, as previously described.[19]

Immunoblotting Analysis. Protein expression of hepatic SirT1, AMPK, p-AMPK, PPARγ, and RXRα were assessed by Western blotting analysis according to the manufacturer's instructions. After the determination of protein concentration, 20 μg of protein was mixed 1:1 with 2× sample buffer (20% glycerol, 4% SDS, 10% 2-ME, 0.05% bromophenol blue, and 1.25 M Tris-buffer, pH 6.8), loaded onto an SDS-PAGE gel (8 or 15%), and run at 150 V for 90 min. The tissue proteins were transferred to an ImmunoBlot polyvinylidene difluoride membrane using a Bio-Rad semidry transfer system. Following blocking, membranes were incubated with primary antibody at dilutions of 1:500−1:1000 at 4 °C overnight, washed three times in PBS, and further incubated with a HRP-conjugated secondary anti-IgG antibody at dilutions of 1:2000−1:20000 for 1 h. After three washings, the immunoreactive proteins were visualized by ECL chemiluminescence detection (Amersham Biosciences, Piscataway, NJ, USA). Equal loading of proteins was verified by β-actin immunoblotting.

Statistical Analysis. A P value <0.05 was deemed to be statistically significant using Duncan's multiple-range test of the Social Package of Statistical Sciences (SPSS) posteriori analysis of variance (ANOVA). All data are expressed as the mean ± standard error.

RESULTS

Effects of α-MG on Body Weight Gain and Food Intake. Effects of α-MG on body weight changes in C57BL/6

DOI: 10.1021/acs.jafc.5b01637
J. Agric. Food Chem. 2015, 63, 8399−8406

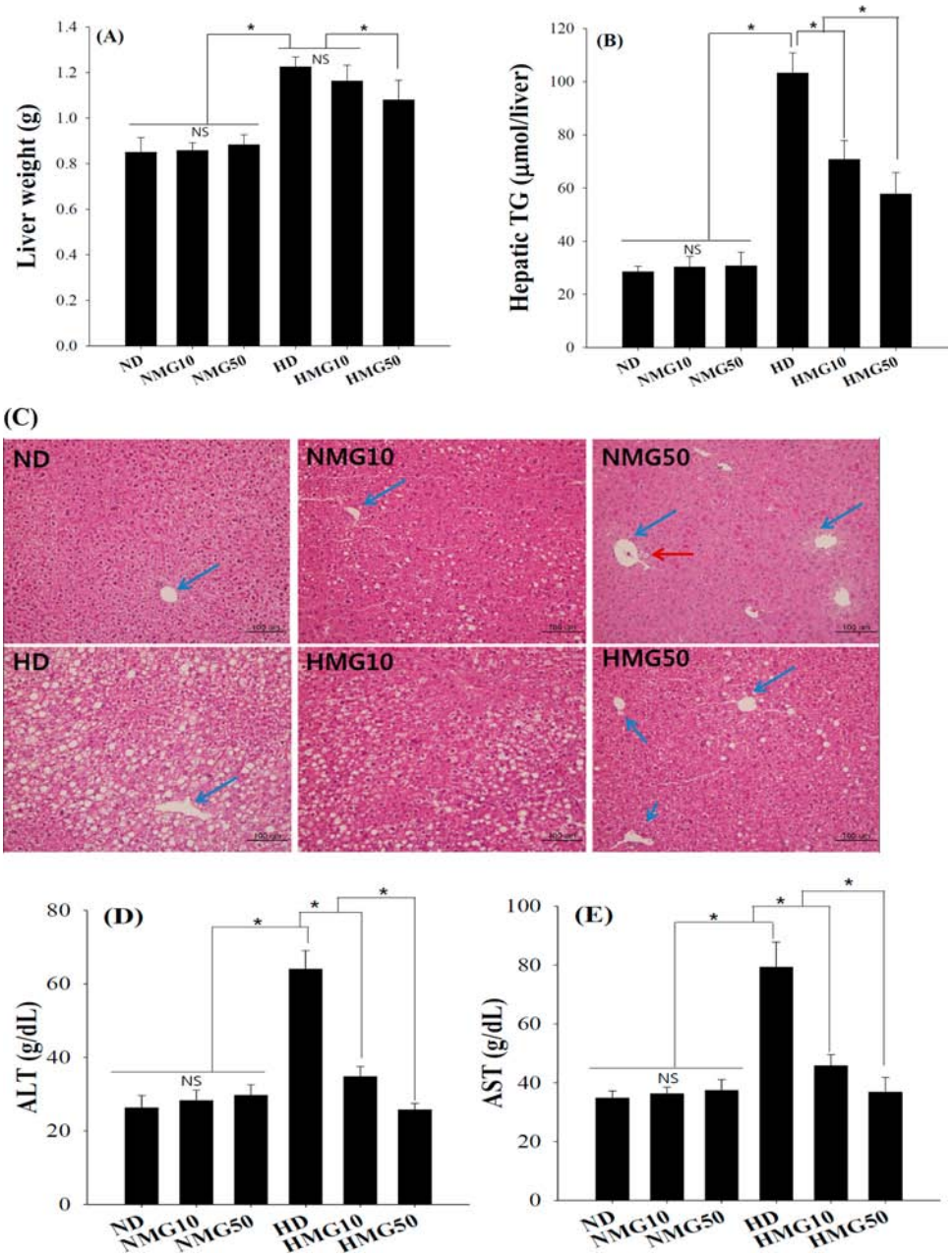

Figure 2. Effects of α-MG on liver from ND, NMG10, NMG50, HD, HMG10, and HMG50 groups. The weights of liver and hepatic TG contents were measured (A, B). Also, the histology of liver was compared after H&E staining: vein (blue arrow); bile duct (red arrow) (C). The liver functions were determined by ALT and AST in serum (D, E). (*) Means not sharing a common symbol differ, $P < 0.05$.

mice fed a normal diet (ND) or a high-fat diet (HD) are shown in Figure 1. The body weight gains in the high-fat diet groups were significantly greater than those in the normal diet groups from day 14 to the end of this experiment (e.g., body weight gain compared with initial body weight: 12.3 vs 28.8% at day 14 and 39.6 vs 130% at day 80, respectively, for the ND and HD groups). The body weight loss appeared 26 days after starting the treatment with 50 mg/kg α-MG (at day 61 after the start of the HD) in the HMG50 group compared with the HD group. However, a body weight loss did not appear in the HMG10 group compared with the HD group. The mean value of body weight in the NMG50 group seemed to be greater than in the ND or NMG10 group; however, there was no significant difference. The food intakes were comparable among all groups of mice (data not shown).

Effects of α-MG on Hepatic Steatosis. In an effort to assess the effect of α-MG on hepatic steatosis, measurements of liver weight and hepatic TG level and histopathological analysis of the liver were conducted. In the HMG50 group, the high-fat diet induced an increase in liver weight and hepatic TG level in the HD group (by 44.1 and 262% increase for liver weight and hepatic TG, respectively, vs the ND group), and the increase in liver weight and hepatic TG level was restored (by 12.2 and 44.1% decrease, respectively, vs the HD group) (Figure 2A,B). As shown in Figure 2C, the histopathological analysis of the liver revealed that HD caused the accumulation of fat droplets in the liver, accompanying hepatic steatosis. Arrestingly, the hepatic fat accumulation decreased in the HMG50 group according to liver histology. The conditions of liver weight, hepatic TG level, and hepatic steatosis in the HMG10 group

DOI: 10.1021/acs.jafc.5b01637
J. Agric. Food Chem. 2015, 63, 8399−8406

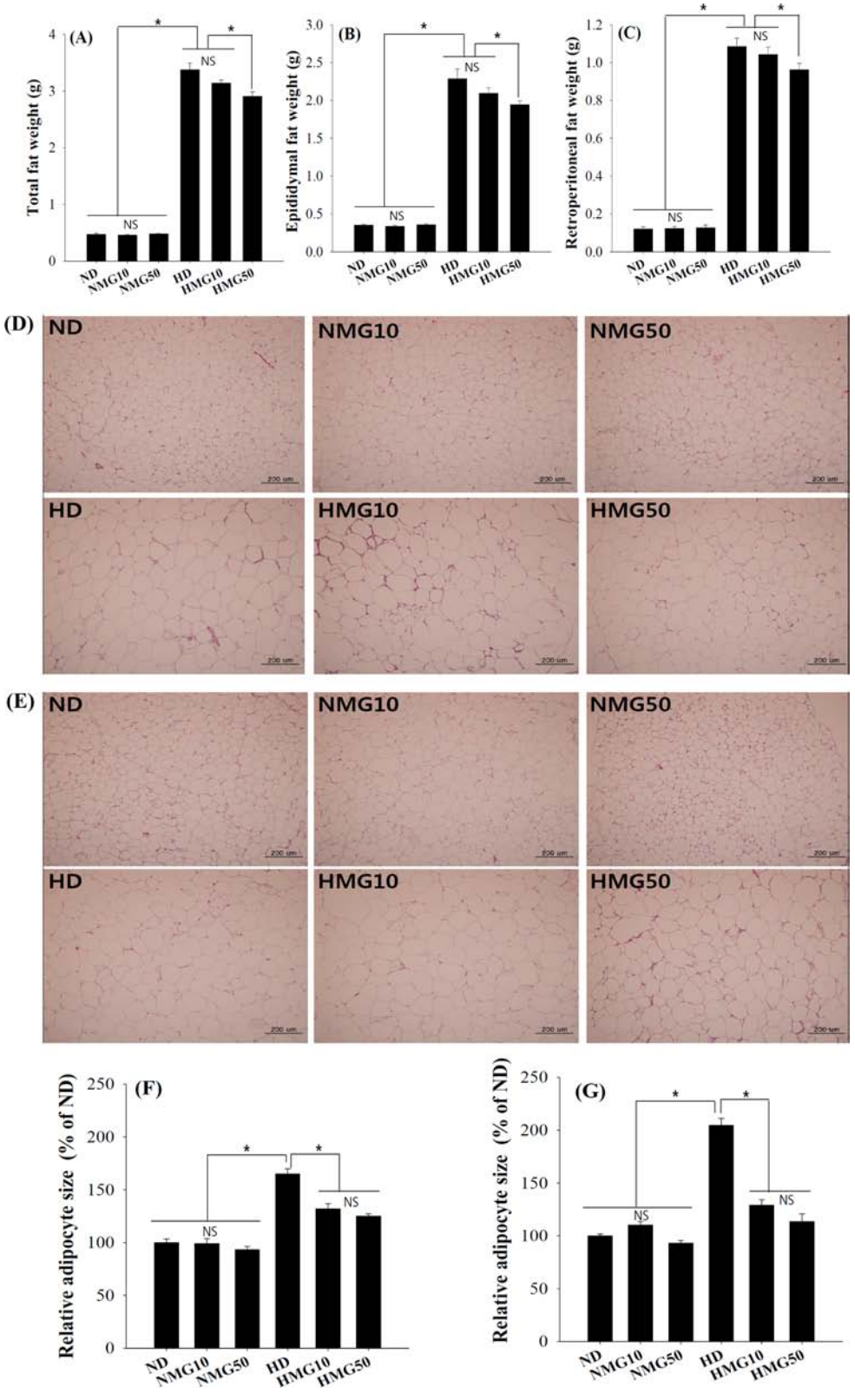

Figure 3. Effects of α-MG on fat from ND, NMG10, NMG50, HD, HMG10, and HMG50 groups. The weights of total fat, epididymal fat, and retroperitoneal fat were measured (A−C). The histologies of epididymal and retroperitoneal fats were compared after H&E staining (D, E). Adipocyte size of epididymal fat (F) and retroperitoneal fat (G) was measured. (∗) Means not sharing a common symbol differ, $P < 0.05$.

were still abnormal and similar to the HD group. According to Figure 2D,E for the measurement of liver functions, the serum ALT and AST levels were significantly higher in the HD group (by 144 and 128% increases respectively, vs the ND group), but were recovered to control levels in the HMG10 (by 45.7 and 42.3% decreases respectively, vs the HD group) and HMG50 (by 59.8 and 53.6% decreases respectively, vs HD group) groups. The albumin levels were comparable among the three

DOI: 10.1021/acs.jafc.5b01637
J. Agric. Food Chem. 2015, 63, 8399−8406

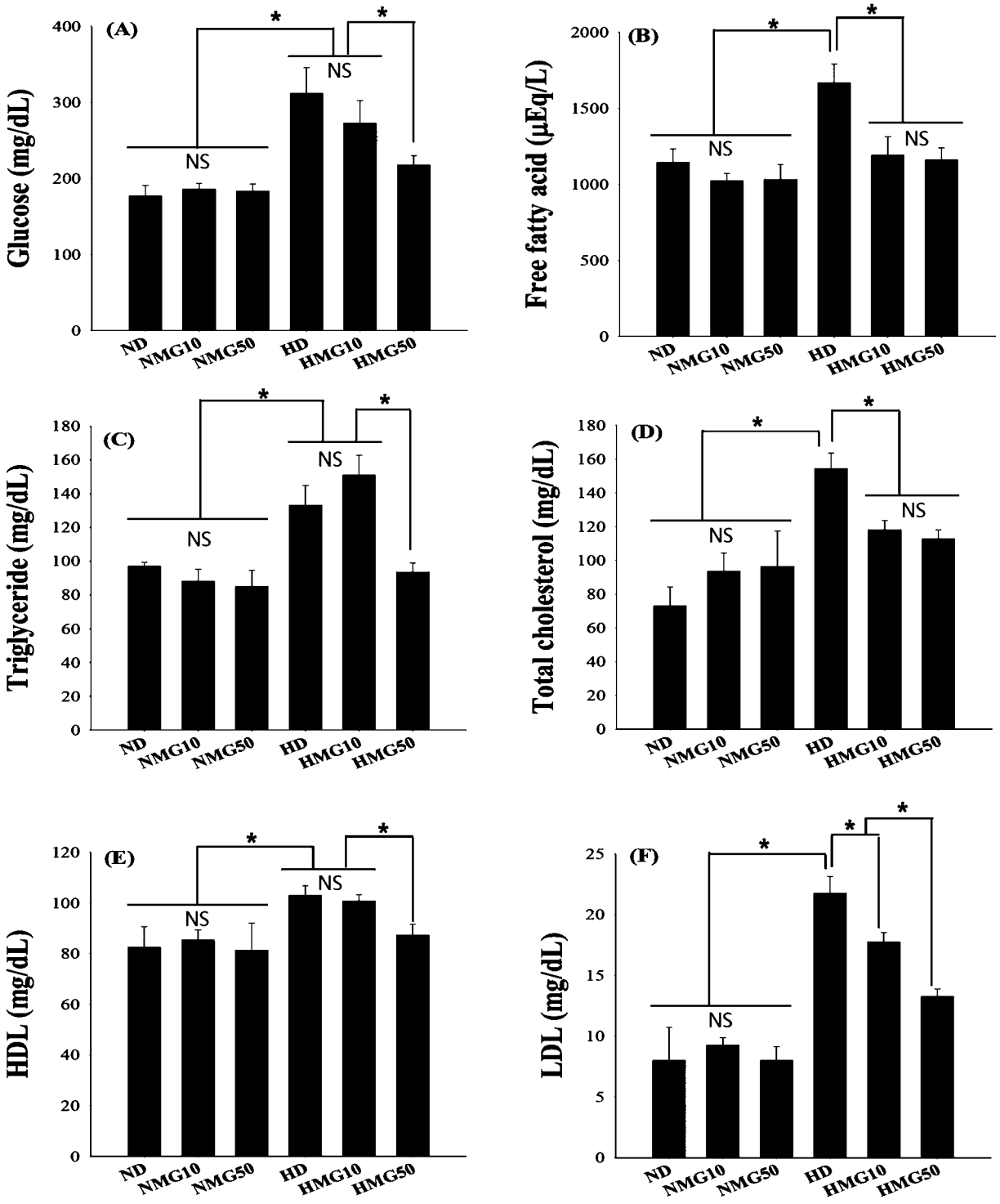

Figure 4. Effects of α-MG on serum profiles in ND, NMG10, NMG50, HD, HMG10, and HMG50 groups. Glucose (A), free fatty acid (B), triglyceride (C), total cholesterol (D), high-density lipoprotein cholesterol (HDL-C) (E), and low-density lipoprotein cholesterol (LDL-C) (F) were assayed. (*) Means not sharing a common symbol differ, $P < 0.05$.

groups of mice fed HD (data not shown). With the ND, in both the NMG10 and NMG50 groups, all conditions of the liver maintained a normal state. Collectively, these results demonstrate that 50 mg/kg α-MG treatment attenuated hepatic steatosis in high-fat diet-fed mice.

Effects of α-MG on Fat Accumulation. To investigate whether α-MG regulated the fat accumulation in adipose tissues, the weight and size of epididymal and retroperitoneal fats were examined. The weights of total, epididymal, and retroperitoneal fats were increased in the HD group (by 614, 549, and 804% increases respectively, vs the ND group), which were significantly reduced (by 13.8, 15.0, and 11.3% decreases respectively, vs HD group) in the HMG50 group (Figure 3A−). As shown in Figure 3D,E, the sizes of epididymal and retroperitoneal fats in the HD group were significantly increased, by 64.9 and 104.6%, respectively, compared with

DOI: 10.1021/acs.jafc.5b01637
J. Agric. Food Chem. 2015, 63, 8399−8406

those of the ND group. In the HMG50 group, the sizes of adipose tissue were slightly reduced, by 24.2 and 44.5% in both epididymal and retroperitoneal fats, respectively, as compared with the HD group (Figure 3F). However, 10 mg/kg α-MG treatment did not significantly affect the fat weights and sizes from the HD group. In normal diet groups (ND, NMG10,and NMG50), there were no changes in fat weights or sizes regardless of treatment with α-MG.

Effects of α-MG on Lipid Metabolism. To determine whether α-MG improved lipid metabolism, the serum glucose, FFA, TG, TC, HDL-C, and LDL-C levels were measured (Figure 4). All parameters in the HD group were higher (by 76.6, 45.7, 37.1, 111, 24.8, and 172% increases respectively) than in the ND group, and all of them were decreased in the HMG50 group (by 30.2, 30.3, 29.7, 26.9, 15.3, and 39.1% decreases respectively, vs the HD group). In the HMG10 group, FFA, TC, and LDL-C levels were reduced (by 28.5, 23.3, and 18.4% decrease, respectively, vs the HD group). In particular, in the HMG50 group, the reduction in the LDL-C level was greater than that of the HDL-C level (by 39.1 and 15.3% decreasesfor LDL-C and HDL-C levels, respectively, vs the HD group). The ratio of HDL-C/LDL-C in the HMG50 group was significantly increased (by 38.5%) compared with the HD group. These results suggest that α-MG improved the serum lipid profile, which may result from the decrease in lipogenesis.

Effects of α-MG on Hepatic Fatty Acid Metabolism through the SirT1-AMPK Pathway. To investigate the involvement of α-MG in hepatic fatty acid metabolism, Western blotting analysis was performed as shown in Figure 5. First, the

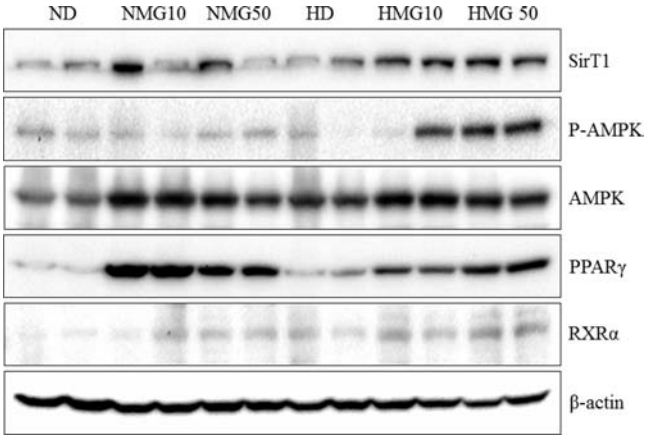

Figure 5. Protein levels of hepatic SirT1, phosphorylated AMPK, AMPK, PPARγ, and RXRα in liver were measured. SirT1, AMPK, PPARγ, and RXRα pathways regulate energy metabolism and hepatic lipid homeostasis.

protein levels of hepatic PPARγ and AMPK were increased in the HD group (vs the ND group); however, those of hepatic SirT1 and phosphorylated AMPK were much the same in the ND and HD groups. When ND-fed mice were supplied with 10 or 50 mg/kg α-MG, the protein levels of hepatic PPARγ and AMPK were remarkably amplified; however, α-MG seemed to negligibly affect the level of SirT1 and phosphorylated AMPK proteins. In HD-fed mice, an α-MG supplement up-regulated the hepatic PPARγ protein level in HD-fed mice, suggesting that α-MG acted as a hepatic PPARγ agonist. Interestingly, the protein levels of hepatic SirT1 and phosphorylated AMPK showed a different phenomenon with the α-MG supplement between ND- and HD-fed mice. In the HMG10 and HMG50 groups, protein levels of both hepatic SirT1 and phosphorylated AMPK were outstandingly increased compared with the HD group, suggesting that the hepatic SirT1 and AMPK axis was implicated in changes in fat accumulation in the liver, in parallel with the induction of hepatic PPARγ by α-MG. On the basis of these results, α-MG regulated the hepatic fatty acid metabolism through the SirT1 and AMPK pathways. Subsequently, the effects of α-MG treatment on the levels of lipogenic genes involved in fatty acid oxidation were determined in the liver. The protein expression of RXRα was stimulated in the HMG10 and HMG50 groups compared with the HD group, suggesting that the activated PPARγ and RXRα may form a heterodimer and bind to responsive DNA elements more effectively, thereby stimulating the transcription of genes related to lipid metabolism in the liver.

DISCUSSION

The present study provides the first in vivo evidence that α-MG attenuated hepatic steatosis through hepatic SirT1-AMPK and PPARγ pathways. As found in the experimental data, the hepatic fat accumulation was significantly attenuated, and the increase in hepatic TG content was decreased by α-MG compared with the HD group. All of these results were consistent with the changes in metabolic parameters.

A metabolic syndrome is defined as the combination of various symptoms of abdominal obesity, dyslipidemia, impaired glucose metabolism, hypertension, inflammatory responses,[18] and hepatic steatosis, the latter of which is referred to as a representative hepatic component of metabolic syndrome.[2,20] Typically, the high-fat diet is emerging as the most common cause for the overproduction and accumulation of lipids (mostly TG) within hepatocytes, which evolves into a line of diagnostic symptoms in hepatic steatosis with obesity patients.[19−22] Hepatic steatosis leads to the elevated influx of fatty acids, hepatic fat accumulation, and impaired export of TG and other cytotoxic factors, including oxidative stress, lipid peroxidation, and inflammatory cytokines[19] after excess intake of nutrients. Thus, the hepatic steatosis model in obese mice induced by a high-fat diet was utilized in this study.

The gross inspection of the HMG50 group indicates a clear recovery in body weight, fat mass, hepatic steatosis, and serum biochemical profiles relevant to lipid metabolism. The average values of food intake for 80 days were comparable among all groups, indicating that α-MG did not control appetite, but had a beneficial influence on fatty acid oxidation or cholesterol homeostasis.[20,23] In particular, the up-regulated serum glucose, FFA, TC, LDL-C, and TG were gradually reduced by α-MG in the HMG10 and HMG50 groups, and notably a significantly increased HDL-C and HDL/LDL-C ratio were observed. Moreover, the decreased TG content may result from decreased lipid synthesis. Because the high HDL-C/LDL-C ratio showed a positive correlation with a lower risk of cardiovascular disease, the 50 mg/kg α-MG treatment showed potential efficacy to ameliorate metabolic diseases.[24,25] In the HMG50 group, hepatic steatosis and abnormal liver function seemed to be recovered by 50 mg/kg α-MG supplementation, but 10 mg/kg α-MG seemed to reduce hepatic steatosis negligibly. The elevated ALT and AST levels in the HD groups were restored in the HMG10 and HMG50 groups, indicating that a high-fat diet resulted in abnormal liver function, and α-MG attenuated hepatic injury. With supplementation of 10 and 50 mg/kg α-MG with the ND, the normal liver state was

DOI: 10.1021/acs.jafc.5b01637
J. Agric. Food Chem. 2015, 63, 8399−8406

maintained, suggesting that α-MG itself did not cause liver injury. In addition, hepatic steatosis was recovered in the HMG50 group with respect to morphological aspects. Furthermore, no renal injuries were observed in any group of mice (Supporting Information 1). Taken together with body weight changes, hepatic steatosis, fat accumulation, and/or lipid metabolism, α-MG seemed to regulate hepatic steatosis and obesity. In particular, the body weight and liver weight changes seemed to be dose-dependent, because 50 mg/kg α-MG treatment significantly decreased body and liver weights, but there was no significant decrease at 10 mg/kg α-MG treatment compared to those in the HD group. A dose of 50 mg/kg of α-MG administered to mice is equivalent to approximately 320 mg/kg in the human adult, according to the interspecies dose conversions of NOAELs and previous reports.[26−28]

The Western blotting results clearly indicate that the hepatic SirT1 and phosphorylated AMPK levels were activated by α-MG in the HMG10 and HMG50 groups. Moreover, the protein expression of hepatic PPARγ and RXRα was stimulated by α-MG in the HMG10 and HMG50 groups.

AMPK, a downstream component of a protein kinase cascade, acts as an intracellular energy sensor to maintain energy balance. This pivotal role of AMPK makes it an ideal candidate for regulating whole-body energy metabolism such as glucose homeostasis and lipid metabolism, and additionally AMPK may play a role in protecting the body from metabolic diseases with obesity.[29,30] Along with AMPK phosphorylation, SirT1, a nuclear protein, plays a key role in controlling the transcription factors related to energy metabolism.[31] The specific SirT1 activator enhances oxidative metabolism in liver and skeletal muscle,[29] which may regulate whole-body glucose metabolism both systemically and locally.[31,32] Activation of SirT1 mimics several metabolic aspects of calorie restriction that enhance selective nutrient utilization and mitochondrial oxidative function.[32] The AMPK/SirT1 signaling pathway is, furthermore, the mechanism by which hormones enhance mitochondrial metabolism.[32,33] Regulation of AMPK and SirT1 is a potential therapeutic target for attenuation of fatty acid oxidation in liver.[33] The functions of these enzymes are like a fuel gauge: they are activated under conditions of high-energy depletion.[33] Phosphorylation of AMPK leads to the down-regulation of lipid biosynthesis by phosphorylating of acetyl-CoA carboxylase, which decreases the amount of malonyl-CoA and, in turn, suppresses carnitine palmitoyl-CoA transferase, resulting in an increase of fatty acid oxidation.[34] In addition, PPARγ forms heterodimers with the RXR that regulate the lipid metabolism.[35,36] SirT1 and PPARγ might coordinate the regulation of adipogenesis.[37−39] We have found that α-MG suppressed lipid accumulation in the mouse model. Although α-MG has also been found to be effective in fatty liver by PPARγ activation, the interplay between the AMPK signaling pathway and regulation of lipid disorders remains unclear.

The administration of α-MG to HF-induced obese mice reduced body-weight gain, adipose mass, serum triglyceride, total cholesterol, and low-density lipoprotein concentration. Our results suggest that α-MG exerts antiobesity effects in HF-induced obese mice by activating hepatic AMPK, SirT1, and PPARγ expression. The antiobesity effect of α-MG in HF-induced mice may support the potential of α-MG to reduce the risks of metabolic diseases.

■ ASSOCIATED CONTENT

Supporting Information

The Supporting Information is available free of charge on the ACS Publications website at DOI: 10.1021/acs.jafc.5b01637.

Effects of α-MG on kidney from ND, NMG10, NMG50, HD, HMG10, and HMG50 groups and effects of α-MG on body weight changes, liver weight, glucose, and fat weights (PDF)

■ AUTHOR INFORMATION

Corresponding Author

*(Y.-W.C.) Phone: 82-31-961-5218. Fax: 82-31-961-5218. E-mail: f2744@dongguk.edu.

Funding

This study was supported by the grant of the National Research Foundation of Korea (NRF) funded by the government of Korea (NRF-2012R1A1A2004424, Y.H.C.), the GRRC program of Gyeonggi province (GRRC DONGGUK2014-B03, Development of functional food to alleviating metabolic syndromes and circulatory disorders), and a National Research Foundation of Korea (NRF) grant funded by the Korean government (MSIP) (NRF-2015R1A2A2A01006736).

Notes

The authors declare no competing financial interest.

■ ACKNOWLEDGMENTS

We acknowledge the persons involved in sample production, sampling, and data collection: Hee Chul Ahn and colleagues from the NMR and animal facilities.

■ REFERENCES

(1) Nawrocki, A. R.; Scherer, P. E. Keynote review: the adipocyte as a drug discovery target. *Drug Discovery Today* **2005**, *10*, 1219−1230.

(2) Eckel, R. H.; Grundy, S. M.; Zimmet, P. Z. The metabolic syndrome. *Lancet* **2005**, *365*, 1415−1428.

(3) Sethi, J. K.; Vidal-Puig, A. J. Thematic review series: adipocyte biology. Adipose tissue function and plasticity orchestrate nutritional adaptation. *J. Lipid Res.* **2007**, *48*, 1253−1262.

(4) Gregoire, F. M. Adipocyte differentiation: from fibroblast to endocrine cell. *Exp. Biol. Med.* **2001**, *226*, 997−1002.

(5) Zhao, Y.; Sedighi, R.; Wang, P.; Chen, H.; Zhu, Y.; Sang, S. Carnosic acid as a major bioactive component in rosemary extract ameliorates high-fat-diet-induced obesity and metabolic syndrome in mice. *J. Agric. Food Chem.* **2015**, *63*, 4843−4852.

(6) Lai, Y. S.; Chen, W. C.; Ho, C. T.; Lu, K. H.; Lin, S. H.; Tseng, H. C.; Lin, S. Y.; Sheen, L. Y. Garlic essential oil protects against obesity-triggered nonalcoholic fatty liver disease through modulation of lipid metabolism and oxidative stress. *J. Agric. Food Chem.* **2014**, *62*, 5897−5906.

(7) Shen, Z.; Liang, X.; Rogers, C. Q.; Rideout, D.; You, M. Involvement of adiponectin-SIRT1-AMPK signaling in the protective action of rosiglitazone against alcoholic fatty liver in mice. *Am. J. Physiol. Gastrointest. Liver Physiol.* **2010**, *298*, G364−G374.

(8) Palomer, X.; Salvado, L.; Barroso, E.; Vazquez-Carrera, M. An overview of the crosstalk between inflammatory processes and metabolic dysregulation during diabetic cardiomyopathy. *Int. J. Cardiol.* **2013**, *168*, 3160−3172.

(9) Towler, M. C.; Hardie, D. G. AMP-activated protein kinase in metabolic control and inuslin signaling. *Circ. Res.* **2007**, *100*, 328−341.

(10) Price, N. L.; Gomes, A. P.; Ling, A. J. Y.; Duarte, F. V.; Martin-Montalvo, A.; North, B. J.; Ye, L.; Ramadori, G.; Teodoro, J. S.; Hubbard, B. P.; Varela, A. T.; Davis, J. G.; Varamini, B.; Hafner, A.; Moaddel, R.; Rolo, A. P.; Coppari, R.; Palmeira, C. M.; Cabo, R.; Baur, J. A.; Sinclair, D. A. SIRT1 is required for AMPK activation and the

DOI: 10.1021/acs.jafc.5b01637
J. Agric. Food Chem. 2015, 63, 8399−8406

beneficial effects of resveratrol on mitochondrial function. *Cell Metab.* **2012**, *15*, 675−690.
(11) Li, Y.; Lazar, M. A. Differentiation gene regulation by PPARγ agonist and constitutively active PPARγ2. *Mol. Endocrinol.* **2002**, *16*, 1040−1048.
(12) Chin, Y.-W.; Kinghorn, A. D. Structural characterization, biological effects, and synthetic studies on xanthones from mangosteen (*Garcinia mangostana*), a popular botanical dietary supplement. *Mini-Rev. Org. Chem.* **2008**, *5*, 355−364.
(13) Bumrungpert, A.; Kalpravidh, R. W.; Chichumroonchokchai, C.; Chung, C. C.; West, T.; McIntosh, M. Xanthones from mangosteen prevent lipopolysaccharide-mediated inflammation and insulin resistance in primary culcures of human adipocytes. *J. Nutr.* **2009**, *139*, 1185−1191.
(14) Cui, J.; Hu, W.; Cai, Z.; Liu, Y.; Li, S.; Tao, W.; Xiang, H. New medical properies of mangostins: analgestic activity and pharmacological characterization of active ingredients from the fruit hull of *Garcinia mangostana*. *Pharmacol., Biochem. Behav.* **2010**, *95*, 166−172.
(15) Jariyapongskul, A.; Areebambud, A.; Suksamrarn, S.; Mekseepralard, C. α-Mangostin attenuation of hyperglycemia-induced ocular hypoperfusion and blood retinal barrier leakage in the early stage of type 2 diabetes rats. *BioMed Res. Int.* **2015**, *2015*, 1.
(16) Chao, A. C.; Hsu, Y. L.; Liu, C. K.; Kuo, P. L. α-Mangosin, a dietary xanthone, induces autopahgic cell death by activating the AMP-activated protin kinase pathway in glioblastoma cells. *J. Agric. Food Chem.* **2011**, *59*, 2086−2096.
(17) Quan, X.; Wang, Y.; Ma, X.; Liang, Y.; Tian, W.; Ma, Q.; Jiang, H.; Zhao, Y. α-Mangostin induces apotosis and suppresses differentiation of 3T3-L1 cells via inhibiting fatty acid synthase. *PLoS One* **2012**, *7*, e33376.
(18) Han, S. Y.; Chin, Y. W.; Kim, D. Y.; Choi, Y. H. Simultanoues determination of α- and γ-mangostins in mouse plasma by HPLC-MS/MS method: application to a pharmacokinetic study of mangosteen extract in mouse. *Chromatographia* **2013**, *76*, 643−650.
(19) Berryman, D. E.; List, E. O.; Sackmann-Sala, L.; Lubbers, E.; Munn, R.; Kopchick, J. J. Growth hormone and adipose tissue: beyond the adipocyte. *Growth Horm. IGF Res.* **2011**, *21*, 113−123.
(20) Kim, Y. W.; Kim, Y. M.; Yang, Y. M.; Kim, T. H.; Hwang, S. J.; Lee, J. R.; Kim, S. C.; Kim, S. G. Inhibition of SREBP-1C-mediated hepatic steatosis and oxidative stress by sauchinone, an AMPK-activating lignin in *Saururus chinensis*. *Free Radical Biol. Med.* **2010**, *48*, 567−578.
(21) Alberti, K. G.; Eckel, R. H.; Grundy, S. M.; Zimmet, P. Z.; Cleeman, J. I.; Donato, K. A.; Fruchart, J. C.; James, W. P.; Loria, C. M.; Smith, S. C., Jr. International Diabetes Federation Task Force on Epidemiology and Prevention. *Circulation* **2009**, *120*, 1640−1645.
(22) Kang, S. W.; Choi, J. S.; Choi, Y. J.; Bae, J. Y.; Li, J.; Kim, D. S.; Kim, J. L.; Shin, S. Y.; Lee, Y. J.; Kwun, I. S.; Kang, Y. H. Licorice isoliquiritigenin dampens angiogenic activity via inhibition of MAPK-responsive signaling pathways leading to induction of matrix metalloproteinases. *J. Nutr. Biochem.* **2010**, *21*, 55−65.
(23) Cornier, M. A.; Dabelea, D.; Hernandez, T. L.; Lindstrom, R. C.; Steig, A. J.; Stob, N. R.; Van Pelt, R. E.; Wang, H.; Eckel, R. H. The metabolic syndrome. *Endocr. Rev.* **2008**, *29*, 777−822.
(24) Weiler Miralles, C. S.; Wollinger, L. M.; Marin, D.; Genro, J. P.; Contini, V.; Morelo Dal Basco, S. Waist-to-height ratio (WHER) and triglyceride to HDL-C ratio (TG/HDL-C) as predictors of cardiometabolic risk. *Nutr. Hosp.* **2015**, *1*, 2115−2121.
(25) LDL-V/HDL-C ratio in subjects with cardiovascular disease and a low HDL-C: results of the RADAR (rosuvastatin and atorvastatin in different doseages and reverse cholesterol transport) study. *Curr. Med. Res. Opin.* **2005**, *21*, 1865−1874.10.1185/030079905X74952
(26) Petiwala, S. M.; Ramaiya, A.; Kumar, A.; Gill, R. K.; Saksena, S.; Johnson, J. J. Pharmacokinetic characterization of mangosteen (*Garcinia mangostana*) fruit extract standardized to α-mangostin in C57BL/6 mice. *Nutr. Res. (N. Y., NY, U. S.)* **2014**, *34*, 336−345.
(27) Ramaiya, A.; Li, G.; Petiwala, S. M.; Johnson, J. J. Single dose oral pharmacokinetic profile of α-mangostin in mice. *Curr. Drug Targets* **2012**, *13*, 1698−1704.
(28) *Guidance for Industry: Estimating the Maximum Safe Starting Dose in Initial Clinical Trials for Therapeutics in Adult Healthy Volunteers*; FDA: Washington, DC, USA, 2015.
(29) Bijland, S.; Mancini, S. J.; Salt, I. P. Role of AMP-activated protein kinase in adipose tissue metabolism and inflammation. *Clin. Sci.* **2013**, *124*, 491−507.
(30) Carling, D. The AMP-activated protein kinase cascade − a unifying system for energy control. *Trends Biochem. Sci.* **2004**, *29*, 18−24.
(31) Cantó, C.; Auwerx, J. Targeting sirtuin 1 to improve metabolism: all you need is NAD(+)? *Pharmacol. Rev.* **2012**, *64*, 166−1687.
(32) Feige, J. N.; Lagouge, M.; Canto, C.; Strehle, A.; Houten, S. M.; Milne, J. C.; Lambert, P. D.; Mataki, C.; Elliott, P. J.; Auwerx, J. Specific SIRT1 activation mimics low energy levels and protects against diet-induced metabolic disorders by enhancing fat oxidation. *Cell Metab.* **2008**, *8*, 347−358.
(33) Iwabu, M.; Yamauchi, T.; Okada-Iwabu, M.; Sato, K.; Nakagawa, T.; Funata, M.; Yamaguchi, M.; Namiki, S.; Nakayama, R.; Tabata, M.; Ogata, H.; Kubota, N.; Takamoto, I.; Hayashi, Y. K.; Yamauchi, N.; Waki, H.; Fukayama, M.; Nishino, I.; Tokuyama, K.; Ueki, K.; Oike, Y.; Ishii, S.; Hirose, K.; Shimizu, T.; Touhara, K.; Kadowaki, T. Adiponectin and AdipoR1 regulate PGC-1α and mitochondria by Ca^{2+} and AMPK/SIRT1. *Nature* **2010**, *464*, 1313−1319.
(34) Hardie, D. G. AMP-activated protein kinase as a drug target. *Annu. Rev. Pharmacol. Toxicol.* **2007**, *47*, 185−210.
(35) Chandra, V.; Huang, P.; Hamuro, Y.; Raghuram, S.; Wang, Y.; Burris, T. P.; Rastinejad, F. Structure of the intact PPAR-γ-RXR-nuclear receptor complex on DNA. *Nature* **2008**, *456*, 350−356.
(36) Gronemeyer, H.; Gustafsson, J. A.; Laudet, V. Principles for modulation of the nuclear receptor superfamily. *Nat. Rev. Drug Discovery* **2004**, *3*, 950−964.
(37) Tontonoz, P.; Hu, E.; Spiegelman, B. M. Stimulation of adipogenesis in fibroblasts by PPARγ 2, a lipid-activated transcription factor. *Cell* **1994**, *79*, 1147−1156.
(38) MacDougald, O. A.; Mandrup, S. Adipogenesis: forces that tip the scales. *Trends Endocrinol. Metab.* **2002**, *13*, 5−11.
(39) Jin, Q.; Zhang, F.; Yan, T.; Liu, Z.; Wang, C.; Ge, X.; Zhai, Q. C/EBPα regulates SIRT1 expression during adipogenesis. *Cell Res.* **2010**, *20*, 470−479.

DOI: 10.1021/acs.jafc.5b01637
J. Agric. Food Chem. 2015, 63, 8399−8406

Table 1. Primer Sequences

gene name	forward (5′→3′)	reverse (5′→3′)
primer sequences of mRNA quantification		
Chrebp	CCAGCCTCAAGGTGAGCAAA	CATGTCCCGCATCTGGTCA
Cox5b	TTCAAGGTTACTTCGCGGAGT	CGGGACTAGATTAGGGTCTTCC
GADPH	AGGTCGGTGTGAACGGATTTG	TGTAGACCATGTAGTTGAGGTCA
Ndufs8	AGTGGCGGCAACGTACAAG	TCGAAAGAGGTAACTTAGGGTCA
Nfkb1	ATGGCAGACGATGATCCCTAC	TGTTGACAGTGGTATTTCTGGTG
Nrf1	AGCACGGAGTGACCCAAAC	TGTACGTGGCTACATGGACCT
Ppargc1a	TATGGAGTGACATAGAGTGTGCT	CCACTTCAATCCACCCAGAAAG
Atgl	GGATGGCGGCATTTCAGACA	CAAAGGGTTGGGTTGGTTCAG
Sirt1	GCTGACGACTTCGACGACG	TCGGTCAACAGGAGGTTGTCT
Srebp1	GCAGCCACCATCTAGCCTG	CAGCAGTGAGTCTGCCTTGAT
Tfam	ATTCCGAAGTGTTTTTCCAGCA	TCTGAAAGTTTTGCATCTGGGT
primer sequences of mtDNA copy number		
MTCO2	CCATAGGGCACCAATGATACTG	AGTCGGCCTGGGATGGCATC
18S rRNA	CTTAGAGGGACAAGTGGCGTTC	CGCTGAGCCAGTCAGTGTAG

study was to evaluate whether EGCG attenuates aging-associated metabolic disorders through modulation of the insulin signaling pathway, mitochondrial function, and lipid metabolism in skeletal muscle and liver using SAMR1 and SAMP8 models.

MATERIALS AND METHODS

Materials. EGCG (TEAVIGO, DSM), a highly purified extract from green tea leaves (*Camellia sinensis*) containing >94% EGCG and <5% other catechins,[16] was a gift from Gemfont Corp. (Taipei, Taiwan). For Western blotting, primary antibodies Akt, phospho-Akt (Thr308), phospho-AS160 (Thr642), AMP-activated protein kinase α (AMPKα), phospho-AMPKα (Thr172), GLUT4, mammalian target of rapamycin (mTOR), phospho-mTOR (Ser2448), and peroxisome proliferator-activated receptor gamma coactivator 1-α (PGC1α) were purchased from Cell Signaling Technology (Danvers, MA, USA). Akt substrate of 160 kDa (AS160) was from Millipore (Billerica, MA, USA), and GAPDH was from GeneTex (Hsinchu City, Taiwan). Secondary antibodies goat anti-rabbit and sheep anti-mouse HRP conjugated antibodies were purchased from Bio-Rad (Hercules, CA, USA) and GE Healthcare Life Sciences (Pittsburgh, PA, USA), respectively.

Animals. The senescence-accelerated mouse-prone 8 (SAMP8, n = 30) and senescence-accelerated mouse-resistant 1 (SAMR1, n = 9) mice were obtained from Providence University (Taichung, Taiwan). Animal experiments were approved by the Institutional Animal Care and Use Committee of National Cheng Kung University. Mice were individually caged in an air-conditioned animal facility at 20 ± 2 °C on a 12 h light/dark cycle and were maintained with free access to water and normal chow diet (LabDiet 5010, St. Louis, MO, USA). Body weight and food intake were measured weekly. At the age of 28 weeks, SAMP8 mice were divided into two groups: SAMP8 mice (n = 15) were fed chow diet; SAMP8 mice administered 0.32% EGCG (n = 15) were fed chow diet consisting of 0.32% EGCG (3.2 g EGCG/kg chow diet) for 12 weeks. The presently used dose of EGCG has been reported to effectively inhibit obesity, metabolic syndrome, and fatty liver disease in high-fat-fed mice.[17] At the age of 40 weeks, animals were fasted overnight and then euthanized. After decapitation, blood was immediately collected and centrifuged at 3000 rpm, and the supernatant was collected. Tissues were isolated immediately and stored at −80 °C for further analysis.

Glucose, Insulin, and Free Fatty Acid Measurement. Serum glucose levels were measured by ACCU-CHEK (Roche, Switzerland). Serum insulin levels were measured by mouse insulin ELISA kit (Mercodia, Uppsala, Sweden) according to the manufacturer's instructions. Serum FFA levels were measured by colorimetric kit (BioVision, Milpitas, CA, USA) according to the manufacturer's instructions.

ALT and AST Activities and TG Measurement. For ALT and AST activities, liver samples (~10 mg) were measured by colorimetric assay kit (BioVision) according to the manufacturer's instructions.

To solubilize TG, liver samples (~50 mg) were homogenized in 5% NP-40. The samples were slowly heated to 100 °C for 5 min and then cooled, and the heating procedure was repeated once more. Samples were centrifuged for 2 min at top speed to remove any insoluble material and were diluted 10-fold with distilled water followed by the manufacturer's instructions (BioVision).

Liver Histology and Oil Red O Staining. Fresh liver tissues were fixed in 10% buffered formaldehyde solution and embedded in paraffin. Embedded liver tissue blocks from SAMP8 and SAMR1 mice were cut into 5 μm sections and stained with hematoxylin and eosin. For oil red O (ORO) staining, frozen liver tissues were embedded in OCT compounds and were cut into 20 μm sections. The sections were stained with 0.4% ORO solution (Sigma, St. Louis, MO, USA) for 5 min and then rinsed in tap water. Images were observed under a microscope (Zeiss, Germany) and captured with a digital camera (Nikon, Japan). Quantification of neutral lipids by ORO analysis in liver was performed using ImageJ.[18]

Western Blot. Skeletal muscle and liver samples were homogenized in ice-cold RIPA buffer (Cell Signaling Technology) containing 1 mM phenylmethanesulfonyl fluoride, and the supernatant was obtained by centrifugation. Total protein in the supernatant was measured by the BCA method (Bio-Rad), and the supernatant was obtained by centrifugation. An equal amount of protein for each preparation was added to 6× Laemmli sample buffer, separated by SDS-PAGE, transferred to PVDF membrane, blocked with 5% nonfat dry milk in 0.1% Tween-Tris buffered saline, and incubated in 5% dry milk Tween-Tris buffered saline with different primary antibodies. Membranes were then washed and incubated with horseradish peroxidase-conjugated secondary antibodies in Tween-Tris buffered saline with 5% nonfat dry milk. Protein bands were visualized using a Chemiluminescence kit (Millipore, Billerica, MA, USA). Quantitative results of Western blotting were performed using the LAS-4000 mini biomolecular imager (GE HealthCare Life Sciences).

RNA Extraction and Real-Time PCR. Total RNA was extracted from skeletal muscle and liver samples by using Trizol/chloroform procedure (Gibco BRL, Rockville, MD, USA) and quantified by using a NanoDrop meter. Total RNA (1 μg) was reverse transcribed into cDNAs by using the kit (Invitrogen, Grand Island, NY, USA) according to the manufacturer's instructions. mRNA levels were quantified using StepOnePlus Real-Time systems (Applied Biosystems, Foster City, CA, USA). Primer sequences are shown in Table 1. Real-time PCR was performed using Fast Start SYBR Green master mix kit (Applied Biosystems). Each cDNA sample was run in triplicate, and GAPDH as an internal control gene was included in each run to correct sample-to-sample variation and to normalize mRNA levels.

DOI: 10.1021/acs.jafc.5b02501
J. Agric. Food Chem. 2015, 63, 8407−8417

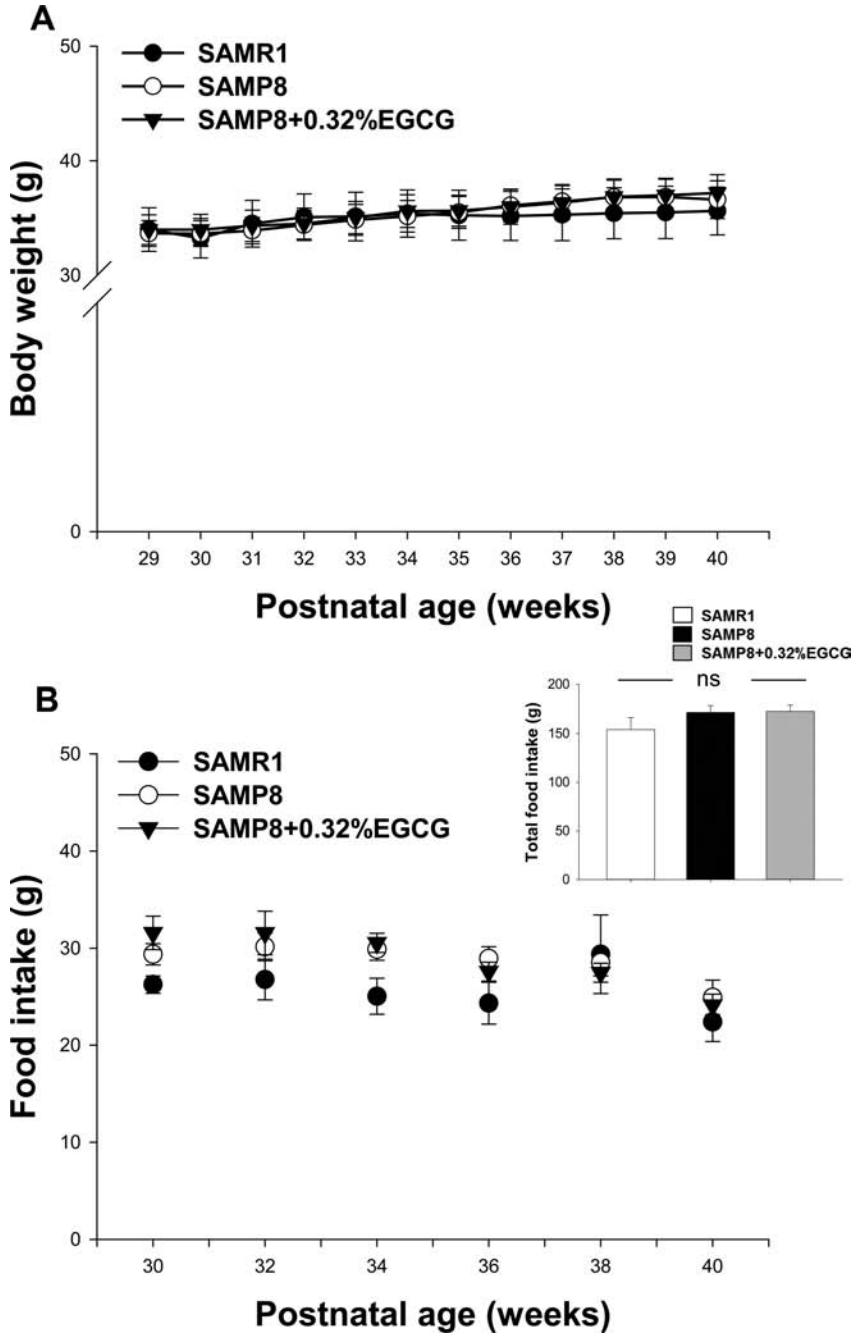

Figure 1. (A) Body weight and (B) mean weekly food intake and total food intake of SAMR1, SAMP8, and SAMP8 + 0.32 EGCG mice. Results are expressed as means ± SEM.

The relative mRNA level was calculated according to the comparative ΔΔCt method.

DNA Extraction and Quantification. Genomic DNA from skeletal muscle and liver samples was prepared using a commercial kit according to the manufacturer's instructions (Zymo Research, Irvine, CA, USA). The relative copy numbers of mitochondrial and nuclear DNA were determined by real-time PCR with specific primers. Ct values were determined for MTCO2 gene encoded by mitochondrial DNA and 18S rRNA gene encoded by the nuclear DNA. The relative mtDNA copy number was calculated by normalizing to 18S rRNA gene copy number.[19] Primer sequences are shown in Table 1.

Statistical Analysis. Results are expressed as means ± SEM. The one-way ANOVA was used to determine the statistical significance of the differences among the groups and following post hoc assessment by Student−Newman−Keuls method correction for multiple comparisons (SigmaPlot 12.0). Different lower case letters indicate significant differences among groups at a P of ≤0.05 by one-way ANOVA.

RESULTS

Body Weight, Food Intake, and Metabolic Parameters. No significant differences in body weight and food intake were observed between SAMR1 and SAMP8 mice (Figure 1). Administration of EGCG for 12 weeks did not affect body weight and food intake of SAMP8 mice. The levels of fasting glucose, insulin, and FFA were significantly increased in SAMP8 mice compared with age-matched SAMR1 at 40 weeks old (Table 2). After administration of EGCG for 12 weeks, the levels of fasting glucose and insulin in SAMP8 mice were similar to those in SAMR1 mice (Table 2).

DOI: 10.1021/acs.jafc.5b02501
J. Agric. Food Chem. 2015, 63, 8407−8417

Table 2. Fasting Serum Glucose, Insulin, and FFA after 12 Weeks of EGCG Treatment[a]

	Glucose (mg/dL)	Insulin (pmol)	FFA (μmol)
SAMR1	246.6 ± 14.9[a]	62.2 ± 19.9[a]	4.12 ± 0.57[a]
SAMP8	286.0 ± 6.7[b]	129.5 ± 9.7[b]	6.42 ± 0.45[b]
SAMP8 + 0.32% EGCG	254.7 ± 7.5[a]	99.1 ± 13.5[ab]	6.76 ± 0.48[b]

[a]Serum samples were collected from 40-week-old SAMR1, SAMP8, and SAMP8+EGCG mice after overnight fasting. Data are means ± SEM (n = 8−14/group). Significance (P < 0.05) among groups is denoted by different letters.

Effects of EGCG on Insulin Signaling Pathway and AMPKα in Skeletal Muscle. The levels of key proteins involved in the insulin signaling pathway (Akt, pAkt, AS160, pAS160, and GLUT4) were measured by Western blotting. Significantly decreased Akt activity, increased AS160 activity, and decreased protein expression of GLUT4 were observed in SAMP8 mice compared with age-matched SAMR1 (Figure 2A−D), supporting insulin-resistant conditions observed in skeletal muscle of SAMP8 mice. EGCG normalized Akt activity and promoted the protein expression of GLUT4 (123%) in SAMP8 mice compared with age-matched SAMR1. AMPK is a key molecule responsible for non-insulin-mediated glucose uptake. A marked increase in AMPKα activity (146%) was observed in SAMP8 mice after 12 weeks administration of 0.32% EGCG (Figure 2E).

Effects of EGCG on Mitochondrial Function in Skeletal Muscle. Mitochondrial dysfunction in skeletal muscle is highly associated with insulin resistance. PGC1α is a master regulator involved in mitochondrial biogenesis and function. Nuclear respiratory factor 1 (Nrf1), a downstream target of PGC1α and an important transcription factor, stimulates the expression of mitochondrial proteins such as oxidative phosphorylation components and regulates the expression of mitochondrial transcription factor A (Tfam), thereby affecting mitochondrial DNA (mtDNA) replication and expression. Significantly decreased PGC1α protein expression (Figure 3A,B) and mtDNA/nuclear DNA ratio (Figure 3C) were observed in SAMP8 mice compared to age-matched SAMR1 mice. EGCG restored mtDNA/nuclear DNA ratio in SAMP8 mice to the level observed in SAMR1 mice (Figure 3C). EGCG did not affect PGC1α protein expression after 12 weeks of administration. Significantly decreased SIRT1 mRNA expression in SAMP8 mice was restored by EGCG (Figure 3D). EGCG resulted in a marked increase in Nrf1 mRNA expression (267%), thereby stimulating gene expression of downstream targets including Tfam (330%), mitochondrial complex I Ndufs8 (178%), and complex IV Cox5b (127%) mRNA expression in comparison with SAMR1 mice and SAMP8 mice without EGCG feeding (Figure 3D).

Effects of EGCG on Histopathology and Function of Liver. As shown in Figure 4B, SAMP8 mice displayed fatty infiltration with macro- and microvesicles in the liver. Staining neutral lipids and lipid droplets with ORO further demonstrated fatty liver in SAMP8 mice (Figure 4E,G). In contrast, lipid droplets were rarely observed in SAMR1 mice (Figure 4D,G). In line with morphological observation, hepatic TG was significantly increased in SAMP8 mice (Figure 4H), which demonstrated excess lipid accumulation in liver of SAMP8 mice. After 12 weeks of EGCG treatment, a marked reduction in hepatocyte ballooning and fewer lipid droplets were observed (Figure 4C,F). Normalization of hepatic TG to the level of SAMR1 mice was also observed after 12 weeks of EGCG treatment (Figure 4H). Significantly increased ALT activity was observed in SAMP8 mice compared with age-matched SAMR1 mice (Figure 4I). EGCG normalized hepatic ALT activity to the level of SAMR1 mice after 12 weeks of treatment (Figure 4I). No significant difference in hepatic AST activity was observed among three groups (Figure 4J).

Effects of EGCG on Lipid Metabolism, Inflammation, and Mitochondrial Function in Liver. Promoted de novo lipogenesis through up-regulated transcription factors by insulin and glucose results in increased hepatic lipid accumulation in liver of SAMP8 mice. Marked increases in sterol regulatory element-binding proteins-1c (SREBP-1c) (277%) and carbohydrate-responsive element-binding protein (ChREBP) (224%), transcription factors involved in the biosynthesis of fatty acids, in conjunction with significant decreased adipose triglyceride lipase (ATGL) gene expression, a rate-limiting enzyme in TG hydrolysis, were observed in liver of SAMP8 mice (Figure 5A). These results indicate that accelerated aging-associated lipid accumulation in liver is through reduced hepatic TG hydrolysis and increased hepatic TG biosynthesis. Furthermore, NFκB, a master regulator of pro-inflammatory signaling pathway, was significantly increased at mRNA level in SAMP8 mice. EGCG significantly suppressed SREBP-1c and attenuated NFκB mRNA expression, but did not affect ChREBP and ATGL mRNA expression (Figure 5A). The mTOR pathway has been shown to activate SREBP-1c expression. Therefore, normalization of SREBP-1c mRNA to the level of SAMR1 (Figure 5A) was, at least in part, attributed to inhibition of mTOR activity via suppressing the positive regulator, Akt, and activating the negative regulator, AMPK, by EGCG (Figure 5B−E). Significantly decreased PGC1α protein expression and mtDNA/nuclear DNA ratio were observed in the liver of SAMP8 mice compared to those of age-matched SAMR1 mice (Figure 6A−C). EGCG did not affect these two at the present dose. No differences in SIRT1, PGC1α, Nrf1, Tfam, mitochondrial complex I, and complex IV at mRNA levels were observed in liver among the three groups (Figure 6D).

DISCUSSION

Aging per se is an independent risk factor for the development of insulin resistance. As a result, impairment of glucose homeostasis in peripheral tissues such as skeletal muscle occurs during the aging progress.[20] In this study, higher levels of glucose and insulin observed in SAMP8 mice compared to the normal aging group, SAMR1 mice, suggest that the accelerated aging mouse model is suitable for studying the underlying mechanism of aging-associated insulin resistance. EGCG, the most abundant component in green tea, improves insulin sensitivity in different rodent models.[16,17,21] In this study, EGCG successfully attenuated aging-associated insulin resistance in SAMP8 mice.

In the present study, hyperglycemia and hyperinsulinemia were observed in SAMP8 mice at the age of 40 weeks. In line with our data, elevated insulin levels and increased insulin resistance index (HOMA-IR) in SAMP8 mice at similar age were reported by another group.[9] Postreceptor defects in skeletal muscle of SAMP8 mice may impair glucose homeostasis, because it is the major peripheral tissue responsible for insulin-mediated glucose uptake.[22] Defective insulin signaling pathway including inhibition of PI3K/Akt pathway and decreased GLUT4 expression, which have been considered as

DOI: 10.1021/acs.jafc.5b02501
J. Agric. Food Chem. 2015, 63, 8407−8417

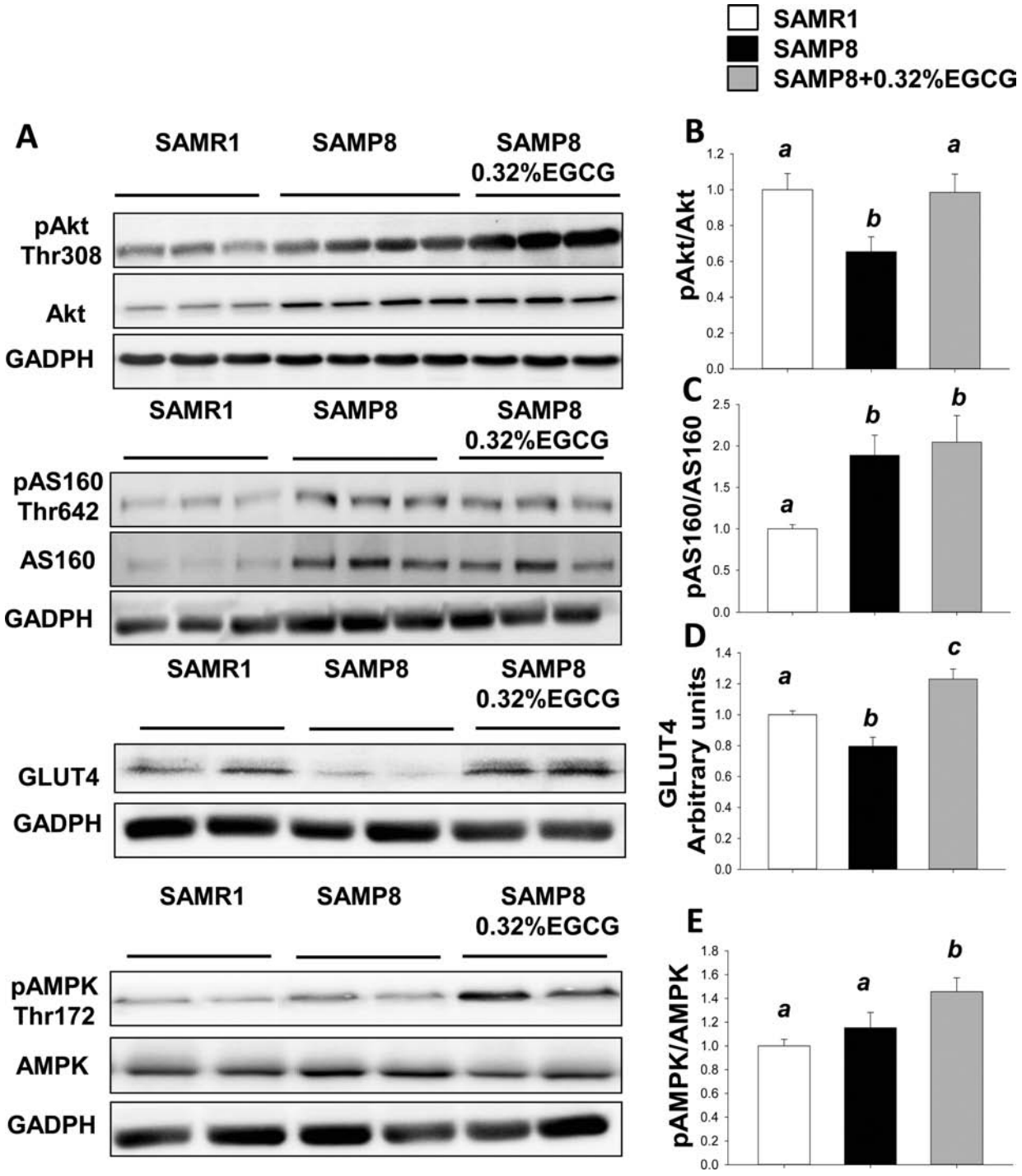

Figure 2. Insulin signaling pathway and AMPKα in skeletal muscle: (A) Representative blots are shown. (B−E) Values presented are means ± SEM (n = 6−8/group). Equal amounts of mouse tissue lysates were analyzed using Western blotting with anti-phospho-Akt (Thr308), anti-Akt, anti-phospho-AS160 (Thr642), anti-AS160, anti-GLUT4, anti-phospho-AMPKα (Thr172), and anti-AMPKα antibodies. Statistical analysis was performed using ANOVA followed by post hoc analysis using Student−Newman−Keuls method. Significance (P < 0.05) among groups is denoted by different letters.

the pathophysiology of skeletal muscle insulin resistance,[23,24] were observed in SAMP8 mice of the present study. In the search for popular natural products, EGCG reveals beneficial effects on obesity and diabetes ranging from in vitro cell models[12,25] to in vivo studies by using different diabetic and/or obese rodent models.[16,17,21,26,27] The underlying mechanism of alleviating FFAs-induced insulin resistance by EGCG was reported to suppress serine phosphorylation of PKCθ and IRS1, enhance AMPK activity, and stimulate GLUT4 translocation in rats.[28] Here, we demonstrated that EGCG exhibited beneficial effects on aging-associated insulin resistance in SAMP8 mice via not only enhanced AMPK activity but also restored Akt activity and stimulated GLUT4 protein expression. Restored GLUT4 expression by EGCG in SAMP8 mice could be attributed to AMPK activation, because AMPK directly

DOI: 10.1021/acs.jafc.5b02501
J. Agric. Food Chem. 2015, 63, 8407−8417

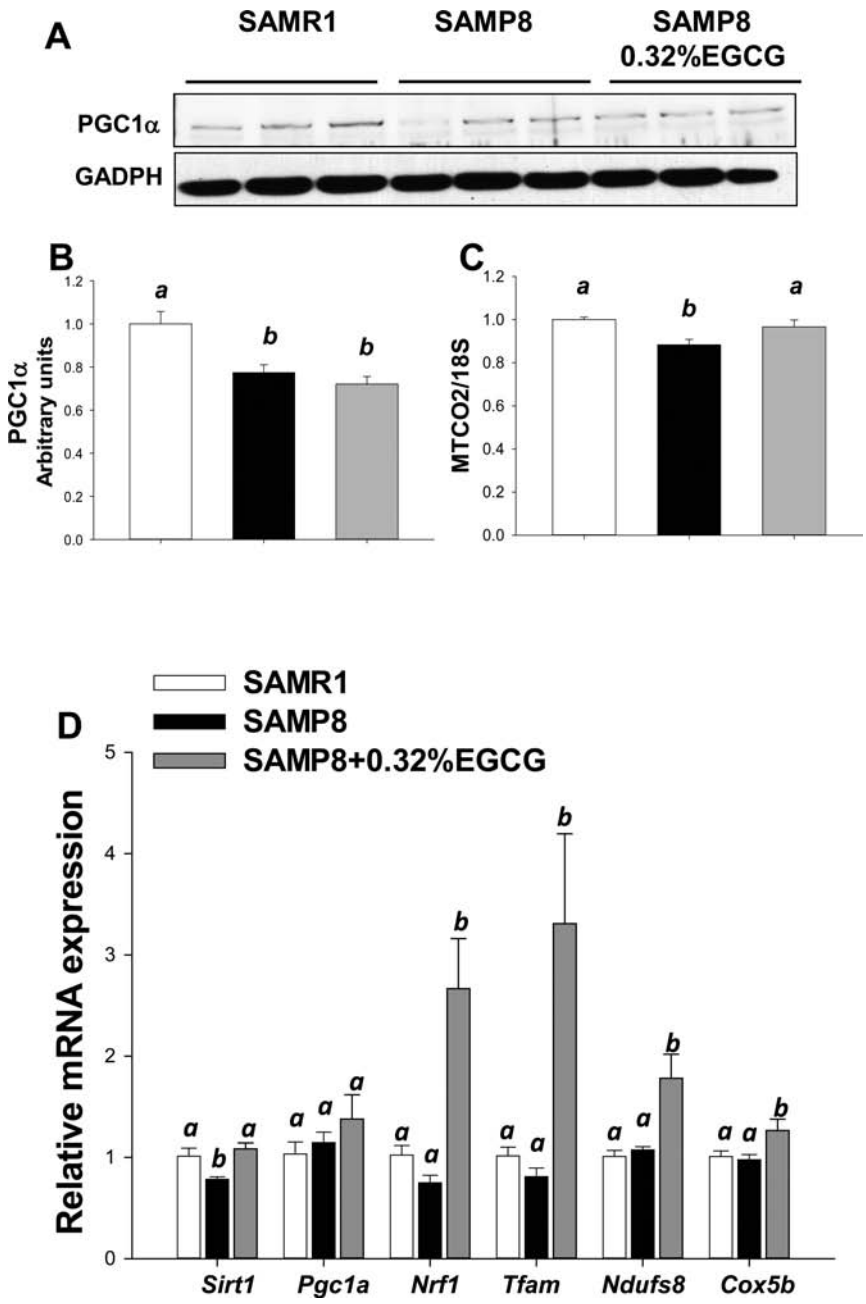

Figure 3. PGC1α transcriptional pathway and mitochondrial biogenesis in skeletal muscle: (A) PGC1α protein expression (n = 6−8/group) and (B) mtDNA copy number were assessed by the ratio of MTCO2/18S (n = 5/group); (C) *Sirt1*, *Pgc1a*, *Nrf1*, *Tfam*, *Ndufs8*, and *COX5b* mRNA expression levels are expressed as mean ratio to control after normalization with GAPDH mRNA levels. Fold differences were calculated using the ΔΔCt method. Values presented are means ± SEM (n = 5−6/group, each in triplicate). Statistical analysis was performed using ANOVA followed by post hoc analysis using Student−Newman−Keuls method. Significance (P < 0.05) among groups is denoted by different letters.

regulates the GLUT4 expression through phosphorylation of histone deacetylase 5.[29]

Distinct from the insulin signaling pathway, perturbation in mitochondrial function has been considered as a novel mechanism involved in the development of insulin resistance, especially in the older age groups.[30,31] Significantly decreased PGC1α and mtDNA copy number in skeletal muscle of SMAP8 mice reveal mechanisms linking defective mitochondrial biogenesis to insulin resistance. Beyond insulin resistance, mitochondrial dysfunction occurred in SAMP8 mice contributes to the shorter lifespan of these mice.[32] Pharmacological and nutritional agents have been used to promote AMPK and SIRT1 activities and subsequently activate PGC1α function and boost mitochondrial biogenesis.[31,33,34] With regard to the effect of EGCG on mitochondrial biogenesis in SAMP8 mice, it restored SIRT1 gene expression and stimulated AMPK activity, leading to enhanced transcription factors such as Tfam and NRF1 accompanied by restored mtDNA copy number and promoted mitochondrial complex I and IV at mRNA levels in the present study.

Fatty liver, including hepatocellular ballooning and lipid accumulation, was observed in SAMP8 mice of our and others' studies.[11,35] The underlying mechanism of spontaneous fatty liver in SAMP8 mice could be due to an imbalance between

DOI: 10.1021/acs.jafc.5b02501
J. Agric. Food Chem. 2015, 63, 8407−8417

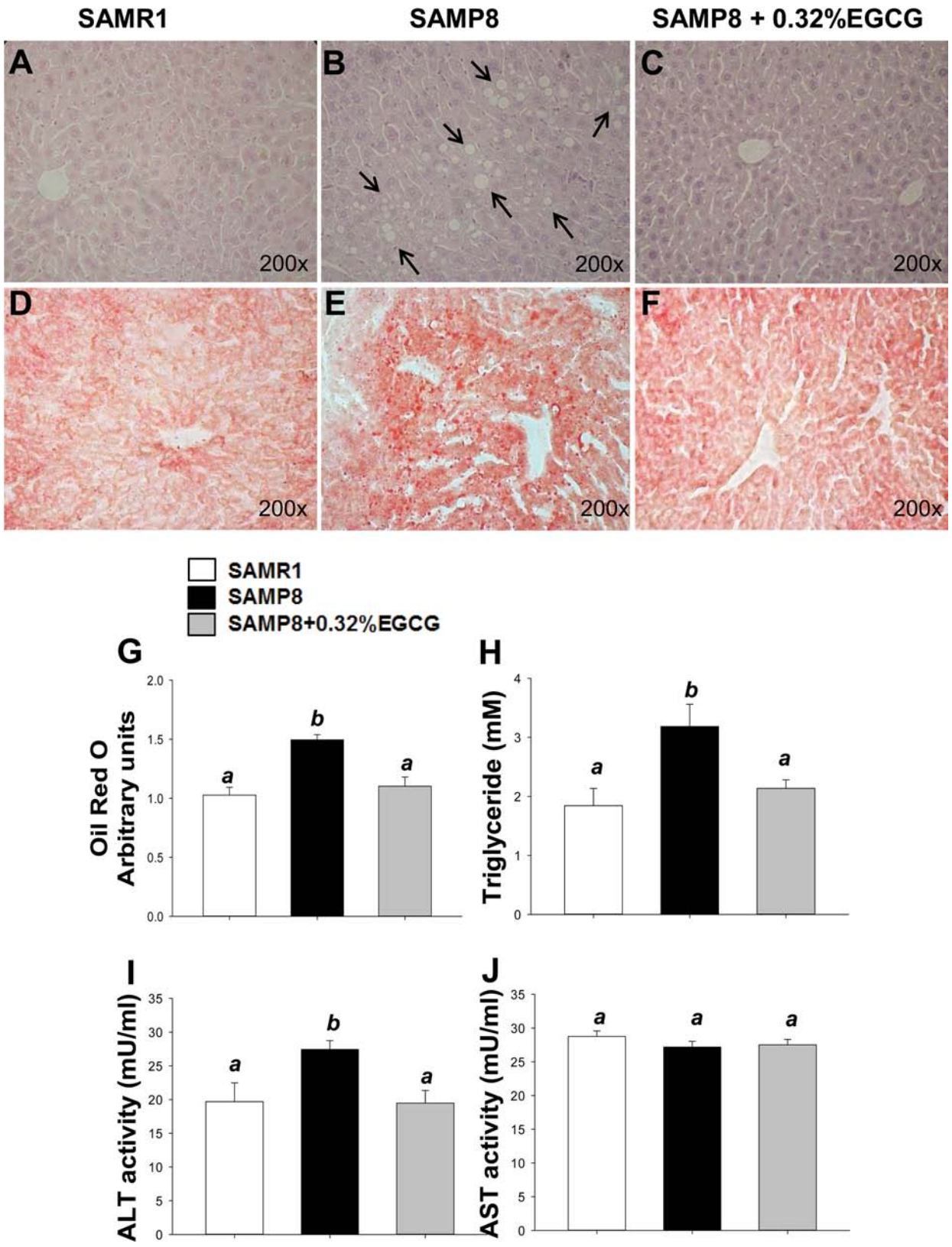

Figure 4. Fatty liver in SAMR1, SAMP8, and SAMP8 + 0.32% EGCG mice: hepatic histological analysis (A–C) stained with hematoxylin and eosin (200×) (arrows indicate the accumulation of TG as macro- or microvesicles (B)); visualization (D–F) and quantification (G) of neutral lipids stained with ORO solution in liver; TG concentration, ALT activity, and AST activity in liver (n = 6–11/group) (H–J).

lipid supply and demand during aging. At the age of 40 weeks, SAMP8 mice elevated serum FFA levels because enhanced TG lipolysis and reduced FFA esterification in adipose tissue result in rising circulating FFA levels under insulin-resistant conditions.[36] It is reasonably assumed that elevated circulating FFA entered hepatocytes and were subsequently esterified into

DOI: 10.1021/acs.jafc.5b02501
J. Agric. Food Chem. 2015, 63, 8407–8417

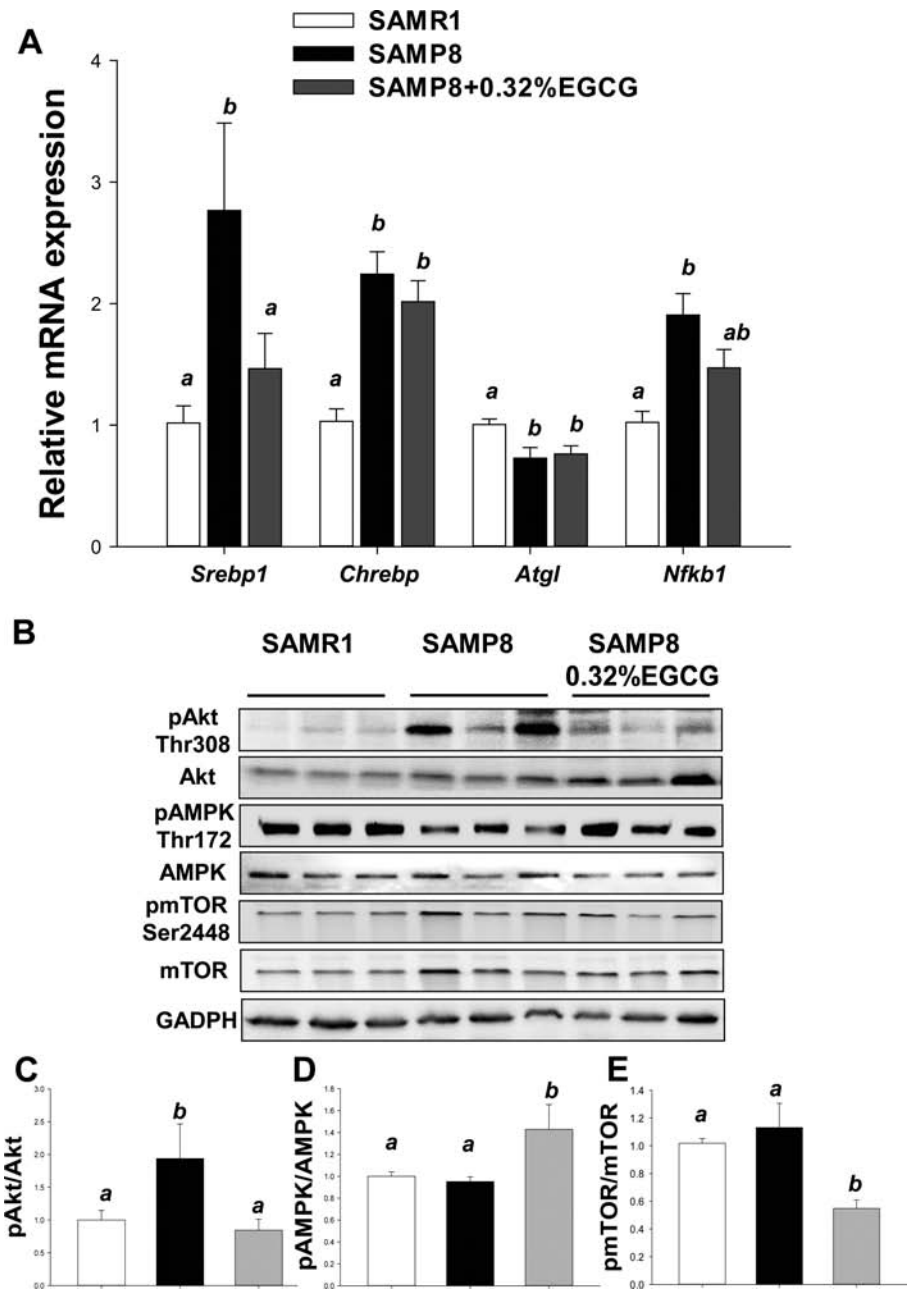

Figure 5. Lipid metabolism and Akt/AMPK/mTOR pathway in liver. (A) *Srebp1*, *Chrebp*, *Atgl*, and *Nfkb1* mRNA expression levels are expressed as mean ratio to control after normalization with GAPDH mRNA levels. Fold differences were calculated using the ΔΔCt method. Values presented are means ± SEM (n = 5−6/group, each in triplicate). (B) Representative blots of Akt, phosphor-Akt (Thr308), AMPKα, phospho-AMPKα (Thr172), mTOR, and phospho-mTOR (Ser2448) are shown. (C−E) Values presented are means ± SEM (n = 5−7/group). Statistical analysis was performed using ANOVA followed by post hoc analysis using Student−Newman−Keuls method. Significance ($P < 0.05$) among groups is denoted by different letters.

TG, leading to excessive accumulation of TG in the liver of SAMP8 mice. Up-regulation of nuclear transcription factors including SREBP-1c and ChREBP, responsible for de novo fatty acid synthesis, was observed in SAMP8 mice. Promoted de novo lipogenesis via the activation of two transcription factors in the liver is attributed to higher levels of insulin and glucose.[10] TG hydrolysis and fatty acid oxidation are essential processes to prevent excessive TG accumulation in the liver. Decreased TG hydrolysis was observed by ATGL knockdown in vitro.[37] Here, we found a marked decrease in ATGL gene expression of SAMP8 mice. Suppressed ATGL expression, the key enzyme for the breakdown of TG, could attenuate intrahepatic TG hydrolysis, thus preventing fatty acid oxidation. Loss of mitochondrial function and impaired fatty acid oxidation are causative factors in excessive TG accumulation in the liver of Otsuka Long-Evans Tokushima Fatty rats.[38] In agreement with the previous study,[38] decreased PGC1α protein expression and mtDNA copy number in SAMP8 mice were correlated with a decrease in mitochondrial biogenesis, which could result in a reduced rate of mitochondrial fatty acid oxidation and consequently cause excessive TG accumulation. Up-regulation of mitochondrial biogenesis was not observed in EGCG treated mice. Meng et al. reported that administration of EGCG (500 mg/kg diet) for 6 months protected mitochondrial integrity

DOI: 10.1021/acs.jafc.5b02501
J. Agric. Food Chem. 2015, 63, 8407−8417

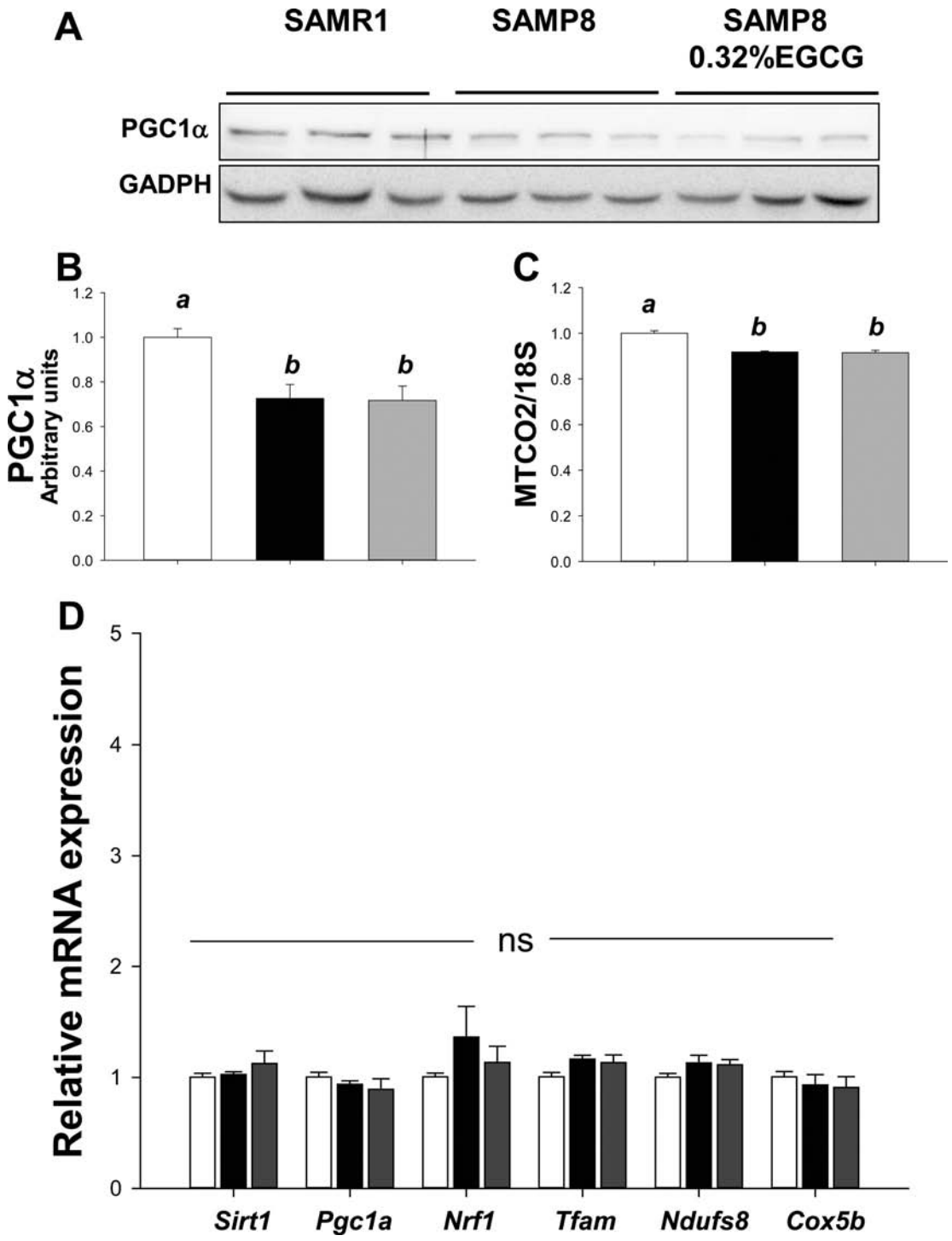

Figure 6. PGC1α transcriptional pathway and mitochondrial biogenesis in liver. (A) PGC1α protein expression (n = 6−8/group) and (B) mtDNA copy number were assessed by the ratio of MTCO2/18S (n = 5/group). (C) *Sirt1*, *Pgc1a*, *Nrf1*, *Tfam*, *Ndufs8*, and *COX5b* mRNA expression levels are expressed as mean ratio to control after normalization with GAPDH mRNA levels. Fold differences were calculated using the ΔΔCt method. Values presented are means ± SEM (n = 5−6/group, each in triplicate). Statistical analysis was performed using ANOVA followed by post hoc analysis using Student−Newman−Keuls method. Significance (P < 0.05) among groups is denoted by different letters.

including restored mitochondrial membrane potential of lymphocytes and increased mitochondrial DNA deletion in the liver of rats.[39] The main discrepancy between their study and ours could be attributed to the duration of administration (6 months vs 12 weeks). In another study, SAMP8 administered melatonin, a direct free radical scavenger and an indirect antioxidant, from 7 to 12 months of age (6 months), led to a significant increase in mitochondrial complex I and IV activities in the liver of melatonin-treated SAMP8 mice.[40] Taken together, these results indicate that the protective effects may depend on the duration of treatment.

Reduced hepatic TG contents by EGCG in SMAP8 mice are consistent with an earlier study using high-fat-fed rodent models.[17] Beneficial effects of EGCG on lowering hepatic TG

DOI: 10.1021/acs.jafc.5b02501
J. Agric. Food Chem. 2015, 63, 8407−8417

levels in SMAP8 mice are attributed to modulation of SREBP-1c expression via inhibiting mTOR activity and/or decreasing insulin levels. Inhibition of mTOR by rapamycin, an mTOR inhibitor, leads to repressed SREBP-1c protein expression and subsequently inhibits lipid accumulation in orotic acid-induced fatty liver.[41] Furthermore, Akt and AMPK, two major upstream regulators of mTOR, were down- and up-regulated by EGCG in SAMP8 mice, respectively. Akt, the positive regulator of mTOR, was suppressed by EGCG within physiologically relevant concentrations;[42] on the other hand, AMPK activation results in the inhibition of mTOR.[41] Therefore, the molecular mechanism underlying the reduction of fatty acid synthesis by EGCG was attributed to suppression of SREBP-1c at mRNA level via inhibiting the mTOR pathway. In addition to mTOR, insulin is a well-known stimulator of lipogenesis and activates hepatic SREBP-1c expression at the transcriptional level.[43] For this reason, it is likely that the restoration of SREBP-1c mRNA in SAMP8 back to the level of SAMR1 mice was due to lower insulin levels by EGCG. Decreased ALT and NFκB activities by EGCG have been reported in NAFLD rodent models.[14,17] In accordance with these studies, we found that EGCG reduced liver injury and inflammatory status, such as decreased ALT activity and attenuated NFκB gene expression in SAMP8 mice. Reduced liver damage via inhibiting the NFκB-induced inflammatory signaling pathway in healthy rats is thought to be the potential mechanism in the extension of lifespan after long-term administration of EGCG.[15]

Decreased respiratory quotient by EGCG has been observed in obese mice, suggesting that EGCG stimulates fatty acid oxidation.[44] Results from the present study indicate that EGCG up-regulates genes related to mitochondrial function in skeletal muscle of SAMP8 mice. Therefore, it is speculated that the increased FFA influx to skeletal muscle, together with the activation of key enzymes in lipid catabolism by EGCG, leads a marked increase in muscle fatty acid oxidation. Simultaneously, fewer FFA are taken up by the liver thereby preventing lipid accumulation in liver. Taken together, it is suggested that skeletal muscle participated in preventing TG accumulation in the liver of SMAP8 mice.

In conclusion, SAMP8 mice exhibited higher levels of insulin, glucose, and FFA, and defective insulin signaling and mitochondrial dysfunction in skeletal muscle are suitable models for the investigation of aging-associated insulin resistance. Increased SREBP-1c and ChREBP involved in lipogenesis and decreased gene responsible for TG hydrolysis result in lipid accumulation leading to the development of fatty liver in SAMP8 mice. Dietary supplementation of SAMP8 mice with EGCG for 12 weeks alleviates aging-associated skeletal muscle insulin resistance via stimulating AMPKα activity, restoring Akt activity and GLUT4 protein expression, and enhancing mitochondrial biogenesis. EGCG prevents fat accumulation in the liver, at least in part, through inhibition of mTOR activity and down-regulation of SREBP-1c mRNA. Overall, our results indicate that EGCG as an antiaging agent is beneficial for aging-associated metabolic disorders.

AUTHOR INFORMATION

Corresponding Author

*(S.-J.C.) Mail: Department of Life Sciences, National Cheng Kung University, 1 University Road, Tainan, Taiwan. E-mail: sjchang@mail.ncku.edu.tw. Fax: +886-6-2742583. Phone: +886-6-2757575, ext. 65542.

Funding

This research was supported by a grant from the National Science Council (now the Ministry of Science and Technology), Taiwan, to S.-J.C. (102-2628-B-006-012-MY3).

Notes

The authors declare no competing financial interest.

ACKNOWLEDGMENTS

We are grateful to Zih-Ling Hong for skillful technical assistance.

ABBREVIATIONS USED

AMPKα: AMP-activated protein kinase α
ATGL: adipose triglyceride lipase
ChREBP: carbohydrate-responsive element-binding protein
EGCG: (−)-epigallocatechin-3-gallate
FFA: free fatty acids
GLUT4: glucose transporter 4
IRS1: insulin receptor substrate 1
mTOR: mammalian target of rapamycin
NAFLD: nonalcoholic fatty liver disease
NFκB: nuclear factor-κB
Nrf1: nuclear respiratory factor 1
ORO: oil red O
PGC1α: proxisome proliferator-activated receptor gamma coactivator 1-α
PI3K: phosphatidylinositol-3-kinases
PKC: protein kinase C
SAM: senescence-accelerated mice
SIRT1: sirtuin1
SREBP-1c: sterol regulatory element binding proteins-1c
Tfam: mitochondrial transcription factor A
TG: triglycerides

REFERENCES

(1) Liu, H.; Li, J. Aging and dyslipidemia: a review of potential mechanisms. *Ageing Res. Rev.* **2015**, *19C*, 43−52.

(2) Dillon, L. M.; Rebelo, A. P.; Moraes, C. T. The role of PGC-1 coactivators in aging skeletal muscle and heart. *IUBMB Life* **2012**, *64*, 231−241.

(3) Tchkonia, T.; Morbeck, D. E.; Von Zglinicki, T.; Van Deursen, J.; Lustgarten, J.; Scrable, H.; Khosla, S.; Jensen, M. D.; Kirkland, J. L. Fat tissue, aging, and cellular senescence. *Aging Cell* **2010**, *9*, 667−684.

(4) Yu, Y. H.; Ginsberg, H. N. Adipocyte signaling and lipid homeostasis: sequelae of insulin-resistant adipose tissue. *Circ. Res.* **2005**, *96*, 1042−1052.

(5) Houtkooper, R. H.; Argmann, C.; Houten, S. M.; Canto, C.; Jeninga, E. H.; Andreux, P. A.; Thomas, C.; Doenlen, R.; Schoonjans, K.; Auwerx, J. The metabolic footprint of aging in mice. *Sci. Rep.* **2011**, *1*, 134.

(6) Takeda, T. Senescence-accelerated mouse (SAM) with special references to neurodegeneration models, SAMP8 and SAMP10 mice. *Neurochem. Res.* **2009**, *34*, 639−659.

(7) Takeda, T.; Matsushita, T.; Kurozumi, M.; Takemura, K.; Higuchi, K.; Hosokawa, M. Pathobiology of the senescence-accelerated mouse (SAM). *Exp. Gerontol.* **1997**, *32*, 117−127.

(8) Butterfield, D. A.; Poon, H. F. The senescence-accelerated prone mouse (SAMP8): a model of age-related cognitive decline with relevance to alterations of the gene expression and protein abnormalities in Alzheimer's disease. *Exp. Gerontol.* **2005**, *40*, 774−783.

(9) Cuesta, S.; Kireev, R.; Garcia, C.; Rancan, L.; Vara, E.; Tresguerres, J. A. Melatonin can improve insulin resistance and aging-induced pancreas alterations in senescence-accelerated prone male mice (SAMP8). *Age* **2013**, *35*, 659−671.

DOI: 10.1021/acs.jafc.5b02501
J. Agric. Food Chem. 2015, 63, 8407−8417

(10) Cohen, J. C.; Horton, J. D.; Hobbs, H. H. Human fatty liver disease: old questions and new insights. *Science* **2011**, *332*, 1519−1523.
(11) Ye, X.; Meeker, H. C.; Kozlowski, P. B.; Wegiel, J.; Wang, K. C.; Imaki, H.; Carp, R. I. Pathological changes in the liver of a senescence accelerated mouse strain (SAMP8): a mouse model for the study of liver diseases. *Histol. Histopathol.* **2004**, *19*, 1141−1151.
(12) Babu, P. V.; Liu, D.; Gilbert, E. R. Recent advances in understanding the anti-diabetic actions of dietary flavonoids. *J. Nutr. Biochem.* **2013**, *24*, 1777−1789.
(13) Ueda, M.; Nishiumi, S.; Nagayasu, H.; Fukuda, I.; Yoshida, K.; Ashida, H. Epigallocatechin gallate promotes GLUT4 translocation in skeletal muscle. *Biochem. Biophys. Res. Commun.* **2008**, *377*, 286−290.
(14) Xiao, J.; Ho, C. T.; Liong, E. C.; Nanji, A. A.; Leung, T. M.; Lau, T. Y.; Fung, M. L.; Tipoe, G. L. Epigallocatechin gallate attenuates fibrosis, oxidative stress, and inflammation in non-alcoholic fatty liver disease rat model through TGF/SMAD, PI3 K/Akt/FoxO1, and NF-kappa B pathways. *Eur. J. Nutr.* **2014**, *53*, 187−199.
(15) Niu, Y.; Na, L.; Feng, R.; Gong, L.; Zhao, Y.; Li, Q.; Li, Y.; Sun, C. The phytochemical, EGCG, extends lifespan by reducing liver and kidney function damage and improving age-associated inflammation and oxidative stress in healthy rats. *Aging Cell* **2013**, *12*, 1041−1049.
(16) Wolfram, S.; Raederstorff, D.; Preller, M.; Wang, Y.; Teixeira, S. R.; Riegger, C.; Weber, P. Epigallocatechin gallate supplementation alleviates diabetes in rodents. *J. Nutr.* **2006**, *136*, 2512−2518.
(17) Bose, M.; Lambert, J. D.; Ju, J.; Reuhl, K. R.; Shapses, S. A.; Yang, C. S. The major green tea polyphenol, (−)-epigallocatechin-3-gallate, inhibits obesity, metabolic syndrome, and fatty liver disease in high-fat-fed mice. *J. Nutr.* **2008**, *138*, 1677−1683.
(18) Mehlem, A.; Hagberg, C. E.; Muhl, L.; Eriksson, U.; Falkevall, A. Imaging of neutral lipids by oil red O for analyzing the metabolic status in health and disease. *Nat. Protoc.* **2013**, *8*, 1149−1154.
(19) Park, J. Y.; Wang, P. Y.; Matsumoto, T.; Sung, H. J.; Ma, W.; Choi, J. W.; Anderson, S. A.; Leary, S. C.; Balaban, R. S.; Kang, J. G.; Hwang, P. M. p53 improves aerobic exercise capacity and augments skeletal muscle mitochondrial DNA content. *Circ. Res.* **2009**, *105*, 705−712 11 p following 712..
(20) Fink, R. I.; Kolterman, O. G.; Griffin, J.; Olefsky, J. M. Mechanisms of insulin resistance in aging. *J. Clin. Invest.* **1983**, *71*, 1523−1535.
(21) Ortsater, H.; Grankvist, N.; Wolfram, S.; Kuehn, N.; Sjoholm, A. Diet supplementation with green tea extract epigallocatechin gallate prevents progression to glucose intolerance in db/db mice. *Nutr. Metab.* **2012**, *9*, 11.
(22) DeFronzo, R. A.; Gunnarsson, R.; Bjorkman, O.; Olsson, M.; Wahren, J. Effects of insulin on peripheral and splanchnic glucose metabolism in noninsulin-dependent (type II) diabetes mellitus. *J. Clin. Invest.* **1985**, *76*, 149−155.
(23) Sesti, G. Pathophysiology of insulin resistance. *Best Pract Res. Clin Endocrinol Metab* **2006**, *20*, 665−679.
(24) Houmard, J. A.; Weidner, M. D.; Dolan, P. L.; Leggett-Frazier, N.; Gavigan, K. E.; Hickey, M. S.; Tyndall, G. L.; Zheng, D.; Alshami, A.; Dohm, G. L. Skeletal muscle GLUT4 protein concentration and aging in humans. *Diabetes* **1995**, *44*, 555−560.
(25) Wang, S.; Moustaid-Moussa, N.; Chen, L.; Mo, H.; Shastri, A.; Su, R.; Bapat, P.; Kwun, I.; Shen, C. L. Novel insights of dietary polyphenols and obesity. *J. Nutr. Biochem.* **2014**, *25*, 1−18.
(26) Kuzu, N.; Bahcecioglu, I. H.; Dagli, A. F.; Ozercan, I. H.; Ustundag, B.; Sahin, K. Epigallocatechin gallate attenuates experimental non-alcoholic steatohepatitis induced by high fat diet. *J. Gastroenterol. Hepatol.* **2008**, *23*, e465−e470.
(27) Yan, J.; Feng, Z.; Liu, J.; Shen, W.; Wang, Y.; Wertz, K.; Weber, P.; Long, J.; Liu, J. Enhanced autophagy plays a cardinal role in mitochondrial dysfunction in type 2 diabetic Goto-Kakizaki (GK) rats: ameliorating effects of (−)-epigallocatechin-3-gallate. *J. Nutr. Biochem.* **2012**, *23*, 716−724.
(28) Li, Y.; Zhao, S.; Zhang, W.; Zhao, P.; He, B.; Wu, N.; Han, P. Epigallocatechin-3-*O*-gallate (EGCG) attenuates FFAs-induced peripheral insulin resistance through AMPK pathway and insulin signaling pathway in vivo. *Diabetes Res. Clin. Pract.* **2011**, *93*, 205−214.
(29) McGee, S. L.; van Denderen, B. J.; Howlett, K. F.; Mollica, J.; Schertzer, J. D.; Kemp, B. E.; Hargreaves, M. AMP-activated protein kinase regulates GLUT4 transcription by phosphorylating histone deacetylase 5. *Diabetes* **2008**, *57*, 860−867.
(30) Toledo, F. G. Mitochondrial involvement in skeletal muscle insulin resistance. *Diabetes* **2014**, *63*, 59−61.
(31) Anderson, R.; Prolla, T. PGC-1alpha in aging and anti-aging interventions. *Biochim. Biophys. Acta, Gen. Subj.* **2009**, *1790*, 1059−1066.
(32) Nakahara, H.; Kanno, T.; Inai, Y.; Utsumi, K.; Hiramatsu, M.; Mori, A.; Packer, L. Mitochondrial dysfunction in the senescence accelerated mouse (SAM). *Free Radical Biol. Med.* **1998**, *24*, 85−92.
(33) Price, N. L.; Gomes, A. P.; Ling, A. J.; Duarte, F. V.; Martin-Montalvo, A.; North, B. J.; Agarwal, B.; Ye, L.; Ramadori, G.; Teodoro, J. S.; Hubbard, B. P.; Varela, A. T.; Davis, J. G.; Varamini, B.; Hafner, A.; Moaddel, R.; Rolo, A. P.; Coppari, R.; Palmeira, C. M.; de Cabo, R.; Baur, J. A.; Sinclair, D. A. SIRT1 is required for AMPK activation and the beneficial effects of resveratrol on mitochondrial function. *Cell Metab.* **2012**, *15*, 675−690.
(34) Jiang, T.; Yin, F.; Yao, J.; Brinton, R. D.; Cadenas, E. Lipoic acid restores age-associated impairment of brain energy metabolism through the modulation of Akt/JNK signaling and PGC1alpha transcriptional pathway. *Aging Cell* **2013**, *12*, 1021−1031.
(35) Liao, J. W.; Hong, L. Z.; Wang, M. F.; Tsai, S. C.; Lin, Y. J.; Chan, Y. C. Mutagenic safety and fatty liver improvement of nanonized black soybeans in senescence-accelerated prone-8 mice. *J. Food Sci.* **2010**, *75*, T82−T90.
(36) Lewis, G. F.; Carpentier, A.; Adeli, K.; Giacca, A. Disordered fat storage and mobilization in the pathogenesis of insulin resistance and type 2 diabetes. *Endocr. Rev.* **2002**, *23*, 201−229.
(37) Ong, K. T.; Mashek, M. T.; Bu, S. Y.; Greenberg, A. S.; Mashek, D. G. Adipose triglyceride lipase is a major hepatic lipase that regulates triacylglycerol turnover and fatty acid signaling and partitioning. *Hepatology* **2011**, *53*, 116−126.
(38) Rector, R. S.; Thyfault, J. P.; Uptergrove, G. M.; Morris, E. M.; Naples, S. P.; Borengasser, S. J.; Mikus, C. R.; Laye, M. J.; Laughlin, M. H.; Booth, F. W.; Ibdah, J. A. Mitochondrial dysfunction precedes insulin resistance and hepatic steatosis and contributes to the natural history of non-alcoholic fatty liver disease in an obese rodent model. *J. Hepatol.* **2010**, *52*, 727−736.
(39) Meng, Q.; Velalar, C. N.; Ruan, R. Regulating the age-related oxidative damage, mitochondrial integrity, and antioxidative enzyme activity in Fischer 344 rats by supplementation of the antioxidant epigallocatechin-3-gallate. *Rejuvenation Res.* **2008**, *11*, 649−660.
(40) Okatani, Y.; Wakatsuki, A.; Reiter, R. J. Melatonin protects hepatic mitochondrial respiratory chain activity in senescence-accelerated mice. *J. Pineal Res.* **2002**, *32*, 143−148.
(41) Jung, E. J.; Kwon, S. W.; Jung, B. H.; Oh, S. H.; Lee, B. H. Role of the AMPK/SREBP-1 pathway in the development of orotic acid-induced fatty liver. *J. Lipid Res.* **2011**, *52*, 1617−1625.
(42) Van Aller, G. S.; Carson, J. D.; Tang, W.; Peng, H.; Zhao, L.; Copeland, R. A.; Tummino, P. J.; Luo, L. Epigallocatechin gallate (EGCG), a major component of green tea, is a dual phosphoinositide-3-kinase/mTOR inhibitor. *Biochem. Biophys. Res. Commun.* **2011**, *406*, 194−199.
(43) Osborne, T. F. Sterol regulatory element-binding proteins (SREBPs): key regulators of nutritional homeostasis and insulin action. *J. Biol. Chem.* **2000**, *275*, 32379−32382.
(44) Klaus, S.; Pultz, S.; Thone-Reineke, C.; Wolfram, S. Epigallocatechin gallate attenuates diet-induced obesity in mice by decreasing energy absorption and increasing fat oxidation. *Int. J. Obes.* **2005**, *29*, 615−623.

DOI: 10.1021/acs.jafc.5b02501
J. Agric. Food Chem. 2015, 63, 8407−8417

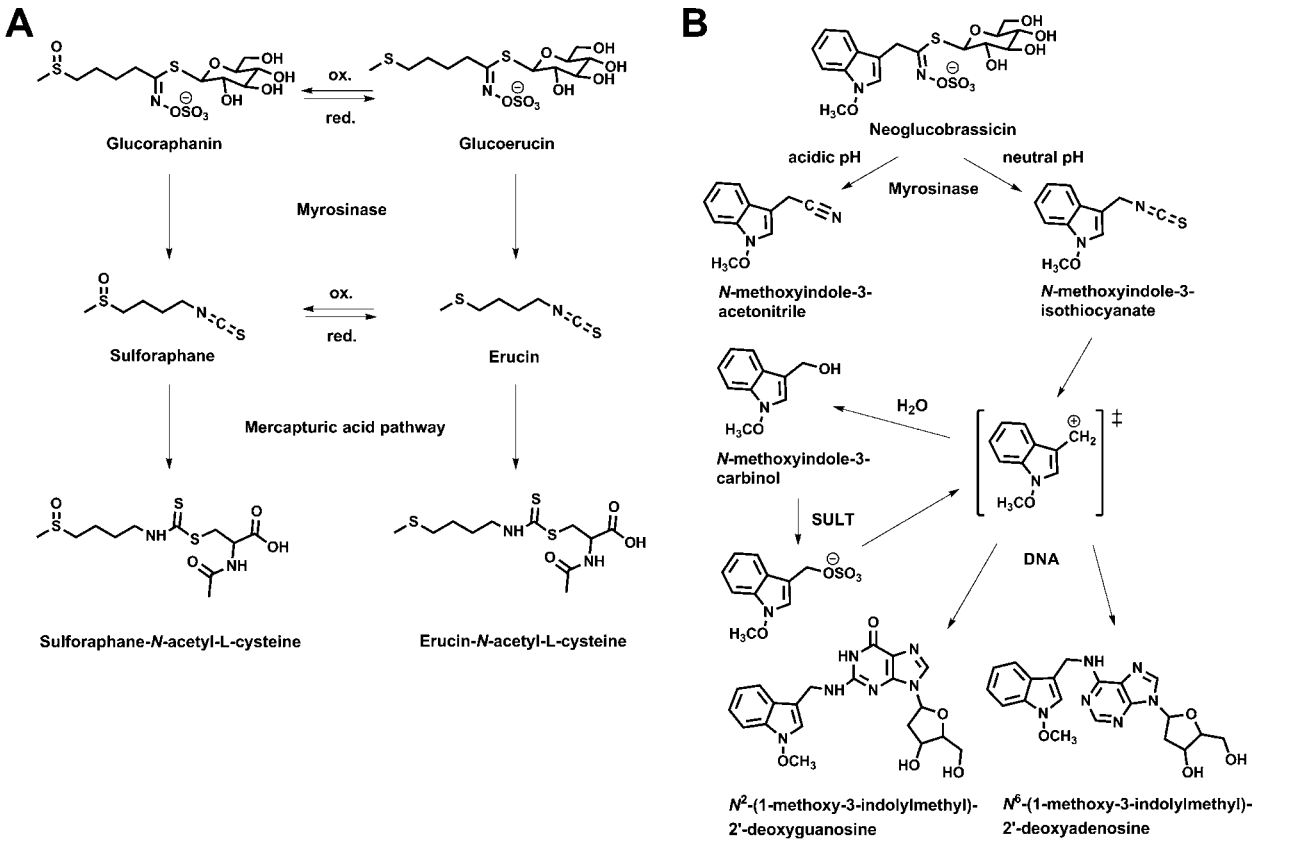

Figure 1. Chemical structures of (A) glucoraphanin, (B) neoglucobrassicin, and their metabolites following myrosinase-catalyzed hydrolysis and further reaction products (mercapturic acids, DNA adducts) investigated in the present study. SULT, sulfotransferase.

(methylthio)butyl glucosinolate, GER] was from Phytolab GmbH & Co. KG (Vestenbergsgreuth, Germany). NGBS was isolated from Pak Choi with a purity of >99% according to Baasanjav-Gerber et al.[3] *N*-Methoxyindole-3-carbinol (NI3C) and *N*-methoxyindole-3-acetonitrile were synthesized and provided by Dr. Albrecht Seidel (Biochemical Institute for Environmental Carcinogens, Professor Dr. Gernot Grimmer-Foundation, Germany) as described previously.[13] Myrosinase, *N*-(*tert*-butoxycarbonyl)-L-cysteine methyl ester (*N*-*t*Boc-Cys-ME), cysteinylglycine, *N*-acetyl-L-cysteine, L-glutathione, and trifluoroacetic acid were purchased from Sigma-Aldrich (Steinheim, Germany). Potassium dihydrogen phosphate, dipotassium hydrogen phosphate, ethyl acetate, L-cysteine, acetonitrile, and MeOH (both HPLC-grade) were obtained from Roth (Karlsruhe, Germany). Ethanol (HPLC-grade) was obtained from VWR (Darmstadt, Germany). All aqueous solutions were prepared with ultrapure water purified with Ultra Clear UV UF (Barsbüttel, Germany). *N*-*t*Boc-Cys-ME stock solution (1.068 M in MeOH) was prepared fresh daily with 100% MeOH and was further diluted to a 427 mM working solution with 60% MeOH (v/v).

Mercapturic acid conjugates of SFN and ERU were prepared as reference substances for the detection and quantification as described by Kassahun[14] and Vermeulen.[15] Briefly, isothiocyanates were dissolved in ethanol and gradually added to the corresponding reagent solution (*N*-acetyl-L-cysteine, L-cysteine, cysteinylglycine, or L-glutathione). The mixture was allowed to react during 24 h of stirring at room temperature. After removal of the solvents using a vacuum centrifuge (Jouan SpeedVac RC 1020, Saint Herblain, France), the structure and purity of all analytical standards were investigated by HPLC-flow-inject electrospray ionization mass spectrometry and nuclear magnetic resonance spectroscopy.

Animals and Treatments. To investigate the role of human gut bacteria in the bioactivation of GRA and NGBS in vivo, animal experiments were carried out using HMA mice in comparison to germ free mice. Animal experiments were conducted in accordance with the institutional and national guidelines for the care and use of laboratory animals. All experimental procedures were approved by the Animal Welfare Committee of the local authority (Landesamt für Verbraucherschutz, Landwirtschaft and Flurneuordnung, Frankfurt/Oder, Germany) under approval number 23-2347-4-2010. The mice were housed in isolators under controlled temperature and lighting conditions (23 °C, 12 h light/dark cycle) and had free access to irradiated food (50 kGy) and autoclaved water.

Eight week old germ free mice were associated with fecal microbiota from a healthy human female donor. A fresh fecal sample was transferred to an anaerobic hood, diluted 1:10 with reduced phosphate buffer (PBS, in g/L: NaCl 8.5, KH_2PO_4 0.3, Na_2HPO_4 0.6, cysteine × HCl × H_2O 0.25, Bacto peptone 0.1, and resazurine 0.001, pH 7) and the resulting slurry subsequently diluted 1:5 with glycerol and stored at −80 °C until use. For association of the germ free mice, 200 μL of the suspension was applied to each animal by gavage. The ability of the donor's microbiota to activate GLS was not affected by this procedure as cecal and colonic contents of the recipient mice displayed similar activities (data not shown).

For practical reasons, animal experiments were carried out consecutively. Inoculation with frozen material ensured the same composition and quality of inoculation material for all experiments, as it is known that the microbial composition of a human donor changes over time.[16] We previously demonstrated that fecal material for inoculation can be stored after freezing and be transferred to germ free rodents by inoculation of the frozen fecal material. Counts of bacterial strains in cecal, colonic, and fecal material were comparable to those of gnotobiotic animals that received the bacteria live.[17]

The stability of the intestinal microbiota composition in mice was monitored throughout the study by PCR-coupled denaturing gradient gel electrophoresis as described previously.[18] The microbiological status of germ free mice was confirmed as described previously.[19] Throughout the study, the fecal microbiota of the HMA mice had up to 51% similarity to that of the human fecal donor sample. Similarity of

DOI: 10.1021/acs.jafc.5b02948
J. Agric. Food Chem. 2015, 63, 8418−8428

fecal microbiota within a human individual usually varies between 65 and 88% within a certain time frame.[16] Similarities did not differ significantly between time points. These data correspond to those reported in a previous long-term study with rats.[20]

Glucoraphanin Treatment. Male, 8-week-old germ free C3H/HeOuJ mice (Charles River Laboratories International, Sulzfeld, Germany, $n = 30$) were associated with human intestinal microbiota by intragastric application of a human fecal suspension (diluted 1:50 in reduced phosphate buffer, pH 7, containing in g/L of 80% glycerol: NaCl 8.5, KH_2PO_4 0.3, Na_2HPO_4 0.6, cysteine × HCl × H_2O 0.25, Bacto peptone 0.1, resazurine 0.001) or water as a control. We investigated fecal samples from several human donors for their glucosinolate-degrading activity in relation to their habitual Brassica intake. However, we did not observe any correlation between the intake of Brassica vegetables and the rate of glucosinolate hydrolysis in their fecal slurries. The animals were fed the standard diet (Altromin, Lage, Germany) for 2 weeks after association to allow bacteria to colonize the animals' gut. Thereafter, they were switched to a GLS-free semisynthetic diet (Altromin C1000f, Lage, Germany).

After 2 weeks on this diet, at 12 weeks of age, 10 mice per group received once an oral dose of glucoraphanin (172 mg/kg body weight) or glucoraphanin in combination with myrosinase (17 U/kg body weight) as a positive control or water as a negative control. The latter served to assess the absorbance by proteins in the sample. For application, glucoraphanin and myrosinase were dissolved in autoclaved ultrapure water and sterilized by membrane filtration (0.22 μm pore diameter). The GRA dose of 7.2 μmol corresponds to approximately 35 or 60% of the total daily GLS dose administered in a recent study to mice in the form of GLS-enriched broccoli or pak choi.[21] The activity of myrosinase administered together with GRA was sufficient to cleave the GRA completely within 22 min in vitro (data not shown).

Urine and feces were collected using metabolic cages (Tecniplast, Hohenpeißenberg, Germany) over 48 h after application. The collected samples were pooled for every 12 h. Urine samples were centrifuged for 5 min at 20.000*g* and 5 °C. The resulting supernatants and the feces were frozen at −80 °C until further analysis. Finally, mice were anesthetized, and blood was taken by cardiac puncture. The blood was centrifuged at 2.000*g* for 10 min at 4 °C, and the resulting plasma was stored at −80 °C. The gastrointestinal tract was removed and divided into three segments: cecum, small intestine, and colon. The tissue and contents from each segment were collected and immediately frozen at −80 °C until further analysis.

Neoglucobrassicin Treatment. The NGBS experiment was conducted in the same way as the GRA experiment but with the following modifications: Since NGBS was not commercially available and isolation from plant material was very time-consuming, the number of animals was reduced to $n = 5$ per group. NGBS (297 mg/kg body weight) or water as a negative control was orally administered to HMA and germ free animals. The latter served to assess the absorbance of proteins in the sample. To identify a dose that causes detectable adduct levels in colonic and cecal tissue of mice in response to the oral administration of neoglucobrassicin, we performed preliminary experiments. We tested doses of 60, 200, and 600 μmol/kg body weight, and the latter dose was considered to be most suitable. The germ free animals received NGBS in combination with myrosinase (29 U/kg body weight) as a positive control. For HMA mice, the positive control was omitted. The activity of myrosinase administered together with NGBS was sufficient to cleave the NGBS completely within 22 min in vitro (data not shown). The mice were killed 8 h after NGBS application, and urine and feces were pooled during this period. Cecal and colonic tissues were shock-frozen in liquid nitrogen and stored at −80 °C until DNA adduct analysis.

Analysis of Glucosinolates and Their Metabolites in Biological Samples. *Glucoraphanin.* The analysis of GRA and its potential metabolites GER, SFN, and ERU was performed as described previously.[22] Briefly, each sample was analyzed twice: SFN and ERU were determined directly after derivatization with *N*-*t*Boc-Cys-ME. GRA and GER were determined indirectly after enzymatic hydrolysis to SFN and ERU, respectively. The GRA and GER contents of a sample were calculated from the difference of the concentrations of the SFN-*N*-*t*Boc-Cys-ME derivative or the ERU-*N*-*t*Boc-Cys-ME derivative before and after myrosinase treatment. The latter represented the sum of the initial GLS and isothiocyanate content, and the former represented the initial sulforaphane or erucin content.

Neoglucobrassicin. For analysis of intact NGBS and its metabolites NI3C and *N*-methoxyindole-3-acetonitrile, urine (30 μL) and plasma (30 μL) were diluted 1:2 (v/v) with phosphate buffer (1 M, pH 6.7) and briefly vortexed. The diluted samples were extracted three times with 300 μL of 1-butanol. After adding 1-butanol, samples were vortexed for 5 min at room temperature and centrifuged at 3.000*g* and 4 °C for 10 min. Feces and intestinal contents (each 30 mg) were diluted 1:10 (w/v) with phosphate buffer (0.1 M, pH 6.7), vortexed for 5 min at room temperature, and then centrifuged for 10 min at 24.652*g* and 4 °C. The resulting supernatants were extracted three times with 900 μL of 1-butanol, vortexed three times, and centrifuged at 3.000*g* at 4 °C for 10 min. The pellets were extracted three times with 300 μL of 20% MeOH in water (v/v), vortexed for 5 min at room temperature, and subsequently centrifuged at 20.000*g* at 4 °C for 10 min. Every supernatant obtained was evaporated until dryness using a vacuum centrifuge. The residue was suspended in 30 μL of 60% acetonitrile in water (v/v), vortexed for 5 min at room temperature, centrifuged at 20.000*g* and 4 °C for 5 min, and the supernatant subjected to HPLC analysis.

Mercapturic Acid Conjugates in Urine. For the analysis of mercapturic acids, urine samples were centrifuged at 20.000*g* and 4 °C for 5 min. Supernatants were diluted with water (1:5, v/v), centrifuged again at 20.000*g* and 4 °C for 5 min, and analyzed immediately by HPLC/DAD. The analysis of potential mercapturic acid conjugates of NGBS was not performed due to the unavailability of reference substances.

DNA-Adduct Analysis. DNA adducts are formed by reaction of nucleophilic sites of the DNA with exogenous or endogenous electrophilic metabolites. Such a highly reactive electrophile, precisely a benzylic carbocation, can be formed after NGBS hydrolysis either from the resulting short-lived isothiocyanate or from an also unstable sulfoconjugate, whose formation from NI3C is catalyzed by sulfotransferase.[13] Adducts in DNA isolated from cecum and colon tissues were determined using isotope-dilution ultraperformance liquid chromatography−electrospray ionization−tandem mass spectrometry (UPLC-ESI-MS/MS) as described previously.[23,24] Briefly, DNA samples (25 μg) were spiked with [$^{15}N_5$]N^2-(1-methoxy-3-indolylmethyl)-2′-deoxyguanosine ([$^{15}N_5$]N^2-(1-MIM)-dG) and [$^{15}N_5$]N^6-(1-methoxy-3-indolylmethyl)-2′-deoxyadenosine ([$^{15}N_5$]N^6-(1-MIM)-dA) as internal adduct standards, hydrolyzed to 2′-deoxynucleosides, and quantified by isotope-dilution multiple reaction monitoring (MRM). The use of a standard DNA isolation protocol[25] resulted in considerable contamination with RNA despite RNase treatment. Therefore, dG was quantified in the DNA hydrolysate by UPLC-ESI-MS/MS using [$^{15}N_5$]dG as an internal standard, and the actual DNA content of the samples was subsequently determined knowing that dG constitutes 21% of all nucleosides in the murine genome.[26]

HPLC and UPLC-ESI-MS/MS Apparatus and Conditions. Metabolites were separated and quantified with a Summit HPLC system (Dionex, Idstein, Germany) consisting of a pump (P680A LPG), an autosampler (ASI-100T), a column oven (TCC-100), and a diode-array detector (UVD 340U PDA). The HPLC was equipped with an analytical C18 LiChrospher reversed-phase column (5 μm, 4.6 × 250 mm, Merck, Darmstadt, Germany) and a C18 LiChrospher guard column (5 μm). The autosampler temperature was set at 5 °C, the flow rate was 1.0 mL/min, and the column temperature was 30 °C. Instrument control, data acquisition, and peak area analysis were done using the Chromeleon 6.40 Chromatography data system (Dionex, Idstein, Germany). GLS and their metabolites were identified by their retention times, and their UV-spectra in comparison to reference substances and calibration curves were used for their quantification.

For the analysis of isothiocyanate-*N*-(*tert*-butoxycarbonyl)-L-cysteine methyl ester (ITC-*N*-*t*Boc-Cys-ME) derivatives, NGBS and its metabolites, the mobile phase consisted of potassium dihydrogen phosphate (50 mM) acidified with phosphoric acid to pH 2.3 (solvent

DOI: 10.1021/acs.jafc.5b02948
J. Agric. Food Chem. 2015, 63, 8418−8428

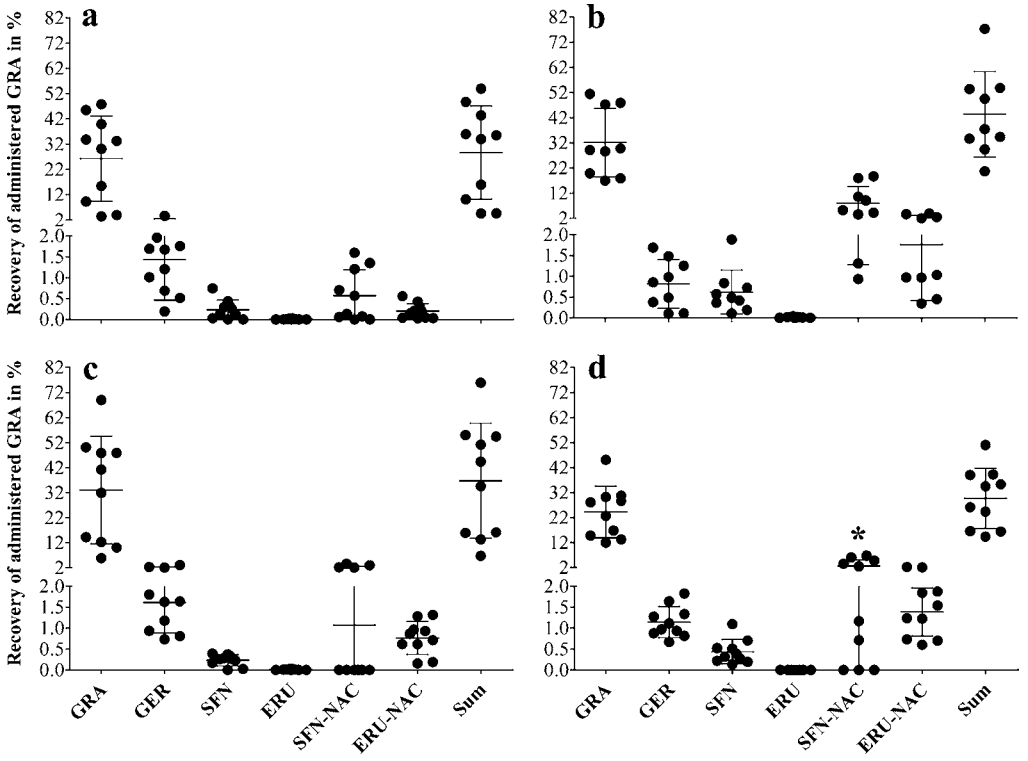

Figure 2. Renal excretion of glucoraphanin (GRA) and its potential metabolites glucoerucin (GER), sulforaphane (SFN), erucin (ERU), sulforaphane-*N*-acetyl-L-cysteine (SFN-NAC), and erucin-*N*-acetyl-L-cysteine (ERU-NAC) within 48 h after GRA application (172 mg/kg body weight) depicted as % recovery of applied GRA in germ free mice without (a) and with (b) myrosinase application and human microbiota-associated (HMA) mice without (c) and with (d) myrosinase application. Each point represents an experimental animal (n = 9 to 10 per group). Depicted are the mean and standard deviation. * translates into the significant difference ($p < 0.05$) between germ free and HMA mice.

A), acetonitrile (solvent B), and ultrapure water (solvent C). ITC-*N*-*t*Boc-Cys-ME derivatives were analyzed as described previously.[22] For the measurement of NGBS and its metabolites, the gradient started with 100% A, changed to 3% B within 4.5 min, from 3% to 25% B within 20.5 min, and from 25% to 60% B within 20 min. The gradient was subsequently switched from 60% B to 100% C and held for 5 min. Then, the column was rinsed with 100% C for 5 min. Finally, the mobile phase returned to the initial solvent composition for 5 min for re-equilibration of the column between single runs.

For the analysis of mercapturic acid conjugates, which were detected at 254 nm, the mobile phase consisted of 0.05% (v/v) trifluoroacetic acid in water (A), 0.1% (v/v) trifluoroacetic acid in acetonitrile (B) and ultrapure water (C). A linear gradient from 0% B to 20% B within 10 min, which was held for 5 min, changed to 35% B within 7.5 min and to 100% B within 5 min, which was held for 5 min. Finally, the mobile phase returned to the initial composition for 5 min for re-equilibration of the column between single runs.

The analysis of the DNA adducts formed from NGBS metabolites was conducted using an Acquity UPLC system equipped with an Acquity UPLC BEH Phenyl column (1.7 μm, 2.1 × 100 mm) coupled to a Xevo TQ triple quadrupole mass spectrometer (all from Waters, Eschborn, Germany) operating in the positive ion mode (ESI+). Conditions for LC separation and MS/MS detection of the analytes have been published previously.[23]

Statistical Analysis. The excretion of GRA, NGBS, and their metabolites via urine, feces, and gut contents of mice was calculated for each animal as percentage recovery of the ingested GLS dose based on molar amount of GLS applied. Statistical analysis was performed using the software SPSS 20.0 (IBM, NY, USA). Values were tested for normal distribution using the Kolmogorov−Smirnov test.[27] Differences were analyzed for normally distributed data on their statistical significance using the unpaired t test and for dependent measurements using the paired t test. Differences of non-normally distributed data were checked for significance using the Mann−Whitney-U-test for unpaired data and the Wilcoxon-test for paired data. Differences in excretion between HMA and germ free mice were considered significant at $p < 0.05$, and a trend was defined as $p < 0.1$. Data are presented as mean values.

RESULTS

Glucoraphanin Is Absorbed Intact and Mainly Excreted via Urine. *Plasma and Urine.* Forty-eight hours after application of GRA with or without myrosinase, no GRA-derived metabolites could be detected in plasma from germ free or HMA mice. Instead, approximately 30% of the applied GRA was excreted in urine in its intact form, mainly within 24 h. The application of GRA (172 mg/kg body weight, corresponding to 362 μmol/kg body weight) to germ free and HMA mice resulted within 12 h in the total renal excretion of GRA and its metabolites in amounts that corresponded to 24 (±17) and 29 (±19)% of administered dose of GRA, respectively, when no myrosinase had additionally been applied and 22 (±17) and 21 (±12)%, respectively, when myrosinase had been applied. When the observation time was extended to 48 h, these values were only slightly increased; they were 29 (±18) and 37 (±23)% in germ free and HMA mice, respectively, without myrosinase, and 43 (±17) and 30 (±12)%, respectively, with myrosinase (Figures 2a−d). Thus, GRA was absorbed intact regardless of the colonization status of the mice and whether myrosinase had been applied. In contrast to the procedure used in our study, Lai et al. administered GRA or SFN directly to the cecal lumen of anesthetized rats using a surgical procedure. In this way, these substances bypassed the small intestine where absorption of GRA preferentially takes place as may be deduced from the appearance of intact GRA in the animals' urine within

DOI: 10.1021/acs.jafc.5b02948
J. Agric. Food Chem. 2015, 63, 8418−8428

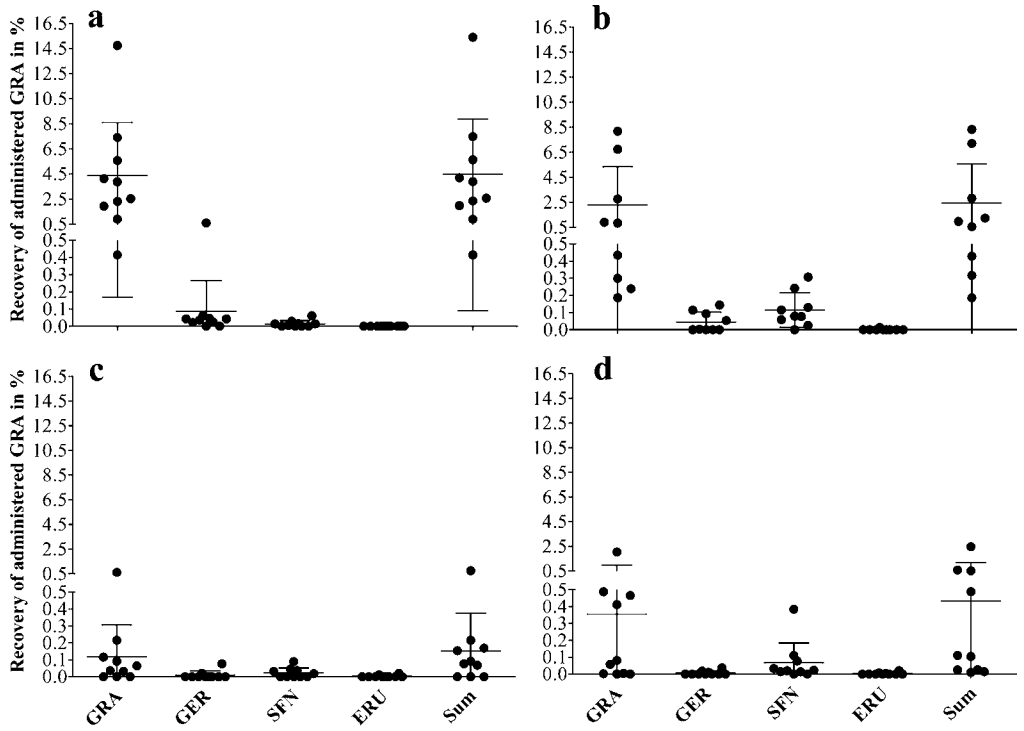

Figure 3. Fecal excretion of glucoraphanin (GRA) and its potential metabolites glucoerucin (GER), sulforaphane (SFN), and erucin (ERU) within 48 h after its application (172 mg/kg body weight) depicted as % recovery of applied GRA in germ free mice without (a) and with (b) myrosinase application and human microbiota-associated (HMA) mice without (c) and with (d) myrosinase application. Each point represents an experimental animal (n = 9 to 10 per group). Depicted are the mean and standard deviation.

12 h after application.[28] A small amount of GER was detected in all groups (the mean varying from 0.8 to 1.6% recovery within 48 h after GRA application, based on the dose of GRA applied to the animals), which suggests that GRA was reduced to GER by the animals' metabolism. The isothiocyanates, SFN and ERU, were excreted in the urine of germ free and HMA mice. However, renal excretion was low for SFN and almost negligible for ERU. The amount of SFN recovered within 48 h after GRA application in germ free and HMA mice corresponded to 0.23 (±0.23) and 0.24 (±0.13)% of the applied GRA dose, when no myrosinase had been applied, and to 0.62 (±0.53) and 0.44 (±0.29)%, respectively, when myrosinase had been applied. Thus, GLS underwent hydrolysis to isothiocyanates in the animals irrespective of the presence or absence of myrosinase. ERU may have been formed either by the reduction of SFN or by hydrolysis of GER, the reduction product of GRA.

SFN and ERU excreted in urine within the first 12 h after application of GRA were mainly present as *N*-acetyl-L-cysteine (NAC) conjugates, also referred to as mercapturic acids. Glutathione or cysteine conjugates were not detected. The amount of NAC-conjugates excreted by the experimental groups differed: Within 48 h after the application of GRA, germ free mice and HMA mice excreted SFN-NAC in amounts corresponding to 0.57 (±0.62) and 1.1 (±1.4)% of the initial administered GRA dose, respectively, as well as ERU-NAC in amounts corresponding to 0.20 (±0.18) and 0.76 (±0.39)% of the initial administered GRA dose. Thus, germ free animals excreted significantly less ERU-NAC than HMA mice (p < 0.05). As expected, the application of myrosinase resulted in increased amounts of SFN-NAC and ERU-NAC excreted by germ free mice and HMA mice: 7.9 (±6.7)% of the GRA dose was recovered within 48 h as SFN-NAC and 1.8 (±1.3)% as ERU-NAC in germ free mice as well as 2.5 (±2.6)% as SFN-NAC and 1.4 (±0.6)% as ERU-NAC in HMA mice (p < 0.05 for SFN-NAC).

Gut Contents and Feces. Neither intact GRA nor its metabolites were detectable in small intestinal, cecal, and colonic contents of HMA mice 48 h after GRA application. However, they were present at low concentrations in small intestinal, cecal, and colonic contents of germ free animals corresponding to 0.05 (±0.03)% with myrosinase and 0.64 (±0.41)% without myrosinase of the applied GRA dose (p < 0.05). Thus, in germ free mice, myrosinase reduced the GRA content in the small intestine, cecum, and colon. In HMA mice, the absence of GRA or isothiocyanates from gut contents was unrelated to the application of myrosinase. Thus, the presence of myrosinase, whether administered orally or as a consequence of bacterial colonization, led to a reduced recovery of GRA in the gut contents. From a total of 10 animals per experimental group, SFN was only detected in the intestinal contents of two germ free animals without and one germ free animal with myrosinase administration (0.004, 0.006 and 0.024%, respectively, of the initial dose of GRA applied to the animals were recovered as SFN).

Fecal excretion of GRA and its metabolites over 48 h was determined for both mouse groups (Figures 3a–d). The germ free mice excreted more intact GRA in their feces than HMA mice, namely, 4.4 (±4.2)% versus 0.12 (±0.19)% of the initial dose of GRA, p < 0.001, without myrosinase supplementation, as well as 2.3 (±3.1)% versus 0.36 (±0.63)% with myrosinase supplementation. As observed for the gut contents, myrosinase administered orally or provided by intestinal bacteria, resulted in an overall reduced recovery of GRA in the feces. GER was detected at very low levels in all groups (the mean varying from

DOI: 10.1021/acs.jafc.5b02948
J. Agric. Food Chem. 2015, 63, 8418–8428

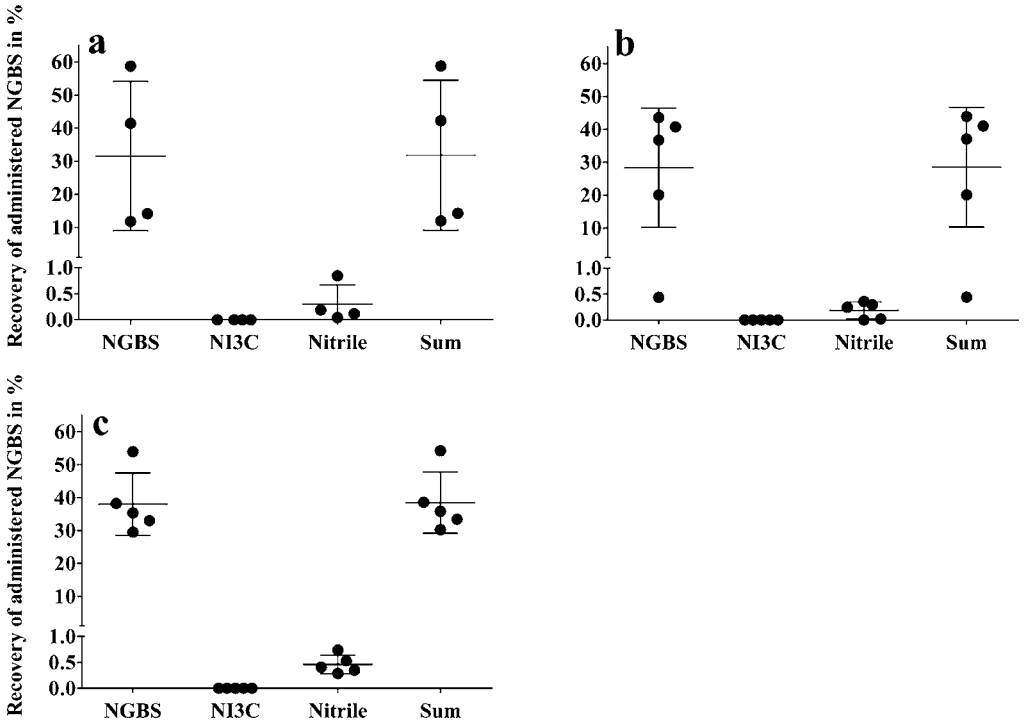

Figure 4. Renal excretion of neoglucobrassicin (NGBS) and its potential metabolites *N*-methoxyindole-3-carbinol (NI3C) and *N*-methoxyindole-3-acetonitrile (Nitrile) within 8 h after its application (297 mg/kg body weight) depicted as % recovery of applied NGBS in germ free mice without (a) and with (b) myrosinase application and in human microbiota-associated (HMA) mice (c). Each point represents an experimental animal (n = 5 per group). Depicted are the mean and standard deviation.

0.007 to 0.09% recovery within 48 h after GRA application, based on the dose of GRA applied to the animals).

Fecal excretion of SFN and ERU by HMA mice corresponded for both isothiocyanates together to 0.07 (±0.12) and 0.025 (±0.035)% of the initial GRA dose, with or without oral myrosinase application, respectively. In germ free mice that received myrosinase, the proportion of orally applied GRA recovered as SFN and ERU was 0.12 (±0.10)%. SFN was also detected in germ free animals, which did not receive myrosinase, but only in very low amounts, corresponding to 0.014 (±0.019)% of the initial GRA dose applied to the animals. Overall, the recovery of GRA and its metabolites in the feces 48 h after its oral administration was low, independent of bacterial colonization of the animals: in germ free and HMA mice, 4.5 (±4.4) and 0.15 (±0.22)% of the applied GRA dose, when no myrosinase had been applied, and 2.5 (±3.1) and 0.43 (±0.75)%, respectively, when myrosinase had been applied.

Neoglucobrassicin Is Also Absorbed Intact and Mainly Excreted via Urine. *Urine and Plasma.* Eight hours after its oral application, NGBS was detected in the plasma of mice from all groups and hence, similar to GRA, was also absorbed intact. The recovery of NGBS in plasma was higher in germ free mice that did not receive myrosinase than in germ free animals that received myrosinase, namely, 0.022 (±0.015) versus 0.005 (±0.004)% of the administered NGBS dose, $p < 0.05$. The recovery of NGBS in the plasma of HMA mice was 0.007%. However, the detection of NGBS was overall low, and metabolites derived from NGBS, i.e., NI3C and *N*-methoxyindole-3-acetonitrile, were not observed.

Independent from bacterial colonization and the application of myrosinase, NGBS was excreted in urine intact. The recovery in urine of germ free animals with and without myrosinase application was 28 (±18) and 32 (±23)% of the administered NGBS dose, respectively, and 38 (±9)% in the urine of HMA mice (Figures 4a–c). NI3C, a stable degradation product of NGBS, which under neutral pH conditions is formed from the respective isothiocyanate, was not detected in urine samples. *N*-Methoxyindole-3-acetonitrile, which is formed under acidic conditions from the isothiocyanate of NGBS, was excreted in very small amounts in all experimental groups. Germfree animals with and without myrosinase application excreted the nitrile at concentrations that correspond to 0.18 (±0.16) and 0.30 (±0.37)% of the administered NGBS dose, respectively, and HMA animals to 0.46 (±0.18)%. Thus, renal excretion of *N*-methoxyindole-3-acetonitrile was higher in HMA mice than in germ free animals that received myrosinase ($p < 0.05$).

Gut Contents and Feces. The recovery of NGBS in gut contents of HMA mice was very low and corresponded to only 0.01 (±0.005)% of the administered NGBS dose. The combined gut contents of germ free mice contained NGBS mainly in its intact form, no matter whether myrosinase had been applied (2.5 ± 5.5% of applied dose) or not (4.2 ± 4.5, $p < 0.05$, Figures 5a–c). Germfree mice contained only small amounts of NI3C in their intestines, corresponding to 0.12 (±0.05) and 0.03 (±0.04)% of the administered NGBS dose, with and without myrosinase application, respectively. However, HMA mice contained even less NI3C in their intestines, corresponding to 0.0002 (±0.0002)% of the applied NGBS dose ($p < 0.05$). *N*-Methoxyindole-3-acetonitrile contents in the cecum and colon of germ free animals were low and corresponded to 0.01 (±0.02)% of the administered NGBS dose with myrosinase application and 0.02 (±0.02)% without, while it was not detected in HMA mice.

Neither NGBS nor its metabolites were detected in feces from HMA mice within 8 h after its application. Independent from the application of myrosinase, fecal excretion of NGBS by

DOI: 10.1021/acs.jafc.5b02948
J. Agric. Food Chem. 2015, 63, 8418–8428

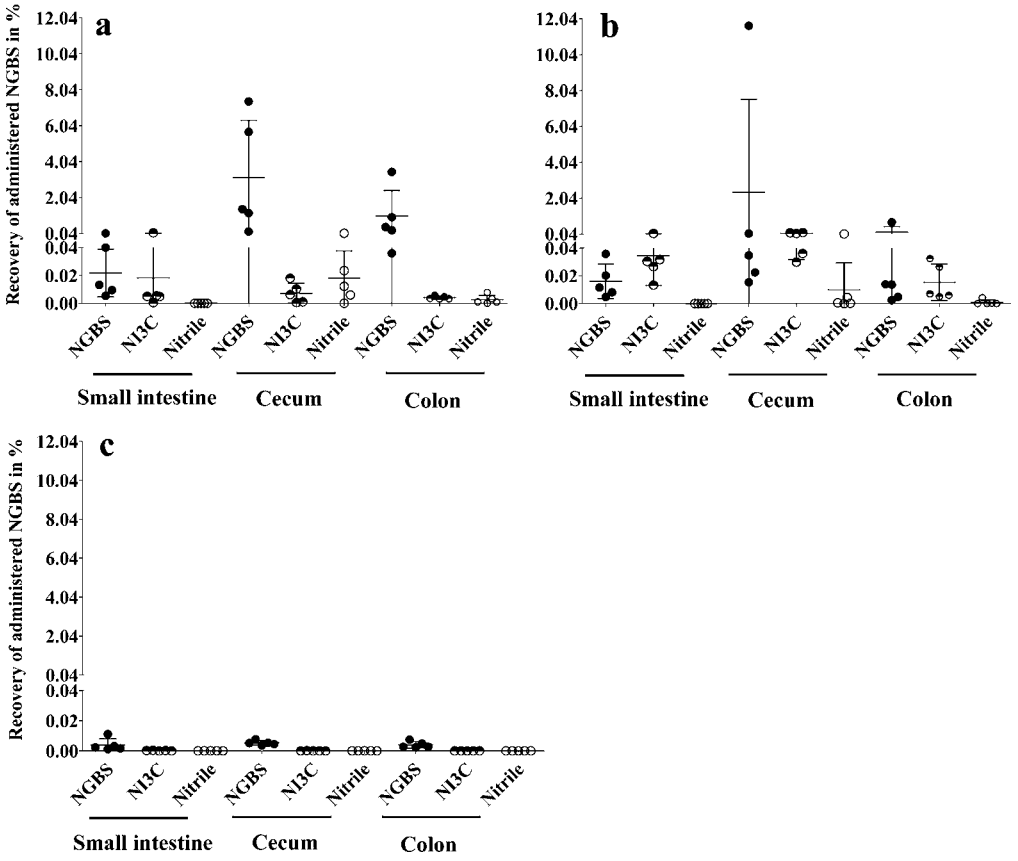

Figure 5. Recovery of neoglucobrassicin (NGBS) and its metabolites *N*-methoxyindole-3-carbinol (NI3C) and *N*-methoxyindole-3-acetonitrile (Nitrile) in gut contents of germ free mice without (a) and with (b) myrosinase application and of human microbiota-associated (HMA) mice (c) 8 h after its application (297 mg/kg body weight). Each point represents an experimental animal (n = 5 per group). Depicted are the mean and standard deviation.

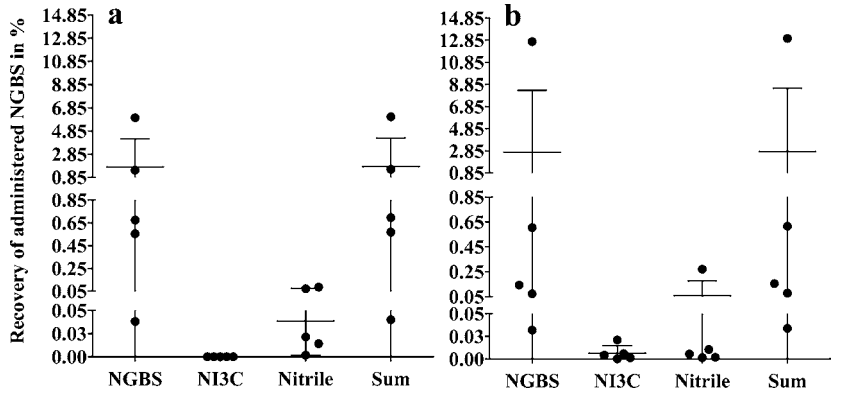

Figure 6. Fecal excretion of neoglucobrassicin (NGBS) and its potential metabolites *N*-methoxyindole-3-carbinol (NI3C) and *N*-methoxyindole-3-acetonitrile (Nitrile) within 8 h after its application (297 mg/kg body weight) depicted as % recovery of applied NGBS in germ free mice without (a) and with (b) myrosinase application. Data from human microbiota-associated (HMA) mice are not depicted as neither NGBS nor its metabolites were detected in their feces. Each point represents an experimental animal (n = 5 per group). Depicted are the mean and standard deviation.

germ free mice in its intact form was low and corresponded to 2.7 (±5.9)% of the administered NGBS dose with myrosinase treatment and 1.7 (±2.4)% without (Figure 6a–b). NI3C was excreted in very small quantities in the myrosinase-treated germ free animals, corresponding to 0.006 (±0.008)% of the applied NGBS dose. Germfree mice also contained very small fecal amounts of *N*-methoxyindole-3-acetonitrile corresponding to 0.06 (±0.12)% of the NGBS dose applied to mice with myrosinase application and 0.04 (±0.04)% without.

DNA Adducts. The genotoxic activity of NGBS depending on the colonization status and/or the myrosinase treatment was studied by LC-MS/MS analysis of adducts in DNA isolated from murine cecum and colon 8 h after administration of NGBS. DNA adducts were detected in the cecum and colon of all NGBS-treated HMA and germ free mice: HMA, 78 (±49) and 54 (±45) DNA adducts (sum of dA- and dG-adducts) per 10^8 nucleotides, respectively. They were also detected in the cecum and colon of germ free mice: 441 (±625) and 333 (±547) DNA adducts per 10^8 nucleotides, respectively, with

DOI: 10.1021/acs.jafc.5b02948
J. Agric. Food Chem. 2015, 63, 8418–8428

myrosinase, and 55 (±51) and 33 (±26) DNA adducts per 10^8 nucleotides, respectively, without myrosinase. Control animals, germ free or HMA, that received the vehicle only showed no DNA adducts originating from NGBS. Thus, without oral application of myrosinase, germ free and HMA mice did not differ from each other with respect to the amount of DNA adducts formed. It may be concluded that the oral application of myrosinase to germ free mice was responsible for the increased numbers of cecal and colonic DNA adducts ($p < 0.05$ and $p < 0.1$, respectively). However, as the amount of DNA adducts formed in the cecum and colon of HMA mice was not significantly different from that of germ free mice not treated with myrosinase (Figure 7), a role of the human-derived bacteria colonizing the gut of HMA mice in NGBS activation is negligible.

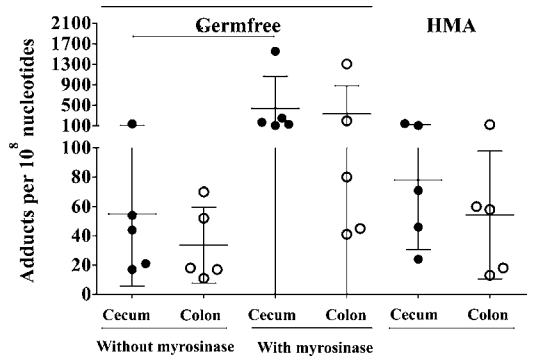

Figure 7. DNA adduct levels (sum of N^6-(1-MIM)-dA and N^2-(1-MIM)-dG) in cecum and colon of germ free mice with and without myrosinase application and of human microbiota-associated (HMA) mice 8 h after application of neoglucobrassicin (297 mg/kg body weight). Each point represents an experimental animal ($n = 5$ per group). Depicted are the mean and standard deviation. *$p < 0.05$.

DISCUSSION

Glucosinolates Are Absorbed Intact and Mainly Excreted via Urine. Mice excreted approximately one-quarter to one-third of orally applied GLS, GRA, and NGBS, intact in their urine. Thus, the amount of hydrolysis products recovered was lower than expected. This finding may be of importance as potential health effects of GLS have mainly been attributed to the hydrolysis products of GLS.

Intact GLS were detected not only in the urine of mice following their application but also in plasma. For example, intact NGBS appeared in the plasma of mice 8 h after NGBS had been administered confirming the absorption of intact GLS into the circulation. Until now, only a few studies have addressed the absorption of intact GLS: intact GRA was observed in plasma of dogs and rats.[29] Rats were also reported to excrete intact GRA, but the proportion of GRA recovered in urine was only 5% of the administered dose.[30] Following the consumption of broccoli, GRA and sinigrin were detected in human urine and plasma, respectively.[31,32,35,36] Studies on everted intestinal sacs of rats provided evidence for a passive transport of intact GLS from the mucosal to the serosal side of the epithelial cells in the small intestine and colon.[33] The transport rate of GLS depends on their chemical structure: transport of the aromatic GLS glucotropaeolin was slightly faster than that of the aliphatic GLS sinigrin. This has been attributed to the lipophilic side chain of sinigrin.[33] However, in the present study urinary excretion of indolic NGBS 8 h after its application was similar to that of aliphatic GRA after 12 h. This indicates a rather fast absorption, distribution, and excretion for both GLS. This is in agreement with data obtained in rats, in which 95% of the total excretion of GRA was observed in urine within 8 h after its application.[30]

Detection of intact GLS in plasma and urine in the present study possibly indicates that physiological effects previously reported for GLS may be at least in part exerted by GLS itself rather than by its degradation products. This has not been studied to any great extent, and the results are in part contradictory. For example, GRA induces chemoprotective phase II enzymes[34] and has shown cytotoxic and genotoxic properties in vitro.[35]

Isothiocyanates Are Excreted in Urine Mainly as Mercapturic Acid Conjugates. After the application of GRA, SFN and ERU appeared in the urine of germ free and HMA mice. ERU is formed either by the reduction of SFN or hydrolysis of GER. The latter is formed by the reduction of GRA.[36] Urinary SFN and ERU were mainly excreted as their NAC-conjugates within 12 h after GRA application. A rapid renal excretion of mercapturic acid conjugates was also reported for humans; it occurred within the first 8 h after the ingestion of broccoli sprouts.[37] However, whereas in humans 40% of the applied GRA dose was detected as SFN-NAC,[6] the excretion of NAC-conjugates in the present mouse study was low, unless myrosinase was given to the mice. These differences might be due to differences between animal species in the catalytic activity and specificity of xenobiotic metabolizing enzymes or to the fact that in the present study GRA was applied as a pure substance, whereas in human studies broccoli or other GLS-containing vegetables were given, in which GRA is embedded in a plant matrix.[38] Studies of the metabolism of isothiocyanate in various species have shown differences in the metabolite profile. The cyclic mercaptopyruvic acid (4-hydroxy-4-carboxy-3-benzylthiazolidin-2-thione) occurred in the urine from guinea-pigs and rabbits after the oral or intravenous administration of benzyl isothiocyanate or its cysteine metabolite.[39] In human individuals, the isothiocyanates are mainly metabolized via the mercapturic acid pathway.[40] However, to the best of our knowledge, mercaptopyruvic acid has not been observed in human intervention studies up to now, and we also did not detect it in our study.

Interindividual Differences in Metabolism of the Glucosinolates. In the present study, considerable differences in the excreted amounts of GRA, NGBS, and their metabolites were observed between individual animals. High interindividual variation in excretion was also observed in human studies after the intake of GLS via *Brassica* vegetables.[41,42] The interindividual differences in the excretion of GLS metabolites observed in the present study may be due to different times of feed intake, as the amount of feed in the stomach varies when animals are fed ad libitum, which in turn would affect transit time and thereby the metabolism of GLS.[43]

Impact of Intestinal Microbiota on the Bioactivation of Glucosinolates Is Low. This is the first study that examines the impact of human intestinal bacteria on the bioavailability of GLS in vivo using HMA mice and germ free animals as a control. As a positive control, myrosinase was applied orally to the mice to achieve enzymatic cleavage of GLS in the animals' digestive tract. This is the first time that intact GLS are reported to be present in feces and gut contents after their oral application, even though in low amounts. Germ free

DOI: 10.1021/acs.jafc.5b02948
J. Agric. Food Chem. 2015, 63, 8418−8428

mice had higher amounts of intact GLS in their feces and gut contents than HMA mice. This difference may result from an increased hydrolysis or a higher absorption of GLS in HMA animals and supports the hypothesis that human intestinal bacteria convert GLS. However, these differences may also be the result of a shortened intestinal transit time reported for colonized animals in comparison to that of their germ free counterparts.[44] The intestinal microbiota modulates the intestinal nervous system and thus stimulates the motility of the intestine[45] such that GLS would stay longer in the intestinal tract of germ free animals.

Only very small amounts of metabolites derived from orally applied GRA or NGBS were detected in plasma, urine, or feces. Unexpectedly, HMA and germ free mice did not differ substantially in the spectra of GLS metabolites formed and hence in their ability to hydrolyze GLS into their respective metabolites. Basal GLS activation in germ free animals was only slightly increased by oral myrosinase application or by bacterial colonization with HMA. This is in agreement with a gnotobiotic rat study, in which intestinal microbiota in contrast to plant myrosinase hardly contributed to the hydrolysis of GLS, which was adminstered as freeze-dried Brussels sprouts (mainly sinigrin).[46] On the basis of these results and the outcome of our study, the impact of human intestinal bacteria on activation of GLS appears to be rather weak in vivo, at least in HMA rodents.

Other factors that could possibly account for GLS hydrolysis in germ free mice were investigated and excluded: an in vitro incubation of GLS with synthetic gastric and intestinal juices and various mouse tissues did not lead to their hydrolysis (data not shown). The detection of intact GRA and NGBS in intestinal contents and feces of mice also argues in favor of a considerable stability of GLS during gastrointestinal passage. Moreover, GRA and NGBS preparations used in the animal experiments remained stable for at least 24 h of incubation at 37 °C (data not shown). A spontaneous cleavage of GLS in germ free mice is therefore unlikely. There was also no indication that the germ free mice investigated in the present study were contaminated with bacteria. Their germ free status was confirmed by Gram staining and checking fecal samples from these animals for growth (data not shown). Thus, the presented results indicate a thioglucosidase activity of the host, which is in contradiction to the literature to date.

However, it cannot be excluded that the HMA animal model is not well suited for studying the bacterial hydrolysis of GLS in vivo. This conclusion may be drawn from the fact that the number of DNA adducts detected in the intestinal tissue did not differ significantly between HMA and germ free mice after the application of NGBS and overall were very low. In contrast, conventional C3H and FVB/N mice treated in the same way as the HMA and germ free C3H mice in the present study showed 5- to 8-fold higher numbers of DNA adducts in the cecum compared to the HMA mice of the present study (conventional C3H mice, 392 (±43) DNA adducts per 10^8 nucleotides (n = 5); conventional FVB/N mice, 616 (±283) DNA adducts per 10^8 nucleotides (n = 10)). This indicates that bacterial hydrolysis of NGBS was higher in conventionally colonized mice than in HMA mice.[4] This difference between conventional and HMA mice indicates that the human microbiota transferred to germ free mice may have lost its ability to hydrolyze GLS following colonization. However, the fact that the fecal samples from both the human donor and the recipient mice efficiently hydrolyzed GRA and NGBS in vitro indicates that the microbial community had not lost this activity (data not shown). Communication between host and microbiota plays an important role in this ecosystem.[47] Therefore, the bacterial metabolism of GLS may have been affected in vivo by the specific host environment. The composition of the intestinal microbiota and the catalytic activity of selected enzymes in the gut of HMA mice are largely comparable to those of the human donor. Therefore, comparing HMA mice with germ free mice is a suitable experimental approach to investigate the complex human gut microbiota in vivo.[48] However, it should be kept in mind that not all human bacteria are able to establish in the mouse gut[49] and that the digestive tract of humans differs from that of mice. Owing to these limitations, the results obtained in this mouse study cannot simply be extrapolated to humans without additional experiments. Nevertheless, our experiments clearly show that the intestinal microbiota plays a minor role in the bioactivation of GLS in HMA mice.

AUTHOR INFORMATION

Corresponding Author

*Arthur-Scheunert-Allee 114-116, 14558 Nuthetal, Germany. Phone +49-33200-882470. Fax: +49-33200882407. E-mail: blaut@dife.de.

Present Address

‖F.S.: Department of Nutritional Toxicology, University of Potsdam, Nuthetal, Germany.

Author Contributions

⊥J.B. and L.H. contributed equally to this work.

Funding

This study was funded by the German Federal Ministry of Education and Research (01EA1310D) and the Gottfried Wilhelm Leibniz Society (SAW 2009).

Notes

The authors declare no competing financial interest.

ACKNOWLEDGMENTS

We thank Ines Gruener and Ute Lehmann for good animal care and Sabine Schmidt for excellent technical assistance. We acknowledge Dr. Renato Iori (Agricultural Research Council, Industrial Crop Research Centre, Italy) for kindly providing GRA and Dr. Albrecht Seidel (Biochemical Institute for Environmental Carcinogens, Professor Dr. Gernot Grimmer-Foundation, Germany) for kindly providing NI3C and *N*-methoxyindole-3-acetonitrile.

ABBREVIATIONS USED

GLS, glucosinolate(s); HMA, human microbiota-associated; GRA, glucoraphanin; SFN, sulforaphane; GER, glucoerucin; ERU, erucin; NGBS, neoglucobrassicin; NI3C, *N*-methoxyindole-3-carbinol; ITC-*N*-*t*Boc-Cys-ME, isothiocyanate-*N*-(*tert*-butoxycarbonyl)-L-cysteine methyl ester

REFERENCES

(1) Hansen, M.; Lausten, A. M.; Olsen, C. E.; Poll, L.; Sorensen, H. Chemical and sensory quality of broccoli (*Brassica oleracea L. var italica*). *J. Food Qual.* **1997**, *20*, 441.

(2) Sarikamis, G. Glucosinolates in crucifers and their potential effects against cancer: Review. *Can. J. Plant Sci.* **2009**, *89*, 953−59.

(3) Baasanjav-Gerber, C.; Monien, B. H.; Mewis, I.; Schreiner, M.; Barillari, J.; Iori, R.; Glatt, H. Identification of glucosinolate congeners able to form DNA adducts and to induce mutations upon activation by myrosinase. *Mol. Nutr. Food Res.* **2011**, *55*, 783−92.

DOI: 10.1021/acs.jafc.5b02948
J. Agric. Food Chem. 2015, 63, 8418−8428

(4) Schumacher, F.; Florian, S.; Schnapper, A.; Monien, B. H.; Mewis, I.; Schreiner, M.; Seidel, A.; Engst, W.; Glatt, H. A secondary metabolite of Brassicales, 1-methoxy-3-indolylmethyl glucosinolate, as well as its degradation product, 1-methoxy-3-indolylmethyl alcohol, forms DNA adducts in the mouse, but in varying tissues and cells. *Arch. Toxicol.* **2014**, *88*, 823−36.
(5) Holst, B.; Williamson, G. A critical review of the bioavailability of glucosinolates and related compounds. *Nat. Prod. Rep.* **2004**, *21*, 425−47.
(6) Conaway, C. C.; Getahun, S. M.; Liebes, L. L.; Pusateri, D. J.; Topham, D. K.; Botero-Omary, M.; Chung, F. L. Disposition of glucosinolates and sulforaphane in humans after ingestion of steamed and fresh broccoli. *Nutr. Cancer* **2000**, *38*, 168−78.
(7) Zhu, N.; Soendergaard, M.; Jeffery, E. H.; Lai, R. H. The impact of loss of myrosinase on the bioactivity of broccoli products in F344 rats. *J. Agric. Food Chem.* **2010**, *58*, 1558−63.
(8) Greer, M. A.; Deeney, J. M. Antithyroid activity elicited by the ingestion of pure progoitrin, a naturally occurring thioglycoside of the turnip family. *J. Clin. Invest.* **1959**, *38*, 1465−74.
(9) Shapiro, T. A.; Fahey, J. W.; Wade, K. L.; Stephenson, K. K.; Talalay, P. Human metabolism and excretion of cancer chemoprotective glucosinolates and isothiocyanates of cruciferous vegetables. *Cancer Epidemiol Biomarkers Prev* **1998**, *7*, 1091−100.
(10) Cheng, D. L.; Hashimoto, K.; Uda, Y. In vitro digestion of sinigrin and glucotropaeolin by single strains of Bifidobacterium and identification of the digestive products. *Food Chem. Toxicol.* **2004**, *42*, 351−7.
(11) Elfoul, L.; Rabot, S.; Khelifa, N.; Quinsac, A.; Duguay, A.; Rimbault, A. Formation of allyl isothiocyanate from sinigrin in the digestive tract of rats monoassociated with a human colonic strain of Bacteroides thetaiotaomicron. *FEMS Microbiol. Lett.* **2001**, *197*, 99−103.
(12) Haack, M.; Löwinger, M.; Lippmann, D.; Kipp, A.; Pagnotta, E.; Iori, R.; Monien, B. H.; Glatt, H.; Brauer, M. N.; Wessjohann, L. A.; Brigelius-Flohe, R. Breakdown products of neoglucobrassicin inhibit activation of Nrf2 target genes mediated by myrosinase-derived glucoraphanin hydrolysis products. *Biol. Chem.* **2010**, *391*, 1281−93.
(13) Glatt, H.; Baasanjav-Gerber, C.; Schumacher, F.; Monien, B. H.; Schreiner, M.; Frank, H.; Seidel, A.; Engst, W. 1-Methoxy-3-indolylmethyl glucosinolate; a potent genotoxicant in bacterial and mammalian cells: Mechanisms of bioactivation. *Chem.-Biol. Interact.* **2011**, *192*, 81−6.
(14) Kassahun, K.; Davis, M.; Hu, P.; Martin, B.; Baillie, T. Biotransformation of the naturally occurring isothiocyanate sulforaphane in the rat: identification of phase I metabolites and glutathione conjugates. *Chem. Res. Toxicol.* **1997**, *10*, 1228−33.
(15) Vermeulen, M.; van Rooijen, H. J.; Vaes, W. H. Analysis of isothiocyanate mercapturic acids in urine: a biomarker for cruciferous vegetable intake. *J. Agric. Food Chem.* **2003**, *51*, 3554−9.
(16) Zoetendal, E. G.; Akkermans, A. D.; Akkermans-van Fliet, W. M.; de Visser, J.; de Vos, W. M. The host genotype affects the bacterial community in the human intestinal tract. *Microb. Ecol. Health Dis.* **2001**, *13*, 129−134.
(17) Becker, N.; Kunath, J.; Loh, G.; Blaut, M. Human intestinal microbiota: characterization of a simplified and stable gnotobiotic rat model. *Gut Microbes* **2011**, *2*, 25−33.
(18) Hanske, L.; Hussong, R.; Frank, N.; Gerhauser, C.; Blaut, M.; Braune, A. Xanthohumol does not affect the composition of rat intestinal microbiota. *Mol. Nutr. Food Res.* **2005**, *49*, 868−73.
(19) Kamlage, B.; Hartmann, L.; Gruhl, B.; Blaut, M. Intestinal microorganisms do not supply associated gnotobiotic rats with conjugated linoleic acid. *J. Nutr.* **1999**, *129*, 2212−7.
(20) Alpert, C.; Sczesny, S.; Gruhl, B.; Blaut, M. Long-term stability of the human gut microbiota in two different rat strains. *Curr. Issues Mol. Biol.* **2008**, *10*, 17−24.
(21) Lippmann, D.; Lehmann, C.; Florian, S.; Barknowitz, G.; Haack, M.; Mewis, I.; Wiesner, M.; Schreiner, M.; Glatt, H.; Brigelius-Flohe, R.; Kipp, A. P. Glucosinolates from pak choi and broccoli induce enzymes and inhibit inflammation and colon cancer differently. *Food Funct.* **2014**, *5*, 1073−81.
(22) Budnowski, J.; Hanschen, F. S.; Lehmann, C.; Haack, M.; Brigelius-Flohe, R.; Kroh, L. W.; Blaut, M.; Rohn, S.; Hanske, L. A derivatization method for the simultaneous detection of glucosinolates and isothiocyanates in biological samples. *Anal. Biochem.* **2013**, *441*, 199−207.
(23) Schumacher, F.; Engst, W.; Monien, B. H.; Florian, S.; Schnapper, A.; Steinhauser, L.; Albert, K.; Frank, H.; Seidel, A.; Glatt, H. Detection of DNA adducts originating from 1-methoxy-3-indolylmethyl glucosinolate using isotope-dilution UPLC-ESI-MS/MS. *Anal. Chem.* **2012**, *84*, 6256−62.
(24) Schumacher, F.; Herrmann, K.; Florian, S.; Engst, W.; Glatt, H. Optimized enzymatic hydrolysis of DNA for LC-MS/MS analyses of adducts of 1-methoxy-3-indolylmethyl glucosinolate and methyleugenol. *Anal. Biochem.* **2013**, *434*, 4−11.
(25) Gupta, R. C. 32P-postlabelling analysis of bulky aromatic adducts. *IARC Sci. Publ* **1993**, 11−23.
(26) Ruvinsky, A.; Marshall Graves, J. A. *Mammalian Genomics*; Wallingford: Oxfordshire, UK, 2005.
(27) Massey, F. J. The Kolmogorov-Smirnov test forgoodness of fit. *J. Am. Stat. Assoc.* **1951**, *46*, 68−78.
(28) Lai, R. H.; Miller, M. J.; Jeffery, E. Glucoraphanin hydrolysis by microbiota in the rat cecum results in sulforaphane absorption. *Food Funct.* **2010**, *1*, 161−6.
(29) Cwik, M. J.; Wu, H.; Muzzio, M.; McCormick, D. L.; Kapetanovic, I. Direct quantitation of glucoraphanin in dog and rat plasma by LC-MS/MS. *J. Pharm. Biomed. Anal.* **2010**, *52*, 544−9.
(30) Bheemreddy, R. M.; Jeffery, E. H. The metabolic fate of purified glucoraphanin in F344 rats. *J. Agric. Food Chem.* **2007**, *55*, 2861−6.
(31) Song, L.; Morrison, J. J.; Botting, N. P.; Thornalley, P. J. Analysis of glucosinolates, isothiocyanates, and amine degradation products in vegetable extracts and blood plasma by LC-MS/MS. *Anal. Biochem.* **2005**, *347*, 234−43.
(32) Egner, P. A.; Chen, J. G.; Wang, J. B.; Wu, Y.; Sun, Y.; Lu, J. H.; Zhu, J.; Zhang, Y. H.; Chen, Y. S.; Friesen, M. D.; Jacobson, L. P.; Munoz, A.; Ng, D.; Qian, G. S.; Zhu, Y. R.; Chen, T. Y.; Botting, N. P.; Zhang, Q.; Fahey, J. W.; Talalay, P.; Groopman, J. D.; Kensler, T. W. Bioavailability of Sulforaphane from two broccoli sprout beverages: results of a short-term, cross-over clinical trial in Qidong, China. *Cancer Prev. Res.* **2011**, *4*, 384−95.
(33) Michaelsen, S.; Otte, J.; Simonsen, L. O.; Sorensen, H. Absorption and degradation of individual intact glucosinolates in the digestive-tract of rodents. *Acta Agric. Scand., Sect. A* **1994**, *44*, 25−37.
(34) Abdull Razis, A. F.; Bagatta, M.; De Nicola, G. R.; Iori, R.; Ioannides, C. Up-regulation of cytochrome P450 and phase II enzyme systems in rat precision-cut rat lung slices by the intact glucosinolates, glucoraphanin and glucoerucin. *Lung Cancer* **2011**, *71*, 298−305.
(35) Paolini, M.; Perocco, P.; Canistro, D.; Valgimigli, L.; Pedulli, G. F.; Iori, R.; Croce, C. D.; Cantelli-Forti, G.; Legator, M. S.; Abdel-Rahman, S. Z. Induction of cytochrome P450, generation of oxidative stress and in vitro cell-transforming and DNA-damaging activities by glucoraphanin, the bioprecursor of the chemopreventive agent sulforaphane found in broccoli. *Carcinogenesis* **2004**, *25*, 61−7.
(36) Clarke, J. D.; Hsu, A.; Riedl, K.; Bella, D.; Schwartz, S. J.; Stevens, J. F.; Ho, E. Bioavailability and inter-conversion of sulforaphane and erucin in human subjects consuming broccoli sprouts or broccoli supplement in a cross-over study design. *Pharmacol. Res.* **2011**, *64*, 456−63.
(37) Ye, L.; Dinkova-Kostova, A. T.; Wade, K. L.; Zhang, Y.; Shapiro, T. A.; Talalay, P. Quantitative determination of dithiocarbamates in human plasma, serum, erythrocytes and urine: pharmacokinetics of broccoli sprout isothiocyanates in humans. *Clin. Chim. Acta* **2002**, *316*, 43−53.
(38) Martignoni, M.; Groothuis, G. M.; de Kanter, R. Species differences between mouse, rat, dog, monkey and human CYP-mediated drug metabolism, inhibition and induction. *Expert Opin. Drug Metab. Toxicol.* **2006**, *2*, 875−94.

DOI: 10.1021/acs.jafc.5b02948
J. Agric. Food Chem. 2015, 63, 8418−8428

(39) Görler, K.; Krumbiegel, G.; Mennicke, W. H.; Siehl, H. U. The metabolism of benzyl isothiocyanate and its cysteine conjugate in guinea-pigs and rabbits. *Xenobiotica* **1982**, *12*, 535−42.
(40) Lamy, E.; Scholtes, C.; Herz, C.; Mersch-Sundermann, V. Pharmacokinetics and pharmacodynamics of isothiocyanates. *Drug Metab. Rev.* **2011**, *43*, 387−407.
(41) Kensler, T. W.; Chen, J. G.; Egner, P. A.; Fahey, J. W.; Jacobson, L. P.; Stephenson, K. K.; Ye, L.; Coady, J. L.; Wang, J. B.; Wu, Y.; Sun, Y.; Zhang, Q. N.; Zhang, B. C.; Zhu, Y. R.; Qian, G. S.; Carmella, S. G.; Hecht, S. S.; Benning, L.; Gange, S. J.; Groopman, J. D.; Talalay, P. Effects of glucosinolate-rich broccoli sprouts on urinary levels of aflatoxin-DNA adducts and phenanthrene tetraols in a randomized clinical trial in He Zuo township, Qidong, People's Republic of China. *Cancer Epidemiol., Biomarkers Prev.* **2005**, *14*, 2605−13.
(42) Fahey, J. W.; Wehage, S. L.; Holtzclaw, W. D.; Kensler, T. W.; Egner, P. A.; Shapiro, T. A.; Talalay, P. Protection of humans by plant glucosinolates: efficiency of conversion of glucosinolates to isothiocyanates by the gastrointestinal microflora. *Cancer Prev. Res.* **2012**, *5*, 603−11.
(43) Conaway, C. C.; Jiao, D.; Kohri, T.; Liebes, L.; Chung, F. L. Disposition and pharmacokinetics of phenethyl isothiocyanate and 6-phenylhexyl isothiocyanate in F344 rats. *Drug Metab. Dispos.* **1999**, *27*, 13−20.
(44) Kashyap, P. C.; Marcobal, A.; Ursell, L. K.; Larauche, M.; Duboc, H.; Earle, K. A.; Sonnenburg, E. D.; Ferreyra, J. A.; Higginbottom, S. K.; Million, M.; Tache, Y.; Pasricha, P. J.; Knight, R.; Farrugia, G.; Sonnenburg, J. L. Complex interactions among diet, gastrointestinal transit, and gut microbiota in humanized mice. *Gastroenterology* **2013**, *144*, 967−77.
(45) Husebye, E.; Hellstrom, P. M.; Midtvedt, T. Intestinal microflora stimulates myoelectric activity of rat small intestine by promoting cyclic initiation and aboral propagation of migrating myoelectric complex. *Dig. Dis. Sci.* **1994**, *39*, 946−56.
(46) Rouzaud, G.; Rabot, S.; Ratcliffe, B.; Duncan, A. J. Influence of plant and bacterial myrosinase activity on the metabolic fate of glucosinolates in gnotobiotic rats. *Br. J. Nutr.* **2003**, *90*, 395−404.
(47) Falk, P. G.; Hooper, L. V.; Midtvedt, T.; Gordon, J. I. Creating and maintaining the gastrointestinal ecosystem: what we know and need to know from gnotobiology. *Microbiol Mol. Biol. Rev.* **1998**, *62*, 1157−70.
(48) Hirayama, K. Ex-germfree mice harboring intestinal microbiota derived from other animal species as an experimental model for ecology and metabolism of intestinal bacteria. *Exp. Anim.* **1999**, *48*, 219−27.
(49) Oh, P. L.; Benson, A. K.; Peterson, D. A.; Patil, P. B.; Moriyama, E. N.; Roos, S.; Walter, J. Diversification of the gut symbiont Lactobacillus reuteri as a result of host-driven evolution. *ISME J.* **2010**, *4*, 377−87.

DOI: 10.1021/acs.jafc.5b02948
J. Agric. Food Chem. 2015, 63, 8418−8428

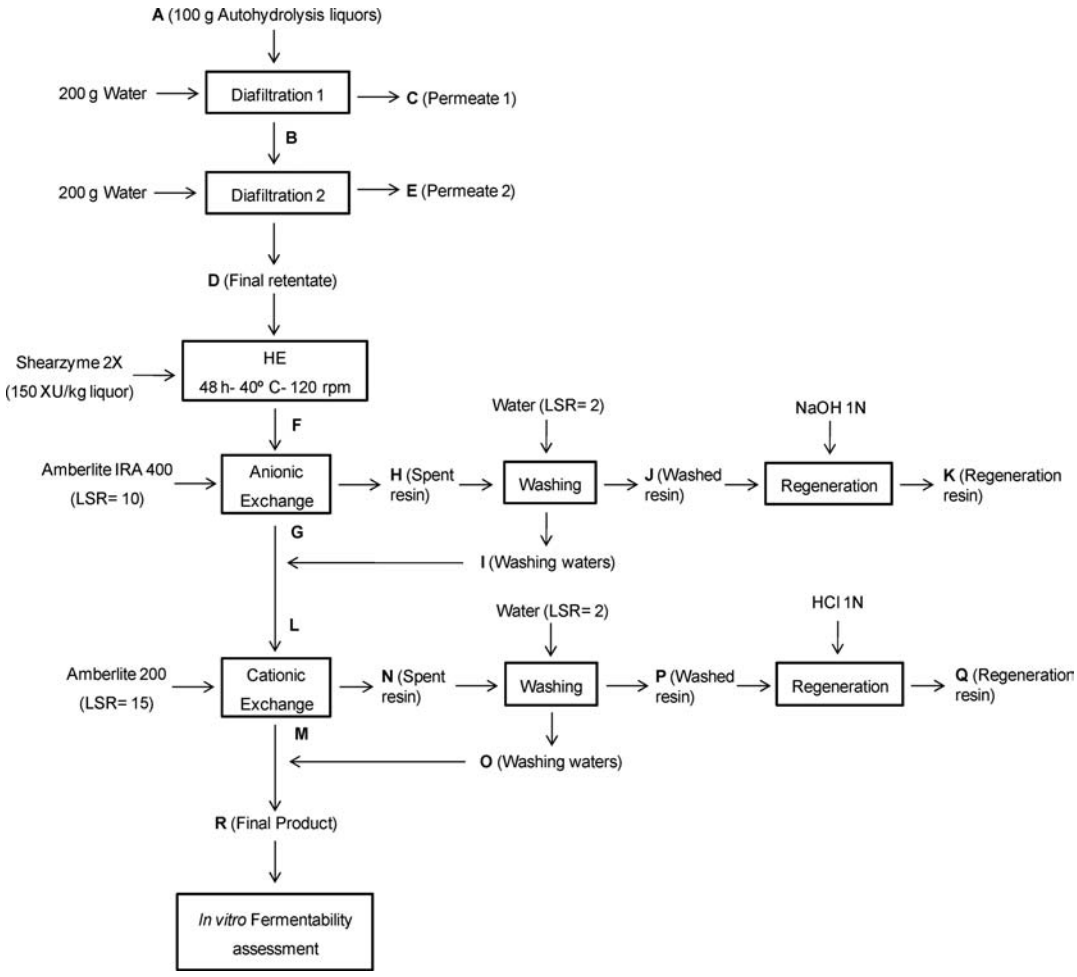

Figure 1. Scheme of the process after obtaining the optimal autohydrolysis conditions.

When BSG is subjected to hydrothermal treatment under selected conditions, hemicelluloses are mainly broken down into oligosaccharides (OS) with a variable degree of polymerization.[16−18] Afterward, if AXOS with a low degree of polimerization (DP) are desired, the enzymatic hydrolysis is a suitable alternative because it is possible to control the reaction, limiting the formation of undesirable products. In addition, no chemicals are used in the process, which is in line with the green chemistry perspective.[11]

However, in addition to AXOS production, other effects occur during the process (including extractives solubilization, monosaccharides production, sugar decomposition product generation, and lignin depolymerization). Because of this, if the AXOS are to be used for food purposes, then the autohydrolysis liquors need to be refined to remove these nondesired impurities. This goal can be achieved by a variety of technologies including liquid−liquid extraction, membrane filtration, or ion exchange.[18−20]

The aims of this work were (1) to evaluate the production of AXOS from BSG by hydrothermal treatment, (2) to modify and refine the AXOS obtained by a combined process of enzymatic hydrolysis, membrane filtration, and ion exchange, and (3) to evaluate the effects of the final purified product on the composition of the colonic microbiota and organic acids production (SCFA and lactate) using fecal inoculum from elderly.

MATERIALS AND METHODS

Raw Material. BSG samples were provided by Customdrinks (Galicia, Spain), dried at room temperature, homogenized in a single lot, and stored.

Starch Extraction and Hydrothermal Processing. Two types of pretreatments were assayed to remove or, at least, to reduce the starch content of BSG: (i) an aqueous treatment at 100 °C for 30 min and (ii) a nonisothermal water extraction (from 60 to 130 °C in 9.3 min).

In both cases, BSG was mixed with distilled water at a liquid−solid mass ratio of 8:1 g/g (oven-dry basis) and introduced into a stirred, stainless-steel reactor (Parr Instr. Co., Moline, IL, USA). Then, the reactor was heated up to achieve the desired temperature, and when the treatment was finished, the suspension was cooled and centrifuged. The solid phases from this first treatment were air-dried and stored until use.

Solids resulting from starch extraction were mixed with distilled water at a liquid−solid mass ratio of 8:1 g/g and subjected to a hydrothermal treatment under nonisothermal operation up to maximum temperatures of 180, 190, 195, 200, 210, or 220 °C. Once the temperature was achieved, the reactor was cooled and opened, and the liquors recovered by centrifugation were analyzed and processed as described below.

With the aim of facilitating the comparison between different reaction conditions, the severity factor (R_0) of each treatment was calculated according to Overend and Chornet.[21] This parameter combines the effects of time and temperature caused by isothermal or nonisothermal processing; it is defined as

DOI: 10.1021/acs.jafc.5b03132
J. Agric. Food Chem. 2015, 63, 8429−8438

$$R_0 = \int_0^t \exp\left[\frac{T(t) - 100}{14.75}\right] dt \quad \text{(eq 1)}$$

(where t and $T(t)$ are the reaction time and the temperature, respectively) and gives a simplified, empirical interpretation of the complex chemistry of polysaccharide degradation in aqueous media.[22]

Because treatments with similar R_0 values should provoke similar effects on the reaction products, a treatment was carried out under isothermal conditions at T = 180 °C and t = 12.2 min, a set of operational conditions that corresponds to a severity factor = 4439.8 min, a value identical to the one calculated for the experiment carried out under selected nonisothermal conditions where the T_{max} was 195 °C.

Processing of Autohydrolysis Liquors. Liquors from the hydrothermal treatment were subjected to membrane filtration (Amicon stirred cell, model 8400, Millipore, Darmstadt, Germany) using the experimental device described by Gómez et al.[23] However, in this work, the operation was carried out only in diafiltration mode (two stages) at room temperature using a transmembrane pressure of 3 bar, as indicated in Figure 1.

Retentate from the second diafiltration stage (stream D in Figure 1) was treated with a commercial endoxylanase (Shearzyme 2×) kindly provided by Novozymes-Spain (more details in Gullón et al.).[24] The xylanases were added to the retentate at the desired enzyme loading (150 XU/kg of liquor), and the solution was kept at 40 °C in an agitated vessel (120 rpm). Hydrolysis was carried out for 48 h, and no buffer was added to the medium.

Liquors from the enzymatic hydrolysis (Figure 1) were treated with Amberlite IRA 400 (a strong-anion-exchange resin) and Amberlite 200 (an acidic cation-exchange resin) to reduce the content of ionic impurities. Both resins were supplied by Sigma-Aldrich (St. Louis, MO, USA). In both cases, liquors and resin were contacted for 24 h with gentle agitation at room temperature using a liquor/resin mass ratio of 10:1 g/g (Amberlite IRA 400) and 15:1 g/g (Amberlite 200). At the end of treatment, the spent resins (streams H and N) were washed with distilled water using a RLS of 2 g of water per gram of resin in order to recover those compounds that could have been retained. The resulting stream (denoted as R) was freeze-dried and stored until use in fermentation experiments.

Fermentation of AXOS Mixtures. Samples of AXOS were fermented using fecal inocula obtained from three healthy elder volunteers (age > 60 years). Fecal samples were collected in sterile vials, kept in an anaerobic cabinet, and used within a maximum of 2 h after the collection. The fecal inoculum (FI) was prepared by dilution in a reduced physiological salt solution (RPS; cysteine-HCl 0.5 g/L and NaCl 8.5 g/L) ratio of 100 g of feces to 1 L of RPS at pH 6.8.

FOS (Sigma-Aldrich, St. Louis, MO, USA) and a medium without any carbon source were included in the study as positive and negative controls, respectively.

The fermentation process was developed according to Gullón et al.[20] An assay was carried out per donor for each substrate (FOS or AXOS), and the data shown correspond to an average of the results from the three different donors (n = 3).

Changes in human fecal bacterial populations were assessed by FISH using the following 16S rRNA probes: Lab158 (*Lactobacillus/Enterococcus* group), Bif164 (*Bifidobacterium* genus), Bac303 (*Bacteroides/Prevotella* group), and His150 (clusters I and II of *Clostridium*), all of which were purchased from Tib Molbiol, Berlin, Germany. For the total cell counting, samples were stained with 4′,6-diamidino-2-phenylindole (DAPI) from Sigma-Aldrich (St. Louis, MO, USA). Bacterial counts were carried out at fixed fermentation times using a fluorescence microscope (Olympus BX41, Tokyo, Japan). One hybridization was made per analyzed sample (one sample was obtained per donor, substrate, and time) and a minimum of 15 fields were counted per hybridized sample.

Differences between bacterial populations and organic acid concentrations were tested using one-way analysis of variance (ANOVA) and Tukey's post hoc test. Differences were considered significant when $p < 0.05$.

Analytical Methods. Aliquots from BSG and spent solids from hydrothermal treatments were subjected to moisture and ash determinations (methods ISO 638 and ISO 776, respectively) and to quantitative acid hydrolysis (method TAPPI T13m). The HPLC analysis of liquors was carried out using a 1100 series Hewlett-Packard chromatograph fitted with a refractive index detector and a Aminex HPX- 87H column from Biorad (Hercules, CA, USA) operating at 50 °C and using as mobile phase H_2SO_4 0.003 M (flow rate = 0.6 mL/min). In addition, uronic acids (UA) were determined by the method of Blumenkrantz and Asboe-Hansen[25] using galacturonic acid (Fluka, parent company of Sigma-Aldrich, St. Louis, MO, USA) as a standard for quantification. Elemental nitrogen was determined with a Thermo Finnegan Flash EATM 1112 analyzer, using 130 and 100 mL/min of He and O_2 and an oven temperature of 50 °C. Protein content was obtained by multiplying the elemental N content by 6.25. The starch content was quantified with an enzymatic kit (Boheringer-Mannheim, R-Biopharm, Darmstadt, Germany). All determinations were made in triplicate.

In contrast, samples of liquors were filtered through 0.45 μm cellulose acetate membranes and assayed for the glucose, xylose, arabinose, acetic acid, formic acid, hydroxymethylfurfural (HMF), and furfural content by HPLC following the method described above. Moreover, an aliquot of the liquors were subjected to quantitative posthydrolysis (with 4% sulfuric acid at 121 °C for 20 min) before HPLC analysis in order to determine the concentrations of oligomers (GlcOS, XOS, and AraOS) present in the media. (The increase in the concentrations of monosaccharides caused by the posthydrolysis is a measure of the oligomers content.) In a similar way, the increase in acetic acid concentration allows us to measure the amount of acetyl groups (AcO) linked to oligosaccharides. Additionally, uronyl substituents were determined by the same method already cited for the raw material, using galacturonic acid as a standard for quantification. Nonvolatile compounds (NVC) were measured by oven-drying at 100 °C until constant weight, whereas the content of impurities (other nonvolatile compounds, ONVC) were calculated as follows: ONVC = (NVC − MS − OS)/ NVC. All the analyses were made by triplicate.

The structural characterization of the refined product (stream R in Figure 1) was carried out by high-performance size-exclusion chromatography (HPSEC) using an Ultimate 3000 system (Dionex Corp., Sunnyvale, CA, USA) and by matrix-assisted laser desorption/ionization-time-of-flight mass spectrometry (MALDI-TOF MS) using an Ultraflex workstation (Bruker Daltonics, Bremen, Germany). More details can be found in the article by Gómez et al.[23]

Cells were harvested by centrifugation (10 000 rpm), and the supernatants were filtered through 0.20 μm cellulose acetate membranes (Sartorius Stedim Biotech, Germany) before HPLC analysis for monosaccharides, oligosaccharides, formate, lactate, succinate, and SCFA (acetic, propionic, and butyric acids) as well as pH measurement. Cell pellets were used for counting the selected bacterial groups by FISH.[20]

RESULTS AND DISCUSSION

Aqueous Extraction and Autohydrolysis. Starch lacks prebiotic potential, and its presence in liquors is a drawback if a high-purity final product is desired. Therefore, a pretreatment is needed to remove it or, at least, to reduce its content in the raw material.[26] Moreover, starch could be used for a variety of processes. Two alternatives (isothermal and nonisothermal aqueous treatment) were assayed, resulting in similar solid yields (~76%) and starch removal percentages (85%), although small losses of target compounds were also found to occur.

Taking this into account, an isothermal pretreatment at 100 °C for 30 min was chosen because lower energy consumption was expected. The composition of both BSG and pretreated solid is shown Table 1. As can be seen, glucan, xylan, acid insoluble residue (AIR), and protein were the major components in both untreated and pretreated solids. As a

DOI: 10.1021/acs.jafc.5b03132
J. Agric. Food Chem. 2015, 63, 8429−8438

Table 1. Chemical Composition of BSG and the Pretreated Solid Obtained by Aqueous Extraction at 100 °C for 30 min

component	BSG (%)	pretreated solid (%)
glucan	24.91	19.73
xylan	13.94	17.43
arabinan	6.68	7.99
acetyl groups	0.80	0.88
UA	6.45	6.13
AIR	22.82	20.77
starch	9.42	2
protein	26.77	24.10
ashes	2.98	

result of the aqueous extraction, a solid enriched in xylan and arabinan with lower starch content was obtained.

Following the process scheme (Figure 1), pretreated solids were subjected to hydrothermal processing, first under nonisothermal conditions (until reaching a temperature of 180, 190, 200, 210, or 220 °C) and second under isothermal conditions (at 180 °C), as explained above.

Figure 2 shows the dependence of monosaccharide and oligosaccharide concentrations on the maximum temperature of the treatment. As can be seen, the xylose concentration increased significantly from 195 to 210 °C, as a result of hydrolysis of oligomers, whereas arabinose showed a maximum at 200 °C and decreased rapidly. The evolution of the oligosaccharides content with temperature is shown in Figure 2b, and maxima of XOS content and their main substituents (uronic acids and acetyl groups) were observed near T_{max}= 200 °C. At 200 °C, up to 77% of the xylan was hydrolyzed into XOS, whereas the percentage of acetyl groups remaining as substituents of XOS exceeded the 60%. Regarding the total OS yield (excluding GlcOS), a maximum of 13.7 g per 100 g of dry BSG was achieved at 195 °C. This value was then selected as the optimum, and it is in agreement with the results published by Carvalheiro et al.[16]

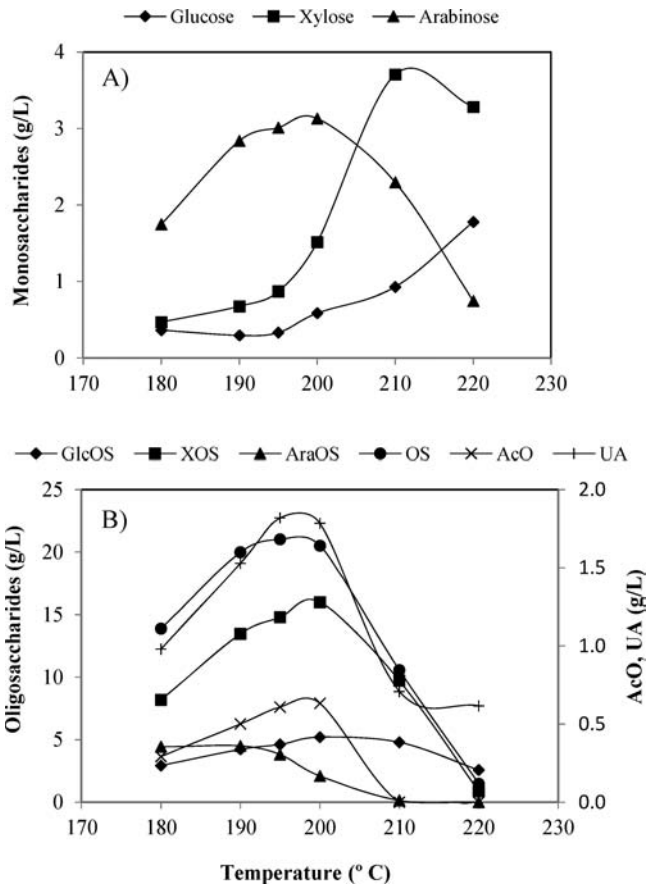

Figure 2. Effect of temperature on the composition of autohydrolysis liquors: (A) monomers expressed in g/L and (B) oligomers expressed in g/L.

Figure 3a shows a fast increase in the acetic acid, formic acid, furfural, and HMF concentrations, which starts at 195 °C and is partially due to the sugar decomposition. As a consequence of the increased severity, a rapid increase in the ONVC impurities concentration can be observed in Figure 3b. Meanwhile, the NVC content shows a maximum at 200 °C (0.048 g/g of liquor) and then decreases because of the decomposition reactions that give volatile compounds as products. These results compared favorably with the ones obtained from barley husks and wheat straw by Garrote et al.[27] and Carvalheiro et al.,[28] respectively.

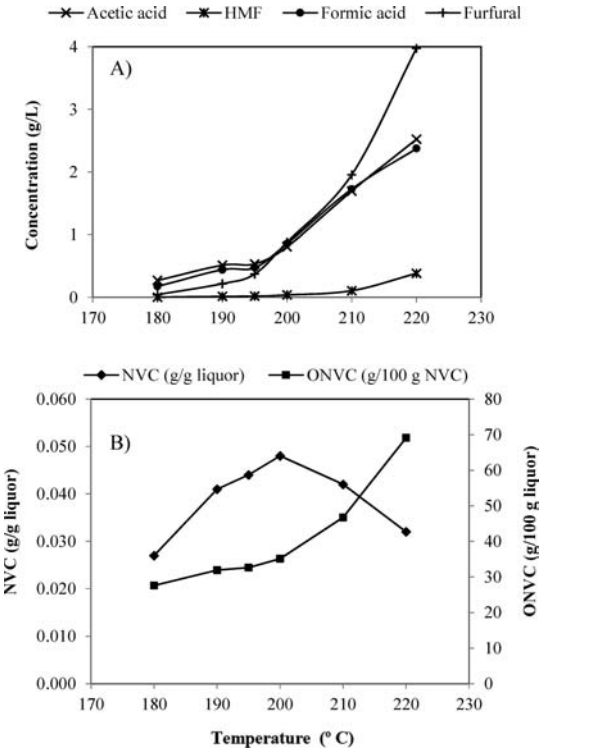

Figure 3. (A) Dependence of the concentrations of organic acids and furans in autohydrolysis liquors. (B) Temperature dependence of the concentrations of NVC and ONVC in reaction liquors (NVC, nonvolatile compounds; ONVC, other nonvolatile compounds or impurities).

Operating under isothermal conditions at the same severity (T = 180 °C and t = 12.2 min), 12.8 g of OS (OS = XOS + AraOS + AcO + UA) were obtained from 100 g of dry BSG. As indicated in Table 2, these liquors (stream A) contained 8% of MS, 61% of OS (including GlcOS), and 31% of ONVC. Most of the ONVC could correspond to products derived from the protein fraction, being necessary to develop a refining process.

Purification of Liquors. Figure 1 shows the purification scheme proposed for reducing the average DP of AXOS and to increase the purity of the final product. Membrane filtration is a

DOI: 10.1021/acs.jafc.5b03132
J. Agric. Food Chem. 2015, 63, 8429−8438

Table 2. Chemical Composition and Material Balances of Streams in Figure 1[a]

	streams of the process						
	A	D	F	G	L	M	R
			Chemical Composition[b]				
NVC	4.20	3.12	3.05	2.51	2.17	1.79	1.63
glucose	0.008	0.004	0.046	0.046	0.045	0.054	0.055
xylose	0.017	0.006	0.008	0.008	0.008	0.010	0.010
arabinose	0.055	0.012	0.011	0.012	0.013	0.015	0.015
acetic acid	0.010	0.002	0.001	0.002	0.002	0.000	0.000
GlcOS	0.104	0.117	0.044	0.053	0.053	0.052	0.053
XOS	0.345	0.392	0.416	0.500	0.500	0.570	0.562
AraOS	0.106	0.109	0.115	0.138	0.136	0.154	0.153
AcO	0.018	0.020	0.020	0.018	0.018	0.021	0.021
UA	0.033	0.038	0.038	0.041	0.040	0.047	0.048
MS	0.080	0.022	0.065	0.066	0.066	0.079	0.080
OS	0.606	0.676	0.633	0.750	0.747	0.844	0.837
ONVC	0.314	0.302	0.302	0.184	0.187	0.077	0.083
			Material Balances[c]				
recovered liquors	100.00	99.19	98.84	92.00	110.85	103.82	117.97
NVC	4.20	3.09	3.01	2.31	2.41	1.85	1.92
glucose	0.03	0.01	0.14	0.11	0.11	0.10	0.11
xylose	0.07	0.02	0.02	0.02	0.02	0.02	0.02
arabinose	0.23	0.04	0.03	0.03	0.03	0.03	0.03
acetic acid	0.04	0.01	0.00	0.01	0.01	0.00	0.00
GlcOS	0.44	0.36	0.13	0.12	0.13	0.10	0.10
XOS	1.45	1.21	1.25	1.16	1.20	1.06	1.08
AraOS	0.45	0.34	0.35	0.32	0.33	0.29	0.29
AcO	0.08	0.06	0.06	0.04	0.04	0.04	0.04
UA	0.14	0.12	0.12	0.10	0.10	0.09	0.09
MS	0.33	0.07	0.20	0.15	0.16	0.15	0.15
OS	2.56	2.09	1.91	1.73	1.80	1.57	1.61
ONVC	1.31	0.93	0.91	0.43	0.46	0.14	0.16

[a]MS, monosaccharides; OS, total oligosaccharides including acetyl groups and uronic substituents. [b]Expressed as mass fractions (kg NVC/kg stream), except for NVC, which is expressed as kg NVC/100 kg stream. [c]On the basis of 100 kg of autohydrolysis liquors obtained under optimal conditions: 180 °C and 12.2 min.

simple technology that has many advantages: it is energetically efficient, not harmful solvents are needed, it is easily scaled-up, and it was even employed successfully for the purification, fractionation, and/or concentration of oligosaccharides.[18,23] In contrast, ion exchange allows change of the ionic composition of a certain solution without introducing undesirable substances. Even though these resins are expensive, they can be reutilized after a simple regeneration with NaOH or HCl and distilled water. The scaling-up of this technique is not difficult, and it is used in several industrial applications. Moreover, ion exchange was also successfully applied to the purification of autohydrolysis liquors.[19,26]

Table 2 lists compositional data of the streams involved in the process as well as the mass balances.

Diafiltration. First, autohydrolysis liquors were diluted with distilled water and concentrated to their original volume using a 1 kDa molecular weight cutoff membrane. This sequence was repeated twice. As a result of this treatment, the concentrations of unwanted compounds (monosaccharides and ONVC) decreased to 79.4 and 28.5%, respectively. In contrast, high recoveries were achieved for oligomers and substituents (83.6% for XOS, 75.7% for AraOS, 81.6% for AcO, and 84.2% for UA). These results confirm the suitability of this technology for refining autohydrolysis liquors as mentioned in the literature.[29−31] Nevertheless, a higher degree of purity is desired because the ONVC content of the stream D is still 30%.

Enzymatic Hydrolysis. Because the DP distribution of AXOS is an important factor affecting their biological properties, the aim of the second step was to reduce the average DP of the oligomers by partial enzymatic hydrolysis using endoxylanases. As can be seen in Table 2, the content of the main part of the components remained almost constant. Some variations were observed for GlcOS and glucose concentrations, demonstrating the presence of cellulase activity in the enzymatic preparation.

Ion Exchange. As observed in previous studies, significant removal of impurities can be reached when XOS-containing liquors are treated by ion-exchange resins.[26,29,32] Taking this into account, an aliquot of stream F (liquors from the enzymatic hydrolysis) was subjected to ion exchange using Amberlite IRA400 (an anion exchange resin) under the conditions mentioned above. As a result of the treatment, a decrease of the ONVC by >50% and losses below 10% of total OS were achieved. The OS losses could be reduced to a value of 6% if the washing waters generated during the resin regeneration stage were recovered and added to the stream G to give stream L.

To increase the purity of the final product, stream L was treated with a cationic exchange resin generating stream M, which was joined with stream O to give the final refined product (stream R, Table 2). The percentages of product recovery in stream R were 80.3% for GlcOS, 89.9% for XOS,

DOI: 10.1021/acs.jafc.5b03132
J. Agric. Food Chem. 2015, 63, 8429−8438

89.9% for AraOS, 93.0% for AcO, and 95.8% for UA, but were just 32.6% for ONVC. As can be seen in Table 2, a final product containing 84% of substituted oligosaccharides (XOS, 56.2%; AraOS, 15.3%) and 8% of nonvolatile impurities was obtained by applying this processing scheme. These results are in agreement with other previous related studies.[29,32]

Structural and Chemical Characterization of the Final Product (Stream R). As a result of the process reflected in Figure 1, AXOS-enriched samples were obtained and freeze-dried in order to obtain a solid product that was evaluated for their prebiotic potential. However, in order to obtain more information about the composition of the product, samples of stream R were further characterized by HPSEC and MALDI-TOF MS. It must be taken into account that the structural features of OS affect their prebiotic potential as confirmed in the literature. Sarbini et al.[33] indicated that low-molecular-mass OS are often more selectively fermented by bifidobacteria and lactobacilli than are their parent high-molecular-weight carbohydrates. According to Sanchez et al.,[34] who used a human colon model system, the chain length of the AXOS is critical in determining the site of fermentation because shorter-chain-length molecules are fermented in the proximal colon, whereas longer molecules (average DP = 29) reach the distal colon and increase SCFA concentrations in all the compartments.

HPSEC analysis (Figure 4) proved the presence of large amounts of OS, including those with DP > 40 (molecular

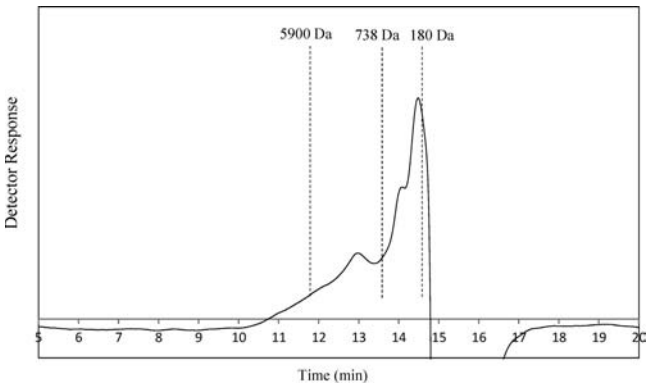

Figure 4. HPSEC chromatogram (including pullulan standards) of stream R.

weight >5900 Da), but the highest area was the one observed in the range 180−738 Da (using pullulan standards), namely, DP ≈ 2−6. This is interesting data taking into account that according to Moura et al.[35] a decrease in XOS consumption by species such as *Bifidobacterium adolescentis* was observed when DP was increased. Moreover, *L. brevis* showed preference for the commercial preparation, which basically constituted of xylobiose.

Likewise, the MALDI-TOF MS analysis data (Figure 5) confirmed the presence of a wide range of OS made up of both unsubstituted (DP = 3−16) and acetyl-substituted (DP = 3−10) pentoses. In accordance with the compositional information shown in Table 2 (XOS/AraOS = 3.67), the oligomers present in the refined product correspond not only to XOS but also to AXOS.

In Vitro Fermentability of the Refined Final Product. To assess the effects of AXOS consumption on the stimulation of four bacterial groups, an in vitro fermentation study was carried out using fecal samples obtained from three volunteers over 60 years old.

SCFA production and pH Evolution in the Fecal Cultures. As is well-known, a variety of the beneficial effects of prebiotics are related to SCFA production and pH reduction in the gut. As shown in Table 3, almost no differences were found between the pH values observed with FOS and AXOS. The decrease of pH was more pronounced during the first 11 h of fermentation, in concordance with the increases in the concentrations of SCFA and with the largest percentage of total OS consumption (Table 4), especially for GlcOS that were consumed up to 90% of their initial amount. In contrast, longer fermentation times resulted in slow decreases in the concentration of substrates, suggesting that some products could have low fermentability and, as a consequence, could reach distal parts of the colon. In fact, some oligomers (10.7 and 17.3% of the initial XOS and AraOS, respectively) remained in the media at the end of fermentation time assayed (45 h). In agreement with our results, a recent study on the prebiotic activity of refined AXOS[26] reported that some XOS and AraOS were not depleted at the end of fermentations (33 h). The incomplete consumption of these compounds could be attributed to the presence of high-DP linear chains because the acetyl groups were metabolized after 7 h, and according to Reis et al.,[36] smaller and highly ramified arabinoxilooligosaccharides are preferably consumed to linear fragments. However, this was not confirmed in this work, and it also should be taken into account that the fermentation pattern adopted by gut microbiota not only depends on the substrate structure but also on the composition of the initial microbiota.

Furthermore, Table 3 also details the generation profiles of SCFA (acetate, propionate, and butyrate), lactate, and formate.

As can be seen, the evolution of the total SCFA content in media containing AXOS was similar to that observed with FOS, and their production mainly took place along the period of 0−11 h (as a result of consumption of the OS). At 29 h, the total organic acids production observed for AXOS was basically acetic acid ≫ butyric acid > propionic acid. In a previous work using XOS derived from rice husks, fermentation times longer than 9 h also resulted in increased SCFA production and a similar product profile.[29] By contrast, a different profile was observed for commercial FOS because lower amounts of acetic acid and significant amounts of lactate (11.6 mM) and formate (19.1 mM) were achieved in the medium. Lactate was usually detected at low concentrations in cultures containing OS, even disappearing in a second fermentation stage (from 11 h), but it is often found at higher concentrations in FOS cultures.[23,37,38] Specifically, the maximum significant amount of lactic acid quantified in this study was 13.96 mM using FOS at 11 h. It has been described as behaving as an intermediary product rapidly converted into SCFAs by the cross-feeding of other bacteria,[36,39,40] which is the likely cause of its decreasing concentration.

In addition to the differences in the organic acids profile, a significant difference (125.04 vs 104.32 mM) was found in total acid concentrations between both substrates at the last time assayed. This fact is in agreement with previous studies; for instance, Reis et al.[36] obtained SCFA average values of 108.4 and 80.6 mM when using arabinoxylan from BSG and FOS, respectively. In the same way, Gullón et al.[26] determined after 33 h of fermentation an average total content of SCFA of 95.0 and 75.6 mM when employing as substrates AXOS from wheat bran and FOS, respectively.

DOI: 10.1021/acs.jafc.5b03132
J. Agric. Food Chem. 2015, 63, 8429−8438

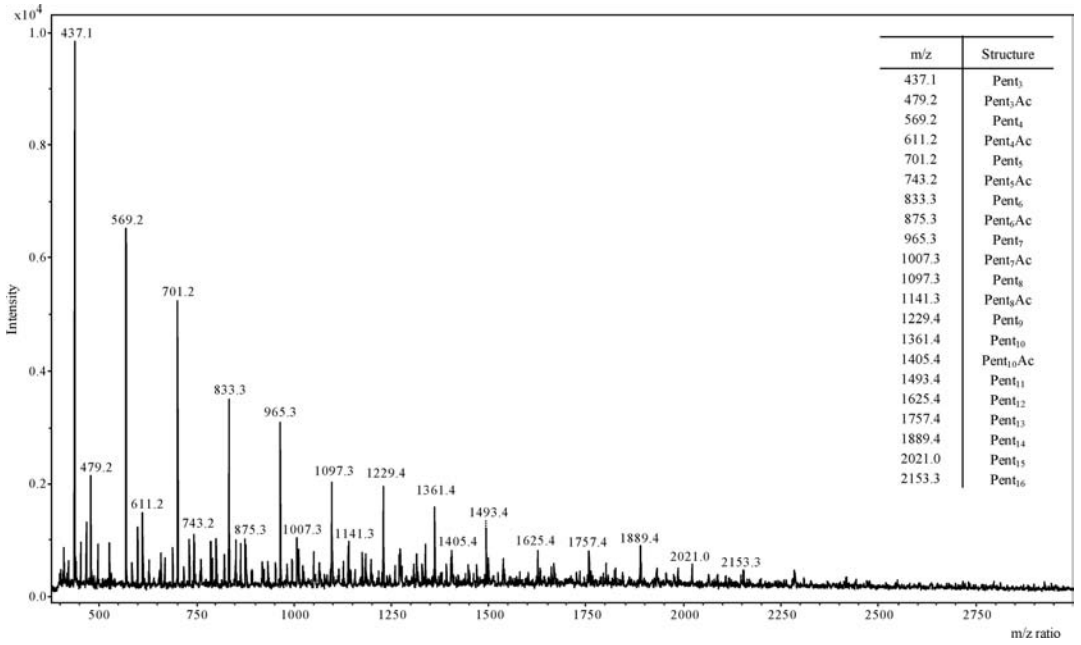

Figure 5. MALDI-TOF mass spectrum of stream R.

Acetate was the main acid in all the experiments, reaching the highest values when AXOS were used as substrate. In fact, observing the data obtained for this acid, significant differences were found between the three substrates assayed from 11 h to the end of fermentation. The acetate proportions (with respect to total acids) and its concentrations obtained at 45 h with AXOS, FOS, and the negative control were 70.7, 42.8, and 70.5% and 88.4, 44.7, 30.9 mM, respectively. This acetogenic potential of XOS was previously observed by Gullón et al.[29] using rice husks as raw material or by Gullón et al.[26] with AXOS from wheat bran. Similarly, the highest propionate concentrations were found in media containing AXOS, which is in agreement with the results reported by Hughes et al.[41] and Gullón et al.,[26] ranging from 6.6 mM in the control assay until to 14.8 mM with AXOS at 45 h. Propionate generation has been associated with the presence of side chains in XOS,[42] and it is utilized primarily by the liver. Its role as a potential modulator of cholesterol synthesis has been proposed.[43]

By comparison, butyrate levels were found in similar amounts in both AXOS and FOS cultures (Table 3), being slightly higher in experiments with FOS. These results were similar to those reported by Gullón et al.[26] with hemicellulose-derived soluble AXOS or by Rivas et al.[44] employing saccharides derived from wood mannan. The butyrate accumulation leads to potent effects on a variety of colonic mucosal functions and may promote satiety.[45] In the case of the negative control, the SCFA generation is associated with the protein degradation, which consequently also lead to increases of the ammonia and phenols (generated in putrefactive processes) levels in the gut.

Dynamics of the Bacterial Populations. Nowadays, potential prebiotic consumers expect from these products the promotion of the growth of specific groups able to enhance their health. Many investigations have focused only on the stimulation of *Bifidobacterium* and *Lactobacillus* species.[46] However, in addition to these two bacterial groups, *Bacteroides* and *Clostridium* also are of great interest and should be included in all the studies. Following the Figure 6 and regarding the number of bifidobacteria, increases in this genus were higher for AXOS, in comparison with commercial FOS, so it can be stated that they have a similar or even greater bifidogenic effect than FOS. On the contrary, the increases in the number of lactobacilli were significantly higher than the ones observed in the control assay but lower than the ones achieved with FOS. This is in agreement with the lactic acid generation in the experiments assayed with FOS, as well as with other studies that demonstrated the potential of FOS to promote the growth of lactobacilli.[23,47,48]

Moreover, the increases in clostridia numbers (often considered harmful bacteria because of their capacity to produce branched-chain fatty acids and a variety of nitrogen- and sulfur-containing compounds) were, in general, lower than those observed in the other bacterial groups, and when AXOS are used as substrate, these increases were slightly lower than those achieved with FOS and similar to the ones observed in the control assays. This means that the growth of clostridia numbers observed in these assays could partially be due to the components of the basal medium. Gullón et al.[20] observed a similar effect on the clostridia population with fermented oligosaccharide mixtures derived from apple pomace using the same nutrient medium.

Meanwhile, the rise in the bacteroides counts was similar in both AXOS and FOS assays after 20 h of fermentation, but almost the same increases were also observed in control experiments because this group of bacteria has saccharolytic and peptolytic activity. Rycroft et al.[48] obtained similar results for *Bacteroides* populations when FOS and XOS were used as substrates, and Jaskari et al.[49] reported that oat xylooligomers were not selectively used by bifidobacteria because *Bacteroides* sp. or *C. difficile* also showed moderate growth on these substrates. By contrast, Yamada et al.[50] reported that wheat arabinoxylan hydrolysates (arabinosylxylobiose, arabinosylxylotriose, arabinosylxylotetraose, and diarabinosylxylotetraose) were utilized by *B. adolescentis* and *Bifidobacterium longum* but not by *Bacteroides* sp.

DOI: 10.1021/acs.jafc.5b03132
J. Agric. Food Chem. 2015, 63, 8429−8438

Table 3. Concentrations of Lactic Acid, Formic Acid, and Short-Chain Fatty Acids (mM) Produced during Fermentation Using AXOS, FOS, and Control (without Carbohydrate Added) and pH Values*

organic acid (mM)	time (h)	carbon source: AXOS	FOS	control
lactic acid	4	1.65 (0.49)[a]	1.84 (0.64)[a]	0.04 (0.04)[a]
	7	4.33 (1.42)[a]	10.61 (4.77)[a]	0.00 (0.00)[a]
	11	3.69 (2.10)[a,b]	13.96 (4.54)[b]	0.00 (0.00)[a]
	20	0.28 (0.15)[a]	11.80 (6.17)[a]	0.00 (0.00)[a]
	29	0.05 (0.05)[a]	11.56 (5.84)[a]	0.00 (0.00)[a]
	45	0.03 (0.03)[a]	4.59 (4.55)[a]	0.00 (0.00)[a]
formic acid	4	1.28 (0.21)[a,b]	1.72 (0.43)[b]	0.16 (0.10)[a]
	7	5.48 (0.97)[a]	13.44 (1.81)[b]	0.85 (0.48)[a]
	11	5.11 (0.70)[b]	18.62 (0.89)[c]	0.46 (0.23)[a]
	20	2.92 (0.10)[a]	18.64 (1.72)[b]	0.00 (0.00)[a]
	29	2.04 (0.06)[b]	19.08 (0.42)[c]	0.00 (0.00)[a]
	45	1.41 (0.56)[a]	18.19 (1.25)[b]	0.00 (0.00)[a]
acetic acid	4	10.31 (2.74)[a]	7.73 (1.97)[a]	3.27 (0.41)[a]
	7	52.50 (8.42)[b]	31.03 (4.78)[a,b]	9.16 (1.08)[a]
	11	78.80 (2.96)[c]	43.58 (1.33)[b]	15.27 (1.43)[a]
	20	82.32 (2.74)[c]	41.15 (2.29)[b]	20.47 (1.64)[a]
	29	84.19 (3.68)[c]	45.11 (1.49)[b]	24.18 (1.57)[a]
	45	88.41 (2.50)[c]	44.70 (2.96)[b]	30.89 (1.87)[a]
propionic acid	4	3.12 (0.19)[a]	2.50 (0.20)[a]	2.25 (0.33)[a]
	7	5.55 (1.39)[a]	4.72 (1.94)[a]	2.87 (0.52)[a]
	11	8.81 (2.57)[a]	6.69 (2.46)[a]	3.37 (0.52)[a]
	20	11.55 (2.21)[a]	7.78 (2.12)[a]	4.72 (0.91)[a]
	29	13.43 (1.03)[b]	9.69 (1.31)[a,b]	5.63 (1.06)[a]
	45	14.77 (0.84)[b]	10.76 (1.20)[a,b]	6.62 (1.28)[a]
butyric acid	4	1.76 (0.33)[a]	1.70 (0.43)[a]	0.84 (0.13)[a]
	7	7.14 (1.26)[b]	8.21 (1.64)[b]	1.68 (0.47)[a]
	11	13.20 (0.66)[b]	15.68 (0.40)[b]	3.16 (0.65)[a]
	20	18.04 (1.86)[b]	18.88 (3.08)[b]	5.06 (0.67)[a]
	29	19.20 (2.53)[b]	21.46 (2.05)[b]	5.94 (0.60)[a]
	45	20.43 (2.49)[b]	26.08 (3.32)[b]	6.33 (0.36)[a]
total	4	18.12 (3.6)[a]	15.49 (3.24)[a]	6.56 (0.36)[a]
	7	74.99 (6.64)[b]	68.00 (11.66)[b]	14.56 (0.73)[a]
	11	109.63 (2.19)[b]	98.53 (3.69)[b]	22.26 (1.38)[a]
	20	115.11 (1.96)[b]	98.25 (7.55)[b]	30.24 (2.67)[a]
	29	118.91 (2.53)[b]	106.91 (3.76)[b]	35.75 (2.58)[a]
	45	125.04 (1.55)[c]	104.32 (4.35)[b]	43.84 (2.12)[a]
pH	0	6.76 (0.09)	6.85 (0.04)	6.87 (0.02)
	4	6.62 (0.08)	6.67 (0.06)	6.89 (0.02)
	7	5.90 (0.27)	5.69 (0.46)	6.92 (0.11)
	11	5.13 (0.05)	5.06 (0.18)	6.97 (0.14)
	20	5.12 (0.07)	5.04 (0.19)	6.84 (0.06)
	29	5.15 (0.07)	5.12 (0.22)	6.84 (0.14)
	45	5.15 (0.06)	5.28 (0.16)	6.72 (0.09)

*Standard error in parentheses (n = 3). Different letters indicate significant differences (p < 0.05) among carbon source for each acid.

Table 4. Oligosaccharide Consumption during Fermentation[a]

time (h)	GlcOS	XOS	AraOS	AcO
4	69.7	13.8	29.8	20.2
7	88.5	69.5	46.2	100.0
11	90.1	79.5	63.4	100.0
20	90.6	85.2	73.8	100.0
29	90.7	87.1	76.8	100.0
45	100.0	89.3	82.7	100.0

[a]Average values expressed as percentage of their initial amounts.

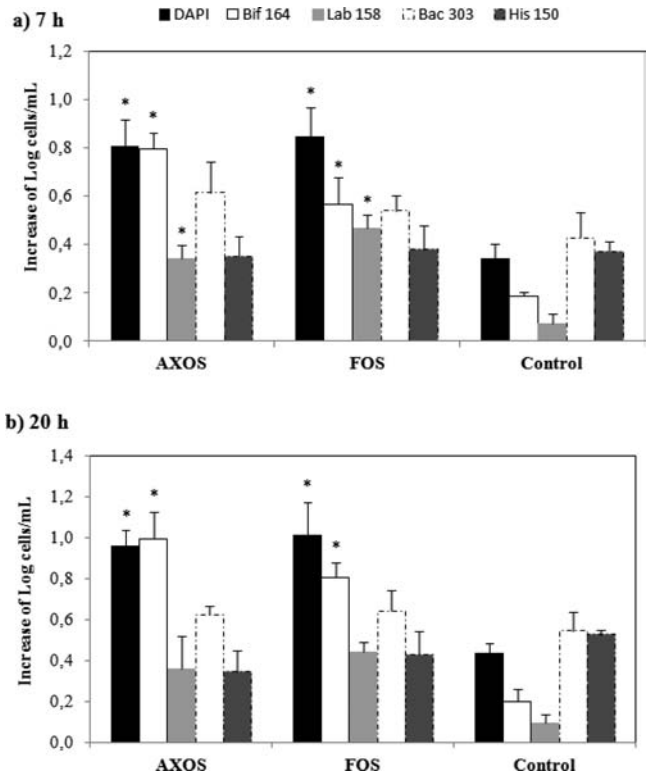

Figure 6. Increase of bacterial populations (expressed as log cells/mL) in fecal batch cultures using three different human inoculums and various substrates: (a) 7 h and (b) 20 h. Error bars indicate standard error (n = 3). Asterisks indicate significant differences (Tukey's test, p < 0.05) between different carbon sources. DAPI: 4′,6-diamidino-2-phenylindole; Bif164: *Bifidobacterium*; Lab158: *Lactobacillus/Enterococcus*; Bac303: *Bacteroides/Prevotella*; and His150: *Clostridium histolyticum* clusters I and II.

This influence of AXOS on the growth of the four bacterial groups (Figure 6) presented a pattern in close correspondence with the substrate consumption because the largest increase in total cell counts took place within the first 7 h of fermentation, coinciding with the largest decrease in the concentration of OS and with the pH decreasing. Also, the highest production of lactic or acetic acids correlated with changes in the numbers of bifidobacteria and lactobacilli. These results are in agreement with Mussatto et al.,[13] who indicated that germinated barley foodstuff is considered to be a mild anti-inflammatory through increases in colonic butyrate concentration and the number of *Bifidobacterium* sp., or with Jaskari et al.,[49] who proved that most of the intestinal bacteria tested (*Bacteroides thetaiotaomicron*, *Bacteroides vulgatus*, *Bacteroides fragilis*, and *C. diffcile*) were able to degrade at least some xylooligomers from oat spelt xylan. In addition, the data obtained by Falck et al.[11] from batch fermentation experiments showed that XOS hydrolysates from cereal xylan (rye flour) and hardwood (birchwood) were fermented by both *B. adolescentis* and *L. brevis*, whereas nontreated polymeric xylans were not fermented by any of the strains. However, Finegold et al.[1] reported that XOS increases the counts of *Bifidodobacterium* without increasing the counts of *Lactobacillus* in healthy adults. Another study assessing the effects of a 4 g per day of XOS on the intestinal microbiota, gastrointestinal function, and nutritional

DOI: 10.1021/acs.jafc.5b03132
J. Agric. Food Chem. 2015, 63, 8429−8438

parameters in elderly patients over a 21 day period concluded that XOS supplementation promoted intestinal health and showed no adverse effects on the elderly study population.[51] This is an important point because a requirement for an effective prebiotic would be the absence of gastrointestinal side effects.

CONCLUSIONS

Brewer's spent grain (BSG) was evaluated as a raw material for obtaining a mixture of arabinoxylooligosaccharides (AXOS) suitable to be use as prebiotics for elderly. After hydrothermal treatment of BSG, AXOS were refined by membrane filtration and ion exchange and modified by enzymatic hydrolysis.

The presence of both substituted (DP = 2−10) and unsubstituted (DP = 2−16) oligosaccharides made up of xylose and arabinose were confirmed in purified mixtures (OS content = 84% w/w) by MALDI-TOF MS. Finally, AXOS were evaluated for their prebiotic activity by in vitro fermentation assays using fecal inocula from elderly people. Experimental results showed that AXOS fermentation resulted in increased bifidobacteria and lactobacilli populations with respect to the negative control cultures as well as the accumulation of SCFA, confirming a stimulatory effect. Moreover, taking into account the variations in the bacterial populations and the production of organic acids, it can be concluded that the results obtained with AXOS are slightly better than the ones achieved with FOS.

Therefore, the intake of this kind of AXOS could enable the improvement of intestinal microbiota and their functions and, as a consequence, the health of the elderly.

AUTHOR INFORMATION

Funding

We are grateful to Xunta de Galicia (project ref GRC2014/018 and "INBIOMED" Project) for the financial support of this work. Both projects were partially funded by the FEDER Program of the European Union ("Unha maneira de facer Europa"). B.G. thanks the Spanish Ministry of Education, Culture, and Sports for her FPU research grant.

Notes

The authors declare no competing financial interest.

ABBREVIATIONS USED

AcO, Acetyl substituents in oligomers; AIR, Acid insoluble residue chromatography; AraOS, Arabinosyl substituents; AXOS, Arabinoxylooligosaccharides; BSG, Brewer's spent grain; DAPI, 4′,6-diamidino-2-phenylindole; DP, Degree of polimerization; FI, Fecal inocula; FISH, Fluorescent in situ hybridization; FOS, Fructooligosaccharides; GalOS, Galactooligosaccharides; GlcOS, Glucooligosaccharides; HMF, Hydroxymethylfurfural; HPLC, High-performance liquid chromatography; HPSEC, High-performance size exclusion; MALDI-TOF MS, Matrix-assisted laser desorption/ionization-time-of-flight; MS, Monosaccharides; NVC, Nonvolatile content; ONVC, Other nonvolatile content; OS, Oligosaccharides; SCFA, Short-chain fatty acids; UA, Uronic acids; XOS, Xylooligosaccharides

REFERENCES

(1) Finegold, S. M.; Li, Z.; Summanen, P. H.; Downes, J.; Thames, G.; Corbett, K.; Dowd, S.; Krak, M.; Heber, D. Xylooligosaccharide increases bifidobacteria but not lactobacilli in human gut microbiota. *Food Funct.* **2014**, *5*, 436−445.

(2) Lecerf, J. M.; Dépeint, F.; Clerc, E.; Dugenet, Y.; Niamba, C. N.; Rhazi, L.; Cayzeele, A.; Abdelnour, G.; Jaruga, A.; Younes, H.; Jacobs, H.; Lambrey, G.; Abdelnour, A. M.; Pouillart, P. R. Xylo-oligosaccharide (XOS) in combination with inulin modulates both the intestinal environment and immune status in healthy subjects, while XOS alone only shows prebiotic properties. *Br. J. Nutr.* **2012**, *108*, 1847−1858.

(3) Woodmansey, E. J. Intestinal bacteria and ageing. *J. Appl. Microbiol.* **2007**, *102*, 1178−1186.

(4) Rowland, I.; Gill, C. Prebiotics and nutrition in the elderly: The concept of healthy aging. In *Handbook of Prebiotics*; Gibson, G. R., Roberfroid, M. B., Eds.; CRC Press: New York, 2008, 405−419.

(5) Scheid, M. M. A.; Moreno, Y. M. F.; Maróstica Junior, M. R.; Pastore, G. M. Effect of prebiotics on the health of the elderly. *Food Res. Int.* **2013**, *53*, 426−432.

(6) Woodmansey, E. J.; McMurdo, M. E. T.; Macfarlane, G. T.; Macfarlane, S. Comparison of compositions and metabolic activities of fecal microbiotas in young adults and in antibiotic-treated and non-antibiotic-treated elderly subjects. *Appl. Environ. Microbiol.* **2004**, *70*, 6113−6122.

(7) Claesson, M. J.; Cusack, S.; O'Sullivan, O.; Greene-Diniz, R.; De Weerd, H.; Flannery, E.; Marchesi, J. R.; Falush, D.; Dinan, T.; Fitzgerald, G.; Stanton, C.; Van Sinderen, D.; O'Connor, M.; Harnedy, N.; O'Connor, K.; Henry, C.; O'Mahony, D.; Fitzgerald, A. P.; Shanahan, F.; Twomey, C.; Hill, C.; Ross, R. P.; O'Toole, P. W. Composition, variability, and temporal stability of the intestinal microbiota of the elderly. *Proc. Natl. Acad. Sci. U. S. A.* **2011**, *108* (Suppl. 1), 4586−4591.

(8) Childs, C. E.; Röytiö, H.; Alhoniemi, E.; Fekete, A. A.; Forssten, S. D.; Hudjec, N.; Lim, Y. N.; Steger, C. J.; Yaqoob, P.; Tuohy, K. M.; Rastall, R. A.; Ouwehand, A. C.; Gibson, G. R. Xylo-oligosaccharides alone or in synbiotic combination with Bifidobacterium animalis subsp. lactis induce bifidogenesis and modulate markers of immune function in healthy adults: A double-blind, placebo-controlled, randomised, factorial cross-over study. *Br. J. Nutr.* **2014**, *111*, 1945−1956.

(9) Samanta, A. K.; Senani, S.; Kolte, A. P.; Sridhar, M.; Sampath, K. T.; Jayapal, N.; Devi, A. Production and *in vitro* evaluation of xylooligosaccharides generated from corn cobs. *Food Bioprod. Process.* **2012**, *90*, 466−474.

(10) Carvalheiro, F.; Garrote, G.; Parajó, J. C.; Pereira, H.; Gírio, F. M. Kinetic modeling of brewery's spent grain autohydrolysis. *Biotechnol. Prog.* **2005**, *21*, 233−243.

(11) Falck, P.; Precha-Atsawanan, S.; Grey, C.; Immerzeel, P.; Stålbrand, H.; Adlercreutz, P.; Nordberg Karlsson, E. Xylooligosaccharides from hardwood and cereal xylans produced by a thermostable xylanase as carbon sources for lactobacillus brevis and bifidobacterium adolescentis. *J. Agric. Food Chem.* **2013**, *61*, 7333−7340.

(12) Kabel, M. A.; Schols, H. A.; Voragen, A. G. J. Complex xylo-oligosaccharides identified from hydrothermally treated Eucalyptus wood and brewery's spent grain. *Carbohydr. Polym.* **2002**, *50*, 191−200.

(13) Mussatto, S. I.; Dragone, G.; Roberto, I. C. Brewers' spent grain: generation, characteristics and potential applications (Review). *J. Cereal Sci.* **2006**, *43*, 1−14.

(14) Treimo, J.; Westereng, B.; Horn, S. J.; Forssell, P.; Robertson, J. A.; Faulds, C. B.; Waldron, K. W.; Buchert, J.; Eijsink, V. G. H. Enzymatic solubilization of brewers' spent grain by combined action of carbohydrases and peptidases. *J. Agric. Food Chem.* **2009**, *57*, 3316−3324.

(15) Robertson, J. A.; I'Anson, K. J. A.; Treimo, J.; Faulds, C. B.; Brocklehurst, T. F.; Eijsink, V. G. H.; Waldron, K. W. Profiling brewers' spent grain for composition and microbial ecology at the site of production. *LWT - Food Sci. Technol.* **2010**, *43*, 890−896.

(16) Carvalheiro, F.; Esteves, M. P.; Parajó, J. C.; Pereira, H.; Gírio, F. M. Production of oligosaccharides by autohydrolysis of brewery's spent grain. *Bioresour. Technol.* **2004**, *91*, 93−100.

(17) Conde, E.; Gullón, P.; Moure, A.; Domínguez, H.; Parajó, J. C. Fractionation of industrial solids containing barley husks in aqueous media. *Food Bioprod. Process.* **2009**, *87*, 208−214.

DOI: 10.1021/acs.jafc.5b03132
J. Agric. Food Chem. 2015, 63, 8429−8438

(18) Gullón, P.; González-Muñoz, M. J.; Parajó, J. C. Manufacture and prebiotic potential of oligosaccharides derived from industrial solid wastes. *Bioresour. Technol.* **2011**, *102*, 6112−6119.
(19) Vegas, R.; Luque, S.; Alvarez, J. R.; Alonso, J. L.; Domínguez, H.; Parajó, J. C. Membrane-assisted processing of xylooligosaccharide-containing liquors. *J. Agric. Food Chem.* **2006**, *54*, 5430−5436.
(20) Gullón, B.; Gullón, P.; Sanz, Y.; Alonso, J. L.; Parajó, J. C. Prebiotic potential of a refined product containing pectic oligosaccharides. *LWT - Food Sci. Technol.* **2011**, *44*, 1687−1696.
(21) Overend, R. P.; Chornet, E.; Gascoigne, J. A. Fractionation of Lignocellulosics by Steam-Aqueous Pretreatments [and Discussion]. *Philos. Trans. R. Soc., A* **1987**, *321* (1561), 523−536.
(22) Garrote, G.; Cruz, J.; Domínguez, H.; Parajó, J. Valorisation of waste fractions from autohydrolysis of selected lignocellulosic materials. *J. Chem. Technol. Biotechnol.* **2003**, *78* (4), 392−398.
(23) Gómez, B.; Gullón, B.; Remoroza, C.; Schols, H. A.; Parajó, J. C.; Alonso, J. L. Purification, characterization and prebiotic properties of pectic oligosaccharides from orange peel wastes. *J. Agric. Food Chem.* **2014**, *62*, 9769−9782.
(24) Gullón, P.; Moura, P.; Esteves, M. P.; Girio, F. M.; Domínguez, H.; Parajó, J. C. Assessment on the fermentability of xylooligosaccharides from rice husks by probiotic bacteria. *J. Agric. Food Chem.* **2008**, *56*, 7482−7487.
(25) Blumenkrantz, N.; Asboe-Hansen, G. New method for quantitative determination of uronic acids. *Anal. Biochem.* **1973**, *54*, 484−489.
(26) Gullón, B.; Gullón, P.; Tavaria, F.; Pintado, M.; Gomes, A. M.; Alonso, J. L.; Parajó, J. C. Structural features and assessment of prebiotic activity of refined arabinoxylooligosaccharides from wheat bran. *J. Funct. Foods* **2014**, *6*, 438−449.
(27) Garrote, G.; Domínguez, H.; Parajó, J. C. Production of substituted oligosaccharides by hydrolytic processing of barley husks. *Ind. Eng. Chem. Res.* **2004**, *43*, 1608−1614.
(28) Carvalheiro, F.; Silva-Fernandes, T.; Duarte, L. C.; Gírio, F. M. Wheat straw autohydrolysis: process optimization and products characterization. *Appl. Biochem. Biotechnol.* **2009**, *153*, 84−93.
(29) Gullón, P.; González-Muñoz, M. J.; van Gool, M. P.; Schols, H. A.; Hirsch, J.; Ebringerová, A.; Parajó, J. C. Production, refining, structural characterization and fermentability of rice husk xylooligosaccharides. *J. Agric. Food Chem.* **2010**, *58*, 3632−3641.
(30) González-Muñoz, M. J.; Santos, V.; Parajó, J. C. Purification of oligosaccharides obtained from Pinus pinaster hemicelluloses by diafiltration. *Desalin. Water Treat.* **2011**, *27*, 48−53.
(31) Gómez, B.; Gullón, B.; Yáñez, R.; Parajó, J. C.; Alonso, J. L. Pectic oligosacharides from lemon peel wastes: Production, purification, and chemical characterization. *J. Agric. Food Chem.* **2013**, *61*, 10043−10053.
(32) Vegas, R.; Alonso, J. L.; Domínguez, H.; Parajó, J. C. Enzymatic processing of rice husk autohydrolysis products for obtaining low molecular weight oligosaccharides. *Food Biotechnol.* **2008**, *22*, 31−46.
(33) Sarbini, S. R.; Kolida, S.; Naeye, T.; Einerhand, A. W.; Gibson, G. R.; Rastall, R. A. The prebiotic effect of α-1,2 branched, low molecular weight dextran in the batch and continuous faecal fermentation system. *J. Funct. Foods* **2013**, *5*, 1938−1946.
(34) Sanchez, J. I.; Marzorati, M.; Grootaert, C.; Baran, M.; Van Craeyveld, V.; Courtin, C. M.; Broekaert, W. F.; Delcour, J. A.; Verstraete, W.; Van De Wiele, T. Arabinoxylan-oligosaccharides (AXOS) affect the protein/carbohydrate fermentation balance and microbial population dynamics of the Simulator of Human Intestinal Microbial Ecosystem. *Microb. Biotechnol.* **2009**, *2*, 101−113.
(35) Moura, P.; Barata, R.; Carvalheiro, F.; Gírio, F.; Loureiro-Dias, M. C.; Esteves, M. P. *In vitro* fermentation of xylo-oligosaccharides from corn cobs autohydrolysis by Bifidobacterium and Lactobacillus strains. *LWT - Food Sci. Technol.* **2007**, *40* (6), 963−972.
(36) Reis, S. F.; Gullón, B.; Gullón, P.; Ferreira, S.; Maia, C. J.; Alonso, J. L.; Domingues, F. C.; Abu-Ghannam, N. Evaluation of the prebiotic potential of arabinoxylans from brewer's spent grain. *Appl. Microbiol. Biotechnol.* **2014**, *98* (22), 9365−9373.
(37) Leijdekkers, A. G. M.; Aguirre, M.; Venema, K.; Bosch, G.; Gruppen, H.; Schols, H. A. *In vitro* fermentability of sugar beet pulp derived oligosaccharides using human and pig fecal inocula. *J. Agric. Food Chem.* **2014**, *62*, 1079−1087.
(38) Mandalari, G.; Nueno-Palop, C.; Bisignano, G.; Wickham, M. S. J.; Narbad, A. Potential prebiotic properties of almond (Amygdalus communis L.) seeds. *Appl. Environ. Microbiol.* **2008**, *74*, 4264−4270.
(39) Flint, H. J.; Barcenilla, A.; Stewart, C. S.; Duncan, S. H.; Hold, G. L. Roseburia intestinalis sp. nov. a novel saccharolytic, butyrateproduction bacterium from human faeces. *Int. J. Syst. Evol. Microbiol.* **2002**, *52*, 1615−1620.
(40) Bourriaud, C.; Robins, R. J.; Martin, L.; Kozlowski, F.; Tenailleau, E.; Cherbut, C.; Michel, C. Lactate is mainly fermented to butyrate by human intestinal microfloras but inter-individual variation is evident. *J. Appl. Microbiol.* **2005**, *99*, 201−212.
(41) Hughes, S. A.; Shewry, P. R.; Gibson, G. R.; McCleary, B. V.; Rastall, R. A. *In vitro* fermentation of oat and barley derived b-glucans by human faecal microbiota. *FEMS Microbiol. Ecol.* **2008**, *64*, 482−493.
(42) Broekaert, W. F.; Courtin, C. M.; Verbeke, K.; Van de Wiele, T.; Verstraete, W.; Delcour, J. A. Prebiotic and other health-related effects of cereal-derived arabinoxylans, arabinoxylan-oligosaccharides, and xylooligosaccharides. *Crit. Rev. Food Sci. Nutr.* **2011**, *51*, 178−194.
(43) Bourquin, L. D.; Titgemeyer, E. C.; Garleb, K. A.; George, C.; Fahey, J. R. Short-chain fatty acid production and fiber degradation by human colonic bacteria: effects of substrate and cell wall fractionation procedures. *J. Nutr.* **1992**, *122*, 1508−1520.
(44) Rivas, S.; Gullón, B.; Gullón, P.; Alonso, J. L.; Parajó, J. C. Manufacture and properties of bifidogenic saccharides derived from wood mannan. *J. Agric. Food Chem.* **2012**, *60*, 4296−4305.
(45) Hamer, H. M.; Jonkers, D.; Venema, K.; Vanhoutvin, S.; Troost, F. J.; Brummer, R. J. Review article: The role of butyrate on colonic function. *Aliment. Pharmacol. Ther.* **2008**, *27*, 104−119.
(46) Scott, K. P.; Martin, J. C.; Duncan, S. H.; Flint, H. J. Prebiotic stimulation of human colonic butyrate-producing bacteria and bifidobacteria, *in vitro*. *FEMS Microbiol. Ecol.* **2014**, *87*, 30−40.
(47) Chen, J.; Liang, R.-H.; Liu, W.; Li, T.; Liu, C.-M.; Wu, S.-S.; Wang, Z.-J. Pectic-oligosaccharides prepared by dynamic high-pressure microfluidization and their *in vitro* fermentation properties. *Carbohydr. Polym.* **2013**, *91*, 175−182.
(48) Rycroft, C. E.; Jones, M. R.; Gibson, G. R.; Rastall, R. A. A comparative *in vitro* evaluation of the fermentation properties of prebiotic oligosaccharides. *J. Appl. Microbiol.* **2001**, *91*, 878−887.
(49) Jaskari, J.; Kontula, P.; Siitonen, A.; Jousimies-Somer, H.; Mattila-Sandholm, T.; Poutanen, K. Oat b-glucan and xylan hydrolysates as selective substrates for Bifidobacterium and Lactobacillus strains. *Appl. Microbiol. Biotechnol.* **1998**, *49*, 175−181.
(50) Yamada, H.; Itoh, K.; Morishita, Y.; Taniguchi, H. Advances in cereal chemistry and technology in Japan. Structure and properties of oligomers from wheat bran. *Cereal Foods World* **1993**, *38*, 490−492.
(51) Chung, Y.; Hsu, C.; Ko, C.; Chan, Y. Dietary intake of xylooligosaccharides improves the intestinal microbiota, fecal moisture, and pH value in the elderly. *Nutr. Res. (N. Y., NY, U. S.)* **2007**, *27*, 756−761.

DOI: 10.1021/acs.jafc.5b03132
J. Agric. Food Chem. 2015, 63, 8429−8438

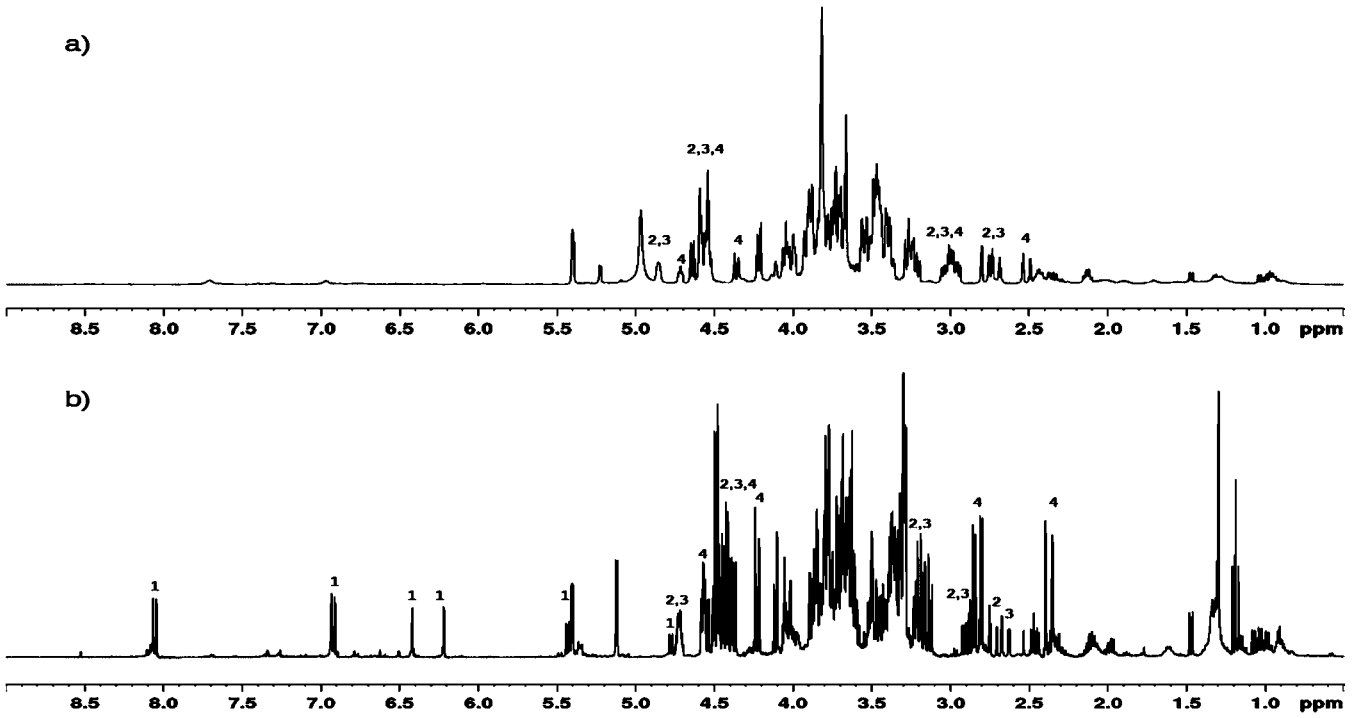

Figure 2. (a) Water-presaturated ^{1}H HR-MAS NMR spectrum of fresh saffron petals and (b) ^{1}H NMR spectrum of the ethanol (95%) extract of fresh saffron petals in D_2O solution.

bone loss preventive, and osteoclastogenesis suppressing.[19] For these reasons, efforts toward efficient synthesis of compounds **2** and **3** by a chemoenzymatic approach have recently been reported.[20]

To gain a deeper insight into this subject and to establish which are the main metabolites present in *C. sativus* petals, we analyzed them by high-resolution magic-angle-spinning nuclear magnetic resonance (HR-MAS NMR) and their ethanol (95%) extract by HR-NMR. HR-MAS NMR spectroscopy allows for the derivation of the biochemical profile of intact (human, animal, or plant) tissues[21] formed by fast-moving small metabolites that give rise to narrow resonances. Through HR-MAS NMR, we tried to have a look inside a complex row matrix without disrupting its structure and avoiding hydrolytic processes that can flank extraction. The purpose of this paper is to contribute to the utilization of *C. sativus* petals directly after the separation from saffron. To the best of our knowledge, this is the first HR-MAS NMR study of petals.

EXPERIMENTAL SECTION

Plant Materials. *C. sativus* flowers were collected in Abruzzo (Italy), in the Aquila Saffron Protected Designation of Origin (PDO) status, at the Farm "Vigna di More" located in Tione degli Abruzzi, in autumn 2011. The flowers grew at 700 m above sea level. The bulbs were planted in August on a ground prepared 1 year before (the soil is employed every 5 years), and the flowers were harvested in October. The bulbs were put at 2−3 cm distance from each other, at least 8 cm depth in rows of two or three, according to the space and land available. Flowers were hand-picked early in the morning, before sunrise before perianth opening, and were placed in traditional wicker baskets. After collection, they were stored at 5 °C and send to the lab, where intact petals were used for HR-MAS NMR measurements within 3 days after collection.

Extraction. Fresh petals (10 g) were extracted with 95% ethanol (Sigma-Aldrich), and the extract was vacuum-evaporated (150 mg). The whole process was carried out quickly at room temperature (about 1 h). The extracts were analyzed in HR-NMR and mass spectrometry (MS).

NMR Measurements. ^{1}H HR-MAS NMR spectra were recorded with a Bruker Avance 400 (Bruker BioSpin) spectrometer operating at a frequency of 400.13 MHz. The instrument was equipped with a ^{1}H,^{13}C HR-MAS probe for semi-solids and with a broadband inverse (BBI) probe for liquids. Before HR-MAS examination, intact saffron petals were introduced in a MAS zirconia rotor (4 mm outer diameter) and 10 μL of D_2O was added to provide deuterium for the lock system, fitted with a 50 μL cylindrical insert to increase sample homogeneity, and then transferred into the probe cooled to 5 °C. Experiments were performed at a temperature of 5 °C controlled by a Bruker cooling unit.

Samples were spun at 4000 Hz, and one-dimensional (1D) and two-dimensional (2D) spectra were acquired using the sequences implemented in the Bruker software. The same experiments were carried out on D_2O extract solution at 25 °C, with a lower number of scans. To record ^{1}H water-presaturated spectrum, a composite pulse sequence (zgcppr) with 2 s water presaturation during the relaxation delay, 8 kHz spectral width, 32 000 data points, and 16−8 scans were used. The 2D correlation spectroscopy (COSY) spectra were acquired using a standard pulse sequence (cosygpprqf), 1 s water presaturation during relaxation delay, 2−4 kHz spectral width, 2000 data points, 4 scans per increment, and 128 increments. The 2D total correlation spectroscopy (TOCSY) spectra were acquired using a standard pulse sequence (mlevgpph19), 1 s water presaturation during relaxation delay, 100 ms mixing (spin-lock) time, 2−4 kHz spectral width, 4000 data points, 4 scans per increment, and 512 increments. The 2D heteronuclear single-quantum coherence (HSQC)-edited spectra were acquired using a standard pulse sequence echo−antiecho phase sensitive (hsqcedetgp), 0.5 s relaxation delay, 1.725 ms evolution time, 2−4 kHz spectral width in f2, 2000 data points, 16−8 scans per increment, 15 kHz spectral width in f1, and 256 increments. The 2D heteronuclear multiple-bond coherence (HMBC) spectra were acquired using a standard pulse sequence (hmbcgplpndqf), 0.5 s relaxation delay, 50 ms evolution time, 2−4 kHz spectral width in f2, 2000 data points, 128−32 scans per increment, 22 kHz spectral width in f1, and 256 increments.

Deconvolution of ^{1}H NMR-selected signals was run with MestReNova 9.1 (2014 Mestrelab Research S.L.).

DOI: 10.1021/acs.jafc.5b03284
J. Agric. Food Chem. 2015, 63, 8439−8444

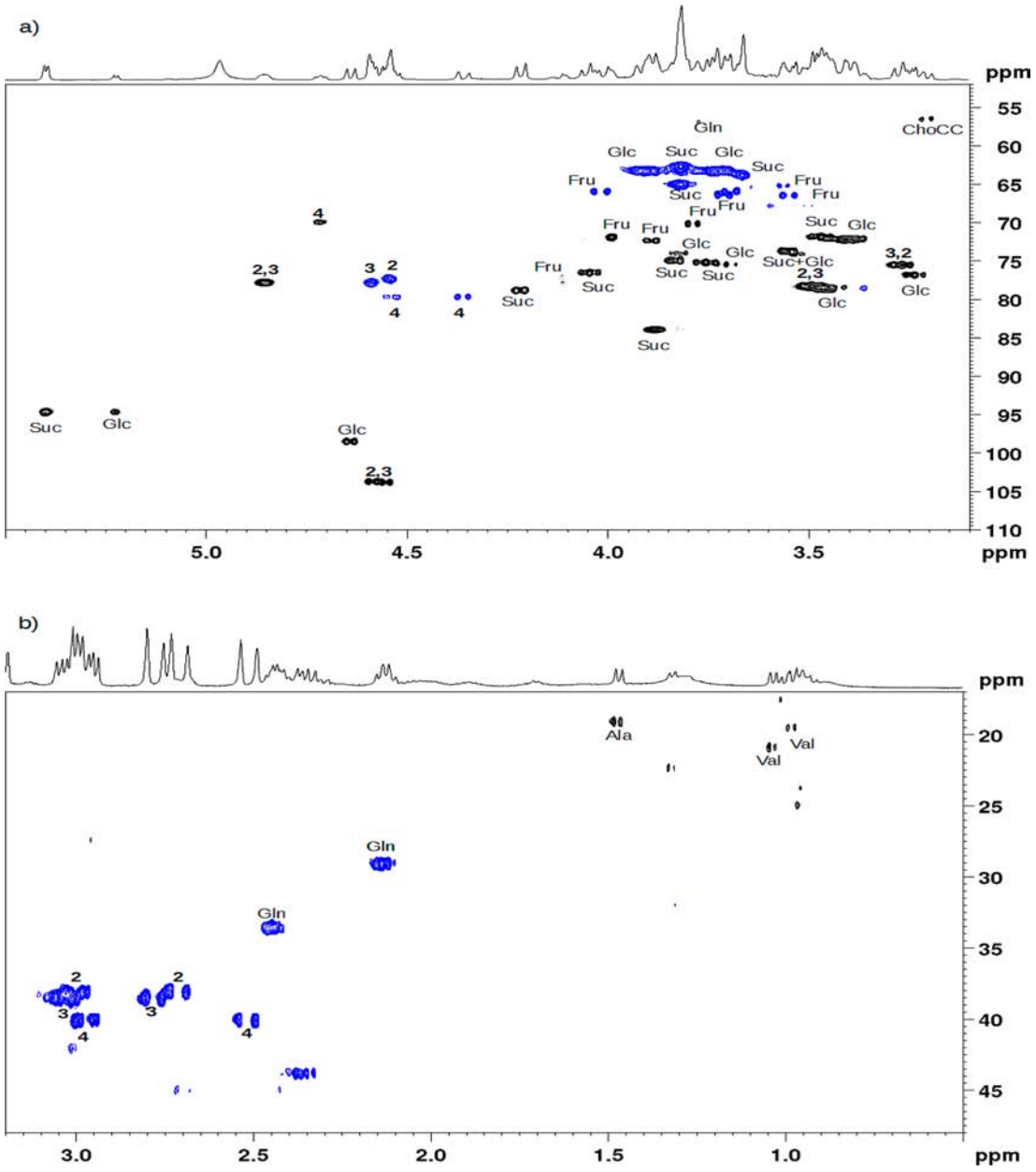

Figure 3. Enlarged (a) carbohydrate and (b) aliphatic regions of the HSQC HR-MAS NMR spectrum of fresh saffron petals. ChoCC = choline-containing compounds.

Electrospray Ionization (ESI) Ion-Trap (IT) MS Measurements. The negative-ion ESI mass spectra and ESI−MS/MS data (collision energies of 10, 15, 20, or 35 eV) were acquired with a LC−MS(n) IT 6310A (Agilent Technologies) coupled with a HPLC Agilent Series 1200 equipped with a Zorbax SB-C18 column, 30 × 2.1 mm inner diameter, 3.5 μm particle size (Agilent). Eluents were acetonitrile, H_2O, and 1% formic acid. Chromatographic runs were performed using a gradient of 1% formic acid in acetonitrile (98 → 10%) and 1% formic acid in water (2 → 90%). The solvent flow rate was 0.2 mL/min; the temperature kept at 25 °C; and the injector volume selected was 2 μL. Total ion current (TIC) chromatograms were acquired in both positive and negative mode in the mass range between m/z 100 and 1400. He was used as the collision gas in MS^2 experiments.

RESULTS AND DISCUSSION

The water-presaturated ^{1}H HR-MAS NMR spectrum of saffron petals (Figure 2a) shows the overlapped signals from a number of metabolites, mainly in the carbohydrate region, whereas only broad and weak signals are found in the aromatic region, at about 6.9 and 7.7 ppm, where multiplets from kaempferol derivatives are expected. These two broad resonances are sometimes assigned to polyphenols, but they have also been attributed to NH protons.[22] On the other hand, some multiplets in the range of 3.1−2.5 ppm, outside the common carbohydrate region, are detected, and other low signals mainly attributable to free amino acids and lipids are present at lower parts per million (ppm).

To disentangle the complex spectral pattern, it was necessary to use 2D NMR homo- and heterocorrelated experiments, such as COSY, TOCSY, HSQC, and HMBC. We were thus able to reconstruct molecular skeletons and compare the chemical shifts and the correlation patterns to those reported in the literature and in NMR databanks, such as the Human Metabolome Database (HMDB; http://www.hmdb.ca/). Using this approach, we found that the majority of signals in the ^{1}H spectrum are due

DOI: 10.1021/acs.jafc.5b03284
J. Agric. Food Chem. 2015, 63, 8439−8444

Table 1. ^{1}H and ^{13}C NMR Data of Compounds 2−4 (ppm[a]) in *C. sativus* Petals As Obtained by HR-MAS NMR and of Compounds 1−4 Extracted with Ethanol (95%) (D_2O)

	2[b]		2[c]		3[b]		3[c]		4[b]		4[c]		1[c]	
	^{1}H	^{13}C	^{1}H	^{13}C	^{1}H	^{13}C	^{1}H	^{13}C	^{1}H	^{13}C	^{1}H	^{13}C	^{1}H	^{13}C
1		182.5		179.7		182.5		180.1		183.0		180.3		
2	2.99, 2.71 dd, 18.1, 6.1 Hz; d, 18.1 Hz)	38.2	2.87, 2.65 (dd, 18.0, 6.4 Hz; ddd, 18.0, 1.9, 0.8 Hz)	37.2	3.03, 2.78 dd, 18.6, 6.1 Hz; d, 18.6 Hz)	38.5	2.89, 2.73 (dd, 18.2, 1.4 Hz; dd, 18.2, 6.4 Hz)	38.1	2.97, 2.51 (dd, 18.1, 6.1 Hz; d, 18.1 Hz)	40.1	2.83, 2.37 (dd, 17.7, 5.8 Hz; dt, 17.7, 1.3 Hz)	39.7		160.3
3	4.86	77.9	4.72	77.2	4.86	77.9	4.73	77.4	4.71 (t, 4.6 Hz)	70.0	4.57 (ddt, 4.3, 5.8, 1.3 Hz)	69.5		136.1
4	4.55	77.4	4.54,[d] 4.49	77.3	4.59	77.9	4.47[d]	76.4	4.54, 4.36 (d, 10.3 Hz)	79.8	4.42, 4.22[d] (dd, 10.0, 4.3 Hz; dt, 10.0, 1.2 Hz)	78.9		nd
4a														106.9
5														164.2
6													6.22	101.0
7														167.2
8													6.42	95.9
8a														159.6
1′	4.55	103.9	4.40[e] (d, 7.8 Hz)	104.8	4.58	103.7	4.38[e] (d, 7.8 Hz)	105.1						123.9
2′	3.27	75.6	3.19	75.9	3.27	75.6	3.19	75.9					8.05	133.5
3′	3.49	78.4	3.36	79.2	3.49	78.4	3.36	79.2					6.92	117.5
4′	*f*	*f*	3.29	72.8	*f*	*f*	3.29	72.8						162.8
5′	*f*	*f*	3.29	79.2	*f*	*f*	3.29	79.2					6.92	117.5
6′	*f*	*f*	3.67, 3.88	63.9	*f*	*f*	3.67, 3.88	63.9					8.05	133.5
1″													5.43[g]	102.2
2″													3.74[h]	84.3
3″													3.61	79.0
4″													3.36	
5″													3.20	79.5
6″													3.49, 3.69	63.7
1‴													4.78	106.0
2‴													3.37	76.8
3‴, 4‴, 5‴’													3.41−3.30	
6‴													3.69, 3.80	63.5

[a]Chemical shifts refer to sucrose 1-H at 5.40 and 94.8 ppm, respectively. [b]Intact petals. [c]Petals extracted with ethanol (95%). [d]Long-range correlation with C═O. [e]Long-range correlations at 4.40/77.2 and 4.38/77.4 ppm in the HMBC spectrum. [f]Overlapped to β-Glc. [g]Long-range correlations with 136.0 ppm of carbon in the HMBC spectrum. [h]Long-range correlations with 102.2 and 106.0 ppm of carbon in the HMBC spectrum.

J. Agric. Food Chem. 2015, 63, 8439−8444
DOI: 10.1021/acs.jafc.5b03284

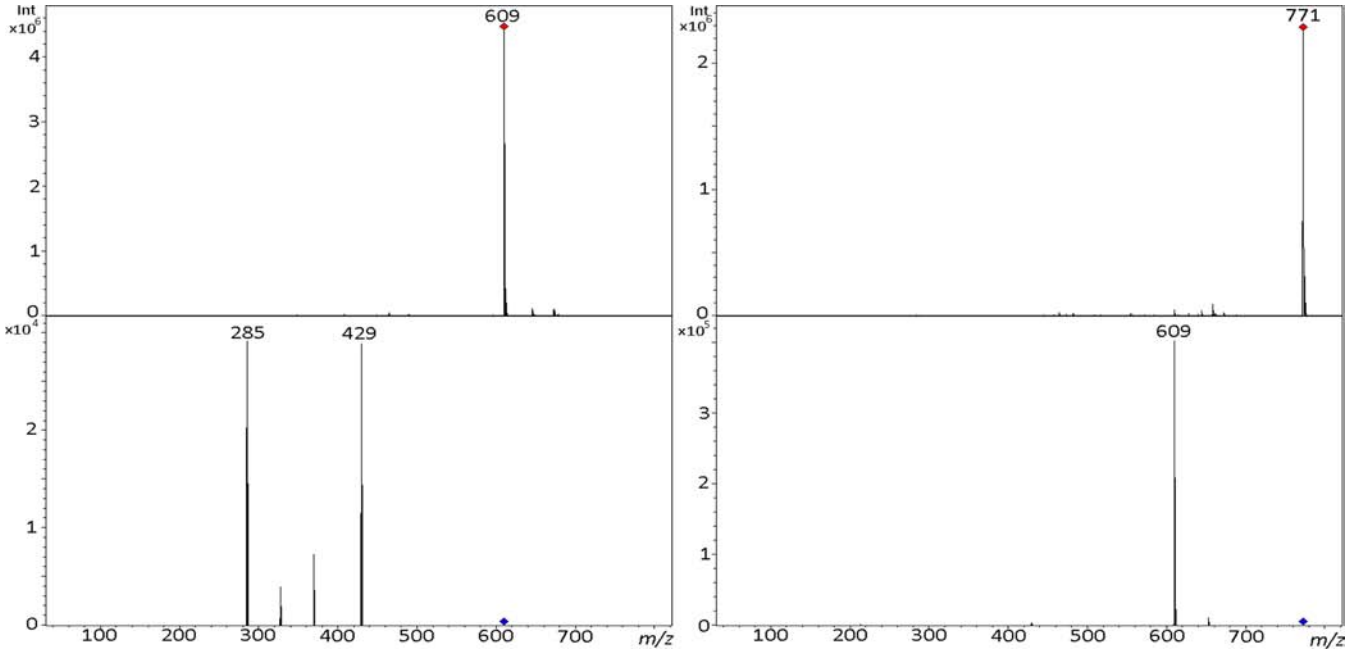

Figure 4. ESI−IT MS/MS spectra of (left) compound **1** and (right) minor kaempferol derivative.

to sucrose (Suc), glucose (Glc), and fructose (Fru), as can be better seen observing HSQC correlations (Figure 3). Apart from those sugars, other resonances as a result of compounds **2**−**4** are detected and assigned, through 2D experiments, as reported in Table 1. The chemical shifts determined by us on intact petals were parallel to those reported in pyridine-d_5 by Zhang et al.[20] Remarkably, even 2D NMR spectra did not highlight signals from kaempferol or its derivatives in the aromatic region, meaning that, in the cell environment of fresh petals, these molecules are not freely tumbling but are probably associated with rigid structures within the cell. Other minor resonances were confirmed to derive from free amino acids (mainly alanine, Ala, glutamine, Gln, and valine, Val).

The molar ratio of total **2**−**4** derivatives relative to the water signal, estimated through deconvolution of 2-H signals of compounds **2**−**4** at 2.8−2.5 ppm and H_2O at 4.97 ppm in the not presaturated ^{1}H NMR spectrum, resulted in around 0.3 mol %. It can be roughly converted to 0.8% in weight with respect to water and then, considering 75% water in petals, to 0.6% of compounds **2**−**4** in intact petals.

Fresh petals were then extracted rapidly with 95% ethanol; the vacuum-evaporated residue was solubilized in D_2O; and 1D and 2D NMR and ESI MS/MS spectra were acquired.

The ^{1}H NMR spectrum of the extract is reported in Figure 2b, and it clearly displays signals in the aromatic region that compare well to those reported by Wolfram et al.[23] and were assigned, together with other resonances in the carbohydrate region, to kaempferol 3-*O*-sophoroside (**1**; Table 1) and to a minor derivative that differs mainly for the 2′,6′-H signals that are found at 8.09 ppm, 8-H at 6.78 ppm (d, 2.2 Hz), 6-H at 6.50 ppm (d, 2.2 Hz), and 1-H_{Glc} at 5.48 ppm (d, 7.6 Hz) and could be a 7-substituted derivative of compound **1**.

Apart from differences in the chemical shifts, as a result of a change from the cell environment to D_2O solution, resonances from compounds **2**−**4** were also detected in the ethanol extract, even though in a ratio different with respect to that observed in intact petals: the (**2** + **3**)/**4** molar ratio passes from 2.5:1 in intact petals to less that 1:1 in the extracts, and at the same time, the free glucose signals enhance with respect to those of sucrose (1-$H_{\alpha\text{-Glc}}$/1-H_{suc} passes from 0.4 to 1.2). Hence, the extraction process, even though carried out rapidly and without acidic conditions, promoted hydrolysis of compounds **2** and **3** to compound **4** and free Glc.

ESI−IT MS was finally employed to confirm the presence of compound **1** and to clarify the structure of the minor flavonol detected in the ethanol extract (Figure 4). The two major peaks detected in negative mode correspond to *m*/*z* 609 and 771 $[M - H]^-$ pseudo-molecular ions. The collision-induced dissociation (CID) with He gas of *m*/*z* 609 (highest) peak gave *m*/*z* 429 $[M - C_6H_{12}O_6 - H]^-$ and *m*/*z* 285 $[\text{kaempferol} - H]^-$ as expected for two subsequent hexose losses starting from compound **1**. On the other hand, CID of *m*/*z* 771 gave *m*/*z* 609, corresponding to a loss of $C_6H_{10}O_5$, demonstrating that this derivative contains a further hexose unit. Minor peaks, corresponding to pseudo-molecular species of *m*/*z* 625 (which decomposes to *m*/*z* 463 through hexose loss) and *m*/*z* 651 (which gives *m*/*z* 471 and 285 under CID), were also detected. The former could be due to quercetin sophoroside, and the latter is probably an acetylated derivative.

In conclusion, this work shows that HR-MAS NMR can be employed to monitor bioactive compounds freely tumbling in the cell environment, directly on intact petals. HR-MAS NMR allows for detection of the presence of compounds **2**, **3**, and **4** directly on intact *C. sativus* petals, without the need of extraction processes. Their content was estimated by HR-MAS NMR to be roughly 0.6%. HR-MAS NMR does not detect instead flavonols, especially compound **1**, that are still contained in petals in a not negligible amount, as demonstrated by ^{1}H NMR analysis of the ethanol extract. This implies that flavonol derivatives in saffron petals have low tumbling rates, which could be due to their close association to macromolecular species in cell walls.[24]

The 3-hydroxybutyrolactone derivatives **2**−**4** contained in *C. sativus* petals are biologically active species that, together with compound **1**, probably contribute to confer hepatoprotective, antihyperglycemic, anti-inflammatory, and other effects to petal

DOI: 10.1021/acs.jafc.5b03284
J. Agric. Food Chem. 2015, 63, 8439−8444

extracts. The extraction process leads to partial hydrolysis of petal constituents; hence, it could be useful to evaluate the direct employment of saffron petals for phytopharmaceutical and nutraceutical purposes, to better exploit a waste product of massive production of commercial saffron.

The data presented in this study strongly support the idea that petals of *C. sativus* are not a waste but can be used for their biological activity in specific foods as well as in herbalist products. This can have a major impact for the community of saffron, the cultivation of which represents an opportunity to improve and develop the economy of the agricultural sector in poor European regions. The exploitation of not only stigmas but also petals as raw material for health-enhancing products would further enhance the economical value of this activity and reduce waste production.

AUTHOR INFORMATION

Corresponding Author

*Telephone: 00390592058636. E-mail: adele.mucci@unimore.it.

Notes

The authors declare no competing financial interest.

ACKNOWLEDGMENTS

The authors are very grateful to Prof. Dario Iarossi and the "Vigna di More" farm, located in Tione degli Abruzzi, for the supply of *C. sativus* petals (http://www.valleaterno.it/vignadimore/).

REFERENCES

(1) Winterhalter, P.; Straubinger, M. Saffron: Renewed interest in an ancient spice. *Food Rev. Int.* **2000**, *16*, 39−59.

(2) Montoro, P.; Tuberoso, C. I. G.; Maldini, M.; Cabras, P.; Pizza, C. Qualitative Profile and Quantitative Determination of Flavonoids from *Crocus sativus* L. Petals by LC-MS/MS. *Nat. Prod. Commun.* **2008**, *3*, 2013−2016.

(3) Zeka, K.; Ruparelia, K. C.; Continenza, M. A.; Stagos, D.; Vegliò, F.; Arroo, R. R. J. Petals of Crocus sativus L. as a potential source of the antioxidants crocin and kaempferol. *Fitoterapia* **2015**.

(4) Omidi, A.; Riahinia, N.; Montazer Torbati, M. B.; Behdani, M. A. Hepatoprotective effect of *Crocus sativus* (saffron) petals extract against acetaminophen toxicity in male Wistar rats. *J. Phytomed.* **2014**, *4*, 330−336.

(5) Vijaya Bhargava, K. Medicinal Uses and Pharmacological Properties of *Crocus sativus* Linn. (Saffron). *Int. J. Pharm. Pharm. Sci.* **2011**, *3*, 22−26.

(6) Hadizadeh, F.; Khalilia, N.; Hosseinzadeh, H.; Khair-Aldine, R. Kaempferol from Saffron Petals. *Iran. J. Pharm. Res.* **2003**, 251−252.

(7) Kubo, I.; Kinst-Hori, I. Flavonols from Saffron Flower: Tyrosinase Inhibitory Activity and Inhibition Mechanism. *J. Agric. Food Chem.* **1999**, *47*, 4121−4125.

(8) Yoon, H.-R.; Han, H.-G.; Paik, Y.-S. Flavonoid glycosides with antioxidant activity from the petals of *Carthamus tinctorius*. *J. Appl. Biol. Chem.* **2007**, *50*, 175−178.

(9) Kim, T. H.; Ku, S.-K.; Lee, I.-C.; Bae, J.-S. Anti-inflammatory effects of kaempferol-3-*O*-sophoroside in human endothelial cells. *Inflammation Res.* **2012**, *61*, 217−224.

(10) Gao, W. Y.; Li, Y. M.; Zhu, D. Y. Phenolic glucosides and a γ-lactone glucoside from the sprouts of *Crocus sativus*. *Planta Med.* **1999**, *65*, 425−427.

(11) Ito, A.; Kasai, R.; Yamasaki, K.; Sugimoto, H. Aliphatic and aromatic glucosides from *Anoectochilus koshunensis*. *Phytochemistry* **1993**, *33*, 1133−1137.

(12) Du, X. M.; Yoshizawa, T.; Shoyama, Y. Butanoic acid glucoside composition of whole body and in vitro plantlets of *Anoectochilus formosanus*. *Phytochemistry* **1998**, *49*, 1925−1928.

(13) Zhang, Y.; Cai, J.; Ruan, H.; Pi, H.; Wu, J. Antihyperglycemic activity of kinsenoside, a high yielding constituent from *Anoectochilus roxburghii* in streptozotocin diabetic rats. *J. Ethnopharmacol.* **2007**, *114*, 141−145.

(14) Du, X. M.; Sun, N. Y.; Chen, Y.; Irino, N.; Shoyama, Y. Hepatoprotective aliphatic glycosides from three Goodyera species. *Biol. Pharm. Bull.* **2000**, *23*, 731−734.

(15) Wu, J.-B.; Lin, W.-L.; Hsieh, C.-C.; Ho, H.-Y.; Tsay, H.-S.; Lin, W.-C. The hepatoprotective activity of kinsenoside from Anoectochilus formosanus. *Phytother. Res.* **2007**, *21*, 58−61.

(16) Hsiao, H. B.; Wu, J. B.; Lin, H.; Lin, W. C. Kinsenoside isolation from *Anoectochilus formosanus* suppresses LPS-stimulated inflammatory reactions inmacrophages and endotoxin shock in mice. *Shock* **2011**, *35*, 184−190.

(17) Du, X.-M.; Sun, N.-Y.; Tamura, T.; Mohri, A.; Sugiura, M.; Yoshizawa, T.; Irino, N.; Hayashi, J.; Shoyama, Y. Higher yielding isolation of kinsenoside in *Anoectochilus* and its antihyperliposis effect. *Biol. Pharm. Bull.* **2001**, *24*, 65−69.

(18) Liu, Z.-L.; Liu, Q.; Xiao, B.; Zhou, J.; Zhang, J.-G.; Li, Y. The vascular protective properties of kinsenoside isolated from *Anoectochilus roxburghii* under high glucose condition. *Fitoterapia* **2013**, *86*, 163−170.

(19) Hsiao, H. B.; Lin, H.; Wu, J. B.; Lin, W. C. Kinsenoside prevents ovariectomy-induced bone loss and suppresses osteoclastogenesis by regulating classical NF-κB pathways. *Osteoporosis Int.* **2013**, *24*, 1663−1676.

(20) Zhang, Y.; Xia, Y.; Lai, Y.; Tang, F.; Luo, Z.; Xue, Y.; Yao, G.; Zhang, Y.; Zhang, J. Antihyperglycemic activity of kinsenoside, a high yielding constituent from *Anoectochilus roxburghii* in streptozotocin diabetic rats. *Molecules* **2014**, *19*, 16950−16958.

(21) Righi, V.; Schenetti, L.; Mucci, A. A new NMR technique: HR-MAS applied to animal and vegetable soft materials. In *New Trends in Analytical, Environmental and Cultural Heritage Chemistry*; Colombini, M. P., Tassi, L., Eds.; Transworld Research Network: Trivandrum, India, 2008; pp 31−42.

(22) Marino, G.; Righi, V.; Simoni, A.; Schenetti, L.; Mucci, A.; Tugnoli, V.; Muzzi, E.; Francioso, O. Effect of a Peat Humic Acid on Morphogenesis in Leaf Explants of *Pyrus communis* and *Cydonia oblonga*. Metabolomic Analysis at an Early Stage of Regeneration. *J. Agric. Food Chem.* **2013**, *61*, 4979−4987.

(23) Wolfram, K.; Schmidt, J.; Wray, V.; Milkowski, C.; Schliemann, W.; Strack, D. Profiling of phenylpropanoids in transgenic low-sinapine oilseed rape (*Brassica napus*). *Phytochemistry* **2010**, *71*, 1076−1084.

(24) Hutzler, P.; Fischbach, R.; Heller, W.; Jungblut, T. P.; Reuber, S.; Schmitz, R.; Veit, M.; Weissenböck, G.; Schnitzler, J.-P. Tissue localization of phenolic compounds in plants by confocal laser scanning microscopy. *J. Exp. Bot.* **1998**, *49*, 953−965.

DOI: 10.1021/acs.jafc.5b03284
J. Agric. Food Chem. 2015, 63, 8439−8444

sulfate, 50 ppm) at 25 °C in the dark. After 90 h of incubation, the monocolonies on the surface of the plates were transferred onto KMV^+ medium several times to purify the strains. These isolated strains were kept on a KMV^+ medium (without antibiotics) as monoclonal cultures, and then we determined their squalene content using gas chromatography.

Molecular and Phylogenetic Analyses. The genomic DNA of selected strains was extracted using a Universal Genomic DNA extraction kit (Takara DV811A, Dalian, China), according to the protocol of the manufacturer. The internal transcribed spacer (ITS) region was amplified using the ITS4 primer P1 (5′-TCCTCCGCTTATTGATATGC-3′) and the ITS5 primer P2 (5′-GGAAGTAAAAGTCGTAACAAGG-3′). The polymerase chain reaction (PCR) products were visualized by agarose gel electrophoresis and purified using the TIANgel Midi Purification Kit (TIANGEN DP209, Beijing, China). The purified PCR products were cloned into the pGEM-T Easy vector (Promega) and then were sequenced by Takara Co., Ltd.

The resulting sequence data were searched using NCBI BLAST, and the sequences were aligned with the ClustalX program. A phylogenetic tree was inferred using the Minimum Evolution method of MEGA, version 5.0. The tree reliability was evaluated by bootstrap analysis of 1000 replicates.

Strains and Cultivation. Strain SD301 was isolated by the methods mentioned above and cultivated in 50 mL of GPY medium (6% glucose, 1% peptone, and 1% yeast extract) containing 1.5% artificial sea salt in a 250 mL flask shaken at 200 rpm and 25 °C.

Optimization of Culture Conditions. To investigate the effects of various cultivation media, eight carbon sources (6% of glucose, D-fructose, D-xylose, maltose, sucrose, lactose, glycerol, and starch) and seven nitrogen sources (2% of yeast extract, peptone, tryptone, urea, ammonium sulfate, sodium glutamate, and sodium nitrate) were tested. Tryptone (2%) was used as the nitrogen source for the carbon source testing, while glucose (6%) was consistently used as the carbon source when the nitrogen source testing was carried out. To investigate the C/N ratio effect on the cell growth and squalene yield of strain SD301, the constant concentration of the C source of 6% and various N source concentrations were used.

The effects of varying concentrations (0−60 g L^{-1}) of sea salt were also studied using the optimized medium. To examine the effects of various growth parameters, various pH values (pH 4.0, 5.0, 6.0, 7.0, 8.0, and 9.0) and different temperatures (15, 20, 25, 30, and 35 °C) were used to cultivate *Pseudozyma* sp. SD301.

All tests were carried out in 250 mL flasks with 50 mL medium shaken at 200 rpm and 25 °C for 5 days.

Batch and Fed-Batch Fermentation Experiments for Squalene Production. A batch fermentation experiment was performed in a 5 L Biostat B plus bioreactor, which was equipped with controllers for pH, temperature, agitation, and dissolved oxygen (DO) concentration. Batch cultures were carried out in 3.5 L of production medium. The temperature was maintained at 25 °C. The agitation speed automatically varied from 300 to 800 rpm at a fixed air flow rate of 1.2 vessel volumes per minute (vvm) to maintain the DO at 20% air saturation. The pH was maintained at 6.0 by adding 2 mol L^{-1} NaOH or 2 mol L^{-1} HCl. To control foam formation, 1 mL of antifoam was added at the beginning of the run. Samples for off-line determination of the glucose concentration, biomass, and squalene yield were withdrawn every 6 h until the end of the fermentation (48 h).

Another fed-batch fermentation experiment was also performed in the 5 L Biostat B plus bioreactor, with the same conditions of the batch fermentation, except that intermittent glucose feeding was supplied to maintain the residual glucose concentration at approximately 5 to 25 g L^{-1} by feeding a 40% (w/v) glucose stock solution. The samples were withdrawn every 10 h until the end of the fermentation (100 h).

The initial fermentation medium contained 60 g L^{-1} glucose and 20 g L^{-1} yeast extract in artificial seawater (artificial sea salt concentration of 15 g L^{-1}). This medium also contained a vitamin solution (2 mL L^{-1}). The vitamin solution was filter-sterilized (0.22 μm) and contained 100 mg/L thiamine, 10 mg/L biotin, and 50 mg/L cyanocobalamin.

Biomass Determination and Glucose Assay. The biomass of *Pseudozyma* sp. SD301 was expressed as DCW. Samples (5 mL) were collected and centrifuged at 7000*g* at 4 °C for 10 min, and they were then freeze-dried to a constant weight at −50 °C for approximately 60 h. The residual glucose in the fermentation medium was analyzed by a biosensor equipped with a glucose oxidase electrode (SBA-40E, Institute of Biology, Shandong Academy of Sciences, Jinan, China).

Observation Using Confocal Laser Scanning Microscopy (CLSM). To investigate the intracellular localization of squalene in *Pseudozyma* sp. SD301, the observation of *in vivo* fluorescence imaging of the cells were carried out using CLSM (FluoView FV1000, Olympus, Tokyo, Japan). First, the cells were dyed by nile red using the method mentioned by Morita et al.[24] In details, 500 μg mL^{-1} nile red was prepared in acetone and stored at 4 °C as the stock solution. Then, the stock solution was added to the culture with a final concentration of 0.1 μg mL^{-1} and incubated at 37 °C for 15 min. Second, the stained cells were observed by CLSM, and the excitation and emission wavelengths were 559 and 612 nm, respectively. The fluorescent images were obtained at 1000× magnification.

Lipid Extraction and Fatty Acid and Squalene Content Analyses. The total lipid content was estimated using a modified miniaturized Bligh−Dyer method.[25] The harvested cells were extracted into 30 mL of chloroform/methanol (2:1, v/v) at room temperature. The lipid extract was dried over anhydrous Na_2SO_4, and the solvent was removed by evaporation.

The total lipid was converted into fatty acid methyl esters (FAMEs), and the fatty acid composition was analyzed using an Agilent 7890-5975 gas chromatography−mass spectrometry (GC−MS) system (Agilent Technologies, Inc., Santa Clara, CA).[26]

Squalene was isolated from the total lipid by saponification,[27] with some modifications. Samples (5 mL, V_1) were freeze-dried and used to extract the total lipid by the methods mentioned above. The extracted total lipid was transferred into 10 mL of 10% KOH−ethanol solution and incubated at 60 °C for 1 h with refluxing for saponification. Then, 4 mL of distilled water was added, and the unsaponifiable compositions were extracted with 2 mL (V_2) of *n*-hexane. Afterward, squalene was separated by Agilent 7890A GC with a 7650A automatic liquid sampler using a HP-5, 30 m × 320 μm × 0.25 μm column; meanwhile, nitrogen was used as a carrier gas. The initial oven temperature was 100 °C and was maintained for 1 min, and then the temperature was raised to 300 °C for 15 °C min^{-1} and, finally, maintained at 300 °C for another minute. Peak detection was performed by a flame ionization detector. The temperature of the injection port and flame ionization port was 300 °C. The injection volume was 1 μL, and the split ratio was 1:10. The squalene concentration (X, μg mL^{-1}) was further quantified using an external standard method. The standard curve (Figure S1) was made from a set of concentrations of commercial squalene standard (>99% squalene, J&K Chemical) by GC analysis. The squalene production (P, g L^{-1}) was calculated by eq 1.

$$P = X\frac{V_2}{V_1} \times 10^{-3} \quad (1)$$

RESULTS AND DISCUSSION

Isolation and Identification of *Pseudozyma* sp. SD301. Samples obtained from a mangrove ecosystem were screened for squalene-producing microorganisms. Almost 100 purified strains were isolated as colonies on the KMV^+ medium plates and microscopically observed. The biomass (DCW) of the strains ranged from 5.29 to 27.61 g L^{-1} when cultivated in the GPY medium, and the squalene contents (percent of DCW) and squalene yields ranged from 0.4 to 5.6% DCW and from 0.1 to 0.9 g L^{-1}, respectively.

Among these tested strains, SD301 showed the highest levels of squalene content and yield. On the basis of morphological

DOI: 10.1021/acs.jafc.5b03539
J. Agric. Food Chem. 2015, 63, 8445−8451

observations, SD301 formed a yeast-like vegetative cell that was ovoid to cylindrical and produced fusiform blastoconidia (Figure 1). These morphological characteristics were common features of the genus *Pseudozyma*.[28] Subsequently, the ITS region of this strain was determined, and SD301 was confirmed to be a *Pseudozyma* strain by phylogenetic analysis using the minimum-evolution (ME) tree (Figure 2). Hence, the newly isolated strain was termed *Pseudozyma* sp. SD301. To find the optimal conditions for squalene production, we further investigated the cell growth and squalene production on various carbon and nitrogen sources and under various temperatures, pH, and osmotic stresses, all of which are necessary for the optimization of the culture conditions.

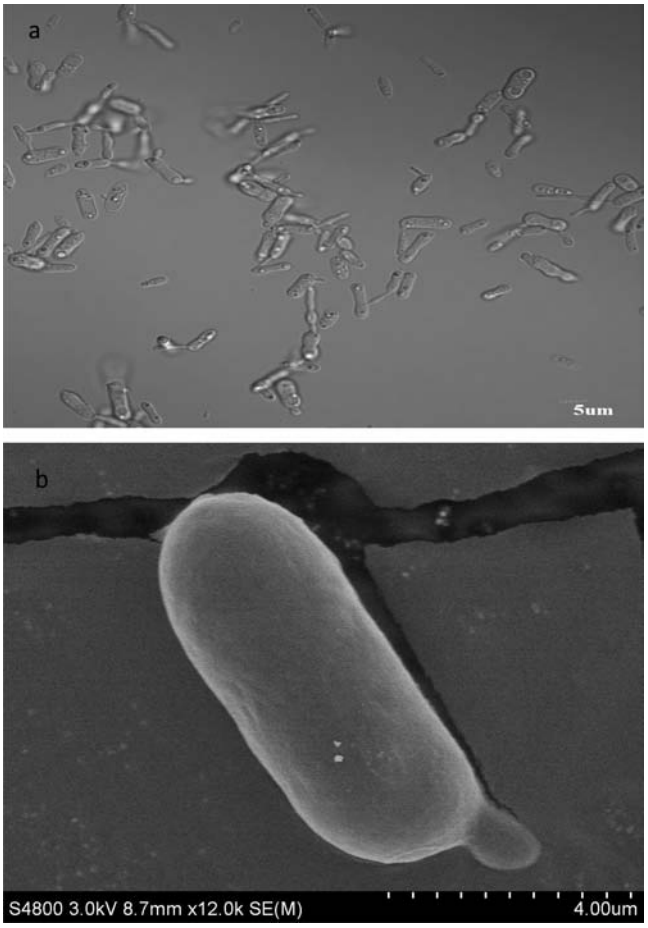

Figure 1. Morphology of *Pseudozyma* sp. SD301 (a, light microscope, 400× magnification; b, scanning electron microscope, 3500× magnification).

Cell Growth and Squalene Production on Various Carbon and Nitrogen Sources. As shown in Figure 3a, glucose, fructose, xylose, maltose, sucrose, starch, glycerol, and lactose were used as carbon sources to investigate the cell growth and squalene yield of *Pseudozyma* sp. SD301. The monosaccharide hexoses, such as glucose and fructose, could be well used by *Pseudozyma* sp. SD301 with a biomass of 24.06 and 19.09 g L^{-1}, respectively, but pentoses (such as xylose) and polysaccharides (e.g., starch) were not efficient substrates for cell growth. Sucrose was a good carbon source for *Pseudozyma* sp. SD301 growth, while maltose, another disaccharide, was not optimal. At the same time, glycerol and lactose were also very suitable for its growth. In contrast, only three carbon sources, glucose, sucrose, and lactose, were fit for optimal squalene production by *Pseudozyma* sp. SD301, with the best squalene yield of 0.79 g L^{-1} (Figure 3a). These results were in agreement with previous data obtained for *Pseudozyma* sp. JCC207.[15]

Peptone, yeast extract, tryptone, urea, sodium glutamate, ammonium sulfate, and sodium nitrate were tested as organic or inorganic nitrogen sources for the growth of *Pseudozyma* sp. SD301 (Figure 3b). When yeast extract was used as a nitrogen source, the highest biomass and squalene production (28.32 and 0.788 g L^{-1}, respectively) were obtained, followed by tryptone, peptone, sodium glutamate, ammonium sulfate, urea, and sodium nitrate. According to our results, organic nitrogen sources, such as yeast extract, tryptone, and peptone, were more suitable for the cell growth and squalene production than inorganic nitrogen sources because these organic nitrogen sources had, in contrast to inorganic nitrogen sources,

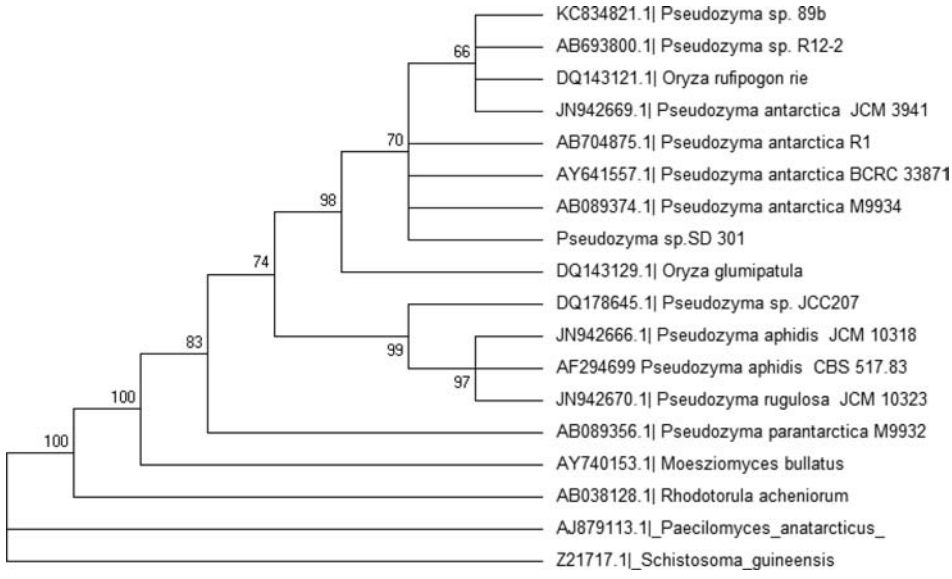

Figure 2. Phylogenetic relationship of *Pseudozyma* species based on the aligned ITS sequences. The tree was constructed using the ME method and 1000 bootstrapped replicates in MEGA5.0.

DOI: 10.1021/acs.jafc.5b03539
J. Agric. Food Chem. 2015, 63, 8445−8451

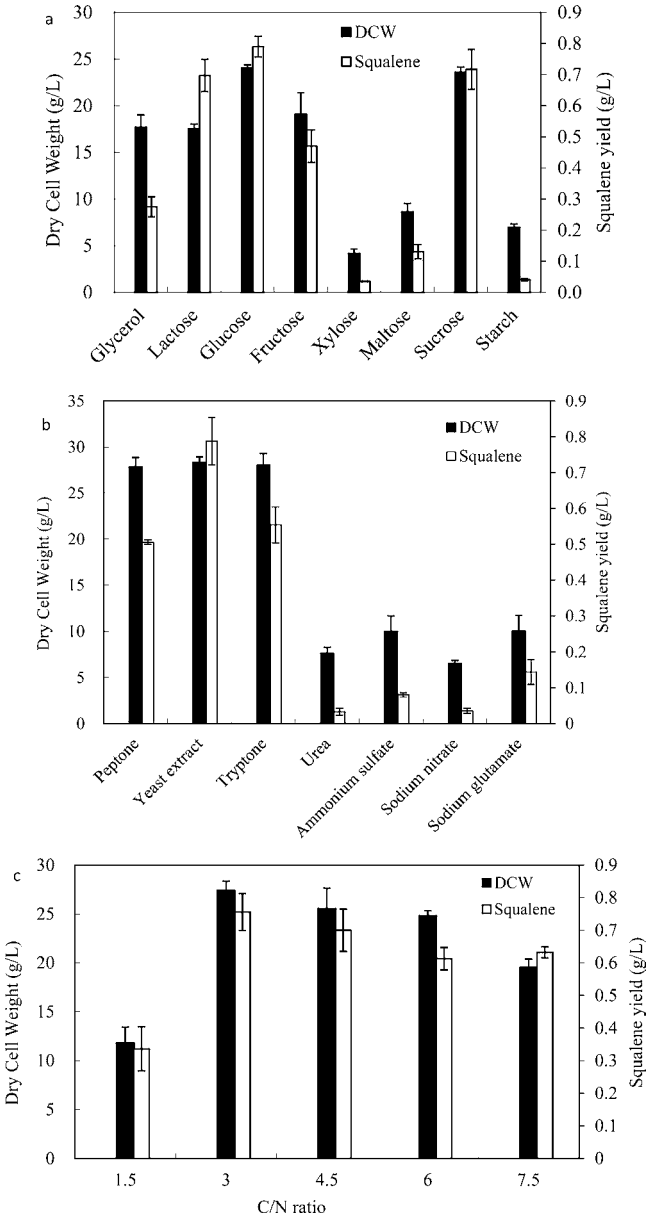

Figure 3. Effects of (a) carbon sources, (b) nitrogen sources, and (c) C/N ratio on the cell growth and squalene yield in *Pseudozyma* sp. SD301.

additional growth factors, such as vitamins and coenzymes, which might be necessary for squalene biosynthesis. These results were slightly different from the results of *Pseudozyma* sp. JCC207,[15] which could also produce squalene with inorganic nitrogen sources.

It is well-known that the C/N ratio of the culture medium dramatically affects the growth of microorganisms. A high C/N ratio is effective for increasing the lipid content in cells.[29] Therefore, the effects of the C/N ratio on the cell growth and squalene yield of strain SD301 were examined (Figure 3c). The cell growth increased to the maximum level by increasing the C/N ratio to 3. The highest squalene yield of 0.756 g L^{-1} was also obtained at this C/N ratio. A further increase of the C/N radio showed a negative effect on both the cell growth and squalene yield. When the C/N ratio reached 7.5, the biomass and squalene production decreased to 19.53 and 0.632 g L^{-1}, respectively. This phenomenon could be explained by the fact that the high C/N ratio might lead to relative nitrogen hunger (or other nutrient hunger, e.g., phosphorus and sulfur), which limits cell growth and increases the biosynthesis of other lipids (such as fatty acids and triglyceride).

Effects of the Sea Salt Concentration and Culture Temperature on Cell Growth. The effects of the sea salt concentration on cell growth and squalene production were examined in a range of 0−6%. *Pseudozyma* sp. SD301 showed a wide salinity tolerance. As shown in Figure 4a, the optimum salt

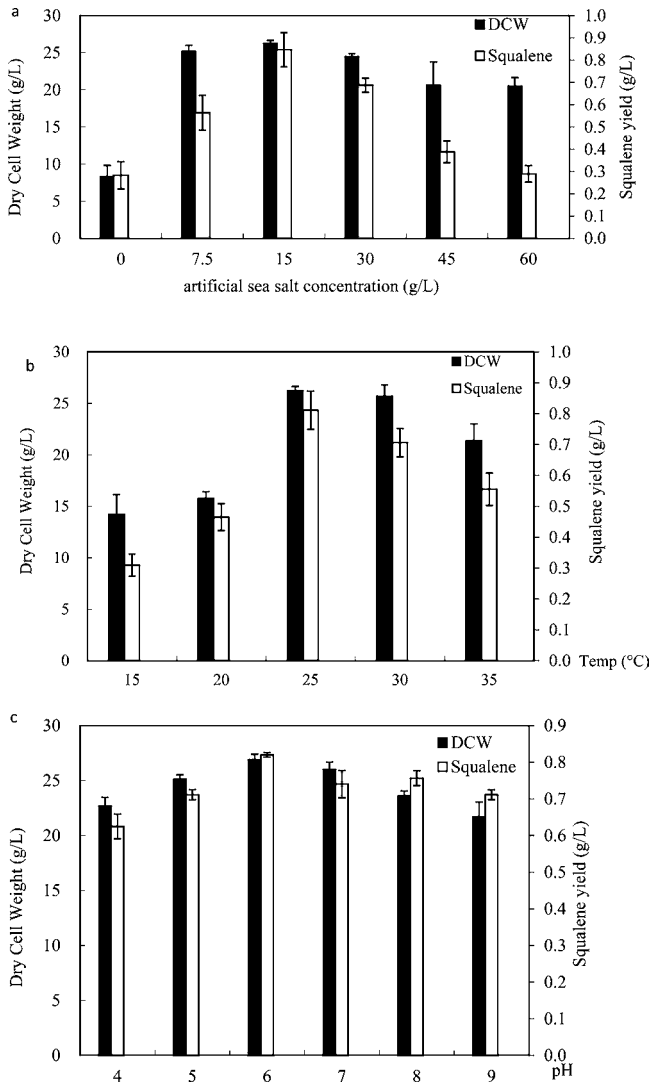

Figure 4. Effect of (a) artificial sea salt concentration, (b) temperature, and (c) initial pH on cell growth and squalene yield in *Pseudozyma* sp. SD301.

concentration was 15 g L^{-1}, with a biomass and squalene yield of 26.25 and 0.847 g L^{-1}, respectively. A slight change in the cell growth was observed in the range of 0.75−3%. Many microorganisms living in the mangrove ecosystem show euryhalinity[30,31] because the salinity of this area often sharply changes as a result of the afflux of fresh water and evaporation.

The effects of the temperature on biomass and squalene yield were tested from 15 to 35 °C. As shown in Figure 4b, there were only slight fluctuations in biomass and squalene yield between the temperatures of 25 and 30 °C. The biomass production was the highest (26.23 g L^{-1}) at 25 °C. However, when the temperature was raised to 35 °C, the biomass

DOI: 10.1021/acs.jafc.5b03539
J. Agric. Food Chem. 2015, 63, 8445−8451

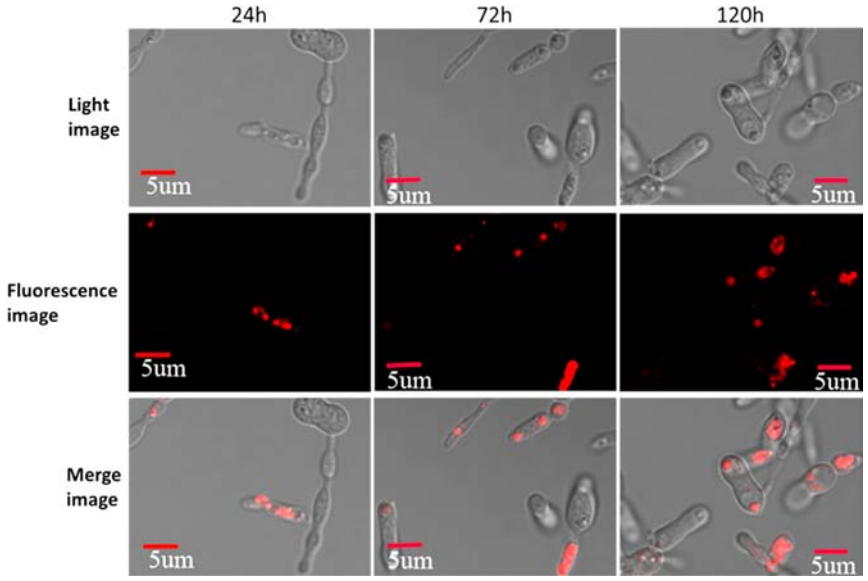

Figure 5. Observation of *Pseudozyma* sp. SD301 using CLSM for locating the lipid droplets and squalene accumulation during cultivation.

decreased to 21.37 g L^{-1} and the squalene yield also decreased significantly, from 0.811 g L^{-1} at 25 °C to 0.555 g L^{-1} at 35 °C. The variation in squalene yields may be the result of the biosynthesis of ergosterol and steroids, which are vital structural and regulatory components in eukaryotic cells.

Effects of Initial pH on Cell Growth. Because the pH value of the medium profoundly affects cell membrane functions, cell metabolism, and the uptake of nutrients and product biosynthesis, the initial pH values of the medium tested in this study ranged from 4.0 to 9.0. The results showed that strain SD301 had a wide adaptability of initial pH (4.0−9.0) for growth and squalene accumulation (Figure 4c). The variation of biomass and squalene yields in the tested pH ranges ranged from 21.70 g L^{-1} (pH 9.0) to 26.90 g L^{-1} (pH 6.0) and from 0.625 g L^{-1} (pH 4.0) to 0.820 g L^{-1} (pH 6.0), respectively. The optimal pH for biomass and squalene yield was 6.0. The wide pH adaptability of *Pseudozyma* sp. SD301 may due to its adaptation to the mangrove ecosystem, in which the pH is constantly changing with tidal actions.

Microscopic Observation and the Fatty Acid Composition of *Pseudozyma* sp. SD301. From the fluorescence imaging of the cells (Figure 5), the lipid droplets containing squalene were distinctly observed at the both ends of the cells and were accumulated along with the cell growth. This phenomenon was coincident with that in *Saccharomyces cerevisiae*.[16,17] The fatty acid composition of SD301 was shown in Table 1, and the main ingredients were the fatty acids with 16 or 18 carbons, such as C16:0, C18:0, C18:1, and C18:2. Along with the cell growth, the content of saturated fatty acids in cells decreased and the content of unsaturated fatty acids reached up to over 51%.

Table 1. Fatty Acid Profiles of *Pseudozyma* sp. SD301

	content (% TFA)		
fatty acid	24 h	72 h	120 h
C14:0	2.03	1.57	1.34
C16:0	30.06	26.46	24.89
C16:1	2.32	2.09	1.45
C17:0	2.44	2.77	1.51
C18:0	24.12	20.99	15.97
C18:1	23.21	29.22	35.94
C18:2	13.87	14.58	16.74
C20:0	1.83	2.28	2.14

Batch and Fed-Batch Fermentation Experiments for Squalene Production. Using the optimized culture conditions described above, the biomass, squalene production, and glucose consumption were examined during batch and fed-batch cultivation.

Glucose was exhausted after 42 h of batch fermentation, reaching the highest biomass and squalene production of 30.24 and 1.649 g L^{-1}, respectively (Figure 6a). The conversion rate from glucose to biomass was approximately 50.4%, and the squalene productivity reached 0.039 g L^{-1} h^{-1}. In contrast, for the fed-batch fermentation, a total glucose concentration of 143 g L^{-1} was consumed and the maximum DCW was 71.53 g L^{-1} with a squalene yield of 2.445 g L^{-1} at 80 h (Figure 6b). In comparison to the batch fermentation, both the glucose conversion rate and the squalene productivity were slightly decreased. This result might be caused by the increasing C/N ratio during glucose feeding, which could influence cell growth and increase fatty acid and triglyceride biosynthesis.

Some strains of *Aurantiochytrium* (*Schizochytrium* or *Thraustochytrium*) were used to produce squalene with the final yield of approximately 1 g during 96 h of fermentation. In comparison to these strains, *Pseudozyma* sp. SD301 had superior squalene productivity and higher squalene yield (Table 2). The squalene yield of 2.445 g L^{-1} by *Pseudozyma* sp. SD301 was 2 times greater than the reported highest yield of *Aurantiochytrium* sp. 18W-13a (1.29 g L^{-1}), and the squalene productivity was approximately 3 times higher than that of *Aurantiochytrium* strains.

In summary, this study characterized a newly isolated yeast-like strain, *Pseudozyma* sp. SD301, which is a promising candidate for commercial squalene production. The results illustrated that the optimized medium for squalene production should contain 60 g L^{-1} glucose, 20 g L^{-1} yeast extract, and 15 g L^{-1} artificial sea salt concentration, with the appropriate cultivation conditions of pH 6.0 and 25 °C.

DOI: 10.1021/acs.jafc.5b03539
J. Agric. Food Chem. 2015, 63, 8445−8451

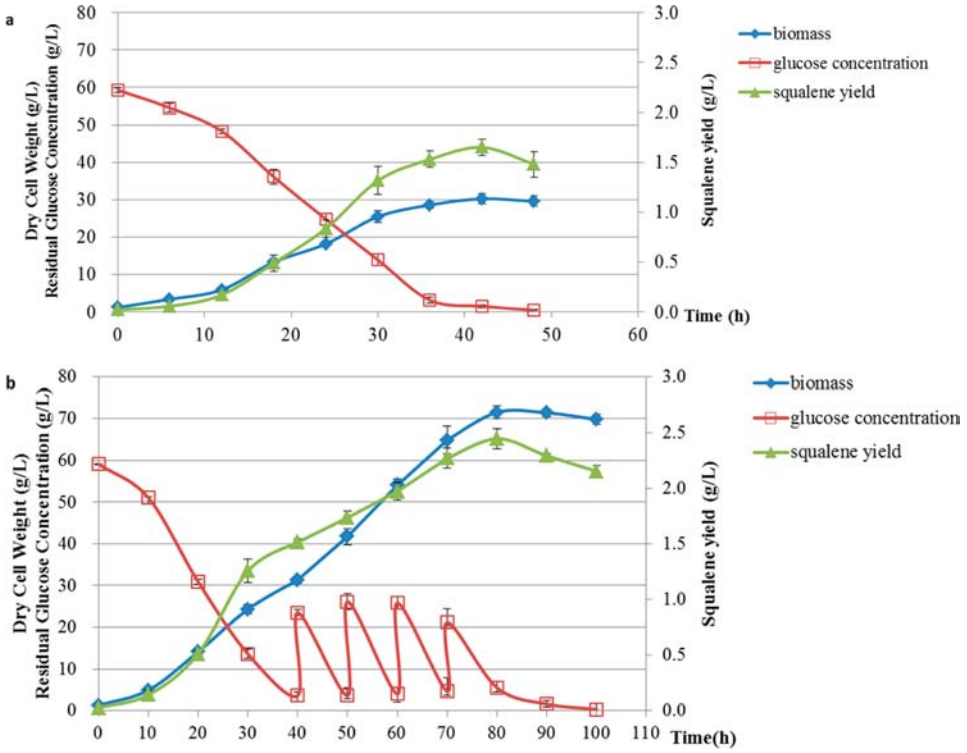

Figure 6. Fermentation experiments of *Pseudozyma* sp. SD301 in a 5 L bioreactor: (a) batch fermentation experiment and (b) fed-batch fermentation experiment: (open squares) residual glucose, (closed diamonds) biomass, and (closed triangles) squalene yield.

Table 2. Comparison of the Squalene Yield by the Strains Mentioned in This Study

strain	squalene yield ($g\ L^{-1}$)	squalene productivity ($g\ L^{-1}\ h^{-1}$)	reference
Aurantiochytrium sp. 18W-13a (2011)	1.29	0.014	20
Aurantiochytrium sp. 18W-13a (2012)	0.9		21
Thraustochytrium (2013)	≈1	0.012	22
Schizochytrium mangrovei PQ6 (2014)	0.992−1.019	0.011	23
Pseudozyma sp. JCC207 (2008)	0.341	0.004	15
Pseudozyma sp. SD301	2.445	0.039	this study

■ ASSOCIATED CONTENT

Supporting Information

The Supporting Information is available free of charge on the ACS Publications website at DOI: 10.1021/acs.jafc.5b03539.

Standard curve of squalene concentrations (Figure S1) (PDF)

■ AUTHOR INFORMATION

Corresponding Authors

*Telephone: +86-532-80662705. Fax: +86-532-80662707. E-mail: songxj@qibebt.ac.cn.
*Telephone: +86-532-80662706. Fax: +86-532-80662707. E-mail: cuiqiu@qibebt.ac.cn.

Funding

This work was financially supported by the National Natural Science Foundation of China (41306132) and the National High Technology Research and Development Program of China (863 Program, 2014AA021701).

Notes

The authors declare no competing financial interest.

■ REFERENCES

(1) Smith, T. J. Squalene: potential chemopreventive agent. *Expert Opin. Invest. Drugs* **2000**, *9*, 1841−1848.
(2) Amarowicz, R. Squalene: A natural antioxidant? *Eur. J. Lipid Sci. Technol.* **2009**, *111*, 411−412.
(3) Spanova, M.; Daum, G. Squalene − biochemistry, molecular biology, process biotechnology, and applications. Eur. *Eur. J. Lipid Sci. Technol.* **2011**, *113*, 1299−1320.
(4) Rao, C. V.; Newmark, H. L.; Reddy, B. S. Chemopreventive effect of squalene on colon cancer. *Carcinogenesis* **1998**, *19*, 287−290.
(5) Smith, T. J.; Yang, G. Y.; Seril, D. N.; Liao, J.; Kim, S. Inhibition of 4-(methylnitrosamino)-1-(3-pyridyl)-1-butanone-induced lung tumorigenesis by dietary olive oil and squalene. *Carcinogenesis* **1998**, *19*, 703−706.
(6) Storm, H. M.; Oh, S. Y.; Kimler, B. F.; Norton, S. Radioprotection of mice by dietary squalene. *Lipids* **1993**, *28*, 555−559.
(7) Aguilera, Y.; Dorado, M. E.; Prada, F. A.; Martinez, J. J.; Quesada, A.; Ruiz-Gutierrez, V. The protective role of squalene in alcohol damage in the chick embryo retina. *Exp. Eye Res.* **2005**, *80*, 535−543.
(8) Chan, P.; Tomlinson, B.; Lee, C. B.; Lee, Y. S. Effectiveness and safety of low-dose pravastatin and squalene, alone and in combination, in elderly patients with hypercholesterolemia. *J. Clin. Pharmacol.* **1996**, *36*, 422−427.
(9) Newmark, H. L. Squalene, olive oil, and cancer risk - review and hypothesis. *Ann. N. Y. Acad. Sci.* **1999**, *889*, 193−203.

DOI: 10.1021/acs.jafc.5b03539
J. Agric. Food Chem. 2015, 63, 8445−8451

(10) Pietsch, A.; Jaeger, P. Concentration of squalene from shark liver oil by short-path distillation. *Eur. J. Lipid Sci. Technol.* **2007**, *109*, 1077−1082.
(11) He, H. P.; Corke, H. Oil and squalene in amaranthus grain and leaf. *J. Agric. Food Chem.* **2003**, *51*, 7913−7920.
(12) García-González, D. L.; Aparicio-Ruiz, R.; Aparicio, R. Virgin olive oil - Chemical implications on quality and health. *Eur. J. Lipid Sci. Technol.* **2008**, *110*, 602−607.
(13) Storelli, M. M.; Ceci, E.; Storelli, A.; Marcotrigiano, G. O. Polychlorinated biphenyl, heavy metal and methylmercury residues in hammerhead sharks: contaminant status and assessment. *Mar. Pollut. Bull.* **2003**, *46*, 1035−1039.
(14) Turoczy, N. J.; Laurenson, L. J.; Allinson, G.; Nishikawa, M.; Lambert, D. F.; Smith, C.; Cottier, J. P.; Irvine, S. B.; Stagnitti, F. Observations on metal concentrations in three species of shark (*Deania calcea*, *Centroscymnus crepidater*, and *Centroscymnus owstoni*) from southeastern Australian waters. *J. Agric. Food Chem.* **2000**, *48*, 4357−4364.
(15) Chang, M. H.; Kim, H. J.; Jahng, K. Y.; Hong, S. C. The isolation and characterization of *Pseudozyma* sp. JCC 207, a novel producer of squalene. *Appl. Microbiol. Biotechnol.* **2008**, *78*, 963−972.
(16) Garaiova, M.; Zambojova, V.; Simova, Z.; Griac, P.; Hapala, I. Squalene epoxidase as a target for manipulation of squalene levels in the yeast *Saccharomyces cerevisiae*. *FEMS Yeast Res.* **2014**, *14*, 310−323.
(17) Mantzouridou, F.; Naziri, E.; Tsimidou, M. Z. Squalene versus ergosterol formation using *Saccharomyces cerevisiae*: combined effect of oxygen supply, inoculum size, and fermentation time on yield and selectivity of the bioprocess. *J. Agric. Food Chem.* **2009**, *57*, 6189−6198.
(18) Fan, K. W.; Aki, T.; Chen, F.; Jiang, Y. Enhanced production of squalene in the thraustochytrid *Aurantiochytrium mangrovei* by medium optimization and treatment with terbinafine. *World J. Microbiol. Biotechnol.* **2010**, *26*, 1303−1309.
(19) Chen, G.; Fan, K. W.; Lu, F. P.; Li, Q.; Aki, T.; Chen, F.; Jiang, Y. Optimization of nitrogen source for enhanced production of squalene from thraustochytrid *Aurantiochytrium* sp. *New Biotechnol.* **2010**, *27*, 382−389.
(20) Kaya, K.; Nakazawa, A.; Matsuura, H.; Honda, D.; Inouye, I.; Watanabe, M. M. Thraustochytrid *Aurantiochytrium* sp. 18W-13a Accummulates High Amounts of Squalene. *Biosci., Biotechnol., Biochem.* **2011**, *75*, 2246−2248.
(21) Nakazawa, A.; Matsuura, H.; Kose, R.; Kato, S.; Honda, D.; Inouye, I.; Kaya, K.; Watanabe, M. M. Optimization of culture conditions of the thraustochytrid *Aurantiochytrium* sp. strain 18W-13a for squalene production. *Bioresour. Technol.* **2012**, *109*, 287−291.
(22) Nakazawa, A.; Kokubun, Y.; Matsuura, H.; Yonezawa, N.; Kose, R.; Yoshida, M.; Tanabe, Y.; Kusuda, E.; Van Thang, D.; Ueda, M.; Honda, D.; Mahakhant, A.; Kaya, K.; Watanabe, M. M. TLC screening of thraustochytrid strains for squalene production. *J. Appl. Phycol.* **2014**, *26*, 29−41.
(23) Hoang, M. H.; Ha, N. C.; Thom, L. T.; Tam, L. T.; Anh, H. T.; Thu, N. T.; Hong, D. D. Extraction of squalene as value-added product from the residual biomass of *Schizochytrium mangrovei* PQ6 during biodiesel producing process. *J. Biosci. Bioeng.* **2014**, *118*, 632−639.
(24) Morita, T.; Konishi, M.; Fukuoka, T.; Imura, T.; Kitamoto, D. Physiological differences in the formation of the glycolipid biosurfactants, mannosylerythritol lipids, between *Pseudozyma antarctica* and *Pseudozyma aphidis*. *Appl. Microbiol. Biotechnol.* **2007**, *74*, 307−315.
(25) Bligh, E. G.; Dyer, W. J. A rapid method of total lipid extraction and purification. *Can. J. Biochem. Physiol.* **1959**, *37*, 911−917.
(26) Xiao, Y.; Zhang, J.; Cui, J.; Feng, Y.; Cui, Q. Metabolic profiles of *Nannochloropsis oceanica* IMET1 under nitrogen-deficiency stress. *Bioresour. Technol.* **2013**, *130*, 731−738.
(27) Dhara, R.; Bhattacharyya, D. K.; Ghosh, M. Analysis of sterol and other components present in unsaponifiable matters of mahua, sal and mango kernel oil. *J. Oleo Sci.* **2010**, *59*, 169−176.
(28) Boekhout, T. PseudozymaBandoni emend. Boekhout, a genus for yeast-like anamorphs of Ustilaginales. *J. Gen. Appl. Microbiol.* **1995**, *41*, 359−366.
(29) Converti, A.; Casazza, A. A.; Ortiz, E. Y.; Perego, P.; Del Borghi, M. Effect of temperature and nitrogen concentration on the growth and lipid content of *Nannochloropsis oculata* and *Chlorella vulgaris* for biodiesel production. *Chem. Eng. Process.* **2009**, *48*, 1146−1151.
(30) Gao, M.; Song, X. J.; Feng, Y. G.; Li, W. L.; Cui, Q. Isolation and characterization of Aurantiochytrium species: high docosahexaenoic acid (DHA) production by the newly isolated microalga, *Aurantiochytrium* sp SD116. *J. Oleo Sci.* **2013**, *62*, 143−151.
(31) Yokochi, T.; Honda, D.; Higashihara, T.; Nakahara, T. Optimization of docosahexaenoic acid production by *Schizochytrium limacinum* SR21. *Appl. Microbiol. Biotechnol.* **1998**, *49*, 72−76.

DOI: 10.1021/acs.jafc.5b03539
J. Agric. Food Chem. 2015, 63, 8445−8451

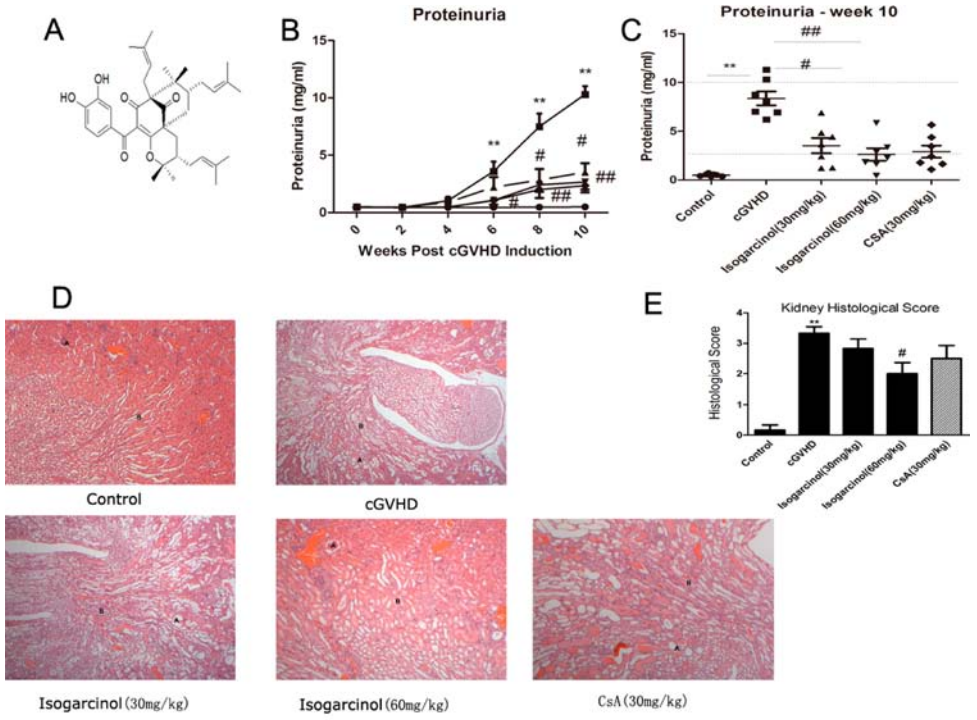

20

Figure 1. Isogarcinol decreased proteinuria and reduced the histopathological changes caused by cGVHD. Chronic GVHD mouse model was induced as mentioned in Materials and Methods. Mice were placed in metabolic cages for urine collection and proteinuria was measured using the Bradford assay. Mice were sacrificed at week 10 to evaluate the histological scores in the kidney with H&E stain. (A) Chemical structure of isogarcinol. (B) Proteinuria during the development of cGVHD. (C) Isogarcinol reduced proteinuria at week 10. (D) Renal histopathology in different groups at week 10. A, glomerulus, and B, tubules. (E) Isogarcinol lowered the histological score in the kidneys. **, $p < 0.01$ versus control; #, $p < 0.05$ versus cGVHD.

allogeneic skin transplantation.[19] In addition, isogarcinol showed a desirable effect on rheumatoid arthritis and its anti-inflammatory effect has also been reported.[20] Furthermore, isogarcinol had lower toxicity on liver and kidney function than did CsA in experimental animals.[19,20] On the basis of our previous study, we hypothesized that isogarcinol can inhibit the stimulation of CD4 T cells and exhibit an anti-inflammatory effect in the cGVHD mouse model, and we aimed both to determine whether orally administered isogarcinol could be a novel and effective agent for the treatment of SLE and to elucidate the potential underlying mechanisms.

MATERIALS AND METHODS

Six- to eight-week-old female DBA/2 and BDF1 (C57BL/6 × DBA/2) mice were purchased from Beijing Vital River. The mice were housed in a controlled environment (12 h light/12 h dark period, 25 ± 1 °C) in the Animal Center of Beijing Normal University for 1 week before gaining access to standard food and water for mice. All animal experimental procedures were conducted according to protocols approved by Ethic and Animal Welfare Committee (NO.CLS-EAW-2013-015) and were conducted in strict accordance with institutional guidelines. Isogarcinol (purity >95%) was extracted and purified in our lab by J.C.

Bradford assay kit was purchased from Bioteke (Beijing, China). Blood urea nitrogen, creatinine, triglyceride, and cholesterol test kits were brought from Reegen (Beijing, China). Calf thymus DNA, 3,3′-5,5′-tetramethylbenzidine (TMB), rabbit antibody against mouse IgG, goat anti-mouse IgG1, lipopolysaccharide (LPS, L2880), phorbol, 12-myristate 13-acetate (PMA), and ionomysin were purchased from Sigma (St. Louis, MO USA). HRP-conjugated rabbit anti-goat IgG and HRP-conjugated goat anti-mouse IgG were brought from CST (Danvers, MA, USA). TRIzol reagent, DMEM, and fetal bovine serum (FBS) were from Life Technologies (Carlsbad, CA, USA). RNA and quantitative real-time PCR (qRT-PCR) reagents such as oligodT primers, TaqMan Reverse Transcription Reagents, and SYBR Premix Ex Taqkit were from TaKaRa Bio (Kusatsu, Shiga, Japan). Flow cytometry antibodies such as FITC-conjugated anti-mouse CD4, PE-conjugated CD8, IFN-γ, and IL-4 and Golgi Stop were brought from BD biosciences (San Jose, CA, USA). Tumor necrosis factor-α (TNF-α), IL-1β, and IL-6 ELISA kits were from Neobioscience (Shenzheng, China).

Murine Model of cGVHD. DBA/2 mice were sacrificed, and spleen cells were filtered through sterile mesh, lysed in hemolysis buffer, washed, and processed into single-cell suspensions. Either 0.9% NaCl (control group) or 6×10^7 DBA/2 spleen cells (other groups) per mouse were twice injected into the tail vein of a BDF1 mouse at day −7 and day 0. For the drug effect study, the mice were divided into 5 groups ($n = 7$): control, cGVHD, isogarcinol 30 mg/kg, isogarcinol 60 mg/kg, and CsA 30 mg/kg. For further mechanism study, the mice were divided into 3 groups ($n = 4–6$): control, cGVHD, and isogarcinol 60 mg/kg group. Isogarcinol is insoluble in water, so isogarcinol and CsA were dissolved in 20% DMSO and 80% distilled water. Isogarcinol and CsA were continuously given daily by gavage from day 1 until the end of the experiment. The control and the cGVHD groups received the same dose of the vehicle (20% DMSO + 80% distilled water, total of 0.2 mL per mouse per day). Animal experiments were repeated twice.

Determination of Proteinuria, Serum Blood Urea Nitrogen, Triglyceride, Creatinine, and Cholesterol Content. Serum and urine were collected every 2 weeks. The mice were placed in metabolic cages for urine collection. Proteinuria was tested using the Bradford assay kit. The serum blood urea nitrogen (BUN), creatinine, triglyceride, and cholesterol levels were measured using an automatic biochemical analyzer (Olympus AU400,Tokyo, Japan).

DOI: 10.1021/acs.jafc.5b03425
J. Agric. Food Chem. 2015, 63, 8452−8459

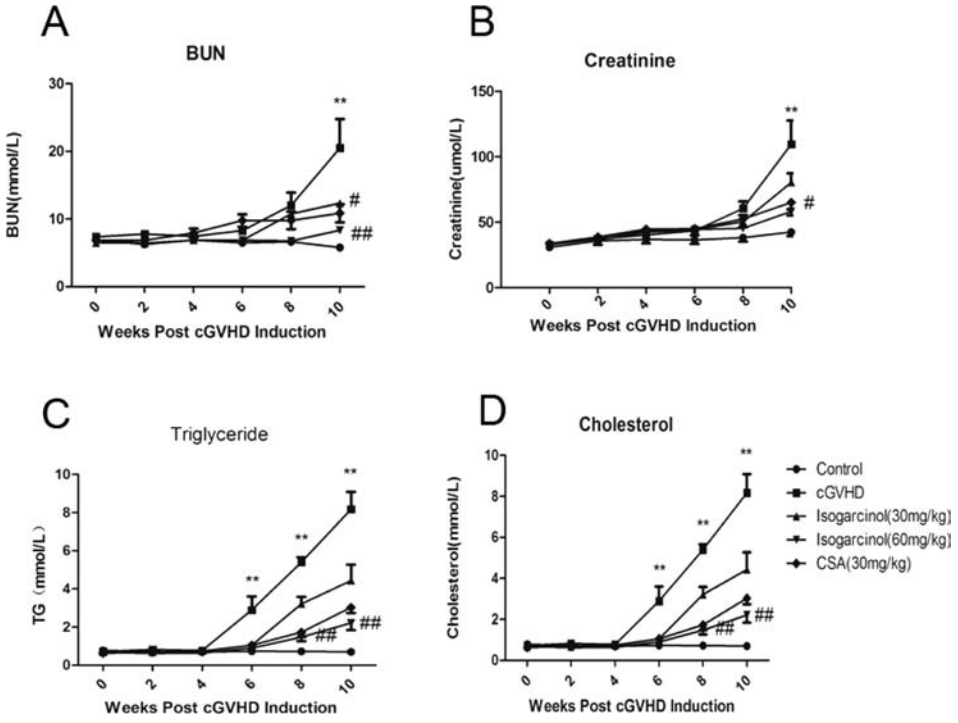

Figure 2. Isogarcinol corrected abnormal serum indices in the cGVHD mice. Chronic GVHD mouse model was induced as mentioned in Materials and Methods. Serum was collected every 2 weeks, and the serum indices were measured by an automatic biochemical analyzer. Isogarcinol lowered (A) blood urea nitrogen, (B) creatinine, (C) triglyceride, and (D) cholesterol in the cGVHD mouse model. The bars show the mean ± SEM ($n = 7$). **, $p < 0.01$ versus control; # and ##, $p < 0.05$ and $p < 0.01$ versus cGVHD, respectively.

Determination of Serum Antibody Production. The serum anti-double-stranded DNA (anti-dsDNA) or total antibody was tested by ELISA as follows: Microtiter plates were coated with calf thymus DNA. Then, HRP-conjugated goat anti-mouse IgG was added, followed by TMB. The reaction was stopped with 2 M H_2SO_4, and the plates were read at 450 nm in a Polarstar Omega (BMG labtech, Cary, NC, USA). Serum IgG1 was measured as follows: Microtiter plates were coated with rabbit antibody against mouse IgG. Goat anti-mouse IgG1 was used as primary antibody. The HRP-conjugated rabbit anti-goat IgG was then added as the secondary antibody. TMB and H_2SO_4 were added in order, and the plates were read at 450 nm. The samples were diluted 1:250.

Real-Time PCR. Mice were sacrificed at the end of the experiment, and total RNA was isolated from the fresh spleen and kidney using TRIzol reagent. Then, cDNA synthesis was initiated by adding oligodT primers and TaqMan Reverse Transcription Reagents. qRT-PCR was performed according to the instructions of SYBR Premix Ex Taqkit in an Applied Biosystems 7500 fast Real-Time PCR system (Thermo Fisher, Grand Island, NY, USA). β-actin was used for normalization, and the sequences of the primers used are as follows: T-bet, gttcaaccagcaccagacagag (forward), tggtccaccaagaccacatc (reverse); GATA-3, ggatgtaagtcgaggcccaag (forward), attgcaaaggtagtgcccggta (reverse); IFN-γ cggcacagtcattgaaagccta (forward), gttgctgatggcctgatt-gtc (reverse); IL-4 acggagatggatgtgccaaac (forward), agcaccttggaa-gccctacaga (reverse), TNF-α, actccaggcggtgcctatgt (forward), gtgagg-gtctgggccatagaa (reverse); IL-1β tccaggatgaggacatgagcac (forward), gaacgtcacacaccagcaggtta (reverse); IL-6 caacgatgatgcacttgcaga (forward), ctccaggtagctatggtactccaga (reverse); β-actin, agagggaaatcg-tgcgtgac (forward), caatagtgatgacctggccgt (reverse).

Flow Cytometry. BDF1 mice were sacrificed at week 8, and spleen cells were filtered through sterile mesh, lysed in hemolysis buffer, washed, and processed into single-cell suspensions. To determine the content of CD4 and CD8, single-cell suspensions were directly used without stimulation of PMA and ionomysin. FITC-conjugated anti-mouse CD4 and PE-conjugated CD8 were used for the flow cytometry assay.

To determine the intracellular cytokine staining, the cells were cultured in 20% FBS DMEM for 2 h. Then, 100 ng/mL PMA and 1000 ng/mL ionomycin together with Golgi Stop were added for an additional 4 h. Next, the cells were harvested, blocked, and stained with FITC-conjugated anti-mouse CD4, PE-conjugated anti-mouse IFN-γ, and PE-conjugated anti-mouse IL-4 according to the respective manufacturer's protocol. Finally, the cells were analyzed on a FACS Calibur flow cytometer system with CellQuest software (BD, San Jose, CA, USA).

Macrophage Preparation and Cytokine Measurement. At the end of the experiment, macrophages of every group of mice were collected and adjusted to 1×10^6/mL in plates. Then, cells were cultured in 20% FBS DMEM at 37 °C for 2 h. Then, cells were stimulated by 10 μg/mL LPS for an additional 12 h before culture supernatants were harvested. Cytokines in culture supernatants, such as TNF-α, IL-1β, and IL-6, were determined using ELISA kits.

Renal Histopathology. The mice were sacrificed at week 10 to evaluate the histological scores in the kidney. After being fixed in 4% formalin and embedded in paraffin, the kidney was sectioned, mounted on slides, and stained with H&E. Each observer was blinded when evaluating each section, scoring the glomeruli, and classifying the lesion.[21] The following scale was applied: 0, normal morphology; 1, moderate expansion of the glomerular matrix without glomerulonephritis; 2, mild glomerulonephritis with mesangial hypercellularity and/or segmental necrosis; 3, moderate glomerulonephritis with extensive sclerosis and/or loop necrosis and/or cellular crescent; 4, severe glomerulonephritis with large area of loop necrosis and cellular crescent.

Statistical Analyses. The results are expressed as the means ± standard error of the mean (SEM). One-way analysis of variation (ANOVA) followed by Bonferroni's multiple comparison test was used to compare experimental groups and the control groups. The statistical analyses were performed in GraphPad Prism 5.0 software. The level of statistical significance was set at $p < 0.05$.

DOI: 10.1021/acs.jafc.5b03425
J. Agric. Food Chem. 2015, 63, 8452−8459

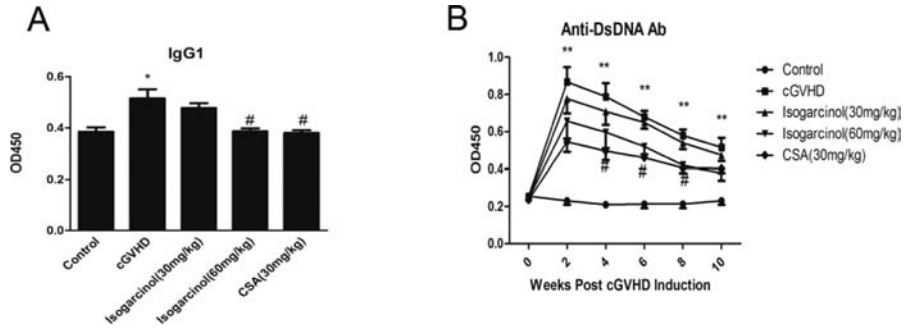

Figure 3. Isogarcinol decreases serum autoantibodies in cGVHD mouse model. Chronic GVHD mouse model was induced as mentioned in Materials and Methods. Serum was collected every 2 weeks and ELISA assay was used to determine the content of serum IgG1 and anti-dsDNA antibody. (A) Isogarcinol reduced the content of serum IgG1 at week 10 ; (B) Isogarcinol reduced the content of serum anti-dsDNA antibody. The bars show the mean ± SEM (n = 7). **, $p < 0.01$ versus control; #, $p < 0.05$ versus cGVHD.

RESULTS

Isogarcinol Reduced Proteinuria and Ameliorated Histopathological Changes Caused by cGVHD. Nephritis is a notable characteristic in both human SLE and the animal SLE model.[10,12] During the experiment, increased proteinuria was observed in cGVHD mice at week 6 and continued to increase in the following weeks. Daily treatment with 30 and 60 mg/kg isogarcinol significantly decreased proteinuria (Figure 1B,C). Renal histopathology was evaluated at week 10 after cGVHD induction with H&E stain (Figure 1D). Severe glomerulonephritis with extensive sclerosis was observed in cGVHD mice, and the renal histopathology score was significantly higher in the cGVHD group compared to that in the control group (3.3 versus 0.2, $p < 0.01$). Treatment with 60 mg/kg isogarcinol lowered the score to 2.0 ($p < 0.05$) (Figure 2E).

Isogarcinol Corrected Abnormal Serum Triglyceride, Creatinine, Blood Urea Nitrogen and Cholesterol in cGVHD Mice. SLE is a systemic autoimmue disease that affects many internal organs in the body. It is reported that during the experiment the biochemical indices such as triglyceride, creatinine, blood urea nitrogen, and cholesterol in serum were increased in similar models.[10,13,22] We measured the concentration of these indices every 2 weeks with an automatic biochemical analyzer and found that the indices of cGVHD group mice exhibited a significant high level. Treatment with 60 mg/kg isogarcinol and 30 mg/kg CsA significantly lowered these indices (Figure 2).

Isogarcinol Reduced Serum anti-dsDNA Antibody and IgG1 Concentrations. Anti-dsDNA antibody is the signature antibody in the cGVHD mouse model and in human SLE. It is documented that IgG1 was also upregulated in this model.[10] Serum was collected every 2 weeks, and levels of anti-dsDNA antibody as well as of IgG1 were determined using ELISA assay. The results manifested that after treatment with isogarcinol the anti-dsDNA and IgG1 antibodies were inhibited (Figure 3A,B). Treatment with 60 mg/kg isogarcinol and 30 mg/kg CsA were equally effective in preventing anti-dsDNA and IgG1 antibody.

Isogarcinol Alleviated the CD4 Activation in the cGVHD Mouse Model. From all of the above results, the new immunosuppressant isogarcinol displayed an outstanding effect in the cGVHD mouse model. Next, we divided the mice into 3 groups: control, cGVHD, and 60 mg/kg isogarcinol for the further mechanism studies (n = 4−6). CD4 T cell activation and interaction with CD8 T cells, together with the antibody-producing B cells, have been a major focus of investigation in SLE-cGVHD, and both CD4 T cell expansion and ineffective CD8 T cells play a role in the model.[23] Flow cytometry was applied to measure the proportion of CD4/spleen cells and the ratio of CD4/CD8. The experimental results exhibited that both were increased in the cGVHD mice, whereas isogarcinol lowered them (Figure 4A,B). These results suggest that isogarcinol might alleviate CD4 activation during the development of cGVHD. Furthermore, we extracted RNA directly from spleen cells, and the gene expression levels of Th1 (T-bet) and Th2 (GATA-3) and their key cytokines IFN-γ and IL-4 were determined. All four genes were significantly upregulated in spleen cells, whereas isogarcinol decreased their expression (Figure 4C−E).

Next, we tried to evaluate the activation form of CD4 T cells. After stimulation by 100 ng/mL PMA and 1000 ng/mL ionomycin and together with Golgi stop for another 4 h, the spleen cells were intracellularly strained for IFN-γ and IL-4. Flow cytometry was used to determine the content of CD4+IFN+ and CD4+IL4+ in spleen cells. We found that both cytokines of CD4 T cells, IFN-γ and IL-4, were increased in the cGVHD mice (Figure 5A). We also calculated the absolute content of IFN-γ+CD4+ and IL-4+CD4+ cells, and treatment with isogarcinol markedly reduced the secretion (Figure 5B). Furthermore, the relative content of the cells was also measured, and the ratio of IFN-γ+ and IL-4+ in CD4+ T cells also decreased after isogarcinol treatment (Figure 5C). In total, these results suggest that isogarcinol alleviated CD4 activation in both inactivated form and under activated condition.

Isogarcinol Exhibited Anti-Inflammatory Effects in the cGVHD Mouse Model. After stimulation with various agents such as LPS, macrophages participate in quite a few autoimmune diseases through a number of mechanisms. A variety of signal pathways are involved in the action of macrophages such as secretion of cytokines. Finally, at week 8 peritoneal macrophages were collected and cultured in vitro for the ELISA test. The levels of inflammatory cytokines TNF-α, IL-1β, and IL-6 were determined after stimulation with LPS. We found that the expression of three kinds of inflammatory cytokines was increased in cGVHD mice, yet the treatment of isogarcinol lowered these levels (Figure 6A).

The overproduction of autoantibodies assembled in kidney and deposition of immune complexes results in inflammation, then finally renal failure. In the process, inflammatory cytokines play a crucial role in the effect of inflammation. At week 8,

DOI: 10.1021/acs.jafc.5b03425
J. Agric. Food Chem. 2015, 63, 8452−8459

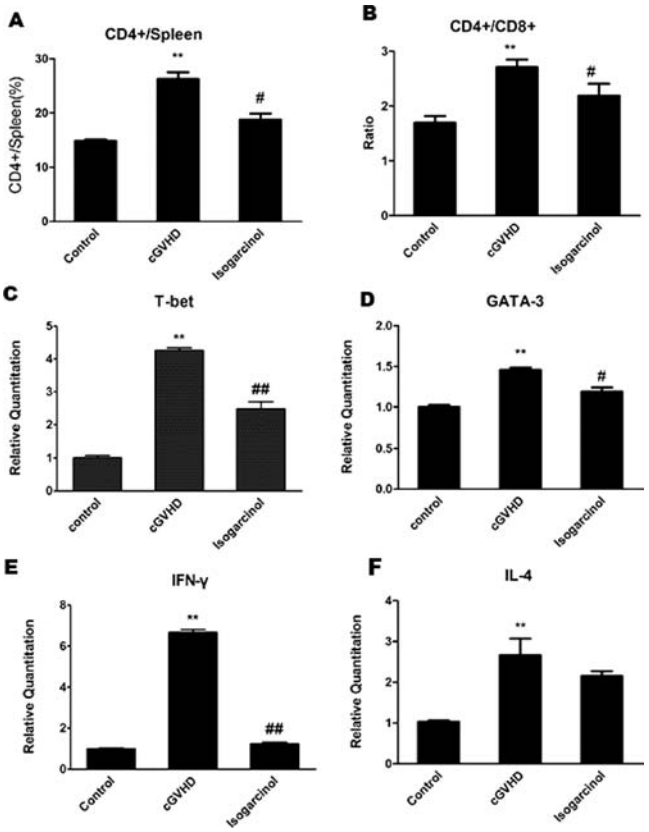

Figure 4. Isogarcinol alleviated the CD4 activation in cGVHD mouse model. At week 8, spleen cells of BDF1 mice were processed into single-cell suspensions and directly stained for flow cytometry test without stimulation. (A) Isogarcinol decreased the CD4 in spleen cells. (B) Isogarcinol reduced the ratio of CD4/CD8. In contrast, total RNA of fresh spleen tissues was extracted, and the expressions of relevant genes were measured using qRT-PCR. The expression levels of (C) T-bet, (D) GATA-3, (E) IFN-γ, and (F) IL-4 were lowered by isogarcinol. The bars show the mean ± SEM (n = 4–6). **, $p < 0.01$ versus control; # and ##, $p < 0.05$ and $p < 0.01$ versus cGVHD, respectively.

mRNA was directly extracted from the kidneys, and qRT-PCR was performed to analyze the inflammatory gene factors. The mRNA expression of TNF-α and IL-6 were prominently reduced in the isogarcinol group compared to expression in the cGVHD group, but we did not find any differences of IL-1β among the groups (Figure 6B). Together, these results suggest that the anti-inflammatory effects of isogarcinol might protect against the disease.

DISCUSSION

Injecting DBA/2 spleen cells into the tail vein of a BDF1 mouse can lead to an SLE-like disease resembling human SLE.[24−26] Compared to the traditional gene SLE models, such as (NZB × NZW) F1 and MRL/lpr mouse models, chronic GVHD models are easier to control, more adjustable, and have a shorter period that are widely used in studying the mechanism of quite a few chronic diseases. In our SLE model, the female donor will make the female host more vulnerable to SLE than a male, which is similar to human SLE.[27] All of these reasons make our mouse model a favorable model for the lupus study. In our present work, we proved that the immunosuppressant isogarcinol (especially 60 mg/kg group) markedly prevented the development of proteinuria and ameliorated lethal renal injury (Figure 1), corrected the abnormal biochemical index in serum (Figure 2), and significantly lowered the serum antibody (Figure 3). Further work with 60 mg/kg isogarcinol treatment inhibited the activation of CD4 T cells (Figures 4 and 5) and inflammation in kidneys and macrophages (Figure 6). The therapeutic effect of isogarcinol may at least partially contribute to the inhibition of CD4 T cells and the inflammation effect. In our further work with 60 mg/kg isogarcinol treatment, we picked week 3 (day 21) and week 8 (day 56) to evaluate the CD4 expansion and inflammatory cytokine secretion. However, we did not find any differences among the groups at week 3 (data not shown).

Recognition of the foreign MHC of the F1 host by parental spleen cells leads to a GVH disease. There are two major types of GVHD: acute and chronic.[28] Compared to acute GVHD, which is more likely to reflect apoptosis and necrosis, chronic GVHD is characterized by inflammatory and fibrotic processes.[29,30] During the development of cGVHD, stimulation of CD4 T cells plays an paramount role in SLE-cGVHD, and both CD4 T cell expansion and ineffective CD8 T cells play a role in this model. Similar reports demonstrated that genetic lupus mice displayed increased CD4 T cell activation at a higher CD4/CD8 ratio.[31,32] In our present study, we compared the ratio of CD4/CD8 and CD4/spleen cells, and we found that treatment with 60 mg/kg isogarcinol could alleviate the activation of CD4 cells.

Depending on the pattern of cytokine production, CD4+ T cells can be divided into at least three different subsets: Th1, Th2, and Th17 cells. Th1 cells preferentially produce IFN-γ and IL-2, which activate macrophages and stimulate production of IgG2a in mice. Th2 cells preferentially produce IL-4 and IL-10, which provide potent B cells and help induce IgG1 production in mice. It has been traditionally reported that the cytokines produced during acute GVHD are Th1 cells, whereas those produced during cGVHD are Th2 cytokines. However, recent studies have suggested that cGVHD could be caused by cytokines secreted by Th1 cells.[33,34] The mechanisms leading to the development of cGVHD are still not completely understood. In similar models, there was a significant expansion of Th2 cells in the early phase (week 2) of the model,[35] whereas some reported that both Th1 and Th2 cells were increased but that the increase of Th2 cells was more significant.[8,12] In our experiment, we found serum IgG1 (Figure 3) and IL-4 (data not shown) increased in cGVHD mice at week 10. These results suggest that there might be Th2 cell expansion in this model. However, the gene expressions of Th1 (T-bet) and Th2 (GATA-3) and their key cytokines IFN-γ and IL-4 were all increased in spleen cells before stimulation (Figure 4). Furthermore, after the stimulation with PMA and ionomysin, we compared the absolute content and relative content of Th1 and Th2 cells, and the results were similar to the inactivated experiments (Figure 5). In addition, we did not find any differences of Th17 cells at week 8 (data not shown). In our previous work, we have reported that isogarcinol significantly inhibited the proliferation of murine spleen T-lymphocytes induced by ConA.[19] These results indicate to us that isogarcinol downregulates both Th1 and Th2 cells and alleviates CD4 activation resulting in attenuation of lupus-like disease.

We also found isogarcinol significantly decreased NO production and inducible nitric oxide synthase mRNA expression in the LPS-stimulated RAW 264.7 macrophages and the anti-inflammatory effect associated with isogarcinol in

DOI: 10.1021/acs.jafc.5b03425
J. Agric. Food Chem. 2015, 63, 8452−8459

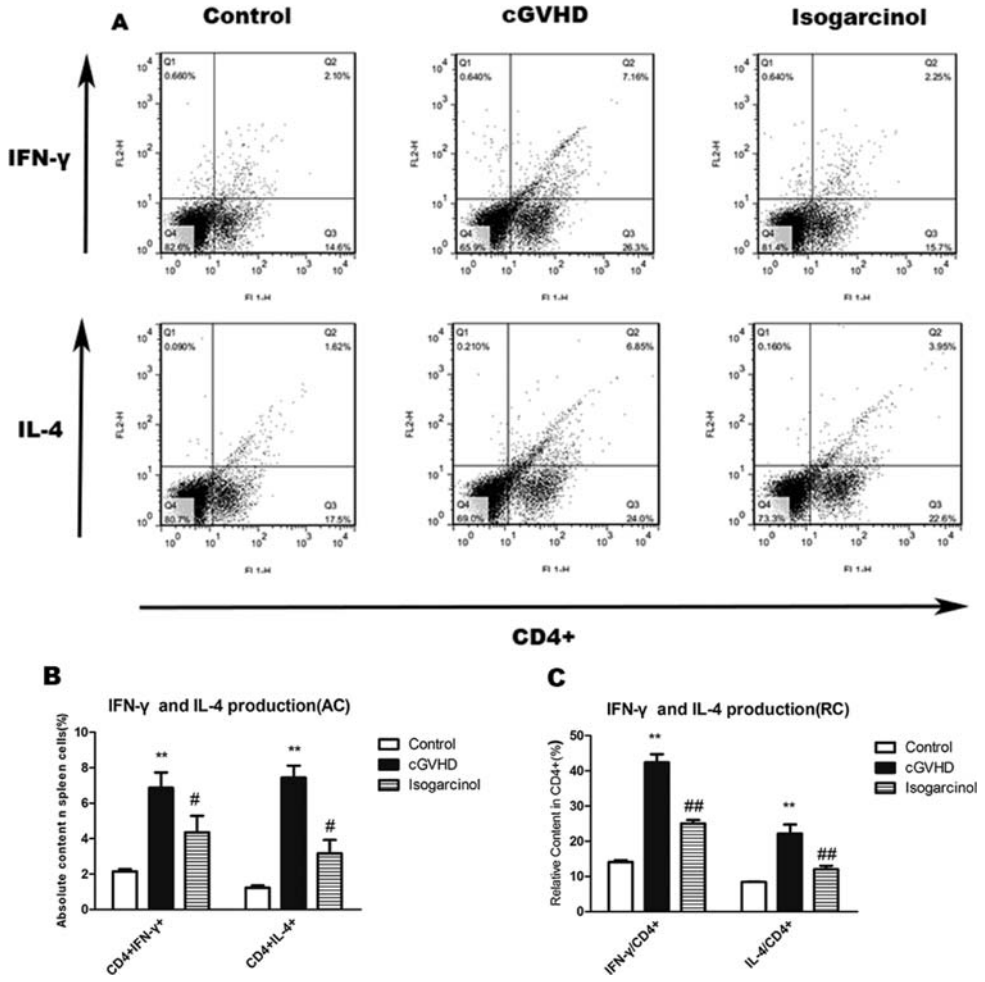

Figure 5. Isogarcinol alleviated PMA/ionomycin induced CD4 activation in cGVHD mouse model. At week 8, spleen cells of BDF1 mice were processed into single-cell suspensions and were cultured in 20% FBS DMEM for 2 h. After stimulatation by 100 ng/mL of PMA and 1000 ng/mL ionomycin and together with Golgi stop for another 4 h, the spleen cells were harvested and then intracellularly strained with IFN-γ and IL-4 on CD4 T cells. Flow cytometry was used to determine the content of CD4+IFN+ and CD4+IL4+ in spleen cells. (A) The content of CD4+IFN+ and CD4+IL4+ cells in the different groups. (B) Isogarcinol lowered the absolute content (AC) of spleen cells. (C) Isogarcinol lowered relative content (RC) of CD4+ cells. AC = IFN-γ+CD4+(IL-4+CD4+)/spleen cells; RC = IFN-γ+CD4+(IL4+CD4+)/Total CD4+ cells. The bars show the mean ± SEM (n = 4–6). **, $p < 0.01$ versus control; # and ##, $p < 0.05$ and $p < 0.01$ versus cGVHD, respectively.

chronic inflammatory arthritis.[19,20] The inflammatory cytokines TNF-α, IL-1β, and IL-6 produced by macrophages play an essential role in responding to infection and inflammation. Moreover, the kidney mRNA levels of TNF-α and IL-1β as well as protein levels in lupus-prone MRL/lpr mice have been found to increase.[36] We first tested the cytokines of the macrophages and found the inflammatory cytokines, such as TNF-α, IL-6, and IL-1β, were highly expressed in cGVHD mice. The gene expression in kidneys of two inflammatory cytokines, TNF-α and IL-6, displayed a similar result (Figure 6). Treatment with 60 mg/kg isogarcinol can effectively reduce inflammatory cytokine secretion and finally protect the injury of the kidneys and prevent proteinuria (Figure 1). These results suggest that the anti-inflammatory effects of isogarcinol may protect from the GVH response.

Antibody- and immune-complex-mediated inflammation in SLE can trigger the development of glomerulonephritis, arthritis, and serositis. The most common cause of death in SLE is renal failure, and the 5-year survival rate is approximately 77%. Current therapies for lupus are broad-spectrum, including steroids and immunosuppressants, which are compromised by toxicity and side effects in the medications. Immunosuppressants, such as CsA, can inhibit the CN pathway and target T cells to regulate GVH responses. In our present research, we found a similar effective therapy between daily oral 60 mg/kg isogarcinol and 30 mg/kg CsA in preventing proteinuria, autoantibodies, and abnormal serum indicators. However, the CsA group manifested a higher renal histological score than did the isogarcinol group (Figure 1). In addition, during the experiment, a significant body weight change in the CsA treatment mice and abdominal edema was observed during the experiment (data not shown), and because of edema, the CsA group mice showed less activity than the other mice group. All of these may have to do with the toxicity of CsA with daily oral treatment. Moreover, we compared the toxicity of CsA and isogarcinol for both in vitro and in vivo experiments. Isogarcinol exhibited a better viability of spleen cells, and the serum indices, such as glutamic-pyruvic transaminase, glytamic-oxalacetic transaminease, total bilirubin, urea nitrogen, and creatinine, were abnormally high in the CsA group compared with the isogarcinol group.[19] Similar experiments regarding the toxicity of CsA were found in the collagen-induced arthritis

DOI: 10.1021/acs.jafc.5b03425
J. Agric. Food Chem. 2015, 63, 8452–8459

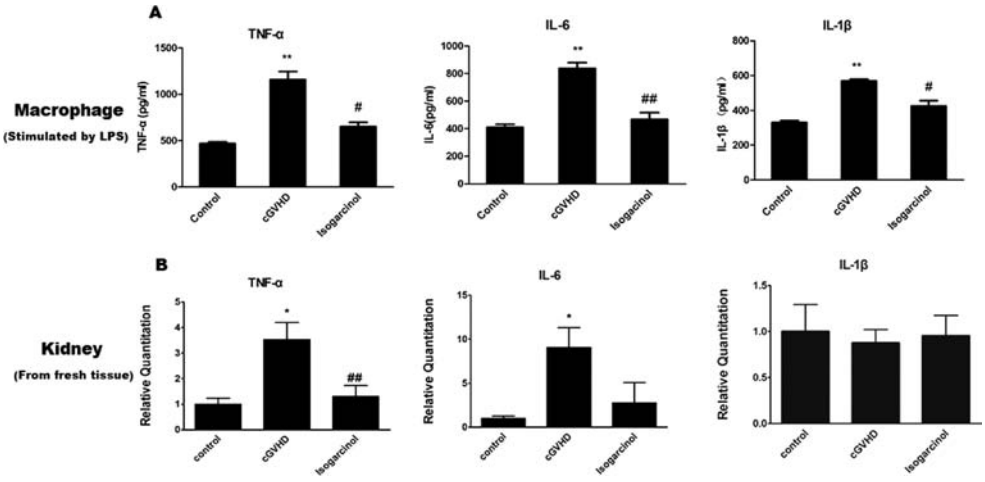

Figure 6. Isogarcinol exhibited an anti-inflammatory effect in the cGVHD mouse model. At week 8, macrophages of BDF1 mice were collected and adjusted to 1×10^6/mL in plates. Cells were cultured in 20% FBS DMEM for 2 h then stimulated with LPS in vitro for 12 h. The supernatants were harvested for the ELISA assay. (A) Isogarcinol reduced the content of TNF-α, IL-1β, and IL-6 expression. Messenger RNA of kidney tissue was directly extracted, and relevant genes were measured using qRT-PCR. (B) The effect of Isogarcinol on gene expression of TNF-α, IL-6, and IL-1β in the kidneys. The bars show the mean ± SEM (n = 4–6). **, $p < 0.01$ versus control; # and ##, $p < 0.05$ and $p < 0.01$ versus cGVHD, respectively.

mouse model.[37] These results all link with the severe hepatotoxicity and nephrotoxicity of CsA. In our present work, we found an immunosuppression and anti-inflammatory effect of isogarcinol extracted from mangosteen fruit. Therefore, we have reason to expect it will become a potential candidate drug in the future.

Isogarcinol is a low-toxicity, peroral compound we extracted from mangosteen fruit. Experimental data in this study elucidated that it is effective against SLE-like disease, and the therapeutic effect was associated with the downregulation of the activation of CD4 T cells and the inflammatory effect.

AUTHOR INFORMATION

Corresponding Author

*Tel.: 86-010-58807365. Fax: 86-010-58807365. E-mail: weiq@bnu.edu.cn.

Funding

The work was supported by the National Natural Science Foundation of China, the National Important Novel Medicine Research Project, and the special fund of the coconstruction project from the Beijing Education Committee.

Notes

The authors declare no competing financial interest.

ABBREVIATIONS

anti-dsDNA, anti-double-stranded DNA; BUN, blood urea nitrogen; cGVHD, chronic graft versus host disease; CN, calcineurin; CsA, cyclosporine A; FBS, fetal bovine serum; IFN-γ, interferon gamma; LPS, lipopolysaccharides; PMA, phorbol, 12-myristate 13-acetate; SLE, systemic lupus erythematosus; TNF-α, tumor necrosis factor-α

REFERENCES

(1) Feskanich, D.; Ziegler, R. G.; Michaud, D. S.; Giovannucci, E. L.; Speizer, F. E.; Willett, W. C.; Colditz, G. A. Prospective study of fruit and vegetable consumption and risk of lung cancer among men and women. *J. Natl. Cancer. Inst* **2000**, *92*, 1812–1823.

(2) Kondo, M.; Zhang, L.; Ji, H.; Kou, Y.; Ou, B. Bioavailability and antioxidant effects of a xanthone-rich Mangosteen (Garcinia mangostana) product in humans. *J. Agric. Food Chem.* **2009**, *57*, 8788–92.

(3) Jung, H. A.; Su, B. N.; Keller, W. J.; Mehta, R. G.; Kinghorn, A. D. Antioxidant xanthones from the pericarp of Garcinia mangostana (Mangosteen). *J. Agric. Food Chem.* **2006**, *54*, 2077–82.

(4) Pedraza-Chaverri, J.; Cardenas-Rodriguez, N.; Orozco-Ibarra, M.; Perez-Rojas, J. M. Medicinal properties of mangosteen (Garcinia mangostana). *Food Chem. Toxicol.* **2008**, *46*, 3227–39.

(5) Eisenberg, R. A.; Via, C. S. T cells, murine chronic graft-versus-host disease and autoimmunity. *J. Autoimmun.* **2012**, *39*, 240–7.

(6) Shlomchik, M. J.; Craft, J. E.; Mamula, M. J. From T to B and back again: positive feedback in systemic autoimmune disease. *Nat. Rev. Immunol.* **2001**, *1*, 147–53.

(7) Wenderfer, S. E.; Ke, B.; Hollmann, T. J.; Wetsel, R. A.; Lan, H. Y.; Braun, M. C. C5a receptor deficiency attenuates T cell function and renal disease in MRLlpr mice. *J. Am. Soc. Nephrol.* **2005**, *16*, 3572–3582.

(8) Kuroiwa, T.; Iwasaki, T.; Imado, T.; Sekiguchi, M.; Fujimoto, J.; Sano, H. Hepatocyte growth factor prevents lupus nephritis in a murine lupus model of chronic graft-versus-host disease. *Arthritis. Res. Ther* **2006**, *8*, R123.

(9) Schorlemmer, H. U.; Brendel, S.; Bartlett, R. R. Malononitrilamides prevent the development of murine systemic lupus erythematosus-like diseases in BDF1 hybrid mice and MRL/lpr autoimmune mice. *Transplant. Proc.* **1996**, *28*, 3040–3042.

(10) Xiao, Z. Y.; Chen, S. H.; Cheng, J. P.; Zhou, W. X.; Zhang, Y. X.; Yang, R. F.; Yun, L. H. Y27, a novel derivative of 4-hydroxyquinoline-3-formamide, prevents the development of murine systemic lupus erythematosus-like diseases in MRL/lpr autoimmune mice and BDF1 hybrid mice. *Arthritis. Res. Ther* **2012**, *14*, R235.

(11) Via, C. S.; Shearer, G. M. T-cell interactions in autoimmunity: insights from a murine model of graft-versus-host disease. *Immunol. Today* **1988**, *9*, 207–13.

(12) Zhang, J. L.; Sun, D. J.; Hou, C. M.; Wei, Y. L.; Li, X. Y.; Yu, Z. Y.; Feng, J. N.; Shen, B. F.; Li, Y.; Xiao, H. CD3 mAb treatment ameliorated the severity of the cGVHD-induced lupus nephritis in mice by up-regulation of Foxp3+ regulatory T cells in the target tissue: kidney. *Transplant Immunol.* **2010**, *24*, 17–25.

(13) Xiao, Z. Y.; Zhou, W. X.; Zhang, Y. X.; Cheng, J. P.; He, J. F.; Yang, R. F.; Yun, L. H. Roquinimex-mediated protection effect on the development of chronic graft-versus-host disease in mice is associated with induction of Th1 cytokine production and inhibition of proinflammatory cytokine production. *Life Sci.* **2007**, *81*, 1403–10.

DOI: 10.1021/acs.jafc.5b03425
J. Agric. Food Chem. 2015, 63, 8452–8459

(14) MacDonald, K. P.; Shlomchik, W. D.; Reddy, P. Biology of graft-versus-host responses: recent insights. *Biol. Blood Marrow Transplant.* **2013**, *19*, S10−4.
(15) Scott, L. J.; McKeage, K.; Keam, S. J.; Plosker, G. L. Tacrolimus: a further update of its use in the management of organ transplantation. *Drugs* **2003**, *63*, 1247−97.
(16) Lei, H.; Luo, J.; Tong, L.; Peng, L. Q.; Qi, Y.; Jia, Z. G.; Wei, Q. Quercetin binds to calcineurin at a similar region to cyclosporin A and tacrolimus. *Food Chem.* **2011**, *127*, 1169−74.
(17) Peng, L.; Qi, Y.; Wu, H.; Wei, Q. Interaction of glycyrol with calcineurin A studied by spectroscopic methods and docking. *IUBMB Life* **2011**, *63*, 14−20.
(18) Cen, J.; Wang, M.; Jiang, G.; Yin, Y.; Su, Z.; Tong, L.; luo, J.; Ma, Y.; Gao, Y.; Wei, Q. The new immunosuppressant, isogarcinol, binds directly to its target enzyme calcineurin, unlike cyclosporin A and tacrolimus. *Biochimie* **2015**, *111*, 119−24.
(19) Cen, J.; Shi, M.; Yang, Y.; Fu, Y.; Zhou, H.; Wang, M.; Su, Z.; Wei, Q. Isogarcinol is a new immunosuppressant. *PLoS One* **2013**, *8*, e66503.
(20) Fu, Y.; Zhou, H.; Wang, M.; Cen, J.; Wei, Q. Immune regulation and anti-inflammatory effects of isogarcinol extracted from Garcinia mangostana L. against collagen-induced arthritis. *J. Agric. Food Chem.* **2014**, *62*, 4127−34.
(21) Senuma, A.; Hagiwara, E.; Nagahama, K.; Okuda, K.; Nakamura, M.; Fukumoto, N.; Shirai, A.; Tani, K.; Ishigatsubo, Y. Therapeutic effect of CpG motifs on the development of chronic graft-versus-host disease in mice. *Cytokine+* **2002**, *20*, 23−29.
(22) Xiao, Z. Y.; Chen, S. H.; Zhou, W. X.; Zhang, Y. X.; Cheng, J. P.; Yang, R. F. H1521, a novel derivative of 4-hydroxyquinoline-3-carboxamide, suppresses the development of lupus in mice by inducing Th1 cytokine profile in T cells. *Int. Immunopharmacol.* **2011**, *11*, 435−43.
(23) Chu, Y. W.; Gress, R. E. Murine models of chronic graft-versus-host disease: insights and unresolved issues. *Biol. Blood Marrow Transplant.* **2008**, *14*, 365−78.
(24) Slayback, D. L.; Dobkins, J. A.; Harper, J. M.; Allen, R. D. Genetic factors influencing the development of chronic graft-versus-host disease in a murine model. *Bone Marrow Transplant.* **2000**, *26*, 931−8.
(25) Gleichmann, E.; Pals, S. T.; Rolink, A. G.; Radaszkiewicz, T.; Gleichmann, H. Graft-versus-host reactions: clues to the etiopathology of a spectrum of immunological diseases. *Immunol. Today* **1984**, *5*, 324−32.
(26) Sasaki, M.; Hasegawa, H.; Kohno, M.; Inoue, A.; Ito, M. R.; Fujita, S. Antagonist of secondary lymphoid-tissue chemokine (CCR ligand 21) prevents the development of chronic graft-versus-host disease in mice. *J. Immunol.* **2003**, *170*, 588−96.
(27) Lang, T. J.; Nguyen, P.; Papadimitriou, J. C.; Via, C. S. Increased severity of murine lupus in female mice is due to enhanced expansion of pathogenic T cells. *J. Immunol.* **2003**, *171*, 5795−801.
(28) Kupers, R. C.; Suiter, T.; Gleichmann, E.; Rose, N. R. The induction of organ-specific antibodies during the graft-vs.-host reaction. *Eur. J. Immunol.* **1988**, *18*, 161−166.
(29) Sullivan, K. M.; Shulman, H. M.; Storb, R.; Weiden, P. L.; Witherspoon, R. P.; McDonald, G. B.; Schubert, M. M.; Atkinson, K.; Thomas, E. D. Chronic graft-versus-host disease in 52 patients: adverse natural course and successful treatment with combination immunosuppression. *Blood* **1981**, *57*, 267−276.
(30) Lee, S. J. New approaches for preventing and treating chronic graft-versus-host disease. *Blood* **2005**, *105*, 4200−6.
(31) Perry, D. J.; Yin, Y.; Telarico, T.; Baker, H. V.; Dozmorov, I.; Perl, A.; Morel, L. Murine lupus susceptibility locus Sle1c2 mediates CD4+ T cell activation and maps to estrogen-related receptor gamma. *J. Immunol.* **2012**, *189*, 793−803.
(32) Yin, Y.; Choi, S. C.; Xu, Z.; Perry, D. J.; Seay, H.; Croker, B. P.; Sobel, E. S.; Brusko, T. M.; Morel, L. Normalization of CD4+ T cell metabolism reverses lupus. *Sci. Transl. Med.* **2015**, *7*, 274ra18.
(33) Zhou, L.; Askew, D.; Wu, C.; Gilliam, A. C. Cutaneous gene expression by DNA microarray in murine sclerodermatous graft-versus-host disease, a model for human scleroderma. *J. Invest. Dermatol.* **2007**, *127*, 281−92.
(34) Nishimori, H.; Maeda, Y.; Teshima, T.; Sugiyama, H.; Kobayashi, K.; Yamasuji, Y.; Kadohisa, S.; Uryu, H.; Takeuchi, K.; Tanaka, T.; Yoshino, T.; Iwakura, Y.; Tanimoto, M. Synthetic retinoid Am80 ameliorates chronic graft-versus-host disease by down-regulating Th1 and Th17. *Blood* **2012**, *119*, 285−95.
(35) Rus, V.; Svetic, A.; Nguyen, P.; Gause, W. C.; Via, C. S. Kinetics of Th1 and Th2 cytokine production during the early course of acute and chronic murine graft-versus-host disease. Regulatory role of donor CD8+ T cells. *J. Immunol.* **1995**, *155*, 2396−2406.
(36) Boswell, J. M.; Yui, M. A.; Burt, D. W.; Kelley, V. E. Increased tumor necrosis factor and IL-1 beta gene expression in the kidneys of mice with lupus nephritis. *J. Immunol.* **1988**, *141*, 3050−3054.
(37) Fu, Y.; Zhou, H.; Wang, S.; Wei, Q. Glycyrol suppresses collagen-induced arthritis by regulating autoimmune and inflammatory responses. *PLoS One* **2014**, *9*, e98137.

DOI: 10.1021/acs.jafc.5b03425
J. Agric. Food Chem. 2015, 63, 8452−8459

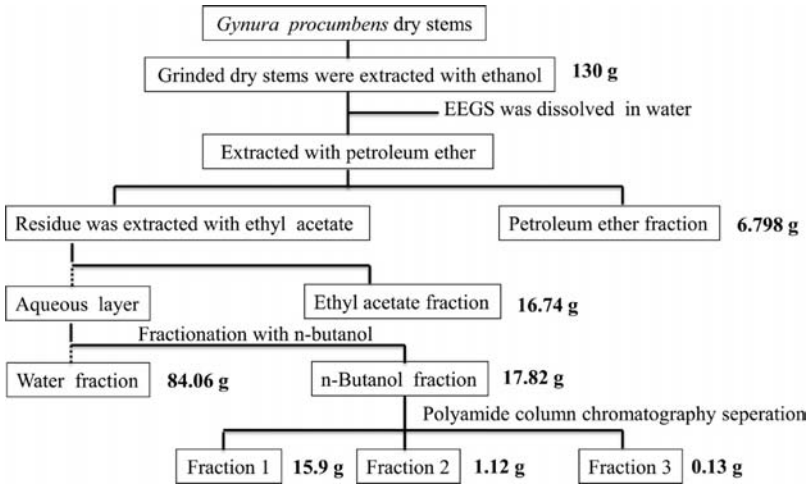

Figure 1. Schematic diagram of the bioguided fractions of *G. procumbens* on alcohol-induced liver injury.

molecular mechanisms underlying the protective effects of *G. procumbens* against ALD.

MATERIALS AND METHODS

Reagents. *G. procumbens* was produced in Shantou, Guangdong, China (identified by Prof. Bingkun Zhang, Wuhan Botany, Chinese Academy of Sciences). P44/42 MAPK (Erk1/2), phospho-p44/42 MAPK (Thr202/Tyr204), p38 MAPK, phospho-p38 MAPK (Thr180/Tyr182), acetyl-CoA carboxylase, phospho-acetyl-CoA carboxylase (Ser79) antibodies were purchased from Cell Signaling Technology (Beverly, MA). SREBP-1 antibody was purchased from Abcam (Cambridge, UK). AMPK1/2 and phospho-AMPK1/2 (Thr172) antibodies were obtained from Santa Cruz Biotechnology (Santa Cruz, CA). The GAPDH antibody was purchased from AB CLONAL Biotechnology (Wuhan, Hubei, China). Chlorogenic acid and silymarin were purchased from Sigma-Aldrich (St. Louis, MO). All other chemicals purchased were of the purest form commercially available.

Animals, Grouping, Treatment, and Sampling. *Preparation of the Ethanol Extract from G. procumbens Stems (EEGS) and Its Subfractions.* Fresh stems were minced, dried in the sun, and powdered for the experiments. The extract was prepared from 1000 g of powder extracted by heat reflux in 10 L of 80% ethanol at 85 °C for 1 h and filtered. The extraction was repeated three times. The filters were combined and evaporated under reduced pressure at 50 °C to remove the solvent. Then, the extract was lyophilized to obtain EEGS with a yield of 18.5%. The yield in the present study is always calculated using the following formula: yield = (weight of the dried extract/weight of sample used for extraction) × 100%.

EEGS was further fractionated according to the schematic diagram shown in Figure 1. EEGS was dissolved in 500 mL of water, and the solution was successively extracted by the same volumes of petroleum, ethyl acetate, and water-saturated *n*-butyl alcohol. Each solvent extraction was repeated three times. The extracts of each solvent were combined and then evaporated under reduced pressure at 50 °C. The crude extracts of the four fractions were classed, yielding petroleum, ethyl acetate, *n*-butyl alcohol, and water at 5.4%, 14.2%, 13.3%, and 67.0%, respectively.

The *n*-butyl alcohol extract was further fractionated on a polyamide glass column (custom-made, inner diameter 2 cm, packing height 40 cm). Elution was started with distilled water followed by 60% ethanol and ending with 95% ethanol, 375 mL each, 2.5 mL/min. The eluted fractions were evaporated under reduced pressure at 50 °C to give fraction 1 (yield 92.74%), fraction 2 (yield 6.49%), and fraction 3 (yield 0.76%).

Analysis of Chlorogenic Acids by HPLC-UV. Five chlorogenic acids—neochlorogenic acid, chlorogenic acid, isochlorogenic acid A, isochlorogenic acid B, and isochlorogenic acid C—have been isolated and identified in EEGS in our previous study. HPLC analysis was carried out with a U3000-Dionex instrument with a 5 μm Acclaim C-18 column (4.6 × 250 mm, Thermo Fisher Scientific, Inc., Waltham, MA). Detection was carried out at 326 nm with a 70 min gradient. Solvent A was acetonitrile, and solvent B was a 0.1% aqueous phosphoric acid solution. The gradient system was A-B (v/v) = 19/81 (0 min) → 27/73 (65 min) → 19/81 (70 min). The flow rate of the mobile phase was 1 mL/min (Figure 2). The contents of neochlorogenic acid, chlorogenic acid, isochlorogenic acid A, isochlorogenic acid B, and isochlorogenic acid C in EEGS as calculated by external standard method were 0.01%, 0.27%, 0.28%, 0.051%, and 0.12%, respectively. The contents of chlorogenic acid in petroleum extract, ethyl acetate extract, *n*-butyl alcohol extract, water extract, fraction 1, fraction 2, and fraction 3 were 0.0078%, 0.38%, 1.0%, 0.03%, 0% (not detectable), 13.6%, and 42.0%, respectively.

Screening of the Active Fraction(s) of EEGS in the Acute Alcohol Exposure Model. The acute alcohol exposure model designed by Carson and Pruett[17] is particularly valuable when used to screen the efficacy of agents that may offer clinical benefits and for the mechanistic and predictive analysis of therapeutic compounds.[18] In the current study, male Kunming mice (body weight 18−22 g) were used, and all experiments followed the WHO Guidance of Humane Care and Use of Laboratory Animals. Ethanol (5 g/kg) was given orally (by gavage) every 12 h for a total of three doses to induce liver injury in the acute alcohol exposure model. EEGS and its fractions were suspended in the ethanol solution so that the mice received ethanol and EEGS or its fractions at the same time. The mice were sacrificed 4 h after the last ethanol treatment, and their blood samples and whole livers were immediately collected. Blood samples were used to test for alanine aminotransferase (ALT) and aspartate aminotransferase (AST) activity. Serum levels of ALT and AST were determined using commercial spectrophotometric kits (Nanjing Jiancheng Bioengineering Institute, Nanjing, Jiangsu, China) according to the manufacturer's instructions. Liver samples were used for RT-PCR, Western blot, triglyceride (TG) content analysis, and histological examination. We performed three rounds of screening with the acute ALD model to evaluate the active fraction(s) of *G. procumbens*. One round of screening was to determine the optimal EEGS dose, and the other two were to screen the active fraction(s) of the EEGS and *n*-butyl alcohol extract.

Estimation of the Effect of EEGS and Fraction 2 in the Chronic Alcohol Exposure. Because acute alcohol exposure in mice induces hepatic steatosis in a manner similar to chronic ethanol administration, the acute model is useful as a screening tool and/or a mechanistic and predictive analysis for agents against liver disease induced by chronic alcohol intake.[18] However, negative health consequences of alcohol use vary according to the drinking pattern, such as acute or chronic.[1] The acute model with three binge-drinking episodes did not evoke the full range of symptoms of chronic alcohol consumption in the liver.[19]

DOI: 10.1021/acs.jafc.5b03504
J. Agric. Food Chem. 2015, 63, 8460−8471

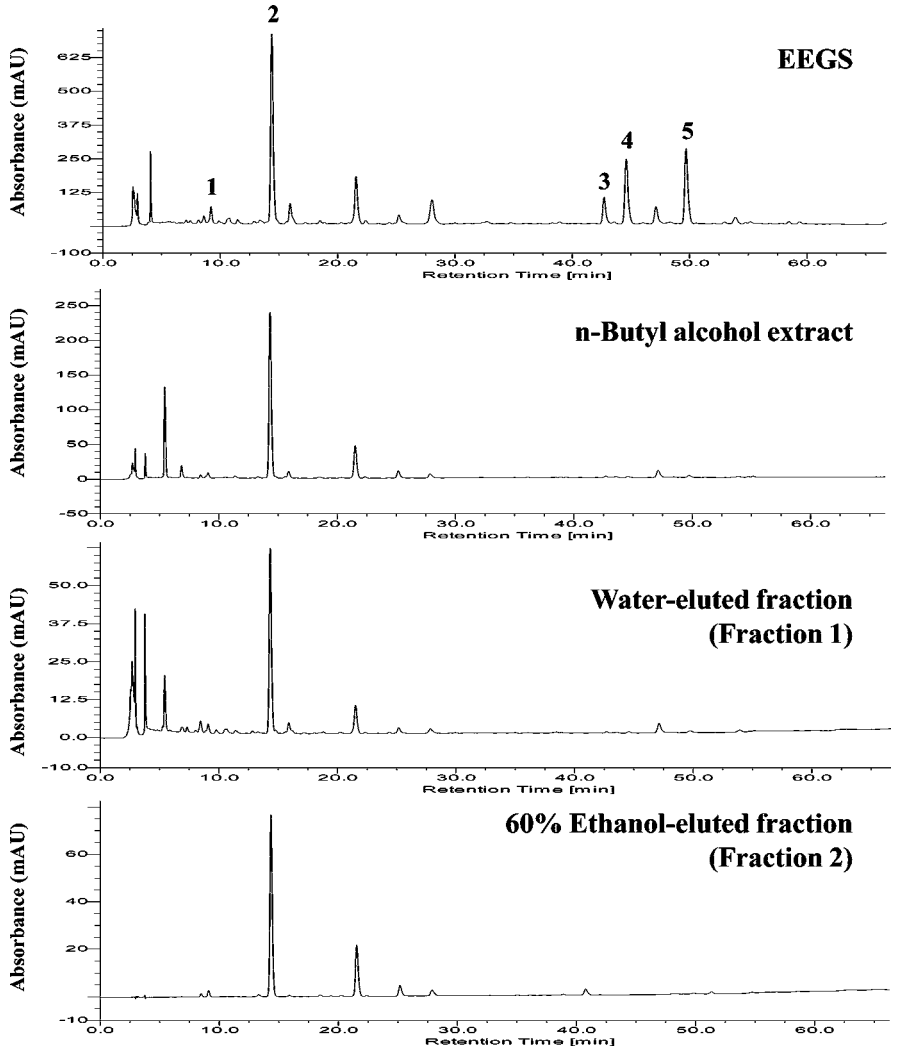

Figure 2. Representative HPLC-UV chromatograms of EEGS and its subfractions. HPLC analysis was carried out with a U3000-Dionex instrument with a 5 μm Acclaim C-18 column (4.6 × 250 mm) (Thermo Fisher Scientific, Inc. Waltham, MA). Detection was carried out at 326 nm with a 70 min gradient. Solvent A was acetonitrile, and solvent B was 0.1% aqueous phosphoric acid solution. The gradient system was A-B (v/v) = 19/81 (0 min) → 27/73 (65 min) → 19/81 (70 min). The flow rate of the mobile phase was 1 mL/min. Peaks: 1, neochlorogenic acid; 2, chlorogenic acid; 3, isochlorogenic acid B; 4, isochlorogenic acid A; and 5, isochlorogenic acid C.

Thus, we also evaluated the protective effect of *G. procubens* on chronic ethanol-induced liver steatosis. Liquid diets were based on the Lieber−DeCarli formulation (Dyets, Inc., Bethlehem, PA). Each mouse was housed in an individual cage and allowed ad libitum access to ethanol-containing diet. Control animals were pair-fed the same diet but with maltodextrin isocalorically substituted for ethanol.[20] Either the ethanol-containing diet or the isocaloric maltose-dextrin (control) diet was fed to the animals for 8 weeks. The ethanol content began at 2.5% and was increased in a stepwise manner 0.5% every 2 days until the end of the first week and then 0.5% every 4 days until 5% was achieved. This level was maintained until the end of the experiment.

Silymarin, a mixture of flavonolignans with anti-oxidant and anti-inflammatory features, is extracted from the seed of *Silybum marianum* and protects against both acute[21] and chronic[22] ethanol-induced liver injury.[2] In view of its nontoxic nature, easy availability, and well-studied quality standard, silymarin was used as the positive control in the present experiment. Blood ethanol concentrations were measured using gas chromatography as previously described.[23,24] Blood alcohol levels ranged between 66 and 186 mg/dL and were similar among the groups.

Histological Assay. Liver tissues were fixed in 4% paraformaldehyde and then embedded in paraffin. Three-micrometer sections were stained with hematoxylin and eosin (H&E) by standard methods and then studied by light microscopy. Hepatic lipids were determined by staining 16 μm thick frozen liver sections with oil red O. Multispectral imaging was performed using the Nuance Multispectral Imaging System (Cambridge Research and Instrumentation Inc., Woburn, MA) as described in our previous study.[25] Briefly, spectral optical density data were automatically acquired from 420 to 720 nm in 10 nm increments. Spectral unmixing was accomplished using Nuance software v1.42 with pure spectral libraries of oil red O (slide stained with only oil red O). For the quantification, three equal-sized fields of each photograph were randomly chosen for each experiment.

Measurement of Liver TG Content. Hepatic levels of TG in mice were measured using a commercially available Tissue Triglyceride Assay kit (Applygen Technologies Inc., Beijing, China). A 20-fold volume of lysate was added to the 40 mg liver preparations. Supernatants were collected after centrifugation at 2000 rpm for 5 min and analyzed for TG content according to the manufacturer's protocol. The TG concentrations were normalized to protein concentrations and expressed as mg of TG/g of protein.

Real-Time PCR Assay. Total RNA was extracted from the stored frozen liver tissues using RNAiso Plus (TaKaRa Bio, Dalian, Liaoning, China) according to the manufacturer's protocol. The isolated RNA was converted into complementary DNA using Advantage RT-for-PCR Kit (TaKaRa Bio, Dalian, Liaoning, China). RT-PCR was

DOI: 10.1021/acs.jafc.5b03504
J. Agric. Food Chem. 2015, 63, 8460−8471

Table 1. Primers Used for Quantitative PCR

gene	forward primer (5′ to 3′)	reverse primer (5′ to 3′)
CPTIA	CTCAGTGGGAGCGACTCTTCA	GGCCTCTGTGGTACACGACAA
Fabp1	AAACTCACCATCACCTATGGAC	ATTGAGTTCAGTCACGGACTTT
Fabp4	GATGTGCGAACTGGACACAG	CATAGGGGGCGTCAAACAG
PPAR-α	TATTCGGCTGAAGCTGGTGTAC	CTGGCATTTGTTCCGGTTCT
Fasn	TCCTGGGAGGAATGTAAACAGC	CACAAATTCATTCACTGCAGCC
SREBP-1	GATGTGCGAACTGGACACAG	CATAGGGGGCGTCAAACAG
PPAR-γ	CGCTGATGCACTGCCTATGA	AGAGGTCCACAGAGCTGATTCC
ApoB	AAGCACCTCCGAAAGTACGTG	CTCCAGCTCTACCTTACAGTTGA
MTTP	ATACAAGCTCACGTACTCCACT	TCCACAGTAACACAACGTCCA
CD68	GTGTCTGATCTTGCTAGGACC	TGTGCTTTCTGTGGCTGTAG
IL-1β	TGGTGTGTGACGTTCCCATT	CAGCACGAGGCTTTTTTGTTG
IL-6	CCACTTCACAAGTCGGAGGCTTA	CCAGTTTGGTAGCATCCATCATTTC
CD163	TCCACACGTCCAGAACAGTC	CCTTGGAAACAGAGACAGGC
Arginase	ATGGAAGAGACCTTCAGCTAC	GCTGTCTTCCCAAGAGTTGGG
TGF-β	GTGTGGAGCAACATGTGGAACTCT	ACGCTGAATCGAAAGCCCTGTA
F4/80	CTTTGGCTATGGGCTTCCAGTC	GCAAGGAGGACAGAGTTTATCGTG
MCP-1	CCAGCCTACTCATTGGGATCA	CTTCTGGGCCTGCTGTTCA
TNF-α	ACCCTCACACTCAGATCATCTTC	TGGTGGTTTGCTACGACGT
GAPDH	TGTGTCCGTCGTGGATCTGA	TTGCTGTTGAAGTCGCAGGAG

performed on the Thermal Cycler Dice TP800 system (TaKaRa Bio, Otsu, Shiga Prefecture, Japan) using SYBR Premix Ex *Taq*II (TaKaRa Bio, Dalian, Liaoning, China) with 30−40 cycles of denaturation at 95 °C for 5 s, annealing, and extension at 60 °C for 30 s. GAPDH was used as an internal standard, and the mRNA expression levels of the target genes were normalized to that of GAPDH. The sequences of both forward and reverse primers are listed in Table 1.

Western Blotting Assay. Total proteins were extracted from liver using Cell Lysis Buffer for Western and IP (Beyotime Institute of Biotechnology, Haimen, Jiangsu, China) containing 1% phenylmethanesulfonyl fluoride (Beyotime Institute of Biotechnology, Haimen, Jiangsu, China) and 1% phosphatase inhibitor cocktail (Roche Diagnostics GmbH, Mannheim, Germany). Protein concentrations were determined by the Lowry method.[26] Twenty micrograms of protein was separated by electrophoresis on a 6%, 8%, or 12% sodium dodecyl sulfate-polyacrylamide gel, and electrophoretically transferred to polyvinylidene difluoride membranes. The blots were incubated with specific primary antibodies for 1 h at room temperature: rabbit anti-AMPKα1/2 antibodies, rabbit anti-phospho-p44/42 MAPK, rabbit p44/42 MAPK, rabbit anti-phospho-p38 MAPK, and rabbit p38 MAPK antibodies (1:200 dilution); mouse anti-SREBP-1 and rabbit anti-phospho-AMPKα1/2 (1:750 dilution); rabbit anti-acetyl-CoA carboxylase and rabbit anti-phospho-acetyl-CoA carboxylase antibodies (1:2000 dilution); and mouse anti-GAPDH antibody (1:10000 dilution) overnight at 4 °C. They were then incubated with a secondary antibody: rabbit polyclonal anti-immunoglobulin G (IgG), or mouse or rabbit monoclonal anti-IgG (1:2000 dilution). Antibody binding was detected using an enhanced chemiluminescence kit with hyper-enhanced chemiluminescence film.

Statistical Analysis. All results were expressed as the mean ± standard deviation (SD). Statistical comparisons were performed using one way analysis of variance (ANOVA) with Dunnett's multiple comparison test or unpaired Student's *t* test. The analyses were performed with SPSS software (version 16.0, SPSS Inc., Chicago, IL). A p value less than 0.05 was considered to be statistically significant. The Western blot and optical histological results were obtained from at least three independent experiments, and the analysis was carried out with triplicate samples.

RESULTS

EEGS Attenuated Acute Ethanol-Induced Lipid Accumulation in the Liver. ALT is released from the cytoplasm of impaired hepatocytes. Its serum activity is most commonly used in clinical practice as a reliable primary indicator for ALD.[5,27] As shown in Figure 3A, acute alcohol gavage significantly increased serum activities of ALT (37.9 ± 6.0 U/L vs 30.5 ± 4.2 U/L); this elevation was significantly diminished by treatment with EEGS at a dose of 50 mg/kg. EEGS at a dose of 25 mg/kg also prevented the increase in ALT activity to a certain extent but with no significant difference compared with Group IB. As shown in Figure 3B, acute alcohol gavage increased serum activities of AST. This elevation was significantly diminished by treatment with 50 mg/kg EEGS. EEGS at a dose of 25 mg/kg also slightly prevented the increase in AST activity, but with no significant difference compared with Group IB. According to the above ALT and AST results, the suppressive effect on ethanol-induced injury occurred in a dose-dependent manner.

To assess the effect of EEGS on hepatic steatosis induced by acute ethanol intake, hepatic lipid accumulation was qualitatively examined by oil red O staining and quantitatively determined by a TG quantification kit. After three doses of ethanol administration via oral gavage, mice from both the ethanol group and ethanol plus EEGS groups exhibited obvious accumulation of neutral lipid droplets in their livers compared with the control group, as illustrated by oil red O staining (Figure 3D,E). The lipid droplets in the livers of the EEGS-treated groups were much fewer than those in the model group. Quantitative analysis (Figure 3F) confirmed the histological results by demonstrating that acute ethanol gavage dramatically increased the hepatic TG content in mice, and this elevation was significantly diminished by treatment of EEGS at doses of 12.5 and 50 mg/kg. These data clearly indicated that EEGS could effectively reverse acute ethanol-induced hepatic lipid accumulation. Although the data from the H&E staining and oil red O staining (Figure 3C−E) indicated the treatment with EEGS at dose of 25 mg/kg exerted a protective effect, the data in Figure 3F showed a tendency without statistical significance. In view of significant effect of both 12.5 and 50 mg/kg EEGS, the medium dose of 25 mg/kg was considered to be a turning point, and EEGS exerted bidirectional regulation in a dose-dependent manner, which usually indicates the involvement of complex active ingredients and multiple pathways. Therefore,

DOI: 10.1021/acs.jafc.5b03504
J. Agric. Food Chem. 2015, 63, 8460−8471

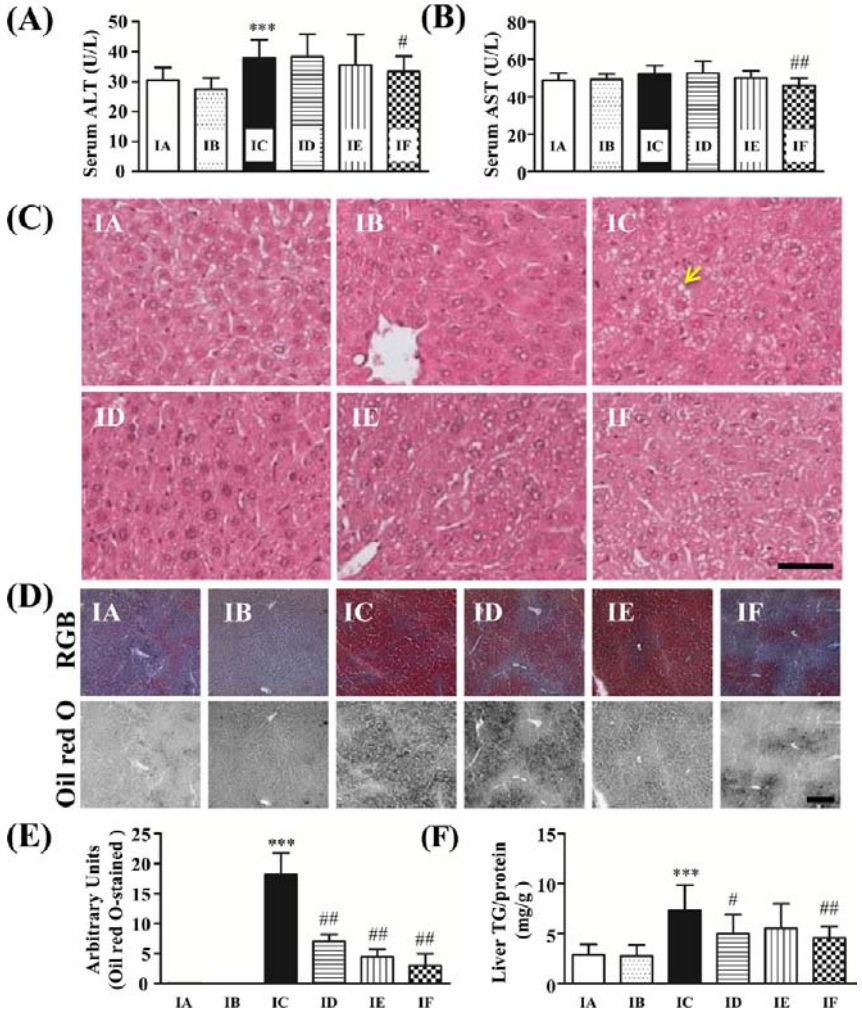

Figure 3. EEGS attenuated acute ethanol-induced liver lipid accumulation. Animals were randomly divided into six groups: Group IA, control (normal saline treated); Group IB received EEGS at a dose of 50 mg/kg only; Groups IC−IF were treated with 5 g/kg ethanol orally every 12 h for a total of three doses; and Groups ID, IE, and IF were treated with EEGS at doses of 12.5, 25, and 50 mg/kg, respectively. The mice were sacrificed 4 h after the last ethanol treatment. (A) Serum alanine aminotransferase (ALT) activity. (B) Serum aspartate aminotransferase (AST) activity. (C) Representative photomicrographs of H&E staining of liver sections. Arrow indicates vacuolated hepatocytes. (D) Representative photomicrographs of oil red O staining of liver sections and (E) densitometric analysis of staining. Red is positive oil red O staining, and blue is hematoxylin counterstain. Top panel in (D): RGB images. Bottom panels: Unmixed oil red O images from the top panel. (F) Quantitation of hepatic triglyceride (TG) content. Data are expressed as the mean ± SD, $n = 15$; $^{***}P < 0.001$ vs control; $^{\#\#}P < 0.001$ vs model. Scale bar = 100 μm.

the medium dose of 25 mg/kg was selected as an optimal dose for further study as specified below.

The *n*-Butanol Fraction Extracted from EEGS Was the Active Fraction of EEGS. Serum ALT activity and hepatic lipid accumulation were used as assessment criteria to screen the active fraction(s) of EEGS. Hepatic lipid accumulation was evaluated by vacuolation in H&E stained sections and quantitatively determined by a TG quantification kit.

As shown in Figure 4B, acute alcohol gavage increased serum ALT activity to a certain extent, and this elevation was significantly diminished by treatment with the *n*-butyl alcohol fraction from EEGS. In addition, the *n*-butyl alcohol fraction significantly reduced the ethanol-induced hepatic lipid accumulation as shown in Figure 4A,C. Again, treatment with EEGS only showed a tendency without statistical significance (Figure 4C), which was consistent with the data in Figure 3F. Moreover, these data provide a further evidence for the existence of bidirectional regulation in protective effect of EEGS against ethanol-induced liver steatosis. Together, the *n*-butanol fraction was determined to be the most active fraction of EEGS and was selected for further fractionation by the polyamide glass column.

Fraction 2 Was the Active Fraction of the *n*-Butyl Alcohol Extract. As shown in Figure 5B, acute alcohol gavage significantly increased serum ALT activity, and this elevation was diminished by treatment of fraction 1, 2, or 3 to a certain extent. In addition, fractions 1 and 2 significantly reduced the ethanol-induced hepatic lipid accumulation as shown in Figure 5A,C. Thus, fractions 1 and 2 were determined to be the active fractions of the *n*-butyl alcohol extract according to the screening criteria mentioned above. Compared with fraction 1, fraction 2 had fewer compounds (Figure 2) and required a lower dose to achieve similar activity. Thus, fraction 2 was selected for further study.

EEGS, Fraction 2, and Chlorogenic Acid Attenuated Chronic Ethanol-Induced Hepatic Lipid Accumulation. As shown in Figure 6D, chronic alcohol treatment increased serum ALT activity, and this elevation was significantly

DOI: 10.1021/acs.jafc.5b03504
J. Agric. Food Chem. 2015, 63, 8460−8471

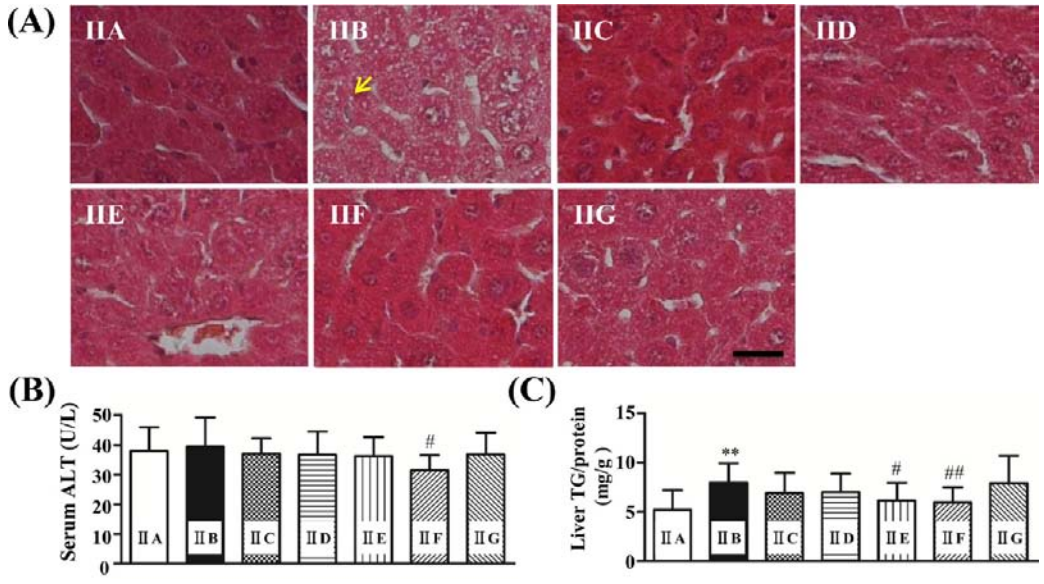

Figure 4. The *n*-butanol fraction was the active fraction of EEGS. Animals were randomly divided into seven groups: Group IIA, control (normal saline treated); Group IIB was treated with 5 g/kg ethanol only; Groups IIC, IID, IIE, IIF, and IIG received oral administration with 5 g/kg ethanol plus EEGS (25 mg/kg), petroleum ether fraction (1.35 mg/kg), ethyl acetate fraction (3.55 mg/kg), *n*-butanol fraction (3.33 mg/kg), or water fraction (16.75 mg/kg), respectively, every 12 h for a total of three doses. (A) Representative photomicrographs of H&E staining of liver sections. The arrow indicates vacuolated hepatocytes. (B) Serum alanine aminotransferase (ALT) activity. (C) Quantitation of hepatic triglyceride (TG) content. Data are expressed as the mean ± SD, $n = 12$; $^{**}P < 0.01$ vs control; $^{\#}P < 0.05$ and $^{\#\#}P < 0.01$ vs model. Scale bar = 100 μm.

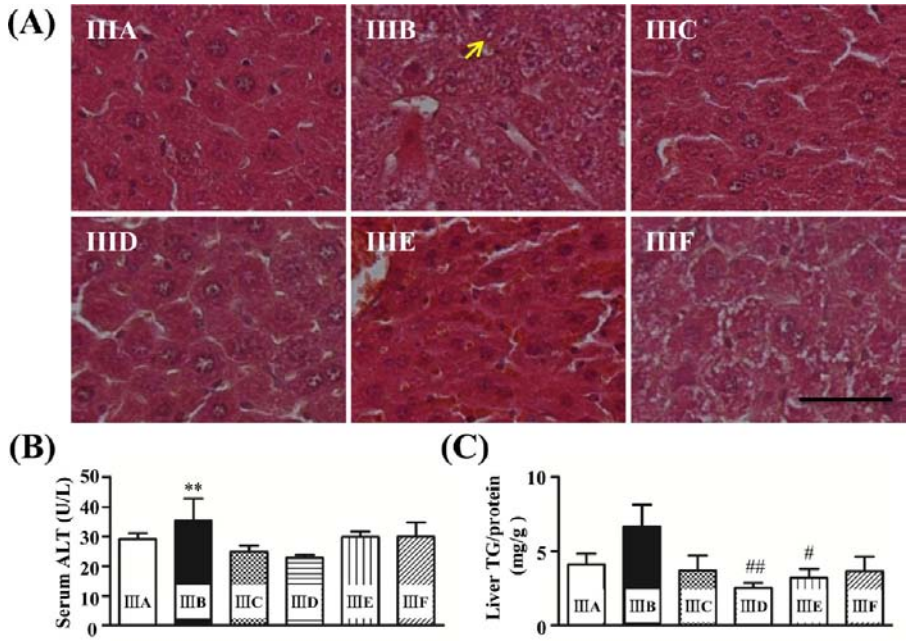

Figure 5. Fraction 2 was the active fraction of the *n*-butyl alcohol extract. Animals were randomly divided into six groups with 6−9 mice per group: Group IIIA, control (normal saline treated); Group IIIB, treated with 5 g/kg ethanol only; Groups IIIC, IIID, IIIE, and IIIF were orally treated with 5 g/kg ethanol plus the *n*-butanol fraction (3.33 mg/kg), fraction 1 (3.10 mg/kg), fraction 2 (0.22 mg/kg), or fraction 3 (0.03 mg/kg), respectively, every 12 h for a total of three doses. (A) Representative photomicrographs of H&E staining of liver sections. The arrow indicates vacuolated hepatocytes. (B) Serum alanine aminotransferase (ALT) activity. (C) Quantitation of hepatic triglyceride (TG) content. Data are expressed as the mean ± SD, $n = 6–9$; $^{**}P < 0.01$ vs control; $^{\#}P < 0.05$ and $^{\#\#}P < 0.01$ vs model. Scale bar = 100 μm.

diminished by treatment with fraction 2. EEGS, chlorogenic acid, and silymarin also prevented the increase in ALT activity to a certain extent, but were not significantly different from Group IVB. Chronic ethanol-induced vacuolation in H&E staining and red staining in the oil red O staining of liver sections were far more serious than that of the acute sections (Figure 6A−C). All of the treatments, including EEGS, fraction 2, chlorogenic acid, and silymarin, attenuated chronic ethanol-induced liver lipid accumulation. EEGS and fraction 2 were more potent than chlorogenic acid and silymarin. Fraction 2 had similar effects as EEGS but was purer and more powerful (10 mg/kg/day vs 75 mg/kg/day).

EEGS Alleviated the Ethanol-Induced Expression of Genes Involved in Lipid Metabolism and Inflammation

DOI: 10.1021/acs.jafc.5b03504
J. Agric. Food Chem. 2015, 63, 8460−8471

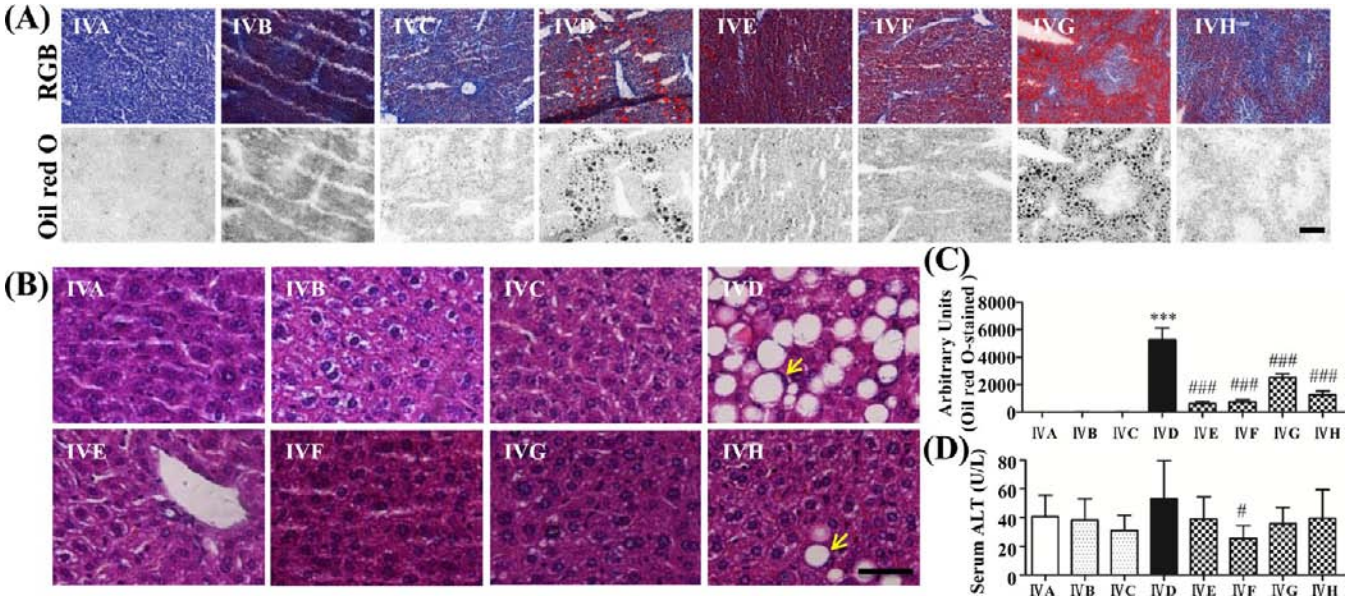

Figure 6. EEGS, fraction 2, and chlorogenic acid attenuated chronic ethanol-induced lipid accumulation in liver. Mice were divided into eight groups with 6−10 mice per group: Group IVA received a standard solid diet and water ad libitum; Group IVB, control (received an isocaloric maltodextrin-containing diet in a pair-fed fashion); Group IVC received an isocaloric maltodextrin-containing diet and was orally treated with EEGS (75 mg/kg/day) for the last 2 weeks; Groups IVD−IVH were treated with an ethanol-containing diet; Groups IVE, IVF, IVG, and IVH were orally treated with EEGS (75 mg/kg/day), fraction 2 (10 mg/kg/day), chlorogenic acid (10 mg/kg/day), or silymarin (100 mg/kg/day), respectively, for the last 2 weeks. Either the ethanol-containing diet or the isocaloric maltodextrin (control) diet was fed to the animals for 8 weeks. (A) Representative photomicrographs of oil red O staining of liver sections and (C) densitometric analysis of staining. Red is positive oil red O staining, and blue is hematoxylin counterstain. Top panels in (A): RGB images. Bottom panels: unmixed oil red O images of the up panel. (B) Representative photomicrographs of H&E staining of liver sections. Arrow indicates vacuolated hepatocytes. (D) Serum alanine aminotransferase (ALT) activity. Data are expressed as the mean ± SD, $n = 6-10$; $^{***}P < 0.001$ vs pair-fed control; $^{\#}P < 0.05$ and $^{\#\#\#}P < 0.001$ vs model. Scale bar for (A) = 100 μm. Scale bar for (B) = 50 μm.

in an Acute Model. Ethanol significantly induced the expression of fatty acid-uptake genes, including *Fabp1* and *Fabp4*, and fatty acid-synthesis genes, including *Fasn* and *SREBP-1*, in the liver (Figure 7A). Intriguingly, EEGS treatment reduced the expression levels of *Fabp1*, *Fabp4*, *Fasn*, and *SREBP-1*. The genes involved in fatty acid *β*-oxidation (*CPT1A*) and TG-secretion (*MTTP*) were also enhanced by ethanol exposure. However, EEGS significantly reduced the mRNA expression of *CPT1A* and *MTTP*. Moreover, ethanol did not show any significant effects on *PPAR-α*, *PPAR-γ*, or *ApoB* mRNA expression when compared to normal controls. *PPAR-γ* and *ApoB* mRNA expressions were upregulated by EEGS in the presence or absence of ethanol.

We also analyzed inflammation markers including *CD68*, *IL-1β*, *IL-6*, *CD163*, *Arginase*, *TGF-β*, *F4/80*, *MCP-1*, and *TNF-α* (Figure 7B). We found that ethanol exposure elevated the expression of almost all of the above genes except for *F4/80* and *TNF-α*. However, EEGS treatment reversed these ethanol-induced mRNA changes. Even *F4/80* and *TNF-α* mRNA expressions were reduced by EEGS treatment. These data indicated that EEGS might relieve ethanol-induced liver damage by regulating of lipid metabolism and reducing inflammatory responses in the liver.

Administration of EEGS, Fraction 2, or Chlorogenic Acid Alleviated Hepatic Steatosis through MAPK/SREBP-1c-Dependent and -Independent Pathways. Premature SREBP-1c (pSREBP-1c) is cleaved and activated in response to ethanol feeding, which is closely associated with an increased expression of hepatic lipogenic genes and the accumulation of TG in the liver.[28] To investigate the possible underlying mechanisms of EEGS-mediated hepatic improvements, we measured the changes of SREBP-1c and its upstream regulators (MAPK and AMPK) and downstream effector (ACC) in the chronic model. There are two obvious bands of SREBP-1c in Figure 8A, the top one is so-called pSREBP-1c, and the bottom one is mSREBP-1c. The pSREBP-1c band in the present study represented both normal and phosphorylated form of premature SREBP-1c. Both the premature and mature forms of SREBP-1c were significantly elevated by chronic ethanol administration. After treatment with EEGS or fraction 2, the influence of ethanol on mSREBP-1c was abolished.

Consequently, we measured the changes of key MAPK members, which suppress SREBP-1c activity by phosphorylation.[15,29] The administration of ethanol significantly decreased the phosphorylation of both p38 MAPK and p44/42 MAPK (Figure 8B). After treatment with EEGS or fraction 2, the influence of ethanol on the phosphorylation of both p38 MAPK and p44/42 MAPK proteins was abolished. In addition, ethanol treatments decreased the total expression of p38 MAPK but not p44/42 MAPK.

Moreover, the effect of ethanol on SREBP-regulated promoter activation was mediated, at least in part, through inhibition of AMPK.[30] However, neither the ethanol nor the EEGS treatments demonstrated any effects on the expression of the total or phosphorylated form of AMPK (Figure 8C). These data indicated that AMPK was not involved in the SREBP-1c pathway in the present study.

The first committed step in fatty acid biosynthesis is carried out by ACC.[10] The regulation of ACC occurs at multiple levels. The first level is regulated by phosphorylation/dephosphorylation, and AMPK phosphorylates and inhibits ACC enzymatic activity.[10,31] The second level is regulated by

DOI: 10.1021/acs.jafc.5b03504
J. Agric. Food Chem. 2015, 63, 8460−8471

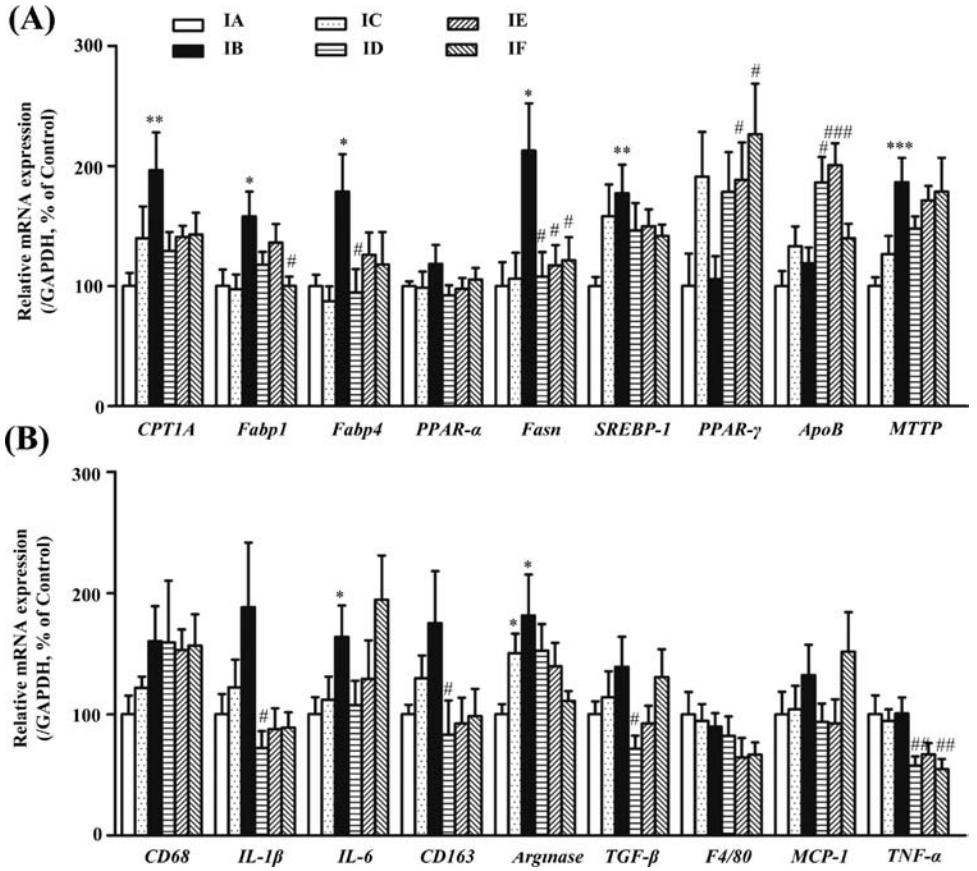

Figure 7. Hepatic expression levels of lipid metabolism-related and inflammation marker genes in mice. Group IA, control (normal saline treated); Group IB received EEGS at a dose of 50 mg/kg only; Groups IC–IF were treated with ethanol orally every 12 h for a total of three doses; Groups ID, IE, and IF were treated with EEGS at a dose of 12.5, 25, and 50 mg/kg, respectively. The mice were sacrificed 4 h after the last ethanol treatment. The mRNA expression of lipid metabolism-related genes (A) and the mRNA expression of inflammation markers (B) were evaluated by quantitative real-time PCR analysis and normalized to the housekeeping gene GAPDH. Data are expressed as the mean ± SD of 15 mice; $^{*}P < 0.05$ and $^{**}P < 0.01$ vs control; $^{\#}P < 0.05$, $^{\#\#}P < 0.01$, and $^{\#\#\#}P < 0.001$ vs model.

transcription, and SREBP-1c increases *ACC* expression.[11,12] In the present study, total ACC and its phosphorylated form were evaluated during chronic ethanol administration (Figure 8C). However, the ratio between the phosphorylated and total ACC forms was progressively decreased by chronic ethanol administration, and after treatment with EEGS or fraction 2, the influence of ethanol on the ratio was abolished.

The administration of EEGS and fraction 2 abolished the influence of ethanol on SREBP-1c activation, its upstream regulators (phosphorylation of both p38 MAPK and p44/42 MAPK) and downstream effectors, such as ACC. Thus, the MAPK/SREBP-1c-dependent pathway participated in the protective effect of EEGS and fraction 2 against hepatic steatosis.

As one of the major active ingredients of fraction 2, chlorogenic acid canceled the negative effect of ethanol on ACC expression and activation. However, unlike fraction 2, chlorogenic acid did not change the MAPK or SREBP-1c activity in the current study. This result indicated that chlorogenic acid inhibited ACC in a MAPK/SREBP-1c-independent manner and that there are other ingredient(s) in fraction 2 that impact the MAPK/SREBP-1c pathway.

DISCUSSION

Over the past decade, dozens of herbs and individual compounds isolated from herbs have been shown to possess protective effects against ethanol-induced liver injury. A previous review has collected 34 herbal medicines and/or active compounds specifically used for that purpose.[27] As summarized by Ding et al. in that review, the underlying mechanisms and active ingredients have not been sufficiently elucidated. In the present study, the capability of EEGS and its fractions to protect against ethanol-induced liver injury were investigated. Emphasis was placed upon the underlying molecular mechanisms and the active ingredient and its contributions to the protective effect.

The ability to prevent increased serum ALT activity and hepatic lipid accumulation in acute ethanol-induced liver steatosis was used as an assessment criterion to screen the active fraction(s) from EEGS. The *n*-butyl alcohol extract was the active fraction of EEGS and was selected for further fractionation by the polyamide glass column. The 60% ethanol-eluted fraction that contained 13.6% chlorogenic acid was the most active fraction, and its effects were further evaluated in the chronic model.

Data in the chronic model demonstrated that treatment with the *n*-butyl alcohol extract, 60% ethanol-eluted fraction, or chlorogenic acid protected against ethanol-induced liver steatosis, indicating that chlorogenic acid, at least in part, contributed to the beneficial effect of *G. procumbens* on alcoholic fatty liver. Compared with the doses of well-known commercial products, such as *Panax notoginseng* saponins

DOI: 10.1021/acs.jafc.5b03504
J. Agric. Food Chem. 2015, 63, 8460–8471

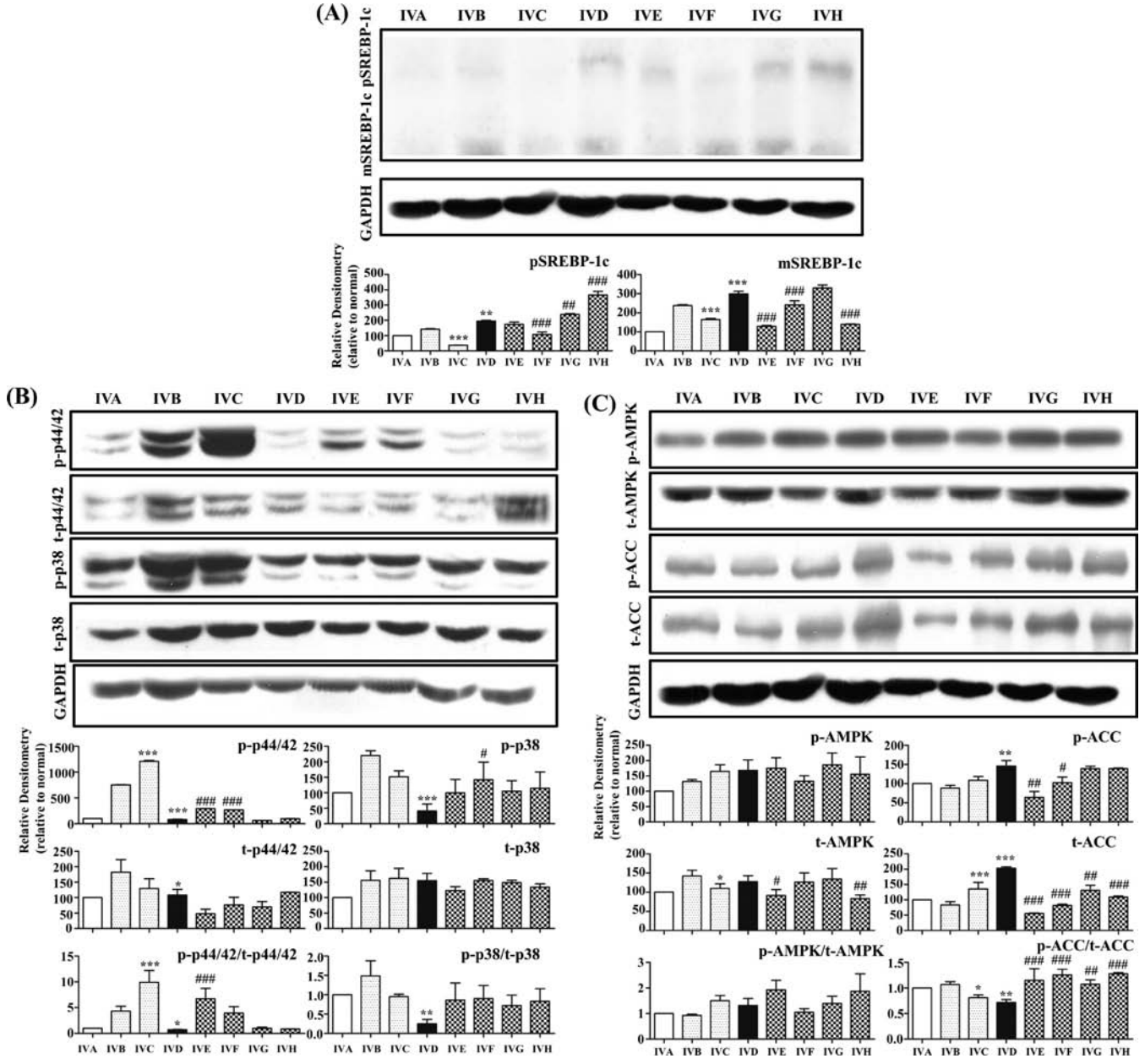

Figure 8. Effect of EEGS, fraction 2, or chlorogenic acid on the protein expression of the MAPK/SREBP-1c/ACC pathway. Mice were divided into eight groups with 6−10 mice per group: Group IVA received a standard solid diet and water ad libitum; Group IVB, control (received an isocaloric maltodextrin-containing diet in a pair-fed fashion); Group IVC received an isocaloric maltodextrin-containing diet and was orally treated with EEGS (75 mg/kg/day) for the last 2 weeks; Groups IVD−IVH were treated with an ethanol-containing diet; Groups IVE, IVF, IVG, and IVH were orally treated with EEGS (75 mg/kg/day), fraction 2 (10 mg/kg/day), chlorogenic acid (10 mg/kg/day), or silymarin (100 mg/kg/day), respectively, for the last 2 weeks. Either the ethanol-containing diet or the isocaloric maltose-dextrin (control) diet was fed to the animals for 8 weeks. Western blot analysis using a specific antibody was used to examine the expression of the proteins in the mouse liver homogenates. Bands densities were determined using ImageJ, normalized to GAPDH, and expressed as a percentage of the standard solid diet control. Representative photographs of Western blots of SREBP-1c (A), p44/42 MAPK and p38 MAPK (B), and ACC and AMPK (C), with quantitative analysis of blots given below each set of photographs, where each bar represents the mean ± SD of the results obtained from three mice. $^{*}P < 0.05$, $^{**}P < 0.01$, and $^{***}P < 0.001$ vs pair-fed control; $^{\#}P < 0.05$, $^{\#\#}P < 0.01$, and $^{\#\#\#}P < 0.001$ vs model.

(100−300 mg/kg/day),[5] silymarin (100−200 mg/kg/day),[21] or most of the above-mentioned herbal medicines, the dose of fraction 2 and chlorogenic acid used in the present study was much lower, just 10 mg/kg/day. In addition, in the present study, fraction 2 showed better potential than chlorogenic acid and silymarin to prevent ethanol-induced liver steatosis.

The mechanism by which ethanol causes fatty liver and liver injury is complicated. Anti-oxidative stress, anti-inflammation, and lipid metabolism regulation are three major mechanisms that are involved in the protective effect of herbal medicines against ALD.[1,27] Alcoholic fatty liver is the earliest and most common response of the liver to alcohol and may be a precursor of more severe forms of liver injury. SREBP-1c is a master regulator of lipid homeostasis, and SREBP-1 knockout mice are completely protected from ALD, indicating a causal involvement of SREBP-1 in ALD.[16] SREBP-1c positively

DOI: 10.1021/acs.jafc.5b03504
J. Agric. Food Chem. 2015, 63, 8460−8471

regulates the expression of genes encoding lipogenic enzymes, including ACC and FAS.[11,12] The most important function of ACC is to provide the malonyl-CoA substrate for the synthesis of fatty acids, and the main function of FAS is to catalyze the synthesis of palmitate. The present study indicated that ethanol induced expression levels of ACC and FAS, which is in accordance with a previous report.[28]

The effect of ethanol on SREBP-regulated promoter activation was mediated, at least in part, through inhibition of AMPK and MAPK.[30] In several studies, AMPK phosphorylation is increased,[32,33] whereas in other studies, AMPK phosphorylation is decreased.[34,35] Ethanol (amount and feeding duration) and fat (type and dose) used in these studies might contribute to the discrepancies.[36] Unlike AMPK, the changes of MAPK were in accordance with SREBP-1c, indicating a possible link between MAPK and SREBP-1c and its downstream genes in the present study. The administration of EEGS and fraction 2 abolished the influence of ethanol on SREBP-1c activation and its upstream regulators and downstream effectors. Thus, the MAPK/SREBP-1c-dependent pathway contributes to the mechanism of the beneficial effect of EEGS and fraction 2 on alcoholic fatty liver.

As one of the major active ingredients of fraction 2, chlorogenic acid was chosen to further investigate the underlying mechanism. Chlorogenic acid has many biological properties, including anti-bacterial, anti-oxidant, and anti-carcinogenic activities. Recently, the roles and applications of chlorogenic acid in relation to hepatic steatosis have been highlighted.[37,38] Chlorogenic acid inhibits the MAPK pathway[39,40] to protect drug-induced liver injury while activating AMPK to improve lipid metabolism in non-alcoholic fatty liver disease.[37] However, unlike fraction 2, chlorogenic acid did not change MAPK or SREBP-1c activity in the current study, which indicated that chlorogenic acid inhibited ACC in a MAPK/SREBP-1c-independent pathway and that there was an addtional ingredient(s) in fraction 2 that impacted the MAPK/SREBP-1c pathway. In addition to AMPK, protein kinase A also has the ability to phosphorylate ACC. Other kinases are also suspected to be important in this regulation, because many other possible phosphorylation sites exist on ACC.[41] Both MAPK/SREBP-1c-dependent and -independent pathways contributed to the regulation of *G. procumbens* on lipid metabolism-related genes, which exerted subsequent protective effects against ethanol-induced hepatic lipid accumulation.

ALD is a complex process. In addition to lipid accumulation, ethanol-induced liver injury is highly linked to inflammatory and oxidative stress.[1] Inflammation and oxidative stress are two etiological factors that have been suggested to play important roles in the development of ethanol-induced liver injury. Silymarin, the positive control in the present study, is a good example of an agent that protects against alcohol-induced liver disease via anti-inflammatory and anti-oxidative features.[21] Increased pro-inflammatory cytokine levels have been well documented in ALD.[42] EEGS treatment alleviated the ethanol-induced upregulation of cytokine levels, which should have resulted in a corresponding attenuation of ethanol-induced liver injury. In addition, because chlorogenic acid is an anti-oxidant and ethanol treatment enhances oxidative stress in the liver,[43] we could assume that the reduction of oxidative stress may also partially contribute to the prevention of liver injury in the present study, but more precise experiments are needed to further confirm that hypothesis.

In summary, our data show that *G. procumbens* protected against ethanol-induced liver steatosis, possibly through ameliorating hepatic lipid accumulation by modulating lipid metabolism-related genes through MAPK/SREBP-1c-dependent and -independent pathways. Our findings also suggest that *G. procumbens* and one of its active ingredients, chlorogenic acid, could potentially be developed as effective agents for acute or chronic ethanol-induced liver injury.

AUTHOR INFORMATION

Corresponding Authors

*(H.-B.T.) Tel/fax: +86 27 6784 2332. E-mail: hbtang2006@mail.scuec.edu.cn.

*(H.-C.S.) Tel/fax: +86 10 8401 2510. E-mail: shanghongcai@126.com.

Author Contributions

#X.-J.L. and Y.-M.M. contributed equally to this work.

Author Contributions

Y.-M.M., T.-T.L., M.-T.Z., Y.-L.Y., and X.-J.L. carried out the experiments. X.-J.L., H.-B.T., and H.-C.S. proposed and designed the research, performed the data analysis, and wrote the paper. Y.-S.L. and W.K.Z. assisted in the data analysis and interpretation.

Funding

This study was supported by grants from the National Natural Science Foundation of China (81403188 and 81373842), the Modernization Engineering Technology Research Center of Ethnic Minority Medicine of Hubei province (2015ZY002), and the Natural Science Foundation of China Hubei (2013CFB451).

Notes

The authors declare no competing financial interest.

ABBREVIATIONS USED

EEGS, ethanol extract from *Gynura procumbens* stems; MAPK, mitogen-activated protein kinase; SREBP-1c, sterol regulatory element binding protein 1c; ALT, alanine transaminase; AST, aspartate transaminase; ALD, alcoholic liver disease; AMPK, 5′-adenosine monophosphate-activated protein kinase; TG, triglyceride; H&E, hematoxylin and eosin; RT-PCR, real-time polymerase chain reaction; IgG, immunoglobulin G; ACC, acetyl-coenzyme A carboxylase; CPT1A, carnitine palmitoyltransferase 1A; Fabp1, fatty acid binding protein 1; Fabp4, fatty acid binding protein 4; PPAR-α, peroxisome proliferator-activated receptor-α; Fas, fatty acid synthase; PPAR-γ, peroxisome proliferator-activated receptor-γ; ApoB, apolipoprotein B; MTTP, microsomal triglyceride transfer protein; CD68, cluster of differentiation 68; IL-1β, interleukin-1β; IL-6, interleukin-6; CD163, cluster of differentiation 163; TGF-β, transforming growth factor-β; F4/80, EGF-like module-containing mucin-like hormone receptor-like 1; MCP-1, monocyte chemotactic protein 1; TNF-α, tumor necrosis factor-α

REFERENCES

(1) Louvet, A.; Mathurin, P. Alcoholic liver disease: mechanisms of injury and targeted treatment. *Nat. Rev. Gastroenterol. Hepatol.* **2015**, *12*, 231−42.

(2) Testino, G.; Leone, S.; Ansaldi, F.; Borro, P. Silymarin and S-adenosyl-L-methionine (SAMe): two promising pharmacological agents in case of chronic alcoholic hepathopathy. A review and a point of view. *Minerva Gastroenterol. Dietol.* **2013**, *59*, 341−56.

DOI: 10.1021/acs.jafc.5b03504
J. Agric. Food Chem. 2015, 63, 8460−8471

(3) Xiao, S. J.; Fu, G. J.; Lv, Y. L.; Zhong, X. N.; Wang, R. H. Prevalence and risk factors of fatty liver disease in young and middle-aged population: one center study in Southwestern China. *J. Gastroenterol. Hepatol.* **2014**, *29*, 358−64.
(4) O'Shea, R. S.; Dasarathy, S.; McCullough, A. J. Alcoholic liver disease. *Am. J. Gastroenterol.* **2010**, *105*, 14−32 (quiz 33).
(5) Ding, R. B.; Tian, K.; Cao, Y. W.; Bao, J. L.; Wang, M.; He, C.; Hu, Y.; Su, H.; Wan, J. B. Protective effect of panax notoginseng saponins on acute ethanol-induced liver injury is associated with ameliorating hepatic lipid accumulation and reducing ethanol-mediated oxidative stress. *J. Agric. Food Chem.* **2015**, *63*, 2413−22.
(6) Algariri, K.; Meng, K. Y.; Atangwho, I. J.; Asmawi, M. Z.; Sadikun, A.; Murugaiyah, V.; Ismail, N. Hypoglycemic and anti-hyperglycemic study of Gynura procumbens leaf extracts. *Asian Pac. J. Trop. Biomed.* **2013**, *3*, 358−66.
(7) Nisa, F.; Hermawan, A.; Murwanti, R.; Meiyanto, E. Antiproliferative effect of gynura procumbens (lour.) Merr. Leaves etanolic extract on 7,12-dimethylbenz(a)antracene induced male rat liver. *Adv. Pharm. Bull.* **2012**, *2*, 99−106.
(8) Shwter, A. N.; Abdullah, N. A.; Alshawsh, M. A.; Alsalahi, A.; Hajrezaei, M.; Almaqrami, A. A.; Salem, S. D.; Abdulla, M. A. Chemoprevention of colonic aberrant crypt foci by Gynura procumbens in rats. *J. Ethnopharmacol.* **2014**, *151*, 1194−201.
(9) Mahmood, A. A.; Mariod, A. A.; Al-Bayaty, F.; Abdel-Wahab, S. I. Anti-ulcerogenic activity of Gynura procumbens leaf extract against experimentally-induced gastric lesions in rats. *J. Med. Plant Res.* **2010**, *4*, 685−91.
(10) Kim, C. W.; Moon, Y. A.; Park, S. W.; Cheng, D.; Kwon, H. J.; Horton, J. D. Induced polymerization of mammalian acetyl-CoA carboxylase by MIG12 provides a tertiary level of regulation of fatty acid synthesis. *Proc. Natl. Acad. Sci. U. S. A.* **2010**, *107*, 9626−31.
(11) Shimano, H. Sterol regulatory element-binding proteins (SREBPs): transcriptional regulators of lipid synthetic genes. *Prog. Lipid Res.* **2001**, *40*, 439−52.
(12) Horton, J. D.; Goldstein, J. L.; Brown, M. S. SREBPs: activators of the complete program of cholesterol and fatty acid synthesis in the liver. *J. Clin. Invest.* **2002**, *109*, 1125−31.
(13) Li, Y.; Xu, S. Q.; Mihaylova, M. M.; Zheng, B.; Hou, X. Y.; Jiang, B. B.; Park, O.; Luo, Z. J.; Lefai, E.; Shyy, J. Y. J.; Gao, B.; Wierzbicki, M.; Verbeuren, T. J.; Shaw, R. J.; Cohen, R. A.; Zang, M. W. AMPK Phosphorylates and Inhibits SREBP Activity to Attenuate Hepatic Steatosis and Atherosclerosis in Diet-Induced Insulin-Resistant Mice. *Cell Metab.* **2011**, *13*, 376−388.
(14) Hong-Brown, L. Q.; Brown, C. R.; Huber, D. S.; Lang, C. H. Alcohol and indinavir adversely affect protein synthesis and phosphorylation of MAPK and mTOR signaling pathways in C2C12 myocytes. *Alcohol.: Clin. Exp. Res.* **2006**, *30*, 1297−307.
(15) Knebel, B.; Lehr, S.; Hartwig, S.; Haas, J.; Kaber, G.; Dicken, H. D.; Susanto, F.; Bohne, L.; Jacob, S.; Nitzgen, U.; Passlack, W.; Muller-Wieland, D.; Kotzka, J. Phosphorylation of sterol regulatory element-binding protein (SREBP)-1c by p38 kinases, ERK and JNK influences lipid metabolism and the secretome of human liver cell line HepG2. *Arch. Physiol. Biochem.* **2014**, *120*, 216−27.
(16) Ji, C.; Chan, C.; Kaplowitz, N. Predominant role of sterol response element binding proteins (SREBP) lipogenic pathways in hepatic steatosis in the murine intragastric ethanol feeding model. *J. Hepatol.* **2006**, *45*, 717−24.
(17) Carson, E. J.; Pruett, S. B. Development and characterization of a binge drinking model in mice for evaluation of the immunological effects of ethanol. *Alcohol.: Clin. Exp. Res.* **1996**, *20*, 132−8.
(18) Massey, V. L.; Arteel, G. E. Acute alcohol-induced liver injury. *Front. Physiol.* **2012**, *3*, 193.
(19) Kanuri, G.; Weber, S.; Volynets, V.; Spruss, A.; Bischoff, S. C.; Bergheim, I. Cinnamon extract protects against acute alcohol-induced liver steatosis in mice. *J. Nutr.* **2009**, *139*, 482−7.
(20) Lieber, C. S.; DeCarli, L. M.; Sorrell, M. F. Experimental methods of ethanol administration. *Hepatology* **1989**, *10*, 501−10.
(21) Song, Z.; Deaciuc, I.; Song, M.; Lee, D. Y.; Liu, Y.; Ji, X.; McClain, C. Silymarin protects against acute ethanol-induced hepatotoxicity in mice. *Alcohol.: Clin. Exp. Res.* **2006**, *30*, 407−13.
(22) Chou, C. H.; Chen, Y. C.; Hsu, M. C.; Tsai, W. L.; Chang, C. Y.; Chiu, C. H. Effect Of Silymarin on Lipid And Alcohol Metabolism In Mice Following Long-Term Alcohol Consumption. *J. Food Biochem.* **2012**, *36*, 369−377.
(23) Zuba, D.; Parczewski, A.; Reichenbacher, M. Optimization of solid-phase microextraction conditions for gas chromatographic determination of ethanol and other volatile compounds in blood. *J. Chromatogr. B: Anal. Technol. Biomed. Life Sci.* **2002**, *773*, 75−82.
(24) Nanji, A. A.; Jokelainen, K.; Lau, G. K. K.; Rahemtulla, A.; Tipoe, G. L.; Polavarapu, R.; Lalani, E. N. Arginine reverses ethanol-induced inflammatory and fibrotic changes in liver despite continued ethanol administration. *J. Pharmacol. Exp. Ther.* **2001**, *299*, 832−839.
(25) Li, Y. S.; Wang, J. X.; Jia, M. M.; Liu, M.; Li, X. J.; Tang, H. B. Dragon's blood inhibits chronic inflammatory and neuropathic pain responses by blocking the synthesis and release of substance P in rats. *J. Pharmacol. Sci.* **2012**, *118*, 43−54.
(26) Lowry, O. H.; Rosebrough, N. J.; Farr, A. L.; Randall, R. J. Protein measurement with the Folin phenol reagent. *J. Biol. Chem.* **1951**, *193*, 265−75.
(27) Ding, R. B.; Tian, K.; Huang, L. L.; He, C. W.; Jiang, Y.; Wang, Y. T.; Wan, J. B. Herbal medicines for the prevention of alcoholic liver disease: a review. *J. Ethnopharmacol.* **2012**, *144*, 457−65.
(28) You, M.; Fischer, M.; Deeg, M. A.; Crabb, D. W. Ethanol induces fatty acid synthesis pathways by activation of sterol regulatory element-binding protein (SREBP). *J. Biol. Chem.* **2002**, *277*, 29342−7.
(29) Xiao, J.; Wang, J.; Xing, F.; Han, T.; Jiao, R.; Liong, E. C.; Fung, M. L.; So, K. F.; Tipoe, G. L. Zeaxanthin dipalmitate therapeutically improves hepatic functions in an alcoholic fatty liver disease model through modulating MAPK pathway. *PLoS One* **2014**, *9*, e95214.
(30) You, M.; Crabb, D. W. Molecular mechanisms of alcoholic fatty liver: role of sterol regulatory element-binding proteins. *Alcohol* **2004**, *34*, 39−43.
(31) Kahn, B. B.; Alquier, T.; Carling, D.; Hardie, D. G. AMP-activated protein kinase: ancient energy gauge provides clues to modern understanding of metabolism. *Cell Metab.* **2005**, *1*, 15−25.
(32) Shearn, C. T.; Smathers, R. L.; Jiang, H.; Orlicky, D. J.; Maclean, K. N.; Petersen, D. R. Increased dietary fat contributes to dysregulation of the LKB1/AMPK pathway and increased damage in a mouse model of early-stage ethanol-mediated steatosis. *J. Nutr. Biochem.* **2013**, *24*, 1436−45.
(33) Everitt, H.; Hu, M.; Ajmo, J. M.; Rogers, C. Q.; Liang, X.; Zhang, R.; Yin, H.; Choi, A.; Bennett, E. S.; You, M. Ethanol administration exacerbates the abnormalities in hepatic lipid oxidation in genetically obese mice. *Am. J. Physiol. Gastrointest. Liver Physiol.* **2013**, *304*, G38−47.
(34) Shen, Z.; Liang, X.; Rogers, C. Q.; Rideout, D.; You, M. Involvement of adiponectin-SIRT1-AMPK signaling in the protective action of rosiglitazone against alcoholic fatty liver in mice. *Am. J. Physiol. Gastrointest. Liver Physiol.* **2010**, *298*, G364−74.
(35) Garcia-Villafranca, J.; Guillen, A.; Castro, J. Ethanol consumption impairs regulation of fatty acid metabolism by decreasing the activity of AMP-activated protein kinase in rat liver. *Biochimie* **2008**, *90*, 460−6.
(36) Shearn, C. T.; Backos, D. S.; Orlicky, D. J.; Smathers-McCullough, R. L.; Petersen, D. R. Identification of 5′ AMP-activated kinase as a target of reactive aldehydes during chronic ingestion of high concentrations of ethanol. *J. Biol. Chem.* **2014**, *289*, 15449−62.
(37) Meng, S.; Cao, J.; Feng, Q.; Peng, J.; Hu, Y. Roles of Chlorogenic Acid on regulating glucose and lipids metabolism: a review. *Evid. Based Complement. Alternat. Med.* **2013**, *2013*, 801457.
(38) Mubarak, A.; Hodgson, J. M.; Considine, M. J.; Croft, K. D.; Matthews, V. B. Correction to Supplementation of a high-fat diet with chlorogenic acid is associated with insulin resistance and hepatic lipid accumulation in mice. *J. Agric. Food Chem.* **2015**, *63*, 1882.
(39) Feng, R. T. The chemopreventive activity of chlorogenic acid is mediated by inhibiting AP-1-MAPKs pathway and inducing phase II

DOI: 10.1021/acs.jafc.5b03504
J. Agric. Food Chem. 2015, 63, 8460−8471

detoxifying enzyme through stimulating Nrf2 signaling. *Cancer Epidem. Biomar.* **2004**, *13*, 1880s.
(40) Ji, L.; Jiang, P.; Lu, B.; Sheng, Y.; Wang, X.; Wang, Z. Chlorogenic acid, a dietary polyphenol, protects acetaminophen-induced liver injury and its mechanism. *J. Nutr. Biochem.* **2013**, *24*, 1911−9.
(41) Brownsey, R. W.; Boone, A. N.; Elliott, J. E.; Kulpa, J. E.; Lee, W. M. Regulation of acetyl-CoA carboxylase. *Biochem. Soc. Trans.* **2006**, *34*, 223−7.
(42) Kawaratani, H.; Tsujimoto, T.; Douhara, A.; Takaya, H.; Moriya, K.; Namisaki, T.; Noguchi, R.; Yoshiji, H.; Fujimoto, M.; Fukui, H. The effect of inflammatory cytokines in alcoholic liver disease. *Mediators Inflammation* **2013**, *2013*, 495156.
(43) Wu, D.; Cederbaum, A. I. Oxidative stress and alcoholic liver disease. *Semin. Liver Dis.* **2009**, *29*, 141−54.

DOI: 10.1021/acs.jafc.5b03504
J. Agric. Food Chem. 2015, 63, 8460−8471

resveratrol and its derivatives, *E*-piceatannol, *E*-ε-viniferin, ampelopsin A, *E*-miyabenol C, *Z*/*E*-vitisin B, hopeaphenol, and isohopeaphenol (Figure 1), between conducting tissues, cortex, and pith has been studied in grape canes from healthy and downy mildew-infected vineyards.

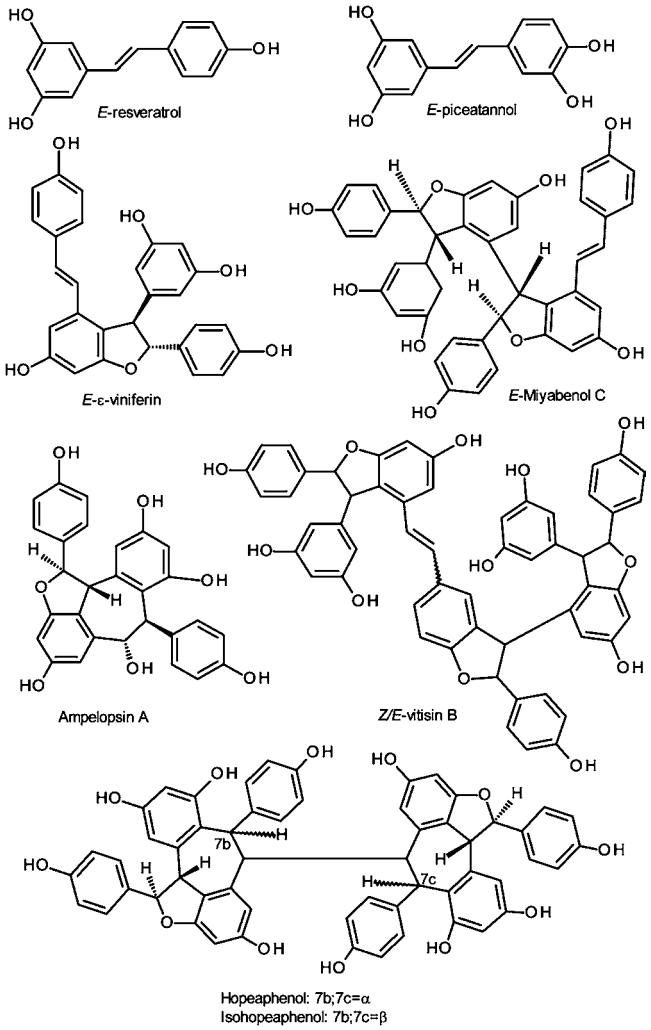

Figure 1. Selected structures of typical stilbenoids present in grape canes.

MATERIALS AND METHODS

Plant Material. The study was conducted on 35-year-old vineyards of the Bourgueil district in the Loire Valley region (France) in vintage 2011. Vineyards were planted with *V. vinifera* cv. Cabernet franc (clone 327 grafted onto 3309 rootstock) on a clay−silica−limestone soil at a spacing of 1 m (within row) × 2 m (between rows) corresponding to 5000 vines ha^{-1}. Two adjacent vineyard parcels (plot A, 47°17′28.82″ N, 0°13′28.51″ E; plot B, 47°17′49.07″ N, 0°14′34.46″ E) were selected for the study, covering areas of 0.18 and 0.233 ha, respectively. Both plots were subjected to organic management with similar practices except for the copper-based fungicide treatments. In plot A, solutions of copper were applied corresponding to 1 kg ha^{-1}. In plot B, the copper treatments were prohibited during the entire growing season to allow fungal infection. Consequently, downy mildew disease intensities at grape harvest were 5 and 95% in plots A (healthy) and B (infected), respectively. Grape canes from both parcels were harvested in December 2011. Grape canes (60 stalks per plot) were randomly pruned across the total area of plots A and B to overcome intraplot variation. Then, grape canes were stored for 10 weeks at 20 °C in the dark as 10 cm long sections.[29] After storage, five lots were constituted within grape canes originating from plots A and B to compare the stilbenoid compositions from healthy and infected vineyards. Wood sections were manually dissected to separate cortex, pith, and conducting tissues.

Stilbenoid Analysis. Whole and dissected tissues of grape canes were ground for 2 min with a cooled analytical grinder (Ika-Werke, Staufen, Germany). A second grinding step was performed using a cutting mill (Polymix PX-MFC 90 D, Kinematica AG, Switzerland) to obtain a powder with an average particle size of 1 mm. Freeze-drying was performed at 0.01 mbar and −20 °C for 48 h with a Christ Alpha I-5 freeze-dryer. For stilbenoid extraction, 50 mg of lyophilized powder was extracted in 1 mL of an ethanol/water solution (60:40; v/v), shaken for 30 min at 1400 rpm and 83 °C, and centrifuged at 18000*g* for 5 min. HPLC analyses were performed on a Waters system (Waters 600 controller, Milford, MA, USA) equipped with a UV−visible photodiode array detector (Waters 996) and a column packed with 3 μm particles (250 × 4 mm, Multospher 120 RP18HP; CS-Service, Langerwehe, Germany) at 24 °C. The mobile phase was aqueous phosphoric acid (0.1% w/v; eluent A) and acetonitrile (eluent B) pumped at 0.5 mL min^{-1}. The gradient started at 5% B and increased linearly to 72.5% after 60 min, followed by washing and reconditioning of the column. Compounds in extracts were identified according to their UV spectra and retention time by comparison with external standards. Quantification was performed using reference standards of *E*-resveratrol, *E*-piceatannol, *E*-ε-viniferin, *Z*/*E*-vitisin B, ampelopsin A, *E*-miyabenol C, and hopeaphenol and five-point calibration curves (0−100 ppm) using the Maxplot detection mode.

Chemicals. *E*-Resveratrol and *E*-piceatannol were purchased from Sigma-Aldrich (St. Louis, MO, USA). *E*-ε-Viniferin, *Z*/*E*-vitisin B, ampelopsin A, *E*-miyabenol C, and hopeaphenol were extracted from grape canes as previously described.[6] Acetonitrile and ethanol were purchased from Thermo Fisher Scientific (Courtaboeuf, France). Ultrapure water was obtained from a Millipore Milli-Q water purification system (Bedford, MA, USA).

Microscopic Analysis. Free-hand cross sections of freshly pruned grape canes from Cabernet franc variety were observed with an epifluorescence microscope (Olympus BX51; Olympus Optical, Tokyo, Japan) equipped with a digital camera (Olympus DP71) and the corresponding software (SIS Cell). The autofluorescence was observed with a UV excitation filter set (Olympus WU2, 330−385 nm excitation filter, 420 nm long pass emission filter).

Fluorescence Spectroscopy. Pure standards of *E*-resveratrol and *E*-ε-viniferin in methanol solution (2 μg mL^{-1}) and 1:100 dilution of grape cane extracts prepared as described above (whole tissues, pith, cortex, or conducting tissues) were used. Excitation and emission spectra were acquired with a spectrofluorometer (Hitachi F-4500; Hitachi, Ltd., Tokyo, Japan). The excitation spectra were acquired with an emission at 390 nm, and the emission spectra were acquired with an excitation at 320 nm.[34]

Statistical Analysis. Data were analyzed with Statistica, version 6.0 (StatSoft Inc., Tulsa, OK, USA). Statistical significance from different treatments was revealed after one-way analysis of variance (ANOVA) followed by post hoc Tukey's honestly significant difference (HSD) test.

RESULTS AND DISCUSSION

Two adjacent vineyard plots planted with the Cabernet franc grape variety both on a clay−silica−limestone soil were selected for this study to avoid stilbenoid changes due to genetic or pedo-climatic variations. The two parcels were subjected to similar agricultural practices with the exception of the copper-based fungicide treatments that were applied to plot A (1 kg ha^{-1}) and absent in plot B. As a result, mildew disease intensities at midveraison were drastically contrasted at 5 and 95% in plots A (healthy) and B (infected), respectively. Specifically in plot B, 95% of the leaves were infected by downy mildew with at least 50% of leaf area being necrotic as well as

DOI: 10.1021/acs.jafc.5b02997
J. Agric. Food Chem. 2015, 63, 8472−8477

the occurrence of clusters turning brown. During winter, grape canes from both parcels were randomly pruned across the total area of plot A and B to overcome intraplot variation and stored for 10 weeks at 20 °C in the dark as 10 cm long sections to allow postpruned stilbenoid accumulation.[29] HPLC chromatograms of grape canes from healthy (plot A) and infected (plot B) vineyards showed differences in stilbenoid composition (Figure 2). *E*-Resveratrol and *E*-ε-viniferin, the two prominent

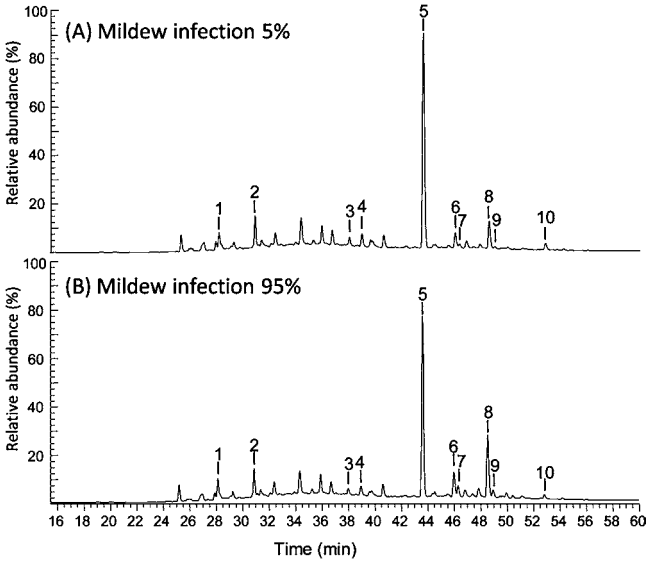

Figure 2. HPLC chromatograms measured in maxplot detection of hydroalcoholic cane extracts of *Vitis vinifera* cv. Cabernet franc from 5% (A) and 95% (B) downy mildew-infected vineyards. Peaks: (1) catechin, (2) epicatechin, (3) ampelopsin A, (4) *E*-piceatannol, (5) *E*-resveratrol, (6) hopeaphenol, (7) isohopeaphenol, (8) *E*-ε-viniferin, (9) *E*-miyabenol C, (10) *Z*/*E*-vitisin B.

compounds, were strongly influenced by downy mildew infection. Surprisingly, the concentration of *E*-resveratrol, a well-characterized grape phytoalexin in leaf and berries, decreased in infected grape canes, whereas *E*-ε-viniferin, the dimer of resveratrol, increased (Figure 3). Interestingly, hopeaphenol, the third most accumulated compound, remained

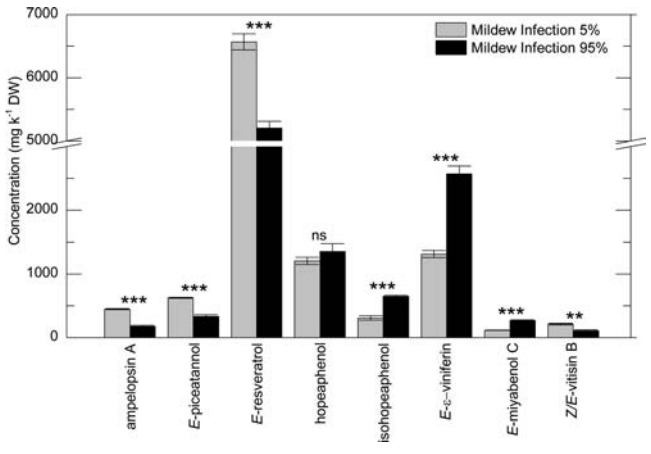

Figure 3. Stilbenoid composition in total tissues of grape canes from 5 and 95% downy mildew-infected vineyards. Asterisks indicate significant differences between the two infection levels (∗, $P < 0.05$; ∗∗, $P < 0.01$; ∗∗∗, $P < 0.001$). NS, no significant differences.

unchanged, whereas other minority stilbenoids either significantly decreased (ampelopsin A, *E*-piceatannol, *E*/*Z* vitisin B) or increased (isohopeaphenol, *E*-miyabenol C) in grape canes from downy mildew-infected vineyards.

Under favorable conditions, *Plasmopara viticola*, the etiological agent of downy mildew, infects leaves via stomata, spreads within the leaf tissue through the intercellular space of the spongy mesophyll, and later forms haustoria that penetrate host cells. Previous studies showed an induction of stilbenoids in necrotic areas after downy mildew infection,[35] but the effect on grape cane stilbenoids was not investigated. The change in stilbenoid composition observed in grape canes might affect the antifungal activity of grape cane extracts. Indeed, the toxicity of ε-viniferin against downy mildew is 2-fold higher than that of resveratrol,[30,36] and the level of resveratrol dimerization is considered as a marker of grapevine resistance to downy mildew.[37,38] The resistance level of grapevine cultivars depends on their ability to rapidly induce high concentrations of stilbenoids at the infection site.[39] Among the *V. vinifera* Cabernet franc clone collection, the resistance level to downy mildew was linked to higher production of stilbenoid phytoalexins in leaves including ε-viniferin and δ-viniferin.[40] δ-Viniferin was not detected in the grape cane extracts of either the present or previous studies.

The stilbenoid composition of stored grape canes results from a sequential accumulation of oligomers and monomers.[29] Oligomers accumulated before pruning and their levels remain unchanged during storage, but monomers (*E*-resveratrol and *E*-piceatannol) are mainly biosynthesized during storage along with an induction of stilbene synthase. In the present study, the stilbenoid composition was affected, but the total concentration was not significantly different between plot A (10792 ± 180 mg kg^{-1} DW) and plot B (10666 ± 331 mg kg^{-1} DW). The high level of *E*-ε-viniferin in grape canes from infected vineyards was offset by a limited accumulation of monomers during postpruning storage, suggesting a tight regulation of stilbenoid metabolism in grape canes. Resveratrol dimerization involves peroxidase isoenzymes located both in the vacuoles and in cell walls.[41] The accumulation of *E*-ε-viniferin in grape canes from downy mildew infected vineyards might result from a local conversion in stems or biosynthesis in leaves at the local infection site followed by phloem-mediated relocation.

To further assess the impact of downy mildew infection during the growing season on winter-harvested grape canes, the change in spatial distribution of stilbenoids was investigated. Stilbenoids emit a blue fluorescence under UV light with an excitation peak around 320 nm and an emission peak at 390 nm.[42] Therefore, fluorescence analyses were used to investigate the spatial distribution of stilbenoids in healthy grapevine tissues. A free-hand cross section of freshly pruned grape canes from Cabernet franc variety was prepared and observed by fluorescence microscopy. Figure 4 reveals the microscopical structure of a healthy grape cane including pith, conducting tissues, and cortex. The blue fluorescence observed in conducting tissues may rely on lignin fluorescence but also suggests a major accumulation of stilbenoids in vascular tissues of grape canes. No changes were observed between healthy and infected grape canes either in the blue fluorescence intensity or in the tissue structure (data not shown). To evaluate the contribution of stilbenoid fluorescence in the observed blue fluorescence, in vitro fluorescence spectra of pure solutions (*E*-resveratrol and *E*-ε-viniferin) and grape cane extracts were compared. Panels A and E of Figure 5 present respectively the

DOI: 10.1021/acs.jafc.5b02997
J. Agric. Food Chem. 2015, 63, 8472−8477

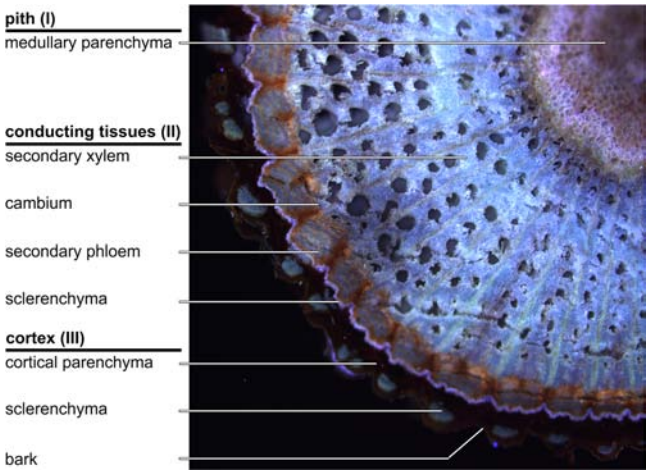

Figure 4. Fluorescence microscopy under UV excitation of a freshly pruned cross section of healthy grape cane from *Vitis vinifera* cv. Cabernet franc.

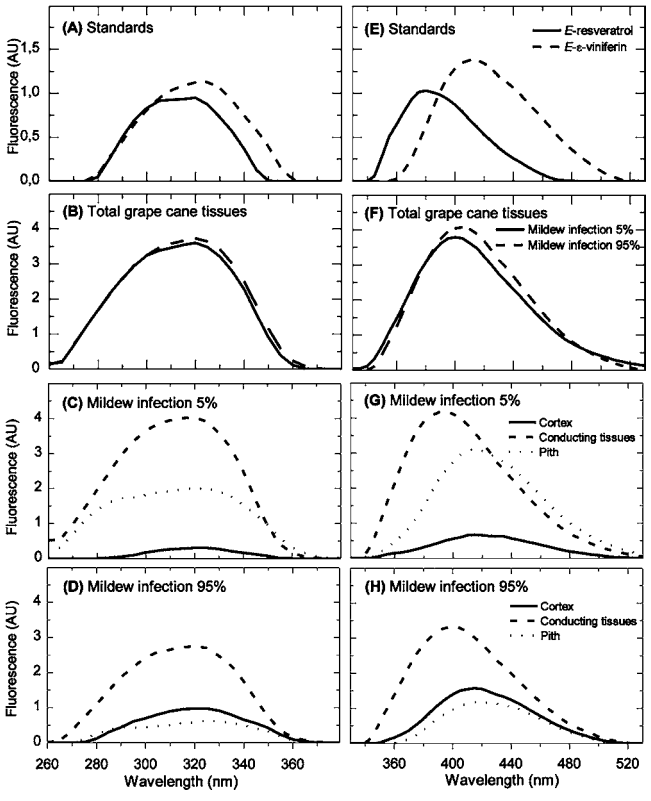

Figure 5. Fluorescence spectra of stilbenoid compounds and grape cane extracts: excitation (A–D) (emission wavelength, 390 nm) and emission (E–H) (excitation wavelength, 320 nm) fluorescence spectra of *E*-resveratrol and *E*-ε-viniferin (A, E) in solution; total tissue extract of grape canes from 5 and 95% downy mildew-infected vineyards (B, F); and dissected tissues of grape canes from 5% (C, G) and 95% (D, H) downy mildew-infected vineyards.

excitation and emission fluorescence spectra of pure *E*-resveratrol and *E*-ε-viniferin with similar broad excitation spectra (290–330 nm) and an emission maximum around 380 nm for *E*-resveratrol and 420 nm for *E*-ε-viniferin. The excitation fluorescence spectrum of the grape cane extract was similar to those of pure stilbenoids, and the emission maximum was around 400 nm, corresponding to an intermediate emission peak between 380 and 420 nm (Figure 5B,F). These results are in agreement with HPLC stilbenoid analyses, where *E*-resveratrol and *E*-ε-viniferin were the major accumulated compounds (Figure 3). Fluorescence analyses have been reported as a rapid technique to localize the stilbenoid distribution in grape leaves.[34,43] Here this technique points out that conducting tissues represent the main site of accumulation for stilbenoids in grape canes. After manual dissections of cortex, pith, and conducting tissues of grape canes, the spatial distribution of stilbenoids from healthy and downy mildew-infected vineyards was evaluated. The emission and excitation spectra indicate that conducting tissues represent the main site of stilbenoid accumulation in grape canes (Figure 5C,G). The emission maximum around 400 nm for conducting tissues and that around 420 nm for cortex and pith suggest a predominance of monomers in conducting tissues and oligomers in cortex and pith. Moreover, fluorescence spectra suggest that downy mildew affects the spatial repartition of stilbenoids with an increase in the cortex and a decrease in the pith (Figure 5C,D,G,H). To ascertain these global trends, HPLC analyses were performed on the corresponding dissected tissues (Figure 6). Striking differences of stilbenoid composition were revealed in the different grape cane tissues. Although the pith represented only 2% of the whole tissues, it contained high levels of oligomers, particularly hopeaphenol, isohopeaphenol, and *E*-ε-viniferin, compared to other tissues and was poor in monomers. Conducting tissues represented 88% of the overall tissues, and as a consequence the specific stilbenoid composition of conducting tissues mainly reflected the composition of the whole grape canes (Figure 3). The cortex representing 10% of the whole tissues was poor in stilbenoids, with hopeaphenol and *E*-ε-viniferin as major compounds. The HPLC tissue-specific analyses allowed a fine description of downy mildew impact on spatial distribution of stilbenoids. Indeed, the levels of all stilbenoid compounds were massively decreased in the pith of canes from infected plants whereas some oligomers were increased in conducting tissues and cortex. It should be noted that there was a drastic increase of *E*-ε-viniferin in conducting tissues (× 2) and cortex (× 3.4) following downy mildew infection.

The spatial characterization of stilbenoids in grape canes as well as the impact of downy mildew on stilbenoid distribution was unprecedented in the literature. Several studies are in agreement with the presence of stilbenoids in conducting tissues of grape canes. In young grape plants, resveratrol was shown to accumulate mainly in the stem.[27] HPLC analyses of xylem sap collected during the bleeding period revealed the presence of resveratrol.[44] Interestingly, in the xylem sap of vines infected by esca-associated fungi, a decrease of resveratrol was observed as in downy mildew-infected grape canes. In Norway spruce bark, the stilbenoids accumulate mainly in phloem parenchyma cells,[45] and after infection with the bark-beetle-associated fungi *Ceratocystis polonica*, an increase in stilbenoid dimers was observed accompanied by the loss of monomers. In grape canes from downy mildew-infected vineyards, resveratrol dimerization might be induced in conducting tissues for transport purpose, whereas in pith, a tissue with storage functions, the oligomer accumulation might be limited. The strong increase of *E*-ε-viniferin in the cortex, a tissue notably involved in protection against mechanical damage and microbial attack, might result from a systemic defense response to protect the plant against upcoming infections. It should be mentioned that a potential effect of copper treatments in plot A

DOI: 10.1021/acs.jafc.5b02997
J. Agric. Food Chem. 2015, 63, 8472–8477

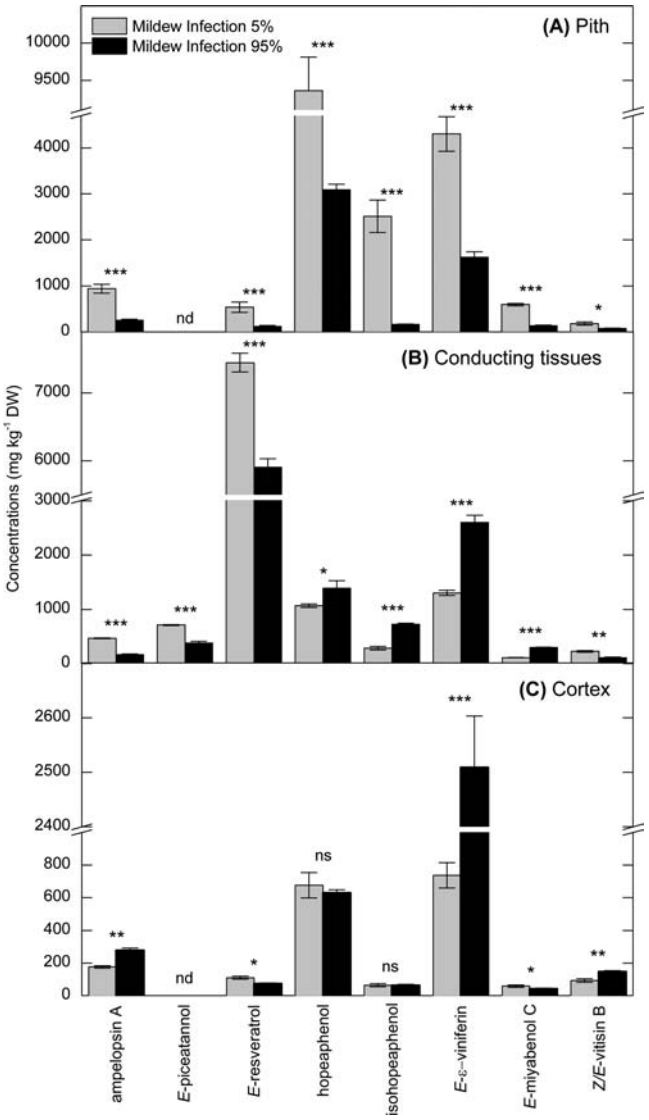

Figure 6. Stilbenoid composition in pith (A), conducting tissues (B), and cortex (C) of grape canes from 5 and 95% downy mildew-infected vineyards. Asterisks indicate significant differences between the two infection levels (*, $P < 0.05$; **, $P < 0.01$; ***, $P < 0.001$). NS, no significant differences; ND, not detected.

on the stilbenoid contents in grape canes cannot be excluded because an elicitation has been reported on excised grape leaves of in vitro grown plants.[46]

In conclusion, this study indicates that stilbenoid composition in winter-pruned grape canes was greatly affected by downy mildew infection over the growing season. A change in spatial distribution of stilbenoids was observed, particularly in conducting tissues, where an increase in *E*-ε-viniferin and a decrease in *E*-resveratrol were seen. These findings suggest that the health status in vineyards could modify the composition of stilbenoids in winter-harvested grape canes. As vineyard management contributes to wine quality, it might also influence the composition of bioactive compounds of grape canes and the resulting potential biological properties of these valuable extracts. Further studies are still required to evaluate the influence of pedo-climatic factors on the variations of stilbenoid contents.

AUTHOR INFORMATION

Corresponding Author

*(A.L.) E-mail: arnaud.lanoue@univ-tours.fr. Phone: +33(0)2 47 36 72 14. Fax: +33(0)2 47 36 72 32.

Funding

This work was supported by Région Centre Grants ACTISARM 201100068678 and VITITERROIR 201300083172.

Notes

The authors declare no competing financial interest.

ACKNOWLEDGMENTS

We thank the Domaine de la Chevalerie (Restignée, France) and the Domaine de la Noiraie (Benais, France) for access to the vineyards.

REFERENCES

(1) Rivière, C.; Pawlus, A. D.; Mérillon, J.-M. Natural stilbenoids: distribution in the plant kingdom and chemotaxonomic interest in Vitaceae. *Nat. Prod. Rep.* **2012**, *29*, 1317−1333.

(2) Shen, T.; Wang, X.-N.; Lou, H.-X. Natural stilbenes: an overview. *Nat. Prod. Rep.* **2009**, *26*, 916−935.

(3) Roupe, K. A.; Remsberg, C. M.; Yáñez, J. A.; Davies, N. M. Pharmacometrics of stilbenes: seguing towards the clinic. *Curr. Clin. Pharmacol.* **2006**, *1*, 81−101.

(4) Milne, J. C.; Lambert, P. D.; Schenk, S.; Carney, D. P.; Smith, J. J.; Gagne, D. J.; Jin, L.; Boss, O.; Perni, R. B.; Vu, C. B.; Bemis, J. E.; Xie, R.; Disch, J. S.; Ng, P. Y.; Nunes, J. J.; Lynch, A. V.; Yang, H.; Galonek, H.; Israelian, K.; Choy, W.; Iffland, A.; Lavu, S.; Medvedik, O.; Sinclair, D. A.; Olefsky, J. M.; Jirousek, M. R.; Elliott, P. J.; Westphal, C. H. Small molecule activators of SIRT1 as therapeutics for the treatment of type 2 diabetes. *Nature* **2007**, *450*, 712−716.

(5) Viswanathan, M.; Kim, S. K.; Berdichevsky, A.; Guarente, L. A role for SIR-2.1 regulation of ER stress response genes in determining *C. elegans* life span. *Dev. Cell* **2005**, *9*, 605−615.

(6) Houillé, B.; Papon, N.; Boudesocque, L.; Bourdeaud, E.; Besseau, S.; Courdavault, V.; Enguehard-Gueiffier, C.; Delanoue, G.; Guerin, L.; Bouchara, J.-P.; Clastre, M.; Giglioli-Guivarc'h, N.; Guillard, J.; Lanoue, A. Antifungal activity of resveratrol derivatives against *Candida* species. *J. Nat. Prod.* **2014**, *77*, 1658−1662.

(7) Zhang, F.; Liu, J.; Shi, J.-S. Anti-inflammatory activities of resveratrol in the brain: role of resveratrol in microglial activation. *Eur. J. Pharmacol.* **2010**, *636*, 1−7.

(8) Bai, Y.; Mao, Q.-Q.; Qin, J.; Zheng, X.-Y.; Wang, Y.-B.; Yang, K.; Shen, H.-F.; Xie, L.-P. Resveratrol induces apoptosis and cell cycle arrest of human T24 bladder cancer cells in vitro and inhibits tumor growth *in vivo*. *Cancer Sci.* **2010**, *101*, 488−493.

(9) Ramprasath, V. R.; Jones, P. J. H. Anti-atherogenic effects of resveratrol. *Eur. J. Clin. Nutr.* **2010**, *64*, 660−668.

(10) Nguyen, T. N. A.; Dao, T. T.; Tung, B. T.; Choi, H.; Kim, E.; Park, J.; Lim, S.-I. L.; Oh, W. K. Influenza A (H1N1) neuraminidase inhibitors from *Vitis amurensis*. *Food Chem.* **2011**, *124*, 437−443.

(11) Rege, S. D.; Geetha, T.; Griffin, G. D.; Broderick, T. L.; Babu, J. R. Neuroprotective effects of resveratrol in Alzheimer disease pathology. *Front. Aging Neurosci.* **2014**, *6*, 218.

(12) Chong, J.; Poutaraud, A.; Hugueney, P. Metabolism and roles of stilbenes in plants. *Plant Sci.* **2009**, *177*, 143−155.

(13) Jeandet, P.; Delaunois, B.; Conreux, A.; Donnez, D.; Nuzzo, V.; Cordelier, S.; Clément, C.; Courot, E. Biosynthesis, metabolism, molecular engineering, and biological functions of stilbene phytoalexins in plants. *BioFactors* **2010**, *36*, 331−341.

(14) Langcake, P.; Cornford, C. A.; Pryce, R. J. Identification of pterostilbene as a phytoalexin from *Vitis vinifera* leaves. *Phytochemistry* **1979**, *18*, 1025−1027.

(15) Fung, R. W. M.; Gonzalo, M.; Fekete, C.; Kovacs, L. G.; He, Y.; Marsh, E.; McIntyre, L. M.; Schachtman, D. P.; Qiu, W. Powdery

DOI: 10.1021/acs.jafc.5b02997
J. Agric. Food Chem. 2015, 63, 8472−8477

mildew induces defense-oriented reprogramming of the transcriptome in a susceptible but not in a resistant grapevine. *Plant Physiol.* **2008**, *146*, 236−249.
(16) Adrian, M.; Jeandet, P. Effects of resveratrol on the ultrastructure of *Botrytis cinerea* conidia and biological significance in plant/pathogen interactions. *Fitoterapia* **2012**, *83*, 1345−1350.
(17) Adrian, M.; Jeandet, P.; Veneau, J.; Weston, L.; Bessis, R. Biological activity of resveratrol, a stilbenic compound from grapevines, against *Botrytis cinerea*, the causal agent for gray mold. *J. Chem. Ecol.* **1997**, *23*, 1689−1702.
(18) Chiron, H.; Drouet, A.; Lieutier, F.; Payer, H. D.; Ernst, D.; Sandermann, H. Gene induction of stilbene biosynthesis in Scots pine in response to ozone treatment, wounding, and fungal infection. *Plant Physiol.* **2000**, *124*, 865−872.
(19) Calderón, A. A.; Zapata, J. M.; Ros Barceló, A. Peroxidase-mediated formation of resveratrol oxidation products during the hypersensitive-like reaction of grapevine cells to an elicitor from *Trichoderma viride*. *Physiol. Mol. Plant Pathol.* **1994**, *44*, 289−299.
(20) Jeandet, P.; Douillet-Breuil, A.-C.; Bessis, R.; Debord, S.; Sbaghi, M.; Adrian, M. Phytoalexins from the Vitaceae: Biosynthesis, phytoalexin gene expression in transgenic plants, antifungal activity, and metabolism. *J. Agric. Food Chem.* **2002**, *50*, 2731−2741.
(21) Torres, P.; Guillermo Avila, J.; Romo de Vivar, A.; García, A. M.; Marín, J. C.; Aranda, E.; Céspedes, C. L. Antioxidant and insect growth regulatory activities of stilbenes and extracts from *Yucca periculosa*. *Phytochemistry* **2003**, *64*, 463−473.
(22) Bavaresco, L.; Pezzutto, S.; Gatti, M.; Mattivi, F. Role of the variety and some environmental factors on grape stilbenes. *Vitis* **2007**, *46*, 57−61.
(23) Jeandet, P.; Bessis, R.; Gautheron, B. The production of resveratrol (3,5,4′-trihydroxystilbene) by grape berries in different developmental stages. *Am. J. Enol. Vitic.* **1991**, *42*, 41−46.
(24) Versari, A.; Parpinello, G. P.; Tornielli, G. B.; Ferrarini, R.; Giulivo, C. Stilbene compounds and stilbene synthase expression during ripening, wilting, and UV treatment in grape cv. corvina. *J. Agric. Food Chem.* **2001**, *49*, 5531−5536.
(25) Fornara, V.; Onelli, E.; Sparvoli, F.; Rossoni, M.; Aina, R.; Marino, G.; Citterio, S. Localization of stilbene synthase in *Vitis vinifera* L. during berry development. *Protoplasma* **2008**, *233*, 83−93.
(26) Gatto, P.; Vrhovsek, U.; Muth, J.; Segala, C.; Romualdi, C.; Fontana, P.; Pruefer, D.; Stefanini, M.; Moser, C.; Mattivi, F.; Velasco, R. Ripening and genotype control stilbene accumulation in healthy grapes. *J. Agric. Food Chem.* **2008**, *56*, 11773−11785.
(27) Wang, W.; Tang, K.; Yang, H.-R.; Wen, P.-F.; Zhang, P.; Wang, H.-L.; Huang, W.-D. Distribution of resveratrol and stilbene synthase in young grape plants (*Vitis vinifera* L. cv. Cabernet Sauvignon) and the effect of UV-C on its accumulation. *Plant Physiol. Biochem.* **2010**, *48*, 142−152.
(28) Gorena, T.; Saez, V.; Mardones, C.; Vergara, C.; Winterhalter, P.; von Baer, D. Influence of post-pruning storage on stilbenoid levels in *Vitis vinifera* L. canes. *Food Chem.* **2014**, *155*, 256−263.
(29) Houillé, B.; Besseau, S.; Courdavault, V.; Oudin, A.; Glévarec, G.; Delanoue, G.; Guérin, L.; Simkin, A. J.; Papon, N.; Clastre, M.; Giglioli-Guivarc'h, N.; Lanoue, A. Biosynthetic origin of *E*-resveratrol accumulation in grape canes during postharvest storage. *J. Agric. Food Chem.* **2015**, *63*, 1631−1638.
(30) Schnee, S.; Queiroz, E. F.; Voinesco, F.; Marcourt, L.; Dubuis, P.-H.; Wolfender, J.-L.; Gindro, K. *Vitis vinifera* canes, a new source of antifungal compounds against *Plasmopara viticola*, *Erysiphe necator*, and *Botrytis cinerea*. *J. Agric. Food Chem.* **2013**, *61*, 5459−5467.
(31) Baechler, S. A.; Schroeter, A.; Dicker, M.; Steinberg, P.; Marko, D. Topoisomerase II-targeting properties of a grapevine-shoot extract and resveratrol oligomers. *J. Agric. Food Chem.* **2014**, *62*, 780−788.
(32) Rayne, S.; Karacabey, E.; Mazza, G. Grape cane waste as a source of *trans*-resveratrol and *trans*-viniferin: high-value phytochemicals with medicinal and anti-phytopathogenic applications. *Ind. Crops Prod.* **2008**, *27*, 335−340.
(33) Lambert, C.; Richard, T.; Renouf, E.; Bisson, J.; Waffo-Téguo, P.; Bordenave, L.; Ollat, N.; Mérillon, J.-M.; Cluzet, S. Comparative analyses of stilbenoids in canes of major *Vitis vinifera* L. cultivars. *J. Agric. Food Chem.* **2013**, *61*, 11392−11399.
(34) Bellow, S.; Latouche, G.; Brown, S. C.; Poutaraud, A.; Cerovic, Z. G. *In vivo* localization at the cellular level of stilbene fluorescence induced by *Plasmopara viticola* in grapevine leaves. *J. Exp. Bot.* **2012**, *63*, 3697−3707.
(35) Poutaraud, A.; Naidenov, A. Quantification of stilbene in grapevine leaves by direct fluorometry and high performance liquid chromatography: spatial localisation and time course of synthesis. *J. Int. Sci. Vigne Vin* **2010**, *44*, 27−32.
(36) Pezet, R.; Gindro, K.; Viret, O.; Richter, H. Effects of resveratrol, viniferins and pterostilbene on *Plasmopara viticola* zoospore mobility and disease development. *Vitis* **2004**, *43*, 145−148.
(37) Dercks, W.; Creasy, L. L. The significance of stilbene phytoalexins in the *Plasmopara viticola*-grapevine interaction. *Physiol. Mol. Plant Pathol.* **1989**, *34*, 189−202.
(38) Pezet, R.; Gindro, K.; Viret, O.; Spring, J. L. Glycosylation and oxidative dimerization of resveratrol are respectively associated to sensitivity and resistance of grapevine cultivars to downy mildew. *Physiol. Mol. Plant Pathol.* **2004**, *65*, 297−303.
(39) Alonso-Villaverde, V.; Voinesco, F.; Viret, O.; Spring, J.-L.; Gindro, K. The effectiveness of stilbenes in resistant Vitaceae: ultrastructural and biochemical events during *Plasmopara viticola* infection process. *Plant Physiol. Biochem.* **2011**, *49*, 265−274.
(40) van Leeuwen, C.; Roby, J.-P.; Alonso-Villaverde, V.; Gindro, K. Impact of clonal variability in *Vitis vinifera* Cabernet franc on grape composition, wine quality, leaf blade stilbene content, and downy mildew resistance. *J. Agric. Food Chem.* **2013**, *61*, 19−24.
(41) Barcelo, A. R.; Pomar, F.; Lopez-Serrano, M.; Pedreno, M. A. Peroxidase: a multifunctional enzyme in grapevines. *Funct. Plant Biol.* **2003**, *30*, 577−591.
(42) Hillis, W. E.; Ishikura, N. Chromatographic and spectral properties of stilbene derivatives. *J. Chromatogr., A* **1968**, *32*, 323−336.
(43) Poutaraud, A.; Latouche, G.; Martins, S.; Meyer, S.; Merdinoglu, D.; Cerovic, Z. G. Fast and local assessment of stilbene content in grapevine leaf by *in vivo* fluorometry. *J. Agric. Food Chem.* **2007**, *55*, 4913−4920.
(44) Bruno, G.; Sparapano, L. Effects of three esca-associated fungi on *Vitis vinifera* L.: II. Characterization of biomolecules in xylem sap and leaves of healthy and diseased vines. *Physiol. Mol. Plant Pathol.* **2006**, *69*, 195−208.
(45) Li, S.-H.; Nagy, N. E.; Hammerbacher, A.; Krokene, P.; Niu, X.-M.; Gershenzon, J.; Schneider, B. Localization of phenolics in phloem parenchyma cells of Norway spruce (*Picea abies*). *ChemBioChem* **2012**, *13*, 2707−2713.
(46) Aziz, A.; Trotel-Aziz, P.; Dhuicq, L.; Jeandet, P.; Couderchet, M.; Vernet, G. Chitosan oligomers and copper sulfate induce grapevine defense reactions and resistance to gray mold and downy mildew. *Phytopathology* **2006**, *96*, 1188−1194.

DOI: 10.1021/acs.jafc.5b02997
J. Agric. Food Chem. 2015, 63, 8472−8477

ment under a water deficit, which provide new insights into the biochemical mechanism of wheat grain development in response to drought stress.

MATERIALS AND METHODS

Wheat Materials, Water Deficit Treatment, and Sampling. The elite Chinese winter wheat cultivar Jing 411 (*Triticum aestivum* L; $2n = 6x = 42$; AABBDD) was used as material in this study, which has been widely cultivated in Beijing and the north wheat production area of China since the 1990s. It has many desirable features such as high yield and good yield stability, strong cold hardiness, wide adaptability, and commendable resistance.[17] The cultivar was grown at the Wuqiao experimental station of the Agricultural University of China during the 2013−2014 growing season. The station is located in Hebei province (latitude 37°41′02″N, longitude 116°37′23″E) with an average amount of annual sunlight of 2690 h, a high temperature of 32 °C, and ∼125 mm of rainfall during the wheat growing season. Plants were grown at three biological replicates, and each plot was 50 m^2. Water stress treatment was conducted as follows. In the control group as local field cultivation management, wheat was watered approximately 750 m^3/ha at sowing, jointing, and flowering stages, while in the stress group, no watering was used after sowing. The soil water content ranged from 13.3 to 9.18% in water deficit conditions and from 18.1 to 13.3% in control conditions at the jointing stage, flowering stage, and mature stage. This soil water content was approximately 20−30% lower in stressed than in control groups. The treatment belonged to medium-to-severe drought stress according to Guttieri.[18] Wheat spikes were immediately marked once they had flowered and collected 15, 21, 26, 30, and 45 days after flowering (DAF). The middle four to six grains of each ear were used as experimental materials. Husks were first removed from seeds, and then the embryo and aleurone layer were separated from the remainder of the seed at low temperatures.[13] Embryo and endosperm samples were stored at −80 °C prior to being used.

Measurement of Physiological Indicators, Agronomic Traits, and Quality Parameters. Flag leaves of five stages (12, 15, 18, 21, and 26 DAF) were sampled. Five biology replications of each period were measured. Physiological indicator testing consisted of the contents of leaf relative water (RWC), malondialdehyde (MDA), soluble sugar, free proline, and chlorophyll. The measurement of RWC was followed by the method of Smart.[19] MDA and soluble sugar contents were based on the procedure of Zhao et al.[20] The free proline content was referenced to the work of Bates et al.[21] The chlorophyll content was according to Arnon[22] with minor modifications.

After the grain matured, the main agronomic traits were measured and the plant samples were collected. The grain yield was measured according to three plot replications, and theoretical and practical yields were obtained. Different grain quality parameters were tested, including the total protein content (14% moisture basis), falling number, gluten content, Farinograph, Extensograph, Mixograph, loaf volume, appearance score, and C-cell properties. The flour protein content was determined according to American Association of Cereal Chemists Approved Methods (AACC) 39-10A with a near-infrared (NIR) analyzer (Instalab610, Dickey-john Co. Ltd.). Falling numbers (Perten) were determined with method AACC 56-81B. The Mixograph index (National Manufacturing), including water absorption rate, peak time, and time × width, was determined according to method AACC 54-40A. The gluten content was measured according to the method of Czuchajowska.[23] Farinograph and Extensograph (Brabender) were followed by methods AACC 54-21 and 54-10, and breadmaking was followed with method AACC 10-10B. The internal structure of bread was tested and evaluated by the means of C-CELL (UK CCFRA Co.). Data analysis was performed using an independent Student's *t* test with SPSS statistical software (version 17.0).

Protein Extraction and Nonlinear Two-Dimensional Electrophoresis (2-DE). Protein was extracted from the embryo and endosperm according to the process of Guo et al.[24] with minor modifications. A total of 500 mg samples were quickly ground into a fine power in liquid nitrogen. Protein extractions were dissolved with lysis buffer (7 M urea, 2 M thiourea, and 4% CHAPS) for ∼5 h. Protein concentrations were evaluated with a 2-D Quant Kit (Amersham Bioscience) using bovine serum albumin (BSA, 2 mg/mL) as the standard.

Nonlinear 2-DE isolation was performed according to the steps of Jiang et al., which can significantly improve the resolution of protein separation compared to that with traditional linear 2-DE.[8] In total, 500 μg protein samples were mixed with 1 mg of DTT, 0.5% IPG buffer (GE Healthcare/Amersham Biosciences), 1 μL of a 1% bromophenol blue solution, and moderate rehydration buffer [7 M urea, 2 M thiourea, and 2% (w/v) CHAPS], and 350 μL of a mixed solution was loaded onto an ImmobilineDryStrip (pH 3−10, 18 cm, nonlinear strip, GE Healthcare) for isoelectric focusing (IEF). After IEF, the strips were treated with equilibration buffer for the second sodium dodecyl sulfate−polyacrylamide gel electrophoresis. At least two technical replicates for each sample were performed to obtain statistically reliable results. Protein spot images were visualized by Coomassie Brilliant Blue staining (R-250/G-250 = 4:1; Sigma) and scanned at 600 dpi with a UMAX Power Look 2100XL scanner (Maxium Tech Inc., Taiwan, China). Image analysis was conducted with ImageMaster 2D Platinum Software version 7.0 (Amersham Bioscience). The abundance of protein spots from biological and technical replicates was estimated by percentage volumes (vol %). Data analysis was conducted using an independent Student's *t* test with SPSS statistical software (version 17.0). Only those with significant and reproducible changes (at least 2-fold increase and/or decrease and p value of <0.05) were considered as differentially expressed protein (DEP) spots.

MALDI-TOF/TOF-MS. DEP spots were manually excised from the gels, digested with trypsin, and identified by matrix-assisted laser desorption ionization time-of-flight/time-of-flight mass spectrometry (MALDI-TOF/TOF-MS). After being bleached, exposed to enzymes, and dried, the peptides were analyzed by using an ABI 4800 Proteomic Analyzer MALDI-TOF/TOF-MS instrument (Applied Biosystems/MDS Sciex). The parameters were set as follows: laser intensity of 4500 and mass range of 900−3500 Da. The MS/MS spectra was searched against Viridiplantae (green plant) sequences in the nonredundant National Center for Biotechnology Information (NCBI) database (November 28, 2012; including 1154529 protein sequences) by using software MASCOT (version 2.1.0) with the following parameter settings: trypsin cleavage, one missed cleavage allowed, peptide mass tolerance set to ±0.3 Da, and fragment tolerance set to ±0.4 Da. Only the proteins with both Protein Score C.I. % and Total Ion Score C.I. % above 95% were identified as credible results.

Multivariate and Cluster Analysis. The multivariate method was conducted by principal component analysis (PCA) in the R language with the average relative abundance of all the identified DEP spots.[25,26] PCA is a way of identifying patterns in data and expressing the data in such a way as to emphasize their similarities and differences. In our study, identified DEP spots of control and stressed embryo and endosperm during the five development stages were analyzed by PCA. Cluster analysis of the differentially abundant protein data was performed by using cluster software (version 3.0). Euclidean distances and Ward's criteria were used for the analysis. Cluster results were displayed by Java Tree view software.

Bioinformatics and Statistical Analysis. The possible functions of identified proteins were classified according to the information from the Uniprot database (www.uniprot.org) and Gene Ontology (GO) database (www.geneontology.org). The sequences of all identified proteins were used for BLAST analysis with the NCBI cluster of eukaryotic Orthologous Groups (KOG) database to obtain the KOG numbers of those proteins. Information about the protein−protein interaction was used with these KOG numbers with the Search Tool for Retrieval of Interacting Genes/Proteins (STRING) database (version 9.1, www.string-db.org) to construct an interaction network graph[27] with a confidence score of potential substrates of at least 0.9. The network was displayed using the cytoscape software (version 3.0).[28] When an unknown named protein was identified, a homologous protein of known function with the highest query cover (>90%) and lowest E value was a blast in the NCBI database.

DOI: 10.1021/acs.jafc.5b00575
J. Agric. Food Chem. 2015, 63, 8478−8487

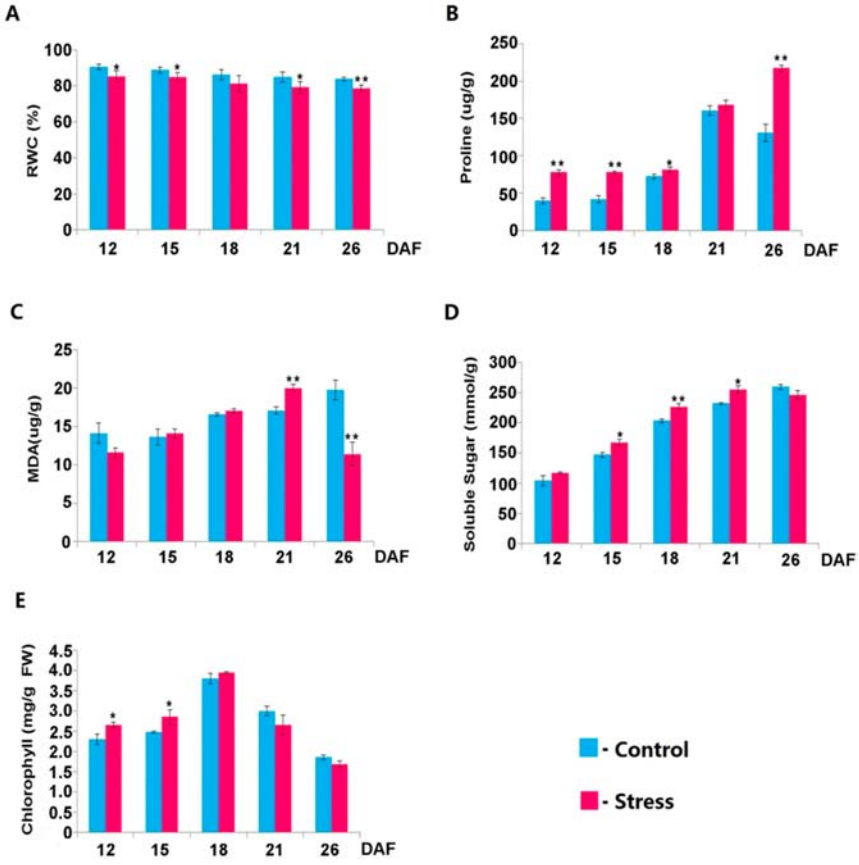

Figure 1. Physiological index changes of wheat flag leaves in the control and water stress samples during the development progress. (A) RWC, relative water content. (B) Proline content. (C) MDA, malondialdehyde content. (D) Soluble sugar content. (E) Chlorophyll content. DAF, day after flower. Control, the control samples. Stress, the water-stressed samples. Two asterisks and one asterisk denote significant differences between the stress and the control samples at 1 and 5% levels, respectively.

Subcellular localizations of identified proteins were forecasted by the UniprotKB (http://www.uniprot.org/) database, WoLF PSORT (http://wolfpsort.org/), and Predotar (http://urgi.versailles.inra.fr/predotar/predotar.html).[29,30] The most likely location of a given protein was determined by similar results from at least two programs.

RESULTS

Changes in Leaf Physiological Indexes, Agronomic Traits, and Breadmaking Quality Properties in Response to a Water Deficit. Results for leaf physiological indexes are shown in Figure 1. RWC displayed a decreasing trend during the five development periods and a significantly lower content in water stress samples. In contrast, the contents of free proline, MDA, and soluble sugar were all significantly higher in the water stress samples. MDA, which can react with proteins and nucleic acids and inhibit protein synthesis, is the final decomposition product of lipid peroxidation and reflects the degree of cell damage, while free proline and soluble sugars help to protect the structure of proteins, adjust the osmotic balance, and protect the proteins from stress damage.[31] The chlorophyll content increased in the first three stages and then decreased during the subsequent stages and displayed significant changes under water stress. These physiological index changes might reflect the general wheat response to a water deficit during grain development.

The results for agronomic traits, yield, and quality performance showed a significant difference between control and water stress samples (Table 1 and Figure S1). Under water stress, the seeds had significant lower spikelet numbers, spike grain numbers, and grain weights and exhibited an approximate 12% reduction in yield compared to that of the control (Table S1). Water stress shortened the time of wheat grain filling, which explains the lower weight and yield under a water deficit. Grain quality analysis showed that total protein and gluten contents were higher in control samples. However, some breadmaking-related parameters of Mixograph, Extensograph, loaf volume, loaf appearance score, and C-cell testing showed significant increases under water-stressed treatment compared with the control values (Table 1).

Proteome Characterization of the Embryo and Endosperm in Response to a Water Deficit during Grain Development. Protein spots for the embryo and endosperm were detected by nonlinear 2-DE during grain development under a water deficit (Figure 2A,B). In total, 876 ± 8 and 752 ± 5 spots on all gels of the embryo and endosperm, respectively, were detected. Of these, 155 DEP spots in the embryo that corresponded to 112 unique proteins and 130 DEP spots in the endosperm that corresponded to 96 unique proteins were successfully identified by MALDI-TOF/TOF-MS (Figures 2A,B and 3 and Tables S2 and S3). Among these DEP spots, 60 representing 47 unique DEPs were found in both embryo and endosperm samples, while 95 representing 76 unique DEPs and 70 representing 60 unique DEPs were identified in the embryo and endosperm, respectively (Figure 3). Detailed peptide information for all of the identified proteins is shown in Table S4. To obtain more information about the unknown/

DOI: 10.1021/acs.jafc.5b00575
J. Agric. Food Chem. 2015, 63, 8478−8487

Table 1. Comparison of Different Breadmaking Quality Parameters of Wheat Cultivar Jing 411 between Normal Cultivation Conditions and Water Deficit Treatment

	basic quality parameters			Mixograph			Farinograph		Extensograph		
treatment	FN[a]	total protein (%)	total gluten content (%)	peak time (min)	time × width (%)	water absorption (%)	DT[b] (min)	stability (min)	energy area (cm^2)	extensibility (mm)	maximal resistance (BU)
control	313 ± 3	12.67 ± 0.05	3.26 ± 0.03	6.34 ± 0.06	5.46 ± 0.8	50.1 ± 0.1	1.9 ± 0.1	3.5 ± 0.1	50 ± 1	161 ± 1	192 ± 4
stress	325 ± 6[c]	12.51 ± 0.02[c]	2.92 ± 0.03[d]	6.33 ± 0.03	6.12 ± 0.84[d]	50 ± 0.1	1.7 ± 0.1[c]	4 ± 0.2[c]	57 ± 1[c]	165 ± 2[c]	208 ± 1[c]

	loaf volume and appearance score		C-cell parameters							
treatment	loaf volume (mL^3)	score (100)	cell diameter (px)	cell contrast	curvature	nonuniformity	no. of cells	slice area (px)	slice brightness	total concavity (%)	volume of holes
control	820 ± 12	59 ± 1	20.03 ± 0.16	0.705 ± 0.005	1383.5 ± 64.5	1.81 ± 0.09	2436 ± 15	270709 ± 348	145.1 ± 0.3	1.75 ± 0.02	0.75 ± 0.25
stress	883 ± 6[c]	67 ± 2[c]	21.00 ± 0.32[d]	0.717 ± 0.001[d]	1788 ± 3[d]	1.04 ± 0.17[d]	2512 ± 37[c]	287615 ± 176[d]	150.9 ± 0.4[d]	3.425 ± 0.08[d]	0.25 ± 0.12[c]

[a]Falling number. [b]Dough development time. [c]Significance at the 5% level. [d]Significance at the 1% level.

Figure 2. Identified differentially expressed protein (DEP) spots in the embryo (A) and endosperm (B) in response to a water deficit during grain development. The protein numbers are same as those in Tables S2 and S3. Abbreviations: NL, nonlinear; EMC15, control embryo 15 days after flowering; EMC21, control embryo 21 days after flowering; EMC26, control embryo 26 days after flowering; EMC30, control embryo 30 days after flowering; EMC45, control embryo 45 days after flowering; EMS15, stressed embryo 15 days after flowering; EMS21, stressed embryo 21 days after flowering; EMS26, stressed embryo 26 days after flowering; EMS30, stressed embryo 30 days after flowering; EMS45, stressed embryo 45 days after flowering; ENC15, control

DOI: 10.1021/acs.jafc.5b00575
J. Agric. Food Chem. 2015, 63, 8478−8487

Figure 2. continued

endosperm 15 days after flowering; ENC21, control endosperm 21 days after flowering; ENC26, control endosperm 26 days after flowering; ENC30, control endosperm 30 days after flowering; ENC45, control endosperm 45 days after flowering; ENS15, stressed endosperm 15 days after flowering; ENS21, stressed endosperm 21 days after flowering; ENS26, stressed endosperm 26 days after flowering; ENS30, stressed endosperm 30 days after flowering; ENS45, stressed endosperm 45 days after flowering. The protein spot was numbered by the order of the first letter of the protein names. The same differential protein spot in the embryo and endosperm has the same number, whereas different protein spots had different numbers.

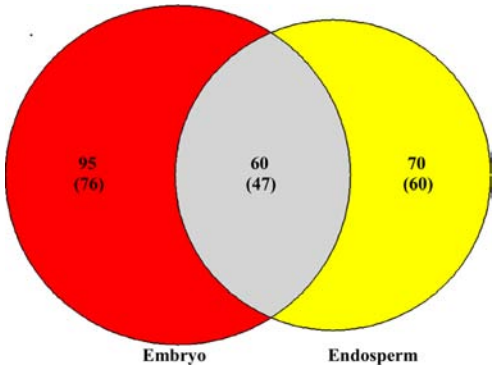

Figure 3. Numbers of identified DEP spots in the embryo and endosperm. Numbers in parentheses are the corresponding numbers of unique proteins.

predicted proteins, their sequences were used to search for homologues by BLASTP. Predicted proteins with a level of sequence similarity of >90% were considered homologues.[14] BLASTP revealed homologues for 20 spots (Table S5).

PCA showed major differences between the two organs during the grain development stages under drought stress. DEP spots of different stages in the endosperm were located in the same plot and were in a different plot of those in the embryo (Figure 4A,B). These results indicate that the difference between organs was dominant over differences during grain development under water stress. Samples from five different development stages were grouped into different plots in these two organs, but differences between control and water deficit samples were modest (Figure 4C,D). Our moderate treatment might explain this phenomenon. Cluster results showed differential protein expression trends in the embryo and endosperm during grain development under a water deficit (Figure S1). Protein expression profiles 15−21 DAF and 30−45 DAF generally showed similar patterns of accumulation in control embryo and protein expression profiles 26 DAF close to those 30−45 DAF (Figure S1A), whereas under a water deficit, protein accumulation 21 DAF was similar to that 26 DAF and different from that 15 DAF (Figure S1B), which might indicate proteins in embryo in response to water deficit mainly from 21 DAF. By comparison of panels C and D of Figure S1, proteins in the endosperm responded to a water deficit mainly from 26 DAF.

According to the protein function, these DEPs could be classified into nine categories in embryo development: stress/defense response, energy metabolism, storage proteins, nitrogen metabolism, protein metabolism/folding, starch metabolism, transport, lipid metabolism, and other important functions (Table S2). The DEP spots identified in endosperm development under a water deficit showed similarly functional classifications (Table S3), except for the absence of lipid metabolism-related proteins. Prediction of protein−protein interactions is shown in Figure 5. Proteins identified in both embryo and endosperm samples were located in the middle. Proteins identified specifically in the embryo and endosperm were located to the left and right, respectively. Glyceraldehyde-3-phosphate dehydrogenase (GAPDH, KOG0657), 70 kDa heat shock-related protein (HSP70, KOG0101), and ubiquitin (KOG0001) had the most connections with other proteins and were located in the center, suggesting their important roles in embryo and/or endosperm development in response to a water deficit. Proteins with different functions were closely connected with each other and formed a large network to play central roles in response to a water deficit. Subcellular localizations of the identified proteins were predicted. They were mainly located in the cytoplasm, mitochondria, vacuole, and nucleus (Tables S2 and S3).

Comparative Proteome Analysis of the Embryo and Endosperm in Grain Development under a Water Deficit. The embryo was identified to have more stress/defense response-related DEP spots and fewer starch metabolism and storage-related proteins than endosperm in this study. Approximately 40 and 34 DEP spots involved in stress/defense response were identified in the embryo and endosperm, respectively (Tables S2 and S3), whereas 10 and 19 DEP spots taking part in starch metabolism were identified, respectively. Aldose reductase-related protein (spot 30), cold-regulated protein (spot 54), peroxidase 1 (spot 151), and stromal 70 kDa heat shock-related protein (spot 164) involved in stress/defense response were identified in only the embryo, while β-amylase (spot 45) with important roles in starch metabolism, storage proteins such as putative avenin-like α precursor (spot 169), and HMW gultenin subunit Dy 12 (spot 115) were identified in only the endosperm (Table 2).

DISCUSSION

Stress/Defense-Related Proteins. Cells suffer harmful damage during grain development because of various biotic and abiotic stresses, especially under a water deficit. Large amounts of ROS accumulate in cells under stress, leading to lipid peroxidation, protein (enzyme) instability, and a loss of osmotic balance.[4] Defense signals are activated in cells in response to stress. Many proteins largely accumulated in cells under stress, such as peroxidase, HSP, and LEA. 1-Cys peroxiredoxin PER1 (spot 3) is involved in ROS scavenging and has been reported to be a dormancy-related protein expressed in the embryo and aleurone layer of barley.[32] This enzyme may help maintain dormancy and prevent germination under unfavorable conditions.[33] It displayed a higher level of expression from 21 DAF in both the embryo and the endosperm under a water deficit and reached a 4.56-fold accumulation level in the embryo 26 DAF compared with 15 DAF, much more than that increased in the endosperm (Tables S2 and S3). The higher level of accumulation improved the ability to survive a harsh environment during grain development. Four peroxidase proteins (spots 150−153) that also take part in ROS scavenging were specifically up-accumulated in the embryo during grain development in response to defense stress (Table 2 and Table S2).[34] Stromal 70 kDa heat shock-related protein (HSP 70), a chaperone, binds extended peptide segments of polypeptides with a net hydrophobic character

DOI: 10.1021/acs.jafc.5b00575
J. Agric. Food Chem. 2015, 63, 8478−8487

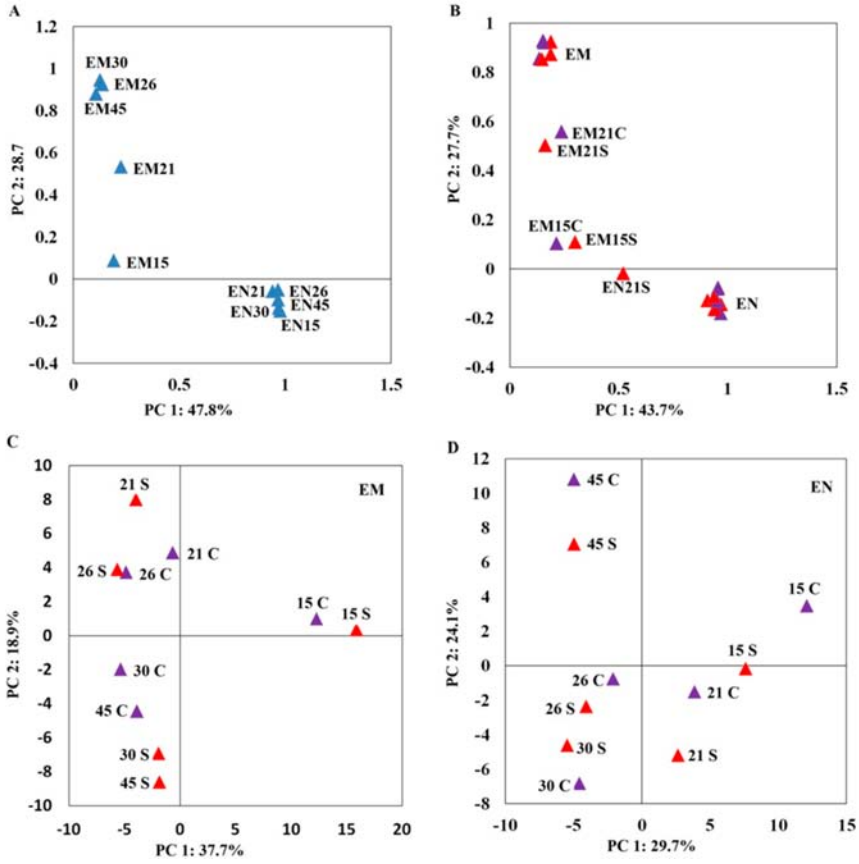

Figure 4. Principal component analysis (PCA) of all the identified DEP spots in embryo and endosperm development under a water deficit. (A) Individual stages in embryo and endosperm development. (B) Individual stages of the embryo and endosperm under a water deficit. (C) Individual stages of embryo development in response to a water deficit. (D) Individual stages of endosperm development in response to a water deficit. Abbreviations: C, control samples; S, stressed samples; EM, embryo; EN, endosperm; 15, 21, 26, 30, and 45, five grain developmental stages 15, 21, 26, 30, and 45 DAF, respectively.

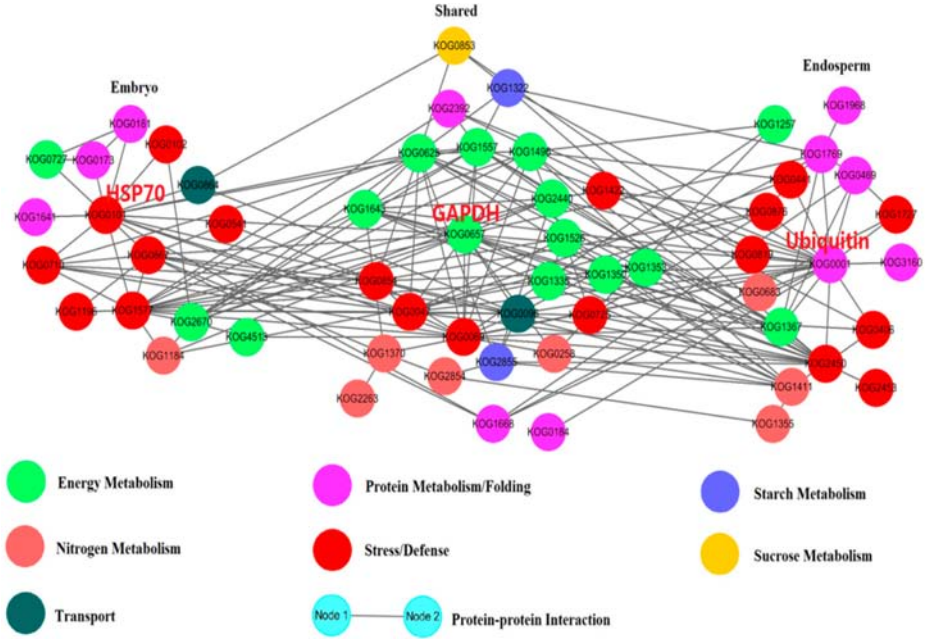

Figure 5. Prediction of protein−protein interaction between some identified proteins with a high confidence score (0.900). Proteins at the left were from the embryo. Proteins at the right were from the endosperm. Proteins in the middle were shared by these two tissues. Different colors display different functions. Abbreviations: GAPDH, cytosolic glyceraldehyde-3-phosphate dehydrogenase; HSP70, stromal 70 kDa heat shock-related protein.

DOI: 10.1021/acs.jafc.5b00575
J. Agric. Food Chem. 2015, 63, 8478−8487

Table 2. Expression Characteristics of Some Important DEP Spots in the Embryo and Endosperm in Response to a Water Deficit during Grain Development

SpotID[a]	GI Number	Protein Name	Average volume (15:21:26:30:45)[b] EMC[c]	EMS[d]	ENC[e]	ENS[f]	Protein Function
48	gi|133872550	Bp2A protein			E	E	Energy Metabolism
6	gi|28172909	Cytosolic 3-phosphoglycerate kinase	E	E			Energy Metabolism
73	gi|461744058	Enolase			E	E	Energy Metabolism
157	gi|18076790	Phosphoglucomutase					Energy Metabolism
175	gi|475604217	Pyrophosphate--fructose 6-phosphate					Energy Metabolism
111	gi|148508784	Glyceraldehyde-3-phosphate dehydrogenase			E	E	Energy Metabolism
113	gi|148508784	Glyceraldehyde-3-phosphate dehydrogenase	N	N			Energy Metabolism
204	gi|11124572	Triosephosphate-isomerase			E	E	Energy Metabolism
205	gi|11124572	Triosephosphate-isomerase					Energy Metabolism
21	gi|32812836	ADP-glucose pyrophosphorylase large subunit					Starch Metabolism
45	gi|32400764	Beta-amylase	E	E			Starch Metabolism
15	gi|474033197	Acyl-[acyl-carrier-protein] desaturase 2, chloroplastic			N	N	Lipid Metabolism
61	gi|1872473	Delta-24-sterol methyltransferase			N	N	Lipid Metabolism
23	gi|475595366	Alanine aminotransferase 2					Nitrogen Metabolism
9	gi|474407512	20 kDachaperonin, chloroplastic			E	E	Protein Folding
49	gi|56606827	Calreticulin-like protein			N	N	Protein Metabolism
69	gi|473753874	Elongation factor 1-beta					Protein Metabolism
182	gi|27735373	Replication factor C like protein					Protein Metabolism
207	gi|68305063	Ubiquitin	N	N			Protein Metabolism
3	gi|475442339	1-Cys peroxiredoxin PER1					Stress/Defense
30	gi|167113	Aldose reductase-related protein			E	E	Stress/Defense
50	gi|474292610	Catalase isozyme 1					Stress/Defense
51	gi|62465514	Class II chitinase					Stress/Defense
54	gi|26017213	Cold regulated protein			N	N	Stress/Defense
71	gi|1169518	Em protein H5			N	N	Stress/Defense
145	gi|474110039	Late embryogenesis abundant protein Lea14-A					Stress/Defense
151	gi|300087071	Peroxidase 1			E	E	Stress/Defense
164	gi|475565760	Stromal 70 kDa heat shock-related protein			E	E	Stress/Defense
169	gi|89143120	Putative avenin-like a precursor	E	E			Storage Protein
87	gi|474411419	Globulin-1 S allele					Storage Protein
102	gi|215398468	Globulin 3C					Storage Protein
115	gi|46981764	HMW glutenin subunit Dy12	E	E			Storage Protein

[a]The protein spots shown in Figure 2. [b]Average relative abundance 15, 21, 26, 30, and 45 DAF. [c]Control embryo. [d]Stressed embryo. [e]Control endosperm. [f]Stressed endosperm. E means the spot did not show significantly at least 2-fold differences. N means the spot did not exist. Green color indicates a relatively lower level of accumulation. Red color indicates a relatively higher level of accumulation.

during translation and membrane translocation and may interact with newly imported proteins to assist in their maturation by protein folding and reassembly.[35] A related study has reported the overexpression of HSP genes in wheat in response to environmental stress.[36] Three HSP DEP spots (spots 164, 191, and 211) were specifically identified in the embryo (Table S2). Spots 191 and 211 (corresponding to KOG 0101) and spot 164 (corresponding to KOG0102) were predicted to interact with many other proteins and played a key role in embryo development[14] (Figure 5). Two other proteins were obtained, 16.8 kDa heat shock protein (spot 133) and predicted 17.9 kDa class I heat shock protein-like (spot 216), the homologous protein of hypothetical protein TRIUR3_03549 and an unnamed protein product, respectively (Table S5). The abundance of small Hsps in plants played a part in binding and stabilizing non-native proteins and might play a role in plant-acquired tolerance to drought and salt.[37] These phenomena enhanced the embryo's ability to tolerate drought and might show the main function in stress/defense response in the embryo under a water deficit. α-Amylase inhibitors (spots 1, 32, 33, 52, 66, 67, 118, 147, and 181) inhibit the degradation of starch and increase the level of accumulation of starch in cells, which are related to the adjustment of the osmotic balance and protecting the cells from damage by insects.[38] It has been reported that the wheat endosperm proteome contained abundant levels (~11% of total proteins) of α-amylase inhibitors and α-amylase/trypsin inhibitors to protect the starch reserves from degradation.[39] Their expressions were upregulated in drought tolerance genotypes but were downregulated in sensitive genotypes.[16] Consistent with our results, nine related DEP spots were identified in the endosperm; seven of them showed higher levels of expression under a water deficit (Table S3). In particular, spot 147 had reached 5.15-, 8.15-, and 7.77-fold levels of accumulation 21, 26, and 45 DAF (compared with 15 DAF), respectively. These results reveal the main function of adjusting starch accumulation in the endosperm under drought.

Energy Metabolism-Related Proteins. Proteins participating in ATP synthesis, glycolysis, and the tricarboxylic acid (TCA) cycle provide plenty of energy and molecular materials for grain development under a water deficit. In this study, many DEPs related to energy metabolism were identified under

DOI: 10.1021/acs.jafc.5b00575
J. Agric. Food Chem. 2015, 63, 8478−8487

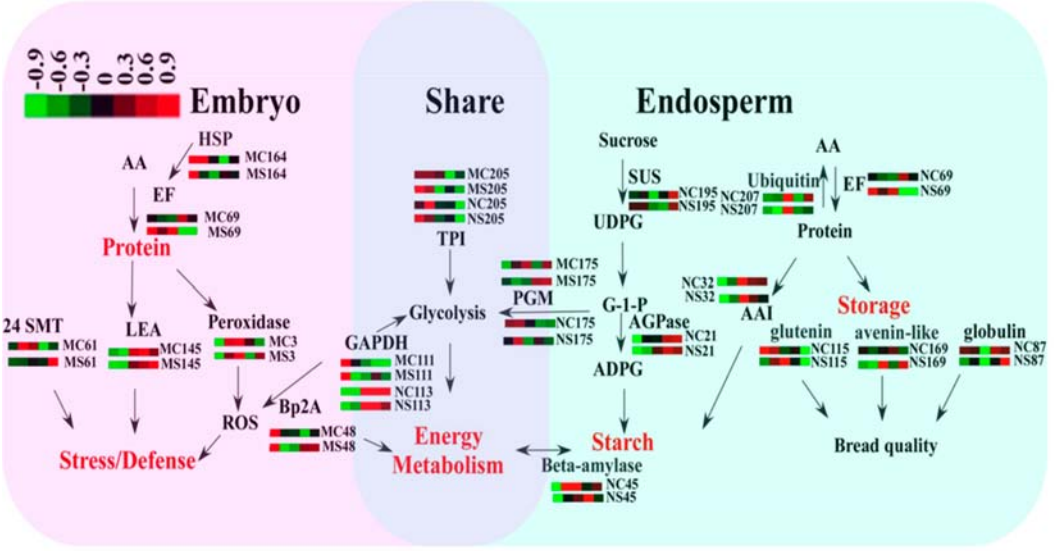

Figure 6. Overview of possible metabolic pathways of embryo and endosperm development in response to a water deficit. Abbreviations: AA, amino acid; AAI, α-amylase inhibitor; ADPG, ADP-glucose; AGPase, ADP-glucose pyrophosphorylase large subunit; Bp2A, Bp2A protein; DHAR, dehydroascorbate reductase; EF, elongation factor; GAPDH, glyceraldehyde-3-phosphate dehydrogenase; G-1-P, glucose 1-phosphate; HSP, heat shock-related protein; LEA, late embryogenesis abundant protein Lea14-A; MC, control embryo; MS, stressed embryo; NC, control endosperm; NS, stressed endosperm; PGM, phosphoglucomutase; ROS, reactive oxygen species; 24SMT, Δ-24-sterol methyltransferase; SUS, sucrose synthase, UDPG, uridinediphosphate glucose.

drought. GAPDH (spots 57 and 110−114), a key enzyme of glycolysis, catalyzes the conversion of D-glyceraldehyde 3-phosphate (G3P) to 3-phospho-D-glyceroyl phosphate. In the study presented here, this enzyme showed a higher level of accumulation in early embryo and late endosperm development and was upregulated 30 DAF in embryo under a water deficit [spot 111 (Table 2)]. This favored embryo cells regulating a stress defense mechanism. Protein−protein interaction analysis showed that many other proteins related to energy metabolism and stress/defense responses were closely connected with GAPDH (Figure 5) and indicated its central role in metabolism. Other energy metabolism-related proteins such as ATP synthase-related proteins, dihydrolipoyl dehydrogenase 1, Bp2A protein, triosephosphate isomerase, etc., were identified in response to a water deficit in the embryo and/or endosperm during grain development. All of these proteins closely interacted with each other and provided enough carbohydrates and energy for embryo and endosperm development under a water deficit.

Starch Metabolism-Related Proteins. The embryo has been reported to be a powerful sink for nutrients and also acquires a moderate level of starch for germination, but many starches were degraded into carbohydrates to improve the desiccation tolerance during development.[40,41] Storage starch mainly accumulates in the endosperm (approximately 70−80% dry weight) and largely determines wheat yield during development. Seven and 10 related proteins were identified in the embryo and endosperm in this study, respectively, and most of them displayed a lower level of accumulation under drought compared with the control, leading to a reduction in yield (Table S1). Sucrose synthase (SUS, spots 192−197) catalyzes the first step in the conversion of sucrose to starch, which provides UDP-glucose and fructose for various metabolic pathways. ADP-glucose pyrophosphorylase large subunit (AGPase, spot 21) is a major rate-limiting enzyme in grain starch biosynthesis. It initiates starch biosynthesis in plants and catalyzes the formation of ADP-glucose from Glc-1-P and ATP. SUS and AGPase are considered to be crucial for development, carbon partitioning, and synthesis of storage starch during grain development and are active when starch accumulates in storage tissues.[42,43] In the study presented here, these two proteins mainly displayed down-accumulation in late embryo and endosperm development under a water deficit. Fructokinase-1-like, a homologue of the hypothetical protein F775_30384 (spot 130), which may help to maintain the flux of carbon toward starch formation,[44] showed a similar decreasing level of expression under drought. β-Amylase (spot 45), which hydrolyzes (1→4)-α-D-glucosidic linkages in polysaccharides and removes successive maltose units from the nonreducing ends of the chains, was specifically identified in the endosperm and downregulated during late development under water stress (Table 2), so the endosperm expressed α-amylase inhibitors to ease the reduced starch under a water deficit.

Storage Proteins. Wheat storage proteins mainly present in the endosperm, especially glutenins and gliadins, have important effects on nutritional quality for humans and livestock and on functional properties in food processing.[45] Under a water deficit, many of them displayed a similar expression pattern and had fewer changes than the control (Table S3). Some globulins displayed downregulation during grain development, which is similar to the previous results of Laino.[15] However, some storage proteins showed a higher level of expression under a water deficit than the control, such as HMW glutenin subunit Dy12 (spot 115), putative avenin-like α precursor (spot 169) (Table 2), and the hypothetical protein F775_27291 (spot 124), a homologue of avenin-3 (Table S5). One gliadin protein spot (spot 84) and four protein spots, globulin-1 S allele (spots 87−90), also displayed >3-fold upregulation during grain development under a water deficit (Table S3). Glutenins and gliadins are two prolamine groups of gluten constituents, contain many cysteine residues that are involved in intramolecular and intermolecular linkages, and

DOI: 10.1021/acs.jafc.5b00575
J. Agric. Food Chem. 2015, 63, 8478−8487

contribute to the viscoelastic properties of gluten that determine dough strength.[46] Avenin-like proteins are also rich in cysteine and may contribute to wheat dough viscoelastic properties via interchain disulfide bonds.[47] Globulins are cross-linked by both disulfide and non-disulfide cross-links, which affects dough and crumb properties.[48] As we all know, there is a great relationship between dough strength and breadmaking quality. Therefore, it is suggested that these proteins have positive significance for the improvement of breadmaking quality. As shown in Table 1, although the amount of gluten decreased, bread quality improved under a water deficit.

Overview of Central Metabolic Changes during Wheat Embryo and Endosperm Development in Response to a Water Deficit. Here, we propose a putative proteomic metabolic pathway during wheat embryo and endosperm development in response to a water deficit, which provides an overview of the main DEP differences between the embryo and endosperm (Figure 6). The embryo mainly synthesized proteins related to stress/defense responses during grain development, such as peroxidase and HSP, while storage starch and storage proteins mainly accumulated in the endosperm. Many energy metabolism-related enzymes were both identified in these two organs. Under a water deficit, most proteins related to energy metabolism and stress/defense responses were upregulated in the embryo. Proteins related to starch were downregulated in the endosperm, which might explain the lower grain weights and reduced yields, but some storage proteins, such as HMW glutenin, globulins, and avenin-like proteins, showed upregulated expression under a water deficit, which might benefit breadmaking quality.

■ ASSOCIATED CONTENT

Supporting Information

The Supporting Information is available free of charge on the ACS Publications website at DOI: 10.1021/acs.jafc.5b00575.

Some agronomic and yield traits of wheat cultivar Jing 411 under control and water deficit treatment (Table S1), identified differentially expression proteins in embryo (Table S2) and endosperm (Table S3) in water deficit response during grain development, peptide information about all the identified proteins (Table S4), and homologous proteins of some unknown proteins (Table S5) (XLS)

Hierarchical clustering of identified proteins in both control and stressed embryo and endosperm during the grain development (Figure S1) (PDF)

■ AUTHOR INFORMATION

Corresponding Author

*College of Life Science, Capital Normal University, Xi San Huan Bei Lu No. 105, 100048 Beijing, P. R. China. Telephone and Fax: 0086-10-68902777. E-mail: yanym@cnu.edu.cn.

Funding

This research was financially supported by grants from the National Natural Science Foundation of China (31271703 and 31471485), the Natural Science Foundation of Beijing City and the Key Developmental Project of Science and Technology, Beijing Municipal Commission of Education (KZ201410028031), the National Key Project for Transgenic Crops in China (2014ZX08009-003), and the International Science & Technology Cooperation Program of China (2013DFG30530).

Notes

The authors declare no competing financial interest.

■ ABBREVIATIONS USED

AGPase, ADP-glucose pyrophosphorylase large subunit; DAF, days after flowering; DEP, differentially expressed protein; 2-DE, two-dimensional electrophoresis; GAPDH, glyceraldehyde-3-phosphate dehydrogenase; HMW, high-molecular weight; HSP 70, stromal 70 kDa heat shock-related protein; IEF, isoelectric focusing; KOG, eukaryotic Orthologous Groups; LEA, late embryogenesis abundant proteins; MALDI-TOF/TOF-MS, matrix-assisted laser desorption ionization time-of-flight/time-of-flight mass spectrometry; MDA, malondialdehyde; NCBI, National Center for Biotechnology Information; PCA, principal component analysis; ROS, reactive oxygen species; RWC, leaf relative water; SUS, sucrose synthase; TCA, tricarboxylic acid cycle

■ REFERENCES

(1) Shewry, P. R. Wheat. *J. Exp. Bot.* **2009**, *60* (6), 1537−1553.

(2) Tester, M.; Langridge, P. Breeding technologies to increase crop production in a changing world. *Science* **2010**, *327* (5967), 818−822.

(3) Kobata, T.; Palta, J. A.; Turner, N. C. Rate of development of postanthesis water deficits and grain filling of spring wheat. *Crop Sci.* **1992**, *32* (5), 1238−1242.

(4) Mittler, R. Oxidative stress, antioxidants and stress tolerance. *Trends Plant Sci.* **2002**, *7* (9), 405−410.

(5) Mittler, R. Abiotic stress, the field environment and stress combination. *Trends Plant Sci.* **2006**, *11* (1), 15−19.

(6) Habash, D. Z.; Kehel, Z.; Nachit, M. Genomic approaches for designing durum wheat ready for climate change with a focus on drought. *J. Exp. Bot.* **2009**, *60* (10), 2805−2815.

(7) Aprile, A.; Mastrangelo, A. M.; De Leonardis, A. M.; Galiba, G.; Roncaglia, E.; Ferrari, F.; De Bellis, L.; Turchi, L.; Giuliano, G.; Cattivelli, L. Transcriptional profiling in response to terminal drought stress reveals differential responses along the wheat genome. *BMC Genomics* **2009**, *10*, 279.

(8) Ge, P.; Ma, C.; Wang, S.; Gao, L.; Li, X.; Guo, G.; Ma, W.; Yan, Y. Comparative proteomic analysis of grain development in two spring wheat varieties under drought stress. *Anal. Bioanal. Chem.* **2012**, *402* (3), 1297−1313.

(9) Jiang, S. S.; Liang, X. N.; Li, X.; Wang, S. L.; Lv, D. W.; Ma, C. Y.; Li, X. H.; Ma, W. J.; Yan, Y. M. Wheat drought-responsive grain proteome analysis by linear and nonlinear 2-DE and MALDI-TOF mass spectrometry. *Int. J. Mol. Sci.* **2012**, *13* (12), 16065−16083.

(10) Ling, H. Q.; Zhao, S.; Liu, D.; Wang, J.; Sun, H.; Zhang, C.; Fan, H.; Li, D.; Dong, L.; Tao, Y.; Gao, C.; Wu, H.; Li, Y.; Cui, Y.; Guo, X.; Zheng, S.; Wang, B.; Yu, K.; Liang, Q.; Yang, W.; Lou, X.; Chen, J.; Feng, M.; Jian, J.; Zhang, X.; Luo, G.; Jiang, Y.; Liu, J.; Wang, Z.; Sha, Y.; Zhang, B.; Wu, H.; Tang, D.; Shen, Q.; Xue, P.; Zou, S.; Wang, X.; Liu, X.; Wang, F.; Yang, Y.; An, X.; Dong, Z.; Zhang, K.; Zhang, X.; Luo, M. C.; Dvorak, J.; Tong, Y.; Wang, J.; Yang, H.; Li, Z.; Wang, D.; Zhang, A.; Wang, J. Draft genome of the wheat A-genome progenitor *Triticum urartu*. *Nature* **2013**, *496* (7443), 87−90.

(11) Jia, J. Z.; Zhao, S. C.; Kong, X. Y.; Li, Y. R.; Zhao, G. Y.; He, W. M.; Appels, R.; Pfeifer, M.; Tao, Y.; Zhang, X. Y.; Jing, R. L.; Zhang, C.; Ma, Y. Z.; Gao, L. F.; Gao, C. A.; Spannagl, M.; Mayer, K.; Li, D.; Pan, S. K.; Zheng, F. Y.; Hu, Q.; Xia, X. C.; Li, J. W.; Liang, Q. S.; Chen, J.; Wicker, T.; Gou, C. Y.; Kuang, H. H.; He, G. Y.; Luo, Y. D.; Keller, B.; Xia, Q. J.; Lu, P.; Wang, J. Y.; Zou, H. F.; Zhang, R. Z.; Xu, J. Y.; Gao, J. L.; Middleton, C.; Quan, Z. W.; Liu, G. M.; Wang, J. International Wheat Genome Sequencing Consortium; Yang, H. M.; Liu, X.; He, Z. H.; Mao, L.; Wang, J. *Aegilops tauschii* draft genome sequence reveals a gene repertoire for wheat adaptation. *Nature* **2013**, *496* (7443), 91−95.

(12) Choulet, F.; Alberti, A.; Theil, S.; Glover, N.; Barbe, V.; Daron, J.; Pingault, L.; Sourdille, P.; Couloux, A.; Paux, E.; Leroy, P.;

DOI: 10.1021/acs.jafc.5b00575
J. Agric. Food Chem. 2015, 63, 8478−8487

Mangenot, S.; Guilhot, N.; Le Gouis, J.; Balfourier, F.; Alaux, M.; Jamilloux, V.; Poulain, J.; Durand, C.; Bellec, A.; Gaspin, C.; Safar, J.; Dolezel, J.; Rogers, J.; Vandepoele, K.; Aury, J. M.; Mayer, K.; Berges, H.; Quesneville, H.; Wincker, P.; Feuillet, C. Structural and functional partitioning of bread wheat chromosome 3B. *Science* **2014**, *345* (6194), 1249721.

(13) Emes, M. J.; Bowsher, C. G.; Hedley, C.; Burrell, M. M.; Scrase-Field, E. S. F.; Tetlow, I. J. Starch synthesis and carbon partitioning in developing endosperm. *J. Exp. Bot.* **2003**, *54* (382), 569−575.

(14) Irar, S.; Brini, F.; Goday, A.; Masmoudi, K.; Pagès, M. Proteomic analysis of wheat embryos with 2-DE and liquid-phase chromatography (ProteomeLab PF-2D) — A wider perspective of the proteome. *J. Proteomics* **2010**, *73* (9), 1707−1721.

(15) Laino, P.; Shelton, D.; Finnie, C.; De Leonardis, A. M.; Mastrangelo, A. M.; Svensson, B.; Lafiandra, D.; Masci, S. Comparative proteome analysis of metabolic proteins from seeds of durum wheat (cv. Svevo) subjected to heat stress. *Proteomics* **2010**, *10* (12), 2359−2368.

(16) Hajheidari, M.; Eivazi, A.; Buchanan, B. B.; Wong, J. H.; Majidi, I.; Salekdeh, G. H. Proteomics Uncovers a Role for Redox in Drought Tolerance in Wheat. *J. Proteome Res.* **2007**, *6* (4), 1451−1460.

(17) Guo, G. F.; Ge, P.; Ma, C. Y.; Li, X. H.; Lv, D. W.; Wang, S. L.; Ma, W. J.; Yan, Y. M. Comparative proteomic analysis of salt response proteins in seedling roots of two wheat varieties. *J. Proteomics* **2012**, *75* (6), 1867−1885.

(18) Guttieri, M. J.; Stark, J. C.; O'Brien, K.; Souza, E. Relative sensitivity of spring wheat grain yield and quality parameters to moisture deficit. *Crop Sci.* **2001**, *41* (2), 327−335.

(19) Smart, R. E. Rapid estimates of relative water content. *Plant Physiol.* **1974**, *53* (2), 258−260.

(20) Zhao, S. J.; Xu, C. C.; Zou, Q.; Meng, Q. W. Improvements of method for measurement of malondialdehvde in plant tissues. *Plant Physiol. Commun.* **1994**, *30* (3), 207−210.

(21) Bates, L. S.; Waldren, R. P.; Teare, I. D. Rapid determination of free proline for water-stress studies. *Plant Soil* **1973**, *39* (1), 205−207.

(22) Arnon, D. I. Copper enzymes in isolated chloroplasts. Polyphenoloxidase in Beta vulgaris. *Plant Physiol.* **1949**, *24* (1), 1−15.

(23) Czuchajowska, Z.; Paszczynska, B. Is wet gluten good for baking? *Cereal chemistry* **1996**, *73* (4), 483−489.

(24) Guo, G. F.; Lv, D. W.; Yan, X.; Subburaj, S.; Ge, P.; Li, X. H.; Hu, Y. K.; Yan, Y. M. Proteome characterization of developing grains in bread wheat cultivars (*Triticum aestivum* L.). *BMC Plant Biol.* **2012**, *12*, 147.

(25) Valledor, L.; Jorrin, J. Back to the basics: maximizing the information obtained by quantitative two dimensional gel electrophoresis analyses by an appropriate experimental design and statistical analyses. *J. Proteomics* **2011**, *74* (1), 1−18.

(26) Kosová, K.; Vítámvás, P.; Planchon, S.; Renaut, J.; Vanková, R.; Prášil, I. T. Proteome Analysis of Cold Response in Spring and Winter Wheat (*Triticum aestivum*) Crowns Reveals Similarities in Stress Adaptation and Differences in Regulatory Processes between the Growth Habits. *J. Proteome Res.* **2013**, *12*, 4830−4845.

(27) Franceschini, A.; Szklarczyk, D.; Frankild, S.; Kuhn, M.; Simonovic, M.; Roth, A.; Lin, J.; Minguez, P.; Bork, P.; von Mering, C.; Jensen, L. J. STRING v9.1: protein-protein interaction networks, with increased coverage and integration. *Nucleic Acids Res.* **2013**, *41* (D1), D808−D815.

(28) Cline, M. S.; Smoot, M.; Cerami, E.; Kuchinsky, A.; Landys, N.; Workman, C.; Christmas, R.; Avila-Campilo, I.; Creech, M.; Gross, B.; Hanspers, K.; Isserlin, R.; Kelley, R.; Killcoyne, S.; Lotia, S.; Maere, S.; Morris, J.; Ono, K.; Pavlovic, V.; Pico, A. R.; Vailaya, A.; Wang, P. L.; Adler, A.; Conklin, B. R.; Hood, L.; Kuiper, M.; Sander, C.; Schmulevich, I.; Schwikowski, B.; Warner, G. J.; Ideker, T.; Bader, G. D. Integration of biological networks and gene expression data using Cytoscape. *Nat. Protoc.* **2007**, *2* (10), 2366−2382.

(29) Horton, P.; Park, K. J.; Obayashi, T.; Fujita, N.; Harada, H.; Adams-Collier, C. J.; Nakai, K. Protein subcellular localization prediction with WOLF PSORT. *Nucleic Acids Res.* **2007**, *35*, W585−587.

(30) Small, I.; Peeters, N.; Legeai, F.; Lurin, C. Predotar: A tool for rapidly screening proteomes for N-terminal targeting sequences. *Proteomics* **2004**, *4* (6), 1581−1590.

(31) Yang, F.; Xu, X.; Xiao, X.; Li, C. Responses to drought stress in two poplar species originating from different altitudes. *Biol. Plant.* **2009**, *53* (3), 511−516.

(32) Aalenf, R. B.; Opsahl-Ferstad, H. G.; Linnestad, C.; Olsen, O. A. Transcripts encoding an oleosin and a dormancy-related protein are present in both the aleurone layer and the embryo of developing barley (*Hordeum vulgare* L.) seeds. *Plant J.* **1994**, *5* (3), 385−396.

(33) Haslekås, C.; Stacy, R. A.; Nygaard, V.; Culiáñez-Macià, F. A.; Aalen, R. B. The expression of a peroxiredoxin antioxidant gene, AtPer1, in Arabidopsis thaliana is seed-specific and related to dormancy. *Plant Mol. Biol.* **1998**, *36* (6), 833−845.

(34) Radyuk, S. N.; Klichko, V. I.; Spinola, B.; Sohal, R. S.; Orr, W. C. The peroxiredoxin gene family in Drosophila melanogaster. *Free Radical Biol. Med.* **2001**, *31* (9), 1090−1100.

(35) Tsugeki, R.; Nishimura, M. Interaction of homologues of Hsp70 and Cpn60 with ferredoxin-NADP$^+$ reductase upon its import into chloroplasts. *FEBS Lett.* **1993**, *320* (3), 198−202.

(36) Duan, Y. H.; Guo, J.; Ding, K.; Wang, S. J.; Zhang, H.; Dai, X. W.; Chen, Y. Y.; Govers, F.; Huang, L. L.; Kang, Z. S. Characterization of a wheat HSP70 gene and its expression in response to stripe rust infection and abiotic stresses. *Mol. Biol. Rep.* **2011**, *38* (1), 301−307.

(37) Krasensky, J.; Jonak, C. Drought, salt, and temperature stress-induced metabolic rearrangements and regulatory networks. *J. Exp. Bot.* **2012**, *63* (4), 1593−1608.

(38) Franco, O. L.; Rigden, D. J.; Melo, F. R.; Grossi-De-Sa, M. F. Plant alpha-amylase inhibitors and their interaction with insect alpha-amylases. *Eur. J. Biochem.* **2002**, *269* (2), 397−412.

(39) Skylas, D. J.; Mackintosh, J. A.; Cordwell, S. J.; Basseal, D. J.; Walsh, B. J.; Harry, J.; Blumenthal, C.; Copeland, L.; Wrigley, C. W.; Rathmell, W. Proteome approach to the characterisation of protein composition in the developing and mature wheat-grain endosperm. *J. Cereal Sci.* **2000**, *32*, 169−188.

(40) Smart, M. G.; O'Brien, T. P. The development of the wheat embryo in relation to the neighbouring tissues. *Protoplasma* **1983**, *114*, 1−13.

(41) Blackig, M.; Corbineau, F.; Grzesikit, M.; Guyi, P.; Côme, D. Carbohydrate metabolism in the developing and maturing wheat embryo in relation to its desiccation tolerance. *J. Exp. Bot.* **1996**, *47*, 161−169.

(42) Sturm, A.; Tang, G. Q. The sucrose-cleaving enzymes of plants are crucial for development, growth and carbon partitioning. *Trends Plant Sci.* **1999**, *4* (10), 401−407.

(43) Weschke, W.; Panitz, R.; Gubatz, S.; Wang, Q.; Radchuk, R.; Weber, H.; Wobus, U. The role of invertases and hexose transporters in controlling sugar ratios in maternal and filial tissues of barley caryopses during early development. *Plant J.* **2003**, *33* (2), 395−411.

(44) Jiang, H.; Dian, W.; Liu, F.; Wu, P. Isolation and characterization of two fructokinasec DNA clones from rice. *Phytochemistry* **2003**, *62* (1), 47−52.

(45) Shewry, P. R.; Halford, N. G. Cereal seed storage proteins: structures, properties and role in grain utilization. *J. Exp. Bot.* **2002**, *53* (370), 947−958.

(46) Branlard, G.; Dardevet, M.; Saccomano, R.; Lagoutte, F.; Gourdon, J. Genetic diversity of wheat storage proteins and bread wheat quality. *Wheat in a global environment*; Springer: Dordrecht, The Netherlands, 2001; Vol. *119*, Issue 1−2, pp 59−67.

(47) Ma, F. Y.; Li, M.; Yu, L. L.; Li, Y.; Liu, Y. Y.; Li, T. T.; Liu, W.; Wang, H. M.; Zheng, Q.; Li, K. X.; Chang, J. L.; Yang, G. X.; Wang, Y. S.; He, G. Y. Transformation of common wheat (*Triticum aestivum* L.) with *avenin-like b* gene improves flour mixing properties. *Mol. Breed.* **2013**, *32* (4), 853−865.

(48) Rasiah, I. A.; Sutton, K. H.; Low, F. L.; Lin, H. M.; Gerrard, J. A. Crosslinking of wheat dough proteins by glucose oxidase and the resulting effects on bread and croissants. *Food Chem.* **2005**, *89* (3), 325−332.

DOI: 10.1021/acs.jafc.5b00575
J. Agric. Food Chem. 2015, 63, 8478−8487

phosphate, disodium hydrogen phosphate, and anhydrous sodium sulfate were purchased from Grüssing (Filsum, Germany). MGO (40%, w/w), DHA, *ortho*-phenylenediamine (*o*PD), and 2,4,6-trimethylpyridine (TMP) were obtained from Sigma-Aldrich (Steinheim, Germany). 5-Hydroxymethylfurfural (HMF) was provided by Alfa Aesar (Karlsruhe, Germany). D(−)-Fructose, D(+)-glucose, D(+)-saccharose, and acetic acid were purchased from Carl Roth (Karlsruhe, Germany). Sodium hydroxide pellets were purchased from Fisher Scientific (Schwerte, Germany). For all experiments, ultrapure water was used, prepared by an ELGA LabWater PURELAB Plus water system (Celle, Germany).

Reversed-Phase High-Performance Liquid Chromatography with Ultraviolet Detection (RP-HPLC−UV) Analysis of MGO and DHA after Derivatization to Quinoxalines. The determination of MGO and DHA was performed according to the literature,[11] with some modifications. Briefly, for quantitation of MGO, 1 mL aliquots of 10% (w/v) honey solutions in 0.5 M phosphate buffer (pH 6.5) were mixed with 300 μL of phosphate buffer (pH 6.5) and 300 μL of *o*PD solution (1% in phosphate buffer at pH 6.5). Samples were incubated in the dark at room temperature overnight and membrane-filtered (0.45 μm). For quantitation of DHA, 1 mL aliquots of 10% honey solutions in 0.5 M acetate buffer (pH 4.0) were mixed with 300 μL of acetate buffer (pH 4.0) and 300 μL of *o*PD solution (1% in acetate buffer at pH 4.0), followed by incubation for 16 h at 37 °C and membrane filtration (0.45 μm).

HPLC analyses were performed using an Äkta basic system from Amersham Pharmacia Biotech (Uppsala, Sweden) with a pump P-900 and an online degasser K-5004 (Knauer, Berlin, Germany) as well as an UV detector UV-900 and an auto sampler A-900. Peak evaluation was managed using the software UNICORN 4.11. The separation of quinoxalines was realized on a stainless-steel column filled with Eurospher 100 RP18 material (250 × 4.6 mm, 5 μm particle size, with integrated pre-column, Knauer, Berlin, Germany). The mobile phase were 0.075% acetic acid in water (solvent A) and a mixture of 80% methanol and 20% solvent A (solvent B). The gradient started with 40% solvent B for 1 min, was elevated linearly to 100% B over a period of 20 min, was changed back to 40% B in 4 min, and was held there for 7 min. The flow rate was 0.9 mL/min; the separation was performed at 30 °C; 20 μL sample solution was injected; and peaks were detected by measurement of UV absorbance at 312 nm. Quantitation was achieved by external calibration with MGO standard solution or the standard addition method for DHA.

RP-HPLC−UV Analysis of HMF. The determination of HMF was performed according to the literature,[15] with some modifications. Briefly, 1 mL aliquots of 10% honey solutions in ultrapure water were membrane-filtered (0.45 μm) and subsequently analyzed via HPLC−UV.

The HPLC system and column was used as mentioned above. The mobile phase consisted of 0.05 M phosphate buffer at pH 5.5 (solvent A) and HPLC-grade methanol (solvent B). The elution was carried out isocratically with 15% solvent B over 30 min. The flow rate was 1.0 mL/min at ambient temperature; 50 μL sample solution was injected; and peaks were detected by measurement of UV absorbance at 283 nm. Quantitation was achieved by external calibration with freshly prepared HMF standard solution.

Analysis of Proline in Honey. A total of 1 g of honey was dissolved in 10 mL of phosphate buffer (0.1 M, pH 2) and subjected to a column (25 × 110 mm) filled with ion-exchange resin Dowex 50WX8, 100−200 mesh. The ion-exchange resin was previously activated with 50 mL of HCl (2 mol/L). The amino acids were eluted with 100 mL of a solution of ammoniac (7 mol/L). The eluate was evaporated to dryness, and the dry residue was dissolved in ultrapure water. After lyophilization, the sample was dissolved in 1 mL of lithium citrate buffer (0.12 M, pH 2.2), diluted (1:10), and subjected to amino acid analysis. The analyses were performed using a SYKAM S4300 amino acid analyzer (Fuerstenfeldbruck, Germany) with conditions according to the instructions of the manufacturer. The ninhydrin derivate of proline was detected at 440 nm.

Gas Chromatography−Mass Spectrometry (GC−MS) Analysis of 2-AP. A total of 10 g of honey was dissolved in 10 mL of ultrapure water. A total of 50 μL of TMP solution (195 mg/L) was added, and the pH was adjusted to 8 with 1 M sodium hydroxide solution. The alkaline honey solution was mixed with 5 mL of dichloromethane, agitated vigorously for 60 s, and centrifuged afterward. The organic layer was collected, and extraction with dichloromethane was repeated once. The collected organic layer was washed with 5 mL of water and dried with anhydrous sodium sulfate. An aliquot of 1 mL was transferred to a GC vial and subjected to GC−MS analysis. Matrix calibration was achieved by adding known amounts of 2-AP to an artificial honey, which was then extracted as described above. The artificial honey was prepared following ref 16. Briefly, 46.5 g of fructose, 35 g of glucose, 1.5 g of saccharose, and 17 g of water were mixed and stirred until a fine crystalline suspension was formed. The artificial honey/2-AP mixture was diluted with pure artificial honey, and 10 g of each mixture was analyzed according to the extraction procedure above. The actual 2-AP concentration of the commercial standard was determined by RP-HPLC with a chemiluminescent nitrogen detector (CLND) according to ref 17.

GC−MS analysis of 2-AP was performed using an Agilent 7890A system, consisting of a 7683 Series injector with a sample tray and a 5975C MS detector working in electron ionization (EI) mode, all from Agilent (Boblingen, Germany). The GC system was equipped with a TR-FFAP capillary column (30.0 m × 0.25 mm inner diameter, with a 0.25 μm film thickness) from Thermo Scientific (Runcorn, U.K.). Helium was used as the carrier gas with a constant flow of 1 mL/min. The injector temperature was set to 250 °C, and a 1 μL sample was injected using the pulsed splitless mode. The auxiliary temperature was set to 235 °C, and the ion source and quadrupole temperatures were set to 230 and 150 °C, respectively. The initial oven temperature was set to 40 °C and held for 2 min, then raised at 2.25 °C/min to 80 °C, finally raised at 30 °C/min to 235 °C, and held for 5 min. The mass spectrometer was working in EI mode at 70 eV in the scan (mass range of m/z 40.0−300.0) and selected ion monitoring (SIM) mode. For quantitation, the SIM mode was used with the monitoring of the following ions: m/z 111 and 83 (2-AP) and m/z 121 and 79 (TMP). The ions underlined were used for quantitation. The retention time of the analytes was 15.0 min for 2-AP and 17.9 min for TMP, respectively. Data acquisition and evaluation were performed with MSD ChemStation software (Agilent, Germany).

Model Studies on 2-AP Formation in Honey. Commercial non-manuka multifloral honey from Germany was mixed with MGO alone (100 mg/kg, labeled as "low", or 500 mg/kg, labeled as "high", respectively) or MGO and DHA in a 1:2 ratio (100 and 200 mg/kg, labeled as "low", or 500 and 1000 mg/kg, labeled as "high", respectively). The samples were stirred vigorously and stored in the dark at room temperature and 37 °C. The storage temperature of 37 °C was chosen to simulate accelerated ripening and to study chemical reactions that occur during longer storage. Samples were taken after 0, 2, 4, 8, and 12 weeks of storage. A control (multifloral honey without added MGO) was stored under the same conditions, and samples were taken after 0, 4, and 12 weeks of storage. The samples were analyzed according to the extraction procedure mentioned above.

Statistics. Results are expressed as mean values of two separate measurements, except otherwise indicated. Hypothesis testing was performed via a two sample t test with a significance level of 0.01. Intraday variation of 2-AP analysis was investigated using five replicate injections of a 2-AP standard solution. Interday precision was determined using four calibration standards, which were analyzed during 8 months.

RESULTS AND DISCUSSION

The aim of this study was to investigate whether 2-AP, a specific flavor compound formed from MGO and proline, is present in manuka honeys from New Zealand. Identification and quantitation of 2-AP in manuka honey was achieved using GC−MS based on a method recently described in the literature for 2-AP analysis.[18] For sample preparation, a crucial step for reliable quantitation of 2-AP, solid-phase microextraction (SPME), or solvent extraction methods are reported.[7,9,18]

DOI: 10.1021/acs.jafc.5b03042
J. Agric. Food Chem. 2015, 63, 8488−8492

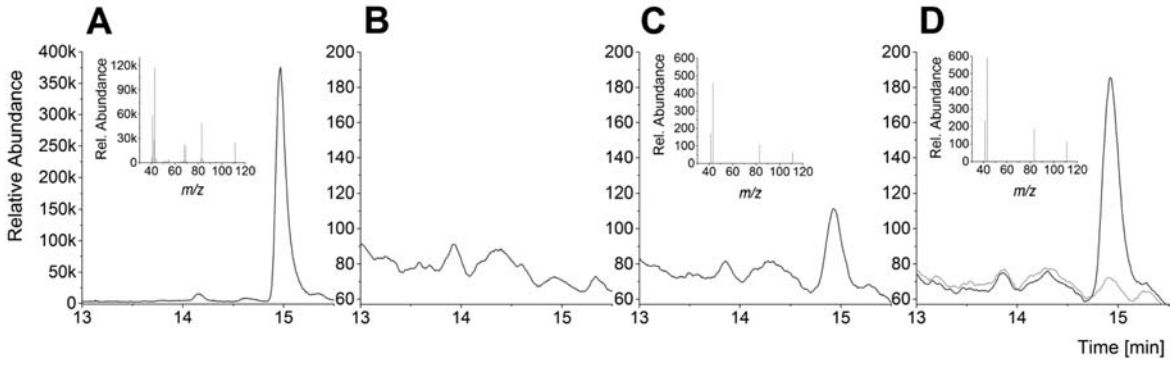

Figure 1. GC−MS data for identification and quantitation of 2-AP: (A) synthetic standard solution, (B) lime honey; (C) manuka honey, and (D) artificial honey spiked with proline and MGO (black line) and DHA (gray line) incubated for 20 weeks at 37 °C.

Because 2-AP formation in manuka honey is probably enhanced by a high temperature, an extraction procedure using dichloromethane without heating was chosen. Furthermore, concentration steps like drying with nitrogen were avoided to prevent a loss of 2-AP during sample preparation. TMP was used as an internal standard to check the recovery during the extraction procedure. Comparing peak areas for 2-AP standard samples extracted from aqueous solutions or from honey matrix calibration resulted in an estimated 60% recovery of 2-AP. Therefore, quantitation was carried out via external matrix calibration, using a synthetic 2-AP standard and artificial honey. The actual 2-AP concentration of the commercial standard was checked with RP-HPLC and chemiluminescent nitrogen detection (CLND) to be 83.3% of the specification given by the supplier. A regression coefficient R^2 of 0.998 was calculated for the linear calibration range from 0.1 to 2.0 mg/kg. The limit of detection (LOD) was 0.04 mg/kg, and the limit of quantitation (LOQ) was 0.09 mg/kg. LOD and LOQ were calculated on the basis of the signal-to-noise-ratio. Inter- and intraday precisions were 3.1 and 6.1%, respectively. 2-AP was unequivocally identified in commercial samples of manuka honey by comparing retention time and corresponding mass spectra of honey samples and standard solutions (panels A and C of Figure 1). The comparison of the fragmentation pattern and the characteristic ratio of the quantifier ion to the qualifier ion (m/z 83 and 111, respectively) of the 2-AP standard and the 2-AP peak in honey yields identical relative intensity ratios. The hypothesis that 2-AP in manuka honey results from the reaction of MGO and proline was confirmed by significantly smaller signals of 2-AP in non-manuka honeys without MGO (Figure 1B) and the detection of 2-AP in an artificial honey containing MGO and proline after 20 weeks of incubation (Figure 1D).

For 11 commercially available manuka honeys, amounts of 2-AP ranging from 0.08 to 0.45 mg/kg were measured (Figure 2). In contrast to this, the majority of non-manuka honeys analyzed in this study contained 2-AP only in very small amounts between 0.08 and 0.11 mg/kg. However, some aromatic non-manuka honeys, namely, buckwheat, lime, and thyme honey, contained 2-AP in concentrations ranging between 0.20 and 0.31 mg/kg. According to the literature, 2-AP has been found in different sorts of food as an aroma active compound. The concentrations vary between 78 μg/kg for white-bread crust and 0.8 mg/kg for cooked rice.[8,9] Concerning honey, 2-AP has already been detected in lime honey from the linden tree.[19] The authors pointed out that 2-AP is an

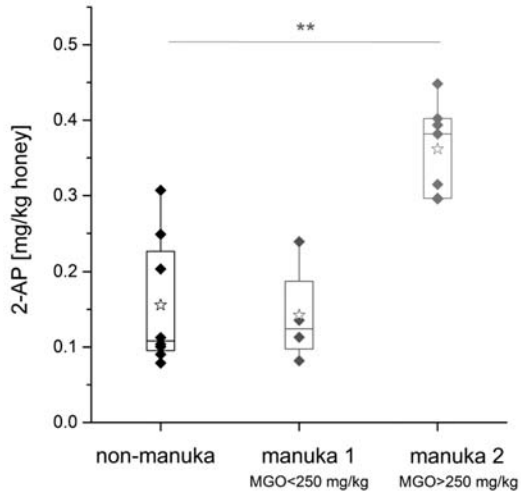

Figure 2. 2-AP concentration of commercial samples of non-manuka honey (n = 8) and manuka honey with MGO below 250 mg/kg (manuka 1) (n = 4) and above 250 mg/kg (manuka 2) (n = 7). Stars indicate the average value for each group.

important odorant of linden honey but did not report on quantitative amounts of 2-AP. Interestingly, no 2-AP was detected in the blossoms of the linden tree, what supports the hypothesis that 2-AP originates from reactions in the honey matrix. The 2-AP concentration of manuka honey with a MGO concentration below 250 mg/kg is comparable to the non-manuka honeys. However, the concentration of 2-AP in manuka honeys with a MGO concentration above 250 mg/kg was significantly increased in comparison to the non-manuka group (Figure 2). The average amount of 2-AP in manuka honeys with MGO contents above 250 mg/kg was 0.36 mg/kg, and the average amount of 2-AP in non-manuka honeys was 0.16 mg/kg. For this samples, the 2-AP content of the analyzed manuka honeys increased with increasing MGO concentrations up to a MGO value of approximately 500 mg/kg honey (see Figure S1). For concentrations of 600−1000 mg of MGO/kg of honey, no further increase of 2-AP was found. Proline is the most abundant amino acid in honey, accounting for 260−890 mg/kg, which represents 70% of the total free amino acids.[14] The analysis of the proline concentration of the studied honeys showed no significant difference between the non-manuka and manuka honeys with varying MGO contents. The proline concentration ranged between 200 and 540 mg/kg and did not correlate with the MGO content (for data on MGO and

DOI: 10.1021/acs.jafc.5b03042
J. Agric. Food Chem. 2015, 63, 8488−8492

proline, see Table S1). In fact, MGO appears to be the crucial factor for 2-AP formation. The observation that MGO contents between 600 and 1000 mg/kg do not lead to a further increase of 2-AP in manuka honeys could be explained by competitive reactions. MGO can react with other honey substances or with another MGO molecule to form adducts or aroma-active compounds, such as furaneol, respectively. To assess whether storage of non-manuka honey containing artificially added MGO or DHA results in the formation of 2-AP, a commercial multifloral honey was spiked with MGO or a 1:2 mixture of MGO and DHA, respectively, and stored at room temperature and 37 °C for 12 weeks. Figure 3A shows the 2-AP concentration depending upon the incubation time. When high amounts of MGO (500 mg/kg) were added to the honey, 2-AP significantly increased after 4 weeks of storage at 37 °C. After 12 weeks, the 2-AP concentration reached the amount that was quantitated in the commercial manuka honey samples

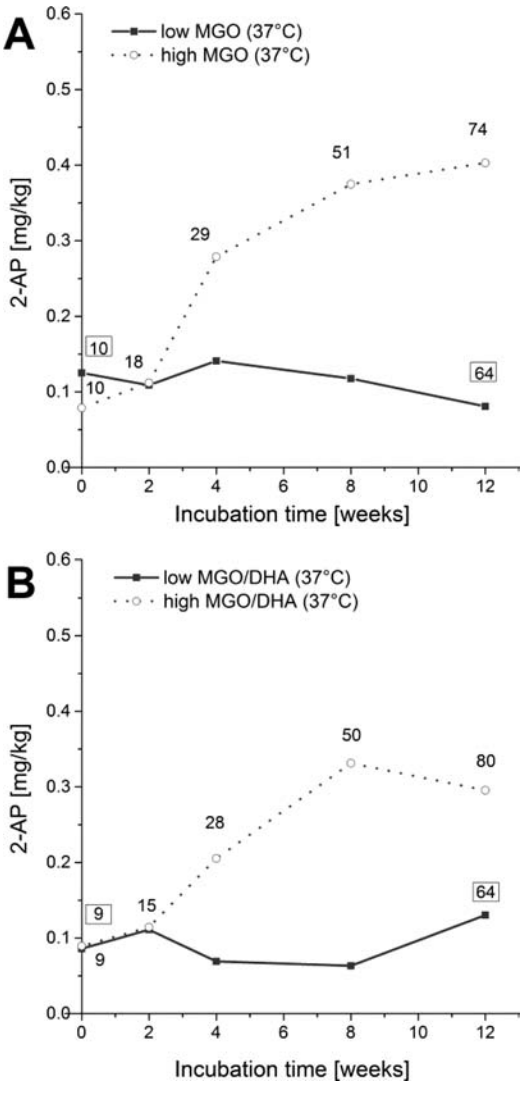

Figure 3. 2-AP formation in a non-manuka multifloral honey with (A) added MGO and (B) added MGO and DHA, stored at 37 °C (n = 2 for each time point and sample). Values above symbols are HMF concentrations (mg/kg) at the given time points (values without boxes belong to samples with a high addition of MGO or MGO/DHA, and values in boxes belong to samples with a low addition of MGO or MGO/DHA).

with high MGO contents, followed by no further increase. No increase of 2-AP was found during storage of non-manuka honey with artificially added MGO at ambient temperature and non-manuka honey without MGO (ambient temperature and 37 °C; data not shown). There was also no increase in 2-AP when low MGO concentrations (100 mg/kg) were added to non-manuka honey and stored at an elevated temperature for 12 weeks (see Figure 3). This is in accordance with the 2-AP amounts of commercial manuka honeys containing MGO below 250 mg/kg. The average 2-AP content of these samples was 0.14 mg/kg. The non-manuka honey with artificially added MGO (low MGO) had approximately the same amount of 2-AP, which did not increase after storage. This indicates that a "threshold level" of MGO of approximately 250 mg/kg is necessary to initiate a reaction of proline and MGO and significantly increase the 2-AP content in manuka honey. Competitive reactions as a possible reason for the disproportionate conversion of MGO and proline to 2-AP were discussed above. The 2-AP concentration in non-manuka honey was not influenced by the addition of DHA and subsequent storage (Figure 3B). For the spiked honey samples, which were stored for 8 weeks or longer at 37 °C, a significant increase in the concentration of HMF in addition to the formation of 2-AP was observed. HMF is used as a quality parameter of honey and should not exceed 40 mg/kg.[20] All commercial manuka honeys in this study were below this threshold level. This result points to the fact that, following "artificial" spiking of a non-manuka honey with MGO, 2-AP concentrations do only increase during storage at elevated temperatures, which also leads to increasing amounts of HMF. 2-AP, therefore, might be an interesting indicator to control the storage conditions and the quality of manuka honey. High amounts of 2-AP, as a result of high MGO levels, together with an increased concentration of HMF may point to a fraudulent addition of MGO and increased temperatures for "artificially" producing high-price manuka honey products. A manuka honey with a high MGO content together with a high 2-AP concentration and a low HMF level has likely been stored at low temperatures over a longer time period. This "natural" ripening process cannot be simulated by MGO addition followed by a high temperature storage. According to the literature, the storage of manuka honey initially leads to a MGO increase as a result of continuous formation from DHA, followed by a MGO decrease, probably as a result of reactions of MGO with other honey components.[21] Further studies are needed to clarify the reaction pathways of MGO and its role in the unique chemistry of manuka honey. In addition to MGO and DHA, 2-AP as a direct reaction product of MGO and proline could be a suitable parameter to characterize the quality of manuka honey.

■ ASSOCIATED CONTENT

Supporting Information

The Supporting Information is available free of charge on the ACS Publications website at DOI: 10.1021/acs.jafc.5b03042.

MGO, HMF, proline, and 2-AP contents of non-manuka and manuka honeys (Table S1) and 2-AP concentration of commercial manuka honey samples (n = 11) with varying MGO contents (Figure S1) (PDF)

DOI: 10.1021/acs.jafc.5b03042
J. Agric. Food Chem. 2015, 63, 8488−8492

AUTHOR INFORMATION

Corresponding Author

*Telephone: +49-351-463-34647. Fax: +49-351-463-34138. E-mail: thomas.henle@chemie.tu-dresden.de.

Funding

The authors gratefully acknowledge financial support for this project from Manuka Health, Ltd., New Zealand. This financial support did not prevent the authors from publishing both positive and negative results. Publishing this research was possible without the prior approval of the sponsor.

Notes

The authors declare no competing financial interest.

ABBREVIATIONS USED

2-AP, 2-acetyl-1-pyrroline; MGO, methylglyoxal; DHA, dihydroxyacetone; GC−MS, gas chromatography−mass spectrometry; LOD, limit of detection; LOQ, limit of quantitation; HMF, 5-hydroxymethylfurfural; *o*PD, *ortho*-phenylenediamine; HPLC, high-performance liquid chromatography; TMP, 2,4,6-trimethylpyridine

REFERENCES

(1) Molan, P. C. The Antibacterial Activity of Honey. *Bee World* **1992**, *73* (1), 5−28.

(2) Mavric, E.; Wittmann, S.; Barth, G.; Henle, T. Identification and quantification of methylglyoxal as the dominant antibacterial constituent of Manuka (Leptospermum scoparium) honeys from New Zealand. *Mol. Nutr. Food Res.* **2008**, *52* (4), 483−489.

(3) Adams, C. J.; Boult, C. H.; Deadman, B. J.; Farr, J. M.; Grainger, M. N. C.; Manley-Harris, M.; Snow, M. J. Isolation by HPLC and characterisation of the bioactive fraction of New Zealand manuka (Leptospermum scoparium) honey. *Carbohydr. Res.* **2008**, *343* (4), 651−659.

(4) Wang, Y.; Ho, C.-T. Flavour chemistry of methylglyoxal and glyoxal. *Chem. Soc. Rev.* **2012**, *41* (11), 4140−4149.

(5) Wang, Y.; Ho, C. T. Formation of 2,5-dimethyl-4-hydroxy-3(2H)-furanone through methylglyoxal: A maillard reaction intermediate. *J. Agric. Food Chem.* **2008**, *56*, 7405−7409.

(6) Hofmann, T.; Schieberle, P. 2-Oxopropanal, Hydroxy-2-propanone, and 1-Pyrrolines Important Intermediates in the Generation of the Roast-Smelling Food Flavor Compounds 2-Acetyl-1-pyrroline and 2-Acetyltetrahydropyridine. *J. Agric. Food Chem.* **1998**, *46*, 2270−2277.

(7) Grimm, C. C.; Champagne, E. T.; Lloyd, I. S. W.; Easson, I. M.; Condon, B.; McClung, A. Analysis of 2-Acetyl-l-Pyrroline in Rice by HSSE/GC/MS. *Cereal Chem.* **2011**, *88* (3), 271−277.

(8) Buttery, R. G.; Ling, L. C.; Mon, T. R. Quantitative Analysis of 2-Acetyl-1-pyrroline in Rice. *J. Agric. Food Chem.* **1986**, *34* (1), 112−114.

(9) Schieberle, P.; Grosch, W. Quantitative analysis of aroma compounds in wheat and rye bread crusts using a stable isotope dilution assay. *J. Agric. Food Chem.* **1987**, *35* (1968), 252−257.

(10) Belitz, H.-D.; Grosch, W.; Schieberle, P. *Lehrbuch der Lebensmittelchemie*, 6th ed.; Springer: Berlin, Germany, 2008.

(11) Weigel, K. U.; Opitz, T.; Henle, T. Studies on the occurrence and formation of 1,2-dicarbonyls in honey. *Eur. Food Res. Technol.* **2004**, *218* (2), 147−151.

(12) Degen, J.; Hellwig, M.; Henle, T. 1,2-Dicarbonyl Compounds in Commonly Consumed Foods. *J. Agric. Food Chem.* **2012**, *60* (28), 7071−7079.

(13) Hellwig, M.; Henle, T. Baking, ageing, diabetes: a short history of the Maillard reaction. *Angew. Chem., Int. Ed.* **2014**, *53* (39), 10316−10329.

(14) Bernal, J. L.; Nozal, M. J.; Toribio, L.; Diego, J. C.; Ruiz, A. A comparative study of several HPLC methods for determining free amino acid profiles in honey. *J. Sep. Sci.* **2005**, *28*, 1039−1047.

(15) Jeuring, H. J.; Kuppers, F. J. High performance liquid chromatography of furfural and hydroxymethylfurfural in spirits and honey. *J. Assoc. Off. Anal. Chem.* **1980**, *63* (6), 1215−1218.

(16) Wahdan, H. A. L. Causes of the antimicrobial activity of honey. *Infection* **1998**, *26* (1), 26−31.

(17) Penndorf, I.; Biedermann, D.; Maurer, S. V.; Henle, T. Studies on N-terminal glycation of peptides in hypoallergenic infant formulas: Quantification of α-*N*-(2-furoylmethyl) amino acids. *J. Agric. Food Chem.* **2007**, *55*, 723−727.

(18) Wu, M.-L.; Chou, K.-L.; Wu, C.-R.; Chen, J.-K.; Huang, T.-C. Characterization and the possible formation mechanism of 2-acetyl-1-pyrroline in aromatic vegetable soybean (Glycine max L.). *J. Food Sci.* **2009**, *74* (5), S192−S197.

(19) Blank, I.; Fischer, K.; Grosch, W. Intensive neutral odourants of linden honey. Differences from honeys of other botanical origin. *Z. Lebensm.-Unters. Forsch.* **1989**, *189* (5), 426−433.

(20) Codex Alimentarius Commission. *Revised Codex Standard for Honey*; Codex Alimentarius Commission: Geneva, Switzerland, 1981.

(21) Atrott, J.; Haberlau, S.; Henle, T. Studies on the formation of methylglyoxal from dihydroxyacetone in Manuka (Leptospermum scoparium) honey. *Carbohydr. Res.* **2012**, *361*, 7−11.

DOI: 10.1021/acs.jafc.5b03042
J. Agric. Food Chem. 2015, 63, 8488−8492

molecular basis. From this information, molecular models composed of fatty acids and bitter substances can be constructed to elucidate the mode of interaction.

MATERIALS AND METHODS

Chemicals. These were obtained from commercial sources. Hexanoic, octanoic, decanoic, linoleic, and linolenic fatty acids as well as sodium thiocyanate, taurine, acesulfame K, saccharin sodium dehydrate, caffeine, thiamine hydrochloride, and amygdalin were obtained from Wako Pure Chemical Industries Ltd. (Osaka, Japan); lauric acid, *N*-phenylthiocarbamide, salicin, berberine hydrochloride monohydrate, and quinine hydrochloride dihydrate were obtained from Nacalai Tesque, Inc. (Kyoto, Japan). The myristoleic, palmitoleic, oleic, and arachidonic fatty acids as well as glycerol monooleate, (±)-propranolol hydrochloride, promethazine hydrochloride, chloramphenicol, yohimbine hydrochloride, colchicine, cromolyn disodium salt, limonin, and ouabain octahydrate were obtained from Sigma-Aldrich Co. (Tokyo, Japan). Methyltryptophan and naringin were obtained from Tokyo Chemical Industry Co., Ltd. (Tokyo, Japan). Acetic acid and antipyrine were obtained from Kanto Chemical Co. Inc. (Tokyo, Japan), and glycerol monolaurate was obtained from Chem-Implex International, Inc. (Wood Dale, IL, USA).

Screening of Bitter Substances. ITC was carried out using a MicroCal iTC200 instrument (Malvern Instruments Japan Corp., Kobe, Japan). The fatty acids were neutralized and solubilized by adding an equimolar amount of sodium hydroxide. The interactions between 22 bitter substances, whose structures are shown in Figure S1-1, and sodium oleate were measured. The concentrations of the bitter substances and sodium oleate were 1.5 and 0.5 mM, respectively. The compounds were dissolved in 5 mM phosphate buffer (pH 7.0). The reference cell was filled with Milli-Q water (Millipore Corp., Billerica, MA, USA). The bitter substances in buffer solutions were titrated into sodium oleate dissolved in 5 mM phosphate buffer (pH 7.0) at a stirring rate of 1000 rpm and at 25 °C. Each titration was carried out with an initial injection volume of 0.4 μL, followed by 18 main injections of 2 μL each at 120 s intervals. The first titration (0.4 μL) was excluded from the analysis. The data corresponding to the dilution of the ligand in the buffer was subtracted from the titration data.

Measurement of Interactions between Fatty Acids and Bitter Substances. The interactions between five bitter substances, QHCl, promethazine hydrochloride (PHCl), propranolol hydrochloride (PrHCl), berberine hydrochloride (BHCl), and yohimbine hydrochloride (YHCl), and sodium salts of eight fatty acids (sodium hexanoate, sodium octanoate, sodium decanoate, sodium laurate, sodium myristoleate, sodium oleate, sodium linoleate, and sodium linolenate) and two monoacylglycerides (glycerol monolaurate and glycerol monooleate) were measured. The concentrations of the fatty acids were 0.5 mM, and those of the bitter substances are given in Table S1. The samples were dissolved in 5 mM phosphate buffer (pH 7.0). Titrations were conducted as described above.

The data were analyzed according to the "one set of sites" model provided in Origin 7.0 software for MicroCal iTC_{200}. The binding constant (K) and enthalpy change (ΔH) of binding were obtained from the fitted curve. The entropy change (ΔS) and free energy change (ΔG) of binding were obtained using the following equation:

$$\Delta G = \Delta H - T\Delta S = -RT \ln K$$

where R is the gas constant and T is the thermodynamic temperature.

Preparation of Crystals. QHCl (3 mmol, 1.08 g) was dissolved in 3 L of Milli-Q water. A solution of sodium laurate (3 mmol, 0.67 g) in Milli-Q water (50 mL) was added to the QHCl solution, and the mixture was thoroughly stirred. The mixture was allowed to stand overnight at room temperature. The precipitated crystals were filtered (No. 5A, Toyo Rishi Kaisha, Ltd., Tokyo, Japan), rinsed with water, and air-dried. Differential scanning calorimetry (DSC) measurements were carried out using a Shimazu DSC-60 (Kyoto, Japan) in the temperature range of 5−60 °C at a heating rate of 5 °C/min under a nitrogen atmosphere.

NMR Spectroscopy. All NMR experiments except for solid-state NMR were conducted on a Varian Inova 500 NMR spectrometer (500 MHz) at 25 °C (Varian Inc., Palo Alto, CA, USA). The bitter substances (32 μmol; QHCl, PHCl, and PrHCl) were measured in the absence and presence of sodium laurate. The samples were dissolved in 600 μL of DMSO-d_6. The ^{1}H NMR measurement conditions were as follows: number of data points: 16 384; acquisition time: 1.75 s; delay time: 5 s; and number of scans: 16. The NOESY (nuclear Overhauser enhancement spectroscopy) measurement conditions were as follows: number of data points: 512 and 1024 for F1 and F2, respectively; digital resolutions of F1 and F2: 5.50 and 8.79 Hz, respectively; delay time: 1.5 s; mixing time: 1.0 s; and number of scans: 16. Solid-state NMR was conducted using an ECA 500 (500 MHz) (JEOL, Tokyo, Japan) at 0 °C to stop the crystals from melting, using 4 mm of CP/MAS (cross-polarization/magic angle spinning) probe at 10 000 rpm. The measurement was as follows: number of data points: 1024; digital resolution: 49.2 Hz; delay time: 5.0 s; and number of scans: 2048.

Molecular Modeling. Initial models of conformations that were consistent with the NOESY data of the three bitter substances in the absence and presence of sodium laurate were manually constructed using GaussView 5.0 (Gaussian, Inc., Wallingford, CT, USA). The geometries were optimized in vacuo at the B3LYP/6-31G (d) level of theory; then, the geometries were optimized in DMSO at the same level of theory. The polarizable continuum model (PCM) was used to calculate solvent effects in DMSO. All calculations were carried out using the Gaussian 09 software package.[27]

RESULTS

ITC Measurements. The interactions between 22 bitter substances and sodium oleate were studied using ITC (Figure S1-2). Five bitter substances, QHCl, PHCl, PrHCl, BHCl, and YHCl were found to interact with sodium oleate. Notably, each of these substances bears a nitrogen atom (Figure 1). The

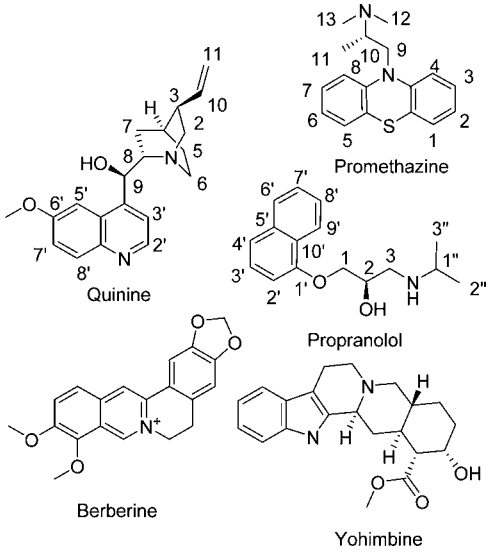

Figure 1. Chemical structures of five bitter substances showing exothermic interactions with sodium oleate.

interactions between these five substances and six fatty acids were then studied (Table 1). The change in Gibbs free energy (ΔG) was negative for all the interactions detected, meaning that these interactions occurred spontaneously. The change in enthalpy (ΔH) contributed to ΔG in all cases, and the change in entropy (ΔS) contributed in some cases (Table 1). In these

DOI: 10.1021/acs.jafc.5b03193
J. Agric. Food Chem. 2015, 63, 8493−8500

Table 1. Thermodynamic Parameters for Association between Five Bitter Substances and Sodium Salts of Fatty Acids

		QHCl	PHCl	PrHCl	BHCl	YHCl
lauric acid (12:1)	ΔH[a]	−25.5 ± 3.5	−20.3 ± 2.6	−16.7 ± 2.3	n.d.[b]	n.d.
	$T\Delta S$[c,d]	−3.5 ± 3.5	0.7 ± 2.6	1.3 ± 2.5	n.d.	n.d.
	ΔG[e]	−22.0 ± 0.1	−21.0 ± 0.0	−18.0 ± 0.1	n.d.	n.d.
myristoleic acid (14:1)	ΔH	−10.8 ± 1.4	−12.6 ± 0.7	n.d.	n.d.	n.d.
	$T\Delta S$	13.7 ± 1.9	11.0 ± 0.6	n.d.	n.d.	n.d.
	ΔG	−24.5 ± 0.5	−23.6 ± 0.1	n.d.	n.d.	n.d.
palmitoleic acid (16:1)	ΔH	−28.0 ± 2.6	−21.8 ± 2.5	−24.4 ± 1.4	n.d.	n.d.
	$T\Delta S$	−0.3 ± 2.8	5.2 ± 3.0	1.3 ± 1.5	n.d.	n.d.
	ΔG	−27.6 ± 0.3	−27 ± 0.6	−25.7 ± 0.1	n.d.	n.d.
oleic acid (18:1)	ΔH	−17.7 ± 0.4	−10.7 ± 0.2	−6.4 ± 0.1	−11.5 ± 0.2	−10.0 ± 0.5
	$T\Delta S$	11.5 ± 0.4	18.3 ± 0.3	22.0 ± 0.1	15.7 ± 0.2	14.6 ± 0.4
	ΔG	−29.2 ± 0.0	−29.0 ± 0.3	−28.4 ± 0.3	−27.2 ± 0.0	−24.6 ± 0.2
linoleic acid (18:2)	ΔH	−27.3 ± 3.1	−21.0 ± 2.3	−28 ± 1.7	n.d.	n.d.
	$T\Delta S$	1.3 ± 3.1	7.5 ± 2.4	−2.1 ± 1.8	n.d.	n.d.
	ΔG	−28.6 ± 0.1	−28.6 ± 0.1	−25.8 ± 0.1	n.d.	n.d.
linolenic acid (18:3)	ΔH	−42.3 ± 2.5	−30.4 ± 3.2	−28.2 ± 3.8	−34.5 ± 0.8	−7.8 ± 1.5
	$T\Delta S$	−15.1 ± 2.5	−2.6 ± 3.2	−2.6 ± 4.0	8.8 ± 8.2	−17.4 ± 1.7
	ΔG	−27.2 ± 0.0	−27.8 ± 0.0	−25.6 ± 0.2	−25.6 ± 0.1	−25.1 ± 0.3

[a] ΔH, enthalpy change (kJ/mol). [b] n.d., not determined by calculation according to "one set of site" model using the titration curve. Mean and standard deviation values are obtained from the fitted data of three independent experiments. [c] T, thermodynamic temperature (K). [d] ΔS, entropy change (kJ/(mol K)). [e] ΔG, Gibbs free energy (kJ/mol).

Table 2. Binding Constant K ($\times 10^3$ M^{-1}) Derived from ITC Profiles for the Association between Five Bitter Substances and Nine Sodium Salts of Fatty Acids and Two Glycerol Esters

	QHCl	PHCl	PrHCl	BHCl	YHCl
hexanoic acid (6:0)	n.d.[a]	n.d.	n.d.	n.d.	n.d.
octanoic acid (8:0)	n.d.	n.d.	n.d.	n.d.	n.d.
decanoic acid (10:0)	n.d.	n.d.	n.d.	n.d.	n.d.
lauric acid (12:0)	7.2 ± 0.2	4.9 ± 0.0	1.4 ± 0.1	n.d.	n.d.
myristoleic acid (14:1)	19.9 ± 4.0	13.7 ± 0.3	n.d.	n.d.	n.d.
palmitoleic acid (16:1)	69.2 ± 6.9	54.8 ± 14.0	32.2 ± 2.2	n.d.	n.d.
oleic acid (18:1)	129 ± 1.2	123.0 ± 14.3	94.8 ± 9.1	59.5 ± 4.8	20.4 ± 1.5
linoleic acid (18:2)	101.1 ± 3.4	100.7 ± 4.9	33.4 ± 0.8	n.d.	n.d.
linolenic acid (18:3)	60.4 ± 0.7	74.2 ± 0.5	31.2 ± 2.2	31.1 ± 1.0	25.8 ± 3.6
glycerol monolaurate	n.d.	n.d.	n.d.	n.d.	n.d.
glycerol monooleate	n.d.	n.d.	n.d.	n.d.	n.d.

[a] n.d., not determined by calculation according to the "one set of site" model using the titration curve. Mean and standard deviation values are obtained from the fitted data of three independent experiments.

cases, the titrated solutions became turbid upon injecting the bitter substances, indicating that insoluble complexes had been formed between the fatty acids and the bitter substances. Of the five bitter substances examined, BHCl and YHCl exhibited relatively weak interactions with the fatty acids (Table 2). Therefore, only the three that had strong interactions with the fatty acids were examined: QHCl, PHCl, and PrHCl.

No interactions were detected between fatty acids with 10 or fewer carbon atoms and the three bitter substances. All three substances showed the greatest binding constants upon binding with sodium oleate, which increased as the number of carbon atoms in the alkyl chain of the fatty acids increased. The binding constant also decreased as the number of double bonds in the fatty acids increased (Table 2). These results suggested that the carbon chain length and the number of double bonds in the fatty acids affected these interactions.

To examine the effect of the carboxyl group in the fatty acids, the interactions between the bitter substances and glycerol monolaurate and glycerol monooleate were also measured. However, no interactions between the bitter substances and these glycerol esters were detected (Table 2).

Overall, carbon chains of a certain length and the presence of carboxyl groups in the fatty acids were necessary to induce interactions with the bitter substances.

NMR Measurements. ITC measurements proved that fatty acids interacted directly with some bitter substances. To examine the mechanism of these interactions, the ^{1}H NMR spectra of three bitter substances (QHCl, PHCl, and PrHCl) were measured in the absence and presence of an equimolar amount of sodium laurate. Because these bitter substances are insoluble in water when sodium laurate is added, DMSO-d_6 was used as the solvent instead.

The three bitter substances contained a nitrogen atom (Figure 1). The signals of the protons on the hydrogen atoms located near the nitrogen atoms was shifted upfield in the presence of sodium laurate (H2, H6, and H8 of QHCl; H9–H13 of PHCl; and H1″ and H3 of PrHCl; Figure 2). The changes in the chemical shift ($\Delta\delta$) of these protons were more than 0.3 ppm for QHCl and PHCl and more than 0.2 ppm for

DOI: 10.1021/acs.jafc.5b03193
J. Agric. Food Chem. 2015, 63, 8493−8500

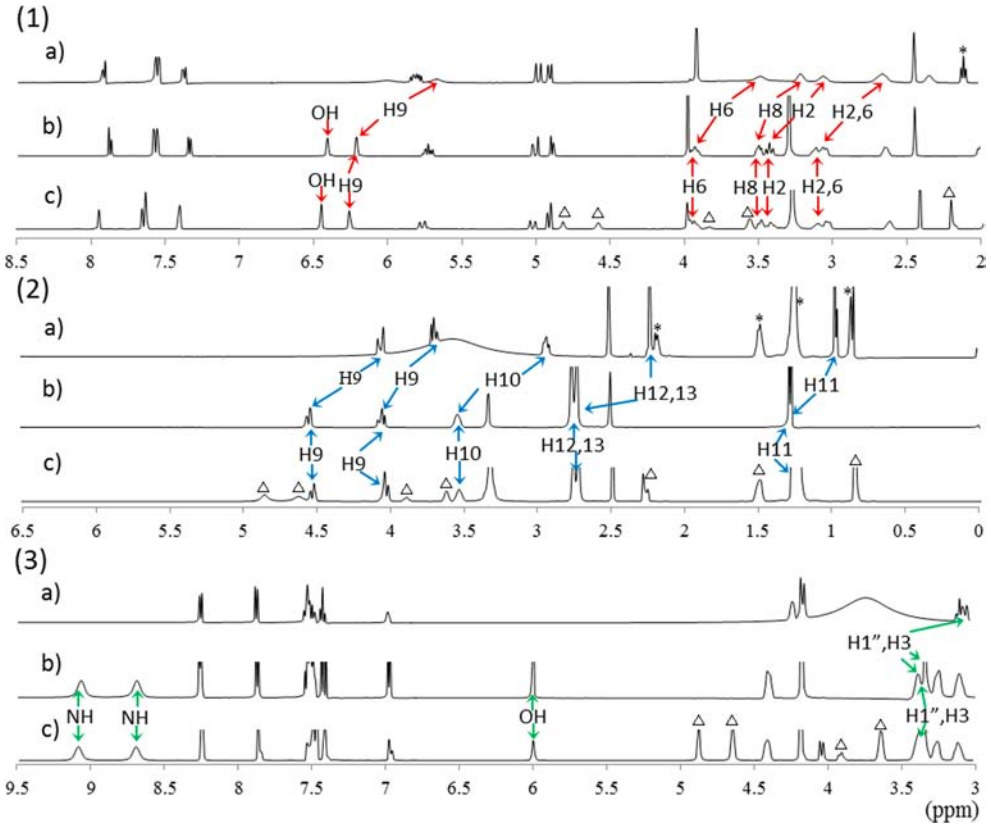

Figure 2. ^{1}H NMR spectra of (1) QHCl, (2) PHCl, and (3) PrHCl. Spectra of (a) bitter substances in the presence of sodium laurate, (b) bitter substances alone, and (c) bitter substances in the presence of glycerol monolaurate. Characteristic protons are indicated by arrows. The broadening of the OH and perturbation of H9 in QHCl and the broadening of OH and NH in PrHCl resulted from the exchange of OH or NH protons with those in the carboxyl moiety in sodium laurate. *, signals of sodium laurate; △, signals of glycerol monolaurate.

PrHCl (Table S2). In the presence of glycerol monolaurate, no significant changes were observed ($\Delta\delta$ < 0.02 ppm) (Table S3).

The ^{1}H NMR spectra of QHCl were also measured in the presence of sodium decanoate (10:0), sodium octanoate (8:0) and sodium hexanoate (6:0) which caused the signals corresponding to H2, H6, and H8 of QHCl (Table S4) to be shifted upfield ($\Delta\delta$ > 0.3 ppm). These results suggested that the hydrogen bond between the nitrogen atom of the bitter substances and the carboxyl group of the fatty acid was formed in DMSO.

In addition, the ^{1}H NMR spectra were measured after changing the molar ratio of sodium laurate to QHCl (0, 0.2, 0.5 and 0.8). The changes in the chemical shifts of H2, H6, and H8 ($\Delta\delta$) were plotted as a function of the molar ratio of sodium laurate (Figure 3). As the chemical shifts depended on the molar ratio of sodium laurate, the exchange between the free and complexed states was faster than the chemical shift difference between the two states.

ITC measurements revealed that the length of the carbon chain and the number of double bonds in the fatty acids affected the binding constants, which suggested that the alkyl chains contributed to the interactions. To examine where the hydrophobic interactions occurred, the NOESY spectra of the bitter substances were measured in the absence and presence of sodium laurate (Figure 4).

In the present study, there were three possible locations for hydrophobic interactions: the first was between the fatty acids and bitter substances, the second was between different molecules of the bitter substances, and the third was between

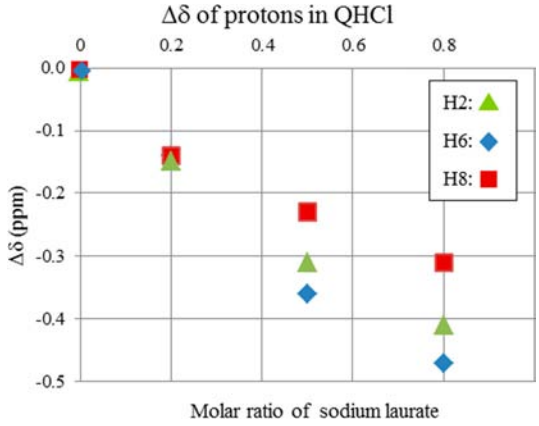

Figure 3. Titration curve corresponding to QHCl (H6, H8, and H2) upon addition of sodium laurate. The change in the chemical shift ($\Delta\delta$) in 32 μmol of QHCl is plotted as a function of the molar ratio of sodium laurate (0, 0.2, 0.5, and 0.8).

different molecules of the fatty acids. Although no cross-peaks were observed between sodium laurate and QHCl, some were observed between H2′ and H8′ of QHCl in the presence of sodium laurate (Figure 4). Because these protons cannot interact with each other within a single molecule of QHCl, intermolecular hydrophobic interactions between two molecules of QHCl occurred in the presence of sodium laurate. However, in the case of PHCl and PrHCl, no interactions between bitter substances and fatty acids and between different molecules of bitter substances were observed (Figure S3 and

DOI: 10.1021/acs.jafc.5b03193
J. Agric. Food Chem. 2015, 63, 8493−8500

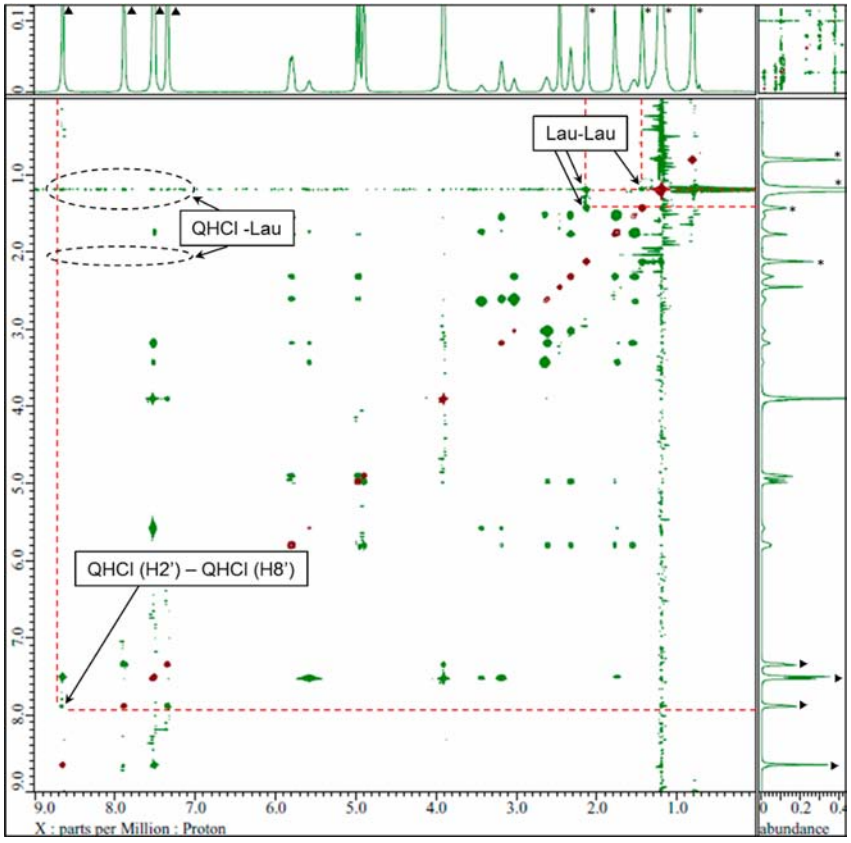

Figure 4. NOESY spectra of QHCl in the presence of sodium laurate. ^{1}H NMR spectra of QHCl/sodium laurate is displayed on X−Y axis. Characteristic cross-peaks are indicated by red circles. *, signals of sodium laurate; ▲, signals of aromatic protons in QHCl.

Table S5). Detailed analysis of the cross-peaks between carbon chains was impossible because many signals overlapped. However, because the length of the carbon chain affected the strength of the interactions in the ITC experiment, we concluded that hydrophobic interactions existed primarily between the carbon chains in an aqueous environment. On the basis of the NOESY results, we constructed molecular models of the binary complexes formed between the bitter substances and sodium laurate in DMSO (Figure 5).

Crystal Analysis of Sodium Laurate and QHCl. Needlelike crystals were observed upon mixing an aqueous solution of sodium laurate and QHCl (Figure 6a). These crystals were composed of an equimolar amount of laurate and quinine, as indicated by ^{1}H NMR. The DSC curve of the crystal revealed a wide exothermic peak (Figure 6b). From CP/MAS NMR spectra, it appeared that C2, C6, and C8 in QHCl resonated at chemical shifts of 62.3, 56.9, and 66.3 ppm, respectively, and each of the signals split into three peaks with a broadened peak width when the crystal was formed with lauric acid (Figure S2). This indicates that at least three states were involved in the crystal. In addition, peak broadening of the methyl and methylene carbon atoms in lauric acid upon formation of crystal demonstrated an incoherent microcrystalline structure. X-ray diffraction analysis was applied to the ground crystal samples using the radial distribution function $4\pi r^2\rho$ (r) to obtain structural information. The sum of the data for QHCl and lauric acid, measured independently, was different from that of the data for the ground crystal sample, implying that specific interactions had been formed in the complex. The crystal seems to be in an intermediate state regarding its amorphosity and crystal style (data not shown).

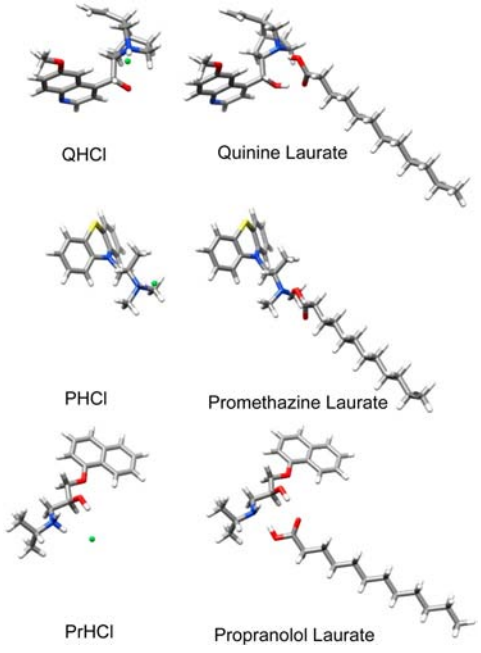

Figure 5. Structures of three bitter substances and their laurates. Atoms are presented as carbon in gray, oxygen in red, sulfur in yellow, nitrogen in blue, and chloride in light green.

These results suggested that the crystal was composed of various conformations. The bitterness of the crystal was significantly less than that of QHCl alone using sensory testing (data not shown).

DOI: 10.1021/acs.jafc.5b03193
J. Agric. Food Chem. 2015, 63, 8493−8500

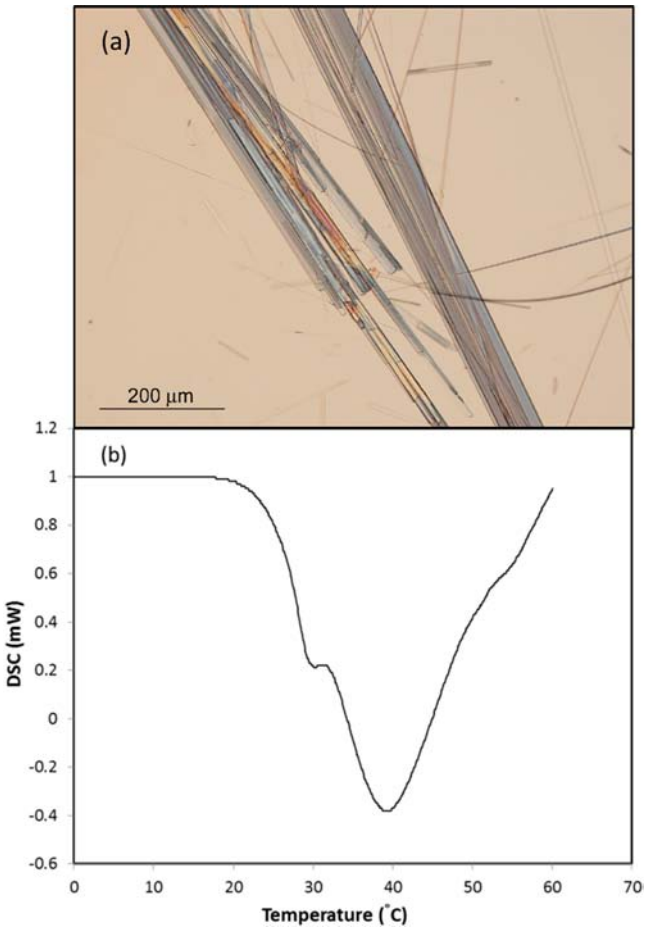

Figure 6. (a) Needlelike crystals formed between sodium laurate and QHCl. (b) DSC thermal curve of the crystal.

DISCUSSION

In a previous report,[26] it was shown that sodium oleate suppressed the bitterness of QHCl. Exothermic interactions were observed when QHCl was added to the fatty acid, associated with masking the bitterness of QHCl by direct interaction with the fatty acids. However, the detailed mechanism of the bitterness-masking reaction has not been elucidated. In the present study, we found that two types of interaction, hydrogen bonds and hydrophobic interactions, were necessary to mask the bitterness of some compounds. Specifically, NMR revealed that hydrogen bonding occurred between the nitrogen atom of the bitter substances (N1 of QHCl, N11 of PHCl, and N4 of PrHCl) and the carboxyl group of the fatty acids in DMSO (Figure 2). In addition, the ITC experiments in water indicated that the strength of the interaction between the bitter substance and the fatty acid depended on the length of the carbon chain of the fatty acid, demonstrating the involvement of hydrophobic interactions.

In aqueous solutions, the bitter substances and fatty acids dissociated as weak bases and acids, respectively.[28] In neutral pH solutions, the dissociation equilibrium of the long-chain fatty acids (RCOOH) shifted to the left of the equilibrium reaction (eq 1), given that the pK_a values of oleic acid, linoleic acid, and linolenic acid are 9.85, 9.24, and 8.28, respectively.[28]

$$RCOOH \leftrightarrows RCOO^- + H^+ \quad (1)$$

However, the dissociation equilibrium of bitter nitrogenous substances (BN) such as quinine, promethazine, and propranolol shifted to the left side of the equilibrium reaction (eq 2), given that the pK_a values of quinine,[29] promethazine,[30] and propranolol[31] are 8.3, 8.6, and 9.2, respectively.

$$BNH^+ \leftrightarrows BN + H^+ \quad (2)$$

The ΔH values for the interactions between the fatty acids and bitter substances were in the range of 10−40 kJ/mol in all cases (Table 1). These results suggested that hydrogen bonds existed between the fatty acids and bitter substances. Two possible mechanisms of hydrogen bond formation are proposed: One involves interaction between RCOOH and BN that comprises a unit of the binary complex, and the other interaction occurs between BH^+ and $RCOO^-$. The former hypothesis can explain the observation that long-chain fatty acids interact with the bitter substances whereas short-chain fatty acids do not. The latter hypothesis can account for the ionic attraction between oppositely charged species.

Of the 22 bitter substances examined, those that exhibited strong interactions with the fatty acids contained secondary or tertiary amino groups. Although some bitter substances that did not interact with the fatty acid also had nitrogen atoms, most of these nitrogen atoms were present in amide groups or in conjugated systems. The rest were present in primary amino groups that might be unsuitable for forming hydrophobic interactions with the carbon chain of the fatty acids.

Regarding hydrophobic interactions, the contribution of the carbon chains was obvious because the length of the carbon chain and the number of double bonds affected the binding constants (Table 2). The NOESY data indicated the possibility of a stacking effect between the aromatic rings of QHCl. However, the $T\Delta S$ values varied widely and were not correlated with ΔG, especially with sodium linoleate (Table 1). This phenomenon was perhaps due to either the conformational variation of the fatty acids or the decreased solubility of the mixture of hydrochloride salts of the bitter substances and the sodium salts of the fatty acids.

On the basis of these results, we propose that the bitterness of substances can be masked with fatty acids by the formation of a binary complex between these species through a hydrogen bond and a hydrophobic interaction (Figure 7). Specifically, the aggregation of a unit of binary complex of fatty acids and bitter substances generated large insoluble complexes. The formation of these complexes made it more difficult for the bitter substances to interact with the bitter taste receptors, thereby masking the bitterness. Particularly in the case of QHCl and sodium laurate, both substances aggregated because of hydrophobic interactions between the carbon chains, forming needlelike crystals (Figure 7). As suggested by DSC, the crystal was probably composed of quinine laurate in various conformations with stacking interactions between the aromatic rings of QHCl.

In the present study, fatty acids have been found to interact directly with bitter substances through hydrogen bonds and hydrophobic interactions. Moreover, both types of interaction played important roles in masking bitterness. This study has been described how direct interactions between bitterness-masking substances and bitter substances can suppress bitterness. The results of this study should lead to the development of new method for masking bitterness, which may be directly applicable to food processing. More research would be needed to investigate the taste and acceptability of

DOI: 10.1021/acs.jafc.5b03193
J. Agric. Food Chem. 2015, 63, 8493−8500

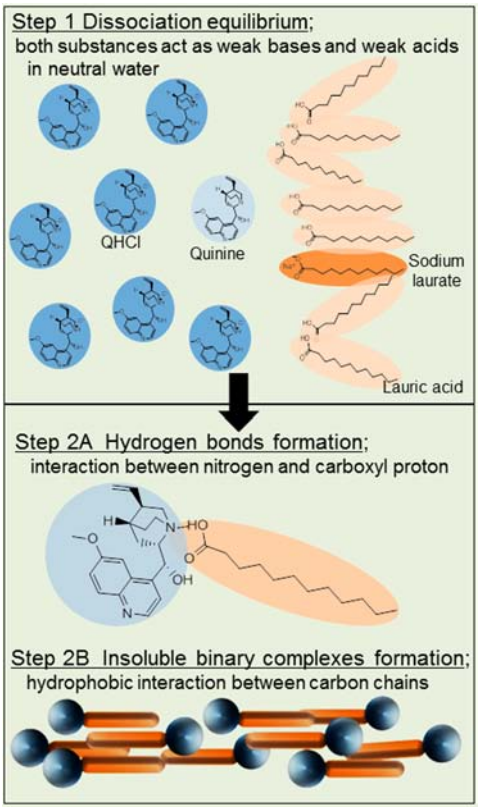

Figure 7. Possible mechanism of interaction between sodium laurate and QHCl. Sodium laurate and QHCl interact weakly via step 1, comprising dissociation equilibrium of QHCl as weak bases and sodium laurate as weak acids. Hydrogen bonding and insoluble binary complexes occur via step 2; for fatty acids with a chain length of 12 or more carbon atoms, hydrogen bonds form between quinine and laurate. The complex model is presented in the lower image. QHCl molecules are colored blue, and sodium laurate is shown in orange. The binary complexes are connected to each other by hydrophobic interactions and grow in a single direction, forming needlelike crystals.

food containing fatty acids and nitrogen-containing bitter compounds.

From this study, we can propose a possible mechanism for how fatty acids mask the bitterness of bitter substances. Both hydrogen bonds and hydrophobic interactions are essential for forming the insoluble binary complexes composed of bitter substances and fatty acids. Nitrogen atoms in the bitter substances and fatty acids with chain lengths of 12 or more carbon atoms are necessary for forming the binary complexes.

■ ASSOCIATED CONTENT

Supporting Information

The Supporting Information is available free of charge on the ACS Publications website at DOI: 10.1021/acs.jafc.5b03193.

The structures of screened substances and the isothermal titration profiles, solid-state NMR spectra of crystal, lauric acid and QHCl, ^{1}H NMR assignments of QHCl, PHCl and PrHCl in the absence and presence of sodium laurate, ^{1}H NMR assignments of QHCl, PHCl and PrHCl in the absence and presence of glycerol monolaurate, ^{1}NMR assignments of QHCl in the absence and presence of sodium decanoate, sodium octanoate and sodium hexanoate, NOESY assignments of QHCl, PHCl and PrHCl in the absence and presence of sodium laurate, NOESY spectra of PHCl and PrHCl in the presence of sodium laurate. (PDF)

■ AUTHOR INFORMATION

Corresponding Author

*Phone/Fax: +81-3-5841-1879. E-mail: asakura@mail.ecc.u-tokyo.ac.jp.

Author Contributions

K.O. and H.Y. contributed equally to this work.

Notes

The authors declare no competing financial interest.

■ ACKNOWLEDGMENTS

This work was supported by a Grant-in-Aid for Scientific Research 20259013 to T.A from the Ministry of Education, Culture, Sports, Science and Technology of Japan. This work was supported by the Council for Science, Technology and Innovation (CSTI), Cross-Ministerial Strategic Innovation Promotion Program (SIP), "Technologies for creating next-generation agriculture, forestry and fisheries"

■ ABBREVIATIONS USED

ITC, isothermal titration calorimetry; ^{1}H NMR, proton nuclear magnetic resonance; NOESY, nuclear Overhauser enhancement spectroscopy; DMSO, dimethyl sulfoxide; T2Rs, taste receptors type 2; K, binding constant; ΔH, enthalpy change of binding; ΔS, entropy change of binding; ΔG, free energy change of binding; R, the gas constant; T, thermodynamic temperature; QHCl, quinine hydrochloride; PHCl, promethazine hydrochloride; PrHCl, propranolol hydrochloride; BHCl, berberine hydrochloride; YHCl, yohimbine hydrochloride; CP/MAS, cross-polarization/magic angle spinning; DSC, differential scanning calorimetry; PCM, polarizable continuum model

■ REFERENCES

(1) Chandrashekar, J.; Hoon, M. A.; Ryba, N. J. P.; Zuker, C. S. The receptors and cells for mammalian taste. *Nature* **2006**, *444*, 288−294.

(2) Drewnowski, A.; Gomez-Carneros, C. Bitter taste, phytonutrients, and the consumer: a review. *Am. J. Clin. Nutr.* **2000**, *72*, 1424−1435.

(3) Degenhardt, A. G.; Hofmann, T. Bitter-tasting and kokumi-enhancing molecules in thermally processed avocado (Persea americana MILL.). *J. Agric. Food Chem.* **2010**, *58*, 12906−12915.

(4) Maehashi, K.; Huang, L. Bitter peptides and bitter taste receptors. *Cell. Mol. Life Sci.* **2009**, *66*, 1661−1671.

(5) Nakamura, T.; Tanigake, A.; Miyanaga, Y.; Ogawa, T.; Akiyoshi, T.; Matsuyama, K.; Uchida, T. The effect of various substances on the suppression of the bitterness of quinine-human gustatory sensation, binding, and taste sensor studies. *Chem. Pharm. Bull.* **2002**, *50*, 1589−1593.

(6) Wilkie, L. M.; Capaldi Phillips, E. D.; Wadhera, D. Sodium chloride suppresses vegetable bitterness only when plain vegetables are perceived as highly bitter. *Chemosens. Percept.* **2014**, *7*, 10−22.

(7) Squier, C. A.; Mantz, M. J.; Wertz, P. W. Effect of menthol on the penetration of tobacco carcinogens and nicotine across porcine oral mucosa ex vivo. *Nicotine Tob. Res.* **2010**, *12*, 763−767.

(8) Slack, J. P.; Brockhoff, A.; Batram, C.; Menzel, S.; Sonnabend, C.; Born, S.; Galindo, M. M.; Kohl, S.; Thalmann, S.; Ostopovici-Halip, L.; Simons, C. T.; Ungureanu, I.; Duineveld, K.; Bologa, C. G.; Behrens, M.; Furrer, S.; Oprea, T. I.; Meyerhof, W. Modulation of bitter taste perception by a small molecule hTAS2R antagonist. *Curr. Biol.* **2010**, *20*, 1104−1109.

DOI: 10.1021/acs.jafc.5b03193
J. Agric. Food Chem. 2015, 63, 8493−8500

(9) Roland, W. S. U.; Gouka, R. J.; Gruppen, H.; Driesse, M.; van Buren, L.; Smit, G.; Vincken, J. P. 6-Methoxyflavanones as bitter taste receptor blockers for hTAS2R antagonist. *PLoS One* **2014**, *9*, e94451.
(10) Greene, T. A.; Alarcon, S.; Thomas, A.; Berdougo, E.; Doranz, B. J.; Breslin, P. A. S.; Rucker, J. B. Probenecid inhibits the human bitter taste receptor TAS2R16 and suppresses bitter perception of salicin. *PLoS One* **2011**, *6*, e20123.
(11) Brockhoff, A.; Behrens, M.; Roudnitzky, N.; Appendino, G.; Avonto, C.; Meyerhof, W. Receptor agonism and antagonism of dietary bitter compounds. *J. Neurosci.* **2011**, *31*, 14775−14782.
(12) Bora, D.; Borude, P.; Bhise, K. Taste masking by spray-drying technique. *AAPS PharmSciTech* **2008**, *9*, 1159−1164.
(13) Joshi, S.; Petereit, H. Film coatings for taste masking and moisture protection. *Int. J. Pharm.* **2013**, *457*, 395−406.
(14) Yan, Y.; Woo, J. S.; Kang, J. H.; Yong, C. S.; Choi, H. Preparation and evaluation of taste-masked donepezil hydrochloride orally disintegrating tablets. *Biol. Pharm. Bull.* **2010**, *33*, 1364−1370.
(15) Khan, S.; Kataria, P.; Nakhat, P.; Yeole, P. Taste masking of ondansetron hydrochloride by polymer carrier system and formulation of rapid-disintegrating tablets. *AAPS PharmSciTech* **2007**, *8*, E127−E133.
(16) Li, S. P.; Martellucci, S. A.; Bruce, R. D.; Kinyon, A. C.; Hay, M. B.; Higgins, J. D., III Evaluation of the film-coating properties of a hydroxyethyl cellulose/hydroxypropyl methylcellulose polymer system. *Drug Dev. Ind. Pharm.* **2002**, *28*, 389−401.
(17) Elder, D. Pharmaceutical applications of ion-exchange resins. *J. Chem. Educ.* **2005**, *82*, 575.
(18) Samprasit, W.; Akkaramongkolporn, P.; Ngawhirunpat, T.; Rojanarata, T.; Opanasopit, P. Formulation and evaluation of meloxicam oral disintegrating tablet with dissolution enhanced by combination of cyclodextrin and ion exchange resins. *Pharm. Dev. Technol.* **2014**, 1−11.
(19) Yewale, C. P.; Rathi, M. N.; Kore, G. G.; Jadhav, G. V.; Wagh, M. P. Formulation and development of taste masked fast-disintegrating tablets (FDTs) of Chlorpheniramine maleate using ion-exchange resins. *Pharm. Dev. Technol.* **2013**, *18*, 367−376.
(20) Prajapati, S. T.; Patel, P. B.; Patel, C. N. Formulation and evaluation of sublingual tablets containing Sumatriptan succinate. *Int. J. Pharm. Investig.* **2012**, *2*, 162−168.
(21) Binello, A.; Cravotto, G.; Nano, G.; Spagliardi, P. Synthesis of chitosan-cyclodextrin adducts and evaluation of their bitter-masking properties. *Flavour Fragrance J.* **2004**, *19*, 394−400.
(22) Izutani, Y.; Kanaori, K.; Imoto, T.; Oda, M. Interaction of gymnemic acid with cyclodextrins analyzed by isothermal titration calorimetry, NMR and dynamic light scattering. *FEBS J.* **2005**, *272*, 6154−6160.
(23) Szejtli, J.; Szente, L. Elimination of bitter, disgusting tastes of drugs and foods by cyclodextrins. *Eur. J. Pharm. Biopharm.* **2005**, *61*, 115−125.
(24) Tokuyama, E.; Shibasaki, T.; Kawabe, H.; Mukai, J.; Okada, S.; Uchida, T. Bitterness suppression of BCAA solutions by L-ornithine. *Chem. Pharm. Bull.* **2006**, *54*, 1288−1292.
(25) Keast, R. S. J.; Breslin, P. A. S Bitterness suppression with zinc sulfate and Na-cyclamate: a model of combined peripheral and central neural approaches to flavor modification. *Pharm. Res.* **2005**, *22*, 1970−1977.
(26) Homma, R.; Yamashita, H.; Funaki, J.; Ueda, R.; Sakurai, T.; Ishimaru, Y.; Abe, K.; Asakura, T. Identification of bitterness-masking compounds from cheese. *J. Agric. Food Chem.* **2012**, *60*, 4492−4499.
(27) Frisch, M. J.; Trucks, G. W.; Schlegel, H. B.; Scuseria, G. E.; Robb, M. A.; Cheeseman, J. R.; Scalmani, G.; Barone, V.; Mennucci, B.; Petersson, G. A.; Nakatsuji, H.; Caricato, M.; Li, X.; Hratchian, H. P.; Izmaylov, A. F.; Bloino, J.; Zheng, G.; Sonnenberg, J. L.; Hada, M.; Ehara, M.; Toyota, K.; Fukuda, R.; Hasegawa, J.; Ishida, M.; Nakajima, T.; Honda, Y.; Kitao, O.; Nakai, H.; Vreven, T.; Montgomery, J. A., Jr.; Peralta, J. E.; Ogliaro, F.; Bearpark, M.; Heyd, J. J.; Brothers, E.; Kudin, K. N.; Staroverov, V. N.; Kobayashi, R.; Normand, J.; Raghavachari, K.; Rendell, A.; Burant, J. C.; Iyengar, S. S.; Tomasi, J.; Cossi, M.; Rega, N.; Millam, J. M.; Klene, M.; Knox, J. E.; Cross, J. B.; Bakken, V.; Adamo, C.; Jaramillo, J.; Gomperts, R.; Stratmann, R. E.; Yazyev, O.; Austin, A. J.; Cammi, R.; Pomelli, C.; Ochterski, J. W.; Martin, R. L.; Morokuma, K.; Zakrzewski, V. G.; Voth, G. A.; Salvador, P.; Dannenberg, J. J.; Dapprich, S.; Daniels, A. D.; Farkas, O.; Foresman, J. B.; Ortiz, J. V.; Cioslowski, J.; Fox, D. J. *Gaussian 09*, revision D.01; Gaussian, Inc.: Wallingford, CT, 2009.
(28) Kanicky, J. R.; Shah, D. O. Effect of degree, type, and position of unsaturation on the p*K*a of long-chain fatty acids. *J. Colloid Interface Sci.* **2002**, *256*, 201−207.
(29) Geiser, L.; Henchoz, Y.; Galland, A.; Carrupt, P.; Veuthey, J. Determination of p*K*a values by capillary zone electrophoresis with a dynamic coating procedure. *J. Sep. Sci.* **2005**, *28*, 2374−2380.
(30) Magnussen, M. P. The effect of ethanol on the gastrointestinal absorption of drugs in the rat. *Acta Pharmacol. Toxicol.* **1968**, *26*, 130−144.
(31) Krämer, S. D.; Braun, A.; Jakits-Deiser, C.; Wunderli-Allenspach, H. Towards the predictability of drug-lipid membrane interactions: the pH-dependent affinity of propranolol to phosphatidylinositol containing liposomes. *Pharm. Res.* **1998**, *15*, 739−744.

DOI: 10.1021/acs.jafc.5b03193
J. Agric. Food Chem. 2015, 63, 8493−8500

Scheme 1. Two-Step Metal-Catalyzed Oxidation of a Phenol To Yield the Intermediate Semiquinone Radical and Subsequently the Quinone and Hydrogen Peroxide

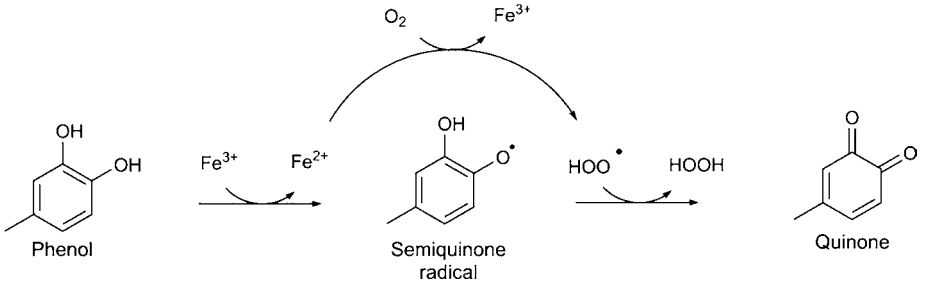

Scheme 2. Nucleophilic Addition between a Quinone and a Protein Thiol Group (A) To Yield a Thiol−Quinone (TQ) Adduct or between a Quinone and a Protein Amino Group To Yield Amino−Quinone (AQ) Adducts by Either Michael Addition (B1) or Formation of Schiff Base-Like Structures (B2)

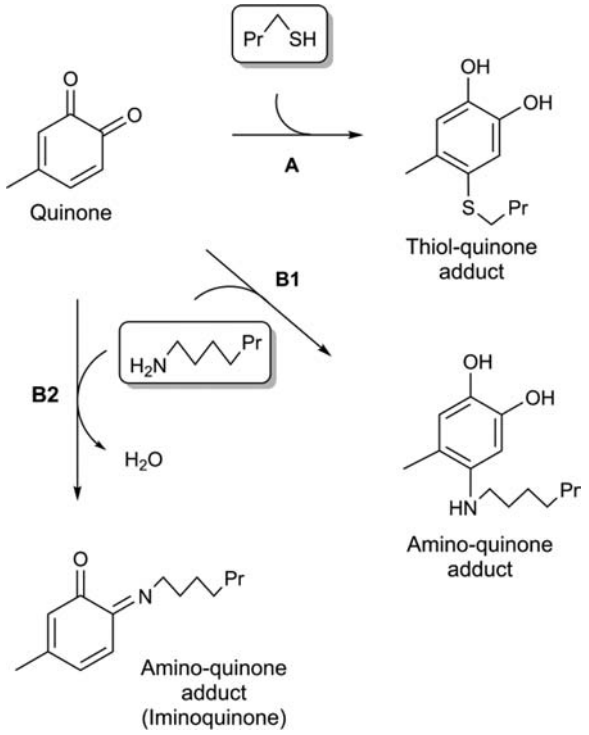

present study was to determine how protein−phenol adduct formation between the quinones of 4-methylcatechol (4MC) or catechin (Cat) affects the metal-catalyzed oxidation of β-lactoglobulin (β-LG). The two phenolic compounds were added in either their reduced phenolic form or in their oxidized quinoic form to identify possible changes in the oxidation pattern of β-LG depending upon the redox status of the phenolic compounds. The oxidation was followed for prolonged incubation times to investigate both early and later stages of oxidation.

2. MATERIALS AND METHODS

2.1. Reagents. β-LG ($M_w \sim 18\,300$) consisting of a mixture of the variants A and B was isolated from bovine milk as described by Kristiansen et al.[13] Malic acid was obtained from Scharlau SL, Sentmenat, Spain. Cat, 4MC, Trizma base, 5,5-dithiobis(2-nitrobenzoic acid) (DTNB), *N*-ethylmaleimide (NEM), Trolox, neocuproine, Amberlyst A26, and fluorescamine was obtained from Sigma-Aldrich, St. Louis, MO. Reagent-grade chemicals and double-deionized (Milli-Q) water were used throughout.

2.2. Peroxidation of Phenols by Periodate Resin. Periodate resin was prepared according to Harrison and Hodge,[14] with slight modifications as recently described by Jongberg et al.[15] 4MC and Cat was oxidized by mixing 158 mg of periodate resin with 12.4 mg of 4MC or 14.5 mg of Cat dissolved in acetonitrile for 3 min during stirring. The amount of 4MC converted to 4-methylbenzoquinone (4MBQ) was estimated to be ∼95% by high-performance liquid chromatography−ultraviolet/visible spectroscopy (HPLC−UV/vis),[16] giving an estimated concentration of ∼95 mM 4MBQ or 47.5 mM catechin−quinone (CatQ). The quinone solutions were used immediately for the preparation of samples.

2.3. Preparation of Samples. Samples were prepared in 0.1 malic acid buffer (pH 5.8) to contain 5.0 mg/mL (273 μM) β-LG alone or with addition of 273 μM 4MC or Cat or their corresponding quinones, 4MBQ or CatQ, and left to react for 10 min at room temperature (20 °C). In parallel, blank phenol and quinone samples were prepared in the same concentrations without the addition of β-LG. NEM-derivatized β-LG was prepared by letting 273 μM β-LG react with 7.2 mM NEM for 90 min at room temperature (20 °C). A corresponding blank NEM sample was prepared in parallel without the addition of protein. In total, 11 samples were prepared in triplicate: 6 samples with protein, β-LG, β-LG−4MC, β-LG−4MBQ, β-LG−Cat, β-LG−CatQ, and β-LG−NEM, and 5 samples without protein, 4MC, 4MBQ, Cat, CatQ, and NEM.

2.4. Metal-Catalyzed Oxidation. Oxidation of all 11 samples was initiated by the addition of 50 μM $FeSO_4$ and 5 mM H_2O_2 both dissolved in Milli-Q water. The samples were oxidized in the dark at 37 °C for up to 20 days with constant stirring. Prior to initiation, day 0 samples were collected for thiol and Schiff base analyses, which were carried out on the same day. Samples for α-aminoadipic semialdehyde (AAS) and γ-glutamic semialdehyde (GGS) quantification were frozen at −80 °C until analysis. Onward, samples were collected at days 1, 3, 5, 8, 12, and 20, and the same procedure as for the day 0 samples was followed.

2.5. Antioxidative Activity by the Cupric Reducing Antioxidant Capacity (CUPRAC) Assay. Samples were prepared as described above (section 2.3), although including additional concentrations of 4MC, 4MBQ, Cat, and CatQ. For each, three concentration levels were added to 273 μM β-LG in 0.1 M malic acid buffer (pH 5.8), namely, 137, 273, or 546 μM, corresponding to the molar ratio between β-LG and the phenol or quinone of 1:0.5, 1:1, or 1:2, respectively. In parallel, blank samples without the addition of β-LG were prepared, containing only 137, 273, or 546 μM 4MC, Cat, 4MBQ, or CatQ, respectively. Samples containing β-LG−NEM and its corresponding blank NEM was prepared as described above. An aliquot of 0.1 mL sample was added to a test tube containing 1.0 mL of 10 mM $CuCl_2$ dissolved in water, 1.0 mL of 1 M ammonium acetate buffer (pH 7.0), 1.0 mL of 7.5 mM neucoproine in ethanol, and 1.0 mL of water. The mixture was mixed and left to react at room temperature (20 °C) for 30 min before the absorbance at 450 nm was read on a HITACHI U-2000 spectrophotometer. Trolox dissolved in 80% ethanol was used as the standard, and data are given as Trolox equivalent antioxidant capacity (TEAC) and presented as millimolar

DOI: 10.1021/acs.jafc.5b02551
J. Agric. Food Chem. 2015, 63, 8501−8509

Trolox equivalents (mean ± standard deviation) of three independent replicates (n = 3). Three different TEAC values are presented: one of the model system containing β-LG, one with of the blank model system without β-LG, and finally, a summarized TEAC, which represents the sum of the TEAC of the blank model system plus the TEAC of β-LG alone.

2.6. Quantification of Thiol Groups. Protein thiol groups in samples prior to oxidation by $FeSO_4/H_2O_2$ were determined by derivatization with DTNB[17] and recently described by Jongberg et al.[15] The thiol concentrations given as nanomoles of thiol per milligram of protein are presented as means ± standard deviation of three independent replicates (n = 3). All protein-containing samples were subtracted from the contribution measured in the corresponding blank sample without protein.

2.7. Quantification of Free Amino Groups. Free amino groups in samples prior to oxidation by $FeSO_4/H_2O_2$ were determined as described by Weigele et al.[18] and Strauss and Gibson.[19] An aliquot of 850 μL of sample containing ~0.01 mg/mL β-LG was added to 2.0 mL of 0.05 M sodium tetraborate (pH 8.5) in a 4 mL quartz spectrofluorometer cell, and 150 μL of 0.7 mM fluorescamine solution in acetone was added. The cell was inverted 4 times, and the resulting fluorescence was measured using 390/485 nm for excitation and emission, respectively, on a PerkinElmer LS45 fluorescence spectrometer (Llantrisant, U.K.). The contribution from malic acid buffer (pH 5.8) was recorded under the same conditions and subtracted all samples. The free amino group concentration was calculated on the basis of a standard curve prepared from lysine diluted in malic acid buffer (pH 5.8). The concentration is given as micromoles of amino groups per milligram of protein and are presented as means ± standard deviation of three independent replicates (n = 3). All protein-containing samples were subtracted from the contribution measured in the corresponding blank sample without protein.

2.8. Quantification of the Semialdehydes AAS and GGS. The protein oxidation products AAS and GGS were quantified in samples from the samples containing protein according to the method described by Utrera et al.[20] An aliquot of 250 μL of sample was precipitated with 1.3 mL of ice-cold 10% trichloroacetic acid (TCA) and centrifuged at 5000 rpm for 30 min and the supernatant was discarded. The pellet was precipitated again with 1.5 mL of ice-cold 5% TCA and centrifuged for 5 min and the supernatant was discarded. The pellet was derivatized by the addition of 0.5 mL of 1% sodium dodecyl sulfate and 1 mM diethylenetriaminepentaacetic acid in 0.25 M MES buffer at pH 6.0 (SDS/DTPA), 0.5 mL of 50 mM aminobenzoic acid in MES buffer (ABA), and 0.25 mL of 100 mM $NaBH_3CN$ in MES buffer. The mixture was incubated at 37 °C for 90 min with stirring every 30 min. Subsequently, the proteins were precipitated twice, first with 0.25 mL of ice-cold 50% TCA and then with 1.5 mL of 5% ice-cold TCA. The precipitates were hydrolyzed in 6 N HCl at 110 °C for 18 h and subsequently dried *in vacuo* at 40 °C using a Savant speed-vac concentrator. Hydrolysates were reconstituted with 0.2 mL of Milli-Q water and filtered through hydrophilic polypropylene GH Polypro (GHP) syringe filters (0.45 μm pore size, Pall Corporation, Port Washington, NY). Samples were analyzed using ultrahigh-pressure liquid chromatography (UHPLC, Shimadzu USA Manufacturing, Inc., Canby, OR) equipped with a COSMOSIL 5 μm C18-AR-II RP-HPLC column (15 cm × 4.6 mm × 5 μm) coupled to a RF-10A XL Shimadzu fluorescence detector (FLD) (excitation and emission wavelengths of 283 and 350 nm, respectively). The mobile phase was a mixture of 50 mM sodium acetate buffer (pH 5.4) and acetonitrile, increasing gradually with a flow rate of 1.0 mL/min of the acetonitrile concentration from 0 to 8% between 0 and 20 min, then from 8 to 90% between 20 and 30 min, and finally, ending up at 100% buffer after 40 min. Identification of both ABA-derivatized semialdehydes in the FLD chromatograms was carried out by comparing their retention times to those from standard AAS and GGS (synthesized *in vitro* according to Akagawa et al.[21]). Data are expressed as nanomoles of carbonyls per milligram of protein as quantified using an ABA standard curve.

2.9. Quantification of Schiff Base Structures. The emission of fluorescence by protein oxidation products (Schiff base structures) was assessed by use of fluorescence spectroscopy.[22] Samples were diluted 50-fold in malic acid buffer and then dispensed in a 4 mL quartz spectrofluorometer cell. The excitation wavelength was set at 350 nm, and emission spectra were recorded from 400 to 500 nm (LS45 PerkinElmer fluorescence spectrometer, Llantrisant, U.K.). Emission spectra of the malic acid buffer (pH 5.8) were recorded under the same conditions and subtracted all sample spectra. Excitation and emission slit widths were set at 10 nm, and data were collected at 500 nm/min in both measurements. The content of Schiff base structures (AU) was expressed as fluorescence intensity units emitted at 440 nm and presented as the mean ± standard deviation of three independent replicates (n = 3). All protein-containing samples were subtracted from the contribution measured in the corresponding blank sample without protein.

2.10. Statistical Data Analysis. Statistical analysis were performed by analysis of variance (ANOVA) using R, version 2.12.1, The R Foundation for Statistical Computing (ISBN 3-900051-07-0).

3. RESULTS

3.1. Phenol- or Quinone-Derived Modifications of β-LG. To evaluate the extent of protein−phenol adduct formation, the concentration of amino and thiol groups of β-LG were evaluated before initiation of oxidation by Fe/H_2O_2. The samples without β-LG were used as blank samples in the analyses to compensate for any interference from the phenols or quinones in the assays. The results showed a significant decrease of 22% amino groups by the addition of 4MBQ to β-LG (upper panel of Figure 1). Higher reactivity of the phenols and quinones was observed for the reaction with thiol groups, where the addition of 4MBQ and 4MC significantly reduced the thiol group concentration by 60 and 12%, respectively

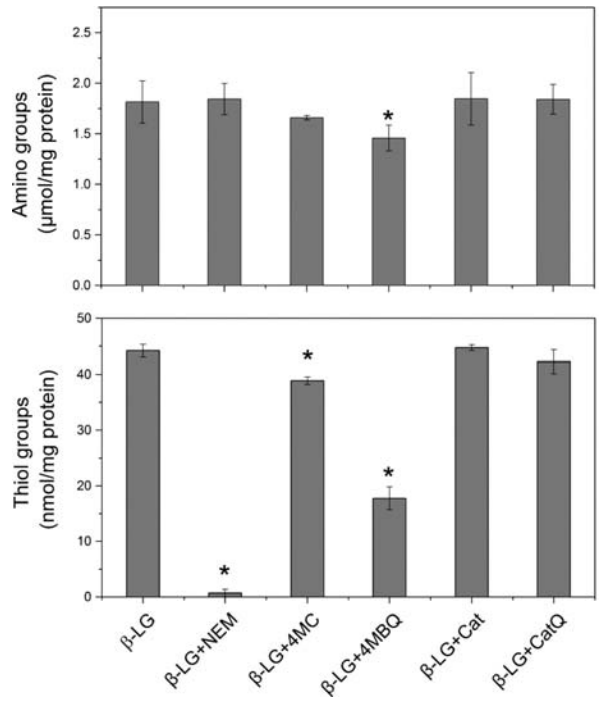

Figure 1. Free amino and thiol groups (mean ± standard deviation; n = 3) in samples (pH 5.8, no oxidants added) containing 273 μM β-LG alone or after reaction with 273 μM 4MC, 4MBQ, Cat, or CatQ for 10 min or after treatment with excess NEM for 90 min at room temperature. The asterisks (∗) indicate that the sample is significantly different (p < 0.05) from the model system containing only β-LG.

DOI: 10.1021/acs.jafc.5b02551
J. Agric. Food Chem. 2015, 63, 8501−8509

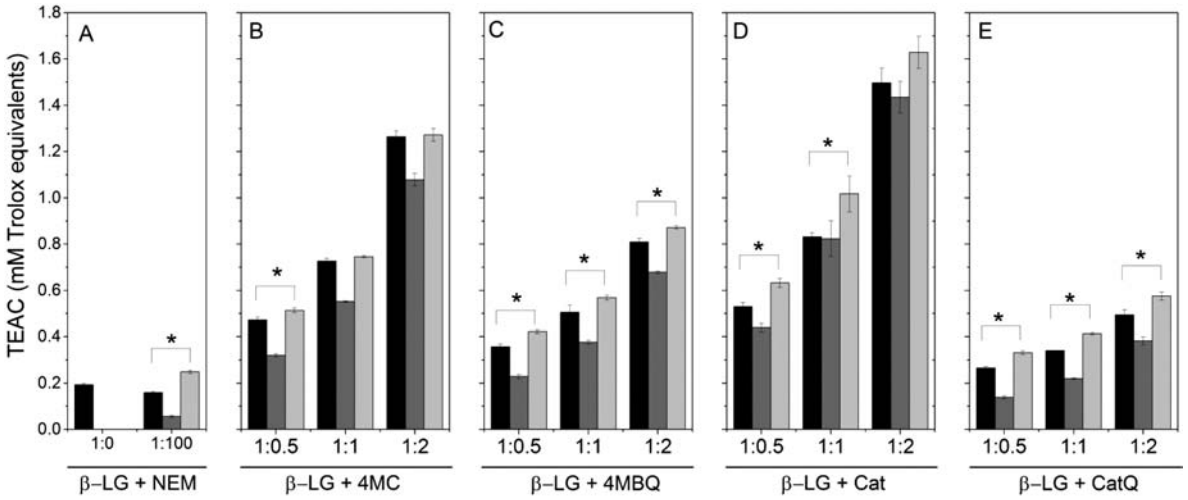

Figure 2. Antioxidative capacity as determined by TEAC (millimolar Trolox equivalents; mean ± standard deviation; $n = 3$) in samples (pH 5.8, no oxidants added) containing 273 μM β-LG (A) alone (1:0) or after treatment with 27.3 mM NEM or after 10 min of reaction at room temperature with 137 μM (1:0.5), 273 μM (1:1), or 546 μM (1:2) (B) 4MC, (C) 4MBQ, (D) Cat, or (E) CatQ. Black bars represent TEAC of the model systems containing β-LG. Dark gray bars represent TEAC of the blank model systems without β-LG. Light gray bars represent the summarized TEAC of the model systems without β-LG added to the TEAC of 273 μM β-LG alone (A, 1:0). The asterisks (∗) denote a statistical significant difference ($p < 0.05$) between the measured TEAC and the summarized TEAC.

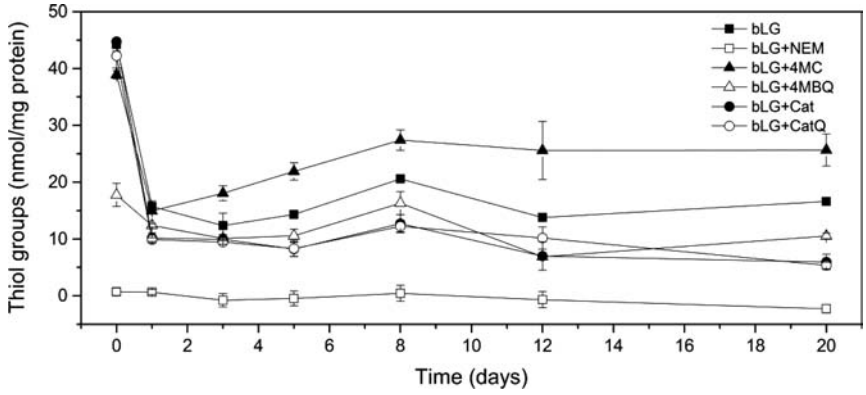

Figure 3. Thiol group concentration (mean ± standard deviation; $n = 3$) during *in vitro* oxidation by Fe(II)/H_2O_2 of samples (pH 5.8, 37 °C) containing 273 μM β-LG alone or after treatment with 27.3 mM NEM (β-LG−NEM) or in the presence of equal molar concentrations of 4MC (β-LG−4MC), 4MBQ (β-LG−4MBQ), Cat (β-LG−Cat), or CatQ (β-LG−CatQ). Data from Figure 1 are included as $t = 0$ day.

(lower panel of Figure 1). As a control, the thiol concentration was also determined in NEM-treated β-LG, and NEM was found to block 98% of the thiol groups.

3.2. Antioxidative Capacity of the β-LG Samples. The antioxidative capacity of the samples prior to oxidation by Fe(II)/H_2O_2 was evaluated by the CUPRAC assay (Figure 2). The overall antioxidative capacity was determined for all samples with or without β-LG, including not only the 1:1 molar ratio between the protein and phenol or quinone, but also the ratios 1:0.5 and 1:2. The TEAC obtained for all samples increased proportionally with the concentration of phenol or quinone (panels B−E of Figure 2). Comparing the measured TEAC of the sample with the summarized TEAC indicates whether the combination of protein and phenol or quinone interact to provide an additive, synergistic, or antagonistic antioxidative capacity. A statistically significant difference (marked by ∗ in Figure 2) between the measured TEAC and the summarized TEAC indicates a synergistic or antagonistic effect, whereas the effect is additive for the samples with no significant difference between the measured and summarized TEAC. In this way, additive effects were observed in the β-LG samples containing 4MC in the ratios 1:1 and 1:2 and in the β-LG sample containing Cat in the ratio 1:2 (panels B and D of Figure 2). All β-LG samples containing quinones (panels C and E of Figure 2) as well as the low ratios of 4MC (1:0.5) and Cat (1:0.5 and 1:1) resulted in antagonistic antioxidative capacities, which means that the combination of β-LG and phenols or quinones in most cases reduces the overall antioxidative capacity. Also, derivatization of β-LG with NEM (Figure 2A) led to a significant decrease of TEAC, as compared to β-LG alone.

3.3. Thiol Loss during *in Vitro* Oxidation. The samples were oxidized by Fe/H_2O_2 at 37 °C for up to 20 days. The results showed that thiols were rapidly lost and reached steady state already at day 1 after initiation for most samples (Figure 3). The samples containing only β-LG reached ∼15 nmol of thiols/mg protein at day 1, and this level was not significantly different from the level at day 20 (Figure 3). The same pattern was observed in the β-LG samples containing 4MBQ, Cat, and CatQ (Figure 3), although with a lower starting point for the 4MBQ as a result of the modifications induced to the protein thiols, as shown in Figure 1. In contrast, a significant increase in

DOI: 10.1021/acs.jafc.5b02551
J. Agric. Food Chem. 2015, 63, 8501−8509

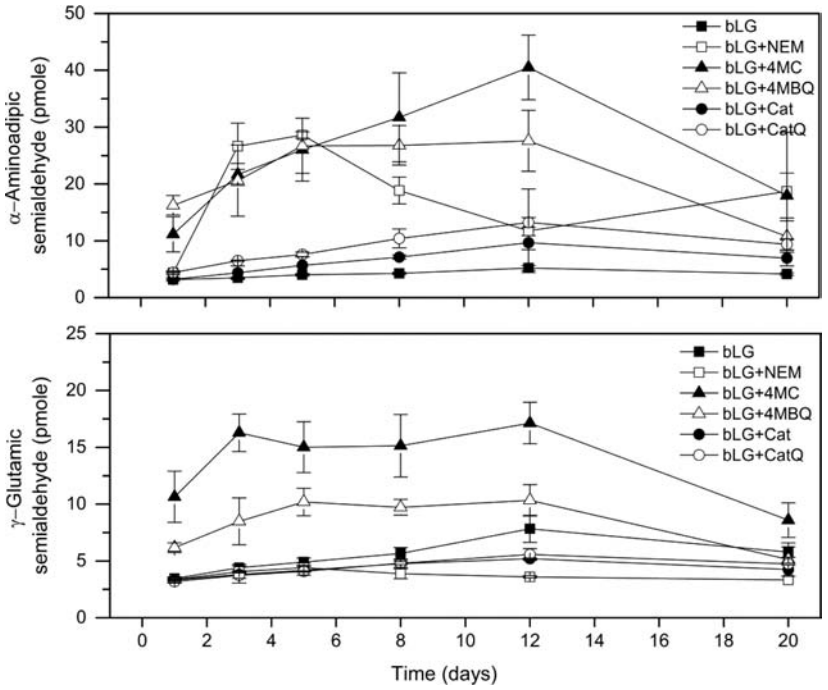

Figure 4. AAS (upper panel) and GGS (lower panel) (mean ± standard deviation; $n = 3$) during *in vitro* oxidation by Fe(II)/H_2O_2 of samples (pH 5.8 and 37 °C) containing 273 μM β-LG alone or after treatment with 27.3 mM NEM (β-LG−NEM) or in the presence of equal molar concentrations of 4MC (β-LG−4MC), 4MBQ (β-LG−4MBQ), Cat (β-LG−Cat), or CatQ (β-LG−CatQ).

the thiol level from days 1 to 8 was found in the β-LG sample containing 4MC, which unfortunately cannot be definitely explained on the basis of the experimental design of the present study.

3.4. AAS and GGS Formation during *in Vitro* Oxidation. Both AAS and GGS were quantified in the β-LG samples, and results showed that limited but significant formation took place up to day 12 in the samples containing only β-LG (Figure 4). In β-LG treated with NEM, where all thiol groups were blocked, a rapid and significant increase in AAS was observed until day 5, where the concentration of carbonyl peaked to decrease afterward. For β-LG containing 4MC, 4MB, Cat, or CatQ, the concentration of AAS increased significantly until day 12 and then subsequently decreased (upper panel of Figure 4). The presence of 4MC or 4MBQ significantly increased the concentration of GGS already at day 1, which continued to be significantly higher until day 12, as compared to β-LG alone, whereas Cat and CatQ had no significant effect on GGS formation in β-LG (lower panel of Figure 4). For β-LG treated with NEM, no GGS was found.

3.5. Formation of Schiff Base Structures during *in Vitro* Oxidation. The reaction between various carbonyl and amino groups leads to the formation of unspecific Schiff base tructures that can be quantified by fluorescence spectroscopy. In the sample containing only β-LG, the Schiff base structures increased significantly after 12 days of storage, whereas in β-LG treated with NEM, the structures increased significantly already from day 1 (Figure 5). In the present study, the emission spectra for the sample containing only β-LG or β-LG and NEM showed a maximum at 420 nm. However, the maximum shifted toward a higher wavelength (440 nm) by the addition of phenols or quinones. Both emission wavelengths were monitored, but because no differences in the overall results were observed, only the data from 440 nm are presented. In the β-LG samples containing 4MC or 4MBQ, significantly elevated

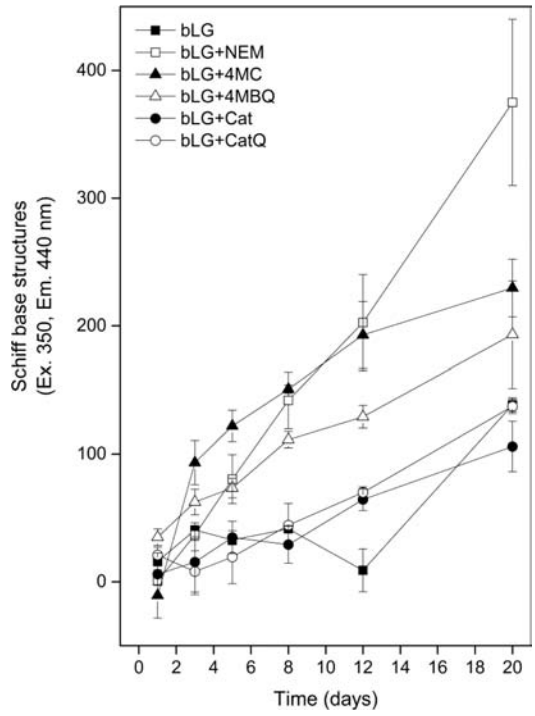

Figure 5. Schiff base structures (mean ± standard deviation; $n = 3$) during *in vitro* oxidation by Fe(II)/H_2O_2 of samples (pH 5.8 and 37 °C) containing 273 μM β-LG alone or after treatment with 27.3 mM NEM (β-LG−NEM) or in the presence of equal molar concentrations of 4MC (β-LG−4MC), 4MBQ (β-LG−4MBQ), Cat (β-LG−Cat), or CatQ (β-LG−CatQ).

fluorescence was observed at day 3, as compared to β-LG alone. In contrast, in β-LG samples containing Cat or CatQ, the Schiff base structures increased significantly after day 8 (Figure 5). No

DOI: 10.1021/acs.jafc.5b02551
J. Agric. Food Chem. 2015, 63, 8501−8509

Scheme 3. Formation of AAS and the Schiff Base Product Azomethine via (A) Metal-Catalyzed Oxidation of a Protein Lysine Residue or (B) Oxidative Deamination Reaction of the AQ Adduct Iminoquinone[a]

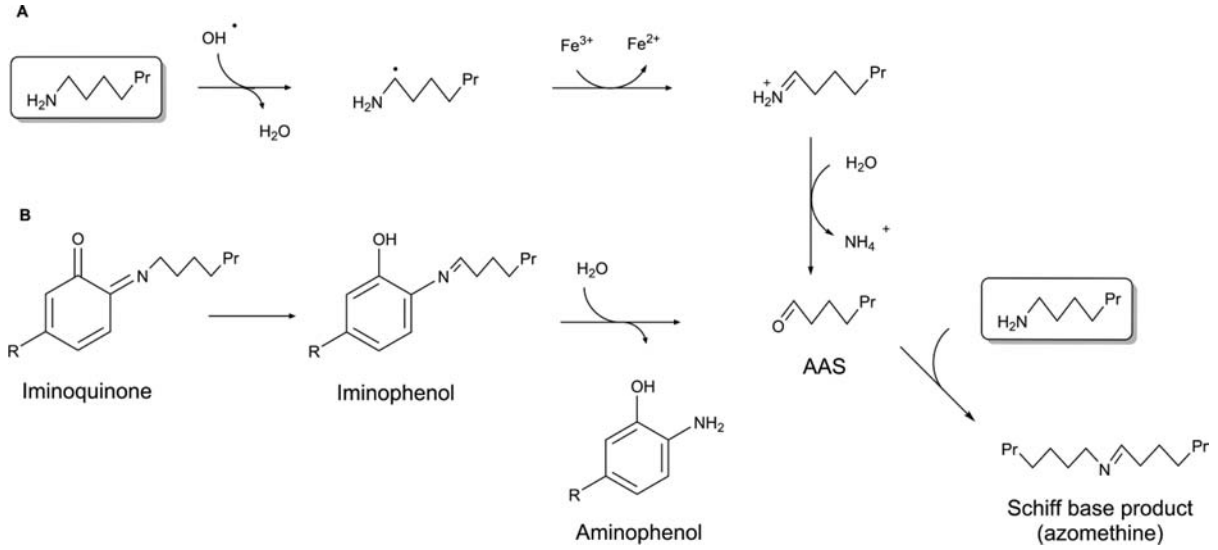

[a]R represents the methyl of 4-MC or the A and C ring of Cat.

apparent differences were observed between Cat and CatQ with regard to Schiff base structures.

4. DISCUSSION

4.1. β-LG Oxidation and Effect of NEM-Blocking of Thiol Groups. The overall antioxidative capacity of β-LG as determined by CUPRAC was significantly reduced after treatment with NEM, indicating that β-LG was less resistant toward oxidation when the thiols were blocked. The CUPRAC assay was selected as a marker of overall antioxidative activity because it also includes the reducing effect of protein thiols,[23] and the result is in accordance with a recent report showing that thiol groups in a myofibrillar protein isolate (MPI) are important for the scavenging of perferrylmyoglobin radicals.[24] In the present study, the thiols were rapidly lost during the first day of storage in the presence of Fe(II) and hydrogen peroxide generating hydroxyl radicals (Figure 3). NEM effectively blocked the thiol groups of β-LG, and consequently, no thiols were available for oxidation in β-LG treated with NEM, which changed the target of the oxidants. This is evident from the rapid formation of AAS during the first days of storage in β-LG treated with NEM as opposed to a slower formation of AAS in untreated β-LG. Similarly, the formation of Schiff base structures also increased more rapidly in NEM-treated β-LG compared to untreated β-LG. These data show that thiols are oxidized more rapidly in our system than alkaline amino acids and are, therefore, better markers of early oxidation events in systems without polyphenols, which is consistent with the higher rate constants reported for the reaction of hydroxyl radicals with thiols than with alkaline amino acids. Sulfur-containing amino acid residues, such as Cys and Met, may act as intramolecular antioxidants in proteins by scavenging radical species.[25] Elias et al.[26] found no loss of Met during oxidation of β-LG but a rather rapid initial loss of thiols, followed by a plateau during continuing oxidation. This sacrificial protection by the protein thiols was not possible in β-LG treated with NEM, and therefore, other susceptible amino acid residues, such as alkaline amino acids, were subsequently attacked by the oxidants.

Concomitantly, in β-LG treated with NEM, AAS increased rapidly during the first days of storage, whereas GGS increased slowly until day 12 together with the formation of Schiff base structures, which continued to increase throughout the reaction period. This finding emphasizes the role of metal-catalyzed oxidation in the carbonylation of β-LG when thiols are not available for oxidation. AAS, GGS, and other protein oxidation products may engage in reactions involving a carbonyl group and an amino group, leading to advanced protein modifications similar to Maillard reactions with the generation of Schiff base structures.[27,28] The overall higher concentration of AAS compared to that of GGS in the β-LG systems is in agreement with previous reports and may be derived from the higher concentration and susceptibility of lysine in β-LG toward metal-catalyzed oxidation compared to other alkaline amino acids.[29]

4.2. Effect of Protein−Phenol Adducts on β-LG Oxidation. In the present study, quantification of amino and thiol groups prior to initiation of oxidation showed that the addition of 4MBQ decreased the concentration of protein amino and thiol groups, suggesting the formation of covalent TQ and AQ adducts for β-LG in the presence of 4MBQ (Scheme 2). In a previous study, it was shown by liquid chromatography−mass spectrometry (LC−MS) analysis that >20% of β-LG was found as protein−phenol adducts when 4MBQ was added in a equimolar ratio at pH 8.0, while 40% of the thiols were lost.[15] In the present study, 60% of the thiols were lost by the addition of an equimolar concentration of 4MBQ at pH 5.8. However, the concentration in the present study was 5 times higher, and pH was lower than in the aforementioned study, which may have led to an increased reaction rate and changes in the protein structure that may have altered the reactivity of specific amino acid side chains as a result of changed exposure to the environment.[30] The smaller loss of amino groups (ca. 20%) suggests that the reaction with quinones was slower than that with thiols. This may be explained by the difference in pK_a of the nucleophilic sites (e.g., pK_a for ε-amino group of Lys is 10.79, and pK_a for thiol group of Cys is 8.37) because a larger proportion of the thiols will be deprotonated and, thereby, more reactive at pH 5.8 compared

DOI: 10.1021/acs.jafc.5b02551
J. Agric. Food Chem. 2015, 63, 8501−8509

to the amines. On the basis of these data, it is not possible to clarify whether the thiol loss is caused by pro-oxidative behavior oxidation or adduct formation. During the *in vitro* oxidation, the thiol level at day 1 was found to be similar in β-LG independent of the presence of 4MC or 4MBQ.

The addition of both 4MC and 4MBQ also caused an increase in the formation of AAS, GGS, and Schiff bases. This apparent pro-oxidative effect was similar to the observation of the NEM-blocked β-LG and may be explained by three different mechanisms. First, it may likely be caused by the elimination of the thiols as oxidation targets or radical scavengers in β-LG, exposing other amino acids to oxidation. Second, phenols may also act as pro-oxidants, forming hydrogen peroxide in the presence of transition metals (Scheme 1). Zhou and Elias[31] showed that 400 μM (−)-epigallocatechin-3-gallate (EGCG) produced 350 μM hydrogen peroxide during 4 days of storage of emulsions in the presence of 25 μM Fe^{3+} (pH 7.0). In the present study, the phenols or quinones (273 μM) and Fe(II) (50 μM) may in a similar manner generate hydrogen peroxide during oxidation as part of a pro-oxidant mechanism. However, 5 mM hydrogen peroxide was added initially as the oxidation initiator, and this concentration indeed exceeds any possible hydrogen peroxide formation by oxidation of the phenols. Previous studies have shown that a similar concentration of whey protein was able to quench 0.45 mM hydrogen peroxide during 3 days of storage.[32] This indicates that any hydrogen peroxide generated by phenol oxidation may be considered insignificant compared to the excess hydrogen peroxide added as an initiator. Finally, besides additions to Cys, quinones may also react, as already mentioned with other nucleophiles, and both Lys and Trp have previously been found as targets.[10] The reaction with amino groups from Lys to yield AQ adducts can occur by two mechanisms: (i) substitution of an aromatic carbon by the 1,4-Michael addition or (ii) formation of a Schiff base, where the oxo group of the quinone reacts with the amino group to yield iminoquinones and the release of water (Scheme 2). As depicted in Scheme 3, the iminoquinone may transform to the iminophenol, which through an oxidative deamination mechanism releases an aminophenol and the corresponding semialdehyde, AAS.[33,34] This carbonyl, in turn, may engage further in advanced reaction pathways to yield Schiff base structures with other amino groups. Extracts from green tea, black tea, and coffee were found to deaminate oxidatively lysine residues of bovine serum albumin in the presence of metal ions, indicating a lysyl oxidase-like activity of the phenolic compounds in the extracts.[34] This pro-oxidant mechanism of certain phenolics has also been described for myofibrillar proteins oxidized *in vitro* by a hydroxyl-radical-generating system[2,35] and also in complex muscle foods.[36] Scheme 3 shows how AAS may be generated through either metal-catalyzed oxidation of Lys (reaction A) or as described above by the oxidative deamination pathway (reaction B). In the present study, the latter pathway seem to be most pronounced, because the presence of phenols and quinones significantly increased AAS and the Schiff base structures in β-LG. Taking these three mechanisms into consideration, the ability of 4MC and 4MBQ to eliminate thiols as an oxidation target and to promote the oxidative deamination pathway may be the major mechanisms behind the apparent pro-oxidative effect of these species toward carbonylation of β-LG.

The chemical structure of 4MC is similar to the B ring of Cat, indicating that the reactivity of the two compounds may be similar. However, the effects of Cat or CatQ were not as clear as that of 4MC or 4MBQ. Neither Cat nor CatQ were found to decrease the concentration of amino groups or thiol groups prior to oxidation. However, significantly lower levels of thiols were detected from day 1 and throughout the *in vitro* oxidation, suggesting other pro-oxidative activities than the TQ adduct formation. The formation of AAS in the presence of Cat or CatQ was found to be higher than that for β-LG alone, indicating again a pro-oxidative activity; however, no significant effect was observed for the formation of GGS, and Schiff bases were only significantly higher at day 12. Utrera and Estévez[35] also found diverse effects of the same phenolic compounds on the different expressions of the oxidative damage caused in proteins by a hydroxyl-radical-generating system. These findings reflect the different chemistry (factors, catalysts, and pathways) behind each of the chemical changes induced in food proteins by oxidants (reviewed by Lund et al.[37]). On the other hand, these results emphasize the specificity of certain phenol−protein interaction mechanisms. For instance, the lysyl oxidase activity of certain phenols is only applicable to alkaline amino acids and promote carbonylation (pro-oxidant effect), while the effect of the same phenolic compound on thiol residues may lead to a different outcome (i.e., antioxidant, pro-oxidant, or no effect at all).

4.3. Redox Chemistry of Phenols and Quinones. No difference was observed between the addition of Cat or CatQ for all protein oxidation products evaluated throughout 20 days of *in vitro* oxidation, indicating that the redox state of Cat did not affect the oxidation of β-LG. This is interesting, because the overall antioxidative activity as determined by the CUPRAC assay showed a large variation between Cat and CatQ (dark gray bars in panels B−E of Figure 2). Indeed, the reducing capacity of Cat was found to be 4-fold higher than the reducing capacity of CatQ, because 1 mol of Cat or CatQ corresponded to 2.4 or 0.6 mol of Trolox, respectively. In contrast, the reducing capacity for 4MC was 1.7-fold higher than that for 4MBQ. The reducing capacity observed for Cat is close to previously published data, showing that 1 mol of Cat corresponded to 3.1 mol of Trolox.[38] The presence of β-LG in the present study was not found to influence these ratios, but the results indicate that the oxidation to the quinoic structures had a larger impact on Cat than on 4MC.

The lack of coherence between the results of the CUPRAC assay and the determination of oxidation products *in vitro* demonstrates the drawback of antioxidant assays and demonstrates how they rarely provide exact information on the antioxidant capacity of a given system and that the reducing capacity or antioxidant activity is highly dependent upon the oxidation substrate and the actual conditions. However, in the present study, the antioxidant assay may provide information on the reaction between the protein and quinones and the effect that their interactions may have on the given system. For the equimolar concentrations applied during the oxidation of β-LG, the presence of 4MBQ, Cat, and CatQ resulted in antagonistic antioxidative effects in β-LG, whereas 4MC showed an additive affect. Antagonistic effects has previously been observed for quercetin-derivatized bovine serum albumin (BSA), where covalent attachment between the phenol to the protein reduced TEAC, as compared to free quercetin.[12]

The formation of covalent TQ or AQ adducts may explain the antagonistic effects because the reaction between the quinone and a nucleophile results in the substitution at a carbon in the aromatic ring of the quinone. The substitution

DOI: 10.1021/acs.jafc.5b02551
J. Agric. Food Chem. 2015, 63, 8501−8509

reduces the quinone to the hydroquinone, and this substitution is commonly considered as the mechanism by which quinones regenerate in cycles of polymerization reactions with other phenols to yield polymeric compounds. In aqueous media, if no nucleophiles or other phenols are available, quinones are reduced spontaneously in a single-step two-electron two-proton process to yield the phenol,[39] and this may explain why a reducing activity was observed for the quinoic compounds, 4MBQ and CatQ, in the CUPRAC assay in the present study. For each polymerization cycle or nucleophile addition reaction, the ability of the quinone to regenerate is reduced, which leads, in turn, to a less antioxidative activity of the compound. The larger difference in reducing capacity observed between Cat and CatQ (4-fold) than that between 4MC and 4MBQ (1.7-fold) may result from different reduction or polymerization mechanisms. It may be hypothesized that Cat preferably is reduced through polymerization and 4MBQ is reduced through spontaneous reduction in the aqueous media. Spontaneous reduction will not compromise the antioxidative capacity in contrast to polymerization, and hence, less difference between the antioxidant capacity of the phenol and quinone may be observed for 4MBQ.

In the present study, the nucleophile reaction between β-LG and the quinones were simulated by the NEM reaction with the thiol groups, which indeed resulted in a change in oxidation targets in β-LG by promoting AAS and Schiff base formation. The CUPRAC assay also showed that the reducing capacity of β-LG was reduced by blocking the thiol groups with NEM. The decrease in the overall reducing capacity of NEM-blocked β-LG may also explain the antagonistic effect observed for the combination of β-LG and 4MBQ, because TQ adducts were generated in this sample. However, this does not explain the antagonistic effects of β-LG combined with Cat or CatQ because neither amino groups nor thiols were lost in those samples prior to oxidation.

In conclusion, after reaction with 4MC and 4MBQ, β-LG had a decrease of thiol groups by 12 and 60%, respectively, and a 22% decrease in amino groups was found by the addition of 4MBQ. The addition of Cat or CatQ did not lead to any instant decrease in either thiol or amino groups. The oxidative stability of β-LG after reaction with 4MC, 4MBQ, Cat, or CatQ was impaired during 20 days of storage in the presence of Fe(II) and hydrogen peroxide. Especially, the presence of 4MC and 4MBQ served as apparent pro-oxidants, and the changes observed were ascribed to the redirection of oxidation as a result of the blocking of thiol groups but also to the oxidative deamination pathway accelerating the production of semialdehydes and subsequently Schiff base structures. The complex chemistry of the interaction mechanisms between phenols and different protein residues urges the necessity of more mechanistic studies in this field. The pro-oxidant effect and, hence, potential harmful effect of certain phenolic compounds on proteins provide advice toward a more detailed toxicological evaluation prior to use of phenolic compounds for food protection and in dietary supplements.

AUTHOR INFORMATION

Corresponding Author

*Telephone: +45-3533-2181. Fax: +45-3533-3344. E-mail: jongberg@food.ku.dk.

Funding

The authors acknowledge The Danish Council for Independent Research|Technology and Production within The Danish Agency for Science Technology and Innovation for granting the project entitled "Antioxidant Mechanisms of Natural Phenolic Compounds against Protein Cross-Link Formation in Meat and Meat Systems" (11-117033). The study was partially supported by the project "IB13132" funded by Gobierno de Extremadura and co-funded by FEDER.

Notes

The authors declare no competing financial interest.

REFERENCES

(1) Tomas-Barberan, F. A.; Andres-Lacueva, C. Polyphenols and Health: Current State and Progress. *J. Agric. Food Chem.* **2012**, *60* (36), 8773−8775.

(2) Estévez, M.; Heinonen, M. Effect of phenolic compounds on the formation of alpha-aminoadipic and gamma-glutamic semialdehydes from myofibrillar proteins oxidized by copper, iron, and myoglobin. *J. Agric. Food Chem.* **2010**, *58* (7), 4448−4455.

(3) Bonoli-Carbognin, M.; Cerretani, L.; Bendini, A.; Almajano, M. P.; Gordon, M. H. Bovine Serum Albumin Produces a Synergistic Increase in the Antioxidant Activity of Virgin Olive Oil Phenolic Compounds in Oil-in-Water Emulsions. *J. Agric. Food Chem.* **2008**, *56* (16), 7076−7081.

(4) Le Bourvellec, C.; Renard, C. M. G. C. Interactions between Polyphenols and Macromolecules: Quantification Methods and Mechanisms. *Crit. Rev. Food Sci. Nutr.* **2012**, *52* (1−3), 213−248.

(5) Kroll, N. G.; Rawel, H. M.; Rohn, S. Reactions of plant phenolics with food proteins and enzymes under special consideration of covalent bonds. *Food Sci. Technol. Res.* **2003**, *9* (3), 205−218.

(6) Cilliers, J. J. L.; Singleton, V. L. Characterization of the Products of Nonenzymic Autoxidative Phenolic Reactions in A Caffeic Acid Model System. *J. Agric. Food Chem.* **1991**, *39* (7), 1298−1303.

(7) Richard-Forget, F. C.; Rouet-Mayer, M. A.; Goupy, P. M.; Philippon, J.; Nicolas, J. J. Oxidation of chlorogenic acid, catechins, and 4-methylcatechol in model solutions by apple polyphenol oxidase. *J. Agric. Food Chem.* **1992**, *40* (11), 2114−2122.

(8) Kalyanaraman, B.; Felix, C. C.; Sealy, R. C. Semiquinone Anion Radicals of Catechol(Amine)S, Catechol Estrogens, and Their Metal-Ion Complexes. *Environ. Health Perspect.* **1985**, *64*, 185−198.

(9) Pierpoint, W. S. o-Quinones formed in plant extracts - their reactions with amino acids and peptides. *Biochem. J.* **1969**, *112* (5), 609−616.

(10) Rawel, H. M.; Kroll, J.; Hohl, U. C. Model studies on reactions of plant phenols with whey proteins. *Nahrung* **2001**, *45* (2), 72−81.

(11) Almajano, M. P.; Delgado, M. E.; Gordon, M. H. Changes in the antioxidant properties of protein solutions in the presence of epigallocatechin gallate. *Food Chem.* **2007**, *101* (1), 126−130.

(12) Rohn, S.; Rawel, H. M.; Kroll, J. Antioxidant activity of protein-bound quercetin. *J. Agric. Food Chem.* **2004**, *52* (15), 4725−4729.

(13) Kristiansen, K. R.; Otte, J.; Ipsen, R.; Qvist, K. B. Large-scale preparation of b-lactoglobulin A and B by ultrafiltration and ion-exchange chromatography. *Int. Dairy J.* **1998**, *8*, 113−118.

(14) Harrison, C. R.; Hodge, P. Polymer-supported periodate and iodate as oxidizing-agents. *J. Chem. Soc., Perkin Trans. 1* **1982**, No. 2, 509−511.

(15) Jongberg, S.; Lund, M. N.; Otte, J. Dissociation and reduction of covalent b-lactoglobulin-quinone adducts by dithiothreitol, tris(2-carboxyethyl)phosphine, or sodium sulfite. *Anal. Biochem.* **2015**, *478* (0), 40−48.

(16) Jongberg, S.; Gislason, N. E.; Lund, M. N.; Skibsted, L. H.; Waterhouse, A. L. Thiol-quinone adduct formation in myofibrillar proteins detected by LC-MS. *J. Agric. Food Chem.* **2011**, *59* (13), 6900−6905.

(17) Ellman, G. L. Tissue sulfhydryl groups. *Arch. Biochem. Biophys.* **1959**, *82* (1), 70−77.

(18) Weigele, M.; DeBernardo, S. L.; Tengi, J. P.; Leimgruber, W. Novel reagent for the fluorometric assay of primary amines. *J. Am. Chem. Soc.* **1972**, *94* (16), 5927−5928.

DOI: 10.1021/acs.jafc.5b02551
J. Agric. Food Chem. 2015, 63, 8501−8509

(19) Strauss, G.; Gibson, S. M. Plant phenolics as cross-linkers of gelatin gels and gelatin-based coacervates for use as food ingredients. *Food Hydrocolloids* **2004**, *18* (1), 81−89.
(20) Utrera, M.; Morcuende, D.; Rodríguez-Carpena, J. G.; Estévez, M. Fluorescent HPLC for the detection of specific protein oxidation carbonyls - [alpha]-aminoadipic and [gamma]-glutamic semialdehydes - in meat systems. *Meat Sci.* **2011**, *89* (4), 500−506.
(21) Akagawa, M.; Sasaki, D.; Ishii, Y.; Kurota, Y.; Yotsu-Yamashita, M.; Uchida, K.; Suyama, K. New method for the quantitative determination of major protein carbonyls, alpha-aminoadipic and gamma-glutamic semialdehydes: Investigation of the formation mechanism and chemical nature in vitro and in vivo. *Chem. Res. Toxicol.* **2006**, *19* (8), 1059−1065.
(22) Estévez, M.; Kylli, P.; Puolanne, E.; Kivikari, R.; Heinonen, M. Fluorescence spectroscopy as a novel approach for the assessment of myofibrillar protein oxidation in oil-in-water emulsions. *Meat Sci.* **2008**, *80* (4), 1290−1296.
(23) Prior, R. L.; Wu, X. L.; Schaich, K. Standardized methods for the determination of antioxidant capacity and phenolics in foods and dietary supplements. *J. Agric. Food Chem.* **2005**, *53* (10), 4290−4302.
(24) Jongberg, S.; Lund, M. N.; Skibsted, L. H.; Davies, M. J. Competitive reduction of perferrylmyoglobin radicals by protein thiols and plant phenols. *J. Agric. Food Chem.* **2014**, *62* (46), 11279−11288.
(25) Levine, R. L.; Berlett, B. S.; Moskovitz, J.; Mosoni, L.; Stadtman, E. R. Methionine residues may protect proteins from critical oxidative damage. *Mech. Ageing Dev.* **1999**, *107* (3), 323−332.
(26) Elias, R. J.; McClements, D. J.; Decker, E. A. Antioxidant activity of cysteine, tryptophan, and methionine residues in continuous phase beta-lactoglobulin in oil-in-water emulsions. *J. Agric. Food Chem.* **2005**, *53* (26), 10248−10253.
(27) Eyre, D. R.; Paz, M. A.; Gallop, P. M. Cross-Linking in Collagen and Elastin. *Annu. Rev. Biochem.* **1984**, *53*, 717−748.
(28) Dolz, R.; Heidemann, E. Reactivity of the allysine aldehyde group. *Connect. Tissue Res.* **1989**, *18* (4), 255−268.
(29) Stadtman, E. R.; Berlett, B. S. Fenton Chemistry - Amino-Acid Oxidation. *J. Biol. Chem.* **1991**, *266* (26), 17201−17211.
(30) Casal, H. L.; Kohler, U.; Mantsch, H. H. Structural and Conformational-Changes of Beta-Lactoglobulin-B - An Infrared Spectroscopic Study of the Effect of Ph and Temperature. *Biochim. Biophys. Acta, Protein Struct. Mol. Enzymol.* **1988**, *957* (1), 11−20.
(31) Zhou, L.; Elias, R. J. Influence of cysteine and methionine availability on protein peroxide scavenging activity and phenolic stability in emulsions. *Food Chem.* **2014**, *146*, 521−530.
(32) Zhou, L.; Elias, R. J. Investigating the hydrogen peroxide quenching capacity of proteins in polyphenol-rich foods. *J. Agric. Food Chem.* **2011**, *59* (16), 8915−8922.
(33) Akagawa, M.; Suyama, K. Amine oxidase-like activity of polyphenols - Mechanism and properties. *Eur. J. Biochem.* **2001**, *268* (7), 1953−1963.
(34) Akagawa, M.; Shigemitsu, T.; Suyama, K. Oxidative deamination of benzylamine and lysine residue in bovine serum albumin by green tea, black tea, and coffee. *J. Agric. Food Chem.* **2005**, *53* (20), 8019−8024.
(35) Utrera, M.; Estevez, M. Impact of trolox, quercetin, genistein and gallic acid on the oxidative damage to myofibrillar proteins: The carbonylation pathway. *Food Chem.* **2013**, *141* (4), 4000−4009.
(36) Cando, D.; Morcuende, D.; Utrera, M.; Estevez, M. Phenolic-rich extracts from Willowherb (Epilobium hirsutum L.) inhibit lipid oxidation but accelerate protein carbonylation and discoloration of beef patties. *Eur. Food Res. Technol.* **2014**, *238* (5), 741−751.
(37) Lund, M. N.; Heinonen, M.; Baron, C. P.; Estévez, M. Protein oxidation in muscle foods: A review. *Mol. Nutr. Food Res.* **2011**, *55* (1), 83−95.
(38) Ozyurek, M.; Guclu, K.; Tutem, E.; Baskan, K. S.; Ercag, E.; Esin Celik, S.; Baki, S.; Yildiz, L.; Karaman, S.; Apak, R. A comprehensive review of CUPRAC methodology. *Anal. Methods* **2011**, *3* (11), 2439−2453.
(39) Guin, P. S.; Das, S.; Mandal, P. C. Electrochemical reduction of quinones in different media: A review. *Int. J. Electrochem.* **2011**, *2011*, 1−22.

DOI: 10.1021/acs.jafc.5b02551
J. Agric. Food Chem. 2015, 63, 8501−8509

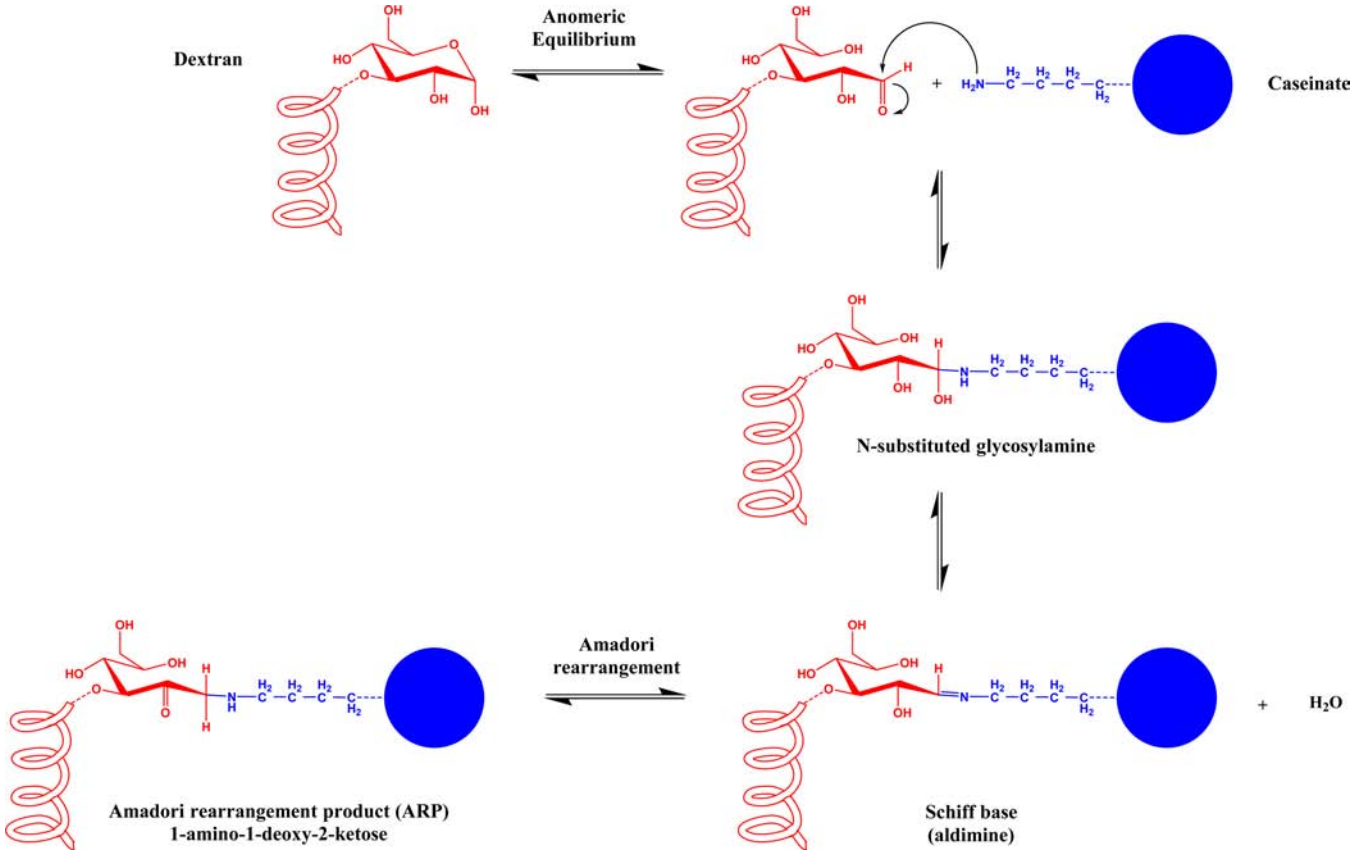

Figure 1. Schematic representation of the Maillard conjugation reaction between the reducing end of a sugar molecule and a free amine group of a protein. This figure only shows the initial phase of the Maillard reaction until the formation of the Amadori products; the further stages of the reaction are not shown.

addition than were emulsions prepared using only β-lactoglobulin.[19,20] Maillard conjugates (MC) between caseinate and maltodextrin have previously been used to stabilize caseinate against precipitation at the isoelectric point.[21] Biopolymer particles fabricated using conjugates of whey protein isolate and maltodextrin displayed better thermal stability than particles produced using nonconjugated biopolymers.[22]

Resveratrol (trans-resveratrol; trans-3,5,4′-trihydroxy-stilbene), a polyphenolic compound that can be isolated from wine byproducts,[23] has been shown to have several potential beneficial effects on human health.[24−26] Nevertheless, its utilization as a nutraceutical ingredient within the food industry is currently limited because of its poor water solubility, low oral bioavailability, and chemical instability.[27−29] There is therefore a need to encapsulate this bioactive component so that it can be used as a functional ingredient in the food and other industries.

On the basis of this background, we hypothesize that the use of MC of caseinate and high-molecular-mass polysaccharides will generate enough steric repulsion to stabilize the zein nanoparticles created by LAS even in the presence of low or zero electrostatic repulsion. Therefore, the aim of the current work was to evaluate the physical stability of zein nanoparticles produced by LAS and coprecipitation with MC of sodium caseinate and polysaccharides with different molecular masses. The physical stability of these particles was assessed under conditions commonly encountered within the food industry, i.e., thermal processing, salt addition, and pH changes. The capacity of this system to encapsulate a grape skin extract (GSE) rich in resveratrol was also assessed by analyzing the encapsulation efficiency. The results of our study will be useful to evaluate the viability of creating stable delivery systems to encapsulate hydrophobic nutraceuticals to enrich a wide variety of food products without compromising their physical quality.

MATERIALS AND METHODS

Materials. Resveratrol standard (purity ≥ 99%), potassium bromide (≥99%), calcium chloride (≥97%), *o*-phthalaldehyde (OPA, ≥ 99%), 2-mercaptoethanol, and dextran (with molecular masses of 37 and 150 kDa) were purchased from Sigma-Aldrich Co. (St. Louis MO, USA). All other chemicals, reagents, and solvents were purchased from Fisher Scientific (Waltham, MA, USA) and were of analytical grade unless stated otherwise. GSE containing 99% resveratrol was purchased from Changsha Organic Herb, Inc. (Changsha, China). Food-grade zein (F4000) was purchased from Flo Chemicals (Ashburnham, MA, USA). Sodium caseinate was purchased from American Caseinate Company (Burlington, NJ, USA). Maltodextrin samples (with a degree of esterification of 6.4 and 17.2 and calculated molecular masses of 1 and 2.8 kDa) were kindly provided by Grain Processing Corporation (Muscatine, IO, USA).

Maillard Conjugate Formation. Sodium caseinate (2.00 w/v %) and the polysaccharides (3.5 w/v %) were individually solubilized overnight at 5 °C in water. The completely solubilized and hydrated samples were subsequently mixed in a 1:1 ratio, which led to a final sodium caseinate concentration of 1.00 w/v %. The mixture was spray-dried (Buchi, Switzerland) using an inlet temperature of 150 °C, a feed rate of 7.5 mL/min, a compressed air pressure of 600 kPa, and an air flow rate of 35 m^3/h.[22] Maillard conjugation reactions were performed by incubating the spray-dried mixture at 60 °C and 76% relative humidity for 48 h.[21,30] After conjugation, the samples were allowed to cool down to room temperature and ground using a mortar and pestle.

DOI: 10.1021/acs.jafc.5b02699
J. Agric. Food Chem. 2015, 63, 8510−8518

The samples were subsequently stored in a desiccator prior to their use.

Maillard Conjugate Characterization. *Conjugation Efficiency.* The conjugation efficiency was determined by measuring the reduction in free amino groups using the OPA assay.[30] The OPA reagent was prepared according to Pan and colleagues.[30] In short, 40 mg of OPA (dissolved in 1.0 mL of 95% ethanol), 25 mL of 0.100 M sodium tetraborate buffer (pH 9.5), 2.5 mL of 20% SDS solution, and 0.10 mL of 2-mercaptoethanol were mixed together and brought to a final volume of 50 mL. The OPA reagent was prepared freshly before use. After dispersing the conjugates, 0.10 mL of the dispersion was mixed with 2.70 mL of OPA reagent and incubated for 1 min at room temperature; the absorbance at 340 nm was measured immediately. The calibration curves were constructed using L-leucine (0.2−5 mM) as a standard amino-group-containing compound.[21,30] The conjugation efficiency was defined as follows:

$$\text{conjugation efficiency (\%)} = \left(1 - \frac{\text{amine groups after conjugation (M)}}{\text{amine groups before conjugation (M)}}\right) \times 100$$

Quantification of Unreacted Protein Using the Lowry Assay. The quantification of the unreacted protein remaining in the system was assessed on the basis of the methodology described by Markman and Livney.[21] The samples were dissolved in double-distilled water at concentrations of 10 mg/mL and subsequently acidified to pH 4.6 with HCl. The sample suspensions were centrifuged at 1000 g for 10 min and then filtered (P5 filter paper, Fisher Scientific, Pittsburgh, PA). The pH of the supernatant was readjusted to 7.0 with NaOH. The protein contents of the suspension (after pH adjustment and before centrifugation) and supernatant were measured by the Lowry method.[31] The amount of protein was subsequently calculated using a calibration curve prepared using sodium caseinate concentrations ranging from 0.2 to 1.0 mg/mL. The conjugation yield was defined as follows:

$$\text{conjugation yield (\%)} = \left(\frac{\text{protein in supernatant (mg/L)}}{\text{protein in the suspension (mg/L)}}\right) \times 100$$

Size Exclusion Chromatography. The conjugation products were analyzed by high-performance size-exclusion chromatography (1260 Infinity, Agilent Technologies, Santa Clara, CA). A 100 μL aliquot of the sample (containing 1.0 w/v % solids) was injected and separated over a OHpak SB-806 M HQ column (Shodex, Showa Denko America Inc., Torrance, CA, USA) at a flow rate of 1.0 mL/min and 20 °C. The mobile phase consisted of 0.200 M NaCl solution. Two detectors were used: a light-scattering detector (Dawn Heleos-II, Wyatt Technology) and a refractive index detector (Optilab, T-rex, Wyatt Technology). The light-scattering data were collected at a cell temperature of 30 °C and with a detector angle of 90°. The cell temperature of the refractive index detector was set to 40 °C.

Fabrication of Nanoparticles. Protein nanoparticles were fabricated by LAS as described in a previous manuscript.[1] Zein (3.0 w/v %) was suspended in 85 v/v % ethanol by stirring for 2 h followed by centrifugation at 9900 g for 12 min. The supernatant was collected, and after overnight storage at 4 °C, it was centrifuged again (9900 g for 12 min) and filtered using filter paper (P5, Fisher Scientific) to remove any precipitated material. The filtered zein solution was subsequently added to the antisolvent at a 1:5 ratio under continuous stirring (440 rpm) at room temperature. Bare zein particles were produced using water (at pH 7.0) as antisolvent, whereas coated particles were produced by coprecipitation in aqueous sodium caseinate and maltodextrin or dextran or conjugate solutions (pH 7.0, final protein concentration of 1.00 w/v %). After addition, the particle suspensions were stirred for an additional 2 min. Ethanol was removed from the mixtures using a rotary evaporator at 30 °C (Buchi RE 111, Flawil, Switzerland). For the nanoparticles loaded with resveratrol, 0.15 w/v % of GSE was added to the solvent phase, i.e., the initial zein solution, stirred for 30 min, and then filtered using Whatman paper (No. 42) prior to particle production. The particle suspensions after the LAS procedure hence contained 0.5 w/v % zein and 0.025 w/v % resveratrol.

Resveratrol Quantification. The resveratrol level contained in the nanoparticles was measured using a UV−vis spectrophotometer (Ultrospec 3000 pro, Biochrom Ltd., Cambridge, UK) at a wavelength of 307 nm. The nanoparticles were dissolved in dimethyl sulfoxide prior the analysis. Nanoparticles without resveratrol were used as blank. Pure resveratrol was dissolved in dimethyl sulfoxide at 100 μg/mL and then diluted to create a calibration curve with concentrations ranging from 0.2 to 6.0 μg/mL.

Characterization of Nanoparticles. *Particle Size and ζ Potential.* Mean particle diameter, polydispersity index, and particle size distribution were obtained using a dynamic light-scattering instrument (Zetasizer Nano ZS, Malvern Instruments, Malvern, UK). The ζ potential was determined by particle electrophoresis using the same instrument. Samples were diluted 40-fold to avoid multiple scattering effects and equilibrated at 25 °C prior to analysis.

Encapsulation Efficiency. The encapsulation efficiency (EE,%) of the nanoparticles prepared by coprecipitation with the physical mixture of caseinate and maltodextrin of 2.8 kDa or dextrans of 37 and 150 kDa as well as those prepared with the Maillard conjugates was determined using the following equation:

$$\text{EE (\%)} = \left(1 - \frac{\text{Res}_\text{F}}{\text{Res}_\text{T}}\right) \times 100$$

in which Res_T is the resveratrol contained in the suspension (M) and Res_F is the amount of free resveratrol (M). The free resveratrol was determined as the amount of resveratrol that was collected by the filtrate receiver after being centrifuged at 1840 g for 60 min using a centrifugal filter (Amicon Ultracel-10 kDa, 2 mL Millipore, Cork Ireland).[6] The recovery yield of resveratrol after passing through the filter (92%) was taken into account to correct the actual amount of resveratrol in the filtrate. The resveratrol contained in the nanoparticles and the filtrate was assessed by diluting the suspension in dimethyl sulfoxide[32] prior to quantification. The suspensions without resveratrol were used as blank samples.

Morphology. The morphology of the conjugated and nonconjugated particles with dextran 37 kDa was analyzed using transmission electron microscopy (2000FX TEM, JEOL, Tokyo, Japan) at a voltage of 200 kV. The sample was diluted 40-fold following the same procedure as that used for the particle size and ζ potential measurements. An aliquot (5 μL) of the diluted sample was drop-cast onto a carbon-coated copper grid (400 mesh). The grid was then air-dried at room temperature before loading it into the microscope. Images of the biopolymer particles were recorded in randomly selected fields.[33]

Particle Stability to Environmental Stresses. *$CaCl_2$ Stability.* After production, the particle dispersions were diluted twofold using $CaCl_2$ solutions (0.0−200 mM) to obtain systems with final $CaCl_2$ concentrations ranging from 0.0 to 100 mM. The samples were then stored for 24 h at room temperature, after which the particle size distribution was analyzed by dynamic light scattering.

Temperature Stability. Freshly prepared particle dispersions were diluted twofold using NaCl solutions (600 and 1200 mM) to obtain systems with final NaCl concentrations ranging of 300 and 600 mM and then incubated in a water bath set at different temperatures (30−90 °C) for 30 min. The samples were then allowed to cool down to 23 °C and were stored for 24 h, after which the particle size distribution was analyzed by dynamic light scattering.

pH Stability. The pH stability of freshly prepared 40-fold-diluted particle dispersions was assessed using an automatic titrator (MPT-2, Malvern Instruments) with NaOH (0.25 M) and HCl (0.10 M) as the titrating base and acid. The particle size distribution and ζ potential were measured from pH 9.0 to pH 3.0 (titrating intervals of 0.5) by dynamic light scattering and particle electrophoresis.

DOI: 10.1021/acs.jafc.5b02699
J. Agric. Food Chem. 2015, 63, 8510−8518

Data Analysis. All experiments were performed at least in duplicate, and the results are given as mean values ± standard deviation.

RESULTS AND DISCUSSION

Conjugation Efficiency and Yield. The conjugation efficiency of the reaction of caseinate with carbohydrates with molecular masses of 1.0, 2.8, 37, or 150 kDa was analyzed by quantifying the unreacted amino groups of the caseinate after the conjugation reaction using the OPA test (Figure 2). The conjugation yield was tested by studying the behavior of the nonconjugated and conjugated protein−carbohydrate samples at the isoelectric point of the protein (pH 4.6). The protein that does not precipitate at this pH is considered to be stabilized by conjugation to the carbohydrate. It is, however, possible that this technique underestimates the real conjugation yield because protein aggregates, although conjugated to dextran molecules, will likely also precipitate under these conditions and hence be considered unconjugated. This technique is also a simple way to purify the conjugated from the nonconjugated proteins (Figure 2).[21] The molecular mass of the polysaccharide had an influence on both the conjugation efficiency and conjugation yield. With an increase in molecular mass of the polysaccharide the conjugation efficiency diminished. The lowest efficiency was reached at 37 kDa, and it did not significantly change upon further increases in molecular mass (Figure 2). Simultaneously, the increase in molecular mass of the polysaccharide substantially increased the conjugation yield. The conjugation of carbohydrates with a higher molecular mass to the proteins clearly stabilized the caseinate proteins against aggregation near the isoelectric point. The conjugation yield, hence, reflects two processes: (i) the conjugation of the carbohydrate and the protein (conjugation efficiency) and (ii) the ability of the carbohydrate to stabilize the protein near its isoelectric point. On the basis of previous studies,[21,30] the average number of amino groups per caseinate molecule available to react with the reducing sugars of the polysaccharides is 13.6. We therefore estimated the average number of carbohydrates conjugated per caseinate molecule in

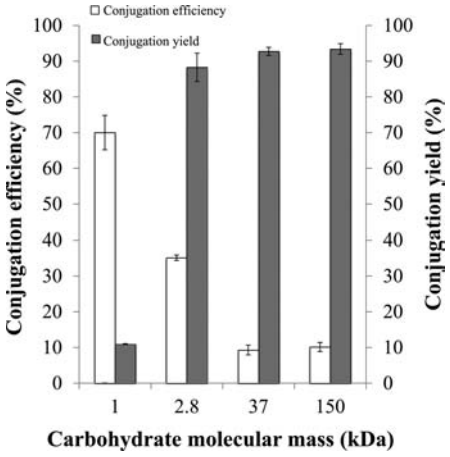

Figure 2. Conjugation yield and efficiency of the conjugation of caseinate to maltodextrin/dextran.

Table 1. Molecular Mass of the Dextran, Nonconjugated Dextran−Caseinate, and Conjugated Dextran−Caseinate Samples as Determined by High-Performance Size-Exclusion Chromatography

	dextran (37 kDa)	dextran (150 kDa)
pure dextran	32 kDa	229 kDa
nonconjugated casein−dextran	34 kDa	231 kDa
conjugated casein−dextran	1402 kDa and 628 kDa	1242 kDa and 682 kDa

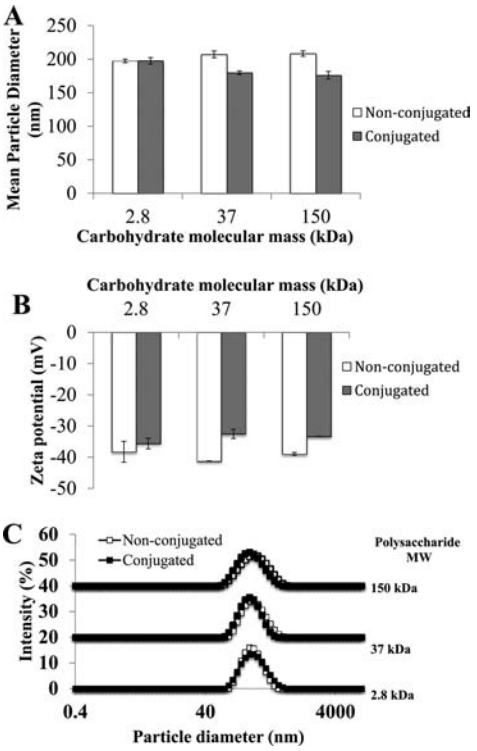

Figure 3. (A) Mean particle diameter, (B) zeta potential, and (C) particle size distribution of zein particles loaded with grape skin extract (GSE) prepared with conjugated (Maillard conjugates of sodium caseinate and dextran) and nonconjugated (physical mixture of unreacted sodium caseinate and dextran) biopolymers in the antisolvent (1.0% (w/v)). The ratio of polysaccharides to sodium caseinate was 1.75−1.0. Zein and GSE concentrations in the particle suspensions were 0.5 and 0.025% (w/v), respectively.

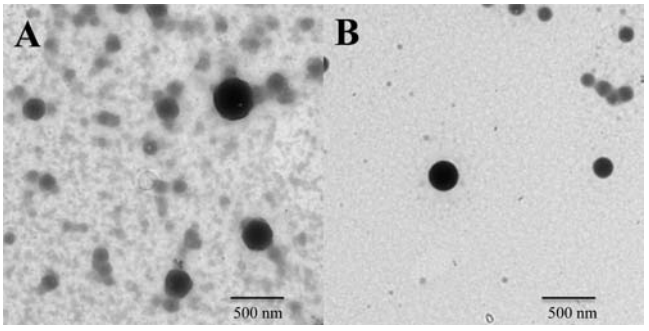

Figure 4. Transmission electron microscopy (TEM) images of zein particles loaded with grape skin extract (GSE) prepared with (A) conjugated (Maillard conjugates of sodium caseinate and dextran) and (B) nonconjugated (physical mixture of unreacted sodium caseinate and dextran) biopolymers in the antisolvent (1.0% (w/v)). The caseinate was conjugated with dextran of 37 kDa. The ratio of polysaccharides to sodium caseinate was 1.75−1.0. Zein and GSE concentrations in the particle suspensions were 0.5 and 0.025% (w/v), respectively.

DOI: 10.1021/acs.jafc.5b02699
J. Agric. Food Chem. 2015, 63, 8510−8518

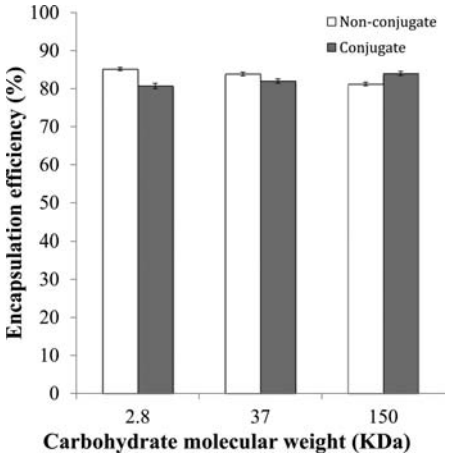

Figure 5. Encapsulation efficiency of zein particles loaded with grape skin extract (GSE) prepared with conjugated (Maillard conjugates of sodium caseinate and dextran) and nonconjugated (physical mixture of unreacted sodium caseinate and dextran) biopolymers in the antisolvent [1.0% (w/v)]. The ratio of polysaccharides to sodium caseinate was 1.75 to 1.0. Zein and GSE concentrations in the particle suspensions were 0.5 and 0.025% (w/v), respectively.

our study to be about 9, 5, 0.7, and 0.7 for the 1.0 and 2.8 maltodextrins and 37 and 150 kDa dextrans, respectively. The reduction in the conjugation efficiency could be explained by an increase in the steric hindrance when longer polysaccharides are conjugated with a protein, reducing the accessibility of the surrounding unconjugated amino groups. The steric hindrance effect using dextrans of 37 and 150 kDa appears to be similar because the number of carbohydrates conjugated per caseinate molecule was equal for both treatments. Furthermore, the molar ratio between the caseinate and the polysaccharides was also reduced by increasing the molecular mass of the carbohydrates, resulting in less reducing sugar ends to conjugate to the protein. The protein−carbohydrate mass ratio used was not changed between the carbohydrate samples because increasing the concentration of the high-molecular-mass dextran to keep the same molar ratio resulted in hazy solutions with incomplete solubilization.

Size-exclusion chromatography confirmed the molecular mass reported by the supplier of the dextrans and showed that the molecular mass of the dextran molecules was not altered by spray-drying the dextran−caseinate mixture (Table 1). The subsequent incubation of the spray-dried caseinate−dextran mixture resulted in the formation of large complexes (Table 1). It was, however, impossible to estimate the ratio of

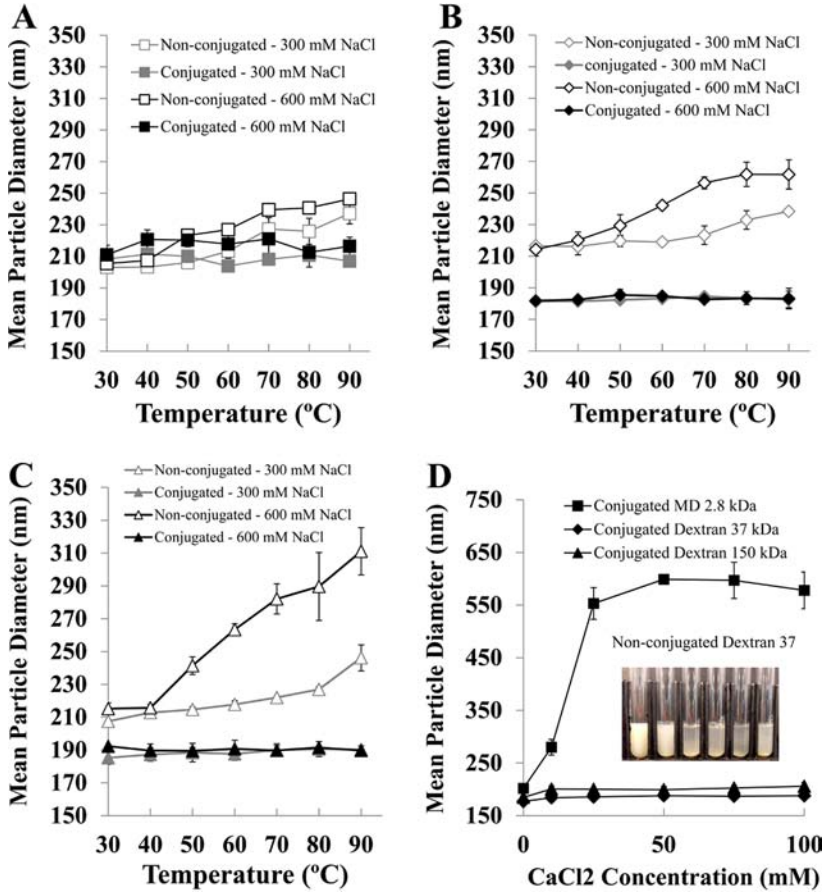

Figure 6. Effect of ions on the particle diameter of zein particles coated with nonconjugated or conjugated caseinate. The particles were incubated in short high-temperature treatments (30 min) and/or elevated salt conditions (300 and 600 mM NaCl and 0−100 mM $CaCl_2$). The effect of the molecular mass of the conjugated carbohydrate was studied for NaCl/temperature treatments (A) maltodextrin (MD) 2.8 kDa, (B) dextran 37 kDa, and (C) dextran 150 kDa and for (D) $CaCl_2$ incubation. Insert in panel D: Appearance of precipitated particles made with the physical mixture of sodium caseinate and dextran 37 kDa in the presence of $CaCl_2$. Zein and GSE concentrations in the particle suspensions were 0.5 and 0.025% (w/v), respectively.

DOI: 10.1021/acs.jafc.5b02699
J. Agric. Food Chem. 2015, 63, 8510−8518

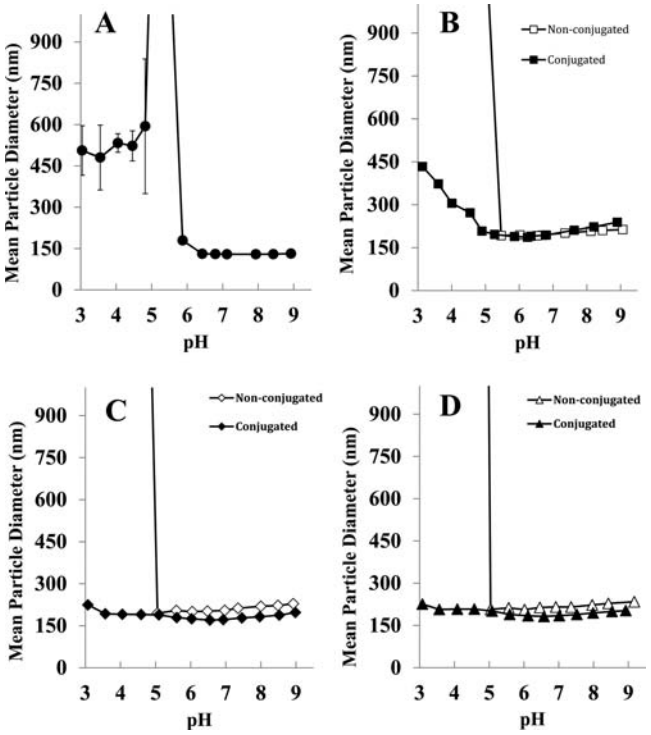

Figure 7. Effect of pH on the mean diameter of (A) plain zein nanoparticles and (B–D) zein nanoparticles prepared with conjugated (Maillard conjugates of sodium caseinate and dextran) and non-conjugated (physical mixture of unreacted sodium caseinate and dextran) biopolymers in the antisolvent (1.0% (w/v)). The effect of the molecular mass of the conjugated carbohydrate was studied as a function of pH: (B) maltodextrin (MD) 2.8 kDa, (C) dextran 37 kDa, and (D) dextran 150 kDa. Zein and GSE concentrations in the particle suspensions were 0.5 and 0.025% (w/v), respectively.

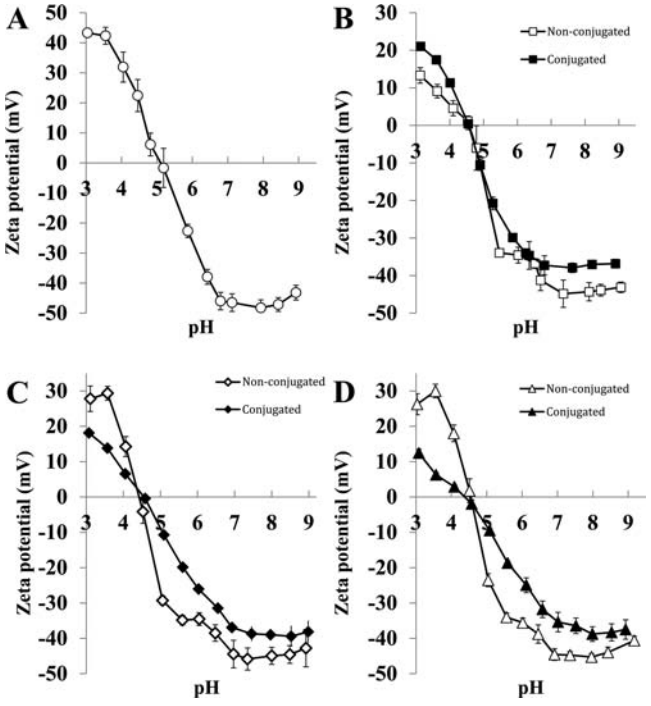

Figure 8. Effect of pH on the zeta potential of (A) plain zein nanoparticles and (B–D) zein nanoparticles prepared with conjugated (sodium caseinate and dextran) and nonconjugated (physical mixture of unreacted sodium caseinate and dextran) in the antisolvent (1.0% (w/v)). The effect of the molecular mass of the conjugated carbohydrate was studied as a function of pH: (B) maltodextrin (MD) 2.8 kDa, (C) dextran 37 kDa, and (D) dextran 150 kDa. Zein and GSE concentrations in the particle suspensions were 0.5 and 0.025% (w/v), respectively.

caseinate to dextran molecules on the basis of these data because caseinate probably does not occur as single molecules but rather as caseinate aggregates.[34] The broad molecular weight distribution of the signals picked up for the conjugated samples could be ascribed to the presence of a variety of conjugation degrees between the caseinate and the dextran molecules or, more likely, to the aggregation or micellization of unreacted protein in the column.[34,35] Around pH 4.6, nonconjugated caseinate has no or a very low net charge, leading to aggregation and precipitation because of the loss of electrostatic repulsion between the protein chains. After conjugation, the stability of the caseinate–carbohydrate conjugates is believed to be driven by steric repulsion. As clearly shown by the conjugation yield data, the steric repulsion caused by the conjugation with the maltodextrin of 1.0 kDa is not enough to stabilize the protein solution near the isoelectric point of the protein. Increasing the molecular mass of the polysaccharide by approximately threefold already had a sharp effect on the stability of the protein by increasing the recovery yield from 10% to almost 90% at pH 4.6. Further increases in the molecular mass of the polysaccharide resulted in even higher yields of up to 93%.

Particles Characterization. MC of caseinate and carbohydrates with molecular masses of 2.8, 37, and 150 kDa were included in the antisolvent phase to study the effect of the glycation of caseinate on the characteristics and the stability of caseinate-coated zein nanoparticles encapsulating resveratrol produced by LAS. The conjugates formed with maltodextrin of 1.0 kDa were not used for further studies because these polysaccharide chains were not long enough to create the steric repulsion needed to stabilize the caseinate at pH 4.6. The mean particle diameter of the resveratrol-loaded particles created with the conjugates and the nonconjugated physical mixture of caseinate and carbohydrates was subsequently analyzed (Figure 3A). All the samples presented a monomodal particle size distribution (Figure 3C). The mean particle diameter remained relatively stable for particles produced with the nonconjugated mixture of caseinate and carbohydrates. Furthermore, the diameter did not change significantly for the particles coprecipitated with the caseinate–maltodextrin (2.8 kDa) conjugates versus those produced in the presence of the nonconjugated mixture of caseinate and maltodextrin (2.8 kDa).

For the zein particles produced with the antisolvent mixtures containing conjugates of caseinate and the higher molecular mass dextrans (37 and 150 kDa), the mean particle diameter decreased relative to that of those particles coprecipitated with nonconjugated protein–carbohydrate mixtures. The reason for this decrease could be a reduction in the packing parameter and an associated increase in the curvature of the coated nanoparticles. The reduction is a consequence of the increase in the bulkiness of the hydrophilic domains of the caseinate protruding into the environment caused by the attachment of the polysaccharide chains.[21] Another possibility to explain the reduction in size is steric repulsion caused by the carbohydrate structures protruding from the particle surface that restrict particle growth because no other zein or caseinate molecules

DOI: 10.1021/acs.jafc.5b02699
J. Agric. Food Chem. 2015, 63, 8510–8518

can approach the inner core of the particles. The increase in the bulkiness of the conjugates with maltodextrin with a molecular mass of 2.8 kDa is not enough to decrease the packing parameter or ensure enough steric repulsion. Conversely, the zein particles coprecipitated with the nonconjugated mixture of caseinate and dextran (37 and 150 kDa) had an increased particle diameter compared to the ones made with 2.8 kDa maltodextrin. A slight aggregation of the particles caused by depletion flocculation could be responsible for the observed increase in mean particle diameter. The long-chain polysaccharides generated a thermodynamic incompatibility with the nanoparticles, pushing the particles together.[36] Electrophoresis measurements of the particles that coprecipitated with the conjugates and the nonconjugated mixtures of caseinate and carbohydrates indicated that the magnitude of the zeta potential decreased upon conjugation (Figure 3B). The decrease, however, was greater for the conjugates made with the dextrans of 37 and 150 kDa. Lesmes and McClements[19] observed similar results with lipid droplets coated by β-lactoglobulin−dextran MC and hypothesized that the reduction in the zeta potential could be explained by two phenomena. First, the number of ionizable groups at the particle surface is reduced because of the formation of the Amadori compounds that consume free amino groups (Figure 1). Second, the decrease in the apparent zeta potential of the nanoparticles can be due to a screening effect in which the distance between the protein charges and the aqueous continuous phase is increased. The presence of resveratrol did not change the size and zeta potential of the nanoparticles (data not shown), which can be attributed to the fact that it is incorporated into the internal hydrophobic core or embedded in the biopolymer network of the particles. Figure 4 shows the microscopic morphology of zein nanoparticles loaded with resveratrol prepared with nonconjugated and conjugated caseinate with dextran 37 kDa. The particles have a spheroid shape and proved to be stable against aggregation. The size of the conjugated particles is smaller, supporting the results obtained with the dynamic light-scattering instrument. The surface of the nonconjugated particles appears to be rougher and less even than the surface of the conjugated particles. The difference in the surface of the particles can be related to the hypothesized differences in molecular arrangements in the particle structure.

Encapsulation Efficiency. The EE was measured for the particles coprecipitated with the nonconjugated mixture of caseinate and the polysaccharides with molecular masses of 2.8, 37, and 150 kDa and for their conjugates. The EE of the particles produced with the nonconjugated and the conjugated caseinate−carbohydrate samples in the antisolvent all varied around 80 and 85% without a clear tendency of increasing or decreasing EE depending on the evaluated treatments (Figure 5). Therefore, it was concluded that the conjugation of caseinate did not negatively affect the EE. Moreover, the percentages are similar to the ones obtained previously, in which resveratrol was encapsulated in zein particles stabilized by sodium caseinate without the addition of carbohydrates.[1] In that research, it was found that resveratrol could form complexes with sodium caseinate in the system that could be part of the particle coating or be dispersed within the continuous phase as a complementary method of resveratrol encapsulation. It is also know that polysaccharides can stabilize resveratrol in aqueous medium mainly through the formation of hydrogen bonds.[37] This can certainly also contribute to a higher EE of resveratrol in these systems.

Particle Stability. The ultimate goal of the use of protein−polysaccharide conjugates to coat the zein particles was to increase the stability of the final nanoparticles without compromising particle functionality, e.g., EE. We therefore tested the influence of a variety of environmental stresses on the stability of the particles.

Sodium ions were included in the aqueous phase of the nanoparticle suspensions that were then subjected to thermal treatments. The ions shield the surface charges on the particles, hence reducing the electrostatic repulsion between them. This approach also more closely matches the conditions encountered in real-world food systems. In accordance with previous research on caseinate-coated zein particles,[38] the mean diameter of zein nanoparticles made with caseinate and maltodextrin (both nonconjugated and conjugated) did not change appreciably with increasing temperature or high salt concentrations (Figure 6A). For both dextran samples, however, the mean diameter increased with increasing temperature for the nonconjugated samples (Figure 6B,C) and presented a multimodal particle size distribution indicating the presence of aggregates (data not shown). This was more pronounced with increasing salt concentration and increasing molecular mass of the carbohydrate moiety. In nonconjugated samples, free dextran molecules will be found in the suspension that promote depletion flocculation and destabilization of the particle suspensions, resulting in increased particle sizes. In this case, the free biopolymers therefore act as an additional destabilization factor. Depletion flocculation occurs because of steric exclusion of polymers from the particle surfaces, which leads to osmotic pressure gradients that increase the attractive forces between the particles.[39] Previous research already indicated that the critical concentration at which depletion flocculation occurs decreases with the molecular mass of the nonadsorbed polymer.[40] Larger molecules will be more easily excluded from the particle surfaces, and their effect will therefore be more pronounced at lower concentrations (assuming similar properties of the polymers). Particle and biopolymer mobility will be increased by higher temperatures, which will speed up the flocculation process. The conjugation of dextran to caseinate molecules coating the zein particles inhibited destabilization due to depletion flocculation, probably because of steric repulsion and the fact that the free dextran concentration in the conjugated samples was also significantly lower than that in the nonconjugated samples. The mean diameter of the conjugated dextran−caseinate zein nanoparticles did not grow significantly with increasing temperature, even in the presence of elevated salt concentrations (Figure 6B,C), and the particle size distribution remained monomodal.

Calcium chloride, as a divalent salt, has a strong cross-linking and destabilizing effect on biopolymer-based nanoparticles,[41] especially when they are only stabilized by electrostatic repulsion. As outlined above, in general protein particles are mainly stabilized by electrostatic repulsion between the particles. Calcium ions can form salt bridges between anionic protein particles. The increase of the steric repulsion by conjugating carbohydrates to the caseinate molecules coating the zein particles is expected to increase the stability of the nanoparticles. The hairy carbohydrate protrusions hamper the formation of calcium bridges between particles. The particles coated with nonconjugated caseinate destabilized in the presence of calcium ions (Figure 6D insert). Conjugation of the carbohydrate with the lowest molecular mass, i.e., maltodextrin, to the coating caseinate only marginally stabilized

DOI: 10.1021/acs.jafc.5b02699
J. Agric. Food Chem. 2015, 63, 8510−8518

the particles against bridging by calcium ions (Figure 6D). Conversely, dextran stabilized the particles against aggregation at elevated calcium concentrations, which can be attributed to the greater steric repulsion generated by the longer carbohydrate molecules (Figure 6D).

Protein particles are especially sensitive to pH changes. Near the isoelectric point of the protein particles, the charge on the particle surface is reduced, which minimizes the electrostatic repulsion between particles and promotes aggregation. Plain zein particles destabilized around pH 5.0 (Figure 7A), where they showed the lowest absolute zeta potential (Figure 8A). This would seriously hamper the use of these protein particles in many food products. Coating of zein particles with caseinate slightly reduced the pH at which the particles aggregated, i.e., to around pH 4.5 (Figure 7B–D),[38] but extensive aggregation still occurred. Conjugation of a carbohydrate to the caseinate coating the zein particles does not significantly affect the isoelectric point of the particles relative to the values found for the nonconjugated samples (Figure 8B–D). However, it did reduce the magnitude of the electrical charge on the particles below and above the isoelectric point. As discussed earlier, this can be attributed to the association of carbohydrates to amino groups on the proteins and to shielding of the particle surface charge by carbohydrate layer. Nonconjugated particles were still destabilized near and below the isoelectric point. However, when the zein particles were coated with caseinate–carbohydrate conjugates, the mean particle diameter did not increase appreciably when the pH was reduced to around and below the isoelectric point. Maltodextrin did not perform as efficiently as the higher molecular mass dextrans. Indeed, the dextran molecules with a molecular mass of 37 kDa were able to completely stabilize the particles against size increments caused by pH effects.

We have shown that the stability of resveratrol-fortified zein nanoparticles can be improved by coating them with MC made from sodium caseinate and neutral carbohydrates. The molecular mass of the carbohydrates used to form the MC had a significant impact on particle stabilization, with the stability of the delivery systems increasing with increasing carbohydrate molecular mass. This is an important result in view of the potential application of zein particles in real-world food applications. The nanoparticles produced in this work were highly stable against environmental stresses that might be encountered by delivery systems in real-life food processing applications, e.g., temperature, pH, and ionic strength changes.

AUTHOR INFORMATION

Corresponding Author

*E-mail: iris.joye@biw.kuleuven.be. Tel.: +32 16376123. Fax.: +32 16321997.

Funding

G.D.-P. is recipient of a postdoctoral fellowship by the Secretaría de Ciencia Tecnología e Innovación del Distrito Federal (SECITI, Mexico City). I.J.J. gratefully acknowledges financial support from the Fonds voor Wetenschappelijk Onderzoek–Vlaanderen (FWO, Brussels, Belgium) and from the European Commission 7th Framework Program (FP7-People-2011-IOF-300408). This material is partly based upon work supported by the U.S. Department of Agriculture, NRI Grants (2011-03539, 2013-03795, 2011-67021, and 2014-67021).

Notes

The authors declare no competing financial interest.

REFERENCES

(1) Davidov-Pardo, G.; Joye, I. J.; McClements, D. J. Encapsulation of resveratrol in biopolymer particles produced using liquid antisolvent precipitation. Part 1: preparation and characterization. *Food Hydrocolloids* **2015**, *45*, 309–316.

(2) Patel, A.; Hu, Y. C.; Tiwari, J. K.; Velikov, K. P. Synthesis and characterisation of zein-curcumin colloidal particles. *Soft Matter* **2010**, *6*, 6192–6199.

(3) Patel, A. R.; Heussen, P. C. M.; Hazekamp, J.; Drost, E.; Velikov, K. P. Quercetin loaded biopolymeric colloidal particles prepared by simultaneous precipitation of quercetin with hydrophobic protein in aqueous medium. *Food Chem.* **2012**, *133*, 423–429.

(4) Parris, N.; Cooke, P. H.; Hicks, K. B. Encapsulation of essential oils in zein nanospherical particles. *J. Agric. Food Chem.* **2005**, *53*, 4788–4792.

(5) Luo, Y. C.; Wang, T. T. Y.; Teng, Z.; Chen, P.; Sun, J. H.; Wang, Q. Encapsulation of indole-3-carbinol and 3,3′-diindolylmethane in zein/carboxymethyl chitosan nanoparticles with controlled release property and improved stability. *Food Chem.* **2013**, *139*, 224–230.

(6) Luo, Y. C.; Zhang, B. C.; Whent, M.; Yu, L. L.; Wang, Q. Preparation and characterization of zein/chitosan complex for encapsulation of alpha-tocopherol, and its in vitro controlled release study. *Colloids Surf., B* **2011**, *85*, 145–152.

(7) Joye, I. J.; McClements, D. J. Production of nanoparticles by anti-solvent precipitation for use in food systems. *Trends Food Sci. Technol.* **2013**, *34*, 109–123.

(8) Hu, K.; McClements, D. J. Fabrication of surfactant-stabilized zein nanoparticles: A pH modulated antisolvent precipitation method. *Food Res. Int.* **2014**, *64*, 329–335.

(9) Joye, I. J.; Nelis, V. A.; McClements, D. J. Gliadin-based nanoparticles: Stabilization by post-production polysaccharide coating. *Food Hydrocolloids* **2015**, *43*, 236–242.

(10) Zhong, Q.; Jin, M. Zein nanoparticles produced by liquid–liquid dispersion. *Food Hydrocolloids* **2009**, *23*, 2380–2387.

(11) Patel, A. R.; Bouwens, E. C. M.; Velikov, K. P. Sodium caseinate stabilized zein colloidal particles. *J. Agric. Food Chem.* **2010**, *58*, 12497–12503.

(12) Li, K. K.; Yin, S. W.; Yin, Y. C.; Tang, C. H.; Yang, X. Q.; Wen, S. H. Preparation of water-soluble antimicrobial zein nanoparticles by a modified antisolvent approach and their characterization. *J. Food Eng.* **2013**, *119*, 343–352.

(13) Chen, H. Q.; Zhong, Q. X. Processes improving the dispersibility of spray-dried zein nanoparticles using sodium caseinate. *Food Hydrocolloids* **2014**, *35*, 358–366.

(14) Hu, K.; McClements, D. J. Fabrication of biopolymer nanoparticles by antisolvent precipitation and electrostatic deposition: Zein-alginate core/shell nanoparticles. *Food Hydrocolloids* **2015**, *44*, 101–108.

(15) McClements, D. J. Protein-stabilized emulsions. *Curr. Opin. Colloid Interface Sci.* **2004**, *9*, 305–313.

(16) Jahanshahi, M.; Babaei, Z. Protein nanoparticle: a unique system as drug delivery vehicles. *Afr. J. Biotechnol.* **2008**, *7*, 4926–4934.

(17) Oliver, C. M.; Melton, L. D.; Stanley, R. A. Creating proteins with novel functionality via the maillard reaction: A review. *Crit. Rev. Food Sci. Nutr.* **2006**, *46*, 337–350.

(18) Ames, J. M. Control of the Maillard reaction in food systems. *Trends Food Sci. Technol.* **1990**, *1*, 150–154.

(19) Lesmes, U.; McClements, D. J. Controlling lipid digestibility: Response of lipid droplets coated by β-lactoglobulin-dextran Maillard conjugates to simulated gastrointestinal conditions. *Food Hydrocolloids* **2012**, *26*, 221–230.

(20) Wooster, T. J.; Augustin, M. A. β-Lactoglobulin-dextran Maillard conjugates: Their effect on interfacial thickness and emulsion stability. *J. Colloid Interface Sci.* **2006**, *303*, 564–572.

DOI: 10.1021/acs.jafc.5b02699
J. Agric. Food Chem. 2015, 63, 8510–8518

(21) Markman, G.; Livney, Y. D. Maillard-conjugate based core-shell co-assemblies for nanoencapsulation of hydrophobic nutraceuticals in clear beverages. *Food Funct.* **2012**, *3*, 262−70.
(22) Shah, B.; Davidson, P. M.; Zhong, Q. Encapsulation of eugenol using Maillard-type conjugates to form transparent and heat stable nanoscale dispersions. *LWT - Food Science and Technology* **2012**, *49*, 139−148.
(23) Walle, T.; Hsieh, F.; DeLegge, M. H.; Oatis, J. E., Jr; Walle, U. K. High absorption but very low bioavailability of oral resveratrol in humans. *Drug Metab. Dispos.* **2004**, *32*, 1377−1382.
(24) Alves, N. E. G. Studies on mechanistic role of natural bioactive compounds in the management of obesity, an overview. *Open Nutraceuticals J.* **2012**, *5*, 193.
(25) Catalgol, B.; Batirel, S.; Taga, Y.; Ozer, N. K. Resveratrol: French paradox revisited. *Front. Pharmacol.* **2012**, *3*, 141 DOI: 10.3389/fphar.2012.00141.
(26) Reis, S.; Neves, A. R.; Lucio, M.; Martins, S.; Lima, J. L. C. Novel resveratrol nanodelivery systems based on lipid nanoparticles to enhance its oral bioavailability. *Int. J. Nanomed.* **2013**, *8*, 177−187.
(27) Hung, C.-F.; Chen, J.-K.; Liao, M.-H.; Lo, H.-M.; Fang, J.-Y. Development and evaluation of emulsion-liposome blends for resveratrol delivery. *J. Nanosci. Nanotechnol.* **2006**, *6*, 2950−2958.
(28) Patel, K. R.; Scott, E.; Brown, V. A.; Gescher, A. J.; Steward, W. P.; Brown, K.; Vang, O.; Das, D. K. Clinical trials of resveratrol. *Ann. N. Y. Acad. Sci.* **2011**, *1215*, 161−169.
(29) Trela, B. C.; Waterhouse, A. L. Resveratrol: Isomeric molar absorptivities and stability. *J. Agric. Food Chem.* **1996**, *44*, 1253−1257.
(30) Pan, X.; Mu, M.; Hu, B.; Yao, P.; Jiang, M. Micellization of casein-graft-dextran copolymer prepared through Maillard reaction. *Biopolymers* **2006**, *81*, 29−38.
(31) Lowry, O. H.; Rosebrough, N. J.; Rarr, L. A.; Randall, R. J. Protein measurement with the Folin phenol reagent. *J. Biol. Chem.* **1951**, *193*, 265−275.
(32) Podaralla, S.; Perumal, O. Influence of formulation factors on the preparation of zein nanoparticles. *AAPS PharmSciTech* **2012**, *13*, 919−927.
(33) Arroyo-Maya, I. J.; McClements, D. J. Biopolymer nanoparticles as potential delivery systems for anthocyanins: Fabrication and properties. *Food Res. Int.* **2015**, *69*, 1−8.
(34) Morris, G. A.; Sims, I. M.; Robertson, A. J.; Furneaux, R. H. Investigation into the physical and chemical properties of sodium caseinate-maltodextrin glyco-conjugates. *Food Hydrocolloids* **2004**, *18*, 1007−1014.
(35) O'Regan, J.; Mulvihill, D. M. Preparation, characterisation and selected functional properties of sodium caseinate−maltodextrin conjugates. *Food Chem.* **2009**, *115*, 1257−1267.
(36) McClements, D. J. *Food Emulsions: Principles, practice, and techniques*; CRC Press: Boca Raton, FL, 2005; p 374.
(37) Zhang, X. P.; Le, Y.; Wang, J. X.; Zhao, H.; Chen, J. F. Resveratrol nanodispersion with high stability and dissolution rate. *LWT-Food Science and Technology* **2013**, *50*, 622−628.
(38) Joye, I. J.; Davidov-Pardo, G.; McClements, D. J. Encapsulation of resveratrol in biopolymer particles produced using liquid antisolvent precipitation. Part 2: Stability and functionality. *Food Hydrocolloids* **2015**, *49*, 127−134.
(39) Walstra, P. *Physical Chemistry of Foods*; Marcel Dekker, Inc.: New York, 2003; p 807.
(40) Burns, J. L.; Yan, Y.; Jameson, G. J.; Biggs, S. The effect of molecular weight of nonadsorbing polymer on the structure of depletion-induced flocs. *J. Colloid Interface Sci.* **2002**, *247*, 24−32.
(41) Agboola, S. O.; Dalgleish, D. G. Calcium-induced destabilization of oil-in-water emulsions stabilized by caseinate of by beta-lactoglobulin. *J. Food Sci.* **1995**, *60*, 399−404.

DOI: 10.1021/acs.jafc.5b02699
J. Agric. Food Chem. 2015, 63, 8510−8518

Table 1. Most Abundant Fatty Acids with a Peak Intensity of $\geq 10^6$ in a Green Tea Infusion As Identified by Means of LC-MS in a Range of m/z 100−1000

fatty acid	rt (min)	$[M - H]^-$ (m/z)	error (ppm)	fragments (m/z)
nonanedioic acid ($C_9H_{16}O_4$)	25.5	187.0971	2	125.0973 ($C_8H_{13}O$; octanone)
dodecenedioic acid ($C_{12}H_{20}O_4$)	29.8	227.1285	1	183.1393 ($C_{11}H_{19}O_2$; $-CO_2$; undecenoic acid), 165.1287 ($C_{11}H_{17}O$; $-H_2O$)
hydroxynonenoic acid ($C_9H_{16}O_3$)	28.9	171.1023	2	127.1130 ($C_8H_{15}O$; $-CO_2$), 153.0924 ($C_9H_{13}O_2$; $-H_2O$)
hydroxynonenediynoic acid ($C_9H_8O_3$)	25.9	163.0396	3	119.0503 (C_8H_7O; $-CO_2$)
hydroxyundecenoic acid ($C_{11}H_{20}O_3$)	28.7	199.1335	2	155.1079 ($C_9H_{15}O_2$; nonenoic acid)
hydroxydodecanedioic acid ($C_{12}H_{22}O_5$)	26.5	245.1389	2	185.1187 ($C_{10}H_{17}O_3$; hydroxydecenoic acid)
hydroxyoctadecatrienoic acid ($C_{18}H_{30}O_3$)	36.8	293.2118	2	275.2025 ($C_{18}H_{27}O_2$; $-H_2O$), 235.1710 ($C_{15}H_{23}O_2$)
dihydroxypalmitic acid ($C_{16}H_{32}O_4$)	30.3	287.2224	1	187.1345 ($C_{10}H_{19}O_3$; hydroxydecanoic acid)
trihydroxystearic acid ($C_{18}H_{36}O_5$)	29.5	331.2484	2	313.2407 ($C_{18}H_{33}O_4$; $-H_2O$), 287.0204 ($C_{17}H_{35}O_3$; $-CO_2$)
trihydroxyoctadecenoic acid ($C_{18}H_{34}O_5$)	29.7	329.2329	1	311.2245 ($C_{18}H_{31}O_4$; $-H_2O$), 171.1036 ($C_9H_{15}O_3$; hydroxynonenoic acid), 229.1445 ($C_{12}H_{21}O_4$; dodecanedioic acid)
trihydroxyoctadecadienoic acid ($C_{18}H_{32}O_5$)	28.9	327.2172	2	309.2099 ($C_{18}H_{29}O_4$; $-H_2O$), 171.1033 ($C_9H_{15}O_3$; oxononanoic acid)
hydroperoxyoctadecadienoic acid ($C_{18}H_{32}O_4$)	35.1	311.2222	2	293.2128 ($C_{18}H_{29}O_3$; $-H_2O$; epoxyoctadecadienoic acid), 171.1028 ($C_9H_{15}O_3$; hydroxynonenoic acid)
hydroperoxyoctadecatrienoic acid ($C_{18}H_{30}O_4$)	31.3	309.2066	1	291.1972 ($C_{18}H_{27}O_3$; $-H_2O$; hydroxyoctadecadienynoic acid), 171.1029 ($C_9H_{15}O_3$; hydroxynonenoic acid)

Germany. Both samples were stored under vacuum prior to analysis. All other chemicals were purchased from Sigma-Aldrich, Vienna, Austria, and Carl Roth, Karlsruhe, Germany.

Sample Preparation. Green and King's oolong tea infusions were prepared by first adding 50 mL of double-distilled, boiling water to 1 g of dried leaves.[14] After 10 min, the infusion was refilled with water to consider evaporated water and was passed through a Whatman cellulose filter with a pore size of 11 μm and a polyvinylidene fluoride syringe filter with a pore size of 0.45 μm. Additionally, samples were prepared to which 50 μL of $CuSO_4$ (300 mM) was added to freshly prepared tea infusions (50 mL) to yield a 300 μM surplus in copper concentration. After filtration, the samples were stored at −20 °C prior to analysis.

LC-MS Analyses. Analyses of the fatty acid profiles of the tea samples were performed on a Nano-LC system (Dionex Ultimate 3000 RSLC, Thermo Fisher Scientific, Vienna, Austria) coupled to a Nano-ESI-LTQ-Orbitrap mass spectrometer (Thermo Fisher Scientific). The trap column (Acclaim PepMap 100, 100 μm × 2 cm nanoViper, C18, 5 μm, Thermo Fisher Scientific) was loaded with 5 μL of sample, which was separated on a nano LC column (Acclaim PepMap 100, 75 μm × 15 cm nanoViper, C18, 3 μm, Thermo Fisher Scientific). The columns were maintained at 35 °C. The gradient program started with 3% acetonitrile in water acidified with 0.1% formic acid (pH 2.69) and increased to 100% acidified acetonitrile (pH 1.66) after 40 min at a flow rate of 300 nL/min. The ESI-MS was operated in the negative mode, scanning a mass range of m/z 100−1000. Ionization of fatty acids as carboxylate anions might be facilitated in the ESI(−) mode.[15] The capillary temperature and the capillary voltage were set at 300 °C and 3.0 kV, respectively. For structural identification, MS/MS experiments were performed by applying higher energy collisional dissociation with a normalized collision energy of 30%. To avoid cross-contamination, water was run as blank after each sample. Quantitation of 13-hydroperoxy-9*Z*,11*E*-octadecadienoic acid in tea samples was performed by external calibration using standard concentrations in the range of 0.01−1 μM. The ion peak with a m/z of 457.0768 was identified as epigallocatechin-3-gallate, which eluted after 22.8 min, and showed characteristic fragments at m/z 305.067 (gallocatechin) and m/z 169.0143 (gallic acid). The ion peak at m/z 457 was used to quantitate epigallocatechin-3-gallate in tea by applying the external calibration method.

Synthesis of 13-Hydroperoxy-9*Z*,11*E*-octadecadienoic Acid. The synthesis of 13-hydroperoxy-9*Z*,11*E*-octadecadienoic acid was performed with slight modifications according to the method of Schieberle et al.[16] Briefly, 0.64 mmol of linoleic acid was emulsified with 8 mL of 0.1% Tween-80 and approximately 2 mL of 1 M NaOH. The pH was adjusted to 9.0 after the addition of 190 mL of 0.02 M sodium borate buffer (pH 9.0). After cooling on ice, the solution was saturated with oxygen and vigorously stirred for 5 min. To start the enzymatic reaction, 4.2 mg of soy lipoxygenase type I dissolved in 1 mL of borate buffer was added to the substrate. The solution was then vigorously stirred and bubbled with oxygen for 2 h. The reaction was stopped by adding 2 M HCl to adjust the pH to 3.0. The reaction mixture was extracted three times with 200 mL of diethyl ether, and the pooled extracts were washed with 200 mL of double-distilled water and dried with Na_2SO_4. The solvent was removed by rotating evaporation. A purity of 98% was determined by mass spectrometry. The synthesized product, 13-hydroperoxy-9*Z*,11*E*-octadecadienoic acid, was identified by means of ESI(−)MS (m/z 311 and 293) and NMR. ^{1}H NMR (500 MHz, $(CD_3)_2SO$): δ (ppm) 4.40 [q, 1 H, CH, C(13)], 5.42 [m, 1 H, J = 11.1 Hz; CH, C(9)], 5.59 [dd, 1 H, J = 15.0 Hz; CH, C(12)], 5.98 [t, 1 H, J = 11.1 Hz; CH, C(10)], 6.46 [dd, 1 H, J = 15.0 Hz; CH, C(11)]. ^{13}C NMR (500 MHz; $(CD_3)_2SO$, HMBC): δ (ppm) 14.3 [CH, C(18)], 85.1 [CH, C(13)], 128 [CH, C(11)], 129 [CH, C(10)], 133 [CH, C(9)], 134 [CH, C(12)], 175 [COOH, C(1)].[17]

Quantitation of Copper in Tea Samples. Total copper concentrations in tea samples were determined using a PinAAcle 900Z graphite furnace atomic absorption spectrometer (PerkinElmer, Vienna, Austria) as described previously.[18] A volume of 8 mL of 34% HNO_3 (TraceSELECT Fluka) was added to 1 mL of each tea sample and heated to 180 °C in a microwave MARS XPRESS system (CEM Corp., Kamp-Lintfort, Germany). After treatment in the microwave oven, double-distilled water was added, leading to a final volume of 20 mL, which was passed through a 0.2 μm polytetrafluoroethylene filter prior to measurement. The limit of detection for copper was determined to be 0.2 μg/L.

EPR Measurement of Copper Complex. Tea extracts (1 g/50 mL H_2O, 100 °C, 10 min) were incubated with Cu(II) (300 μM) at pH 7.5 and recorded by a Bruker ESP300e EPR spectrometer at room temperature, using a TM_{110} resonator ER 4103 equipped with a quartz flat cell using the following parameters: center field, 3203.5 G; field range, 1507 G; microwave frequency, 9.796 GHz; microwave power, 20 mW; modulation frequency, 100 kHz; modulation amplitude, 10.8 G; receiver gain, 1 × 10^4; time constant, 81.9 ms; conversion time, 81.9 ms; 1024 data points; 5 scans accumulated.

DOI: 10.1021/acs.jafc.5b02792
J. Agric. Food Chem. 2015, 63, 8519−8526

Table 2. Most Abundant Fatty Acids with a Peak Intensity of $\geq 10^6$ in Oolong Tea Infusion As Identified by Means of LC-MS in a Range of m/z 100−1000

fatty acid	rt (min)	$[M - H]^-$ (m/z)	error (ppm)	fragments (m/z)
nonanedioic acid ($C_9H_{16}O_4$)	25.6	187.0971	2	125.0972 ($C_8H_{13}O$; octanone)
hydroxy dodecenoic acid ($C_{12}H_{22}O_3$)	30.3	213.1493	1	195.1394 ($C_{12}H_{19}O_2$; $-H_2O$; dodecadienoic acid), 183.1396 ($C_{11}H_{19}O_2$; undecenoic acid)
dihydroxy palmitic acid ($C_{16}H_{32}O_4$)	30.3	287.2224	1	187.1345 ($C_{10}H_{19}O_3$; hydroxydecanoic acid)
dihydroxyoctadecenoic acid ($C_{18}H_{34}O_4$)	33.9	313.2378	1	269.2156 ($C_{16}H_{29}O_3$; hydroxyhexadecenoic acid)
trihydroxystearic acid ($C_{18}H_{36}O_5$)	29.4	331.2485	1	313.2407 ($C_{18}H_{33}O_4$; $-H_2O$), 287.0204 ($C_{17}H_{35}O_3$; $-CO_2$)
trihydroxyoctadecenoic acid ($C_{18}H_{34}O_5$)	29.7	329.2329	1	311.2250 ($C_{18}H_{31}O_4$; $-H_2O$), 171.1032 ($C_9H_{15}O_3$; hydroxynonenoic acid), 229.1454 ($C_{12}H_{21}O_4$; dodecanedioic acid)

Data Processing. The statistical analysis program XCMS online[19] was applied to identify (i) the fatty acid profile in the tea samples by comparing tea infusions with the water blank, (ii) the difference with regard to fatty acids between green and oolong teas, and (iii) the differences of fatty acid patterns between untreated and copper-treated tea samples. Prior to data processing, the raw data files were converted to the mzXML format using MSConvert.[20] The centWave algorithm was applied for highly sensitive feature detection.[21] A maximally tolerated m/z deviation in consecutive runs of 2.5 ppm and a peak width range of 10−90 s were chosen for feature detection. Retention time correction was performed with the OBI-Warp method.[22] Chromatographic alignment of the mass spectrometry data was defined by (i) a minimum fraction of samples of 0.5 in at least one of the sample groups, (ii) a 5 s bandwidth of the Kernel smoother, and (iii) a m/z 0.015 width of overlapping m/z slices. To minimize the false discovery rate for peak annotations of isotopes and adducts, the parts per million error and the m/z absolute error were set to 5 and 0.015, respectively. The METLIN metabolomics database[23,24] was consulted for structural identification of $[M - H]^-$ adducts. The tolerance for this database search was set to 5 ppm.

Statistical Analysis. All experiments were performed three to four times independently with two technical replicates each. Principal component analysis (PCA) was performed to assess any effects of copper on the fatty acid profile. For identifying the fatty acid profiles, the copper-induced changes in the tea samples, and the differences between tea samples in fatty acid profiles, the unpaired Welch t test was applied. A difference was considered significant when the p value was ≤ 0.01. The signal intensity was $\geq 10^5$ or $\geq 10^6$, as indicated in the table titles and figure captions, and at least 2-fold changes were detected. Differences in copper concentrations between the oolong and green teas were determined by Kruskal−Wallis one-way ANOVA on Ranks, where a p value of <0.05 was considered significant. Differences between non- and copper-treated tea samples with regard to 13-hydroperoxy-9*Z*,11*E*-octadecadienoic acid were calculated by one-way ANOVA, where also a p value of <0.05 was considered significant.

RESULTS AND DISCUSSION

Fatty Acid Profile in Green and Oolong Teas. Tables 1 and 2 show the most abundant fatty acids in the green and oolong tea samples, as identified by high-resolution MS, and MS/MS fragmentation. A total of 13 fatty acids were identified in the green tea, but only 6 fatty acids with a peak intensity of at least 10^6 au were detected in the oolong tea sample. In both the green and oolong tea samples, the vast majority of the fatty acids was already oxidized and appeared as hydroxy or hydroperoxy derivatives of medium- and long-chain saturated and unsaturated fatty acids. By comparing the fatty acid profiles of the green and oolong tea samples, five oxidized fatty acids were identified as having a >2-fold higher abundance in green tea than in oolong tea, although more oxidized fatty acids were expected in the semifermented oolong tea. The most pronounced difference between the green and oolong teas with regard to the oxidized fatty acids was obtained for hydroperoxyoctadecatrienoic acid and hydroxyoctadecatrienoic acid. An at least 2-fold higher abundance of hydroxyundecenoic acid (2.3-fold), hydroxynonenoic acid (4.4-fold), hydroperoxyoctadecadienoic acid (2.3-fold), trihydroxyoctadecadienoic acid (3.4-fold), hydroperoxyoctadecatrienoic acid (16-fold), and hydroxyoctadecatrienoic acid (38-fold) could be shown in the green tea compared to the oolong tea sample.

Copper Content in Green and Oolong Teas. To explain the higher abundance of oxidized fatty acids in nonfermented green tea, which was not subjected to oxidation after harvest, the amount of copper was quantitated. The total copper concentration represents the maximum concentration of copper, which might, however, be partially bound to traces of tea proteins or amino acids, thereby restricting its participation in redox reactions. It could be shown that copper bound to proteins or amino acids led to a reduced formation of reactive oxygen species compared to free copper.[25] In the current study, the total copper concentrations in the green tea and oolong tea infusions were determined by atomic absorption spectroscopy to be 1.52 ± 0.38 and 0.25 ± 0.05 μM, respectively (Figure 1).

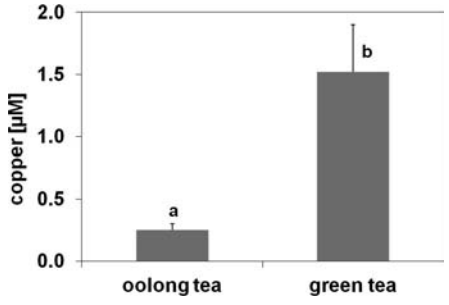

Figure 1. Concentration (μM) of copper in green and oolong tea infusions. Data are expressed as the mean ± SD (n = 4). Different letters indicate statistically significant differences between the tea samples ($p < 0.05$).

Thus, the approximately 6-fold higher copper concentration in the green tea compared to the oolong tea ($p < 0.05$) may be an explanation for the higher abundance of oxidized fatty acids in this sample. Gallaher et al.[26] reported a relatively narrow concentration range of 0.79 ± 0.05 μM copper in various teas, whereas other researchers quantified larger differences among different tea varieties. For example, Wong et al.[11] quantitated a concentration of 0.96 ± 0.17 μM copper in a 1% aqueous

DOI: 10.1021/acs.jafc.5b02792
J. Agric. Food Chem. 2015, 63, 8519−8526

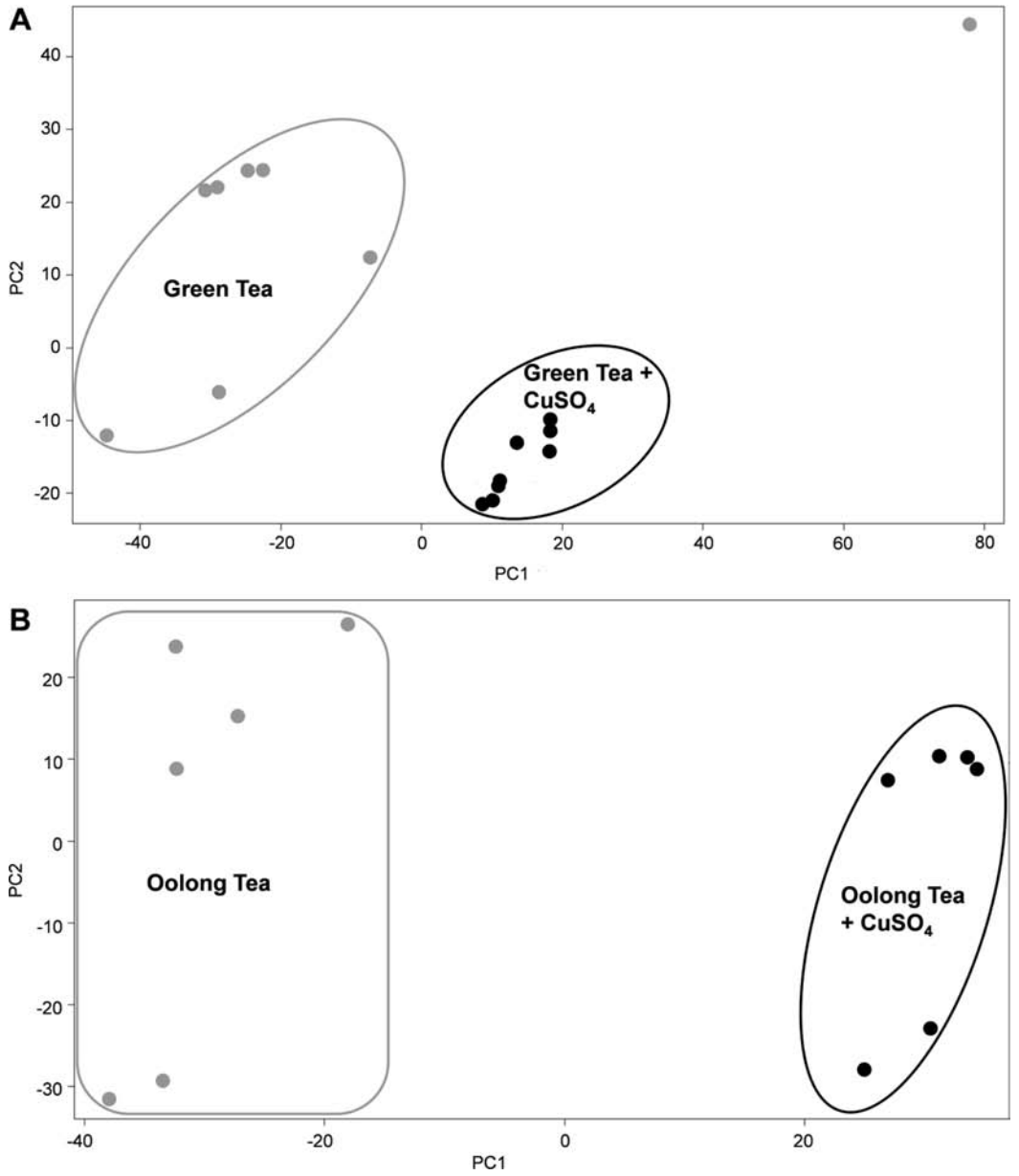

Figure 2. PCA scores plot obtained from green tea (A) and oolong tea (B) without or with addition of 300 μM $CuSO_4$.

Table 3. A More than 2-Fold Higher or Lower Abundance ($p \leq 0.01$) of Oxidized Fatty Acids with a Peak Intensity of $\geq 10^5$ in Green Tea Compared to Green Tea Infusion Supplemented with 300 μM $CuSO_4$ As Identified by Means of LC-MS in a Range of m/z 100−1000

fatty acid	rt (min)	$[M-H]^-$ (m/z)	error (ppm)	fragments (m/z)	effect of Cu^{2+} addition on the relative abundance of fatty acid
isopropylhexanoic acid ($C_9H_{18}O_2$)	35.0	157.1232	1	113.0612 ($C_6H_9O_2$; hexenoic acid)	↑ 2.2
methyltetradecanedioic acid ($C_{15}H_{28}O_4$)	34.9	271.1913	1	253.1814 ($C_{15}H_{25}O_3$; $-H_2O$), 209.1912 ($C_{14}H_{25}O$)	↓ 5.8
octadecatetraenoic acid ($C_{18}H_{28}O_2$)	36.6	275.2015	1	231.2118 ($C_{17}H_{27}$; $-CO_2$), 177.1647 ($C_{13}H_{21}$)	↓ 22
hydroxyoctadecatrienoic acid ($C_{18}H_{30}O_3$)	36.8	293.2118	2	275.2022 ($C_{18}H_{27}O_2$; $-H_2O$; octadecatetraenoic acid), 235.1708 ($C_{15}H_{23}O_2$)	↓ 3.3
methylhydroperoxy bisepidioxy eicosadienoate ($C_{21}H_{34}O_8$)	31.8	413.2178	0	221.1549 ($C_{14}H_{21}O_2$; dodecatrienyl acetate)	↑ 3.0

extract green tea, but only 0.46 ± 0.39 μM in a similar extract of oolong tea. Similarly, Xie et al.[12] also determined copper contents of 1.14 ± 0.38 and 0.49 ± 0.04 μM, respectively, in 2% aqueous extracts of green and oolong teas. Thus, the higher concentration of copper in the green tea sample compared to the oolong tea sample of the present work was not unexpected. As reported previously, the concentration of copper in a tea infusion was shown to be >8 times higher than the

DOI: 10.1021/acs.jafc.5b02792
J. Agric. Food Chem. 2015, 63, 8519−8526

Table 4. A More than 2-Fold Higher or Lower Abundance ($p \leq 0.01$) of Oxidized Fatty Acids with a Peak Intensity of $\geq 10^5$ in Oolong Tea Compared to Oolong Tea Infusion Supplemented with 300 μM $CuSO_4$ As Identified by Means of LC-MS in a Range of m/z 100−1000

fatty acid	rt (min)	$[M-H]^-$ (m/z)	error (ppm)	fragments (m/z)	effect of Cu^{2+} addition on the relative abundance of fatty acid (x-fold change)
hydroxynonanoic acid ($C_9H_{18}O_3$)	31.0	173.1181	1		↑ 12
hydroxydecenoic acid ($C_{10}H_{18}O_3$)	31.6	185.1180	2	167.1079 ($C_{10}H_{15}O_2$; $-H_2O$), 115.0400 ($C_5H_7O_3$)	↑ 7.3
hydroxyundecenoic acid ($C_{11}H_{20}O_3$)	28.7	199.1335	2	155.1079 ($C_9H_{15}O_2$; nonenoic acid)	↓ 3.5
undecenoic acid ($C_{11}H_{20}O_2$)	30.0	183.1387	2	139.1128 ($C_9H_{15}O$)	↓ 6.4
dodecadienoic acid ($C_{12}H_{20}O_2$)	34.7	195.1389	1		↓ 4.3
methyldodecanedioic acid ($C_{13}H_{24}O_4$)	32.1	243.1599	1	225.1499 ($C_{13}H_{21}O_3$; $-H_2O$), 163.0406 ($C_9H_7O_3$)	↓ 11
hydroxyoctadecadienoic acid ($C_{18}H_{32}O_3$)	38.3	295.2276	0	277.2186 ($C_{18}H_{29}O_2$; $-H_2O$), 230.9827	↓ 49
trihydroxyoctadecenoic acid ($C_{18}H_{34}O_5$)	29.7	329.2329	1	311.2245 ($C_{18}H_{31}O_4$; $-H_2O$), 171.1021 ($C_9H_{15}O_3$; hydroxynonenoic acid), 229.1444 ($C_{12}H_{21}O_4$; dodecanedioic acid)	↓ 15
trihydroxyoctadecadienoic acid ($C_{18}H_{32}O_5$)	28.9	327.2172	2	309.2099 ($C_{18}H_{29}O_4$; $-H_2O$), 171.1033 ($C_9H_{15}O_3$; oxononanoic acid)	↓ 3.7
hydroperoxyoctadecadienoic acid ($C_{18}H_{32}O_4$)	35.4	311.2225	1	293.2128 ($C_{18}H_{29}O_3$; $-H_2O$; epoxyoctadecadienoic acid), 171.1028 ($C_9H_{15}O_3$; hydroxynonenoic acid)	↓ 2.2
hydroperoxyhydroxy octadecatrienoic acid ($C_{18}H_{30}O_5$)	29.2	325.2015	1		↓ 2.4
hydroperoxydihydroxyoctadecenoic acid ($C_{18}H_{34}O_6$)	29.2	345.2275	2	171.1025 ($C_9H_{15}O_3$; hydroxynonenoic acid), ($C_{12}H_{19}O_4$; dioxododecanoic acid)	↓ 5.6

concentration of iron.[27] Other factors may also influence the copper contents of tea infusions. Soil pH influences the uptake of trace metals by tea plants,[28] and elements including copper are more readily taken up from acidic soils.[10,28]

Effect of Copper Addition on the Fatty Acid Profiles in Green and Oolong Tea Samples. In addition to copper in tea infusions, copper in foods consumed together with tea might also affect the profiles of fatty acids and oxidized fatty acids in tea infusions. For example, 28.3 g of beef liver contains 4.13 mg of copper.[29] If this amount is consumed together with 250 mL of tea, a total amount of approximately 16 mg (about 260 μM) of copper would result in the stomach. Thus, to model the effect of copper from other food or nonfood sources on the fatty acid profiles of green and oolong teas, 300 μM $CuSO_4$ was added to freshly prepared tea infusions. It was also aimed to simulate a copper enrichment occurring, for example, as a result of the use of copper-containing pesticides, fertilizers, or equipment during tea production.[10,13] PCA was performed to determine any effects of copper on the fatty acid profile. Figure 2 demonstrates a distinct difference between copper-enriched tea and tea without copper addition. By applying nontargeted profiling, at least 2-fold changes in the abundance of five fatty acids with a peak intensity of a minimum of 10^5 au were caused by the addition of copper to the green tea sample (Table 3). Compared to the untreated sample, copper supplementation of the green tea resulted in significant decreases of methyl tetradecadioic acid (5.8-fold decrease), octadecatetraenoic acid (22-fold decrease), and hydroxyoctadecatrienoic acid (3.3-fold decrease), whereas methyl hydroperoxy bis-epidioxy eicosadienoate (3.0-fold increase) and isopropylhexanoic acid (2.2-fold increase) were increased. In the oolong tea sample, 12 fatty acids with a peak intensity of $\geq 10^5$ au showed at least a 2-fold change as a result of copper addition (Table 4). Most of these were oxidized fatty acids such as hydroxy- and hydroperoxy derivatives. Ten of these were significantly reduced, and only hydroxynonanoic acid and hydroxydecenoic acid were increased. The types of fatty acids affected by the addition of copper to oolong tea were comparable to those in copper-supplemented green tea. The long-chain unsaturated fatty acids were decreased after the addition of copper to oolong tea, the most pronounced effect being observed with hydroxyoctadecadienoic acid (49-fold decrease). Overall, the addition of copper resulted in more pronounced changes in the fatty acid profile in the oolong tea than in green tea. The different susceptibility to oxidation of the fatty acids in green and oolong tea as a result of the copper addition was also observed by quantitative analysis of 13-hydroperoxy-9Z,11E-octadecadienoic acid (Figure 3). Whereas

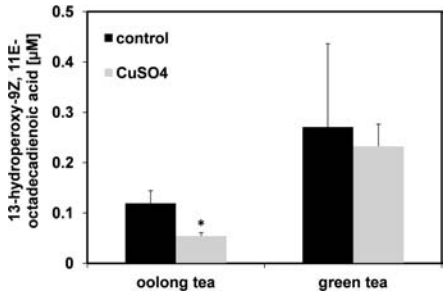

Figure 3. Concentration of 13-hydroperoxy-9Z,11E-octadecadienoic acid in green and oolong tea infusions with or without addition of 300 μM $CuSO_4$. Data are expressed as the mean ± SD (n = 4). The asterisk indicates statistically significant difference versus control (p < 0.05).

copper addition did not induce significant changes in the concentration of 13-hydroperoxy-9Z,11E-octadecadienoic acid in green tea, it resulted in a clear reduction from 0.12 ± 0.02 to 0.05 ± 0.01 μM in the oolong tea. This result suggests that green tea, but not oolong tea, contains substances that might interact with copper to inhibit the copper-induced degradation of the oxidized fatty acids.

Effect of Addition of Copper on the Concentration of Epigallocatechin-3-gallate in Green and Oolong Tea Samples. To investigate a possible cause for the different susceptibilities of the green and oolong tea samples to copper-

DOI: 10.1021/acs.jafc.5b02792
J. Agric. Food Chem. 2015, 63, 8519−8526

induced fatty acid oxidation, changes in the abundance of epigallocatechin-3-gallate, the major polyphenol in untreated tea leaves, were also investigated for the green and oolong tea samples in the presence and absence of 300 μM $CuSO_4$. The green tea polyphenols, such as epicatechin, epicatechin-3-gallate, epigallocatechin, and epigallocatechin-3-gallate, constitute 25−35% of the dry weight of green tea leaves[30−33] and represent approximately 50 mg/g tea infusion,[34] whereas in black tea, the more highly condensed thearubigin and theaflavin represent the main polyphenolic compounds.[35] In the current study, extracted ion chromatograms for m/z 457.0765−457.0780, representing epigallocatechin-3-gallate, are illustrated in Figure 4. Epigallocatechin-3-gallate was approximately 2-fold

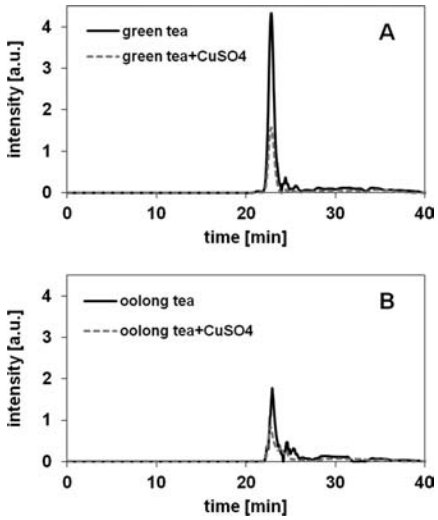

Figure 4. Extracted ion chromatogram of epigallocatechin-3-gallate in green (A) and oolong tea (B) samples in the presence or absence of 300 μM $CuSO_4$ at a mass range of m/z 457.0765−457.0780. Representative chromatogram of four experimental and two technical replicates.

higher in the green tea sample than in the oolong tea sample and is, thus, a candidate for mitigating the copper-induced degradation of oxidized fatty acids in green tea.

The antioxidative activity of tea flavanols has been demonstrated in several in vitro and in vivo studies.[36−38] Higdon and Frei[39] reported a 2−15% increase in plasma antioxidant activity after consumption of tea. In vitro experiments revealed that epigallocatechin-3-gallate is a more effective radical scavenger than other major green tea polyphenols.[38] It has been proposed that catechin polyphenols exert their antioxidant activities by chelating redox-active transition metals, such as copper, thereby preventing the formation of free radical and nonradical oxidation products.[40,41] Mira et al.[41] showed that catechins chelate Cu(II) ions at the *o*-catechol group at pH 7.4. Similar results were obtained by Yoshioka et al.,[42] who confirmed the copper-coordinating activity of catechins by showing that 125 μM epigallocatechin-3-gallate formed a complex with 63 μM Cu(II) ions in phosphate buffer. Furthermore, the green tea polyphenols gallic acid and epigallocatechin-3-gallate tend to form polymeric complexes with Cu(II) at acidic and neutral pH values and precipitate from pure solutions.[43] However, in the present study, the concentration of epigallocatechin-3-gallate was not only substantially decreased by a factor of 2 in the green tea sample (from 252 ± 7.97 to 128 ± 4.00 μM) but also decreased in oolong tea sample (from 129 ± 4.07 to 59.3 ± 1.87 μM) after the addition of 300 μM $CuSO_4$, suggesting that epigallocatechin-3-gallate was not the predominant "antioxidant" source in the green tea sample.

EPR Measurements of Green and Oolong Teas with Cu(II) at Neutral pH. In the present study, the LC-MS experiments did not reveal any copper-derived compounds in the copper-treated teas, possibly because of instability of the complexes during the ionization process in the mass spectrometer. However, EPR measurements by Goodman et al.[44] indicated the formation of a number of Cu(II) complexes in copper-supplemented teas at neutral and weakly acidic pH values. Goodman et al.[44] proposed involvement of tea-containing amino acids, such as theanine, because the EPR results were inconsistent with the formation of soluble Cu(II) chelates of epigallocatechin-3-gallate. Goodman et al.[44] also observed a substantial reduction in the EPR-detectable Cu(II) in tea solutions at these pH values, a result that is consistent with the formation of polymeric species or precipitates as observed in reactions of Cu(II) with solutions of the green tea polyphenols gallic acid and epigallocatechin-3-gallate.[43,45] In the current study, the EPR spectra of all tea extracts were dominated by a six-line signal from solvated Mn(II) (not shown), which has been discussed previously,[44,46] and was subtracted from all spectra to record the Cu(II) signals resulting from the addition of 300 μM $CuSO_4$ (Figure 5). Both

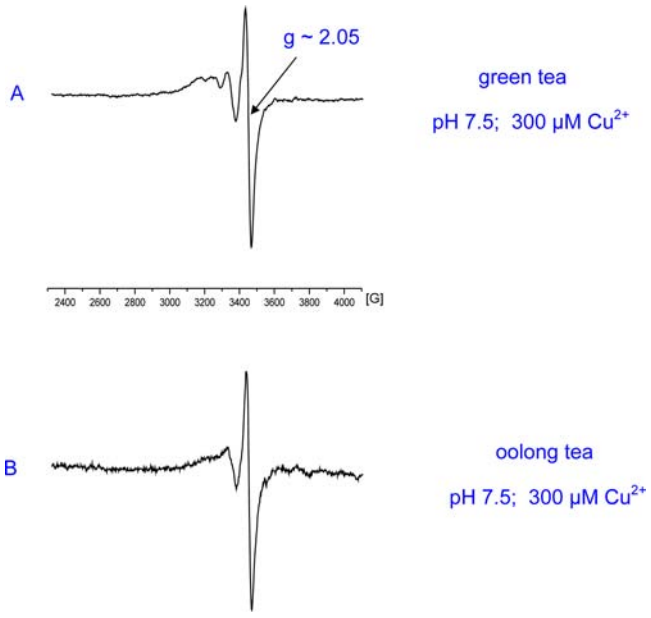

Figure 5. EPR measurements of copper complexes formed at pH 7.5 by adding 300 μM $CuSO_4$ to green (A) or oolong (B) tea infusions.

tea samples showed EPR signals at pH 7.5 that are similar to those reported previously for green and black teas (a_{Cu} = 70 G; g = 2.138).[44] The line width variation in these spectra is the result of incomplete averaging of the anisotropy through molecular motion and is a normal phenomenon in the EPR solution spectra of Cu(II) complexes. In addition, the better resolution of the spectrum from the green tea sample compared to that from the oolong tea is indicative of more rapid molecular motion and, hence, a lower molecular mass complex. Because the EPR signals of the individual Cu complexes could be obtained only after a series of spectral subtractions, the

DOI: 10.1021/acs.jafc.5b02792
J. Agric. Food Chem. 2015, 63, 8519−8526

reported values for the spectral parameters must be considered to be approximate, because unequivocal assignment to a specific complex was not possible. However, the parameters obtained from the green tea spectrum are consistent with Cu(II) bis(amino acid) complexes[47] and the bis complex of Cu(II) with theanine showing solution spectral parameters of a_{Cu} = 70 G and g = 2.135.[44] Polyphenols, on the other hand, tend to form EPR-silent complexes and precipitate in solutions around neutral pH, and although a spectrum was observed with Cu(II)/epigallocatechin-3-gallate solutions,[43] it has greater line width anisotropy than that observed with the green tea solution. Therefore, the spectrum in Figure 5A does not correspond to a bis complex of Cu(II) with epigallocatechin-3-gallate, although the involvement of catechins in mixed complexes with amino acids cannot be discounted. This tentative assignment to mixed complexes is consistent with the differences between the Cu(II) spectra from the green and oolong teas (Figure 5), because of the overall higher molecular mass of the polyphenolic components in fermented teas.

Thus, green tea polyphenols and other low-molecular-weight compounds, such as amino acids, might help to protect the oxidized fatty acids from copper-induced degradation (Figure 6). A redox reaction of oxidized fatty acids or polyphenols with

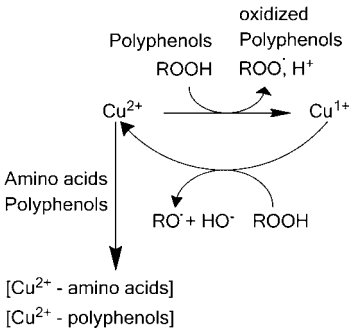

Figure 6. Proposed reaction explaining the fate of oxidized fatty acids in the presence of cupric sulfate in non- and semifermented teas.

Cu(II) resulting in the formation of Cu(I) and peroxy radicals[17,48,49] is illustrated in Figure 6. Reoxidation of Cu(I) by hydroperoxides produces alkoxy radicals, which might further decompose into aldehydes.[50] Formation of polymeric Cu(II) species by reaction with green tea polyphenols[43,45] or amino acids[47] could remove Cu(II) from the reaction cycle and, therefore, inhibit the degradation of oxidized fatty acids. However, the higher copper concentration of the green tea sample and the higher abundance of fatty acid oxidation products prior to copper addition might have contributed to the less pronounced effect of copper administration compared to oolong tea.

Overall, the present study suggests that low concentrations of copper, which occur naturally in teas, might contribute to the oxidation of tea fatty acids, whereas higher concentrations of copper may lead to degradation of these oxidized fatty acids. Future mechanistic studies should verify whether copper-induced decomposition of oxidized fatty acids might be hampered by green tea polyphenols and amino acids. Because fatty acids are among the precursors of aroma molecules, such reactions may contribute to the aroma characteristics of tea infusions.

AUTHOR INFORMATION

Corresponding Author

*(M.P.) Mail: Althanstraße 14, 1090 Vienna, Austria. Phone: +43 1 4277 70621. Fax: +43 1 4277 9706. E-mail: marc.pignitter@univie.ac.at.

Notes

The authors declare no competing financial interest.

ACKNOWLEDGMENTS

We thank Prof. Dr. Peter Schieberle, Head of the German Research Centre for Food Chemistry in Freising, Germany, for carefully reading the manuscript and providing constructive comments. We also gratefully acknowledge Prof. Dr. Galanski for recording the NMR spectra.

REFERENCES

(1) Harbowy, M. E.; Balentine, D. A. Tea chemistry. *Crit. Rev. Plant Sci.* **1997**, *16*, 415−480.
(2) Wang, H.; You, X.; Chen, Z. The chemistry of tea volatiles. In *Tea − Bioactivity and Therapeutic Potential*; Zhen, Y., Chen, Z., Cheng, S., Chen, M., Eds.; Taylor & Francis: London, UK, 2002; pp 89−120.
(3) Wright, A. J.; Fishwick, M. J. Lipid degeneration during manufacture of black tea. *Phytochemistry* **1979**, *18*, 1511−1513.
(4) Mahanta, P. K.; Hazarika, M.; Takeo, T. Flavor volatiles and lipids in various components of tea shoots *Camellia sinensis*, (L.), O. Kuntze. *J. Sci. Food Agric.* **1985**, *36*, 1130−1132.
(5) Sanderson, G. W.; Grahamm, H. N. Formation of black tea aroma. *J. Agric. Food Chem.* **1973**, *21*, 576−585.
(6) Robinson, J. M.; Owuor, P. O. Tea aroma. In *Tea Cultivation to Consumption*; Willson, K. C., Clifford, M. N., Eds.; Chapman and Hall: London, UK, 1992; 18, pp 603−647.
(7) Mahanta, P. K.; Tamuli, P.; Bhuyan, L. P. Changes of fatty-acid contents, lipoxygenase activities, and volatiles during black tea manufacture. *J. Agric. Food Chem.* **1993**, *41*, 1677−1683.
(8) Yoshida, Y.; Niki, E. Oxidation of methyl linoleate in aqueous dispersions induced by copper and iron. *Arch. Biochem. Biophys.* **1992**, *295*, 107−114.
(9) Karak, T.; Bhagat, R. M. Trace elements in tea leaves, made tea and tea infusion: a review. *Food Res. Int.* **2010**, *43*, 2234−2252.
(10) Jin, C. W.; Du, S. T.; Zhang, K.; Lin, X. Y. Factors determining copper concentration in tea leaves produced at Yuyao County, China. *Food Chem. Toxicol.* **2008**, *46*, 2054−2061.
(11) Wong, M. H.; Zhang, Z. Q.; Wong, J. W. C.; Lan, C. Y. Trace metal contents (Al, Cu and Zn) of tea: tea and soil from two tea plantations, and tea products from different provinces of China. *Environ. Geochem. Health* **1998**, *20*, 87−94.
(12) Xie, M.; von Bohlen, A.; Klockenkamper, R.; Jian, X.; Gunther, K. Multielement analysis of Chinese tea (*Camellia sinensis*) by total-reflection X-ray fluorescence. *Z. Lebensm. Unters. Forsch* **1998**, *207*, 31−38.
(13) Saha, D.; Mandal, S.; Saha, A. Copper induced oxidative stress in tea (*Camellia sinensis*) leaves. *J. Environ. Biol.* **2012**, *33*, 861−866.
(14) Martin, L. C. *Tea: The Drink That Changed the World*, 1st ed.; Tuttle Publishing: North Clarendon, VT, USA, 2007.
(15) Levison, B. S.; Zhang, R. L.; Wang, Z. N.; Fu, X. M.; DiDonato, J. A.; Hazen, S. L. Quantification of fatty acid oxidation products using online high-performance liquid chromatography tandem mass spectrometry. *Free Radical Biol. Med.* **2013**, *59*, 2−13.
(16) Schieberle, P.; Tsoukalas, B.; Grosch, W. Decomposition of linoleic-acid hydroperoxides by radicals. 1. Structures of products of methyl 13-hydroperoxy-cis,trans-9,11-octadecadienoate. *Z. Lebensm.-Unters. Forsch.* **1979**, *168*, 448−456.
(17) Schieberle, P.; Grosch, W. Decomposition of linoleic-acid hydroperoxides. 2. Breakdown of methyl 13-hydroperoxy-cis-9-trans-11-octadecadienoate by radicals or copper-II ions. *Z. Lebensm.-Unters. Forsch.* **1981**, *173*, 192−198.

DOI: 10.1021/acs.jafc.5b02792
J. Agric. Food Chem. 2015, 63, 8519−8526

(18) Otachi, E. O.; Korner, W.; Avenant-Oldewage, A.; Fellner-Frank, C.; Jirsa, F. Trace elements in sediments, blue spotted tilapia *Oreochromis leucostictus* (Trewavas, 1933) and its parasite *Contracaecum multipapillatum* from Lake Naivasha, Kenya, including a comprehensive health risk analysis. *Environ. Sci. Pollut. Res.* **2014**, *21*, 7339−7349.
(19) Tautenhahn, R.; Patti, G. J.; Rinehart, D.; Siuzdak, G. XCMS Online: a web-based platform to process untargeted metabolomic data. *Anal. Chem.* **2012**, *84*, 5035−5039.
(20) Chambers, M. C.; Maclean, B.; Burke, R.; Amodei, D.; Ruderman, D. L.; Neumann, S.; Gatto, L.; Fischer, B.; Pratt, B.; Egertson, J.; Hoff, K.; Kessner, D.; Tasman, N.; Shulman, N.; Frewen, B.; Baker, T. A.; Brusniak, M. Y.; Paulse, C.; Creasy, D.; Flashner, L.; Kani, K.; Moulding, C.; Seymour, S. L.; Nuwaysir, L. M.; Lefebvre, B.; Kuhlmann, F.; Roark, J.; Rainer, P.; Detlev, S.; Hemenway, T.; Huhmer, A.; Langridge, J.; Connolly, B.; Chadick, T.; Holly, K.; Eckels, J.; Deutsch, E. W.; Moritz, R. L.; Katz, J. E.; Agus, D. B.; MacCoss, M.; Tabb, D. L.; Mallick, P. A cross-platform toolkit for mass spectrometry and proteomics. *Nat. Biotechnol.* **2012**, *30*, 918−920.
(21) Tautenhahn, R.; Bottcher, C.; Neumann, S. Highly sensitive feature detection for high resolution LC/MS. *BMC Bioinf.* **2008**, *9*, 504.
(22) Prince, J. T.; Marcotte, E. M. Chromatographic alignment of ESI-LC-MS proteomics data sets by ordered bijective interpolated warping. *Anal. Chem.* **2006**, *78*, 6140−6152.
(23) Tautenhahn, R.; Cho, K.; Uritboonthai, W.; Zhu, Z.; Patti, G. J.; Siuzdak, G. An accelerated workflow for untargeted metabolomics using the METLIN database. *Nat. Biotechnol.* **2012**, *30*, 826−828.
(24) Smith, C. A.; O'Maille, G.; Want, E. J.; Qin, C.; Trauger, S. A.; Brandon, T. R.; Custodio, D. E.; Abagyan, R.; Siuzdak, G. METLIN: a metabolite mass spectral database. *Ther. Drug Monit.* **2005**, *27*, 747−751.
(25) Letelier, M. E.; Lepe, A. M.; Faundez, M.; Salazar, J.; Marin, R.; Aracena, P.; Speisky, H. Possible mechanisms underlying copper-induced damage in biological membranes leading to cellular toxicity. *Chem.-Biol. Interact.* **2005**, *151*, 71−82.
(26) Gallaher, R. N.; Gallaher, K.; Marshall, A. J.; Marshall, A. C. Mineral analysis of ten types of commercially available tea. *J. Food Compos. Anal.* **2006**, *19*, S53−S57.
(27) Street, R.; Szakova, J.; Drabek, O.; Mladkova, L. The status of micronutrients (Cu, Fe, Mn, Zn) in tea and tea infusions in selected samples imported to the Czech Republic. *Czech J. Food Sci.* **2006**, *24*, 62−71.
(28) Han, W. Y.; Zhao, F. J.; Shi, Y. Z.; Ma, L. F.; Ruan, J. Y. Scale and causes of lead contamination in Chinese tea. *Environ. Pollut.* **2006**, *139*, 125−132.
(29) U.S. Department of Agriculture, Agricultural Research Service. USDA National Nutrient Database for Standard Reference, release 26; Nutrient Data Laboratory Home Page, 2013; http://www.ars.usda.gov/ba/bhnrc/ndl.
(30) Abdel-Rahman, A.; Anyangwe, N.; Carlacci, L.; Casper, S.; Danam, R. P.; Enongene, E.; Erives, G.; Fabricant, D.; Gudi, R.; Hilmas, C. J.; Hines, F.; Howard, P.; Levy, D.; Lin, Y.; Moore, R. J.; Pfeiler, E.; Thurmond, T. S.; Turujman, S.; Walker, N. J. The safety and regulation of natural products used as foods and food ingredients. *Toxicol. Sci.* **2011**, *123*, 333−348.
(31) Balentine, D. A.; Wiseman, S. A.; Bouwens, L. C. M. The chemistry of tea flavonoids. *Crit. Rev. Food Sci. Nutr.* **1997**, *37*, 693−704.
(32) Graham, H. N. Green tea composition, consumption, and polyphenol chemistry. *Prev. Med.* **1992**, *21*, 334−350.
(33) Zaveri, N. T. Green tea and its polyphenolic catechins: medicinal uses in cancer and noncancer applications. *Life Sci.* **2006**, *78*, 2073−2080.
(34) Zuo, Y.; Chen, H.; Deng, Y. Simultaneous determination of catechins, caffeine and gallic acids in green, oolong, black and pu-erh teas using HPLC with a photodiode array detector. *Talanta* **2002**, *57*, 307−316.
(35) Mukhtar, H.; Ahmad, N. Tea polyphenols: prevention of cancer and optimizing health. *Am. J. Clin. Nutr.* **2000**, *71*, 1698s−1702s.
(36) Henning, S. A.; Niu, Y.; Liu, Y.; Lee, N. H.; Hara, Y.; Thames, G. D.; Minutti, R. R.; Carpenter, C. L.; Wang, H.; Heber, D. Bioavailability and antioxidant effect of epigallocatechin gallate administered in purified form versus as green tea extract in healthy individuals. *J. Nutr. Biochem.* **2005**, *16*, 610−616.
(37) Rietveld, A.; Wiseman, S. Antioxidant effects of tea: evidence from human clinical trials. *J. Nutr.* **2003**, *133*, 3285s−3292s.
(38) Nanjo, F.; Mori, M.; Goto, K.; Hara, Y. Radical scavenging activity of tea catechins and their related compounds. *Biosci., Biotechnol., Biochem.* **1999**, *63*, 1621−1623.
(39) Higdon, J. V.; Frei, B. Tea catechins and polyphenols: health effects, metabolism, and antioxidant functions. *Crit. Rev. Food Sci. Nutr.* **2003**, *43*, 89−143.
(40) van Acker, S. A. B. E.; van den Berg, D. J.; Tromp, M. N. J. L.; Griffioen, D. H.; van Bennekom, W. P.; van der Vijgh, W. J. F.; Bast, A. Structural aspects of antioxidant activity of flavonoids. *Free Radical Biol. Med.* **1996**, *20*, 331−342.
(41) Mira, L.; Fernandez, M. T.; Santos, M.; Rocha, R.; Florencio, M. H.; Jennings, K. R. Interactions of flavonoids with iron and copper ions: a mechanism for their antioxidant activity. *Free Radical Res.* **2002**, *36*, 1199−1208.
(42) Yoshioka, H.; Senba, Y.; Saito, K.; Kimura, T.; Hayakawa, F. Spin-trapping study on the hydroxyl radical formed from a tea catechin-Cu(II) system. *Biosci., Biotechnol., Biochem.* **2001**, *65*, 1697−1706.
(43) Pirker, K. F.; Baratto, M. C.; Basosi, R.; Goodman, B. A. Influence of pH on the speciation of copper(II) in reactions with the green tea polyphenols, epigallocatechin gallate and gallic acid. *J. Inorg. Biochem.* **2012**, *112*, 10−16.
(44) Goodman, B. A.; Severino, J. F.; Pirker, K. F. Reactions of green and black teas with Cu(II). *Food Funct.* **2012**, *3*, 399−409.
(45) Severino, J. F.; Goodman, B. A.; Reichenauer, T. G.; Pirker, K. F. Is there a redox reaction between Cu(II) and gallic acid? *Free Radical Res.* **2011**, *45*, 115−124.
(46) Pirker, K. F.; Severino, J. F.; Reichenauer, T. G.; Goodman, B. A. Free radical processes in green tea polyphenols (GTP) investigated by electron paramagnetic resonance (EPR) spectroscopy. *Biotechnol. Annu. Rev.* **2008**, *14*, 349−401.
(47) Goodman, B. A.; McPhail, D. B.; Powell, H. K. J. Electron spin resonance study of copper(II)−amino-acid complexes: evidence for cis and trans isomers and the structures of copper(II)−histidinate complexes in aqueous solution. *J. Chem. Soc., Dalton Trans.* **1981**, 822−827.
(48) Waters, W. A. Kinetics and mechanism of metal-catalyzed autoxidation. *J. Am. Oil Chem. Soc.* **1971**, *48*, 427−433.
(49) Marino, D. C.; Sabino, L. Z.; Armando, J., Jr.; De Andrade Ruggiero, A.; Moya, H. D. Analysis of the polyphenols content in medicinal plants based on the reduction of Cu(II)/bicinchoninic complexes. *J. Agric. Food Chem.* **2009**, *57*, 11061−11066.
(50) Patel, R. P.; Svistunenko, D.; Wilson, M. T.; Darley-Usmar, V. M. Reduction of Cu(II) by lipid hydroperoxides: implications for the copper-dependent oxidation of low-density lipoprotein. *Biochem. J.* **1997**, *322*, 425−433.

DOI: 10.1021/acs.jafc.5b02792
J. Agric. Food Chem. 2015, 63, 8519−8526

If NPs are not emitting any signal when mixed within food samples, it is difficult to find them. However, some NPs present in food samples, such as carbon dots, could emit fluorescent signals; hence, they can be extracted easily by using size exclusion chromatography. Carbon dots belong to a new class of quantum dot-like NPs that have wavelength-tunable emission properties, good photostability, and biocompatibility.[7−13] They are considered promising candidates for potential biomedical applications because they are safer and nontoxic both in vitro and in vivo.[7,8,14−17] The preparation, physicochemical properties, and applications of carbon dots in metal ion sensing, cell imaging, and photochemical catalysis have been intensively documented worldwide since the original report in 2004.[15,18−20] We have discovered that the fluorescence of Nescafé Original instant coffee originated from the presence of carbon dots,[6] which has motivated us to analyze the presence of carbon dots in other common beverages.

Carbon dots in beverages are being consumed constantly with no known toxicity. Thus, it is reasonable to believe that they may be safely utilized in many biological applications. In this study, the presence of carbon dots in common beverages including fermented beverages (kvass, pony malta, pilsner beer) and sport beverages (Vivant and Profit) were investigated. The extraction methods of carbon dots were established and their fluorescence properties were characterized. The representative carbon dots from kvass were systematically studied, including their surface chemistry, fluorescence lifetime, stability, and cytotoxicity. Their application as bioimaging agents in tumor cells and onion epidermal cells was also explored.

MATERIALS AND METHODS

Materials. Kvass was purchased from Harbin Tyurin in Dawes Food Co., Ltd. (Harbin, China). Pony malta was purchased from Cervecería Nacional Cn S.A. Co. (Guayaquil, Ecuador). Pilsner beer was also purchased from Cervecería Nacional Cn S.A. Co. Vivant Storm was purchased from Corporation Azende S.A. Co. (Guayaquil, Ecuador). Profit was purchased from Industrias Lácteas Toni S.A. (Guayaquil, Ecuador). Quinine sulfate was purchased from Aladdin Reagent Co. (Shanghai, China). Sephadex gel G-25 was purchased from Sigma-Aldrich Co. LLC (St. Louis, MO, USA). 3-(4,5-Dimethylthiazol-2-yl)-2,5-diphenyltetrazolium bromide (MTT) was purchased from Aladdin Reagents Co., Ltd. (Shanghai, China). Chinese hamster ovary (CHO) cell line was a gift kindly provided by the Institute of Biochemistry and Cell Biology, Shanghai Institute for Biological Sciences, Chinese Academy of Sciences. RPMI-1640 medium was purchased from HyClone Laboratories (Logan, UT, USA). Onion was purchased from the local market. Human tongue squamous carcinoma cell line Tca-8113 was purchased from the Cell Bank of Type Culture Collection of the Chinese Academy of Sciences (Shanghai, China).

Instrumentation. Absorption spectra were recorded at room temperature on a UV-2550 UV−vis spectrophotometer (Shimadzu, Japan). The fluorescence spectra were measured by an LS55 fluorescence spectrometer (PerkinElmer, USA). The steady-state fluorescence and time-resolved fluorescence decays were recorded using a FluoroMax-4 spectrofluorometer (Horiba Scientific Co., Albany, NY, USA) with a 376 nm laser as the excitation source. Transmission electron microscopy (TEM) measurements were performed on a model JEM-2000EX transmission electron microscope (JEOL, Akishima, Japan) for characterization of the shape and size of the carbon dots by deposition on 400-mesh C-coated Cu grids. X-ray photoelectron spectroscopy (XPS) spectra were used to characterize the chemical composition using an Escalab 250 Xi X-ray photoelectron spectrometer (Thermo Scientific, USA). The Fourier transform infrared spectroscopy (FTIR) spectra were measured by VECTOR 22 (Bruker, Germany) with the KBr pellet technique ranging from 500 to 4000 cm^{-1}. Fluorescent microscope imaging was conducted with a laser-based point scanning FV1000 confocal fluorescent microscope (Olympus, Japan), equipped with a 40× objective lens in *xy* mode with 600 × 600 pixel resolution; 405 and 488 nm lasers were used for excitation of carbon dots with emitted light collected between 425 and 475 nm and between 500 and 600 nm, respectively.

Carbon Dots Extraction. Beverages were concentrated and purified. For kvass, 150 mL of sample was added to a beaker and stirred at room temperature for 4 h to remove the gas. The kvass was then lyophilized. To further purify the kvass, 1 mL of the concentrated aqueous solution was added to a Sephadex G-25 column and the fluorescent fractions were collected. Other soluble fractions were retained on the column and eluted after the C-dots were collected. The resulting fluorescent carbon dot fractions (∼20 mL) were further lyophilized and stored in the dark at 4 °C for further characterization and use.

Fluorescence Quantum Yield and Lifetime Measurement. To calculate fluorescence quantum yield (Φ), eq 1 was used

$$\Phi_1 = \Phi_2 I_1 A_2 \eta_1^{\,2} / I_2 A_1 \eta_2^{\,2} \quad (1)$$

where I_1 and I_2 are fluorescence intensities of carbon dots and the quinine sulfate standard, respectively; A_1 and A_2 are optical densities of carbon dots and the standard, respectively; η_1 and η_2 are refractive indices of carbon dots and the standard, respectively. The standard quantum yield of Φ_2 was 0.54 for quinine sulfate at 360 nm in 0.1 M H_2SO_4 (refractive index: $\eta_2 = 1.2$), and carbon dots were dissolved in water (refractive index: $\eta_1 = 1.2$). Absorbance values of each solution in cuvette were maintained under 0.1 at the excitation wavelength to minimize reabsorption effects. Excitation and emission slit widths were both 4.5 nm for the fluorescence spectra measurement. The fluorescence lifetime (τ) of the C-dots was calculated using eq 2[7]

$$\tau = (A_1\tau_1 + A_2\tau_2 + A_3\tau_3)/(A_1 + A_2 + A_3) \quad (2)$$

where A_i is the fractional contributions of time-resolved decay lifetime of τ_i. The average fluorescence lifetime of carbon dots from kvass was calculated to be 10.59 ns.

pH Effect on Fluorescence Intensity. Various pH (pH 2−11) solutions were prepared by adding different amounts of 0.2 mmol/L NaOH solution to the Britton−Robinson buffer consisting of 0.04 M H_3BO_3, 0.04 M H_3PO_4, and 0.04 M CH_3COOH. To 2 mL of Britton−Robinson buffer solution was added 200 μL of carbon dots solution (1 mg/mL), and the fluorescence intensity was recorded with a fluorescence spectrometer using a 330 nm excitation wavelength and a 1200 nm/min scan rate. Measurements were done in triplicate.

Cytotoxicity Assay. CHO cells were seeded in 96-well plates at a density of 5 × 10^3 cells/well and cultured for 24 h in 10% serum containing DMEM (Sigma-Aldrich Co. LLC) supplemented with penicillin (100 units/mL) and streptomycin (100 μg/mL) in a humidified atmosphere with 5% CO_2 at 37 °C. After incubation with different concentrations (0, 0.31, 0.63, 1.25, 2.5, 5.0, 10.0, 20.0, and 40.0 mg/mL, $n = 3$) of carbon dots from kvass for 24 h, 20 μL of MTT (5 mg/mL) reagent was added to each cell well. After further incubation for 3 h, the cells were washed with PBS three times, and 100 μL of dimethyl sulfoxide (DMSO) was added. The optical density (OD) of the mixture was measured at 570 nm using a microplate reader. The cell viability was estimated according to eq 3

$$\text{cell viability (\%)} = (\text{OD}_{\text{treated}}/\text{OD}_{\text{control}}) \times 100\% \quad (3)$$

where $\text{OD}_{\text{control}}$ is measured in the absence of agent and $\text{OD}_{\text{treated}}$ is the intensity of carbon dots from kvass. The viability was expressed as the percentages of viable cells compared to the survival of a control group (untreated cells as controls of 100% viability).

In Vitro Tumor Cell Imaging. Human tongue squamous carcinoma (Tca)-8113 cells were cultured and maintained in DMEM containing 10% FBS, antibiotic−antimycotic solution L-glutamine (2 mmol/L), and nonessential amino acids (1%) in 5% CO_2 at 37 °C. After the cells were trypsinized and seeded in tissue culture plates at an initial cell density of 1 × 10^5 cells/well, they were

DOI: 10.1021/acs.jafc.5b04216
J. Agric. Food Chem. 2015, 63, 8527−8533

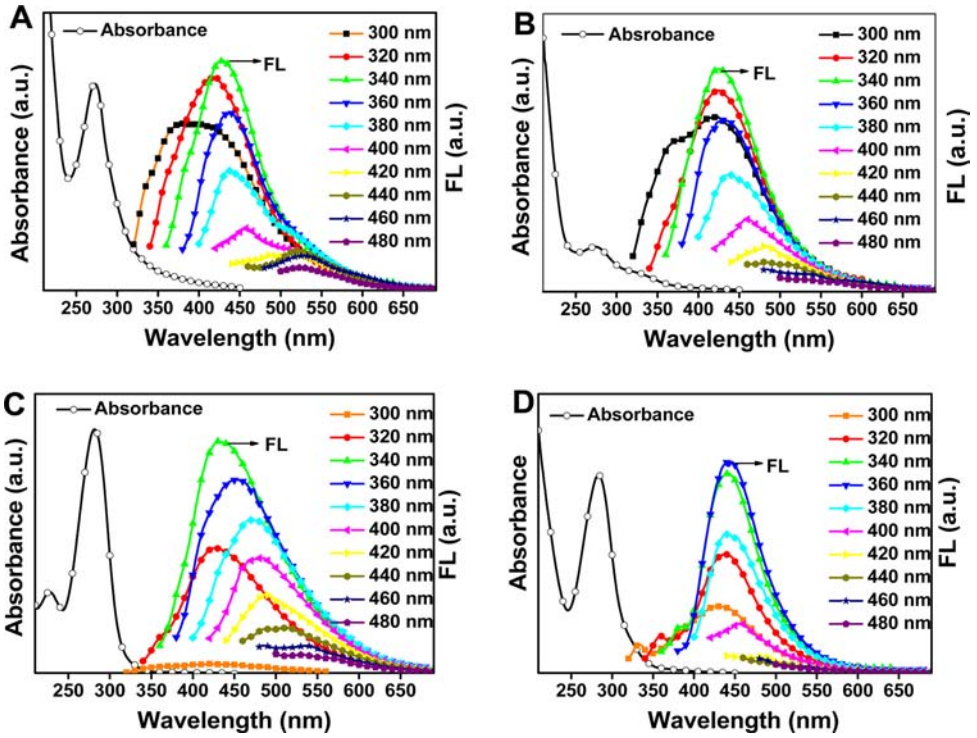

Figure 1. UV−vis absorption and fluorescence (FL) spectra of (A) pony malta, (B) pilsner beer, (C) Vivant, and (D) Profit.

treated with the carbon dots from kvass at a concentration of 10 mg/mL. After incubation at 37 °C for 24 h, the Tca-8113 cells were washed three times with fresh media and imaged with a laser confocal fluorescent microscope with excitation of 405 and 488 nm laser and emission of 425−475 and 500−600 nm for blue and green region imaging, respectively.

Onion Epidermal Cells Imaging. A small piece of the epidermal membrane of a fresh onion was laid flat on the surface of a slide, and 0.9% saline containing 40 mg/mL kvass carbon dots was added. The sample was then covered with a thin glass coverslip ensuring that there were no air bubbles. After 6 h, onion epidermal cells were imaged with a laser confocal fluorescent microscope with excitation of a 405 nm laser, and the collecting wavelengths were 425−475 nm for blue emission.

RESULTS AND DISCUSSION

Extraction of Carbon Dots and Their Fluorescent Properties. The beverages, such as fermented beverages (kvass, pony malta, pilsner beer) and sport beverages (Vivant Storm and Profit), are all common drinks. Carbon dots were extracted from all five beverages by using a size exclusion Sephadex G-25 column. The extraction of carbon dots from the five commercial beverages can be simply done by column chromatographic separation. Sephadex G-25 was used here because it was a well-established gel filtration medium prepared by cross-linking dextran with epichlorohydrin for desalting. The overall production yield of the carbon dots is about 2−5% w/w calculated from the beverages. Similar results were also reported as 2−3% w/w of carbon dots present in bread, jaggery, corn flakes, and biscuit.[2] The aqueous solution of carbon dots from the five beverages exhibited strong fluorescence under excitation of ultraviolet light at 365 nm. The UV−vis absorption and fluorescence spectra of the aqueous solution of carbon dots are shown in Figure 1. A strong absorption feature centered at 275 nm in the UV−vis absorption spectra was observed for all of the carbon dots derived from the four beverages, indicating the presence of aromatic π orbitals. When excited in the range of 300−480 nm, these carbon dots emit fluorescence around 430−450 nm. The emission peaks shift to longer wavelengths accompanied by a remarkable fluorescence intensity decrease. The bathochromic emission phenomenon is consistent with previous reports on carbon dots.[16] Their fluorescent properties are summarized in Table 1. The fluorescent quantum yields of C-dots from the five beverages are in the range of 1.48−11.9%. The morphology of carbon dots from pony malta, pilsner beer, Vivant Storm, and Profit was characterized using TEM by dropping a dilute aqueous solution of the carbon dots on a carbon-coated copper grid. The carbon dots are nearly spherical in shape and well dispersed, with average sizes of 23.5, 39.1, 2.8, and 17.5 nm for pony malta, pilsner beer, Vivant Storm, and Profit, respectively (Figure 2; Table 1). This indicates the presence of nanoparticles in the four beverages. An organic macromolecule that has absorbed a small fluorescence molecule might not be visible in the classic TEM without counterstaining, due to the low contrast of the light elements such as carbon and hydrogen.

Table 1. Fluorescent Properties of the Carbon Dots from Beverages

C-dots	av size (nm)	max ex (nm)	max em (nm)	fwhm (nm)	quantum yield (%)
pony malta	23.5	352	447	100	6.10
pilsner	39.1	329	414	101	1.48
Vivant Storm	2.8	326	399	107	1.90
Profit	17.5	352	447	80	11.90
kvass	5.0	328	411	106	2.22

Pony malta is a nonalcoholic malt beverage. Currently the drink is produced and marketed in several countries in South and Central America, including Colombia, Peru, Ecuador,

DOI: 10.1021/acs.jafc.5b04216
J. Agric. Food Chem. 2015, 63, 8527−8533

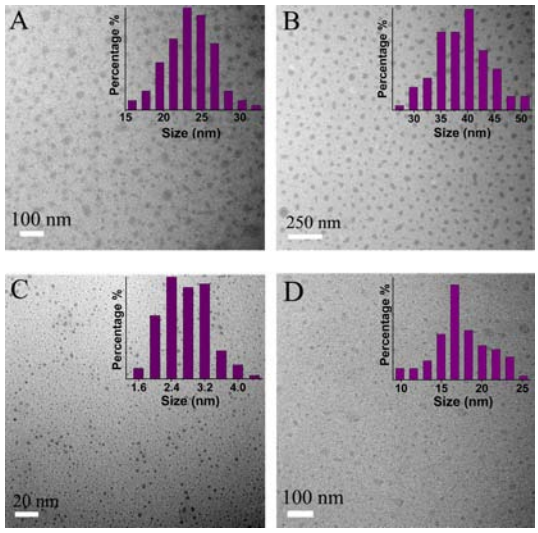

Figure 2. TEM images of (A) pony malta, (B) pilsner beer, (C) Vivant, and (D) Profit carbon dots. (Insets) Corresponding particle size histograms.

Panama, and Venezuela. The beverage is made from barley malt, sugar, fiber, protein, niacin, thiamin, riboflavin, and calcium. The origin of carbon dots from pony malta possibly is due to the heating of the starting materials, such as sugar, which has been reported to form carbon dots in food products.[2] Pilsner beer is an alcoholic beverage produced by the saccharification of starch and the subsequent fermentation of the resulting sugar. The basic ingredients of pilsner beer are water, malt, hops, and yeast. The preparation of beer is called brewing. Any starting materials involved in the heating process could produce the carbon dots. Sugar is a common ingredient in the other two beverages, Vivant Storm and Profit, as well. We believe the origin of carbon dots in all four beverages is due to the heating of sugar during the manufacturing process.

Characterization of Carbon Dots from Kvass. The carbon dots derived from kvass were selected as representative nanoparticles, and their properties were investigated thoroughly. Kvass is a fermented beverage made from black or regular rye bread and is classified as a nonalcoholic drink by Russian and Ukrainian standards, as the alcohol content from fermentation is typically <1.2%. Carbon dots have been found in bread, where the baking process involves heating of the starting materials.[2] Because carbon dots are highly water-soluble, they might be dissolved in the beverage kvass during the fermentation process. Therefore, the origin of carbon dots from kvass could be attributed to the bread. The kvass carbon dots were analyzed by UV−vis and fluorescence spectroscopy, respectively. Figure 3A shows the typical absorption and fluorescence emission spectra measured from the kvass carbon dots in aqueous solution. The absorption spectrum exhibits only one peak around 265 nm, which extends to 500 nm without noticeable fine structures. Similar to previous studies, the peak at 265 nm denotes $\pi-\pi^*$ transition of aromatic C═C bonds.[21] The fluorescence emission spectrum displays an emission maximum at 425 nm for excitation at 360 nm, and the emission wavelength and intensity show clear excitation wavelength dependency, similar to that of previously reported carbon dots.[22] This complex behavior might be associated with a variety of emitting centers present in the carbon dots suspension.[23] It clearly indicates the presence of carbon dots in kvass. The inset in Figure 3A shows the optical image of kvass carbon dots in aqueous solution irradiated by a 365 nm UV lamp, and the fluorescence was strong enough to be seen with the naked eye. A typical luminescence lifetime (τ) was also measured (Figure 3B), where a value of 10.59 ns was obtained. The decay of fluorescence emission was non-monoexponential for the kvass carbon dots suspension. The possible mechanism of fluorescence might be attributed to the radiative recombination of the energy-trapping sites on the carbon dots.[6,18] Using quinine bisulfate (QY = 0.54 in 0.1 M H_2SO_4) as reference, the QY of the kvass carbon dots in aqueous solution was determined to be 2.22%, comparable to previous results.[2]

The TEM image (Figure 4A) illustrates that the kvass carbon dots are spherical in shape and well dispersed, with an average size of 5.0 ± 0.7 nm, in good agreement with sizes of carbon dots observed previously.[6] The TEM result further confirmed

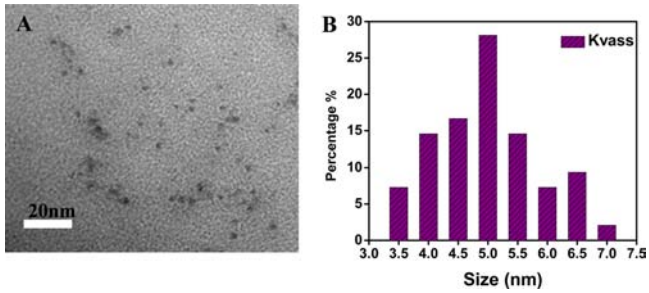

Figure 4. (A) Representative TEM image of kvass carbon dots and (B) particle size histogram.

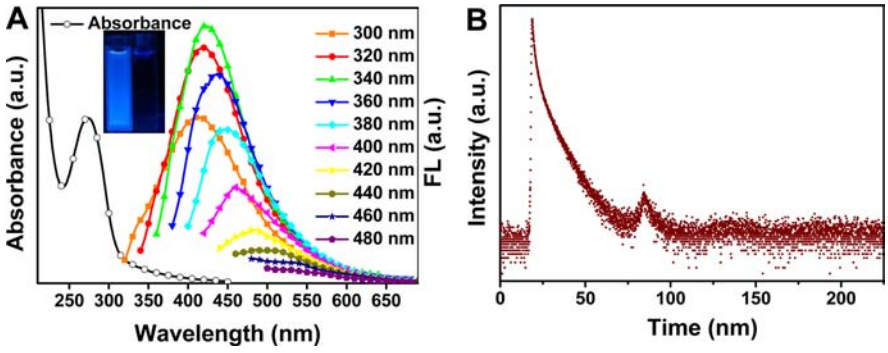

Figure 3. (A) UV−vis absorption and fluorescence (FL) spectra and (B) fluorescence decay curve of kvass carbon dots. (Inset) Photograph of the kvass carbon dot aqueous solution and water under the excitation of UV light.

DOI: 10.1021/acs.jafc.5b04216
J. Agric. Food Chem. 2015, 63, 8527−8533

the presence of carbon dots in the kvass beverage. The size distribution of the carbon dots was relatively narrow, with the majority falling within 3.5−7.0 nm based on the statistical analysis of 100 particles (Figure 4B). The ultrasmall size of the kvass carbon dots may facilitate their entry into live cells for bioimaging applications.

XPS elemental analysis revealed the composition of the kvass carbon dots to be C 83.17%, O 13.83%, and N 3.00%, thus indicating these dots are carbon-rich nanodots. Figure 5A

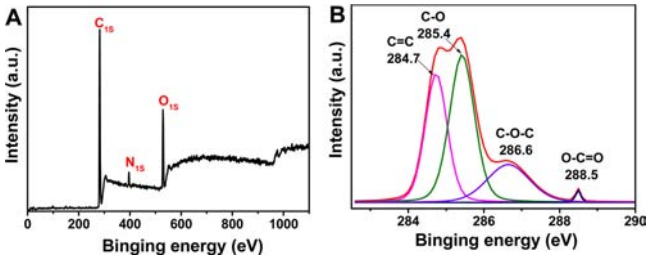

Figure 5. (A) XPS spectrum and (B) high-resolution XPS spectra of C 1s of kvass carbon dots.

shows the XPS spectrum of kvass carbon dots, in which three peaks were observed at 285, 532, and 399.4 eV, corresponding to carbon, oxygen, and nitrogen, respectively. Figure 5B shows the high-resolution C 1s peak of the carbon dots, which could be fitted into four peaks at 284.7, 285.4, 286.6, and 288.5 eV. They were attributed to C═C, C—O, C—O—C, and O—C═O bonds, respectively.[21] These data show that the kvass carbon dots are mainly composed of graphitic carbon (sp2) and carbon defects (sp3), and abundant hydroxy and carbonyl/carboxylate groups are found at their surfaces.[24]

FTIR spectroscopy was used to gain further structural insights about the kvass carbon dots. As shown in Figure 6, a

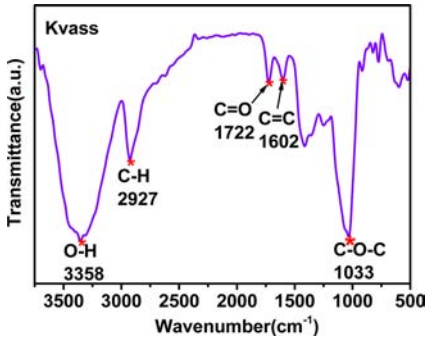

Figure 6. FTIR spectra of kvass carbon dots.

broad and intense peak around 3358 cm^{-1} was attributed to the O—H stretching vibration, indicating the existence of large numbers of hydroxyl groups. The peak at 2927 cm^{-1} corresponds to the C—H vibrations of methylene. The predominant peak of a C═O group at 1722 cm^{-1} and C═C double bonds at 1602 cm^{-1} can also be observed, consistent with the XPS results. Another strong peak with high intensity at 1033 cm^{-1} indicates the existence of aromatic alkoxy bonds in the kvass carbon dots. These results revealed that there are many carboxyl/hydroxyl groups on the surface of the kvass carbon dots. These hydrophilic groups greatly improve the aqueous dispersibility and stability of the carbon dots in aqueous solution and may facilitate their applications in biomedical fields.[21]

Interestingly, the fluorescence intensity of the kvass carbon dots appeared to be pH independent with the pH ranging from 2 to 11. This is quite similar to the carbon dots extracted from Nescafe Original instant coffee,[6] whereas the carbon dots from candle soot displayed a pH-dependent fluorescence intensity.[25] These results indicated that the radiative recombination of the energy-trapping sites on the kvass carbon dots was not affected by changing pH from alkaline to acidic. Moreover, the effect of sodium chloride concentration on fluorescence intensity of the kvass carbon dots was also investigated. When the sodium chloride concentration increased from 0 to 2.5 mol/L, the fluorescence intensity decreased only 20%. The good stability of the kvass carbon dots in a wide range of pH and NaCl concentration suggested that these carbon dots might find good biological applications.

Cytotoxicity Study of the Kvass Carbon Dots. The cytotoxicity of the kvass carbon dots was assessed by MTT assay with CHO cells. Figure 7 shows the cell viability profile

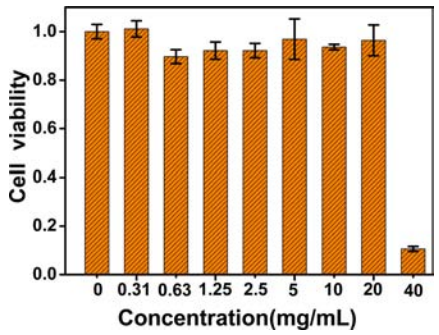

Figure 7. Cytotoxicity of kvass carbon dots with increasing concentrations from 0 to 40 mg/mL in CHO cells. All values are the average of triplicate measurements.

after incubation with the kvass carbon dots at concentrations of 0.31−40 mg/mL for 24 h. The results suggested that the cytotoxicity of the kvass carbon dots was negligible up to a concentration of 20 mg/mL, whereas most of synthesized carbon dots are toxic at 2 mg/mL.[15,17,26] However, the cell viability fell significantly when the concentration of the kvass carbon dots became >20 mg/mL. Overall, the cytotoxicity of the kvass carbon dots was only marginal even at relatively high concentration (20 mg/mL), which makes them suitable for bioimaging applications. Moreover, further experiments are required to study their safety issue for the new carbon nanomaterials in future biomedical applications, although carbon is not considered an intrinsically toxic element.

In Vitro Tumor Cell Imaging. To illustrate the bioimaging potential of the kvass carbon dots, we studied their in vitro uptake by human tongue squamous carcinoma (Tca-8113) cells. Cells were cultured and maintained in DMEM containing the kvass carbon dots for 24 h. Figure 8 shows confocal images of Tca-8113 cells treated with the kvass carbon dots at bright field; excitation wavelengths were 488 and 405 nm, respectively. The human tongue squamous carcinoma cells incubated with the kvass carbon dots became bright at λ_{ex} 405 and 488 nm, as compared to the control cells without the addition of the carbon dots. The fluorescent images of Tca-8113 cells clearly show the agglomeration of blue and green fluorescent carbon dots distributed inside the cytoplasm area of the tumor cells.

DOI: 10.1021/acs.jafc.5b04216
J. Agric. Food Chem. 2015, 63, 8527−8533

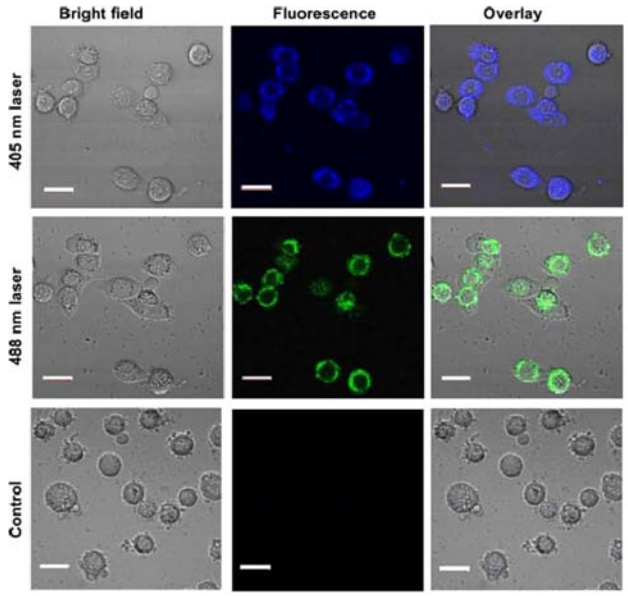

Figure 8. Laser scanning confocal microscopy images of Tca-8113 cells under bright field, by excitation at 488 and 405 nm. Cells without carbon dots were used as a control. Scale bar = 30 μm.

Notably, the excitation-dependent fluorescence of the kvass carbon dots made it possible for multicolor (blue and green) cell imaging.

Onion Epidermal Cell Imaging. The kvass carbon dots were also used for imaging onion epidermal cells inside the onion skin. The kvass carbon dots were directly applied to the onion skin. After 6 h, the onion epidermal cells were imaged at bright field, with an excitation wavelength of 405 nm. As shown in Figure 9, strong fluorescence of the kvass carbon dots was

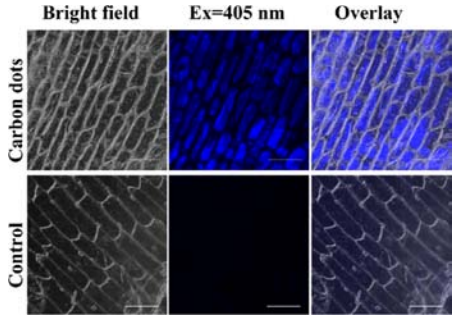

Figure 9. Laser scanning confocal microscopy images of onion epidermal cells under bright field, by excitation at 405 nm. Cells without carbon dots were used as a control. Scale bar = 200 μm.

observed as compared to the control, indicating that the fluorescence was from the carbon dots. It can be clearly seen that the kvass carbon dots were uniformly disturbed in the cytoplasm area, emitting strong blue fluorescence. The carbon dots obtained from kvass can serve as a potential substitute for organic dyes or semiconductor quantum dots in bioimaging.

In the present study, the fluorescent carbon dots were extracted from five beverages, kvass, pony malta, pilsner beer, Vivant, and Profit. TEM analysis demonstrated that the extracted carbon dots are in the nanosize range. Carbon dots from the five beverages exhibited an excitation-dependent emission behavior. XPS elemental analysis revealed the kvass carbon dots are carbon-rich nanodots with excellent pH and ion strength stability and excellent biocompatibility. The kvass carbon dots can be directly applied in the imaging of human tongue squamous carcinoma and onion epidermal cells. The discovery of the NPs in human beverages may provide valuable insights into their safety, distribution, and potential biological imaging applications.

AUTHOR INFORMATION

Corresponding Author

*(M.T.) Phone: +86-411-86323262. Fax: +86-411-86323262. E-mail: 2468750030@qq.com.

Funding

This work was supported by the National Nature Science Foundation of China (91227126), the National Key Scientific Instrument and Equipment Development Project of China (2013YQ17046307), the Nature Science Foundation of Liaoning Province, China (2013020177), and Proyecto Prometeo and Secretaría de Educación Superior, Ciencia, Tecnología e Innovación, Ecuador.

Notes

The authors declare no competing financial interest.

REFERENCES

(1) Institute of Medicine (US) Food Forum. *Nanotechnology in Food Products: Workshop Summary. Safety and Efficacy of Nanomaterials in Food Products*; National Academy Press: Washington, DC, USA, 2009.

(2) Sk, M. P.; Jaiswal, A.; Paul, A.; Ghosh, S. S.; Chattopadhyay, A. Presence of amorphous carbon nanoparticles in food caramels. *Sci. Rep.* **2012**, *2*, DOI: 10.1038/srep00383.

(3) Blasco, C.; Picó, Y. *Nanoparticles in Foods, Determination of*; Wiley: Hoboken, NJ, USA, 2013.

(4) Weir, A.; Westerhoff, P.; Fabricius, L.; Hristovski, K.; von Goetz, N. Titanium dioxide nanoparticles in food and personal care products. *Environ. Sci. Technol.* **2012**, *46*, 2242−2250.

(5) von der Kammer, F.; Legros, S.; Larsen, E. H.; Loeschner, K.; Hofmann, T. Separation and characterization of nanoparticles in complex food and environmental samples by field-flow fractionation. *TrAC, Trends Anal. Chem.* **2011**, *30*, 425−436.

(6) Jiang, C.; Wu, H.; Song, X.; Ma, X.; Wang, J.; Tan, M. Presence of photoluminescent carbon dots in Nescafe original instant coffee: applications to bioimaging. *Talanta* **2014**, *127*, 68−74.

(7) Yan, H.; Tan, M.; Zhang, D.; Cheng, F.; Wu, H.; Fan, M.; Ma, X.; Wang, J. Development of multicolor carbon nanoparticles for cell imaging. *Talanta* **2013**, *108*, 59−65.

(8) Feng, L.; Yang, X.; Shi, X.; Tan, X.; Peng, R.; Wang, J.; Liu, Z. Polyethylene glycol and polyethylenimine dual-functionalized nano-graphene oxide for photothermally enhanced gene delivery. *Small* **2013**, *9*, 1989−1997.

(9) Liu, Z. Y.; Zhang, C. L.; Luo, L.; Chang, Z.; Sun, X. M. One-pot synthesis and catalyst support application of mesoporous N-doped carbonaceous materials. *J. Mater. Chem.* **2012**, *22*, 12149−12154.

(10) Mitra, S.; Chandra, S.; Kundu, T.; Banerjee, R.; Pramanik, P.; Goswami, A. Rapid microwave synthesis of fluorescent hydrophobic carbon dots. *RSC Adv.* **2012**, *2*, 12129−12131.

(11) Zhang, Y. Q.; Ma, D. K.; Zhuang, Y.; Zhang, X.; Chen, W.; Hong, L. L.; Yan, Q. X.; Yu, K.; Huang, S. M. One-pot synthesis of N-doped carbon dots with tunable luminescence properties. *J. Mater. Chem.* **2012**, *22*, 16714−16718.

(12) Zhao, Q. L.; Zhang, Z. L.; Huang, B. H.; Peng, J.; Zhang, M.; Pang, D. W. Facile preparation of low cytotoxicity fluorescent carbon nanocrystals by electrooxidation of graphite. *Chem. Commun.* **2008**, 5116−5118.

(13) Wang, B. B.; Wang, Y. F.; Wu, H.; Song, X. J.; Guo, X.; Zhang, D. M.; Ma, X. J.; Tan, M. Q. A mitochondria-targeted fluorescent probe based on TPP-conjugated carbon dots for both one- and two-photon fluorescence cell imaging. *RSC Adv.* **2014**, *4*, 49960−49963.

DOI: 10.1021/acs.jafc.5b04216
J. Agric. Food Chem. 2015, 63, 8527−8533

(14) Qiao, Z. A.; Wang, Y. F.; Gao, Y.; Li, H. W.; Dai, T. Y.; Liu, Y. L.; Huo, Q. S. Commercially activated carbon as the source for producing multicolor photoluminescent carbon dots by chemical oxidation. *Chem. Commun.* **2009**, *46*, 8812−8814.
(15) Salinas-Castillo, A.; Ariza-Avidad, M.; Pritz, C.; Camprubi-Robles, M.; Fernandez, B.; Ruedas-Rama, M. J.; Megia-Fernandez, A.; Lapresta-Fernandez, A.; Santoyo-Gonzalez, F.; Schrott-Fischer, A.; Capitan-Vallvey, L. F. Carbon dots for copper detection with down and upconversion fluorescent properties as excitation sources. *Chem. Commun.* **2013**, *49*, 1103−1105.
(16) Tan, M.; Zhang, L.; Tang, R.; Song, X.; Li, Y.; Wu, H.; Wang, Y.; Lv, G.; Liu, W.; Ma, X. Enhanced photoluminescence and characterization of multicolor carbon dots using plant soot as a carbon source. *Talanta* **2013**, *115*, 950−956.
(17) Baker, S. N.; Baker, G. A. Luminescent carbon nanodots: emergent nanolights. *Angew. Chem., Int. Ed.* **2010**, *49*, 6726−6744.
(18) Sun, Y. P.; Zhou, B.; Lin, Y.; Wang, W.; Fernando, K. A. S.; Pathak, P.; Meziani, M. J.; Harruff, B. A.; Wang, X.; Wang, H. F.; Luo, P. J. G.; Yang, H.; Kose, M. E.; Chen, B. L.; Veca, L. M.; Xie, S. Y. Quantum-sized carbon dots for bright and colorful photoluminescence. *J. Am. Chem. Soc.* **2006**, *128*, 7756−7757.
(19) Chen, P. C.; Chen, Y. N.; Hsu, P. C.; Shih, C. C.; Chang, H. T. Photoluminescent organosilane-functionalized carbon dots as temperature probes. *Chem. Commun.* **2013**, *49*, 1639−1641.
(20) Anilkumar, P.; Cao, L.; Yu, J. J.; Tackett, K. N.; Wang, P.; Meziani, M. J.; Sun, Y. P. Crosslinked carbon dots as ultra-bright fluorescence probes. *Small* **2013**, *9*, 545−551.
(21) Jia, X. F.; Li, J.; Wang, E. K. One-pot green synthesis of optically pH-sensitive carbon dots with upconversion luminescence. *Nanoscale* **2012**, *4*, 5572−5575.
(22) Jiang, J.; He, Y.; Li, S. Y.; Cui, H. Amino acids as the source for producing carbon nanodots: microwave assisted one-step synthesis, intrinsic photoluminescence property and intense chemiluminescence enhancement. *Chem. Commun.* **2012**, *48*, 9634−9636.
(23) Li, Q.; Ohulchanskyy, T. Y.; Liu, R. L.; Koynov, K.; Wu, D. Q.; Best, A.; Kumar, R.; Bonoiu, A.; Prasad, P. N. Photoluminescent carbon dots as biocompatible nanoprobes for targeting cancer cells in vitro. *J. Phys. Chem. C* **2010**, *114*, 12062−12068.
(24) Wang, J.; Wang, C. F.; Chen, S. Amphiphilic egg-derived carbon dots: rapid plasma fabrication, pyrolysis process, and multicolor printing patterns. *Angew. Chem., Int. Ed.* **2012**, *51*, 9297−9301.
(25) Liu, H. P.; Ye, T.; Mao, C. D. Fluorescent carbon nanoparticles derived from candle soot. *Angew. Chem., Int. Ed.* **2007**, *46*, 6473−6475.
(26) Sahu, S.; Behera, B.; Maiti, T. K.; Mohapatra, S. Simple one-step synthesis of highly luminescent carbon dots from orange juice: application as excellent bio-imaging agents. *Chem. Commun.* **2012**, *48*, 8835−8837.

DOI: 10.1021/acs.jafc.5b04216
J. Agric. Food Chem. 2015, 63, 8527−8533

It has recently been proposed that *excipient foods* can be designed to boost the bioavailability of nutraceuticals in fruits and vegetables.[31,32] The type, concentration, and structural organization of the ingredients in an excipient food are specifically selected to enhance nutraceutical bioavailability by altering their bioaccessibility, absorption, and/or transformation in the GIT.[22] The first step in the design of an excipient food involves identifying the major factors that normally limit the bioavailability of the desired nutraceuticals[22] An excipient food is then designed to overcome these factors by incorporating specific ingredients or structures within it.[31]

The objective of the present study was to investigate the utilization of excipient emulsions to increase the bioaccessibility of carotenoids from yellow peppers. Peppers are known to be a good source of carotenoids,[33−35] and so their consumption may be beneficial to human health. The overall bioavailability of carotenoids is often limited due to their relatively low bioaccessibility, which may be due to poor release from the plant cell tissues and/or due to poor solubilization within the GIT fluids.[22] In this study, we examined the effectiveness of oil-in-water excipient emulsions containing either digestible or indigestible lipids on the bioaccessibility of carotenoids from yellow peppers.[36] Our hypothesis was that digestible lipids would be rapidly digested within the small intestine phase of the GIT and form mixed micelles capable of solubilizing any carotenoids released from the yellow peppers. In addition, we examined the influence of lipid phase type, long chain triglycerides (LCT), medium chain triglycerides (MCT), and indigestible oil (orange oil), since this factor has previously been shown to impact the bioaccessibility of carotenoids encapsulated in colloidal delivery systems.[37,38] The information obtained from this study would facilitate the rational design of excipient foods that can boost the bioavailability of health promoting nutrients and nutraceuticals from natural sources.

MATERIALS AND METHODS

Chemicals. Fresh yellow peppers and corn oil (a source of LCTs) were obtained from a local supermarket. Miglyol 812 (a source of MCTs) was obtained from SASOL (Houston, TX). Orange oil (OO, 10× decolorized) was obtained from the Chemistry Store (Cayce, SC). β-Carotene (≥93%), gallic acid (≥99%), lipase (porcine pancreas, type II), bile extract, and calcium chloride were purchased from Sigma-Aldrich (St. Louis, MO). All other chemicals were of analytical grade. All aqueous solutions were prepared using double-distilled water from a water purification system.

Preparation of Excipient Emulsion and Yellow Pepper. An aqueous phase was prepared by dispersing 1.5% nonionic surfactant (Tween 20) in buffer solution (10 mM phosphate, pH7.0). An organic phase was prepared that contained LCT, MCT, or orange oil. A coarse emulsion was then prepared by blending the organic phase (8%, w/w) with the aqueous phase (92%, w/w) using a high-shear mixer (10 000 rpm, 2 min). Excipient emulsions were then formed by passing the coarse emulsion through a microfluidizer (Model 101, Microfluidics, Newton, MA) three times at a homogenization pressure of 9000 psi.

Yellow peppers were cut into small pieces that were used directly ("raw") or were subjected to a thermal treatment ("boiled") by heating them in a pan of boiling water for 5 min. These two treatments were used to take into account that peppers may be consumed raw (e.g., in salads) or they may be cooked (e.g., in sauces).

Simulated Gastrointestinal Tract. The yellow peppers were converted into a puree by grinding with a mortar and pestle to simulate tissue breakdown in the mouth due to mastication. The pureed yellow pepper (6 g) was then mixed with excipient food (6 g of buffer or emulsion), and the resulting mixture was passed through a static simulated GIT:[37,38]

Mouth Phase. Simulated saliva fluid (SSF) was prepared by dispersing mucin and various salts in water and then stirring overnight, as described previously.[39] The pepper/excipient sample (12 g) was then mixed with SSF (12 g), and the system was adjusted to pH 6.8 with sodium hydroxide solution. The resulting mixture was incubated at 37 °C for 10 min with continuous agitation (100 rpm).

Stomach Phase. Simulated gastric fluid (SGF) was prepared by dissolving 2 g of sodium chloride and 7 mL of hydrogen chloride (37%) in 1 L of water and then dispersing 0.064 g of pepsin into 20 mL of this solution followed by stirring for 45 min. The sample resulting from the mouth phase (20 g) was then mixed with SGF (20 g), and adjusted to pH 2.5 with sodium hydroxide solution. The stomach sample was placed in an incubator at 37 °C for 2 h with continuous swirling at 100 rpm to simulate gastric digestion.

Small Intestine. A sample from the stomach phase (30 g) was placed in a temperature-controlled (37 °C) water bath, and the pH value was adjusted to pH 7.0. Then, 4 mL of bile salt solution (187.5 mg/4 mL) and 1.5 mL of simulated small intestine solution (10 mM of calcium chloride and 150 mM of sodium chloride) were added into the mixture, and the mixture was adjusted to pH 7.0. Afterward, 4 mL of freshly prepared lipase suspension (187.5 mg/4 mL) dissolved in phosphate buffer was added to the mixture. The pH of the mixture was monitored, and the volume of 0.25 M NaOH (mL) necessary to neutralize the free fatty acids (FFA) released from the lipid digestion was recorded over 2 h using an automatic titration (pH stat) method (Metrohm USA Inc., Riverview, FL). The percentage of FFA released was calculated using the following equation:

$$\mathrm{FFA}(t) = 100 \times \left(\frac{V_{\mathrm{NaOH}}(t) \cdot C_{\mathrm{NaOH}} \cdot M_{\mathrm{Oil}}}{2 \cdot m_{\mathrm{Oil}}} \right) \quad (1)$$

Here, $V_{\mathrm{NaOH}}(t)$ is the volume of NaOH solution required to neutralize the FFAs produced at digestion time t (L), C_{NaOH} is the molarity of the NaOH solution used to titrate the sample (mol/L), M_{oil} is the molecular weight of the oil (g/mol), and m_{oil} is the total mass of lipid initially present in the incubation cell (g).The molecular weights of the LCT and MCT were taken to be 872 and 492 g/mol, respectively.

Particle Characterization in Excipient Emulsions and Digesta. The mean particle diameter, particle size distribution, and electrical charge of the samples were monitored after exposure to each stage of the simulated GIT. The mean particle diameter and particle size distribution were measured using static light scattering (Mastersizer 2000, Malvern Instruments Ltd., Worcestershire, UK). The samples were diluted in 10 mM phosphate buffer (pH 7.0) prior to measurement to avoid multiple scattering effects. The particle size was reported as the surface-weighted mean diameter (d_{32}). The electrical charge (ζ-potential) on the particles in the samples was measured using a particle electrophoresis method (Nano ZS, Malvern Instruments, Malvern, UK).

Bioaccessibility. The bioaccessibility of β-carotene was determined after each sample had been subjected to the full *in vitro* digestion process using a method described previously.[37,38] After the small intestine stage, raw digesta samples were collected and centrifuged (4400 rpm for 1 h), which resulted in samples that contained a sediment at the bottom with a supernatant above. The supernatant was collected and assumed to be the "micelle" fraction, in which the carotenoids were solubilized. The bioaccessibility was calculated from the concentrations of total carotenoids determined in the micelle fraction and supernatant using a procedure described previously.[37,38] The bioaccessibility of total carotenoids was calculated using the following equation:

$$\mathrm{Bioaccessibility} = 100 \times \left(\frac{C_{\mathrm{Micelle}}}{C_{\mathrm{Raw\ Digesta}}} \right)$$

where C_{micelle} and $C_{\mathrm{Raw\ Digesta}}$ are the concentrations of total carotenoids in the micelle fraction and in the overall sample (raw digesta) after the simulated intestinal digestion experiment, respectively. The carotenoid content of each sample was determined according to the method described previously.[40]

DOI: 10.1021/acs.jafc.5b04217
J. Agric. Food Chem. 2015, 63, 8534−8543

Microstructure Analysis. The microstructure of the samples initially and after exposure to various GIT phases was characterized using optical and confocal scanning fluorescence microscopy (Nikon D-Eclipse C1 80i, Nikon, Melville, NY). The samples analyzed by confocal microscopy were stained with a lipophilic fluorescent dye (Nile Red) to highlight the location of the lipid phase. The Nile red was dissolved in absolute ethyl alcohol at a concentration of 1 mg/mL. Then, before analysis 2 mL samples were mixed with 20 μL of Nile Red solution (1 mg/mL ethanol) to dye the oil phase. All images were captured with a 10× eyepiece and a 60× objective lens (oil immersion).

Statistical Analysis. All experiments were conducted in at least duplicate, and analyses of each sample were also carried out in duplicate. Results are expressed as the mean and the standard deviation of these measurements. Variance analyses were performed by statistical analysis software (SPSS19.0, IBM). Multiple comparisons were conducted to determine the significant differences at the 5% level ($p < 0.05$).

RESULTS AND DISCUSSION

The potential impact of excipient emulsions on the gastrointestinal fate of the nutraceuticals in the yellow peppers was assessed using a static *in vitro* digestion model: mouth, stomach, and small intestine.

Properties of Initial Excipient Emulsions. Initially, the size and charge of the lipid droplets in the excipient emulsions was characterized before mixing them with the raw or boiled pureed yellow pepper samples. The mean particle diameter (d_{32}) of the excipient emulsions containing digestible lipids was relatively small: 0.14 and 0.18 μm for the MCT and LCT emulsions, respectively (Figure 1). In addition, these two emulsions had monomodal particle size distributions (Figure 2c and d) and exhibited no visible phase separation throughout storage for 1 week (data not shown). Optical and confocal microscopy images indicated that the droplets in these emulsions were relatively small and evenly distributed throughout the samples (Figure 3). Thus, microfluidization was an effective means of preparing stable excipient emulsions from these types of triglyceride oils. Conversely, the initial excipient emulsions containing the indigestible lipids (orange oil) had relatively large mean particle diameters (0.64 μm) as measured by light scattering (Figure 1a), and there were some large droplets observed in the particle size distributions (Figure 2b) and microscopy images (Figure 3). After a few hours of storage, the orange oil emulsions separated into a cream layer at the top and a serum layer at the bottom (data not shown). The reason for the relatively large droplet size in these emulsions can be attributed to Ostwald ripening: orange oil is a relatively polar lipid, and so a substantial amount may diffuse from the small droplets to the large droplets due to a thermodynamic driving force associated with differences in interfacial curvature.[41] The resulting increase in droplet size due to this process leads to enhanced creaming and coalescence of the droplets, which accounts for the visual appearance of phase separation.

The lipid droplets in all the excipient emulsions were moderately anionic, with ζ-potentials of −11, −14, and −19 mV for the MCT, LCT, and orange oil emulsions, respectively (Figure 4a). The negative charge on the droplets can be attributed to the presence of anionic impurities (such as free fatty acids) in the nonionic surfactant or lipid ingredients used to fabricate the emulsions.[42]

Influence of Mouth Phase. The pureed yellow peppers (raw or boiled) were mixed with either excipient emulsion (MCT, LCT, or orange oil) or buffer solution (control) and then exposed to simulated mouth conditions. Samples were collected at the end of the incubation period, and then their particle sizes, microstructures, and electrical characteristics were measured (Figures 1−4).

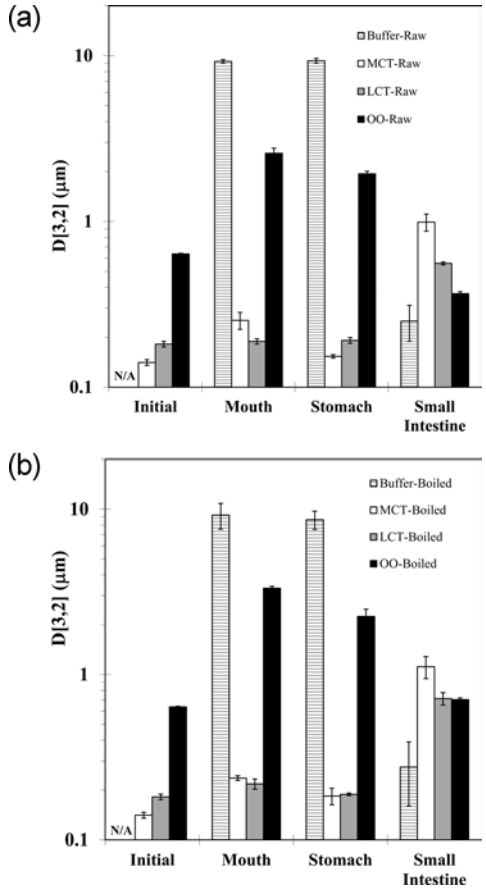

Figure 1. (a) Influence of passage through a simulated GIT on the mean particle diameter (d_{32}) of samples containing raw yellow pepper and either buffer solution (control) or excipient emulsions with different oil types: long chain triglycerides (LCT), medium chain triglycerides (MCT), or orange oil (OO). (b) Influence of passage through a simulated GIT on the mean particle diameter (d_{32}) of samples containing boiled yellow pepper and either buffer solution (control) or excipient emulsions with different oil types: long chain triglycerides (LCT), medium chain triglycerides (MCT), or orange oil (OO).

In the absence of lipid droplets (control), the light scattering measurements indicated that both the raw and boiled yellow pepper samples contained relatively large particles ($d_{32} \approx 10$ μm) after exposure to the mouth phase (Figure 1). These large particles were presumably fragments of yellow pepper generated during the simulated mastication process. Indeed, the optical microscopy images clearly showed the presence of a number of relatively large particles within these samples (Figure 3b and d). There was evidence of bright regions within the confocal microscopy images for the yellow pepper in buffer samples, which suggests that the Nile red dye may have been localized within some hydrophobic regions in the plant tissue (Figure 3a and c). The fragments in both the raw and boiled yellow pepper control samples had fairly high negative charges ($\zeta \approx -18$ mV), which may have been due to the presence of anionic biopolymers (e.g., pectin) at the surfaces of the yellow pepper pieces. Interestingly, the raw and boiled samples

DOI: 10.1021/acs.jafc.5b04217
J. Agric. Food Chem. 2015, 63, 8534−8543

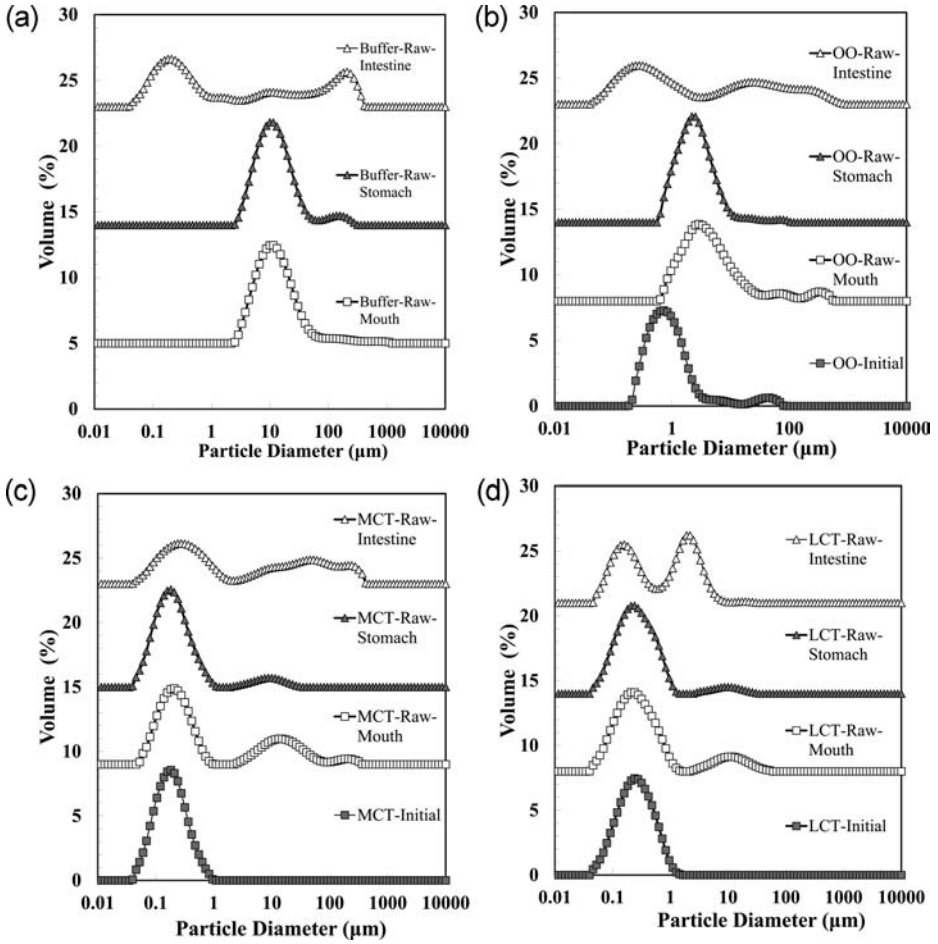

Figure 2. (a) Influence of gastrointestinal stage on the particle size distribution of mixed systems containing raw yellow pepper and buffer solution (control). (b) Influence of gastrointestinal stage on the particle size distribution of mixed systems containing raw yellow pepper and orange oil excipient emulsions. (c) Influence of gastrointestinal stage on the particle size distribution of mixed systems containing raw yellow pepper and MCT excipient emulsions. (d) Influence of gastrointestinal stage on the particle size distribution of mixed systems containing raw yellow pepper and LCT excipient emulsions.

behaved very similarly throughout the GIT (see later). These results suggest that boiling did not have a major impact on the initial size or electrical properties of the yellow pepper fragments. Nevertheless, there are likely to have been other changes that would not be detected by light scattering or microscopy methods, such as tissue softening.

In the presence of the excipient emulsions, the mean particle diameter measured by light scattering was much smaller than that for the yellow pepper alone, particularly for the MCT and LCT samples (Figure 1a and b). Conversely, the optical and confocal microscopy images clearly suggested that there were large particles in these samples (Figure 3). These large particles appeared to be tissue fragments from the yellow pepper, as well as some clumps of droplets. These apparent contradictory results may be attributed to the ability of the mucin molecules from the simulated saliva fluids to promote depletion flocculation of the lipid droplets.[43] The lipid droplets were coated by a nonionic surfactant with a polymeric headgroup (Tween 20), and so one would not expect the mucin molecules to strongly adhere to the droplet surfaces. However, the presence of nonadsorbed biopolymers in the aqueous phase surrounding the droplets generates an osmotic attraction between them that causes them to become flocculated.[44] The forces holding the droplets together in aggregates formed by depletion flocculation are usually relatively weak, and reduced when the sample is diluted and stirred for light scattering measurements. Hence, the droplets may have been highly aggregated in the original samples, but appear to be relatively small in the light scattering measurements. The mixtures containing orange oil emulsions and yellow pepper had much larger mean particle diameters than the ones containing digestible lipids. In addition, the particle size distribution data showed that most of these samples had a bimodal distribution with a population of small particles around 0.1−0.3 μm and a population of large particles around 10 μm (Figure 2b). The small particles were likely to be the lipid droplets, and the large particles, the yellow pepper fragments. The large mean particle size in these samples can be attributed to the contribution of large orange oil droplets formed due to Ostwald ripening.[41] Nevertheless, the microscopy images also indicated that extensive droplet flocculation still occurred under oral conditions, which can be attributed to the depletion flocculation mechanism discussed earlier.

The electrical charges on the particles in the mixed systems were more highly negative than those in the control systems (Figure 4), but they followed a similar trend to those observed in the initial emulsions, with the charge becoming increasingly negative in the following order: control < MCT < LCT <

DOI: 10.1021/acs.jafc.5b04217
J. Agric. Food Chem. 2015, 63, 8534−8543

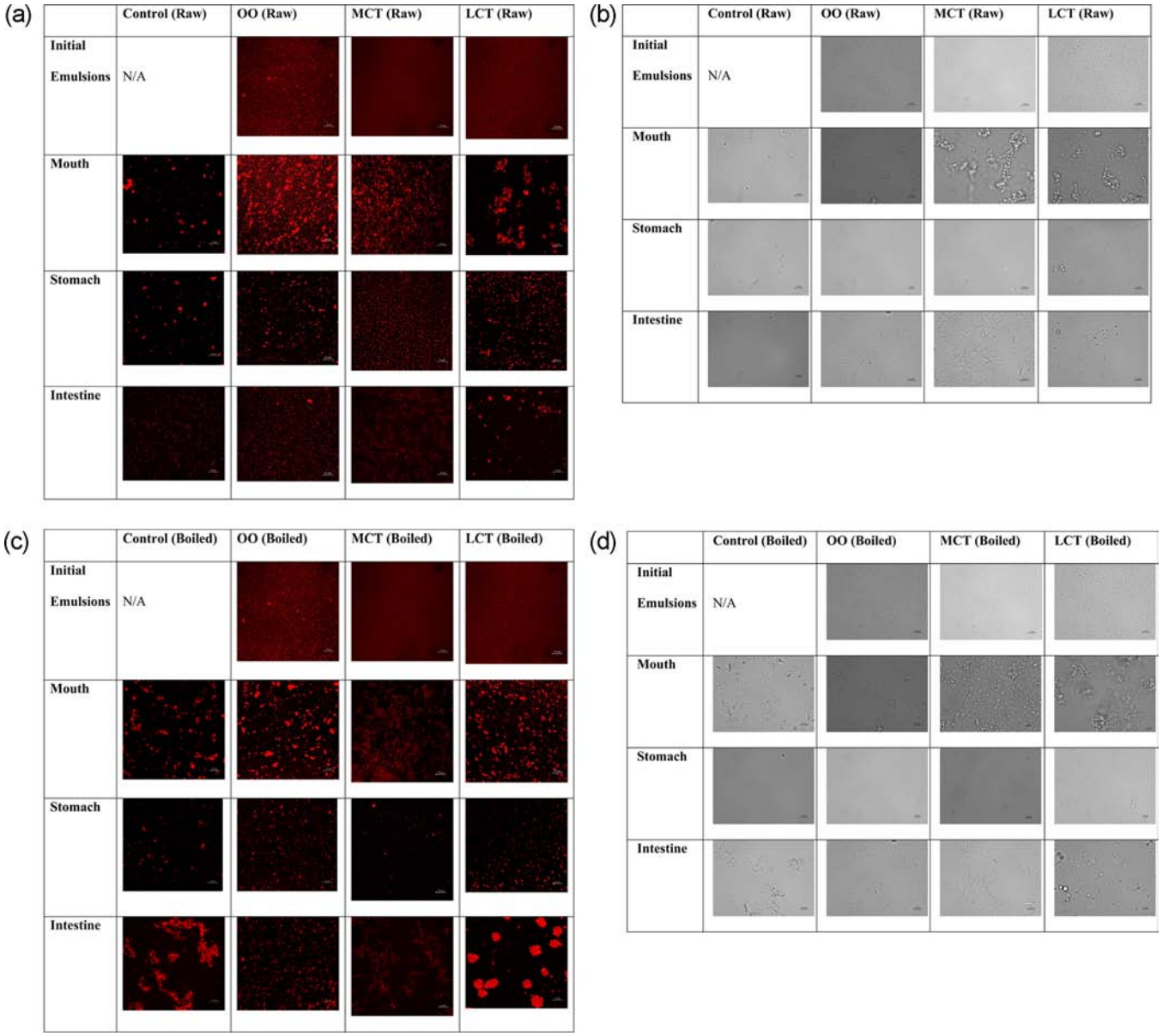

Figure 3. (a) Change in microstructure of raw yellow pepper samples as they passed through the simulated GIT as observed by confocal fluorescent microscopy using a lipid dye. (b) Change in microstructure of raw yellow pepper samples as they passed through the simulated GIT as observed by optical microscopy. (c) Change in microstructure of boiled yellow pepper samples as they passed through the simulated GIT as observed by confocal fluorescent microscopy using a lipid dye. (d) Change in microstructure of boiled yellow pepper samples as they passed through the simulated GIT as observed by optical microscopy.

orange oil. The negative charge on the particles in the mixed systems is due to the fact that they contained a mixture of anionic lipid droplets and anionic yellow pepper fragments.

Influence of Stomach Phase. The samples resulting from the oral phase were incubated in simulated gastric fluids, and then their size, microstructure, and charge were measured (Figures 1–4). In the yellow pepper controls (no lipids), the particle size remained relatively large after exposure to gastric conditions, $d_{32} \approx 10$ μm (Figure 1). Hence, the highly acidic environment of the gastric fluids did not appear to breakdown the yellow pepper tissue fragments. On the other hand, the mean particle diameter remained relatively small in the presence of the digestible lipid droplets (MCT and LCT), which suggests that these droplets were resistant to droplet coalescence under gastric conditions. In addition, the mean particle diameter of the mixtures containing the orange oil emulsions remained relatively high, which can be attributed to droplet growth by Ostwald ripening. The optical and confocal micrographs indicated that the large clumps of droplets observed in the excipient emulsions in the mouth stage were not present after exposure to the gastric phase (Figure 3). The breakdown of these clumps may have been because the emulsions were diluted (1:1) with simulated gastric fluids, which weakened the attractive osmotic forces acting between the droplets, thereby reducing the tendency for depletion flocculation to occur.[44] In addition, the change in solution pH and ionic strength may have altered the relative magnitude of the other attractive and repulsive colloidal interactions operating between the lipid droplets, leading to changes in the tendency for droplets to come together. The particle size distribution data also showed that there was a reduction in the population of large particles after exposure to gastric conditions

DOI: 10.1021/acs.jafc.5b04217
J. Agric. Food Chem. 2015, 63, 8534–8543

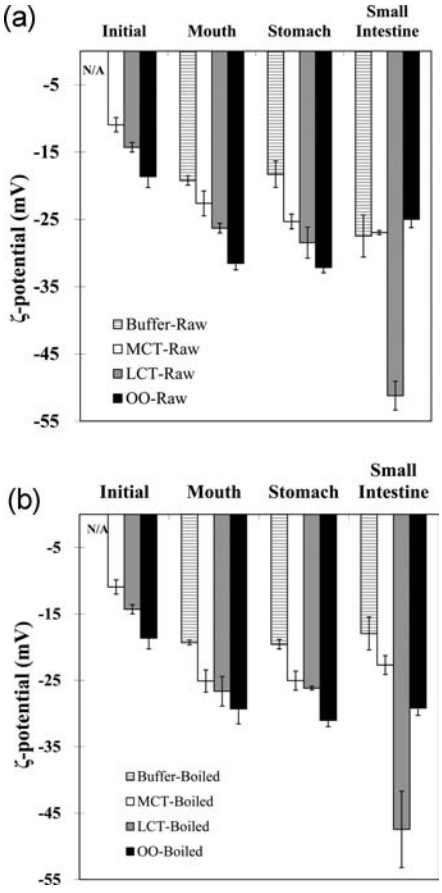

Figure 4. (a) Influence of passage through a simulated GIT on the electrical characteristics of the particles (ζ-potential) of samples containing raw yellow pepper and either buffer solution (control) or excipient emulsions with different oil types: long chain triglycerides (LCT), medium chain triglycerides (MCT), or orange oil (OO). (b) Influence of passage through a simulated GIT on the electrical characteristics of the particles (ζ-potential) of samples containing boiled yellow pepper and either buffer solution (control) or excipient emulsions with different oil types: long chain triglycerides (LCT), medium chain triglycerides (MCT), or orange oil (OO).

(Figure 2). This observation suggests that the presence of the lipid droplets somehow promoted the disruption of the yellow pepper fragments under simulated gastric conditions, although the origin of this effect is currently unknown.

The ζ-potential of the gastric samples was measured under the same solution conditions (pH 7) as those used for the other stages of the simulated GIT, so that alterations in interfacial properties could be directly compared between different samples. The ζ-potential on the particles in all the samples became slightly more negative after they were exposed to stomach conditions (Figure 3), which suggests that there was some alteration in the interfacial composition of the lipid droplets and/or the yellow pepper fragments. This alteration may have occurred due to adsorption of anionic species to their surfaces, such as mucin or pepsin.

Influence of Small Intestine Phase. The gastric samples were then exposed to simulated small intestine conditions and their particle size, microstructure, and charge were measured at the end of the incubation period (Figures 1−4). In the control yellow pepper samples (no lipid), there was an appreciable decrease in the mean particle size measured by light scattering (Figure 1), which may have been due to some breakdown of the yellow pepper fragments, or due to the contribution of particles originating from the small intestine fluids to the light scattering signal (such as mixed micelles formed by bile salts or insoluble aggregates from the lipase extract). The optical microscopy images of both the raw and boiled yellow pepper samples indicate that there were still some large fragments present (Figure 3b and d), which suggests that the small sizes measured by light scattering were probably due to particles arising from the simulated small intestinal fluids. These results highlight the importance of confirming light scattering results using microscopy analysis.

In the presence of lipid droplets, there was an appreciable change in the mean particle diameter after exposure to small intestine conditions: the particle size increased in the mixtures containing digestible lipid droplets, but decreased in the mixtures containing indigestible lipid droplets (Figure 1). This change in particle dimensions can be attributed to the formation of a complex mixture of different colloidal particles that can scatter light, such as undigested lipid droplets, micelles, vesicles, insoluble calcium soaps, and liquid crystals. The number, type, and dimensions of these particles formed is likely to depend strongly on lipid composition. Consequently, it is difficult to interpret the results from light scattering measurements in such complex colloidal mixtures. The optical and confocal microscopy images indicated that various kinds of structures were formed in the small intestinal fluids depending on lipid type (Figure 3). In the orange oil emulsions, there appeared to be a fairly even distribution of relatively small particles spread through the system.

Interestingly, both the raw and boiled yellow peppers, containing MCT emulsions, contained an interwoven network of hair-like structures after digestion. These long thin structures may have been liquid crystals formed from the medium chain fatty acids and other substances in the digesta. To the authors' knowledge this is the first time this kind of structure has been observed, and their origin and nature are currently unknown. The samples that initially contained LCT excipient emulsions contained a number of large lipophilic spheroids after digestion, which may have been undigested fat droplets or large vesicle-like structures. These structures were particularly apparent in the boiled yellow pepper sample. Overall, our microscopy results show that there is a large change in the microstructures formed within the digesta produced in the small intestine phase. Other studies have also indicated that various kinds of structures may be formed in simulated small intestine fluids depending on the nature of the lipid phase used.[45,46]

In the presence of lipid droplets, there was evidence that the population of large particles observed in the particle size distribution was reduced, which also suggested that there was some breakdown of the yellow pepper fragments under simulated small intestine conditions. Cellular disruption may have occurred because the surface-active bile salts, free fatty acids, and monoacylglycerols present in the intestinal fluids penetrated into the plant tissues and disrupted the bonds between them. After exposure to the small intestine phase the system containing MCT emulsions exhibited two major peaks around 0.27 and 46 μm for raw yellow pepper and 0.21 and 35 μm for boiled, respectively. LCT emulsions exhibited two major peaks around 0.16 and 2.2 μm for raw but three major peaks around 0.18, 2.2, and 180 μm for boiled, respectively, which suggests that different kinds of colloidal structures were formed after digestion. These larger particles may have been undigested lipid droplets or liposomes formed from the long

DOI: 10.1021/acs.jafc.5b04217
J. Agric. Food Chem. 2015, 63, 8534−8543

chain fatty acids released by lipid digestion or yellow pepper fragments.

The electrical charge on the particles in the small intestine phase was negative for all of the samples studied (Figure 3), which can be attributed to the presence of anionic species in the small intestinal fluids, such as bile salts, free fatty acids, peptides, and mucin. Nevertheless, the negative charge was much higher for the samples containing LCT, which may have been because lipid digestion generated long chain fatty acids that accumulated at the surfaces of the lipid droplets or were incorporated into micelle micelles. Again, the results were very similar for the samples containing raw and boiled yellow pepper.

Lipid Digestion. The digestion of the lipid phase in the mixtures containing excipient emulsions was followed using an automatic titration (pH-stat) method. The volume of alkaline solution that had to be titrated into the reaction vessel to neutralize the free fatty acids (and any other acids) released during digestion of the raw and cooked yellow pepper was measured (Figure 5a and b). These data were then used to calculate the percentage of free fatty acids released from the lipid phase for the two digestible oils, i.e., LCT and MCT (Figure 6a and b). The volume of alkaline determined for the control sample (no lipid) was subtracted from the volume measured for the samples containing digestible lipids prior to making these calculations so as to account for any changes of pH due to the reactants employed.

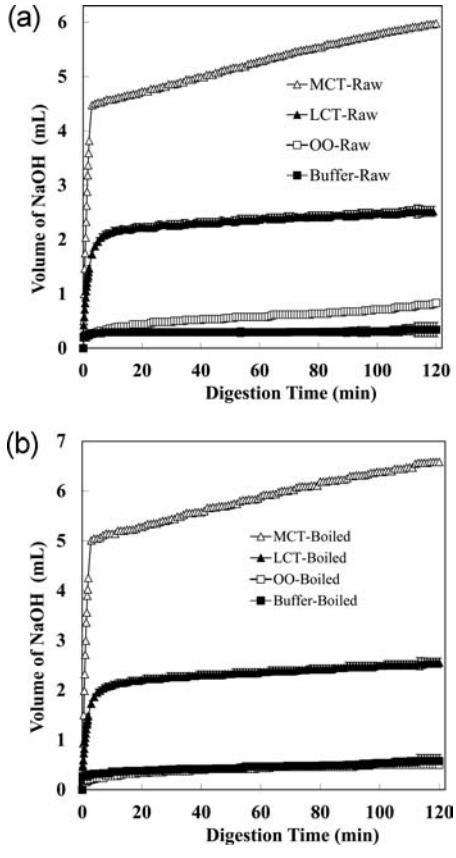

Figure 5. (a) Volume of alkaline solution (0.25 M NaOH) required to maintain the pH at neutral under simulated small intestine conditions: The samples analyzed originally contained raw yellow pepper and either buffer solution (control) or excipient emulsions with different oil types: LCT, MCT, or orange oil. (b) Volume of alkaline solution (0.25 M NaOH) required to maintain the pH at neutral under simulated small intestine conditions: The samples analyzed originally contained boiled yellow pepper and either buffer solution (control) or excipient emulsions with different oil types: LCT, MCT, or orange oil.

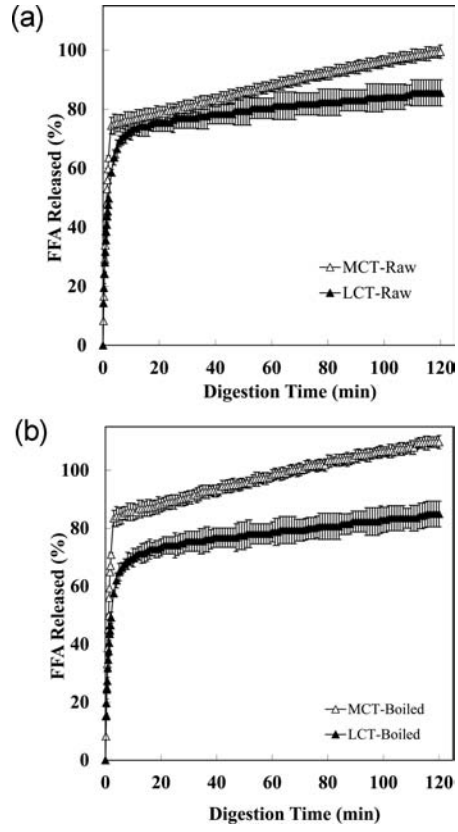

Figure 6. (a) Percentage of free fatty acids released under simulated small intestine conditions for samples initially containing raw yellow pepper and excipient emulsions with different digestible oil types: LCT or MCT. (b) Percentage of free fatty acids released under simulated small intestine conditions for samples initially containing boiled yellow pepper and excipient emulsions with different digestible oil types: LCT or MCT.

In the absence of digestible lipids (control and orange oil sample), there was only a slight increase in the volume of alkaline solution added to the reaction chamber during the course of the experiment (Figure 5), which may be due to the digestion of some components in the reagents (such as bile salts or lipase). The volume of alkaline solution titrated into the mixture containing LCT was appreciably lower than that titrated into the one containing MCT, which is at least partly due to the higher molecular weight of LCT.[47]

For both digestible lipids, and for both raw and boiled samples, there was a rapid increase in free fatty acids released during the first few minutes, followed by a much slower increase at later times (Figure 6a and b). The rate of increase in FFAs released at later times appeared to be higher for the MCT system than for the LCT system. Consequently, by the end of the 2 h digestion period only about 80% of the LCT had been digested, but over 100% of the MCT had been digested. These calculations are based on the assumption that every triglyceride molecule produces two free fatty acids, so that the high value determined for MCT may be because more than two FFAs were released per triglyceride molecule.[48] In addition, previous studies have shown that lipid digestion may be inhibited in LCT emulsions because of accumulation of long chain fatty

DOI: 10.1021/acs.jafc.5b04217
J. Agric. Food Chem. 2015, 63, 8534−8543

acids at the lipid droplet surfaces.[49] These long chain FFAs form a liquid crystalline shell around the lipid droplets that restricts the access of lipase to the remaining triglycerides, thereby inhibiting further digestion. The lipase can continue to function properly once the long chain free fatty acids are removed from the droplet surfaces by solubilization within mixed micelles or by precipitation by calcium ions. It is therefore possible that there was insufficient bile salts or calcium present in the simulated small intestinal fluids used in our study to completely remove all of the long chain FFAs from the LCT droplet surfaces. Finally, at neutral pH not all of the carboxylic acid groups on the fatty acids may be ionized, therefore inhibiting proton release.[48]

Bioaccessibility. Finally, we measured the bioaccessibility of the carotenoids released from the yellow pepper tissue after their passage through the simulated GIT (Figure 7). The

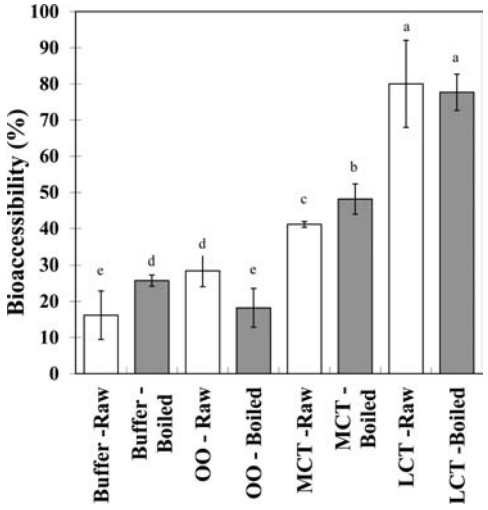

Figure 7. Bioavailability of carotenoids released under simulated GIT conditions from samples initially containing boiled yellow pepper and either buffer solutions or excipient emulsions with different oil types: LCT, MCT, and orange oil.

bioaccessibility was calculated by measuring the carotenoid concentrations in the mixed micelle phase and the total digesta. The bioaccessibility of the carotenoids in the control samples (no lipids) and in the samples containing indigestible oil (orange oil) were relatively low (<30%). This phenomenon can be attributed to the fact that there were no free fatty acids produced that could form mixed micelles with the bile salts and increase the solubilization capacity of the small intestinal fluids. In this case, the carotenoids released from the yellow pepper tissue were probably solubilized in simple micelles that only consisted of bile salts. There was a significant increase in the bioaccessibility of the carotenoids for the yellow peppers (raw and boiled) that had been mixed with the excipient emulsions containing digestible lipids (MCT and LCT). This effect can be attributed to the fact that the free fatty acids produced by lipid digestion were incorporated into mixed micelles with bile salts, which increases the solubilization capacity of the small intestinal fluids.[50] Moreover, the bioaccessibility of the carotenoids was significantly higher for the samples containing LCT droplets than for those containing MCT droplets, which agrees with earlier studies that have reported that the bioaccessibility of carotenoids encapsulated in emulsion-based delivery systems is higher for LCT than MCT.[37,38] This effect can be attributed to the ability of the long chain free fatty acids arising from LCT digestion to form mixed micelles that have hydrophobic regions big enough to accommodate long nonpolar molecules.[45,46] Conversely, the hydrophobic regions in the mixed micelles formed by MCT are insufficiently large to incorporate the carotenoid molecules. This result has important implications for the design of excipient emulsions to boost the bioavailability of large hydrophobic nutraceuticals, such as carotenoids. Boiling the yellow peppers appeared to have little impact on their overall bioaccessibility. In previous studies, it has been reported that certain types of domestic cooking (such as stir-frying) lead to a major improvement in carotenoid bioaccessibility, whereas others (such as boiling) only cause a modest increase.[30] Presumably, the oil used in stir-frying helps to solubilize the carotenoids and to form mixed micelles in the gastrointestinal tract.

In conclusion, this study has shown that excipient emulsions can boost the bioaccessibility of carotenoids in yellow pepper, with the magnitude of the effect depending strongly on lipid phase type. Excipient emulsions fabricated from LCT gave a significantly higher bioaccessibility than those fabricated from MCT, which can be attributed to the greater solubilizing power of mixed micelles formed from long chain fatty acids. Boiling the yellow peppers had little influence on their gastrointestinal fate or on carotenoid bioaccessibility. Overall, these results highlight the potential of designing excipient emulsions to boost the fraction of beneficial nutraceuticals present in natural fruits and vegetables. For example, it may be possible to design an excipient dressing to pour on raw peppers in salads, or an excipient creamy sauce to pour on cooked peppers.

AUTHOR INFORMATION

Corresponding Author

*Tel: 413 545-1019. Fax: 413 545-1262. E-mail: mcclements@foodsci.umass.edu.

Funding

This work was partly supported by the China Scholarship Council (No. 201303250031). This material was also partly based upon work supported by the Cooperative State Research, Extension, Education Service, United State Department of Agriculture, Massachusetts Agricultural Experiment Station (Project No. 831) and United States Department of Agriculture, NRI Grants (2011-03539, 2013-03795, 2011-67021, and 2014-67021). This project was also partly funded by the Deanship of Scientific Research (DSR), King Abdulaziz University, Jeddah, under Grant Nos. 330-130-1435-DSR, 299-130-1435-DSR, and 87-130-35-HiCi. The authors, therefore, acknowledge with thanks DSR technical and financial support.

Notes

The authors declare no competing financial interest.

REFERENCES

(1) Ghosh, D.; Bagchi, D.; Konishi, T. *Clinical Aspects of Functional Foods and Nutraceuticals*; CRC Press: Boca Raton, FL, 2014.

(2) Paliyath, G.; Bakovic, M.; Shetty, K. *Functional Foods, Nutraceuticals and Degenerative Disease Prevention*; Wiley-Blackwell: New York, NY, 2011.

(3) Gupta, S. C.; Kim, J. H.; Prasad, S.; Aggarwal, B. B. Regulation of survival, proliferation, invasion, angiogenesis, and metastasis of tumor cells through modulation of inflammatory pathways by nutraceuticals. *Cancer Metastasis Rev.* **2010**, *29*, 405−434.

DOI: 10.1021/acs.jafc.5b04217
J. Agric. Food Chem. 2015, 63, 8534−8543

(4) Chen, Z.-Y.; Peng, C.; Jiao, R.; Wong, Y. M.; Yang, N.; Huang, Y. Anti-hypertensive nutraceuticals and functional foods. *J. Agric. Food Chem.* **2009**, *57*, 4485−4499.
(5) Paredes-Lopez, O.; Cervantes-Ceja, M. L.; Vigna-Perez, M.; Hernandez-Perez, T. Berries: Improving human health and healthy aging, and promoting quality of life-A review. *Plant Foods Hum. Nutr.* **2010**, *65*, 299−308.
(6) Tapas, A. R.; Sakarkar, D. M.; Kakde, R. B. Flavonoids as nutraceuticals: A review. *Trop. J. Pharm. Res.* **2008**, *7*, 1089−1099.
(7) Ullah, M. F.; Khan, M. W. Food as Medicine: Potential therapeutic tendencies of plant derived polyphenolic compounds. *Asian Pacific J. Cancer Prevention* **2008**, *9*, 187−195.
(8) Bagchi, D.; Preuss, H. G.; Swaroop, A. *Nutraceuticals and Functional Foods in Human Health and Disease Prevention*. CRC Press: Boca Raton, FL, 2015.
(9) Huang, Q.; Yu, H.; Ru, Q. Bioavailability and delivery of nutraceuticals using nanotechnology. *J. Food Sci.* **2010**, *75*, R50−R57.
(10) McClements, D. J.; Decker, E. A.; Park, Y.; Weiss, J. Structural design principles for delivery of bioactive components in nutraceuticals and functional foods. *Crit. Rev. Food Sci. Nutr.* **2009**, *49*, 577−606.
(11) Velikov, K. P.; Pelan, E. Colloidal delivery systems for micronutrients and nutraceuticals. *Soft Matter* **2008**, *4*, 1964−1980.
(12) Ortega, R. M. Importance of functional foods in the Mediterranean diet. *Public Health Nutr.* **2006**, *9*, 1136−1140.
(13) Fardet, A. Complex foods versus functional foods, nutraceuticals and dietary supplements: differential health impact (Part 1). *Agro Food Industry Hi-Tech* **2015**, *26*, 20−24.
(14) Shahidi, F. Nutraceuticals and functional foods: whole versus processed foods. *Trends Food Sci. Technol.* **2009**, *20*, 376−387.
(15) Jeffery, J. L.; Turner, N. D.; King, S. R. Carotenoid bioaccessibility from nine raw carotenoid-storing fruits and vegetables using an in vitro model. *J. Sci. Food Agric.* **2012**, *92*, 2603−2610.
(16) van het Hof, K. H.; West, C. E.; Weststrate, J. A.; Hautvast, J. G. A. J. Dietary factors that affect the bioavailability of carotenoids. *J. Nutr.* **2000**, *130*, 503−506.
(17) Ryan, L.; O'Connell, O.; O'Sullivan, L.; Aherne, S. A.; O'Brien, N. M. Micellarisation of carotenoids from raw and cooked vegetables. *Plant Foods Hum. Nutr.* **2008**, *63*, 127−133.
(18) Lemmens, L.; Colle, I.; Van Buggenhout, S.; Palmero, P.; Van Loey, A.; Hendrickx, M. Carotenoid bioaccessibility in fruit- and vegetable-based food products as affected by product (micro) structural characteristics and the presence of lipids: A review. *Trends Food Sci. Technol.* **2014**, *38*, 125−135.
(19) Jeffery, J.; Holzenburg, A.; King, S. Physical barriers to carotenoid bioaccessibility. Ultrastructure survey of chromoplast and cell wall morphology in nine carotenoid-containing fruits and vegetables. *J. Sci. Food Agric.* **2012**, *92*, 2594−2602.
(20) Rodriguez-Roque, M. J.; Rojas-Graue, M. A.; Elez-Martinez, P.; Martin-Belloso, O. In vitro bioaccessibility of health-related compounds as affected by the formulation of fruit juice- and milk-based beverages. *Food Res. Int.* **2014**, *62*, 771−778.
(21) Schweiggert, R. M.; Mezger, D.; Schimpf, F.; Steingass, C. B.; Carle, R. Influence of chromoplast morphology on carotenoid bioaccessibility of carrot, mango, papaya, and tomato. *Food Chem.* **2012**, *135*, 2736−2742.
(22) McClements, D. J.; Li, F.; Xiao, H., The nutraceutical bioavailability classification scheme: Classifying nutraceuticals according to factors limiting their oral bioavailability. *Annu. Rev. Food Sci. Technol.* **2015**, *6*, pp 299−32710.1146/annurev-food-032814-014043.
(23) Hornero-Méndez, D.; Mínguez-Mosquera, M. I. Bioaccessibility of carotenes from carrots: Effect of cooking and addition of oil. *Innovative Food Sci. Emerging Technol.* **2007**, *8*, 407−412.
(24) Ornelas-Paz, J. D. J.; Failla, M. L.; Yahia, E. M.; Gardea-Bejar, A. Impact of the stage of ripening and dietary fat on in vitro bioaccessibility of beta-carotene in 'Ataulfo' mango. *J. Agric. Food Chem.* **2008**, *56*, 1511−1516.
(25) Goltz, S. R.; Sapper, T. N.; Failla, M. L.; Campbell, W. W.; Ferruzzi, M. G. Carotenoid bioavailability from raw vegetables and a moderate amount of oil in human subjects is greatest when the majority of daily vegetables are consumed at one meal. *Nutr. Res. (N. Y., NY, U. S.)* **2013**, *33*, 358−366.
(26) Failla, M. L.; Thakkar, S. K.; Kim, J. Y. In Vitro Bioaccessibility of beta-carotene in orange fleshed sweet potato (ipomoea batatas, lam.). *J. Agric. Food Chem.* **2009**, *57*, 10922−10927.
(27) Huo, T.; Ferruzzi, M. G.; Schwartz, S. J.; Failla, M. L. Impact of fatty acyl composition and quantity of triglycerides on bioaccessibility of dietary carotenoids. *J. Agric. Food Chem.* **2007**, *55*, 8950−8957.
(28) Veda, S.; Platel, K.; Srinivasan, K. Influence of food acidulants and antioxidant spices on the bioaccessibility of beta-carotene from selected vegetables. *J. Agric. Food Chem.* **2008**, *56*, 8714−8719.
(29) Veda, S.; Platel, K.; Srinivasan, K. Varietal Differences in the bioaccessibility of beta-carotene from mango (mangifera indica) and papaya (carica papaya) fruits. *J. Agric. Food Chem.* **2007**, *55*, 7931−7935.
(30) Veda, S.; Platel, K.; Srinivasan, K. Enhanced bioaccessibility of beta-carotene from yellow-orange vegetables and green leafy vegetables by domestic heat processing. *Int. J. Food Sci. Technol.* **2010**, *45*, 2201−2207.
(31) McClements, D. J.; Xiao, H. Excipient foods: designing food matrices that improve the oral bioavailability of pharmaceuticals and nutraceuticals. *Food Funct.* **2014**, *5*, 1320−1333.
(32) McClements, D. J. Utilizing food effects to overcome challenges in delivery of lipophilic bioactives: structural design of medical and functional foods. *Expert Opin. Drug Delivery* **2013**, *10*, 1621−1632.
(33) Abdel-Aal, E.-S. M.; Akhtar, H.; Zaheer, K.; Ali, R. Dietary sources of lutein and zeaxanthin carotenoids and their role in eye health. *Nutrients* **2013**, *5*, 1169−1185.
(34) Hernandez-Carrion, M.; Hernando, I.; Quiles, A. Tissue microstructure, physicochemical properties, and bioactive compound locations in different sweet pepper types. *Food Sci. Technol. Int.* **2015**, *21*, 3−13.
(35) O'Sullivan, L.; Jiwan, M. A.; Daly, T.; O'Brien, N. M.; Aherne, S. A. Bioaccessibility, uptake, and transport of carotenoids from peppers (capsicum spp.) using the coupled in vitro digestion and human intestinal Caco-2 cell model. *J. Agric. Food Chem.* **2010**, *58*, 5374−5379.
(36) McClements, D. J.; Li, Y. Structured emulsion-based delivery systems: Controlling the digestion and release of lipophilic food components. *Adv. Colloid Interface Sci.* **2010**, *159*, 213−228.
(37) Qian, C.; Decker, E. A.; Xiao, H.; McClements, D. J. Nanoemulsion delivery systems: Influence of carrier oil on beta-carotene bioaccessibility. *Food Chem.* **2012**, *135*, 1440−1447.
(38) Salvia-Trujillo, L.; Qian, C.; Martin-Belloso, O.; McClements, D. J. Modulating beta-carotene bioaccessibility by controlling oil composition and concentration in edible nanoemulsions. *Food Chem.* **2013**, *139*, 878−884.
(39) Zou, L.; Zheng, B.; Liu, W.; Liu, C.; Xiao, H.; McClements, D. J. Enhancing nutraceutical bioavailability using excipient emulsions: Influence of lipid droplet size on solubility and Bioaccessibility of Powdered Curcumin. *J. Funct. Foods* **2015**, *15*, 72−83.
(40) Mun, S.; Kim, Y.-R.; McClements, D. J. Control of beta-carotene bioaccessibility using starch-based filled hydrogels. *Food Chem.* **2015**, *173*, 454−461.
(41) McClements, D. J.; Henson, L.; Popplewell, L. M.; Decker, E. A.; Choi, S. J. Inhibition of ostwald ripening in model beverage emulsions by addition of poorly water soluble triglyceride oils. *J. Food Sci.* **2012**, *77*, C33−C38.
(42) Mun, S.; Decker, E. A.; McClements, D. J. Influence of droplet characteristics on the formation of oil-in-water emulsions stabilized by surfactant-chitosan layers. *Langmuir* **2005**, *21*, 6228−6234.
(43) Vingerhoeds, M. H.; Blijdenstein, T. B. J.; Zoet, F. D.; van Aken, G. A. Emulsion flocculation induced by saliva and mucin. *Food Hydrocolloids* **2005**, *19*, 915−922.
(44) Jenkins, P.; Snowden, M. Depletion flocculation in colloidal dispersions. *Adv. Colloid Interface Sci.* **1996**, *68*, 57−96.
(45) Sek, L.; Porter, C. J. H.; Kaukonen, A. M.; Charman, W. N. Evaluation of the in-vitro digestion profiles of long and medium chain

DOI: 10.1021/acs.jafc.5b04217
J. Agric. Food Chem. 2015, 63, 8534−8543

glycerides and the phase behaviour of their lipolytic products. *J. Pharm. Pharmacol.* **2002**, *54*, 29−41.
(46) Christensen, J. O.; Schultz, K.; Mollgaard, B.; Kristensen, H. G.; Mullertz, A. Solubilisation of poorly water-soluble drugs during in vitro lipolysis of medium- and long-chain triacylglycerols. *Eur. J. Pharm. Sci.* **2004**, *23*, 287−296.
(47) Li, Y.; McClements, D. J. New Mathematical Model for Interpreting pH-Stat Digestion Profiles: Impact of Lipid Droplet Characteristics on in Vitro Digestibility. *J. Agric. Food Chem.* **2010**, *58*, 8085−8092.
(48) Benito-Gallo, P.; Franceschetto, A.; Wong, J. C. M.; Marlow, M.; Zann, V.; Scholes, P.; Gershkovich, P. Chain length affects pancreatic lipase activity and the extent and pH-time profile of triglyceride lipolysis. *Eur. J. Pharm. Biopharm.* **2015**, *93*, 353−362.
(49) Devraj, R.; Williams, H. D.; Warren, D. B.; Mullertz, A.; Porter, C. J. H.; Pouton, C. W. In vitro digestion testing of lipid-based delivery systems: Calcium ions combine with fatty acids liberated from triglyceride rich lipid solutions to form soaps and reduce the solubilization capacity of colloidal digestion products. *Int. J. Pharm.* **2013**, *441*, 323−333.
(50) Porter, C. J. H.; Wasan, K. M. Lipid-based systems for the enhanced delivery of poorly water soluble drugs. *Adv. Drug Delivery Rev.* **2008**, *60*, 615−616.

DOI: 10.1021/acs.jafc.5b04217
J. Agric. Food Chem. 2015, 63, 8534−8543

produce more aromatic alcohols per cell than yeast cells at low population density.[4,12]

In the present study, we aimed to correlate our previously implemented quantitative kinetics model to monitor the aromatic alcohols 2-phenylethanol, tryptophol, and tyrosol in *S. cerevisiae*[15] and the expression of the *ARO8*, *ARO9*, and *ARO10* genes. Additionally, we were interested in whether, and to what extent, the parameters to which yeast are exposed during wine fermentation affect the production of these quorum-sensing molecules. Of the multiple stresses that can affect yeast vitality during fermentation, here ethanol stress was selected, with examination of the possible effects on 2-phenylethanol, tyrosol, and tryptophol production. Thus, after ethanol addition to the medium to create stress, the relative expression levels of the *ARO8*, *ARO9*, and *ARO10* genes were compared to the kinetics of the production of these quorum-sensing aromatic alcohols.

MATERIALS AND METHODS

Strains and Inoculum Preparation. This study was performed with the wine-yeast strain *S. cerevisiae* ZIM 1927, which was originally isolated from the must of 'Malvasia' wine grapes. The strain was obtained from the Collection of Industrial Microorganisms (ZIM) at the Biotechnical Faculty, University of Ljubljana, Ljubljana, Slovenia. The preparation of the inoculum and the fermentation were carried out using MS300 synthetic must, as described previously,[16] with some modifications. The medium contained 100 g/L glucose and 100 g/L fructose, and no anaerobic factors were used. It contained also 460 mg/L ammonium chloride, a mixture of 19 amino acids (612.6 mg/L L-proline, 505.3 mg/L L-glutamine, 374.4 mg/L L-arginine, 179.3 mg/L L-tryptophan, 145.3 mg/L L-alanine, 120.4 mg/L L-glutamic acid, 78.5 mg/L L-serine, 759.2 mg/L L-threonine, 48.4 mg/L L-leucine, 44.5 mg/L L-aspartic acid, 44.5 mg/L L-valine, 37.9 mg/L L-phenylalanine, 32.7 mg/L isoleucine, 32.7 mg/L L-histidine, 31.4 mg/L L-methionine, 18.3 mg/L L-tyrosine, 18.3 mg/L L-glycine, 17.0 mg/L lysine, 13.1 mg/L L-cysteine), mineral salts (750 mg/L KH_2PO_4, 500 mg/L K_2SO_4, 250 mg/L $MgSO_4{\cdot}7H_2O$, 155 mg/L $CaCl_2{\cdot}2H_2O$, 200 mg/L NaCl, 4 mg/L $MnSO_4{\cdot}H_2O$, 4 mg/L $ZnSO_4$, 1 mg/L $CuSO_4{\cdot}5H_2O$, 1 mg/L KI, 0.4 mg/L $CoCl_2{\cdot}6H_2O$, 1 mg/L H_3BO_3, 1 mg/L $NaMoO_4{\cdot}2H_2O$), and vitamins (20 mg/L *myo*-inositol, 2 mg/L nicotinic acid, 1.5 mg/L calcium panthothenate, 0.25 mg/L thiamin HCl, 0.25 mg/L pyridoxine HCl, 0.003 mg/L biotin). The medium supports 300 mg of assimilable nitrogen, as provided by 460 mg/L ammonium chloride (corresponding to 120 mg of nitrogen) as well as by the mixture of 19 amino acids (corresponding to 180 mg of nitrogen). The inoculum was prepared aerobically in 100 mL Erlenmeyer flasks on a rotary shaker at 220 rpm constant shaking, at 22 °C. After 48 h of cultivation, the inoculum was centrifuged at 1500*g* and resuspended in 5 mL of fresh MS300 medium. The concentration of the yeast cells was determined by automatic counting of viable cells using ImageJ software, as described previously.[15] The yeast suspensions were diluted with MS300 to obtain two different initial concentrations, 1.2×10^7 cells/mL and a 20-fold dilution for 6×10^5 cells/mL, with 1.5 mL of the inoculated medium distributed in four repetitions into perforated 2 mL microcentrifuge tubes.

Fermentation Conditions. The mini-fermentations were carried out at 22 °C, as described previously.[15] Throughout the 42 h of the mini-fermentations, four of the microcentrifuge tubes were sampled every 2 h, to determine the concentrations of viable cells and quorum-sensing molecules (i.e., 2-phenylethanol, tryptophol, tyrosol), and to collect cell biomass for RNA analysis.

Determination of Viable Cell Concentrations. The viable cell concentrations were determined as described previously.[15] Briefly, 20 μL of the cell suspensions was collected from each fermenter and diluted 1:1 (v/v) with methylene blue. The stained suspension was transferred to a Bürker–Türk hemocytometer, and bright-field microscope images were recorded using an attached camera. The viable cells were then counted using ImageJ software.

Determination of the 2-Phenylethanol, Tryptophol, and Tyrosol Concentrations. The monitoring and kinetics analyses for 2-phenylethanol, tryptophol, and tyrosol were performed as described previously.[15] Briefly, high-performance liquid chromatography (HPLC) analysis was performed using a reverse phase column (XBridge Phenyl, 5 μm, 4.6 mm × 150 mm; Waters) and H_2O/acetonitrile (80:20, v/v) as the mobile phase. Prior to the HPLC analysis, 1 mL of the samples was centrifuged (initially 1500*g* for 5 min, then 6500*g* for 5 min) and filtered through 0.2 μm filters (Phenex, Phenomenex, Italy). 2-Phenylethanol, tryptophol, and tyrosol were detected using a fluorescence detector (Shimadzu RF551, Japan), at their optimal wavelengths of 255/285, 280/368, and 275/315 nm, respectively.

Quorum-Sensing Kinetics. We described the quorum-sensing kinetics with the recently implemented parameter of "production rate", which was calculated on the basis of the data from the measurements of the cell concentrations and the quorum-sensing molecule concentrations. The production rate of the quorum-sensing molecules (R_{QSM}) on the interval (t_1, t_2) was calculated as

$$R_{\mathrm{QSM}\left(\frac{t_1+t_2}{2}\right)} = \frac{\left(c_{\mathrm{QSM}(t_2)} - c_{\mathrm{QSM}(t_1)}\right)}{\left(\frac{c_{t_1}+c_{t_2}}{2}\right) \times (t_2 - t_1)} [\mathrm{fmol/cells/h}] \quad (1)$$

where t is time, c_{QSM} is the concentration of the quorum-sensing molecule, c is the concentration of the cells, and $dc_{QSM}/dt \approx (c\mathrm{QSM}(t_2) - c\mathrm{QSM}(t_1))/(t_2 - t_1)$. To plot R_{QSM}, curve fitting for the concentration of cells and the quorum-sensing molecules was performed, from which 100 data points were generated. These data points from the fitted curves were then used in eq 1.

RNA Isolation. From samples with an initial cell concentration of 1.2×10^7 cells/mL, the total RNA was isolated after 0, 4, 12, 16, 24, and 32 h of cultivation; in samples with an initial cell concentration of 6×10^5 cells/mL, total RNA was isolated after 0, 18, 26, 30, 34, and 38 h of cultivation. RNA was isolated using the commercial Qiagen RNeasy mini kits, as described by the manufacturer. Briefly, cell lysates were prepared using 350 μL of lysis buffer (RLT; Qiagen GmbH) containing β-mercaptoethanol (10 μL/L RLT buffer), acid-washed glass beads (diameter = 420–600 μm; Sigma), and a homogenizer (Bullet Blender Storm, Next Advance). After this, the samples were centrifuged (12000*g*, 10 min) and 900 μL of supernatant was transferred to new centrifuge tubes. To remove the residual DNA, on-column DNase digestion with the RNase-free DNase set (Qiagen) was performed. Total RNA was eluted in 50 μL of RNase-free water (Qiagen) and stored at −80 °C until use.

The quantity and purity of the total RNA were measured with a spectrophotometer (Lambda Bio, PerkinElmer), and visualized by agarose gel electrophoresis.

Reverse Transcription and cDNA Synthesis. The reverse transcription reaction was performed using commercial Superscript VILO cDNA synthesis kits (Invitrogen), according to the manufacturer's instructions, with some modifications. For each single reaction, we combined 2 μL of 5-fold concentrated VILO reaction mix, 1 μL of 10-fold concentrated Superscript enzymatic mix, the RNA, and diethylpyrocarbonate-treated water, to a final reaction volume of 10 μL. The RNA concentrations in the samples were determined spectrophotometrically, and the starting RNA concentration was normalized to 650 ng. The reaction mixtures were successively incubated for 10 min at 25 °C, for 60 min at 42 °C, and for 5 min at 85 °C.

Primer and Probe Design. The primers and probes for the *ARO8*, *ARO9*, and *ARO10* target genes and the *ACT1*, *18S rRNA*, *TEF1* reference genes were designed with the Primer 3 software package.[17] The oligonucleotides and probes used were designed in silico, using the NCBI database. The probes were labeled at their 5′-end using 6-carboxyfluorescein (FAM) and at their 3′-end using 5′-tetramethylrhodamine-5(6)-carboxamide (TAMRA).

Controls. Each sample was analyzed as three biological repetitions and two technical repetitions. To check for residual DNA, each RNA sample was also subjected to a cDNA synthesis reaction without addition of the reverse transcriptase enzyme (NoRT control). When a

DOI: 10.1021/acs.jafc.5b03400
J. Agric. Food Chem. 2015, 63, 8544–8550

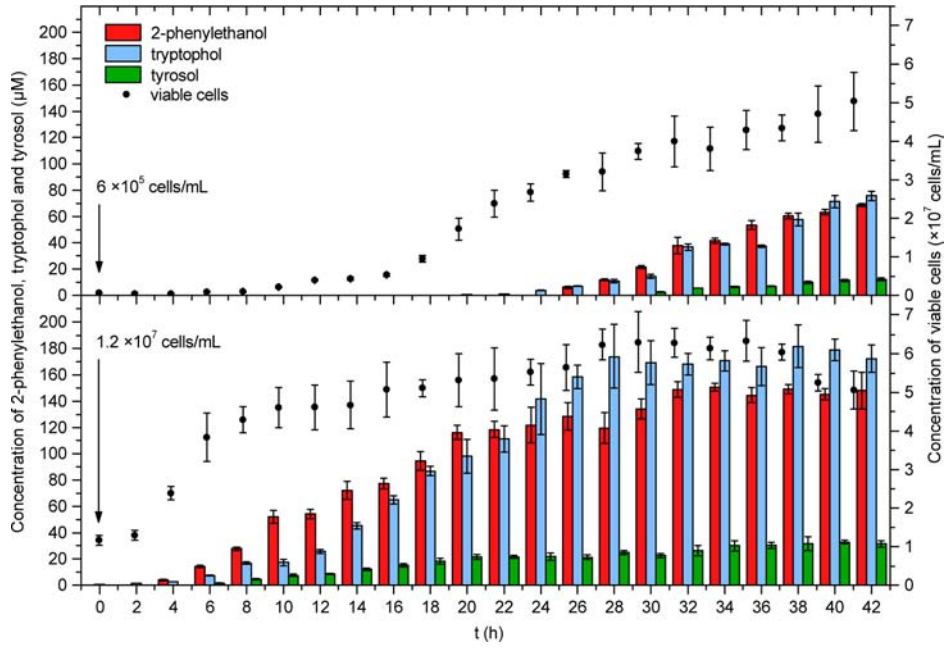

Figure 1. Concentrations of viable cells (circles) and production of 2-phenylethanol, tryptophol, and tyrosol (histograms, as indicated) over 42 h of mini-fermentations with *S. cerevisiae* at the initial cell concentrations of 6×10^5 cells/mL (top) and 1.2×10^7 cells/mL (bottom).

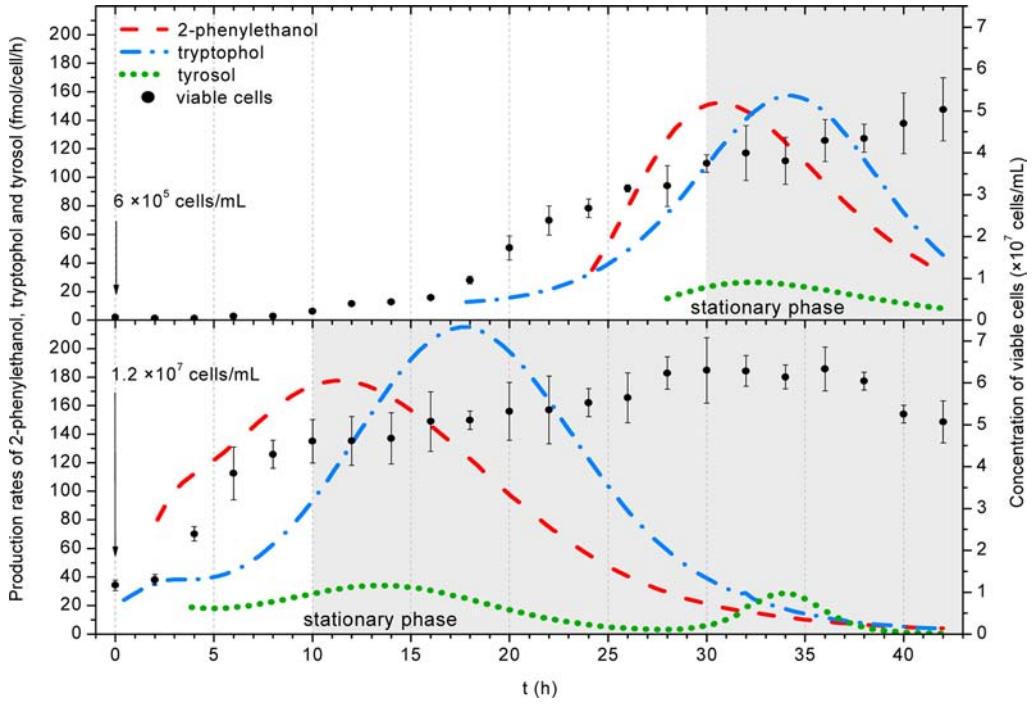

Figure 2. Production rates of 2-phenylethanol (dashed line), tryptophol (dash-dotted line), and tyrosol (dotted line) over 42 h of mini-fermentations with *S. cerevisiae* at the initial cell concentrations of 6×10^5 cells/mL (top) and 1.2×10^7 cells/mL (bottom). The production rates were calculated from concentrations of aromatic alcohols and cells presented in Figure 1.

ΔC_t of >4 between the sample and its respective NoRT control was obtained, the DNA contamination level was considered negligible. Negative control templates consisted of the master mixture with sterile water as the template.

Real-Time Quantitative PCR. Real-time quantitative PCR was carried out with the ABI PRISM 7900 HT Sequence Detection System, using the SDS 3.2 application software (Applied Biosystems). For each reaction, 5 μL of EXPRESS qPCR SuperMix Universal was mixed with 0.02 μL of passive reference dye (ROX), 2.25 μL of 125 nM probe, the optimal oligonucleotide concentration (300 or 600 nM), and nuclease-free water, to give a final volume of 8 μL. The 8 μL reaction mixture and 2 μL of diluted cDNA (final concentration = 1 ng/μL) were transferred to each well of 384-well optical reaction plates (MicroAmp, Applied Biosystems). The following cycle profile was used: one cycle at 50 °C for 15 min, one cycle at 95 °C for 2 min, 40 cycles at 95 °C for 15 s, and 60 °C for 1 min. The C_t values obtained by real-time PCR were quantified using a relative standard curve. For this purpose, a stock solution of cDNA was prepared, from which 2-fold serial dilutions were made.

DOI: 10.1021/acs.jafc.5b03400
J. Agric. Food Chem. 2015, 63, 8544−8550

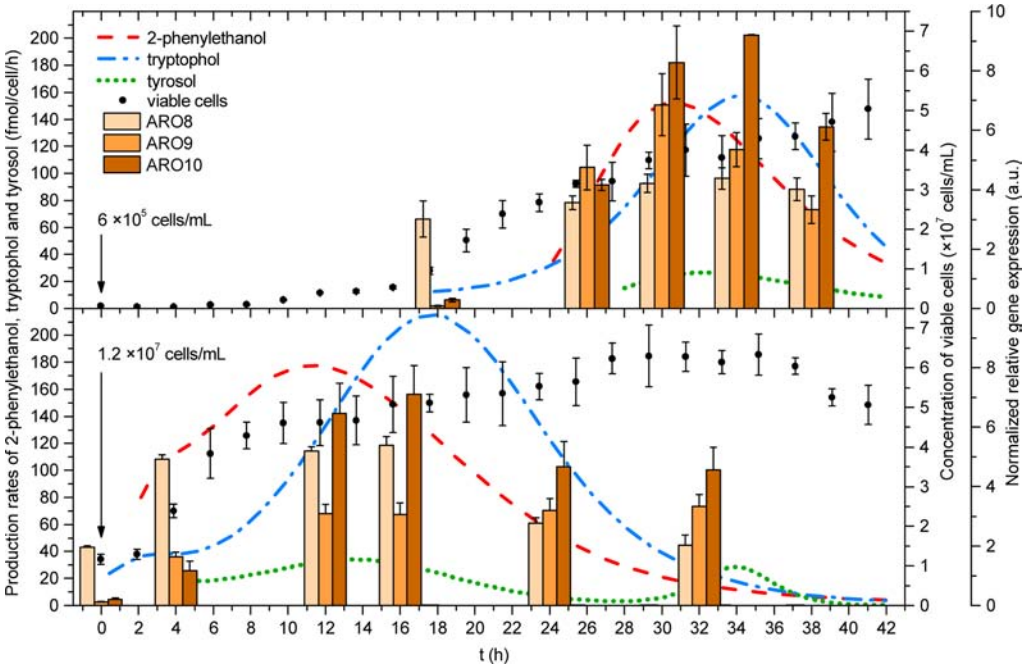

Figure 3. Relative expression of the *ARO8*, *ARO9*, and *ARO10* genes (as indicated) and correlation with the production rates of 2-phenylethanol (dashed line), tryptophol (dash-dotted line), and tyrosol (dotted line) over 42 h of mini-fermentations with *S. cerevisiae* at the initial cell concentrations of 6×10^5 cells/mL (top) and 1.2×10^7 cells/mL (bottom).

Analysis of the Relative Expression Levels of *ARO8*, *ARO9*, and *ARO10*. To analyze the variability of the housekeeping genes used, the software program geNorm^{PLUS} was used.[18] This program calculates first the gene stability measure M (which must be <1.5) for each housekeeping gene used and, second, the normalization factor for the housekeeping genes used, which is applied in the data processing. The relative *ARO8*, *ARO9*, and *ARO10* gene expression levels were normalized to the relative quantities of the three different housekeeping genes using geNorm^{PLUS}.

Effects of Ethanol on *ARO* Gene Expression and Production of Quorum-Sensing Molecules in *S. cerevisiae*. At the start of the mini-fermentations in MS300 medium, where the initial cell count was 2×10^7 cells/mL, 2, 6, 8, and 12% ethanol were added to the medium (as final concentrations). Cell viability and quorum-sensing molecule production was monitored after 0, 4, 8, 12, 24, and 28 h of cultivation and compared to the control sample with no ethanol added. The total RNA was isolated from the control sample and from the sample with initial 2% ethanol, after 0, 4, 8, 12, and 24 h, whereas the RNA was isolated from the sample with initial 6% ethanol after 0, 8, 12, 24, and 28 h, as described above. *ARO8*, *ARO9*, and *ARO10* gene expression levels were compared to the kinetics of the 2-phenylethanol, tryptophol, and tyrosol production.

RESULTS AND DISCUSSION

In our previous study,[15] we claimed that in *S. cerevisiae*, the kinetics of the production of 2-phenylethanol, tryptophol, and tyrosol indicate their involvement in the mechanism of quorum sensing. We showed that the kinetics can be calculated from the concentrations of these quorum-sensing molecules and the viable cells, as we took into consideration that only live cells with active permeases,[19] transaminases, decarboxylases, and reductases[20,21] can produce 2-phenylethanol, tryptophol, and tyrosol. As the mechanism of quorum sensing starts with the activation of the *ARO* genes,[13,14] in the present study, we aimed to correlate the kinetics model that we had previously developed with the expression of the *ARO* genes that are responsible for 2-phenylethanol, tryptophol, and tyrosol biosynthesis (i.e., *ARO8*, *ARO9*, *ARO10*). In addition, to show the correlation of the quorum-sensing kinetics and cell concentration, we conducted two parallel fermentations with low (6×10^5 cells/mL) and high (1.2×10^7 cells/mL) initial concentrations of the yeast cells.

Quorum-Sensing Kinetics in *S. cerevisiae* Correlate with Expression of the *ARO8*, *ARO9*, and *ARO10* Genes. The monitored parameters of the two fermentations with low and high initial cell concentrations are presented in Figure 1. Here, it can be seen that the first quorum-sensing molecules in the medium were detected in both cases when the concentrations of viable cells were between 1×10^7 and 2×10^7 cells/mL (i.e., the quorum was reached), despite the differences in the slopes of the growth curves. To examine the kinetics of these quorum-sensing molecules, eq 1 was used, and the production rates obtained for each quorum-sensing molecule are plotted in Figure 2.

From the peaks of these production rates, the kinetics of the quorum sensing can be determined; namely, at both low and high cell concentrations, cells in the exponential phase started with an intense production of tryptophol, which was then closely followed by 2-phenylethanol. At both cell concentrations, when the peak production of 2-phenylethanol was first achieved (at 30 and 12 h, respectively), the cell growth curves showed that the cells were in the declining growth phase. The peak of the tryptophol production rate appeared around 4 and 6 h later in the case of the low and high cell concentrations, respectively, which corresponded also to the declining growth phase, whereas the tyrosol production rate reached its peak between the peaks of 2-phenylethanol and tryptophol. The production of all three aromatic alcohols reached its peak in the declining growth phase, which is earlier than reported by others, who connected quorum-sensing molecule release with stationary growth phase.[12]

An interesting phenomenon appeared after 30 h of fermentation with the initial high cell concentration. At this point, a slight decrease in cell growth was observed together

DOI: 10.1021/acs.jafc.5b03400
J. Agric. Food Chem. 2015, 63, 8544−8550

with the increased tyrosol production rate, similar to the growth decline after 10 h of fermentation, when the first tyrosol peak was determined. This cell response might have implications on a quorum-sensing mechanism where the regulation differs from that of 2-phenylethanol and tryptophol. With regard to its stimulative effect on germ-tube formation in the yeast *C. albicans*,[5] the increase of tyrosol in the declining growth phase could be similarly explained as an antagonistic mechanism against the effect of 2-phenylethanol and tryptophol. However, the second peak at 34 h did not result in increased cell growth as observed after the first peak, but this could be explained by the high concentration of already accumulated 2-phenylethanol and tryptophol in the medium. On the other hand, this increased tyrosol concentration in the medium might represent the consequence of intracellular tyrosol release from lysed cells, especially after 30 h of fermentation.

Through the prism of quorum-sensing theory, these observations indicate that the accumulation of aromatic alcohols in the medium is growth-phase dependent and is regulated by the cell concentration. This is in agreement with previous findings,[12] despite some major differences in experimental approach. Indeed, Chen and Fink[12] estimated the cell concentrations by OD_{600} measurements, which did not take differences between live and dead cells into consideration, and they used silica gel thin layer chromatography for the detection of quorum-sensing molecules. They also analyzed only one time point, which did not make it possible to study the production kinetics of the putative quorum-sensing molecules. The development of better experimental techniques has now provided us with a more detailed view into this biological phenomenon. Thus, from the data in the present study, it can be hypothesized that cells start to regulate their concentration first with the intense release of tryptophol, which is then followed by the release of 2-phenylethanol and tyrosol. When the cells reach the stationary phase, the intensity of the production of these quorum-sensing molecules decreases, most likely because their production is repressed either by autoregulation or by some other event that occurs during this phase (e.g., nutrient limitation). As well as these more detailed kinetics of the quorum-sensing molecules 2-phenylethanol and tryptophol in the present study, the correlation of tyrosol production with cell concentration in *S. cerevisiae* has also not been reported previously, to the best of our knowledge.

If the established model is valid, the peak production rates of 2-phenylethanol, tryptophol, and tyrosol should match the peak expression of the genes that are responsible for their synthesis. In this regard, these quorum-sensing kinetics were correlated with *ARO8*, *ARO9*, and *ARO10* expression (Figure 3).

The expression of the *ARO* genes was normalized to the mean *M* (i.e., the gene stability measure; see Materials and Methods) of the selected housekeeping genes *ACT1*, *18S rRNA*, and *TEF1*. The small differences between these *M* values (0.690, 0.707, 0.742, respectively) indicated that each of these housekeeping genes was constitutively expressed under the experimental conditions and that they were therefore suitable as internal controls.

The expression of the selected *ARO* genes was monitored after 0, 4, 12, 16, 24, and 32 h of cultivation for the low initial cell concentration and after 0, 18, 26, 30, 34, and 38 h of cultivation for the high initial cell concentration. In both cases, the *ARO8* gene, which encodes the aminotransferase enzyme that is responsible for early synthesis of aromatic alcohols, was the first of these three genes to be activated, which occurred early in the exponential growth phase. This was followed by *ARO9* and *ARO10* gene expression in the declining growth phase, which thus paralleled later peak activities (Figure 3). These kinetics are in agreement with the kinetics of the quorum-sensing molecules in the medium determined as described above. Moreover, the peak expression of these *ARO* genes corresponded relatively closely to the peak production rates of the quorum-sensing molecules (Figure 3).

Positive feedback regulation by 2-phenylethanol and tryptophol,[4,12] and maybe by tyrosol, would explain the continued relatively high expression of these *ARO* genes into the late stationary phase. It should be stressed that despite the apparent decrease in the production rates of these quorum-sensing molecules after entry into the stationary phase (Figure 2), they were still present in the medium at high concentrations, also at the last measurement time (see Figure 1).

Ethanol Addition Affects the Production of Quorum-Sensing Molecules at the Metabolic and Transcriptomic Levels. To date, there have not been any studies on the kinetics of the quorum-sensing molecules 2-phenylethanol, tryptophol, and tyrosol during alcoholic fermentation. In the present study, ethanol was selected from among several potential stress factors, as its toxicity is one of the major stress factors that undermine the fermentative abilities of yeast.[22] Although *S. cerevisiae* is ethanol tolerant, relatively high ethanol concentrations inhibit cell growth and viability, which limits fermentation productivity and ethanol yield.[23,24] The effects of ethanol on the production of the quorum-sensing molecules 2-phenylethanol, tryptophol, and tyrosol in the medium were thus examined under addition of different ethanol concentrations at an initial cell count of 2×10^7 cells/mL. At the same time, the cell growth and the expression of the *ARO* genes were measured.

Here, the addition of 2% ethanol to the medium did not alter the cell growth of *S. cerevisiae*, whereas the kinetics of tryptophol and tyrosol production were weakly repressed when compared to the control with no ethanol addition (Figure 4). For 6% ethanol addition, a significant delay in the peak production of all three of these aromatic alcohols was detected, most probably due to weak suppression of cell growth. At 8% ethanol addition, the suppression of cell growth escalated, which resulted in a complete suppression of tryptophol production, whereas the other two measured aromatic alcohols were delayed and only weakly expressed. With the highest ethanol addition to the medium (12% initial concentration), no additional cell growth was seen, which is in agreement with previously reported findings;[25] moreover, cell viability dropped to 47% from the point of inoculation to 28 h, when none of these three aromatic alcohols were detected (data not shown).

An interesting observation in this part of the study can be noted. The times when the aromatic alcohols were first detected in the medium highly correlated with the specific cell concentrations; that is, in all cases of ethanol addition, the production of 2-phenylethanol, tryptophol, and tyrosol still started when the cells reached a concentration between 2×10^7 and 3×10^7 cells/mL, between 3×10^7 and 4×10^7 cells/mL, and between 2×10^7 and 4×10^7 cells/mL, respectively, despite the differences in the cell growth curves. These concentrations appear to represent the quorums that are specific for each of these three aromatic alcohols when they are synthesized under defined conditions of wine fermentation. On the other hand, the shapes of the production rate curves show

DOI: 10.1021/acs.jafc.5b03400
J. Agric. Food Chem. 2015, 63, 8544−8550

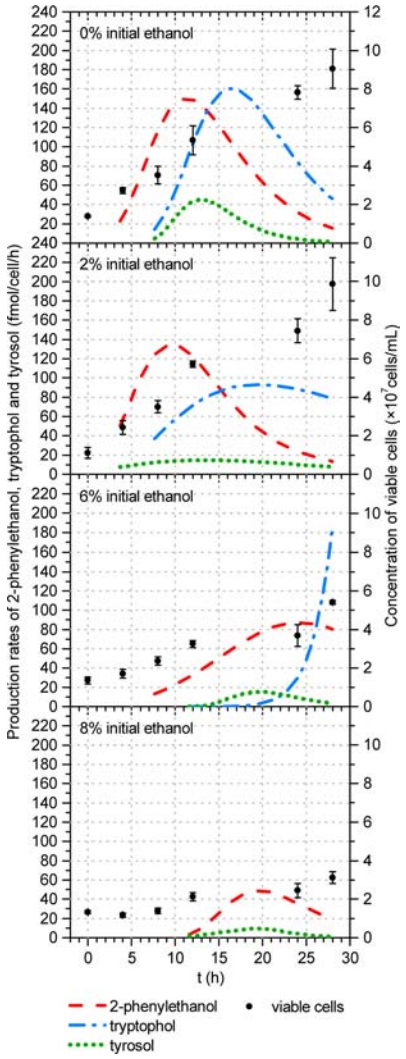

Figure 4. Production rates of 2-phenylethanol (dashed line), tryptophol (dash-dotted line), and tyrosol (dotted line) over 28 h of mini-fermentations with *S. cerevisiae* at the initial cell concentration of 1.2×10^7 cells/mL, without and with the addition of ethanol at 2, 6, and 8% (as indicated).

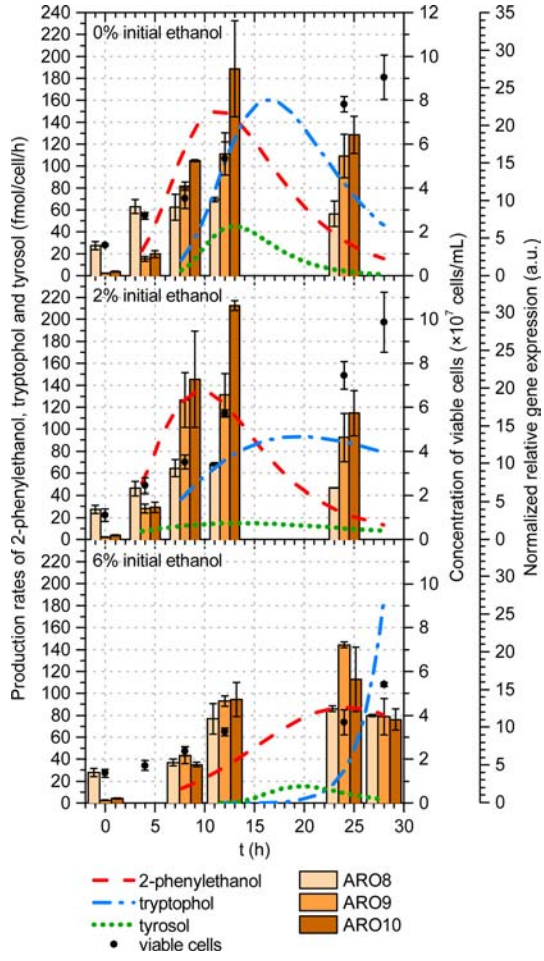

Figure 5. Relative expression of the *ARO8*, *ARO9*, and *ARO10* genes (as indicated) and correlation with the production rates of 2-phenylethanol (dashed line), tryptophol (dash-dotted line), and tyrosol (dotted line) over 28 h of mini-fermentations with *S. cerevisiae* at the initial cell concentration of 1.2×10^7 cells/mL, without and with the addition of ethanol at 2 and 6% (as indicated).

that ethanol addition had either a direct or an indirect effect on the production of all three monitored quorum-sensing molecules. It seems that cell concentration and ethanol addition influenced the start and the intensity of the production of quorum-sensing molecules, respectively.

To enrich these findings, we also measured the relative expression of the *ARO8*, *ARO9*, and *ARO10* genes during these mini-fermentations with the addition of ethanol. As seen in Figure 3, only *ARO8* expression was detected at the start of the fermentation, probably due to its involvement in the early stages of aromatic alcohol synthesis. As before, with the addition of 2 and 6% ethanol to the medium, the relative expression levels of these *ARO* genes that are responsible for the production of 2-phenylethanol, tryptophol, and tyrosol showed the same trends as the production rates of these three aromatic alcohols (Figure 5). This also again confirms the usability of the HPLC/microscopy methods developed here.

The experiments with added ethanol clearly showed that ethanol has a direct or an indirect effect on aromatic alcohol production rates. With the increased concentration of added ethanol, the production rates of 2-phenylethanol, tryptophol, and tyrosol seem to decrease, which is most probably correlated with the general disruption of numerous cell processes caused by ethanol stress including decreased cell growth and viability, amino acid and glucose transport systems, membrane structure and function, etc.[26] However, the addition of 6% of ethanol resulted in a significant increase of tryptophol production rate, which could be connected to the increased biosynthesis of tryptophan during ethanol stress as reported by Hirasawa et al. On the other hand, *ARO10* gene (coding for phenylpyruvate decarboxylase) was down-regulated, which might be the consequence of some specific ethanol involvement in decarboxylases and dehydrogenases regulation reported also by other authors.[27] In the case of the initial 8% ethanol addition, no tryptophol was detected and the cell concentration did not exceed the threshold that we showed here to be specific for the onset of tryptophol production, that is, around 3.5×10^7 cells/mL (Figure 4).

In the present study, we have demonstrated that the expression of the *ARO8*, *ARO9*, and *ARO10* genes correlates with the kinetics of the release of the aromatic alcohols 2-phenylethanol, tryptophol, and tyrosol. This thus demonstrates the connection between these activated quorum-sensing-related genes and their corresponding products that are released into

DOI: 10.1021/acs.jafc.5b03400
J. Agric. Food Chem. 2015, 63, 8544−8550

the medium. Furthermore, this study confirms the adequacy of our previously implemented model[15] for the study of these quorum-sensing kinetics. It also recognizes the quorums (i.e., the cell concentrations) at which *S. cerevisiae* start to produce 2-phenylethanol, tryptophol, and tyrosol, apparently as a response to their abundant growth. These findings thus open a new field of research that is aimed at the control of yeast quorum-sensing during wine fermentation or, even more specifically, at the control of yeast fermentation through the use of such quorum-sensing molecules themselves.

AUTHOR INFORMATION

Corresponding Authors

*(M.A.) Phone: +386-1-3203762. Fax: +386-1-2574092. E-mail: martina.avbelj@bf.uni-lj.si.

*(P.R.) Phone: +386-5-6626463. Fax: +386-5-6626480. E-mail: peter.raspor@fvz.upr.si.

Funding

This study was supported financially by the Slovenian Research Agency (ARRS).

Notes

The authors declare no competing financial interest.

ACKNOWLEDGMENTS

We thank Neža Čadež, the curator of the Collection of Industrial Microorganisms (ZIM) at the Biotechnical Faculty, Slovenia, for providing us with the yeast strain.

REFERENCES

(1) Bassler, B. L. Small talk. Cell-to-cell communication in bacteria. *Cell* **2002**, *109*, 421−424.

(2) Atkinson, S.; Williams, P. Quorum sensing and social networking in the microbial world. *J. R. Soc., Interface* **2009**, *6*, 959−978.

(3) Williams, P.; Winzer, K.; Chan, W. C.; Cámara, M. Look who's talking: communication and quorum sensing in the bacterial world. *Philos. Trans. R. Soc., B* **2007**, *362*, 1119−1134.

(4) Wuster, A.; Babu, M. M. Transcriptional control of the quorum sensing response in yeast. *Mol. BioSyst.* **2009**, *6*, 134−141.

(5) Chen, H.; Fujita, M.; Feng, Q.; Clardy, J.; Fink, G. R. Tyrosol is a quorum-sensing molecule in *Candida albicans*. *Proc. Natl. Acad. Sci. U. S. A.* **2004**, *101*, 5048−5052.

(6) Leeder, A. C.; Palma-Guerrero, J.; Glass, N. L. The social network: deciphering fungal language. *Nat. Rev. Microbiol.* **2011**, *9*, 440−451.

(7) Hazelwood, L. A.; Daran, J. M.; van Maris, A. J.; Pronk, J. T.; Dickinson, J. R. The Ehrlich pathway for fusel alcohol production: a century of research on *Saccharomyces cerevisiae* metabolism. *Appl. Environ. Microbiol.* **2008**, *74*, 2259−2266.

(8) Dickinson, J. R.; Salgado, L. E.; Hewlins, M. J. The catabolism of amino acids to long chain and complex alcohols in *Saccharomyces cerevisiae*. *J. Biol. Chem.* **2003**, *278*, 8028−8034.

(9) Dujon, B. Yeasts illustrate the molecular mechanisms of eukaryotic genome evolution. *Trends Genet.* **2006**, *22*, 375−387.

(10) Etschmann, M. M.; Bluemke, W.; Sell, D.; Schrader, J. Biotechnological production of 2-phenylethanol. *Appl. Microbiol. Biotechnol.* **2002**, *59*, 1−8.

(11) Fabre, C. E.; Blanc, P. J.; Goma, G. Production of 2-phenylethyl alcohol by *Kluyveromyces marxianus*. *Biotechnol. Prog.* **1998**, *14*, 270−274.

(12) Chen, H.; Fink, G. R. Feedback control of morphogenesis in fungi by aromatic alcohols. *Genes Dev.* **2006**, *20*, 1150−1161.

(13) Iraqui, I.; Vissers, S.; Cartiaux, M.; Urrestarazu, A. Characterisation of *Saccharomyces cerevisiae* ARO8 and ARO9 genes encoding aromatic aminotransferases I and II reveals a new aminotransferase subfamily. *Mol. Gen. Genet.* **1998**, *257*, 238−248.

(14) Iraqui, I.; Vissers, S.; André, B.; Urrestarazu, A. Transcriptional induction by aromatic amino acids in *Saccharomyces cerevisiae*. *Mol. Cell. Biol.* **1999**, *19*, 3360−3371.

(15) Zupan, J.; Avbelj, M.; Butinar, B.; Kosel, J.; Šergan, M.; Raspor, P. Monitoring of quorum-sensing molecules during minifermentation studies in wine yeast. *J. Agric. Food Chem.* **2013**, *61*, 2496−2505.

(16) Bely, L.; Sablayrolles, J. M.; Barre, P. Description of alcoholic fermentation kinetics: its variability and significance. *Am. J. Enol. Vitic.* **1990**, *40*, 319−324.

(17) Rozen, S.; Skaletsky, H. J. Primer3 on the WWW for general users and for biologist programmers. In *Methods in Molecular Biology: Bioinformatics Methods and Protocols*; Krawetz, S., Misener, S., Eds.; Humana Press: Totowa, NJ, USA, 1999; Vol. 132, 365−386.10.1385/1-59259-192-2:365

(18) Vandesompele, J.; De Preter, K.; Pattyn, F.; Poppe, B.; Van Roy, N.; De Paepe, A.; Speleman, F. Accurate normalization of real-time quantitative RT-PCR data by geometric averaging of multiple internal control genes. *Genome Biol.* **2002**, *3*, 1−12.

(19) Didion, T.; Grauslund, M.; Kielland-Brandt, M. C.; Andersen, H. A. Amino acids induce expression of BAP2, a branched-chain amino acid permease gene in *Saccharomyces cerevisiae*. *J. Bacteriol.* **1996**, *178*, 2025−2029.

(20) Ehrlich, F. Über die Bedingungen der Fuselolbildung und über ihren Zusammenhang mit dem Eiweissaufbau der Hefe. *Ber. Dtsch. Chem. Ges.* **1907**, *40*, 1027−1047.

(21) Sentheshanmuganathan, S. The mechanism of the formation of higher alcohols from amino acids by *Saccharomyces cerevisiae*. *Biochem. J.* **1960**, *47*, 558−576.

(22) Carmona-Gutierrez, D.; Sommer, C.; Andryushkova, A.; Kroemer, G.; Madeo, F. A higher spirit: avoiding yeast suicide during alcoholic fermentation. *Cell Death Differ.* **2012**, *19*, 913−914.

(23) Aguilera, F.; Peinado, R. A.; Millan, C.; Ortega, J. M.; Mauricio, J. C. Relationship between ethanol tolerance, H+ ATPase activity and the lipid composition of the plasma membrane in different wine yeast strains. *Int. J. Food Microbiol.* **2006**, *110*, 34−42.

(24) Ansanay-Galeote, V.; Blondin, B.; Dequin, S.; Sablayrolles, J. M. Stress effects of ethanol on fermentation kinetics by stationary-phase cells of *Saccharomyces cerevisiae*. *Biotechnol. Lett.* **2001**, *23*, 677−681.

(25) Costa, V.; Reis, E.; Quintanilha, A.; Moradas-Ferreira, P. Acquisition of ethanol tolerance in *Saccharomyces cerevisiae*: the key role of the mitochondrial superoxide dismutase. *Arch. Biochem. Biophys.* **1993**, *300*, 608−614.

(26) Chandler, M.; Stanley, G. A.; Rogers, P.; Chambers, P. A genomic approach to defining the ethanol stress response in the yeast *Saccharomyces cerevisiae*. *Ann. Microbiol.* **2004**, *54*, 427−454.

(27) Hirasawa, T.; Yoshikawa, K.; Nakakura, Y.; Nagahisa, K.; Furusawa, C.; Katakura, Y.; Shimizu, H.; Shioya, S. Identification of target genes conferring ethanol stress tolerance to *Saccharomyces cerevisiae* based on DNA microarray data analysis. *J. Biotechnol.* **2007**, *131*, 34−44.

DOI: 10.1021/acs.jafc.5b03400
J. Agric. Food Chem. 2015, 63, 8544−8550

chemicals responsible for flavors and fragrances, bitterness, acidity, viscosity, mouth feel, etc., is reached.

Fructose is a reducing sugar that exists as a mixture of five isomers, when dissolved in water. The different isomers in the form of β-pyranose, α-pyranose, β-furanose, α-furanose, and ketohexose (Figure 1) are distinct compounds, differing from

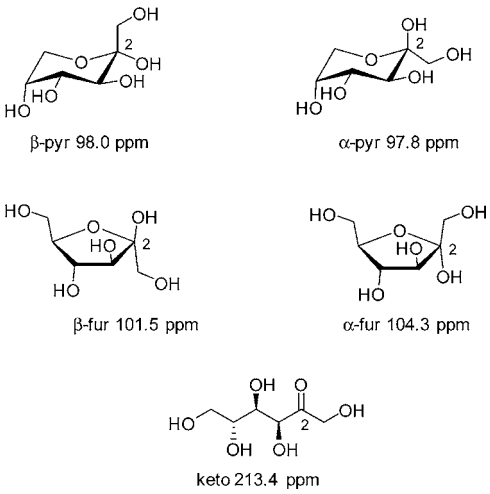

Figure 1. Structures of fructose isomers, with the chemical shift of carbon 2 in wines indicated.

each other in their chemical, physical, and biological properties.[14] These forms can be observed by nuclear magnetic resonance (NMR) spectroscopy, and their proportion in the equilibrium mixture can be measured. However, because of the low sensitivity of ^{13}C NMR, the majority of the studies have been performed with ^{1}H NMR and mainly in pure water solutions. The sweetness arising from fructose is the most variable among the naturally occurring sugars (this variation is directly related to the mutarotational behavior), and it is well-known that the sweetness of aqueous solutions containing fructose markedly decreases as the temperature increases.[15] The β-pyranose isomer is reported as the major form in aqueous solution and as the isomer responsible for sweetness, while β-furanose and α-furanose are nearly void of taste; the decrease in sweetness with increasing temperature is attributed to the lesser proportion of the β-pyranose isomer.[15] Analytical techniques, including gas chromatography (GC), high-performance liquid chromatography (HPLC),[16−20] and solid-phase microextraction (SPME),[21,22] and spectroscopic techniques, such as infrared (IR),[23] have been applied to the detection and measurement of fructose and other carbohydrates in wines. However, some of these analytical procedures are somewhat restricted and usually require time-consuming sample preparation procedures. ^{1}H NMR spectroscopy has been used extensively for identifying carbohydrates and other compounds in wines, but its application is limited in that the spectral region where the carbohydrate signals are observed is highly congested as a result of the presence of overlapping resonances, requiring multidimensional NMR approaches for deconvolution. Consistent analyses of ^{1}H NMR spectra of wine are further complicated by the large number of compounds present and also by the variations in ^{1}H chemical shifts that can occur as a result of changes in the pH, concentration, and presence of other compounds. For this reason, proper analysis typically requires sophisticated data treatment techniques, or alternatively, samples need to be pH-buffered and ideally have accurate pH adjustments made to minimize chemical shift variations, so that reliable assignment of specific resonances to individual compounds is possible.[24] Even with these sample manipulations prior to spectral acquisition, peak alignment and fine adjustments are often still required before spectral analyses can be reliably undertaken.[25] Although the qualitative and quantitative measurements of sugars in wine based on ^{1}H NMR spectra are challenging, advances have been made possible by the availability of innovative statistical analysis methods[25,26] and modern chemometric tools.[27] There have been multi-site demonstrations for the methodology of the Wine-Screener,[28] which showed the use of identical (400 MHz) NMR instrumentation, in conjunction with standardized, optimized sample preparation, data acquisition, data processing, and data analysis protocols for chemical analysis of wines and fruit juices based on ^{1}H NMR spectra.[24,29]

Although ^{13}C NMR has been used for the identification of individual components within complex mixtures, relatively few papers have described its use for quantitative analysis of carbohydrates in natural mixtures.[30,31] Analytical evaluation of honey by ^{13}C quantitative nuclear magnetic resonance (qNMR), aimed at revealing its origin and possible adulteration, which used a cryogenically cooled NMR probe to achieve higher sensitivity, has been reported.[32,33] Duquesnoy et al. developed a procedure using ^{13}C qNMR spectroscopy, which allowed for the direct identification and quantification of the carbohydrates in ethanolic extracts of two conifers, using an internal standard method.[34] Concerning wine analysis, a first quantitative analysis of contaminants (diethylene glycol and natural compounds, such as sugars, sugar alcohols, glycerol, and sugar acids) by ^{13}C NMR was reported in the mid-1980s.[35] Most recently, with the introduction of advanced technologies for direct sample analysis, full-bottle ^{13}C NMR was applied for the measurement of acetic acid content in wine.[36] Although the method was not practical for the quantification of wine components, such as tannins, flavonoids, phenols, and aldehydes, it was perfectly suitable for the study of the specific enological problem of acetic acid spoilage and the quality of fine wines.

We describe herein the use of ^{13}C qNMR for the quantitative determination of the relative fructose isomer composition and the total fructose content in wines. The method is also applicable to the detection and quantification of other compounds, including ethanol, other sugars, such as glucose and sucrose, or additional chemicals, as long as they have at least one ^{13}C signal that does not overlap with resonances from other compounds present.

MATERIALS AND METHODS

NMR Sample Preparation. Fructose, sucrose, and ethanol−OD (CH_3CH_2OD, 99.95% pure) were purchased from Sigma-Aldrich. D-[UL-$^{13}C_6$] fructose was purchased from Omicron Biochemicals. White wines produced from different grape varieties, including Baccus Weiss (2012 vintage), Pinot Gris (2013), Chardonnay Blanc (2013), and a late-harvest Riesling (2012), were purchased from wine stores in British Columbia, Canada. A sweet Moscato wine (2013) was purchased from an Italian winery. The 600 MHz grade, 5 mm NMR tubes (from Bruker) were filled with 550 μL of the wine or solution to be analyzed.

^{13}C NMR Spectra. Spectra were acquired on a Bruker AVANCE II digital spectrometer operating at 600.33 MHz for ^{1}H and 150.90 MHz for ^{13}C equipped with a Bruker 5 mm quadruple nucleus probe (QNP) cryoprobe. This direct-detect probe for ^{13}C has cold (~20 K) ^{13}C, ^{1}H, and ^{2}H coils, and the ^{13}C and ^{1}H preamplifier channels are both cooled to 77 K. The sample temperature was maintained at the desired temperature (283, 293, and 310 K) using a Bruker BVT-3000 and a Bruker BCU-05 air controller to regulate the sample temperature by

DOI: 10.1021/acs.jafc.5b03641
J. Agric. Food Chem. 2015, 63, 8551−8559

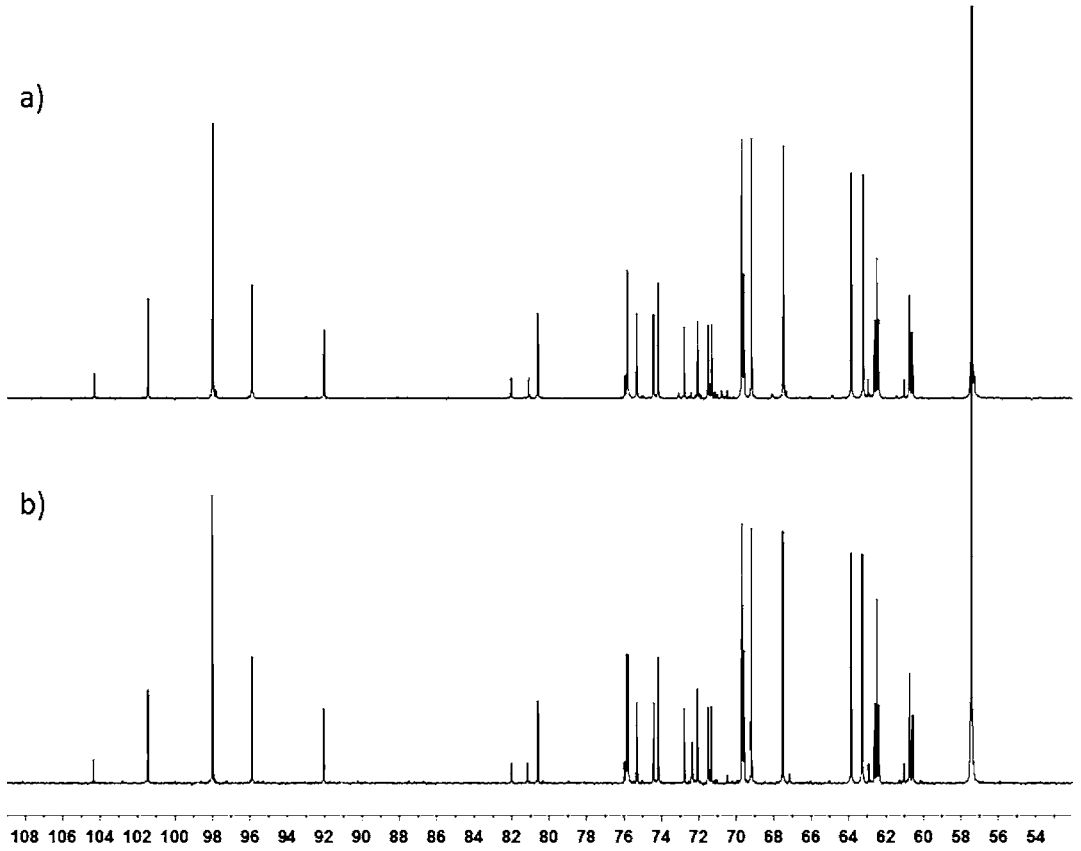

Figure 2. ^{13}C qNMR spectra of two wines analyzed: (a) Moscato and (b) late-harvest Riesling.

actively controlling the temperature of flow of heated air over the NMR tubes. The air flows ranged from 670 L/h for 293 K to 800 L/h for 310 K. These higher than normal flows compared to those used on conventional NMR probes are necessary to compensate for the cooling effect of the cold but vacuum-insulated NMR radio frequency (rf) coils surrounding the sample. The sample temperature was calibrated using 99.9% methanol[37] and was found to show a variation of less than 0.1 K from the displayed value. An inversion recovery pulse sequence was used to measure ^{13}C T^1 values for the carbons of interest with a recycle delay of 120 s and an array of 12 different recovery delays covering the range from 100 ms to 120 s. Relaxation data were fit using the T_1/T_2 analysis routines in the Topspin software. T_1 relaxation times for the C-2 carbons of fructose in 15 vol % ethanol at 298 K were 11.3 s for ketohexose, 8.9 s for α-furanose, 8.2 s for β-furanose, 8.5 s for β-pyranose, and 10.2 s for α-pyranose. Quantitative proton-decoupled ^{13}C NMR spectra were acquired using an inverse-gated pulse sequence to eliminate nuclear Overhauser effect (NOE) enhancements.[38] The ^{13}C transmitter frequency was set to 100 ppm, a spectral width of 250 ppm was used, and 32 scans, each consisting of 131 072 complex points, were accumulated with a recycle delay of 120 s between scans (65 min per spectrum). Proton decoupling was performed using the WALTZ-64 decoupling sequence (^{1}H pulses of 100 μs, with the ^{1}H transmitter set to 4.00 ppm).[39] A total of 5−12 spectra were recorded for each sample.

Dependence of the Equilibrium Composition of Fructose in Wine upon the Temperature. Fructose was dissolved in 15% ethanol−OD and 85% H_2O (fructose concentration of 1.11 M). Upon complete dissolution, the samples were transferred to 5 mm NMR tubes and equilibrated at three different temperatures (283, 293, and 310 K). ^{13}C qNMR experiments of 32 scans (65 min for each spectrum) were recorded, and six experiments were performed for each temperature. The effect of pH on the isomeric composition was evaluated by dissolving fructose (fructose concentration of 1.11 M) in 15% ethanol−OD and 85% H_2O solution, with the addition of diluted HCl or NaOH to the desired pH (pH 2.0 and 6.2, respectively). ^{13}C qNMR spectra of 32 scans were recorded for each sample, and six experiments were performed for each temperature (283, 293, and 310 K). For direct wine analysis, NMR tubes containing 550 μL of pure Riesling and Moscato were were prepared and five ^{13}C qNMR spectra (32 scans each) were acquired for each wine at each temperature.

Equilibrium Composition of Fructose at 293 K. Samples at different pH were prepared by dissolving fructose (1.11 M) in 15% ethanol−OD and 85% H_2O, previously acidified with diluted HCl and NaOH to the desired pH (pH 2.0, 3.0, 5.0, and 6.2, respectively). Samples containing different volume percentages of ethanol were prepared by dissolving fructose (1.11 M) in 5, 10, 20, and 30% ethanol−OD, respectively. Six ^{13}C qNMR spectra (32 scans) were recorded for each sample at 293 K.

Quantitative Determination Using the PULCON Method. An aqueous solution of sucrose of accurately known concentration (0.293 M) was prepared in 15 vol % ethanol−OD for the external reference sample, and ^{13}C qNMR spectra were recorded at 283, 293, and 310 K, respectively. For ethanol quantification, a solution of ethanol−OD (99.95% pure) was used as an external reference and ^{13}C qNMR spectra were recorded at 293 K. Samples of 550 μL of unaltered Baccus Weiss, Pinot Gris, and Chardonnay Blanc wines were added to separate NMR tubes, and five successive ^{13}C qNMR spectra (32 scans) were recorded of each wine at 293 K.

Analysis of ^{13}C NMR Spectra. Fourier transformation of the free induction decays (FIDs) was performed with 2-fold zero-filling and application of an exponential apodization (line broadening of 2 Hz). Spectra were manually phased and baseline-corrected using Bruker TopSpin software. The resulting series of ^{13}C qNMR spectra were deconvoluted using procedures coded in a Mathematica 5.1 notebook written by Dr. Darren Brouwer.[36] Because ^{13}C satellite peaks may be comparable to resonances of low-concentration components, deconvolution was applied and the contribution of satellites was taken into account (see the Supporting Information). An initial, automated deconvolution over the chemical shift range of interest for the carbon signals of fructose isomers was performed by reading in the phased, baseline-corrected spectrum. Experimental spectra were fit using the

DOI: 10.1021/acs.jafc.5b03641
J. Agric. Food Chem. 2015, 63, 8551−8559

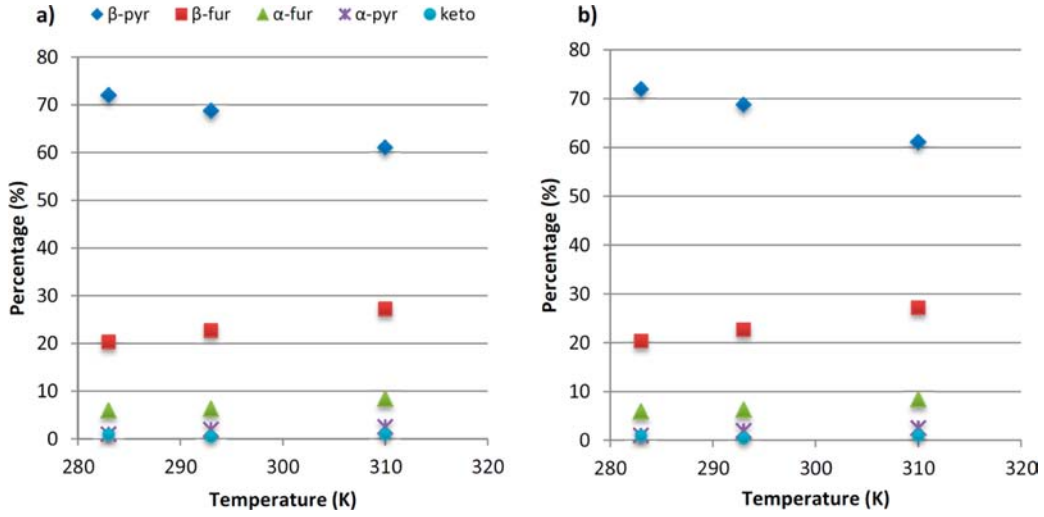

Figure 3. Equilibrium composition of fructose isomers (β-pyranose, β-furanose, α-furanose, α-pyranose, and ketohexose in order of abundance) and dependence of the individual components with increasing temperatures in wines: (a) Moscato and (b) late-harvest Riesling.

least-squares "nonlinearRegress" function in Mathematica. Starting from the initial parameters, the peak positions, peak widths at half height, and optimal combination of Lorentzian and Gaussian peaks were allowed to vary, to reach the best match for the resonances of the specific sample.

RESULTS AND DISCUSSION

^{13}C qNMR experiments were initially carried out on wine-like mixtures made by dissolving fructose in water containing up to 15% ethanol by volume to determine accurately the relative isomer ratios. High-resolution spectra and accurate quantification using peak area integration and peak deconvolution analyses of these data permitted accurate measurements of relative ratios of the fructose isomers. ^{13}C qNMR analysis of wines at 293 K was then carried out (Figure 2). Late-harvest and dessert wines are made with naturally dehydrated grapes and are very concentrated in sugars. A few hours of data acquisition using a cryoprobe provided ^{13}C NMR spectra with signal-to-noise ratios suitable for reliable quantification, and less than 1 mL aliquot of wine was required to perform the analysis. Here, we describe the application of the PULCON method[38] to ^{13}C qNMR spectra of wines for measuring fructose concentrations in wines sampled directly from the bottle and added to a NMR tube by using a sucrose solution as the external quantification standard. PULCON is a method that correlates the absolute intensities of two spectra measured in different solution conditions.[40] It overcomes the need to add an additional reference compound (internal standard) of known concentration to the sample being analyzed. PULCON therefore permits direct comparisons of integrals from different spectra and, thus, also different samples.[41] The use of ^{13}C NMR is inherently selective for the fructose isomers in wine because these sugars are present in the highest concentrations after water (which has no ^{13}C signal and is therefore not detected) and ethanol (whose ^{13}C signals are well-resolved from those of the sugars). Other organic compounds are present at much lower concentrations and do not interfere with the identification of the sugar resonances or peak area determinations of these signals. The protocol used in the present study only requires that an accurately measured volume of wine be transferred directly to the NMR tube. No solvents, standards, or buffer solutions are added, and no pH adjustments, chemical separations, derivatizations, or other pretreatments are carried out. The high spectral dispersion and narrow peak widths in ^{13}C NMR spectra, when coupled with the field stability and slow drift rates of the main magnet field available on most modern, shielded superconducting magnets, also make it possible to turn off the usual ^{2}H-based field locking if desired. This approach eliminates the need to add a deuterated solvent, which means that the wine can be tested and analyzed in its native condition.

The limit of detection (LOD) for ^{13}C qNMR, assuming a signal-to-noise of 3:1 for a 1 h acquisition on the 600 MHz QNP cryoprobe, is 0.6 g/L. The LOD was measured with samples of fructose of known concentration in wine-like solution. By comparison using ^{1}H NMR, the reported limits of quantification (LOQs) for the WineScreener are 0.2 g/L for sucrose and 0.5 g/L for glucose and fructose. Assuming that the LOQ is based on a 10:1 signal-to-noise ratio, we can estimate that WineScreener LODs are approximately one-third of the LOQ values. The ^{13}C-NMR-based methodology presented in the current work provides a useful, straightforward, and alternative analytical technique for analyzing sugars in wine (and other beverages). ^{13}C NMR removes the need to suppress the strong water and ethanol signals (which ^{1}H-NMR-based WineScreener requires), eliminates the need for pH adjustments (because ^{13}C chemical shifts do not vary much for the range of pH that most wines have), does not require a specific brand of NMR spectrometer or type of NMR probe, and can be carried out at any magnetic field strength, making it possible to implement it on virtually all NMR spectrometers designed for analyzing liquid samples. Furthermore, in the current ^{13}C NMR method, 550 μL of intact, unmodified wine is simply added directly to a NMR tube; there is no extra time, special equipment, or chemical addition required. The WineScreener protocol requires several pretreatment steps, including adding buffer and adjusting the pH.

Equilibrium Composition of Fructose in Wine: Variation with the Temperature. Previous investigations aimed at determining fructose isomeric composition resulted sometimes in inconsistent data, essentially as a result of the complexity of the mutarotation phenomenon and the limitations of the different methods employed.[42,43] Isomeric composition studies have been performed in different solvents, suggesting different relative compositions but also giving rise to confusing and incorrect interpretations.[44,45] ^{13}C qNMR spectroscopy has been considered unsuitable for determination of the isomeric ratios of fructose because of its low sensitivity and the difficulties in

DOI: 10.1021/acs.jafc.5b03641
J. Agric. Food Chem. 2015, 63, 8551−8559

Table 1. ^{13}C NMR Quantification of Individual Isomers of Fructose at Equilibrium, Using the Relative Molar Ratios

reference	method	pH	solvent	β-pyr (%)	β-fur (%)	α-fur (%)	α-pyr (%)	keto (%)
Barclay et al.[45] [a]	^{1}H NMR	[b]	D_2O	68.23	22.35	6.24	2.67	0.50
Mega et al.[46] [c]	^{13}C NMR	[b]	30% D_2O	69.6	21.1	5.7	3.0	0.5
this research[a]	^{13}C NMR	[b]	15% EtOD	67.22	23.96	6.18	2.01	0.63
	^{13}C NMR	2.0	15% EtOD	69.70	22.35	5.62	1.84	0.48
	^{13}C NMR	3.0	15% EtOD	67.58	23.49	5.91	2.15	0.87
	^{13}C NMR	5.0	15% EtOD	67.86	23.48	5.95	1.98	0.72
	^{13}C NMR	6.2	15% EtOD	69.30	22.71	5.73	1.70	0.57
	^{13}C NMR	3.0	wine 1[d]	68.72	22.68	6.26	1.90	0.44
	^{13}C NMR	3.9	wine 2[e]	68.72	22.60	6.22	1.92	0.54

[a]Measured at 293 K. [b]Unbuffered solvent. [c]Measured at 294 K. [d]Late-harvest Riesling (10% EtOH). [e]Moscato (15.5% EtOH).

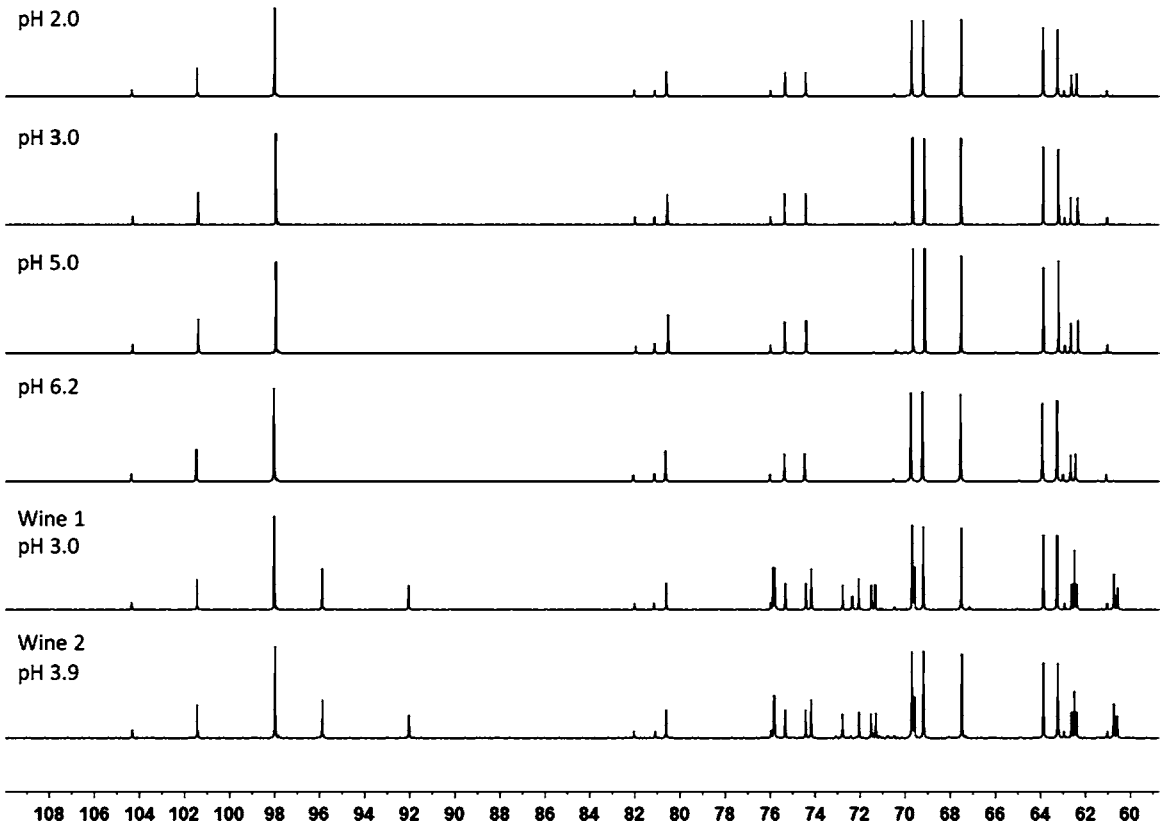

Figure 4. Representative ^{13}C NMR spectra of wine-like solutions at 293 K at different pH (pH 2.0, 3.0, 5.0, and 6.2 from the top) and for wines: wine 1, late-harvest Riesling at pH 3.0; wine 2, Moscato at pH 3.9.

detecting minor isomers, such as α-pyranose and keto forms.[46] However, in our cryprobe-enhanced experiments, ^{13}C signals for all five isomers of fructose (Figure 1) at a reasonable concentration (about 1 M) were observed. The analyses were performed on the resonances corresponding to the C-2 carbon of each isomer: β-pyranose (98.0 ppm), α-pyranose (97.8 ppm), β-furanose (101.5 ppm), α-furanose (104.3 ppm), and ketohexose (213.4 ppm). These signals were chosen because they generally do not overlap with other signals in wine samples. To guarantee the quantitative reliability of ^{13}C spectroscopy, it is necessary to set an interscan delay at least 5 times as long as the longest T_1 value, before applying another pulse, combined with a 90° pulse, to allow for complete relaxation of each carbon of the wine compounds to be analyzed. Quantitative spectra can also be obtained using a fast train of short pulses, which leads to a minor change in the steady-state magnetization as T_1 is varied. The integration of these two approaches usually provides excellent results.[32] We measured the T_1 values of all of the carbons for pure fructose in 15% ethanol solution, finding T_1 values ranging from 0.2 to 11.3 s. The highest T_1 values were observed for carbon 2 (11.3 s for the keto form). On the basis of the largest T_1 value, the interscan delay was fixed at 120 s (10 times the highest T_1) to ensure accurate signal intensities. WALTZ-16 composite pulse decoupling was used to minimize any rf-induced heating of the samples. The main objective of this set of experiments was to confirm the general trend observed for changes in the relative ratios of the fructose isomers in wines as the temperature of the samples was altered. The dependence of the individual components with increasing temperatures in Moscato and late-harvest Riesling is shown in Figure 3 and is very similar to wine-like solutions at different pH (see the Supporting Information).

The relative amounts of the various isomers of fructose, including the contribution of the keto form, were recently reported by Barclay et al. based on ^{1}H NMR spectroscopic

DOI: 10.1021/acs.jafc.5b03641
J. Agric. Food Chem. 2015, 63, 8551−8559

measurements of pure fructose in D_2O.[47] An accurate quantitative analysis of isomeric forms by ^{13}C qNMR spectroscopy was reported by Mega et al., who used ^{13}C-enriched fructose in water solution (30% D_2O and 70% H_2O).[48]

To the best of our knowledge, the current analysis of the relative ratios of the various fructose isomers is the first using real wine samples. These results provide useful information about the actual isomeric composition in aqueous ethanolic solutions and wines at different temperatures and help to resolve the previous inconsistencies in the literature regarding the equilibrium fructose concentrations in ethanolic solutions.[43] Our results correlate with those reported by Barclay et al.[45] and Mega et al.,[46] suggesting no significant variation in the equilibrium isomeric ratios with either the pH, solvent composition (pure water, aqueous solution containing 15% ethanol by volume, or wines) or a combination of these parameters.[45,46] No significant differences in the relative amounts of the various isomers were apparent in our measurements when comparing the ratios obtained at different pH or fructose concentrations in the presence of ethanol or in wines. The absolutely critical parameter to fix *a priori* for a quantitative evaluation of fructose is the temperature; therefore, for all other evaluations of the fructose content, the temperature was held constant at 293 K. The dependence of the fructose isomeric composition in wines upon temperature variation gives rise to fascinating speculations about the suggested serving temperatures for white wines. Although there are a number of factors responsible for the complexity of wine taste, the temperature should be taken into consideration for its contribution to sweetness, which is determined primarily by fructose isomer proportions.

Equilibrium Composition of Fructose at a Constant Temperature. Equilibrium compositions of fructose at 293 K of wine and wine-like samples at different pH are reported in Table 1. The negligible variability of peak chemical shifts and invariability of fructose isomer peak intensities from spectra recorded on different samples is shown in Figure 4. Table wines generally have a pH between 2.5 and 4.5. However, considering that late-harvest Riesling and Moscato wine have pH 3.0 and 3.9, respectively, a range between 2.0 and 6.2 was examined in this study. Table 1 shows the variations among the set of ethanolic solutions at different pH, revealing a slight percentage variation in the wide range considered. The values reported by Barclay et al.[45] and Mega et al.[46] are included for comparison. Although the pH has been reported to have an influence on the rate of the mutarotation of fructose[46] (which is often approximated using a simple first-order process representing just the conversion of β-pyranose to the furanose forms), it was previously also reported that the isomeric composition at equilibrium was not significantly affected by variations in pH,[46] as corroborated by our data. To find a mean percentage value reflecting the distribution of the isomeric forms at a constant temperature, we combined data generated from samples at different pH and selected ethanol contents ranging from 5 to 30 vol % ethanol (without pH buffering). As a consequence, the small variations observed are considered to derive from random effects and, thus, mimic the case of directly analyzing wines without pretreatment and without knowledge of the actual pH or ethanol concentration.

Artificial mixtures of fructose were investigated, and mean values of the molar percent ratios were obtained and compared to the values measured using different methods of analyzing the ^{13}C qNMR spectra (see the Supporting Information). Three different techniques were used: (1) mean values determined using integration of the peaks for all of the carbons, including the contributions from the associated ^{13}C satellite peaks, (2) mean values from peak areas obtained by peak deconvolutions of signals from all carbons, including the ^{13}C satellite peaks, and (3) values calculated using peak areas from peak fitting (deconvolution) using the main resonance and the associated satellite peaks for the signals related to only carbon 2 for each isomer (Figure 6). These satellite peaks arise from the coupling of the

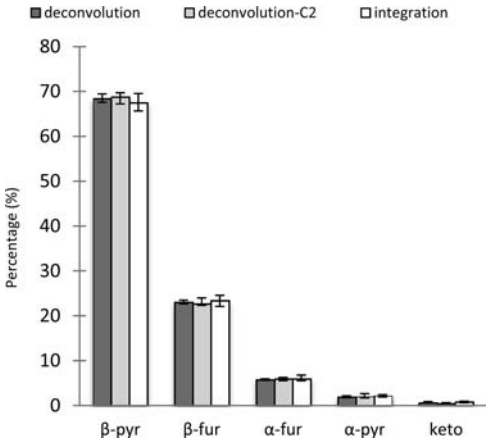

Figure 5. Variation in the equilibrium composition of fructose isomers (β-pyranose, β-furanose, α-furanose, α-pyranose, and ketohexose in order of abundance) in wine-like solutions at 293 K. Averages values are reported in the graph. The error bars reflect the range of the standard deviation. For each isomer, the three bars reflect different methods of data analysis (in order from left to right, deconvolution of all carbon peaks, deconvolution applied to C-2 peaks, and integration of all carbon peaks).

observed ^{13}C nuclei to an adjacent (directly bonded) ^{13}C at natural abundance, have separations of 30−70 Hz as expected for $^1J_{C-C}$ couplings, and are not due to incomplete proton decoupling. In the latter case, C-2 was selected because it exhibited a well-resolved, reasonably strong peak for all five fructose isomers. Histograms describing the isomeric composition depending upon the different analysis methods employed are reported in Figure 5. The largest standard deviations were found when the integration method was used. The smallest spread about the average was achieved using deconvolution analysis for all signals, even though deconvolution applied to just carbon 2 of each isomer also yielded a smaller standard deviation than integration. However, the data obtained from deconvolutions just at carbon 2 of each isomer (Table 2) represent a good compromise between speed and accuracy and were thus considered more appropriate for further evaluation of the fructose content in wine. The mean values also match perfectly with the isomeric ratios obtained from a fully ^{13}C-enriched fructose sample in 15% ethanolic solution (Table 2).

Fructose Quantification in Wine. Concentration measurements with the PULCON method use the principle of reciprocity, which indicates that the lengths of a 90° or 360° pulse are inversely proportional to the NMR signal intensity.[49,50] When the concentration of the external reference sample is known precisely, the unknown concentrations of different samples can be obtained using eq 1, where U and R indices stand for unknown and reference, respectively (fructose and sucrose, respectively)

DOI: 10.1021/acs.jafc.5b03641
J. Agric. Food Chem. 2015, 63, 8551−8559

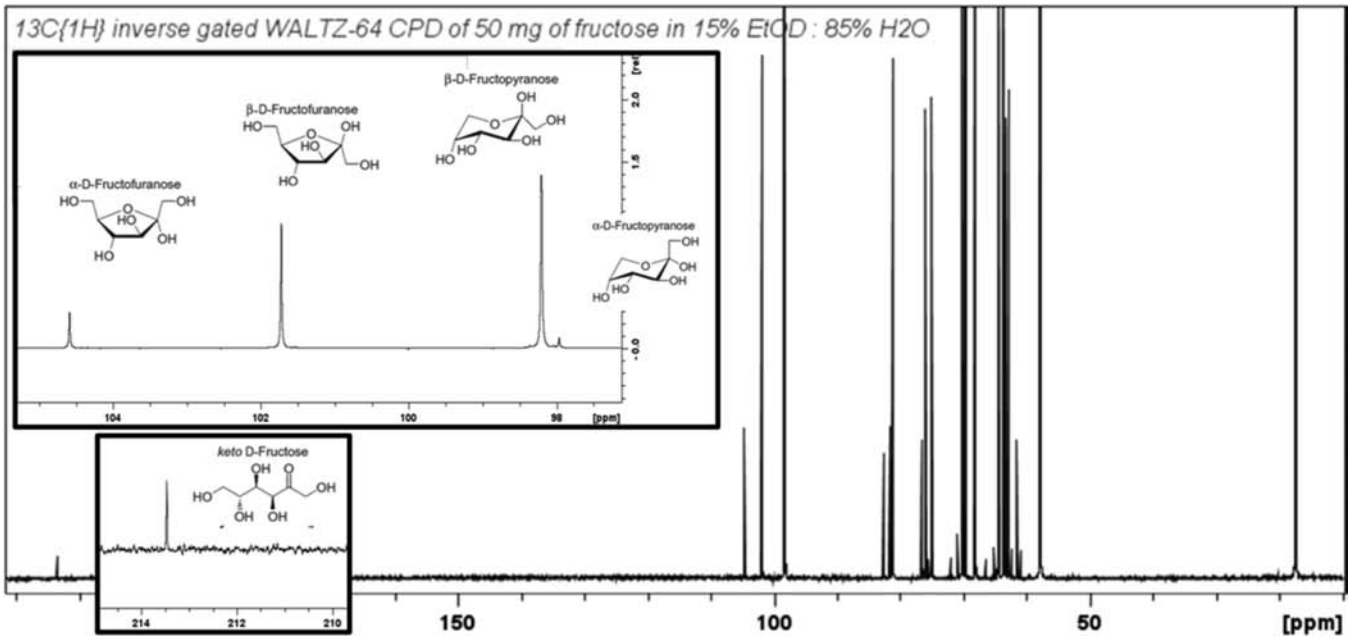

Figure 6. Portion of the ^{13}C qNMR spectrum of fructose in ethanolic solvents, showing the expansion of the area containing carbon 2 from fructose isomers. Each isomer is shown close to its corresponding C-2 peak.

Table 2. Fructose Isomer Percentage Determination from Peak Deconvolution at C-2

ppm	isomer	mean	minimum	maximum	σ (g/L)	$^{13}C_6$ fructose
98.0	β-pyr	68.12	65.65	69.70	1.28	68.42
104.3	β-fur	23.16	22.08	24.55	0.77	22.93
101.5	α-fur	5.94	5.50	6.79	0.36	5.72
97.9	α-pyr	2.10	1.70	2.63	0.25	2.35
213.4	keto	0.68	0.44	0.97	0.15	0.59

$$c_U = kc_R \frac{A_U T_U \theta_{90}^U n_R}{A_R T_R \theta_{90}^R n_U} \quad (1)$$

where C is the concentration, T is the temperature, θ^{90} is the 90° pulse length, n is the number of transients used for the experiments, and k is a correction factor taking into account the use of different receiver gains for measurement of the reference and unknown samples or incomplete relaxation. In our experiments T and n have the same values for both the reference and unknown samples; therefore, the formula could be further simplified. The reference sucrose spectra were measured 5 times, and areas were calculated for all of the carbon signals, averaged, and used in the PULCON equation (A_R; eq 1). We investigated the reliability of the PULCON method for the determination of the fructose content with wines already analyzed, comparing our results to those from a WineScreener analysis carried out on different bottles of the (supposedly) identical wines. ^{13}C qNMR spectra of the Baccus Weiss, Pinot Gris, and Chardonnay Blanc wines were measured. The most important cause of different signal strength (peak areas) between spectra derives from differences in conductivities of the samples, which results in a variation of the 90° rf pulse length. However, as long as the probe is properly tuned and matched for each sample, this effect can be compensated for by applying the principle of reciprocity.[47] For each sample, the magnetic field was shimmed to provide symmetrical peak shapes and the actual duration required for a true 90° rf pulse was determined, keeping the power of the rf pulse fixed. All other acquisition and processing parameters remained unaltered. The quantitative reliability of the NMR peak area measurements can suffer if the delay between successive rf pulse scans is too short to allow for full recovery of the magnetization. An interscan delay of 120 s was employed, which afforded >99.9% recovery of magnetization for the fructose carbons having the largest longitudinal relaxation times (C-2 in the keto form; T_1 = 11.3 s). For fructose quantification, the information obtained from relative isomer composition (Table 2) was used and eq 1 was modified, leading to a simpler formula for calculating the fructose concentrations in wine samples. Just considering the area of the region between 97.0 and 99.9 ppm (related to the β-pyranose and α-pyranose isomers) which from reported evaluations (Table 2) accounts for 70% of the total concentration of fructose, the fructose content in wine samples could be expressed as reported in eq 2, where c_R is the molar concentration of a sucrose reference sample and A_* is the area of the 97.0−99.9 ppm region.

$$\text{fructose}\left(\frac{g}{L}\right) = M\frac{100}{P^U}c_R\frac{A_*\theta_{90}^U}{A_R\theta_{90}^R} \quad (2)$$

Fructose concentrations (in g/L) can be directly calculated using eq 2 by measuring the peak areas related to the two isomers (^{13}C satellite peaks included) and applying a multiplication factor determined from the product of the molecular weight of fructose M (180 g/mol) and the fractional amount of total fructose (on the basis of a percentage estimation of the isomers being used; $100/P^U$, where P^U is 70).

The values obtained compare remarkably well to those measured using the ^1H-NMR-based WineScreener analysis (Table 3). These ^{13}C-NMR-based concentration measurements were repeated 5 times for each wine sample, and the precision of the measurements was estimated using the standard deviations calculated from these separate measurements. Equation 2 can be extended to measure other carbohydrates, such as glucose and sucrose, present in wine, by measuring the peak areas related to one of the two isomers for glucose (β-pyranose and α-pyranose isomers) or measuring the peak area of one isolated signal for

DOI: 10.1021/acs.jafc.5b03641
J. Agric. Food Chem. 2015, 63, 8551−8559

Table 3. Fructose Content Determination in Wine

	WineScreener (g/L)	eq 2 (g/L)	σ (g/L)[a]
Baccus Weiss	8.7	8.7	1.2
Pinot Gris	5.3	5.1	1.1
Chardonnay Blanc	4.5	4.5	0.4

[a]Standard deviation related to the concentrations obtained from five experiments. Each experiments used a $^{13}C\{^1H\}$ inverse-gated WALTZ-64 CPD, SFU Bruker AV II 600 with a QNP cryoprobe (unlocked; T = 293 K; $D1$ = 120 s; NS = 32; 65 min).

sucrose (which exists as a single isomer, *O*-α-D-glucopyranosyl-(1−2)-β-D-fructofuranoside). The multiplication factor M and percentage estimation of the isomers should be adapted to the carbohydrate to be measured. Baccus Weiss wine contained 1.6 g/L sucrose (WineScreener), which we could detect readily by ^{13}C qNMR peaks at 81.3 and 103.6 ppm (see the Supporting Information). From the same spectra, ethanol concentrations could also be determined. An external reference, a sample of 99.95% ethanol−OD, was used, and eq 3 was employed.

$$\text{ethanol (vol\%)} = 99.95 c_R \frac{A_U \theta_{90}^U}{A_R \theta_{90}^R} \quad (3)$$

These results are also in close agreement with those obtained using the official WineScreener analyses and printed on the bottle labels (Table 4), especially for the volume percent ethanol

Table 4. Ethanol Content Determination in Wine

	label	WineScreener (%)	eq 3 (%)	σ (%)[a]
Baccus Weiss	12.9	13.5	13.3	0.07
Pinot Gris	13.4	13.5	13.3	0.09
Chardonnay Blanc	13.8	14.0	13.5	0.05

[a]Standard deviation related to the ethanol percentage measured from five experiments.

contents. The one outlier was the Baccus Weiss wine, which yielded a significantly (more than 1% by volume) higher alcohol content based on the two independent NMR-based analyses than reported on the label.

In conclusion, a straightforward method is described for the direct determination of fructose isomers and total contents in wines without chemically altering the samples. ^{13}C qNMR analysis works essentially as a sensitivity "filter", removing the problem of water and ethanol suppression (which are the highest abundance components of wines) on the one hand and avoiding the detection of minor components and low abundance substances on the other hand. This type of analysis can also be readily performed on 400 MHz NMR spectrometers, extending the acquisition to a simple overnight experiment (see the Supporting Information). This method can detect and quantify ethanol and multiple sugars (and other compounds) at all stages of wine production, including grape must, during fermentation, and before and after bottling, providing a way to monitor possible back-blending practices. The method is also applicable to the analysis of fruit juices (up to 100 g/L sugar), carbonated soft drinks (100−120 g/L sugar), and certain energy drinks (up to 160 g/L sugar).

■ ASSOCIATED CONTENT

Supporting Information

The Supporting Information is available free of charge on the ACS Publications website at DOI: 10.1021/acs.jafc.5b03641.

^{13}C NMR spectra and tables (PDF)

■ AUTHOR INFORMATION

Corresponding Authors

*Telephone: 778-782-5650. Fax: 778-782-3765. E-mail: cinzia_colombo@sfu.ca.

*Telephone: 778-782-5650. Fax: 778-782-3765. E-mail: bpinto@sfu.ca.

Funding

This work was supported by the Natural Sciences and Engineering Research Council of Canada, through a Discovery Grant to B. Mario Pinto.

Notes

The authors declare no competing financial interest.

■ ACKNOWLEDGMENTS

We thank M. Spraul, H. Schaefer, and B. Schuetz at the Bruker NMR Applications Group in Rheinstetten, Germany, for collecting and providing the WineScreener NMR data.

■ ABBREVIATIONS USED

GC, gas chromatography; HPLC, high-performance liquid chromatography; IR, infrared; LOD, limit of detection; LOQ, limit of quantification; NMR, nuclear magnetic resonance; ^{13}C qNMR, ^{13}C quantitative nuclear magnetic resonance; rf, radio frequency; SPME, solid-phase microextraction

■ REFERENCES

(1) Davies, C.; Robinson, S. P. Sugar Accumulation in Grape Berries. *Plant Physiol.* **1996**, *111*, 275−283.

(2) Wu, B.; Liu, H.; Guan, L.; Fan, P.; Li, S. Carbohydrate metabolism in grape cultivars that differ in sucrose accumulation. *Vitis* **2011**, *50*, 51−57.

(3) Reboredo-Rodríguez, P.; González-Barreiro, C.; Rial-Otero, R.; Cancho-Grande, B.; Simal-Gándara, J. Effects of Sugar Concentration Processes in Grapes and Wine Aging on Aroma Compounds of Sweet Wines-A Review. *Crit. Rev. Food Sci. Nutr.* **2015**, *55*, 1053−1073.

(4) Robinson, J. *The Oxford Companion to Wine*; Oxford University Press: Oxford, U.K., 1984; pp 927−928.

(5) Jackson, R. S. *Wine Science: Principles and Applications*, 4th ed.; Academic Press: Waltham, MA, 2014; p 689.

(6) White, J. S.; Hobbs, L. J.; Fernandez, S. Fructose content and composition of commercial HFCS-sweetened carbonated beverages. *Int. J. Obes.* **2015**, *39*, 176−182.

(7) Cox, T. M. The genetic consequences of our sweet tooth. *Nat. Rev. Genet.* **2002**, *3*, 481−487.

(8) Bray, G. A. Fructose: should we worry? *Int. J. Obes.* **2008**, *32*, S127−S131.

(9) Hanover, L. M.; White, J. S. Manufacturing, composition, and applications of fructose. *Am. J. Clin. Nutr.* **1993**, *58*, 724S−732S.

(10) Lawless, H. T.; Horne, J.; Spiers, W. Contrast and range effects for category, magnitude and labeled magnitude scales in judgements of sweetness intensity. *Chem. Senses* **2000**, *25*, 85−92.

(11) Galindo-Cuspinera, V.; Winnig, M.; Bufe, B.; Meyerhof, W.; Breslin, P. A. S. A TAS1R receptor-based explanation of sweet 'water-taste'. *Nature* **2006**, *441*, 354−357.

(12) Eggers, S. C.; Acree, T. E.; Shallenberger, R. S. Sweetness chemoreception theory and sweetness transduction. *Food Chem.* **2000**, *68*, 45−49.

(13) Green, B. G.; Cruz, A. Thermal stimulation of taste. *Nature* **2000**, *403*, 889−892.

(14) Angyal, S. J. The composition of reducing sugars in solution. *Advances in Carbohydrate Chemistry and Biochemistry*; Elsevier: Amsterdam, Netherlands, 1984; Vol. *42*, pp 15−68, DOI: 10.1016/S0065-2318(08)60122-5

DOI: 10.1021/acs.jafc.5b03641
J. Agric. Food Chem. 2015, 63, 8551−8559

(15) Shallenberger, R. S. Intrinsic Chemistry of Fructose. *Pure Appl. Chem.* **1978**, *50*, 1409−1420.
(16) Sassaki, G. L.; Gorin, P. A.; Reis, R. A.; Serrato, R. V.; Elifio, S. L.; Iacomini, M. Carbohydrate, glycolipid, and lipid components from the photobiont (Scytonema sp.) of the lichen, Dictyomema glabratum. *Carbohydr. Res.* **2005**, *340*, 1808−1817.
(17) Kakasy, A.; Füzfai, Z.; Kursinszki, L.; Molnár-Perl, I.; Lemberkovics, É. Analysis of Non-volatile Constituents in Dracocephalum Species by HPLC and GC-MS. *Chromatographia* **2006**, *63*, S17−S22.
(18) Slimestad, R.; Vâgen, I. M. Thermal stability of glucose and other sugar aldoses in normal phase high performance liquid chromatography. *J. Chromatogr. A* **2006**, *1118*, 281−284.
(19) Andersen, R.; Sørensen, A. Separation and determination of alditols and sugars by high-pH anion-exchange chromatography with pulsed amperometric detection. *J. Chromatogr. A* **2000**, *897*, 195−204.
(20) Moro, E.; Majocchi, R.; Ballabio, C.; Molfino, S.; Restani, P. A Rapid and Simple Method for Simultaneous Determination of Glycerol, Fructose, and Glucose in Wine. *Am. J. Enol. Vitic.* **2007**, *58*, 279−282.
(21) Castro, R.; Natera, R.; Benitez, P.; Barroso, C. G. Comparative analysis of volatile compounds in "fino" sherry wine by rotatory and continuous liquid−liquid extraction and solid-phase microextraction in conjunction with gas chromatography-mass spectrometry. *Anal. Chim. Acta* **2004**, *513*, 141−150. (6) Tao, Y. S.; Li, H.; Wang, H.; Zhang, L. Volatile compounds of young Cabernet Sauvignon red wine from Changli County (China). *J. Food Compos. Anal.* **2008**, *21*, 689−694.
(22) Tao, Y. S.; Li, H.; Wang, H.; Zhang, L. Volatile compounds of young Cabernet Sauvignon red wine from Changli County (China). *J. Food Compos. Anal.* **2008**, *21*, 689−694.
(23) Cozzolino, D. Near infrared spectroscopy in natural products analysis. *Planta Med.* **2009**, *75*, 746−756.
(24) Godelmann, R.; Fang, F.; Humpfer, E.; Schütz, B.; Bansbach, M.; Schäfer, H.; Spraul, M. Targeted and non-targeted wine analysis by ^{1}H NMR spectroscopy combined with multivariate statistical analysis. Differentiation of important parameters: geographical origin, year of vintage. *J. Agric. Food Chem.* **2013**, *61*, 5610−5619.
(25) Papotti, G.; Bertelli, D.; Graziosi, R.; Silvestri, M.; Bertacchini, L.; Durante, C.; Plessi, M. Application of One- and Two-Dimensional NMR Spectroscopy for the Characterization of Protected Designation of Origin Lambrusco Wines of Modena. *J. Agric. Food Chem.* **2013**, *61*, 1741−1746.
(26) López-Rituerto, E.; Savorani, F.; Avenoza, A.; Busto, J. H.; Peregrina, J. M.; Engelsen, S. B. Investigations of La Rioja terroir for wine production using 1H NMR metabolomics. *J. Agric. Food Chem.* **2012**, *60*, 3452−3461.
(27) Larsen, F. H.; van den Berg, F.; Engelsen, S. B. An exploratory chemometric study of 1H NMR spectra of table wines. *J. Chemom.* **2006**, *20*, 198−208.
(28) Spraul, M.; Link, M.; Schaefer, H.; Fang, F.; Schuetz, B. Wine analysis to check quality and authenticity by fully-automated ^{1}H-NMR. *BIO Web of Conferences* **2015**, *5*, 02022.
(29) Spraul, M.; Schütz, B.; Rinke, P.; Koswig, S.; Humpfer, E.; Schäfer, H.; Mörtter, M.; Fang, F.; Marx, U. C.; Minoja, A. NMR-Based Multi Parametric Quality Control of Fruit Juices: SGF Profiling. *Nutrients* **2009**, *1*, 148−155.
(30) Tamate, J.; Bradbury, H. Determination of sugars in tropical root crops using ^{13}C N.m.r spectroscopy: Comparison with the h.p.l.c. method. *J. Sci. Food Agric.* **1985**, *36*, 1291−1302.
(31) De Bruyn, A.; Van Loo, J. The identification by ^{1}H- and ^{13}C-n.m.r. spectroscopy of sucrose, 1-kestose, and neokestose in mixtures present in plant extracts. *Carbohydr. Res.* **1991**, *211*, 131−136.
(32) Mazzoni, V.; Bradesi, P.; Tomi, F.; Casanova, J. Direct qualitative and quantitative analysis of carbohydrate mixtures using ^{13}C NMR spectroscopy: application to honey. *Magn. Reson. Chem.* **1997**, *35*, S81−S90.
(33) Pelczer, I. Quality and Authenticity of Complex Natural Mixtures: Analysis of Honey Using NMR Spectroscopy and Statistics. In *Botanicals: Methods and Techniques for Quality & Authenticity*; Reynertson, K., Mahmood, K., Eds.; CRC Press: Boca Raton, FL, 2015; Chapter 12, pp 183−198, DOI: 10.1201/b17987-13
(34) Duquesnoy, E.; Castola, V.; Casanova, J. Identification and quantitative determination of carbohydrates in ethanolic extracts of two conifers using ^{13}C NMR spectroscopy. *Carbohydr. Res.* **2008**, *343*, 893−902.
(35) Rapp, A.; Markowetz, A.; Spraul, M.; Humpfer, E. Nachweis und quantitative Bestimmung von Zuckern, Zuckeralkoholen und Zuckersäuren in Wein mit ^{13}C NMR-Spektrokopie. *Z. Lebensm.-Unters. Forsch.* **1989**, *188*, 138−143.
(36) Weekley, A. J.; Bruins, P.; Sisto, M.; Augustine, M. P. Using NMR to study full intact wine bottles. *J. Magn. Reson.* **2003**, *161*, 91−98.
(37) Findeisen, M.; Brand, T.; Berger, S. A ^{1}H-NMR thermometer suitable for cryoprobes. *Magn. Reson. Chem.* **2007**, *45*, 175−178.
(38) Berger, S.; Braun, S. *200 and More NMR Experiments: A Practical Course*; Wiley-VCH: Weinheim, Germany, 2004; p 128.
(39) Shaka, A. J.; Freeman, R. J. Composite pulses with dual compensation. *J. Magn. Reson.* **1983**, *55*, 487−493.
(40) Wider, G.; Dreier, L. Measuring Protein Concentrations by NMR Spectroscopy. *J. Am. Chem. Soc.* **2006**, *128*, 2571−2576.
(41) Burton, I. W.; Quilliam, M. A.; Walter, J. A. Quantitative 1H NMR with External Standards: Use in Preparation of Calibration Solutions for Algal Toxins and Other Natural Products. *Anal. Chem.* **2005**, *77*, 3123−3131.
(42) Yaylayan, V. A.; Ismail, A. A.; Mandeville, S. Quantitative determination of the effect of pH and temperature on the keto form of Fructose by FT IR spectroscopy. *Carbohydr. Res.* **1993**, *248*, 355−360.
(43) Hyvönen, L.; Varo, P.; Koivistoinen, P. Tautomeric equilibria of D-glucose and fructose. NMR spectrometric measurements. *J. Food Sci.* **1977**, *42*, 657−659.
(44) Schneider, B.; Lichtenthaler, F. W.; Steinle, G.; Schiweck, H. Distribution of furanoid and pyranoid tautomers of fructose in water, dimethyl sulfoxide, and pyridine via ^{1}H NMR intensities of anomeric hydroxy groups in [D_6]DMSO. *Liebigs Ann. Chem.* **1985**, *1985*, 2443−2453.
(45) Flood, A. E.; Johns, M. R.; White, E. T. Mutarotation of Fructose in aqueous-ethanolic solutions and its influence on crystallisation. *Carbohydr. Res.* **1996**, *288*, 45−56.
(46) Horton, D.; Walaszek, Z. Tautomeric equilibria of some sugars by partially relaxed, ^{13}C pulse Fourier transform, nuclear magnetic resonance spectroscopy. *Carbohydr. Res.* **1982**, *105*, 145−153.
(47) Barclay, T.; Ginic-Markovic, M.; Johnston, M. R.; Cooper, P.; Petrovsky, N. Observation of the keto tautomer of Fructose in D_2O using ^{1}H NMR spectroscopy. *Carbohydr. Res.* **2012**, *347*, 136−141.
(48) Mega, T. L.; Cortes, S.; Van Etten, R. L. The ^{18}O Isotope Shift in ^{13}C nuclear magnetic resonance spectroscopy. Oxygen exchange at the anomeric carbon of D-glucose, D-mannose, and D-fructose. *J. Org. Chem.* **1990**, *55*, 522−528.
(49) Hoult, D. I.; Richards, R. E. The signal-to-noise ratio of the nuclear magnetic resonance experiment. *J. Magn. Reson.* **1976**, *24*, 71−85.
(50) Hoult, D. I. The principle of reciprocity in signal strength calculations-A mathematical guide. *Concepts Magn. Reson.* **2000**, *12*, 173−187.

DOI: 10.1021/acs.jafc.5b03641
J. Agric. Food Chem. 2015, 63, 8551−8559

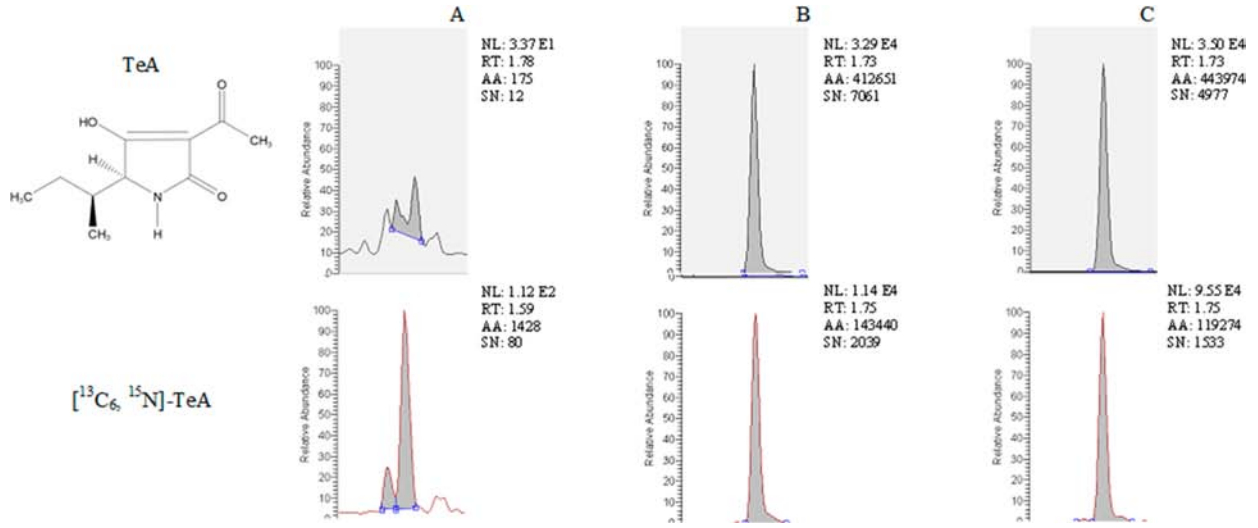

Figure 1. Chemical structure of tenuazonic acid (TeA, left) and LC-MS/MS chromatograms of (A) a blank pig plasma sample, (B) a spiked pig plasma sample (TeA concentration = 100 ng/mL), and (C) an incurred pig plasma sample that was taken at 0.5 h pa of a single oral dose of 0.05 mg TeA/kg body weight (TeA concentration = 129 ng/mL). The upper trace presents TeA, and the lower trace presents the internal standard ([$^{13}C_6$, ^{15}N]-TeA).

of TeA in food without the need for derivatization have been described.[5,13,14] Therefore, the present study aimed to develop a LC-MS/MS method without a derivatization step.

Next, toxicokinetic and plasma protein binding studies in both animal species were performed. The absolute oral bioavailability (F) and the main toxicokinetic parameters were calculated: area under the plasma concentration−time curve (AUC), maximum concentration after oral administration (C_{max}), plasma concentration at time of intravenous injection (C_0), time to maximal plasma concentration (t_{max}), elimination rate constant (k_{el}), elimination half-life ($t_{1/2el}$), total body clearance (Cl), volume of distribution (V_d), and mean residence time (MRT).

MATERIALS AND METHODS

Chemicals, Products, and Reagents. The analytical standard of TeA (purity ≥ 99%) was purchased from Fermentek (Jerusalem, Israel). The chemical structure of this compound is presented in Figure 1. The internal standard (IS) [$^{13}C_6$, ^{15}N]-TeA was synthesized according to the method of Asam et al.[15] TeA and the IS were stored at ≤ −15 °C. Water, methanol (MeOH), and acetonitrile (ACN) were of LC-MS grade and obtained from Biosolve (Valkenswaard, The Netherlands). Ammonium bicarbonate (purity ≥ 99.5%) and ammonium formate (purity > 99.0%) were of analytical grade and purchased from Sigma-Aldrich (Diegem, Belgium). Absolute ethanol was of analytical grade and obtained from VWR (Leuven, Belgium). Millex-GV PVDF filters (0.22 μm) and Amicon Ultra-0.5 mL centrifugal filter devices (molecular weight cutoff = 30 kDa) were purchased from Merck-Millipore (Overijse, Belgium).

Preparation of Stock and Working Solutions. Stock solutions of TeA (1 mg/mL) and IS (100 μg/mL) were prepared in MeOH. Working solutions (WS) of 1, 0.1, and 0.01 μg TeA/mL were prepared daily by appropriate dilution of the stock solution and WS with water. A WS (1 μg/mL) of IS was made by further dilution of the stock solution in MeOH. Stock solutions of TeA and stock and WS of IS were stored at ≤ −15 °C.

Animal Experiments. Toxicokinetic studies with TeA were performed in eight 10-week-old male piglets (Seghers hybrids, Ratterlow Seghers Holding, Lokeren, Belgium) and five 4-week-old broiler chickens (Ross 308, Geluveld, Belgium) of mixed gender. The mean BW was 33.44 ± 1.71 and 1.56 ± 0.20 kg for pigs and broilers, respectively. Both animal trials were designed as a two-way crossover. After an acclimatization period of at least 3 days, each pig or broiler chicken received either an oral (po) or intravenous (iv) dose of 0.05 mg TeA/kg BW. The analytical standard of TeA was dissolved in ethanol at a concentration of 1.75 or 1.00 mg TeA/mL for pigs or chickens, respectively. The stock solution was further diluted with water (po) or saline (iv) up to a final concentration that corresponded with a dose of 0.05 mg/kg BW.

Animals were deprived of feed from 12 h before until 4 h after administration of TeA. Pigs and broiler chickens had ad libitum access to drinking water at all times. Oral bolus administrations were given in the crop (chickens) or by gastric gavage (pigs), whereas iv injections were performed in the wing vein (*vena basilica*, chickens) or through a double-lumen catheter (*vena jugularis externa*, pigs).[16] About 1 mL of blood was sampled via the catheter (pigs) or the leg vein (*vena metatarsalis plantaris superficialis*, broilers) and collected in EDTA-coated tubes just before (0 h) and at different time points postadministration (pa), that is, at 0.08, 0.25, 0.5, 0.75, 1, 1.5, 2, 3, 4, 6, 8, and 10 h pa for pigs and at 0.08, 0.16, 0.32, 0.50, 1, 2, 4, 6, 8, and 10 h pa for broiler chickens. The blood samples were centrifuged (2095*g*, 10 min, 4 °C), and plasma samples (aliquots of 250 μL) were stored at ≤ −15 °C until analysis.

The animal experiments were approved by the Ethical Committee of the Faculty of Veterinary Medicine and Bioscience Engineering of Ghent University (EC 2013/145).

Plasma Sample Preparation. To 250 μL of plasma was added 12.5 μL of the IS WS (1 μg/mL). After a vortex-mixing step, 750 μL of ACN was added followed by vortex-mixing and centrifugation (8517*g*, 10 min, 4 °C). The supernatant was evaporated under a gentle nitrogen (N_2) stream (45 ± 5 °C). The dry residue was dissolved in 262.5 μL of water/MeOH (80:20, v/v) for pig plasma and in 5 mM ammonium formate in water (pH 9)/MeOH (95:5, v/v) for chicken plasma. After a vortex-mixing step, the sample was filtered through a Millex-GV PVDF filter (0.22 μm) and transferred to an autosampler vial. A 10 μL aliquot was injected onto the LC-MS/MS instrument.

Plasma Protein Binding. Plasma protein binding of TeA was assessed by spiking fresh blank pig and broiler chicken plasma at 10, 50, and 100 ng/mL. At each concentration level, one aliquot (aliquot 1) followed the plasma sample treatment (vide supra), but without filtering through a Millex-GV filter. A second aliquot and a third aliquot (aliquots 2 and 3) were incubated in a hot water bath, set at 37 and 41 °C for pig and broiler chicken plasma, respectively. After 1 h, aliquots 2 and 3 were transferred onto Amicon Ultra-0.5 centrifugal filter devices. Following centrifugation (8517*g*, 15 min, 37 or 41 °C), aliquots 2 and 3 were treated in a similar way as aliquot 1.

DOI: 10.1021/acs.jafc.5b02828
J. Agric. Food Chem. 2015, 63, 8560−8567

Corresponding calibration curves were used to quantify TeA in each aliquot. Plasma protein binding was calculated at each level (10, 50, and 100 ng/mL) using the following equation:[17]

$$\text{plasma protein binding} = \frac{(C_{\text{aliquot 1}} - C_{\text{av in aliquots 2 and 3}}) \times 100}{C_{\text{aliquot 1}}} \quad (1)$$

Liquid Chromatography. The LC system consisted of a quaternary, low-pressure mixing pump with vacuum degassing (type Surveyor MSpump Plus, ThermoFisher Scientific, Breda, The Netherlands) connected to an autosampler with a temperature-controlled tray and column oven (type Autosampler Plus, ThermoFisher Scientific). Chromatographic separation was achieved on a Zorbax Eclipse Plus column (C18; i.d., 3.0 × 100 mm; d.p., 3.5 μm) in combination with a guard column of the same type (i.d., 2.1 × 12.5 mm; d.p., 5 μm), both from Agilent Technologies (Sint-Katelijne-Waver, Belgium).

Mobile phase A consisted of 0.1 mM ammonium bicarbonate in water/MeOH (95:5, v/v) or 5 mM ammonium formate in water (pH 9) for pig and chicken plasma analysis, respectively. Mobile phase B consisted of MeOH. For the analysis of pig plasma samples, the following gradient elution program was run: 0.0−0.5 min (70% A, 30% B), 0.5−2.0 min (linear gradient to 20% A, 80% B), 2.0−7.0 min (20% A, 80% B), 7.0−7.5 min (linear gradient to 70% A, 30% B), 7.5−12.5 min (70% A, 30% B). For the analysis of broiler plasma samples, the gradient elution program was as follows: 0.0−2.0 min (90% A, 10% B), 2.0−2.5 min (linear gradient to 2% A, 98% B), 2.5−8.5 min (2% A, 98% B), 8.5−9.0 min (linear gradient to 90% A, 10% B), 9.0−12.5 min (90% A, 10% B). The flow rate was set at 300 μL/min. The column oven and tray temperature were set at 50 and 5 °C, respectively.

Mass Spectrometry. The LC column effluent was interfaced to a TSQ Quantum Ultra triple-quadrupole mass spectrometer, equipped with a heated electrospray ionization (h-ESI) probe operating in the negative ionization mode (all from ThermoFisher Scientific). Instrument parameters were optimized by syringe infusion of a WS (1 μg/mL) of TeA and the IS. The following MS/MS parameters were used: spray voltage, 4000 V; vaporizer temperature, 250 °C; sheath gas pressure, 40 arbitrary units (au); ion sweep gas pressure, 2.0 au; auxiliary gas pressure, 23 au; capillary temperature, 300 °C; source CID collision energy, 5 eV; and collision pressure, 1.5 mTorr. The resolution for Q1 and Q3 was set at 0.7 full width at half-maximum (fwhm).

Acquisition was performed in the selected reaction monitoring (SRM) mode. The following transitions (m/z) were monitored for qualification and quantification, respectively, for TeA, 196 → 112 and 196 → 139, and for IS, 203 → 142 and 203 → 113. Tube lens offset was set at 98 and 84 V for TeA and IS, respectively.

Method Validation. The method was validated according to a validation protocol previously described by De Baere et al., using spiked blank plasma samples obtained from healthy, untreated animals.[18] A set of parameters that were in compliance with the recommendations and guidelines defined by the European Community and with criteria described in the literature were evaluated.[18−22] These include evaluation of linearity, within- and between-run accuracy and precision, limit of quantitation (LOQ), limit of detection (LOD), specificity, carry-over, extraction recovery (R_E), and matrix effects (signal suppression or enhancement, SSE).

Linearity. Linearity was evaluated by preparing three matrix-matched calibration curves on three different days. Additionally, freshly prepared calibration curves were included during the analysis of the samples obtained from the toxicokinetic study. Calibration curve samples (range of 5−200 ng/mL) were prepared by applying standard working solutions directly onto the blank plasma samples, followed by a vortex mixing step. After 5 min of equilibration, the calibration curve samples were treated in a similar way as the unknown samples. The correlation coefficients (r) and goodness-of-fit coefficients (g) were calculated and had to be ≥0.99 and ≤20%, respectively.[18,21,22] The following equation was used to calculate g:

$$g = \sqrt{\frac{\sum (\%\text{difference})^2}{n-1}} \quad (2)$$

$$\text{with \% difference} = \frac{x_{\text{back-calculated}} - x_{\text{nominal}}}{x_{\text{nominal}}} \times 100$$

Accuracy and Precision. Within-run accuracy and precision (repeatability) were determined by analyzing six blank samples that were spiked at 5, 10, and 100 ng/mL in the same run. The between-run accuracy and precision (reproducibility) were determined by analyzing two blank samples per concentration level (5, 10, and 100 ng/mL) on three different days (n = 6). The acceptance criteria for accuracy were −30% to +10% and −20% to +10% for concentration levels between 1 and 10 ng/mL and ≥10 ng/mL, respectively. The precision was evaluated by the determination of the relative standard deviation (RSD), which had to be below the RSD_{max} value. For the within-day precision, RSD_{max} is fixed at 25, 15, and 10% for concentrations of 5, 10, and 100 ng/mL respectively,[20] whereas for between-run precision, the RSD had to be below the RSD_{max} calculated by the Horwitz equation:

$$RSD_{max} = 2^{(1-0.5\log(\text{concn}))} \quad (3)$$

Limit of Quantitation. The LOQ was the lowest concentration of the analyte for which the method was validated with an accuracy and precision that fell within the recommended ranges (see Accuracy and Precision). The LOQ was also established as the lowest point of the calibration curve. The LOQ was determined by analyzing six samples spiked at a TeA concentration level of 5 ng/mL, on the same day.

Limit of Detection. The LOD was defined as the lowest concentration that could be recognized by the detector with a signal-to-noise (S/N) ratio of ≥3. The LOD values were calculated using the samples spiked at the LOQ level.

Specificity. The specificity of the method was verified by analyzing 20 different blank plasma samples from both pigs and broiler chickens. The eventual analyte concentration of a peak in the elution zone of TeA or the IS had to be below the LOD.

Carry-over. The absence of carry-over was verified by analyzing the reconstitution solvent injected after the highest calibration sample (200 ng/mL). If a peak was observed in the elution zone of TeA or the IS, it had to be below the LOD.

Extraction Recovery and Matrix Effects. The slopes of three calibration curves were used to determine the extraction recovery (R_E) and the matrix effects (SSE) as described by Matuszewski et al.[23] The first calibration curve was made by spiking blank plasma samples before extraction at concentration levels of 1, 2, 5, 10, 20, 50, 100, and 200 ng/mL (= spiked samples). The second calibration curve was made by spiking blank plasma samples after extraction (= spiked extracts), whereas the third curve was prepared using standard solutions in the reconstitution solvent (= standard solutions). No IS was added, and absolute areas were used to calculate the R_E and SSE through the following equations:

$$R_E = \frac{\text{slope curve spiked samples}}{\text{slope curve spiked extracts}} \quad (4)$$

$$\text{SSE} = \frac{\text{slope curve spiked extracts}}{\text{slope curve standard solutions}} \quad (5)$$

Toxicokinetic Analysis. Noncompartmental toxicokinetic analysis was performed with WinNonlin 6.3 (Pharsight, St. Louis, MO, USA). The following main toxicokinetic parameters were calculated for iv and po administration in both animal species: area under the plasma concentration−time curve from time 0 to last concentration (AUC_{0-t}, ng·h/mL), area under the plasma concentration−time curve from time 0 to infinity (AUC_{0-inf}, ng·h/mL), maximum concentration after oral administration (C_{max}, ng/mL), plasma concentration at time of iv injection (C_0, ng/mL), time to maximal plasma concentration (t_{max}, h), elimination rate constant (k_{el}, h^{-1}), elimination half-life ($t_{1/2el}$, h), total body clearance (Cl, mL/h/kg), volume of distribution (V_d, mL/kg),

DOI: 10.1021/acs.jafc.5b02828
J. Agric. Food Chem. 2015, 63, 8560−8567

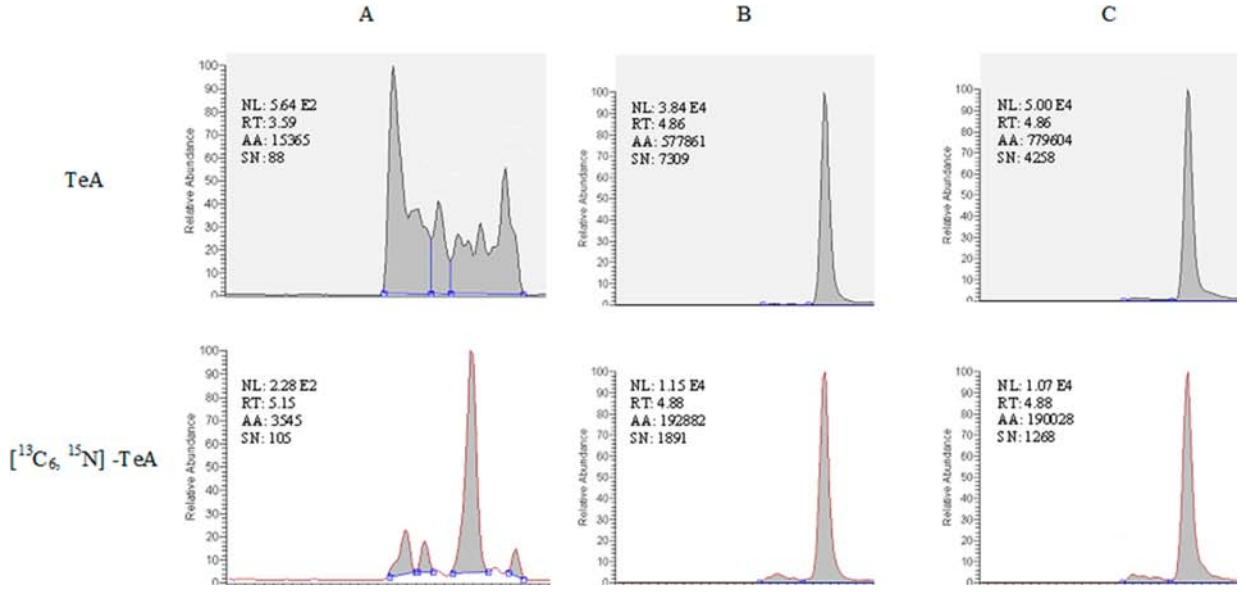

Figure 2. LC-MS/MS chromatograms of (A) a blank broiler plasma sample, (B) a spiked broiler plasma sample (tenuazonic acid (TeA) concentration = 100 ng/mL), and (C) an incurred broiler plasma sample that was taken at 2 h pa of a single oral dose of 0.05 mg TeA/kg BW (TeA concentration = 139 ng/mL). The upper trace presents TeA, and the lower trace presents the internal standard ([$^{13}C_6$, ^{15}N]-TeA).

Table 1. Results of the Evaluation of Linearity (Goodness-of-fit Coefficient (g), Correlation Coefficient (r)), Extraction Recovery (R_E), Matrix Effects (Signal Suppression or Enhancement, SSE), Limit of Quantitation (LOQ), and Limit of Detection (LOD) for the Analysis of Tenuazonic Acid in Plasma from Pigs and Broiler Chickens[a]

matrix	calibration range (ng/mL)	g (%)	r	R_E (%)	SSE (%)	LOQ (ng/mL)	LOD (ng/mL)
pig plasma	5−200	3.17	0.9996	91.8	37.8	5.0	0.01
broiler chicken plasma	5−200	5.96	0.9992	86.2	102.5	5.0	0.22

[a]Acceptance criteria: $g \leq 20\%$, $r \geq 0.99$.

and mean residence time (MRT, h). The absolute oral bioavailability (F) was calculated using the following equation:

$$F = \frac{AUC_{0-inf\,po}}{AUC_{0-inf\,iv}} \quad (6)$$

Cl and V_d after po administration were corrected for F. The mean absorption time (MAT, h) was calculated using the following equation:

$$MAT_{po} = MRT_{po} - MRT_{iv} \quad (7)$$

Statistical Analysis. To assess the repeatability and reproducibility, a one-way analysis of variance (ANOVA, SPSS 21, IBM, Armonk, NY, USA) was performed at each calibrator concentration level (5, 10, and 100 ng/mL) for both broiler chicken and pig plasma. Furthermore, ANOVA was performed on all toxicokinetic parameters in both animal species and between both routes of administration. $AUC_{0-inf\,iv}$, $AUC_{0-t\,iv}$, $t_{1/2el\,iv}$, MRT_{iv}, $t_{max\,po}$, $t_{1/2el\,po}$, and MRT_{po} were compared between broilers and pigs using a Kruskal−Wallis test. The level of significance was set at 0.05.

RESULTS

LC-MS/MS Method. In the present study, the use of a double end-capped Zorbax Eclipse Plus column resulted in good chromatographic properties because TeA and the IS eluted as a sharp peak in both pig and broiler plasma (Figures 1 and 2). The use of ammonium bicarbonate and MeOH as mobile phases in a gradient elution program gave reproducible results in pig plasma. For the analysis of chicken plasma, the mobile phase ammonium bicarbonate in water/MeOH was replaced by ammonium formate in water and the gradient was adjusted. This resulted in a better chromatographic performance and a more robust method for TeA in broiler plasma (Figure 2).

Table 1 summarizes the validation results obtained for TeA in pig and chicken plasma. Linear matrix-matched calibration curves were reached (range of 5−200 ng/mL) with g and r values falling well within the acceptance criteria. The LOQ was 5.0 ng/mL in both pig and broiler plasma, whereas the LODs were 0.01 and 0.22 ng/mL in pig and chicken plasma, respectively. Furthermore, the protein precipitation sample treatment yielded high extraction recoveries, that is, 91.8% in pig plasma and 86.2% in broiler chicken plasma. There was a strong suppression of the signal of TeA in pig plasma (SSE = 37.8%), but not in broiler chicken plasma (SSE = 102.5%).

The within-day and between-day precision and accuracy fell within the acceptance ranges and are presented in Table 2. There was no statistically significant difference in within-day and between-day precision for both pig and broiler chicken plasma at the concentration levels tested (5, 10, and 100 ng/mL). The method was specific in both pig and broiler plasma because no interfering peaks could be detected in any of the blank samples at the retention time of TeA. Moreover, no significant carry-over was present, because no TeA was detected with a concentration higher than the LOD in the reconstitution solvent injected after the highest calibration sample (data not shown).

Toxicokinetic Studies. No general side effects were observed after the po or iv administration of 0.05 mg TeA/kg BW as a single dose. The plasma concentration−time profile of TeA in pigs and broiler chickens is shown in panels A and B of Figure 3, respectively. Table 3 summarizes the main

DOI: 10.1021/acs.jafc.5b02828
J. Agric. Food Chem. 2015, 63, 8560−8567

Table 2. Results of the Within- and Between-Run Precision and Accuracy Evaluation for the Analysis of Tenuazonic Acid in both Pig and Broiler Chicken Plasma[a]

matrix	theor concn (ng/mL)	mean concn ± SD (ng/mL)	precision, RSD (%)	accuracy (%)
pig plasma	5[b]	4.6 ± 0.55	12.0	−8.8
	5[c]	4.7 ± 0.44	9.2	−5.4
	10[b]	10.5 ± 0.51	4.9	4.9
	10[c]	10.0 ± 0.96	9.6	−0.5
	100[b]	103.7 ± 3.78	3.6	3.7
	100[c]	101.0 ± 5.93	5.9	1.0
broiler chicken plasma	5[b]	5.2 ± 0.63	12.1	4.6
	5[c]	5.1 ± 0.77	15.0	2.1
	10[b]	9.2 ± 0.74	8.1	−8.1
	10[c]	10.0 ± 0.78	7.7	0.1
	100[b]	101.2 ± 7.50	7.4	1.2
	100[c]	100.8 ± 4.17	4.1	0.8

[a]SD, standard deviation; RSD, relative standard deviation. Acceptance criteria: accuracy, 1−10 ng/L, −30% to +10%, and ≥10 ng/mL, −20% to +10%. Within-run precision (RSD_{max}): 5 ng/mL, 25.0%; 10 ng/mL, 15.0%; and 100 ng/mL, 10.0%. Between-run precision: 5 ng/mL, 35.5%; 10 ng/mL, 32.0%; and 100 ng/mL, 22.6%. [b]Within-run. [c]Between-run.

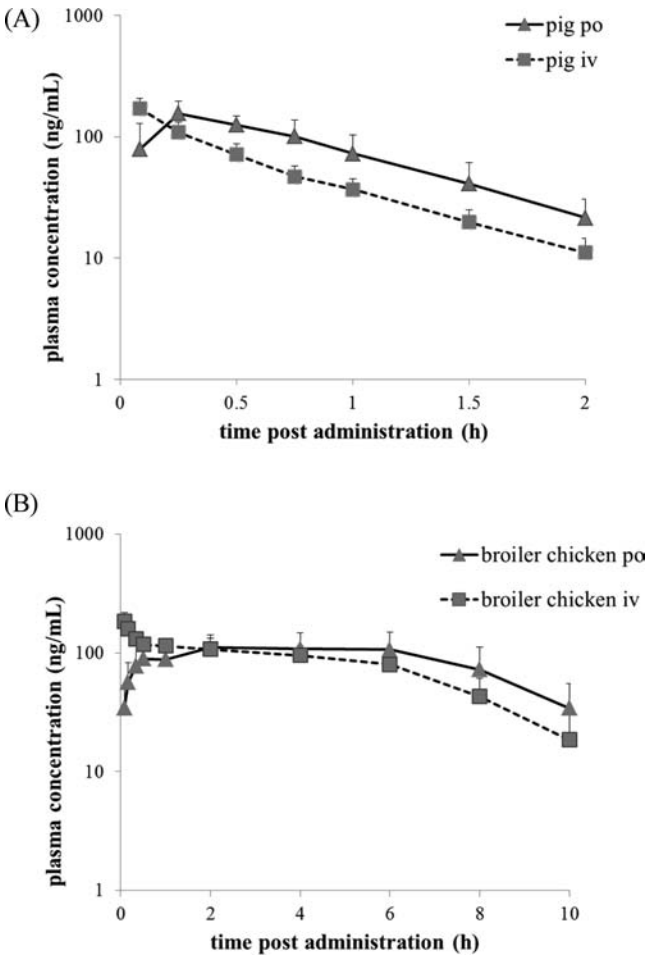

Figure 3. Plasma concentration−time profile of tenuazonic acid in (A) pigs (n = 8) and (B) broiler chickens (n = 5) after oral (po) and intravenous (iv) administration. Values are presented as mean ± SD.

toxicokinetic parameters. Mean AUC_{0-t} values were 108.9 and 151.7 ng·h/mL in pigs and 805.6 and 893.2 ng·h/mL in broiler chickens after iv and po administration, respectively. Consequently, TeA was completely absorbed after oral administration in pigs (mean F = 1.47) and broiler chickens (mean F = 1.24). Mean maximum concentration after oral administration was reached at 0.32 h pa in pigs and at 2.60 h in broiler chickens. Furthermore, TeA was rapidly eliminated after po administration in pigs, but not in broiler chickens. In pigs, $t_{1/2el}$ was 0.51 and 0.55 h after iv and po administration, respectively. In contrast, $t_{1/2el}$ was much longer in broiler chickens, that is, 2.03 and 2.45 h after iv and po administration, respectively. The mean Cl values were 448.4 and 446.1 mL/h/kg in pigs and 59.3 and 59.2 mL/h/kg in broiler chickens after iv and po administration, respectively. The mean V_d values were 325.8 and 358.4 mL/kg in pigs and 164.6 and 207.2 mL/kg in broiler chickens after iv and po administration, respectively. The mean MRT values were 0.70 and 0.94 h in pigs and 4.46 and 5.52 h in broiler chickens after iv and po administration, respectively. In both animal species, the k_{el}, $t_{1/2el}$, Cl, and V_d did not statistically differ after iv or po administration. Plasma protein binding did not significantly differ between both animal species and was 72.8 ± 3.4 and 58.1 ± 9.2% in broiler chickens and pigs, respectively (p = 0.06).

DISCUSSION

LC-MS/MS Method. First, a sensitive and specific LC-MS/MS method was developed and validated to quantify TeA in pig plasma. Next, minor modifications were made for quantification of TeA in chicken plasma.

The sample pretreatment consisted of a plasma protein precipitation method using ACN. Initially, a rather extensive sample preparation procedure for chicken plasma was evaluated. Three solid-phase extraction (SPE) columns were tested, that is, HybridSPE-Phospholipid cartridges (Sigma-Aldrich), C18 Bond elut (Agilent Technologies), and Oasis HLB columns (Waters, Zellik, Belgium). Compared to the protein precipitation method, the signal was reduced by factors of approximately 100 and 10 when using the Bond elut and HLB columns, respectively. The signal was completely lost when using the HybridSPE-Phospholipid cartridges. Therefore, the protein precipitation method was preferred as the final sample preparation method in both chicken and pig plasma. Protein precipitation is a frequently used sample preparation method for the LC-MS/MS analysis of several mycotoxins in pig and broiler chicken plasma.[24−27] Despite several benefits of this extraction procedure, such as high throughput and cost effectiveness, a main drawback is the sustainability of the LC-MS equipment due to remaining matrix compounds such as phospholipids in chicken plasma. Clotting was prevented by adjusting the mobile phase and gradient elution program for the analysis of TeA in chicken plasma, which resulted in a delayed retention time. Also, the divert valve was set to send as much effluent as possible to the waste.

With regard to chromatographic performance, TeA has been described as a troublesome compound because of its acidic and metal-chelating properties. To obtain better chromatographic properties, modifiers such as $Zn(II)SO_4$ were added to the mobile phase. However, these modifiers were not suited for MS.[5,12,13] Shephard et al. improved the chromatographic performance of TeA by using an end-capped C18 column, which prevented interactions between the amine moiety of TeA and active silanol groups on the column.[14] In the present study,

DOI: 10.1021/acs.jafc.5b02828
J. Agric. Food Chem. 2015, 63, 8560−8567

Table 3. Main Toxicokinetic Parameters of Tenuazonic Acid after Intravenous (iv) and Oral (po) Administration (0.05 mg/kg BW) to Pigs (n = 8) and Broiler Chickens (n = 5)[a]

	pig		broiler	
toxicokinetic parameter	iv	po	iv	po
AUC $_{0-t}$ (ng·h/mL)	108.9 ± 21.5 a	151.7 ± 28.6 b	805.6 ± 148.1 c	893.2 ± 275.3 c
AUC $_{0-inf}$ (ng·h/mL)	117.2 ± 23.8 a	169.8 ± 36.0 b	874.1 ± 182.2 c	1026.7 ± 353.1 c
F		1.47 ± 0.28 a		1.24 ± 0.51 a
C_{max} (ng/mL)		170.6 ± 32.2 a		133.3 ± 20.6 b
C_0 (ng/mL)	216.6 ± 53.0 a		218.5 ± 53.5 a	
t_{max} (h)		0.32 ± 0.21 a		2.60 ± 2.38 b
k_{el} (h^{-1})	1.38 ± 0.14 a	1.29 ± 0.23 a	0.41 ± 0.17 b	0.30 ± 0.09 b
$t_{1/2el}$ (h)	0.51 ± 0.05 a	0.55 ± 0.10 a	2.03 ± 1.04 b	2.45 ± 0.68 b
Cl (mL/h/kg)	448.4 ± 107.1 a	446.1 ± 110.8 a	59.3 ± 13.6 b	59.2 ± 13.2 b
V_d (mL/kg)	325.8 ± 75.1 a	358.4 ± 118.3 a	164.6 ± 62.8 b	207.2 ± 62.0 b
MRT (h)	0.70 ± 0.08 a	0.94 ± 0.20 b	4.46 ± 1.06 c	5.52 ± 1.23 c
MAT (h)		0.24 ± 0.24 a		1.06 ± 1.53 a

[a]Values are presented as the mean ± SD. AUC_{0-t}, area under the plasma concentration−time curve from time 0 to last concentration > LOQ; AUC_{0-inf}, area under the plasma concentration−time curve from time 0 to infinity; F, oral bioavailability; C_{max}, maximal plasma concentration; C_0, plasma concentration at time 0; t_{max}, time to maximal plasma concentration; k_{el}, elimination rate constant; $t_{1/2el}$, elimination half-life; Cl, total body clearance corrected for F; V_d, volume of distribution corrected for F; MRT, mean residence time; MAT, mean absorption time. Values sharing a lower case online letter for the same parameter do not differ from one another at the 5% global significance level.

the use of a double end-capped Zorbax Eclipse Plus column resulted in good chromatographic properties because TeA and the IS eluted as a sharp peak in both pig and broiler chicken plasma. Furthermore, the addition of ammonium bicarbonate to the mobile phase has been described to give reliable chromatographic properties of TeA in tomato and pepper product extracts, and ammonium formate has been used in LC-MS/MS analysis of TeA in different food commodities.[5,13] However, it must be mentioned that the use of ammonium formate resulted in a more robust method in the long term, because it produces no precipitation of the transfer tube, in contrast to ammonium bicarbonate.

The validation results (Tables 1 and 2) demonstrate the applicability of the developed LC-MS/MS method for a proper quantification of TeA in plasma samples taken during the toxicokinetic studies. Notwithstanding the strong suppression of the signal of TeA in pig plasma, a correct quantification was attained by using a stable isotopically labeled IS. Moreover, the IS was added before the start of the sample pretreatment and thus compensates for analyte losses during the extraction and cleanup procedure.[28,29]

Toxicokinetic Studies. The single dose of 0.05 mg/kg BW administered in the study presented corresponds with a daily intake of feed (approximately 1.5 kg for pigs and 150 g for broiler chickens) contaminated with realistic levels and covers the range between the median and maximum levels detected by Streit et al., namely, 68 and 1983 μg/kg feed, respectively.[3] Comparison of the toxicokinetic parameters after po and iv administration of TeA in both pigs and broiler chickens reveals no statistically significant difference in k_{el}, $t_{1/2el}$, Cl, and V_d between both routes of administration. However, both AUC_{0-t} and AUC_{0-inf} are higher after po administration compared to iv administration (Table 3). The higher AUC after po administration results in an F > 1, for both animal species. Toutain and Bousquet-Mélou list various reasons why a bioavailability >100% is regularly reported.[30] In the study presented, the dose and Cl, two factors influencing AUC, did not differ between both routes of administration. Furthermore, the plasma samples obtained after iv and po administration of one animal were analyzed on the same day, using the same procedure, to exclude analytical variation. The percentage extrapolated AUC_{t-inf} was <20% in both animals, indicating appropriate and sufficient selection of blood collection time points pa.[30] On the other hand, some earlier blood sample collection immediately after iv administration (<5 min pa) could possibly more accurately estimate the AUC and initial phase after iv bolus administration.[30] This could result in a higher AUC after iv administration, especially in pigs, which showed a rapid Cl. Consequently, a higher AUC after iv administration could result in a bioavailability approximating 100%.

The toxicokinetic behavior of TeA is noticeably different between pigs and broiler chickens. Although TeA was completely absorbed after oral administration in both animal species, the absorption rate was deemed to be slower in broilers.

Furthermore, the shorter $t_{1/2el}$ demonstrates the significantly more rapid elimination of TeA in pigs. V_d is rather small in both pigs and broiler chickens. Although statistically significant, the difference in V_d between pigs and broiler chickens is negligible in comparison to the striking difference in Cl between both animal species. Thus, the longer $t_{1/2el}$ is most likely due to the significantly lower Cl of TeA in broilers.

The total body Cl of a compound equals the sum of all clearances, with the most important organs being the liver and kidney. Remarkably, our results indicate a distinctly lower Cl in broilers, suggesting clear differences in elimination processes between both animal species. Because only non-plasma protein bound compounds are eliminated by glomerular filtration,[31] TeA plasma protein binding was determined in the present study. Mean plasma protein binding did not significantly differ between broiler chickens (72.8%) and pigs (58.1%). However, differences in Cl between pigs and broilers could also be attributed to species differences in active tubular secretion and/or reabsorption.[31] Another hypothesis for the slower elimination of TeA in broiler chickens could be zero-order biotransformation kinetics, in which a saturation of biotransformation enzymes or a clear inhibition of these enzymes occurs.[32] However, in humans, metabolization of TeA seems limited, because 90% of the ingested dose was excreted

DOI: 10.1021/acs.jafc.5b02828
J. Agric. Food Chem. 2015, 63, 8560−8567

unchanged in the urine.[6] Additionally, considering complete oral bioavailability, no first-pass effect by the liver was seen in pigs or broiler chickens. Because, to our knowledge, no in vitro nor in vivo information about the biotransformation of TeA is available, further research is needed to elucidate phase I and II metabolites in pigs and broiler chickens.

Few toxicity studies have been performed in chickens. After chronic exposure, Giambrone et al. noted a decreased weight gain and lowered feed efficiency when TeA was given at 10 mg/kg feed or by daily esophageal intubation (1.25 or 2.5 mg/kg BW) for 3 weeks. Other symptoms in the chickens receiving TeA via intubation were an enlarged and mottled spleen, erosions of the gizzard, and hemorrhages.[9] Because the maximum feed contamination level detected by Streit et al. was <2 mg TeA/kg feed, the 10 mg TeA/kg feed administered daily by Giambrone et al. is rather high.[3,9] Nevertheless, more subtle toxic effects could possibly occur when broiler chickens are fed daily highly contaminated feed, especially because the elimination rate is low and accumulation could occur. Accumulation of TeA in tissues and edible offal of broiler chickens could implicate health risks for human consumers. Therefore, future tissue residue studies are recommended. To our knowledge, no studies concerning the toxicity of TeA in pigs have been performed. Further research is imperative for a better understanding of the possible harmful effects of TeA in both animal species and humans. Moreover, the toxicokinetic parameters and toxic effects in pigs could be an indication for those in humans, because pigs possess multiple anatomical, physiological, and biochemical characteristics that closely resemble humans.[33−35]

In conclusion, a LC-MS/MS method to quantitate TeA in pig and broiler chicken plasma was successfully developed and validated. Using this method, TeA plasma concentrations were determined after single po and iv administration of 0.05 mg TeA/kg BW in pigs and broiler chickens, in a two-way crossover design. This study demonstrated the complete absolute oral bioavailability and significant differences in the toxicokinetic profile of TeA between pigs and broiler chickens. The elimination of TeA was slower in broiler chickens ($t_{1/2el,\ iv}$, 2.03 h; Cl_{iv}, 59.3 mL/h/kg) compared to pigs ($t_{1/2el,\ iv}$, 0.51 h; Cl_{iv}, 448.4 mL/h/kg). Tissue residue studies are recommended to assess the carry-over of TeA from feed to edible tissues and offal. Further research is needed to elucidate the biotransformation and excretion processes of TeA and other *Alternaria* mycotoxins in animal species and humans for a better understanding of the possible toxicity of these mycotoxins.

AUTHOR INFORMATION

Corresponding Author

*(S.F.) E-mail: sophie.fraeyman@ugent.be. Phone: +32 9 264 73 50. Fax: +32 9 264 74 97.

Notes

The authors declare no competing financial interest.

ACKNOWLEDGMENTS

We are grateful to Elke Gasthuys, Elke Plessers, Anneleen Watteyn, and Heidi Wyns for their assistance during the animal trials. Furthermore, we thank Jelle Lambrecht for her aid in laboratory experiments.

REFERENCES

(1) Ostry, V. Alternaria mycotoxins: an overview of chemical characterization, producers, toxicity, analysis and occurrence in foodstuffs. *World Mycotoxin J.* **2008**, *1*, 175−188.

(2) Müller, M. E. H.; Korn, U. Alternaria mycotoxins in wheat − a 10 years survey in the northeast of Germany. *Food Control* **2013**, *34*, 191−197.

(3) Streit, E.; Schwab, C.; Sulyok, M.; Naehrer, K.; Krska, R.; Schatzmayr, G. Multi-mycotoxin screening reveals the occurrence of 139 different secondary metabolites in feed and feed ingredients. *Toxins* **2013**, *5*, 504−523.

(4) Asam, S.; Lichtenegger, M.; Liu, Y.; Rychlik, M. Content of the *Alternaria* mycotoxin tenuazonic acid in food commodities determined by a stable isotope dilution assay. *Mycotoxin Res.* **2012**, *28*, 9−15.

(5) Lohrey, L.; Marschik, S.; Cramer, B.; Humpf, H. U. Large-scale synthesis of isotopically labeled $^{13}C_2$-tenuazonic acid and development of a rapid HPLC-MS/MS method for the analysis of tenuazonic acid in tomato and pepper products. *J. Agric. Food Chem.* **2013**, *61*, 114−120.

(6) Asam, S.; Habler, K.; Rychlik, M. Determination of tenuazonic acid in human urine by means of a stable isotope dilution assay. *Anal. Bioanal. Chem.* **2013**, *405*, 4149−4158.

(7) Shigeura, H. T.; Gordon, C. N. The biological activity of tenuazonic acid. *Biochemistry* **1963**, *2*, 1132−1137.

(8) Smith, E. R.; Fredrickson, T. N.; Hadidian, Z. Toxic effects of the sodium and the N,N′-dibenzylethylenediamine salts of tenuazonic acid (NSC-525816 and NSC-82260). *Cancer Chemother. Rep. Part 1* **1968**, *52*, 579−585.

(9) Giambrone, J. J.; Davis, N. D.; Diener, U. L. Effect of tenuazonic acid on young chickens. *Poult. Sci.* **1978**, *57*, 1554−1558.

(10) Griffin, G. F.; Chu, F. S. Toxicity of the *Alternaria* metabolites alternariol, alternariol methyl-ether, altenuene, and tenuazonic acid in the chicken-embryo assay. *Appl. Environ. Microbiol.* **1983**, *46*, 1420−1422.

(11) European Food Safety Authority on Contaminants in the Food Chain. Scientific opinion on the risks for animal and public health related to the presence of *Alternaria* toxins in feed and food. *EFSA J.* **2011**, *9* (10), 2407 [97 pp].10.2903/j.efsa.2011.2407

(12) Scott, P. M. Analysis of agricultural commodities and foods for *Alternaria* mycotoxins. *J. AOAC Int.* **2001**, *84*, 1809−1817.

(13) Asam, S.; Lichtenegger, M.; Muzik, K.; Liu, Y.; Frank, O.; Hofmann, T.; Rychlik, M. Development of analytical methods for the determination of tenuazonic acid analogues in food commodities. *J. Chromatogr. A* **2013**, *1289*, 27−36.

(14) Shephard, G. S.; Thiel, P. G.; Sydenham, E. W.; Vleggaar, R.; Marasas, W. F. Reversed-phase high-performance liquid chromatography of tenuazonic acid and related tetramic acids. *J. Chromatogr., Biomed. Appl.* **1991**, *566*, 195−205.

(15) Asam, S.; Liu, Y.; Konitzer, K.; Rychlik, M. Development of a stable isotope dilution assay for tenuazonic acid. *J. Agric. Food Chem.* **2011**, *59*, 2980−2987.

(16) Gasthuys, F.; De Boever, S.; Schauvliege, S.; Reyns, T.; Levet, T.; Cornillie, P.; Casteleyn, C.; De Backer, P.; Croubels, S. Transsplenic portal catheterization combined with a jugular double-lumen catheter for pharmacokinetic and presystemic metabolization studies in pigs. *J. Vet. Pharmacol. Ther.* **2009**, *32*, 137−145.

(17) Garré, B.; Shebany, K.; Gryspeerdt, A.; Baert, K.; van der Meulen, K.; Nauwynck, H.; Deprez, P.; De Backer, P.; Croubels, S. Pharmacokinetics of acyclovir after intravenous infusion of acyclovir and after oral administration of acyclovir and its prodrug valacyclovir in healthy adult horses. *Antimicrob. Agents Chemother.* **2007**, *51*, 4308−4314.

(18) De Baere, S.; Goossens, J.; Osselaere, A.; Devreese, M.; Vandenbroucke, V.; De Backer, P.; Croubels, S. Quantitative determination of T-2 toxin, HT-2 toxin, deoxynivalenol and deepoxy-deoxynivalenol in animal body fluids using LC-MS/MS detection. *J. Chromatogr. B: Anal. Technol. Biomed. Life Sci.* **2011**, *879*, 2403−2415.

(19) Commission Decision 2002/657/EC implementing Council Directive 96/23/EC concerning the performances of analytical

DOI: 10.1021/acs.jafc.5b02828
J. Agric. Food Chem. 2015, 63, 8560−8567

methods and the interpretation of results, Official Journal of the European Communities, No. L221, 17/08/2002, Decision of 12 August 2002, European Commission, Directorate General for Public Health and consumers Protection.
(20) VICH GL 49 (2012-Final), Guidance for Industry. Studies to evaluate the metabolism and residue kinetics of veterinary drugs in food producing animals: validation of analytical methods used in residue depletion studies, February 2011.
(21) Knecht, J.; Stork, G. Prozentuales und logarithmisches Verfahren zur Berechnung von Eichkurven. *Fresenius' Z. Anal. Chem.* **1974**, *270*, 97−99.
(22) Hill, H. M.; Causey, A. G.; Lessard, D.; Selinger, K.; Herman, J. Choice and optimization of calibration functions. In *Bioanalytical Approaches for Drugs, including Anti-asthmatics and Metabolites*; Royal Society of Chemistry: London, UK, 1992; Vol. 20, pp 111−118.
(23) Matuszewski, B. K.; Constanzer, M. L.; Chavez-Eng, C. M. Strategies for the assessment of matrix effect in quantitative bioanalytical methods based on HPLC-MS/MS. *Anal. Chem.* **2003**, *75*, 3019−3030.
(24) De Baere, S.; Osselaere, A.; Devreese, M.; Vanhaecke, L.; De Backer, P.; Croubels, S. Development of a liquid-chromatography tandem mass spectrometry and ultra-high-performance liquid chromatography high-resolution mass spectrometry method for the quantitative determination of zearalenone and its major metabolites in chicken and pig plasma. *Anal. Chim. Acta* **2012**, *756*, 37−48.
(25) Devreese, M.; De Baere, S.; De Backer, P.; Croubels, S. Quantitative determination of several toxicological important mycotoxins in pig plasma using multi-mycotoxin and analyte-specific high performance liquid chromatography-tandem mass spectrometric methods. *J. Chromatogr. A* **2012**, *1257*, 74−80.
(26) Devreese, M.; Osselaere, A.; Goossens, J.; Vandenbroucke, V.; De Baere, S.; Eeckhout, M.; De Backer, P.; Croubels, S. New bolus models for in vivo efficacy testing of mycotoxin-detoxifying agents in relation to EFSA guidelines, assessed using deoxynivalenol in broiler chickens. *Food Addit. Contam., Part A* **2012**, *29*, 1101−1107.
(27) Devreese, M.; De Baere, S.; De Backer, P.; Croubels, S. Quantitative determination of the *Fusarium* mycotoxins beauvericin, enniatin A, A1, B and B1 in pig plasma using high performance liquid chromatography-tandem mass spectrometry. *Talanta* **2013**, *106*, 212−219.
(28) Antignac, J. P.; de Wasch, K.; Monteau, F.; De Brabander, H.; Andre, F.; Le Bizec, B. The ion suppression phenomenon in liquid chromatography-mass spectrometry and its consequences in the field of residue. *Anal. Chim. Acta* **2005**, *529*, 129−136.
(29) Rychlik, M.; Asam, S. Stable isotope dilution assays in mycotoxin analysis. *Anal. Bioanal. Chem.* **2008**, *390*, 617−628.
(30) Toutain, P. L.; Bousquet-Mélou, A. Bioavailability and its assessment. *J. Vet. Pharmacol. Ther.* **2004**, *27*, 455−466.
(31) Riviere, J. E. Renal elimination. In *Comparative Pharmacokinetics*, 2nd ed.; Wiley-Blackwell: Ames, IA, USA, 2011 ; p 95.
(32) Riviere, J. E. Nonlinear models. In *Comparative Pharmacokinetics*, 2nd ed.; Wiley-Blackwell: Ames, IA, USA, 2011; pp 207−223.
(33) Bode, G.; Clausing, P.; Gervais, F.; Loegsted, J.; Luft, J.; Nogues, V.; Sims, J. The utility of the minipig as an animal model in regulatory toxicology. *J. Pharmacol. Toxicol. Methods* **2010**, *62*, 196−220.
(34) Roth, W. J.; Kissinger, C. B.; McCain, R. R.; Cooper, B. R.; Marchant-Forde, J. N.; Vreeman, R. C.; Hannou, S.; Knipp, G. T. Assessment of juvenile pigs to serve as human pediatric surrogates for preclinical formulation pharmacokinetic testing. *AAPS J.* **2013**, *15*, 763−774.
(35) Swindle, M. M.; Makin, A.; Herron, A. J.; Clubb, F. J., Jr.; Frazier, K. S. Swine as models in biomedical research and toxicology testing. *Vet. Pathol.* **2012**, *49*, 344−356.

DOI: 10.1021/acs.jafc.5b02828
J. Agric. Food Chem. 2015, 63, 8560−8567

roasting until it turns to dark brown. After roasting, sometimes the roasted coffee beans are brought to the family members or visitors to allow them to experience the aroma. Afterwards, it will be ground to a fine powder using a traditional wooden mortar and pestle. The powder is poured into boiled water in a special local coffee clay pot called a "jebena". Coffee will be ready to serve when the steam with an attractive flavor starts to come out from the nozzle. After that, the jebena is placed on ground for about 3 min to let the coffee sludge settle to the bottom. The brewed coffee is then poured into small cups and served (personal observation). In general, coffee is an important crop for domestic consumption as well as a source of hard currency for the nation.

However, studies have indicated that coffee beans have different pesticide residues. Even though coffee is the most important agricultural product for human consumption as well as for the economic growth of the producing countries, the beans might have different pesticide residues that can expose consumers to hazardous agrochemicals.[7] Because of the high consumption of coffee and its economic importance, people from the producer, exporter, and consumer countries give more attention to its safety.[8] Even though pesticide contamination in green coffee beans is limited during agricultural treatments, there may be contamination during transportation and storage.[9] Different studies have stated that coffee is contaminated by different classes of pesticides applied in the field. According to the U.S. Food and Drug Administration, from a survey of 60 imported green coffee bean samples, some of them contained different pesticide residues, such as chlorpyrifos at a concentration ranging from 0.01 to 0.04 mg/kg and pirimiphos methyl at 0.01 mg/kg.[10] From a study done in Brazil, the residues of different pesticides, such as endosulfan, chlorpyrifos, cypermethrin, and captafol, have been detected in coffee beans from either registered or illegal use.[11] Additionally, from the previous study done in Ethiopia, DDT, cypermethrin, permethrin, deltamethrin, chlorpyrifos ethyl, and endosulfan (α and β) were detected in coffee beans at concentrations ranging from 0.011 to 1.115 mg/kg[7].

The pesticide residues, to a variable extent, left in the food materials after harvesting, are beyond the control of consumers and may have deleterious effects on human health. Because Ethiopia is the largest producer, exporter, and consumer of coffee in Africa, a pragmatic solution should be developed to tackle the problem of coffee safety. Different studies have revealed that food processing can be one important solution that has a significant role for the reduction of pesticide residues in different food items.[2−4,12] Nowadays, there is an increasing need for information on the effect of various food processes on pesticide residues. Few studies have indicated the effect of coffee roasting on the reduction of pesticide residues.[13,14] However, no studies are available on the effect of household coffee processing (washing, roasting, and brewing) methods on pesticide residues. Therefore, the main aim of the present study is to evaluate the effect of household processing on pesticide residues in coffee and to determine the processing factor (PF) for each of the processing steps.

2. MATERIALS AND METHODS

2.1. Chemicals and Reagents. Analytical grade acetonitrile (99.9% purity) was supplied by VWZ-prolabo. High performance liquid chromatography grade *n*-hexane (98% purity) and acetone (98.9% purity) that were obtained from ALLthec were used to extract the pesticide residues from the raw coffee beans and after different processing steps. Thermo Fisher Scientific supplied $MgSO_4$ (98% purity), NaAc (99% purity), the 50 mL centrifuge tube, the 15 mL dispersive solid phase extraction cleanup tube packed with primary secondary amine (PSA: 99% purity), magnesium sulfate ($MgSO_4$, 98% purity), and octadecyl (C18, 99% purity). The pesticides under study ($p'p$-DDE (99.9%), $p'p$-DDD (99.3%), $o'p$-DDT (100%), $p'p$-DDT (99%), endosulfan α (98.5%), endosulfan β (98%), Permethrin (98%), cypermethrin (98%), deltamethrin (99%), Chlorpyrifos ethyl (99.5%), Heptachlor epoxide (99.5%) and hexachlorobenzene (98%)) with their highest analytical purity, were obtained from Supelco and delivered by Sigma-Aldrich Logistic Analytical. The physicochemical properties of the pesticides studied in the present study are presented in Table 1.

Table 1. Physicochemical Properties of the Pesticides under Study[a]

pesticides	water solubility (mg/L)	log k_{ow}	vapor pressure (mmHg)	mode of action
$p'p$-DDE	0.025	6.91	1.6×10^{-7}	contact
$p'p$-DDD	0.120	6.51	1.4×10^{-6}	contact
$o'p$-DDT	0.090	6.02	6.0×10^{-6}	contact
$p'p$-DDT	0.085	6.79	1.1×10^{-7}	contact
endosulfan α	0.530	3.83	1×10^{-5}	contact
endosulfan β	0.280	3.62	1×10^{-5}	contact
permethrin	0.006	6.10	2.15×10^{-8}	contact
cypermethrin	0.009	5.40	2.3×10^{-7}	contact
deltamethrin	0.002	6.10	1.5×10^{-8}	contact
heptachlor epoxide	0.350	5.40	3.0×10^{-4}	contact
hexachlorobenzene	0.006	5.73	1.09×10^{-5}	systemic
chlorpyrifos ethyl	1.400	4.70	1.9×10^{-5}	contact

[a]log k_{ow} = logarithm of octanol-water partion coefficient.

2.2. Sampling. A 3 kg portion of green coffee beans was bought from a local market in Jimma zone, southwestern Ethiopia in August, 2014 and served as a blank and spiked sample. Samples were packed in polyethylene plastic bags, after which they were sealed and labeled properly. The samples were transported to the laboratory and stored at −20 °C until extraction was done.

2.3. Quality Control. *2.3.1. Linearity.* The quantitative determination of the pesticide residues in processed and unprocessed coffee beans was done on the basis of an external standard method. The calibration curves were obtained by injecting five different concentrations of the pesticide standards in the range of 0.005−1 mg/L. The regression coefficient (r^2) was >0.995 for all the pesticides under study. Identification and quantification of the pesticides were done on the basis of the retention time and peak area, respectively.

2.3.2. Recovery Study. To evaluate the performance of the analytical procedures recovery (% recovery), studies were undertaken for each pesticide. A 10 g sample of pesticide-free coffee beans was weighed on the analytical balance and spiked with 40 μL of 100 mg/L of each pesticide in three replicates. The extraction was performed in a similar way with the samples. The percent recovery was derived from the equation: (amount of pesticide observed)/(amount of pesticides spiked) × 100. The percent relative standard deviation (% RSD) was obtained by dividing the standard deviations by the average concentration and multiplying the result by 100.

DOI: 10.1021/acs.jafc.5b03327
J. Agric. Food Chem. 2015, 63, 8568−8573

2.4. Treatment of Raw Coffee Bean. A 10 g portion of raw coffee beans was weighed on an analytical balance and spiked with 40 μL of a 100 mg/L solution of each pesticides under study (DDT metabolites, cypermethrin, deltamethrin, permethrin, endosulfan [α, β] and chlorpyrifos ethyl, heptachlor epoxide, and hexachlorobenzene) in three replicates to increase the reliability of the results. Spiking was done for each household coffee processing method (washing, roasting, and brewing). The pesticides selected for this study were detected in the previous study done on Ethiopian coffee beans,[7] except for heptachlorepoxide and hexachlorobenzene, in which the investigators expected them from previous application in the environment. The spraying of the coffee beans was done in a Petri dish to get equal distribution of the pesticides for each bean. After spraying, the Petri dishes were covered with aluminum foil and placed in refrigerator at 4 °C for 24 h to increase the contact time between the pesticides and the matrix. After 1 day, the processing methods (washing, roasting, brewing) and the extraction, clean up, and analysis were followed as stated below.

2.5. Extraction and Cleanup of the Samples. To assess the effect of washing, roasting, and brewing of coffee on pesticide residues, the extraction and cleanup of the raw and processed coffee beans were done using the modified Quick, Easy, Cheap, Effective, Rugged and Safe (QuEChERS) method combined with a dispersive solid phase extraction cleanup (d-SPE) method. The analytical procedure was based on the method AOAC 2007.01.[15] The subsequent processing steps of the coffee beans were done to correspond, as closely as possible, to the actual traditional household coffee processing in Ethiopia. Blank coffee bean (nonspiked) was also analyzed together with the raw and processed coffee beans. The extraction and cleanup procedures for raw coffee beans and processed coffee beans were as follows:

2.5.1. Raw coffee beans. After holding the spiked samples for 1 day, the treated raw coffee bean was ground and homogenized using a coffee grinder with a knife in it. A 15 mL portion of acetonitrile was added, and the sample was shaken by hand for 30 s. Then 6 g of $MgSO_4$/1.5 g of NaCl/1.5 g of Na_3citrate·$2H_2O$/0.750 g of Na_2Hcitrate was added, and the mixture was again shaken for 5 min to prevent formation of agglomerates between the water and $MgSO_4$. Then the samples were centrifuged at 5000 rpm for 5 min. The upper organic layer was taken for cleanup using a 15 mL dispersive solid phase extraction tube (d-SPE) containing 300 mg of PSA, 900 mg of $MgSO_4$, and 150 mg of C18 and then shaken for 30 s. The cleaned extracts were centrifuged to get a clear solution. After centrifugation, 5 mL of the upper layer was taken into a 100 mL flat bottom flask and evaporated to dryness using a rotary evaporator (N18673 Rotavapor; Buchi) at a temperature of 40 °C. A 2 mL portion of *n*-hexane/acetone (9:1 V/V) was added for solvent exchange to make the sample amenable for GC/ECD analysis. The blank coffee bean was also extracted in a similar way, as were with the spiked samples. Then the extract was placed into a vial for GC/ECD analysis.

2.5.2. Washed Coffee Beans. The spiked coffee beans were washed thoroughly for 5 min under normal tap water (25−30 °C), which resembles coffee bean washing at the household level. Then all other procedures for the unprocessed coffee beans were applied for the extraction, cleanup, and analysis for the presence of pesticides.

2.5.3. Roasted Coffee Beans. The spiked coffee beans were roasted on a stove at a temperature range of 230−240 °C (light to medium) roasting and an average time of 12−14 min until the characteristics aroma or flavor of coffee appears. The roasting temperature and duration of roasting was based on a study done by Moon and Shibamoto.[16] The roasting processes were done in a way similar to the traditional Ethiopian household coffee roasting procedures. Then the other procedures for extraction and cleanup used for raw coffee beans were applied.

2.5.4. Brewed Coffee Beans. Some heat-resistant pesticides may be detected in a cup of coffee after the coffee beans were roasted. To determine the effect of brewing on the pesticides under study, the brewing process was also undertaken. The roasted coffee beans were ground to a fine powder using a coffee grinder (type 4041, 220-230 V/150w). The fine coffee powder was added to a coffee pot traditionally called a "Jebena" containing 100 mL boiled water and brewed for 10−12 min in a way similar to that of the tradition Ethiopian coffee brewing processes (personal observation). After brewing, the coffee pot was picked up from the stove and put on the ground until the infusion of the coffee was cooled and the coffee powder or sludge had settled to the bottom of the coffee pot. Then the upper liquid layer was removed carefully to the cups, and then extraction, cleanup and analysis of the brewed coffee solution was done in a way similar to that of the raw coffee beans.

2.6. Determination of Processing Factor (PF). The effect of household processing on the level of pesticides often correlates with the physicochemical properties of the pesticides under study, so it is important to adequately monitor the processing factor. The processing factor (PF) for all transformation steps was calculated as the ratio between the pesticide concentrations in the processed commodity (mg/kg) to the pesticide concentration in unprocessed (raw) commodity (mg/kg). According to Bonnechere and his colleagues,[17] a PF of <1 indicated that there is reduction of pesticides by the processing method (PF < 1 = reduction factor), whereas >1 indicated no reduction in weight or volume, (PF > 1 = a concentration factor). The processing factor is the proportional amount by which residues change when food is processed. For this study, it is calculated by the formula below:

$$\text{processing factor (PF)} = \frac{\text{concentration of pesticides in processed coffee beans (mg/kg)}}{\text{concentration of pesticides in raw coffee beans (mg/kg)}}$$

After obtaining the processing factor, the percent reduction (% reduction) for each processing method was calculated as follows: % reduction = (1 − PF) × 100.

2.7. Wash Water and Coffee Sludge Remaining at the Bottom of Pot after Coffee Brewing. Before the coffee was roasted, it was washed with water (which may remove some residues on the surface of the coffee beans). Additionally, after the coffee was brewed, there is sludge (powder or coffee residue) remaining in the bottom of the coffee pot, which may contain some pesticide residue that can evade the roasting process. Traditionally, this wash water and coffee sludge is often disposed of in the environment, which may contaminate food grown there. To check whether the wash water from the samples and the sludge of the coffee contain pesticide residues, these two samples were analyzed. The procedure was as follows: A 10 mL portion of the wash water (assuming 10 g of water) and 6−8 g of coffee sludge were weighed on an analytical balance and placed into a 50 mL centrifuge tube.

DOI: 10.1021/acs.jafc.5b03327
J. Agric. Food Chem. 2015, 63, 8568−8573

Then the extraction, cleanup, and analysis were done in a way similar to that of the raw coffee bean.

2.8. Analytical equipment. Quantitative estimations and chromatographic separation of each pesticide were done by gas chromatography with an electron capture detector (GC−ECD, Agilent Technologies 6890N) with an auto sampler. The coffee bean processing was undertaken to see their effect on the pesticides previously detected in Ethiopian green coffee beans,[7] so the chromatographic conditions for this study were the same as the previous paper, as explained below. A HP-5 capillary column of 30 m × 0.25 mm i.d. × 0.25 μm film thickness coated with 5% phenyl methyl siloxane (model no. Agilent 19091J-433) was used in combination with the following oven temperature program: initial temperature, 80 °C; ramp at 30 °C min^{-1} to 180 °C; ramp at 3 °C min^{-1} to 205 °C; held for 4 min; ramp at 20 °C min^{-1} to 290 °C; held for 8 min; ramp at 50 °C min^{-1} to 325 °C. For deltamethrin, the oven temperature was maintained initially at 130 °C, held for 1 min, ramped at 30 °C min^{-1} to 280 °C, held for 16 min, ramped at 50 °C min^{-1} to 325 °C, and held for 3 min. The total GC run time was 27.92 min. Helium (99.9999% purity) was used as a carrier gas at a flow rate of 20 mL min^{-1}, and nitrogen was the makeup gas at a flow rate of 60 mL min^{-1}. An aliquot of 1 μL was injected in split mode at a split ratio of 50:1 and injection temperature of 280 °C. The pesticide residues were detected with an electron capture detector (μ-ECD) operated at a temperature of 300 °C. For the reliability of the results, each sample was analyzed in triplicate, and the mean concentration was computed accordingly.

2.9. Statistical Analysis. All the treatments for the three processing methods were done in three replicates, and values are shown as mean ± SD. Statistical significance was checked using the Kruskal−Wallis test to see if the processing methods (washing, roasting, and brewing) are different in the percent reduction of the pesticides under study. Differences at $P < 0.05$ were considered as significant.

3. RESULTS AND DISCUSSION

3.1. Quality Control Studies. The mean percent recovery for most of the pesticides was 80−120% and the percent relative standard deviation (% RSD) was below 10% for all the pesticides under study, except for cypermethrin and deltamethrin. All pesticides were in the acceptable analytical range (70−120% recovery and RSD < 20%). The regression coefficients (r^2) were >0.995 for all the pesticides. This method is accurate and precise for the analysis of the pesticides under study and fulfilled the requirement of European Document no. SANCO/12495/2011.[18] The results are indicated in Table 2.

3.2. Effect of Household Processing of Coffee Beans on Pesticide Residues. This study investigated the effect of household processing of coffee (washing, roasting, and brewing) on the stability of 12 pesticides, including metabolites and isomers. The concentration of the pesticides under study in raw and processed coffee beans are presented in Figure 1. Among the household processes, washing decreased the pesticide residues by 14.63−57.69%. This effect may be due to the fact that most of the pesticides have contact action and are found on the surface of the coffee beans. This washing process may help for the removal of the pesticides with the silverskin of the coffee (very thin layer of a coffee bean located just above the main part of the coffee beans), dust, or soil. Reports indicated that surface residues are easily amenable to removal by simple washing processes with water.[4] The majority

Table 2. Results of Regression Coefficient, Percent Recovery and Percent RSD[a]

pesticides	r^2	% recovery	% RSD
endosulfan α	0.998	80	6.3
endosulfan β	0.997	130	3.8
chlorpyrfos ethyl	0.995	122.5	2.0
permethrin	0.998	112.5	8.9
cypermethrin	0.999	127.5	19.6
deltamethrin	0.999	100	15.0
$p'p$-DDE	0.999	102.5	2.4
$p'p$-DDD	0.999	102.5	4.9
$o'p$-DDT	0.998	125	4.0
$p'p$-DDT	0.988	125	2.0
heptachlorepoxide	0.999	117.5	10.6
hexachlorobenzene	0.999	120	0.20

[a]RSD = relative standard deviation.

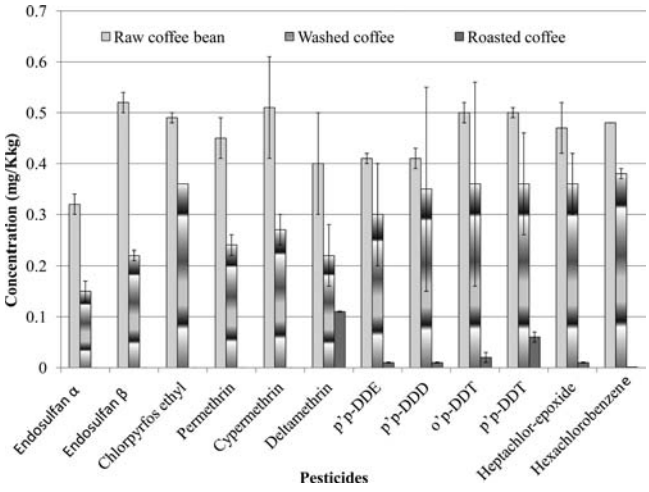

Figure 1. Mean pesticide residues (mg/kg) at different coffee processing steps. The error bars indicate standard deviation. Pesticides from brewed coffee were not detected and are not shown in this graph.

of the pesticides applied to agricultural crops are confined to the surface and a much smaller amount undergoes penetration to the plant system.[19] As a result, they can easily be acquiescent to being washed, trimmed, or peeled from the surface of the crop. The maximum reduction was observed for endosulfan α and β, for which the residue decreased by 53.13−57.69%, respectively. A similar result was observed from a study done in India: washing of the vegetable brinjal with tap water decreased endosulfan residue up to 55%; however, a lesser removal of heptachlor epoxide in cucumber was observed.[20]

The rinsability of some pesticides by washing with water may not always correlate with its water solubility.[21] As indicated in Table 1, most of the pesticides under study have low water solubility and high octanol-water partition coefficient (log k_{ow} > 3). Washing was found comparatively less effective in reducing the residues of $p'p$-DDD (14.63%), hexachlorobenzene (20.83%), heptachlor epoxide (23.40%), chlorpyrifos ethyl (26.53%), $o'p$-DDT ((28%), and $p'p$-DDT (28%).

In this study, roasting was found to be effective in affecting the stability of pesticide residues in coffee beans. By this process, reductions of the residues of the pesticides were in the range of 72.5−99.8%. The maximum reductions were observed in hexachlorobenzene (99.8%), heptachlor epoxide (97.9%), $p'p$-DDE, $p'p$-DDD (97.6%), and $o'p$-DDT (96%). Five of the

DOI: 10.1021/acs.jafc.5b03327
J. Agric. Food Chem. 2015, 63, 8568−8573

spiked pesticides (chlorpyrifos ethyl, permethrin, cypermethrin, and endosulfan α and β) were not detected after the roasting process. This may be due to the instability of these pesticides to the heat applied during the roasting process. Thermal processing treatments such as cooking, backing, blanching, steaming, and boiling have been found effective for the breakdown of various pesticides, depending on the type of pesticide.[22] Additionally, there may be a loss of the pesticides during the application of heat depending on their physicochemical properties, such as evaporation or thermal degradations.[23] From a study done in Japan on the behavior of pesticides in coffee beans, the pesticide residues decreased a significant amount after the coffee beans were roasted.[14]

After the coffee brewing process, none of the pesticides under study were detected. This process is found to be the most effective for the breakdown of the pesticides under study. As it has been explained by Abou-Arab and Abou Donia,[24] the elimination of the pesticide residue from the boiled extract (brewed coffee) may be due to the decomposition of the pesticide residue by the application of heat during brewing. The pesticide residues were significantly influenced by the roasting and brewing processes. In general, the three household coffee bean processing methods have a cumulative effect in the reduction of pesticides and help in solving health problems that can occur from exposure to pesticides in coffee.

3.3. Determination of the Processing Factor. The processing factor for each pesticide from each processing step was determined. The PFs for coffee samples after each processing step was <1, which indicated that the processing methods have an effect on pesticide residues. A study done by Bonnechere et al[17] has also indicated that a PF of less than a unit is an indication of pesticide residue reduction due to a specific food processing step. The PFs for the detected pesticides in the roasting process were the lowest, particularly for hexachlorobenzene. Heptachlorepoxide, $p'p$-DDE, $p'p$-DDD, and $o'p$-DDT ranged from 0.001 to 0.04. This indicated that the roasting process played the most important role in removing the pesticides from coffee beans compared with the washing process. The processing factor was not calculated for the pesticides not detected after the processing (Table 3).

The Kruskal–Wallis test showed that there is a strong variation in the stability of pesticide residues in coffee beans among the processing methods (P = 0.00001). The reduction of pesticide residues due to washing is significantly lower than roasting (p = 0.0001) and brewing processes (P = 0.00001); however, there is no significant difference between coffee roasting and coffee brewing (P > 0.05). According to Hasmukh et al.,[25] the washing process may depend on different factors, such as location, age of residue, water solubility, and temperature; this may be the reason for the variation. From the household processing methods, roasting and brewing are the most effective in decreasing the pesticides in coffee beans.

Table 3. Processing Factor for the Effect of Washing, Roasting and Brewing Processes[a]

Pesticide	PF Washing	PF Roasting	PF Brewing
endosulfan α	0.47	*a*	*a*
endosulfan β	0.42	*a*	*a*
chlorpyrefos ethyl	0.73	*a*	*a*
permethrin	0.53	*a*	*a*
cypermethrin	0.53	*a*	*a*
deltamethrin	0.55	0.28	*a*
$p'p$-DDE	0.73	0.02	*a*
$p'p$-DDD	0.85	0.02	*a*
$o'p$-DDT	0.72	0.04	*a*
$p'p$-DDT	0.72	0.12	*a*
heptachlor epoxide	0.77	0.02	*a*
hexachlorobenzene	0.79	0.001	*a*

[a]Not detected and the processing factor is not calculated.

3.4. Pesticide Residue in Wash Water and Coffee Sludge. To determine the level of pesticide liquid waste (wash water) and the coffee sludge that settled to the bottom of the coffee pot after the coffee was brewed, these two samples were analyzed. The result of the analyses revealed that all DDT metabolites ($p'p$-DDE, $p'p$-DDD, $o'p$-DDT, and $p'p$-DDT) and deltamethrin were detected in the wash water (Figure 2). This

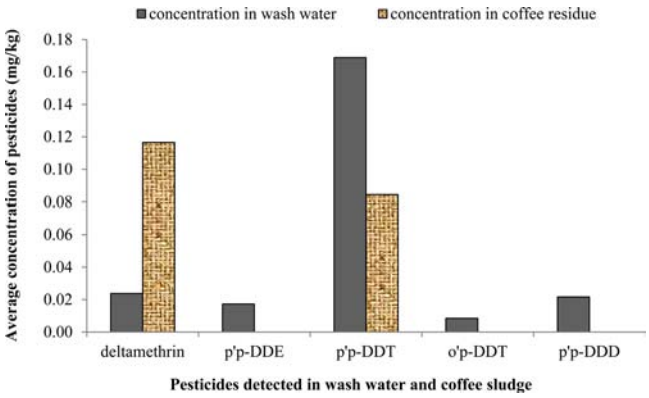

Figure 2. Average concentrations of pesticides detected in wash water and coffee sludge (mg/kg).

may be due to the fact that these pesticides have contact action (acting on surface) and may be removed with the coffee silverskin and found in the wash water. Most of the pesticides disappeared from the coffee beans during the roasting process. In the meantime, pesticides were not detected in the coffee sludge after brewing, except for deltamethrin and $p'p$-DDT. This may be because the percent reductions of deltamethrin (72.5%) and $p'p$-DDT (88%) after roasting of the coffee beans were low compared with other pesticides under study (Figure 2). The results indicated that the coffee sludge should not be scored when pouring the brewed coffee into a cup before human consumption. After brewing, it is necessary to wait some time until the sludge of the coffee completely settles to the bottom of the coffee pot.

In Ethiopia, the wash water from coffee beans and the residue from the brewed coffee are discarded to the open environment, which may pose contamination, so care should be taken during the disposal of both the liquid (wash water) and semi-solid coffee sludge) waste. In addition, during pouring of the coffee solution to drink or serve coffee, only the upper layer (not mixed with the sludge at the bottom of the pot) should be used for the safety of the consumers.

AUTHOR INFORMATION

Corresponding Author

*Phone: +32 (0)9264 60 12 Fax: +32 (0)9 264 62 49. E-mails: sebleworkmekonen.shegen@ugent.be; seblework2001@yahoo.com.

Notes

The authors declare no competing financial interest.

DOI: 10.1021/acs.jafc.5b03327
J. Agric. Food Chem. 2015, 63, 8568–8573

■ ACKNOWLEDGMENTS

The authors are very grateful for a special research fund (BOF) of Ghent University for sponsoring this study and Jimma University for supporting the study. The authors also would like to acknowledge Lillian Goeteyn and Claudine Schollaert for their assistant in the laboratory work.

■ REFERENCES

(1) Kaushik, G.; Satya, S.; Naik, S. N. Food processing a tool to pesticide residue dissipation − A review. *Food Res. Int.* **2009**, *42* (1), 26−40.

(2) Satpathy, G.; Tyagi, Y. K.; Gupta, R. K. Removal of Organophosphorus (OP) Pesticide Residues from Vegetables Using Washing Solutions and Boiling. *J. Agric. Sci.* **2012**, *4* (2). DOI: 10.5539/jas.v4n2p69

(3) Pal, P.; Sahah, P. G. Effect of storage and processing on dissipation of five insecticides on wheat. *Pestic. Res. J.* **2008**, *20* (2), 253−258.

(4) Ahmed, A.; Randhawa, M. A.; Yusuf, M. V.; Khalid, N. Effect of processing on pesticide residues in food crops-Ariview. *J. Agric. Res.* **2011**, *49* (3).379390

(5) Yeretzian, C.; Jordan, A.; Lindinger, W. Analysing the headspace of coffee by proton-transfer-reaction mass-spectrometry. *Int. J. Mass Spectrom.* **2003**, *223−224*, 115−139.

(6) ICO. Ethiopian coffee challenges and opportunities. *ICO Annual Review* 2012.

(7) Mekonen, S.; Ambelu, A.; Spanoghe, P. Pesticide residue evaluation in major staple food items of Ethiopia using the QuEChERS method: A case study from the Jimma Zone: Pesticide residues in food items. *Environ. Toxicol. Chem.* **2014**, *33* (6), 1294−1302.

(8) Yang, X.; Wang, J.; Xu, D. C.; Qiu, J. W.; Ma, Y.; Cui, J. Simultaneous Determination of 69 Pesticide Residues in Coffee by Gas Chromatography−Mass Spectrometry. *Food. Anal. Methods* **2011**, *4*, 186−195.

(9) Durand, N.; Gueule, D.; Fourny, G. Contaminants in coffee. *Cah. Agric.* **2006**, 2−3, 192−196.

(10) Jacobs, R. M.; Yess, N. J. Survey of imported green coffee beans for pesticide residues. *Food Addit. Contam.* **1993**, *10* (5), 575−577.

(11) Pizzutti, I. R.; de Kok, A.; Dickow Cardoso, C.; Reichert, B.; de Kroon, M.; Wind, W.; Weber Righi, L.; Caiel da Silva, R. A multi-residue method for pesticides analysis in green coffee beans using gas chromatography−negative chemical ionization mass spectrometry in selective ion monitoring mode. *J. Chromatogr. A* **2012**, *1251*, 16−26.

(12) Keikotlhaile, B. M.; Spanoghe, P.; Steurbaut, W. Effects of food processing on pesticide residues in fruits and vegetables: A meta-analysis approach. *Food Chem. Toxicol.* **2010**, *48* (1), 1−6.

(13) Cetinkaya, M.; von Düszeln, J.; Thiemann, W.; Silwar, R. [Organochlorine pesticide residues in raw and roasted coffee and their degradation during the roasting process]. *Z. Lebensm.-Unters. Forsch.* **1984**, *179* (1), 5−8.

(14) Sakamoto, K.; Nishizawa, H.; Manabe, N. Behavior of pesticides in coffee beans during the roasting process. *Shokuhin Eiseigaku Zasshi* **2012**, *53* (5), 233−236.

(15) Lehotay, S. J. Determination of Pesticide Residues in Foods by Acetonitrile Extraction and Partitioning with Magnesium Sulfate: Collaborative Study. *J. AOAC Int.* **2007**, *90* (2), 485−520.

(16) Moon, J.-K.; Shibamoto, T. Role of Roasting Conditions in the Profile of Volatile Flavor Chemicals Formed from Coffee Beans. *J. Agric. Food Chem.* **2009**, *57* (13), 5823−5831.

(17) Bonnechere, A.; Hanot, V.; Jolie, R.; Hendrickx, M.; Bragard, C.; Bedoret, T.; Van Loco, J. Processing Factors of Several Pesticides and Degradation Products in Carrots by Household and Industrial Processing. *J. Food Res.* **2012**, *1* (3), DOI: 10.5539/jfr.v1n3p68

(18) Method validation and quality control procedures for pesticide residues analysis in food and feed. *Document No. SANCO/12495/2011*; National Food Administration: Uppsala, Sweden, 2011.

(19) Toker, İ.; Bayındırlı, A. Enzymatic peeling of apricots, nectarines and peaches. *LWT - Food Sci. Technol.* **2003**, *36* (2), 215−221.

(20) Yoshida, S.; Murata, H.; Imaida, M. Distribution of Pesticide Residues in Vegetables and Fruits and Removal by Washing. *Nippon Nogei Kagaku Kaishi* **1992**, *66* (6), 1007−1011.

(21) Cengiz, M. F.; Certel, M.; Karakaş, B.; Göçmen, H. Residue contents of captan and procymidone applied on tomatoes grown in greenhouses and their reduction by duration of a pre-harvest interval and post-harvest culinary applications. *Food Chem.* **2007**, *100* (4), 1611−1619.

(22) Bajwa, U.; Sandhu, K. S. Effect of handling and processing on pesticide residues in food- a review. *J. Food Sci. Technol.* **2014**, *51* (2), 201−220.

(23) Sharma, J.; Satya, S.; Kumar, V.; Tewary, D. K. Dissipation of pesticides during bread-making. *Chem. Health Saf.* **2005**, *12* (1), 17−22.

(24) Abou-Arab, A. A. K.; Abou Donia, M. Pesticide residues in some Egyptian spices and medicinal plants as affected by processing. *Food Chem.* **2001**, *72*, 439−445.

(25) Hasmukh, J.; Neha, T.; Praful, J. Effect of Household Processing on Reduction of Pesticide Residues in Cauliflower (*Brassica oleraceae* var. botrytis). *Eur. J. Exp. Biol.* **2012**, *2* (5), 1639−1645.

DOI: 10.1021/acs.jafc.5b03327
J. Agric. Food Chem. 2015, 63, 8568−8573

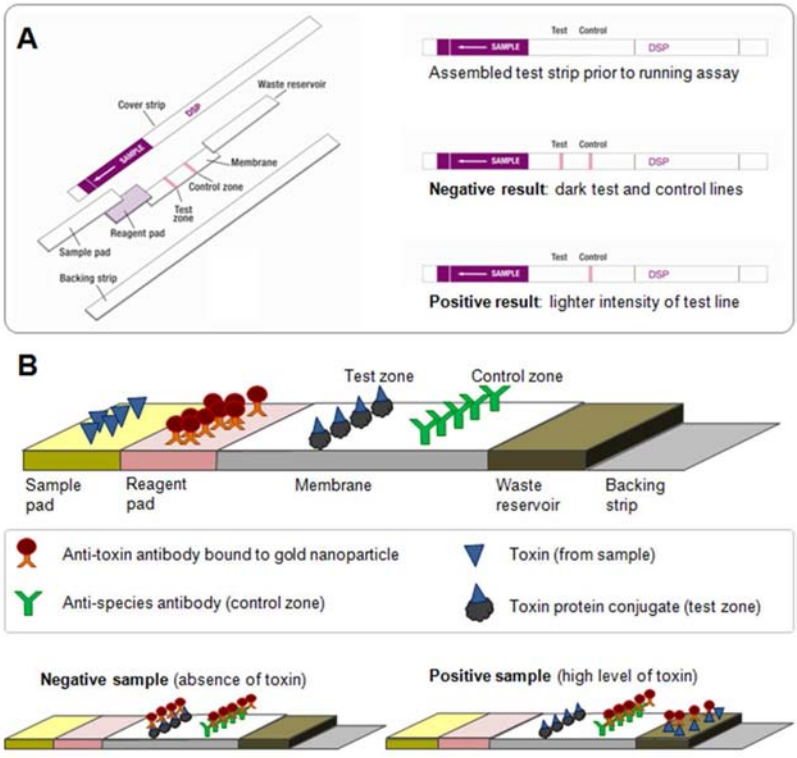

Figure 2. Diagrammatic views of the lateral flow immunoassay. Representations of the architecture and assembled test strips (A) and schematics of key interactions (B) are illustrated.

(TEFs) have been assigned equally for OA and DTX1 (1.0) and lower for DTX2 (0.6).[20] Acyl-derivatives (DTX3) have the TEF corresponding to the parent unesterified toxin. DTX3 esters cannot usually be detected directly via analytical methods, functional assays, or immunoassays because of their high molecular weight, lipophilicity, variability in structure, and/or lack of standards. Alkaline hydrolysis is a widely employed procedure to revert the esters back to the parent toxins by removal of the fatty acids, allowing an estimation of total toxicity.[21,22]

In Europe, the two main reference methods employed by national reference laboratories are the mouse bioassay (MBA) and liquid chromatography coupled with tandem mass spectrometry (LC-MS/MS). Alternative or complementary methods can be used if they are appropriately validated and are shown to provide an equivalent level of public health protection. In the United States, regulatory monitoring of OA toxins has been established in recent years, and LC-MS/MS is the preferred method.[13,23] The MBA has been regarded as a simple and generally effective method, keeping consumers safe.[24] However, limitations include low sensitivity (close to the MPL), the risk of false results, possible interference from hydrophilic toxins such as domoic acid and saxitoxin, in addition to moral and ethical concerns.[4,25] LC-MS/MS methods provide a more sensitive and specific option, but require high-cost equipment and skilled personnel, and fully replaced the MBA in the EU at the end of last year.[26]

As a result of the characteristics of the current method, there is an accepted need for rapid and low-cost screening tools which are sufficiently sensitive and specific.[25,27] Two main approaches which have been developed to help meet this need are functional assays based on protein phosphatase 2A (PP2A) receptor inhibition activity or immunoassays based on competitive antibody ligand reactions. PP2A is one of the enzymes inhibited by OA group toxins[28] and this enzymatic response has been employed to produce functional assays. Immunoassays, such as enzyme linked immunosorbent assays (ELISAs), provide another option. Both aforementioned methods are sensitive and specific while being faster than conventional confirmatory methods. However, these functional assays can be cumbersome, requiring multiple steps, laborious sample preparation, and often have longer time to results. Therefore, these assays do not fully meet the desired criteria for a rapid test. The lateral flow immunoassay (LFIA) format has higher potential to meet the criteria for a rapid and simple test. However, previous attempts at developing a suitable LFIA have not possessed the desired speed, cross-reactivity, sensitivity, or accuracy in addition to notable matrix effects.[27,29,30]

Furthermore, current extraction methods typically require relatively high solvent volumes, centrifugation, and in some cases expensive 0.2 or 0.45 μM membrane filtration, none of which were desired for a rapid and low-cost test.

As there are currently no means for rapid and effective screening for OA toxins in shellfish, the goals were to develop a simple to use and accurate LFIA which would have the potential for laboratory or field use.[31] In the LFIA system reported here, simple extraction and test procedures were developed in conjunction with an antibody possessing a favorable cross-reactivity profile.[32] A sample could be qualitatively screened for the presence of free toxins (OA, DTX1, DTX2) in less than 20 min, including sample extraction. Total toxins, including DTX3, could be detected with an additional hydrolysis step. There were no requirements for extensive equipment, calibration standards, or analyses of results.

DOI: 10.1021/acs.jafc.5b01254
J. Agric. Food Chem. 2015, 63, 8574−8583

Once developed, the LFIA was validated to determine accuracy, sensitivity, cross reactivity, matrix effects, reproducibility, robustness, ruggedness, and stability.

In the present study, the development and validation of a rapid and simple LFIA for the screening of the OA group of toxins, at concentrations relevant to regulations, is reported.

MATERIALS AND METHODS

Safety. OA group toxins are responsible for incidents of DSP. Therefore, special care should be taken when using OA toxin standard solutions or contaminated shellfish. Gloves and eye protection should be worn at all times. Appropriate disposal methods should also be utilized.

Toxins. Certified reference standards (CRM-OA-c, CRM-DTX1, CRM-DTX2) were obtained from the National Research Council of Canada (NRCC, Halifax NS, Canada).

Equipment and Apparatus. *Extraction Materials.* Methanol (Fisher, U.K.) was used as the extraction solvent. Microperforated filter bags (280 μM) (BagPage +100, Interscience, France) and metal seam rollers (Trade1st, U.K.) were used for the manual extraction. Extracted samples were filtered using a glass fiber filter syringe (Product 9420, Neogen, U.S.).

Materials Required for Hydrolysis Procedure (to Include Detection of DTX3 Toxins). Sodium hydroxide (Sigma, U.K.), hydrochloric acid (Fisher, U.K.), a block heater (Stuart SBH130D), and screw cap glass vials (600000751CV, Waters, U.K.) were employed for the hydrolysis procedure.

LFIA Readers. Portable electronic LFIA readers (Reveal AccuScan PRO) were supplied by Neogen Corporation (MI, U.S.).

Sources and Treatment of Samples. Certified negative mussel samples (CRM-Zero-Mus) and contaminated mussel tissues (CRM-DSP-Mus-B) were obtained from the NRCC. LC-MS/MS and/or MBA verified toxin-free and OA group contaminated samples (mussels, oysters, scallops, clams) were obtained from the Agri-Food and Biosciences Institute (U.K.); CFSAN, FDA (MD, U.S.); or RIKILT (Netherlands, EU) or were locally sourced. Fresh samples were cleaned and opened by cutting the adductor muscles. Tissue was removed from the shell, transferred to strainers, and drained prior to homogenization using a blender or Ultra Turrax. Homogenates were distributed into aliquots and stored at −20 °C for up to three years until analysis.

Principle of LFIA Test Strips. The LFIA is a single-step test based on a competitive immunoassay format (Figure 2). Antibody production for the detection of okadaic acid and DTXs was previously described elsewhere.[32] The sample was wicked through a reagent zone containing antibodies specific for OA-group toxins that were conjugated to colloidal gold particles. If OA toxins were present, they would be captured by the particle−antibody complexes. The complexes wicked onto a nitrocellulose membrane, which contained a stationary capture zone of a toxin−protein conjugate (test zone). The test zone would capture any particle−antibody complexes which had not bound to toxin. Therefore, as the concentration of toxins in the sample increased, the test zone intensity decreased. The membrane also contained a stationary control zone, consisting of antispecies antibodies, which would always form regardless of the level of toxins.

Sample Preparation. Two grams of homogenized shellfish tissue were weighed into each filter bag. Compliant samples, containing less than the limit of detection of 25 μg OA eq/kg via LC-MS/MS, were spiked with fixed volumes of the relevant standard concentration of OA toxins for the preparation of spiked matrix samples.

Procedure for the Extraction of Free Toxins (OA, DTX1, DTX2). Methanol (8 mL) was added to 2 g of shellfish tissue and a roller applied for 30 s. The filtrate was passed through a filter syringe.

Procedure for the Detection of Total OA Toxins (OA, DTX1, DTX2, DTX3). Filtered methanolic extract (800 μL), obtained using the free toxin procedure described above, was mixed with 100 μL of 2.5 M sodium hydroxide for 30 s in a glass vial. The vial was placed in a heat block set at 76 °C for 40 min. The vial was cooled to room temperature (18−25 °C), and 100 μL of 2.5 M hydrochloric acid was mixed with the extract for 30 s.

One variation of the standard LFIA extraction protocol was also evaluated, whereby the filter bag and roller method was replaced with centrifugation for 10 min (2000 *g*).

Analysis by the LFIA. For the detection of free toxins (OA, DTX1, DTX2), 100 μL of the unhydrolysed extract was added to 1.4 mL of buffer and mixed for 30 s. For the detection of total OA toxins (i.e., including DTX3), 100 μL of the hydrolyzed extract was added to 1.1 mL of buffer and mixed for 30 s. The buffers contained salts and surfactants optimized for the assay. A 100 μL portion of buffered sample extract was added to a microwell. A test strip was placed within the microwell for 15 min prior to immediate placement into an LFIA reader to obtain the result. The qualitative result generated using the electronic reader was derived from numerical test and control line readings obtained from the test strip. Because of the competitive nature of the assay, the optical density reading of the test line was greatest in the absence of toxin and the derived values were therefore assigned response values of 100% in dose−response graphs.

Comparative Analysis of LFIA with LC-MS/MS Analysis. Two different LC-MS/MS reference methods, based on McNabb[33] and Gerssen,[34] were employed to quantify toxin concentrations in spiked or naturally contaminated samples. Except where stated, the Gerssen protocol was employed for analyses, with the uncertainty of the in-house method stated as 26.1% and a limit of detection of 25 μg/kg.

LFIA Method Validation. *Extraction Efficiency.* Two studies were conducted to determine extraction efficiencies from naturally contaminated samples in terms of toxin recoveries from LFIA extracts in comparison to LC-MS/MS extracts. Oyster samples (n = 4) known to contain acyl-OA (DTX3) at high levels (90−98%) were employed for the initial study. Samples consisting of mussels (n = 4) and clams (n = 1) known to contain primarily DTX1 and acyl-DTX1 (DTX3) were employed for the second study. Extracts prepared using LC-MS/MS methodologies were compared to those prepared via the standard LFIA extraction method (n = 2 extractions per each condition). All extractions were carried out in parallel, and analyses were carried out at a single site. LFIA extracts were analyzed using LC-MS/MS to determine toxin recoveries. The LFIA extraction protocol had two key differences from the standard LC-MS/MS procedures: the absence of sample centrifugation and a lower solvent to sample ratio. LFIA extracts were diluted to match extracts from LC-MS/MS methods with respect to matrix dilution factors and amount of solvent. Hydrolysed LFIA extracts were diluted to contain equivalent levels of acid and base. All LFIA extracts analyzed via LC-MS/MS were subsequently filtered through a 0.2 μM PVDF syringe filter.

Toxin Response Calibration Curves for Sensitivity and Specificity. Toxin standard concentrations ranging from 0−200 ng/mL were prepared using CRM-OA-c, CRM-DTX1, and CRM-DTX2 to generate dose−response graphs to determine sensitivity and specificity. The optimal matrix dilution factor to effectively screen samples containing suspect levels of OA toxins was determined based on the dose−response data. The dilution factors were selected based on three criteria: the region on the curve which would (1) provide sufficient resolution at the target cutoff for noncompliant results, (2) allow for a simple and practical dilution scheme, and (3) be large enough to reduce or eliminate nonspecific interference on assay performance from various shellfish matrices. OA spiked mussel samples and naturally contaminated oyster samples, containing acyl-derivatives of OA (DTX3), were also evaluated at a range of concentrations.

Accuracy Study for the LFIA Device. A study to determine the accuracy of the LFIA method relative to LC-MS/MS verification was conducted using four species (mussels, oysters, scallops, and clams) spiked at various concentrations of OA toxins ranging from 0 to 320 μg OA eq/kg.

LC-MS/MS verified naturally contaminated samples (mussels, oysters, clams, and scallops) were also used as part of the validation to determine the accuracy and toxin recovery with real samples.

Matrix Effects. A two-operator study was conducted to determine the extent of matrix effects with respect to sensitivity and cross reactivity across various species (mussels, scallops, oysters, and clams)

DOI: 10.1021/acs.jafc.5b01254
J. Agric. Food Chem. 2015, 63, 8574−8583

Table 1. Extraction Efficiencies of LFIA Extracts in Comparison to LC-MS/MS Extracts

study	sample (source: US)	species	toxin profile	% DTX3 (LC-MS/MS extract)	LC-MS/MS analysis of hydrolyzed extracts: LC-MS/MS extract (μg OA eq/kg)	LC-MS/MS analysis of hydrolyzed extracts: LFIA extract (μg OA eq/kg)	LFIA recovery
1	1	oysters	OA	>90%	190*	130*	68.4%
	2	oysters	OA	>90%	280*	350*	125.0%
	3	oysters	OA	>90%	410*	230*	56.1%
	4	oysters	OA	>90%	440*	700*	159.1%
2	5	mussels	DTX1	5.4% ± 2.8%**	483 ± 18**	513 ± 23**	106.2%
	6	mussels	DTX1	9.9% ± 5.4%**	822 ± 21**	866 ± 28**	105.4%
	7	clams	DTX1	95.0% ± 0.6%**	540 ± 31**	556 ± 28**	103.0%
	8	mussels	DTX1	8.3% ± 1.3%**	1382 ± 86**	1863 ± 176**	134.8%
	9	mussels	DTX1	11.8% ± 3.5%**	1983 ± 201**	2372 ± 117**	119.6%

*McNabb protocol (LC-MS/MS extracts analyzed 2008, U.S.; LFIA extracts analyzed 2011, U.K.). **Mean ± SD (n = 2 extractions per sample). LC-MS/MS standard working range of 25−1600 μg/kg.

spiked at 0, 40, and 160 μg OA eq/kg of each of the toxins (n = 3 tests per condition). Samples were extracted and assayed according to both free toxin (unhydrolysed) and total toxin (hydrolysis) LFIA procedures.

Interspecies CVs across the range of concentrations and for both extraction procedures were calculated based on quantitative readings.

All studies were conducted randomized blind and, except where stated, all samples were evaluated using five LFIA tests per each condition.

Naturally Contaminated Samples and Comparisons with Reference Methods. A comparative study of various naturally contaminated shellfish samples was performed in two different laboratories (lab 1, n = 72; lab 2, n = 40) using the LFIA method and standard reference method. For laboratory 1, samples consisted of mussels, oysters, clams, and scallops sourced from the EU and United States, and samples from laboratory 2 consisted of mussels, oysters, and scallops.

Robustness. Robustness studies were performed to determine the uncertainty, associated with the method, to various intrinsic and extrinsic factors (including operators, days, LFIA lots, extractions, and readers). A multiday (n = 3) study consisting of multiple LFIA lots (n = 3), readers (n = 3), and operators (n = 3) was conducted. Each operator carried out two extractions of 10 spiked shellfish tissues each day. A total of 190 mussel samples were prepared and consisted of OA (40, 120, 160 μg OA eq/kg), DTX1 (40, 120, 160 μg OA eq/kg), DTX2 (80, 160, 320 μg OA eq/kg), and a toxin-free sample (methanol only). Higher concentrations of DTX2 were employed to take account of the cross reactivity profile of the assay to this analyte, in addition to its lower toxic potency. Each different sample was extracted and analyzed according to LC-MS/MS protocols to determine spiking accuracy.

Interlaboratory Evaluations (Free Toxins). A study involving six mussel samples, two samples each at concentrations less than 40, 120, and 170 μg OA eq/kg, was conducted by three external participants. Samples were extracted and assayed according to the unhydrolysed LFIA procedure (n = 2 tests per condition).

RESULTS AND DISCUSSION

Extraction Efficiencies. The results for the comparison of the LFIA and LC-MS/MS extract for extraction efficiencies are presented in Table 1 and demonstrate equivalence of results for the oyster samples with a mean recovery of 102.2% ± 48.4% (n = 4). The large standard deviation was possibly due to several reasons, including (1) poor sample homogeneity and/or (2) that LC-MS/MS and LFD extractions were carried out in two different laboratories in 2008 and 2012, respectively.

For mussel and clam samples, the results shown in Table 1 demonstrate equivalence with a mean recovery of 113.8% ± 13.4% (n = 5) and 105% ± 1.7% (n = 3 samples with results within the standard working range).

Toxin Response Calibration Curves for Sensitivity and Specificity. The linear portion of the dynamic range of the assay was approximately 0.5−10 ng/mL for each of the toxins, as shown in Figure 3. To ensure samples were effectively screened at the desired 160 μg OA eq/kg cutoff, a matrix dilution factor of approximately 60 fold was selected. As the intention of the assay was to provide a qualitative screening result for suspect samples, the cutoff for noncompliant results was selected at 60% response, which equated to the equivalent of approximately 120 μg OA/kg (75% MPL), 140 μg DTX1/kg (88% MPL), and 240 μg DTX2/kg (90% MPL) in shellfish, based on the dilution factor. OA spiked mussel samples and naturally contaminated oyster samples, containing acyl-derivatives of OA (DTX3), were also evaluated at a range of concentrations, as shown in Figure 3. No matrix effects were observed, with comparable sensitivity and specificity for these toxins.

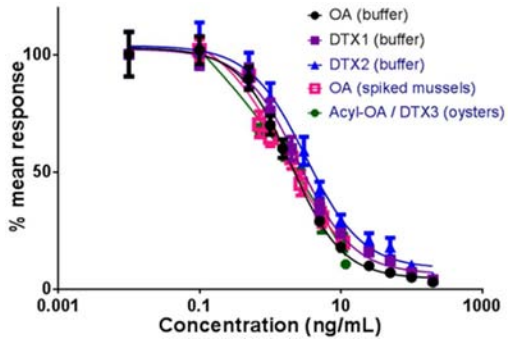

Figure 3. Spiked buffer dose−response graph. Plots are of mean response ± SD (n = 3) for various concentrations of OA and DTXs in buffer and shellfish, using data derived from the electronic reader. The qualitative cutoff for noncompliant results was generated based on a predetermined mean response value of 60%. Note: Acyl-OA/DTX3 (oysters) indicates that DTX3, specifically acyl-OA, was present in the analyzed oyster sample. The detected toxins were derived using alkaline hydrolysis.

Accuracy Study. The accuracy study showed that for OA all samples spiked at 0 or 40 μg/kg were correctly identified as compliant to the action level. A 95% accuracy level at correctly identifying 60 μg/kg samples as compliant was observed. Samples containing 120 μg/kg generated 85% noncompliant results, and all samples spiked at or above 140 μg/kg generated noncompliant results.

DOI: 10.1021/acs.jafc.5b01254
J. Agric. Food Chem. 2015, 63, 8574−8583

Table 2. LFIA Results in Comparison to Reference Methods[a]

sample (source region)	species	toxin profile	LC-MS/MS, unhydrolysed (μg OA eq/kg)	LC-MS/MS, hydrolyzed (μg OA eq/kg)	MBA result	LFIA result, unhydrolysed	LFIA result, hydrolyzed	confirmatory result
1 (EU)	mussels	ND	<25	<25	NA	C	C	C
2 (EU)	mussels	OA	24.5	81	NA	C	C	C
3 (EU)	mussels	OA	55	122	NA	C	C	C
4 (EU)	mussels	NA	NA	125	NA	C	NC	C
5 (EU)	mussels	OA	59	170	NA	C	NC	NC
6 (EU)	mussels	OA (98%), DTX1 (2%)	96	269	NA	NC	NC	NC
7 (EU)	mussels	OA (74%), DTX1 (18%), DTX2 (8%)	149	336	NA	NC	NC	NC
8 (EU)	mussels	OA (99%), DTX1 (1%)	215	386	NA	NC	NC	NC
9 (EU)	mussels	OA (92%), DTX2 (8%)	320	415	NA	NC	NC	NC
10 (EU)	mussels	OA (99%), DTX1 (1%)	269	569	NA	NC	NC	NC
11 (EU)	mussels	OA (99%), DTX1 (1%)	254	569	NA	NC	NC	NC
12 (EU)	mussels	OA (99%), DTX1 (1%)	276	618	NA	NC	NC	NC
13 (US)	mussels	ND	<25	<25	NA	C	C	C
14 (US)	oysters	ND	<25	<25	NA	C	C	C
15 (US)	oysters	OA	<25	190	NA	C	NC	NC
16 (US)	oysters	OA	<25	376	NA	C	NC	NC
17 (US)	oysters	OA	<40	410	NA	C	NC	NC
18 (US)	oysters	ND	<25	<25	NA	C	C	C
19 (US)	oysters	OA	<40	440	NA	C	NC	NC
20 (US)	oysters	OA	<40	450	NA	C	NC	NC
21 (US)	oysters	OA	<40	470	NA	C	NC	NC
22 (US)	oysters	ND	<25	<25	NA	C	C	C
23 (US)	clams	ND	<25	<25	NA	C	C	C
24 (US)	clams	DTX1	32	515	NA	C	NC	NC
25 (US)	clams	ND	<25	<25	NA	C	C	C
26 (EU)	mussels	ND	<25	<25	NA	C	C	C
27 (US)	mussels	DTX1	485	524	NA	NC	NC	NC
28 (US)	mussels	DTX1	841	944	NA	NC	NC	NC
29 (US)	mussels	DTX1	1382	>1600	NA	NC	NC	NC
30 (US)	mussels	DTX1	>1600	>1600	NA	NC	NC	NC
31 (EU)	mussels	OA	83	132	NA	C	C	C
32 (EU)	scallops	OA	41	66	NA	C	C	C
33 (EU)	scallops	OA (51%), DTX2 (49%)	60	200	NA	C	NC	NC
34 (EU)	scallops	ND	<25	<25	NA	C	C	C
35 (EU)	mussels	OA (37%), DTX1 (15%), DTX2 (49%)	151	299	NA	NC	NC	NC
36 (EU)	mussels	OA (38%), DTX1 (57%), DTX2 (5%)	109	168	NA	NC	NC	NC
37 (EU)	mussels	OA (63%), DTX2 (37%)	127	243	NA	NC	NC	NC
38 (EU)	oysters	OA (50%), DTX2 (50%)	206	401	NA	NC	NC	NC
39 (EU)	mussels	OA (82%), DTX1 (18%)	231	757	NA	NC	NC	NC
40 (EU)	mussels	OA (85%), DTX2 (15%)	63	85	NA	C	C	C
41 (EU)	clams	OA (70%), DTX1 (13%), DTX2 (17%)	491	1293	NA	NC	NC	NC
42 (EU)	oysters	OA (56%), DTX1 (8%), DTX2 (37%)	139	371	NA	NC	NC	NC

DOI:10.1021/acs.jafc.5b01254
J. Agric. Food Chem. 2015, 63, 8574−8583

Table 2. continued

sample (source region)	species	toxin profile	LC-MS/MS, unhydrolysed (μg OA eq/kg)	LC-MS/MS, hydrolyzed (μg OA eq/kg)	MBA result	LFIA result, unhydrolysed	LFIA result, hydrolyzed	confirmatory result
43 (EU)	cockles	ND	<25	<25	C	C	C	C
44 (EU)	cockles	ND	<25	<25	C	C	C	C
45 (EU)	clams	ND	<25	<25	C	C	C	C
46 (EU)	oysters	ND	<25	<25	C	C	C	C
47 (EU)	mussels	ND	<25	<25	C	C	C	C
48 (EU)	mussels	ND	<8	<8	C	C	C	C
49 (EU)	mussels	OA (91%), DTX1 (2%), DTX2 (7%)	244	326	NA	NC	NC	NC
50 (EU)	mussels	OA (55%), DTX1 (27%), DTX2 (18%)	10	11	NA	C	C	C
51 (EU)	mussels	OA (48%), DTX1 (9%), DTX2 (43%)	191	695	NC	NC	NC	NC
52 (EU)	mussels	OA (47%), DTX1 (10%), DTX2 (43%)	324	707	NC	NC	NC	NC
53 (EU)	mussels	OA (75%), DTX1 (4%), DTX2 (21%)	65	215	NC	C	NC	NC
54 (EU)	mussels	OA (78%), DTX1 (5%), DTX2 (17%)	59	127	NC	C	NC	C (LC-MS/MS); NC (MBA)
55 (EU)	mussels	OA (72%), DTX1 (3%), DTX2 (25%)	71	162	NC	NC	NC	NC
56 (EU)	mussels	OA (76%), DTX1 (24%)	1211	2796	NC	NC	NC	NC
57 (EU)	mussels	OA (70%), DTX1 (30%)	1751	3410	NC	NC	NC	NC
58 (EU)	mussels	NA	271	452	NC	NC	NC	NC
59 (EU)	mussels	ND	<8	<8	C	C	C	C
60 (EU)	mussels	ND	<8	<8	C	C	C	C
61 (EU)	mussels	OA (36%), DTX1 (64%)	152	176	NC	NC	NC	NC
62 (EU)	mussels	NA	NA	552	NA	NA	NC	NC
63 (EU)	mussels	NA	NA	554	NA	NA	NC	NC
64 (EU)	mussels	NA	NA	263	NA	NA	NC	NC
65 (EU)	mussels	NA	NA	373	NA	NA	NC	NC
66 (EU)	mussels	NA	NA	164	NA	NA	NC	NC
67 (EU)	mussels	NA	NA	>400	NC	NA	NC	NC
68 (EU)	mussels	NA	NA	NA	NC	NA	NC	NC
69 (EU)	mussels	ND	<8	<8	C	NA	C	C
70 (EU)	mussels	OA	58	125	NA	C	NC	C
71 (EU)	mussels	OA (99%), DTX1 (1%)	276	618	NA	NC	NC	NC
72 (EU)	mussels	ND	<8	<8	C	C	C	C

[a]NA = no data. ND = not detected. C = compliant. NC = noncompliant.

DOI: 10.1021/acs.jafc.5b01254
J. Agric. Food Chem. 2015, 63, 8574−8583

Table 3. LFIA Results in Comparison to Reference Methods (Laboratory 2)[a]

sample (EU)	species	toxin profile	LC-MS/MS, unhydrolysed (μg OA eq/kg)	LC-MS/MS, hydrolyzed (μg OA eq/kg)	MBA result	LFIA result, unhydrolysed	LFIA result, hydrolyzed	confirmatory result
1	mussel	OA (93%), DTX1 (7%)	12	151	NA	C	C	C
2	mussel	OA	<8	149	NA	C	C	C
3	mussel	OA (96%), DTX1 (4%)	6	180	NA	NC	NC	NC
4	mussel	OA (97%), DTX1 (3%)	42	189	NA	NC	NC	NC
5	mussel	OA (36%), DTX1 (64%)	152	176	NA	NC	NC	NC
6	mussel	ND	<8	<8	NA	C	C	C
7	mussel	OA (7%), DTX1 (93%)	69	181	NA	NC	NC	NC
8	mussel	OA (57%), DTX1 (43%)	30	176	NA	NC	NC	NC
9	mussel	OA (8%), DTX1 (91%), DTX2 (2%)	38	130.2	NA	C	NC	C
10	mussel	OA (67%), DTX1 (33%)	48	177	NA	NC	NC	NC
11	mussel	OA (51%), DTX2 (49%)	37	60	NA	C	C	C
12	scallops	NA	NA	NA	DSP C; ASP NC	C	C	C
13	scallops	OA (85%), DTX1 (15%)	33	177	DSP C; ASP NC	C	NC	NC (LC-MS/MS); C (MBA)
14	scallops	NA	NA	NA	DSP C; ASP NC	C	C	C
15	oyster	NA	NA	NA	DSP C	C	C	C
16	oyster	NA	NA	NA	DSP C	C	C	C
17	scallops	NA	NA	NA	DSP C; ASP NC	C	C	C
18	scallops	NA	NA	NA	DSP C	C	C	C
19	scallops	NA	NA	NA	DSP C	C	C	C
20	scallops	NA	NA	NA	DSP C	C	C	C
21	scallops	NA	NA	NA	DSP C	C	C	C
22	scallops	NA	NA	NA	DSP C	C	C	C
23	scallops	NA	NA	NA	DSP C; ASP NC	C	C	C
24	scallops	NA	NA	NA	DSP C; ASP NC	C	C	C
25	scallops	NA	NA	NA	DSP C; ASP NC	C	C	C
26	scallops	NA	NA	NA	DSP C; ASP NC	C	C	C
27	scallops	NA	NA	NA	DSP C	C	C	C
28	mussel	OA (77%), DTX1 (23%)	71	149	NA	NC	NC	C
29	mussel	OA (77%), DTX1 (23%)	42	83.7	NA	C	C	C
30	mussel	NA	529	850	NA	NC	NC	NC
31	mussel	NA	750	1141	NA	NC	NC	NC
32	mussel	OA (75%), DTX1 (4%), DTX2 (21%)	65	215	NA	C	NC	NC
33	mussel	OA (76%), DTX1 (24%)	1211	2796	NA	NC	NC	NC
34	mussel	OA (43%), DTX1 (4%), DTX2 (53%)	324	365	NA	NC	NC	NC
35	mussel	OA (54%), DTX1 (11%), DTX2 (35%)	191	695	NA	NC	NC	NC
36	mussel	OA (71%), DTX1 (7%), DTX2 (22%)	271	452	NA	C	NC	NC
37	scallops	NA	NA	NA	DSP C; ASP NC	C	C	C
38	scallops	NA	NA	NA	DSP C; ASP NC	C	C	C
39	scallops	NA	NA	NA	DSP C; ASP NC	C	C	C
40	scallops	OA	18	18	DSP C; ASP NC	C	C	C

[a]NA = no data. ND = not detected. C = compliant. NC = noncompliant.

J. Agric. Food Chem. 2015, 63, 8574−8583 DOI: 10.1021/acs.jafc.5b01254

For DTX1, all samples spiked at 0 or 40 μg/kg were correctly identified as compliant. A 95% accuracy level at correctly identifying 100 μg/kg samples as compliant was observed. A 50% accuracy level was observed at 120 μg/kg, with 95% accuracy to generate noncompliant results at 140 μg/kg. All samples containing at or above 160 μg/kg correctly generated noncompliant results.

For DTX2, all samples spiked at 0 or 66 μg/kg were correctly identified as compliant. A 95% accuracy level at correctly identifying 133 μg/kg samples as compliant was observed. Samples containing 267 μg/kg (160 μg OA eq/kg) generated 50% noncompliant results, and all samples spiked at or above 400 μg/kg (240 μg OA eq/kg) correctly generated noncompliant results.

Matrix Effects. Results indicated matrix effects on performance were negligible with CVs calculated as 1.9% and 2.6% for operators one and two, respectively.

The equivalency of data generated by both unhydrolysed and hydrolyzed extracts when containing equivalent levels of toxin indicated a low level of variation between extraction methods with CVs of 4.0% and 5.6% for operators one and two, respectively.

Naturally Contaminated Samples and Comparisons with Reference Methods. For laboratory 1, there were no false compliant results with the LFIA method in comparison to the LC-MS/MS results (Table 2). All samples generating a noncompliant result by the unhydrolysed LFIA procedure were also noncompliant to the action level by LC-MS/MS. Samples 4, 54, and 70 generated false noncompliant results by the hydrolyzed LFIA procedure and contained 125, 127, and 125 μg OA eq/kg via LC-MS/MS, respectively. It should be noted, however, that sample 54 was also noncompliant by MBA.

The comparison of results for laboratory 2 are shown in Table 3. There were no false compliant results with the hydrolysis procedure, and all samples producing a noncompliant result with the unhydrolysed extracts also produced a noncompliant result with the hydrolyzed extracts. The hydrolyzed LFIA method generated false noncompliant results with samples 9 and 28, which were quantified via LC-MS/MS to contain 130 and 149 μg OA eq/kg, respectively. Sample 13 was compliant by the unhydrolysed LFIA procedure and MBA, but noncompliant with the hydrolyzed LFIA procedure and LC-MS/MS (177 μg OA eq/kg).

Method Robustness. For the robustness studies all compliant (toxin-free) samples generated compliant results by LFIA. Samples containing OA at 40 μg/kg (LC-MS/MS, 35 ± 9 μg/kg), 120 μg/kg (LC-MS/MS, 95 ± 25 μg/kg), and 160 μg/kg (LC-MS/MS, 123 ± 32 μg/kg) generated 14%, 67%, and 98% noncompliant results, respectively. Samples containing DTX1 at 40 μg/kg (LC-MS/MS, 36 ± 9 μg/kg), 120 μg/kg (LC-MS/MS, 117 ± 30 μg/kg), and 160 μg/kg (LC-MS/MS, 139 ± 36 μg/kg) generated 9%, 51%, and 94% noncompliant results, respectively. Samples containing DTX2 at 80 μg OA eq/kg (LC-MS/MS, 57 ± 15 μg OA eq/kg), 160 μg OA eq/kg (LC-MS/MS, 178 ± 46 μg OA eq/kg), and 320 μg OA eq/kg (LC-MS/MS, 343 ± 89 μg OA eq/kg) generated 31%, 90%, and 100% noncompliant results, respectively. The overall mean CV of the method, based on test and control line readings, was 5.9% ± 2.9% (n = 10 samples), which indicated the sum of inter- and intra- variability (operators, readers, extractions, LFIA lots, days). Because of errors in extraction (mainly operator 3, day 1), data from 12 samples were not analyzed.

Interlaboratory Evaluations (Free Toxins). The overall accuracy for the interlaboratory study, to indicate compliant results to the action level below 40 μg/kg and noncompliant results at 170 μg/kg, was 100%. Samples containing 120 μg/kg generated 75% noncompliant tests (n = 12).

Summary of Results and Discussion. The use of LFIAs has been previously exploited for the detection of marine biotoxins from extracts of shellfish tissues. However, two major weaknesses identified with past attempts have been the cross reactivity profile and the subjective nature of the interpretation of results. The reported LFIA was designed as a reader-based assay to eliminate any subjective element, with a qualitative cutoff for noncompliant results at concentrations relevant to the regulatory limits. It also allowed the option of both free toxins and/or total toxins to be rapidly screened from the same initial sample extract. Sample homogenates could be screened in 20 min for free toxins (including extraction and assay time) while waiting for hydrolysis. If a sample was deemed noncompliant, then the hydrolyzed extract would not need to be screened. If the sample was deemed compliant, the hydrolyzed extract would be screened to determine total toxicity (including any esters). Because of the nature of antibody-based assays (immunoassays), which are based on structure as opposed to function, cross reactivity to structural analogues will often vary from the parent compound to which the antibody was raised. In some cases, the cross reactivity profile may mirror the defined toxicity of the compounds.[32] In the reported assay, the cross reactivity profile to DTX1 and DTX2 resembles the toxicity closer than any previously reported, portable immunoassays for this toxin group. Furthermore, although the possibility of false compliant results was observed with samples spiked with DTX2, validation data demonstrated the occurrence of no false compliant results with naturally contaminated samples (various toxin profiles and matrices) containing 160 μg OA eq/kg or greater. Furthermore, results indicated no false noncompliant results with samples containing up to approximately 80 μg OA eq/kg.

Therefore, we report on the development and validation of an LFIA which is a practical, simple, and accurate screening method for shellfish contaminated with OA group toxins. The assay can be utilized as a rapid screening tool for use within the shellfish industry including shipboard or remote locations, providing added protection of shellfish consumers. There is also a significant potential for this method to be used in regulatory laboratories to complement the costly LC-MS/MS- or MBA-based tests that are routinely employed as part of national monitoring programmes because the assay utilizes the simplest OA group extraction and detection systems reported to date, allowing reliable results to be obtained significantly faster and at lower costs. Such simple to use and low-cost methods are ideal for laboratories in developing countries where the ability to purchase, run, and maintain expensive LC-MS/MS equipment is very difficult or the MBA method is not feasible or desirable to conduct routinely.

AUTHOR INFORMATION

Corresponding Author

*Tel.: +44 1292 525553. Fax: +44 1292 525601. E-mail: wjawaid01@qub.ac.uk.

Funding

The authors acknowledge that the work was partly funded by a Knowledge Transfer Partnership (KTP) program.

DOI: 10.1021/acs.jafc.5b01254
J. Agric. Food Chem. 2015, 63, 8574−8583

Notes

The authors declare the following competing financial interest(s): The research was funded in part from Innovate UK (75%) and Scottish Enterprise (25%) with Grant KTP007048. This research was supported by Neogen Europe Limited and may lead to the development of products in which Neogen has a business and financial interest.

■ ACKNOWLEDGMENTS

The authors express their thanks to Cowan Higgins (AFBI, U.K.) for provision of samples, assisting with method validations, and performing LC-MS/MS analyses; Arjen Gerssen (RIKILT, Netherlands) for provision of samples used in an interlaboratory study; Jonathon Deeds (CFSAN/FDA, U.S.) for the provision of samples, performing LC-MS/MS analyses, and assisting with method validations; and NRCC for provision of prerelease reference standards. The authors also thank (in alphabetical order): Begona Ben Gigirey at the European Union Reference Laboratory for Marine Biotoxins (EURLMB, Spain, EU), Brian Bill at NOAA's Northwest Fisheries Science Center (U.S.), Gerhard Thielert at CVUA Sigmaringen (Germany), and Gordon Goldsworthy at Loch Fyne Seafarms (U.K.) for participation in the interlaboratory trials; in addition to BioPol (Iceland), Lenger Seafoods (Netherlands, EU), MacDuff Shellfish (U.K.), and Shetland Seafood Quality Control (U.K.); Frank Klein, James Clarke, Ron Sarver, Steven Schadler, and Tim Goldy (Neogen Corporation) for key technical input; Brett Greer (Queen's University, Belfast), Clothilde Baker (CEFAS, England), and Paul Muirhead (Neogen) for valuable advice and/or performing LC-MS/MS analyses; Mark Hooper (Neogen) for development and validation efforts; and Nate Banner and Sharon Graham (Neogen) for their valuable input. Note: External organizations listed above do not endorse or promote the LFIA.

■ ABBREVIATIONS USED

LFIA, lateral flow immunoassay; OA, okadaic acid; DTX, dinophysis toxin; MPL, maximum permitted level; MBA, mouse bioassay; LC-MS/MS, liquid chromatography tandem mass spectrometry; HAB, harmful algal bloom; OA eq, okadaic acid equivalents; TEF, toxicity equivalency factor; PP2A, protein phosphatase 2A; ELISA, enzyme linked immunosorbent assay

■ REFERENCES

(1) Sobel, J.; Painter, J. Illnesses caused by marine toxins. *Clin. Infect. Dis.* **2005**, *41*, 1290−1296.

(2) Yasumoto, T.; Murata, M. Marine Toxins. *Chem. Rev.* **1993**, *93*, 1897−1909.

(3) Food and Agriculture Organization of the United Nations. *Marine Biotoxins*; FAO Food and Nutrition Paper 80, Food and Agriculture Organization: Rome, Italy, 2004. Available at URL: http://www.fao.org/docrep/007/y5486e/y5486e00.HTM.

(4) European Food Safety Authority. Opinion of the Scientific Panel on Contaminants in the Food chain on a request from the European Commission on marine biotoxins in shellfish − okadaic acid and analogues. *EFSA J.* **2008**, *589*, 1−62.

(5) Committee on Toxicity. COT statement on risk assessment of marine toxins of the okadaic acid, pectenotoxin, azaspiracid and yessotoxin groups in support of human health, 2006, 1−44. Available at URL: http://cot.food.gov.uk/committee/committee-on-toxicity/cotstatements/cotstatementsyrs/cotstatements2006/389771

(6) Davidson, K.; Bresnan, E. Shellfish toxicity in UK waters: a threat to human health. *Environ. Health* **2009**, *8* (1), S12.

(7) MacKenzie, L.; Beuzenberg, V.; Holland, P.; McNabb, P.; Suzuki, T.; Selwood, A. Pectenotoxin and okadaic acid-based toxin profiles in Dinophysis acuta and Dinophysis acuminata from New Zealand. *Harmful Algae* **2005**, *4* (1), 75−85.

(8) Kat, M. Diarrhetic mussel poisoning in the Netherlands related to the dinoflagellate Dinophysis acuminata. *Antonie van Leeuwenhoek* **1983**, *49* (4−5), 417−427.

(9) Torgersen, T.; Aasen, J.; Aune, T. Diarrhetic shellfish poisoning by okadaic acid esters from Brown crabs (Cancer pagurus) in Norway. *Toxicon* **2005**, *46* (5), 572−578.

(10) Trainer, V. L.; Moore, L.; Bill, B. D.; Adams, N. G.; Harrington, N.; Borchert, J.; da Silva, D.; Eberhart, B.-T. Diarrhetic shellfish toxins and other lipophilic toxins of human health concern in Washington State. *Mar. Drugs* **2013**, *11* (6), 1815−1835.

(11) Vale, P.; Botelho, M. J.; Rodrigues, S. M.; Gomes, S. S.; Sampayo, M. A. D. Two decades of marine biotoxin monitoring in bivalves from Portugal (1986−2006): a review of exposure assessment. *Harmful Algae* **2008**, *7* (1), 11−25.

(12) Elgarch, A.; Vale, P.; Rifai, S.; Fassouane, A. Detection of Diarrheic Shellfish Poisoning and Azaspiracids Toxins in Moroccan Mussels: Comparison of LC-MS Method with the Commercial Immunoassay Kit. *Mar. Drugs* **2008**, *6* (4), 587−594.

(13) Deeds, J. R.; Wiles, K.; Heideman, G. B.; White, K. D.; Abraham, A. First US report of shellfish harvesting closures due to confirmed okadaic acid in Texas Gulf coast oysters. *Toxicon* **2010**, *55* (6), 1138−1146.

(14) Yasumoto, T.; Murata, M.; Oshima, Y.; Sano, M.; Matsumoto, G. K.; Clardy, J. Diarrhetic shellfish toxins. *Tetrahedron* **1985**, *41* (6), 1019−1025.

(15) Fux, E.; Smith, J. L.; Tong, M.; Guzman, L.; Anderson, D. M. Toxin profiles of five geographical isolates of Dinophysis spp. from North and South America. *Toxicon* **2011**, *57*, 275−287.

(16) Lagos, N. Microalgal blooms A global issue with negative impact in Chile. *Biol. Res.* **1998**, *31*, 375−386.

(17) Prassopoulou, E.; Katikou, P.; Georgantelis, D.; Kyritsakis, A. Detection of okadaic acid and related esters in mussels during diarrhetic shellfish poisoning (DSP) episodes in Greece using the mouse bioassay, the PP2A inhibition assay and HPLC with fluorimetric detection. *Toxicon* **2009**, *53* (2), 214−227.

(18) European Commission. Regulation (EC) No. 2074/2005 under regulations (EC) nos. 853/2004 and 854/2004. *Off. J. Eur. Comm.* **2005**, *358*, 27.

(19) Codex Alimentarius: Codex standard 292, Standard for live and raw bivalve molluscs, Codex Alimentarius Commission: Rome, Italy, 2008.

(20) Aune, T.; Larsen, S.; Aasen, J. A.; Rehmann, N.; Satake, M.; Hess, P. Relative toxicity of dinophysistoxin-2 (DTX-2) compared with okadaic acid, based on acute intraperitoneal toxicity in mice. *Toxicon* **2007**, *49* (1), 1−7.

(21) Mountfort, D. O.; Suzuki, T.; Truman, P. Protein phosphatase inhibition assay adapted for determination of total DSP in contaminated mussels. *Toxicon* **2001**, *39*, 383−390.

(22) van den Top, H. J.; Gerssen, A.; McCarron, P.; Van Egmond, H. P. Quantitative determination of marine lipophilic toxins in mussels, oysters and cockles using liquid chromatography-mass spectrometry: inter-laboratory validation study. *Food Addit. Contam., Part A* **2011**, *28* (12), 1745−1757.

(23) Lloyd, J. K.; Duchin, J. S.; Borchert, J.; Flores-Quintana, H.; Robertson, A. Diarrhetic Shellfish Poisoning, Washington, USA, 2011. *Emerging Infect. Dis.* **2013**, *19* (8), 1314−1316.

(24) Yasumoto, T.; Oshima, Y.; Yamaguchi, M. Occurrence of a new type of shellfish poisoning in the Tohoku district. *Nippon Suisan Gakkaishi* **1978**, *44*, 1249−1255.

(25) Expert group: Methods for the detection of lipophilic marine biotoxins. London, U.K., 2007 http://collections.europarchive.org/tna/20101209122142/http://www.food.gov.uk/multimedia/pdfs/publication/methodslipophilic

DOI: 10.1021/acs.jafc.5b01254
J. Agric. Food Chem. 2015, 63, 8574−8583

(26) Commission Regulation (EU). 15/2011 of 10 January 2011 amending Regulation (EC) No 2074/2005 as regards recognised testing methods for detecting marine biotoxins in live bivalve molluscs. *Off. J. Eur. Comm.* **2011**, *L6*, 3−6.
(27) Eberhart, B.-T.; Moore, L. K.; Harrington, N.; Adams, N. G.; Borchert, J.; Trainer, V. L. Screening tests for the rapid detection of diarrhetic shellfish toxins in Washington State. *Mar. Drugs* **2013**, *11* (10), 3718−3734.
(28) Cohen, P.; Brewis, N. D.; Hughes, V.; Mann, D. J. Protein serine/threonine phosphatases; an expanding family. *FEBS Lett.* **1990**, *268* (2), 355−359.
(29) Laycock, M. V.; Jellett, J. F.; Easy, D. J.; Donovan, M. A. First report of a new rapid assay for diarrhetic shellfish poisoning toxins. *Harmful Algae* **2006**, *5* (1), 74−78.
(30) Vale, P.; Gomes, S. S.; Lameiras, J.; Rodrigues, S. M.; Botelho, M. J.; Laycock, M. V. Assessment of a new lateral flow immunochromatographic (LFIC) assay for the okadaic acid group of toxins using naturally contaminated bivalve shellfish from the Portuguese coast. *Food Addit. Contam., Part A* **2009**, *26* (2), 214−220.
(31) Jawaid, W.; Meneely, J. P.; Campbell, K.; Hooper, M.; Melville, K.; Holmes, S. J.; Rice, J.; Elliott, C. T. Development and validation of the first high performance-lateral flow immunoassay (HP-LFIA) for the rapid screening of domoic acid from shellfish extracts. *Talanta* **2013**, *116*, 663−669.
(32) Stewart, L.; Elliott, C. T.; Walker, A. D.; Curran, R. M.; Connolly, L. Development of a monoclonal antibody binding okadaic acid and dinophysistoxins-1,-2 in proportion to their toxicity equivalence factors. *Toxicon* **2009**, *54* (4), 491−498.
(33) McNabb, P.; Selwood, A. I.; Holland, P. T. Multiresidue method for determination of algal toxins in shellfish: single-laboratory validation and interlaboratory study. *J. AOAC Int.* **2005**, *88* (3), 761−772.
(34) Gerssen, A.; van Olst, E. H. W.; Mulder, P. P. J.; de Boer, J. In-house validation of a liquid chromatography tandem mass spectrometry method for the analysis of lipophilic marine toxins in shellfish using matrix-matched calibration. *Anal. Bioanal. Chem.* **2010**, *397*, 3079.

DOI: 10.1021/acs.jafc.5b01254
J. Agric. Food Chem. 2015, 63, 8574−8583

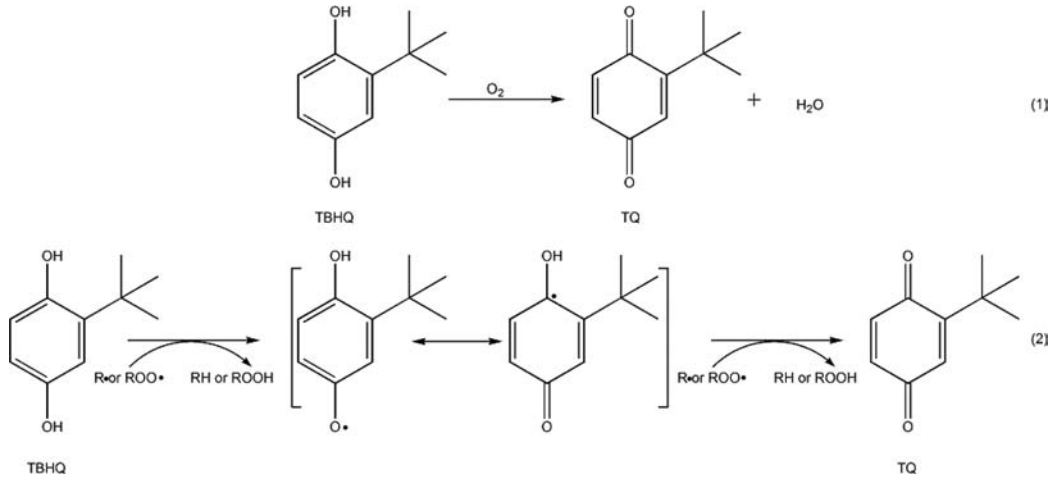

Figure 1. Two pathways of TBHQ converting to TQ.

MATERIALS AND METHODS

Chemicals. Standards of TBHQ (purity > 99.0%) and TQ (purity > 98.0%) were purchased from Sigma-Aldrich (St. Louis, MO). Fresh refined SBO (acid value of 0.13 mg of KOH/g and peroxide value of 1.22 mmol/kg) with no synthetic antioxidants was obtained from Henan Sunshine Oils and Fats Co., Ltd. (Zhengzhou, China). Fresh refined lard (acid value of 0.10 mg of KOH/g and peroxide value of 1.03 mmol/kg) with no antioxidants was purchased from Tianjin Tianyuan Oils & Fats Co., Ltd. (Tianjin, China). Liquid chromatography (LC) solvents (methanol, *n*-hexane, isopropanol, ethyl acetate, and acetonitrile) were of HPLC grade, obtained from VBS Biologic, Inc. (New York), and used after filtration by a 0.45 μm organic membrane. Glacial acetic acid (purity > 99.8%, HPLC grade) was purchased from Kerch Chemical Reagent Co., Ltd. (Tianjin, China). All other solvents were analytical-grade and used without further purification.

Apparatus. The RP-HPLC spectra were measured with a 2695 separation module and an ultraviolet (UV)/visible-2489 detector (Waters, Milford, MA). The NP-HPLC spectra were measured with a 2695 separation module and an UV/visible-2487 detector (Waters, Milford, MA). The vortex mixer (Staufen, German), SCQ-250B ultrasonic apparatus (Shanghai, China), and 800 low-speed centrifuge (Jintan, China) were also used in the experiments.

Preparation and Storage of TBHQ or TQ Standard Solutions. To prepare a standard stock solution, 0.10 g (accurately weighted to 0.1 mg, similarly hereinafter) of TBHQ or TQ was individually weighted into a 100 mL amber volumetric flask and dissolved with methanol. The stock solutions were stored in a refrigerator (4 °C) and away from light for a maximum of 1 month. Before use, standard working solutions of variable concentrations (0.10, 1.00, 2.00, 5.00, 10.00, 20.00, 50.00, 100.00, 200.00, and 500.00 μg/mL) were prepared daily by diluting appropriate volumes of the stock solution in methanol.

Preparation of SBO or Lard Containing 2000 mg/kg of TBHQ or TQ. Lard was preheated at 40 °C until completely melted. A total of 0.12 g of TBHQ or TQ was added to 59.88 g of refined SBO or lard and then shaken until homogeneous.

Preparation of SBO or Lard Containing 50, 100, and 200 mg/kg of TBHQ or TQ. Lard was preheated at 40 °C until completely melted. A total of 1.50, 3.00, and 6.00 g of SBO or lard containing 2000 mg/kg of TBHQ or TQ were diluted to 60.00 g with control SBO or lard and then shaken until homogeneous.

Preparation of SBO or Lard Containing 150 mg/kg of TBHQ Plus 50 mg/kg of TQ, 100 mg/kg of TBHQ Plus 100 mg/kg of TQ, and 50 mg/kg of TBHQ Plus 150 mg/kg of TQ. Lard was preheated at 40 °C until completely melted. A total of 4.50, 3.00, or 1.50 g of SBO or lard containing 2000 mg/kg of TBHQ and 1.50, 3.00, or 4.50 g of SBO or lard containing 2000 mg/kg of TQ were diluted to 60.00 g with SBO or lard without TBHQ and TQ and then shaken until homogeneous.

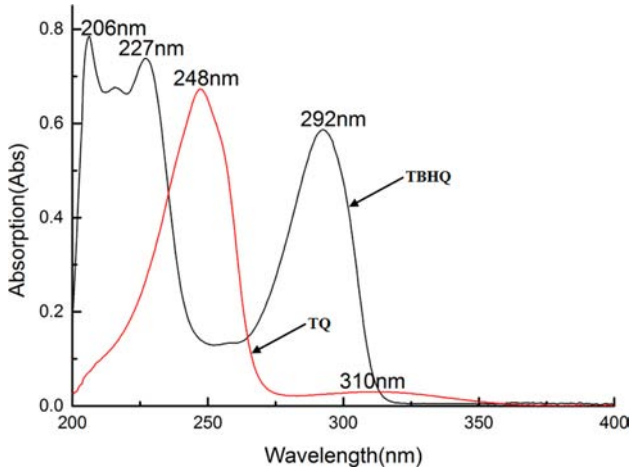

Figure 2. UV absorption spectra of TBHQ and TQ.

Extraction Procedure. The extraction procedure was in accordance with previous methods.[16,21,23] A total of 0.50 g of each of the oil samples was weighed into a 10 mL test tube, and 4 mL of methanol was added. The mixture was agitated for 3 min using a vortex mixer and then centrifuged at 3000 rpm for 2 min at room temperature. The supernatant was quantitatively transferred to a 10 mL flask. The extraction procedure was repeated twice, adding 3 mL of methanol each time. Finally, sufficient methanol was added to achieve a 10 mL solution. The solution was filtered through a 0.45 μm membrane before HPLC analysis.

Analysis of TBHQ and TQ. The conditions of RP-HPLC analysis were as follows:[16,24,25] the injection volume for TBHQ or TQ samples was 20 μL; the column was Symmetry C18 (4.6 × 250 mm, 5 μm, Waters); the solvent system was methanol−H_2O containing 0.5% AcOH (65:35, v/v); the flow rate was 0.8 mL/min; the dual detection wavelengths were 280 nm for TBHQ and 310 nm for TQ; and the column temperature was 35 °C. Methanol and H_2O containing 0.5% AcOH were both degassed for 15 min by an ultrasonic apparatus.

The conditions of NP-HPLC analysis were as follows: the injection volume for TBHQ or TQ samples was 20 μL; the column was Sunfire Prep Silica (4.6 × 250 mm, 5 μm, Waters); the solvent system was *n*-hexane containing 5% ethyl acetate (solvent A) and *n*-hexane containing 5% isopropanol (solvent B); the gradient elution was isocratic mode of 8% solvent B for 10 min, linear gradient from 8 to 100% solvent B for 5 min, and then isocratic mode of 100% solvent B for 12 min; the flow rate was 0.8 mL/min; the dual detection wavelengths were 280 nm for TBHQ and 310 nm for TQ; and the column temperature was 30 °C. Solvents A and B were both degassed for 40 min by an ultrasonic apparatus. Identification of compounds was

DOI: 10.1021/acs.jafc.5b03002
J. Agric. Food Chem. 2015, 63, 8584−8591

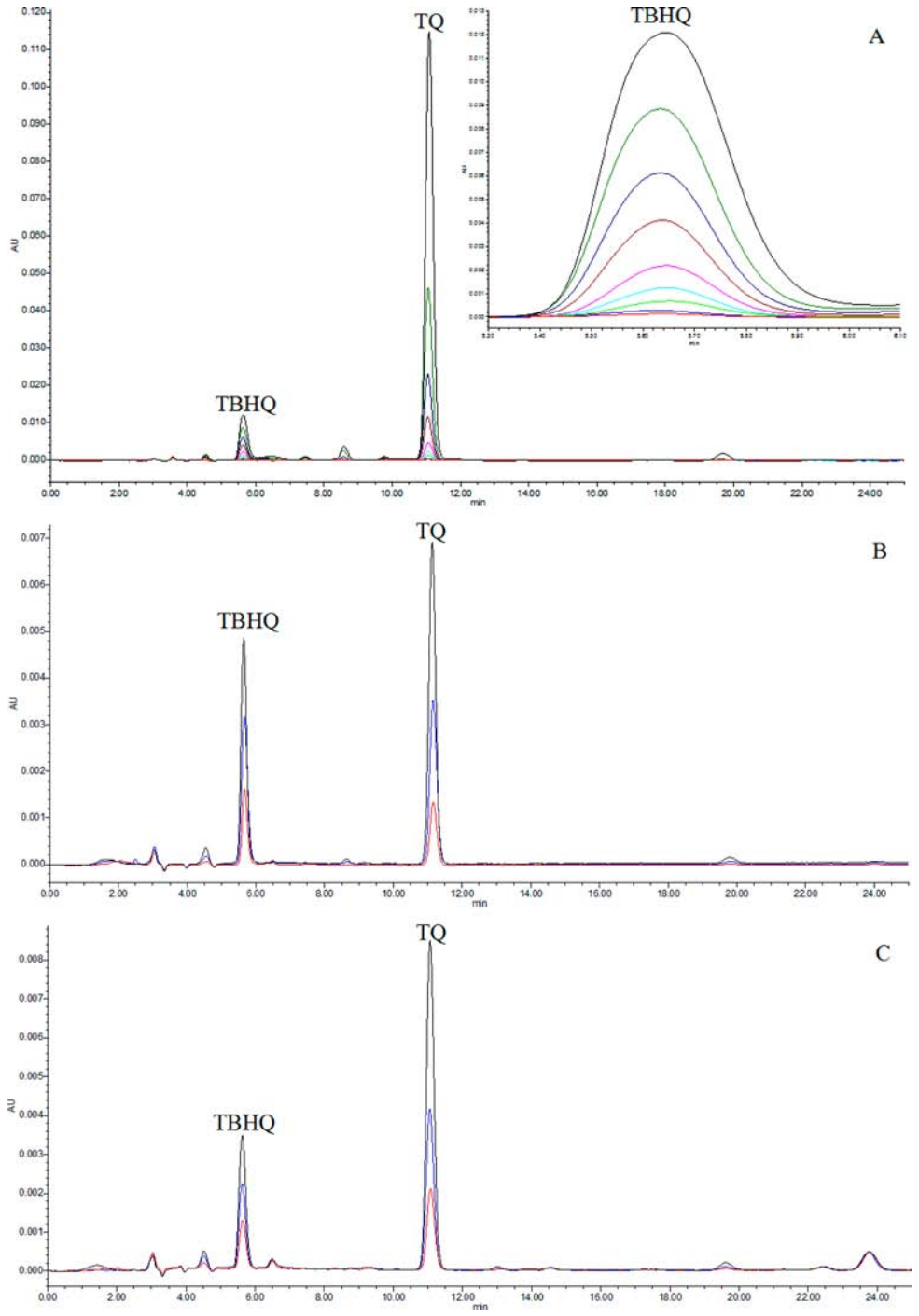

Figure 3. Superimposed RP-HPLC chromatograms of variable concentrations of (A) TQ standard solutions, (B) methanol extracting solutions of SBO adding 50, 100, and 200 mg/kg of TQ, and (C) methanol extracting solutions of lard adding 50, 100, and 200 mg/kg of TQ. Analysis conditions: the injection volume for TQ samples was 20 μL; the column was Symmetry C18 (4.6 × 250 mm, 5 μm, Waters); the solvent system was methanol−H_2O containing 0.5% AcOH (65:35, v/v); the flow rate was 0.8 mL/min; the dual detection wavelengths were 280 nm for TBHQ and 310 nm for TQ; and the column temperature was 35 °C. Methanol and H_2O containing 0.5% AcOH were both degassed for 15 min by an ultrasonic apparatus.

achieved by comparing their retention times to those of standards. Data were collected and processed using Empower 2.0 software (Waters Corporation).

Statistical Analyses. All experiments were performed at least in duplicate. All data were presented as the mean ± standard deviation (SD).

RESULTS AND DISCUSSION

Wavelength Screening. The UV absorption spectra of TBHQ and TQ were shown in Figure 2. The characteristic absorption wavelengths of TBHQ were 206, 227, and 292 nm. The characteristic absorption wavelengths of TQ were 248 and 310 nm. According to the American Oil Chemists' Society (AOCS) method,[24] 280 nm was selected as the appropriate detection wavelength for TBHQ. As a result of 248 nm less than the UV cutoff wavelength of ethyl acetate (254 nm)[26] and weak absorption of TQ at 280 nm (Figure 2), 310 nm was selected as an appropriate detection wavelength for TQ. Finally,

DOI: 10.1021/acs.jafc.5b03002
J. Agric. Food Chem. 2015, 63, 8584−8591

dual wavelengths (280 and 310 nm) were selected to detect TBHQ and TQ.

Determination of TBHQ by RP-HPLC. *Specificity, Linearity, Limit of Detection (LOD), and Limit of Quantification (LOQ) of TBHQ.* Specificity of the RP method for TBHQ detection was verified by comparing the chromatograms of TBHQ standard solution, oil samples, and lard samples before and after spiking with TBHQ. In oil and lard blank samples, no signal of TBHQ was detected.

The calibration curve was constructed by plotting the measured peak area versus the concentration of TBHQ. Excellent linearity was obtained within the concentration range of 0.10−500.00 μg/mL for TBHQ (R^2 > 0.9999).

The instrumental LOD was estimated and defined as the average response (n = 3) of the lower concentration level of the calibration curve for TBHQ plus 3 times the standard deviation.[27] The instrumental LOQ was taken as 10/3.3 times LOD.[28] The results showed that LOD and LOQ of TBHQ were below 0.06 and 0.18 μg/mL, respectively, which were both lower than that reported by Saad et al.[20]

Intra- and Interday Precision and Accuracy of TBHQ. The precision of the RP-HPLC system was demonstrated by intra- and interday variation studies.[29] In the intraday studies, six repeated injections of TBHQ standard solutions (5.00, 10.00, and 20.00 μg/mL) were made in 1 day and its relative standard deviation (RSD) and bias were calculated. In the interday variation studies, three repeated injections of TBHQ standard solutions (5.00, 10.00, and 20.00 μg/mL) were performed on 3 consecutive days and its RSD and bias were also calculated. Results showed that intra- and interday precisions of TBHQ with the RP-HPLC system were acceptable, with its RSD lower than 0.58% and bias lower than 1.52% (Table S1 of the Supporting Information).

Recoveries and Precision of TBHQ in SBO or Lard. Recoveries of TBHQ were determined using SBO or lard spiking with TBHQ. The recovery experiments were carried out at three levels of 50, 100, and 200 mg/kg (n = 6), and the percentage recoveries were calculated and presented in Table S2 of the Supporting Information. Recoveries of TBHQ in SBO and lard were in the ranges of 96.45−99.02 and 94.23−99.56%, respectively, with the RSD less than 0.64 and 0.45%.

Determination of TQ by RP-HPLC. *Specificity of TQ.* Verification of specificity of the RP-HPLC method for TQ detection was similar to that of TBHQ. In oil or lard blank samples, no signal of TQ was detected. However, in TQ standard solution (Figure 3A) and oil samples (Figure 3B) and lard samples (Figure 3C) spiking with TQ, there were all signals of TBHQ and the peaks were symmetric, which indicated that, during the injection, TQ was reduced to TBHQ by reduced hydrogen ([H]). Reduction ratios of TQ were calculated (Figure S1 of the Supporting Information), and specific results were presented in Tables 1 and 2. The [H] was from the mobile phase (water and acid solution) of the RP-HPLC system (Figure S2 of the Supporting Information).

Determination of TBHQ and TQ by NP-HPLC. *Specificity, Linearity, LOD, and LOQ of TBHQ and TQ.* Verification of specificity of the NP-HPLC method for TBHQ and TQ detections was also similar to that of the RP-HPLC method for TBHQ. In oil or lard blank samples, no signal of TBHQ and TQ was detected. In TBHQ standard solution, no signal of TQ was detected (Figure 4A). In TQ standard solution, no signal of TBHQ was also detected (Figure 4B).

Table 1. Reduction Ratios and Precision of Variable Concentrations of TQ Standard Solutions with the RP-HPLC System[a]

concentration of TQ (μg/mL)	reduction yield of TQ (%)[b]	RSD (%)
1.00	9.55 ± 0.36	3.77
2.00	9.70 ± 0.14	1.44
5.00	8.70 ± 0.38	4.37
10.00	8.03 ± 0.42	5.23
20.00	7.24 ± 0.56	7.73
50.00	5.55 ± 0.61	10.99
100.00	4.30 ± 0.42	9.77
200.00	3.17 ± 0.14	4.41
500.00	1.89 ± 0.22	11.64

[a]Analysis conditions: the injection volume for TQ samples was 20 μL; the column was Symmetry C18 (4.6 × 250 mm, 5 μm, Waters); the solvent system was methanol−H_2O containing 0.5% AcOH (65:35, v/v); the flow rate was 0.8 mL/min; the dual detection wavelengths were 280 nm for TBHQ and 310 nm for TQ; and the column temperature was 35 °C. Methanol and H_2O containing 0.5% AcOH were both degassed for 15 min by an ultrasonic apparatus. [b]Mean ± SD.

Table 2. Reduction Ratios and Precision of the Spiked TQ from SBO and Lard with the RP-HPLC System[a]

sample	concentration of TQ (mg/kg)	reduction yield of TQ (%)[b]	RSD (%)
SBO	50	7.98 ± 0.47	5.89
	100	8.26 ± 0.59	7.15
	200	5.94 ± 0.60	10.13
lard	50	5.71 ± 0.04	0.62
	100	6.14 ± 0.14	2.30
	200	5.15 ± 0.14	2.74

[a]Analysis conditions: the injection volume for TQ samples was 20 μL; the column was Symmetry C18 (4.6 × 250 mm, 5 μm, Waters); the solvent system was methanol−H_2O containing 0.5% AcOH (65:35, v/v); the flow rate was 0.8 mL/min; the dual detection wavelengths were 280 nm for TBHQ and 310 nm for TQ; and the column temperature was 35 °C. Methanol and H_2O containing 0.5% AcOH were both degassed for 15 min by an ultrasonic apparatus. [b]Mean ± SD.

These results indicated that the redox reaction of TBHQ and TQ did not happen during the NP-HPLC analysis.

Constructions of calibration curves of TBHQ and TQ with the NP-HPLC system were similar to that of TBHQ with the RP-HPLC system. Excellent linearity was obtained within the concentration range of 0.10−500.00 μg/mL for TBHQ and TQ (R^2 > 0.9999).

The estimations and definitions of instrumental LOD and LOQ with the NP-HPLC system were similar to that of the RP-HPLC system. Results showed that LOD and LOQ of TBHQ were below 0.30 and 0.91 μg/mL, respectively, which were both lower than those of Saad et al.[20] The LOD and LOQ of TQ were below 0.10 and 0.30 μg/mL, respectively.

Intra- and Interday Precision and Accuracy of TBHQ and TQ. The demonstration of the precision of the NP-HPLC system was similar to that of the RP-HPLC system. Corresponding RSD and bias were calculated and presented in Table S3 of the Supporting Information. Results showed that intra- and interday precisions of TBHQ and TQ with the NP-HPLC system were acceptable, with the RSD lower than 1.76% and the bias lower than 5.55%.

Selection of the Extraction Solvent. In general, phenolic antioxidants in edible oils can often be extracted using some polar solvents, such as methanol, acetonitrile, etc.[30] Nonpolar

DOI: 10.1021/acs.jafc.5b03002
J. Agric. Food Chem. 2015, 63, 8584−8591

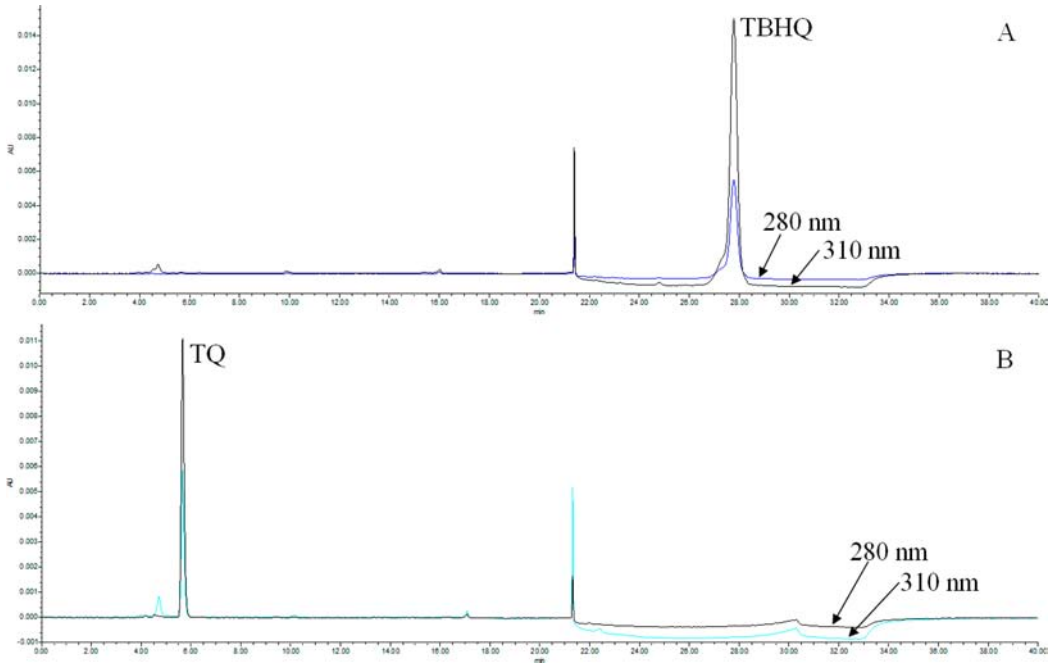

Figure 4. NP-HPLC chromatograms of (A) TBHQ and (B) TQ standard solutions. Analysis conditions: the injection volume for TBHQ or TQ samples was 20 μL; the column was Sunfire Prep Silica (4.6 × 250 mm, 5 μm, Waters); the solvent system was *n*-hexane containing 5% ethyl acetate (solvent A) and *n*-hexane containing 5% isopropanol (solvent B); the gradient elution was isocratic mode of 8% solvent B for 10 min, linear gradient from 8 to 100% solvent B for 5 min, and then isocratic mode of 100% solvent B for 12 min; the flow rate was 0.8 mL/min; the dual detection wavelengths were 280 nm for TBHQ and 310 nm for TQ; and the column temperature was 30 °C. Solvents A and B were both degassed for 40 min by an ultrasonic apparatus.

Table 3. Recoveries and Precision of the Spiked TBHQ or TQ from SBO and Lard Determined by NP-HPLC[a]

	TBHQ (n = 6)			TQ (n = 6)		
sample	added (mg/kg)	recovery (%)[b]	RSD (%)	added (mg/kg)	recovery (%)[b]	RSD (%)
SBO	50	98.92 ± 0.38	0.38	50	100.58 ± 1.73	1.71
	100	100.69 ± 0.39	0.38	100	96.68 ± 0.29	0.30
	200	102.34 ± 0.37	0.36	200	96.28 ± 0.55	0.58
lard	50	96.17 ± 1.23	1.28	50	98.83 ± 3.54	3.58
	100	99.42 ± 0.56	0.57	100	99.24 ± 1.28	1.29
	200	96.11 ± 1.98	2.06	200	99.00 ± 0.39	0.39

[a]Analysis conditions: the injection volume for TBHQ or TQ samples was 20 μL; the column was Sunfire Prep Silica (4.6 × 250 mm, 5 μm, Waters); the solvent system was *n*-hexane containing 5% ethyl acetate (solvent A) and *n*-hexane containing 5% isopropanol (solvent B); the gradient elution was isocratic mode of 8% solvent B for 10 min, linear gradient from 8 to 100% solvent B for 5 min, and then isocratic mode of 100% solvent B for 12 min; the flow rate was 0.8 mL/min; the dual detection wavelengths were 280 nm for TBHQ and 310 nm for TQ; and the column temperature was 30 °C. Solvents A and B were both degassed for 40 min by an ultrasonic apparatus. [b]Mean ± SD.

Table 4. Recoveries and Precision of the Spiked TBHQ and TQ from SBO and Lard Determined by NP-HPLC[a]

	TBHQ/TQ						
sample	added ((mg/kg)/(mg/kg))	recovery of TBHQ (%)[b]	RSD (%)	recovery of TQ (%)[b]	RSD (%)	recovery of TBHQ plus TQ (%)[b]	RSD (%)
SBO	150/50	95.12 ± 0.95	1.00	101.57 ± 0.17	0.17	98.72 ± 0.95	0.96
	100/100	96.73 ± 0.88	0.91	97.86 ± 0.18	0.18	97.96 ± 0.22	0.22
	50/150	97.41 ± 0.85	0.87	97.57 ± 0.17	0.17	97.83 ± 0.50	0.51
lard	150/50	98.42 ± 0.58	0.59	101.61 ± 0.80	0.79	99.30 ± 0.43	0.43
	100/100	96.73 ± 2.26	2.33	98.85 ± 2.19	2.21	97.81 ± 2.20	2.25
	50/150	94.14 ± 0.63	0.67	97.87 ± 0.92	0.94	96.93 ± 0.83	0.86

[a]Analysis conditions: the injection volume for TBHQ and TQ samples was 20 μL; the column was Sunfire Prep Silica (4.6 × 250 mm, 5 μm, Waters); the solvent system was *n*-hexane containing 5% ethyl acetate (solvent A) and *n*-hexane containing 5% isopropanol (solvent B); the gradient elution was isocratic mode of 8% solvent B for 10 min, linear gradient from 8 to 100% solvent B for 5 min, and then isocratic mode of 100% solvent B for 12 min; the flow rate was 0.8 mL/min; the dual detection wavelengths were 280 nm for TBHQ and 310 nm for TQ; and the column temperature was 30 °C. Solvents A and B were both degassed for 40 min by an ultrasonic apparatus. [b]Mean ± SD.

solvents, such as *n*-hexane, can often be used to remove the oil matrix coextracted. However, because of the polarity of TQ of less than that of TBHQ, TQ can be easily dissolved in nonpolar solvents, such as *n*-hexane. To obtain a specific distribution

DOI: 10.1021/acs.jafc.5b03002
J. Agric. Food Chem. 2015, 63, 8584−8591

Table 5. Contents of TBHQ and TQ in SBO or Lard Containing 200 mg/kg of TBHQ during Storage at Room Temperature Determined by NP-HPLC[a]

	SBO				lard			
storage time (week)	C_2 (mg/kg)[b]	C_3 (mg/kg)[b]	C_1 (mg/kg)[b]	C_0 (mg/kg)	C_2 (mg/kg)[b]	C_3 (mg/kg)[b]	C_1 (mg/kg)[b]	C_0 (mg/kg)
0	197.35 ± 0.56	0.00 ± 0.00	197.35 ± 0.56	200	198.50 ± 0.19	0.00 ± 0.00	198.50 ± 0.19	200
2	183.50 ± 0.93	11.17 ± 0.51	194.67 ± 1.44	200	154.37 ± 1.36	41.79 ± 0.83	196.16 ± 2.19	200
4	182.98 ± 0.14	14.17 ± 0.42	197.15 ± 0.56	200	146.99 ± 0.31	51.07 ± 0.71	198.06 ± 1.02	200
6	180.79 ± 0.37	16.61 ± 0.68	197.40 ± 1.05	200	108.22 ± 2.01	77.25 ± 0.89	185.47 ± 2.90	200
8	178.59 ± 1.21	16.15 ± 0.81	194.74 ± 2.02	200	87.25 ± 0.94	95.32 ± 0.64	182.57 ± 1.58	200

[a]Analysis conditions: the injection volume for TBHQ and TQ samples was 20 μL; the column was Sunfire Prep Silica (4.6 × 250 mm, 5 μm, Waters); the solvent system was *n*-hexane containing 5% ethyl acetate (solvent A) and *n*-hexane containing 5% isopropanol (solvent B); the gradient elution was isocratic mode of 8% solvent B for 10 min, linear gradient from 8 to 100% solvent B for 5 min, and then isocratic mode of 100% solvent B for 12 min; the flow rate was 0.8 mL/min; the dual detection wavelengths were 280 nm for TBHQ and 310 nm for TQ; and the column temperature was 30 °C. Solvents A and B were both degassed for 40 min by an ultrasonic apparatus. C_0, original added load of TBHQ in SBO or lard; C_1, content of TBHQ plus TQ detected in SBO or lard; C_2, content of TBHQ detected in SBO or lard; and C_3, content of TQ detected SBO or lard. [b]Mean ± SD.

Table 6. Contents of TBHQ and TQ in Some Commercial Vegetable Oils Determined by NP-HPLC[a]

	original commercial oils			commercial oils stored for 2 months without seal			
sample type	TBHQ (mg/kg)[b]	TQ (mg/kg)	TBHQ plus TQ (mg/kg)[b]	TBHQ (mg/kg)[b]	TQ (mg/kg)[b]	TBHQ plus TQ (mg/kg)[b]	conversion yield of TBHQ (%)
SBO	64.46 ± 0.12	–[c]	64.46 ± 0.12	56.28 ± 0.41	7.02 ± 0.39	63.30 ± 0.44	10.89
	26.19 ± 0.30	–	26.19 ± 0.30	23.18 ± 0.09	3.53 ± 0.52	26.72 ± 0.61	13.48
	73.44 ± 0.55	–	73.44 ± 0.55	64.75 ± 0.29	9.96 ± 0.11	74.72 ± 0.18	13.62
edible blended oil	19.36 ± 1.70	–	19.36 ± 1.70	16.07 ± 0.15	3.82 ± 0.22	19.89 ± 0.37	19.73
	90.18 ± 0.67	–	90.18 ± 0.67	76.62 ± 1.32	12.18 ± 0.48	88.79 ± 1.80	13.51
sunflower seed oil	57.85 ± 2.47	–	57.85 ± 2.47	46.34 ± 0.85	10.09 ± 0.42	56.43 ± 0.43	17.44

[a]Analysis conditions: the injection volume for TBHQ and TQ samples was 20 μL; the column was Sunfire Prep Silica (4.6 × 250 mm, 5 μm, Waters); the solvent system was *n*-hexane containing 5% ethyl acetate (solvent A) and *n*-hexane containing 5% isopropanol (solvent B); the gradient elution was isocratic mode of 8% solvent B for 10 min, linear gradient from 8 to 100% solvent B for 5 min, and then isocratic mode of 100% solvent B for 12 min; the flow rate was 0.8 mL/min; the dual detection wavelengths were 280 nm for TBHQ and 310 nm for TQ; and the column temperature was 30 °C. Solvents A and B were both degassed for 40 min by an ultrasonic apparatus. [b]Mean ± SD. [c]"–" represents no TBHQ or TQ found.

ratio of TQ in *n*-hexane and methanol (or acetonitrile), 5 mL of *n*-hexane was added to 5 mL of 500.00 μg/mL TQ methanol solution (or acetonitrile solution). The mixtures were mixed for 2 min using a vortex mixer and then centrifuged at 3000 rpm for 2 min at room temperature. After filteration using 0.45 μm organic membrane, the *n*-hexane fraction and methanol fraction (or acetonitrile fraction) were analyzed. Results showed that the distribution ratios of TQ in *n*-hexane and methanol were 44.91 and 54.62%, respectively; the distribution ratios of TQ in *n*-hexane and acetonitrile were 33.84 and 66.16%, respectively. Therefore, in the work, if nonpolar solvents were used to remove the oil matrix coextracted, approximately half or one-third of TQ was removed from methanol or acetonitrile extracting solution and dissolved in nonpolar solvents. In addition, mobile phases of NP-HPLC were low polarity or nonpolar solvents,[31,32] which can easily dissolve the oil matrix coextracted. The oil matrix coextracted could be eluted from stationary phase by mobile phases, which has little effect on the lifetime of the silica gel column and the baseline (Figure S3 of the Supporting Information). Therefore, the process of removing the oil matrix coextracted could be left out. In addition, considering the higher toxicity and cost of acetonitrile than that of methanol,[33] methanol was used to extract TBHQ and TQ from the edible oils.

Recoveries and Precision of TBHQ or TQ in Edible Oil Samples. The determination of recoveries of TBHQ or TQ with the NP-HPLC system was similar to that of TBHQ with the RP-HPLC system. The recoveries were calculated and presented in Table 3. Recoveries of TBHQ in SBO and lard were in the ranges of 98.92–102.34 and 96.11–99.42%, with the RSD less than 0.38 and 2.06%, respectively. Recoveries of TQ in SBO and lard were in the ranges of 96.28–100.58 and 98.83–99.24%, with the RSD less than 1.71 and 3.58%, respectively.

Recoveries and Precision of TBHQ and TQ in Edible Oil Samples. Recoveries of TBHQ and TQ were determined using SBO and lard spiking with TBHQ and TQ. The recovery experiments were carried out at three levels of 150/50, 100/100, and 50/150 (mg/kg)/(mg/kg) (n = 6), and the recoveries of TBHQ and TQ were calculated and presented in Table 4. Recoveries of TBHQ and TQ in SBO and lard were in the ranges of 97.83–98.72 and 96.93–99.30%, with the RSD less than 0.96 and 2.25%, respectively, which indicated that the NP-HPLC method can be used to evaluate the original added load of TBHQ in edible oils (Figure S4 of the Supporting Information).

Analysis of Contents of TBHQ and TQ in SBO and Lard during Storage at Room Temperature. On the basis of the NP-HPLC method, the contents of TBHQ and TQ in SBO and lard containing 200 mg/kg of TBHQ during storage at room temperature were determined. Results showed that, with the increase of the storage time, the contents of TBHQ in SBO and lard decreased gradually, while the contents of TQ in SBO and lard increased (Table 5). For example, the original added

DOI: 10.1021/acs.jafc.5b03002
J. Agric. Food Chem. 2015, 63, 8584–8591

load of TBHQ in SBO was 197.35% without TQ. After SBO samples were stored for 1 and 2 months, the contents of TBHQ were 182.98 and 178.59 mg/kg, respectively, and the contents of TQ were 14.17 and 16.15 mg/kg, respectively. The original added load of TBHQ in lard was 198.50% without TQ as well. After lard samples were stored for 1 and 2 months, the contents of TBHQ were 146.99 and 87.25 mg/kg, respectively, and the contents of TQ were 51.07 and 95.32 mg/kg, respectively. Meanwhile, contents of TBHQ converting to TQ in SBO were less than those in lard, which might be attributed to the presence of tocopherols (approximately 1000 mg/kg[34]) in SBO. Partial oxidation of tocopherols can consume partial oxygen dissolved in SBO, which can slow the conversion of TBHQ to TQ.

Analysis of TBHQ and TQ in Some Commercial Vegetable Oils. Some commercial oil samples were analyzed using the NP-HPLC method. Results showed that TBHQ existed in all original oil samples but TQ was not detected, which might be no oxygen presented in the commercial bottled oils before opening. However, when the package of the original samples was unclosed and stored at 25 °C for 2 months, TQ can be detected (Table 6). Conversion ratios of TBHQ to TQ were in the ranges of 10−20% in all commercial vegetable oils tested. These results indicated that, after the continuous exposure of oils in air, TBHQ can be converted to TQ in the presence of oxygen and free radicals of oils. In addition, none of the positive samples violated the legal limit (200 mg/kg[3]).

In conclusion, in comparison to the RP-HPLC system, the NP-HPLC method overcame the reduction of TQ, can simultaneously and accurately analyze the contents of TBHQ and TQ in edible oils, and was also successfully applied to evaluate the original added load of TBHQ in edible oils.

■ ASSOCIATED CONTENT

Supporting Information

The Supporting Information is available free of charge on the ACS Publications website at DOI: 10.1021/acs.jafc.5b03002.

Calculation of reduction ratios of TQ (Figure S1), reduction reaction of TQ by protonation (Figure S2), baseline of NP-HPLC before and after elution of the sample directly extracted with methanol (Figure S3), equation for calculating the original added load of TBHQ (Figure S4), values of the intra- and interday precision and accuracy assay of TBHQ determined by RP-HPLC (Table S1), recoveries and precision of the spiked TBHQ from SBO and lard determined by RP-HPLC (Table S2), and values of the intra- and interday precision and accuracy assay of TBHQ and TQ determined by NP-HPLC (Table S3) (PDF)

■ AUTHOR INFORMATION

Corresponding Author

*Telephone/Fax: +86-0371-67758022. E-mail: yanlanbi@hotmail.com.

Funding

This work was financially supported by the National Natural Science Foundation of China (31271883).

Notes

The authors declare no competing financial interest.

■ ABBREVIATIONS USED

TBHQ, tertiary butylhydroquinone; TQ, 2-*tert*-butyl-1,4-benzoquinone; SBO, soybean oil; HPLC, high-performance liquid chromatography; RP, reverse phase; NP, normal phase; [H], reduced hydrogen; LOD, limit of detection; LOQ, limit of quantification; SD, standard deviation; RSD, relative standard deviation

■ REFERENCES

(1) Hamama, A. A.; Nawar, W. W. Thermal decomposition of some phenolic antioxidants. *J. Agric. Food Chem.* **1991**, *39*, 1063−1069.

(2) Ramanathan, L.; Das, N. P. Studies on the control of lipid oxidation in ground fish by some polyphenolic natural products. *J. Agric. Food Chem.* **1992**, *40*, 17−21.

(3) U.S. Food and Drug Administration (FDA). *Code of Federal Regulations 21, Food and Drugs*; Office of the Federal Register (OFR): Washington, D.C., 1980.

(4) Macari, E. R.; Schaeffer, E. K.; West, R. J.; Lowrey, C. H. Simvastatin and t-butylhydroquinone suppress KLF1 and BCL11A gene expression and additively increase fetal hemoglobin in primary human erythroid cells. *Blood* **2013**, *121*, 830−839.

(5) Eskandani, M.; Hamishehkar, H.; Ezzati Nazhad Dolatabadi, J. Cytotoxicity and DNA damage properties of tert-butylhydroquinone (TBHQ) food additive. *Food Chem.* **2014**, *153*, 315−320.

(6) Choe, E.; Min, D. B. Mechanisms and factors for edible oil oxidation. *Compr. Rev. Food Sci. Food Saf.* **2006**, *5*, 169−186.

(7) Kim, C. M.; Pratt, D. E. Degradation products of 2-tert-butylhydroquinone at frying temperature. *J. Food Sci.* **1990**, *55*, 847−847.

(8) Buck, D. F. Antioxidants in soya oil. *J. Am. Oil Chem. Soc.* **1981**, *58*, 275−278.

(9) Asap, T.; Augustin, M. A. Effect of TBHQ on quality characteristics of RBD olein during frying. *J. Am. Oil Chem. Soc.* **1986**, *63*, 1169−1172.

(10) Marmesat, S.; Morales, A.; Velasco, J.; Dobarganes, M. C. Action and fate of natural and synthetic antioxidants during frying. *Grasas Aceites* **2010**, *61*, 333−340.

(11) Braeuning, A.; Vetter, S.; Orsetti, S.; Schwarz, M. Paradoxical cytotoxicity of tert-butylhydroquinone in vitro: what kills the untreated cells? *Arch. Toxicol.* **2012**, *86*, 1481−1487.

(12) Morimoto, K.; Tsuji, K.; Iio, T.; Miyata, N.; Uchida, A.; Osawa, R.; Kitsutaka, H.; Takahashi, A. DNA damage in forestomach epithelium from male F344 rats following oral administration of tert-butylquinone, one of the forestomach metabolites of 3-BHA. *Carcinogenesis* **1991**, *12*, 703−708.

(13) Schilderman, P.; Rhijnsburger, E.; Zwingmann, I.; Kleinjans, J. C. S. Induction of oxidative DNA damage and enhancement of cell proliferation in human lymphocytes in vitro by butylated hydroxyanisole. *Carcinogenesis* **1995**, *16*, 507−512.

(14) Matsunaga, T.; Endo, S.; Takemura, M.; Soda, M.; Yamamura, K.; Tajima, K.; Miura, T.; Terada, T.; El-Kabbani, O.; Hara, A. Reduction of cytotoxic p-quinone metabolites of tert-butylhydroquinone by human aldo-keto reductase (AKR) 1B10. *Drug Metab. Pharmacokinet.* **2012**, *27*, 553−558.

(15) Kahl, R.; Weinke, S.; Kappus, H. Production of reactive oxygen species due to metabolic activation of butylated hydroxyanisole. *Toxicology* **1989**, *59*, 179−194.

(16) Li, J.; Bi, Y. L.; Liu, W.; Sun, S. D.; Liu, C. F.; Ma, S. M. Effect of acid value on TBHQ and BHT losses in heating oils: identification of the esterification products of TBHQ and free fatty acids. *J. Am. Oil Chem. Soc.* **2014**, *91*, 1763−1771.

(17) Kurechi, T.; Aizawa, M.; Kunugi, A. Studies on the antioxidants XVIII: oxidation product of tertiary butyl hydroquinone (TBHQ) (I). *J. Am. Oil Chem. Soc.* **1983**, *60*, 1878−1882.

(18) Lin, F. S.; Warner, C. R.; Fazio, T. Alteration of phenolic antioxidants in heated vegetable oil. *J. Am. Oil Chem. Soc.* **1981**, *58*, A789−A792.

DOI: 10.1021/acs.jafc.5b03002
J. Agric. Food Chem. 2015, 63, 8584−8591

(19) Kurechi, T.; Kunugi, A. Studies on the antioxidants XIX: Photooxidation products of tertiary butyl hydroquinone (TBHQ) (II). *J. Am. Oil Chem. Soc.* **1983**, *60*, 1882−1887.
(20) Saad, B.; Sing, Y. Y.; Nawi, M. A.; Hashim, N.; Mohamedali, A.; Saleh, M. I.; Sulaiman, S. F.; Talib, K. M.; Ahmad, K. Determination of synthetic phenolic antioxidants in food items using reversed-phase HPLC. *Food Chem.* **2007**, *105*, 389−394.
(21) Perrin, C.; Meyer, L. Quantification of synthetic phenolic antioxidants in dry foods by reversed-phase HPLC with photodiode array detection. *Food Chem.* **2002**, *77*, 93−100.
(22) Li, X. Q.; Ji, C.; Sun, Y. Y.; Yang, M. L.; Chu, X. G. Analysis of synthetic antioxidants and preservatives in edible vegetable oil by HPLC/TOF-MS. *Food Chem.* **2009**, *113*, 692−700.
(23) Guo, L.; Xie, M. Y.; Yan, A. P.; Wan, Y. Q.; Wu, Y. M. Simultaneous determination of five synthetic antioxidants in edible vegetable oil by GC−MS. *Anal. Bioanal. Chem.* **2006**, *386*, 1881−1887.
(24) American Oil Chemists' Society (AOCS). Antioxidants—Lipid chromatographic method. *Official Methods and Recommended Practices of the American Oil Chemists' Society*, 5th ed.; AOCS Press: Champaign, IL, 1997; Official Method Ce 6-8.
(25) AOAC International. Phenolic antioxidants in oils, fats and butter oil liquid chromatographic method. *Official Methods of the Association of Official Analytical Chemists*; AOAC Press: Rockville, MD, 1994; Official Method 983.15.
(26) Yao, S.; Luo, J. G.; Huang, X. F.; Kong, L. Y. Application of preparative high-speed counter-current chromatography/preparative high-performance liquid chromatography mode in rapid separation of saponins. *J. Chromatogr. B: Anal. Technol. Biomed. Life Sci.* **2008**, *864*, 69−77.
(27) Koesukwiwat, U.; Jayanta, S.; Leepipatpiboon, N. Validation of a liquid chromatography-mass spectrometry multi-residue method for the simultaneous determination of sulfonamides, tetracyclines and pyrimethamine in milk. *J. Chromatogr. A* **2007**, *1140*, 147−156.
(28) Wang, J. Y.; Wu, H. L.; Sun, Y. M.; Gu, H. W.; Liu, Z.; Liu, Y. J.; Yu, R. Q. Simultaneous determination of phenolic antioxidants in edible vegetable oils by HPLC−FLD assisted with second-order calibration based on ATLD algorithm. *J. Chromatogr. B: Anal. Technol. Biomed. Life Sci.* **2014**, *947−948*, 32−40.
(29) Chen, M.; Hu, X. J.; Tai, Z. G.; Qin, H.; Tang, H. N.; Liu, M. S.; Yang, Y. L. Determination of four synthetic phenolic antioxidants in edible oils by high-performance liquid chromatography with cloud point extraction using Tergitol TMN-6. *Food Anal. Method.* **2013**, *6*, 28−35.
(30) Antolovich, M.; Prenzler, P.; Robards, K.; Ryan, D. Sample preparation in the determination of phenolic compounds in fruits. *Analyst* **2000**, *125*, 989−1009.
(31) Ansari, G. A. S. High-performance liquid chromatographic separation of the isomers of butylated hydroxyanisole. *J. Chromatogr. A* **1983**, *262*, 393−396.
(32) Panfili, G.; Fratianni, A.; Irano, M. Normal phase high-performance liquid chromatography method for the determination of tocopherols and tocotrienols in cereals. *J. Agric. Food Chem.* **2003**, *51*, 3940−3944.
(33) Concha-Herrera, V.; Torres-Lapasió, J. R.; Vivó-Truyols, G.; García-Álvarez-Coque, M. C. A comparative study of the performance of acetonitrile and methanol in the multi-linear gradient separation of proteic primary amino acids. *Anal. Chim. Acta* **2007**, *582*, 250−258.
(34) Lim, H.; Woo, S.; Kim, H. S.; Jong, S.-K.; Lee, J. Comparison of extraction methods for determining tocopherols in soybeans. *Eur. J. Lipid Sci. Technol.* **2007**, *109*, 1124−1127.

DOI: 10.1021/acs.jafc.5b03002
J. Agric. Food Chem. 2015, 63, 8584−8591

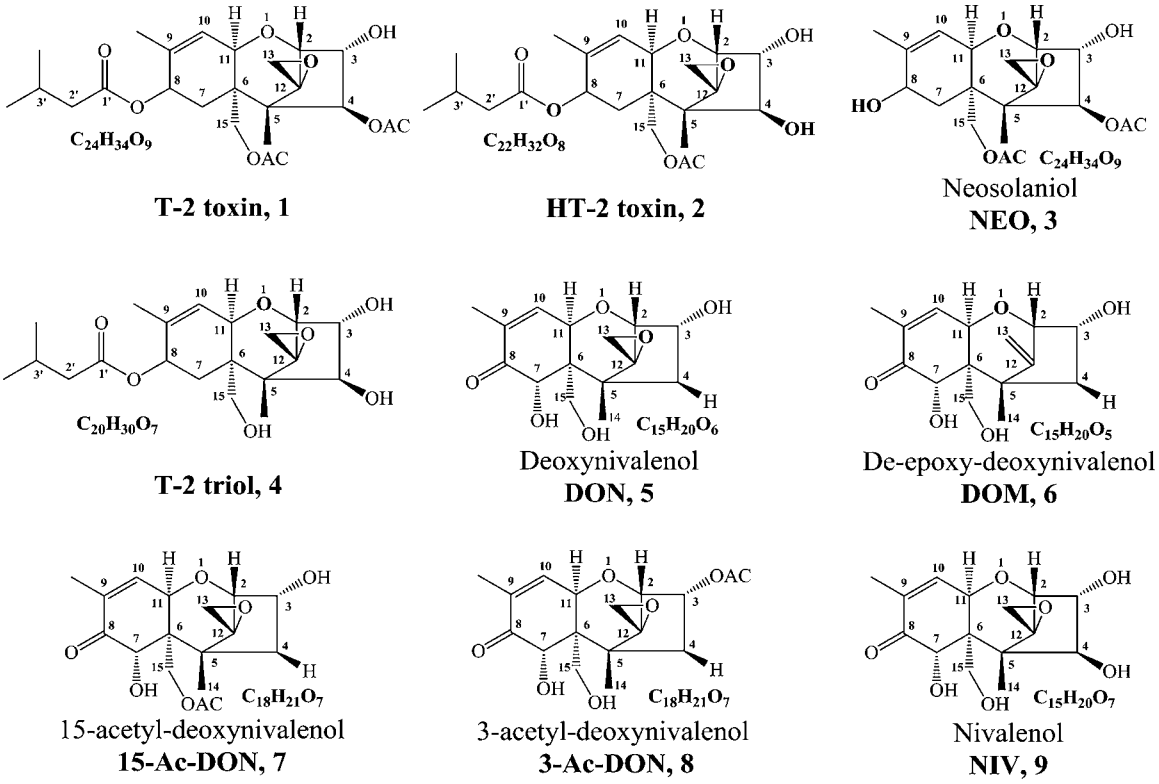

Figure 1. Chemical structures of T-2 toxin, HT-2 toxin, NEO, T-2-triol, DON, DOM, 15-Ac-DON, 3-Ac-DON, and NIV.

be rapidly deacetylated, such as 3-acetyldeoxynivalenol (3-Ac-DON) (**7**), where deacetylation was the predominant biotransformation reaction and minimal deepoxidation occurred.[2,7] On the other hand, 15-acetyldeoxynivalenol (15-Ac-DON) (**8**) showed only small amounts of the deacetylation products, but produced large amounts of products having both the acetyl and epoxy functionalities removed.[2] However, in the metabolism of nivalenol (NIV) (**9**), only one deepoxy metabolite was found.[2]

Accurate and reliable methods for the detection and quantitation of these compounds, and their metabolites, are required for studying the toxicodynamics or concentration levels in naturally contaminated samples. A variety of methods have been published for the determination of trichothecenes, including thin-layer chromatography (TLC), enzyme-linked immunosorbent assays (ELISAs), gas chromatography−electron capture detection (GC−ECD), gas chromatography−mass spectrometry (GC−MS), and liquid chromatography coupled with ultraviolet detection (HPLC−UV).[10−14] However, since liquid chromatography coupled with tandem mass spectrometry (LC−MS/MS) offers more accurate quantitation, better selection, and higher sensitivity compared to other analytical methods, it plays an increasingly important role in the analysis of mycotoxins.[4] Numerous LC−MS/MS methods have been developed for determination of trichothecenes.[15−19] However, these methods are primarily focused on cereals and their derivative foods,[15−19] because there is a high likelihood that trichothecenes or their metabolites can enter the human food chain via meat products or secondary animal products, such as eggs and milk, as the result of livestock eating contaminated feed.[2] Currently, many publications have reported mycotoxins in urine, milk, and eggs.[17,20−24] For animal meat, such as chicken and pork, only one available publication reported a method to detect DON and T-2 toxin in meat.[25] In fact, when T-2 toxin and DON are ingested by food animals, they are rapidly metabolized to HT-2 toxin, DOM, and other metabolites.[2] In comparison with T-2 toxin and DON, their metabolites were more likely to be present at high levels in meat products, especially HT-2 toxin.[1,2] Therefore, it is necessary to develop a method for also detecting the main metabolites of these mycotoxins in animal tissues.

The aim of this study was to develop and validate an accurate and sensitive LC−MS/MS method for simultaneous determination of type A and type B trichothecenes, and their main metabolites, in animal tissues. Such a method would be valuable for studies of metabolism, residue elimination, and safety evaluation.

MATERIALS AND METHODS

Standards. The standards of T-2 toxin, HT-2 toxin, T-2-triol, NEO, DON, 3-Ac-DON, 5-Ac-DON, DOM, and NIV were purchased from Fermentek Biotechnology (Jerusalem, Israel). Stock standard solutions (100 mg/L) of individual compounds were prepared in acetonitrile and stored at −20 °C in darkness. Working solutions (5 mg/L) of the standards were prepared by diluting stock solutions with a mixture of acetonitrile/water (10:90, v/v) and stored at 4 °C in the dark.

Chemicals and Reagents. Acetonitrile and methanol were HPLC and MS grade, purchased from Fisher Chemical Co. (Fair Lawn, NJ). Ammonium hydroxide (28% NH_3) was purchased from Alfa-Aesar (Ward Hill, MA). Analytical grade ethyl acetate and *n*-hexane were purchased from Sinopharm Chemical Reagent Co., Ltd. (Beijing, China). Water was purified using a Milli-Q system (resistivity 18.2 MΩ, Millipore, Bedford, MA). Oasis HLB cartridges (3 cm^3, 60 mg) were purchased from Waters Co. (Milford, MA). Other reagents were of analytical grade and were obtained from the Beijing Reagent Co. (Beijing, China).

Samples. A total of 15 blank samples, including 3 of chicken meat, 3 of pork, 6 chicken livers, and 3 whole pig livers, were purchased from randomly chosen local supermarkets in Beijing, China. All samples

DOI: 10.1021/acs.jafc.5b03281
J. Agric. Food Chem. 2015, 63, 8592−8600

were homogenized before use in a high-speed food blender. Then the samples were stored at −20 °C until analysis.

Animal Study. Twelve chickens (1.1 ± 0.1 kg) were purchased from Beijing Huadu Co. Ltd. (Beijing, China). The experimental protocol was approved by the University Ethics Committee and conformed to the China Agricultural University regulations concerning protection of animals used for scientific purposes (2010-SYXK-0037). Chickens were given a single oral dose of T-2 (3 mg/kg of body weight (bw), dissolved in ethanol/water (30:70, v/v)). Muscle and liver tissues were collected 6, 12, 24, and 48 h after oral administration. All samples were frozen at −20 °C until analysis.

Sample Preparation. One gram of sample was extracted with 8 mL of acetonitrile/ethyl acetate (1:3, v/v) during 5 min on a vortex shaker. The sample extract was then centrifuged at 10141*g* for 10 min, and the supernatant was transferred into a new tube. The residue was extracted a second time with 5 mL of the extraction solution according to the above procedure. The supernatants were combined and placed in a −80 °C freezer to remove the fat. After 20 min, the tubes were taken out and centrifuged at 10141*g* for 10 min at 4 °C. The supernatant was removed and dried with N_2 gas at 40 °C. Then the residue was reconstituted in 600 μL of acetonitrile/water (10:90, v/v) and diluted by 10 mL of water. Afterward, the obtained solution was further cleaned up using Oasis HLB cartridges. First, the cartridges were preconditioned with 3 mL of methanol, followed by 3 mL of water. The sample extract was loaded onto an HLB cartridge, which was washed by 3 mL of water and then 3 mL *n*-hexane, and finally eluted with 5 mL of dichloromethane. The elution was dried under N_2 gas at 40 °C, and the residue was redissolved with 1 mL of acetonitrile/water (10:90, v/v) and filtered with a 0.22 μm syringe filter into a UPLC−MS/MS autosampler vial for analysis.

UPLC−MS/MS Analysis. Chromatographic analysis was performed on an Acquity ultraperformance liquid chromatography system equipped with a degasser and an autosampler (Waters, Milford, MA). The MS/MS detection was performed using a Quattro LC triple-quadrupole mass spectrometer equipped with an electrospray ionization (ESI) source (Micromass, Manchester, U.K.). The separation was performed on a 50 mm × 2.1 mm i.d., 1.7 μm Acquity BEH RP18 column (Waters) using a gradient elution program consisting of mobile phase A (0.005 mmol/L ammonia) and mobile phase B (acetonitrile). The gradient elution program was as follows: 0 min, 100% A; 0−1 min, A linearly decreased to 90%; 1−6 min, A linearly decreased to 20%; 6−6.5 min, A increased to 100%. The column temperature was maintained at 30 °C, and the injection volume was 10 μL with a flow rate of 0.3 mL/min.

The UPLC system was connected to the mass spectrometer via an ESI interface. The analysis was performed in ESI positive mode with the capillary voltage set at 3.0 kV. The extractor and radio frequency (rf) lens voltages were at 3.0 and 0.5 V, respectively. The source temperature was held constant at 100 °C and the desolvation temperature at 350 °C. Nitrogen was used as the desolvation gas at a flow rate of 600 L/h, while the cone gas flow rate was 30 L/h. Collision-induced dissociation was performed using argon as the collision gas at a pressure of 2.5×10^{-3} mbar in the collision cell. The monitoring mode was set to multiple-reaction monitoring (MRM), with the detailed parameters for each analyte shown in Table S1.

Method Validation. To validate the method, spiked blank samples were used, in accordance with a validation protocol provided by the European Community and the FDA.[26] These validation experiments included linearity, accuracy, precision, LODs, and LOQs.

Because a matrix effect was observed on the ESI source, matrix-matched calibration curves were used for quantitation. Linearity was tested using matrix-matched calibration curves by spiking blank extracted animal tissues at seven concentration levels.

Recovery and intraday precision were studied with spiked samples at three concentration levels. The interday precision was obtained using three spiked levels of standards, and the recoveries were determined on three separate days. LODs and LOQs were determined on the basis of signal-to-noise ratios (S/N) of ≥3 and ≥10, respectively.

RESULTS AND DISCUSSION

Optimization of the UPLC Conditions. The choice of mobile phase is important for ionization efficiency and also for protection of the chromatography column and MS. To obtain a high response intensity, trace levels of ammonium acetate and/or acetic acid are usually added to the mobile phase.[10] According to our previous study, ammonia could improve the ionization of T-2 toxin and HT-2 toxin under ESI positive mode.[15] In the present study, different concentrations of ammonia (0.001, 0.003, 0.005, 0.010, and 0.020 mmol/L) were tested in mobile phase A (water). Satisfactory results were obtained for all analytes when 0.005 mmol/L ammonia was added to water. Therefore, water containing 0.005 mmol/L ammonia (mobile phase A) and acetonitrile (mobile phase B) were selected as the mobile phases. All analytes were eluted with high selectivity and good sensitivity in less than 6.5 min using the gradient elution program described above.

In general, type B trichothecenes are highly polar compounds. This is especially true for NIV, which is hardly retained by the column. However, type A compounds, such as T-2 toxin and HT-2 toxin, have relatively weak polarity. Therefore, a reversed-phase C_{18} (RP18) column may be the best choice considering the wide differences in polarity between the trichothecenes. The ACQUITY UPLC BEH C_{18} and ACQUITY UPLC BEH Shield RP18 chromatography columns were compared in this work. The RP18 column exhibited reasonable retention effects and separation efficiency for all analytes.

Optimization of the MS/MS Determination. Both positive and negative ion modes of the electrospray ion source were tested to evaluate the ionization of every analyte. Most of the compounds exhibited precursor ions and product ions with reasonably high signal intensities in ESI positive mode. For optimization of MS and MS/MS parameters, individual standard solutions at 100 μg/L prepared in acetonitrile/water (10:90, v/v) were injected at different values of the cone voltage (5−50 V) and collision energy (5−60 eV). According to European Union (EU) convention, at least two product ions should be selected for each analyte.[26] The most abundant product ion is used for quantitation, and another product ion is monitored for confirmation of the identity. The parameters of the optimized MRM transitions for all compounds are detailed in Table S1.

All type A trichothecenes tend to generate the precursor ions $[M + NH_4]^+$, $[M + Na]^+$, and $[M + K]^+$ in ESI positive mode. Although $[M + Na]^+$ adducts exhibited the highest intensities, this precursor ion was not suitable due to a lack of fragmentation in further MS/MS experiments. The addition of 0.005 mmol/L ammonia in mobile phase A suppressed the formation of $[M + Na]^+$, as reported by Sulyok et al.[19] Therefore, the ammonium $[M + NH_4]^+$ adducts were chosen as precursor ions for T-2 toxin, HT-2 toxin, NEO, and T-2-triol. Other studies have reported that type B trichothecenes give a higher response in ESI negative mode, and $[M - H]^-$ and $[M + CH_3COO]^-$ were selected as their precursor ions.[21,22,27] Under experimental conditions, the protonated molecules of $[M + H]^+$ were observed for all type B trichothecenes in ESI positive mode, giving higher signal intensities than the related $[M - H]^-$ species. In ESI positive mode, the mass value of DON at *m/z* 297 ($[M + H]^+$) showed an almost 7-fold intensity in comparison with that at *m/z* 295 ($[M - H]^-$), which was obtained in ESI negative mode. Therefore, $[M + H]^+$

DOI: 10.1021/acs.jafc.5b03281
J. Agric. Food Chem. 2015, 63, 8592−8600

ions were selected as the precursor ions for DON, NIV, 15-Ac-DON, 3-Ac-DON, and DOM due to their relatively higher responses.

The chemical structure of 3-Ac-DON is similar to that of 15-Ac-DON; the difference is the position of the acetyl group (Figure 1). Due to the similar polarities of these two mycotoxins, it is difficult to achieve chromatographic separation, as reported by Monbaliu et al.[28] However, the selective detection power of MS/MS can facilitate their identification. Although the protonated molecules of $[M + H]^+$ have the same m/z 339.3, separate identification can be achieved due to the difference in characteristic daughter ions in MRM mode, identified as m/z 339.5 > 137.2 and 339.5 > 321.1 and m/z 339.5 > 213.0 and 339.5 > 230.9 for 15-Ac-DON and 3-Ac-DON, respectively.

Sample Pretreatment Optimization: Selection of the Extraction Solvent. In the present study, a total of nine mycotoxins served as target analytes. It was difficult to recover all mycotoxins equally during sample preparation, because their chemical structures are diverse. Thus, a compromise method had to be made. Many extraction methods have been reported in previous works. Methanol/water (84:16, v/v), acetonitrile/water (84:16, v/v), and methanol/water/acetic acid (79:20:1, v/v/v) were frequently used to extract mycotoxins.[16,18,19] However, these methods were mainly used to extract multiple mycotoxins in cereals and derived products. For meat and liver samples, limited information was available. In comparison with cereal samples, the sample matrix of meat and liver is very complex, containing lipids, proteins, inorganic salts, etc.[25] To reduce matrix effects, choosing a suitable extraction solvent is of critical importance. Acetonitrile and acetonitrile/water/acetic acid (79:20:1, v/v/v) have been reported to give good results for extracting multiple mycotoxins from meat and fish samples.[25,27] However, in the present study, we found that when acetonitrile was used during the extraction process, the meat tissue precipitated to a "cake" consistency, which would lead to poorer recoveries of the analytes. To select a suitable extraction solvent, acetonitrile, ethyl acetate, and acetonitrile/ethyl acetate solutions of different ratios were successively tested. As a result, better recoveries were obtained for all analytes when acetonitrile/ethyl acetate (1:3, v/v) was employed as the extraction solvent.

Optimization of Cleanup. To minimize matrix interferences, a cleanup procedure after extraction is necessary. A Waters Oasis HLB cartridge, which is suitable for the extraction of both polar and nonpolar compounds, was investigated first. According to reports, HLB cartridges have been used for the successful analysis of T-2 toxin and DON in meat and fish samples.[25,27] However, our results indicate that it failed to retain the more polar compounds of DON and NIV when standard protocols were used. To get a high recovery of DON and NIV, a modified protocol was applied, wherein water/methanol (95:5, v/v) was replaced by pure water at the washing step. Due to a significant proportion of fatty matrix compounds present in animal tissues, an *n*-hexane defatting step was also added. In this way, polar compounds could be recovered and the fatty matrix compounds removed. To further reduce background noise and the matrix effect, several eluents were tested, such as methanol, ethyl acetate, and dichloromethane. As shown in Figure 2, a higher relative response intensity was found for all analytes when dichloromethane was the elution solvent. Additionally, higher recovery values ranging from

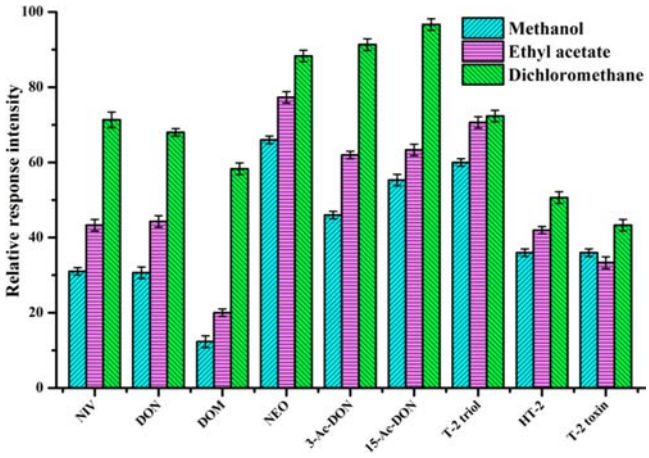

Figure 2. Effects of three eluents (methanol, ethyl acetate, and dichloromethane) on the response of analytes after cleanup using an Oasis HLB cartridge in pork.

74.1% to 96.9% were obtained for all analytes, as shown in Table 1.

Evaluation of Matrix Effects. Coelution of the matrix can affect the ionization efficiency of the analytes, leading to either suppression or artificial enhancement of the signal. The matrix effect is an important consideration since the ESI source can be easily influenced. Although the use of isotopic internal standards can overcome matrix effects, these compounds are usually expensive and suitable candidates cannot easily be obtained for all applications. Therefore, matrix-matched calibration curves are generally adopted. To evaluate the matrix effect, the slope of the matrix-matched calibration standards was compared to that of standard calibration in pure solvent. Referred to as the signal suppression/enhancement (SSE) value, this was calculated for each analyte. The results indicated that signal suppression can be observed for both strongly and weakly polar compounds, such as DON and T-2 toxin, no matter which matrix was chosen.

Method Validation. *Selectivity.* Twenty blank samples of chicken muscle, pork, chicken liver, and swine liver were analyzed to evaluate the selectivity of this method. The samples were prepared according to the developed method. Blank samples were spiked with standard solutions and analyzed; the resultant MRM chromatograms are depicted in Figure 3. As shown, there were no interferences in the analyte peaks, compared with the standards made in solvent, demonstrating the high selectivity of the method.

Linearity. Four matrix-matched calibration curves for all analytes were made at concentrations ranging from 3 to 1000 μg/kg to evaluate the linearity of the method. a linear relationship was observed with correlation coefficients (r) higher than 0.9900 for all analytes. These results are summarized in Table 1, demonstrating that this method could be used to monitor these analyte residues in animal tissues.

Accuracy and Precision. Accuracy and precision were evaluated by comparing the recoveries of each analyte at three spiked levels, with six replicates, on three separate days. The mean recoveries and coefficients of variation of target compounds are shown in Table 1. According to the criteria of SANCO Protocol No. 12495/2011, the acceptable recoveries for analytes should be in the range of 70−120%.[29] In the present study, all compounds were recovered satisfactorily, with

DOI: 10.1021/acs.jafc.5b03281
J. Agric. Food Chem. 2015, 63, 8592−8600

Table 1. Recoveries, Intra- and Interday Precision, Standard Curve, LOD, and LOQ for T-2 Toxin, DON, and NIV and Their Metabolites in Different Tissues

matrix	compd	added level (μg/kg)	mean recovery (%)	intraday RSD (%)	interday RSD (%)	linearity range (μg/kg)	LOD (μg/kg)	LOQ (μg/kg)
chicken muscle	NIV	50	87.1	3.6	7.8	15.0−1000.0	5.0	15.0
		200	84.2	5.7				
		1000	85.6	4.4				
	DON	20	85.6	4.6	4.8	6.0−750.0	2.0	6.0
		200	84.8	6.1				
		750	89.6	2.6				
	DOM	20	83.3	2.6	5.9	6.0−750.0	2.0	6.0
		200	90.2	5.9				
		750	88.0	5.0				
	NEO	10	89.4	3.8	5.3	3.0−500.0	1.0	3.0
		50	86.9	5.8				
		500	86.7	7.8				
	3-Ac-DON	20	83.9	5.5	6.4	6.0−750.0	2.0	6.0
		200	87.0	7.1				
		750	80.1	3.5				
	15-Ac-DON	50	82.2	5.8	5.6	15.0−1000.0	5.0	15.0
		200	85.6	5.8				
		1000	82.1	5.3				
	T-2-triol	50	84.1	5.2	5.5	15.0−1000.0	5.0	15.0
		200	87.1	5.1				
		1000	88.0	6.2				
	HT-2 toxin	20	80.8	5.1	7.5	6.0−750.0	2.0	6.0
		200	86.8	6.1				
		750	81.9	5.5				
	T-2 toxin	10	91.4	2.2	7.2	3.0−500.0	1.0	3.0
		50	80.4	4.1				
		500	84.7	3.6				
chicken liver	NIV	50	85.6	5.9	6.8	15.0−1000.0	5.0	15.0
		200	84.6	7.1				
		1000	80.8	8.4				
	DON	20	88.3	4.6	5.7	6.0−750.0	2.0	6.0
		200	89.4	5.9				
		750	92.2	3.5				
	DOM	20	89.5	4.6	5.1	6.0−750.0	2.0	6.0
		200	94.0	4.1				
		750	95.5	2.6				
	NEO	10	83.0	5.5	6.8	3.0−500.0	1.0	3.0
		50	90.0	3.6				
		500	85.8	6.8				
	3-Ac-DON	20	92.6	6.1	4.6	6.0−750.0	2.0	6.0
		200	93.4	4.1				
		750	92.2	1.7				
	15-Ac-DON	50	95.1	5.7	5.1	15.0−1000.0	5.0	15.0
		200	87.8	5.8				
		1000	96.4	7.8				
	T-2-triol	50	91.8	6.8	9.1	15.0−1000.0	5.0	15.0
		200	85.0	5.4				
		1000	95.2	2.0				
	HT-2 toxin	20	88.8	7.2	5.8	6.0−750.0	2.0	6.0
		200	84.9	6.4				
		750	92.4	4.2				
	T-2 toxin	10	87.6	1.4	5.6	3.0−500.0	1.0	3.0
		50	86.4	7.1				
		500	96.9	2.7				
pork	NIV	50	82.3	9.4	7.8	15.0−1000.0	5.0	15.0
		200	82.5	6.1				
		1000	83.4	5.8				
	DON	20	91.0	4.7	4.9	6.0−750.0	2.0	6.0
		200	83.3	3.4				

DOI: 10.1021/acs.jafc.5b03281
J. Agric. Food Chem. 2015, 63, 8592−8600

Table 1. continued

matrix	compd	added level (μg/kg)	mean recovery (%)	intraday RSD (%)	interday RSD (%)	linearity range (μg/kg)	LOD (μg/kg)	LOQ (μg/kg)
		750	93.4	4.6				
	DOM	20	84.3	3.9	4.3	6.0−750.0	2.0	6.0
		200	90.3	3.6				
		750	90.8	3.3				
	NEO	10	83.1	5.5	5.4	3.0−500.0	1.0	3.0
		50	83.1	5.3				
		500	90.2	5.6				
	3-Ac-DON	20	83.8	6.0	5.9	6.0−750.0	2.0	6.0
		200	88.5	4.1				
		750	79.2	8.8				
	15-Ac-DON	50	90.9	5.4	5.1	15.0−1000.0	5.0	15.0
		200	93.0	3.6				
		1000	96.6	6.0				
	T-2-triol	50	83.5	5.7	5.6	15.0−1000.0	5.0	15.0
		200	84.9	5.9				
		1000	83.0	5.3				
	HT-2 toxin	20	88.2	8.3	8.3	6.0−750.0	2.0	6.0
		200	88.1	8.6				
		750	90.7	4.9				
	T-2 toxin	10	86.7	4.8	6.3	3.0−500.0	1.0	3.0
		50	81.2	8.7				
		500	84.8	5.8				
swine liver	NIV	50	81.3	7.1	6.1	15.0−1000.0	5.0	15.0
		200	84.1	7.4				
		1000	84.4	4.5				
	DON	20	86.5	7.2	4.8	6.0−750.0	2.0	6.0
		200	91.0	4.3				
		750	91.1	3.8				
	DOM	20	88.2	5.4	5.0	6.0−750.0	2.0	6.0
		200	87.1	4.8				
		750	90.0	3.3				
	NEO	10	91.0	3.8	5.5	3.0−500.0	1.0	3.0
		50	86.8	5.4				
		500	86.3	7.3				
	3-Ac-DON	20	84.3	5.4	5.2	6.0−750.0	2.0	6.0
		200	83.6	5.7				
		750	81.8	9.8				
	15-Ac-DON	50	93.1	4.7	4.0	15.0−1000.0	5.0	15.0
		200	90.3	2.7				
		1000	87.2	6.8				
	T-2-triol	50	82.9	5.0	9.0	15.0−1000.0	5.0	15.0
		200	80.6	8.4				
		1000	85.6	4.8				
	HT-2 toxin	20	88.3	3.4	8.2	6.0−750.0	2.0	6.0
		200	89.3	5.0				
		750	88.8	4.2				
	T-2 toxin	10	84.1	8.3	6.2	3.0−500.0	1.0	3.0
		50	74.8	2.9				
		500	79.7	9.9				

mean values in the range of 80.1−91.4% for chicken muscle, 79.2−96.6% for pork, 80.8−96.9% for chicken liver, and 74.1−93.1% for swine liver. Additionally, the intraday and interday RSD values were in the range of 1.4−9.9% and 4.3−9.1%, respectively. These results indicate that the developed method is suitable for the detection of type A and B trichothecenes, and their main metabolites, in food animal tissues.

Limit of Detection and Limit of Quantitation. The LOD is defined as the lowest analyte concentration reliably detected in the samples, and the LOQ is defined as the lowest concentration that can be reliably measured. For each analyte in each investigated matrix, the LODs and LOQs were determined by diluting the stock standard solutions with the blank matrixes. According to the IUPAC (International Union of Pure and Applied Chemistry) settings, the S/N ratios of LODs and LOQs should be more than 3 and 10, respectively.[18,28] Table 1 outlines LOD and LOQ values for every analyte in each investigated matrix, which ranged from 3.0 to 15.0 μg/kg and from 10.0 to 50.0 μg/kg, respectively. The European Commission has set maximum levels for *Fusarium*

DOI: 10.1021/acs.jafc.5b03281
J. Agric. Food Chem. 2015, 63, 8592−8600

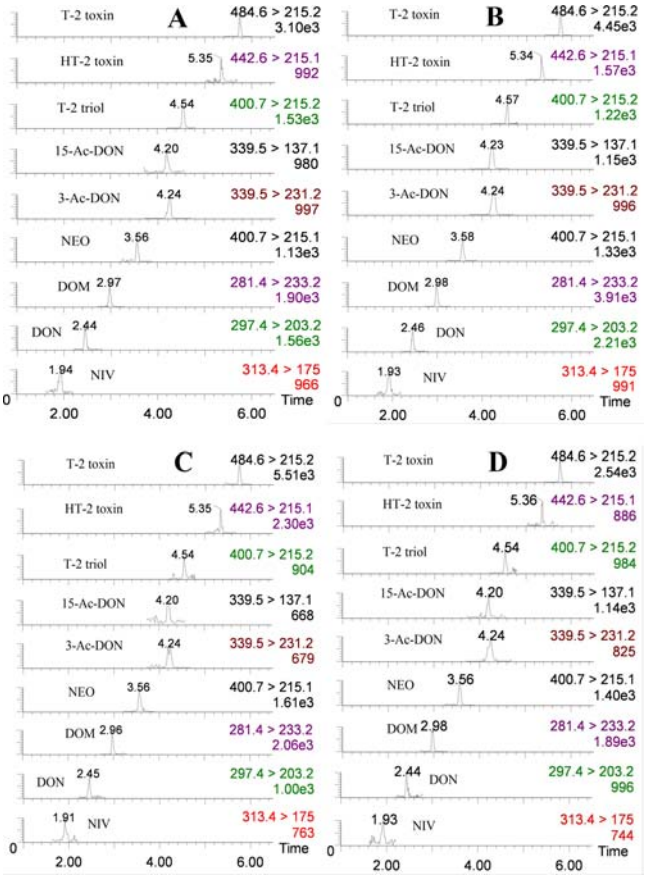

Figure 3. UPLC−MS/MS chromatograms of quantitative ions of (A) chicken muscle, (B) pork, (C) chicken liver, and (D) swine liver with concentrations of 15 μg/kg for NIV, 15-Ac-DON, and T-2-triol, 6 μg/kg for DON, DOM, 15-Ac-DON, and HT-2 toxin, and 3 μg/kg for NEO and T-2 toxin.

toxins in maize and maize products.[30] Regarding animal tissues for food, no regulatory limits have been set for these mycotoxins. According to the reports published by the European Food Safety Authority (EFSA), the tolerable daily intake (TDI) for DON together with its acetyl derivatives, 3-Ac-DON and 15-Ac-DON, was set at 1 μg/kg of bw per day.[31] For NIV, a TDI of 1.2 μg/kg of bw per day was established.[32] Considering that T-2 toxin is rapidly metabolized to a large number of products, HT-2 toxin being a major metabolite, a group TDI of 100 ng/kg of bw for the sum of T-2 and HT-2 toxins was recommended by EFSA.[33] In the present study, the UPLC−MS/MS method developed could detect all target analytes at parts per billion (μg/kg) levels, meaning it could effectively be applied to analyze mycotoxins in meat and liver samples. Only one publication reported the LOQs of T-2 toxin and DON in chicken meat and pork, 0.007 and 0.02 μg/kg, respectively.[25] In addition, another paper reported the LOQs of T-2 toxin, HT-2 toxin, and DON in fish samples, ranging from 0.5 to 3.0 μg/kg.[27]

Application of the Proposed Method to Real Samples.

Twelve chickens were given T-2 toxin at levels of 3 mg/kg of bw by oral administration. Muscle and liver tissues were collected 6, 12, 24, and 48 h after dose. The tissue samples were then analyzed using the methods developed here. The detailed results are shown in Table 2. Within 6 h after oral administration, only trace amounts of T-2 toxin could be detected, indicating that T-2 toxin was rapidly metabolized in the chicken. A large amount of HT-2 toxin was found in chicken muscle and liver. Even 48 h later, it was also detected in the liver, which suggested that HT-2 toxin was a main metabolite of T-2 toxin. In addition, the other two metabolites of T-2 toxin, NEO and T-2-triol, were also detected in both tissues at trace levels. These results suggest that, compared with T-2 toxin, it is more important to develop the method to detect its metabolites, especially HT-2 toxin.

In summary, a UPLC−MS/MS method for simultaneous analysis of DON, T-2 toxin, NIV, 3-Ac-DON, and 15-Ac-DON and their main metabolites DOM, HT-2 toxin, NEO, and T-2-triol, in chicken meat, pork, chicken liver, and swine liver was developed in the present work. The analytical method was developed and validated, and the resulting data demonstrated good accuracy and precision, indicating that this method was reliable, sensitive, and convenient. In addition, this method was successfully applied to the analysis of chicken muscle and liver taken from chickens that received an oral dose of T-2 toxin. The proposed analytical procedure can therefore be used for the determination of DON, T-2 toxin, NIV, 3-Ac-DON, and 15-Ac-DON and four of their major metabolites in animal tissues.

■ ASSOCIATED CONTENT

Supporting Information

The Supporting Information is available free of charge on the ACS Publications website at DOI: 10.1021/acs.jafc.5b03281.

Figures showing the full mass scan of DON in the negative and positive ion modes, the MS/MS spectra of 3-Ac-DON and 15-Ac-DON, the slope ratios between matrix-matched and solvent calibration of the target analytes in different animal tissues, and the UPLC−MS/MS chromatograms of quantitative ions in the blank samples of four different animal tissues and tables presenting the parameters of the MRM conditions for each analyte and the concentration points of the matrix-matched calibration curve for four matrixes (PDF)

Table 2. Determination of T-2 Toxin and Its Main Metabolites in Chicken Tissues

	chicken muscle				chicken liver			
compd	6 h	12 h	24 h	48 h	6 h	12 h	24 h	48 h
T-2 toxin	16.2	<LOQ[a]	<LOQ[a]	ND	20.4	<LOQ[a]	<LOQ[a]	ND
HT-2 toxin	96.0	76.6	28.7	<LOQ[a]	126.8	87.4	69.3	21.7
NEO	10.3	33.1	<LOQ[a]	ND	40.2	24.8	13.2	ND
T-2-triol	<LOQ[a]	<LOQ[a]	<LOQ[a]	ND	<LOQ[a]	19.1	<LOQ[a]	ND

[a] <LOQ refers to samples that were >LOD, but <LOQ.

DOI: 10.1021/acs.jafc.5b03281
J. Agric. Food Chem. 2015, 63, 8592−8600

AUTHOR INFORMATION

Corresponding Author

*Phone: +86-10-6273-4565. Fax: +86-10-6273-1032. E-mail: suxia@cau.edu.cn.

Funding

This work was supported by the National Natural Science Foundation of China (NSFC) (Grant U1301214), the International Science & Technology Cooperation Program of China (Grant 2012DFG31840), and the Special Fund for Agro-scientific Research in the Public Interest (Grant 201203040).

Notes

The authors declare no competing financial interest.

ACKNOWLEDGMENTS

We acknowledge Xiaoli Song, Chenglong Li, Haixia Wu, Kaili Liu, and Lu Zhang for their practical work.

ABBREVIATIONS USED

LC−MS/MS, liquid chromatography−tandem mass spectrometry; UPLC−MS/MS, ultraperformance liquid chromatography coupled with triple-quadruple mass spectrometry; NEO, neosolaniol; DON, deoxynivalenol; 3-Ac-DON, 3-acetyldeoxynivalenol; 15-Ac-DON, 15-acetyldeoxynivalenol; DOM, deepoxydeoxynivalenol; NIV, nivalenol; ESI, electrospray ionization; MRM, multiple-reaction monitoring; LOD, limit of detection; LOQ, limit of quantitation; ATA, alimentary toxic aleukia; TLC, thin-layer chromatography; ELISAs, enzyme-linked immunosorbent assays; GC−ECD, gas chromatography−electron capture detection; GC−MS, gas chromatography−mass spectrometry; HPLC−UV, liquid chromatography coupled with ultraviolet detection; S/N, signal-to-noise ratio; SSE, signal suppression/enhancement; EFSA, European Food Safety Authority

REFERENCES

(1) Li, Y.; Wang, Z.; Beier, R. C.; Shen, J.; De Smet, D.; De Saeger, S.; Zhang, S. T-2 toxin, a trichothecene mycotoxin: review of toxicity, metabolism, and analytical methods. *J. Agric. Food Chem.* **2011**, *59*, 3441−3453.

(2) Wu, Q.; Dohnal, V.; Huang, L.; Kuca, K.; Yuan, Z. Metabolic pathways of trichothecenes. *Drug Metab. Rev.* **2010**, *42*, 250−267.

(3) EFSA Panel on Contaminants in the Food Chain (CONTAM).. Scientific Opinion on risks for animal and public health related to the presence of nivalenol in food and feed. *EFSA J.* **2013**, *11*, 3262.

(4) Meneely, J. P.; Ricci, F.; van Egmond, H. P.; Elliott, C. T. Current methods of analysis for the determination of trichothecene mycotoxins in food. *TrAC, Trends Anal. Chem.* **2011**, *30*, 192−203.

(5) Wu, Q.; Dohnal, V.; Kuca, K.; Yuan, Z. Trichothecenes: structure-toxic activity relationships. *Curr. Drug Metab.* **2013**, *14*, 641−660.

(6) McCormick, S. P.; Stanley, A. M.; Stover, N. A.; Alexander, N. J. Trichothecenes: from simple to complex mycotoxins. *Toxins* **2011**, *3*, 802−814.

(7) Wu, Q. H.; Wang, X.; Yang, W.; Nussler, A. K.; Xiong, L. Y.; Kuca, K.; Dohnal, V.; Zhang, X. J.; Yuan, Z. H. Oxidative stress-mediated cytotoxicity and metabolism of T-2 toxin and deoxynivalenol in animals and humans: an update. *Arch. Toxicol.* **2014**, *88*, 1309−1326.

(8) Marin, S.; Ramos, A. J.; Cano-Sancho, G.; Sanchis, V. Mycotoxins: occurrence, toxicology, and exposure assessment. *Food Chem. Toxicol.* **2013**, *60*, 218−237.

(9) Yang, S.; Li, Y.; Cao, X.; Hu, D.; Wang, Z.; Wang, Y.; Shen, J.; Zhang, S. Metabolic pathways of T-2 toxin in in vivo and in vitro systems of Wistar rats. *J. Agric. Food Chem.* **2013**, *61*, 9734−9743.

(10) Sokolović, M.; Šimpraga, B. Survey of trichothecene mycotoxins in grains and animal feed in Croatia by thin layer chromatography. *Food Control* **2006**, *17*, 733−740.

(11) Li, Y.; Luo, X.; Yang, S.; Cao, X.; Wang, Z.; Shi, W.; Zhang, S. High specific monoclonal antibody production and development of an ELISA method for monitoring T-2 toxin in rice. *J. Agric. Food Chem.* **2014**, *62*, 1492−1497.

(12) Valle-Algarra, F. M.; Medina, A.; Gimeno-Adelantado, J. V.; Llorens, A.; Jimenez, M.; Mateo, R. Comparative assessment of solid-phase extraction clean-up procedures, GC columns and perfluoroacylation reagents for determination of type B trichothecenes in wheat by GC-ECD. *Talanta* **2005**, *66*, 194−201.

(13) Rodriguez-Carrasco, Y.; Molto, J. C.; Manes, J.; Berrada, H. Development of a GC-MS/MS strategy to determine 15 mycotoxins and metabolites in human urine. *Talanta* **2014**, *128*, 125−131.

(14) Pascale, M.; Panzarini, G.; Visconti, A. Determination of HT-2 and T-2 toxins in oats and wheat by ultra-performance liquid chromatography with photodiode array detection. *Talanta* **2012**, *89*, 231−236.

(15) Wang, Y.; Cao, X. Y.; Li, Y. S.; Yang, S. P.; Shen, J. Z.; Zhang, S. X. Simultaneous determination of type-A and type-B trichothecenes in rice by UPLC-MS/MS. *Anal. Methods* **2012**, *4*, 4077−4082.

(16) De Boevre, M.; Di Mavungu, J. D.; Maene, P.; Audenaert, K.; Deforce, D.; Haesaert, G.; Eeckhout, M.; Callebaut, A.; Berthiller, F.; Van Peteghem, C.; De Saeger, S. Development and validation of an LC-MS/MS method for the simultaneous determination of deoxynivalenol, zearalenone, T-2-toxin and some masked metabolites in different cereals and cereal-derived food. *Food Addit. Contam., Part A* **2012**, *29*, 819−835.

(17) Frenich, A. G.; Romero-Gonzalez, R.; Gomez-Perez, M. L.; Vidal, J. L. Multi-mycotoxin analysis in eggs using a QuEChERS-based extraction procedure and ultra-high-pressure liquid chromatography coupled to triple quadrupole mass spectrometry. *J. Chromatogr. A* **2011**, *1218*, 4349−4356.

(18) Diana Di Mavungu, J.; Monbaliu, S.; Scippo, M. L.; Maghuin-Rogister, G.; Schneider, Y. J.; Larondelle, Y.; Callebaut, A.; Robbens, J.; Van Peteghem, C.; De Saeger, S. LC-MS/MS multi-analyte method for mycotoxin determination in food supplements. *Food Addit. Contam., Part A* **2009**, *26*, 885−895.

(19) Sulyok, M.; Berthiller, F.; Krska, R.; Schuhmacher, R. Development and validation of a liquid chromatography/tandem mass spectrometric method for the determination of 39 mycotoxins in wheat and maize. *Rapid Commun. Mass Spectrom.* **2006**, *20*, 2649−2659.

(20) Tsiplakou, E.; Anagnostopoulos, C.; Liapis, K.; Haroutounian, S. A.; Zervas, G. Determination of mycotoxins in feedstuffs and ruminant's milk using an easy and simple LC-MS/MS multiresidue method. *Talanta* **2014**, *130*, 8−19.

(21) Huybrechts, B.; Martins, J. C.; Debongnie, P.; Uhlig, S.; Callebaut, A. Fast and sensitive LC-MS/MS method measuring human mycotoxin exposure using biomarkers in urine. *Arch. Toxicol.* **2014**, DOI: 10.1007/s00204-014-1358-8.

(22) Broekaert, N.; Devreese, M.; De Mil, T.; Fraeyman, S.; De Baere, S.; De Saeger, S.; De Backer, P.; Croubels, S. Development and validation of an LC-MS/MS method for the toxicokinetic study of deoxynivalenol and its acetylated derivatives in chicken and pig plasma. *J. Chromatogr. B: Anal. Technol. Biomed. Life Sci.* **2014**, *971*, 43−51.

(23) Warth, B.; Sulyok, M.; Krska, R. LC-MS/MS-based multi-biomarker approaches for the assessment of human exposure to mycotoxins. *Anal. Bioanal. Chem.* **2013**, *405*, 5687−5695.

(24) Song, S.; Ediage, E. N.; Wu, A.; De Saeger, S. Development and application of salting-out assisted liquid/liquid extraction for multi-mycotoxin biomarkers analysis in pig urine with high performance liquid chromatography/tandem mass spectrometry. *J. Chromatogr. A* **2013**, *1292*, 111−120.

(25) Zou, Z.; He, Z.; Li, H.; Han, P.; Tang, J.; Xi, C.; Li, Y.; Zhang, L.; Li, X. Development and application of a method for the analysis of two trichothecenes: deoxynivalenol and T-2 toxin in meat in China by HPLC-MS/MS. *Meat Sci.* **2012**, *90*, 613−617.

DOI: 10.1021/acs.jafc.5b03281
J. Agric. Food Chem. 2015, 63, 8592−8600

(26) Commission Decision 2002/657/EC of 12 August 2002 implementing Council Directive 96/23/EC, concerning the performances of analytical methods and the interpretation of results. *Off. J. Eur. Commun.* **2002**, *L221*, 8−36.
(27) Sun, W.; Han, Z.; Aerts, J.; Nie, D.; Jin, M.; Shi, W.; Zhao, Z.; De Saeger, S.; Zhao, Y.; Wu, A. A reliable liquid chromatography-tandem mass spectrometry method for simultaneous determination of multiple mycotoxins in fresh fish and dried seafoods. *J. Chromatogr. A* **2015**, *1387*, 42−48.
(28) Monbaliu, S.; Van Poucke, K.; Heungens, K.; Van Peteghem, C.; De Saeger, S. Production and migration of mycotoxins in sweet pepper analyzed by multimycotoxin LC-MS/MS. *J. Agric. Food Chem.* **2010**, *58*, 10475−10479.
(29) The Directorate General for Health and Consumer Affairs. Document No. SANCO/12495/2011, 2011. http://ec.europa.eu/food/plant/protection/pesticides/docs/qualcontrol-en.pdf (accessed Jan 1, 2011).
(30) Commission Regulation (EC). No. 1126/2007 of 28 September 2007 amending Regulation (EC) No. 1881/2006 setting maximum levels for certain contaminants in foodstuffs as regards Fusarium toxins in maize and maize products. *Off. J. Eur. Commun.* **2007**, *L255*, 14−17.
(31) European Food Safety Authority (EFSA).. Evaluation of the increase of risk for public health related to a possible temporary derogation from the maximum level of deoxynivalenol, zearalenone and fumonisins for maize and maize products. *EFSA J.* **2014**, *12*, 3699.
(32) EFSA Panel on Contaminants in the Food Chain (CONTAM).. Scientific Opinion on risks for animal and public health related to the presence of nivalenol in food and feed. *EFSA J.* **2013**, *11*, 3262.
(33) EFSA Panel on Contaminants in the Food Chain (CONTAM).. Scientific Opinion on the risks for animal and public health related to the presence of T-2 and HT-2 toxin in food and feed. *EFSA J.* **2011**, *9*, 2481.

DOI: 10.1021/acs.jafc.5b03281
J. Agric. Food Chem. 2015, 63, 8592−8600

For example, Pinalate, a yellowish mutant of Navelate orange (*Citrus sinensis* L. Osbeck), accumulates linear carotenes;[31] and both Hong Anliu, a red-flesh mutant of sweet orange (*C. sinensis* L. Osbeck),[30] and Cara Cara, a red-flesh mutant of Navel orange (*C. sinensis* L. Osbeck),[32] accumulate lycopene. However, very few studies have been focused on other biological processes that may be affected by the altered carotenoid profile in these mutants.

Similar to other perishable agricultural products, citrus fruits are susceptible to the damage caused by physical disorder and pathogenic diseases during shipping, storing, and marketing.[33] Citrus green mold rot, which is caused by *Penicillium digitatum*, leads to huge postharvest losses in the citrus industry.[34] Although the application of artificial fungicide proved inexpensive and effective to control this disease, it is greatly limited by the emergence of new resistant fungal strains as well as by its low potency, poisonousness, poor solubility, and nonbiodegradability.[34,35] Enhancing the natural defense of the fruit by reprogramming its physiological status would be a promising alternative strategy in the prevention of this pathogen.[33−35] Flavonoids are a group of polyphenolic compounds that include flavanone, flavanone- and flavone-*O*-glycosides, flavone-*C*-glycosides, flavone, and polymethoxyflavone aglycones.[35] The PMFs in citrus are a class of flavones found in glycosylated and aglycone states, showing a great variety of compounds with their structure frequently multisubstituted by hydroxyl and/or methoxyl groups.[36] Flavonoids, especially polymethoxylated flavones (PMFs) which are rich in citrus peel, have proved essential barriers against pathogen attack and can be induced to accumulate in citrus fruits.[34,36−38]

A nontargeted metabolomic analysis revealed significantly different primary and secondary metabolites in fruits between the bud mutant Hong Anliu and its parent.[39] Enhanced carotenoid accumulation in citrus calli by overexpressing *CrtB* affected redox status and starch metabolism and was linked with flavonoid/anthocyanin accumulation.[2] These results indicate that the altered carotenoid accumulation might affect other metabolisms potentially associated with carotenoids. However, no studies have tested the influences of the carotenoid-associated changes of metabolism on the abiotic and biotic stress resistance in fruits of these citrus mutants. A yellowish bud mutant has been identified from Ponkan (*C. reticulata* Blanco), which has reduced xanthophyll accumulation in fruits. Here, we used this bud mutant to explore the possible alterations in primary and secondary metabolisms, especially flavonoid accumulation, which is strongly related to the resistance against abiotic and biotic stresses. The feasibility of applying this bud mutant to improve postharvest performance of fruits was further tested by storage experiment and inoculation with *P. digitatum*.

MATERIALS AND METHODS

Plant Materials. The yellowish bud mutant of Ponkan (*C. reticulata* Blanco) (PK) was found in year 2008 by Quzhou Bureau of Agriculture Economic Specialty Station from the grafted seedlings of PK in orchard. The yellowish coloring in fruits of YP was confirmed to be stable by an investigation of six years. The materials of YP and PK used for the present study were grown following commercial cultivation practices in the same orchard in Quzhou, Zhejiang Province, China. Ripening fruits were harvested on November 10 (coloring stage 1, CS1), November 20 (coloring stage 2, CS2), and November 30 (coloring stage 3, CS3) in 2013 and 2014.

Thirty fruits grouped as one sample were peeled and immediately frozen in liquid nitrogen. One half of the pulp was immediately frozen in liquid nitrogen, whereas the other half was used for quality analysis. All samplings were performed in three biological repeats. Frozen samples were kept at −80 °C until use. The transverse and longitudinal diameters of leaves were determined by a vernier caliper.

Chemicals. Acetonitrile, methanol, formic acid, and authentic standards of flavonoids were of HPLC grade and were provided as follows: acetonitrile and methanol by Fisher (Fisher Scientific, USA), formic acid by Guangfu (Tianjin Guangfu Fine Chemical Research Institute, China), eriocitrin (ERI), narirutin (NART), hesperidin (HES), didymin (DID), nobiletin (NOB), and tangeretin (TAN) (purity ≥98%) by YiFang S&T (Tianjin, China), sinensetin (SIN) from Chromadex (Santa Ana, CA, USA), and 5-demethyl-nobiletin (DEM) from MeiLian (Shanghai, China). Deionized water was prepared by distilled water through a Milli-Q A10 system (Millipore, Milford, MA, USA).

Color Measurement. Fruit color was measured by a color analyzer (KONICA MINOLTA CR-400, Japan). The red to green was expressed as $+a$ to $-a$, yellow to blue was expressed as $+b$ to $-b$, and brightness was expressed as L. The color index (CI) was calculated by the eq 1:

$$\mathrm{CI} = \frac{1000a}{Lb} \tag{1}$$

Analysis of Titratable Acid and Total Soluble Solids. Hand-squeezed juice from sliced pulp was filtered and subjected to titratable acid (TA) and total soluble solids (TSS) analysis. TA was determined by a Fruit Acidity Meter (GMK-835F, G-WON HITECH CO.,LTD, Korea), and TSS was determined by a Brix Refractometer (Pocket PAL-1, ATAGO, Japan).

Carotenoid Extraction and HPLC Analysis. Carotenoid extraction and analysis by reverse-phase high-performance liquid chromatography (RP-HPLC) were performed according to a previous work.[31] Retention time and UV spectrum of isolated carotenoids are listed in Table 1 of the Supporting Information.

Analysis of Abscisic Acid. Abscisic acid (ABA) was extracted from 1.0 g of fresh sample with 4 mL of extraction solution (MeOH/water = 4:1, 1 mM BHT, 2, 6-di*tert*-butyl-4-methyl-phenol) at 4 °C as previously described.[40] Samples and standard solutions were analyzed by the indirect enzyme-linked immunosorbent assay (ELISA). The ELISA kit was kindly supplied by Professor Baomin Wang (China Agricultural University).

Analysis of Primary Metabolites by GC-MS. Primary metabolites were extracted and analyzed by GC-MS as previously described.[33]

Flavonoid Analysis by UPLC. A 1.0 g aliquot of flavedo or 4.0 g of pulp was ground by liquid nitrogen and extracted using 80% MeOH more than three times. After centrifugation, the supernatants were collected and metered to volume (25 mL for flavedo and 10 mL for pulp). After the filtering through a 0.22 um filtration membrane (Millipore, USA), a 2 uL sample was injected and analyzed in a Waters H-Class UPLC system (eλ PDA detector, HSS T3 column: 150 mm × 3.0 mm i.d., 1.8 um particle, Waters, USA). Optimum mobile phase was composed of phase A (water/acetonitrile/formic acid = 100:2:0.1) and phase B (acetonitrile containing 0.1% formic acid). The elution program was performed as follows (min, % A): (0, 100), (2, 95), (8, 75), (12, 55), (20, 25), and (23, 0). The equilibration time after gradient analysis was 5 min. The flow rate was 0.5 mL/min, and the column temperature was kept at 35 °C. Detection was at 283 nm for flavanones and at 330 nm for PMFs. The concentration range, LOD, LOQ, and linearity of standards were listed in Table 2 of the Supporting Information. The structure and UV spectrum of the identified flavonoids were listed in Table 3 of the Supporting Information.

Fruit Storage and Sampling. The fruits from CS3 were stored at 16−20 °C with relative humidity (RH) at 80−90%. The flavedo of fruits from 0, 15, 25, 35, and 45 days after storage (DAS) was sampled, immediately frozen in liquid nitrogen, and kept at −80 °C until analysis.

***P. digitatum* Inoculation and Sampling.** Fruits from 35 DAS were used for *P. digitatum* inoculation according to the previous work.[33] Each group of nine fruits was incubated in a storage chamber

DOI: 10.1021/acs.jafc.5b02807
J. Agric. Food Chem. 2015, 63, 8601−8614

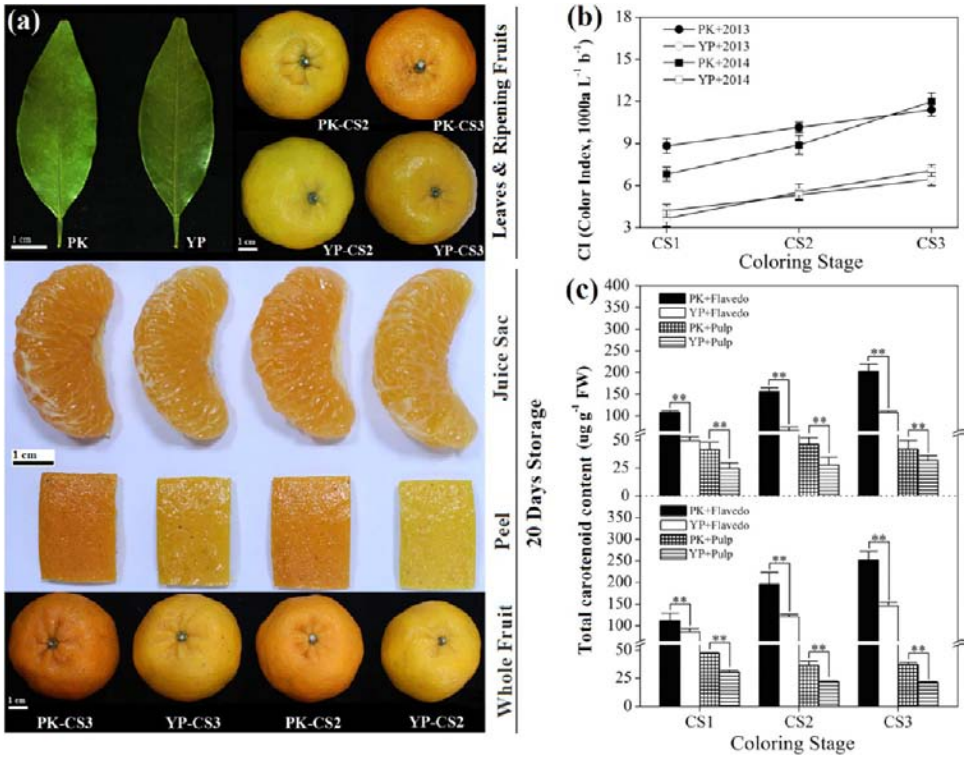

Figure 1. Phenotype of Ponkan and its mutant. (a) Coloring and shape of leaves and fruits. Top: leaves and fruits were harvested on tree; bottom: pulp (juice sac), flavedo, and whole fruits from 20 days after storage. (b) CI of PK and YP at three coloring stages for two consecutive years. (c) Total content of carotenoids and xanthophylls in flavedo and pulp at three coloring stages. Top, year 2013, and bottom, year 2014. Error bars represent SDs of the means ($n \geq 3$, biological triplicates). Results were averaged values plus SDs of the means and statistically analyzed using a paired-samples *t*-test. *, $p < 0.05$, and **, $p < 0.01$; CS1/2/3: coloring stage 1/2/3.

(25 °C, 95% RH). Disease incidence rate and lesion diameter were calculated on the basis of the following equations (eq 2−4):

$$\text{Infection rate of inoculated fruits (IRIF, \%)} = \frac{\sum \text{number of infected fruits}}{9 \times 100} \quad (2)$$

$$\text{Infection rate of inoculated fruits (IRIF, \%)} = \frac{\sum \text{number of infected spots}}{18 \times 100} \quad (3)$$

$$\text{Lesion diameter (LD, cm)} = \frac{\sum \text{lesion diameter of decaying spots}}{\text{total number of decaying spots}} \quad (4)$$

Two groups were sampled each time at 0, 2, 6, 12, 24, 48, and 72 hours after inoculation (HAI). Samples with a radius of 1.5 cm were cut off from the inoculated YP flavedo (IYPF) and inoculated PK flavedo (IPKF) spots, respectively. Samples peeled from the uninoculated YP flavedo (UYPF) and uninoculated PK flavedo (UPKF) spots at 6, 12, 24, 48, and 72 HAI were used as the control of IYPF and IPKF, respectively. The inoculated and the uninoculated flavedo were cut off from the same fruit. Groups for investigation of pathogenesis process were kept until 240 HAI and also sampled finally. All the samples were immediately frozen in liquid nitrogen and kept at −80 °C until flavonoid analysis.

Transmission Electron Microscopy. Fruits from CS3 without damage were used for transmission electron microscope (TEM) analysis according to a previous method.[41] More than one hundred individual cells from 30 fields of vision were used to obtain statistics of plastids by ImageJ.

RNA Isolation and Quantitative Real Time PCR Analysis. Total RNA was extracted according to the method of a previous work.[31] Integrity of RNA was electrophoretically verified; then, its concentration as well as A_{260}/A_{280}, and A_{230}/A_{260} absorption ratios were detected by Nanodrop (Agilent 2100, USA). Potential contamination with DNA was eliminated by treatment with DNase I (RNase-free, Fermentas MBI). A 1 μg aliquot of total RNA from each sample was used to synthesize the first-strand cDNA using the RevertAid First Strand cDNA Synthesis Kit (Fermentas, Thermo Fisher Scientific, Waltham, MA), following the manufacturer's recommendations. Quantitative reverse transcription PCR (qRT-PCR) was carried out in an ABI PRISM 9600 Sequence Detection System (Applied Biosystems) using SYBR Green Supermix according to the manufacturer's instructions, under the thermal cycle conditions of an initial denaturation step (94 °C for 10 min), followed by 40 cycles of 94 °C for 15 s and 60 °C for 31 s for annealing, and a final step of extension at 72 °C for 7 min. The expression levels of the selected genes were calculated by the $\delta-\delta$-Ct method.[42] The expression level of β-actin is more stable than that of GPADH; thus, the β-actin gene was used as reference gene for data normalizations. Each biological sample was examined in duplicate with three technical replicates. Genes and primers for qRT-PCR analysis are listed in Table 4 of the Supporting Information.

Western Blot Analysis. Total proteins were extracted as described previously[43] and quantified using a RC DC protein assay kit (Bio-Rad, Hercules, CA, USA). Then, 30 ug of total flavedo protein or 50 ug of total pulp protein was separated by SDS-PAGE (12.5%) and blotted onto PVDF membranes (Millipore, USA). The subsequent Western blot analyses were conducted as previously described.[41] The primary antibodies (1:3000, v/v) were rabbit anti-plastoglobulin 35 (PGL35) antibody (Agrisera, Sweden) and mouse anti-plant actin (as an internal reference, Abbkine, USA); the secondary antibodies (1:15 000, v/v) were peroxidase-conjugated immunopure goat anti-rabbit or goat anti-mouse IgG [H+L] (Pierce, USA). The signal was detected using a Clarity Western ECL Substrate (Bio-Rad, Hercules, CA, USA) according to the manufacturer's instructions. The chemiluminescence signal was imaged using a ChemiDoc XRS (Bio-Rad) and quantified using Quantity One software (Bio-Rad, USA). The calculated intensity volumes were fitted with a variable-slope dose−response relationship using ImageJ.

DOI: 10.1021/acs.jafc.5b02807
J. Agric. Food Chem. 2015, 63, 8601−8614

Table 1. Internal Quality of PK and YP Fruits at Three Coloring Stages[a]

	year 2013			year 2014		
material	TSS	TA	TSS/TA	TSS	TA	TSS/TA
PK+CS1	13.70 ± 0.38 abc	2.12 ± 0.05 d	6.47 ± 0.25 a	11.12 ± 0.49 a	1.37 ± 0.07 c	8.14 ± 0.15 a
YP+CS1	13.25 ± 0.28 a	2.04 ± 0.10 d	6.49 ± 0.19 a	11.53 ± 0.30 a	1.35 ± 0.03 c	8.55 ± 0.06 a
PK+CS2	13.42 ± 0.15 ab	1.71 ± 0.08 ab	7.84 ± 0.29 c	11.57 ± 0.16 a	1.18 ± 0.07 b	9.83 ± 0.50 b
YP+CS2	13.80 ± 0.10 c	2.03 ± 0.23 d	6.87 ± 0.78 ab	12.50 ± 0.09 b	1.30 ± 0.07 c	9.66 ± 0.45 b
PK+CS3	13.97 ± 0.44 cd	1.56 ± 0.13 a	8.98 ± 0.46 d	12.41 ± 0.16 b	1.00 ± 0.08 a	12.47 ± 0.88 d
YP+CS3	14.30 ± 0.00 d	1.89 ± 0.03 bc	7.57 ± 0.12 bc	12.74 ± 0.17 c	1.17 ± 0.02 b	10.92 ± 0.07 c

[a]TSS: total soluble solids; TA: titratable acid; and CS1/2/3: coloring stage 1/2/3. Results were averaged values plus SDs of the means ($n \geq 3$, biological triplicates). Different letters at each parameter indicate significant differences according to Duncan's multiple tests ($p < 0.05$).

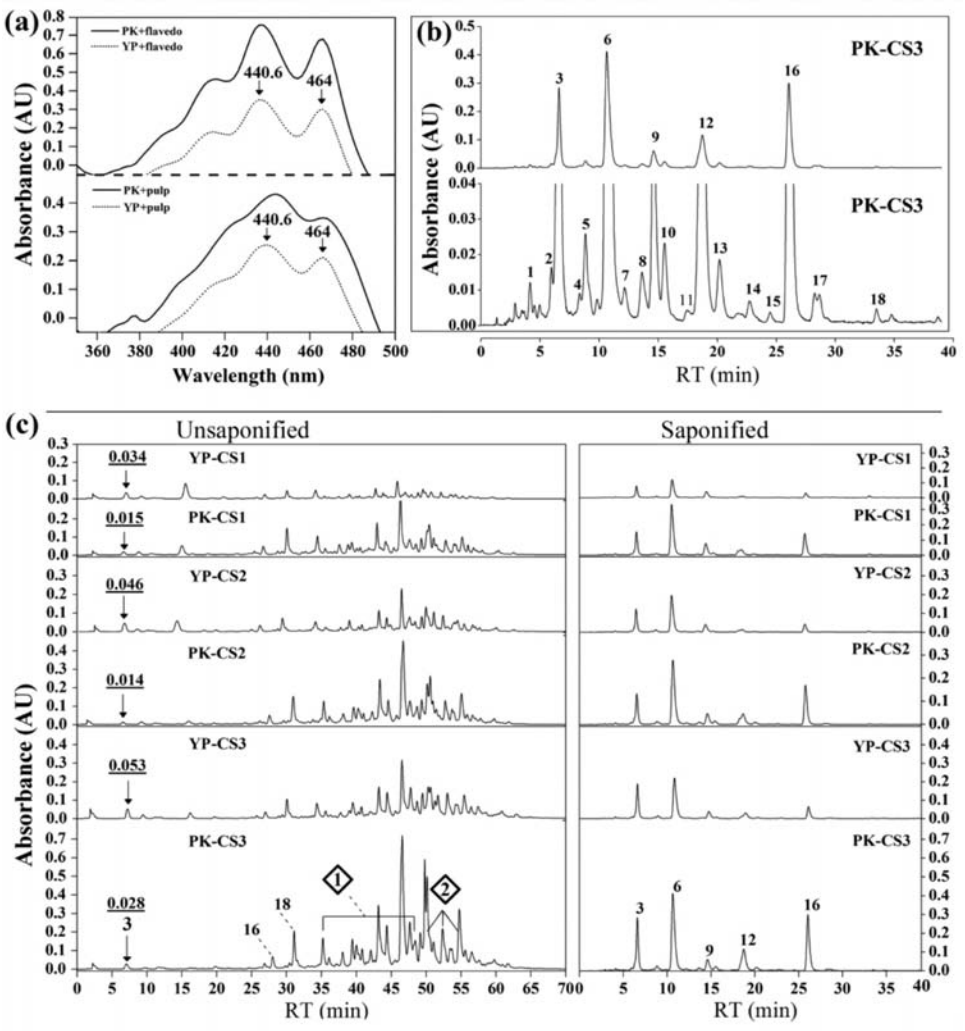

Figure 2. Carotenoid profile analysis. (a) Representative absorbance spectra of *n*-hexane solutions of unsaponified carotenoid extracts from fruits of CS3. Black line: PK; dotted line: YP. Numbers above the arrows represent the maximum wavelengths of absorbance. (b) Representative HPLC chromatogram of saponified carotenoid extract in PK flavedo of CS3. The bottom half is a magnified image of the top part. Peaks were extracted at 450 nm and labeled as 1, violaxanthin; 2, unknown; 3, 9-*cis*-violaxanthin 1; 4, unknown; 5, luteoxanthin; 6, 9-*cis*-violaxanthin 2; 7, neoxanthin 1; 8, neoxanthin 2; 9, lutein; 10, zeaxanthin; 11, lutein isomer 1; 12, lutein isomer; 13, lutein isomer 2; 14, α-cryptoxanthin; 15, all-trans-phytoene; 16, β-cryptoxanthin; 17, α-carotene; and 18, β-carotene. (c) Representative HPLC chromatogram of unsaponified (left) and saponified (right) carotenoid extracts in flavedo from both genotypes. Left: Peak 3 violaxanthin (free type) was marked by arrows, and their absorbances were shown by underlining. 16, β-cryptoxanthin (free type), and 18, β-carotene (free type). Arabic numerals in Rhombic blocks: 1, violaxanthin esters; 2, β-cryptoxanthin esters. Right: The main peaks were shown and labeled according to b. All the samples used above were from year 2013. CS1/2/3: coloring stage 1/2/3.

The relative value of plastoglobulin 35 was calculated by normalization using actin value.

Measurement of H_2O_2. A 0.5 g aliquot of flavedo powder was homogenized by liquid nitrogen and extracted in 5 mL of physiological saline. Measurement of H_2O_2 was conducted as previously described.[33]

Statistical Analysis. The variance of data was analyzed using SPSS software package release 16.0 (SPSS Inc. Chicago, IL). Multiple comparisons were performed by one-way ANOVA based on Duncan's multiple range tests, whereas paired-samples *t* tests were performed to test the statistical significance between two genotypes.

DOI: 10.1021/acs.jafc.5b02807
J. Agric. Food Chem. 2015, 63, 8601−8614

RESULTS AND DISCUSSION

YP Is Characterized by Yellowish Coloring with Reduced Carotenoid and Xanthophyll Accumulation and Better Postharvest Performance. Yellowish coloring in both the flavedo and pulp was observed in YP at not only ripening stage but also the postharvest stage. No difference in leaf morphology was found between YP and PK (Figure 1a). The lower CI in YP indicates a slower coloring (Figure 1b). Compared with that of PK, the total content of carotenoids and xanthophylls in YP was decreased by half in flavedo and by one-quarter in pulp (Figure 1c, top: year 2013, bottom: year 2014). Along with the ripening, TSS showed an increased accumulation, whereas TA showed an obvious decrease in both YP and PK. However, the slower decrease of TA in YP resulted in a less remarkable increase of TSS/TA in YP (Table 1). These results indicate a slight difference of internal quality between YP and PK. We also observed a better postharvest performance of YP, as indicated by a lower decay rate (Figure S2a) and better quality in YP during storage (Figure S2b,c). These phenotypes were confirmed to be stable by consecutive investigations for several years.

Xanthophyll Esters Are Reduced in YP. Information concerning the natural binding form of carotenoids is usually lost because of the saponification procedure, a commonly used step in carotenoid analysis.[20] To obtain a comprehensive understanding of the carotenoid and xanthophyll accumulation process, flavedo samples with and without alkaline saponification were analyzed (Figure 2). In unsaponified samples, YP shared the maximum wavelengths (440.6 and 464 nm) of absorbance with PK (Figure 2a). In detail, in YP samples, violaxanthin esters and cryptoxanthin esters showed a significantly lower absorbance, but unesterificated carotenoids showed a higher absorbance at each coloring stage (Figure 2c, left).

In the flavedo, the contents of α-carotene, β-carotene, zeaxanthin, and lutein isomers were onefold or more lower in YP than in PK, whereas the content of lutein was onefold lower in the year 2013 but showed no decrease in the year 2014 in YP (Figures 2c, right, and 3a, respectively). Violaxanthin and 9-*cis*-violaxanthins in YP showed about onefold decrease in the year 2013 but only a slight decrease in the year 2014 (Figure S3a). This inconsistency was speculated to be caused by the varying coloring behaviors in different years (Figure 1b). It is noteworthy that YP flavedo showed a fivefold lower accumulation of β-cryptoxanthin in both years. Compared with contents in the pulp of PK, in the pulp of YP, a consistent onefold decrease in the contents of β-cryptoxanthin, lutein, and lutein isomers was observed in both years, whereas the contents of violaxanthin, neoxanthin, and zeaxanthin showed no consistent decrease. In addition, it was noted that the content of β-carotene was stably decreased by fourfold or more (Figures 3b and S3b).

As compared with violaxanthin-abundant citrus, the main contributor to the orange-reddish appearance in Ponkan pulp is β-cryptoxanthin (violaxanthins and β-cryptoxanthin in flavedo).[29] However, unlike the fruits of both violaxanthin-abundant type and β-cryptoxanthin-abundant type, YP showed steadily reduced contents of total carotenoids and xanthophylls (mainly β-cryptoxanthin) in both the pulp and flavedo. These results indicate different behaviors of carotenoid accumulation and esterification between YP and PK. It is noteworthy that the carotenoid profile of YP was also different from that of Pinalate, a yellowish mutant of Navelate orange (*C. sinensis* L. Osbeck) which accumulates linear carotenes.[31]

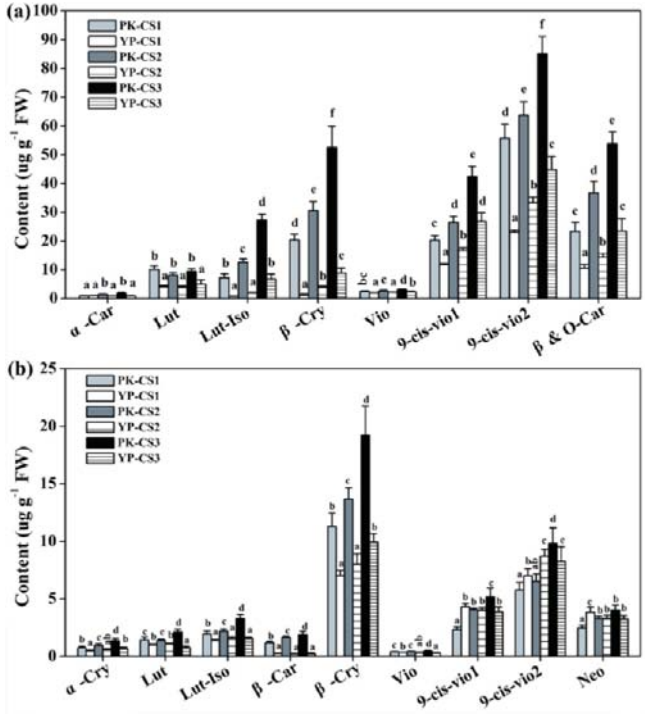

Figure 3. Changes in contents of carotenoids and xanthophylls in fruits of three coloring stages: (a) flavedo and (b) pulp. All the samples used were from year 2013. Abbreviations: α-Car: α-carotene; α-Cry: α-cryptoxanthin; Lut: lutein; Lut-Iso: lutein isomer; β-Car: β-carotene; β- and O-Car: β-carotene and other carotenoids; β-Cry: β-cryptoxanthin; Vio: violaxanthin; 9-*cis*-vio1: 9-*cis*-violaxanthin1; 9-*cis*-vio2: 9-*cis*-violaxanthin 2; Neo: neoxanthin. Error bars represent SDs of the means ($n \geq 3$, biological triplicates). Columns with different letters at each sample indicate significant differences according to Duncan's multiple tests ($p < 0.05$). CS1/2/3: coloring stage 1/2/3.

Abscisic Acid Accumulation Is Higher in YP at Earlier Coloring Stages. To investigate whether ABA accumulation is influenced by altered carotenoid composition in YP, quantification of ABA was performed in flavedo and pulp (Table 2). In the flavedo, ABA content started to decrease at CS2 in PK but was maintained at higher levels at CS1 and CS2 in YP. In the pulp of both genotypes, ABA content increased from CS1 to CS3. However, YP pulp showed a higher accumulation of ABA at CS1 (about a twofold increase) and CS3 (38% increase) when compared with PK pulp. In total, YP has a higher accumulation of ABA at the earlier period. Results indicated that the reduced accumulation of xanthophylls showed strong correlation with the ABA accumulation in YP. This conclusion was supported by the expression of *NCED5* in the later mentioned results (Figure 6).

Organic Acids and Flavonoid Are the Main Differentially Accumulated Metabolites during Coloring. A total of 52 and 57 identified primary metabolites were detected in the pulp and flavedo, respectively, mainly including sugars, organic acids, amino acids, alcohols, fatty acids, and several other metabolites (Table 3). All together there were 41 metabolites in the pulp and 48 metabolites in the flavedo that had significantly different accumulations between YP and PK. It is noteworthy that the accumulations of four metabolites (xylose, ribofuranose, succinic acid, and 10,12-tricosadiynoic acid) in the pulp and isocitric acid in the flavedo were significantly different at all three CSs between YP and PK ($p < 0.01$). Briefly, the dominant sugars were lower in YP pulp, whereas the dominant organic acids were

DOI: 10.1021/acs.jafc.5b02807
J. Agric. Food Chem. 2015, 63, 8601−8614

Table 2. Abscisic Acid Contents in the Flavedo and Pulp of PK and YP[a]

	ABA content (ng g^{-1} FW)			
coloring stage	PK+flavedo	YP+flavedo	PK+pulp	YP+pulp
CS1	88.29 ± 3.43	100.98 ± 21.40 ns.	37.39 ± 13.18	108.62 ± 27.07 **
CS2	50.50 ± 3.21	106.40 ± 3.96 **	80.59 ± 8.67	108.69 ± 16.48 ns.
CS3	46.77 ± 12.96	41.34 ± 14.36 ns.	98.91 ± 12.96	135.74 ± 14.66 **

[a]Results were averaged value plus SDs of the means and statistically analyzed using a paired-samples *t*-test. *: significant difference, $p < 0.05$;**: significant difference, $p < 0.01$; ns.: no significant difference. CS1/2/3: coloring stage 1/2/3.

higher in both the flavedo and pulp of YP when compared with in the flavedo and pulp of PK.

Analyses of secondary metabolites were performed on coloring fruits by LC-MS/MS. Except for flavonoid, other phenolic acids (protocatechuic acid, *p*-hydroxybenzoic acid, caffeic acid, vanillic acid, coumaric acid, ferulic acid, and sinapic acid) showed no significant difference between YP and PK (data not shown). Five flavanones (eriocitrin, ERI; hesperidin, HES; poncitrin, PON; narirutin, NART; and didymin, DID) and four PMFs (sinensetin, SIN; nobiletin, NOB; sinensetin, SIN; and 5-demethylnobiletin, DEM) were indentified (Figure 4a and Tables S2 and S3) and quantified for the two consecutive years (Figures 4b and S4). In flavedo, higher accumulations of ERI, HES, and PON were found in YP compared with those in PK in the year 2013. Similar accumulations of HES and PON were observed in YP in the year 2014. NART and DID showed no significant difference between YP and PK in the year 2013, whereas NART showed lower accumulation at CS2 and CS3 in YP in the year 2014. Furthermore, in YP flavedo, all the PMFs at CS2 and CS3 were significantly higher in the year 2013, whereas NOB at CS2 and SIN and DEM at CS3 showed a significantly higher level of accumulation in year 2014, as compared with those in PK flavedo (Figures 4b and S4a). In YP pulp, a significantly higher level of HES was found at CS1 in the year 2013 and at CS2 and CS3 in the year 2014. Interestingly, in YP pulp, higher accumulations of PMFs were found at CS1 and CS2 in the year 2013 but at CS1 and CS3 in the year 2014 (Figure S4b,c).

The results showed that in addition to some sugars and the dominant organic acids (citric acid, malic acid, succinic acid, and isocitric acid), PMFs were the main different metabolites between YP and PK. Because of the anticancer and antivirus activities as well as the other benefits of PMFs to humans, the YP fruits might be more attractive as fresh fruit for their higher level of PMFs. Furthermore, higher levels of PMFs mean higher antimicrobial activity in YP flavedo.[36]

YP Has Enhanced Resistance Against *P. digitatum*. *P. digitatum* was used as an elicitor to test the resistance of fruits from 45 DAS to pathogen infection (Figure 5). After inoculation, infection lesions appeared on PK fruits at 60 HAI, whereas no infection lesion was found on YP fruits (Figure 5a). Inhibited development of *P. digitatum* and a lower rotting rate were found during the infection process of *P. digitatum* in all YP groups when compared with in PK groups (Figure 5a,b). Statistical results of IRIS, IRIF, and LD from 60 to 144 HAI indicated a higher infection rate in PK than in YP, though the infection rate varied among three groups of the same genotype (Figure 5c−e). We previously found that YP showed a lower rotting rate and better internal quality in storage experiments for three consecutive years (Figure S2). We speculated that the antimicrobial activity might be improved in YP flavedo. Here, our results indicated that the development of *P. digitatum* was more effectively inhibited in YP compared with in PK.

Increase in Expression of Carotenoid Catabolism Genes Exceeds That of Biosynthesis Genes in YP versus PK. To understand the regulation of carotenoid accumulation at the transcription level, the relative expression of carotenoid-related genes was investigated (Figure 6). The dominantly expressed deoxy-D-xylulose 5-phosphate synthase (DXS) gene *DXS1* showed significantly lower expression at CS1 and CS2 in YP as compared with expression in PK. Interestingly, deoxy-D-xylulose 5-phosphate reducto-isomerase (*DXR*) and 1-hydroxy-2-methyl-2-(E)-butenyl 4-diphosphate synthase (*HDS*) showed significantly higher expression at all CSs, whereas isopentenyl diphosphate isomerase (*IPI*) and GGPP synthase (*GGPS*) showed several-fold higher expression at CS3 in YP relative to PK. In YP pulp, *DXS1* and *DXS2* showed relatively higher expression at all CSs, whereas *IPI* and *GGPS* showed higher expression at CS3 (Figure 6).

In the flavedo, most of the carotenoid biosynthesis genes except for ζ-carotene desaturase (*ZDS*) showed higher expression during coloring, especially at CS3 in YP than in PK (Figure 6a). In the pulp, most of these genes showed decreased expression at CS1 but no different expression or only slightly increased expression at the last two CSs in YP relative to PK (Figure 6). It is noteworthy that the dominantly expressed phytoene synthase (*PSY*) gene, *PSY1*, showed 12-fold higher expression in YP flavedo and 3-fold higher expression in YP pulp at CS3 compared with that in PK flavedo and pulp (Figure 6).

The upregulation of the expression of most of the genes for ABA synthesis and carotenoid cleavage was stronger than that of the genes of MEP pathway and carotenoid biosynthesis at the later CSs in YP (Figure 6). The expression of 9-*cis*-epoxycarotenoid dioxygenase 3 (*NCED3*) was stable and showed no significant difference between YP and PK, whereas *NCED5* showed more than 20-fold higher expression in YP flavedo at all three CSs and 3-fold higher expression in YP pulp at CS3 when compared with its expression in PK. In addition, the expression of *CCD1* and *CCD4b1* was two or three folds higher at all CSs in YP flavedo, whereas *CCD1* showed no difference in expression between YP and PK in the pulp. Surprisingly, *CCD4b1* was only detected in YP pulp. However, compared with expression in PK pulp, more than fivefold higher expression of *CCD4b2* was found in YP pulp at CS2 and in YP flavedo at CS3, and more than sevenfold higher expression of *CCD4c* was observed in YP pulp at CS3 in the present study (Figure 6).

NCED5 and NCED3 cleave 9-*cis*-violaxanthin at the 11−12 position to form xanthoxin, a precursor of ABA, whereas CitCCD1 protein cleaves β-cryptoxanthin, zeaxanthin, and all-trans-violaxanthin at the 9−10 and 9′−10′ positions and 9-*cis*-violaxanthin at the 9′−10′ position.[26] The 20-fold higher expression of *NCED5* might result in the higher accumulation of ABA in YP flavedo (Table 2). It is noteworthy that CCD4b1 in citrus (CitCCD4) was shown to produce a fruit-specific C_{30} apocarotenoid (β-citraurin) from cryptoxanthin and zeaxanthin.[27,28] However, β-citraurin was not detected in either YP or PK. Thus, except for the production of

DOI: 10.1021/acs.jafc.5b02807
J. Agric. Food Chem. 2015, 63, 8601−8614

Table 3. Differentially Accumulated Primary Metabolites in YP Compared with Those in PK[a]

pulp				flavedo			
metabolite	CS1	CS2	CS3	metabolite	CS1	CS2	CS3
			sugars				
sucrose	0.97	0.94	0.78*	sucrose	1.13*	0.96	1.02
glucose	0.94	0.95	0.84**	fructose	1.05	0.94	0.88*
fructose	0.86**	0.98	0.92	glucose	1.10**	0.96	1.01
sorbose	1.06	1.05	0.91	sorbose	1.10*	1.11	1.06
turanose	0.94	0.82	0.77*	turanose	1.01	1.31*	1.10
galactose	1.00	1.02	0.89	galactose	1.38**	1.05	1.18**
allofuranose	1.05	0.92	1.32	allofuranose	1.21*	1.07	1.13*
glucopyranoside	0.85*	0.96	down	lyxose	0.98	0.78**	0.78**
lyxose	0.97	1.01	0.85**	cellobiose	1.28*	1.14	1.29*
xylose	1.28**	1.29**	0.77*	xylose	1.02	0.89**	0.91*
mannopyranoside	0.69	0.68**	0.58**	ribofuranose	1.01	0.75**	0.77**
ribofuranose	0.75*	0.54**	0.69*	mannobiose	1.31**	1.07	0.86*
tagatose	1.12	1.04	0.96	mannopyranoside	1.46**	0.55*	0.87
D-ribose	1.06	1.00	0.66**	tagatose	1.59**	1.10	1.01
hexopyranose	2.30	up	7.81	4-keto-glucose	0.72*	0.84	0.70*
cellobiose	down	0.92	5.98*	hexopyranose	0.83	1.47	0.56
				lactulose	1.21**	0.94	1.11
				glucopyranoside	1.11	0.95	0.61**
				D-ribose	0.91	0.84**	0.78**
				inososе	0.97	0.55**	0.74
				glycoside	1.73**	BN	1.20**
				ribo-hexos-3-ulose	1.58**	down	1.34**
				tagatofuranose	9.06**	down	1.09
			organic acids				
citric acid	0.88	1.35*	1.47*	isocitric acid	1.24**	1.19**	1.34**
malic acid	1.47**	1.43**	0.89	malic acid	0.98	1.09	1.09
succinic acid	0.49**	0.44**	0.39**	arabino-hexonic acid	1.12	0.87	0.69**
isocitric acid lactone	1.13*	1.26**	1.07	erythro-pentonic acid	0.93	0.81	1.28**
fumaric acid	0.85	0.37**	0.29**	D-ribonic acid	1.15*	1.10	1.18*
acetic acid	0.15**	BN	BN	trihydroxybutyric acid	1.35**	1.16	1.23*
L-ascorbic acid	1.00	1.25*	0.96	acetic acid	0.72	BN	BN
3-fumaric acid	0.56**	down	down	succinic acid	1.15	1.22**	1.56**
arabino-hexonic acid	0.74	0.66**	0.76*	gluconic acid	0.89	0.00	0.93
aconitate acid	0.69*	down	down	fumaric acid	1.28*	1.30	2.23*
D-ribonic acid	0.87*	1.05	down	galacturonic acid	1.39*	1.13	1.20
erythro-pentonic acid	down	0.29**	1.01	cinnamic acid	1.22	0.93	BN
				propanoic acid	0.89	0.56**	2.54**
				L-ascorbic acid	4.15**	2.91**	1.78
			amino acids				
L-proline	0.47**	1.04	0.63*	L-proline	1.11	0.67*	0.97
threonine	0.72	down	down	threonine	1.03	0.76	0.35**
aminoacetamide	down	down	down	γ-aminobutyric acid	0.88	up	down
valine	down	BN	BN	glycine	down	0.38**	2.08**
asparagine	down	BN	BN	alanine	BN	BN	up
alanine	BN	BN	0.40	serine	up	up	up
glycine	up	0.23**	0.37	DL-ornithine	up	BN	0.42
			alcohols				
inositol	1.04	1.10	0.91	inositol	1.14**	0.97	1.06
glycerol	1.01	0.86	1.22*	glycerol	0.91	1.31*	0.65
D-sorbitol	down	1.00	0.85				
tert-hexadecanethiol	down	1.00	0.61**				
			fatty acids				
hexadecanoic acid	0.79*	1.01	1.10	hexadecanoic acid	0.93	0.93	0.74*
10,12-tricosadiynoic acid	1.37*	1.31**	0.62**	10,12-tricosadiynoic acid	1.06	1.46*	1.03
octadecanoic acid	1.01	0.79*	0.66*	octadecanoic acid	0.83	0.94	0.77
9,12-octadecadienoic acid	0.19	3.85	2.29	13-*cis*-retinoic acid	0.91	0.96	1.24*
			others				
1,3-benzoxazol-2-amine	0.95	0.95	0.94	1,3-benzoxazol-2-amine	0.91	1.11	1.00
pentadecane	1.27	1.01	BN	phosphoric acid	0.97	1.26	BN

DOI: 10.1021/acs.jafc.5b02807
J. Agric. Food Chem. 2015, 63, 8601−8614

Table 3. continued

pulp				flavedo			
metabolite	CS1	CS2	CS3	metabolite	CS1	CS2	CS3
others							
alfacalcidol	0.10**	0.78	0.75*	(+)-α-tocopherol	0.82	0.87	down
hydroxybutyric-acid-ketone	down	1.15*	0.99	hydroxybutyric acid ketone	0.99	1.02	down
octadecane	2.56**	1.00	0.60**	bisnorhopane	0.82	0.95	1.03
heptadecane	BN	1.12	1.57	pentadecane	1.04	0.75	1.21
1-monolinoleoylglycerol	1.79	1.12	7.65				
phosphoric acid	BN	up	up				
squalene	up	up	up				

[a]Results are shown as the YP/PK ratio of each compound. *: $p < 0.05$; **: $p < 0.01$; up: detected the YP but not in PK; down: detected in the PK but not in YP; BN: undetected in both genotypes; and CS1/2/3: coloring stage 1/2/3. Metabolites in each category were arranged in an order of absolute contents.

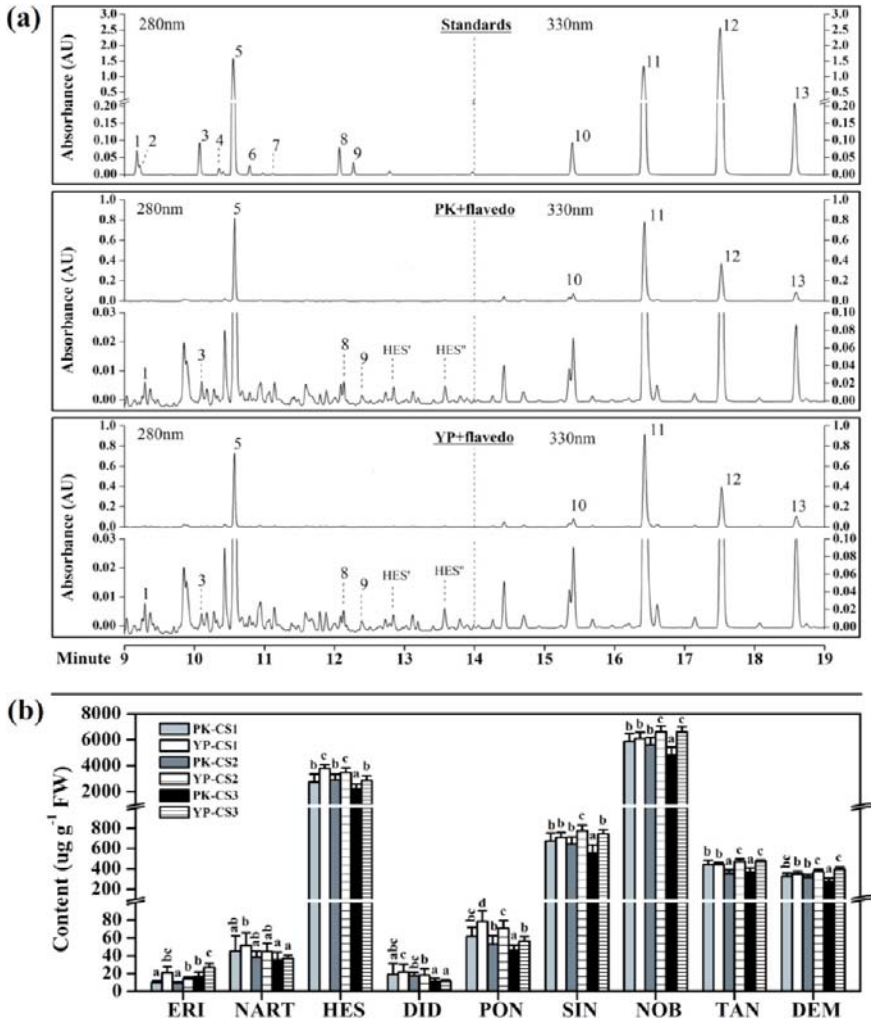

Figure 4. Separation and quantity of flavonoid in flavedo by UPLC analysis. (a) UPLC profiles of flavonoid standards (top) and flavonoid extracts in flavedo from PK (middle) and YP (bottom) of CS3. Peaks: 1, eriocitrin; 2, rutin; 3, narirutin; 4, naringin; 5, hesperidin; 6, neohesperidin; 7, scutellarein; 8, didymin; 9, poncirin; 10, sinensetin; 11, nobiletin; 12, tangeretin; and 13, 5-demethylnobiletin. HES′ and HES″ were deduced to be analogues of hesperidin by their UV absorption characteristics (HES′: 224, 282.3, 328.9; HES″: 224, 282.3, 328.9). (b) Compositions and contents of flavonoid in flavedo from both genotypes at three coloring stages. Error bars represent SDs of the means ($n \geq 3$, biological triplicates). Columns with different letters at each substance indicate significant differences according to Duncan's multiple tests ($p < 0.05$). CS1/2/3: coloring stage 1/2/3.

β-citraurin, CCD4b1 might be involved in other catalytic reactions. *CCD4c* is restricted to petals and may be related to the cleavage of carotenoids to colorless volatile apocarotenoids (C_9–C_{13}). *CCD4a* transcripts were detected in all pulp, peel, leaf, stem, root, and petal samples but were relatively higher in leaf.[28] For their unclarified functions and low absolute expression levels, the relationship between *CCD4a*, *CCD4b2*, or *CCD4c* and carotenoid catabolism in citrus fruits has to be further investigated.

DOI: 10.1021/acs.jafc.5b02807
J. Agric. Food Chem. 2015, 63, 8601−8614

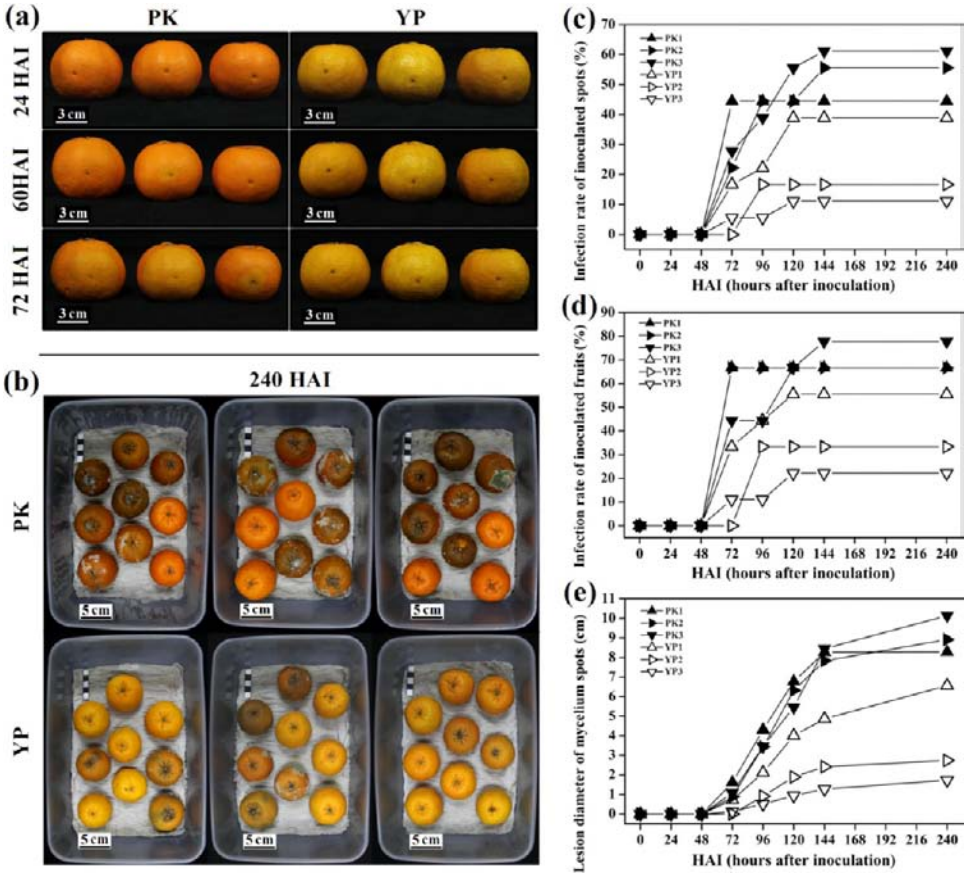

Figure 5. Inoculation experiment of *P. digitatum* in PK and YP fruits. (a) Invasion process of *P. digitatum* in PK and YP. (b) Infection of *P. digitatum* on fruits of PK and YP up to 240 HAI. (c) IRIS, (d) IRIF, and (e) LD of *P. digitatum* were investigated during 240 HAI. PK1, PK2, and PK3 represent three biological repeats of inoculations of PK fruits, and YP1, YP2, and YP3 represent independent biological repeats of inoculations of YP fruits.

Although the expression of upstream genes (*DXR, HDS, IPI, GGPS*, and *PSY*) was unexpectedly upregulated in YP, the reduced carotenoid accumulation of YP might be due to the fact that the increase in expression of carotenoid catabolism genes exceeds that of biosynthesis genes in YP versus PK. The unexpected upregulation of upstream genes for carotenoid biosynthesis in YP at CS3 might be due to the feedback regulation by the higher accumulation of ABA at the earlier coloring stages and a potential higher oxidative stress, as indicated by the higher H_2O_2 level (Figure S8). Furthermore, it was recently reported that OR controls carotenoid biosynthesis via posttranscriptional regulation of PSY in plants.[18] Thus, the transcripts of these upregulated genes may not always be translated to active proteins because of the potential regulation at posttranscriptional level.

Carotenoid Sequestration Capacity and Compartment of Chromoplastid Are Reduced in YP. Western blot analysis was performed to detect fibrillin/PGL35 protein, a lipoprotein in plastoglobulus related to lipid storage and carotenoid and tocopherol synthesis.[17] Compared with expression in PK flavedo and pulp, a significant lower abundance of PGL35 at CS1 and CS2 was found in YP flavedo (Figure 7a), whereas a lower abundance of PGL35 at CS1 was found in YP pulp (Figure 7b).

As shown in Figure S5a, to investigate the compartment of chromoplastid in flavedo, more than 100 cells from 30 TEM sections were used to obtain statistics for chromoplastids. The average number and density of plastids were lower in YP flavedo than in PK flavedo: 38.78% of the investigated YP cells held one plastid, which is obviously higher than that of PK (20.69%), whereas only 3.06% of YP cells held four chromoplastids, which is far less than that of PK (15.86%) (Figure S5b). In addition, more plastids with areas of 0.00−7.00 um^2 were found, whereas fewere plastids with areas of 7.01−16.00 um^2 were found in YP compared with those in PK (Figure S5c). Similarly, more cells with 0.00−10.00% total plastid compartment area (TPCA) were present in YP relative to in PK, whereas fewer cells with 12.00 to over 30.00% TPCA were present in YP relative to in PK (Figure S5d). In summary, compared with those from PK, plastids from YP were characterized by lower density, smaller size, and smaller TPCA. These results indicate reduced storage capacity for carotenoids and xanthophylls in YP.

The relatively lower abundance of PGL35 in YP fruits at earlier stages indicates reduced capacity of carotenoid sequestration during coloring. Recently, the QTL with the largest effect on β-cryptoxanthin content was detected. This QTL includes the Gn0005 locus, a marker derived from the *CitPAP* cDNA sequence (GenBank: AB011797).[44] Although the relation between *CitPAP* and carotenoid accumulation has not been clarified in citrus, the reduced abundance of PGL35 in YP at the earlier stages of coloring showed a strongly positive correlation with the reduced carotenoid accumulation. Thus, our results suggest that the carotenoid accumulation in YP is the integrated result of the disequilibrium between carotenoid catabolism and biosynthesis and the weakened storage capacity of carotenoids.

PMFs Levels Are Stabilized and H_2O_2 Accumulation Is Increased in YP during *P. digitatum* Expansion. As shown in Figure S6, compared with in PK, *PAL1* expression was upregulated in YP flavedo but was not upregulated in YP pulp during coloring. However, the accumulation of PMFs was increased

DOI: 10.1021/acs.jafc.5b02807
J. Agric. Food Chem. 2015, 63, 8601−8614

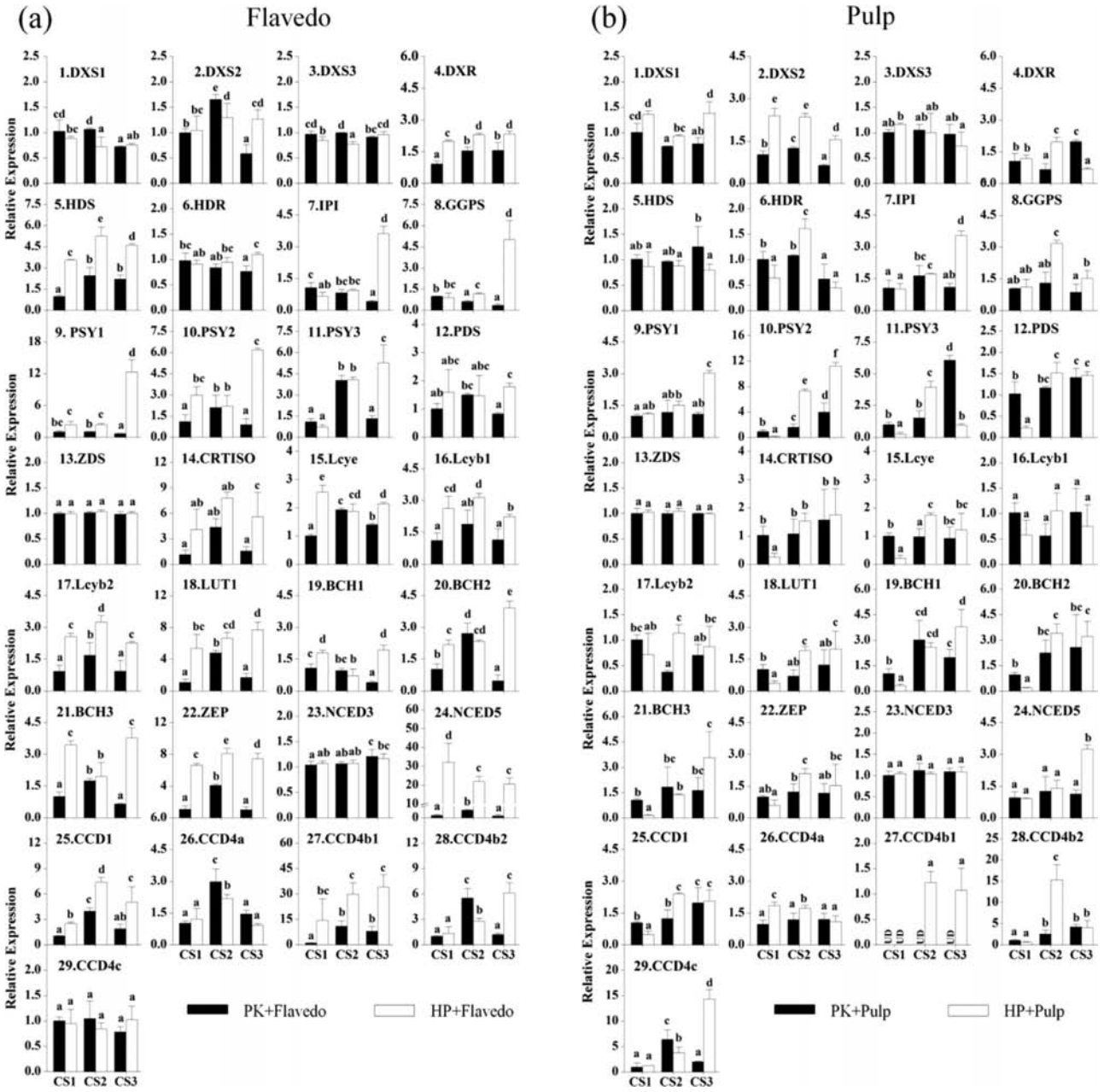

Figure 6. Expression of genes involved in carotenoid biosynthesis and catabolism: (a) flavedo and (b) pulp. DXS1/2/3: DXP (deoxy-D-xylulose 5-phosphate) synthase 1/2/3; DXR: DXP reducto-isomerase; HDS: 1-hydroxy-2-methyl-2-(*E*)-butenyl 4-diphosphate synthase; HDR: 1- hydroxy-2-methyl-2-(*E*)-butenyl 4-diphosphate reductase; IPI: isopentenyl diphosphate isomerase; GGPS: GGPP synthase; PSY1/2/3: phytoene synthase 1/2/3; PDS: phytoene desaturase; ZDS: ζ-carotene desaturase; CRTISO: carotenoid isomerase; Lcye: lycopene ε-cyclase; Lcyb1/b2: lycopene β-cyclase b1/b2; LUT1: an ε-carotene hydroxylase; BCH1/2/3: β-carotene hydroxylase 1/2/3; ZEP: zeaxanthin epoxidase; NCED3/5:9-*cis*-epoxy-carotenoid dioxygenase 3/5; CCD1/4*a*/4b1/4b2/4c: carotenoid cleavage dioxygenase 1/4*a*/4b1/4b2/4c. Error bars represent the SDs of the means ($n \geq 3$). Columns with different letters indicate significant differences according to Duncan's multiple range tests ($p < 0.05$). CS1/2/3: coloring stage 1/2/3.

in both of the flavedo and pulp of YP when compared with that in PK (Figures 4b and S4). Thus, the correlation between the expression of *PAL1* and PMFs accumulation might be tissue-specific because flavedo is the interface to environment and is subjected to various stresses. In addition, the expression of *PAL*1 showed positive correlation with the abscisic acid content in flavedo. An ABRE cis element was found in the promoter of *PAL*1. Thus, we speculated that the increased accumulation of ABA might increase the flavonoid accumulation by upregulating the expression of *PAL*1.

During 45 days of postharvest storage, the levels of PMFs fluctuated and reached the highest value at 15 DAS, but overall they were significantly higher in YP flavedo compared with levels in PK flavedo, except for NOB, DEM, and TAN (tangeretin) at 35 DAS (Figure S7). Thus, higher levels of PMFs in YP at both coloring and storage stages might be a biochemical basis for the enhanced resistance. Consistent with this deduction, the YP fruits from 45 DAS showed enhanced resistance against *P. digitatum* (Figure 5).

To understand the biochemical basis for the enhanced resistance against *P. digitatum*, a sequential monitoring of secondary metabolites was conducted in inoculated or uninoculated flavedo by UPLC (Figure 8) and LC-MS/MS. In previously reported

DOI: 10.1021/acs.jafc.5b02807
J. Agric. Food Chem. 2015, 63, 8601−8614

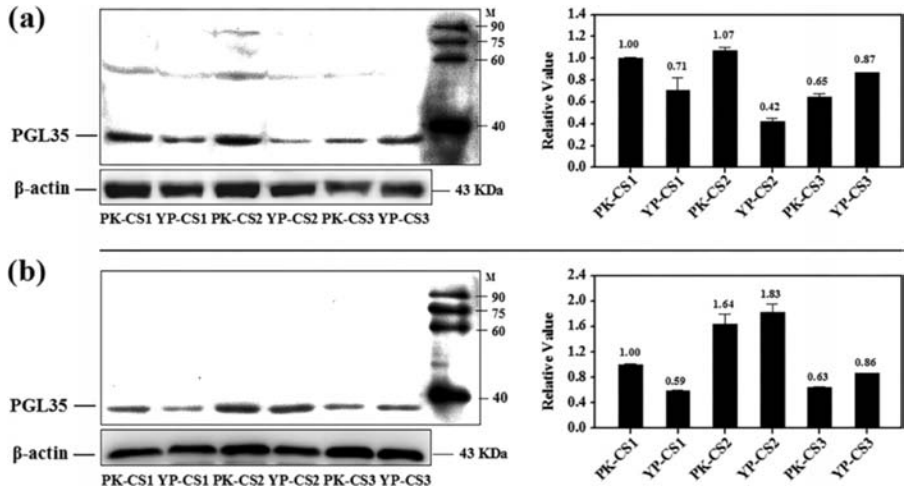

Figure 7. Western blot analysis of PGL35 protein: (a) flavedo and (b) pulp. Exposure time was 2 and 3 min for flavedo and pulp samples, respectively. CS1/2/3: coloring stage 1/2/3.

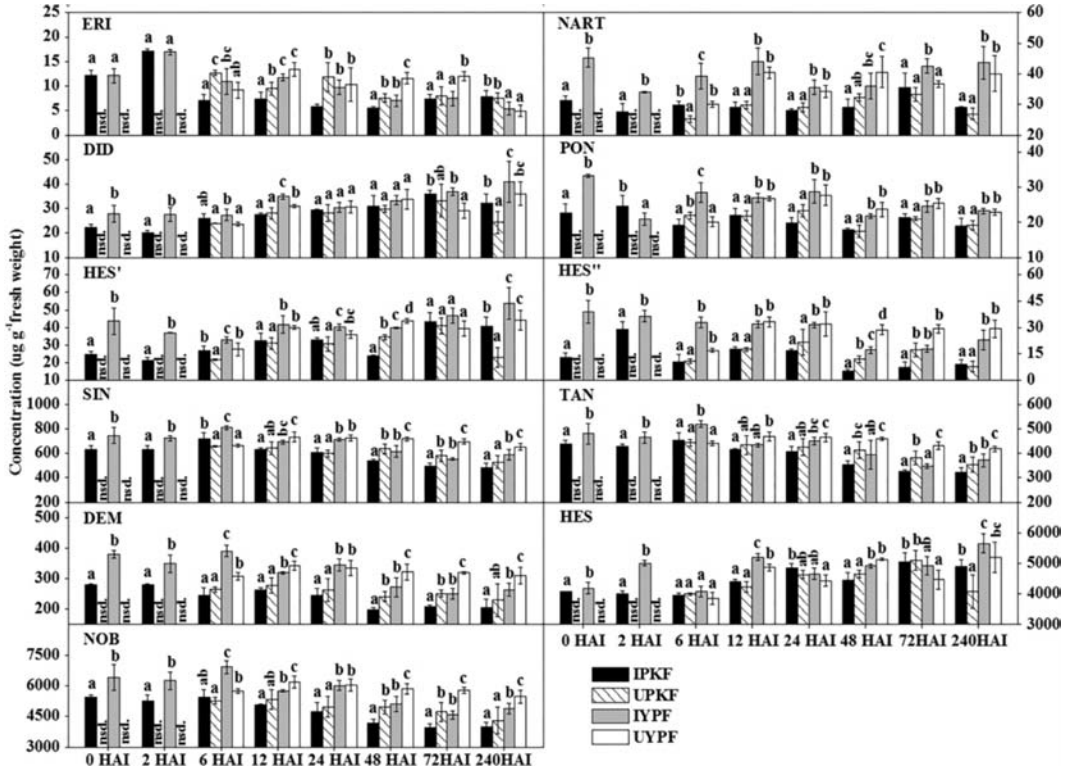

Figure 8. Flavonoid contents in flavedo inoculated with *P. digitatum* or uninoculated flavedo during 240 h. Error bars represent SDs of the means ($n \geq 3$, biological triplicates). Columns with different letters at each substance indicate significant differences according to Duncan's multiple tests ($p < 0.05$). IPKF: inoculated PK flavedo; UPKF: uninoculated PK flavedo; IYPF: inoculated YP flavedo; UYPF: uninoculated YP flavedo; nsd: not sampled for detection; and HAI: hours after inoculation.

studies, the inoculated and uninoculated materials for monitoring flavonoids were sampled from different fruits.[34,37,38,45] In contrast to these methods, we sampled the inoculated and uninoculated flavedo materials for flavonoid detection from the same fruit. Because the same fruit represents the same physiological background, our sampling method should be more reliable. No novel metabolite derived from the inoculation was found (data not shown). The contents of all the flavonones fluctuated but in general showed higher levels in YP (IYPF/UYPF) relative to those in PK (IPKF/UPKF) during 240 HAI. HES′ was deduced to be hesperetin 7-*o*-glucoside in previous document, which is the probable product of HES hydrolysis by enzymes from fungi.[45] It is noteworthy that the levels of HES′ and HES″ (another unknown flavonone) were increased by folds in YP relative to those in PK at 240 HAI. The contents of PMFs in IPKF and UPKF did not increase and started to decrease from 12 to 24 HAI, respectively, whereas their contents in IYPF and UYPF were increased and reached peak values at 6 and 12 HAI, respectively. It is noteworthy that the PMFs in UYPF stayed unchanged from 12 to 72 HAI and started to decrease slowly afterward. Our results indicate that the stabilized level of PMFs in the uninoculated flavedo in YP help to construct an effective barrier against the attack of *P. digitatum*.

DOI: 10.1021/acs.jafc.5b02807
J. Agric. Food Chem. 2015, 63, 8601−8614

H_2O_2 was shown to be an important secondary messenger for the induction of the expression of defense genes.[46] It is noteworthy that H_2O_2 level was higher in both inoculated and uninoculated spots in YP flavedo than that in PK flavedo during *P. digitatum* expansion (Figure S8). The integration of reactive oxygen species/redox status and sugars/carbon status can account for most of the effects of the major environmental factors that influence carotenoid biosynthesis, and carotenoids or their derivatives can in turn act as stress signaling molecules.[47] Reasonably, H_2O_2 might participate in the regulation of carotenoid biosynthesis and the induction of the expression of defense-related genes. A more efficient transduction of the H_2O_2 signal from the inoculated spots to healthy tissues may facilitate the establishment of barriers against pathogens, such as the accumulation of PMFs in YP.

The volatile oil in flavedo is another group of important metabolites that might be related to the resistance against *P. digitatum*.[35,48] We conducted a comparative analysis of chemical composition of the volatile oil in flavedo between YP and PK. The previously proven antifungal components against *P. digitatum*, D-limonene, γ-terpinene, and β-linalool showed lower accumulation, whereas α-terpineol and octanal showed higher accumulation in YP flavedo when compared with levels in PK flavedo. (Table S5 and Figure S9). However, the antifungal activity of α-terpineol and octanal against *P. digitatum* might be weak because of their low accumulation in flavedo (Table S5). In total, the content of antifungal components was lower in YP than in PK. Thus, volatile oil might not contribute to the enhanced resistance in YP.

Our results demonstrate that the disequilibrium between catabolism and biosynthesis and the reduced sink capacity of carotenoids are responsible for the reduced xanthophylls and the yellowish coloring in YP fruits. Through a comprehensive investigation of YP by analysis of its primary and secondary metabolites and resistance against abiotic and biotic stresses, this study reveals that reprogramming of metabolisms may help to enhance the resistance against abiotic and biotic stresses in YP. However, the improvement of postharvest performance was at the expense of a part of nutritional quality such as carotenoids, but higher PMFs might compensate for this loss of nutrition in the pulp. Taken together, our work is the first report that confirms the practicability of using the reprogramming of metabolisms in mutants to improve the postharvest performance of citrus fruit.

■ ASSOCIATED CONTENT

Supporting Information

The Supporting Information is available free of charge on the ACS Publications website at DOI: 10.1021/acs.jafc.5b02807.

Retention time and UV spectrum of isolated carotenoids in HPLC analysis; structure and UV spectrum information on identified flavonoids by UPLC analysis; data for calibration curve of 13 flavonoid standards; specific primers used in real-time reverse transcriptase PCR; chemical composition and relative content of the volatile oil from flavedo of YP and PK; pathway for carotenoid biosynthesis and cleavage; changes in rotting rate and internal quality during postharvest storage; carotenoid contents from fruits of year 2014 at three coloring stages; compositions and contents of flavonoids in fruits at coloring stages; statistics of plastids according to transmission electron microscope of flavedo; expression of *PAL1* in flavedo and pulp in both genotypes; changes in compositions and contents of flavonoids in flavedo during 45 day storage; H_2O_2 contents in flavedo of PK and YP during *P. digitatum* infection; and GC-MS analysis of chemical composition of the volatile oil from flavedo of PK and YP. (PDF)

■ AUTHOR INFORMATION

Corresponding Author

*Phone: +86-2787281796. Fax: +86-2787280622. E-mail: yjcheng@mail.hzau.edu.cn.

Funding

This work was supported by Huazhong Agricultural University Scientific & Technological Self-innovation Foundation, the National Natural Science Foundation of China (NSFC, grant nos. 31221062 and 31271968), the Program for New Century Excellent Talents in University (NCET-12-0859), the National Modern Agriculture (Citrus) Technology Systems of China (grant no. CARS-27) and the Special Fund for Agro-scientific Research in the Public Interest (grant no. 201303093).

Notes

The authors declare no competing financial interest.

■ ACKNOWLEDGMENTS

We are grateful to Prof. Zuoxiong Liu (Foreign Language College of Huazhong Agricultural University) for reading and revising the manuscript.

■ REFERENCES

(1) Nisar, N.; Li, L.; Lu, S.; Khin; Nay, C.; Pogson; Barry, J. Carotenoid metabolism in plants. *Mol. Plant* **2015**, *8*, 68−82.

(2) Cao, H.; Wang, J.; Dong, X.; Han, Y.; Ma, Q.; Ding, Y.; Zhao, F.; Zhang, J.; Chen, H.; Xu, Q.; Xu, J.; Deng, X. Carotenoid accumulation affects redox status, starch metabolism, and flavonoid/anthocyanin accumulation in citrus. *BMC Plant Biol.* **2015**, *15*, 27.

(3) Gonzalez-Jorge, S.; Ha, S. H.; Magallanes-Lundback, M.; Gilliland, L. U.; Zhou, A.; Lipka, A. E.; Nguyen, Y. N.; Angelovici, R.; Lin, H.; Cepela, J.; Little, H.; Buell, C. R.; Gore, M. A.; DellaPenna, D. *CAROTENOID CLEAVAGE DIOXYGENASE4* is a negative regulator of β-carotene content in *Arabidopsis* seeds. *Plant Cell* **2013**, *25*, 4812−4826.

(4) Cazzonelli, C. I.; Pogson, B. J. Source to sink: regulation of carotenoid biosynthesis in plants. *Trends Plant Sci.* **2010**, *15*, 266−274.

(5) Maass, D.; Arango, J.; Wüst, F.; Beyer, P.; Welsch, R. Carotenoid crystal formation in *Arabidopsis* and carrot roots caused by increased phytoene synthase protein levels. *PLoS One* **2009**, *4*, e6373.

(6) Gady, A. L. F.; Vriezen, W. H.; Van de Wal, M. H. B. J.; Huang, P.; Bovy, A. G.; Visser, R. G. F.; Bachem, C. W. B. Induced point mutations in the phytoene synthase 1 gene cause differences in carotenoid content during tomato fruit ripening. *Mol. Breed.* **2012**, *29*, 801−812.

(7) Fu, X.; Feng, C.; Wang, C.; Yin, X.; Lu, P.; Grierson, D.; Xu, C.; Chen, K. Involvement of multiple phytoene synthase genes in tissue- and cultivar-specific accumulation of carotenoids in loquat. *J. Exp. Bot.* **2014**, *65*, 4679−4689.

(8) Harjes, C. E.; Rocheford, T. R.; Bai, L.; Brutnell, T. P.; Kandianis, C. B.; Sowinski, S. G.; Stapleton, A. E.; Vallabhaneni, R.; Williams, M.; Wurtzel, E. T.; Yan, J.; Buckler, E. S. Natural genetic variation in *lycopene epsilon cyclase* tapped for maize biofortification. *Science* **2008**, *319*, 330−333.

(9) Zhou, X.; McQuinn, R.; Fei, Z.; Wolters, A.-M. A.; Van Eck, J.; Brown, C.; Giovannoni, J. J.; Li, L. I. Regulatory control of high levels of carotenoid accumulation in potato tubers. *Plant, Cell Environ.* **2011**, *34*, 1020−1030.

(10) Arango, J.; Jourdan, M.; Geoffriau, E.; Beyer, P.; Welsch, R. Carotene hydroxylase activity determines the levels of both α-Carotene and total carotenoids in orange carrots. *Plant Cell* **2014**, *26*, 2223−2233.

(11) Cookson, P. J.; Kiano, J. W.; Shipton, C. A.; Fraser, P. D.; Romer, S.; Schuch, W.; Bramley, P. M.; Pyke, K. A. Increases in cell elongation,

DOI: 10.1021/acs.jafc.5b02807
J. Agric. Food Chem. 2015, 63, 8601−8614

plastid compartment size and phytoene synthase activity underlie the phenotype of the high *pigment-1* mutant of tomato. *Planta* **2003**, *217*, 896−903.
(12) Kolotilin, I.; Koltai, H.; Tadmor, Y.; Bar-Or, C.; Reuveni, M.; Meir, A.; Nahon, S.; Shlomo, H.; Chen, L.; Levin, I. Transcriptional profiling of *high pigment-2^{dg}* tomato mutant links early fruit plastid biogenesis with Its overproduction of phytonutrients. *Plant Physiol.* **2007**, *145*, 389−401.
(13) Galpaz, N.; Wang, Q.; Menda, N.; Zamir, D.; Hirschberg, J. Abscisic acid deficiency in the tomato mutant *high-pigment 3* leading to increased plastid number and higher fruit lycopene content. *Plant J.* **2008**, *53*, 717−730.
(14) Powell, A. L. T.; Nguyen, C. V.; Hill, T.; Cheng, K. L.; Figueroa-Balderas, R.; Aktas, H.; Ashrafi, H.; Pons, C.; Fernández-Muñoz, R.; Vicente, A.; Lopez-Baltazar, J.; Barry, C. S.; Liu, Y.; Chetelat, R.; Granell, A.; Van Deynze, A.; Giovannoni, J. J.; Bennett, A. B. *Uniform ripening* encodes a *Golden 2-like* transcription factor regulating tomato fruit chloroplast development. *Science* **2012**, *336*, 1711−1715.
(15) Kilambi, H. V.; Kumar, R.; Sharma, R.; Sreelakshmi, Y. Chromoplast-specific carotenoid-associated protein appears to be important for enhanced accumulation of carotenoids in *hp1* tomato fruits. *Plant Physiol.* **2013**, *161*, 2085−2101.
(16) Kilcrease, J.; Rodriguez-Uribe, L.; Richins, R. D.; Arcos, J. M. G.; Victorino, J.; O'Connell, M. A. Correlations of carotenoid content and transcript abundances for fibrillin and carotenogenic enzymes in *Capsicum annum* fruit pericarp. *Plant Sci.* **2015**, *232*, 57−66.
(17) Simkin, A. J.; Gaffé, J.; Alcaraz, J.-P.; Carde, J.-P.; Bramley, P. M.; Fraser, P. D.; Kuntz, M. Fibrillin influence on plastid ultrastructure and pigment content in tomato fruit. *Phytochemistry* **2007**, *68*, 1545−1556.
(18) Zhou, X.; Welsch, R.; Yang, Y.; Álvarez, D.; Riediger, M.; Yuan, H.; Fish, T.; Liu, J.; Thannhauser, T. W.; Li, L. Arabidopsis OR proteins are the major posttranscriptional regulators of phytoene synthase in controlling carotenoid biosynthesis. *Proc. Natl. Acad. Sci. U. S. A.* **2015**, *112*, 3558−3563.
(19) Breithaupt, D. E.; Bamedi, A. Carotenoid esters in vegetables and fruits: a screening with emphasis on β-cryptoxanthin esters. *J. Agric. Food Chem.* **2001**, *49*, 2064−2070.
(20) Hornero-Méndez, D. m.; Mínguez-Mosquera, M. I. Xanthophyll esterification accompanying carotenoid overaccumulation in chromoplast of *Capsicum* annuum. ripening fruits is a constitutive process and useful for ripeness index. *J. Agric. Food Chem.* **2000**, *48*, 1617−1622.
(21) Ariizumi, T.; Kishimoto, S.; Kakami, R.; Maoka, T.; Hirakawa, H.; Suzuki, Y.; Ozeki, Y.; Shirasawa, K.; Bernillon, S.; Okabe, Y.; Moing, A.; Asamizu, E.; Rothan, C.; Ohmiya, A.; Ezura, H. Identification of the carotenoid modifying gene *PALE YELLOW PETAL1* as an essential factor in xanthophyll esterification and yellow flower pigmentation in tomato (*Solanum lycopersicum*). *Plant J.* **2014**, *79*, 453−465.
(22) Chiou, C.-Y.; Pan, H.-A.; Chuang, Y.-N.; Yeh, K.-W. Differential expression of carotenoid-related genes determines diversified carotenoid coloration in floral tissues of *Oncidium* cultivars. *Planta* **2010**, *232*, 937−948.
(23) Vallabhaneni, R.; Bradbury, L. M. T.; Wurtzel, E. T. The carotenoid dioxygenase gene family in maize, sorghum, and rice. *Arch. Biochem. Biophys.* **2010**, *504*, 104−111.
(24) Brandi, F.; Bar, E.; Mourgues, F.; Horváth, G.; Turcsi, E.; Giuliano, G.; Liverani, A.; Tartarini, S.; Lewinsohn, E.; Rosati, C. Study of 'Redhaven' peach and its white-fleshed mutant suggests a key role of CCD4 carotenoid dioxygenase in carotenoid and norisoprenoid volatile metabolism. *BMC Plant Biol.* **2011**, *11*, 24.
(25) Han, Y.; Wang, X.; Chen, W.; Dong, M.; Yuan, W.; Liu, X.; Shang, F. Differential expression of carotenoid-related genes determines diversified carotenoid coloration in flower petal of *Osmanthus fragrans*. *Tree Genet. Genomes* **2014**, *10*, 329−338.
(26) Kato, M. The role of carotenoid cleavage dioxygenases in the regulation of carotenoid profiles during maturation in citrus fruit. *J. Exp. Bot.* **2006**, *57*, 2153−2164.
(27) Ma, G.; Zhang, L.; Matsuta, A.; Matsutani, K.; Yamawaki, K.; Yahata, M.; Wahyudi, A.; Motohashi, R.; Kato, M. enzymatic formation of β-citraurin from β-cryptoxanthin and zeaxanthin by Carotenoid Cleavage Dioxygenase 4 in the flavedo of citrus fruit. *Plant Physiol.* **2013**, *163*, 682−695.
(28) Rodrigo, M. J.; Alquezar, B.; Alos, E.; Medina, V.; Carmona, L.; Bruno, M.; Al-Babili, S.; Zacarias, L. A novel carotenoid cleavage activity involved in the biosynthesis of Citrus fruit-specific apocarotenoid pigments. *J. Exp. Bot.* **2013**, *64*, 4461−4478.
(29) Rodrigo, M. J.; Alquézar, B.; Alós, E.; Lado, J.; Zacarías, L. Biochemical bases and molecular regulation of pigmentation in the peel of Citrus fruit. *Sci. Hortic.* **2013**, *163*, 46−62.
(30) Liu, Q.; Xu, J.; Liu, Y.; Zhao, X.; Deng, X.; Guo, L.; Gu, J. A novel bud mutation that confers abnormal patterns of lycopene accumulation in sweet orange fruit (*Citrus sinensis* L. Osbeck). *J. Exp. Bot.* **2007**, *58*, 4161−4171.
(31) Rodrigo, M.-J.; Marcos, J. F.; Alférez, F.; Mallent, M. D.; Zacarías, L. Characterization of Pinalate, a novel *Citrus sinensis* mutant with a fruit-specific alteration that results in yellow pigmentation and decreased ABA content. *J. Exp. Bot.* **2003**, *54*, 727−738.
(32) Alquezar, B.; Rodrigo, M. J.; Zacarías, L. Regulation of carotenoid biosynthesis during fruit maturation in the red-fleshed orange mutant Cara Cara. *Phytochemistry* **2008**, *69*, 1997−2007.
(33) Yun, Z.; Gao, H.; Liu, P.; Liu, S.; Luo, T.; Jin, S.; Xu, Q.; Xu, J.; Cheng, Y.; Deng, X. Comparative proteomic and metabolomic profiling of citrus fruit with enhancement of disease resistance by postharvest heat treatment. *BMC Plant Biol.* **2013**, *13*, 44.
(34) Ortuño, A.; Báidez, A.; Gómez, P.; Arcas, M. C.; Porras, I.; García-Lidón, A.; Río, J. A. D. *Citrus paradisi* and *Citrus sinensis* flavonoids: Their influence in the defence mechanism against *Penicillium digitatum*. *Food Chem.* **2006**, *98*, 351−358.
(35) Jing, L.; Lei, Z.; Li, L.; Xie, R.; Xi, W.; Guan, Y.; Sumner, L. W.; Zhou, Z. Antifungal Activity of Citrus Essential Oils. *J. Agric. Food Chem.* **2014**, *62*, 3011−3033.
(36) Del Río, J. A.; Arcas, M. C.; Benavente-García, O.; Ortuño, A. Citrus poly- methoxylated flavones can confer resistance against *Phytophthora citrophthora*, *Penicillium digitatum*, and *Geotrichum* Species. *J. Agric. Food Chem.* **1998**, *46*, 4423−4428.
(37) Ortuño, A.; Díaz, L.; Alvarez, N.; Porras, I.; García-Lidón, A.; Del Río, J. A. Comparative study of flavonoid and scoparone accumulation in different Citrus species and their susceptibility to *Penicillium digitatum*. *Food Chem.* **2011**, *125*, 232−239.
(38) Ballester, A.-R.; Teresa Lafuente, M.; González-Candelas, L. Citrus phenyl- propanoids and defence against pathogens. Part II: Gene expression and metabolite accumulation in the response of fruits to *Penicillium digitatum* infection. *Food Chem.* **2013**, *136*, 285−291.
(39) Pan, Z.; Li, Y.; Deng, X.; Xiao, S. Non-targeted metabolomic analysis of orange (*Citrus sinensis* [L.] Osbeck) wild type and bud mutant fruits by direct analysis in real-time and HPLC-electrospray mass spectrometry. *Metabolomics* **2014**, *10*, 508−523.
(40) Deng, A.; Tan, W.; He, S.; Liu, W.; Nan, T.; Li, Z.; Wang, B.; Li, Q. X. Monoclonal antibody-based enzyme linked Immunosorbent assay for the analysis of Jasmonates in Plants. *J. Integr. Plant Biol.* **2008**, *50*, 1046−1052.
(41) Cao, H.; Zhang, J.; Xu, J.; Ye, J.; Yun, Z.; Xu, Q.; Xu, J.; Deng, X. Comprehending crystalline β-carotene accumulation by comparing engineered cell models and the natural carotenoid-rich system of citrus. *J. Exp. Bot.* **2012**, *63*, 4403−4417.
(42) Schmittgen, T. D.; Livak, K. J. Analyzing real-time PCR data by the comparative C_T method. *Nat. Protoc.* **2008**, *3*, 1101−1108.
(43) Isaacson, T.; Damasceno, C. M. B.; Saravanan, R. S.; He, Y.; Catalá, C.; Saladié, M.; Rose, J. K. C. Sample extraction techniques for enhanced proteomic analysis of plant tissues. *Nat. Protoc.* **2006**, *1*, 769−774.
(44) Sugiyama, A.; Omura, M.; Matsumoto, H.; Shimada, T.; Fujii, H.; Endo, T.; Shimizu, T.; Nesumi, H.; Ikoma, Y. Quantitative trait loci (QTL) analysis of carotenoid content in *Citrus* fruit. *J. Jpn. Soc. Hortic. Sci.* **2011**, *80*, 136−144.
(45) Kim, H. G.; Kim, G.-S.; Lee, J. H.; Park, S.; Jeong, W. Y.; Kim, Y.-H.; Kim, J. H.; Kim, S. T.; Cho, Y. A.; Lee, W. S.; Lee, S. J.; Jin, J. S.; Shin, S. C. Determination of the change of flavonoid components as the defence materials of *Citrus unshiu* Marc. fruit peel against *Penicillium*

DOI: 10.1021/acs.jafc.5b02807
J. Agric. Food Chem. 2015, 63, 8601−8614

digitatum by liquid chromatography coupled with tandem mass spectrometry. *Food Chem.* **2011**, *128*, 49−54.
(46) Orozco-Cárdenas, M. L.; Narváez-Vásquez, J.; Ryan, C. A. Hydrogen peroxide acts as a second messenger for the induction of defense genes in tomato plants in response to wounding, systemin, and methyl jasmonate. *Plant Cell* **2001**, *13*, 179−191.
(47) Fanciullino, A. L.; Bidel, L. P. R.; Urban, L. Carotenoid responses to environmental stimuli integrating redox and carbon controls into a fruit model. *Plant, Cell Environ.* **2014**, *37*, 273−289.
(48) Tao, N.; Jia, L.; Zhou, H. Anti-fungal activity of Citrus reticulata Blanco essential oil against *Penicillium italicum* and *Penicillium digitatum*. *Food Chem.* **2014**, *153*, 265−271.

DOI: 10.1021/acs.jafc.5b02807
J. Agric. Food Chem. 2015, 63, 8601−8614

compounds in urine or plasma. To monitor intake frequency in individuals, it is extremely helpful to have a noninvasive biomarker in hand that is specific to coffee and sensitive enough for detection with straightforward analytical chemistry tools.[36] Several biomarkers for coffee have been proposed, including caffeine, polyphenols, and trigonelline.[37−41] Ingestion of caffeine results in excretion of caffeine and other xanthine derivatives;[37] chlorogenic acid leads to excretion of different quinic acids and hippuric acids;[38−40] and trigonelline and its roasting product *N*-methylpyridinium are also directly excreted in urine.[41] However, most detected markers to date are not specific to coffee consumption. For example, caffeine can be found in other stimulatory beverages, and the excretion of polyphenol-derived markers is not specific to coffee because fruits, vegetables, and tea are also rich in polyphenols.[38,42] Furthermore, metabolism of polyphenols is dependent on the gut microbiota and therefore subject to high interindividual variation in humans.[43−45]

Nontargeted metabolic profiling has in the past been shown to deliver novel food biomarkers, without prior knowledge of ingredients or processing and metabolism steps.[46−48] Here, we conducted a multistep approach for sequentially elucidating novel biomarkers for coffee consumption and established their temporal excretion profiles using ^{1}H NMR based metabolic profiling of a coffee intervention study.

MATERIALS AND METHODS

Dietary Intervention Study. A nutritional intervention study was designed to detect urinary biomarkers of different food consumption by using a nontargeted metabolic profiling approach. The study involved eight volunteers (seven women and one man; age range, 28−45 years) who met the following inclusion criteria: healthy, aged 18−45 years, nonsmokers, body mass index (BMI; in kg/m^2) 18−25, absence of regular drug intake and regular food supplement intake, and no antibiotic use within the previous 3 months. Participants consumed a standardized breakfast, lunch, and dinner that comprised whole-grain bread and cheese (breakfast), a ham sandwich (lunch), and different dinners on each day (dinner) from the run-in day (day 0) until lunch on day 7. Participants were allowed to drink coffee between 8 am and 12 (i.e., for breakfast and as desired, until 12 am). Urine was collected 4 times/day (first morning urine, before lunch, before dinner, and at bedtime), from the morning of day 1 until the evening of day 6. Urine specimens were collected into sterile tubes (Sterilin, Aberbargoed, UK) and kept in the refrigerator for a maximum of 12 h before storage at −40 °C until analysis. The study was approved by Imperial College London Research Ethics Committee and is registered at clinicaltrials.gov as NCT01102049.

Coffee Study. A food study was undertaken to characterize the excretion profile of 2-furoylglycine after coffee consumption. Five volunteers (three women and two men; age range: 24−34 years) who met the inclusion criteria of being self-assessed as healthy, aged 18−45 years, nonsmokers, a BMI of 18−30 kg/m^2, and an absence of regular drug intake and regular food supplement intake were recruited. The number of volunteers was based on power calculations with values from the previous dietary intervention study with $\alpha = 0.05$ and power of the test 0.80. Other than coffee consumption, participants were not restricted in their choice of foods for the duration of the study. Day 0 served as a run-in day, where no coffee consumption was allowed; a coffee challenge (1 espresso with or without milk) was administered on day 1 at 10 am and spot urine specimens were collected on day 1 (i.e., baseline samples, 6 times/d, collected at 8 am, 10 am, 12 am, 4 pm, and 8 pm and at bedtime); and at 8 am and 10 am on day 2 (study finish). Urine specimens were collected in sterile tubes (Sterilin) and kept in the refrigerator before they were stored at −80 °C until analysis.

Standard Spiking Experiment. The chemical standard of 2-furoylglycine was purchased from Sigma-Aldrich, was dissolved in NMR buffer, and was analyzed with ^{1}H NMR spectroscopy. Furthermore, a representative urine sample from time point "12 am" was analyzed with the same spectroscopic settings as the standard. Lastly, a ^{1}H NMR spectrum of the same urine, spiked with 2-furoylglycine in appropriate physiological amounts, was acquired, and the resulting spectrum was compared with the original spectrum.

Coffee Analysis. Three different kinds of coffee were analyzed: espresso, instant espresso, and chicory coffee. Coffees were prepared as per normal consumption, i.e., 12.5 g of bean powder per 50 mL of extraction water, 15 g of instant espresso powder per 50 mL of water, and 8 g of chicory coffee powder per 200 mL of water, and an aliquot of 50 μL was mixed with 200 μL of NMR buffer (90% D_2O 500 mM PO_4 buffer with 0.1% TSP, pH 7.4), centrifuged, and transferred to 3 mm outer diameter NMR Bruker Match tubes (Hilgenberg GmbH, Malsfeld, Germany).

NMR Spectroscopic Analysis. *Urine Analysis.* An aliquot of each urine sample was analyzed by ^{1}H NMR analysis. Urine and NMR buffer were mixed 2:1 and centrifuged, and 550 uL of the supernatant was transferred to 5 mm (dietary intervention study) or 120 uL to 3 mm (coffee study) outer diameter NMR Bruker Match tubes. Urine specimens of the dietary intervention study were acquired on a Bruker 600 MHz spectrometer (Bruker Biospin, Rheinstetten, Germany) that operated at 600.13 MHz. The spectrometer used a standard one-dimensional (1D) pulse-sequence [recycle delay (RD)-90°-t1-90°-mixing time (tm)-90°-acquire] free-induction decay (FID) with water-suppression irradiation during a RD of 2 s with tm set to 100 ms and a 90° pulse set to 10 μs. Spectra were acquired with 128 scans into 32 K data points with a spectral width of 12000 Hz. Urine specimens from the coffee study were analyzed on a Bruker 800 MHz spectrometer operating at 800.35 MHz with a quadrupole inverse cryogenic probe. A standard 1-dimensional pulse sequence [recycle delay (RD)-90°-t1-90°-tm-90°-acquire FID] was acquired, with water suppression irradiation during RD of 2 s, mixing time (tm) set on 200 ms, and a 90° pulse set to 10.13 μs, collecting 512 scans into 64 K data points with a spectral width of 12 ppm. All spectra were manually phased, baseline corrected, and calibrated to TSP (δ 0.00) with TopSpin 3.2 (Bruker BioSpin, Rheinstetten, Germany). Data were imported to Matlab (Mathworks, Massachusetts, US) and further processed, i.e., water region removed (δ 4.70−5.21). The spectra were normalized by using a probabilistic quotient normalization algorithm[49] to account for urinary dilution effects and aligned by using a recursive segment-wise peak-alignment algorithm.[50] Relative quantification of metabolites of interest was done by integration of the area under the curve (AUC), as outlined in Heinzmann et al.[46] and expressed as relative measure to creatinine concentration.

Coffee Analysis. Coffee samples were analyzed with a Bruker 800 MHz spectrometer equipped with a quadrupole inverse cryogenic probe, wherewith ^{1}H NMR spectra and 2D spectra (total correlation spectroscopy (TOCSY) and heteronuclear single quantum coherence (HSQC)) were acquired. For 2D NMR spectra, phase-sensitive sensitivity-improved 2D TOCSY with water suppression by gradient tailored excitation (WATERGATE) (3-9-19) and using decoupling in the presence of scalar interactions (DIPSI-2), were acquired. For each spectrum, 19228 × 1024 data points were collected using 32 scans per increment, an acquisition time of 1 s, and 16 dummy scans. The spectral widths were set to 12 and 12 ppm in the F2 and F1 dimensions, respectively. For the 2D ^{1}H−^{13}C HSQC spectra, phase-sensitive ge-2D-HSQC using preservation of equivalent pathways (PEP) and adiabatic pulses for inversion and refocusing with gradients were used. For each 2D spectrum, 4096 × 1024 data points were collected using 32 scans per increment, an acquisition time of 0.25 s, and 16 dummy scans. The spectral widths were set to 12 and 230 ppm in the proton and carbon dimensions, respectively. Processing of the spectra was carried out in TopSpin 3.2. FIDs were multiplied by an exponential decaying function corresponding to a line broadening of 0.3 Hz before Fourier transformation. All spectra were manually phased, baseline corrected, and calibrated to TSP (δ 0.00).

Multivariate Analysis. All timed urine specimens of the dietary intervention study that were collected at lunchtime were defined as "coffee samples", all others (first morning urine, before dinner, and

DOI: 10.1021/acs.jafc.5b03040
J. Agric. Food Chem. 2015, 63, 8615−8621

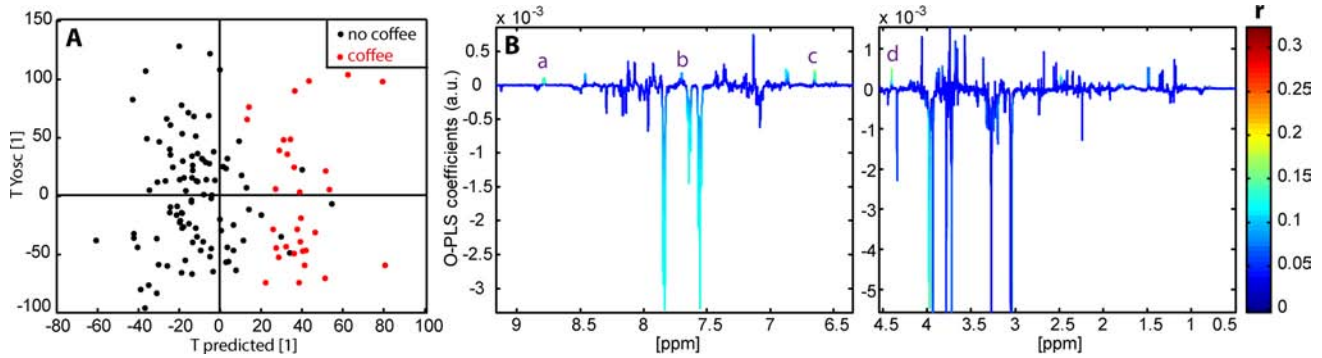

Figure 1. OPLS-DA scores and loadings plots of urine specimen after coffee challenge (12 am) vs all other urine collection (8 am, 8 pm, bedtime). (A) The scores plot shows a clear separation of coffee vs no coffee groups with a goodness of fit (R^2Y) of 0.58 and predictive value (Q^2Y) of 0.22. (B) Loadings plot of the coffee challenge indicates putative biomarkers with chemical shifts at a δ 8.79 (d), b δ 7.20, c δ 6.65 (dd), d δ 4.40 (s), with highest correlation coefficient for δ 6.65 (dd).

Figure 2

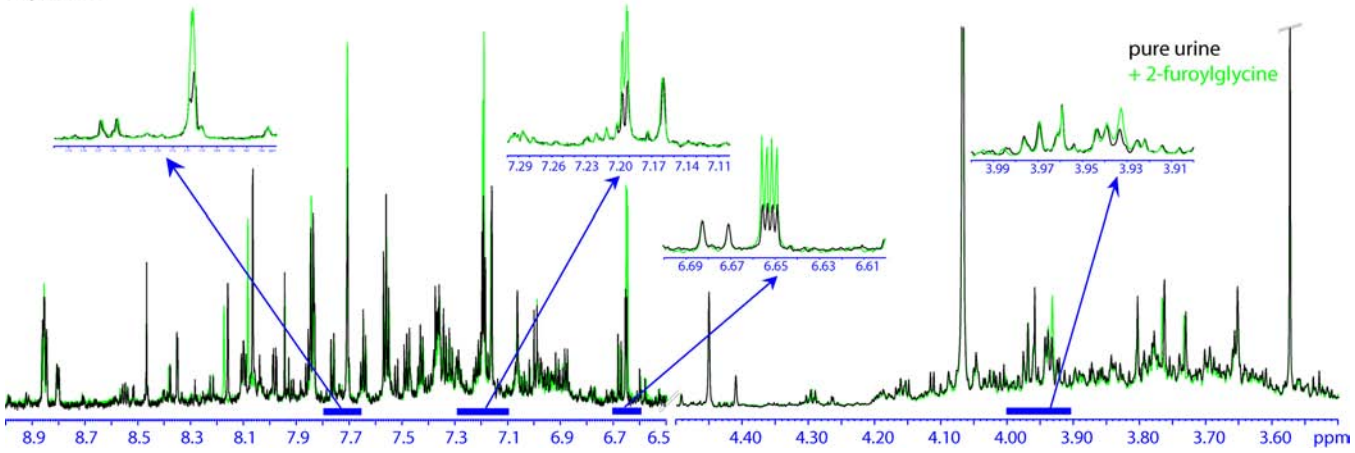

Figure 2. Standard addition experiment of 2-furoylglycine to a urine sample. Black, urine sample collected after coffee consumption; green, spiking of 2-furoylglycine to the same urine sample for confirmation of the assumed chemical structure of the biomarker. Chemical shifts are δ 7.71 (d), δ 7.20 (dd), δ 6.65 (dd), and δ 3.93 (s).

before bed) as "no coffee samples". Volunteers participated in the dietary intervention trial for 6 days; therefore, 24 urine samples per participant were collected. Pairwise orthogonal partial least-squares discriminant analysis (OPLS-DA)[51] was carried out with Matlab software. The OPLS-DA loading plots were created with an in-house Matlab script according to the method of Cloarec et al.[52]

RESULTS AND DISCUSSION

Discovery Phase: Nontargeted ^{1}H NMR Metabolic Profiling of Urine from a 6-Day Dietary Intervention Study. To discover novel biomarkers of food consumption, we performed a human dietary intervention trial (n = 8), where participants consumed a standardized breakfast and lunch and varying dinner each day (for more details, see also Heinzmann et al.[46]). As part of the dietary protocol, participants were allowed coffee for breakfast and until 12 am each day (SI Figure 1). Six participants chose coffee, one participant consumed chicory coffee, and one deviated from the protocol and drank Earl Grey tea every day. Urinary metabolite profiles were acquired to enable comparison of metabolites excreted after coffee consumption. OPLS-DA analysis of the urines from coffee-drinking volunteers revealed putative biomarker(s) with chemical shifts at δ 8.79 (d), δ 7.20, δ 6.65 (dd), δ 4.40 (s) (Figure 1B). 2D HSQC NMR suggested these shifts derived from two different metabolites (see SI Figure 2), namely 2-furoylglycine (2-FG) and *N*-methylpyridinium (NMP). Confirmation of the chemical structures was carried out by standard spiking experiments of the chemical standards 2-FG and NMP into urine samples (Figure 2 and SI Figure 3). ^{1}H NMR shifts of 2-FG standard were δ 6.65 (dd, H-C4 of furoyl), δ 7.20 (dd, H-C3 of furoyl), δ 7.71 (d, H-C5 of furoyl), δ 3.93 (s, CH_2 of glycine). The standard matched the prediction from the OPLS-DA analysis, with the exception of the two latter signals, which were overlapped with other metabolites and did not resolve in the OPLS-DA loadings plot. NMP has previously been linked to coffee consumption by Lang et al.[41] Urinary excretion of the glycine conjugate of derivatized furan, 2-FG, has not, to our knowledge, been reported to be associated with coffee consumption. In serum, however, it has been previously detected.[53] Integration of the H-C3 of furoyl signal confirmed high excretion of 2-FG in coffee consumers especially in the urine samples at lunch time. Neither chicory coffee nor Earl Grey tea consumption resulted in excretion of 2-FG with urine (Figure 3), and inspection of urine spectra after consumption of these coffee alternatives did not show ^{1}H NMR-detectable quantities of 2-FG (SI Figure 4). Interestingly, hippurate, which is discussed as a potential biomarker for coffee consumption,[37] correlated negatively with coffee consumption. The coffee consumption period was closely aligned with breakfast, which

DOI: 10.1021/acs.jafc.5b03040
J. Agric. Food Chem. 2015, 63, 8615−8621

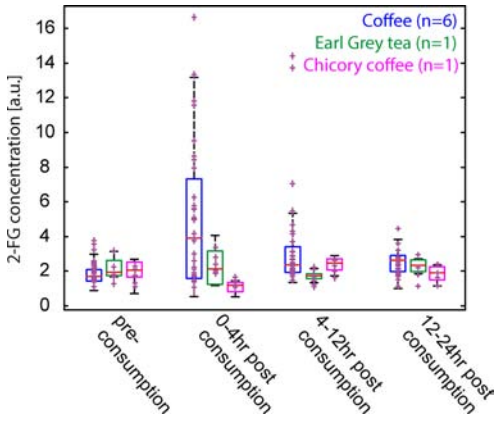

Figure 3. Boxplot and individual measurement points (purple) of urinary 2-furoylglycine excretion in volunteers at the four different time points. Boxplots are divided into blue, "coffee consumption"; green, "alternative consumption of Earl Grey tea"; and magenta, "alternative consumption of Chicory coffee".

was not rich in polyphenols, while dinner (i.e., part of the "noncoffee sample" group) was always rich in fruit and vegetables,[46] and polyphenols can be metabolized to hippurate.[45,54]

Dietary Sourcing Phase: Possible Sources of 2-Furoylglycine in Coffee. To investigate the origin of 2-FG in participant's urine samples after coffee consumption, we interrogated existing literature on furan derivates in different coffees, their concentration, and possible degradation pathways in humans after consumption (Figure 4). Indeed, furan metabolites arise through roasting of coffee beans via the Maillard reaction,[55] and the highest concentrations can be found in roasted ground coffee (6900 μg/kg) and considerably lower amounts in instant coffee (569 μg/kg).[56−59] The amount of furan varies, depending on coffee bean species and roast degree.[33] Other sources of furan exist but provide much lower quantities, e.g., baby foods with up to 29 μg/kg, soups and sauces (<24 μg/kg), and 0−4 μg/kg in tea,[55,60,61] and are therefore not expected to interfere with 2-FG excretion. Dependent on the chosen coffee brewing procedure, about 2−50% of the bean-derived furans get extracted into coffee.[59] Moon et al. have identified furans in coffee and found seven different furan derivatives such as furfuryl alcohol and furfural.[34] After consumption, furans undergo conversion to furfural and 2-furoic acid, then conjugation with glycine to 2-FG, which can then be excreted via the kidney,[62−64] see Figure 4. Remarkably, while the roasting process can potentially produce furan and various 2-furan metabolites, the human metabolism reduces such diversity to a single metabolite being excreted, namely 2-FG.

From our ^{1}H NMR spectral analysis, we detected furan derivatives such as 2-furoic acid and furfuryl alcohol in relatively high quantities in espresso (Figure 5 and SI Figure 6). Instant espresso also contained 2-furoic acid, and much lower quantities were found in chicory coffee. This overview of furan derivates is in consensus with suggested furan concentrations in existing literature.[33,34,57−59] Furfuryl alcohol was not found in instant espresso or chicory coffee. Trigonelline and its roasting product NMP could be found in espresso and instant espresso but not in chicory coffee. An additional furan derivate, 5-hydroxymethylfurfural, appeared in instant espresso and in high amounts in chicory coffee, and only little amounts in espresso. This metabolite is proposed to get metabolized to 5-hydroxymethylfuroic acid and 2,5-furandicarboxylfuroic acid and their glycine adducts[65] and is therefore not expected to influence 2-FG excretion in the chicory coffee or instant espresso consumer.

Confirmation Phase: Excretion Kinetics of 2-Furoylglycine after Coffee Consumption. To confirm the putative biomarker and investigate the mode of excretion, we carried out an additional coffee intervention study where participants avoided coffee for 24 h and then collected several timed spot urine samples over 24 h after a single dose of espresso.

Excretion of 2-FG was quantified by the ratio of area under the curve integration of 2-FG (δ 6.640−6.653) and creatinine (δ 4.0405−4.0475). All participants showed a maximal

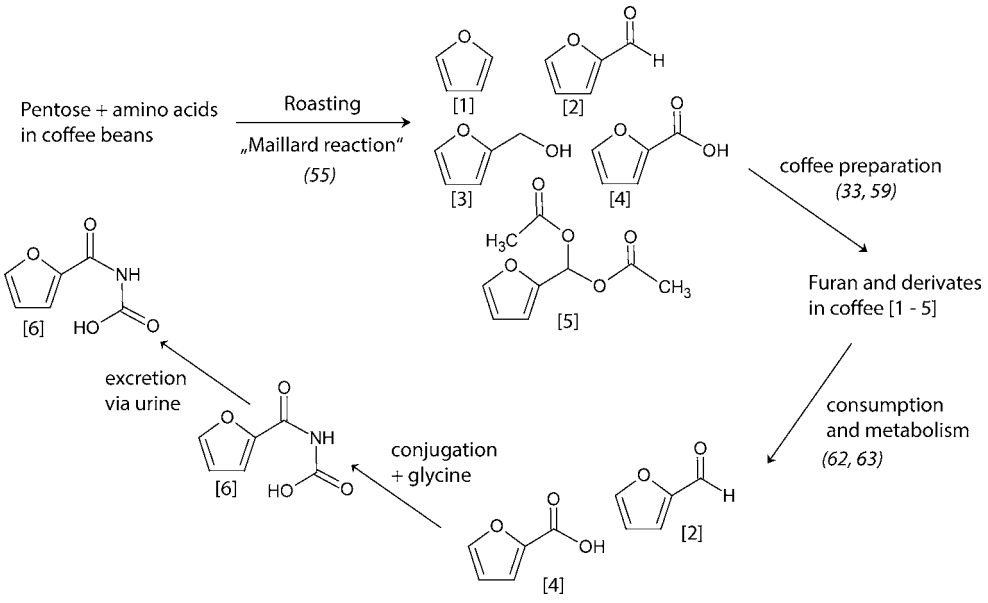

Figure 4. Summary of origin, extraction, metabolism, and excretion of furan metabolites and 2-furoylglycine. Abbreviations: 1, furan; 2, furfural; 3, 2-furoic acid; 4, furfuryl alcohol; 5, furfural diacetate; and 6, 2-furoylglycine.

DOI: 10.1021/acs.jafc.5b03040
J. Agric. Food Chem. 2015, 63, 8615−8621

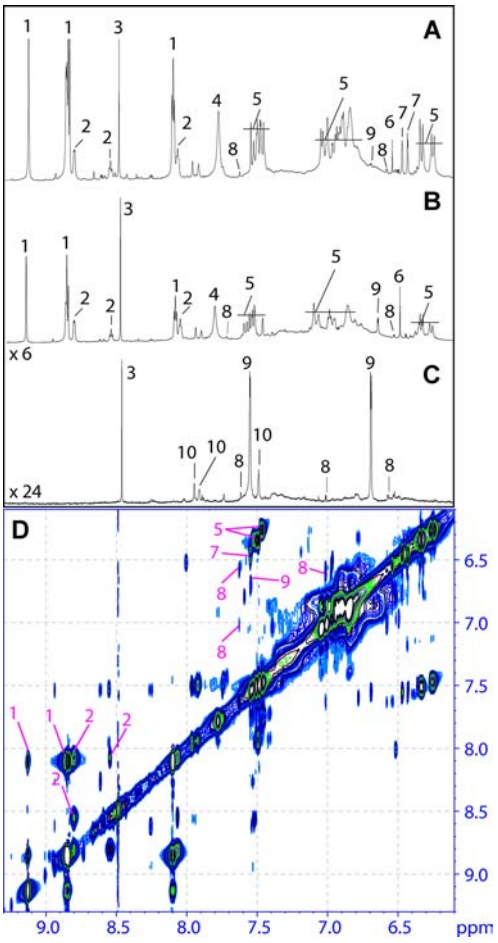

Figure 5. ^{1}H NMR spectrum of (A) espresso coffee, (B) instant espresso, and (C) chicory coffee with main peaks labeled. Spectra of B and C are enlarged by ×6 and ×24, respectively. (D) Two-dimensional NMR spectroscopy (^{1}H−^{1}H-TOCSY) of the aromatic area (δ 9.3−6.0) of espresso coffee: 1, trigonelline; 2, *N*-methylpyridinium; 3, formate; 4, caffeine; 5, chlorogenic acids; 6, fumarate; 7, furfurylalcohol; 8, 2-furoic acid; 9, 5-hydroxymethylfurfural (5-HMF); and 10, unknown compound (signals linked in TOCSY).

excretion of 2-FG after 2 h (p = 0.0002) and a rapid decline to near baseline after 24 h (p = 0.74), as shown in Figure 6. In more detail, the mean value of 2-FG/creatinine ratio was 0.0038 and 0.0041 2 and 0 h before coffee consumption, where this value is a result of baseline and other peak background integration. At 2 h after consumption, the value increased to 0.031, dropped rapidly to 0.011 4 h after consumption, and further declined to 0.0044 after 24 h. The interindividual variation was minimal, and all participants showed a similar trajectory (Figure 6). Deviation of the excretion curve, e.g. volunteer A did not decline to baseline after 24 h, was largely attributed to peak overlap in the spectral region of 2-FG. Overall, the excretion can be described as first-order excretion kinetics, as evidenced by a fast accumulation of the metabolite in urine and decline to baseline within 24 h. It can be discussed, however, that more sensitive analytical chemistry measurements such as UPLC-MS might allow detection of 2-FG for a longer period.[66] This has been shown by Lang et al.,[41] where NMP could be detected up to 5 days after coffee consumption. For comparison, NMP showed excretion kinetics similar to that of 2-FG (SI Figure 5).

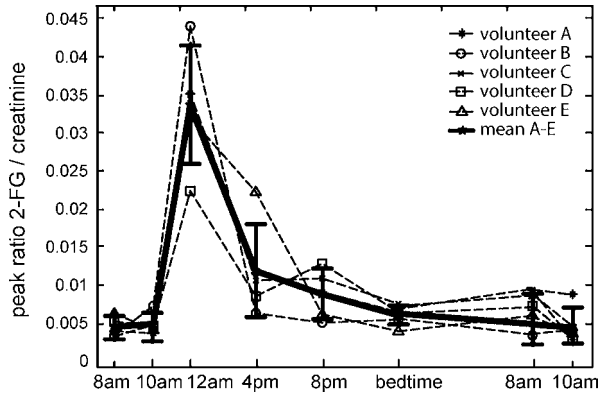

Figure 6. Excretion kinetics of 2-furoylglycine after coffee consumption (n = 5) over 26 h. Coffee was consumed at 10 am. 2-FG was relatively quantified by integration of the spectral region δ 6.640−6.654, including the doublet of doublets at δ 6.647 in relation to creatinine (δ 4.056−4.072). The five individuals showed similar trajectory in 2-FG excretion with maximal excretion of the biomarker at 2 h post coffee consumption and little interindividual variation.

In summary, we introduced a novel biomarker for coffee consumption by combining nontargeted ^{1}H NMR metabolic profiling in a nutritional intervention study, investigation of possible dietary sources of the biomarker, and finally validation of the putative marker in a second food intervention study. In contrast to previously identified biomarkers such as caffeine and chlorogenic acid degradation products, we identified a biomarker that is dependent on the roasting procedure of the coffee bean and therefore not influenced by consumption of tea, fruit and vegetables, or caffeine-containing energy drinks, which makes it highly specific to coffee. As a next step, the biomarker could now be further validated in a larger cohort, where coffee drinking behavior, different coffee types, and varying amounts of ingested coffee are recorded and matching urine samples are available for quantification of 2-FG to assess its quantitative rather than qualitative value. A combination of data from a well-monitored coffee drinking cohort as assessed by urinary 2-FG quantification with, e.g., CVD risk factors such as blood pressure, blood lipid parameters, and BMI, should deliver valuable information on potential health benefit of coffee consumption on disease risk and disease progression. For example, urinary metabolic profiling data from the INTERMAP study highlighted the here-assigned coffee biomarker to be inversely associated with BMI.[67] Taking advantage of the fact that different coffee biomarkers derive from different ingredients of coffee, a simultaneous analysis of several coffee biomarkers should pave the way for designing a biomarker pattern for sensitive and highly specific detection of coffee consumption in individuals and allow researchers to reach meaningful conclusions on the influence of coffee consumption on health and disease.

■ ASSOCIATED CONTENT

Supporting Information

The Supporting Information is available free of charge on the ACS Publications website at DOI: 10.1021/acs.jafc.5b03040.

Study design for the 6-day dietary intervention study; two-dimensional HSQC spectrum of spiked urine; ^{1}H NMR urine profiles of a sample obtained after coffee consumption with standard addition of 2-furoylglycine and *N*-methylpyridinium; urine spectral region of 2-FG

DOI: 10.1021/acs.jafc.5b03040
J. Agric. Food Chem. 2015, 63, 8615−8621

(6.63−6.67 ppm) in all volunteers; excretion kinetics of 2-furoylglycine and *N*-methylpyridinium after coffee consumption; and 2D NMR spectroscopy (^{1}H−^{1}H-TOCSY) of espresso coffee, instant espresso, and chicory coffee (PDF)

AUTHOR INFORMATION

Corresponding Author

*E-mail: silke.heinzmann@helmholtz-muenchen.de. Phone: +49 89 3187 3308. Fax: +49 89 3187 2705.

Notes

The authors declare no competing financial interest.

ACKNOWLEDGMENTS

The authors thank Roman Lang and Thomas Hofmann from Technische Universität München for the kind donation of the chemical standard *N*-methylpyridinium.

ABBREVIATIONS USED

NMR, nuclear magnetic resonance; TSP, trimethylsilyl-tetradeuteropropionic acid; FID, free induction decay; HSQC, heteronuclear single quantum coherence; TOCSY, total correlation spectroscopy; DIPSI, decoupling in the presence of scalar interactions; OPLS-DA, orthogonal partial least-squares discriminant analysis; PEP, preservation of equivalent pathways; WATERGATE, water suppression by gradient tailored excitation; 2-FG, 2-furoylglycine; NMP, *N*-methylpyridinium; AUC, area under the curve

REFERENCES

(1) Fredholm, B. B.; Battig, K.; Holmen, J.; Nehlig, A.; Zvartau, E. E. Actions of caffeine in the brain with special reference to factors that contribute to its widespread use. *Pharmacol. Rev.* **1999**, *51*, 83−133.

(2) Gilbert, R. M. Caffeine consumption. *Prog. Clin. Biol. Res.* **1984**, *158*, 185−213.

(3) Myers, M. G. Effects of caffeine on blood pressure. *Arch. Intern. Med.* **1988**, *148*, 1189−1193.

(4) Hindmarch, I.; Rigney, U.; Stanley, N.; Quinlan, P.; Rycroft, J.; Lane, J. A naturalistic investigation of the effects of day-long consumption of tea, coffee and water on alertness, sleep onset and sleep quality. *Psychopharmacology* **2000**, *149*, 203−216.

(5) Smith, A. P.; Brockman, P.; Flynn, R.; Maben, A.; Thomas, M. Investigation of the effects of coffee on alertness and performance during the day and night. *Neuropsychobiology* **1993**, *27*, 217−23.

(6) Doherty, M.; Smith, P. M. Effects of caffeine ingestion on rating of perceived exertion during and after exercise: a meta-analysis. *Scand. J. Med. Sci. Sports* **2005**, *15*, 69−78.

(7) Doherty, M.; Smith, P. M. Effects of caffeine ingestion on exercise testing: A meta-analysis. *Int. J. Sport Nutr. Exercise Metab.* **2004**, *14*, 626−646.

(8) Dulloo, A. G.; Geissler, C. A.; Horton, T.; Collins, A.; Miller, D. S. Normal caffeine consumption: influence on thermogenesis and daily energy expenditure in lean and postobese human volunteers. *Am. J. Clin. Nutr.* **1989**, *49*, 44−50.

(9) Koot, P.; Deurenberg, P. Comparison of changes in energy expenditure and body temperatures after caffeine consumption. *Ann. Nutr. Metab.* **1995**, *39*, 135−42.

(10) Bracco, D.; Ferrarra, J. M.; Arnaud, M. J.; Jequier, E.; Schutz, Y. Effects of caffeine on energy metabolism, heart rate, and methylxanthine metabolism in lean and obese women. *Am. J. Physiol* **1995**, *269*, E671−8.

(11) Maia, L.; de Mendonca, A. Does caffeine intake protect from Alzheimer's disease? *Eur. J. Neurol.* **2002**, *9*, 377−382.

(12) Santos, C.; Costa, J.; Santos, J.; Vaz-Carneiro, A.; Lunet, N. Caffeine Intake and Dementia: Systematic Review and Meta-Analysis. *J. Alzheimer's Dis.* **2010**, *20*, S187−S204.

(13) Eskelinen, M. H.; Kivipelto, M. Caffeine as a Protective Factor in Dementia and Alzheimer's Disease. *J. Alzheimer's Dis.* **2010**, *20*, S167−S174.

(14) Hernán, M. A.; Takkouche, B.; Caamano-Isorna, F.; Gestal-Otero, J. J. A meta-analysis of coffee drinking, cigarette smoking, and the risk of Parkinson's disease. *Ann. Neurol.* **2002**, *52*, 276−284.

(15) Hu, G.; Bidel, S.; Jousilahti, P.; Antikainen, R.; Tuomilehto, J. Coffee and tea consumption and the risk of Parkinson's disease. *Mov. Disord.* **2007**, *22*, 2242−2248.

(16) Ross, G. W.; Abbott, R. D.; Petrovitch, H.; Morens, D. M.; Grandinetti, A.; Tung, K. H.; Tanner, C. M.; Masaki, K. H.; Blanchette, P. L.; Curb, J. D.; Popper, J. S.; White, L. R. Association of coffee and caffeine intake with the risk of Parkinson disease. *JAMA, J. Am. Med. Assoc.* **2000**, *283*, 2674−2679.

(17) Klatsky, A. L.; Morton, C.; Udaltsova, N.; Friedman, G. D. Coffee, cirrhosis, and transaminase enzymes. *Arch. Intern. Med.* **2006**, *166*, 1190−1195.

(18) Gallus, S.; Tavani, A.; Negri, E.; La Vecchia, C. Does coffee protect against liver cirrhosis? *Ann. Epidemiol.* **2002**, *12*, 202−205.

(19) Larsson, S. C.; Wolk, A. Coffee consumption and risk of liver cancer: A meta-analysis. *Gastroenterology* **2007**, *132*, 1740−1745.

(20) Sinha, R.; Cross, A. J.; Daniel, C. R.; Graubard, B. I.; Wu, J. W.; Hollenbeck, A. R.; Gunter, M. J.; Park, Y.; Freedman, N. D. Caffeinated and decaffeinated coffee and tea intakes and risk of colorectal cancer in a large prospective study. *Am. J. Clin. Nutr.* **2012**, *96*, 374−381.

(21) Lopez-Garcia, E.; van Dam, R. M.; Willett, W. C.; Rimm, E. B.; Manson, J. E.; Stampfer, M. J.; Rexrode, K. M.; Hu, F. B. Coffee consumption and coronary heart disease in men and women - A prospective cohort study. *Circulation* **2006**, *113*, 2045−2053.

(22) Sofi, F.; Conti, A. A.; Gori, A. M.; Eliana Luisi, M. L.; Casini, A.; Abbate, R.; Gensini, G. F. Coffee consumption and risk of coronary heart disease: A meta-analysis. *Nutr., Metab. Cardiovasc. Dis.* **2007**, *17*, 209−223.

(23) Larsson, S. C.; Orsini, N. Coffee Consumption and Risk of Stroke: A Dose-Response Meta-Analysis of Prospective Studies. *Am. J. Epidemiol.* **2011**, *174*, 993−1001.

(24) Huxley, R.; Lee, C. M. Y.; Barzi, F.; Timmermeister, L.; Czernichow, S.; Perkovic, V.; Grobbee, D. E.; Batty, D.; Woodward, M. Coffee, Decaffeinated Coffee, and Tea Consumption in Relation to Incident Type 2 Diabetes Mellitus A Systematic Review With Meta-analysis. *Arch. Intern. Med.* **2009**, *169*, 2053−2063.

(25) Ding, M.; Bhupathiraju, S. N.; Chen, M.; van Dam, R. M.; Hu, F. B. Caffeinated and Decaffeinated Coffee Consumption and Risk of Type 2 Diabetes: A Systematic Review and a Dose-Response Meta-analysis. *Diabetes Care* **2014**, *37*, 569−586.

(26) Lopez-Garcia, E.; van Dam, R. M.; Li, T. Y.; Rodriguez-Artalejo, F.; Hu, F. B. The relationship of coffee consumption with mortality. *Ann. Intern. Med.* **2008**, *148*, 904.

(27) Bidel, S.; Hu, G.; Qiao, Q.; Jousilahti, P.; Antikainen, R.; Tuomilehto, J. Coffee consumption and risk of total and cardiovascular mortality among patients with type 2 diabetes. *Diabetologia* **2006**, *49*, 2618−2626.

(28) Spiller, M. A. The chemical components of coffee. *Prog. Clin. Biol. Res.* **1984**, *158*, 91−147.

(29) Yanagimoto, K.; Ochi, H.; Lee, K. G.; Shibamoto, T. Antioxidative activities of fractions obtained from brewed coffee. *J. Agric. Food Chem.* **2004**, *52*, 592−596.

(30) Urgert, R.; Katan, M. B. The cholesterol-raising factor from coffee beans. *Annu. Rev. Nutr.* **1997**, *17*, 305−324.

(31) Casiglia, E.; Spolaore, P.; Ginocchio, G.; Ambrosio, G. B. Unexpected effects of coffee consumption on liver enzymes. *Eur. J. Epidemiol.* **1993**, *9*, 293−297.

(32) Moser, G. J.; Foley, J.; Burnett, M.; Goldsworthy, T. L.; Maronpot, R. Furan-induced dose-response relationships for liver

DOI: 10.1021/acs.jafc.5b03040
J. Agric. Food Chem. 2015, 63, 8615−8621

cytotoxicity, cell proliferation, and tumorigenicity (furan-induced liver tumorigenicity). *Exp. Toxicol. Pathol.* **2009**, *61*, 101−111.
(33) Arisseto, A. P.; Vicente, E.; Ueno, M. S.; Tfouni, S. A. V.; De Figueiredo Toledo, M. C. Furan Levels in Coffee As Influenced by Species, Roast Degree, and Brewing Procedures. *J. Agric. Food Chem.* **2011**, *59*, 3118−3124.
(34) Moon, J.-K.; Shibamoto, T. Role of Roasting Conditions in the Profile of Volatile Flavor Chemicals Formed from Coffee Beans. *J. Agric. Food Chem.* **2009**, *57*, 5823−5831.
(35) Bingham, S. A. Limitations of the various methods for collecting dietary intake data. *Ann. Nutr. Metab.* **1991**, *35*, 117−127.
(36) Bates, C. J., Biochemical markers of nutrient intake. In *Design Concepts in Nutritional Epidemiology*; Nelson, B. M. M. M., Ed.; Oxford University Press: Oxford, 1991; pp 192−165.
(37) Rothwell, J. A.; Fillatre, Y.; Martin, J.-F.; Lyan, B.; Pujos-Guillot, E.; Fezeu, L.; Hercberg, S.; Comte, B.; Galan, P.; Touvier, M.; Manach, C. New Biomarkers of Coffee Consumption Identified by the Non-Targeted Metabolomic Profiling of Cohort Study Subjects. *PLoS One* **2014**, *9*, e93474.
(38) Lloyd, A. J.; Beckmann, M.; Haldar, S.; Seal, C.; Brandt, K.; Draper, J. Data-driven strategy for the discovery of potential urinary biomarkers of habitual dietary exposure. *Am. J. Clin. Nutr.* **2013**, *97*, 377−389.
(39) Stalmach, A.; Mullen, W.; Barron, D.; Uchida, K.; Yokota, T.; Cavin, C.; Steiling, H.; Williamson, G.; Crozier, A. Metabolite Profiling of Hydroxycinnamate Derivatives in Plasma and Urine after the Ingestion of Coffee by Humans: Identification of Biomarkers of Coffee Consumption. *Drug Metab. Dispos.* **2009**, *37*, 1749−1758.
(40) Ito, H.; Gonthier, M. P.; Manach, C.; Morand, C.; Mennen, L.; Remesy, C.; Scalbert, A. Polyphenol levels in human urine after intake of six different polyphenol-rich beverages. *Br. J. Nutr.* **2005**, *94*, 500−509.
(41) Lang, R.; Wahl, A.; Stark, T.; Hofmann, T. Urinary N-methylpyridinium and trigonelline as candidate dietary biomarkers of coffee consumption. *Mol. Nutr. Food Res.* **2011**, *55*, 1613−1623.
(42) Mennen, L. I.; Sapinho, D.; Ito, H.; Bertrais, S.; Galan, P.; Hercberg, S.; Scalbert, A. Urinary flavonoids and phenolic acids as biomarkers of intake for polyphenol-rich foods. *Br. J. Nutr.* **2006**, *96*, 191−198.
(43) Hervert-Hernandez, D.; Goni, I. Dietary Polyphenols and Human Gut Microbiota: a Review. *Food Rev. Int.* **2011**, *27*, 154−169.
(44) Walker, A. W.; Ince, J.; Duncan, S. H.; Webster, L. M.; Holtrop, G.; Ze, X.; Brown, D.; Stares, M. D.; Scott, P.; Bergerat, A.; Louis, P.; McIntosh, F.; Johnstone, A. M.; Lobley, G. E.; Parkhill, J.; Flint, H. J. Dominant and diet-responsive groups of bacteria within the human colonic microbiota. *ISME J.* **2011**, *5*, 220−230.
(45) Heinzmann, S. S.; Merrifield, C. A.; Rezzi, S.; Kochhar, S.; Lindon, J. C.; Holmes, E.; Nicholson, J. K. Stability and Robustness of Human Metabolic Phenotypes in Response to Sequential Food Challenges. *J. Proteome Res.* **2011**, *11*, 643.
(46) Heinzmann, S. S.; Brown, I. J.; Chan, Q.; Bictash, M.; Dumas, M.-E.; Kochhar, S.; Stamler, J.; Holmes, E.; Elliott, P.; Nicholson, J. K. Metabolic profiling strategy for discovery of nutritional biomarkers: proline betaine as a marker of citrus consumption. *Am. J. Clin. Nutr.* **2010**, *92*, 436−443.
(47) O'Sullivan, A.; Gibney, M. J.; Brennan, L. Dietary intake patterns are reflected in metabolomic profiles: potential role in dietary assessment studies. *Am. J. Clin. Nutr.* **2011**, *93*, 314−321.
(48) Lloyd, A. J.; Fave, G.; Beckmann, M.; Lin, W.; Tailliart, K.; Xie, L.; Mathers, J. C.; Draper, J. Use of mass spectrometry fingerprinting to identify urinary metabolites after consumption of specific foods. *Am. J. Clin. Nutr.* **2011**, *94*, 981−991.
(49) Dieterle, F.; Ross, A.; Schlotterbeck, G.; Senn, H. Probabilistic quotient normalization as robust method to account for dilution of complex biological mixtures. Application in H-1 NMR metabonomics. *Anal. Chem.* **2006**, *78*, 4281−4290.
(50) Veselkov, K. A.; Lindon, J. C.; Ebbels, T. M. D.; Crockford, D.; Volynkin, V. V.; Holmes, E.; Davies, D. B.; Nicholson, J. K. Recursive Segment-Wise Peak Alignment of Biological 1H NMR Spectra for Improved Metabolic Biomarker Recovery. *Anal. Chem.* **2009**, *81*, 56−66.
(51) Trygg, J.; Wold, S. PLS regression on wavelet compressed NIR spectra. *Chemom. Intell. Lab. Syst.* **1998**, *42*, 209−220.
(52) Cloarec, O.; Dumas, M. E.; Craig, A.; Barton, R. H.; Trygg, J.; Hudson, J.; Blancher, C.; Gauguier, D.; Lindon, J. C.; Holmes, E.; Nicholson, J. Statistical total correlation spectroscopy: An exploratory approach for latent biomarker identification from metabolic H-1 NMR data sets. *Anal. Chem.* **2005**, *77*, 1282−1289.
(53) Guertin, K. A.; Loftfield, E.; Boca, S. M.; Sampson, J. N.; Moore, S. C.; Xiao, Q.; Huang, W.-Y.; Xiong, X.; Freedman, N. D.; Cross, A. J.; Sinha, R. Serum biomarkers of habitual coffee consumption may provide insight into the mechanism underlying the association between coffee consumption and colorectal cancer. *Am. J. Clin. Nutr.* **2015**, *101*, 1000−1011.
(54) van Duijnhoven, F. J. B.; Bueno-De-Mesquita, H. B.; Ferrari, P.; Jenab, M.; Boshuizen, H. C.; Ros, M. M.; Casagrande, C.; Tjonneland, A.; Olsen, A.; Overvad, K.; Thorlacius-Ussing, O.; Clavel-Chapelon, F.; Boutron-Ruault, M. C.; Morois, S.; Kaaks, R.; Linseisen, J.; Boeing, H.; Nothlings, U.; Trichopoulou, A.; Trichopoulos, D.; Misirli, G.; Palli, D.; Sieri, S.; Panico, S.; Tumino, R.; Vineis, P.; Peeters, P. H. M.; van Gils, C. H.; Ocke, M. C.; Lund, E.; Engeset, D.; Skeie, G.; Suarez, L. R.; Gonzalez, C. A.; Sanchez, M. J.; Dorronsoro, M.; Navarro, C.; Barricarte, A.; Berglund, G.; Manjer, J.; Hallmans, G.; Palmqvist, R.; Bingham, S. A.; Khaw, K. T.; Key, T. J.; Allen, N. E.; Boffetta, P.; Slimani, N.; Rinaldi, S.; Gallo, V.; Norat, T.; Riboli, E. Fruit, vegetables, and colorectal cancer risk: the European Prospective Investigation into Cancer and Nutrition. *Am. J. Clin. Nutr.* **2009**, *89*, 1441−1452.
(55) Maarse, H.; Visscher, C. A.; Willimsens, L. C. *Volatile Compounds in Food: Qualitative and Quantitative Data*, 7th ed.; Centraal Instituut voor Voedingsonderzoek, TNO: Zeist, 1994; Vol. 3.
(56) Hasnip, S.; Crews, C.; Castle, L. Some factors affecting the formation of furan in heated foods. *Food Addit. Contam.* **2006**, *23*, 219−227.
(57) Zoller, O.; Sager, F.; Reinhard, H. Furan in food: Headspace method and product survey. *Food Addit. Contam.* **2007**, *24*, 91−107.
(58) Kuballa, T.; Stier, S.; Strichow, N. Furan in Kaffee und Kaffeegetränken. *Dtsch. Lebensm.-Rundsch.* **2005**, *101*, 229−235.
(59) Guenther, H.; Hoenicke, K.; Biesterveld, S.; Gerhard-Rieben, E.; Lantz, I. Furan in coffee: pilot studies on formation during roasting and losses during production steps and consumer handling. *Food Addit. Contam., Part A* **2010**, *27*, 283−290.
(60) Moro, S.; Chipman, J. K.; Wegener, J.-W.; Hamberger, C.; Dekant, W.; Mally, A. Furan in heat-treated foods: Formation, exposure, toxicity, and aspects of risk assessment. *Mol. Nutr. Food Res.* **2012**, *56*, 1197−1211.
(61) Stofberg, J.; Grundschober, F. Consumption ratio and food predominance of flavouring materials. *Perfum. Flavor.* **1987**, *12*, 27.
(62) Rice, E. W. Furfural: exogenous precursor of certain urinary furans and possible toxicologic agent in humans. *Clin. Chem.* **1972**, *18*, 1550−1551.
(63) Nomeir, A. A.; Silveira, D. M.; McComish, M. F.; Chadwick, M. Comparative metabolism and disposition of furfural and furfuryl alcohol in rats. *Drug Metab. Dispos.* **1992**, *20*, 198−204.
(64) Parkash, M. K.; Caldwell, J. Metabolism and excretion of 14C furfural in the rat and mouse. *Food Chem. Toxicol.* **1994**, *32*, 887−95.
(65) Hardt-Stremayr, M.; Mattioli, S.; Greilberger, J.; Stiegler, P.; Matzi, V.; Schmid, M. G.; Wintersteiger, R. Determination of metabolites of 5-hydroxymethylfurfural in human urine after oral application. *J. Sep. Sci.* **2013**, *36*, 670−676.
(66) Wishart, D. S. Advances in metabolite identification. *Bioanalysis* **2011**, *3*, 1769−1782.
(67) Elliott, P.; Posma, J. M.; Chan, Q.; Garcia-Perez, I.; Wijeyesekera, A.; Bictash, M.; Ebbels, T. M. D.; Ueshima, H.; Zhao, L.; van Horn, L.; Daviglus, M.; Stamler, J.; Holmes, E.; Nicholson, J. K. Urinary metabolic signatures of human adiposity. *Sci. Transl. Med.* **2015**, *7*, 285ra62.

DOI: 10.1021/acs.jafc.5b03040
J. Agric. Food Chem. 2015, 63, 8615−8621

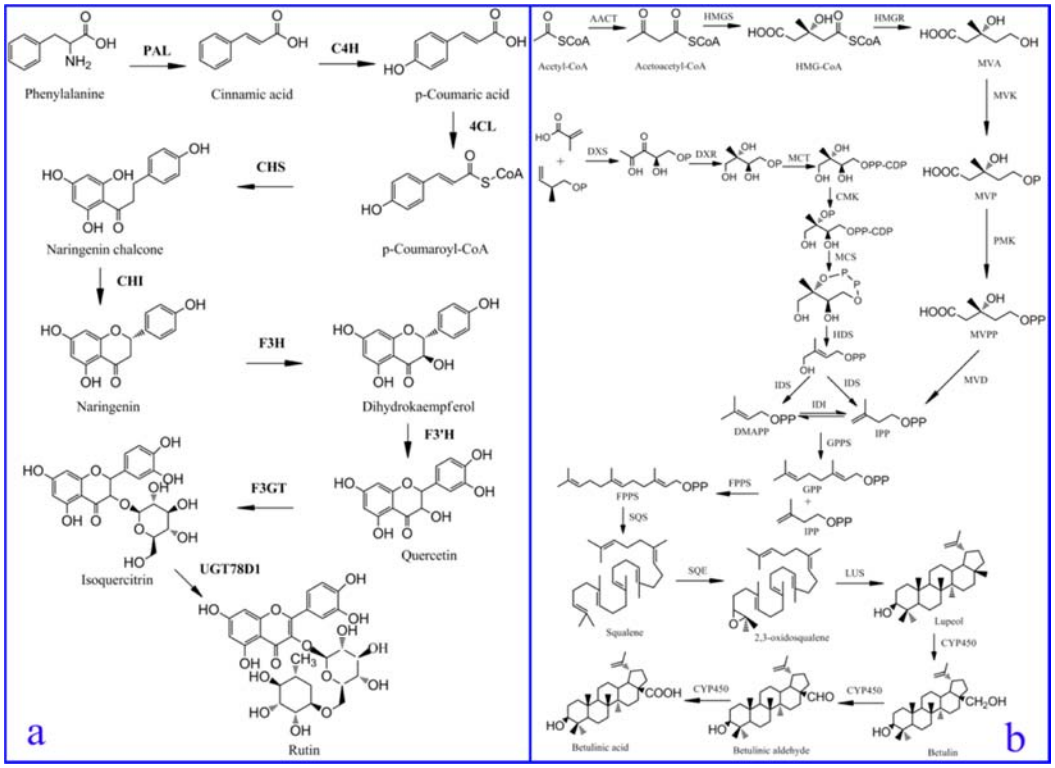

Figure 1. Schematics of (a) rutin biosynthesis and (b) betulin and betulinic acid biosynthesis. PAL, phenylalanine ammonia lyase; C4H, cinnamic acid 4-hydroxylase; 4CL, 4-coumarate-CoA ligase; CHS, chalcone synthase; CHI, chalcone isomerase; F3H, flavone 3-hydroxylase; F3′H, flavonoid 3′-hydroxylase; F3GT, flavonol 3-*O*-glucosyltransferase; UGT78D1, flavonol-3-*O*-glucoside L-rhamnosyltransferase; AACT, acetyl-CoA acetyltransferase; HMGS, hydroxymethylglutaryl-CoA synthase; HMGR, 3-hydroxy-3-methylglutaryl-coenzyme A reductase; MVK, mevalonate kinase; PMK, phosphomevalonate kinase; MVD, diphosphomevalonate decarboxylase; DXS, 1-deoxyxylulose-5-phosphate synthase; DXR, 1-deoxy-D-xylulose-5-phosphate reductoisomerase; MCT, 2-C-methyl-D-erythritol 4-phosphate cytidylyltransferase; CMK, 4-diphosphocytidyl-2-C-methyl-D-erythritol kinase; MCS, 2-C-methyl-D-erythritol 2,4- cyclodiphosphate synthase; HDS, 4-hydroxy-3-methylbut-2-enyl diphosphate synthase; IDS, 4-hydroxy-3-methylbut-2-enyl diphosphate reductase; IDI, Isopentenyl-diphosphate delta-isomerase; GPPS, geranyl diphosphate synthase; FPPS, farnesyl diphosphate synthase; SQS, squalene synthetase; SQE, squalene epoxidase; and LUS, lupeol synthase.

(MEP) pathway at the initial period (Figure 1b). These pathways generate the same products: isopentenyl diphosphate (IPP) and dimethylallyl diphosphate (DMAPP). Then, geranyl diphosphate synthase (GPPS) catalyzes the condensation of IPP and DMAPP to form geranyl pyrophosphate (GPP). GPP then unites with another molecule of IPP to form farnesyl pyrophosphate (FPP), catalyzed by farnesyl pyrophosphate synthetase. Next, squalene synthase (SQS) and squalene epoxide (SQE) catalyze two NADPH-requiring reactions to form squalene and 2,3-oxidosqualene, respectively; 2,3-oxidosqualene is the common precursor of triterpenes through different pathways. In betulinic acid biosynthesis, 2,3-oxidosqualene is converted to lupeol by lupeol synthase (LUP), and betulinic acid is derived from lupeol followed by successive oxidation at the C-28 position by the cytochrome P450 family.

Mulberry (*Morus alba* L., Moraceae) is used in traditional Chinese medicine and is the sole food source of the silkworm. The medicinal value of mulberry is derived from the many important secondary metabolites compounds it produces and includes protection against liver damage as well as antidiabetic, antioxidant, anticancer, and antifever effects.[11−17] Secondary metabolites produced by *M. alba* include flavonoid compounds[18−20] such as anthocyanin and rutin,[16,21] which have strong antioxidant and anti-inflammatory effects.[22,23]

Mulberry contains many more phenolic and flavonoid compounds than do other fruits and vegetables.[24] Some studies have assessed the rutin content in mulberry leaves,[25,26] but the contents of betulin and betulinic acid have not been evaluated for this plant. Although the draft genome sequence has been reported for another mulberry species, *Morus notabilis*,[27] and although most phenylpropanoid and triterpene biosynthetic genes have been identified, currently the genetic background is not clear for *M. alba*. In a previous study, our group sequenced the transcriptome of *M. alba* L. by using an NGS sequencing platform (unpublished), which is the first report of transcriptome analysis for *M. alba*. Here, we investigated the expression levels of genes related to phenylpropanoid and triterpene biosynthesis with reference to this transcriptome data and analyzed the rutin and betulinic acid contents in different organs by using quantitative real-time PCR (qRT-PCR) and high-performance liquid chromatography (HPLC), respectively. Our results are expected to provide baseline information toward elucidating the mechanism of astragaloside biosynthesis in *M. alba*.

MATERIALS AND METHODS

Plant Materials. *M. alba* plants were grown at the experimental farm of National Academy of Agricultural Science, Rural Development Administration (Wanju, Korea). The fruits, flowers, leaves, stems ,and roots were excised from mature plants. The samples were immediately frozen in liquid nitrogen and stored at −80 °C and/or freeze-dried for RNA isolation and/or HPLC analysis.

DOI: 10.1021/acs.jafc.5b03221
J. Agric. Food Chem. 2015, 63, 8622−8630

Table 1. Comparison of Phenylpropanoid Biosynthetic Genes of *Morus alba* L. with the Most Orthologous Genes

M. alba (accession no.)	length (amino acids)	orthologous genes (accession no.)	identity (%)
MaPAL1	722	*Morus notabilis* PAL (XM_010113926)	97
		Ricinus communis PAL (XM_002531631)	84
		Nelumbo nucifera PAL (XM_010264565)	84
MaPAL2	749	*Morus notabilis* PAL (XM_010109218)	97
		Boehmeria nivea PAL (KP100114)	87
		Jatropha curcas PAL (XM_012226984)	86
MaPAL3	344	*Morus notabilis* PAL (XM_010091807)	99
		Jatropha curcas PAL (XM_012221611)	78
		Nelumbo nucifera PAL (XM_010263680)	78
MaC4H1	525	*Morus notabilis* C4H (XM_010108644)	98
		Lonicera japonica C4H (JX068605)	81
		Theobroma cacao C4H (XM_007014477)	84
MaC4H2	507	*Morus notabilis* C4H (XM_004249173)	99
		Jatropha curcas C4H (XM_012222786)	92
		Rubus occidentalis C4H (FJ554629)	91
Ma4CL2	365	*Morus notabilis* 4CL2 (XM_010089179)	99
		Vitis vinifera 4CL (JN858959)	85
		Prunus persica 4CL (XM_007219446)	84
Ma4CL7-1	547	*Morus notabilis* 4CL7 (XM_010103319)	97
		Prunus mume 4CL7 (XM_008243188)	73
		Cucumis melo 4CL7 (XM_008444488)	67
Ma4CL7-2	539	*Morus notabilis* 4CL7 (XM_010113516)	97
		Malus domestica 4CL7 (XM_008386493)	81
		Betula pendula 4CL (KM099197)	80
Ma4CL9	471	*Morus notabilis* 4Cl9 (XM_010106939)	81
		Prunus mume 4CL9 (XM_008241147)	70
		Malus domestica 4CL9 (XM_008394619)	68
MaCHS1	257	*Morus notabilis* CHS (XM_010100833)	99
		Vaccinium ashei CHS (AB694902)	93
		Hypericum perforatum CHS (AF461105)	93
MaCHS2	259	*Citrus sinensis* CHS2 (XP_006468926)	86
		Clausena lansium CHS (KP064028)	86
		Elaeis guineensis CHS2 (XM_010931189)	87
		Citrus limon CHS (KP720587)	66
MaCHS3	399	*Populus alba* CHS (DQ371803)	65
		Cochlearia danica CHS (AF144532)	64
		Morus notabilis CHS9 (XM_010090374)	98
MaCHS9	218	*Ricinus communis* CHS (XM_002529211)	84
		Vitis vinifera CHS (XM_002276617)	84
		Morus notabilis CHI (XM_010103211)	95
MaCHI1	228	*Prunus cerasifera* CHI (KP772274)	57
		Camellia nitidissima CHI (HQ269805)	57
		Morus notabilis CHI (KF438043)	98
MaCHI2	308	*Prunus avium* CHI1 (GU990525)	80
		Populus trichocarpa CHI (XM_002315222)	77
		Morus notabilis CHI (XM_010105346)	98
MaCHI3	208	*Actinidia chrysantha* CHI (KM453235)	77
		Gossypium hirsutum CHI (GU295063)	77
		Morus notabilis F3H1 (KF438044)	99
MaF3H	228	*Dimocarpus longan* F3H (EF468104)	92
		Vitis vinifera F3H (XM_002275527)	91
		Morus notabilis F3H (XM_010107524)	97
MaF3′H1	354	*Prunus avium* F3′H1 (GU990527)	74
		Vitis vinifera F3′H3 (AB213604)	73
		Morus notabilis F3′H (XM_010107523)	97
MaF3′H2	177	*Prunus persica* F3′H (KJ484546)	73
		Vitis vinifera F3′H (AJ880357)	73
		Morus notabilis UGT85A1 (XM_010089319)	95
MaF3GT	339	*Theobroma cacao* UGT85A2 (XM_007047847)	78
		Prunus mume UGT85A5 (XM_008235943)	72
		Morus notabilis UGT85A2 (XM_010100315)	99
MaUGT78D1	447	*Prunus mume* UGT85A2 (XM_008221095)	74
		Theobroma cacao UGT85A2 (XM_007042858)	73

RNA Isolation and cDNA Synthesis. Samples (200 mg) of different organs of *M. alba* L. were ground with a mortar and pestle in liquid nitrogen. RNA was isolated separately using a Plant Total RNA Mini Kit (Geneaid, Taiwan) according to the manufacturer's instructions. The quality and concentration of total extracted RNA were determined by 1.2% formaldehyde RNA agarose-gel electrophoresis and NanoVue Plus spectrophotometer analysis (code no. 28956058, GE Healthcare, UK), respectively. For cDNA synthesis, 1 μg of total RNA was reverse transcribed (RT) using a ReverTra Ace-R kit (Toyobo, Osaka, Japan) and oligo (dT) 20 primer according to the

DOI: 10.1021/acs.jafc.5b03221
J. Agric. Food Chem. 2015, 63, 8622−8630

Table 2. Comparison of Triterpene Biosynthetic Genes of *Morus alba* L. with the Most Orthologous Genes

M. alba (accession no.)	length (amino acids)	orthologous genes (accession no.)	identity (%)
MaAACT1	403	*Morus notabilis* AACT1 (XM_010090057)	98
		Camellia oleifera AACT (GU594059)	92
		Sesamum indicum AACT1 (XM_011102210)	91
MaAACT2	416	*Morus notabilis* AACT2 (XM_010093715)	99
		Prunus mume AAC1 (XM_008226416)	84
		Cicer arietinum AACT2 (XM_004507531)	83
MaHMGS	464	*Morus notabilis* HMGS (XM_010109749)	98
		Ricinus communis HMGS (XM_002509646)	88
		Jatropha curcas HMGS (XM_012231634)	88
MaHMGR1	548	*Morus notabilis* HMGR1 (XM_010096207)	97
		Betula platyphylla HMGR (KJ452334)	85
		Hevea brasiliensis HMGR1 (P29057)	81
MaHMGR2	586	*Morus notabilis* HMGR2 (XM_010092425)	98
		Prunus mume HMGR1 (XM_008237609)	82
		Cucumis melo HMGR1 (XM_008452963)	80
MaMVK	356	*Morus notabilis* MVK (XM_010107540)	99
		Prunus mume MVK (XM_008248266)	83
		Jatropha curcas MVK (XM_012233688)	82
MaPMK	507	*Morus notabilis* PMK (XM_010112088)	91
		Prunus mume PMK (XM_008239928)	84
		Jatropha curcas PMK (XM_012236623)	82
MaMVD	421	*Morus notabilis* MVD (XM_010090485)	95
		Astragalus membranaceus MVD (KF355964)	86
		Glycine max MVD (XM_003555822)	87
MaIDI	295	*Morus notabilis* IDI2 (XM_010112783)	99
		Pueraria montana IDI (AY315650)	89
		Glycine soja IDI2 (KN645832)	88
MaDXS	714	*Morus notabilis* DXS (XM_010115150)	98
		Prunus mume DXS2 (XM_008238129)	84
		Ricinus communis DXS (XM_002532338)	85
MaDXR	363	*Morus notabilis* DXR (XM_010102910)	99
		Populus trichocarpa DXR (EU693020)	92
		Hevea brasiliensis DXR (AB294701)	91
MaMCT	243	*Morus notabilis* MCT (XM_010090393)	87
		Populus trichocarpa MCT (EU693021)	82
		Prunus mume MCT (XM_008220406)	71
MaCMK	254	*Morus notabilis* CMK (XM_010095512)	99
		Prunus mume CMK (XM_008229149)	81
		Cicer arietinum CMK (XM_004499380)	78
MaMCS	248	*Morus notabilis* MCS (XM_010114326)	96
		Fragaria vesca MCS (XM_004298785)	88
		Prunus mume MCS (XM_008240732)	74
MaHDS	740	*Morus notabilis* HDS (XM_010099896)	99
		Vitis vinifera HDS (XM_002285094)	90
		Theobroma cacao HDS1 (XM_007016661)	91
MaIDS	461	*Morus notabilis* IDS (XM_010097923)	97
		Prunus mume IDS (XM_008238530)	85
		Hevea brasiliensis IDS (AB294708)	85
MaGPPS	380	*Morus notabilis* GPPS (XM_010096985)	95
		Corylus avellana GPPS (EF553534)	77
		Elaeagnus umbellata GPPS (FJ827762)	78
MaFPPS	182	*Morus notabilis* FPPS1 (XM_010105650)	99
		Cucumis sativus FPPS1 (XM_004149361)	89
		Nelumbo nucifera FPPS1 (XM_010246724)	88
MaSQS	408	*Morus notabilis* L484 (XM_010111466)	98
		Cicer arietinum SQS (XM_004507443)	85
		Diospyros kaki SQS (FJ687954)	85
MaSES	524	*Theobroma cacao* SQE1 (XM_007018355)	86
		Cucumis melo SQE (XM_008454464)	86
		Jatropha curcas SQE (XM_012212770)	83
MaLUS	754	*Eucalyptus grandis* LUS (XM_010050218)	74
		Morus notabilis LUS (XM_010096904)	72
		Theobroma cacao LUS1 (XM_007014650)	73

manufacturer's protocol. A 20-fold dilution of 20 μL of the resulting cDNA was used as a template for qRT-PCR.

Sequence Analysis. To identify the phenylpropanoid and triterpene biosynthetic gene sequences in our mulberry NGS database, all generated sequences were blasted against related phenylpropanoid biosynthetic genes in GenBank using BioEdit version 7.0.9.0. The deduced amino acid sequences of the phenylpropanoid and triterpene biosynthetic genes were analyzed for homology by blasting against the

DOI: 10.1021/acs.jafc.5b03221
J. Agric. Food Chem. 2015, 63, 8622−8630

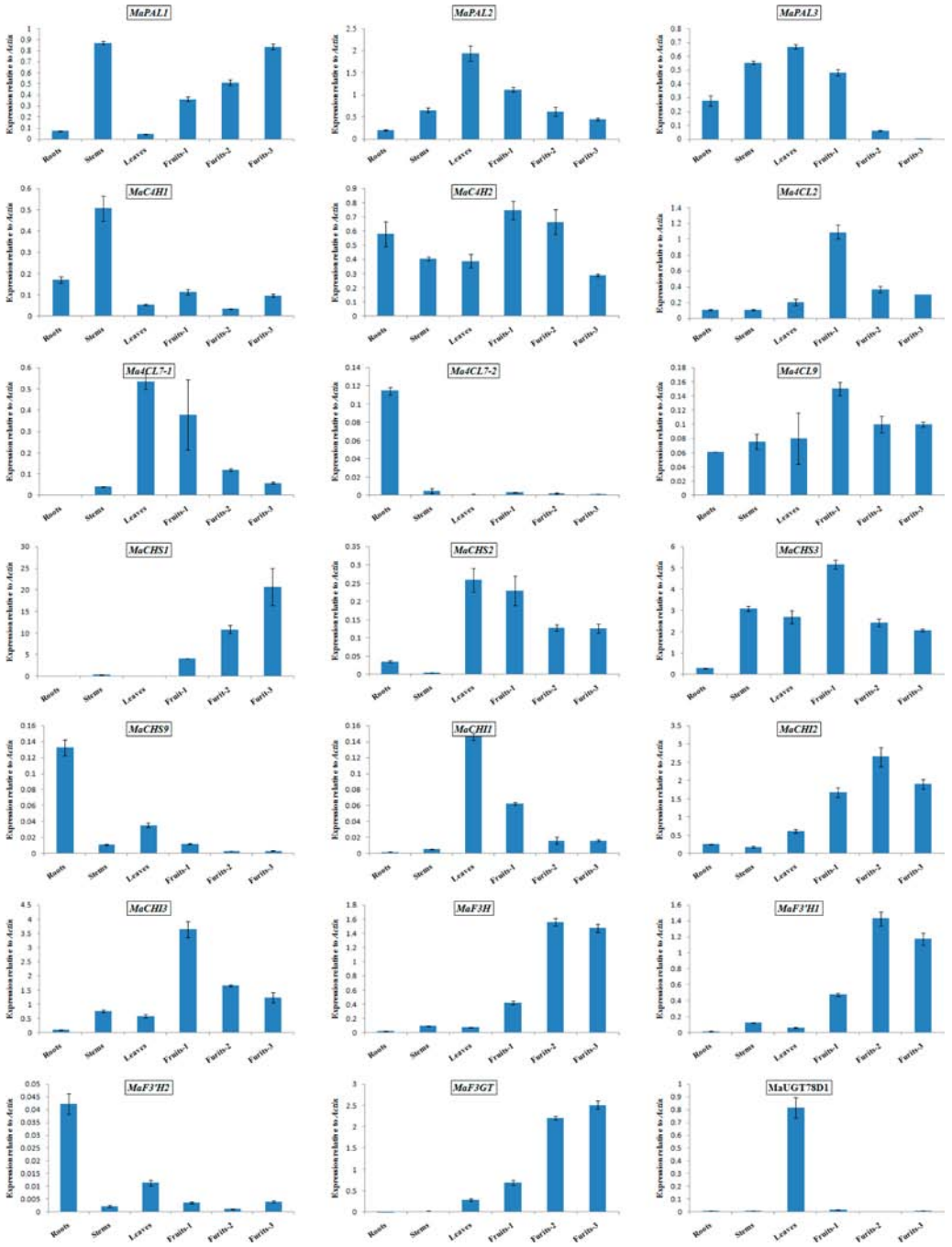

Figure 2. Expression levels of phenylpropanoid biosynthetic genes in different organs of mulberry (*Morus alba* L.) calculated by relative quantification with the mulberry *actin* housekeeping gene. Each value is the mean of three replicates, and error bars indicate standard deviation.

GenBank database. Identified gene sequences were submitted to GenBank.

Quantitative Real-Time Polymerase Chain Reaction. On the basis of the published gene sequences of *MaPAL1, MaPAL2, MaPAL3, MaC4H1, MaC4H2, Ma4CL2, Ma4CL7-1, Ma4CL7-2, Ma4CL9, MaCHS1, MaCHS2, MaCHS3, MaCHS9, MaCHI1, MaCHI2, MaCHI3, MaF3H, MaF3′H1, MaF3′H2, MaF3GT, and MaUGT78D1* (DNA Data Bank of Japan (DDBJ) accession nos. KJ616395−KJ616404 and KT630878−KT630889) for phenylpropanoid biosynthesis and those of *MaAACT1, MaAACT2, MaHMGS, MaHMGR1, MaHMGR2, MaMVK, MaPMK, MaMVD, MaIDI, MaDXS, MaDXR, MaMCT, MaCMK, MaMCS, MaHDS, MaIDS, MaGPPS, MaFPPS, MaSQS, MaSQE, and MaLUP* (DDBJ accession nos. KR080458−KR080471 and KR132245−KR132251), real-time PCR primers were designed using the Primer 3 web site (http://frodo.wi.mit.edu/primer3/) (Table S1). The expression of these genes was calculated by relative quantification with the *actin* housekeeping gene (DDBJ accession no. KJ616403) of *M. alba* as a reference. For quantification of the standard, PCR products amplified from cDNA were purified, and the concentration of the products was measured to calculate the number of cDNA copies. qRT-PCR was performed in a 20 μL reaction mixture including 5 μL of template cDNA, 10 μL of 1× SYBR Green Real-time PCR Master Mix (Toyobo, Osaka, Japan), 0.5 μL of each primer (10 μL), and DEPC-treated water. Thermal cycling conditions were as follows: 95 °C for 15 min and 41 cycles of 95 °C for 20 s, 55 °C for 40 s, and 72 °C for 30 s. The PCR reactions were performed on a CFX96 Real-Time system (Bio-Rad Laboratories, Hercules, CA). PCR products were analyzed with the Bio-Rad CFX Manager 2.0 software. Three replications per sample were used for the real-time PCR analysis, and values were expressed as means ± SD.

DOI: 10.1021/acs.jafc.5b03221
J. Agric. Food Chem. 2015, 63, 8622−8630

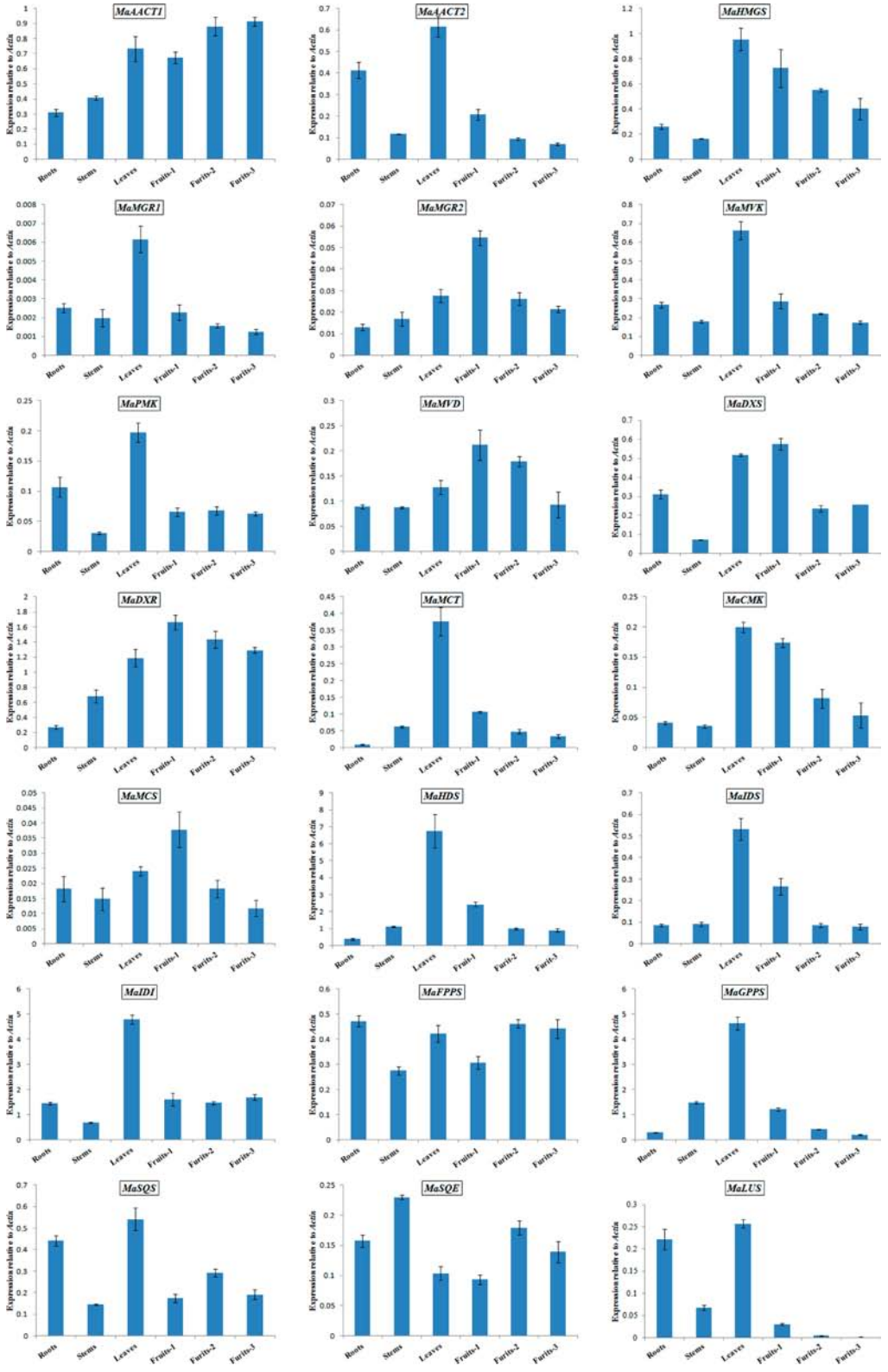

Figure 3. Expression levels of triterpene biosynthetic genes in different organs of mulberry (*Morus alba* L.) calculated by relative quantification with the mulberry *actin* housekeeping gene. Each value is the mean of three replicates, and error bars indicate standard deviations.

High-Performance Liquid Chromatography Analysis. Different organs of *M. alba* L. were freeze-dried at −80 °C for 48 h and then ground into a fine powder using a mortar and pestle. Rutin was released from the samples (50 mg) by adding 3 mL of 80% methanol containing 0.1% ascorbic acid (w/v) at 60 °C for 1 h. After centrifuging the extract (3000 g), the supernatant was filtered with a 0.22 μm Acrodisc syringe filter (Pall Corp.; Port Washington, NY) and analyzed by HPLC. The phenylpropanoids were separated on a C18 column (250 × 4.6 mm^2, 5 μm; RStech, Daejeon, Korea) using an Agilent 1100 HPLC system (Agilent Technologies, Massy, France) equipped with a photodiode array detector. The mobile phase consisted of methanol, water, and 0.2% acetic acid, and the column

DOI: 10.1021/acs.jafc.5b03221
J. Agric. Food Chem. 2015, 63, 8622−8630

was maintained at 30 °C. The parameters were as follows: the flow rate was maintained at 1.0 mL/min, the injection volume was 20 μL, and the detection wavelength was 280 nm. Pentacyclic triterpenes were released from the *M. alba* samples (500 mg) by adding 5 mL of 95% methanol containing 250 μL of 1% hydrogen chloride, sonicating for 15 min, and then allowing to stand for 30 min. After centrifugation and filtration, pentacyclic triterpenes were separated on a ProntoSIL 120–5 C18 ace-EPS (150 × 4.6 mm^2, 5 μm; ProntoSIL, Bollinger, Germany) using a Futex NS-4000 HPLC system (Futex Chromatography, Daejeon, Korea). The parameters were as follows: the mobile phase consisted of acetonitrile and water (9:1), the column was maintained at 25 °C, the flow rate was 1.0 mL/min, the injection volume was 20 μL, and the detection wavelength was 210 nm. The concentrations of compounds were determined by using a standard curve. All samples were analyzed in triplicate. Values were expressed as means ± SD.

RESULTS AND DISCUSSION

Sequence Analyses of Phenylpropanoid and Triterpene Biosynthetic Genes from Mulberry. Full-length cDNAs encoding PAL1, PAL2, C4H1, C4H2, 4CL7-1, 4CL7-2, CHS3, CHI1, CHI3 AACT1, AACT2, HMGS, PMK, MVD, IDI, DXS, MCS, HDS, IDS, GPPS, SQE, and LUS, and partial-length cDNA clones encoding PAL3, 4CL2, 4CL9, CHS1, CHS2, CHS9, CHI2, F3H, F3′H1, F3′H2 F3GT, UGT78D1, HMGR1, HMGR2, MVK, DXR, MCT, CMK, FPPS, and SQS were identified. They were confirmed for homology with the BLAST program and designated as MaPAL1 (722 amino acids [aa]), MaPAL2 (749 aa), MaPAL3 (344 aa), MaC4H1 (525 aa), MaC4H2 (507 aa), Ma4CL2 (365 aa), Ma4CL7-1 (547 aa), Ma4CL7-2 (539 aa), Ma4CL9 (471 aa), MaCHS1 (257 aa), MaCHS2 (259 aa), MaCHS3 (399 aa), MaCHS9 (218 aa), MaCHI1 (228 aa). MaCHI2 (308 aa), MaCHI3 (208 aa), MaF3H (228 aa), MaF3′H1 (354 aa), MaF3′H2 (177 aa), MaF3GT (339 aa), MaUGT78D1 (447 aa), MaAACT1 (403 aa), MaAACT2 (416 aa), MaHMGS (464 aa), MaHMGR1 (548 aa), MaHMGR2 (586 aa), MaMVK (356 aa), MaPMK (507 aa), MaMVD (421 aa), MaIDI (295 aa), MaDXS (714 aa), MaDXR (363 aa), MaMCT (243 aa), MaCMK (254 aa), MaMCS (248 aa), MaHDS (740 aa), MaIDS (461 aa), MaGPPS (380 aa), MaFPPS (182 aa), MaSQS (408 aa), MaSQE (524 aa), and LcLUS (754 aa). The data provided in Tables 1 and 2 showed that the mulberry phenylpropanoid and triterpene biosynthetic genes exhibited high identity with other orthologous genes.

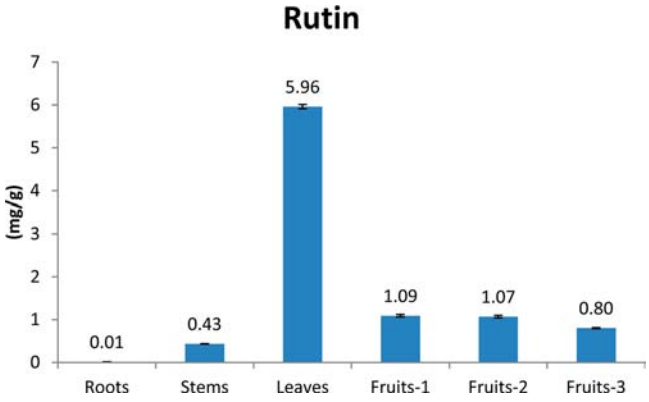

Figure 4. Accumulation of rutin in different organs of mulberry (*Morus alba* L.). Each value is the mean of three replicates, and error bars indicate standard deviation.

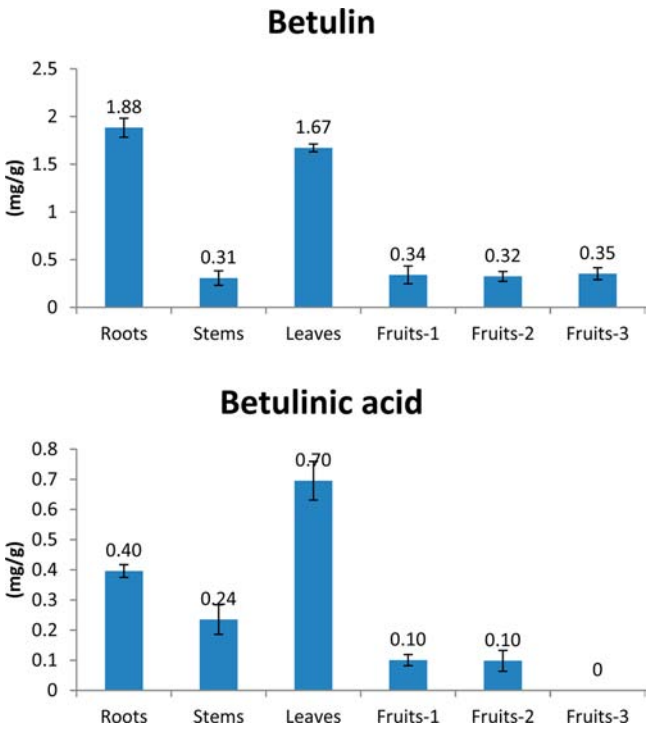

Figure 5. Accumulation of betulin and betulinic acid in different organs of mulberry (*Morus alba* L.). Each value is the mean of three replicates, and error bars indicate standard deviation.

Expression of Phenylpropanoid and Triterpene Biosynthetic Genes in Mulberry. The expression of phenylpropanoid and triterpene biosynthetic genes was analyzed in roots, stems, and leaves as well as in three fruit stages (unripe: fruits-1, semiripe: fruits-2, and fully ripe: fruits-3) by qRT-PCR (Figure 2). The expression patterns of phenylpropanoid biosynthetic genes differ among species.[28−32] In *M. alba*, the expression level of three isoform *PAL* genes were different: *MaPAL1* was expressed at the highest levels in stems and fully ripe fruits; however, *MaPAL2* and *MaPAL3* were highly expressed in leaves. The expression level of *MaC4H1* was the highest in the stems relative to expression in the other organs, whereas the expression level of MaC4H2 was similar in all mulberry organs. The expression levels of *Ma4CL2* and *Ma4CL9* were high in unripe fruits. *Ma4CL7-1* was highly expressed in the leaves, and *Ma4CL7-2* was highly expressed in the roots. *MaCHS1* showed high expression levels in fruits; *MaCHS2* was highly expressed in the leaves and unripe fruits, intermediately expressed in semi- and fully ripe fruits, and showed low expression in the roots and stems. However, *MaCHS9* was highly expressed in the root. *MaCHI1* was highly expressed in the leaves, whereas *MaCHI2* and *MaCHI3* was mainly expressed in the fruits. The expression patterns of *MaF3H*, *MaF3′H1*, and *MaF3GT* were similar, with relatively higher expression in fruits than in roots, stems, and leaves. However, *MaF3′H2* was different from *MaF3′H1*, with the highest expression level in roots. *MaUGT78D1* showed significantly higher expression in leaves than in other organs. During fruit ripening, the expression of *MaPAL2*, *MaPAL3*, *MaC4H2*, *Ma4CL*, *MaCHS2*, *MaCHS3*, *MaCHS9*, and *MaCHI3* declined gradually. In contrast, the expression of *MaPAL1*, *MaCHS1*, *MaCHI*, *MaF3H*, *MaF3′H*, and *MaF3GT* increased gradually as fruit ripened. In the triterpene biosynthetic pathway, most genes were highly expressed in

DOI: 10.1021/acs.jafc.5b03221
J. Agric. Food Chem. 2015, 63, 8622−8630

leaves (Figure 3). During fruit development, the expression of most triterpene biosynthetic genes decreased, including that of *MaAACT2*, *MaHMGS*, *MaHMGR1*, *MaHMGR2*, *MaMVK*, *MaMVD*, *MaDXS*, *MaDXR*, *MaMCT*, *MaCMK*, *MaMCS*, *MaHDS*, *MaIDS*, *MaGPPS*, and *MaLUS*. *MaIDI* and *MaPMK* were expressed at the same level in the three fruit-ripening stages. In contrast, *MaAACT1*, *MaFPPS*, *MaSQS*, and *MaSQE* showed increased expression during ripening. Possibly, these genes were relative with fruit maturation.

There are various explanations for the diverse expression levels of phenylpropanoid biosynthetic genes among plant species, including the existence of different gene isoforms in different organs. Xu et al.[33] cloned three isoforms of *PAL* in *Scutellaria baicalensis* and found different transcript levels in different organs. Expression of isoform *SbPAL1* was highest in stems, *SbPAL2* was highest in leaves, and *SbPAL3* expression was highest in roots. Li et al.[28] compared two isoforms of *4CL* in buckwheat and found that *Fe4CL1* was most strongly expressed in roots, whereas *Fe4CL2* had the highest expression in stems. Biotic and abiotic environmental factors can also influence phenylpropanoid gene expression because of the protective function of phenylpropanoid compounds. Ozone can modify phenylpropanoid and lignin expression pathways in leaves and stems of poplar.[34] Gene expression in leaves was stimulated by ozone exposure, but in stems, gene expression was decreased by ozone. Xu et al.[33] also found that different concentrations of methyl jasmonate (a plant hormone) and wounding treatments affected the transcript levels of phenylpropanoid genes.

A few reports have examined differences in transcription levels of triterpene biosynthetic genes in different plant organs. Huang et al.[35] investigated the expression of amyrin synthase (AS) and amyrin oxidase (AO) in *Catharanthus roseus* and found that both genes were more highly expressed in leaves. Here, we isolated 21 triterpene biosynthesis-related genes and examined their expression levels in different organs. Similarly, we found that most genes were highly expressed in leaves. The transcription level of *MaLUS* was very high in leaves and roots, which was related to higher levels of betulin and betulinic acid in these organs. We propose that *MaLUS* is the key regulator of betulin and betulinic acid accumulation in mulberry; however, further studies are needed to confirm this.

Rutin, Betulin, and Betulinic Acid Content. Mulberry fruits have been used for centuries as food, tea, and traditional medicine in southwestern Asia. The same plant materials used for qRT-PCR were used for the HPLC analysis of rutin, botulin, and betulinic acid accumulation (Figure 4). Rutin contents in various species have been shown to differ depending on environmental factors and growth stages.[28,36] Our results indicated that larger amounts of rutin (6−7-fold higher) were detected in leaves than in fruits and that rutin content decreased during fruit maturation (Figure 4). Small quantities of rutin were detected in the stems. As mentioned above, *MaUGT78D1* was highly expressed in leaves (Figure 2); we speculate that *MaUGT78D1* may play an important regulatory role in the rutin biosynthetic pathways, which would require further confirmation by transformation experiments. UGT78D1, a flavonol-specific glycosyltransferase, has been shown to be responsible for transferring rhamnose or glucose to the 3-OH position in vitro.[37]

The natural compound, betulinic acid, has been shown to have potent anticancer activity in cancer cells and thus is a new and promising experimental anticancer agent for the treatment of human cancers.[38] Large amounts of betulin were found in the roots and leaves (Figure 5), whereas only a little was detected in the stems and fruits (average of approximately 0.3 μg/mg DW). Leaves contained the highest levels of betulinic acid, followed by the roots and stems; little or no betulinic acid was detected in the fruit (Figure 5).

We conducted detailed investigations of the phenylpropanoid and triterpenoid biosynthetic pathways in the mulberry plant. To our knowledge, this is the first study on expression of triterpenoid biosynthetic pathway genes in mulberry. We identified 18 phenylpropanoid and 21 triterpenoid biosynthetic genes with different isoforms showing varied levels of expression. In addition, we found abundant rutin in mulberry leaves and abundant betulin and betulinic acid in the roots and leaves. Because of the significant medicinal functions of these compounds, we believe that our results will provide the basic data for research on the significant health benefits and medicinal potential of mulberry roots and leaves. Furthermore, the molecular characterization of genes involved in the phenylpropanoid and triterpene biosynthesis broadens our understanding of the molecular mechanisms in these biosynthesis pathways in *Morus alba*.

■ ASSOCIATED CONTENT

Supporting Information

The Supporting Information is available free of charge on the ACS Publications website at DOI: 10.1021/acs.jafc.5b03221.

Primers used for qRT-PCR. (PDF)

■ AUTHOR INFORMATION

Corresponding Author

*Phone: +82-42-821-5730. Fax: +82-42-822-2631. E-mail: supark@cnu.ac.kr.

Notes

The authors declare no competing financial interest.

■ ACKNOWLEDGMENTS

This research was supported by Basic Science Research Program through the National Research Foundation of Korea (NRF) funded by the Ministry of Education (NRF-2014R1A1A4A01008939)

■ REFERENCES

(1) Vogt, T. Phenylpropanoid Biosynthesis. *Mol. Plant* **2010**, *3*, 2−20.

(2) Vijayalakshmi, A.; Kumar, P. R.; Sakthi Priyadarsini, S.; Meenaxshi, C. In Vitro Antioxidant and Anticancer Activity of Flavonoid Fraction from the Aerial Parts of Cissus quadrangularis Linn. against Human Breast Carcinoma Cell Lines. *J. Chem.* **2013**, 1.

(3) Li, X. H.; Park, N. I.; Xu, H.; Woo, S. H.; Park, C. H.; Park, S. U. Differential Expression of Flavonoid Biosynthesis Genes and Accumulation of Phenolic Compounds in Common Buckwheat (Fagopyrum esculentum). *J. Agric. Food Chem.* **2010**, *58*, 12176−12181.

(4) Beirith, A.; Santos, A. R.; Calixto, J. B.; Hess, S. C.; Messana, I.; Ferrari, F.; Yunes, R. A. Study of the antinociceptive action of the ethanolic extract and the triterpene 24-hydroxytormentic acid isolated from the stem bark of Ocotea suaveolens. *Planta Med.* **1999**, *65*, 50−55.

(5) Matsuda, H.; Murakami, T.; Yashiro, K.; Yamahara, J.; Yoshikawa, M. Antidiabetic principles of natural medicines. IV. Aldose reductase and qlpha-glucosidase inhibitors from the roots of Salacia oblonga Wall. (Celastraceae): structure of a new friedelane-type triterpene, kotalagenin 16-acetate. *Chem. Pharm. Bull.* **1999**, *47*, 1725−9.

DOI: 10.1021/acs.jafc.5b03221
J. Agric. Food Chem. 2015, 63, 8622−8630

(6) Ma, C.; Nakamura, N.; Miyashiro, H.; Hattori, M.; Shimotohno, K. Inhibitory effects of constituents from Cynomorium songaricum and related triterpene derivatives on HIV-1 protease. *Chem. Pharm. Bull.* **1999**, *47*, 141−5.
(7) Zhu, M.; Chang, Q.; Wong, L. K.; Chong, F. S.; Li, R. C. Triterpene antioxidants from ganoderma lucidum. *Phytother. Res.* **1999**, *13*, 529−31.
(8) Dehelean, C. A.; Soica, C.; Ledeti, I.; Aluas, M.; Zupko, I.; Găluşcan, A.; Cinta-Pinzaru, S.; Munteanu, M. Study of the betulin enriched birch bark extracts effects on human carcinoma cells and ear inflammation. *Chem. Cent. J.* **2012**, *6*, 137.
(9) Soica, C.; Dehelean, C.; Danciu, C.; Wang, H. M.; Wenz, G.; Ambrus, R.; Bojin, F.; Anghel, M. Betulin complex in gamma-cyclodextrin derivatives: properties and antineoplasic activities in in vitro and in vivo tumor models. *Int. J. Mol. Sci.* **2012**, *13*, 14992−5011.
(10) Wick, W.; Grimmel, C.; Wagenknecht, B.; Dichgans, J.; Weller, M. Betulinic acid-induced apoptosis in glioma cells: A sequential requirement for new protein synthesis, formation of reactive oxygen species, and caspase processing. *J. Pharmacol. Exp. Ther.* **1999**, *289*, 1306−12.
(11) Liu, J. D. Study of the etiology of low-fever among female silk-weaving workers: extrinsic allergic alveolitis due to mulberry silk dust exposure. *Zhonghua yu fang yi xue za zhi* **1985**, *19*, 354−7.
(12) Kim, H.; Yoon, Y. J.; Shon, J. H.; Cha, I. J.; Shin, J. G.; Liu, K. H. Potent inhibition of human liver CYP3A activity by mulberry juice. *Drug Metab Rev.* **2006**, *38* (Suppl. 3), 50−50.
(13) Hemmati, A. A.; Jalai, M. T.; Rashidi, I.; Hormozi, T. K. Effects of aqueous extract of black mulberry (Morus nigra) on liver and kidney of diabetic mice. *Toxicol. Lett.* **2008**, *180*, S48−S49.
(14) Heo, S. I.; Jin, Y. S.; Jung, M. J.; Wang, M. H. Antidiabetic properties of 2,5-dihydroxy-4,3 ′-di(beta-D-glucopyranosyloxy)-trans-stilbene from mulberry (Morus bombycis Koidzumi) root in streptozotocin-induced diabetic rats. *J. Med. Food* **2007**, *10*, 602−607.
(15) Wang, Y. H.; Xiang, L. M.; Wang, C. H.; Tang, C.; He, X. J. Antidiabetic and Antioxidant Effects and Phytochemicals of Mulberry Fruit (Morus alba L.) Polyphenol Enhanced Extract. *PLoS One* **2013**, *8*, e71144.
(16) Jiang, D. Q.; Guo, Y.; Xu, D. H.; Huang, Y. S.; Yuan, K.; Lv, Z. Q. Antioxidant and anti-fatigue effects of anthocyanins of mulberry juice purification (MJP) and mulberry marc purification (MMP) from different varieties mulberry fruit in China. *Food Chem. Toxicol.* **2013**, *59*, 1−7.
(17) Naowaratwattana, W.; De-Eknamkul, W.; De Mejia, E. G. Phenolic-containing organic extracts of mulberry (Morus alba L.) leaves inhibit HepG2 hepatoma cells through G2/M phase arrest, induction of apoptosis, and inhibition of topoisomerase IIalpha activity. *J. Med. Food* **2010**, *13*, 1045−56.
(18) Radojkovic, M. M.; Zekovic, Z. P.; Vidovic, S. S.; Kocar, D. D.; Maskovic, P. Z. Free radical scavenging activity and total phenolic and flavonoid contents of mulberry (Morus spp. L., Moraceae) extracts. *Hem. Ind.* **2012**, *66*, 545−550.
(19) Jia, D. D.; Li, S. F.; Gu, Z. P. Preparative Isolation of Flavonoids from Mulberry (Morus Alba L.) Leaves by Macroporous Resin Adsorption. *J. Food Process Eng.* **2011**, *34*, 1319−1337.
(20) Kumar, R. V.; Babu, G. S.; Chauhan, S.; Srivastava, A.; Rao, Y.; Kumar, D. Total phenolics and flavonoids content in ripened and unripened fruits of different mulberry (Morus alba) varieties. *Indian J. Agr Sci.* **2012**, *82*, 277−279.
(21) Lee, Y.; Lee, D. E.; Lee, H. S.; Kim, S. K.; Lee, W.; Kim, S. H.; Kim, M. W. Influence of auxins, cytokinins, and nitrogen on production of rutin from callus and adventitious roots of the white mulberry tree (Morus alba L.). *Plant Cell, Tissue Organ Cult.* **2011**, *105*, 9−19.
(22) Lotito, S. B.; Frei, B. Consumption of flavonoid-rich foods and increased plasma antioxidant capacity in humans: cause, consequence, or epiphenomenon? *Free Radical Biol. Med.* **2006**, *41*, 1727−46.
(23) Guardia, T.; Rotelli, A. E.; Juarez, A. O.; Pelzer, L. E. Anti-inflammatory properties of plant flavonoids. Effects of rutin, quercetin and hesperidin on adjuvant arthritis in rat. *Farmaco* **2001**, *56*, 683−7.
(24) Lin, J.-Y.; Tang, C.-Y. Determination of total phenolic and flavonoid contents in selected fruits and vegetables, as well as their stimulatory effects on mouse splenocyte proliferation. *Food Chem.* **2007**, *101*, 140−147.
(25) Yan, J. W.; Wang, M.; Lu, J. D. Determination of rutin, quercetin, and chlorogenic acid in mulberry leaves by capillary zone electrophoresis. *Anal. Lett.* **2004**, *37*, 3287−3297.
(26) Li, J. R.; Han, X. X. Ultrahigh-pressure extraction for mulberry leaf rutin. *Chinese J. Anal. Chem.* **2008**, *36*, 365−368.
(27) He, N.; Zhang, C.; Qi, X.; Zhao, S.; Tao, Y.; Yang, G.; Lee, T. H.; Wang, X.; Cai, Q.; Li, D.; Lu, M.; Liao, S.; Luo, G.; He, R.; Tan, X.; Xu, Y.; Li, T.; Zhao, A.; Jia, L.; Fu, Q.; Zeng, Q.; Gao, C.; Ma, B.; Liang, J.; Wang, X.; Shang, J.; Song, P.; Wu, H.; Fan, L.; Wang, Q.; Shuai, Q.; Zhu, J.; Wei, C.; Zhu-Salzman, K.; Jin, D.; Wang, J.; Liu, T.; Yu, M.; Tang, C.; Wang, Z.; Dai, F.; Chen, J.; Liu, Y.; Zhao, S.; Lin, T.; Zhang, S.; Wang, J.; Wang, J.; Yang, H.; Yang, G.; Wang, J.; Paterson, A. H.; Xia, Q.; Ji, D.; Xiang, Z. Draft genome sequence of the mulberry tree Morus notabilis. *Nat. Commun.* **2013**, *4*, 2445.
(28) Li, X.; Kim, J. K.; Park, S. Y.; Zhao, S.; Kim, Y. B.; Lee, S.; Park, S. U. Comparative analysis of flavonoids and polar metabolite profiling of tanno-original and tanno-high rutin buckwheat. *J. Agric. Food Chem.* **2014**, *62*, 2701−8.
(29) Tuan, P. A.; Park, N. I.; Li, X.; Xu, H.; Kim, H. M.; Park, S. U. Molecular Cloning and Characterization of Phenylalanine Ammonia-lyase and Cinnamate 4-Hydroxylase in the Phenylpropanoid Biosynthesis Pathway in Garlic (Allium sativum). *J. Agric. Food Chem.* **2010**, *58*, 10911−10917.
(30) Tuan, P. A.; Park, W. T.; Xu, H.; Park, N. I.; Park, S. U. Accumulation of Tilianin and Rosmarinic Acid and Expression of Phenylpropanoid Biosynthetic Genes in Agastache rugosa. *J. Agric. Food Chem.* **2012**, *60*, 5945−5951.
(31) Zhao, S.; Li, X.; Cho, D. H.; Arasu, M. V.; Al-Dhabi, N. A.; Park, S. U. Accumulation of kaempferitrin and expression of phenylpropanoid biosynthetic genes in kenaf (Hibiscus cannabinus). *Molecules* **2014**, *19*, 16987−97.
(32) Zhao, S.; Tuan, P. A.; Li, X.; Kim, Y. B.; Kim, H.; Park, C. G.; Yang, J.; Li, C. H.; Park, S. U. Identification of phenylpropanoid biosynthetic genes and phenylpropanoid accumulation by transcriptome analysis of Lycium chinense. *BMC Genomics* **2013**, *14*, 802.
(33) Xu, H.; Park, N. I.; Li, X.; Kim, Y. K.; Lee, S. Y.; Park, S. U. Molecular cloning and characterization of phenylalanine ammonia-lyase, cinnamate 4-hydroxylase and genes involved in flavone biosynthesis in Scutellaria baicalensis. *Bioresour. Technol.* **2010**, *101*, 9715−22.
(34) Richet, N.; Tozo, K.; Afif, D.; Banvoy, J.; Legay, S.; Dizengremel, P.; Cabane, M. The response to daylight or continuous ozone of phenylpropanoid and lignin biosynthesis pathways in poplar differs between leaves and wood. *Planta* **2012**, *236*, 727−737.
(35) Huang, L.; Li, J.; Ye, H.; Li, C.; Wang, H.; Liu, B.; Zhang, Y. Molecular characterization of the pentacyclic triterpenoid biosynthetic pathway in Catharanthus roseus. *Planta* **2012**, *236*, 1571−81.
(36) Kim, H. J.; Park, K. J.; Lim, J. H. Metabolomic analysis of phenolic compounds in buckwheat (Fagopyrum esculentum M.) sprouts treated with methyl jasmonate. *J. Agric. Food Chem.* **2011**, *59*, 5707−13.
(37) Ren, G.; Hou, J.; Fang, Q.; Sun, H.; Liu, X.; Zhang, L.; Wang, P. G. Synthesis of flavonol 3-O-glycoside by UGT78D1. *Glycoconjugate J.* **2012**, *29*, 425−32.
(38) Fulda, S. Betulinic Acid for cancer treatment and prevention. *Int. J. Mol. Sci.* **2008**, *9*, 1096−107.

DOI: 10.1021/acs.jafc.5b03221
J. Agric. Food Chem. 2015, 63, 8622−8630

methyl-*N*-(trimethylsilyl)trifluoroacetamide (MSTFA), methoxyamine hydrochloride, pyridine, kojic acid, mushroom tyrosinase (1000 units/mL), L-tyrosine, and commercial standard compounds were obtained from Sigma Chemical Co. (St. Louis, MO). Disodium hydrogen phosphate 12-water and sodium dihydrogen phosphate dehydrate were obtained from Junsei chemical (Tokyo, Japan).

Plant Materials. The samples were prepared as follows; germination was initially triggered in a climate-controlled greenhouse with day and night temperatures of 26 and 20 °C, respectively. After 5 weeks, they were transplanted into an experimental field shelter, located at Geumsan-gun, Chungcheongnam-do, in the Republic of Korea (36°13′N, 127°23′E; elevation of 170 m). The leaves and stems of *L. maximowiczii* were collected 3, 4, 6, 8, 15, and 18 months after germination from the shelter. All sampling was conducted between June 2013 and September 2014. The samples were identified by J. Lee at the Department of Environment and Forest Resources of Chungnam National University (Daejeon, Republic of Korea), and voucher specimens were deposited at the herbarium (KRIB). The harvested plant samples were dried under shade conditions and ground into fine homogeneous powders using a grinder (sieve size mesh no. 8, Jworldtech, Seoul, Korea). The samples were stored at −20 °C prior to extraction. The information regarding the *L. maximowiczii* samples used in this study is listed in Table 1.

Table 1. List of *L. maximowiczii* Harvested during Different Growth Periods after Germination[a]

growth period (after germination) (months)	length (cm) (size)[b]	harvest date	growing conditions (temperature[c]/ precipitation[d]/ duration of sunshine[e])	collected part
3	10−15 (Δ 4)	June 2013	23 °C/118 mm/ 169 h	leaves, stems
4	20−30 (Δ 12.5)	July 2013	26 °C/217 mm/ 113 h	leaves, stems
6	70 (Δ 22.5)	September 2013	20 °C/81 mm/ 147 h	leaves, stems
8	80 (Δ 5)	November 2013	5 °C/55 mm/ 136 h	leaves, stems
15	110−120	June 2014	22 °C/46 mm/ 146 h	leaves, stems
18	>120	September 2014	20 °C/91 mm/ 157 h	leaves, stems

[a]All samples were cultivated in Chungcheongnam-do, Republic of Korea. Growing conditions were those in the harvest month. [b]The Δ value means the average value of the elongated length per month. [c]Monthly average temperature. [d]Monthly average precipitation. [e]Monthly average duration of sunshine.

Sample Extraction and Derivatization for GC-MS. Approximately 1 g of dried leaves and 2 g of dried stems were extracted at room temperature with 40 mL of methanol for 24 h at 200 rpm using a Twist Shaker (Biofree, Seoul, Korea). The resulting mixture was centrifuged at 5000 rpm and 4 °C for 15 min (Hettich Zentrifugen, Universal 320). The supernatant was then concentrated using a speed-vacuum machine (Modulspin 31, Biotron). The samples were then dissolved in methanol and filtered through a 0.2 μm PTFE filter for the UPLC-Q-TOF-MS and ultra-high-performance liquid chromatography-electrospray ionization-mass spectrometry/mass spectrometry (UHPLC-ESI-MS/MS) analyses. For the GC-MS analysis, the dried extract was oximated with 50 μL of methoxyamine hydrochloride in pyridine (20 mg/mL) for 90 min at 30 °C using a thermomixer (Eppendorf, Hamburg, Germany). Then, the oximated samples were silylated with 50 μL of MSTFA for 30 min at 37 °C, using a thermomixer. The final concentration of the samples was 5 mg/mL for UPLC-Q-TOF-MS, UHPLC-ESI-MS/MS, and GC-TOF-MS analyses. All MS analyses were conducted with five analytical replications.

GC-TOF-MS Analysis. GC-MS analysis was performed on an Agilent 7890A GC system (Agilent, Atlanta, GA) equipped with an Agilent 7693 autosampler coupled to a Pegasus HT TOF-MS (Leco Corp., St. Joseph, MI) system. An Agilent HP-5MS capillary column with an internal diameter of 0.25 mm, a film thickness of 0.25 μm, and a length of 30 m was employed for the separation. Chromatographic-grade helium with a constant flow of 1.0 mL/min served as the carrier gas. The injector and transfer line temperatures were both set at 240 °C. The oven temperature was held at 75 °C for 2 min, then increased to 300 °C at a rate of 15 °C/min, and maintained at 300 °C for 3 min. The mass data collected in electron ionization mode with an ionization energy of 70 eV were used to conduct a full scan at m/z 50−1000. One microliter of each derivatized sample was injected into the GC-TOF-MS instrument without split.

UPLC-Q-TOF-MS and UHPLC-ESI-MS/MS Analyses. UPLC was performed using a Waters Micromass Q-TOF Premier with a UPLC Acquity system (Waters Corp., Milford, MA) equipped with a binary solvent delivery system, an autosampler, and an ultraviolet (UV) detector. The UPLC system was set up with an Acquity UPLC BEH C18 column [100 mm × 2.1 mm, 1.7 μm particle size (Waters Corp.)]. The mobile phase consisted of 0.1% (v/v) formic acid in water (A) and 0.1% (v/v) formic acid in acetonitrile (B). The solvent gradient system was as follows: 5% B for 1 min, increased to 100% B for 9 min, held at 100% for 1 min, decreased to 5% B over 2 min, and finally held at 5% B for 1 min. Five microliters of a sample extract solution was injected, and the flow rate was maintained at 0.3 mL/min. The waters Q-TOF Primer (Micromass MS Technologies, Manchester, U.K.) was operated in quadrupole mode for the MS data, and the TOF data were collected in the range of m/z 100−1000 in both negative (−) and positive (+) ion modes. The operating parameters were as follows: ion source temperature, 100 °C; desolvation gas flow, 650 L/h at 200 °C; capillary voltage, 2.3 kV; and cone voltage, ≤35 V. The V mode of the mass spectrometer was used, and data were collected in the centroid mode with a scan accumulation time of 0.2 s. Leucine enkephalin was used as a reference lock mass ([−] m/z 554.2615, [+] m/z 556.2771, 10 μL/min) to ensure accuracy and reproducibility, by independent LockSpray interference.

LC-MS data were analyzed using an LTQ XL linear ion trap mass spectrometer/mass spectrometer from Thermo Fischer Scientific (San Jose, CA) coupled with an RS autosampler, RS column compartment, RS diode array detector, and DIONEX UltiMate 3000 RS pump (Dionex Corp., Sunnyvale, CA). The separation was performed on a Thermo Scientific Syncronis C18 UHPLC column with a particle size of 1.7 μm. The mobile phases were 0.1% (v/v) formic acid in water (A) and acetonitrile (B). The gradient system was as follows: from 10 to 100% solvent B over 18 min and then re-equilibrated to initial conditions over 4 min. The flow rate was 0.3 mL/min, and the injection volume was 10 μL. Mass spectra were obtained using ion traps in both negative (−) and positive (+) modes within a range of m/z 100−1000. A photodiode array was set for detection at 200−600 nm and managed using 3DField. The operating parameters were as follows: source voltage, ±5 kV; capillary temperature, 350 °C; and capillary voltage, 39 V. Tandem MS analysis was conducted via scan-type turbo data-dependent scanning (DDS) under the same conditions used for MS scanning.

Tyrosinase Inhibitory Activity. The analysis of tyrosinase inhibitory activity was performed as previously described with slight modifications.[20] The reaction mixture, consisting of 125 μL of 0.1 M sodium phosphate buffer (pH 6.5), 5 μL of the methanol extract of *L. maximowiczii* dissolved in 100% methanol, 40 μL of 1.5 mM L-tyrosine, and 30 μL of mushroom tyrosinase (1000 units/mL), was added to a 96-well plate. After incubation at 37 °C for 20 min, the absorbance was measured at 490 nm every 0 and 20 min with a spectrophotometer (Spectronic Genesys 6, Thermo Electron, Madison, WI). Kojic acid was used as a positive control. The percentage inhibition of tyrosinase activity was expressed using the following formula:

DOI: 10.1021/acs.jafc.5b03566
J. Agric. Food Chem. 2015, 63, 8631−8639

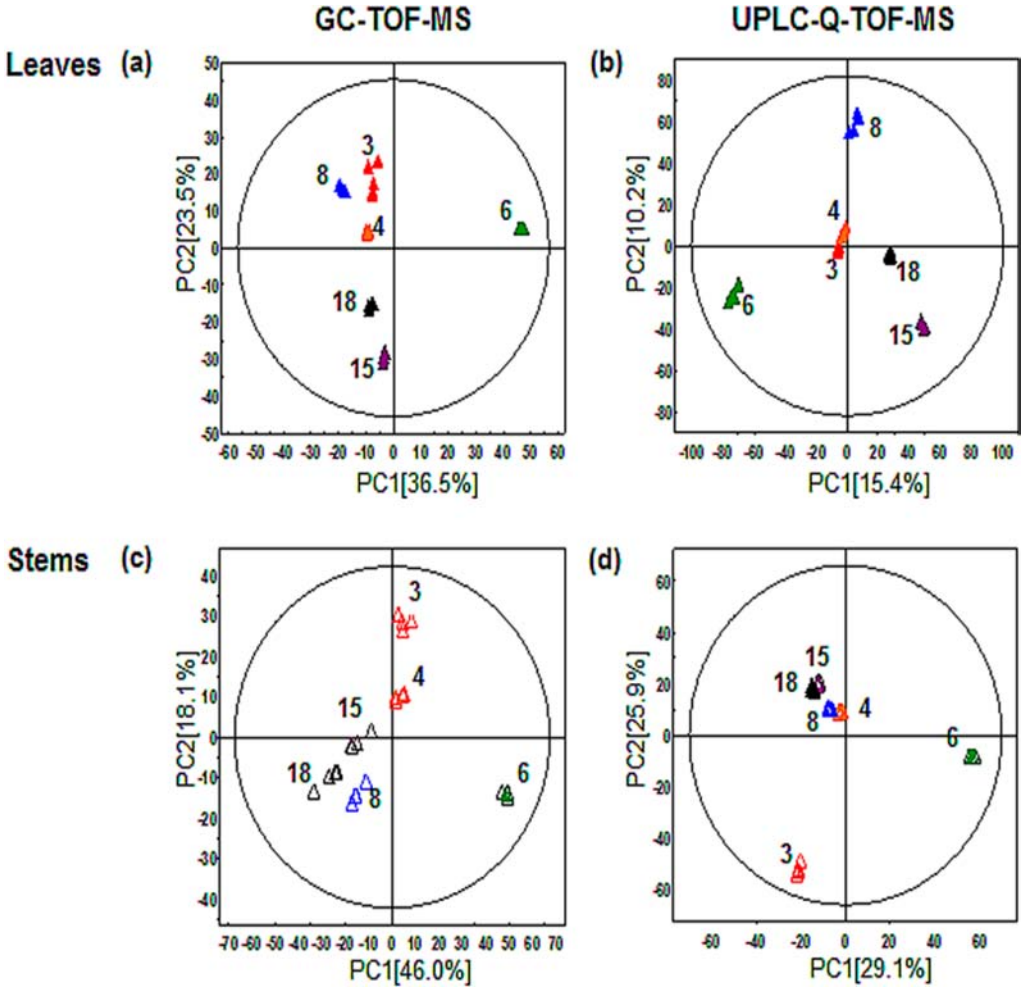

Figure 1. Principal component analysis (PCA) score plots of leaves (a and b) and stems (c and d) collected during different growth periods of *L. maximowiczii* and analyzed by GC-TOF-MS (a and c) and UPLC-Q-TOF-MS (b and d). Each symbol represents a growth period after germination, in either the leaves or stems of *L. maximowiczii* (filled triangles, leaves; empty triangles, stems): red for 3 months (harvest date, June 2013), orange for 4 months (July 2013), green for 6 months (September 2013), blue for 8 months (November 2013), purple for 15 months (June 2014), and black for 18 months (September 2014). PLS-DA models were fitted using the following quality parameters. (a) $R^2X_{(cum)} = 0.941$; $R^2Y_{(cum)} = 0.992$; $Q^2_{(cum)} = 0.989$. (b) $R^2X_{(cum)} = 0.425$; $R^2Y_{(cum)} = 0.992$; $Q^2_{(cum)} = 0.843$. (c) $R^2X_{(cum)} = 0.935$; $R^2Y_{(cum)} = 0.997$; $Q^2_{(cum)} = 0.991$. (d) $R^2X_{(cum)} = 0.835$; $R^2Y_{(cum)} = 0.994$; $Q^2_{(cum)} = 0.999$. The p values were below 0.05 in all analyses.

$$\%\ \text{inhibition rate} = [(C_{20\ \text{min}} - C_{0\ \text{min}}) - (S_{20\ \text{min}} - S_{0\ \text{min}}) / (C_{20\text{min}} - C_{0\ \text{min}})] \times 100$$

where $C_{20\ \text{min}}$ and $C_{0\ \text{min}}$ are the absorbance of the control after 20 and 0 min, respectively, whereas $S_{20\ \text{min}}$ and $S_{0\ \text{min}}$ are the absorbance of the sample after 20 and 0 min, respectively.

Data Processing and Multivariate Analysis. GC-TOF-MS data files were converted to CDF format (*.cdf) using the Leco ChromaTOF software program (version 4.44, Leco Corp.). Data processing for the UPLC-Q-TOF-MS analysis was conducted using MassLynx software, and raw data files were converted into netCDF (*.cdf) format using Waters DataBridge version 4.1. After conversion, the MS data were processed using the metAlign software package (http://www.metalign.nl) to obtain a data matrix containing retention times, accurate masses, and normalized peak intensities. The resulting data were exported to Excel (Microsoft, Redmond, WA), and multivariate statistical analysis was performed using SIMCA-P+ (version 12.0, Umetrics, Umea, Sweden). Unsupervised PCA and supervised PLS-DA models were used to compare the production of different metabolites among growth periods in the leaves and stems of *L. maximowiczii*, respectively. The OPLS-DA was also performed to compare metabolite differences at 6 months of the growth period between leaves and stems of *L. maximowiczii*. Metabolites with variable importance as determined by a projection (VIP) value of >0.7 and a p value of <0.05 were selected. To visualize differences in metabolites among samples, heat map analyses were performed using Mev software program version 4.8 (http://www.tm4.org). Significant differences were tested by one-way analysis of variance (ANOVA) using the STATISCA program (version 7.0, StaSoft Inc., Tulsa, OK). Differences in tyrosinase inhibitory activity were analyzed by one-way ANOVA and Duncan's multiple-range test using PASW Statistics 18 (SPSS Inc., Chicago, IL). Pairwise correlations between secondary metabolites and tyrosinase inhibitory activity were calculated by Pearson's correlation coefficient test using PASW Statistics 18, and correlation maps were generated by the MEV software program.

RESULTS

The Differentiated Metabolites in the Leaves and Stems of *L. maximowiczii* during Different Growth Periods Using GC-TOF-MS Analysis. Differences between the growth periods of the leaves and stems of *L. maximowiczii* were clearly visible in the principal component analysis (PCA) and partial least-squares discriminant analysis (PLS-DA) score plots, respectively (panels a and c of Figure 1, respectively). In particular, both leaves and stems harvested 6 months after

DOI: 10.1021/acs.jafc.5b03566
J. Agric. Food Chem. 2015, 63, 8631−8639

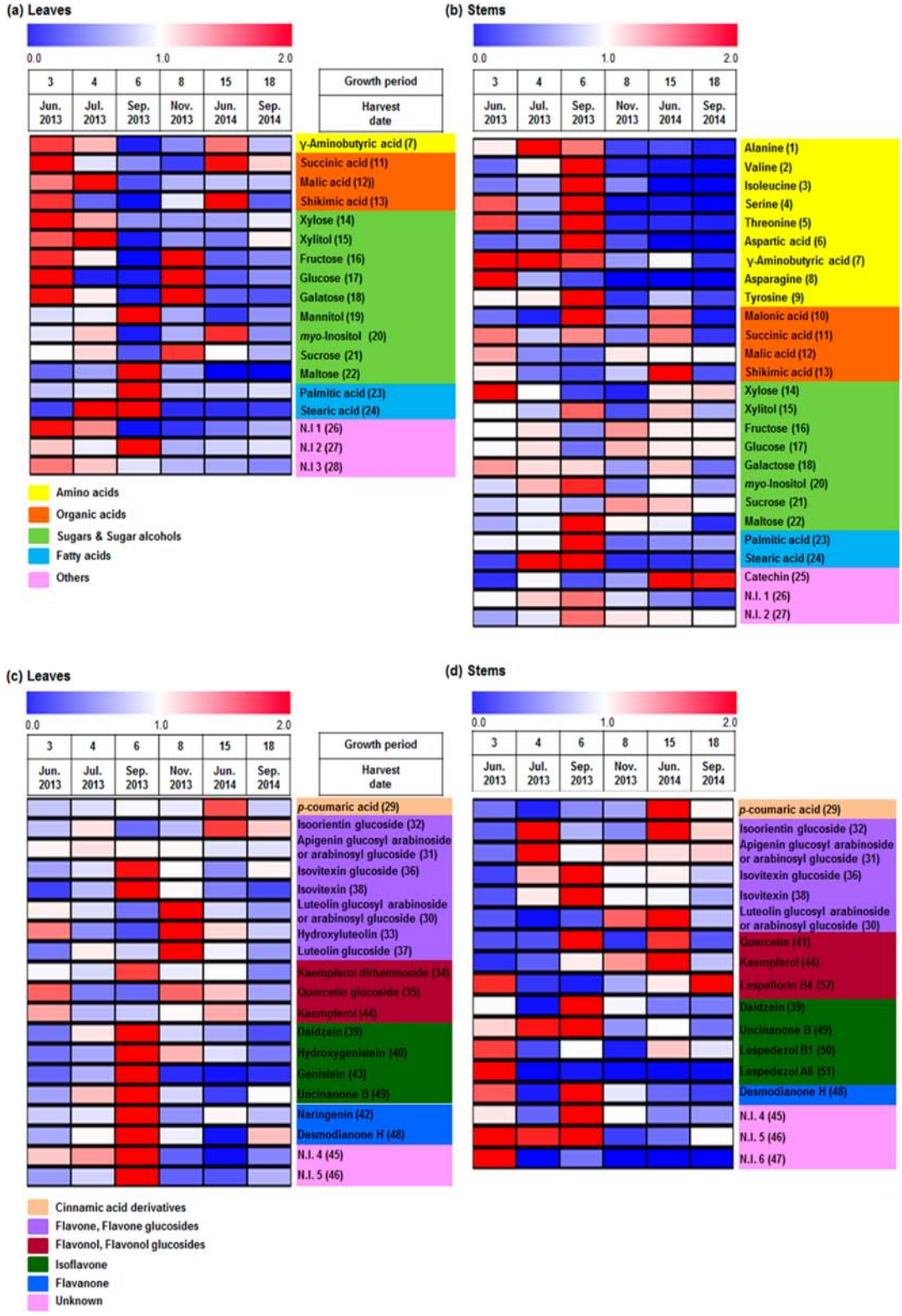

Figure 2. Heat maps of different metabolites from the leaves (a and c) and stems (b and d) of *L. maximowiczii* during different growth periods, from GC-TOF-MS (a and b) and UPLC-Q-TOF-MS (c and d) analysis. Growth periods after germination are shown in each column, with colors representing relative abundance, and relative intensities indicated by the heat scale. The numbering of metabolites is identical to that in Tables S1 and S2.

germination were significantly distinguished from those harvested during other months. Significantly different metabolites were selected as variables by PLS1 and PLS2 in the PLS-DA score plot, based on variable importance in the projection (VIP) value (>0.7) and p value (<0.05). As shown in the Supporting Information (Table S1), 18 and 26 metabolites in the leaves and stems, respectively, were selected as variables, which changed with growth period. Metabolites in leaves and

DOI: 10.1021/acs.jafc.5b03566
J. Agric. Food Chem. 2015, 63, 8631−8639

stems, including amino acids, organic acids, sugars and sugar alcohols, fatty acids, and catechin, were identified on the basis of their retention times and mass fragmentation, using the NIST library, and compared to the commercial standards.

Among discriminated variables according to the growth period in leaves, most primary metabolites, except for mannitol (**19**), maltose (**22**), palmitic acid (**23**), stearic acid (**24**), and nonidentified metabolite (**27**), were produced in relatively smaller quantities 6 months after germination than during other months (Figure 2a). Four metabolites, including fructose (**16**), glucose (**17**), galactose (**18**), and sucrose (**21**), were detected in the largest quantities in *L. maximowiczii* leaves harvested in November (at 8 months).

However, the following metabolites were detected in the largest quantities in stems 6 months after germination (Figure 2b): amino acids such as valine (**2**), isoleucine (**3**), serine (**4**), threonine (**5**), aspartic acid (**6**), and tyrosine (**9**); sugars such as xylitol (**15**), *myo*-inositol (**20**), and maltose (**22**); malonic acid (**10**); palmitic acid (**23**); and two nonidentified metabolites (**26** and **27**). The levels of sugars such as fructose (**16**), glucose (**17**), and sucrose (**21**) were higher in stems harvested in November (at 8 months) than in stems harvested during other months.

The Discriminated Metabolites in Leaves and Stems of *L. maximowiczii* during Different Growth Periods Using UPLC-Q-TOF-MS Analysis. In the UPLC-Q-TOF-MS analysis, the leaves and stems of *L. maximowiczii* samples were observed to produce different patterns in the PCA and PLS-DA score plots, according to growth period (3, 4, 6, 8, 15, and 18 months). In terms of overall secondary metabolites, leaves harvested 6 months after germination were significantly different from those harvested during other months (Figure 1b). As seen in Figure 1d, the stem samples collected 6 months after germination are clearly separated by PC1 (29.1%) from those collected at other times. To reveal the differences in secondary metabolites produced in the leaves and stems during different growth periods, both a VIP value of >0.7 and a p value of <0.05 of variables obtained from PLS1 and PLS2 were applied. As shown in the Supporting Information (Table S2), these metabolites were tentatively identified according to retention time, molecular weight, elemental composition, error and i-Fit, from the UPLC-Q-TOF-MS and UV spectral data, MS^n fragmentation patterns obtained via UHPLC-ESI-MS/MS, and comparisons with reference compounds.

A total of 19 metabolites, including *p*-coumaric acid (**29**), luteolin glucosyl arabinoside or arabinosyl glucoside (**30**), apigenin glucosyl arabinoside or arabinosyl glucoside (**31**), isoorientin glucoside (**32**), hydroxyluteolin (**33**), kaempferol dirhamnoside (**34**), quercetin glucoside (**35**), isovitexin glucoside (**36**), luteolin glucoside (**37**), isovitexin (**38**), daidzein (**39**), hydroygenistein (**40**), naringenin (**42**), genistein (**43**), kaempferol (**44**), desmodianone H (**48**), uncinanone B (**49**), and two nonidentified metabolites (**45** and **46**), were found to be significant metabolites for distinguishing each growth period of the leaves of *L. maximowiczii* (Table S2).

In stems, 10 metabolites (**29**−**32**, **36**, **38**, **39**, **44**, **48**, and **49**) selected from the leaf data, as well as quercetin (**41**), lespedezol B1 (**50**), lespedezol A6 (**51**), lespeflorin B4 (**52**), and three nonidentified metabolites (**45**−**47**), were selected as variables suitable for the study of the stem metabolites of *L. maximowiczii* during different growth periods (Supporting Information, Table S2).

To explain the changes in the secondary metabolite contents of leaves and stems of *L. maximowiczii* over the growth period, heat maps were generated (Figure 2). In both leaves and stems, most metabolites were present in relatively larger quantities 6 months after germination than in other months. Eleven secondary metabolites, including kaempferol dirhamnoside (**34**), isovitexin glucoside (**36**), isovitexin (**38**), daidzein (**39**), hydroygenistein (**40**), naringenin (**42**), genistein (**43**), desmodianone H (**48**), uncinanone B (**49**), and two non-identified metabolites (**45** and **46**), were found to be present at higher levels in leaves harvested at 6 months than other samples from different harvest periods (Figure 2c). In particular, luteolin glucosyl arabinoside or arabinosyl glucoside (**30**), hydroxyluteolin (**33**), and luteolin glucoside (**37**) were present in the largest quantities during November (at 8 months) in *L. maximowiczii* leaves.

As shown in Figure 2d, eight metabolites were present in large quantities in stems collected 6 months after germination: isovitexin glucoside (**36**), isovitexin (**38**), daidzein (**39**), quercetin (**41**), desmodianone H (**48**), uncinanone B (**49**), and two nonidentified metabolites (**45** and **46**).

Correlation between Tyrosinase Inhibitory Activity and Secondary Metabolites in the Leaves and Stems of *L. maximowiczii*. Both the leaves and stems of *L. maximowiczii* collected 6 months after germination showed the highest levels of tyrosinase inhibitory activity, while those harvested 8 months after germination showed the lowest activity (Figure 3a,b). The tyrosinase inhibitory activity in leaves (54.6%) at 6 months was significantly higher than that in stems at the same harvest time (20.3%).

To visualize the correlations between tyrosinase inhibitory activity and secondary metabolites in the leaves and stems of *L. maximowiczii*, correlation maps are presented (Figure 3c,d). The Pearson's correlation coefficients (r) of all secondary metabolites were calculated and represented as positive correlations when $0 < r < 1$ and negative correlations when $-1 < r < 0$. The results indicate that nine secondary metabolites were positively correlated with tyrosinase inhibitory activity in the leaves: kaempferol dirhamnoside (**34**), isovitexin glucoside (**36**), isovitexin (**38**), daidzein (**39**), hydroxygenistein (**40**), naringenin (**42**), genistein (**43**), desmodianone H (**48**), and uncinanone B (**49**). Meanwhile, seven secondary metabolites were strongly positively correlated with tyrosinase inhibitory activity in the stems: isovitexin (**38**), daidzein (**39**), quercetin (**41**), desmodianone H (**48**), uncinanone B (**49**), and two nonidentified metabolites (**45** and **46**). Of the secondary metabolites that were positively correlated with tyrosinase inhibition activity, four metabolites were present in the largest quantities in both leaves and stems 6 months after germination: isovitexin (**38**), daidzein (**39**), desmodianone H (**48**), and uncinanone B (**49**).

Differences in the Tyrosinase Inhibitory Activity and Metabolite Composition According to Plant Parts. The result that tyrosinase inhibitory activity in leaves of *L. maximowiczii* was higher than that in stems irrespective of the growth period was considered on the basis of difference in metabolite composition between them. Therefore, we applied PCA and PLS-DA from LC-MS data sets to identify metabolite differences between the plant parts, leaves and stems. The PLS-DA models demonstrated the differences between samples: $R^2X_{(cum)} = 0.647$, $R^2Y_{(cum)} = 0.992$, $Q^2_{(cum)} = 0.877$, and $p < 0.05$. Leaves and stems were clearly separated by PLS1 (Supporting Information, Figure 1Sa). Eight metabolites were

DOI: 10.1021/acs.jafc.5b03566
J. Agric. Food Chem. 2015, 63, 8631−8639

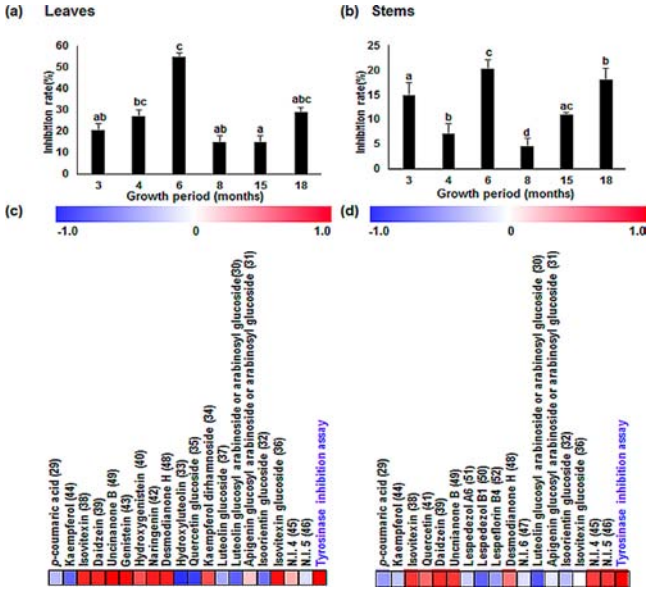

Figure 3. Tyrosinase inhibitory activity in (a) leaves and (b) stems of *L. maximowiczii* during different growth periods, and a correlation map of metabolites and tyrosinase inhibitory activity in the (c) leaves and (d) stems of *L. maximowiczii*. Data were evaluated using a one-way ANOVA followed by Duncan's multiple-range test. Means with different letters, e.g., "a" or "b", are statistically different. Differences were considered significant at p values of <0.05. All assays were conducted in triplicate. Each square (c and d) indicates the r (Pearson's correlation coefficient values) for a pair of averaged values from either metabolites or tyrosinase inhibitory activity. Red represents positive ($0 < r < 1$) correlations, and blue represents negative ($-1 < r < 0$) correlations.

determined to be significantly different in the PLS-DA score plot: *p*-coumaric acid (**29**), luteolin glucosyl arabinoside or arabinosyl glucoside (**30**), isoorientin glucoside (**32**), isovitexin (**38**), daidzein (**39**), kaempferol (**44**), nonidentified metabolites (**46**), and uncinanone B (**49**). Among these metabolites, the contents of five metabolites (**29**, **30**, **38**, **39**, and **49**) were higher in leaves than in stems. On the other hand, the contents of three metabolites (**32**, **44**, and **46**) were lower in leaves than in stems (Supporting Information, Figure 1Sb).

Furthermore, leaves and stems showed a big difference up to 40% in tyrosinase inhibitory activity 6 months after germination. To compare the differences in secondary metabolites closely associated with bioactivity between leaves and stems at 6 months, we applied an orthogonal projection to latent structures discriminate analysis (OPLS-DA) model from the LC-MS data sets. In Figure 2Sa of the Supporting Information, the OPLS-DA model showed a clear separation between the leaves and stems of *L. maximowiczii* harvested at 6 months of the growth period along with discriminating the goodness of fit parameter, R^2 (0.52), and the predictive ability parameter, Q^2 (0.97). A clear difference between the leaves and stems at 6 months was seen in the first OPLS component ($t[1]$ = 45%). The OPLS score plot and loading S plot were conducted using *par* scaling to identify the metabolites contributing to the difference. Eleven metabolites were determined to be significantly different using the VIP values (VIP > 0.7) and p value ($p < 0.05$) of the S plot (Supporting Information, Figure 2Sb): *p*-coumaric acid (**29**), isoorientin glucoside (**32**), kaempferol dirhamnoside (**34**), daidzein (**39**), hydroxygenistein (**40**), quercetin (**41**), genistein (**43**), kaempferol (**44**), N.I. 5 (**46**), desmodianone H (**48**), and uncinanone B (**49**). Of these variables, eight leaf secondary metabolites (**29**, **34**, **39**, **40**, **43**, **46**, **48**, and **49**) placed in the positive section were present in larger quantities in leaves, whereas three metabolites (**32**, **41**, and **44**) in the negative section were present in smaller quantities in leaves.

DISCUSSION

In this study, we determined that *L. maximowiczii* underwent the most significant changes in metabolites in both the leaves and the stems 6 months after germination. This was determined by comprehensive MS-based metabolite profiling. Tyrosinase inhibitory activity was also significantly affected by secondary metabolite changes. Six months after germination, many primary metabolites were present in smaller quantities in the leaves, while most metabolites were present in larger quantities in the stems than in other months (Figure 2a,b). In particular, amino acids were more abundant in stems than in leaves and were present in high concentrations 6 months after germination. Amino acids are the major metabolic carbon and nitrogen sources for plant metabolic engineering during growth and development.[21] Our data also showed that primary metabolites such as sugars, organic acids, and fatty acids were present in larger quantities in stems than in leaves. Among them, the level of sucrose, an important product from photosynthesis, was elevated in both leaves and stems harvested at 3 and 4 months, which are the summer quarter, from June to July. In general, the rate of photosynthesis during the summer season is higher than in other seasons because more sunlight and higher temperatures elevate the rate of photosynthesis. In plants, primary metabolites are essential for growth, development, respiration, and photosynthesis.[22] As is shown in Table 1, the *L. maximowiczii* plants grew to 70 cm within 6 months of germination. The rate of vertical growth was also the highest 6 months after germination. These data indicate that the morphological changes observed are largely related to changes in metabolite production during growth.

We also detected variations with growth period in the production of many flavonoids, such as isoflavone, flavanone, flavonol, flavone, flavone glucosides, and flavonol glucosides. Our results show a remarkable difference between the chemical contents and constituents of *L. maximowiczii* leaves and stems 6 months after germination and other months during the growth period (Figure 2c,d). Moreover, our data showed significant tyrosinase inhibitory activity in both leaves and stems during the same period. The activity in the leaves was significantly higher than in the stems 6 months after germination. In the correlation map (Figure 3c,d), four metabolites, isovitexin (**38**), daidzein (**39**), desmodianone H (**48**), and uncinanone B (**49**), which were strongly positively correlated with each other, were reported to be regulatory agents of melanogenesis.[9,23,24] As these metabolites were present with the largest quantities in samples harvested 6 months after germination, they may be the most active 6 months after germination. The samples at this time were harvested in September, which is the start of the fall season in Korea. Among the secondary metabolites, the accumulation of isoflavones and flavanones contributed to high tyrosinase inhibitory activity in the fall (September 2013). On the other hand, a correlated decline in isoflavones and flavanone resulted in relatively low tyrosinase inhibitory activity in winter (November). For a year after germination, the tyrosinase inhibitory activity at 15 months (June 2014) was lower than after 3 months (June 2013). This was identically

DOI: 10.1021/acs.jafc.5b03566
J. Agric. Food Chem. 2015, 63, 8631−8639

shown between 6 months (September 2013) and 18 months (September 2014). Moreover, the phenotypes of *L. maximowiczii* showed differences in the same period of the two different years. The leaves and stems within 1 year of germination were smaller and thinner than others. On the other hand, the shapes of leaves and stems harvested in the same period of the second year were larger and thicker than those of leaves and stems harvested within one year. These differences were closely associated with metabolite changes. These results indicated that differences in phytochemicals for the one year interval were attributed to the contents of secondary metabolites, such as flavonoids, affecting tyrosinase inhibitory activity in each growth period. Also, the tyrosinase inhibitory activity in both leaves and stems harvested in September was higher than those in June. Therefore, our study suggests that harvesting *L. maximowiczii* in the fall will be useful in bioactivities because the inhibition properties of melanogenesis were the highest during this season.

In the winter season, the changes in metabolites for surviving with cold tolerance were greater than those related to tyrosinase inhibitory activity. We found the changes in the production of some sugars 8 months after germination to be particularly significant. One of the environmental factors potentially affecting plant growth is temperature.[25] Low temperature, in particular, subjects growing plants to cold stress and induces carbohydrate changes in many plant species.[26] Sugar metabolism plays an important role in the survival of cold stress. Sucrose is well-known as one of the soluble sugars, which accumulate in plants as a reserve carbon source in preparation for cold conditions.[27,28] Our results showed that the levels of fructose (**16**), glucose (**17**), and sucrose (**21**) were significantly increased in both leaves and stems harvested in November (Figure 2), which is the beginning of the winter season to start at a low temperature (average temperature of 5 °C) in Korea. These results suggest that changes in sugars are associated with seasonal variations depending on the growth period. Various derivatives of luteolin dominated the metabolite profiles of leaves harvested in November (8 months after germination), including luteolin glucosyl arabinoside or arabinosyl glucoside (**30**), hydroxyluteolin (**33**), and luteolin glucoside (**37**). Phenolic compounds play an important role by replacing other compounds in cellular metabolism during the winter.[29] Phenolic compound contents are affected by environmental factors such as temperature, UV light, rainfall, and soil conditions.[30] Our data suggest that the accumulation of phenolic compounds in the leaves might be an adaptation to low-temperature stress during the winter. From the overall results, the relationship between metabolite changes and tyrosinase inhibitory activity in *L. maximowiczii* during the growth period is briefly summarized in Figure 4.

In addition, the variation of metabolites from *L. maximowiczii* was largely influenced by the monthly average precipitation within a year of germination. In the summer rainy season, the levels of organic acids such as succinic acid and shikimic acid were significantly decreased. In the fall dry season, amino acid contents were generally increased (Figure 2).

Moreover, we determined a significant difference in the contents of metabolites and tyrosinase inhibition activity between the plant parts, leaves and stems. Many researchers reported that gene expression varied between plant parts, in spite of being subjected to the same environmental factors. For this reason, they predicted that there are differences also in the metabolite composition of plant parts.[31] Also, our team

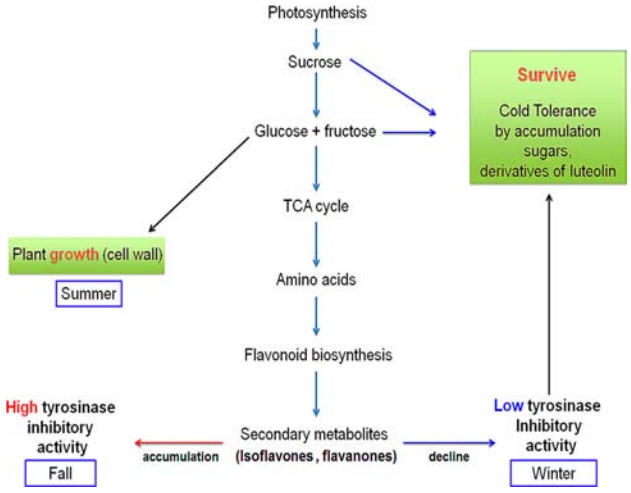

Figure 4. Suggested mechanism of seasonal metabolite changes resulting in tyrosinase inhibitory activity.

previously studied the fact that phytochemical production was dependent on the particular parts of the plant in *Lespedeza*.[32]

Leaves are exposed to much higher levels of UV radiation than stems, and therefore, photosynthesis in the leaves is heavily influenced by leaf structure characteristics such as thickness and density.[33,34] Thus, we assume that metabolite production in the leaves is more strongly affected by these conditions than that in the stems. In particular, these tendencies were remarkably shown 6 months after germination (Supporting Information, Figure 2S). Isoflavonoids such as daidzein (**39**), hydroxygenistein (**40**), genistein (**43**), and uncinanone B (**49**) were closely associated with tyrosinase inhibitory activity,[24] and their contents in leaves were superior to those in stems 6 months after germination in our data. This phenomenon was also observed in the different distributions of isoflavones in different parts of red clover and in red clover harvested at different growing stages.[35] This study demonstrated the two different parts of *L. maximowiczii* plants exhibited different levels of tyrosinase inhibitory activity due to differences in bioactive metabolites. These results suggest these metabolites are the variables discriminated from the plant parts in *L. maximowiczii* and affect its activity.

In conclusion, we confirmed that the production of primary and secondary metabolites in the leaves and stems of *L. maximowiczii* changed in response to seasonal variations. Furthermore, *L. maximowiczii* was found to undergo remarkable changes in morphology and activity after germination along with seasonal variations. The tyrosinase inhibitory activity was high in the fall because secondary metabolites involved in the activity accumulated. Both leaves and stems possessed the capacity to produce melanogenesis-regulatory substances, but the leaves had tyrosinase inhibitory activity higher than that of stems. This study revealed the relationship between metabolite changes and activity in *L. maximowiczii* during the growth period. This MS-based metabolomics approach can be applied to understand correlation between bioactivities and the changes in metabolites according to seasonal variations of any other plants.

■ ASSOCIATED CONTENT

Supporting Information

The Supporting Information is available free of charge on the ACS Publications website at DOI: 10.1021/acs.jafc.5b03566.

DOI: 10.1021/acs.jafc.5b03566
J. Agric. Food Chem. 2015, 63, 8631−8639

PLS-DA score plot and box and whisker plots using UPLC-Q-TOF-MS from the leaves and stems of *L. maximowiczii*, OPLS-DA score plot and S plot using UPLC-Q-TOF-MS from the leaves and stems of *L. maximowiczii*, harvested at 6 months, and a list of metabolites discriminated by different growth periods using GC-TOF-MS and UPLC-Q-TOF-MS (PDF)

AUTHOR INFORMATION

Corresponding Author

*Telephone: +82-2-2049-6177. Fax: +82-2-455-4291. E-mail: chlee123@konkuk.ac.kr.

Funding

This paper was supported by Konkuk University in 2014.

Notes

The authors declare no competing financial interest.

ABBREVIATIONS USED

MSTFA, *N*-methyl-*N*-(trimethylsilyl)trifluoroacetamide; PCA, principal component analysis; PLS-DA, partial least-squares discriminant analysis; OPLS-DA, orthogonal projection to latent structures discriminate analysis; VIP, variable importance in the projection; GC-TOF-MS, gas chromatography-time-of-flight-mass spectrometry; UPLC-Q-TOF-MS, ultraperformance liquid chromatography-quadrupole/time-of-flight-mass spectrometry; UHPLC-ESI-MS/MS, ultra-high-performance liquid chromatography-electrospray ionization-mass spectrometry/mass spectrometry; N.I., nonidentified metabolites; N.D., not detected

REFERENCES

(1) Kim, S. M.; Kang, K.; Jho, E. H.; Jung, Y. J.; Nho, C. W.; Um, B. H.; Pan, C. H. Hepatoprotective effect of flavonoid glycosides from *Lespedeza cuneata* against oxidative stress induced by tert-butyl hyperoxide. *Phytother. Res.* **2011**, *25*, 1011−1017.

(2) Wong, B. M.; Houseman, G. R.; Hinman, S. E.; Foster, B. L. Targeting vulnerable life-stages of Sericea Lespedeza (*Lespedeza cuneata*) with prescribed burns. *Invasive Plant Sci. Manage.* **2012**, *5*, 487−493.

(3) Raj Sharma, B.; Kim, M. S.; Yokozawa, T.; Rhyu, D. Y.; et al. Anti-oxidant and anti-diabetic activities of *Lespedeza cuneata* water extract. *J. Med. Plants Res.* **2014**, *8*, 935−941.

(4) Mori-Hongo, M.; Takimoto, H.; Katagiri, T.; Kimura, M.; Ikeda, Y.; Miyase, T. Melanin synthesis inhibitors from *Lespedeza floribunda*. *J. Nat. Prod.* **2009**, *72*, 194−203.

(5) Mori-Hongo, M.; Yamaguchi, H.; Warashina, T.; Miyase, T. Melanin synthesis inhibitors from *Lespedeza crytobotrya*. *J. Nat. Prod.* **2009**, *72*, 63−71.

(6) Woo, H. S.; Kim, D. W.; Curtis-Long, M. J.; Lee, B. W.; Lee, J. H.; Kim, J. Y.; Kang, J. E.; Park, K. H. Potent inhibition of bacterial neuraminidase activity by pterocarpans isolated from the roots of *Lespedeza bicolor*. *Bioorg. Med. Chem. Lett.* **2011**, *21*, 6100−6103.

(7) Park, H. Y.; Kim, G. B.; Kwon, Y. S. Two new dihydrofuranoisoflavanones from the leaves of *Lespedeza maximowiczi* and their inhibitory effect on the formation of advanced glycation end products. *Arch. Pharmacal Res.* **2010**, *33*, 1159−1163.

(8) Yoo, H. H.; Kim, T.; Ahn, S.; Kim, Y. J.; Kim, H. Y.; Piao, X. L.; Park, J. H. Evaluation of the estrogenic activity of leguminosae plants. *Biol. Pharm. Bull.* **2005**, *28*, 538−540.

(9) Heo, D. Y.; Kim, Y. M.; Lee, J.; Park, S. H.; Kim, J.; Park, H. M.; Lee, C. H. Desmodianone H and uncinanone B, potential tyrosinase inhibitors obtained from *Ledpedeza maximowiczii* by using bioactivity-guided isolation. *Biosci., Biotechnol., Biochem.* **2014**, *78*, 943−945.

(10) Kim, J. H.; Baek, S. H.; Kim, D. H.; Choi, T. Y.; Yoon, T. J.; Hwang, J. S.; Kim, M. R.; Kwon, H. J.; Lee, C. H. Downregulation of melanin synthesis by haginin A and its application to in vivo lightening model. *J. Invest. Dermatol.* **2008**, *128*, 1227−1235.

(11) Lee, L. S.; Choi, J. H.; Son, N.; Kim, S. H.; Park, J. D.; Jang, D. J.; Jeong, Y.; Kim, H. J. Metabolomic analysis of the effect of shade treatment on the nutritional and sensory qualities of green tea. *J. Agric. Food Chem.* **2013**, *61*, 332−338.

(12) Tugizimana, F.; Piater, L.; Dubery, I. Plant metabolomics: A new frontier in phytochemical analysis. *S. Afr. J. Sci.* **2013**, *109*, 1−11.

(13) Brunetti, C.; George, R. M.; Tattini, M.; Field, K.; Davey, M. P. Metabolomics in plant environmental physiology. *J. Exp. Bot.* **2013**, *64*, 4011−4020.

(14) Ku, K. M.; Choi, J. N.; Kim, J.; Kim, J. K.; Yoo, L. G.; Lee, S. J.; Hong, Y. S.; Lee, C. H. Metabolomics analysis reveals the compositional differences of shade grown tea (*Camellia sinesis* L.). *J. Agric. Food Chem.* **2010**, *58*, 418−426.

(15) Mediani, A.; Abas, F.; Ping, T. C.; Khatib, A.; Lajis, N. H. Influence of growth stage and season on the antioxidant constituents of *Cosmos caudatus*. *Plant Foods Hum. Nutr.* **2012**, *67*, 344−350.

(16) t'Kindt, R.; Morreel, K.; Deforce, D.; Boerjan, W.; Van Bocxlaer, J. Joint GC-MS and LC-MS platforms for comprehensive plant metabolomics: repeatability and sample pre-treatment. *J. Chromatogr. B: Anal. Technol. Biomed. Life Sci.* **2009**, *877*, 3572−3580.

(17) Ogbemudia, F. O.; Thompsonm, E. O. Variation in plants secondary metabolites and potential ecological roles. *Int. J. Modern Biol. Med.* **2014**, *5*, 111−130.

(18) del Bano, M. J.; Lorente, J.; Castillo, J.; Benavente-Garcia, O.; del Rio, J. A.; Ortuno, A.; Quirin, K. W.; Gerard, D. Phenolic diterpenes, flavones, and rosmarinic acid distribution during the development of leaves, flowers, stems, and roots of *Rosmarinus officinalis*. Antioxidant activity. *J. Agric. Food Chem.* **2003**, *51*, 4247−4253.

(19) Lee, S.; Do, S. G.; Kim, S. Y.; Kim, J.; Jin, Y.; Lee, C. H. Mass spectrometry-based metabolite profiling and antioxidant activity of Aloe vera (*Aloe barbadensis* Miller) in Different Growth Stages. *J. Agric. Food Chem.* **2012**, *60*, 11222−11228.

(20) Lee, M. Y.; Kim, J. H.; Choi, J. N.; Kim, J.; Hwang, G. S.; Lee, C. H. The melanin synthesis inhibition and radical scavenging activities of compounds isolated from the aerial part of *Lespedeza crytobotrya*. *J. Microbiol. Biotechnol.* **2010**, *20*, 988−994.

(21) Arnold, A.; Sajitz-Hermstein, M.; Nikoloski, Z. Effects of varying nitrogen sources on amino acid synthesis costs in *Arabidopsis thaliana* under different light and carbon-source conditions. *PLoS One* **2015**, *10*, e0116536.

(22) Gomez-Romero, M.; Segura-Carretero, A.; Fernandez-Gutierrez. Metabolite profiling and quantification of phenolic compounds in methanol extracts of tomato fruit. *Phytochemistry* **2010**, *71*, 1848−1864.

(23) Yao, Y.; Cheng, X.; Wang, L.; Wang, S.; Ren, G. Mushroom tyrosinase inhibitors from mung bean (*Vigna radiatae* L.) extracts. *Int. J. Food Sci. Nutr.* **2012**, *63*, 358−361.

(24) Chang, T. S.; Ding, H. Y.; Lin, H. C. Identifying 6,7,4'-Trihydroxyisoflavone as a Potent Tyrosinase Inhibitor. *Biosci., Biotechnol., Biochem.* **2005**, *69*, 1999−2001.

(25) Morison, J. I. L.; Lawlor, D. W. Interactions between increasing CO_2 concentration and temperature on plant growth. *Plant, Cell Environ.* **1999**, *22*, 659−682.

(26) Theocharis, A.; Clement, C.; barka, E. A. Physiological and molecular changes in plant grown at low temperatures. *Planta* **2012**, *235*, 1091−1105.

(27) Savitch, L. V.; Harney, T.; Huner, N. P. A. Sucrose metabolism in spring and winter wheat in response to high irradiance, cold stress and cold acclimation. *Physiol. Plant.* **2000**, *108*, 270−278.

(28) Wong, B. L.; Baggett, K. L.; Rye, A. H. Seasonal patterns of reserve and soluble carbohydrates in mature sugar maple (*Acer saccharum*). *Can. J. Bot.* **2003**, *81*, 780−788.

(29) Olenichenko, N. A.; Ossipov, V. I.; Zagoskina, N. V. Effect of cold hardening on the phenolic complex of winter wheat leaves. *Russ. J. Plant Physiol.* **2006**, *53*, 495−500.

DOI: 10.1021/acs.jafc.5b03566
J. Agric. Food Chem. 2015, 63, 8631−8639

(30) Borges, L. L.; Alves, S. F.; Sampaio, B. L.; Conceicao, E. C.; F. Bara, M. T.; Paula, J. R. Environmental factors affecting the concentration of phenolic compounds in *Myrcia tomentosa* leaves. *Rev. Bras. Farmacogn.* **2013**, *23*, 230−238.
(31) Juhasz, Z.; Boldizsar, A.; Nagy, T.; Kocsy, G.; Marincs, F.; Galiba, G.; Banfalvi, Z. Pleiotropic effect of chromosome 5A and the mvp mutation on the metabolite profile during cold acclimation and the vegetative/generative transition in wheat. *BMC Plant Biol.* **2015**, *15*, 57.
(32) Kim, Y. M.; Lee, J.; Park, S.; Lee, C.; Lee, J. W.; Lee, D.; Kim, N. H.; Lee, D.; Kim, H. Y.; Lee, C. H. LC-MS-based chemotaxonomic classification of wild-type *Lespedeza* sp. and its correlation with genotype. *Plant Cell Rep.* **2012**, *31*, 2085−2097.
(33) Chabot, B. F.; Chabot, J. F. Effects of light and temperature on leaf anatomy and photosynthesis in *Fragaria vesca*. *Oecologia.* **1977**, *26*, 363−377.
(34) Garnier, E.; Salager, J. L.; Laurent, G.; Sonie, L. Relationships between photosynthesis, nitrogen and leaf structure in 14 grass species and their dependence on the basis of expression. *New Phytol.* **1999**, *143*, 119−129.
(35) Tsao, R.; Papadopoulos, Y.; Yang, R.; Young, J. C.; Mcrae, K. Isoflavone profiles of Red Clovers and their distribution in different parts harvested at different growing stages. *J. Agric. Food Chem.* **2006**, *54*, 5797−5805.
(36) Langdale, G. W.; Giddens, J. E. Phytotoxic phenolic compounds in *Sericea Lespedeza* Residues. *Agron J.* **1967**, *59*, 581−584.
(37) Plazonic, A.; Bucar, F.; Males, Z.; Mornar, A.; Nigovic, B.; Kujundzic, N. Identification and quantification of flavonoids and phenolic acids in Burr Parsley (*Caucalis platyacarpos*), using high-performance liquid chromatography with diode array detection and electrospray ionization mass spectrometry. *Molecules* **2009**, *14*, 2466−2490.
(38) Jung, E. S.; Lee, S.; Lim, S. H.; Ha, S. H.; Liu, K. H.; Lee, C. H. Metabolite profiling of the short-term responses of rice leaves (*Oryza sativa* cv. Ilmi) cultivated under different LED lights and its correlations with antioxidant activities. *Plant Sci.* **2013**, *210*, 61−69.
(39) Siraichi, J. T.; Felipe, D. F.; Brambilla, L. Z.; Gatto, M. J.; Terra, V. A.; Cecchini, A. L.; Cortez, L. E.; Rodrigues-Filho, E.; Cortez, D. A. Antioxidant capacity of the leaf extract obtained from Arrabidaea chica cultivated in Southern Brazil. *PLoS One* **2013**, *8*, e72733.
(40) Sanchez-Rabaneda, F.; Jauregui, O.; Casals, I.; Andres-Lacueva, C.; Izquierdo-Pulido, M.; Lamuela-Raventos, R. M. Liquid chromatographic/electrospray ionization tandem mass spectrometric study of the phenolic composition of cocoa (*Theobroma caao*). *J. Mass Spectrom.* **2003**, *38*, 35−42.
(41) Matsuzaki, K.; Wang, Y.; Takahashi, K.; Okuyama, T. Flavonoid Glycosides of *Lespedeza* Species. *Shoyakugaku Zasshi* **1990**, *44*, 251−253.
(42) Miyase, T.; Ueno, A.; Noro, T.; Fukushima, S. Studies on the constitutents of *Lespedeza crytobotrya* MIQ. I. The structures of a new chalcone and two new isoflav-3-ens. *Chem. Pharm. Bull.* **1980**, *28*, 1172−1177.
(43) Klejdus, B.; Vitamvasova-Sterbova, D.; Kuban, V. Identification of isoflavone conjugates in red clover (*Trifolium pretense*) by liquid chromatography mass-spectrometry after two-dimensional solid-phase extraction. *Anal. Chim. Acta* **2001**, *450*, 81−97.
(44) Wojakowska, A.; Piasecka, A.; Garcia-Lopez, P. M.; Zamora-Natera, F.; Krajewski, P.; Marczak, L.; Kachlicki, P.; Stobiecki, M. Structural analysis and profiling of phenolic secondary metabolites of Mexican lupine species using LC-MS techniques. *Phytochemistry* **2013**, *92*, 71−86.
(45) Kwon, D. J.; Kim, J. K.; Ham, Y. H.; Bae, Y. S. Flavone glycosides from the aerial parts of *Lespedeza cuneata* G.Don. *J. Korean Soc. Appl. Biol. Chem.* **2007**, *50*, 344−347.
(46) Miyase, T.; Sano, M.; Nakai, H.; Muraoka, M.; Nakazawa, M.; Suzuki, M.; Yoshino, K.; Nishihara, Y.; Tanai, J. Antioxidants from *Lespedeza homoloba* (I). *Phytochemistry* **1999**, *52*, 303−310.
(47) Miyase, T.; Sano, M.; Yoshino, K.; Nonaka, K. Antioxidants from *Lespedeza homoloba* (II). *Phytochemistry* **1999**, *52*, 311−319.

DOI: 10.1021/acs.jafc.5b03566
J. Agric. Food Chem. 2015, 63, 8631−8639

JOURNAL OF AGRICULTURAL AND FOOD CHEMISTRY

Addition/Correction

pubs.acs.org/JAFC

Correction to Photodegradation of Imidacloprid in Aqueous Solution by the Metal-Free Catalyst Graphitic Carbon Nitride using an Energy-Saving Lamp

Xue Liu, Xiaoli Wu, Zhen Long, Che Zhang, Yongqiang Ma,* Xianghong Hao, Hongyan Zhang, and Canping Pan

J. Agric. Food Chem. **2015**, *63* (19), 4754−4760. DOI: 10.1021/acs.jafc.5b01105

Supporting Information

An incorrect Supporting Information file was made available with the original publication of this paper. The correct file is available with this correction, and it has also been replaced in the original document.

■ ASSOCIATED CONTENT

Supporting Information

The Supporting Information is available free of charge on the ACS Publications website at DOI: 10.1021/acs.jafc.5b04445.

FT-IR spectra of M-g-C_3N_4 and U-g-C_3N_4 samples (Figure S1), C1s and O1s XPS spectra of g-C_3N_4 synthesized from different precursors (Figure S2), ratios of bonds within the N1s core level peak (Table S1), and percentage breakdown of different bonds within the N1s spectrum (Table S2) (PDF)

Published: September 16, 2015

ACS Publications © 2015 American Chemical Society

DOI: 10.1021/acs.jafc.5b04445
J. Agric. Food Chem. 2015, 63, 8640−8640

Table 1. Coordinates of Locations Where Fruits of Wild Bilberry (*Vaccinium myrtillus*, Vm) and Cultivated Blueberry (*Vaccinium corymbosum* cv. Brigitta Blue, Vc) Were Harvested during Two Consecutive Seasons (2013 and 2014)[a]

							n		harvest date	
location	site	species	latitude (° N)	longitude (° E)	altitude (m asl)	soil pH	2013	2014	2013	2014
Val di Cembra	Vm1	*V. myrtillus*	46.22	11.26	1166	5.1	13	18	July 17	July 3
Val di Cembra	Vm2	*V. myrtillus*	46.22	11.26	1261	4.4	7	18	July 24	July 3−10
Val di Cembra	Vm3	*V. myrtillus*	46.22	11.24	1404	4.8	11	23	July 24	July 10
Monte Paganella	Vm4	*V. myrtillus*	46.17	11.04	1520	4.7	2	11	Aug 21	Aug 1
Monte Paganella	Vm5	*V. myrtillus*	46.16	11.04	1617	4.8	1	11	Aug 21	Aug 28
Monte Paganella	Vm6	*V. myrtillus*	46.16	11.03	1829	4.3	12	23	Sept 3	Aug 28
Telve	Vc1	*V. corymbosum*	46.07	11.49	495		4	4	July 22	July 7
Spera	Vc2	*V. corymbosum*	46.08	11.51	749		4	4	July 22	Aug 12
Pinè	Vc3	*V. corymbosum*	46.03	11.28	1034		4	4	Aug 12	Aug 12

[a] *n* = number of individuals collected on the site. For bilberry, also pH of soil is reported.

majority of ACs found in blueberries, constituting about 70% of total ACs.[18] Acylated ACs are also found in blueberries and bilberries, but they account for only a small portion of the total amount.[18,19]

Latitude appears to influence the accumulation of ACs in bilberries, as a clear increasing trend in AC production toward the north has been reported in high latitudes. Higher AC content was reported in northern (63−70° N) latitudes of northern Europe, compared to southern latitudes (54−62° N).[10,11] The berries of the northernmost clones have been shown to contain higher total content of ACs and higher proportions of the more hydroxylated anthocyanidins, Dps and Mvs, whereas Cys accumulated more in the more southern populations of northern Europe (latitudes 54−62° N). Studies have also been performed in relation to different altitudes, although they have given contradictory results. Spinardi et al.[20] reported higher levels of ACs and ascorbic acid in blueberries grown at 600 m asl compared with the same cultivar grown at 450 m asl in Valtellina (northern Italy). In a two-year study in Austria,[7] decreasing AC contents were found in bilberry fruits along with increasing altitude (between 800 and 1500 m asl). In studies performed in the areas of northern Europe, where altitudinal differences are less pronounced, no clear relationship with elevation and AC concentration has been found.[11,21]

In the present study, we investigated the effect of the altitude on the accumulation of ACs in the berries of two *Vaccinium* species (*V. myrtillus* L., bilberry, and *V. corymbosum* L. cv. Brigitta Blue) growing in northern Italy over two growing seasons. The aim was to investigate the effect of temperature and light conditions on the accumulation of ACs. The AC profiles of six wild bilberry populations growing in the Alps of northern Italy along an altitudinal gradient of about 650 m were analyzed and compared with the AC profile of one of the most popular varieties of highbush blueberry (cv. Brigitta Blue), which is cultivated in a range of about 550 m. Furthermore, temperature and light conditions monitored along the altitudinal gradient were compared with AC profiles of berries. The study provides detailed information about the AC composition of *Vaccinium* berries, which is valuable for food quality control in the berry industry. With specific regard to the wild species, the metabolic profile of individuals within each bilberry population may also allow selection of specific genotypes for cultivation and breeding purposes.

MATERIALS AND METHODS

Plant Material and Altitudinal Gradients. The field trials were established along altitudinal gradients in the region of Trentino (Italy). Permissions for field work were granted by the municipalities of Grumes, Valda, and Zambana and the Province of Trento (Italy). Six sites were identified for bilberry (*V. myrtillus* L., Vm) experimental fields. The gradient was established between Val di Cembra (46.22° N, 11.26° E) and Monte Paganella (46.16° N, 11.04° E) at 1166, 1261, 1406, 1520, 1620, and 1829 m asl (Table 1). In each site 10−25 individual bilberry plants within an area of about 20 m^2 were considered for AC analysis of the berries.

Blueberries (*V. corymbosum* L., Vc) of cv. Brigitta Blue were collected from plants cultivated by farmers of Valsugana valley (46.08° N, 11.50° E). Three sites, located in Telve (495 m asl.), Spera (749 m asl), and Pinè (1034 m asl) were considered for the altitudinal gradient (Table 1). Plants were cultivated according to conventional farming methods. Fruits were collected from five plants chosen randomly on five different rows of plants in the field in an area of 100 m^2.

Fruit Harvesting. The study was conducted in two consecutive growing seasons (years 2013 and 2014). Bilberries were harvested when fruits reached the full development in size and color, and total soluble solid content (TSSC) was >6.0 °Brix. In 2013, bilberry fruits from Val di Cembra were collected between July 17 (in lowest location, site Vm1) and July 24 (in middle-high locations, sites Vm2 and Vm3), whereas on Monte Paganella, on sites Vm4 and Vm5, bilberries were collected on August 21 and bilberries from the highest location (site Vm6) on September 3. In 2014, the growing season was anticipated in Val di Cembra, as the berry harvesting started on June 20 in the lowest site (Vm1). The harvest continued on July 3 on sites Vm2 and Vm3, on August 1 for Vm4, and on August 28 on sites Vm5 and Vm6 (Table 1).

Blueberry fruits were manually picked at the commercial ripening stage, when berries were fully developed in size and color, with TSSC content >10 °Brix, and at least 80% of berries on the plant reached ripeness. Fruit collection started on July 22, 2013, in sites of Telve (Vc1) and Spera (Vc2) and ended on August 12, 2013, in the highest location, Pinè (Vc3). In the following year, 2014, fruits were harvested on the same plants, starting from Telve on July 7 and finishing on August 12 in Spera and Pinè (Table 1).

Berries were placed in plastic tubes and stored on ice to prevent sample degradation during transport from the field to the laboratories, where they were stored at −80 °C. Metabolic analyses were performed within 3 months from the collection.

Total Soluble Solid Content Analysis. TSSC analyses were conducted on mature fruits, as homogeneous as possible for size and color. TSSC was measured with a DBR35 refractometer.

AC Extraction. Frozen ripe berries were ground into a fine powder with a cryomill (Retsch, Haan, Germany). The homogenized samples (1 g fresh weight, FW, of at least 10 g of fresh berries) were extracted twice in 1.5 mL of 80% methanol under shaking for 1 h. Samples were centrifuged at 12000*g* for 2 min. Supernatants were pooled and brought to a volume of 5 mL. Samples were filtered (0.22 μm PVDF filters), transferred to glass vials, and randomized before analysis by UPLC-MS/MS.[22]

DOI: 10.1021/acs.jafc.5b02833
J. Agric. Food Chem. 2015, 63, 8641−8650

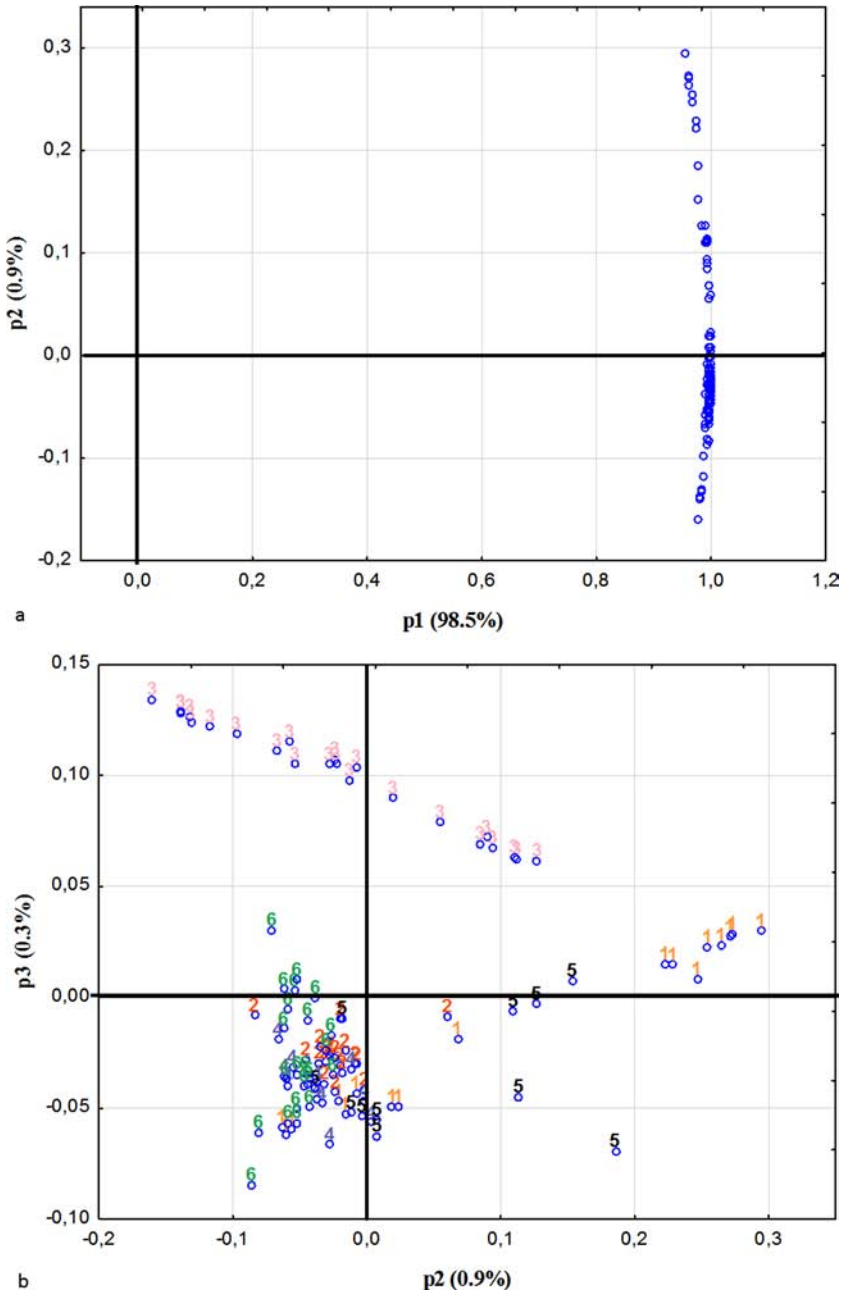

Figure 1. AC variability estimated by PCA among bilberry individuals from six bilberry populations in northern Alps of Italy: variability explained by first and second PCA components (a) and by second and third PCA components (b).

UPLC Analysis. Analytical separation of ACs was performed in an Acquity ultraperformance liquid chromatographic (UPLC) system (Waters, UK) operating under MassLynx XS software. The system was coupled to a mass spectrometer detector Waters Xevo TQ MS (Milford, MA, USA) equipped with an electrospray (ESI) source. All samples were analyzed on a reverse phase Acquity UPLC BEH C18, 1.7 μm, 2.1 × 150 mm column (Waters), protected with an Acquity UPLC BEH C18, 1.7 μm, 2.1 × 5 mm precolumn (Waters) at 40 °C and under mobile phase flow rate of 0.4 mL/min. Water was used as weak eluting solvent (A) and methanol as strong eluting solvent (B); formic acid 5% v/v was used as additive in both eluents. The multistep linear gradient used was as follows: from 95 to 60% for the first 4 min, from 60 to 45% A from 4 to 9 min, from 45 to 5% A from 9 to 11 min, and an isocratic hold for 3 min to clean the column. The equilibration time was 4 min, and the injection volume was 2 μL. 4-Hydroxystilbene was used as internal standard (2.5 ppm) to check that the sensitivity of the machine was kept constant during the analysis. A quality control standard mixture was injected periodically to check that the sensitivity of the machine was kept constant during the analysis.

Identification and Quantification (MS/MS). ACs were detected by multiple reaction monitoring (MRM), by screening the MS/MS transitions and using the parameters earlier optimized for grape wine.[22] The method was slightly modified to allow the detection of gal and ara anthocyanidins that have earlier been described for bilberry. For some of the compounds, there were no standards available, but they could be tentatively identified on the basis of their MRM transitions and the relative retention time with respect to known compounds and considering previous results (Supplementary Table 1).[19]

For quantification, external calibration curves were prepared by injecting authentic standards of each compound at different concentrations. When the authentic standard was not available, the ACs were quantified relative to Mv-3-*O*-glu, using the Mv-3-*O*-glu calibration curve (Supplementary Table 1). Data processing was done

DOI: 10.1021/acs.jafc.5b02833
J. Agric. Food Chem. 2015, 63, 8641−8650

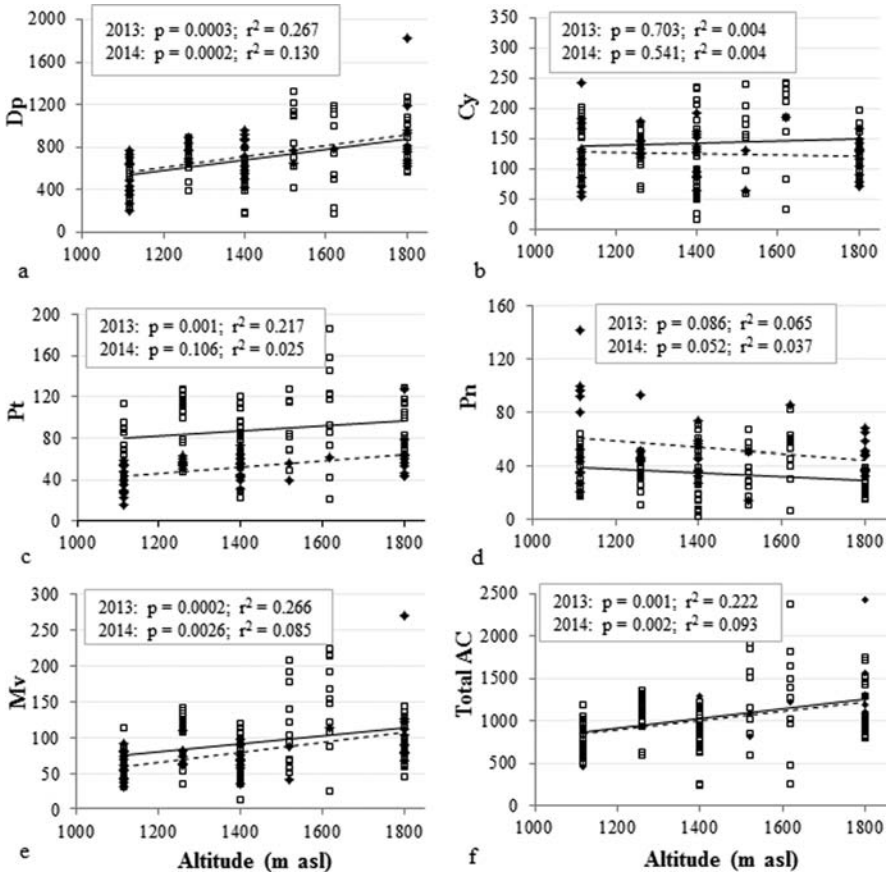

Figure 2. AC accumulation (mg/100 g FW) in bilberries along altitudinal gradient in two consecutive seasons (2013−2014). Regression analysis was performed, and coefficient of determination r^2 and p value were calculated for each class of anthocyanidin (a, Dp; b, Cy; c, Pn; d, Pt; e, Mv) and the total AC content (f). (■) 2013 samples; (□) 2014 samples; (broken line) regression line of 2013 samples; (solid line) regression line of 2014 samples.

using Waters MassLynx 4.1 and TargetLynx software. The amount of anthocyanidin classes (Dp, Cy, Mv, Pn, and Pt) and total ACs was calculated by summing the amounts of single AC compounds identified.

Air Temperature Measurement. The air temperature was measured along the altitudinal gradient, between 410 and 2125 m asl, at the meteorological stations of the Protezione Civile of Trento (Italy). Among all of the stations present in the province of Trento, the ones chosen were the nearest to the experimental fields. In detail, stations were located in Telve (T0392, 46.06° N, 11.47° E, 410 m asl), Bieno (T0015, 46.08° N, 11.56° E, 843 m asl), Lavarone (T0032, 45.94° N, 11.25° E, 1155 m asl), Monte Bondone (T0368, 46.01° N, 11.05° E, 1490 m asl), and Monte Paganella (T0099, 46.14° N, 11.04° E, 2125 m asl). Maximum daily temperatures were recorded in 2013 and 2014 during berry growing season (June 1−August 31). Data are available online at www.meteotrentino.it.

Solar Radiation and Light Quality Measurements. Light at the tops of canopies was measured with a USB 2000 spectrometer (Ocean Optics, Dunedin, FL, USA). Measurements were recorded during fruit development and ripening at noon on sunny days under a clear sky, within a range of altitude between 495 and 1404 m asl (at locations Vc1, Vc2, Vc3, Vm1, Vm2, and Vm3). The quality of light reaching the plants was measured as photosynthetic active radiation (PAR) by integrating the area between 200 and 850 nm for full sunlight spectra, 200−380 nm for UV light, 380−750 nm for visible light, 380−495 nm for blue components, 590−710 nm for red components, and 710−750 nm for far-red components.[23] Spectra and integration of light were measured from five consecutive scans of the sunlight, after calibration of the instrument according to the manufacturer's instructions.

Soil pH. For bilberry, in every location, five points were spotted out of the edges of the bilberry matrix frame for soil sampling. In these spots, about 1 kg of soil between 20 and 50 cm underground was collected. The samples were first cleaned of plant roots, leaves, and small stones and then pooled together. A pooled sample of 80 g was dissolved in 200 mL of distilled water[24] and stirred overnight, and the next day the pH was measured with Crison PH 25+ (Hach Lange Srl, Derio, Spain).

Statistics. All data were analyzed using Statistica 9 software (StatSoft Inc., Tulsa, OK, USA). Two-way ANOVA followed by pairwise comparison using Fisher's least significant difference (LSD) test was made between the variables: metabolites versus altitude and year of collection, light conditions versus altitude, and temperature versus altitude. Differences were considered significant when $p < 0.05$.

Principal component analysis (PCA) was performed on bilberries' AC composition to investigate the variation within bilberry populations and to discriminate geographic areas of collection. Regression analyses were made on the full set of bilberry samples to measure the coefficient of determination r^2 and p value between the anthocyanidin classes (Dp, Cy, Pn, Pt, Mv), total ACs, and altitude.

■ RESULTS AND DISCUSSION

AC Profile of Bilberry Populations. AC profiles of bilberry fruits as well as AC variation among native bilberry populations in the Alps of northern Italy were systematically analyzed. The ACs identified were Dp, Cy, Pn, Pt, and Mv, conjugated with glu, gal, and ara, and their acylated forms, including acetylated and para-coumaroylated ACs. In small amounts, also Cy 3 sambubioside and Pg were identified (Supplementary Table 2). The amounts of Dp glycosides were higher than of Cy glycosides on average, similarly to the profiles

DOI: 10.1021/acs.jafc.5b02833
J. Agric. Food Chem. 2015, 63, 8641−8650

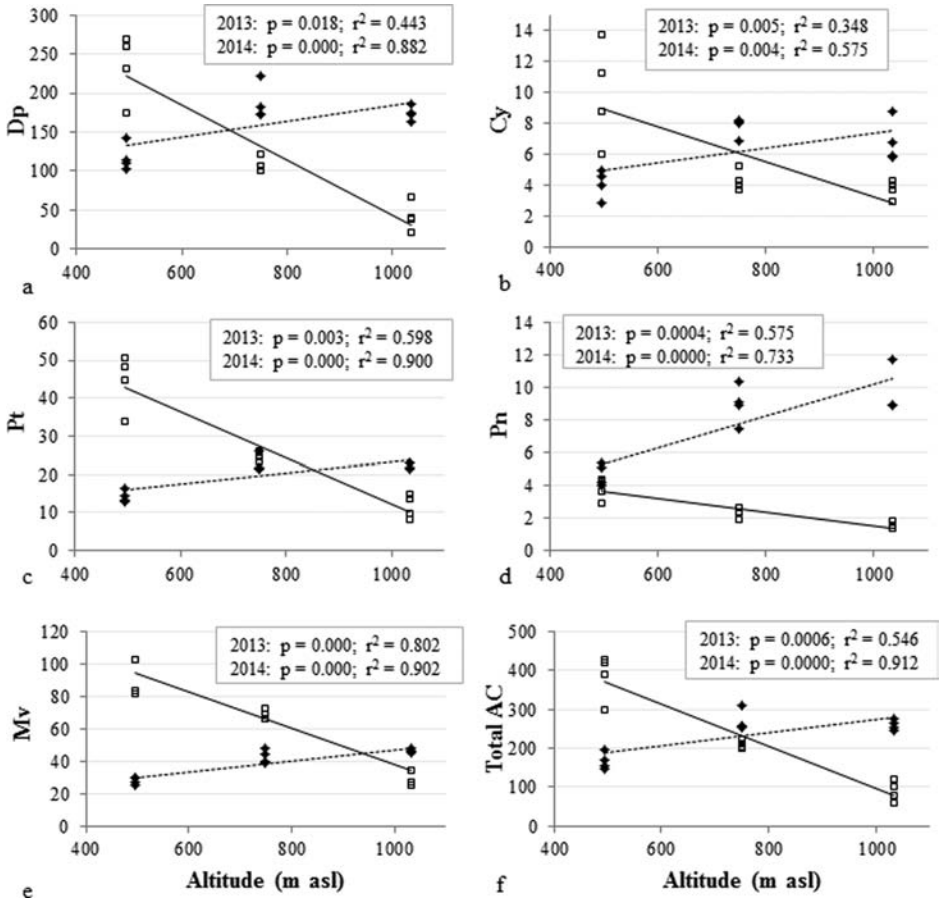

Figure 3. AC accumulation (mg/100 g FW) in blueberries (cv. Brigitta Blue) along altitudinal gradient in two consecutive seasons (2013−2014). Regression analysis was performed, and coefficients of determination r^2 and p value were calculated for each class of anthocyanidin (a, Dp; b, Cy; c, Pn; d, Pt; e, Mv) and the total AC content (f). (■) 2013 samples; (□) 2014 samples; (broken line) regression line of 2013 samples; (solid line) regression line of 2014 samples.

detected in other southern European bilberries, for example, from Austria,[7] Slovenia,[8] and Montenegro,[25] but also in northern European bilberries, for example, from Finland.[10,19] However, the comparison between bilberries from Finland[19] and Italy (presented in this study) which were analyzed with the same analytical method[22] revealed differences in the sugar moiety. In bilberries growing in northern Europe >60% of the ACs was conjugated with glu, whereas the remaining 40% was shared equally between gal and ara.[19] In the present study, ACs were equally conjugated with the three sugars (about 30% each), which is in line with the results of the study on Slovenian bilberries.[8] In the present study, also climate differences affected accumulation of acetylated compounds, which were more abundant in 2013 than in 2014 (Supplementary Table 2).

The AC variability among bilberry populations, estimated through PCA, was minimal as the first axis explained the 98.5% of the diversity, but grouped all samples in a single cluster (Figure 1a). However, the second and third axes, which respectively explained 0.9 and 0.3% of the diversity, separated the populations from sites Vm1, Vm3, and Vm5 (Figure 1b), indicating that the AC profile may be used as a discriminative factor of bilberry populations from close geographical sites.

AC Profile of Blueberries (cv. Brigitta Blue). The AC profile was typical for the cv. Brigitta Blue,[26] with Dp and Mv as predominant anthocyanidins, followed by Pt and in lowest proportion Cy and Pn (Supplementary Table 3). AC compounds were conjugated with glu, gal, and ara sugars, but were not uniformly distributed among the anthocyanidins. Dp was equally conjugated with glu and ara, whereas very little Dp 3 gal was detected. On the contrary, Mv and Pt (which are methylated forms of Dps[27]) and the monohydroxylated Cy and Pn were equally conjugated with gal and ara and to a small extent with glu. No acylated forms were identified in blueberries (Supplementary Table 3).

AC Accumulation in Wild and Cultivated *Vaccinium* spp. along Altitudinal Gradients. The two *Vaccinium* species, bilberry and blueberry, showed important differences in the accumulation of ACs along the altitudinal gradient. Our results indicated an increase in the accumulation of ACs in bilberries along a gradient of about 650 m, which was consistent over the two growing seasons (Figure 2). Indeed, regression analysis of total AC concentration gave a significant positive correlation between altitude and total AC accumulation in berries ($p = 0.001$ in 2013 and $p = 0.002$ in 2014) in both years (Figure 2). The trend was due to a significant increase in the trihydroxylated anthocyanidins such as Dp ($p = 0.0003$ in 2013, $p = 0.0002$ in 2014) and Mv ($p = 0.0002$ in 2013, $p = 0.0026$ in 2014). To a small extent also Pt increased with increasing altitude ($p = 0.001$ in 2013). The accumulation of the monohydroxylated Cy and Pn glycosides, instead, was not affected by the altitude (Figure 2).

The results of the present study are in line with those of Jovancevic et al.,[25] who showed that bilberries collected in sunny locations contained higher amounts of ACs with

DOI: 10.1021/acs.jafc.5b02833
J. Agric. Food Chem. 2015, 63, 8641−8650

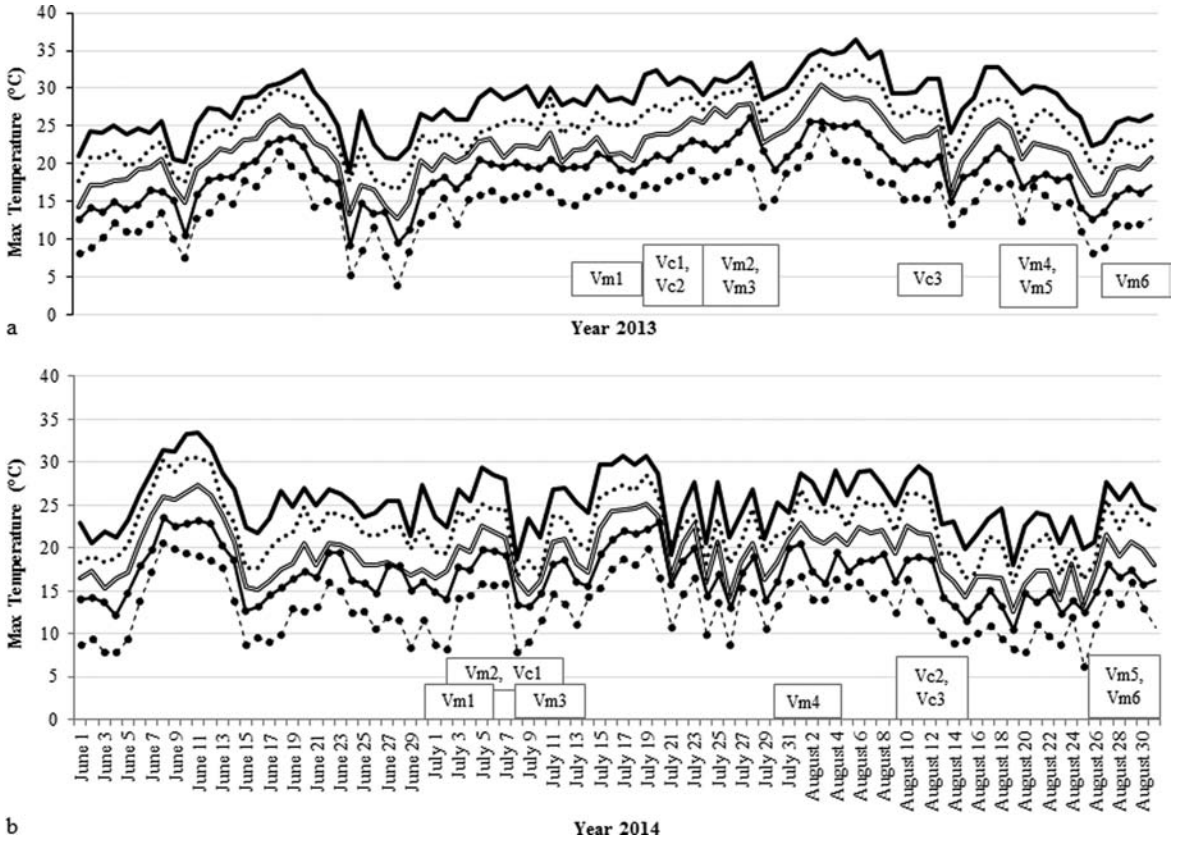

Figure 4. Maximum daily temperatures recorded along the altitudinal gradient during berry ripening (June 1−September 4) in 2013 (a) and 2014 (b). The temperatures were recorded at the meteorological stations in Telve (410 m asl, solid line), Bieno (843 m asl, broken line), Lavarone (1155 m asl, double line), Monte Bondone (1490 m asl, solid line with dots), and Monte Paganella (2125 m asl, broken line with dots) in the region of Trentino (northern Italy). The harvest date for each location is provided.

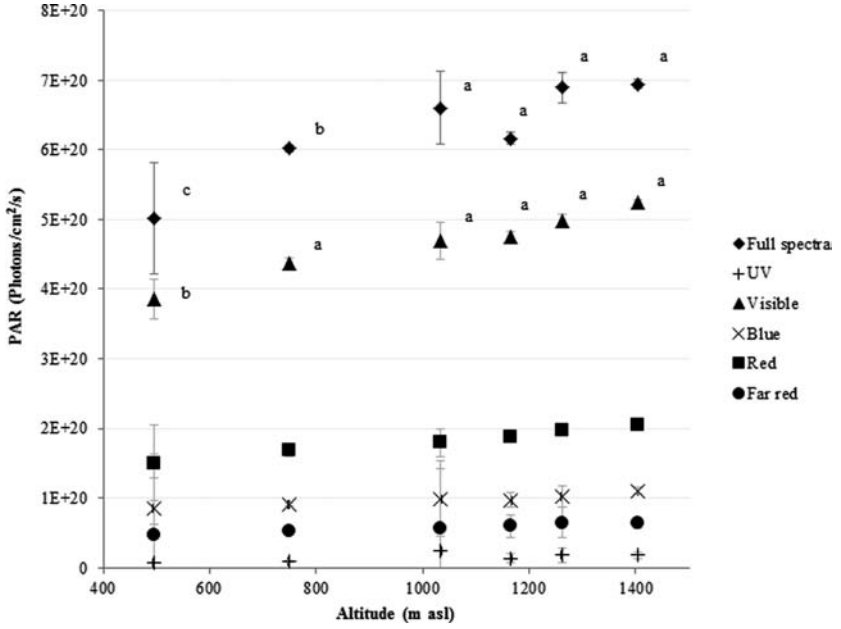

Figure 5. Solar radiation PAR measured along the altitudinal gradient. PAR was measured in six locations between 495 and 1404 m asl by integrating the spectra between 200 and 850 nm for full sunlight spectra, 200−380 nm for UV light, 380−750 nm for visible light, 380−495 nm for blue components, 590−710 nm for red components, and 710−750 nm for far-red components.

increasing altitude. In particular, an increase in Dp-type ACs was observed in locations above 1500 m asl.[25] Contrasting results were reported by Rieger et al.[7] in bilberries collected at different altitudes in Austria, where decreasing amounts of ACs were observed with increasing altitude. However, results by Rieger et al.[7] are also in contrast with the same analysis

DOI: 10.1021/acs.jafc.5b02833
J. Agric. Food Chem. 2015, 63, 8641−8650

performed within the same study on other plant species (*Calluna vulgaris* L. and *Sambucus nigra* L.). Moreover, no information about the exposure and climatic conditions of the bilberry collection sites was presented. The content and composition of ACs in bilberries are highly affected by environmental factors such as light intensity, light quality, and temperature,[19,28−30] which need to be taken into consideration to explain the accumulation of metabolites in fruits growing in natural environments.

In blueberry, an opposite trend was observed during the two years in the present study; in 2013 the accumulation of total AC was positively increasing toward higher altitudes (p = 0.0006), whereas in 2014 accumulation was negatively correlated with altitude (p = 0.0000; Figure 3). In the case of blueberry, only the cultivar (Brigitta Blue) was used in the study and, therefore, the seasonal differences in the AC content were considered to be connected to environmental effects.

Environmental Effect on AC Accumulation. In all types of fruits, environmental factors affect the quantitative and qualitative composition of ACs in the ripening fruit.[31] In general, the genetic background of the species/variety determines the AC content in fruit, yet the environmental factors can affect the concentration of diverse ACs in different ways. Temperature, solar radiation, and soil are considered the major environmental factors affecting the accumulation of ACs in fruits.[32] All of these factors may vary markedly along latitudinal gradients, where changes in phenolic content of bilberries were recorded with changing environments from southern to northern latitudes.[10,11,21]

In the present study we observed that the same factors vary markedly also along an altitudinal gradient. Maximum daily temperatures decreased progressively with increasing altitude (Figure 4). Moreover, differences in temperatures were recorded throughout the two growing seasons, which significantly affected the accumulation of ACs in berries (p < 0.05; Supplementary Table 2). Higher temperatures were recorded during the year 2013, when also higher accumulation of AC was found in bilberries, with higher proportion of acylated forms of ACs (Supplementary Table 2) in line with findings in grape berries (cv. Merlot)[33] and in our previous study on bilberry.[30]

Light conditions were also measured in six locations along the gradient, within 495 and 1404 m asl; Figure 5). Sunlight PAR (full spectra) increased constantly toward increasing altitudes, and significant changes (p < 0.001) were recorded between locations at 495 and 756 m asl and locations higher than 1034 m asl. The increase was due to a progressive increase of visible light along with altitude, although the blue and red components were not significantly affected with increasing altitude. The UV radiation accounted for only 1.3−3.8% of the total radiation and was not significantly affected by altitude. The soil pH ranged between 4.3 and 5.1 (Table 1), which is optimal for the growth of bilberry,[35] but did not show any particular trend connected with altitude.

Our results suggest that lower temperatures have a major effect on the accumulation of ACs in bilberry. Decreasing temperatures observed with increasing altitude, positively influenced the accumulation of ACs in bilberries being in line with the results of Uleberg et al.,[28] who showed that higher amounts of Dp derivatives are produced at low temperatures (12 °C) compared to higher temperatures (18 °C). Recently, we also observed that when plants from the same bilberry populations were moved from higher to lower altitude (485 m asl), in open-field conditions with higher temperature, berries accumulated lower amounts of ACs, confirming the role of temperature in the determination of the final AC profile of berries.[30] Thus, the difference in the average daily temperature in the original locations (Vm1−Vm6) was at least 5 °C lower than in the test field at 485 m asl and the AC accumulation was almost 2-fold higher in the original site. Excessive light stress appeared to inhibit AC accumulation,[30] but considering the present results, where light intensity is higher at altitudes above 1034 m asl compared to fields at altitude 495 m asl (Figure 5), light intensity appears to have less influence than temperature on AC accumulation in bilberry fruits growing in natural environments. Supporting this assumption, in the locations above 1034 m asl, where bilberry populations were growing, no significant difference in the intensity of the light reaching the plants was detected (Figure 5). Therefore, we hypothesized that bilberry plants grown at higher altitudes may have developed genetic adaptation mechanisms which respond to low temperatures with an increased production in ACs, in particular of the Dp type.

The biosynthesis of Dp-type ACs is driven by the flavanone 3′5′-hydroxylase (*F3′5′H*) gene, which is responsible for the hydroxylation at the 3′,5′-positions of the B-ring of the precursor dihydrokaempferol into Dp and the methylated derivatives Mv and Pt and which also shifts the biosynthesis from the Cy and Pn branch toward the branch of the flavonoid pathway producing Dp, Mv, and Pt as final core structures of ACs.[27] Studies conducted on blueberry,[27] bog bilberry (*Vaccinium uliginosum* L.),[36] and grape berries (*Vitis vinifera* L.)[37] showed that the *F3′5′H* gene is weakly expressed during the earliest ripening stages and is abundant only during the late ripening stages, closely paralleling the appearance of ACs. In blueberry, as the fruit ripens and the exocarp color changes from mostly green to partially pink, blue-purple Dp-type ACs begin to accumulate. The appearance of the trihydroxylated anthocyanidin Dp and its derivatives Mv and Pt is coordinated with the abundance of *VcF3′5′H* transcripts at developmental stage S5 (at the initiation of ripening).[27] On the basis of the conservation of the flavonoid pathway in diverse species, *VmF3′5′H* gene expression is expected to increase at the late ripening stages of bilberry as well as when exposed to low temperatures, as found in the present study and as suggested for grapevine.[38]

In blueberry, marked differences in AC content were recorded in the same locations during the two seasons. The accumulation of ACs in blueberries is developmentally regulated and occurs during the pink and purple-blue (full ripe) stages of berry development.[27] At the lowest location, Vc1, the berries started in 2013 to visibly turn color and to accumulate ACs on June 30, and they reached full ripeness on July 22, whereas in 2014 the berries started to turn color on June 10 and reached ripeness by July 7. In the central location Vc2, blueberries started to turn color on June 30 in 2013 and reached ripeness on July 22 (as in location Vc1), whereas in 2014 the ripening was delayed by almost 3 weeks as berries started AC accumulation on August 1 and ripened on August 12. In the highest location, Vc3, the ripening of berries was more uniform during the two seasons and the berries started to turn color around August 1 in both years and were ready for picking on August 12.

The accumulation of AC in blueberries is regulated also by environmental factors.[30] To our knowledge, very little information is known about the effect of temperature on AC

DOI: 10.1021/acs.jafc.5b02833
J. Agric. Food Chem. 2015, 63, 8641−8650

biosynthesis in blueberries. Therefore, in the present study, the cultivation of blueberries at different altitudes allowed us to investigate the effect of natural differences in temperature on the AC composition of the berries at harvest. The meteorological station present in location Vc1 (Telve, Figure 4) recorded maximum daily temperatures ranging from 26 °C at the beginning of the pink stage that progressively increased to 32.5 °C at full ripeness in 2013. In 2014, during the pink stage, the temperature peaked at 33.5 °C and later decreased, fluctuating around an average of 26 °C until ripening (Figure 4). In correspondence with the temperature flow recorded in 2014 (i.e., high temperatures during the pink stage followed by lower temperatures during the last ripening phase), blueberries ripened more quickly and accumulated the highest content of AC (385 ± 59 mg/100 g FW), which was doubled compared to the amount recorded in 2013 (168 ± 22 mg/100 g FW; Figure 3f; Supplementary Table 3). Meteorological stations were not present on the site for the other two localities (Vc2 and Vc3), and therefore information from the closest meteorological stations (Bieno, 6 km from Vc2, and Lavarone, 43 km from Vc3, respectively) was used. In location Vc2, temperatures recorded were almost constant throughout the pink and purple stages of berry development in both years (Figure 4). Consistently, the difference in the content of ACs in berries between the two seasons was not as marked as in the other two localities (270 ± 28 mg/100 g FW in 2013 and 210 ± 11 mg/100 g FW in 2014; Figure 3f; Supplementary Table 3). In location Vc3, a difference of 5−10 °C between the two seasons markedly affected the accumulation of AC in blueberries. In 2013, temperatures ranged between 20 and 28 °C during berry ripening (Figure 4) and the AC content of blueberries was 260 ± 13 mg/100 g FW. In 2014, accumulation of total ACs was only 91 ± 27 mg/100 g FW due to the lower temperatures (between 14 and 25 °C) during the berry-ripening stage. The optimum temperatures for blueberry fruit set, size, and ripening are 20−26 °C during the day and 16 °C during the night.[39] However, the temperature conditions registered in location Vc1 during 2014 appeared to be optimal for AC accumulation in blueberries (Figure 3f; Supplementary Table 3). The present results are comparable with studies conducted on grape berries, in which the highest concentration of ACs was recorded in berries grown in temperature regimens with maximum daily temperatures of 25 °C.[40] The AC content instead dramatically dropped when the maximum daily temperatures reached 35 °C.[40]

The present study suggests that temperature is the major environmental factor affecting AC concentration and composition in berries of the *Vaccinium* species under examination. This information will be helpful when the effects of climate change on the species under examination are considered. If the scenarios of global warming to be continued in the future become true, the distribution of bilberry populations may change both in Nordic countries and Alpine environments, and the nutritional value of berries may change consequently. Furthermore, the proportions of specific ACs such as Dp- and Mv-glycosides in bilberry along increasing altitude followed the same trend along increasing latitude, indicating that temperature conditions are related to adaptation of bilberry to the environment.[10,11] The present study indicates that for production of high-quality berries with regard to AC production, bilberry plants located at high latitudes or altitude should be preferred for propagation. However, it is important to take environmental conditions and suitable bilberry genotypes into consideration during the establishment of field propagation. For this purpose, the metabolic profile of individuals within each bilberry population may allow selection of potential genotypes for cultivation and breeding purposes. This aspect is also important to blueberry growers, who may have to compromise agro-economical needs to offer berries with high nutritional value to consumers.

■ ASSOCIATED CONTENT

Supporting Information

The Supporting Information is available free of charge on the ACS Publications website at DOI: 10.1021/acs.jafc.5b02833.

Identification (retention time, MRM transition) and quantification of individual anthocyanins (PDF)

Average content of each anthocyanin detected in bilberries, collected at six different altitudes in the Alps of northern Italy during two consecutive seasons (PDF)

Average content of each anthocyanin detected in blueberries cultivated at three different altitudes in the Alps of northern Italy during two consecutive seasons (PDF)

■ AUTHOR INFORMATION

Corresponding Author

*(L.Z.) Phone: +39 328 8110052. E-mail: laura.zoratti@oulu.fi.

Funding

This research was funded at FEM-CRI by the ADPs 2013-2015 (Autonomous Province of Trento) and by the Finnish Doctoral Program in Plant Science (to L.Z.). L.J. received funding from the Kone Foundation (Grant 35- 539 2405).

Notes

The authors declare no competing financial interest.

■ ACKNOWLEDGMENTS

We acknowledge the municipalities of Grumes, Valda, and Zambana (Trentino, Italy) and the Province of Trento (Italy) for permission to perform our bilberry studies within forests of Trentino's region; the blueberry farmers (Paolo Vinante and Andrea Ioriatti for having made available their fields for the experiments); and the Centro funzionale di Protezione Civile of Trento (Italy) for the meteorological data. We thank also our collaborators Stefan Martens, Paolo Loretti, Matteo Ajelli, Marcella Grisenti, and Domenico Masuero in the Edmuch Mach Foundation, Italy.

■ ABBREVIATIONS USED

asl, above sea level; AC, anthocyanin; ara, monoarabinoside; Cy, cyanidin; Dp, delphinidin; FW, fresh weight; Mv, malvidin; gal, monogalactoside; glu, monoglucoside; PCA, principal component analysis; Pg, pelargonidin; Pn, peonidin; Pt, petunidin; TSSC, total soluble solid content; Vm, *Vaccinium myrtillus*; Vc, *Vaccinium corymbosum*

■ REFERENCES

(1) Prior, R. L.; Cao, G. H.; Martin, A.; Sofic, E.; McEwen, J.; O'Brien, C.; Lischner, N.; Ehlenfeldt, M.; Kalt, W.; Krewer, G.; Mainland, C. M. Antioxidant capacity as influenced by total phenolic and anthocyanin content, maturity, and variety of *Vaccinium* species. *J. Agric. Food Chem.* **1998**, *46* (7), 2686−2693.

(2) Landete, J. M. Updated knowledge about polyphenols: functions, bioavailability, metabolism, and health. *Crit. Rev. Food Sci. Nutr.* **2012**, *52* (10), 936−948.

DOI: 10.1021/acs.jafc.5b02833
J. Agric. Food Chem. 2015, 63, 8641−8650

(3) Barizza, E.; Guzzo, F.; Fanton, P.; Lucchini, G.; Sacchi, G. A.; Lo Schiavo, F.; Nascimbene, J. Nutritional profile and productivity of bilberry (*Vaccinium myrtillus* L.) in different habitats of a protected area of the Eastern Italian Alps. *J. Food Sci.* **2013**, *78* (13), 673−678.
(4) Woodward, F. I. Ecophysiological studies on the shrub *Vaccinium myrtillus* L. taken from a wide altitudinal range. *Oecologia* **1986**, *70* (4), 580−586.
(5) Giovanelli, G.; Buratti, S. Comparison of polyphenolic composition and antioxidant activity of wild Italian blueberries and some cultivated varieties. *Food Chem.* **2009**, *112* (4), 903−908.
(6) Beccaro, G.; Mellano, M. G.; Botta, R.; Chiabrando, V.; Bounous, G. Phenolic and anthocyanin content and antioxidant activity in fruits of bilberry (*Vaccinium myrtillus* L.) and of highbush blueberry (*V. corymbosum* L.) cultivars in North Western Italy. *Proceedings of the 8th International Symposium on Vaccinium Culture* **2004**, *715*, 553−557.
(7) Rieger, G.; Muller, M.; Guttenberger, H.; Bucar, F. Influence of altitudinal variation on the content of phenolic compounds in wild populations of *Calluna vulgaris*, *Sambucus nigra*, and *Vaccinium myrtillus*. *J. Agric. Food Chem.* **2008**, *56* (19), 9080−9086.
(8) Moze, S.; Polak, T.; Gasperlin, L.; Koron, D.; Vanzo, A.; Poklar Ulrih, N.; Abram, V. Phenolics in Slovenian bilberries (*Vaccinium myrtillus* L.) and blueberries (*Vaccinium corymbosum* L.). *J. Agric. Food Chem.* **2011**, *59* (13), 6998−7004.
(9) Connor, A. M.; Luby, J. J.; Tong, C. B. S.; Finn, C. E.; Hancock, J. F. Genotypic and environmental variation in antioxidant activity, total phenolic content, and anthocyanin content among blueberry cultivars. *J. Am. Soc. Hortic. Sci.* **2002**, *127* (1), 89−97.
(10) Lätti, A. K.; Riihinen, K. R.; Kainulainen, P. S. Analysis of anthocyanin variation in wild populations of bilberry (*Vaccinium myrtillus* L.) in Finland. *J. Agric. Food Chem.* **2008**, *56* (1), 190−196.
(11) Åkerstrom, A.; Jaakola, L.; Bang, U.; Jäderlund, A. Effects of latitude-related factors and geographical origin on anthocyanidin concentrations in fruits of *Vaccinium myrtillus* L. (bilberries). *J. Agric. Food Chem.* **2010**, *58* (22), 11939−11945.
(12) Kong, J. M.; Chia, L. S.; Goh, N. K.; Chia, T. F.; Brouillard, R. Analysis and biological activities of anthocyanins. *Phytochemistry* **2003**, *64* (5), 923−933.
(13) Castaneda-Ovando, A.; Pacheco-Hernandez, M. D.; Paez-Hernandez, M. E.; Rodriguez, J. A.; Galan-Vidal, C. A. Chemical studies of anthocyanins: a review. *Food Chem.* **2009**, *113* (4), 859−871.
(14) Kalt, W.; McDonald, J. E.; Ricker, R. D.; Lu, X. Anthocyanin content and profile within and among blueberry species. *Can. J. Plant Sci.* **1999**, *79* (4), 617−623.
(15) Määtta-Riihinen, K. R.; Kähkonen, M. P.; Törrönen, A. R.; Heinonen, I. M. Catechins and procyanidins in berries of *Vaccinium* species and their antioxidant activity. *J. Agric. Food Chem.* **2005**, *53* (22), 8485−8491.
(16) Mikulic-Petkovsek, M.; Slatnar, A.; Stampar, F.; Veberic, R. HPLC-MSn identification and quantification of flavonol glycosides in 28 wild and cultivated berry species. *Food Chem.* **2012**, *135* (4), 2138−46.
(17) Lätti, A. K.; Jaakola, L.; Riihinen, K. R.; Kainulainen, P. S. Anthocyanin and flavonol variation in bog bilberries (*Vaccinium uliginosum* L.) in Finland. *J. Agric. Food Chem.* **2010**, *58* (1), 427−433.
(18) Norberto, S.; Silva, S.; Meireles, M.; Faria, A.; Pintado, M.; Calhau, C. Blueberry anthocyanins in health promotion: a metabolic overview. *J. Funct. Foods* **2013**, *5* (4), 1518−1528.
(19) Zoratti, L.; Sarala, M.; Carvalho, E.; Karppinen, K.; Martens, S.; Giongo, L.; Häggman, H.; Jaakola, L. Monochromatic light increases anthocyanin content during fruit development in bilberry. *BMC Plant Biol.* **2014**, *14*, 10.
(20) Spinardi, A.; Mignani, I.; Folini, L.; Beghi, R. Quality and nutraceutical content of blueberries (*Vaccinium corymbosum*) grown at two different altitudes (450 and 650 m above sea level). *IX International Vaccinium Symposium* **2008**, *810*, 817−822.
(21) Martz, F.; Jaakola, L.; Julkunen-Tiitto, R.; Stark, S. Phenolic composition and antioxidant capacity of bilberry (*Vaccinium myrtillus*) leaves in northern Europe following foliar development and along environmental gradients. *J. Chem. Ecol.* **2010**, *36* (9), 1017−1028.
(22) Arapitsas, P.; Perenzoni, D.; Nicolini, G.; Mattivi, F. Study of Sangiovese wines pigment profile by UHPLC-MS/MS. *J. Agric. Food Chem.* **2012**, *60* (42), 10461−10471.
(23) Stagnari, F.; Galieni, A.; Cafiero, G.; Pisante, M. Application of photo-selective films to manipulate wavelength of transmitted radiation and photosynthate composition in red beet (*Beta vulgaris* var. conditiva Alef.). *J. Sci. Food Agric.* **2014**, *94* (4), 713−720.
(24) Giandon, P.; Bortolami, P. *L'interpretazione delle analisi del terreno. Strumento per la sostenibilità ambientale*; ARPAV, 2007.
(25) Jovancevic, M.; Balijagic, J.; Menkovic, N.; Savikin, K.; Zdunic, G.; Jankovic, T.; Dekic-Ivankovic, M. Analysis of phenolic compounds in wild populations of bilberry (*Vaccinium myrtillus* L.) from Montenegro. *J. Med. Plants Res.* **2011**, *5* (6), 910−914.
(26) Rodriguez-Mateos, A.; Cifuentes-Gomez, T.; Tabatabaee, S.; Lecras, C.; Spencer, J. P. E. Procyanidin, anthocyanin, and chlorogenic acid contents of highbush and lowbush blueberries. *J. Agric. Food Chem.* **2012**, *60* (23), 5772−5778.
(27) Zifkin, M.; Jin, A.; Ozga, J. A.; Zaharia, L. I.; Schernthaner, J. P.; Gesell, A.; Abrams, S. R.; Kennedy, J. A.; Constabel, C. P. Gene expression and metabolite profiling of developing highbush blueberry fruit indicates transcriptional regulation of flavonoid metabolism and activation of abscisic acid metabolism. *Plant Physiol.* **2012**, *158* (1), 200−224.
(28) Uleberg, E.; Rohloff, J.; Jaakola, L.; Trost, K.; Junttila, O.; Häggman, H.; Martinussen, I. Effects of temperature and photoperiod on yield and chemical composition of northern and southern clones of bilberry (*Vaccinium myrtillus* L.). *J. Agric. Food Chem.* **2012**, *60* (42), 10406−10414.
(29) Jaakola, L.; Määtta-Riihinen, K.; Kärenlampi, S.; Hohtola, A. Activation of flavonoid biosynthesis by solar radiation in bilberry (*Vaccinium myrtillus* L.) leaves. *Planta* **2004**, *218* (5), 721−728.
(30) Zoratti, L.; Jaakola, L.; Häggman, H.; Giongo, L. Modification of sunlight radiation through colored photo-selective nets affects anthocyanin profile in *Vaccinium* spp. berries. *PLoS One* **2015**, *10*, e0135935.
(31) Jaakola, L. New insights into the regulation of anthocyanin biosynthesis in fruits. *Trends Plant Sci.* **2013**, *18* (9), 477−483.
(32) Carbone, F.; Preuss, A.; De Vos, R. C. H.; D'Amico, E.; Perrotta, G.; Bovy, A. G.; Martens, S.; Rosati, C. Developmental, genetic and environmental factors affect the expression of flavonoid genes, enzymes and metabolites in strawberry fruits. *Plant, Cell Environ.* **2009**, *32* (8), 1117−1131.
(33) McKown, A. D.; Guy, R. D.; Klapste, J.; Geraldes, A.; Friedmann, M.; Cronk, Q. C. B.; El-Kassaby, Y. A.; Mansfield, S. D.; Douglas, C. J. Geographical and environmental gradients shape phenotypic trait variation and genetic structure in *Populus trichocarpa*. *New Phytol.* **2014**, *201* (4), 1263−1276.
(34) Tarara, J. M.; Lee, J. M.; Spayd, S. E.; Scagel, C. F. Berry temperature and solar radiation alter acylation, proportion, and concentration of anthocyanin in Merlot grapes. *Am. J. Enol. Vitic.* **2008**, *59* (3), 235−247.
(35) Gabriela, O. M.; Gabriela, L.; Emília, O.; Alena, G. In vitro propagation of *Vaccinium* species. *Acta Univ. Latviensis, Biol.* **2004**, *676* (3), 207−212.
(36) Primetta, A. K.; Karppinen, K.; Riihinen, K. R.; Jaakola, L. Metabolic and molecular analyses of white mutant Vaccinium berries show down-regulation of MYBPA1-type R2R3MYB regulatory factor. *Planta* **2005**, *242* (3), 631−634.
(37) Castellarin, S. D.; Di Gaspero, G.; Marconi, R.; Nonis, A.; Peterlunger, E.; Paillard, S.; Adam-Blondon, A. F.; Testolin, R. Colour variation in red grapevines (*Vitis vinifera* L.): genomic organisation, expression of flavonoid 3′-hydroxylase, flavonoid 3′,5′-hydroxylase genes and related metabolite profiling of red cyanidin-/blue delphinidin-based anthocyanins in berry skin. *BMC Genomics* **2006**, *7*, 12.
(38) Mori, K.; Goto-Yamamoto, N.; Kitayama, M.; Hashizume, K. Effect of high temperature on anthocyanin composition and

DOI: 10.1021/acs.jafc.5b02833
J. Agric. Food Chem. 2015, 63, 8641−8650

transcription of flavonoid hydroxylase genes in 'Pinot noir' grapes (*Vitis vinifera*). *J. Hortic. Sci. Biotechnol.* **2007**, *82* (2), 199−206.
(39) Gough, E. R. *The Highbush Blueberry and Its Management*; Haworth Press−Food Production Press: New York, 1993; p 288.
(40) Mori, K.; Goto-Yamamoto, N.; Kitayama, M.; Hashizume, K. Loss of anthocyanins in red-wine grape under high temperature. *J. Exp. Bot.* **2007**, *58* (8), 1935−1945.

DOI: 10.1021/acs.jafc.5b02833
J. Agric. Food Chem. 2015, 63, 8641−8650

Table 1. Chemical Names, HPLC Retention Times, and TLC R_f Values for (*Z*)-(1*R*,3*R*)-Profluthrin and Its Metabolites

compound	chem name	HPLC t_R [min]	TLC R_f value syst A	syst B
(*Z*)-(1*R*,3*R*)-profluthrin	2,3,5,6-tetrafluoro-4-methylbenzyl (*Z*)-(1*R*,3*R*)-2,2-dimethyl-3-(prop-1-enyl) cyclopropanecarboxylate	50.8	ND[a]	ND
M1	2,3,5,6-tetrafluoro-4-(hydroxymethyl)benzoic acid	11.0	ND	ND
M2	1,4-bis(hydroxymethyl)-2,3,5,6-tetrafluorobenzene	16.0	0.82	0.43
M3	*N*-acetyl-*S*-[2,3,5,6-tetrafluoro-4-(hydroxymethyl)benzyl]cysteine	21.0	ND	ND
M4	2,3,5,6-tetrafluoro-4-methylbenzoic acid	34.1	0.76	0.41
M5	2,3,5,6-tetrafluoro-4-methylbenzyl alcohol	36.6	0.89	0.63
M6	2,3,5,6-tetrafluoro-4-(hydroxymethyl)benzyl (1*R*,3*R*)-2-(1,2-dihydroxypropyl)-3,3-dimethylcyclopropanecarboxylate	30.7, 31.9, 33.9, 35.3[b]	0.71	0.15
M7	2,3,5,6-tetrafluoro-4-(hydroxymethyl)benzyl (*Z*)-(1*R*,3*R*)-2-carboxy-2-methyl-3-(prop-1-enyl) cyclopropanecarboxylate	41.1	0.86	0.45
M8	2,3,5,6-tetrafluoro-4-methylbenzyl (*Z*)-(1*R*,3*R*)-2-(2-carboxyvinyl)-3,3-dimethylcyclopropanecarboxylate	45.2	0.91	0.66

[a]ND: Not determined. [b]This metabolite contains 4 isomers and can be separated under the HPLC conditions.

R_f values for authentic metabolite standards are shown in Table 1, and their structures are shown in Figure 5. Unlabeled (*Z*)-(1*R*,3*R*)-profluthrin (purity: 99.3%) and 6 authentic standards of M1, M2, M4, M5, M6, and M8 were synthesized, and their structures were confirmed using nuclear magnetic resonance (NMR) and mass spectrometry (MS). The spectroscopic information on these 6 metabolites is as follows. M1: ^{1}H NMR (DMSO-d_6, δ in ppm) 4.597 (t, 2H, J = 2 Hz, PhCH_2OH); APCI-MS (negative), m/z = 223 ([M − H]$^-$). M2: ^{1}H NMR (CD_3OD, δ in ppm) 4.716 (t, 4H, J = 1 Hz, PhCH_2OH); ESI-MS (positive), m/z = 218 ([M + Na + H]$^+$). M4: ^{1}H NMR (CD_3OD, δ in ppm) 2.346 (t, 3H, J = 3 Hz, PhCH_3); ESI-MS (negative), m/z = 207 ([M − 1]$^-$). M5: ^{1}H NMR (CD_3OD, δ in ppm) 2.274 (t, 3H, J = 2 Hz, PhCH_3), 4.687 (t, 2H, J = 2 Hz, PhCH_2OH); ESI-MS (positive), m/z = 234 ([M + Na + H]$^+$). M6: ^{1}H NMR (CD_3OD, δ in ppm) 1.111 (d, 3H, J = 6 Hz, CH(OH)CH_3), 1.175 (m, 6H, C(CH_3)$_2$), 1.505 (m, 1H, C*H*CH(OH)), 1.602 (d, 1H, J = 6 Hz, C*H*COO), 3.054 (m, 1H, CHC*H*(OH)CH(OH)), 3.630 (m, 1H, CH(OH)C*H*(OH)CH_3), 4.718 (t, 2H, J = 1 Hz, PhCH_2OH), 5.251 (q, 2H, J = 2, 5 Hz, PhCH_2OCO); ESI-MS (negative), m/z = 379 ([M − H]$^-$). M8: ^{1}H NMR ($CDCl_3$, δ in ppm) 1.219 (s 3H, CCH_3), 1.342 (s, 3H, CCH_3), 1.727 (d, 1H, J = 7 Hz, C*H*COO), 3.313 (m, 1H, CH═CHC*H*), 5.227 (s, 2H, PhCH_2OCO), 5.918 (m, 1H, CHC*H*═CH), 5.918 (m, 1H, CH═C*H*COOH); ESI-MS (negative), m/z = 359 ([M − H]$^-$).

The two other authentic standards, those of M3 and M7, were isolated and purified in our laboratory. Their spectroscopic information is described in Identification of Isolated Metabolites in Results. Other chemicals were reagent grade and were purchased from Nacalai Tesque (Japan) or Wako Pure Chemicals (Japan).

Chromatographic Procedures. HPLC was conducted with a system consisting of an HPLC pump (L-2130, Hitachi, Tokyo, Japan), a UV detector (L-2400, Hitachi), and an online radioactivity monitor (Radiomatic 610TR, PerkinElmer, Waltham, MA, USA) fitted with an ODS column (Atlantis dC18, 5 μm, 4.6 mm i.d. × 150 mm, Waters, MA, USA). The mobile phases were A, 0.05% trifluoroacetic acid, and B, acetonitrile, and gradient conditions were % B = 5% (0 min), 5% (5 min), 25% (15 min), 25% (30 min), 100% (50 min), 100% (55 min) for metabolite analyses and % B = 10% (0 min), 60% (30 min) for purification and for purity analysis of metabolites, at a flow rate of 1 mL/min.

Precoated silica gel 60 F254 chromatoplate (20 × 20 cm, 0.25 or 0.5 mm layer thickness, Merck, Darmstadt, Germany) was used for TLC. The solvent systems were A, ethyl acetate/water/formic acid (35:2:2, v/v/v), and B, toluene/ethyl acetate/formic acid (50:50:1, v/v/v). Unlabeled standards on TLC plates were detected by viewing under UV light (around 254 nm). Radioactivity on TLC plates was detected by scraping−LSC (liquid scintillation counter) method or autoradiography using an imaging plate processed with a fluoro-image analyzer (FLA-5000, Fujifilm, Tokyo, Japan).

Spectroscopic and Spectrometric Analysis. Chemical structures of purified metabolites were determined using NMR spectrometry and mass spectrometry together with high performance liquid chromatography (LC/MS). ^{1}H NMR spectra were obtained with a Unity 400 plus spectrometer (Varian, Palo Alto, CA, USA) operating at 400 MHz with methanol-d_4, DMSO-d_6, or chloroform-d as the solvent. LC/MS spectra were obtained with an LTQ XL (Thermo Fisher Scientific, Waltham, MA, USA).

Treatment of Animals. Male and female Crl:CD(SD) untreated rats at the age of 6 weeks and bile duct cannulated rats at the age of 8 weeks were purchased from Charles River Japan Inc. (Kanagawa, Japan) and maintained under constant environmental conditions: room temperature of 21−25 °C; relative humidity of 55 ± 15%; ventilation of 10 air exchanges per hour; and artificial lighting from 8:00 am to 8:00 pm. Animals had free access to pelleted diet and water throughout the study. All animal experiments were conducted in accordance with the Guidance for the Care and Use of Laboratory Animals in our laboratory, which corresponds to the Guidelines for Proper Conduct of Animal Experiments (Science Council of Japan). All tested animals except bile duct cannulated rats showed normal weight gain and no abnormal clinical symptoms during 7 days of quarantine and acclimation, and their body weights were 250−306 g for males and 177−215 g for females when dosed. Bile duct cannulated rats were dosed on the day of arrival. All animals were euthanized by bleeding from the abdominal artery under anesthesia.

Preparation of Dosing Solutions. [Benzyl-α-^{14}C]-labeled (*Z*)-(1*R*,3*R*)-profluthrin was radiochemically diluted with unlabeled (*Z*)-(1*R*,3*R*)-profluthrin with a specific activity of 6.51 MBq/mg for low dose and 108 kBq/mg for high dose. The test compound was dissolved in corn oil to give 1 and 60 mg/5 mL in the dosing solutions. The radiochemical purities of the ^{14}C-labeled compound in the dosing formulations were analyzed by HPLC, and were confirmed to be 100% for all the dose groups.

^{14}C-Excretion Study. Male and female rats at 7 weeks old were given a single oral dose of [benzyl-α-^{14}C]-labeled (*Z*)-(1*R*,3*R*)-profluthrin at 1 and 60 mg/kg/5 mL of corn oil at 4 animals per group, and the animals were housed separately in glass metabolism cages (Metabolica CO_2, Sugiyamagen Iriki, Tokyo, Japan) to collect urine, feces, and expired air. Urine and feces from each rat were collected at 6 and 12 h (urine only), and 1, 2, 3, 5, and 7 days after administration. Expired air was passed through an alkaline trap containing 10% NaOH solution for 1 day after administration to collect expired CO_2 gas. Following the collection of feces and urine, each metabolism cage was washed with water to recover the remaining ^{14}C (cage-wash). Radioactivity in the cage-wash was included in the urinary excretion.

Biliary Excretion Study. Bile duct cannulated rats at 8 weeks old were given a single oral dose of [benzyl-α-^{14}C]-labeled (*Z*)-(1*R*,3*R*)-profluthrin at 1 mg/kg/5 mL of corn oil at 4 animals per group, and the animals were housed separately in glass metabolism cages. In addition to collecting urine and feces, bile was collected with a free

DOI: 10.1021/acs.jafc.5b03321
J. Agric. Food Chem. 2015, 63, 8651−8661

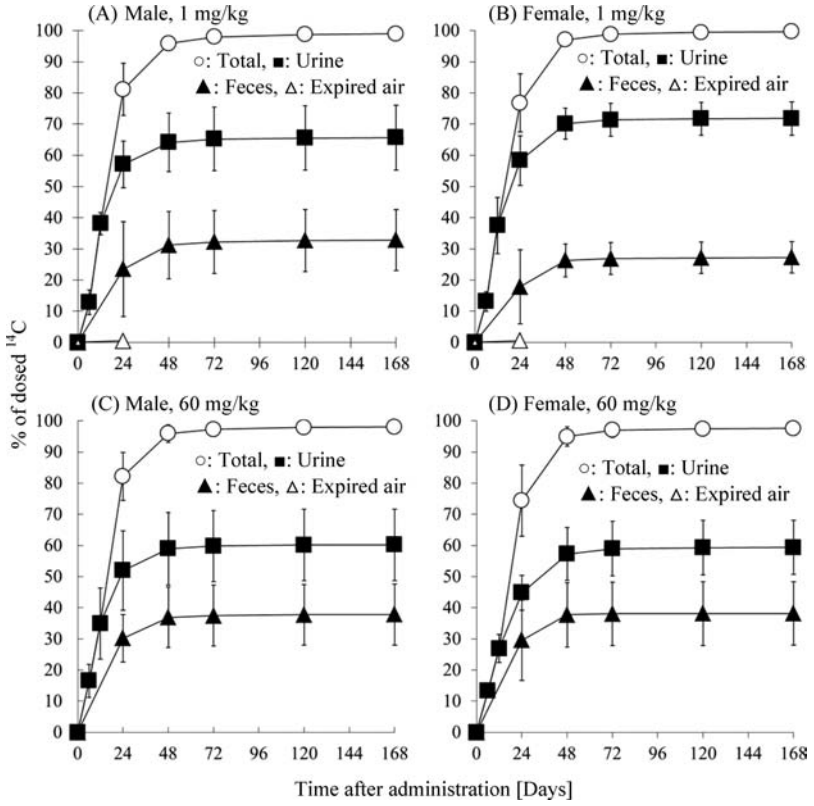

Figure 2. Cumulative ^{14}C-excretion after single oral administration of [benzyl-α-^{14}C]-labeled (*Z*)-(1*R*,3*R*)-profluthrin to rats. Points and bars are mean values and standard deviations for data from four rats.

moving system adapted to the cages at 6 and 12 h (urine and bile), and 1, 2, and 3 days after administration.

Plasma ^{14}C Concentration Study. Male and female rats at 7 weeks old were given a single oral dose of [benzyl-α-^{14}C]-labeled (*Z*)-(1*R*,3*R*)-profluthrin at 1 and 60 mg/kg/5 mL of corn oil at 3 animals per group. Blood samples were collected from tail vein at 15 and 30 min, and 1, 2, 4, 6, 8, 12, 24, 48, 72, 120, and 168 h after the administration, and aliquoted into vials. The rest of the blood was centrifuged at 3000*g* for 10 min, and separated blood cells and plasma were transferred to vials. Maximum plasma concentration (C_{max}, μg equiv of (*Z*)-(1*R*,3*R*)-profluthrin/g) and time to peak concentration (T_{max}, h) were obtained from the actual measured values. Area under the concentration−time curve to 168 h (AUC_{0-168h}, μg equiv of (*Z*)-(1*R*,3*R*)-profluthrin·h/g) was determined by trapezoid method for the time interval of actual measurement of concentration, assuming the value of "0 μg/mL" as the concentration at time 0. Half-life of radioactivity was obtained by calculating ln 2/α of the slope (α) of a regression line fitted to the β phase of plasma concentration curve (48 to 168 h without including values less than the quantification limit), with the least-squares method.

^{14}C-Tissue Distribution Study. Male and female rats at 7 weeks old were given a single oral dose of [benzyl-α-^{14}C]-labeled (*Z*)-(1*R*,3*R*)-profluthrin at 1 and 60 mg/kg/5 mL of corn oil at 4 time points per dose and sex, and 3 or 4 animals each per group. The animals were euthanized after the defined time points, and the tissues were dissected for the radioanalysis. Duplicate aliquots of blood were collected, and the remaining blood was separated into blood cells and plasma by centrifugation at 2000*g* for 10 min. The residual carcasses were solubilized with 3 M KOH alkaline solution. The percentage of the ^{14}C-distribution to tissue was calculated on the basis of the weight of each tissue dissected, except blood, bone, fat, muscle, and skin, for which the actual weight cannot be measured.

Measurement of Radioactivity. Radioactivity in urine, cage wash, bile, $^{14}CO_2$-trapped alkaline solution, solubilized carcass (decolorized by hydrogen peroxide), and organosoluble fraction was directly quantified with a Tri-Carb 2700TR liquid scintillation (LS) analyzer (PerkinElmer) after mixing with scintillation cocktail, Emulsifier Scintillator Plus or Hionic Fluor (PerkinElmer). Feces (homogenized with 2 times weight of water), blood, plasma, blood cell, tissues, and unextractable fecal residues were combusted with a 308 sample oxidizer (PerkinElmer) prior to LS analysis. As the $^{14}CO_2$ absorbent and the scintillator, 8 mL of Carbo Sorb and 8 mL of Permafluor E$^+$ (PerkinElmer) were used, respectively.

Isolation and Purification of Metabolites. Two metabolites (M3 and M7 in Table 1) were isolated from rat excreta by HPLC and TLC. Three female rats were given a single oral dose of [benzyl-α-^{14}C]-labeled (*Z*)-(1*R*,3*R*)-profluthrin at 50 mg/kg/5 mL of corn oil and housed in metabolism cages. Urine sample was collected 1 day after administration, and a small part of the sample was applied to HPLC analysis. Fractions eluted at 22 and 42 min were collected, and these fractions were used as crude standards for the further purification procedures of M3 and M7, respectively. The rest of the urine sample was applied to preparative TLC analysis (solvent system A) after extraction with ethyl acetate or HCl-acidified ethyl acetate. Separated organosoluble fractions were collected, concentrated, and then applied to preparative HPLC for purification. The purified metabolites were identified by spectroanalyses, and then used as metabolite standards of M3 and M7.

Metabolite Analysis. Urine, bile, and homogenate of feces in the excretion study and plasma and homogenate of liver and kidney in the tissue distribution study were analyzed with HPLC. Homogenates of feces, liver, and kidney and plasma samples were applied to HPLC after extraction with 3-fold volume of methanol and concentrated. Major unknown metabolites were isolated by HPLC and applied to enzyme hydrolysis under the following conditions: metabolites were incubated with β-glucuronidase/aryl sulfatase (from *Helix pomatia*, Merck) in 0.2 M acetic acid buffer (pH 5.0) with or without β-glucuronidase inhibitor, D-saccharic acid 1,4-lactone, at 37 °C for 4 h. Assay was terminated by adding 2 times of acetonitrile, and the supernatant was applied to 2D TLC analysis (first D, solvent system A; second D, solvent system B). Consistency of metabolites was confirmed against authentic standards by 2 of the following 3

DOI: 10.1021/acs.jafc.5b03321
J. Agric. Food Chem. 2015, 63, 8651−8661

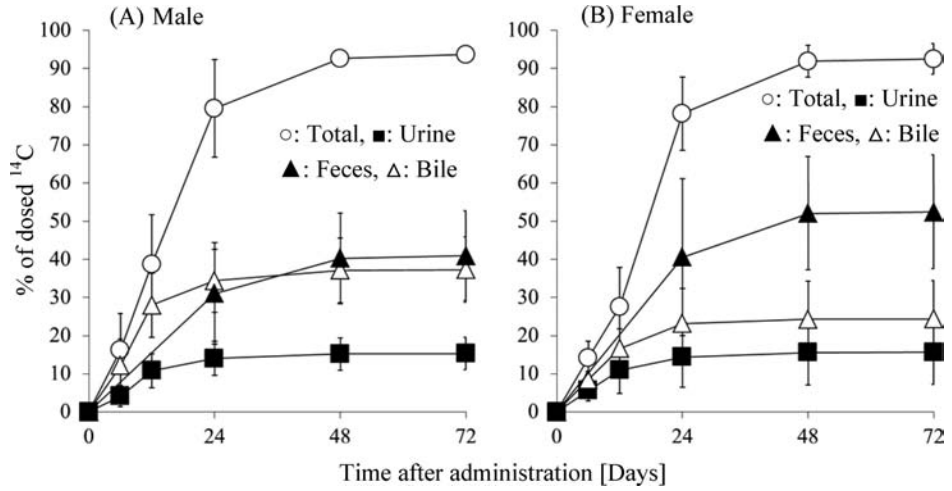

Figure 3. Cumulative ^{14}C-excretion after single oral administration of [benzyl-α-^{14}C]-labeled (*Z*)-(1*R*,3*R*)-profluthrin at the dose of 1 mg/kg to bile duct cannulated rats. Points and bars are mean values and standard deviations for data from four rats.

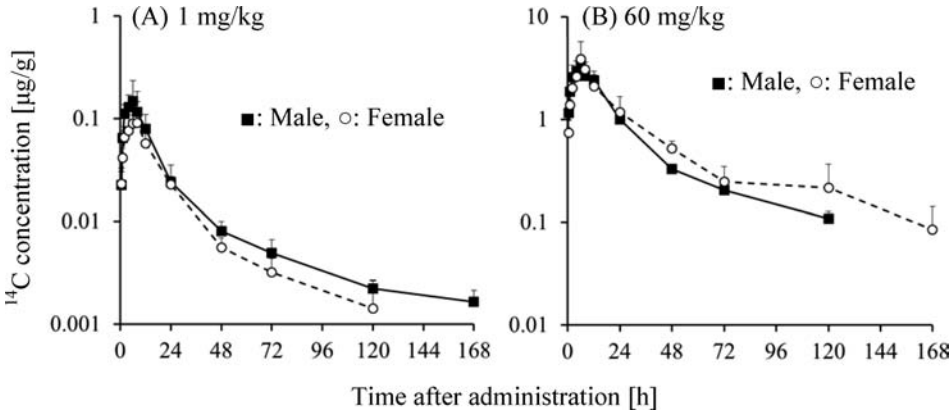

Figure 4. Plasma concentration after single oral administration of [benzyl-α-^{14}C]-labeled (*Z*)-(1*R*,3*R*)-profluthrin to rats.

methods: (1) comparing their retention time in radio-HPLC analysis against coeluted authentic standards, (2) cochromatography of TLC analysis, and (3) comparing MS and MS/MS spectra in LC/MS analysis against those of authentic standards.

RESULTS

^{14}C-Elimination into Urine, Feces, and Bile. ^{14}C-Excretion profiles into urine, feces, and expired air during 7 days after a single oral administration of [benzyl-α-^{14}C]-labeled (*Z*)-(1*R*,3*R*)-profluthrin to normal rats are shown in Figure 2. ^{14}C was rapidly and almost completely excreted into urine and feces when dosed at 1 and 60 mg/kg. ^{14}C-Excretion into expired air was not more than 1% at 1 day after the administration at low dose, thus it was not examined further nor at high dose since it could be regarded as negligible. ^{14}C-Excretion within 7 days after administration was 99.0% (feces, 32.8%; urine, 65.6%; and expired air, 0.5%) in male rats and 99.7% (feces, 27.3%; urine, 71.8%; and expired air, 0.6%) in female rats at 1 mg/kg groups. At high dose, ^{14}C-excretion was 98.1% (feces, 37.8%; and urine, 60.2%) in male rats and 97.6% (feces, 38.2%; and urine, 59.4%) in female rats, which revealed that the ratio excreted through urine was approximately 10% lower at high dose. No marked sex-related differences were observed in the rate of ^{14}C-elimination.

The ^{14}C-excretion rates within 2 days after a single oral administration of [benzyl-α-^{14}C]-labeled (*Z*)-(1*R*,3*R*)-profluthrin at a dose of 1 mg/kg (low dose) to bile duct cannulated rats are shown in Figure 3. ^{14}C-Excretion was rapid in both males and females with average rates for 3 animals of 93.6% in males (41.0% in feces, 15.3% in urine, and 37.3% in bile), and 92.5% in females (52.4% in feces, 15.7% in urine, and 24.4% in bile) within 3 days after administration.

Plasma ^{14}C Concentration Study. The plasma−concentration curves after a single oral administration of [benzyl-α-^{14}C]-labeled (*Z*)-(1*R*,3*R*)-profluthrin at low and high doses are shown in Figure 4, and the kinetic parameters are shown in Table 2. At both low and high dose, plasma ^{14}C concentration was rapidly increased and reached C_{max} at 6 to 8 h after the

Table 2. Pharmacokinetic Parameters of ^{14}C in Plasma after Single Oral Administration of [Benzyl-α-^{14}C]-Labeled (*Z*)-(1*R*,3*R*)-Profluthrin to Male and Female Rats at 1 and 60 mg/kg

	1 mg/kg		60 mg/kg	
parameters	male	female	male	female
T_{max} [h]	6	8	6	6
C_{max} [μg equiv of profluthrin/g of plasma]	0.148	0.091	3.54	3.87
$T_{1/2}$ [h]	52.2	37.3	46.2	51.8
AUC [μg equiv of profluthrin·h/g of plasma]	2.82	1.97	88.9	104.8

DOI: 10.1021/acs.jafc.5b03321
J. Agric. Food Chem. 2015, 63, 8651−8661

Table 3. Concentrations of Radioactivity in Tissues after Single Oral Administration of [Benzyl-α-^{14}C]-Labeled (*Z*)-(1*R*,3*R*)-Profluthrin to Male and Female Rats at 1 mg/kg

	μg equiv of (*Z*)-(1*R*,3*R*)-profluthrin/g of tissue (ppm)							
	male				female			
tissue	6 h	12 h	48 h	168 h	8 h	12 h	48 h	168 h
adrenal	0.0572	0.0347	0.0079	0.0024	0.0595	0.0298	0.0079	0.0018
blood	0.0781	0.0347	0.0056	0.0016	0.0656	0.0312	0.0066	0.0017
blood cell	0.0409	0.0190	0.0046	0.0025	0.0350	0.0183	0.0048	0.0025
plasma	0.115	0.0495	0.0064	0.0010	0.0953	0.0462	0.0079	0.0009
bone	0.0163	0.0081	0.0015	0.0007	0.0186	0.0185	0.0017	0.0007
bone marrow	0.0351	0.0192	0.0039	0.0007	0.0365	0.0468	0.0053	<0.0007
brain	0.0147	0.0053	0.0012	<0.0004	0.0167	0.0087	0.0018	<0.0004
eye	0.0212	0.0139	0.0022	<0.0008	0.0210	0.0125	0.0022	0.0013
fat	0.0344	0.0267	0.0067	0.0026	0.0367	0.0428	0.0080	0.0019
hair and skin	0.0950	0.0466	0.0083	0.0017	0.0623	0.0751	0.0127	0.0011
heart	0.0372	0.0165	0.0025	0.0008	0.0320	0.0167	0.0031	0.0006
kidney	0.381	0.160	0.0179	0.0036	0.322	0.130	0.0180	0.0030
liver	0.686	0.492	0.155	0.0369	0.502	0.278	0.0646	0.0194
lung	0.0525	0.0261	0.0056	0.0018	0.0485	0.0256	0.0065	0.0013
mandibular gland	0.0472	0.0244	0.0030	0.0008	0.0352	0.0198	0.0040	0.0007
muscle	0.0234	0.0124	0.0028	0.0006	0.0286	0.0147	0.0030	<0.0004
ovary					0.0680	0.0471	0.0135	0.0014
pancreas	0.0574	0.0336	0.0046	0.0008	0.0676	0.0283	0.0079	0.0006
pituitary gland	0.0605	0.0142	0.0116	<0.0076	0.0373	0.0385	<0.0098	<0.0070
sciatic nerve	0.0350	0.0319	0.0058	<0.0030	0.0173	0.0755	0.0026	<0.0048
spleen	0.0367	0.0183	0.0040	0.0011	0.0409	0.0204	0.0052	0.0010
spinal cord	0.0180	0.0150	0.0016	0.0005	0.0201	0.0125	0.0015	<0.0010
testis	0.0271	0.0107	0.0029	0.0005				
thymus	0.0282	0.0158	0.0039	0.0006	0.0284	0.0132	0.0040	0.0005
thyroid	0.129	0.420	0.0402	<0.0060	0.0786	0.0613	0.0115	<0.0077
uterus					0.0663	0.0632	0.0075	0.0009
cecum	0.271	0.550	0.124	0.0017	1.51	0.770	0.135	0.0016
large intestine	0.248	0.286	0.0902	0.0013	0.282	0.200	0.0986	0.0010
small intestine	2.01	0.873	0.0775	0.0018	2.54	0.428	0.205	0.0019
stomach	1.18	0.332	0.0125	0.0008	0.822	0.183	0.0547	0.0008
cecum contents	2.40	10.0	0.312	0.0031	7.88	8.55	0.342	0.0019
large intestine contents	0.334	7.21	0.274	0.0042	2.98	7.62	0.248	0.0018
small intestine contents	13.5	6.74	0.337	0.0029	12.2	5.76	0.979	0.0031
stomach contents	3.41	1.70	0.0042	<0.0004	6.48	0.604	0.0152	<0.0004

administration. The elimination of ^{14}C was comparatively slow, and the half-lives were around 2 days. C_{max} and AUC of the high dose group were 24−43 times and 32−53 times higher at high dose when compared to low dose, respectively. There were no marked sex-related differences in kinetics of (*Z*)-(1*R*,3*R*)-profluthrin.

^{14}C Concentrations in Tissues. The ^{14}C concentration−time profiles in tissues after a single oral administration of [benzyl-α-^{14}C]-labeled (*Z*)-(1*R*,3*R*)-profluthrin at low and high doses are shown in Tables 3 and 4, respectively. The ^{14}C concentrations in most of the tissues other than gastrointestinal tract were highest at first sampling time, 6 to 8 h after administration, and thereafter decreased rapidly. For almost all groups and all time points, liver showed the highest radioactivity, followed by fat, thyroid gland, uterus, ovary, kidney, skin with hair, blood cells, and adrenal gland. At the last time point, 7 days after the administration, total residual radioactivity was no more than 0.3% of administered dose, which indicates that the dosed (*Z*)-(1*R*,3*R*)-profluthrin was rapidly excreted from the body, and showed no accumulation to specific organs or tissues.

Identification of Isolated Metabolites. The unknown metabolites detected in urine were purified and identified by both NMR spectroscopic technique and MS spectrometric analysis. ^{1}H NMR data of identified metabolites are shown in Table 5.

M3. In the ^{1}H NMR spectrum, the signal from the benzyl proton at 5.23 ppm (2H, t) detected in (*Z*)-(1*R*,3*R*)-profluthrin was observed as the methylene signal at 3.89 ppm (2H, dd), and the signal from the 4-methyl group at 2.29 ppm (3H, t) was observed as the hydroxymethyl group at 4.70 ppm (2H, s). In addition, signals from one methyl group and one methine group were observed at 1.99 ppm (3H, s) and 4.51 ppm (1H, m), and one methylene group was observed at 2.89 ppm (1H, dd) and 3.09 ppm (1H, dd), respectively. In APCI-MS measurement in the positive ion mode, protonated ion peak m/z = 356 $[M + H]^+$ was observed, and from the MS/MS analysis of the protonated ion, dehydrated ion, m/z = 338 $[M + H - H_2O]^+$, and the ion supposed to be derived from *N*-acetyl-L-cysteine, m/z = 162 $[C_5H_8NO_3S]^+$, were also detected. Based on these results, M3 was considered to be an *N*-acetyl-L-cysteine (mercapturic acid) conjugate of M2.

DOI: 10.1021/acs.jafc.5b03321
J. Agric. Food Chem. 2015, 63, 8651−8661

Table 4. Concentrations of Radioactivity in Tissues after Single Oral Administration of [Benzyl-α-^{14}C]-Labeled (*Z*)-(1*R*,3*R*)-Profluthrin to Male and Female Rats at 60 mg/kg

	μg equiv of (*Z*)-(1*R*,3*R*)-profluthrin/g of tissue (ppm)							
	male				female			
tissue	6 h	24 h	48 h	168 h	6 h	12 h	72 h	168 h
adrenal	3.03	1.04	0.45	<0.16	4.14	1.98	0.37	0.14
blood	2.44	0.67	0.35	0.09	2.52	1.28	0.16	0.06
blood cell	1.56	0.37	0.31	0.14	1.52	0.81	0.18	0.11
plasma	3.39	0.88	0.37	0.04	3.56	1.74	0.16	0.03
bone	0.78	0.23	0.19	0.05	0.89	0.64	0.09	0.04
bone marrow	1.76	0.56	0.41	0.06	1.90	1.18	0.17	<0.06
brain	0.76	0.17	0.06	<0.02	0.97	0.45	0.05	<0.02
eye	0.74	0.23	0.09	<0.06	0.97	0.50	0.08	<0.04
fat	2.75	1.68	0.74	0.19	2.97	2.47	0.60	0.15
hair and skin	2.27	2.50	0.70	0.08	2.32	1.51	0.33	0.07
heart	1.59	0.42	0.16	0.03	1.61	0.81	0.10	0.03
kidney	15.0	3.47	1.02	0.13	11.7	5.73	0.37	0.10
liver	15.1	7.18	3.74	1.02	10.1	6.37	1.14	0.33
lung	1.92	0.64	0.35	0.09	2.05	1.21	0.23	0.07
mandibular gland	1.77	0.46	0.21	0.04	1.89	0.99	0.11	0.04
muscle	1.07	0.30	0.10	0.03	1.46	0.59	0.07	<0.02
ovary					3.52	2.62	0.39	0.08
pancreas	2.31	0.67	0.31	0.03	3.80	1.58	0.16	0.04
pituitary gland	1.62	1.47	<0.59	<0.57	3.22	1.21	<0.55	<0.54
sciatic nerve	1.45	0.48	0.25	<0.28	1.13	0.99	<0.28	<0.25
spleen	1.56	0.47	0.25	0.05	2.09	0.95	0.16	0.06
spinal cord	0.89	0.26	0.09	<0.05	0.88	0.54	0.07	<0.03
testis	1.08	0.31	0.12	0.03				
thymus	1.38	0.60	0.19	<0.03	1.37	0.78	0.13	0.04
thyroid	11.6	5.94	0.71	<0.43	7.64	3.63	0.47	<0.41
uterus					3.05	3.46	0.40	0.07
cecum	9.12	17.4	4.52	0.10	6.07	34.4	1.47	0.11
large intestine	8.17	10.3	2.61	0.06	7.92	15.3	0.97	0.06
small intestine	75.2	31.4	5.95	0.08	60.3	25.9	1.24	0.10
stomach	50.1	4.73	1.12	0.03	46.1	13.3	0.43	0.05
cecum contents	334	72.1	11.7	0.12	162	531	4.45	0.32
large intestine contents	135	92.0	8.45	0.17	21.4	580	2.28	0.36
small intestine contents	589	117	24.9	0.13	664	545	8.19	0.20
stomach contents	151	3.95	0.15	<0.03	283	120	0.29	0.15

Table 5. ^{1}H NMR Analysis Data for (*Z*)-(1*R*,3*R*)-Profluthrin and Isolated Metabolites

	(*Z*)-(1*R*,3*R*)-profluthrin		M3		M7	
	δ (CD_3OD)	*J* (Hz)	δ (CD_3OD)	*J* (Hz)	δ (CD_3OD)	*J* (Hz)
Ha	2.29 (3H, t)	2.0	4.70 (2H, s)		4.71 (2H, s)	
Hb	5.23 (2H, t)	1.4	3.89 (2H, dd)	26.0, 13.6	5.24 (2H, dd)	39.6, 12.4
Hc	1.50 (1H, d)	5.6			1.63 (1H, d)	5.6
Hd	1.14 (3H, s)				1.33 (3H, s)	
	1.23 (3H, s)					
He	2.12 (1H, m)				2.76 (1H, m)	
Hf	5.16 (1H, m)				5.16 (1H, m)	
Hg	5.60 (1H, m)				5.64 (1H, m)	
Hh	1.68 (3H, m)				1.74 (3H, m)	
CH_3CO-			1.99 (3H, s)			
$-CH_2CH-$			2.89 (1H, dd)	13.2, 8.0		
			3.09 (1H, dd)	13.2, 4.4		
$-CH_2CH-$			4.51 (1H, m)			

M7. In the ^{1}H NMR spectrum, the signal from proton of 4-methyl group at 2.29 ppm (3H, t) detected in (*Z*)-(1*R*,3*R*)-profluthrin was observed as the methylene signal at 4.71 ppm (2H, s), and the signal from the methyl group at 1.14 ppm (3H, s) was not observed. In APCI-MS measurement in the positive ion mode, molecular ion peak m/z = 377 $[M + H]^+$ was obtained, and as its product ions in the MS/MS analysis, dehydrated ion, m/z = 359, and the ion supposed to be derived

DOI: 10.1021/acs.jafc.5b03321
J. Agric. Food Chem. 2015, 63, 8651−8661

from acid side (i.e., 2,2-dimethyl-3-(prop-1-enyl)-cyclopropanecarboxylate), m/z = $[C_9H_{11}O_3]^+$, were detected. M7 was considered to be formed from (*Z*)-(1*R*,3*R*)-profluthrin via hydroxylation of 4-methyl group and oxidation of one of the methyl groups bound to the 2-cyclopropane ring to give a carboxylic acid.

Amounts of Metabolites in Urine, Feces, and Bile. Amounts of metabolites (% of the dose ^{14}C) in urine and feces within 2 days after single oral administration of [benzyl-α-^{14}C]-labeled (*Z*)-(1*R*,3*R*)-profluthrin to normal rats are presented in Table 6. In feces, (*Z*)-(1*R*,3*R*)-profluthrin was the most abundant, especially at high dose. Only M7 was identified as a metabolite in the feces, but the amount was not so large (not more than 2.11%). In urine, 8 metabolites, including 3 glucuronides, were identified. A glucuronide of M5 (M5-glu) was the most abundant in urine, followed by a glucuronide of M2 (M2-glu). The sum of these two metabolites was 44 to 51% of dosed ^{14}C in all groups. M1 and M4, which are oxidized metabolites of M2 and M5, and M3, which is a mercapturic acid conjugate of M2, were also detected in urine, but the amounts were each around 2 to 5% of the dosed ^{14}C. As the ester-retaining metabolites, only M7 and its glucuronide were detected. The sums of these metabolites in urine and feces were 1 to 12%, which indicates that (*Z*)-(1*R*,3*R*)-profluthrin is easily cleaved at its ester bond.

Table 6. Amounts of Metabolites in Urine and Feces within 2 Days after Single Oral Administration of [Benzyl-α-^{14}C]-Labeled (*Z*)-(1*R*,3*R*)-Profluthrin to Rats

		% of the dosed ^{14}C			
		1 mg/kg		60 mg/kg	
	metabolite	male	female	male	female
urine					
	M1	2.95	3.30	1.90	2.25
	M2-glu	16.77	14.90	10.83	11.50
	M2	0.18	0.38	0.20	0.11
	M3	2.53	3.46	1.14	2.48
	M5-glu	32.11	29.49	40.44	33.80
	M4	3.59	5.42	3.50	5.30
	M7-glu	1.25	5.25	ND[a]	0.42
	M7	2.30	6.01	0.05	0.73
	others	2.51	1.89	0.84	0.72
	total of urine	64.20	70.10	58.90	57.30
feces					
	M7	2.11	0.40	0.66	ND
	(*Z*)-(1*R*,3*R*)-profluthrin	23.13	22.49	34.53	35.98
	others	2.56	0.75	0.31	0.30
	subtotal	27.79	23.64	35.50	36.28
	unextractable	3.41	2.76	1.40	1.52
	total of feces	31.20	26.40	36.90	37.80

[a]ND: Not detected.

Amounts of metabolites (% of the dosed ^{14}C) in urine, feces, and bile within 2 days after single oral administration of [benzyl-α-^{14}C]-labeled (*Z*)-(1*R*,3*R*)-profluthrin to bile duct cannulated rats are shown in Table 7. Ten metabolites, including 4 glucuronides, were identified in bile and urine. Composition of metabolites identified in urine of bile-cannulated rats was similar to that of normal rats. In bile, M5-glu was most abundant followed by M2-glu, M6-glu, M8, M7, and M7-glu. As the nonhydrolytic metabolites that were not observed in urine, M6-glu and M8 were detected in bile and the amounts were small (0 to 3%). No unchanged (*Z*)-(1*R*,3*R*)-profluthrin was detected in bile or urine, and the major components in bile were almost similar to those in urine. Also, the metabolites identified in bile were rarely detected in feces of normal rats, which suggests that the metabolites excreted via bile were mostly reabsorbed in the intestinal tract, and finally excreted via urine.

Table 7. Amounts of Metabolites in Urine, Feces, and Bile within 2 Days after Single Oral Administration of [Benzyl-α-^{14}C]-Labeled (*Z*)-(1*R*,3*R*)-Profluthrin to Bile Duct Cannulated Rats

		% of the dosed ^{14}C	
		1 mg/kg	
	metabolite	male	female
urine			
	M1	0.46	0.34
	M2-glu	2.77	1.84
	M2	0.13	0.19
	M3	0.04	0.15
	M5-glu	10.94	10.72
	M4	0.49	0.33
	M7-glu	0.18	1.12
	M7	0.03	0.68
	others	0.17	0.13
	total of urine	15.20	15.50
bile			
	M2-glu	3.33	1.96
	M2	0.85	ND[a]
	M6-glu	3.05	1.57
	M5-glu	14.32	13.82
	M7-glu	4.06	1.19
	M7	2.25	1.10
	M8	0.54	0.24
	others	8.72	4.42
	total of bile	37.10	24.30
feces			
	(*Z*)-(1*R*,3*R*)-profluthrin	39.92	51.65
	unextractable	0.38	0.45
	total of feces	40.30	52.10

[a]ND: Not detected.

Metabolites in Blood, Kidney, and Liver. Concentrations of metabolites in liver, kidney, and plasma of rats after a single oral administration of [benzyl-α-^{14}C]-labeled (*Z*)-(1*R*,3*R*)-profluthrin at low dose and high dose are presented in Table 8. In kidney, the components of metabolites in the methanol-extractable fraction were almost similar to those in urine, and M5-glu was the most abundant metabolite, followed by M7, M7-glu, M2, M2-glu, and M3. In liver, the ratios of the ester metabolites were higher than those in urine or kidney, and M7 and its glucuronide were the most abundant. As another ester metabolite that was not observed in urine, M8 was also detected in liver. This metabolite was also detected in plasma of the low dose group. M5-glu, M7, M2, and its glucuronide were also observed in plasma.

DISCUSSION

There were no significant sex- or dose-related differences on the ADME profile of (*Z*)-(1*R*,3*R*)-profluthrin. After single oral administration of [benzyl-α-^{14}C]-labeled (*Z*)-(1*R*,3*R*)-proflu-

DOI: 10.1021/acs.jafc.5b03321
J. Agric. Food Chem. 2015, 63, 8651−8661

Table 8. Concentrations of Metabolites in Liver, Kidney and Plasma after Single Oral Administration of [Benzyl-α-^{14}C]-Labeled (Z)-(1R,3R)-Profluthrin at 1 or 60 mg/kg to Male and Female Rats

	μg equiv of (Z)-(1R,3R)-profluthrin/g of tissue (ppm)							
	1 mg/kg				60 mg/kg			
	male		female		male		female	
metabolite	6 h	12 h	8 h	12 h	6 h	24 h	6 h	12 h
liver								
M2	0.065	0.017	0.084	0.045	3.7	1.4	3.0	1.5
M3	0.035	ND[a]	ND	ND	ND	ND	ND	ND
M5-glu	0.030	0.018	ND	0.023	ND	ND	ND	1.4
M7-glu	0.115	0.035	0.090	0.035	ND	2.0	3.8	1.2
M7	0.189	0.169	0.145	0.093	4.1	ND	1.1	0.7
M8	0.119	0.030	0.103	0.016	2.2	ND	1.1	0.6
others	ND	0.029	ND	0.011	2.8	ND	ND	ND
subtotal	0.553	0.297	0.422	0.224	12.7	3.4	9.0	5.3
unextractable	0.133	0.195	0.080	0.054	2.4	3.8	1.1	1.1
total of liver	0.686	0.492	0.502	0.278	15.1	7.2	10.1	6.4
kidney								
M2-glu	0.020	0.015	0.052	0.013	2.8	ND	2.2	1.4
M2	0.039	0.016	0.026	0.021	2.1	ND	1.3	0.8
M3	ND	ND	0.021	ND	ND	ND	ND	ND
M5-glu	0.166	0.046	0.129	0.051	9.8	2.6	5.1	3.2
M7-glu	0.058	0.043	0.056	0.016	ND	0.5	ND	ND
M7	0.047	0.032	0.029	0.024	ND	ND	ND	ND
others	0.041	ND	ND	ND	ND	ND	2.8	ND
subtotal	0.371	0.152	0.313	0.125	14.6	3.1	11.5	5.5
unextractable	0.010	0.008	0.008	0.005	0.4	0.4	0.2	0.2
total of kidney	0.381	0.160	0.322	0.130	15.0	3.5	11.7	5.7
plasma								
M2-glu	ND	ND	ND	0.005	ND	ND	0.8	ND
M2	0.022	0.009	0.021	0.007	1.1	ND	1.1	0.7
M5-glu	0.022	0.005	0.010	0.007	2.0	0.4	1.3	0.8
M7	ND	0.009	0.015	0.006	ND	0.3	ND	ND
M8	0.039	0.006	0.018	0.006	ND	ND	ND	ND
others	0.024	0.012	0.022	0.008	ND	ND	ND	ND
subtotal	0.107	0.041	0.087	0.039	3.1	0.6	3.2	1.5
unextractable	0.008	0.008	0.009	0.007	0.3	0.3	0.3	0.3
total of plasma	0.115	0.050	0.095	0.046	3.4	0.9	3.6	1.7

[a]ND: Not detected.

thrin to male and female rats, the ^{14}C concentration in plasma rapidly reached C_{max} (0.148 and 0.091 μg equiv/g at low dose and 3.54 and 3.87 μg equiv/g at high dose, respectively) at 6 to 8 h after the administration. Radioactivity in plasma was time-dependently decreased with a half-life of 37.3 to 52.2 h, and the tendency of elimination of ^{14}C in tissues and organs was almost the same as that in plasma. ^{14}C concentrations in major tissues reached a peak within 6 to 8 h for both low and high dose, and thereafter decreased rapidly to low levels on the seventh day. Remaining ^{14}C in whole body was less than 0.3% of the dosed ^{14}C at 168 h after the administration, and no organ-specific accumulation was observed.

Dosed ^{14}C was rapidly and almost completely excreted within 2 days after administration with the major route of urine. The amounts of excreted ^{14}C into the urine and feces were 59.3 to 71.7% and 27.2 to 38.2%, respectively, with total recoveries of 98.1 to 99.7%. The amount of ^{14}C excreted into urine (59.3% to 71.7% of the dose) was considered to be absorbed from the gastrointestinal (GI) tract and excreted. In the biliary excretion study, the amounts of excreted ^{14}C into urine, bile, and feces were 15.3 to 15.7%, 24.4 to 37.3%, and 41.0 to 52.4%, respectively. GI absorption rates were evaluated to be 53.2% and 40.3% for males and females, respectively, as the sum of ^{14}C detected in urine, bile, and residual carcass, and they were lower than the amount excreted into urine from normal rats. It has been reported[12−14] that the decreased intestinal absorption due to the lack of bile components (i.e., taurocholate) in the intestinal fluid was observed by bile duct cannulation, and the situation was supposed to occur also for (Z)-(1R,3R)-profluthrin. Since no parent compound was detected in bile and almost all of the ^{14}C components in feces were derived from the unchanged (Z)-(1R,3R)-profluthrin, it was suggested that the amount of ^{14}C excreted into feces can be regarded as unabsorbed, and it was considered that the amount of ^{14}C excreted into urine under normal conditions can alter the intestinal absorption rate. On these bases, intestinal absorption rates were determined to be approximately 65.6 to 71.8% at low dose and 59.4 to 60.2% at high dose, which suggests a 6 to 12% decrease in intestinal absorption at high dose. The obtained parameters of AUC in the kinetic study were 32−53 times higher at high dose, and were lower than the actual dose ratio,

DOI: 10.1021/acs.jafc.5b03321
J. Agric. Food Chem. 2015, 63, 8651−8661

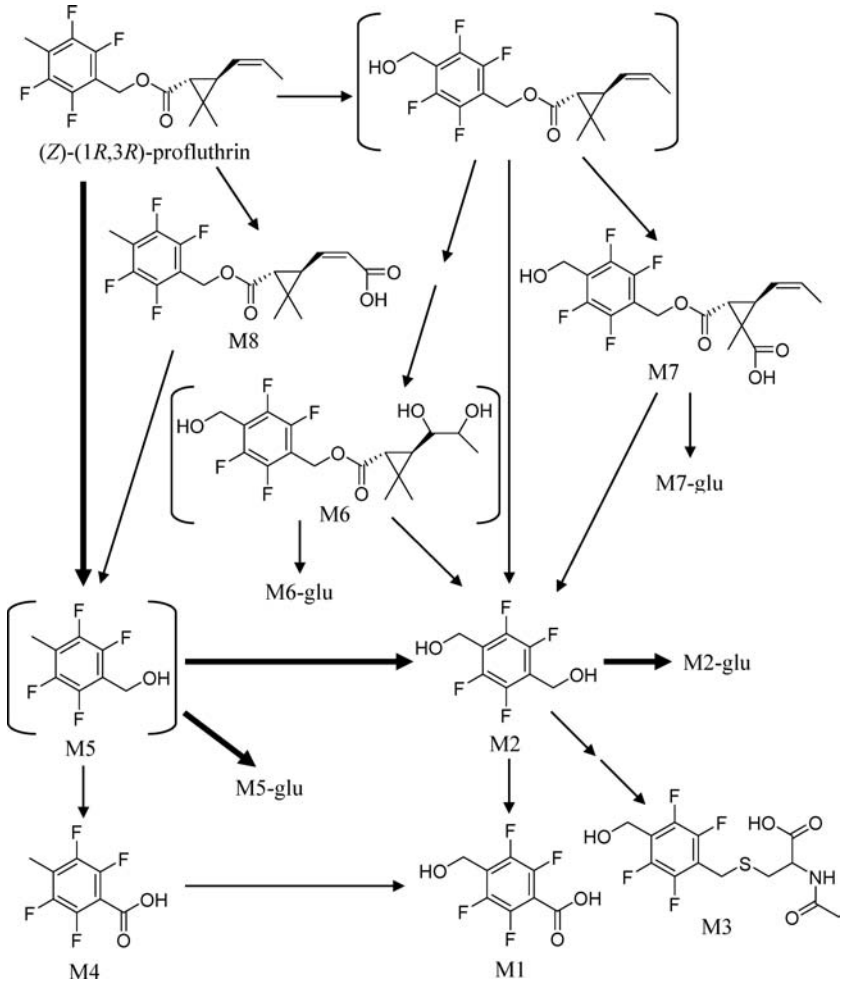

Figure 5. Proposed metabolic pathways of (*Z*)-(1*R*,3*R*)-profluthrin in rats.

60 vs 1 mg/kg. These results were also considered to support the saturation of absorption at the high dose.

As shown in Tables 6 and 7, 10 metabolites, including 4 glucuronides, were identified in bile, feces, and urine within 2 days after single oral administration of [benzyl-α-^{14}C]-labeled (*Z*)-(1*R*,3*R*)-profluthrin. In both urine and bile, glucuronic acid conjugate of the ester-hydrolyzed metabolite, M5-glu, was most abundant, followed by M2, M7, and their glucuronides. Only in urine, M4, M1, and M3 (a mercapturic acid conjugate of M2) were detected. M6-glu and M8 were both ester metabolites, and were only detected in bile and in small amounts. The composition of metabolites identified in urine of bile-cannulated rats was similar to that of normal rats.

The proposed metabolic pathways of (*Z*)-(1*R*,3*R*)-profluthrin are shown in Figure 5. The main metabolic reactions are the cleavage of the ester bond, hydroxylation of the methyl group on the C4 of the phenyl ring, and monoglucuronidation of these metabolites. Also, oxidation of the methyl group on the C2 of the cyclopropane ring, hydration of the double bond of propenyl group following the epoxidation, ω-hydroxylation of propenyl group, and oxidation and conjugation with mercapturic acid of benzyl alcohol were observed as minor reactions.

As described previously, it is commonly observed for synthetic pyrethroids that they are mostly metabolized via cleavage of ester bond followed by oxidation and glucuronidation,[1,4,5] and these reactions were also observed with (*Z*)-(1*R*,3*R*)-profluthrin. The extent of metabolic transformation of (*Z*)-(1*R*,3*R*)-profluthrin is summarized in Table 9. In urine and feces, 55% to 58% of dosed ^{14}C was excreted as ester-cleaved metabolites, while 1% to 12% (not including unchanged (*Z*)-(1*R*,3*R*)-profluthrin in feces) was confirmed to be ester-retaining. As we indicated above, the existence or nonexistence of cyano moiety on its α-position of the alcohol side and the stereochemical conformations of the 1- and 3-positions of cyclopropane can affect the ratio of ester linkage-retained metabolites.[1,4,6−8] Since (*Z*)-(1*R*,3*R*)-profluthrin does not have cyano moiety on its α-position of the alcohol side and its steric conformation about the substituent of 1- and 3-cyclopropane is *trans*, it was supposed to be easily hydrolyzed. Actually, the amount of ester metabolites in excreta was between 1 and 16%,

Table 9. Extents of Metabolic Transformations (%)

	1 mg/kg		60 mg/kg	
	male	female	male	female
cleavage of ester linkage	58	57	58	55
(ester remaining[a])	6	12	1	1
hydroxylation of Ph−C4 moiety	28	34	15	17
oxidation of Ph−C1 or C4 alcohol	7	9	5	8
glucuronidation of Ph−C1 or C4 alcohol	52	50	52	46
mercapturic acid conjugate	3	3	1	2

[a]Not including unchanged (*Z*)-(1*R*,3*R*)-profluthrin.

DOI: 10.1021/acs.jafc.5b03321
J. Agric. Food Chem. 2015, 63, 8651−8661

relatively low, and thus in agreement with the known rules for pyrethroid metabolism.

As also shown in Table 9, the amounts of ester metabolites in excreta, which consisted of M7 and its glucuronide, were significantly higher at low dose than at high dose, and in contrast, the amount of C4-hydroxylated metabolites, which consisted of M1, M2-glu, M2, M3, M4, M5-glu, M7, and M7-glu, decreased at high dose, probably due to the saturation of C4 hydroxylation at high dose. The reason for the decrease in ester-retaining metabolites remains unclear, but it is considered a possibility that the polarization step of Ph−C4 hydroxylation was saturated at high dose, and the rate of ester cleavage relatively increased.

As an S-containing metabolite, M3 (a mercapturic acid conjugate of M2) was detected in urine, bile, and tissues in small amount. The metabolic pathway of mercapturic acid conjugate has been well characterized for many pesticides and chemicals previously.[15−20] van Doorn et al. reported mercapturic acid conjugation of benzyl group in the metabolism of toluene and xylene.[17] M3 was also supposed to be produced via conjugation of glutathione, amide cleavage of glutamate and glycine, and addition of acetyl group to the amino group of the cysteine moiety.

In this study, only alcohol side labeled compound was used to determine the metabolic fate of (*Z*)-(1*R*,3*R*)-profluthrin, and thus the further metabolism of the acid side following the ester cleavage has not been investigated. The acid side, 2,2-dimethyl-3-(prop-1-enyl)cyclopropanecarboxylic acid, is almost similar to chrysanthemic acid, with the only difference being the presence of methyl moiety of the 2-propenyl moiety. There are many pyrethroids with chrysanthemic acid as an acid moiety, i.e., tetramethrin, phenothrin, cyphenothrin, empenthrin, and allethrin. The metabolic fate of chrysanthemic acid is well characterized.[6−8] In short, the ω-position of chrysanthemic acid is oxidized to alcohol and carboxylic acid, and/or conjugated to glucuronide, and rapidly excreted mainly in urine. These previous reports, including the metabolism of chrysanthemic acid, provide sufficient basis on which to estimate the metabolic pathways of the acid side of (*Z*)-(1*R*,3*R*)-profluthrin; however, further experimentation with acid side labeled (*Z*)-(1*R*,3*R*)-profluthrin or other compound that has the same substructure is considered to be prudent to elucidate the whole metabolic fate of (*Z*)-(1*R*,3*R*)-profluthrin.

In conclusion, the metabolic fate of (*Z*)-(1*R*,3*R*)-profluthrin in rat is almost completely revealed. Dosed (*Z*)-(1*R*,3*R*)-profluthrin was absorbed approximately 70% in intestine, and excreted rapidly, mainly via urine. Absorbed ^{14}C was once excreted into bile as metabolites, but most of this was reabsorbed, underwent enterohepatic circulation, and finally was excreted into urine. The plasma concentration reached the peak at 6 to 8 h, and decreased with a half-life of 37 to 52 h. ^{14}C concentration in tissues also decreased at basically the same rate as in plasma. When dosed at 60 mg/kg, saturation of the absorption occurred, and the rate decreased to approximately 60%. There were no marked differences in the kinetics or ^{14}C distribution to tissues and organs. The most abundant metabolite in urine was M5-glu, followed by M2-glu. As minor metabolites, M3 (a mercapturic acid conjugate of M2), M1, and M4 (oxidized metabolites of M2 and M5) and M7 and its glucuronide were also detected. In the feces, most of the detected radioactivity was derived from unabsorbed (*Z*)-(1*R*,3*R*)-profluthrin, especially in the high dose group. The main routes of the metabolism are the cleavage of the ester bond, hydroxylation of the methyl group on the C4 of the phenyl ring, and its glucuronidation. Also, oxidation of the methyl group on the C2 of the cyclopropane ring, hydration of the double bond of propenyl group following the epoxidation, ω-hydroxylation of propenyl group, and oxidation and conjugation with mercapturic acid of benzyl alcohol were observed as minor reactions. Decreased ester metabolites were observed at high dose, and it was probably due to the saturation of Ph−C4 hydroxylation; however, there were no qualitative differences between high dose and low dose. No marked sex-related differences were observed in ^{14}C-elimination, ^{14}C-distribution, or metabolite profiles.

AUTHOR INFORMATION

Corresponding Author

*Tel: +81-6-6466-5321. E-mail: abej@sc.sumitomo-chem.co.jp.

Notes

The authors declare no competing financial interest.

REFERENCES

(1) Kaneko, H. Pyrethroids: mammalian metabolism and toxicity. *J. Agric. Food Chem.* **2011**, *59*, 2786−2791.

(2) Casida, J. E.; Quistad, G. B. Golden age of insecticide research: past, present, or future? *Annu. Rev. Entomol.* **1998**, *43*, 1−16.

(3) Ujihara, K.; Sugano, M.; Nakada, K.; Iwakura, K.; Nishihara, K.; Katoh, H. Discovery and development of profluthrin (Fairytale®), a new active ingredient of moth proofer. *Sumitomo Kagaku* **2010**, *2*, 13−23.

(4) Mikata, K.; Isobe, N.; Kaneko, H. Biotransformation and enzymatic reactions of synthetic pyrethroids in mammals. *Top. Curr. Chem.* **2011**, *314*, 113−135.

(5) Yang, D.; Wang, X.; Chen, Y.; Deng, R.; Yan, B. Pyrethroid insecticides: isoform-dependent hydrolysis, induction of cytochrome P450 3A4 and evidence on the involvement of the pregnane X receptor. *Toxicol. Appl. Pharmacol.* **2009**, *237*, 49−58.

(6) Kaneko, H.; Matsuo, M.; Miyamoto, J. Comparative metabolism of stereoisomers of cyphenothrin and phenothrin isomers in rats. *J. Pestic. Sci.* **1984**, *9*, 237−247.

(7) Kaneko, H.; Izumi, T.; Ueda, Y.; Matsuo, M.; Miyamoto, J. Metabolism and placental transfer of stereoisomers of tetramethrin isomers in pregnant rats. *J. Pestic. Sci.* **1984**, *9*, 249−258.

(8) Kaneko, H.; Ohkawa, H.; Miyamoto, J. Metabolism of tetramethrin isomers in rats. *J. Pestic. Sci.* **1981**, *6*, 425−435.

(9) Mori, T.; Ujihara, K.; Matsumoto, O.; Yanagi, K.; Matsuo, N. Synthetic studies of fluorine-containing compounds for household insecticides. *J. Fluorine Chem.* **2007**, *128*, 1174−1181.

(10) Ujihara, K.; Mori, T.; Iwasaki, T.; Sugano, M.; Shono, Y.; Matsuo, N. Metofluthrin: A potent new synthetic pyrethroid with high vapor activity against mosquitoes. *Biosci., Biotechnol., Biochem.* **2004**, *68*, 170−174.

(11) Ujihara, K.; Matsuo, N.; Kitahara, T. Synthesis of all stereoisomers of the norchrysanthemic acid methyl ester. *Synth. Commun.* **2004**, *34*, 1001−1010.

(12) Holm, R.; Tønsberg, H.; Jørgensen, E. B.; Abedinpour, P.; Farsad, S.; Müllertz, A. Influence of bile on the absorption of halofantrine from lipid-based formulations. *Eur. J. Pharm. Biopharm.* **2012**, *81*, 281−287.

(13) van Hasselt, P. M.; Janssens, G. E. P. J.; Slot, T. K.; van der Ham, M.; Minderhoud, T. C.; Talelli, M.; Akkermans, L. M.; Rijcken, C. J. F.; van Nostrum, C. F. The influence of bile acids on the oral bioavailability of vitamin K encapsulated in polymeric micelles. *J. Controlled Release* **2009**, *133*, 161−168.

(14) Humberstone, A. J.; Porter, C. J. H.; Charman, W. N. A physicochemical basis for the effect of food on the absolute oral bioavailability of halofantrine. *J. Pharm. Sci.* **1996**, *85*, 525−529.

DOI: 10.1021/acs.jafc.5b03321
J. Agric. Food Chem. 2015, 63, 8651−8661

(15) Tomigahara, Y.; Shiba, K.; Isobe, N.; Kaneko, H.; Nakatsuka, I.; Yamada, H. Identification of two new types of S-linked conjugates of Etoc in rat. *Xenobiotica* **1994**, *24*, 839−852.
(16) Delbressine, L. P. C.; van Balen, H. C. J. G.; Seutter-Berlage, F. Isolation and identification of mercapturic acid metabolites of phenyl substituted acrylate esters from urine of rats. *Arch. Toxicol.* **1982**, *49*, 321−330.
(17) van Doorn, R.; Bos, R. P.; Brouns, R. M. E.; Leijdekkers, C.-M.; Henderson, P. T. Effect of toluene and xylenes on liver glutathione and their urinary excretion as mercapturic acids in rats. *Arch. Toxicol.* **1980**, *43*, 293−304.
(18) Pratt, I. S.; Lock, E. A. Deacetylation and further metabolism of the mercapturic acid of hexachloro-1,3-butadiene by rat kidney cytosol in vitro. *Arch. Toxicol.* **1988**, *62*, 341−345.
(19) Bernauer, U.; Birner, G.; Dekant, W.; Henschler, D. Biotransformation of trichloroethene: dose-dependent excretion of 2,2,2-trichloro-metabolites and mercapturic acids in rats and humans after inhalation. *Arch. Toxicol.* **1996**, *70*, 338−346.
(20) Ou, Y. H.; Lin, J. K. Biotransformation of butachlor through mercapturic acid pathway in rat tissue homogenates. *J. Toxicol. Environ. Health* **1992**, *35*, 19−28.

DOI: 10.1021/acs.jafc.5b03321
J. Agric. Food Chem. 2015, 63, 8651−8661

indicated that ~50% and ~70% of them, respectively, were bioaccessible upon in vitro gastrointestinal digestion conditions. The authors did not detect free crocetin in the saffron extract digestate, a finding verified a few years later by Lautenscläger et al. (2015).[8] In vivo studies, however, point out that crocetin is the form detected in biological fluids,[9−11] suggesting that this is the most biologically relevant form. In addition, Lautenscläger et al. (2015)[8] detected free crocetin in the digestate only when they added a freshly prepared tissue homogenate from purged small mouse intestine to their in vitro model. However, no information is available in the literature for the intestinal absorption and metabolism of picrocrocin.

The present study aimed at investigating the cellular transport of the second major saffron apocarotenoid picrocrocin as this glucoside is coextracted with crocetin sugar esters using water or alcoholic mixtures. A Caco-2 cell model coupled with an in vitro digestion procedure was employed. Caco-2 cells are human colon adenocarcinoma cells, which can be differentiated to resemble small intestinal epithelial cells.[12] This cell line is a well-established tool for the in vitro assessment of cellular transport and prediction of the bioavailability of nutrients and non-nutrient bioactive compounds (e.g., carotenoids and phenols). Using the same model, the cellular transport of pure picrocrocin was also investigated in comparison to that of the other two major saffron apocarotenoids, i.e., *trans*-crocetin (di-β-D-gentiobiosyl) ester (*trans*-4-GG crocetin ester) and crocetin. Moreover, the potential biological activity of picrocrocin in terms of protection against oxidant-induced DNA damage in U937 cells and antiproliferative effects in Caco-2 and HepG2 cells were also investigated using the Comet and MTT assays, respectively. The data of the present study will add to existing knowledge on the degree of cellular transport of polar apocarotenoids and also to the limited information regarding the bioactivity of picrocrocin. Our findings may also be useful to the requirements of food legislation regarding saffron preparations.

MATERIALS AND METHODS

Chemicals. Authentic Greek saffron (harvest year 2013, Category I according to ISO 3632-1 specifications[13]) was donated by the Saffron Cooperative of Kozani (Greece).

All of the chemicals were of the highest purity needed for each assay. In particular, the enzymes (pepsin, pancreatin) and bile salts used were from Sigma Chemical Co. (Dublin, Ireland). Fetal bovine serum (FBS) was purchased from Invitrogen (Paisley, Scotland, UK). Dulbecco's Modified Eagle's Medium (DMEM), Hank's Balanced Salt Solution (HBSS), and RPMI-1640 medium were from Sigma Chemical Co. (Dublin, Ireland). Cell culture plastics were supplied by Cruinn Diagnostics (Dublin, Ireland). Corning 24 mm transwell plates with collagen coated PTFE membrane and 0.4 μm pore size (product code: CLS3491) were supplied by Sigma Chemical Co. (Dublin, Ireland). All solvents used were of HPLC grade. Ultrahigh purity water was produced in the laboratory using a SG Ultra Clear Basic UV system (SG Wasseraufbereitung and Regenerierstation GmbH, Barsbüttel, Germany).

Apocarotenoid Isolation. Individual apocarotenoids were isolated and characterized as follows:

Picrocrocin Isolation. Picrocrocin was isolated according to Sánchez et al. (2009).[14] Purity (91%) of the isolated compound was checked chromatographically by RP-HPLC-DAD (HPLC system I) and calculated as the percentage of the total peak area at 250 nm. The HPLC system I consisted of a pump, model P4000 (Thermo Separation Products, San Jose, CA, USA), a Midas autosampler (Spark, Emmen, The Netherlands), and a UV 6000 LP diode array detector (DAD) (Thermo Separation Products, San Jose, CA, USA). Separation was carried out on a LiChroCART Superspher 100 C18 (125 mm × 4 mm i.d.; 4 μm) column (Merck, Darmstadt, Germany). The elution system used consisted of a mixture of water:acetic acid (1%, v/v) (A) and acetonitrile (B). The linear gradient was 20−100% B in 20 min. The flow rate was 0.5 mL/min. Chromatographic data were processed using the ChromQuest Version 3.0 software (Thermo Separation Products, San Jose, CA, USA). Monitoring was in the range of 200−550 nm. Its identity was confirmed by LC-ESI-MS analysis (model 2010 EV, Shimadzu, Kyoto, Japan) and by nuclear magnetic resonance (NMR) spectroscopy recording the ^{1}H 1D spectra at 300 MHz on a Bruker 300AM spectrometer (Rheinstetten, Germany) (see Supporting Information I).

trans-4-GG Crocetin Ester Isolation. The procedure described below was according to Kyriakoudi et al. (2012).[3] In particular, saffron stigmas were carefully ground with an agate pestle and mortar and passed through a 0.4 mm sieve just prior to further analysis. Finely ground saffron (0.36 g) was extracted with ultrahigh purity water (20 mL) with the aid of ultrasounds for 30 min. Sample temperature was kept at 15 ± 0.5 °C in a thermostated water bath. The extract was centrifuged (4100 rpm, 15 min, 4 °C), and the supernatant was lyophilized and stored at −22 °C until further use. *trans*-4-GG crocetin ester was then isolated by semipreparative RP-HPLC (HPLC system II). The system consisted of two Marathon IV series HPLC pumps (Rigas Laboratories, Thessaloniki, Greece), a Rheodyne injection valve (model 7125) with a 250 μL fixed loop (Rheodyne, Cotati, CA), and a diode array linear UVIS-206 multiple wavelength detector (Linear Instruments, Fermont, CA). Separation was carried out on a Nucleosil 100 C18 (250 mm × 10 mm i.d.; 7 μm) chromatographic column (Macherey-Nagel, Düren, Germany). The gradient elution system used consisted of water (A) and methanol (B). The gradient was: 0 min, 30% (B), 0−10 min, 45% (B), 10−20 min, 70% (B), 20−30 min, 100% (B), 30−40 min, 100% (B), 40−50 min, 30% (B) with a flow rate of 3.0 mL/min. Monitoring was at 440 nm. Purity (97%) of isolated *trans*-4-GG crocetin ester was checked chromatographically by RP-HPLC-DAD (HPLC system I) in the range 200−550 nm and calculated as the percentage of the total peak area at 440 nm. The identity of the isolated *trans*-4-GG crocetin ester was confirmed by LC-ESI-MS analysis and by NMR spectroscopy, recording the ^{1}H 1D spectra at 300 MHz on a Bruker 300AM spectrometer (Rheinstetten, Germany) (see Supporting Information II).

Crocetin Preparation. Crocetin was prepared from an aqueous saffron extract by acid hydrolysis according to a protocol described by Ordoudi et al. (2009).[15] Purity (99%) of isolated crocetin was checked chromatographically by RP-HPLC-DAD (HPLC system I) in the range of 200−550 nm and calculated as the percentage of the total peak area at 440 nm. Its identity was confirmed by LC-ESI-MS analysis and by NMR spectroscopy recording the ^{1}H 1D spectra at 500 MHz on a Agilent spectrometer (California, United States) (see Supporting Information III).

Preparation and Characterization of Saffron Aqueous Extract. Saffron was carefully ground with a pestle and mortar just prior to analysis. The finely ground plant material (0.05 g) was extracted with ultrahigh purity water (100 mL) by rigorous agitation (~500 rpm) at ambient temperature for 1 h. All manipulations were performed under subdued (yellow) light to minimize photodecomposition of crocetin esters. The characterization was achieved using RP-HPLC. The HPLC system (HPLC system III) (Finnigan Spectra system; Thermo Scientific, Philadelphia, PA) consisted of a P2000 pump, a AS300 autosampler, and a diode array detector (DAD; Finnigan Spectra system; Thermo Scientific, Philadelphia, PA). Separation was carried out on the same chromatographic column [LiChroCART Superspher 100 C18 (125 mm × 4 mm i.d.; 4 μm) column (Merck, Darmstadt, Germany)]. The elution system consisted of a mixture of water:acetic acid (1%, v/v) (A) and acetonitrile (B). The linear gradient was 20−100% B in 20 min. The flow rate was 0.5 mL/min, and the injection volume was 20 μL. Chromatographic data were processed using ChromQuest software (version 4.2, Thermo Fisher Scientific). Monitoring was in the range of 200−550 nm. Quantification of picrocrocin was accomplished with the aid of a

DOI: 10.1021/acs.jafc.5b03363
J. Agric. Food Chem. 2015, 63, 8662−8668

proper calibration curve ($y = 12830x - 2950$; $R^2 = 1.00$; 9.8−570 ng/20 μL injected volume; $n = 6$). The total and major individual crocetin esters content of saffron was also determined by constructing a calibration curve of pure *trans*-4-GG crocetin ester ($y = 35561x - 381548$; $R^2 = 0.99$; 12−600 ng/20 μL injected volume; $n = 6$).

In Vitro Gastrointestinal Digestion Procedure. The in vitro digestion procedure was carried out as previously described by Kyriakoudi et al. (2013).[7] Briefly, aliquots (2 mL) of the saffron aqueous extract were transferred into amber bottles and HBSS was added to a final volume of 20 mL. To each bottle, 1 mL of freshly prepared pepsin (0.04 g pepsin/0.1 mol/L HCl) was added and the pH was acidified to 2.0 using 1 mol/L HCl. The samples were overlaid with nitrogen gas and incubated at 37 °C for 1 h in a shaking water bath (Grant, OLS200; Keison Products, Chelmsford, Essex, UK) at 95 rpm to mimic the gastric phase of human digestion. The intestinal phase involved increasing the pH to 5.3 with 0.9 mol/L sodium bicarbonate, followed by the addition of 200 μL of bile salts glycodeoxycholate (0.8 mmol/L), taurodeoxycholate (0.45 mmol/L), and taurocholate (0.75 mmol/L) and 100 μL of porcine pancreatin (0.08 g/mL HBSS). The final pH was adjusted to 7.4 using 1 mol/L NaOH. Samples were overlaid with a layer of nitrogen gas and incubated at 37 °C for 2.5 h to mimic the duodenal phase of human digestion. After the intestinal phase, the digestate was centrifuged at 14000*g* using a Sigma 4K15 centrifuge (SIGMA Laborzentrifugen GmbH, Osterode am Harz, Germany) for 60 min at 4 °C. After centrifugation, the supernatants were collected and filtered through a 0.45 μm membrane filter. The resulting filtrates were stored at −80 °C until further analysis.

Cellular Transport of Picrocrocin. Human colon adenocarcinoma Caco-2 cells were purchased from the European Collection of Animal Cell Cultures (Salisbury, Wilts, UK). Cells were maintained in the DMEM supplemented with 10% (v/v) fetal bovine serum and 1% (v/v) nonessential amino acids. Cells were grown at 37 °C in a humidified incubator with 5% CO_2 in the absence of antiobiotics. Culture medium was replaced three times a week. Caco-2 cells were seeded at a density of 1.0×10^5 cells/mL on transwell inserts in 6-well transwell plates. Cells were maintained in DMEM (10% FBS) for 21−25 days to obtain a differentiated cell monolayer; media was changed every 2−3 days. Transepithelial electrical resistance (TEER) measurements were taken before each transport experiment by a transepithelial electrical resistance voltohmmeter (Millicel-ERS, Merck Millipore, Merck KgaA, Darmstadt, Germany) to ensure that the monolayer was intact. Only inserts with TEER values >250 $\Omega \cdot cm^2$ in culture medium were selected for transport experiments. At the beginning of each experiment, the insets were washed twice with 2 mL of HBSS.

Saffron Extract Digestate. The apical (mucosal) compartment received increasing volumes of the saffron extract digestate diluted with HBSS up to a final volume of 2 mL. The basolateral (serosal) compartment received 1.5 mL of HBSS.

Pure Compounds. The cellular transport of pure picrocrocin was determined after its dissolution in HBSS at a concentration range between 8 and 24 μM. Pure *trans*-4-GG crocetin ester and crocetin were also examined at equimolar concentrations for comparison.

The incubation time of the cells with the tested samples was 3 h for all experiments. Following incubation, the TEER values were determined again, and wells with TEER values <250 $\Omega \cdot cm^2$ were discounted. Media from both the apical and basolateral chambers was isolated and stored at −80 °C until further analysis. Samples were analyzed by RP-HPLC (HPLC system III) as detailed above. The injection volume was 90 μL. Quantification of picrocrocin, *trans*-4-GG crocetin ester, and crocetin was accomplished with the aid of proper calibration curves. Cellular transport was the quantity measured in the basolateral chamber expressed as a percentage of the concentration of the compound that was initially added to the Caco-2 cells.

In Vitro Bioactivity Studies of Picrocrocin and Other Major Saffron Apocarotenoids. *Cell Cultures.* Caco-2 cells were maintained in the DMEM supplemented with 10% (v/v) fetal bovine serum (FBS) and 1% (v/v) nonessential amino acids. HepG2 cells were maintained in DMEM supplemented with 10% (v/v) FBS. U937 cells were maintained in RPMI-1640 supplemented with 10% (v/v) FBS. The cells were grown at 37 °C and 5% (v/v) CO_2 in a humidified incubator. Cells were cultured in the absence of antibiotics and were subcultured every two to 3 days.

Sample Preparation for Bioactivity Assays. A 5000 μM stock solution of picrocrocin and *trans*-4-GG crocetin ester in water as well as crocetin in DMSO:PBS (10:90, v/v) were prepared. Samples were filtered through a 0.45 μm membrane filter. The resulting filtrates were stored at −20 °C until further analysis.

Determination of DNA Damage (Comet Assay). U937 cells (1×10^5 cells/mL) were supplemented with increasing nontoxic concentrations of individual apocarotenoids, i.e., picrocrocin, *trans*-4-GG crocetin ester, and crocetin (25 μM) in 6-well plates with a final volume of 2 mL and incubated for 24 h at 37 °C. The cytotoxicity of the tested compounds against this cell line was determined by the fluorescein diacetate/ethidium bromide (FDA/EtBr) assay as previously detailed.[7] Following incubation, cells were treated with 75 μM H_2O_2 for 30 min. Cells were harvested, suspended in a low melting point (LMP) agarose, placed on microscope slides, and allowed to solidify. Slides were placed in cold lysis solution [2.5 M NaCl, 100 mM EDTA, 10 mM Tris, pH = 10, 1% (w/v) sodium sarcosinate], with 1% (v/v) Triton X-100 and 10% (v/v) DMSO, added freshly before each use, for 1.5 h. Slides were then placed in a horizontal gel electrophoresis tank containing fresh electrophoresis solution (1 mM EDTA, 300 mM NaOH) for 30 min. Subsequently, electrophoresis was carried out for 25 min at 4 °C with a current of 25 V (300 mA) using a compact power supply. After electrophoresis, the slides were washed three times with neutralizing buffer (0.4 M Tris, pH = 7.5) at 4 °C for 5 min each. Slides were stained with ethidium bromide (20 μg/mL) and covered with coverslips. Komet 5.5 image analysis software (Kinetic Imaging Ltd., Bromborough, UK) was utilized to measure the level of DNA damage, which was expressed as percentage tail DNA.

Cell Proliferation. The antiproliferative effects of individual apocarotenoids (picrocrocin, *trans*-4-GG crocetin ester, crocetin) were examined in the Caco-2 and HepG2 cell lines using the (4,5-dimethylthiazol-2-yl)-2,5-diphenyltetrazolium bromide (MTT) assay (MTT I proliferation kit, Roche Diagnostics, West Sussex, United Kingdom). Caco-2 and HepG2 cells were seeded at a density of 1×10^5 cells/mL in 96-well plates and allowed to adhere overnight. Cells were then exposed to increasing concentrations of individual apocarotenoids. After 24 h incubation at 37 °C, 5 μL of MTT solution was added to each of the samples and incubated for 4 h at 37 °C. Following incubation, 100 μL of the solubilization solution (10% SDS in 0.01 M HCl) was added. A further incubation period of 24 h at 37 °C followed. Absorbance was read using a Tecan Spectrafluor Plus microplate reader at a wavelength of 570 nm with a reference wavelength of 690 nm. Cell proliferation was expressed as a percentage of the control, untreated cells. GraphPad Prism version 4.00 software (San Diego, USA) was used to determine IC_{50} values for each of the samples in Caco-2 and HepG2 cells.

Statistical Analysis. Statistical comparisons of the mean values were performed by one-way ANOVA, followed by the multiple comparison Duncan test ($p < 0.05$ confidence level) using the SPSS 14.0 software (SPSS Inc., Chicago, IL, USA).

RESULTS AND DISCUSSION

Chemical Characterization of Saffron Aqueous Extract. The RP-HPLC-DAD profile of the saffron aqueous extract at 250 and 440 nm indicated the presence of picrocrocin and crocetin sugar esters, respectively, as expected. The picrocrocin content (14.4 ± 0.7 g/100 g dry stigmas) and that of total crocetin sugar esters (29.3 ± 0.5 g/100 g dry stigmas) and major individual ones, i.e., *trans*-4-GG crocetin ester (15.6 ± 0.3 g/100 g dry stigmas) and *trans*-crocetin (β-D-glucosyl)-(β-D-gentiobiosyl) ester (*trans*-3-Gg crocetin ester) (7.4 ± 0.2 g/100 g dry stigmas) were representative of those of high quality saffron and of similar size to reported data.[3,14,16]

DOI: 10.1021/acs.jafc.5b03363
J. Agric. Food Chem. 2015, 63, 8662−8668

Bioaccessibility of Picrocrocin in Saffron Aqueous Extract. Treatment of the saffron aqueous extract under the simulated digestion conditions showed that ~75% of the initial amount of picrocrocin survived the harsh gastrointestinal conditions, in agreement with the results of our previous study.[7] Picrocrocin was found to be more stable under these conditions than the total crocetin sugar esters of the saffron extract (~40% loss), in agreement with previous results.[7,8] Picrocrocin is reported to be resistant to thermal treatment,[17] however, there is no information available about the effect of pH and/or digestive enzymes to its degradation rate.

Cellular Transport of Picrocrocin and Other Major Saffron Apocarotenoids. *Saffron Extract Digestate.* The cellular transport of picrocrocin was then examined by applying the saffron digestate to the Caco-2 cell monolayer. As the digestate itself can be toxic to the Caco-2 cells due to the presence of proteolytic and lipolytic enzymes, it was first diluted with medium (HBSS), at least 1:2 (v/v), and then added to the cell monolayer. Blank digestates that contained all the digestive enzymes except for the saffron extract were also examined. Dilutions that resulted in TEER values <250 $\Omega \cdot cm^2$ were not examined further. After a 3 h incubation period in the Caco-2 cells with three increasing concentrations of the saffron digestate corresponding to 2.3, 2.6, and 2.8 mg picrocrocin/L digestate, no picrocrocin was detected in the basolateral compartment even though a high fraction of its initial amount was bioaccessible. This observation could be attributed to the presence of the sugar moiety that results in lack of affinity toward the cellular membranes and does not allow passive diffusion.[18] Numerous studies have demonstrated that hydrolysis by digestive enzymes or intestinal microflora may be necessary for the absorption of glucosides of phenolic compounds due to their structural complexicity. Two metabolic pathways have been reported for the absorption of glucosides.[19] Glucosides may be hydrolyzed by lactase phloridizin hydrolase (LPH), which is located on the brush border of small intestinal epithelial cells into the aglycone, or alternatively, they may be absorbed by means of the active sodium-dependent glucose transporter (SGLT-1) and then they can be hydrolyzed within the intestinal cells by cytosolic β-glucosidase. In the present study, however, no sign of picrocrocin hydrolysis and release of the aglycone 4-hydroxy-2,6,6-trimethyl-1-cyclohexene-1-carboxaldehyde (HTCC)[1] was evidenced on the chromatogram at 250 nm [relative retention time (RRT) toward picrocrocin = 1.53]. It has also been observed in the literature that other glucosides, such as quercetin-4′-glucoside,[20] *trans*-piceid,[21] genistin, and daidzein,[22] are not transported across the Caco-2 cell monolayer, possibly due to an absence of β-glucosidase activity in this in vitro model. The crocetin sugar esters of the saffron extract digestate were found to be barely transported across the Caco-2 cell monolayer (data not shown). In particular, only 0.4% of the bioaccessible fraction of total crocetin sugar esters was found to be transported to the basolateral compartment, i.e., was bioavailable. Similarly, the major crocetin ester, *trans*-4-GG, which accounts for ~60% of the total crocetin esters content of saffron, was transported by ~0.4−0.5%. *trans*-3-Gg crocetin ester was detected in the basolateral chamber but at concentrations below the limit of quantification (LOQ) of the specific analytical method employed. No evidence of the hydrolysis of crocetin sugar esters to release the aglycone crocetin was evidenced during cellular transport experiments, probably due to the reasons detailed above. Lautenschläger et al. (2015)[8] also found that only 0.34% of pure *trans*-4-GG crocetin ester was transported across the Caco-2 cells monolayer with no concomitant generation of free crocetin during absorption. However, the presence of free crocetin has been observed in rodent plasma after the oral administration of either a mixture of crocetin esters or pure *trans*-4-GG crocetin ester, derived from the dried fruits of *Gardenia jasminoides* Ellis.[9,10] Moreover, when human volunteers consumed a cup of saffron tea, no crocetin esters but only crocetin was detected in their bloodstream.[11] Compounds that are not absorbed in the small intestine are expected to reach the colon, where they may exert their biological effects.

Pure Compounds. The cellular transport of pure picrocrocin versus that of the other two major saffron apocarotenoids, i.e., *trans*-4-GG crocetin ester and crocetin, was then examined at equimolar concentrations (8−24 μM) using the same in vitro model. The pure compounds were applied directly onto the Caco-2 cell monolayer. In this case, the cellular transport of picrocrocin was found to be ~0.2% (Figure 2). The observed

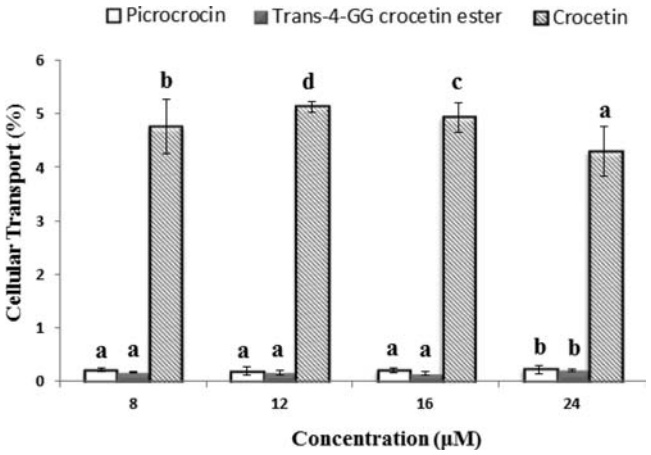

Figure 2. Cellular transport (%) of pure picrocrocin, *trans*-4-GG crocetin ester, and crocetin across the Caco-2 cell monolayer. Cells were incubated with increasing concentrations (8−24 μM) of the compounds for 3 h. Data are mean values ± SD of three independent experiments (n = 3) and were analyzed by one-way ANOVA. Different lowercase letters for each compound indicate significant difference according to Duncan's test at $p < 0.05$.

cellular transport in comparison to that found for picrocrocin in the saffron extract digestate could be attributed to antagonistic interactions with other copresent constituents (e.g., crocetin sugar esters) that may have similar mechanisms of absorption.[23] Data in Figure 2 showed a 10-fold higher cellular transport of the aglycone crocetin (~5% in the range 8−24 μM) compared to that of picrocrocin and also its natural sugar ester forms. Lautenschläger et al. (2015)[8] measured the absorption of *trans*-crocetin in Caco-2 cells and found an average permeation rate of 32%; they also found that the absorption was similar for each concentration in the range of 10−114 μM and was not dose dependent. In addition, there was no specific transporter associated with the transport of *trans*-crocetin and the authors concluded that transport was via the paracellular route. Several experimental factors such as the pH of the transport buffer, the solvent used to deliver the test compound,[24] and the TEER values of the Caco-2 monolayers can affect transport across Caco-2 cells.[25] Theoretically, crocetin is expected to be efficiently absorbed after oral administration as it meets the Lipinski's requirements for optimal oral bioavailability.[26]

DOI: 10.1021/acs.jafc.5b03363
J. Agric. Food Chem. 2015, 63, 8662−8668

According to Lipinski's rule,[27] a compound is expected to display optimum gastrointestinal absorption if "it has a molecular mass of equal or less than 500 g/mol, less than five hydrogen bond donors, and less than ten hydrogen bond acceptors and a calculated partition coefficient (log *P*) less than five". Therefore, crocetin, with a molecular mass of 328.40 g/mol, four hydrogen bond acceptors, two hydrogen bond donors, and a value of log *P* equal to 4.72,[28] may fulfill better these requirements in comparison to the more polar apocarotenoids.

Once carotenoids are absorbed by the intestinal cells, metabolism becomes the major barrier to their bioavailability.[29] The metabolism of apocarotenoids derived from saffron has not been fully eludidated, however, β-carotene 9′,10′-oxygenase (BOC2), which is expressed in mammalian tissues, has a broad substrate specificity and has been shown to metabolize xanthophylls.[30] In the present study, however, peaks at retention times earlier than those of picrocrocin and *trans*-4-GG crocetin ester were not detected on the chromatograms of the basolateral medium. Similar observations have been also made in the case of quercetin from red onions[31] and apples[32] using the same cell line. It is well documented that conjugation via glucuronidation occurs to a greater extent in the liver where the expression of glucuronosyltranferases (UGTs) is much higher compared to that in the small intestine.[33]

DNA Protective Effects of Picrocrocin and Other Major Saffron Apocarotenoids. To determine the protective effects of the individual major saffron apocarotenoids against oxidant-induced DNA damage, the Comet assay was employed. The Comet assay is a sensitive tool for measuring DNA single-strand breaks in individual cells.[34] In the present study, the addition of 75 μM H_2O_2 to U937 cells caused an increase in DNA damage to 52.6% tail DNA compared to the unchallenged control (4% tail DNA) (Figure 3). Cell supplementation with a nontoxic concentration (data not shown) of pure picrocrocin and *trans*-4-GG crocetin ester (25 μM) did not exhibit a significant ($p < 0.05$) DNA protective effect under these experimental conditions. When the aglycone crocetin was examined at an equimolar concentration (25 μM), it caused a significant ($p < 0.05$) decrease in DNA damage (~43% tail DNA). It has been shown that saffron compounds including crocetin may form a complex with DNA and scavenge free radicals which can protect DNA from oxidant induced damage.[35] Literature data focus on the protective effects of saffron extracts and pure *trans*-4-GG crocetin ester against oxidant-induced DNA damage. In particular, Kyriakoudi et al. (2013)[7] reported a significant decrease (13.2% tail DNA) in DNA damage induced by hydrogen peroxide after supplementation of U937 cells with a saffron aqueous extract. *trans*-4-GG crocetin ester has previously demonstrated a dose dependent decrease in H_2O_2-induced DNA damage, as determined by the Comet assay, in a mouse lymphoma (L5178Y) cell line, however, it did not protect against methylmethanesulfonate (MMS)-induced DNA damage in the same study.[36] The protective effect of a saffron extract and pure *trans*-4-GG crocetin ester has been also reported in vivo against methylmethanesulfonate-induced DNA damage in mice organs using the Comet assay.[37]

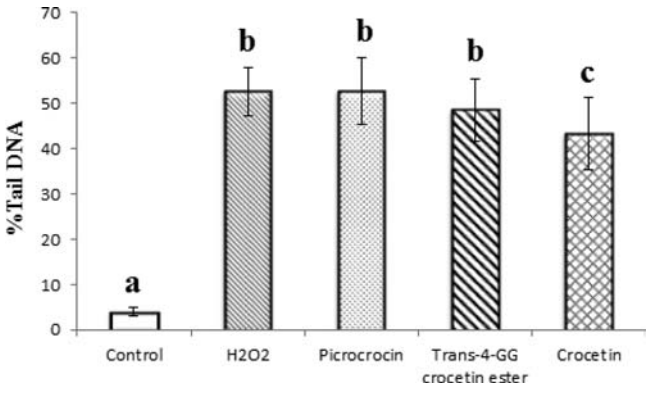

Figure 3. DNA damage in U937 cells following pretreatment with or without pure picrocrocin, *trans*-4-GG crocetin ester, and crocetin (25 μM) for 24 h followed by exposure to 75 μM H_2O_2 for 30 min at 37 °C. DNA damage was assessed by the comet assay. Data are the mean values of six independent experiments, with standard errors represented by vertical bars. Statistical comparisons of the mean values were performed by one-way ANOVA followed by Duncan's test. (a,b,c) Mean value was significantly different from that for H_2O_2-challenged cells ($p < 0.05$).

Antiproliferative Effects of Picrocrocin and Other Major Saffron Apocarotenoids in Human Cancer Cell Lines. Several constituents of saffron have shown antitumor effects through an inhibition of cancer cell growth. The antiproliferative effects of saffron extracts have been demonstrated in breast cancer cells (MCF-7), hepatocarcinoma cells (HepG2), colorectal cancer cells (HCT-116, SW-480, HT-29), and lung cancer cells (NSCLC), among others.[38] Additionally, ethanolic extracts of saffron have demonstrated selective toxicity to cancer cells and did not induce toxicity in normal, noncancerous cells.[39] The effect of picrocrocin, *trans*-4-GG crocetin ester, and crocetin on the in vitro proliferation of human tumoral cells was studied using the human adenocarcinoma, Caco-2, and the human hepatocellular carcinoma, HepG2, cell lines. As illustrated in Figure 4A, picrocrocin and *trans*-4-GG crocetin ester reduced Caco-2 cell proliferation in a dose-dependent manner. Crocetin was found to stimulate cell growth at the lower concentrations (125 and 250 μM) but reduced cell proliferation at higher ones. The IC_{50} value for each compound is presented in Table 1. These values were found to range from 840 to 1700 μM, with crocetin exhibiting the highest antiproliferative effect followed by picrocrocin and *trans*-4-GG crocetin ester. Picrocrocin had an IC_{50} value of 3000 μM in TC-1, malignant murine, cells following a 48 h incubation and *trans*-4-GG crocetin ester had an IC_{50} value of 1500 μM.[40] The differences in IC_{50} values for the various saffron constituents could result from differences in the uptake, transport, and retention of these compounds. In the HepG2 cell line, it was found that picrocrocin triggered a dose-dependent decrease in cell proliferation (Figure 4B), similar to the trend observed in the Caco-2 cell line. In this cell line, *trans*-4-GG crocetin ester and crocetin were found to increase cell viability at the lower concentrations examined, 125 and 250 μM, but decreased cell proliferation at higher concentrations. The IC_{50} values for the tested apocarotenoids were found to be similar in both the HepG2 and the Caco-2 cell lines (Table 1). These data indicate that picrocrocin, *trans*-4-GG crocetin ester, and crocetin may have chemopreventative effects. The ability of crocetin to impede cancer cell growth has been related to an enhancement of the cellular antioxidant systems, the inhibition of nucleic acid synthesis, and the induction of apoptosis.[41]

In conclusion, even though picrocrocin is the most bioaccesible among the major saffron apocarotenoids, it was found to be transported across the Caco-2 cell monolayer at

DOI: 10.1021/acs.jafc.5b03363
J. Agric. Food Chem. 2015, 63, 8662−8668

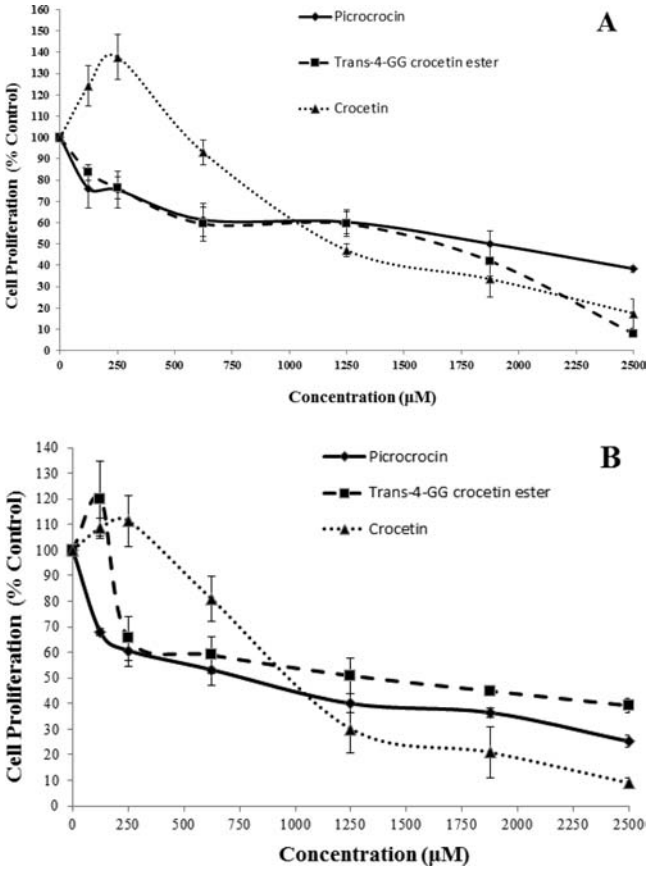

Figure 4. Cell proliferation in Caco-2 (A) and HepG2 (B) cell lines following 24 h exposure to picrocrocin, *trans*-4-GG crocetin ester, and crocetin. Cell proliferation was assessed using the MTT assay. Data are the mean values ± SD of six independent experiments (n = 6).

Table 1. IC_{50} Values for Picrocrocin, *Trans*-4-GG Crocetin Ester, and Crocetin in Human Colon Adenocarcinoma Caco-2 Cells and Human Hepatocarcinoma HepG2 Cells

	IC_{50} values (μM)[a]	
	Caco-2 cells	HepG2 cells
picrocrocin	1160 ± 0.88	1100 ± 0.13
trans-4-GG crocetin ester	1700 ± 0.11	1250 ± 0.03
crocetin	840 ± 0.21	750 ± 0.25

[a]Each value is the mean of triplicate determinations ± SD.

very low levels. When pure picrocrocin was examined at equimolar concentrations with other major saffron apocarotenoids, i.e., *trans*-4-GG crocetin ester and crocetin using the same in vitro model, its cellular transport was found to be approximately similar to that of *trans*-4-GG crocetin ester and ∼10-fold lower than that of the aglycone crocetin. To the best of our knowledge, this is the first time that the data on the cellular transport of picrocrocin itself or in the presence of other saffron apocarotenoids are presented. Picrocrocin also demonstrated antiproliferative activity in human cancer cell lines. This study highlights the relevance of picrocrocin to investigations of the bioavailability and bioactivity of saffron extracts.

■ ASSOCIATED CONTENT

Supporting Information

The Supporting Information is available free of charge on the ACS Publications website at DOI: 10.1021/acs.jafc.5b03363.

LC-ESI-MS and NMR data for the identification of picrocrocin (I), *trans*-4-GG crocetin ester (II), and crocetin(III) (PDF)

■ AUTHOR INFORMATION

Corresponding Author

*Phone: +353 21 4902884. Fax: +353 21 4270244. E-mail: nob@ucc.ie.

Funding

A.K. thanks the Foundation of State Scholarships (IKY, Athens, Greece) for financial support for doctoral studies.

Notes

The authors declare no competing financial interest.

■ ABBREVIATIONS USED

trans-4-GG crocetin ester, *trans*-crocetin (di-β-D-gentiobiosyl) ester; *trans*-3-Gg crocetin ester, *trans*-crocetin (β-D-glucosyl)-(β-D-gentiobiosyl) ester; TEER, transepithelial electrical resistance; FBS, fetal bovine serum; HBSS, Hank's Balanced Salt Solution; DMEM, Dulbecco's Modified Eagle's Medium; MTT, (4,5-dimethylthiazol-2-yl)-2,5-diphenyltetrazolium bromide; FDA-EtBr, fluorescein diacetate/ethidium bromide; LOQ, limit of quantification; H_2O_2, hydrogen peroxide; RP-HPLC-DAD, reversed phase high performance liquid chromatography diode array detector; RRT, relative retention time; NMR, nuclear magnetic resonance; ANOVA, analysis of variance

■ REFERENCES

(1) Carmona, M.; Zalacain, A.; Alonso, G. L. *the Chemical Composition of Saffron: Color, Taste and Aroma*, 1st ed.; Editorial Bomarzo S.L.: Albacete, Spain, 2006; Chapter 4, pp 77−104.

(2) Frusciante, S.; Diretto, G.; Bruno, M.; Ferrante, P.; Pietrella, M.; Prado-Cabrero, A.; Rubio-Moraga, A.; Beyer, P.; Gomez-Gomez, L.; Al-Babili, S.; Giuliano, G. Novel carotenoid cleavage dioxygenase catalyzes the first dedicated step in saffron crocin biosynthesis. *Proc. Natl. Acad. Sci. U. S. A.* **2014**, *111*, 12246−12251.

(3) Kyriakoudi, A.; Chrysanthou, A.; Mantzouridou, F.; Tsimidou, M. Z. Revisiting extraction of bioactive apocarotenoids from *Crocus sativus* L. dry stigmas (saffron). *Anal. Chim. Acta* **2012**, *755*, 77−85.

(4) Kyriakoudi, A.; Ordoudi, S. A.; Roldán-Medina, M.; Tsimidou, M. Z. Saffron, a functional spice. *Austin J. Nutr. Food Sci.* **2015**, *3*, 1059−1063.

(5) Giaccio, M. Crocetin from Saffron: An Active Component of an Ancient Spice. *Crit. Rev. Food Sci. Nutr.* **2004**, *44*, 155−172.

(6) Alavizadeh, S. H.; Hosseinzadeh, H. Bioactivity assessment and toxicity of crocin: A comprehensive review. *Food Chem. Toxicol.* **2014**, *64*, 65−80.

(7) Kyriakoudi, A.; Tsimidou, M. Z.; O'Callaghan, Y. C.; Galvin, K.; O'Brien, N. M. Changes in total and individual crocetin esters upon in vitro gastrointestinal digestion of saffron aqueous extracts. *J. Agric. Food Chem.* **2013**, *61*, 5318−5327.

(8) Lautenschläger, M.; Sendker, J.; Hüwel, S.; Galla, H. J.; Brandt, S.; Düfer, M.; Riehemann, K.; Hensel, A. Intestinal formation of *trans*-crocetin from saffron extract (*Crocus sativus* L.) and in vitro permeation through intestinal and blood brain barrier. *Phytomedicine* **2015**, *22*, 36−44.

(9) Asai, A.; Nakano, T.; Takahashi, M.; Nagao, A. Orally administrated crocetin and crocins are absorbed into blood plasma

DOI: 10.1021/acs.jafc.5b03363
J. Agric. Food Chem. 2015, 63, 8662−8668

as crocetin and its glucuronide conjugates in mice. *J. Agric. Food Chem.* **2005**, *53*, 7302−7306.
(10) Xi, L.; Qian, Z.; Du, P.; Fu, J. Pharmacokinetic properties of crocin (crocetin digentiobiose ester) following oral administration in rats. *Phytomedicine* **2007**, *14*, 633−636.
(11) Chryssanthi, D. G.; Lamari, F. N.; Georgakopoulos, C. D.; Cordopatis, P. A new validated SPE-HPLC method for monitoring crocetin in human plasma - Application after saffron tea consumption. *J. Pharm. Biomed. Anal.* **2011**, *55*, 563−568.
(12) Sambruy, Y.; Ferruzza, S.; Ranaldi, G. I.; De Angelis, I. Intestinal cell culture models. Applications in toxicology and pharmacology. *Cell Biol. Toxicol.* **2001**, *17*, 301−317.
(13) *ISO 3632-1 Saffron (Crocus sativus Linneaus) Part 1: Specifications*; International Organization for Standardization: Geneva, 2011.
(14) Sánchez, A. M.; Carmona, M.; del Campo, C. P.; Alonso, G. L. Solid-phase extraction for picrocrocin determination in the quality control of saffron spice (*Crocus sativus* L.). *Food Chem.* **2009**, *116*, 792−798.
(15) Ordoudi, S. A.; Befani, C. D.; Nenadis, N.; Koliakos, G. G.; Tsimidou, M. Z. Further examination of antiradical properties of *Crocus sativus* stigmas extract rich in crocins. *J. Agric. Food Chem.* **2009**, *57*, 3080−3086.
(16) Sánchez, A. M.; Carmona, M.; Ordoudi, S. A.; Tsimidou, M. Z.; Alonso, G. L. Kinetics of individual crocetin ester degradation in aqueous extracts of saffron (*Crocus sativus* L.) upon thermal treatment in the dark. *J. Agric. Food Chem.* **2008**, *56*, 1627−1637.
(17) Sánchez, A. M.; Carmona, M.; Jarén-Galán, M.; Mínguez Mosquera, M. I.; Alonso, G. L. Picrocrocin kinetics in aqueous saffron spice extracts (*Crocus sativus* L.) upon thermal treatment. *J. Agric. Food Chem.* **2011**, *59*, 249−255.
(18) Murota, K.; Shimizu, S.; Chujo, H.; Moon, J. H.; Terao, J. Efficiency of absorption and metabolic conversion of quercetin and its glucosides in human intestinal cell line Caco-2. *Arch. Biochem. Biophys.* **2000**, *384*, 391−397.
(19) Nemeth, K.; Plumb, G. W.; Berrin, J. G.; Juge, N.; Jacob, R.; Naim, H. Y.; Williamson, G.; Swallow, D. M.; Kroon, P. A. Deglycosylation by small intestinal epithelial cell β-glucosidases is a critical step in the absorption and metabolism of dietary flavonoid glycosides in humans. *Eur. J. Nutr.* **2003**, *42*, 29−42.
(20) Walgren, R. A.; Walle, U. K.; Walle, T. Transport of quercetin and its glucosides across human intestinal epithelial Caco-2 cells. *Biochem. Pharmacol.* **1998**, *55*, 1721−1727.
(21) Henry, C.; Vitrac, X.; Decendit, A.; Ennamany, R.; Krisa, S.; Mérillon, J. M. Cellular uptake and efflux of *trans*-piceid and its aglycone *trans*-resveratrol on the apical membrane of human intestinal Caco-2 cells. *J. Agric. Food Chem.* **2005**, *53*, 798−803.
(22) Steensma, A.; Noteborn, P. J. M.; van der Jagt, R. C. M.; Polman, T. H.G.; Mengelers, M. J. B.; Kuiper, H. A. Bioavailability of genistein, daidzein, and their glycosides in intestinal epithelial Caco-2 cells. *Environ. Toxicol. Pharmacol.* **1999**, *7*, 209−212.
(23) D'Archivio, M.; Filesi, C.; Varì, R.; Scazzocchio, B.; Masella, R. Bioavailability of the polyphenols: status and controversies. *Int. J. Mol. Sci.* **2010**, *11*, 1321−1342.
(24) Yamashita, S.; Furubayashi, T.; Kataoka, M.; Sakane, T.; Sezaki, H.; Tokuda, H. Optimized conditions for prediction of intestinal drug permeability using Caco-2 cells. *Eur. J. Pharm. Sci.* **2000**, *10*, 195−204.
(25) Wallace, C. J.; Medina, S. H.; ElSayed, M. E. H. Effect of rhamnolipids on permeability across Caco-2 cell monolayers. *Pharm. Res.* **2014**, *31*, 887−894.
(26) Abourashed, E. A. Bioavailability of plant-derived antioxidants. *Antioxidants* **2013**, *2*, 309−325.
(27) Lipinski, C. A.; Lombardo, F.; Dominy, B. W.; Feeney, P. J. Experimental and computational approaches to estimate solubility and permeability in drug discovery and development settings. *Adv. Drug Delivery Rev.* **2001**, *46*, 3−26.
(28) *ChemSpider: Search and Share Chemistry*; Royal Society of Chemistry, http://www.Chemspider.com (accessed on 01/07/2015).
(29) von Lintig, J. Provitamin A metabolism and functions in mammalian biology. *Am. J. Clin. Nutr.* **2012**, *96* (suppl), 1234S−1244S.
(30) Bonet, M. L.; Canas, J. A.; Ribot, J.; Palou, A. Carotenoids and their conversion products in the control of adipocyte function, adiposity and obesity. *Arch. Biochem. Biophys.* **2015**, *572*, 112−125.
(31) Walgren, R. A.; Karnaky, K. J.; Lindenmayer, G. E.; Walle, T. Efflux of Dietary flavonoid quercetin 4′-β-glucoside across human intestinal Caco-2 cell monolayers by apical multidrug resistance-associated protein-21. *J. Pharmacol. Exp. Ther.* **2000**, *294*, 830−836.
(32) Boyer, J.; Brown, D.; Liu, R. H. Uptake of quercetin and quercetin 3-glucoside from whole onion and apple peel extracts by Caco-2 cell monolayers. *J. Agric. Food Chem.* **2004**, *52*, 7172−7179.
(33) Gao, S.; Hu, M. Bioavailability challenges associated with development of anti-cancer phenolics. *Mini-Rev. Med. Chem.* **2010**, *10*, 550−567.
(34) Liao, W.; McNutt, M. A.; Zhu, W. G. The comet assay: A sensitive method for detecting DNA damage in individual cells. *Methods* **2009**, *48*, 46−53.
(35) Kanakis, C. D.; Tarantilis, P. A.; Pappas, C.; Bariyanga, J.; Tajmir-Riahi, H. A.; Polissiou, M. G. An overview of structural features of DNA and RNA complexes with saffron compounds: Models and antioxidant activity. *J. Photochem. Photobiol., B* **2009**, *95*, 204−212.
(36) Choi, H. Y.; Kim, Y. J.; Ryu, J. C. Study of genotoxicity of crocin, a component of gardenia fruit, in bacterial and mammalian cell systems. *Mol. Cell Toxicol.* **2008**, *4*, 285−292.
(37) Hosseinzadeh, H.; Abootorabi, A.; Sadeghnia, H. R. Protective effect of *Crocus* sativus stigma extract and crocins (*trans*-crocin 4) on methyl methanesulfonate−induced DNA damage in mice organs. *DNA Cell Biol.* **2008**, *27*, 657−664.
(38) Bolhassani, A.; Khavari, A.; Bathaie, S. Z. Saffron and natural carotenoids: Biochemical activities and anti-tumor effects. *Biochim. Biophys. Acta, Rev. Cancer* **2014**, *1845*, 20−30.
(39) Li, C. Y.; Huang, W. F.; Wang, Q.-L.; Wang, F.; Cai, F. W.; Hu, B.; Du, J.-C.; Wang, J.; Chen, R.; Cai, X. J.; Feng, J.; Li, H. H. Crocetin induces cytotoxicity in colon cancer cell lines via p53-independent mechanisms. *Asian Pac. J. Cancer Prev.* **2012**, *13*, 3757−3761.
(40) Khavari, A.; Bolhassani, A.; Alizadeh, F.; Bathaie, S. Z.; Balaram, P.; Agi, E.; Vahabpour, R. Chemo-immunotherapy using saffron and its ingredients followed by E7-NT (gp96) DNA vaccine generates different anti-tumor effects against tumors expressing the E7 protein of human papillomavirus. *Arch. Virol.* **2015**, *160*, 499−508.
(41) Gutheil, W. G.; Reed, G.; Ray, A.; Anant, S.; Dhar, A. Crocetin: an agent derived from saffron for prevention and therapy from cancer. *Curr. Pharm. Biotechnol.* **2012**, *13*, 173−179.

DOI: 10.1021/acs.jafc.5b03363
J. Agric. Food Chem. 2015, 63, 8662−8668

Therefore, we need to develop a new system for a more efficient delivery of β-carotene with an enhanced stability.

It is well-known that the carboxyl groups can coordinate with divalent and trivalent ions, such as Ca^{2+} or Fe^{3+}. In this way, the carboxyl-containing polymers are physically cross-linked by those ions, leading to a gel formation. For example, calcium alginate microspheres for prolonged drug release were prepared by ionic gelation of alginate with calcium chloride ($CaCl_2$).[20] A gelation of poly(acrylic acid) (PAA) polymers can be induced by coordination with Fe^{3+} ions.[21] Polysaccharide microspheres can be obtained by cross-linking carboxylmethyl konjac glucomannan via Fe^{3+} ions.[22] We have reported a polysaccharide microsphere prepared of oxidized konjac glucomannan where the carboxyl (COO^-) groups are physically cross-linked by Fe^{3+} ions.[23] On the basis of the literature, we propose to prepare a new microsphere by cross-linking COO^- groups on oxidized starch with Fe^{3+} ions by an emulsion-cross-linking method. Oil-in-water-in-oil (O/W/O) double emulsions have a high potential for application in the food processing industry to encapsulate or protect sensitive and hydrophobic components.[24] β-carotene can be dissolved in the inner oil phase, and the oxidized starch can be solidified by Fe^{3+} in the middle water phase. In this way, β-carotene can be encapsulated inside oxidized starch microspheres via the double-emulsion method.

The objective of this study is to develop an oral delivery system that specifically delivers β-carotene to the intestine, aiming to improve its water solubility and stability. First, β-carotene-loaded oxidized starch microspheres were made of 90% degree of oxidation (DO) oxidized starch polymer, where the COO^- groups are physically cross-linked via ferric ions (Fe^{3+}) through O/W/O double-emulsion methods. Second, the surface morphology and distribution of the oil phase inside microspheres were observed by scanning electron microscopy (SEM) and confocal laser scanning microscopy (CLSM). The properties of microspheres, such as size distribution and ζ-potential, as a function of pH and ionic strength were characterized. Then, the *in vitro* release of β-carotene from the oxidized starch microspheres in simulated gastric and intestinal fluids was measured. Finally, the scavenging activity of encapsulated β-carotene after heat treatment was measured by 1,1-diphenyl-2-picrylhydrazyl radical, 2,2-diphenyl-1-(2,4,6-trinitriphenyl) (DPPH), methods. The storage stability of encapsulated β-carotene at room temperature was tested as well. The results indicated that oxidized starch microspheres can be potentially used to deliver β-carotene into intestine with an enhanced stability.

MATERIALS AND METHODS

Materials. Native potato starch polymer was kindly provided by AVEBE, Netherlands. The oxidation catalyst TEMPO was purchased from Merck, Germany. Whey protein isolate (WPI) was kindly provided by Davisco Foods International, Inc. (Le Sueur, MN). β-carotene (purity > 97%) was purchased from TCI, Japan. DPPH was purchased from Sigma. Sodium hypochlorite, ferrous sulfate ($FeSO_4 \cdot 7H_2O$), paraffin liquid, Tween 80, and Span 80 were purchased from Beijing Chemical Reagent Factory, China. Pepsin was obtained from Biosharp, China. Pancreatin powder was purchased from AOBOX Biotechnology Company, China. All other chemicals used were of analytical grade. Deionized water was used throughout.

Preparation of the β-carotene-Loaded Oxidized Starch Microsphere. By TEMPO-mediated oxidation, the primary alcohol groups at the C-6 position on potato starch polymer were selectively oxidized into carboxyl groups. In this way, starch polymers of 90% DO were prepared, following the procedure described by de Nooy et al.[14] The DO was controlled by the amount of sodium hypochlorite added during oxidation. The oxidation was performed at a constant pH (pH 10) using 2 M NaOH at 10 °C.

An emulsion cross-linking method was used to prepare the oxidized starch microsphere. O/W/O double emulsion was used to prepare the β-carotene-loaded oxidized starch microsphere. First, 10% (w/w) crystalline β-carotene was dissolved in corn oil to obtain the inner oil phase (O_I). Then, 1% (w/v) WPI was dissolved in aqueous buffer solution (0.02 M citric acid−phosphate buffer at pH 3) to obtain aqueous phase I (W_I). The volume ratio of O_I to aqueous phase I (W_I) was 1:4 (O_I/W_I). The O_I/W_I emulsion was prepared by ultrasonic emulsification (32 W for 5 min). Then, 20 mg of 90% DO oxidized starch polymer and 5 mg of $FeSO_4 \cdot 7H_2O$ were dissolved in 100 μL to prepare aqueous phase II (W_{II}). The 100 μL (O_I/W_I) emulsion and 100 μL water phase II (W_{II}) were mixed to obtain primary emulsion [$O_I/(W_I + W_{II})$]. A total of 0.67 g of Span 80 was dissolved in 20 g of paraffin oil to obtain continuous oil phase II (O_{II}). The volume ratio of primary emulsion [$O_I/(W_I + W_{II})$] to O_{II} was 1:100. The primary emulsion was gradually added to O_{II} under stirring at 1000 rpm to make the double emulsion. Later, oxygen gas was pumped into the double emulsion during stirring at 35 °C for 20 min to oxidize Fe^{2+} to Fe^{3+}, leading to the gel formation caused by the coordination between Fe^{3+} and carboxyl groups on oxidized starch. Finally, the micropheres were washed 2 times with hexane and 2 times with methanol. After each washing step, the system was centrifuged (3000 rpm for 2 min), then the liquid was decanted, and the particles were redispersed in pH 3 HCl solution. In the end, the β-carotene-loaded oxidized starch microspheres were obtained.

Morphology of the β-carotene-Loaded Oxidized Starch Microsphere. The surface morphology of the β-carotene-loaded oxidized starch microsphere was examined by SEM using a scanning electron microscope (S-4700, Hitachi Company, Tokyo, Japan) with an accelerating voltage of 15 kV. The microspheres were sputter-coated with gold prior to observation.

CLSM. Because β-carotene is a natural fluorescent pigment, the distribution of β-carotene in oxidized starch microspheres can be directly observed by CLSM (TCS SP2, Leica, Wetzlar, Germany). The excitation wavelength for β-carotene is 488 nm, and the emission wavelength is 560 nm.

Determination of β-carotene Encapsulated Inside the Oxidized Starch Microspheres by High-Performance Liquid Chromatography (HPLC). The β-carotene content was determined using a standard curve created from a series of β-carotene solutions at different concentrations. β-carotene encapsulated inside the oxidized starch microspheres was extracted by hexane under sonication. HPLC was used to determine its concentration with 450 nm as a detection wavelength. The HPLC parameters of the experiment were as follows: A Diamonsil C_{18} chromatographic column (250 × 4.6 mm, 5 μm, Dikma) was employed at 28 °C. The mixture of acetonitrile and dichloromethane with a volume ratio of 3:1 was used as the mobile phase. The flow rate was 1.5 mL/min, and 20 μL of each sample was injected.

The loading capacity (L) was calculated according to the following formula:

$$\text{loading capacity}\left(\frac{\text{mg}}{\text{g}}\right) = \frac{\text{mg of β-carotene encapsulated}}{\text{g of oxidized starch polymers in microspheres}} \quad (1)$$

The loading capacity was 2.3 mg of β-carotene/g of oxidized starch microspheres.

Chemical Structure Analysis by Fourier Transform Infrared (FTIR) Spectra. The FTIR spectroscopy technique was used to analyze the chemical structures of non-oxidized starch polymers, oxidized starch polymers, and the microspheres. A total of 200 mg of KBr and 8 mg of sample were pressed under 10 MPa for 10 min to obtain a tablet that was investigated using a FTIR spectrophotometer (Araffinity-1, Shimadzu, Kyoto, Japan).

DOI: 10.1021/acs.jafc.5b03575
J. Agric. Food Chem. 2015, 63, 8669−8675

Size Distribution and ζ-Potential Measurements of the β-carotene-Loaded Oxidized Starch Microsphere. The size distribution of oxidized starch microspheres in suspension was determined by dynamic light scattering (DLS, MasterSizer 2000, Malvern, London, U.K.). The microspheres in suspension were measured at 25 °C. The weight concentration of particles used in measurement was 0.05 mg/mL. Before the measurements, suspensions were sonicated for 2 min, to obtain finely dispersed microphores.

The ζ-potential of oxidized starch microspheres in suspension was determined using a DLS system (Zetasizer Nano ZS series, Malvern, London, U.K.). The temperature of all samples was controlled at 25 °C. The weight concentration of oxidized starch microspheres used in measurement was 0.3 mg/mL in citric acid−phosphate buffer (0.02 M, pH 3−7) with different ionic strengths. Before the measurements, the suspensions were sonicated for 2 min, to obtain finely dispersed particles.

***In Vitro* Release of β-carotene from Oxidized Starch Microspheres in Simulated Gastrointestinal Fluids.** The simulated gastrointestinal fluids were prepared according to previously described methods.[19] The percentage of released β-carotene was defined as the ratio of the weight of released β-carotene to the weight of absorbed gross. The percentage of β-carotene released $A_{released}$ was calculated from the measured released β-carotene concentration ($C'_{\beta\text{-C}}$) as

$$A_{released} = (C'_{\beta\text{-C}} V_{extracted})/(Lm_{microspheres}) \times 100\% \quad (2)$$

where $V_{extracted}$ is the volume of released β-carotene, L is the loading capacity, and $m_{microspheres}$ is the weight of β-carotene encapsulated inside oxidized starch microspheres.

Following standard pharmacopoeia methods, the β-carotene-loaded oxidized starch microspheres were first incubated for 120 min in simulated gastric fluid at 37 °C and the percentage of released β-carotene were measured at times 0, 15, 30,45, 60, 75, 90, and 120 min. Thereafter, the microspheres were transferred into simulated intestinal fluid for continuous release for another 3 h. The percentage of released β-carotene was measured at times 0, 15, 30, 45, 60, 90, 120, 150, and 180 min in stimulated intestinal fluid. All of the samples were centrifuged under 3000 rpm for 2 min. Released β-carotene in the supernatant was extracted with solvent [*n*-hexane/ethanol (v/v) = 2:1]. The absorbance of β-carotene under 450 nm was measured by HPLC. The concentration of β-carotene released was calculated from a standard calibration curve.

DPPH Radical-Scavenging Activity of Oxidized Starch Microspheres That Encapsulated β-carotene. The oxidized starch microsphere loaded with β-carotene and free β-carotene were heated at 80 °C for 40 h and sampling at different time intervals (0, 4, 8, 22, 26, 32, and 40 h). DPPH was dissolved in ethanol (0.4 mmol). β-carotene loaded by 10 mg of microspheres was extracted by hexane. Free β-carotene in hexane solution was adjusted to the same concentration as the extract. A total of 200 μL of β-carotene extracted from microspheres and free β-carotene hexane solution were added to 3.8 mL of DPPH solution. The mixtures were stirred 30 min to scavenge free radicals. The absorbance of solution was determined at 517 nm to measure the scavenging rate. A_0 is the absorbance of initial DPPH solution before scavenging, and A_t is the absorbance of DPPH solution after scavenging at 30 min.

The scavenging rate A_{scan} (%) could be calculated as

$$A_{scan}\ (\%) = (A_0 - A_t)/A_0 \times 100\% \quad (3)$$

Storage Stability of Oxidized Starch Microspheres That Encapsulated β-carotene. The β-carotene-loaded oxidized starch microsphere and free β-carotene were placed in a storage chamber with a constant temperature of 25 °C. The β-carotene concentration was determined daily, and the sampling lasted for 10 days. The collected samples were detected by HPLC, described in a previous section. The storage stability of β-carotene was expressed as a residual rate in percent: C_t/C_0, where C_t is the β-carotene concentration after storage for a period of time t and C_0 is the β-carotene content at the time of preparation.

Statistical Analysis. Each experiment was performed in triplicate. A spreadsheet statistical package was used to analyze the mean of the three measurements and standard deviations.

RESULTS AND DISCUSSION

Distribution of β-carotene Inside Oxidized Starch Microspheres. By means of an O/W/O double-emulsion method, in the water phase, TEMPO oxidized starch polymers, of which the carboxyl groups are cross-linked via Fe^{3+} ions and in which β-carotene can be simultaneously incorporated in the inner oil phase. The left image of Figure 1a showed that β-carotene did not dissolve in water. In the contrast, after loading it in the oxidized starch microspheres, the dispersibility of β-carotene in water was improved. It was demonstrated by the homogeneous yellow suspension of β-carotene-loaded starch microsphere solution (right image of Figure 1a). The surface morphology of the β-carotene-loaded starch microspheres was shown in panels b and c of Figure 1. Their diameter ranged from 10 to 40 μm. They possessed a rough surface, which was related to the heterogeneous cross-link reaction. The optical microscopic image of β-carotene-loaded microspheres was shown in Figure 1d. It can be clearly seen that the oil droplets were encapsulated inside the oxidized starch microspheres. Because of the fluorescent nature of β-carotene, the distribution of β-carotene inside the microspheres was further observed by CLSM. Red-colored β-carotene molecules were present in the inner oil phase (Figure 1e). The above results suggested that β-carotene was successfully incorporated inside oxidized starch microspheres and its dispersibility in aqueous solution was improved.

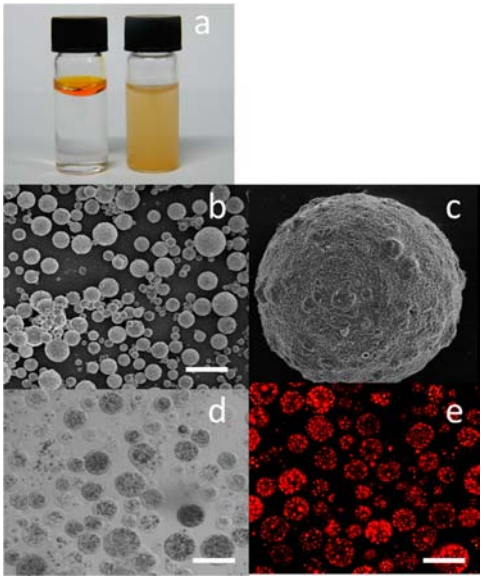

Figure 1. (a) Photograph of the aqueous solution of non-encapsulated (left) and oxidized starch microspheres that encapsulated β-carotene (right). (b) Surface morphology of oxidized starch microspheres and (c) magnified image by SEM. (d) Optical images of β-carotene-loaded oxidized starch microspheres. (e) CLSM images of β-carotene-loaded oxidized starch microspheres. Scale bar = 50 μm.

Characterization of the Physical and Chemical Properties of Oxidized Starch Microspheres. The chemical structure of the Fe^{3+} cross-linked oxidized starch microspheres was mesured by FTIR spectrometry. As shown in Figure 2, the asymmetric vibration ν_{as} and symmetric vibration

DOI: 10.1021/acs.jafc.5b03575
J. Agric. Food Chem. 2015, 63, 8669−8675

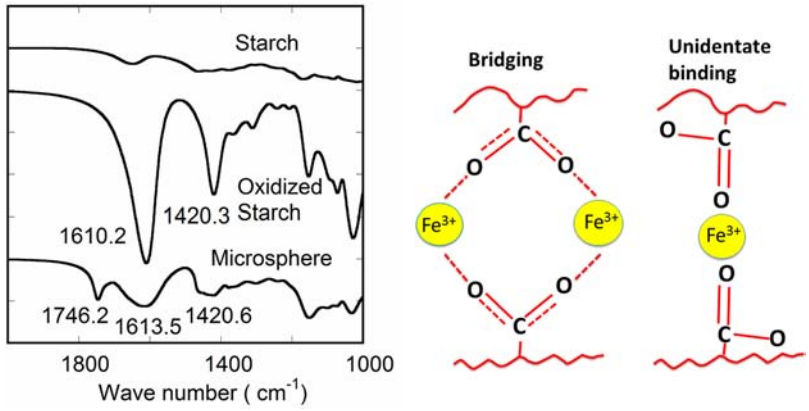

Figure 2. (Left) FTIR spectra of starch, TEMPO-oxidized starch, and oxidized starch microspheres. (Right) Schematic illustration of unidentate binding and bridging between COO^- and Fe^{3+} in the oxidized starch microspheres.

ν_s of COO^- in the oxidized starch polymer appear at 1610.2 and 1420.3 cm^{-1}, suggesting the successful oxidation of primary alcohol groups on starch polymers to carboxyl groups. For Fe^{3+} cross-linked starch, we found that the asymmetric vibration peak of COO^- (1610.2 cm^{-1}) for the oxidized starch polymer was split into two peaks at 1746.2 and 1613.5 cm^{-1}. It is well-known in the literature that the wavenumber separation between the asymmetric and symmetric stretching vibrations, $\Delta\nu_{as-s} = \nu_{as}(COO^-) - \nu_s(COO^-)$, of COO^- groups reflects their coordination state.[25] $\Delta\nu_{as-s} \gg 200$ cm^{-1} points to unidentate binding, and $\Delta\nu_{as-s} \approx 200$ cm^{-1} indicates binding by bridging. The symmetric vibration ν_s for the gel is at 1421.3 cm^{-1}. Thus, two wavenumber separations $\Delta\nu_{as-s}$, 1746.2−1420.6 and 1613.5−1420.6 cm^{-1}, suggested the coexistence of unidentate binding ($\Delta\nu_{as-s} \gg 200$ cm^{-1}) and bridging ($\Delta\nu_{as-s} \approx 200$ cm^{-1}) between COO^- and Fe^{3+} in the oxidized starch microspheres (illustrated in the left image of Figure 2). This explained the mechanism of the gel formation between the oxidized starch polymer and Fe^{3+}. It is consistent with the FTIR results of Fe^{3+} cross-linked oxidized konjac glucomannan microspheres.[23]

Figure 3A showed the particle size distribution for oxidized starch microspheres in pH 3 HCl solution, revealing a diameter

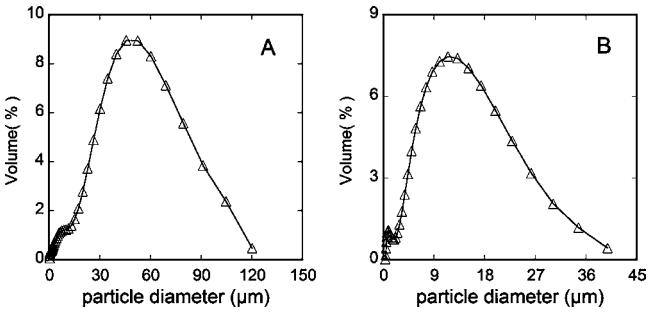

Figure 3. Size distribution of oxidized starch microspheres in (A) pH 3 HCl solution and (B) ethanol.

distribution between 10 and 90 μm, with an average of 39 μm. The size of microspheres in pH 3 HCl solution was slightly bigger than that at the dry state (SEM in Figure 1b) probably as a result of the swelling of microspheres in water. Figure 3B presented the size distribution of oxidized starch microspheres in ethanol, and it has an average size of 10.5 μm. The shrinkage of oxidized starch microspheres in ethanol was caused by the dehydration of oxidized starch polymers as a result of competitive binding of water by ethanol. It suggested that microspheres contained a large amount of water, and this swelling capacity may provide a large space for accommodating more bioactive ingredients.

The pH dependence of the ζ-potential of oxidized starch microspheres is shown in Figure 4A. The negative value of the ζ-potential increases with increasing pH. It approached a maximum near pH 5, where the dissociation of the carboxyl groups reached completion. An increasing salt concentration lowered the ζ potential of oxidized starch microspheres (Figure 4B), reaching a plateau value at 0.1 M NaCl. This is due to screening of the negative charges in the oxidized starch microspheres by counterions, i.e., Na^+. Apparently, charge screening reached a maximum at 0.1 M salt. This result is consistent with the salt dependence of oxidized starch microgel made of trimetaphosphate cross-linked oxidized starch polymers.[15]

***In Vitro* Release Kinetics of Encapsulated Ingredients from Oxidized Starch Microspheres in Simulated Gastrointestinal Fluids.** The *in vitro* release experiment under simulated gastrointestinal conditions is an important indication for their behavior in a physiological environment. The *in vitro* release of β-carotene from oxidized starch microspheres was studied under simulated gastric and intestinal fluids. Inset microscopic images of Figure 5A showed that the structure of microspheres remained intact when incubated in simulated gastric fluid for 120 min. Around 10% of β-carotene was released from oxidized starch microspheres after 120 min. According to the literature, the degradation of β-carotene in nanoemulsion is faster at an acidic pH value, such as gastric pH (pH < 2).[26,27] Therefore, a carrier system is needed to prevent the early release of β-carotene under gastric pH. Obviously, the oxidized starch microspheres were largely protected from acid degradation, so that β-carotene remained stable in microspheres. Then, β-carotene-containing microspheres were transferred to simulated intestinal fluid (pH 7.0) to continue their release. At intestinal conditions, oxidized starch microspheres will be dissociated gradually because the cross-linker Fe^{3+} may react with OH^- at pH 7. The degradation of microspheres led to a release of the encapsulated drugs from the spheres into the intestine. As shown in Figure 5B, about 83% of β-carotene was released after 180 min in simulated intestinal fluid. It has been reported that the absorption and metabolism of β-carotene mainly occur in the small intestine.[1,28,29] It is desirable to have a

DOI: 10.1021/acs.jafc.5b03575
J. Agric. Food Chem. 2015, 63, 8669−8675

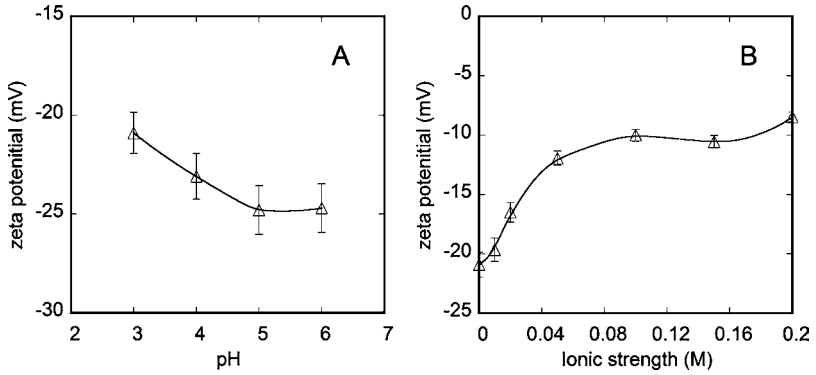

Figure 4. (A) ζ-Potential of oxidized starch microspheres as a function of pH, with no salt added, and (B) as a function of the ionic strength at pH 3.

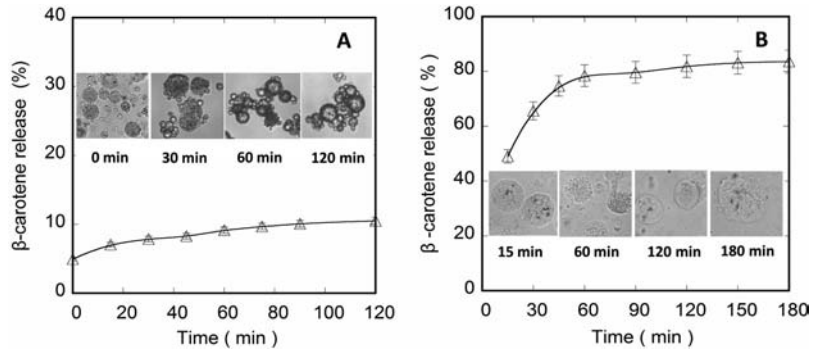

Figure 5. (A) *In vitro* release kinetics of *β*-carotene from oxidized starch microspheres during incubation in simulated gastric fluid. The inset microscopic images represented loaded microspheres incubated at times 0, 30, 60, and 120 min. (B) *In vitro* release kinetics of *β*-carotene from oxidized starch microspheres during incubation in simulated intestinal fluid. The inset microscopic images represented loaded microspheres incubated at times 15, 60, 120, and 180 min.

slow release at gastric conditions for the oral delivery system, because the gastric degradation of encapsulated carotenoids can be reduced, so that the active molecules available for absorption in the intestine can be increased. These results indicated that oxidized starch microspheres can potentially be used in targeted simultaneous delivery of hydrophobic drugs to the intestine. Yi et al. have reported a *β*-carotene nanocarrier made of *β*-lactoglobulin−dextran Maillard conjugates.[30] Their *in vitro* release experiments showed that *β*-carotene was protected at acidic gastric conditions and released at intestinal conditions. They explained that their particles were more accessible to trypsin at intestinal conditions rather than pepsin at stomach conditions. Later, they found that encapsulated *β*-carotene had a high transport rate through a Caco-2 cell monolayer. They concluded that the bioavailability of *β*-carotene was improved by nanoparticle encapsulation. Tan et al. also found that the release of *β*-carotene from liposomes was inhibited in a simulated gastric fluid, while a slow and sustained release was achieved in a simulated intestinal fluid. They explained that the liposomes were disrupted under intestinal conditions by penetration of bile salts and pancreatin, leading to the release of encapsulated *β*-carotene.[9] However, the heat stability of above-mentioned *β*-lactoglobulin−dextran nanoparticles may be low as a result of the protein presented. The high tendency of oxidation of liposome may cause uncontrolled leakage of the encapsulated ingredients. Therefore, the carrier system made of polysaccharides may have advantages over proteins and lipids on this point.

Enhancement of Antioxidant Activity against Heat and Storage Stability of *β*-carotene in Oxidized Starch Microspheres.

It is well-known that *β*-carotene is sensitive to heat.[26,27] Encapsulation in oxidized starch microspheres may protect them from degradation by heat. To study the stabilizing effect of *β*-carotene in oxidized starch microspheres, antioxidant activity (eq 1), i.e., scavenging DPPH radicals, of *β*-carotene-loaded oxidized microspheres and individual components were measured during continuous heating at 80 °C. Figure 6 showed

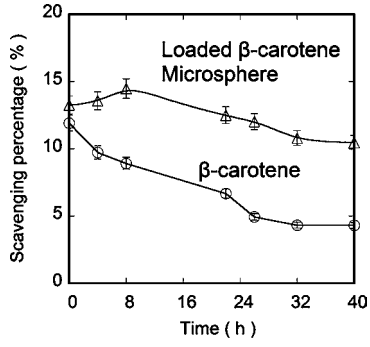

Figure 6. DPPH scavenging percentage (%) for oxidized starch microspheres that encapsulated *β*-carotene and free *β*-carotene after a continuous heating at 80 °C.

that the loaded microspheres exhibited a stronger antioxidant activity than those of individual *β*-carotene upon prolonged heating at 80 °C. It suggested that the stability of *β*-carotene against heat was improved by encapsulation inside oxidized starch microspheres. Recent studies suggested that antioxidant activity of *β*-carotene was improved when loaded it in chitosan-

DOI: 10.1021/acs.jafc.5b03575
J. Agric. Food Chem. 2015, 63, 8669−8675

graft-poly(lactide) nanomicelles.[31] Besides, β-carotene can be self-assembled into the core of casein micelles, which improved their heat stability during processing.[10,11] It can be seen that microencapsulation is an effective way to protect heat-sensitive bioactives during processing and storage. It already proved that the structure of oxidized starch microspheres was stable against heat and acid. It can be a good candidate for β-carotene stabilization against hazard conditions, such as acid and heat.

In addition to the damage of β-carotene under heat, it may also suffer from light and oxygen oxidation during storage. Therefore, the storage stability of β-carotene-loaded oxidized starch microspheres was investigated. The residual rate C_t/C_0 (β-carotene concentration after storage for a period time C_t/the initial concentration C_0) was measured daily for 10 days at room temperature (Figure 7). Both encapsulated and non-

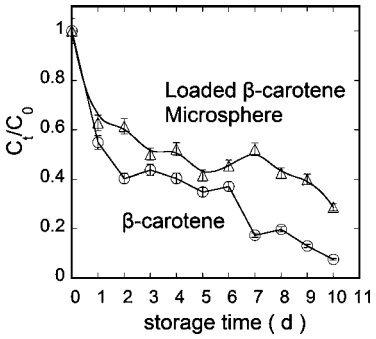

Figure 7. Residual rate C_t/C_0 of β-carotene for oxidized starch microspheres that encapsulated β-carotene and free β-carotene stored at ambient temperature for a prolonged 10 days.

encapsulated β-carotene have a decreasing trend. However, the residual rate for encapsulated β-carotene was around 30%, and that for non-encapsulated β-carotene approached 0%. It seems that, without any protection, β-carotene was totally destroyed after 10 days of storage. It showed that encapsulation by oxidized starch microspheres had delayed the β-carotene degradation. It indicates that the oxidized starch microspheres are able to protect β-carotene during storage to some extent. However, cross-linker Fe^{3+} of the microspheres may undergo light reduction, which may cause the disruption of the microsphere network, leading to a weakened stabilizing effect. Chen et al. had reported that the storage stability of β-carotene at 37 °C was improved by inclusion inside ferritin nanocages.[8] However, the heat stability of ferritin protein still needs to be a concern. Spada et al. have reported that the storage stability of encapsulated β-carotene by hydrolyzed pinhão starches after freeze-drying was improved under ultraviolet light at 25 °C and under dark at 25 and 4 °C. They postulated that the high content of amylose in pinhão starches may form a network by hydrogen bonds, which can entrap and protect β-carotene from degradation.[32] The starch network in our case may function in a similar way. It was also reported that the degradation of β-carotene in microemulsions formulated with peppermint oil was inhibited undergoing ultraviolet radiation and thermal treatments at 60 and 80 °C.[33] They explained that antioxidants in peppermint oil may play an important role against oxidative and thermal degradation. Similarly, the stabilizing effect of our oxidized starch microspheres may be improved by replacing the inner oil phase soybean oil with the oil rich in antioxidants.

In this study, oxidized starch microspheres for releasing β-carotene to intestine and improving their thermal and storage stabilities were developed. It is based on TEMPO-oxidized starch, a carboxyl polysaccharide, which can be cross-linked by Fe^{3+} ions, leading to an oil-in-water (O/W) polymer network formation that is able to simultaneously incorporate hydrophobic components. The oxidized starch microspheres were found to be stable at acidic stomach conditions (pH < 2), whereas at neutral intestinal conditions (pH 7.0), they disrupt to release loaded β-carotene. The results showed that β-carotene-loaded starch microspheres possessed an improved antioxidant activity against heat and enhanced storage stability. Thus, oxidized starch microspheres showed a potential in delivering the hydrophobic bioactives to the specific sites with an enhanced stability.

AUTHOR INFORMATION

Corresponding Author

*Telephone: +86-10-64447747. Fax: +86-10-64416428. E-mail: liyuan@mail.buct.edu.cn.

Author Contributions

†Shanshan Wang and Yuying Chen contributed equally to this work.

Funding

The financial support of the National Natural Science Foundation of China (NSFC, 31201334 and 31471577), the Fundamental Research Funds for the Central Universities (ZZ1404, ZY1329, and YS1407), and the Scientific Research Foundation for the Returned Overseas Chinese Scholars, State Education Ministry (LXJJ201304), is gratefully acknowledged.

Notes

The authors declare no competing financial interest.

ABBREVIATIONS USED

TEMPO, 2,2,6,6-tetramethyl-1-piperidinyloxy; WPI, whey protein isolate; DPPH, 1,1-diphenyl-2-picrylhydrazyl radical, 2,2-diphenyl-1-(2,4,6-trinitriphenyl); CLSM, confocal laser scanning microscopy

REFERENCES

(1) Failla, M. L.; Huo, T.; Thakkar, S. K. In vitro screening of relative bioaccessibility of carotenoids from foods. *Asia Pac. J. Clin. Nutr.* **2008**, *17*, 200−203.

(2) Delgado-Vargas, F.; Jimenez, A. R.; Paredes-Lopez, O. Natural pigments: carotenoids, anthocyanins, and betalains−characteristics, biosynthesis, processing, and stability. *Crit. Rev. Food Sci. Nutr.* **2000**, *40*, 173−289.

(3) Nishino, H.; Tokuda, H.; Murakoshi, M.; Satomi, Y.; Masuda, M.; Onozuka, M.; Yamaguchi, S.; Takayasu, J.; Tsuruta, J.; Okuda, M.; Khachik, F.; Narisawa, T.; Takasuka, N.; Yano, M. Cancer prevention by natural carotenoids. *BioFactors* **2000**, *13*, 89−94.

(4) Hennekens, C. H.; Buring, J. E.; Manson, J. E.; Stampfer, M.; Rosner, B.; Cook, N. R.; Belanger, C.; LaMotte, F.; Gaziano, J. M.; Ridker, P. M.; Willett, W.; Peto, R. Lack of effect of long-term supplementation with beta carotene on the incidence of malignant neoplasms and cardiovascular disease. *N. Engl. J. Med.* **1996**, *334*, 1145−9.

(5) Tapiero, H.; Townsend, D. M.; Tew, K. D. The role of carotenoids in the prevention of human pathologies. *Biomed. Pharmacother.* **2004**, *58*, 100−110.

(6) Boon, C. S.; McClements, D. J.; Weiss, J.; Decker, E. A. Factors Influencing the Chemical Stability of Carotenoids in Foods. *Crit. Rev. Food Sci. Nutr.* **2010**, *50*, 515−532.

(7) Mensi, A.; Choiset, Y.; Haertlé, T.; Reboul, E.; Borel, P.; Guyon, C.; de Lamballerie, M.; Chobert, J. M. Interlocking of b-carotene in

DOI: 10.1021/acs.jafc.5b03575
J. Agric. Food Chem. 2015, 63, 8669−8675

beta-lactoglobulin aggregates produced under high pressure. *Food Chem.* **2013**, *139*, 253−260.
(8) Chen, L.; Bai, G.; Yang, R.; Zang, J.; Zhou, T.; Zhao, G. Encapsulation of beta-carotene within ferritin nanocages greatly increases its water-solubility and thermal stability. *Food Chem.* **2014**, *149*, 307−12.
(9) Tan, C.; Xue, J.; Abbas, S.; Feng, B.; Zhang, X.; Xia, S. Liposome as a delivery system for carotenoids: comparative antioxidant activity of carotenoids as measured by ferric reducing antioxidant power, DPPH assay and lipid peroxidation. *J. Agric. Food Chem.* **2014**, *62*, 6726−35.
(10) Saiz-Abajo, M. J.; Gonzalez-Ferrero, C.; Moreno-Ruiz, A.; Romo-Hualde, A.; Gonzalez-Navarro, C. J. Thermal protection of beta-carotene in re-assembled casein micelles during different processing technologies applied in food industry. *Food Chem.* **2013**, *138*, 1581−7.
(11) Ge, W.; Li, D.; Chen, M.; Wang, X.; Liu, S.; Sun, R. Characterization and antioxidant activity of beta-carotene loaded chitosan-graft-poly(lactide) nanomicelles. *Carbohydr. Polym.* **2015**, *117*, 169−76.
(12) Lu, D. R.; Xiao, C. M.; Xu, S. J. Starch-based completely biodegradable polymer materials. *eXPRESS Polym. Lett.* **2009**, *3*, 366−375.
(13) Qi, Z. Starch-based ingredients for flavor encapsulation starch. *Cereal Foods World* **1999**, *44*, 460−466.
(14) de Nooy, A. E. J.; Besemer, A. C.; Vanbekkum, H. Highly selective tempo mediated oxidation of primary alcohol groups in polysaccharides. *Recl. Trav. Chim. Pays-Bas* **1994**, *113*, 165−166.
(15) Li, Y.; de Vries, R.; Slaghek, T.; Timmermans, J.; Cohen Stuart, M. A.; Norde, W. Preparation and characterization of oxidized starch polymer microgels for encapsulation and controlled release of functional ingredients. *Biomacromolecules* **2009**, *10*, 1931−1938.
(16) Li, Y.; de Vries, R.; Kleijn, M.; Slaghek, T.; Timmermans, J.; Stuart, M. C.; Norde, W. Lysozyme uptake by oxidized starch polymer microgels. *Biomacromolecules* **2010**, *11*, 1754−1762.
(17) Li, Y.; Kadam, S.; Abee, T.; Slaghek, T. M.; Timmermans, J. W.; Cohen Stuart, M. A.; Norde, W.; Kleijn, M. J. Antimicrobial lysozyme-containing starch microgel to target and inhibit amylase-producing microorganisms. *Food Hydrocolloids* **2012**, *28*, 28−35.
(18) Wang, Z. R.; Li, Y.; Chen, L.; Xin, X. L.; Yuan, Q. P. A study of controlled uptake and release of anthocyanins by oxidized starch microgels. *J. Agric. Food Chem.* **2013**, *61*, 5880−5887.
(19) Wang, S. S.; Chen, X. D.; Shi, M. X.; Zhao, L. H.; Li, W.; Chen, Y. Y.; Lu, M. L.; Wu, J. D.; Yuan, Q. P.; Li, Y. Absorption of whey protein isolated (WPI)-stabilized β-Carotene emulsions by oppositely charged oxidized starch microgels. *Food Res. Int.* **2015**, *67*, 315−322.
(20) Cho, A. R.; Chun, Y. G.; Kim, B. K.; Park, D. J. Preparation of alginate-CaCl2 microspheres as resveratrol carriers. *J. Mater. Sci.* **2014**, *49*, 4612−4619.
(21) Peng, F.; Li, G. Z.; Liu, X. X.; Wu, S. Z.; Tong, Z. Redox-responsive gel-sol/sol-gel transition in poly(acrylic acid) aqueous solution containing Fe(III) Ions switched by light. *J. Am. Chem. Soc.* **2008**, *130*, 16166−16167.
(22) Wang, B.; Liao, L.; Huang, Q.; Cheng, Y. Adsorption behaviors of benzonic acid by carboxyl methyl konjac glucomannan gel micropheres cross-linked with Fe3+. *J. Chem. Eng. Data* **2012**, *57*, 72−77.
(23) Chen, X. D.; Wang, S. S.; Lu, M. L.; Chen, Y. Y.; Zhao, L. H.; Li, W.; Yuan, Q. P.; Norde, W.; Li, Y. Formation and characterization of light-responsive TEMPO-oxidized konjac glucomannan microspheres. *Biomacromolecules* **2014**, *15*, 2166−71.
(24) Benichou, A.; Aserin, A.; Garti, N. O/W/O double emulsions stabilized with WPI−polysaccharide conjugates. *Colloids Surf., A* **2007**, *297*, 211−220.
(25) Lan, Y.; Xu, L.; Yan, Y.; Huang, J.; de Keizer, A.; Besseling, N. A. M.; Cohen Stuart, M. A. Promoted formation of coordination polyelectrolytes by layer-by-layer assembly. *Soft Matter* **2011**, *7*, 3565−3570.
(26) Qian, C.; Decker, E. A.; Xiao, H.; McClements, D. J. Physical and chemical stability of beta-carotene-enriched nanoemulsions: Influence of pH, ionic strength, temperature, and emulsifier type. *Food Chem.* **2012**, *132*, 1221−1229.
(27) Xu, D.; Wang, X.; Jiang, J.; Yuan, F.; Decker, E. A.; Gao, Y. Influence of pH, EDTA, alpha-tocopherol, and WPI oxidation on the degradation of beta-carotene in WPI-stabilized oil-in-water emulsions. *Food Sci. Technol.* **2013**, *54*, 236−241.
(28) Salvia-Trujillo, L.; Qian, C.; Martin-Belloso, O.; McClements, D. J. Influence of particle size on lipid digestion and beta-carotene bioaccessibility in emulsions and nanoemulsions. *Food Chem.* **2013**, *141*, 1472−1480.
(29) During, A.; Harrison, E. H. An in vitro model to study the intestinal absorption of carotenoids. *Food Res. Int.* **2005**, *38*, 1001−1008.
(30) Yi, J.; Lam, T. I.; Yokoyama, W.; Cheng, L. W.; Zhong, F. Controlled Release of beta-Carotene in beta-Lactoglobulin-Dextran-Conjugated Nanoparticles' in Vitro Digestion and Transport with Caco-2 Monolayers. *J. Agric. Food Chem.* **2014**, *62*, 8900−8907.
(31) Ge, W.; Li, D.; Chen, M.; Wang, X.; Liu, S.; Sun, R. Characterization and antioxidant activity of beta-carotene loaded chitosan-graft-poly(lactide) nanomicelles. *Carbohydr. Polym.* **2015**, *117*, 169−176.
(32) Spada, J. C.; Noreña, C. P. Z.; Marczak, L. D. F.; Tessaro, I. C. Study on the stability of β-carotene microencapsulated with pinhão (Araucaria angustifolia seeds) starch. *Carbohydr. Polym.* **2012**, *89*, 1166−1173.
(33) Chen, H.; Zhong, Q. Thermal and UV stability of beta-carotene dissolved in peppermint oil microemulsified by sunflower lecithin and Tween 20 blend. *Food Chem.* **2015**, *174*, 630−636.

DOI: 10.1021/acs.jafc.5b03575
J. Agric. Food Chem. 2015, 63, 8669−8675

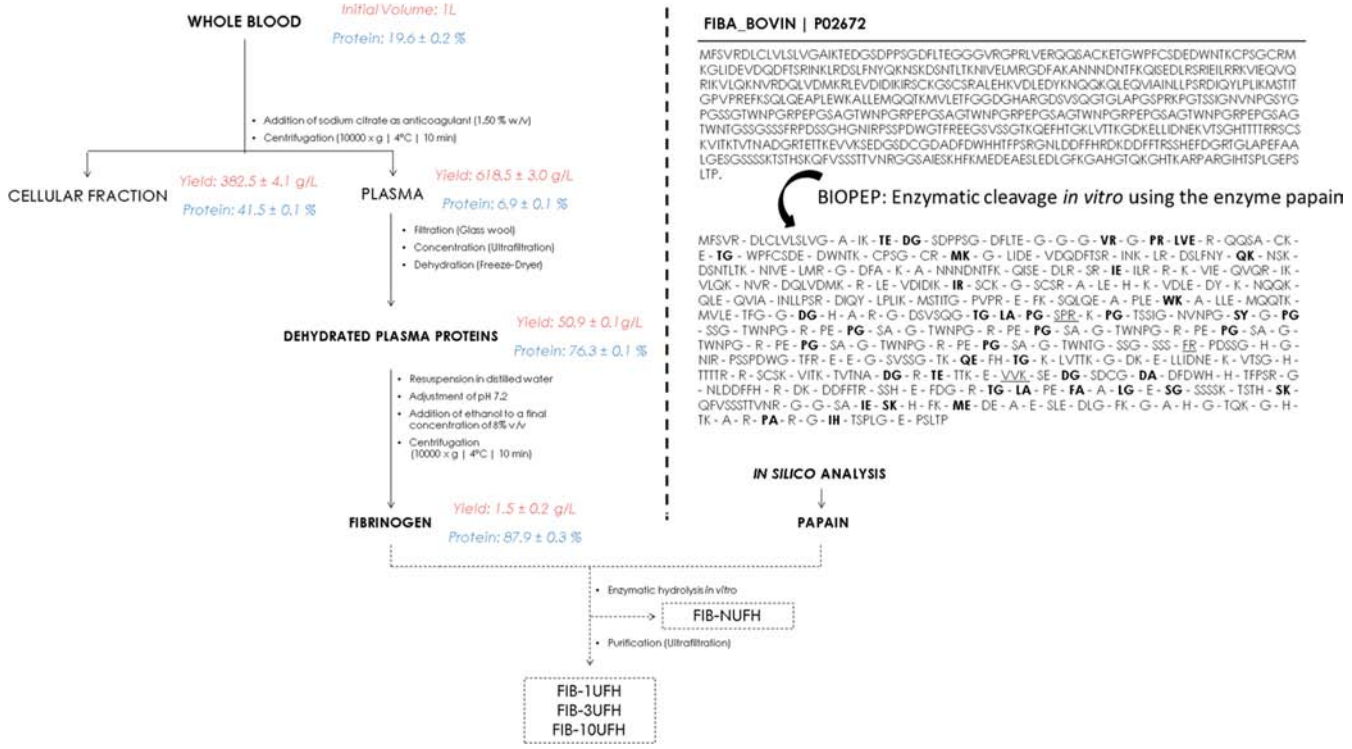

Figure 1. Schematic representation of the procedure followed for the generation of bioactive peptides from bovine fibrinogen. Blood plasma was separated from the cellular fraction by centrifugation at 10000*g* for 10 min. Plasma was frozen and freeze-dried. A protein fraction rich in fibrinogen was obtained by cold ethanol precipitation, frozen, and freeze-dried. In silico analysis was used for enzyme selection. Papain was chosen as the most efficient enzyme for the generation of a hydrolysate with ACE-I-, renin-, and DPP-I-inhibiting properties. Di- and tripeptides in bold are known ACE-I, renin, or DPP-IV inhibitors available in BIOPEP. Bovine fibrinogen was hydrolyzed using papain, and four fractions were generated by ultrafiltration: FIB-NUFH, FIB-1UFH, FIB-3UFH, and FIB-10UFH.

following this process. Selected peptides were chemically synthesized for in vitro confirmation of their renin and ACE-I inhibitory activities. Moreover, the concentration of peptide required to inhibit the activity of ACE-I and renin by half (IC_{50}) was calculated for identified active renin and ACE-I inhibitory peptides, and their resistance to gastrointestinal digestion and bitter taste were predicted using in silico analysis.

MATERIALS AND METHODS

Materials and Reagents. Formic acid (FA), glycerol, tricine, dithiothreitol, ethanol, dimethyl sulfoxide (DMSO), acetonitrile (ACN), sodium citrate, papain from *Carica papaya*, the specific renin inhibitor Z-Arg-Arg-Pro-Phe-His-Sta-Ile-His-Lys-(Boc)-OMe, and the ACE-I inhibitor captopril were supplied by Sigma-Aldrich (Dublin, Ireland). The DPP-IV inhibitor screening assay kit, containing the DPP-IV inhibitor and positive control sitagliptin, and the renin inhibitor screening assay kit were supplied by Cambridge BioSciences (Cambridge, UK). The ACE-I inhibition assay kit was supplied by NBS Biologicals Ltd. (Cambridgeshire, UK). Tris-Tricine 10−20% SDS gels, sodium dodecyl sulfate (SDS), Coomassie Blue G-250, Coomassie Brilliant Blue R-250 destaining solution, and the Bio-Safe Coomassie Blue G-250 stain were purchased from Fischer Scientific (Dublin, Ireland). All other chemicals used were of analytical grade.

Blood Collection and Fractionation Procedure. Whole bovine blood was collected at time of slaughter under hygienic conditions in the abattoir at the Teagasc Food Research Centre, Ashtown, Dublin 15, Ireland. All animals slaughtered were female, Charolais cross heifer breed and were aged between 23 and 24 months. Sodium citrate solution was used as an anticoagulant and was added immediately to blood following collection at a final concentration of 1.5% (w/v). Blood was chilled to 4 °C and handled carefully to minimize hemolysis.

Whole blood cells were separated from plasma by centrifugation at 4 °C and 10000*g* for 10 min using a Sigma 6K10 centrifuge (Sigma Laborzentrifugen GmbH, Osterode am Harz, Germany). Plasma was kept at 4 °C, filtered through glass wool, and freeze-dried using an industrial scale freeze-drier, FD 80 model (Cuddon Engineering, Marlborough, New Zealand). The temperature was maintained at <35 °C during the freeze-drying process. A fibrinogen-rich protein fraction was obtained from the freeze-dried extract by precipitation following a previously described method.[13] Briefly, dehydrated plasma proteins were resuspended in Milli-Q water to a final concentration of 35 g/L, the pH was adjusted using 0.1 M HCl, and ethanol was added as the fractionation agent. A protein fraction rich in fibrinogen was obtained by precipitation after the addition of ethanol to plasma at a final concentration of 8% (v/v) and adjustment of the pH to 7.2. Ethanol was added drop by drop, and the process was carried out at temperatures close to 0 °C to minimize protein denaturation. Fibrinogen was separated by centrifugation at 4 °C and 10000*g* for 5 min, resuspended in water, frozen, and freeze-dried.

The total protein content was determined using a LECO FP628 Protein analyzer (LECO Corp., St. Joseph, MI, USA) based on the Dumas method and according to AOAC method 992.15, 1990. The conversion factor of 6.25 was used to convert total nitrogen to protein. The total protein content was calculated as shown in Figure 1.

In Silico Analysis. The amino acid sequence of bovine fibrinogen (UniProt ID: FIBA_BOVIN | UniProt AC: P02672; UniProt ID: FIBB_BOVIN | UniProt AC: P02676 and UniProt ID: FIBG_BOVIN | UniProt AC: P12799) was accessed from the UniProt database, available at http://www.uniprot.org/. The predicted cleavage sites of fibrinogen using the enzymes papain, pepsin (EC 3.4.23.1), trypsin (EC 3.4.21.4), bromelain (EC 3.4.22.4), ficain (EC 3.4.22.3), and thermolysin (EC 3.4.24.27) were calculated using BIOPEP, available at http://www.uwm.edu.pl/biochemia/index.php/pl/biopep.[14] These

DOI: 10.1021/acs.jafc.5b03167
J. Agric. Food Chem. 2015, 63, 8676−8684

enzymes were selected on the basis of the availability of cleavage information and their documented ease of use in the meat industry and in previous hydrolysis studies. The database BIOPEP was also used to compare the peptides generated in silico and the peptides identified by de novo peptide sequencing with previously reported ACE-I-, DPP-IV-, and renin-inhibiting bioactive peptides. PeptideRanker, available at http://bioware.ucd.ie, was used to predict peptides with bioactivities.[15]

Computer simulations of proteolysis were used to study the bioavailability of selected peptides after simulated gastrointestinal digestion using ExPASy PeptideCutter, available at http://web.expasy.org/peptide_cutter/, and gastrointestinal enzymes including pepsin (pH 1.3 and pH >2), trypsin (EC 3.4.21.4) and chymotrypsin (EC 3.4.21.1). The bitterness of the synthesized peptides was predicted using the "Q rule" in accordance with a previously published method.

Enzymatic Hydrolysis. Papain hydrolysates of the bovine fibrinogen enriched fraction were prepared in triplicate using a BioFlo 110 Modular Benchtop Fermentor (New Brunswick Scientific Co., Cambridge, UK) with agitation, temperature, and pH control. A substrate solution was prepared by resuspending the dried bovine fibrinogen in Milli-Q purified water at a concentration of 10 g/L at a total volume of 500 mL. Agitation, temperature, and pH conditions were adjusted to 350 rpm, 65 °C, and 6.5, respectively. The pH was kept constant using 0.1 M NaOH. Once the optimum pH and temperature conditions were achieved, the enzyme papain (activity ≥ 3 U/mg) was added in a substrate to enzyme ratio of 100:1 (w/w). After 24 h, papain was heat-deactivated at 95 °C for 10 min in a Grant JB Aqua 12 water bath (Grant Instruments, Cambridge, UK).

The non-ultrafiltered hydrolysate and the 1, 3, and 10 kDa permeate fractions obtained using MWCO membranes (Millipore, Tullagreen, Carrigtwohill, Co. Cork, Ireland) were labeled FIB-NUFH, FIB-1UFH, FIB-3UFH, and FIB-10UFH, respectively. All fractions were frozen, freeze-dried, and stored at −20 °C until further use.

Electrophoretic Separation Using Tris-Tricine Peptide Gels. Electrophoresis was carried out using a Bio-Rad Mini-PROTEAN 3 cell System (Bio-Rad Laboratories Ltd., Hertfordshire, UK) and a 10-well Mini-PROTEAN Tris-Tricine gel according to the manufacturer's instructions. Commercial low (1.7−42 kDa in size) and high (2−250 kDa in size) molecular weight (MW) markers were used.

Renin Inhibition Assay. This assay was carried out following a previously described method using a renin inhibitor screening assay kit in accordance with the manufacturer's instructions.[5] All fractions were assayed at a concentration of 1 mg sample/mL DMSO in triplicate and standard deviations (SD) calculated. Fluorescence intensity was recorded with a FLUOstar Omega microplate reader (BMG LABTECH GmbH, Offenburg, Germany) using an excitation wavelength of 340 nm and an emission wavelength of 500 nm. The known renin inhibitor Z-Arg-Arg-Pro-Phe-His-Sta-Ile-His-Lys-(Boc)-OMe was used as a positive control, and renin IC_{50} values were determined in triplicate for active peptides and hydrolysates by plotting the percentage of renin inhibition as a function of the concentration of test compound.

ACE-I Inhibition Assay. This assay was carried out following a previously described method using an ACE-I inhibitor assay kit and in accordance with the manufacturer's instructions.[5] All fractions were assayed at a concentration of 1 mg/mL HPLC grade water in triplicate, and means and SD were calculated. The known ACE-I inhibitor captopril was used as a positive control at a concentration of 1 mg/mL. Absorbance was measured with a FLUOstar Omega microplate reader (BMG LABTECH GmbH) at 450 nm. ACE-I IC_{50} values were determined for active hydrolysates and peptides by plotting the percentage of inhibition as a function of the concentration of test compound.

DPP-IV Inhibition Assay. This assay was carried out following a previously described method using a DPP-IV inhibitor screening assay kit and in accordance with the manufacturer's instructions.[5] All hydrolysates were assayed in triplicate, and means and SD were calculated. The known DPP-IV inhibitor sitagliptin was used as a positive control. Fluorescence intensity was recorded with a FLUOstar Omega microplate reader (BMG LABTECH GmbH) using an excitation wavelength of 355 nm and an emission wavelength of 460 nm. DPP-IV IC_{50} values were determined for active hydrolysates by plotting the percentage of inhibition as a function of the concentration of test compound.

De Novo Peptide Sequencing. The FIB-1UFH fraction of the papain hydrolysate of bovine fibrinogen was resuspended in HPLC grade water at a concentration of 1 mg/mL and filtered through a 0.45 μm CHROMAFIL Xtra PVDF-45/25 syringe filter (Macherey-Nagel GmbH & Co., Düren, Germany). The filtered hydrolysate was analyzed using a Q-TOF Premier mass spectrometer (Waters Corp., Milford, MA, USA), coupled to an Alliance 2695 HPLC system (Waters Corp.). The chromatographic separation was carried out at a flow rate of 0.2 mL/min with an injection volume of 10 μL on an Atlantis dC18 column, 100 mm × 2.1 mm, 3 μm particle size (Waters Corp.). Peptides were separated using 0.1% FA in HPLC grade water (solvent A) and 0.1% FA in ACN (solvent B). Column temperature was maintained at 40 °C. The gradient program was as follows: (i) 0 min, 98% A; (ii) 0−0.1 min, 98% A; (iii) 0.1−18 min, 90% A; (iv) 18−20 min, 85% A; (v) 20−21 min, 40% A; (vi) 21−22 min, 20% A; (vii) 22−25 min, 98% A; and (viii) 25−30 min, 98% A. HPLC-MS/MS was performed using a data-dependent acquisition (DDA) on electrospray ionization (ESI) in positive ion mode at 1 s scan. Argon was used as collision gas with the collision energy ramp from 15 eV for low MW peptides to 60 eV for high MW peptides. The tandem mass spectrometry (MS/MS) spectral data were deconvoluted using the MaxEnt 3 algorithm, and their amino acid sequences were determined using the peptide sequencing software available in the Waters Biolynx software package.

Chemical Synthesis. Peptides were synthesized by microwave-assisted solid phase peptide synthesis (MW-SPPS) performed on a Liberty CEM microwave peptide synthesizer (Mathews, NC, USA). Peptides were synthesized on H-Ala-HMPB-ChemMatrix and H-Ile-HMPB-ChemMatrix resins (PCAS Biomatrix Inc., Quebec, Canada) and purified using RP-HPLC on a Semi Preparative Jupiter Proteo (4u, 90A) column (Phenomenex, Cheshire, UK). Fractions containing the desired molecular mass were identified using matrix-assisted laser desorption ionization time-of-flight mass spectrometry (MALDI-TOF-MS) and were pooled and freeze-dried on a Genevac HT 4X lyophilizer (Genevac Ltd., Ipswich, UK).

Statistical Analysis. All tests were replicated three times, and mean values and SD were calculated. ANOVA one-way analysis was carried out using Minitab v17 (Minitab Ltd., UK). When significant differences were present, a Tukey pairwise comparison of the means was conducted to identify where the sample differences occurred.

RESULTS AND DISCUSSION

In Silico Analysis. In silico analysis was previously shown to be an efficient method to predict the release of bioactive peptides with prolyl endopeptidase- (PEP; EC 3.4.21.26), ACE-I-, and DPP-IV-inhibiting properties.[5−7,16] In this work, a bovine fibrinogen enriched protein fraction was generated and hydrolyzed using papain to generate bioactive peptides with ACE-I, renin, and DPP-IV inhibitory activities. Bovine fibrinogen is composed of two sets of disulfide-bridged α-, β-, and γ-chains.[17] The amino acid sequences of bovine fibrinogen α-, β-, and γ-chains were accessed from the UniProt database. In silico analysis was carried out using BIOPEP to select a suitable enzyme to generate a hydrolysate rich in bioactive peptides with potential to inhibit ACE-I, renin, and DPP-IV (Figure 1). A number of enzymes including papain, pepsin, trypsin, ficain, bromelain, and thermolysin were trialled using in silico analysis to generate peptides from bovine fibrinogen. Table 1 describes the number of known ACE-I-, renin-, and DPP-IV-inhibiting peptides, available in BIOPEP, which were generated in this study from bovine fibrinogen using selected enzymes in silico. Few renin inhibitory peptides were predicted to be released from bovine fibrinogen by in silico cleavage

DOI: 10.1021/acs.jafc.5b03167
J. Agric. Food Chem. 2015, 63, 8676−8684

Table 1. Number of ACE-I, Renin, and DPP-IV Inhibitory Sequences Found within Bovine Fibrinogen after in Silico Hydrolysis with BIOPEP

enzyme used for in silico hydrolysis	no. of known bioactive peptides		
	ACE-I inhibitors[a]	renin inhibitors[a]	DPP-IV inhibitors[a]
papain (EC 3.4.22.2)	72	3	48
pepsin (EC 3.4.23.1)	3	0	8
trypsin (EC 3.4.21.4)	5	2	4
bromelain (EC 3.4.22.4)	45	0	22
thermolysin (EC 3.4.24.27)	28	1	22
ficain (EC 3.4.22.3)	58	0	61

[a]Data accessed from BIOPEP, available at http://www.uwm.edu.pl/biochemia/index.php/pl/biopep on April 2015.

compared to ACE-I and DPP-IV inhibitory peptides. This may be due to the limited reports that exist regarding the generation of renin inhibitors from natural sources. Renin and DPP-IV inhibitory peptides generated in silico include the peptides IR and FA, corresponding to $f(180-181)$ and $f(533-534)$ of the α-chain of bovine fibrinogen. The peptide FA was previously reported to inhibit DPP-IV,[18] and the peptide IR was previously generated from pea protein and was reported to have a renin IC_{50} value of 9.2 ± 0.2 mM.[19] Papain was the enzyme selected for use in vitro in this study. Papain was used previously to generate ACE-I and renin inhibitors as well as antioxidant peptides from seaweed as well as bovine proteins.[20,21] Moreover, papain was found to generate the largest number of known ACE-I- and renin-inhibiting peptides from fibrinogen. In addition, application of papain to bovine fibrinogen generated 48 DPP-IV-inhibiting peptides. This compared favorably to the enzymes pepsin, trypsin, bromelain,

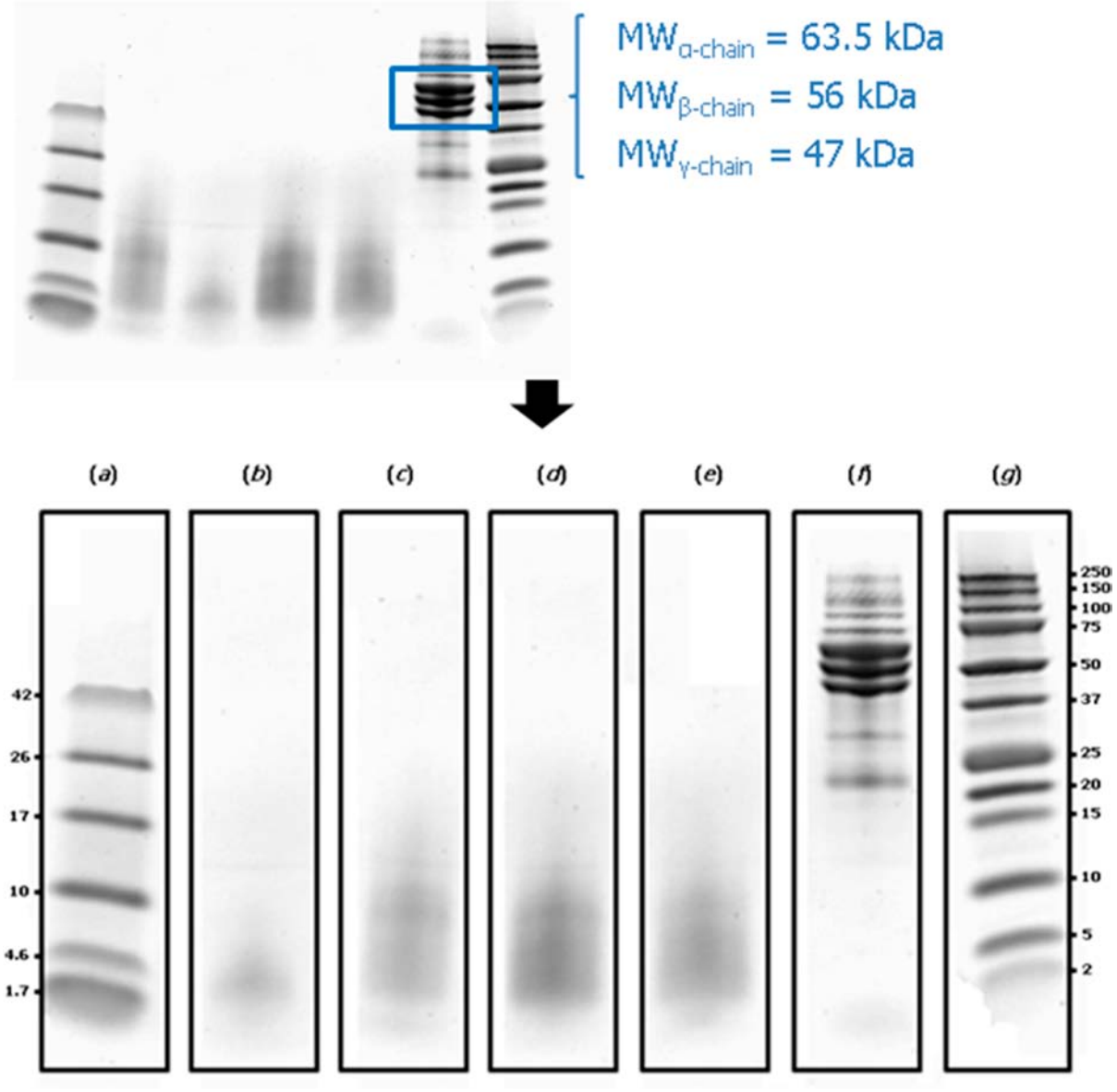

Figure 2. Tris-tricine peptide gel of the isolated fibrinogen protein and fractions generated by hydrolysis and ultrafiltration. Low and high MW markers are shown in columns (*a*) and (*g*), respectively. The isolated fibrinogen-rich fraction is shown in column (*f*). FIB-1UFH, FIB-3UFH, FIB-10UFH, and FIB-NUFH are shown in columns (*b*), (*c*), (*d*), and (*e*), respectively.

DOI: 10.1021/acs.jafc.5b03167
J. Agric. Food Chem. 2015, 63, 8676−8684

and thermolysin, which generated 8, 4, 22, and 22 DPP-IV inhibitory peptides, respectively, following in silico analysis (Table 1).

Generation of a Bovine Fibrinogen-Enriched Protein Fraction. Plasma constitutes approximately 65−70% of the total weight of blood and can be separated from the cellular fraction by centrifugation.[22] Yields for cellular and plasma fractions were calculated as 61.65 ± 0.31 and 38.35 ± 0.32% for the plasma and the cellular fraction, respectively. Moreover, the yield of the fibrinogen-rich fraction was found to be 1.5 ± 0.2 g/L. This fraction was analyzed by electrophoresis using a Tris-Tricine 10−20% peptide gel. Results, shown in Figure 2, suggest that although some impurities were present in the isolated fraction, fibrinogen was the main constituent with bands shown at 63.5 kDa (α-chain), 56 kDa (β-chain), and 47 kDa (γ-chain). In addition, the total protein content of the fibrinogen-rich fraction generated following the procedure described in Figure 1 was determined as 87.9 ± 0.3% using the LECO method. This value is comparable to the protein contents obtained in previous hydrolysis studies where high protein yields were obtained following hydrolysis of peanut.[23] In addition, the use of fibrinogen in combination with the enzyme thrombin was determined as safe for human consumption by the European Food Safety Authority (EFSA) in 2005.[24] Bovine blood proteins including hemoglobin and serum albumin have previously been used for the generation of bioactive proteins,[1,4] but to the best of our knowledge, no ACE-I, renin, or DPP-IV inhibitors have been generated from bovine fibrinogen to date. The identification of bioactive peptides within the sequence of bovine fibrinogen adds further value to this protein product. Electrophoresis results, shown in Figure 2, demonstrate that the generated fibrinogen protein fraction was hydrolyzed by papain and that the fractions generated by MWCO filtration consist mainly of peptides with MW <10 kDa. This is clear from the gel as the bands present at positions 63.5, 56, and 47 kDa no longer appear in the 10, 3, and 1 kDa fractions. Bands are shown in the low molecular weight range (1.7−10 kDa range).

ACE-I and Renin Inhibitory Activities in Vitro. The in vitro ACE-I and renin inhibitory activities of the generated hydrolysates were calculated and are shown in Figure 3. At a concentration of 1 mg/mL, fraction FIB-1UFH inhibited ACE-I by >50% compared to the positive control captopril, which had an ACE-I inhibitory activity of 88.10 ± 4.75%. The ACE-I IC_{50} values of FIB-NUFH, FIB-1UFH, FIB-3UFH, and FIB-10UFH were calculated and determined as 1.86 ± 0.12, 0.92 ± 0.08, 1.41 ± 0.09, and 1.55 ± 0.09 mg/mL, respectively. Ultrafiltration of FIB-NUFH led to increased ACE-I inhibitory activity, and the FIB-1UFH fraction had the lowest ACE-I IC_{50} value compared to the FIB-NUFH, FIB-10UFH, and FIB-3UFH fractions ($p < 0.05$). These results are consistent with the fact that peptidic ACE-I inhibitors usually consist of short amino acid sequences.[25] Results are comparable to inhibition values obtained for other protein hydrolysates, where sequential ultrafiltration of blood protein hydrolysates with 10, 3, and 1 kDa membranes resulted in increased ACE-I-inhibiting activity.[26]

Furthermore, the renin inhibitory activity of the generated hydrolysates was measured at a concentration of 1 mg/mL. Again, MWCO led to a significant increase in the renin-inhibiting activity of the FIB-1UFH fraction compared to the FIB-NUFH, FIB-10UFH, and FIB-3UFH fractions ($p < 0.05$). These results are consistent with the fact that dipeptides were

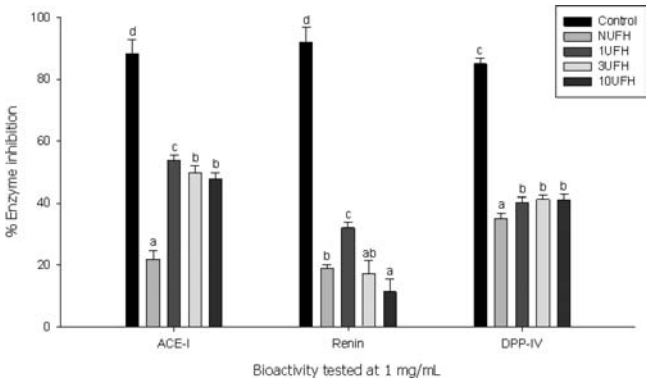

Figure 3. ACE-I-, renin-, and DPP-IV-inhibiting properties in vitro of studied papain hydrolysates and ACE-I, renin, and DPP-IV inhibitory bioactivities of papain hydrolysates of bovine fibrinogen when tested in vitro at a sample concentration of 1 mg/mL. Z-Arg-Arg-Pro-Phe-His-Sta-Ile-His-Lys-(Boc)-OMe, sitagliptin, and captopril were used as positive controls for renin, DPP-IV, and ACE-I, respectively. Enzyme inhibition is expressed as percent inhibition, and the values represent the means of three independent experiments ± SD. For each bioactivity tested, bars with different letters have mean values that are significantly different ($p < 0.05$).

previously suggested as the most effective for renin inhibition.[19] Furthermore, long peptides present within a hydrolysate can mask the activity of small active peptides. The activity of the FIB-10UFH fraction was lower than that of FIB-NUFH ($p < 0.05$). This may be due to the presence of one or more polypeptides with renin inhibitory properties within the FIB-NUFH fraction, as longer peptides such as IRLIIVLMPILMA have been reported to inhibit renin.[21] The fraction FIB-1UFH was the most active and inhibited renin by 32.09 ± 1.93%. This result concurs with previously reported research on flaxseed protein hydrolysates and renin inhibitory activities.[27] In this work, flaxseed was hydrolyzed with Thermoase and only a marginal improvement in renin inhibitory activity was observed for virtually all samples after membrane ultrafiltration.[27] No studies regarding the use of blood proteins for the generation of renin-inhibiting hydrolysates and peptides have been carried out to date.

In Vitro DPP-IV Inhibitory Activity. The in vitro DPP-IV inhibitory activity of the studied fractions was calculated, and results are shown in Figure 3. All studied fractions showed a moderate inhibition of DPP-IV. The most active fraction, FIB-3UFH, inhibited DPP-IV by 41.29 ± 1.17% when tested at a concentration of 1 mg/mL. The DPP-IV IC_{50} value of this fraction was calculated and was 1.03 ± 0.01 mg/mL. A slight increase in the DPP-IV-inhibiting activity of the ultrafiltered fractions compared to the nonultrafiltered fraction was observed ($p < 0.005$). The removal of higher MW fractions previously led to an increase in the DPP-IV inhibitory activity in vitro.[28] Moreover, most of the peptides with DPP-IV inhibitory activity described in the literature to date are between two and eight amino acid residues in length.[7] The DPP-IV-inhibiting activities of the papain hydrolysates generated in this study were comparable to those of other hydrolysates from natural sources. These include the trypsin hydrolysates of *Amaranthus hypochondriacus* L. proteins, with IC_{50} values ranging from 1.2 to 2.0 mg/mL, depending on the enzyme to substrate ratio,[28] and a Flavourzyme hydrolysate of Atlantic salmon gelatin with an IC_{50} value of 1.35 mg/mL.[29] The IC_{50} values obtained herein were also similar to those

DOI: 10.1021/acs.jafc.5b03167
J. Agric. Food Chem. 2015, 63, 8676−8684

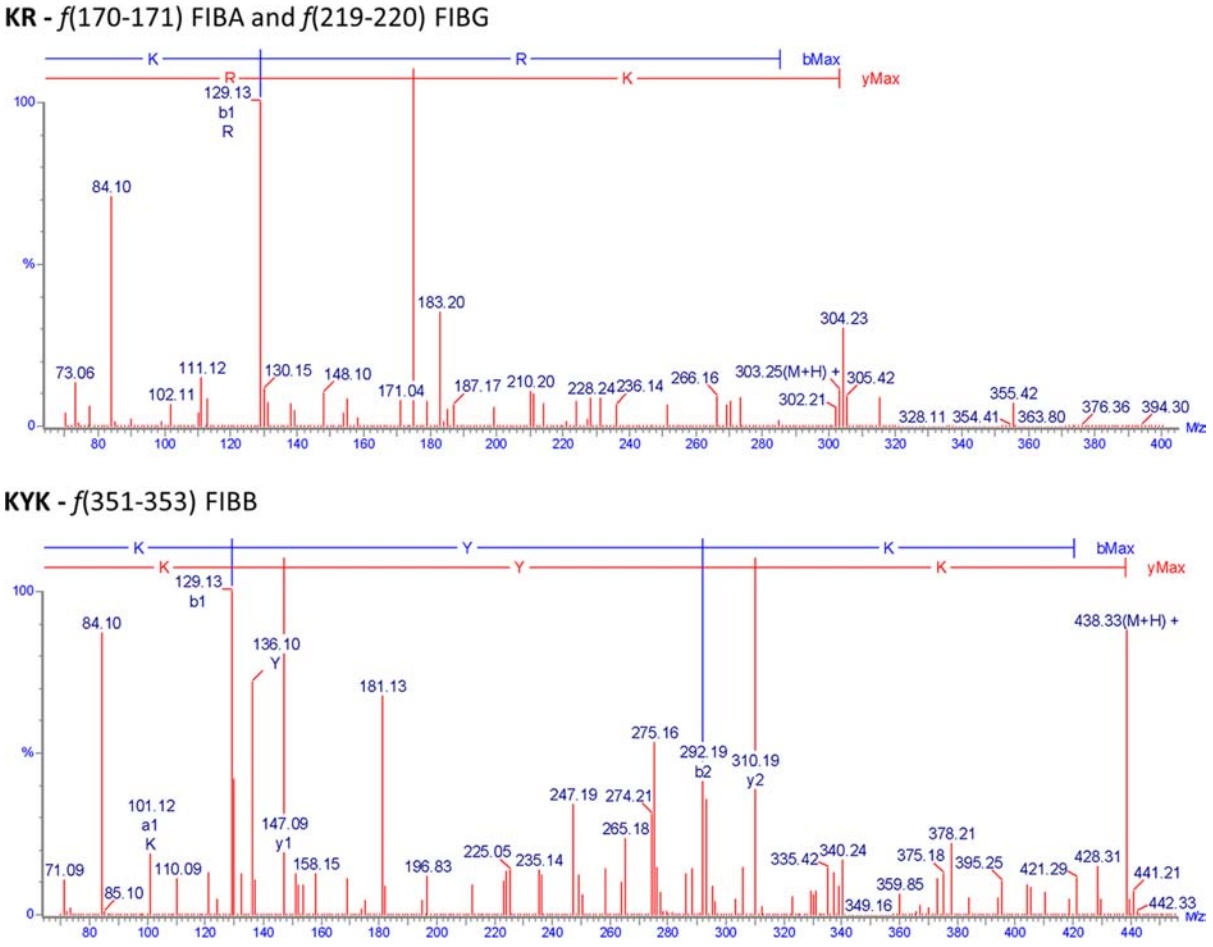

Figure 4. ESI-MS/MS spectra for de novo sequence determination of peptides KR and KYK. Peptides KR, FR, YF, RR, YR, SLK, SPR, and KYK were identified by de novo peptide sequencing software within the BioLynx software package (Waters Corp., Milford, MA, USA).

obtained from a trypsin hydrolysate of whey protein, which had an IC_{50} value of 1.51 mg/mL. The pentapeptide IPAVF, corresponding to β-lactoglobulin $f(78-82)$, had an IC_{50} value of 44.7 μM and was responsible for the observed DPP-IV inhibitory activity.[30]

Peptide Identification by de Novo Peptide Sequencing. The characterization of bioactive peptides within an active protein hydrolysate is of key importance. To identify bioactive peptides, it is often necessary to fractionate and purify the whole hydrolysate using filtration and chromatography methods. Today, widely used methods for peptide fractionation and enrichment include ultrafiltration and liquid chromatography.[31] In this study, the identification of peptides contained in FIB-1UFH was carried out using HPLC-MS/MS. A total of 20 di-, tri-, and tetrapeptides were identified by de novo peptide sequencing as represented in Figure 4. These peptides are listed in Table 2 together with their position in the parent protein and their observed masses as well as their calculated masses. Identified bioactive peptides were compared to previously reported ACE-I, DPP-IV, and renin inhibitors available in the database BIOPEP.[14] A number of the identified peptides were bioactive and were previously generated from various natural sources. For example, the peptide RR was generated by the action of dipeptidyl peptidases purified from porcine skeletal muscle and was reported to inhibit ACE-I.[32] There were sequence similarities between the peptides identified in this study and previously reported ACE-I and DPP-IV inhibitors available in BIOPEP, as shown in Table 2. For example, the peptide RR, corresponding to $f(145-147)$ and $f(452-453)$ of the α-chain of bovine fibrinogen, was found to share the same peptides at the C-terminus of the peptide with the previously reported DPP-IV inhibitor WRR, which had a reported DPP-IV IC_{50} value of 570 $\pm$ 62 μM.[33]

Chemical Synthesis and Confirmation of Bioactivity. A number of the identified peptides were selected for chemical synthesis and bioassay assessment. PeptideRanker scores were calculated for each peptide and are shown in Table 2. Peptide selection for chemical synthesis was based on the current knowledge of bioactive peptides, the known attributes of ACE-I and renin inhibitors, and the score assigned by PeptideRanker to each peptide (Table 2). The amino acids tryptophan, tyrosine, proline, and phenylalanine were reported previously as the most effective amino acids in an ACE-I-inhibiting peptide when they are present at the C-terminal side of a dipeptide.[34] A quantitative structure−activity relationships study (QSAR), which modeled biological activity of ACE-I-inhibiting peptides as a function of molecular structure, suggested that amino acid residues with large bulky chains as well as hydrophobic side chains such as found in the amino acids phenylalanine, tryptophan, and tyrosine are the most effective residues in a dipeptide.[25] Amino acid residues with small as well as hydrophobic side chains, which include valine, leucine, and isoleucine, were suggested for the N-terminal side of ACE-I inhibitory peptides. Hydrophobic amino acid residues with high

DOI: 10.1021/acs.jafc.5b03167
J. Agric. Food Chem. 2015, 63, 8676−8684

Table 2. Peptides Identified from Bovine Fibrinogen by HPLC-MS/MS

amino acid sequence	parent protein	obtained mass charge (Da)	calcd mass (Da)	PeptideRanker score[a]	similar ACE-I-inhibiting peptides[b]	similar DPP-IV-inhibiting peptides[b]
KR	*f*(170−171) FIBA and *f*(219−220) FIBG	302.17	302.20	0.21	**KR**, FQKP**KR**, IPALL**KR**	**KR**
FR	*f*(388−389; 408−409) FIBA	321.17	321.18	0.99	**FR**, WT**FR**, AFKDEDTEEVP**FR**	**FR**, EQLTKCEV**FR**
YF	*f*(464−465) FIBB and *f*(191−192; 305−306) FIBG	327.87	328.14	0.98	**YF**YPEL	**YF**
RR	*f*(145−146; 452−453) FIBA	330.17	330.21	0.57	**RR**, YLYEIA**RR**	W**RR**
YR	*f*(48−49; 243−244) FIBB and *f*(299−300) FIBG	337.17	337.17	0.53	**YR**PY	**RR**, W**RR**
PAR	*f*(599−601) FIBA	342.17	342.20	0.60	ALKAWSVA**R**, YLYEIA**R**	**PA**CGGFYISGRPG
VVK	*f*(476−478) FIBA	344.27	344.24	0.03	LYP**VK**, **VK**, AFDAVG**VK**, AHEP**VK**	**VK**SVVAL, **VK**
TVK	*f*(163−165) FIBB and *f*(166−168) FIBG	346.17	346.22	0.03	LYP**VK**, **VK**, AFDAVG**VK**, AHEP**VK**	**VK**SVVAL, **VK**
LVK	*f*(85−87) FIBG	358.17	358.25	0.07	LYP**VK**, **VK**, AFDAVG**VK**, AHEP**VK**	**LV**SGM, **VK**SVVAL, **VK**
SPR	*f*(288−290) FIBA	358.17	358.19	0.62	Y**PR**, **PR**, IY**PR**, WN**PR**, QLGFLG**PR**	**SP**
VSR	*f*(114−146) FIBB	360.27	360.21	0.09	N/A	N/A
KAR	*f*(596−598) FIBA	373.28	373.24	0.17	ALKAWSVA**R**, YLYEIA**R**	N/A
SLR	*f*(35−37) FIBB	374.28	374.22	0.40	LDAQSAP**LR**	**SL**
EAR	*f*(80−82) FIBG	374.18	374.19	0.09	ALKAWSVA**R**, YLYEIA**R**	N/A
VLR	*f*(174−176) FIBB and *f*(270−272) FIBG	386.28	386.26	0.20	LDAQSAP**LR**	**VL**GP, **VL**VLDTDYK
YSK	*f*(379−381) FIBG	396.28	396.20	0.13	NMAINP**SK**	N/A
NLR	*f*(181−183) FIBB and *f*(147−149) FIBG	401.28	401.23	0.34	LDAQSAP**LR**	N/A
DSSD	*f*(323−326) FIBG	421.98	422.12	0.10	N/A	N/A
KYK	*f*(351−353) FIBB	437.28	437.26	0.11	VLDTD**YK**, VLAQ**YK**, G**YK**, I**YK**, **YK**	VLVLDTD**YK**
EVVK	*f*(475−478) FIBA	473.28	473.28	0.02	LYP**VK**, **VK**, AFDAVG**VK**, AHEP**VK**	**EV**TFPA

[a]Data accessed from PeptideRanker, available at http://bioware.ucd.ie/ in April 2015. [b]Data accessed from BIOPEP, available at http://www.uwm.edu.pl/biochemia/index.php/pl/biopep in April 2015.

electronic properties such as proline, phenylalanine, and tryptophan are usually found at the C-terminal end of active ACE-I inhibitory tripeptides.[25] Furthermore, dipeptides with hydrophobic residues at the N-terminus and a bulky or aromatic group at the C-terminus were observed to be the most effective peptides for renin inhibition.[19]

The dipeptides KR, FR, YF, RR, and YR and the tripeptides SLR and KYK were chemically synthesized by MW-SPPS and tested for ACE-I- and renin-inhibiting properties in vitro. The IC_{50} values were determined for active peptides by plotting the percentage of enzyme inhibition as a function of the concentration of test compound. At a concentration of 1 mg/mL, the peptides KR, FR, YF, YR, SLR, and KYK inhibited ACE-I by >60%. ACE-I IC_{50} values were calculated for active peptides and were found to be 383.76 ± 1.64, 425.12 ± 21.49, 94.62 ± 5.83, 124.12 ± 8.40, 171.95 ± 25.44, and 280.12 ± 33.14 μM for KR, FR, YF, YR, SLR, and KYK, respectively. The peptide RR is a known ACE-I inhibitor with an IC_{50} value of 267.1 ± 11.3 μM.[32] No ACE-I peptide inhibitors have been generated from bovine fibrinogen to date. However, the ACE-I-inhibiting activity of the peptides identified in this study compared favorably to ACE-I-inhibiting peptides generated from bovine blood proteins such as hemoglobin.[35] These include the peptides corresponding to *f*(67−106), *f*(73−105), and *f*(100−105) of the α-chain of bovine hemoglobin, which inhibited the activity of ACE-I by half at a concentration of 366, 518, and 1095 μM, respectively.[35] Selected peptides were also screened for their ability to inhibit renin. Only the dipeptide YR and the tripeptide SLR were found to inhibit renin with IC_{50} values of 8.78 ± 0.37 and 7.29 ± 0.16 mM, respectively. These results compare favorably to previously describe renin inhibitors including the peptides IR and IRLIIVLMPILMA, generated by enzymatic hydrolysis of pea and seaweed proteins and with calculated IC_{50} values of 9.2 and 3.3 mM, respectively.[19,21]

Prediction of Resistance to Gastrointestinal Degradation and Bitterness. The use of bioactive peptides as functional ingredients is usually limited by a number of issues including low stability of the peptides against gastrointestinal degradation. Although bioavailability should be assessed in vivo, resistance of a peptide to degradation can be predicted by computer simulations of proteolysis. In this study, the in silico tool ExPASy PeptideCutter was used to predict the stability of the identified bioactive peptides after a simulated gastrointestinal digestion. Results suggest that the peptide RR may be resistant to degradation by pepsin, trypsin, and chymotrypsin. The peptides FR, YR, and YF were predicted to be cleaved by both pepsin and chymotrypsin into the amino acids phenylalanine and arginine, tyrosine and arginine, and tyrosine and phenylalanine, respectively. Moreover, the peptide KR was

DOI: 10.1021/acs.jafc.5b03167
J. Agric. Food Chem. 2015, 63, 8676−8684

predicted to be degraded by trypsin, and the tripeptides SLR and KYK were predicted to be broken down into the dipeptides SL and LR and KY and YK, respectively. The peptides SL and KY are known DPP-IV inhibitors, and the peptides KY and YK were both previously reported to inhibit ACE-I and are available in BIOPEP.

Bioactive hydrolysates and peptides are usually bitter in taste, and Western consumers do not seem to be willing to compromise taste for health benefits.[36] A number of methods have been used to predict the bitterness of a peptide. The "Q rule" formulated by Ney[37] quantifies the bitterness of a peptide on the basis of its amino acid composition, whereby a Q value is calculated from the solubility data of the individual amino acids. According to this method, when the Q value of a peptide, with a MW under 6 kDa, exceeds 1400 cal/mol, this peptide will be almost certainly bitter. The Q values for the peptides KR, FR, YF, RR, YR, SLR, and KYK were 1125.0, 1337.0, 2400.0, 750.0, 1525.0, 950.0, and 1766.6 cal/mol, respectively. Obtained Q values suggest that the peptides YF, YR, and KYK may be bitter in taste. Moreover, the Q value of peptides generated by the action of digestive enzymes in silico was also calculated. The peptides SL, LR, KY, and YK, which were predicted to be generated by the cleavage of the tripeptides SLR and KYK, had Q values of 1050.0, 1275.0, 1900.0, and 1900.0 cal/mol, respectively. The peptide KYK was predicted to be degraded by gastrointestinal enzymes and to be cleaved into the peptides KY and YK, which had higher predicted Q values and therefore could have enhanced bitterness following digestion. Ney's rule can be applied to the majority of known peptides, but there are exceptions. For example, a recent study characterized the flavor, chemical properties, and hydrophobicity of a number of peptides derived from two commercial enzymatic hydrolysates of soy protein. The obtained hydrophobicity data based on Q values did not support Ney's rule as a predictor of bitterness.[38]

In this work a sequential fractionation and enrichment methodology was used to generate fibrinogen-enriched fractions with inhibitory activities against the enzymes ACE-I, DPP-IV, and renin. This is the first report that evaluates the ACE-I, renin, and DPP-IV inhibitory activity from papain hydrolysates of bovine fibrinogen. Results presented in this study show the presence of biologically active peptides with renin- and ACE-I-inhibiting properties. These peptides were encrypted in bovine fibrinogen and released by enzymatic cleavage with the food-grade enzyme papain. The generated papain hydrolysates and peptides were found to inhibit renin, ACE-I, and DPP-IV, and the percentage inhibition values obtained compared favorably with those found previously for hydrolysates and peptides isolated from animal and plant sources. A number of known as well as novel bioactive peptides were generated and identified. The peptides identified herein were predicted to be bitter and to be degraded by digestive enzymes in silico. However, in silico analysis is not enough to predict the resistance of a peptide to degradation and its taste, and in vivo studies in animal models are required to assess the bioavailability of a peptide after ingestion. These results demonstrate the potential of bovine fibrinogen as a resource for bioactive peptide generation and opens new commercial opportunities for its use beyond its current applications in the food industry.

AUTHOR INFORMATION

Corresponding Author

*(M.H.) Phone: +353 (0) 1 8059957. E-mail: maria.hayes@teagasc.ie.

Funding

T.L. is in receipt of a Teagasc Walsh Fellowship. This work forms part of the ReValueProtein Research Project (Grant Award 11/F/043), which is supported by the Irish Department of Agriculture, Food and the Marine (DAFM) and the Food Institutional Research Measure (FIRM), both funded by the Irish government under National Development Plan 2007-2013.

Notes

The authors declare no competing financial interest.

ABBREVIATIONS USED

1UFH, hydrolysate ultrafiltrated with a 1 kDa membrane; 3UFH, hydrolysate ultrafiltered with a 3 kDa membrane; 10UFH, hydrolysate ultrafiltered with a 10 kDa membrane; ACE-I, angiotensin-I-converting enzyme; ACN, acetonitrile; DDA, data-dependent acquisition; DMSO, dimethyl sulfoxide; DPP-IV, dipeptidyl peptidase-IV; EFSA, European Food Safety Authority; ESI, electrospray ionization; FA, formic acid; GIP, gastric inhibitory peptide; GLP-1, glucagon-like peptide-1; HPLC, high-performance liquid chromatography; MALDI, matrix-assisted laser desorption/ionization; MS, mass spectrometry; MS/MS, tandem mass spectrometry; MW, molecular weight; MWCO, molecular weight cutoff; MW-SPPS, microwave-assisted solid phase peptide synthesis; NUFH, non-ultrafiltered hydrolysate; PEP, prolyl endopeptidase; SD, standard deviation; TOF, time-of-flight; QSAR, quantitative structure−activity relationship

REFERENCES

(1) Bah, C. S. F.; Bekhit, A. E.-D. A.; Carne, A.; McConnell, M. A. Slaughterhouse blood: an emerging source of bioactive compounds. *Compr. Rev. Food Sci. Food Saf.* **2013**, *12*, 314−331.

(2) Lalor, F.; Wall, P. G. Health claims regulations. *Br. Food J.* **2011**, *113*, 298−313.

(3) Korhonen, H.; Pihlanto, A. Bioactive peptides: production and functionality. *Int. Dairy J.* **2006**, *16*, 945−960.

(4) Lafarga, T.; Hayes, M. Bioactive peptides from meat muscle and by-products: generation, functionality and application as functional ingredients. *Meat Sci.* **2014**, *98*, 227−239.

(5) Lafarga, T.; O'Connor, P.; Hayes, M. Identification of novel dipeptidyl peptidase-IV and angiotensin-I-converting enzyme inhibitory peptides from meat proteins using in silico analysis. *Peptides* **2014**, *59*, 53−62.

(6) Cheung, I. W. Y.; Nakayama, S.; Hsu, M. N. K.; Samaranayaka, A. G. P.; Li-Chan, E. C. Y. Angiotensin-I converting enzyme inhibitory activity of hydrolysates from oat (*Avena sativa*) proteins by in silico and in vitro analyses. *J. Agric. Food Chem.* **2009**, *57*, 9234−9242.

(7) Lacroix, I. M. E.; Li-Chan, E. C. Y. Evaluation of the potential of dietary proteins as precursors of dipeptidyl peptidase (DPP)-IV inhibitors by an in silico approach. *J. Funct. Foods* **2012**, *4*, 403−422.

(8) Mora, L.; Hayes, M. Cardioprotective cryptides derived from fish and other food sources: generation, application, and future markets. *J. Agric. Food Chem.* **2015**, *63*, 1319−1331.

(9) López-Barrios, L.; Gutiérrez-Uribe, J. A.; Serna-Saldívar, S. O. Bioactive peptides and hydrolysates from pulses and their potential use as functional ingredients. *J. Food Sci.* **2014**, *79*, R273−R283.

(10) Hernández-Ledesma, B.; García-Nebot, M. J.; Fernández-Tomé, S.; Amigo, L.; Recio, I. Dairy protein hydrolysates: peptides for health benefits. *Int. Dairy J.* **2014**, *38*, 82−100.

DOI: 10.1021/acs.jafc.5b03167
J. Agric. Food Chem. 2015, 63, 8676−8684

(11) Atlas, S. A. The renin-angiotensin aldosterone system: pathophysiological role and pharmacologic inhibition. *J. Managed Care Pharm.* **2007**, *13*, S9−S20.
(12) Drucker, D. J. Enhancing incretin action for the treatment of type 2 diabetes. *Diabetes Care* **2003**, *26*, 2929−2940.
(13) Álvarez, C.; García, V.; Rendueles, M.; Díaz, M. Functional properties of isolated porcine blood proteins modified by Maillard's reaction. *Food Hydrocolloids* **2012**, *28*, 267−274.
(14) Minkiewicz, P.; Dziuba, J.; Iwaniak, A.; Dziuba, M.; Darewicz, M. BIOPEP database and other programs for processing bioactive peptide sequences. *J. AOAC Int.* **2008**, *91*, 965−980.
(15) Mooney, C.; Haslam, N. J.; Pollastri, G.; Shields, D. C. Towards the improved discovery and design of functional peptides: common features of diverse classes permit generalized prediction of bioactivity. *PLoS One* **2012**, *7*, e45012.
(16) Lafarga, T.; O'Connor, P.; Hayes, M. In silico methods to identify meat-derived prolyl endopeptidase inhibitors. *Food Chem.* **2015**, *175*, 337−343.
(17) Mosesson, M. W. Fibrinogen and fibrin structure and functions. *J. Thromb. Haemostasis* **2005**, *3*, 1894−1904.
(18) Bella, A. M., Jr; Erickson, R. H.; Kim, Y. S. Rat intestinal brush border membrane dipeptidyl-aminopeptidase IV: Kinetic properties and substrate specificities of the purified enzyme. *Arch. Biochem. Biophys.* **1982**, *218*, 156−162.
(19) Li, H.; Aluko, R. E. Identification and inhibitory properties of multifunctional peptides from pea protein hydrolysate. *J. Agric. Food Chem.* **2010**, *58*, 11471−11476.
(20) Di Bernardini, R.; Mullen, A. M.; Bolton, D.; Kerry, J.; O'Neill, E.; Hayes, M. Assessment of the angiotensin-I-converting enzyme (ACE-I) inhibitory and antioxidant activities of hydrolysates of bovine brisket sarcoplasmic proteins produced by papain and characterisation of associated bioactive peptidic fractions. *Meat Sci.* **2012**, *90*, 226−235.
(21) Fitzgerald, C. n.; Mora-Soler, L.; Gallagher, E.; O'Connor, P.; Prieto, J.; Soler-Vila, A.; Hayes, M. Isolation and characterization of bioactive pro-peptides with in vitro renin inhibitory activities from the macroalga Palmaria palmata. *J. Agric. Food Chem.* **2012**, *60*, 7421−7427.
(22) Duarte, R. T.; Carvalho Simões, M. C.; Sgarbieri, V. C. Bovine blood components: fractionation, composition, and nutritive value. *J. Agric. Food Chem.* **1999**, *47*, 231−236.
(23) Jamdar, S. N.; Rajalakshmi, V.; Pednekar, M. D.; Juan, F.; Yardi, V.; Sharma, A. Influence of degree of hydrolysis on functional properties, antioxidant activity and ACE inhibitory activity of peanut protein hydrolysate. *Food Chem.* **2010**, *121*, 178−184.
(24) EFSA Opinion of the Scientific Panel on food additives, flavourings, processing aids and materials in contact with food (AFC) related to use of an enzyme preparation based on thrombin:fibrinogen derived from cattle and/or pigs as a food additive for reconstituting food. *EFSA J.* **2005**, *214*, 1−810.2903/j.efsa.2005.214.
(25) Wu, J.; Aluko, R. E.; Nakai, S. Structural requirements of angiotensin I-converting enzyme inhibitory peptides: quantitative structure-activity relationship study of di- and tripeptides. *J. Agric. Food Chem.* **2006**, *54*, 732−738.
(26) Hyun, C. K.; Shin, H. K. Utilization of bovine blood plasma proteins for the production of angiotensin I converting enzyme inhibitory peptides. *Process Biochem.* **2000**, *36*, 65−71.
(27) Nwachukwu, I. D.; Girgih, A. T.; Malomo, S. A.; Onuh, J. O.; Aluko, R. E. Thermoase-derived flaxseed protein hydrolysates and membrane ultrafiltration peptide fractions have systolic blood pressure-lowering effects in spontaneously hypertensive rats. *Int. J. Mol. Sci.* **2014**, *15*, 18131−18147.
(28) Velarde-Salcedo, A. J.; Barrera-Pacheco, A.; Lara-González, S.; Montero-Morán, G. M.; Díaz-Gois, A.; González de Mejia, E.; Barba de la Rosa, A. P. In vitro inhibition of dipeptidyl peptidase IV by peptides derived from the hydrolysis of amaranth (*Amaranthus hypochondriacus* L.) proteins. *Food Chem.* **2013**, *136*, 758−764.
(29) Li-Chan, E. C. Y.; Hunag, S. L.; Jao, C. L.; Ho, K. P.; Hsu, K. C. Peptides derived from Atlantic salmon skin gelatin as dipeptidyl-peptidase IV inhibitors. *J. Agric. Food Chem.* **2012**, *60*, 973−978.
(30) Silveira, S. T.; Martínez-Maqueda, D.; Recio, I.; Hernández-Ledesma, B. Dipeptidyl peptidase-IV inhibitory peptides generated by tryptic hydrolysis of a whey protein concentrate rich in β-lactoglobulin. *Food Chem.* **2013**, *141*, 1072−1077.
(31) Agyei, D.; Danquah, M. K. Industrial-scale manufacturing of pharmaceutical-grade bioactive peptides. *Biotechnol. Adv.* **2011**, *29*, 272−277.
(32) Sentandreu, M. A.; Toldrá, F. Evaluation of ACE inhibitory activity of dipeptides generated by the action of porcine muscle dipeptidyl peptidases. *Food Chem.* **2007**, *102*, 511−515.
(33) Lan, V. T. T.; Ito, K.; Ito, S.; Kawarasaki, Y. Trp-Arg-Xaa tripeptides act as uncompetitive-type inhibitors of human dipeptidyl peptidase IV. *Peptides* **2014**, *54*, 166−170.
(34) Cheung, H. S.; Wang, F. L.; Ondetti, M. A.; Sabo, E. F.; Cushman, D. W. Binding of peptide substrates and inhibitors of angiotensin-converting enzyme. Importance of the COOH-terminal dipeptide sequence. *J. Biol. Chem.* **1980**, *255*, 401−407.
(35) Adje, E.; Balti, R.; kouach, M.; Guillochon, D.; Nedjar-Arroume, N. α 67−106 of bovine hemoglobin: a new family of antimicrobial and angiotensin I-converting enzyme inhibitory peptides. *Eur. Food Res. Technol.* **2011**, *232*, 637−646.
(36) Grasso, S.; Brunton, N. P.; Lyng, J. G.; Lalor, F.; Monahan, F. J. Healthy processed meat products − regulatory, reformulation and consumer challenges. *Trends Food Sci. Technol.* **2014**, *39*, 4−17.
(37) Ney, K. Prediction of bitterness of peptides from their amino acid composition. *Z. Lebensm.-Unters. Forsch.* **1971**, *147*, 64−68.
(38) Cho, M. J.; Unklesbay, N.; Hsieh, F.-H.; Clarke, A. D. Hydrophobicity of bitter peptides from soy protein hydrolysates. *J. Agric. Food Chem.* **2004**, *52*, 5895−5901.

DOI: 10.1021/acs.jafc.5b03167
J. Agric. Food Chem. 2015, 63, 8676−8684

Table 1. Enzymatic Activities of Depol 761P and Viscoferm*

enzyme preparation	xylanase, pH 6.0	β-glucanase, pH 6.0	polygalacturonase, pH 5.5	acidic protease, pH 5.5	cellulase (FPU), pH 5.0	endoglucanase, pH 5.0
Depol 761P	35828	1625	1317	ND	ND	ND
Viscoferm	15715	NA	50	2.5	13036	149

*NA = not analyzed. ND = not detected.

offering an array of tools to valorize bran matrix without altering its nutritional benefits.[2,9] Bioprocessing of rye and wheat bran with microbes and hydrolytic enzymes improved the bioaccessibility of phenolic compounds, significantly impacted the dietary fiber and protein fraction, and enhanced the overall nutritional quality.[10−12] Fermentation with *Lactobacillus brevis* E95612 and *Kazachstania exigua* C81116 in the presence of an enzyme mixture having carbohydrase activity improved the nutritional properties of wheat bran fractions, including proteins.[10] In a recent study, bran treatment with proteolytic enzymes was shown to significantly increase the solubilization of the protein mostly in the subaleurone layer, whereas they were less effective on the proteins in the aleurone cells.[13] Innovative and simple transformation processes are the key to exploit the nutritional quality of bran matrix and are also applicable to industrial production. However, more knowledge on the mechanisms underlying protein bioaccessibility should still be acquired to enhance the potential of the protein component of bran.

This article will focus on the release and modification of the protein fraction of wheat bran after enzymatic and microbial bioprocessing. A coarse bran fraction, characterized by a more-intact cell wall structure[11] was used in order to assess the role of the endogenous enzymatic activity, alone or in combination with cell-wall-degrading enzymes and microbial fermentation, on protein changes during bioprocessing. The effects on in vitro protein digestibility, phytase activity, and release of total phenols were also evaluated.

MATERIALS AND METHODS

Raw Material, Enzymes, And Microorganisms. The commercial wheat bran used in this study (Fazer Mills, Lahti, Finland) had a particle size of 750 μm and the following chemical composition: total dietary fiber, 44.3 ± 0.60%; starch, 16.8 ± 0.16%; fermentable sugars, 3.57 ± 0.24%; protein, 15.98 ± 0.12%; and fat, 4.1 ± 0.10%.

Two commercial enzymes, Depol 761P (Biocatalysts Ltd., Cardiff, UK) and Viscoferm, were used for bran treatments. The xylanase, β-glucanase, polygalacturonase, acidic protease, cellulase, endoglucanse, and ferulic acid esterase activity were measured according to the methods reported by Santala et al.[14] The resulting activity profile of the two enzymes is described in Table 1.

L. brevis E-95612 and *Candida humilis* E-96250, belonging to VTT Culture Collection (VTT, Technical Research Centre of Finland), were used as starters for fermentation. *L. brevis* E95612 was cultivated for 24 h at 30 °C in MRS (Oxoid LTD, Basingstoke, Hampshire, UK) under anaerobic conditions, whereas *C. humilis* E-96250 was cultivated for 24 h at 25 °C in YM (3 g/L malt extract, 3 g/L peptone, and 10 g/L dextrose). After the late exponential phase of growth was reached, cells were recovered by centrifugation (10 000 g for 10 min), successively washed twice in 0.05 M phosphate buffer (pH 7.0), and resuspended in tap water (ca. 15% of the initial volume of the culture).

Bioprocessing of Bran. A mixture of wheat bran and water (20:80 w/v) was treated with the addition of enzymes, antibiotics, and/or lactic acid bacteria and yeast according to Table 2, obtaining six different bioprocessing combinations. In three samples, aiming at the evaluation of the enzymatic activity of endogenous (End), exogenous (E), and endogenous + exogenous enzymes (End/E) respectively, the antibiotics cycloheximide (0.01% w/w) and chloramphenicol (0.01% w/w) were added into the mixture to prevent microbial growth. The pH of samples End and End/E was adjusted to 4.5 by an organic acid buffer (lactic acid/acetic acid at a 4:1 molar ratio) in order to activate the endogenous enzymes of wheat bran.[15] The enzyme preparations were dosed at 100 nkat/g bran according to their xylanase activity, and the enzymes were added at the beginning of fermentation to the samples E, End/E, St/E, and Sp/E. In controlled fermentations (St and St/E), the starter microorganisms *L. brevis* E-95612 and *C. humilis* E-96250 were both inoculated at a cell density of ca. 6.0 log cfu/g of sample. Sample Sp/E was incubated only with the addition of enzymes to evaluate the effect of the spontaneous fermentation. All the samples were incubated for 24 h at 30 °C. A control (ct) sample, corresponding to a mixture of bran and water prepared as described above, was frozen at −20 °C after preparation (time 0).

Table 2. Bioprocessing Combinations of the Bran/Water Mixtures*

sample	bioprocessing (bran/water mixture 20:80 w/v)	Depol 761P and Viscoferm	starter	antibiotics	chemical acidification
ct	no bioprocessing (time 0)				
End	endogenous enzymes activity			+	4.5
E	enzymatic processing (exogenous enzymes)	+		+	
End/E	enzymatic processing (endogenous + exogenous enzymes)	+		+	4.5
St	controlled fermentation		+		
St/E	controlled fermentation + exogenous enzymes	+	+		
Sp/E	spontaneous fermentation + exogenous enzymes	+			

*All the mixtures were incubated at 30°C for 24 h except for control bran (ct). The initial pH of samples End and End/E was adjusted with a solution lactic acid/acetic acid in 4:1 molar ratio.

Water/salt-soluble extracts (WSE) were prepared from each sample according to the method originally described by Osborne and modified by Weiss et al.[16] An aliquot of sample (37.5 g) was diluted with 30 mL of Tris-HCl 50 mM (pH 8.8), held for 1 h at room temperature under stirring conditions, and centrifuged at 20 000 g for 20 min. The supernatants, containing the water/salt-soluble nitrogen fraction were freeze-dried and used for further analyses.

Microbiological Analyses and pH Determination. Bran samples (10 g) were homogenized with 90 mL of sterile saline in a Stomacher 400 lab blender (Seward Medical, London). Serial dilutions were made, and enumeration of the main microbial groups was carried out. Lactic acid bacteria count was obtained by plating on MRS agar (Oxoid) at 30 °C for 48 h; yeasts were counted on YM agar after incubation at 25 °C for 48 h. Total *Enterobacteriaceae* were counted on VRGBA agar (Oxoid) after incubation at 37 °C for 24 h, and total aerobic bacteria count was carried out on PCA agar (Oxoid) at 30 for 48 h. The pH value was measured on-line by a Foodcare pH meter HI99161 (Hanna Instruments, Woonoscket, USA).

Chemical Analyses. The moisture contents of the samples were determined by drying in oven at 130 °C for 1 h. Aiming at the determination of the protein and protein derivatives, the organic

DOI: 10.1021/acs.jafc.5b03495
J. Agric. Food Chem. 2015, 63, 8685−8693

Table 3. WE-Pentosan Content, Reducing Sugars, Total Solubilized Nitrogen Ratio, Soluble Protein Content by Bradford Method, Peptide Content by OPA Method, Peptides Area Obtained through RP-FPLC Analysis and Total Amino Acid Content of the Water-Salt Soluble Extract from Control and Bioprocessed Wheat Bran*

sample	WE-pentosan content (%)	reducing sugars (mg/L)	total solubilized nitrogen ratio (%)	soluble protein content by Bradford method (mg/mL)	peptide content by OPA method (mg/mL)	peptides area (mAu mL)	total amino acid content (mg AA/kg bran)
ct	1.4^{a,b}	9.7^{a}	14.0^{a}	0.34^{a}	6.9^{a}	4200^{a}	1954^{a}
End	2.0^{b}	230.9^{c}	74.7^{e}	1.2^{d}	15.2^{b}	8877^{b,c}	2148^{b}
E	3.9^{c}	287.3^{d}	39.1^{b}	1.1^{d}	17.7^{b}	10119^{c}	2588^{c}
End/E	4.9^{d}	364.7^{e}	62.6^{d}	1.2^{d}	15.0^{a,b}	9541^{b,c}	2309^{b}
St	0.9^{a}	10.6^{a}	52.1^{c}	0.8^{c}	13.2^{a,b}	6898^{a,b,c}	3477^{e}
St/E	1.9^{b}	26.6^{a}	52.0^{c}	0.5^{b}	13.4^{a,b}	5968^{a,b}	4391^{f}
Sp/E	3.3^{c}	189.2^{b}	34.2^{b}	0.6^{b}	17.2^{b}	8506^{b,c}	2953^{d}

*Samples with same letter among the group and column have no statistical difference ($p > 0.05$). Values in the same column with different letter differ significantly ($p < 0.05$). RP-FPLC chromatograms are available in the Supporting Information.

nitrogen concentration of samples and corresponding WSE was analyzed with the Kjeldahl method (AACC) 46-11A.[17] The organic nitrogen solubilized after bioprocessing was calculated as follows:

$$\text{Solubilized organic nitrogen ratio (\%)} = \frac{\text{organic nitrogen in WSE}}{\text{total organic nitrogen}} \times 100$$

To evaluate the degree of proteolysis during bioprocessing, the concentration of proteins, peptides and free amino acids was determined in WSE. In details, the concentration of proteins was determined by Bradford method.[18] The concentration of peptides in the WSE was determined by the *o*-phtaldialdehyde (OPA) method as described by Church et al.[19] Peptide profiles were obtained by reversed-phase fast protein liquid chromatography (RP-FPLC), using a Resource RPC column and ÄKTA FPLC equipment, with a UV detector operating at 214 nm (GE Healthcare Bio-Sciences AB, Uppsala, Sweden) as described in Coda et al.[11] Free amino acids were analyzed by a Biochrom30 series Amino Acid Analyzer (Biochrom Ltd., Cambridge Science Park, UK) with a Na-cation-exchange column (20 cm × 0.46 cm internal diameter) as reported in Coda et al.[11]

The water-extractable pentosan (WE-pentosan) content was analyzed as described by Santala et al.,[21] and the reducing sugars content was estimated with the dinitrosalicylic acid method.[22] Phytase activity was measured as described by Shimuzu[23] and expressed as the amount of inorganic orthophosphate released from the phytic acid by phytase.

Analysis of total phenols was carried out in agreement with the method of Slinkard and Singleton[24]on methanolic extracts. The concentration of total phenols was expressed as gallic acid equivalent (mmol/100 g).

In Vitro Protein Digestibility. The in vitro digestibility of the samples was determined by the method of Akeson and Stahmann.[20] A known amount of sample was incubated with 1.5 mg of pepsin in 15 mL of 0.1 M HCl at 37 °C for 3 h. After neutralization with 2 M NaOH and addition of 4 mg of pancreatin in 7.5 mL of phosphate buffer (pH 8.0), 1 mL of toluene was added to prevent microbial growth, and the solution was incubated for 24 h at 37 °C. After 24 h, the enzyme was inactivated by addition of 10 mL of trichloroacetic acid (20%, wt/vol), and the undigested protein was precipitated. The volume was increased to 100 mL with distilled water, and the mixture was centrifuged at 5000 rpm for 20 min. The precipitate was subjected to protein extraction, according to Weiss et al.,[16] and the concentration of protein was determined. The in vitro protein digestibility of the bran samples was expressed as the percentage of the total protein that was solubilized after the in vitro enzyme hydrolysis mimicking the in vivo digestion in the gastrointestinal tract.[20]

Electrophoresis. The water/salt-soluble protein fraction was extracted from the freeze-dried sample as described by Weiss et al.[16] using 50 mM tris-HCl (pH 8.8). The extracts were analyzed by sodium dodecyl sulfate polyacrylamide gel electrophoresis (SDS-PAGE)[25] The samples were mixed at a ratio of 1:1 with SDS sample buffer, boiled for 10 min, and 10 μL of sample was pipetted to NuPage Bis-tris 12% minigels (Invitrogen, Waltham, MA). As a protein standard, Novex Sharp Prestained was used (10−250 mol/g, LC5800, Invitrogen, Waltham, MA). After the run (2 h, 200 V, 100 mA), the gels were stained overnight by Coomassie blue and destained with water until clear gels were achieved.

Statistical Analyses. The results were calculated as means of at least four analysis results. The data was analyzed by one-way ANOVA with using a Bonferroni adjustment to test for significance ($p > 0.05$) among the replicates. The statistics were carried out with IBM SPSS Statistics, version 22. When the response differed significantly ($p < 0.05$), it was indicated with a different letter. Biochemical properties of the bran samples were analyzed through principal component analysis[26] (PCA), using the software Statistica 8.0 (StatSoft Inc., Tulsa, USA).

RESULTS AND DISCUSSION

Effect of Bioprocessing on Microbiological Quality, Acidity, and Cell-Wall Degradation of Bran. Microbiological analysis was carried out before and after bioprocessing to monitor the impact of the microbial population on the different treatments. Before bioprocessing, the bran/water mixture (time 0) was characterized by total mesophilic bacteria cell density varying from 5.0 ± 0.3 to 6.6 ± 0.1 log cfu/g, total *Enterobacteriaceae* cell density of 4.0 ± 0.1 log cfu/g, and lactic acid bacteria and yeast cell densities below 3.0 and 2.0 log cfu/g, respectively. After bioprocessing, no microbial growth was detected in the samples that were chemically acidified and/or that had enzymes added (End, E, and End/E), confirming the efficiency of the antibiotic. In the treatments in which *L. brevis* E-95612 and *C. humilis* E-96250 were used as starters for fermentation (St and St/E), the cell density of lactic acid bacteria showed an increase of ca. 3 log cycles after fermentation, reaching values of 9.9 ± 0.1 log cfu/g in the case of enzyme-added sample (St/E). The yeast cell density increased of ca. 2 log cycles, reaching a final value of 8.6 ± 0.1 log cfu/g (St/E). No *Enterobacteriaceae* were detected in 10 g of sample in conditions of controlled fermentation. In comparison with controlled fermentation, the sample subjected to spontaneous fermentation (Sp/E) was characterized by similar lactic acid bacteria cell density (9.4 ± 0.0 log/cfu g), higher total enterobacteria cell density (7.8 ± 0.1 log cfu/g), and lower yeast density (4.0 ± 0.2 log/cfu g). The total mesophilic bacteria count was comparable among all the fermented samples, varying from 9.4 ± 0.7 to 9.9 ± 0.0 log cfu/g. No significant difference between the controlled fermentations was observed in terms of microbial growth because similar cell counts were obtained for both the starters, with or without

DOI: 10.1021/acs.jafc.5b03495
J. Agric. Food Chem. 2015, 63, 8685−8693

the addition of enzymes. On the contrary, spontaneous fermentation was characterized by a different microflora, even though a high cell density of lactic acid bacteria was still present. The initial values of pH for enzyme-added bran (E) and for chemically acidified bran (End and End/E) were 6.7 or 4.5, respectively, and did not show any significant variation throughout bioprocessing. From an initial pH value of 6.7, after 24 h of fermentation, samples St, St/E, and Sp/E reached pH values in the range 4.3−3.7, showing the lowest value when starter and enzymes were added (St/E).

Spontaneous fermentations are the result of competitive activities of a variety of autochthonous and contaminating microorganisms, and compared to controlled fermentation, they are characterized by a more complex microbiota. This also reflects on the acidification properties of the fermented matrix, which typically occurs faster when starter cultures are used independent of the final cell density of lactic acid bacteria.[27] The interaction between exogenous enzymes and starter microorganisms is evident in the final pH value of the controlled fermentation. It was already shown that in the presence of xylose, ribose, or arabinose not only a higher acidification rate but also higher growth rate and cell yield can be expected.[28]

WE-pentosan and reducing sugar content were determined to monitor the effect of the treatments on cell wall degradation (Table 3). In the chemically acidified and/or enzyme-added treatments, (End, E, and End/E), the addition of hydrolytic enzymes increased WE-pentosan and reducing sugar content by 2.7−3.5- and 24−37-fold, respectively, in comparison with those of ct. The highest amount of soluble carbohydrates were shown by treatment End/E (4.9% and 364.7 mg/L of WE-pentosan and reducing sugar, respectively), where the action of endogenous hydrolytic activity was supported by enzyme addition. Also, the high cellulase activity of Viscoferm (Table 1) could have impacted on the final carbohydrate content of the chemically acidified sample End/E. The consumption of carbohydrates during fermentation was visible as the lower content of WE-pentosans and reducing sugar of the fermented samples in comparison with those of the previous samples. The higher content of reducing sugar observed in the spontaneous fermentation Sp/E (189.2 g/L) confirms a slower growth/acidification process if compared to that of the controlled fermentation (Table 3). Because controlled fermentation was characterized by higher cell density of the starters relative to the beginning of bioprocessing, microbial metabolism occurred at a faster rate, therefore affecting the final carbohydrate concentration.

Impact of Bioprocessing on Protein Solubility and Proteolysis. The solubility of wheat bran proteins and protein derivatives (peptides and free amino acids) after different treatments was evaluated in the water/salt-soluble extract by different methods. The Kjeldahl method, determining the organic nitrogen, was used to estimate the overall solubilization of all the proteinaceous compounds, whereas the degree of proteolysis was investigated by the determination of the concentration of proteins, peptides, and free amino acids (Table 3). In untreated bran (ct), the total solubilized organic nitrogen ratio was 14%. The most significant increase of solubilized organic nitrogen (corresponding to 74.7%) was achieved by treatment End, representing the sole activity of bran endogenous enzymes. In this treatment, the pH of the sample was adjusted to ca. 4.5 to achieve rapid activation of the endogenous proteinases.[15] A significantly lower solubilization value (39.1%) was observed for the treatment in which only the added enzymes were active (treatment E), as a consequence of the high pH (ca. 6.7) maintained throughout the processing. An intermediate value of organic nitrogen solubilization (62.6%), was obtained through the combined activity of endogenous and exogenous enzymes (End/E), which was also subjected to pH adjustment. In the fermented samples, the use of starters alone or with the addition of enzymes (St and St/E, respectively) did not show significantly different values of solubilized organic nitrogen (52%), whereas the lowest increase (34.2%) was observed for the bran spontaneously fermented in the presence of enzymes (Sp/E). This difference might be due to the acidification conditions during fermentation because optimal pH values for bran proteases were reached in a longer time when spontaneous fermentation occurred, in comparison with the faster acidification due to the starter metabolism. This could also explain the lowest value of nitrogen solubilization observed in Sp/E, in which the acidification process was the slowest among the fermented samples. Overall, pH values during bioprocessing seemed to have the strongest impact on protein solubilization and were enhanced in the treatment in which pH 4.5 was kept throughout the bioprocessing (End and End/E) or when optimal pH was achieved by a more effective acidification (St and St/E). The protein concentration in the water/salt-soluble extract as measured by Bradford assay was highest (1.2−1.1 mg/mL) in the samples in which only the activity of endogenous and/or added enzymes was involved (End, E, and End/E) with no significant difference among the samples. In the fermented samples, the use of the starters alone (St) showed the highest protein concentration (0.8 mg/mL), whereas no significant difference was shown by the treatments St/E and Sp/E, showing the lowest amount of protein (Table 3). The water/salt-soluble extracts, containing low-molecular-mass peptides naturally present in samples or deriving from protein degradation during bioprocessing, were analyzed with OPA method and liquid chromatography. The peptide content of the water/salt-soluble extract of the bioprocessed brans ranged from 15.0 to 17.7 mg/mL. Overall, the highest peptide concentration was found for E and Sp/E, in which low protease activity or a slow fermentation occurred. The lowest peptide content was observed for the controlled fermentation samples (St and St/E) with no significant variation between them. The peptide area, intended here as the total peak area in the chromatogram, confirmed the tendency observed about peptide amount in the different treatments. This data was used together with OPA analysis to avoid the interference of high concentration of FAA with the OPA reagent. The highest areas, indicating a moderate proteolysis, were found for the samples treated with enzymes E, End/E, and Sp/E, with the only exception of St/E, in which the lowest peptide content/area was found, indicating that a more intense proteolysis occurred in this sample. In the fermented samples, the addition of enzymes to the microbial inoculum enhanced peptide degradation to amino acids as consequence of improved microbial activity. Generally, the free amino acids content after bioprocessing ranged from 2148 to 4391 mg/kg of bran and was in agreement with the data previously analyzed, showing a smaller increase in the treatments chemically acidified and/or with added enzymes and a larger increase in the fermented samples. The effect of enzyme addition during starter fermentation (St/E) led to the highest amount of free amino acids, increasing the total amino acids content up to 55% in comparison with that of untreated bran (ct). Overall, the

DOI: 10.1021/acs.jafc.5b03495
J. Agric. Food Chem. 2015, 63, 8685−8693

differences among the proteolytic end-products of the treatments were mostly due to the activity of the microorganisms involved in the fermentation, and a marked effect of the starter microorganisms in comparison with the spontaneous microflora was also evident. In cereal fermentation, during primary proteolysis, oligopeptides are released mainly by the activity of cereal endoproteases, whereas secondary proteolysis releases free amino acids and small-sized peptides and occurs through microbial peptidase activity, especially that of lactic acid bacteria.[29] In particular, the proteolytic activity of the lactic acid bacteria was enhanced under the condition of fermentation controlled by the addition of enzymes.

Polypeptide, Amino Acid Profiles, and In Vitro Digestibility of Wheat Bran Proteins after Bioprocessing. The profile of the water/salt-soluble proteins of bioprocessed bran was analyzed by SDS-PAGE (Figure 1).

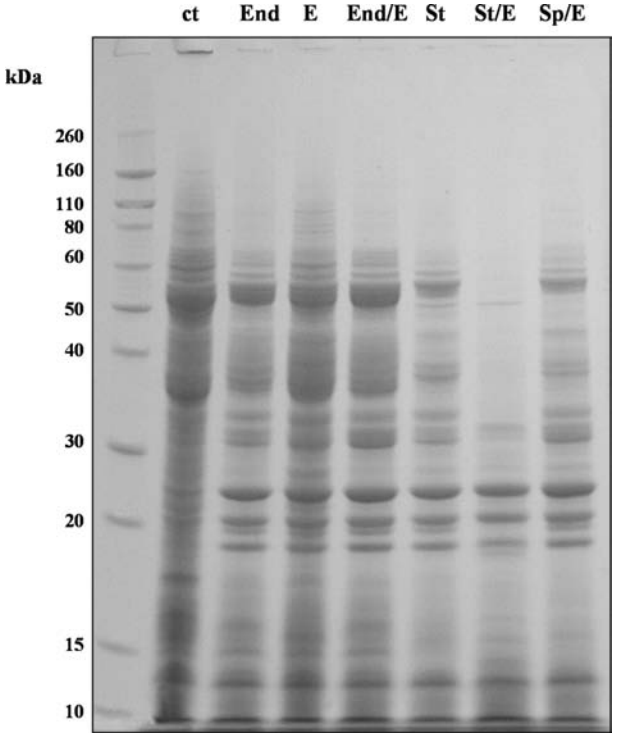

Figure 1. SDS-PAGE of water/salt-soluble extracts polypeptides from control and bioprocessed wheat bran. ct: untreated bran (time 0); End, endogenous enzymes; E: exogenous enzymes; End/E: endogenous and exogenous enzymes; St: controlled fermentation; St/E, controlled fermentation and exogenous enzymes; and Sp/E, spontaneous fermentation and exogenous enzymes.

Analysis of the untreated bran soluble fraction (ct) showed a distribution of polypeptides throughout the length of the gel, with most of the bands ranging from 70 to 20 kDa. Compared to that of the ct, the profile of the bioprocessed bran appeared modified in all the cases but with different intensities. Overall, more intense bands were observed in the lower range of the gel (32−18 kDa). Only minor differences could be detected between the chemically acidified and/or enzyme-added treatments (samples End, E, and End/E) in comparison with untreated bran, showing very similar polypeptide profiles. Nevertheless, weaker signals for many bands ranging from 35 to 45 kDa were found compared to ct, indicating hydrolysis to some extent. As expected, an intense proteolysis was found in these samples for polypeptides having high molecular weight as the consequence of the activity of the endogenous proteinases. Similar to wheat flour, in which proteolytic activity is mainly due to aspartic proteinases and serine carboxypeptidases located in the endosperm that are active under acidic conditions, wheat bran has serine carboxypeptidases with an optimum peptidase pH of 4−4.5.[30] Compared to the untreated bran and to the chemically acidified and/or enzyme-added samples, microbial fermentation intensely modified the polypeptides profile, especially in the range 55−35 kDa (St, St/E, and Sp/E). A clear difference in the overall quality of the proteolysis was also visible among the fermented samples. In particular, all the high-molecular-weight polypeptides were almost completely hydrolyzed in St/E.

This difference is also highlighted in the free amino acids profiles as reported in Figure 2. In the water/salt-soluble extract of untreated bran (ct), Arg, Ser, Lys, Leu, Phe, and Asp were the most abundant amino acids, ranging from 135 to 208 mg/kg for Asp and Arg, respectively. Compared to ct, almost all the amino acids increased after bioprocessing, with very few exceptions, such as Tyr and Arg, which decreased in the fermented samples. Generally, the observed increase ranged from 8% of Cys in the chemically acidified sample (End) up to 90% of Glu in the starter fermented sample (St). The highest increase was observed for Glu, Pro, and Orn, which were, respectively, found at a concentration of 650, 544, and 325 mg/kg of bran in the controlled fermentation with added enzymes (St/E). Very few differences were shown among the chemically acidified and/or enzyme-added treatments End, E, and End/E, except for Thr, Glu, Gly, and Pro, which were significantly more abundant in E. On the contrary, more differences were detected among the fermented samples, particularly Glu, Phe, Orn, and Pro, which had higher concentrations when starters were used together with enzymes (St/E), followed by the use of starters alone and spontaneous fermentation (St and Sp/E, respectively). Lactic acid bacteria and yeast activity are known to be responsible for amino acid level increase when compared to chemically acidified doughs.[31] Also, the composition of the fermentation microbiota has an effect on the overall proteolytic events and can strongly influence the composition and the concentration of amino acids in fermented flour. In our case, for instance, the high amount of Orn in the controlled fermentation could derive from the yeast biomass or arginine metabolism of lactic acid bacteria.[32] Bioprocessing with starter and enzymes allowed doubling of the amount of Phe, His, Leu, and Val, some of the essential amino acids, whereas it increased the concentration of Pro and Glu of 5−9-fold, respectively. The high amount of Pro and Glu could also partly originate from prolamin degradation. This is in agreement with the data previously observed by Coda et al.[11] for wheat bran bioprocessing in the presence of hydrolytic enzymes. Thus, these results showed that in the fermented samples the primary proteolysis was followed by degradation to peptides and amino acids as a consequence of microbial metabolism. Particularly in the case of controlled fermentation (St/E), the addition of enzymes, favoring a faster growth and acidification of the starters, led to a higher accumulation of amino acids and improved free amino acid composition.

A multistep protocol, which mimics the in vivo gastrointestinal digestion, was used to estimate the in vitro protein digestibility of bran (Table 4). The in vitro digestibility gives information on both the stability of protein hydrolyzates and how they withstand digestive processes. Overall, all the bioprocessing methods significantly increased the protein

DOI: 10.1021/acs.jafc.5b03495
J. Agric. Food Chem. 2015, 63, 8685−8693

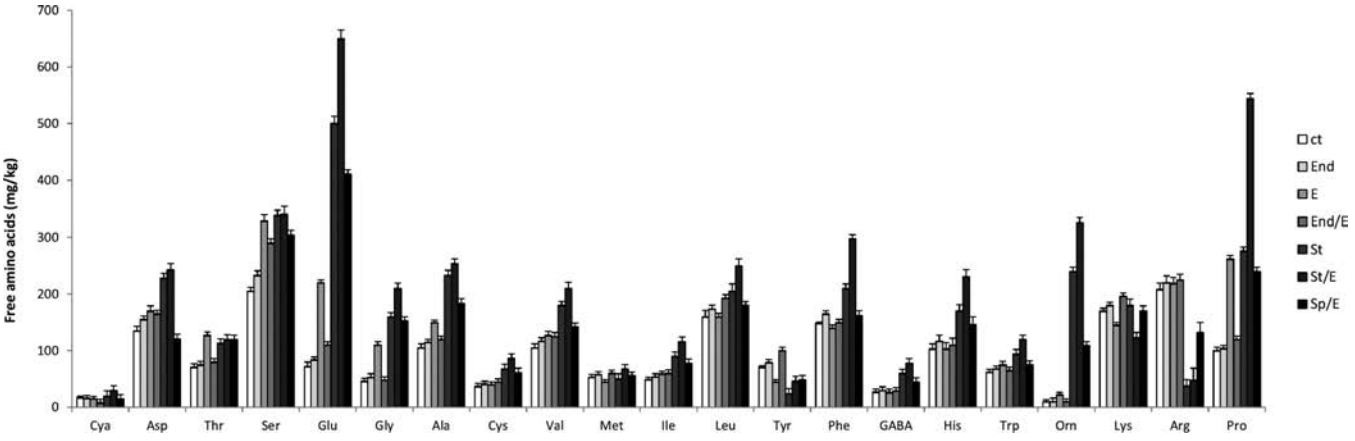

Figure 2. Free amino acid concentrations (mg/kg) of water/salt-soluble extracts from control and bioprocessed wheat bran. Ct: untreated bran (time 0); End, endogenous enzymes; E: exogenous enzymes; End/E: endogenous and exogenous enzymes; St: controlled fermentation; St/E, controlled fermentation and exogenous enzymes; and Sp/E, spontaneous fermentation and exogenous enzymes.

Table 4. In Vitro Protein Digestibility, Phytase Activity, And Total Phenols Of Control And Bioprocessed Wheat Bran*

sample	in vitro protein digestibility (%)	phytase activity (U)**	total phenols (mM gallic acid)
ct	14.6[a]	7.1a	1.2[a]
End	20.0[b]	10.8[b,c]	4.1[b]
E	25.3[c]	8.9[a,b]	5.6[c]
End/E	18.4[b]	11.0[b,c]	3.8[b]
St	32.7[e]	12.1[c]	6.7[c,d]
St/E	39.1[f]	12.1[c]	6.8[d]
Sp/E	28.7[d]	10.0[b,c]	4.4[b]

*Values in the same column with different superscript letter differ significantly ($p < 0.05$). Samples with same letter among the group and column have no statistical difference ($p > 0.05$). **One unit (U) of phytase activity represents the amount of enzyme required to release 1 μmol of phosphate/min under the assay conditions.

digestibility. Among the chemically acidified and/or enzyme-added samples, the use of the exogenous enzymes (E) corresponded to significantly higher values of the protein digestibility compared to the effect of the sole endogenous enzymes activation (End). The digestibility of the End/E sample was similar to that found for the End sample, probably as a consequence of the lower activity of exogenous enzymes in acidic conditions. The highest values of in vitro protein digestibility were observed for the fermented samples, varying from 32.7 to 39.1%. The microbial activity clearly affected the overall digestibility, also due to a more intense proteolysis, and showed the highest value when the starters were used in combination with enzymes (St/E), in agreement with the data previously reported. Compared to an analogous study on wheat bran,[11] the in vitro digestibility found under these conditions, including control bran, was lower; nonetheless, the increase observed after bioprocessing was higher (up to 2.7-fold the initial value) than that previously reported.

Effect of Bran Bioprocessing on Phytase Activity and Total Phenols. After bioprocessing, the phytase activity increased in all the samples (Table 4). In the chemically acidified treatments with or without the addition of enzymes (End and End/E), the phytase activity was significantly higher in comparison with the sole addition of exogenous enzymes (E). This is probably due to the activation of endogenous enzymes, including phytases, as a consequence of pH lowering during bioprocessing because endogenous wheat phytases have optimal activity at around pH 5.[6,33] A further increase of phytase activity (12.1 U) was found in the controlled fermentations (St and St/E) and was most probably due to the activity of lactic acid bacteria and yeast phytases. This seems a possible explanation also for the lowest phytase activity during spontaneous fermentation in the presence of enzymes (Sp/E), characterized by a more diverse microflora and slower acidification rate. The increase of phytase activity during bioprocessing of bran was previously reported.[11,34] Under the conditions here applied, fermentation with lactic acid bacteria and yeast showed the best performance in terms of an increase of phytase activity, independent of the addition of enzymes, indicating an important role of the microbial activity compared to the endogenous phytases alone.

Phenolic acids of wheat bran are mostly hydroxycinnamic acids, of which ferulic acid represents a structural component of the cell walls of aleurone and pericarp, mainly esterified with arabinoxylans.[12] The concentration of total phenols significantly increased in all of the treatments in comparison with ct bran (Table 4). Among the chemically acidified and/or enzyme-added samples, the highest content of total phenols (5.6 mmol/100 g) was obtained for sample E, in which the higher pH of the treatment allowed a predominant activity of the exogenous enzymes, especially xylanase, thus leading to a more intense release of phenols. The highest increase of total phenols was obtained with controlled fermentation (St and St/E), but no significant difference was found with the addition of enzymes. Phenolic acids can be released during bioprocessing by ferulic acid esterase activity of bran, whereas xylanase activity further releases hydroxycinnamic acids from its bound form.[35] The enhanced degradation of wheat bran during bioprocessing is also reflected in the increase of phenols release, which is probably also a consequence of an increased amount of WE-pentosans. This is in agreement with previous findings where bioprocessing with enzymes and lactic acid bacteria fermentation have been shown to increase the content of free phenols.[10−12,35] However, in contrast with previous results, in our study, no further release of phenols was observed during controlled fermentation with added enzymes (St/E), probably because the enzyme preparation here used did not possess ferulic acid esterase activity.

Total Variance and Correlation between the Biochemical Components after Bioprocessing. Data collected

DOI: 10.1021/acs.jafc.5b03495
J. Agric. Food Chem. 2015, 63, 8685−8693

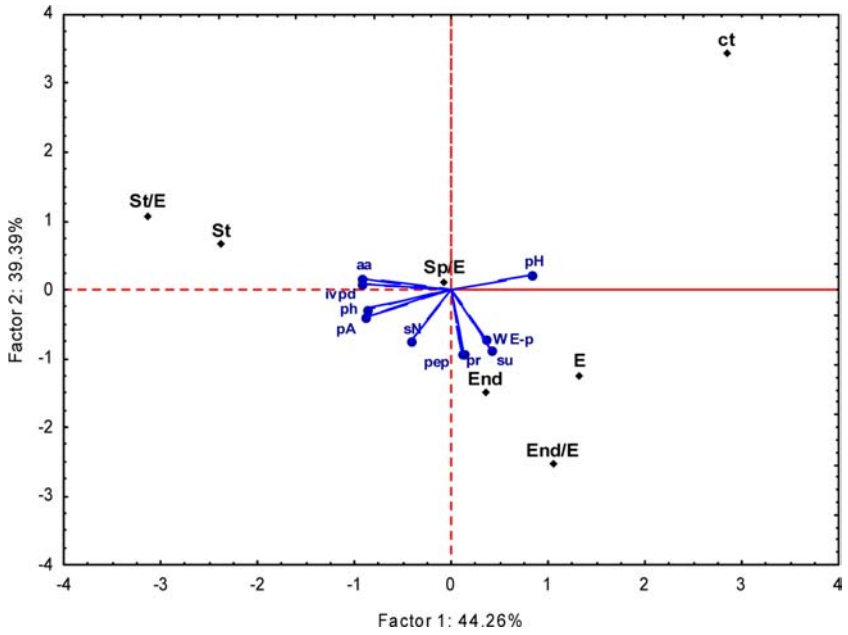

Figure 3. Principal component analysis (PCA) on the basis of the biochemical characteristics of control and bioprocessed wheat bran. Bioprocessing options are listed in Table 1. aa: free amino acids concentration; ivpd: in vitro protein digestibility; pA: phytase activity; pep: peptide concentration; ph: total phenols concentration; pr: soluble protein concentration; sN: solubilized nitrogen ratio; su: reducing sugars concentration; and WE-p: water-soluble pentosans concentration.

Table 5. Pearson Correlation Matrix of the Biochemical Parameters Analyzed from Control and Bioprocessed Wheat Bran*

	pep	aa	ivpd	ph	pA	WE-p	su	sN	pr	pH
pep	1.000	−0.219	−0.077	0.268	0.214	0.756	**0.899**	0.530	**0.864**	−0.036
aa	−0.219	1.000	**0.974**	**0.819**	0.692	−0.288	−0.474	0.130	−0.353	−0.638
ivpd	−0.077	**0.974**	1.000	**0.889**	0.695	−0.261	−0.401	0.158	−0.261	−0.624
ph	0.268	**0.819**	**0.889**	1.000	0.776	−0.084	−0.101	0.436	0.176	−0.575
pA	0.214	0.692	0.695	0.776	1.000	−0.076	−0.025	0.754	0.265	**-0.929**
WE-p	0.756	−0.288	−0.261	−0.084	−0.076	1.000	**0.902**	0.158	0.549	0.174
su	**0.899**	−0.474	−0.401	−0.101	−0.025	**0.902**	1.000	0.421	**0.817**	0.151
sN	0.530	0.130	0.158	0.436	0.754	0.158	0.421	1.000	0.739	−0.618
pr	**0.864**	−0.353	−0.261	0.176	0.265	0.549	**0.817**	0.739	1.000	−0.045
pH	−0.036	−0.638	−0.624	−0.575	**−0.929**	0.174	0.151	−0.618	−0.045	1.000

*Bioprocessing treatments are listed in Table 1. pep: peptide concentration; aa: free amino acids concentration; ivpd: in vitro protein digestibility; ph: total phenols concentration; pA: phytase activity; WE-p: water-soluble pentosans concentration; su: reducing sugars concentration; sN: solubilized nitrogen ratio; pr: soluble protein concentration; and pH: final pH of the bioprocessed bran. Values in bold indicate the variables with the largest correlation ($-0.80 > p > 0.80$).

from chemical characterization and related to bioprocessing conditions were subjected to principal component analysis (PCA) and shown in Figure 3. Factor 1, representing 44.26% of the total variance, displayed a continuous variance between the samples, whereas factor 2, representing 39.39% of the total variance, clearly separated the untreated bran from the other samples. The fermented samples St and St/E were grouped in the same area of the plot because they shared several features (highest free amino acids, total phenols concentration, phytase activity, and in vitro protein digestibility; lowest reducing sugars, WE-pentosans, and peptide concentrations). Similarly, the chemically acidified and/or enzyme-added samples End, E, and End/E were grouped together, opposite to the fermented samples because of their different chemical characteristics. Spontaneously fermented bran (Sp/E) was not grouped with any of the other samples because of its intermediate characteristics. The correlation matrix among the biochemical properties of the samples clearly showed a strong positive relationship among in vitro protein digestibility, free amino acids, and total phenols and, to a lesser extent, phytase activity (Table 5). On the contrary, a large negative correlation was observed between not only pH and phytase activity but also free amino acids and total solubilized nitrogen ratio. The correlations among all the parameters were considered, and protein solubilization were less strong in comparison with the in vitro protein digestibility, suggesting the role of several concurrent factors in the release and solubilization of proteins from wheat bran. The effect of pH was crucial for the activation of endogenous enzymes and the primary solubilization of protein derivatives from wheat bran. However, even if the activity of the sole endogenous enzymes was more effective in solubilizing the proteins, the in vitro digestibility was lower after treatment with microbes. The use of exogenous cell-wall-degrading enzymes showed a lower impact on the overall protein solubility but positively affected the digestibility especially when microbes were involved. The use of starter

DOI: 10.1021/acs.jafc.5b03495
J. Agric. Food Chem. 2015, 63, 8685−8693

cultures affected the release and composition of free amino acids and the release of phenols as well as showing a stronger impact on the in vitro digestibility of protein, in particular when in combination with cell-wall-degrading enzymes, thus conferring the best nutritional characteristics to wheat bran.

■ ASSOCIATED CONTENT

Supporting Information

The Supporting Information is available free of charge on the ACS Publications website at DOI: 10.1021/acs.jafc.5b03495.

RP-FPLC chromatograms of the water/salt-soluble extracts from control and bioprocessed wheat bran. (PDF)

■ AUTHOR INFORMATION

Corresponding Author

*E-mail: rossana.coda@helsinki.fi. Tel.: +358 408428330.

Funding

The authors are grateful to Era-Net SUSFOOD for funding this research.

Notes

The authors declare no competing financial interest.

■ REFERENCES

(1) Prückler, M.; Siebenhandl-Ehn, S.; Apprich, S.; Höltinger, S.; Haas, C.; Schmid, E.; Kneifel, W. Wheat bran-based biorefinery 1: Composition of wheat bran strategies of functionalization. *LWT − Food Sci. Technol.* **2014**, *56*, 211−221.

(2) Apprich, S.; Tirpanalan, Ö.; Hell, J.; Reisinger, M.; Böhmdorfer, S.; Siebenhandl-Ehn, S.; Novalin, S.; Kneifel, W. Wheat bran-based biorefinery 2: valorization of products. *LWT − Food Sci. Technol.* **2014**, *56*, 222−231.

(3) Poutanen, K.; Sozer, N.; Della Valle, G. How can technology help deliver more of grain in cereal foods for a healthy diet? *J. Cereal Sci.* **2014**, *59*, 327−336.

(4) Di Lena, G.; Patroni, E.; Quaglia, G. B. Improving the nutritional value of wheat bran by a white-rot fungus. *Int. J. Food Sci. Technol.* **1997**, *32*, 513−519.

(5) Antoine, C.; Peyron, S.; Mabille, F.; Lapierre, C.; Bouchet, B.; Abecassis, J.; Rouau, X. Individual contribution of grain outer layers and their cell wall structure to the mechanical properties of wheat bran. *J. Agric. Food Chem.* **2003**, *51*, 2026−2033.

(6) Guo, J.; Bian, Y. Y.; Zhu, K. X.; Guo, X. N.; Peng, W.; Zhou, H. M. Activation of endogenous phytase and degradation of phytate in wheat bran. (2015). *J. Agric. Food Chem.* **2015**, *63*, 1082−1087.

(7) Servi, S.; Özkaya, H.; Colakoglu, A. S. Dephytinization of wheat bran by fermentation with bakers' yeast, incubation with barley malt flour and autoclaving at different pH levels. *J. Cereal Sci.* **2008**, *48*, 471−476.

(8) van den Borne, J. J. G. C.; Kabel, M. A.; Briens, M.; van der Poel, A. F. B.; Hendriks, W. H. Effects of pretreatment of wheat bran on the quality of protein-rich residue for animal feeding and on monosaccharide release for ethanol production. *Bioresour. Technol.* **2012**, *124*, 446−454.

(9) Coda, R.; Katina, K.; Rizzello, C. G. Bran bioprocessing for enhanced functional properties. *Current Opinion in Food Science.* **2015**, *1*, 50−55.

(10) Nordlund, E.; Katina, K.; Aura, A. M.; Poutanen, K. Changes in bran structure by bioprocessing with enzymes and yeast modifies the in vitro digestibility and fermentability of bran protein and dietary fibre complex. *J. Cereal Sci.* **2013**, *58*, 200−208.

(11) Coda, R.; Rizzello, C. G.; Curiel, J. A.; Poutanen, K.; Katina, K. Effect of bioprocessing and particle size on the nutritional properties of wheat bran fractions. Innov. *Innovative Food Sci. Emerging Technol.* **2014**, *25*, 19−27.

(12) Anson, N. M.; Selinheimo, E.; Havenaar, R.; Aura, A. M.; Mattila, I.; Lehtinen, P.; Bast, A.; Poutanen, K.; Haenen, G. R. M. M. Bioprocessing of wheat bran improves in vitro bioaccessibility and colonic metabolism of phenolic compounds. *J. Agric. Food Chem.* **2009**, *57*, 6148−6155.

(13) Arte, E.; Katina, K.; Holopainen-Mantila, U.; Nordlund, E. *Cereal Chem* **2015**, submitted.

(14) Santala, O.; Nordlund, E.; Poutanen, K. Treatments with xylanase at high (90%) and low (40%) water content have different impacts on physicochemical properties of wheat bran. *Food Bioprocess Technol.* **2013**, *6*, 3102−3112.

(15) Loponen, J.; Sontag-Strohm, T.; Venäläinen, J.; Salovaara, H. Prolamin hydrolysis in wheat sourdoughs with differing proteolytic activities. *J. Agric. Food Chem.* **2007**, *55*, 978−984.

(16) Weiss, W.; Vogelmeier, C.; Görg, A. Electrophoretic characterization of wheat grain allergens from different cultivars involved in bakerś asthma. *Electrophoresis* **1993**, *14*, 805−816.

(17) AACC International. AACCI Method 46-11.02 Crude Protein -- Improved Kjeldahl Method, Copper Catalyst Modification. In *Approved Methods of Analysis*, 11th ed.; AACC International: St. Paul, MN, 2003. http://methods.aaccnet.org/summaries/46-11-02.aspx.

(18) Bradford, M. M. A rapid and sensitive method for the quantification of microgram quantities of protein utilizing the principle of protein-dye binding. *Anal. Biochem.* **1976**, *72*, 248−254.

(19) Church, F. C.; Swaisgood, H. E.; Porter, D. G.; Catignani, G. L. Spectrophotometric assay using *o*-phtaldialdehyde for determination of proteolysis in milk and isolated milk proteins. *J. Dairy Sci.* **1983**, *66*, 1219−1227.

(20) Akenson, W. R.; Stahmann, M. A. A pepsin pancreatin digest index of protein quality evaluation. *J. Nutr.* **1964**, *83*, 257−261.

(21) Santala, O.; Lehtinen, P.; Nordlund, E.; Suortti, T.; Poutanen, K. Impact of water content on the solubilisation of arabinoxylan during xylanase treatment of wheat bran. *J. Cereal Sci.* **2011**, *54*, 187−194.

(22) Bernfeld, P. Amylase α and β. In *Methods in Enzymology*; Colowick, S. P., Kaplan, N. O., Eds; Academic Press: New York, 1955; Vol. *1*, pp 149−158.

(23) Shimizu, M. Purification and characterization of phytase from *Bacillus subtilis* (natto) N-77. *Biosci., Biotechnol., Biochem.* **1992**, *56*, 1266−1269.

(24) Slinkard, K.; Singleton, V. L. Total phenol analysis: Automation and comparison with manual methods. *Am. J. Enol. Viticult.* **1997**, *28*, 49−55.

(25) Laemmli, U. K. Cleavage of structural proteins during the assembly of the head of bacteriophage T4. *Nature* **1970**, *227*, 680−685.

(26) Dijksterhuis, G. B.. *Multivariate data analysis in sensory and consumer science*. Food and Nutrition Press: Trumbull, CT, 1997.

(27) Nionelli, L.; Curri, N.; Curiel, J. A.; Di Cagno, R.; Pontonio, E.; Cavoski, I.; Gobbetti, M.; Rizzello, C. G. Exploitation of Albanian wheat cultivars: characterization of the flours and lactic acid bacteria microbiota, and selection of starters for sourdough fermentation. *Food Microbiol.* **2014**, *44*, 96−107.

(28) Gobbetti, M.; Lavermicocca, P.; Minervini, F.; De Angelis, M.; Corsetti, A. Arabinose fermentation by Lactobacillus plantarum in sourdough with added pentosans and $\alpha\alpha$-L-arabinofuranosidase: a tool to increase the production of acetic acid. *J. Appl. Microbiol.* **2000**, *88*, 317−324.

(29) Gänzle, M., Gobbetti, M. Physiology and biochemistry of lactic acid bacteria. In *Handbook on Sourdough Biotechnology*; Gänzle, M., Gobbetti, M., Eds.; Springer Science & Business Media: New York, 2013; Vol. *1*, pp 183−216.

(30) Breddam, K. Carboxypeptidase S-1 from Penicillium janthinellum: Enzymatic properties in hydrolysis and aminolysis reactions. *Carlsberg Res. Commun.* **1988**, *53*, 309−320.

(31) Thiele, C.; Gänzle, M. C.; Vogel, R. F. Contribution of sourdough lactobacilli, yeast, and cereal enzymes to the generation of amino acids in dough relevant for bread flavor. *Cereal Chem.* **2002**, *79*, 45−51.

DOI: 10.1021/acs.jafc.5b03495
J. Agric. Food Chem. 2015, 63, 8685−8693

(32) Gänzle, M. G.; Vermeulen, N.; Vogel, R. F. Carbohydrate, peptide and lipid metabolism of lactic acid bacteria in sourdough. *Food Microbiol.* **2007**, *24*, 128−138.
(33) Kumar, V.; Sinha, A. K.; Makkar, H. P. S.; Becker, K. Dietary roles of phytate and phytase in human nutrition: A review. *Food Chem.* **2010**, *120*, 945−959.
(34) Rizzello, C. G.; Coda, R.; Mazzacane, F.; Minervini, D.; Gobbetti, M. Micronized by-products from debranned durum wheat and sourdough fermentation enhanced the nutritional, textural and sensory features of bread. *Food Res. Int.* **2012**, *46*, 304−313.
(35) Savolainen, O.; Coda, R.; Suomi, K.; Katina, K.; Juvonen, R.; Hanhineva, K.; Poutanen, K. The role of oxygen in the liquid fermentation of wheat bran. *Food Chem.* **2014**, *153*, 424−431.

DOI: 10.1021/acs.jafc.5b03495
J. Agric. Food Chem. 2015, 63, 8685−8693

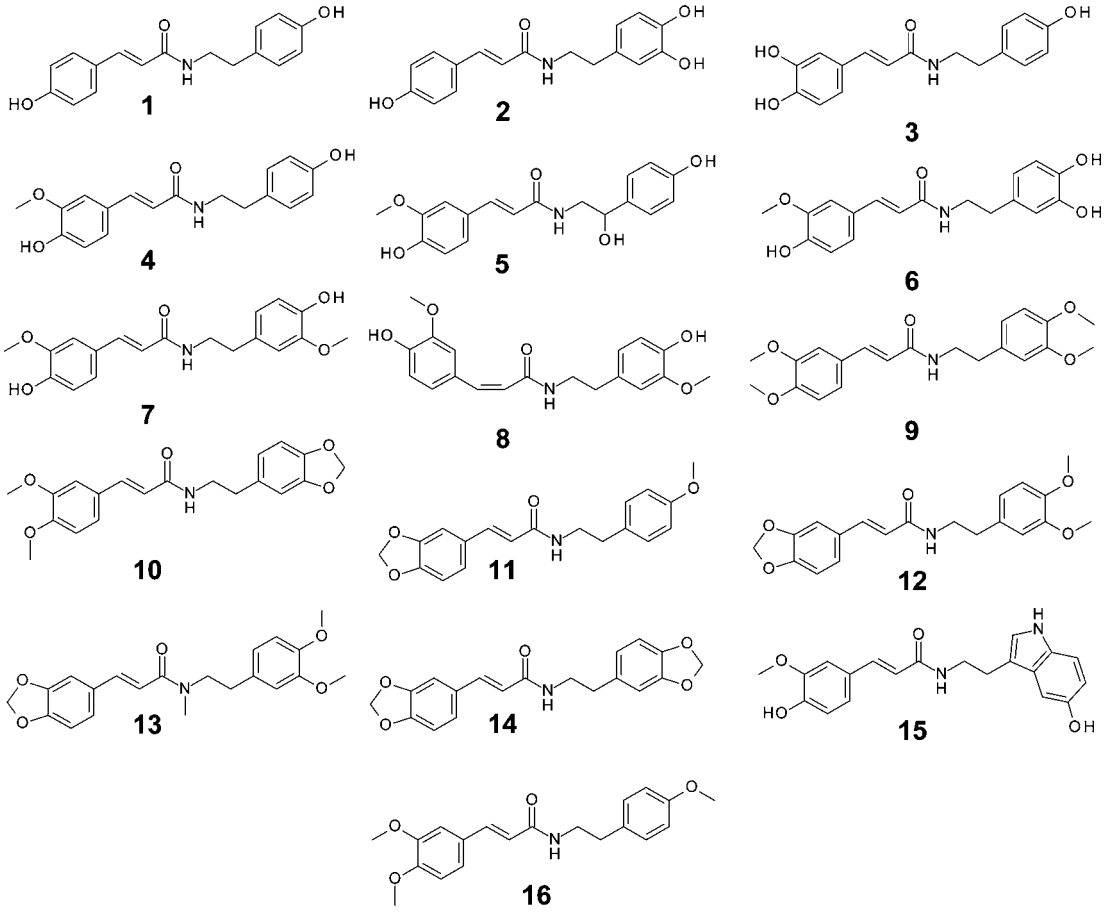

Figure 1. Structures of naturally occurring *N*-cinnamoyl amines **1**–**16**; for natural occurrence, see Table 1.

have been described as weakly pungent substances[18] and some avenanthramides show cooling properties.[19] Until recently, no data about the umami effect of these secondary metabolites where reported, but during the reviewing process for this paper, a study was published showing the umami effects of rubemamine (**9**) and its homologue *N*-3,4-dimethoxycinnamoyl-4-methoxyphenethylamine (**16**).[20]

To identify potential umami-modulating compounds, a series of naturally occurring *N*-cinnamoyl derivatives of substituted phenethylamines and serotonin was prepared (Figure 1; natural occurrence, Table 1) and tested by a sensory panel. In addition, advanced sensory studies investigated the potential of these compounds to function as general taste modifiers and synergistic umami taste modulators. Furthermore, in order to identify a biological basis for the observed sensory effects, the compounds were tested by means of an in vitro TAS1R1-TAS1R3 receptor assay for their intrinsic and synergistic activity together with MSG.

MATERIALS AND METHODS

General. Reagents, solvents, and consumables were purchased from commercial suppliers (Acros Organics, Geel, Belgium; Sigma-Aldrich, Steinheim, Germany; Alfa Aesar GmbH & Co KG, Karlsruhe, Germany) or produced by Symrise and used without further purification or drying. Monosodium glutamate (MSG) was obtained from Oskar Berg GmbH, Germany. Monitoring of the reaction was accomplished by thin-layer chromatography on silica-gel GF254 plates with either UV detection or by use of a staining reagent consisting of ammonium molybdate, cerium sulfate, and sulfuric acid. Purity was determined via GC chromatography using either an Agilent 6890N or Agilent 7890N (Agilent Technologies, Santa Clara, USA) system equipped with DB-WAX and DB-1 columns (length, 20 m; inside diameter, 0.18 mm; film, 0.18 μm; flow rate, 0.5–3.0 mL min^{-1}; injector, split ratio 1/70, 12 °C/s, 80–250 °C; carrier gas, H_2; and detector, FID, 275 °C (Agilent Technologies, Santa Clara, USA)) or a high-temperature MXT column (length, 15 m; inside diameter, 0.25 mm; film, 0.10 μm; flow rate, 1.0–5.0 mL min^{-1}; injector, split ratio 1/100, 10 °C/s, 60–380 °C; carrier gas, H_2; and detector, FID, 420 °C (Restek, Bad Homburg, Germany)). If the purity could not be determined via GC because of decomposition, then the below-mentioned NMR and UPLC instruments were used to determine the purity. The purity of all reported compounds was ≥95%. ^{1}H and ^{13}C nuclear magnetic resonance spectra were recorded on a Varian Gemini, Varian Mercury Plus or Varian Unity Innova spectrometer (Varian, Darmstadt, Germany) using tetramethylsilane as an internal reference. GC-MS spectra (EI, 70 eV, detector: quadrupole) were obtained by using either a Shimadzu GC2010/QP2010 (Shimadzu Corporation, Kyoto, Japan) or an Agilent 6890N (Agilent Technologies, Santa Clara, USA) system. HR-MS spectra (EI, 70 eV, detector: TOF) were recorded on a coupled system consisting of a Bruker micrOTOF Q-II (Bruker Daltonik GmbH, Bremen, Germany) and a Waters Acquity UPLC (Waters, Eschborn, Germany).

General Procedure A for the Synthesis of Amides 1–7, 11, 12, and 15. A 1.0 equiv amount of the corresponding cinnamic acid derivative and a 1.0 equiv amount of the *N*-hydroxysuccinimide were dissolved in 2.5–5.0 mL/mmol dioxane at 35 °C. Subsequently, 1.0 equiv of DCC in 1.5–2.5 mL/mmol dioxane was added, and the resulting mixture was stirred overnight at room temperature. The formed solid was removed by filtration and washed with dioxane. This mixture was added slowly to a suspension of 1.1–1.5 equiv of the corresponding amine in 2.0–3.0 mL/mmol water containing 1.0–2.5 equiv of $NaHCO_3$, keeping the temperature below 40 °C; after completion of the addition, the mixture is stirred at room temperature

DOI: 10.1021/acs.jafc.5b04402
J. Agric. Food Chem. 2015, 63, 8694–8704

Table 1. Structural Analogs Investigated as Potential Umami Compounds[a]

name, occurrence	sensory screening in water
N-coumaroyltyramine (**1**), *Aristolochia manshuriensis*[39]	10 ppm: no taste 50 ppm: coffee, card board, burned, anis 100 ppm: anis, bitter
N-coumaroyldopamine (**2**), *Atraphaxis spinosa* L., var. *sinaica* Boiss.[40]	10 ppm: dry, coffee 50 ppm: dry, coffee, bitter 100 ppm: bitter, coffee
N-caffeoyltyramine (**3**), *Capsicum annuum*[41]	10 ppm: roasty, coffee 50 ppm: bitter, flowery, coffee 100 ppm: bitter, plastic
N-feruloyltyramine (**4**), e.g., *Beta vulgaris*[42]	10 ppm: neutral 50 ppm: neutral 100 ppm: bitter, dry, chalky
N-feruloyloctopamine (**5**), *Salsolia tetranda*[43]	10 ppm: neutral, weakly bitter 50 ppm: glue, coffee
N-feruloyldopamine (**6**), *Amaranthus* spp.[44]	10 ppm: vanille 50 ppm: vanille, dry 100 ppm: bitter, plastic
N-feruloyl-3-methoxytyramine (**7**), e.g., *Beta vulgaris*[42]	10 ppm: neutral, weakly pungent 50 ppm: bitter, scratchy dry 100 ppm: bitter
N-*cis*-feruloyl-3-methoxytyramine (**8**), *Cinnamomum reticulatum*[45]	10 ppm: dry 50 ppm: dull, dry 100 ppm: strongly dry
rubemamine (**9**), *Chenopodium album*, *Zanthoxylum rubescens*[32,46]	10 ppm: **weakly umami** 50 ppm: **umami**, weakly sweet 100 ppm: **strongly umami**
rubescenamine (**10**), *Z. rubescens*[21]	10 ppm: **umami**, quick onset 50 ppm: **strongly umami**, soapy
armatamide (**11**), *Zanthoxylum armatum*[47]	10 ppm: neutral, dry 50 ppm: weakly pungent 100 ppm: weakly sour, weakly sweet, tingling
zanthosine (**12**), *Z. rubescens*[48]	10 ppm: bitter 50 ppm: bitter 100 ppm: bitter
zanthosinamide (**13**), *Z. rubescens*[48]	10 ppm: alcoholic 50 ppm: bitter, **weakly umami** 100 ppm: strongly bitter, **umami aftertaste**
dioxamine (**14**), *Z. rubescens*[46]	10 ppm: neutral 50 ppm: neutral, weakly bitter 100 ppm: bitter, acidic, weakly sweet
moschamine (**15**), *Carthamus tinctorius* L.[49]	10 ppm: neutral 50 ppm: neutral 100 ppm: bitter

[a]All compounds were tested by a trained consensus panel (n = 8) in water. For structures of **1**–**15**, see Figure 1.

and monitored by TLC. After the reaction is finished, 10% aqueous HCl is added to adjust the pH to 1.5, and the reaction mixture is extracted two times with ethyl acetate. The combined organic layers are consecutively washed with saturated aqueous $NaHCO_3$ solution and brine before being dried over $NaSO_4$. (If necessary, activated charcoal can be added during the drying process.) After removal of the solvent, the products were subjected to crystallization, flash chromatography, or preparative HPLC for final purification.

General Procedure B for the Synthesis of Amides 9, 10, 13, and 14. A 1.05–1.2 equiv amount of oxalyl chloride was slowly added to a mixture of 1.0 equiv of the corresponding cinnamic acid derivative in 2.0–4.0 mL/mmol of dichloromethane. The mixture was allowed to stir overnight before refluxing for an additional 30 min. After evaporation of the solvent, the crude acid chloride was dissolved in 1.0–2.0 mL/mmol of acetone and added to a mixture of the amine (or the corresponding hydrochloride) in 1.0–2.0 mL/mmol acetone and 1.0–2.0 mL/mmol water containing 1.0 equiv (or 2.0 equiv if the hydrochlorides are used) of sodium hydroxide. The mixture is allowed to stir for an additional 2 h before the product is filtered out and washed several times with water. Further purification is possible where needed by recrystallization.

Spectral data of all compounds were in accordance with those reported in the literature as listed in Table S.1.

N-*E*-Coumaroyltyramine (**1**) was prepared following procedure A starting from *p*-coumaric acid and tyramine hydrochloride. Final purification was possible via crystallization from ethyl acetate.

^{1}H NMR (200 MHz, CD_3OD): 2.74 (dd, J = 8.1, 6.6 Hz, 2H), 3.44 (dd, J = 8.2, 6.5 Hz, 2H), 3.64 (s, 1H), 6.40 (d, J = 15.7 Hz, 1H), 6.73 (m, 2H), 6.80 (m, 2H), 7.07 (m, 2H), 7.41 (m, 2H), 7.49 (d, J = 15.8, 1H) ppm. HR-MS (ESI$^+$): 284.1281 ([$M^{+\cdot}$ + H], $C_{17}H_{19}NO_3^+$; calcd 284.1281).

N-(*E*)-Coumaryldopamine (**2**) was prepared following procedure A starting from *p*-coumaric acid and dopamine hydrochloride. Final purification was possible via two consecutive flash chromatography steps (first chromatography employing ethyl acetate as eluent; second chromatography employing chloroform/methanol 10:1 as eluent).

^{1}H NMR (200 MHz, CD_3OD): 2.69 (dd, J = 8.1, 6.5 Hz, 2H), 3.44 (m, 2H), 6.38 (d, J = 15.7 Hz, 1H), 6.54 (dd, J = 7.9, 2.2 Hz, 1H), 6.67 (d, J = 2.1 Hz, 1H), 6.71 (d, J = 8.0, 1H), 6.78 (m, 2H), 7.39 (m, 2H), 7.48 (d, J = 15.7, 1H) ppm. HR-MS (ESI$^+$): 300.1235 ([$M^{+\cdot}$ + H], $C_{17}H_{18}NO_4^+$; calcd 300.1230).

N-(*E*)-Caffeoyltyramine (**3**) was prepared following procedure A starting from caffeic acid and tyramine. Final purification was possible via crystallization from chloroform/methanol 10:1.

^{1}H NMR (400 MHz, CD_3OD): 2.74 (dd, J = 8.0, 6.9 Hz, 2H), 3.45 (m, 2H), 6.32 (d, J = 15.7 Hz, 1H), 6.71 (m, 2H), 6.74 (d, J = 8.2 Hz, 1H), 6.88 (ddd, J = 8.2, 2.1, ~0.5 Hz, 1H), 6.98(d, J = 2.1 Hz, 1H), 7.05 (m, 2H), 7.37 (d, J = 15.6 Hz, 1H) ppm. HR-MS (ESI$^+$): 300.1235 ([$M^{+\cdot}$ + H], $C_{17}H_{18}NO_4^+$; calcd 300.1230).

N-(*E*)-Feruloyltyramine (**4**) was prepared following procedure A starting from ferulic acid and tyramine. Final purification was possible via flash chromatography employing ethyl acetate as eluent.

^{1}H NMR (400 MHz, CD_3OD): 2.75 (t, J = 7.4 Hz, 2H), 3.35 (s, 1H), 3.46 (m, 2H), 3.88 (s, 3H), 6.38 (dd, J = 15.5, 1.1 Hz, 1H), 6.72 (m, 2H), 6.77 (dd, J = 8.3, 1.1 Hz, 1H), 7.01 (dd, J = 8.3, 1.9 Hz, 1H), 7.05 (m, 2H), 7.10 (d, J = 1.9 Hz, 1H), 7.43 (d, J = 15.7 Hz, 1H) ppm. GC/EI-MS: 343 (6, [$M^{+\cdot}$]), 329 (20), 194(12), 193(10), 192(10), 177(40), 151(10), 150(100), 149(9), 145(14), 137(11), 89(8).

N-(*E*)-Feruloyloctopamine (**5**) was prepared following procedure A starting from ferulic acid and octopamine hydrochloride. Final purification was possible via flash chromatography employing ethyl acetate as eluent.

^{1}H NMR (400 MHz, CD_3OD): 3.43 (dd, J = 13.6, 7.9 Hz, 1H), 3.53 (dd, J = 13.6, 5.0 Hz, 1H), 3.88 (s, 3H), 4.72 (m, 1H), 6.45 (d, J = 15.7, 1H), 6.76 (m, 2H), 6.79 (d, J = 8.2, 1H), 7.02 (dd, J = 8.1, 2.0 Hz, 1H), 7.12 (d, J = 2.0 Hz, 1H), 7.22 (m, 2H), 7.44 (d, J = 15.6 Hz, 1H) ppm. HR-MS (ESI$^+$): 330.1335 ([$M^{+\cdot}$ + H], $C_{18}H_{20}NO_5^+$; calcd 330.1336).

N-(*E*)-Feruloyldopamine (**6**) was prepared following procedure A starting from ferulic acid and dopamine hydrochloride. Final purification was possible via two consecutive flash chromatography steps (first chromatography employing ethyl acetate as eluent; second chromatography employing chloroform/methanol 10:1 as eluent).

^{1}H NMR (400 MHz, CD_3OD): 2.70 (t, J = 7.4 Hz, 2H), 3.45 (dd, J = 8.0, 6.7 Hz, 2H), 3.87 (s, 3H), 6.40 (dd, J = 15.7, 0.4 Hz, 1H), 6.55 (dd, J = 8.0, 2.1 Hz, 1H), 6.67 (d, J = 2.1 Hz, 1H), 6.69 (d, J = 8.0 Hz, 1H), 6.79 (d, J = 8.2 Hz, 1H), 7.02 (dd, J = 8.2, 2.0, 1H), 7.11 (d, J = 2.0 Hz, 1H), 7.43 (d, J = 15.7 Hz, 1H) ppm. GC/EI-MS: 329 (20,

DOI: 10.1021/acs.jafc.5b04402
J. Agric. Food Chem. 2015, 63, 8694–8704

[$M^{+\cdot}$]), 194 (64), 193 (13), 192 (29), 177 (100), 145 (30), 136 (38), 123 (13), 117 (14), 89 (15).

N-(*E*)-Feruloyl-3-methoxytyramine (**7**) was prepared following procedure A starting from ferulic acid and 3-methoxytyramine hydrochloride. Final purification was possible via two consecutive flash chromatography steps (first chromatography employing ethyl acetate as eluent; second chromatography employing chloroform/methanol 10:1 as eluent).

^{1}H NMR (200 MHz, CD_3OD): 2.74 (t, *J* = 7.2 Hz, 2H), 3.44 (dd, *J* = 7.9, 6.5 Hz, 2H), 3.76 (s, 3H), 3.81 (s, 3H), 6.48 (d, *J* = 15.5 Hz, 1H), 6.73 (dd, *J* = 8.0, 1.8 Hz, 1H), 6.79 (d, *J* = 8.1 Hz, 1H), 6.83 (d, *J* = 8.2 Hz, 1H), 6.88 (d, *J* = 1.9 Hz, 1H), 7.09 (m,1H), 7.17 (d, *J* = 1.9 Hz, 1H), 7.49 (d, J = 15.6 Hz, 1H) ppm. GC/EI-MS: 343 (6, [$M^{+\cdot}$]), 194 (12), 193 (10), 192 (10), 177 (40), 151 (10), 150 (100), 149 (9), 145 (14), 137 (11), 89 (8).

N-(*Z*)-Feruloyl-3-methoxytyramine (**8**) was prepared by dissolving *N*-*E*-feruloyl-3-methoxytyramine (**7**) in 100 mL/g ethanol and subsequently treating it with UV irradiation (LW 366) for 100 h. The resulting *E*/*Z* mixture of isomers was purified by HPLC chromatography.

^{1}H NMR (400 MHz, CD_3OD): 2.70 (t, *J* = 7.3 Hz, 2H), 3.42 (dd, *J* = 7.9, 6.7 Hz, 2H), 3.78 (s, 3H), 3.82 (s, 3H), 5.81 (d, *J* = 12.7, 1H), 6.60 (dd, *J* = 8.0, 2.0, 1H), 6.62 (d, *J* = 12.6 Hz, 1H), 6.69 (d, *J* = 8.0 Hz, 1H), 6.73 (d, *J* = 8.2 Hz, 1H), 6.77 (d, *J* = 2.0 Hz, 1H), 6.92 (dd, *J* = 8.2, 2.0 Hz, 1H), 7.36 (d, *J* = 2.0 Hz, 1H) ppm. GC/EI-MS: 343 (5, [$M^{+\cdot}$]), 194 (12), 193 (8), 177 (39), 151 (11), 150 (100), 145 (19), 137 (10), 135 (8), 117 (9), 89 (10).

Rubemamine (**9**) was prepared following procedure B starting from (*E*)-3,4-dimethoxy cinnamic acid and 3,4-dimethoxyphenylethylamine. If necessary, further purification is possible via crystallization from n-propanol/*n*-hexane 2:3. Spectral data were in accordance with those reported in the literature.[21]

^{1}H NMR (400 MHz, $CDCl_3$): 2.84 (t, *J* = 6.9 Hz, 2H), 3.64 (td, *J* = 6.9, 5.9 Hz, 2H), 3.87 (s, 3H), 3.87 (s, 3H), 3.90 (s, 3H), 3.90 (s, 3H), 5.58 (t, *J* = 5.9 Hz, 1H), 6.20 (d, *J* = 15.5 Hz, 1H), 6.75 (d, *J* = 2.0 Hz, 1H), 6.77 (dd, *J* = 8.0, 1.9 Hz, 1H), 6.83 (d, J = 8.0 Hz, 1H), 6.85 (d, *J* = 8.3 Hz, 1H), 7.00 (d, *J* = 2.0 Hz, 1H), 7.07 (ddd, *J* = 8.2, 2.0, ∼0.5 Hz, 1H), 7.56 (d, *J* = 15.5 Hz, 1H) ppm. GC/EI-MS: 371 (6, [$M^{+\cdot}$]), 207 (3), 206 (10), 192 (5), 191 (29), 165 (11), 164 (100), 163 (5), 151 (7), 149 (6).

Rubescenamine (**10**) was prepared following procedure B starting from (*E*)-3,4-dimethoxy cinnamic acid and 2-(1,3-benzodioxol-5-yl)ethanamine hydrochloride. If necessary, further purification is possible via crystallization from n-propanol/*n*-hexane 2:3. Spectral data were in accordance with those reported in the literature.[21]

^{1}H NMR (400 MHz, $CDCl_3$): 2.80 (t, *J* = 6.8 Hz, 2H), 3.61 (td, *J* = 6.8, 5.9 Hz, 2H), 3.90 (s, 6H), 5.56 (t, *J* = 6.1 Hz, 1H), 5.94 (s, 2H), 6.20 (d, *J* = 15.5 Hz, 1H), 6.67 (dd, *J* = 7.8, 1.7 Hz, 1H), 6.72 (d, *J* = 1.7 Hz, 1H), 6.77 (d, *J* = 7.9 Hz, 1H), 6.85 (d, *J* = 8.3 Hz, 1H), 7.01 (d, *J* = 2.0 Hz, 1H), 7.07 (dd, *J* = 8.3, 2.0 Hz, 1H), 7.56 (d, *J* = 15.5 Hz, 1H) ppm. GC/EI-MS: 355 (17, [$M^{+\cdot}$]), 207 (58), 206 (79), 192 (12), 191 (69), 163 (11), 149 (11), 148 (100), 147 (13), 77 (11).

Armatamide (**11**) was prepared following procedure A starting from (*E*)-3,4-methylendioxy cinnamic acid and 2-(4-methoxyphenyl)-ethanamine. Final purification was possible via crystallization from ethyl acetate.

^{1}H NMR (200 MHz, CD_3OD): 2.77 (dd, *J* = 8.0, 6.6 Hz, 2H), 3.46 (m, 2H), 3.73 (s, 3H), 6.02 (s, 2H), 6.42 (d, *J* = 15.6 Hz, 1H), 6.83 (d, *J* = 8.1, 1H), 6.86 (d, *J* = 8.7 Hz, 2H), 7.04 (ddd, *J* = 8.0, 1.7, ∼0.5 Hz, 1H), 7.11 (m, 1H), 7.16 (m, 2H), 7.44 (d, *J* = 15.6, 1H) ppm. HR-MS (ESI$^+$): 326.1387 ([$M^{+\cdot}$ + H], $C_{19}H_{20}NO_4^+$; calcd 326.1387).

Zanthosine (**12**) was prepared following procedure A staring from (*E*)-3,4-methylendioxy cinnamic acid and 3,4-dimethoxyphenylethylamine. For final purification, the product was dissolved in ethyl acetate under reflux. After cooling down to room temperature, the product was precipitated by the addition of diethyl ether.

^{1}H NMR (200 MHz, $CDCl_3$): 2.83 (t, *J* = 6.9 Hz, 2H), 3.63 (td, *J* = 6.9, 5.9 Hz, 2H), 3.87 (s, 3H), 3.87 (s, 3H), 5.66 (m, 1H), 5.99 (s, 2H), 6.15 (d, *J* = 15.5 Hz, 1H), 6.70−6.88 (m, 4H), 6.92−7.02 (m, 2H), 7.53 (d, *J* = 15.5 Hz, 1H) ppm. HR-MS (ESI$^+$): 356.1490 ([$M^{+\cdot}$ + H], $C_{20}H_{22}NO_5^+$; calcd 356.1492).

Zanthosinamide (**13**) was prepared following procedure B staring from (*E*)-3,4-methylendioxy cinnamic acid and 2-(3,4-dimethoxyphenyl)-*N*-methyl-ethanamine. As the expected, product did not precipitate from the reaction mixture; the product is extracted with ethyl acetate. After evaporation of the solvent, no further purification was necessary.

^{1}H NMR (100 °C, 400 MHz, $CDCl_3$): 2.81 (m, 2H), 2.99 (s, 3H), 3.62 (m, 2H), 3.77 (s, 3H), 3.80 (s, 3H), 5.94 (s, 2H), 6.50 (d, *J* = 15.3 Hz, 1H), 6.70 (s, 2H), 6.72 (d, *J* = 2.0 Hz, 1H), 6.78 (d, *J* = 8.3 Hz, 1H), 6.80 (d, *J* = 8.1 Hz, 1H), 6.92 (d, *J* = 6.5 Hz, 2H), 7.46 (d, *J* = 15.3 Hz, 1H) ppm. GC/EI-MS: 369 (7, [$M^{+\cdot}$]), 176 (9), 175 (78), 165 (11), 164 (100), 151 (7), 149 (4), 145 (25), 117 (12), 89 (15). HR-MS (ESI$^+$): 353.1369 ([$M^{+\cdot}$ + H], $C_{20}H_{21}N_2O_4^+$; calcd 353.1496).

Dioxamine (**14**) was prepared following procedure B starting from (*E*)-3,4-methylendioxy cinnamic acid and 2-(1,3-benzodioxol-5-yl)-ethanamine hydrochloride.

^{1}H NMR (200 MHz, CD_3OD): 2.80 (t, *J* = 6.8 Hz, 2H), 3.60 (td, *J* = 6.8, 5.9 Hz, 2H), 5.54 (s, 1H), 5.94 (s, 2H), 5.99 (s, 2H), 6.14 (d, *J* = 15.5 Hz, 1H), 6.66 (dd, *J* = 7.8, 1.6 Hz, 1H), 6.71 (d, *J* = 1.5 Hz, 1H), 6.76 (d, *J* = 7.8, 1H), 6.79 (dd, *J* = 7.6, ∼0.8 Hz, 1H), 6.96 (dd, *J* = 7.6, 1.7, 1H), 6.98 (s, 1H), 7.53 (d, *J* = 15.5 Hz, 1H) ppm. HR-MS: 340.1172 ([$M^{+\cdot}$ + H], $C_{19}H_{18}NO_5$; calcd 340.1179).

Moschamine (**15**) was prepared following procedure A starting from ferulic acid and serotonine hydrochloride. Final purification was possible via flash chromatography employing ethyl acetate as eluent with subsequent recrystallization from ethyl acetate.

^{1}H NMR (400 MHz, $CD_3S{=}OCD_3$): 2.78 (t, *J* = 7.4 Hz, 2H), 3.43 (m, 2H), 3.80 (s, 3H), 6.45 (d, *J* = 15.7 Hz, 1H), 6.59 (dd, *J* = 8.6, 2.3 Hz, 1H), 6.79 (d, *J* = 8.1 Hz, 1H), 6.85 (d, *J* = 2.4 Hz, 1H), 6.98 (dd, *J* = 8.1, 1.9 Hz, 1H), 7.05 (d, *J* = 2.5 Hz, 1H), 7.12 (d, *J* = 2.0 Hz, 1H), 7.13 (dd, *J* = 8.8, ∼0.6 Hz, 1H), 7.33 (d, *J* = 15.7 Hz, 1H), 8.03 (t, *J* = 5.7 Hz, 1H), 8.59 (s, 1H), 10.48 (d, *J* = 2.4 Hz, 1H) ppm. HR-MS: 353.1374 ([$M^{+\cdot}$ + H], $C_{20}H_{21}N_2O_4$; calcd 353.1496).

Sensory Tests. Sensory tests were carried out with healthy and trained panelists without known taste disorders. Panelists were fully informed about procedure and intention of the project and had given written consent. Because of the FEMA/GRAS status of rubemamine (**9**)[22] and rubescenamine (**10**)[23] and the positive evaluation EFSA for rubemamine (**9**),[24] the other compounds were considered to be a low risk for the screening phase. In addition, the panelists were advised not to swallow the samples (maximum 10 mL of solution) but rather to use the sip and spit method. The tests were conducted in sensory panel rooms under standardized conditions, and they were blind and randomized. For the preparation of the test solutions, Vittel water was used. The panelists had participated earlier at regular intervals in sensory work and were, therefore, familiar with the techniques applied.

Pre-Evaluation. A number of 5−8 trained panelists received each compound in a dosage of 10, 50, and 100 ppm in a 0.5% salt and a 5.0% sugar solution, and were asked to describe the sample and give a qualitative statement for the umami intensity. No additional reference (e.g., MSG) was presented during this session.

Using as the base an American beef extract (Beef Meat Extract Stock Type, Symrise), a corresponding base mixed with MSG, or a corresponding base mixed with MSG, the test compound was in each case administered blindly and individually to 15−25 trained panelists at slightly elevated temperatures (30−35 °C) for profiling. Using the descriptors previously decided upon by discussion (mouth feel, salty, metallic, meaty, bitter, mouth-watering, barbecued−roasted, sweet, sour, and lingering), the strength of each of these was assessed on a scale from 0 (imperceptible) to 9 (very strong). The individual results of the panelists were averaged.

The taste detection threshold for rubemamine (**9**) in water (Vittel) was determined by a forced-choice ascending concentration series method of limits according to the established ASTM protocol.[25] Threshold for rubescenamine (**10**) was determined at elevated temperature (∼30 °C) according to the same method.

Quantification of Taste Modulation Effects of Rubemamine (9) and Rubescenamine (10) on Umami Taste of MSG

DOI: 10.1021/acs.jafc.5b04402
J. Agric. Food Chem. 2015, 63, 8694−8704

(Yamaguchi Protocol). For the quantification of the synergistic effects, the intrinsic and positive umami-modulating activity of the test compound in comparison to MSG was determined by means of a paired choice comparison test as proposed by Yamaguchi.[2] For the determination of the intrinsic activity, a binary solution (pH 6.0) containing the test compound in water (fixed sample) was compared to a series of aqueous solutions containing logarithmically increasing concentrations of MSG (reference samples; 30% intervals: 0.17, 0.22, 0.28, 0.37, 0.49, 0.63, 0.82, 1.07, 1.4, and 1.82% w/w). For the determination of the modulating activity, a binary solution (pH 6.0) containing the umami compound and MSG (0.17% or 0.22%) in water (fixed sample) was compared to a series of aqueous solutions containing logarithmically increasing concentrations (30% intervals) of MSG (reference samples). In each sensory session, the assessors were asked to evaluate four sample pairs presented in randomly coded cups and to identify the sample exhibiting the stronger umami taste using a forced choice methodology (2-AFC). The panelists wore nose clips during tasting. Each test was repeated three times for each panelist. To control for significance, Student's t test was conducted, and the level of significance was set to $p < 0.1$ because of the relatively low panelist number ($n = 14–18$).

Activation of TAS1R1-TAS1R3 Umami Receptor in Transfected HEK 293 Cells. To elucidate umami receptor activation by the test compounds, a cell-based assay was used as described elsewhere.[26] In brief, functional experiments were carried out using HEK293-PEAKrapid cells (American Type Culture Collection) modified for stable expression of human TAS1R1 (hTAS1R1) subunit and the promiscuous G protein subunit Gα15. For umami receptor expression, cells were transiently transfected with vector encoding for the rat Tas1r3 (rTas1r3) subunit using Lipofectamine2000 (Invitrogen). Transfection was carried out 24 h prior to calcium imaging experiments.

To enable functional calcium imaging, transfected cells were loaded with 2 μM Fluo4-AM (Molecular Probes) in serum-free DMEM low-glucose Glutamax (Gibco) medium containing 2.5 mM probenecide. After 1 h of incubation at 37 °C, cells were washed three times with bath solution (130 mM NaCl, 5 mM KCl, 10 mM Hepes, 2 mM $CaCl_2$, pH 7.4) and incubated for 20 min at room temperature in the dark between washing steps to allow complete de-esterification of the dye. Calcium imaging experiments were carried out using a fluorimetric imaging plate reader (FLIPR^{tetra}, Molecular Devices). This allows automated substance application and simultaneous fluorescence measurements. Compounds were solved and applied in bath solution or low concentrations of DMSO (0.03–0.3%) for better solubility. Subsequent to application of test compounds, isoproterenol was applied onto the cells to control for cell number and vitality. Cells transfected with empty vector were used to control for unspecific responses of the cellular background. To control for responses of the diluent, cells were treated with bath solution or the respective concentration of DMSO.

Raw fluorescence changes were corrected for unspecific fluorescence changes of empty vector expressing cells using ScreenWorks 2.0. Relative fluorescence change was then calculated ($\Delta F = F_{max} - F_{min}$) and normalized to baseline fluorescence ($\Delta F/F$). To calculate concentration–response curves, $\Delta F/F$ values were plotted half-logarithmically against concentration of the test compound. Half-maximal effective agonist concentrations (EC_{50}) were calculated using nonlinear regression to the sigmoidal function $f(x) = \min + (\max - \min/(1 + [x/EC_{50}]^{Hillslope}))$ (SigmaPlot 9.01, Systat Software). To control for significance, one-way analysis of variance was carried out using SPSS.

RESULTS AND DISCUSSIONS

To investigate their possible potential as modulators of umami taste, a subset of the known naturally occurring *N*-cinnamoyl phenethylamines similar to rubemamine (**9**) and rubescenamine (**10**) with various substitution patterns were prepared. In Figure 1, the synthesized structures are shown; their natural occurrence is listed in Table 1. Depending on the substitution pattern, there are several methods known to obtain these *N*-cinnamoyl amines. In the case of free hydroxyl groups, the cinammic acid has to be activated as the corresponding *N*-hydroxysuccinimide ester, employing *N*,*N*-dicyclohexylcarbodiimide as coupling reagent.[27] These intermediates were reacted with an appropriate amine to obtain the desired compounds. The target compounds could be purified by column chromatography or crystallization. Alternatively, if the cinnamic acid moiety contains no hydroxyl groups, then it may be more convenient to transfer the cinnamic acid into the corresponding acid chloride by using oxalyl chloride and subsequent reaction with a suitable amine under Schotten–Baumann conditions. Usually, no further purification step is necessary; in the Supporting Information, the ^{1}H NMR and GC-MS or LC-MS spectra for rubemamine (**9**) and rubescenamine (**10**) are shown to demonstrate purity. The best method to obtain (*Z*) isomers of the parent (*E*)-configured cinnamic acid amides is an isomerization reaction under UV[28] as described for *N*-(*Z*)-feruloyl-3-methoxytyramine (**8**).

All synthesized compounds were evaluated at 10, 50, and 100 ppm in pure water by a panel of eight experts (Table 1). Although many of these *N*-cinnamoyl derivatives mostly evoked bitterness or mouth drying or were associated with trigeminal sensations at 100 ppm, only rubemamine (**9**) and rubescenamine (**10**) showed an intrinsic umami taste. Zanthosinamide (**13**) was found to elicit umami taste at 100 ppm as well but it also was rated very bitter at the same concentration. Just recently, the umami taste of **9** was reported,[20] but from the remaining umami active cinnamoyl amines, only the homologue *N*-3,4-dimethoxycinnamoyl-4-methoxyphenethylamine (**16**) could be identified in natural sources. According to the study, a 3,4-dimethoxycinnamic acid moiety seems to be necessary for a strong umami activity, which is very well reflected by the results shown in Table 1 for the series of naturally occurring *N*-cinnamoyl phenethylamines.

Besides the well-known umami taste of foodstuffs or raw materials rich in amino acids, ribonucleotides, peptides, their derivatives, or their reaction products generated during food processing,[1,13,29] there are only singular reports about plant secondary metabolites exhibiting or modulating umami taste. For example, the malic acid derivative morelid was found in morel mushrooms and weakly modulates umami taste evoked by MSG,[30] and the polyphenol theogallin was identified to be one component of the umami character of green tea.[31] The reason for this paucity may be the very low concentration of such substances in the original botanical sources, e.g., rubemamine (**9**) was found in white goosefoot (*Chenopodium album*)[32] at a level of 6 mg kg^{-1}, *N*-3,4-dimethoxycinnamoyl-4-methoxyphenethylamine (**16**) as a trace compound in *Zanthoxylum piperitum*,[20] and rubescenamine (**10**) was present at a level of 10 ppm in the bark of *Zanthoxylum rubescens*.[21] The detection threshold for rubemamine (**9**) in water was determined to be a level of 2263 ppb. Therefore, even for white goosefoot, which is at least sporadically consumed in Western European countries as salad or greens, the effective amount in food prepared from goosefoot is near or even below the threshold for the pure compound. Because of the limited solubility of rubescenamine (**10**), the threshold of the neat compound was determined at elevated temperatures (30 °C) to be 903 ppb. *Z. piperitum* bark is reported to be used solely for pharmaceutical treatments; therefore, only limited sensorial data are available.

DOI: 10.1021/acs.jafc.5b04402
J. Agric. Food Chem. 2015, 63, 8694–8704

The ability of the investigated *N*-cinnamoyl amines **1**−**15** to activate the heterodimeric umami receptor in a heterologous cell system was investigated via calcium imaging. Of the synthesized compounds, only rubemamine (**9**) and rubescenamine (**10**) showed activation of the heterologously expressed umami receptor hTAS1R1-rTas1r3 (Figures 2 and 3). Because

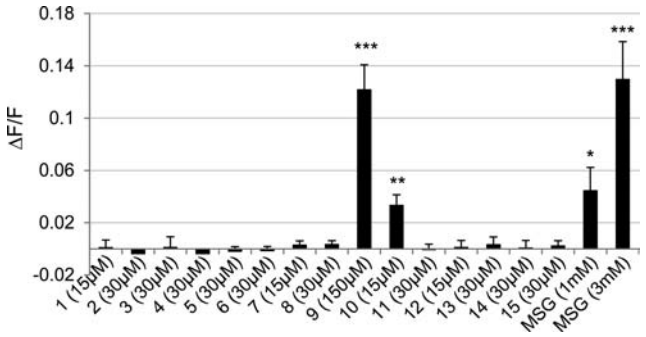

Figure 2. Test for umami receptor hTAS1R1-rTas1r3 activation in HEK293 cell model by *N*-cinnamoyl amines **1**−**15** and MSG measured in calcium imaging experiments. Data represent mean ± standard deviation of three independent experiments, each measured in triplicates. One-way variance analysis was carried out to test differences between substances, including vehicle. Contrast tests, with a multiple comparison Bonferroni adjustment, were carried out between substances and their respective vehicle. *, $p < 0.05$; **, $p < 0.01$; and ***, $p < 0.001$.

glutamate and nucleotides were shown to interact with the TAS1R1 subunit of the receptor,[6] it can be assumed that the functionally expressed umami receptor resembles the native human umami receptor in taste cells. Moreover, the EC_{50} value we found for the prototypical umami substance glutamate (MSG) is in the range of other in vitro data and also correlated well with the in vivo threshold for glutamate.[3,33−36] To compare the potency and efficacy of these newly identified umami compounds, concentration−response curves were established. Figure 3 demonstrates that rubemamine (**9**) is a powerful umami receptor agonist that is ∼40-fold more potent than MSG and equally efficient. In contrast, rubescenamine (**10**) has a much lower efficacy. However, this compound (**10**) is able to activate the receptor at even lower concentrations than rubemamine (**9**) and therefore has a 200-fold higher potency than does MSG. This is can be seen by the lower EC_{50} value of rubescenamine (**10**) (7.5 ± 0.4 μM) compared to those of rubemamine (**9**) (44 ± 8.0 μM) and MSG (1704 ± 335 μM). Although the difference in the EC_{50} value of rubemamine and rubescenamine is statistically not significant by one-way analysis of variance, the higher potency of rubescenamine (**10**) relative to that of rubemamine (**9**) to act on the umami receptor is also reflected by their detection thresholds in water (903 vs 2263 ppb).

Furthermore, the potential of the two naturally occurring compounds to modulate umami receptor activation by MSG and MSG + IMP was evaluated. Rubemamine (**9**) and rubescenamine (**10**) were both able to positively modulate the receptor response to MSG, yet the effect mediated by **9** was much larger than that mediated by (**10**). For rubescenamine (**10**), no further effect was observed in the presence of IMP (Figure 4). Most remarkably, rubemamine (**9**) further positively influenced the IMP-enhanced receptor responses to MSG, whereas IMP did not further enhance the receptor response to MSG and **9**. Thus, the data do not us allow to decide if IMP and **9** bind to the same site or different sites in

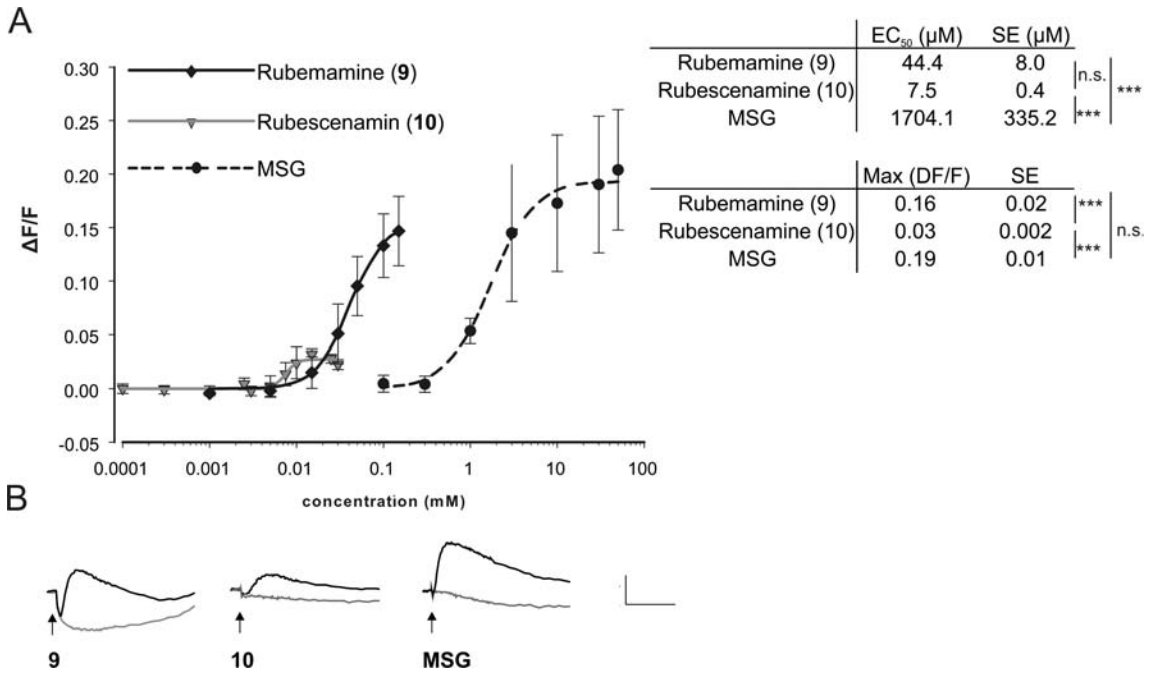

Figure 3. (A) Concentration response curve of rubemamine (**9**) and rubescenamine (**10**) in HEK293-cell model compared to that of MSG. Data represent mean ± standard deviation of three independent experiments measured in triplicate. To test for significant differences in maximal signal amplitude (Max $\Delta F/F$) and between EC_{50} values of the compounds, one-way variance analyses were carried out followed by Bonferroni posthoc test (*, $p < 0.05$; **, $p < 0.01$; and ***, $p < 0.001$). (B) Original calcium traces of hTAS1R1-rTas1r3-expressing HEK293 cells (black) and control cells (gray) in response to the application (↑) of rubemamine (**9**) (150 μM), rubescenamine (**10**) (15 μM), and MSG (3 mM); scale bar: $y = 100$ relative fluorescence units, $x = 100$ s.

DOI: 10.1021/acs.jafc.5b04402
J. Agric. Food Chem. 2015, 63, 8694−8704

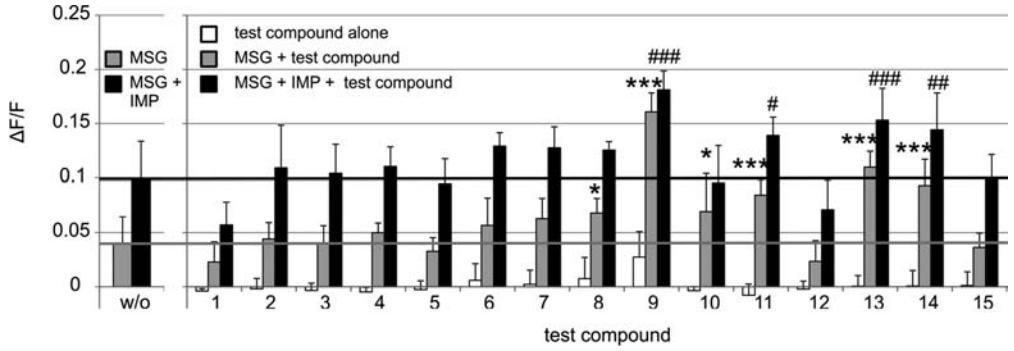

Figure 4. Umami-receptor-modulating ability of *N*-cinnamoyl amines determined by comparing the relative fluorescence elicited by the application of MSG and MSG plus IMP to the coapplication with the different test compounds. Isolated compounds were applied in nonactivating concentrations (compounds **2**−**6**, **8**, **11**, and **13**−**15**: 30 μM; compounds **1**, **9**, and **12**: 15 μM; compound **7**: 6 μM; and compound **10**: 5 μM) alone (white bars), with 1 mM MSG (gray bars), and with 1 mM MSG + 0.1 mM IMP (black bars). Gray and black horizontal lines indicate the mean fluorescence change induced the application of MSG and MSG plus IMP, respectively. Data represent mean ± standard deviation of three independent experiments, each measured in duplicate or triplicate. One-way variance analysis was carried out to test differences between substances and their respective controls (MSG or MSG plus IMP), followed by a Dunett multiple comparison posthoc test (MSG response: *, $p < 0.05$; **, $p < 0.01$; and ***, $p < 0.001$; MSG plus IMP response: $^{\#}$, $p < 0.05$; $^{\#\#}$, $p < 0.01$; and $^{\#\#\#}$, $p < 0.001$).

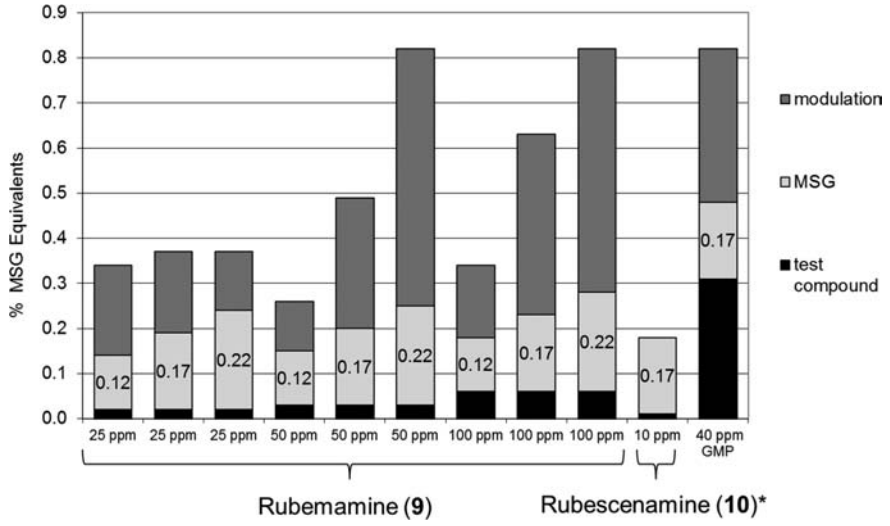

Figure 5. Quantification of positive modulating effects of rubemamine (**9**) and rubescenamine (**10**) on umami taste of MSG and comparison to that of GMP/MSG mixture according to Yamaguchi.[2] A binary solution (pH 6 0.0) containing the test compound in water was compared by forced choice methodology (2-AFC) to a series of aqueous solutions (0.17−1.82% w/w) with increasing concentrations of MSG. For the determination of the modulating activity, a binary solution (pH 6.0) containing the umami compound and MSG (0.17%) in water was compared to the same series of MSG solutions. Each test was repeated three times for each panelist.

hTAS1R1-rTas1r3, yet the data demonstrate that **9** positively modulates MSG-mediated receptor responses to an extent that cannot be further enlarged by IMP. Substances **8**, **11**, **13**, and **14**, which showed no receptor activation when applied alone onto the cells, were also capable of positively modulating receptor activation by MSG even though their effects were smaller than that of **9**. Additionally, similar to compound **9**, compounds **11**, **13**, and **14** enlarged the IMP-enhanced TAS1R1-Tas1r3 responses to MSG. However, there are differences between the effects mediated by **9** or by **11**, **13**, and **14**. First, the positive effect of rubemamine (**9**) on IMP-enhanced MSG-mediated receptor responses is smaller than that contributed by **11**, **13**, and **14**. Second, and more importantly, unlike the case of **9**, the effect of the latter compounds on MSG-mediated receptor response can be further enhanced by IMP. These findings suggest that the binding sites for **11**, **13**, and **14** differ from that of IMP. Positive modulation of a ribonucleotide-enhanced MSG-mediated umami receptor responses was also shown for another amide.[37] However, the reported effect was much smaller than effects elicited by **9**, **11**, **13**, and **14**.

Although binding and sensory studies need to confirm these results, the data show that little differences in molecular structure can have large impact on receptor responses. For the related sweet taste receptor TAS1R2-TAS1R3 that has the TAS1R3 subunit in common with the umami receptor binding of structurally related substances has been described to occur in similar regions.[7,8,38] Although umami receptor positive modulation by nucleotides is described to occur via the TAS1R1 subunit,[6] the known sweet- and umami-taste inhibitor lactisole negatively modulates the umami receptor via the transmembrane regions of the TAS1R3 subunit.[7,8] Also, the positively umami-taste-modulating compound S807 (*N*-(heptan-4-yl)benzo[*d*][1,3]dioxole-5-carboxamide) has been demonstrated to interact with the transmembrane region of the TAS1R1 subunit.[6] If the binding occurred via the rTas1r3

DOI: 10.1021/acs.jafc.5b04402
J. Agric. Food Chem. 2015, 63, 8694−8704

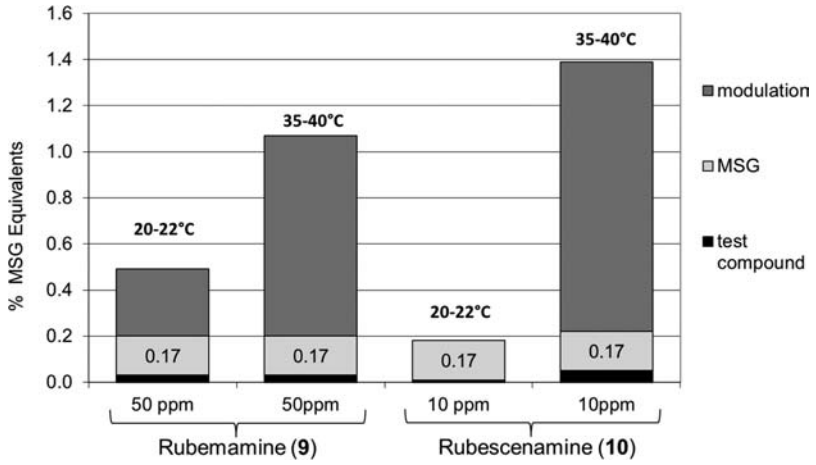

Figure 6. Positive modulation effect of rubemamine (**9**) and rubescenamine (**10**) on umami taste of MSG in ambient (20−22 °C) and warm application. Conditions were the same as those in Figure 5, but the solutions in columns 2 and 4 were warmed to 30−35 °C before tasting.

subunit, then the modulatory effect was not seen in human sensory studies, but the regions of the receptor that are targets for interaction with the *N*-cinnamoyl amides are currently unknown and need to be determined exactly in further investigations.

To quantify the modulating effects for the naturally occurring *N*-cinnamoyl amines **9**−**11**, **13**, and **14** in vivo, further sensory studies according to the method described by Yamaguchi[2] were carried out; amide **8** was not evaluated because of its disturbing dry off-taste. Generally, it is very difficult to quantify umami effects because of the strong lingering character of this taste quality. Specifically, a single experimental comparison of a test solution against a full concentration series of MSG within a single sensory session fails because of carry-over effects. Therefore, Yamaguchi proposed a series of forced-choice paired tests that compare mixtures of a standard MSG concentration (e.g., 0.17%) and the test compound with each sample of an MSG concentration series (here, from 0.17 up to 1.82% MSG). Multiple sessions for each panelist are necessary to get data on the full series of dilutions. In a single test, the panelist has only to decide which solution is stronger in umami. At the end, all experiments are ranked according to the answers of the panelists. The same experiment is done with the test compound alone, and finally, the MSG equivalent concentration is calculated as the last concentration where the mixture of MSG and test compound is nonsignificantly weaker than the MSG reference solution. The known synergistic effect for GMP[2] was used for the validation of the panel; 40 ppm GMP (corresponds to 0.37% MSG) and 0.17% MSG were described to elicit the same intensity of umami taste as an MSG solution of 0.8%. Therefore, GMP exhibited a clear and expected synergistic effect on umami taste for the panelists.

Amides **11** (10 ppm) and **13** (50 ppm) showed no significant modulating effect in the Yamaguchi sensory protocol (data not shown). Dioxamine (**14**) at 25 ppm in combination with 0.17% MSG exhibited a sensory equivalent to 0.37% MSG. Because of the limited solubility of **14**, the latter test was done at increased temperature (35−40 °C). Unfortunately, some bitterness was detected that could potentially mislead the panelists; therefore, the tests with **14** were not extended in depth. For rubemamine (**9**), positive modulating effects were found and are summarized in Figure 5. For all tested combinations of rubemamine (**9**) with MSG (columns 1−9), the compound shows a positive synergistic effect. In contrast, rubescenamine (**10**) (50 ppm column 10, 0.17% MSG) showed no effect at room temperature (20−22 °C; Figure 5, column 10), but the experiment was repeated with a warmed solution also in comparison with rubemamine (**9**) (Figure 6). At increased temperature, for **9** the effect is still more pronounced compared to ambient conditions, and rubescenamine (**10**) also shows positive modulating properties on the umami taste of MSG. The limited solubility of **10** at ambient conditions noticed in this experiment might be also the reason for the lower efficacy of **10** compared to rubemamine (**9**) seen in the dose−response studies on the hTAS1R1-rTas1r3 receptor.

Although the interaction sites of the cinnamoyl amides at the umami receptor remain to be elucidated, the quantitative sensory results support the studies using the receptor assays and the proposal of two different binding sites: Only **9** and **10** are able to induce strong intrinsic umami effects and cause a positive modulation of the MSG umami taste in vitro and in vivo. In contrast, the potential modulators **11**, **13**, and **14** putatively binding to an alternative receptor site exhibited only weak or no intrinsic umami effects. Only **14** showed some modulating effect on MSG in vivo that was slightly disturbed by limited solubility and bitterness. For the observed differences between the umami modulation in vitro and in vivo by the compounds **11** and **13**, it must be considered that we used the rat Tas1r3 in the heterologous expression system that could be responsible for this effect. To evaluate the potential of rubemamine (**9**) and rubescenamine (**10**) as flavor substances showing also general taste modifying properties, advanced profiling studies in a model broth were carried out with a larger panel (n = 16−20) on an American beef extract already containing the typical umami tastants such as glutamate and nucleotides. In this case, the attribute "umami" itself was excluded because of some uncertainty of its description in a complex flavor environment. Instead, umami-related attributes such as "mouth watering" or "meaty" were used. In Figure 7, the differences of these descriptors in relation to the ratings for the base are shown: 0.05% MSG increases most of the attributes significantly. Rubemamine (**9**) at 50 ppm significantly raises the important descriptors mouth feel, meaty, and mouth-watering; however, with the exception for the parameter mouth-watering, this amount is not able to match the intensity of the positive control (base with 0.05% MSG added, Figure 7A). Rubescenamine (**10**) at 5 ppm and especially at 10 ppm is able to boost significantly mouth feel, meaty, mouth-watering,

DOI: 10.1021/acs.jafc.5b04402
J. Agric. Food Chem. 2015, 63, 8694−8704

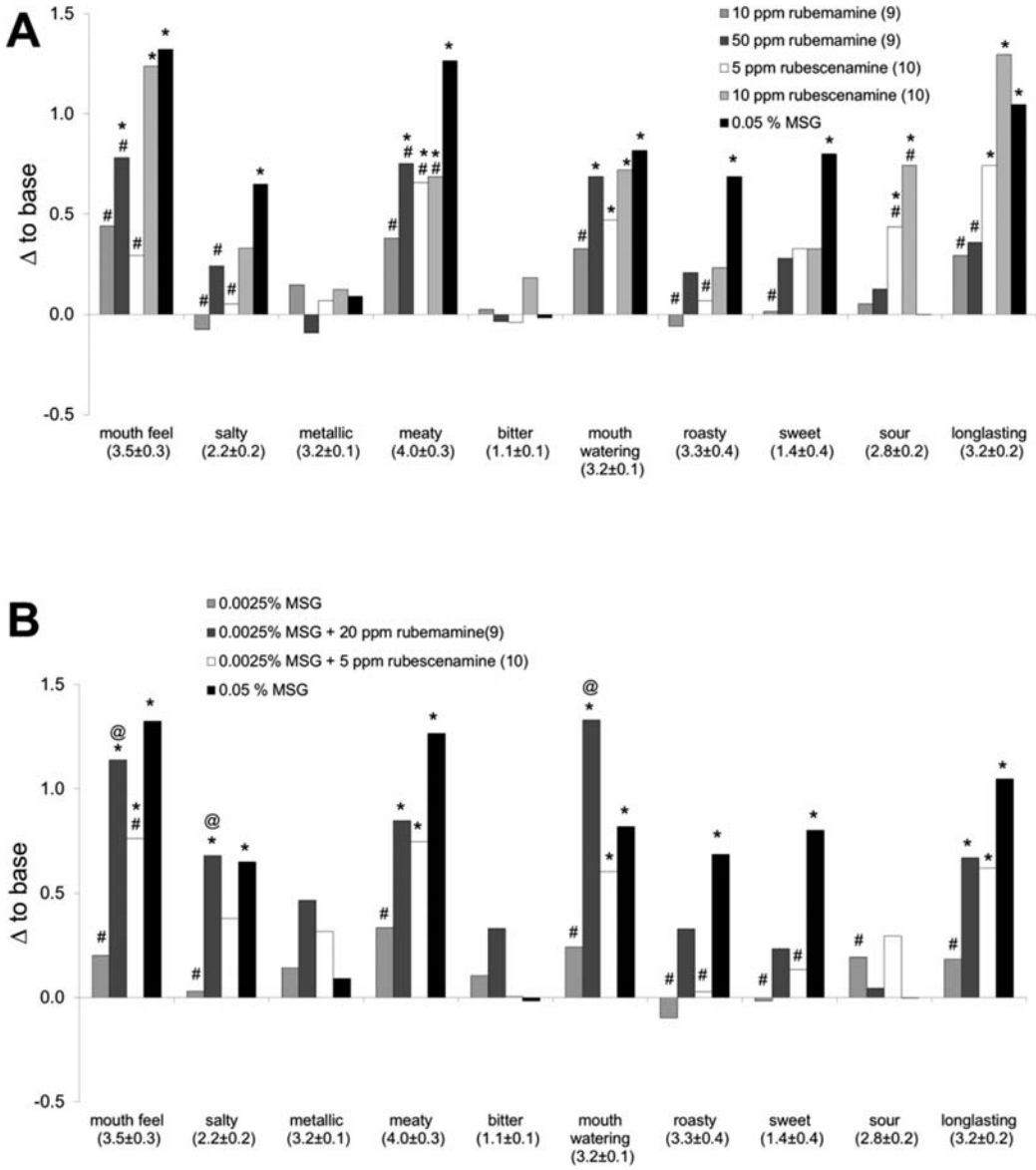

Figure 7. Taste-modulating effects of rubemamine (**9**) and rubescenamine (**10**) in an American beef extract (base) by sensory profiling at slightly elevated temperatures (30−35 °C) by a panel of trained subjects (n = 16−20). The descriptors used and their average ratings (0 through 9) and standard deviations for the base a shown on the x axis. The mean values are shown as differences of the ratings of the test samples to the respective ratings of the base. (A) Differences (Δ) between the base and base with added rubemamine (**9**) or rubescenamine (**10**) and a positive control with added MSG. Significant differences ($p < 0.05$) as determined by Student's t test (nonpaired, two-sided): *, between base and test sample, and #, between test sample and positive control. (B) Differences (Δ) between the base and base with added MSG, base with added MSG and rubemamine (**9**), base with added MSG and rubescenamine (**10**), and positive control. Significant differences ($p < 0.05$) as determined by Student's t test (nonpaired, two-sided): *, between base and test sample; @, between between test sample and base with 0.0025% added MSG; and #, between test sample and positive control.

sour, and long-lasting (Figure 7A) and shows at 10 ppm no significant difference to the positive control for mouth feel, saltiness, and mouth-watering, reflecting its higher potential as a flavor modifier. In Figure 7B, the potential of **9** and **10** to boost the flavor profile of a low concentration of added MSG in the model broth is shown. The effect of a mixture of low MSG and rubemamine (**9**) matches most ratings of the attributes of the positive control. Rubescenamine (**10**) at 5 ppm in combination with 0.0025% MSG is also able to boost the profile of the base, showing mostly significant changes compared to the base but nonsignificant differences compared to the positive control.

As result of the study, besides the known umami tastant rubemamine (**9**), also the naturally occurring rubescenamine (**10**) was found to modulate complex flavor systems. Both are able to synergistically modulate the umami sensation of MSG and act on the umami receptor as shown in heterologous cell models. New insights for the binding mode can be deduced from the combined sensory and in vitro experiments that lead to further studies to validate the binding mode and binding site within the umami receptor.

■ ASSOCIATED CONTENT

Supporting Information

The Supporting Information is available free of charge on the ACS Publications website at DOI: 10.1021/acs.jafc.5b04402.

DOI: 10.1021/acs.jafc.5b04402
J. Agric. Food Chem. 2015, 63, 8694−8704

References for spectral data; additional NMR, GC, and UPLC data for compounds **9** and **10**. (PDF)

AUTHOR INFORMATION

Corresponding Author

*jakob.ley@symrise.com.

Funding

The study was partly funded by BMBF (Federal Ministry of Education and Research, Germany), FKZ 01EA1324C.

Notes

The authors declare the following competing financial interest(s): Michael Backes, Katja Obst, Susanne Paetz, Katharina V. Reichelt, Gerhard E. Krammer, and Jakob P. Ley are employees of Symrise AG.

ACKNOWLEDGMENTS

We thank Maria Blings, Petra Hoffmann-Lücke, Carsten Strempel, Bernd Wiedwald, and Susanne Mundt for technical support. We also gratefully acknowledge Dr. Anne Brockhoff (Nuthetal) for her continuous advice how to run the umami receptors assays.

REFERENCES

(1) Behrens, M.; Meyerhof, W.; Hellfritsch, C.; Hofmann, T. Sweet and Umami Taste: Natural Products, Their Chemosensory Targets, and Beyond. *Angew. Chem., Int. Ed.* **2011**, *50*, 2220−2242.

(2) Yamaguchi, S. The Synergistic Taste Effect of Monosodium Glutamate and Disodium 5′-Inosinate. *J. Food Sci.* **1967**, *32*, 473−478.

(3) Nelson, G.; Chandrashekar, J.; Hoon, M. A.; Feng, L.; Zhao, G.; Ryba, N. J. P.; Zuker, C. S. An amino-acid taste receptor. *Nature* **2002**, *416*, 199−202.

(4) Nelson, G.; Hoon, M. A.; Chandrashekar, J.; Zhang, Y.; Ryba, N. J.; Zuker, C. S. Mammalian sweet taste receptors. *Cell* **2001**, *106*, 381−390.

(5) Voigt, A.; Hubner, S.; Lossow, K.; Hermans-Borgmeyer, I.; Boehm, U.; Meyerhof, W. Genetic labeling of Tas1r1 and Tas2r131 taste receptor cells in mice. *Chem. Senses* **2012**, *37*, 897−911.

(6) Zhang, F.; Klebansky, B.; Fine, R. M.; Xu, H.; Pronin, A.; Liu, H.; Tachdjian, C.; Li, X. Molecular mechanism for the umami taste synergism. *Proc. Natl. Acad. Sci. U. S. A.* **2008**, *105*, 20930−20934.

(7) Xu, H.; Staszewski, L.; Tang, H.; Adler, E.; Zoller, M.; Li, X. Different functional roles of T1R subunits in the heteromeric taste receptors. *Proc. Natl. Acad. Sci. U. S. A.* **2004**, *101*, 14258−14263.

(8) Winnig, M.; Bufe, B.; Meyerhof, W. Valine 738 and lysine 735 in the fifth transmembrane domain of rTas1r3 mediate insensitivity towards lactisole of the rat sweet taste receptor. *BMC Neurosci.* **2005**, *6*, 22−22.

(9) Kurobayashi, Y.; Katsumi, Y.; Fujita, A.; Morimitsu, Y.; Kubota, K. Flavour Enhancement of Chicken Broth from Boiled Celery Constituents. *J. Agric. Food Chem.* **2008**, *56*, 512−516.

(10) Starkenmann, C.; Cayeux, I.; Birkbeck, A. A. Exploring Natural Products for New Taste Sensations. *Chimia* **2011**, *65*, 407−410.

(11) Kuroda, M. *Proteins and Peptides with Taste*; CRC Press: Boca Raton, FL, 2012; p 277−296.

(12) Backes, M.; Paetz, S.; Vössing, T.; Ley, J. P. Synthesis and Sensory Studies of Umami-Active Scaffolds. *Chem. Biodiversity* **2014**, *11*, 1782−1797.

(13) Winkel, C.; de Klerk, A.; Visser, J.; de Rijke, E.; Bakker, J.; Koenig, T.; Renes, H. New Developments in Umami (Enhancing) Molecules. *Chem. Biodiversity* **2008**, *5*, 1195−1203.

(14) Bassard, J.-E.; Ullmann, P.; Bernier, F.; Werck-Reichhart, D. Phenolamides: Bridging polyamines to the phenolic metabolism. *Phytochemistry* **2010**, *71*, 1808−1824.

(15) Stark, T.; Hofmann, T. Isolation, Structure Determination, Synthesis, and Sensory Activity of N-Phenylpropenoyl-L-amino Acids from Cocoa (*Theobroma cacao*). *J. Agric. Food Chem.* **2005**, *53*, 5419−5428.

(16) Koyama, N.; Kuribayashi, K.; Seki, T.; Kobayashi, K.; Furuhata, Y.; Suzuki, K.; Arisaka, H.; Nakano, T.; Amino, Y.; Ishii, K. Serotonin Derivatives, Major Safflower (*Carthamus tinctorius L.*) Seed Antioxidants, Inhibit Low-Density Lipoprotein (LDL) Oxidation and Atherosclerosis in Apolipoprotein E-Deficient Mice. *J. Agric. Food Chem.* **2006**, *54*, 4970−4976.

(17) Bratt, K.; Sunnerheim, K.; Bryngelsson, S.; Fagerlund, A.; Engman, L.; Andersson, R. E.; Dimberg, L. H. Avenanthramides in oats (*Avena sativa L.*) and Structure-Antioxidant activity relationships. *J. Agric. Food Chem.* **2003**, *51*, 594−600.

(18) Ley, J. P.; Krammer, G.; Kindel, G.; Bertram, H.-J. Pungency of Various Substituted Hydroxycinnamic Amides of Hydroxyphenethylamines. In *Polyphenol Communications 2004*; Hoikkala, A., Soidinsalo, O., Wähälä, K., Eds.; University of Helsinki: Helsinki, Finland, 2004; pp 269−270.

(19) Bassoli, A.; Borgonovo, G.; Busnelli, G.; Morini, G. Use of amide derivatives as taste-modifying agents, flavouring compositions and products containing them. WO 2006 117,602.

(20) Frerot, E.; Neirynck, N.; Cayeux, I.; Yuan, Y.; Yuan, Y.-M. New Umami Amides: Structure-Taste Relationship Studies of Cinnamic Acid-Derived Amides and Natural Occurrence of an Intense Umami Amide in *Zanthoxylum piperitum*. *J. Agric. Food Chem.* **2015**, *63*, 7161−7168.

(21) Adesina, S. K. Three new amides from *Zanthoxylum rubescens*. *Planta Med.* **1989**, *55*, 324−326.

(22) Waddell, W. J.; Cohen, S. M.; Feron, V. J.; Goodman, J. I.; Marnett, L. J.; Portoghese, P. S.; Rietjens, I. M. C. M.; Smith, R. L.; Adams, T. B.; Gavin, C. L.; McGowen, M. M.; Williams, M. C. GRAS flavoring substances 23. *Food Technol.* **2007**, *61*, 22−21.

(23) Marnett, L. J.; Cohen, S. M.; Fukushima, S.; Gooderham, N. J.; Hecht, S. S.; Rietjens, I. M. C. M.; Smith, R. L.; Adams, T. B.; Hallagan, J. B.; Harman, C.; McGowen, M. M.; Taylor, S. V. GRAS Flavoring Substances 26. *Food Technol.* **2013**, *67*, 38−56.

(24) Sundh, U. B.; Binderup, M.-L.; Bolognesi, C.; Brimer, L.; Castle, L.; Di Domenico, A.; Engel, K.-H.; Franz, R.; Gontard, N.; Gurtler, R.; Husoy, T.; Jany, K.-D.; Kolf-Clauw, M.; Mennes, W.; Milana, M. R.; Pratt, I.; Svensson, K.; de Fatima Tavares Pocas, M.; Toldra, F.; Wolfle, D. Scientific opinion on flavouring group evaluation 94, revision 2 (FGE.94Rev2): consideration of aliphatic amines and amides evaluated in an addendum to the group of aliphatic and aromatic amines and amides evaluated by the JECFA (68th meeting). *EFSA Journal* **2015**, *12*, 3622.

(25) ASTM Subcommittee E18.04 *Standard Practice for Determination of Odor and Taste Thresholds By a Forced-Choice Ascending Concentration Series Method of Limits*. Practice E679-04(2011); ASTM International: West Conshohocken, PA, 2011, . DOI: 10.1520/E0679-91R97

(26) Suess, B.; Brockhoff, A.; Degenhardt, A.; Billmayer, S.; Meyerhof, W.; Hofmann, T. Human Taste and Umami Receptor Responses to Chemosensorica Generated by Maillard-type N2-Alkyl- and N2-Arylthiomethylation of Guanosine 5′-Monophosphates. *J. Agric. Food Chem.* **2014**, *62*, 11429−11440.

(27) Anderson, G. W.; Zimmerman, J. E.; Callahan, F. M. N-Hydroxysuccinimide Esters in Peptide Synthesis. *J. Am. Chem. Soc.* **1963**, *85*, 3039−3039.

(28) Yoshihara, T.; Yamaguchi, K.; Takamatsu, S.; Sakamura, S. A New Lignan Amide, Grossamide, from Bell Pepper *Capsicum annuum* var. *grossum*. *Agric. Biol. Chem.* **1981**, *45*, 2593−2598.

(29) Suess, B.; Brockhoff, A.; Meyerhof, W.; Hofmann, T. Structures, Orosensory Activity, and T1R1/T1R3-Receptor Activation of Amides Generated by Lactone Aminolysis Using Food-Related Processing Conditions. *Eur. Food Res. Technol.* **2013**, *237*, 57−70.

(30) Rotzoll, N.; Dunkel, A.; Hofmann, T. Activity-Guided Identification of (*S*)-Malic Acid 1-O-D-Glucopyranoside (Morelid) and -Aminobutyric Acid as Contributors to Umami Taste and Mouth-Drying Oral Sensation of Morel Mushrooms (*Morchella deliciosa* Fr.). *J. Agric. Food Chem.* **2005**, *53*, 4149−4156.

DOI: 10.1021/acs.jafc.5b04402
J. Agric. Food Chem. 2015, 63, 8694−8704

(31) Kaneko, S.; Kumazawa, K.; Masuda, H.; Henze, A.; Hofmann, T. Molecular and Sensory Studies on the Umami Taste of Japanese Green Tea. *J. Agric. Food Chem.* **2006**, *54*, 2688−2694.
(32) Cutillo, F.; D'Abrosca, B.; DellaGreca, M.; Di Marino, C.; Golino, A.; Previtera, L.; Zarrelli, A. Cinnamic acid amide from *Chenopodium album*: effects on seeds germination and plant growth. *Phytochemistry* **2003**, *64*, 1381−1387.
(33) Raliou, M.; Grauso, M.; Hoffmann, B.; Schlegel-Le-Poupon, C.; Nespoulous, C.; Débat, H.; Belloir, C.; Wiencis, A.; Sigoillot, M.; Preet Bano, S.; Trotier, D.; Pernollet, J.-C.; Montmayeur, J.-P.; Faurion, A.; Briand, L. Human Genetic Polymorphisms in T1R1 and T1R3 Taste Receptor Subunits Affect Their Function. *Chem. Senses* **2011**, *36*, 527−537.
(34) Li, X.; Staszewski, L.; Xu, H.; Durick, K.; Zoller, M.; Adler, E. Human receptors for sweet and umami taste. *Proc. Natl. Acad. Sci. U. S. A.* **2002**, *99*, 4692−4696.
(35) Xu, H.; Staszewski, L.; Tang, H.; Adler, E.; Zoller, M.; Li, X. Different functional roles of T1R subunits in the heteromeric taste receptors. *Proc. Natl. Acad. Sci. U. S. A.* **2004**, *101*, 14258−14263.
(36) Shigemura, N.; Shirosaki, S.; Sanematsu, K.; Yoshida, R.; Ninomiya, Y. Genetic and Molecular Basis of Individual Differences in Human Umami Taste Perception. *PLoS One* **2009**, *4*, e6717−e6717.
(37) Suess, B.; Brockhoff, A.; Meyerhof, W.; Hofmann, T. Structures, orosensory activity, and T1R1/T1R3 receptor activation of amides generated by lactone aminolysis using food-related processing conditions. *Eur. Food Res. Technol.* **2013**, *237*, 57−70.
(38) Masuda, K.; Koizumi, A.; Nakajima, K.; Tanaka, T.; Abe, K.; Misaka, T.; Ishiguro, M. Characterization of the modes of binding between human sweet taste receptor and low-molecular-weight sweet compounds. *PLoS One* **2012**, *7*, e35380−e35380.
(39) Wu, P.-L.; Su, G.-C.; Wu, T.-S. Constituents from the Stems of *Aristolochia manshuriensis*. *J. Nat. Prod.* **2003**, *66*, 996−998.
(40) El-Gamal, A. A.; Takeya, K.; Itokawa, H.; Halim, A. F.; Amer, M. M.; Saad, H. E. A.; Awad, S. A. Studies on the chemical constituents of *Atraphaxis spinosa L.*, var. *sinaica* Boiss. *Nat. Med. (Tokyo, Jpn.)* **1994**, *48*, 304−306.
(41) Chen, C.-Y.; Yeh, Y.-T.; Yang, W.-L. Amides from the Stem of *Capsicum annuum*. *Nat. Prod. Com.* **2011**, *6*, 227−229.
(42) Kujala, T. S.; Vienola, M. S.; Klika, K. D.; Loponen, J. M.; Pihlaja, K. Betalain and phenolic compositions of four beetroot (*Beta vulgaris*) cultivars. *Eur. Food Res. Technol.* **2002**, *214*, 505−510.
(43) Oueslati, M. H.; Ben Jannet, H. B.; Mighri, Z.; Chriaa, J.; Abreu, P. M. Phytochemical constituents from *Salsolia tetranda*. *J. Nat. Prod.* **2006**, *69*, 1366−1369.
(44) Pedersen, H. A.; Steffensen, S. K.; Christophersen, C.; Mortensen, A. G.; Jørgensen, L. N.; Niveyro, S.; de Troiani, R. M.; Rodríguez-Enríquez, R. J.; Barba-de la Rosa, A. P.; Fomsgaard, I. S. Synthesis and Quantitation of Six Phenolic Amides in *Amaranthus spp*. *J. Agric. Food Chem.* **2010**, *58*, 6306−6311.
(45) Chen, C.-Y.; Yeh, H.-C. A new amide from the stems of *Cinnamomum reticulatum* Hay. *Nat. Prod. Res.* **2011**, *25*, 26−30.
(46) Adesina, S. K.; Reisch, J. Amides from *Zanthoxylum rubescens*. *Phytochemistry* **1989**, *28* (3), 839−842.
(47) Kalia, N. K.; Singh, B.; Sood, R. P. A New Amide from *Zanthoxylum armatum*. *J. Nat. Prod.* **1999**, *62*, 311−312.
(48) Adesina, S. K.; Olatunji, O. A.; Bergenthal, D.; Reisch, J. Natural product chemistry. Part 122. Transcinnamoylamides from *Zanthoxylum rubescens* pericarbs. *Pharmazie* **1988**, *43*, 517−518.
(49) Kang, G.-H.; Chang, E.-J.; Choi, S.-W. Antioxidative activity of phenolic compounds in roasted safflower (*Carthamus tinctorius L.*) seeds. *J. Food Sci. Nutr.* **1999**, *4*, 221−225.

DOI: 10.1021/acs.jafc.5b04402
J. Agric. Food Chem. 2015, 63, 8694−8704

health-promoting properties, such as cardioprotective and antioxidant effects.[16−18] However, our group previously demonstrated the stability of maqui anthocyanins to be comparably poor,[10] stating that deeper insights into the degradation of the contained anthocyanin 3-*O*-glycosides as well as 3,5-*O*- and 3,7-*O*-diglycosides are urgently required.

Therefore, the present study aimed at evaluating the stability of maqui anthocyanins by thermal treatment of differently purified liquid maqui preparations, including "total matrix", "matrix-depleted", and "matrix-free" anthocyanin samples to investigate the influence of concomitant polar low-molecular-weight matrix constituents (e.g., sugars and citric acid) and non-anthocyanin phenolics. In addition, the effect of pH was studied by adjusting the preparations to pH 2.2 and 3.6 prior to thermal treatment. Moreover, the stability of maqui anthocyanins in the total matrix and matrix-depleted maqui preparations was monitored during long-term storage at 4 and 20 °C in the dark, also testing the effect of illumination during storage at 20 °C. The results were compared to those obtained after storing the respective dried preparations (powders). Besides detailed HPLC-DAD analyses on anthocyanins and initial non-anthocyanin phenolic compounds, changes in antioxidant activity (trolox equivalent antioxidant capacity, TEAC assay) and color parameters (CIE $L^*a^*b^*$) were studied in the stored samples.

MATERIALS AND METHODS

Chemicals. Cyanidin 3-*O*-glucoside, cyanidin 3,5-*O*-diglucoside, delphinidin 3-*O*-glucoside, and delphinidin 3,5-*O*-diglucoside were obtained from Extrasynthèse (Genay, France). Myricetin 3-*O*-glucoside was from Sigma-Aldrich (St. Louis, MO, USA), isoquercetin from Carl Roth (Karlsruhe, Germany,) and ellagic acid from Serva (Heidelberg, Germany). Maltodextrin (dextrose equivalent DE 19) was from Agrana (Vienna, Austria). 2,2′-Azinobis(3-ethylbenzthiazoline-6-sulfonic acid) diammonium salt (ABTS), 2,2′-azobis(2-amidinopropane) dihydrochloride (ABAP), and Folin−Ciocalteu reagent were purchased from Sigma-Aldrich. All further solvents and reagents were at least of analytical grade and obtained from Merck and VWR (Darmstadt, Germany). Ultrapure water (Milli-Q system) from EMD Millipore (Bedford, MA, USA) was used throughout.

Production of Liquid and Dried Maqui Preparations with Different Matrix Degrees. Maqui berries originating from the Aysén region near Coihaique in Patagonia (Chile) were harvested by the end of February 2013 and sent frozen to Stuttgart on dry ice by express airmail. Processing of maqui berries into a juice was conducted as described previously.[10] The term "total matrix" will be used to refer to preparations made from the juice by dilution with buffer, that is, without selective purification steps. The "matrix-depleted" preparation was prepared by removal of polar low-molecular-weight juice constituents (e.g., sugars and citric acid) according to a previously reported procedure[8] with the following modifications. The maqui juice was applied to a conditioned and equilibrated column filled with Lewatit VP OC 1064 MD PH, 1.4 L bed volume (BV) (Lanxess, Langenfeld, Germany), instead of Amberlite XAD-16 HP. For column conditioning, washing, and elution, methanol and trifluoroacetic acid were replaced by ethanol and aqueous hydrochloric acid (HCl) at pH 2. After conditioning with 1.0 BV of ethanol and washing with 1.8 BV of aqueous HCl (pH 2), 50 mL of the maqui juice (diluted 1:1 with water) was applied to the column, and nonadsorbent juice matrix components were eluted with aqueous HCl (4.0 BV). The deeply red-colored phenolic fraction was eluted from the column using 2.0 BV of ethanol with aqueous hydrochloric acid (95:5, v/v) and concentrated in vacuo to remove the solvent. To achieve an almost "matrix-free" anthocyanin extract, the non-anthocyanin phenolics present in the matrix-depleted extract were separated from anthocyanins by extracting them with ethyl acetate as previously reported.[10] Pure anthocyanin preparations were obtained by dissolving authentic standards in the respective buffers (only for cyanidin 3-*O*-glucoside, cyanidin 3,5-*O*-diglucoside, delphinidin 3-*O*-glucoside, and delphinidin 3,5-*O*-diglucoside).

In addition to the liquid samples, dried preparations (powders) were produced from the aforementioned total matrix and matrix-depleted preparations. For this purpose, aliquots of these samples were combined with 15% (w/v) of maltodextrin, homogenized for 5 min using a T25 Ultra-Turrax (IKA, Staufen, Germany), transferred to plastic pans (30 mm deep), and frozen at −20 °C prior to freeze-drying. Freeze-drying was carried out at 5 Pa for 72 h with a condenser and final plate temperatures of −60 and 30 °C, respectively. Dried preparations containing maltodextrin were manually ground and then sequentially sieved (mesh sizes of 1.0 and 0.5 mm) (Retsch, Haan, Germany). Only the powder fraction with particle sizes between 0.5 and 1.0 mm was used for the storage experiment and further analyses. Moisture contents of the powders were measured by infrared drying at 105 °C with an infrared moisture analyzer (Sartorius, Göttingen, Germany).

Storage Experiments Using Liquid and Dried Maqui Preparations. Liquid preparations for storage stability tests were obtained by adjusting the maqui juice (total matrix) and the matrix-depleted extract to a total anthocyanin concentration of 1000 μmol/L using a sodium acetate buffer solution (pH 3.6). This pH was chosen, being the genuine pH of the maqui juice used. Subsequently, the concentration-adjusted maqui preparations were filtered (0.45 μm) into transparent, previously sterilized glass bottles (50 mm × 18 mm) with plastic snap-on caps. Additionally, aliquots of 6 g powdered samples were placed in rectangular molded transparent plastic bags (PA/PE, ∼90 × 20 mm), flattened to a height of 1 mm, and sealed under vacuum. Liquid and dried samples were placed in a controlled climate chamber (Binder, Tuttlingen, Germany), where temperature (20 °C) and illumination (L36W/840 and LT36W/009) (Osram, Munich, Germany) were controlled. Sample positions were rotated periodically (twice per week) to ensure uniform light exposure. In addition to illuminated storage, liquid preparations were stored at 4 and 20 °C in the dark. All samples were stored for up to 85 days, and anthocyanin stabilities were assessed by HPLC-DAD after membrane filtration (0.45 μm) into amber HPLC vials. Moreover, the pH values, total soluble solids (refractometer, RX-5000) (Atago, Tokyo, Japan), antioxidant activities (trolox equivalent antioxidant capacity, TEAC assay), and color parameters (CIE $L^*a^*b^*$) of the samples were analyzed at selected storage days.

Heating Experiments Using Liquid Maqui Preparations and Standard Solutions. Prior to heating, the above-mentioned liquid total matrix, matrix-depleted, and matrix-free samples as well as standard solutions of cyanidin 3-*O*-glucoside, cyanidin 3,5-*O*-diglucoside, delphinidin 3-*O*-glucoside, and delphinidin 3,5-*O*-diglucoside were adjusted to pH 3.6 and 2.2 by using a sodium acetate buffer solution (pH 3.6) and aqueous hydrochloric acid (pH 2.2), respectively. Aliquots of 900 μL of the samples were heated in Eppendorf tubes in a thermoshaker at 85 °C and 1400 rpm. After 30, 60, 90, 120, 240, and 420 min, tubes were cooled in an ice bath to stop thermal anthocyanin degradation. An aliquot of each sample as well as of the unheated samples was membrane-filtered (0.45 μm) into amber HPLC vials for subsequent anthocyanin analyses by HPLC-DAD.

HPLC-DAD Analyses. Liquid heated and stored samples were prepared for HPLC analyses as described above, whereas aliquots of the dried preparations (5.0 g) were resuspended in 50 mL of deionized water prior to HPLC-DAD analysis. Identification and quantitation of anthocyanins and non-anthocyanin phenolics in liquid and dried maqui samples were carried out by HPLC-DAD-ESI/MS^n and HPLC-DAD as previously described.[10] Although quantitative analyses of anthocyanins were conducted for all maqui samples, quantitation of non-anthocyanin phenolics was executed only for the determination of their initial contents in the total matrix and matrix-depleted preparations used for the storage experiments. For this purpose, non-anthocyanin phenolics in the samples were extracted twice with ethyl acetate. The extracts were combined, evaporated to dryness by a gentle stream of nitrogen, and resuspended in methanol as previously

DOI: 10.1021/acs.jafc.5b03471
J. Agric. Food Chem. 2015, 63, 8705−8714

reported.[10] Dried preparations were dissolved in a defined volume of aqueous hydrochloric acid (pH 1.5) prior to ethyl acetate extraction.

Quantitation of maqui anthocyanins (Figure 1) was carried out using linear calibration curves of authentic standards. A delphinidin 3-*O*-glucoside calibration was used for quantitating delphinidin 3-*O*-sambubioside-5-*O*-glucoside (**1**), delphinidin 3,5-*O*-diglucoside (**2**), delphinidin 3-*O*-sambubioside (**5**), and delphinidin 3-*O*-glucoside (**6**), whereas a cyanidin 3-*O*-glucoside calibration was used for the quantitation of cyanidin 3-*O*-sambubioside-5-*O*-glucoside (**3**), cyanidin 3,5-*O*-diglucoside (**4**), cyanidin 3-*O*-sambubioside (**7**), and cyanidin 3-*O*-glucoside (**8**). In particular, compounds **3** and **4** as well as compounds **7** and **8** were quantitated together due to the lack of HPLC baseline separation. Moreover, it should be mentioned that the proposed position of sugar moieties at the delphinidin and cyanidin 3,5-*O*-diglucosides, **2** and **4**, has not yet been unambiguously confirmed by NMR spectroscopy, to the best of our knowledge. Because the differentiation between a 5-*O*- and a 7-*O*-glycosylation is most intricate if not impossible without NMR, these compounds might also represent the respective 3,7-*O*-diglucoside derivatives.[10]

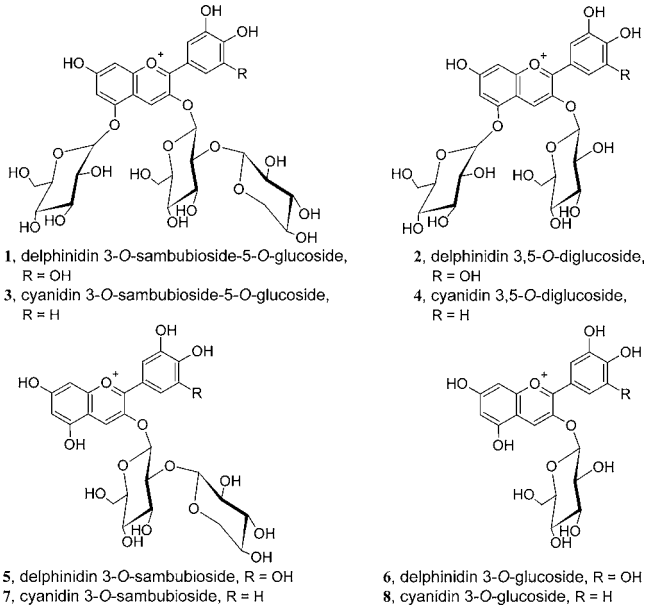

Figure 1. Chemical structures of the studied 3-*O*- and 3,5-*O*-glycosylated cyanidin and delphinidin derivatives, naturally present in maqui. Compounds are numbered according to their elution order from the HPLC column.

Initial non-anthocyanin phenolic contents were quantitated on the basis of calibration curves of authentic standards. A myricetin 3-*O*-glucoside calibration was used for myricetin 3-*O*-galloyl-glucoside (**9**), myricetin 3-*O*-galactoside (**10**), and myricetin 3-*O*-glucoside (**11**), whereas the two quercetin galloyl-hexosides, (**12**) and (**13**), dimethoxylated quercetin (**17**) and quercetin (**18**) were quantitated using an isoquercetin calibration. Due to the lack of HPLC baseline separation, ellagic acid (**14**), quercetin 3-*O*-rutinoside (**15**), and quercetin 3-*O*-galactoside (**16**) were quantitated together by using the calibration curve of the main compound (ellagic acid (**14**)). Compounds **10** and **11** as well as compounds **12** and **13** were also quantitated together.

Degradation Kinetics. The stability of individual and total anthocyanins was expressed as the ratio $A_t/A_0 \times 100\%$ (anthocyanin retention), where A_t represents the anthocyanin content after a given period t during storage or thermal treatment and A_0 the initial anthocyanin content before storage or thermal treatment. In agreement with previous papers,[19−21] first-order reaction kinetics ($A_t = A_0\, e^{-kt}$; k = reaction rate coefficient, t = storage time) were used to fit the analytical data. According to previously published papers,[19−22]

Table 1. Initial Concentrations[a] of Anthocyanins and Non-anthocyanin Phenolics in Differently Purified Liquid and Dried Preparations (Powders) and Total Soluble Solids[a] in Liquid Samples as well as Moisture Contents[a] in Dried Samples

	preparation			
compd	liquid total matrix	dried total matrix	liquid matrix-depleted	dried matrix-depleted
	Anthocyanin Contents (μmol/L, Liquid)/(μmol/kg, Dried)			
1	291.7 ± 38.2	1610.9 ± 2.1	312.8 ± 22.9	1789.8 ± 7.4
2	164.7 ± 17.2	888.1 ± 14.3	174.6 ± 9.5	971.7 ± 29.3
3 + **4**	98.0 ± 12.7	529.9 ± 7.1	105.6 ± 7.6	601.3 ± 1.7
5	187.8 ± 14.9	1038.2 ± 47.4	200.3 ± 4.2	1142.2 ± 61.7
6	163.1 ± 1.8	923.9 ± 97.3	168.5 ± 17.8	984.1 ± 93.6
7 + **8**	79.8 ± 4.9	425.0 ± 20.8	82.9 ± 0.2	468.0 ± 36.9
total 3,5-*O*-diglycosyl anthocyanins	555.4 ± 68.0	3028.8 ± 23.5	593.0 ± 40.0	3362.8 ± 38.4
total 3-*O*-glycosyl anthocyanins	430.8 ± 17.9	2387.2 ± 165.5	451.6 ± 13.8	2594.3 ± 192.2
total anthocyanins (*a*)	**985.2 ± 86.0**	**5416.0 ± 189.9**	**1044.6 ± 26.2**	**5957.2 ± 230.6**
	Non-Anthocyanin Phenolic Contents (μmol/L, Liquid)/(μmol/kg, Dried)			
9, myricetin 3-*O*-galloylglucoside	3.6 ± 0.1	10.1 ± 0.4	4.7 ± 0.6	9.3 ± 0.8
10, myricetin 3-*O*-galactoside + **11**, myricetin 3-*O*-glucoside	6.9 ± 0.3	19.3 ± 0.6	7.6 ± 0.1	18.4 ± 1.4
12, quercetin galloylhexoside + **13**, quercetin galloylhexoside	3.6 ± 0.1	25.4 ± 1.5	4.3 ± 0.3	22.9 ± 3.1
14, ellagic acid + **15**, quercetin 3-*O*-rutinoside + **16**, quercetin 3-*O*-glucoside	29.7 ± 0.2	113.3 ± 0.3	53.9 ± 2.7	110.1 ± 5.7
17, dimethoxylated quercetin	8.1 ± 0.2	21.9 ± 0.4	9.2 ± 0.2	21.7 ± 3.8
18, quercetin	1.3 ± 0.0	3.8 ± 0.5	1.3 ± 0.0	5.1 ± 1.2
total non-anthocyanin phenolics (*b*)	**53.2 ± 0.8**	**193.7 ± 1.0**	**63.0 ± 4.0**	**187.5 ± 16.0**
ratio copigment (*b*):pigment (*a*)	1:19	1:28	1:17	1:32
total soluble solids (°Brix)	1.3 ± 0.0	nd	0.7 ± 0.0	nd
moisture content (%)	nd	3.4 ± 0.3	nd	3.5 ± 0.5

[a]Values expressed as the mean ± standard deviation, n = 2 (anthocyanin and non-anthocyanin phenolic contents and TSS) and n = 3 (moisture contents). For assignment of compound numbers, see Figure 1.

DOI: 10.1021/acs.jafc.5b03471
J. Agric. Food Chem. 2015, 63, 8705−8714

half-life ($t_{1/2}$) values were determined by plotting the natural logarithms of the A_t/A_0 ratios against the storage time in days or heating time in hours [$\ln(A_t/A_0) = -kt$]. The slope of the linear regression curve yielded $-k$, enabling exact calculations of $t_{1/2}$ values [$t_{1/2} = (\ln 2)/k$]. The $t_{1/2}$ values of individual anthocyanins, total delphinidins, total cyanidins, and total anthocyanins were calculated.

Antioxidant Activity and Color Measurement during Storage. The TEAC assay was used to determine the antioxidant activity as described by van den Berg et al.,[23] and values were expressed as trolox equivalents in millimoles per liter (liquid preparations) and millimoles per kilogram DM (dried preparations). If required, samples and calibration solutions were diluted in deionized water. A Power Wave XS microplate spectrophotometer (Biotek Instruments, Bad Friedrichshall, Germany) was used for the test assay. Color measurements (CIE $L^*a^*b^*$) were carried out using a Minolta Chromameter CR-300 (Illuminant D65 and 10° observer angle) (Konica Minolta, Osaka, Japan) calibrated with a standard white tile ($L^* = 97.43$, $a^* = 0.01$, $b^* = 1.64$). On the basis of a^* and b^* values, chromaticity C* [$C^* = (a^{*2} + b^{*2})^{1/2}$] and hue angle $h°$ [$h° = \arctan(b^*/a^*)$] were determined.

Statistical Analysis. HPLC-DAD and TEAC analyses were conducted in duplicate, whereas color measurements (CIE $L^*a^*b^*$) were performed in a five-fold determination. Moisture contents, moisture adsorptions, and glass transition temperatures for the characterization of maqui powders were determined in triplicate. Results were expressed as means ± standard deviation. Analysis of variance (ANOVA) including the Tukey test were conducted with JMP 6 (SAS, Cary, NC, USA) to determine significant differences of means at $p < 0.05$.

RESULTS AND DISCUSSION

Physicochemical Characterization of Liquid and Dried Preparations Used for Storage Experiments. After adjustment to a consistent initial total anthocyanin concentration (~1000 μmol/L) and pH of 3.6, the total soluble solids (TSS) in the liquid preparation derived from the total matrix juice (1.3 ± 0.0 °Brix) were expectedly higher than those of the matrix-depleted extract (0.7 ± 0.0 °Brix) (Table 1). The pH and TSS of the liquid preparations remained constant during the whole storage period under all conditions applied.

Anthocyanins present in the samples were composed of delphinidin and cyanidin derivatives substituted with different sugar moieties (glucose and sambubiose) at position 3-*O*- and/or 5-*O*- as also previously reported (Figure 1 and Table 1).[10,17,18] When water was removed from the maltodextrin-containing liquid samples, initial total anthocyanin contents in the obtained dried preparations (powders) increased from 985 μmol/L to 5416 μmol/kg (when prepared from total matrix juice) and from 1045 μmol/L to 5958 μmol/kg (when prepared from matrix-depleted extract). In both liquid and dried preparations, proportions of total delphinidins (82% of total anthocyanins) were higher than the proportions of total cyanidins (18%). Delphinidin 3-*O*-sambubioside 5-*O*-glucoside (**1**) was the predominant anthocyanin, accounting for ca. 30% of total anthocyanins in all samples, followed by delphinidin 3-*O*-sambubioside (19%; **5**), delphinidin 3-*O*-glucoside (16%; **6**), and delphinidin 3,5-*O*-diglucoside (17%; **2**). Cyanidin derivatives were less abundant [sum of cyanidin 3-*O*-sambubioside-5-*O*-glucoside (**3**) and cyanidin 3,5-*O*-diglucoside (**4**), 10% of total anthocyanins; sum of cyanidin 3-*O*-sambubioside (**7**) and cyanidin 3-*O*- glucoside (**8**) 8% of total anthocyanins].

In agreement with a previous study,[10] non-anthocyanin phenolics in the maqui samples mostly consisted of ellagic acid (**14**) as well as derivatives of myricetin and quercetin (compounds **9**–**13** and **15**–**18**) (Table 1). Initial non-anthocyanin phenolic contents in the total matrix (53 μmol/L, liquid sample; 194 μmol/kg, powder) and matrix-depleted preparations (63 μmol/L, liquid sample; 188 μmol/kg, powder) were determined to be 17–32-fold lower than the initial total anthocyanin contents. Non-anthocyanin phenolic compounds were quantitated due to their potential importance for anthocyanin stabilization. So-called intermolecular copigmentation effects between non-anthocyanin phenolics (copigment) and anthocyanins may increase pigment stability, however, being reported to occur at high copigment/pigment ratios of, for example, 31:1, in a liquid anthocyanin extract based on grapes.[24] Despite markedly lower copigment/pigment ratios of ca. 1:24 on average determined in our maqui samples, the possible stabilizing effect caused by intermolecular copigmentation was further investigated in storage and heat experiments described below.

Residual moisture contents in the dried preparations were within the range of 3–5% (Table 1), at which quality attributes such as color, odor and taste were previously reported to be retained during long-term storage,[25] resulting in free-flowing, nonsticky powders.

Impact of Different Storage Conditions on the Stability of Total Anthocyanins. In all liquid samples investigated (Figure 2 and Table 2), total anthocyanin degradation was strongly influenced by the storage temperature and light exposure. For instance, the fastest anthocyanin degradation to ca. 22% of its initial content was observed after 28 days at 20 °C under permanent illumination [half-life ($t_{1/2}$) = ca. 12 days]. When samples were stored at the same temperature (20 °C) in the dark, anthocyanin retentions below ca. 22% were obtained much later, that is, after 63 days ($t_{1/2}$ =

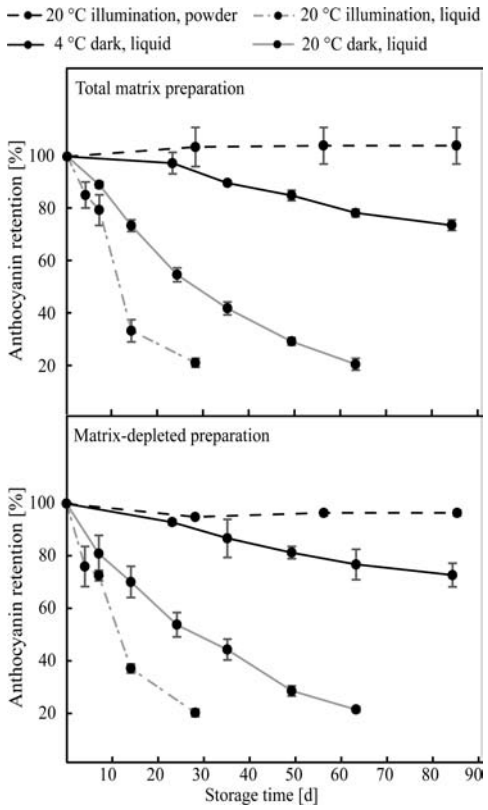

Figure 2. Anthocyanin retention (%) of liquid and dried (powder) total matrix and matrix-depleted maqui preparations at different storage conditions.

DOI: 10.1021/acs.jafc.5b03471
J. Agric. Food Chem. 2015, 63, 8705–8714

Table 2. Half-Life Values ($t_{1/2}$)[a] of Anthocyanins in Total Matrix and Matrix-Depleted Liquid Samples and Anthocyanin Retention[a] of the Respective Dried Preparations (Powders) during Storage at Different Temperatures with and without Illumination

	$t_{1/2}$ (days)			retention (%)
compd	20 °C, illumination (28 days of storage)	20 °C, dark (63 days of storage)	4 °C, dark (84 days of storage)	20 °C, illumination (85 days of storage)
Liquid/Dried Total Matrix Preparation				
1	18.2 ± 2.2a	45.3 ± 2.0a	270.0 ± 0.1ab	103.8 ± 0.1a
2	16.9 ± 0.9a	42.3 ± 2.0a	211.2 ± 2.4bc	102.9 ± 2.7a
3 + 4	17.0 ± 1.7a	44.2 ± 3.2a	214.2 ± 8.7bc	103.4 ± 1.6a
5	7.0 ± 0.0d	17.2 ± 0.3de	87.7 ± 2.8f	105.1 ± 8.2a
6	6.6 ± 0.6d	17.3 ± 0.4de	88.0 ± 4.9f	105.3 ± 23.7a
7 + 8	7.2 ± 0.1cd	17.7 ± 0.7de	89.2 ± 0.8f	106.3 ± 9.5a
total anthocyanins	**12.0 ± 0.2b**	**28.2 ± 1.8bc**	**141.2 ± 4.4def**	**104.2 ± 7.0a**
total delphinidins	12.2 ± 0.2b	28.6 ± 1.7bc	146.0 ± 4.2def	104.1 ± 7.4a
total cyanidins	11.9 ± 0.4b	28.6 ± 2.5bc	137.9 ± 2.3def	104.7 ± 5.1a
Liquid/Dried Matrix-Depleted Preparation				
1	17.0 ± 1.7a	43.9 ± 5.8a	300.9 ± 49.9a	96.9 ± 0.3a
2	16.9 ± 1.5a	40.8 ± 4.9a	227.5 ± 27.8b	95.9 ± 1.3a
3 + 4	15.2 ± 1.8ab	37.8 ± 4.5ab	223.7 ± 23.5b	95.4 ± 0.6a
5	7.1 ± 0.4d	16.3 ± 0.8de	99.8 ± 3.0def	96.7 ± 1.7a
6	6.7 ± 0.2d	16.1 ± 0.6e	95.6 ± 15.0ef	97.1 ± 1.2a
7 + 8	7.0 ± 0.4d	15.6 ± 0.6e	98.1 ± 0.6def	95.6 ± 4.8a
total anthocyanins	**11.7 ± 0.6b**	**28.0 ± 1.8bc**	**152.6 ± 0.2cde**	**96.5 ± 1.1a**
total delphinidins	12.0 ± 0.6b	29.0 ± 1.8bc	158.3 ± 0.2 cd	96.7 ± 0.8a
total cyanidins	11.2 ± 0.8bc	26.5 ± 1.8cd	146.8 ± 4.7def	95.5 ± 2.4a

[a]Values expressed as the mean ± standard deviation, $n = 2$ (correlation coefficients, R^2 of half-life values = 0.914−0.999). Significant differences between values in the same column are indicated by different letters ($P < 0.05$). For assignment of compound numbers, see Figure 1.

ca. 28 days), demonstrating the detrimental influence of light on color retention. Interestingly, total anthocyanin stability was only marginally affected by the food matrix. As shown in Figure 2, when samples were stored at 20 °C in the dark, stabilities of anthocyanins in the total matrix and the matrix-depleted preparations were almost identical ($t_{1/2} \sim 28$ days for both) (Table 2). Therefore, the presence of low-molecular-weight and non-phenolic matrix compounds appears to be irrelevant for maqui anthocyanin stability.

Expectedly, the reduction of the storage temperature from 20 to 4 °C significantly enhanced the total anthocyanin stability in liquid samples (Figure 2 and Table 2). Similar anthocyanin stabilities were found when total matrix and matrix-depleted samples were compared, exhibiting $t_{1/2}$ values ranging from ca. 141 to 153 days. For comparison, anthocyanin-rich vegetables mostly comprising high amounts of acylated anthocyanins have been shown to possess markedly higher pigment stabilities. For instance, substantially higher $t_{1/2}$ values of >365 days at 2 °C and 70 days at 25 °C have been reported in liquid anthocyanin preparations extracted from red potatoes (pH 3.5), which, however, contain high proportions of highly stable acylated anthocyanins.[26]

After drying, total anthocyanins remained stable over the whole period of storage (85 days) at 20 °C under illumination (total anthocyanin retentions ca. 100 ± 5%, Figure 2). Because the high stability of anthocyanins in dried samples hampered the deduction of reliable $t_{1/2}$ values, the retention of total anthocyanins (%) at the end of storage (85 days) is shown in Table 2 instead of $t_{1/2}$ values. The improved anthocyanin stability in the dried preparations was expected, most likely due to impaired hydration reactions by the removal of water.[27] In addition, embedding in maltodextrin has been previously reported to improve anthocyanin stability against oxidation reactions.[28] Accordingly, enhanced anthocyanin stabilities to decreasing storage temperatures and/or when liquid anthocyanin samples were processed into powders have been previously reported.[29,30] Thus, lowering the storage temperature or processing liquid maqui products into fruit powders may be a useful tool to obtain high-performance food colorants exhibiting long shelf life.

Antioxidant Activity and Color Changes (CIE *L*a*b) during Storage.** Differences in antioxidant activity were insignificant during storage of both liquid and dried maqui preparations (Table 3). Unexpectedly, antioxidant activities did not correlate with anthocyanin concentrations. Whereas the latter were reduced over time, antioxidant activities remained statistically unchanged, fluctuating between 88 and 115% in all samples. Possibly, the yet unknown anthocyanin degradation products exhibited antioxidant properties similar to those of their precursors.[31] These findings were in accordance with previous results, suggesting the formation of antioxidant polymeric compounds from anthocyanin degradation.[32]

As expected, observed color changes mostly followed those of anthocyanin concentrations. For instance, color changes were negligible during storage of the dried and liquid maqui samples at 4 °C in the dark (Table 3), in accordance with their high anthocyanin stability described above. However, color changes were notable when liquid preparations were stored at 20 °C in the dark and under illumination. Increases in lightness L^*, redness a^*, and yellowness b^* and in chromaticity C^* (only for illuminated samples) over time proved discoloration of the red color at 20 °C, resulting in a light brownish hue. Additionally, significant increases were observed in hue angles $h°$, also confirming the visually observed brownish color of the samples. In accordance with the literature, color changes were

DOI: 10.1021/acs.jafc.5b03471
J. Agric. Food Chem. 2015, 63, 8705−8714

Table 3. Antioxidant Capacity (TEAC)[a] and CIE $L^*a^*b^*$ as well as C^* and $h°$ Color Values[a] of Total Matrix and Matrix-Depleted Liquid and Dried Maqui Preparations after Storage under Different Conditions

	beginning of storage, day 0	4 °C, dark, day 84	20 °C, dark, day 63	20 °C, illumination, day 28
Liquid Total Matrix Preparation				
TEAC (mmol/L)	8.0 ± 0.7b	8.0 ± 0.2b	8.0 ± 0.1b	7.0 ± 0.0b
CIE L^*	13.2 ± 0.1c	12.8 ± 0.0d	17.4 ± 0.0b	20.5 ± 0.1a
CIE a^*	37.9 ± 0.2c	35.1 ± 0.1d	41.1 ± 0.1b	42.9 ± 0.0a
CIE b^*	1.5 ± 0.1c	0.0 ± 0.0d	8.0 ± 0.1b	11.2 ± 0.1a
CIE C^*	38.0 ± 0.2b	35.1 ± 0.1d	37.8 ± 0.5c	44.3 ± 0.1a
CIE $h°$	2.2 ± 0.2c	0.1 ± 0.1d	9.0 ± 0.6b	14.6 ± 0.1a
Dried Total Matrix Preparation				
TEAC (mmol/kg DM)	39.6 ± 2.6a	nd	nd	40.6 ± 3.1a
CIE L^*	38.5 ± 0.6b	nd	nd	42.4 ± 0.8a
CIE a^*	17.1 ± 0.1a	nd	nd	16.0 ± 0.3b
CIE b^*	−5.0 ± 0.0b	nd	nd	−4.6 ± 0.1a
CIE C^*	17.8 ± 0.1a	nd	nd	16.6 ± 0.3b
CIE $h°$	343.6 ± 0.1b	nd	nd	344.0 ± 0.1a
Liquid Matrix-Depleted Preparation				
TEAC (mmol/L)	6.9 ± 1.0b	7.2 ± 0.3b	7.4 ± 0.0b	7.0 ± 0.2b
CIE L^*	14.3 ± 0.1c	13.6 ± 0.1d	21.2 ± 0.1b	23.2 ± 0.1a
CIE a^*	41.1 ± 0.2c	37.8 ± 0.3d	45.6 ± 0.1a	45.2 ± 0.1b
CIE b^*	3.1 ± 0.1c	1.5 ± 0.2d	13.0 ± 0.1b	14.2 ± 0.1a
CIE C^*	41.2 ± 0.2b	37.9 ± 0.3d	39.9 ± 0.1c	47.4 ± 0.1a
CIE $h°$	4.3 ± 0.2c	2.3 ± 0.2d	8.9 ± 0.1b	17.5 ± 0.1a
Dried Matrix-Depleted Preparation				
TEAC (mmol/kg DM)	39.1 ± 2.6a	nd	nd	42.0 ± 2.6a
CIE L^*	40.2 ± 0.6b	nd	nd	43.2 ± 0.7a
CIE a^*	14.0 ± 0.3b	nd	nd	15.1 ± 0.3a
CIE b^*	−6.6 ± 0.1b	nd	nd	−6.3 ± 0.1a
CIE C^*	15.5 ± 0.3b	nd	nd	16.4 ± 0.3a
CIE $h°$	334.9 ± 0.1b	nd	nd	337.2 ± 0.2a

[a]Values expressed as the mean ± standard deviation, $n = 2$ (TEAC) and $n = 5$ (CIE $L^*a^*b^*$). Significant differences between values in the same row are indicated by different letters ($P < 0.05$).

reported to result from both anthocyanin degradation, and the formation of higher molecular-weight brown pigments.[33,34]

Storage Stability of Individual Anthocyanins. On the basis of the half-life ($t_{1/2}$) values listed in Table 2, degradation kinetics of total delphinidins and cyanidins were unexpectedly similar under a given storage condition ($p < 0.05$), in contrast to their thermal stability. Their $t_{1/2}$ values amounted to 158 days on average when stored at 4 °C in the dark, whereas $t_{1/2}$ values were 5 and 12 times smaller when samples were stored at 20 °C in the dark and under illumination, respectively (Table 2). Half-lives of total cyanidins and delphinidins of total matrix preparations were similar to those of matrix-depleted samples. Therefore, matrix constituents such as sugars and acids were suggested to have no or only a marginal impact on anthocyanin stability. These findings are in agreement with previous results,[30] in which the type of anthocyanidin core and the purity of the extract were found to have only insignificant effects when compared with anthocyanin storage stability of standard solutions to that of matrix-depleted anthocyanin extracts derived from grape pomace, purple corn, and black rice.[30] Conversely, stabilizing effects of polymeric matrix compounds, such as pectin, or even destabilizing effects (addition of citrate) on the storage stability of anthocyanins derived from black currant, strawberry, elderberry, and black carrot have been shown in other papers.[35−37]

In contrast to the marginal influence of the anthocyanidin core type and matrix constituents, the number of glycosyl moieties directly attached to the anthocyanidin apparently played a major role for stability. Irrespective of the anthocyanidin type, anthocyanins carrying two glycosylated hydroxyl functions (3,5-*O*- or 3,7-*O*-) showed $t_{1/2}$ values about 2.4 times higher (e.g., $t_{1/2}$ = ca. 15−18 days, 20 °C, illuminated) than those with only one glycosylated hydroxyl function (e.g., $t_{1/2}$ = ca. 7 days, 20 °C, illuminated) as shown in Table 2. The stability of diglycosylated maqui anthocyanins was further enhanced to $t_{1/2}$ values of ca. 38−45 and 211−301 days by light exclusion (20 °C) and cooled storage at 4 °C, respectively. A similarly improved stability was also observed for the monoglycosylated anthocyanins (Table 2), although being consistently ca. 2.5−2.6-fold less stable than their diglycosylated counterparts at a given storage condition ($t_{1/2}$ = ca. 16−18 days, 20 °C, dark; $t_{1/2}$ = ca. 88−100 days, 4 °C, dark).

In agreement with our findings, Robinson et al. reported enhanced stability of 3,5-*O*-diglucosylated anthocyanins when comparing to the corresponding 3-*O*-monoglucosides.[38] More recently, a faster degradation of 3-*O*-glucosides than of the 3,5-*O*-diglucosides has been determined during storage of a pomegranate juice (pH 3.8), which like maqui contained both 3-*O*- and 3,5-*O*-diglucosides.[39] Because sugar substitution at C5 lowers the nucleophilicity of the aromatic C6 and C8 positions of the anthocyanins, 3,5-*O*-diglycosylated anthocyanins have been suggested to be less prone to an electrophilic attack than those carrying a nonglycosylated A-ring.[40] Therefore, 3,5-*O*-diglycosylated anthocyanins were assumed to be more stable, particularly, because electrophilic attacks are followed by the fission of the C ring and subsequent chalcone

DOI: 10.1021/acs.jafc.5b03471
J. Agric. Food Chem. 2015, 63, 8705−8714

Table 4. Half-Life ($t_{1/2}$, h)[a] Values of Liquid Maqui Samples and Standard Anthocyanin Solutions at pH 2.2 and 3.6, Respectively, after 7 h of Thermal Treatment at 85 °C

compd.	liquid maqui samples and standard solutions			
	total matrix preparation	matrix-depleted preparation	matrix-free preparation	standard solution
		pH 3.6		
1	3.6 ± 0.1ef	2.5 ± 0.0fg	2.0 ± 0.0efg	3.5 ± 0.1de
2	2.5 ± 0.1gh	1.9 ± 0.0gh	1.4 ± 0.0fg	2.6 ± 0.0e
4 (+ **3**)	10.4 ± 0.5a	11.4 ± 0.3b	8.0 ± 0.3b	6.3 ± 0.2b
6 (+ **5**)	6.1 ± 0.3c	7.6 ± 0.3c	5.1 ± 0.0c	5.1 ± 0.2bc
7	4.0 ± 0.2de	2.8 ± 0.1efg	2.3 ± 0.0ef	nd
8	2.7 ± 0.1fgh	2.1 ± 0.1gh	1.6 ± 0.0efg	nd
total anthocyanins	**3.8 ± 0.2de**	**3.4 ± 0.1ef**	**2.6 ± 0.0def**	
		pH 2.2		
1	1.1 ± 0.1i	1.1 ± 0.0h	1.2 ± 0.0g	1.2 ± 0.0f
2	2.3 ± 0.0h	2.7 ± 0.2efg	2.8 ± 0.0de	2.5 ± 0.0e
4 (+ **3**)	6.7 ± 0.4c	7.0 ± 0.5 cd	6.2 ± 0.1c	4.4 ± 0.1 cd
6 (+ **5**)	8.9 ± 0.5b	13.8 ± 0.7a	12.4 ± 1.1a	8.6 ± 0.8a
7	2.6 ± 0.2gh	2.5 ± 0.2fg	2.7 ± 0.0def	nd
8	4.7 ± 0.2d	6.3 ± 0.3d	6.4 ± 0.0c	nd
total anthocyanins	**3.4 ± 0.2efg**	**3.8 ± 0.3e**	**3.9 ± 0.0d**	

[a]Values expressed as means ± standard deviation, n = 2 (correlation coefficients, R^2, of half-life values = 0.951−0.999). Significant differences between values in the same column are indicated by different letters (P < 0.05). For assignment of compound numbers, see Figure 1.

formation, thus often representing the first step of a detrimental breakdown cascade.[8,41,42] To provide deeper insights into the differing stabilities of 3-*O*- and 3,5-*O*-glycosylated anthocyanins, a series of heating experiments was conducted.

Influence of Glycosylation on Thermal Anthocyanin Stability in Acidic Solutions. To further investigate the influence of sugar substitution at the 3-*O* and 3,5-*O* positions on anthocyanin degradation, total matrix, matrix-depleted, and matrix-free preparations as well as aqueous solutions of standards (3-*O*-glucosides and 3,5-*O*-diglucosides of cyanidin and delphinidin) were heated for 7 h at 85 °C at pH 2.2 and 3.6, respectively, the latter representing the genuine maqui pH.

During thermal treatment at pH 3.6, degradation patterns of differently glycosylated cyanidin and delphinidin derivatives were similar to those observed during the storage experiment at 20 °C. For instance, in total matrix preparations, delphinidin 3-*O*-glucoside (**6**) and 3-*O*-sambubioside (**5**) were about 1.5 times less stable ($t_{1/2}$ = 2.6 h) than their respective diglycosylated derivatives, that is, delphinidin 3,5-*O*-diglucoside (**2**) and 3-*O*-sambubioside-5-*O*-glucoside (**1**; $t_{1/2}$ = 3.8 h). By analogy, the cyanidin 3-*O*-glucoside (**8**; $t_{1/2}$ = 6.1 h) was more rapidly degraded than its diglycosylated derivatives cyanidin 3,5-*O*-diglucoside (**4**) and 3-*O*-sambubioside-5-*O*-diglucoside (**3**; $t_{1/2}$ = 10.4 h).

A similar stability behavior was observed when the matrix-depleted maqui extract, the extract being devoid of the plant matrix (matrix-free), and the individual anthocyanin standards were examined at pH 3.6. Thus, 3-*O*-glycosylated anthocyanins were considered significantly less stable at pH 3.6 than their 3,5-*O*-diglycosylated counterparts, irrespective of the food matrix.

Whereas diglycosylated anthocyanins were more heat-stable than 3-*O*-glycosylated ones at pH 3.6, a reversed behavior was encountered at pH 2.2 as expressed by the respective half-life values (Table 4) and anthocyanin degradation kinetics exemplified by the total matrix preparation and the individual standard solutions (Figure 3). These observations were consistent in all samples independent of their matrix composition including the standard solutions. Similar to pH

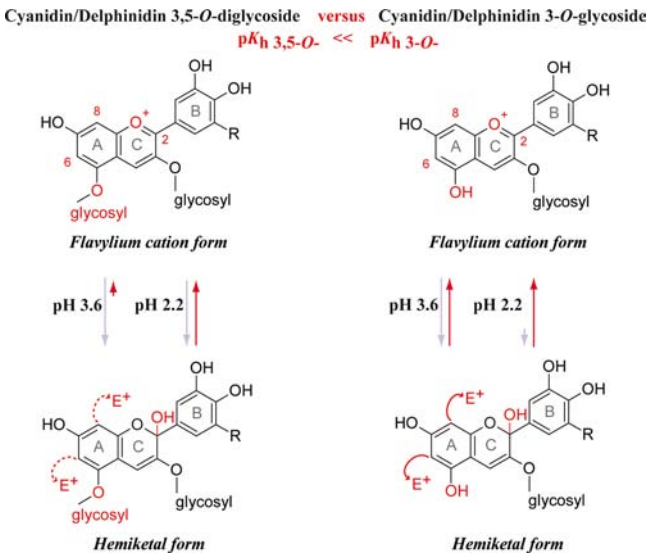

Figure 3. Anthocyanin retention (%) of delphinidin and cyanidin 3,5-*O*-diglycosides versus 3-*O*-monoglycosides of total matrix maqui preparations and standard solutions upon thermal treatment at 85 °C at pH 3.6 and 2.2. Lowered reactivity of electrophilic attacks at positions C6 and C8 of the hemiketal form is indicated by a dotted electron arrow. Enhanced reactivity is indicated by solid electron arrows. R = OH (delphinidin) / R = H (cyanidin).

3.6, stabilities of maqui anthocyanins were shown to be widely independent of matrix constituents. To provide a mechanistic hypothesis for these observations, the general pH-dependent behavior of anthocyanins in aqueous solution is briefly summarized.

Although depending slightly on the anthocyanidin type and the number of aromatic substituents, anthocyanins mainly exist in their stable flavylium cation form at low pH (pH < ∼1.0) (Figure 4). When the pH is increased (pH > ∼2), a nucleophilic attack of water at the C2 position of the pyrylium ring (C ring) leads to the formation of colorless hemiketals and, after ring fission, to chalcones. The pH-dependent behavior of

DOI: 10.1021/acs.jafc.5b03471
J. Agric. Food Chem. 2015, 63, 8705−8714

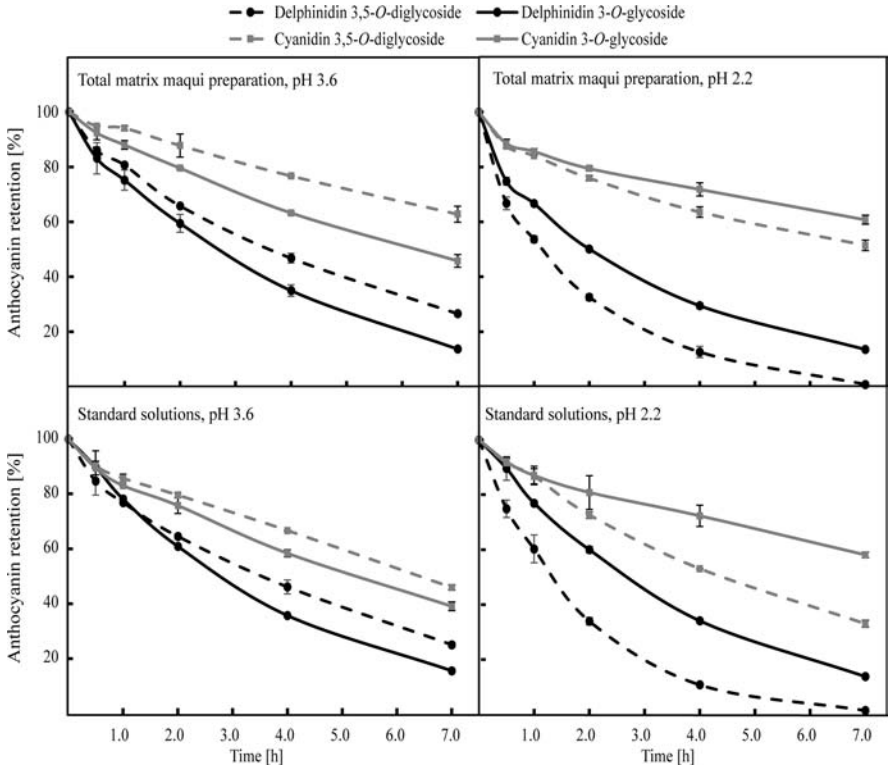

Figure 4. Impact of the hydration equilibrium constant pK_h of 3,5-*O*-diglycosylated and 3-*O*-monoglycosylated delphinidin and cyanidin on the formation of flavylium cation and colorless hemiketal species at pH 3.6 and 2.2. Lowered reactivity of electrophilic attack at positions C6 and C8 of the hemiketal form is indicated by a dotted electron arrow. Enhanced reactivity is indicated by solid electron arrows. R = OH (delphinidin)/H (cyanidin).

3-*O*-glycosylated and 3,5-*O*-diglycosylated anthocyanins was well described previously by their overall hydration equilibrium constants pK_h ranging from 1.79 to 3.02.[43−46] The pK_h constants indicate at which pH a 50:50 equilibrium of flavylium cation:hemiketal is reached. Lower hydration constants were found for 3,5-*O*-diglycosides [pK_h = 1.79 (delphinidin)[43]−2.23 (cyanidin)[44,46]] than for 3-*O*-glycosides [pK_h = 2.36 (delphinidin)[43]−3.02 (cyanidin)[45,46]], because glycosylation at position 5-*O*- decreases the electron density of the pyrylium ring, thus favoring the nucleophilic attack by water.[43,47] Therefore, in our experiments at pH 2.2, a major proportion [>50% (delphinidin); ≫50% (cyanidin)] of 3-*O*-monoglycosylated anthocyanins prevailed as flavylium cation, whereas a substantial proportion of 3,5-*O*-diglycosylated anthocyanins occurred in the hemiketal/chalcone form [≫ 50% (delphinidin); ∼50% (cyanidin)]. At pH 3.6, both 3-*O*- and particularly 3,5-*O*-glycosylated anthocyanins were present as hemiketal/chalcone to a large extent. As a result, 3,5-*O*-diglycosides should be considered more stable in their hemiketal/chalcon forms than as flavylium cation according to our findings. These hemiketals/chalcones might be particularly stable due to their glycosyl moiety at position 5-*O*- (or 7-*O*-), making the positions C6 and C8 less susceptible to electrophilic attacks as described above. Hence, the 3,5-*O*-diglycosylated anthocyanins were more stable at pH 3.6 than at pH 2.2. These findings are in agreement with previous studies,[39,40,46,48] even stating that 3,5-*O*-diglucosides of cyanidin, peonidin, delphinidin, petunidin, and malvidin show their optimum stability at pH 5.0,[48] that is, when completely occurring in their hemiketal and chalcone forms. In contrast, our results indicate that 3-*O*-glycosides were more stable as flavylium cation than as hemiketal/chalcone. The two hydroxyl groups of the anthocyanidin A-ring exert a strong positive mesomeric effect (+M), favoring electrophilic attacks at positions C6 and C8 positions (ortho/para). Thus, the stability of 3-*O*-glycosylated anthocyanins was lower at pH 3.6 than at pH 2.2 (Figure 4). Similar findings of an enhanced color stability of 3-*O*-glycosylated anthocyanins in more acidic media have been reported previously.[49,50]

In conclusion, because both 3-*O*-mono- and 3,5-*O*-diglycosylated anthocyanins occur approximately at a ratio of 50:50 in maqui samples, the resulting effect of their differing stability on total anthocyanin retention was almost outweighed when heating experiments at pH 2.2 ($t_{1/2}$ = 3.4−3.9 h) and at pH 3.6 ($t_{1/2}$ = 2.6−3.8 h) were compared (Table 4).

Influence of the Anthocyanidin Core on Thermal Anthocyanin Stability in Acidic Solutions. Besides the pH-dependent stability differences among differently glycosylated anthocyanins, the anthocyanin core type played a greater role during thermal treatment than during the above-described storage experiment, where identically glycosylated cyanidins and delphinidins were found to be similarly stable (Table 2). During thermal treatment at both pH 2.2 and 3.6, cyanidin derivatives were significantly more stable than the respective delphinidin derivatives (Table 4). This relationship was consistently found, irrespective of the level of food matrix present in the different maqui samples. The lower thermal stability of delphinidins as compared to cyanidins might be related to an increasing susceptibility to oxidation with increasing number of hydroxyl functions at the B ring.[48] Such oxidative degradation of the phenolic B ring might be the predominant degradation reaction at elevated temperatures,

DOI: 10.1021/acs.jafc.5b03471
J. Agric. Food Chem. 2015, 63, 8705−8714

being only of marginal importance at lower temperatures (4 and 20 °C).

In conclusion, two important features of maqui anthocyanins should be considered when maqui preparations are applied as coloring foodstuff or colorants. First, the major proportion of total anthocyanins is represented by delphinidin derivatives (73−82%), which per se were shown to be less stable when heated than the concomitant cyanidin derivatives (18−27% of total anthocyanins). Thus, heat exposure should be minimized during maqui processing. Second, although the pH value had an enormous effect on the differing stability of 3-*O*- and 3,5-*O*-glycosylated anthocyanins, their co-occurrence at a ratio of ∼50:50 may equally allow the application of maqui preparations between pH 2.2 and 3.6. According to our results, they might be preferably used in acidic chilled or frozen food products, such as sorbet and ice cream, because their storage stability was found to be best at low temperatures. In addition, application of maqui anthocyanins to food with low water activity, such as confectionery and cake glaze, may be a suitable option, as their stability was substantially increased after they were converted into powders. Nevertheless, maqui preparations should also be suitable for coloring beverages, fruit purees, fruit spreads, and jams when stored in the dark and, if possible, at cool temperatures.

■ ASSOCIATED CONTENT

Supporting Information

The Supporting Information is available free of charge on the ACS Publications website at DOI: 10.1021/acs.jafc.5b03471.

Materials and Methods and Results and Discussion: Determination of glass transition temperatures and water adsorptions of dried maqui preparations. Figure S1: Equilibrium moisture contents of the dried total matrix and matrix-depleted preparations at given relative humidities. Table S1: Initial concentrations of anthocyanins in differently purified, liquid maqui samples and in standards solutions before thermal treatment at 85 °C. Table S2: Anthocyanin retentions in differently purified, liquid maqui samples and standard solutions at pH 2.2 and 3.6 after 7 h of thermal treatment at 85 °C (PDF)

■ AUTHOR INFORMATION

Corresponding Author

*(R.M.S.) Phone: +49-(0)-711-459-22995. Fax: +49-(0)-711-459-24110. E-mail: ralf.schweiggert@uni-hohenheim.de.

Funding

We are grateful to Prof. Dr. H. C. Rainer Wild and the Dr. Rainer Wild Holding for generous financial support of this work.

Notes

The authors declare no competing financial interest.

■ ACKNOWLEDGMENTS

Salus Chile (Villarrica, Chile) is acknowledged for providing fruit samples.

■ REFERENCES

(1) Gultekin, F.; Doguc, D. K. Allergic and immunologic reactions to food additives. *Clin. Rev. Allergy Immunol.* **2013**, *45*, 6−29.

(2) McCann, D.; Barrett, A.; Cooper, A.; Crumpler, D.; et al. Food additives and hyperactive behaviour in 3-year-old and 8/9-year-old children in the community: a randomised, double-blinded, placebo-controlled trial. *Lancet* **2007**, *370*, 1560−1567.

(3) Cliff Burrows. Update regarding cochineal extract. http://blogs.starbucks.com/blogs/customer/archive/2012/03/29/update-regarding-cochineal-extract.aspx (accessed Aug 26, 2015).

(4) Cliff Burrows. Cochineal extract update. http://blogs.starbucks.com/blogs/customer/archive/2012/04/19/cochineal-extract-update.aspx (accessed Aug 26, 2015).

(5) Yamakawa, Y.; Oosuna, H.; Yamakawa, T.; Aihara, M.; Ikezawa, Z. Cochineal extract-induced immediate allergy. *J. Dermatol.* **2009**, *36*, 72−74.

(6) He, J.; Giusti, M. M. Anthocyanins: natural colorants with health-promoting properties. *Annu. Rev. Food Sci. Technol.* **2010**, *1*, 163−187.

(7) Giusti, M.; Wrolstad, R. E. Acylated anthocyanins from edible sources and their applications in food systems. *Biochem. Eng. J.* **2003**, *14*, 217−225.

(8) Sadilova, E.; Stintzing, F. C.; Carle, R. Thermal degradation of acylated and nonacylated anthocyanins. *J. Food Sci.* **2006**, *71*, C504−C512.

(9) Kammerer, D.; Carle, R.; Schieber, A. Quantification of anthocyanins in black carrot extracts (*Daucus carota* ssp. *sativus* var. *atrorubens* Alef.) and evaluation of their color properties. *Eur. Food Res. Technol.* **2004**, *219*, 479−486.

(10) Brauch, J. E.; Buchweitz, M.; Schweiggert, R. M.; Carle, R. Detailed analyses of fresh and dried maqui (*Aristotelia chilensis* (Mol.) Stuntz) berries and juice. *Food Chem.* **2016**, *190*, 308−316.

(11) Benn Brothers, France. *Colouring Wine* **1890**, *36*, 417.

(12) Kew Royal Botanic Gardens.. Maqui berries for colouring wine (*Aristotelia maqui*). *Bull. Misc. Inf. (R. Gardens, Kew)* **1890**, *38*, 34−36.

(13) Gironés-Vilaplana, A.; Mena, P.; García-Viguera, C.; Moreno, D. A. A novel beverage rich in antioxidant phenolics: maqui berry (*Aristotelia chilensis*) and lemon juice. *LWT−Food Sci. Technol.* **2012**, *47*, 279−286.

(14) Gironés-Vilaplana, A.; Calín-Sánchez, Á.; Moreno, D. A.; Carbonell-Barrachina, Á. A.; García-Viguera, C. Novel maqui liquor using traditional pacharán processing. *Food Chem.* **2015**, *173*, 1228−1235.

(15) Torres, C. A.; Romero, L. A.; Diaz, R. I. Quality and sensory attributes of apple and quince leathers made without preservatives and with enhanced antioxidant activity. *LWT−Food Sci. Technol.* **2015**, *62*, 996−1003.

(16) Céspedes, C. L.; El-Hafidi, M.; Pavon, N.; Alarcon, J. Antioxidant and cardioprotective activities of phenolic extracts from fruits of Chilean blackberry *Aristotelia chilensis* (Elaeocarpaceae), maqui. *Food Chem.* **2008**, *107*, 820−829.

(17) Céspedes, C. L.; Valdez-Morales, M.; Avila, J. G.; El-Hafidi, M.; et al. Phytochemical profile and the antioxidant activity of Chilean wild black-berry fruits, *Aristotelia chilensis* (Mol) Stuntz (Elaeocarpaceae). *Food Chem.* **2010**, *119*, 886−895.

(18) Fredes, C.; Yousef, G. G.; Robert, P.; Grace, M. H.; et al. Anthocyanin profiling of wild maqui berries (*Aristotelia chilensis* [Mol.] Stuntz) from different geographical regions in Chile. *J. Sci. Food Agric.* **2014**, *94*, 2639−2648.

(19) Cisse, M.; Vaillant, F.; Acosta, O.; Dhuique-Mayer, C.; Dornier, M. Thermal degradation kinetics of anthocyanins from blood orange, blackberry, and roselle using the Arrhenius, Eyring, and Ball models. *J. Agric. Food Chem.* **2009**, *57*, 6285−6291.

(20) Harbourne, N.; Jacquier, J. C.; Morgan, D. J.; Lyng, J. G. Determination of the degradation kinetics of anthocyanins in a model juice system using isothermal and non-isothermal methods. *Food Chem.* **2008**, *111*, 204−208.

(21) Fischer, U. A.; Carle, R.; Kammerer, D. R. Thermal stability of anthocyanins and colourless phenolics in pomegranate (*Punica granatum* L.) juices and model solutions. *Food Chem.* **2013**, *138*, 1800−1809.

(22) Buchweitz, M.; Brauch, J.; Carle, R.; Kammerer, D. R. Colour and stability assessment of blue ferric anthocyanin chelates in liquid pectin-stabilised model systems. *Food Chem.* **2013**, *138*, 2026−2035.

(23) van den Berg, R.; Haenen, G. R.; van den Berg, H.; Bast, A. Applicability of an improved Trolox equivalent antioxidant capacity (TEAC) assay for evaluation of antioxidant capacity measurements of mixtures. *Food Chem.* **1999**, *66*, 511−517.
(24) Malien-Aubert, C.; Dangles, O.; Amiot, M. J. Color stability of commercial anthocyanin-based extracts in relation to the phenolic composition. Protective effects by intra- and intermolecular copigmentation. *J. Agric. Food Chem.* **2001**, *49*, 170−176.
(25) Saydi, D.; Hatamipour, M. S. Analysis of the effective parameters on potato powder quality produced by a spray dryer. *Iranian J. Chem. Eng.* **2012**, *9*, 55−62.
(26) Rodriguez-Saona, L. E.; Giusti, M. M.; Wrolstad, R. E. Color and pigment stability of red radish and red-fleshed potato anthocyanins in juice model systems. *J. Food Sci.* **1999**, *64*, 451−456.
(27) Patras, A.; Brunton, N. P.; O'Donnell, C.; Tiwari, B. K. Effect of thermal processing on anthocyanin stability in foods; mechanisms and kinetics of degradation. *Trends Food Sci. Technol.* **2010**, *21*, 3−11.
(28) Mahdavee Khazaei, K.; Jafari, S. M.; Ghorbani, M.; Hemmati Kakhki, A. Application of maltodextrin and gum Arabic in microencapsulation of saffron petal's anthocyanins and evaluating their storage stability and color. *Carbohydr. Polym.* **2014**, *105*, 57−62.
(29) Fracassetti, D.; Del Bo', C.; Simonetti, P.; Gardana, C.; et al. Effect of time and storage temperature on anthocyanin decay and antioxidant activity in wild blueberry (*Vaccinium angustifolium*) powder. *J. Agric. Food Chem.* **2013**, *61*, 2999−3005.
(30) West, M. E.; Mauer, L. J. Color and chemical stability of a variety of anthocyanins and ascorbic acid in solution and powder forms. *J. Agric. Food Chem.* **2013**, *61*, 4169−4179.
(31) Sadilova, E.; Carle, R.; Stintzing, F. C. Thermal degradation of anthocyanins and its impact on color and *in vitro* antioxidant capacity. *Mol. Nutr. Food Res.* **2007**, *51*, 1461−1471.
(32) Brownmiller, C.; Howard, L. R.; Prior, R. L. Processing and storage effects on monomeric anthocyanins, percent polymeric color, and antioxidant capacity of processed blueberry products. *J. Food Sci.* **2008**, *73*, H72−H79.
(33) Giusti, M.; Wrolstad, R. E. Characterization and measurement of anthocyanins by UV-visible spectroscopy. In *Handbook of Food Analytical Chemistry*; Wrolstad, R. E., Acree, T. E., Decker, E. A., Penner, M. H., et al., Eds.; Wiley: Hoboken, NJ, USA, 2004; pp 19−31.
(34) Skrede, G.; Wrolstad, R. E.; Lea, P.; Enersen, G. Color stability of strawberry and blackcurrant syrups. *J. Food Sci.* **1992**, *57*, 172−177.
(35) Buchweitz, M.; Speth, M.; Kammerer, D. R.; Carle, R. Impact of pectin type on the storage stability of black currant (*Ribes nigrum* L.) anthocyanins in pectic model solutions. *Food Chem.* **2013**, *139*, 1168−1178.
(36) Buchweitz, M.; Speth, M.; Kammerer, D.; Carle, R. Stabilisation of strawberry (*Fragaria* × *ananassa* Duch.) anthocyanins by different pectins. *Food Chem.* **2013**, *141*, 2998−3006.
(37) Sadilova, E.; Stintzing, F. C.; Kammerer, D. R.; Carle, R. Matrix dependent impact of sugar and ascorbic acid addition on color and anthocyanin stability of black carrot, elderberry and strawberry single strength and from concentrate juices upon thermal treatment. *Food Res. Int.* **2009**, *42*, 1023−1033.
(38) Robinson, W. B.; Weirs, L. D.; Bertino, L. D.; Mattick, L. R. The relation of anthocyanin composition to color stability of New York state wines. *Am. J. Enol. Vitic.* **1966**, *17*, 178−184.
(39) Martí, N.; Pérez-Vicente, A.; García-Viguera, C. Influence of storage temperature and ascorbic acid addition on pomegranate juice. *J. Sci. Food Agric.* **2002**, *82*, 217−221.
(40) Timberlake, C. F.; Bridle, P. Anthocyanins: colour augmentation with catechin and acetaldehyde. *J. Sci. Food Agric.* **1977**, *28*, 539−544.
(41) Markakis, P.; Livingston, G. E.; Fellers, C. R. Quantitative aspects of strawberry pigment degradation. *J. Food Sci.* **1957**, *22*, 117−130.
(42) Piffaut, B.; Kader, F.; Girardin, M.; Metche, M. Comparative degradation pathways of malvidin 3,5-diglucoside after enzymatic and thermal treatments. *Food Chem.* **1994**, *50*, 115−120.
(43) Figueiredo, P.; Elhabiri, M.; Toki, K.; Saito, N.; et al. New aspects of anthocyanin complexation. Intramolecular copigmentation as a means for colour loss? *Phytochemistry* **1996**, *41*, 301−308.
(44) Mazza, G.; Brouillard, R. Color stability and structural transformations of cyanidin 3,5-diglucoside and four 3-deoxyanthocyanins in aqueous solutions. *J. Agric. Food Chem.* **1987**, *35*, 422−426.
(45) Stintzing, F. C.; Stintzing, A. S.; Carle, R.; Frei, B.; Wrolstad, R. E. Color and antioxidant properties of cyanidin-based anthocyanin pigments. *J. Agric. Food Chem.* **2002**, *50*, 6172−6181.
(46) Timberlake, C. F.; Bridle, P. Flavylium salts, anthocyanidins and anthocyanins. I. Structural transformations in acid solutions. *J. Sci. Food Agric.* **1967**, *18*, 473−478.
(47) Dangles, O.; Elhajji, H. Synthesis of 3-methoxy- and 3-(β-D-glucopyranosyloxy)flavylium Ions. Influence of the flavylium substitution pattern on the reactivity of anthocyanins in aqueous solution. *Helv. Chim. Acta* **1994**, *77*, 1595−1610.
(48) Hrazdina, G.; Borzell, A. J.; Robinson, W. B. Studies on the stability of the anthocyanidin-3,5-diglucosides. *Am. J. Enol. Vitic.* **1970**, *21*, 201−204.
(49) Abdel-Aal, E.-S. M.; Hucl, P. Composition and stability of anthocyanins in blue-grained wheat. *J. Agric. Food Chem.* **2003**, *51*, 2174−2180.
(50) Bao, J.; Cai, Y.; Sun, M.; Wang, G.; Corke, H. Anthocyanins, flavonols, and free radical scavenging activity of chinese bayberry (*Myrica rubra*) extracts and their color properties and stability. *J. Agric. Food Chem.* **2005**, *53*, 2327−2332.

DOI: 10.1021/acs.jafc.5b03471
J. Agric. Food Chem. 2015, 63, 8705−8714

averaged structural information on the mass distribution and shape of noncrystalline molecules in a nondestructive manner. Hence, it has been utilized widely for the nanoscale structural analysis of soft matters such as polymer gels, emulsions, and liquid crystals.[26,27] The characteristic merits of SAXS also can be used effectively for the structural analysis of proteins such as gliadins, not only of the gliadin molecule itself but also of aggregated forms at high concentrations. Some results have been reported to date concerning the structural analysis on gluten proteins by SAXS. Matsushita et al. investigated the structure of high-molecular-weight glutenin subunits by SAXS in 1-propanol/acetic acid/water mixed solutions in the concentration range of 1.0−10.0 mg/mL.[28] From Guinier and cross-section Guinier plots, they determined glutenins to have a rod-like shape. In another SAXS study, Thomson et al.[20,29] examined α-, γ-, and ω-gliadins and high-molecular-weight glutenin subunits in the alcohol/water mixed solutions in the concentration range of about 1−10 mg/mL and analyzed their SAXS profiles by means of Guinier and cross-section Guinier plots. They found that gliadins in this concentration range have a prolate ellipsoid shape with a length of 15−20 nm and a diameter of about 3.5 nm. These results shed light on the nanostructure of gluten protein molecules in dilute solution, but their structure in the alcohol-containing water is not necessarily the same as that in alcohol-free water. In addition, the structure of gluten proteins at high concentrations is still unclear. In this study, we focus on gliadins extracted with distilled water and report on the SAXS analysis of their structures over a wide range of concentrations in aqueous solutions. We also correlate the results of an electrophoresis measurement and a sedimentation velocity experiment with the nanostructure of gliadins established by SAXS.

MATERIALS AND METHODS

Materials. Gliadins used in this study were prepared by the following procedure, the details of which are described in our previous paper.[25] Dough was prepared by mixing and kneading 100 g of wheat flour (Super King, Nisshin Flour Milling, Inc.; 13.8% protein, 0.42% ash, 14% water) with 67 mL of 0.5 M NaCl in a mixer (KN-200, Taisho Denki, Tokyo, Japan) for 20 min and then repeatedly kneaded with one hand in 500 mL of distilled water for 15 min at 15 °C. The first and second wash solutions were discarded. The third to sixth wash solutions were collected and centrifuged at 18000g for 10 min at 20 °C. After NaCl was added to the supernatant to adjust its concentration to 0.5 M, the precipitated gliadins were collected by centrifugation at 18000g for 20 min at 20 °C, suspended in 300 mL of distilled water, dialyzed five times against 3 L of distilled water for 8 h at 4 °C, and finally freeze-dried. The gliadins were also extracted from wheat flour with 70% ethanol according to the method described by Tatham and Shewry.[13] Protein was assayed with an RC.DC protein assay kit from Bio-Rad Laboratories (Hercules, CA, USA).

Sedimentation Velocity Experiments. Sedimentation velocity experiments on 0.02 wt % gliadins dissolved in distilled water were performed with an Optima XL-I unit (Beckman Coulter, Inc., Brea, CA, USA) using an An50Ti rotor at 20 °C. Charcoal-filled Epon double-sector cells were used with the reference sectors filled with distilled water. All data were acquired without time intervals between successive scans. The sedimentation coefficient distribution function, $c(s)$, was obtained by use of the SEDFIT program.[30,31] The partial specific volume of gliadin was set to 0.73, which is the default value.[32] A protocol for calculating the molecular weight corresponding to each peak using the Svedberg equation was implemented in SEDFIT, where a common frictional ratio, f/f_0, was assumed for all molecular species.

Electrophoretic Analysis of Gliadin Preparations. Gliadins extracted into distilled water or 70% ethanol were subjected to 2D-PAGE isoelectric focusing and SDS-PAGE.[33,34] Gliadins were treated with a 2D cleanup kit (GE Healthcare UK Ltd.) and applied to 7 cm Ready-Strip IPG Strips (Bio-Rad Laboratories). Isoelectric focusing was performed using a Protean IEF Cell (Bio-Rad Laboratories). The strips were then subjected to SDS-PAGE and stained with Coomassie Brilliant Blue R-250.

SAXS Experiments. The SAXS experiments were carried out at the beamline BL-10C of Photon Factory, a synchrotron radiation facility of Institute of Materials Structure Science, High Energy Accelerator Research Organization (KEK). Dilute solution samples were measured in a 1 mm thick aluminum cell with 20 μm thick quartz windows. Viscous hydrated solids were measured in a 1 mm thick PTFE sandwich cell with windows of 7.5 μm thick Kapton films (TORAY-DuPont). The X-ray wavelength was 0.1488 nm, and the observed range of scattering vector (denoted q) was 0.06−2.5 nm^{-1} as calibrated with silver behenate. The scattered beam was detected with two-dimensional area detectors. The typical X-ray exposure time was 300 s. Samples were used for SAXS measurements at least 4 days after preparation. Measured two-dimensional data were converted into one-dimensional scattering profiles followed by the standard procedure of data correction for cell and background scatterings, transmission, and beam intensity.

Cross-Linking Experiments. Gliadin solutions were incubated with and without 5 mM 3,3′-dithiobis(sulfosuccinimidyl propionate) (DTSSP) from Dojindo (Tokyo Japan) at 25 °C for 60 min. After the addition of *N*-ethylmaleimide (20 mM), the solutions were incubated for 10 min at room temperature and then freeze-dried. Laemmli's SDS sample buffer[31] without reducing reagent was added to the gliadin solutions, which were then boiled for 5 min. The suspension was centrifuged at 10000g for 40 min at room temperature. The supernatant (30 μg of protein) was subjected to SDS-PAGE under nonreducing conditions. Another part of the supernatant (100 μg protein) was subjected to SDS-PAGE with a native PAGE 3−12% gel (Invitrogen, Carlsbad, CA, USA) and electrophoresed with 50 mM bis(2-hydroxyethyl)amino-tris(hydroxymethyl)methane-HCl (Bis-Tris HCl) buffer having a pH of 6.8, including 50 mM tricine and 0.1% SDS as running buffer, under nonreducing conditions. After electrophoresis, the sample lane was cut from the gel and immersed in Laemmli's SDS sample buffer with 5% 2-mercaptoethanol for 30 min and subjected to SDS-PAGE under reducing conditions. The proteins were stained with Coomassie Brilliant Blue R-250.

RESULTS AND DISCUSSION

Gliadin-Rich Proteins Extracted from NaCl-Containing Dough with Distilled Water. Previously we found that gliadins can be extracted with distilled water from dough prepared with wheat flour and a 0.51 M NaCl aqueous solution.[25] When the dough made with 100 g of wheat flour was washed with 500 mL of distilled water, starch, albumins, and globulins were eluted from the dough into the first and second wash solutions. However, gliadins were eluted into the third to sixth wash solutions when the NaCl content in the dough became <5 mg/100 g dough.[25] In the present study, we also observed abundant gliadins in the third and subsequent extracts by repeating the extraction procedure. The amount of extracted proteins (2.63 g from 100 g of flour) was almost the same as that of gliadins extracted with 70% ethanol (2.53 g from 100 g of flour). 2D-PAGE shows that the composition of proteins extracted by our procedure was almost the same as that of gliadins extracted with 70% ethanol except for a minor spot at 75 kDa in distilled water, which is probably due to contamination (Figure 1).

The gliadins obtained by our procedure can be dissolved in distilled water to yield a transparent solution at concentrations of ≤10 wt %, whereas they form gel-like hydrated solids at concentrations of ≥15 wt %. Gliadins resting in a plastic tube at ≥40 wt % do not flow even when the tube is turned upside down, which suggests the presence of a network structure.

DOI: 10.1021/acs.jafc.5b02902
J. Agric. Food Chem. 2015, 63, 8715−8721

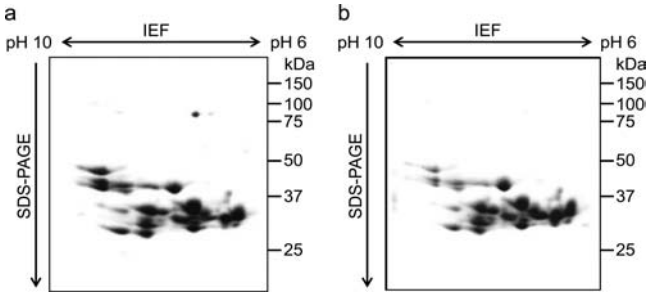

Figure 1. Two-dimensional PAGE of gliadin fractions: (a) gliadin extracted from dough made with wheat flour and a 0.5 M NaCl solution by washing with distilled water; (b) gliadin extracted from wheat flour with 70% ethanol.

Molecular Weight Distribution. A sedimentation velocity analysis revealed the molecular weight distribution of the gliadin in 0.02% distilled water solutions as shown in Figure 2. The distribution curve shows the largest peak at a sedimentation coefficient corresponding to a molecular weight of 25.7 kDa, indicating that most of the extracted gliadins are in the monomeric form. A small, broad peak found at a molecular weight of ca. 103 kDa suggests that associated gliadins exist in addition to monomeric gliadins.

Nanostructure of Gliadins in Distilled Water As Revealed by SAXS. Figure 3 shows SAXS profiles of gliadins in distilled water at various concentrations: (a) solution components of low-concentration samples (≤10 wt %) and (b) high-concentration gel-like solid samples (≥15 wt %). Because of a large difference in the physical state between the two regions, we discuss each concentration region separately.

In the low-concentration region, the scattering intensity increases gradually with increasing concentration. A small shoulder appears near $q = 0.3$ nm^{-1} at 0.5 wt % and gradually shifts to 0.13 nm^{-1} at 10 wt % with increasing intensity. The emergence of this shoulder indicates the presence of considerable interparticle interference. Therefore, it is required that the behavior of isolated gliadin molecules be observed at concentrations <0.5 wt %. We first attempted to evaluate the size of gliadin molecules at concentrations <0.5 wt % by means of a Guinier analysis of the scattering curves. However, the results could not be well fitted with a simple Guinier relationship, $I = A \exp(-R_g^2 q^2/3)$, indicating a polydispersity of scatterers. Thus, we employed the three-component Guinier equation expressed as $I(q) = A_1 \exp(-R_{g1}^2 q^2/3) + A_2 \exp(-R_{g2}^2 q^2/3) + A_3 \exp(-R_{g3}^2 q^2/3)$. As shown in Figure 4a, the scattering profiles are well fitted by this equation; the fitting parameters are summarized in Table 1. The value of the smallest radius of gyration ranges from 4.10 to 6.46 nm. Thomson et al.[20] previously reported R_g values of 3.55, 3.80, and 4.60 nm for α-, γ-, and ω-gliadins in 70% ethanol, respectively. By comparing their data with the R_{g1} values of our data, we can say that gliadin molecules are present as monomers in the 0.025 wt % solution, although some molecules with larger R_g values such as gliadin dimers and oligomers are also present. The presence of these larger molecules is consistent with the results of the sedimentation velocity experiment described above. The values of R_{g1} increase slightly with increasing concentration, indicating that some gliadin monomers associate to dimers at higher concentrations. The parameters R_{g2} and R_{g3} in Table 1 are much larger than that of gliadin monomers and likely correspond to larger aggregates or a high-molecular-weight contaminant (e.g., glutenin).

When anisotropic particles, such as those possessing a rod-like shape, are examined by SAXS, a cross-section Guinier plot may be used to obtain information about the cross-section size. Figure 4b shows the cross-section Guinier plots for the three low-concentration samples. The scattering curves in the low-q region were well fitted with straight lines obeying the relationship $qI(q) = A \exp(-R_c^2 q^2/2)$. The resulting values for the cross-sectional radius of gyration, R_c, are listed in Table 2. These values are more than twice as large as those reported by Thomson et al.[20] The reason for this is due in part to the aggregation of gliadin molecules, but also may be ascribable to structural differences between gliadins in ethanol and in water. The rod length, Λ, obtained from the equation, $R_g^2 - R_c^2 = \Lambda^2/12$, is also presented in Table 2. The radii and length become larger at 0.5 wt %. However, we think that this change is due to an increasing number of aggregated gliadins rather than to a change of molecular size itself; accordingly, the average value of each dimension becomes larger.

In the 1−10 wt % concentration range, Guinier plots do not yield reasonable physical values due to interparticle interference. Instead, the correlation length, L, was obtained from the Bragg equation, $L = 2\pi/q_s$, where q_s is the magnitude of the scattering vector of the shoulder appearing above 1 wt %. As shown in Table 3, L increases with increasing concentration,

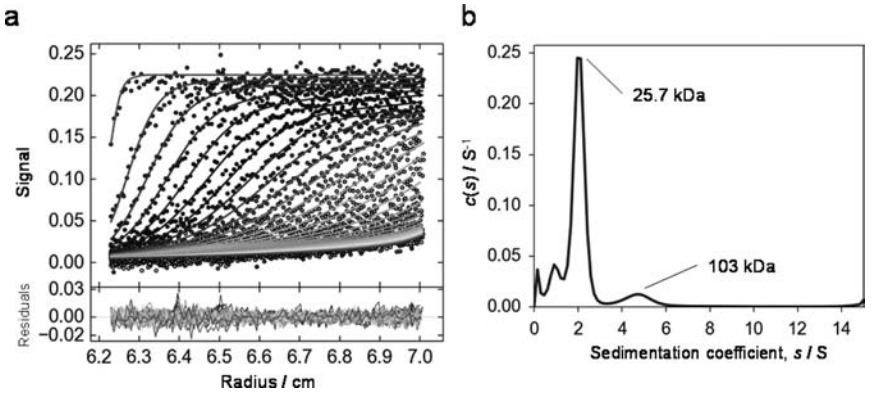

Figure 2. Sedimentation velocity analysis of 0.02 wt % gliadins in distilled water: (a) raw data of sedimentation velocity scans with best-fit curves based on the distribution shown in (b); (b) concentration distribution versus the sedimentation coefficient, s, obtained from the fitting result of (a) (the peaks appearing at 2.06 and 4.76 S correspond to molecular weights of 25.7 and 103 kDa, respectively).

DOI: 10.1021/acs.jafc.5b02902
J. Agric. Food Chem. 2015, 63, 8715−8721

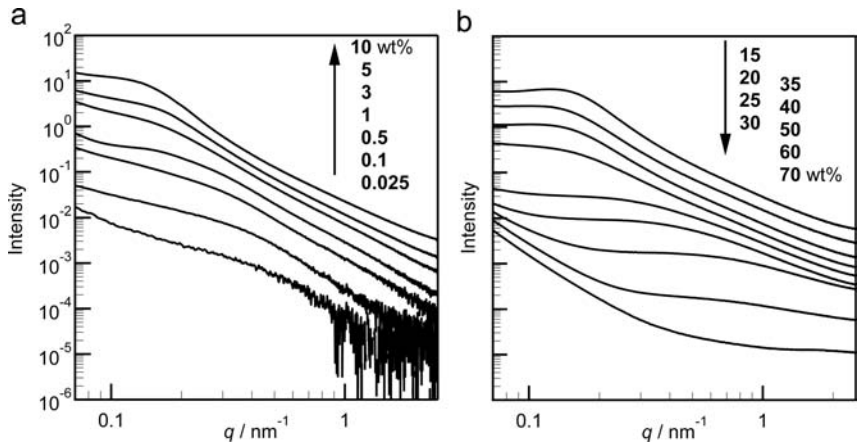

Figure 3. SAXS profiles of gliadins in distilled water: (a) solution components at low concentrations; (b) gel-like solid samples at high concentrations. The curves are vertically shifted for clarity.

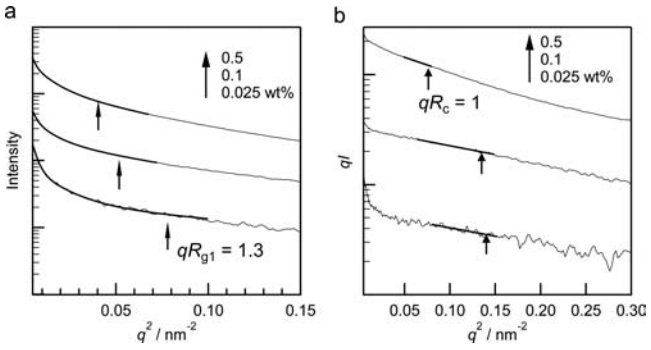

Figure 4. (a) Guinier plots for dilute aqueous solutions of gliadins. Scattering profiles are fitted by a three-component Guinier equation (thick lines). Small arrows indicate the points at which the relationship $qR_{g1} = 1.3$ holds (R_{g1}: smallest radius of gyration). (b) Cross-section Guinier plots for aqueous solutions of gliadins. Small arrows indicate the points at which the relationship $qR_c = 1$ holds (R_c: cross-sectional radius of gyration).

Table 1. Radius of Gyration Calculated by Fitting with a Three-Component Guinier Equation

concn (wt %)	R_{g1} (nm)	R_{g2} (nm)	R_{g3} (nm)
0.025	4.10 ± 0.74	13.7 ± 1.1	33.2 ± 0.9
0.1	5.68 ± 0.20	16.4 ± 0.7	34.9 ± 1.2
0.5	6.46 ± 0.05	16.7 ± 0.1	40.0 ± 0.3

Table 2. Radius of Gyration (R_{g1}), Cross-Sectional Radius of Gyration (R_c), and Rod Length (Λ) Calculated from Guinier and Cross-Section Guinier Plots

concn (wt %)	R_{g1} (nm)	R_c (nm)	Λ (nm)
0.025	4.10 ± 0.74	2.65 ± 0.05	10.8 ± 3.4
0.1	5.68 ± 0.20	2.71 ± 0.01	17.3 ± 0.8
0.5	6.46 ± 0.05	3.59 ± 0.003	18.6 ± 0.2

which suggests that the size of aggregated gliadins becomes larger and that the distance between aggregates increases under these conditions.

At concentrations above 15 wt %, gliadins are insoluble in water and form gel-like hydrated solids. The SAXS profiles in this region are displayed in Figure 3b. The scattering curve at 15 wt % is similar to that of the 10 wt % solution. This fact indicates that the nanostructures of these two samples are similar despite the difference in water solubility. It is suggested that only intermolecular association occurs in this concentration range without a significant change in the size and distribution of aggregated gliadins. As concentration increases further, the shoulder near 0.13 nm^{-1} diminishes while the upturn in the low-q region grows and a broad shoulder appears in the higher q region. When the low-q changes are examined closely, the 0.13 nm^{-1} shoulder shifts to the even lower q and finally protrudes out of the observable q range. This transition suggests the evolving formation of gliadin aggregates. As concentration increases, isolated gliadin aggregates coalesce to form larger aggregates, resulting in the growth of the low-q upturn. Concurrently, the density fluctuation inside the aggregates also increases, which is manifested as a broad peak in the high-q region. The characteristic peaks observed in this region are summarized in Table 3. When the concentration reaches 70 wt %, the broad shoulder is almost unrecognizable, and only the upturn in the low-q region remains.

Table 3. Peak positions (q_s) and Correlation Lengths (L) from Bragg's Law

concn (wt %)	q_s (nm^{-1})	L (nm)
1	0.210 ± 0.003	29.9 ± 0.4
3	0.169 ± 0.002	37.2 ± 0.4
5	0.165 ± 0.001	38.0 ± 0.2
10	0.139 ± 0.003	45.3 ± 0.8
15	0.150 ± 0.004	41.9 ± 1.0
20	0.144 ± 0.002	43.4 ± 0.5
25	0.145 ± 0.001	42.7 ± 0.4
30	0.147 ± 0.002	40.7 ± 0.4
35	0.304 ± 0.005	20.6 ± 0.3
40	0.434 ± 0.001	14.5 ± 0.05
50	0.665 ± 0.002	9.45 ± 0.04
60	0.741 ± 0.008	8.48 ± 0.09

Association of Gliadins Examined by Cross-Linking Experiments. The SAXS analysis described above indicates noncovalent association of gliadins in solution. Thus, cross-linking experiments were performed with DTSSP, a cross-linking molecule that is cleavable with reducing agents after cross-linking, to examine the specificity of association between gliadin molecules. By applying nonreducing SDS-PAGE to the soluble fraction after centrifugation, it is found that the gliadin bands disappear almost entirely from the DTSSP-treated samples at concentrations of ≥8 wt % (Figure 5a). This

DOI: 10.1021/acs.jafc.5b02902
J. Agric. Food Chem. 2015, 63, 8715−8721

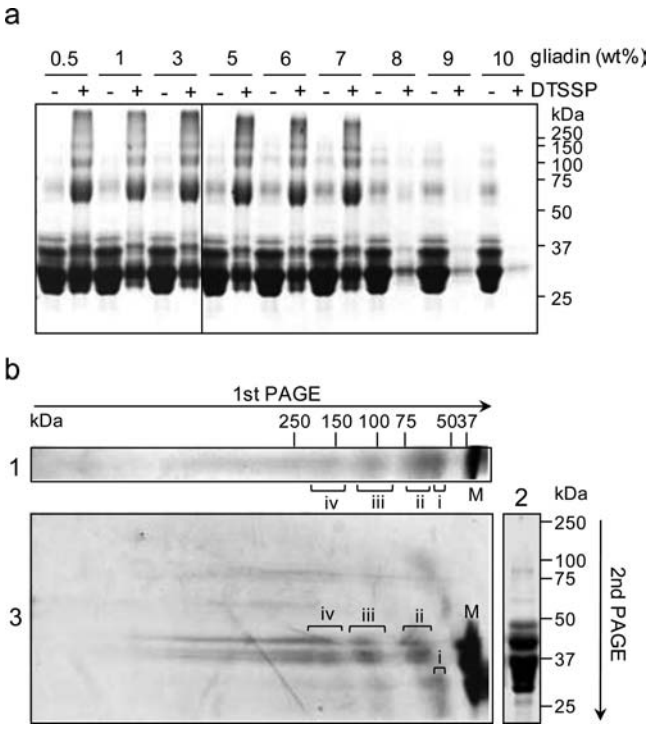

Figure 5. Detection of the self-assembled gliadins in solution. Gliadin solutions (0.5, 1, 3, 5, 6, 7, 8, 9, 10 wt % in distilled H_2O) were incubated at 25 °C for 60 min in the absence (−) or presence of 5 mM DTSSP (+). After NEM treatment for 10 min, the solutions were boiled in Laemmli's SDS sample buffer without reducing agent. The soluble fraction was separated by centrifugation and then subjected to nonreducing SDS-PAGE (a). Gliadins from the 7 wt % solution treated with DTSSP were separated by nonreducing SDS-PAGE on 3−12% gel with Bis-Tris running buffer (b, panel 1), reducing SDS-PAGE (b, panel 2), and 2D-PAGE of nonreducing SDS-PAGE on 3−12% gel with Bis-Tris running buffer and reducing SDS-PAGE (b, panel 3). Proteins were stained with Coomassie Brilliant Blue.

suggests that gliadins cross-link to form large polymers at ≥8 wt % and become insoluble in an SDS solution. Monomeric and cross-linked gliadins are detected in the supernatant for 0.5−7 wt % samples treated with DTSSP. The most prominent bands of cross-linked gliadins correspond to 50−75 kDa in size. Gliadins at 7 wt % were analyzed by 2D-PAGE (Figure 5b). By the first nonreducing SDS-PAGE with bis-Tris-HCl buffer containing tricine, cross-linked gliadins were detected as ∼55−65 kDa (i), ∼65−75 kDa (ii), ∼90−120 kDa (iii), ∼140−180 kDa (iv) in addition to the large smear bands (Figure 5b, panel 1). The cross-linked gliadins were cleaved to monomers in the gel after the first nonreducing SDS-PAGE by reduction with 2-mercaptoethanol and separated by the second reducing SDS-PAGE. The cross-linked ∼55−65 kDa bands on the first nonreducing SDS-PAGE are composed of 30−35 kDa gliadins, which have been shown to be a mixture of α- and γ-gliadins by N-terminal amino acid sequence analysis.[25] The 65−75 kDa bands on the first nonreducing SDS-PAGE are composed of ∼37 and ∼40 kDa gliadins, which have been identified as α-gliadins.[25] These results suggest that some gliadins associate specifically in distilled water. The cross-linked ∼55−65 and ∼65−75 kDa bands are predicted to be dimers on the basis of their sizes. In addition, the 90−120 and 140−180 kDa smear bands on the first nonreducing SDS-PAGE were shown to be composed of 30−35, ∼37, and ∼40 kDa gliadins, suggesting that these bands originate from the formation of oligomers.

Plausible Model for Gliadin Association in Distilled Water. From the above results, we present the model shown in Figure 6 for the nanoscale structures of gliadins in distilled water. In the 0.025−0.5 wt % concentration range, gliadins are dispersed in water as isolated particles (Figure 6a), because no shoulder peak is found due to interparticle interference. Most of the particles are monomers, but small populations of dimers and oligomers are also present on the basis of the results of the sedimentation velocity measurement and the SAXS analyses. Thomson et al. reported that α-, γ-, and ω-gliadins in 70% ethanol show R_g values of 3.55, 3.80, and 4.60 nm, respectively, at concentrations <1 wt %. However, the R_g values obtained in this study are slightly larger. This suggests that the structures of gliadin monomers in distilled water differ somewhat from those in ethanol. The cross-sectional radius of gyration and the length of gliadins at the lowest concentration are 2.50 and 11.3 nm, respectively, which is consistent with a rod-like shape. Although some gliadins form dimers and oligomers at the lowest concentration, the shape of the associated particles is rod-like. The frictional ratio of 1.52 obtained from the sedimentation velocity analysis supports the rod-like model.

In the 0.5−10 wt % concentration range, gliadin molecules self-assemble and form small soluble aggregates (Figure 6b) by noncovalent interactions. Interparticle interference is apparent, but gliadins remain soluble in distilled water up to at least 10 wt %. This interparticle interference arises from the electrostatic repulsion between small aggregates, which is confirmed by the fact that the SAXS shoulder peak vanishes when NaCl is added to the solution at a concentration of 10 mM (data not shown). The correlation length among small aggregates gradually increases with increasing concentration, indicating that the interparticle distance is becoming greater.

At 15−20 wt %, gliadins become insoluble in distilled water, but the SAXS profiles are similar to those at 10 wt % concentration (Figure 6c). We suggest that the small aggregates become more closely spaced and come in contact with one another to form a continuous network without significantly changing aggregation structure. In the SAXS profiles at concentrations >30 wt %, the shoulder near 0.13 nm^{-1} disappears and broad peaks at 0.3−1.0 nm^{-1} become noticeable. In this region, the space is almost entirely filled with gliadin molecules and a definite correlation length disappears; however, density fluctuation is present inside the aggregated gliadins (Figure 6d). Above 50 wt % (Figure 6e), the broad peaks diminish and only the upturn in the low-q region remains, suggesting that gliadins form large aggregates of >100 nm in size.

Finally the influence of NaCl on the structure of associated gliadins should be noted. In this study, NaCl acts as a water solubilizer of gliadins in dough, but it is well-known that NaCl also causes the precipitation of gliadin in aqueous solutions.[25] Because these two observations appear to be contradictory, it is of interest to clarify the effect of NaCl addition on the state of association of gluten proteins in relation to the intermolecular interactions among them. This issue will be addressed in our next paper, which will focus on the difference between the association states of highly concentrated gliadins hydrated with distilled water and the precipitates produced by NaCl addition.

In conclusion, SAXS analyses have clarified the state of association of gliadins in distilled water over a wide concentration range. At low concentrations (≤0.5 wt %), gliadin molecules are present as monomers plus a minor amount of dimers and oligomers. At greater concentrations,

DOI: 10.1021/acs.jafc.5b02902
J. Agric. Food Chem. 2015, 63, 8715−8721

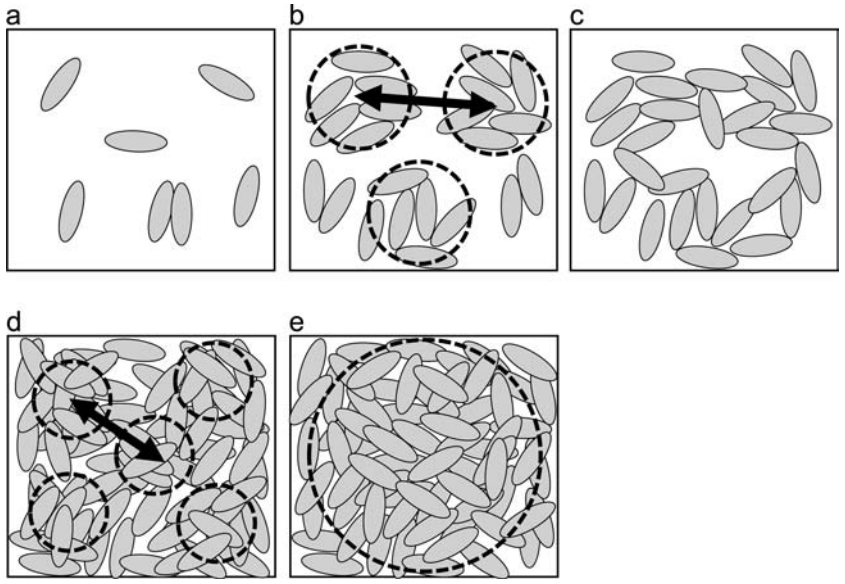

Figure 6. Schematic illustrations of the nanostructures of gliadin assemblies in distilled water over a wide range of concentrations. (a) Gliadins are present as water-soluble isolated monomers and a few dimers at 0.025−0.5 wt %. (b) Gliadin molecules self-assemble to form small aggregates (dashed line circles) at 0.5−10 wt %. The distance between the aggregates is estimated to be ∼40 nm. (c) Gliadins begin to form continuous networks at 15−20 wt %. (d) Gliadin molecules fill the space, but condensed regions due to density fluctuation (dashed line circles) appear above 30 wt %. The distance between dense domains is estimated to be 14 nm at 40 wt %. (e) Above 50 wt % the density fluctuation almost vanishes, but large aggregates over 100 nm in size are formed.

gliadin molecules begin to coalesce (0.5−1 wt %) and then show interparticle interference among aggregated molecules (1−10 wt %). In these regions, the correlation length increases as concentration increases, because the aggregates grow in size and their mutual separation distance increases. Cross-linking experiments indicate that association of gliadin molecules at 0.5−10 wt % occurs in a specific manner. Both dimers and oligomers are formed, but some are preferentially composed only of α-gliadins instead of a mixture of α- and γ-gliadins. Gliadin becomes insoluble at 15 wt %, although the SAXS profile does not show a significant difference from that at 10 wt %. This is due to the formation of a continuous network of aggregated gliadins. As concentration increases further, the space is filled with gliadin molecules while a density fluctuation remains at ∼40 wt %, and finally the large aggregates are formed.

AUTHOR INFORMATION

Corresponding Authors

*(N.S.) Phone: +81 72 451 2499. Fax: +81 72 451 2633. E-mail: sato-n@rri.kyoto-u.ac.jp.
*(M.S.) Phone: +81 72 451 2670. Fax: +81 72 451 2670. E-mail: sugiyama@rri.kyoto-u.ac.jp.
*(R.U.) Phone: +81 774 38 3760. Fax: +81 774 38 3765. E-mail: urade@kais.kyoto-u.ac.jp.

Funding

This work was supported in part by JSPS KAKENHI Grant 26660111 (R.U.), 15H02042 (M.S.), and 24310068 (M.S.), MEXT KAKENHI Grant 26102524 (M.S.), and a grant from the Tojuro Iijima Foundation for Food Science and Technology (R.U.).

Notes

The authors declare no competing financial interest.

ACKNOWLEDGMENTS

This work has been performed under the approval of the Photon Factory Program Advisory Committee (Proposals 2014G127 and 2014G162).

ABBREVIATIONS USED

SDS, sodium dodecyl sulfate; PAGE, polyacrylamide gel electrophoresis; Bis-Tris, bis(2-hydroxyethyl)amino-tris-(hydroxymethyl)methane; DTSSP, 3,3′-dithiobis-[sulfosuccinimidylpropionate]; SAXS, small-angle X-ray scattering

REFERENCES

(1) Hamer, R. J.; MacRitchie, F.; Weegels, P. L. Structure and functional properties of gluten. In *Wheat: Chemistry and Technology*, 4th ed.; Khan, K., Schewry, P. R., Eds.; AACC International Press: St. Paul, MN, USA, 2009; pp 153−178.
(2) Shewry, P. R.; D'Ovidio, R.; Lafiandra, D.; Jenkins, J. A.; Mills, E. N. C.; Békés, F. Wheat grain proteins. In *Wheat: Chemistry and Technology*, 4th ed.; Khan, K., Schewry, P. R., Eds.; AACC International Press: St. Paul, MN, USA, 2009; pp 223−298.
(3) Cornec, M.; Popineau, Y.; Lefebvre, J. Characterisation of gluten subfractions by SE-HPLC and dynamic rheological analysis in shear. *J. Cereal Sci.* **1994**, *19*, 131−139.
(4) Anjum, F. M.; Khan, M. R.; Din, A.; Saeed, M.; Pasha, I.; Arshad, M. U. Wheat gluten: high molecular weight glutenin subunits — structure, genetics, and relation to dough elasticity. *J. Food Sci.* **2007**, *72*, R56−R63.
(5) Uthayakumaran, S.; Gras, P. W.; Stoddard, F. L.; Békés, F. Effect of varying protein content and glutenin-to-gliadin ratio on the functional properties of wheat dough. *Cereal Chem.* **1999**, *76*, 389−394.
(6) Kasarda, D. D.; Adalstein, A. E.; Laird, N. F. γ-Gliadins with α-type structure coded on chromosome 6B of the wheat (*Triticum aestivum* L.) cultivar 'Chinese Spring'. In *Proceedings of the 3rd International Workshop on Gluten Proteins*; Laztity, A., Békés, F., Eds.; World Scientific Publishing: Singapore, 1988; pp 20−29.

DOI: 10.1021/acs.jafc.5b02902
J. Agric. Food Chem. 2015, 63, 8715−8721

(7) Martling, S. E.; Mulvaney, S. J.; Cohen, C. Effect of moisture content on viscoelastic properties of hydrated gliadin. *Cereal Chem.* **2004**, *81*, 207−219.
(8) Fido, R. J.; Békés, F.; Gras, P. W.; Tatham, A. S. Effects of α-, β-, γ- and ω-gliadins on the dough mixing properties of wheat flour. *J. Cereal Sci.* **1997**, *26*, 271−277.
(9) Khatkar, B. S.; Fido, R. J.; Tatham, A. S.; Schofield, J. D. Functional properties of wheat gliadins. II. Effects on dynamic rheological properties of wheat gluten. *J. Cereal Sci.* **2002**, *35*, 307−313.
(10) Khatkar, B. S.; Barak, S.; Mudgil, D. Effects of gliadin addition on the rheological, microscopic and thermal characteristics of wheat gluten. *Int. J. Biol. Macromol.* **2013**, *53*, 38−41.
(11) Lee, C. C.; Mulvaney, S. J. Dynamic viscoelastic and tensile properties of gluten and glutenin gels of common wheats of different strength. *J. Agric. Food Chem.* **2003**, *51*, 2317−2327.
(12) Kasarda, D. D.; Bernardin, J. E.; Gaffield, W. Circular dichroism and optical rotatory dispersion of α-gliadin. *Biochemistry* **1968**, *7*, 3950−3957.
(13) Tatham, A. S.; Shewry, P. R. The conformation of wheat gluten proteins. The secondary structures and thermal stabilities of α-, β-, γ- and ω-gliadins. *J. Cereal Sci.* **1985**, *3*, 103−113.
(14) Tatham, A. S.; Field, J. M.; Smith, S. J.; Shewry, P. R. The conformations of wheat gluten proteins, II*, aggregated gliadins and low molecular weight subunits of glutenin. *J. Cereal Sci.* **1987**, *5*, 203−214.
(15) Tatham, A. S.; Masson, P.; Popineau, Y. Conformational studies of peptides derived by the enzymic hydrolysis of a gamma-type gliadin. *J. Cereal Sci.* **1990**, *11*, 1−13.
(16) Purcell, J. M.; Kasarda, D. D.; Wu, C-S. C. Secondary structures of wheat α- and ω-gliadin proteins: Fourier transform infrared spectroscopy. *J. Cereal Sci.* **1988**, *7*, 21−32.
(17) Blanch, E. W.; Kasarda, D. D.; Hecht, L.; Nielsen, K.; Barron, L. D. New insight into the solution structures of wheat gluten proteins from Raman optical activity. *Biochemistry* **2003**, *42*, 5665−5673.
(18) Cole, E. W.; Kasarda, D.; Lafiandra, D. The conformational structure of α-gliadin: intrinsic viscosities under conditions approaching the native state and under denaturing conditions. *Biochim. Biophys. Acta, Protein Struct. Mol. Enzymol.* **1984**, *787*, 244−251.
(19) Shewry, P. R.; Miles, M. J.; Thomson, N. H.; Tatham, A. S. Scanning probe microscopes − applications in cereal science. *Cereal Chem.* **1997**, *74*, 193−199.
(20) Thomson, N. H.; Miles, M. J.; Popineau, Y.; Harries, J.; Shewry, P.; Tatham, A. S. Small angle X-ray scattering of wheat seed-storage proteins: α-, γ- and ω-gliadins and the high molecular weight (HMW) subunits of glutenin. *Biochim. Biophys. Acta, Protein Struct. Mol. Enzymol.* **1999**, *1430*, 359−366.
(21) Shewry, P. R.; Tatham, A. S. The characteristics, structures and evolutionary relationship of prolamins. In *Seed Proteins*; Shewry, P. R., Ed.; Kluwer Academic Publications: Dordrecht, The Netherlands, 1999; pp 11−33.
(22) Osborne, T. B. *The Proteins of Wheat-Kernel*; Carnegie Institution: Washington, DC, USA, 1907.
(23) Blish, M. J.; Sandstedt, R. M. An improved method of the preparation of wheat gliadin. *Cereal Chem.* **1926**, *3*, 144−149.
(24) Bernerdin, J. E.; Kasarda, D. D.; Mecham, D. K. Preparation and characterization of α-gliadin. *J. Biol. Chem.* **1967**, *242*, 445−450.
(25) Ukai, T.; Matsumura, Y.; Urade, R. Disaggregation and reaggregation of gluten proteins by sodium chloride. *J. Agric. Food Chem.* **2008**, *56*, 1122−1130.
(26) Guinier, A.; Fournet, G. *Small-Angle Scattering of X-rays*; Wiley-Interscience: New York, 1955.
(27) Glatter, O.; Kratky, O. *Small Angle X-ray Acattering*; Academic Press: London, UK, 1982.
(28) Matsushima, N.; Danno, G.; Sasaki, N.; Izumi, Y. Small-angle X-ray scattering study by synchrotron orbital radiation reveals that high molecular weight subunit of glutenin is a very anisotropic molecule. *Biochem. Biophys. Res. Commun.* **1992**, *186*, 1057−1064.
(29) Thomson, N. H.; Miles, M. J.; Tatham, A. S.; Shewry, P. R. Molecular images of cereal proteins by STM. *Ultramicroscopy* **1992**, *42*, 1204−1213.
(30) Schuck, P. Size distribution analysis of macromolecules by sedimentation velocity ultracentrifugation and Lamm equation modeling. *Biophys. J.* **2000**, *78*, 1606−1619.
(31) Schuck, P.; Perugini, M. S.; Gonzales, N. R.; Howlett, G. J.; Schubert, D. Size-distribution analysis of proteins by analytical ultracentrifugation: strategies and application to model systems. *Biophys. J.* **2002**, *82*, 1096−1111.
(32) Laue, T. M.; Shah, B. D.; Ridgeway, T. M.; Pelletier, S. L. Computer-aided interpretation of analytical sedimentation data for proteins. In *Analytical Ultracentrifugation in Biochemistry and Polymer Science*; Harding, S. E., Rowe, A. J., Horton, J. C., Eds.; Royal Society of Chemistry: Cambridge, UK, 1992; pp 90−125.
(33) O'Farrell, P. H. High resolution two-dimensional electrophoresis of proteins. *J. Biol. Chem.* **1975**, *250*, 4007−4021.
(34) Laemmli, U. K. Cleavage of structural proteins during the assembly of the head of bacteriophage T4. *Nature* **1970**, *227*, 680−685.

DOI: 10.1021/acs.jafc.5b02902
J. Agric. Food Chem. 2015, 63, 8715−8721

about 50% that of apigenin in an in situ rat intestinal single-pass perfusion model. This result is consistent with the observation that oral bioavailability of luteolin (30.4%) from a *Flos chrysanthemi* extract was significantly lower than that of apigenin (51.1%).[13] Unfortunately, reports on diglucuronidation of luteolin in situ or in vivo are rare. This process might be a feasible method for eliminating luteolin and thereby controlling its bioavailability.

Given that over 35% of all drugs are metabolized via phase II enzymes, especially UGTs,[14] bioavailability of herbal medicines may be altered when their metabolism is modulated by coadministered drugs, namely, drug−drug interactions. The UGT inhibitor is also involved in many drug−drug interactions, and studies have reported that metabolic clearance of these drugs is inhibited by glucuronidation, such as zidovudine−fluconazole interactions. Fluconazole increases exposure to zidovudine, a typical probe for UGT2B7, to 74% owing to its inhibition of zidovudine glucuronidation.[15] Thus, the effect of the UGT inhibitor on luteolin remains to be elucidated.

In this study, we sought to systematically elucidate the time course of glucuronidation of luteolin by 12 human UDP-glucuronosyltransferases and to further determine the absorption characteristics and metabolic processes of luteolin using an in situ mice intestinal single-pass perfusion model. Specifically, probenecid, a nonspecific UGT inhibitor,[16] was used in this perfusion model. Our findings help us to understand first-pass metabolism and disposition of luteolin via enteric recycling.

MATERIALS AND METHODS

Chemicals and Reagents. Luteolin, propiophenone, probenecid, formic acid (HPLC grade), and testosterone were purchased from Aladdin Reagent Company (Shanghai, China). Mebubarbital was purchased from Center of Reagent, Southern Medical University (Guangzhou, China). Uridine diphosphoglucuronic acid (UDPGA), D-saccharic-1,4-lactone monohydrate, HEPES, and Hanks' balanced salt (powder form) were purchased from Sigma-Aldrich (St. Louis, MO, USA). Alamethicin was purchased from Hui Cheng Biological Technology Co. Ltd. (Shanghai, China). Human-expressed UGT isoforms (UGTs 1A1, 1A3, 1A4, 1A6, 1A7, 1A8, 1A9, 1A10, 2B4, 2B7, 2B15, and 2B17) were also obtained from BD Gentest Corp. (Woburn, MA, USA). Acetonitrile and methanol were typically analytical grade or better (≥99%, HPLC grade), and were used as received.

Animals. Use of all animals was approved by the Ethics Committee of Southern Medical University. Male KM mice weighing between 22 and 25 g were obtained from Laboratory Animal Centre of Southern Medical University. Mice were then fasted overnight with free access to water before the experiment.

Determination of the Concentration Conversion Factor (*K* Values). To quantify each metabolite, the concentration conversion factor (*K*), which represents the ratio between the molar extinction coefficient of each glucuronide and luteolin, was determined following a previously described method.[17] To calculate the *K* values, each metabolite was separated via HPLC, collected for blow drying in nitrogen, dissolved in 50 mM potassium phosphate (KPi, pH 7.4), and then divided into two parts, one of which was analyzed directly and the other was analyzed after being hydrolyzed with β-glucuronidase (100 units/mL) at 37 °C for 2 h. To determine the conjugation position of diG's, the metabolites were separated, collected, and then hydrolyzed with β-glucuronidase for 1 h to ensure that the diG's were not completely hydrolyzed and could produce two related G's. Retention time of the metabolites is a determinant for the conjugation position of luteolin (e.g., 3′,7-diG and 4′,7-diG). Relationships between the peak areas of the metabolites before hydrolysis and the peak areas of aglycones after hydrolysis were used to establish the *K* values needed to quantify the amounts of luteolin conjugates.

Luteolin Glucuronidation by 12 Expressed Human UGTs and the Time-Dependent Experiment. Magnesium chloride (0.88 mM), D-saccharic-1,4-lactone monohydrate (4.4 mM), alamethicin (0.022 mg/mL), 12 UGT isoforms (UGTs 1A1, 1A3, 1A4, 1A6, 1A7, 1A8, 1A9, 1A10, 2B4, 2B7, 2B15, and 2B17, with final concentrations between 0.0528 and 0.264 mg/mL), 1 mM luteolin (final concentration of 10 μM) in 50 mM KPi (pH 7.4), and uridine 5′-diphospho-glucuronic acid (UDPGA, 3.5 mM, added last) were mixed together. The UGT reaction was incubated for different times at 37 °C in a shaking water bath (50 rpm). About 60 μL of iced methanol containing 0.5 μg/mL propiophenone was added to stop the reaction. All experiments were performed in triplicate. The samples were centrifuged at 13 000 rpm at 4 °C for 30 min, and the supernatant was then analyzed by ultra-performance liquid chromatography (UPLC).

To elucidate the characteristics of luteolin glucuronidation by expressed human UGTs, the incubation time was set to 6 h. For the time-dependence metabolism experiment, the UGT reaction system was incubated at 37 °C for 30, 60, 90, and 120 min for each UGT isoform. The rest of the procedures were performed as described above. To identify the product of diglucuronides, the incubation time of luteolin in 12 UGTs was prolonged to 6 h, and the metabolite amount was calculated as nmol per mg.

Animal Surgery. Male KM mice weighing between 22 and 25 g were obtained from the Laboratory Animal Centre of Southern Medical University. The mice were fasted overnight with free access to water before commencing the experiment. The experiments were done with permission from the Ethics Committee of Southern Medical University. Mice were then anesthetized with an i.p. injection of 0.026 mL/g mebubarbital (0.3% m/v). The intestinal surgical procedures were essentially the same as those described in previous publications with minor modifications.[18] We perfused two segments of the intestine (small intestine and colon), with each segment 8−10 cm long. Blood circulation to the liver and intestine was not disrupted in this perfusion model. During the surgery, the body temperature was maintained at 37 °C using a heating lamp. The inlet cannulate was flushed with luteolin in HBSS, which was kept warm at 37 °C by a circulating water bath.

Perfusion Experiments. First, mice gall bladders were obtained, and two segments of mice intestine (small intestine and colon) were simultaneously perfused with a perfusate containing 10 and 20 μM luteolin using an infusion pump at a flow rate of 10 mL/h. To terminate substrate hydrolysis of the enzymes contained in the perfused sample, 0.5 mL of acetonitrile (a stop solution) was added into the receiving container prior to sample collection. Addition of acetonitrile prevented hydrolysis of luteolin and stabilized it. After 15 min of washout period, the samples were collected every 30 min. At the end of the experiment, we measured the intestinal length as described in a previous study[18] About 200 μL of acetonitrile containing 10 μg/mL propiophenone was added into 400 μL of perfusate. The samples were analyzed via UPLC after centrifugation at 13000 rpm at 4 °C for 30 min.

Effect of UGT Inhibitor on Luteolin Glucuronidation in Situ. Probenecid is a potent nonspecific inhibitor of UGTs that significantly inhibits luteolin glucuronidation in vivo. Animal surgery was done as described above. Probenecid was added at 0.5 and 1 mM to perfusate containing 10 and 20 μM luteolin, respectively. About 200 μL of 10 μg/mL propiophenone was added to 400 μL of perfusate. The samples were centrifuged at 13 000 rpm at 4 °C for 30 min, and 10 μL of the supernatant was then analyzed via UPLC. The method for analyzing luteolin was the same as previously described.[10]

UPLC Analysis of Luteolin and Its Glucuronide. The validated method for analyzing luteolin was as follows: system, Waters Acquity UPLC; column, HSS T3, 1.8 μm, 2.1 mm × 100 mm; mobile phase A, 100% acetonitrile; mobile phase B, 0.1% (v/v) formic acid; flow rate, 0.25 mL/min; gradient 0−5 min, 95−45% B, 5−5.5 min, 45−30% B, 5.5−7 min, 30−95% B; wavelength, 340 nm for luteolin and the respective glucuronides, 254 nm for propiophenone; and injection volume, 10 μL. The tested linear response range was 0.3125−40 μM (for a total of eight concentrations) for luteolin. Analytical methods for each test compound were validated for inter-day and intra-day variation using six samples at three concentrations (40, 10, and 2 μM).

DOI: 10.1021/acs.jafc.5b02827
J. Agric. Food Chem. 2015, 63, 8722−8733

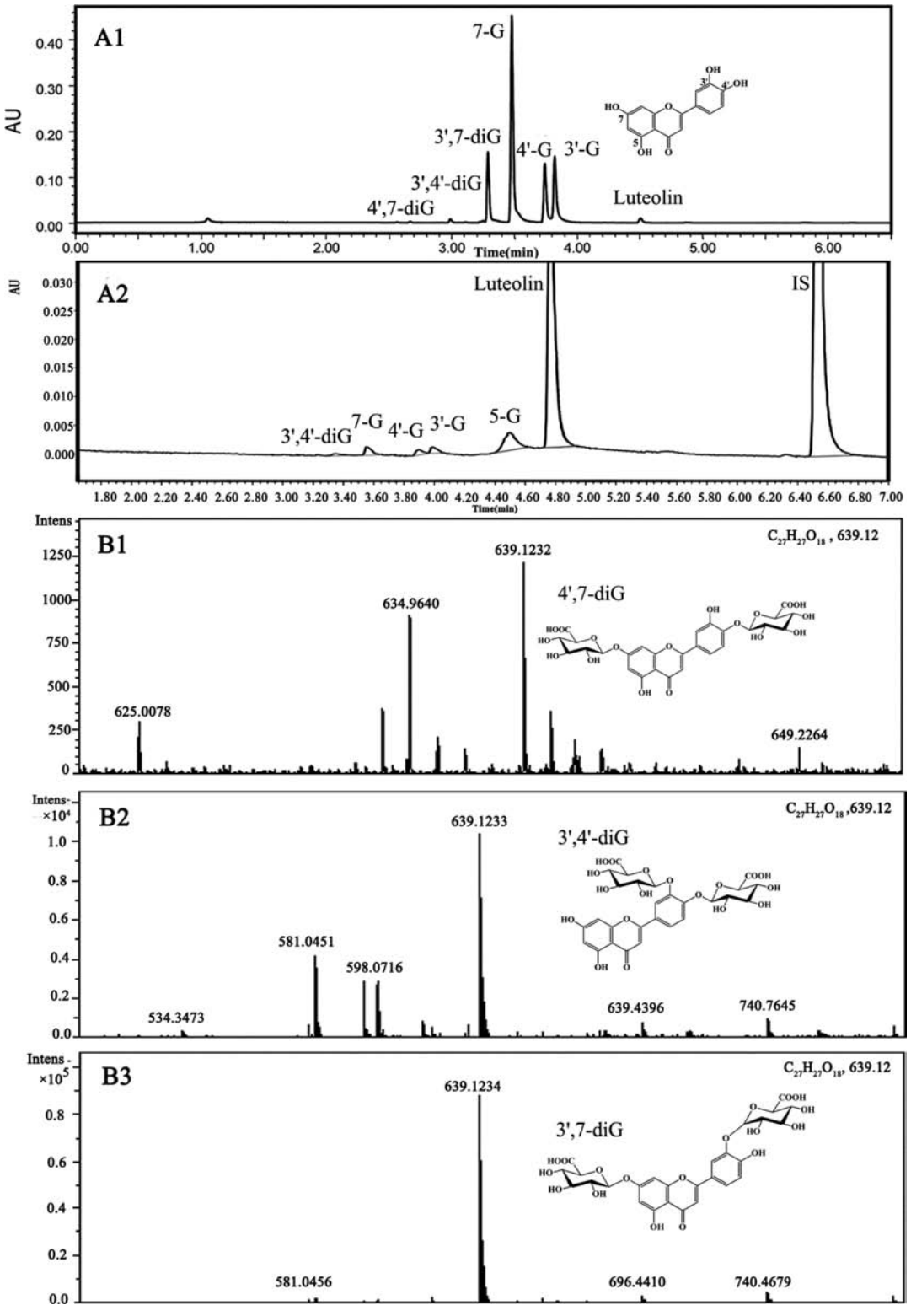

Figure 1. continued

DOI: 10.1021/acs.jafc.5b02827
J. Agric. Food Chem. 2015, 63, 8722−8733

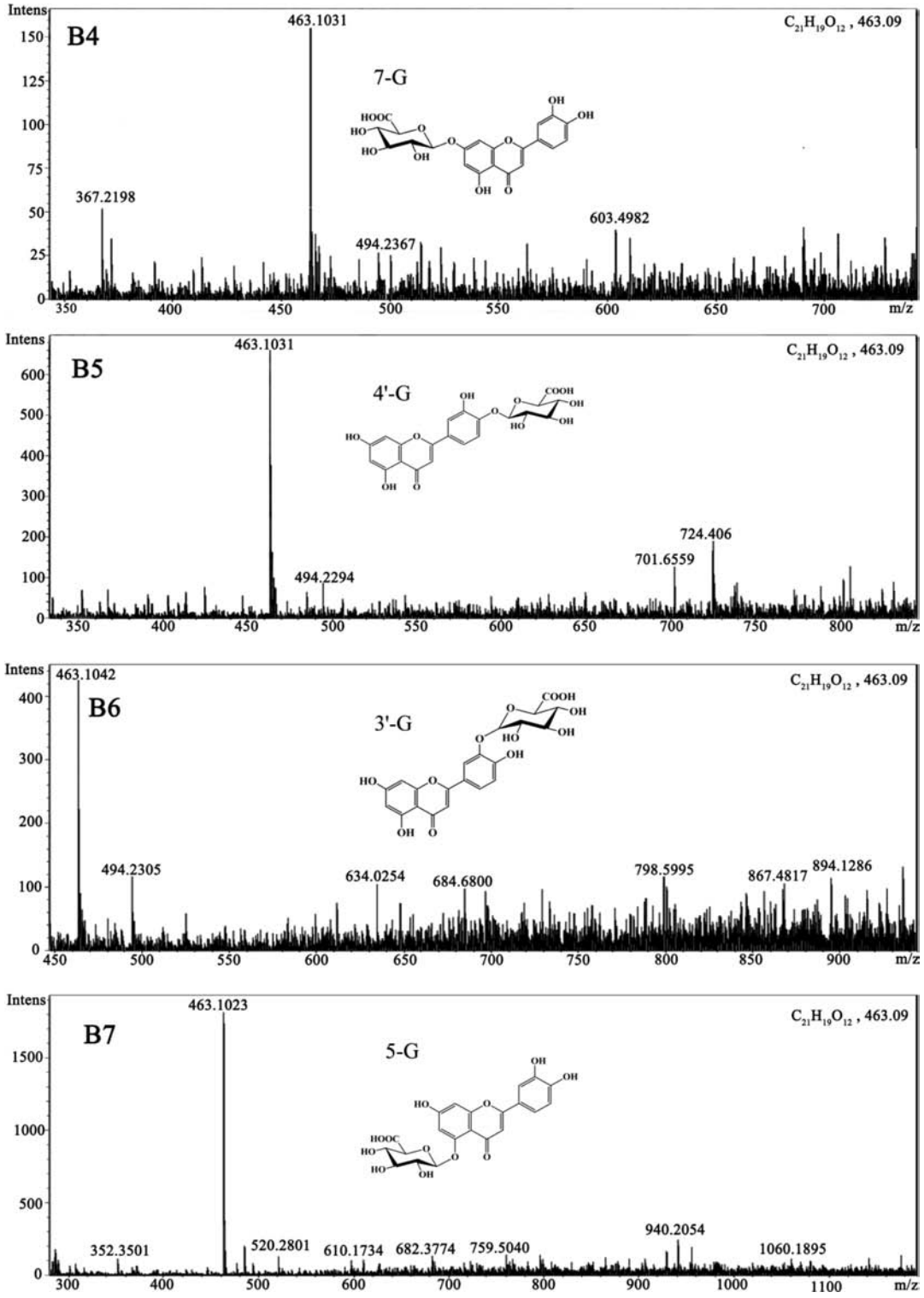

Figure 1. UPLC and HRMS profiles of luteolin and its metabolites, and the structures of the metabolites. UPLC was used to separate and quantify luteolin and its metabolites in the experimental samples generated from incubation with human UGTs and perfusate. (A1) Chromatograms of luteolin and its metabolites in sample incubated with human UGTs. (A2) Chromatograms of luteolin and its metabolites in perfusate. (B1−B3) HRMS scan of diglucuronides (diG's). (B4−B7) HRMS scans of monoglucuronides.

Precision and accuracy for luteolin were in an acceptable range (<10%). Propiophenone was used as internal standard since it is stable in the experimental system and its retention time is 6.4 min, which would not affect luteolin and its metabolites.

Determination of Luteolin Glucuronide Structure by HRMS. A quadrupole time-of-flight tandem mass spectrometer (Bruker, USA) fitted with an Agilent HPLC was used to determine the molecular weight of luteolin and its metabolites. The main working parameters for the mass spectrometers were set as follows: capillary voltage, 3.8 kV; dry heater temperature, 180 °C; nebulizer voltage, 1.0 bar; dry gas flow rate, 6.0 L/min; column, Agilent ZORBAX SB-C18, 5 μm, 4.6 mm × 150 mm; mobile phase B, 100% acetonitrile; mobile phase A, 100% aqueous buffer (0.1% formic acid); flow rate, 1 mL/min; gradient, 0 to 5 min, 92% to 80% A, 5 to 10 min, 80% to 40% A, 10 to

DOI: 10.1021/acs.jafc.5b02827
J. Agric. Food Chem. 2015, 63, 8722−8733

16.5 min, 40% to 0%, 16.5 to 17 min, 0% to 90% A, 17 to 20 min, 90% A to 90% A; wavelength, 340 nm; and injection volume, 50 μL. The MS/MS spectra were produced by collision-induced dissociation of the selected precursor ions. Data were analyzed using Bruker Daltonics software (version 4.0, Bruker, USA).

Kinetic Analysis. Permeability of luiteolin was represented by P^*_{eff}, which was obtained as described before. Likewise, the amount of luteolin absorbed (M_{ab}), amount of conjugated luteolin excreted into the intestinal lumen (M_{gut}), and the percentage absorbed and percentage metabolized values were calculated as described before.

M_{ab} and M_{gut} were expressed as eqs 1 and 2:

$$M_{ab} = Q\tau(CA_{in} - CA_{out}) \quad (1)$$

$$M_{gut} = Q\tau CA_{out} \quad (2)$$

where Q is the flow rate of perfusion (mL/min), τ is the interval time of sampling (30 min), and CA_{in} and CA_{out} are the inlet and outlet concentrations. %Absorbed and %Metabolized were calculated as

$$\%\text{Absorbed in the intestine} = \frac{M_{ab}}{M_{total}} \quad (3)$$

$$\%\text{Metabolites excreted in the intestine} = \frac{M_{gut}}{M_{total}} \quad (4)$$

where M_{total} is the total amount of compound perfused over the first 30 min period.

Rates of metabolism of human UDP-glucuronosyltransferases were expressed as the amount of metabolites formed (nmol/min/mg), as shown in eq 5:

$$V_G = \frac{P_G/P_{IS}}{C_{protein}a_G t} = \frac{P_G/P_{IS}}{C_{protein}Kat} \quad (5)$$

where V_G is the reaction rate, P_G is the peak area of the metabolites, P_{IS} is the peak area of internal standard, $C_{Protein}$ is the protein concentration of UGTs, K is the concentration conversion factor, a is the slope of the standard curve of luteolin, and t is the incubation time for the reaction system.

Statistical Analysis. One-way ANOVA with or without Tukey–Kramer multiple comparison and Student's t test were used to evaluate differences between control and treatment. Differences were considered significant if p values were less than 0.05 or 0.01.

RESULTS

Determination of Luteolin and Its Glucuronides via UPLC and HRMS. The developed UPLC method used to analyze luteolin had a run time of 7 min (Figure 1-1A). The mass spectra of the four metabolites exhibited a pseudomolecule ion $[M + H]^+$ of m/z 463.1031 in the full-scan mass spectra (Figure 1-2B), indicating that they had a molecular formula of $C_{21}H_{18}O_{12}$. On the basis of previously published data, the metabolites were identified as luteolin-7-G, luteolin-4′-G, and luteolin-3′-G. Luteolin has four hydroxyl groups, and a new G was confirmed to be luteolin-5-G (Figure 1-2B7). The mass spectra of the three metabolites showed a pseudomolecular ion $[M + H]^+$ of m/z 639.1232, whose molecular formula was $C_{27}H_{26}O_{18}$. This result suggested that the metabolites were diG's (Figure 1-1 B). Although luteolin-3′,4′-diG has previously been reported,[10] the other two metabolites have not. The two diG's were collected, and each was hydrolyzed into its respective monoglucuronides. One of the diG's was hydrolyzed to 7-G and 4′-G, and the other was hydrolyzed to 7-G and 3′-G. The retention time of the hydrolyzed G's is a determinant for the conjugation position of luteolin diG's. We confirmed the structure of the two new diG's to be luteolin-4′,7-diG and luteolin-3′,7-diG based on retention time and theory of UGT fingerprinting.[5,10,17]

Determination of the Concentration Conversion Factor of Each Luteolin Glucuronide. The extracted samples containing only luteolin glucuronides were hydrolyzed using β-glucuronidase to their corresponding G's and luteolin. The concentration conversion factors of 7-G, 4′-G, 3′-G, and 5-G were 3.63 ± 0.13, 6.36 ± 0.35, 5.74 ± 0.77, and 5.24 ± 0.31, respectively. The conversion factors of 4′,7-diG, 3′,4′-diG, and 3′,7-diG were 5.07 ± 1.14, 3.72 ± 0.12, and 2.73 ± 0.11, respectively (Table 1).

Table 1. Luteolin Metabolites in the UGT Reaction System and in Mice Perfusate

glucuronide	molecular formula	molecular mass	structural formula	K (conversion factor)
Metabolites in UGT Enymes				
7-G	$C_{21}H_{19}O_{12}$	462	luteolin-7-*O*-monoglucuronide	3.63
4′-G	$C_{21}H_{19}O_{12}$	462	luteolin-4′-*O*-monoglucuronide	6.36
3′-G	$C_{21}H_{19}O_{12}$	462	luteolin-3′-*O*-monoglucuronide	5.74
4′,7-G	$C_{27}H_{27}O_{18}$	638	luteolin-4′,7-*O*-diglucuronide	5.07
3′,4′-diG	$C_{27}H_{27}O_{18}$	638	luteolin-3′,4′-*O*-diglucuronide	3.72
3′,7-diG	$C_{27}H_{27}O_{18}$	638	luteolin-3′,7-*O*-diglucuronide	2.73
Metabolites in Mice				
7-G	$C_{21}H_{19}O_{12}$	462	luteolin-7-*O*-monoglucuronide	3.63
4′-G	$C_{21}H_{19}O_{12}$	462	luteolin-4′-*O*-monoglucuronide	6.36
3′-G	$C_{21}H_{19}O_{12}$	462	luteolin-3′-*O*-monoglucuronide	5.74
5-G	$C_{21}H_{19}O_{12}$	462	luteolin-5-*O*-monoglucuronide	5.24
3′,4′-diG	$C_{27}H_{27}O_{18}$	638	luteolin-3′,4′-*O*-diglucuronide	3.72

Metabolism of Luteolin in Human-Expressed UGTs. Twelve human-expressed UGTs were used to catalyze luteolin glucuronidation. The results showed that different glucuronides were mainly generated by different UGT isoforms. 7-G was mainly generated by UGT1A9 (the amount generated was 32.64 ± 0.99 nmol/mg), and then by UGTs 1A1, 1A3, 1A6, 1A7, 1A8, 1A10, and 2B15; UGTs 1A1, 1A3, 1A7, 1A8, 1A9, and UGT1A10 all catalyzed the formation of 4′-G, with UGT1A1 and UGT1A9 showing the highest activities (the amount was 4.11 ± 0.13 and 3.85 ± 0.11 nmol/mg); UGTs 1A1, 1A7, 1A8, 1A9, and 2B7 catalyzed the formation of 3′-G, with UGT1A9 showing the highest activity (18.71 ± 0.53 nmol/mg). All UGT isoforms catalyzed the biotransformation of luteolin to 4′,7-diG, except for UGT1A6. UGT1A1 was the most active among the 12 isoforms; 3′,4′-diG was mainly catalyzed by UGT1A7 (1.23 ± 0.10 nmol/mg), UGT1A9 (1.39 ± 0.11 nmol/mg), and UGT1A10 (1.30 ± 0.17 nmol/mg), and then by UGT1A1, UGT1A3, and UGT1A8. For conversion of luteolin to 3′,7-diG, all isoforms showed activities except UGT1A3, and UGT1A1 showed the highest activity (Figure 2A–F).

DOI: 10.1021/acs.jafc.5b02827
J. Agric. Food Chem. 2015, 63, 8722–8733

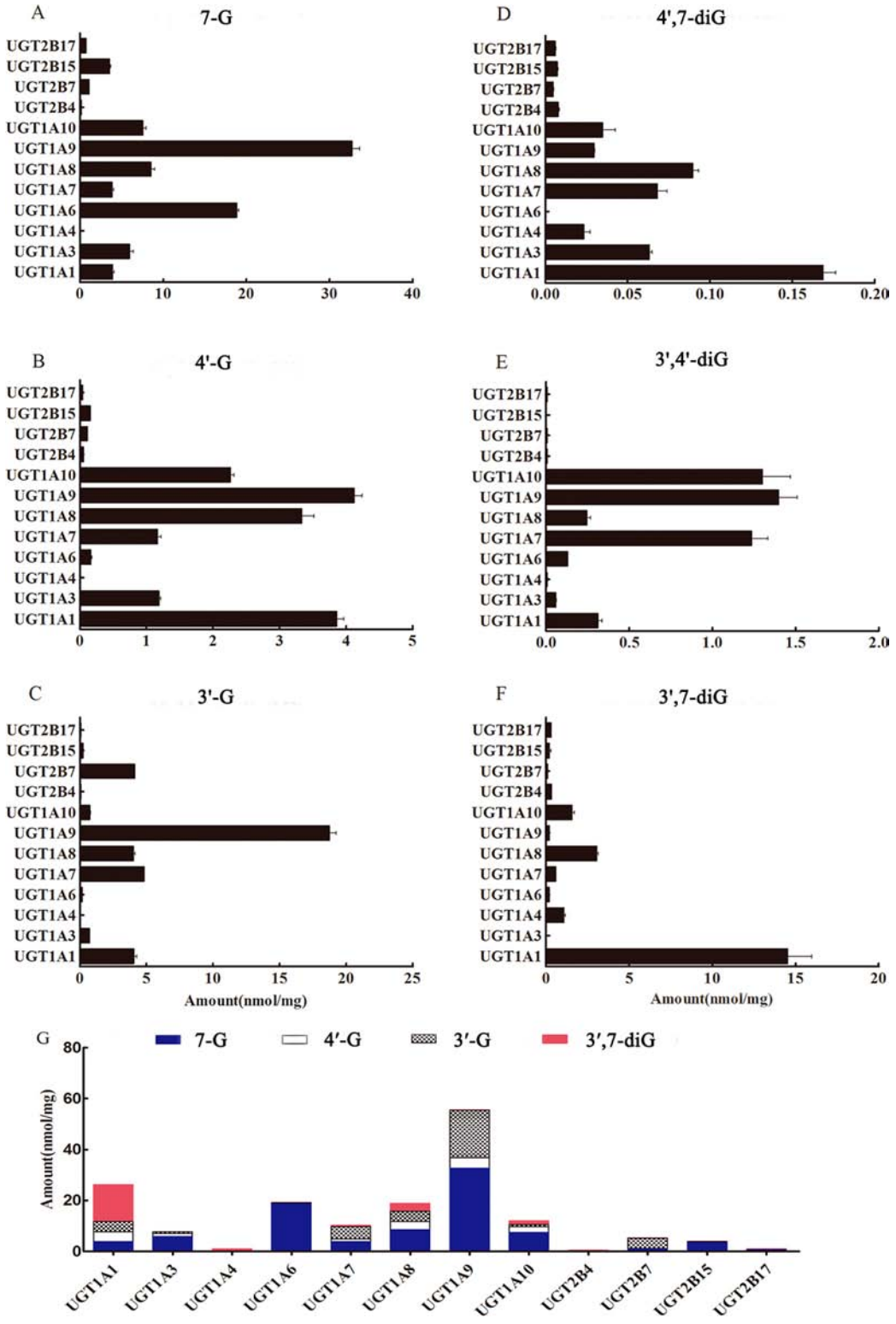

Figure 2. Luteolin glucuronidation by human-expressed UGTs. Human-expressed UGT1As and UGT2Bs were involved in glucuronation of luteolin. UGTs were incubated with luteolin for 6 h. The amount of glucuronidation was calculated as nmol/mg of protein required to obtain steady concentration. Each column represents the average of three determinations, with the error bar representing SD (n = 3).

Luteolin glucuronidation is mediated mainly by UGT1A1, UGT1A9, and UGT1A6. UGT1A1 showed the highest activity in the production of diG's, especially 3′,7-diG. UGT1A9 mainly catalyzed the production of G's, and UGT1A9 mainly catalyzed the production of 7-G (Figure 2G).

Time Dependence of Luteolin Glucuronidation via UGTs. Conducting the experiments for 30, 60, 90, and 120 min revealed that production of luteolin glucuronides was time-dependent and followed a sequential process. For UGT1A1, the amounts of luteolin-3′-G and luteolin-4′-G decreased sharply after 30 min of incubation (from 1.94 ± 0.08 to 0.84 ±

DOI: 10.1021/acs.jafc.5b02827
J. Agric. Food Chem. 2015, 63, 8722−8733

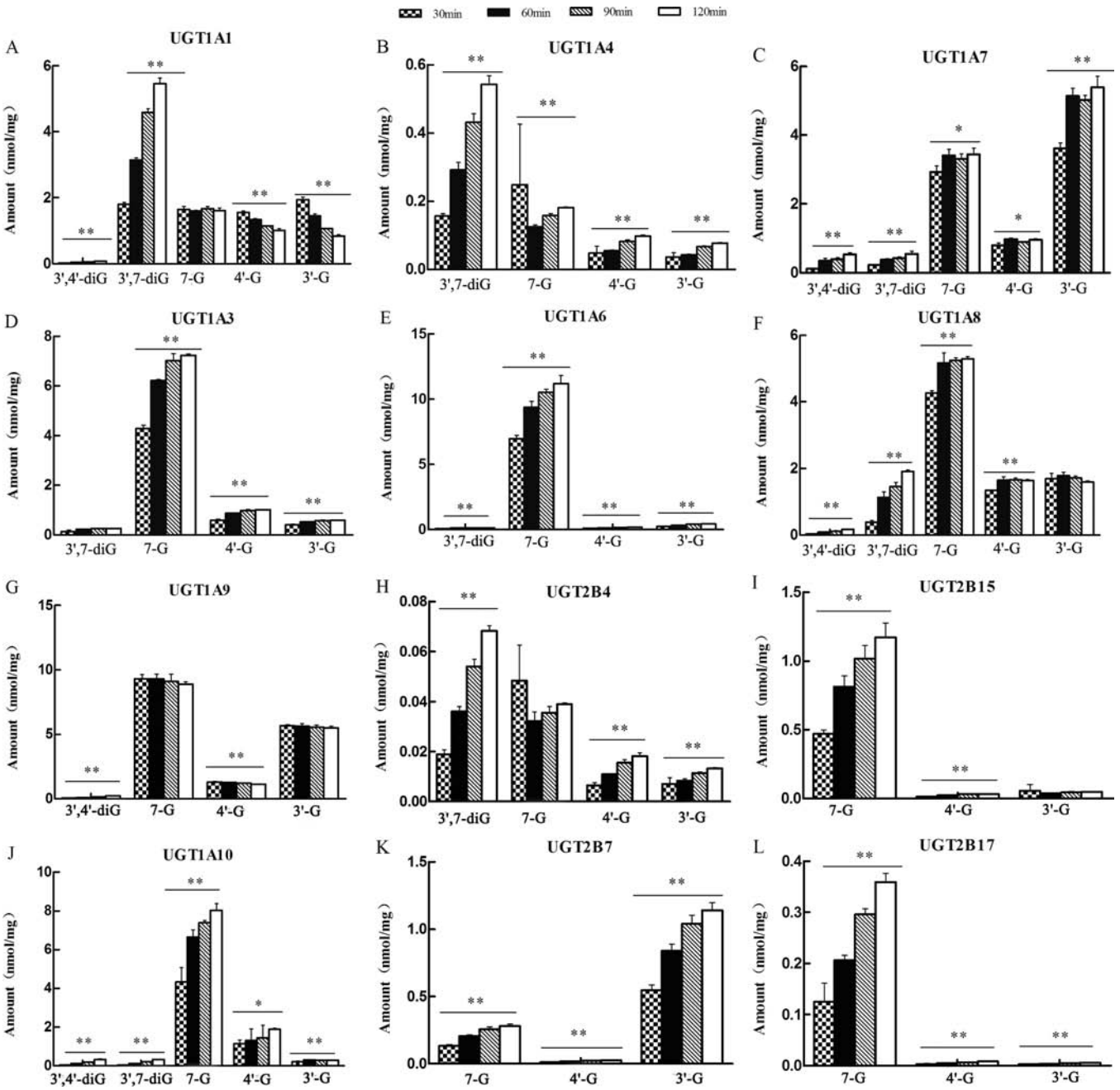

Figure 3. Time-dependent characteristics of luteolin glucuronidation. Twelve human-expressed UGT isoforms were incubated with 10 μM luteolin at 30, 60, 90, and 120 min; glucuronidation was found to be isoform-specific and time-dependent. Each column represents the average of three determinations, and the error bars indicate SD of the mean (n = 3). *p < 0.05; **p < 0.01.

0.04 nmol/mg, and from 1.55 ± 0.04 to 1.01 ± 0.05 nmol/mg, respectively). However, the amount of luteolin-7-G remained the same (1.60 ± 0.09 nmol/mg), while that of luteolin-3′,7-diG increased rapidly, and that of luteolin-3′,4′-diG increased slowly. For UGT1A9, no luteolin-3′,7-diG was produced, and the amount of 4′-G decreased very slowly. The amount of 3′,4′-diG increased slowly after 30 min of incubation, whereas those of luteolin-3′-G and luteolin-7-G had no change. In UGTs 1A3, 1A4, 1A6, 1A7, 1A8, and 1A10, the production of the three G's and diG's increased within 120 min of incubation. In UGT2B's, all the glucuronides increased slowly after 120 min of incubation time (Figure 3).

Intestinal Luteolin Absorption. The amount of luteolin absorbed was significantly different at 10 and 20 μM (p < 0.05) in the small intestine and the colon. The absorption percentage and amount were both markedly higher in the small intestine than those in the colon (amounts in small intestine and colon were 20.85 ± 3.57 and 12.29 ± 2.70 nmol at 10 μM, and 52.57 ± 5.20 and 25.26 ± 4.17 nmol at 20 μM) (Figure 4). When the nonspecific UGT inhibitor probenecid was used along with the in situ mice perfusion model at two substrate concentrations, the absorbed rate/amount of luteolin remained steady, which indicated that probenecid did not affect luteolin absorption (Figure 5).

Intestinal Metabolism of Luteolin. The excretion percentage and amount of luteolin were concentration-dependent in the small intestine and colon, but the same cannot be said for excretion rate in the colon (Figure 6). When

DOI: 10.1021/acs.jafc.5b02827
J. Agric. Food Chem. 2015, 63, 8722−8733

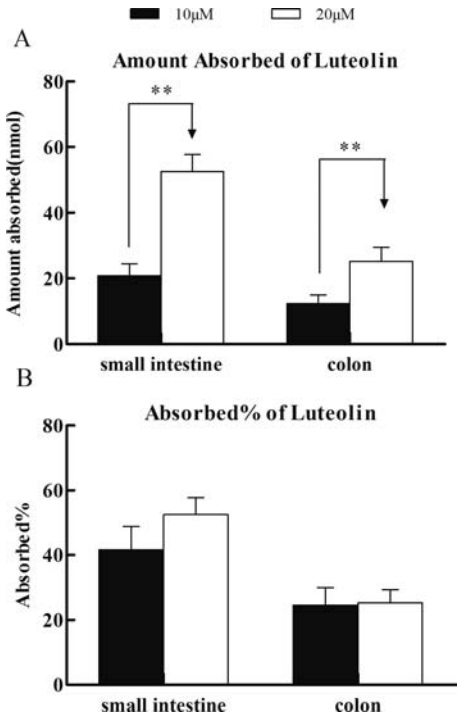

Figure 4. Luteolin absorption in mouse intestine. (A) Amount of luteolin absorbed at 10 and 20 μM in the small intestine and colon. (B) Percentage of luteolin absorbed in the small intestine and colon. Each column represents the average of greater than three determinations, with the error bar representing the SD of the mean. *p < 0.05; **p < 0.01.

probenecid was added, the amount of luteolin glucuronides excreted changed that the excreted amounts of 3′,4-diG decreased from 0.37 ± 0.02 to 0.15 ± 0.06 nmol at 20 μM and from 0.07 ± 0.02 to 0.04 ± 0.02 nmol at 10 μM in the small intestine. The amount of 3′-G decreased from 1.62 ± 0.19 to 0.94 ± 0.22 nmol at 20 μM and from 0.32 ± 0.08 to 0.18 ± 0.05 nmol at 10 μM in the small intestine. Similar decreasing trends were observed for 4′-G and 3′-G. However, the amount of 5-G increased (the excreted amounts increased from 2.02 ± 0.15 to 3.94 ± 1.05 nmol at 20 μM and from 0.72 ± 0.17 to 1.66 ± 0.62 nmol at 10 μM in the small intestine), and the amount of total glucuronides did not change at all (Figure 7).

DISCUSSION

The focus of this study was on determining time-dependent production of luteolin glucuronides via UGTs and investigating the absorption and metabolism of luteolin in our in situ models of the intestines. Three new glucuronides (3′,7- and 4′,7-diG's and luteolin-5-*O*-monoglucuronide) of luteolin were identified in vitro and in vivo. The structure of the unknown diG's was speculated to be 3′,7-diG and 4′,7-diG.

This study is the first to determine the positional preference of luteolin diglucuronidation by human-expressed UGTs. The results reveal that glucuronidation of UGT1A1 is unique, compared to other UGT isoforms. UGT1A1 showed the highest activity in production of diG's, especially 3′,7-diG, among the 12 UGT isoforms (Figure 2G). Diglucuronidation at 7-OH and 3′-OH was observed to be the favored pathway, which is consistent with previous studies, including our own,

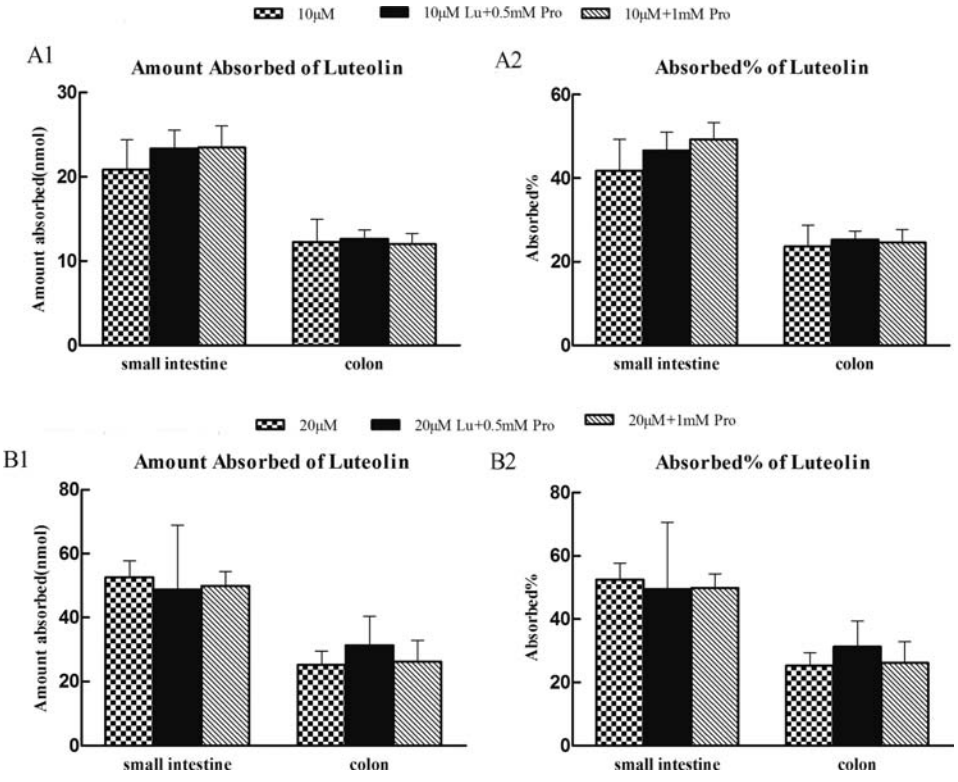

Figure 5. Effect of UGT inhibitor probenecid on glucuronide absorption. (A1,A2) Amount absorbed and absorption percentage of luteolin (10 μM) when probenecid was added (0.5 and 1 mM) in the small intestine and colon. (B1,B2) Amount absorbed and absorption percentage of luteolin (20 μM) when probenecid was added (0.5 and 1 mM) in the small intestine and colon. Each column represents the average of three determinations, with the error bar representing SD (n = 3). *p < 0.05; **p < 0.01.

DOI: 10.1021/acs.jafc.5b02827
J. Agric. Food Chem. 2015, 63, 8722−8733

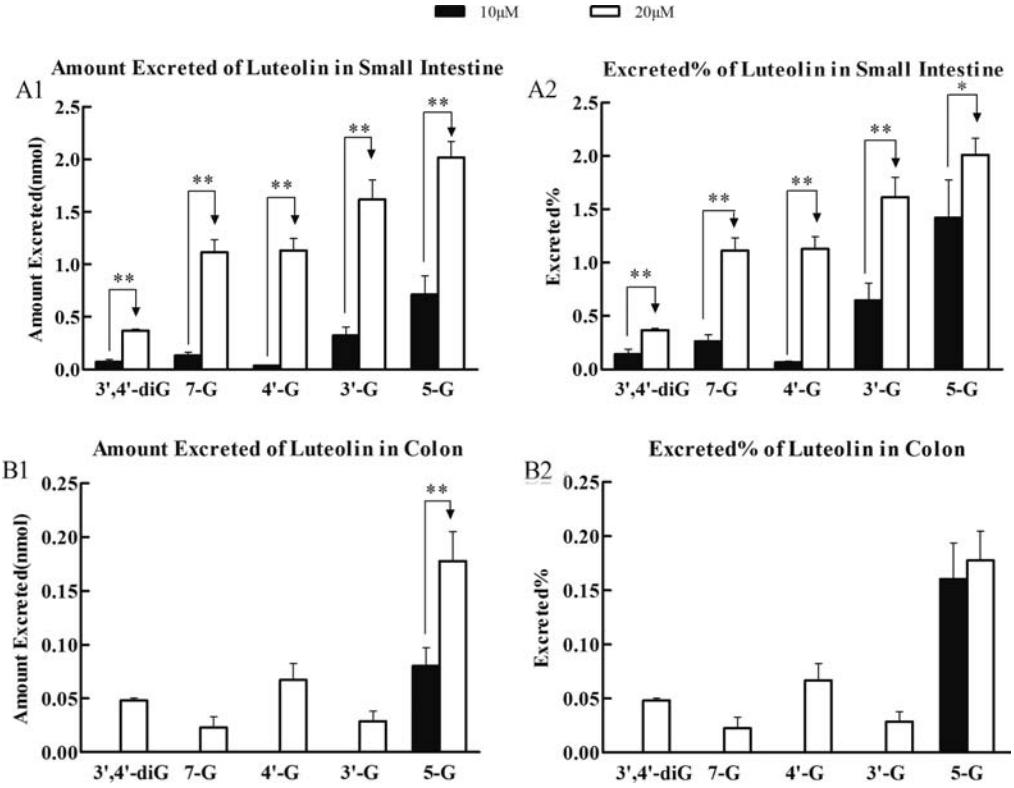

Figure 6. Excretion amount and excretion percentage of luteolin glucuronides in the small intestine and colon. (A1) Excretion of luteolin glucuronides at 10 and 20 μM in the small intestine. (A2) Excretion percentage of glucuronides. (B1) Excretion of luteolin glucuronides at 10 and 20 μM in the colon. (B2) Excretion percentage of glucuronides in the colon. Each column represents the average of three determinations, with the error bar representing SD (n = 3). *p < 0.05; **p < 0.01.

where the 7-OH group was found to be the most reactive for glucuronidation even in more complex flavones with two phenolic groups.[17−23] In addition, the 3′-OH group was found to be highly reactive.[21−23] A hypothesis that can explain the lack of a 3′ hydroxyl group in the flavonoids is that glucuronidation only occurred at position 7, and those containing this functional group also formed 3′-*O*-glucuronides and sometimes 4′-*O*-glucuronides. Thus, the presence or absence of the 3′-OH group is a major determinant of regioselectivity of glucuronidation. Moreover, the specific distribution of multiple glucuronide products (7-O, 3′-O, 4′-O) is governed by the hydroxyl group of flavonoids.[20] We also detected very small amounts of 4′,7-diG, produced mainly by UGT1A1. For 3′,4′-diG, another minor diG, UGTs 1A1, 1A7, 1A8, 1A9, and 1A10 were all identified to be the major isoforms responsible for its production. In UGT1A9, three G's and 3′,4′-diG (very small amounts) were identified. These results indicated that UGT1A9 was the most active isoform in catalyzing the formation of G's (Figure 2A). UGT1A6 was one of the top six isoforms (UGTs 1A1, 1A6, 1A7, 1A8, 1A9, and 1A10) with high activity but could only catalyze 7-G formation (Figure 2B). All UGT isoforms catalyzed the biotransformation of luteolin to 7-G and 4′-G, except UGT1A4. These findings are consistent with those of our previous study, in which luteolin metabolism was found to be mediated chiefly by UGT1A1, UGT1A9, and UGT1A6.[10]

We systematically defined the time dependence of luteolin diglucuronidation in 12 human-expressed UGT isoforms. From the beginning of the incubation up until 30 min, the amounts of 3′-G, 4′-G, 7-G, and 3′,7-diG produced in UGT1A1 were all about 2 nmol/mg. However, the outcome changed after 30 min of incubation. The amount of 7-G remained the same from 30 to 120 min. However, the amount of 3′-G decreased sharply (by 24% every 30 min), whereas that of 3′,7-diG increased rapidly (by 32% every 30 min) with time (Figure 3A). These interesting new findings suggest that UGT1A1 may conjugate to 7-OH of 3′- G to generate 3′,7-diG sequentially from 30 to 120 min (Figure 8). This process also happens during production of 3′,4′-diG (Figure 3A). The amount of 3′,7-diG produced was far greater than that of 3′,4′-diG (>80-fold higher). This surprising discovery demonstrated that UGT1A1 prefers 7-OH and 3′-OH more than 4′-OH. Furthermore, this result also revealed a sequential time-dependent process in which when the production of 7-G reaches a balance in time, UGT1A1 tends to catalyze glucuronic acid to the 3′-OH position of 7-G to produce 3′,7-diG (Figures 3A and 8). Unlike production of the three G's, which peaked within 30 min of incubation and remained stable thereafter, production of 3′,4′-diG slowly increased within 120 min of incubation. However, in UGTs 1A3, 1A4, 1A6, 1A7, 1A8, and 1A10, the amount of diG's (3′,7-diG or 3′,4′-diG) increased steadily with the three G's from the beginning to the end (0 to 120 min). In UGT2B's, the amounts of all the glucuronides slowly increased after 120 min of incubation.

Among these isoforms, UGT1A1 and UGT2B7 are well expressed in both the intestine and the liver, whereas UGT1A9 is well expressed in the liver and the kidneys[24] but either poorly expressed[14] or not expressed at all in the intestine.[25] In contrast, UGT1A8 and UGT1A10 are well expressed in the intestine but not in the liver.[24,25] Thus, we could speculate that the liver, kidney, and intestine are all major organs for luteolin glucuronidation. Moreover, since UGT1A1, UGT1A8, and

DOI: 10.1021/acs.jafc.5b02827
J. Agric. Food Chem. 2015, 63, 8722−8733

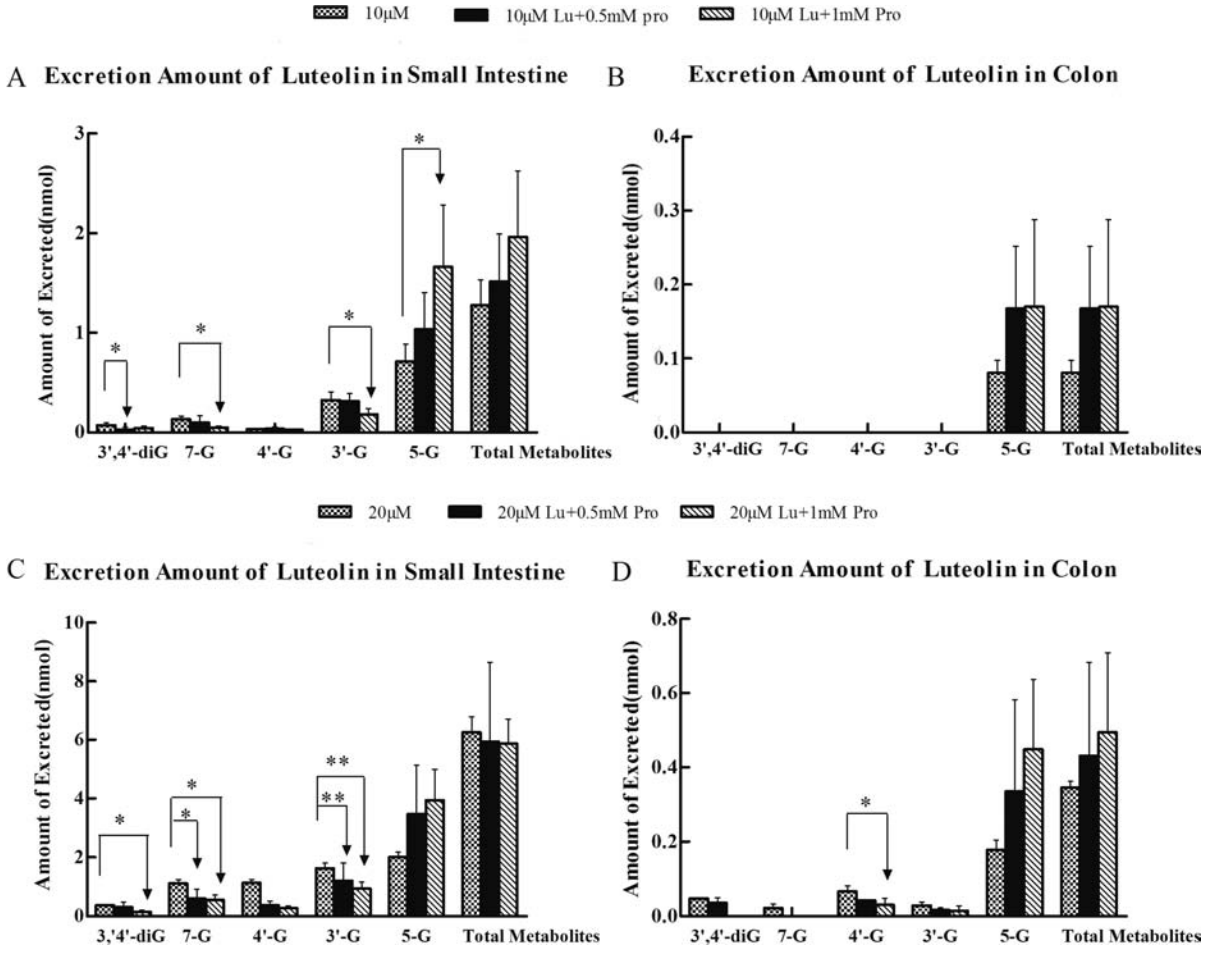

Figure 7. Effect of the UGT-specific inhibitor probenecid on glucuronide excretion: amount of luteolin glucuronides excreted in the absence or presence of probenecid at 0.5 and 1 mM in the small intestine and colon. Each column represents the average of three determinations, with the error bar representing SD (n = 3). *p < 0.05; **p < 0.01.

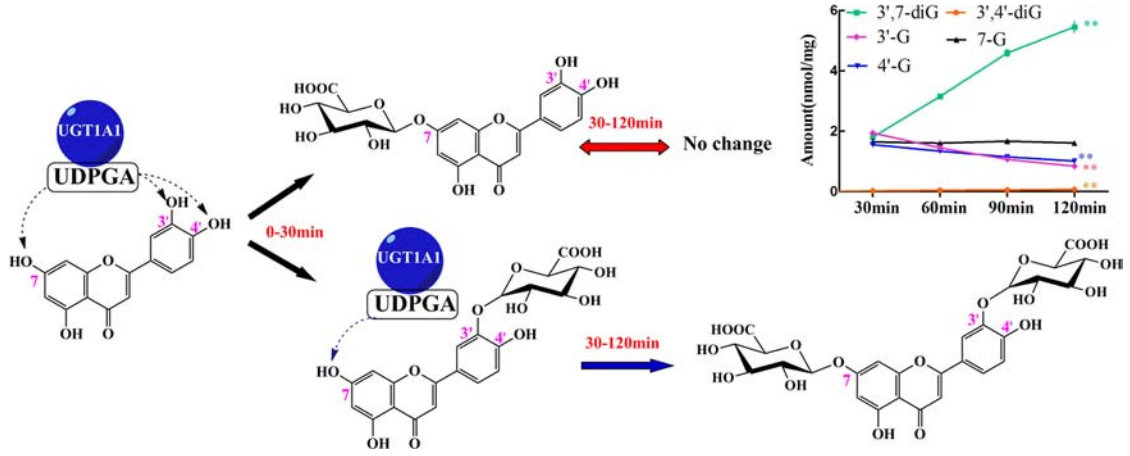

Figure 8. Glucuronic pathways for conversion of luteolin to luteolin-3′,7-*O*-diglucuronide and the sequential time-dependent process in human UGT1A1.

UGT1A10 are not expressed in the kidney, we speculate that diG's may not be produced in the kidney.

Several studies have shown that some nuclear receptors, such as constitutive androstane receptor (CAR),[26] pregnane X receptor (PXR),[27] and aryl hydrocarbon receptor (AhR), are all involved in UGT modulation. These factors play important roles in the modulation of glucuronidation of natural products through UGTs. It has been demonstrated that AhR, which can induce activities of human UGT1A1, is involved in modulation of UGT1A1 by luteolin.[28] These results suggest that more attention should be paid to drug−drug interactions by UGTs, which have brought lots of studies upon the mechanism.

In situ glucuronidation is quite different from the process that occurs in vitro because four G's and 3′,4′-diG were found

DOI: 10.1021/acs.jafc.5b02827
J. Agric. Food Chem. 2015, 63, 8722−8733

in mice perfusate in the current study. The novel 5-G was not found in UGT reaction systems. Most research on flavonoid glucuronidation in vivo and in vitro indicates that metabolism of the 5-hydroxyl group is slow or lacking, which may be due to the fact that the 5-OH group favors the formation of an intramolecular hydrogen bond with the carbonyl group at the C-4 position.[17,18,22,23] For 5-hydroxyflavone, in UGTs 1A1, 1A8, 1A9, 1A10, and 2B7, glucuronidation was apparent, but the other UGT isoforms did not metabolize it.[17,18] Thus, 5-G could be detected in mice intestine, although it was not produced in the 12 UGT isoforms.

Unexpectedly, the amount of 5-G was the highest for all glucuronides in situ. Two explanations are proposed: (1) difference in species might have caused this disparity; (2) other enzymes might be involved in the phase II reaction of luteolin. G's are the major glycoside species of mammals, and members of UGT1 and UGT2 are involved in their formation. However, the UGTs involved in the formation of most glycosides have not been identified and may belong to the UGT3A family.[29] Recently, a novel UGT2A1-mediated glucuronidation has been reported, and we speculate that 5-G may also be catalyzed by UGT2A1.[30] Further refinement of our approach is needed by incorporating additional UGT isoforms, including the newly cloned UGT3A family (UGT3A1/2) and UGT2A1.

The absorption/metabolism of luteolin was also investigated in mice. The absorption amount as well as the absorption rate of luteolin were significantly different ($p < 0.05$) at 10 and 20 μM, which were markedly higher in the small intestine than in the colon. These results are consistent with those reported previously in rat.[11] Thus, luteolin was passively absorbed in the intestine of mice, and absorption was found to be more efficient in the small intestine than in the colon (Figure 4). The amount of excreted luteolin was significant in the small intestine and colon, thereby indicating that luteolin metabolism is concentration-dependent (Figure 6). Surprisingly, probenecid (0.5 and 1 mM) had no effect on luteolin absorption (Figure 5); the excreted amounts of 7-, 4′-, 3′-G, and 3′,4′-diG decreased, but that of 5-G increased when probenecid was used. Moreover, high concentrations of probenecid resulted in production of high amounts of 5-G. The amount of total metabolites remained almost unchanged (Figure 7). We speculate that probenecid is not an inhibitor of UGT3A, since it could not inhibit 5-G production. When UGT1A and UGT2B are inhibited, a compensatory pathway may turn on for activation of other UGTs.

Many luteolin glucosides, such as luteolin 7-*O*-β-glucopyranoside and the C-glucoside homo-orientin (luteolin 6-C-glucoside),[31] are found in vivo and in vitro. Therefore, cleavage of the glucoside by gut bacteria or at the intestinal wall associated with transporters would affect the overall uptake and metabolism/metabolic fate of luteolin. We note that it is important to conduct in vivo experiments with luteolin glucosides in mice to validate these findings.

In conclusion, two novel luteolin diG's, namely 3′,7- and 4′,7-diG, were detected in UGTs for the first time, and a novel G, namely 5-G, was found in situ. UGT1A1, UGT1A6, and UGT1A9 shared the same preference for production of monoglucuronides but displayed unique preferences in diG production such that UGT1A1 preferred to generate diG. Production of 3′,7-diG exhibited time dependence based on the consumption of 3′-G and 7-G by UGT1A1. A compensatory pathway for a newly discovered UGT isoform capable of metabolizing phenols might be responsible for metabolism of luteolin in mice.

AUTHOR INFORMATION

Corresponding Authors

*Tel./fax: +86 20-61648596. E-mail: liusw@smu.edu.cn.

*E-mail: tl405@smu.edu.cn.

Author Contributions

#L.W. and J.L. contributed equally to this paper.

Funding

This work was supported by the Foundation for Distinguished Young Teachers in Higher Education of Guangdong (Yq2013-037), Foundation for graduate education innovation project of Guangdong (Sybzzxm201224), and the Foundation of science and technology of Guangdong (2014A010107012), as well as the Program for Pearl River New Stars of Science and Technology in Guangzhou (2012J2200048).

Notes

The authors declare no competing financial interest.

ACKNOWLEDGMENTS

We thank Ai-Jun Sun and Yun Zhang at South China Sea Institute of Oceanology (SCSIO, CAS) for their assistance in LC-HRMS experiments.

REFERENCES

(1) Lopez-Lazaro, M. Distribution and biological activities of the flavonoid luteolin. *Mini-Rev. Med. Chem.* **2009**, *9* (1), 31−59.

(2) Hara, K.; Haranishi, Y.; Terada, T.; Takahashi, Y.; Nakamura, M.; Sata, T. Effects of intrathecal and intracerebroventricular administration of luteolin in a rat neuropathic pain model. *Pharmacol., Biochem. Behav.* **2014**, *125*, 78−84.

(3) Sak, K. Cytotoxicity of dietary flavonoids on different human cancer types. *Pharmacogn. Rev.* **2014**, *8* (16), 122−46.

(4) Seelinger, G.; Merfort, I.; Schempp, C. M. Anti-oxidant, anti-inflammatory and anti-allergic activities of luteolin. *Planta Med.* **2008**, *74* (14), 1667−77.

(5) Boersma, M. G.; van der Woude, H.; Bogaards, J.; Boeren, S.; Vervoort, J.; Cnubben, N. H.; van Iersel, M. L.; van Bladeren, P. J.; Rietjens, I. M. Regioselectivity of phase II metabolism of luteolin and quercetin by UDP-glucuronosyl transferases. *Chem. Res. Toxicol.* **2002**, *15* (5), 662−70.

(6) Lin, L. C.; Pai, Y. F.; Tsai, T. H. Isolation of Luteolin and Luteolin-7-O-glucoside from Dendranthema morifolium Ramat Tzvel and Their Pharmacokinetics in Rats. *J. Agric. Food Chem.* **2015**, *63*, 7700.

(7) Shimoi, K.; Okada, H.; Furugori, M.; Goda, T.; Takase, S.; Suzuki, M.; Hara, Y.; Yamamoto, H.; Kinae, N. Intestinal absorption of luteolin and luteolin 7-O-beta-glucoside in rats and humans. *FEBS Lett.* **1998**, *438* (3), 220−4.

(8) Shimoi, K.; Saka, N.; Kaji, K.; Nozawa, R.; Kinae, N. Metabolic fate of luteolin and its functional activity at focal site. *BioFactors* **2000**, *12* (1−4), 181−6.

(9) Yasuda, M. T.; Fujita, K.; Hosoya, T.; Imai, S.; Shimoi, K. Absorption and metabolism of luteolin and its glycosides from the extract of Chrysanthemum morifolium flowers in rats and Caco-2 cells. *J. Agric. Food Chem.* **2015**, *63*, 7693.

(10) Tang, L.; Li, Y.; Chen, W. Y.; Zeng, S.; Dong, L. N.; Peng, X. J.; Jiang, W.; Hu, M.; Liu, Z. Q. Breast cancer resistance protein-mediated efflux of luteolin glucuronides in HeLa cells overexpressing UDP-glucuronosyltransferase 1A9. *Pharm. Res.* **2014**, *31* (4), 847−60.

(11) Zhou, P.; Li, L. P.; Luo, S. Q.; Jiang, H. D.; Zeng, S. Intestinal absorption of luteolin from peanut hull extract is more efficient than that from individual pure luteolin. *J. Agric. Food Chem.* **2008**, *56* (1), 296−300.

DOI: 10.1021/acs.jafc.5b02827
J. Agric. Food Chem. 2015, 63, 8722−8733

(12) Simons, A. L.; Renouf, M.; Murphy, P. A.; Hendrich, S. Greater apparent absorption of flavonoids is associated with lesser human fecal flavonoid disappearance rates. *J. Agric. Food Chem.* **2010**, *58* (1), 141−7.
(13) Chen, Z.; Tu, M.; Sun, S.; Kong, S.; Wang, Y.; Ye, J.; Li, L.; Zeng, S.; Jiang, H. The exposure of luteolin is much lower than that of apigenin in oral administration of Flos Chrysanthemi extract to rats. *Drug Metab. Pharmacokinet.* **2012**, *27* (1), 162−8.
(14) Guillemette, C. Pharmacogenomics of human UDP-glucuronosyltransferase enzymes. *Pharmacogenomics J.* **2003**, *3* (3), 136−58.
(15) Sahai, J.; Gallicano, K.; Pakuts, A.; Cameron, D. W. Effect of fluconazole on zidovudine pharmacokinetics in patients infected with human immunodeficiency virus. *J. Infect. Dis.* **1994**, *169* (5), 1103−7.
(16) Aceves Baldo, P.; Anzures-Cabrera, J.; Bentley, D. In vivo evaluation of drug-drug interactions linked to UGT inhibition: the effect of probenecid on dalcetrapib pharmacokinetics. *Int. J. Clin. Pharmacol. Ther.* **2013**, *51* (3), 215−8. Aceves Baldo, P.; Anzures-Cabrera, J.; Bentley, D. Effect of fluconazole on zidovudine pharmacokinetics in patients infected with human immunodeficiency virus. *J. Infect Dis.* **1994**, *169* (5), 1103−7.
(17) Tang, L.; Ye, L.; Singh, R.; Wu, B.; Lv, C.; Zhao, J.; Liu, Z.; Hu, M. Use of glucuronidation fingerprinting to describe and predict mono- and dihydroxyflavone metabolism by recombinant UGT isoforms and human intestinal and liver microsomes. *Mol. Pharmaceutics* **2010**, *7* (3), 664−79.
(18) Tang, L.; Zhou, J.; Yang, C.; Xia, B.; Hu, M.; Liu, Z. Systematic Studies of Sulfation and Glucuronidation of 12 Flavonoids in the Mouse Liver S9 Fraction Reveals both Unique and Shared Positional Preferences. *J. Agric. Food Chem.* **2012**, *60* (12), 3223−3233.
(19) Ruan, J. Q.; Yan, R. Regioselective glucuronidation of the isoflavone calycosin by human liver microsomes and recombinant human UDP-glucuronosyltransferases. *Chem.-Biol. Interact.* **2014**, *220*, 231−40.
(20) Davis, B. D.; Brodbelt, J. S. Regioselectivity of human UDP-glucuronosyl-transferase 1A1 in the synthesis of flavonoid glucuronides determined by metal complexation and tandem mass spectrometry. *J. Am. Soc. Mass Spectrom.* **2008**, *19* (2), 246−56.
(21) Justino, G. C.; Santos, M. R.; Canario, S.; Borges, C.; Florencio, M. H.; Mira, L. Plasma quercetin metabolites: structure-antioxidant activity relationships. *Arch. Biochem. Biophys.* **2004**, *432* (1), 109−21.
(22) Fan, Y.; Tang, L.; Zhou, J.; Feng, Q.; Xia, B.; Liu, Z. Simultaneous determination of sulfation and glucuronidation of flavones in FVB mouse intestine in vitro and in vivo. *J. Appl. Toxicol.* **2013**, *33* (4), 273−80.
(23) Yang, C. H.; Tang, L.; Lv, C.; Ye, L.; Xia, B. J.; Hu, M.; Liu, Z. Q. Sulfation of selected mono-hydroxyflavones by sulfotransferases in vitro: a species and gender comparison. *J. Pharm. Pharmacol.* **2011**, *63* (7), 967−70.
(24) Harbourt, D. E.; Fallon, J. K.; Ito, S.; Baba, T.; Ritter, J. K.; Glish, G. L.; Smith, P. C. Quantification of Human Uridine-Diphosphate Glucuronosyl Transferase 1A Isoforms in Liver, Intestine, and Kidney Using Nanobore Liquid Chromatography-Tandem Mass Spectrometry. *Anal. Chem.* **2012**, *84* (1), 98−105.
(25) Ohno, S.; Nakajin, S. Determination of mRNA expression of human UDP-glucuronosyltransferases and application for localization in various human tissues by real-time reverse transcriptase-polymerase chain reaction. *Drug Metab. Dispos.* **2009**, *37* (1), 32−40.
(26) Mutoh, S.; Osabe, M.; Inoue, K.; et al. Dephosphorylation of threonine 38 is required for nuclear translocation and activation of human xenobiotic receptor CAR (NR1I3). *J. Biol. Chem.* **2009**, *284*, 34785−34792.
(27) Liddle, C.; Goodwin, B. Regulation of hepatic drug metabolism: Role of the nuclear receptors PXR and CAR. *Semin. Liver Dis.* **2002**, *22* (2), 115−122.
(28) Zhang, T.; Kimura, Y.; Jiang, S.; et al. Luteolin modulates expression of drug-metabolizing enzymes through theAhR and Nrf2 pathways in hepatic cells. *Arch. Biochem. Biophys.* **2014**, *557* (1), 36−46.
(29) MacKenzie, P. I.; Rogers, A.; Elliot, D. J.; Chau, N.; Hulin, J. A.; Miners, J. O.; Meech, R. The novel UDP glycosyltransferase 3A2: cloning, catalytic properties, and tissue distribution. *Mol. Pharmacol.* **2011**, *79* (3), 472−8.
(30) Bushey, R. T.; Lazarus, P. Identification and functional characterization of a novel UDP-glucuronosyltransferase 2A1 splice variant: potential importance in tobacco-related cancer susceptibility. *J. Pharmacol. Exp. Ther.* **2012**, *343* (3), 712−24.
(31) Braune, A.; Engst, W.; Blaut, M.; et al. Identification and functional expression of genes encoding flavonoid O- and C-glycosidases in intestinal bacteria. *Environ. Microbiol.* **2015**, DOI: 10.1111/1462-2920.12864.

DOI: 10.1021/acs.jafc.5b02827
J. Agric. Food Chem. 2015, 63, 8722−8733

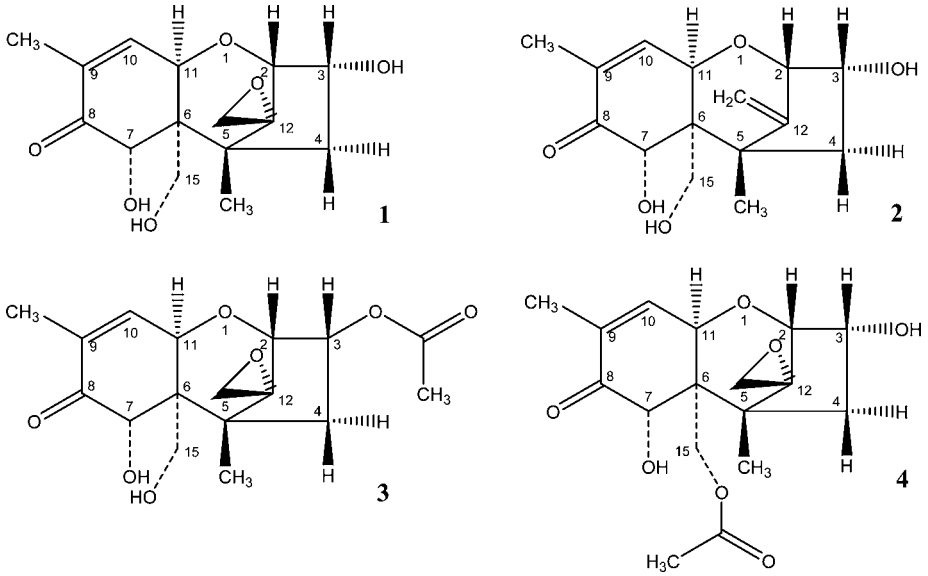

Figure 1. Structures of **1**, 3α,7α,15-trihydroxy-12,13-epoxytrichothec-9-en-8-one (deoxynivalenol or DON); **2**, a main in vivo metabolite, 3α,7α,15-trihydroxytrichothec-9,12-dien-8-one (deepoxydeoxynivalenol or DOM-1); and two acetylated forms of DON, **3**, 3α-acetoxy-7α,15-dihydroxy-12,13-epoxytrichothec-9-en-8-one (3-acetyldeoxynivalenol or 3ADON), and **4**, 15-acetoxy-3α,7α-dihydroxy-12,13-epoxytrichothec-9-en-8-one (15-acetyldeoxynivalenol or 15ADON).

expression of intestinal epithelial cell tight junction proteins.[10] It was suggested that 3ADON is less toxic than DON and, in contrast, that the toxicity of 15ADON is higher or comparable to DON. A comparison of the effect of these compounds on the interleukin-8 (IL-8) secretion in Caco-2 cells, indicating activation of the innate immune system, and intestinal transepithelial transport over Caco-2 cells has been performed.[11] The study revealed a significantly higher intestinal absorption of 15ADON compared to DON and 3ADON. Furthermore, the authors showed that the ability to induce IL-8 secretion was ranked as follows: 3ADON < DON < 15ADON. Similar effects were previously reported for the cytotoxicity on cultured human myeloid and lymphoid cell lines (K-562 and MINGL1),[12] and for DNA inhibition in Swiss mouse 3T3 fibroblasts.[13] Furthermore, one of the main in vivo metabolites, 3α,7α,15-trihydroxy-trichothec-9,12-dien-8-one (deepoxydeoxynivalenol or DOM-1), **4** (Figure 1), was included in the latter study and was found to be the least toxic compound, due to absence of the epoxide ring. In conclusion, these compounds have a distinct degree of toxicity, which can be ranked in order of increasing toxicity: DOM-1 < 3ADON < DON $\leq$ 15ADON.

A key question concerning the in vivo disposition is whether conversion of 3ADON and 15ADON to DON by in vivo hydrolysis in humans and animals would occur and posssibly imply an underestimation of the degree of contamination and the toxicity. Several in vitro studies described the hydrolysis of ADONs to DON in humans, pigs, and poultry.[14−16] In contrast, only a limited number of in vivo studies are available on the hydrolysis and metabolism of ADONs. The hydrolysis of 3ADON and 15ADON after oral administration to rats has been investigated,[17] as well as the hydrolysis and toxicokinetics of 3ADON orally administered to pigs.[18] Both studies demonstrated that an in vivo hydrolysis of ADONs to DON is possible. However, it was not reported if the hydrolysis occurs presystemically or systemically. No in vivo data are available for broiler chickens, although these animals have a high exposure to these mycotoxins because of their mainly cereal-based diet.

The goal of this study was to determine the absolute oral bioavailability, the degree of hydrolysis (differentiating between presystemic and systemic hydrolysis), and toxicokinetic characteristics of 3- and 15ADON in broiler chickens and pigs. Species selection was based, as stated above, on the high exposure of these animals to the toxins, due to their mainly cereal-based diet and the high prevalence of mycotoxins in these diets. Additionally, pigs were included because of their sensitivity to DON. Animal species susceptibility to DON can be ranked as pigs > mice > rats > poultry $\approx$ ruminants.[19] Differences in absorption, distribution, metabolism, and elimination of DON among animal species might account for this differential sensitivity.[2] Furthermore, the data from pig studies are highly relevant to humans because of the anatomical and physiological similarities of the gastrointestinal (GI) tract, liver, kidneys, and cardiovascular system in both species.[20,21]

MATERIALS AND METHODS

Chemicals, Products, and Reagents. DON, 3ADON, and 15ADON had >99% purity (Fermentek, Jerusalem, Israel). The mycotoxins were dissolved in analytical grade ethanol (EtOH) (Merck, Brussels, Belgium), yielding a stock solution of 10 mg/mL, and were used for both animal and analytical experiments. As internal standard (IS), $^{13}C_{15}$-DON (50 μg/mL) stock solution in acetonitrile was used (Romer Laboratories, Tulln, Austria). All stock solutions were stored at ≤ -15 °C. Individual working standard solutions of 10 μg/mL, used for the analytical experiments, were prepared by diluting the above stock solutions with ULC-MS grade acetonitrile (Biosolve, Valkenswaard, The Netherlands). All working standard solutions were stored at ≤ -15 °C. Standard mixture working solutions containing DON, 3ADON, and 15ADON of 1 and 0.1 μg/mL were prepared by mixing appropriate dilutions of the individual working standard solutions in ULC-MS acetonitrile and were stored at 2−8 °C. Solutions of DON in acetonitrile have been reported to be stable for 24 months at room temperature,[22] whereas the supplier reported a stability of at least 6 months at 4 °C for 100 μg/mL solutions of 3ADON and 15ADON in acetonitrile.

Water, methanol, and glacial acetic acid were of ULC-MS grade (Biosolve). Microfilters Millex GV-PVDF 0.22 μm were obtained to filter deproteinized plasma samples (Millex, Overijse, Belgium).

DOI: 10.1021/acs.jafc.5b03270
J. Agric. Food Chem. 2015, 63, 8734−8742

Animal Trials. Eighteen broiler chickens (Ross 308) were purchased from the Institute for Agriculture and Fisheries Research (Melle, Belgium), at the age of 3 weeks, as hatched and had an average bw ± standard deviation (SD) of 1210 ± 172 g. The broilers were randomly allocated to three groups of six animals. Water and feed were given ad libitum. The pen was climate controlled with temperatures between 21 and 25 °C, a relative humidity between 40 and 60%, and an applied light schedule similar to commercial installations (18 h light/6 h dark). After 1 week of acclimatization, the animals were treated with either DON (group 1), 3ADON (group 2), or 15ADON (group 3) by intravenous bolus injection (IV, administration in *vena basilica*) (three animals/group) or *per os* (PO, by means of gavage in the crop) (three animals/group) in a two-way crossover design. The administered doses were based on the European Union (EU) maximum guidance level of 5 mg DON/kg poultry feed.[23] Given the average feed consumption of 4-week-old broiler chickens was 100 g feed/kg bw/day, 500 μg DON/kg bw was administered. For the ADONs, an equimolar dose of 571 μg/kg bw was administered. The calculated volume of stock solution (10 mg/mL in EtOH) was diluted with saline (0.9% NaCl) (VWR, Leuven, Belgium) to a volume of 0.5 mL (IV) or 1 mL (PO). After oral administration of the toxins, 1 mL of tap water was administered to flush the gavage syringe. A washout period of 3 days was maintained between treatments. Feed was withheld for 12 h before administration and until 3 h post administration (PA). Blood (0.5−1 mL) was sampled from the leg vein by venipuncture at 0 min (before administration) and at 5, 10, 20, 30, 45, 60, 90, 120, and 240 min PA. Blood samples were centrifuged (2851*g*, 10 min, 4 °C), and plasma was stored at ≤ −15 °C until analysis.

For the pig study, nine clinically healthy male pigs (11 weeks of age, 28.6 ± 2.8 kg bw) were individually housed with feed and water ad libitum. Natural lighting was provided, the enclosure was climate controlled to keep the temperature between 20 and 24 °C and the relative humidity between 20 and 40%. After a 1 week acclimatization period, the animals were treated with either DON (n = 3), 3ADON (n = 3), or 15ADON (n = 3) by IV bolus injection using a surgically placed jugular catheter as previously described[24] or PO (by means of gavage in the stomach) in a crossover design. For this design pigs were randomly divided into groups of three pigs. Each group received four treatments (two IV and two PO treatments), resulting in a crossover for each compound in six animals. A washout period of 24 h was maintained between treatments. Twelve hours before administration of the mycotoxins, the animals were fasted until 4 h PA. The administered doses were calculated as for the broiler chicken trial. The EU maximum guidance level in pig feed is 0.9 mg/kg DON.[23] Pigs at 12 weeks of age consume on average 40 g feed/kg bw/day. This resulted in the administration of 36 μg DON/kg bw. For the ADONs, an equimolar dose of 41 μg/kg bw was administered. The calculated amount of toxin for each animal, dissolved in EtOH at 10 mg/mL, was diluted with saline to a volume of 1 mL (IV) or 10 mL (PO). After oral administration of the toxins, 50 mL of tap water was administered to flush the gavage tube. Blood (1−2 mL) was sampled from the jugular vein at 0 min (before administration) and at 5, 10, 20, 30, 45, 60, 90, 120, 240, 360, and 480 min PA. Blood samples were centrifuged (2851*g*, 10 min, 4 °C), and plasma was stored at ≤ −15 °C until analysis.

Both animal trials were approved by the Ethical Committee of the Faculty of Veterinary Medicine and Bioscience Engineering of Ghent University (EC2013/64).

LC-MS/MS Analysis. Sample pretreatment and chromatography-tandem mass spectrometry (LC-MS/MS) analysis were performed as previously described.[25] In brief, 250 μL of plasma was supplemented with IS, 5 μL of a 1 μg/mL $^{13}C_{15}$-DON working solution. After vortex mixing for 15 s, acetonitrile was added to a volume of 1 mL to precipitate plasma proteins. The samples were vortex mixed, followed by a centrifugation step (8517*g*, 10 min, 4 °C). The supernatant was transferred and evaporated to dryness under a (gentle) nitrogen stream at 45 ± 5 °C. The dry residue was redissolved in 200 μL of ULC/MS-grade water, microfiltered through a Millex GV-PVDF filter (0.22 μm), and transferred to an autosampler vial. A 10 μL aliquot was injected onto the LC-MS/MS instrument. Broiler plasma was analyzed on a Surveyor type MS pump Plus and Autosampler Plus HPLC in combination with a TSQ Quantum Ultra triple-quadrupole mass spectrometer (Thermo Fisher Scientific, Breda, The Netherlands). Pig plasma was analyzed on an Acquity UPLC system coupled to a Xevo TQ-S triple-quadrupole mass spectrometer (Waters, Zellik, Belgium).

Chromatographic separation of the analytes was achieved on a 50 mm × 2.1 mm i.d., 1.9 μm, Hypersil Gold column with a guard column of the same type (Thermo Fisher Scientific). All compounds were eluted with a gradient of ULC-MS grade water containing 0.1% glacial acetic acid (mobile phase A) and ULC-MS grade methanol containing 0.1% glacial acetic acid (mobile phase B) at a total flow rate of 300 μL/min. The following gradient elution program was run: 0−1 min, 5% B; 1.0−1.1 min, linear gradient to 20% B; 1.1−5.0 min, 20% B; 5.0−5.1 min, linear gradient to 50% B; 5.1−8.0 min, 50% B; 8.0−8.1 min, linear gradient to 95% B; 8.1−9.0 min, 95% B; 9.0−9.1 min, linear gradient to 5% B; 9.1−12.0 min, 5% B. The mass spectrometer was operated in the multiple reaction monitoring (MRM) mode with two ion transitions for each target analyte. Limits of quantitation (LOQs) varied from 0.1 ng/mL (DON in pig) to 1.0 ng/mL (ADONs in pig, DON and 3ADON in chicken) to 2.0 ng/mL (15ADON in chicken).

Toxicokinetic Modeling and Statistical Analysis. Toxicokinetic analysis was performed using WinNonlin Professional version 5.2.1. (Pharsight, St. Louis, MO, USA). Plasma concentrations below the LOQ were not taken into account. For the toxicokinetic analysis, all values were recalculated to their molar concentrations, expressed as nanomoles per milliliter. For the analysis of DON IV and PO data in chickens, a tailor-made two-compartmental model (central compartment (Vc) and peripheral compartment (Vp)) with first-order absorption and first-order elimination was applied. For the IV and PO data of ADONs in chickens, a one-compartmental model was used in combination with the two-compartmental model for DON. The fraction of the dose of DON, 3ADON, or 15ADON that was absorbed after PO administration (in any form, thus as DON and/or ADON) was indicated as FRAC (%). BioADON was the fraction of the absorbed dose that entered the systemic circulation in its unchanged form, thus as ADON (%). Consequently, the product of FRAC and BioADON indicates the absolute oral bioavailability of ADON (F, %), that is, the fraction of ADON absorbed in the systemic circulation in its unchanged form. The product of FRAC and (1-BioADON) then indicates the absorbed fraction that was presystemically hydrolyzed to DON and that entered the systemic circulation as DON (presystemic hydrolysis, %). Systemic hydrolysis was set at 100% for 3ADON and 15ADON in pigs and in broiler chickens, as the hydrolysis to DON was the only assumed clearance (CL) of ADON in the model. In Figure 2 a graphical representation of the constructed model is given for DON (IV and PO) and ADON (IV and PO) in chickens.

The constructed models for pigs were identical to those for chickens, except for the ADON PO model. Insufficient or no ADON data above the LOQ after PO administration of ADONs led to the exclusion of the ADON compartment for this administration route in pigs. This model therefore assumes a full presystemic conversion of ADON to DON.

A $1/\hat{y}$ weighing was applied for all calculations with both the chicken and pig data. For all of the described models, the Gauss−Newton (Levenberg and Hartley) algorithm was used and a maximum of 50 iterations was allowed.

The following primary and secondary toxicokinetic parameters were calculated for IV and PO administration: absorption rate constant (k_a) (identical for DON and ADONs), intercompartmental flow for DON (Q_{DON}), total body clearance of DON (CL_{DON}), total body clearance of ADON to DON (CL_{ADON}), central volume of distribution for DON (Vc_{DON}), peripheral volume of distribution for DON (Vp_{DON}), and central volume of distribution for ADONs (Vc_{ADON}). The elimination rate constant for DON (k_{eDON}) was calculated by dividing CL_{DON} by the sum of Vc_{DON} and Vp_{DON} for each animal. Additionally, for PO data the descriptive toxicokinetic parameters maximal plasma concentration (C_{max}) and time to C_{max} (t_{max}) were given for DON.

Statistical analysis of these parameters consisted of one-way ANOVA with post hoc Scheffé tests (p value < 0.05) for both animal

DOI: 10.1021/acs.jafc.5b03270
J. Agric. Food Chem. 2015, 63, 8734−8742

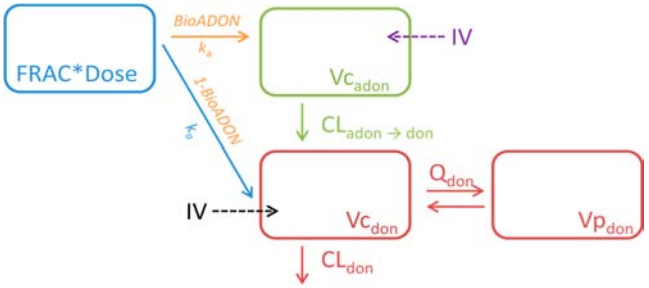

Figure 2. Graphical representation of the applied models in broiler chicken for DON IV (black and red sections), DON PO (blue and red sections), ADON iv (purple, green, and red sections), and ADON PO (blue, orange, green, and red sections). IV, intravenous administration; k_a, absorption rate constant (1/min); CL_{DON}, clearance of DON (mL/min/kg); Q_{DON}, intercompartment flow for DON (mL/min/kg); Vc_{DON} = central volume of distribution for DON (mL/kg); Vp_{DON} = peripheral volume of distribution for DON (mL/kg); CL_{ADON} = clearance of ADON to DON (mL/min/kg); Vc_{ADON} = central volume of distribution for ADON (mL/kg); FRAC = fraction of dose absorbed; BioADON = fraction of the absorbed dose that enters systemic circulation as ADON; 1-BioADON = fraction of the absorbed dose that enters systemic circulation as DON.

species (SPSS 20.0, IBM, Chicago, IL, USA). All variables were log transformed to fulfill the equality of variances criterion as determined by the Levene test for homogeneity of variances (p value > 0.01).

RESULTS AND DISCUSSION

The goal of this study was to determine the absolute oral bioavailability of 3- and 15ADON, the degree of in vivo hydrolysis (differentiating between presystemic and systemic hydrolysis), and the toxicokinetic parameters in broiler chickens and pigs. The plasma concentration−time profiles were analyzed by a tailor-made compartmental toxicokinetic model. This model has the advantage, compared to noncompartmental analysis, that for a given compound, PO and IV data can be fitted simultaneously for each animal. This is more accurate because certain toxicokinetic parameters, such as CL and Vd, are independent of the administration route, and thus more data are available to allow a reliable estimate. Furthermore, this model allows prediction of the plasma concentrations for scenarios that have not been studied yet, whereas noncompartmental analysis uses only observed values. For both ADONs, only a hydrolysis to DON is assumed in the model after IV and PO administration in broilers and pigs. It needs to be mentioned that also formation of glucuronide conjugates and possibly other metabolites can take place. Therefore, high-resolution mass spectrometry (HRMS) analysis on pig and broiler chicken plasma samples from three animals after IV and PO administration of DON was performed. The methodology applied was similar as in a previously described study.[26] After IV and PO administration of DON in pigs, mean peak area ratios of DON-glucuronide/DON of 4.98 and 4.95 were found, respectively (results not shown). Therefore, presystemic glucuronidation in pigs is considered neglibile. For chickens, only trace amounts of DON-glucuronide were detected.[26] Consequently, the impact on estimated volumes of distribution, clearances, absorption, and elimination rate constants are expected to be very small. Furthermore, this study also included IV administration and was set up as a crossover design, generating IV and PO data in the same animals, thereby minimizing variability and compensating for possible other metabolites formed systemically. The developed model allows an estimation of the degree of presystemic and systemic hydrolysis after PO administration, which is not possible using noncompartmental analysis only.

Plasma concentration−time profiles for DON, 3ADON, and 15ADON are presented in Figures 3 and 4, respectively, for broiler chickens and pigs. Each profile represents the mean of six animals ± standard deviation (SD). For broiler chickens, no adverse effects were observed during the animal trial following PO and IV bolus administration of the mycotoxins. Similarly, no adverse effects were observed during the pig trial following PO administration. Following IV dosing of DON, 3ADON, and 15ADON, respectively, three, two, and two of six pigs vomited within 0.5 h PA. However, this had no observable influence on the results as these pigs were IV dosed.

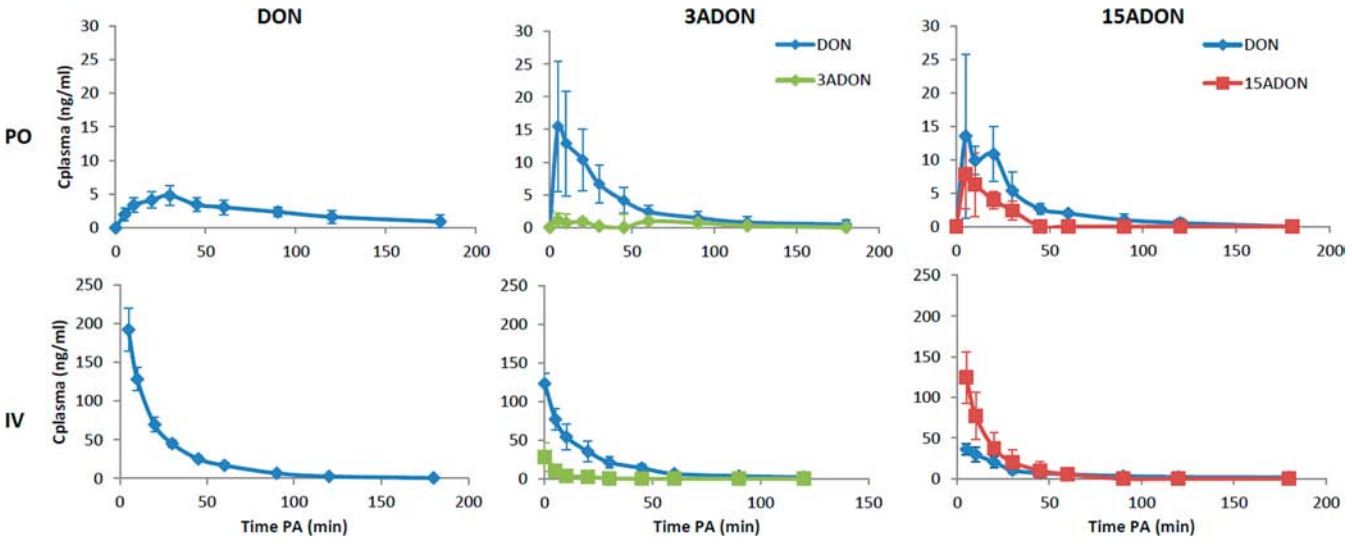

Figure 3. Plasma concentration−time profiles of deoxynivalenol (DON), 3-acetyldeoxynivalenol (3ADON), and 15-acetyldeoxynivalenol (15ADON) after oral (PO) and intravenous (IV) administration (post administration = PA) of DON (dose = 500 μg DON/kg bw), 3ADON (dose = 571 μg 3ADON/kg bw), and 15ADON (dose = 571 μg 15ADON/kg bw) to broiler chickens (n = 6 for each toxin). Values are presented as means ± SD.

DOI: 10.1021/acs.jafc.5b03270
J. Agric. Food Chem. 2015, 63, 8734−8742

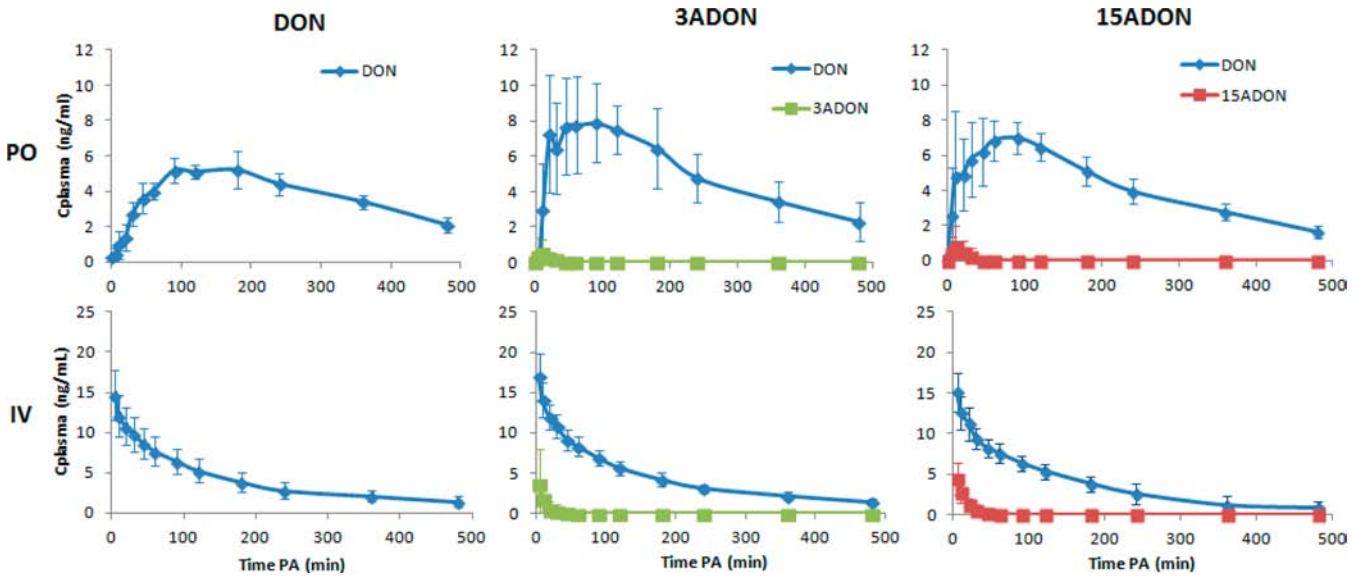

Figure 4. Plasma concentration−time profiles of deoxynivalenol (DON), 3-acetyldeoxynivalenol (3ADON), and 15-acetyldeoxynivalenol (15ADON) after oral (PO) and intravenous (IV) administration (post administration = PA) of DON (dose = 36 μg DON/kg bw), 3ADON (dose = 41 μg 3ADON/kg bw), and 15ADON (dose = 41 μg 15ADON/kg bw) to pigs (n = 6 for each toxin). Values are presented as means ± SD.

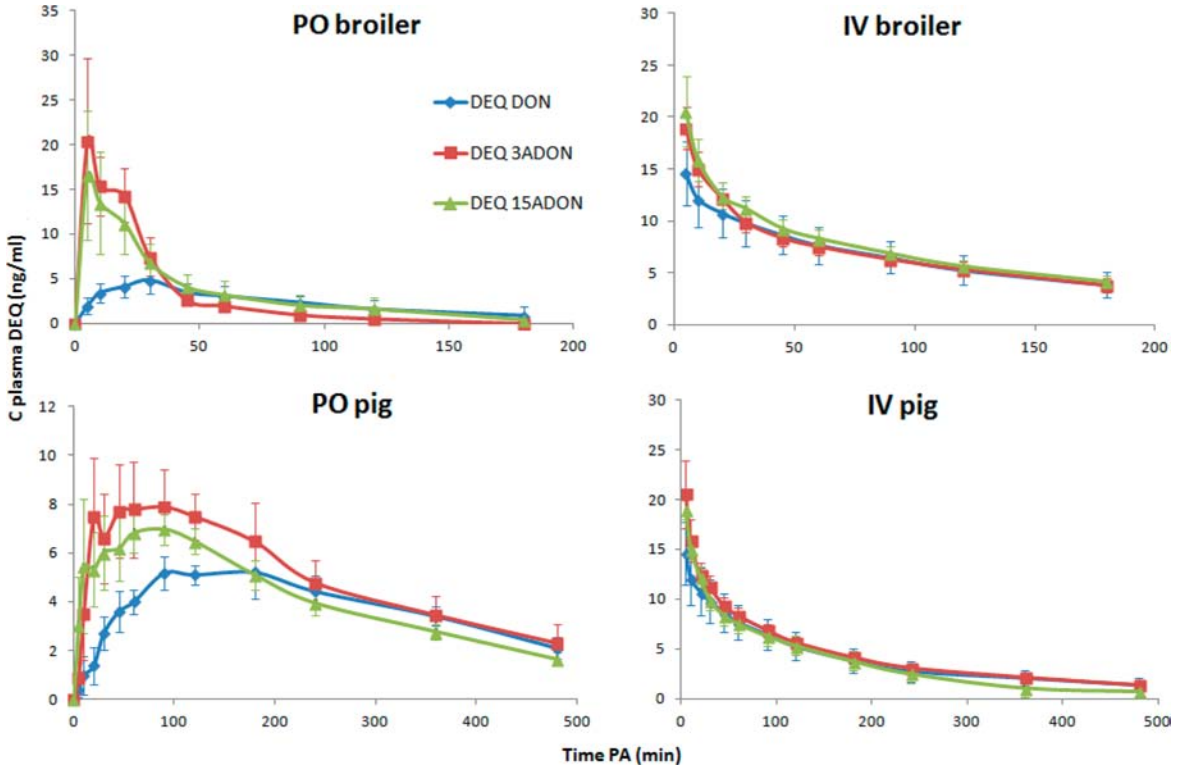

Figure 5. DON equivalent (DEQ) plasma concentration−time profiles after oral (PO) and intravenous (IV) administration of deoxynivalenol (DON), 3-acetyldeoxynivalenol (3ADON), and 15-acetyldeoxynivalenol (15 ADON) in broiler chickens and pigs (n = 6 animals for each toxin). DEQ is calculated by dividing the plasma concentration of the ADONs by their molar mass (338.3 g/mol) and by multiplying by that of DON (296.3 g/mol) and by adding this to DON plasma concentrations. Values are presented as means ± SD.

The plasma concentration−time profiles were also expressed as DON equivalents (DEQ). For this, the ADON concentrations were converted, added to the DON concentrations, and reported as DON equivalent concentrations. This was done by dividing the plasma concentration of the ADONs by their molar mass (338.3 g/mol) and by multiplying by the molar mass of DON (296.3 g/mol). The results for pigs and chickens are shown in Figure 5. Clear differences can be seen for PO administration between DON, 3ADON, and 15ADON in pigs as well as broiler chickens, whereas the IV profiles were similar, which can be regarded as a quality control of the utilized setup. Toxicokinetic parameters, absolute oral bioavailability (F, %) and degree of presystemic hydrolysis (%) were calculated using compartmental modeling, the results of which are given in Table 1.

DOI: 10.1021/acs.jafc.5b03270
J. Agric. Food Chem. 2015, 63, 8734−8742

Table 1. Toxicokinetic Parameters, Presystemic Hydrolysis of the Bioavailable Fraction, and Absolute Oral Bioavailability of DON, 3ADON, and 15ADON after IV and PO Administration to Broiler Chickens and Pigs ($n = 6$)[a]

animal species	adm	k_a (1/min)	k_{ADON} (1/min)	CL_{DON} (mL/min/kg)	Q_{DON} (mL/min/kg)	Vc_{DON} (mL/kg)	Vp_{DON} (mL/kg)	CL_{ADON} (mL/min/kg)	Vc_{ADON} (mL/kg)	FRAC (%)	BioADON (%)	pres hydr (%)	F (%)	$C_{max\,DON}$ (ng/mL)	$t_{max\,DON}$ (min)
broiler chicken	DON	0.0203 ± 0.0101 a	0.0388 ± 0.0062	102 ± 12 a	59.8 ± 25.2 a	1656 ± 426 a	1025 ± 142 a			10.6 ± 4.6 a			10.6 ± 4.6 a	4.2 ± 0.9 a	32 ± 11 a
	3ADON	0.0722 ± 0.0497 a		151 ± 16 a	155 ± 65 a	109 ± 66b	3490 ± 840 a	1506 ± 615 a	15918 ± 11620 a	18.2 ± 5.5 a	0	18.2 ± 5.5 a	0b	15.0 ± 8.8 b	5.0 ± 0 b
	15ADON	0.0289 ± 0.0216 a		340 ± 132 b	287 ± 118 b	1861 ± 1220 a	18154 ± 14573 b	236 ± 63 b	3692 ± 1707 b	42.2 ± 12.5 b	24.6	31.9 ± 14.8 b	10.4 ± 3.6 a	16.2 ± 7.6 ab	9.0 ± 6.5 b
pig	DON	0.0164 ± 0.0161 a	0.00405 ± 0.00076	15.1 ± 3.8 a	21.1 ± 12.7 a	2605 ± 570 a	1174 ± 600 a			100 a			100 a	6.3 ± 2.4 a	109 ± 41 a
	3ADON	0.0179 ± 0.0100 a		14.0 ± 2.4 a	202 ± 50 b	175 ± 96 b	2579 ± 406 b	1428 ± 1162 a	13001 ± 11625 a	100 a	0	100 a	0b	7.5 ± 1.7 a	101 ± 45 a
	15ADON	0.0136 ± 0.0044 a		15.3 ± 2.1 a	113 ± 6.0 c	31.6 ± 31.7 b	2895 ± 241 b	426 ± 231 a	7151 ± 2427 a	100 a	0	100 a	0b	6.5 ± 1.2 a	78 ± 39 a

[a]Values are presented as means ± SD. Statistical analysis was performed within each animal species; results that do not share the same letter in each column are significantly different ($p < 0.05$). Adm, administered mycotoxin; k_a, absorption rate constant (1/min); k_{ADON}, elimination rate constant for DON (1/min) (k_{eADON} could theoretically also be calculated after administration of ADONs, as data for DON were); CL_{DON}, clearance of DON (mL/min/kg); Q_{DON}, intercompartmental flow for DON (mL/min/kg); Vc_{DON}, central volume of distribution for DON (mL/kg); Vp_{DON}, peripheral volume of distribution for DON (mL/kg); CL_{ADON}, clearance of ADON to DON (mL/min/kg); Vc_{ADON}, central volume of distribution for ADON (mL/kg); FRAC, absorbed fraction; BioADON, fraction of the absorbed dose that entered the systemic circulation as ADON (%); pres hydr, percentage of the total dose that is hydrolyzed presystemically to DON and absorbed as DON (%); F, absolute oral bioavailability (%); C_{max}, maximum plasma concentration for DON (ng/mL); t_{max}, time to maximum plasma concentration for DON (min).

The absorbed fractions of 3ADON (18.2%) and 15ADON (42.2%) in broiler chickens correspond to approximately double and quadruple that of DON (10.6%), respectively. However, no statistical difference ($p = 0.061$) could be demonstrated between the absorbed fraction of DON and 3ADON in broiler chickens. The absorbed fraction of 15ADON, on the other hand, was found to be significantly higher than that of DON and 3ADON ($p < 0.05$). An increase in absorbed fractions for the ADONs might be expected as these acetylated mycotoxins are less polar and have a more favorable log D value for absorption by passive nonionic diffusion compared to DON (estimated log D_{ADON} and log D_{DON} at physiological pH are −0.5 and −1, respectively).[27] For pigs, on the other hand, the absorbed fractions of DON, 3ADON, and 15ADON were 100%. The relatively low absorbed fraction for chickens compared to pigs has been discussed[28] and may be partially due to the rapid transit time in the GI tract of chickens, leading to a reduced time for complete absorption. As another contributing factor, the high bacterial content in the GI tract of birds before the main site of absorption is proposed. These bacteria could metabolize DON and/or ADONs, thereby decreasing their bioavailability and toxicity.[27]

To correlate the absorbed fraction to the absolute oral bioavailability (F, %), the degree of in vivo hydrolysis must be considered. As the ADONs can be hydrolyzed presystemically to DON, their absorbed fraction may represent a combination of absorption as DON and as ADON and can thus differ from their oral bioavailability, which is represented by the absorption as ADON. However, this is not the case for DON. For chickens, the F value for DON is equal to its absorbed fraction, being 10.6 ± 4.6% in this study. For DON in broiler chickens, an oral F of 19.3 ± 7.42% has been observed,[29] which is in the same range. In contrast in pigs, a complete absorbed fraction and complete oral bioavailability of DON was found in fasted pigs. Prior studies in pigs observed oral F values for DON after chronic and acute exposure of 62.8 and 54.1%, respectively.[30,31] Differences in F for acute exposure can be attributed to either the prandial state (fed versus fasted) or the administration of a bolus of DON (dissolved in, e.g., ethanol) versus the administration of DON in contaminated feed. The oral absorption as well as oral bioavailability of the ADONs in pigs and chickens has thus far not been investigated.

In broiler chickens, both ADONs have a significantly different degree of presystemic hydrolysis ($p < 0.05$). Whereas for 3ADON the fraction of the dose absorbed was completely hydrolyzed presystemically, the absorbed fraction of 15ADON that entered the systemic circulation as such (BioADON) was 24.6% and was consequently 75.4% as DON. As the fraction of the dose absorbed for 3ADON was completely hydrolyzed presystemically, an F value of 0% was obtained, whereas for 15ADON an F value of 10.4% was calculated. Differences in hydrolysis/metabolism between both ADONs in broiler chickens has already been demonstrated in vitro.[14] After anaerobic incubation of 3ADON for 72 h with microbiota from the GI tract of chickens, deacetylation was the predominant reaction (94%) with only minimal subsequent de-epoxidation (6%); there was no evidence for de-epoxidation only. However, for 15ADON, a large fraction proved to have both the acetyl and epoxy moieties removed (±93%), whereas only small quantities showed either solely de-epoxidation (±1%) or deacetylation (±7%), leaving no 15ADON. The role of GI microbiota in our in vivo study has little to no influence on the

DOI: 10.1021/acs.jafc.5b03270
J. Agric. Food Chem. 2015, 63, 8734−8742

presented results as the high degree of hydrolysis after IV administration indicates a systemic biotransformation rather than the result of the action of GI microbiota. Additionally, the microbiota from the aforementioned in vitro study were isolated from the large intestine. At this site in the GI tract the absorption of the toxins will be negligible and transformation here will not be reflected by changes in plasma concentrations. Furthermore, the average GI transit time for chickens is 3−4 h, whereas the experimental setup of this in vitro study consisted of a 72 h anaerobic incubation.[14,32]

In pigs, 3ADON and 15ADON exhibited a presystemic hydrolysis of >99%, also leading to F values of 0%. These findings for the in vivo hydrolysis of 3ADON in pigs correspond with an earlier study.[18] Five castrated pigs were fed twice daily for 3 days 2.5 mg 3ADON/kg feed. No 3ADON, or DOM-1, could be detected in plasma. The only detected metabolite in plasma was DON as such. After incubation of the plasma samples with β-glucuronidase, an increase of 72% DON was seen, indicating the presence of DON-glucuronide. The rapid deacetylation prior to absorption, as suspected,[18] has been confirmed in our study. These data can be related to several in vitro and in vivo studies in other species. One study investigated the hydrolysis and metabolism of 3ADON and 15ADON after oral administration to rats.[17] One hour PA of 3ADON or 15ADON, 12% of the dose could be detected in the stomach as free DON, indicating a likely hydrolysis of both ADONs in the stomach. It was also observed that both ADONs were glucuronidated in the stomach (5% of the administered dose) without prior deacetylation. Another in vitro study incubated human fecal samples under anaerobic conditions for 48 h with 3ADON.[16] Of the administered dose, 78 ± 30% was recovered as DON, clearly indicating the capability of human large intestinal microbiota to hydrolyze 3ADON to DON. Remarkably, a rapid and complete hydrolysis of 3ADON and 15ADON to DON was also observed after IV administration.

The relatively higher absorbed fractions for ADONs compared to DON in broilers are also reflected by significantly higher observed maximal DON plasma concentrations after PO administration of 3ADON (C_{max} = 15.0 ± 8.8 ng/mL) and 15ADON (C_{max} = 16.2 ± 7.6 ng/mL) compared to PO administration of DON (C_{max} = 4.2 ± 0.9 ng/mL), as depicted in Table 1 and Figure 3. When transformed to DEQ plasma concentrations, this difference between DON and ADONs becomes even more explicit, as can be seen in Figure 5. Furthermore, in broiler chickens, the administration of ADONs appears to lead to a more rapid absorption of DON, reflected by a shorter t_{max} for DON after 3ADON administration (t_{max} = 5.0 ± 0 min) and after 15ADON administration (t_{max} = 9.0 ± 6.5 min) compared to after administration of DON itself (t_{max} = 32 ± 11 min). For pigs, no significant changes were seen in C_{max} or t_{max} of DON after PO administration of DON, 3ADON, or 15ADON.

In this study, an absorption rate constant k_a for DON of 0.0164 ± 0.0161/min was found in pigs, compared to 0.00995 ± 0.00292/min[18] and 0.0310 ± 0.0238/min.[30] However, these results are difficult to compare because the aforementioned study[30] utilized a contaminated feed strategy (chronic exposure), whereas this study was based on a single bolus model with fasted animals. The k_a values in broiler chickens are approximately twice the values obtained for pigs, indicating indeed a fast presystemic hydrolysis of ADONs and a fast GI transit and absorption in poultry.

The CL of DON after DON administration in broilers is approximately 10 times higher compared to that in pigs. The CL of DON in pigs, approximately 15 mL/min/kg, is comparable to a previously reported value for acute DON administration of 9.3 mL/min/kg.[30] The CL of 3ADON in broilers and pigs is remarkably higher compared to that of DON and 15ADON. In contrast, compared to DON, 15ADON showed a faster CL in pigs and a slower clearance in broiler chickens. The intercompartmental flow Q for DON is similar in both animal species. The Vc values for ADONs are in the same order of magnitude for pigs and broilers. The model had difficulties in estimating the central and peripheral volumes of distribution for DON individually. However, when making the sum of both volumes of distribution, the values are found to be in a range of 2.6−3.8 L/kg, except for 15ADON in chickens, for which the Vp was estimated to be approximately 18 L/kg, but with a higher uncertainty. It was therefore attempted to fix the value of this parameter to a lower one, but this led to a poorly fitted model. For 15ADON administration to broilers, DON and 15ADON were clearly measurable for a relatively long period of time, unlike for 15ADON in pigs and 3ADON in broilers as well as pigs. This possibly increased the difficulty for the model to correctly fit all parameters. The mean elimination rate constants for DON (k_{eDON}) in broilers and pigs were 0.0388 ± 0.0062/min and 0.00405 ± 0.00076/min, respectively. This corresponds to mean elimination half-lives for DON in broilers and pigs, calculated as $0.693/k_{eDON}$, of 17.9 and 171 min (2.85 h), respectively. For pigs elimination half-lives of 5.3 ± 2.4 h (acute PO, two-compartmental model),[30] 2.39 ± 0.71 h (acute PO, one-compartmental model),[18] and 2.73 ± 0.477 (acute PO, one-compartmental model)[33] were observed, in contrast to a value of 15.2 ± 12.9 h observed for IV (two-compartmental model).[30] For broiler chickens elimination half-lives of 27.9 ± 6.9 min (IV) and 38.2 ± 11.2 min (acute PO) were observed.[29]

When combining the above-mentioned results for the absorbed fraction, oral bioavailability, and presystemic hydrolysis of 3ADON and 15ADON in pigs, it can be concluded that the administered dose of both ADONs is completely absorbed and both show a complete presystemic hydrolysis. Therefore, both ADONs can be regarded as toxic as DON itself in pigs with regard to systemic toxicity. Moreover, the ADONs may also exert a local toxic effect in the intestine as previously proposed.[10] For broiler chickens, the absorbed fractions of 3ADON and especially 15ADON are higher than or at least equal to that of DON. Furthermore, 3ADON, which is reported to be less toxic than DON, is completely hydrolyzed presystemically to DON, whereas 15ADON is reported to be more toxic and not fully hydrolyzed. This results in a "worst case scenario" for broilers, where each mole of 15ADON could be as toxic as 4 mol of DON and where the less toxic 3ADON can be regarded as equally toxic as DON because it is completely hydrolyzed presystemically.

In conclusion, both pigs and broiler chickens are exposed to DON after oral intake of ADONs. When these findings are combined with the frequent cocontamination of ADONs and DON in food and feed, this demonstrates the possible need to consider the establishment of a TDI for 3ADON and 15ADON or the inclusion of the ADONs in a group TDI for DON-related substances.

DOI: 10.1021/acs.jafc.5b03270
J. Agric. Food Chem. 2015, 63, 8734−8742

■ ASSOCIATED CONTENT

Supporting Information

The Supporting Information is available free of charge on the ACS Publications website at DOI: 10.1021/acs.jafc.5b03270.

Dosing design for the pig trial (S1), and the written code of the utilized model (S2), together with the fits of the median plasma concentration−time profiles of DON, 3ADON, and 15ADON in broiler chickens and pigs (semilog) (S3) (PDF)

■ AUTHOR INFORMATION

Corresponding Author

*(N.B.) Phone: +32 9 264 73 24. Fax: +32 9 264 74 97. E-mail: nathan.broekaert@ugent.be.

Funding

This research was funded by a Ghent University Special Research Fund Grant (I/00105/01).

Notes

The authors declare no competing financial interest.

■ ACKNOWLEDGMENTS

We are grateful to Anneleen Watteyn, Elke Plessers, and Heidi Wyns for experienced assistance during the animal trials.

■ REFERENCES

(1) Doll, S.; Dänicke, S. The *Fusarium* toxins deoxynivalenol (DON) and zearalenone (ZON) in animal feeding. *Prev. Vet. Med.* **2011**, *102*, 132−145.

(2) Pestka, J. J. Deoxynivalenol: mechanisms of action, human exposure, and toxicological relevance. *Arch. Toxicol.* **2010**, *84*, 663−679.

(3) Van Asselt, E. D.; Azambuja, W.; Moretti, A.; Kastelein, P.; De Rijk, T. C.; Stratakou, I.; Van Der Fels-Klerx, H. J. A Dutch field survey on fungal infection and mycotoxin concentrations in maize. *Food Addit. Contam., Part A* **2012**, *29*, 1556−1565.

(4) Rychlik, M.; Humpf, H. U.; Marko, D.; Dänicke, S.; Mally, A.; Berthiller, F.; Klaffke, H.; Lorenz, N. Proposal of a comprehensive definition of modified and other forms of mycotoxins including "masked" mycotoxins. *Mycotoxin Res.* **2014**, *30*, 197−205.

(5) Yoshizawa, T.; Morooka, N. Biological modification of trichothecene mycotoxins: acetylation and deacetylation of deoxynivalenols by *Fusarium* spp. *Appl. Microbiol.* **1975**, *29*, 54−58.

(6) De Boevre, M.; Di Mavungu, J. D.; Maene, P.; Audenaert, K.; Deforce, D.; Haesaert, G.; Eeckhout, M.; Callebaut, A.; Berthiller, F.; Van Peteghem, C.; De Saeger, S. Development and validation of an LC-MS/MS method for the simultaneous determination of deoxynivalenol, zearalenone, T-2-toxin and some masked metabolites in different cereals and cereal-derived food. *Food Addit. Contam., Part A* **2012**, *29*, 819−835.

(7) Gareis, M.; Schothorst, R. C.; Vidnes, A.; Bergsten, C.; Paulsen, B.; Brera, C.; Miraglia, M. Collection of occurrence data of *Fusarium* toxins in food and assessment of dietary intake by the population of EU Member States. Report of Experts Participating in SCOOP Task 3.2.10, 2003; http://europa.eu.int/comm/food/fs/scoop/task3210.pdf (accessed May 2015).

(8) Broekaert, N.; Devreese, M.; De Baere, S.; De Backer, P.; Croubels, S. Modified *Fusarium* mycotoxins unmasked: from occurrence in cereals to animal and human excretion. *Food Chem. Toxicol.* **2015**, *80*, 17−31.

(9) De Boevre, M. D.; Graniczkowska, K.; De Saeger, S. D. Metabolism of modified mycotoxins studied through in vitro and in vivo models: an overview. *Toxicol. Lett.* **2015**, *233*, 24−28.

(10) Pinton, P.; Tsybulskyy, D.; Lucioli, J.; Laffitte, J.; Callu, P.; Lyazhri, F.; Grosjean, F.; Bracarense, A. P.; Kolf-Clauw, M.; Oswald, I. P. Toxicity of deoxynivalenol and its acetylated derivatives on the intestine: differential effects on morphology, barrier function, tight junction proteins, and mitogen-activated protein kinases. *Toxicol. Sci.* **2012**, *130*, 180−190.

(11) Kadota, T.; Furusawa, H.; Hirano, S.; Tajima, O.; Kamata, Y.; Sugita-Konishi, Y. Comparative study of deoxynivalenol, 3-acetyldeoxynivalenol, and 15-acetyldeoxynivalenol on intestinal transport and IL-8 secretion in the human cell line Caco-2. *Toxicol. In Vitro* **2013**, *27*, 1888−1895.

(12) Visconti, A.; Minervini, F.; Lucivero, G.; Gambatesa, V. Cytotoxic and immunotoxic effects of *Fusarium* mycotoxins using a rapid colorimetric bioassay. *Mycopathologia* **1991**, *113*, 181−186.

(13) Sundstol Eriksen, G.; Pettersson, H.; Lundh, T. Comparative cytotoxicity of deoxynivalenol, nivalenol, their acetylated derivatives and de-epoxy metabolites. *Food Chem. Toxicol.* **2004**, *42*, 619−624.

(14) Young, J. C.; Zhou, T.; Yu, H.; Zhu, H.; Gong, J. Degradation of trichothecene mycotoxins by chicken intestinal microbes. *Food Chem. Toxicol.* **2007**, *45*, 136−143.

(15) Eriksen, G. S.; Pettersson, H.; Johnsen, K.; Lindberg, J. E. Transformation of trichothecenes in ileal digesta and faeces from pigs. *Arch. Tierernaehr.* **2002**, *56*, 263−274.

(16) Sundstol Eriksen, G.; Pettersson, H. Lack of de-epoxidation of type B trichothecenes in incubates with human faeces. *Food Addit. Contam.* **2003**, *20*, 579−582.

(17) Versilovskis, A.; Geys, J.; Huybrechts, B.; Goossens, E.; De Saeger, S.; Callebaut, A. Simultaneous determination of masked forms of deoxynivalenol and zearalenone after oral dosing in rats by LC-MS/MS. *World Mycotoxin J.* **2012**, *5*, 303−318.

(18) Eriksen, G. S.; Pettersson, H.; Lindberg, J. E. Absorption, metabolism and excretion of 3-acetyl DON in pigs. *Arch. Anim. Nutr.* **2003**, *57*, 335−345.

(19) Prelusky, D. B.; Gerdes, R. G.; Underhill, K. L.; Rotter, B. A.; Jui, P. Y.; Trenholm, H. L. Effects of low-level dietary deoxynivalenol on haematological and clinical parameters of the pig. *Nat. Toxins* **1994**, *2*, 97−104.

(20) Helke, K. L.; Swindle, M. M. Animal models of toxicology testing: the role of pigs. *Expert Opin. Drug Metab. Toxicol.* **2013**, *9*, 127−139.

(21) Swindle, M. M.; Makin, A.; Herron, A. J.; Clubb, F. J., Jr.; Frazier, K. S. Swine as models in biomedical research and toxicology testing. *Vet. Pathol.* **2012**, *49*, 344−356.

(22) Widestrand, J.; Pettersson, H. Effect of time, temperature and solvent on the stability of T-2 toxin, HT-2 toxin, deoxynivalenol and nivalenol calibrants. *Food Addit. Contam.* **2001**, *18*, 987−992.

(23) Commission Recommendation of 17 August 2006 on the presence of deoxynivalenol, zearalenone, ochratoxin A, T-2 and HT-2 and fumonisins in products intended for animal feeding. *Off. J. Eur. Communities* **2006**, *L229*, 7−9.

(24) Gasthuys, F.; De Boever, S.; Schauvliege, S.; Reyns, T.; Levet, T.; Cornillie, P.; Casteleyn, C.; De Backer, P.; Croubels, S. Transsplenic portal catheterization combined with a jugular double-lumen catheter for pharmacokinetic and presystemic metabolization studies in pigs. *J. Vet. Pharmacol. Ther.* **2009**, *32*, 137−145.

(25) Broekaert, N.; Devreese, M.; De Mil, T.; Fraeyman, S.; De Baere, S.; De Saeger, S.; De Backer, P.; Croubels, S. Development and validation of an LC-MS/MS method for the toxicokinetic study of deoxynivalenol and its acetylated derivatives in chicken and pig plasma. *J. Chromatogr. B: Anal. Technol. Biomed. Life Sci.* **2014**, *971*, 43−51.

(26) Devreese, M.; Antonissen, G.; Broekaert, N.; De Mil, T.; De Baere, S.; Vanhaecke, L.; De Backer, P.; Croubels, S. Toxicokinetic study and oral bioavailability of deoxynivalenol in turkey poults, and comparative biotransformation between broilers and turkeys. *World Mycotoxin J.* **2015**, *8* (4), 533−539.

(27) Maresca, M. From the gut to the brain: journey and pathophysiological effects of the food-associated trichothecene mycotoxin deoxynivalenol. *Toxins* **2013**, *5*, 784−820.

(28) Prelusky, D. B.; Hamilton, R. M.; Trenholm, H. L.; Miller, J. D. Tissue distribution and excretion of radioactivity following administration of 14C-labeled deoxynivalenol to White Leghorn hens. *Toxicol. Sci.* **1986**, *7*, 635−645.

DOI: 10.1021/acs.jafc.5b03270
J. Agric. Food Chem. 2015, 63, 8734−8742

(29) Osselaere, A.; Devreese, M.; Goossens, J.; Vandenbroucke, V.; De Baere, S.; De Backer, P.; Croubels, S. Toxicokinetic study and absolute oral bioavailability of deoxynivalenol, T-2 toxin and zearalenone in broiler chickens. *Food Chem. Toxicol.* **2013**, *51*, 350−355.
(30) Goyarts, T.; Dänicke, S. Bioavailability of the *Fusarium* toxin deoxynivalenol (DON) from naturally contaminated wheat for the pig. *Toxicol. Lett.* **2006**, *163*, 171−182.
(31) Prelusky, D. B.; Hartin, K. E.; Trenholm, H. L.; Miller, J. D. Pharmacokinetic fate of ^{14}C-labeled deoxynivalenol in swine. *Toxicol. Sci.* **1988**, *10*, 276−286.
(32) Golian, A.; Maurice, D. V. Dietary poultry fat and gastrointestinal transit time of feed and fat utilization in broiler chickens. *Poult. Sci.* **1992**, *71*, 1357−1363.
(33) Devreese, M.; Antonissen, G.; De Backer, P.; Croubels, S. Efficacy of active carbon towards the absorption of deoxynivalenol in pigs. *Toxins* **2014**, *6*, 2998−3004.

DOI: 10.1021/acs.jafc.5b03270
J. Agric. Food Chem. 2015, 63, 8734−8742

promising alternative to GC and even NIRS analyses.[31] With the ATR technique, monolayers of analytes can be investigated through direct contact between the sample and the infrared (IR) crystal. Hence, the surface trichomes of sage are easily accessible to the ATR crystal with a low background from the plant matrix.[32]

Therefore, the aim of this study was to investigate the use of ATR−FTIR for the direct qualitative and quantitative analysis of the EO composition of dried intact leaves of sage, including the effect of different varieties, leaf age, and date of harvest. On the basis of reference analysis of solvent extracts from the plant material by gas chromatography coupled with mass spectrometry or flame ionization detection (GC−MS or GC−FID, respectively), appropriate calibration models for the EO content and composition can be developed that include the chemical diversity of different sage accessions.

Table 1. Denotation and Botanical Description of the Considered *S. officinalis* L. Accessions

denotation	geographical origin	accession name
SALV13	D: Botanical Garden University of Budapest	
SALV15	D: Botanical Garden University of Mainz	
SALV25	D: Botanical Garden University of Athens	
SALV28	D: VEB Arzneimittel Dresden, Forschungsstelle Artern	Extrakta
SALV29	D: Botanical Garden Cluji-Napoca (Dr. T. A. Szabó)	
SALV30	D: Botanical Garden Cluji-Napoca (Dr. T. A. Szabó)	
SALV31	E: Landraces CSSR 1981 (Western Slovakia): 67	
SALV34	D: Institute of Applied Botany, Pyongyang University	
SALV36	D: Redwood City Seed Co.: 6	Garden Sage
SALV63	D: Federal Centre for Breeding Research on Cultivated Plants, Braunschweig, Genetic Resources Centre: 61443	
SALV65	D: Federal Centre for Breeding Research on Cultivated Plants, Braunschweig Genetic Resources Centre: 61862	Salbei
SALV67	D: Federal Centre for Breeding Research on Cultivated Plants, Braunschweig Genetic Resources Centre: 55892	Echter Salbei
BG	Bingenheimer Saatgut GmbH, Echzell, Germany	K58

MATERIALS AND METHODS

Chemicals. Pure standard substances (α- and β-thujone, α- and β-pinene, 1,8-cineole, camphor, and carvacrol) were purchased as analytical standards (at least >96%) for GC reference analysis from Roth (Karlsruhe, Germany) and Sigma-Aldrich (Taufkirchen, Germany). Isooctane [>99%, high-performance liquid chromatography (HPLC) grade] for solvent extraction of essential oil components (EOCs) was obtained from Sigma-Aldrich.

Plant Material. Seeds of 12 different sage (*S. officinalis* L.) accessions maintained in a gene bank were obtained from the Leibniz Institute of Plant Genetics and Crop Plant Research in Gatersleben (Germany) and cultivated at the experimental field of the Julius Kühn Institute in Berlin (Germany). For further botanical description, see Table 1. Five fully developed young (leaf size: maximum length, 30 mm; maximum width, 10 mm) and old (leaf size: minimum length, 50 mm; minimum width, 15 mm) leaves of 10 individual plants per accession were collected at two different harvests in 2013 (July 25, H1; September 25, H2). In the second harvest, withering meant that less than 10 plants were available for some accessions (SALV13, 7; SALV25, 9; SALV28, 9; SALV29, 6; SALV30, 8; and SALV34, 5). For external validation, 3 times 10 plants grown from seeds from a commercial sage accession (article number k58, *S. officinalis*, Bingenheimer Saatgut GmbH, Echzell, Germany) were cultivated and sampled under identical conditions as described for gene bank material. At both harvests, old and young leaves were sampled (H1, 30 plants; H2, 29 plants), and the spectra were collected by ATR−FTIR prior to extraction and GC analysis. All leaves were dried at 35 °C for 48 h prior to ATR−FTIR and GC analyses and were stored in paper bags at room temperature in desiccators.

ATR−FTIR. The mid-infrared (MIR) spectra of intact dried sage leaves and pure standards were recorded from 4000 to 375 cm^{-1} with a portable ATR diamond crystal infrared spectrometer (Alpha, Bruker Optics GmbH, Ettlingen, Germany). Approximately 5−10 mg of the standards was placed on the surface of the diamond crystal and measured directly. Intact dried sage leaves were analyzed by gently pressing the adaxial leaf side in the region of the central lamina onto the ATR crystal. Use of the standard pressing mechanism of the instrument allowed for a constant pressure for all measurements. All spectra were composed of 32 scans and acquired with a spectral resolution of 4 cm^{-1}. For each plant per accession and harvest, five old and five young leaves were measured once and the five repeated spectra per experiment were averaged and used for later chemometric analysis.

Table 2. Statistical Results for GC Analysis of All 448 Investigated Sage Plants Averaged over All 12 Considered *S. officinalis* L. Accessions Including Both Harvests and Both Developmental Stages of Leaves

component	mean[b]	SD[a]	maximum[b]	minimum[b]	Q1[b]	Q3[b]	mean[c]
EOC content	3.109	1.215	7.330	0.575	2.188	3.961	
α-thujone	0.610	0.383	2.136	0.008	0.328	0.849	19.6
β-thujone	0.236	0.255	1.311	0.000	0.050	0.343	7.6
camphor	0.511	0.268	1.782	0.005	0.325	0.644	16.4
1,8-cineole	0.254	0.151	0.946	0.017	0.140	0.337	8.2
α-pinene	0.094	0.089	0.634	0.008	0.039	0.111	3.0
β-pinene	0.048	0.042	0.355	0.007	0.020	0.062	1.5
camphene	0.121	0.086	0.546	0.014	0.066	0.145	3.9
myrcene	0.024	0.013	0.079	0.003	0.016	0.029	0.8
limonene	0.037	0.018	0.109	0.006	0.025	0.043	1.3
borneol	0.039	0.034	0.185	0.000	0.015	0.051	1.3
α-caryophyllene	0.251	0.169	0.943	0.025	0.123	0.338	8.1
β-caryophyllene	0.129	0.120	0.911	0.008	0.051	0.161	4.2
manool	0.283	0.166	1.037	0.041	0.162	0.372	9.1
not identified[d]	0.156	0.106	0.633	0.000	0.078	0.213	5.2

[a]SD, standard deviation; Q1 and Q3, quantiles 1 and 3, respectively. [b]In units of mL 100 g^{-1} of DM. [c]In units of %. [d]Retention time = 30.94 min.

DOI: 10.1021/acs.jafc.5b03852
J. Agric. Food Chem. 2015, 63, 8743−8750

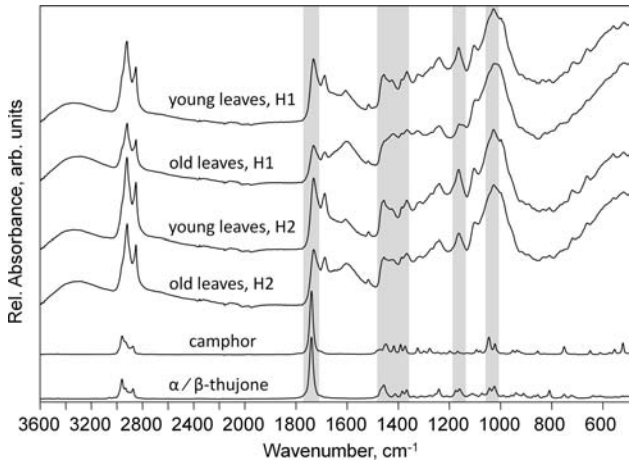

Figure 1. ATR−FTIR spectra of old and young leaves of *S. officinalis* L. for both harvest dates (July 25, 2013/H1 and September 25, 2013/H2) as averaged spectra of all considered gene bank accessions. The highlighted ranges indicate appropriate signals resulting from EO terpenoids as shown by spectra of the appropriate standards α- and β-thujone and camphor, respectively.

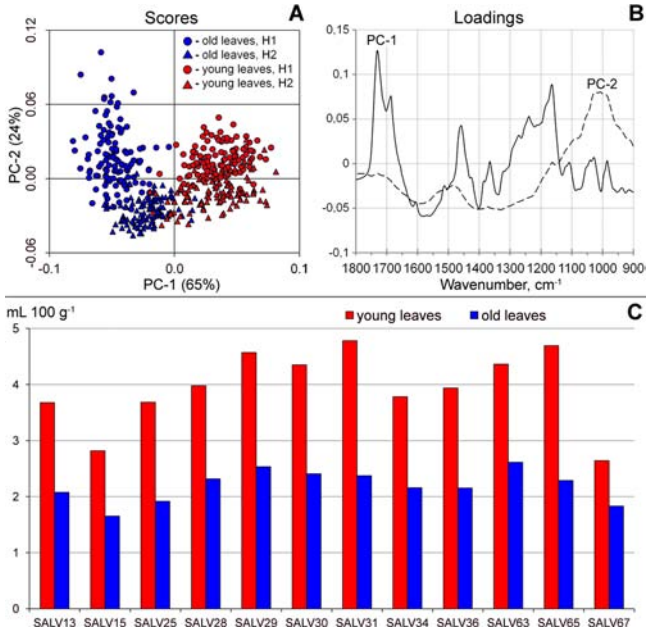

Figure 2. (A) PCA scores plot constructed from ATR−FTIR spectra of old (blue) and young (red) leaves of *S. officinalis* L., (B) corresponding loadings for PC1 and PC2, and (C) averaged EOC content for both harvests and all accessions as determined by GC−FID.

Reference GC−FID and GC−MS Analyses. For reference analysis, 200 mg of air-dried sage leaves were homogenized in 1.0 mL of isooctane [containing 1:2000 (v/v) carvacrol as the internal standard] with a Retsch ball mill MM2000 (Retsch GmbH, Germany). After centrifugation (10 min at 2415*g*), extracts were analyzed by GC−FID using an Agilent gas chromatograph 6890N, fitted with a HP-5 column (50 m × 0.32 mm i.d., with a film thickness of 0.52 μm). This GC instrument is routinely used for EO analysis and regularly validated with external standards. Hence, no repeated extraction was performed, and each sample was investigated once. Detector and injector temperatures were set at 280 and 250 °C, respectively. The following oven temperature program was used: heating from 80 to 220 °C at a rate of 8° min^{-1}. This final temperature was held for 10 min. Hydrogen was used as carrier gas with a constant

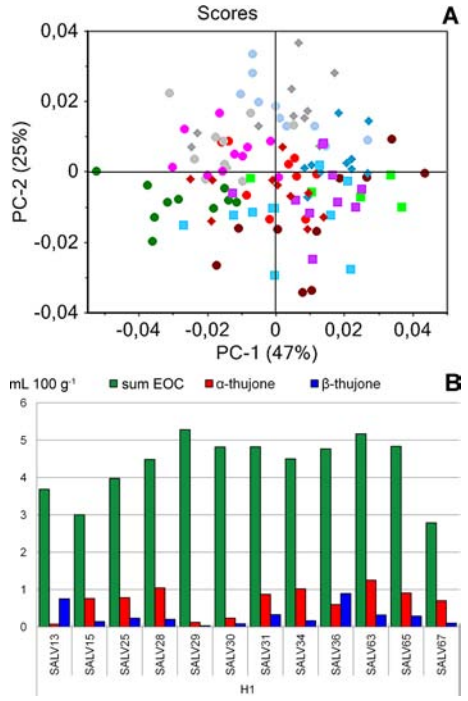

Figure 3. (A) PCA scores plot constructed from ATR−FTIR spectra of dried intact leaves of *S. officinalis* L. for harvest 1 (each color indicates one of the 12 accessions) and (B) GC reference data for the EOC content (green) and amounts of α-thujone (red) and β-thujone (blue) for the 12 different accessions.

flow rate of 1 mL min^{-1}. (split of 1:20). Analyses of the sage extracts were performed using an Agilent MSD 5972/HP 5890 Series II, equipped with a 30 m × 0.25 mm i.d., see above, 0.5 μm HP-5MS column. The column temperature was increased from 60 to 120 °C at a rate of 3° min^{-1}, finally increased to 220 °C at 8° min^{-1}, and held for 10 min. Helium was used as carrier gas with a constant flow rate of 1.1 mL min^{-1} and a split of 1:10. Injector and detector temperatures were set at 250 and 280 °C, respectively. The ionization energy was set at 70 eV. Identification of the detected compounds was based on their relative retention time and their mass spectra in comparison to those observed for the above-mentioned pure standard substances. The other compounds were tentatively identified using the NBS75K and Wiley 138 spectral library databases of the GC−MS system. The percentage composition of the volatile fraction was computed from the GC peak areas using peak area normalization.

Chemometrics. To estimate the variability of the samples, principal component analysis (PCA) was used based on the instrument software package OPUS 7.2 (Quant 2 module, Bruker Optik GmbH, Germany) and Unscrambler X (Camo, Norway).

Relevant spectral ranges were determined by comparison of sample spectra to those of appropriate reference standards and PCA. Calibration models were validated by 10-fold cross-validation ("leave 10% out") using a partial least-squares (PLS) algorithm. Appropriate models designated by cross-validation were further tested by test set validation with an external sample set. Therefore, spectra and GC data of all 30 plants of the commercial accession were averaged, resulting in 12 test samples related to the four treatments (old/young and harvest July 25, 2013/harvest September 25, 2013).

RESULTS AND DISCUSSION

Reference Analysis for *S. officinalis* L. According to the European Pharmacopoeia, EO is analyzed by hydrodistillation and GC methods.[14] Because of the comprehensive sample set and the small sample amounts (five individual leaves per sample) investigated in the present study, solvent extraction

DOI: 10.1021/acs.jafc.5b03852
J. Agric. Food Chem. 2015, 63, 8743−8750

instead of hydrodistillation was performed to describe "essential oil components (EOCs)" following previously published research on various EO plants.[17,21,30,33] Even if solvent extracts instead of hydrodistillates were investigated by GC, the term EOCs has been retained because solvent extraction and hydrodistillation of sage leaves both lead to isolates of comparable chemical composition.[34] Table 2 presents the summarized results of GC analysis of EOC composition for all accessions and all treatments.

The EOC extract was composed of about 85−90% terpenoids, which are known constituents of sage EO. As indicated by the statistical characteristics, there was a high degree of variability in the content of individual compounds in the accessions that were investigated.

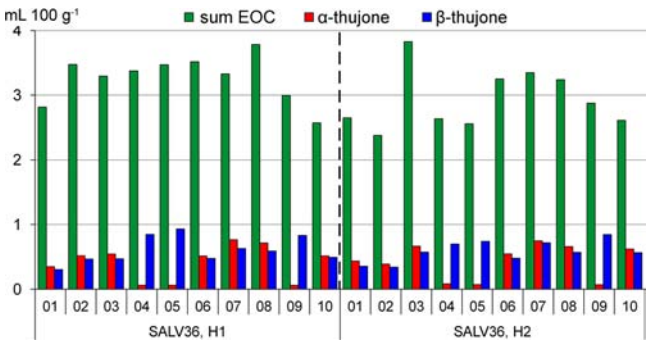

Figure 4. GC reference data for the EOC content (green) and amounts of α-thujone (red) and β-thujone (blue) for the 10 plant repetitions and both harvests of accession SALV36.

Chemotaxonomic Variability of *S. officinalis* L. Sage is known to show a large variety in the EO content and composition.[3,4,19] Therefore, the impact of genetic and geographic origin (12 gene bank accessions), age, and date of harvest on the spectroscopic and chemical variability of the EO composition was investigated, resulting in 448 individual samples (for lost plants, see the Plant Material section).

Figure 1 presents the ATR−FTIR spectra of old and young leaves at both harvests (H1 and H2) as means of all gene bank accessions and the spectra for α- and β-thujone and camphor as main constituents of sage EO.

The spectral ranges highlighted in Figure 1 indicate distinct EO terpenoid-derived signals in the spectra of the plant material compared to spectra of pure standards. Both camphor and α- and β-thujone contain keto groups substituted on a cyclopentane ring system, resulting in a characteristic stretch vibration for the C═O bond at around 1740 cm^{-1}. Furthermore, both terpenoids contain dimethyl-substituted methylene groups with a characteristic two-band deformation vibration pattern around 1390 and 1370 cm^{-1}. Besides matrix signals from cellulose around 1100 cm^{-1}, contributions of these diagnostic IR bands are also found in the spectra of sage leaves. Hence, evaluation of this fingerprint region offers a promising tool for quantification of those metabolites and differentiating sage samples based on their camphor and/or α- and β-thujone contents.

Averaging of the spectra from the adaxial leaf surface of plants followed by PCA resulted in clustering of old and young leaves separated by principal component 1 (PC1), as shown in Figure 2a. The differentiation among the clusters is caused by

Table 3. Data Preprocessing and Spectral Ranges Used for the Developed Calibration Models of the Individual EOCs

n	component	data preprocessing	spectral ranges (cm^{-1})
448	EOC content	min−max[a]	3037−2952; 1781−1709; 1705−1661; 1295−1133
	α-thujone	1. derivative + MSC[b]	3037−2952; 2938−2771; 1781−1709; 1119−905
	β-thujone	SNV[c]	1472−1305; 1295−1133; 1119−905
	camphor	SNV[c]	1705−1661; 1472−1305
	1,8-cineole	2. derivative	1781−1709; 1705−1661; 1546−1489; 1295−1133
	α-pinene	1. derivative	3500−3175; 3037−2952; 2938−2771; 1705−1661; 1472−1305; 1295−1133; 1119−905
	β-pinene	1. derivative	3500−3175; 3037−2952; 2938−2771; 1705−1661; 1472−1305; 1295−1133; 1119−905
48	EOC content	1. derivative + MSC[b]	3037−2952; 2938−2801; 1781−1709; 1705−1661; 1472−1305; 1295−1133; 1117−954
	α-thujone	1. derivative + SNV[c]	2938−2801; 1705−1661; 1295−1133; 1117−954
	β-thujone	2. derivative	3037−2952; 1781−1709; 1648−1552; 1546−1489; 1295−1133; 1117−954
	camphor	1. derivative + MSC[b]	3037−2952; 1781−1709; 1472−1305; 1295−1133; 1117−954
	1,8-cineole	min−max[a]	1705−1661; 1472−1305; 927−639
	α-pinene	SNV[c]	1705−1661; 1472−1305; 1295−1133; 927−639
	β-pinene	1. derivative + SLS[d]	2938−2801; 1546−1489; 1472−1305; 1295−1133

[a]min−max = minimum−maximum normalization. [b]MSC = multiple scatter correction. [c]SNV = standard normal variate. [d]SLS = straight line subtraction.

Table 4. Statistical Parameters for 10-Fold Cross-Validation of ATR−FTIR and GC Data by Correlation of Averaged Spectra for Each Plant (n = 448)

component	R^2	RMSECV[a]	bias[a]	range[a]/mean[a]	LV[b]
EOC content	0.67	0.743	0.00135	0.575−6.744/3.058	6
α-thujone	0.75	0.19	−0.00109	0.008−1.943/0.541	10
β-thujone	0.75	0.125	−0.00164	0.000−1.311/0.218	10
camphor	0.17	0.275	0.00878	0.005−1.782/0.557	7
1,8-cineole	0.76	0.0824	−0.00022	0.018−0.946/0.252	6
α-pinene	0.55	0.0594	0.00306	0.008−0.464/0.091	8
β-pinene	0.58	0.0321	0.00291	0.007−0.355/0.05	8

[a]In units of mL 100 g^{-1} of DM. [b]LV = number of latent variables.

DOI: 10.1021/acs.jafc.5b03852
J. Agric. Food Chem. 2015, 63, 8743−8750

the varying amounts of EOCs with different contents of thujone and camphor, as shown by the characteristic IR signals appearing in the corresponding loadings of PC1 given in Figure 2b. Young leaves generally contain up to 2-fold more EOCs compared to old leaves, as observed for all accessions and both harvests by GC reference analysis (Figure 2c). The strong differences in the amount of EOCs are already clear in the appropriate spectra of old and young leaves presented in Figure 1. Furthermore, PC2 separates samples from harvests 1 and 2 based on signals belonging mostly to the leaf matrix (Figure 2b; PC2 around 1000 cm^{-1}). A similar approach for discrimination of different citrus oils by PCA based on characteristic key Raman bands was described in a previous study.[35]

In contrast, spectroscopic differentiation according to the origin/accession of the material was not possible, as shown in Figure 3a, nor by GC reference data (see Figure S1 of the Supporting Information). Subsequent analysis of the EOCs of each accession revealed a large range in content and relative proportions of α- and β-thujone, as presented in Figure 3b.

These results show a group of accessions with either low overall thujone content (SALV29 and SALV30) or only a low ratio of α-/β-thujone (SALV13 and SALV36). In contrast, the majority of accessions is characterized by a high content of α-thujone (SALV15, SALV25, SALV28, SALV31, SALV34, SALV63, SALV65, SALV67, and BG).

However, the different accessions could not be discriminated possibly because of the large degree of scattering in the data. This might be explained by the genetic variability and heterogeneity of the plant material within the accessions. Generally, gene bank accessions are defined as sample collections taken from nature, and are characterized by the location and time of sampling. Therefore, a certain genetic diversity even within the accessions has to be considered. As indicated by the GC data for the 10 individual plants of accession SALV36 shown in Figure 4, large variations in EOCs, overall amount of thujone, and ratio of α-/β-thujone can be observed for both harvests. Such a high variability in not only the yield of EOC or sum of thujone but also the ratio of both stereoisomers results in insufficient clustering. Hence, because of the clear genetic variation discrimination into individual accessions based on ATR−FTIR spectra of intact dry leaves can only be achieved for those few accessions with an unusual chemical composition containing low amounts of α-thujone and/or high concentrations of β-thujone (Figure 3a).

Nevertheless, information about chemical heterogeneity of the accessions is highly relevant for the development of suitable calibration models with ATR−FTIR spectroscopy (where only a small amount of material is used with each measurement) because it determines an appropriate sampling (e.g., number of individual plants sampled and measurement replicates per leaf) and statistical evaluation. Therefore, a representative number of plants (repetitions per accession) has to be incorporated, and a greater degree of averaging ATR−FTIR spectra (summarizing variability by reduction of data points) has to be applied.

Quantitative Analysis of EOCs by ATR−FTIR. On the basis of the results above, quantification models for the sum of EOCs and individual compounds were validated by 10-fold cross-validation. As a first step, averaged spectra for each age and harvest (resulting in 448 samples) were correlated with GC reference data for the EOC yield as well as α-thujone, β-thujone, camphor, 1,8-cineole, α-pinene, and β-pinene. In Table 3, data preprocessing and the appropriate spectral ranges

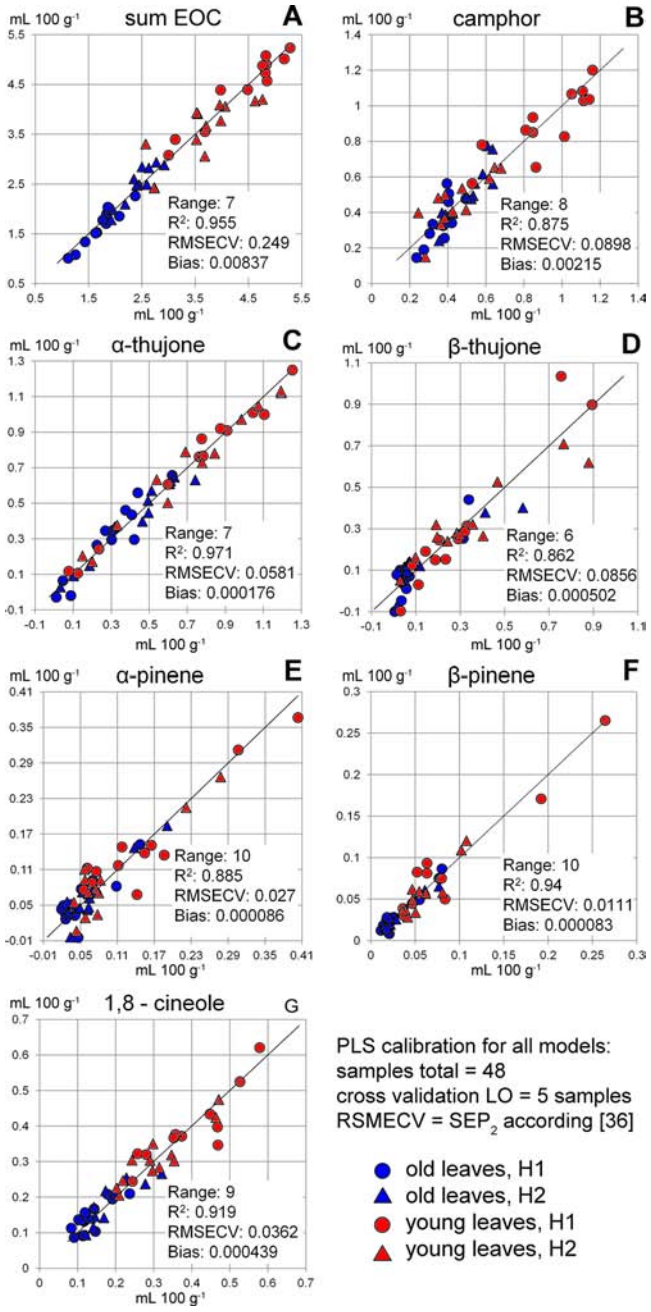

Figure 5. Results of 10-fold cross-validation of ATR−FTIR and GC data for the (A) EOC content, (B) camphor, (C) α-thujone, (D) β-thujone, (E) α-pinene, (F) β-pinene, and (G) 1,8-cineole by correlation of averaged spectra for each accession (n = 48). Blue color, old leaves; red color, young leaves; circle, harvest 1 (July 25, 2013); and triangle, harvest 2 (September 25, 2013).

are summarized, whereas Table 4 provides an overview of the statistical parameters of the corresponding models.

For all components, insufficiently good predictions were obtained, as indicated by low values for the coefficient of determination R^2 and relatively high values for the root-mean-square error of cross-validation (RMSECV) compared to the individual concentration ranges. The low correlation between ATR−FTIR and GC analyses is likely caused by the different amounts of sample used in the two methods. Spectroscopic data were composed of five measurement points of approximately 1 mm^2 in size (size of ATR diamond crystal) distributed

DOI: 10.1021/acs.jafc.5b03852
J. Agric. Food Chem. 2015, 63, 8743−8750

Table 5. Statistical Parameters for Test Set Validation of the Developed Prediction Models of Plant-wise Averaged Spectra (n = 48) with 12 Independent Samples from the Commercial Accession

component	R^2	RMSEP[a]	bias[a]	range[a]/mean[a]	LV[b]
EOC content	0.98	0.174	0.0371	2.223−5.514/3.869	7
α-thujone	0.74	0.124	0.061	0.547−1.268/0.908	8
β-thujone	0.80	0.0778	0.0375	0.085−0.593/0.339	5
camphor	0.74	0.09	−0.0768	0.253−0.895/0.574	7
1,8-cineole	0.87	0.0482	0.0241	0.142−0.598/0.37	6
α-pinene	0.55	0.0471	0.0184	0.056−0.312/0.184	7
β-pinene	0.84	0.0111	0.00267	0.02−0.103/0.0615	8

[a]In units of mL 100 g^{-1} of DM. [b]LV = number of latent variables.

over five individual leaves per plant. In contrast, for GC, the entire five leaves were extracted (see the Reference GC−FID and GC−MS Analyses section), and hence, variability within one plant might not be comparable.

For a better match between the amount of sample used for spectroscopy and GC, the number of ATR−FTIR measurement repetitions per plant should be increased. This will enlarge the amount of leaf area investigated by ATR−FTIR but will lead to longer measurement times. Another option could be averaging more comparable spectra, e.g., all of those belonging to the same accession and treatment (old/young and H1/H2), to make them more representative of a larger sample, e.g., a genuine batch of drug or the yield from an entire parcel of land.

Figure 5 presents the graphical results for cross-validation regarding averaged ATR−FTIR spectra from all plants belonging to the same accession, age, and time of harvest, resulting in 48 individual samples. Data preprocessing and relevant spectral ranges are summarized in Table 3.

The use of spectra averaged across accessions leads to an improved prediction for not only the EOC yield and major constituents (α-thujone, β-thujone, and camphor) but also components with lower concentrations (in per mill range), such as α- or β-pinene and 1,8-cineole.

For all EOCs, coefficients of determination higher than 0.86 were obtained with low values for bias and RMSECV of less than 10% of the corresponding mean values.

The robustness of the cross-validated models was investigated with an additional test set validation of 12 independent samples (3 sets of 10 plants, old/young and H1/H2) which came from the commercial sage accession. As shown by the values of R^2, root-mean-square error of prediction (RMSEP), and bias given in Table 5, for EOCs, a robust and reliable prediction model could be achieved with R^2 = 0.98. For the individual compounds, prediction quality was at best for 1,8-cineole (R^2 = 0.87), with R^2 = 0.74 and 0.80 for α- and β-thujone, respectively. The relatively low prediction accuracy for individual metabolites could again be explained by the genetic and chemotaxonomic diversity of sage. The accession used for test set validation was not included in the calibration model. The impacts of the plant matrix or variation in the ratio of α- and β-thujone were not considered in the calibration. Hence, application of calibration models to unknown samples of different origin might be limited, and the genetic and chemotaxonomic diversity must be taken into account. The RMSEP values were calculated according to the definition of Fearn as SEP_2.[36]

In conclusion, all cross-validated calibration models verified against an external test set resulted in reliable prediction models for the overall yield of EOCs, their major constituents (α- and β-thujone and camphor), and even minor components (α- and β-pinene and 1,8-cineole). An initial screening by ATR−FTIR enabled a rapid assessment of the chemical variability of the samples, which allowed us to adjust sampling protocols (e.g., more measurement repetitions by ATR−FTIR for better representation of sample variability). This, in turn, permitted an improvement of quantification models by different statistical pretreatments (e.g., higher degree of averaging) with only minor additional time required.

In the current ATR−FTIR quantification protocol, plant material only needs to be dried and spectral measurements take only a few minutes. This allows for rapid quality control of the material when it is first received for processing compared to the time-consuming analysis recommended in the Pharmacopoeia. Transfer of the current analytical protocol to fresh material and application in the field is currently under investigation. This will undoubtedly improve growing and quality control for both plant breeding and cultivation and assist in evaluating the chemical variation of breeding populations and identifying optimal points for harvest.

■ ASSOCIATED CONTENT

Supporting Information

The Supporting Information is available free of charge on the ACS Publications website at DOI: 10.1021/acs.jafc.5b03852.

Results of GC−FID data for the leaf material from all 12 accessions of *S. officinalis* L. (Figure S1) and graphical results of 10-fold cross-validation of ATR−FTIR for the individual EOCs for single-plant investigation (n = 448; Figure S2) (PDF)

■ AUTHOR INFORMATION

Corresponding Author

*Telephone: +49-30-8304-2210. Fax: +49-30-8304-2503. E-mail: andrea.kraehmer@jki.bund.de.

Funding

The authors gratefully acknowledge the financial support obtained from the Deutsche Forschungsgemeinschaft (DFG) in Bonn, Germany (Project Schu 566/14-1).

Notes

The authors declare no competing financial interest.

■ ACKNOWLEDGMENTS

The authors thank Bärbel Zeiger and Mario Harke for their support in sample preparation and spectroscopic and GC analyses as well as Dr. Andreas Börner and Dr. Ulrike Lohwasser from the Leibniz Institute of Plant Genetics and Crop Plant Research in Gatersleben (Germany) for providing the seed material. Furthermore, the authors thank Dr. William

DOI: 10.1021/acs.jafc.5b03852
J. Agric. Food Chem. 2015, 63, 8743−8750

Foley from the School of Botany and Zoology, Australian National University, Canberra (Australia), for his valuable comments on the manuscript.

■ ABBREVIATIONS USED

ATR−FTIR, attenuated total reflectance−Fourier transform infrared spectroscopy; GC, gas chromatography; PLS, partial least squares; PCA, principal component analysis; RMSECV, root-mean-square error of cross-validation; RMSEP, root-mean-square error of prediction; SEP, standard error of prediction; SNV, standard normal variate; MSC, multiplicative scattering correction; min−max, minimum−maximum normalization; SLS, straight line subtraction; LV, latent variable; EOC, essential oil component; DM, dry matter; PC, principal component; GC−MS, gas chromatography−mass spectrometry; GC−FID, gas chromatography−flame ionization detection; NIRS, near-infrared spectroscopy; HPLC, high-performance liquid chromatography; SALV, accession name for gene bank material of *S. officinalis* L.

■ REFERENCES

(1) Al-Qudah, M. A.; Al-Jaber, H. I.; Abu Zarga, M. H.; Abu Orabi, S. T. Flavonoid and phenolic compounds from *Salvia palaestina* L. growing wild in Jordan and their antioxidant activities. *Phytochemistry* **2014**, *99*, 115−120.

(2) Ben Farhat, M.; Jordan, M. J.; Chaouech-Hamada, R.; Landoulsi, A.; Sotomayor, J. A. Variations in Essential Oil, Phenolic Compounds, and Antioxidant Activity of Tunisian Cultivated *Salvia officinalis* L. *J. Agric. Food Chem.* **2009**, *57*, 10349−10356.

(3) Grausgruber-Gröger, S.; Schmiderer, C.; Steinborn, R.; Novak, J. Seasonal influence on gene expression of monoterpene synthases in *Salvia officinalis* (Lamiaceae). *J. Plant Physiol.* **2012**, *169*, 353−359.

(4) Lamien-Meda, A.; Schmiderer, C.; Lohwasser, U.; Börner, A.; Franz, C.; Novak, J. Variability of the essential oil composition in the sage collection of the Genebank Gatersleben: a new viridiflorol chemotype. *Flavour Fragrance J.* **2010**, *25*, 75−82.

(5) Martins, N.; Barros, L.; Santos-Buelga, C.; Henriques, M.; Silva, S.; Ferreira, I. C. Evaluation of bioactive properties and phenolic compounds in different extracts prepared from *Salvia officinalis* L. *Food Chem.* **2015**, *170*, 378−385.

(6) Benkherara, S.; Bordjiba, O.; Djahra, A. In vitro evaluation of the antibacterial activity of essential oil of *Salvia officinalis*. *Phytotherapie* **2015**, *13*, 14−18.

(7) Tosun, A.; Khan, S.; Kim, Y. S.; Calin-Sanchez, A.; Hysenaj, X.; Carbonell-Barrachina, A. Essential Oil Composition and Anti-Inflammatory Activity of *Salvia officinalis* L (Lamiaceae) in Murin Macrophages. *Trop. J. Pharm. Res.* **2014**, *13*, 937−942.

(8) Kozics, K.; Klusova, V.; Srancikova, A.; Mucaji, P.; Slamenova, D.; Hunakova, L.; Kusznierewicz, B.; Horvathova, E. Effects of *Salvia officinalis* and *Thymus vulgaris* on oxidant-induced DNA damage and antioxidant status in HepG2 cells. *Food Chem.* **2013**, *141*, 2198−2206.

(9) Moreira, M. R.; Souza, A. B.; Moreira, M. A.; Bianchi, T. C.; Carneiro, L. J.; Estrela, F. T.; dos Santos, R. A.; Januario, A. H.; Martins, C. H.; Ambrosio, S. R.; Veneziani, R. C. RP-HPLC analysis of manool-rich *Salvia officinalis* extract and its antimicrobial activity against bacteria associated with dental caries. *Rev. Bras. Farmacogn.* **2013**, *23*, 870−876.

(10) Russo, A.; Formisano, C.; Rigano, D.; Senatore, F.; Delfine, S.; Cardile, V.; Rosselli, S.; Bruno, M. Chemical composition and anticancer activity of essential oils of Mediterranean sage (*Salvia officinalis* L.) grown in different environmental conditions. *Food Chem. Toxicol.* **2013**, *55*, 42−47.

(11) Ehrnhöfer-Ressler, M. M.; Fricke, K.; Pignitter, M.; Walker, J. M.; Walker, J.; Rychlik, M.; Somoza, V. Identification of 1,8-Cineole, Borneol, Camphor, and Thujone as Anti-inflammatory Compounds in a *Salvia officinalis* L. Infusion Using Human Gingival Fibroblasts. *J. Agric. Food Chem.* **2013**, *61*, 3451−3459.

(12) Bauer, J.; Kuehnl, S.; Rollinger, J. M.; Scherer, O.; Northoff, H.; Stuppner, H.; Werz, O.; Koeberle, A. Carnosol and Carnosic Acids from *Salvia officinalis* Inhibit Microsomal Prostaglandin E-2 Synthase-1. *J. Pharmacol. Exp. Ther.* **2012**, *342*, 169−176.

(13) Miroddi, M.; Navarra, M.; Quattropani, M. C.; Calapai, F.; Gangemi, S.; Calapai, G. Systematic Review of Clinical Trials Assessing Pharmacological Properties of *Salvia* Species on Memory, Cognitive Impairment and Alzheimer's Disease. *CNS Neurosci. Ther.* **2014**, *20*, 485−495.

(14) Salbeiblätter-*Salvia officinalis* folium. *European Pharmacopoeia 8.1, Grundwerk 2014*; Deutscher Apotheker Verlag: Stuttgart, Germany, 2014; pp 2050−2051.

(15) Generalic, I.; Skroza, D.; Surjak, J.; Mozina, S. S.; Ljubenkov, I.; Katalinic, A.; Simat, V.; Katalinic, V. Seasonal Variations of Phenolic Compounds and Biological Properties in Sage (*Salvia officinalis* L.). *Chem. Biodiversity* **2012**, *9*, 441−457.

(16) Gudi, G.; Schütze, W.; Schulz, H. Rapid analysis of rosmarinic acid in lemon balm (*Melissa officinalis* L.). *Asian Chem. Lett.* **2011**, *15*, 1−10.

(17) Gudi, G.; Krähmer, A.; Krüger, H.; Hennig, L.; Schulz, H. Discrimination of fennel chemotypes applying IR and Raman spectroscopy - discovery of a new γ-asarone chemotype. *J. Agric. Food Chem.* **2014**, *62*, 3537−3547.

(18) Krähmer, A.; Gudi, G.; Weiher, N.; Gierus, M.; Schütze, W.; Schulz, H. Characterization and quantification of secondary metabolite profiles in leaves of red and white clover species by NIR and ATR-IR spectroscopy. *Vib. Spectrosc.* **2013**, *68*, 96−103.

(19) Lakusic, B. S.; Ristic, M. S.; Slavkovska, V. N.; Stojanovic, D. L.; Lakusic, D. V. Variations in essential oil yields and compositions of *Salvia officinalis* (Lamiaceae) at different developmental stages. *Bot. Serb.* **2013**, *37*, 127−139.

(20) Krüger, H. Essential oils—Variability in medicinal and spice plants. *Julius Kühn Arch.* **2009**, 70−76.

(21) Krüger, H. Characterisation of Chamomile Volatiles by Simultaneous Distillation Solid-Phase Extraction in Comparison to Hydrodistillation and Simultaneous Distillation Extraction. *Planta Med.* **2010**, *76*, 843−846.

(22) Miraldi, E. Comparison of the essential oils from ten *Foeniculum vulgare* Miller samples of fruits of different origin. *Flavour Fragrance J.* **1999**, *14*, 379−382.

(23) Pank, F.; Krüger, H.; Quilitzsch, R. Selection of essential oil rich populations of bitter fennel (*Foeniculum vulgare* MILL. ssp *vulgare* var. *vulgare*) with reduced estragole content. *Z. Arznei- Gewuerzpflanzen* **2008**, *13*, 161−166.

(24) Pfefferkorn, A.; Krüger, H.; Pank, F. Chemical composition of *Satureja hortensis* L essential oils depending on ontogenetic stage and season. *J. Essent. Oil Res.* **2008**, *20*, 303−305.

(25) Thompson, J.; Chalchat, J. C.; Michet, A.; Linhart, Y.; Ehlers, B. Qualitative and Quantitative Variation in Monoterpene Co-Occurrence and Composition in the Essential Oil of *Thymus vulgaris* Chemotypes. *J. Chem. Ecol.* **2003**, *29*, 859−880.

(26) Fiedler, A.; Baranska, M.; Schulz, H. FT-Raman spectroscopy - a rapid and reliable quantification protocol for the determination of natural indigo dye in *Polygonum tinctorium*. *J. Raman Spectrosc.* **2011**, *42*, 551−557.

(27) Krähmer, A.; Engel, A.; Kadow, D.; Ali, N.; Umaharan, P.; Kroh, L. W.; Schulz, H. Fast and neat - Determination of biochemical quality parameters in cocoa using near infrared spectroscopy. *Food Chem.* **2015**, *181*, 152−159.

(28) Naumann, A.; Kurtze, L.; Krähmer, A.; Hagels, H.; Schulz, H. Discrimination of Solanaceae Taxa and Quantification of Scopolamine and Hyoscyamine by ATR-FTIR Spectroscopy. *Planta Med.* **2014**, *80*, 1315−1320.

(29) Schulz, H.; Baranska, M. Identification and quantification of valuable plant substances by IR and Raman spectroscopy. *Vib. Spectrosc.* **2007**, *43*, 13−25.

(30) Elementi, S.; D'Antuono, L. F.; Schulz, H.; Krüger, H.; Schütze, W.; Steuer, B. *Salvia officinalis* L. essential oil and carnosic acid analysis by means of NIR spectroscopy. *Acta Hortic.* **2006**, 243−248.

DOI: 10.1021/acs.jafc.5b03852
J. Agric. Food Chem. 2015, 63, 8743−8750

(31) Charchari, S.; Chafaa, I.; Kassoussi, K.; Zekri, M. M.; Benhalla, A.; Boudina, N. Glandular Trichomes, Secretory Cavities and Essential Oil of Sage (*Salvia officinalis* L.). *J. Essent. Oil-Bear. Plants* **2010**, *13*, 267−274.
(32) Hind, A. R.; Bhargava, S. K.; McKinnon, A. At the solid/liquid interface: FTIR/ATR - the tool of choice. *Adv. Colloid Interface Sci.* **2001**, *93*, 91−114.
(33) Schulz, H.; Quilitzsch, R.; Drews, H.; Krüger, H. Estimation of minor components in caraway, fennel and carrots by NIRS-comparison of results from dispersive and Fourier-transform instruments. *Int. Agrophys.* **2000**, *14*, 249−253.
(34) Grassi, P.; Novak, J.; Steinlesberger, H.; Franz, C. A direct liquid, non-equilibrium solid-phase micro-extraction application for analysing chemical variation of single peltate trichomes on leaves of *Salvia officinalis*. *Phytochem. Anal.* **2004**, *15*, 198−203.
(35) Schulz, H.; Schrader, B.; Quilitzsch, R.; Steuer, B. Quantitative analysis of various citrus oils by ATR/FT-IR and NIR-FT Raman Spectroscopy. *Appl. Spectrosc.* **2002**, *56*, 117−124.
(36) Fearn, T. Assessing Calibrations: SEP, RPD, RER and R^2. *NIR News* **2002**, *13*, 12−14.

DOI: 10.1021/acs.jafc.5b03852
J. Agric. Food Chem. 2015, 63, 8743−8750

spreading to India, China, the Mediterranean basin, and eastern Europe.[7]

Saffron is widely used mainly as a spice and as a coloring and flavoring agent in both the agro-food and cosmetic industries. The saffron spice is a complex mixture of volatile and nonvolatile compounds and carotenoid derivatives, which all contribute to the overall aroma and flavor of the spice.[8,9] In addition to its color, taste, and aroma, saffron displays a variety of health benefits.[10] Saffron shows analgesic and sedative properties[11] and is a potential anticancer agent.[12,13] Furthermore, saffron is beneficial for the treatment of mental disorders such as depression[14] and dementia.[15]

AGRONOMICAL IMPROVEMENT OF SAFFRON PRODUCTION

The ideal condition for improving crop yield would be the optimization of all metabolic cues together with the environmental conditions where the crop develops.[16] For such a purpose, the rates of all important processes should be optimized and also their interactions and duration, which are generally determined by genetic mechanisms often influenced by the environment. Cultivation of saffron occurs in temperate regions. The life cycle of saffron is adapted to the climate of the Mediterranean regions and is quite similar in all producing countries, but with wide differences in the timing of events.[17] In the Mediterranean region, saffron flowers in autumn, after the formation of replacement corms at the base of the shoots is initiated. At the beginning of the dry season (April−May), the leaves senesce and wither, and the corms go into dormancy. The transition from the vegetative to the reproductive stage occurs before summer in the apex of the buds of underground corms, which do not have roots or foliage leaves.[17] Not all of the newly developed corms are able to produce flowers. Flower formation is directly related to corm size.[18] Therefore, the adequate production of corms is extremely important to guarantee flower production.

During the past decades, the area traditionally dedicated to saffron cultivation in many European countries has fallen dramatically,[19,20] mainly due to the intensive manual labor required for saffron harvest and processing (0.25−2.5 million flowers ha^{-1}). However, in recent years this tendency has reversed, and saffron production in Europe and other developed countries outside Eurasia, for example, in Tasmania (Australia), is increasing, with a specific emphasis on the production of high-quality saffron. A technological breakthrough to increase the quality of saffron cultivation would entail the cultivation under controlled conditions in containers to facilitate the mechanization of flower harvesting and stigma separation.[21] To achieve this, the flowering season must be extended as much as possible to maximize the use of harvesting installations and thus reduce overall installation and running costs. Thus, an in-depth knowledge about the regulation of the flowering process could help to increase the yield of the spice.

Another important factor that limits the areas in which saffron is cultivated is the difficulty in obtaining high-quality propagation material with guaranteed levels of purity, homogeneity, and health. It is a slow-growing species from which three to four daughter corms per mother corm are obtained each season under natural field conditions. Low multiplication and fungal diseases of corms reduce the productivity and quality, thereby restraining the availability of planting material and the widespread use of improved genotypes obtained in the future.

Every sprouting bud in the mother corm has the potential to produce a new corm, but saffron corms show only a few sprouting apical buds plus many axillary dormant buds. Furthermore, there is a heterogeneity in bud emergence and development, which results in heterogeneous flower emergence.[17] This process must therefore be controlled to establish industrial production. In this context, environmental and genetic factors affecting corm development, dormancy, and sprouting, as well as the identification of environmental signals and the genetic and regulatory mechanisms that promote or inhibit flowering in saffron, constitute the most relevant processes to be elucidated for implementing a technological breakthrough and achieving agronomical improvements in this crop.

WHAT IS KNOWN ABOUT FLOWERING AND CORM DEVELOPMENT IN SAFFRON?

Saffron Flowering. The transition from the vegetative to the reproductive stage in saffron occurs early in July when the apex becomes dome shaped and increases in size. This process is followed by the formation of the leaf primordia. By mid July the sheathing leaves begin to grow relatively quickly. Then follows the bract primordia stage, the formation of stamen primordia, the initiation of the perianth, and the formation of gynoecium. All of the flower parts are already differentiated by the end of August (Figure 2). High temperatures are required to release bud dormancy and for flower initiation, which is optimal between 23 and 27 °C[21] and occurs during early spring to mid summer, depending on location.[22−24] The release of bud dormancy could be accelerated by curing the corms at 30 °C for a short time. Storage of corms at 2 °C after flower initiation results in a time-dependent abortion of those flowers already initiated. Corms stored in the cold before flower initiation will form flowers when incubated after storage at 21−25 °C. When corms are maintained for a long time at very low temperatures (1−10 °C), the meristem does not give rise to flower primordia but to a new

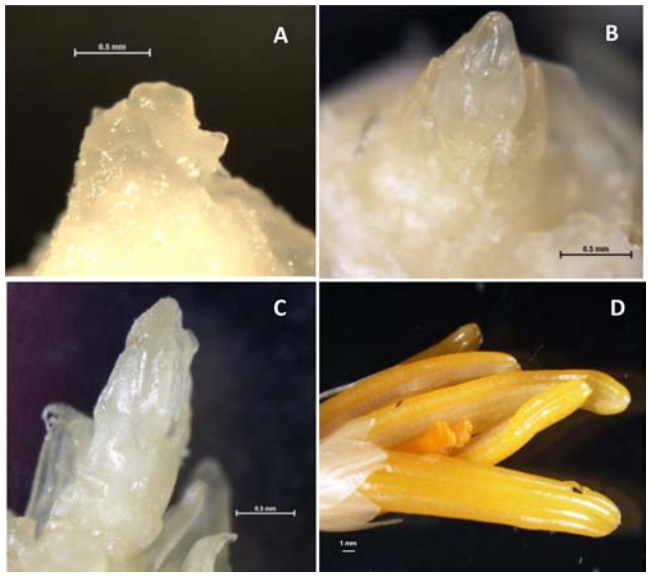

Figure 2. Saffron flower development during summer: (A) resting bud at the end of June; (B) stamen formation in early-mid August; (C) first whorl of tepals is already initiated in the flower at mid-late August; (D) gynoecium has reached half of the length of the stamens in mid September. Scale bars in panels A−C = 0.5 mm. Scale bar in panel D = 1 mm.

DOI: 10.1021/acs.jafc.5b03194
J. Agric. Food Chem. 2015, 63, 8751−8764

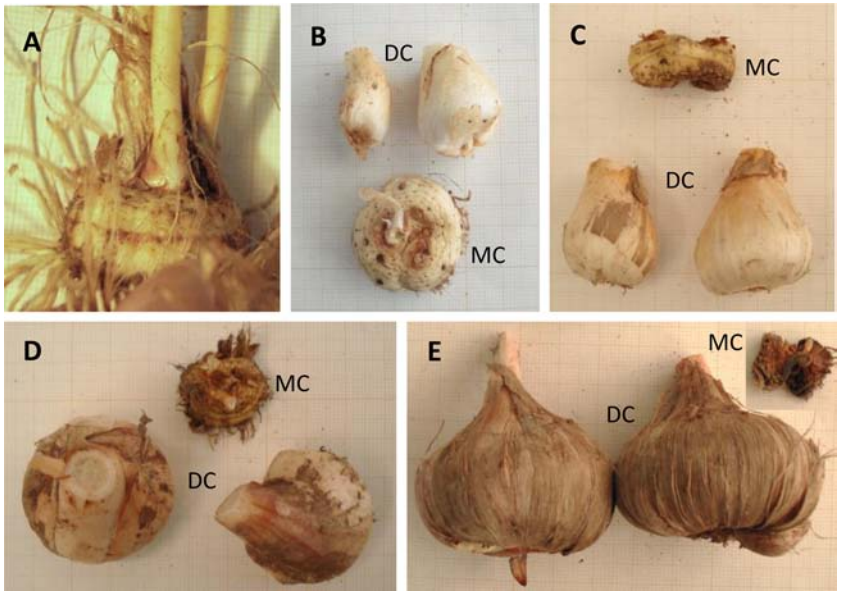

Figure 3. Development of saffron daughter corms (DC) in the field (Valencia, Spain): relationship between mother corm (MC) and daughter corm sizes (flowering took place in November): (A) in early December; (B) by the end of January; (C) in mid February; (D) by the end of February; (E) by the end of April.

corm.[19] Root development and flower emergence occur in late autumn at a markedly lower temperature, in the range of 15−17 °C.[21,25] This contrasts with spring-flowering bulbous species, which require a warm−cold−warm temperature sequence to flower.[26] The research carried out so far on saffron has produced extensive knowledge related to the influence of temperature on flower induction and flowering and the extension of the harvesting period over several months,[17,21,22] but this strategy has reached its peak.

Few works[27,28] have addressed the role of hormones on flowering. In these works flowering development is related to GA activity. The involvement of other environmental or endogenous factors has not been studied, and the molecular mechanisms controlling these processes are largely unknown. The *CEN/TFL1*-like gene (*CENTRORADIALIS/TERMINAL FLOWER1*) has been cloned and characterized in saffron.[29] *CsatCEN/TFL1* transcripts were detected in corms and flower organs but not in leaves, and their role in saffron flowering control is still unclear. Three *FLOWERING LOCUS T* (*FT*)-like genes, designated *CsatFT1*-like, *CsatFT2*-like, and *CsatFT3*-like, have been isolated.[30] The expression analysis indicated differences in the expression of the three *FT*-like genes in different organs. However, the expression has been measured in flowers already developed and in immature flowers, but not in the run-up to floral transition. Hence, the role of the *FT*-like genes awaits further progress.

In relation to the molecular mechanisms controlling flower development in cultivated *Crocus*, different full-length cDNA sequences encoding MADS-box transcription factor proteins involved in flower formation have been cloned and characterized. Homologues of the major ABC and E types from *Crocus* have been isolated and named *Csat AP1/FUL*,[31] CsatAP2,[29] *CsatAP3* and *CsatPI*,[32] and *CsatAG*[33] and *CsatSEP3*.[34] However, the expression analysis did not always show consistent results with the ABC model, and a functional understanding has to be clarified. For example, the three isolated *CsatAP1* genes were expressed in leaves, as well as in the three mature flower parts: tepals, stamen, and carpel. Furthermore, an expanded expression of class B genes in whorls 1 and 4 was also detected. The expression of class B genes into whorl 1 fits the modified ABC model for monocots; however, the additional expression is not consistent with this model.

Corm Development. There is limited knowledge about the physiology of vegetative development of saffron (Figure 3). The relative contribution of different carbon sources (leaf photosynthetic activity and mother corm reserves) to the growth of vegetative organs and the influence of internal and external factors on the photosynthetic processes sustaining corm growth have been studied.[19] After flowering, most of the remaining reserves in the mother corm are depleted during root and leaf development. Once these organs reach their maximum size, the growth of replacement corms is initiated, and this development primarily relies on photosynthesis. During this vegetative development, the reserves from the mother corm contribute to only 10% of the biomass. The photosynthetic rate is consistently high and constant (26 μmol m^{-2} s^{-1}) throughout the year, as has also been reported in *C. vernus*.[35,36] Plants with larger corms show reduced photosynthetic rate, although a significantly higher total leaf area is present.[19] A sink capacity limitation arises during growth of replacement corms because the increase of biomass is limited before total leaf senescence. A reduction in the demand of photoassimilates can lead to sugar accumulation in leaves, which in turn can promote leaf senescence.[37] The studies carried out in *C. vernus*, a spring ephemeral, support the hypothesis that corm sink strength is the most important factor determining leaf duration.[35,38] Differences in sink strength have been associated with differential carbon partitioning between sugar forms in the newly formed corms. A higher availability in hexoses at the beginning of the development of the daughter corms would affect cell division and elongation and, thus, higher corm size that allowed prolonged sink activity.[36] However, an in-depth knowledge about the environmental and genetic factors controlling the final size and the sink strength of the saffron corm still seems far from being achieved.

Sprouting Control in Saffron. Sprouting is another important aspect in saffron research. As stated previously,

DOI: 10.1021/acs.jafc.5b03194
J. Agric. Food Chem. 2015, 63, 8751−8764

every sprouted bud produces a corm and factors affecting apical dominance (para-dormancy) are highly important for corm production. However, the control of dormancy (endo-dormancy) is also crucial in solving the many problems associated with storage and distribution of corms and for extending the flowering and harvesting periods. Physiological and molecular studies support the concept that the mechanisms of flowering induction and dormancy are interrelated.[39] It has been suggested that dormancy-associated *MADS-box* (*DAM*) genes induced by cold temperatures in leafy spurge negatively regulates *FT* or similar genes, which regulate growth cessation and dormancy induction. Most of these studies were performed on species showing winter dormancy, where dormancy was regulated by low temperature and a short photoperiod. However, saffron shows summer dormancy, which is common in typical bulbous species. This plant strategy has been correlated with superior survival and high persistence under severe drought conditions. Summer dormancy is therefore of great interest because intense drought and heat are increasing due to climate change and may affect plant persistence. However, this type of dormancy is relatively uncharacterized at a molecular level. Recently, the characterization of summer dormancy in the bulbous species *Narcissus tazetta* and the role of FTs in summer dormancy has been reported.[40] In saffron, *FT* genes and *CEN/TFL1*-like genes that could be related with the dormancy pathway have been isolated.[30]

Dormancy interacts at some level with the mechanisms involved in cell cycle regulation, which also involves hormonal signals.[39,41] Studies of the hormonal regulation of dormancy in geophytes are abundant.[42] Clear roles for abscisic acid (ABA), such as inducing dormancy, have been revealed. ABA has been recognized to control dormancy in the corm tissue of *C. sativus*, where it declines at the time of dormancy release.[28] It has been proposed that ABA is synthesized from carotenoids (C40) in plants, and three genes that participate in ABA biosynthesis have been isolated and characterized in several plant species. They encode zeaxanthin epoxidase (ZEP[43]), 9-*cis*-epoxycarotenoid dioxygenase (NCED[44]), and abscisic aldehyde oxidase (AAO[45]). ZEP catalyzes the epoxidation of zeaxanthin to produce epoxycarotenoid; NCED catalyzes the cleavage reaction of epoxycarotenoids to produce xanthoxin (the first C15 intermediate) and is considered to be the regulatory enzyme of ABA biosynthesis; and AAO catalyzes the final step of ABA biosynthesis, which converts ABA aldehyde to ABA. Homologue genes for *ZEP*, *AAO*, and *NCED* have been identified in saffron. However, only one *NCED* gene, *CsNCED*, has been studied in detail.[46] *CsNCED* is expressed in floral and corm tissues. In stigmas, *CsNCED* transcript abundance closely mirrors ABA content with a maxima a day after anthesis, and it has been suggested that the ABA levels in the stigma could be related to the initiation of the senescent process in this tissue.[47] During corm development, zeaxanthin levels are correlated with the increase in *CsNCED* expression, suggesting a coordinate regulation of the carotenoid and ABA biosynthetic pathways during corm dormancy.[46]

Mature saffron corms usually show one to three apical dominant buds, which will sprout in the following season plus many axillary dormant buds.[22] Each axillary bud has the same developmental potential as the primary shoot apical meristem in its ability to produce a growing shoot axis (Figure 4). However, axillary buds enter a dormant state after forming only a few leaves. Plant hormones are major players in the control of axillary bud outgrowth. In particular, auxin, strigolactone, and cytokinin

Figure 4. Apical dominance in saffron: (A) corm with the main bud sprouting and dormant axillary buds; (B) axillary bud growth after removal of the main bud.

are involved in this control.[48] In saffron, auxin is supplied from the apical bud and, together with the strigolactones (SL), represses axillary bud outgrowth. By contrast, the cytokinins, produced in the adventitious roots, directly induce the sprout of the axillary buds.[49] Gibberellins (GAs) seem to be involved in apical sprout growth after dormancy break, but not in dormancy maintenance or release.[28]

SLs are derived from the oxidative cleavage of carotenoids and have been implicated in many processes including root growth, root hair and stem elongation, lateral root formation, adventitious rooting, secondary growth, leaf expansion, leaf senescence, and drought and salinity responses but most prominently in shoot branching.[48] SLs seem to act systemically to dampen the polar auxin transport stream, which enhances competition among buds for a common auxin sink.[50] To date, four loci involved in SL biosynthesis and three loci involved in SL signaling have been identified.[51−53] The first steps of SL biosynthesis involve isomerization by the plastidial-isomerase, followed by the sequential cleavage activity of CCD7 and CCD8 carotenoid cleavage dioxygenases. MAX1 encodes a cytP450 predicted to act downstream from CCD7 and CCD8 and is required for synthesis of active SL. Among all of the identified components of the strigolactone biosynthetic pathway, *CsCCD7* and *CsCCD8* genes have been recently isolated and studied in saffron.[54] SL production related to bud dormancy in saffron seems to be controlled at the *CsCCD8* level. In addition, CsCCD8 seems to play an important role in the development of the vasculature of the axillary buds in saffron. Recent evidence shows that SLs positively regulate cambial activity, and this function is conserved among species. Saffron is a monocot without cambial activity. However, given the relationship between cambial and procambial cells, it can be postulated that SLs could also positively regulate procambium activity and the development of vascular tissues in growing buds of monocots.

THE PHYTOCHEMISTRY OF SAFFRON: COMPOUNDS IDENTIFIED FROM SAFFRON FLOWERS AND CORMS

Apocarotenoids in Saffron Flowers, Biosynthesis, and Properties. Apocarotenoids are the products of the oxidative cleavage of carotenoids by specific carotenoid cleavage oxygenases (CCDs) that recognize and specifically cleave one or two double bonds.[55] If sufficient numbers of conjugated double bonds are maintained in the cleavage products they can show coloration, like their parent carotenoids. This is the case of the crocetin molecule (8,8′-diapo-8,8′-carotene-dioic acid) (Figure 5), widely used as a colorant in foods and cosmetics. The crocetin

DOI: 10.1021/acs.jafc.5b03194
J. Agric. Food Chem. 2015, 63, 8751−8764

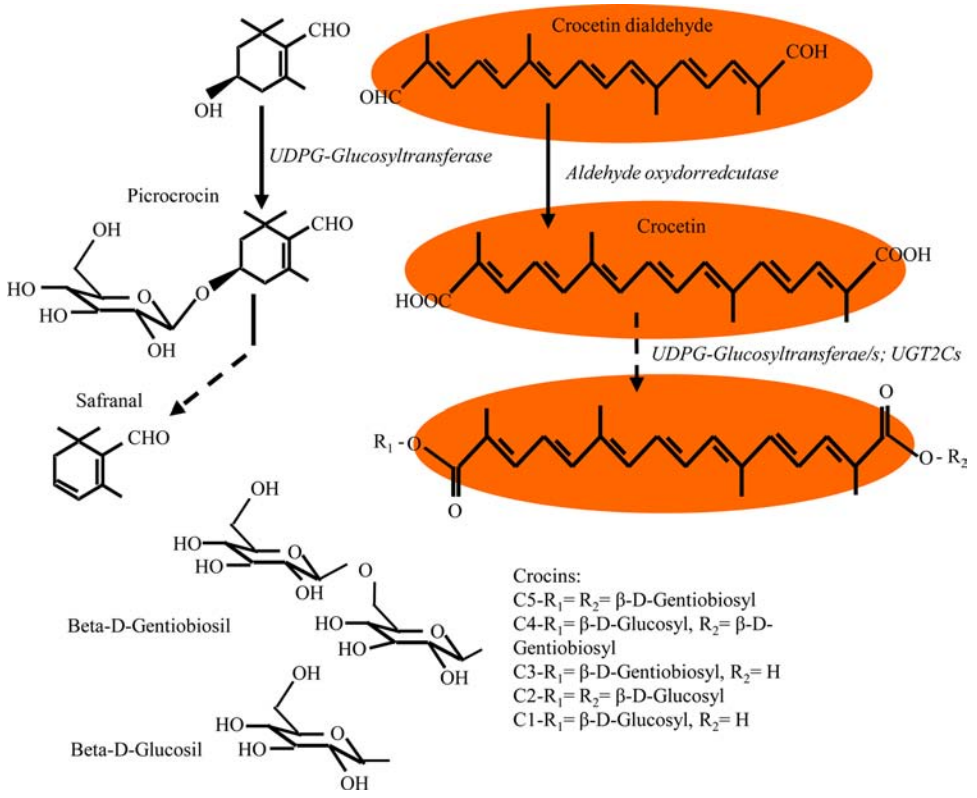

Figure 5. Pathway for crocin and picrocrocin biosynthesis in saffron stigmas.

molecule is further modified by the activity of glucosyltransferases,[56,57] which add different numbers of glucose molecules to produce characteristic crocins, these being the major components of the stigmas of saffron and which confer solubility.[58,59] Crocins are widely present in the species of the genus *Crocus*,[60] but have been also identified in *Buddleja officinalis*,[61] in *Jacquinia angustifolia*,[62] in *Coleus forskolii*,[63] in *Nyctanthes abor-tristis*,[64] in the fruits of *Artocarpus heterophyllus*,[65] *Gardenia jasminoides*,[66] and even in the cyanobacterium *Microcystis*.[67]

Crocetin is formed from the enzymatic cleavage of zeaxanthin on the 7−8/7′−8′ double bonds (Figure 6).[68,69] The resulting products are crocetindial and hydroxyl-β-cyclocitral, which is further glucosylated to form picrocrocin (β-D-glucopyranoside-hydroxyl-β-cyclocitral), the degradation product of which is the odor-active safranal.[69] Carotenoid biosynthesis, cleavage activities, and the expression of corresponding genes have been studied during the development of the stigma of *C. sativus*. A total of five CCD genes belonging to two classes of cleavage enzymes were identified from *C. sativus*.[68,70,71] Heterologous expression of CsCCD1a, CsCCD1b, CsCCD4a, CsCCD4b, and CsCCD4c sequences reduced accumulation of β-carotene in *Escherichia coli* strains engineered for the accumulation of this carotenoid.[68,72] As for volatile cleavage products produced in these strains, only C13 β-ionone could be detected, but no C10 apocarotenoids, whereas a 9−10/9′−10′ cleavage activity for both types of enzymes is predicted (Figure 6). Analysis of stigma volatiles in different stages of flower development indicated high production of β-ionone shortly before and at anthesis.[68,73] In the plant, CsCCD1a and CsCCD4a/b differ if their subcellular location is cytosolic or plastidial, respectively.[68] CsCCD4a sequences, most likely constituting an allelic variant of CsCCD4b (98% of identity) turned out to be identical to a *Crocus* ZCD sequence,[70] albeit CsZCD is a truncated sequence compared to CsCCD4a, with 200 fewer amino acids. For CsZCD a 7−8/7′−8′ cleavage activity in vitro was reported.[70] However, CsZCD lacks important residues and domains for a dioxygenase activity,[74] and no activity was found for this CsZCD in later trials.[68,75] Mining of an EST database from *C. sativus* stigmas has provided further information on potential saffron biosynthetic genes but no candidate for a novel CCD with 7−8/7′−8′ cleavage specificity.[76] Therefore, the previously isolated enzymes were analyzed against a battery of different carotenoids, including zeaxanthin and lutein,[77] and an enzyme, CsCCD2, with a confirmed specificity for the 7−8/7′−8′ double bonds was identified, showing 97% identity with the initially identified CsCCD1b[68] (Figure 6A). On the basis of the in vitro results, lutein and zeaxanthin, but not β-carotene, are good substrates for CsCCD2, and the availability or accessibility to the enzyme would determine the specificity. Accumulation of apocarotenoids in saffron is stigma specific and appears to be developmentally regulated.[73] Higher levels of saffron apocarotenoids increase as stigmas develop and reach their peak in the red stage,[73] and it is likely that the genes involved in their biosynthesis may be stimulated during the process and enhanced in the stigma tissue. *CsCCD1b* and *CsCCD2* expressions are limited to the stigma tissue and detected in the earlier developmental stages, when crocetin accumulation takes place.[68] Analysis of saffron EST collections obtained from the stigma at different developmental stages revealed that *CsCCD2* ESTs were more highly represented in libraries obtained from early stages.[77] Recently, homologues of *CsCCD2* have been identified in spring *Crocus* species, which accumulate crocins in stigmas and tepals.[78] All together, the CCD2 enzymes constitute a new CCD subfamily with no homologues identified in other plant species so far.

Apocarotenoid Properties. The stigmas of *C. sativus* have been used in folk medicine to alleviate different health

DOI: 10.1021/acs.jafc.5b03194
J. Agric. Food Chem. 2015, 63, 8751−8764

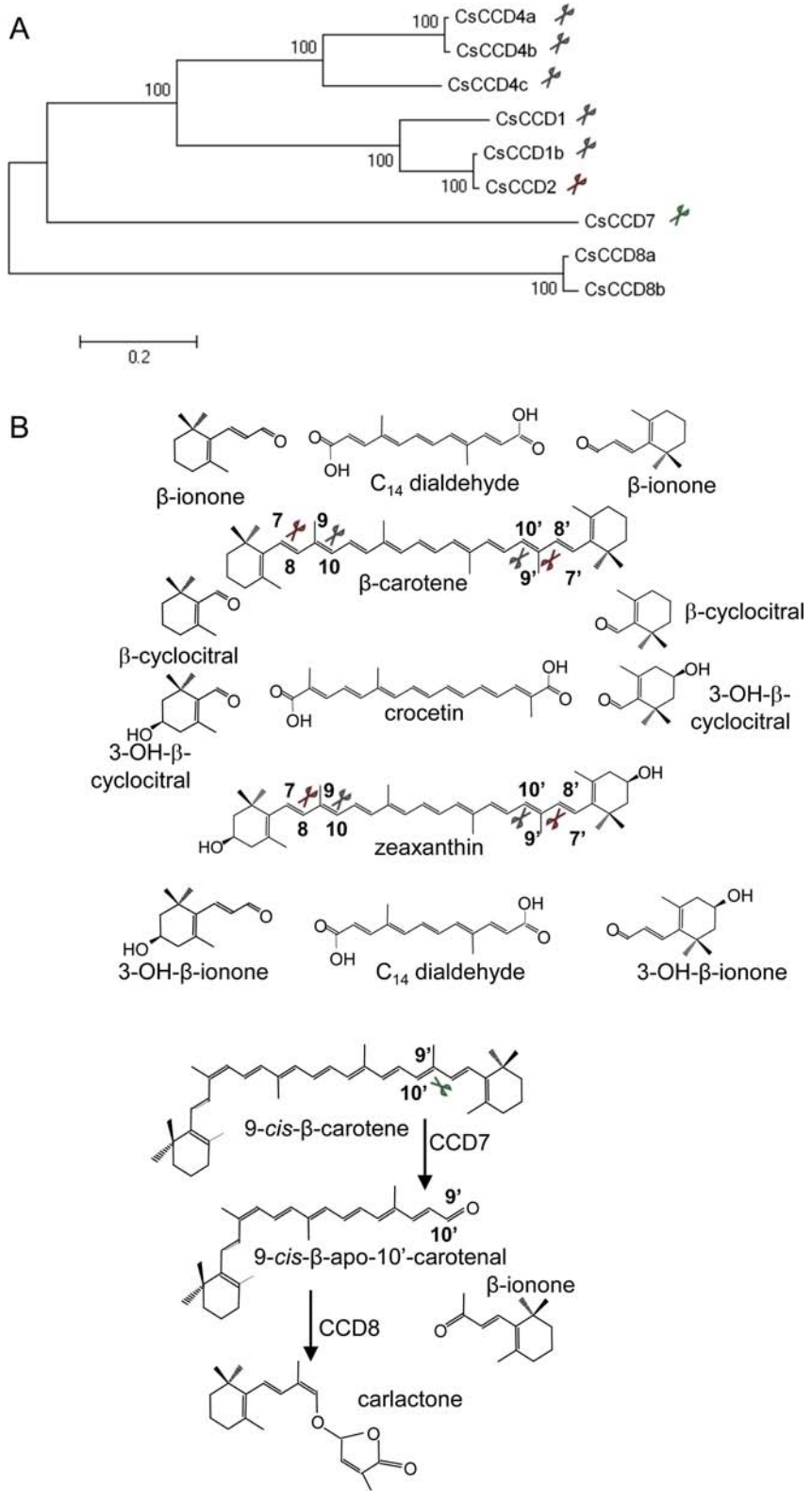

Figure 6. Carotenoid cleavage dioxygenases identified in the stigma of saffron: (A) phylogenetic relationships among the isolated CsCCDs; (B) cleavage activity for the isolated CsCCDs enzymes.

problems.[79] Recent pharmacological studies have demonstrated that crude extracts from saffron and purified chemicals possess antitumor effects, display anti-inflammatory properties, and counteract atherosclerosis and hepatic damage.[11,12] In studies on animal models, it has been shown that crocetin has several pharmacological properties, including antioxidant,[80,81] anti-inflammatory,[82] antiatherosclerotic,[83] insulin resistance improvement,[84] attenuation of physical fatigue,[85] and sleep.[86] Crocetin also alters the growth of cancer cells by inhibiting replication, inducing apoptosis, and enhancing the antioxidative system.[87]

DOI: 10.1021/acs.jafc.5b03194
J. Agric. Food Chem. 2015, 63, 8751−8764

Crocetin shows neuroprotective effects.[88,89] Crocetin inhibits in vitro amyloid-β aggregation,[90] and a clinical pilot study revealed significant improvements in cognition after the treatment of mild-to-moderate Alzheimer's disease patients with crocetin.[91] Crocins had protective effects on neuronal injury,[92] and attenuated the symptoms of obsessive compulsive disorder, a common psychiatric disorder defined by the presence of obsessive thoughts and repetitive compulsive actions.[93] Safranal, the main constituent of the volatile oil fraction, attenuated cerebral ischemia[94] and retinal degeneration.[95,96]

Flavonoids in Saffron Flowers. Flavonoids are among the best-characterized plant secondary metabolites in terms of chemistry, coloration mechanism, biochemistry, genetics, and molecular biology. With a basic structure of C6−C3−C6, they are widely distributed among land plants. Flavonoids are the result of the contribution of two pathways, the flavonoid branch of the phenylpropanoid and the acetate−malonate metabolic pathway. Although the central pathway for flavonoid biosynthesis is conserved in plants, depending on the species, a group of enzymes, such as isomerases, reductases, hydroxylases, and several Fe^{2+}/2-oxoglutarate-dependent dioxygenases, modify the basic flavonoid skeleton, leading to the different flavonoid subclasses.[97] Finally, transferases modify the flavonoid backbone with sugars, methyl groups, and/or acyl moieties, modulating the physiological activity of the resulting flavonoid by altering its solubility, reactivity, and interaction with cellular targets.[98] In *C. sativus*, flavonols are usually glycosylated at their 3-OH, 7-OH and 4′-OH positions,[8,99,100] producing a complex pattern of flavonols. In *C. sativus* stigmas three main glucosides of kaempferol have been identified: kaempferol 7-*O*-sophoroside, kaempferol 3-*O*-sophoroside-7-*O*-glucopyranoside, and kaempferol 3,7,4′-triglucoside. By contrast, 21 different glycosides of isorhamnetin, kaempferol, myricetin, naringenin, quercetin, tamarixetin, and taxifolin have been identified in tepals,[101] kaempferol and kaempferol glycosides being the most dominant class of flavonoids in this tissue (70 and 90% of the total content of flavonoids) followed by quercetin glycosides (5−10%).[102] In pollen kaempferide, a methylated kaempferol and the isorhamnetin glycosides isorhamnetin-3,4′-diglucoside, isorhamnetin-3-*O*-robinobioside, and isorhamnetin-3-β-D-glucoside are detected.[100] In addition, the anthocyanins delphinidin, petunidin, and malvidin have been identified in tepals, with different sugar substitutions,[102] and are responsible for their blue color.

Transcriptome analysis of saffron stigmas has allowed the identification of genes encoding for key enzymes of the flavonol pathway, and putative UDP-glycosyltransferase enzymes have been identified (data not shown). To date three genes encoding flavonol glycosyltransferases have been characterized in saffron.[99,103] The saffron CsGT45 (UGT75P1) protein showed specificity toward flavonoid aglycones and was found to be active on the C-7 position of kaempferol, kaempferol 7-*O*-sophoroside being the most abundant kaempferol glucoside present in the stigma tissue. The UGT707B1 enzyme was recently characterized as a flavonol-3-*O*-glucoside: 2″-glucosyltransferase. The expression of *UGT707B1* in the floral organs of *C. sativus* allowed the accumulation of a specific set of flavonols that influence the transport of the plant hormone auxin and could be responsible for the characteristic morphology of the stigma.[103] The last UGT characterized in saffron involved in flavonoid glucosylation is UGT703B1.[104] This enzyme recognizes isorhamnetin and kaempferol as substrates in vitro. In addition, UGT703B1 expression was found to be highly correlated with the presence of kaempferol 7-*O*-biglucoside-3-*O*-β-glucoside and isorhamnetin-3,7-*O*-diglucoside. These flavonols are present in the flowers of *Crocus* sp. from the series Crocus, but absent in *Crocus* species from other series, and could be used for quimiotaxonomic purposes.

Flavonoid Properties. In plants, flavonoids have many diverse functions including UV protection, defense, allelopathy, flower coloring to attract pollinators, auxin transport inhibition, plant−microorganism communication, and regulation of reactive oxygen species, and in many species they are required for pollen viability.[105] A number of biological processes, such as signal transduction, transcriptional regulation, and cell-to-cell communication, are also influenced by flavonoids. In addition, they play crucial roles in human nutrition, and many therapeutic benefits of flavonoids are known in animal systems. Flavonoids have antioxidant, anti-inflammatory, antitumor, antiproliferative, cardioprotective, and pro-apoptotic activities.[106−109]

The main flavonoid present in saffron tepals is kaempferol-3-*O*-β-D-glucopyranosyl-(1−2)-β-D-glucopyranoside (kaempferol 3-*O*-β-sophoroside).[103] Interestingly, this glucosylated flavonoid is not present in all *Crocus* species, and its presence is relegated to a few series, including the Crocus series. Kaempferol 3-*O*-β-sophoroside has been reported to have analgesic activity.[110] Furthermore, kaempferol 3-*O*-β-sophoroside inhibits the vascular endothelial inflammatory responses and is considered a promising target for the treatment of vascular diseases such as atherosclerosis, shock, heart attack, and sepsis.[111,112] The identification in saffron of the first UGT involved in the formation of this glucosylated flavonoid opens new possibilities for the production of this compound in other crop species or in other heterologous systems.

SAPONINS IN SAFFRON CORMS

Saponin Biosynthesis. Saponins are a widespread group of terpenoids. Saponins are important plant defense compounds, which are determinant for disease resistance due to their antimicrobial, fungicidal, allelopathic, and insecticidal activities.[113] Humans exploit saponins for their medicinal properties and antimicrobial activity. The composition of saponins depends on the genetic background of the plant material, the tissue type, and the age and physiological state of the plant as well as environmental factors.[114] The name saponin is derived from *sapo*, soap in Latin, because the surfactant properties produce soap-like foams in aqueous solution. This trait is the result of the amphiphilic nature of saponins due to linkage of the lipophilic sapogenin to hydrophilic saccharide side chains.

According to the chemical nature of the aglycone (known as sapogenin), the saponins are divided into steroidal and triterpenoid saponins. Steroidal saponins are produced especially in some families of the monocotyledons, for example, Agavaceae, Alliaceae, Asparagaceae, Convallariaceae, Dioscoreaceae, Liliaceae, Smilacaceae, and Trilliacea. In dicotyledons, steroidal saponins are detected only in a few families, for example, Fabaceae, Solanaceae, and Scrophulariaceae.[115] Cholesterol is considered the starting molecule for the biosynthesis of steroidal saponins.[116] The first committed step in the biosynthesis of triterpenoid saponins and phytosterols is the cyclization of 2,3-oxidosqualene by oxidosqualene cyclases (OSGs). The high number of possibilities for establishing different internal linkages during cyclization gives rise to a vast array of different triterpene skeletons.[117] Following formation of basal sapogenin backbone structures mediated by OSCs, various modifications take place prior to glycosylation, the most common being the addition of small functional groups such as aldehyde, hydroxyl, keto, and

DOI: 10.1021/acs.jafc.5b03194
J. Agric. Food Chem. 2015, 63, 8751−8764

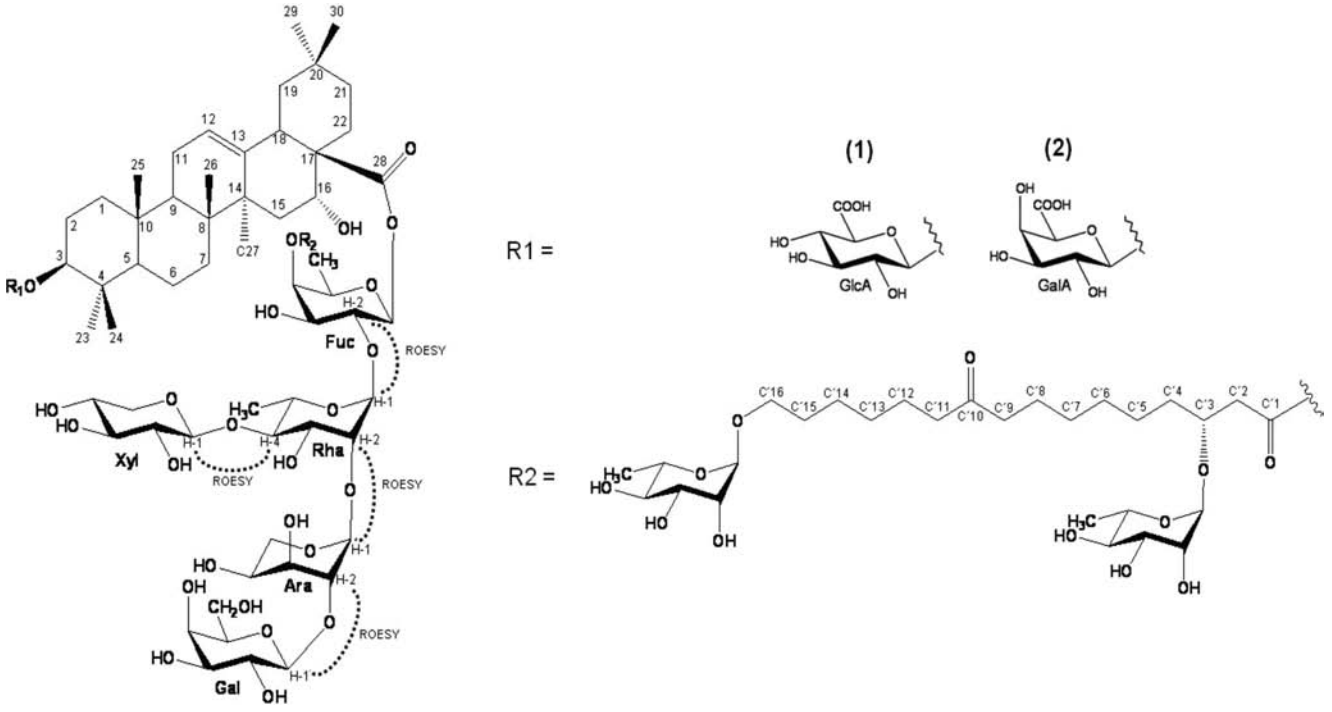

Figure 7. Structures of the triterpenic saponins, azafrines 1 and 2, identified in the corm.

carboxyl moieties at different positions of the backbone, most of them introduced by cytochromes P450 enzymes.[118] Saponin glycosylation involves sequential activity of different UGTs.[98] Typical triterpenoid saponin glycosylation patterns consist of oligomeric sugar chains, two to five monosaccharide units, which are most often linked at position C3 and/or C28.

In saffron, two triterpenic saponins have been identified in the corm, azafrines 1 and 2[119] (Figure 7). Azafrine 1 contains 3-*O*-*β*-D-glucopyranosiduronic acid echinocystic acid as prosapogenin, and azafrine 2 contains 3-*O*-*β*-D-galactopyranosiduronic acid echinocystic acid as prosapogenin. Both prosapogenins are substituted at the C28 position with a pentasaccharide consisting of *β*-D-galactopyranosyl-(1→2)-*α*-L-arabinopyranosyl-(1→2)-[*β*-D-xylopyranosyl-(1→4)]-*α*-L-rhamnopyranosyl-(1→2)-*β*-D-fucopyranose, and a 4-*O*-di-*α*-L-rhamnopyranosyl-3,16-dihydroxy-10-oxo-hexadecanoyl group is linked to C-4 of the *β*-D-fucopyranosyl residue. Azafrines 1 and 2 are localized in the external part of the corms, suggesting their involvement in plant defense.[119,120]

Saponin Properties. Saponins or saponin-containing plant extracts are exploited by the pharmaceutical industry. Several saponins, including the ones identified in saffron, exhibit pharmacological activities and thus attract attention as a target for drug discovery. Saponins are valuable adjuvants, and the first saponin-based vaccines have been introduced commercially.[121] In addition, a recent study demonstrates the potential use of azafrines 1 and 2 in human immunotherapeutic vaccines,[122] and they can also be used for further industrial applications, for instance, preservatives, flavor modifiers, and agents for removal of cholesterol from dairy products[123]

PROSPECTS FOR IMPROVING AND INNOVATING SAFFRON PRODUCTION: THE ROLE OF GENOMIC TOOLS AND BIOTECHNOLOGICAL APPLICATIONS

All over the world saffron is known as one cultivar. The continuous vegetative cultivation of saffron offers certain advantages in terms of preservation of the genetic characteristics of the plant, but makes any genetic improvement difficult. Variability studies with saffron from different countries and locations showed the absence of or very low variability among entries.[124−126] This insufficient genetic variability makes the use of this plant difficult for selection programs,[127,128] whereas the induction of genetic variability through mutagenesis has been addressed using corms at different developmental stages. Even though mutations have been identified as resulting from experimental as well as natural mutagenesis,[129,130] these are not maintained because they are not heritable.

In *C. sativus*, many experiments have been performed to obtain seeds[131] and in vitro regenerated plants[132] without success. As an alternative, researchers have been trying to elucidate how the triploid species was generated to identify the progenitors or at least the closest relatives of *C. sativus*. An autotriploid origin was initially suggested for saffron. However, an allotriploid origin from two wild species has been proposed in different papers,[102,133,134] *C. cartwrightianus* being one of the accepted progenitors.[5,34,135] Nevertheless, no such effort has been undertaken to exploit the closet relatives and hybrid generation.

A first EST collection from saffron was developed in 2007[76] comprising 6603 high-quality ESTs from a saffron mature stigma cDNA. The rapid evolution of next-generation DNA sequencing technologies has allowed the analysis of the transcriptome of six different developmental stages from saffron stigma (unpublished results). This will allow deciphering key players involved in one of the most important processes in saffron from the biotechnological point of view such as apocarotenoid metabolism.

However, it is necessary to point out that one of the most important problems in applying modern biotechnological approaches to saffron and geophytes in general is the lack of high-frequency transformation systems. Further efforts should be made to work in that direction.

DOI: 10.1021/acs.jafc.5b03194
J. Agric. Food Chem. 2015, 63, 8751−8764

Secondary Metabolism and Biotechnological Applications. The current state of the art regarding secondary metabolism in saffron has been discussed above. The identification of the key enzymes involved in apocarotenoid formation represents a very important tool for future biotechnological applications in other crop species where the substrates for crocetin formation are present. This is the case of maize and tomato, where introduction of these enzymes will provide intense red colors and higher nutritional quality, due to the higher bioavailability of the saffron apocarotenoids compared with carotenoids.[136] In addition, rice and tobacco are also good candidates to increase the production of crocins, providing added value to the crop, in the case of rice, or using the plant as a cheaper way to produce crocetin in sufficient quantities for different industrial applications. In this regard, it is also important to consider other *Crocus* species as alternative sources of saffron apocarotenoids, paying special attention to those that accumulate crocins in both stigma and tepals,[60] providing an attractive crop from an economic standpoint, due to the reduction of processing costs.

With regard to corm saponins, the genetic machinery required for the elaboration of this important family of plant secondary metabolites is as yet largely uncharacterized in saffron, despite the considerable commercial interest in this important group of natural products. The development of transcriptomes from the corm combined with metabolomic analyses will allow the identification of key enzymes involved in their biosynthesis.

Nevertheless, still little is known about the genetics that control quantitatively and qualitatively the biosynthesis of these secondary metabolites in saffron and its allies. In addition, knowledge of the regulation of these pathways is practically nonexistent, and such knowledge is of crucial importance to bypass the possibilities of low product yield of these secondary metabolites in other plants or plant cell cultures.

Control of Flower Development. Understanding flowering regulation at the molecular level in saffron, and also in other spring and autumn *Crocus*, would provide the potential for more accurately controlling both flowering time and the development of transcriptional markers for flower initiation to increase genetic variation of saffron for flowering time from spring *Crocus* using biotechnological and *omics* tools.

Although several key flowering genes (*FT*, *CEN/TFL1*, and *AP1*) have been found in saffron, understanding floral inductive pathways in *Crocus* requires not only the identification of some possible regulator genes but a precise knowledge of their expression in the different developmental stages and their control by environmental or internal factors. To date, we are far from achieving this knowledge. Limited information is available on the flower transition of bulbous species, which require high temperature for flower differentiation in species such as saffron. The results obtained by Li et al.[137] working on *Narcissus tazetta*, a bulbous species that requires high temperature for flower differentiation, showed that *Narcissus FLOWERING LOCUS T1 (NFT1)* transcripts were abundant during flower initiation in mature bulbs and were up-regulated by high temperature, suggesting that NFT1 possibly takes part in flower transition control in response to this factor. Given the similarities in the floral induction process of saffron and narcissus, the same up-regulation of *FT* by high temperature could be expected to happen in saffron, although this needs to be confirmed.

Also, the role of *CsatCEN/TFL1* needs to be clarified. Although the involvement of *TFL1* genes in floral transition and axillary meristem identity has been demonstrated in other monocot species,[138] their role in saffron is not clear.

As previously mentioned, treating dry saffron corms with GA in June−July accelerated flower formation and promoted the formation of additional flower buds from undifferentiated meristems. Furthermore, some observations point out that GAs and nutrients act through a common signaling pathway to promote flowering.[139] This pathway controlling flowering in response to gibberellin and nutrients is highly recommended to be studied in saffron. Because flower differentiation takes place in summer when the corm is located underground with no foliage or roots, the involvement of the photoperiod and vernalization pathways seems unlikely, but they should not be entirely ruled out. Another important aspect is related to the decision to bloom, which requires lower temperatures than for flower induction. The genetic control of this process has not yet been studied.

Understanding flower induction in saffron could reveal ways to extend the harvesting period, but the introduction of genetic variation from other *Crocus* species by means of biotechnological tools should also be considered. Furthermore, the development of new genotypes from *C. cartwrightianus* should not be excluded. There is a high variability for flowering time in the *Crocus* genus. This fact enables us to establish a research line aimed at acquiring in-depth knowledge about the differences in the flowering processes at the molecular level between autumn and spring *Crocus* species and making use of this knowledge to extend the saffron flowering period.

Another interesting biotechnological prospect has been pointed out by Tsaftaris and co-workers.[33] It would be desirable to have mutants without stamen formation in saffron flowers, because removal of stamens and separation of stigmas by hand is very labor intensive, leading to high costs. More interesting would be the transformation of stamens to carpel, which should increase saffron production in a single flower. However, it is not at all clear that saffron production would be doubled. The identification of saffron flower development genes that has been already carried out, as mentioned above, will facilitate the achievement of these objectives, and the usefulness of these materials can be tested.

Control of Saffron Sprouting. The understanding and control of dormancy are critical for effectively managing crop production, commercial handling, and storage. Control of endo-dormancy in saffron store corms is a requirement for staggering the production, and reliable markers for endo-dormancy in saffron and other geophytes are one of the most important issues in horticultural practice. The saffron genes *ZEP*, *AAO*, *NCED*, and dormancy-associated MADS-box (*DAM*) genes could be used as markers to determine the exact time at which environmental or internal factors trigger dormancy. It is evident that the application of molecular techniques is indispensable for clarifying the precise mechanism(s) of dormancy induction and release in bulbous species, and the establishment of such a model system is crucial for further research on dormancy of bulbous species.[42]

Another important aspect of dormancy regulation in the *Crocus* genus is the differential response of various plant organs to environmental signals as has been pointed out by Okubo.[42] The genus includes both synanthous and hysteranthous species. In both types, flower initiation occurs in summer, and the initiation orders of the leaves and flowers are similar. However, a time interval takes place between leaf elongation and anthesis in hysteranthous species, when compared to synanthous species (Figure 8). Hence, different organs might vary in their dormancy

DOI: 10.1021/acs.jafc.5b03194
J. Agric. Food Chem. 2015, 63, 8751−8764

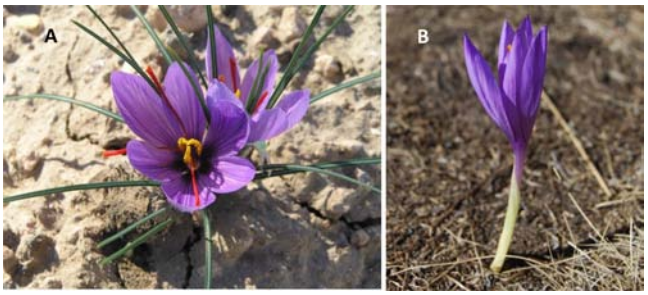

Figure 8. *Crocus* genus includes both (A) synanthous (e.g., *Crocus sativus*) and (B) hysteranthous (e.g., *Crocus nudiflorus*) species.

requirements, and the process might be controlled by both external and internal signals. The absence of leaves at flowering time is of great interest in saffron collection to make harvest work easier, and the understanding of that differential response of leaves and flowers in hysteranthous species takes on great importance.

The rate of propagation in saffron is directly related to axillary meristem formation and outgrowth, and it has been shown that there is a control exerted by the main shoot apex of the corm over the outgrowth of the lateral buds mediated by a hormonal balance. Auxin and strigolactones inhibit bud outgrowth, and cytokinins promote it. A bud-specific gene that promotes bud arrest could be the key element to integrate the bud outgrowth pathway.[140] Such a gene exists in maize (*Teosinte branched 1TB1*),[141] and there is evidence that the gene *BRANCHED1 (BRC1)* acts as an integrator of branching signals within axillary buds of *Arabidopsis*.[142] BCR1 is up-regulated by SLs and down-regulated by cytokinins. Because outgrowth of axillary buds seems to be the major limiting factor in vegetative propagation of bulbs and corms, the SL signaling pathway and *BRC1*-like genes are important targets of choice to study and optimize vegetative propagation.[140]

Improvement of Corm Growth. The manipulation of assimilate partitioning and allocation within the plant is a key factor in the improvement of corm growth. This goal could be achieved through biotechnological approaches based on the identification of the involved genes and regulatory pathways.

Photosynthesis efficiency can be improved through different targets. In relation to light reactions, it could be achieved by increasing the efficiency of light capture, energy transduction, and photoprotective processes, and for carbon fixation reactions by reducing limitations in the diffusion of CO_2 to the site of carboxylation (e.g., mesophyll conductance), in the capacity for carboxylation/oxygenation of Rubisco, and in the regeneration of RuBP.[143] In addition, other processes involving carbon metabolism, such as starch and sucrose synthesis, photorespiration, or respiration, also determine net photoassimilate production.[144]

Despite the potential of biotechnological approaches in optimizing the photosynthetic process, the study of natural genetic variation on photosynthesis within species and between related species is a valuable undertaking.[145] A survey performed on 60 different accessions of *C. sativus* in the field revealed significant differences in the photosynthetic rate and in the quantum efficiency of photosystem II (unpublished data). Research is currently being conducted to characterize the sources of variation within the photosynthetic process and to assess the relationship to biomass production in saffron and related *Crocus* species. This would provide insight into the selective forces that act on this trait and extend our understanding of the regulation of photosynthesis, ultimately increasing the productivity of crops.

Several experimental manipulations suggest that photosynthesis and sink utilization of carbohydrates are closely coordinated.[146] The regulation of carbon partitioning between sources and sinks has a great impact on plant growth and yield and is directly linked to the mechanisms of assimilate transport and allocation. Depending on the main sugar transported and the phloem loading/unloading mechanisms working, different transporters can be involved (e.g., SWEET, H^+/sucrose symporters). The biotechnological manipulation of the transport systems has been reported to positively alter carbon and also nitrogen partitioning and consequently improve crop yields, although pleiotropic effects limiting these gains can also occur.[147] However, at this time no information is available about sugar transport in *Crocus*.

The growth capacity of the sinks is a measure of its strength and depends on sink size and activity. Sink size includes cell number and cell size and is potentially regulated by hormones (gibberellins and cytokinins) along with the supply of assimilates. Bigger corms are formed when photoassimilate availability is higher.[19] Despite the genetic basis, corm size has been proposed to be influenced in *Crocus* by the content and type of soluble sugar content at earlier stages of corm development.[36] Sink activity includes multiple components and key enzymes of carbohydrate metabolism and storage, thus maintaining an assimilate gradient and transport between source and sink.[148] Sucrose is the main transported sugar in many species, and several key enzymes are involved in carbon partitioning. Cell wall and vacuole invertases (INV) in apoplastic unloaders have been related to sink strength, although other activities such as sucrose phosphate phosphatase (SPP), sucrose synthase (SS), or sucrose phosphate synthase (SPS) may also be involved. In addition, final storage products, for example, starch, are the ultimate sinks, and genes involved in their metabolism also influence sink strength.[149]

The integration of carbon assimilation and growth of organs is highly regulated, and hormonal regulation of source-sink relations has been well stated, although many aspects are not fully understood.[148,150] Another interesting approach would be the use of transcription factors to alter the activity of several genes involved in a given process. Several studies in recent years point out this possibility to enhance photosynthesis and biomass production.[150]

CONCLUSIONS

On the basis of this review, we conclude that the molecular and physiological approaches to analyzing and addressing saffron production processes and the exploitation of their secondary metabolism products remain largely unexplored. It is essential to integrate crop physiology and genomic approaches to provide a useful framework in which synergies can be explored between technology and systems-oriented approaches. This review provides a starting point for key aspects in saffron biotechnology.

AUTHOR INFORMATION

Corresponding Author

*(L.G.-G.) E-mail: Marialourdes.gomez@uclm.es. Phone: +34 967599200.

DOI: 10.1021/acs.jafc.5b03194
J. Agric. Food Chem. 2015, 63, 8751−8764

Funding

This work was supported by the Spanish Ministerio de Economía y Competitividad (BIO2013-44239-R).

Notes

The authors declare no competing financial interest.

REFERENCES

(1) Tsoktouridis, G.; Krigas, N.; Karamplianis, T.; Constantinidis, T.; Maloupa, E. In *Genetic Differences among Wild Greek Crocus Taxa and Cultivated Saffron (Crocus sativus L.)*, 3rd International Symposium on Saffron: Forthcoming Challenges in Cultivation Research and Economics, Kozani, Greece; ISHS: Leuven, Belgium, 2009; p 37.

(2) CoskunK, F.; Selvi, S.; Satil, F. Phylogenetic relationships of some Turkish *Crocus* (Iridaceae) taxa based on morphological and anatomical characters. *Turk J. Bot* **2010**, *34*, 171−178.

(3) Mathew, B. *The Crocus − a Revision of the Genus Crocus*; Timber Press: Portland, OR, USA, 1982.

(4) Seberg, O.; Petersen, G. How many loci does it take to DNA barcode a crocus? *PLoS One* **2009**, *4*, e4598.

(5) Castillo, R.; Fernandez, J. A.; Gomez-Gomez, L. Implications of carotenoid biosynthetic genes in apocarotenoid formation during the stigma development of Crocus sativus and its closer relatives. *Plant Physiol.* **2005**, *139*, 674−689.

(6) Negbi, M. Saffron cultivation: past, present and future prospects In *Saffron. Crocus sativus L.*; Negbi, M., Ed.; Harwood Academic Publishers: Reading, UK, 1999; pp 1−18.

(7) Srivastava, R.; Ahmed, H.; Dixit, R. K.; Dharamveer; Saraf, S. A. *Crocus sativus* L.: a comprehensive review. *Pharmacogn. Rev.* **2010**, *4*, 200−208.

(8) Tarantilis, P. A.; Tsoupras, G.; Polissiou, M. Determination of saffron (*Crocus sativus* L.) components in crude plant extract using high-performance liquid chromatography-UV-visible photodiode-array detection-mass spectrometry. *J. Chromatogr A* **1995**, *699*, 107−118.

(9) Winterhalter, P.; Straubinger, M. Saffron-renewed interest in an ancient spice. *Food Rev. Int.* **2000**, *16*, 39−59.

(10) Bathaie, S. Z.; Mousavi, S. Z. New applications and mechanisms of action of saffron and its important ingredients. *Crit. Rev. Food Sci. Nutr.* **2010**, *50*, 761−786.

(11) Abdullaev, F. I. Biological effects of saffron. *Biofactors* **1993**, *4*, 83−86.

(12) Abdullaev, F. I.; Espinosa-Aguirre, J. J. Biomedical properties of saffron and its potential use in cancer therapy and chemoprevention trials. *Cancer Detect. Prev.* **2004**, *28*, 426−432.

(13) Feizzadeh, B.; Afshari, J. T.; Rakhshandeh, H.; Rahimi, A.; Brook, A.; Doosti, H. Cytotoxic effect of saffron stigma aqueous extract on human transitional cell carcinoma and mouse fibroblast. *Urol. J.* **2008**, *5*, 161−167.

(14) Schmidt, M.; Betti, G.; Hensel, A. Saffron in phytotherapy: pharmacology and clinical uses. *Wien. Med. Wochenschr.* **2007**, *157*, 315−319.

(15) Howes, M. J.; Perry, E. The role of phytochemicals in the treatment and prevention of dementia. *Drugs Aging* **2011**, *28*, 439−468.

(16) Rossi, M.; Bermudez, L.; Carrari, F. Crop yield: challenges from a metabolic perspective. *Curr. Opin. Plant Biol.* **2015**, *25*, 79−89.

(17) Molina, R. V.; Valero, M.; Navarro, Y.; Guardiola, J. L.; García-Luis, A. Temperature effects on flower formation in saffron (*Crocus sativus* L.). *Sci. Hortic.* **2005**, *103*, 361−379.

(18) Negb, M.; Dagan, B.; Dror, A.; Basker, D. Growth, flowering, vegetative reproduction, and dormancy in the saffron crocus (*Crocus-sativus* L). *Isr. J. Bot.* **1989**, *38*, 95−113.

(19) Renau-Morata, B.; Nebauer, S. G.; Sánchez, M.; Molina, R. V. Effect of corm size, water stress and cultivation conditions on photosynthesis and biomass partitioning during the vegetative growth of saffron (*Crocus sativus* L.). *Ind. Crops Prod.* **2012**, *39*, 40−46.

(20) de Juan, J. A.; Corcoles, H. L.; Munoz, R. M.; Picornell, M. R. Yield and yield components of saffron under different cropping systems. *Ind. Crops Prod.* **2009**, *30*, 212−219.

(21) Molina, R. V.; Valero, M.; Navarro, Y.; Garcia-Luis, A.; Guardiola, J. L. Low temperature storage of corms extends the flowering season of saffron (*Crocus sativus* L.). *J. Hortic. Sci. Biotechnol.* **2005**, *80*, 319−326.

(22) Molina, R.; Valero, M.; Navarro, Y.; Garcia-Luis, A.; Guardiola, J. L. The effect of time of corm lifting and duration of incubation at inductive temperature on flowering in the saffron plant (*Crocus sativus* L.). *Sci. Hortic.* **2004**, *103*, 79−91.

(23) Milyaeva, E. L.; Azizbekova, N. S. Cytophysiological changes in course of development of stem apices of saffron crocus. *Soviet Plant Physiol.* **1978**, *25*, 227−233.

(24) Koul, K. K.; Farooq, S. Growth and differentiation in the shoot apical meristem of saffron plant (*Crocus sativus* L.). *J. Indian Bot. Soc.* **1982**, *63*, 153−160.

(25) Plessner, O.; Negbi, M.; Ziv, M.; Basber, D. Effects of temperature on the flowering of the saffron crocus (*Crocus sativus* L.): induction of hysteranthy. *Isr. J. Bot.* **1989**, *38*, 7.

(26) Wilkins, H. F. *Crocus vernus, Crocus sativus.* In *Handbook of Flowering*; Halevy, A. H., Ed.; CRC Press: Boca Raton, FL, USA, 1985; Vol. 2, pp 350−355.

(27) Azizbekova, N. S. H.; Milyaeva, E. L.; Lobova, N. V.; Chailakhyan, M. K. H. Effects of gibberellin and kinetin on formation of flower organs in saffron crocus. *Fiziol. Rast* **1978**, *25*, 6.

(28) Farooq, S.; Koul, K. K. Changes in gibberellin-like activity in corms of saffron plant (*Crocus sativus* L.) during dormancy and sprouting. *Biochem. Physiol. Pflanz.* **1983**, *178*, 685−689.

(29) Tsaftaris, A.; Pasentsis, K.; Kalivas, A.; Michailidou, S.; Madesis, P.; Argiriou, A. Isolation of a CENTRORADIALIS/TERMINAL FLOWER1 homolog in saffron (*Crocus sativus* L.): characterization and expression analysis. *Mol. Biol. Rep.* **2012**, *39*, 7899−7910.

(30) Tsaftaris, A.; Pasentsis, K.; Argiriou, A. Cloning and characterization of FLOWERING LOCUS T-like genes from the perennial geophyte saffron crocus (*Crocus sativus*). *Plant Mol. Biol. Rep.* **2013**, *31*, 1558−1568.

(31) Tsaftaris, A.; Pasentsis, K.; Iliopoulos, I.; Polidoros, A. N. Isolation of three homologous AP1-like MADS-box genes in crocus (*Crocus sativus* L.) and characterization of their expression. *Plant Sci.* **2004**, *166*, 1235−1243.

(32) Tsaftaris, A. S.; Polidoros, A. N.; Pasentsis, K.; Kalivas, A. Cloning, structural characterization, and phylogenetic analysis of flower MADS-box genes from crocus (*Crocus sativus* L.). *Sci. World J.* **2007**, *7*, 1047−1062.

(33) Tsaftaris, A. S.; Pasentsis, K.; Polidoros, A. N. Isolation of a differentially spliced C-type flower specific AG-like MADS-box gene from crocus (*Crocus sativus*) and characterization of its expression. *Biol. Plant.* **2005**, *49*, 499−504.

(34) Tsaftaris, A.; Pasentsis, K.; Makris, A.; Darzentas, N.; Polidoros, A.; Kalivas, A.; Argiriou, A. The study of the E-class SEPALLATA3-like MADS-box genes in wild-type and mutant flowers of cultivated saffron crocus (*Crocus sativus* L.) and its putative progenitors. *J. Plant Physiol.* **2011**, *168*, 1675−1684.

(35) Badri, M. A.; Minchin, P. E. H.; Lapointe, L. Effects of temperature on the growth of spring ephemerals: *Crocus vernus* (L.) Hill. *Physiol. Plant.* **2007**, *130*, 67−76.

(36) Lundmark, M.; Vaughan, H.; Lapointe, L. Low temperature maximizes growth of *Crocus vernus* (L.) Hill via changes in carbon partitioning and corm development. *J. Exp. Bot.* **2009**, *60*, 2203−2213.

(37) Wingler, A.; Masclaux-Daubresse, C.; Fischer, A. M. Sugars, senescence, and ageing in plants and heterotrophic organisms. *J. Exp. Bot.* **2009**, *60*, 1063−1066.

(38) Lapointe, L. How phenology influences physiology in deciduous forest spring ephemerals. *Physiol. Plant.* **2001**, *113*, 151−157.

(39) Horvath, D. Common mechanisms regulate flowering and dormancy. *Plant Sci.* **2009**, *177*, 523−531.

(40) Feng, Y.; Zhu, L.; Pan, T.; Guo, Z.; Zhong, X.; Ding, A.; Pan, D. Characterization of summer dormancy in *Narcissus tazetta* var. *chinensis* and the role of NtFTs in summer dormancy and flower differentiation. *Sci. Hortic.* **2015**, *183*, 109−117.

DOI: 10.1021/acs.jafc.5b03194
J. Agric. Food Chem. 2015, 63, 8751−8764

(41) Horvath, D. P.; Anderson, J. V.; Chao, W. S.; Foley, M. E. Knowing when to grow: signals regulating bud dormancy. *Trends Plant Sci.* **2003**, *8*, 534−50.
(42) Okubo, H. Dormancy. In *Ornamental Geophytes: From Basic Science to Sustainable Production*;Okubo, R. K. a. H., Ed.;CRC Press: Boca Raton, FL, USA, 2013; pp 233−260.
(43) Marin, E.; Nussaume, L.; Quesada, A.; Gonneau, M.; Sotta, B.; Hugueney, P.; Frey, A.; Marion-Poll, A. Molecular identification of zeaxanthin epoxidase of *Nicotiana plumbaginifolia*, a gene involved in abscisic acid biosynthesis and corresponding to the ABA locus of *Arabidopsis thaliana*. *EMBO J.* **1996**, *15*, 2331−2342.
(44) Schwartz, S. H.; Tan, B. C.; Gage, D. A.; Zeevaart, J. A.; McCarty, D. R. Specific oxidative cleavage of carotenoids by VP14 of maize. *Science* **1997**, *276*, 1872−1874.
(45) Seo, M.; Koiwai, H.; Akaba, S.; Komano, T.; Oritani, T.; Kamiya, Y.; Koshiba, T. Abscisic aldehyde oxidase in leaves of *Arabidopsis thaliana*. *Plant J.* **2000**, *23*, 481−488.
(46) Ahrazem, O.; Rubio-Moraga, A.; Trapero, A.; Gomez-Gomez, L. Developmental and stress regulation of gene expression for a 9-cis-epoxycarotenoid dioxygenase, CstNCED, isolated from *Crocus sativus* stigmas. *J. Exp. Bot.* **2012**, *63*, 681−694.
(47) Rubio-Moraga, A.; Trapero, A.; Ahrazem, O.; Gomez-Gomez, L. Crocins transport in *Crocus sativus*: the long road from a senescent stigma to a newborn corm. *Phytochemistry* **2010**, *71*, 1506−1513.
(48) Cheng, X.; Ruyter-Spira, C.; Bouwmeester, H. The interaction between strigolactones and other plant hormones in the regulation of plant development. *Front. Plant Sci.* **2013**, *4*, 199.
(49) Rubio-Moraga, A.; Ahrazem, O.; Perez-Clemente, R. M.; Gomez-Cadenas, A.; Yoneyama, K.; Lopez-Raez, J. A.; Molina, R. V.; Gomez-Gomez, L. Apical dominance in saffron and the involvement of the branching enzymes CCD7 and CCD8 in the control of bud sprouting. *BMC Plant Biol.* **2014**, *14*, 171.
(50) Domagalska, M. A.; Leyser, O. Signal integration in the control of shoot branching. *Nat. Rev. Mol. Cell Biol.* **2011**, *12*, 211−221.
(51) Zhao, J.; Wang, T.; Wang, M.; Liu, Y.; Yuan, S.; Gao, Y.; Yin, L.; Sun, W.; Peng, L.; Zhang, W.; Wan, J.; Li, X. Dwarf3 participates in an SCF complex and associates with Dwarf14 to suppress rice shoot branching. *Plant Cell Physiol.* **2014**, *55*, 1096.
(52) Waldie, T.; McCulloch, H.; Leyser, O. Strigolactones and the control of plant development: lessons from shoot branching. *Plant J.* **2014**, *79*, 607.
(53) Jiang, L.; Liu, X.; Xiong, G.; Liu, H.; Chen, F.; Wang, L.; Meng, X.; Liu, G.; Yu, H.; Yuan, Y.; Yi, W.; Zhao, L.; Ma, H.; He, Y.; Wu, Z.; Melcher, K.; Qian, Q.; Xu, H. E.; Wang, Y.; Li, J. DWARF 53 acts as a repressor of strigolactone signalling in rice. *Nature* **2013**, *504*, 401−405.
(54) Rubio-Moraga, A.; Ahrazem, O.; Perez-Clemente, R. M.; Gomez-Cadenas, A.; Yoneyama, K.; Lopez-Raez, J. A.; Molina, R. V.; Gomez-Gomez, L. Apical dominance in saffron and the involvement of the branching enzymes CCD7 and CCD8 in the control of bud sprouting. *BMC Plant Biol.* **2014**, *14*, 171.
(55) Walter, M. H.; Floss, D. S.; Strack, D. Apocarotenoids: hormones, mycorrhizal metabolites and aroma volatiles. *Planta* **2010**, *232*, 1−17.
(56) Moraga, A. R.; Nohales, P. F.; Perez, J. A.; Gomez-Gomez, L. Glucosylation of the saffron apocarotenoid crocetin by a glucosyltransferase isolated from *Crocus sativus* stigmas. *Planta* **2004**, *219*, 955−966.
(57) Dufresne, C.; Cormier, F.; Dorion, S. In vitro formation of crocetin glucosyl esters by *Crocus sativus* callus extract. *Planta Med.* **1997**, *63*, 150−153.
(58) Kuhn, R.; Winterstein, A. Über einen lichtempfindlichen Carotin-Farbstoff aus Safran. *Ber. Dtsch. Chem. Ges. B* **1933**, *66*, 209−214.
(59) Bouillon-Lagrange, E.-J. B. *Analyse du Safran*; 1811.
(60) Rubio Moraga, A.; Ahrazem, O.; Rambla, J. L.; Granell, A.; Gomez Gomez, L. Crocins with high levels of sugar conjugation contribute to the yellow colours of early-spring flowering crocus tepals. *PLoS One* **2013**, *8*, e71946.
(61) Liao, Y. H.; Houghton, P. J.; Hoult, J. R. Novel and known constituents from Buddleja species and their activity against leukocyte eicosanoid generation. *J. Nat. Prod.* **1999**, *62*, 1241−1245.
(62) Eugster, C. H.; Hürlimann, H.; Leuenberger, H. J. Crocetindialdehyd und crocetinhalbaldehyd als blütenfarbstoffe von *Jacquinia angustifolia*. *Helv. Chim. Acta* **1969**, *52*, 806−807.
(63) Tandon, J.; Katti, S.; Rüedi, P.; Eugster, C. Crocetin-dialdehyde from *Coleus forskohlii*. *Helv. Chim. Acta* **1979**, *62*, 2706−2707.
(64) Gadgoli, C.; Shelke, S. Crocetin from the tubular calyx of Nyctanthes arbor-tristis. *Nat. Prod. Res.* **2010**, *24*, 1610−1615.
(65) Priyadarshani, A. M. B.; Jansz, E.; Peiris, H. Studies on the carotenoids of jakfruit (*Artocarpus heterophyllus* Lam.) from Matale and Kurunegala districts. *J. Natl. Sci. Found. Sri Lanka* **2007**, *35*, 259−262.
(66) Pfister, S.; Steck, A.; Pfander, H. Isolation and structure elucidation of carotenoid glycoslyesters on gardenia fruits (*Gardenia jasminoides*) and saffron (*Crocus sativus*). *J. Agric. Food Chem.* **1996**, *44*, 2612−2615.
(67) Jüttner, F.; Höflacher, B. Evidence of β-carotene 7,8(7′,8′) oxygenase (β-cyclocitral, crocetindial generating) in Microcystis. *Arch. Microbiol.* **1985**, *141*, 337−343.
(68) Rubio, A.; Rambla, J. L.; Santaella, M.; Gomez, M. D.; Orzaez, D.; Granell, A.; Gomez-Gomez, L. Cytosolic and plastoglobule-targeted carotenoid dioxygenases from *Crocus sativus* are both involved in β-ionone release. *J. Biol. Chem.* **2008**, *283*, 24816−24825.
(69) Pfander, H.; Schurtenberger, H. Biosynthesis of C20-carotenoids in *Crocus sativus*. *Phytochemistry* **1982**, *21*, 1039−1042.
(70) Bouvier, F.; Suire, C.; Mutterer, J.; Camara, B. Oxidative remodeling of chromoplast carotenoids: identification of the carotenoid dioxygenase CsCCD and CsZCD genes involved in *Crocus* secondary metabolite biogenesis. *Plant Cell* **2003**, *15*, 47−62.
(71) Ahrazem, O.; Trapero, A.; Gomez, M. D.; Rubio-Moraga, A.; Gomez-Gomez, L. Genomic analysis and gene structure of the plant carotenoid dioxygenase 4 family: a deeper study in *Crocus sativus* and its allies. *Genomics* **2010**, *96*, 239−250.
(72) Rubio-Moraga, A.; Rambla, J. L.; Fernandez-de-Carmen, A.; Trapero-Mozos, A.; Ahrazem, O.; Orzaez, D.; Granell, A.; Gomez-Gomez, L. New target carotenoids for CCD4 enzymes are revealed with the characterization of a novel stress-induced carotenoid cleavage dioxygenase gene from *Crocus sativus*. *Plant Mol. Biol.* **2014**, *86*, 555−569.
(73) Moraga, A. R.; Rambla, J. L.; Ahrazem, O.; Granell, A.; Gomez-Gomez, L. Metabolite and target transcript analyses during *Crocus sativus* stigma development. *Phytochemistry* **2009**, *70*, 1009−1016.
(74) Kloer, D. P.; Schulz, G. E. Structural and biological aspects of carotenoid cleavage. *Cell. Mol. Life Sci.* **2006**, *63*, 2291−2303.
(75) Sergeant, M. J.; Li, J. J.; Fox, C.; Brookbank, N.; Rea, D.; Bugg, T. D.; Thompson, A. J. Selective inhibition of carotenoid cleavage dioxygenases: phenotypic effects on shoot branching. *J. Biol. Chem.* **2009**, *284*, 5257−5264.
(76) D'Agostino, N.; Pizzichini, D.; Chiusano, M. L.; Giuliano, G. An EST database from saffron stigmas. *BMC Plant Biol.* **2007**, *7*, 53.
(77) Frusciante, S.; Diretto, G.; Bruno, M.; Ferrante, P.; Pietrella, M.; Prado-Cabrero, A.; Rubio-Moraga, A.; Beyer, P.; Gomez-Gomez, L.; Al-Babili, S.; Giuliano, G. Novel carotenoid cleavage dioxygenase catalyzes the first dedicated step in saffron crocin biosynthesis. *Proc. Natl. Acad. Sci. U. S. A.* **2014**, *111*, 12246−12251.
(78) Ahrazem, O.; Rubio-Moraga, A.; Berman, J.; Capell, T.; Christou, P.; Zhu, C.; Gomez-Gomez, L. The carotenoid cleavage dioxygenase CCD2 catalyzing the synthesis of crocetin in spring crocuses and saffron is a plastidial enzyme. *New Phytol.* **2015**, 13609.
(79) Rios, J. L.; Recio, M. C.; Ginger, R. M.; Manz, S. An update review of saffron and its active constituents. *Phytother. Res.* **1996**, *10*, 189.
(80) Tseng, T. H.; Chu, C. Y.; Huang, J. M.; Shiow, S. J.; Wang, C. J. Crocetin protects against oxidative damage in rat primary hepatocytes. *Cancer Lett.* **1995**, *97*, 61−67.
(81) Kanakis, C. D.; Tarantilis, P. A.; Tajmir-Riahi, H. A.; Polissiou, M. G. Crocetin, dimethylcrocetin, and safranal bind human serum albumin: stability and antioxidative properties. *J. Agric. Food Chem.* **2007**, *55*, 970−977.
(82) Kazi, H. A.; Qian, Z. Crocetin reduces TNBS-induced experimental colitis in mice by downregulation of NFkB. *Saudi J. Gastroenterol.* **2009**, *15*, 181−187.

DOI: 10.1021/acs.jafc.5b03194
J. Agric. Food Chem. 2015, 63, 8751−8764

(83) Zheng, S.; Qian, Z.; Sheng, L.; Wen, N. Crocetin attenuates atherosclerosis in hyperlipidemic rabbits through inhibition of LDL oxidation. *J. Cardiovasc. Pharmacol.* **2006**, *47*, 70−76.
(84) Sheng, L.; Qian, Z.; Shi, Y.; Yang, L.; Xi, L.; Zhao, B.; Xu, X.; Ji, H. Crocetin improves the insulin resistance induced by high-fat diet in rats. *Br. J. Pharmacol.* **2008**, *154*, 1016−1024.
(85) Mizuma, H.; Tanaka, M.; Nozaki, S.; Mizuno, K.; Tahara, T.; Ataka, S.; Sugino, T.; Shirai, T.; Kajimoto, Y.; Kuratsune, H.; Kajimoto, O.; Watanabe, Y. Daily oral administration of crocetin attenuates physical fatigue in human subjects. *Nutr. Res. (N. Y., NY, U. S.)* **2009**, *29*, 145−150.
(86) Kuratsune, H.; Umigai, N.; Takeno, R.; Kajimoto, Y.; Nakano, T. Effect of crocetin from *Gardenia jasminoides* Ellis on sleep: a pilot study. *Phytomedicine* **2010**, *17*, 840−843.
(87) Gutheil, W. G.; Reed, G.; Ray, A.; Anant, S.; Dhar, A. Crocetin: an agent derived from saffron for prevention and therapy for cancer. *Curr. Pharm. Biotechnol.* **2012**, *13*, 173−179.
(88) Ahmad, A. S.; Ansari, M. A.; Ahmad, M.; Saleem, S.; Yousuf, S.; Hoda, M. N.; Islam, F. Neuroprotection by crocetin in a hemi-parkinsonian rat model. *Pharmacol., Biochem. Behav.* **2005**, *81*, 805−813.
(89) Nam, K. N.; Park, Y. M.; Jung, H. J.; Lee, J. Y.; Min, B. D.; Park, S. U.; Jung, W. S.; Cho, K. H.; Park, J. H.; Kang, I.; Hong, J. W.; Lee, E. H. Anti-inflammatory effects of crocin and crocetin in rat brain microglial cells. *Eur. J. Pharmacol.* **2010**, *648*, 110−116.
(90) Papandreou, M. A.; Kanakis, C. D.; Polissiou, M. G.; Efthimiopoulos, S.; Cordopatis, P.; Margarity, M.; Lamari, F. N. Inhibitory activity on amyloid-beta aggregation and antioxidant properties of *Crocus sativus* stigmas extract and its crocin constituents. *J. Agric. Food Chem.* **2006**, *54*, 8762−8768.
(91) Akhondzadeh, S.; Sabet, M. S.; Harirchian, M. H.; Togha, M.; Cheraghmakani, H.; Razeghi, S.; Hejazi, S.; Yousefi, M. H.; Alimardani, R.; Jamshidi, A.; Zare, F.; Moradi, A. Saffron in the treatment of patients with mild to moderate Alzheimer's disease: a 16-week, randomized and placebo-controlled trial. *J. Clin. Pharm. Ther.* **2010**, *35*, 581−588.
(92) Ochiai, T.; Shimeno, H.; Mishima, K.; Iwasaki, K.; Fujiwara, M.; Tanaka, H.; Shoyama, Y.; Toda, A.; Eyanagi, R.; Soeda, S. Protective effects of carotenoids from saffron on neuronal injury in vitro and in vivo. *Biochim. Biophys. Acta, Gen. Subj.* **2007**, *1770*, 578−584.
(93) Georgiadou, G.; Tarantilis, P. A.; Pitsikas, N. Effects of the active constituents of *Crocus sativus* L., crocins, in an animal model of obsessive-compulsive disorder. *Neurosci. Lett.* **2012**, *528*, 27−30.
(94) Hosseinzadeh, H.; Sadeghnia, H. R. Safranal, a constituent of *Crocus sativus* (saffron), attenuated cerebral ischemia induced oxidative damage in rat hippocampus. *J. Pharm. Pharm. Sci.* **2005**, *8*, 394−399.
(95) Fernández-Sánchez, L.; Lax, P.; Esquiva, G.; Martín-Nieto, J.; Pinilla, I.; Cuenca, N. Safranal, a saffron constituent, attenuates retinal degeneration in P23H rats. *PLoS One* **2012**, *7*, e43074.
(96) Hooshmandi, Z.; Rohani, A. H.; Eidi, A.; Fatahi, Z.; Golmanesh, L.; Sahraei, H. Reduction of metabolic and behavioral signs of acute stress in male Wistar rats by saffron water extract and its constituent safranal. *Pharm. Biol.* **2011**, *49*, 947.
(97) Winkel-Shirley, B. Flavonoid biosynthesis. A colorful model for genetics, biochemistry, cell biology, and biotechnology. *Plant Physiol.* **2001**, *126*, 485−493.
(98) Bowles, D.; Lim, E. K.; Poppenberger, B.; Vaistij, F. E. Glycosyltransferases of lipophilic small molecules. *Annu. Rev. Plant Biol.* **2006**, *57*, 567−597.
(99) Moraga, A. R.; Mozos, A. T.; Ahrazem, O.; Gomez-Gomez, L. Cloning and characterization of a glucosyltransferase from *Crocus sativus* stigmas involved in flavonoid glucosylation. *BMC Plant Biol.* **2009**, *9*, 109.
(100) Li, C. Y.; Wu, T. S. Constituents of the pollen of *Crocus sativus* L. and their tyrosinase inhibitory activity. *Chem. Pharm. Bull.* **2002**, *50*, 1305−1309.
(101) Termentzi, A.; Kokkalou, E. LC-DAD-MS (ESI+) analysis and antioxidant capacity of crocus sativus petal extracts. *Planta Med.* **2008**, *74*, 573−581.
(102) Nørbæk, R.; Brandt, K.; Kvist Nielsen, J.; Ørgaard, M.; Jacobsen, N. Flower pigment composition of *Crocus* species and cultivars used for a chemotaxonomic investigation. *Biochem. Syst. Ecol.* **2002**, *30*, 763.
(103) Trapero-Mozos, A.; Ahrazem, O.; Rubio-Moraga, A.; Jimeno, M. L.; Gomez, M. D.; Gomez-Gomez, L. Characterization of a glucosyltransferase enzyme involved in the formation of kaempferol and quercetin sophorosides in *Crocus sativus*. *Plant Physiol.* **2012**, *159*, 1335.
(104) Ahrazem, O.; Rubio-Moraga, A.; Mozos, A. T.; Gómez-Gómez, M. L. Genomic organization of a UDP-glucosyltransferase gene determines differential accumulation of specific flavonoid glucosides in tepals. *Plant Cell, Tissue Organ Cult.* **2014**, *119*, 227.
(105) Buer, C. S.; Imin, N.; Djordjevic, M. A. Flavonoids: new roles for old molecules. *J. Integr. Plant Biol.* **2010**, *52*, 98−111.
(106) Williams, R. J.; Spencer, J. P.; Rice-Evans, C. Flavonoids: antioxidants or signalling molecules? *Free Radical Biol. Med.* **2004**, *36*, 838−849.
(107) Gutierrez-Merino, C.; Lopez-Sanchez, C.; Lagoa, R.; Samhan-Arias, A. K.; Bueno, C.; Garcia-Martinez, V. Neuroprotective actions of flavonoids. *Curr. Med. Chem.* **2011**, *18*, 1195−1212.
(108) Rendeiro, C.; Guerreiro, J. D.; Williams, C. M.; Spencer, J. P. Flavonoids as modulators of memory and learning: molecular interactions resulting in behavioural effects. *Proc. Nutr. Soc.* **2012**, *71*, 246−262.
(109) Mulvihill, E. E.; Huff, M. W. Antiatherogenic properties of flavonoids: implications for cardiovascular health. *Can. J. Cardiol.* **2010**, *26* (Suppl.A), 17A−21A.
(110) Palanichamy, S.; Nagarajan, S. Analgesic activity of *Cassia alata* leaf extract and kaempferol 3-*O*-sophoroside. *J. Ethnopharmacol.* **1990**, *29*, 73−78.
(111) Kim, T. H.; Ku, S. K.; Bae, J. S. Inhibitory effects of kaempferol-3-*O*-sophoroside on HMGB1-mediated proinflammatory responses. *Food Chem. Toxicol.* **2012**, *50*, 1118−1123.
(112) Kim, T. H.; Ku, S. K.; Lee, I. C.; Bae, J. S. Anti-inflammatory effects of kaempferol-3-*O*-sophoroside in human endothelial cells. *Inflamm. Res.* **2012**, *61*, 217−224.
(113) Sparg, S. G.; Light, M. E.; van Staden, J. Biological activities and distribution of plant saponins. *J. Ethnopharmacol.* **2004**, *94*, 219−243.
(114) Haralampidis, K.; Trojanowska, M.; Osbourn, A. E. Biosynthesis of triterpenoid saponins in plants. *Adv. Biochem. Eng. Biotechnol* **2002**, *75*, 31−49.
(115) Voigt, G.; Hiller, K. Advances in the chemistry and biology of the steroid saponins. *Sci. Pharm.* **1987**, *55*, 201−222.
(116) Vincken, J. P.; Heng, L.; de Groot, A.; Gruppen, H. Saponins, classification and occurrence in the plant kingdom. *Phytochemistry* **2007**, *68*, 275−297.
(117) Xu, R.; Fazio, G. C.; Matsuda, S. P. On the origins of triterpenoid skeletal diversity. *Phytochemistry* **2004**, *65*, 261−291.
(118) Augustin, J. M.; Kuzina, V.; Andersen, S. B.; Bak, S. Molecular activities, biosynthesis and evolution of triterpenoid saponins. *Phytochemistry* **2011**, *72*, 435−457.
(119) Rubio-Moraga, A.; Gerwig, G. J.; Castro-Díaz, N.; Jimeno, M. L.; Escribano, J.; Fernández, J. A.; Kamerling, J. P. Triterpenoid saponins from corms of *Crocus sativus*: localization, extraction and characterization. *Ind. Crops Prod.* **2011**, *34*, 1401.
(120) Rubio-Moraga, A.; Gómez-Gómez, L.; Trapero, A.; Castro-Díaz, N.; Ahrazem, O. Saffron corm as a natural source of fungicides: the role of saponins in the underground. *Ind. Crops Prod.* **2013**, *49*, 915.
(121) Adams, M. M.; Damani, P.; Perl, N. R.; Won, A.; Hong, F.; Livingston, P. O.; Ragupathi, G.; Gin, D. Y. Design and synthesis of potent *Quillaja* saponin vaccine adjuvants. *J. Am. Chem. Soc.* **2010**, *132*, 1939−1945.
(122) Castro-Diaz, N.; Salaun, B.; Perret, R.; Sierro, S.; Romero, J. F.; Fernandez, J. A.; Rubio-Moraga, A.; Romero, P. Saponins from the Spanish saffron *Crocus sativus* are efficient adjuvants for protein-based vaccines. *Vaccine* **2012**, *30*, 388−397.
(123) Güçlü-Üstündag, Ö.; Mazza, G. Saponins: properties, applications and processing. *Crit. Rev. Food Sci. Nutr.* **2007**, *47*, 231.

DOI: 10.1021/acs.jafc.5b03194
J. Agric. Food Chem. 2015, 63, 8751−8764

(124) Grilli-Caiola, M. G.; Caputo, P.; Zanier, R. RAPD analysis in *Crocus sativus* L. accessions and related *Crocus* species. *Biol. Plant.* **2004**, *48*, 375.
(125) Rubio-Moraga, A.; Castillo-Lopez, R.; Gomez-Gomez, L.; Ahrazem, O. Saffron is a monomorphic species as revealed by RAPD, ISSR and microsatellite analyses. *BMC Res. Notes* **2009**, *2*, 189.
(126) Nemati, Z.; Mohsen, M.; Majidian, P.; Zeinalabedini, M.; Pirseyedi, S. M.; Bahadori, M. Saffron (*Crocus sativus* L.), a monomorphic or polymorphic species? *Span. J. Agric. Res.* **2014**, *12*, 753.
(127) Agayev, Y.; Shakib, A.; Soheilivand, S.; Fathi, M. In *Breeding of Saffron (Crocus sativus): Possibilities and Problems*, II International Symposium on Saffron Biology and Technology 739; ISHS: Leuven, Belgium, 2006; pp 203−207.10.17660/ActaHortic.2007.739.25
(128) Mir, J.; Ahmed, N.; Singh, D.; Khan, M.; Zaffer, S.; Shafi, W. Breeding and biotechnological opportunities in saffron crop improvement. *Afr. J. Agric. Res.* **2015**, *10*, 970−974.
(129) Khan, M. A.; Nagoo, S.; Naseer, S.; Nehvi, F. A.; Zargar, S. M. Induced mutation as a tool for improving corm multiplication in saffron (*Crocus sativus* L.). *J. Phytol.* **2011**, *3*, 8−10.
(130) Dar, S.; Makhdoomi, M.; Allie, B.; Mir, Z.; Nehvi, F.; Wani, S. In *Biological Interventions for Enhancing Saffron Productivity in Kashmir*, II International Symposium on Saffron Biology and Technology 739; ISHS: Leuven, Belgium, 2006; pp 25−3210.17660/ActaHortic.2007.739.1.
(131) Grilli-Caiola, M.; Canini, A. Saffron reproductive biology. *Acta Hortic.* **2004**, *650*, 25−37.
(132) Souret, F.; Weathers, P. *Crocus sativus* L. (saffron): cultivation, in vitro culture, secondary metabolite production and phytopharmacognosy. *J. Herbs, Spices Med. Plants* **2000**, *6*, 99−116.
(133) Agayev, Y. M. New features in karyotype structure and origin of saffron, *Crocus sativus* L. *Cytologia* **2002**, *67*, 245−252.
(134) Grilli-Caiola, M.; Canini, A. Looking for saffron's (*Crocus sativus* L.) parents. In *Functional Plant Science and Biotechnology, Saffron Special Issue*; Husaini, A. M., Ed.; Global Science Books: London, UK, 2010; Vol. 4, pp 1−14.
(135) Grilli-Caiola, M.; Leonardi, D.; Canini, A. Seed structure in *Crocus sativus* L. × , *C. cartwrightianus* Herb., *C. thomasii* Ten., and *C. hadriaticus* Herb. at SEM. *Plant Syst. Evol.* **2010**, *285*, 111−120.
(136) Abourashed, E. A. Bioavailability of plant-derived antioxidants. *Antioxidants* **2013**, *2*, 309−325.
(137) Li, X. F.; Jia, L. Y.; Xu, J.; Deng, X. J.; Wang, Y.; Zhang, W.; Zhang, X. P.; Fang, Q.; Zhang, D. M.; Sun, Y.; Xu, L. FT-like NFT1 gene may play a role in flower transition induced by heat accumulation in Narcissus tazetta var. chinensis. *Plant Cell Physiol.* **2013**, *54*, 270−281.
(138) Jensen, C. S.; Salchert, K.; Nielsen, K. K. A TERMINAL FLOWER1-like gene from perennial ryegrass involved in floral transition and axillary meristem identity. *Plant Physiol.* **2001**, *125*, 1517−1528.
(139) Eriksson, S.; Bohlenius, H.; Moritz, T.; Nilsson, O. GA4 is the active gibberellin in the regulation of LEAFY transcription and *Arabidopsis* floral initiation. *Plant Cell* **2006**, *18*, 2172−2181.
(140) Leeggangers, H. A.; Moreno-Pachon, N.; Gude, H.; Immink, R. G. Transfer of knowledge about flowering and vegetative propagation from model species to bulbous plants. *Int. J. Dev. Biol.* **2013**, *57*, 611−620.
(141) Doebley, J.; Stec, A.; Hubbard, L. The evolution of apical dominance in maize. *Nature* **1997**, *386*, 485−8.
(142) Aguilar-Martinez, J. A.; Poza-Carrion, C.; Cubas, P. Arabidopsis BRANCHED1 acts as an integrator of branching signals within axillary buds. *Plant Cell* **2007**, *19*, 458−472.
(143) Long, S. P.; Marshall-Colon, A.; Zhu, X. G. Meeting the global food demand of the future by engineering crop photosynthesis and yield potential. *Cell* **2015**, *161*, 56−66.
(144) Zhu, X. G.; Long, S. P.; Ort, D. R. Improving photosynthetic efficiency for greater yield. *Annu. Rev. Plant Biol.* **2010**, *61*, 235−261.
(145) Flood, P. J.; Harbinson, J.; Aarts, M. G. Natural genetic variation in plant photosynthesis. *Trends Plant Sci.* **2011**, *16*, 327−335.
(146) Ainsworth, E. A.; Yendrek, C. R.; Skoneczka, J. A.; Long, S. P. Accelerating yield potential in soybean: potential targets for biotechnological improvement. *Plant, Cell Environ.* **2012**, *35*, 38−52.
(147) Yadav, U. P.; Ayre, B. G.; Bush, D. R. Transgenic approaches to altering carbon and nitrogen partitioning in whole plants: assessing the potential to improve crop yields and nutritional quality. *Front. Plant Sci.* **2015**, *6*, 275.
(148) Albacete, A. A.; Martinez-Andujar, C.; Perez-Alfocea, F. Hormonal and metabolic regulation of source-sink relations under salinity and drought: from plant survival to crop yield stability. *Biotechnol. Adv.* **2014**, *32*, 12−30.
(149) Bihmidine, S.; Hunter, C. T., 3rd; Johns, C. E.; Koch, K. E.; Braun, D. M. Regulation of assimilate import into sink organs: update on molecular drivers of sink strength. *Front. Plant Sci.* **2013**, *4*, 177.
(150) Saibo, N. J.; Lourenco, T.; Oliveira, M. M. Transcription factors and regulation of photosynthetic and related metabolism under environmental stresses. *Ann. Bot.* **2009**, *103*, 609−623.

DOI: 10.1021/acs.jafc.5b03194
J. Agric. Food Chem. 2015, 63, 8751−8764

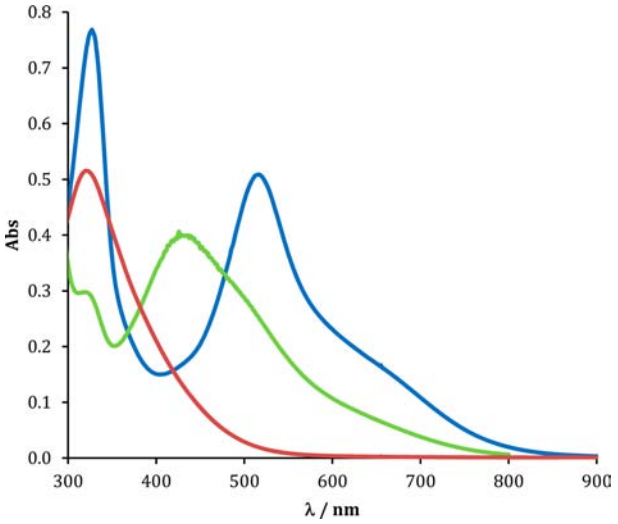

Figure 2. UV−vis spectra of DPPH• (blue, 4.7×10^{-5} M), DPPH−H (maroon, 4.2×10^{-5} M), and the anion DPPH$^-$ (green, 7×10^{-5} M) in methanol at ambient temperature.

plants or single compounds (mostly phenols).[6] The potentially good intentions of the users of this test are, however, blurred by the interpretation of the data pulled from it, particularly the incorrect interpretation of the "efficient concentration"[15] (EC_{50}) as a parameter related to the antioxidant properties of chemicals.

The DPPH• radical is poorly soluble in apolar solvents, whereas in various polar organic solvents it shows a significant solubility. In water, its solubility at ambient temperature is practically nil, and this has hampered the study of the effects that this extraordinary solvent might have on the chemistry of the radical. To fill this current void of knowledge, nanoparticles of DPPH• soluble in water and *β*-cyclodextrin incorporating DPPH• were recently prepared.[13b,16] These forms could help in the understanding of the effects of water on the (electron transfer) mechanism of reactions involving biologically relevant water-soluble antioxidants (ascorbic acid, uric acid, bilirubin, glutathione, etc.). Indeed, in these past 20 years DPPH• has been very useful in the comprehension of (biologically relevant) solvent effects[17] on the rate of reactions of antioxidants + radicals and in the formulation of new[17b,18] electron transfer (ET) mechanisms involving phenols (vide infra).

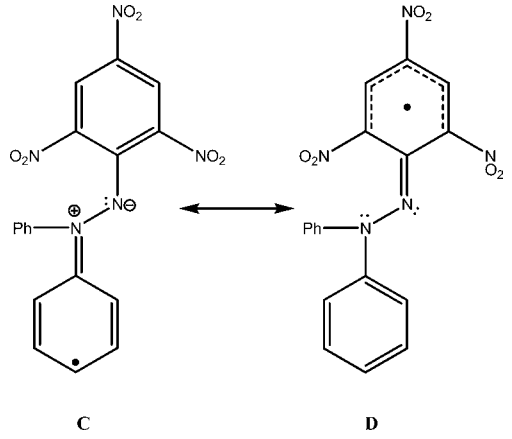

CHEMISTRY OF DPPH•

The DPPH• radical reacts selectively with radicals and H-atom donors at different reaction sites. Whereas radicals usually attack the phenyl rings (or the picryl ring) (see the canonical structures **C** and **D** below), H-atom donors react with the divalent N atom. The limited space around the N atom (see Figure 1) prevents the addition of cumbersome radicals at this site. H-atom donors can approach the N atom and can release their H-atom therein with the formation of the hydrazine DPPH−H.

Molecular oxygen in its triplet-ground state, $^3O_2$, despite being a radical, does not react with DPPH• (or it does very slowly), and solutions of DPPH• kept *in the dark*[19] are stable for long times. Furthermore, the radical does not dimerize and in solution as well as in the solid[9] state is present in the free monomeric form only.

Balaban et al.[11,20] and Ionita[21] have published several papers concerning the reaction products of DPPH• with radicals and nonradical oxidant species. Some of these data are gathered in Table 1. Several oxygen radicals afford para-substitution products at the phenyl and picryl rings along with minor quantities of *p*-NO_2-DPPH−H and fragmentation products (diphenylamine, Ph_2NH, and tetraphenylhydrazine, Ph_2N-NPh_2).[11,20,21] The aryloxyl radicals of syringaldehyde and methyl syringate (two phenolic compounds) react in dichloromethane with excess DPPH• to yield para-substitution products at the picryl ring (see Figure 3).[11] Interestingly, the supramolecular complex of the anion of syringaldehyde with crown ethers yields instead a para-substitution product at the *phenyl* rings (see Figure 3).[11]

Table 1. Products Isolated from the Reaction of Several Radicals and Oxidant Species with DPPH• (in Percent) from Reference 21

reactant	DPPH−H	NO_2-DPPH−H	HO-DPPH−H	notes
hydroxyl radical	10	5	traces	
TEMPO				no reaction
galvinoxyl				no reaction
sodium peroxide	55	33	0	
potassium superoxide	60	25	traces	
potassium hydroxide	25	12	traces	
sodium peroxynitrite	30	55	0	
hydrogen peroxide	100	0	0	
tert-butylperoxide	0	9	0	85% DPPH• recovered
tert-butylhydro-peroxide	30	40	traces	

DOI: 10.1021/acs.jafc.5b03839
J. Agric. Food Chem. 2015, 63, 8765−8776

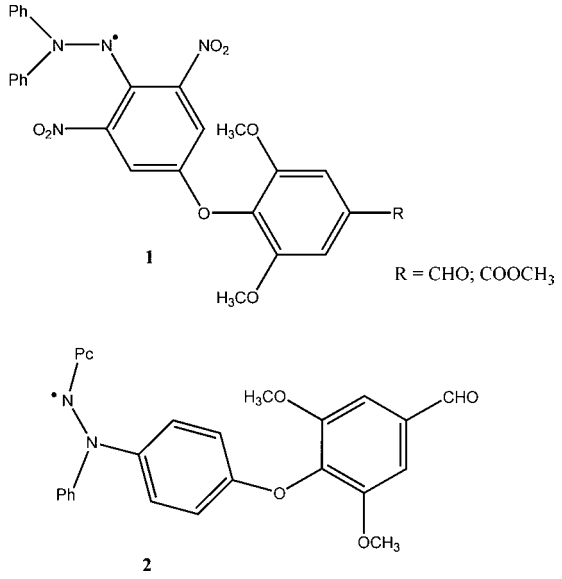

Figure 3. Structures of the compounds formed in the reaction of DPPH• with the aryloxyl radicals of syringaldehyde and methyl syringate (compound **1**) and with the anion of syringaldehyde (compound **2**) from ref 11.

■ REACTIONS OF DPPH• WITH H-ATOM DONORS

Several chemicals react with DPPH• by H-atom donation or electron transfer. Phenols (ArOH) are probably the most reactive and the most important ones, although nontertiary aromatic amines[22] and thiols[23] are of interest, too. These reactions are often used for probing the antiradical or "antioxidant" ability of natural compounds (see below). The importance of these reactions is clearly witnessed by the number of publications. Scopus lists more than 17000 papers for the decade 2005−2015 combining the words "DPPH" and "antioxidants". Most of these papers include outcomes of the so-called "DPPH test", which consists of the addition of a certain amount of a (potential) antioxidant to a DPPH• solution and the evaluation of the pecentage of DPPH• quenched after an *arbitrary* and often *variable* time[24] (minutes to hours). This test is based on the ability of DPPH• to abstract H-atoms from A−H bonds (reaction 1). The H-atom abstraction includes those reactions that occur via electron transfer followed or preceded by proton transfer and which could be classified as *formal* H-atom transfer reactions. With natural extracts, the DPPH• test gives therefore an estimation of the total content in reducers present in solution.

Reaction 1 proceeds relatively quickly only when three constraints are met: (i) the A−H bond is relatively weak (low bond dissociation enthalpy, BDE); (ii) the radical A• is stabilized by resonance; and (iii) A is a heteroatom (O, N, S).

$$A{-}H + DPPH^{\bullet} \rightarrow A^{\bullet} + DPPH{-}H \quad (1)$$

$$A^{\bullet} + DPPH^{\bullet} \rightarrow \text{closed shell products} \quad (2)$$

$$2A^{\bullet} \rightarrow \text{closed shell products} \quad (3)$$

Hydrocarbons act very rarely as H-donors to DPPH•, and when they do, the rate constants are small (see below). 1,4-Cyclohexadiene (C−H BDE = 77.9 kcal/mol),[25a] for instance, reacts with DPPH• in CCl_4 at 298 K with a rate constant of ~0.00025 M^{-1} s^{-1} per H-atom.[12] On the other hand, α-tocopherol, the O−H BDE of which (equal to 77.2 kcal/mol) is very similar to the C−H BDE in 1,4-cyclohexadiene, reacts instead with a bimolecular rate constant of 3.6×10^3 M^{-1} s^{-1},[12,25a] that is, 14,000,000 times faster![25b]

The reasons as to why DPPH• reacts quickly with phenolic O−H bonds and slowly with C−H bonds are probably very similar to those formulated for the isoelectronic peroxyl radicals (ROO•) by Ingold and Pratt[26] in their recent review on antioxidants. Two interlinked factors have been used to explain the rate acceleration of H-atom transfers between *heteroatoms*: (1) the presence of a H-bond between the H-donor and the radical (through one of its lone-pairs) in a prereaction complex and (2) a different mechanism for H-abstraction from O−H or N−H versus C−H.

In the past, it was thought (and still is now for C−H bonds), that the H-atom (proton + valence electron) simply moved from A−H toward the SOMO of the radical along the straight line A—H—SOMO.[27] We usually refer to this mechanism with the generic expression of hydrogen atom transfer (HAT), but its domain of definition has now become less clear.[28] The accepted mechanism for the H-atom exchange between two heteroatoms (e.g., ArO-H/•OOR) is now very different. Formation of a H-bond, in the prereaction complex, involving the ArO−H and *a lone-pair* of the radical ROO• (ArO−H···:ȮOR) gives rise to a peculiar exchange of the H-atom (see Figure 4). In this complex, in fact, only the nucleus (proton) of

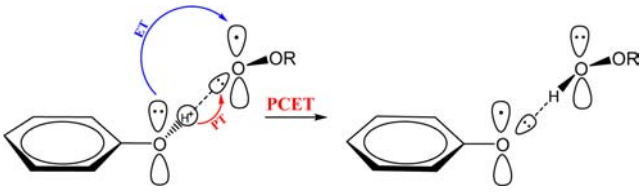

Figure 4. PCET mechanism in the reaction of phenol with an ROO• radical. The nucleus H^+ of the H-atom moves along the line O−H−O, leaving behind its valence electron. An electron is simultaneously transferred from the O lone pair to the ROO SOMO (see ref 26).

the H-atom moves toward the radical, leaving behind its bonding electron. The motion of the proton stimulates a simultaneous electron transfer from one lone pair of ArÖH toward the SOMO of ROO•, yielding the final complex (ArȮ:···H−ÖOR) in a single step. This mechanism is known as "proton-coupled electron-transfer" (PCET) because there is a concerted (single step) delivery of $1e^-$ and $1H^+$ from the donor (phenol) to the acceptor (radical) without the formation of ions.[28,29] There are cases, however (see below), in which electrons and protons are transferred to different acceptors (separated PCET),[30] and for neutral radicals (like DPPH•) this implies the formation of ion pairs. H-atom transfer via PCET is faster than HAT because the H-bond reduces the width and height of the reaction barrier.[26] As suggested by calculations, PCET is energetically favored for the exchange of H between heteroatoms. However, cases of PCET involving H exchange between C/C[31] and C/N[7] are also known. Alternative mechanisms may include electron transfer (ET) followed or preceded by proton transfer (PT) in distinct steps with the formation of high-energy intermediates (see below).

Phenols with electron-rich substituents are excellent H donors because they respond to all three requisites cited above. They are able to quickly quench ROO• radicals via PCET (see above).

DOI: 10.1021/acs.jafc.5b03839
J. Agric. Food Chem. 2015, 63, 8765−8776

$$ArOH + ROO^{\bullet} \rightarrow ArO^{\bullet} + ROOH \quad (4)$$

$$ArO^{\bullet} + ROO^{\bullet} \rightarrow \text{products} \quad (5)$$

The antioxidant abilities of ArOH are quantified by the rate constant of reaction 4, k_{ROO}. Typical values of k_{ROO} for excellent phenolic antioxidants, such as α-tocopherol, are $\sim 10^6$ M^{-1} s^{-1}.[26,33]

Up to now, reactions 4 and 5 have been considered to be of great industrial and biological importance because these reactions reduce the rate of oxidation of organic matter exposed to air (including us, of course).[26,33] In the past decade, however, the opinion that the antioxidant abilities can play a marginal role in the health benefits of dietary antioxidants such as polyphenols has taken shape.[34] This is because the in vivo concentration of these compounds is very low, and hence other mechanisms are being searched for.[34]

The study of reaction 4 can be difficult because peroxyl radicals require special precursors for their formation; moreover, they generally react rapidly with ArOH, and so sophisticated instruments are required to monitor their reaction.[35] On the contrary, the DPPH$^{\bullet}$ radical is commercially available, is colored, and is far less reactive than ROO$^{\bullet}$. In apolar solvents, the rate constant of reaction 1 for nonhindered phenols is some 3 orders of magnitude smaller than k_{ROO}; however, the two values are related because $k_{ROO} \approx 4000 \times k_1^{2/3}$.[36] Ordinary spectrophotometers can therefore be used to monitor reaction 1 (for exceptions, see below), and this has generated an explosion of works aimed at determining the *antioxidant* abilities of phenols in the general belief that the two radicals (ROO$^{\bullet}$ and DPPH$^{\bullet}$) could simply be swapped. Furthermore, kinetic solvent effects are often erroneously undervalued, and reaction 1 is made to occur in protic solvents (methanol and ethanol) because of the limited solubility of many plant-derived phenols in solvents that are not hydrogen bond acceptors, that is, alkanes. As will be shown in the pertinent section, these omissions and misconceptions make many published results and their interpretations quite improbable. This is because in polar solvents several mechanisms may coexist for ArOH + DPPH$^{\bullet}$, and the rate constants in these media do not necessarily correlate with the antioxidant ability of ArOH. Moreover, in a great many cases reaction 1 is an equilibrium reaction because the N−H BDE of DPPH−H is only 78.9 ± 0.5 kcal/mol.[10] Unreacted DPPH$^{\bullet}$ remains, for instance, in the reaction with 2,6-dimethoxyphenol (OH BDE = 82.1 kcal/mol)[7] even with a concentration ratio [ArOH]/[DPPH$^{\bullet}$] of 52:1.[10] Of course, if the initial [DPPH$^{\bullet}$] > [ArOH] (typical conditions in the DPPH$^{\bullet}$ test), then it is likely that some 2,6-dimethoxyphenol remains unreacted in solution, thereby yielding a larger EC_{50}. In both cases, slow radical/radical reactions, reactions 2 and 3, shift the equilibrium to the right.[10]

KINETIC DETERMINATION OF ArO−H BDES IN APOLAR SOLVENTS

A useful application of the kinetics of ArOH + DPPH$^{\bullet}$ was inspired by the observed relationship between the rates of ArOH + DPPH$^{\bullet}$ in apolar solvents and the phenolic O−H BDEs.[7] This correlation allowed the determination of the ArO−H BDEs of several phenols with great precision and simplicity (see Figure 5).[7]

The experimental measurement of the A−H BDE can generally be done by three broadly applicable techniques, which require considerable care: the study of radical kinetics; photoionization mass spectrometry; and the acidity/electron affinity cycle.[38] In addition, a simple and reliable EPR equilibration technique was quite recently developed by Lucarini and co-workers for the determination of ArO−H BDEs.[39a−c] This technique is based on the EPR determination of the aryloxyl radical's concentration in mixtures of 2,4,6-tri*tert*-butylphenol (*t*-BuPhOH) + ArOH submitted to continuous photolysis in the presence of di-*tert*-butylperoxide. Equilibration of the aryloxyl radicals following H-atom transfer, *t*-BuPhO$^{\bullet}$ + ArOH ⇆ *t*-BuPhOH + ArO$^{\bullet}$, is usually rapid.[40] The ΔS^0 for H-atom exchange reactions is usually very small and can be neglected. The equilibrium constant, K_{eq}, therefore, affords the value of ArO−H BDE relative to 2,4,6-tri-*tert*-butylphenol,[39c] $\Delta BDE = \Delta H^0 \cong \Delta G^0 = -RT \ln K_{eq}$.[39a] Finally, this EPR equilibration technique is valid in general and is not limited to phenols only. Recently, it was used to measure, for instance, the O−H BDE of ascorbic acid[39d] and selenenic acids[39e] (RSeOH).

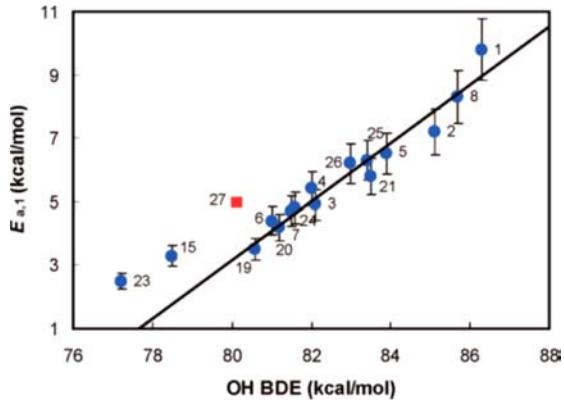

Figure 5. Plot of the activation energy for reaction 1 (A−H = ArOH) versus ArO-H BDE from ref 7. Blue circles are for 16 phenols in the group **1**−**26**. Phenols **15** and **23** were considered outliers and were excluded from the solid correlation line: $E_{a,1}$ = 0.918(O−H BDE) − 70.27 (r^2 = 0.95). The red square is for 2,4,6-tri*tert*-butylphenol, **27**.

In addition to the techniques cited above, one simple method to measure the ArO−H BDEs in apolar solvents is based on the bimolecular rate constants of ArOH + DPPH$^{\bullet}$, which correlate with the strength of the O−H bond (linear free energy relationship). Generally, this method has no critical limitations[41] except for the solubility of ArOH in apolar media. The rate constants of ArOH + DPPH$^{\bullet}$, k_{DPPH}, are easily obtainable with standard procedures, and when there are any kinetic complications, they can be obtained from the initial rates. The observed rate differences are largely due to differences in the activation energy, the Arrhenius pre-exponential factor being essentially constant, ranging from 10^5 to 10^6 M^{-1} s^{-1}.[42,43] Electronic effects of the substituents and intramolecular H-bonds influence both the ArO−H strengths and the activation energies. The equation that correlates these two parameters (in kcal/mol) is

$$E_{a,1} = 0.918 \times (\text{ArO−H BDE}) - 70.27$$

This equation can be converted in such a way that the rate constant k_{DPPH} (M^{-1} s^{-1}) appears in place of $E_{a,1}$.[43] For moderately hindered and nonhindered phenols the equations are OH BDE = 84.3 − 0.64 × ln k_{DPPH} and O−H BDE = 85.4 − 0.64 × ln k_{DPPH}, respectively, where the enthalpies are in kilocalories per mole. A single rate constant, k_{DPPH}, determined

DOI: 10.1021/acs.jafc.5b03839
J. Agric. Food Chem. 2015, 63, 8765−8776

at 298 K in apolar solvents yields by the previous equations the OH BDE of the phenol in use.[7]

SOLVENT EFFECTS: THE ROLE OF THE H-BOND

Polar solvents (PS) exert a strong influence on rates and mechanisms of H-atom abstraction by radicals. In the overwhelming majority of cases, they cause a rate *reduction*,[17a] but a few well-documented cases[44] of rate *acceleration* are also known. These kinetic solvent effects (KSEs) were fully rationalized by Ingold and co-workers in their pioneering studies done in the past 20 years.[17] The DPPH$^{\bullet}$ radical had a pivotal role in these studies[17] in combination with phenols as H-atom donors. Phenols are important antioxidants,[33] and the influence that polar environments have on their in vivo antioxidant and antiradical activities is of great importance. Phenols protect cellular membranes from peroxidation reducing the concentration of peroxyl radicals present in the membrane; they may also quench radicals in the cytoplasm, preventing cell damage. Both reactions are subjected to KSEs.

Phenols form H-bonded complexes with PS, ArOH—PS, in which the H-atom is made inaccessible by the presence of two bulky heteroatoms around. Because of this steric congestion, free radicals cannot react with these species (at least until a PCET mechanism is involved) and react only with the free fraction of ArOH (see Figure 6). Because the concentration of free ArOH decreases as the HB strength increases, the rate of reaction diminishes proportionally to the HB strength.[17a] These "standard" KSEs are observed in the vast majority of ArOH + DPPH$^{\bullet}$ reactions.

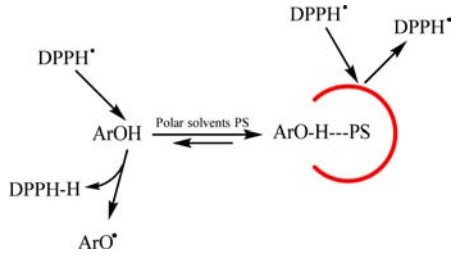

Figure 6. In polar solvents, free radicals can abstract an H-atom from the free fraction of ArOH only. H-bonded ArOHs to PSs are unable to react for steric reasons.

Nevertheless, a change in the mechanism of reaction from PCET to *separated* PCET, ET-PT, or PT-ET can have major effects on the rates because these mechanisms can bypass the steric hindrance in the H-bonded complexes.[32] Solvation of high-energy species such as ArO^{-} and ArOH$^{\bullet+}$, formed by initial PT or ET, can make the stepwise mechanisms competitive with the e^{-}/H^{+} concerted PCET (see Figure 7). These ET-PT and PT-ET mechanisms usually cause "abnormal" KSEs. In this context, Litwinienko and Ingold[45] and Foti et al.[18] discovered independently that in ionizing solvents (methanol, ethanol, water, and their mixtures) phenols react with DPPH$^{\bullet}$ essentially via ET from their anions in a PT-ET process (reactions 5 − 7), which was called sequential proton-loss electron transfer (SPLET) (see the green reaction path in Figure 7). This mechanism was proposed because (i) the KSEs in these solvents were "abnormal"[45] in that the rate constants for reaction 1 (A−H = ArOH) were found to be higher than predicted on the basis of the HB-accepting properties of alcohols;[18,17a] (ii) the rate constants decreased or increased following the addition of acids or bases, respectively;

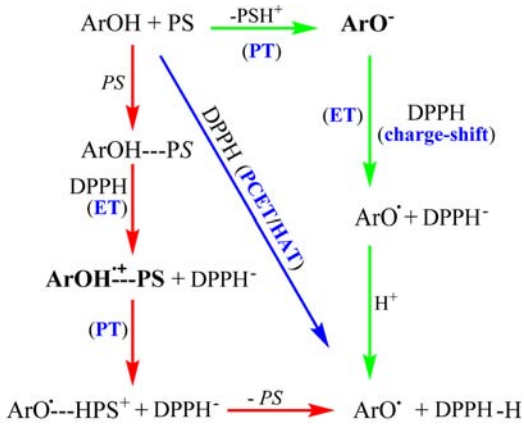

Figure 7. Reaction of phenols with DPPH$^{\bullet}$ can occur via PCET/HAT, ET-PT, or PT-ET mechanisms. The predominance of one mechanism over the others depends on various factors including the medium polarity, the ionization potentials, etc. PCET does not form any intermediate and usually prevails in both apolar and polar solvents (see text). However, for phenols with pendant bases or in a few polar solvents, for example, pyridine, separated PCET (see the corresponding paragraph) and ET-PT can be predominant despite the formation of a high-energy intermediate, ArOH$^{\bullet+}$. On the other hand, ionizing solvents support the stepwise PT-ET mechanism where the anion ArO^{-} is the high-energy intermediate. Solvation of these polar intermediates can facilitate the intervention of these stepwise mechanisms.

and (iii) the methyl esters of cinnamic acids (see Figure 8) were 3−5 times more reactive than their nonesterified counterparts.[18] The reduced reactivity of cinnamic acids relative to their esters showed that the species responsible for the DPPH$^{\bullet}$ scavenging were the phenolic anions (reaction 6). Ionization of the free COOH group reduced the amount of phenolic anions present in solution.

$$\mathrm{ArOH} \leftrightarrows \mathrm{ArO^-} + \mathrm{H^+} \quad (5)$$

$$\mathrm{ArO^-} + \mathrm{DPPH^\bullet} \rightarrow \mathrm{ArO^\bullet} + \mathrm{DPPH^-} \quad (6)$$

$$\mathrm{DPPH^-} + \mathrm{H^+} \rightarrow \mathrm{DPPH{-}H} \quad (7)$$

All of these kinetic observations led to the formulation of SPLET as a predominant mechanism for ArOH + DPPH$^{\bullet}$ reactions in protic solvents. Given the usually high oxidation potentials of phenol anions and the high reduction potentials of several biologically relevant radicals,[46] it is likely that in numerous in vivo ArOH + radical reactions the formal H-atom transfer occurs via stepwise ET mechanisms (e.g., SPLET). The E^0_{red} of DPPH$^{\bullet}$ is +0.23 V/SCE in acetonitrile[47] and perhaps larger in methanol.[48] Therefore, radicals such as $NO_2^{\bullet}$, $CO_3^{\bullet-}$, and HOO$^{\bullet}$ characterized[49] by $E^0_{red} > 0.23$ V can very likely react with phenols via ET from the anions or the neutral species. It is well-known that strongly oxidizing peroxyl radicals (e.g., halogenated peroxyls, peroxyacetyl radical $CH_3(CO)OO^{\bullet}$, etc.) react via ET with several substrates including phenolate, ascorbate, and inorganic anions, producing the corresponding radicals.[50]

REMOTE H-BOND EFFECTS AND SEPARATED PCET

Phenols with pendant piperidine **1**−**3** represent an interesting case of ArOH + DPPH$^{\bullet}$ reactions.[44a] In **1** and **2**, the presence of an intramolecular H-bond has a profound influence on the rate of H-atom abstraction from both the O−H involved in the

DOI: 10.1021/acs.jafc.5b03839
J. Agric. Food Chem. 2015, 63, 8765−8776

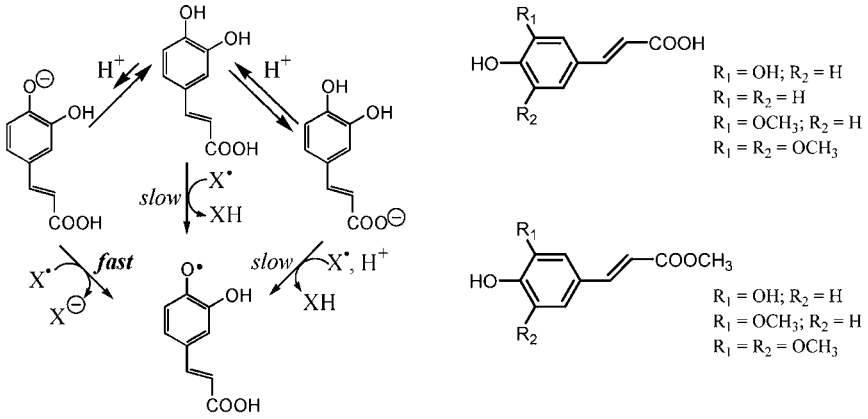

Figure 8. Cinnamic acids react with DPPH• (symbolized as X•) in methanol and ethanol via SPLET, and their rate constant k_1 decreases as the concentration of cinnamic acid increases. This happens because as the concentration of cinnamic acid rises, ionization of the COOH group limits more and more the formation of phenolic anions (the reactive species) (see ref 18). The rate constants k_1 of the methyl esters are instead large and essentially independent of their concentration.

HB (compound **1**) and the HB-free *p*-OH (compound **2**). The rate constants measured in cyclohexane at 298 K for **1**, **2**, and **3** are 2.5, 7800, and 400 M^{-1} s^{-1}, respectively (Table 2). The mechanism involved in these reactions in cyclohexane is most likely PCET/HAT.

Table 2. Rate Constants for the Reactions of 1−3 with DPPH• at 25 °C from Reference 44a

	k_{DPPH} (M^{-1} s^{-1})	
phenol	cyclohexane	acetonitrile
1	2.5 ± 0.5	1200 ± 60
2	7800 ± 30	2340 ± 25
3	400 ± 30	280 ± 60

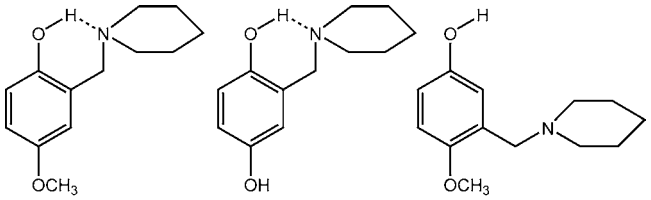

The low reactivity of **1** relative to **3** shows the "protective role" that a H-bond may have on phenolic H-atoms. Generally, free radicals react slowly with intramolecularly H-bonded phenols because the HB increases the energy required to pull the H-atom out. In a great many cases, natural polyphenols are intramolecularly H-bonded to methoxy groups, which probably serve as a sort of "padlock" to protect phenols from radicals and facilitate their arrival at the final reaction site.

On the other hand, the rate constants show that phenol **2** is much more reactive than both **1** and **3** (Table 2). The higher reactivity relative to **1** suggests immediately that the reaction site in phenol **2** is the H-bond free O−H. Interestingly, phenol **2** is also some 20 times more reactive than **3** because of the effects of the "remote H-bond".[51] H-bond effects have been observed in many other dihydroxybenzenes with catechol-, hydroquinone-, and resorcinol-like structure and also in 1,8-naphthalenediols.[37,51] The orientation of the remote H-bond determines the sign of the variation: para → meta H-bonds cause an *increase* in the rate of H-abstraction (as in the case of phenol **2**), whereas meta → para orientations determine a *decrease* in the rate relative to molecules lacking H-bonds.[51b]

The explanation given for these effects is that the −O• in the aryloxyl radical has strong electron-withdrawing character (see Figure 9). This causes an O−H group in the para position of

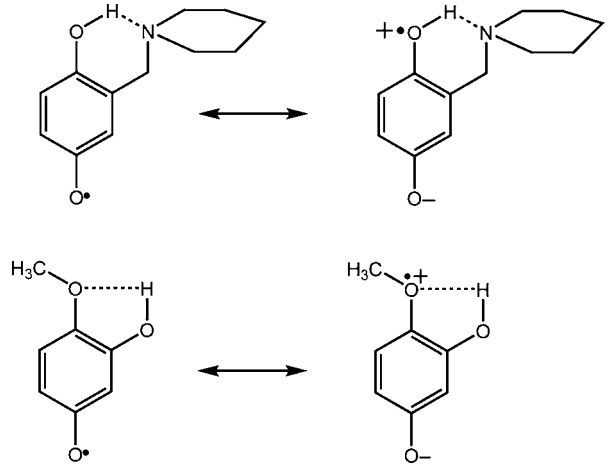

Figure 9. Canonical structures for aryloxyl radicals with remote H-bonds. In both radicals, the presence of the electron-withdrawing −O• group determines a decrease in the electron density of the O atom in the para position. This causes opposite effects in the two radicals. In the aryloxyl with para → meta oriented H-bond (upper case), the increased acidity of the H-bonded O−H determines a reinforcement of the H-bond. This stabilization is reflected in the transition state of the reaction and hence causes an increase in the reactivity of the parent phenol. Conversely, the strength of the H-bond decreases in the aryloxyl with meta → para orientation, and this causes a reduction in the reactivity of the parent phenol because the transition state is destabilized.

ArO• to become more acidic than in the parent molecules and hence capable of forming stronger H-bonds with HB-acceptors in the meta position. For the same reasons, HB-acceptors (such as OCH_3) in the para position become more electron-deficient and form therefore weaker HBs in the aryloxyl radicals than in the parent molecules (see Figure 9). These thermochemistries influence the transition states and thus the kinetics of H-abstraction from phenols by free radicals.

DOI: 10.1021/acs.jafc.5b03839
J. Agric. Food Chem. 2015, 63, 8765−8776

When the solvent is changed from cyclohexane to acetonitrile, the new rate constants showed clearly that the mechanism of DPPH• quenching had changed (see Table 2). The rate constant of **1** increased in acetonitrile by a factor of 480 (k_1 = 1200 M^{-1} s^{-1}), whereas those of **2** and **3** decreased a bit, but the decrease was confined within a factor of 1.4−3.3 (the expected reduction for a PCET/HAT mechanism in acetonitrile would be by a factor of about 70!).[17a]

An apparently reasonable mechanism for **3** + DPPH• in acetonitrile, consistent with the above kinetic data, was suggested by the thermodynamically plausible self-ionization of **3** (reaction 8). The equilibrium constant for this auto-

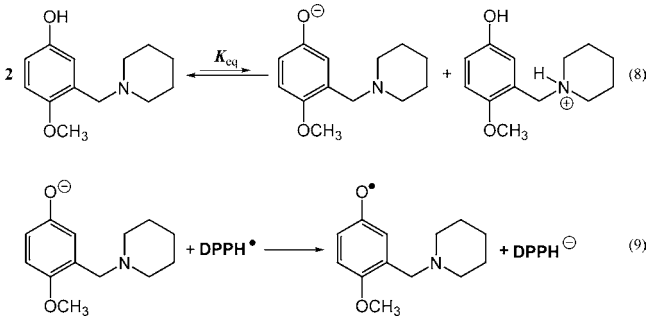

ionization was estimated[44a] to be ∼10^{-8}, a value much greater than the typical K_a ∼ 10^{-25}−10^{-20} of phenols in acetonitrile.[32] Thereby, comparatively large quantities of phenol anions[52] were formed in solution by reaction 8, and these most likely reacted via ET to DPPH• (reaction 9). The overall process represents a special case of SPLET in a nonprotic solvent (acetonitrile) stimulated by the presence of the nitrogen base.

On the other hand, it appears highly probable that phenols **1** and **2** reacted both through a separated[30] PCET pathway, with e^- and H^+ being transferred to DPPH• and piperidine nitrogen, respectively (see reactions 10 and 11) (see also Figure 10). Nevertheless, the kinetic behaviors of the two phenols were very different. Whereas **2** reacted with a pseudo-first-order process, the kinetics of **1** + DPPH• showed a biphasic behavior with an initial fast process (first 300 ms) followed by a second slower DPPH• loss for some tens of seconds. Kinetic evaluations led the first step to be attributed to the equilibrium formation of a metastable distonic radical cation in contact with $DPPH^-$, whereas the second slow step to the dissolution of the ion pair (see reaction 10).

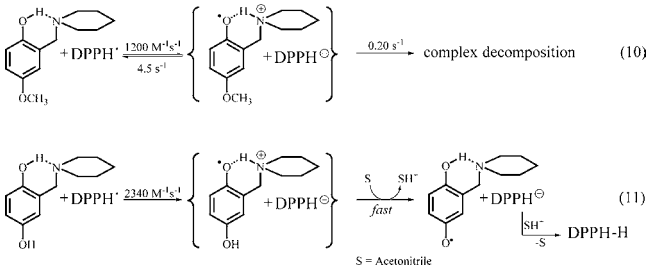

The different kinetic behaviors of the two phenols were interpreted as due to the fact that the distonic radical cation of **2**, unlike the other case, was able to rapidly "shoot" an H^+ from the free OH into the bulk solution because radical cations of phenols are very acidic.[53] This fast process impeded the formation of the equilibrium that was instead attained with **1**, and thus the initial step became rate-determining (reaction 11).

THE REMARKABLE CASE OF QUERCETIN + DPPH• REACTION

Quercetin (QH_2) is a flavonoid widely distributed in the plant kingdom.[54] A balanced daily diet supplies us with a few tens of milligrams of flavonoids chiefly constituted by quercetin.[55] Generally, flavonoids are believed to provide certain health benefits that are usually attributed to their ability to trap free radicals. This ability is actually common to all phenols and does not necessarily reflect their "antioxidant properties" (see above). As most phenols, QH_2 is in fact able to quench both DPPH• and ROO• radicals. This might seem rather trivial in view of the nature of the molecule. The quenching process of DPPH• in methanol/water deserves, however, our attention because it shows how insidious the analysis of the DPPH• kinetics can be and how dissimilar these kinetics are from those of the ROO• radical.[56]

The reported values in the literature of the rate constant for QH_2 + DPPH• in methanol at room temperature surprisingly span a large range from a low of 264 M^{-1} s^{-1} to a high of 6433 M^{-1} s^{-1}.[57] These values were actually measured with conventional spectrophotometers at 519 nm (λ_{max} DPPH•) in a time frame long after the "true" reaction of DPPH• with QH_2 had occurred. This was deduced by using stopped-flow spectrophotometers, which allowed us to observe that the QH_2 + DPPH• reaction in methanol/water 80:20 v/v was over after only 100−300 ms![56] So what was actually being measured when the apparent loss of DPPH• was monitored with conventional spectrophotometers at $t \gg 300$ ms?

To answer this question, it is necessary to re-examine the chemistry of quercetin oxidation.[58] The two-electron oxidation of QH_2 yields quinone/quinomethide products (reaction 12), which are intensely colored.[58] Several tautomers can exist in solution, but according to quantum chemical calculations,[58] the tautomer Q shown in reaction 12 is the most stable and the most abundant in solution. The striking aspect of these compounds is that their UV−vis spectra and color are fortuitously very similar to those of DPPH•.[56] This has created

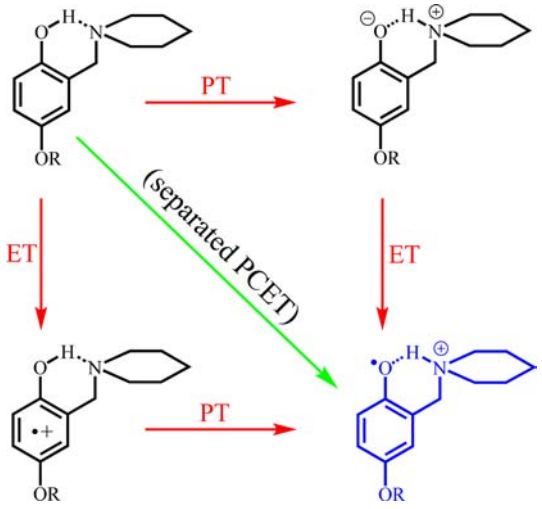

Figure 10. Peripheral pathways to the distonic radical cation shown with red arrows include high-energy species and hence may be kinetically disfavored. The diagonal path (PCET) is instead favored because e^- and H^+ are transferred simultaneously to their respective acceptors, that is, DPPH• and piperidine N, without formation of intermediates.

DOI: 10.1021/acs.jafc.5b03839
J. Agric. Food Chem. 2015, 63, 8765−8776

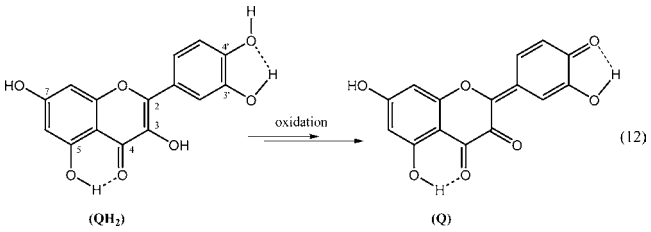

a grave problem of interpretation of the 519 nm absorbance decay at long times, because this decay has been interpreted as a relatively slow loss of DPPH• caused by QH_2. Actually, the QH_2 + DPPH• reaction is so fast that DPPH• is consumed long before any measurements in conventional spectrophotometers can be made.[56] This is because the 2e oxidation of QH_2 by DPPH• proceeds in methanol/water via SPLET in a sequence of reactions shown in Figure 11. The rate law of this process is first-order in DPPH• but only ca. 0.38 order in QH_2, which suggests that the charge-shift occurs in a complex, maybe formed by π-stacking of the reactants, $\{QH^-/DPPH^•\} \rightarrow \{QH^•/DPPH^-\}$.[56] The semiquinone radical QH• generated is likely to rapidly ionize (the Brønsted base being either the DPPH anion in the complex or the solvent) because this radical is expected to be more acidic than QH_2 for the electron-withdrawing character of the −O• group (see above).[53] The radical anion $Q^{•-}$ so derived gives rise to a second ET process to DPPH• with formation of colored quinones/quinomethides, Q (see reaction 12 and Figure 11).

The kinetics at t > 300 ms, monitored with ordinary spectrophotometers, are due to the decay of the quinomethide Q by solvent (MeOH, H_2O) and QH_2 addition. Such addition products have been identified by several workers.[56,57a,59] The quinonemethide, Q, can in fact be regarded as a highly stabilized benzylic carbocation[60] (see Figure 12), which can readily undergo a proton-assisted (Michael-type) nucleophilic addition.

The above case clearly shows how unwise is the evaluation of kinetic or chemical properties from measurements made away from the initial time (the rapid mixing of the reactants) relying particularly on the reaction color. In truth, it is very important to check the initial stage of the reaction with a stopped-flow instrument to get a clear insight into the reaction path.

The above example also shows that the kinetics of DPPH• + flavonoids in alcohols can be very complicated because they involve flavonoid ionization, complexation, and ET mechanisms.[61] These kinetics can prudently be untangled because the DPPH• radical can be directly "observed". In the case of ArOH + ROO•,[62] the most likely mechanism of reaction is PCET (although strongly oxidizing ROO• may react via ET, see above) and thus the estimate of the antioxidant properties of ArOH from the kinetics of ArOH + DPPH• in alcohols can be mistaken.

"THE DPPH• TEST"

The DPPH• test for appraising the antioxidant activity of chemicals (AH) was first suggested by Blois in 1958.[8] Then, the test was developed by Brand-Williams et al.[15] in 1995 in the form adopted by the vast majority of researchers. Briefly, different AH concentrations are used in such a way to determine the concentration of AH that quenches 50% of the initial DPPH• radical in a specific, although arbitrary, time interval. This concentration is called (efficient concentration) EC_{50} or, sometimes, (inhibitory concentration) IC_{50}. In truth, this EC_{50} designation has a proper scientific usage under a different name (LD_{50}) in drug testing. It is likely that the term was "hijacked" to put a veneer of respectability on a questionable measurement using DPPH•. At any rate, it seems obvious that the lower the EC_{50}, the higher the antiradical ability of AH. There are, however, many issues associated with the EC_{50} parameter and its interpretation.

First is the time interval. EC_{50} is time-dependent, and the effect of time can vary from compound to compound.[63] Usually, increasing the reaction time may improve the evaluation of a given compound (lower EC_{50}), and hence the test can be tailored so that a poor antiradical/antioxidant appears to be an excellent antiradical/antioxidant. It is clear therefore that the interpretation of this test is quite arbitrary, and any comparison between results from different laboratories is not possible if the adopted reaction time is different. In general, short reaction times are better than long times in the questionable evaluation of the antioxidant abilities of chemicals from the DPPH• test.[63]

Second, EC_{50} is *not* a kinetic parameter (it is just a concentration), and as such it cannot express the antioxidant or antiradical ability of a compound, because this ability must be

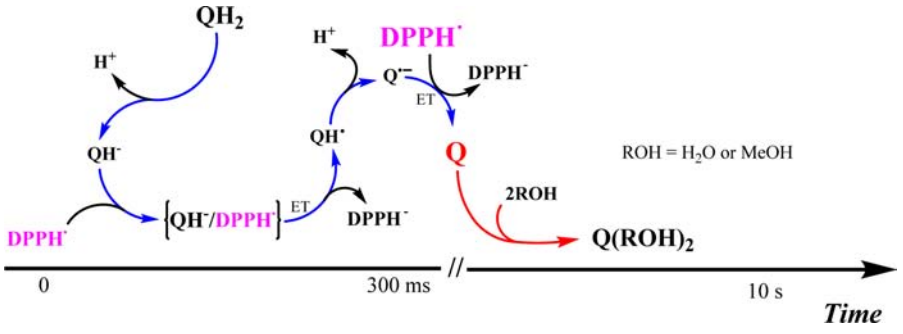

Figure 11. Time evolution of the reaction QH_2 + DPPH• in methanol/water 80:20 v/v at room temperature. The pathway in blue shows the conversion of quercetin into quinomethide Q in a time scale of about 100−300 ms. The pathway in red represents instead the slow (time scale of seconds) decay of Q by solvent and QH_2 addition (see text). The electron donor is the quercetin anion (from the 7-OH) because the addition of acetic acid blocks the reaction. On the other hand, the rate law suggests that QH^- and DPPH• are associated in a complex before reaction. π-Stacked complexes $\{QH^-/DPPH^•\}$ are likely to be present in solution and can convert into the ET products, QH• and $DPPH^-$. Ionization of the semiquinone radical QH• (see text) yields the radical anion $Q^{•-}$, which can give rise to a second ET to DPPH• with formation of quinones/quinomethides intensely colored, Q. These compounds can add solvent and QH_2 molecules forming *colorless* compounds.

DOI: 10.1021/acs.jafc.5b03839
J. Agric. Food Chem. 2015, 63, 8765−8776

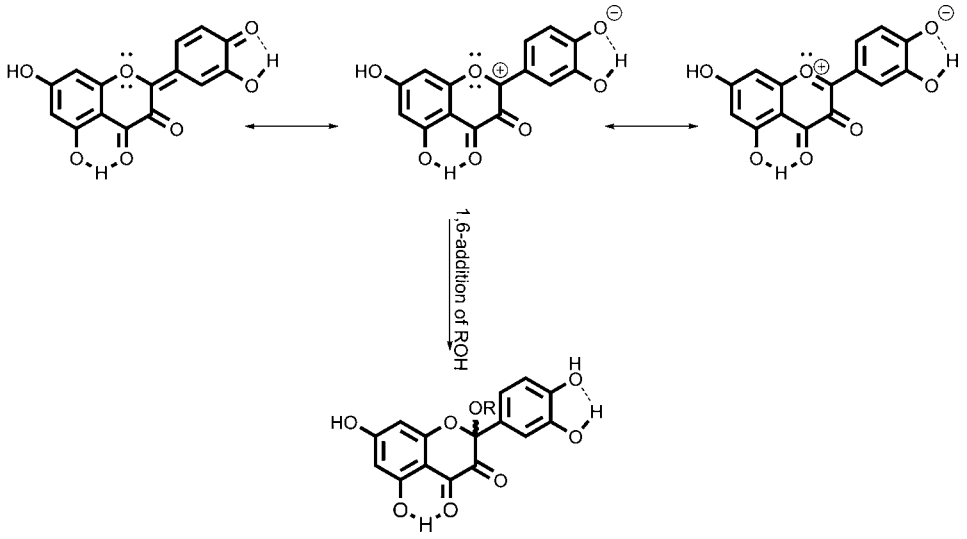

Figure 12. Carbon C2 in Q is electrophilic because of the effects of the quinone moiety. Addition of solvent can therefore easily happen with the formation of colorless compounds.

represented by a kinetic parameter. To establish whether AH is or is not a good antioxidant, it is necessary in fact to compare the *rate* at which AH quenches peroxyl radicals to the *rate* at which peroxyl radicals attack the substrate. The value of EC_{50} is instead essentially related to the stoichiometric factor, *n*, of reaction 13, which is an important complementary parameter for antioxidants (for good antioxidants, $n \geq 2$) that can be easily obtained from the DPPH$^\bullet$ test ($n = ((\Delta[DPPH])/[AH])$ at long times). If reaction 13 is complete, EC_{50} is inversely proportional to *n* because $EC_{50} = [DPPH]_0/2n$ and thus phytochemicals with large stoichiometric factors, *n*, can be classified by the test as powerful antioxidants (low values of EC_{50}) despite the fact that the quenching of DPPH$^\bullet$ may have occurred in one century! Furthermore, the stoichiometric factor *n* (and thus the EC_{50}) may depend on the concentration of AH used in the experiments[6] (see Figure 13). This dependence can be explained via the radical/radical reactions 2 and 3, which take place after the formation of the radical A$^\bullet$ (reaction 1).

$$AH + n\text{DPPH}^\bullet \rightarrow \text{products} \quad (13)$$

It is clear that if reaction 2 is faster than reaction 3, then $n \rightarrow 2$ per single H-atom donated by AH, whereas in the opposite case $n \rightarrow 1$. Anyhow, as the concentration of AH is increased, reaction 3 tends to predominate over reaction 2 and $n \rightarrow 1$ (see Figure 13). Finally, the products formed in reactions 2 and 3 may react with DPPH$^\bullet$, increasing the value of *n*. Obviously, this circumstance is extremely positive because these products contribute to the quenching of DPPH$^\bullet$ and therefore may have antioxidant properties.

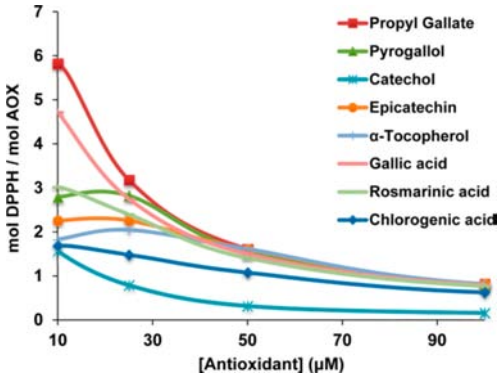

Figure 13. Stoichiometric coefficients for reaction 13 at various concentrations of the H-atom donors. Reprinted from ref 6. Copyright 2014 American Chemical Society.

Third, the quenching mechanisms of DPPH$^\bullet$ and ROO$^\bullet$ may differ. In this case, the evaluation of the antioxidant ability from the DPPH$^\bullet$ test can be deceptive. Usually, the DPPH$^\bullet$ test is done in methanol or ethanol for the ease of solubilization of many phytochemicals including phenols. In alcoholic solutions, however, phenols ionize and thus react with DPPH$^\bullet$ via SPLET (see above), that is, via ET from their anions. In many cases, acidic phenols react relatively rapidly with DPPH$^\bullet$ but slowly with ROO$^\bullet$ because this radical reacts via PCET and the O−H bonds, in this case, have large BDEs. The antioxidant ability of phenols in fact correlates in apolar media with the gas-phase ArO−H BDE (see above). One good example displaying this discrepancy is the following. The 4-cyano-2,6-di-*tert*-butylphenol shows in methanol a higher reactivity toward DPPH$^\bullet$ than the 4-methoxy- and 4-methyl-2,6-di-*tert*-butylphenol. The values of the rate constants are 16, 3.9, and 3.7 M^{-1} s^{-1}, respectively.[63−65] On the other hand, the antioxidant abilities follow the order 4-methoxy- > 4-methyl- ≫ 4-cyano-2,6-di-*tert*-butylphenol.[63]

In conclusion, the "three points" exposed above show pretty well that the much-vaunted DPPH$^\bullet$ test is in fact unsuitable to provide the information for which it was created. The antioxidant properties of phytochemicals must be expressed by a kinetic parameter that can be obtained by studying the DPPH$^\bullet$ decay versus time in appropriate solvents (alkanes, THF, CH_3CN, and other nonionizing solvents), where the complications of ionic mechanisms do not emerge, and with appropriate instruments (conventional vs stopped-flow spectrophotometers). The second-order rate constant k_{DPPH} of reaction 1 is one of the best surrogate parameters useful to prudently evaluate the antioxidant properties of chemicals. For pure compounds, the DPPH$^\bullet$ test can be used to determine the stoichiometric factor *n*, whereas for natural mixtures it serves to titrate the content in H-atom donors (or more in general "reducers") present in the sample. In these cases, the test can be

DOI: 10.1021/acs.jafc.5b03839
J. Agric. Food Chem. 2015, 63, 8765−8776

done in any solvents including alcohols because it is likely that neither *n* nor the content in H-donors is significantly influenced by the solvent.

Despite all of these complications, the DPPH• radical has contributed much to the enlargement of scientific knowledge. The long "scientific life" of this radical has allowed the study and understanding of many chemical phenomena such as kinetic solvent effects, remote H-bond effects, reaction mechanisms involving free radicals, antioxidant properties of phenols, and the strength of the ArO−H bond to name but a few. However, the extreme importance of antioxidant chemistry, as a major theme of free radical chemistry,[26] continues to be used to justify the main usage of this artificial radical: the search for the "perfect antioxidant"!

AUTHOR INFORMATION

Corresponding Author

*Phone: +39 095 733 8343. Fax: +39 095 733 8310. E-mail: mario.foti@cnr.it.

Notes

Partially presented at the "International Conference on Hydrogen Atom Abstraction" (iCHAT) held in Rome in 2014. The authors declare no competing financial interest.

ACKNOWLEDGMENTS

I wish to express my sincere appreciation to all of the reviewers of this work for their helpful and constructive advice.

REFERENCES

(1) π-Radicals are those in which the SOMO is orthogonal to the local molecular plane; in the case of σ-radicals the orbital lies in the plane.

(2) Goldschmidt, S.; Renn, K. Zweiwertiger sticlstoff: über das α,α-diphenyl-β-trinitrophenyl hydrazyl. *Ber. Dtsch. Chem. Ges. B* **1922**, *B55*, 628−643.

(3) Hicks, R. G. Verdazyls and related radicals containing the hydrazyl [R_2N-NR] group. In *Stable Radicals: Fundamentals and Applied Aspects of Odd-Electron Compounds*; Hicks, R. G., Ed.; Wiley: Hoboken, NJ, USA, 2010; pp 245−279.

(4) Fargere, T.; Abdennadher, M.; Delmas, M.; Boutevin, B. Determination of peroxides and hydroperoxides with 2,2-diphenyl-1-picrylhydrazyl (DPPH). Application to ozonized ethylene vinyl acetate copolymers (EVA). *Eur. Polym. J.* **1995**, *31*, 489−497.

(5) Yordanov, N. D.; Christova, A. DPPH as a primary standard for quantitative EPR spectrometry. *Appl. Magn. Reson.* **1994**, *6*, 341−345.

(6) Xie, J.; Schaich, K. M. Re-evaluation of the 2,2-diphenyl-1-picrylhydrazyl free radical (DPPH) assay for antioxidant activity. *J. Agric. Food Chem.* **2014**, *62*, 4251−4260.

(7) Foti, M. C.; Daquino, C.; Mackie, I. D.; DiLabio, G. A.; Ingold, K. U. Reaction of phenols with the 2,2-diphenyl-1-picrylhydrazyl radical. Kinetics and DFT calculations applied to determine ArO-H bond dissociation enthalpies and reaction mechanism. *J. Org. Chem.* **2008**, *73*, 9270−9282.

(8) Blois, M. S. Antioxidant determinations by the use of a stable free radical. *Nature* **1958**, *181*, 1199−1200.

(9) Boucherle, J. X.; Gillon, B.; Maruani, J.; Schweizer, J. Spin distribution in the diphenylpicrylhydrazyl (DPPH) radical measured by neutron diffraction. *Mol. Phys.* **1987**, *60*, 1121−1142. Williams, D. E. Structure of 2,2-diphenyl-1-picrylhydrazyl free radical. *J. Am. Chem. Soc.* **1966**, *88*, 5665−5666. Williams, D. E. Crystal structure of 2,2-diphenyl-1-picrylhydrazyl free radical. *J. Am. Chem. Soc.* **1967**, *89*, 4280−4287.

(10) Foti, M. C.; Daquino, C. Kinetic and thermodynamic parameters for the equilibrium reactions of phenols with the dpph• radical. *Chem. Commun.* **2006**, 3252−3254.

(11) Hristea, E. N.; Covaci-Cimpeanu, I. C.; Ionita, G.; Ionita, P.; Draghici, C.; Caproiu, M. T.; Hillebrand, M.; Constantinescu, T.; Balaban, A. T. Reactions of 2,2-diphenyl-1-picrylhydrazyl (DPPH) with two syringylic phenols or one aroxide derivative. *Eur. J. Org. Chem.* **2009**, *2009*, 626−634 and refs cited therein.. See also: Smith, M. B.; March, J. In *March's Advanced Organic Chemistry*, 6th ed.; Wiley: Hoboken, NJ, USA, 2007.

(12) Valgimigli, L.; Ingold, K. U.; Lusztyk, J. Solvent effects on the reactivity and free spin distribution of 2,2-diphenyl-1-picrylhydrazyl radicals. *J. Org. Chem.* **1996**, *61*, 7947−7950.

(13) (a) Kawai, A.; Shibuya, K. Energy separation between quartet and doublet spin states of radical-triplet encounter pairs; unusual ferromagnetic interaction in a 1,1-diphenyl-2-picrylhydrazyl and triplet coronene pair. *J. Phys. Chem. A* **2002**, *106*, 12305−12314. (b) Chen, O.; Zhuang, J.; Guzzetta, F.; Lynch, J.; Angerhofer, A.; Cao, Y. C. Synthesis of water-soluble 2,2′-diphenyl-1-picrylhydrazyl nanoparticles: a new standard for electron paramagnetic resonance spectroscopy. *J. Am. Chem. Soc.* **2009**, *131*, 12542−12543.

(14) For instance, λ_{max} (nm) and ε (M^{-1} cm^{-1}) in acetone are, respectively, 517 and 11680; in cyclohexane, 513 and 12000; in methanol, 515 and 10870; in acetonitrile, 518 and 12400; and in dichloromethane, 528 and 12000.

(15) Brand-Williams, W.; Cuvelier, M. E.; Berset, C. Use of a free radical method to evaluate antioxidant activity. *LWT−Food Sci. Technol.* **1995**, *28*, 25−30.

(16) Nakanishi, I.; Ohkubo, K.; Imai, K.; Kamibayashi, M.; Yoshihashi, Y.; Matsumoto, K.-I.; Fukuhara, K.; Terada, K.; Itoh, S.; Ozawag, T.; Fukuzumi, S. Solubilisation of a 2,2-diphenyl-1-picrylhydrazyl radical in water by β-cyclodextrin to evaluate the radical-scavenging activity of antioxidants in aqueous media. *Chem. Commun.* **2015**, *51*, 8311−8314.

(17) (a) Snelgrove, D. W.; Lusztyk, J.; Banks, J. T.; Mulder, P.; Ingold, K. U. Kinetic solvent effects on hydrogen-atom abstractions: reliable, quantitative predictions via a single empirical equation. *J. Am. Chem. Soc.* **2001**, *123*, 469−477. (b) Litwinienko, G.; Ingold, K. U. Solvent effects on the rates and mechanisms of reaction of phenols with free radicals. *Acc. Chem. Res.* **2007**, *40*, 222−230.

(18) Foti, M. C.; Daquino, C.; Geraci, C. Electron-transfer reaction of cinnamic acids and their methyl esters with the DPPH radical in alcoholic solutions. *J. Org. Chem.* **2004**, *69*, 2309−2314.

(19) The following reference reports that molecular oxygen does not react with DPPH• dissolved in acetone and kept in the dark. However, in the presence of light the authors claim that oxygen *does* react with DPPH•. See: Ozcelik, B.; Lee, J. H.; Min, D. B. Effects of light, oxygen, and pH on the absorbance of 2,2-diphenyl-1-picrylhydrazyl. *J. Food Sci.* **2003**, *68*, 487−490.

(20) Hristeac, E. N.; Caproiu, M. T.; Pencu, G.; Hillebrand, M.; Constantinescu, T.; Balaban, A. T. Reaction of 2,2-diphenyl-1-picrylhydrazyl with HO•, O_2•−, HO^-, and HOO^- radicals and anions. *Int. J. Mol. Sci.* **2006**, *7*, 130−143.

(21) Ionita, P. Is DPPH stable free radical a good scavenger for oxygen active species? *Chem. Pap.* **2005**, *59*, 11−16.

(22) Ismail, H.; Mirza, B.; Haq, I.; Shabbir, M.; Akhter, Z.; Basharat, A. Synthesis, characterization, and pharmacological evaluation of selected aromatic amines *J. Chem.* **2015**, *2015*, article ID 465286, 9 pp10.1155/2015/465286.

(23) Hunsaker, D. B. The determination of thiols with diphenylpicrylhydrazyl as a spectrophotometric reagent. *Talanta* **1983**, *30*, 475−480. Flood, J.; Russell, K. E. Kinetic, Electron spin resonance, and product studies of the reaction between 2,2-diphenyl-1-picrylhydrazyl and 2,4,6-tri-t-butylbenzenethiol. *Can. J. Chem.* **1975**, *53*, 1123−1128.

(24) Pyrzynska, K.; Pękal, A. Application of free radical diphenylpicrylhydrazyl (DPPH) to estimate the antioxidant capacity of food samples. *Anal. Methods* **2013**, *5*, 4288−4295.

(25) (a) Amorati, R.; Foti, M. C.; Valgimigli, L. Antioxidant Activity of Essential Oils. *J. Agric. Food Chem.* **2013**, *61*, 10835−10847. (b) The overall experimental rate constant is 0.001 M^{-1} s^{-1}.[12] However, in 1,4-cyclohexadiene there are four bis-allylic H-atoms, and thus the rate

DOI: 10.1021/acs.jafc.5b03839
J. Agric. Food Chem. 2015, 63, 8765−8776

constant per H-atom is 0.001/4 = 0.00025 M^{-1} s^{-1}. In ref 25a, the *overall* rate constant of 1,4-cyclohexadiene was used for the comparison that of α-tocopherol..

(26) Ingold, K. U.; Pratt, D. A. Advances in radical-trapping antioxidant chemistry in the 21st century: a kinetics and mechanisms perspective. *Chem. Rev.* **2014**, *114*, 9022−9046.

(27) Zavitsas, A. A.; Melikian, A. A. Hydrogen abstractions by free radicals. Factors controlling reactivity. *J. Am. Chem. Soc.* **1975**, *97*, 2757−2763.

(28) (a) Huynh, M. H. V.; Meyer, T. J. Proton-coupled electron transfer. *Chem. Rev.* **2007**, *107*, 5004−5064. (b) Mayer, J. M.; Hrovat, D. A.; Thomas, J. L.; Borden, W. T. Proton-coupled electron transfer versus hydrogen atom transfer in benzyl/toluene, methoxyl/methanol, and phenoxyl/phenol self-exchange reactions. *J. Am. Chem. Soc.* **2002**, *124*, 11142−11147. (c) Warren, J. J.; Mayer, J. M. Moving protons and electrons in biomimetic systems. *Biochemistry* **2015**, *54*, 1863−1878.

(29) In the case of $DPPH^{\bullet}$ the transition states for the reactions with phenol and 3- and 4-methoxyphenol show that the reactions cannot be described as occurring exclusively by either a HAT or a PCET mechanism (see ref 7). Also, the formation of a prereaction complex is hampered by the NO_2 groups of the radical. The H-bonded complexes with these groups keep phenols off the reaction path (see ref 32).

(30) Markle, T. F.; Rhile, I. J.; DiPasquale, A. G.; Mayer, J. M. Probing concerted proton−electron transfer in phenol−imidazoles. *Proc. Natl. Acad. Sci. U. S. A.* **2008**, *105*, 8185−8190.

(31) DiLabio, G. A.; Johnson, E. R. Lone pair−π and π−π interactions play an important role in proton-coupled electron transfer reactions. *J. Am. Chem. Soc.* **2007**, *129*, 6199−6203 (see also ref 7)..

(32) Foti, M. C. Solvent effects on the activation parameters of the reaction between an α-tocopherol analogue and $dpph^{\bullet}$: the role of H-bonded complexes. *Int. J. Chem. Kinet.* **2012**, *44*, 524−531.

(33) Foti, M. C. Antioxidant properties of phenols. *J. Pharm. Pharmacol.* **2007**, *59*, 1673−1685.

(34) (a) Forman, H. J.; Davies, K. J. A.; Ursini, F. How do nutritional antioxidants really work: nucleophilic tone and para-hormesis versus free radical scavenging in vivo. *Free Radical Biol. Med.* **2014**, *66*, 24−35. (b) Niki, E. Role of vitamin E as a lipid-soluble peroxyl radical scavenger: in vitro and in vivo evidence. *Free Radical Biol. Med.* **2014**, *66*, 3−12.

(35) Alfassi, Z. In *Peroxyl Radicals*; Wiley: Chichester, UK, 1997.

(36) This empirical equation was obtained by correlating the rate constants of ArOH + $DPPH^{\bullet}$ reactions with those involving polystyrylperoxyls as abstracting radicals (see refs 10 and 37).

(37) Foti, M. C.; Johnson, E. R.; Vinqvist, M. R.; Wright, J. S.; Barclay, L. R. C.; Ingold, K. U. Naphthalene diols: a new class of antioxidants intramolecular hydrogen bonding in catechols, naphthalene diols, and their aryloxyl radicals. *J. Org. Chem.* **2002**, *67*, 5190−5196.

(38) Blanksby, S. J.; Ellison, G. B. Bond dissociation energies of organic molecules. *Acc. Chem. Res.* **2003**, *36*, 255−263.

(39) (a) Lucarini, M.; Pedrielli, P.; Pedulli, G. F.; Cabiddu, S.; Fattuoni, C. Bond dissociation energies of OH bonds in substituted phenols from equilibration studies. *J. Org. Chem.* **1996**, *61*, 9259−9263. (b) Brigati, G.; Lucarini, M.; Mugnaini, V.; Pedulli, G. F. Determination of the substituent effect on the OH bond dissociation enthalpies of phenolic antioxidants by the EPR radical equilibration technique. *J. Org. Chem.* **2002**, *67*, 4828−4832. (c) Mulder, P.; Korth, H.-G.; Pratt, D. A.; DiLabio, G. A.; Valgimigli, L.; Pedulli, G. F.; Ingold, K. U. Critical re-evaluation of the O-H bond dissociation enthalpy in phenol. *J. Phys. Chem. A* **2005**, *109*, 2647−2655. (d) Amorati, R.; Pedulli, G. F.; Valgimigli, L. Kinetic and thermodynamic aspects of the chain-breaking antioxidant activity of ascorbic acid derivatives in non-aqueous media. *Org. Biomol. Chem.* **2011**, *9*, 3792−3800. (e) Zielinski, Z.; Presseau, N.; Amorati, R.; Valgimigli, L.; Pratt, D. A. Redox Chemistry of selenenic acids and the insight it brings on transition state geometry in the reactions of peroxyl radicals. *J. Am. Chem. Soc.* **2014**, *136*, 1570−1578.

(40) Foti, M.; Ingold, K. U.; Lusztyk, J. The surprisingly high reactivity of phenoxyl radicals. *J. Am. Chem. Soc.* **1994**, *116*, 9440−9447.

(41) The straight-line used to calculate ArO-H BDEs from $k_{DPPH}^{\bullet}$ (see Figure 5) was built using well-established values of ArO-H BDEs determined with the EPR equilibration technique. These values are based on the OH BDE of 2,4,6-tri-*tert*-butylphenol, which was recently reviewed (see ref 39c).

(42) The *A* value of strongly hindered phenols, such as 2,4,6-tri*tert*-butylphenol, is much lower, ∼10^3 M^{-1} s^{-1}. These phenols were not included in the group of phenols used to construct the E_a/ArO-H BDE relationship.

(43) The *A* values for moderately hindered phenols and nonhindered phenols are 2.2 × 10^5 and 1.2 × 10^6 M^{-1} s^{-1}, respectively (see ref 7).

(44) (a) Amorati, R.; Menichetti, S.; Viglianisi, C.; Foti, M. C. Proton−electron transfer pathways in the reactions of peroxyl and dpph˙ radicals with hydrogen-bonded phenols. *Chem. Commun.* **2012**, *48*, 11904−11906. (b) Amorati, R.; Franchi, P.; Pedulli, G. F. Intermolecular hydrogen bonding modulates the hydrogen-atom-donating ability of hydroquinones. *Angew. Chem., Int. Ed.* **2007**, *46*, 6336−6338.

(45) (a) Litwinienko, G.; Ingold, K. U. Abnormal solvent effects on hydrogen atom abstractions. 1. The reactions of phenols with 2,2-diphenyl-1-picrylhydrazyl (dpph) in alcohols. *J. Org. Chem.* **2003**, *68*, 3433−3438. (b) Litwinienko, G.; Ingold, K. U. Abnormal solvent effects on hydrogen atom abstraction. 2. Resolution of the curcumin antioxidant controversy. The role of sequential proton loss electron transfer. *J. Org. Chem.* **2004**, *69*, 5888−5896.

(46) Buettner, G. R. The pecking order of free radicals and antioxidants: lipid peroxidation, α-tocopherol, and ascorbate. *Arch. Biochem. Biophys.* **1993**, *300*, 535−543.

(47) In ref 44a we erroneously reported this E_{red}^{0} as +0.69 V/NHE. The correct value is reported in: Nakanishi, I.; Kawashima, T.; Ohkubo, K.; Waki, T.; Uto, Y.; Kamada, T.; Ozawa, T.; Matsumoto, K.; Fukuzumi, S. Disproportionation of a 2,2-diphenyl-1-picrylhydrazyl radical as a model of reactive oxygen species catalysed by Lewis and/or Brønsted acids. *Chem. Commun.* **2014**, *50*, 814−816.

(48) Taras-Goslinska, K.; Jonsson, M. Solvent effects on the redox properties of thioethers. *J. Phys. Chem. A* **2006**, *110*, 9513−9517.

(49) Bartberger, M. D.; Liu, W.; Ford, E.; Miranda, K. M.; Switzer, C.; Fukuto, J. M.; Farmer, P. J.; Wink, D. A.; Houk, K. N. The reduction potential of nitric oxide (NO) and its importance to NO biochemistry. *Proc. Natl. Acad. Sci. U. S. A.* **2002**, *99*, 10958−10963. Shafirovich, V.; Dourandin, A.; Huang, W.; Geacintov, N. E. The carbonate radical is a site-selective oxidizing agent of guanine in double-stranded oligonucleotides. *J. Biol. Chem.* **2001**, *276*, 24621−24626.

(50) See Chapters 8 and 9 of ref 35.

(51) (a) Foti, M.; Ruberto, G. Kinetic solvent effects on phenolic antioxidants determined by spectrophotometric measurements. *J. Agric. Food Chem.* **2001**, *49*, 342−348. (b) Foti, M. C.; Amorati, R.; Pedulli, G. F.; Daquino, C.; Pratt, D. A.; Ingold, K. U. Influence of "remote" intramolecular hydrogen bonds on the stabilities of phenoxyl radicals and benzyl cations. *J. Org. Chem.* **2010**, *75*, 4434−4440.

(52) Of course, significant quantities of the zwitterionic form could also be present in solution.

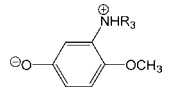

(53) Dixon, W. T.; Murphy, D. Determination of the acidity constants of some phenol radical cations by means of electron spin resonance. *J. Chem. Soc., Faraday Trans. 2* **1976**, *72*, 1221−1230.

(54) *The Science of Flavonoids*; Groteworld, E., Ed.; Springer Science + Business Media: New York, 2006.

(55) Conquer, J. A.; Maiani, G.; Azzini, E.; Raguzzini, A.; Holub, B. J. Supplementation with quercetin markedly increases plasma quercetin

DOI: 10.1021/acs.jafc.5b03839
J. Agric. Food Chem. 2015, 63, 8765−8776

concentration without effect on selected risk factors for heart disease in healthy subjects. *J. Nutr.* **1998**, *128*, 593−597.
(56) Foti, M. C.; Daquino, C.; DiLabio, G. A.; Ingold, K. U. Kinetics of the oxidation of quercetin by 2,2-diphenyl-1-picrylhydrazyl (dpph$^{\bullet}$). *Org. Lett.* **2011**, *13*, 4826−4829.
(57) (a) Villano, D.; Fernandez-Pachon, M. S.; Moya, M. L.; Troncoso, A. M.; Gaecia-Parrilla, M. C. Radical scavenging ability of polyphenolic compounds towards DPPH free radical. *Talanta* **2007**, *71*, 230−235. (b) Tsimogiannis, D. I.; Oreopoulou, V. The contribution of flavonoid C-ring on the DPPH free radical scavenging efficiency. A kinetic approach for the 3′,4′-hydroxy substituted members. *Innovative Food Sci. Emerging Technol.* **2006**, *7*, 140−146. Musialik, M.; Kuzmicz, R.; Pawłowski, T. S.; Litwinienko, G. Acidity of hydroxyl groups: an overlooked influence on antiradical properties of flavonoids. *J. Org. Chem.* **2009**, *74*, 2699−2709.
(58) Boersma, M. G.; Vervoort, J.; Szymuslak, H.; Lemanska, K.; Tyrakowska, B.; Cenas, N.; Segura-Aguilar, J.; Rietjens, I. M. C. M. Regioselectivity and reversibility of the glutathione conjugation of quercetin quinone methide. *Chem. Res. Toxicol.* **2000**, *13*, 185−191.
(59) Dangles, O.; Fargeix, G.; Dufour, C. One-electron oxidation of quercetin and quercetin derivatives in protic and non protic media. *J. Chem. Soc., Perkin Trans. 2* **1999**, 1387−1395. Alluis, B.; Dangles, O. Quercetin (=2-(3,4-dihydroxyphenyl)-3,5,7-trihydroxy-4*H*-1-benzopyran-4-one) glycosides and sulfates: chemical synthesis, complexation, and antioxidant properties. *Helv. Chim. Acta* **2001**, *84*, 1133−1156. Goupy, P.; Dufour, C.; Loonis, M.; Dangles, O. Quantitative kinetic analysis of hydrogen transfer reactions from dietary polyphenols to the DPPH radical. *J. Agric. Food Chem.* **2003**, *51*, 615−622. Hvattum, E.; Stenstrøm, Y.; Ekeberg, D. Study of the reaction products of flavonols with 2,2-diphenyl-1-picrylhydrazyl using liquid chromatography coupled with negative electrospray ionization tandem mass spectrometry. *J. Mass Spectrom.* **2004**, *39*, 1570−1581.
(60) Toteva, M. M.; Richard, J. P. Structure-reactivity relationships for addition of sulfur nucleophiles to electrophilic carbon: resonance, polarization, and steric/electrostatic effects. *J. Am. Chem. Soc.* **2000**, *122*, 11073−11083. Toteva, M. M.; Moran, M.; Amyes, T. L.; Richard, J. P. Substituent Effects on carbocation stability: the pK_R for *p*-quinone methide. *J. Am. Chem. Soc.* **2003**, *125*, 8814−8819.
(61) Similar kinetics were observed with the ABTS radical, see: Pannala, A. S.; Chan, T. S.; O'Brien, P. J.; Rice-Evans, C. A. Flavonoid B-ring chemistry and antioxidant activity: fast reaction kinetics. *Biochem. Biophys. Res. Commun.* **2001**, *282*, 1161−1168.
(62) It is important to observe that the antioxidant properties of ArOH expressed by the value of k_{ROO} (reaction 4) are not measured by monitoring ArOH + ROO$^{\bullet}$. The rate constant k_{ROO} is obtained from the (inhibited) rate of oxygen uptake by oxidizable substrates undergoing peroxidation in the presence of ArOH (see ref 33).
(63) Amorati, R.; Valgimigli, L. Advantages and limitations of common testing methods for antioxidants. *Free Radical Res.* **2015**, *49*, 633−649.
(64) At short reaction times, it is likely (see ref 63) that the EC_{50} values of these three phenols will follow the same order of reactivity.
(65) The 4-cyano-2,6-di-*tert*-butylphenol + DPPH$^{\bullet}$ reaction is an equilibrium reaction largely shifted to the left. The degree of conversion into the reaction products (aryloxyl radical + DPPH−H) is therefore low.

DOI: 10.1021/acs.jafc.5b03839
J. Agric. Food Chem. 2015, 63, 8765−8776

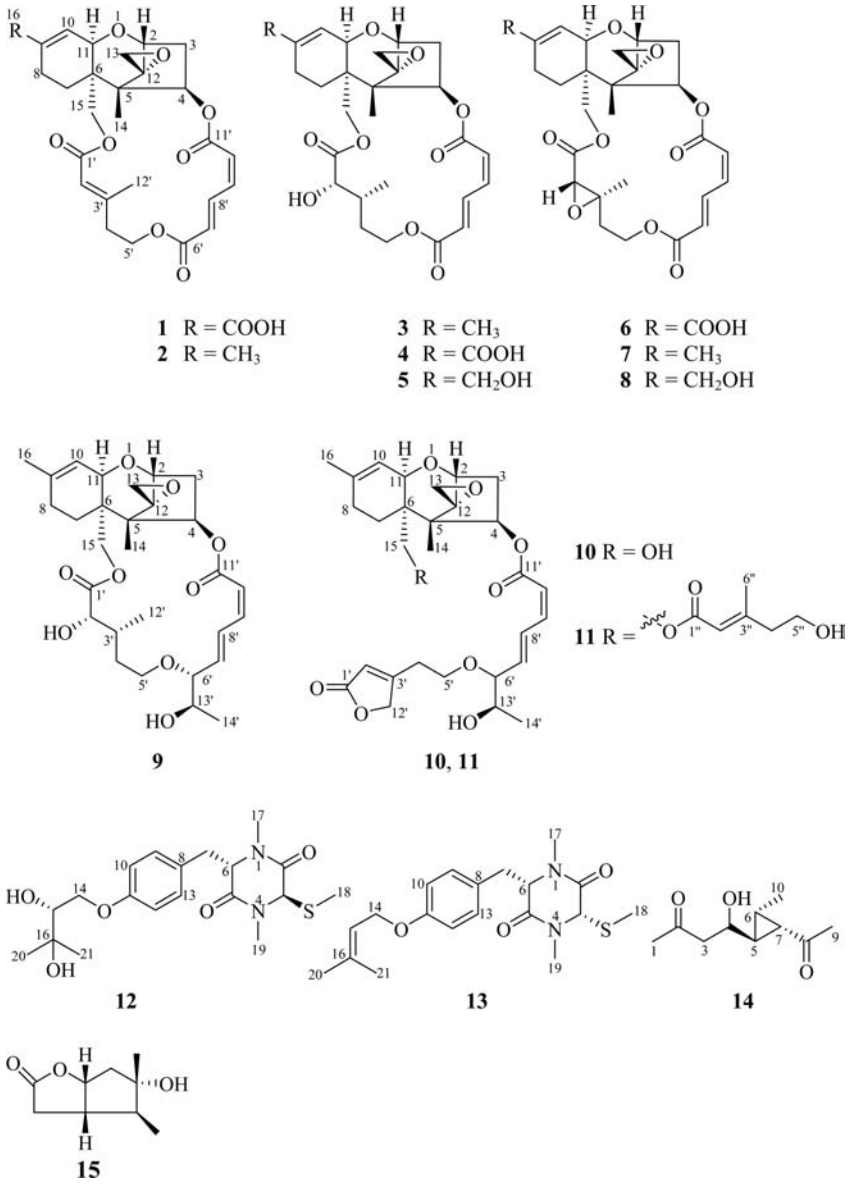

Figure 1. Structures of compounds **1**−**15**.

report the structure determination and biological activities of compounds **1**−**12**, **14**, and **15** (Figure 1) isolated from this fungus.

MATERIALS AND METHODS

Safety Information. Trichothecenes are highly toxic inhibitors of the protein biosynthesis. They may penetrate the skin and have been discussed as potential biological warfare agents ("yellow rain").

General Experimental Procedures. Optical rotation values were measured on a PerkinElmer polarimeter, model 241, at the sodium D line (λ = 589 nm). The NMR spectra were recorded on a Mercury-300 (300.141 MHz), a Varian Inova 500 (125.707 MHz for ^{13}C NMR spectra), and a Varian Inova 600 (599.740 MHz) spectrometer. IR spectra were taken on a Jasco FT/IR-4100 type A instrument. Chemical shifts (δ) were referenced to CH_3OH at 3.30 for ^{1}H and at 49.0 for ^{13}C and to $CHCl_3$ at 7.24 for ^{1}H and at 77.0 for ^{13}C. ESI-HRMS spectra were acquired on a micrOTOF 10237. Size exclusion chromatography was performed on Sephadex LH-20 purchased from Sigma-Aldrich Chemie, Steinheim, Germany. Open column chromatography was done on silica gel 60 (0.063−0.20 mm), and PTLC was performed on silica gel P/UV_{254} (both obtained from Macherey-Nagel, Düren, Germany). Mosher's reagent and nystatin were bought from Sigma-Aldrich, Steinheim, Germany. Ciprofloxacin was obtained from Square Pharmaceutical Co., Bangladesh. Solvents used for extraction and chromatography were distilled prior to use. For HPLC-MS, HPLC grade solvents (LiChrosolv, Merck AG, Darmstadt, Germany) were used.

Fungal Material and Identification. Healthy stems (∼4 cm length) of *D. metel* were collected from the garden of medicinal plants, Department of Pharmacy, Rajshahi University, Bangladesh, and kept in plastic zipper packs at 4 °C for 2 months. The surface sterilization of each stem was done according to a previously described procedure.[2] The sterilized stems were air-dried on sterile filter paper, and the bark was removed by a sterile knife. Pieces of the stem (∼1 × 1.5 cm) were then placed on a water-agar Petri dish (18 g agar per L tap water) and incubated at 25 °C. The outgrowing endophytic fungal strain M10 was isolated and maintained on M_2 agar medium (10 g of glucose, 4 g of yeast extract, 4 g of malt extract, 18 g of agar, and 1 L of tap water). The strain M10 was identified by its ITS and morphological features. The ITS sequence of M10 showed 99.8% homology to the ITS sequence of *M. roridum* strain CBS 331.51 (GenBank accession no. HQ115647). The M10 strain is kept in the Microbial Culture Collection at the Institute for Organic and Bimolecular Chemistry,

DOI: 10.1021/acs.jafc.5b02366
J. Agric. Food Chem. 2015, 63, 8777−8786

Georg-August-University Göttingen, Germany, under the curatorship of Prof. Laatsch.

Fermentation and Isolation. For the seed culture, the fungal strain M10 was subcultured on M_2 agar medium and incubated at 25 °C for 3 days. For the batch fermentation, 200 g of rice and 150 mL of tap water were added to each of 24 P-flasks (28 × 17 × 7 cm) and then sterilized for 15 min at 121 °C. From the seed culture, the mycelium was scraped out using a sterile loop, spread in 200 mL of sterile water, and then added into each P-flask containing the rice medium. The flasks were incubated at 30 °C for 20 days, and then the whole culture was extracted with EtOAc and filtered through Celite (diatomaceous earth). The filtrate was concentrated to dryness in vacuo using a rotary evaporator at 40 °C to obtain a reddish gum. The concentrated extract was dissolved in MeOH and treated with cyclohexane to remove fats. The methanol was then evaporated, and the extract was partitioned between EtOAc and distilled water. The water phase was evaporated to dryness (1.5 g) and separated into 30 fractions (F1−F30) using Sephadex LH-20 column chromatography, eluting with CH_2Cl_2/MeOH (1:1). Compounds **3** (6.0 mg from F7−F9) and **4** (4.5 mg from F16−F26) were isolated by PTLC using 10% MeOH in CH_2Cl_2. Compounds **5** (10.0 mg), **10** (6.0 mg), and **11** (6.5 mg) were obtained from F12 in a similar way, eluting with $CHCl_3$/*n*-hexane/MeOH (4:1:1).

The EtOAc phase was also evaporated to dryness (10.0 g) and fractionated by silica gel column chromatography using a stepwise gradient: 2% MeOH in CH_2Cl_2 (F1−F24), 7% MeOH in CH_2Cl_2 (F25−F35), and 12% MeOH in CH_2Cl_2 (F36−F43). Compounds **1** (5.4 mg from F34), **2** (5.0 mg, F25), **6** (4.5 mg, F34), **7** (5.0 mg, F24), **8** (13.0 mg, F24), **9** (15.0 mg, F36−F37), **12** (6.0 mg, F28), **14** (1.0 mg, F10), and **15** (5.0 mg, F29) were isolated by first subfractionating each fraction on Sephadex LH-20 (CH_2Cl_2/MeOH 4:6) and finally by PTLC (**2**, **8**, **9**, and **12** with $CHCl_3$/MeOH/*n*-hexane 2:0.4:0.6; **1**, **6**, and **7** with EtOAc/$CHCl_3$/*n*-hexane 1:1:1; **14** and **15** with CH_2Cl_2/MeOH 95:5).

Verrucarin Y (**1**): colorless, amorphous solid; $[\alpha]_D^{20}$ +6 (*c* 0.54, $CHCl_3$); IR (neat) ν_{max} 3221, 2963, 1711, 1650, 1414, 1359, 1266, 1219, 1184, 1086, 1040 cm^{-1}; ^1H and ^{13}C NMR data ($CDCl_3$), see Table 1; (+)-ESI-HRMS *m*/*z* 537.1731 $[M + Na]^+$ (calcd for $C_{27}H_{30}O_{10}Na$, 537.1731).

Verrucarin Z (**6**): colorless, amorphous solid; $[\alpha]_D^{20}$ +22 (*c* 0.12, $CHCl_3$); IR (neat) ν_{max} 3166, 2927, 1711, 1411, 1198, 1082, 1002, 962 cm^{-1}; ^1H and ^{13}C NMR data ($CDCl_3$), see Table 1; (+)-ESI-HRMS *m*/*z* 553.1680 $[M + Na]^+$ (calcd for $C_{27}H_{30}O_{11}Na$, 553.1680).

Bilain D (**12**): colorless crystals; $[\alpha]_D^{20}$ −24 (*c* 0.47, $CHCl_3$); IR (neat) ν_{max} 3434, 2929, 1652, 1507, 1450, 1399, 1295, 1240, 1173, 1088, 1025 cm^{-1}; ^1H and ^{13}C NMR data ($CDCl_3$), see Table 2; (+)-ESI-HRMS *m*/*z* 419.1611 $[M + Na]^+$ (calcd for $C_{19}H_{28}N_2O_5SNa$, 419.1611).

Hamavellone C (**14**): colorless, amorphous solid; $[\alpha]_D^{20}$ +8 (*c* 0.05, $CHCl_3$); IR (neat) ν_{max} 3427, 2927, 1697, 1365, 1177, 1070, 981 cm^{-1}; ^1H and ^{13}C NMR data (CD_3OD), see Table 2; (+)-ESI-HRMS *m*/*z* 207.0992 $[M + Na]^+$ (calcd for $C_{10}H_{16}O_3Na$, 207.0991).

Preparation of the (*S*)-MTPA Ester (10a) of 10. Compound **10** (1.6 mg) was dissolved in 300 μL of pyridine, 10 μL of (*R*)-(−)-MTPA-Cl was added, and the mixture was stirred at 20 °C for 16 h. The reaction mixture was dried under air flow and purified by PTLC ($CHCl_3$/*n*-hexane/MeOH 1:0.8:0.2) to obtain **10a** (1.9 mg).

Compound **10a**: colorless oil; selected ^1H NMR data ($CDCl_3$, 600 MHz) δ_H 1.28 (H_3-14′, d, *J* = 6.5 Hz), 5.16 (H-13′, m), 3.89 (H-6′, t, *J* = 7.3 Hz), 5.68 (H-7′, dd, *J* = 15.5, 7.3 Hz), 7.59 (H-8′, dd, *J* = 15.5, 11.3 Hz), 6.53 (H-9′, t, *J* = 11.3 Hz), 3.43 (H-5′a, dt, *J* = 9.2, 5.5 Hz), 3.57 (H-5′b, m), 2.51 (H_2-4′, m); (+)-ESI-HRMS *m*/*z* 985.3204 $[M + Na]^+$ (calcd for $C_{49}H_{52}F_6O_{13}Na$, 985.3204).

Preparation of the (*R*)-MTPA Ester (10b) of 10. The (*R*)-MTPA ester of compound **10** (1.4 mg) was prepared with (*S*)-(+)-MTPA-Cl and purified in the same way as **10a** to obtain **10b** (1.3 mg).

Compound **10b**: colorless oil; selected ^1H NMR data ($CDCl_3$, 600 MHz) δ_H 1.21 (H_3-14′, d, *J* = 6.5 Hz), 5.17 (H-13′, m), 3.95 (H-6′, t, *J* = 7.0 Hz), 5.78 (H-7′, dd, *J* = 15.7, 7.0 Hz), 7.63 (H-8′, dd, *J* = 15.7, 11.3 Hz), 6.58 (H-9′, t, *J* = 11.3 Hz), 3.51 (H-5′a, m), 3.67 (H-5′b, m), 2.62 (H_2-4′, m); (+)-ESI-HRMS *m*/*z* 985.3204 $[M + Na]^+$ (calcd for $C_{49}H_{52}F_6O_{13}Na$, 985.3204).

Table 1. ^{13}C (125 MHz) and ^1H (600 MHz) NMR Data for 1 and 6 in $CDCl_3$

	1			6		
no.	δ_C	type	δ_H, mult (*J* in Hz)	δ_C	type	δ_H, mult (*J* in Hz)
2	79.4	CH	3.87, d (4.8)	79.4	CH	3.75, d (4.8)
3	34.9	CH_2	2.18, dt (15.0, 4.8)	34.9	CH_2	2.22, dt (15.8, 4.8)
			2.53, m			2.52, dd (15.8, 8.2)
4	75.0	CH	5.98, dd (10.0, 5.0)	75.3	CH	5.83, dd (8.2, 4.7)
5	48.8	C		49.2	C	
6	43.1	C		43.9	C	
7	20.2	CH_2	1.87, dd (12.6, 5.5)	19.6	CH_2	1.86, td (12.6, 5.4)
			1.92, dd (12.0, 5.5)			1.94, m
8	21.7	CH_2	2.14, m	21.6	CH_2	2.16, m
			2.54, overlapped			2.54, m
9	133.6	C		133.9	C	
10	135.1	CH	6.89, brd (6.0)	134.5	CH	6.87, brd (6.0)
11	66.4	CH	3.89, brd (6.0)	66.3	CH	3.75, brd (6.0)
12	65.2	C		64.9	C	
13	48.0	CH_2	2.82, d (4.2)	47.9	CH_2	2.82, d (4.2)
			3.10, d (4.2)			3.12, d (4.2)
14	7.0	CH_3	0.82, s	7.7	CH_3	0.88, s
15	62.8	CH_2	3.84, d (13.2)	63.3	CH_2	4.28, d (13.6)
			4.43, d (13.2)			4.37, d (13.6)
16	170.5	C		170.3	C	
1′	165.8	C		167.6	C	
2′	117.8	CH	5.79, brs	58.3	CH	3.37, s
3′	157.0	C		61.8	C	
4′	40.2	CH_2	2.52, m	36.9	CH_2	1.69, ddd (15.5, 9.1, 3.8)
						2.29, ddd (15.5, 6.0, 2.9)
5′	60.4	CH_2	4.12, ddd (11.5, 9.7, 3.8)	60.8	CH_2	4.30, m
			4.43, dt (11.5, 4.2)			4.33, m
6′	165.5	C		165.3	C	
7′	127.5	CH	5.99, d (15.6)	127.6	CH	6.04, d (15.6)
8′	139.0	CH	8.03, dd (15.6, 11.7)	138.2	CH	7.87, dd (15.6, 11.4)
9′	139.7	CH	6.60, t (11.7)	138.8	CH	6.62, t (11.4)
10′	125.2	CH	6.07, d (11.7)	125.7	CH	6.14, d (11.4)
11′	165.7	C		166.2	C	
12′	17.2	CH_3	2.24, s	16.0	CH_3	1.53, s

Preparation of 11a and 11b from 11. To prepare the (*S*)- and (*R*)-MTPA esters **11a** and **11b**, two separate amounts of compound **11** (1.0 mg and 1.2 mg) were esterified with (*R*)-(−)- and (*S*)-(+)-MTPA-Cl, respectively, using the procedure described above, to obtain **11a** (1.2 mg) and **11b** (1.2 mg).

Compound **11a**: colorless oil; selected ^1H NMR data ($CDCl_3$, 600 MHz) δ_H 1.27 (H_3-14′, d, *J* = 6.5 Hz), 5.14 (H-13′, m), 3.87 (H-6′, dd, *J* = 8.0, 6.0 Hz), 5.61 (H-7′, dd, *J* = 15.4, 8.0 Hz), 7.56 (H-8′, dd, *J* = 15.4, 11.3 Hz), 6.45 (H-9′, t, *J* = 11.3 Hz), 3.41 (H-5′a, dt, *J* = 9.2, 5.6 Hz), 3.57 (H-5′b, m), 2.53 (H_2-4′, m); (+)-ESI-HRMS *m*/*z* 1097.3729 $[M + Na]^+$ (calcd for $C_{55}H_{60}F_6O_{15}Na$, 1097.3728).

Compound **11b**: colorless oil; selected ^1H NMR data ($CDCl_3$, 600 MHz) δ_H 1.19 (H_3-14′, d, *J* = 6.5 Hz), 5.15 (H-13′, m), 3.93 (H-6′, dd, *J* = 8.0, 6.8 Hz), 5.73 (H-7′, dd, *J* = 15.0, 6.8 Hz), 7.62 (H-8′, dd, *J* =

DOI: 10.1021/acs.jafc.5b02366
J. Agric. Food Chem. 2015, 63, 8777−8786

Table 2. ^{13}C and ^{1}H NMR Data for 12 and 14

	12			14		
no.	δ_C[a]	type	δ_H,[b] mult (J in Hz)	δ_C[c]	type	δ_H,[d] mult (J in Hz)
1				30.8	CH_3	2.15, s
2	163.7	C		210.0	C	
3	64.7	CH	3.82, s	51.1	CH_2	2.63, dd (12.0, 4.0)
4				70.4	CH	3.62, td (7.3, 4.0)
5	165.1	C		36.1	CH	1.48, td (7.3, 4.9)
6	62.7	CH	4.24, t (3.5)	25.4	CH	1.57, m
7	36.5	CH_2	3.09, dd (14.2, 3.5)	32.5	CH	2.12, dd (9.2, 4.9)
			3.22, dd (14.2, 3.5)			
8	126.4	C		208.9	C	
9	130.8	CH	6.90, d (8.6)	32.0	CH_3	2.22, s
10	114.5	CH	6.78, d (8.6)	11.5	CH_3	1.07, d (6.2)
11	158.0	C				
12	114.5	CH	6.78, d (8.6)			
13	130.8	CH	6.90, d (8.6)			
14	69.1	CH_2	3.94, dd (9.6, 7.5)			
			4.06, dd (9.6, 3.0)			
15	75.7	CH	3.76, dd (7.5, 3.0)			
16	71.6	C				
17	33.0	CH_3	3.09, s			
18	11.3	CH_3	1.89, s			
19	32.4	CH_3	2.81, s			
20	26.4	CH_3	1.28, s			
21	24.9	CH_3	1.24, s			

[a]Measured at 125 MHz in $CDCl_3$. [b]Recorded at 300 MHz in $CDCl_3$. [c]Measured at 125 MHz in CD_3OD. [d]Recorded at 600 MHz in CD_3OD.

15.0, 11.3 Hz), 6.54 (H-9′, t, J = 11.3 Hz), 3.63 (H-5′a, m), 3.69 (H-5′b, m), 2.60 (H_2-4′, m); (+)-ESI-HRMS m/z 1097.3729 $[M + Na]^+$ (calcd for $C_{55}H_{60}F_6O_{15}Na$, 1097.3728).

Preparation of 12a and 12b. The (*S*)-MTPA (**12a**) and (*R*)-MTPA (**12b**) esters were prepared by derivatization of **12** (1.5 mg each case) with (*R*)-(−)- and (*S*)-(+)-MTPA-Cl, following the procedure described earlier, to obtain **12a** (1.8 mg) and **12b** (1.7 mg), respectively.

Compound **12a**: colorless oil; ^{1}H NMR ($CDCl_3$, 600 MHz) δ_H 3.79 (H-3, s), 4.24 (H-6, t, J = 3.5 Hz), 3.10 (H-7a, dd, J = 14.2, 3.5 Hz), 3.22 (H-7b, dd, J = 14.2, 3.5 Hz), 6.90 (H-9, d, J = 8.5 Hz), 6.70 (H-10, d, J = 8.5 Hz), 6.70 (H-12, d, J = 8.5 Hz), 6.90 (H-13, d, J = 8.5 Hz), 4.04 (H-14a, dd, J = 10.5, 8.1 Hz), 4.23 (H-14b, dd, J = 10.5, 3.0 Hz), 5.38 (H-15, dd, J = 8.0, 3.0 Hz), 3.10 (H_3-17, s), 1.90 (H_3-18, s), 2.79 (H_3-19, s), 1.29 (H_3-20, s), 1.29 (H_3-21, s), 3.49 (OMe, s), 7.36 (H_3, m), 7.55 (H_2, dd, J = 7.1, 1.8); (+)-ESI-HRMS m/z 635.2011 $[M + Na]^+$ (calcd for $C_{29}H_{35}N_2F_3SO_7Na$, 635.2009).

Compound **12b**: colorless oil; ^{1}H NMR ($CDCl_3$, 600 MHz) δ_H 3.85 (H-3, s), 4.26 (H-6, t, J = 3.6 Hz), 3.13 (H-7a, dd, J = 14.2, 3.6 Hz), 3.24 (H-7b, dd, J = 14.2, 3.6 Hz), 6.94 (H-9, d, J = 8.6 Hz), 6.77 (H-10, d, J = 8.6 Hz), 6.77 (H-12, d, J = 8.6 Hz), 6.94 (H-13, d, J = 8.6 Hz), 4.13 (H-14a, dd, J = 10.6, 8.3 Hz), 4.32 (H-14b, dd, J = 10.6, 2.7 Hz), 5.40 (H-15, dd, J = 8.3, 2.7 Hz), 3.11 (H_3-17, s), 1.92 (H_3-18, s), 2.81 (H_3-19, s), 1.21 (H_3-20, s), 1.24 (H_3-21, s), 3.54 (OMe, s), 7.32–7.27 (H_2, m), 7.35 (H_1, d, J = 7.4 Hz), 7.58 (H_2, d, J = 7.8 Hz); (+)-ESI-HRMS m/z 635.2011 $[M + Na]^+$ (calcd for $C_{29}H_{35}N_2F_3SO_7Na$, 635.2009).

Zoospores' Motility Inhibitory and Lysis Activity Assays. The test pathogen *P. nicotianae* was isolated from leaves collected in June 2014 from the plant *Catharanthus roseus*, grown in the nursery beds of Bangabandhu Sheikh Mujibur Rahman Agricultural University, Gazipur, Bangladesh. Infected leaves of *C. roseus* were placed in water to develop sporangia. Abundant sporangia were produced overnight, and mycelia developed after 2 days. The bioassay was carried out as described previously.[11,12]

Antimicrobial Test. The antimicrobial test was performed according to a previously described procedure.[13]

RESULTS

The structure determinations of the new compounds **1**, **6**, **12**, and **14** were achieved using selected NMR experiments and by comparison of these data with published values. Using AntiBase,[10] the structures of the known compounds were identified as verrucarin A (**3**),[14] 16-hydroxyverrucarin A (**5**),[15] verrucarin B (**7**),[16] 16-hydroxyverrucarin B (**8**),[17] verrucarin J (**2**),[18] verrucarin X (**4**),[15] roridin A (**9**),[19] roridin L-2 (**10**),[20] trichoverritone (**11**),[21] and myrotheciumone A (**15**).[22]

Trichothecenes are sesquiterpene alcohols or esters that have a tricyclic skeleton in common, the trichothecane, typically with a double bond between C-9 and C-10 and a 12,13-epoxide ring.[23] There are two classes of trichothecenes: those that have only a central sesquiterpenoid structure and those that have an additional macrocyclic or opened ring (simple and macrocyclic trichothecenes, respectively).[24] Macrocyclic trichothecenes are further subdivided as either verrucarins (generally C_{27} compounds) or roridins (generally C_{29} compounds).[23] The ester groups involved in forming the macrocyclic ring or open chain are attached at positions 4β and 15 of the trichothecane core.

Compound **1** was isolated as a colorless, optically active, amorphous solid by PTLC. The ^{1}H NMR spectrum showed similarities to that of verrucarin J (**2**), and the (+)-ESI-HR mass spectrum showed a molecular ion peak at m/z 537.1731 $[M + Na]^+$ corresponding to the molecular formula $C_{27}H_{30}O_{10}$ (13 DBEs), indicating a new verrucarin-like trichothecene derivative. The ^{13}C NMR spectrum displayed 27 carbon resonances that were attributed, with the help of a phase-sensitive HSQC spectrum, to 2 methyl, 7 methylene, 9 methine (including 6 olefinic), and 9 quaternary carbons (Table 1). Because analysis of the NMR data suggested that the molecule contains four C,C double bonds and 4 carbonyl groups, 5 rings were expected.

The basic trichothecene moiety was identified by the HMBC spectrum, with signals nearly overlapping with those of verrucarin J (**2**), and confirmed by a detailed NMR analysis (Figure 2). Besides the trichothecene skeleton, two further structural subunits were observed. Using a COSY correlation between H_2-4′ and H_2-5′ and HMBC correlations of H-2′ to C-1′, -3′, -4′, and -12′ (Figure 2), the first of these was established as a 5-hydroxy-3-methylpent-2-enoic acid, a subunit also found in verrucarin J (**2**).

The second subunit was identified as hexa-2,4-dienedioic acid by COSY correlations from H-7′ to H-10′ and HMBC correlations of H-8′ to C-6′ and H-10′ to C-11′. Finally, these subunits were connected via an ester linkage to each other and to the trichothecene moiety. The resulting structure **1** was confirmed by additional HMBC correlations (H-4/C-11′, H_2-15/C-1′, and H_2-5′/C-6′, Figure 2) and was named verrucarin Y.

The configuration of **1** was elucidated by the analysis of coupling constants and ^{1}H chemical shifts and by considering its biosynthesis. The coupling constants of H-7′ (J = 15.6 Hz)

DOI: 10.1021/acs.jafc.5b02366
J. Agric. Food Chem. 2015, 63, 8777–8786

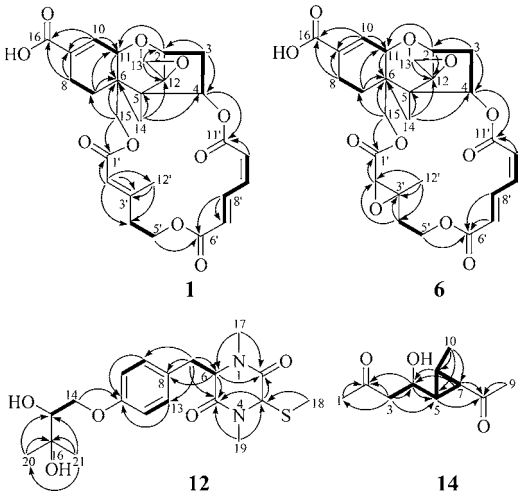

Figure 2. $^{1}H-^{1}H$ COSY (bold line) and HMBC (H→C) correlations for **1**, **6**, **12**, and **14**.

and H-10′ (J = 11.7 Hz) indicated $\Delta^{7'}$-(E) and $\Delta^{9'}$-(Z) geometries for **1**. The $\Delta^{2'}$ geometry was derived from the influence on the protons in the neighborhood. In the case of macrocyclic trichothecenes, the proton shifts, especially of H_2-15, H_2-4′, and H_2-5′, are strongly dependent on the geometry of the $\Delta^{2'}$ double bond,[18] as shown for 2′-(Z)- and 2′-(E)-verrucarin J (**2**) in Table S1 (Supporting Information).[18,25] Analysis of the current data clearly indicated a $\Delta^{2'}$-(E) configuration for **1** (Table S1).

Because the trichothecene ring in the various derivatives can be assumed to originate from common biosynthetic pathways, it is plausible that the six chiral centers in the core of **1** are (2*R*,4*R*,5*S*,6*R*,11*R*,12*S*), as is found in other trichothecenes.[24] NOE correlations between H-2β/H_2-13, H-2β/H-3β, H-13b/H_3-14β, H-4α/H_2-15, and H-4α/H-11α supported these configurations. The configurations were further confirmed by the closely related shifts for the trichothecene core in **1** compared to other verrucarins and also by the simultaneous formation of **1** and **2** by the same strain.

The molecular formula of verrucarin Z (**6**) was deduced as $C_{27}H_{30}O_{11}$ by ESI-HRMS, indicating 13 DBEs. 1D and 2D NMR data of **6** were nearly identical to those of **1**. The only differences were at C-2′ and C-3′, where an epoxide group in **6** replaced the double bond in **1**. The presence of a 2′,3′-epoxide was confirmed by the appearance of two signals of oxygenated carbons (δ_C 58.3, 61.8) in the ^{13}C NMR spectrum of **6** [replacing the two olefinic signals observed in **1** (Table 1)] and by the HMBC correlations of H_2-4′ to C-2′ and -3′ (Figure 2).

The configurations of the double bonds at $\Delta^{7'}$ and $\Delta^{9'}$ were determined as E and Z, respectively, on the basis of the observed coupling constants (Table 1). The chemical shifts of H-2′ and H_3-12′ in **6** were δ_H 3.37 and 1.53, respectively, indicating the epoxide ring was *trans* substituted[26] as in verrucarin B[16] (δ_H 3.41 and 1.56). This was also supported by an NOE correlation between H-2′β and H_2-4′. For the same reasons as in **1**, an identical core configuration can be assumed, resulting in (2*R*,4*R*,5*S*,6*R*,11*R*,12*S*,2′*S**,3′*R**)-**6**.[19,24]

In addition to the verrucarins, roridins were also isolated from strain M10. Whereas the verrucarins contain a hexadienedicarboxylic acid unit in the macrolactone ring, in all of the approximately 40 currently known roridins,[10] the dicarboxylic acid is substituted by a chiral 6,7-dihydroxyoctadienoic acid.[27]

^{1}H and ^{13}C resonances of the three roridins isolated here were identical to those published for roridin A (**9**), roridin L-2 (**10**), and trichoverritone (**11**); however, the configuration at C-6′ and C-13′ had been reported only for compound **9**.[20,21,27] Consequently, the modified Mosher's method was applied to determine the configuration of C-13′ in **10** and **11**.[28] A positive $\Delta\delta_H$ value for H_3-14′ and negative values for the rest of the selected protons (Figure 3) indicated that the 13′*R* configuration was present in both **10** and **11**, as in **9**.

Bilain D (**12**) was isolated as an optically active, colorless crystals. The molecular formula $C_{19}H_{28}N_2O_5S$ (7 DBEs) was inferred on the basis of (+)-ESI-HRMS data. The ^{1}H NMR spectrum revealed 5 methyl singlets, 2 methylene ABX signals, and 3 sp^3 methine resonances. Two aromatic 2H doublets at δ_H 6.78 and 6.90 indicated a 1,4-disubstituted benzene ring in the molecule (Table 2). With the help of an HSQC spectrum, the 19 carbon resonances were established to be 5 methyl, 2 methylene, 3 aliphatic oxymethine, 4 methine (2 signals of double intensity), and 5 quaternary carbons (Table 2).

COSY and HMBC correlations revealed three structural fragments: a phenol unit, an oxidized isopentane, and a diketopiperazine fragment (Figure 2). The typical A_2B_2 pattern and the shift values indicated a *para*-substituted phenol derivative. The phenolic carbon showed an HMBC correlation with an aliphatic methylene group, which must be connected via an ether bond. A COSY correlation indicated that C-14 was connected to an oxymethine group and then to a dimethylcarbinol (indicated by HMBC correlations; Figure 2), resulting in the presence of a dihydroxylated isoprene phenol ether.

Among the remaining signals, two *N*-methyl groups were identified as a result of their C and H shifts. Both showed HMBC correlations with CH groups and amide carbonyls (e.g., Me-17 with C-2 and C-6); further HMBC and COSY correlations resulted in an *N*,*N*-dimethyl diketopiperazine skeleton. The open bond at C-3 was determined to be

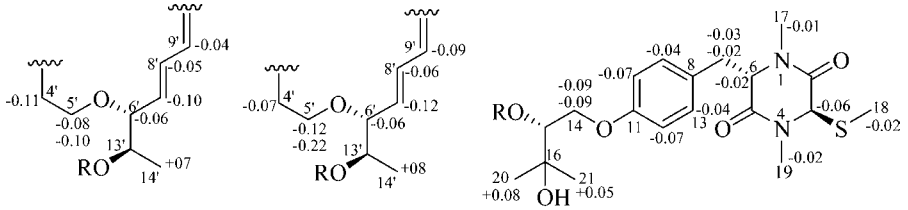

Figure 3. Selected $\Delta\delta_H$ ($\Delta\delta_H = \delta_S - \delta_R$) values for MTPA esters **10a**/**10b**, **11a**/**11b**, and for MTPA esters **12a**/**12b**.

DOI: 10.1021/acs.jafc.5b02366
J. Agric. Food Chem. 2015, 63, 8777−8786

occupied by a thiomethyl (*S*-Me) group, and the diketopiperazine ring was established to be connected to the phenol unit via a methylene group (CH_2-7), as indicated by COSY and HMBC correlations, resulting in structure **12** (Figure 2). This is a new bilain, assigned the letter D.

The configuration of C-15 in **12** was determined by using the modified Mosher's method.[28] All proton signals of the resultant two ester derivatives, **12a** and **12b**, were assigned by $^1H-^1H$ COSY experiments and through comparison of their chemical shifts with those from the original ^1H NMR data of **12**; the shift differences ($\Delta\delta_H = \delta_S - \delta_R$) are shown in Figure 3. The positive $\Delta\delta_H$ values of H_3-20 and H_3-21, but negative $\Delta\delta_H$ values of all other protons, indicated the *R* configuration at C-15.[28] The relative configurations of the further two stereocenters in **12** were established by comparing the chemical shifts with those of the synthetic thiodiketopiperazine **13** and via NOE correlations. The chemical shifts of H-3 and H-6 in the *cis*-diketopiperazine (3*S*,6*S*)-methylthiosilvatin (**13**) were δ_H 4.58 and 4.22,[29] but those in **12** were δ_H 3.82 and 4.24, respectively, indicating that the substituents at C-3 and C-6 are *trans*-oriented in **12**. This was confirmed by the observance of the expected NOE correlation between the *S*-Me group at δ_H 1.89 and H-6, and by signals between H-3 and the aromatic protons. Therefore, a (3*R**,6*S**) configuration can be assigned for **12**. Calculation of the optical rotations (see Supporting Information) indicated that this is also the absolute configurations, so that finally (3*R*,6*S*,15*R*) resulted for **12**.

Among the >200 known microbial diketopiperazines, some from fungal sources carry characteristic 3- or 6-thiomethyl or 3,6-di(thiomethyl) groups, with or without *N*-methyl and *N*,*N*′-dimethyl groups in the ring. These compounds are mostly derived from phenylalanine; however, fewer than 20 derivatives (including the bilains) contain the *O*-prenylated tyrosine unit.[30−36] In all previously described Phe-derived monothiomethyl diketopiperazines, the *S*-Me group is present at C-6; bilain D (**12**), isolated here, is the only example with an *S*-Me group at C-3.[36] It can be speculated that the bilains function as signaling compounds, as do the related benzylidene-diketopiperazines.[37]

Hamavellone C (**14**), an unusual cyclopropyl diketone,[38] was obtained as an amorphous, colorless solid, for which the molecular formula was determined as $C_{10}H_{16}O_3$ by ESI-HRMS, indicating 3 DBEs. The IR spectrum exhibited a broad absorption band centered at 3427 cm^{-1} and a sharp band at 1697 cm^{-1}, indicating hydroxy and carbonyl functionalities, respectively. Analysis of ^1H, ^{13}C, and HSQC spectra revealed two keto carbonyls (δ_C 210.0, 208.9). An oxymethine proton resonated at δ_H 3.62 (δ_C 70.4), methylene protons appeared at δ_H 2.63 (δ_C 51.1), three methine protons were observed at δ_H 1.48, 1.57, and 2.12 (δ_C 36.1, 25.4, and 32.5), and three methyl signals appeared at δ_H 1.07, 2.22, and 2.15 (δ_C 11.5, 30.8, and 32.0).

Analysis of the 1D and 2D NMR spectra of **14** revealed the spin system $C^3H_2-C^4H-C^5H(C^7H)-C^6H(C^{10}H_3)-C^7H$ and two independent methyl singlets (Figure 2). Besides the two carbonyl groups, the ^{13}C NMR spectrum showed no further double bonds; compound **14** must therefore be monocyclic. The HMBC and COSY correlations of a methyl doublet (C-10) with C-5, C-6, and C-7 established a cyclopropane moiety (Figure 2). HMBC correlations of the methyl protons H_3-1 and H_3-9 with the keto carbons C-2 and C-8, respectively, indicated their terminal positions. The methine H-5 (δ_H 1.48, td, J = 7.3, 4.9 Hz) of the cyclopropane ring was *trans*-oriented with respect to H-6 and H-7 (δ_H 2.12, dd, J = 9.2, 4.9 Hz), as indicated by the NOESY correlations between H-6 and H-7, between H-5 and Me-10, and between Me-9 and Me-10, but not between H-5 and H-6/7 (Figure 4). This was confirmed by

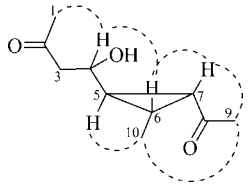

Figure 4. Key NOESY correlations for **14**.

the small coupling constant between H-5/H-6 (J = 4.9 Hz) and H-5/H-7 (J = 4.9 Hz), indicating a *trans* orientation, and by the high coupling value between H-7 and H-6 (J^{cis} = 9.2 Hz) (Table 2). Typically, *trans*-oriented protons of the cyclopropyl ring show a coupling of 4.2−5.9 Hz, whereas 8.4−9.7 Hz is indicative of a *cis* orientation.[39] It was not possible to address the absolute configuration of C-4 in **14** due to the limited amount of compound available.

Open chain alkyl-cyclopropyl ketones are very unusual in natural sources. To the best of our knowledge, hamavellones A and B, isolated from a soil fungus, are the only two microbial compounds known that are similar to **14**, which we therefore named hamavellone C.[38] Other known cyclopropyl ketones are cyclic sesquiterpenes and are mainly produced by mushrooms.[40,41]

The compounds **1**−**12**, **14**, and **15** were tested against zoospores of *P. nicotianae* and a few other microorganisms; results are presented in Tables 3 and 4, respectively. Motility inhibitory and lytic activities against zoospores clearly increased to the maximum applied dose (Table 3). None of the macrocyclic trichothecenes tested here showed motility inhibitory and lytic activities, except for those with certain distinct structural features. Compounds **6**, **7**, **9**, and **14** exhibited IC_{50} values against zoospores at a concentration of 50 μg/mL after 30, 45, 45, and 30 min, whereas double the concentration (IC_{50} = 100 μg/mL) was required for **3** and **5** to produce the same effect after 45 and 60 min of treatment, respectively (Table 3). Compound **8** showed a 50% inhibitory concentration (IC_{50}) of 250 μg/mL after 5 min of treatment. On treatment with higher concentrations (100−900 μg/mL), all of these motility inhibitors caused lysis of zoospores (zoosporicidal activity) (Table 3). Compounds **1**, **2**, **4**, **10**, **11**, **12**, and **15** did not show any motility inhibitory or lytic activities against zoospores within 60 min up to 900 μg/mL.

In the case of compounds **3**−**5**, the presence of a methyl or hydroxymethyl group at C-9 increased the motility halting activity, whereas the presence of a carboxy group (**4**) at the same position led to a complete loss of activity (Table 3). Verrucarins or roridins with double bonds at C-2′ became inactive, irrespective of their functionalities at C-9 (**1** and **2**). For the verrucarins, either a CH_3, COOH, or CH_2OH moiety at C-9 in the presence of an epoxide group at C-2′,3′ (**6**−**8**) resulted in motility inhibitory activity followed by lysis of zoospores (Figure 1 and Table 3). When the macrocyclic ring was opened (**10** and **11**), no activity was observed against the zoospores.

DOI: 10.1021/acs.jafc.5b02366
J. Agric. Food Chem. 2015, 63, 8777−8786

Table 3. Motility Inhibitory and Zoosporicidal Activities of 1−12, 14, and 15 against the Late Blight Pathogen *P. nicotianae*[a]

		motility inhibitory and zoosporicidal activities over control[b] (% ± SE)											
		5 min		10 min		15 min		30 min		45 min		60 min	
compd	dose (μg/mL)	inhibited motility	lysed	inhibited motility	lysed	inhibited motility	lysed	inhibited motility	lysed	inhibited motility	lysed	inhibited motility	lysed
3	900	100 ± 0	0 ± 0	100 ± 0	0 ± 0	100 ± 0	10 ± 4	100 ± 0	25 ± 2	100 ± 0	30 ± 6	100 ± 0	55 ± 7
	800	100 ± 0	0 ± 0	100 ± 0	0 ± 0	100 ± 0	0 ± 0	100 ± 0	5 ± 2	100 ± 0	0 ± 0	100 ± 0	10 ± 3
	700	80 ± 9	0 ± 0	100 ± 0	0 ± 0	100 ± 0	0 ± 0	100 ± 0	0 ± 0	100 ± 0	0 ± 0	100 ± 0	0 ± 0
	600	70 ± 6	0 ± 0	80 ± 4	0 ± 0	100 ± 0	0 ± 0	100 ± 0	0 ± 0	100 ± 0	0 ± 0	100 ± 0	0 ± 0
	500	50 ± 5	0 ± 0	70 ± 8	0 ± 0	80 ± 6	0 ± 0	100 ± 0	0 ± 0	100 ± 0	0 ± 0	100 ± 0	0 ± 0
	400	30 ± 7	0 ± 0	50 ± 9	0 ± 0	60 ± 6	0 ± 0	80 ± 7	0 ± 0	100 ± 0	0 ± 0	100 ± 0	0 ± 0
	300	10 ± 4	0 ± 0	25 ± 5	0 ± 0	40 ± 5	0 ± 0	70 ± 8	0 ± 0	90 ± 7	0 ± 0	100 ± 0	0 ± 0
	250	0 ± 0	0 ± 0	15 ± 5	0 ± 0	30 ± 7	0 ± 0	50 ± 5	0 ± 0	70 ± 6	0 ± 0	80 ± 8	0 ± 0
	100	0 ± 0	0 ± 0	0 ± 0	0 ± 0	20 ± 4	0 ± 0	30 ± 4	0 ± 0	50 ± 8	0 ± 0	60 ± 5	0 ± 0
5	900	100 ± 0	0 ± 0	100 ± 0	0 ± 0	100 ± 0	0 ± 0	100 ± 0	5 ± 2	100 ± 0	15 ± 5	100 ± 0	25 ± 6
	800	80 ± 9	0 ± 0	100 ± 0	0 ± 0	100 ± 0	0 ± 0	100 ± 0	5 ± 3	100 ± 0	7 ± 3	100 ± 0	10 ± 3
	700	75 ± 6	0 ± 0	100 ± 0	0 ± 0	100 ± 0	0 ± 0	100 ± 0	0 ± 0	100 ± 0	0 ± 0	100 ± 0	0 ± 0
	600	60 ± 5	0 ± 0	85 ± 8	0 ± 0	100 ± 0	0 ± 0	100 ± 0	0 ± 0	100 ± 0	0 ± 0	100 ± 0	0 ± 0
	500	30 ± 3	0 ± 0	50 ± 7	0 ± 0	100 ± 0	0 ± 0	100 ± 0	0 ± 0	100 ± 0	0 ± 0	100 ± 0	0 ± 0
	400	25 ± 4	0 ± 0	45 ± 4	0 ± 0	60 ± 5	0 ± 0	100 ± 0	0 ± 0	100 ± 0	0 ± 0	100 ± 0	0 ± 0
	300	20 ± 4	0 ± 0	30 ± 3	0 ± 0	50 ± 8	0 ± 0	80 ± 8	0 ± 0	100 ± 0	0 ± 0	100 ± 0	0 ± 0
	250	10 ± 2	0 ± 0	20 ± 2	0 ± 0	35 ± 3	0 ± 0	55 ± 4	0 ± 0	70 ± 4	0 ± 0	80 ± 8	0 ± 0
	100	0 ± 0	0 ± 0	0 ± 0	0 ± 0	5 ± 2	0 ± 0	15 ± 7	0 ± 0	35 ± 3	0 ± 0	50 ± 5	0 ± 0
	50	0 ± 0	0 ± 0	0 ± 0	0 ± 0	0 ± 0	0 ± 0	0 ± 0	0 ± 0	5 ± 3	0 ± 0	10 ± 3	0 ± 0
6	900	100 ± 0	100 ± 0	nt	nt	nt	nt	nt	nt	nt	nt	nt	nt
	800	100 ± 0	80 ± 5	100 ± 0	100 ± 0	nt	nt	nt	nt	nt	nt	nt	nt
	700	100 ± 0	60 ± 6	100 ± 0	75 ± 5	100 ± 0	80 ± 9	100 ± 0	100 ± 0	nt	nt	nt	nt
	600	100 ± 0	10 ± 2	100 ± 0	30 ± 2	100 ± 0	50 ± 6	100 ± 0	60 ± 6	100 ± 0	90 ± 8	100 ± 0	100 ± 0
	500	100 ± 0	5 ± 3	100 ± 0	15 ± 8	100 ± 0	25 ± 7	100 ± 0	40 ± 5	100 ± 0	65 ± 7	100 ± 0	90 ± 9
	400	100 ± 0	0 ± 0	100 ± 0	10 ± 5	100 ± 0	20 ± 2	100 ± 0	30 ± 2	100 ± 0	50 ± 2	100 ± 0	70 ± 4
	300	100 ± 0	0 ± 0	100 ± 0	0 ± 0	100 ± 0	2 ± 2	100 ± 0	10 ± 9	100 ± 0	25 ± 8	100 ± 0	50 ± 8
	250	60 ± 4	0 ± 0	80 ± 3	0 ± 0	100 ± 0	0 ± 0	100 ± 0	5 ± 4	100 ± 0	20 ± 2	100 ± 0	30 ± 3
	100	0 ± 0	0 ± 0	50 ± 8	0 ± 0	65 ± 3	0 ± 0	80 ± 6	0 ± 0	100 ± 0	0 ± 0	100 ± 0	5 ± 2
	50	0 ± 0	0 ± 0	0 ± 0	0 ± 0	25 ± 2	0 ± 0	50 ± 2	0 ± 0	70 ± 2	0 ± 0	80 ± 7	0 ± 0
7	900	100 ± 0	100 ± 0	nt	nt	nt	nt	nt	nt	nt	nt	nt	nt
	800	100 ± 0	80 ± 8	100 ± 0	100 ± 0	nt	nt	nt	nt	nt	nt	nt	nt
	700	100 ± 0	50 ± 4	100 ± 0	60 ± 5	100 ± 0	70 ± 5	100 ± 0	90 ± 9	100 ± 0	100 ± 0	nt	nt
	600	100 ± 0	0 ± 0	100 ± 0	10 ± 2	100 ± 0	30 ± 3	100 ± 0	50 ± 6	100 ± 0	70 ± 5	100 ± 0	100 ± 0
	500	80 ± 7	0 ± 0	100 ± 0	0 ± 0	100 ± 0	0 ± 0	100 ± 0	20 ± 3	100 ± 0	50 ± 7	100 ± 0	70 ± 6
	400	70 ± 4	0 ± 0	90 ± 8	0 ± 0	100 ± 0	0 ± 0	10 0 ± 0	10 ± 4	10 0 ± 0	20 ± 5	100 ± 0	30 ± 4
	300	50 ± 5	0 ± 0	70 ± 8	0 ± 0	80 ± 7	0 ± 0	100 ± 0	0 ± 0	10 0 ± 0	0 ± 0	100 ± 0	5 ± 2
	250	50 ± 4	0 ± 0	60 ± 5	0 ± 0	70 ± 4	0 ± 0	100 ± 0	0 ± 0	100 ± 0	0 ± 0	100 ± 0	0 ± 0

DOI: 10.1021/acs.jafc.5b02366
J. Agric. Food Chem. 2015, 63, 8777−8786

Table 3. continued

		motility inhibitory and zoosporicidal activities over control[b] (% ± SE)											
		5 min		10 min		15 min		30 min		45 min		60 min	
compd	dose (μg/mL)	inhibited motility	lysed	inhibited motility	lysed	inhibited motility	lysed	inhibited motility	lysed	inhibited motility	lysed	inhibited motility	lysed
	100	15 ± 3	0 ± 0	30 ± 2	0 ± 0	50 ± 3	0 ± 0	60 ± 4	0 ± 0	80 ± 5	0 ± 0	100 ± 0	0 ± 0
	50	0 ± 0	0 ± 0	0 ± 0	0 ± 0	10 ± 2	0 ± 0	25 ± 2	0 ± 0	50 ± 6	0 ± 0	70 ± 7	0 ± 0
	25	0 ± 0	0 ± 0	0 ± 0	0 ± 0	5 ± 2	0 ± 0	30 ± 3	0 ± 0	45 ± 4	0 ± 0	50 ± 5	0 ± 0
8	900	100 ± 0	0 ± 0	100 ± 0	0 ± 0	100 ± 0	30 ± 3	100 ± 0	50 ± 7	100 ± 0	80 ± 6	100 ± 0	100 ± 0
	800	100 ± 0	0 ± 0	100 ± 0	0 ± 0	100 ± 0	10 ± 3	100 ± 0	20 ± 5	100 ± 0	50 ± 8	100 ± 0	60 ± 6
	700	90 ± 7	0 ± 0	100 ± 0	0 ± 0	100 ± 0	0 ± 0	100 ± 0	0 ± 0	100 ± 0	10 ± 3	100 ± 0	15 ± 3
	600	80 ± 4	0 ± 0	100 ± 0	0 ± 0	100 ± 0	0 ± 0	100 ± 0	0 ± 0	100 ± 0	0 ± 0	100 ± 0	5 ± 2
	500	70 ± 8	0 ± 0	80 ± 9	0 ± 0	100 ± 0	0 ± 0	100 ± 0	0 ± 0	100 ± 0	0 ± 0	100 ± 0	0 ± 0
	400	65 ± 6	0 ± 0	70 ± 6	0 ± 0	80 ± 5	0 ± 0	90 ± 7	0 ± 0	100 ± 0	0 ± 0	100 ± 0	0 ± 0
	300	60 ± 5	0 ± 0	50 ± 7	0 ± 0	65 ± 7	0 ± 0	80 ± 8	0 ± 0	100 ± 0	0 ± 0	100 ± 0	0 ± 0
	250	50 ± 7	0 ± 0	55 ± 5	0 ± 0	60 ± 4	0 ± 0	70 ± 5	0 ± 0	80 ± 6	0 ± 0	90 ± 7	0 ± 0
	100	0 ± 0	0 ± 0	0 ± 0	0 ± 0	5 ± 2	0 ± 0	10 ± 3	0 ± 0	25 ± 2	0 ± 0	40 ± 6	0 ± 0
9	900	100 ± 0	0 ± 0	100 ± 0	0 ± 0	100 ± 0	15 ± 4	100 ± 0	100 ± 0	nt	nt	nt	nt
	800	50 ± 7	25 ± 0	80 ± 8	50 ± 0	100 ± 0	80 ± 0	100 ± 0	100 ± 0	nt	nt	nt	nt
	700	30 ± 4	0 ± 0	60 ± 5	0 ± 0	75 ± 2	0 ± 0	100 ± 0	70 ± 0	100 ± 0	100 ± 0	nt	nt
	600	25 ± 6	0 ± 0	60 ± 7	0 ± 0	70 ± 9	0 ± 0	100 ± 0	20 ± 0	100 ± 0	50 ± 4	100 ± 0	100 ± 0
	500	15 ± 2	0 ± 0	35 ± 5	0 ± 0	50 ± 6	0 ± 0	80 ± 7	5 ± 0	100 ± 0	30 ± 3	100 ± 0	80 ± 8
	400	15 ± 3	0 ± 0	25 ± 3	0 ± 0	35 ± 3	0 ± 0	65 ± 3	5 ± 3	80 ± 5	45 ± 7	100 ± 0	60 ± 4
	300	0 ± 0	0 ± 0	20 ± 5	0 ± 0	30 ± 9	0 ± 0	55 ± 8	0 ± 0	70 ± 8	20 ± 6	100 ± 0	50 ± 8
	250	0 ± 0	0 ± 0	20 ± 5	0 ± 0	25 ± 5	0 ± 0	50 ± 5	0 ± 0	70 ± 3	10 ± 3	100 ± 0	30 ± 5
	100	0 ± 0	0 ± 0	0 ± 0	0 ± 0	15 ± 8	0 ± 0	35 ± 9	0 ± 0	60 ± 6	0 ± 0	100 ± 0	5 ± 3
	50	0 ± 0	0 ± 0	0 ± 0	0 ± 0	10 ± 9	0 ± 0	25 ± 2	0 ± 0	50 ± 4	0 ± 0	75 ± 5	0 ± 0
	25	0 ± 0	0 ± 0	0 ± 0	0 ± 0	0 ± 0	0 ± 0	0 ± 0	0 ± 0	10 ± 4	0 ± 0	35 ± 4	0 ± 0
14	900	100 ± 0	90 ± 7	100 ± 0	100 ± 0	nt	nt	nt	nt	nt	nt	nt	nt
	800	100 ± 0	75 ± 5	100 ± 0	100 ± 0	nt	nt	nt	nt	nt	nt	nt	nt
	700	100 ± 0	50 ± 0	100 ± 0	80 ± 5	100 ± 0	100 ± 0	nt	nt	nt	nt	nt	nt
	600	100 ± 0	30 ± 0	100 ± 0	50 ± 4	100 ± 0	65 ± 3	100 ± 0	90 ± 5	100 ± 0	100 ± 0	nt	nt
	500	100 ± 0	0 ± 0	100 ± 0	0 ± 0	100 ± 0	5 ± 7	100 ± 0	30 ± 4	100 ± 0	50 ± 3	100 ± 0	65 ± 9
	400	80 ± 3	0 ± 0	100 ± 0	0 ± 0	100 ± 0	0 ± 0	100 ± 0	15 ± 9	100 ± 0	35 ± 8	100 ± 0	50 ± 7
	300	70 ± 7	0 ± 0	90 ± 5	0 ± 0	100 ± 0	0 ± 0	100 ± 0	5 ± 2	100 ± 0	35 ± 4	100 ± 0	45 ± 2
	250	35 ± 5	0 ± 0	50 ± 4	0 ± 0	80 ± 4	0 ± 0	100 ± 0	0 ± 0	100 ± 0	10 ± 3	100 ± 0	25 ± 5
	100	30 ± 5	0 ± 0	40 ± 7	0 ± 0	70 ± 7	0 ± 0	100 ± 0	0 ± 0	100 ± 0	5 ± 2	100 ± 0	10 ± 3
	50	0 ± 0	0 ± 0	10 ± 3	0 ± 0	20 ± 3	0 ± 0	50 ± 3	0 ± 0	75 ± 9	0 ± 0	100 ± 0	0 ± 0
	25	0 ± 0	0 ± 0	0 ± 0	0 ± 0	0 ± 0	0 ± 0	20 ± 9	0 ± 0	30 ± 3	0 ± 0	60 ± 7	0 ± 0

[a]Compounds **1**, **2**, **4**, **10**, **11**, **12**, and **15** did not show inhibitory and lytic activities up to 900 μg/mL. [b]Data represented here are average values ± SE (standard error) of at least three replicates of each dose of compound. nt, not tested.

DOI: 10.1021/acs.jafc.5b02366
J. Agric. Food Chem. 2015, 63, 8777−8786

Table 4. Antimicrobial Activity of 1−12, 14, and 15

	diameter of inhibition zone in mm at 50 μg/disk				
compd[a]	*C. albicans*	*M. miehei*	*B. subtilis*	*E. coli*	*S. aureus*
1	–[b]	–	–	–	–
2	12	36	–	–	–
3	16	38	–	–	–
4	–	–	–	–	–
5	–	–	–	–	–
6	–	24	–	–	–
7	20	46	–	–	–
8	–	20	–	–	–
9	16	32	–	–	–
10	–	–	–	–	–
11	–	16	–	–	–
12	–	–	–	–	–
14	–	–	–	–	–
15	–	11	–	–	–
nystatin	17	21	–	–	–
ciprofloxacin	–	–	28	22	24

[a]Nystatin and ciprofloxacin were used as positive control. [b]–, not active at 50 μg/disk.

DISCUSSION

Motility inhibition followed by lytic activities against phytopathogenic Peronosporomycete zoospores has been reported previously for several plant and microbial metabolites, including polyflavonoid tannins from *Lannea coromandelica*,[11] polyketides from an endophytic fungus *Cryptosporiopsis* sp.,[42] lipopeptides from *Bacillus subtilis*,[12] indolocarbazole alkaloids from *Streptomyces* sp.,[43] and phloroglucinols from *Pseudomonas fluorescens*,[44] among others. However, motility inhibition and subsequent lysis of *P. nicotianae* zoospores by trichothecenes, as reported here, were previously unknown.

In our experiments with Peronosporomycetes, we observed a distinct relationship between structural features and activity in trichothecenes, as described previously by others.[45] In the agar diffusion assay for antifungal activity, among the macrocyclic trichothecenes tested here, only the 9-methyl trichothecenes (**2**, **3**, **7**, and **9**) showed noteworthy activities against *Candida albicans* and *Mucor miehei* at a concentration of 50 μg/disk when compared with nystatin (Table 4). The most notable activity against *C. albicans* and *M. miehei* was exhibited by compound **7**. It gave inhibition zones of 20 and 46 mm in diameter against *C. albicans* and *M. miehei*, whereas nystatin, a clinically used antifungal drug, gave 17 and 21 mm zones, respectively. The presence of the COOH or CH_2OH group at C-9 rendered the trichothecenes inactive against fungi, whereas among the verrucarins, the 2′,3′-epoxide ring was required for zoosporicidal activity.

The mechanisms by which trichothecenes produce cytotoxic effects in eukaryotic cells primarily involve inhibition of the macromolecule biosynthesis:[46] verrucarin A is 10 times more active than actinomycin D, one of the most active chemotherapeutic drugs. There is, however, no activity against prokaryotes (see Table 4), as also observed by others.[15]

In conclusion, trichothecenes are a large family of biologically active mycotoxins, with pronounced differential toxicity for eukaryotes[47] and strong structure-activity relationships. On the basis of these differential toxicities, trichothecenes may well be useful compounds for the development of effective agrochemicals and also as therapeutic leads.

ASSOCIATED CONTENT

Supporting Information

The Supporting Information is available free of charge on the ACS Publications website at DOI: 10.1021/acs.jafc.5b02366.

^{1}H and ^{13}C NMR spectra of compounds **1**, **6**, **12**, and **14**; ^{1}H NMR spectra of **10a**, **10b**, **11a**, **11b**, **12a**, and **12b**; selected ^{1}H chemical shifts for verrucarin J (**2**) isomers and verrucarin Y (**1**); calculation of ORD data to determine the absolute configuration of bilain D (**12**) (PDF)

AUTHOR INFORMATION

Corresponding Author

*(H.L.) Phone: +49 551 3933211. Fax: +49 551 399660. E-mail: hlaatsc@gwdg.de.

Funding

This work was financially supported by the Alexander von Humboldt Foundation through a Georg Forster Fellowship to M.A.M.M. and was also supported by the World Bank (CP 2071 to MTI).

Notes

The authors declare no competing financial interest.

ACKNOWLEDGMENTS

We are indebted to Dr. H. Frauendorf and Dr. M. John for MS and NMR measurements, respectively. We thank F. Lissy for technical assistance and Dr. S. Hickford for careful linguistic corrections of the manuscript.

ABBREVIATIONS USED

COSY, correlation spectroscopy; DBEs, double-bond equivalents; ESI-HRMS, electrospray ionization high-resolution mass spectrometry; EtOAc, ethyl acetate; HMBC, heteronuclear multiple-bond correlation; HSQC, heteronuclear single-quantum coherence; IC_{50}, 50% motility inhibitory concentration in μg/mL; IR, infrared; ITS, internal transcribed spacer sequence; Sephadex LH-20, type of lipophilic hydrophilic Sephadex for size exclusion chromatography; MTPA-Cl, α-methoxy-α-(trifluoromethyl)phenylacetyl chloride; NMR, nuclear magnetic resonance; NOE, nuclear Overhauser effect; P-flasks, *Penicillium* flasks; PTLC, preparative thin layer chromatography

REFERENCES

(1) Erwin, D. C.; Ribiero, O. K. *Phytophthora Diseases Worldwide*; APS Press: St. Paul, MN, USA, 1996.

(2) Kim, H. Y.; Choi, G. J.; Lee, H. B.; Lee, S. W.; Lim, H. K.; Jang, K. S.; Son, S. W.; Lee, S. O.; Cho, K. Y.; Sung, N. D.; Kim, J. C. Some fungal endophytes from vegetable crops and their anti-oomycete activities against tomato late blight. *Lett. Appl. Microbiol.* **2007**, *44*, 332−337.

(3) Schulz, B.; Boyle, C.; Draeger, S.; Römmert, A.-K.; Krohn, K. Endophytic fungi: a source of novel biologically active secondary metabolites. *Mycol. Res.* **2002**, *106*, 996−1004.

(4) Zhang, D. X.; Nagabhyru, P.; Schardl, C. L. Regulation of a chemical defense against herbivory produced by symbiotic fungi in grass plants. *Plant Physiol.* **2009**, *150*, 1072−1082.

(5) Clay, K.; Cheplick, G. P. Effect of ergot alkaloids from fungal endophyt-infected grasses on fall armyworm (*Spodoptera frugiperda*). *J. Chem. Ecol.* **1989**, *15*, 169−182.

(6) Patterson, C. G.; Potter, D. A.; Fannin, F. F. Feeding deterrency of alkaloids from endophyte-infected grasses to Japanese beetle grubs. *Entomol. Exp. Appl.* **1991**, *61*, 285−289.

DOI: 10.1021/acs.jafc.5b02366
J. Agric. Food Chem. 2015, 63, 8777−8786

(7) Prestidge, R. A.; Ball, O. J. -P. A catch 22: the utilization of endophytic fungi for pest management. In *Multitrophic Interactions in Terrestrial Systems*; Gange, A. C., Brown, V. K., Eds.; Blackwell Scientific Press: Oxford, UK, 1997; pp 171−192.
(8) Panneerselvam, A.; Ramya, S.; Gopinath, K.; Periyathambi, N.; Jayakumararaj, R.; Devaraj, A. Biopesticidal effect of ethyl acetate leaf extracts of *Datura metel* L. (Solanaceae) on the larvae of *Helicoverpa armigera* (Hübner). *Int. J. Pharm. Sci. Rev. Res.* **2013**, *18*, 150−154.
(9) Kuriakose, G. C.; Singh, S.; Rajvanshi, P. K.; Surin, W. R.; Jayabaskaran, C. *In vitro* cytotoxicity and apoptosis induction in human cancer cells by culture extract of an endophytic *Fusarium solani* strain isolated from *Datura metel* L. *Pharm. Anal. Acta* **2014**, *5*, 1−8.
(10) Laatsch, H. *AntiBase, a Database for Rapid Structural Determination of Microbial Natural Products, and Annual Updates*; Wiley-VCH: Weinheim, Germany, 2013; see http://wwwuser.gwdg.de/~ucoc/laatsch/AntiBase.htm.
(11) Islam, M. T.; Ito, T.; Sakasai, M.; Tahara, S. Zoosporicidal activity of polyflavonoid tannin identified in *Lannea coromandelica* stem bark against phytopathogenic oomycete *Aphanomyces cochlioides*. *J. Agric. Food Chem.* **2002**, *50*, 6697−6703.
(12) Tareq, F. S.; Lee, M. A.; Lee, H.; Lee, J. S.; Hasan, C. M.; Islam, M. T.; Shin, J. S. Gageotetrins A−C, noncytotoxic antimicrobial linear lipopeptides from a marine bacterium *Bacillus subtilis*. *Org. Lett.* **2014**, *16*, 928−931.
(13) Fandi, K.; Al-Muaikel, N.; Al-Momani, F. Antimicrobial activities of some thermophiles isolated from Jordan hot springs. *Int. J. Chem., Environ. Biol. Sci.* **2014**, *2* (1).
(14) Shimada, A.; Takeuchi, S.; Kusano, M.; Fujioka, S.; Kimura, Y. Roridin A and verrucarin A, inhibitors of pollen development in *Arabidopsis thaliana*, produced by *Cylindrocarpon* sp. *Plant Sci.* **2004**, *166*, 1307−1312.
(15) Schoettler, S.; Bascope, M.; Sterner, O.; Anke, T. Isolation and characterization of two verrucarins from *Myrothecium roridum*. *Z. Naturforsch. C. J. Biosci.* **2006**, *61*, 309−314.
(16) Gutzwiller, J.; Tamm, C. The structure elucidation of verrucarin B. *Helv. Chim. Acta* **1965**, *48*, 177−182.
(17) Pavanasasivam, G.; Jarvis, B. B. Microbial transformation of macrocyclic trichothecenes. *Appl. Environ. Microbiol.* **1983**, *2*, 480−483.
(18) Smitka, T. A.; Bunge, R. H.; Bloem, R. J.; French, J. C. Two new trichothecenes, PD 113,325 and PD 113,326. *J. Antibiot.* **1984**, *37*, 823−828.
(19) Jarvis, B. B.; Midiwo, J. O. Stereochemistry of roridins. *J. Nat. Prod.* **1982**, *45*, 440−448.
(20) Bloem, R. J.; Smitka, T. A.; Runge, R. H.; French, J. C. Roridin L-2, a new trichothecene. *Tetrahedron Lett.* **1983**, *24*, 249−252.
(21) Jarvis, B. B.; Vrudhula, V. M.; Pavanasasivam, G. Trichoverritone and 16-hydroxyroridin L-2, new trichothecenes from *Myrothecium roridum*. *Tetrahedron Lett.* **1983**, *24*, 3539−3542.
(22) Lin, T.; Wang, G.; Shan, W.; Zeng, D.; Ding, R.; Jiang, X.; Zhu, D.; Liu, X.; Yang, S.; Chen, H. Myrotheciumones: bicyclic cytotoxic lactones isolated from an endophytic fungus of *Ajuga decumbens*. *Bioorg. Med. Chem. Lett.* **2014**, *24*, 2504−2507.
(23) Grove, J. F. Macrocyclic trichothecenes. *Nat. Prod. Rep.* **1993**, *10*, 429−448.
(24) Tamm, C.; Breitenstein, W. The biosynthesis of trichothecene mycotoxins. In *The Biosynthesis of Mycotoxins: A Study in Secondary Metabolism*; Steyn, P. S., Ed.; Academic Press: New York, 1980; pp69−101.
(25) Roush, W. R.; Blizzard, T. A. Synthesis of epoxytrichothecenes: verrucarin J and verrucarin J isomers. *J. Org. Chem.* **1984**, *49*, 1772−1783.
(26) Breitenstein, W.; Tamm, C. The absolute configuration of the fungal metabolite verrucarin B. Biosynthetic consequences. *Helv. Chim. Acta* **1979**, *62*, 2699−2705.
(27) Jarvis, B. B.; Wang, S. Stereochemistry of the roridins. Diastereomers of roridin E. *J. Nat. Prod.* **1999**, *62*, 1284−1289.
(28) Ohtani, I.; Kusumi, T.; Kashman, Y.; Kakisawa, H. High-Field FT NMR application of Mosher's method. The absolute configurations of marine terpenoids. *J. Am. Chem. Soc.* **1991**, *113*, 4092−4096.
(29) Yonezawa, Y.; Shimizu, K.; Uchiyama, M.; Kagawa, N.; Shin, C.-g. Total syntheses of naturally occurring bis(methylthio)silvatin and its three stereoisomers. *Heterocycles* **1997**, *45*, 1151−1159.
(30) Capon, R. J.; Stewart, M.; Ratnayake, R.; Lacey, E.; Gill, J. H. Citromycetins and bilains A−C: new aromatic polyketides and diketopiperazines from australian marine-derived and terrestrial *Penicillium* spp. *J. Nat. Prod.* **2007**, *70*, 1746−1752.
(31) Amagata, T.; Minoura, K.; Numata, A. Cytotoxic metabolites produced by a fungal strain from a *Sargassum* alga. *J. Antibiot.* **1998**, *51*, 432−434.
(32) Rahbaek, L.; Sperry, S.; Piper, J. E.; Crews, P. Deoxynortrichoharzin, a new polyketide from the saltwater culture of a sponge-derived *Paecilomyces* fungus. *J. Nat. Prod.* **1998**, *61*, 1571−1573.
(33) Wang, G.-Y.-S.; Abrell, L. M.; Avelar, A.; Borgeson, B. M.; Crews, P. New hirsutane based sesquiterpenes from salt water cultures of a marine sponge-derived fungus and the terrestrial fungus *Coriolus consors*. *Tetrahedron* **1998**, *54*, 7335−7342.
(34) Hanson, J. R.; O'Leary, M. A. New piperazinedione metabolites of *Gliocladium deliquescens*. *J. Chem. Soc., Perkin Trans. 1* **1981**, 218−220.
(35) Chu, M.; Mierzwa, R.; Truumees, I.; Gentile, F.; Gullo, M. P. V.; Chan, T.-M.; Puar, M. S. Two novel diketopiperazines isolated from the fungus *Tolypocladium* sp. *Tetrahedron Lett.* **1993**, *34*, 7537−7540.
(36) Ayer, W. A.; Altena, I. V.; Browne, L. M. Three piperazinediones and a drimane diterpenoid from *Penicillium brevi-compactum*. *Phytochemistry* **1990**, *29*, 1661−1665.
(37) Matselyukh, B.; Mohammadipanah, F.; Laatsch, H.; Rohr, J.; Efremenkova, O.; Khilya, V.; Matselyukh, O. *N*-Methylphenylalanyl-dehydrobutyrine diketopiperazine, an A-factor mimic that restores antibiotic biosynthesis and morphogenesis in *Streptomyces globisporus* 1912-B2 and *Streptomyces griseus* 1439. *J. Antibiot.* **2015**, *68*, 9−14.
(38) Isaka, M.; Chinthanom, P.; Veeranondha, S.; Supothina, S.; Luangsa-ard, J. J. Novel cyclopropyl diketones and 14-membered macrolides from the soil fungus *Hamigera avellanea* BCC 17816. *Tetrahedron* **2008**, *64*, 11028−11033.
(39) Snyman, L. D.; Kellerman, T. S.; Vleggaar, R.; Flett, B. C.; Basson, K. M.; Schultz, R. A. Diplonine, a neurotoxin isolated from cultures of the fungus *Stenocarpella maydis* (berk.) sacc. that induces diplodiosis. *J. Agric. Food Chem.* **2011**, *59*, 9039−9044.
(40) Clericuzio, M.; Cassino, C.; Corana, F.; Vidari, G. Terpenoids from *Russula lepida* and *R. amarissima* (Basidiomycota, Russulaceae). *Phytochemistry* **2012**, *84*, 154−159.
(41) Kanokmedhakul, S.; Lekphrom, R.; Kanokmedhakul, K.; et al. Cytotoxic sesquiterpenes from luminescent mushroom *Neonothopanus nambi*. *Tetrahedron* **2012**, *68*, 8261−8266.
(42) Talontsi, F. M.; Facey, P.; Tatong, M. D.; Islam, T. M.; Frauendorf, H.; Draeger, S.; Tiedemann, Av.; Laatsch, H. Zoosporicidal metabolites from an endophytic fungus *Cryptosporiopsis* sp. of *Zanthoxylum leprieurii*. *Phytochemistry* **2012**, *83*, 87−94.
(43) Islam, M. T.; von Tiedemann, A.; Laatsch, H. Protein kinase C is likely to be involved in zoosporogenesis and maintenance of flagellar motility in the peronosporomycete zoospores. *Mol. Plant-Microbe Interact.* **2011**, *24*, 938−947.
(44) Islam, M. T.; von Tiedemann, A. 2,4-Diacetylphloroglucinol suppresses zoosporogenesis and impairs motility of peronosporomycete zoospores. *World J. Microbiol. Biotechnol.* **2011**, *27*, 2071−2079.
(45) Wu, Q.; Dohnal, V.; Yuan, Z. Trichothecenes: structure-toxic activity relationships. *Curr. Drug Metab.* **2013**, *14*, 641−660.
(46) Rocha, O.; Ansari, K.; Doohan, F. M. Effects of trichothecene mycotoxins on eukaryotic cells: a review. *Food Addit. Contam.* **2005**, *22*, 369−378.
(47) Abbas, H. K.; Johnson, B. B.; Shier, W. T.; Tak, H.; Jarvis, B. B.; Boyette, C. D. Phytotoxicity and mammalian cytotoxicity of macrocyclic trichothecene mycotoxins from *Myrothecium verrucaria*. *Phytochemistry* **2002**, *59*, 309−313.

DOI: 10.1021/acs.jafc.5b02366
J. Agric. Food Chem. 2015, 63, 8777−8786

spectra were determined with a Bruker AM-400BB (400 MHz) spectrometer (Bruker, Ltd., Karlsruhe, Germany). Values of δ in parts per million (ppm) are relative to tetramethylsilane (TMS). Values of J are given in hertz (Hz). High-resolution electrospray ionization mass spectrometry (HRESIMS) was performed with a Bruker APEX-II mass spectrometer (Bruker, Ltd., Karlsruhe, Germany), and results are presented in terms of m/z.

Fungal Material. The fungus was isolated from the healthy stems of *E. tangutorum*, collected in Qinghai Province, China. The fungus was identified on the basis of morphology and molecular phylogenetic data. The organism was determined to be a common ancestor with an *E. bromicola* strain from *Hordeum brevisubulatum*. Therefore, the isolate was defined as *E. bromicola* (NI_201216) and was deposited at the College of Pastoral Agriculture Science and Technology, Lanzhou University.[13]

Preparative Scale Culture. *E. bromicola* was grown on a sterilized moistened rice medium in 1000 mL flasks (100 g/flask × 100) at 27 °C for 30 days to produce white moldy rice.

Extraction, Isolation, and Purification Process. The rice culture was extracted with EtOAc 4 times to yield 18 g of the crude extract. The crude extract was applied to a silica gel column (90 × 15 cm) and eluted with $CHCl_3$/MeOH (4 L, 1:0−0:1 gradient system) to give four fractions labeled Fr-A−Fr-D.

Fr-A was chromatographed on a Sephadex LH-20 column (120 × 2.5 cm, $CHCl_3$/MeOH, 500 mL, 1:1) and silica gel column (30 × 4 cm, petroleum ether/acetone, 800 mL, 1:0−0:1) to yield compounds **1** (478.0 mg), **2** (13.0 mg), **6** (6.6 mg), **8** (20.9 mg), and **12** (5.8 mg).

Fr-B was subjected to a Sephadex LH-20 column (120 × 2.5 cm, pure MeOH, 200 mL) and then silica gel column (20 × 4 cm, $CHCl_3$/EtOAc, 700 mL, 1:0−0:1) to produce compounds **3** (98.0 mg), **13** (5.3 mg), **15** (7.5 mg), and **16** (6.9 mg).

Fr-C was purified by column chromatography on a RP-18 column (30 × 2 cm, 500 mL, H_2O/MeOH, 1:0−0:1) and PTLC ($CHCl_3$/acetone, 80 mL, 1:0−0:1) to afford compounds **4** (5.3 mg), **5** (12.6 mg), **7** (9.7 mg), **10** (5.1 mg), **11** (5.4 mg), and **14** (2.9 mg).

Fr-D was isolated by a RP-18 column (30 × 2 cm, H_2O/MeOH, 600 mL, 1:0−0:1) and then a silica gel column (20 × 4 cm, $CHCl_3$/MeOH, 550 mL, 1:0−0:1) to give compounds **9** (18.0 mg), and **17** (102.0 mg).

Cyclosporin T, **1**, was a white powder with $[\alpha]_D^{22}$ −197 (c 0.10 in MeOH). HRESIMS indicated m/z 1188.8337 $[M + H]^+$ (calculated for $[C_{61}H_{110}O_{12}N_{11}]$ 1188.8330). The spot color of compound **1** was red with 10% H_2SO_4 in EtOH, followed by heating and under Dragendorff's reagent. ^1H and ^{13}C NMR spectra of compound **1** in $CDCl_3$ were consistent with those reported in the literature.[14]

3-(2′-(4″-Hydroxyphenyl)acetoxy)-2*S*-methylpropanoic acid, **7**, was a yellow oil with $[\alpha]_D^{22}$ +50 (c 0.10 in MeOH). IR parameters (νKBr_{max}) were 3423, 1714, and 1632 cm^{-1}. ^1H and ^{13}C NMR data are in Table 1.

Theoretical Calculations. To identify the absolute configuration of compound **7**, quantum mechanical calculations were performed. The B3LYP functional with the 6-31G(d, p) basis set was used.[15,16] The calculations were performed using the Gaussian 09 suite of programs.[17]

General Procedure for Synthesis of Compounds 7a and 7b. Thionyl chloride (0.65 mL, 8.9 mmol) and dimethylformamide (100.0 μL, 1.3 mmol) were added to a solution of 2-phenylacetic acid (0.40 g, 3.0 mmol) in dichloromethane (10.0 mL). After the mixture was stirred at room temperature for 1 h, the solvent was removed *in vacuo* to obtain 2-phenylacetyl chloride (0.45 g, 98%) as yellow oil, which was used directly in the next step.

To a solution of 2-phenylacetyl chloride (0.45 g, 2.9 mmol) in dichloromethane (2.0 mL), a solution of methyl 3-hydroxy-2*R*/*S*-methylpropanoate (0.21 g, 1.8 mmol) in dichloromethane (5.0 mL) was added. After the reaction mixture was stirred for 4 h, the reaction was quenched by the addition of ice water and the organic phase was separated. The aqueous phase was then extracted with dichloromethane (2 × 10.0 mL). The organic phase was dried with $MgSO_4$, and the solvent was removed *in vacuo*. Purification by flash chromatography (ethyl acetate/petroleum ether, 1:10) gave methyl 2*R*-methyl-3-(2-phenylacetoxy)propanoate (**7a**) or methyl 2*S*-methyl-3-(2-phenylacetoxy)propanoate (**7b**) as an oil (0.31 g, 73%).

Table 1. ^1H and ^{13}C NMR Data of Metabolite 7[a]

	7	
number	δ_H multi (J in Hz)	δ_C
1″		125.5
2″	7.09 d (8.4)	130.4
3″	6.72 d (8.4)	115.5
4″		154.8
5″	7.09 d (8.4)	130.4
6″	6.72 d (8.4)	115.5
1′	3.55 brs	38.8
2′		172.1
1		179.4
2	4.83 m	40.4
3	4.20 dd (7.2, 10.8)	65.6
	4.28 dd (7.2, 10.8)	
4	1.21 d (7.2)	13.5

[a] ^1H (400 MHz) and ^{13}C (100 MHz) NMR, TMS, measured in $CDCl_3$.

*Methyl 2R-Methyl-3-(2-phenylacetoxy)propanoate (**7a**).* The colorless oil exhibited $[\alpha]_D^{22}$ −70 (c 0.10 in MeOH). ^1H NMR (400 MHz, $CDCl_3$) δ_H: 7.27−7.34 (m, 5H, ArH), 4.19, 4.25 (dd, J = 7.2 and 10.8 Hz, 2H, $-CH_2O-$), 3.64 (s, 3H, $-OCH_3$), 3.61 (s, 2H, $-CH_2-$), 2.78 (m, 1H, −CH−), 1.16 (d, J = 7.2 Hz, Me−H). ^{13}C NMR (100 MHz, $CDCl_3$) δ_C: 174.1 (−C═O), 171.2 (−C═O), 133.8, 129.2, 129.2, 128.5, 128.5, 127.1 (ArC × 6), 65.8 ($-CH_2O-$), 51.8 ($-OCH_3$), 41.2 (−CH−), 38.9 ($-CH_2-$), 13.7 (Me−C). HRESIMS: m/z 237.1118 $[M + H]^+$ (calculated for $[C_{13}H_{17}O_4]$ 237.1121).

*Methyl 2S-Methyl-3-(2-phenylacetoxy)propanoate (**7b**).* The colorless oil exhibited $[\alpha]_D^{22}$ +70 (c 0.10 in MeOH). Compounds **7b** and **7a** shared the same NMR data. HRESIMS: m/z 237.1120 $[M + H]^+$ (calculated for $[C_{13}H_{17}O_4]$ 237.1121).

Antifungal Assay. Antifungal activity against pathogenic fungi was tested using the previously reported method.[18] A sample was dissolved in dimethyl sulfoxide (DMSO) to give a test solution at a defined concentration. This solution (0.1 mL) was thoroughly mixed with 20 mL of potato dextrose agar (PDA) molten agar medium. The mixture was then equally poured onto three Petri dishes (6 cm diameter) to prepare treated culture. DMSO without a sample was processed similarly to give control culture media. Chlorothalonil served as the positive control. Discs (0.4 cm) of hyphae were cut from the edge of a colony. These hyphae were placed in the middle surface of the culture medium with the hyphae downward. The inhibition rate was obtained according to the following formula: inhibition rate (%) = $(C - T)/(C - 0.4\ cm)$, where T is the average diameter of mycelia on PDA treated with sample and C is the average number of mycelia on PDA treated with control compounds. The EC_{50} values of the tested compounds were thus determined. Each assay was performed in triplicate.

Phytotoxicity Bioassay. With glyphosate as the positive control, phytotoxic effects on *Lolium perenne* and *Poa crymophila* were examined using the method described in the literature.[19] The seedlings were soaked in cold water for 100 min, then dipped in ethanol for 5 min, and repeatedly rinsed until odorless. A 12-well microplate was placed on two sheets of aseptic filter paper. The samples to be tested were dissolved in MeOH and applied to the paper. Upon evaporation of MeOH, aseptic water was added to the wells. *L. perenne* and *P. crymophila* seedlings of uniform size and shape were put on the papers. The seedlings were kept for 5 and 9 days, respectively, at 22 °C under dark conditions. The phytotoxicities were observed after 72 and 120 h, respectively. Methanol was used as a blank control. Each experimental result was expressed as the mean ± standard deviation (SD) of three trials.

Cytotoxicity Assay. MDBK cells were purchased from the Shanghai cell bank of the Chinese Academy of Sciences and maintained at 37 °C under an atmosphere of 95% air and 5% CO_2

DOI: 10.1021/acs.jafc.5b04260
J. Agric. Food Chem. 2015, 63, 8787−8792

in Dulbecco's modified Eagle's medium (DMEM) containing 10% fetal bovine serum and 1% antibiotic/antimicrobial solution. A cytotoxicity assay was performed as previously described.[20] MDBK cells were seeded in 96-well plates at a cell concentration of 5000 cells per well in 100 μL of DMEM. After incubation of the cells for 24 h at 37 °C, various concentrations of compounds were added and the incubation was continued for 24 h. Untreated cells were used as controls. After that, 10 μL of 5 mg/mL resazurin solution was added into each well and incubation was continued for 2 h at 37 °C. The fluorescence intensity was measured using FlexStation 3 (Molecular Devices, Sunnyvale, CA) at excitation/emission wavelengths of 555/585 nm. Each assay was performed in triplicate.

RESULTS AND DISCUSSION

Cultivation, Isolation, and Structure Elucidation. The fungal strain was cultured in rice medium at 27 °C for 30 days.

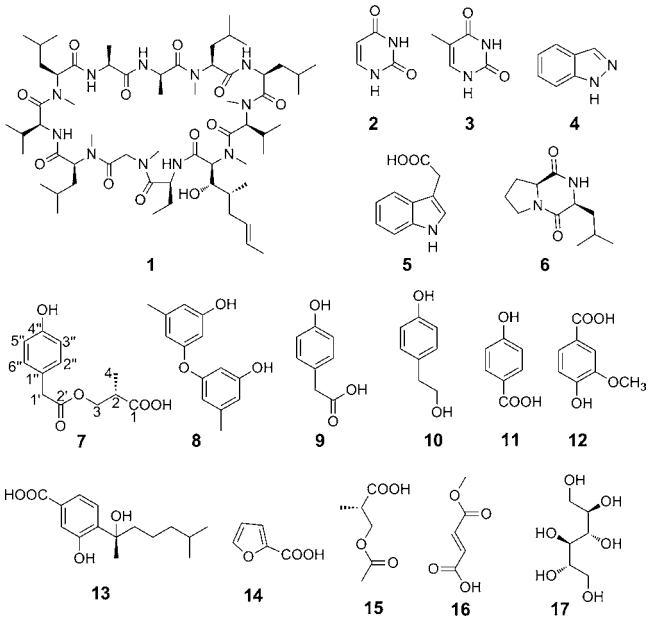

Figure 1. Structures of compounds **1**–**17**.

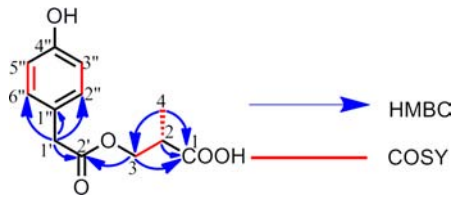

Figure 2. HMBC and COSY of compound **7**.

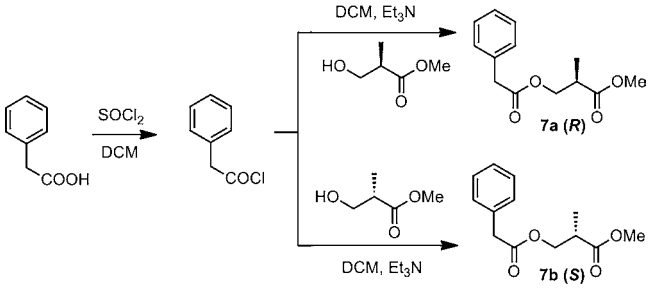

Figure 3. Synthesis of compounds **7a** and **7b**.

The cultured material was extracted 4 times with EtOAc. The EtOAc extract was then fractionated by means of chromatography on silica gel, Sephadex LH-20, PTLC, and RP-18. A new compound (**7**) and 16 known compounds (**1**–**6** and **8**–**17**), including a cyclic peptide (**1**) (Figure 1) were obtained from the EtOAc extract. It should be noted that these isolated compounds were not detected in the rice medium without the fungus (*E. bromicola*). The structures of these obtained compounds were determined by combining the extensive

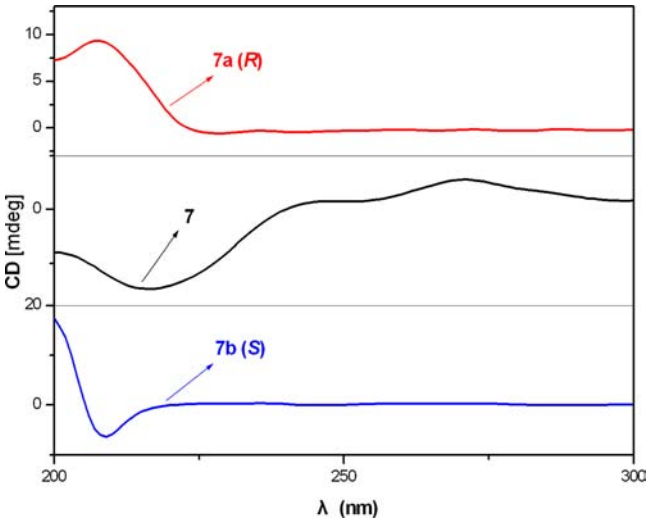

Figure 4. ECD spectra of compounds **7**, **7a**, and **7b** (in MeOH).

Table 2. Antifungal Activities of Metabolites 1, 3, 9, and 17 against Four Pathogenic Fungi (EC_{50}, μM)

compound	*A. alternata*	*B. sorokiniana*	*F. avenaceum*	*C. lunata*
1	5.3	3.9	0.7	2.9
3	>200	>200	>200	>200
9	>150	>100	>100	>100
17	>200	>200	>200	>200
chlorothalonil	56.8	66.4	13.5	38.8

Table 3. Inhibitory Effects of Metabolites 1–17 on the Growth of *L. perenne* Seedlings[a]

	inhibition ratio (%)[b]	
compound	root	shoot
1	16.4 ± 1.1	9.1 ± 1.0
2	23.4 ± 2.1	35.6 ± 2.7
3	0	9.3 ± 3.4
4	19.3 ± 1.9	1.5 ± 1.4
5	74.8 ± 3.5	48.5 ± 3.2
6	5.6 ± 2.3	3.7 ± 2.1
7	10.1 ± 3.3	5.2 ± 2.1
8	83.9 ± 2.9	59.8 ± 2.1
9	55.8 ± 3.8	28.4 ± 1.7
10	13.8 ± 2.6	2.8 ± 5.7
11	2.6 ± 2.3	3.1 ± 2.2
12	8.7 ± 2.9	0
13	0	0
14	1.9 ± 1.3	2.5 ± 2.0
15	21.1 ± 3.8	11.9 ± 2.3
16	3.2 ± 1.9	2.6 ± 1.4
17	0	0
glyphosate	72.0 ± 3.5	82.3 ± 2.8

[a]All of the metabolites were tested at the concentration of 200 ppm. [b]Mean ± SD.

DOI: 10.1021/acs.jafc.5b04260
J. Agric. Food Chem. 2015, 63, 8787–8792

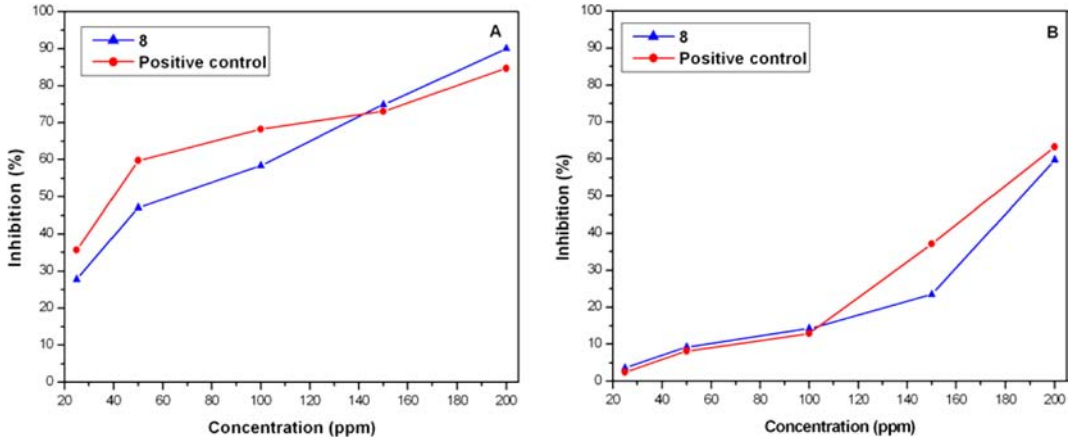

Figure 5. Phytotoxic activities of compound **8** and positive control on *P. crymophila*: (A) root and (B) shoot ($p < 0.05$).

Table 4. Cytotoxic Activities of Metabolites 1−17 against MDBK Cells[a]

compound	inhibition ratio (%) at the concentration of 12.5 μM
1	−1.8
2	−2.9
3	−5.8
4	−5.3
5	−17.0
6	−12.1
7	−11.1
8	−11.1
9	−8.1
10	−8.8
11	−9.7
12	−5.1
13	−5.9
14	−1.5
15	−7.9
16	−1.6
17	−4.8
ergonovine	29.3

[a]The IC_{50} values of metabolites **1−17** and ergonovine were above 100 μM.

spectroscopic analysis with computational optical rotation, chemical reaction, and comparison to the data in the literature.

Compound **7** was obtained as optically active yellow oil. The ^{13}C NMR and distortionless enhancement by polarization transfer (DEPT) spectra together with the molecular ion peak in the HRESIMS indicated a molecular formula of $C_{12}H_{14}O_5$. The IR spectrum of compound **7** showed absorption bands of hydroxyl (3423 cm^{-1}) and carbonyl (1632 and 1714 cm^{-1}) groups. The ^1H NMR spectrum of compound **7** showed four aromatic protons at δ_H 6.72 (2H, d, J = 8.4 Hz) and 7.09 (2H, d, J = 8.4 Hz), implying that the aromatic ring had a 1,4-disubstitution pattern. Moreover, the ^1H NMR spectrum revealed the presence of a set of oxygenated methylene protons at δ_H 4.20 and 4.28 (dd, J = 7.2, 10.8 Hz), a set of methylene proton at δ_H 3.55 (s), a methine proton at δ_H 2.82 (m), and a secondary methyl group at δ_H 1.21 (d, J = 7.2 Hz). The ^{13}C NMR and DEPT spectra of compound **7** displayed six aromatic carbons at δ_C 115.5, 115.5, 125.5, 130.4, 130.4, and 154.8, two carbonyl carbons at δ_C 172.1 and 179.4, an oxygenated methylene carbon at δ_C 65.6, a methylene carbon at δ_C 38.8, a methine carbon at δ_C 40.4, and a secondary methyl carbon at δ_C 13.5. The $^1H-^1H$ correlation spectroscopy (COSY) spectrum of compound **7** revealed a spin-coupling system of H_2-3, H-2, and H_3-4, and the heteronuclear multiple-bond correlations (HMBC) of H-4 (δ_H 1.21) with C-3 and C-1, H-3 (δ_H 4.20 and 4.28) with C-2′ and C-1, and H-1′ (δ_H 3.55) with C-2′ suggested that compound **7** has a C_6 side chain. The C_6 side chain was positioned at C-1″ according to the HMBC of the methylene group H-1′ (δ_H 3.55) with C-1″, C-2″, and C-6″ (Figure 2). With the above information taken into account, the hydroxyl was positioned at C-4″. Accordingly, the whole planar structure of compound **7** was completely elucidated.

A detailed analysis of the stereochemistry of compound **7** indicated only one chiral center at C-2, thus making it possible to identify two candidate stereostructures as either 2*S* or 2*R*. The computational optical rotation approach was used to determine the configuration of C-2. All optical rotation calculations were performed using the integral equation formalism polarizable continuum model (IEF-PCM) solvation model, and in agreement with the experimental condition, MeOH was specified as the solvent. The calculated optical rotation for 2*S* was 84.9°, while the value of 2*R* was −84.9°. The former is closer to the experimental value of 50.0°. Therefore, the absolute configuration of C-2 was 2*S*.

To further verify the absolute configuration of compound **7**, two model compounds (**7a** and **7b**) were synthesized through the esterification reactions using methyl 3-hydroxy-2*R*-methylpropanoate or methyl 3-hydroxy-2*S*-methylpropanoate as the substrates (Figure 3). The electron capture dissociation (ECD) spectra of compounds **7a** and **7b** were tested in MeOH (Figure 4), and the ECD spectrum of compound **7b** is similar to that of compound **7**. Therefore, the absolute configuration of C-2 of compound **7** is 2*S*. Accordingly, the structure of the novel compound **7** was established and named as 3-(2′-(4″-hydroxyphenyl)acetoxy)-2*S*-methylpropanoic acid.

The spectral data (MS and ^1H and ^{13}C NMR spectra) of compounds **1−6** and **8−17** were identical to those reported in the previous literature. Accordingly, their structures were identified as those of cyclosporin T (**1**),[14] uracil (**2**),[21] 5-methyluracil (**3**),[21] 1*H*-indazole (**4**),[22] 1*H*-indazole-3-acetic acid (**5**),[23] cyclo-(L-leucyl-L-prolyl) (**6**),[24] 3,3′-dihydroxy-5,5′-dimethyldiphenyl ether (**8**),[25] (4-hydroxyphenyl)-acetic acid (**9**),[26] 2-(4-hydroxyphenyl)-ethanol (**10**),[27] *p*-hydroxybenzoic acid (**11**), vanillic acid (**12**),[28] (−)-sydonic acid (**13**),[29] furan-2-

DOI: 10.1021/acs.jafc.5b04260
J. Agric. Food Chem. 2015, 63, 8787−8792

carboxylic acid (**14**),[30] 3-acetoxy-2*S*-methylpropanoic acid (**15**),[31] fumaric acid, methyl ester (**16**),[32] and dulcose (**17**).[33]

The obtained compounds were different from those alkaloids previously found in the fermentation of *Epichloë* spp., which may be due to the alteration of the cultivation parameters to one strain.[34] Analysis of the structures of the presently obtained compounds indicated that compounds **1** and **6** are peptides. In particular, compound **1** is a polypeptide. Compounds **2** and **3** are nucleobases. Compound **4** is an indazole. Compounds **7** and **9** are phenylacetic acid derivatives. Compounds **8** and **13** are a dimethyldiphenyl ether and a sesquiterpene, respectively. Compound **10** is 2-(4-hydroxyphenyl)-ethanol. Compounds **11** and **12** are substituted benzoic acids. The other compounds (**14**−**17**) were acids and sugar. These metabolites, except the alkaloid 1*H*-indole-3-acetic acid (**5**), were isolated from the genus *Epichloë* for the first time through a literature search.

Antifungal Activity of Metabolites. To determine the effects of these metabolites from *E. bromicola* on different phytopathogenic fungi, metabolites **1**, **3**, **9**, and **17** were tested for their inhibition of *Alternaria alternata*, *Bipolaris sorokiniana*, *Fusarium avenaceum*, and *Curvularia lunata in vitro* (there were insufficient quantities of compounds **2**, **4**−**8**, and **10**−**16**). The phytopathogenic fungi were chosen because they are very common in the cool-season subfamily of Pooideae grasses and caused a substantial reduction in the yield of herbage.[35] As shown in Table 2, compound **1** was the most active among the assayed compounds. The other tested compounds were weaker than chlorothalonil as the positive control, with EC_{50} values from 13.5 to 66.4 μM.[36] The EC_{50} values of compound **1** against *A. alternata*, *B. sorokiniana*, *F. avenaceum*, and *C. lunata* were 5.3, 3.9, 0.7, and 2.9 μM, respectively, suggesting that it had broad-spectrum inhibitory activity against these four plant pathogenic fungi and was stronger than chlorothalonil. Therefore, compound **1** may be considered as a lead compound for the development of new fungicides for suppression of common plant diseases, especially those caused by these tested phytopathogenic fungi. Furthermore, compound **1** was the most abundant of the 17 isolated metabolites, indicating that compound **1** plays an important role in host disease resistance against these pathogens. Thus, *E. bromicola* is a promising lead organism for the development of a natural microorganism fungicide to allow *E. tangutorum* to resist plant pathogenic fungi.

Phytotoxic Activity of Metabolites. Metabolites **1**−**17** of *E. bromicola* were tested for their phytotoxic activities against *L. perenne* seedlings. As shown in Table 3, compound **8** was the most active against the roots and shoots, with the inhibitory rates of 83.9 and 59.8%, respectively. Compound **5** (74.8%) showed similar activity with glyphosate (72.0%) in inhibiting the root growth; it displayed weaker inhibition of the shoots (48.5%) than glyphosate as the positive control (82.3%). This result was consistent with reported literature.[37] Compound **9** exhibited moderate activity against the roots and shoots, with inhibitory rates of 55.8 and 28.4%, respectively. Other metabolites showed weak activity toward the shoots and roots, with the inhibition rates ranging from 0 to 35.6%.

To determine whether compound **8** possesses inhibitory activity against *P. crymophila*, its phytotoxic effects were assayed at different concentrations. As shown in Figure 5, at high concentrations of 150−200 ppm, compound **8** exhibited inhibition rates in the range of 74.9−90.1% against roots, which was as active as glyphosate (73.1−84.7%); it displayed weaker activity (23.5−59.8%) than glyphosate (37.1−63.3%) toward the shoots. At low concentrations of 25−100 ppm, compound **8** weakly inhibited the roots (27.8−58.4%) relative to glyphosate (35.7−68.3%); however, its inhibitory rates (3.6−14.2%) were similar to that of glyphosate (2.4−12.9%) against shoots. The results showed that compound **8** displayed marked phytotoxic effects toward the roots and shoots of various seedlings at concentrations of 50−200 ppm. Therefore, compound **8** may play a crucial role for *E. tangutorum* in inhibiting the growth of other grasses, and it has potential as a new type of natural microbial herbicide. The compound may be the reason for the wide distribution of *E. tangutorum* and its high frequency of infection of *Epichloë* spp. in China. Moreover, this is the first report of phytotoxic effects of dimethyldiphenyl ethers.

Cytotoxicity of Metabolites. Metabolites **1**−**17** were tested for their cytotoxicity against MDBK cells. As shown in Table 4, none of the obtained metabolites exerted cytotoxicity toward MDBK cells. The IC_{50} values were above 100 μM. Moreover, the inhibition rates of the metabolites were between −1.6 and −17.0% at a concentration of 12.5 μM, indicating that they may promote mammalian cell growth at low concentrations. Thus, the metabolites did not exhibit cytotoxicity to MDBK cells. The results were quite different from those observed with the alkaloids isolated from *Epichloë* spp.; those alkaloids produced detrimental effects on their hosts.[6] The present results indicate that it may be safe for animals to eat *E. tangutorum* grass that is infected with *E. bromicola*. Accordingly, *E. bromicola* may be a beneficial fungus with desirable phytotoxic and antifungal properties and a lack of cytotoxicity toward mammalian cells. The results indicate the possibility of raising new varieties of herbage with resistance against infection and competition.

AUTHOR INFORMATION

Corresponding Authors

*E-mail: zhibiao@lzu.edu.cn.

*E-mail: npchem@lzu.edu.cn.

Funding

This work was funded by the Research Program 973 of China (2014CB138702), the Fundamental Research Funds for the Central Universities (lzujbky-2014-81), and the National Natural Science Foundation of China (31502001).

Notes

The authors declare no competing financial interest.

REFERENCES

(1) Leuchtmann, A.; Bacon, C. W.; Schardl, C. L.; White, J. F.; Tadych, M. Nomenclatural realignment of *Neotyphodium* species with genus. *Mycologia* **2014**, *106*, 202−215.

(2) Bush, L. P.; Wilkinson, H. H.; Schardl, C. L. Bioprotective alkaloids of grass fungal endophyte symbioses. *Plant Physiol.* **1997**, *114*, 1−7.

(3) Schardl, C. L.; Grossman, R. B.; Nagabhyru, P.; Faulkner, J. R.; Mallik, U. P. Loline alkaloids: currencies of mutualism. *Phytochemistry* **2007**, *68*, 980−996.

(4) Marks, S.; Clay, K.; Cheplick, G. P. Effects of fungal endophytes on interspecific and intraspecific competition in the grass *Festuca arundinacea* and *Lolium perenne*. *J. Appl. Ecol.* **1991**, *28*, 194−204.

(5) Zhang, Y. P.; Nan, Z. B. Growth and anti-oxidative systems changes in *Elymus dahuricus* is affected by *Neotyphodium* endophyte under contrasting water availability. *J. Agron. Crop Sci.* **2007**, *193*, 377−386.

(6) Yang, S.; Li, C. J.; Chai, Q.; Huang, X.; Nan, Z. B. Allelopathic effects of *Neotyphodium* endophytes of *Elymus dahuricus* on seeds and

DOI: 10.1021/acs.jafc.5b04260
J. Agric. Food Chem. 2015, 63, 8787−8792

seedlings of three turf grass species. *Acta Pratacult. Sin.* **2010**, *19*, 33−40.
(7) Ma, M. Z.; Christensen, M. J.; Nan, Z. B. Effects of the endophyte *Epichloe festucae* var. *lolii* of perennial ryegrass (*Lolium perenne*) on indicators of oxidative stress from pathogenic fungi during seed germination and seedling growth. *Eur. J. Plant Pathol.* **2015**, *141*, 571−583.
(8) Bush, L. P.; Fannin, F. F.; Siegel, M. R.; Dahlman, D. L.; Burton, H. R. Chemistry, occurrence and biological effects of saturated pyrrolizidine alkaloids associated with endophyte-grass interactions. *Agric., Ecosyst. Environ.* **1993**, *44*, 81−102.
(9) Johnson, M. C.; Dahlman, D. L.; Siegel, M. R.; Bush, L. P.; Latch, G. C. M.; Potter, D. A.; Varney, D. R. Insect feeding deterrents in endophyte-infected tall fescue. *Appl. Environ. Microbiol.* **1985**, *49*, 568−571.
(10) Zhang, X. X.; Nan, Z. B.; Li, C. J.; Gao, K. Cytotoxic effect of ergot alkaloids in *Achnatherum inebrians* infected by the *Neotyphodium gansuense* endophyte. *J. Agric. Food Chem.* **2014**, *62*, 7419−7422.
(11) Nan, Z. B.; Li, C. J. Roles of the grass-*Neotyphodium* association in pastoral agriculture systems. *Acta Ecol. Sin.* **2004**, *24*, 605−616.
(12) Yan, X.; Guo, Y.; Zhou, H.; Lu, B.; Wang, K. Genetic patterns of ten *Elymus* species from the Tibetan and Inner Mongolian plateaus of China. *Grass Forage Sci.* **2006**, *61*, 398−404.
(13) Song, H.; Nan, Z. B. Origin, divergence, and phylogeny of asexual *Epichloë* endophyte in *Elymus* species from Western China. *PLoS One* **2015**, *10*, e0127096.
(14) Traber, R.; Hofmann, H.; Loosli, H. R.; Ponelle, M.; von Wartburg, A. Neue cyclosporine aus *Tolypocladium inflatum*. Die cyclosporine K−Z. *Helv. Chim. Acta* **1987**, *70*, 13−36.
(15) Lee, C.; Yang, W.; Parr, R. G. Development of the Colle-Salvetti correlation-energy formula into a functional of the electron density. *Phys. Rev. B: Condens. Matter Mater. Phys.* **1988**, *37*, 785−789.
(16) Becke, A. D. Density-functional thermochemistry. III. The role of exact exchange. *J. Chem. Phys.* **1993**, *98*, 5648−5652.
(17) Frisch, M. J.; Trucks, G. W.; Schlegel, H. B.; Scuseria, G. E.; Robb, M. A.; Cheeseman, J. R.; Scalmani, G.; Barone, V.; Mennucci, B.; et al. *Gaussian 09, Revision a.02*; Gaussian, Inc.: Wallingford, CT, 2009.
(18) Song, Q. Y.; Qi, W. Y.; Li, Z. M.; Zhao, J.; Chen, J. J.; Gao, K. Antifungal activities of triterpenoids from the roots of *Astilbe myriantha* Diels. *Food Chem.* **2011**, *128*, 495−499.
(19) Li, H.; Xiao, J.; Gao, Y. Q.; Tang, J. J.; Zhang, A. L.; Gao, J. M. Chaetoglobosins from *Chaetomium globosum*, An endophytic fungus in *Ginkgo biloba*, and their phytotoxic and cytotoxic activities. *J. Agric. Food Chem.* **2014**, *62*, 3734−3741.
(20) Lu, R. L.; Bao, G. H.; Hu, F. L.; Huang, B.; Li, C. R.; Li, Z. Z. Comparison of cytotoxic extracts from fruiting bodies, infected insects and cultured mycelia of *Cordyceps formosana*. *Food Chem.* **2014**, *145*, 1066−1071.
(21) Qi, S. H.; Zhang, S.; Gao, C. H.; Li, Q. X. Purine and pyrimidine derivatives from the South China Sea gorgonian *Subergorgia suberosa*. *Chem. Pharm. Bull.* **2008**, *56*, 993−994.
(22) Chabukswar, A.; Kuchekar, B.; Lokhande, P.; Tryambake, M.; Pagare, B.; Kadam, V.; Jagdale, S.; Chabukswar, V. Design, synthesis and evaluation of antibacterial activity of novel indazole derivatives. *Curr. Bioact. Compd.* **2013**, *9*, 263−269.
(23) Okamoto, T.; Koizumi, T.; Isogai, Y. Studies on plant growth regulators. II. isolation of indole-3-acetic acid, phenylacetic acid, and several plant growth inhibitors from etiolated seedlings of *Phaseolus*. *Chem. Pharm. Bull.* **1967**, *15*, 159−167.
(24) Sawadsitang, S.; Mongkolthanaruk, W.; Suwannasai, N.; Sodngam, S. Antimalarial and cytotoxic constituents of *Xylaria cf. cubensis* PK108. *Nat. Prod. Res.* **2015**, *29*, 2033−2036.
(25) Lan, W. J.; Liu, W.; Liang, W. L.; Xu, Z.; Le, X.; Xu, J.; Lam, C. K.; Yang, D. P.; Li, H. J.; Wang, L. Y. Pseudaboydins A and B: novel isobenzofuranone derivatives from marine fungus *Pseudallescheria boydii* associated with starfish *Acanthaster planci*. *Mar. Drugs* **2014**, *12*, 4188−4199.
(26) Xifeng, L.; Kim, S. K.; Kang, J. S.; Choi, H. D.; Son, B. W. Radical scavenging hydroxyphenyl ethanoic acid derivatives from a marine-derived fungus. *J. Microbiol. Biotechnol.*. **2006**, *16*, 637−638.
(27) Zhang, Y. G.; Yuan, W. P.; Xia, X. K.; Jia, A. R.; Liu, X.; Zhang, M. S.; Liu, C. H. Secondary metabolites from fungus *Paecilomyces* sp. *J. Chin. Med. Mater.* **2011**, *34*, 707−709.
(28) Cheng, M. J.; Wu, M. D.; Chen, J. J.; Cheng, Y. C.; Hsieh, M. T.; Hsieh, S. Y.; Yuan, G. F.; Su, Y. S. Secondary metabolites from the endophytic fungus *Annulohypoxylon stygium* BCRC 34024. *Chem. Nat. Compd.* **2014**, *50*, 237−241.
(29) Li, D.; Xu, Y.; Shao, C. L.; Yang, R. Y.; Zheng, C. J.; Chen, Y. Y.; Fu, X. M.; Qian, P. Y.; She, Z. G.; de Voogd, N. J.; Wang, C. Y. Antibacterial bisabolane-type sesquiterpenoids from the sponge-derived fungus *Aspergillus* sp. *Mar. Drugs* **2012**, *10*, 234−241.
(30) Abdel-Lateff, A.; Fisch, K. M.; Wright, A. D.; König, G. M. A new antioxidant isobenzofuranone derivative from the algicolous marine fungus *Epicoccum* sp. *Planta Med.* **2003**, *69*, 831−834.
(31) Matsumoto, T.; Takahashi, M.; Kashihara, Y. Pyrrolizidine Alkaloids. The synthesis and absolute configuration of all stereo-isomers of monocrotalic acid. *Bull. Chem. Soc. Jpn.* **1979**, *52*, 3329−3336.
(32) Daengrot, C.; Rukachaisirikul, V.; Tansakul, C.; Thongpanchang, T.; Phongpaichit, S.; Bowornwiriyapan, K.; Sakayaroj, J. Eremophilane sesquiterpenes and diphenyl thioethers from the soil fungus *Penicillium copticola* PSU-RSPG138. *J. Nat. Prod.* **2015**, *78*, 615−622.
(33) Tu, P. F.; Shi, H. M.; Song, Z. H.; Jiang, Y.; Zhao, Y. Y. Chemical constituents of *Cistanche sinensis*. *J. Asian Nat. Prod. Res.* **2007**, *9*, 79−84.
(34) Zhang, Q.; Wang, S. Q.; Tang, H. Y.; Li, X. J.; Zhang, L.; Xiao, J.; Gao, Y. Q.; Zhang, A. L.; Gao, J. M. Potential allelopathic indole diketopiperazines produced by the plant endophytic *Aspergillus fumigatus* using the one strain−many compounds method. *J. Agric. Food Chem.* **2013**, *61*, 11447−11452.
(35) Ma, M. Z.; Nan, Z. B. Effects of fungal endophytes from perennial ryegrass on the growth of plant pathogens. *Pratacult. Sci.* **2011**, *28*, 962−968.
(36) Song, Q. Y.; Gao, K.; Nan, Z. B.; Tian, P.; Song, H. The preparation methods and applications of cyclosporin T. Chinese Patent Application 201510298350.5, 2015.
(37) Fejer, S. Effects of gibberellic acid, indole-acetic acid, coumarin and perloline on perennial ryegrass (*Lolium perenne* L.). *N. Z. J. Agric. Res.* **1960**, *3*, 734−743.

DOI: 10.1021/acs.jafc.5b04260
J. Agric. Food Chem. 2015, 63, 8787−8792

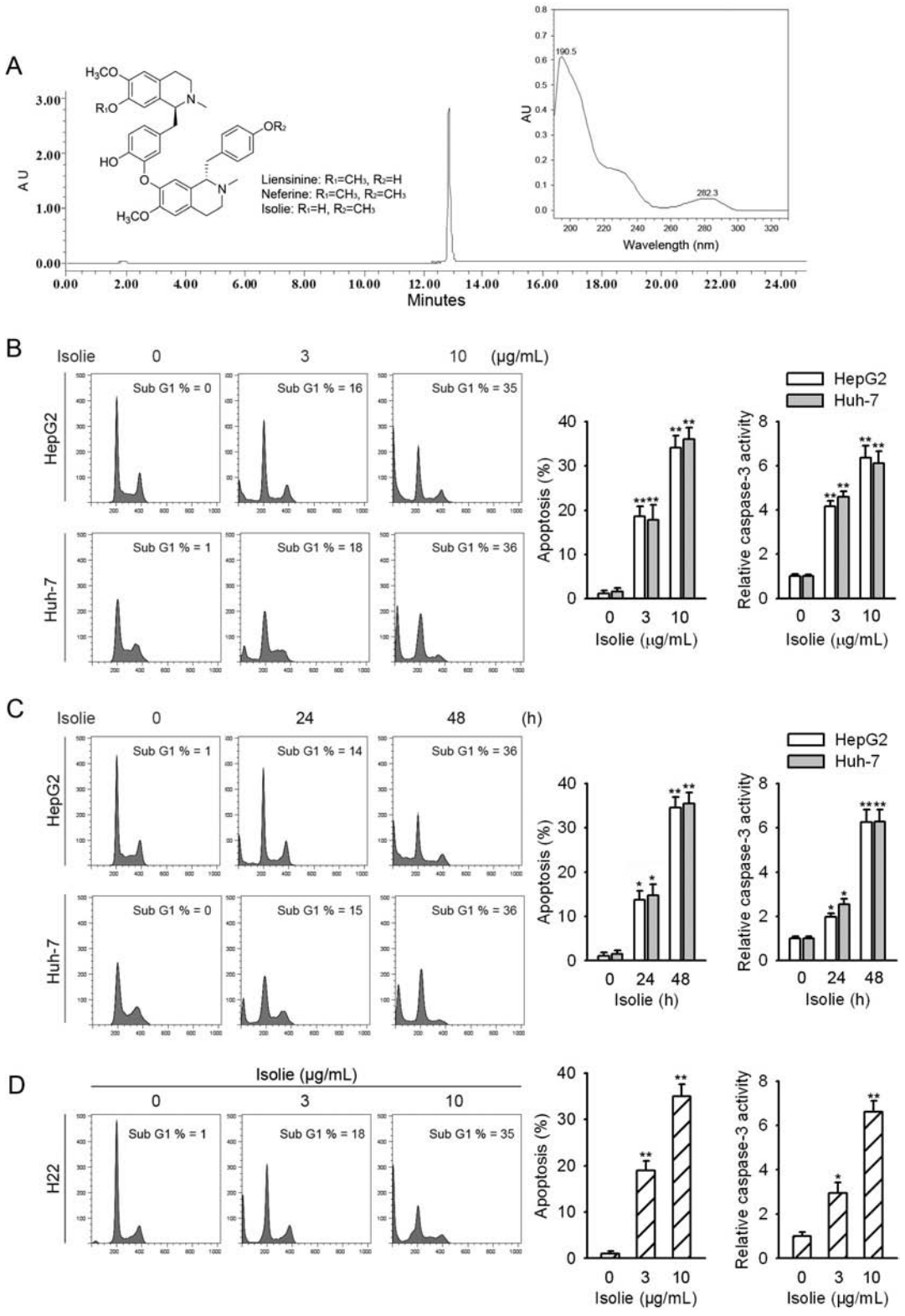

Figure 1. Isolie dose- and time-dependently provoked human and murine HCC cell apoptosis in vitro. (A) Chemical structures of liensinine, isolie, and neferine are shown. The purity of isolie was determined by both HPLC and UV spectrum analysis. (B) HCC cells were treated with indicated concentrations of isolie. After 48 h, cell apoptosis was examined by FACS (left and middle, both representative FACS diagrams and statistics are shown) and caspase-3 activity assay (right). (C) HepG2 and Huh-7 cells were treated with 10 μg/mL isolie for indicated times. Then, cell apoptosis was examined by FACS (left and middle) and caspase-3 activity assay (right). (D) H22 cells were incubated with indicated concentrations of isolie. Cell apoptosis was examined by FACS (left and middle) and caspase-3 activity assay (right) 48 h later. *$p < 0.05$ and **$p < 0.01$ versus HCC cells without isolie treatment.

DOI: 10.1021/acs.jafc.5b02993
J. Agric. Food Chem. 2015, 63, 8793−8803

Table 1. Cytotoxic Effects of Liensinine, Isolie, and Neferine on HCC Cells and Untransformed Hepatocytes

	IC50[a] (μg/mL)					
compound	PMH[b]	HL-7702	Huh-7	HepG2	Hep3B	Bel-7402
liensinine	53.7	49.3	9.7	11.7	14.1	15.5
isolie	72.9	70.1	4.5	4.2	6.0	5.7
neferine	23.2	20.8	6.2	8.3	10.1	9.8

[a]IC50, the concentration of a compound at which cell viability was reduced by 50%. [b]PMH, primary mouse hepatocytes.

HCC cell apoptosis. The bioavailability and toxic impact of isolie were also assessed on tumor-bearing mice.

MATERIALS AND METHODS

Isolation and Purification of Isolie. The embryos of *N. nucifera* were purchased from Jointown Pharmaceutical Group Co. Ltd. (Wuhan, Hubei Province, PR China) in September 2011 and identified by Prof. Dingrong Wan from the College of Pharmacy, South-Central University for Nationalities, Wuhan, China. Voucher specimens (2011009N) were deposited in the Herbarium of the College of Pharmacy, South-Central University for Nationalities. Air-dried embryos of *N. nucifera* (1.0 kg) were ground into powder and extracted using 90% EtOH (4 × 3.0 L). After evaporation of the collected percolate, the crude extract was acidified with diluted HCl (5%) to a pH of 1−2 and partitioned between hexane (3 × 1.5 L) and the acid water layer. The aqueous part was basified with aqueous NH_3 to a pH of 9−10 and extracted with $CHCl_3$ to yield 14.5 g of crude alkaloid. A portion of the crude alkaloid (14 g) was then subjected to column chromatography over silica gel (300−400 mesh) and eluted with the isocratic gradient solvent system of CH_2Cl_2, methanol, and diethylamide (100:5:2) to yield five major fractions (F1−F5) (F1, 1.8 L; F2, 2.4 L; F3, 1.7 L; F4, 2.6 L; F5, 3.5 L). After evaporation under vacuum, crude isolie (1.8 g) was obtained from F4 and then dissolved in anhydrous acetone (50 mL). The solution was acidified with drops of diluted $HClO_4$ (10%) to a pH of 2−3. The acidized isolie solution was kept at 4 °C to crystallize and yielded 1.9 g of pure isolie perchloride. The isolie perchloride (1.8 g) was dissolved in 50 mL of water, and this solution was basified with aqueous NH_3 to a pH of 9−10. The solution was extracted with $CHCl_3$ to give 1.3 g of the free isolie. ^1H, ^{13}C NMR and LC-ESIMS data were obtained to support the identification of isolie (Supplementary Figure 1). The isolie was analyzed by high-performance liquid chromatography (HPLC) on a Waters 1525 HPLC instrument by a single injection of 20 μL with an analytical C18 HPLC column (Betasil 150 × 4.6 mm, 5 μm) detected at 254 nm. Gradient conditions: 90% H_2O (0.1% TFA) + 10% MeCN (0.1% TFA) → 100% MeCN (0.1% TFA), 20 min, 100% MeCN (0.1% TFA), 25 min. Flow rate: 1.0 mL/min. The purity of the isolie was above 95% as detected by HPLC and UV spectrum analysis (Figure 1A).

Cells, Reagents, Kits, and Antibodies. Human HL-7702 untransformed hepatocytes and murine H22 ascitic hepatoma cells were supplied by the China Center for Type Culture Collection. HepG2 and Hep3B human HCC cells were from the American Type Culture Collection. Huh-7 HCC cells, Panc-1 pancreatic carcinoma cells, and HT-29 colon carcinoma cells were obtained from the Cell Bank of Shanghai Institute of Biological Sciences. Primary mouse hepatocytes were separated and cultured as described previously.[13] Dulbecco's modified Eagle medium (DMEM) was obtained from Hyclone (Logan, UT, USA). Fetal calf serum (FCS), penicillin, and streptomycin for cell culture and TRIzol reagents for RNA extraction were purchased from Invitrogen (Carlsbad, CA, USA). FuGENE reagents for cell transfection were purchased from Roche (Penzberg, Germany). 3-(4,5-Dimethylthiazol-2-yl)-2,5-diphenyltetrazolium bromide (MTT) and propidium iodide were purchased from Wolsen Biotechnology (Xi'an, Shanxi Province, PR China). Caspase-3 activity assay kits, BCA protein quantification kits, and JC-1, which is a fluorescent probe for mitochondrial membrane potential, were purchased from Beyotime Biotechnology (Nantong, Jiangsu Province, PR China). NF-κB-dependent luciferase reporters, pRL-TK plasmids, and Dual Reporter assay systems for the determination of intercellular luciferase activity were obtained from Promega (Fitchburg, WI, USA). The pRL-TK plasmid encodes the *Renilla* luciferase gene driven by the promoter of herpes simplex virus thymidine kinase gene and is used as an internal control in luciferase activity assays. Reverse transcriptase ReverTra Ace-α were obtained from Toyobo (Osaka, Japan). Primary antibodies against Bcl-2 (SC-492), Bcl-xL (SC-8392), MMP9 (SC-6841), p65 (SC-372), and IκBα (SC-371) and secondary antibodies conjugated with horseradish peroxidase were from Santa Cruz Biotechnology (Santa Cruz, CA, USA). Antibodies against Ser536-phosphorylated p65 (No. 13346), myc tag (No. 2278), and β-actin (No. 3700) were obtained from Cell Signaling Technology (Danvers, MA, USA).

Cells Culture and Transfection. Cells were maintained in DMEM containing 10% FCS, 100 U/mL penicillin, and 100 μg/mL streptomycin at 37 °C in a humidified atmosphere with 5% CO_2. To overexpress p65 phosphorylation mimics in which Ser536 is mutated into an Asp (p65-S536D), the encoding gene of human p65-S536D was cloned into the vector pcDNA3.1A. Plasmids were transfected into HCC cells using FuGENE reagents, according to the manufacturer's instructions.

Cell Viability Assay and Calculation of IC50 Value. Cells were incubated with different concentrations of the indicated compounds. After 48 h, MTT cell viability assays were performed as described previously.[14] The IC50 value of a compound is defined as the concentration at which cell viability was reduced by 50% as determined by MTT cell viability assays and calculated by using the Origin Software.

Flow Cytometry Analysis (FACS). FACS was performed as described previously.[15] Briefly, after undergoing treatment as indicated in the text, the cells were trypsinized and fixed with cold 70% ethanol (stored at −20 °C) for at least 2 h. Samples were then pelleted and washed with PBS containing 20 mM EDTA. Intracellular RNA was removed by incubating samples with 1 mg/mL RNaseA at 37 °C for more than 2 h. Finally, cells were stained with 30 μg/mL propidium iodide and subjected to FACS (Becton Dickinson FACSCalibur, Franklin Lakes, NJ, USA). Cells in Sub G1 phase were considered to be apoptotic.

Caspase-3 Activity Assay. Caspase-3 activity assay kits were used to measure caspase-3 activity in the total lysates of cultured cells or tumors tissues, according to the manufacturer's instructions.

NF-κB Luciferase Reporter Assay. Cells were cultured for 24 h in 24-well plates prior to transfection. Then, NF-κB luciferase reporters and pRL-TK plasmids were cotransfected into HCC cells using FuGENE reagents. After 24 h, the medium was replaced and cells were incubated with various stimuli as indicated in the text. The Dual Reporter assay system was used to measure luciferase activity in cell lysates, according to the manufacturer's instructions.

RNA Isolation, Reverse Transcription, and Real-Time Polymerase Chain Reaction (PCR). RNA was extracted from cultured HCC cells or in vivo tumor tissues by TRIzol reagent, according to the manufacturer's instructions. To get cDNA from each sample, 3 μg of total RNA was reverse transcribed at 42 °C for 30 min using ReverTra Ace-α. mRNA levels of indicated genes were analyzed by real-time PCR. Glyceraldehyde-3-phosphate dehydrogenase (GAPDH) was used as the loading control.

Chromatin Immunoprecipitation (ChIP). ChIP assay was performed as previously described.[16] Relative binding of p65 to promoter regions of Bcl-2 and Bcl-xL encoding genes was measured by real-time PCR.

Assessment of Mitochondria Dysfunction by JC-1 Staining. JC-1 is a fluorescent dye which forms aggregates in normal mitochondria and emits red fluorescence. However, JC-1 monomers emit green fluorescence in cells with mitochondrial dysfunction. Cells were seeded in 24-well plates and stimulated as indicated in the text. After the treatment, the medium was discarded and replaced by 500 μL of fresh medium containing 5 μg/mL JC-1. After incubating for 1

DOI: 10.1021/acs.jafc.5b02993
J. Agric. Food Chem. 2015, 63, 8793−8803

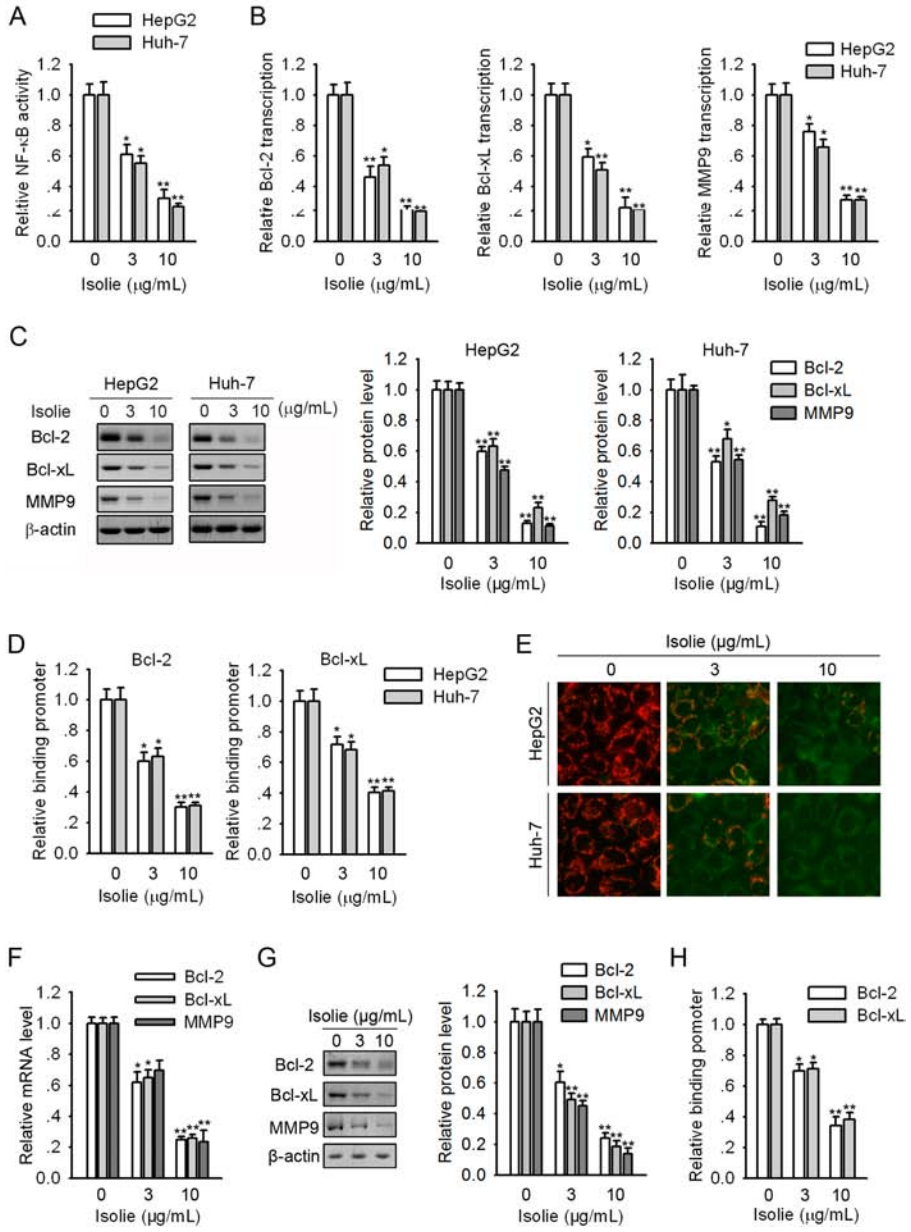

Figure 2. Isolie inhibited NF-κB activity in HCC cells. (A) Plasmids encoding *Renilla* luciferase and NF-κB-dependent luciferase reporter were cotransfected into HepG2 and Huh-7 cells. After 24 h, these cells were treated with indicated concentrations of isolie, using vehicle as the negative control. Cells were subjected to luciferase activity assay 24 h later. (B–D) HCC cells were treated with different concentrations of isolie. After 24 h, mRNA and protein levels of NF-κB target genes were determined by real-time PCR (B) and immunoblotting (C, left). Density values of immunoreactive bands of Bcl-2, Bcl-xL, and MMP9 were normalized to those of β-actin (C, middle and right). Association between p65 protein and promoter regions of indicated genes was detected by ChIP (D). (E) HepG2 and Huh-7 cells were treated with indicated concentrations of isolie for 24 h and then subjected to JC-1 staining assays. (F–H) H22 cells were treated with indicated concentrations of isolie for 24 h. Then mRNA and protein levels of Bcl-2, Bcl-xL, and MMP9 were determined by real-time PCR (F) and immunoblotting (G). Association between p65 and promoter regions of Bcl-2 and Bcl-xL were quantified by ChIP (H). *$p < 0.05$ and **$p < 0.01$ versus HCC cells without isolie treatment.

h, cells were washed twice with PBS and photographed at a magnification of 100× under a fluorescence microscope.

Animals. Male athymic nude mice (6 weeks old) and Kunming mice, weighing between 18 and 22 g, were obtained from the Center of Experimental Animals, Institute of Health and Epidemic Prevention (Wuhan, PR China), and housed under standard specific pathogen-free conditions with access to sterilized water and food ad libitum. All of the animal experimental procedures were performed in accordance with the terms approved by the Experimental Animal Care and Use Committee of South-Central University for Nationalities (Wuhan, PR China).

Huh-7 Xenograft Tumor Growth in Nude Mice. Huh-7 cells (1×10^6) were suspended in 0.2 mL of serum-free DMEM with 50% Matrigel (BD Biosciences, Bedford, MA, USA) and subcutaneously injected into the dorsal flanks of nude mice. Mice were randomly divided into groups of 6 mice each. When the xenograft tumor volume reached about 200 mm^3, isolie was administrated at the indicated dosages once daily, for 3 weeks, via intraperitoneal (ip) injection; normal saline (0.9% NaCl) was used as the negative control. Tumor volumes were monitored every 3 days by the following formula: tumor volume = length × width × width/2. Blood samples were collected from animals anesthetized with diethyl ether. All mice were then

DOI: 10.1021/acs.jafc.5b02993
J. Agric. Food Chem. 2015, 63, 8793–8803

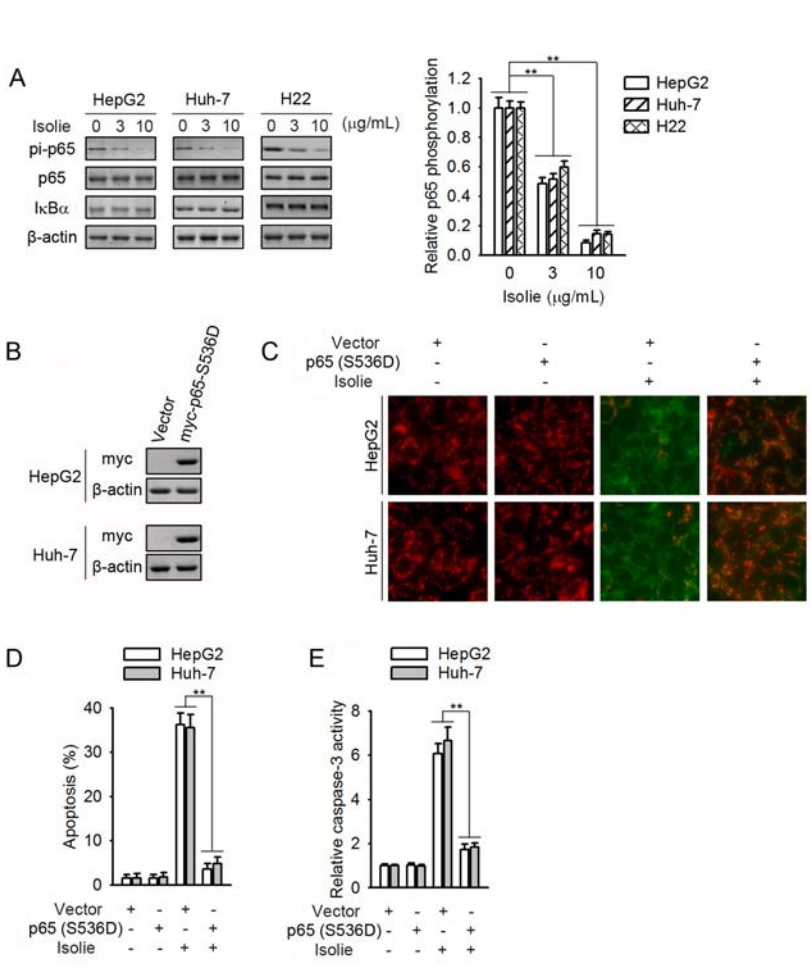

Figure 3. Isolie decreased constitutive phosphorylation of p65 protein at Ser536. (A) Effects of 24-h isolie treatment on protein levels of phosphorylated p65 (Ser536), p65 and IκB*α* in HCC cells were detected by immunoblotting (left). Density values of immunoreactive bands of Ser536-phosphorylated p65 were normalized to those of total p65 (right). (B) Myc-tagged p65-S536D was transfected into indicated HCC cells. After 24 h, exogenous p65-S536D proteins were determined by immunoblotting using the primary antibody against myc tag. (C) Cells transfected with indicated plasmids were incubated with or without 10 μg/mL isolie and subjected to JC-1 staining assays after 24 h. (D, E) Empty or p65-S536D encoding plasmids were transfected into HepG2 and Huh-7 cells. After 24 h, HCC cells were incubated with or without 10 μg/mL isolie. Cell apoptosis was examined 48 h later by FACS (D) and caspase-3 activity assay (E). *$p < 0.05$ and **$p < 0.01$ versus the indicated control.

euthanized, and the livers and xenograft tumors were immediately resected for further analysis.

H22 Transplanted Tumor Establishment and Isolie Administration. H22 cells (1×10^6) were subcutaneously transplanted into the dorsal flanks of Kunming mice. Mice were randomly divided into groups of 10 mice each. Drug treatment began 24 h later. Drugs were administrated once daily, for 10 days, via ip injection or gavage as indicated in the text. Isolie groups received different dosages (3 and 10 mg/kg). The vehicle control group received normal saline. A group of mice without tumor transplantation was also included. Tumor volumes were monitored every 2 days. At last, blood samples were collected under diethyl ether anesthesia. Immediately after all animals were euthanized, transplanted tumors and corresponding organs were resected for further analysis. The organ index was calculated using the following formula: organ index = organ weight (g)/body weight (g) × 1000.

Blood and Serum Physiochemical Indexes Determination. An automatic blood cell count apparatus (Mindray, Shenzhen, Guangdong Province, PR China) was used to record the amount of white blood cells (WBC), red blood cells (RBC), hemoglobins (HGB), and platelets (PLT). Serum was prepared by centrifuging blood samples at 4500*g* for 10 min. Serum hepatic and renal function parameters, including aspartate aminotransferace (AST), alanine aminotransferace (ALT), blood urea nitrogen (BUN), uric acid (UA), and creatinine (CRE), were measured by an automatic biochemical analyzer (Sysmex, Kobe, Japan) according to the manufacturer's instructions.

Statistical Analysis. Data shown in this study are representatives or statistics (mean value ± standard deviation) of the results from at least three independent experiments or all mice of each group. One-way analysis of variance (ANOVA) was performed to determine the statistical significance. If the treatment involved more than one concentration or dosage, Dunnett's *t* tests were further conducted to determine the statistical significance of each concentration/dosage group compared to the negative control. A *p* value of <0.05 was considered to be statistically significant and indicated by "*". A *p* value of <0.01 was considered to be statistically very significant and indicated by "**".

More detailed materials and methods are provided in the Supporting Information.

RESULTS

Isolie Induced HCC Cell Apoptosis in Vitro. To assess the ability of isolie to provoke HCC cell apoptosis, human HepG2 and Huh-7 HCC cells were treated with 3 and 10 μg/mL isolie. After 48 h, ratios of Sub-G1 DNA in the cell populations were quantified by FACS. The result showed that

DOI: 10.1021/acs.jafc.5b02993
J. Agric. Food Chem. 2015, 63, 8793−8803

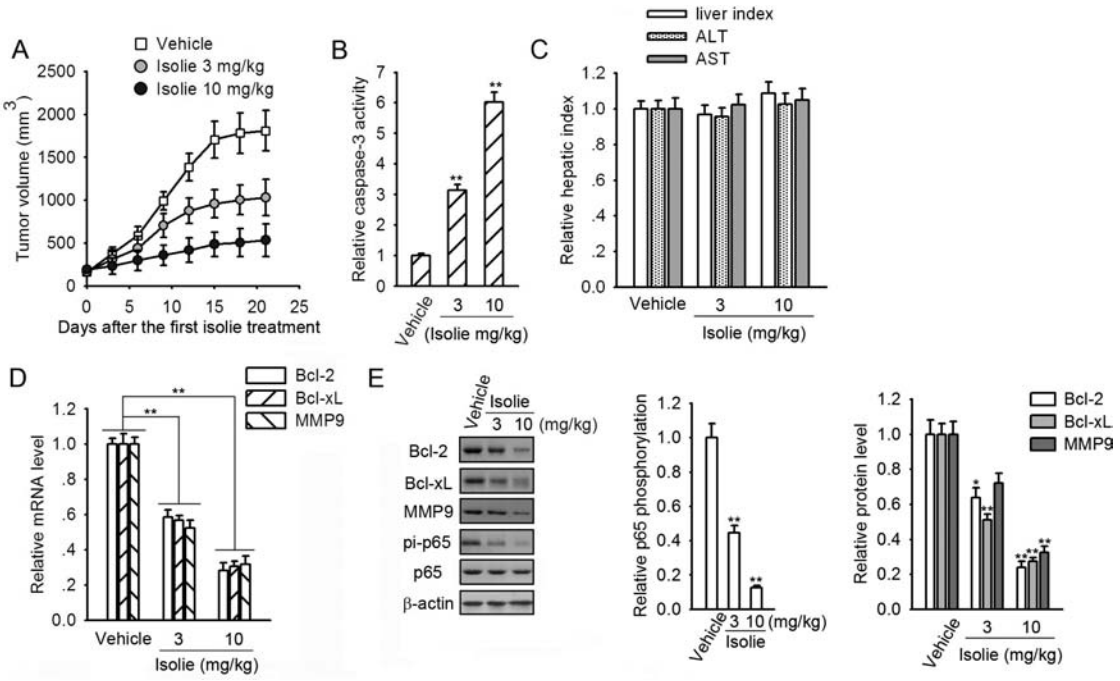

Figure 4. Isolie suppressed the growth of Huh-7 xenografts in nude mice. (A) Vehicle or indicated dosages of isolie were intraperitoneally injected into tumor-bearing nude mice for 3 weeks, and tumor growth was monitored every 3 days. (B) At the end of the study, tumor lysates were prepared and subjected to caspase-3 activity assay. (C) Serum and livers were collected from tumor-bearing mice. Serum activities of ALT and AST were detected, and liver indexes were calculated. Values were normalized to those from the vehicle control group. (D, E) At the end of isolie treatment, transcription levels of indicated genes were detected by real-time PCR (D). Levels of indicated proteins were detected by immunoblotting (E, left). Densitometric values of phosphorylated p65 at Ser536 were normalized to those of total p65 (E, middle). Densitometric values of Bcl-2, Bcl-xL, and MMP9 were normalized to those of β-actin (E, right). $^{**}p < 0.01$ versus tumors dissected from mice treated with saline.

48-h isolie treatment dose-dependently increased the ratio of Sub-G1 DNA (Figure 1B, left and middle). In addition, caspase-3 activity was dose-dependently elevated in HCC cells by isolie (Figure 1B, right). Similarly, as shown by FACS and caspase-3 activity assay, isolie time-dependently triggered HepG2 and Huh-7 cell apoptosis (Figure 1C). Moreover, isolie dose-dependently induced murine H22 ascitic hepatoma cell apoptosis (Figure 1D). These data demonstrated that isolie is capable of provoking HCC cell apoptosis in vitro.

Isolie Suppressed NF-κB Activity in HCC Cells. To understand the molecular mechanisms underlying isolie-mediated HCC cell apoptosis, we first evaluated the impacts of isolie on an array of signaling pathways that regulate cell apoptosis including p53, STAT3, Foxo3a, and NF-κB using corresponding luciferase reporter assays. Isolie showed few effects on the activity of p53, STAT3, or Foxo3a (data not shown), but substantially decreased the basal level of NF-κB activity in both HepG2 and Huh-7 HCC cells (Figure 2A). Consistently, mRNA and protein levels of typical NF-κB target genes, such as Bcl-2, Bcl-xL, and MMP9, in HCC cells were also downregulated by isolie (Figure 2B,C). ChIP assay confirmed that isolie suppressed the interaction between NF-κB p65 subunit and promoter regions of Bcl-2 and Bcl-xL encoding genes (Figure 2D). In HepG2 and Huh-7 cells without isolie treatment, mitochondria were intact and emitted red fluorescence after JC-1 staining. Isolie reduced the red fluorescence signal emitted by JC-1, but elevated the green fluorescence signal, indicating that isolie induced mitochondrial dysfunction in HCC cells (Figure 2E). In murine H22 HCC cells, isolie dose-dependently inhibited transcription and translation of NF-κB responsive genes (Figure 2F and G). Interactions between p65 proteins and promoter regions of Bcl-2 and Bcl-xL were also reduced by isolie (Figure 2H). These data suggested that isolie suppresses NF-κB activity in HCC cells.

Isolie Provoked Dephosphorylation of p65 Protein at Ser536. Degradation of IκBα protein is an important molecular event that activates NF-κB signaling. However, IκBα remained unchanged in response to isolie (Figure 3A). Phosphorylation of NF-κB p65 subunit at Ser536 plays important roles in promoting NF-κB-dependent gene transcription. Isolie dose-dependently suppressed p65 Ser536 phosphorylation in HCC cells (Figure 3A). To confirm the role of p65 dephosphorylation at Ser536 in isolie-induced HCC cell apoptosis, plasmids encoding myc-tagged p65-S536D, which is a p65 phosphorylation mimic at Ser536, were transfected into HCC cells (Figure 3B). Overexpressing p65-S536D dramatically alleviated isolie-induced mitochondrial dysfunction (Figure 3C). Accordingly, isolie-induced HCC cell apoptosis was also considerably abrogated (Figure 3D,E). These findings suggested that p65 dephosphorylation at Ser536 is a critical molecular event accounting for isolie-induced NF-κB inhibition and apoptosis in HCC cells.

Isolie Suppressed Huh-7 Xenograft Tumor Growth in Nude Mice. To explore whether the proapoptotic activity of isolie on HCC cell lines has any potential clinical implications, we evaluated the in vivo impacts of isolie on the proliferation of Huh-7 HCC xenograft tumors. Isolie substantially attenuated the proliferation of xenograft tumors as compared to vehicle (Figure 4A). Isolie-induced HCC cell apoptosis in vivo was verified by caspase-3 activity assay (Figure 4B). To assess side impacts of isolie on normal hepatocytes of tumor-bearing mice, its effects on host liver indexes and serum markers of liver function including ALT and AST were tested immediately at

DOI: 10.1021/acs.jafc.5b02993
J. Agric. Food Chem. 2015, 63, 8793−8803

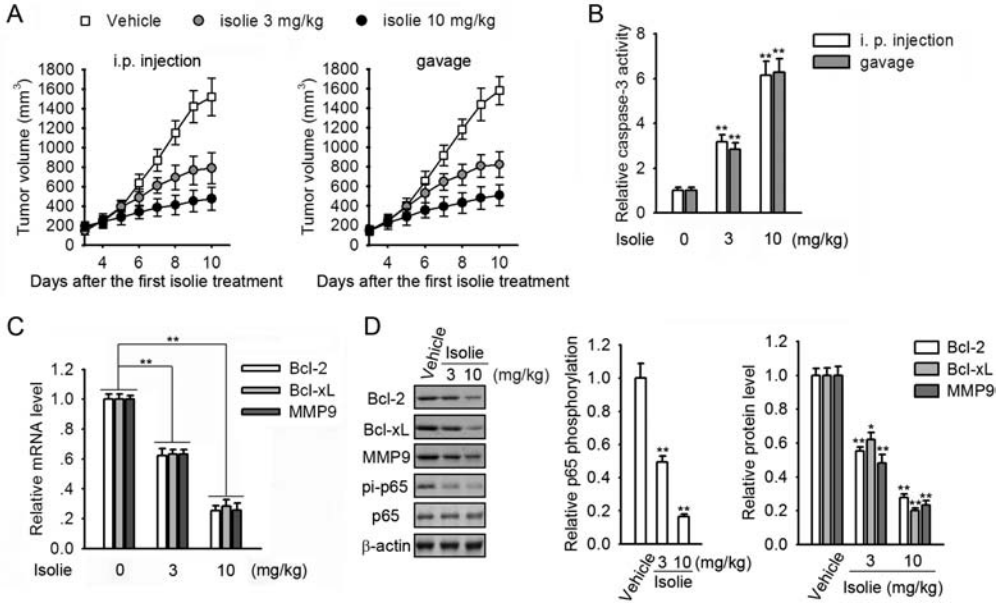

Figure 5. Effects of isolie on transplanted H22 HCC cells in Kunming mice. (A, B) Kunming mice bearing H22 tumors were treated with indicated dosages of isolie by ip injection (left) or gavage (right) for 10 d, and tumor growth was monitored every day (A). At the end of isolie treatment, tumor lysates were prepared and subjected to caspase-3 activity assay (B). (C, D) Tumor-bearing mice were treated with indicated dosages of isolie by gavage for 10 d. At the end of the study, mRNA levels of Bcl-2, Bcl-xL, and MMP9 were detected by reverse transcription real-time PCR (C). Indicated proteins were examined by immunoblotting (D). Densitometric values of phosphorylated p65 at Ser536 were normalized to those of total p65 (D, middle). Densitometric values of Bcl-2, Bcl-xL, and MMP9 were normalized to those of β-actin (D, right). $^{**}p < 0.01$ versus tumors dissected from mice treated with saline.

Table 2. Effects of Ip Injection of Isolie on WBC, RBC, HGB, and PLT in Kunming mice

		concn of blood cells (L^{-1})			
group	dosage (mg/kg)	WBC (10^9)	RBC (10^{12})	HGB (g)	PLT (10^9)
nontumor		6.62 ± 0.47	5.57 ± 0.73	109 ± 11	666 ± 63
vehicle		6.35 ± 0.55	6.48 ± 0.66	121 ± 12	680 ± 70
isolie	3	7.07 ± 0.58	5.91 ± 0.73	115 ± 12	662 ± 69
isolie	10	6.83 ± 0.62	6.61 ± 0.69	117 ± 13	692 ± 66

the end of the treatment. There was no significant change in any of these parameters in response to ip injection of isolie (Figure 4C). To correlate the tumor-suppressing activity in vivo with mechanisms of action identified in vitro, effects of isolie on p65 phosphorylation and NF-κB activity in Huh-7 xenograft tumors were detected. Isolie dose-dependently decreased p65 Ser536 phosphorylation (Figure 4E, left and middle). Moreover, mRNA and protein levels of NF-κB responsive genes were dose-dependently declined in xenograft tumors as shown by real-time PCR (Figure 4D) and immunoblotting (Figure 4E, left and right). These data suggested that, in Huh-7 xenograft HCC tumors, isolie provokes p65 dephosphorylation at Ser536 that reduces NF-κB activity and leads to cell apoptosis. Toxic impacts of isolie on normal livers were undetectable.

Effects of Isolie on Transplanted H22 HCC Cell Growth in Kunming Mice. To explore the anti-HCC activity of isolie in hosts with intact immune systems that is closer to clinical situations, effects of isolie on the proliferation of H22 HCC cells subcutaneously transplanted into the dorsal flanks of Kunming mice were evaluated. Two routes of drug administration, including ip injection and gavage, were both tested in this model. As shown in Figure 5A,B, isolie given by both routes dose-dependently reduced the growth of H22 transplanted tumors and elevated caspase-3 activity in tumor tissues. Additionally, gavage of isolie dose-dependently reduced constitutive phosphorylation of p65 at Ser536 in transplanted tumor tissues (Figure 5D, left and middle). There were also dramatic decreases in mRNA and protein levels of NF-κB target genes (Figure 5C,D, left and right). To understand isolie uptake by mice, the concentration of isolie in the blood was quantified by ultraperformance liquid chromatography tandem mass spectrometry (UPLC-MS/MS). After ip injection of isolie at the dosage of 10 mg/kg, the maximum absorption peak of isolie appeared at 15 min with the concentration of 1356.3 ng/mL in plasma. The concentration of isolie in plasma declined to 469.1 ng/mL at 30 min, and further to 95.5 ng/mL at 2 h (Supplementary Figure 2). These data provided more evidence to support the capacity of isolie to inhibit NF-κB signaling and induce apoptosis in HCC cells in vivo.

Effects of Isolie on Tumor-Bearing Mice. Finally, we evaluated toxic impacts of ip injection of isolie on Kunming mice. We found that ip injection of isolie (10 mg/kg) showed few effects on body weight of tumor-bearing mice (data not shown). Moreover, amounts of WBC, RBC, HGB, and PLT were comparable among all experimental groups (Table 2). In addition, effects of isolie on serum levels of liver function parameters including ALT and AST were unobvious. BUN, UA, and CRE are serum renal function indicators. These parameters remained almost unchanged after ip injection of isolie (Table 3). Moreover, isolie showed little influence on indexes of

DOI: 10.1021/acs.jafc.5b02993
J. Agric. Food Chem. 2015, 63, 8793−8803

Table 3. Effects of Ip Injection of Isolie on Serum Parameters of Liver and Kidney Functions in Kunming Mice

group	dosage (mg/kg)	serum params of hepatic and renal functions (U/L)				
		BUN	UA	CRE	ALT	AST
nontumor		6.5 ± 0.49	140 ± 8.8	45.8 ± 5.4	121 ± 13	589 ± 48
vehicle		6.7 ± 0.53	139 ± 9.4	44.7 ± 4.7	133 ± 17	611 ± 52
isolie	3	6.6 ± 0.55	135 ± 8.9	46.4 ± 5.1	118 ± 16	618 ± 46
isolie	10	6.6 ± 0.47	136 ± 9.5	47.1 ± 4.9	126 ± 15	577 ± 49

thymus, spleens, and livers of tumor-bearing mice (Table 4). These data suggested that toxic effects of isolie at the dosage of 10 mg/kg on vital organs of tumor-bearing mice are undetectable.

Table 4. Effects of Ip Injection of Isolie on Organ Indexes of Kunming Mice

group	dosage (mg/kg)	organ indexes (mg/g)		
		thymus	spleen	liver
nontumor		2.72 ± 0.12	8.60 ± 0.40	48.2 ± 5.2
vehicle		2.70 ± 0.09	8.95 ± 0.35	47.9 ± 4.2
isolie	3	2.82 ± 0.11	8.90 ± 0.37	48.6 ± 4.8
isolie	10	2.84 ± 0.11	8.97 ± 0.42	48.1 ± 5.1

DISCUSSION

In this study, we prepared isolie from embryos of *N. nucifera*. The ^{1}H NMR, ^{13}C NMR, and LC-ESIMS data of isolie we isolated are as followed. ^{1}H NMR data ($CDCl_3$, 500 MHz): δ_H 3.65 (1H, m, H-1), 3.73 (1H, m, H-1′), 2.46 (1H, s, 2-NCH_3), 2.56 (1H, s, 2′-NCH_3), 3.12 (1H, m, H_1-3), 2.76 (1H, m, H_1-3), 3.18 (1H, m, H_1-3′), 3.00 (1H, m, H_1-3′), 2.73 (2H, m, H-4), 2.74 (1H, m, H_1-4′), 2.72 (1H, m, H_1-4′), 6.65 (1H, s, H-5), 6.48 (1H, s, H-5′), 3.80 (3H, s, 6-OCH_3), 3.82 (3H, s, 6′-OCH_3), 6.25 (1H, s, H-8), 6.29 (1H, s, H-8′), 2.89 (1H, dd, J = 12.0, 8.7 Hz, H_1-9), 2.81 (1H, J = 12.0, 5.1 Hz, H_2-9), 3.12 (1H, m, H_1-9′), 2.72 (1H, J = 13.8, 6.9 Hz, H_2-9′), 6.90 (1H, d, J = 8.6 Hz, H-11, H-15), 6.43 (1H, d, J = 1.8 Hz, H-15′), 6.70 (1H, d, J = 8.6 Hz, H-12, H-14), 3.73 (3H, s, 13-OCH_3), 6.83 (1H, d, J = 8.2 Hz, H-14′), 6.76 (1H, 1H, dd, J = 8.2, 1.8 Hz, H-11′). ^{13}C NMR data ($CDCl_3$, 125 MHz): δ 64.3 (C-1), 64.5 (C-1′), 42.3 (2-NCH_3, 2′-NCH_3), 47.1 (C-3), 46.6 (C-3′), 25.7 (C-4), 24.9 (C-4′), 130.1 (C-4a), 130.5 (C-4a′), 112.4 (C-5), 110.6 (C-5′), 149.2 (C-6), 145.4 (C-6′), 55.8 (6-OCH_3), 56.0 (6′-OCH_3), 142.9 (C-7), 143.7 (C-7′), 120.0 (C-8), 113.9 (C-8′), 130.1 (C-8a), 125.4 (C-8a′), 40.4 (C-9), 39.1 (C-9′), 130.8 (C-10), 131.0 (C-10′), 130.5 (C-11, C-15), 125.4 (C-11′), 113.6 (C-12, C-14), 144.5 (C-12′), 157.9 (C-13), 145.4 (C-13′), 55.2 (13-OCH_3), 115.5 (C-14′), 119.1 (C-15′). ESI-MS: m/z 611 $[M + H]^+$. Compared with the spectroscopic data of isolie reported in the previous literature,[17] this compound we purified from embryos of *N. nucifera* could be unambiguously determined as isolie. Although isolie has been recognized for decades, it still remains poorly understood whether it possesses any proapoptotic activity against HCC cells. Here, we showed that isolie time- and dose-dependently induced apoptosis in HepG2, Huh-7, and H22 HCC cells in vitro. Additionally, isolie also displayed strong cytotoxic effects on HT-29 colon carcinoma cells and Panc-1 pancreatic carcinoma cells (Supplementary Figure 3). These data suggested that isolie is able to inhibit other cancer cells such as colon and pancreatic cancer cells.

On the basis of its favorable in vitro proapoptotic activity against HCC cells, effects of isolie on Huh-7 xenograft tumors in nude mice were assessed. It was revealed that ip injection of isolie dramatically decreased growth of xenografted Hun-7 tumors. Caspase-3 activity assay further demonstrated that isolie has the capacity of provoking apoptosis in xenografted HCC tissues in vivo. Similarly, ip injection of isolie inhibited transplanted H22 tumor growth and induced H22 HCC cell apoptosis in Kunming mice. Gavage is a safer and more convenient route than ip injection. We thus also tested the anti-HCC activity of isolie given by gavage. Excitingly, isolie gavage achieved a similar tumor-suppressing effect as compared to that of ip injection, implying a possibility that this compound is stable in the digestive tract of animals and can be efficiently absorbed into the circulatory system.

An important part of cancer chemotherapy is that the agent used should induce malignant cell death with low toxic effects on their normal counterparts. Cisplatin is a conventional chemotherapeutic anticancer drug with a high tumor-suppressing activity. However, it exhibits severe hepatotoxicity and nephrotoxicity in patients, leading to a very poor prognosis.[18] Sorafenib is one of few targeted therapeutic reagents for treating advanced HCC approved by the US Food and Drug Administration. Unfortunately, sorafenib has also been shown to exert side effects on some vital organs including the liver itself.[19,20] In this study, isolie exerted its in vivo anti-HCC effects at the dosage of 10 mg/kg. At this dosage, ip injection of isolie showed few changes in liver indexes and serum parameters of liver function in nude mice. Toxic effects of ip injection of isolie at 10 mg/kg on Kunming mice were unobvious as well. Consistently, our unpublished data showed that the median lethal dosage of isolie given by ip injection is greater than 1.2 g/kg for mice. These observations can be supported by the fact that the plant *N. nucifera* is widely consumed as food. Previous studies showed that the mass fraction of isolie in the crude extract of embryos of *N. nucifera* was 45.7 mg/g. In their report, the yield of the crude extract from embryos of *N. nucifera* was 593 g/10 kg = 5.93%.[21] The mass fraction of isolie in the raw plant material was thereby 2.71 mg/g. Hence, the dosage of isolie (10 mg/kg) in our in vivo experiment should be equivalent to an intake of about 3.69 g/kg embryos of *N. nucifera* for mice. According to the notion of animal surface area, this dosage is equivalent to 0.3 g/kg for human.[22] Thus, a person weighting 65 kg would need to consume about 20 g of embryos of *N. nucifera* every day, which is in fact a feasible dosage.

Among three alkaloids including liensinine, isolie, and neferine, isolie exhibited the most prominent cytotoxic activity on HCC cells. Cytotoxic activity of neferine on HCC cells was less potent than that of isolie, but stronger than that of liensinine. Similar to our observations, a very recent study reported that, among these three alkaloids, cytotoxic activity of isolie on MDA-MB-231 breast cancer cells was the most potent and liensinine was the least potent.[23] Based on these data,

DOI: 10.1021/acs.jafc.5b02993
J. Agric. Food Chem. 2015, 63, 8793−8803

structure−activity relationships of these three alkaloids can be summed up as follows (positions R1 and R2 are indicated in Figure 1A). Replacing the hydrogen atom at the R2 position by a methyl group is conducive to enhancing the cytotoxic potency of the compound. But the same substitution at the R1 position can potentially decline its cytotoxic potency. Mechanistically, neferine-mediated malignant cell death is associated with the inhibition of Akt signaling,[24,25] while liensinine sensitizes cancer cells to chemotherapy through DNM1L-mediated mitochondrial fission.[26] Here, we reported that suppression of NF-κB signaling is the key molecular event mediating isolie-induced HCC cell apoptosis.

Epidemiological studies revealed that viral infection and steatohepatitis are significant risk factors of HCC. Both of them have the potential to activate hepatic NF-κB, suggesting the important role of persistently activated NF-κB in hepatocarcinogenesis.[27,28] At the molecular level, activation of NF-κB has the potential to promote transcription of genes antagonizing apoptosis such as Bcl-2 and Bcl-xL as well as enzymes degrading extracellular matrix such as MMP9.[29,30] These NF-κB-responsive genes are important contributors to the survival and metastasis of HCC. Our current study clearly displayed that, in HCC cells, isolie dramatically declined their transcription and translation both in vitro and in vivo. These data suggested that isolie inhibited NF-κB in HCC cells. Similarly, previous studies reported that an array of reagent with the capacity of suppressing NF-κB signaling induced HCC cell apoptosis.[31−34] These findings not only supported the feasibility of considering NF-κB as a potential target in HCC chemotherapy but also implied a possible participation of hyperactivated NF-κB for maintaining HCC cell survival.

Declined p65 phosphorylation at Ser536 was implicated in isolie-mediated inhibition of NF-κB, which could be supported by lines of evidence in this study. First, isolie suppressed p65 phosphorylation at Ser536 both in vitro and in vivo, and p65 dephosphorylation at Ser536 was associated with HCC cell apoptosis. Second, transfection of p65 Ser536 phosphorylation mimics abrogated isolie-induced mitochondrial injury and apoptosis in HCC cells. It has been reported by previous studies that p65 phosphorylation at Ser536 plays critical roles in the proliferation and invasion of cancer cells of different origins.[35−37] In addition, aberrant p65 phosphorylation at Ser536 has been detected in some other malignant tissues dissected from human cancers and correlates with cancer progression.[38−41] A series of kinases are involved in the phosphorylation of p65 protein at Ser536. For example, activation of kinases, such as Akt and IKK, is positively associated with elevated p65 protein phosphorylation at Ser536.[42−44] Dysregulation of Akt and IKK are increasingly implicated in the pathogenesis of HCC.[45,46] In addition, Akt- and IKK-related signaling pathways have been considered as potential targets for the clinical management of HCC.[47,48] It is thus reasonable to speculate that the possible interaction between isolie and these pathways in HCC cells plays roles in isolie-mediated dephosphorylation of p65 at Ser536.

For a brief summary, in this study, proapoptotic effects of isolie on HCC cells were tested and possible molecular mechanisms underlying isolie-induced HCC cell apoptosis were explored. It was unveiled that isolie dose- and time-dependently provoked HepG2, Huh-7, and H22 HCC cell apoptosis. Mechanistically, isolie gave rise to a substantial decrease in NF-κB activity in HCC cells. Isolie dramatically declined constitutive phosphorylation of NF-κB p65 subunit at Ser536. Overexpressing p65 Ser536 phosphorylation mimics abrogated HCC cell apoptosis induced by isolie. Moreover, ip injection of isolie inhibited the growth of Huh-7 xenografts in nude mice. In Huh-7 xenografts, isolie triggered p65 Ser536 dephosphorylation and inhibited NF-κB activity. In addition, isolie given by both ip injection and gavage had the capacity of diminishing in vivo proliferation of transplanted H22 cells in Kunming mice. Toxic effects of isolie on tumor-bearing mice were undetectable. Our findings provided strong evidence for the potential anti-HCC capacity of isolie. Suppression of NF-κB via p65 dephosphorylation at Ser536 is implicated in isolie-induced HCC cell apoptosis.

■ ASSOCIATED CONTENT

Supporting Information

The Supporting Information is available free of charge on the ACS Publications website at DOI: 10.1021/acs.jafc.5b02993.

Methods and figures depicting spectroscopic data, pharmacokinetics, and cytotoxic activity (PDF)

■ AUTHOR INFORMATION

Corresponding Author

*Phone/fax: + 86 27 6784 1196. E-mail: xinzhou_yang@163.com.

Funding

This work is supported by the Natural Science Foundation of China (31301147, 81573561).

Notes

The authors declare no competing financial interest.

■ ABBREVIATIONS USED

isolie, isoliensinine; HCC, hepatocellular carcinoma; NF-κB, nuclear factor κB

■ REFERENCES

(1) Siegel, R.; Naishadham, D.; Jemal, A. Cancer statistics, 2012. *Ca-Cancer J. Clin.* **2012**, *62*, 10−29.

(2) Verslype, C.; Libbrecht, L. The multidisciplinary management of gastrointestinal cancer. The diagnostic and therapeutic approach for primary solid liver tumours in adults. *Best Pract. Res. Clin. Gastroenterol.* **2007**, *21*, 983−996.

(3) Verstrepen, L.; Beyaert, R. Receptor proximal kinases in NF-kappaB signaling as potential therapeutic targets in cancer and inflammation. *Biochem. Pharmacol.* **2014**, *92*, 519−529.

(4) Glauert, H. P. Role of NF-kappaB in hepatocarcinogenesis and its potential inhibition by dietary antioxidants. *Curr. Cancer Drug Targets* **2012**, *12*, 1160−1172.

(5) Oeckinghaus, A.; Ghosh, S. The NF-kappaB family of transcription factors and its regulation. *Cold Spring Harbor Perspect. Biol.* **2009**, *1*, a000034.

(6) Shu, G.; Tang, Y.; Zhou, Y.; Wang, C.; Song, J. G. Zac1 is a histone acetylation-regulated NF-kappaB suppressor that mediates histone deacetylase inhibitor-induced apoptosis. *Cell Death Differ.* **2011**, *18*, 1825−1135.

(7) Chen, G.; Han, K.; Xu, X.; Du, X.; Zhang, Z.; Tang, J.; Shi, M.; Wang, M.; Li, J.; Cao, B.; Mao, X. An anti-leishmanial thiadiazine agent induces multiple myeloma cell apoptosis by suppressing the nuclear factor kappaB signalling pathway. *Br. J. Cancer* **2014**, *110*, 63−70.

(8) Xu, X. X.; Jiang, H. R.; Li, H. B.; Zhang, T. N.; Zhou, Q.; Liu, N. Apoptosis of stomach cancer cell SGC-7901 and regulation of Akt signaling way induced by bovine lactoferrin. *J. Dairy Sci.* **2010**, *93*, 2344−2350.

DOI: 10.1021/acs.jafc.5b02993
J. Agric. Food Chem. 2015, 63, 8793−8803

(9) Wu, C. H.; Hong, B. H.; Ho, C. T.; Yen, G. C. Targeting cancer stem cells in breast cancer: potential anticancer properties of 6-shogaol and pterostilbene. *J. Agric. Food Chem.* **2015**, *63*, 2432−2441.
(10) Yuan, L.; Wei, S.; Wang, J.; Liu, X. Isoorientin induces apoptosis and autophagy simultaneously by reactive oxygen species (ROS)-related p53, PI3K/Akt, JNK, and p38 signaling pathways in HepG2 cancer cells. *J. Agric. Food Chem.* **2014**, *62*, 5390−5400.
(11) Kim, S. P.; Nam, S. H.; Friedman, M. The tomato glycoalkaloid α-tomatine induces caspase-independent cell death in mouse colon cancer CT-26 cells and transplanted tumors in mice. *J. Agric. Food Chem.* **2015**, *63*, 1142−1150.
(12) Newman, D. J.; Cragg, G. M. Natural products as sources of new drugs over the 30 years from 1981 to 2010. *J. Nat. Prod.* **2012**, *75*, 311−335.
(13) Pan, X.; Wang, X.; Lei, W.; Min, L.; Yang, Y.; Song, J. Nitric oxide suppresses transforming growth factor-beta1-induced epithelial-to-mesenchymal transition and apoptosis in mouse hepatocytes. *Hepatology* **2009**, *50*, 1577−1587.
(14) Liu, C.; Lin, J.-J.; Yang, Z.-Y.; Tsai, C.-C.; Hsu, J.-L.; Wu, Y.-J. Proteomic Study Reveals a Co-occurrence of Gallic Acid-Induced Apoptosis and Glycolysis in B16F10 Melanoma Cells. *J. Agric. Food Chem.* **2014**, *62*, 11672−11680.
(15) Shu, G.; Yang, J.; Zhao, W.; Xu, C.; Hong, Z.; Mei, Z.; Yang, X. Kurarinol induces hepatocellular carcinoma cell apoptosis through suppressing cellular signal transducer and activator of transcription 3 signaling. *Toxicol. Appl. Pharmacol.* **2014**, *281*, 157−165.
(16) Shu, G.; Yang, T.; Wang, C.; Su, H.; Xiang, M. Gastrodin stimulates anticancer immune response and represses transplanted H22 hepatic ascitic tumor cell growth: Involvement of NF-kappaB signaling activation in CD4+ T cells. *Toxicol. Appl. Pharmacol.* **2013**, *269*, 270−279.
(17) Yang, J.; Zhou, K. NMR spectroscopic analysis of neferine and isoliensinine. *Magn. Reson. Chem.* **2004**, *42*, 994−997.
(18) Cayir, K.; Karadeniz, A.; Simsek, N.; Yildirim, S.; Karakus, E.; Kara, A.; Akkoyun, H. T.; Sengul, E. Pomegranate seed extract attenuates chemotherapy-induced acute nephrotoxicity and hepatotoxicity in rats. *J. Med. Food* **2011**, *14*, 1254−1262.
(19) Llovet, J. M.; Ricci, S.; Mazzaferro, V.; Hilgard, P.; Gane, E.; Blanc, J. F.; de Oliveira, A. C.; Santoro, A.; Raoul, J. L.; Forner, A.; Schwartz, M.; Porta, C.; Zeuzem, S.; Bolondi, L.; Greten, T. F.; Galle, P. R.; Seitz, J. F.; Borbath, I.; Haussinger, D.; Giannaris, T.; Shan, M.; Moscovici, M.; Voliotis, D.; Bruix, J. Sorafenib in advanced hepatocellular carcinoma. *N. Engl. J. Med.* **2008**, *359*, 378−390.
(20) Shah, R. R.; Morganroth, J.; Shah, D. R. Hepatotoxicity of tyrosine kinase inhibitors: clinical and regulatory perspectives. *Drug Saf.* **2013**, *36*, 491−503.
(21) Chen, Y.; Fan, G.; Wu, H.; Wu, Y.; Mitchell, A. Separation, identification and rapid determination of liensine, isoliensinine and neferine from embryo of the seed of Nelumbo nucifera GAERTN. by liquid chromatography coupled to diode array detector and tandem mass spectrometry. *J. Pharm. Biomed. Anal.* **2007**, *43*, 99−104.
(22) Reagan-Shaw, S.; Nihal, M.; Ahmad, N. Dose translation from animal to human studies revisited. *FASEB J.* **2008**, *22*, 659−661.
(23) Zhang, X.; Wang, X.; Wu, T.; Li, B.; Liu, T.; Wang, R.; Liu, Q.; Liu, Z.; Gong, Y.; Shao, C. Isoliensinine induces apoptosis in triple-negative human breast cancer cells through ROS generation and p38 MAPK/JNK activation. *Sci. Rep.* **2015**, *5*, 12579.
(24) Poornima, P.; Quency, R. S.; Padma, V. V. Neferine induces reactive oxygen species mediated intrinsic pathway of apoptosis in HepG2 cells. *Food Chem.* **2013**, *136*, 659−667.
(25) Poornima, P.; Weng, C. F.; Padma, V. V. Neferine from Nelumbo nucifera induces autophagy through the inhibition of PI3K/Akt/mTOR pathway and ROS hyper generation in A549 cells. *Food Chem.* **2013**, *141*, 3598−3605.
(26) Zhou, J.; Li, G.; Zheng, Y.; Shen, H. M.; Hu, X.; Ming, Q. L.; Huang, C.; Li, P.; Gao, N. A novel autophagy/mitophagy inhibitor liensinine sensitizes breast cancer cells to chemotherapy through DNM1L-mediated mitochondrial fission. *Autophagy* **2015**, *11*, 1259−1279.
(27) Kao, J. H.; Chen, P. J.; Chen, D. S. Recent advances in the research of hepatitis B virus-related hepatocellular carcinoma: epidemiologic and molecular biological aspects. *Adv. Cancer Res.* **2010**, *108*, 21−72.
(28) Park, E. J.; Lee, J. H.; Yu, G. Y.; He, G.; Ali, S. R.; Holzer, R. G.; Osterreicher, C. H.; Takahashi, H.; Karin, M. Dietary and genetic obesity promote liver inflammation and tumorigenesis by enhancing IL-6 and TNF expression. *Cell* **2010**, *140*, 197−208.
(29) Ni, H.; Zhao, W.; Kong, X.; Li, H.; Ouyang, J. NF-kappa B modulation is involved in celastrol induced human multiple myeloma cell apoptosis. *PLoS One* **2014**, *9*, e95846.
(30) Chen, Y. Y.; Lu, H. F.; Hsu, S. C.; Kuo, C. L.; Chang, S. J.; Lin, J. J.; Wu, P. P.; Liu, J. Y.; Lee, C. H.; Chung, J. G. Bufalin inhibits migration and invasion in human hepatocellular carcinoma SK-Hep1 cells through the inhibitions of NF-kB and matrix metalloproteinase-2/-9-signaling pathways. *Environ. Toxicol.* **2015**, *30*, 74−82.
(31) Zhao, B.; Ma, Y.; Xu, Z.; Wang, J.; Wang, F.; Wang, D.; Pan, S.; Wu, Y.; Pan, H.; Xu, D.; Liu, L.; Jiang, H. Hydroxytyrosol, a natural molecule from olive oil, suppresses the growth of human hepatocellular carcinoma cells via inactivating AKT and nuclear factor-kappa B pathways. *Cancer Lett.* **2014**, *347*, 79−87.
(32) Xiang, M.; Su, H.; Hu, Y.; Yang, T.; Shu, G. Chemical composition of total flavonoids from Salvia chinensia Benth and their pro-apoptotic effect on hepatocellular carcinoma cells: potential roles of suppressing cellular NF-kappaB signaling. *Food Chem. Toxicol.* **2013**, *62*, 420−426.
(33) Yu, W.; Gu, K.; Yu, Z.; Yuan, D.; He, M.; Ma, N.; Lai, S.; Zhao, J.; Ren, Z.; Zhang, X.; Shao, C.; Jiang, G. L. Sorafenib potentiates irradiation effect in hepatocellular carcinoma in vitro and in vivo. *Cancer Lett.* **2013**, *329*, 109−117.
(34) Wong, L. L.; Lam, I. P.; Wong, T. Y.; Lai, W. L.; Liu, H. F.; Yeung, L. L.; Ching, Y. P. IPA-3 inhibits the growth of liver cancer cells by suppressing PAK1 and NF-kappaB activation. *PLoS One* **2013**, *8*, e68843.
(35) Zhang, L.; Shao, L.; Creighton, C. J.; Zhang, Y.; Xin, L.; Ittmann, M.; Wang, J. Function of phosphorylation of NF-kB p65 ser536 in prostate cancer oncogenesis. *Oncotarget* **2015**, *6*, 6281−6294.
(36) Zou, Z.; Zeng, F.; Xu, W.; Wang, C.; Ke, Z.; Wang, Q. J.; Deng, F. PKD2 and PKD3 promote prostate cancer cell invasion by modulating NF-kappaB- and HDAC1-mediated expression and activation of uPA. *J. Cell Sci.* **2012**, *125*, 4800−4811.
(37) Yang, Z. Y.; Qu, Y.; Zhang, Q.; Wei, M.; Liu, C. X.; Chen, X. H.; Yan, M.; Zhu, Z. G.; Liu, B. Y.; Chen, G. Q.; Wu, Y. L.; Gu, Q. L. Knockdown of metallopanstimulin-1 inhibits NF-kappaB signaling at different levels: the role of apoptosis induction of gastric cancer cells. *Int. J. Cancer* **2012**, *130*, 2761−2770.
(38) MacKenzie, L.; McCall, P.; Hatziieremia, S.; Catlow, J.; Adams, C.; McArdle, P.; Seywright, M.; Tanahill, C.; Paul, A.; Underwood, M.; Mackay, S.; Plevin, R.; Edwards, J. Nuclear factor kappaB predicts poor outcome in patients with hormone-naive prostate cancer with high nuclear androgen receptor. *Hum. Pathol.* **2012**, *43*, 1491−1500.
(39) Lewander, A.; Gao, J.; Carstensen, J.; Arbman, G.; Zhang, H.; Sun, X. F. NF-kappaB p65 phosphorylated at serine-536 is an independent prognostic factor in Swedish colorectal cancer patients. *Int. J. Colorectal Dis.* **2012**, *27*, 447−452.
(40) Wang, Y. P.; Liu, I. J.; Chiang, C. P.; Wu, H. C. Astrocyte elevated gene-1 is associated with metastasis in head and neck squamous cell carcinoma through p65 phosphorylation and upregulation of MMP1. *Mol. Cancer* **2013**, *12*, 109.
(41) McCall, P.; Bennett, L.; Ahmad, I.; Mackenzie, L. M.; Forbes, I. W.; Leung, H. Y.; Sansom, O. J.; Orange, C.; Seywright, M.; Underwood, M. A.; Edwards, J. NFkappaB signalling is upregulated in a subset of castrate-resistant prostate cancer patients and correlates with disease progression. *Br. J. Cancer* **2012**, *107*, 1554−1563.
(42) Bhattacharyya, S.; Sen, P.; Wallet, M.; Long, B.; Baldwin, A. S., Jr.; Tisch, R. Immunoregulation of dendritic cells by IL-10 is mediated through suppression of the PI3K/Akt pathway and of IkappaB kinase activity. *Blood* **2004**, *104*, 1100−1109.

DOI: 10.1021/acs.jafc.5b02993
J. Agric. Food Chem. 2015, 63, 8793−8803

(43) Adli, M.; Baldwin, A. S. IKK-i/IKKepsilon controls constitutive, cancer cell-associated NF-kappaB activity via regulation of Ser-536 p65/RelA phosphorylation. *J. Biol. Chem.* **2006**, *281*, 26976−26984.
(44) Sakurai, H.; Chiba, H.; Miyoshi, H.; Sugita, T.; Toriumi, W. IkappaB kinases phosphorylate NF-kappaB p65 subunit on serine 536 in the transactivation domain. *J. Biol. Chem.* **1999**, *274*, 30353−30356.
(45) Hu, T. H.; Huang, C. C.; Lin, P. R.; Chang, H. W.; Ger, L. P.; Lin, Y. W.; Changchien, C. S.; Lee, C. M.; Tai, M. H. Expression and prognostic role of tumor suppressor gene PTEN/MMAC1/TEP1 in hepatocellular carcinoma. *Cancer* **2003**, *97*, 1929−1940.
(46) Jiang, R.; Xia, Y.; Li, J.; Deng, L.; Zhao, L.; Shi, J.; Wang, X.; Sun, B. High expression levels of IKKalpha and IKKbeta are necessary for the malignant properties of liver cancer. *Int. J. Cancer* **2010**, *126*, 1263−1274.
(47) Zhou, Q.; Lui, V. W.; Yeo, W. Targeting the PI3K/Akt/mTOR pathway in hepatocellular carcinoma. *Future Oncol.* **2011**, *7*, 1149−1167.
(48) Huang, J. J.; Chu, H. X.; Jiang, Z. Y.; Zhang, X. J.; Sun, H. P.; You, Q. D. Recent advances in the structure-based and ligand-based design of IKKbeta inhibitors as anti-inflammation and anti-cancer agents. *Curr. Med. Chem.* **2014**, *21*, 3893−3917.

DOI: 10.1021/acs.jafc.5b02993
J. Agric. Food Chem. 2015, 63, 8793−8803

Table 1. Overview on the Main Virulence Factors of Uropathogenic *E. coli*

virulence factor	gene	functions	features
		1. Adhesins	
			host receptor specificity
type 1 fimbriae	*fim*	mediates mannose-sensitive adhesion in urinary tract epithelium and tissue matrix, invasion, biofilm formation; present in >90% of patients	mannosylated glycoproteins (e.g., UPIa and CD48), Tamm–Horsfall protein, type I and type IV collagens, laminin, fibronectin
P fimbriae	*pap*	mediates mannose-resistant adhesion, cytokine induction; present in 40–60% of UPEC isolates, identified in 80% of pyelonephritis-causing UPEC	GbO3, GbO4, GbO5; P-blood group antigen specific glycosphingolipids (α-D-Gal-(1→4)-β-D-Gal)
S fimbriae	*sfa*	adhesion to bladder, kidney mucosal epithelium and to brain endothelium, involved in NMEC	neuraminic acids/sialic acid residues, plasminogen/β-GalNac-(1→4)-β-Gal
F1C fimbrae	*foc*	adhesion to mucosal and endothelial cells, cytokine induction	lactosylceramide containing glycolipids, β-GalNac-(1→4)-β-Gal
Dr fimbriae	*dra*	involved in adhesion and invasion	Dr blood group antigen present on the complement cascade regulator factor, DAF (CD55), CD66e, type IV collagen, $\alpha_5\beta_1$ integrin
afimbrial adhesin	*afa*	adhesion to mucosal epithelium	decay accelerating factor (DAF)
nonfimbrial adhesin	*nfa*	adhesion	glycophorin A
thin aggregative fimbriae (curli)	*csg*	promotes colonization of perneal area, biofilm formation, adhesion	matrix and plasma proteins (fibronectin, laminin, plasminogen, H-kininogen)
M-adhesin	*bma*	adhesion	A^M determinant of M blood group antigen
G-adhesin		adhesion	GlcNac
UPEC autotransporter adhesin	*upa*	autotransporter that promotes cell aggregation and the formation of biofilms, adhesion to bladder epithelial cells	fibronectin, laminin/localization: cell surface
		2. Host Defense Evasion	
capsular polysaccharide (K antigen)	*kps*	antiphagocytic, anticomplement, and involved in serum resistance	localization: cell surface
lipopolysaccharide (LPS; O-antigen)	*rfa*, *rfb*, *rfc*	endotoxic effects, cytokine induction, serum resistance, immunoadjuvant, leading to inflammation and exfoliation of host cells	localization: cell surface
serum resistance	*colV*, *traT*	confers resistance to killing of bacteria by serum (membrane attack system (MAC) of the complement); it can function individually or combined with effects of capsular polysaccharide, *O*-polysaccharide side chains, and surface proteins	localization: cell surface, involved proteins: Iss, TraT, Bor
TcpC	-	TcpC suppresses innate immunity by homology to TIR domain of TLR	
		3. Toxins	
α-hemolysin	*hly*	cytotoxicity, hemolysis	toxin of Rtx type/localization: exported
cytotoxic necrotizing factor	*cnf*	interference with phagocytosis and apoptosis	localization: exported
secreted autotransporter toxin	*sat*	cytotoxicity	localization: exported
vacuolating autotransporter toxin	*vat*	cytotoxicity	localization: exported
cytolethal distending toxin	*cdt*	cytotoxicity	localization: exported
		4. Iron Acquisition System	
aerobactin siderophore	*iutA*	growth under iron restriction	hydroxamate type/localization: exported
enterobactin siderophore	*ent*	growth under iron restriction	catechol type/localization: exported
hemin uptake system	*chu*	heme transporter	localization: exported
salmochelin siderophore	*iro*	growth under iron restriction	catechol type/localization: exported
yersiniabactin siderophore	*fyuA*	growth under iron restriction	localization: exported

J. Agric. Food Chem. 2015, 63, 8804–8818
DOI: 10.1021/acs.jafc.5b03030

Table 1. continued

virulence factor	gene	functions	features
5. Others			
flagellum (H-antigen)	*fliC*	motility, fitness, facilitates ascending route	localization: cell surface
outer membrane proteins	*ireA, iha, ompA/C/T*	receptor and transport function, OmpA is involved in bacterial invasion by facilitating IBC maturation and chronic bacterial persistence	;ocalization: cell surface
CPA24/CP1	*guaA/argC*	urine growth factor	localization: exported
antigen 43	*flu*	autoaggregation phenotype of UPEC during biofilm formation, autotransporter	localization: cell surface

increased biofilm formation after in vivo intake of cranberry juice for 20% of the UPEC strains.

With regard to the clinical efficacy, a recent Cochrane meta-study concluded that cranberry products are not significantly different from standard antibiotic treatment for preventing UTI, but the evidence for a potentially significant benefit seems too small for a clear recommendation for the prevention of UTI.[11] One major reason for this nonconvincing outcome of the Cochrane review is the use of nonstandardized cranberry products for clinical investigations and the high drop-out numbers of patients during the long-term studies. The need for the development of quantified and standardized cranberry preparations is therefore obvious.[11]

During examination of the very complex literature published on cranberry activity against UPEC, we found it astonishing that most of the authors claim PACs to be responsible for the antiadhesive activity.[7] On the other hand, recent studies have shown that PACs are absorbed over the intestinal barrier only to a very limited extent and, in principle, are not bioavailable in relevant concentrations.[12,13] Interestingly, polyphenols known to be microbial-derived metabolites of PACs such as phenylacetic acid, 3,4-dihydroxyphenylacetic acid, and catechol have recently been identified as antiadhesive compounds against UPEC,[14] and also myricetin has been pinpointed as an antiadhesive compound in human urine from volunteers after cranberry uptake.[15] From the current state of knowledge it might be assumed that PACs are not dominantly responsible for the antiadhesive effects of cranberry, whereas PAC metabolites, formed during the intestinal passage, or cranberry-associated flavonoids are bioavailable to a significant extent and can be found as potential antiadhesive compounds in the urine.

The purpose of this investigation was to initiate studies for systematic evaluation of (i) the influence of PAC-containing and PAC-depleted cranberry extracts on the bacterial adhesion of UPEC to bladder cells in ex vivo studies and (ii) the influence of PAC-containing and PAC-depleted cranberry extracts on UPEC virulence factors.

MATERIALS AND METHODS

Materials. If not stated otherwise, solvents, reagents, and consumables were obtained from VWR International (Darmstadt, Germany). All solvents and reagents were of analytical quality. Water was produced by a MilliporeSimplicity 185 system (Schwalbach, Germany).

The cranberry dry extract (Extract High PAC Special, batch 903514/product code HC23174; Frutarom, Londerzeel, Belgium) from the fruits of *V. macrocarpon* Ait. is certified for use as a food product. A voucher sample (IPBP-281) has been stored in the archives of the Institute of Pharmaceutical Biology and Phytochemistry, University of Münster, Germany.

Preparation of *V. macrocarpon.* (*V.m.*) Extract. Cranberry dry extract contained excipients to ensure optimal powder technology, which were insoluble in EtOH/water (1:1, v/v). These compounds were removed from 20 g of the dry extract after rotor-stator homogenization by Ultraturrax (Ika, Staufen, Germany) in 200 mL of EtOH/water (1:1, v/v) three times for 5 min. The suspension was centrifuged for 5 min at 3000*g*. The remaining residue was re-extracted again three times until the insoluble material was colorless. The combined extracts were lyophilized. The dried extract was stored under an argon atmosphere at −20 °C and is termed in the following as *V.m.* extract.

Proanthocyanidins in *V.m.* extract were quantified according to the European Pharmacopeia[16] and the content of PACs calculated as cyanidine. Quantification was performed with $n = 6$ independent determinations, using 350 mg of *V.m.* extract.

DOI: 10.1021/acs.jafc.5b03030
J. Agric. Food Chem. 2015, 63, 8804−8818

Preparation of *V.m.* Extract$^{\neq PAC}$. One hundred milligrams of *V.m.* extract was dissolved in 100 mL of water. One thousand milligrams of Polyclar AT (G.A.F. Corp., USA), a water-insoluble polyvinylpyrrolidone, was added. Polyphenols were precipitated under gentle stirring of the reaction vessel for 30 min. The suspension was centrifuged at 3000*g* for 5 min. The supernatant was filtered through a paper filter, and clear filtrates were combined, evaporated, and lyophilized to yield 66 mg of *V.m.* extract$^{\neq PAC}$. Proanthocyanidin depletion was proven by thin layer chromatography, using vanillin−hydrochloric acid reagent for specific PAC detection.

LC-MS Dereplication of *V.m.* Extracts. For the preparation of LC-MS samples, *V.m.* extract and *V.m.* extract$^{\neq PAC}$ were dissolved in methanol to a concentration of 10 mg/mL. Separation was performed on a Dionex Ultimate 3000 RS liquid chromatography system over a Dionex Acclaim RSLC 120, C18 column (2.1 × 100 mm, 2.2 μm) with a binary gradient (A, water with 0.1% formic acid; B, acetonitrile with 0.1% formic acid) at 0.4 mL/min: 0−5 min, isocratic at 5% B; 5−37 min, linear from 5 to 100% B; 37−47 min, isocratic at 100% B; 47−48 min, linear from 100 to 5% B; 48−55 min, isocratic at 5% B. The injection volume was 2 μL. Eluted compounds were detected using a Dionex Ultimate DAD-3000 RS over a wavelength range of 200−800 nm and a Bruker Daltonics micrOTOF-QII time-of-flight mass spectrometer equipped with an Apollo electrospray ionization source in positive mode at 2 Hz over a mass range of m/z 50−1500 using the following instrument settings: nebulizer gas nitrogen, 4 bar; dry gas nitrogen, 9 L/min, 200 °C; capillary voltage, −4500 V; end plate offset, −500 V; transfer time, 100 μs; prepulse storage, 6 μs; collision energy, 8 eV. MS/MS scans were triggered by AutoMS2 settings within a range of m/z 200−1500, using a collision energy of 40 eV and a collision cell RF of 130 Vpp. Internal data set calibration (HPC mode) was performed for each analysis using the mass spectrum of a 10 mM solution of sodium formate in 50% isopropanol that was infused during LC re-equilibration using a divert valve equipped with a 20 μL sample loop.

Manufacture of Cranberry Extract-Containing Capsules. Cranberry dry extract, certified as a food product for use in humans, was used for the ex vivo pilot study. Encapsulation of 150 mg of extract, without addition of further additives, was performed into hard gelatin capsules (size 0/cream colored, batch 13E27-N13; WEPA, Hilscheid, Germany). The uniformity of mass of single-dose preparations was analyzed by a weight variation test according to the requirements of the European Pharmacopoeia.[17] Capsules were stored in plastic containers protected from heat and light at room temperature.

Study Design. Four male individuals, who gave informed consent, volunteered to consume cranberry capsules over a 7 day period, with urine sampling at days 0, 3, and 7 for ex vivo studies. Exclusion criteria included antibiotic treatment 2 weeks prior to and during the study. Before starting the trial, the volunteers were instructed to abstain from consumption of any other products containing cranberry or phytochemically or botanically similar fruits (especially from the plant family Ericaceae) 2 weeks before and during the study. Each subject was asked to take two cranberry capsules of 150 mg in the morning and in the evening after a meal, equivalent to 600 mg of cranberry extract per day for 7 days. Generally, the first midstream urine of the day was collected and used for functional and analytical investigations. A control urine sample (S0) was collected prior to the consumption of the capsules. The second urine sample (S1) was collected at day 3 of medication, and the third sample (S2) was collected on the last day of cranberry capsule intake. The urine samples were centrifuged at 3000*g* for 5 min, filtered (0.22 μm pore size), and stored at −20 °C until use.

Cell Culture and Microbiology. T24 cells (ATCC HTB-4) represent a human epithelial bladder cell line, derived from the bladder carcinoma of an 82-year-old Swedish female.[18] These cells have been already demonstrated to be suitable for adhesion and invasion in vitro assays with UPEC[19] and were kindly provided by Prof. Straube (University of Jena, Germany). The influence of test compounds on the viability of T24 cells was monitored by MTT assay.[20] T24 cells were seeded in 96-well plates with 2.5 × 10^4 cells per well (100 μL) and incubated for 24 h at 37 °C with 5% CO_2. T24 cells were washed with 200 μL/well PBS. Incubation of the cells with test extracts (100 μL) was performed for 24 h at 37 °C with 5% CO_2. After the incubation with extracts, the supernatant was removed and cells were washed twice with PBS, 200 μL/well. Fifty microliters of MTT reagent was added to each well, and the 96-well plate was incubated for a further 4 h at 37 °C/5% CO_2. MTT reagent was tapped off the 96-well plate, and 50 μL of DMSO was added to dissolve the formazan crystals. After the plate had been shaken for 10 min, the absorption of the formazan was determined at λ = 492 nm and a reference wavelength of λ = 690 nm.

Bacterial strains included *E. coli* strain 2980 (DSM 10791), provided by Prof. Straube (University of Jena, Germany); UPEC NU14, a clinical cystitis isolate, provided by Prof. Dobrindt (University of Münster, Germany); and J96 provided by Inga Benz (University of Münster, Germany).

Bacteria from passages 2 to 4 were used for all tests and were cultivated from frozen stocks. For adhesion assays agar-grown bacteria were harvested and used for inoculation of Loeb agar supplemented with 0.2% $CaCl_2$, which is supposed to increase the type 1 fimbria expression.[21] For liquid culture 1 colony-forming unit (CFU) of agar-grown bacteria was transferred to 10 mL of UPEC broth in 50 mL tubes and incubated under shaking (200 rpm/37 °C) until mid-logarithmic phase.

For the agar diffusion assay, agar-grown bacteria were harvested, suspended in sterile PBS, and adjusted to an $OD_{640\ nm}$ of 0.2/mL. One hundred microliters of the bacterial suspension was transferred to a Loeb agar plate and spread homogeneously. Subsequently, five sterile BD Sensi-Disks (BD Biosciences, Franklin Lakes, NJ, USA) were distributed circularly in equal intervals on the agar plate with sterile tweezers. Twenty microliters of the respective test solutions (sterile filtered, 0.22 μm) were pipetted on the disks. Norfloxacin (50 μg/mL) (Fluka, Buchs, Switzerland) served as positive control. Plates were incubated for 48 h at 37 °C.

To monitor bacterial growth in liquid culture, 1 CFU of agar-grown bacteria was suspended in 10 mL of liquid medium and cultivated overnight in an incubator rotary shaker (200 rpm at 37 °C). Bacteria were adjusted to an $OD_{640\ nm}$ of 1.0/mL in liquid medium and pipetted in 100 μL aliquots into a 96-well plate. Additionally, 100 μL of fresh liquid medium was added to the wells plus 50 μL of sterile filtered (0.22 μm) test solution. Liquid medium served as negative control, and gentamicin (100 μg/mL) (PAA, Pasching, Austria) was used as positive control. The plate was incubated at 37 °C, and bacterial growth was monitored by measuring the optical density every 30 min over a 6 h period at λ = 640 nm.

Adhesion Assay with Urine Samples by Quantitative Flow Cytometry. In general, FITC labeling of UPEC and flow cytometric adhesion assay was performed as described in refs 22 and 23. T24 cells (2.5 × 10^5 cells/well) were seeded in 6-well plates and incubated at 37 °C and 5% CO_2 until 90% confluence was reached (corresponding to 800,000 cells, after approximately 24 h of incubation). After this incubation, T24 cell culture medium was removed, cells were washed once with PBS, and 2 mL of DMEM was added to each well. All further steps with FITC-labeled *E. coli* ($OD_{640\ nm}$ 0.4/1000 μL (corresponding to 8 × 10^7 CFU/mL) were carried out under light protection. For adhesion experiments a bacterial cell ratio (BCR) of 100:1 was used. After addition of UPEC to T24 cells, the interaction was accelerated by short centrifugation (200*g*, 1 min) of the 6-well plate, followed by 2 h of incubation at 37 °C. Subsequently, unattached UPEC were removed by gently washing the T24 cells three times with 1 mL of PBS/well. T24 cells were detached by the addition of 600 μL trypsin/EDTA for 3 min at 37 °C. Trypsination was stopped by the addition of 2 mL of DMEM. The content of each well was transferred to tubes and centrifuged for 5 min at 400*g*. The supernatant was discarded and the cell pellet suspended, dependent on the visually observable size of the pellet, in 500−1000 μL of PBS. Finally, the fluorescence of the cell suspension was measured by flow cytometer. For data evaluation 10000 counts for each sample were used. For quantitative in vitro flow cytometric adhesion assay with urine samples the adhesion assay was performed similarly to the assay described above with the following changes to the described protocol: 10 mL of sterile urine, containing 5% of UPEC liquid medium, was inoculated with 1 CFU of agar-grown bacteria and incubated in a rotary shaker (200 rpm at 37 °C) until mid-logarithmic growth phase was reached. In pre-experiments the growth rate of *E. coli* in urine, supplemented with 5% broth, had been monitored, revealing

DOI: 10.1021/acs.jafc.5b03030
J. Agric. Food Chem. 2015, 63, 8804−8818

that the mid-logarithmic growth phase was reached after 3.5 h. Additionally, a negative control sample was prepared with each urine sample from each volunteer which had not been inoculated with *E. coli* in order to prove sterility of urine samples. Bacteria were centrifuged after an incubation time of 3.5 h at 3000*g* for 5 min and washed with PBS, and the suspension was adjusted to an $OD_{640\ nm}$ of 0.5/100 μL in saline solution for FITC labeling. After fluorescence labeling, the density of bacteria was adjusted to an $OD_{640\ nm}$ of 0.4/mL in DMEM. Bacteria were added to T24 cells in 6-well plates and incubated for 2 h at 37 °C. Finally, bacterial adhesion was quantified by flow cytometry. Urine samples S0 of each volunteer served as untreated control.

In Vitro Adhesion Assay by Confocal Laser Scanning Microscopy with UPEC and T24 Cells. T24 cells (6×10^4 cells/well) were seeded on 8-well silicone FlexiPERM chambers (Greiner bio-one, Kremsmünster, Austria) and grown to 90% confluence. The supernatant was removed, the monolayer washed with PBS, and 350 μL/well DMEM was added. Agar-grown bacteria were harvested, labeled with FITC, and adjusted to an $OD_{640\ nm}$ of 2.0/mL. Fifty microliters of the bacteria suspension was mixed with 300 μL of test solution and incubated for 30 min at 37 °C. Bacteria in test solution were applied to T24 cells at a BCR of 100:1 for 2 h at 37 °C. After bacterial infection, cells were washed three times with PBS and fixed by 20 min of incubation with 3.7% paraformaldehyde in PBS. Subsequently, the fixed cells were permeabilized by incubation with 0.2% Triton X-100 in PBS for 5 min at room temperature. T24 cells were blocked with PBS containing 3% BSA for 20 min, followed by staining F-actin with Texas Red-conjugated phalloidin (Life Technologies, Carlsbad, CA, USA) for 30 min at room temperature. Nuclei were stained with 1 μg/mL DAPI for 30 min at 4 °C. Subsequently, cells were washed three times with PBS, and the FlexiPERM chamber was removed. Cells were fixed with Dako fluorescent mounting medium (Dako, Carpinteria, CA, USA), covered with a coverslip, and sealed with nail polish. Confocal laser scanning microscopy was accomplished with a Leica TCS SP2 fluorescence microscope (Leica, Wetzlar, Germany) at λ 405/420−480 nm for DAPI, 488/500−580 for FITC, and 594/620−700 for Texas Red.

In Vitro Adhesion Assay by Scanning Electron Microscopy. T24 cells (1×10^5 cells/well) were seeded on Transwell inserts (Corning, Corning, NY, USA) in 12-well plates and grown to confluence. After washing with PBS, 500 μL, respectively, of 1500 μL of DMEM was added. Agar-grown bacteria were harvested and adjusted to an $OD_{640\ nm}$ of 0.4/100 μL. Fifty microliters of the bacteria suspension was mixed with 450 μL of test solution and incubated for 30 min at 37 °C, followed by addition to the T24 cells for 2 h at 37 °C. After the incubation, cells were washed three times with PBS. The samples were prepared for electron microscopy using standard procedures[24] and a high-resolution scanning electron microscope Auriga (Zeis, Jena, Germany).

Quantitative biofilm assay was performed as described in ref 25. Quantitative Congo Red binding assay was performed as described in ref 26.

Methods of Molecular Biology. *Bacterial RNA Extraction, DNase I Treatment, and cDNA Synthesis.* For the isolation of total RNA from *E. coli* 2980 and *E. coli* NU14, bacteria were incubated in the presence of T24 cells (bacteria-host cell contact, BCR 100:1) or without T24 cells in DMEM (untreated control), respectively, containing different concentrations of the test extracts over a time period of 1.5 h at 37 °C and 5% CO_2.

After the incubation time of 1.5 h, bacteria in wells without T24 cells were transferred directly to fresh tubes. The medium in wells with T24 cells was discarded, and cells were washed three times with PBS. Subsequently, T24 cells were detached using a cell scraper and also transferred to fresh tubes. After centrifugation (6500*g*, 5 min), the cell pellets were suspended in PBS and transferred into tubes containing RNAprotect Bacteria reagent (Qiagen, Germany) and mixed by vortexing for 5 s. After 5 min of incubation at room temperature and centrifugation (5000*g*, 10 min), the cells were lysed by mixing with TE buffer containing lysozyme (1 mg/mL, Sigma-Aldrich), followed by incubation for 8 min at room temperature and 500 rpm. The stabilized RNA was purified with an RNeasy Mini Kit (Qiagen, Germany) according to the manufacturer's protocol. The quality and quantity of eluted RNA were determined by measuring the samples at λ = 260 nm and λ = 280 nm by using a BioPhotometer plus and a μCuvette G1.0 (both Eppendorf, Germany).

Potential coeluted DNA was digested by treatment of the isolated RNA with DNase I (Life Technologies, USA) for 15 min at room temperature followed by an inactivation of the enzyme by the addition of EDTA and heating to 65 °C for 10 min. After DNA digestion, samples were controlled again by measuring the $OD_{260\ nm}$ and $OD_{280\ nm}$.

For each RNA sample, 0.5 μg of RNA was transcribed into cDNA by using the Masterscript Kit (5 Prime, Germany) and a random hexamer primer (Thermo Scientific, USA) following the manufacturer's instructions. Here, minus-room temperature controls were also performed, which did not comprise the reverse transcriptase during cDNA synthesis.

Quantitative Real-Time PCR (qRT-PCR). qRT-PCR was performed with an equivalent of 25 ng of total RNA by using the iTaq Universal SYBR Green supermix (BioRad, Germany) according to the protocol recommended by the manufacturer and the CFX96 Real-Time System C1000 Touch (BioRad, Germany). The qPCR parameters were as follows: polymerase activation and initial denaturation for 15 s at 95 °C followed by 39 cycles of 5 s at 95 °C and 30 s at 60 °C. Afterward, an additional melt curve analysis was performed (65−95 °C, ramp 0.5 °C pro cycle, 1 cycle = 5 s, 60 cycles in total). Data were evaluated with the BioRad CFX Manager 3.0 software based on the comparative C_T method ($2^{-\Delta\Delta CT}$ method) and were normalized to the endogenous reference gene16S rRNA.

Primers for the qPCR were designed with the Universal ProbeLibrary Assay design Center (Roche, Switzerland), and the oligonucleotides were obtained from Eurofins MWG Operon, Luxembourg. Primer sequences used for the differential gene expression analysis are listed in Table 2.

Statistical Analysis. Statistical results were obtained by use of SPSS statistics (version 20) (IBM, Armonk, NY, USA). Results are expressed as the mean value (MV) ± standard deviation (±SD). Data ($n \geq 3$) were processed by analysis of variance (one-way ANOVA). A subsequent post hoc test was conducted using Dunnett's test (two-sided) to determine the statistical significance of differences between mean values of two with each other compared groups. *P* values <0.05 were considered as significant.

RESULTS AND DISCUSSION

Antiadhesive Activity of Urine Obtained from Volunteers after 7 Days of Intake of Cranberry Extract. EtOH-/water (1:1, v/v) soluble compounds of a commercially available food grade cranberry dry extract were characterized using LC-ESI-qTOF-DAD-MS (Figure 1). Peaks were assigned as displayed in Table 3 on the basis of a comparison of pseudomolecular ions and major fragments' exact *m*/*z* values with published data of *V. macrocarpon* constituents.

V. m. extract was used within an in vivo study with *n* = 4 male human subjects to ensure potential antiadhesive effects of the urine obtained from the volunteers. The extract was administered for 7 days at 600 mg per day. Urine samples for ex vivo analysis were collected at three time points from the first midstream urine of the day: A control urine sample (S0) was collected at day 0 prior to the application of the cranberry extract. The second urine sample (S1) was collected at day 3, and the third sample (S2) was collected after day 7. For investigation of potential antiadhesive effects of the urine samples an ex vivo antiadhesion assay was performed. A defined amount of UPEC strain NU14 from mid-logarithmic growth phase was incubated for 3.5 h in urine, supplemented with 5% of UPEC growth medium. Subsequently, bacteria were isolated, fluorescent-labeled with fluorescein isothiocyanate, followed by co-incubation with T24 bladder cells for 2 h to allow bacterial adhesion to the host cells. The amount of bacteria, attached to the eukaryotic cells was quantified by flow cytometry. As displayed in Figure 2 significant

DOI: 10.1021/acs.jafc.5b03030
J. Agric. Food Chem. 2015, 63, 8804−8818

Table 2. Primer Sequences for UPEC[a]

primer	gene ID (ref)	sequence: 5′→3′
afaE1-f	433882	CCAAGACGGCGGTGTATATTA
afaE1-r		TCGTACGATGAACACCATCTG
afaE2-f	299929324	GGAACCTCAAGGGCACAA
afaE2-r		ACTGGAATGAAGCTCGTTTTG
afaE3-f	55670384	ACGACCGACAATGGTGTCTT
afaE3-r		CTACGTAGATCCCGATAGTTCCA
agn 43-f	386261151	TGGCACCATCAGCCTGCGTG
agn 43-r		CGTACCACTGTTGCCGGCGT
csgA-f	190907313	GTAGCAGCAATTGCAGCAATCG
csgA-r		TTAGATGCAGTCTGGTCAACAG
fimH-f	3286745	CAATGGTACCGCAATCCCTA
fimH-r		GCAGGCGCAAGGTTTACA
fliC-f	26108594	ACAGCCTCTCGCTGATCACTCAAA
fliC-r		GCGCTGTTAATACGCAAGCCAGAA
focG-f	239708	TGGCCACCGGTCTTATTAAC
focG-r		CCCTCCCTGTAACAGTAATCGT
hlyA-f	146377	TTGCTTCTGTTGTGACACT
hlyA-r		CTCTATTTTATTGGCACGTTTA
nfa-f	7239822	TGAATCTCGTTACCCCGAAC
nfa-r		GTGATTTCGCGGTTTGCTA
papGI-f	42290	GTCAGGCGGTAATGATGCTT
papGI-r		TCGTTAAAAGCATAAAACATGACATT
papGII-f	147093	GAAATTTTCGGTTGGTCTGG
papGII-r		TCCACCCCGTTAACTGAAAC
papGIII-f	7407206	AGCAATTTTCGGTTGGTCTG
papGIII-r		TCCACGCCATTAATCGAAAT
prsGIII-f	42529	CAATTTTCGGTTGGTCTGG
prsGIII-r		CGATGGTCAGGTTTTGTG
sfaS-f	S53210	CCCGTCACAGTAATCGTCGT
sfaS-r		CCCGTCACAGTAATCGTCGT
16S rRNA-f	85674274	GGCGCATACAAAGAGAAG
16S rRNA-r		ATGGAGTCGAGTTGCAGA

[a]f, forward primer; r, reverse primer; ref, reference.

inhibition of bacterial adhesion was obvious for S1 (−39%) and S2 (−48%) compared to the control samples S0. These data clearly indicate in vivo antiadhesive activity of the cranberry extract and confirmed a similar study on antiadhesive properties of urine obtained after the ingestion of cranberry preparations.[32]

Molecular Characterization of UPEC Strains. For detailed in vitro investigations on these antiadhesive effects three different UPEC strains were investigated and characterized. Strain J96, isolated from a human patient with pyelonephritis and frequently used in UTI research, has been described to carry the genes coding for type 1 fimbriae (*fimH*), P fimbriae (*papGI/III*), and F1C fimbriae (*focG*) and for the toxins cytotoxic necrotizing factor 1 (CNF1) (*cnf1*) and α-hemolysin (*hlyA*).[33] This strain could not be used for any adhesion experiments in the following studies due to the secretion of α-hemolysin and CNF1, which, after incubation with T24 cells, led to strong cytotoxic effects against the eukaryotic cells.

Subsequently, adhesion studies were carried out with two further UPEC strains: 2980 (isolated from human feces, characterized as an UTI-causing strain,[34] positive for the *fimH*, *papGII/III*, *focG*, *sfaS*, and *hlyA* genes; and NU14, isolated from a patient with clinical cystitis, frequently used for studies of molecular mechanisms of pathogenesis of UTI, positive for the *papGI/II*, *sfaS*, *fimH*, *hlyA*, *cnf*, and *fliC* virulence-associated genes of UPEC.[35]

For verification of these literature-based characteristics both strains were investigated for gene expression by quantitative real-time PCR (qRT-PCR) using a strain-specific sequence of the 16S rRNA from *E. coli* K-12 (clone W3110) as endogenous control. Surprisingly, no or only very limited gene expression of most of the relevant virulence factors was observed after 0.5−2 h of incubation of the bacteria in liquid medium. Thus, it was concluded that the bacteria need a stimulant which induces the expression of virulence factors. Therefore, UPEC were incubated in DMEM in the presence of T24 bladder cells (BCR 100:1, 1.5 h of incubation). This experimental setup evoked a clear up-regulation of several virulence factors, whereas others were not impaired.

For strain 2980, expression of the genes *afaE3*, *nfa*, *papGI*, *papGIII*, and *sfa* was not detectable, regardless of whether bacteria were incubated with T24 cells or not. The biofilm related protein antigen 43 (*agn43*) and the toxin α-hemolysin (*hlyA*) were expressed independent of a T24 stimulus. The presence of T24 cells significantly induced expression of the adhesins *focG*, *papGII*, and *prsGIII* (Figure 3A).

In addition, time course experiments indicated that the level of gene expression for these three adhesins was time dependent: prolonged incubation time of bacteria with T24 cells led to higher expression rates of *papGII* and *prsGIII*, whereas *hlyA* was down-regulated (Supporting Information Figure S1). Thus, *E. coli* strain 2980 is P- and F1C-fimbriae dominated, leading to mannose-resistant adhesion.

For NU14, expression of *fimH*, *papGIII*, *fliC*, *csgA*, and *agn43* was recorded for bacteria incubated in medium alone. The presence of T24 cells evoked significant up-regulation of *fimH* transcripts, whereas *papGIII* transcription was significantly down-regulated (Figure 3B). Thus, NU14 is type 1 fimbriae dominated, and mannose could be used for the inhibition of bacterial adhesion as positive control.

By comparison of both strains it became obvious that NU14 and 2980 have only one adhesin, *papGIII*, in common, which gets down-regulated in the presence of T24 cells in NU14. Therefore, *papGIII* seems not to be essential for bacterial attachment of NU14 to T24 cells.

In summary, both strains 2980 and NU14 are suitable for comparative adhesion experiments and target identification of specific adhesin inhibitors. Furthermore, NU14 and the other strains used in this study can be used for the investigation of curli (*csgA*) and biofilm (*agn43*) formation, as well as for motility studies (*fliC*).

Influence of Cranberry Extract on Bacterial in Vitro Adhesion to T24 Bladder Cells. From the cranberry dry extract used for the in vivo study, standardized on 1.24% PACs and containing >80% of non-cranberry excipients to ensure

DOI: 10.1021/acs.jafc.5b03030
J. Agric. Food Chem. 2015, 63, 8804−8818

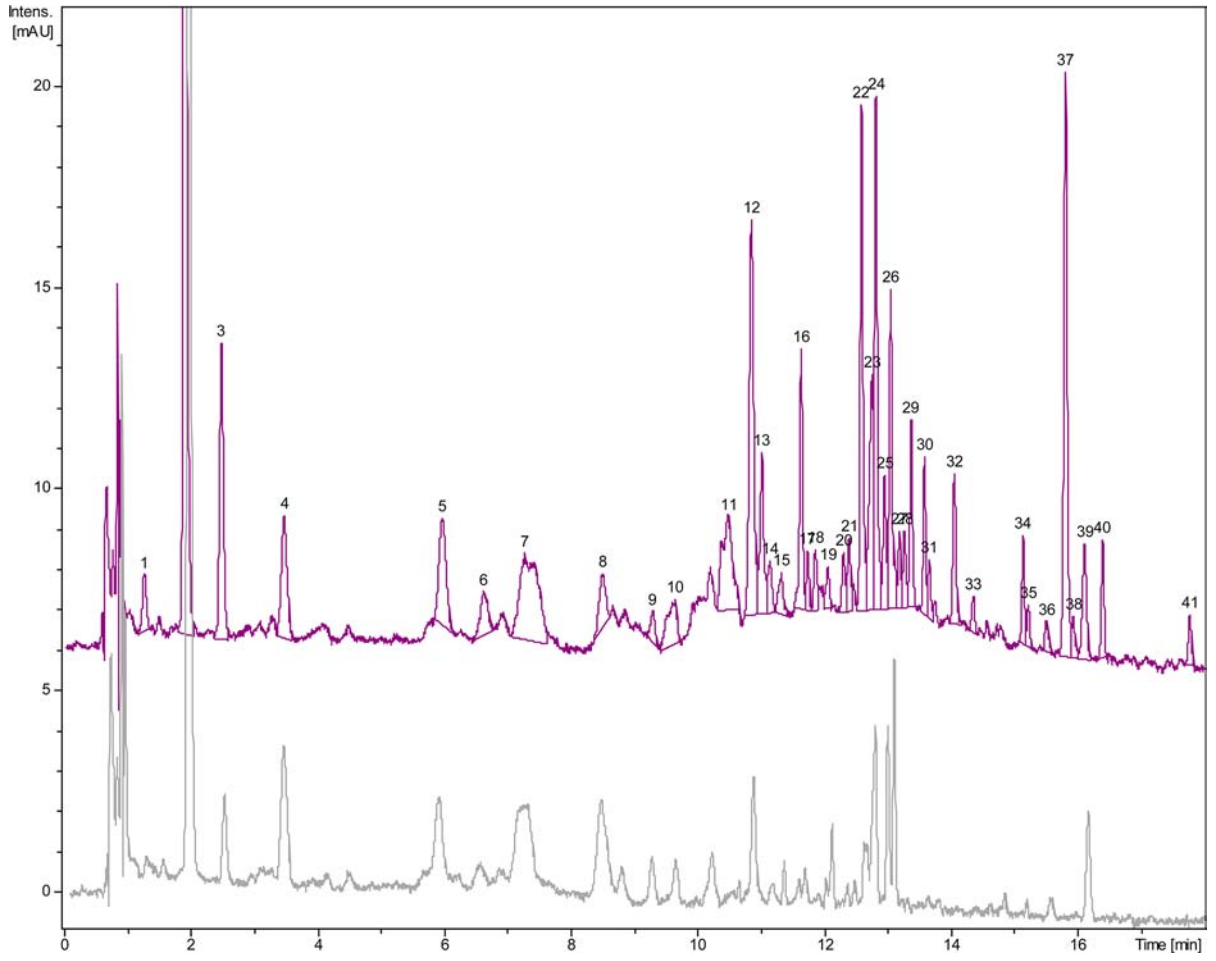

Figure 1. HPLC-UV chromatograms of *V.m.* extract (upper plot) and *V.m.* extract$^{\neq PAC}$ (lower plot) (λ = 280 nm). Peak assignment by MS. See Table 3.

optimized free floating powder technology, EtOH/water (1:1, v/v) soluble compounds were extracted. The resulting lyophilized product, *V.m.* extract, had a PAC content of 21.1 ± 1.9%, HPLC fingerprint as displayed in Figure 1, and compound dereplication as displayed in Table 3.*V.m.* extract was investigated for potential cytotoxic effects against *E. coli* 2980 by agar diffusion test over 24 h. Up to 1000 μg/mL, no inhibition of bacterial growth was observed (data not shown). *V.m.* extract up to concentrations of 250 μg/mL did not influence viability of eukaryotic T24 bladder cells over 24 h of incubation time as analyzed by MTT assay (data not shown).

Treatment of *E. coli* 2980 and NU14 with *V.m.* extract (10−100 μg/mL), addition of the suspension to T24 cells, and evaluation of bacterial adhesion to the host cells by flow cytometry resulted in a concentration-dependent increase in bacterial adhesion, due to the aggregation and clustering of the bacteria. Comparable results were also obtained in the case of a 2 h preincubation of *E. coli* 2980 with *V.m.* extract, followed by removal of extract components by successive washing steps prior to the addition of the *V.m.* extract-pretreated bacteria to the T24 cells (Figure 4). Semiquantitative evaluation of these data obtained by fluorescence microscopy confirmed these findings and clearly indicated a huge bacterial burden attached to the bladder cells (Figure 5).

Laser scanning microscopy was performed for investigating the localization of UPEC within the T24 cells. A top view of the cells indicated strongly individualized UPEC on the cell surface in the untreated control group, whereas bacterial clusters were visible for the *V.m.* extract (25 μg/mL) treated groups (Supplementary Data Figure S2).

Systematic section scanning of the monolayer preparations (30 steps, 0.2 μm) demonstrated the occurrence of mainly intracellular bacteria for the untreated control (Figure 6, series A) with most bacteria found within the cytoplasm (1−3 μm). In contrast, most of the bacteria in the *V.m.* extract-treated groups were detected as clusters on the cell surface (4−5 μm), whereas nearly no bacterial internalization was observed (Figure 6, series B).

To prove that *V.m.* extract leads to increased formation of UPEC clusters on the surface of the bladder cells, a third methodology, scanning electron microscopy (SEM), was performed. As expected, untreated control cells showed individualized bacteria on the cell surface (Figure 6A), whereas *V.m.* extract-treated UPEC formed clusters (Figure 7B). Increased magnification proved the presence of agglomerates (Figure 7C), and also the integration of the bacteria within a thin meshed film network was observed (Figure 7D). From these data it was concluded that *V.m.* extract at low concentrations under in vitro condition has the ability to agglomerate UPEC, which are strongly fixed to the T24 cell surface, and cannot be removed by repeated washing steps.

From these data a strong tendency of agglomeration of bacteria by cranberry extract was obvious. This phenomenon was also reproduced using different cranberry extracts from different suppliers and also by cranberry extract prepared directly from fresh fruits.

DOI: 10.1021/acs.jafc.5b03030
J. Agric. Food Chem. 2015, 63, 8804−8818

Table 3. LC-qTOF-MS Peak Characteristics As Obtained by Integrating a UV Chromatogram of *V. m.* Extract (λ = 280 nm)[a]

peak	tR (min)	m/z (ion)	ion	fragment m/z	λ_{max} (nm)	area fraction (%)	name	ref
1	1.29	na	na		217, 273	0.9	not identified	
2	1.94	149.0207	base peak		284	19.9	not identified	
3	2.51	339.1021	M + Na	137	205, 216, 260, 295	4.3	not identified	
4	3.49	349.0912	M + Na	165	287	2.6	coumaroyl-hexose	31
5	5.97	365.0860	M + Na	181	298sh, 316	2.8	caffeoyl glucose	31
6	6.63	355.1043	M + H	163	298sh, 319	1.2	chlorogenic acid	31
7	7.27	349.0906	M + Na	165	na	5.7	coumaroyl-hexose	31
8	8.49	307.0802	M + Na	163, 123, 105	234, 278	1.3	benzoyl hexose	
9	9.28	439.1237	M + Na	295, 285, 163, 133, 123, 105	234, 278	0.0	benzoyl pentosylhexose	
10	9.63	379.1012	base peak	195	290, 328sh	1.6	not identified	
11	10.46	463.1263	M^+	301[b]	280, 516	3.5	peonidin-3-galactoside	27, 30
12	10.83	545.1964	M + Na	165, 147	310	6.5	coumaroyl derivative	
13	11.00	433.1157	M^+	301[b]	na	2.3	peonidin-3-arabinoside	27, 30
		865.2033	M + H	713, 695, 533, 413, 301, 287, 271, 259, 139[b]	280		procyandin A-type trimer	27
14	11.13	373.1151	M + H	197, 177	na	0.8	dihydroferulic acid 4-*O*-β-D-glucuronide	31
15	11.30	1153.2661	M + H		280	0.7	procyanidin A-type tetramer	27
16	11.62	481.1035	M + H	319	258, 306sh, 355	2.8	myricetin-3-β-galactoside	28, 30, 31
17	11.72	457.1166	base peak		265, 298	0.6	not identified	
18	11.84	865.2031	M + H	577	280	0.8	procyandin A-type trimer	
19	12.03	177.0593	base peak		232, 299, 325	0.5	not identified	
20	12.28	451.0919	M + H	319	na	0.7	myricetin-3-α-xylopyranoside	28,30
21	12.37	451.0904	M + H	319	263. 355	0.9	myricetin-3-α-arabinofuranoside	28,30,31
22	12.56	465.1089	M + H	303	257, 302sh, 354	5.3	quercetin-3-β-galactoside	28,30,31
23	12.73	545.2085	base peak		230	3.3	not identified	
24	12.79	577.1380	M + H	287[b], 425	280	5.6	procyanidin A-type dimer	27,31
25	12.92	561.1641	M+Na	377, 359, 147	na	1.5	10-p-*trans*-coumaroyl-1*S*-dihydromonotropein	29
26	13.02	435.0951	M + H	303	na	3.7	quercetin-3-α-xylopyranoside	28,30,31
		561.1602	M + Na	377, 359, 341, 147	229. 314		10-p-*cis*-coumaroyl-1*S*-dihydromonotropein	29
27	13.16	435.0930	M + H	303	256, 304sh, 354	0.7	quercetin-3-α-arabinopyranoside	28,30,31
28	13.24	169.0515	base peak		221, 275, 293	0.8	not identified	
29	13.34	435.0934	M + H	303	258, 306sh, 355	1.8	quercetin-3-α-arabinofuranoside	28
30	13.55	449.1062	M + H	303	256, 306sh, 350	1.5	quercetin-3-rhamnopyranoside	28,30,31
		479.1162	M + H	317	256, 306sh, 350		3′-methylquercetin-3-β-galactoside	28,31
31	13.63	509.1305	M + H	347	260, 357	0.6	dimethylmyricetin-hexoside	28
32	14.02	319.0469	M + H	217, 153	255, 374	1.7	myricetin	30,31
33	14.32	449.1066	M + H	317	na	0.4	methylquercetin-pentoside	28
34	15.10	469.1131	M + Na	267, 249, 163	232, 298sh, 316	1.0	biochanin-A-7-*O*-glucoside	31
35	15.18	611.1416	M + H		na	0.4	prodelphinidin B4	31
36	15.47	585.1253	M + H	319, 105[b]	264, 360	0.4	myricetin-benzoylhexoside	
37	15.47	303.0510	M + H	257, 229, 201, 153, 137[b]	257, 370	7.2	quercetin	30,31
38	15.89	333.0610	M + H		252, 372	0.5	not identified	
39	16.07	569.1288	M + H	303	n.a.	1.7	quercetin-benzoylhexoside	
40	16.35	569.1264	M + H	303, 105[b]	256, 355	1.1	quercetin-3-*O*-(6″-benzoyl)-β-galactoside	28
41	17.72	317.0657	M + H		255, 367	0.5	methylquercetin	

[a]Peaks were assigned to known constituents of *V. macrocarpon* as denominated in the refs27−31. Assignment of stereoisomers is based on published RP18 elution order and relative peak areas.[27−31] Assignments without reference are based on the interpretation of MS, MS^2, and UV spectra. Peaks 13, 26, and 30 are constituted of two compounds, respectively. Chemical structures are displayed in the cited literature. na, not accessible. [b]Preceding fragment m/z values were obtained from MS^2-CID experiments (collision energy = 40 eV) or from peak background-corrected full MS spectra (ISCID 0 eV, collision energy = 8 eV).

At this point of the investigation this phenomenon seemed confusing in relation to already published data. Most publications on antiadhesive cranberry preparations used similar in vitro protocols: Bacteria were pre-incubated with extracts or test compounds (e.g., PACs), followed by incubation with bladder cells; unattached bacteria were removed and cells fixed and stained with Giemsa. Bacterial adhesion was calculated throughout the literature by using light microscopy and determining the average number of bacteria attached to a certain number of human cells.[36−40]

DOI: 10.1021/acs.jafc.5b03030
J. Agric. Food Chem. 2015, 63, 8804−8818

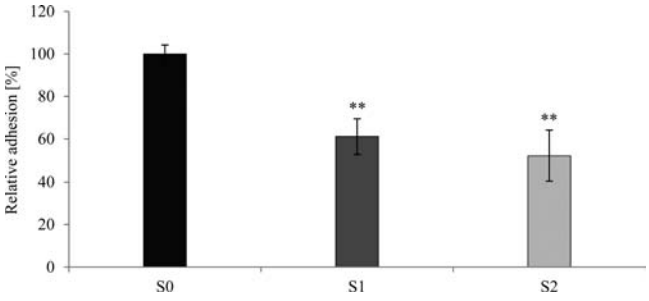

Figure 2. Relative adhesion of UPEC, strain NU14, to T24 bladder cells after 3.5 h of cultivation of bacteria in urine obtained from cranberry extract treated volunteers (n = 4, 600 mg extract for 7 days). S0, control urine, prior to cranberry consumption; S1, urine obtained at day 3 during cranberry extract application; S2, urine obtained at day 7 during cranberry extract application. Data are related to the initial adhesion values determined for S0 (=100%). (**) $p < 0.01$. Values represent the mean ± SD.

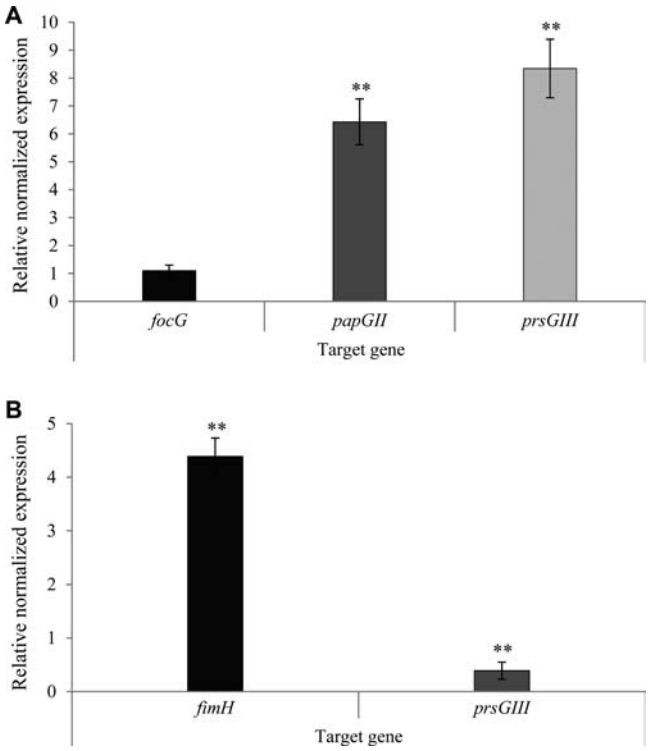

Figure 3. Relative gene expression of selected virulence factors from *E. coli* strain 2980 (A) and strain NU14 (B) as determined by qRT-PCR: comparison of relative expressions of *focG*, *papGII*, and *papGIII* (strain 2980) as well as *fimH* and *papGIII* (NU14) in UPEC incubated for 1.5 h in medium (alone) with bacteria incubated for 1.5 h in the presence of T24 cells. The relative expression of genes from bacteria in the absence of T24 cells (alone) has been set to 1. Expression levels have been normalized to the expression of the endogenous control gene 16S rRNA. (**) $p < 0.01$. Values represent the mean ± SD of six independent assays with two technical replicates for each experiment.

We speculate that during this evaluation bacterial agglomerates or clusters were not taken in account as they appear typically as dark, undefinable, spots in the microscope. Additionally, when bacteria are agglomerated and clustered, this could also imply a lower number of individual bacteria for counting. Another bias could occur during microscopy: as shown by SEM (Figure 6) the cluster-bearing host cells have typically some areas where the bacteria are strongly agglomerated in a three-dimensional mash, but many areas, if not most, of the cell surface are free of bacteria or clusters. In cases when only these cluster-free parts of a cell are evaluated, a strongly reduced number of bacteria might be counted, compared to the untreated control groups where the bacterial load is distributed very regularly over the host cell surface. For these different reasons published data on anti-adhesive cranberry activity should be reviewed very carefully concerning the respective quantitative evaluation protocols.

On the other hand, it seems not very astonishing that PAC-enriched extracts should agglomerate bacteria by an unspecific, astringent, tannin-like effect.

Another essential aspect is the limited absorption of PACs after oral intake: recent publications have shown that oligomeric PACs have a very limited bioavailability from the gut, which implies that these polyphenolic compounds will not appear in the lower urinary tract to a higher extent. To investigate the influence of PACs within the *V.m.* extract on bacterial adhesion, tannins were precipitated quantitatively from the extract by polyvinylpyrrolidone. From 100 mg of *V.m.* extract 66 mg of a PAC-free extract was obtained, designated in the following as *V.m.* extract$^{\neq PAC}$. TLC studies of this PAC-depleted extract indicated the absence of vanillin−HCl-positive spots, typically for flavan-3-ols and PACs. Also, comparative HPLC-MS (Figure 1) studies against *V.m.* extract demonstrated the disappearance of PACs in *V.m.* extract$^{\neq PAC}$: PVP treatment removed the majority of polyphenolic substances from the extract, with anthocyanidins and flavonol aglyca depleted by 100% (below the limit of detection), anthocyans and flavonoid glycosides by 97%, phenylpropane glycosides by 56%, iridoid glycosides by 42%, and benzoyl glycosides by 5% (averaged values).

Evaluation of the bacterial adhesion assay with *V.m.* extract$^{\neq PAC}$ indicated that the agglomerating effects against UPEC on the T24 cell surface did not occur (Figure 4): strain 2980, treated with the PAC-depleted extract, did not show any differences compared to the untreated control groups (Figure 4A), whereas strain NU14, treated with *V.m.* extract$^{\neq PAC}$, showed significantly decreased adhesion to the host cells, which was similar to the inhibiting effect of the positive control, 10 mmol of mannose. From these experiments it can be deduced that PAC-free cranberry extracts can interact significantly and in a dose-dependent manner with the adhesion of UPEC to T24 cells, which should be due to a more or less specific effect against *FimH* adhesin. In contrast, P-fimbriae-mediated adhesion is not influenced by cranberry extracts. The finding that PACs are not responsible for the antiadhesive effects is also in accordance with recently published data indicating that after oral cranberry intake, myricetin derivatives have been identified in the urine, which again seem to exert significant antiadhesive effects against UPEC.[41] On the other hand, *V.m.* extract$^{\neq PAC}$ used in our study was also strongly depleted from myricetin, which again might indicate that other extract compounds are responsible for the antiadhesive activity of this extract.

Influence of Cranberry Extracts of Gene Expression of Bacterial Adhesins. To investigate the influence of PAC-containing and PAC-depleted cranberry extracts on the gene expression of relevant bacterial adhesins, both *E. coli* strains 2980 and NU14 were treated with either *V.m.* or *V.m.* extract$^{\neq PAC}$ (100 μg/mL) for 1.5 h in the presence or absence of T24 cells; gene expression was monitored by qRT-PCR.

In the case of incubation of *E. coli* 2980 with *V.m.* extract in the absence of T24 cells *papGII* and *focG*, transcript levels were slightly up-regulated, whereas the transcript levels of *papGIII* remained unchanged (Figure 8A). In contrast, treatment of strain

DOI: 10.1021/acs.jafc.5b03030
J. Agric. Food Chem. 2015, 63, 8804−8818

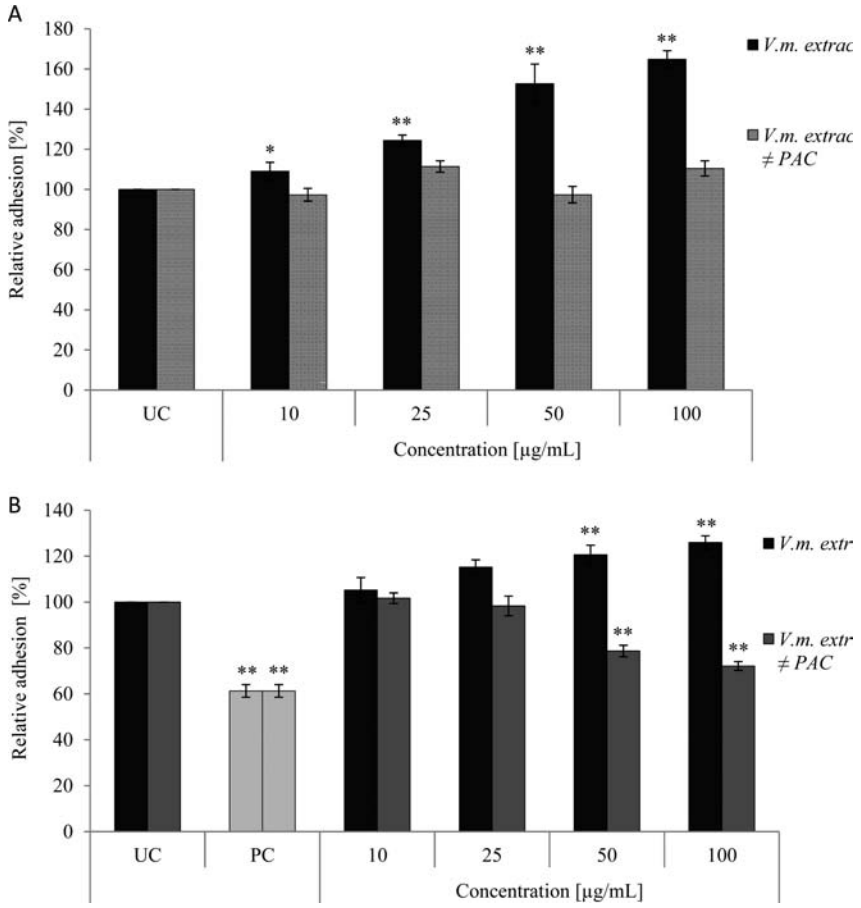

Figure 4. Influence of different concentrations of *V.m.* extract and *V.m.* extract$^{\neq PAC}$ on the adhesion of FITC-labeled *E. coli*, strain 2980 (A) and strain NU14 (B) to T24 cells after 2 h of pre-incubation of bacteria with the extracts. Data indicate the adhesion related to the untreated control (UC = 100%). For strain NU14 (B) mannose (10 mmol) served as positive control (PC). (∗) $p < 0.05$ and (∗∗) $p < 0.01$. Values represent the mean ± SD of six independent assays.

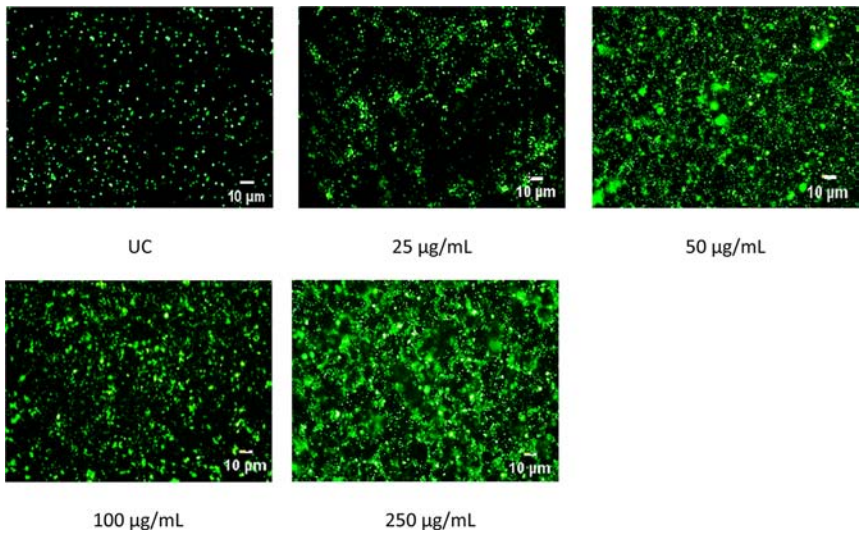

Figure 5. Influence of different concentrations of *V.m.* extract (25−250 µg/mL) on the bacterial adhesion of FITC-labeled *E. coli*, strain 2980, against T24 bladder cells (BCR 115:1) after 2 h of pretreatment of *E. coli* as determined by fluorescence microscopy. Magnification: 10×. UC, untreated control.

2980 with *V.m.* extract$^{\neq PAC}$ did not have any influence (Figure 8B). Similar experiments, but in the presence of T24 cells, indicated down-regulation of *papGII* and *focG* by *V.m.* extract (Figure 8A), whereas *V.m.* extract$^{\neq PAC}$ in the presence of T24 cells did not influence gene expression (Figure 8B).

Incubation of *E. coli* NU14 with *V.m.* extract had almost no impact on the gene expression level of adhesins (Figure 8C). Only the expression of *fimH* was slightly increased when bacteria were incubated in the absence of T24 cells. In contrast, *V.m.* extract$^{\neq PAC}$ induced transcription of *fimH*, whereas *papGIII*

DOI: 10.1021/acs.jafc.5b03030
J. Agric. Food Chem. 2015, 63, 8804−8818

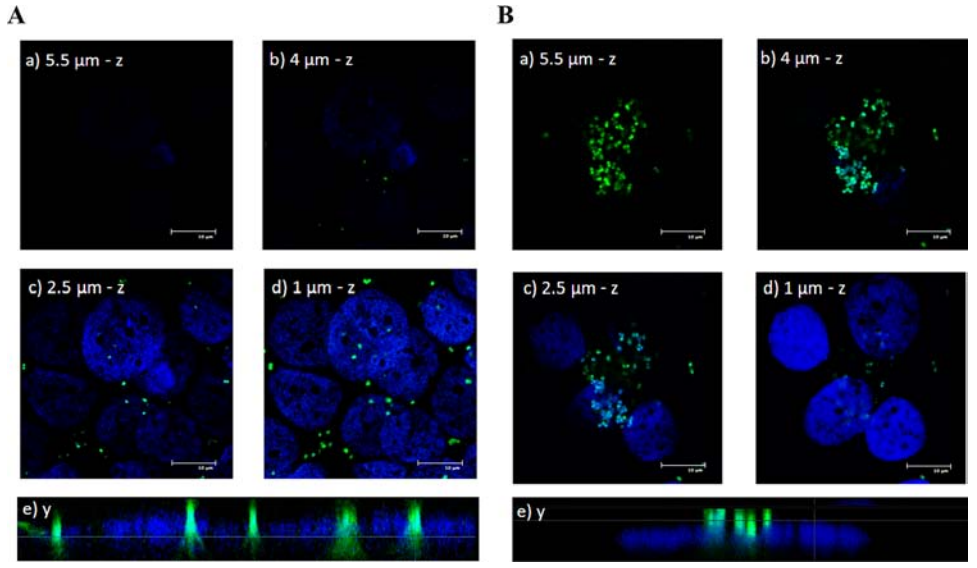

Figure 6. Sectional confocal laser scanning microscopic analysis of adhesion of UPEC to T24 bladder cells. T24 cells were incubated for 2 h with FITC-labeled *E. coli*, strain 2980. Staining of cell nuclei with DAPI is indicated by blue color, that of F-actin with Texas Red by orange color, and that of bacteria with FITC by yellow-green color. Scale bars = 47.6 μm. The images represent four 1.5 μm steps (a–d) in horizontal (z) and one image (e) side view (y) of a 30-step–0.2 μm (z-position) sectional scanning of the preparation. Scale bars = 10 μm. Series A: untreated UPEC, buffer only. Series B, UPEC pretreated with *V. m.* extract, 25 μg/mL.

transcript levels remained on a comparable level to the untreated control in the absence of T24 cells (Figure 8D). In cases when T24 cells were present, the expression of both adhesin genes, *fimH* as well as *papGIII*, was up-regulated (Figure 8D). The specific up-regulation of *fimH* transcription by both extracts, *V.m.* extract as well as *V.m.* extract$^{\neq PAC}$, is in good agreement with the inhibitory activity of the extracts against FimH: blocking of this adhesin will lead to a controlled feedback mechanism of NU14 toward a higher expression rate to ensure interaction with the host cell.

The findings concerning the reactivity of *E. coli* 2980 are more complicated and must be related to a central study in cranberry research, which is related to the finding that the *papGII* protein should be inhibited by the cranberry-specific trimeric A-type PAC.[5] In this study PAC-pretreated bacteria have been investigated concerning their interaction with an immobilized synthetic P-receptor analogue and agglutination of human red blood cells; the authors found significant lower agglutination of beads or blood cells between PAC-treated *E. coli* compared to untreated controls. Compared to our findings, we assume that the reduced agglutination of beads or blood cells might be due to inactivation of UPEC by formation of tannin-induced clustering and interaction leading to a decreased ability for bacterial adhesion. On the other hand, our finding indicates that the extract also induces up-regulation of *papGII* and *focG*, but also of *fimH* transcription. The increased expression of *focG* in *E. coli* 2980 could then be a feedback consequence of inhibition of P-fimbriae. On the basis of these results it can be assumed that bacteria which are already agglomerated by tannins exhibit additionally an enhanced density of adhesins (papGII and FocG) on their surface. Therefore, although papGII is inhibited, the bacterial clusters are still able to interact with host cells because of the availability of the second up-regulated adhesin (FocG). Thus, we conclude that the impact of cranberry extracts on UPEC adhesion is much more complicated than is described in the recent literature, where mostly UPEC strains have been used with multifunctional adhesins. Whereas non-PAC cranberry constituents block type 1 fimbriae, PAC seems additionally to inhibit P-fimbriae, which again will lead to up-regulation of F1C-fimbriae. In total, reduced bacterial inhibition is observed onlyin cases where the feedback regulation toward increased adhesins expression is not balanced by the adhesion-blocking effects of the cranberry extracts against *fimH*.

From the literature,[5] it is known that cranberry trimeric PACs interact with *papGII*. By using *V. m.* extract this leads to an up-regulation of this adhesin as shown in Figure 8. Additionally *V.m.* extract stimulates a further bacterial adhesin *fFocG* (Figure 8). This means that incubation of *E. coli* 2980 with *V. m* extract increases the density of different adhesins on the bacterial surface.

In the case when T24 bladder cells are present in combination with *V. m.* extract, we observe a different gene expression profile, where the stimulation of the adhesins is much lower (Figure 8), probably due to the fact that the bacteria attach to the cells and do not need the additional adhesins anymore. This strong adhesion is also monitored in the adhesion assay (Figure 4), where *V. m.* extract leads to a strong and dose-dependent increase in adhesion to the T24 cells.

From the gene expression data for *V.m.* extract$^{\neq PAC}$, no influence on the expression of the adhesins is observed. This indicates that PACs are responsible for induction of the bacterial adhesins. This again is in good correlation with the data from the adhesion assay (Figure 4) where no influence of *V.m.* extract$^{\neq PAC}$ on the amount of adhering *E. coli* 2980 is observed.

For UPEC NU14 it is interesting that a decreased adhesion takes place, which indicates the presence of compounds in the extract with inhibitory effects against *fimH* (Figure 4). On the other hand, NU14 up-regulates *fimH* and *papGII* expression after treatment with *V.m.* extract$^{\neq PAC}$, which means the bacteria recognize the blocking of FimH by extract compounds and counter-regulate by increasing the gene expression of this and a second adhesin.

Cranberry Extract Does Not Influence Curli and Biofilm Formation. *V.m.* extract and *V.m.* extract$^{\neq PAC}$ (50 and 100 μg/mL)

DOI: 10.1021/acs.jafc.5b03030
J. Agric. Food Chem. 2015, 63, 8804–8818

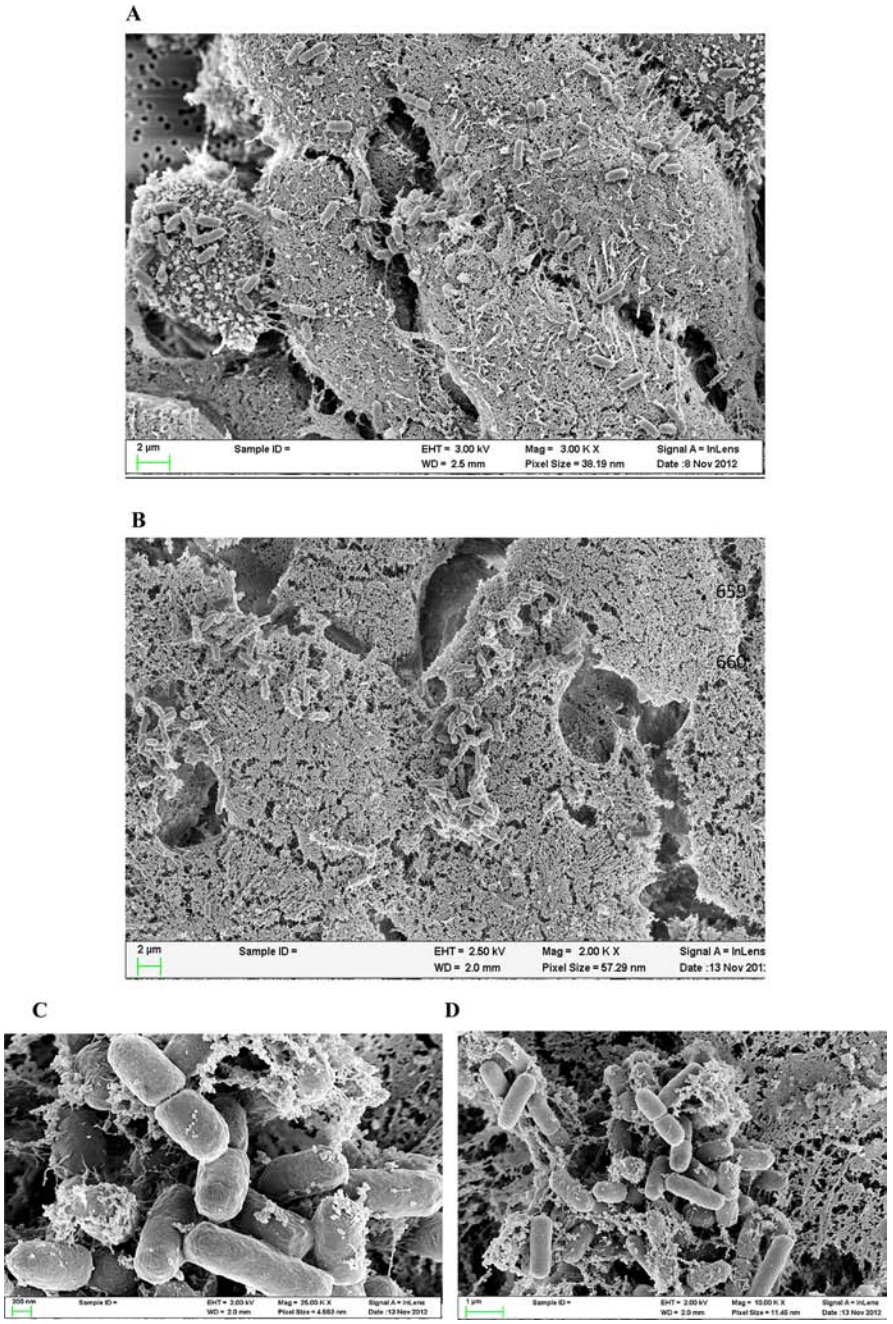

Figure 7. Scanning electron microscopy of T24 bladder cells incubated for 2 h with *E. coli* strain 2980 after pretreatment of the bacteria with *V.m.* extract (25 μg/mL) (B, C, D at different magnifications) versus untreated bacteria (A). (A) Untreated *E. coli*, buffer only; (B) *E. coli* pretreated with *V.m.* extract, 25 μg/mL; (C) *E. coli* pretreated with *V.m.* extract, 25 μg/mL; (D) *E. coli* pretreated with *V.m.* extract, 25 μg/mL.

were investigated concerning their ability to inhibit adhesion by interaction with bacterial curli formation by using the Congo Red assay.[21] On the basis of the information on gene expression analysis, *E. coli* strain NU14 should exhibit curli as it expresses *csgA*. The quantitative Congo Red binding assay confirmed this finding. The assay indicated that neither *V.m.* extract nor *V.m.* extract$^{\neq PAC}$ interacted with the formation of curli (Supplementary Data, Figure S3).

By gene expression analysis, both strains, 2980 and NU14, have been shown to express Agn43, an autotransporter protein involved in biofilm formation. Therefore, a biofilm assay[21] was performed with *V.m.* extract and *V.m.* extract$^{\neq PAC}$ in a concentration range of 25−200 μg/mL. The biofilm mass produced by *E. coli* 2980 after incubation with *V.m.* extract was slightly, but not significantly, increased. *V.m.* extract$^{\neq PAC}$ had no influence on biofilm formation of strain 2980 (Supplementary Data, Figure S4A). Incubation of *E. coli* NU14 with both extracts led to biofilm masses that were comparable to the biofilm mass determined for the untreated control (Supplementary Data, Figure S4B).

Summarizing this study, the data indicate that PAC-depleted cranberry extracts inhibit the FimH-mediated adhesion of UPEC to bladder cells, which again implies that further studies are needed to evaluate the clinical relevance of this finding, as well as the phytochemical search for the active compounds in cranberry extracts.

DOI: 10.1021/acs.jafc.5b03030
J. Agric. Food Chem. 2015, 63, 8804−8818

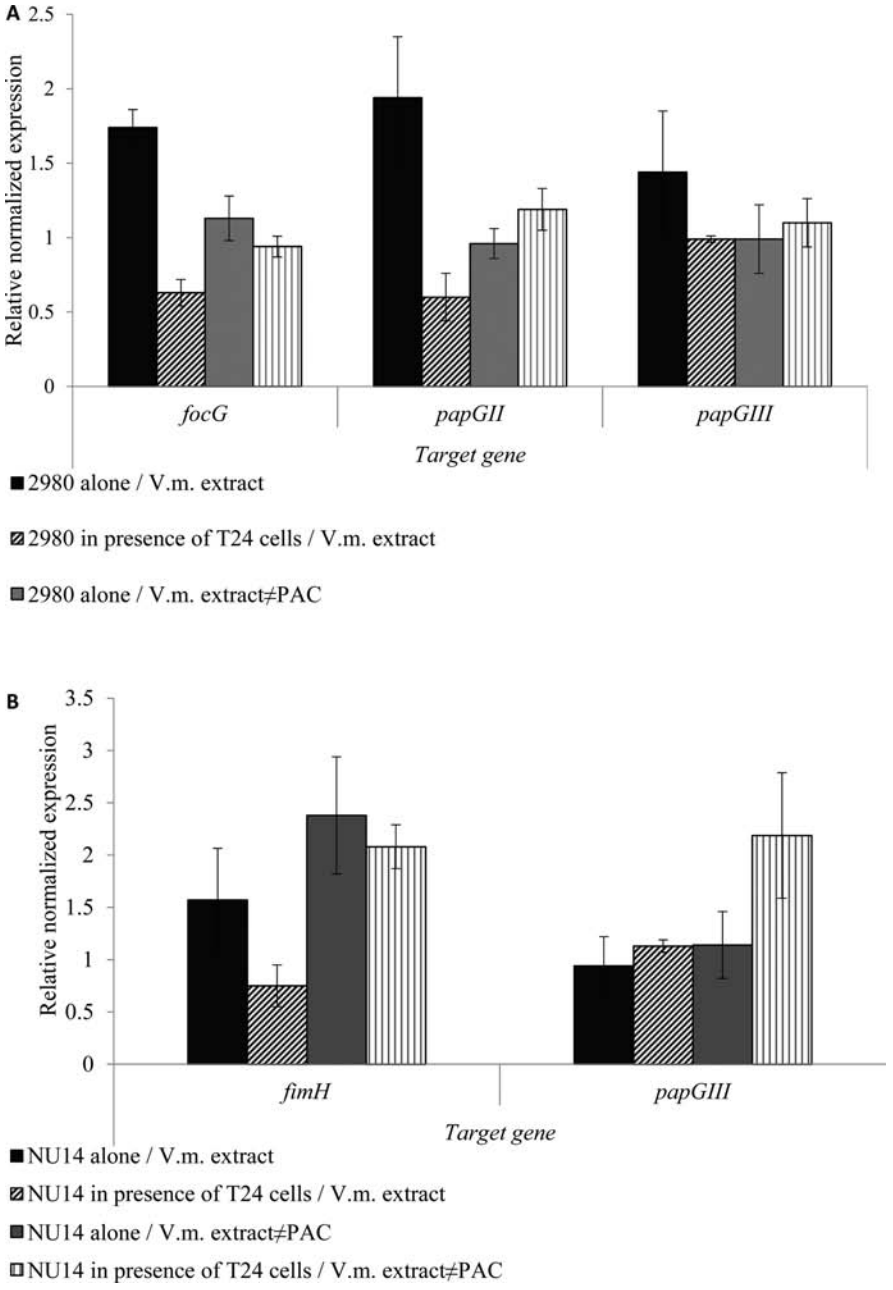

Figure 8. Influence of PAC-containing cranberry extract (*V.m.* extract, 100 μg/mL) and PAC-depleted cranberry extract (*V.m.* extract$^{\neq PAC}$, 100 μg/mL) on the relative gene expression of *E. coli* strains 2980 (A) and NU14 (B) in the presence or absence of T24 bladder cells. Relative expression levels of *focG*, *papGII*, and *papGIII* were determined for strain 2980 and *fimH* and *papGIII* for strain NU14 after incubation for 1.5 h with the respective extracts in absence or presence of T24 bladder cells. Respective expression levels are normalized to the endogenous control 16S rRNA; relative gene expression of untreated control groups = 1. Data are the mean ± SD from three independent assays with two technical replicates.

■ ASSOCIATED CONTENT

Ⓢ Supporting Information

The Supporting Information is available free of charge on the ACS Publications website at DOI: 10.1021/jf5b03030

Supplementary Figures S1−S4 (PDF)

■ AUTHOR INFORMATION

Corresponding Author

*(A.H.) Phone: +49 251 8333380. Fax: +49 838341. E-mail: ahensel@uni-muenster.de.

Author Contributions

N.R. performed the experiments, S.B. provided assistance to gene expression experiments, J.S. performed the LC-MS studies, U.D. provided UPEC strains and advised microbiological investigations, and A.H. designed and mentored the study and wrote the manuscript.

Funding

The study has been completely financed by intramural grants of the University of Münster, Germany. The cranberry extract has been supplied free of charge by Frutarom, Londerzeel, Belgium; the company did not have any influence on the study design, the experiments performed, or the evaluation of the data.

DOI: 10.1021/acs.jafc.5b03030
J. Agric. Food Chem. 2015, 63, 8804−8818

Notes

The authors declare no competing financial interest.

■ ACKNOWLEDGMENTS

We thank Richard Klöpsch and Katharina Schäper for their support concerning SEM.

■ ABBREVIATIONS USED

BCR, bacteria/cell ratio; CLSM, confocal laser scanning microscopy; DMEM, Dubelco's minimum essential medium; PAC, proanthocyanidins; qRTPCR, quantitative real-time polymerase chain reaction; SEM, scanning electron microscopy; UPEC, uropathogenic *E. coli*; UTI, uncomplicated urinary tract infections; VF, virulence factor; V.m., *Vaccinium macrocarpon*; *V.m.* extract, proanthocyanidin-enriched cranberry extract; *V.m.* extract$^{\neq PAC}$, proanthocyanidin-depleted cranberry extract

■ REFERENCES

(1) Dhakal, B. K.; Kulesus, R. R.; Mulvey, M. A. Mechanisms and consequences of bladder cell invasion by uropathogenic *Escherichia coli*. *Eur. J. Clin. Invest.* **2008**, *38*, 2−11.

(2) Cusumano, C. K.; Pinkner, J. S.; Han, Z.; Greene, S. E.; Ford, B. A.; Crowley, J. R.; Henderson, J. P.; Janetka, J. W.; Hultgren, S. J. Treatment and prevention of urinary tract infection with orally active FimH inhibitors. *Sci. Transl. Med.* **2011**, *3*, 109ra115.

(3) Chorell, E.; Pinkner, J. S.; Bengtsson, C.; Banchelin, T. S.; Edvinsson, S.; Linusson, A.; Hultgren, S. J.; Almqvist, F. Mapping pilicide anti-virulence effect in *Escherichia coli*, a comprehensive structure−activity study. *Bioorg. Med. Chem.* **2012**, *20*, 3128−3142.

(4) Stapleton, A. E.; Au-Yeung, M.; Hooton, T. M.; Fredricks, D. N.; Roberts, P. L.; Czaja, C. A.; Yarova-Yarovaya, Y.; Fiedler, T.; Cox, M.; Stamm, W. E. Randomized, placebo-controlled phase 2 trial of a *Lactobacillus crispatus* probiotic given intravaginally for prevention of recurrent urinary tract infection. *Clin. Infect. Dis.* **2011**, *52*, 1212−1217.

(5) Foo, L.; Lu, Y.; Howell, A. B.; Vorsa, N. A-type proanthocyanidin trimers from cranberry that inhibit adherence of uropathogenic P-fimbriated *Escherichia coli*. *J. Nat. Prod.* **2000**, *63*, 1225.

(6) Hidalgo, G.; Chan, M.; Tufenkji, N. Inhibition of *Escherichia coli* CFT073 fliC expression and motiluity by cranberry materials. *Appl. Environ. Microbiol.* **2011**, *77*, 6852−6857.

(7) Zafriri, D.; Ofek, I.; Adar, R.; Pocino, M.; Sharon, N. Inhibitory activity of cranberry juice on adherence of type 1 and type P fimbriated *Escherichia coli* to eucaryotic cells. *Antimicrob. Agents Chemother.* **1989**, *33*, 92.

(8) DiMartino, P.; Agniel, R.; Gaillard, J. L.; Denys, P. Effects of cranberry juice on uropathogenic *Escherichia coli in vitro* biofilm formation. *J. Chemother.* **2005**, *17*, 563−565.

(9) Valentova, K.; Stejskal, D.; Bednar, P.; Vostalova, J.; Cihalik, C.; Vecerova, R.; Koukalova, D.; Kolar, M.; Reichenbach, R.; Sknouril, L.; Ulrichova, J.; Simanek, V. Biosafety, antioxidant status, and metabolites in urine after consumption of dried cranberry juice in healthy women: a pilot double-blind placebo-controlled trial. *J. Agric. Food Chem.* **2007**, *55*, 3217−3224.

(10) Tapiainen, T.; Jauhiainen, H.; Jaakola, L.; Salo, J.; Sevander, J.; Ikäheimo, I.; Pirttilä, A. M.; Hohtola, A.; Uhari, M. Biofilm formation and virulence of uropathogenic *Escherichia coli* in urine after consumption of cranberry-lingoberry juice. *Eur. J. Clin. Microbiol. Infect. Dis.* **2012**, *31*, 655−662.

(11) Jepson, R. G.; Williams, G.; Craig, J. C. Cranberries for preventing urinary tract infections. *Cochrane Database Syst. Rev.* **2012**, *10*, CD001321.

(12) Rzeppa, S.; Bittner, K.; Döll, S.; Dänicke, S.; Humpf, H. U. Urinary excretion and metabolism of procyanidins in pigs. *Mol. Nutr. Food Res.* **2012**, *56*, 653−665.

(13) Zumdick, S.; Deters, A.; Hensel, A. *In vitro* transport of oligomeric procyanidins (DP2 to 4) across monolayers of Caco-2 cells. *Fitoterapia* **2012**, *83*, 1210−1217.

(14) de Llano, D. G.; Esteban-Fernandez, A.; Sanchez-Patan, F.; Martin-Alvarez, P. J.; Moreno-Arribas, V.; Bartolome, B. Anti-adhesive activity of cranberry phenolic compounds and their microbial-derived metabolites against uropathogenic *Escherichia coli* in bladder epithelial cell cultures. *Int. J. Mol. Sci.* **2015**, *16*, 12119−12310.

(15) Kimble, L. L.; Mathison, B. D.; Kaspar, K. L.; Koo, C.; Chew, B. P. Development of a fluorimetric microplate antiadhesion assay using uropathogenic *Escherichia coli* and human uroepithelial cells. *J. Nat. Prod.* **2014**, *77*, 1102−1110.

(16) European Pharmacopoeia. 7.0/1220, *Monograph Weißdornfrüchte Crataegi fructus*; Deutscher Apothekerverlag: Stuttgart, Germany, 2011; Vol. 1, pp 1934−1935.

(17) European Pharmacopoeia 7.0/1220, *General Methodology, Prüfung auf Gleichförmigkeit der Masse einzeldosierter Arzneiformen*; Govi-Verlag: Eschborn, Germany, 2011; Vol. 1, Chapter 2.9.5; p 374.

(18) Bubenik, J.; Baresova, M.; Viklicky, V.; Jakoubkova, J.; Sainerova, H.; Donner, J. Established cell line of urinary bladder carcinoma (T24) containing tumour-spcific amtigen. *Int. J. Cancer* **1973**, *11*, 765−773.

(19) Miyazaki, J.; Ba-Thein, W.; Kumato, T.; Obata Yasuoka, M.; Akaza, H.; Hayshi, H. Type 1, P and S fimbriae, and afimrial adhesion I are not essential for uropathogenic *Escherichia coli* FEMS. *FEMS Immunol. Med. Microbiol.* **2002**, *33*, 23−26.

(20) Mosmann, M. Rapid colorimetric assay for cellular growth and survival: application to proliferation and cytotoxicity assays. *J. Immunol. Methods* **1983**, *65*, 55−63.

(21) Connell, I.; Agace, W.; Klemm, P.; Schembri, M.; Marild, S.; Svanborg, C. Type 1 fimbrial expression enhances *Escherichia coli* virulence for the urinary tract. *Proc. Natl. Acad. Sci. U. S. A.* **1996**, *93*, 9827−9832.

(22) Rafsanjany, N.; Lechtenberg, M.; Petereit, F.; Hensel, A. Antiadhesion as a functional concept for protection against uropathogenic *E. coli*: *in vitro* studies with traditionally used herbal extracts as antiadhesive entities against uncomplicated urinary tract infections. *J. Ethnopharmacol.* **2013**, *145*, 591−597.

(23) Messing, J.; Thöle, C.; Niehues, M.; Shevtsova, A.; Borén, T.; Hensel, A. Antiadhesive properties from *Abelmoschus esculentus* (Okra) immature fruit extract against *Helicobacter pylori* adhesion. *PLoS One* **2014**, *9*, e84836.

(24) Bozzola, J. J.; Rusell, L. D. In *Electron Microscopy: Principles and Techniques for Biologists*, 2nd ed.; Jones & Bartlett Learning: Burlington, MA, USA, 1999; pp 658−690.

(25) O'Toole, G. A.; Kolter, R. Initiation of biofilm formation in *Pseudomonas fluorescens* WCS365 proceeds via multiple, convergent signalling pathways: a genetic analysis. *Mol. Microbiol.* **1998**, *28*, 449−461.

(26) Klunk, W. E.; Jacob, R. F.; Mason, R. P. Quantifying amyloid by congo red spectral shift assay. *Methods Enzymol.* **1999**, *309*, 285−305.

(27) Prior, R. L.; Lazarus, S. A.; Cao, G.; Muccitelli, H.; Hammerstone, J. F. Identification of procyanidins and anthocyanins in blueberries and cranberries (*Vaccinium* spp.) using high-performance liquid chromatography/mass spectrometry. *J. Agric. Food Chem.* **2001**, *49*, 1270−1276.

(28) Vvedenskaya, I. O.; Rosen, R. T.; Guido, J. E.; Russell, D. J.; Mills, K. A.; Vorsa, N. Characterization of flavonols in cranberry (*Vaccinium macrocarpon*) powder. *J. Agric. Food Chem.* **2004**, *52*, 188−195.

(29) Turner, A.; Chen, S. N.; Nikolic, D.; van Breemen, R.; Farnsworth, N. R.; Pauli, G. F. Coumaroyl iridoids and a depside from cranberry (*Vaccinium macrocarpon*). *J. Nat. Prod.* **2007**, *70*, 253−258.

(30) Lin, L. Z.; Harnly, J. M. A screening method for the identification of glycosylated flavonoids and other phenolic compounds using a standard analytical approach for all plant materials. *J. Agric. Food Chem.* **2007**, *55*, 1084−1096.

(31) Iswaldi, I.; Gómez-Caravaca, A. M.; Arráez-Román, D.; Uberos, J.; Lardón, M.; Segura-Carretero, A.; Fernández-Gutiérrez, A. Characterization by high-performance liquid chromatography with diode-array detection coupled to time-of-flight mass spectrometry of the phenolic fraction in a cranberry syrup used to prevent urinary tract diseases, together with a study of its antibacterial activity. *J. Pharm. Biomed. Anal.* **2012**, *58*, 34−41.

DOI: 10.1021/acs.jafc.5b03030
J. Agric. Food Chem. 2015, 63, 8804−8818

(32) Sobota, A. E. Inhibition of bacterial adherence by cranberry juice: potential use for the treatment of urinary tract infections. *J. Urol.* **1984**, *131*, 1013−1016.
(33) Johnson, J. R.; Stell, A. L. Extended virulence genotypes of *Escherichia coli* strains from patients with urosepsis in relation to phylogeny and host compromise. *J. Infect. Dis.* **2000**, *181*, 261−272.
(34) Dobrindt, U.; Blum-Oehler, G.; Hartsch, T.; Gottschalk, G.; Ron, E. Z.; Funfstuck, R.; Hacker, J. S-Fimbria-encoding determinant sfa(I) is located on pathogenicity island III(536) of uropathogenic *Escherichia coli* strain 536. *Infect. Immun.* **2001**, *69*, 4248−4256.
(35) Johnson, J. R.; Weissman, S. J.; Stell, A. L.; Trintchina, E.; Dykhuizen, D. E.; Sokurenko, E. V. Clonal and pathotypic analysis of archetypal *Escherichia coli* cystitis isolate NU14. *J. Infect. Dis.* **2001**, *184*, 1556−1565.
(36) Di Martino, P.; Agniel, R.; David, K.; Templer, C.; Gaillard, J.; Denys, P.; Botto, H. Reduction of *Escherichia coli* adherence to uroepithelial bladder cells after consumption of cranberry juice: a double-blind randomized placebo-controlled cross-over trial. *World J. Urol.* **2006**, *24*, 21−27.
(37) Gupta, K.; Chou, M.; Howell, A.; Wobbe, C.; Grady, R.; Stapleton, A. Cranberry products inhibit adherence of P-fimbriated *Escherichia coli* to primary cultured bladder and vaginal epithelial cells. *J. Urol.* **2007**, *177*, 2357−2360.
(38) Howell, A. B.; Foxman, B. Cranberry juice and adhesion of antibiotic-resistant uropathogens. *JAMA, J. Am. Med. Assoc.* **2002**, *287*, 3082−3083.
(39) Howell, A. B.; Reed, J. D.; Krueger, C. G.; Winterbottom, R.; Cunningham, D. G.; Leahy, M. A-type cranberry proanthocyanidins and uropathogenic bacterial anti-adhesion activity. *Phytochemistry* **2005**, *66*, 2281−2291.
(40) Lavigne, J.; Bourg, G.; Combescure, C.; Botto, H.; Sotto, A. *In vitro* and *in vivo* evidence of dose−dependent decrease of uropathogenic *Escherichia coli* virulence after consumption of commercial *Vaccinium macrocarpon* (cranberry) capsules. *Clin. Microbiol. Infect.* **2008**, *14*, 350−355.
(41) Kimble, L. L.; Mathison, B. D.; Kaspar, K. L.; Khoo, C.; Chew, B. P. *J. Nat. Prod.* **2014**, *77*, 1102−1110.

DOI: 10.1021/acs.jafc.5b03030
J. Agric. Food Chem. 2015, 63, 8804−8818

in the investigation of peptides could provide information about the presence of an analyte or evaluate the general constitutions of a peptide mixture based upon retardation factor (R_f value);[16−18] it also was used for the separation and/or identification of certain peptides with known characteristics in combination with other analytical techniques.[15,16] However, to the best of our knowledge, there have been no reports on the fractionation and isolation of the more effective components from complex protein hydrolysates, mainly by means of the common silica TLC, for the identification of potent bioactive peptides.

Therefore, the objective of this work was to develop a two-dimensional silica TLC (2D-TLC) technique using two coupled plates with different eluents to separate and divide the trypsin/chymotrypsin-treated goat casein hydrolysates into fractions with different potencies of DPP-IV inhibition, and to verify its feasibility and efficiency by RP−HPLC at different stages. The more efficient DPP-IV-inhibitory components were then isolated and their peptidic inhibitors were identified.

MATERIALS AND METHODS

Materials. Skim milk powder from Saanen goat (*Capra hircus*) was provided by Ausnutria Hyproca Dairy Group BV (Changsha, China). Trypsin (from porcine pancreas, with trypsin ≥250NF U/mg, chymotrypsin ≤75NF U/mg) was from Amresco LLC (Solon, OH). DPP-IV (from porcine kidney, ≥10 U/mg protein) and Gly-Pro-*p*-nitroanilide (H-Gly-Pro-*p*NA HCl) were purchased from Sigma-Aldrich (St. Louis, MO). Ile-Pro-Ile (diprotin A) was prepared by Qiangyao Biological Technology Co. Ltd. (Shanghai, China). Chloroform, 25% ammonia, *n*-butanol, and acetic acid were from Beijing Chemical Works (Beijing, China). Acetonitrile, methanol, trifluoroacetic acid (TFA), and formic acid (FA) were HPLC-grade and from Fisher Scientific (Fair Lawn, NJ). All other chemicals were of analytical grade.

Preparation of Hydrolysates. Goat milk casein was prepared by the acidic precipitation method, in which pH is adjusted to the isoelectric point of goat casein, 4.2. The obtained casein precipitate was lyophilized by LGJ-12 vacuum freeze-dryer (Songyuan Huaxing Technology Development Co. Ltd., Beijing, China), and the freeze-dried casein powder consisted of 95.2 ± 1.1% protein. The casein powder was dissolved in 0.05 M NaOH to 5% (w/w, protein basis) and stirred until complete dissolution; then the solution was preincubated at enzymatic temperature for 10 min, and the hydrolysis was initiated by adding commercial trypsin with a 3% (w/w) substrate-to-enzyme ratio and conducted at pH 8.0 and 37 °C for 3 h, with constant temperature and pH (holding with 1 M NaOH). After hydrolysis, the resulting hydrolysates were heated in boiling water for 10 min to inactive the enzyme, then cooled with ice water bath and centrifuged with TGL-20 M high-speed centrifuge (Pingfan Instrument Co. Ltd., Changsha, China) at 1800 × *g* (4 °C) for 20 min. The supernatant was adjusted to pH 8.0, sequentially filtered through a 0.22-μm syringe filter (Jinteng Corporation, Tianjin, China) and Amicon Ultra-15 centrifugal filter device (Millipore Corporation, Bedford, MA) with molecular-mass cutoff of 5 kDa. The <5 kDa fraction was used for further chromatographic separation and DPP-IV-inhibitory activity assay.

Analyses of <5 kDa Fraction of Hydrolysates by 2D-TLC. The <5 kDa fraction of the hydrolysates, labeled SF-0, was developed and analyzed by 2D-TLC. The TLC was carried out on a glass-backed 100 × 100 × 0.2−0.25 mm ready-use silica gel 60 TLC plate (Haiyang Corporation, Qingdao, China). The suitability of different development solvent systems for the fractionation and separation of protein hydrolysates was tested. Freeze-dried SF-0 (3 μL of 100 mg/mL dissolved in ddH_2O) was spotted (<3 mm diameter spot) onto the TLC plate origin. After air-drying under an air stream at 50 °C, the plate was developed with chloroform/methanol/25% ammonia (2:2:1, v/v/v) eluent until the solvent front reached a distance of 7.5 cm in a vertical chamber (XinYi, Shanghai, China). The control sample for this first-dimension TLC was spotted on the horizontally opposite side of the plate (1.5 μL SF-0). After the first-dimension separation, the developed plate was dried in air at room temperature to remove eluent and turned 90°; the second-dimension TLC development was carried out at a 90° angle to the first-dimension TLC development with another type of solvent (*n*-butanol/acetic acid/water, 4:1:1, v/v/v) until the solvent front reached ca. 7.5 cm. The control sample (1.5 μL of SF-0) for the second-dimension TLC was similarly located at the horizontally opposite side. After air-drying at room temperature, 0.05% (w/v) ninhydrin in ethanol was sprayed onto the plate, and peptide coloration was developed at 95 °C for 15 min.

Semipreparation of Peptide Fractions and/or Subfractions by TLC. The semipreparative 2D-TLC process was conducted by two coupled silica gel 60 plates with the same solvents and development order as above. The SF-0 sample was first fractionated by the first-dimension TLC, and the recovered fraction was transferred to a new TLC plate for the second-dimension separation. Briefly, 2.5 μL of SF-0 (100 mg/mL) was spotted onto a TLC plate with 12 repeats along the starting line (2 spots were used for peptide visualization, and the other 10 spots were used for semipreparation of the fractions after TLC development with the first- or second-dimension development solvents). Thus, 2.5 mg of SF-0 was loaded and separated on the first-dimension TLC plate. Separated peptide bands were scraped according to the R_f value of the ninhydrin-colored spots, and the silica powders were extracted twice with ddH_2O at 20 °C for 20 min (oscillation with an interval of 4 min) to recover the adsorbed peptides completely, then centrifuged at 12 000 × *g* at 4 °C for 20 min (repeated twice) to exclude the silica. The supernatant for each fraction or subfraction was adjusted to 500 μL as the initial volume of SF-0 (equivalent to 5 mg/mL concentration), and then the DPP-IV-inhibitory activity was assayed.

RP−HPLC Verification. The peptide samples from the fractions or subfractions of the first- or second-dimension semipreparative TLC were analyzed by RP−HPLC, performed on a Chuangxin Tongheng LC3050 HPLC system. A 20-μL aliquot of sample dissolved in ddH_2O was injected into an analytical C18 column with 250 × 4.6 mm i.d., 5 μm, 100 Å (Chuangxin Tongheng Science and Technology Co. Ltd., Beijing, China), and eluted with 0.1% TFA in water (solvent A) and 0.1% TFA in acetonitrile (solvent B) as follows: 10% B, followed by a linear gradient from 10 to 50% B from 5 to 45 min, at a flow rate of 1 mL/min at 30 °C. The elution was monitored at 215 nm with a UV/vis detector; the peptide peaks were collected when needed, and the separation was repeated multiple times to obtain enough samples for analysis. After removing acetonitrile by evaporation, each subfraction was also adjusted to the same initial volume as SF-0 (500 μL at 5 mg/mL concentration) for assaying their effect on DPP-IV activity as the semipreparative 2D-TLC.

Identification of Peptide Sequences by Liquid Chromatography−Tandem Mass Spectrometry. The peptide subfractions with the most efficient DPP-IV-inhibitory activities were subjected to sequence identification by LC−ESI−MS/MS (ESI = electrospray ionization) using a nanoAcquity nano HPLC system (Waters, Milford, MA) coupled to Q-Exactive high-resolution mass spectrometer (Thermo Scientific, Waltham, MA). The sample was injected into a trap column of 2 cm × 100 μm i.d. fused silica capillary (Polymicro, Phoenix, AZ) and separated on a 10 cm × 50 μm i.d. microanalytical column of the same material, which was packed with C18 stationary phase of Aqua 5 μm, 125 Å, and Aqua 3 μm, 125 Å, respectively (Phenomenex, Torrance, CA). The eluting program was conducted with 0.1% FA in water (solvent A) and 0.1% FA in acetonitrile (solvent B) following a linear gradient from 1 to 40% B from 0 to 40 min, at a flow rate of 200 nL/min. The eluate was directly injected into the MS system. A spray voltage of 2000 V was applied to the electrospray tip; the capillary temperature was 320 °C. MS analysis was operated with the following scan parameters: data-dependent MS^2 and positive ion mode, full scan mass range 100−1500 m/z, full scan resolution 70 000, MS/MS scan resolution 17 500, mass selection window 4 Da, dynamic exclusion 10 s. The 10 most intensive peptide signals from the full scan were selected for MS/MS scans. The MS/MS data were preprocessed

DOI: 10.1021/acs.jafc.5b03062
J. Agric. Food Chem. 2015, 63, 8819−8828

with Mascot Distiller 2.4 (Matrix Science, London, U.K.) for peak picking and further searched against protein data of *Capra hircus* from UniProtKB/Swiss-Prot database[19] using Mascot 2.4 search engine (Matrix Science, London, U.K.) to confirm the amino acid sequence of peptides.

Peptide Synthesis. Peptides identified by nano LC−MS/MS were synthesized by conventional 9-fluorenylmethyloxycarbonyl (Fmoc) solid-phase synthesis by China Peptides Co. Ltd. (Shanghai, China). The purity of these synthesized peptides was ≥95%, and their DPP-IV-inhibitory activity was determined.

Assay for DPP-IV-Inhibitory Activity. DPP-IV-inhibitory activity was measured according to the method described by Aart et al.[4] with minor modifications. Briefly, peptide samples were diluted in 100 mM Tris−HCl buffer pH 8.0 to the desired concentration. In a 96-well microplate, 25 μL of diluted sample was preincubated with 25 μL of Gly-Pro-*p*-nitroanilide (1.6 mM) at 37 °C for 10 min; then 50 μL of DPP-IV (8 U/L) was added, and the mixture was incubated at 37 °C for 60 min. The reaction was stopped by adding 100 μL of 1 M sodium acetate buffer, pH 4.0, and the absorbance was measured at 405 nm by Multiskan MK3 ELISA plate reader (Thermo Labsystems, Franklin, MA). Diprotin A was used as a reference inhibitor. The DPP-IV-inhibition (DI) was calculated as

$$\mathrm{DI}(\%) = \left(1 - \frac{A_{405}(\text{sample}) - A_{405}(\text{sample control})}{A_{405}(\text{negative reaction}) - A_{405}(\text{negative control})}\right) \times 100 \quad (1)$$

where A_{405}(sample) is the optical density at 405 nm (OD_{405}) in the presence of DPP-IV, its substrate Gly-Pro-*p*-nitroanilide, and inhibitor peptide sample; A_{405}(sample control) is the OD_{405} when DPP-IV is replaced with Tris-HCl buffer (100 mM, pH 8.0) as sample assay; A_{405}(negative reaction) is OD_{405} of DPP-IV and substrate with no addition of inhibitor; and A_{405}(negative control) is OD_{405} of the assay with no DPP-IV and inhibitor.

The IC_{50} value of the tested sample was determined by the plot of percent DPP-IV inhibition (%) against $\log_{10}$ (sample concentration), and Lineweaver−Burk plots were used to visualize the modes of DPP-IV inhibition.[20] After TLC separation, the total DPP-IV inhibition (totalDI) was calculated as the sum of each fraction or subfraction DPP-IV inhibition (DI_i):

$$\mathrm{totalDI}(\%) = \sum_{i=\text{SF-1 or SF-16-1}}^{n} \mathrm{DI}_i(\%) \quad (2)$$

where *i* is the fraction or subfraction serial number (SF-*i* or SF-16-*i*), *i* = 1 to *n*.

Data Analysis. All experiments were carried out at least three times, and data were expressed as means with standard deviation (SD). Significant differences ($P < 0.05$) between means were identified by Tukey's procedures using SPSS 17.0 (SPSS Inc., Chicago, IL).

RESULTS AND DISCUSSION

Fractionation of SF-0 by 2D-TLC. Our previous assays have confirmed that the DPP-IV-inhibitory activity of the trypsin/chymotrypsin-treated goat casein hydrolysates is largely distributed among peptides with molecular mass below 5 kDa (unpublished results). Therefore, the <5 kDa fraction of the hydrolysates, SF-0, was used as the starting peptide mixture for the following 2D-TLC separation in this study. Figure 1 shows the 2D-TLC profile of the SF-0 fraction after ninhydrin coloration. A weakly alkaline lower-polar solvent (chloroform/methanol/25% ammonia, 2:2:1) was adopted as the first-dimension TLC eluent, while the second-dimension TLC used to further separate the fractions was performed with a weakly acidic polar solvent (*n*-butanol/acetic acid/water, 4:1:1). Compared to one-dimensional TLC in either alkaline or acid solvent, the SF-0 was developed and separated more efficiently and divided into more constituents by the 2D-TLC. In total,

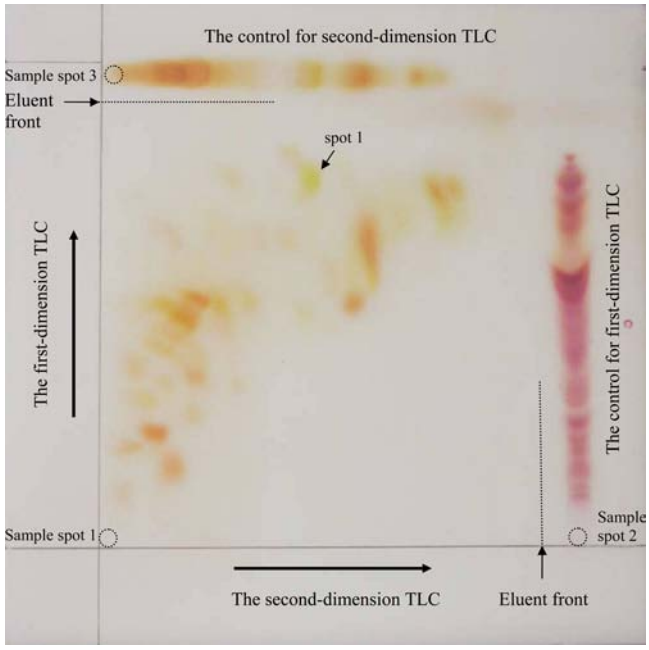

Figure 1. Two-dimensional silica thin-layer chromatography (2D-TLC) profile of the <5 kDa fraction of goat casein hydrolysates (SF-0) after ninhydrin coloration.

more than 35 visible spots were displayed on the 2D-TLC with different color tints (Figure 1), indicating the separation of potential bioactive peptide fractions from the casein hydrolysates. Therefore, semipreparation of individual fractions by 2D-TLC with two coupled plates was carried out to analyze their DPP-IV-inhibitory activities and isolate the relatively more efficient active components among the SF-0.

First-Dimension TLC Fractionation. The first-dimension of the semipreparative TLC separation of SF-0 gave 18 bands (fractions SF-1−SF-18) (Figure 2A) with different DPP-IV inhibition values (Figure 2B). We assayed their DPP-IV-inhibitory activity as was done for the initial volume of SF-0 (500 μL of 5 mg/mL) for each corresponding fraction. Of these, fraction SF-16 was found to be most effective at inhibiting the enzyme (36.1 ± 2.8% inhibition value); next were fractions SF-14, SF-15, and SF-17 with 19.1 ± 0.2, 20.9 ± 3.0, and 19.8 ± 0.9% inhibition values, respectively; fractions SF-12 and SF-13 exhibited about 10% inhibition, whereas fractions SF-1 to SF-11, as well as SF-18, showed quite low DPP-IV-inhibitory activity (inhibition value <5%) (Figure 2B).

As a type of adsorption chromatography, TLC can separate sample mixtures by elution based on a multistage distribution process. The R_f value has an important relationship with the sample's polarity: the smaller the R_f value, the stronger is the adsorption of the silica gel and the higher is the hydrophilicity of the material in question.[21] With the weakly alkaline lower-polar solvent, goat casein-derived peptides migrated rapidly on the TLC plate, as shown in Figure 2B; the dominant DPP-IV-inhibitory activities were distributed among the fractions with higher R_f values (fractions SF-12−SF-17). Peptides with larger chains and/or enriched in hydrophobic amino acids could give them relatively lower polarity, and thus the active DPP-IV-inhibitory fractions in the SF-0 might be made up of oligopeptides with the above characteristics.

At the same time, we found that the total DPP-IV-inhibition value of fractions SF-1 to SF-18 from the first-dimension TLC

DOI: 10.1021/acs.jafc.5b03062
J. Agric. Food Chem. 2015, 63, 8819−8828

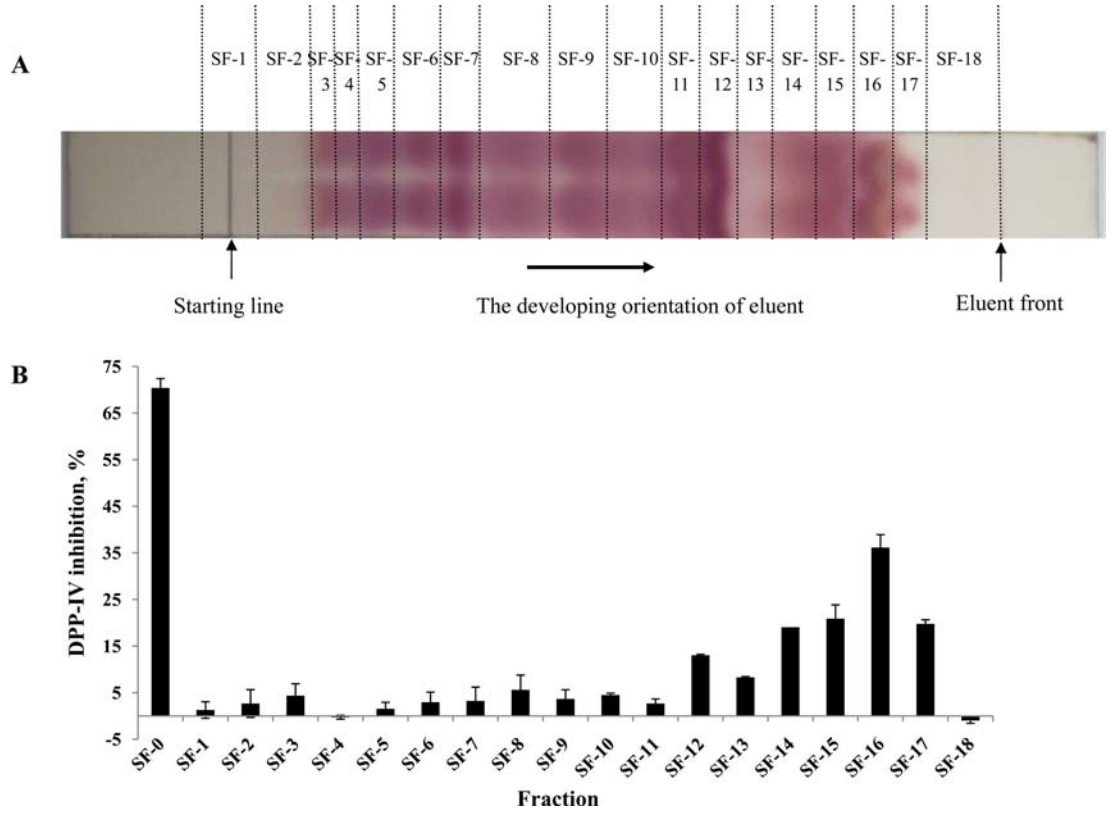

Figure 2. (A) Fractionated peptide bands and (B) fractions' DPP-IV-inhibitory activities from the <5 kDa fraction of goat casein hydrolysates prepared by the first-dimension TLC. Bars indicate standard deviations.

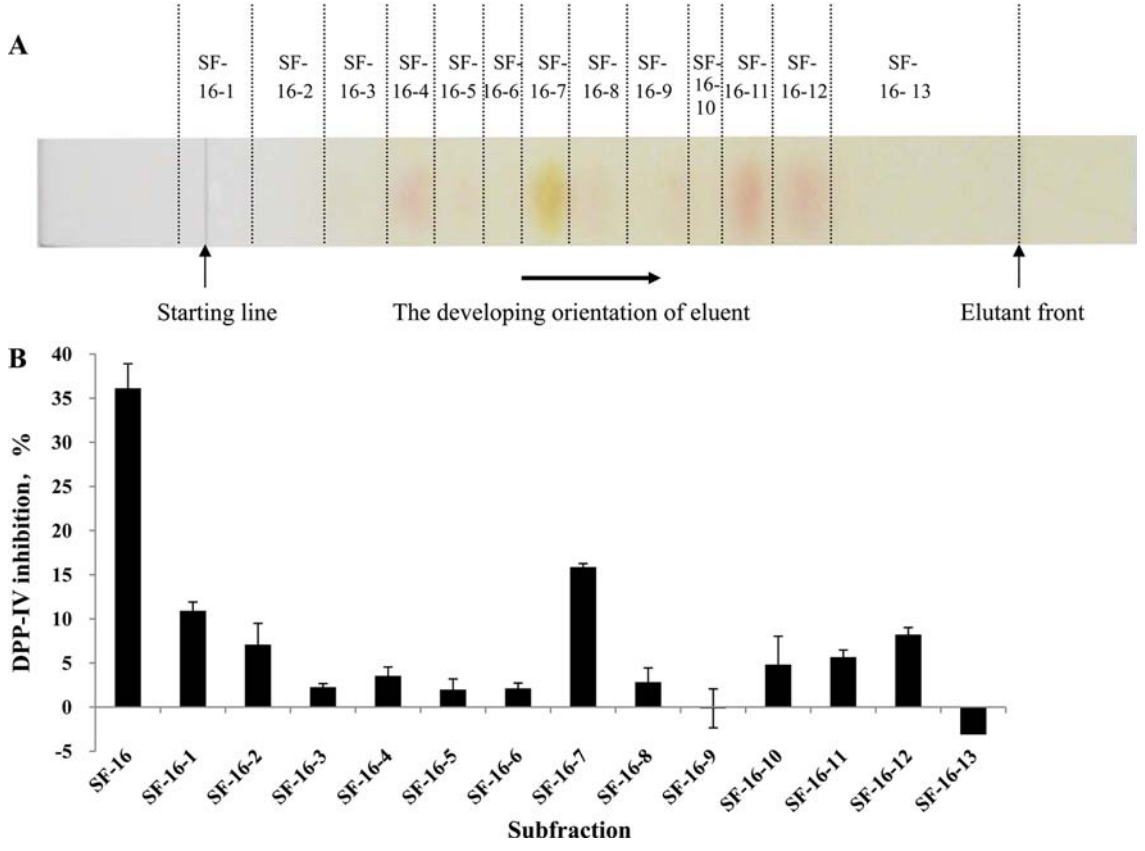

Figure 3. (A) Fractionated peptide bands and (B) fractions' DPP-IV-inhibitory activities from fraction SF-16 subjected to second-dimension TLC. Bars indicate standard deviations.

DOI: 10.1021/acs.jafc.5b03062
J. Agric. Food Chem. 2015, 63, 8819−8828

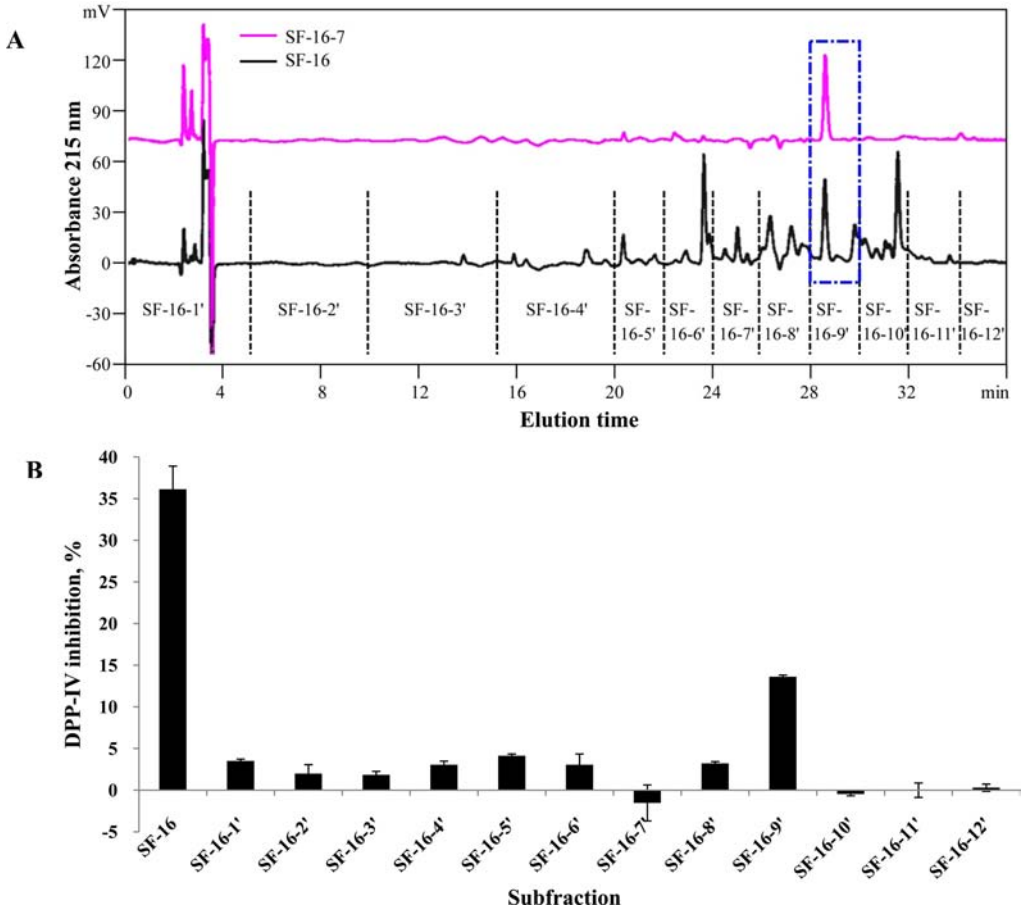

Figure 4. (A) RP−HPLC profiles of fraction SF-16 and subfraction SF-16-7 obtained from the first- and second-dimension TLC separation, respectively, and (B) DPP-IV-inhibitory activities of subfractions of SF-16 separated by RP−HPLC. The dotted line frame indicates the partial coincidence of t_R values in the RP−HPLC profiles of fraction SF-16 and subfraction SF-16-7. Bars indicate standard deviations.

separation (totalDI_{SF-0}) is ∼150%, markedly higher than the initial inhibition value of the SF-0 (DI_{SF-0}, 70.4 ± 2.0%). This suggested the interactive effects of various inhibitory peptides in mixed hydrolysates for the overall DPP-IV inhibition.[22] Among the first-dimension TLC fractions, SF-16 displayed the greatest DPP-IV-inhibitory activity (DI_{SF-16}, 36.1%) up to 50% of DI_{SF-0}, so we selected SF-16 for the second-dimension TLC separation.

Second-Dimension TLC Fractionation. Figure 3A shows separation of fraction SF-16 into 13 bands on the second-dimension TLC, designated subfractions SF-16-1 to SF-16-13. As shown in Figure 3B, except for SF-16-9 and SF-16-13, these subfractions showed widely varying DPP-IV-inhibitory activity. SF-16-7 had markedly higher DPP-IV-inhibition value ($DI_{SF-16-7}$, 15.9 ± 0.4%) than the other subfractions (Figure 3B), and it made up 44% and 23% of DI_{SF-16} and DI_{SF-0}, respectively. In addition, subfraction SF-16-7 showed yellowish-brown color (Figure 3A), contrasting with all of the other spots in the first- and second-dimension TLC (Figures 2A and 3A), indicating a certain number of secondary amine (e.g., from Trp residue) and/or acylamino structures (e.g., from Asn or Gln residue) of its contained peptide sequences.[23,24] SF-16-7 was also seen on the 2D-TLC plate as spot 1, by which it could be seen as one of the main constitutions of SF-0 (Figure 1). In addition, similar interactive effects on DPP-IV inhibition, albeit less strong, were observed after the second-dimension TLC: the total inhibition value of SF-16 subfractions (totalDI_{SF-16}, 62.0%) was significantly (1.7 times) higher than that of initial SF-16 (DI_{SF-16}, 36.1%).

During the screening of a suitable developing solvent system for TLC separation of protein hydrolysates, most of the tested solvents failed due to either incomplete development for the raw sample or ambiguous separation of the fractionated peptide components (data not shown). In contrast, two kinds of eluents described in the foregoing first-/second-dimension TLC gave satisfactory experimental results. In the first-dimension TLC, fraction SF-1, which also refers to the spotted position of raw SF-0, without ninhydrin coloration and DPP-IV inhibition (Figure 2A and B), demonstrated that the SF-0 was fully eluted by the solvent chloroform/methanol/25% ammonia (2:2:1). Moreover, apparently fractionated peptide bands distributed in the entire developing space of the first-dimension TLC plate, and fractions with obviously different DPP-IV-inhibitory activities were obtained (Figure 2A and B). This suggests that the eluent is a suitable solvent for DPP-IV-inhibitory peptides separation and concentration. The second-dimension TLC with the solvent *n*-butanol/acetic acid/water (4:1:1) further separated the narrow fraction (SF-16) into different bands with widely different R_f values (Figure 3A), confirming the satisfactory and complementary efficiency and selectivity of two coupled TLC eluents for peptide separation. Reversing the application order of the two types of TLC eluents was not recommended: when *n*-butanol/acetic acid/water (4:1:1) was used as the initial separation solvent, the SF-0 separated into

DOI: 10.1021/acs.jafc.5b03062
J. Agric. Food Chem. 2015, 63, 8819−8828

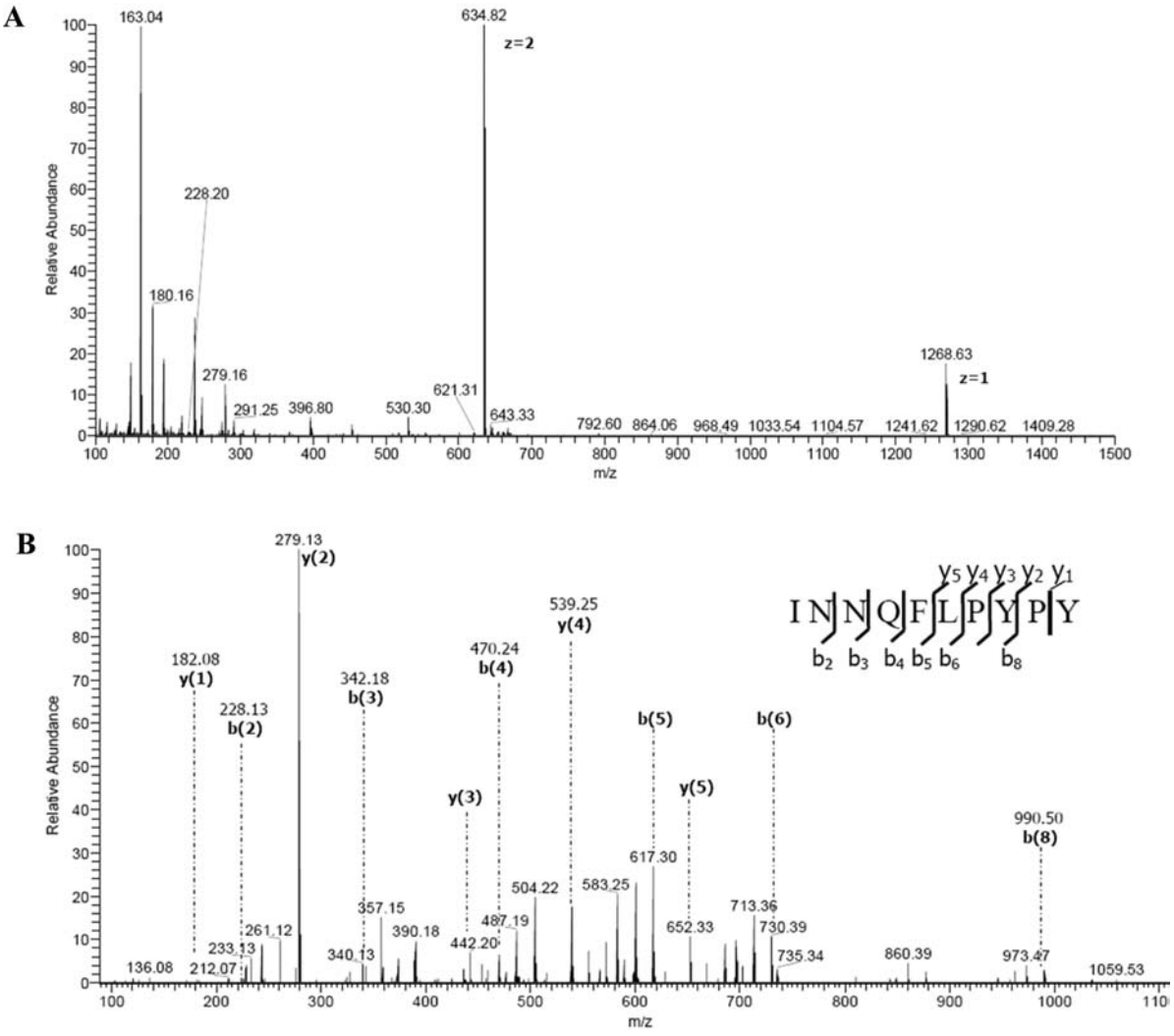

Figure 5. Identification of DPP-IV-inhibitory peptides. (A) LC−MS spectrum and (B) LC−MS/MS spectrum of single-charged ion with m/z 1268.63. Following sequence interpretation and database searching, the MS/MS spectrum of ion with m/z 1268.63 was matched to peptide INNQFLPYPY. Peptide sequence is displayed with ion fragments observed in the spectrum.

only four main fractions, whereas the chloroform/methanol/25% ammonia (2:2:1) eluent could separate the SF-0 into a dozen fractions, therefore simplifying and refining the second-dimension TLC separation of peptides (Figure 1). The contrasting results suggest the latter was more suitable as the first-dimension TLC eluent.

Use of RP−HPLC to Verify TLC Fractionation. To monitor and estimate the compositional changes of the peptide fractions by TLC separation, RP−HPLC analysis was applied to fraction SF-16 and its subfraction SF-16-7. Figure 4A shows the changes in the RP−HPLC profile of SF-16 before and after the second-dimension TLC separation. SF-16 subjected to RP−HPLC displayed a multipeak pattern and was divided into 12 subfractions (SF-16-1′−16-12′) with different retention times (t_R). Of these, SF-16-9′, with t_R of 28−30 min, displayed the highest inhibitory activity ($DI_{SF\text{-}16\text{-}9'}$, 13.6 ± 0.2%); next was SF-16-5′ with t_R 20−22 min ($DI_{SF\text{-}16\text{-}5'}$, 4.1 ± 0.2%), while other subfractions had quite weak inhibitory activity (Figure 4B). SF-16-9′ from the RP−HPLC profile showed a relatively stronger hydrophobic property, in line with the view that most DPP-IV-inhibitory peptides contain abundant hydrophobic amino acids in their sequences.[14] As the subfractions with the highest DI, SF-16-7 and SF-16-9′, from the second-dimension TLC and RP-HPLC, respectively, showed partial coincidence of t_R values in the RP−HPLC profiles (Figure 4A) and nearly equivalent DPP-IV-inhibitory activities (Figures 3B and 4B), indicating that the two subfractions were expected to contain some bioactive sequences in common. In addition, RP−HPLC analysis of SF-16-7 and SF-16-9′ revealed a single and two main peptide peak profiles, respectively, under a rather shallow elution gradient with a 1% change in acetonitrile concentration per minute (Figure 4A), suggesting that the bioactive fractions have reached adequate purity and are suitable for LC−MS/MS to identify the peptide sequences, and both TLC/TLC or TLC/RP−HPLC are feasible methods for the separation and isolation of bioactive peptide from protein hydrolysates.

Identification of Peptide Sequences Present in Subfractions SF-16-7 and SF-16-9′ by Nano LC−MS/MS. As the most effective DPP-IV-inhibitory components, subfractions SF-16-7 from the second-dimension TLC and SF-16-9′ from RP−HPLC were analyzed by nano LC−MS/MS to identify their constituent peptides. As an example, Figure 5A showed the mass spectrum of a double-charged ion with m/z at 634.82 and/or single-charged ion of 1268.63, which matched the sequence INNQFLPYPY corresponding to goat milk κ-casein f(51−60), by MS/MS sequence interpretation and

DOI: 10.1021/acs.jafc.5b03062
J. Agric. Food Chem. 2015, 63, 8819−8828

Table 1. LC−MS/MS Identification of Peptides and DPP-IV-Inhibitory Activity and Modes of Inhibition for Synthetic Peptides[a]

peptide sequence	fraction(s)	calculated mass	observed molecular ion, m/z (charge)	origin	pI	DPP-IV inhibition[b] ± SD (%) 500 μM	DPP-IV inhibition[b] ± SD (%) 125 μM	IC_{50}[c] ± SD (μM)	mode of inhibition
MHQPPQPL	SF-16-9′	946.47	474.24(2)/ 947.48(1)	β-CN f(144−151)	7.85	58.57 ± 0.95	26.32 ± 2.42	350.41 ± 4.1	noncompetitive
TQTPVVVPPF	SF-16-7, SF-16-9′	1084.29	542.81(2)/ 1084.60(1)	β-CN f(78−87)	6.01	0.20 ± 1.11	/	/	/
SPTVMFPPQSVL	SF-16-7, SF-16-9′	1302.57	659.85(2)/ 1318.67(1)	β-CN f(152−163)	6.01	43.48 ± 1.92	7.51 ± 0.64	676.31 ± 12.6	noncompetitive
VMFPPQSVL	SF-16-7, SF-16-9′	1017.26	509.28(2)/ 1017.55(1)	β-CN f(155−163)	6.01	12.58 ± 3.99	/	/	/
INNQFLPYPY	SF-16-7, SF-16-9′	1268.45	634.82(2)/ 1268.63(1)	κ-CN f(51−60)	5.87	87.89 ± 0.38	74.28 ± 0.49	40.08 ± 5.0	uncompetitive
NNQFLPYPY	SF-16-7	1155.28	1155.50(1)	κ-CN f(52−60)	6.2	/	/	/	/
TTMPLW	SF-16-9′	747.89	764.37(1)	α_{s1}-CN f(194−199)	6.01	/	/	/	/
AWPQYL	SF-16-9′	776.89	777.23(1)	α_{s2}-CN f(176−181)	6.2	18.16 ± 1.24	5.71 ± 0.62	/	/
AQAQSLVYPF	SF-16-9′	1122.57	562.29(2)/ 1123.58(1)	β-CN f(53−62)	6.2	/	/	/	/
IPI[d]	/	341.45	/	diprotin A	6.01	NA	NA	6.36 ± 1.2	competitive

[a]CN, casein; /, not determined; NA, not applicable; SD, standard deviation. [b]DPP-IV-inhibition values are means of triplicate determinations and measured under assay concentration of peptides. [c]IC_{50} was calculated as the peptide concentration required to inhibit 50% of DPP-IV activity under the assay conditions. [d]Inhibitory activity and mode of inhibition of diprotin A (IPI) were included as reference.

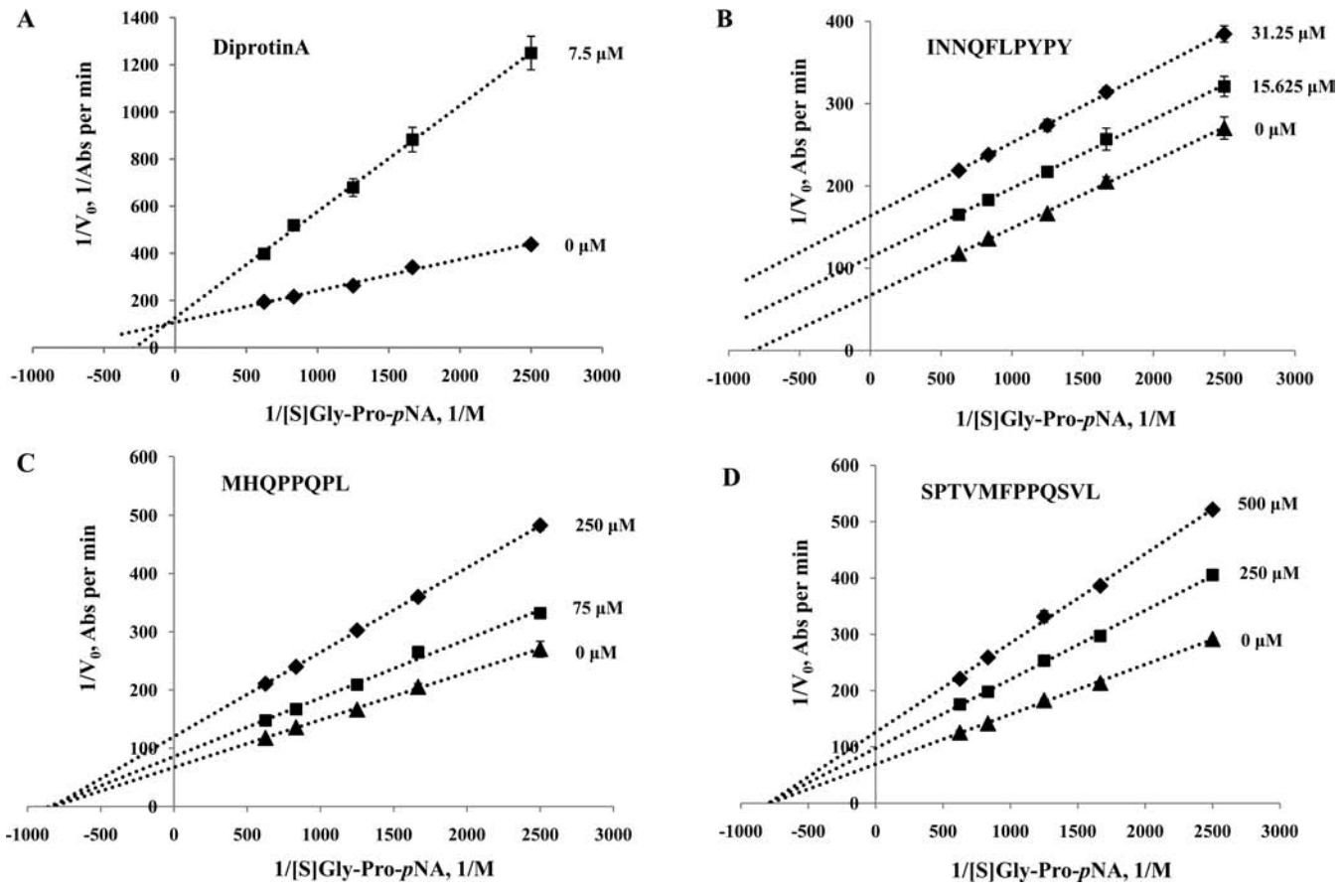

Figure 6. Lineweaver−Burk double-reciprocal plot for DPP-IV activity in the absence and presence of casein-derived peptides at different inhibitory concentrations. (A) Diprotin A (0 and 7.5 μM) as reference, (B) peptide INNQFLPYPY (0, 15.625, and 31.25 μM assay concentration), (C) peptide MHQPPQPL (0, 75, and 250 μM assay concentration), and (D) peptide SPTVMFPPQSVL (0, 250, and 500 μM assay concentration). Bars indicate standard deviations.

database searching (Figure 5B). A total of nine peptides were identified from subfractions SF-16-7/9′, mainly distributed in the β- and κ-casein chains, with lengths ranging from 6 to 12 amino acids (Table 1). The trypsin/chymotrypsin used for this study was a commercially available trypsin containing a certain amount of chymotrypsin in total activities, and therefore, the

DOI: 10.1021/acs.jafc.5b03062
J. Agric. Food Chem. 2015, 63, 8819−8828

Table 2. Interactive Effects on DPP-IV Inhibition between Pure Peptidic Inhibitors with Different Modes of Action[a]

peptide inhibitors	DPP-IV inhibition[b] (%) ± SD					
	low inhibitor concentration		intermediate inhibitor concentration		high inhibitor concentration	
	calculated value	measured value	calculated value	measured value	calculated value	measured value
GPFPILV	/	15.46 ± 0.86 D	/	28.58 ± 1.38 GH	/	45.50 ± 0.90 M
INNQFLPYPY	/	12.55 ± 0.69 C	/	27.57 ± 1.87 G	/	43.54 ± 2.31 L
MHQPPQPL	/	5.42 ± 0.40 A	/	10.96 ± 0.44 B	/	20.85 ± 1.08 EF
GPFPILV+ INNQFLPYPY	28.01 b	28.71 ± 1.01 bGH	56.15 b	47.21 ± 2.10 cM	89.04 b	67.11 ± 1.33 cP
GPFPILV+ MHQPPQPL	20.88 b	19.26 ± 2.09 bEF	39.54 b	36.50 ± 1.16 cJK	66.35 b	52.53 ± 0.29 cNO
INNQFLPYPY+ MHQPPQPL	17.97 b	18.44 ± 1.08 bE	38.53 b	35.30 ± 1.73 cJ	64.39 b	51.58 ± 1.52 cN
GPFPILV+ INNQFLPYPY+ MHQPPQPL	33.43 b	32.07 ± 1.90 bI	67.11 b	51.65 ± 0.48 cN	109.89 b	69.33 ± 0.67 cQ

[a]/, not determined; SD, standard deviation. [b]DPP-IV inhibition values are means of triplicate determinations and measured under different assay concentrations of peptide inhibitors: low concentration (GPFPILV 31.25 μM; INNQFLPYPY 7.815 μM; MHQPPQPL 62.5 μM), intermediate concentration (GPFPILV 62.5 μM; INNQFLPYPY 15.63 μM; MHQPPQPL 125 μM), high concentration (GPFPILV 125 μM; INNQFLPYPY 31.25 μM; MHQPPQPL 250 μM). Calculated values refer to the sum of the corresponding single peptide inhibitors. Different lowercase letters for calculated and measured values of individual samples at the same concentration and capital letters for all the measured values of inhibitor alone and in combinations indicate significant difference ($P < 0.05$).

hydrolysates were a mixture of peptides hydrolyzed by trypsin's tendency to cleave at the C-terminal Arg and Lys, whereas chymotrypsin cleaved at C-terminal hydrophobic amino acids such as Phe, Trp, Leu, and Tyr.[25] This was also reflected by the C-terminal amino acid residues of these identified sequences, for example, the C-terminal Tyr in INNQFLPYPY and Leu in MHQPPQPL, etc. (Table 1).

Among these peptides, the fragment f(194−199) of α_{s1}-casein corresponding to sequence TTMPLW has been verified to be a weak DPP-IV inhibitor by our previous in silico trypsin hydrolysis of goat casein and peptide synthesis (unpublished data), while the inhibitory activities of the other identified peptides have never been described. The most preferred inhibitory peptides reported in the literature tend to have lengths varying from dipeptides to octapeptides with molecular masses between 200 and 1000 Da,[14,26] whereas larger peptides presenting DPP-IV-inhibitory activity may act as different type of inhibitors via completely different inhibitory mechanisms.[8,20] It is interesting to note that most of our identified peptides were relatively longer peptides with 8−12 amino acid residues in length, and the structures of these identified peptides did not have the common Xaa-Pro- and Xaa-Xaa-Pro- motifs at their N termini, which are supposed to be typical of DPP-IV-inhibitory peptides;[14,26,27] on the other hand, all identified sequences contained dominant amounts of hydrophobic amino acids (such as Phe, Tyr, Leu, Ile, Trp, Val, and Met) and Pro residues in their sequences. In addition, four common peptide sequences, TQTPVVVPPF, SPTVMFPPQSVL, VMFPPQSVL, and INNQFLPYPY, were identified in both SF-16-9′ and SF-16-7 (Table 1), coinciding with the partially overlapping region in RP−HPLC elution profiles of the two subfractions (Figure 4A). Therefore, these four peptides, as well as MHQPPQPL and AWPQYL, were synthesized and evaluated for their potential inhibition of DPP-IV activity.

Table 1 shows the DPP-IV-inhibitory activity of the standard diprotin A (IPI) and the peptides identified in our hydrolysates, as well as their IC_{50} values as assayed in this study. The synthesized peptides found to cause greater inhibition of DPP-IV were further investigated to determine their modes of action on the enzyme (Figure 6). Diprotin A displayed IC_{50} of 6.36 ± 1.2 μM and behaved as a competitive inhibitor (Table 1 and Figure 6A), in accordance with reports in the literature.[12,14]

It is highlighted that, among the selected peptides, the κ-casein-derived peptide INNQFLPYPY f(51−60) displayed the highest and most notable inhibitory activity with an IC_{50} value of 40.08 ± 5.0 μM (Table 1), much lower than that of peptide LPYPY reported previously (IC_{50}, 108.3 μM).[28] Moreover, the Lineweaver−Burk plot of INNQFLPYPY showed apparently uncompetitive inhibition of DPP-IV (Figure 6B), contrasting to the competitive behavior of LPYPY that interacts with the active site of DPP-IV by involving both hydrogen bonds and hydrophobicity.[28] This suggested that addition of residues Phe, Gln, Asn, Asn, and Ile at the N terminus of the peptide LPYPY led to not only a significant increase in its DPP-IV-inhibitory activity but also the alteration of targeting domains and binding sites on DPP-IV.

The β-casein-derived octapeptide MHQPPQPL f(144−151) and dodecapeptide SPTVMFPPQSVL f(152−163) showed moderate inhibitory activities with IC_{50} values of 350.41 ± 4.1 and 676.31 ± 12.6 μM, respectively (Table 1), and they behaved as noncompetitive inhibitors (Figure 6C and 6D). SPTVMFPPQSVL contains a Pro at the second position of its N-terminal, in contrast to the general assumption of competitive DPP-IV-inhibition manner for smaller peptides with the same Pro-motif.[7,20,26] This indicates that the amino acid residues of SPTVMFPPQSVL may spatially block the interaction between the second Pro residue and the DPP-IV active site, while conversely facilitating the dodecapeptide binding to the domains outside the DPP-IV catalytic center; it also suggests that not only amino acid composition but also peptide length influences the DPP-IV-inhibition mechanism. Velarde-Salcedo et al.[8] showed that some DPP-IV-inhibitory peptides larger than 13 residues blocked the formation of the active dimeric form of DPP-IV by stagnating at the dimerization interface, using ligand−enzyme docking simulations. Moreover, the peptide VMFPPQSVL from β-casein f(155−163), lacking the N-terminal tripeptide sequence compared to SPTVMFPPQSVL, also inhibited DPP-IV but to a lesser extent (Table 1). The relationship between the structure and the bioactivity of different DPP-IV-inhibitory peptides supported the notion that the binding to DPP-IV is strongly influenced by the N-terminal amino acids, especially the tripeptide sequence of the inhibitors.[27] The N-terminal tripeptide SPT of SPTVMFPPQSVL is also indispensable for

DOI: 10.1021/acs.jafc.5b03062
J. Agric. Food Chem. 2015, 63, 8819−8828

its DPP-IV-inhibitory activity, even though other residues might determine the mode of inhibition of the dodecapeptide. In addition, another hexapeptide from goat α_{s2}-casein f(176−181), AWPQYL, was also identified to be a weak DPP-IV inhibitor, whereas the decapeptide TQTPVVVPPF had no effect on the activity of the enzyme (Table 1).

Furthermore, the alignment of goat (*Capra hircus*) α_{s2}-, β-, or κ-casein with other five main livestock including sheep (*Ovis aries*), cow (*Bos taurus*), yak (*Bos grunniens*), buffalo (*Bubalus bubalis*), and horse (*Equus caballus*) found that the goat β-casein-derived peptide VMFPPQSVL and κ-casein-derived peptide INNQFLPYPY also exist in sheep, cow, yak, and buffalo β-/κ-casein chain but not in horse; the consensus sequence MHQPPQPL was conserved in β-casein and AWPQYL in α_{s2}-casein of goat, sheep, and buffalo, while SPTVMFPPQSVL was only found in goat β-casein.

The interactive effects on DPP-IV inhibition between pure peptidic inhibitors GPFPILV (a competitive DPP-IV-inhibitory peptide obtained by our previous trypsin virtual hydrolysis of goat β-casein f(201−207), unpublished results), MHQPPQPL, and INNQFLPYPY with different types of inhibitory behaviors were tested in three levels of concentrations labeled as low, intermediate, and high concentration with a dose ratio 1:2:4 and the maximum concentration of single inhibitor no more than its IC_{50} value. As shown in Table 2, simply additive effects on inhibition were observed for the binary or ternary combination of peptide inhibitors at low concentration, which might suggest the targeting of different domains of DPP-IV without mutual interference, by GPFPILV binding to the active site while MHQPPQPL and INNQFLPYPY interfere outside the catalytic center of the enzyme or enzyme−substrate complex.[20] However, combined inhibitors at intermediate or high concentration caused greater inhibition compared to a single inhibitor rather than the sum of the individual peptides acting alone, and the higher the concentration of the peptidic inhibitor and the more the overlap among the peptides with different acting modes, the more obvious are interactive effects on DPP-IV inhibition (Table 2), which also corroborates the different extents of interactions on DPP-IV inhibition between the fractions from the first-dimension TLC (Figure 2B) or subfractions from the second-dimension TLC (Figure 3B). This might partially attribute to the apparently spatial conflicts between different targeting domains for different inhibitors caused at higher peptide concentration; varying interactive effects on DPP-IV-inhibitory properties were observed for certain binary peptide mixtures with different ratios in a previous report.[22] Besides, it also might result from that the combinations of inhibitors accelerate the tendency to plateau and/or saturation effect compared with a single inhibitor at the same concentration; a similar phenomenon has been shown in whey-derived inhibitory peptides in combination with sitagliptin.[29] In addition, Ohno et al.[30] have shown that an uncompetitive-type tripeptide inhibitor Trp-Arg-Glu could cover the binding substrate-mimicking competitive inhibitor Glu-Pro-Ala and act as a synergistic inhibitor to DPP-IV at a concentration equivalent to their respective 1/2 IC_{50} value. However, in this study, the DPP-IV-inhibition values of a combination of uncompetitive inhibitor INNQFLPYPY with competitive inhibitor GPFPILV at low (28.71 ± 1.01%) and intermediate (47.21 ± 2.10%) concentrations showed no significant ($P > 0.05$) difference compared to that of GPFPILV alone at intermediate (28.58 ± 1.38%) and high (45.50 ± 0.90%) concentrations, respectively, suggesting no positive synergistic effect between the two peptides, possibly due to the slight impact of INNQFLPYPY on substrate-binding affinity or the nonsubstrate-like competitive inhibition of GPFPILV.[30,31]

As a separation technique with characteristics of convenience, simplicity, rapidity, and lower cost, 2D-TLC method was set up to separate casein hydrolysates and was verified by RP−HPLC to be feasible and efficient. By virtue of TLC/TLC or TLC/RP−HPLC separation in combination with nano LC−MS/MS analysis, we successfully isolated components with higher efficiency and identified several new goat casein-derived DPP-IV-inhibitory peptides with different extents of bioactivities and modes of actions. Further investigation of the stability and absorbability of oligopeptides in the gastrointestinal tract, as well as the efficacy of goat milk casein-derived DPP-IV-inhibitory peptides in vivo, is warranted, so that it may serve as a natural food ingredient in the prevention of or coadjuvant therapy for the management of type 2 diabetes.

■ ASSOCIATED CONTENT

Supporting Information

The Supporting Information is available free of charge on the ACS Publications website at DOI: 10.1021/acs.jafc.5b03062.

Identification of DPP-IV-inhibitory peptides and alignment of caseins from six livestock (PDF)

■ AUTHOR INFORMATION

Corresponding Author

*Tel.: +86-10-62738663. Fax: +86-10-62731157. E-mail: swchen@cau.edu.cn.

Funding

This work was financially supported by the project 2011BAD09B03 of the National 12th Five-year Plan of China in Rural Areas.

Notes

The authors declare no competing financial interest.

■ REFERENCES

(1) WHO. Definition and diagnosis of diabetes mellitus and intermediate hyperglycemia: Report of a WHO/IDF consultation. World Health Organization: Geneva, Switzerland, 2006; pp 5.

(2) Mentlein, R. Therapeutic assessment of glucagons-like peptide-1 agonists compared with dipeptidyl peptidase IV inhibitors as potential antidiabetic drugs. *Expert Opin. Invest. Drugs* **2005**, *14*, 57−64.

(3) Sebokova, E.; Christ, A. D.; Boehringer, M.; Mizrahi, J. Dipeptidyl peptidase IV inhibitors: the next generation of new promising therapies for the management of type 2 diabetes. *Curr. Top. Med. Chem.* **2007**, *7*, 547−555.

(4) Aart, V. A.; Catharina M. J.; Zeeland-Wolbers V.; Maria L. A.; Gilst V.; Hendrikus W.; Buikema; Hendrik, J.; Nelissen; Maria, J. W. P. Egg protein hydrolysates. Int. Pat. WO 2009/128713 A1, 2009.

(5) Huang, S. L.; Jao, C. L.; Ho, K. P.; Hsu, K. C. Dipeptidyl-peptidase IV inhibitory activity of peptides derived from tuna cooking juice hydrolysates. *Peptides* **2012**, *35*, 114−121.

(6) Lacroix, I. M. E.; Li-Chan, E. C. Y. Dipeptidyl peptidase-IV inhibitory activity of dairy protein hydrolysates. *Int. Dairy J.* **2012**, *25*, 97−102.

(7) Hatanaka, T.; Inoue, Y.; Arima, J.; Kumagai, Y.; Usuki, H.; Kawakami, K.; Kimura, M.; Mukaihara, T. Production of dipeptidyl peptidase IV inhibitory peptides from defatted rice bran. *Food Chem.* **2012**, *134*, 797−802.

(8) Velarde-Salcedo, A. J.; Barrera-Pacheco, A.; Lara-González, S.; Montero-Morán, G. M.; Díaz-Gois, A.; González de Mejia, E.; Barba de la Rosa, A. P. *In vitro* inhibition of dipeptidyl peptidase IV by

DOI: 10.1021/acs.jafc.5b03062
J. Agric. Food Chem. 2015, 63, 8819−8828

peptides derived from the hydrolysis of amaranth (*Amaranthus hypochondriacus* L.) proteins. *Food Chem.* **2013**, *136*, 758−764.
(9) Lacroix, I. M. E.; Li-Chan, E. C. Y. Evaluation of the potential of dietary proteins as precursors of dipeptidyl peptidase (DPP)-IV inhibitors by an *in silico* approach. *J. Funct. Foods* **2012**, *4*, 403−422.
(10) Uenishi, H.; Kabuki, T.; Seto, Y.; Serizawa, A.; Nakajima, H. Isolation and identification of casein-derived dipeptidyl-peptidase 4 (DPP-4)-inhibitory peptide LPQNIPPL from gouda-type cheese and its effect on plasma glucose in rats. *Int. Dairy J.* **2012**, *22*, 24−30.
(11) Nongonierma, A. B.; FitzGerald, R. J. Inhibition of dipeptidyl peptidase IV (DPP-IV) by proline containing casein-derived peptides. *J. Funct. Foods* **2013**, *5*, 1909−1917.
(12) Boots, J.-W. P. Protein hydrolysate enrichened peptides inhibiting DPP-IV and their use. Patent 11/722,667 (US 2009/0075904), 2009.
(13) Li, S. Z. Livestock (Ming Dynasty). *Illustration of Compendium of Materia Medica*, 1st ed.; Zhao, Q. X., Eds.; Hebei Science and Technology Publishing House: Shijiazhuang, China, 2013; pp 587.
(14) Silveira, S. T.; Martínez-Maqueda, D.; Recio, I.; Hernández-Ledesma, B. Dipeptidyl peptidase-IV inhibitory peptides generated by tryptic hydrolysis of a whey protein concentrate rich in β-lactoglobulin. *Food Chem.* **2013**, *141*, 1072−1077.
(15) Urbanova, I.; Svec, F. Monolithic polymer layer with gradient of hydrophobicity for separation of peptides using two-dimensional thin layer chromatography and MALDI-TOF-MS detection. *J. Sep. Sci.* **2011**, *34*, 2345−2351.
(16) Bhushan, R.; Mahesh, V. K.; Mallikharjun, P. V. Thin layer chromatography of peptides and proteins: a review. *Biomed. Chromatogr.* **1989**, *3*, 95−104.
(17) Matsumoto, J. J.; Suzuki, T.; Asaka, Y.; Tamaki, N.; Minaguchi, H.; Utsugi, S.; Tamiya, T. Stimulating effect of fur seal muscle hydrolysate peptides on contractile activity of actomyosin. *Nippon Suisan Gakkaishi* **1976**, *42*, 1033−1040.
(18) Popp, R. A. The separation and amino acid composition of the tryptic peptides of the α chain of hemoglobin from C57BL mice. *J. Biol. Chem.* **1965**, *240*, 2863−2867.
(19) UniProtKB results. http://www.uniprot.org/uniprot/?query=*&fil=reviewed%3Ayes (accessed Nov 4, 2014).
(20) Lacroix, I. M. E.; Li-Chan, E. C. Y. Isolation and characterization of peptides with dipeptidyl peptidase-IV inhibitory activity from pepsin-treated bovine whey proteins. *Peptides* **2014**, *54*, 39−48.
(21) Liu, Y.; Liu, Y. G. Q&A for thin layer chromatography. *Handbook of thin layer chromatography*; People's Medical Publishing House: Beijing, China, 2011; pp 6−20.
(22) Nongonierma, A. B.; FitzGerald, R. J. Utilisation of the isobole methodology to study dietary peptide−drug and peptide−peptide interactive effects on dipeptidyl peptidase IV (DPP-IV) inhibition. *Food Funct.* **2015**, *6*, 313−320.
(23) Friedman, M. Applications of the ninhydrin reaction for analysis of amino acids, peptides, and proteins to agricultural and biomedical sciences. *J. Agric. Food Chem.* **2004**, *52*, 385−406.
(24) Thin layer chromatography of amino acids and short peptides. http://www.reachdevices.com/TLC_aminoacids.html (accessed Aug 23, 2015).
(25) PeptideMass. Instructions for PeptideMass peptide characterisation software. http://web.expasy.org/peptide_mass/peptide-mass-doc.html#table1 (accessed Aug 23, 2015).
(26) Li-Chan, E. C. Y.; Hunag, S. L.; Jao, C. L.; Ho, K. P.; Hsu, K. C. Peptides derived from Atlantic salmon skin gelatin as dipeptidyl-peptidase IV inhibitors. *J. Agric. Food Chem.* **2012**, *60*, 973−978.
(27) Lorey, S.; Stöckel-Maschek, A.; Faust, J.; Brandt, W.; Stiebitz, B.; Gorrell, M. D.; Kähne, T.; Mrestani-Klaus, C.; Wrenger, S.; Reinhold, D.; Ansorge, S.; Neubert, K. Different modes of dipeptidyl peptidase IV (CD26) inhibition by oligopeptides derived from the N-terminus of HIV-1 Tat indicate at least two inhibitor binding sites. *Eur. J. Biochem.* **2003**, *270*, 2147−2156.
(28) Nongonierma, A. B.; Mooney, C.; Shields, D. C.; FitzGerald, R. J. *In silico* approaches to predict the potential of milk protein-derived peptides as dipeptidyl peptidase IV (DPP-IV) inhibitors. *Peptides* **2014**, *57*, 43−51.
(29) Nongonierma, A. B.; FitzGerald, R. J. Dipeptidyl peptidase IV inhibitory properties of a whey protein hydrolysate: Influence of fractionation, stability to simulated gastrointestinal digestion and food−drug interaction. *Int. Dairy J.* **2013**, *32*, 33−39.
(30) Ohno, M.; Ito, K.; Lan, V. T. T.; Kusubata, M.; Tometsuka, C.; Koyama, Y.; Motoyama, T.; Ito, S.; Kawarasaki, Y. Synergistic inhibition of human dipeptidyl peptidase IV by combinations of peptides. *Peptides* **2015**, *69*, 115−117.
(31) Lan, V. T. T.; Ito, K.; Ito, S.; Kawarasaki, Y. Trp-Arg-Xaa tripeptides act as uncompetitive-type inhibitors of human dipeptidyl peptidase IV. *Peptides* **2014**, *54*, 166−170.

DOI: 10.1021/acs.jafc.5b03062
J. Agric. Food Chem. 2015, 63, 8819−8828

used to design the properties of the hydrogel network.[43−46] In particular, the porosity (mesh size) of biopolymer hydrogels can be tailored by factors impacting structuring elements (volume fraction, distribution and sizes of pores. etc.) of the gel such as chemical (e.g., hydrogen, covalent bonds, enzymatic cross-linking)/physical bondings (e.g., hydrophobic bonds).[44−48] For example, Klak et al. recently demonstrated that the release of different molecular weight dextrans could be retarded by transglutaminase cross-linked gelatin gels (5 wt %).[49] Klak et al. also demonstrated that the release of high molecular weight dextran was accelerated due to enzymatic degradation of the gel, highlighting that the polymer release from the hydrogels can occur via a combination of diffusion control and surface erosion.[49] Emulsions have also been incorporated into biopolymer gels to impact the textural and flavor release properties of complex food systems.[50−55] Somewhat surprisingly, there has been only limited work on the control of lipid emulsion digestion.[23,24] Li et al. encapsulated MCT emulsions stabilized by β-lactoglobulin into calcium alginate beads and demonstrated that the kinetics of fatty acid release was affected (modestly) by alginate bead size and considerably by alginate volume fraction and calcium concentration.[23] Another recent study by Guo et al. suggested that the microstructure as well as gel strength of whey protein emulsion gel had an effect on the extent of gastric proteolysis; however, the effect on intestinal digestion of lipids was not investigated.[25]

Whilst Li et al.[23] related the retardation of lipolysis to the microstructure of a polysaccharide gel, mechanistic understanding of how gel architecture (particularly gel digestibility, porosity, and network architecture) impacts the transport of enzymes/digesta through a protein hydrogel and how this relates to the rate of lipolysis is missing. Therefore, the present study sought to understand how the microstructure of protein gels affects lipolysis of gelled emulsions. The selected system consists of an oil-in-water (o/w) emulsion embedded within a gelatin gel. The microstructure of the gel was modulated with different protein concentrations. In vitro digestion of the systems was performed, and the impact of different gel microstructures on lipase diffusion was assessed. In addition, model experiments were conducted in order to understand the mechanism by which protein gels slow/retard the access of lipase to the fat droplets (diffusion control vs surface erosion).

EXPERIMENTAL PROCEDURES

Materials. For the preparation of emulsion, sunflower oil (Coop, Switzerland) and whey protein isolate (WPI) containing 95.8% protein (Bipro, Davisco Foods International, USA) were used without any further purification. Commercial gelatin type B was obtained from Gelita (240 Bloom, 30 mesh, 98% protein). Milli-Q water (water purified by treatment with a Milli-Q apparatus; Millipore Corp., Bedford, MA, USA) was used as the solvent for all of the experiments. Pepsin (porcine, 882 U/mg activity, Sigma-Aldrich, P7000), pancreatin (porcine, USP × 8, Sigma-Aldrich P7545), and bile extract porcine (total bile salt content = 49 wt %; with 10−15% glycodeoxycholic acid, 3−9% taurodeoxycholic acid, 0.5−7% deoxycholic acid; phospholipids 5 wt %) were used as obtained from Sigma-Aldrich (B8631).

Methods. *Emulsion Preparation.* The aqueous phase containing 5 wt % protein was prepared by dissolving WPI in Milli-Q water, and the pH was adjusted to pH 8. Protein dispersion was stirred at ambient conditions for 1 h. Sunflower oil was then added to the aqueous protein solution to form final emulsions containing 40 wt % oil. Pre-emulsion was prepared by homogenizing the mixture of the aqueous phase with the oil phase using a Silverson L5M-A rotor-stator mixer (Silverson Machines, UK) at 7000 rpm for 2 min. Then the pre-emulsion was further homogenized by two passes through a two-stage valve homogenizer (NIRO Soavi Panda, GEA, France) operating at 1000 bar for the first stage and at 160 bar for the second stage. Sodium azide (0.05 wt %) was added to avoid microbial growth. Emulsions were stored for not more than 1 week at 4 °C.

Gelled Emulsion Preparation for in Vitro Digestion. Gelatin was solubilized of different concentrations (2.5−15 wt %) in 0.1 M NaCl solution at 60 °C. The pH of the gelatin solution was adjusted to pH 7.0 using 1 M NaOH. Sodium azide (0.05 wt %) was added to avoid microbial growth. Stock gelatin gels were prepared by allowing gelation in 100 mL glass containers at 4 °C for 24 h.

For the preparation of gelatin-gelled emulsions, the emulsion prepared as above and the gelatin dispersion were placed in a water bath at 60 °C. Emulsion was gently added to the gelatin solutions (10−25 wt %) to reach final concentrations of 10 wt % oil, 0.7 wt % WPI, and 2.5−15 wt % gelatin in 100 mM NaCl at pH 8. The emulsion/gelatin dispersion was mixed at 60 °C in a water bath in a 100 mL glass container for 30 min and cooled by storage in a refrigerator set at 4 °C for 24 h to allow the gels to set. These gels were further used for in vitro digestion and microscopy measurements.

Confocal Microscopy. For the confocal imaging, the gels were sliced manually into 1 × 1 × 0.2−0.3 mm slices and then stained overnight in a 10^{-6} M solution of Rhodamine 6G (Sigma 83697) containing Nile red (Sigma N3013:100 μL of a 0.025% ethanol solution per 10 mL of the rhodamine solution). The confocal imaging was carried out with a Zeiss LSM 710 confocal microscope, at excitation wavelengths of 514 nm for the Rhodamine 6G (emission bandwidth, 520−560 nm) and 561 nm for the Nile red (emission bandwidth, 565−700 nm).

Lipase Diffusion Measurements. (1) Lipase Labeling. High-purity porcine pancreatic lipase EPC B.141 (1×10^6 units/22 mg protein) was purchased from Elastin Products (LC 298) and covalently labeled with fluorescein isothiocyanate according to the following procedure: 26.4 mg of FITC (Sigma F3652) was dissolved in 5 mL of DMSO (Serva 20385.01). Then, 0.5 mL of this FITC−DMSO solution was diluted in 1 mL of borate buffer (Fluka 15662), pH 8.5; 44 mg of the lipase was dissolved in 1.5 mL of Milli-Q water and mixed with 1.5 mL of the DMSO−borate FITC solution. The final mixture was incubated for 2 h at 50 °C. Finally, the free FITC was eliminated using Amicon Ultra-15 centrifugal (10 centrifugations) devices (Millipore catalog no. UFC900524).

(2) Lipase Diffusion Experiment. For the diffusion experiments, the gels were cooled in Petri dishes and punched with the capillary end of glass Pasteur pipets. This capillary end, with the sample inside, was then glued at the bottom of a 3 mm deep Plexiglas observation chamber. Finally, this experimental setup was covered with the solution containing the lipase (50 μL of labeled lipase in 1 mL of PBS). Continuous image acquisition was carried out at an excitation wavelength of 488 nm for 30 min (120 images per run). The experiments were carried out in triplicate.

Characterization of Viscoelastic Properties of Gelled Emulsion by Small Deformation Rheology. Oscillatory measurements were carried out using a Physica MCR 501 rheometer (Anton Paar, Graz, Austria). The measuring geometry was a concentric cylinder (CC-27; the inner diameter of the cup is 24.5 mm, and the diameter of bob is 23 mm) with a Peltier temperature control system. Twenty milliliters of emulsion/gelatin dispersion described under Gelled Emulsion Preparation for in Vitro Digestion and, as control, the corresponding gelatin dispersion with a similar concentration were placed in the measuring cell at 60 °C, and the surface of the sample was covered with mineral oil to avoid evaporation. The sample was then submitted to temperature ramp mimicking the temperature ramp of sample prepared for in vitro digestion protocol allowing gelation in situ of equipment. Temperature was decreased from 60 to 4 °C at −5 °C/min. Then, the temperature was maintained for 2 h at 4 °C. Finally, the temperature was raised to 25 °C at 5 °C/min. The temperature ramp was done within a linear regime with strain of 0.5% at 1 Hz frequency. A frequency sweep test was then performed from 0.1 to 100 Hz at 0.5% strain at 25 °C. Finally, a strain sweep test was performed

DOI: 10.1021/acs.jafc.5b03700
J. Agric. Food Chem. 2015, 63, 8829−8837

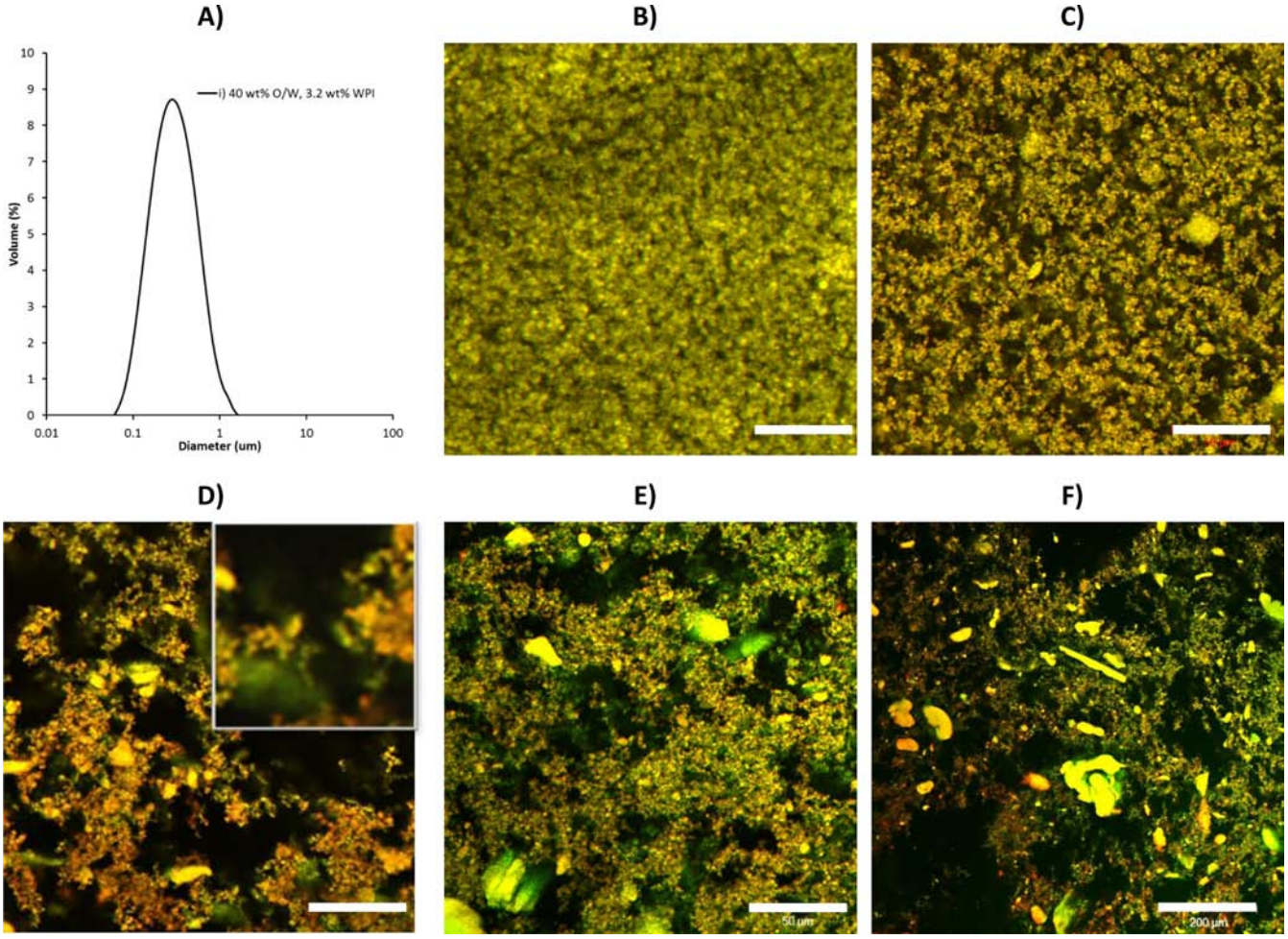

Figure 1. Emulsion and gelled emulsion (micro)structure: (A) particle size distribution of the parent WPI-stabilized emulsion; (B−F) confocal laser scanning microscope images of 10 wt % WPI emulsion (Nile) dispersed within gelatin gels (Rhodamine 6G, pH 8.0, 100 mM NaCl) containing (B) 2.5 wt % gelatin, (C) 5 wt % gelatin, (D) 7.5 wt % gelatin. (E) 10 wt % gelatin, and (F) 15 wt % gelatin. Scale bar represents 50 μm (B−E) or 200 μm (F). The inset in (D) is 2.5 times magnification of the original image.

from 0.1 to 20% strain at 0.1 Hz at 25 °C. Critical gelation temperature was defined as G', G'' crossover.[56,57] Final gel strength was defined as final G' modulus obtained at 25 °C after the temperature ramp was completed. Triplicate gelatin measurements were performed for each system.

In Vitro Digestion. The digestion kinetics of gelled emulsion systems was examined using a simulated intestinal digestion model at 25 °C with conditions similar to those of Wooster et al.[24] Briefly, a single piece of gelled emulsion (20 × 20 × 5 mm, ~2 g) was mixed with 8.5 mL of simulated intestinal fluid (SIF) to achieve a final composition of 10 mM $CaCl_2$, 12 mM mixed bile salts, 0.75 mM phospholipid, 150 mM NaCl, and 4 mM tris(hydroxymethyl)-aminomethane buffer. The temperature and pH were stabilized for at least 2 min at 37 ± 0.5 °C and 6.8 ± 0.02, respectively; the titration was then initialized with the addition of pancreatin solution (200 μL, containing 150 mM NaCl, 4 mM Tris-HCl, and 125 mg/mL pancreatin). The digestion was carried out over 3 h while the pH was maintained at 6.8 by the addition of 0.05 M NaOH using a pH-STAT (TIM 854, Radiometer). During the intestinal phase of digestion, the kinetics of digestion were followed using a pH-STAT technique and expressed as titratable acid (rather than fatty acid) and were calculated by the equation

$$\mathrm{TA} = V_{\mathrm{NaOH}} \times 0.05 \times 1000 \quad (1)$$

where TA is total titratable acid released (μmol) and V_{NaOH} is the volume of NaOH used to titrate the released acid in 3 h (mL).

RESULTS AND DISCUSSION

Microstructure of Gelled Emulsions Observed by CLSM. The mixing of the WPI-stabilized emulsion with different gelatin concentrations led to the formation of gels having microstructure that changed with increasing gelatin concentration (Figure 1). The WPI-stabilized emulsion itself presents as individual droplets with a log-normal particle distribution and an average diameter, $D_{4,3}$ of 0.32 μm (Figure 1A). Mixing WPI emulsion (10 wt %) with 2.5 wt % gelatin and gelling at 4 °C result in a homogeneous structure in which emulsion droplets are evenly distributed throughout the gel (Figure 1B). Increasing the gelatin concentration to 5 wt % (Figure 1C) results in a change in gelled emulsion structure; the emulsion droplets appear as aggregates, and light green voids appear between the aggregates of droplets. The voids between the emulsion droplets consist of regions rich in gelatin as indicated by the dark green hue in the confocal images (Figure 1D, inset) and by visual observations that these gels are very firm. Increasing the gelatin concentration to 7.5, 10, and 15 wt % causes an increase in the size/number of both the emulsion aggregates and the void spaces between the aggregates (Figure 1D−F). These observations indicate that as gelatin concentration is increased, the resulting structure is a discontinuous network of aggregated emulsion droplets

DOI: 10.1021/acs.jafc.5b03700
J. Agric. Food Chem. 2015, 63, 8829−8837

(mesoscale) contained within a continuous network of gelatin (microscale). The aggregation of the emulsion droplets in the gel could be due to either the presence of salt (100 mM) or the addition of gelatin. Given the strong increase in aggregation with increasing gelatin concentration, and the fact that similar emulsions (stabilized with β-lactoglobulin, the main protein of WPI) have been shown to be (relatively) stable to the presence of 120 mM NaCl,[58] we suggest that the main driving force for aggregation is depletion interactions caused by the self-association of gelatin during the gelation process.

Viscoelastic Properties of Gelled Emulsion. The gelation behavior of gelatin is known to be mainly driven by temperature and gelatin concentration such that lower temperatures and higher concentrations resulted in faster and stronger gel formation.[52,59] Figure 2 shows the time-dependent

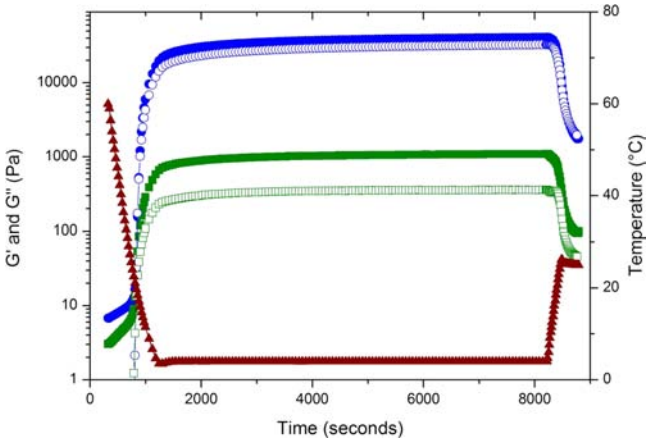

Figure 2. Kinetics of gelation of gelatin gels (empty symbols) and corresponding filled emulsion gels (10.0 wt % oil, 0.7 wt % WPI, 15.0 wt % gelatin) (filled symbols). The crossover of G' (blue circles) and G'' (green circles) indicates the gel point. Temperature curve is represented by the red triangles.

storage modulus G' and loss modulus G'' of 15.0 wt % gelatin-gelled emulsion and the corresponding 15 wt % gelatin gel as a function of temperature. Steep increases in G' and G'' were observed as the temperature was decreased to 4 °C, after which they remained fairly constant during aging at 4 °C for 2 h. Both G' and G'' decreased upon heating to 25 °C, due to weakening of the H-bonded triple helix. Similar changes in G' and G'' as a function of temperature were observed for all gelatin concentrations used to make simple gels or gelled emulsion systems (data not shown).

In order to understand the impact that incorporating an emulsion has on the properties of gelatin gels, dynamic oscillatory rheological experiments were conducted to assess gel point and viscoelastic properties of different systems as a function of gelatin concentration. Figure 3 shows the gel point (A) and storage/loss moduli (B) (at 25 °C) for simple gels and gelled emulsion systems as a function of gelatin concentration. As gelatin concentration increased from 2.5 to 10 wt %, the gel points of both systems increased linearly from 7 to 20 °C and then increased slightly to 23 °C at 15 wt % gelatin. No significant differences in gel point were found between the gelled emulsion systems and simple gelatin gels. The magnitude of the storage modulus G' at 25 °C increased from 0.95 ± 0.26 to 2325 Pa for the gelled emulsion system as the gelatin concentration increased from 2.5 to 15.0 wt %. Simple gels containing 2.5 wt % gelatin showed a higher storage modulus

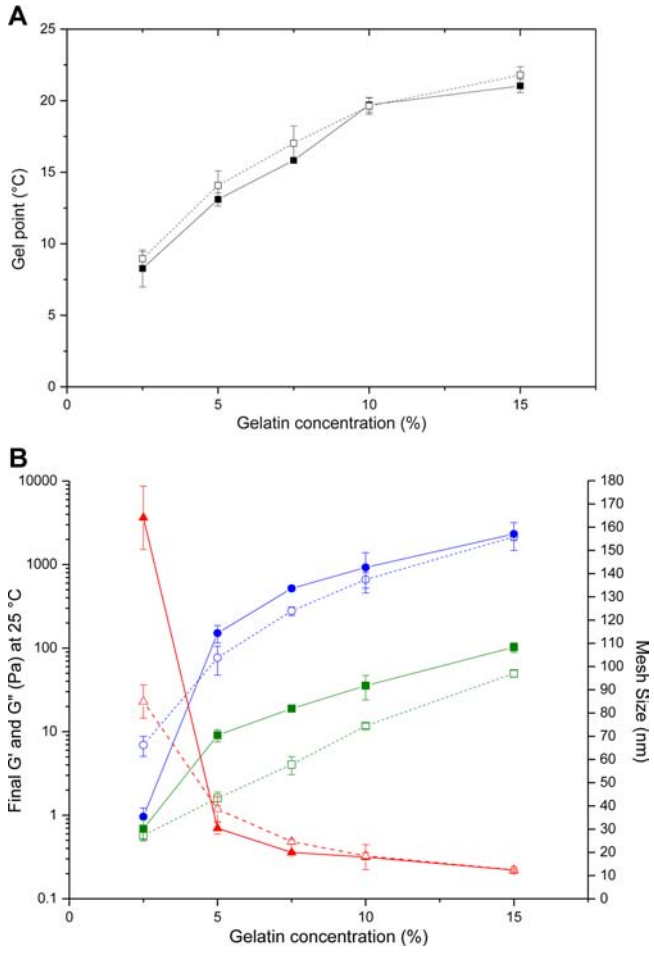

Figure 3. (A) Gel point of gelatin gels (empty squares) and corresponding gelled emulsions (10.0 wt % oil, 0.7 wt % WPI, 2.5−15.0 wt % gelatin) (filled squares) as a function of gelatin concentration. (B) Final G' (blue circles) and G'' (green squares) of gelatin gels (empty symbols) and corresponding gelled emulsions (10.0 wt % oil, 0.7 wt % WPI, 2.5−15.0 wt % gelatin) (filled symbols) as a function of gelatin concentrations; average mesh size (red triangles) of gelatin gels (empty symbols) and corresponding filled emulsion gels (10.0 wt % oil, 0.7 wt % WPI, 2.5−15.0 wt % gelatin) (filled symbols) as a function of gelatin concentrations at temperature of digestion (25 °C).

(6.9 ± 2.7 vs 0.95 ± 0.26 Pa) and a similar loss modulus (0.57 ± 0.06 vs 0.69 ± 0.19 Pa) compared to gelled emulsion systems. At and above 5 wt % gelatin, the gelled emulsion systems exhibited higher loss and storage moduli than the simple gelatin gels (Figure 3B).

A frequency sweep test of selected gelled emulsions containing different concentrations of gelatin as well as simple gelatin gels is shown in Figure 4. Similar behavior was observed for both systems at all concentrations >5.0 wt % (data not shown for 7.5 and 15%). In the presence of 5−15 wt % gelatin, a strong gel-like behavior is observed characterized by the predominance of G' over G'', the absence of crossover points between G' and G'', and also weak dependence on frequency.[60] The dependence was slightly higher at 5 wt % than at ≥10 wt % gelatin. In contrast, gelled emulsion containing 2.5 wt % gelatin presented a mechanical behavior of rather a weak gel with G' close to G'' at low frequency with little differences between the moduli and cross-over at high frequency.[57] An additional strain sweep test (not shown) formed with 2.5 wt % gelatin broke at

DOI: 10.1021/acs.jafc.5b03700
J. Agric. Food Chem. 2015, 63, 8829−8837

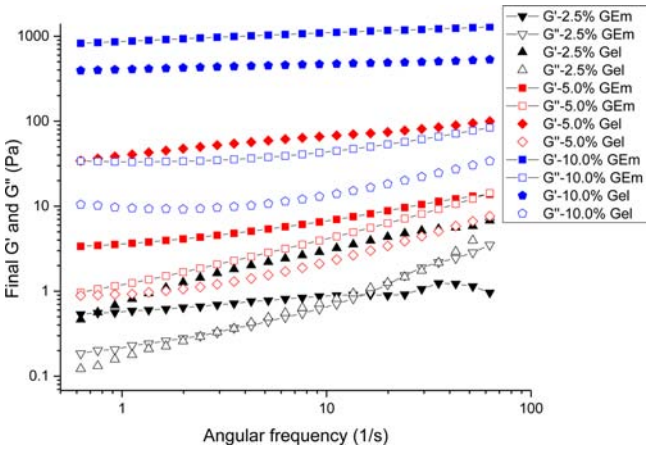

Figure 4. Frequency sweep test of gelatin gels (empty symbols) and corresponding gelled emulsions (10.0 wt % oil, 0.7 wt % WPI, 2.5, 5.0, 10.0 wt % gelatin) (filled symbols) at temperature of digestion (25 °C).

very low strain (0.2%), whereas gelled emulsion systems with higher gelatin concentration did not break in the strain range tested. Similarly, the gelatin gel showed strain breakage only for 2.5 wt % gelatin gels but at higher strain level (16.2%).

Overall results suggest that the rheology of gelled emulsion systems is mostly governed by gelatin gelation at concentrations ≥5 wt % gelatin, leading to strong gels with higher moduli than the corresponding simple gelatin gels. At 2.5 wt % gelatin, the gelled emulsion system was weaker than simple gelatin gel, suggesting a different structure. This mechanical behavior confirms the above description of the microstructure observed by CLSM, suggesting a discontinuous network of aggregated emulsion droplets (mesoscale) dispersed within a continuous network of gelatin (microscale), which governs the overall mechanical properties of the gelled emulsion. At gelatin concentration >2.5 wt %, aggregation of emulsion droplets was visible, which could be related to the higher storage modulus of the gelled emulsion compared to simple gelatin gels. Previous studies have shown that incorporation of particles or oil droplets could lead to an increase in gelatin gel rigidity depending upon the gelatin concentration.[51,61] Oil droplets seem to contribute to the stiffening of the gel as they are mechanically connected to the gel matrix and so contribute to the gel strength.[50] At 2.5 wt %, the lower storage modulus compared to the gelatin system might be related to the discontinuous dispersion of emulsion within the continuous gelatin network.[53,62]

Estimation of Gel Porosity Using Rheological Data. A key hypothesis of this work is that the digestion of gelled emulsions is related to gelatin network structure through the decrease in network porosity within increasing gelatin concentration. In order to understand this relationship, the average mesh size (i.e., pore size) of simple gelatin gels and gelled emulsions was calculated using eq 2[49]

$$\xi^3 = \kappa_B T / G' \quad (2)$$

where ξ is the mesh size, G' represents the final storage modulus (Pa), K_B is the Boltzmann constant, and T is the temperature.

Figure 3B shows the variation of mesh size as a function of gelatin concentration for gelled emulsion systems and simple gelatin gels. The mesh size of gelled emulsion systems decreases from 164 to 20 nm with increase in gelatin concentration from 2.5 to 7.5 wt % and to 12 nm with 15 wt % gelatin. The corresponding simple gelatin gels showed slightly higher mesh sizes at 5 and 7.5 wt % gelatin (38, 30 nm vs 24, 20 nm) and similar mesh sizes at 10 and 15 wt % gelatin (18.5 and 12 nm). At 2.5 wt % gelatin, the simple gelatin gels had significantly smaller average mesh size (85 nm) as compared to gelled emulsion (164 nm). These results can be understood from the structural changes observed by CLSM and viscoelastic response measured. The presence of emulsion within the gelatin network at 2.5 wt % modified its structure, suggesting a less dense network structure than that of the simple gelatin gel. Thus, the gelled emulsion has an increased mesh size as compared to the gelatin system. As gelatin concentration increased, this effect was less visible because the emulsion droplets start to aggregate locally and the gelatin network becomes the main continuous network in the gelled emulsion systems. Consequently, the average mesh size decreased in the gelled emulsion as compared to the corresponding pure gelatin gels. Overall, these results suggest that at 2.5 wt % gelatin, the emulsion droplets are evenly distributed in the gelatin network, decreasing its connectivity and overall gel strength compared to gelatin systems. At 5 and 7.5 wt % gelatin, the increase in gelatin concentration leads to a decrease in average mesh size, and the local aggregation of the emulsion droplets further contributes to the increase in gel strength compared to gelatin systems. As gelatin concentration increases further (10 and 15 wt %), fewer differences compared to gelatin systems were visible, suggesting that the local aggregation of emulsion droplet does not contribute significantly to the overall mechanical behavior of gelled emulsion. Above 10 wt % gelatin, the structure is mainly governed by the gelatin continuous network, and thus mesh sizes decreased to a minimum level as gelatin concentration increased in both the gelatin gel and gelled emulsion systems.

Impact of Gelatin Gels on Fat Emulsion Digestion. A central concept of this work is that surrounding a fat emulsion in a protein gel will slow the digestion of the fat because the protein network slows lipase diffusion to the emulsion droplet. To assess the impact of gelatin gels on the digestion of emulsions, gelled emulsions of differing gelatin concentrations were assessed by simulating only the intestine phase of digestion (at 25 °C) using a pH-STAT technique (Figure 5).[65] As a control, the digestion of emulsion alone was also measured. The emulsion underwent rapid digestion with an initial acid release rate of 100 μmol min^{-1} and released 580 μmol acid after 15 min before going through a point of inflection after which the rate of acid release slowed to 0.6 μmol min^{-1}. Surrounding the emulsion in a gelatin gel progressively decreased the rate of acid release (Table 1). The WPI emulsion in 2.5 wt % gelatin had an initial acid release rate of 35 μmol min^{-2}; this systematically slows, being 11 μmol min^{-2} at 7.5 wt % gelatin and 3.5 μmol min^{-2} at 15 wt % gelatin. Each sample released a similar maximum amount of acid of 700 μmol. Each exhibited an inflection point in the acid release curve from fast to slow acid release at increasingly longer times as gelatin concentration increased. A solution of 10 wt % gelatin had an acid release rate of 0.32 μmol min^{-2} and released 17.5 μmol acid after 60 min, showing that proteolysis of the gelatin itself contributed minimally to the observed differences in acid release and that the kinetics of acid release can essentially be regarded as the kinetics of fat digestion.

DOI: 10.1021/acs.jafc.5b03700
J. Agric. Food Chem. 2015, 63, 8829−8837

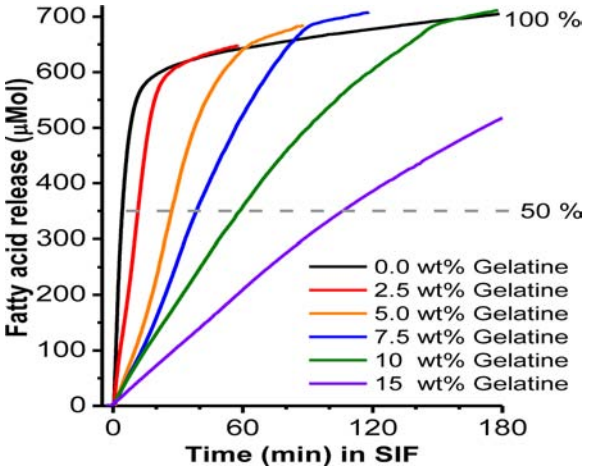

Figure 5. Acid release profiles obtained from 10 wt % O/W emulsions (stabilized by 0.7 wt % WPI) alone (i) or entrapped in various amounts of bovine gelatin (Bloom 240) as a gelled emulsion. Acid release profiles were obtained during single-step pH-STAT simulated intestinal lipolysis at pH 6.8 and 25 °C.

Table 1. Gelatin Concentration in Gelled Emulsions

	gelatin concentration in 10 wt % gelled emulsions					
	0 wt %	2.5 wt %	5 wt %	7.5 wt %	10 wt %	15 wt %
K_{lip} (μmol min^{-1})	100	35	18.5	11	6	3.5
t_{infect} (min)	13	24.5	55	90	149	260

It is apparent from Figure 5 and Table 1 that there is a systematic relationship between gelatin concentration in emulsion gelled and the kinetics of lipolysis. As described earlier, the gelatin concentration affects overall gel structure and, in particular, its porosity. It is well-known that the porosity of a gel will affect the diffusion of large molecules through the gel. Hence, an understanding of the porosity of these gelled emulsions as a function of gelatin concentration was obtained from rheology data using eq 2.[49] Figure 6 shows the relationship between the kinetics of lipolysis and mesh size of each gelled emulsion. It is apparent that there is a direct, almost linear, relationship between gel mesh size and the kinetics of lipolysis. This suggests that smaller mesh size of the gelatin gel (at higher gelatin concentration) restricts the transport of lipase to the emulsion droplet. The question is whether digestion is slowed because lipase diffusion through the gel is slowed or because lipase is not able to diffuse into the gel and proteolysis of the gel is first required for lipolysis to occur.

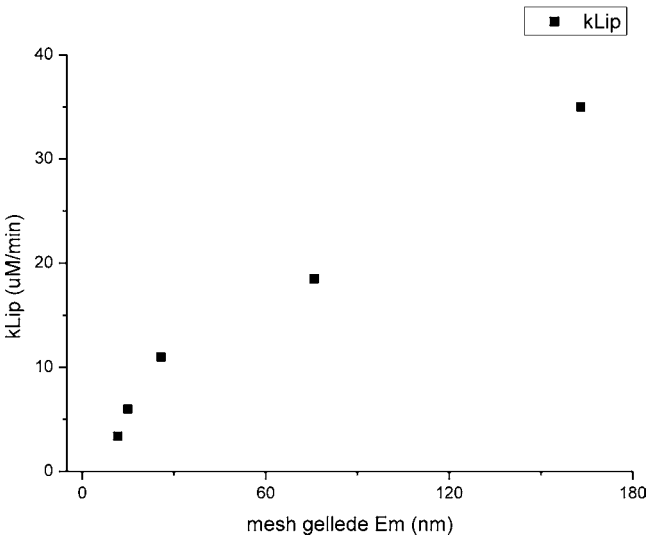

Figure 6. Relationship between the rate of acid release (lipolysis – K_{lip}) and the average mesh size calculated from G' at 25 °C using eq 2.

In order to understand the mechanisms by which protein gels slow the digestion of gelled emulsions, two experiments were conducted: (i) digestions of the gelled emulsion in the presence of pure lipase (Figure 7); (ii) measurement of lipase transport through pure gelatin control gels (Figure 8). Figure 7 compares the digestion of the 10 wt % o/w emulsion embedded within 10 wt % gelatin gel by pancreatin and pure pancreatic lipase in the presence of 12 mM mixed bile and 10 mM $CaCl_2$ at pH 6.8 and 25 °C. Digestion of the gelled emulsion by pancreatin results in a moderate rate of acid release, having a constant rate of 8.9 ± 0.3 μmol min^{-1} over the first 60 min, gradually slowing over the next 60 min to reach 90% digestion after 120 min. In contrast, digestion of the same composition by pure pancreatic lipase (with colipase) resulted in a 10-fold decrease in digestion kinetics (Figure 7ii). After an initial lag phase of ~30 min, acid release reaches a constant rate of 0.76 ± 0. 095 μmol min^{-1} between 60 and 180 min (2–15% digestion) and a constant rate of 0.45 ± 0.036 μmol min^{-1} between 420 and 840 min (30–60% digestion). The differences between digestion by pancreatin and pure pancreatic lipase correspond to an 11-fold reduction during the initial stages of digestion and a 20-fold reduction during the majority of digestion. What is interesting

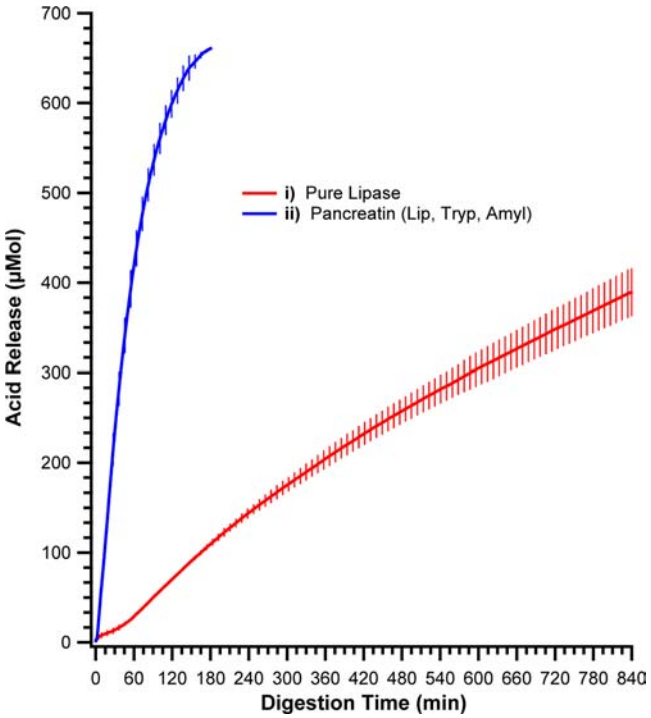

Figure 7. Kinetics of acid release (lipolysis) from 10 wt % gelatin, 10 wt % o/w gelled emulsions when they are exposed to (i) pure pancreatic lipase (11000 U, 250 U/mL), (ii) pancreatin containing pancreatic lipase (2700 U, 63 U/mL), trypsin (16575 U), and amylase (20250 U). Lines represent the average of three measurements; error bars, ±1 standard deviation.

DOI: 10.1021/acs.jafc.5b03700
J. Agric. Food Chem. 2015, 63, 8829–8837

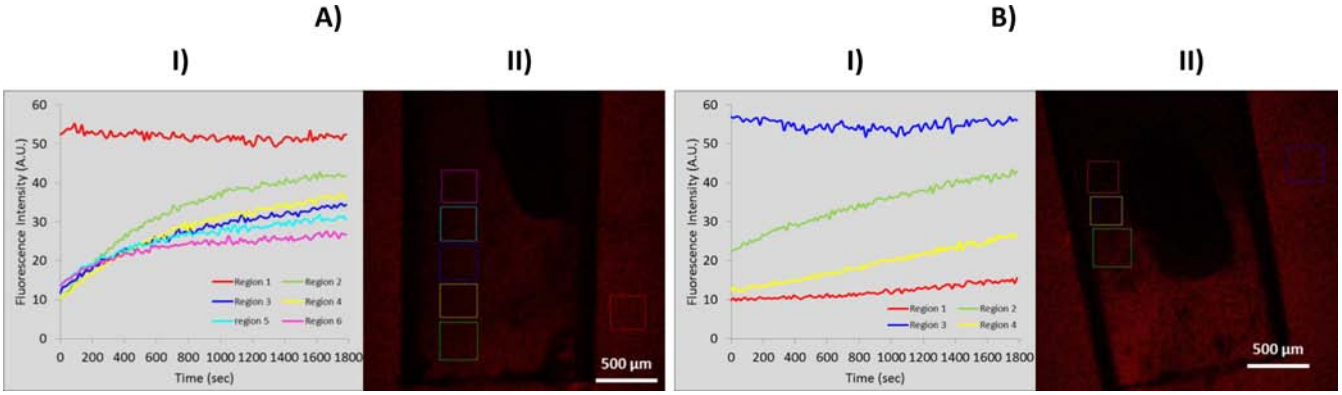

Figure 8. Diffusion of fluorescently labeled (fluorescein isothiocyanate, FITC) porcine pancreatic lipase into (A) 5 wt % gelatin gel and (B) 10 wt % gelatin gel. (I) The fluorescence intensity within different regions of the gel and (II) the external buffer (constant intensity) was monitored over time. Gel pieces were contained within glass capillaries; the faster rate of fluorescence intensity equilibration within the 5 wt % gelatin gel compared to the 10 wt % gel highlights much faster diffusion of the fluorescently labeled lipase.

is that the rate of acid release from the gelled emulsion digested with pancreatin is 10 times lower than the rate of digestion of the parent emulsion or the melted gelled emulsion (100 μmol min^{-1}). These results highlight that the gelatin gel is able to slow the diffusion of both lipase and proteases.

This dramatic reduction in lipolysis can be understood from the fact that the tight mesh of the gelatin gel restricts lipase transport to the emulsion droplets embedded within the gel. The average pore size of this system was estimated to be 18.5 nm (10 wt % gelatin), and the radius of gyration of the pancreatic lipase/co-lipase complex is 25−26 Å.[63] Given that the average pore size is approximately 3−4 times larger than the pancreatic lipase/co-lipase complex, lipase should be able to diffuse through the gel, which was confirmed by digestion experiments with pure lipase. In addition, confocal microscopy measurements show that the diffusion of lipase through 5 wt % gelatin gels is much faster than the diffusion through 10 wt % gelatin gels (Figure 8). Whilst it is apparent that lipase can diffuse through the gelatin gel, the lipolysis rate is considerably retarded compared to the free emulsion (~130 times slower), indicating that the gel provides a (restricted) diffusion barrier to the digestion of the emulsion. The fact that digestion occurs 10−20 times faster in the presence of protease indicates that the main mechanism driving gel degradation is surface erosion of the gel by proteases. A limitation of this work is that the gel systems studied are thermoreversible and melt at in-body temperatures. However, these results do demonstrate that protein gels can act to slow lipolysis. Some might consider that the gel pieces at 20 × 20 × 5 mm are too large to empty from the stomach and anyway would undergo erosion during chewing and trituration.[64] However, the effective diffusion distance is the thinnest dimension of the gel, which at 5 mm is within the range of particles that empty from the stomach.[64] Overall, this work highlights a new approach to control the digestion of lipid emulsions by controlling lipase access to the interface of emulsions via a diffusion barrier adjacent to the interface. The new insights generated in this work provide new design principles for the controlled digestion of food to impact on satiety and weight management or the controlled delivery of active ingredients at different times and/or places within the digestive tract.

Summary and Conclusions. The present study sought to understand how the structure of protein gels affects lipolysis of gelled emulsions. The selected system consisted of an o/w emulsion embedded within gelatin gels. The microstructure of the gel was modulated with different protein concentrations. In vitro digestion of the systems was performed, and the impact of different gel microstructures on lipase diffusion was assessed. The gelatin-gelled emulsions consisted of a discontinuous network of aggregated emulsion droplets (mesoscale), dispersed within a continuous network of gelatin (microscale). Rheological measurements found that the base gelatin gel exhibited thermoreversible elastic type behavior characteristic of gelatin. Incorporation the emulsion into low protein concentration gels weakened the gels due to interruption of network connectivity. Incorporation of the emulsion into gels with ≥5 wt % gelatin led to a slight strengthening of the gel. The rheology of the gelled emulsions was dominated by the rheological behavior of the gelatin network for gelatin concentrations >2.5 wt %; at no point was yielding or brittle fracture observed, suggesting a gelatin continuous microstructure rather than a bicontinuous gel. The rate of fat digestion of gelatin-gelled emulsion correlated with protein concentration within the gel. The average gel mesh size (ξ) was estimated from the storage modulus eq 2, and a direct relationship between lipolysis kinetics (K_{lip}) and average gel mesh size was found. This direct relationship between K_{lip} and ξ indicates that the digestion of fat within gelatin-gelled emulsions is controlled by the gel's ability to slow lipase diffusion to the interface of fat droplets. Additional studies using pure lipase identified that the tortuous gelatin network significantly slowed lipase diffusion into the gel, but did not stop it. The main mechanism of gel breakdown was surface erosion catalyzed by proteases. Overall, this work has demonstrated that protein gels can significantly slow the kinetics of lipolysis of gelled emulsions. This information can be of great use in the design of foods and nutraceuticals to control fat digestion.

AUTHOR INFORMATION

Corresponding Author

*(T.J.W.) E-mail: timothyjames.wooster@rdls.nestle.com.

Notes

The authors declare no competing financial interest.

ACKNOWLEDGMENTS

The authors would like to thank Christine Mettraux for conducting the lipase diffusion work and Thomas Fischer from

DOI: 10.1021/acs.jafc.5b03700
J. Agric. Food Chem. 2015, 63, 8829−8837

Gelita German GmbH for generous donation of the sample of gelatin. T.J.W. would also like to thank Tsugaike Kogen for technical support.

REFERENCES

(1) Golding, M.; Wooster, T. J. The influence of emulsion structure and stability on lipid digestion. *Curr. Opin. Colloid Interface Sci.* **2010**, *15*, 90−101.
(2) Chan, M. In *Opening Address at the 8th Global Conference on Health Promotion*, 8th Global Conference on Health Promotion, Helsinki, Finland, 2013.
(3) Porter, C. J. H.; Trevaskis, N. L.; charman, w. n. lipids and lipid-based formulations: optimizing the oral delivery of lipophilic drugs. *Nat. Rev. Drug Discovery* **2007**, *6*, 231−248.
(4) Fave, G.; Coste, T. C.; Armand, M. Physicochemical properties of lipids: new strategies to manage fatty acid bioavailability. *Cell. Mol. Biol.* **2004**, *50*, 815−831.
(5) Carey, M. C.; Small, D. M.; Bliss, C. M. Lipid digestion and absorption. *Annu. Rev. Physiol.* **1983**, *45*, 651−677.
(6) Christensen, J. O.; Schultz, K.; Mollgaard, B.; Kristensen, H. G.; Mullertz, A. Solubilization of poorly water-soluble drugs during in vitro lipolysis of medium- and long-chain triacylglycerols. *Eur. J. Pharm. Sci.* **2004**, *23*, 287−296.
(7) Borel, P.; Grolier, P.; Armand, M.; Partier, A.; Lafont, H.; Lairon, D.; Azaisbraesco, V. Carotenoids in biological emulsions: solubility, surface-to-core distribution, and release from lipid droplets. *J. Lipid Res.* **1996**, *37*, 250−261.
(8) Ostlund, R. E., Jr. Phytosterols in human nutrition. *Annu. Rev. Nutr.* **2002**, *22*, 533−549.
(9) McClements, D. J.; Decker, E. A.; Park, Y. Controlling lipid bioavailability through physicochemical and structural approaches. *Crit. Rev. Food Sci. Nutr.* **2008**, *49*, 48−67.
(10) Maldonado-Valderrama, J.; Wilde, P.; Macierzanka, A.; Mackie, A. The role of bile salts in digestion. *Adv. Colloid Interface Sci.* **2011**, *165*, 36−46.
(11) Armand, M. Lipases and lipolysis in the human digestive tract: where do we stand? *Curr. Opin. Clin. Nutr. Metab. Care* **2007**, *10*, 156−164.
(12) Carriere, F.; Grandval, P.; Gregory, P. C.; Renou, C.; Henniges, F.; Sander-Struckmeier, S.; Laugier, R. Does the pancreas really produce much more lipase than required for fat digestion? *J. Pancreas* **2005**, *6*, 206−215.
(13) Mattes, R. D. The role of macronutrients in appetite regulation. *Can. J. Dietetic Pract. Res.* **2007**, *68*.
(14) Feinle, C.; Christen, M.; Grundy, D.; Faas, H.; Meier, O.; Otto, B.; Fried, M. Effects of duodenal fat, protein or mixed-nutrient infusions on epigastric sensations during sustained gastric distension in healthy humans. *Neurogastroenterol. Motil.* **2002**, *14*, 205−213.
(15) Maljaars, P. W. J.; Peters, H. P. F.; Mela, D. J.; Masclee, A. A. M. Ileal brake: a sensible food target for appetite control. A review. *Physiol. Behav.* **2008**, *95*, 271−281.
(16) Maljaars, P. W. J.; Symersky, T.; Kee, B. C.; Haddeman, E.; Peters, H. P. F.; Masclee, A. A. M. Effect of ileal fat perfusion on satiety and hormone release in healthy volunteers. *Int. J. Obes.* **2008**, *32*, 1633−1639.
(17) Matzinger, D.; Degen, L.; Drewe, J.; Meuli, J.; Duebendorfer, R.; Ruckstuhl, N.; D'Amato, M.; Rovati, L.; Beglinger, C. The role of long chain fatty acids in regulating food intake and cholecystokinin release in humans. *Gut* **2000**, *46*, 689−693.
(18) Little, T. J.; Russo, A.; Meyer, J. H.; Horowitz, M.; Smyth, D. R.; Bellon, M.; Wishart, J. M.; Jones, K. L.; Feinle-Bisset, C. Free fatty acids have more potent effects on gastric emptying, gut hormones, and appetite than triacylglycerides. *Gastroenterology* **2007**, *133*, 1124−1131.
(19) Pilichiewicz, A. N.; Little, T. J.; Brennan, I. M.; Meyer, J. H.; Wishart, J. M.; Otto, B.; Horowitz, M.; Feinle-Bisset, C. Effects of load, and duration, of duodenal lipid on antropyloroduodenal motility, plasma CCK and PYY, and energy intake in healthy men. *Am. J. Physiol.−Regul. Integr. Comp. Physiol.* **2006**, *290*, R668−R677.
(20) Marciani, L.; Wickham, M.; Singh, G.; Bush, D.; Pick, B.; Cox, E.; Fillery-Travis, A.; Faulks, R.; Marsden, C.; Gowland, P. A.; Spiller, R. C. Delaying gastric emptying and enhancing cholecystokinin release and satiety by using acid stable fat emulsions. *Gastroenterology* **2006**, *130*, A227.
(21) Sjostrom, L.; Rissanen, A.; Andersen, T.; Boldrin, M.; Golay, A.; Koppeschaar, H. P. F.; Krempf, M. Randomized placebo-controlled trial of orlistat for weight loss and prevention of weight regain in obese patients. *Lancet* **1998**, *352*, 167−173.
(22) Seimon, R. V.; Wooster, T.; Otto, B.; Golding, M.; Day, L.; Little, T. J.; Horowitz, M.; Clifton, P. M.; Feinle-Bisset, C. The droplet size of intraduodenal fat emulsions influences antropyloroduodenal motility, hormone release, and appetite in healthy males. *Am. J. Clin. Nutr.* **2009**, *89*, 1729−1736.
(23) Li, Y.; Hu, M.; Du, Y.-M.; Xiao, H.; McClements, D. J. Control of lipase digestibility of emulsified lipids by encapsulation within calcium alginate beads. *Food Hydrocolloids* **2010**, *25*, 122−130.
(24) Wooster, T. J.; Day, L.; Xu, M.; Golding, M.; Oiseth, S.; Keogh, J.; Clifton, P. Impact of different biopolymer networks on the digestion of gastric structured emulsions. *Food Hydrocolloids* **2014**, *36*, 102−114.
(25) Guo, Q.; Ye, A.; Lad, M.; Dalgleish, D.; Singh, H. Effect of gel structure on the gastric digestion of whey protein emulsion gels. *Soft Matter* **2014**, *10*, 1214−1223.
(26) Armand, M.; Pasquier, B.; Borel, P.; Andre, M.; Senft, M.; Peyrot, J.; Salducci, J.; Lairon, D. Emulsion and absorption of lipids: the importance of physicochemical properties. *OCL−Oleagineux Corps Gras Lipides* **1997**, *4*, 178−185.
(27) Golding, M.; Wooster, T. J. The influence of emulsion structure and stability on lipid digestion. *Curr. Opin. Colloid Interface Sci.* **2010**, *15*, 90−101.
(28) Carriere, F.; Grandval, P.; Gregory, P. C.; Renou, C.; Henniges, F.; Sander-Struckmeier, S.; Laugier, R. Does the pancreas really produce much more lipase than required for fat digestion? *J. Pancreas* **2005**, *6*, 206−215.
(29) Daher, G. C.; Cooper, D. A.; Zorich, N. L.; King, D.; Riccardi, K. A.; Peters, J. C. Olestra ingestion and dietary fat absorption in humans. *J. Nutr.* **1997**, *127*, 1694S−1698S.
(30) Carriere, F.; Renou, C.; Ransac, S.; Lopez, V.; De Caro, J.; Ferrato, F.; De Caro, A.; Verger, R.; Laugier, R. Effect of Orlistat on lipolysis following standard test meals. *Gastroenterology* **1999**, *116*, A543.
(31) Wickham, M.; Garrood, M.; Leney, J.; Wilson, P. D. G.; Fillery-Travis, A. Modification of a phospholipid stabilized emulsion interface by bile salt: effect on pancreatic lipase activity. *J. Lipid Res.* **1998**, *39*, 623−632.
(32) Chu, B. S.; Rich, G. T.; Ridout, M. J.; Faulks, R. M.; Wickham, M. S. J.; Wilde, P. J. Modulating pancreatic lipase activity with galactolipids: effects of emulsion interfacial composition. *Langmuir* **2009**, *25*, 9352−9360.
(33) Sandra, S.; Decker, E. A.; McClements, D. J. Effect of interfacial protein cross-linking on the in vitro digestibility of emulsified corn oil by pancreatic lipase. *J. Agric. Food Chem.* **2008**, *56*, 7488−7494.
(34) Maldonado-Valderrama, J.; Wilde, P.; Macierzanka, A.; Mackie, A. The role of bile salts in digestion. *Adv. Colloid Interface Sci.* **2011**, *165*, 36−46.
(35) Golding, M.; Wooster, T. J.; Day, L.; Xu, M.; Lundin, L.; Keogh, J.; Clifton, P. Impact of gastric structuring on the lipolysis of emulsified lipids. *Soft Matter* **2011**, *7*, 3513−3523.
(36) Sjostrom, L.; Rissanen, A.; Andersen, T.; Boldrin, M.; Golay, A.; Koppeschaar, H. P. F.; Krempf, M. Randomized placebo-controlled trial of orlistat for weight loss and prevention of weight regain in obese patients. *Lancet* **1998**, *352*, 167−173.
(37) Hennink, W. E.; van Nostrum, C. F. Novel crosslinking methods to design hydrogels. *Adv. Drug Delivery Rev.* **2002**, *54*, 13−36.
(38) Lin, C. C.; Metters, A. T. Hydrogels in controlled release formulations: network design and mathematical modeling. *Adv. Drug Delivery Rev.* **2006**, *58*, 1379−1408.

DOI: 10.1021/acs.jafc.5b03700
J. Agric. Food Chem. 2015, 63, 8829−8837

(39) Lau, H. K.; Kiick, K. L. Opportunities for multicomponent hybrid hydrogels in biomedical applications. *Biomacromolecules* **2015**, *16*, 28−42.
(40) Kopecek, J.; Yang, J. Hydrogels as smart biomaterials. *Polym. Int.* **2007**, *56*, 1078−1098.
(41) Tabata, Y.; Ikada, Y. Protein release from gelatin matrices. *Adv. Drug Delivery Rev.* **1998**, *31*, 287−301.
(42) Young, S.; Wong, M.; Tabata, Y.; Mikos, A. G. Gelatin as a delivery vehicle for the controlled release of bioactive molecules. *J. Controlled Release* **2005**, *109*, 256−274.
(43) Wang, Y.; Bamdad, F.; Song, Y.; Chen, L. Hydrogel particles and other novel protein-based methods for food ingredient and nutraceutical delivery systems. *Woodhead Publ. Ser. Food Sci., Technol. Nutr.* **2012**, *239*, 412−450.
(44) Clark, A. H.; Ross-Murphy, S. B. Structural and mechanical properties of biopolymer gels. *Adv. Polym. Sci.* **1987**, *83*, 57−192.
(45) Norton, I. T.; Frith, W. J. Microstructure design in mixed biopolymer composites. *Food Hydrocolloids* **2001**, *15*, 543−553.
(46) Zasypkin, D. V.; Braudo, E. E.; Tolstoguzov, V. B. Multicomponent biopolymer gels. *Food Hydrocolloids* **1997**, *11*, 159−170.
(47) Schuster, E.; Eckardt, J.; Hermansson, A.-M.; Larsson, A.; Loren, N.; Altskaer, A.; Stroem, A. Microstructural, mechanical and mass transport properties of isotropic and capillary alginate gels. *Soft Matter* **2014**, *10*, 357−366.
(48) Walkenstrom, P.; Kidman, S.; Hermansson, A.-M.; Rasmussen, P. B.; Hoegh, L. Microstructure and rheological behaviour of alginate/pectin mixed gels. *Food Hydrocolloids* **2003**, *17*, 593−603.
(49) Klak, M.-C.; Picard, J.; Giraudier, S.; Larreta-Garde, V. Mastered proteolysis of gelatin gel can control delivery kinetics of entrapped large molecules. *Soft Matter* **2012**, *8*, 4750−4755.
(50) Dickinson, E. Emulsion gels: The structuring of soft solids with protein-stabilized oil droplets. *Food Hydrocolloids* **2012**, *28*, 224−241.
(51) Dickinson, E.; Stainsby, G.; Wilson, L. An adsorption effect on the gel strength of dilute gelatin-stabilized oil-in-water emulsions. *Colloid Polym. Sci.* **1985**, *263*, 933−934.
(52) Sala, G.; van Vliet, T.; Cohen Stuart, M.; van de Velde, F.; van Aken, G. A. Deformation and fracture of emulsion-filled gels: effect of gelling agent concentration and oil droplet size. *Food Hydrocolloids* **2009**, *23*, 1853−1863.
(53) Van Vliet, T. Rheological properties of filled gels. Influence of filler matrix interaction. *Colloid Polym. Sci.* **1988**, *266*, 518−524.
(54) Lian, G.; Malone, M. E.; Homan, J. E.; Norton, I. T. A mathematical model of volatile release in mouth from the dispersion of gelled emulsion particles. *J. Controlled Release* **2004**, *98*, 139−155.
(55) Malone, M. E.; Appelqvist, I. A. M. Gelled emulsion particles for the controlled release of lipophilic volatiles during eating. *J. Controlled Release* **2003**, *90*, 227−241.
(56) Power, D. J.; Rodd, A. B.; Paterson, L.; Boger, D. V. Gel transition studies on nonideal polymer networks using small amplitude oscillatory rheometry. *J. Rheol. (Melville, NY, U. S.)* **1998**, *42*, 1021−1037.
(57) Winter, H. H. Can the gel point of a crosslinking polymer be detected by the G′-G″ crossover? *Polym. Eng. Sci.* **1987**, *27*, 1698−1702.
(58) Zhai, J.; Wooster, T. J.; Hoffmann, S. V.; Lee, T.-H.; Augustin, M. A.; Aguilar, M.-I. Structural rearrangement of β-lactoglobulin at different oil-water interfaces and its effect on emulsion stability. *Langmuir* **2011**, *27*, 9227−9236.
(59) Djabourov, M.; Lechaire, J. P.; Gaill, F. Structure and rheology of gelatin and collagen gels. *Biorheology* **1993**, *30*, 191−205.
(60) Lorenzo, G.; Checmarev, G.; Zaritzky, N.; Califano, A. Linear viscoelastic assessment of cold gel-like emulsions stabilized with bovine gelatin. *LWT−Food Sci. Technol.* **2010**, *44*, 457−464.
(61) Ring, S.; Stainsby, G. Filler reinforcement of gels. *Prog. Food Nutr. Sci.* **1982**, *6*, 323−329.
(62) Jampen, S.; Britt, I. J.; Yada, S.; Tung, M. A. Rheological properties of gellan gels containing filler particles. *J. Food Sci.* **2001**, *66*, 289−293.
(63) Pignol, D.; Ayvazian, L.; Kerfelec, B.; Timmins, P.; Crenon, I.; Hermoso, J.; Fontecilla-Camps, J. C.; Chapus, C. Critical role of micelles in pancreatic lipase activation revealed by small angle neutron scattering. *J. Biol. Chem.* **2000**, *275*, 4220−4224.
(64) Marciani, L.; Gowland, P. A.; Fillery-Travis, A.; Manoj, P.; Wright, J.; Smith, A.; Young, P.; Moore, R.; Spiller, R. C. Assessment of antral grinding of a model solid meal with echo-planar imaging. *Am. J. Physiol.* **2001**, *280*, G844−G849.
(65) A highly artificial digestion model was used to test the concept that protein gels can slow fat digestion. A temperature of 25 °C was used to prevent gelatin melting; this is not representative of human physiology (37 °C). In addition, oral or gastric steps of digestion were omitted; both phases are likely to affect digestion through trituration and proteolysis.

DOI: 10.1021/acs.jafc.5b03700
J. Agric. Food Chem. 2015, 63, 8829−8837

and assembled into the active NADPH oxidase.[8,9] The active oxidase has emerged as an important source of cytosolic-derived ROS for signal transduction. During monocyte−macrophage differentiation, up-regulation of subunit NOX2 expression and p47phox membrane translocation are known to be highly induced, resulting in ROS production and contributing to pathological changes in cell function and the development of atherosclerosis.[8,10] Smooth muscle cells in mice deficient for p47phox exhibited decreased superoxide production and cell proliferation. Additionally, deletion of p47phox led to amelioration of atherosclerotic plaques in apolipoprotein E-deficient ($ApoE^{-/-}$) mice.[11,12] Therefore, reducing ROS production by limiting NADPH oxidase activity may be beneficial for the blockage of atherosclerotic progression.

Turmeric is prepared from the dried rhizomes of *Curcuma longa* and has been used as a foodstuff, in cosmetics, and as a therapeutic application in traditional Asian medicine.[13] Curcuminoids consist of a mixture of curcumin, demethoxycurcumin (DMC), and bisdemethoxycurcumin (BDMC) (Figure 1); the major active ingredients are responsible for

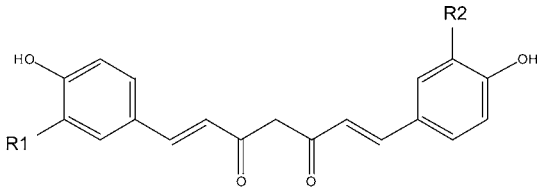

	R1	R2
Curcumin	OCH_3	OCH_3
Demethoxycurcumin (DMC)	OCH_3	H
Bisdemethoxycurcumin (BDMC)	H	H

Figure 1. Chemical structures of curcumin, demethoxycurcumin (DMC), and bisdemethoxycurcumin (BDMC).

the predominant medicinal properties of turmeric. Curcuminoids have been reported to possess several desirable characteristics, including antioxidant, anti-inflammatory, antidiabetic, neuroprotective, and anticancer activities.[14−17] Numerous reports have suggested possible beneficial effects of curcuminoids on hypocholesterolemic and antiatherosclerotic activities. Turmeric intake has been reported to reduce fibrinogen levels in patients with atherosclerosis.[18] Curcumin administration decreased serum lipid peroxides and cholesterol in healthy volunteers.[19] In animal studies, dietary supplementation with curcumin, DMC, and BDMC in rats fed a moderately high fat diet exhibited triacylglycerol- and cholesterol-lowing potency,[20] and long-term administration of curcumin lowered serum and hepatic cholesterol and suppressed atherosclerotic lesions in high-fat-fed $LDLR^{-/-}$ mice.[21] In in vitro studies, curcumin has been reported to increase LDLR expression in hepatic cell lines.[22] Recently, curcumin was demonstrated to increase LDL uptake through the down-regulation of PCSK9 gene expression in HepG2 cells.[23] Curcumin suppressed lipid accumulation in peritoneal macrophages isolated from $LDLR^{-/-}$ mice fed a high-fat diet.[24] Moreover, curcuminoids attenuated oxLDL-induced CD36 and scavenger receptor-A (SR-A) expression and reduced oxLDL uptake during monocyte to macrophage differentiation.[25]

The THP-1 cell is an acute monocytic leukemia cell line that is the most widely exploited monocyte-like cell line. THP-1 cells are used to induce monocyte to macrophage differentiation by phorbol-12-myristate-13-acetate (PMA) in studies related to atherosclerosis.[26] Curcumin, DMC, and BDMC are usually found in mixtures in natural foods. However, their individual effects on monocyte to macrophage differentiation remain unclear. In the present study, we investigated the effects and underlying mechanisms of curcumin, DMC, and BDMC on monocyte invasion during PMA-induced THP-1 to macrophage differentiation.

MATERIALS AND METHODS

Chemicals. Curcumin (purity ≥98.5%), Gö6976, DAPH-7, and rottlerin were purchased from Enzo Life Sciences (Ann Arbor, MI). Demethoxycurcumin (DMC, purity ≥98%), bisdemethoxycurcumin (BDMC, purity ≥98%), dimethyl sulfoxide (DMSO), phorbol-12-myristate-13-acetate (PMA), ECM gel, gelatin, *N*-acetyl-L-cysteine, RPMI-1640 medium, nonessential amino acids (NEAA), and other chemicals, unless otherwise indicated, were purchased from Sigma-Aldrich Co. (St. Louis, MO). Bisindolylmaleimide I (BIM) was purchased from Cayman Chemical (Ann Arbor, MI).

Cell Culture and Treatment of Cells with Curcumin, DMC, and BDMC. The THP-1 monocytelike cell line was obtained from Bioresource Collection and Research Center (Hsinchu, Taiwan) and maintained in RPMI-1640 medium supplemented with 10% fetal bovine serum (FBS) (Invitrogen, Carlsbad, CA) and 1% NEAA in a 5% CO_2 incubator at 37 °C. For monocyte to macrophage differentiation, THP-1 cells were seeded onto six-well plates (1×10^6/mL) in RPMI medium and treated with vehicle (0.1% DMSO), curcumin, DMC, or BDMC (10−20 μM) for 1 h, followed by stimulation with PMA (30 nM) for 24 h. For inhibitors treatment, THP-1 cells were treated with the inhibitors for 30 min and then curcuminoids for 1 h, followed by the addition of PMA for an additional 24 h of incubation.

Cell Invasion Assay. Polycarbonate membrane Transwell permeable supports (pore size, 8 μm) (Corning Inc.) were coated with ECM gel (5 mg/mL). THP-1 cells (3×10^5) in 300 μL of serum-free RPMI medium were inoculated into the upper chamber, and 500 μL of RPMI containing 10% FBS was added to the lower chamber. Cells were treated with vehicle or the indicated curcuminoids (20 μM) for 1 h and then incubated with PMA (30 nM). After 24 h of incubation, the Transwell inserts were fixed with 3.7% formaldehyde and stained with Wright stain buffer. The invasive cells were observed and counted under a microscope.

Gelatin Zymography Analysis. THP-1 cells (1×10^6/mL) were seeded in serum-free RPMI medium and treated with vehicle or the indicated curcuminoids (20 μM) for 1 h, followed by exposure to PMA (30 nM) for 24 h. For secreted protein preparation, the serum-free medium of the cultured cells was collected and centrifuged to remove the cells. The proteins in the media were separated with an 8% sodium dodecyl sulfate−polyacrylamide gel (SDS−PAGE) containing 0.1% gelatin. The gels were incubated in 2.5% Triton X-100 to remove the SDS. After a 30 min incubation, the gels were incubated in an enzyme buffer (40 mM Tris-HCl, 10 mM $CaCl_2$, and 0.01% NaN_3, pH 8.0) at 37 °C for 12 h. After incubation, the gels were stained in buffer containing 0.125% Coomassie Blue and destained in 20% methanol with 10% acetic acid.

Reverse-Transcription Quantitative Polymerase Chain Reaction (RT-Q-PCR) Analysis. Total cellular RNA was prepared using a Total RNA Mini Kit (Geneaid, Taipei, Taiwan). Reverse transcription was performed using a high-capacity cDNA reverse transcription kit (Applied Biosystems, Foster City, CA). Quantitative real-time PCR was performed in a reaction mixture containing cDNA, specific primers (Supporting Information, Table S1), and the Maxima SYBR Green/ROX qPCR Master Mix (Fermentas, Burlington, CA). The following PCR conditions were used: 58 °C for 2 min, 94 °C for 4 min, and 45 cycles of 94 °C for 1 min, 58 °C for 1 min, and 72 °C for 1 min. The ΔΔCt method was used for data analysis. The PCR amplification was carried out in a Roche LightCycler-480 Real-Time PCR System, and the levels of mRNA expression were determined in triplicate samples and normalized to the mRNA level of

DOI: 10.1021/acs.jafc.5b04083
J. Agric. Food Chem. 2015, 63, 8838−8848

glyceraldehyde-3-phosphate dehydrogenase (GAPDH) in the same samples.

Detection of CD11b Expression by Flow Cytometry Analysis. CD11b on the cell surface was detected by flow cytometry, as previously described.[27] Briefly, THP-1 cells were washed with PBS and incubated in PBS containing 5% bovine serum albumin (BSA) at 37 °C for 1 h. Then, the cells were incubated with a fluorescein isothiocyanate (FITC)-conjugated antihuman CD11b monoclonal antibody (eBioscience, San Diego, CA) for 30 min in the dark at 4 °C. After washing, the cells were suspended in PBS and measured on the FACSCalibur (FACScan, BD Biosciences, San Jose, CA). The data were analyzed using Cell Quest Pro software (BD Biosciences). CD11b expression on the cell surface was calculated and expressed as the relative percentage of the geometric mean fluorescence intensity.

Analysis of Reactive Oxygen Species Generation. The level of ROS was measured by flow cytometry analysis, as previously described.[28] Briefly, THP-1 cells (1×10^6/mL) were seeded onto six-well plates in RPMI medium and treated with vehicle or the indicated curcuminoids (20 μM) for 1 h, followed by exposure to PMA (30 nM) for 24 h. Then, H_2DCFDA (10 μM) was added, and the cells were incubated at 37 °C in the dark for 30 min. After incubation, the cells were harvested for ROS analysis. Three independent samples of 10 000 cells were analyzed via flow cytometry using the FL1 emission filter. The data were expressed as the relative percentage of the geometric mean fluorescence intensity.

Western Blot Analysis. THP-1 cells (1×10^6/mL) were seeded and subsequently incubated with the indicated reagents for the indicated time periods. Cells were harvested and total cellular lysates were extracted in RIPA buffer (Thermo Fisher Scientific, Inc., Rockford, IL). For membrane and cytosolic protein preparations, the cells were harvested using a Mem-PER Plus Membrane Protein Extraction Kit (Thermo Fisher Scientific) according to the manufacturer's instructions. The proteins were separated by 10% SDS–PAGE and subsequently transferred onto a polyvinylidene fluoride membrane (PerkinElmer, Boston, MA). The blots were incubated with the following specific antibodies: anti-MMP-9, anti-p47phox (anti-NCF1) (GeneTex, Irvine, CA), antiphosphor-PKCδ (Tyr311), anti-Na,K-ATPase (Cell Signaling Technology, Danvers, MA), and monoclonal anti-β-actin (Sigma-Aldrich). Then, the membranes were incubated with the appropriate horseradish peroxidase-conjugated secondary antibodies (Santa Cruz Biotechnology, Santa Cruz, CA) for 1 h. The proteins were detected using the Amersham ECL Prime Western Blotting Detection Reagent, and the signal was visualized on an Amersham Hyperfilm ECL (GE Healthcare, Buckinghamshire, UK).

Analysis of Protein Kinase C Activity. Protein kinase C (PKC) activity analysis was performed as previously described.[29] The cellular proteins were harvested using RIPA buffer, and PKC activity was measured using the Nonradioactive PKC Kinase Activity Kit (Enzo Life Sciences) according to the manufacturer's instructions. The 96-well microplate was read at 450 nm in a microplate reader.

Statistical Analysis. All experiments were repeated at least three times, and the data were expressed as the mean ± SD. Statistic calculations were carried out using IBM SPSS Statistics 22.0 software. Comparisons between results were made by analysis of variance (ANOVA). Statistic differences were assessed using one-way ANOVA with Dunnett's posthoc test. A value of $p < 0.05$ was considered statistically significant.

RESULTS

Curcumin, DMC, and BDMC Suppressed Matrix Invasion during PMA-Induced THP-1 Differentiation. The matrix invasion of macrophages into the subendothelium plays a critical role in the initial stage of atherosclerosis. To examine the effects of curcumin, DMC, and BDMC on matrix invasion during PMA-induced THP-1 differentiation, the invasion assay was performed as described in the Materials and Methods. As shown in Figure 2, PMA significantly increased the extracellular matrix (ECM) invasion ability to

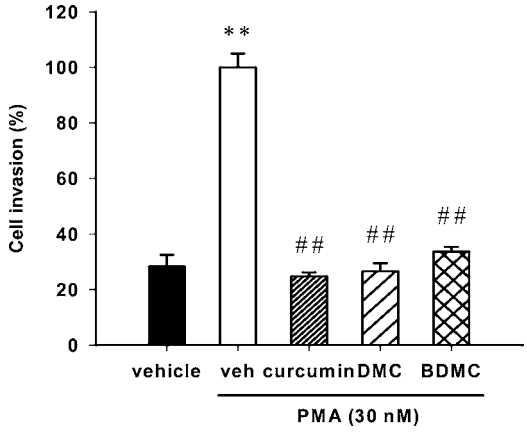

Figure 2. Curcumin, DMC, and BDMC suppressed matrix invasion during PMA-induced THP-1 differentiation. THP-1 cells were inoculated into the transwell chamber containing the ECM gel-coating filter and pretreated with vehicle (0.1% DMSO), curcumin, DMC, or BDMC (20 μM) for 1 h followed by incubation with PMA (30 nM) for 24 h. The transwell filters were fixed and stained with Wright stain buffer. The number of THP-1 cells that invaded the ECM gel was calculated, and the data are presented as the means ± SD from three independent experiments. **$p < 0.01$ represents a significant difference compared to the PMA-untreated cells (vehicle group). ##$p < 0.01$ represents a significant difference compared to the PMA-alone-treated cells (veh group).

100.0 ± 5.0% in THP-1 cells relative to cells without PMA exposure (28.3 ± 4.2%). The transwell invasion ability of cells pretreated with curcumin, DMC, and BDMC (20 μM) was markedly decreased from 100.0 ± 5.0% to 24.8 ± 1.4%, 26.6 ± 2.9%, and 33.7 ± 1.7% in PMA-treated THP-1 cells, respectively ($p < 0.01$). Curcumin, DMC, and BDMC showed similar activity on the inhibition of matrix invasion in PMA-treated THP-1 cells. These data indicate that curcuminoids suppress extracellular matrix invasion during PMA-induced THP-1 differentiation.

Effects of Curcumin, DMC, and BDMC on CD11b Expression during PMA-Induced THP-1 Differentiation. The adhesion molecule CD11b is a major marker of monocyte differentiation toward adherent macrophages.[30] To investigate the effect of curcumin, DMC, and BDMC on CD11b expression during PMA-induced THP-1 differentiation, the cells were pretreated with the three curcuminoids (10 and 20 μM) for 1 h, followed by incubation with PMA (30 nM) for 24 h. CD11b mRNA expression was measured by RT-Q-PCR. As shown in Figure 3A, CD11b mRNA expression in THP-1 cells was significantly induced by PMA. Pretreatment of THP-1 cells with the indicated curcumin, DMC, and BDMC at 20 μM concentration equally reduced CD11b mRNA expression by approximately 62%, 60%, and 65%, respectively, compared to the PMA alone-treated group ($p < 0.01$). Next, we examined the effect of curcuminoids on cell surface expression of CD11b on PMA-treated THP-1 cells by flow cytometry. The level of cell surface CD11b induced by PMA was significantly attenuated in curcumin-, DMC- and BDMC-treated cells, respectively (Figure 3B). This data showed that the inhibition ability of curcuminoids is in the order of BDMC > curcumin ≈ DMC in PMA-treated THP-1 cells. These data reveal that curcuminoids inhibit CD11b mRNA expression during PMA-induced monocyte to macrophage differentiation. The inhibitory activity against surface-CD11b expression was associated

DOI: 10.1021/acs.jafc.5b04083
J. Agric. Food Chem. 2015, 63, 8838−8848

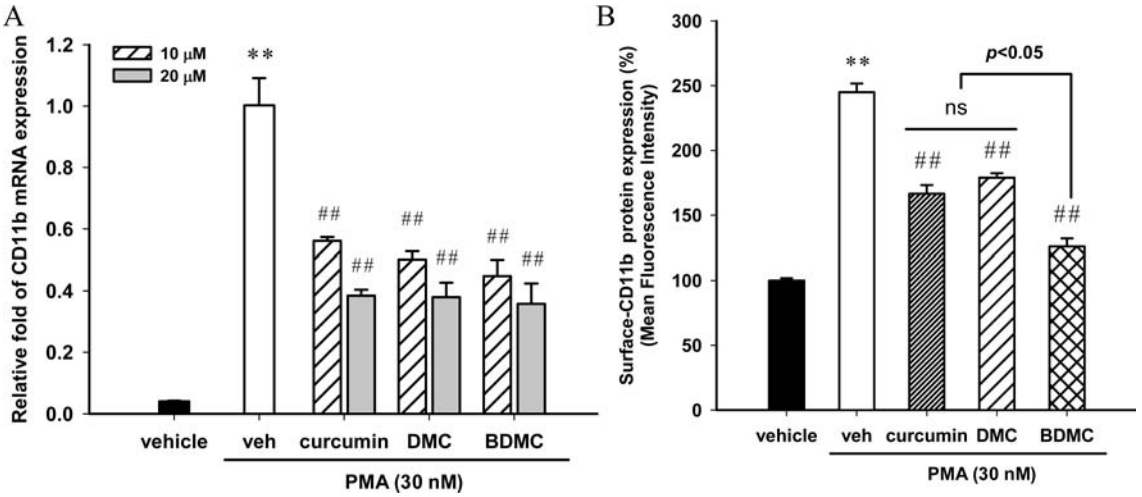

Figure 3. Curcumin, DMC, and BDMC suppressed CD11b expression during PMA-induced THP-1 differentiation. (A) THP-1 cells were pretreated with vehicle, curcumin, DMC, or BDMC (10 or 20 μM) for 1 h and then treated with PMA for 24 h. CD11b mRNA expression was measured by RT-Q-PCR. (B) Summary of cell-surface CD11b levels. The cells were pretreated with vehicle or the curcuminoids (20 μM) for 1 h and then treated with PMA for 24 h. The level of cell-surface CD11b was determined by flow cytometry analysis, as described in the Materials and Methods. The data are presented as the means ± SD from three independent experiments. $^{**}p < 0.01$ represents a significant difference compared to the PMA-untreated cells (vehicle group). $\#\#p < 0.01$ represents a significant difference compared to the PMA-alone-treated cells (veh group). ns: no significant differences.

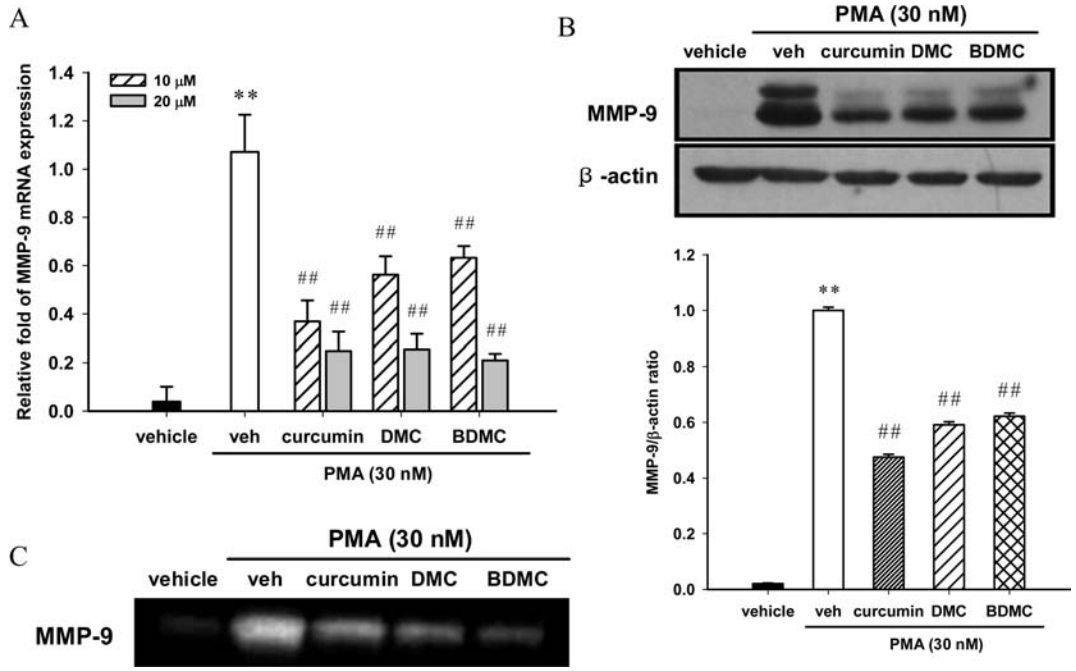

Figure 4. Curcumin, DMC, and BDMC inhibited MMP-9 expression and activity during PMA-induced THP-1 differentiation. (A) THP-1 cells were pretreated with vehicle, curcumin, DMC, or BDMC (10–20 μM) for 1 h and then treated with PMA for 24 h. MMP-9 mRNA expression was measured by RT-Q-PCR. (B) Cells were pretreated with vehicle or curcuminoids (20 μM) for 1 h and then incubated with PMA for 24 h. The MMP-9 and β-actin protein levels were analyzed via Western blot analysis. The experiments were replicated three times, and a representative blot is shown. The intensity of MMP-9 normalized to the β-actin protein is presented as the mean ± SD of three independent experiments. $^{**}p < 0.01$ represents a significant difference compared to the PMA-untreated cells (vehicle group). $\#\#p < 0.01$ represents a significant difference compared to the PMA-alone-treated cells (veh group). (C) The extracellular MMP-9 activity was measured by gelatin zymography, as described in the Materials and Methods. The experiments were replicated three times, and a representative graph is shown.

more with BDMC and less with curcumin or DMC during PMA-differenced THP-1 cells.

Effects of Curcumin, DMC, and BDMC on MMP-9 Expression and Activity during PMA-Induced THP-1 Differentiation. The invasion of monocytes into the vascular intima requires the destruction of the extracellular matrix (ECM) by matrix metalloprotease-9 (MMP-9), which is involved in early atherosclerotic processes.[5] Therefore, we investigated the effect of curcumin, DMC, and BDMC on MMP-9 gene expression and activity during PMA-induced THP-1 differentiation. As shown in Figure 4A,B, THP-1 cells treated with PMA markedly induced MMP-9 mRNA and

DOI: 10.1021/acs.jafc.5b04083
J. Agric. Food Chem. 2015, 63, 8838–8848

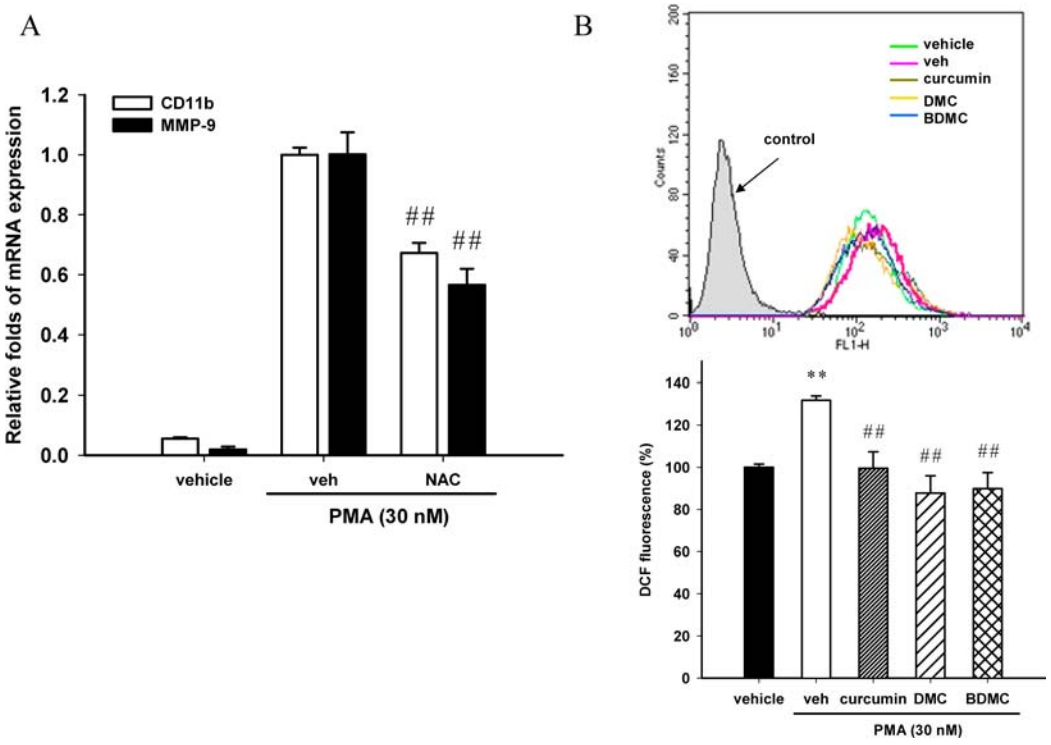

Figure 5. Curcumin, DMC, and BDMC suppressed ROS generation during PMA-induced THP-1 differentiation. (A) THP-1 cells were pretreated with NAC (10 mM) for 30 min, followed by incubation with PMA for 24 h. CD11b, MMP-9, and GAPDH mRNA expression levels were measured by RT-Q-PCR. (B) The summary of the ROS levels. THP-1 cells were pretreated with curcuminoids for 1 h and then treated with PMA for 24 h. The level of ROS was analyzed using flow cytometry, as described in the Materials and Methods. A representative histogram is shown. The data are presented as the mean ± SD from three independent experiments. $^{**}p < 0.01$ represents a significant difference compared to the PMA-untreated cells (vehicle group). $\#\#p < 0.01$ represents a significant difference compared to the PMA-alone-treated cells (veh group).

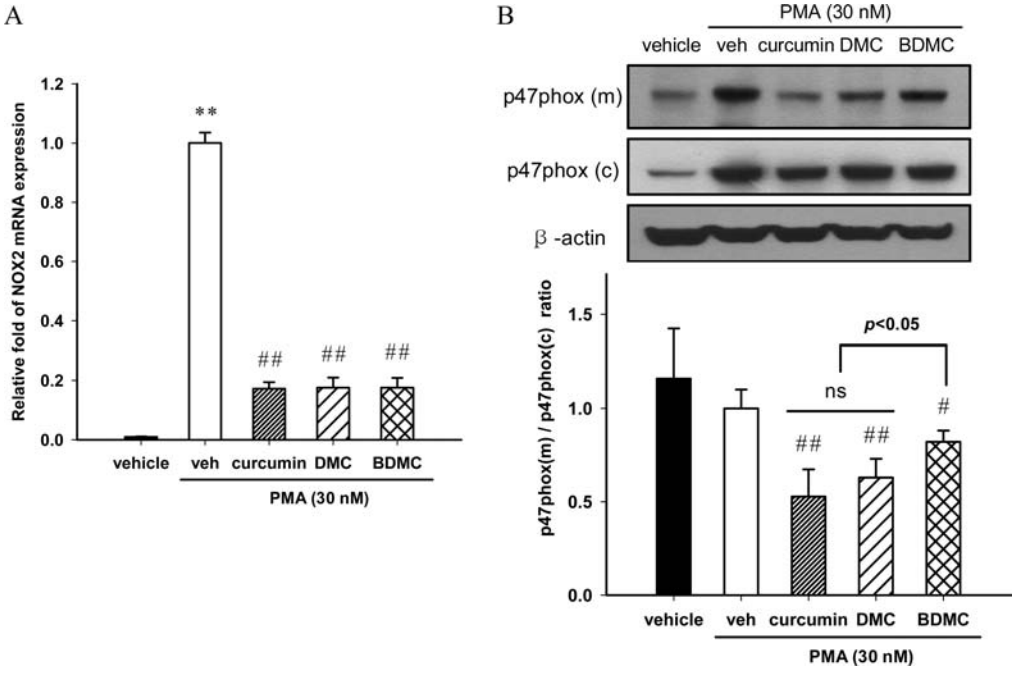

Figure 6. The effects of curcuminoids on NOX2 expression and p47phox activation during PMA-induced THP-1 differentiation. THP-1 cells were treated with vehicle or the indicated curcuminoids for 1 h and then treated with PMA for 24 h. (A) NOX2 and GAPDH mRNA expression was measured by RT-Q-PCR. (B) The membrane form of p47phox (m) and the cytosolic p47phox (c) proteins were analyzed using Western blot analysis. The experiments were replicated at least three times, and a representative blot is shown. The normalized intensity of p47phox (m) versus p47phox (c) is presented as the mean ± SD of three independent experiments. $^{**}p < 0.01$ represents a significant difference compared to the PMA-untreated cells (vehicle group). $\#p < 0.05$ and $\#\#p < 0.01$ represent a significant difference compared to the PMA-alone-treated cells (veh group). ns: no significant differences.

DOI: 10.1021/acs.jafc.5b04083
J. Agric. Food Chem. 2015, 63, 8838−8848

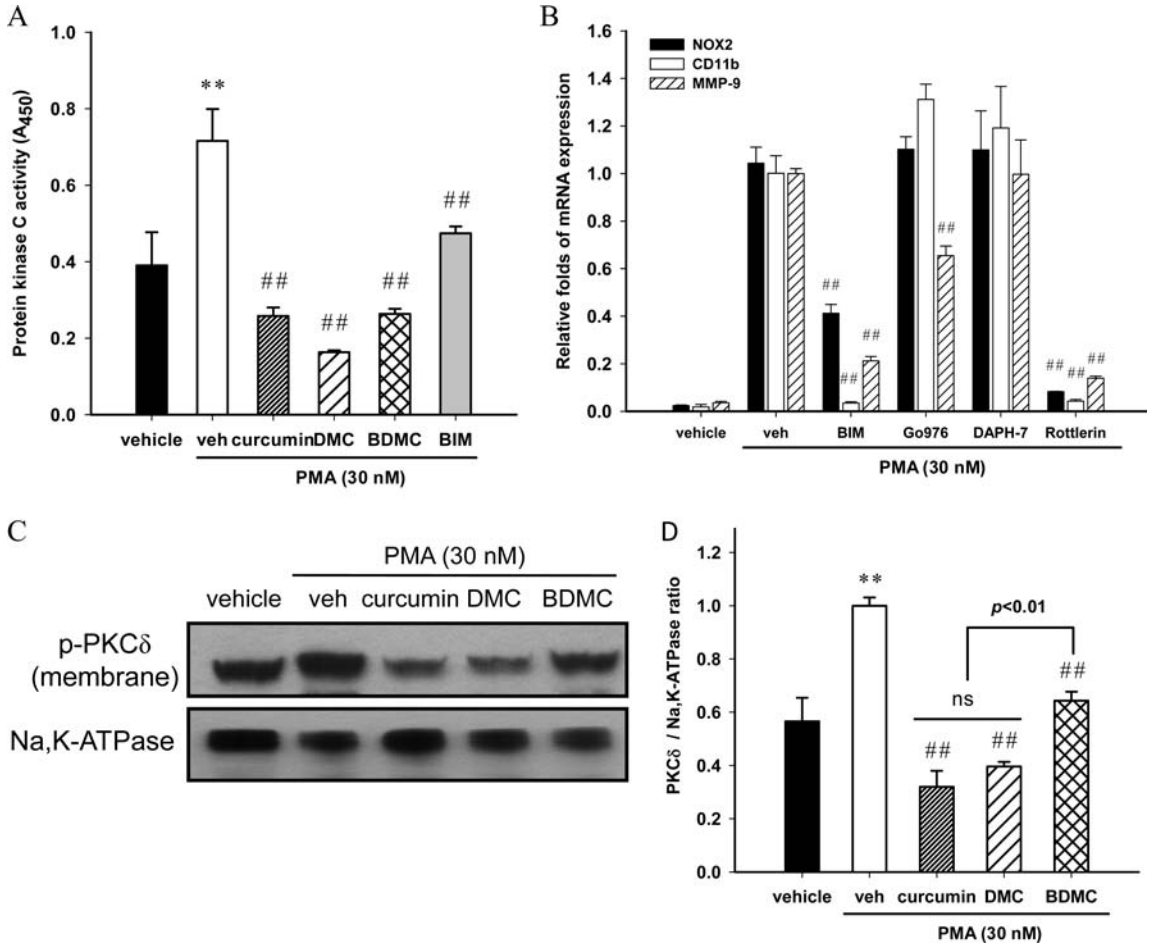

Figure 7. The effects of curcumin, DMC, and BDMC on protein kinase C (PKC) activity during PMA-induced THP-1 differentiation. (A) THP-1 cells were treated with vehicle, curcuminoids (20 μM), or PKC inhibitor (BIM) for 1 h and then treated with PMA for 24 h. PKC activity was detected using an PKC assay kit, as described in the Materials and Methods. The data represent the mean ± SD of three independent experiments. (B) THP-1 cells were pretreated for 30 min with vehicle or one of the following inhibitors: Gö6976 (1 μM), DAPH-7 (1 μM), and rottlerin (10 μM). The mRNA levels of NOX2, CD11b, and MMP-9 were determined via RT-Q-PCR. (C) The membrane form of p-PKCδ and the Na,K-ATPase internal control protein were analyzed using Western blot analysis. The experiments were replicated at least three times, and a representative blot is shown. (D) The normalized intensity of p-PKCδ versus the Na,K-ATPase internal control is presented as the mean ± SD of three independent experiments. **$p < 0.01$ represents a significant difference compared to the PMA-untreated cells (vehicle group). ##$p < 0.01$ represents a significant difference compared to the PMA-alone-treated cells (veh group). ns: no significant differences.

protein expression in THP-1 cells, which was significantly suppressed by pretreatment with curcumin, DMC, and BDMC (10 or 20 μM). We investigated the effect of curcuminoids on extracellular MMP-9 activity using gelatin zymography analysis. As shown in Figure 4C, extracellular MMP-9 activity was strongly induced after PMA stimulation for 24 h. In contrast, pretreatment of the cells with curcumin, DMC, or BDMC (20 μM) significantly reduced extracellular MMP-9 activity in PMA-treated THP-1 cells. These results indicate that curcumin, DMC, and BDMC suppress MMP-9 expression and activity during PMA-induced THP-1 differentiation.

Curcumin, DMC, and BDMC Reduced ROS Generation during PMA-Induced THP-1 Differentiation. Reactive oxygen species (ROS) generation is involved in monocyte adhesion and infiltration. To test whether ROS generation induced by PMA was involved in the CD11b and MMP-9 up-regulation in THP-1 cells, the cells were pretreated with 10 mM of the ROS scavenger *N*-acetyl-L-cysteine (NAC) for 30 min, and then PMA (30 nM) was added for an additional 24 h of incubation. CD11b and MMP-9 mRNA expression was determined by RT-Q-PCR. We found that pretreatment of THP-1 cells with NAC significantly decreased CD11b and MMP-9 mRNA expression in the PMA-treated cells (Figure 5A). These data verified the involvement of ROS in PMA-induced CD11b and MMP-9 expression. We further investigated the effect of curcumin, DMC, and BDMC on ROS production during PMA-induced differentiation. As shown in Figure 5B, treatment of THP-1 cells with PMA alone increased DCF fluorescence to 126.7 ± 2.1% compared to the PMA-untreated cells (100.0 ± 2.9%). Preincubation of the cells with curcumin, DMC, and BDMC (20 μM) markedly decreased PMA-induced intracellular ROS to 99.5 ± 7.8%, 87.8 ± 8.2%, and 89.8 ± 7.6%, respectively ($p < 0.01$). These findings suggest that ROS reduction by curcuminoids is involved in the suppression of CD11b and MMP-9 expression during PMA-induced THP-1 differentiation.

Effects of Curcumin, DMC, and BDMC on NADPH Oxidase Activation during PMA-Induced THP-1 Differentiation. During monocyte to macrophage differentiation, ROS is primarily generated by the NADPH oxidase.[31,32] Therefore, the effect of curcumin, DMC, and BDMC on NOX2/gp91phox mRNA expression in PMA-treated THP-1

DOI: 10.1021/acs.jafc.5b04083
J. Agric. Food Chem. 2015, 63, 8838−8848

cells was investigated. Figure 6A shows that curcumin, DMC, and BDMC (20 μM) significantly decreased PMA-induced NOX2 mRNA expression by approximately 80% compared to the PMA-alone-treated group ($p < 0.01$). Next, we examined the effect of curcumin, DMC, and BDMC on PMA-induced membrane translocation of p47phox in THP-1 cells. As shown in Figure 6B, treatment of THP-1 cells with PMA significantly increased both the levels of p47phox protein expression and membrane translocation of p47phox. In contrast, pretreatment of the cells with curcumin, DMC, and BDMC (20 μM) significantly inhibited the PMA-triggered membrane translocation of p47phox. The inhibition activity of curcuminoids is in the order of curcumin ≈ DMC > BDMC in PMA-treated THP-1 cells. These results indicate that curcuminoids inhibit NADPH oxidase activation via the down-regulation of NOX2/gp91phox mRNA expression and the attenuation of p47phox membrane translocation, leading to reduced ROS generation during monocyte to macrophage differentiation.

Effects of Curcumin, DMC, and BDMC on PKC Activity during PMA-Induced THP-1 Differentiation. PMA is known to activate protein kinase C (PKC); specifically, activation of the isoforms PKCα, -β, and -δ is thought to be involved in PMA-induced monocyte to macrophage differentiation.[33,34] Therefore, we analyzed the effects of curcumin, DMC, and BDMC on PKC activity during PMA-induced THP-1 differentiation. As shown in Figure 7A, treatment of THP-1 cells with PMA significantly increased PKC activity, as expected. When the cells were pretreated with curcumin, DMC, and BDMC (20 μM) or a PKC inhibitor (bisindolylmaleimide I, BIM; 2.5 μM), the PMA-induced PKC activity was significantly attenuated.

Furthermore, the possible involvement of PKC isoforms in NOX2, CD11b, and MMP-9 expression during PMA-induced cell differentiation was investigated using specific isoform inhibitors for PKCα (Gö6976), PKCβ (DAPH-7), and PKCδ (rottlerin). The THP-1 cells were pretreated with Gö6976 (1 μM), DAPH-7 (1 μM), and rottlerin (10 μM) for 30 min, and then PMA was added for an additional 24 h of incubation. The NOX2, CD11b, and MMP-9 mRNA expression levels were determined by RT-Q-PCR. As shown in Figure 7B, pretreatment of THP-1 cells with the inhibitor rottlerin significantly decreased NOX2 and CD11b mRNA expression in the PMA-treated cells. However, NOX2 and CD11b mRNA expression was not affected by treatment with the inhibitors Gö6976 or DAPH-7. PMA-induced MMP-9 expression was suppressed by the inhibitors Gö6976 and rottlerin but not by the inhibitor DAPH-7. These results reveal the involvement of PKCδ-dependent pathway activation in PMA-induced NOX2, CD11b, and MMP-9 mRNA expression.

Finally, we examined the effect of curcumin, DMC, and BDMC on PKCδ activation during PMA-induced THP-1 differentiation. The expression of membrane proteins prepared from curcuminoids-treated cells and the phosphorylated PKCδ (p-PKCδ) and Na,K-ATPase (as an internal protein control of the membrane fraction) was determined by Western blot analysis. As shown in Figure 7C,D, the level of membrane-bound p-PKCδ proteins induced by PMA was significantly decreased in THP-1 cells by the addition of curcumin, DMC, and BDMC (20 μM). This data showed that the PKCδ inhibition activity of three curcuminoids is in the order of curcumin ≈ DMC > BDMC. These data indicate that curcuminoids' inhibition of the PKCδ activity during PMA-induced THP-1 differentiation may be associated with suppression of monocyte invasion.

DISCUSSION

Monocyte recruitment, adhesion, and secretion of matrix metalloproteases (MMPs) are crucial for the initiation and progression of atherosclerotic lesions. The suppression of monocyte adhesion and infiltration and macrophage accumulation is thought to exert antiatherosclerotic effects via the attenuation of atherosclerotic plaque formation and a decrease in the plaque rupture. Therefore, investigation into the effects of curcuminoids on monocyte to macrophage differentiation could help elucidate their roles in the prevention or development of therapeutic application for atherosclerosis. In the present study, we found that curcumin, DMC, and BDMC suppressed monocytes−macrophages invasion through the inhibition of PKCδ-dependent NADPH oxidase-derived ROS generation. Attenuation of ROS production by curcumin, DMC, and BDMC led to down-regulation of the key adherent and invasive molecules (including CD11b and MMP-9) during PMA-induced THP-1 differentiation (Figure 8).

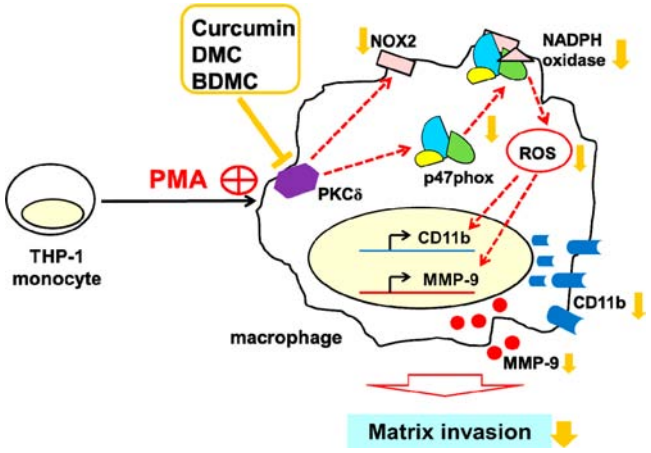

Figure 8. Hypothetical mechanism by which the curcuminoids inhibited monocyte invasion during PMA-induced THP-1 differentiation. During PMA-induced THP-1 differentiation, curcumin, DMC, and BDMC suppressed monocyte invasion through the inhibition of PKCδ-dependent NADPH oxidase-derived ROS generation, which led to the down-regulation of CD11b and MMP-9 expression.

PMA-treated THP-1 cells are generally used as a model to study the function and regulation of monocyte−macrophage differentiation. PMA differentiates THP-1 cells into macrophage-like cells with morphological changes, including a higher level of adherence and higher cell-surface CD11b and metalloprotease MMP-9 expression.[35,36] In the present study, we demonstrated that curcumin, DMC, and BDMC suppressed the matrix invasive ability associated with monocyte−macrophage differentiation. Furthermore, we found that curcumin, DMC, and BDMC decreased CD11b and MMP-9 expression in PMA-differentiated THP-1 cells. Inhibition of the adherent molecule CD11b and protease MMP-9 expression by curcuminoids may lead to a reduction in the invasive ability of monocytes−macrophages. In the present study, we found that BDMC reduced the surface-CD11b protein level more effectively than curcumin and DMC during PMA-induced THP-1 differentiation, despite its similar effect on mRNA

DOI: 10.1021/acs.jafc.5b04083
J. Agric. Food Chem. 2015, 63, 8838−8848

expression. Whether BDMC distinctly modulates the surface-CD11b level through post-transcriptional regulation remains to be investigated. Dietary curcuminoids have been reported to possess antioxidative and antiatherosclerosis activities. Treatment of THP-1 cells with PMA leads to a reduction in LDL receptor expression and an increase in scavenger receptors, such as CD36.[30] Curcuminoids exerted antioxidant activities, regulated heme oxygenase-1 (HO-1) expression and effectively attenuated ox-LDL-induced CD36 expression and activity in PMA-treated THP-1 cells.[25] Our findings supported the hypothesis that the suppression of monocyte invasion by curcuminoids might result in decreased monocyte recruitment and invasion, thereby preventing atherosclerosis initiation.

Curcumin has been reported to possess low toxicity at high doses and is considered to be safe for human subjects.[37] The oral bioavailability of curcuminoids is limited due to their water insolubility, low absorption rate, and rapid metabolism.[38,39] The phase I and II metabolites of curcuminoids, such as hydroxyl or glucuronide/sulfate conjugations, have been reported in in vivo studies. Hoehle et al. reported that the major phase I reduced metabolites of curcuminoids were tetrahydro-, hexahydro- and octahydro-products found in the precision-cut liver slices from rats.[40] During phase II metabolism, curcuminoids and their reduced metabolites are majorly conjugated with glucuronide and a mixed glucuronide/sulfate that are present in the blood circulation in rats.[41] Recently, it has been reported that most orally administrated curcumin is converted to curcumin glucuronide, but residual curcumin or its metabolites other than glucuronide conjugations may be bioactive.[42] In the present study, we demonstrated the cellular response to curcuminoids at micromolar concentrations ranging from 10 to 20 μM, which are widely used in vitro cell culture conditions,[15,23,25] although they are much higher than what can be achieved in vivo. Additionally, the curcuminoid concentrations (10−20 μM) used in this study showed no cytotoxic effects on the THP-1 cells (data not shown). To reach the concentrations employed in this study, novel formulations or delivery systems such as nanoparticle or excipient emulsions may be required to enhance their absorption and improve the bioavailability of curcuminoids.[43,44]

Elevated ROS production causing oxidative stress has been implicated in hypercholesterolemia, atherosclerosis, and heart failure.[45] ROS, especially H_2O_2, is known to be a second messenger in the activation of signaling pathways that induce monocyte adhesion, invasion, and smooth muscle cell migration in atherosclerosis.[6] The H_2O_2 molecules generated from superoxide radicals ($O_2^{\bullet-}$) by superoxide dismutase regulate the expression of several genes by modulating signaling molecules such as mitogen-activated protein kinase (MAPK) and nuclear factor κB (NF-κB).[46] PMA exposure has been reported to induce ROS generation, resulting in cell growth inhibition and monocyte−macrophage differentiation in THP-1 cells.[47] In the present study, we found that depletion of ROS by the antioxidant ROS scavenger NAC led to a reduction in CD11b and MMP-9 mRNA expression in PMA-treated cells. We further demonstrated that curcumin, DMC, and BDMC markedly suppressed ROS production during PMA-induced THP-1 differentiation. Recently, Makino et al. reported that treatment of THP-1 cells with PMA induced CD11b expression via ROS production.[48] Kim et al. reported that MMP-9 expression and cell migration were controlled by ROS production in macrophages.[49] Our current results also revealed that ROS depletion by curcuminoids resulted in a reduction in PMA-induced CD11b and MMP-9 expression in THP-1 cells. Overproduction of ROS has been reported to activate AP-1, SP1, or NF-κB, which are the most well known redox-dependent transcriptional factors and regulate genes involved in inflammation, including MMP-9 in macrophages.[50,51] Whether inhibition of ROS-dependent signaling by curcumin, DMC, and BDMC causes a reduction in the transcriptional activities of AP-1, SP1, or NF-κB remains to be investigated.

Active NADPH oxidase produces superoxide ($O_2^{\bullet-}$) by transferring one electron from cytosolic NADPH to oxygen in polymorphonuclear neutrophils (PMNs) and phagocytes in response to stimuli. Up-regulation of the NOX2 mRNA increased intracellular oxidative stress in macrophages and was associated with the severity of atherosclerosis.[6] Additionally, NOX2 upregulation was correlated with plaque macrophage content in human coronary atherosclerosis.[7] PMA is known to activate this oxidase by promoting the phosphorylation and translocation of cytosolic p47phox, which then leads to active NADPH oxidase assembly. Recently, it was reported that curcumin could act not only as a ROS-scavenging agent but also as an inhibitor of NADPH oxidase activity in a cell-free assay system.[52] In this study, we demonstrated that curcumin, DMC, and BDMC down-regulated NOX2 mRNA expression and also attenuated membrane-bound p47phox translocation during PMA-induced THP-1 to macrophage differentiation. Our current findings reveal that curcumin, DMC, and BDMC may contribute to intracellular ROS reduction through inactivation of the NADPH oxidase and modulation of cell adhesion and invasion during monocyte to macrophage differentiation. The antiatherosclerotic effect of curcuminoids is proposed to reduce ROS production by limiting NADPH oxidase activity in monocytes/macrophages.

Studies have shown that the activation of protein kinase C (PKC) modulates endothelial cells, vascular smooth muscle cells, and monocyte−macrophage functions, suggesting important roles for the PKC signaling pathway in regulating the atherosclerotic process.[53] PMA activates PKC by translocating the kinase from the cytoplasm to the membrane, causing THP-1 differentiation. Additionally, PKC signaling is important for NOX2 and CD11b expression in PMA-primed cells.[32,35] In the current study, we found that curcumin, DMC, and BDMC inhibited PMA-induced PKC activity in THP-1 cells. A change in the expression of PKC isoforms is involved in the cellular differentiation of a variety of cell types, including monocytes. Among the PKC isoforms, PKCα, -β, and -δ are thought to play major roles in many steps in the pro-atherogenic process. In PMA-treated THP-1 cells, PKCα was slightly expressed and PKCδ was highly expressed during monocyte−macrophage differentiation.[35] Activation of PKCα promoted the differentiation of THP-1 cells; however, PKCβ acted in an antagonistic role.[54] In the present study, we demonstrated that inhibition of pan-PKC activity by the inhibitor bisindolylmaleimide I resulted in the down-regulation of NOX2, CD11b, and MMP-9 mRNA expression. Our findings suggest that PKCδ is the most critical isoform of PKC involved in PMA-induced THP-1 differentiation. Furthermore, we found that PMA-induced NOX2, CD11b, and MMP-9 expression in THP-1 cells was also decreased by exposure to the PKCδ-specific inhibitor rottlerin. PKCδ is classified as a member of the new/novel PKC (nPKC) isoenzyme and is widely expressed among cells and tissues. It has been reported that PKCδ is activated by diacylglycerol or PMA. PMA enhanced PKCδ tyrosine phosphorylation and increased the enzyme

DOI: 10.1021/acs.jafc.5b04083
J. Agric. Food Chem. 2015, 63, 8838−8848

activity and translocation from the cytosol to the membrane in various cells.[55] Our current results showed that curcumin, DMC, and BDMC attenuated the membrane translocation of actively phosphorylated PKCδ in PMA-treated THP-1 cells. Recently, curcumin derivative compounds were reported to inhibit PKCδ and NADPH oxidase in equine neutrophils.[52] Taken together, these results suggested that curcuminoids suppressed the activation of the PKCδ/NADPH oxidase/ROS pathway during PMA-induced THP-1 differentiation. Several recent studies supported the hypothesis that treatment of inflammation with a low dose of a PKC isoform inhibitor (such as a PKCδ-specific inhibitor) might prevent or decrease fat accumulation and improve glucose tolerance and foam cell formation in obesity- or hyperlipidemia-associated atherosclerosis.[56,57] Our current findings suggested that curcuminoids may serve as PKCδ inhibitors and provide advantages in modulating the process of atherosclerosis.

In conclusion, this study reports the novel antiatherosclerotic mechanisms of curcuminoids. Our findings reveal for the first time that curcuminoids suppress matrix invasion via the regulation of the PKCδ/NADPH oxidase/ROS signaling pathway during monocyte to macrophage differentiation. Several comparative studies on the biological activities of curcuminoids have shown that curcumin, DMC, and BDMC possessed similar biological activities. Recently, Kou et al. reported that curcumin, DMC, and BDMC distinctly exert antioxidant activities and atheroprotective effects in PMA-differentiated THP-1 macrophage.[25] In the current study, in comparison, the rank order of PKCδ and p47phox translocation inhibition is curcumin ≈ DMC > BDMC during monocyte to macrophage differentiation. These results implied that the *o*-methoxy group of curcuminoids may be more effectively involved in the down-regulation of PKCδ-dependent NADPH oxidase activation. Our results also demonstrated that BDMC showed less activity than curcumin and DMC on PKCδ inhibition; however, equal inhibitory efficacy was demonstrated by these curcuminoids on pan-PKC activity, ROS production, CD11b/MMP-9 mRNA expression, and matrix invasion during PMA-induced THP-1 differentiation. These finding implied that a distinct PKC-isoform-dependent or different signaling pathways downstream of PKC may partly account for BDMC-mediated antiatherosclerotic effects. In addition, the relative cellular uptake of these curcuminoids may also contribute to their efficacy. Therefore, curcuminoids, despite structural similarities, may exhibit different atheroprotective effects.

■ ASSOCIATED CONTENT

Supporting Information

The Supporting Information is available free of charge on the ACS Publications website at DOI: 10.1021/acs.jafc.5b04083.

Primers used in RT-Q-PCR (Table S1) (PDF)

■ AUTHOR INFORMATION

Corresponding Author

*Tel: +886-3-856-5301, ext 2683. Fax: +886-3-856-1422. E-mail: imyenjh@mail.tcu.edu.tw.

Author Contributions

S.-L.H. and P.-Y.C. contributed equally to this work.

Funding

This research was supported by grants MOST-102-2313-B-320-001-MY3 (to J.-H.Y.) and MOST-102-2320-B-041-003-MY3 (to M.-J.W.) from the Ministry of Science and Technology and by grant TCRD-103-17 (to P.-Y.C.) from Buddhist Tzu Chi General Hospital, Taiwan.

Notes

The authors declare no competing financial interest.

■ REFERENCES

(1) Woollard, K. J.; Geissmann, F. Monocytes in atherosclerosis: subsets and functions. *Nat. Rev. Cardiol.* **2010**, *7*, 77−86.

(2) Moore, K. J.; Tabas, I. Macrophages in the pathogenesis of atherosclerosis. *Cell* **2011**, *145*, 341−55.

(3) Rahaman, S. O.; Lennon, D. J.; Febbraio, M.; Podrez, E. A.; Hazen, S. L.; Silverstein, R. L. A CD36-dependent signaling cascade is necessary for macrophage foam cell formation. *Cell Metab.* **2006**, *4*, 211−21.

(4) Weber, C.; Erl, W.; Weber, P. C. Enhancement of monocyte adhesion to endothelial cells by oxidatively modified low-density lipoprotein is mediated by activation of CD11b. *Biochem. Biophys. Res. Commun.* **1995**, *206*, 621−8.

(5) Stuve, O.; Chabot, S.; Jung, S. S.; Williams, G.; Yong, V. W. Chemokine-enhanced migration of human peripheral blood mononuclear cells is antagonized by interferon beta-1b through an effect on matrix metalloproteinase-9. *J. Neuroimmunol.* **1997**, *80*, 38−46.

(6) Park, J. G.; Oh, G. T. The role of peroxidases in the pathogenesis of atherosclerosis. *BMB Rep* **2011**, *44*, 497−505.

(7) Sorescu, D.; Weiss, D.; Lassegue, B.; Clempus, R. E.; Szocs, K.; Sorescu, G. P.; Valppu, L.; Quinn, M. T.; Lambeth, J. D.; Vega, J. D.; Taylor, W. R.; Griendling, K. K. Superoxide production and expression of nox family proteins in human atherosclerosis. *Circulation* **2002**, *105*, 1429−1435.

(8) Babior, B. M. NADPH oxidase: An update. *Blood* **1999**, *93*, 1464−1476.

(9) El Benna, J.; Faust, L. R. P.; Johnson, J. L.; Babior, B. M. Phosphorylation of the respiratory burst oxidase subunit p47phox as determined by two-dimensional phosphopeptide mapping. Phosphorylation by protein kinase C, protein kinase A, and a mitogen-activated protein kinase. *J. Biol. Chem.* **1996**, *271*, 6374−8.

(10) Babior, B. M.; Lambeth, J. D.; Nauseef, W. The neutrophil NADPH oxidase. *Arch. Biochem. Biophys.* **2002**, *397*, 342−4.

(11) Barry-Lane, P. A.; Patterson, C.; van der Merwe, M.; Hu, Z.; Holland, S. M.; Yeh, E. T.; Runge, M. S. p47phox is required for atherosclerotic lesion progression in ApoE$^{(-/-)}$ mice. *J. Clin. Invest.* **2001**, *108*, 1513−22.

(12) Judkins, C. P.; Diep, H.; Broughton, B. R.; Mast, A. E.; Hooker, E. U.; Miller, A. A.; Selemidis, S.; Dusting, G. J.; Sobey, C. G.; Drummond, G. R. Direct evidence of a role for Nox2 in superoxide production, reduced nitric oxide bioavailability, and early atherosclerotic plaque formation in ApoE$^{-/-}$ mice. *Am. J. Physiol Heart Circ Physiol* **2010**, *298*, H24−32.

(13) Hatcher, H.; Planalp, R.; Cho, J.; Torti, F. M.; Torti, S. V. Curcumin: from ancient medicine to current clinical trials. *Cell. Mol. Life Sci.* **2008**, *65*, 1631−52.

(14) Kim, K. M.; Pae, H. O.; Zhung, M.; Ha, H. Y.; Ha, Y. A.; Chai, K. Y.; Cheong, Y. K.; Kim, J. M.; Chung, H. T. Involvement of anti-inflammatory heme oxygenase-1 in the inhibitory effect of curcumin on the expression of pro-inflammatory inducible nitric oxide synthase in RAW264.7 macrophages. *Biomed. Pharmacother.* **2008**, *62*, 630−6.

(15) Liao, K. K.; Wu, M. J.; Chen, P. Y.; Huang, S. W.; Chiu, S. J.; Ho, C. T.; Yen, J. H. Curcuminoids promote neurite outgrowth in PC12 cells through MAPK/ERK- and PKC-dependent pathways. *J. Agric. Food Chem.* **2012**, *60*, 433−43.

(16) Na, L. X.; Li, Y.; Pan, H. Z.; Zhou, X. L.; Sun, D. J.; Meng, M.; Li, X. X.; Sun, C. H. Curcuminoids exert glucose-lowering effect in type 2 diabetes by decreasing serum free fatty acids: a double-blind, placebo-controlled trial. *Mol. Nutr. Food Res.* **2013**, *57*, 1569−77.

(17) Chen, W. C.; Lai, Y. A.; Lin, Y. C.; Ma, J. W.; Huang, L. F.; Yang, N. S.; Ho, C. T.; Kuo, S. C.; Way, T. D. Curcumin suppresses doxorubicin-induced epithelial-mesenchymal transition via the inhib-

DOI: 10.1021/acs.jafc.5b04083
J. Agric. Food Chem. 2015, 63, 8838−8848

ition of TGF-beta and PI3K/AKT signaling pathways in triple-negative breast cancer cells. *J. Agric. Food Chem.* **2013**, *61*, 11817−24.
(18) Ramirez Bosca, A.; Soler, A.; Carrion-Gutierrez, M. A.; Pamies Mira, D.; Pardo Zapata, J.; Diaz-Alperi, J.; Bernd, A.; Quintanilla Almagro, E.; Miquel, J. An hydroalcoholic extract of Curcuma longa lowers the abnormally high values of human-plasma fibrinogen. *Mech. Ageing Dev.* **2000**, *114*, 207−10.
(19) Soni, K. B.; Kuttan, R. Effect of oral curcumin administration on serum peroxides and cholesterol levels in human volunteers. *Indian J. Physiol. Pharmacol.* **1992**, *36*, 273−5.
(20) Asai, A.; Miyazawa, T. Dietary curcuminoids prevent high-fat diet-induced lipid accumulation in rat liver and epididymal adipose tissue. *J. Nutr.* **2001**, *131*, 2932−5.
(21) Shin, S. K.; Ha, T. Y.; McGregor, R. A.; Choi, M. S. Long-term curcumin administration protects against atherosclerosis via hepatic regulation of lipoprotein cholesterol metabolism. *Mol. Nutr. Food Res.* **2011**, *55*, 1829−40.
(22) Peschel, D.; Koerting, R.; Nass, N. Curcumin induces changes in expression of genes involved in cholesterol homeostasis. *J. Nutr. Biochem.* **2007**, *18*, 113−9.
(23) Tai, M. H.; Chen, P. K.; Chen, P. Y.; Wu, M. J.; Ho, C. T.; Yen, J. H. Curcumin enhances cell-surface LDLR level and promotes LDL uptake through downregulation of PCSK9 gene expression in HepG2 cells. *Mol. Nutr. Food Res.* **2014**, *58*, 2133−45.
(24) Zingg, J. M.; Hasan, S. T.; Cowan, D.; Ricciarelli, R.; Azzi, A.; Meydani, M. Regulatory effects of curcumin on lipid accumulation in monocytes/macrophages. *J. Cell. Biochem.* **2012**, *113*, 833−40.
(25) Kou, M. C.; Chiou, S. Y.; Weng, C. Y.; Wang, L.; Ho, C. T.; Wu, M. J. Curcuminoids distinctly exhibit antioxidant activities and regulate expression of scavenger receptors and heme oxygenase-1. *Mol. Nutr. Food Res.* **2013**, *57*, 1598−610.
(26) Kohro, T.; Tanaka, T.; Murakami, T.; Wada, Y.; Aburatani, H.; Hamakubo, T.; Kodama, T. A comparison of differences in the gene expression profiles of phorbol 12-myristate 13-acetate differentiated THP-1 cells and human monocyte-derived macrophage. *J. Atheroscler. Thromb.* **2004**, *11*, 88−97.
(27) Chen, P. Y.; Yen, J. H.; Kao, R. H.; Chen, J. H. Down-regulation of the oncogene PTTG1 via the KLF6 tumor suppressor during induction of myeloid differentiation. *PLoS One* **2013**, *8*, e71282.
(28) Chen, P. Y.; Ho, Y. R.; Wu, M. J.; Huang, S. P.; Chen, P. K.; Tai, M. H.; Ho, C. T.; Yen, J. H. Cytoprotective effects of fisetin against hypoxia-induced cell death in PC12 cells. *Food Funct.* **2015**, *6*, 286−95.
(29) Chiu, S. P.; Wu, M. J.; Chen, P. Y.; Ho, Y. R.; Tai, M. H.; Ho, C. T.; Yen, J. H. Neurotrophic action of 5-hydroxylated polymethoxyflavones: 5-demethylnobiletin and gardenin A stimulate neuritogenesis in PC12 cells. *J. Agric. Food Chem.* **2013**, *61*, 9453−63.
(30) Qin, Z. The use of THP-1 cells as a model for mimicking the function and regulation of monocytes and macrophages in the vasculature. *Atherosclerosis* **2012**, *221*, 2−11.
(31) Brown, D. I.; Griendling, K. K. Nox proteins in signal transduction. *Free Radical Biol. Med.* **2009**, *47*, 1239−53.
(32) Makino, J.; Nakanishi, R.; Kamiya, T.; Hara, H.; Ninomiya, M.; Koketsu, M.; Adachi, T. Luteolin suppresses the differentiation of THP-1 cells through the Inhibition of NOX2 mRNA expression and the membrane translocation of p47phox. *J. Nat. Prod.* **2013**, *76*, 1285−90.
(33) Nishizuka, Y. Intracellular signaling by hydrolysis of phospholipids and activation of protein kinase C. *Science* **1992**, *258*, 607−14.
(34) Kent, J. D.; Sergeant, S.; Burns, D. J.; McPhail, L. C. Identification and regulation of protein kinase C-delta in human neutrophils. *J. Immunol* **1996**, *157*, 4641−7.
(35) Schwende, H.; Fitzke, E.; Ambs, P.; Dieter, P. Differences in the state of differentiation of THP-1 cells induced by phorbol ester and 1,25-dihydroxyvitamin D3. *J. Leukocyte Biol.* **1996**, *59*, 555−61.
(36) Wong, B.; Lumma, W. C.; Smith, A. M.; Sisko, J. T.; Wright, S. D.; Cai, T. Q. Statins suppress THP-1 cell migration and secretion of matrix metalloproteinase 9 by inhibiting geranylgeranylation. *J. Leukocyte Biol.* **2001**, *69*, 959−62.
(37) Vareed, S. K.; Kakarala, M.; Ruffin, M. T.; Crowell, J. A.; Normolle, D. P.; Djuric, Z.; Brenner, D. E. Pharmacokinetics of curcumin conjugate metabolites in healthy human subjects. *Cancer Epidemiol., Biomarkers Prev.* **2008**, *17*, 1411−7.
(38) Hoehle, S. I.; Pfeiffer, E.; Solyom, A. M.; Metzler, M. Metabolism of curcuminoids in tissue slices and subcellular fractions from rat liver. *J. Agric. Food Chem.* **2006**, *54*, 756−64.
(39) Hasan, S. T.; Zingg, J. M.; Kwan, P.; Noble, T.; Smith, D.; Meydani, M. Curcumin modulation of high fat diet-induced atherosclerosis and steatohepatosis in LDL receptor deficient mice. *Atherosclerosis* **2014**, *232*, 40−51.
(40) Hoehle, S. I.; Pfeiffer, E.; Solyom, A. M.; Metzler, M. Metabolism of curcuminoids in tissue slices and subcellular fractions from rat liver. *J. Agric. Food Chem.* **2006**, *54*, 756−64.
(41) Asai, A.; Miyazawa, T. Occurrence of orally administrated curcuminoid as glucuronide and glucuronide/sulfate conjugates in rat plasma. *Life Sci.* **2000**, *67*, 2785−93.
(42) Shoji, M.; Nakagawa, K.; Watanabe, A.; Tsuduki, T.; Yamada, T.; Kuwahara, S.; Kimura, F.; Miyazawa, T. Comparison of the effects of curcumin and curcumin glucuronide in human hepatocellular carcinoma HepG2 cells. *Food Chem.* **2014**, *151*, 126−32.
(43) Zou, L.; Liu, W.; Liu, C.; Xiao, H.; McClements, D. J. Utilizing food matrix effects to enhance nutraceutical bioavailability: increase of curcumin bioaccessibility using excipient emulsions. *J. Agric. Food Chem.* **2015**, *63*, 2052−62.
(44) Gangwar, R. K.; Tomar, G. B.; Dhumale, V. A.; Zinjarde, S.; Sharma, R. B.; Datar, S. Curcumin conjugated silica nanoparticles for improving bioavailability and its anticancer applications. *J. Agric. Food Chem.* **2013**, *61*, 9632−7.
(45) Warnholtz, A.; Nickenig, G.; Schulz, E.; Macharzina, R.; Brasen, J. H.; Skatchkov, M.; Heitzer, T.; Stasch, J. P.; Griendling, K. K.; Harrison, D. G.; Bohm, M.; Meinertz, T.; Munzel, T. Increased NADH-oxidase-mediated superoxide production in the early stages of atherosclerosis: evidence for involvement of the renin-angiotensin system. *Circulation* **1999**, *99*, 2027−33.
(46) Hancock, J. T.; Desikan, R.; Neill, S. J. Role of reactive oxygen species in cell signalling pathways. *Biochem. Soc. Trans.* **2001**, *29*, 345−50.
(47) Traore, K.; Trush, M. A.; George, M., Jr.; Spannhake, E. W.; Anderson, W.; Asseffa, A. Signal transduction of phorbol 12-myristate 13-acetate (PMA)-induced growth inhibition of human monocytic leukemia THP-1 cells is reactive oxygen dependent. *Leuk. Res.* **2005**, *29*, 863−79.
(48) Makino, J.; Kamiya, T.; Hara, H.; Adachi, T. TPA induces the expression of EC-SOD in human monocytic THP-1 cells: involvement of PKC, MEK/ERK and NOX-derived ROS. *Free Radical Res.* **2012**, *46*, 637−44.
(49) Kim, S. Y.; Lee, J. G.; Cho, W. S.; Cho, K. H.; Sakong, J.; Kim, J. R.; Chin, B. R.; Baek, S. H. Role of NADPH oxidase-2 in lipopolysaccharide-induced matrix metalloproteinase expression and cell migration. *Immunol. Cell Biol.* **2010**, *88*, 197−204.
(50) Han, K. Y.; Kwon, T. H.; Lee, T. H.; Lee, S. J.; Kim, S. H.; Kim, J. Suppressive effects of Lithospermum erythrorhizon extracts on lipopolysaccharide-induced activation of AP-1 and NF-kappaB via mitogen-activated protein kinase pathways in mouse macrophage cells. *BMB Rep* **2008**, *41*, 328−33.
(51) Chuang, S. Y.; Yang, S. H.; Chen, T. Y.; Pang, J. H. Cilostazol inhibits matrix invasion and modulates the gene expressions of MMP-9 and TIMP-1 in PMA-differentiated THP-1 cells. *Eur. J. Pharmacol.* **2011**, *670*, 419−26.
(52) Derochette, S.; Franck, T.; Mouithys-Mickalad, A.; Ceusters, J.; Deby-Dupont, G.; Lejeune, J. P.; Neven, P.; Serteyn, D. Curcumin and resveratrol act by different ways on NADPH oxidase activity and reactive oxygen species produced by equine neutrophils. *Chem.-Biol. Interact.* **2013**, *206*, 186−93.
(53) Fan, H. C.; Fernandez-Hernando, C.; Lai, J. H. Protein kinase C isoforms in atherosclerosis: pro- or anti-inflammatory? *Biochem. Pharmacol.* **2014**, *88*, 139−49.

DOI: 10.1021/acs.jafc.5b04083
J. Agric. Food Chem. 2015, 63, 8838−8848

(54) Dieter, P.; Schwende, H. Protein kinase C-alpha and -beta play antagonistic roles in the differentiation process of THP-1 cells. *Cell. Signalling* **2000**, *12*, 297−302.
(55) Kikkawa, U.; Matsuzaki, H.; Yamamoto, T. Protein kinase C delta (PKC delta): activation mechanisms and functions. *J. Biochem.* **2002**, *132*, 831−9.
(56) Huang, W.; Bansode, R. R.; Bal, N. C.; Mehta, M.; Mehta, K. D. Protein kinase Cbeta deficiency attenuates obesity syndrome of ob/ob mice by promoting white adipose tissue remodeling. *J. Lipid Res.* **2012**, *53*, 368−78.
(57) Bezy, O.; Tran, T. T.; Pihlajamaki, J.; Suzuki, R.; Emanuelli, B.; Winnay, J.; Mori, M. A.; Haas, J.; Biddinger, S. B.; Leitges, M.; Goldfine, A. B.; Patti, M. E.; King, G. L.; Kahn, C. R. PKCdelta regulates hepatic insulin sensitivity and hepatosteatosis in mice and humans. *J. Clin. Invest.* **2011**, *121*, 2504−17.

DOI: 10.1021/acs.jafc.5b04083
J. Agric. Food Chem. 2015, 63, 8838−8848

function of miR528 in the adaptive response to environmental factors in rice remains unclear.

Thus, in the present study, a construct carrying the overexpressed miR528 precursor was subsequently transferred to the *japonica* rice Nipponbare cultivar, which is more tolerant to As(III) than Minghui 86. As expected, the transgenic rice plants became more sensitive to As(III) compared with WT plants. On this basis, the physiological and molecular mechanisms of miR528-mediated As(III) sensitivity were preliminarily investigated.

MATERIALS AND METHODS

Rice Cultivation and Treatments. The *japonica* rice cv. Nipponbare was used in all experiments. Rice seeds were surface sterilized with 0.5% NaOCl for 15 min, then rinsed thoroughly, and soaked in deionized water overnight. Next, the seeds were placed on filter paper and germinated for 5 days by supplying a 0.5 mM $CaCl_2$ solution. Subsequently, the rice seedlings were transferred to 10 L containers filled with half-strength Kimura solution[21] for an additional 21 days of hydroponic cultivation in a growth chamber under a 16 h light (30 °C)/8 h dark (20 °C) photoperiod. Then, the seedlings were treated with 25 μM sodium arsenite ($NaAsO_2$) for 6 days. During rice cultivation and treatment, the nutrient solution was renewed every 3 days. At different time points in the As(III) treatment (6, 24, 72, and 144 h), rice roots, shoots, and leaves were sampled separately for further analyses. At harvest, the As(III)-treated seedling roots were first immersed in an ice-cold desorption solution for 10 min to remove apoplastic As. The desorption solution was composed of 1 mM K_2HPO_4, 0.5 mM $Ca(NO_3)_2$, and 5 mM MES (pH 5.5).[21]

Cloning of miR528 and Rice Transformation. A 400 bp fragment harboring the miR528 precursor sequence was amplified from the genomic DNA of cv. Nipponbare using the primers 5′-AAA GAG CTC CCA CCC TTC ACC AAT GGA TGC ATC-3′ (forward) and 5′-AAA GGA TCC GAA ATG GAT ATG AAT TCA GAC CTG G-3′ (reverse). The amplified PCR product was cloned into the Ubiquitin promoter cassette of pCAMBIA1300 between the *Sac*I and *Bam*HI restriction sites, and this construct was subsequently transformed into *Escherichia coli* strain DH5α for proliferation. After confirmation through sequencing, the plasmid carrying pCAMBIA1300-*MIR528* was electroporated into *Agrobacterium tumefaciens* EHA105, which was then transformed into rice to generate transgenic plants. T_3 homozygous lines were used for all experiments.

Real-Time Quantitative RT-PCR (qPCR). Total RNA and small RNAs from different tissues were extracted using the RNAiso plus and RNAiso for small RNA Kits (TaKaRa, Shiga, Japan), respectively. For real-time RT-PCR analysis, a universal reverse primer and two pairs of specific primers were designed for miR528-5p and -3p, respectively (Supplementary Table 1). The real-time qPCR mix included 5 μL of cDNA, 5 μL of primers, and 10 μL of 2× SYBR Green Mix, in a final volume of 20 μL. Real-time qPCR was carried out in a Mastercycler ep realplex system (Eppendorf, Hauppauge, NY, USA) using the SYBR PrimeScript miRNA RT-PCR Kit (TaKaRa) under conditions of 95 °C for 1 min, followed by 40 cycles of 95 °C for 15 s and 60 °C for 30 s.

The expression analyses of the target genes and six functional genes were also performed using real-time qPCR. In these analyses, the RNA was first treated with DNase I and then reverse transcribed using an oligo(dT) primer. The PrimeScript RT Reagent Kit (TaKaRa) was used to generate cDNA, at 50 °C for 30−60 min. The primers employed for PCR amplification are listed in Supplementary Table 1. The Mastercycler ep realplex system (Eppendorf) was also used to carry out real-time qPCR with the SYBR Premix Ex Taq Kit (TaKaRa).

The relative expression level was calculated using the comparative CT method. The results were normalized to the expression of *U6* or β-tubulin. Each experiment was replicated at least three times.

Quantification of Total As and Copper (Cu). After 6 days of As(III) treatment, the contents of total As and Cu in the samples were quantified via inductively coupled plasma mass spectrometry (ICP-MS, Agilent 7500a; Agilent Technologies, Santa Clara, CA, USA). Briefly, the roots and shoots of the rice seedlings were separately sampled and oven-dried, after apoplastic As in the roots was removed by treatment with desorption solution for 10 min. The samples were then powdered using a ball mill (Retsch, MM301, Germany), and 0.3 g of the ground powder from each sample was digested with 0.5 mL of H_2O_2 and 2 mL of nitric acid at 120 °C for 24 h. When the digestion solution had cooled, deionized water was added to a final volume of 20 mL for the quantification of total As and Cu through ICP-MS.

Antioxidant Enzyme Assays. After 3 and 6 days of As(III) treatment, fresh root and leaf samples from each treatment were used to assess the activity of antioxidant enzymes, including superoxide dismutase (SOD), catalase (CAT), and ascorbate peroxidase (APX). The procedures and methods applied for the enzymatic activity analyses were as described previously.[22]

Amino Acid Analysis. Fresh root and leaf samples from each treatment were milled to a fine powder for amino acid analysis. Briefly, 0.3 g of the ground samples was digested with 10 mL of HCl (6 mol L^{-1}) at 110 °C for 24 h. After cooling, the digestion solution was diluted by adding 15 mL of deionized water to a final volume of 25 mL. Then, 1 mL of the diluted digestion solution was transferred to a glass tube and dried in a vacuum oven at 50 °C. After being dried completely, the sample was redried once more after the addition of 1 mL of deionized water. After redrying, 1 mL of deionized water, 0.5 mL of triethylamine hexanenitrile (14%), 0.5 mL of phenyl isothiocyanate, and 2 mL of *n*-hexane were successively added to the glass tube. The mixture was rocked intensely for 2 min and was then placed on a table for a static duration of 1 h. Finally, the obtained subnatant was filtered and injected into a Waters HPLC system to quantify the contents of different amino acids.

Statistical Analysis. All of the data are presented as the mean value ± standard error (SE) of three or four replicates. The data were analyzed via two-way analysis of variance to confirm the variability and validity of the results and using the least significant difference (LSD) test to examine the significant differences between treatments in SPSS 19.0.

RESULTS

Analysis of the Expression Pattern of miR528 at Different Developmental Stages in Transgenic Plants. To better understand the relationship between plant growth and miR528 expression, we investigated the expression patterns of miR528-5p and -3p at four different stages of development in WT and transgenic plants under normal field conditions. As clearly shown in Figure 1, both miR528-5p and -3p were highly expressed in transgenic seedlings compared with WT plants. With the time of plant growth, the expression levels of the two miR528s decreased significantly (Figure 1). Both miR528-5p and -3p reached their minimum expression level at the booting stage and then rebounded at the heading stage. Notably, the expression levels of both miR528s were >5-fold higher in the transgenic plants than in their WT counterparts at booting stage. These observations indicated that miR528 was indeed highly expressed throughout all stages of development in *Ubi::MIR528* transgenic plants.

Comparison of the Phenotypes of WT and *Ubi::MIR528* Transgenic Plants under Arsenite Stress. Under normal growth conditions, the transgenic plants showed no apparent phenotypic changes compared with WT plants, although miR528 was highly expressed throughout all developmental stages in the transgenic plants (Figure 1). However, when challenged with 25 μM As(III) for 3 days, almost the entire *Ubi::MIR528* seedling exhibited the typical As-poisoning phenotype, with chlorosis being observed in the leaves and shrinking or necrosis in aerial parts, in contrast to

DOI: 10.1021/acs.jafc.5b04191
J. Agric. Food Chem. 2015, 63, 8849−8861

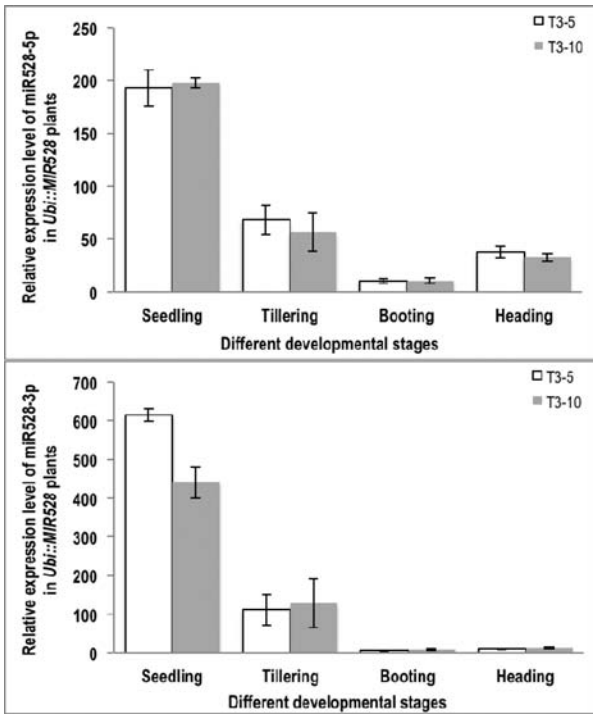

Figure 1. Expression pattern of miR528-5p and -3p in leaves during different developmental stages in rice. The leaves of WT and transgenic plants (#5 and #10) were harvested at four different developmental stages: seedling, tillering, booting, and heading stages. The rice plants were grown in the field under normal conditions. Total RNA was extracted from the harvested leaves, and real-time RT-PCR was performed to assess the relative expression levels of miR528-5p and -3p at the different stages of development. The expression levels of miR528-5p and -3p were normalized to the level of *U6* snRNA. Fold changes in expression levels were estimated using the $2^{-\Delta\Delta CT}$ method relative to levels in the leaves of WT plants at the same developmental stage. Data are reported as the mean ± SE for three independent experiments.

WT (Figure 2). The observed sensitivity of *Ubi::MIR528* plants to As(III) revealed that miR528 is directly involved in the process of As tolerance in rice.

Moreover, compared with WT plants, *Ubi::MIR528* plants accumulated a significantly lower total As level in the roots

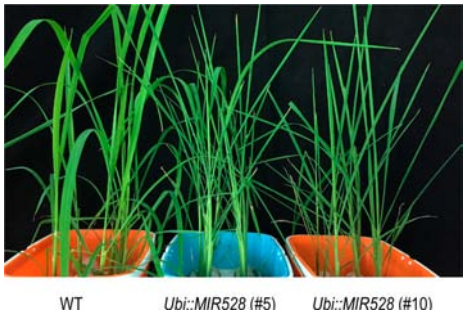

Figure 2. Phenotype of WT and *Ubi::MIR528* transgenic plants under arsenite stress. *Ubi::MIR528* plants were more sensitive to arsenite stress. Plants 5 and 10 are two different *Ubi::MIR528* transgenic lines. Plants were grown hydroponically in half-strength Kimura solution[21] for 21 days under growth conditions with a 16 h light (30 °C)/8 h dark (20 °C) photoperiod and then treated with a 25 μM concentration of arsenite in the form of $NaAsO_2$ for 3 days.

(485.2 ± 21.8 vs 1153.7 ± 69.2 mg kg^{-1}) but showed a higher concentration in the shoots (39.8 ± 1.63 vs 25.7 ± 1.15 mg kg^{-1}). Total As was decreased by 137.8% in the roots, but was increased by 54.9% in the shoots of transgenic plants. Accordingly, transgenic plants overexpressing *MIR528* exhibited significantly weaker As uptake and accumulation (588.0 ± 29.4 vs 1213.2 ± 60.7 mg kg^{-1}; $p < 0.01$) but stronger translocation from the roots to the shoots (0.082 ± 0.004 vs 0.022 ± 0.001 mg kg^{-1}; $p < 0.01$). Interestingly, significant increments of the copper content (166.8 and 440.0%) were observed in the roots (65.1 ± 5.7 vs 24.4 ± 0.7 mg kg^{-1}) and shoots (29.7 ± 1.2 vs 5.5 ± 0.3 mg kg^{-1}) of transgenic plants compared with WT plants.

Spatial−Temporal Expression Analysis of miR528 in WT and Transgenic Plants under Arsenite Stress. According to the annotation in miRBase (release 21), the rice miR528 may produce two mature miRNAs, designated miR528-5p and -3p. Therefore, the spatial−temporal expression patterns of miR528-5p and -3p were assayed in the roots and leaves of WT and *Ubi::MIR528* seedlings at different time points of As(III) treatment via real-time RT-PCR (Figure 3).

As shown in Figure 3, the two mature miRNAs exhibited similar expression patterns in the roots of WT and transgenic plants under challenge with As(III). In WT seedling roots, the expression of both miR528-5p and -3p was consistently increased from 6 to 72 h, reaching the maximum expression level at 72 h and then decreasing at 144 h after treatment with As(III). A similar phenomenon was observed in transgenic plants, where the maximum expression level was detected at 72 h of As(III) exposure (Figure 3). However, inhibition of miR528-3p expression was observed after 24 h of treatment in the roots of transgenic plants. In the leaves, both miR528-5p and -3p were highly up-regulated and reached their highest expression level at 144 h after As(III) treatment in WTs (Figure 3b,d). In contrast, the expression of miR528-3p was down-regulated throughout the treatment stages, although a slight increase was observed at 144 h in the *Ubi::MIR528* plants (Figure 3b). With the exception of the slightly induced expression of miR528-5p detected at 6 h, the expression of miR528-5p remained unchanged or was slightly inhibited during the later treatment times in the different transgenic lines (Figure 3d).

As expected, both miR528s were highly expressed in the roots and leaves of the transgenic plants compared with WT plants (Supplementary Figure 1). The highest expression was observed at 0 h of As(III) treatment, after which the difference between WT and *Ubi::MIR528* plants decreased with increasing treatment time (Supplementary Figure 1). Specifically, the expression of miR528-3p in the leaves was significantly inhibited in *Ubi::MIR528* plants under As(III) stress (from 6 to 144 h) compared with that under control conditions (0 h). Given that overexpression of miR528 confers sensitivity to As(III), it is reasonable to infer the involvement of miR528 in the As(III) response and tolerance of rice.

Time Course Analysis of miR528 and Its Target Genes in Response to Arsenite. In total, 12 and 9 genes were predicted to be potential target genes of miR528-5p and -3p, respectively (Table 1), using psRNATarget with the default parameters (http://plantgrn.noble.org/psRNATarget/). Considering that some genes showed significantly low abundance in the roots or exhibited mismatches with miR528-5p and/or -3p at 10−11 sites, 9 of the predicted target genes were used for expression analysis (Table 1). In addition, a laccase-encoding

DOI: 10.1021/acs.jafc.5b04191
J. Agric. Food Chem. 2015, 63, 8849−8861

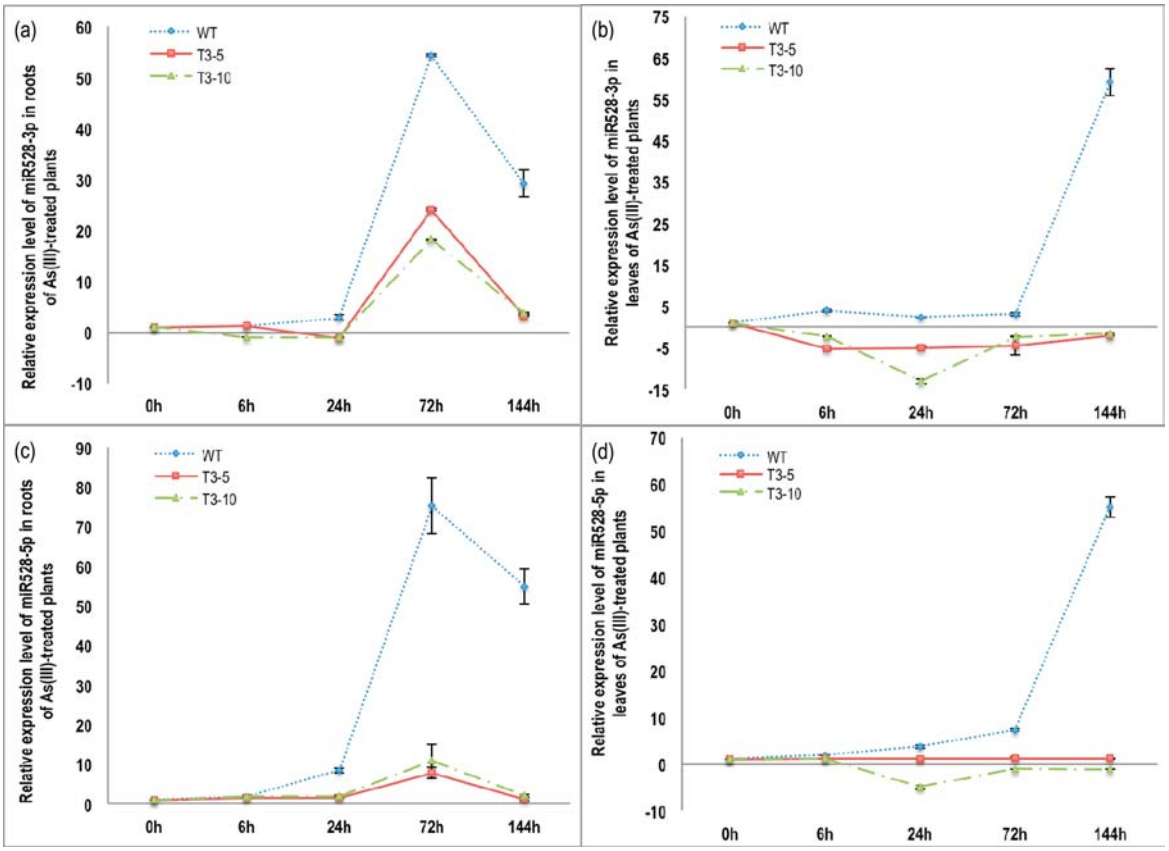

Figure 3. Expression profiles of miR528-5p and -3p in the roots (a, c) and leaves (b, d) of As(III)-treated *Ubi::MIR528* and WT plants. Both miR528-5p and -3p exhibited similar expression profiles in the roots but different profiles in the leaves in response to arsenite stress in transgenic and WT plants. Plants were grown hydroponically and treated with a 25 μM dose of arsenite for 6, 24, 72, or 144 h. Total RNA was isolated from the harvested roots and leaves. The expression levels of miR528-5p and -3p were examined using real-time RT-PCR and normalized to *U6* snRNA levels. Fold changes in expression levels were estimated using the $2^{-\Delta\Delta CT}$ method relative to the levels in *Ubi::MIR528* and WT samples without As(III) treatment (0 h). Data are reported as the mean ± SE for three independent experiments.

gene, *LOC_Os01g62600.1*, that was previously reported to be one of the targets of miR528-5p[17] was also analyzed.

The tested target genes were all expressed in the roots of the As(III)-treated WT and *Ubi::MIR528* plants (Figure 4). Both miR528-5p and -3p were significantly up-regulated at 72 h and then strongly down-regulated at 144 h in both WT and transgenic plants (Figure 4). In contrast, the 10 potential targets could be classified into two groups on the basis of their expression patterns. The first group contained seven target genes of which the expression profile was nearly exactly complementary to miR528-5p or -3p (Figure 4). These genes included one plastocyanin-like protein gene (*LOC_Os07g38290.1*), two multi-copper oxidase genes (*LOC_Os01g03640.1*, *LOC_Os01g03620.1*), two laccase-encoding genes (*LOC_Os01g62600.1*, *LOC_Os01g44330.1*), and two galactosyltransferase family protein-coding genes (*LOC_Os12g41956.1* and *LOC_Os07g09690.1*). In particular, *LOC_Os01g62600.1* and *LOC_Os07g38290.1* showed an exact negative expression pattern in comparison with miR528-5p in the roots of WT and *Ubi::MIR528* (#5) plants, respectively. The negative correlation in the expression pattern further validated the regulatory role of miR528 in relation to these target genes in the response to As(III) tolerance in rice.

The remaining three genes (*LOC_Os06g06050.1*, *LOC_Os09g33800.2*, and *LOC_Os03g40800.1*) were representatives of the second group. Their expression profiles showed no clear negative correlation with miR528s (Figure 4). The results suggested that these three potential target genes either were not true targets of miR528 or might not be involved in the process of miR528-mediated arsenite tolerance in rice.

Alteration of Antioxidant Enzyme Activity and Amino Acid Profiles under Arsenite Stress in Transgenic Plants. In plants, regulation of the expression of antioxidant enzymes, such as SOD, APX, and CAT, is an efficient detoxification mechanism for protecting plants against oxidative stress. To preliminarily elucidate the physiological mechanisms of miR528-mediated As sensitivity, the activity of the antioxidant enzymes SOD, APX, and CAT was assayed in transgenic and WT plants. Compared with the controls (CK), As(III)-treated WT plants exhibited a significant increase of SOD activity at 3 days in the roots and at 6 days in the leaves, whereas a strong decrease was observed at 6 days in the roots and at 3 days in the leaves. However, both the roots and leaves showed more SOD activity after 6 days of treatment with As(III) compared with the 3 day treatment in WT plants; in contrast, with the exception of the 6 day As(III) treatment in the leaves, SOD activity was extensively inhibited in both tested tissues in the transgenic plants upon As exposure (Figure 5a,d).

In the roots, the changes in APX activity were similar between the transgenic and WT plants (Figure 5b). However, transgenic plants exhibited APX activity in the leaves that was distinct from that observed in As(III)-treated WT plants (Figure 5e). In *Ubi::MIR528* plants, excess As strongly elevated APX activity at 3 days but decreased APX activity at 6 days of

DOI: 10.1021/acs.jafc.5b04191
J. Agric. Food Chem. 2015, 63, 8849−8861

Table 1. Summary of the Predicted Target Genes of miR528-5p and -3p in Rice[a]

target accession	expectation	UPE[b]	target start	target end	target description
					miR528-5p
LOC_Os08g04310.1	2	20.806	247	267	cDNAplastocyanin-like domain containing protein, putative, expressed
LOC_Os06g06050.1[c]	1.5	9.118	2648	2668	cDNAOsFBL27-F-box domain and LRR containing protein, expressed
LOC_Os01g40150.1	2.5	18.749	2693	2713	cDNAeukaryotic translation initiation factor 5B, putative, expressed
LOC_Os06g37150.1	2.5	16.324	2000	2020	cDNAL-ascorbate oxidase precursor, putative, expressed
LOC_Os07g38290.1[c]	2	19.606	528	547	cDNAplastocyanin-like domain containing protein, putative, expressed
LOC_Os01g44330.1[c]	3	18.884	41	61	cDNAllaccase precursor protein, putative, expressed
LOC_Os09g33800.2[c]	3	11.738	371	391	cDNAlarabinogalactan protein, putative, expressed
LOC_Os08g44770.2	2.5	4.381	299	319	cDNAlcopper/zinc superoxide dismutase, putative, expressed
LOC_Os08g44770.1	2.5	4.381	299	319	cDNAlcopper/zinc superoxide dismutase, putative, expressed
LOC_Os12g13295.1	3	18.55	79	99	cDNAlexpressed protein
LOC_Os01g03620.1[c]	3	15.308	59	79	cDNAlmulticopper oxidase domain containing protein, expressed
LOC_Os01g03640.1[c]	3	12.644	45	65	cDNAlmulticopper oxidase domain containing protein, expressed
					miR528-3p
LOC_Os01g14160.1	2	12.133	787	807	cDNAlretrotransposon, putative, centromere-specific, expressed
LOC_Os12g11440.1	2	13.01	427	447	cDNAlretrotransposon protein, putative, unclassified, expressed
LOC_Os07g09690.1[c]	3	22.044	1991	2011	cDNAlgalactosyltransferase family protein, putative, expressed
LOC_Os01g09200.1	3	22.495	1708	1728	cDNAlAGC_AGC_other_NDRh_TRCd.1-ACG kinases include homologues to PKA, PKG, and PKC, expressed
LOC_Os03g58920.1	3	23.385	3155	3175	cDNAlgalactosyltransferase family protein, putative, expressed
LOC_Os03g58920.2	3	23.385	1985	2005	cDNAlgalactosyltransferase family protein, putative, expressed
LOC_Os12g41956.1[c]	3	20.704	1779	1799	cDNAlgalactosyltransferase family protein, putative, expressed
LOC_Os03g40800.1[c]	2.5	19.274	207	227	cDNAlexpressed protein

[a]Target prediction was performed using the psRNATarget web server with the default parameters by searching against the rice cDNA sequence database (MSU v7). [b]Target accessibility allowed maximum energy to unpair the target site. [c]Predicted target genes that were used for expression analysis in this study.

As(III) exposure in the leaves. In contrast, APX activity was significantly inhibited at 3 days, but strongly induced at 6 days in the leaves of As(III)-treated WT plants (Figure 5e). Interestingly, elevation of CAT activity was observed after 3 days of As(III) exposure in both the roots and leaves of transgenic and WT plants (Figure 5c,f). However, a reverse tendency of the change in CAT activity was detected at 6 days after As(III) treatment in the roots and leaves (Figure 5c,f).

Amino acid (AA) profiles were also analyzed in the leaves and/or roots of transgenic and WT plants to examine the alterations of various AAs under As-induced oxidative stress (Figure 6). The total contents of three (Pro, Met, and Cys) and six of the examined AAs (Asp, Glu, Ser, Gly, Arg, and Tyr) were significantly greater and lower, respectively, in the leaves of *Ubi::MIR528* plants than in WT plants under normal conditions. However, a significant decrease in contents of all 16 tested AAs, with the greatest reduction occurring for Pro, was observed in both transgenic and WT plants under As(III) stress (Figure 6a). In contrast, there were 3 (Glu, Pro, and Met) and 4 AAs (His, Ala, Tyr, and Val) whose total content was significantly increased or decreased, respectively, whereas 9 of 16 AAs showed no obvious changes in the roots of transgenic plants after treatment with As(III) (Figure 6b). Furthermore, most of the AAs examined (12 of 16) significantly accumulated in the roots of WT plants compared with transgenic plants under As exposure, whereas the contents of three stress-responsive AAs (Glu, Ala, and Pro) were much more abundant in transgenic plants (Figure 6c).

Regulation of the Expression of Genes Involved in As(III) Uptake, Translocation, and Tolerance in Transgenic Plants. Previous research has identified some of the genes functioning in As(III) uptake, translocation, and tolerance in rice.[9,23,24] To preliminarily investigate the possible mechanisms underlying the sensitivity of *Ubi::MIR528* plants to As(III), the expression profiles of six functional genes were further analyzed and compared in the roots and leaves of the *Ubi::MIR528* and WT plants under As(III) stress.

The mRNA transcripts of four of the six tested genes (*NIP2;1*, *Lsi2*, *PIP2;4*, and *PIP2;6*) were strongly decreased during the entire period (from 6 to 144 h) of As(III) treatment in both WT and *Ubi::MIR528* transgenic plants (Supplementary Figure 2). In contrast, the transcripts of *NRAMP1* and *PIP2;7* were found to be highly accumulated at all treatment time points in the transgenic plants but were strongly reduced in WT plants from 72 to 144 h and from 6 to 144 h of As(III) exposure (Supplementary Figure 2).

Furthermore, we compared the expression changes in all of the tested genes in the roots between WT and transgenic plants at each time point (Figure 7). Without As(III) treatment (0 h), *NIP2;1*, *NARAMP1*, and *PIP2;7* were weakly expressed in the transgenic plants compared with WT plants, whereas the remaining genes (*Lsi2*, *NIP2;4*, and *NIP2;6*) showed a reverse expression pattern in relation to the first group of genes (Figure 7). However, under As(III) stress, the expression of *NIP2;1* and *PIP2;7* was differentially induced during the entire treatment period in transgenic plants. *NRAMP1* was also found to be up-regulated from 6 to 72 h but was then down-regulated at 144 h with the addition of As(III). In contrast, *PIP2;4* and *PIP2;6* were highly down-regulated by As(III) treatment, with the exception of *PIP2;4* at 72 h. Notably, *Lsi2* was strongly expressed at 72 h but suppressed at 24 and 144 h the exposure to As(III) in *Ubi::MIR528* plants (Figure 7).

A more complex expression pattern was observed in the leaves of WT and *Ubi::MIR528* plants (Supplementary Figure 3). Compared with the expression pattern observed in WT plants, *NIP2;1* and *Lsi2* were slightly and highly expressed at 6

DOI: 10.1021/acs.jafc.5b04191
J. Agric. Food Chem. 2015, 63, 8849−8861

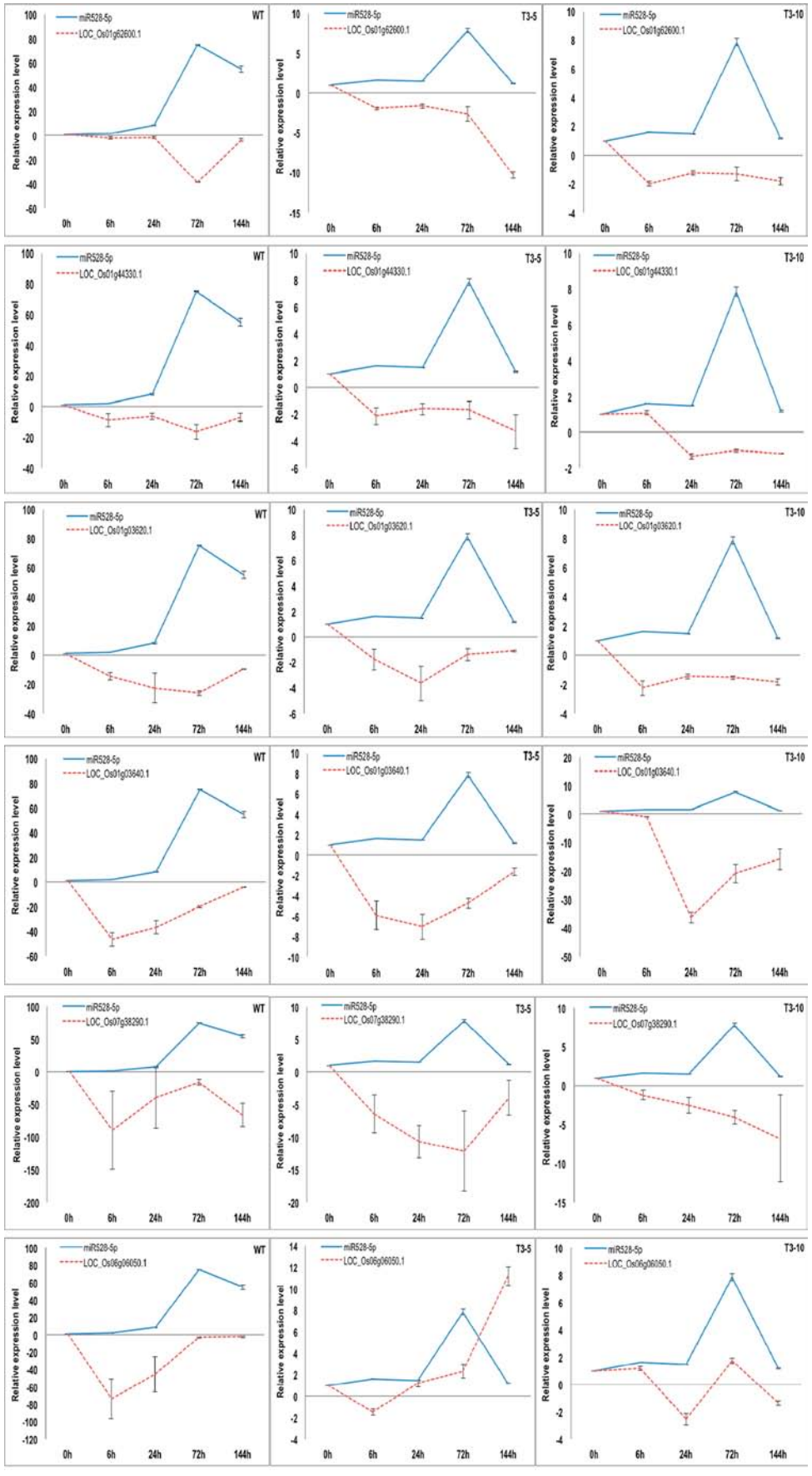

Figure 4. continued

DOI: 10.1021/acs.jafc.5b04191
J. Agric. Food Chem. 2015, 63, 8849−8861

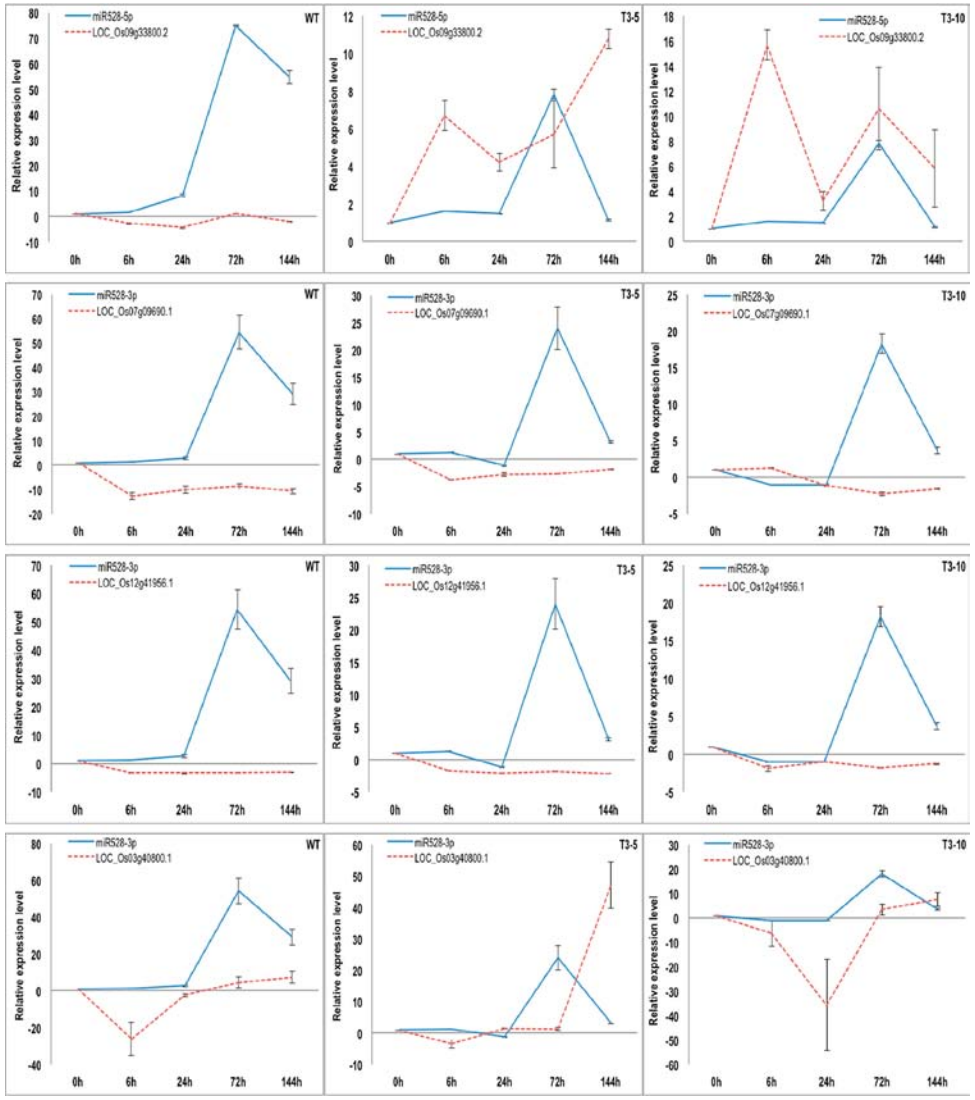

Figure 4. Spatial−temporal expression profiles of miR528 and target genes in the roots of As(III)-treated WT and *Ubi::MIR528* plants. Five genes (*LOC_Os07g38290.1*, *LOC_Os01g03640.1*, *LOC_Os01g03620.1*, *LOC_Os01g62600.1*, *LOC_Os01g44330.1*) and two target genes (*LOC_Os12g41956.1*, *LOC_Os07g09690.1*) showed a clear negative correlation with miR528-5p and -3p in terms of expression. Plants were grown hydroponically and treated with a 25 μM dose of arsenite for 6, 24, 72, or 144 h. Total RNA was isolated using the RNAiso Kit. Relative quantification of miR528 and target gene expression was carried out via real-time RT-PCR analysis. Expression levels were normalized to those of *U6* snRNA and β-tubulin. Fold changes in expression levels were estimated using the $2^{-\Delta\Delta CT}$ method relative to those in WT and *Ubi::MIR528* plants after 0 h of As(III) treatment. The results are reported as the mean ± SE for three biological replicates.

and 144 h, respectively, but were greatly inhibited at 24 and 72 h of As(III) exposure in transgenic plants (Figure 8). A similar case was also observed for *NIP2;4*, which reached its highest expression level at 144 h. With one exception (24 h), the transcripts of *NRAMP1* were highly abundant during the entire treatment period in transgenic plants. Interestingly, *NIP2;6* and *NIP2;7* showed contradictory expression patterns, with the former gene being strongly down-regulated from 0 to 72 h but then rebounding at 144 h, while the expression of the latter gene was slightly increased under As(III) challenge but decreased under normal conditions (0 h) in transgenic plants compared with WT plants (Figure 8).

DISCUSSION

Unlike animals, sessile plants are easily challenged by various environmental factors. During evolution, plants have evolved several strategies to overcome such stress challenges. One of the best-known strategies involves miRNA-mediated gene regulation. Acting as key gene expression regulators,[13] miRNAs have been found to be widely involved in the stress responses and/or tolerance of plants.[12] In the past 10 years, a monocot-specific miR528 has been identified in rice,[16] wheat,[25] maize,[26] sorghum,[26] and sugar cane,[18,27] respectively. In most monocot species, the genome encodes only one miR528, in contrast to the two members observed in maize.[26] miR528 has been demonstrated to be stress-responsive and is differentially expressed under zinc deficiency,[28] low nitrate conditions,[29] drought,[27] and arsenic stress,[16,30] respectively; nevertheless, its biological function has remained unclear thus far. Here, using an overexpression strategy, we established the defining role of miR528 in arsenite tolerance in rice, providing the first evidence contributing to a better understanding of the functions of miR528 in the stress response and/or tolerance of plants.

DOI: 10.1021/acs.jafc.5b04191
J. Agric. Food Chem. 2015, 63, 8849−8861

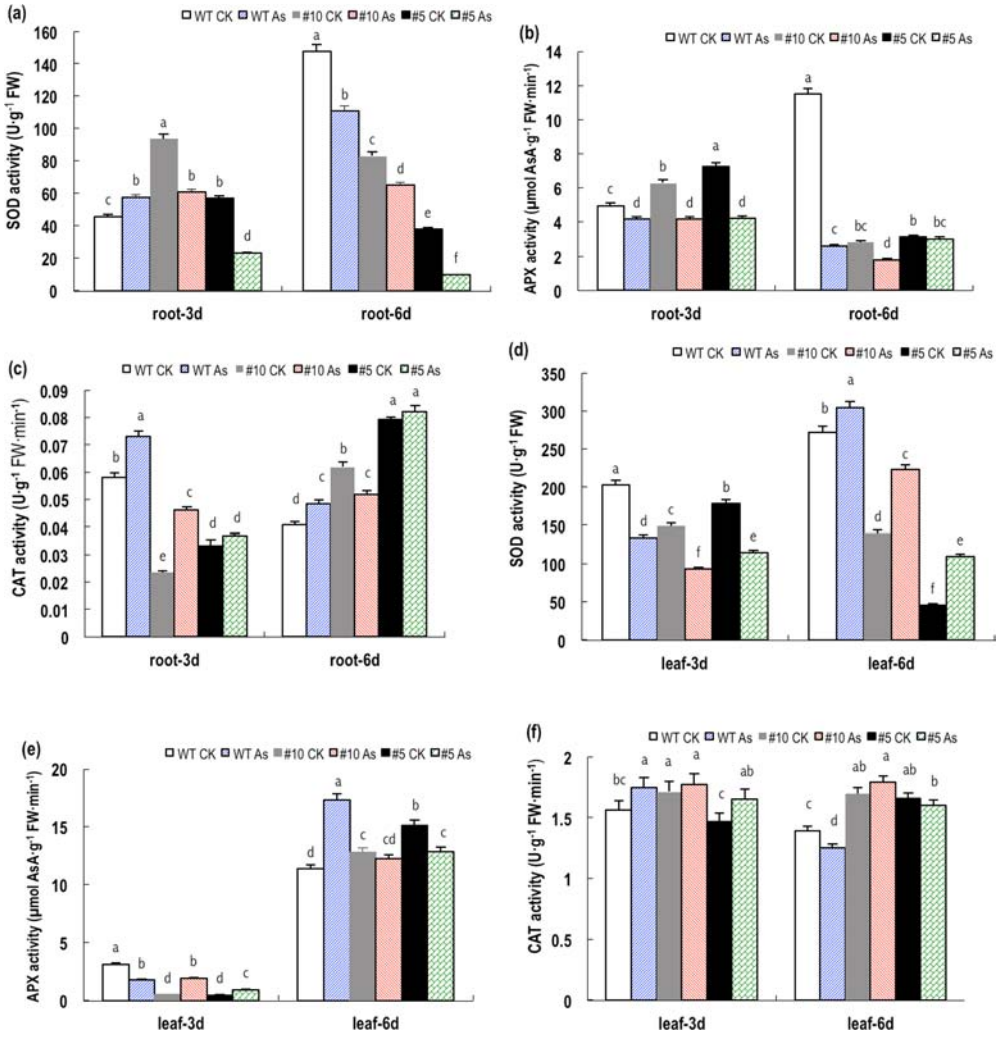

Figure 5. Effect of arsenite exposure on the activity of the antioxidant enzymes SOD, APX, and CAT in the roots (a–c) and leaves (d–f) of WT and *Ubi::MIR528* transgenic plants. Plants were grown hydroponically in a nutrient solution containing 0 or 25 μM sodium arsenite for 3 or 6 days, respectively. Data are reported as the mean ± SE of three replicates. Different letters indicate a significant difference between treatments (LSD; ANOVA analysis; $p \leq 0.05$). WT CK, WT plants without As(III) treatment; WT As, WT plants with 25 μM As(III) treatment; #10 CK, control plants of the 10th transgenic line; #10 As, 10th transgenic line plants treated with 25 μM As(III); #5 CK, control plants of the 5th transgenic line; #5 As, 5th transgenic line plants treated with 25 μM As(III).

In nature, arsenite [As(III)] and arsenate [As(V)] are the predominant forms of As under anaerobic and aerobic conditions, respectively.[1] As(III) might be rapidly oxidized to As(V) in aerobic soils under certain conditions.[1] Additionally, Guo et al.[31] revealed that approximately 10–20% of As(III) added to a nutrient solution might be oxidized to As(V) in the absence of rice seedlings. However, as discussed by Hu et al.,[22] As(III) is expected to be the dominant As species when rice seedlings are cultivated in half-strength Kimura solution with a pH of 5.5,[21] due to the relatively higher redox potential, lack of iron plaque formation,[22] and limited contribution of O_2 loss in the root rhizosphere to the oxidization of As(III) to As(V) under hydroponic culture conditions.[32]

Interestingly, in this study, a significant increment of the Cu content was observed in the roots and shoots of transgenic plants, which could be partially attributed to the following factors: (1) the remarkable deficiency of transcripts of targeted Cu protein-coding genes because of the high induction of miR528 (Table 1 and Figure 4) as well as miR408 and miR397 under arsenite stress;[16,33,34] (2) the potential acceleration of Cu uptake, translocation, and transport in As(III)-stressed transgenic plants, as in lettuce and red clover plants, Cu accumulation has been observed to increase with increasing concentrations of As;[35,36] and (3) the promoter of *MIR528*, like those of *MIR397*, *MIR398*, *MIR408*, and *MIR857*,[33,34,37] contains multiple CuRE-responsive elements (GTAC motif) that bind with AtSPL7 in *Arabidopsis* and play a crucial role in Cu homeostasis.[34] Some transcription factors, for example, OsSPL9, which is an orthologue of AtSPL7,[38] could be strongly activated and, thus, enhance the activity of Cu transporters in the roots and shoots of transgenic plants overexpressing miR528.

We found that the expression patterns of miR528-5p and -3p were similar in the roots, but dissimilar in the leaves between WT and transgenic plants (Figure 3). However, their expression levels were significantly higher in transgenic plants compared with WT plants under either normal or stress conditions (Supplementary Figure 1). Accordingly, overexpression of miR528 would result in the severe inhibition of the expression of its target genes in transgenic plants. As

DOI: 10.1021/acs.jafc.5b04191
J. Agric. Food Chem. 2015, 63, 8849–8861

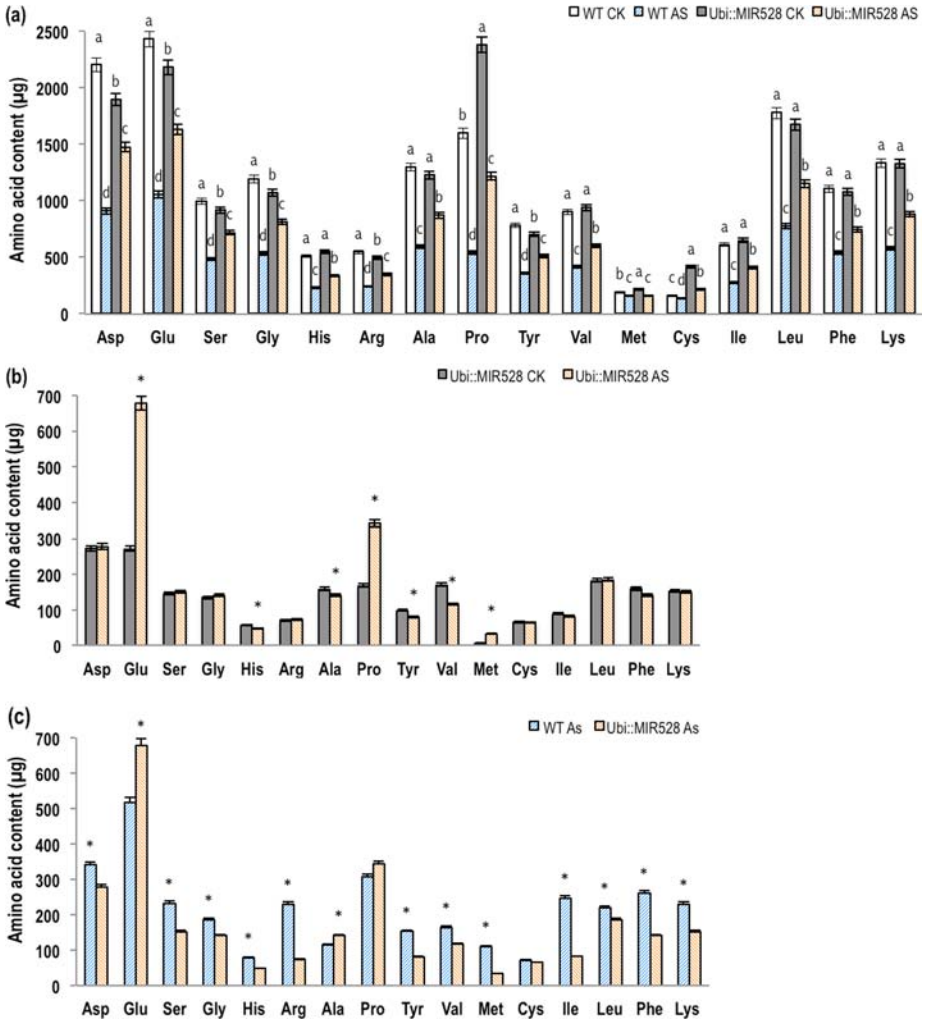

Figure 6. Differential amino acid profiles in response to arsenite stress in the leaves (a) and roots (b, c) of *Ubi::MIR528* and WT plants. The changes in amino acid contents in the roots were significantly different between WT and *Ubi::MIR528* plants. The 21-day-old seedlings were grown for 6 days in a nutrient solution containing 0 or 25 μM sodium arsenite. All values are reported as the mean of triplicates ± SE. Different letters (ANOVA) and asterisks (t test) indicate significantly different amino acid contents between treatments or genotypes ($p \leq 0.05$).

discussed above, the suppression of Cu^{2+}-binding proteins, which are potential targets of miR528-5p (Table 1), might destroy copper homeostasis in transgenic plants, as excess copper is harmful to living cells. On the other hand, two galactosyltransferase family genes were predicted to be potential targets of miR528-3p (Table 1). In plants, galactosyltransferases are reported to function in embryo[39] and anther development,[40] in cell wall synthesis, and in the determination of salt stress tolerance,[41] respectively. Thus, the observed high accumulation of miR528-5p and -3p transcripts could further lead to distortions in copper homeostasis and disorders of the development and growth of roots and leaves of transgenic plants, which might partially explain the observed sensitivity of transgenic plants to arsenite.

In two studies, Dave et al.[42] and Tripathi et al.[43] established that tolerant rice cultivars were prone to accumulate much higher levels of amino acids than sensitive cultivars. We found that the accumulation of 12 of the 16 examined amino acids was significantly lower in the roots of *Ubi::MIR528* plants under As exposure, including that of some essential AAs, such as Met, Val, Ile, Leu, Phe, and Lys (Figure 6), which are highly susceptible to free radicals.[44] However, no significant difference in the total content of Cys, which is a central metabolite that is involved in antioxidant defense and metal detoxification through GSH/PC synthesis,[45] was found between transgenic and WT plants under As stress. Several studies have demonstrated that Pro plays a protective role against active oxygen or hydroxyl radicals in plants.[44,46,47] However, increasing evidence has shown that Pro accumulation is not an indicator of stress tolerance but, merely, a consequence of stress.[48,49] The significant accumulation of free Pro detected in the roots could therefore be reasonably interpreted as a hyperirritability to arsenite in transgenic plants overexpressing miR528. In plants, Pro is known to be mainly synthesized from glutamate,[46] which is another metabolite involved in GSH and PC syntheses.[45] The strong accumulation of the two stress-responsive AAs (Glu and Pro) indicated that Glu should be the major source used for Pro biosynthesis in As-stressed transgenic plant roots. Alternatively, the observed phenomenon might have been due to increased oxidation of Pro to glutamate.[46] However, other possible explanations for the observed high abundance of Pro (for example, protein degradation) cannot be arbitrarily ruled out. Furthermore, a significant increase in glutamic acid was reported in the As-sensitive rice cv. IET-4786, which accumulates remarkably less As than the As-tolerant Triguna,[50] a phenomenon consistent

DOI: 10.1021/acs.jafc.5b04191
J. Agric. Food Chem. 2015, 63, 8849−8861

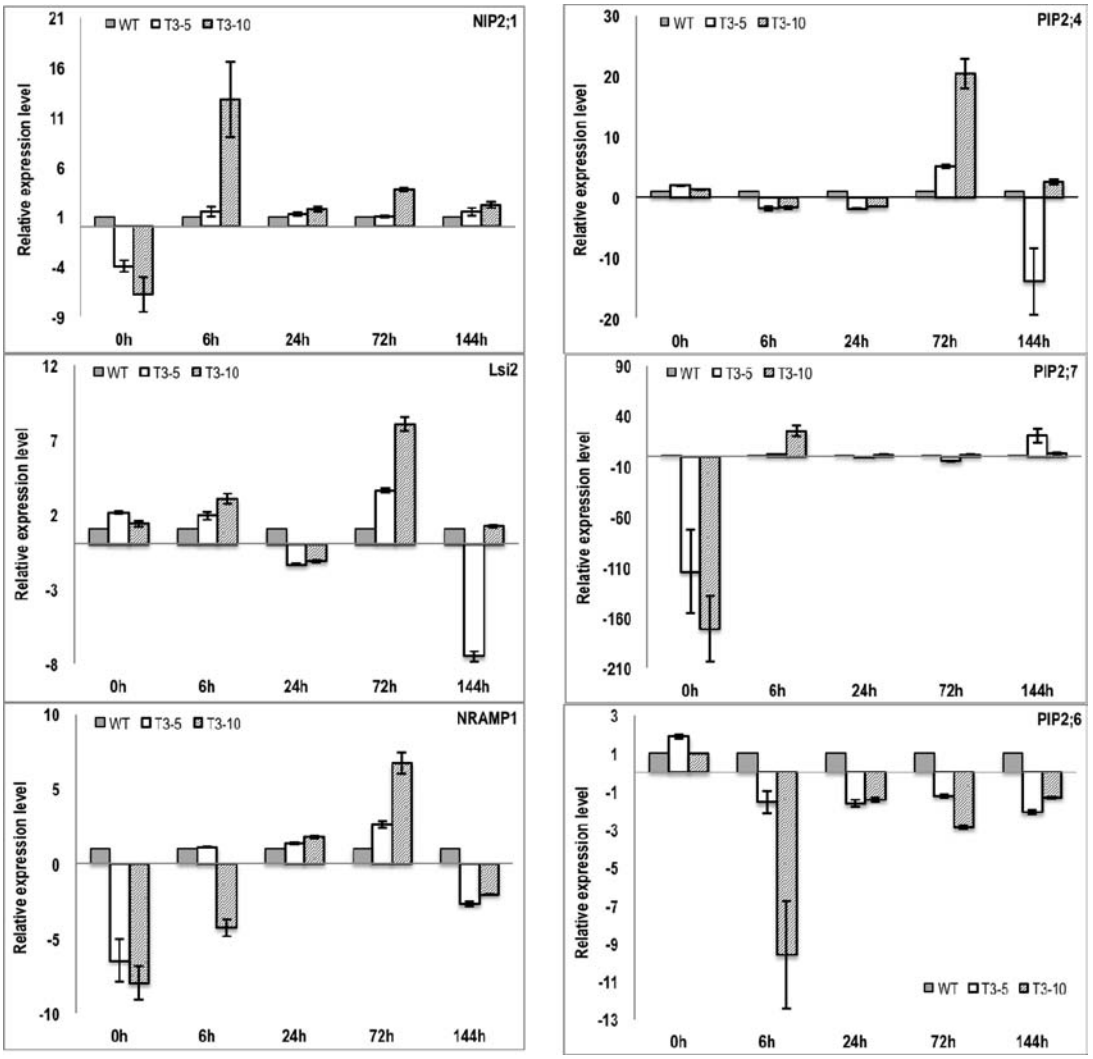

Figure 7. Temporal expression analysis of genes functioning in arsenite uptake, translocation, and tolerance in the roots of *Ubi::MIR528* plants. Plants were grown hydroponically and treated with 25 μM arsenite for 6, 24, 72, and 144 h. Total RNA was isolated using the RNAiso Kit, and expression levels were quantified through real-time RT-PCR analysis. The expression levels of the tested functional genes were normalized to that of β-tubulin. Fold changes in expression levels were estimated via the $2^{-\Delta\Delta CT}$ method relative to levels in the roots of WT plants at the same time point of As(III) treatment (6, 24, 72, or 144 h). The results are presented as the mean ± SE of three biological replicates. *NRAMP1*, *PIP2;6*, *PIP2;4*, and *PIP2;7* were identified as As tolerance related, whereas *NIP2;1* and *Lsi2* function in As(III) uptake, translocation, and accumulation in rice.

with our observations. Moreover, another stress-responsive AA, Ala, was also found to be prominent in transgenic plants under As stress. In general, it appears that the overall reduction of essential and most nonessential AAs in the roots is likely to contribute to the As(III) sensitivity of *Ubi::MIR528* plants.[43]

In rice, a number of genes have been recently identified and characterized as functioning in As(III) uptake, translocation, and tolerance.[9,23,24] To better understand the molecular mechanisms of miR528-mediated As(III) sensitivity in rice, the expression patterns of six genes were investigated in this study. We found that most of the tested genes showed similar expression patterns in the roots of WT and transgenic plants, with two exceptions: *NRAMP1* and *PIP2;7* (Supplementary Figure 2). However, we surprisingly found that *NIP2;1*, which represents the major route of As(III) influx and efflux in rice,[21,23] was slightly induced by As(III) treatment in transgenic plants compared with WT plants (Figure 7). Considering the weak accumulation of As in the transgenic plants, we speculate that the slight activation of *NIP2;1* expression might accelerate the efflux of As(III) into the external media. Another possibility is that other genes that are involved in As(III) uptake in rice,[23] including *NIP2;2*, *NIP1;1*, *NIP3;2*, and *NIP3;1*, could be extensively down-regulated by As(III) in the roots of transgenic plants. In comparison, *Lsi2* was shown to be strongly expressed at 72 h in the roots and at 144 h in the leaves upon As exposure (Figures 7 and 8). This observation better explains why *Ubi::MIR528* plants exhibited greater As translocation. In addition, the expression of two PIP subfamily members, *PIP2;4* and *PIP2;6*, which might function in As tolerance,[9] was clearly suppressed by As(III) at most treatment time points (Figures 7 and 8). Therefore, the observed sensitivity of *Ubi::MIR528* transgenic plants to As(III) might be partly attributable to the significant inhibition of the expression of the corresponding genes in the roots and leaves. *PIP2;7* and *NRAMP1* have also been reported to be related to As tolerance.[9,10] However, the expression of these two genes was increased extensively in both the roots and leaves of transgenic plants (Figures 7 and 8), suggesting that *PIP2;7* and *NRAMP1* may play minor roles in miR528-mediated As tolerance in rice. Nevertheless, the relationship between the expression of functional genes and

DOI: 10.1021/acs.jafc.5b04191
J. Agric. Food Chem. 2015, 63, 8849−8861

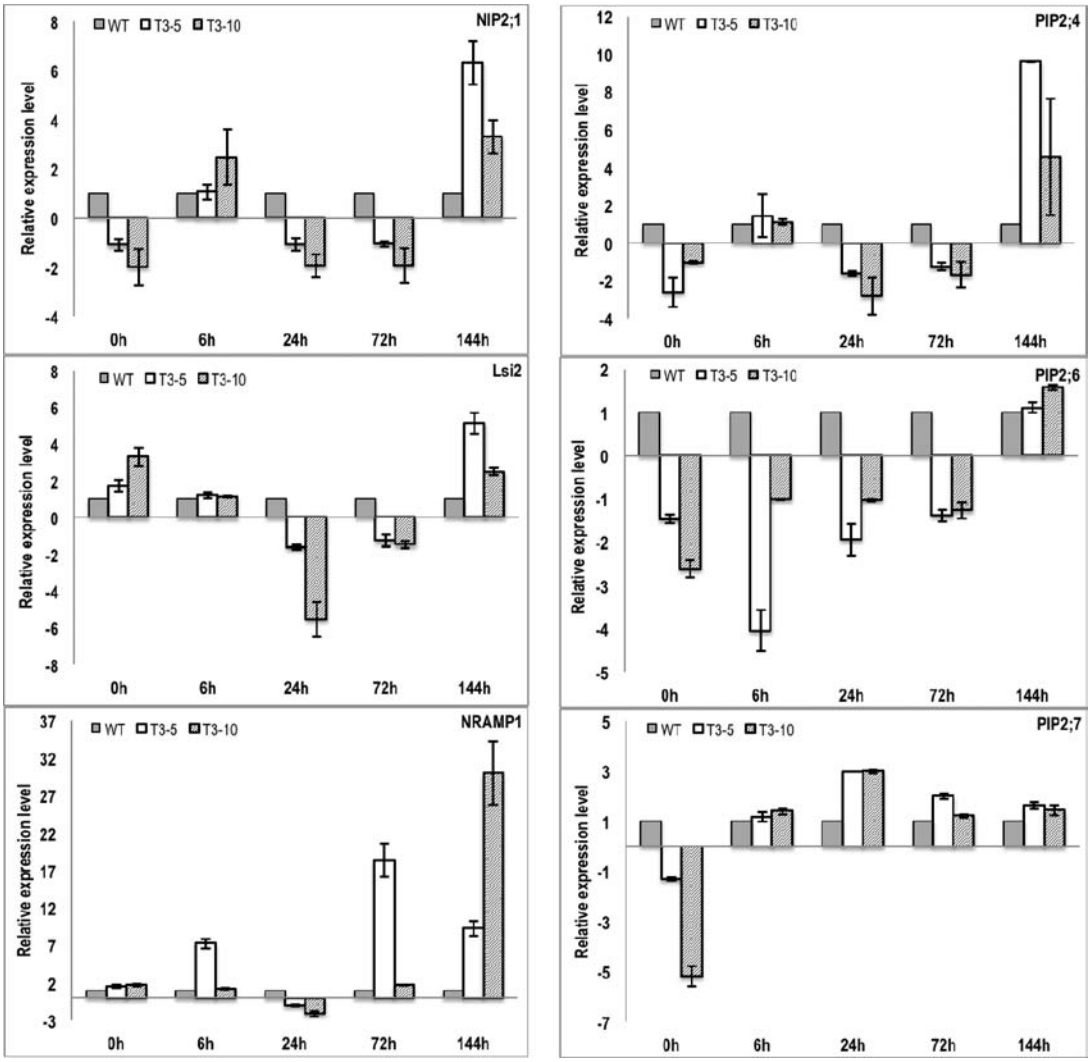

Figure 8. Regulation of the expression of genes with functions in arsenite uptake, translocation, and tolerance in the leaves of *Ubi::MIR528* plants. Plants were grown in half-strength Kimura solution[21] and treated with 25 μM arsenite for 6, 24, 72, or 144 h. Relative quantification of the expression levels of the tested functional genes was conducted using real-time RT-PCR. Expression levels were normalized to that of β-tubulin. Fold changes in expression levels were estimated using the $2^{-\Delta\Delta CT}$ method relative to levels in the leaves of WT plants at the same time point of As(III) treatment (6, 24, 72, or 144 h). The results are presented as the mean ± SE for three biological replicates. Four of six tested genes (*NRAMP1*, *PIP2;6*, *PIP2;4*, and *PIP2;7*) were reported to be involved in As tolerance, whereas *NIP2;1* and *Lsi2* are related to As(III) uptake, translocation, and accumulation in rice.

As tolerance needs to be further validated experimentally in rice.

■ ASSOCIATED CONTENT

Supporting Information

The Supporting Information is available free of charge on the ACS Publications website at DOI: 10.1021/acs.jafc.5b04191.

Supplementary Table 1, RT-PCR primers (XLS)

Supplementary Figure 1, Expression levels of miR528-5p, -3p in the roots and leaves of As(III)-treated Ubi::MIR528 plants (PDF)

Supplementary Figure 2, Temporal expression analysis of genes functioning in arsenite uptake, translocation, and tolerance in the roots of WT and Ubi::MIR528 plants (PDF)

Supplementary Figure 3, Expression profiles of genes functioning in arsenite uptake, translocation, and tolerance in the leaves of WT and Ubi::MIR528 plants (PDF)

■ AUTHOR INFORMATION

Corresponding Authors

*(Q.L.) Phone: 86-0571-63742087. Fax: 86-0571-63741276. E-mail: liuqp@zafu.edu.cn.

*(H.Z.) E-mail: zhhengmu@tsinghua.org.cn.

Author Contributions

‖H.H. and L.Z. contributed equally to this work.

Funding

This work was financially supported by grants from the National Natural Science Foundation of China (31471431), the Zhejiang Provincial Natural Science Foundation of China (LY14B070015, Y3090152), and the Training Program for Outstanding Young Talents of Zhejiang A&F University to Q.L.

Notes

The authors declare no competing financial interest.

DOI: 10.1021/acs.jafc.5b04191
J. Agric. Food Chem. 2015, 63, 8849−8861

■ ACKNOWLEDGMENTS

We thank the anonymous reviewers and Prof. Hanne Christine Bertram for their valuable and constructive suggestions and comments on our earlier manuscript.

■ REFERENCES

(1) Moreno-Jiménez, E.; Esteban, E.; Peñalosa, J. M. The fate of arsenic in soil-plant systems. *Rev. Environ. Contam. Toxicol.* **2012**, *215*, 1−37.

(2) Brammer, H.; Ravenscroft, P. Arsenic in groundwater: a threat to sustainable agriculture in South and South-East Asia. *Environ. Int.* **2009**, *35*, 647−654.

(3) Cubadda, F.; Ciardullo, S.; D'Amato, M.; Raggi, A.; Aureli, F.; Carcea, M. Arsenic contamination of the environment−food chain: a survey on wheat as a test plant to investigate phytoavailable arsenic in Italian agricultural soils and as a source of inorganic arsenic in the diet. *J. Agric. Food Chem.* **2010**, *58*, 10176−10183.

(4) Signes-Pastor, A. J.; Mitra, K.; Sarkhel, S.; Hobbes, M.; Burló, F.; de Groot, W. T.; Carbonell-Barrachina, A. A. Arsenic speciation in food and estimation of the dietary intake of inorganic arsenic in a rural village of West Bengal, India. *J. Agric. Food Chem.* **2008**, *56*, 9469−9474.

(5) Rahman, M. A.; Rahman, M. M.; Reichman, S. M.; Lim, R. P.; Naidu, R. Arsenic speciation in Australian-grown and imported rice on sale in Australia: implications for human health risk. *J. Agric. Food Chem.* **2014**, *62*, 6016−6024.

(6) Su, Y. H.; McGrath, S. P.; Zhao, F. J. Rice is more efficient in arsenite uptake and translocation than wheat and barley. *Plant Soil* **2010**, *328*, 27−34.

(7) Williams, P. N.; Villada, A.; Deacon, C.; Raab, A.; Figuerola, J.; Green, A. J.; Feldmann, J.; Meharg, A. A. Greatly enhanced arsenic shoot assimilation in rice leads to elevated grain levels compared to wheat and barley. *Environ. Sci. Technol.* **2007**, *41*, 6854−6859.

(8) Dasgupta, T.; Hossain, S. A.; Meharg, A. A.; Price, A. H. An arsenate tolerance gene on chromosome 6 of rice. *New Phytol.* **2004**, *163*, 45−49.

(9) Mosa, K. A.; Kumar, K.; Chhikara, S.; Mcdermott, J.; Liu, Z.; Musante, C.; White, J. C.; Dhankher, O. P. Members of rice plasma membrane intrinsic proteins subfamily are involved in arsenite permeability and tolerance in plants. *Transgenic Res.* **2012**, *21*, 1265−1277.

(10) Tiwari, M.; Sharma, D.; Dwivedi, S.; Singh, M.; Tripathi, R. D.; Trivedi, P. K. Expression in *Arabidopsis* and cellular localization reveal involvement of rice NRAMP, OsNRAMP1, in arsenic transport and tolerance. *Plant, Cell Environ.* **2014**, *37*, 140−152.

(11) Lim, S. D.; Hwang, J. G.; Han, A. R.; Park, Y. C.; Lee, C.; Ok, Y. S.; Jang, C. S. Positive regulation of rice RING E3 ligase OsHIR1 in arsenic and cadmium uptakes. *Plant Mol. Biol.* **2014**, *85*, 365−379.

(12) Gupta, O. P.; Sharma, P.; Gupta, R. K.; Sharma, I. MicroRNA mediated regulation of metal toxicity in plants: present status and future perspectives. *Plant Mol. Biol.* **2014**, *84*, 1−18.

(13) Moreno-Moya, J. M.; Vilella, F.; Simón, C. MicroRNA: key gene expression regulators. *Fertil. Steril.* **2014**, *101*, 1516−1523.

(14) Ding, Y.; Qu, A.; Gong, S.; Huang, S.; Lv, B.; Zhu, C. Molecular identification and analysis of Cd-responsive microRNAs in rice. *J. Agric. Food Chem.* **2013**, *61*, 11668−11675.

(15) Li, T.; Li, H.; Zhang, Y. X.; Liu, J. Y. Identification and analysis of seven H_2O_2-responsive miRNAs and 32 new miRNAs in the seedlings of rice (*Oryza sativa* L. ssp. *indica*). *Nucleic Acids Res.* **2011**, *39*, 2821−2833.

(16) Liu, Q.; Zhang, H. Molecular identification and analysis of arsenite stress-responsive miRNAs in rice. *J. Agric. Food Chem.* **2012**, *60*, 6524−6536.

(17) Campo, S.; Peris-Peris, C.; Siré, C.; Moreno, A. B.; Donaire, L.; Zytnicki, M.; Notredame, C.; Llave, C.; San Segundo, B. Identification of a novel microRNA (miRNA) from rice that targets an alternatively spliced transcript of the Nramp6 (natural resistance-associated macrophage protein 6) gene involved in pathogen resistance. *New Phytol.* **2013**, *199*, 212−227.

(18) Zanca, A. S.; Vicentini, R.; Ortiz-Morea, F. A.; EV Del Bem, L.; da Silva, M. J.; Vincentz, M.; Nogueira, F. T. S. Identification and expression analysis of microRNAs and targets in the biofuel crop sugarcane. *BMC Plant Biol.* **2010**, *10*, 260.

(19) Nakamura, K.; Go, N. Function and molecular evolution of multicopper blue proteins. *Cell. Mol. Life Sci.* **2005**, *62*, 2050−2066.

(20) Kosman, D. J. Multicopper oxidases: a workshop on copper coordination chemistry, electron transfer, and metallophysiology. *JBIC, J. Biol. Inorg. Chem.* **2010**, *15*, 15−28.

(21) Zhao, F. J.; Ago, Y.; Mitani, N.; Li, R. Y.; Su, Y. H.; Yamaji, N.; McGrath, S. P.; Ma, J. F. The role of the rice aquaporin Lsi1 in arsenite efflux from roots. *New Phytol.* **2010**, *186*, 392−399.

(22) Hu, H.; Zhang, J.; Wang, H.; Li, R.; Pan, F.; Wu, J.; Feng, Y.; Ying, Y.; Liu, Q. Effect of silicate supplementation on the alleviation of arsenite toxicity in 93−11 (*Oryza sativa* L. *indica*). *Environ. Sci. Pollut. Res.* **2013**, *20*, 8579−8589.

(23) Kumar, S.; Dubey, R. S.; Tripathi, R. D.; Chakrabarty, D.; Trivedi, P. K. Omics and biotechnology of arsenic stress and detoxification in plants: current updates and prospective. *Environ. Int.* **2015**, *74*, 221−230.

(24) Wang, X.; Peng, B.; Tan, C.; Ma, L.; Rathinasabapathi, B. Recent advances in arsenic bioavailability, transport, and speciation in rice. *Environ. Sci. Pollut. Res.* **2015**, *22*, 5742−5750.

(25) Kurtoglu, K. Y.; Kantar, M.; Budak, H. New wheat microRNA using whole-genome sequence. *Funct. Integr. Genomics* **2014**, *14*, 363−379.

(26) Zhang, L.; Chia, J. M.; Kumari, S.; Stein, J. C.; Liu, Z.; Narechania, A.; Maher, C. A.; Guill, K.; McMullen, M. D.; Ware, D. A genome-wide characterization of microRNA genes in maize. *PLoS Genet.* **2009**, *5*, e1000716.

(27) Ferreira, T. H.; Gentile, A.; Vilela, R. D.; Costa, G. G.; Dias, L. I.; Endres, L.; Menossi, M. microRNAs associated with drought response in the bioenergy crop sugarcane (*Saccharum* spp.). *PLoS One* **2012**, *7*, e46703.

(28) Li, Y.; Zhang, Y.; Shi, D.; Liu, X.; Qin, J.; Ge, Q.; Xu, L.; Pan, X.; Li, W.; Zhu, Y.; Xu, J. Spatial-temporal analysis of zinc homeostasis reveals the response mechanisms to acute zinc deficiency in *Sorghum bicolor*. *New Phytol.* **2013**, *200*, 1102−1115.

(29) Nischal, L.; Mohsin, M.; Khan, I.; Kardam, H.; Wadhwa, A.; Abrol, Y. P.; Iqbal, M.; Ahmad, A. Identification and comparative analysis of microRNAs associated with low-N tolerance in rice genotypes. *PLoS One* **2012**, *7*, e50261.

(30) Sharma, D.; Tiwari, M.; Lakhwani, D.; Tripathi, R. D.; Trivedi, P. K. Differential expression of microRNAs by arsenate and arsenite stress in natural accessions of rice. *Metallomics* **2015**, *7*, 174−187.

(31) Guo, W.; Zhang, J.; Teng, M.; Wang, L. H. Arsenic uptake is suppressed in a rice mutant defective in silicon uptake. *J. Plant Nutr. Soil Sci.* **2009**, *172*, 867−874.

(32) Moore, K. L.; Schröder, M.; Wu, Z.; Martin, B. G. H.; Hawes, C. R.; McGrath, S. P.; Hawkesford, M. J.; Ma, J. F.; Zhao, F. J.; Grovenor, C. R. M. Highresolution secondary ion mass spectrometry reveals the contrasting subcellular distribution of arsenic and silicon in rice roots. *Plant Physiol.* **2011**, *156*, 913−924.

(33) Abdel-Ghany, S. E.; Pilon, M. MicroRNA-mediated systemic down-regulation of copper protein expression in response to low copper availability in *Arabidopsis*. *J. Biol. Chem.* **2008**, *283*, 15932−15945.

(34) Zhang, H.; Li, L. *SQUAMOSA promoter binding protein-like7* regulated microRNA408 is required for vegetative development in *Arabidopsis*. *Plant J.* **2013**, *74*, 98−109.

(35) Gusman, G. S.; Oliveira, J. A.; Farnese, F. S.; Cambraia, J. Mineral nutrition and enzymatic adaptation induced by arsenate andarsenite exposure in lettuce plants. *Plant Physiol. Biochem.* **2013**, *71*, 307−314.

(36) Mascher, R.; Lippmann, B.; Holzinger, S.; Bergmann, H. Arsenate toxicity: effects on oxidative stress response molecules and enzymes in red clover plants. *Plant Sci.* **2002**, *163*, 961−969.

DOI: 10.1021/acs.jafc.5b04191
J. Agric. Food Chem. 2015, 63, 8849−8861

(37) Naya, L.; Paul, S.; Valdés-López, O.; Mendoza-Soto, A. B.; Nova-Franco, B.; Sosa-Valencia, G.; Reyes, J. L.; Hernández, G. Regulation of copper homeostasis and biotic interactions by microRNA 398b in common bean. *PLoS One* **2014**, *9*, e84416.
(38) Yang, Z.; Wang, X.; Gu, S.; Hu, Z.; Xu, H.; Xu, C. Comparative study of SBP-box gene family in *Arabidopsis* and rice. *Gene* **2008**, *407*, 1−11.
(39) Geshi, N.; Johansen, J. N.; Dilokpimol, A.; Rolland, A.; Belcram, K.; Verger, S.; Kotake, T.; Tsumuraya, Y.; Kaneko, S.; Tryfona, T.; Dupree, P.; Scheller, H. V.; Höfte, H.; Mouille, G. A galactosyltransferase acting on arabinogalactan protein glycans is essential for embryo development in *Arabidopsis*. *Plant J.* **2013**, *76*, 128−137.
(40) Wang, D.; Skibbe, D. S.; Walbot, V. Maize Male sterile 8 (Ms8), a putative *β*-1,3-galactosyltransferase, modulates cell division, expansion, and differentiation during early maize anther development. *Plant Reprod.* **2013**, *26*, 329−338.
(41) Li, W.; Guan, Q.; Wang, Z. Y.; Wang, Y.; Zhu, J. A bi-functional xyloglucan galactosyltransferase is an indispensable salt stress tolerance determinant in *Arabidopsis*. *Mol. Plant* **2013**, *6*, 1344−1354.
(42) Dave, R.; Tripathi, R. D.; Dwivedi, S.; Tripathi, P.; Dixit, G.; Sharma, Y. K.; Trivedi, P. K.; Corpas, F. J.; Barroso, J. B.; Chakrabarty, D. Arsenate and arsenite exposure modulate antioxidants and amino acids in contrasting arsenic accumulating rice (*Oryza sativa* L.) genotypes. *J. Hazard. Mater.* **2013**, *262*, 1123−1131.
(43) Tripathi, P.; Tripathi, R. D.; Singh, R. P.; Dwivedi, S.; Chakrabarty, D.; Trivedi, P. K.; Adhikari, B. Arsenite tolerance in rice (*Oryza sativa* L.) involves coordinated role of metabolic pathways of thiols and amio acids. *Environ. Sci. Pollut. Res.* **2013**, *20*, 884−896.
(44) Rai, V. K. Role of amino acids in plant responses to stresses. *Biol. Plant.* **2002**, *45*, 481−487.
(45) Sharma, S. S.; Dietz, K. J. The significance of amino acids and amino acid-derived molecules in plant responses and adaptation to heavy metal stress. *J. Exp. Bot.* **2006**, *57*, 711−726.
(46) Szabados, L.; Savouré, A. Proline: a multifunctional amino acid. *Trends Plant Sci.* **2010**, *15*, 89−97.
(47) Tripathi, P.; Singh, R. P.; Sharma, Y. K.; Tripathi, R. D. Arsenite stress variably stimulates pro-oxidant enzymes, anatomical deformities, photosynthetic pigment reduction, and antioxidants in arsenic-tolerant and sensitive rice seedlings. *Environ. Toxicol. Chem.* **2015**, *34*, 1562.
(48) Liu, J.; Zhu, J. K. Proline accumulation and salt-stress-induced gene expression in a salt-hypersensitive mutant of *Arabidopsis*. *Plant Physiol.* **1997**, *114*, 591−596.
(49) Schat, H.; Vooijs, R. Multiple tolerance and co-tolerance to heavy metals in *Silene vulgarisa* co-segregation analysis. *New Phytol.* **1997**, *136*, 489−496.
(50) Dwivedi, S.; Tripathi, R. D.; Tripathi, P.; Kumar, A.; Dave, R.; Mishra, S.; Singh, R.; Sharma, D.; Rai, U. N.; Chakrabarty, D.; Trivedi, P. K.; Adhikari, B.; Bag, M. K.; Dhankher, O. P.; Tuli, R. Arsenate exposure affects amino acids, mineral nutrient status and antioxidants in rice (*Oryza sativa* L.) genotypes. *Environ. Sci. Technol.* **2010**, *44*, 9542−9549.

DOI: 10.1021/acs.jafc.5b04191
J. Agric. Food Chem. 2015, 63, 8849−8861

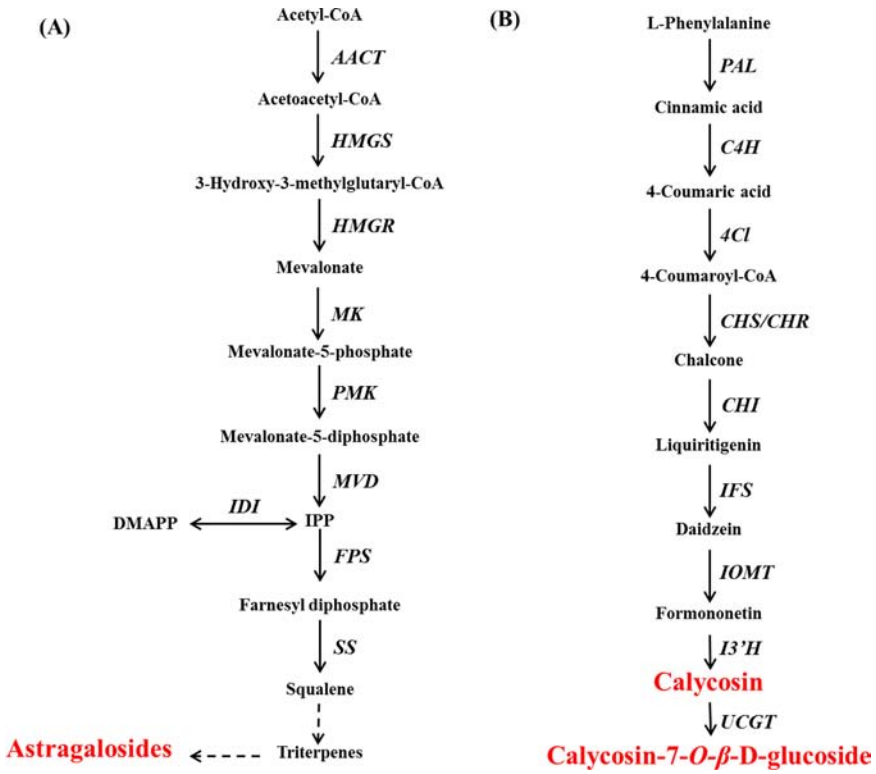

Figure 1. Putative scheme of biosynthetic pathway leading to (A) astragaloside and (B) calycosin and calycosin-7-*O*-*β*-D-glucoside. AACT, acetoacetyl-CoA thiolase; HMGS, HMG-CoA synthase; HMGR, HMG-CoA reductase; MK, mevalonate kinase; PMK, phosphomevalonate kinase; MVD, mevalonate diphosphate decarboxylase; IDI, isopentenyl diphosphate isomerase; FPS, farnesyl diphosphate synthase; DMAPP, dimethylallyl diphosphate; IPP, isoprenyl diphosphate; FPP, farnesyl diphosphate; SS, squalene synthase; PAL, phenylalanine ammonia-lyase; C4H, cinnamate-4-hydroxylase; 4CL, 4-coumarate:coenzyme A-ligase; CHS, chalcone synthase; CHR, chalcone reductase; CHI, chalcone isomerase; IFS, isoflavone synthase; IOMT, isoflavone *O*-methyltransferase; I3′H, isoflavone 3′-hydroxylase; UCGT, calycosin 7-*O*-glucosyltransferase.

by ramification into sterol and triterpene.[17] The first diversifying step in triterpenoid biosynthesis is the cyclization of 2,3-oxidosqualene, which is catalyzed by oxidosqualene cyclase (OSC); this step enables the synthesis of more than 100 variations of triterpenoids in plants.[18] Several OSCs, including cycloartenol synthase (CAS) and lanosterol synthase (LAS), are involved in both sterol biosynthesis and triterpenoid biosynthesis in higher plants.[19] Squalene synthase (SS) synthesizes 2,3-oxidosqualene from FPP and is the main backbone for the synthesis of ursane, oleanane, dammarane, and lupeol, which are the major triterpenoid skeletons.[18,20]

In the plant system isoflavones calycosin and CG are metabolically produced via the phenylpropanoid pathway (Figure 1B). Phenylalanine ammonia-lyase (PAL) is the starting enzyme, which converts L-phenylalanine into *trans*-cinnamic acid. Furthermore, cinnamate-4-hydroxylase (C4H) and 4-coumarate:coenzyme A-ligase (4CL) subsequently act on *trans*-cinnamic acid to produce *p*-coumarate CoA ester, respectively.[21] After that, *p*-coumaroyl-CoA condenses with three molecules of malonyl-CoA to synthesize chalcone by the catalytic action of chalcone synthase (CHS). In the next reaction, naringenin (5,7,4′-trihydroxyflavanone) was produced using the isomerization reaction of chalcone isomerase (CHI). In species that synthesize isoflavones, the enzyme isoflavone synthase (IFS), which catalyzes the formation of all isoflavones, has two roles: diverting naringenin into genistein production and catalyzing daidzein.[22] A methyl group is then added to daidzein by isoflavone *O*-methyltransferase (IOMT) to form formononetin.[23] Finally, calycosin is synthesized by hydroxylation of isoflavone 3′-hydroxylase (I3′H), and this compound can be modified to CG by calycosin 7-*O*-glucosyltransferase (UCGT).[24]

Through these well-characterized pathways, the common components of *A. membranaceus* are synthesized and promote the beneficial effects of the herb. In addition to these well-known synthetic pathways, *A. membranaceus* is also a good candidate for natural product isolation due to its long history in traditional medicine and abundance of beneficial compounds. Commonly called "Hwang Qi", the traditional medicine from *A. membranaceus* is prepared from the dried roots of the plant, and studies have characterized the phytochemistry, pharmacology, and clinical applications of the preparation.[25] However, to the best of our knowledge, no studies have compared the contents and expression profiles of genes involved in biosynthetic pathways between seedling roots (SRs), adventitious roots (ARs), and hairy roots (HRs) of *A. membranaceus*.

In vitro root culture is the well-known method for the bulk level production of novel plant metabolites with nutraceutical, pharmaceutical, and industrial applications.[26,27] In vitro culturing of ARs with the supply of optimized concentration of phytohormone comparatively produces valuable secondary metabolites.[27] Establishment of AR suspension culture systems has indicated that effective culture systems can promote large-scale multiplication, strain improvement, and species conservation.[28] Genetically transformed HR cultures have several beneficial properties, including rapid growth, genetic and biochemical stability, relatively low-cost culture obligation, and growth in hormone-free medium.[29] Additionally, HRs

DOI: 10.1021/acs.jafc.5b02525
J. Agric. Food Chem. 2015, 63, 8862−8869

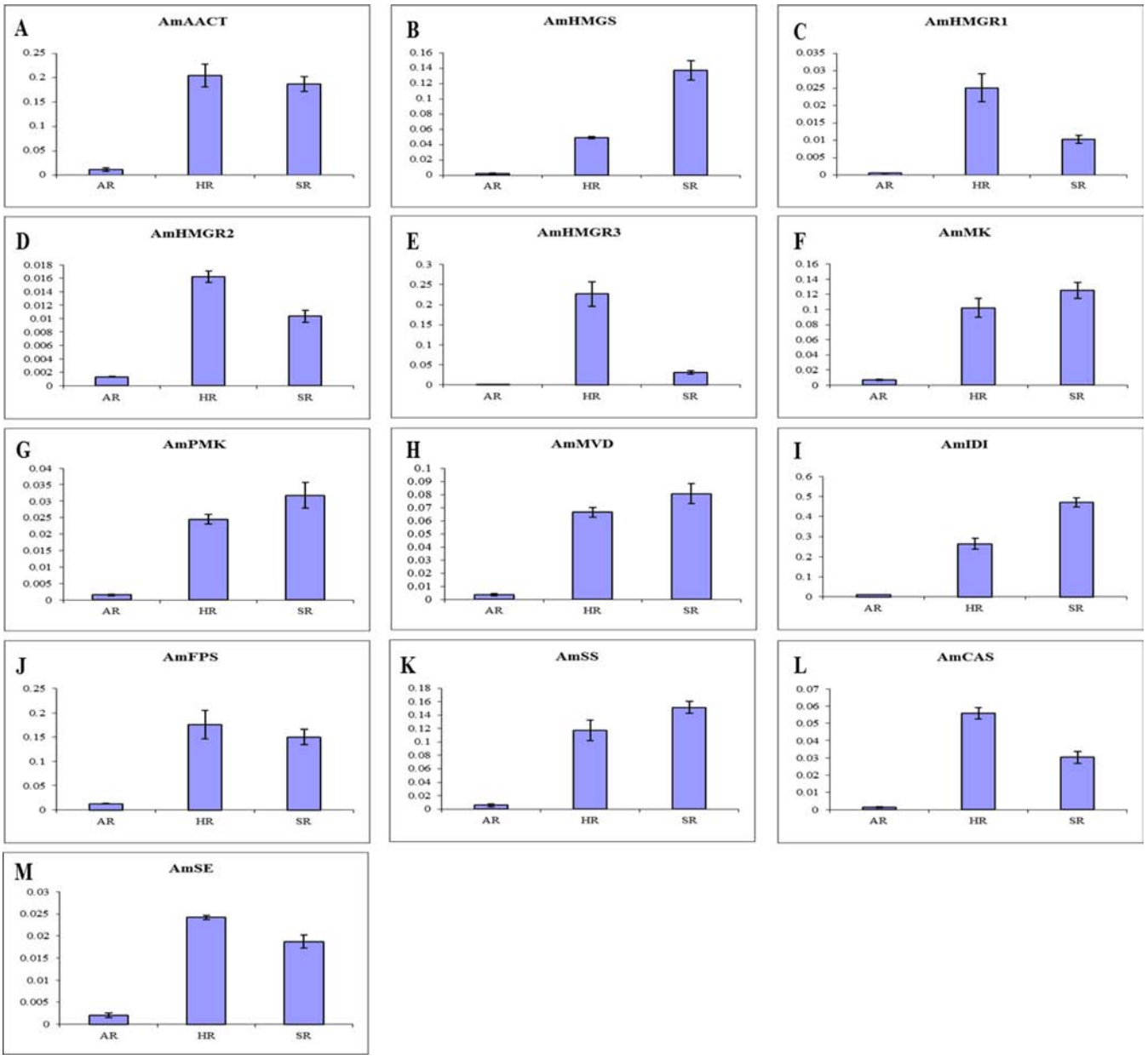

Figure 2. Accumulation of genes related to astragaloside biosynthetic in three different types of roots. AR, adventitious root; SR, seedling root; HR, hairy root. The height of each bar and the error bars indicate the means and standard errors, respectively, from three independent measurements.

derived from *Agrobacterium rhizogenes* by infection into plants exhibit multienzyme biosynthetic potential similar to or greater than those of the parent plants.[30]

Metabolomics provides a biochemical snapshot of an organism's phenotype. This technique provides the chance for in-depth identification of markers for the individual metabolite specific to species, cultivar, certain stages of development, or conditions such as disease, stress, or daily and seasonal changes, respectively.[31] A combination of gas chromatography and mass spectrometry (GC-MS) has allowed for the identification and robust quantification of several hundred metabolites within a single extract. Recently, several metabolomics studies have classified diverse biological samples varying in status, origin, and quality using GC-time-of-flight (TOF)-MS.[32−34] However, no metabolite profiles of the *A. membranaceus* have been reported to date.

In this study, we aimed to compare the expression levels of genes related to AST, calycosin, and CG biosynthetic pathways among SRs, ARs, and HRs. Moreover, ASTs, calycosin, and CG extracted from these three different types of root cultures of *A. membranaceus* were quantified using high-performance liquid chromatography (HPLC). These results demonstrated an efficient root culture system for the production of secondary metabolites in *A. membranaceus*. In addition, the levels of hydrophilic metabolites were analyzed from different root materials using GC-TOF-MS.

MATERIALS AND METHODS

Induction of HRs and ARs. Hairy roots were initiated from excised leaves of *A. membranaceus* after being infected with *Agrobacterium rhizogenes* R1000. Briefly, the excised leaves (1.0 × 1.0 cm) were washed thoroughly with distilled water and dipped into the *A. rhizogenes* for 10 min. Immediately after that, the leaves were

DOI: 10.1021/acs.jafc.5b02525
J. Agric. Food Chem. 2015, 63, 8862−8869

collected and kept in sterile filter paper for the removal of the liquid and then placed on autoclaved sterile solidified MS medium.[35] After that, the samples were kept in an incubator at 25 °C and maintained in the dark for 2 days. After that, the explants tissue was cultivated in the hormone-free MS medium for 3−4 weeks. Upon emergence of the hairy roots, they were removed from the flask and cultivated in MS medium containing 200 mg/L timentin at 25 °C under dark conditions. Furthermore, the roots were routinely cultivated by transferring them into fresh medium to collect the fresh hairy roots. Rapidly growing adventitious roots were carefully collected and initiated from leaf explants of *A. membranaceus* maintained on agar-solidified MS media containing 1.0 mg/L 1-naphthaleneacetic acid (NAA) as described by Thwe et al.[36] Seedling roots excised from *A. membranaceus* plantlets were grown in vitro.

The above obtained three types of root cultures were collected and further subcultured in hormone-free MS liquid medium, cultivated at 25 °C on a shaker (100 rpm) under dark conditions for 24 h. After 20 days of incubation, the hairy roots were harvested for the extraction of total RNA and analysis of phytochemicals. The harvested samples were immediately stored at −80 °C for further molecular and chemical analysis.

Quantitative Real-Time Reverse Transcription Polymerase Chain Reaction (qRT-PCR). On the basis of the sequences of *AmAACT*, *AmIDI*, *AmSS*, *AmPAL1*, *Am4CL*, *AmCHS1*, *AmCHI*, and *AmIOMT*, we designed real-time PCR primers using the Primer3 Web site (http://frodo.wi.mit.edu/primer3/). Total RNA was extracted from each collected sample using a modified trizol method. The first strand of cDNA was synthesized using 1 μg of total RNA according to the manufacturer's method (ReverTra ace, Toyobo, Japan). The reverse-transcribed cDNA products were used as templates for gene expression analysis with gene-specific primers. Real-time PCR products were tested for specificity of fragment sizes, melting curves, and sequences by PCR, qRT-PCR, and cloning into a T-Blunt vector for sequencing, respectively. The housekeeping phosphoribosyl transferase gene (NCBI GenBank accession no. KF355974) was used to normalize the relative expression of the targeted genes. qRT-PCR was performed on a CFX96 real time system (Bio-Rad Laboratories, Hercules, CA, USA) with the 2× real-time PCR Smart mix (BioFACT, Korea) under the following conditions: 95 °C for 15 min, followed by 40 cycles of 95 °C for 15 s, annealing for 15 s at 55 °C, and elongation for 20 s at 72 °C. Three replications for each sample were used in the real-time analyses.

HPLC Analysis. The materials were freeze-dried and ground into a fine powder. Briefly, 100 mg samples were extracted with 1.5 mL of MeOH and sonicated for 60 min. The samples were vortexed every 20 min during sonication. After centrifugation at 4000 rpm at room temperature for 10 min, the supernatant was filtered through a 0.45 μm PTFE syringe filter (Advantec DISMIC-13HP; Toyo Roshi Kaisha, Ltd., Tokyo, Japan) for HPLC analysis. HPLC grade methanol (MeOH) was purchased from J. T. Baker (Phillipsburg, NJ, USA). Formic acid was purchased from Sam Chun Pure Chemical Co., Ltd. (Gyeonggi, Korea). AST-I, AST-II, AST-III, AST-IV, calycosin, and CG were obtained from ChromaDex (Irvine, CA, USA). HPLC analysis was performed using a C_{18} column (250 × 4.6 mm, 5 μm; RStech; Daejeon, Korea). The flow rate was maintained at 1.0 mL/min, the column was maintained at 30 °C, and the injection volume was 20 μL. The mobile phases consisted of 0.3% formic acid in water (A) and acetonitrile (B), and a gradient elution protocol was used. The ultraviolet (UV) detection wavelength was 260 nm for isoflavonoids. The drift tube temperature for evaporating light scattering detection (ELSD) was 70 °C, and the nebulizing gas flow rate was 3.0 L/min. The concentration of each compound was determined using a standard curve. All samples were analyzed in triplicate.

Metabolite Analysis Using GC-TOF-MS. Analytical grade reagents and chemicals were used in this experiment. Chloroform and methanol were procured from J. T. Baker. *N*-Methyl-*N*-trimethylsilyltrifluoroacetamide (MSTFA) and ribitol and were procured from Sigma Chemical Co. (St. Louis, MO, USA). Pyridine and methoxyamine hydrochloride were procured from Thermo Fisher Scientific (Pittsburgh, PA, USA). The extraction of polar metabolite was performed as described by Kim et al.[33] The sample preparation methods, chemicals and reagents, silylation procedures, GC-TOF-MS instrument operating conditions, analytical methods for the separation of the samples and the scanning and the detection of the compounds rang were as implemented as described in our previous research paper Kim et al.[34] ChromaTOF software was used to assist with peak location. Peak identification was performed by comparison with reference compounds and the use of an in-house library.

Statistical Analysis. The data for gene expression and each constituent were analyzed using Statistical Analysis System software (SAS version 9.2). Treatment means were compared using Duncan's multiple-range test. Quantification data acquired from GC-TOF-MS were subjected to principal component analysis (PCA) (SIMCA-P version 13.0; Umetrics, Umea, Sweden) to evaluate differences among groups of multivariate data. The data file was scaled with unit variance scaling for the multivariate analysis. The PCA output consisted of score plots to visualize the contrast between different samples and loading plots to explain the cluster separation.

RESULTS AND DISCUSSION

Transcription Levels of Genes Related to AST Biosynthetic Pathways in Different Root Cultures of *A. membranaceus*. To investigate the mechanisms controlling AST biosynthesis in different root cultures of *A. membranaceus*, the expression levels of genes encoding AST-synthesizing enzymes were analyzed in SRs, ARs, and HRs. The expression levels of *AmAACT*, *AmHMGS*, *AmHMGR1*, *AmHMGR2*, *AmHMGR3*, *AmMK*, *AmPMK*, *AmMVD*, *AmIDI*, *AmFPS*, *AmSS*, *AmCAS*, and *AmSE* are shown in Figure 2. The expression patterns of *AmAACT*, *AmFPS*, *AmCAS*, and *AmSE* were similar, with observably higher expression in HRs than in SRs. Additionally, AmHMGRs (*AmHMGR1*, *AmHMGR2*, and *AmHMGR3*) exhibited lower expression in SRs than in HRs. In contrast, *AmHMGS*, *AmMK*, *AmPMK*, *AmMVD*, *AmIDI*, and *AmSS* exhibited high expression in SRs, but were moderately expressed in HRs. Although the transcripts encoding all of these enzymes were expressed in ARs, ARs exhibited the lowest expression levels for these genes.

Quantitative Analysis of ASTs. A total of four ASTs (AST-I, AST-II, AST-III, and AST-IV) were extracted and quantified in three different root cultures (Table 1). All of the identified compounds were found to be present at high levels in SRs (AST-I, 2532.87 μg/g dry wt; AST-II, 1342.25 μg/g dry wt; AST-III, 1712.40 μg/g dry wt; and AST-IV, 620.97 μg/g dry wt). ARs exhibited the least AST-I (177.34 μg/g dry wt), AST-II (189.63 μg/g dry wt), and AST-III (280.38 μg/g dry wt) and moderate levels of AST-IV (120.84 μg/g dry wt). The levels of these compounds were relatively higher in HRs than in ARs (AST-I, 785.87 μg/g dry wt; AST-II, 391.35 μg/g dry wt; AST-III, 378.92 μg/g dry wt), whereas the level of AST-IV was slightly lower in HRs (119.44 μg/g dry wt) than in ARs.

Table 1. AST Contents (μg/g Dry Weight) in Different Types of Roots of *A. membranaceus*[a]

compound	AR	HR	SR
AST-I	177.34 ± 6.72	785.87 ± 37.56	2532.87 ± 61.91
AST-II	189.63 ± 3.32	391.35 ± 12.63	1342.25 ± 2.84
AST-III	280.38 ± 8.58	378.92 ± 42.06	1712.40 ± 111.69
AST-IV	120.84 ± 5.93	119.44 ± 2.35	620.97 ± 5.46

[a]Each value is from three determinations ± SD. AR, adventitious root; SR, seedling root; HR, hairy root.

Expression Analysis of Calycosin and CG Biosynthetic Genes in Different Root Cultures of *A. membranaceus*.

DOI: 10.1021/acs.jafc.5b02525
J. Agric. Food Chem. 2015, 63, 8862−8869

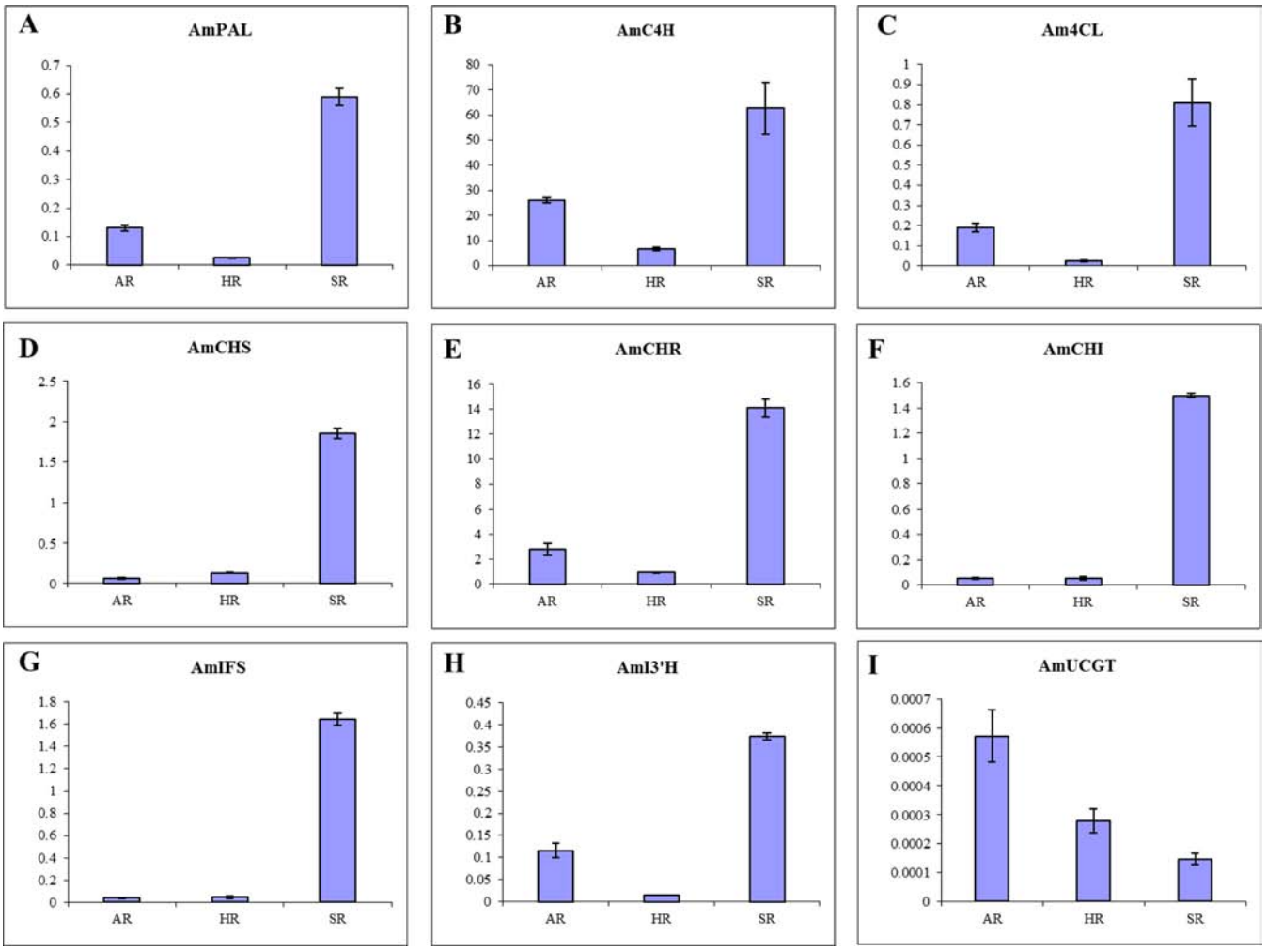

Figure 3. Expression levels in the three types of roots of genes related to the calycosin and calycosin-7-*O*-*β*-D-glucoside biosynthetic pathways: (A) *AmPAL*; (B) *AmC4H*; (C) *Am4CL*; (D) *AmCHS*; (E) *AmCHR*; (F) *AmCHI*; (G) *AmIFS*; (H) *AmI3′H*; (I) *AmUCGT*. AR, adventitious root; SR, seedling root; HR, hairy root. The height of each bar and the error bars indicate the means and standard errors, respectively, from three independent measurements.

To investigate the control of calycosin and CG biosynthesis, we examined the expression levels of genes related to calycosin biosynthesis in ARs, HRs, and SRs using qRT-PCR. The expression levels of *AmPAL*, *AmC4H*, *Am4CL*, *AmCHS*, *AmCHR*, *AmCHI*, *AmIFS*, *AmI3′H*, and *AmUCGT* are shown in Figure 3. The expression levels of these genes, with the exception of *AmUCGT*, were highest in SRs, demonstrating that *AmUCGT* exhibited a different expression profile than the other genes. The expression of *AmUCGT* was extremely low compared to that of other genes and was highest in ARs. The expression patterns of *AmPAL*, *AmC4H*, *Am4Cl*, *AmCHR*, and *AmI3′H* were similar, with observably higher expression in ARs than in HRs. However, the expression levels of *AmCHS*, *AmCHI*, and *AmIFS* were higher in ARs than in HRs.

Calycosin and CG Contents in Different Root Cultures. Next, we assessed the contents of two different flavonoids, calycosin and CG, in the three types of roots. As shown in Table 2, CG and calycosin accumulated at 5.64 and 3.56 μg/g dry wt, respectively, in ARs. The levels of CG and calycosin produced in HRs were 2.84 and 2.93 μg/g dry wt, respectively. However, calycosin (5.70 μg/g dry wt) was more abundant than CG (3.10 μg/g dry wt) in SRs; this was correlated with low expression of *AmUCGT*, which converts calycosin to CG.

Table 2. Analysis of Isoflavone Contents, Including Calycosin and CG Contents, in Different Types of Roots from *A. membranaceus*[a]

compound	AR	HR	SR
calycosin	3.56 ± 0.54	2.93 ± 1.04	5.70 ± 0.11
CG	5.64 ± 0.12	7.14 ± 3.43	3.10 ± 0.62

[a]Each value is from three determinations ± SD. AR, adventitious root; SR, seedling root; HR, hairy root.

Although *AmUCGT* transcript levels were relatively higher in ARs than in HRs, the CG content was high in HRs.

GC-TOF-MS Analysis of Polar Metabolites in Different Root Cultures. GC-TOF-MS was used to identify and quantify low-molecular-weight hydrophilic compounds in *A. membranaceus* samples. We were able to identify 40 compounds including 13 organic acids, 12 amino acids, 6 sugar alcohols, 5 sugars, 3 carbohydrates, and 1 amine in these samples (Supporting Information 1). The corresponding retention times agreed with our previous data.[34] Quantification was performed using selected ions, and the quantitative calculations of all analytes were based on the peak area ratios relative to that of the IS.

DOI: 10.1021/acs.jafc.5b02525
J. Agric. Food Chem. 2015, 63, 8862−8869

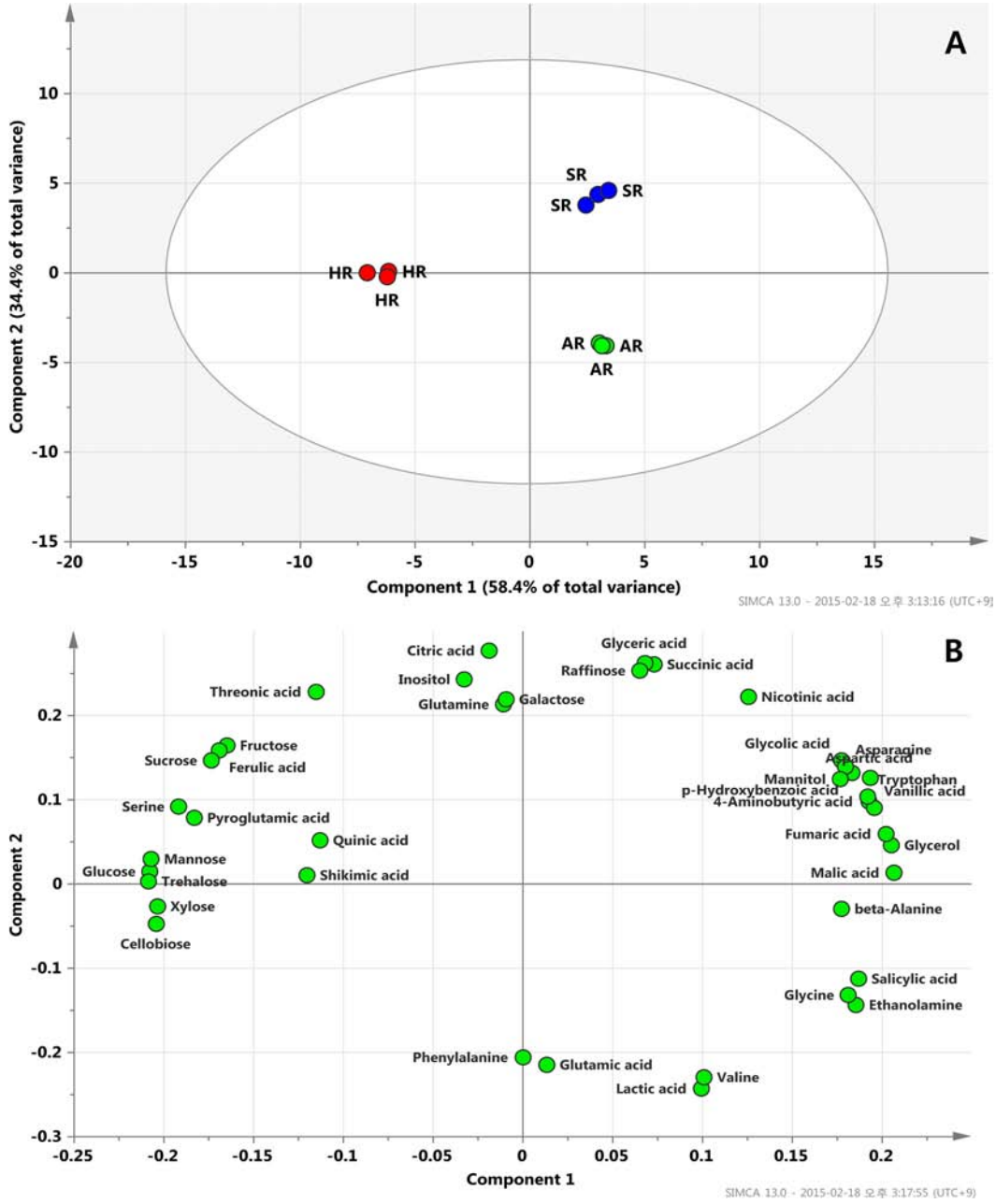

Figure 4. Scores (A) and loading plots (B) of principal components 1 and 2 from the PCA results obtained from polar metabolite data for different types of roots from *A. membranaceus*. AR, adventitious root; SR, seedling root; HR, hairy root.

PCA was used to explore the data structure obtained by GC-TOF-MS. PCA reduces the dimensionality of complex data sets and thereby facilitates the visualization of inherent patterns in the data. PCA transforms the original variables, using an orthogonal linear transformation, to a new set of uncorrelated variables known as principal components (PCs). As shown in Figure 4, the first and second PCs of the PCA score plot represented 58.4 and 34.4% of the total variance of the samples, respectively. The variance of the differences among roots was successfully captured in the two PCs. The first PC resolved the metabolite profiles of HRs and other roots. The metabolomes between SRs and ARs were separated by PC 2. The loading plot of the PCA revealed the magnitude and direction of correlation of the original variables with PCs. Correlation analysis is a common statistical method used to establish relationships between metabolite signals belonging to a biological system.[37] Sugars such as glucose, fructose, mannose, and sucrose were clustered in the left of the loading plot, indicating that the level of sugars in HRs was higher than that in other roots. In plant systems, the building blocks for secondary metabolites are derived from primary metabolism. In this study, free glucose, a building block of CG, was higher in HRs, whereas CG content was lower in HRs than in SRs and ARs (Supporting Information 2). The loading plot of PC 2 indicated that a higher amount of phenylalanine was present in ARs than in SRs and HRs and that TCA-cycle intermediates such as citric acid and succinic acid were higher in SRs than in others. Phenylalanine is a major amino acid donor for the synthesis of CG. Thus, metabolomics can assist in dissecting the

DOI: 10.1021/acs.jafc.5b02525
J. Agric. Food Chem. 2015, 63, 8862−8869

mechanisms that regulate the conversion of primary metabolites into secondary metabolites in plants.

The objective of the present study was to examine an efficient root culture system for ASTs, calycosin, and CG accumulation and the levels of hydrophilic metabolites in different root types of *A. membranaceus*. The results indicate that the highest amounts of ASTs were produced in SRs of this plant with high expression levels of genes associated with this biosynthetic pathway. Also, we observed that ARs and HRs accumulate more CG than calycosin, but SRs showed the reverse. Totally, 40 metabolites were distinguished among three samples of *A. membranaceus*. We demonstrated that HRs were clearly separate from other root cultures because of the high levels of sugars and clusters derived from closely related biochemical pathways.

In vitro root culture has been considered as an alternative method to produce secondary metabolites based on year-round cultivation and high-level quality and quantity.[38] Many researchers have demonstrated new possibilities using in vitro cultures for accumulation of useful phytochemicals in plants. Development of an AR culure system could promote large-scale multiplication, strain improvement, and species conservation,[28] but optimal conditions are necessary to boost root biomass and secondary metabolites.[39−42] AR cultures from many plant species including *Raphanus sativus*,[43] *Panax notoginseng*,[44] *Cornus capitata*,[45] and *Rhus javanica*[46] have been conducted and cultured for production of valuable phytochemicals.[27] Total saponin and flavonoid contents of 40-day-old AR derived from *A. membranaceus* were shown to be higher than those of 1-year-old roots under field cultivation.[47] HR cultures offer a remarkable experimental tool to investigate the various sides of biosynthesis related to biologically effective compounds. Numerous successful examples for HR cultures have been based on phytochemical production from medicinal plants. Du et al.[48] have reported that AST-IV and polysaccharides are produced in HR of *A. membrananceus* on a large scale. Even though we demonstrated that SRs contain the largest amounts of ASTs, ARs or HRs of *A. membranaceus* are great materials for ASTs, calycosin, and CG production possibly using optimal conditions for yield.

■ ASSOCIATED CONTENT

Supporting Information

The Supporting Information is available free of charge on the ACS Publications website at DOI: 10.1021/acs.jafc.5b02525.

Metabolites identified in GC-TOF-MS chromatograms from *A. membranaceus* extracts and their composition in different types of roots (PDF)

■ AUTHOR INFORMATION

Corresponding Authors

*(N. A. Al-Dhabi) Mail: Department of Botany and Microbiology, Addiriyah Chair for Environmental Studies, College of Science, King Saud University, P.O. Box 2455, Riyadh 11451, Saudi Arabia. Phone: +966-1- 467-5829. Fax: +966-1- 469-7204. E-mail: naldhabi@ksu.edu.sa.

*(S. U. Park) Mail: Department of Crop Science, Chungnam National University, 99 Daehak-ro, Yuseong-gu, Daejeon, 305-764, Korea. Phone: +82-42-821-5730. Fax: +82-42-822-2631. E-mail: supark@cnu.ac.kr.

Funding

The project was fully financially supported by King Saud University, through the Vice Deanship of Research Chairs.

Notes

The authors declare no competing financial interest.

■ ABBREVIATIONS USED

AST, astrogaloside; CG, calycosin-7-*O*-β-D-glucoside; SR, seedling root; AR, adventitious root; HR, hairy root; qRT-PCR, quantitative real-time polymerase chain reaction; HPLC, high-performance liquid chromatography; GC-TOF-MS, gas chromatography−time-of-light mass spectrometry; PCA, principal component analysis; DMAPP, dimethylallyl diphosphate; IPP, isoprenyl diphosphate; FPP, farnesyl diphosphate; OSC, oxidosqualene cyclase; CAS, cycloartenol synthase; LAS, lanosterol synthase; SS, squalene synthase; PAL, phenylalanine ammonia-lyase; C4H, cinnamate-4-hydroxylase; 4CL, 4-coumarate:coenzyme A-ligase; CHS, chalcone synthase; CHR, chalcone reductase; CHI, chalcone isomerase; IFS, isoflavone synthase; IOMT, isoflavone *O*-methyltransferase; I3′H, isoflavone 3′-hydroxylase; UCGT, calycosin 7-*O*-glucosyltransferase; ELSD, evaporating light scattering detection; TMS, trimethylsilyl; MSTFA, *N*-methyl-*N*-(TMS)-trifluoroacetamide; AACT, acetoacetyl-CoA thiolase; HMGS, HMG-CoA synthase; HMGR, HMG-CoA reductase; MK, mevalonate kinase; PMK, phosphomevalonate kinase; MVD, mevalonate diphosphate decarboxylase; IDI, isopentenyl diphosphate isomerase; FPS, farnesyl diphosphate synthase

■ REFERENCES

(1) Wojciechowski, M. F.; Sanderson, M. J.; Hu, J. M. Evidence on the monophyly of Astragalus (Fabaceae) and its major subgroups based on nuclear ribosomal DNA ITS and chloroplast DNA trnL intron data. *Syst. Bot.* **1999**, *24*, 409−437.

(2) Tang, W.; Eisenbrand, G. Therapeutic use. In *Chinese Drugs of Plant Origin. Chemistry Pharmacology, and Use in Traditional and Modern Medicine*; Springer Verlag: Berlin, Germany, 1992; pp 191−197.

(3) Sun, Y.; Hersh, E. M.; Talpaz, M.; Lee, S. L.; Wong, W.; Loo, T. L.; Mavligit, G. M. Immune restoration and/or augmentation of local graft versus host reaction by traditional Chinese medicinal herbs. *Cancer* **1983**, *52*, 70−73.

(4) Hikino, H.; Funayama, S.; Endo, S. Hypotensive principle of *Astragalus* and *Hedysarum* roots. *Planta Med.* **1976**, *30*, 297−302.

(5) Rios, J. L.; Waterman, P. G. A review of the pharmacology and toxicology of *Astragalus*. *Phytother. Res.* **1997**, *11*, 411−418.

(6) Tang, L.; Liu, Y.; Wang, Y.; Long, C. Phytochemical analysis of an antiviral fraction of *Radix astragali* using HPLC-DAD-ESIMS/MS. *J. Nat. Med.* **2010**, *64*, 182−186.

(7) Wong, B. Y. Y.; Lau, B. H. S.; Tadi, P. P.; Teel, R. W. Chinese medicinal herbs modulate mutagenesis, DNA binding and metabolism of aflatoxin B1. *Mutat. Res., Genet. Toxicol. Test.* **1992**, *279*, 209−216.

(8) Song, Z. H.; Ji, Z. N.; Lo, C. K.; Dong, T. T. X.; Zhao, K. J.; Li, O. T. X.; Haines, C. J.; Kung, S. D.; Tsim, K. W. K. Chemical and biological assessment of a traditional Chinese herbal decoction prepared from Radix Astragali and Radix Angelicae Sinensis: orthogonal array design to optimize the extraction of chemical contituents. *Planta Med.* **2004**, *70*, 1222−1227.

(9) Wu, F.; Chen, X. A review of pharmacological study on *Astragalus membranaceus* (Fisch.) Bge. *Zhongyaocai (J. Chinese Med. Mater.)* **2004**, *27*, 232−234.

(10) Kwon, H. J.; Hwang, J.; Lee, S. K.; Park, Y. D. Astragaloside content in the periderm, cortex, and xylem of *Astragalus membranaceus* root. *J. Nat. Med.* **2013**, *67*, 850−855.

DOI: 10.1021/acs.jafc.5b02525
J. Agric. Food Chem. 2015, 63, 8862−8869

(11) Toda, S.; Shirataki, Y. Inhibitory effects of isoflavones in roots of *Astragalus membranaceus* Bunge (Astragali Radix) on lipid peroxidation by reactive oxygen species. *Phytother. Res.* **1998**, *12*, 59−61.
(12) Dazheng, W.; Yi, F.; Zhifen, H. Effect of flavonoids isolated from *Astragalus membranaceus* on the changes of endothelial permeability induced by low osmolarity. *Pharmacol. Clin. Chin. Mater. Med.* **2000**, *16*, 16−18.
(13) Liu, Z. Q.; Li, Q. Z.; Qin, G. J. Effect of *Astragalus* injection on platelet function and plasma endothelin in patients with early stage diabetic nephropathy. *Chinese J. Integr. Med.* **2001**, *21*, 274−276.
(14) Fan, Y.; Wu, D. Z.; Gong, Y. Q.; Zhou, J. Y.; Hu, Z. B. Effects of calycosin on the impairment of barrier function induced by hypoxia in human umbilical vein endothelial cells. *Eur. J. Pharmacol.* **2003**, *481*, 33−40.
(15) Choi, S.; Park, S. R.; Heo, T. R. Inhibitory effect of astragali radix on matrix degradation in human articular cartilage. *J. Microbiol. Biotechnol.* **2005**, *15*, 1258−1266.
(16) Lichtenthaler, H. K.; Rohmer, M.; Schwender, Jorg. Two independent biochemical pathway for isopentenyl diphosphate and isoprenoid biosynthesis in higher plants. *Physiol. Plant.* **1997**, *101*, 643−652.
(17) Ding, Y. X.; Ou-Yang, X.; Shang, C. H.; Ren, A.; Shi, L.; Li, Y. X.; Zhao, M. W. Molecular cloning, characterization, and differential expression of a farnesyl-diphosphate synthase gene from the basidiomycetous fungus *Ganoderma lucidum*. *Biosci., Biotechnol., Biochem.* **2008**, *72*, 1571−1579.
(18) Abe, I.; Rohmer, M.; Prestwich, G. D. Enzymatic cyclization of squalene and oxidosqualene to sterols and triterpenes. *Chem. Rev.* **1993**, *93*, 2189−2206.
(19) Ohyama, K.; Suzuki, M.; Kikuchi, J.; Saito, K.; Muranaka, T. Dual biosynthetic pathways to phytosterol via cycloartenol and lanosterol in *Arabidopsis*. *Proc. Natl. Acad. Sci. U. S. A.* **2009**, *106*, 725−730.
(20) He, F.; Zhu, Y.; He, M.; Zhang, Y. Molecular cloning and characterization of the gene encoding squalene epoxidase in Panax notoginseng. *DNA Sequence* **2008**, *19*, 270−273.
(21) Russell, D. W. The metabolism of aromatic compounds in higher plants. X. Properties of the cinnamic acid 4-hydroxylase of pea seedlings and some aspects of its metabolic and developmental control. *J. Biol. Chem.* **1971**, *246*, 3870−3878.
(22) Yu, O.; McGonigle, B. Metabolic Engineering of isoflavone biosynthesis. *Adv. Agron.* **2005**, *86*, 147−195.
(23) Akashi, T.; Sawada, Y.; Shimada, N.; Sakurai, N.; Aoki, T.; Ayabe, S. cDNA cloning and biochemical characterization of *S*-adenosyl-L-methionine: 2,7,4′-trihydroxyisoflavanone 4′-*O*-methyltransferase, a critical enzyme of the legume isoflavonoid phytoalexin pathway. *Plant Cell Physiol.* **2003**, *44*, 103−112.
(24) Lee, J.; Kim, Y. B.; Uddin, M. R.; Cho, J. W.; Park, S. U. Terpenoid and flavonoid biosynthesis in *Astragalus membranaceus*. *Life Sci. J.* **2013**, *10*, 970−973.
(25) Liu, J.; Zhao, Z. Z.; Chen, H. B. Review of Astragali Radix. *Chinese Herbal Med.* **2011**, *3*, 90−105.
(26) Verpoorte, R.; Contin, A.; Memelink, J. Biotechnology for the production of plant secondary metabolites. *Phytochem. Rev.* **2002**, *1*, 13−25.
(27) Murthy, H. N.; Hahn, E. J.; Paek, K. Y. Adventitious roots and secondary metabolism. *Chinese J. Biotechnol.* **2008**, *24*, 711−716.
(28) Holobiuc, I.; Blindu, R. In vitro culture introduction for ex situ conservation of some rare plant species. *Rom. J. Biol.−Plant Biol.* **2006**, 51−52.
(29) Shanks, J. V.; Morgan, J. Plant 'hairy root' culture. *Curr. Opin. Biotechnol.* **1999**, *10*, 151−155.
(30) Banerjee, S.; Rahman, L.; Uniyal, G. C.; Ahuja, P. S. Enhanced production of valepotriates by *Agrobacterium rhizogenes* induced hairy root cultures of *Valeriana wallichii* DC. *Plant Sci.* **1998**, *131*, 203−208.
(31) Jung, Y.; Lee, J.; Kim, H. K.; Moon, B. C.; Ji, Y.; Hwang, G.-S. Metabolite profiling of *Curcuma* species grown in different regions using 1 H NMR spectroscopy and multivariate analysis. *Analyst* **2012**, *137*, 5597−5606.
(32) Park, S.-Y.; Park, W. T.; Park, Y. C.; Ju, J. I.; Park, S. U.; Kim, J. K. Metabolomics for the quality assessment of *Lycium chinense* fruits. *Biosci., Biotechnol., Biochem.* **2012**, *76*, 2188−2194.
(33) Kim, J. K.; Choi, S. R.; Lee, J.; Park, S.-Y.; Song, S. Y.; Na, J.; Kim, S. W.; Kim, S.-J.; Nou, I.-S.; Lee, Y. H. Metabolic differentiation of diamondback moth (*Plutella xylostella* (L.)) resistance in cabbage (*Brassica oleracea* L. ssp. *capitata*). *J. Agric. Food Chem.* **2013**, *61*, 11222−11230.
(34) Park, S.-Y.; Lim, S.-H.; Ha, S.-H.; Yeo, Y.; Park, W. T.; Kwon, D. Y.; Park, S. U.; Kim, J. K. Metabolite profiling approach reveals the interface of primary and secondary metabolism in colored cauliflowers (*Brassica oleracea* L. ssp. *botrytis*). *J. Agric. Food Chem.* **2013**, *61*, 6999−7007.
(35) Murashige, T.; Skoog, F. A revised medium for rapid growth and bio assays with tobacco tissue cultures. *Physiol. Plant.* **1962**, *15*, 473−497.
(36) Thwe, A. A.; Mai, N. T. T.; Li, X.; Kim, Y.; Kim, Y. B.; Uddin, M. R.; Kim, Y. S.; Bae, H.; Kim, H. H.; Lee, M. Y.; Park, S. U. Production of astragaloside and flavones from adventitious root cultures of *Astragalus membranaceus* var. *mongholicus*. *Plant Omics* **2012**, *5*, 466−470.
(37) Park, S.-Y.; Choi, S. R.; Lim, S.-H.; Yeo, Y.; Kweon, S. J.; Bae, Y.-S.; Kim, K. W.; Im, K.-H.; Ahn, S. K.; Ha, S.-H.; Park, S. U.; Kim, J. K. Identification and quantification of carotenoids in paprika fruits and cabbage, kale, and lettuce leaves. *J. Korean. Soc. Appl. Biol. Chem.* **2014**, *57*, 355−358.
(38) Steingroewer, J.; Bley, T.; Georgiev, V.; Ivanov, I.; Lenk, F.; Marchev, A.; Pavlov, A. Bioprocessing of differentiated plant in vitro systems. *Eng. Life Sci.* **2013**, *13*, 26−38.
(39) Choi, S. M.; Son, S. H.; Yun, S. R.; Kwon, O. W.; Seon, J. H.; Paek, K. Y. Pilot-scale culture of adventitious roots of ginseng in a bioreactor system. *Plant Cell, Tissue Organ Cult.* **2000**, *62*, 187−193.
(40) Yu, K.-W.; Gao, W. Y.; Hahn, E.-J.; Paek, K.-Y. Effects of macro elements and nitrogen source on adventitious root growth and ginsenoside production in ginseng (*Panax ginseng* CA Meyer). *J. Plant Biol.* **2001**, *44*, 179−184.
(41) Kim, Y.-S.; Hahn, E.-J.; Murthy, H. N.; Paek, K.-Y. Effect of polyploidy induction on biomass and ginsenoside accumulations in adventitious roots of ginseng. *J. Plant Biol.* **2004**, *47*, 356−360.
(42) Lee, E. J.; Mobin, M.; Hahn, E. J.; Paek, K. Y. Effects of sucrose, inoculum density, auxins, and aeration volume on ceil growth of *Gymnema sylvestre*. *J. Plant Biol.* **2006**, *49*, 427−431.
(43) Betsui, F.; Tanaka-Nishikawa, N.; Shimomura, K. Anthocyanin production in adventitious root cultures of *Raphanus sativus* L. cv. Peking Koushin. *Plant Biotechnol.* **2004**, *21*, 387−391.
(44) Gao, X.; Zhu, C.; Jia, W.; Gao, W.; Qiu, M.; Zhang, Y.; Xiao, P. Induction and characterization of adventitious roots directly from the explants of *Panax notoginseng*. *Biotechnol. Lett.* **2005**, *27*, 1771−1775.
(45) Tanaka, N.; Tanaka, T.; Fujioka, T.; Fujii, H.; Mihashi, K.; Shimomura, K.; Ishimaru, K. An ellagic compound and iridoids from *Cornus capitata* root cultures. *Phytochemistry* **2001**, *57*, 1287−1291.
(46) Taniguchi, S.; Yazaki, K.; Yabu-uchi, R.; Kawakami, K.-y.; Ito, H.; Hatano, T.; Yoshida, T. Galloylglucoses and riccionidin A in *Rhus javanica* adventitious root cultures. *Phytochemistry* **2000**, *53*, 357−363.
(47) Wu, S. Q.; Lian, M. L.; Gao, R.; Park, S. Y.; Piao, X. C. Bioreactor application on adventitious root culture of *Astragalus membranaceus*. *In Vitro Cell. Dev. Biol.: Plant* **2011**, *47*, 719−724.
(48) Du, M.; Wu, X. J.; Ding, J.; Hu, Z. B.; White, K. N.; Branford-White, C. J. Astragaloside IV and polysaccharide production by hairy roots of *Astragalus membranaceus* in bioreactors. *Biotechnol. Lett.* **2003**, *25*, 1853−1856.

DOI: 10.1021/acs.jafc.5b02525
J. Agric. Food Chem. 2015, 63, 8862−8869

also studied the relationship between the calcium content and hardness of cooked soybean cotyledons. PMEs are commonly present in plants and microorganisms such as fungi and bacteria.[8,9] Evidence indicates that pectins are synthesized and methylesterified in the Golgi and thereafter secreted into the cell wall in a highly methylesterified state.[10−12] Subsequently, they are deesterified by wall-associated PMEs that convert the methoxyl groups into carboxyl groups on the polygalacturonic acid chain and release both methanol and protons. It appears that most plant PMEs deesterify pectins in a blockwise fashion, e.g., linearly along the chain, which favors pectin gelation and concomitant cell wall stiffening due to the formation of cooperative Ca^{2+} crossbridges between free carboxyl groups of adjacent pectin chains.[13]

During the cooking process, it has been postulated that middle lamella pectin of the cell walls is depolymerized by β-elimination of methyl-esterified polygalacturonic acids, promoting an increase in cell separation, and this softens the tissues.[14] In legume seeds, tissue softening seems to be achieved mainly through the middle lamella polymer solubilization, which allows cell separation, producing a mealy texture.[15] However, no report has been found on the effect of endogenous PME on the hardness of cooked beans.

In this report, we discuss the role of an endogenous PME gene on the hardness of cooked beans, which has been demonstrated here in the soybean.

MATERIALS AND METHODS

Materials. An RIL population derived from a cross between two Japanese cultivars, Natto-shoryu and Hyoukei-kuro 3, was prepared according to a previously described method.[7] To survey the candidate genetic region and validate the effect of a major QTL (*qHbs3-1*), we selected a heterozygous plant of the fifth filial generation (F_5) from the RIL population using DNA markers in the region proximal to the QTL. The residual heterozygous line (RHL)[16] in the F_5 generation was self-fertilized, and the resultant F_6 plants were harvested individually in 2011. Furthermore, F_9 seeds showing different recombinant genotypes around the QTL region were obtained by self-fertilization and DNA-marker analysis, and F_9 plants were grown in the experimental field. Seeds were harvested from 1−7 F_9 plants for each genotype and were used for texture analysis of cooked beans. Another two F_2 populations derived from a cross between two cultivars, "Enrei" and "LD00-3309" and between "Satonohohoemi" and "Sakukei 98", were used to confirm the effect of the candidate gene in this report. Soybeans were planted and grown in the experimental field at NARO Institute of Crop Science (NICS), Ibaraki, Japan, in 2013 according to the method previously described.[7] The sowing date of Natto-shoryu, Hyoukei-kuro 3, and their progenies was June 25, and that of other cultivars was June 18. Soybean cultivars grown in different locations in 2013 were collected from Kumamoto (Southern area of Japan) and Akita (Northern region of Japan) prefectures as described in Table 1. The sowing date in Akita was June 4, and those in Kumamoto were July 2, 9, or 10. Mature seeds were harvested in October or November, according to the maturing time. Moisture contents of the seeds were from 8 to 12% (Table S1). Soybean seeds were stored at 4 °C until use. The hardness of the cooked soybean cotyledons was analyzed from April 4 to June 18 in 2014.

Texture Analysis of Cooked Beans. Cooked beans were prepared and the breaking stress of the cotyledons was measured according to methods described previously.[7] Briefly, 30 seeds were soaked in 100 mL of deionized water at 20 °C for 22 ± 2 h. Imbibed seeds were boiled for 10 min in 200 mL of deionized water in a 500 mL tall glass beaker (HARIO Ltd., Tokyo, Japan) using a hot stirrer (IKA RCT basic, IKA japan K.K., Osaka, Japan). After cooking, the seeds were cooled in water at room temperature and the water was drained well. The seed coat and embryo axis were removed from the

Table 1. Soybean Cultivars and Locations Used in This Study

cultivar	genotype of *Glyma03g03360*	location
Akishirome	B	NICS, Ibaraki, Japan
		KARC,† Kumamoto, Japan
Enrei	B	NICS, Ibaraki, Japan[a]
		NICS, Ibaraki, Japan[b]
		KARC,† Kumamoto, Japan
		TARC,‡ Akita, Japan[a]
		TARC,‡ Akita, Japan[b]
Fukuibuki	A	NICS, Ibaraki, Japan
		TARC,‡ Akita, Japan[a]
		TARC,‡ Akita, Japan[b]
Fukuminori	A′	NICS, Ibaraki, Japan
		KARC,† Kumamoto, Japan
Fukuyutaka	A′	NICS, Ibaraki, Japan
		KARC,† Kumamoto, Japan
Himeshirazu	B	NICS, Ibaraki, Japan
		KARC,† Kumamoto, Japan
Hyoukei-kuro 3	B	NICS, Ibaraki, Japan
Kosuzu	A	TARC,‡ Akita, Japan[a]
		TARC,‡ Akita, Japan[b]
Kotoyutaka	B	NICS, Ibaraki, Japan
		KARC,† Kumamoto, Japan
LD00-3309	A	NICS, Ibaraki, Japan
Natto-shoryu	A	NICS, Ibaraki, Japan
Oosuzu	B	NICS, Ibaraki, Japan
		TARC,‡ Akita, Japan[a]
		TARC,‡ Akita, Japan[b]
Ryuuhou	B	NICS, Ibaraki, Japan
		TARC,‡ Akita, Japan[a]
		TARC,‡ Akita, Japan[b]
Sachiyutaka	A′	NICS, Ibaraki, Japan
		KARC,† Kumamoto, Japan
Sakukei 98	A′	NICS, Ibaraki, Japan
Satonohohoemi	B	NICS, Ibaraki, Japan[a]
		NICS, Ibaraki, Japan[b]
		TARC,‡ Akita, Japan[a]
		TARC,‡ Akita, Japan[b]
Shuurei	B′	NICS, Ibaraki, Japan
Suzukaren	A′	NICS, Ibaraki, Japan
		KARC,† Kumamoto, Japan
Suzukari	A	TARC,‡ Akita, Japan[a]
		TARC,‡ Akita, Japan[b]
Suzuyutaka	A	NICS, Ibaraki, Japan
		TARC,‡ Akita, Japan[a]
		TARC,‡ Akita, Japan[b]
Tachinagaha	B	NICS, Ibaraki, Japan
		KARC,† Kumamoto, Japan
		TARC,‡ Akita, Japan[a]
		TARC,‡ Akita, Japan[b]
Tachiyutaka	B	NICS, Ibaraki, Japan
		TARC,‡ Akita, Japan[a]
		TARC,‡ Akita, Japan[b]
Tamadaikoku	B′	TARC,‡ Akita, Japan[a]
		TARC,‡ Akita, Japan[b]
Tamahomare	A	NICS, Ibaraki, Japan

†NARO Kyushu Okinawa Agricultiral Research center. ‡NARO Tohoku Agricultiral Research Center. Different letters mean different field plots.

DOI: 10.1021/acs.jafc.5b02896
J. Agric. Food Chem. 2015, 63, 8870−8878

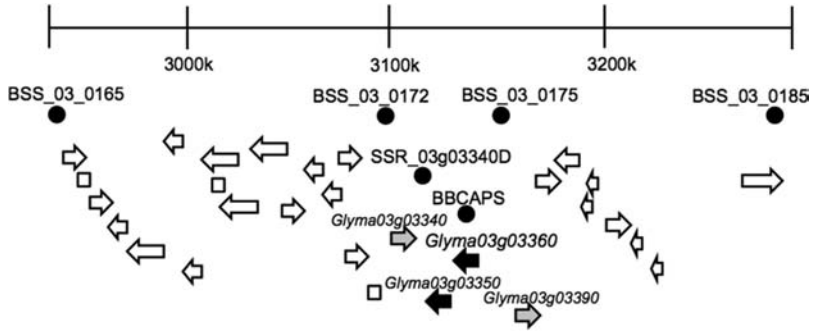

Figure 1. Locations of DNA markers (closed circles) and two genes (arrows in black; *Glyma03g03350* and *Glyma03g03360*) on chromosome 3. Physical positions on the chromosome are indicated above. SSR_03g03340D is located downstream of *Glyma03g03340* (an arrow in gray). BARCSOYSSR_03_0175 (BSS_03_0175) is located upstream of *Glyma03g03390* (an arrow in gray).

boiled seeds; then, the two cotyledons were separated from each other. The puncture strength was measured using a Rheoner RE-3305S texture analyzer (Yamaden Corp., Tokyo, Japan) fitted with a cylindrical probe (3 mm outside diameter) and a 2 kg capacity load cell. The adaxial (flat) side of a piece of cotyledon was placed facing downward on the stage of the analyzer, and the hardness was measured. The probe was operated at a distance of 2.45 mm and a speed of 1 mm/s. Puncture strength was determined as maximum force (pascals). The average score for more than 40 samples was used as an index of cooked seed hardness for each sample. The seed hardness measured by this method was positively correlated with the hardness of embryos ($r = 0.918$, $p < 0.001$) and that of whole beans ($r = 0.926$, $p < 0.001$) measured by the AACC approved method[17] after 40 min of cooking.

The 100-seed weight was calculated from the number and weight of air-dried seeds before soaking, and the water absorption ratio was calculated as the ratio of the seed weight after soaking to that before soaking.

DNA Isolation and Marker Analysis. Genomic DNA was isolated from young leaves of F_2 plants, F_9 plants, and cultivars (see Materials) using a previously described method.[7] Leaves were crushed in 400 μL of DNA extraction buffer (0.1 M Tris−HCl, pH 8.0; 0.05 M EDTA, pH 8.0; 0.5 M NaCl; 43.3 mM SDS; 10 mM dithiothreitol) with a SHAKE MASTER ball mill (Inter Bio Techno, Ltd., Tokyo, Japan), and homogenates were centrifuged at 2750*g* in a Himac CF 5RX centrifuge (Hitachi, Ltd., Tokyo, Japan) for 10 min. An aliquot of the supernatant was mixed with 100 μL of 5 M potassium acetate buffer and incubated at 5 °C for 10 min. The samples were centrifuged again at 2750*g* at 5 °C for 10 min. After centrifugation, 300 μL of the supernatant was gently mixed with 300 μL of isopropyl alcohol and incubated at 5 °C for 10 min. The total DNA was precipitated and segregated by centrifugation at 2750*g* at 5 °C for 10 min, then washed with 500 μL of 99.5% ethyl alcohol, and suspended in distilled water.

The four SSR markers used in this study were BARCSOYSSR_03_0165, BARCSOYSSR_03_0172, BARCSOYSSR_03_0175, and BARCSOYSSR_03_0185, all located on chromosome 3.[18] These markers are described in Table S2 and can be obtained from Soybase (http://soybase.org/).[19] An SSR marker located between BARCSOYSSR_03_0172 and BARCSOYSSR_03_0175 was designed and named "SSR_03g03340D". Polymerase chain reaction (PCR) was performed, and the products were analyzed by electrophoresis according to the methods described previously.[7] Amplification was performed with an initial incubation for 2 min at 95 °C, then 33 cycles of 1 min at 92 °C, 1 min at 58 or 60 °C (depending on the primers used), and 1 min at 68 °C, followed by a final incubation for 5 min at 72 °C. PCR products of SSR_03g03340D were determined using the LabChip GX electrophoresis system (PerkinElmer, MA, US).

DNA Sequencing. DNA fragments containing the open reading frame (ORF) regions of *Glyma03g03350* and *Glyma03g03360* were amplified by PCR using genomic DNA as a template. Information about predicted ORF regions was obtained from Phytozome (http://www.phytozome.net/). The primers used for amplification are described in Table S3. PCR was performed in a 20 μL reaction volume using *LA Taq* Hot Start Version according to the manufacturer's instruction (TAKARA, Shiga, Japan). Amplification was performed using the same conditions as described above. For DNA sequence analysis, DNA fragments were purified with a MonoFas DNA purification kit I (GL Sciences Inc., Tokyo, Japan) after electrophoresis using agarose gel. Sequencing reactions of purified PCR products were done with Big Dye terminators (Applied Biosystems, Foster City, CA). DNA sequences were determined with an ABI 3730xl automated sequencer (Applied Biosystems).

cDNA Synthesis and RT-PCR. Total RNA extracts were prepared using RNeasy Plant Mini Kit (Qiagen, Tokyo, Japan), followed by treatment with DNaseI using Turbo DNA-free Kit (Life Technologies Japan, Tokyo, Japan). For each sample, 1.5 μg of extracted RNA was reverse-transcribed using SuperScript Vilo cDNA Synthesis Kit (Life Technologies Japan). The RT-PCR mixture contained 1 μL of cDNA synthesis reaction mixture, 450 nM of each primer, and 10 μL of 2× KAPA2G Robust HS RM with dye (NIPPON Genetics Co, Ltd., Tokyo, Japan). Amplification was performed with an initial incubation for 3 min at 95 °C, then 33 cycles of 15 s at 95 °C; 10 s at 56, 58, or 60 °C (depending on the primers used); and 10 s at 72 °C.

Measurement of Calcium and Magnesium. Soybeans were ground into powder and 0.25 g of the sample was placed in a porcelain crucible for ashing at 500 °C for 16 h. After ashing, samples were extracted with 1 N HCl and diluted to 100 mL total. The contents of calcium and magnesium in the diluted samples were determined using ICP-AES Optima 4300 DV (PerkinElmer Japan Co., Ltd., Kanagawa, Japan).

Statistical Analysis. Statistical analysis was performed using the SPSS software package (version 22, IBM Japan, Tokyo, Japan).

RESULTS AND DISCUSSION

A *qHbs3-1* Candidate Gene and DNA Sequence Analysis. In our previous study, the analysis using progeny of the RHL derived from a cross between two Japanese cultivars, Natto-shoryu and Hyoukei-kuro 3, delimited the candidate region for *qHbs3-1* between BARCSOYSSR_03_0165 and BARCSOYSSR_03_0185, a physical distance of approximately 330 kb according to the information from Phytozome (Figure 1).[7] For further analysis to identify the gene responsible for *qHbs3-1*, F_7 and F_8 RHL progenies showing different recombinant genotypes of BARCSOYSSR_03_0165, BARCSOYSSR_03_0172, BARCSOYSSR_03_0175, and BARCSOYSSR_03_0185 were selected and the F_9 RHL progenies were obtained by self-fertilization. An SSR marker SSR_03g03340D and a cleaved amplified polymorphic sequence (CAPS) marker "BBCAPS" were further designed (Figure 1, Table S2). The breaking stress of cotyledons was compared among RHL progenies showing

DOI: 10.1021/acs.jafc.5b02896
J. Agric. Food Chem. 2015, 63, 8870−8878

Table 2. Comparison of the Breaking Stress of Progenies of the RHL Derived from a Cross between Two Japanese Cultivars, Natto-shoryu and Hyoukei-kuro 3, Showing Different Genotypes of BARCSOYSSR_03_0165, BARCSOYSSR_03_0172, SSR_03g03340D, BARCSOYSSR_03_0175, BARCSOYSSR_03_0185, and BBCAPS[a]

		Marker						
Cultivar		BSS_03_0165	BSS_03_0172	SSR_03g03340D	BBCAPS	BSS_03_0175	BSS_03_0185	Breaking stress (kPa)
Hyoukei-kuro 3		B	B	B	B	B	B	701
KYS13_1		B	B	B	B	B	B	1061
KYS16-4		B	B	B	B	B	B	1083
KYS17_10		B	B	B	B	B	B	1153
KYS17_14		B	B	B	B	B	B	1155
KYS7		A	B	B	B	B	B	945
KYS8		A	B	B	B	B	B	1014
KYS14_20		A	A	A	B	B	B	905
KYS14_17		A	A	A	B	B	B	910
KYS14_4		A	A	A	B	B	B	931
KYS14_16		A	A	A	B	B	B	934
KYS4		A	A	A	B	B	B	946
KYS14_21		A	A	A	B	B	B	986
KYS13_14		B	B	B	B	A	A	903
KYS13_6		B	B	B	B	A	A	991
KYS3		B	B	B	B	A	A	1011
KYS16-3		B	B	B	B	B	A	981
KYS10		B	B	B	B	B	A	987
KYS11		B	B	B	B	B	A	1093
KYS17_18		B	A	A	A	A	A	1210
KYS17_4		B	A	A	A	A	A	1399
KYS17_8		B	A	A	A	A	A	1430
KYS12		B	A	A	A	A	A	1454
KYS17_17		B	A	A	A	A	A	1674
KYS9		A	A	A	A	A	A	1595
Natto-shoryu		A	A	A	A	A	A	1634
Average of breaking stress of RHL progenies	A genotype	1019^{ns}	1198^{ns}	1198^{ns}	1460***	1296*	1227*	
	B genotype	1172	1031	1031	999	1006	1002	

[a]A indicates the same genotype as Natto-shoryu. B indicates the same genotype as Hyoukei-kuro 3. Breaking stress values more than 1200 kPa are shown in white type with a black background. *, ***: Values are significantly different from the B genotype at the 0.05 or 0.001 level, respectively. ^{ns}No siginificant difference was detected.

different genotypes of BARCSOYSSR_03_0165, BARCSOYSSR_03_0172, SSR_03g03340D, BARCSOYSSR_03_0175, BARCSOYSSR_03_0185, and BBCAPS. The graphical genotypes of RHL progenies and their breaking stress values indicated that *qHbs3-1* is located in the region between SSR_03g03340D and BARCSOYSSR_03_0175, where 2 genes, *Glyma03g03350* and *Glyma03g033360*, were presumed to be encoded (Soybase, Table 2 and Figure 1). BBCAPS, which is located between SSR_03g03340D and BARCSOYSSR_03_0175, detects a single base substitution of *Glyma03g03360* in Hyoukei-kuro 3 (Figures 1 and 2a, Table S2). The PCR products using BBCAPS primers were digested with a DNA restriction enzyme *Bst*1107I, which detects the GTATAC sequence of *Glyma03g03360* in Natto-shoryu (Figure 2b). All RHL progenies showing the same genotype as Hyoukei-kuro 3 at BBCAPS showed higher breaking stress values than that of Hyoukei-kuro 3, probably due to the effect of *qHbs6-1*, because all the RHL progenies examined showed the same genotypes as Natto-shoryu at SSR markers around the *qHbs6-1* region, Satt 100, Satt 277, and Satt 307.[7] Minor QTLs[7] may potentially affect the breaking stress values of RHL progenies.

The DNA sequence of the ORFs of the two genes *Glyma03g03350* and *Glyma03g03360* was analyzed. Primers used for amplification of exons of these genes are described in Table S3. Only the sequence in the third exon of *Glyma03g03360* showed a difference between Natto-shoryu and Hyoukei-kuro 3: a single DNA substitution detected by BBCAPS, resulting in a truncated protein in Hyoukei-kuro 3 (Figure 2a,b). Glyma03g03360 is predicted to be a pectin methylesterase (PME) with an inhibitor domain at the N terminus[20,21] according to Soybase. Glyma03g03360 of Hyoukei-kuro 3 is presumed to lack amino acids that are catalytically important (Figure 2a,b).[22]

PMEs deesterify pectins in the cell wall, converting methoxyl groups into carboxyl groups on the polygalacturonic acid chain and releasing both methanol and protons. The carboxyls can be cross-linked by calcium, which structurally rigidifies the cell wall.[23,24] Transcripts of *Glyma03g03360* were detected in embryo and seed coats at 45 days after anthesis (DAA) from Natto-shoryu by RT-PCR (Figure 3a). The transcripts were also detected in embryo from Hyoukei-kuro 3, although the band that was observed was fainter than that for Natto-shoryu (Figure 3b). It has been reported that mutation in the coding region affected the stability of mRNA and reduced the amount of transcripts, because premature termination of gene translation occasionally leads to transcript instability.[25] It is also possible that the amount of transcripts was affected by mutation in the promoter or flanking regions of *Glyma03g03360*. These results suggested that deesterification of pectins in the cell wall

DOI: 10.1021/acs.jafc.5b02896
J. Agric. Food Chem. 2015, 63, 8870−8878

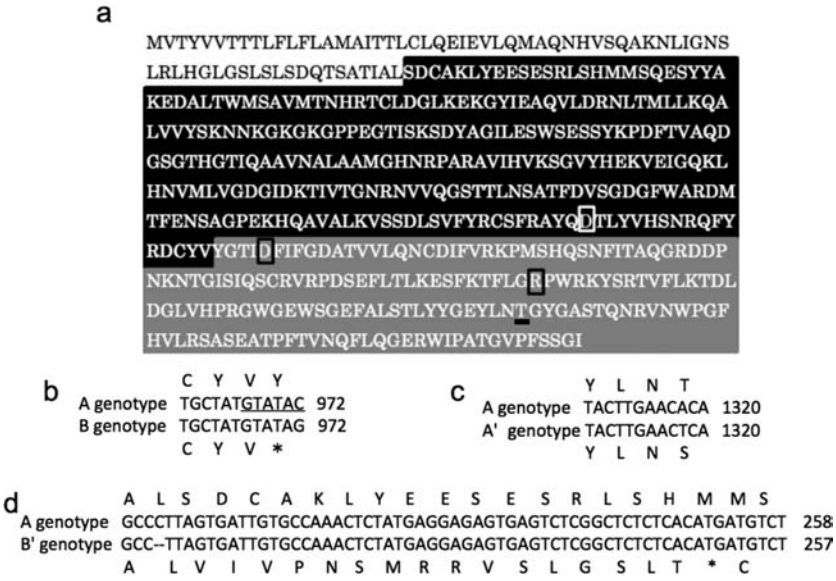

Figure 2. (a) Predicted amino acid sequence of Glyma03g03360 of Natto-shoryu (A genotype). Quadrilaterals indicate the position of catalytically important residues.[22] Glyma03g03360 of the B genotype lacks the sequence in gray. Glyma03g03360 of the B′ genotype lacks the sequence in gray and black. Underlined T indicates a single base substitution of the A′ genotype. (b) Comparison of DNA and predicted amino acid sequences of Glyma03g03360 between genotypes A and B. The nucleotides included in a *Bst*1107I restriction site are underlined. (c) Comparison of DNA and predicted amino acid sequences of Glyma03g03360 between genotypes A and A′. (d) Comparison of DNA and predicted amino acid sequences of Glyma03g03360 between genotypes A and B′.

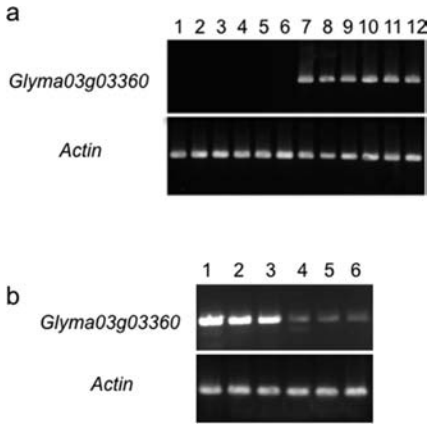

Figure 3. (a) RT-PCR analysis of RNA isolated from leaves (lanes 1−3), embryos 21 days after anthesis (DAA; lanes 4−6), embryos 45 DAA (lanes 7−9), and immature seed coats 45 DAA (lanes 10−12) from Natto-shoryu. RNAs were isolated from three independent tissues. Specific primers for *Glyma03g03360* (upper) and *actin* control (lower) were used. (b) RT-PCR analysis of RNA isolated from embryos 45 DAA from Natto-shoryu (lanes 1−3) and Hyoukei-kuro 3 (lanes 4−6). RNAs were isolated from three independent tissues. Specific primers for *Glyma03g03360* (upper) and *actin* control (lower) were used.

is preceded by the activation of Glyme03g03360 at the late stage of seed development, in both the embryo and seed coat.

Glyma03g03350 is a methionine aminopeptidase-like protein. In living organisms, proteins are synthesized with methionine as the first residue, which is specifically removed from the most mature proteins.[26−28] The free amino-terminal methionine is removed by methionine aminopeptidase. Soybase indicates that Glyma03g03350 is expressed in all tissues examined, including the leaf, flower, pod, seed, root, and nodule. Transcripts of *Glyma03g03350* were detected in embryos both from Natto-shoryu and from Hyoukei-kuro 3, even though the intensities of the bands were different among samples (Figure S1).

Cultivar Differences in the Cooked Seed Hardness and Genotype of *Glyma03g03360*. Genotypes of *Glyma03g03360* and breaking stress of cotyledons were further analyzed using 24 cultivars grown at different locations in 2013 (Table 1). CAPS analysis using the BBCAPS marker in the 24 cultivars resulted in three patterns of DNA fragments (Figure 4): one shows a single, main band designating Hyoukei-kuro 3; another shows two main bands and a minor band designating Natto-shoryu; and the last shows only two main bands. The sizes of the larger main bands were different between the latter two fragment patterns.

DNA sequence analysis indicated that four polymorphisms exist in *Glyma03g03360* among the 24 cultivars, and we named them A, A′, B, and B′. Polymorphisms A and B are the same as that of Natto-shoryu and Hyoukei-kuro 3, respectively. Polymorphism A′, which shows the third pattern by BBCAPS, contains a single base substitution in exon 3, resulting in an amino acid substitution from threonine to serine (Figure 2a,c). Because this amino acid is not predicted to be important for enzymatic activity,[22] Glyma03g03360 of this group is presumably active. Polymorphism B′, which also shows the third pattern by BBCAPS and the same pattern as polymorphism A′, contains a single base deletion in exon 1, resulting in a truncated protein. This protein is also presumed to lack amino acids that are catalytically important. (Figure 2a,d). The upper primer sequence of BBCAPS is located in the intron of *Glyma03g03360* between the second and third exons, and the lower primer sequence is located in the third exon. The expected sizes of *Bst*1107I restriction fragments from the sequence data are 434 bp and 233 bp for Natto-shoryu. The fragment pattern shown in Figure 4 agrees with the sequence data. The size difference in the larger main bands between A, and A′ and B′ genotypes is probably due to the difference in the

DOI: 10.1021/acs.jafc.5b02896
J. Agric. Food Chem. 2015, 63, 8870−8878

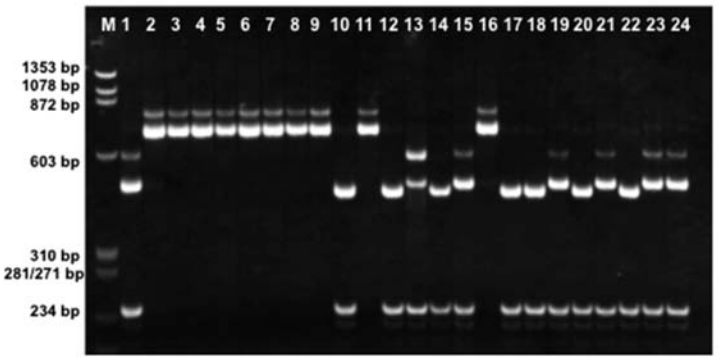

Lane	Cultivar	Genotype
1	Natto-shoryu	A
2	Satonohohoemi	B
3	Hyoukei-kuro 3	B
4	Tachinagaha	B
5	Oosuzu	B
6	Akishirome	B
7	Ryuuhou	B
8	Kotoyutaka	B
9	Tachiyutaka	B
10	Fukuyutaka	A′
11	Enrei	B
12	Sachiyutaka	A′
13	Suzuyutaka	A
14	Fukuminori	A′
15	Fukuibuki	A
16	Himeshirazu	B
17	Suzukaren	A′
18	Tamadaikoku	B′
19	Suzukari	A
20	Shuurei	B′
21	Kosuzu	A
22	Sakukei 98	A′
23	Tamahomare	A
24	LD00-3309	A

Figure 4. Products of BBCAPS from 24 soybean cultivars. M indicates DNA marker (phiX 174/*Hae*III). The migration of size markers is shown to the left of the gel.

intron sequence. The genotypes of *Glyma03g03360* for the full 24 cultivars are described in Table 1 and Figure 4.

The breaking stress values of cotyledons were compared using the 22 cultivars (without Natto-shoryu and Hyoukei-kuro 3) grown in different locations described in Table 1. The averages of these values were 1572, 1568, and 1456 kPa for A or A′ genotypes in Ibaraki (NICS), Kumamoto (KARC), and Akita (TARC), respectively. The averages of the values were 979, 1117, and 870 kPa for B or B′ genotypes in Ibaraki, Kumamoto, and Akita, respectively (Figure 5). Statistical

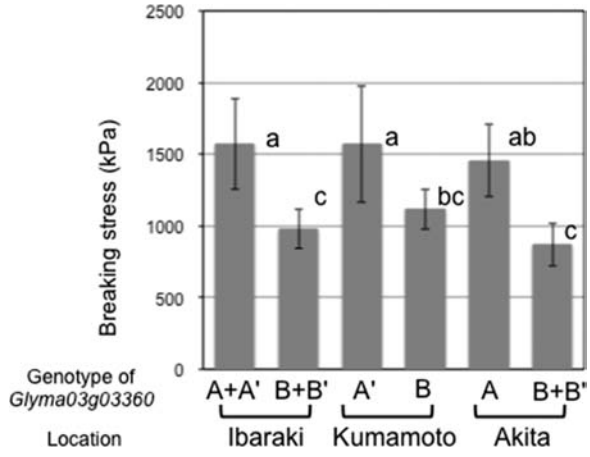

Figure 5. Averages of the breaking stress for A, A′, B, and B′ genotypes. Different letters indicate a significant difference at the 0.05 level by Tukey's test. Bars indicate SD.

analysis indicated that the breaking stress of A and A′ genotypes is significantly different from that of B and B′ genotypes in each location. However, there was no significant difference shown between the A genotype and the A′, or between the B genotype and the B′ (data not shown). These results indicated that Glyma03g03360 significantly affects the cooked seed hardness in many soybean cultivars.

Phenotypic and Genomic Variation of an F_2 Population from Enrei and LD00-3309, and Satonohohoemi and Sakukei 98. The breaking stress of cotyledons and genotypes of *Glyma03g03360* were analyzed using F_2 populations from a cross between Enrei (B genotype) and LD00-3309 (A genotype), and between Satonohohoemi (B genotype) and Sakukei 98 (A′ genotype). The averages of the breaking stress values were 1467 and 1059 kPa for progenies from Enrei and LD00-3309 with an A genotype and those with a B, respectively. The breaking stress of progenies from Enrei and LD00-3309 showing the A genotype was significantly higher than that of the progenies showing the B genotype ($p < 0.05$, Figure 6a). The breaking stress of progenies from Satonohohoemi and Sakukei 98 showing an A′ genotype was significantly higher than that of the progenies showing a B genotype ($p < 0.05$, Figure 6b). Moreover, all the progenies of the A′ genotype showed breaking stress values higher than those of the B genotype. From these results, we concluded that *Glyma03g03360*, a PME homologue, is most certainly *qHbs3-1*.

Effect of Seed Size, Water Absorption Ratio, and Calcium Content on the Cooked Seed Hardness. Negative correlations between cooked seed hardness and 100-seed weight or degree of water absorption have been reported.[29,30] However, no significant negative correlation between the breaking stress and 100-seed weight or water absorption ratio was detected using RHL populations from Natto-shoryu and Hyoukei-kuro 3 ($n = 24$), which showed no significant difference in the 100-seed weight and the water absorption ratio between progenies of the A genotype and those of the B genotype (Table 3). In contrast, statistical analysis using soybean samples described in Table 1 indicated that the 100-seed weight and water absorption ratio are significantly correlated with the breaking stress value ($r = -0.408$ and -0.391, respectively; $p < 0.01$, Table 4). Soybeans with the A and A′ genotypes showed 100-seed weight and water absorption ratio significantly lower than those with B and B′. The averages of the 100-seed weight were 24.69 and 33.24 g for A + A′ genotypes and B + B′ genotypes, respectively. The

DOI: 10.1021/acs.jafc.5b02896
J. Agric. Food Chem. 2015, 63, 8870−8878

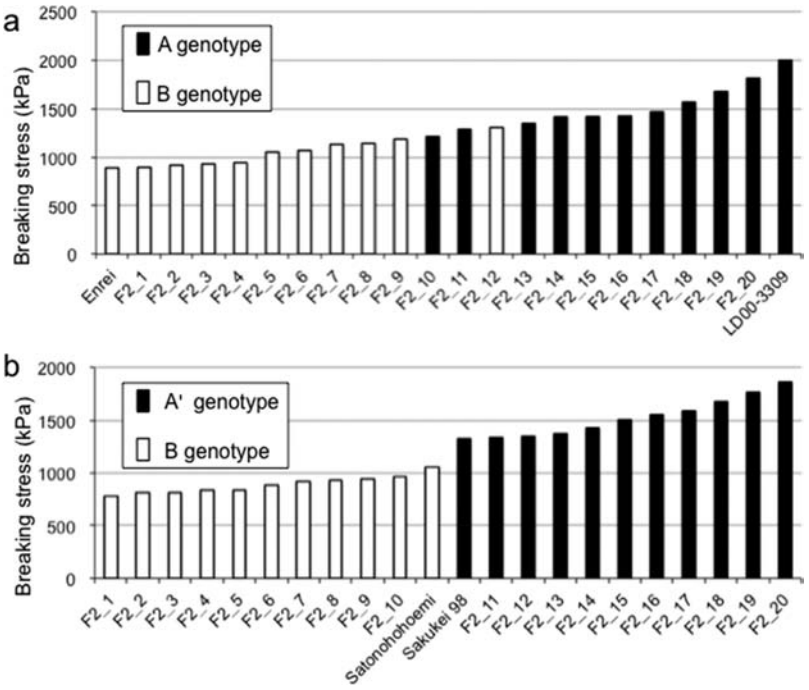

Figure 6. (a) Breaking stress of cotyledons of F_2 progenies from a cross between Enrei and LD00-3309. Black bars indicate the progenies with an A genotype, while white bars indicate progenies with a B genotype. (b) Breaking stress of cotyledons of F_2 progenies from a cross between Satonohohoemi and Sakukei 98. Black bars indicate the progenies with an A′ genotype, while white bars indicate progenies with a B genotype.

Table 3. Correlation of 100-Seed Weight and Water Absorption Ratios and the Breaking Stress Values and the Average Values of 100-Seed Weight and Water Absorption Ratio for RHL Progenies between Natto-shoryu and Hyoukei-kuro 3

	correlation with the breaking stress values	average for each genotype of *Glyma03g03360*
100-seed weight	0.44*	19.14 g (A genotype)
		20.49 g (B genotype)
water absorption ratio	−0.041	2.55 (A genotype)
		2.53 (B genotype)

*Significant at the 0.05 level.

Table 4. Correlation of Calcium and Magnesium Contents, 100-Seed Weight, Water Absorption Ratios, and the Breaking Stress Values between the Groups of Cultivars Showing A, A′, B, and B′ Genotypes

	all samples (n = 54)	A+A′ genotypes (n = 22)	B+B′ genotypes (n = 32)
100-seed weight	−0.408**	−0.015	−0.225
water absorption ratio	−0.391**	−0.235	0.273
Ca content	0.424**	0.702***	0.457**
Mg content	0.309*	0.245	0.132

,,***: Significant at the 0.05, 0.01, or 0.001 level, respectively.

averages of the water absorption ratio were 2.26 and 2.33 for A + A′ genotypes and B + B′ genotypes, respectively. No significant correlation between the breaking stress and 100-seed weight or water absorption ratio was detected within the A + A′ genotypes and within the B + B′ genotypes. One possible explanation for the discordance in the relationship between the 100-seed weight or the water absorption ratio and breaking stress is that Glyma03g03360 may have an effect on the 100-seed weight and the water absorption ratio, which are also affected by other factors. Another possibility is that a gene close to the *qHbs3-1* may have an effect on the 100-seed weight and the water absorption ratio, with no difference in amino-acid sequence and expression between Natto-shoryu and Hyoukei-kuro 3. In our previous study, no QTL was identified in the same chromosomal region as that of *qHbs3-1* for 100-seed weight or water absorption ratio using an RIL population derived from a cross between Natto-shoryu and Hyoukei-kuro 3, although the 100-seed weight of Hyoukei-kuro 3 was more than 4 times higher than that of Natto-shoryu.[7]

It has been reported that a PME inhibitor plays a role in the early stage of radicle emergence.[31] Glyma03g03360 likely has a role in the rigidification of the cell wall and elongation of the cell through PME activity, which may partly affect 100-seed weight and water absorption ratio. Seed weight, also characterized as seed mass or seed size generally, has been widely accepted as a complex trait controlled by polygenes.[32] Hemicellulose content of seed coat fractions, particularly xylans, has been reported to be correlated with water uptake ratio and occurrence of hard seeds (stone seeds).[33]

Calcium content was significantly correlated with breaking stress using soybean samples described in Table 1 (r = 0.424, p < 0.01, Table 4). Soybeans of A and A′ genotypes showed a correlation between calcium content and breaking stress (r = 0.702, p < 0.001, Table 4 and Figure 7) higher than those of B and B′ genotypes (r = 0.457 p < 0.01, Table 4, and Figure 7). These results imply that the Ca^{2+} crossbridges between free carboxyl groups of adjacent pectin chains play an important role in the cooked seed hardness of soybeans. B and B′ genotypes also showed a significant correlation between calcium content and breaking stress, probably due to the expression of the other PME genes. According to SoyBase, more than 100 PME-like

DOI: 10.1021/acs.jafc.5b02896
J. Agric. Food Chem. 2015, 63, 8870−8878

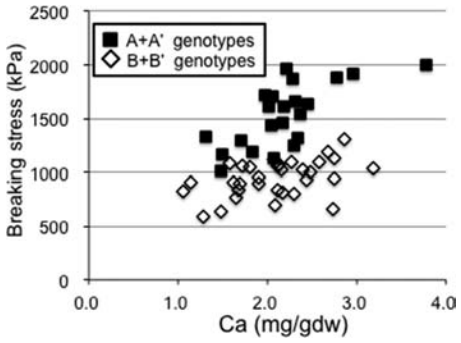

Figure 7. Correlation between calcium content and breaking stress of cotyledons of cultivars with an A or A′ genotype (black squares) and those with a B or B′ genotype (white rhombuses).

genes are found in soybean. Magnesium was also significantly correlated with breaking stress (r = 0.309, p < 0.05, Table 3). Magnesium can cross-link the carboxyl groups of pectins in a similar manner. Magnesium content showed less correlation with breaking stress than calcium, probably due to less variation of magnesium content than that of calcium content (Table 5).

Table 5. Average, Standard Deviations (SDs), and Coefficients of Variations (CVs) of Calcium and Magnesium Contents

		all samples (n = 54)	A+A′ genotypes (n = 22)	B+B′ genotypes (n = 32)
Ca content (mg/gdw)	average	2.13	2.19	2.09
	SD	0.52	0.53	0.52
	CV	0.25	0.24	0.25
Mg content (mg/gdw)	average	2.48	2.54	2.44
	SD	0.20	0.22	0.17
	CV	0.08	0.09	0.07

Sajjaanantakul et al. demonstrated that β-elimination of pectins was primary responsible for the heat degradation at pH 6.1 and that the rate of the β-eliminative cleavage of the prepared pectin depended on the degree of esterification.[34] It has been proposed that a decrease in degree of methylesterification necessitates both endogenous and exogenous calcium to form Ca^{2+} crossbridges between the free carboxyl groups of adjacent pectin molecules.[35] Because Ca^{2+} and Mg^{2+} are bound to protein and/or phytate,[36−38] other mechanisms in the relationship between the calcium and/or magnesium contents and the hardness of cotyledons may possibly be involved. Further studies are required to clarify the relationship between the calcium content in soybean and the degree of methylesterification.

In this study, we conclude that *Glyma03g03360*, a PME homologue, is *qHbs3-1*, a stable QTL for hardness of cooked soybean cotyledons. The contribution of the F_5 generation grown in 2010 to the total phenotypic variance of *qHbs3-1* was 47.4% and that of the F_6 generation grown in 2011 was 44.3%.[7] No QTL was identified in the same chromosomal region as that of *qHbs3-1* for 100-seed weight, also implying that *Glyma03g03360* is useful for the improvement of soybean cultivars through breeding, because larger seeds are preferable for nimame, while smaller seeds are preferable for natto. DNA markers used in this study would be useful both for DNA marker-assisted selection and for the evaluation of seed quality, because it is otherwise time-consuming and laborious to evaluate cooked seed hardness. RT-PCR indicated that Glyma03g03360 is expressed both in embryos and seed coats (Figure 3), suggesting the possible effect of Glyma03g03360 on the texture of the seed coat, although it was not analyzed in this study. The mechanisms underlying how PME activity affects cooked seed hardness still remain to be clarified, although previous studies have shown that the demethylesterification of pectins has dramatic consequences on the rheological properties of the cell wall.[14,39] Hardness after cooking is also important for other beans, such as carioca bean,[40] fava bean,[41] and chickpea.[42] Further studies may help reveal ways to improve the quality of soyfoods and of food products of other beans.

■ ASSOCIATED CONTENT

Ⓢ Supporting Information

The Supporting Information is available free of charge on the ACS Publications website at DOI: 10.1021/acs.jafc.5b02896.

100-seed weight, water absorption ratio, breaking stress, Ca content, Mg content, and moisture content in soybeans listed in Table 1 (Table S1); information about SSR and CAPS markers (Table S2); information about primers used for DNA amplification and RT-PCR (Table S3); RT-PCR analysis of RNA isolated from embryos 45 DAA from Natto-shoryu and Hyoukei-kuro 3 (Figure S1) (PDF)

■ AUTHOR INFORMATION

Corresponding Author

*E-mail: kyokot@affrc.go.jp. Tel: +81-29-838-8503.

Author Contributions

†K.T. and K.H.: These authors contributed equally to this work.

Notes

The authors declare no competing financial interest.

■ ACKNOWLEDGMENTS

The authors are grateful to the Hyogo Prefectural Research Center of Agriculture, Forestry and Fisheries for providing "Hyoukei-kuro 3" seeds. The authors are also grateful to the Nagano Vegetable and Ornamental Crops Experiment Station for providing "Enrei," "Tachinagaha," and "Tamadaikoku" seeds.

■ ABBREVIATIONS USED

CAPS, cleaved amplified polymorphic sequence; CV, coefficients of variations; DAA, days after anthesis; F_2, second filial generation; F_5, fifth filial generation; F_6, sixth filial generation; F_7, seventh filial generation; F_8, eighth filial generation; F_9, ninth filial generation; ORF, open reading frame; PCR, polymerase chain reaction; PME, pectin methylesterase; QTL, quantitative trait locus; RIL, recombinant inbred line; SD, standard deviations; SSR, simple sequence repeat

■ REFERENCES

(1) Taira, H. Quality of soybeans for processed foods in Japan. *JARQ* **1990**, *24*, 224−230.

(2) Yoshioka, K.; Sekine, M.; Suzuki, M.; Otobe, K. Influence of soaking and steaming conditions on the hardness of steamed soybeans and fermented soybeans (natto). *Nippon Shokuhin Kagaku Kogaku Kaishi* **2009**, *56*, 40−47.

DOI: 10.1021/acs.jafc.5b02896
J. Agric. Food Chem. 2015, 63, 8870−8878

(3) Zhang, B.; Chen, P.; Chen, C. Y.; Wang, D.; Shi, A.; Hou, A.; Ishibashi, T. Quantitative trait loci mapping of seed hardness in soybean. *Crop Sci.* **2008**, *48*, 1341−1349.
(4) Makabe, Y. Effect of salts on cooked beans. *Bull. Soc. Sea Water Sci., Jpn.* **2006**, *60*, 342−347.
(5) Yasui, T.; Sasaki, T.; Kohyama, K.; Hajika, M. Variation in firmness of whole beans, embryos, and testas of cooked soybean (*Glycine max*) cultivars. *Cereal Chem.* **2014**, *91*, 419−424.
(6) Orazaly, M.; Chen, P.; Zeng, A.; Zhang, B. Identification and confirmation of quantitative trait loci associated with soybean seed hardness. *Crop Sci.* **2015**, *55*, 688−694.
(7) Hirata, K.; Masuda, R.; Tsubokura, Y.; Yasui, T.; Yamada, T.; Takahashi, K.; Nagaya, T.; Sayama, T.; Ishimoto, M.; Hajika, M. Identification of quantitative trait loci associated with boiled seed hardness in soybean. *Breed. Sci.* **2015**, *64*, 362−370.
(8) Giovane, A.; Servillo, L.; Balestrieri, C.; Raiola, A.; D'Avino, R.; Tamburrini, M.; Ciardiello, M. A.; Camardella, L. Pectin methylesterase inhibitor. *Biochim. Biophys. Acta, Proteins Proteomics* **2004**, *1696*, 245−252.
(9) Pelloux, J.; Rustérucci, C.; Mellerowicz, E. J. New insights into pectin methylesterase structure and function. *Trends Plant Sci.* **2007**, *12*, 267−277.
(10) Li, Y. Q.; Faleri, C.; Geitmann, A.; Zhang, H. Q.; Cresti, M. Immunogold localization of arabinogalactan proteins, unesterified and esterified pectins in pollen grains and pollen tubes of *Nicotiana tabacum* L. *Protoplasma* **1995**, *189*, 26−36.
(11) Staehelin, L. A.; Moore, I. The plant Golgi-apparatus-structure, functional organization and trafficking mechanisms. *Annu. Rev. Plant Physiol. Plant Mol. Biol.* **1995**, *46*, 261−288.
(12) Sterling, J. D.; Quigley, H. F.; Orellana, A.; Mohnen, D. The catalytic site of the pectin biosynthetic enzyme alpha-1,4-galacturonosyltransferase is located in the lumen of the Golgi. *Plant Physiol.* **2001**, *127*, 360−371.
(13) Catoire, L.; Pierron, M.; Morvan, C.; du Penhoat, C. H.; Goldberg, R. Investigation of the action patterns of pectinmethylesterase isoforms through kinetic analyses and NMR spectroscopy-implications in cell wall expansion. *J. Biol. Chem.* **1998**, *273*, 33150−33156.
(14) Pirhayati, M.; Soltanizadeh, N.; Kadivar, M. Chemical and microstructural evaluation of 'hard-to-cook' phenomenon in legumes (pinto bean and small-type lentil). *Int. J. Food Sci. Technol.* **2011**, *46*, 1884−1890.
(15) Ilker, R.; Szczesniak, A. Structural and chemical base for texture of plant foodstuffs. *J. Texture Stud.* **1990**, *21*, 1−36.
(16) Yamanaka, N.; Watanabe, S.; Toda, K.; Hayashi, M.; Fuchigami, H.; Takahashi, R.; Harada, K. Fine mapping of the *FT1* locus for soybean flowering time using a residual heterozygous line derived from a recombinant inbred line. *Theor. Appl. Genet.* **2005**, *110*, 634−639.
(17) AACC International. Method 56-36.01: Firmness of cooked pulses; *Approved Methods of Analysis*, 11th ed.; AACC International: St. Paul, MN, Approved August, 2012.
(18) Song, Q.; Jia, G.; Zhu, Y.; Grant, D.; Nelson, R. T.; Hwang, E. Y.; Hyten, D. L.; Cregan, P. B. Abundance of SSR motifs and development of candidate polymorphic SSR markers (BARC-SOYSSR_1.0) in soybean. *Crop Sci.* **2010**, *50*, 1950−1960.
(19) Grant, D.; Nelson, R. T.; Cannon, S. B.; Shoemaker, R. C. Soybase, the USDA-ARS soybean genetics and genomic database. *Nucleic Acids Res.* **2010**, *38* (suppl 1), D843−D846.
(20) Giovane, A.; Balestrieri, C.; Quagliuolo, L.; Castaldo, D.; Servillo, L. A glycoprotein inhibitor of pectin methylesterase in kiwi fruit. Purification by affinity chromatography and evidence of a ripening-related precursor. *Eur. J. Biochem.* **1995**, *233*, 926−929.
(21) Camardella, L.; Carratore, V.; Ciardiello, M. A.; Servillo, L.; Balestrieri, C.; Giovane, A. Kiwi protein inhibitor of pectin methylesterase amino-acid sequence and structural importance of two disulfide bridges. *Eur. J. Biochem.* **2000**, *267*, 4561−4565.
(22) Bosch, M.; Cheung, A. Y.; Hepler, P. K. Pectin methylesterase, a regulator of pollen tube growth. *Plant Physiol.* **2005**, *138*, 1334−1346.
(23) Goldberg, R.; Morvan, C.; Roland, J. C. Composition, properties and localization of pectins in young and mature cells of the mung bean hypocotyl. *Plant Cell Physiol.* **1986**, *27*, 417−429.
(24) Holdaway-Clarke, T. L.; Hepler, P. K. Control of pollen tube growth: role of ion gradients and fluxes. *New Phytol.* **2003**, *159*, 539−563.
(25) Daar, I. O.; Maquat, L. E. Premature translation termination mediates triosephosphate isomerase mRNA degradation. *Mol. Cell. Biol.* **1988**, *8*, 802−813.
(26) Meinnel, T.; Mechulam, Y.; Blanquet, S. Methionine as translation start signal: a review of the enzymes of the pathway in *Escherichia coli*. *Biochimie* **1993**, *75*, 1061−1075.
(27) Bradshaw, R. A.; Brickey, W. W.; Walker, K. W. N-terminal processing: the methionine aminopeptidase and N alpha-acetyl transferase families. *Trends Biochem. Sci.* **1998**, *23*, 263−267.
(28) Giglione, C.; Meinnel, T. Organellar peptide deformylases: universality of the N-terminal methionine cleavage mechanism. *Trends Plant Sci.* **2001**, *6*, 566−572.
(29) Hirota, T.; Takahata, K.; Ogawa, T.; Iwai, M.; Inoue, Y. Quality of soybean seeds grown in Hyogo prefecture. *Bull. Hyogo Prefect. Technol. Cent. Agric., For. Fish., Agric. Sect.* **2005**, *53*, 6−12.
(30) Motoki, S.; Yamada, N.; Tanaka, N.; Takamatsu, M.; Takahashi, N. Studies on selection of soybean for high processing suitability in bean paste (miso). *Hokuriku Crop Sci.* **1999**, *34*, 118−119.
(31) Müller, K.; Levesque-Tremblay, G.; Bartels, S.; Weitbrecht, K.; Wormit, A.; Usadel, B.; Haughn, G.; Kermode, A. R. Demethylesterification of cell wall pectins in *Arabidopsis* plays a role in seed germination. *Plant Physiol.* **2013**, *161*, 305−316.
(32) Liu, J.; Hua, W.; Yang, H. L.; Zhan, G. M.; Li, R. J.; Deng, L. B.; Wang, X. F.; Liu, G. H.; Wang, H. Z. The *BnGRF2* gene (*GRF2-like* gene from *Brassica napus*) enhances seed oil production through regulating cell number and plant photosynthesis. *J. Exp. Bot.* **2012**, *63*, 3727−3740.
(33) Mullin, W. J.; Xu, W. Study of soybean seed coat components and their relationship to water absorption. *J. Agric. Food Chem.* **2001**, *49*, 5331−5335.
(34) Sajjaanantakul, T.; Van Buren, J. P.; Downing, D. L. Effect of ester content on heat degradation of chelater-soluble carrot pectin. *J. Food Sci.* **1989**, *54*, 1272−1277.
(35) Sila, D. N.; Smout, C.; Vu, T. S.; Hendrickx, M. E. Effects of high-pressure pretreatment and calcium soaking on the texture degradation kinetics of carrots during thermal processing. *J. Food Sci.* **2004**, *69*, E205−E211.
(36) de Rham, O.; Jost, T. Phytate-protein interaction in soybean extracts and low-phytate soy protein products. *J. Food Sci.* **1979**, *44*, 596−600.
(37) Prattley, C. A.; Stanley, D. W. Protein-phytate interaction in soybeans. I. Localization of phytate in protein bodies and globoids. *J. Food Biochem.* **1982**, *6*, 243−254.
(38) Rao, A. G. A.; Rao, M. S. N. Binding of Ca (II), Mg (II), and Zn (II) by 7S fraction of soybean proteins. *J. Agric. Food Chem.* **1976**, *24*, 490−494.
(39) Sénéchal, F.; Wattier; Rustérucci, C.; Pelloux, J. Homogalacturonan-modifying enzymes: structure, expression, and roles in plants. *J. Exp. Bot.* **2014**, *65*, 5125−5160.
(40) Siqueira, B. d. S.; Vianello, R. P.; Fernandes, K. F.; Bassinello, P. Z. Hardness of carioca beans (*Phaseolus vulgaris* L.) as affected by cooking methods. *LWT Food Sci. Technol.* **2013**, *54*, 13−17.
(41) Nasar-Abbas, S. M.; Plummer, J. A.; Siddique, K. H. M.; White, P.; Harris, D.; Dods, K. Cooking quality of faba bean after storage at high temperature and the role of lignins and other phenolics in bean hardening. *LWT* **2008**, *41*, 1260−1267.
(42) Güzel, D.; Sayar, S. Effect of cooking methods on selected physicochemical and nutritional properties of barlotto bean, chickpea, faba bean, and white kidney bean. *J. Food Sci. Technol.* **2012**, *49*, 89−95.

DOI: 10.1021/acs.jafc.5b02896
J. Agric. Food Chem. 2015, 63, 8870−8878

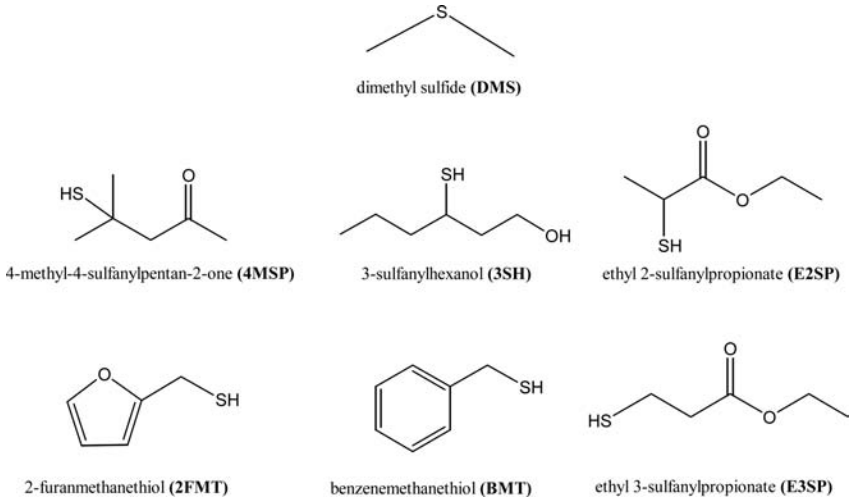

Figure 1. Chemical structures of the volatile sulfur compounds analyzed.

highly odor-active compounds with multiple influences on wine aroma. Originally associated with off flavors, they are now recognized as important contributors to wine aroma, depending on their concentrations, aromatic properties, and synergist effects.[5]

Among these compounds, DMS constitutes an interesting case since its influence on wine aroma is perceived either positively or negatively, depending on the concentration and type of wine.[9] In red wines, its positive contribution to the aroma of Cabernet Sauvignon wines has been reported,[10] and it is also known to accentuate truffle and undergrowth sensory attributes in wines.[9,11] Polyfunctional thiols are a series of volatile sulfur odorants that have received a great deal of research attention over the past decade. The group includes 4-methyl-4-sulfanyl-pentan-2-one (4MSP) and 3-sulfanylhexanol (3SH), associated with the typical fruity nuances in varietal aroma,[12−17] and 2-methyl-3-furanthiol (2M3F), benzenemethanethiol (BMT), ethyl 2-sulfanylpropionate (E2SP), and ethyl 3-sulfanylpropionate (E3SP), responsible for empyreumatic notes acquired during aging.[4,18−20] A sulfur-based furan, 2-furanmethanethiol (2FMT), belongs to another group of pleasant-smelling thiols formed in wine during oak-barrel aging and contributes to the toasty, cooked meat, and roasted coffee characteristics of oak-matured wines.[15,21,22]

Although the involvement of these volatile sulfur compounds in the pleasant truffle, toasty, and smoky aromas of aged fine wines is known and their aromatic descriptors overlap with the main characteristics of the olfactory representation of the aging bouquet concept,[7] this is the first time that a study was aimed to closely examine the combined impact of these aroma compounds on the sensory perception of the aging bouquet of red Bordeaux wines. More precisely, this study was designed to answer the following questions: (i) Do these selected volatile odorant sulfur compounds play a specific role in the typicality of the aging bouquet of red Bordeaux wines? (ii) How are their concentrations related to the occurrence, evolution, and intensity of the sensory nuances perceived in the aging bouquet of Bordeaux red wines during bottle aging?

This work was based on an approach combining sensory and quantitative chemical data, supported by several statistical methodologies, including multivariate tools, such as partial least square (PLS) analysis[23] and principal component analysis (PCA),[24] for relating sensory and compositional data.

MATERIALS AND METHODS

Chemicals. The chemical structures of the six volatile sulfur compounds are presented in Figure 1. Standard compounds were obtained from commercial sources as follows: DMS (>99%), thiophene (>99%), 2FMT (>98%), E3SP (>99%), BMT (>99%) 3SH (>98%), 6-sufanylhexanol (6SH; 97%), L-cysteine (98%), sodium acetate trihydrate (99%), and *p*-hydroxymercuribenzoic acid (*p*-HMB; > 95%) were supplied by Sigma-Aldrich (Saint-Quentin-Fallavier, France). E2SP (>98%) was obtained from Lancaster (MA, USA), 4MSP (1%; v/v ethylene glycol) solution from Interchim (Montluçon, France), and 3-methoxymethylbutanethiol (3MMB; 97%) from Oxford Chemicals (Hartlepool, United Kingdom).

Wines. During the first stage of the study, 24 commercial red wines were studied. They were selected by a panel of wine professionals with the aim of covering a wide range of red Bordeaux wines appellations, vineyards, and vintages. Nine different Bordeaux appellations were retained, from 19 vineyards and various vintages, from 1994 to 2005 inclusive were retained (Table 1). All these wines were oak-barrel matured before bottling.

In the second stage, three sets of wines were studied, each covering a 17- to 19-year period in the same vineyard. They represented three different Bordeaux appellations: Margaux (MX series: 7 wines, 19-year period, and vintages from 1995 to 2013), Pomerol (P series: 7 wines, 17-year period, and vintages from 1996 to 2012), and Saint-Emilion (SEM series: 8 wines, 18-year period, and vintages from 1995 to 2012).

The wines were tasted by two professionals of the tasting panel as soon as the bottles were opened to ascertain the absence of olfactory defects. None of the wines included in the tasting presented off-flavors, such as premature aging character or cork taint. All of the wines were tasted by the panel within 30 min after opening and subjected to both sensory and chemical analyses.

Sensory Analyses. *Professional Wine-Tasting Panel.* A panel of 13 wine professionals was recruited (4 women and 9 men; age range, 30−70; mean age, 42 years). All of the panelists were French native speakers, consumed wine regularly, worked in the Bordeaux area, and had considerable experience in tasting Bordeaux wines. They were informed about the context of the study but not given prior common training.

Experimental Design. The sensory experiments were organized in three different tasting sessions. During the first session, the aging bouquet typicality of the 24 selected wines was assessed, using the previously validated methodology.[7]

To avoid any aging bias, the 24 wines were randomized and separated into four sets of six wines. The panelists performed an ortho- and retronasal typicality evaluation task, according to their own concept of the wine aging bouquet. Wines (20 mL) were poured into clear INAO glasses with plastic covers, coded with three-digit random

DOI: 10.1021/acs.jafc.5b03977
J. Agric. Food Chem. 2015, 63, 8879−8889

Table 1. Characteristics of the 24 Wines Tasted (Appellation, Vintage, and Code)[a]

appellation	vintage	code	aging bouquet typicality score/10 (mean value ± SD)
Listrac-Médoc	2001	LMC01	4.0 ± 0.6
Margaux	1998	**MX98**	**6.5 ± 0.8**
Margaux	2001	MX01	4.9 ± 1.2
Margaux	2004	**MX04**	**7.2 ± 0.5**
Médoc	2001	MC01	5.3 ± 1.3
Pauillac	1994	PC94	4.6 ± 0.7
Pauillac	1996	PC96	4.7 ± 1.4
Pauillac	2001	PC01	5.2 ± 1.2
Pessac-Léognan	2004	PL04	5.2 ± 1.4
Pomerol	1998	P98-1	6.7 ± 0.6
Pomerol	1998	**P98-2**	**6.8 ± 0.7**
Pomerol	2001	P01	3.9 ± 0.9
Pomerol	2004	**P04**	**4.3 ± 1.1**
Saint-Emilion	1998	**SEM98**	**6.0 ± 0.5**
Saint-Emilion	1999	SEM99	5.5 ± 1.1
Saint-Emilion	2000	**SEM00**	**4.0 ± 0.3**
Saint-Emilion	2002	**SEM02**	**2.4 ± 0.4**
Saint-Emilion	2003	SEM03-1	6.8 ± 1.0
Saint-Estèphe	1997	**SE97**	**3.9 ± 0.5**
Saint-Estèphe	1999	SE99	4.5 ± 1.1
Saint Julien	1995	SJ95	5.1 ± 1.1
Saint Julien	1997	SJ97	4.7 ± 0.9
Saint Julien	2001	**SJ01**	**6.0 ± 0.5**
Saint Julien	2005	**SJ05**	**3.9 ± 0.2**

[a]In bold are the 10 wines selected for sensory profiling on four aromatic descriptors of the wine aging bouquet.

numbers, and served in a different order to each taster. The presentation order was randomized among the panelists. Wine samples were tasted in a dedicated room at 18 °C (ISO 8589:2007). The instructions given were as follows: "*Imagine that you have to explain the aging bouquet of red Bordeaux wines to someone. For each wine tasted, please answer the following question: do you think this wine is a good or a poor example of reductive aging bouquet?*". Panelists answered on a 10 cm unstructured scale, ranging from "poor example" on the left to "good example" on the right (one scale per sample, one set of 6 wines per sheet). The distance between the left end and the score-mark made by each wine professional was measured and converted into a figure between 0 and 10, which corresponded to "the typicality score" (Table 1).

During the second tasting, a subset of 10 wines was chosen among the 24 wines evaluated in the first series, according to their degree of correspondence to the wine aging bouquet concept. Five wines were chosen among the group of highly typical wines and five from the less-typical group (Table 1 and Figure S1 in Supporting Information). The choice was designed to maximize the diversity of wine appellations.

In order to assess the reproducibility of the panel's perception, these 10 wines were subjected to the same typicality task as the larger group. After a 15 min break, each wine was subjected to sensory profiling to evaluate the intensity of the four aromatic descriptors previously identified as most representative of a typical aging bouquet: undergrowth, truffle, toasted, and fresh red- and black-berry fruit.[7] The panelists rated the intensity of these descriptors in each sample on a 10 cm unstructured scale, ranging from "not very intense" on the left to "very intense" on the right. The distance between the left end and the score-mark made by each wine professional was measured and converted into a figure between 0 and 10, indicating the sensory intensity of the corresponding aroma attribute. The panelists were not given prior common training.

The third tasting session involved three specific sets of wines, each from a single Bordeaux vineyard, comprising vintages from 1995 to 2013, inclusive. To avoid any vintage effect, these 22 wines were poured into black INAO glasses with plastic covers, coded with three-digit random numbers. They were presented to the panelists in a randomized order. As in the two previous sessions, wine samples were tasted in a dedicated room at 18 °C (ISO 8589:2007). The typicality task and sensory profiling were conducted in the same way as that in the previous session, with the empyreumatic note reminiscent of smoke added to the initial core group of four aromatic descriptors.

Quantitative Chemical Analysis. *DMS Analysis.* DMS was quantified by Solid Phase Micro Extraction coupled to Gas Chromatography–Mass Spectrometry (SPME-GC/MS), according to the method developed by Fedrizzi et al.,[25] but with slight modifications.

At the end of each tasting session, two 10 mL wine samples were taken from the bottles used for sensory assessment. Each 10 mL sample was added to a 20 mL headspace vial with 3 g of sodium chloride (final concentration 5 M) and 10 μL of internal standard thiophene solution (3.9 mM in ethanol solution, 50%, v/v). Extractions were performed using carboxen-polydimethylsiloxane-divinylbenzene (CAR-PDMS-DVB, 50/30 μm × 2 cm) (Supelco, Bellefonte, PA, USA) coated fiber. The basic program for the fiber selected consisted of swirling the vial at 500 rpm for 5 min at 35 °C, then inserting the fiber into the headspace for 30 min at 35 °C as the solution was swirled again, and then transferring the fiber to the injector for desorption at 250 °C for 5 min. Chromatographic analyses were carried out using an HP 5890 GC system (Agilent, Palo Alto, CA, USA) coupled to a HP 5972 quadrupole mass spectrometer (Agilent), equipped with a Gerstel MPS2 autosampler (Gerstel GmbH, Mulheim, Germany) and a BP21 capillary column (50 m × 0.32 mm, 0.25 μm; SGE). The carrier gas was Helium N55 with column head pressure at 7 psi. The oven temperature was raised from 32 °C (1 min) to 40 °C at a rate of 1 °C/min and then ramped at a rate of 10 °C/min to 220 °C (final isotherm for 15 min). The MS source temperature was set at 280 °C. DMS detection was performed in electron ionization (70 eV) and SIM mode, selecting the following ions at the corresponding m/z: 45, 47, and 62. The internal standard was identified using the following ions, m/z: 45, 58, and 84. Ions chosen for quantitation were m/z 62 and 84 for DMS and internal standard, respectively. Each wine was analyzed in duplicate.

Analysis of Polyfunctional Thiols. *Extraction.* Wine samples used for thiol analysis came from the bottles opened for the sensory evaluation. At the end of the tasting session, these bottles were refilled with N_2 and kept at 4 °C until extraction, which was carried out within a maximum of 48 h. The volatile thiols were specifically extracted by reversible combination with sodium *p*-hydroxymercuribenzoate (*p*-HMB), according to the methodology validated by Tominaga and Dubourdieu,[22] with some modifications.

p-HMB solution (7.5 mL, 2 mM in 0.1 M Tris) was added to 50 mL of wine containing 50 nmol 3MMB and 6SH as internal standards. Samples were adjusted to pH 7 and subjected to magnetic stirring for 10 min. The wine samples were then percolated on a Dowex column (Dowex 1 × 2, 50–100 mesh, 1.5 × 3 cm; Acros Organics, Noisy-le-Grand, France) previously reactivated using 0.1 M hydrochloric acid solution. The column was rinsed with 50 mL of sodium acetate buffer (0.1 M, pH 7). The volatile thiols were released from the thiol-*p*HMB conjugate fixed on the column by 50 mL of cysteine solution (0.1 M, pH 7). The eluate containing the volatile thiols was collected in a 100 mL flask, and 0.5 mL of ethyl acetate was added. The final solution was extracted twice, using 4 mL and then 3 mL of dichloromethane with magnetic stirring (5 min at 500 rpm). The organic fractions obtained were collected, dried over anhydrous sodium sulfate, and concentrated to 50 μL under a gentle nitrogen stream. Duplicate extractions were performed on each wine sample.

GC/MS Analysis. The concentrates were injected into a gas chromatograph/mass spectrometer (GC/MS) within 24 h. Analyses were performed on an Optima-Wax capillary column (60 m × 0.25 mm, 0.25 μm, Macherey-Nagel, Hoerd, France), and an Agilent 6890 GC system (Agilent, Palo Alto, CA, USA) coupled to an HP 5973b series mass-selective detector (MSD, Agilent) was used. The carrier gas was Helium N55 with column-head pressure at 19 psi and injector temperature at 230 °C. The temperature program was as follows:

DOI: 10.1021/acs.jafc.5b03977
J. Agric. Food Chem. 2015, 63, 8879–8889

Table 2. Aroma Perception Thresholds of DMS (μg/L) and Volatile, Odor-Active Thiols (ng/L), and Their Concentration Ranges in the 24 Red Bordeaux Wines, According to Their Correlation with Aging Bouquet Typicality

	range of typicality score		DMS (μg/L)	2FMT (ng/L)	3SH (ng/L)	BMT (ng/L)	4MSP (ng/L)	E2SP (ng/L)	E3SP (ng/L)
		aroma perception threshold	1.74[a34]	0.4[a15]	60[a14]	0.3[a20]	0.8[a 14]	500[a60]	200[a45]
			27[b9]						
highly-typical wines (HTW) n = 10	5.2−7.2	range	55−146	57−150	313−634	2−21	7−10	102−314	910−2243
		mean value	**101 a**	**91 a**	**431 a**	9	8	160	1635
		SD	37	36	101	4	1	68	551
		confidence interval (95%)	24	23	66	6	1	44	360
intermediate wines (IW) n = 9	4.5−5.9	range	31−67	14−73	230−471	2−22	3−8	83-210	1014−2693
		mean value	**54 b**	**51 b**	**342 b**	8	7	142	1816
		SD	16	35	134	4	6	56	646
		confidence interval (95%)	10	22	83	6	1	34	400
less-typical wines (LTW) n = 5	2.4−4.0	range	23−65	29−71	100−259	1−13	7−20	90−229	864−1891
		mean value	**51 b**	**35 b**	**206 b**	6	11	123	1449
		SD	16	24	92	2	2	18	380
		confidence interval (95%)	18	21	80	2	5	16	333
		p-value	**0.014***	**0.019***	**0.03***	0.068	0.107	0.350	0.401

[a]In hydroalcoholic solution (12% v/v). [b]In wine. Letters following mean concentrations and the asterisk indicate significant differences at $p < 0.05$ using a Kruskal−Wallis test at a significance level of 95% among HTW and LTW and IW groups.

isotherm at 45 °C for 3 min, then raised to 212 °C at 5 °C/min, and then to 255 °C at 20 °C/min (final isotherm for 10 min). The MS source temperature was set at 250 °C. Quantitation was carried out in electron ionization (70 eV) and SIM mode, based both on the retention time of each compound and the selection of specific ions as follows (the quantifier ions are underlined): m/z 53, 81 and 114 for 2FMT, m/z 61, 88 and 134 for E2SP and E3SP (retention time: 20.28 and 24.25 min, respectively), m/z 91 and 124 for BMT, m/z 75, 99 and 132 for 4MSP, and m/z 100 and 134 for 3SH. All compounds were quantified using 3MMB as internal standard (m/z: 75, 100 and 134), except 3SH, which was quantified using 6SH (m/z: 101 and 116).

Statistical Analysis. Data obtained on the 24 wines in the first wine tasting session were compiled in a wines × judges matrix. A hierarchical cluster analysis (HCA), using the Ward method (dissimilarity criteria), was also applied to the wine typicality score. This methodology was used to measure the degree of similarity among wine samples and sort them according to their typicality score. A Kruskal−Wallis nonparametric statistical test was applied to the three HCA clusters of red Bordeaux wines (less -typical, intermediate, and highly-typical wines) for all the quantitative variables (aroma compound concentrations, typicality scores, and aromatic descriptor intensities), using the Dunn test at a significance level of 95%. A PLS regression was applied to the wine age and typicality score (Y) over the concentration of sulfur odor active compounds (X). Components were added according to the Q^2 criterion, explained by Tenenhaus et al.,[23] with a confidence interval of 95%.

For the sensory profile test on the subset of 10 wines, descriptor intensities were mean-centered per wine professional and scaled to unit variance. A Mann−Whitney nonparametric statistical test at a significance level of 95% was applied to differences in the less- and highly typical wines clusters. Data on the 22 red Bordeaux wines studied in the second stage were analyzed using PCA. For each wine, the correlation matrix included mean values for the intensity of each aromatic descriptor, typicality, and DMS, 2FMT, and 3SH concentrations. Pearson product − moment correlations were also computed among typicality, aromatic intensity ratings, and aroma compounds concentrations at a significance level of $\alpha = 0.05$.

All statistical analyses were conducted using XLSTAT software (Addinsoft, Paris, France, 2015, version 17.1).

RESULTS AND DISCUSSION

Identification of Sulfur Odorants as Key Compounds in the Wine Aging Bouquet. The initial aim of the first wine tasting was to classify the 24 9- to 20-year-old red Bordeaux wines according to their typicality score (Table 1). Wines were clustered into three main groups by HCA (Figure S1, Supporting Information). Cluster 1 consisted of 10 wines with the highest average typicality scores (typicality range: 5.2−7.2), thus considered the most representative of the aging-bouquet concept. This group was called "highly-typical wines" (HTW). Cluster 3 consisted of 5 wines with the lowest average typicality scores (typicality range: 2.4−4.3), described as "less-typical wines" (LTW). Finally, cluster 2 included 9 wines that had no clearly defined correlation with the aging bouquet concept. As their typicality assessment varied drastically among the panel of wine professionals, they were considered "intermediate wines" (IW) in terms of aging bouquet (typicality range: 3.9−5.5). As previously reported[7] and in agreement with other studies on olfactory concepts in Chardonnay and Riesling wines,[26−28] no strict categorization was established of typical vs atypical examples of the wine aging bouquet, and typicality scores formed a gradient from less- to highly typical wines. This continuum was independent of vintage (in the range considered) and geographical origin, within the Bordeaux area. The results of the Kruskall-Wallis test showed that, whereas the HTW and LTW groups presented significant differences in typicality scores (test U; p-value = 0.001), no difference was detected between the LTW and IW clusters.

Following this clusterization of studied wines, sulfur volatiles were quantified in all groups to identify differences in the chemical profile of wines according to their representativeness of the wine aging bouquet. These DMS and volatile thiol quantitation data are summarized in Table 2, which is divided into three sections, corresponding to the HTW, IW, and LTW groups, according to HCA typicality rankings. DMS levels in the wines ranged from 23 to 146 μg/L, in agreement with previous published data on aged wines.[2,10,29,30] Interestingly,

DOI: 10.1021/acs.jafc.5b03977
J. Agric. Food Chem. 2015, 63, 8879−8889

Table 3. Aromatic Descriptor Intensities Based on the Sensory Profile of Ten Selected Red Bordeaux Wines (Five from Each of the HTW and LTW Groups)[a]

	highly typical wines n = 5			less-typical wines n = 5			
	mean intensity (±SD)	min. intensity	max. intensity	mean intensity (±SD)	min. intensity	max. intensity	p-value
undergrowth	4.9 ± 0.8	4.0	5.3	3.8 ± 0.6	2.2	4.9	**0.007** **
truffle	3.8 ± 0.4	3.4	4.0	2.6 ± 0.5	2.3	2.9	**0.001** ***
toasted	3.9 ± 0.7	3.1	5.4	4.4 ± 0.6	3.7	4.9	0.345
fresh red- and black-berry fruit	3.0 ± 1.1	1.9	4.8	3.6 ± 1.2	1.9	6.3	0.145

[a]Aromatic descriptors which discriminated significantly between highly- and less-typical wines are in bold. ** and *** indicate significant differences at p-value < 0.01 and p-value < 0.001, respectively, using a Mann−Whitney test at a significance level of 95%.

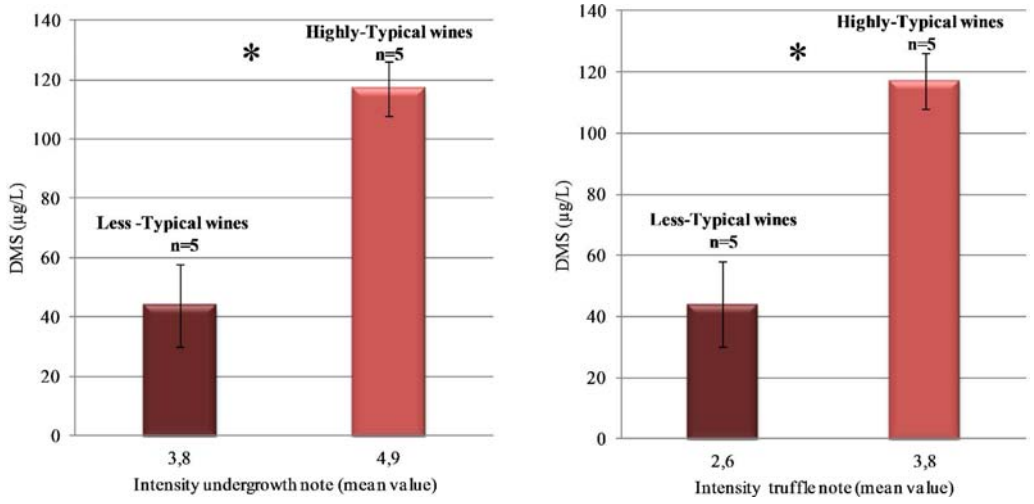

Figure 2. Mean DMS concentrations (±confidence interval) according to the typicality classification, applied to a selected set of 10 red Bordeaux wines. * indicates a significant difference using a Mann−Whitney test at a significance level of 95%.

DMS levels were significantly higher in the HTW group (test U; p-value = 0.014), with concentrations up to twice those found in the LTW group (mean values: 101 µg/L and 51 µg/L, respectively, Table 2). Except for one wine, all DMS concentrations exceeded their perception threshold in red wine (Table 2). Even if the perception threshold concept is currently subject to debate and does not necessarily account for the way complex interactions in odorant mixtures impact the perception of individual compounds,[6,31,32] the high DMS levels assayed compared to its olfactory detection threshold suggested that this compound contributed directly to the aromatic features of the wine aging bouquet. DMS was previously found to enhance truffle and undergrowth aromas when 100 µg/L was added to Syrah wines.[11] It was also shown to accentuate the fruity notes in some high-quality red wines, via complex interactions with other volatile compounds, including C13-norisoprenoids[32,33] and esters.[34] Furthermore, DMS has been reported to contribute a noticeable complexity to the aroma of aged wines.[35−37]

Aromatic profiling was carried out by the wine professional panel on a subset of 10 wines, chosen from among the 24 wines tasted during the typicality task (5 wines from the HTW group and 5 from the LTW group (Table 1). Table 3 shows their aromatic intensities for undergrowth, truffle, toasted, and fresh red- and black-berry fruit attributes. Undergrowth and truffle were the two descriptors that significantly differentiated between the highly- and less-typical groups (p-value = 0.007 and p = 0.001, respectively). Thus, the group of five HTW had significantly higher mean intensities for undergrowth and truffle (4.9 and 3.8, respectively) than the five LTW (3.8 and 2.6, respectively). As shown in Figure 2, when these sensory results were associated with quantitative DMS data, the five HTW also had significantly higher DMS concentrations than the five LTW (mean values, 117 and 44 µg/L, respectively; p-value = 0.004). Besides, a significant correlation was observed for DMS concentrations and truffle note (r = 0.664; p-value = 0.022), whereas a slight correlation with the undergrowth attribute was found (r = 0.440, p-value = 0.04). Overall, the current results demonstrated that high DMS levels, in the vicinity of 100 µg/L, contributed to the expression of the wine aging bouquet and particularly its truffle and undergrowth aromas.

Volatile thiols, with the exception of E2SP, were present in all 24 red Bordeaux wines at concentrations above their olfactory detection thresholds (Table 2). Varietal polyfunctional thiols have been reported to make a relevant contribution to wine aroma and are noted for their low perception thresholds, with 4MSP and 3SH detectable in wine at concentrations in the ng/L range.[4,14,15,38−40] Quantitative analysis of the 9- to 20-year-old red Bordeaux wines considered here revealed that concentrations ranged from 3 to 20 ng/L for 4MSP and 100 to 634 ng/L for 3SH. As shown in Table 2, no significant difference in 4MSP concentrations was found in the wines, irrespective of their aging bouquet typicality classification. Hence, 4MSP was unlikely to have any relevant impact on the fruity aroma component of the wine aging bouquet.

In contrast, 3SH was found to discriminate significantly high typical from low typical wines (test U; p-value = 0.03) between the HTW and LTW groups. Indeed, 3SH concentrations in the HTW group reached twice those found in the LTW group (mean values: 431 ng/L and 206 ng/L, respectively). The

DOI: 10.1021/acs.jafc.5b03977
J. Agric. Food Chem. 2015, 63, 8879−8889

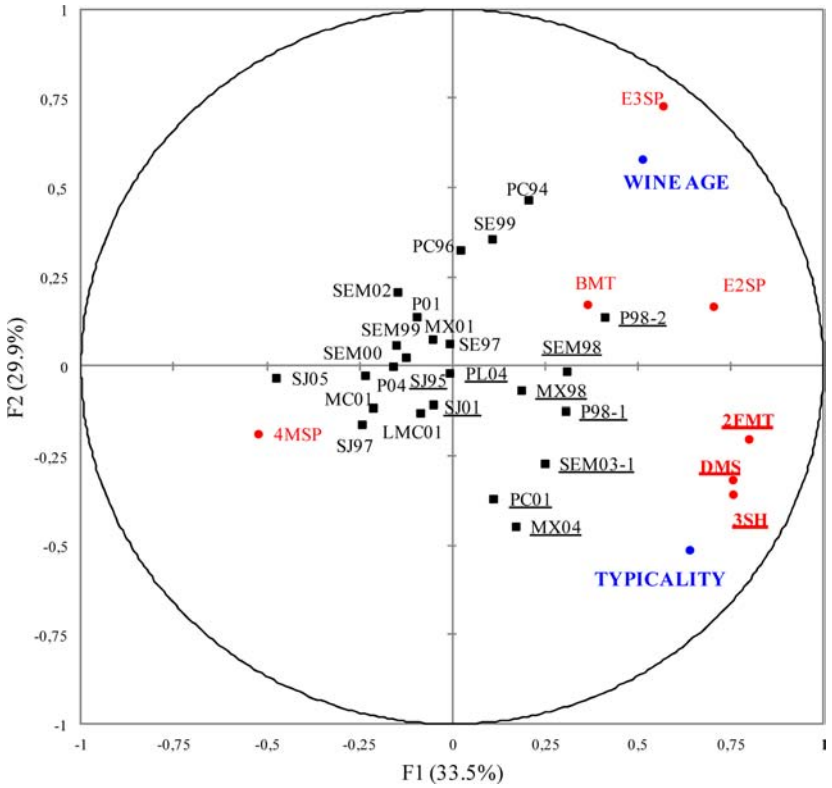

Figure 3. Partial least square (PLS) regression of the sulfur compounds studied (X matrix), typicality score, and wine age (Y matrix). Volatile compounds in bold were correlated with the typicality of the aging bouquet. Underlined labels correspond to wines identified in the HCA as highly typical wines (HTW).

presence of 3SH has been reported in red Bordeaux wines made from Cabernet Sauvignon and Merlot and, more recently, in wines made from other red grape varieties, such as Syrah and Grenache, at levels ranging from several hundred ng up to a few μg/L.[17,40] In addition, 3SH has been shown to enhance the perception of fruity aroma in rosé and red wines[17,40−43] and has also been reported to influence the overall aroma of aged red wines.[44] These results, based on quantitative data, are in agreement with a relevant involvement of 3SH in the overall aromatic balance of wines with an aging bouquet. However, its specific contribution to their fruity freshness requires further clarification, as no conclusive difference was detected between the HTW and LTW groups for fresh red- and black-berry fruit aromas (Table 3).

Three other nonvarietal volatile thiols, 2FMT, BMT, and E3SP, identified in red and white *Vitis vinifera* wines, represented a specific interest in the context of this study. It has been suggested that they contribute actively to the empyreumatic odors, evocative of smoke, toasty nuances, roasted coffee, and cooked meat, which are commonly acquired by fine wines during aging. Tominaga et al.[4,15,20] identified and quantified BMT and 2FMT for the first time in both white (Chardonnay, Semillon, Sauvignon Blanc, and Petit Manseng) and red (Merlot and Cabernet Sauvignon) wines, as well as 15-year-old Champagnes. E3SP has already been identified in both *Vitis labrusca*[45] and *Vitis vinifera* wines[19,46] and has also been shown to play a role in the empyreumatic character of old Champagne.[4] Quantitative data acquired in our study detected BMT and E3SP levels ranging from 1 to 22 ng/L and 864 to 2693 ng/L, respectively (Table 2). However, no significant difference in concentration was observed between the different clusters (Table 2). Hence, these two thiols were unlikely to have any relevant impact on the aging bouquet. In contrast, 2FMT discriminated significantly (test U; p-value = 0.019) between wines in the HTW and LTW groups. Concentrations in the 24 wines ranged from 14 to 150 ng/L (i.e., the same order of magnitude as those previously reported in red wines[15,22]), 2FMT levels were in the upper range of concentrations in the HTW group (mean value: 91 ng/L) compared to the LTW group (mean value: 35 ng/L), indicating its relevant involvement in the overall aromatic balance of wines with an aging bouquet. However, at this stage, the contribution of 2FMT to a specific sensory note requires further clarification, as no significant difference was determined between the HTW and LTW groups concerning the intensity of the toasted attribute (Table 3).

Sensory and quantitative chemical data were statistically processed using PLS regression at 5% significance. The first two components (Q^2 = 0.44) explained 33.5% of the volatile space variance and 29.9% of the typicality and wine age space variance (Figure 3). The typicality score and wine age were both projected on the positive side of the first component, in the same way as DMS, 2FMT, 3SH, BMT, E2SP, and E3SP. However, 4MSP was loaded on the negative side of the first component, indicating that this compound did not actively contribute to either the typicality score or wine aging characteristics. The second component contrasted wine bottle aging and typicality scores. This once again emphasized the good correlation between the typicality score and DMS, 2FMT, and 3SH concentrations. Wine age was correlated with E2SP and E3SP concentrations. BMT also followed the same trend but was positioned further from the correlation circle than E2SP and E3SP, indicating its minor importance as an aging marker. Besides, the regression coefficients for each volatile

DOI: 10.1021/acs.jafc.5b03977
J. Agric. Food Chem. 2015, 63, 8879−8889

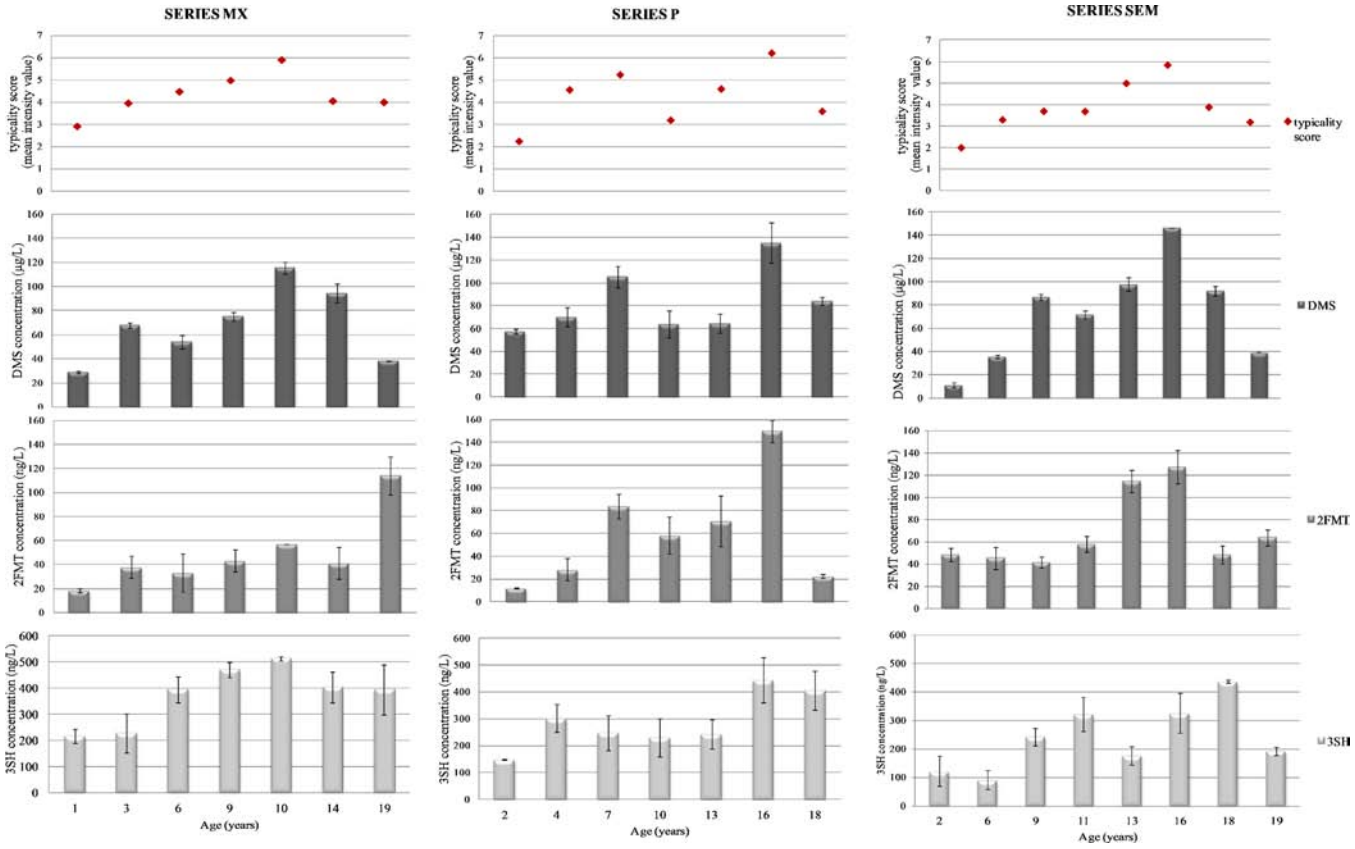

Figure 4. Variations in typicality scores and DMS, 2FMT, and 3SH concentrations during bottle aging for red Bordeaux wines from three vineyards in different appellations (series MX, P, and SEM).

sulfur compound on the first two components associated with the typicality score are presented in Figure S2 (Supporting Information). These coefficients measured the contribution of each variable in the regression model. DMS, 2FMT, and 3SH had positive regression coefficients on the first component and all loaded on the positive side on the same component (Figure 3). E3SP exhibited negative regression coefficients, indicating that this compound did not contribute to aging bouquet typicality. Finally, the regression coefficients of BMT, 4MSP, and E2SP were not significant, indicating that they probably had no influence on typicality scores. As seen in Figure 3, PLS analysis also validated the wine typicality clustering produced by HCA, indicating a good agreement between the two statistical methods in sorting the wines.

Results from this series of 24 red Bordeaux wines demonstrated that highly-typical wines contained significantly higher concentrations of DMS, 2FMT, and 3SH than the less-typical wines. PLS analysis did not reveal any strict correlation between aging bouquet typicality scores and the bottle age of the wines. To explore this point in greater detail, under conditions designed to minimize the variability factors linked to viticultural and enological practices, the next stage in this study focused on three series of wines (MX, P, and SEM), each came from a single vineyard. These three vineyards were selected from the HTW group as representative of different Bordeaux red wine appellations (MX04, P98-2, and SEM98; Table 1).

Whereas the high DMS concentrations in the HTW group were associated with intense truffle and undergrowth notes, no link was demonstrated between fresh-fruit and toasted attributes and 3SH and 2FMT concentrations. Insofar as thiol aromas were frequently associated with empyreumatic notes reminiscent of smoke (soot, smoke, and hearth),[4,20] also used to describe aging bouquet,[7] a sensory evaluation of this attribute was included in the second stage of the study.

Variations in Aging Bouquet Typicality Compared to DMS, 2FMT, and 3SH Levels during Wine Aging. Figure 4 shows the variations in aging bouquet typicality and DMS, 2FMT, and 3SH concentrations during bottle-aging.

Overall, typicality curves did not follow a linear pattern during aging but reached a maximum after 10 (MX) or 16 years (P and SEM) in bottles, with DMS, 3SH, and 2FMT levels following the same trend. The Pearson correlation test showed significant correlation between typicality ratings and DMS (r = 0.816, p-value = 0.0001), 2FMT (r = 0.630, p-value = 0.002) and 3SH levels (r = 0.609, p-value = 0.003). Indeed, in almost all cases, high levels of the three compounds were aligned with high typicality scores. In addition, with the exception of DMS in young wines, levels were above the perception thresholds in all wines analyzed. For the P series, the typicality curve, as well as the DMS and 2FMT concentration profiles, peaked in the 7-year-old wine, possibly revealing a specific vintage effect in this vineyard.

Interestingly, closer examination of the DMS profile revealed that high concentrations perfectly accounted for high typicality scores. Indeed, levels in all series increased during bottle aging, reaching a peak at 10 years for MX (115 µg/L) and 16 years for P and SEM (135 and 146 µg/L, respectively), while the secondary peak in the P series at 7 years reached 105 µg/L. These results are in agreement with those reported in the first stage of this study, highlighting a link between high DMS concentrations (around or above 100 µg/L) and high aging-bouquet typicality scores.

DOI: 10.1021/acs.jafc.5b03977
J. Agric. Food Chem. 2015, 63, 8879−8889

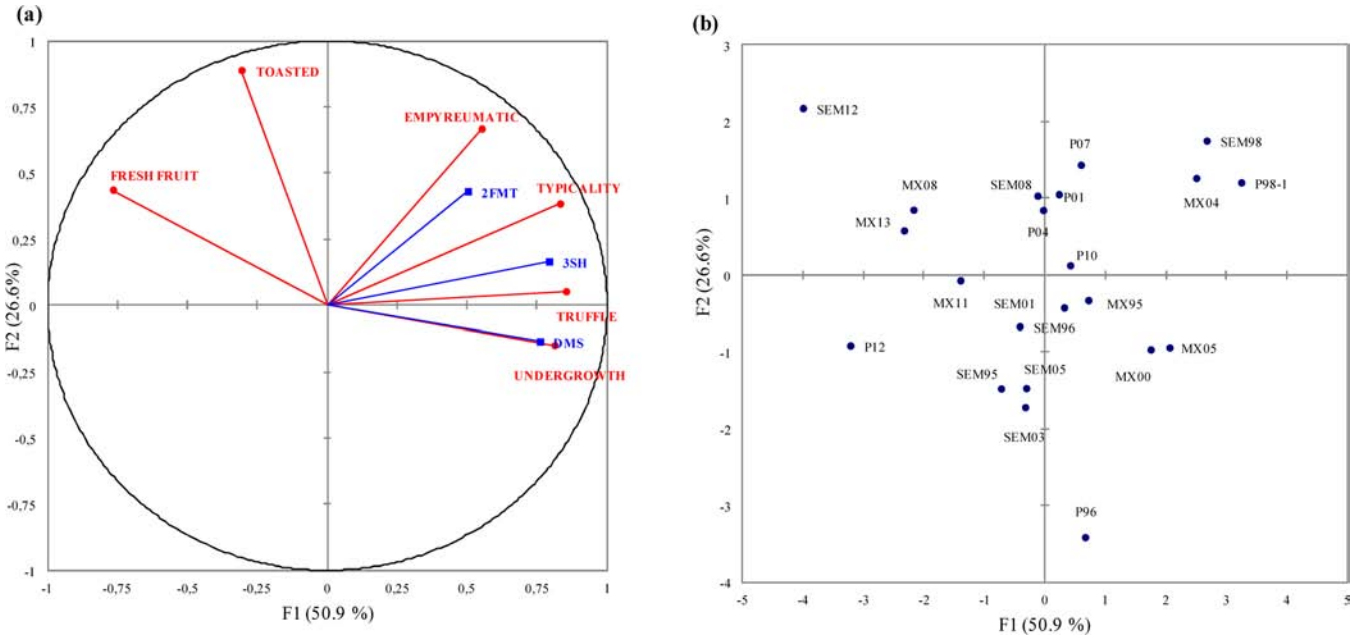

Figure 5. PCA correlation circle of (total variability: 77.5%) presenting typicality scores, aromatic descriptors, and chemical compounds (a) with the corresponding projection map of wines (b).

DMS is generated from several precursors during yeast fermentation but due to its high volatility, it is mainly stripped off during the first steps of winemaking so that its levels in young bottled wines are generally below its perception threshold.[9−11,46] This trend was also observed in this case, as the most recent vintages in all three vineyard series exhibited the lowest DMS concentrations.

An upward trend in free DMS concentrations in wine has frequently been described during aging.[9−11,36,47] The current results confirmed an increase in DMS concentrations during aging and highlighted a maximum DMS content (after 10 or 16 years in our case), which was always aligned with the maximum value for aging bouquet typicality. Different kinetics in the occurrence of this DMS peak are not surprising, bearing in mind the multiple factors reported to govern both PDMS content at bottling and DMS release and stability during bottle storage.[8,29,36,48]

Considering the evolution of 3SH and 2FMT levels in wines during aging, the results reported here revealed a less obvious correlation than for DMS between their concentrations and the corresponding typicality notes. In most cases, high thiol levels corresponded to high typicality scores, thus confirming the results obtained in the first part of the study. However, the highest thiol concentrations did not always correspond to the highest typicality scores, with the exception of the 16-year-old wine in the P series (Figure 4). Interestingly, 2FMT and DMS may have a combined effect on the typicality score: a comparison of 14- and 19-year-old wines in the MX series showed that they both maintained the same typicality note, as though the marked increase in 2FMT offset a corresponding, significant DMS loss.

While high thiol levels were generally associated with high typicality scores, the reported data tended to emphasize the influence of a subtle balance among the three sulfur volatiles. Hence, within the MX series, the 10-year-old wine exhibited the highest typicality score (5.9), as well as both the highest DMS (115 μg/L) and 3SH (494 ng/L) concentrations in the series, but only medium-range 2FMT (57 ng/L). The results obtained from the three different vineyards were not sufficiently comprehensive to draw clear-cut conclusions about the evolution of 3SH or 2FMT concentrations during bottle aging. Similarly, published data do not describe a clear trend in variations in these two thiols during wine aging. The 3SH content of red Bordeaux wines has been reported to decrease considerably during barrel aging.[41] However, under conditions that prevented a decrease in the reducing potential of the wine, 3SH was shown to be very stable,[49] but no significant correlation has been demonstrated between 3SH levels and bottle-aging time, in either wine or Champagne.[4]

2FMT is produced from furfural released from toasted oak via the yeast sulfur metabolism[49,50] and some published studies are in favor of its upward formation from furfural and hydrogen sulfide in the reductive atmosphere in bottles.[4] In our study, 2FMT levels tended to increase in the 3 series but with variable timing. The increase was observed at a later stage in the MX series, whereas it occurred earlier in the other two series and was followed by a marked decrease after 16 years. Such a decrease after a long period of bottle aging may be explained by the known reactivity of the thiol function with quinones and other reactive SH-bearing compounds in wine.

Figure 5a shows the loadings of typicality scores and sensory attribute intensities, as well as DMS, 2FMT, and 3SH levels of the first two components of the PCA. The first principal component explained 50.9% of total variance and was positively correlated with the typicality score. Furthermore, the loading plots for DMS, 2FMT, and 3SH were projected on the same positive side of the first axis and closed to the correlation circle, meaning that these three sulfur markers were well correlated with the typicality of the wine aging bouquet, thus confirming the data shown in Figure 4.

As far as aromatic intensities are concerned, the first principal component contrasted fresh-fruit and toasted notes with truffle, undergrowth, and empyreumatic notes. The latter attributes were loaded on the same positive side as the typicality score and sulfur compounds. The aromatic contribution of DMS to undergrowth and truffle notes, reported in the first part of this

DOI: 10.1021/acs.jafc.5b03977
J. Agric. Food Chem. 2015, 63, 8879−8889

Table 4. Characteristics and Sensory Data of the 22 Red Wines from Three Bordeaux Vineyards (Series MX, P, and SEM)

					aromatic intensity scores (mean values ± SD)				
code series	appellation	age (years)	wine code	typicality score (mean value ± SD)	undergrowth	truffle	toasted	empyreumatic	fresh fruit
MX	Margaux	19	MX95	4.0 ± 1.5	1.9 ± 0.5	4.3 ± 1.3	3.9 ± 1.3	3.8 ± 1.6	2.0 ± 0.8
		14	MX00	4.1 ± 1.1	5.1 ± 1.2	4.3 ± 1.4	3.5 ± 1.0	4.2 ± 1.4	2.6 ± 1.3
		10	MX04	5.9 ± 0.7	4.7 ± 1.1	3.6 ± 1.3	4.5 ± 0.8	4.3 ± 1.1	3.2 ± 1.1
		9	MX05	5.0 ± 1.3	4.9 ± 1.3	3.6 ± 1.1	3.4 ± 0.6	4.1 ± 0.9	2.8 ± 1.0
		6	MX08	4.5 ± 1.2	3.6 ± 1.0	2.9 ± 1.1	4.5 ± 1.3	4.4 ± 1.1	4.4 ± 1.2
		3	MX11	4.0 ± 1.2	2.6 ± 0.9	2.3 ± 1.2	4.2 ± 1.0	3.1 ± 1.3	4.2 ± 1.2
		1	MX13	2.9 ± 0.8	2.6 ± 1.3	2.0 ± 1.0	5.4 ± 1.1	3.9 ± 1.2	4.3 ± 0.6
P	Pomerol	18	P96	3.6 ± 0.7	4.4 ± 1.4	3.3 ± 0.7	2.8 ± 1.1	3.4 ± 1.1	0.9 ± 0.3
		16	P98	6.2 ± 0.8	4.7 ± 0.8	5.0 ± 0.9	5.0 ± 0.9	5.0 ± 1.3	1.9 ± 0.4
		13	P01	4.6 ± 1.3	3.1 ± 1.0	2.2 ± 0.5	4.7 ± 0.9	4.8 ± 1.2	3.6 ± 1.1
		10	P04	3.2 ± 1.0	4.0 ± 1.1	2.5 ± 0.6	4.7 ± 1.2	4.6 ± 1.4	3.7 ± 1.2
		7	P07	5.2 ± 1.4	2.9 ± 0.8	2.7 ± 0.9	4.9 ± 1.2	4.3 ± 1.2	3.3 ± 0.7
		4	P10	4.6 ± 1.2	4.0 ± 0.9	3.4 ± 1.2	4.3 ± 1.2	4.1 ± 1.3	3.9 ± 1.3
		2	P12	2.2 ± 0.6	2.9 ± 0.6	1.6 ± 0.9	4.1 ± 1.4	3.0 ± 0.8	4.9 ± 1.2
					aromatic intensity scores (mean values ± SD)				
code series	appellation	age (years)	wine code	typicality score (mean value ± SD)	undergrowth	truffle	toasted	empyreumatic	fresh fruit
SEM	Saint-Emilion	19	SEM95	3.2 ± 1.7	3.2 ± 1.5	2.4 ± 1.7	3.6 ± 1.4	3.5 ± 1.8	2.4 ± 0.9
		18	SEM96	3.9 ± 1.3	3.9 ± 1.4	2.0 ± 1.0	3.7 ± 1.2	3.5 ± 1.2	3.4 ± 1.4
		16	SEM98	5.9 ± 1.5	4.7 ± 0.9	4.8 ± 1.1	5.5 ± 1.0	4.4 ± 1.3	3.3 ± 1.5
		13	SEM01	5.0 ± 1.5	4.1 ± 1.1	2.1 ± 1.1	4.3 ± 1.2	4.5 ± 1.3	2.6 ± 1.2
		11	SEM03-2	3.7 ± 1.1	3.5 ± 1.1	3.1 ± 1.2	3.0 ± 1.0	3.7 ± 1.3	3.4 ± 1.2
		9	SEM05	3.7 ± 0.9	3.9 ± 1.3	2.5 ± 1.1	4.0 ± 1.2	4.0 ± 1.4	2.2 ± 0.9
		6	SEM08	3.3 ± 1.3	2.7 ± 1.1	2.3 ± 0.9	5.4 ± 1.7	2.9 ± 1.3	4.7 ± 1.4
		2	SEM12	2.0 ± 0.8	1.1 ± 0.8	1.0 ± 0.8	5.6 ± 2.0	4.1 ± 2.1	6.0 ± 1.4

study, was confirmed in the second stage since DMS well correlated with undergrowth (r = 0.743; p-value = 0.001) and truffle (r = 0.587; p-value = 0.004) notes as the PCA circle shows (Figure 5a). Furthermore, in all three vineyard series, these two aromatic descriptors were also perceived as relatively more intense in the wines with both the highest typicality scores and DMS levels (MX 04, P98, and SEM 98; Table 4 and Figure 4).

The empyreumatic attribute was correlated with 2FMT (r = 0.541; p-value = 0.009) which was confirmed by the PCA plot (Figure 5a), meaning that this compound contributed to the empyreumatic nuances perceived in all highly-typical wines. However, no correlation was found between toasted nuances and 2FMT levels. Interestingly, young wines (MX13 and SEM12) had the highest toasted score in the MX and SEM series (5.4 and 5.6, respectively; Table 4 and Figure 5b). These results were not surprising, due to the release of oak wood aromas during barrel aging, which probably confers stronger toasted aromas on young bottle-aged wines than 2FMT does. During bottle storage, fine wines acquire complexity, and the differentiated sensory impact of 2FMT and other volatile compounds released by the wood probably becomes less marked and more finely blended with the other aromas in older wines.[1]

Loading plots of the PCA and Pearson test revealed that 3SH did not contribute in the fresh fruity expression (r = 0.284, p-value = 0.156). Besides, although DMS is a known enhancer of fruity aroma,[34] no significant correlation was found between DMS levels and fresh-fruit notes (r = 0.143, p-value = 0.207). As shown in the projection of wines issued from the PCA (Figure 5b), the highest scores for this descriptor (Table 4) were mainly associated with youngest wines (MX08, MX11, MX13, and SEM12) whose scores for aging bouquet typicality were low. This logically reflects the expected fresh, fruitiness of young wines, with primary aromas that have not yet evolved toward the more complex, finer tertiary nuances that feature in an aging bouquet.

To our knowledge, the combined impact of DMS, 3SH, and 2FMT on the development of aging bouquet in red Bordeaux wines over time have not previously been described. Our results revealed that concentrations of these three sulfur compounds discriminated between wines with typical and atypical aging bouquets. The development of a bouquet during bottle aging was found to follow specific, nonlinear kinetics, associated with a subtle balance of these three sulfur compounds. The direct contribution of DMS to truffle and undergrowth attributes, as well as its key role in the overall complexity and balance of wine aroma, was highlighted. In our context, 2FMT was associated with empyreumatic nuances reminiscent of smoke, but not toasted notes, while the sensory impact of 3SH requires further investigation, as it was not directly correlated with the expected fresh-fruit attribute.

However, while these three volatile compounds have been identified as being responsible for some of the most representative aromatic notes in a typical aging bouquet, it seems unlikely that they are the only aroma compounds to account for its overall complexity. Accordingly, further work is still required to identify other marker molecules and obtain a more comprehensive understanding of the links between aroma compounds and the sensory perception of an aging bouquet in wine. In this respect, a two-tier approach is indicated, both studying the role of other targeted chemical classes and implementing wine fractionation and reconstitution experiments.

DOI: 10.1021/acs.jafc.5b03977
J. Agric. Food Chem. 2015, 63, 8879−8889

■ ASSOCIATED CONTENT

Supporting Information

The Supporting Information is available free of charge on the ACS Publications website at DOI: 10.1021/acs.jafc.5b03977.

HCA of the 24 red Bordeaux wines, according to their typicality belonging to the wine aging bouquet concept and regression coefficients for each volatile compound given by PLS analysis for the two first components and related to the typicality score (PDF)

■ AUTHOR INFORMATION

Corresponding Author

*Tel: +33 0 5 57 57 58 41. Fax: +33 0 5 57 57 58 13. E-mail: magali.picard@u-bordeaux.fr.

Funding

This work received financial support from the Regional Council of Aquitaine, FranceAgriMer, and the Bordeaux Wine Council (CIVB).

Notes

The authors declare no competing financial interest.

■ ACKNOWLEDGMENTS

We express our thanks to the Châteaux in the Bordeaux area whose owners kindly provided wine samples. Special thanks are also expressed to the wine professionals who participated in the sensory sessions during this study.

■ ABBREVIATIONS USED

DMS, dimethyl sulfide; BMT, benzenemethanethiol; 2FMT, 2-furanmethanethiol; 3SH, 3-sulfanylhexanol; E2SP, ethyl 2-sulfanylpropionate; E3SP, ethyl 3-sulfanylpropionate; 4MSP, 4-methyl-4sulfanyl-2pentanone; 3MMB, 3-methoxymethylbutanethiol; 6SH, 6-sufanylhexanol; *p*-HMB, *p*-hydroxymercuribenzoate; PDMS, potential dimethyl sulfide; HCA, hierarchical cluster analysis; HTW, highly-typical wines; IW, intermediate wines; LTW, less-typical wines; PCA, principal component analysis; PLS, partial least squares

■ REFERENCES

(1) Peynaud, E.; Blouin, J. In *Le goût du vin. Le grand livre de la dégustation*; 4th ed.; Dunod: Paris, 2006.

(2) Simpson, R. Aroma composition of bottle aged white wine. *Vitis* **1979**, *18*, 148−154.

(3) Rapp, A..Wine Aroma Substances from Gas Chromatographic Analysis. In *Wine Analysis*; Linskens, H. F., Jackson, J. F., Eds.; Springer-Verlag: Berlin, Germany, 1998; pp 29−66.

(4) Tominaga, T.; Guimbertau, G.; Dubourdieu, D. Role of certain volatile thiols in the bouquet of aged champagne wines. *J. Agric. Food Chem.* **2003**, *51*, 1016−1020.

(5) Francis, I. L.; Newton, J. L. Determining wine aroma from compositional data. *Aust. J. Grape Wine Res.* **2005**, *11*, 114−126.

(6) Robinson, A. L.; Boss, P. K.; Solomon, P. S.; Trengove, R. D.; Heymann, H.; Eleber, S. E. Origin of grape and wine aroma. *Am. J. Enol. Vitic.* **2014**, *65*, 1−24.

(7) Picard, M.; Tempere, S.; de Revel, G.; Marchand, S. A sensory study of the aging bouquet of red Bordeaux wines: A three-step approach for exploring a complex olfactory concept. *Food Qual. Prefer.* **2015**, *42*, 110−122.

(8) Ugliano, M. Oxygen Contribution to Wine Aroma Evolution during Bottle Aging. *J. Agric. Food Chem.* **2013**, *61*, 6125−6136.

(9) Anocibar Beloqui, A. Contribution à l'étude des composés soufrés volatils des vins rouges. Thesis, Université de Bordeaux 2, 1998.

(10) De Mora, S. J.; Knowles, S. J.; Eschenbruch, R.; Torrey, W. J. Dimethyl sulfide in some Australian red wines. *Vitis* **1987**, *26*, 79−84.

(11) Segurel, M. A.; Razungles, A.; Riou, C.; Salles, M.; Baumes, R. Contribution of dimethyl sulfide to the aroma of syrah and grenache noir wines and estimation of Its potential in grapes of these varieties. *J. Agric. Food Chem.* **2004**, *52*, 7084−7093.

(12) Darriet, P.; Tominaga, T.; Lavigne, V.; Boidron, J. N.; Dubourdieu, D. Identification of a powerful aromatic component of *Vitis vinifera* L. var. Sauvignon wines: 4-Mercapto-4-methylpentan-2-one. *Flavour Fragrance J.* **1995**, *10*, 385−392.

(13) Guth, H. Quantitation and sensory studies of character impact odorants of different white wine varieties. *J. Agric. Food Chem.* **1997**, *45*, 3027−3032.

(14) Tominaga, T.; Murat, M.-L.; Dubourdieu, D. Development of a method for analyzing the volatile thiols involved in the characteristic aroma of wines made from *Vitis vinifera* L. Cv. Sauvignon Blanc. *J. Agric. Food Chem.* **1998**, *46*, 1044−1048.

(15) Tominaga, T.; Blanchard, L.; Darriet, P.; Dubourdieu, D. A powerful aromatic volatile thiol, 2-Furanmethanethiol, exhibiting roast coffee aroma in wines made from Several *Vitis vinifera* grape varieties. *J. Agric. Food Chem.* **2000**, *48*, 1799−1802.

(16) Murat, M.-L.; Masneuf, I.; Darriet, P.; Lavigne, V.; Tominaga, T.; Dubourdieu, D. Effect of *Saccharomyces cerevisiae* Yeast Strains on the Liberation of Volatile Thiols in Sauvignon blanc Wine. *Am. J. Enol. Vitic.* **2001**, *52*, 136−139.

(17) Rigou, P.; Triay, A.; Razungles, A. Influence of volatile thiols in the development of blackcurrant aroma in red wine. *Food Chem.* **2014**, *142*, 242−248.

(18) Bouchilloux, P.; Darriet, P.; Dubourdieu, D. Identification du 2-méthyl-3-furanthiol, un compose très odorant dans les vins. *Vitis* **1998**, *37* (4), 177−180.

(19) Blanchard, L. Caractérisation de la fraction volatile de nature soufrée dans les vins de cabernet et merlot. Etude de son évolution au cours de l'élevage en barriques. *Oenologie 99*, 6th Symposium Bordeaux, Tec et Doc Lavoisier: Paris, 1999; pp 501−505.

(20) Tominaga, T.; Guimbertau, G.; Dubourdieu, D. Contribution of benzenemethanethiol to smoky aroma of certain *Vitis vinifera* L. Wines. *J. Agric. Food Chem.* **2003**, *51*, 1373−1376.

(21) Marchand, S.; de Revel, G.; Bertrand, A. Approaches to wine aroma: release of aroma compounds from reactions between cysteine and carbonyl compounds in Wine. *J. Agric. Food Chem.* **2000**, *48*, 4890−4895.

(22) Tominaga, T.; Dubourdieu, D. Novel method for quantitation of 2-Methyl-3-furanthiol and 2-Furanmethanethiol in wines made from *Vitis vinifera* grape varieties. *J. Agric. Food Chem.* **2006**, *54*, 29−33.

(23) Tenenhaus, M.; Pagés, J.; Ambroisine, L.; Guinot, C. PLS methodology to study relationships between hedonic judgements and product characteristics. *Food Qual. Prefer.* **2005**, *16* (4), 315−325.

(24) Ferreira, V.; Fernandez, P.; Escudero, A.; Cacho, J. F.; Pena, C. Investigation on the role played by fermentation esters in the aroma of young Spanish wines by multivariate analysis. *J. Sci. Food Agric.* **1995**, *67* (3), 381−392.

(25) Fedrizzi, B.; Magno, F.; Moser, S.; Nicolini, G.; Versini, G. Concurrent quantitation of light and heavy sulphur volatiles in wine by headspace solid-phase microextraction coupled with gas chromatography/mass spectrometry. *Rapid Commun. Mass Spectrom.* **2007**, *21*, 707−714.

(26) Ballester, J.; Dacremont, C.; Le Fur, Y.; Etievant, P. The role of olfaction in the elaboration and use of the Chardonnay wine concept. *Food Qual. Prefer.* **2005**, *16*, 351−359.

(27) Jaffré, J.; Valentin, D.; Meunier, J.-M.; Siliani, A.; Bertuccioli, M.; Le Fur, Y. The Chardonnay wine olfactory concept revisited: A stable core of volatile compounds, and fuzzy boundaries. *Food Res. Int.* **2011**, *44*, 456−464.

(28) Schüttler, A.; Friedel, M.; Jung, R.; Rauhut, D.; Darriet, P. Characterizing aromatic typicality of Riesling wines: merging volatile compositional and sensory aspects. *Food Res. Int.* **2015**, *69*, 26−37.

(29) Dagan, L. Potentiel aromatique des raisins de *Vitis vinifera* L. *cv.* Petit Manseng et Gros Manseng. Contribution à l'arôme des vins de

DOI: 10.1021/acs.jafc.5b03977
J. Agric. Food Chem. 2015, 63, 8879−8889

pays Côtes de Gascogne. Thesis, Ecole Nationale Superieure Agronomique de Montpellier, 2006.
(30) Anocibar Beloqui, A.; Kotseridis, Y.; Bertrand, A. Détermination de la teneur en sulfure de diméthyle dans quelques vins rouges. *J. Int. Sci. Vigne Vin* **1996**, *30*, 167−170.
(31) Pineau, B.; Barbe, J. C.; Van Leeuwen, C.; Dubourdieu, D. Examples of perceptives interactions involved in specific ≪ red-black-berry ≫ aromas in red wines. *J. Agric. Food Chem.* **2009**, *57*, 3702−3708.
(32) Villamor, R.; Ross, C. F. Wine Matrix Compounds affect perception of wine aromas. *Annu. Rev. Food Sci. Technol.* **2013**, *4*, 1−20.
(33) Escudero, A.; Campo, E.; Fariña, L.; Cacho, J.; Ferreira, V. Analytical characterization of the aroma of five premium red wines. Insights into the role of odor families and the concept of fruitiness of wines. *J. Agric. Food Chem.* **2007**, *55*, 4501−4510.
(34) Lytra, G.; Tempere, S.; Zhang, S.; Marchand, S.; De Revel, G.; Barbe, J.-C. Olfactory impact of dimethyl sulfide on red wine fruity esters aroma expression in model solution. *J. Int. Sci. Vigne Vin* **2014**, *48*, 75−85.
(35) Du Plessis, C.; Loubser, G. The bouquet of "late harvest" wine. *Agrochemophysica* **1974**, *6*, 49−52.
(36) Marais, J. Effect of storage time and temperature on the formation of dimethyl sulfide and on white wine quality. *Vitis* **1979**, *18*, 254−260.
(37) Spedding, D. J.; Raut, P. The influence of dimethyl sulfide and carbon disulphide in the bouquet of wines. *Vitis* **1982**, *21*, 240−246.
(38) Swiegers, J.; Pretorius, I. S. Modulation of volatile sulfur compounds by wine yeast. *Appl. Microbiol. Biotechnol.* **2007**, *74*, 954−960.
(39) Dubourdieu, D.; Tominaga,T. Polyfunctional Thiol Compounds. In *Wine Chemistry and Biochemistry*. Springer: New York, 2009; pp 275−295.
(40) Bouchilloux, P.; Darriet, P.; Henry, R.; Lavigne-Cruège, V.; Dubourdieu, D. Identification of volatile and powerful odorous thiols in Bordeaux red wine varieties. *J. Agric. Food Chem.* **1998**, *46*, 3095−3099.
(41) Blanchard, L.; Darriet, P.; Dubourdieu, D. Reactivity of 3-mercaptohexanol in red wine: impact of oxygen, phenolic fractions, and Sulfur Dioxide. *Am. J. Enol. Vitic.* **2004**, *55*, 115−120.
(42) Ferreira, V.; Ortin, N.; Escudero, A.; Lopez, R.; Cacho, J. Chemical characterization of the aroma of Grenache rose wines: aroma extract dilution analysis, quantitative determination and sensory reconstitution studies. *J. Agric. Food Chem.* **2002**, *50*, 4048−4054.
(43) Masson, G.; Schneider, R. Key compounds of Provence rosé wine flavor. *Am. J. Enol. Vitic.* **2009**, *60*, 116−122.
(44) Cullere, L.; Escudero, A.; Cacho, J.; Ferreira, V. Gas chromatography-olfactometry and chemical quantitative study of the aroma of six premium quality Spanish aged red wines. *J. Agric. Food Chem.* **2004**, *52*, 1653−1660.
(45) Kolor, M. G. Identification of an important new flavor compound in concord grape: ethyl 3-mercaptopropionate. *J. Agric. Food Chem.* **1983**, *31*, 1125−1127.
(46) Segurel, M. A.; Razungles, A.; Riou, C.; Trigueiro, M. G. L.; Baumes, R. Ability of possible DMS precursors to release DMS during wine aging and in the conditions of heat-alkaline treatment. *J. Agric. Food Chem.* **2005**, *53*, 2637−2645.
(47) Fedrizzi, B.; Magno, F.; Badocco, D.; Nicolini, G.; Versini, G. Aging effects and grape variety dependence on the content of sulfur volatiles in wine. *J. Agric. Food Chem.* **2007**, *55*, 10880−10887.
(48) De Royer Dupré, N.; Schneider, R.; Payan, J. C.; Salançon, E.; Razungles, A. Effects of Vine Water Status on Dimethyl Sulfur Potential, Ammonium, and Amino Acid Contents in Grenache Noir Grapes (*Vitis Vinifera*). *J. Agric. Food Chem.* **2014**, *62*, 2760−2766.
(49) Blanchard, L. Recherches sur la contribution de certains thiols volatils à l'arôme des vins rouges. Etude de leur genèse et de leur stabilité. Thesis, Université de Bordeaux 2, 2000.
(50) Blanchard, L.; Tominaga, T.; Dubourdieu, D. Formation of furfurylthiol exhibiting a strong coffee aroma during oak barrel fermentation from furfural released by toasted staves. *J. Agric. Food Chem.* **2001**, *49*, 4833−4835.

DOI: 10.1021/acs.jafc.5b03977
J. Agric. Food Chem. 2015, 63, 8879−8889

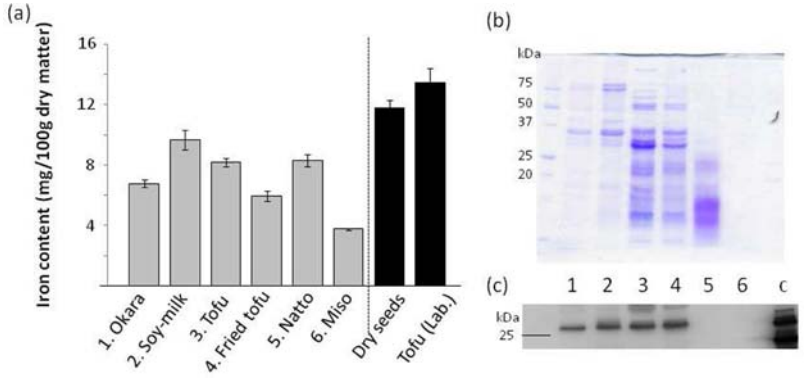

Figure 1. Iron contents and ferritin distribution in various soy-derived foods. (a) Iron contents of soy-derived foods. Blocks 1−6 indicate iron contents of soy-derived foods [soy-seed debris (okara), soymilk, tofu, fried tofu, natto, and miso] purchased at a local market. In addition, the iron contents of dry soybean seeds and tofu prepared in the laboratory are also shown. Error bars indicate SE of three independent analyses. (b) Reduced SDS−PAGE analysis of soy-derived food extracts. The gel was stained with Coomassie Brilliant Blue R-250. Lane 1, soy-seed debris (*okara*); lane 2, soymilk; lane 3, tofu; lane 4, fried tofu; lane 5, natto; and lane 6, miso. (c) Immunoblot analysis of soy-derived food extracts. Lane numbers indicate the same samples as panel b. Lane C indicates the control load of purified soybean ferritin.

storage. Here, I present the structural features of ferritin from tofu and describe the transition of iron contents during the processing of soybeans to tofu. The results presented here demonstrate the structural stability of soybean ferritin and its contribution to the iron content of soy-derived foods.

MATERIALS AND METHODS

Soybean Seeds, Soybean-Derived Foods, and Chemicals. Soybean dry seeds (*Glycine max* Merr. cv. Toyomasari) harvested in 2013 were purchased from a local market. All of the reagents used were of analytical grade or, if not available, special grade. Iron standards (Wako Pure Chemical, Tokyo, Japan) for atomic absorption spectrometry were diluted using distilled water for high-performance liquid chromatography (HPLC) grade (Nacalai, Kyoto, Japan). Commercially available soymilk, tofu, fried tofu, natto, and miso were purchased at local markets.

Preparation of Tofu. First, 250 g of dried soybean seeds was immersed in 1 L of distilled water at room temperature for 20 h. Subsequently, the water-absorbed seeds were homogenized using an electric cooking mixer. The homogenate was poured in a pan in which 1 L of distilled water was boiling. Subsequently, this soy homogenate was boiled in the pan with gently mixing for 10 min. The soymilk was squeezed from the boiled soybean seeds using cooking cloth and stored at 4 °C until the next procedure. A half volume (1 L) of the prepared soymilk was heated to 80 °C, and then 5.0 g of calcium sulfate dihydrate (Nacalai) was added to the soymilk to initiate the gelation. The resultant gel was gathered in a box and pushed gently to form tofu. The wept solution from the tofu, designated here as tofu supernatant, was also kept for further analyses. The moisture of tofu was determined by a moisture analyzer (MOC63u, Shimadzu, Kyoto, Japan).

Purification and Detection of Soybean Ferritin. Ferritin was purified from dry soybean seeds, tofu, and its supernatant by the following processes. The purification procedure of native soybean ferritin from dry soybean seeds was as described previously.[29] Ferritin was purified from tofu and its supernatant in a similar way. In brief, extraction buffer (20 mM TrisHCl at pH 7.7) was added to an equal volume of tofu (the average water content was 86.5%), followed by mixing with an electric cooking mixer and centrifugation (6000*g* for 15 min). The supernatant obtained here was designated as tofu extract. Subsequently, tofu ferritin was salted out by 30% saturated ammonium sulfate. The precipitant was dissolved in the extraction buffer followed by dialysis against the same extraction buffer. Ferritin was purified from the solution by anion-exchange chromatography (Q-toyopearl, Tosoh, Tokyo, Japan) and size-exclusion chromatography (SEC, Superdex 200 pg 16/60, GE Healthcare, Piscataway, NJ). Recombinant human H chain ferritin (rHuHF) was used as a size standard in SEC analysis. The preparation of rHuHF was described elsewhere.[30] To determine the oligomeric state of tofu ferritin, the SEC column (flow rate of 0.8 mL/min) was calibrated using the elution volumes of protein standards [rHuHF (506 000), γ-globulin (158 000), bovine serum albumin (BSA) (66 300), ovalbumin (42 700), and chymotripsinogen A (25 700)] (Figure S1). The oligomeric states of tofu ferritins were estimated using this calibration.

Ferritin was also purified from the tofu supernatant by the same procedure. Soybean ferritin was detected by sodium dodecyl sulfate−polyacrylamide gel (acrylamide concentration of 12.5%) electrophoresis (SDS−PAGE) followed by Coomassie Brilliant Blue R-250 staining and immunoblotting using anti-soybean ferritin antiserum.[29] Horseradish peroxidase (HRP)-labeled anti-rabbit immunoglobulin G (IgG, Promega, Madison, WI) was used as the secondary antibody. The signal was visualized using Chemilumi-one (Nacalai) and a laser imager (LAS-4000, GE Healthcare).

For the estimation of the recovery of ferritin in the purification steps, a dot-blot analysis was performed using the diluted recombinant soybean ferritin H-1 (rSFER1) subunit as a standard. The N-terminal amino acid sequences of purified ferritins from soybean seeds, tofu, and its supernatant were determined using the protein sequencer Procise HT (Life Technologies, Carlsbad, CA).

Iron Content Analyses. Lyophilized soy-derived food and milled soybean seeds were further dried at 120 °C for 4 h. Then, 0.5 g (dry weight) of each sample was wet-ashed with a solution of 14 mL of HNO_3 (60%, Nacalai) and 0.5 mL of H_2O_2 (Wako) for 5 h at 250 °C using a graphite block acid digestion system, Ecopre (Actac, Tokyo, Japan). The resulting digested solution of each sample was diluted with distilled water (HPLC grade, Nacalai), followed by the measurement of the iron concentration using an atomic absorption spectrophotometer (AAS, AA-6800, Shimadzu) equipped with a graphite furnace atomizer. The iron concentrations of lab-prepared soymilk, tofu supernatant, and soluble fractions after the purification steps were analyzed by the AAS after dilution. The concentration of each sample was determined from an average of three independent samples. An analysis of variance (ANOVA) with Tukey−Kramer's multiple comparison test was used to compare the iron contents among the various food products. Mean differences were considered significant at $p < 0.01$.

Circular Dichroism (CD) Measurements. Far-ultraviolet (UV) CD measurements were performed on a Jasco-720 spectropolarimeter (Jasco International, Tokyo, Japan) equipped with a temperature control unit (PTC-348, Jasco), using a spectral bandwidth of 2 nm and a cell path length of 1.0 mm. The protein concentration of recombinant soybean ferritin (rSFER1), ferritin purified from tofu, and its supernatant were adjusted to 0.2 mg/mL using a protein assay (BioRad, Hercules, CA). In temperature-controlled experiments, the molar ellipticity at a wavelength of 222 nm was taken in the range of 25−90 °C

DOI: 10.1021/acs.jafc.5b03080
J. Agric. Food Chem. 2015, 63, 8890−8895

[denaturation temperature (DT) = 0.5 °C] with an acquisition time of 0.2 s after an equilibration time of 30 s at each temperature step.

RESULTS

Iron Measurement and Ferritin Detection in Commercially Available Soy-Derived Foods. The iron contents of soy-derived foods that are available at ordinary grocery stores in Japan are shown in Figure 1a. The iron contents of these foods ranged from 3.6 to 9.6 mg/100 g of dry weight. The ferritins in the foods was detected by immunoblotting using an anti-soybean ferritin antibody. Ferritin was detected in soy-seed debris (okara), soymilk, tofu, and fried tofu, whereas it was absent in fermented foods, such as natto and miso (Figure 1c). Not only ferritin but also most of the proteins were digested in these fermented soy-derived foods (Figure 1b). Although available okara contained a detectable amount of ferritin (Figure 1c), the oligomeric form was not detected in okara (Figure S2). In contrast, oligomeric ferritin was apparently present in tofu and fried tofu purchased at a local market, suggesting that ferritin in okara or debris was aggregated or dissociated to a smaller structure (Figure S2). The iron content of tofu prepared in the laboratory was also determined as 13.5 mg/100 g of dry weight (Figure 1a). This value was higher than the value of the commercially available tofu assayed here. However, to determine the transition of iron and ferritin during the food processing of soybean seeds, the laboratory-prepared tofu was used in the subsequent experiments.

Oligomeric States and Subunit Composition of Ferritin in Tofu. For the determination of whether the oligomeric shell of ferritin is stably maintained after the heat treatment during food processing, ferritin was extracted and purified from soybean seeds and lab-prepared tofu, which included both the solid part (tofu extract) and the wept solution (tofu supernatant) (Figure 2a). All of the ferritin purified was amber-colored proteins,

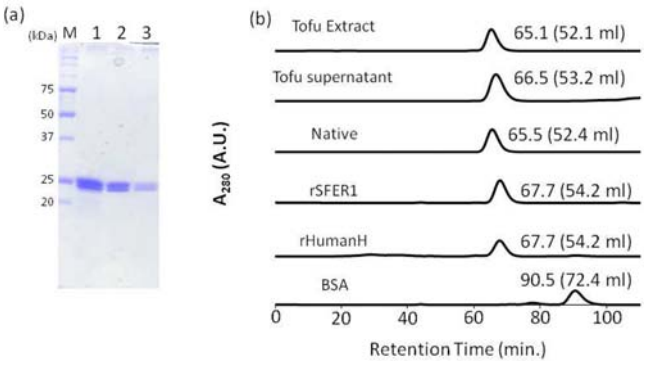

Figure 2. Purification of ferritin from tofu. (a) Purified ferritin from dry soybean seeds (lane 1), tofu extract (lane 2), and tofu supernatant (lane 3). (b) Elution chart of SEC. From the top to the bottom, the chart indicates tofu ferritin from the extract (tofu extract) and from the supernatant (tofu supernatant), native soybean ferritin (native), recombinant soybean ferritin H-1 (rSFER1), recombinant human H chain ferritin (rHumanH), and BSA (MW ≈ 66 300) as a control.

indicating that the proteins were an iron-containing form. Consistent with the observation described previously,[29] native soybean seed ferritin is composed of two types of subunits, H-1 (26.5 kDa, upper band) and H-2 (28 kDa, lower band) (Figure 2a). The ferritin purified from the tofu gel and tofu supernatant was also composed of two types of subunits, which showed similar mobility to that of native ferritin on the acrylamide gel (Figure 2a). The N-terminal amino acid sequences of these two bands (generally defined as 28 and 26.5 kDa) were ASNAPA and ASTVPL, respectively. This means that the subunit compositions of the ferritin from dry seeds and that from tofu were identical.

The oligomeric states of purified ferritins from tofu were estimated by SEC, which was adopted as the final purification step of these proteins. The elution volumes of tofu extract, tofu supernatant, native soybean ferritin, rSFER1, and rHumanH ferritins were calculated to 52.1, 53.2, 52.4, 54.2, and 54.2 mL, respectively, from the elution time of each sample (Figure 2b). Judging from the calibration plot (Figure S1), both of tofu ferritin (tofu extract and tofu supernatant) also formed a similar oligomer composed of 24 subunits.

Secondary Structure and Heat Stability of Purified Tofu Ferritin. Figure 3a shows the far-ultraviolet (UV) CD spectra of ferritin samples purified from tofu extract, tofu supernatant, and recombinant rSFER1 subunit 24-mer. These spectra commonly had the typical characteristics of α-helical proteins, i.e., local minimums of ellipticity at 207 and 222 nm and maximum ellipticity at 196 nm. In addition, the CD spectrum of tofu ferritin after heat treatment (90 °C for 10 min) showed no apparent difference from the tofu and recombinant ferritin (Figure S3); i.e., it showed a typical α-helix spectrum, and the peak intensities were not changed. These spectra indicated that the secondary structure of soybean ferritin was not denatured in the heating process of tofu preparation.

The heat denaturation processes of these proteins were followed by measuring the transition of molar ellipticity at 222 nm in the temperature range of 25−90 °C (Figure 3b). Generally, this type of plot shows the disorder in the secondary structure, especially the α-helical structure, induced by heat treatment. BSA was also treated similarly as a control. Typical proteins show a sigmoidal denaturation curve similar to that of BSA (Figure 3b). The DT can be determined by the fitting of such plots. However, tofu ferritin and recombinant soybean ferritin were not denatured completely at 90 °C, although partial denaturation in the α-helical structure was initiated in the temperature range higher than 80 °C. The secondary structure of tofu ferritin was nearly identical, even after this heating experiment (Figure S3), suggesting that soybean ferritin can recover its structure spontaneously after the partial heat denaturation state.

Iron Recovery during the Purification Steps and Iron Contents of the Purified Ferritins. The average iron content of soybean dry seed (*G. max*, Merr. cv. Toyomasari) used in this experiment was 11.8 ± 0.493 mg/100 g of dry weight (Figure 1a), while the iron concentration of soymilk prepared here was 10.1 ± 0.321 ppm [mean ± standard error (SE)] as the liquid body. In this experimental condition, 125 g of dry seeds produced approximately 1 L of soymilk. This result indicated that approximately two-thirds of iron (10.1 mg in soymilk of 14.8 mg of iron in dry seeds) were present as a soluble form in soymilk. Further, this soymilk (approximately 1 L) produced 330 g of tofu, whose moisture content was 86.5% on average. The iron content of prepared tofu was 13.5 mg/100 g of dry weight (Figure 1a). Thus, the prepared tofu was estimated to contain approximately 6 mg of iron.

On the other hand, the extractable iron amounts in the tofu and its supernatant, which were prepared from 125 g of dry soybean seed, were 807 μg (Figure 4a) and 339 μg (Figure 4c) on average, respectively. Finally, 179 and 45.5 μg of iron were recovered with purified ferritin from tofu extract and its supernatant. The recoveries of iron were 24.6 and 13.4% from

DOI: 10.1021/acs.jafc.5b03080
J. Agric. Food Chem. 2015, 63, 8890−8895

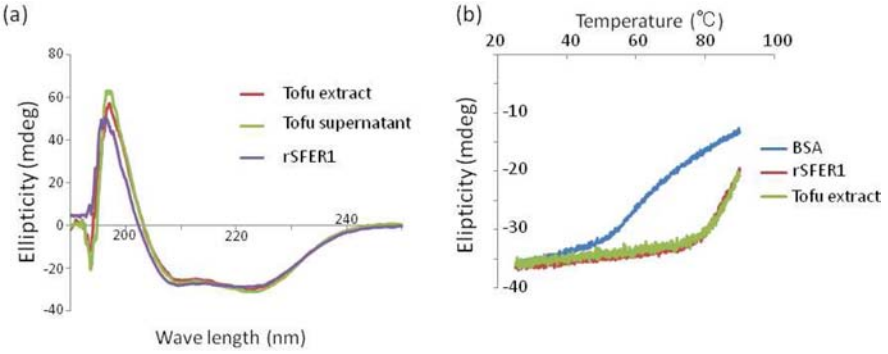

Figure 3. CD spectra of purified ferritin from tofu. (a) CD spectra of tofu ferritin purified from the extract and supernatant and rSFER1. Molar ellipticity in the far-UV region was recorded by scanning the wavelength from 250 to 190 nm. (b) Molar ellipticity at a wavelength of 222 nm was taken in the temperature range of 25−90 °C (DT = 0.5 °C) with an acquisition time of 0.2 s after an equilibration time of 30 s at each temperature step.

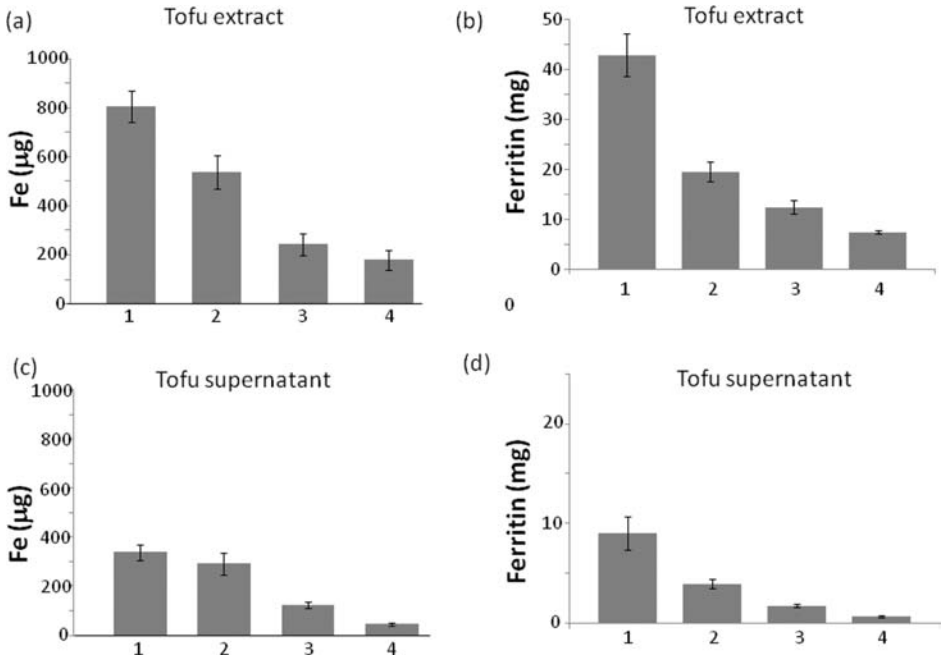

Figure 4. Iron and ferritin recovery during the purification steps. (a and c) Average iron recovery during the ferritin purification step from the tofu extract and supernatant, respectively. Error bars indicate SE of three to five independent analyses. (b and d) Ferritin recovery, which was estimated by dot-blot analyses. In these panels, numbers 1, 2, 3, and 4 mean the following purification steps: 1, crude sample; 2, after salting out and dialysis; 3, after anion-exchange chromatography; and 4, after SEC (the final purification step).

the tofu extract and supernatant, respectively. The ferritin recovery was estimated by a simple quantification of the dot-blot analysis at each purification step (Figure 4). The recoveries of ferritin from the tofu extract and supernatant were estimated to be 17.3 and 8.05%, respectively. These results indicated that large portions of soluble iron were present in ferritin, were maintained in the tofu gel, and not eluted out.

The iron contents of the purified ferritin samples are shown in Table 1. The average iron contents in the purified ferritin samples from soybean seed, tofu extract, and tofu supernatant were 2590, 1148, and 1000 atom per one oligomer, respectively (Table 1). The iron content of native soybean seed ferritin was significantly higher than those of the two types of purified tofu ferritin, whereas there was no significant difference in the iron contents of the ferritins from the tofu extract and supernatant. These results suggest that over half of the iron in soybean ferritin was lost during tofu preparation.

Table 1. Iron Contents of Purified Ferritin Oligomer[a]

ferritin source	number of iron atom per ferritin oligomer
dry seed	2590 ± 143[b]
tofu extract	1148 ± 130
tofu supernatant	1000 ± 62.6

[a]The iron contents of purified ferritin from dry seed, tofu extract, and tofu supernatant were calculated from the protein and iron concentration of each sample. Values indicate the mean ± SE. [b]Significant difference at $p < 0.01$.

DISCUSSION

One of the well-known characteristics of ferritin family proteins is the heat stability. In general, the oligomeric structure of ferritin is maintained and stabilized by large amounts of inter-subunit interactions, such as hydrophobic interactions, electrostatic interactions, hydrogen bonds, and salt bridges. In previous reports, I discussed the structural aspect that provides the heat

DOI: 10.1021/acs.jafc.5b03080
J. Agric. Food Chem. 2015, 63, 8890−8895

stability of plant-type ferritin in relation to the contribution of the plant ferritin-specific extension peptide.[31,32] The results of the present study demonstrated that the fundamental structure of soybean seed ferritin, such as the oligomeric form, secondary structure, and subunit composition, was maintained in tofu even after heat treatment.

Earlier findings obtained using differential scanning calorimetry also showed that the DT of a plant-type ferritin from green alga, *Ulva pertusa*, is higher than 90 °C.[31] Because of the high heat stability of this algal ferritin, the denaturation temperature could not be determined without some denaturant or chaotrope.[31] In the present study, the heat denaturation plots measured by a spectropolarimeter also showed that the secondary structure of soybean ferritin, regardless of the native or recombinant origin, was not completely disrupted in the temperature range of 25−90 °C. These data also support the heat stability of plant-type ferritin.

However, the number of iron atoms per ferritin oligomer was significantly decreased in the tofu ferritin, from both tofu extract and supernatant, compared to the native seed ferritin (Table 1). This indicates a loss of iron to some extent from ferritin in the process of tofu preparation. The heat denaturation plot of the native and tofu ferritin indicated that the secondary structures were affected by the heating, especially at a temperature higher than 80 °C. Such partial disorder would enhance the iron release from the ferritin oligomer. In fact, iron release from a ferritin shell, which is triggered by the partial disorder of the structure, was also reported in some vertebrate ferritins and a bacterial mini-ferritin.[33−36]

Although ferritin iron was partly released from the oligomeric protein shell during food processing, ferritin largely contributed to the soluble iron content in tofu. Ferritin is under scrutiny lately as a nutritional iron source with good bioavailability. The bioavailability of ferritin iron has been studied *in vivo* and *in vitro*, but this topic is still controversial. Initially, there was skepticism regarding the value of ferritin as a nutritional iron source,[37,38] but the appreciation of ferritin as a well-utilized iron source has become dominant.[10−12,15−17,19,26,39−41]

The two major advantages of ferritin iron as nutrition are as follows: (1) intestinal absorption via an independent pathway of heme iron or ferrous iron salts[15−17] and (2) absorption not affected by some dietary factors that have an inhibitory effect on iron absorption, such as phytic acid.[14] In addition, another advantage of the plant-type ferritin is its possibility as a nutritional phosphate source. The structural analysis of the ferritin core suggests that plant-type ferritin contains a large amount of phosphate as well as iron (Fe/P ratio of 2.8),[42] whereas the ratio is generally approximately 20 in vertebrate ferritin.[43] This fact indicates that tofu, which contains the oligomeric plant-type ferritin, may also serve as a dietary phosphate source. The endocytic pathway of ferritin absorption in intestinal epithelial cells was found in a Caco-2 cell experimental system.[16] Further characterization of the molecular mechanism in ferritin iron uptake is expected.

The question of whether ferritin originating from foods is still intact and forms the iron-containing oligomer when it reaches the duodenal epithelium where iron is mainly absorbed is another matter of controversy. Hopper et al. indicated that most plant ferritin degrades during *in vitro* gastric digestion,[44] whereas Lv et al. showed that both ferritins of plant origin and those of mammal origin are stable in simulated human digestive solution.[39] The difference in these findings could be caused by the experimental conditions used, such as pH. Hopper et al. also suggested that ferritin iron is reduced and well-utilized via DMT1 at a level similar to those of other inorganic iron forms, even though the protein shell is degraded during digestion.[44] Consistent with these *in vitro* studies, human trials in iron absorption have demonstrated the efficiency of ferritin as a nutritional iron source.[12,15,40]

The results of the present study demonstrated the fate of soybean ferritin during the processing to tofu. In tofu gel, ferritin maintained a similar oligomeric structure, which contained thousands of iron. We can presume that ferritin is present in various foods, including those of plant origin.[45,46] Despite such significant nutritional values, soybeans are not always regarded as an important staple food for humans worldwide. In addition to nutritional evaluations, further research on the utilization and development of soybean seeds as a substantial food material is needed.

■ ASSOCIATED CONTENT

Supporting Information

The Supporting Information is available free of charge on the ACS Publications website at DOI: 10.1021/acs.jafc.5b03080.

Calibration plot of the SEC column (Figure S1), immunoblot analysis of soy-derived food extracts after non-reducing SDS−PAGE without heat treatment (Figure S2), and CD spectra of purified ferritin from the tofu extract after the heat denaturation experiment (Figure S3) (PDF)

■ AUTHOR INFORMATION

Corresponding Author

*Telephone/Fax: +81-774-38-3765. E-mail: masutaro@kais.kyoto-u.ac.jp.

Funding

This research was supported by a research grant from the Fuji Foundation for Protein Research and the Takano Life Science Research Foundation.

Notes

The authors declare no competing financial interest.

■ REFERENCES

(1) Zimmermann, M. B.; Hurrell, R. F. Nutritional iron deficiency. *Lancet* **2007**, *370*, 511−20.

(2) Gunshin, H.; Mackenzie, B.; Berger, U. V.; Gunshin, Y.; Romero, M. F.; Boron, W. F.; Nussberger, S.; Gollan, J. L.; Hediger, M. A. Cloning and characterization of a mammalian proton-coupled metal-ion transporter. *Nature* **1997**, *388*, 482−8.

(3) McKie, A. T.; Barrow, D.; Latunde-Dada, G. O.; Rolfs, A.; Sager, G.; Mudaly, E.; Mudaly, M.; Richardson, C.; Barlow, D.; Bomford, A.; Peters, T. J.; Raja, K. B.; Shirali, S.; Hediger, M. A.; Farzaneh, F.; Simpson, R. J. An iron-regulated ferric reductase associated with the absorption of dietary iron. *Science* **2001**, *291*, 1755−1759.

(4) Harrison, P. M.; Arosio, P. Ferritins: Molecular properties, iron storage function and cellular regulation. *Biochim. Biophys. Acta, Bioenerg.* **1996**, *1275*, 161−203.

(5) Briat, J. F.; Ravet, K.; Arnaud, N.; Duc, C.; Boucherez, J.; Touraine, B.; Cellier, F.; Gaymard, F. New insights into ferritin synthesis and function highlight a link between iron homeostasis and oxidative stress in plants. *Ann. Bot.* **2010**, *105*, 811−22.

(6) Ambe, S.; Ambe, F.; Nozaki, T. Mossbauer study of iron in soybean seeds. *J. Agric. Food Chem.* **1987**, *35*, 292−296.

(7) Theil, E. C. Iron, ferritin, and nutrition. *Annu. Rev. Nutr.* **2004**, *24*, 327−343.

DOI: 10.1021/acs.jafc.5b03080
J. Agric. Food Chem. 2015, 63, 8890−8895

(8) Hoppler, M.; Zeder, C.; Walczyk, T. Quantification of ferritin-bound iron in plant samples by isotope tagging and species-specific isotope dilution mass spectrometry. *Anal. Chem.* **2009**, *81*, 7368−7372.
(9) Lukac, R. J.; Aluru, M. R.; Reddy, M. B. Quantification of ferritin from staple food crops. *J. Agric. Food Chem.* **2009**, *57*, 2155−2161.
(10) Zielinska-Dawidziak, M.; Hertig, I.; Piasecka-Kwiatkowska, D.; Staniek, H.; Nowak, K. W.; Twardowski, T. Study on iron availability from prepared soybean sprouts using an iron-deficient rat model. *Food Chem.* **2012**, *135*, 2622−7.
(11) Beard, J. L.; Burton, J. W.; Theil, E. C. Purified ferritin and soybean meal can be sources of iron for treating iron deficiency in rats. *J. Nutr.* **1996**, *126*, 154−160.
(12) Davila-Hicks, P.; Theil, E. C.; Lonnerdal, B. Iron in ferritin or in salts (ferrous sulfate) is equally bioavailable in nonanemic women. *Am. J. Clin. Nutr.* **2004**, *80*, 936−940.
(13) Lonnerdal, B. The importance and bioavailability of phytoferritin-bound iron in cereals and legume foods. *Int. J. Vitam. Nutr. Res.* **2007**, *77*, 152−7.
(14) Kalgaonkar, S.; Lönnerdal, B. Effects of dietary factors on iron uptake from ferritin by Caco-2 cells. *J. Nutr. Biochem.* **2008**, *19*, 33−9.
(15) Theil, E. C.; Chen, H.; Miranda, C.; Janser, H.; Elsenhans, B.; Nunez, M. T.; Pizarro, F.; Schumann, K. Absorption of iron from ferritin is independent of heme iron and ferrous salts in women and rat intestinal segments. *J. Nutr.* **2012**, *142*, 478−83.
(16) San Martin, C. D.; Garri, C.; Pizarro, F.; Walter, T.; Theil, E. C.; Nunez, M. T. Caco-2 intestinal epithelial cells absorb soybean ferritin by mu2 (AP2)-dependent endocytosis. *J. Nutr.* **2008**, *138*, 659−666.
(17) Kalgaonkar, S.; Lonnerdal, B. Receptor-mediated uptake of ferritin-bound iron by human intestinal Caco-2 cells. *J. Nutr. Biochem.* **2009**, *20*, 304−11.
(18) Shayeghi, M.; Latunde-Dada, G. O.; Oakhill, J. S.; Laftah, A. H.; Takeuchi, K.; Halliday, N.; Khan, Y.; Warley, A.; McCann, F. E.; Hider, R. C.; Frazer, D. M.; Anderson, G. J.; Vulpe, C. D.; Simpson, R. J.; McKie, A. T. Identification of an intestinal heme transporter. *Cell* **2005**, *122*, 789−801.
(19) Theil, E. C. Iron homeostasis and nutritional iron deficiency. *J. Nutr.* **2011**, *141*, 724S−728S.
(20) Masuda, H.; Aung, M. S.; Nishizawa, N. K. Iron biofortification of rice using different transgenic approaches. *Rice (N Y)* **2013**, *6*, 40.
(21) Yoshihara, T.; Takaiwa, F.; Goto, F.; Shigemoto, N.; Toki, S. Iron fortification of rice seed by the soybean ferritin gene. *Nat. Biotechnol.* **1999**, *17*, 282−286.
(22) Drakakaki, G.; Christou, P.; Stoger, E. Constitutive expression of soybean ferritin cDNA in transgenic wheat and rice results in increased iron levels in vegetative tissues but not in seeds. *Transgenic Res.* **2000**, *9*, 445−452.
(23) Drakakaki, G.; Marcel, S.; Glahn, R. P.; Lund, E. K.; Pariagh, S.; Fischer, R.; Christou, P.; Stoger, E. Endosperm-specific co-expression of recombinant soybean ferritin and Aspergillus phytase in maize results in significant increases in the levels of bioavailable iron. *Plant Mol. Biol.* **2005**, *59*, 869−80.
(24) Wirth, J.; Poletti, S.; Aeschlimann, B.; Yakandawala, N.; Drosse, B.; Osorio, S.; Tohge, T.; Fernie, A. R.; Gunther, D.; Gruissem, W.; Sautter, C. Rice endosperm iron biofortification by targeted and synergistic action of nicotianamine synthase and ferritin. *Plant Biotechnol. J.* **2009**, *7*, 631−44.
(25) Kumar, G. B.; Srinivas, L.; Ganapathi, T. R. Iron fortification of banana by the expression of soybean ferritin. *Biol. Trace Elem. Res.* **2011**, *142*, 232−41.
(26) Zielińska-Dawidziak, M. Plant Ferritin-A Source of iron to prevent its deficiency. *Nutrients* **2015**, *7*, 1184−1201.
(27) Renkema, J. M.; van Vliet, T. Heat-induced gel formation by soy proteins at neutral pH. *J. Agric. Food Chem.* **2002**, *50*, 1569−73.
(28) Riblett, A. L.; Herald, T. J.; Schmidt, K. A.; Tilley, K. A. Characterization of beta-conglycinin and glycinin soy protein fractions from four selected soybean genotypes. *J. Agric. Food Chem.* **2001**, *49*, 4983−9.
(29) Masuda, T.; Goto, F.; Yoshihara, T. A novel plant ferritin subunit from soybean that is related to a mechanism in iron release. *J. Biol. Chem.* **2001**, *276*, 19575−19579.
(30) Masuda, T.; Goto, F.; Yoshihara, T.; Mikami, B. The universal mechanism for iron translocation to the ferroxidase site in ferritin, which is mediated by the well conserved transit site. *Biochem. Biophys. Res. Commun.* **2010**, *400*, 94−99.
(31) Masuda, T.; Morimoto, S.-I.; Mikami, B.; Toyohara, H. The extension peptide of plant ferritin from sea lettuce contributes to shell stability and surface hydrophobicity. *Protein Sci.* **2012**, *21*, 786−796.
(32) Masuda, T.; Goto, F.; Yoshihara, T.; Mikami, B. Crystal structure of plant ferritin reveals a novel metal binding site that functions as a transit site for metal transfer in ferritin. *J. Biol. Chem.* **2010**, *285*, 4049−4059.
(33) Theil, E. C.; Liu, X. S.; Tosha, T. Gated pores in the ferritin protein nanocage. *Inorg. Chim. Acta* **2008**, *361*, 868−874.
(34) Williams, S. M.; Chandran, A. V.; Vijayabaskar, M. S.; Roy, S.; Balaram, H.; Vishveshwara, S.; Vijayan, M.; Chatterji, D. A histidine aspartate ionic lock gates the iron passage in miniferritins from Mycobacterium smegmatis. *J. Biol. Chem.* **2014**, *289*, 11042−58.
(35) Hasan, M. R.; Tosha, T.; Theil, E. C. Ferritin contains less iron (59Fe) in cells when the protein pores are unfolded by mutation. *J. Biol. Chem.* **2008**, *283*, 31394−400.
(36) Jin, W.; Takagi, H.; Pancorbo, B.; Theil, E. C. ″Opening″ the ferritin pore for iron release by mutation of conserved amino acids at interhelix and loop sites. *Biochemistry* **2001**, *40*, 7525−32.
(37) Skikne, B.; Fonzo, D.; Lynch, S. R.; Cook, J. D. Bovine ferritin iron bioavailability in man. *Eur. J. Clin. Invest.* **1997**, *27*, 228−33.
(38) Bejjani, S.; Pullakhandam, R.; Punjal, R.; Nair, K. M. Gastric digestion of pea ferritin and modulation of its iron bioavailability by ascorbic and phytic acids in caco-2 cells. *World J. Gastroenterol.* **2007**, *13*, 2083−2088.
(39) Lv, C.; Zhao, G.; Lönnerdal, B. Bioavailability of iron from plant and animal ferritins. *J. Nutr. Biochem.* **2015**, *26*, 532−540.
(40) Murray-Kolb, L. E.; Welch, R.; Theil, E. C.; Beard, J. L. Women with low iron stores absorb iron from soybeans. *Am. J. Clin. Nutr.* **2003**, *77*, 180−184.
(41) Lönnerdal, B. Soybean ferritin: implications for iron status of vegetarians. *Am. J. Clin. Nutr.* **2009**, *89*, 1680S−1685S.
(42) Wade, V. J.; Treffry, A.; Laulhere, J. P.; Bauminger, E. R.; Cleton, M. I.; Mann, S.; Briat, J. F.; Harrison, P. M. Structure and composition of ferritin cores from pea seed (*Pisum sativum*). *Biochim. Biophys. Acta, Protein Struct. Mol. Enzymol.* **1993**, *1161*, 91−96.
(43) Treffry, A.; Harrison, P. M.; Cleton, M. I.; de Bruijn, W. C.; Mann, S. A note on the composition and properties of ferritin iron cores. *J. Inorg. Biochem.* **1987**, *31*, 1−6.
(44) Hoppler, M.; Schonbachler, A.; Meile, L.; Hurrell, R. F.; Walczyk, T. Ferritin-iron is released during boiling and in vitro gastric digestion. *J. Nutr.* **2008**, *138*, 878−884.
(45) Morimoto, S.; Masuda, T.; Sugihara, I.; Toyohara, H. Identification and characterization of a ferritin gene and its product from the multicellular green alga *Ulva pertusa*. *Biosci., Biotechnol., Biochem.* **2012**, *76*, 1913−9.
(46) Masuda, T.; Yamamoto, A.; Toyohara, H. The iron content and ferritin contribution in fresh, dried, and toasted nori. *Biosci., Biotechnol., Biochem.* **2015**, *79*, 74−81.

NOTE ADDED AFTER ASAP PUBLICATION

Due to a production error, this article published September 30, 2015 with an incorrect Supporting Information file. The correct SI file published October 14, 2015.

DOI: 10.1021/acs.jafc.5b03080
J. Agric. Food Chem. 2015, 63, 8890−8895

MATERIALS AND METHODS

Preparation of MFP. Longissimus muscle (pH 5.6−5.9) was collected from three pork carcasses (48 h post-mortem). Individual samples (~90 g each) were vacuum-packaged and kept in a freezer (−30 °C) until use (less than 6 months). Frozen muscle samples were tempered at 4 °C for 5 h prior to MFP extraction using an isolation buffer of 0.1 M sodium chloride (NaCl), 10 mM sodium phosphate, 2 mM $MgCl_2$, and 1 mM ethylene glycol bis(2-aminoethyl ether)-*N*,*N*,*N*′,*N*′-tetraacetic acid (EGTA) (pH 7.0).[18] The pH of MFP suspension in 0.1 M NaCl at the last wash was adjusted to 6.25 before centrifugation (at 2000*g* for 15 min). The protein concentration of MFP pellet was measured by the Biuret method using bovine serum albumin (BSA) as a standard. The MFP pellet was kept on ice and used within 2 days.

Preparation of Emulsions. Commercial refined soybean oil was purchased from a local grocery; the high-performance liquid chromatography (HPLC) analysis confirmed that its tocopherol content was slightly greater than 100 mg/100 g (18.6 mg/100 g α-tocopherol, 87.6 mg/100 g γ-tocopherol, and 26.3 mg/100 g δ-tocopherol), agreeing with the reported literature.[19] Tween-20-stabilized emulsions were prepared from the mixture of 10% (v/v) soybean oil and 90% (v/v) pre-chilled buffer (25 mM phosphate at pH 6.25 containing 0.6 M NaCl at 4 °C) with 2% (w/v) Tween 20 by homogenization for 2 min with a Polytron blender (Brinkmann Instruments, Inc., Westbury, NY). A low-foaming probe (PTA-20TS) and a speed of 17 500 rpm were used. The pre-homogenized crude emulsion was then finely homogenized with a laboratory-scale jet homogenizer (NanoDeBee, B.E.E. International, Inc., Easton, MA) at an overall pressure of 35 MPa for one pass. During emulsification, the high-pressure pipeline was kept cool with ice pouches; thus, the temperature of outlet emulsion did not exceed 15 °C.

MFP-stabilized emulsions were prepared from the mixture of 10% (v/v) soybean oil and 90% (v/v) MFP in 25 mM phosphate at pH 6.25 containing 0.6 M NaCl. Three MFP concentrations (0.25, 0.5, and 1%, w/v) were used to allow for the determination of the protein concentration effect. The same two-stage homogenization process as above was used for the emulsion preparation.

Oxidation. To oxidize, Tween 20-stabilized and MFP-stabilized emulsions were incubated at 4 °C with hydroxyl radicals produced by an Fe^{2+}-recycling solution comprised of 10 μM $FeCl_3$/100 μM ascorbic acid/5 mM H_2O_2 for 0, 2, and 24 h. The oxidative reaction was terminated by propyl gallate/Trolox/EDTA (1 mM each).[18] In addition, MFP at a final concentration of 0.25, 0.5, or 1% (w/v) was added to the Tween 20 emulsion by gently mixing, followed by oxidation as described above. Because proteins would not adsorb at the interface in Tween emulsion, it was deemed appropriate to determine the antioxidative efficacy of MFP in the continuous phase, as compared to the other emulsion systems.

Measurement of the Emulsion Particle Size and Morphology. Emulsion samples for droplet size distribution were diluted with 25 mM phosphate buffer (pH 6.25, with a refractive index of 1.34) at a 1:50 emulsion/buffer ratio (v/v). The emulsion particle size was analyzed by ZetaSizer Nano-ZS (Malvern Instruments, Worcestershire, U.K.) at 22.5 °C with the following settings: measurement angle, 90°; equilibration time, 120 s; number of runs, 3; run duration, 10 s; number of measurements, 3; and delay between measurements, 10 s. The morphology of emulsified oil droplets was observed under a MICROPHOT-FXA Nikon photomicroscope equipped with a built-in digital camera (Nikon, Inc., Garden City, NY).

Fluorescence microscopy was applied to visualize the microstructure of emulsions and evidence the formation of protein coating around lipid droplets. The oil phase in the emulsions was stained with Nile Red dye (0.1%, v/v), and protein was stained with fluorescein isothiocyanate dye (0.1%, v/v). The dye-treated samples were placed in small cylindrical containers (10 μL) and incubated at room temperature in the dark for 20 min. Fluorescence was produced by excitation with a blue light (488 nm) and emission in the green region (514 nm) using a model Nikon Eclipse E800 fluorescent microscope. Furthermore, total internal reflection fluorescence (TIRF) was measured to probe dynamic morphological changes in protein-coated emulsion particles. An EMCCD (Andor) camera was mounted on the top of a Nikon Ti-U inverse microscope with a 100× oil-type objective. To detect the fluorescence of the fluorescein dye (emission wavelength of 514 nm), a 532 nm excitation filter and a 575 nm emission filter were used. An Olympus ZDC2 auto focus module was applied to limit focal drift. All of the images were obtained with a 100 ms frame rate.

Recovery of Adsorbed and Unadsorbed Proteins. Control and oxidized Tween 20-stabilized emulsions with added MFP (1%) were centrifuged (at 35000*g* for 60 min and 4 °C); the serum phase was collected, and the cream phase was discarded. Care was taken to avoid any cream or oil residue in the collected serum samples. First, the separated cream layer was removed using a spatula, and then a hole was pricked at the bottom of the plastic centrifuge tube using a needle to collect the clear part of the serum phase. The upper part of the serum phase was discarded to avoid oil residues. When MFP was added to Tween-stabilized emulsion, most proteins stayed in the continuous phase because, thermodynamically, it was difficult for them to displace the small surfactant (Tween 20).

Similarly, MFP-stabilized emulsions (1%) with or without the oxidative stress were centrifuged (at 35000*g* for 60 min and 4 °C) to separate the serum phase from the cream phase that contained oil and adsorbed protein. The serum phase was carefully collected as described above to obtain unadsorbed MFP. The cream layer was washed 2 times with deionized water and then subjected to the recovery of adsorbed protein using Tween 20 as the desorbing (displacing) agent.[20] To do so, washed cream was dispersed in 25 mM phosphate buffer (pH 6.25, with the same volume as the removed serum phase) containing 2% (v/v) Tween 20 by stirring at 4 °C for 3 h and then centrifuging at 35000*g* for 60 min and 4 °C. The cream layer was removed with a spatula, and the aqueous solution containing originally adsorbed MFP was collected. The concentration of adsorbed and unadsorbed protein was measured by the Bradford method.[21]

Determination of Lipid Oxidation. Evaluation of oxidative changes in control and oxidized emulsion samples was performed by monitoring the formation of conjugated diene hydroperoxides and 2-thiobarbituric acid reactive substances (TBARS).[22,23] For conjugated dienes, emulsion samples (0.5 mL) were mixed with 5 mL of extracting solvent (3:2, v/v, hexane/isopropanol) and vortexed for 1 min. After centrifugation at 2000*g* for 5 min, the absorbance (233 nm) of the supernatant was recorded and the value converted to conjugated dienes using the molar extinction coefficient of 25 200 M^{-1} cm^{-1}.[24]

For the measurement of TBARS, emulsion samples were mixed into the assay solution containing trichloroacetic acid (TCA) and thiobarbituric acid (TBA), followed by boiling for 30 min. The supernatant of the cooled solution was treated with chloroform and centrifuged at 2000*g* for 5 min. The absorbance of the upper phase containing the pinkish TBA−malonaldehyde adducts was measured at 532 nm, and the molar extinction coefficient of 152 000 M^{-1} cm^{-1} was used to calculate the TBARS content.[25]

Measurement of Protein Oxidation and Structural Changes. Protein modifications were examined over time through monitoring the oxidation and structural changes using the following analytical indexes.

Carbonyl. The content of protein carbonyl derivatives in control and oxidatively stressed emulsion samples was estimated using the 2,4-dinitrophenylhydrazine (DNPH) colorimetric method.[26] Briefly, the DNPH-reacted MFP samples after 20% TCA precipitation were recovered by centrifugation (at 11000*g* for 10 min) and then washed with ethanol/ethyl acetate (1:1, v/v) solvent to remove unbound pigments. The final MFP pellets were dissolved in guanidine hydrochloride (6.0 M), and the absorbances at 370 and 280 nm were recorded for the determination of carbonyl and protein concentrations, respectively. A molar extinction coefficient of 22 000 M^{-1} cm^{-1} was used for carbonyl content computation.

Sulfhydryl. Free sulfhydryl content in emulsion samples was determined by reaction with Ellman's reagent [5,5′-dithio-bis(2-nitrobenzoic acid) (DNTB)] as detailed by Beveridge et al.[27] Blanks

DOI: 10.1021/acs.jafc.5b03377
J. Agric. Food Chem. 2015, 63, 8896−8904

were run with 25 mM phosphate buffer (pH 6.25) containing 0.6 M NaCl. The sulfhydryl concentration was calculated using a molar extinction coefficient of 13 600 M^{-1} cm^{-1}.

Electrophoresis. Sodium dodecyl sulfate−polyacrylamide gel electrophoresis (SDS−PAGE) was performed with a 4% polyacrylamide stacking gel and a 10% polyacrylamide separating gel. Adsorbed and unadsorbed (continuous phase) proteins prepared as described above were dissolved in the SDS−PAGE sample buffer with and without 10% β-mercaptoethanol (βME) to obtain a final protein concentration of 2 mg/mL and then boiled for 3 min. Into each well, 60 μg of prepared sample was loaded.

Circular Dichroism (CD). Far-ultraviolet (UV) (190−260 nm) CD spectra of collected MFP samples were obtained on a Jasco J-810 spectropolarimeter (Hachioji City, Tokyo, Japan) using a 0.1 cm path length cuvette. The protein samples were concentrated on a centrifugal filter device (Amicon Ultra-15, Billerica, MA) with a molecular weight cutoff of 10 000 and then diluted to 0.2 mg/mL with a 0.45 M NaCl and 25 mM phosphate buffer (pH 7.0). After filtering through a 0.22 μm Millipore filter [polyvinylidene fluoride (PVDF)] to reduce light scattering, the spectrum was obtained immediately.[28] The results were expressed as ellipticity, θ (mdeg). The same phosphate buffer without adding MFP was used as the control. The scan rate, response, bandwidth, and step resolution were 100 nm/min, 0.25 s, 1.0 nm, and 0.5 nm, respectively. Values from three scans were averaged to obtain one spectrum.

Intrinsic Tryptophan Fluorescence. The procedure described by Estévez et al.,[29] with slight modifications, was followed to observe a fluorescence pattern and intensity of protein samples. Recovered adsorbed and unadsorbed MFPs (100 μL) were diluted in 5 mL of 25 mM phosphate buffer (pH 6.25) containing 0.6 M NaCl and then subjected to fluorescence testing in a Fluoromax-3 fluorometer (Horiba Jobin Yvon, Inc., Edison, NJ). The excitation and emission wavelengths were 283 and 300−400 nm, respectively, and the scanning speed was 1 nm/s.

Statistical Analysis. Data were collected from two independent experimental trials (replicates) with different batches of MFP isolation. All analyses were performed on triplicate samples, and the results were subjected to the analysis of variance using the procedure of the general linear model of the Statistix software 9.0 (Analytical Software, Tallahassee, FL). All pairwise multiple comparisons [least significant difference (LSD)] were used to identify significant differences ($p < 0.05$) between means.

RESULTS AND DISCUSSION

Structural Characteristics and Physical Stability of Emulsions. The light microscopy of freshly made emulsions is shown in Figure 1A. The oil droplets in Tween emulsion with added MFP exhibited a highly homogeneous distribution, while the oil droplets in MFP-stabilized emulsions (a, b, and c) were less evenly distributed, depending upon the protein concentration. The emulsion with 1% protein (c) contained the smallest oil droplets (mean diameter of 670 nm) that appeared better distributed in the continuous phase when compared to the emulsion (mean diameter of 1126 nm) prepared with 0.25% MFP (a). At lower protein concentrations, for example, 0.25% MFP, most MFP was found to accumulate at the interface as adsorbed protein, with an unmeasurable amount being present in the continuous phase. A higher protein concentration allows for greater surface loading to achieve better emulsifying capability,[12] while excess unadsorbed proteins would restrict the mobility of oil droplets as a result of enhanced viscosity of the continuous phase. Other researchers have reported a similar phenomenon that decreasing the initial concentration of emulsifier resulted in an increased average droplet size and rapid physical destabilization of emulsions.[30] In contrast, Tween 20 as a more surface-active small surfactant can effectively adsorb to

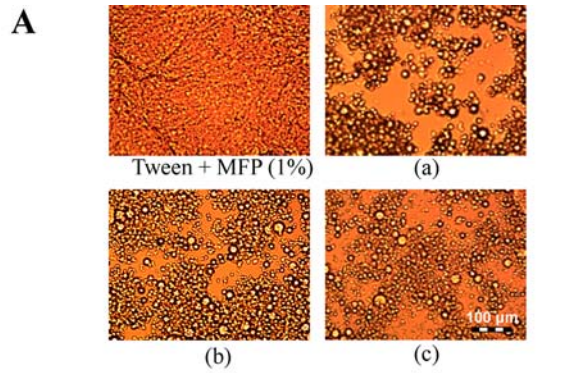

Sample	Peak1 (d, nm)	Peak2 (d, nm)	Z-Ave (d, nm)
Tween 20	20	73	26
(a) MFP (0.25%)	1126	0	1220
(b) MFP (0.5%)	1185	0	1165
(c) MFP (1%)	670	0	706

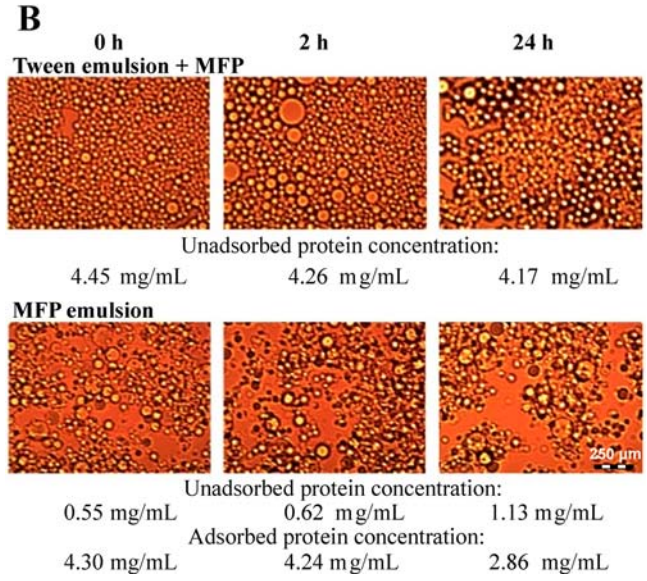

Figure 1. (A) Microscope images of freshly prepared emulsions: Tween emulsion with added MFP (1%) and emulsions prepared with (a) 0.25% MFP, (b) 0.5% MFP, and (c) 1% MFP. Cumulant size (Z average) and peak size are shown in the inset (d = diameter). (B) Microscope images and protein distributions of emulsions during oxidation: (upper panel) Tween emulsions with 1% added MFP and (lower panel) 1% MFP emulsions. Note the bar scale of 100 μm in panel A and 250 μm in panel B.

the oil droplet surface under a high pressure. This thin surfactant film surrounding nanolevel oil droplets lowered surface tension and provided long-term stability with respect to droplet flocculation, coalescence, and creaming.

To illustrate the role of the interfacial membrane in the oxidative stability of emulsions (which will be described later), morphological changes of emulsions prepared with 1% MFP or Tween 20 with added MFP (1%) during oxidation up to 24 h were compared (Figure 1B). The Tween emulsions with added MFP appeared to be relatively stable, and the concentration of the unadsorbed protein in their continuous phase did not change significantly ($p > 0.05$) over the entire oxidation period (upper panel), while droplets present in the MFP emulsions exhibited notable flocculation in 2 h and aggregates in 24 h

DOI: 10.1021/acs.jafc.5b03377
J. Agric. Food Chem. 2015, 63, 8896−8904

(lower panel). This morphological shift for the latter emulsion system was a dynamic process characterized by the partial release of protein from the oil−water interface, which was initially non-appreciable (2 h; $p > 0.05$) but became remarkable (24 h; $p < 0.05$); the adsorbed MFP was reduced to 2.86 mg/mL (or 72% of the total protein) from its fresh state at 4.30 mg/mL (or 89% of the total protein). Oxidant-induced structural changes and aggregation of interfacial proteins facilitated the release of protein and, consequently, destabilization (flocculation) of the emulsion. Flocculation and partial protein desorption were also observed in non-oxidized MFP control emulsions that did not exhibit any measurable oxidative change. Flocculation was not seen in the Tween emulsions even in the presence of MFP added to the continuous phase as a result of the lack of protein as an interfacial constituent. Despite its less physical stability, the MFP emulsion retained much of the membrane structure, which may serve as a barrier against radical attack.

To visualize in greater detail the effect of protein coating on the emulsion droplet morphology and distribution, fluorometry and total internal reflection fluorescence (TIRF) microscopy (Figure 2) were employed. The fluorescence image of MFP-

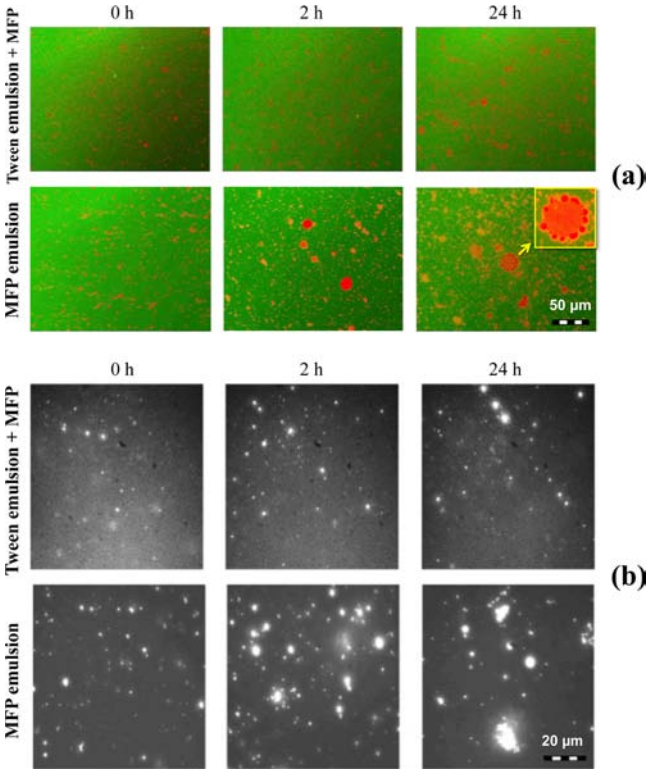

Figure 2. (a) Fluorescence microscopy and (b) TIRF images of (upper panel) Tween-stabilized emulsion with 1% added MFP and (lower panel) 1% MFP-stabilized emulsion with different oxidation times. In panel a, a large particle surrounded by small droplets in 24 h oxidized MFP emulsion is enlarged for visibility.

stabilized emulsions illuminated with two different fluorescent dyes demonstrated the coverage of oil droplets by MFP and the rearrangement of oil droplets during oxidation (Figure 2a). In 2 h, the MFP emulsion displayed a broad droplet size distribution with an obviously larger mean diameter when compared to the Tween emulsions as a result of flocculation and coalescence of small droplets. Interestingly, after 24 h of oxidation, many of the small droplets coated with protein migrated to the surface of the large, coalesced oil droplets, forming neo-interfacial clusters (pointed by arrow), resembling a milk fat emulsion stabilized by casein micelles.[31] In comparison, a different morphological image was observed for emulsions prepared with Tween 20, where oil droplets were not only much smaller but also well-separated, showing no apparent flocculation after 24 h, which was in accordance with light microscopy imaging (Figure 1b).

The above microscopic observation was corroborated by the image captured with TIRF (Figure 2b). The TIRF technique produces a live microscopic profile of dynamic aggregation of protein in MFP emulsions and reversible Brownian flocculation in Tween emulsions. Isolated fluorescent dots in the TIRF image (Figure 2b) were attributed to the emission of protein dye in the emulsion, allowing for the differentiation of morphological variations between MFP emulsions and Tween emulsions with added MFP under oxidative stress. In the MFP emulsions, flocculation occurred within 2 h, followed by partial coalescence in 24 h. The Tween emulsion samples with added MFP also showed a few fluorescent dots, and their presence exhibited no remarkable change. These were protein aggregates rather than oil droplets because of the weaker surface activity of proteins relative to Tween 20 and,[32] therefore, less likely for the continuous-phase MFP to displace the adsorbed Tween at the interface.

Lipid Oxidation. The time course of the oxidative reaction was monitored by the measurement of primary (conjugated dienes) and secondary (TBARS) products of lipid oxidation. Conjugated dienes, which mirror the production of hydroperoxides, are unstable, especially in an intense oxidative environment. Their content typically increases for a short time and then decreases as a result of spontaneous degradation into secondary products.[33] In Figure 3a, conjugated dienes decreased within 24 h oxidation in all emulsion samples, except for 1% MFP-stabilized emulsion. The relatively high protein concentration in the 1% MFP emulsion conspicuously prolonged the lag phase, thereby slowing the production of hydroperoxide-conjugated dienes, hence, the increasing pattern within 24 h. The protein concentration effect was also observed by Kiokias et al.,[34] who reported that an increasing whey protein concentration led to a decrease in the emulsion droplet size but an increase in lipid oxidative stability. At an equal protein concentration, the conjugated diene content in MFP-stabilized emulsions was approximately a half of Tween 20-stabilized emulsions with added MFP (Figure 3a). This was strong evidence that MFP, when acting as an emulsifier surrounding the oil droplets, as opposed to being in the aqueous phase, could effectively delay lipid oxidation. Moreover, the Tween emulsion mixed with MFP had a relatively high conjugated diene value at time zero when compared to MFP emulsion samples, suggesting the early protective role that MFP played in the emulsifying process.

The TBARS results are depicted in Figure 3b. The Tween emulsions with or without added MFP (0.25, 0.5, or 1%) both showed remarkably higher ($p < 0.05$) TBARS values, including time 0, when compared to MFP-generated emulsions. Therefore, interface-adsorbed protein acted as an effective mechanism for the inhibition of lipid oxidation during the homogenization process as well as during prolonged oxidative stress. The result was consistent with the conjugated diene inhibition (Figure 3a). For each emulsion sample, oxidation up to 2 h caused no significant increase in TBARS ($p > 0.05$). After 24 h of

DOI: 10.1021/acs.jafc.5b03377
J. Agric. Food Chem. 2015, 63, 8896−8904

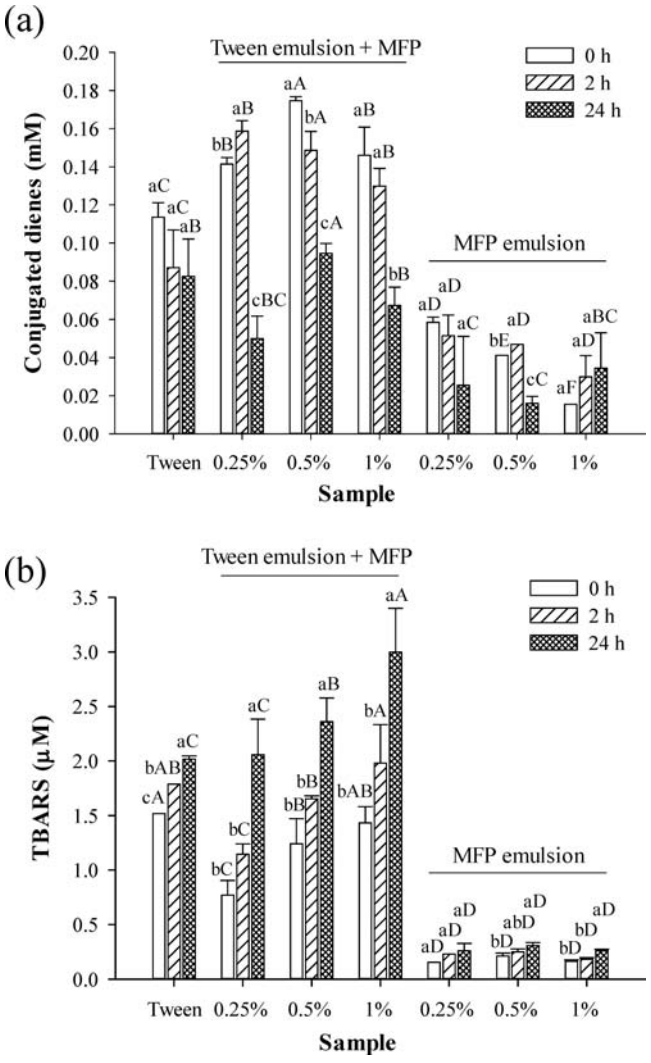

Figure 3. Formation of (a) conjugated dienes and (b) TBARS in emulsions during oxidation. (A–E) Means within the same oxidation time between different emulsions with different capital letters differ significantly ($p < 0.05$). (a–c) Means within the same emulsion between different oxidation times with different lowercase letters differ significantly ($p < 0.05$).

oxidation, the TBARS content rose significantly in Tween emulsions compared to MFP emulsions that had minimal changes.

Protein Oxidation. To confirm the role of MFP as a sacrificing antioxidant to protect protein-stabilized emulsions and delineate the specific actions of interfacial and continuous-phase MFP, oxidative changes at the primary, secondary, and tertiary levels of the emulsions and separated proteins are presented below. The results obtained when compared to lipid oxidation were applied to explain in detail the sequential oxidative change of the two main emulsion constituents.

Sulfhydryl and Carbonyl Derivatives. Modification of amino acid residue side-chain groups is the primary consequence of oxidative attack of proteins. The loss of sulfhydryls and formation of carbonyls are two common measures of protein changes in oxidized muscle foods.[6,35] As presented in Table 1, the sulfhydryl content decreased, while the carbonyls increased continuously during oxidation ($p < 0.05$). For the thiol groups, almost all of the loss occurred within the first 2 h, preceding the onset of lipid oxidation,

Table 1. Sulfhydryl and Carbonyl Contents in Two Different Emulsion Systems as Affected by Oxidation (0, 2, and 24 h)[a]

	sulfhydryl (nmol/mg of protein)			carbonyl (μmol/g of protein)		
emulsion	0 h	2 h	24 h	0 h	2 h	24 h
			Tween + MFP			
0.25% protein	85.0 ± 1.3 aA (21.3)[b]	67.1 ± 1.6 bA (16.8)	66.6 ± 3.4 bA (16.7)	3.01 ± 0.91 aA (0.75)	4.24 ± 0.50 aAB (1.06)	4.78 ± 0.08 aCD (1.20)
0.5% protein	81.2 ± 0.1 aC (40.6)	46.3 ± 0.3 bB (23.2)	46.0 ± 4.0 bC (23)	2.66 ± 0.15 bAB (1.33)	2.90 ± 0.07 bC (1.45)	4.03 ± 0.17 aD (2.02)
1% protein	83.0 ± 2.5 aB (83.0)	42.4 ± 1.9 bB (42.4)	42.1 ± 2.2 bB (42.1)	2.76 ± 0.06 bAB (2.76)	3.26 ± 0.11 aBC (3.26)	4.51 ± 0.99 aCD (4.51)
			MFP			
0.25% protein	76.1 ± 0.3 aCD (19.0)	22.1 ± 3.1 bD (5.5)	21.0 ± 2.8 bE (5.3)	2.32 ± 0.29 cABC (0.58)	4.46 ± 0.78 bA (1.12)	8.41 ± 0.10 aA (2.10)
0.5% protein	74.0 ± 7.0 aE (37.0)	24.3 ± 0.9 bE (12.2)	17.0 ± 4.4 bDE (8.5)	1.61 ± 0.02 cC (0.81)	3.15 ± 0.45 bC (1.58)	6.10 ± 0.12 aB (3.05)
1% protein	77.9 ± 3.4 aC (77.9)	31.1 ± 0.3 bC (31.1)	27.4 ± 4.4 bCD (27.4)	1.62 ± 0.07 cC (1.62)	2.71 ± 0.27 bC (2.71)	5.30 ± 0.36 aBC (5.30)

[a](a–c) Means ± standard deviations within the same emulsion (row) between different oxidation times without a common lowercase letter differ significantly ($p < 0.05$). (A–E) Means ± standard deviations within the same oxidation time (column) between different emulsions without a common capital letter differ significantly ($p < 0.05$). [b]Values in parentheses denote net sulfhydryl (nmol) and carbonyl (μmol) contents on an equal volume basis (100 mL emulsion).

DOI: 10.1021/acs.jafc.5b03377
J. Agric. Food Chem. 2015, 63, 8896–8904

which took place mostly between 2 and 24 h (Figure 3). However, the extent of sulfhydryl reduction was quite different between the two types of emulsions, i.e., 21.1−49.0% for Tween emulsions with added MFP compared to 60.1−71.0% for MFP-generated emulsions, irrespective of the protein concentration. Thus, interface-adsorbed MFP was more prone to hydroxyl radicals than continuous-phase MFP.

Table 1 also summarizes the protein carbonyl content in different emulsions. It is noteworthy that freshly prepared emulsions already had measurable amounts of carbonyls produced during the MFP isolation and emulsion preparation. Oxidative stress resulted in a gradual rise of the carbonyl content in MFP in both emulsion systems. For Tween emulsions, the content of carbonyls on a protein basis (μmol/g of protein) was generally not affected by the amount of MFP added ($p > 0.05$), indicating that proteins in the continuous phase were equally susceptible to radicals. However, when calculated on the basis of the volume, the net amount of carbonyl derivatives in the emulsion (μmol/100 mL) increased with the level of MFP addition. The latter value suggests that the extra oxidized proteins may serve as initiators for lipid oxidation as previously described.

In comparison, the MFP emulsions had a more rapid carbonyl formation during oxidation, with the net increase in 24 h ranging from 3.68 to 6.09 μmol/g of protein versus about 1.5 μmol/g of protein for Tween emulsions ($p < 0.05$) (Table 1). This result again substantiates the premise that interfacial protein in MFP-stabilized emulsions played a sacrificing role as an antioxidant to protect lipids. Interestingly, the pattern of sulfhydryl reduction (completed in 2 h) was not in parallel with the increase in carbonyls (progressive throughout 24 h), suggesting an independent nature of the two oxidative processes. During oxidation, free thiol groups can be readily converted to disulfide bonds, while the formation of carbonyl derivatives appeared to be progressive, which may involve lysine, arginine, proline, and threonine side-chain groups.[36] In strong agreement, results from SDS−PAGE showed disulfide-dependent polymerization of myosin because the polymers were dissociated when oxidized samples were treated with βME, a reducing agent (Figure 4). Moreover, the myosin heavy chain in adsorbed MFP completely vanished within 2 h of oxidation (see the arrows in Figure 4a), suggesting more extensive polymerization compared to the MFP in the continuous phase (Figure 4b). The observation further confirms the high reactivity of interfacial proteins relative to their counterpart in the bulk phase.

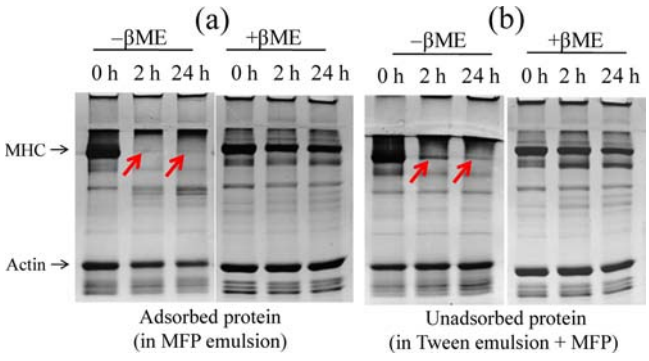

Figure 4. SDS−PAGE of (a) adsorbed protein in MFP emulsion (1%) and (b) unadsorbed protein in Tween emulsion with added MFP (1%) during oxidation. βME, β-mercaptoethanol (a disulfide-bond-breaking agent); MHC, myosin heavy chain.

Secondary and Tertiary Structures. The characteristic CD spectra of MFP in the far-UV region are depicted in panels a and b of Figure 5. The adsorbed protein recovered from MFP-stabilized emulsions exhibited a negative band near 208 and 222 nm and a strong peak at 200 nm (Figure 5a), resembling a typical α-helix curve. While the pattern of the CD spectrum changed very little, the ellipticity attenuated with the oxidation time, indicating destabilization of the secondary structures. However, the results suggest that, even after oxidation, α-helix was still a major structural component in adsorbed MFP, which can be largely ascribed to the myosin helical rod. In contrast, oxidation significantly disrupted the secondary structure of proteins present in the continuous phase of Tween emulsions with added MFP. The conformational changes were evidenced by the reduced ellipticity, the shift of the wavelength, and roughness of the CD curves (Figure 5b).

Intrinsic tryptophan fluorescence was used to assess oxidative changes in the tertiary structure of adsorbed and unadsorbed MFP, and the results are shown in panels c and d of Figure 5. Desorbed MFP from 2 h oxidized emulsion samples exhibited greater losses of fluorescence than continuous-phase MFP, confirming that interface-adsorbed proteins were more oxidizable than unadsorbed protein. This finding was in accordance with Rampon et al.[37] and Berton et al.,[38] who studied emulsions stabilized by BSA/β-lactoglobulin/β-casein and demonstrated that adsorbed proteins were more readily modified than unadsorbed proteins in the aqueous phase.

The remarkable oxidative protection by interfacial MFP can be attributed to multiple mechanisms. First, MFP surrounding the lipid droplets can prevent direct contact between radicals and the enclosed lipid, which has been demonstrated in other protein-stabilized O/W emulsions as well.[4,5] Besides radical protection, the idea of oxygen blockage by a protein interface was brought forth by Toikkanen et al.,[39] who showed that a well-formed protein viscoelastic layer was able to effectively reduce the oxygen permeability. Therefore, the inhibition of oxygen transport by the protein interface might be considered as another reason to prevent lipid from oxidation. Furthermore, induced cross-linking of the interfacial proteins from radical attack would impart a stronger coverage on lipid droplets, which, in turn, would reinforce the physical shielding effect. This premise was also discussed in caseinate-stabilized emulsion systems; the cross-linking of sodium caseinate at the emulsion interface improved the oxidative stability of emulsion.[40]

On the other hand, as a result of the adsorption to the oil droplets, MFP will unfold at the interface,[12] exposing the susceptible amino acid side-chain groups capable of scavenging radicals and donating electrons more readily than unsaturated fatty acids.[36] The reaction rate constant of many proteins, such as albumin and collagen, with a hydroxyl radical has been reported to be a magnitude higher than that of linoleic acid.[41] Therefore, protein modification occurred earlier than lipid oxidation during the oxidative chain reactions in the emulsions, in agreement with the literature report.[38]

The oxidative stability of emulsions depends upon the type of emulsifier. According to Berton et al.,[30] emulsions prepared with milk proteins (β-lactoglobulin, BSA, and β-casein) were less stable than emulsion prepared with Tween 20 or Tween 80. The authors attributed the difference to the heterogeneity and porosity of the protein membrane versus the polysorbate surfactants. While porosity, hence, oxygen diffusion, of a milk-

DOI: 10.1021/acs.jafc.5b03377
J. Agric. Food Chem. 2015, 63, 8896−8904

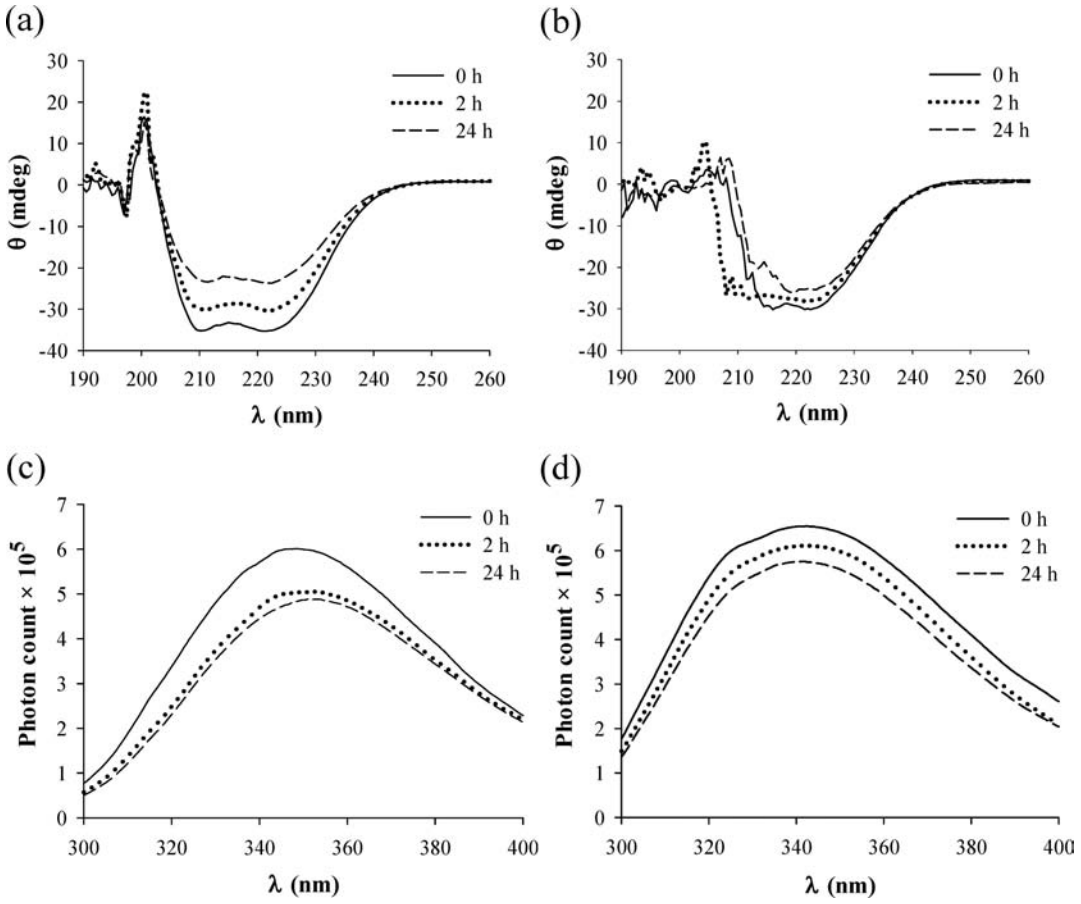

Figure 5. CD spectra of (a) adsorbed protein in MFP emulsion (1%) and (b) unadsorbed protein in Tween emulsion with added MFP (1%) during oxidation and fluorescence of (c) adsorbed protein in MFP emulsion (1%) and (d) unadsorbed protein in Tween emulsion with added MFP (1%) during oxidation.

protein-based interfacial membrane has also been reported by other researchers,[42,43] this did not seem to be applicable to MFP, which is enriched with myosin that is known for its strong surface activity and interface-stabilizing capacity in salt solutions.[44] In addition, the strong adsorption of MFP at the O/W interface (Figure 1B) would lead to a moderately thick interfacial layer when compared to Tween-only emulsions. Indeed, interfacial thickness has been shown to impact the antioxidant potential of a casein-based membrane.[45] The influence of the oil droplet size and interfacial area (larger for MFP emulsions than for Tween emulsions) on lipid oxidation would be negligible based on recent evidence.[46,47]

While interfacial proteins possess an antioxidative effect, the proteins present in the continuous phase exhibited a rather complex behavior. Comparison between Tween emulsions with and without 0.25% added MFP indicated considerable reductions of TBARS at 0 and 2 h when MFP was present in the aqueous phase (Figure 3b). This was probably due to the radical-stabilizing effect of free (unadsorbed) MFP, for example, myosin.[48] It has been reported that continuous-phase proteins, for example, whey protein isolate, soy protein isolate, and sodium caseinate, could inhibit lipid oxidation as a result of free radical scavenging and metal chelation.[49] Presumably, as a favorite target of the hydroxyl radical, MFP had a consequential "sparing" effect to protect lipids. This hypothesis is consistent with the extent of protein oxidation because, at the equal 10% oil, the net amount (μmol) of protein carbonyl derivatives produced increased ($p < 0.05$) with the concentration of MFP; i.e., the higher the MFP concentration, the more oxidation (carbonyl net amount) (Table 1), corresponding to a trend of reduction in lipid oxidation products (Figure 3). Similarly, Estévez et al.[29] reported an inverse relationship between the degree of muscle protein oxidative modification and the amount of conjugated dienes generated in an O/W emulsion incubated at 37 °C. Interestingly, the accumulation of protein oxidation products during oxidation (notably within the initial 2 h), which was moderately significant for Tween emulsion samples with 0.25% added MFP and strongly significant in samples with higher levels of MFP addition (Table 1), appeared to stimulate lipid oxidation subsequently (TBARS formation).

In conclusion, MFP present either at the interface or in the continuous aqueous solution, notably myosin, proves to be a kinetically preferred target of free radicals when compared to lipids in O/W emulsions. This is due to the high reactivity of protein thiol groups. The physical location of the proteins within the complex emulsion systems dictates their antioxidative efficacy; interfacial MFP compared to continuous-phase MFP imparts strong protection, giving rise to a remarkable oxidative stability of emulsified lipids. Hence, capable of building a cohesive interfacial membrane, MFP can be used to prepare oil-based pre-emulsions suitable for functional sausage products. Because the system complexity of meat emulsions and the diverse behaviors of emulsifiers (e.g., surface activity and partitioning efficiency) often lead to contradictory results,[50] further research is needed to explore other kinds of

DOI: 10.1021/acs.jafc.5b03377
J. Agric. Food Chem. 2015, 63, 8896−8904

protein sources for the construction of antioxidative membranes in formulated meat emulsions or batter products.

AUTHOR INFORMATION

Corresponding Author

*Telephone: 859-257-3822. Fax: 859-257-5318. E-mail: ylxiong@uky.edu.

Funding

This is publication number 15-07-050 of the Kentucky Agricultural Experiment Station and is published with the approval of the Director. This work is supported by the National Institute of Food and Agriculture, U.S. Department of Agriculture, Hatch Project 1005724, and the China Scholarship Council through an Overseas Study Fellowship (to Jiayi Yang).

Notes

The authors declare no competing financial interest.

REFERENCES

(1) Walstra, P.; van Vliet, T. Dispersed systems: Basic considerations. In *Fennema's Food Chemistry*, 4th ed.; Srinivasa, D., Parkin, K. L., Fennema, O. R., Eds.; CRC Press (Taylor & Francis Group): Boca Raton, FL, 2008; pp 784−843.

(2) Eskandani, M.; Hamishehkar, H.; Ezzati Nazhad Dolatabadi, J. Cyto/genotoxicity study of polyoxyethylene (20) sorbitan monolaurate (Tween 20). *DNA Cell Biol.* **2013**, *32*, 498−503.

(3) Calicioglu, M.; Kaspar, C. W.; Buege, D. R.; Luchansky, J. B. Effectiveness of spraying with Tween 20 and lactic acid in decontaminating inoculated *Escherichia coli* O157:H7 and indigenous *Escherichia coli* biotype I on beef. *J. Food Prot.* **2002**, *65*, 26−32.

(4) Hu, M.; McClements, D. J.; Decker, E. A. Lipid oxidation in corn oil-in-water emulsions stabilized by casein, whey protein isolate, and soy protein isolate. *J. Agric. Food Chem.* **2003**, *51*, 1696−1700.

(5) Jiang, J.; Zhu, B.; Liu, Y.; Xiong, Y. L. Interfacial structural role of pH-shifting processed pea protein in the oxidative stability of oil/water emulsions. *J. Agric. Food Chem.* **2014**, *62*, 1683−1691.

(6) Díaz, M.; Decker, E. A. Antioxidant mechanisms of casein-ophosphopeptides and casein hydrolysates and their application in ground beef. *J. Agric. Food Chem.* **2004**, *52*, 8208−8213.

(7) Kaul, S.; Sharma, S. S.; Mehta, I. K. Free radical scavenging potential of L-proline: evidence from in vitro assays. *Amino Acids* **2008**, *34*, 315−320.

(8) Dickinson, E. Structure and composition of adsorbed protein layers and the relationship to emulsion stability. *J. Chem. Soc., Faraday Trans.* **1992**, *88*, 2973−2983.

(9) Evers, C. H. J.; Andersson, T.; Lund, M.; Skepö, M. Adsorption of unstructured protein β-casein to hydrophobic and charged surfaces. *Langmuir* **2012**, *28*, 11843−11849.

(10) Galluzzo, S. J.; Regenstein, J. M. Role of chicken breast muscle proteins in meat emulsion formation: myosin, actin and synthetic actomyosin. *J. Food Sci.* **1978**, *43*, 1761−1765.

(11) Zhai, J.; Wooster, T. J.; Hoffmann, S. V.; Lee, T. H.; Augustin, M. A.; Aguilar, M. I. Structural rearrangement of β-lactoglobulin at different oil−water interfaces and its effect on emulsion stability. *Langmuir* **2011**, *27*, 9227−9236.

(12) Damodaran, S. Protein stabilization of emulsions and foams. *J. Food Sci.* **2005**, *70*, R54−R66.

(13) Gordon, A.; Barbut, S.; Schmidt, G. Mechanisms of meat batter stabilization: a review. *Crit. Rev. Food Sci. Nutr.* **1992**, *32*, 299−332.

(14) Asuming-Bediako, N.; Jaspal, M. H.; Hallett, K.; Bayntun, J.; Baker, A.; Sheard, P. R. Effects of replacing pork backfat with emulsified vegetable oil on fatty acid composition and quality of UK-style sausages. *Meat Sci.* **2014**, *96*, 187−194.

(15) Brewer, M. S. Reducing the fat content in ground beef without sacrificing quality: A review. *Meat Sci.* **2012**, *91*, 385−395.

(16) Wu, M.; Xiong, Y. L.; Chen, J. Role of disulphide linkages between protein-coated lipid droplets and the protein matrix in the rheological properties of porcine myofibrillar protein−peanut oil emulsion composite gels. *Meat Sci.* **2011**, *88*, 384−390.

(17) Jiménez-Colmenero, F.; Triki, M.; Herrero, A. M.; Rodríguez-Salas, L.; Ruiz-Capillas, C. Healthy oil combination stabilized in a konjac matrix as pork fat replacement in low-fat, PUFA-enriched, dry fermented sausages. *LWT-Food Sci. Technol.* **2013**, *51*, 158−163.

(18) Park, D.; Xiong, Y. L.; Alderton, A. L. Concentration effects of hydroxyl radical oxidizing systems on biochemical properties of porcine muscle myofibrillar protein. *Food Chem.* **2007**, *101*, 1239−1246.

(19) Carpenter, A. P. Determination of tocopherols in vegetable oils. *J. Am. Oil Chem. Soc.* **1979**, *56*, 668−671.

(20) Lee, S. H.; Lefèvre, T.; Subirade, M.; Paquin, P. Effects of ultra-high pressure homogenization on the properties and structure of interfacial protein layer in whey protein-stabilized emulsion. *Food Chem.* **2009**, *113*, 191−195.

(21) Bradford, M. M. A rapid and sensitive method for the quantitation of microgram quantities of protein utilizing the principle of protein-dye binding. *Anal. Biochem.* **1976**, *72*, 248−254.

(22) Srinivasan, S.; Xiong, Y. L.; Decker, E. A. Inhibition of protein and lipid oxidation in beef heart surimi-like material by antioxidants and combinations of pH, NaCl, and buffer type in the washing media. *J. Agric. Food Chem.* **1996**, *44*, 119−125.

(23) Sinnhuber, R. O.; Yu, T. C. The 2-thiobarbituric acid reaction, an objective measure of the oxidative deterioration occurring in fats and oils. *J. Jpn. Oil Chem. Soc.* **1977**, *26*, 259−267.

(24) O'Brien, P. J. Intracellular mechanisms for the decomposition of a lipid peroxide. I. Decomposition of a lipid peroxide by metal ions, heme compounds, and nucleophiles. *Can. J. Biochem.* **1969**, *47*, 485−492.

(25) Witte, V. C.; Krause, G. F.; Bailey, M. E. A new extraction method for determining 2-thiobarbituric acid values of pork and beef during storage. *J. Food Sci.* **1970**, *35*, 582−585.

(26) Levine, R. L.; Garland, D.; Oliver, C. N.; Amici, A.; Climent, I.; Lenz, A. G.; Ahn, B. W.; Shaltiel, S.; Stadtman, E. R. Determination of carbonyl content in oxidatively modified proteins. *Methods Enzymol.* **1990**, *186*, 464−478.

(27) Beveridge, T.; Toma, S. J.; Nakai, S. Determination of SH- and SS- groups in some food proteins using Ellman's reagent. *J. Food Sci.* **1974**, *39*, 49−51.

(28) Greenfield, N. J. Using circular dichroism spectra to estimate protein secondary structure. *Nat. Protoc.* **2007**, *1*, 2876−2890.

(29) Estévez, M.; Kylli, P.; Puolanne, E.; Kivikari, R.; Heinonen, M. Fluorescence spectroscopy as a novel approach for the assessment of myofibrillar protein oxidation in oil-in-water emulsions. *Meat Sci.* **2008**, *80*, 1290−1296.

(30) Berton, C.; Ropers, M. H.; Viau, M.; Genot, C. Contribution of the interfacial layer to the protection of emulsified lipids against oxidation. *J. Agric. Food Chem.* **2011**, *59*, 5052−5061.

(31) Xiong, Y. L.; Aguilera, J. M.; Kinsella, J. E. Emulsified milkfat effects on rheology of acid-induced milk gels. *J. Food Sci.* **1991**, *56*, 920−925.

(32) Dimitrova, T. D.; Leal-Calderon, F. Forces between emulsion droplets stabilized with Tween 20 and proteins. *Langmuir* **1999**, *15*, 8813−8821.

(33) Frankel, E. N. *Lipid Oxidation*, 2nd ed.; PJ Barnes & Associates: Bridgewater, U.K., 2005.

(34) Kiokias, S.; Dimakou, C.; Tsaprouni, I.; Oreopoulou, V. Effect of compositional factors against the thermal oxidative deterioration of novel food emulsions. *Food Biophys.* **2006**, *1*, 115−123.

(35) Li, C.; Xiong, Y. L.; Chen, J. Oxidation-induced unfolding facilitates myosin cross-linking in myofibrillar protein by microbial transglutaminase. *J. Agric. Food Chem.* **2012**, *60*, 8020−8027.

(36) Stadtman, E. R. Protein oxidation in aging and age-related diseases. *Ann. N. Y. Acad. Sci.* **2001**, *928*, 22−38.

(37) Rampon, V.; Lethuaut, L.; Mouhous-Riou, N.; Genot, C. Interface characterization and aging of bovine serum albumin stabilized oil-in-water emulsions as revealed by front-surface fluorescence. *J. Agric. Food Chem.* **2001**, *49*, 4046−4051.

DOI: 10.1021/acs.jafc.5b03377
J. Agric. Food Chem. 2015, 63, 8896−8904

(38) Berton, C.; Ropers, M. H.; Guibert, D.; Solé, V.; Genot, C. Modifications of interfacial proteins in oil-in-water emulsions prior to and during lipid oxidation. *J. Agric. Food Chem.* **2012**, *60*, 8659−8671.
(39) Toikkanen, O.; Lähteenmäki, M.; Moisio, T.; Forssell, P.; Partanen, R.; Murtomäki, L. Study of oxygen transfer across milk proteins at an air−water interface with scanning electrochemical microscopy. *J. Agric. Food Chem.* **2014**, *62*, 2284−2288.
(40) Ma, H.; Forssell, P.; Kylli, P.; Lampi, A. M.; Buchert, J.; Boer, H.; Partanen, R. Transglutaminase catalyzed cross-linking of sodium caseinate improves oxidative stability of flaxseed oil emulsion. *J. Agric. Food Chem.* **2012**, *60*, 6223−6229.
(41) Buxton, G. V.; Greenstock, C. L.; Helman, W. P.; Ross, A. B.; Tsang, W. Critical review of rate constants for reactions of hydrated electrons, hydrogen atoms and hydroxyl radicals ($\cdot OH/\cdot O^-$) in aqueous solution. *J. Phys. Chem. Ref. Data* **1988**, *17*, 513−886.
(42) Wilde, P.; Mackie, A.; Husband, F.; Gunning, P.; Morris, V. Proteins and emulsifiers at liquid interfaces. *Adv. Colloid Interface Sci.* **2004**, *108*−*109*, 63−71.
(43) Tikekar, R. V.; Johnson, A.; Nitin, N. Real-time measurement of oxygen transport across an oil−water emulsion interface. *J. Food Eng.* **2011**, *103*, 14−20.
(44) Xiong, Y. L. Structure−functionality relationships of muscle proteins. In *Food Proteins and Their Applications*; Damodaran, S., Paraf, A., Eds.; Marcel Dekker, Inc.: New York, 1997; pp 341−392.
(45) García-Moreno, P. J.; Horn, A. F.; Jacobsen, C. Influence of casein−phospholipid combinations as emulsifier on the physical and oxidative stability of fish oil-in-water emulsions. *J. Agric. Food Chem.* **2014**, *62*, 1142−1152.
(46) Dimakou, C.; Kiokias, S.; Tsaprouni, I.; Oreopoulou, V. Effect of processing and storage parameters on the oxidative deterioration of oil-in-water emulsions. *Food Biophys.* **2007**, *2*, 38−45.
(47) Osborn, H. T.; Akoh, C. C. Effect of emulsifier type, droplet size, and oil concentration on lipid oxidation in structured lipid-based oil-in-water emulsions. *Food Chem.* **2004**, *84*, 451−456.
(48) Lund, M. N.; Luxford, C.; Skibsted, L. H.; Davies, M. J. Oxidation of myosin by haem proteins generates myosin radicals and protein cross-links. *Biochem. J.* **2008**, *410*, 565−574.
(49) Faraji, H.; McClements, D. J.; Decker, E. A. Role of continuous phase protein on the oxidative stability of fish oil-in-water emulsions. *J. Agric. Food Chem.* **2004**, *52*, 4558−4564.
(50) Berton-Carabin, C. C.; Ropers, M. H.; Genot, C. Lipid oxidation in oil-in-water emulsions: involvement of the interfacial layer. *Compr. Rev. Food Sci. Food Saf.* **2014**, *13*, 945−977.

DOI: 10.1021/acs.jafc.5b03377
J. Agric. Food Chem. 2015, 63, 8896−8904

and Analysis of the University of Hohenheim. Ultrapure water was used throughout the study (Milli-Q system, Millipore, France).

HPLC-PDA-ESI/MS^n Analyses. The inner bark of *Q. saponaria* Molina was crushed with a food processor until a fine powder was obtained. An aliquot of 3.8 g of the sample powder was combined with 20 mL of water, the pH was adjusted to pH 2 with diluted formic acid, and the mixture was stirred at room temperature for 12 h in the dark under nitrogen atmosphere. Samples were consecutively filtered through a folded filter (5−8 μm, cellulose) and a membrane filter (0.45 μm, regenerated cellulose) to obtain the crude bark extract. In contrast to the crude bark extract, the commercial *Quillaja* extract was dissolved in 1% (v/v) aqueous formic acid and membrane filtered (0.45 μm, regenerated cellulose). Subsequent HPLC-PDA-ESI/MS^n analyses were performed as previously described by Maier et al.[5]

Preparative Isolation of *p*-Coumaroyl Sucrose Esters. Due to the availability of larger quantities, the compounds of interest were only isolated from commercial *Quillaja* extracts. The similarity of the isolated compounds to those found in the natural bark was verified by HPLC-PDA-MS^n. Preparative isolation of phenolic constituents from *Quillaja* extracts was conducted as previously described by Maier et al.[5] Briefly, the targeted phenolic compounds present in the above-described extracts were separated with an Ultimate 3000 preparative HPLC system equipped with two solvent delivery modules, a diode array detector (DAD-3000), and an automatic fraction collector (AFC-3000). The separation column was a preparative 250 × 21.1 mm i.d., 5 μm particle size, 125 Å pore size, Phenomenex Aqua C18 reversed-phase column. The used eluents were water (eluent A) and methanol (eluent B), both being acidified to pH 2 with formic acid. Separation was started by isocratic elution at 20% B for 10 min, followed by a linear gradient from 20 to 40% B over 18 min. After isocratic elution at 40% B for 20 min, a linear gradient from 40 to 100% B within 2 min was applied. After 8 min of isocratic elution at 100% B, a linear gradient to 20% B was applied within 2 min, and the system was equilibrated at 20% B for 10 min. Total run time was 70 min at a constant flow rate of 8 mL/min. The injection volume was 1000 μL. The retention times of the compounds to be isolated, **14** and **15** (Table 1), were 40.2 and 41.0 min, respectively. Compounds were monitored at 280 and 310 nm. After solvent evaporation under reduced pressure (T_{max} = 40 °C), the collected fractions were freeze-dried and stored at −20 °C until further use. Aliquots of the isolated compounds were dissolved in aqueous 4 N HCl and heated to ∼85 °C for 120 min. After subsequent neutralization with aqueous NaOH, the hydrolysate was membrane filtered (0.45 μm) and analyzed by HPLC-PDA-MS^n as described above.

High-Resolution ESI-MS Analyses. High-resolution ESI-MS analyses of the isolated compounds **14** and **15** were performed using a Q-Exactive Plus mass spectrometer (Thermo Fisher Scientific, Bremen, Germany) equipped with an API ion source and a HESI-II probe. The instrument was operated in negative ionization mode and was externally calibrated according to the manufacturer's guidelines. Compounds isolated by preparative HPLC were redissolved in 100 μL of aqueous methanol (50%, v/v) and were analyzed by direct infusion at a flow rate of 5 μL/min. The MS conditions were as follows: capillary temperature, 250 °C; spray voltage, −3200 V; sheath gas and auxiliary gas were not applied. Mass spectra were acquired in the range of *m/z* 150−2000 at resolution of 70000 (at *m/z* 200). Mass spectrometric data were analyzed using Xcalibur 3.0.63 software (Thermo Fisher Scientific).

High-resolution mass data for minor compounds **5**, **6**, **9**, **11**−**13**, and **16**−**29** were determined by HPLC-ESI-HR-MS. An Agilent 1200 series, set up according to the above-mentioned HPLC method,[5] was coupled online to a micrOTOF-Q mass spectrometer (Bruker Daltonics, Bremen, Germany) operated in negative electrospray ionization mode. Capillary voltage was set at +4.5 kV. Nebulizing and drying gas was both nitrogen applied at 3.0 bar and 8.8 L/min. Drying gas was heated to 250 °C. Mass spectra were recorded at 20 Hz (2 GHz sampling rate) in the range of *m/z* 250−2500 at a resolution of 12900 (at *m/z* 996.8). The instrument was calibrated with sodium formate according to the manufacturer's instructions. Chemical formulas were generated by accurate mass measurements and DataAnalysis 3.4 software.

Determination of the Absolute Configuration of the Sugar Moieties. Isolated compounds (ca. 1 mg) were heated with aqueous TFA (2 M) at 85 °C for 2 h, subsequently evaporated in vacuo to 0.2 mL (45 °C). Toluene and pyridine (both 4 × 3.0 mL) were used consecutively to remove TFA and water without evaporating to dryness to avoid the degradation of apiose. Subsequently, the sample was combined with 0.1 mL of L-cysteine methyl ester hydrochloride in pyridine (120 mg/mL) and heated at 65 °C for 1 h. After the addition of 0.2 mL of the silylation reagent, heating was continued for a further 0.5 h. Analytes were partitioned between hexane and H_2O (0.3 mL each), and the hexane layer was analyzed by GC-MS equipped with a 30 m × 0.25 mm, d_f = 0.25 μm, HP-5ms column (temperature program: 100 °C for 1 min, raised at 15 °C/min to 200 °C, raised at 3 °C/min to 240 °C, raised at 15 °C/min to 300 °C, and held for 5 min; carrier gas, helium at 1.2 mL/min). Reference standards were subjected directly to the derivatization reaction (0.2 mL, 0.1 g/L in pyridine). In contrast, 10 μL of aqueous L-apiose was derivatized according to the protocol given above without TFA hydrolysis.

Retention times (retention indices relative to *n*-alkanes) of the derivatives obtained were as follows: D-apiose, 14.0 min (2240); L-rhamnose, 15.7 min (2336); D-fructose, 17.3 min (2426); and D-glucose, 18.5 min (2483). The D-rhamnose, L-fructose, and L-glucose derivatives revealed retention times (indices) of 15.9 min (2347), 17.1 min (2412), and 18.8 min (2502). An authentic standard of L-apiose was unavailable. EI-MS (70 eV) base peak fragment ions were *m/z* 217 (apiose, rhamnose, glucose) and *m/z* 248 (fructose).

NMR Spectroscopy. ^{1}H and ^{13}C NMR spectra of isolated compounds were recorded on a Varian Unity Inova 500 MHz spectrometer (Darmstadt, Germany). Compounds **14** and **15** (Figure 1) were dissolved in DMSO-d_6 (plus a drop of D_2O) and pyridine-d_5, respectively. The ^{1}H and ^{13}C chemical shifts were referenced to residual solvent signals at $\delta_{H/C}$ 2.49/39.5 (DMSO-d_6) and 8.71/149.8 (pyridine-d_5) relative to TMS. Adiabatic 2D broadband and band-selective gHSQC and gHMBC, gDQFCOSY, ROESY, and TOCSY as well as selective 1D TOCSY spectra were recorded using CHEMPACK 4.0 pulse sequences (implemented in Varian VnmrJ 2.1B software). Coupling constants *J* (in hertz) were directly taken from the spectra and are not averaged.

RESULTS AND DISCUSSION

Comparison of Freshly Prepared Bark Extracts and Commercially Available Wood Extracts of *Q. saponaria* Molina. A total of 31 phenolic compounds were previously described to be present in commercially available *Quillaja* wood extracts,[5] which are widely used as emulsifiers in foods (e.g., as E999 in the EU) and cosmetics. In the present study, we compared the composition of such commercial extracts to that of a freshly prepared aqueous extract of the inner bark. The HPLC-PDA-MS^n-based comparison revealed a highly similar phenolic pattern (Figure 2; Table 1). In agreement with our previous work,[5] (+)-piscidic acid, **1**, was found to be the major phenolic, whereas several vanillic acid derivatives (**2**, **3**), syringic acid derivatives (**4**, **8**), and catechin derivatives (**7**, **10**) were found at minor signal intensities. However, we previously described several unknown *p*-coumaric acid derivatives (**5**, **6**, **9**, **11**−**29**), two of them (**14**, **15**) at very high signal intensities. Notably, we were unable to identify some trace compounds in the inner bark extracts, which were previously detected in commercial extracts.[5] The latter compounds were mostly free phenolic acids, such as vanillic, syringic, *p*-coumaric, and ferulic acid, possibly representing artifacts generated during the manufacture of the commercial extracts.

Characterization of New *p*-Coumaroyl Sucrose Esters. After preparative isolation, compound **14** was obtained as a

DOI: 10.1021/acs.jafc.5b03532
J. Agric. Food Chem. 2015, 63, 8905−8911

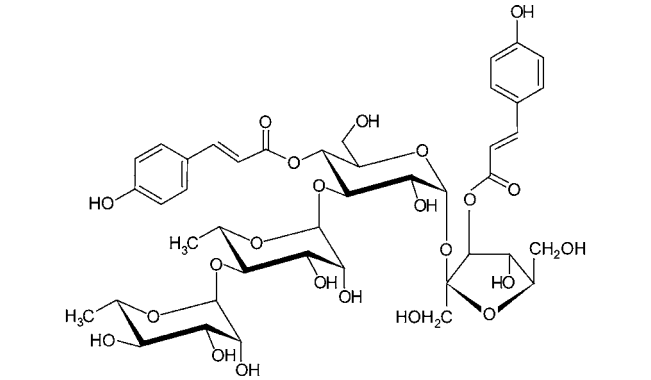

Quillajaside A (**15**)

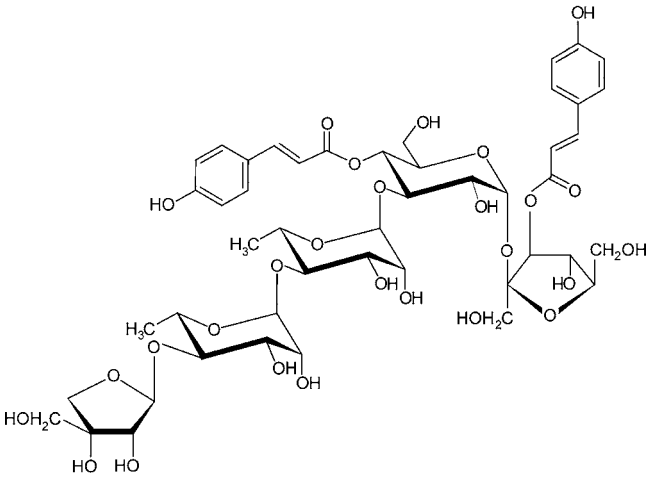

Quillajaside B (**14**)

Figure 1. Chemical structures of the new compounds quillajaside A and quillajaside B extracted from the inner bark of *Q. saponaria* Molina.

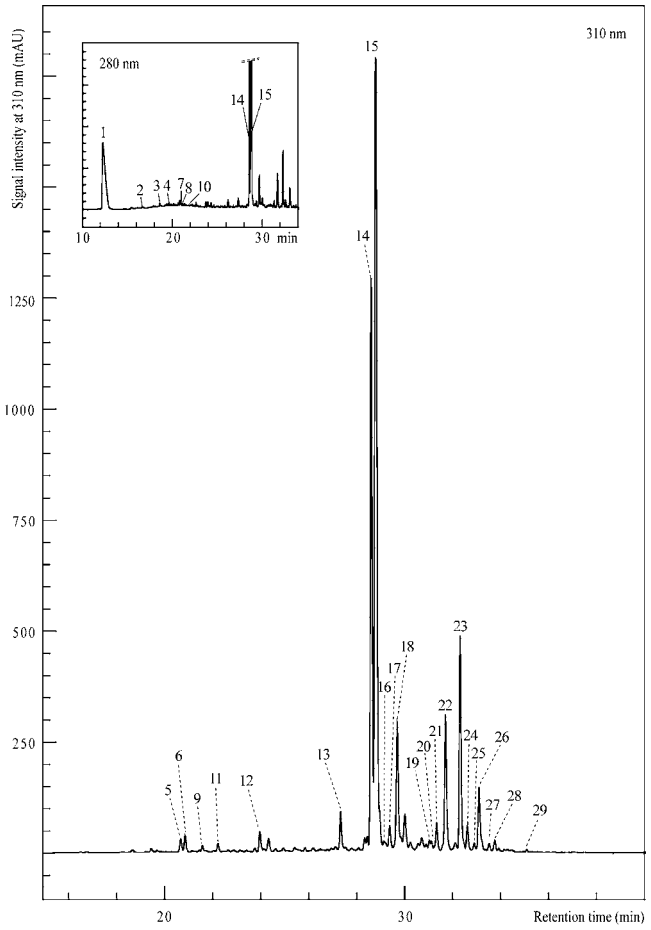

Figure 2. HPLC separation of phenolic compounds from an aqueous extract of the inner bark of *Q. saponaria* Molina at 280 and 310 nm.

white amorphous powder. HR-FT-ESI-MS measurements indicated a molecular formula of $C_{47}H_{62}O_{27}$ (see Table 1). The acidic hydrolysis yielded free *p*-coumaric acid as its only phenolic constituent as shown by HPLC-PDA-MS^n data of an authentic standard. In HPLC-ESI(−)-MS experiments, the nonhydrolyzed compound yielded a pseudomolecular ion $[M - H]^-$ at *m/z* 1057. Collision-induced dissociation (CID) experiments yielded a predominant fragment at $[M - H - 146]^-$ at *m/z* 911 (Table 1), indicating the presence of a deoxy-hexose moiety. The second most abundant, nonisotopic fragment ion $[M - H - 132]^-$ at *m/z* 925 was possibly produced after the potential loss of the pentose moiety. The fragment ion at *m/z* 779 may have resulted from the consecutive loss of the above-mentioned deoxy-hexose (146 Da) and pentose (132 Da) moieties. The fragment ion at *m/z* 633 may represent the additional loss of a deoxy-hexose moiety (146 Da loss), that is, being a fragment species $[M - H - 146 - 146 - 132]^-$ produced by the loss of two deoxy-hexose (146 Da) and one pentose moiety (132 Da). In agreement, a fragment ion $[M - H - 146 - 146]^-$ at *m/z* 765 generated by the loss of two deoxy-hexose (146 Da) units was also observed (Table 1). Further fragments at lower *m/z* values were unavailable due to insufficient signal intensity.

In agreement with the MS/MS-based proposition of one pentose and two deoxy-hexose moieties, analyses of the ^{13}C NMR spectrum showed a total of 17 characteristic signals of one apiosyl and two rhamnosyl moieties (Table 2; Figure 3). Each of the sugar moieties was assigned by evaluation of the gDQFCOSY, TOCSY, selective 1D TOCSY, and gHSQC spectra. Moreover, ROESY correlations (Figure 3A) and HMBC correlations of the H-4‴″ with C-1‴″, C-2‴″, and C-3‴″ as well as correlations of H-5‴″a/b with C-2‴″ and C-3‴″ unambiguously established apiose as one sugar moiety in **14** (Figure 3B). The downfield-shifted rhamnosyl C-4‴′ (δ 77.81) as well as long-range HMBC and ROESY correlations between the rhamnosyl H-4‴′ and the apiosyl C-1‴″ revealed a 1,4 linkage between both sugar moieties. The observation of a doublet at δ 5.17 with a coupling constant of *J* 2.5 Hz of H-1‴″, established the β-configuration of the apiose according to previous papers.[6−10] The absence of downfield-shifted C atoms other than the anomeric C-1‴″ indicated the terminal localization of the apiosyl moiety (Figure 3). The downfield-shifted C-4‴″ (δ 80.02) of the second rhamnose along with long-range HMBC interactions of H-4‴ with C-1‴′ and H-1‴′ with C4‴ as well as an ^1H NMR signal of H-1‴′ at δ 4.82 (bs) suggested the α-1,4 linkage of the two rhamnosyl moieties (Figure 3).

Besides rhamnose and apiose, the ^{13}C NMR spectrum displayed 12 carbon signals of a glucose- and fructose-based disaccharide. Analysis of the homo- and heteronuclear 1D and 2D NMR spectra ascertained the disaccharide to be a trisubstituted sucrose (Figure 3B). The glucosyl C-3″ revealed a characteristic downfield shift at δ 78.49 and displayed a long-

DOI: 10.1021/acs.jafc.5b03532
J. Agric. Food Chem. 2015, 63, 8905−8911

Table 1. Identification of Phenolic Compounds in Crude Aqueous Extracts from the Inner Bark of *Quillaja saponaria* Molina by HPLC-PDA-MS^n

no.	compd identity	ret time (min)	HPLC-PDA abs max (nm)	HPLC-ESI-(−)-HR-MS meas m/z (calcd m/z) $[M - H]^-$[a]	HPLC-ESI-MS^n expt (m/z)[b]
1	(+)-piscidic acid	12.3	275	na[c]	[255]: 209(5), 193(21), 179(5), 166(10), 165(100), 149(5)
2	vanillic acid 4-hexoside	16.7	254/293	na	na
3	vanillic acid 4-hexosyl-pentoside	18.4	254/292	na	[461]: 329(4). 192(4), 178(4), 168(9), 167(100), 161(8), 152(11), 143(5)
4	glucosyringic acid	19.6	262/292sh	na	[359]: 197(100), 182(12), 123(3)
5	*p*-coumaroyl sucrose	20.7	313	487.1417 (487.1457)	[487]: 341(9), 323(3), 307(53), 217(2), 179(1), 163(34), 145(100)
6	*p*-coumaroyl dirhamnosyl sucrose	20.9	313	779.2581 (779.2615)	[779]: 635(3), 634(36), 633(100), 616(5), 615(11), 599(3), 487(2), 453(2), 433(2), 341(2), 307(2)
7	catechin hexoside	21.0	280	na	[451]: 289(100), 245(7),, 161(4)
8	syringic acid hexosyl-pentoside	21.2	262/293sh	na	[491]: 455(6), 359(3), 197(100), 182(28), 167(5), 153(4)
9	*p*-coumaroyl dirhamnosyl monoapiosyl sucrose	21.6	315	911.3010 (911.3038)	[911]: 779(4), 766(19), 765(100), 749(12), 747(17), 732(4), 731(27), 633(3), 585(11), 509(4)
10	catechin hexosyl der[d]	21.6	280	na	na
11	*p*-coumaroyl rhamnosyl sucrose	22.2	313	633.2022 (633.2036)	[633]: 615(1), 597(1), 488(19), 487(100), 469(9), 341(2), 307(5), 217(1), 179(1)
12	*p*-coumaroyl dirhamnosyl sucrose	24.0	313	779.2564 (779.2615)	[779]: 635(3), 634(34), 633(100), 616(3), 615(8), 487(2), 453(1), 433(1), 341(2), 307(1)
13	di-*p*-coumaroyl trirhamnosyl monoapiosyl sucrose	27.3	313	1203.3957 (1203.3985)	[1203]: 1204(5), 1203(9), 1072(5), 1071(10), 1058(40), 1057(100), 925(4), 912(6), 911(17), 893(8), 779(3), 633(1)
14	quillajaside B	28.6	314	1057.3346 // 1057.34131 (1057.3406)[a]	[1057]: 1057(18), 926(7), 925(18), 912(39), 911(100), 893(3), 779(9), 765(6), 745(3), 731(3), 633(1) [1057 → 633]: 487(72), 341(100),
15	quillajaside A	28.8	314	925.2980 // 925.29932 (925.2983)[a]	[925]: 780(28), 779(100), 761(5), 634(2), 633(17), 615(3) [925 → 633]: 487(63), 471(61), 341(100), 231(19)
16	quillajaside B isomer	29.0	312	1057.3341 (1057.3406)	[1057]: 1058(7), 1057(17), 937(2), 926(4), 925(20), 912(37), 911(100), 893(4), 779(8), 765(8), 747(3), 731(3), 633(1)
17	quillajaside B isomer	29.4	314	1057.3354 (1057.3406)	[1057]: 1057(18), 926(7), 925(22), 912(37), 911(100), 893(4), 779(7), 765(5), 747(3), 731(3), 633(1)
18	quillajaside A isomer	29.7	314	925.2964 (925.2983)	[925]: 780(31), 779(100), 761(4), 634(2), 633(21), 615(5)
19	*p*-coumaroyl sucrose der	31.0	314	na (low signal)	[1057]: 1058(5), 1057(14),, 925(5), 912(38), 911(100), 893(6), 779(4), 765(7), 633(1)
20	*p*-coumaroyl sucrose der	31.1	314	na (low signal)	[1057]: 1057(14), 926(5), 925(16), 912(34), 911(100), 893(4), 779(6), 765(5), 731(3), 633(1)
21	quillajaside A isomer	31.3	314	925.2979 (925.2983)	[925]: 780(31), 779(100), 762(2), 761(7), 634(2), 633(13), 615(3)
22	tri-*p*-coumaroyl trirhamnosyl monoapiosyl sucrose	31.7	312	1349.4365 (1349.4353)	[1349]: 1350(30), 1349(80), 1218(18), 1217(41), 1071(17), 1058(19), 1057(40), 1204(45), 1203(100), 925(6), 911(5), 895(5), 779(2), 731(1), 633(1)
23	tri-*p*-coumaroyl trirhamnosyl sucrose	32.3	311	1217.3897 (1217.3930)	[1217]: 1072(41), 1071(100), 926(14), 925(50), 907(7), 779(7), 633(2)
24	tri-*p*-coumaroyl trirhamnosyl monoapiosyl sucrose	32.6	304	1349.4390 (1349.4353)	[1349]: 1350(7), 1349(16), 1217(2), 1204(51), 1203(100), 1072(7), 1071(15), 1058(7), 1057(20), 926(2), 925(5), 911(7), 799(1), 731(1), 633(1)
25	tri-*p*-coumaroyl trirhamnosyl sucrose	32.9	313	1217.3859 (1217.3930)	[1217]: 1072(46), 1071(100), 1053(4), 926(12), 925(53), 907(7), 779(6), 761(2), 633(2)
26	tri-*p*-coumaroyl trirhamnosyl sucrose	33.1	304	1217.3917 (1217.3930)	[1217]: 1072(41), 1071(100), 926(5), 925(26), 779(6), 633(1)
27	tri-*p*-coumaroyl dirhamnosyl sucrose	33.5	304	1071.3344 (1071.3351)	[1071]: 926(22), 925(100), 780(4), 779(20), 633(2), 487(0.3)
28	tri-*p*-coumaroyl dirhamnosyl sucrose	33.7	312	1071.3311 (1071.3351)	[1071]: 926(40), 925(100), 780(12), 779(47), 761(5), 633(2)
29	tri-*p*-coumaroyl trirhamnosyl sucrose	35.1	314	1217.3864 (1217.3930)	[1217]: 1072(43), 1071(100), 926(13), 925(44), 907(7), 779(7), 633(1)

[a]First displayed m/z was measured by HPLC-HR-MS; second displayed m/z was measured by direct HR-MS of the isolated compound. [b]Most reported signals of pseudomolecular ions $[M - H]^-$ also occurred as chloride adducts $[M + 35]^-$. [c]na, not available. [d]der, derivative.

J. Agric. Food Chem. 2015, 63, 8905−8911 DOI: 10.1021/acs.jafc.5b03532

Table 2. ^{1}H (500 MHz) and ^{13}C (125 MHz) NMR Data of Quillajaside B, 14 (*β*-D-api*f*-(1→4)-*α*-L-rha*p*-(1→4)-*α*-L-rha*p*-(1→3)-(4-*O*-*p*-coumaroyl)-*α*-D-glu*p*-(1→2)-(3-*O*-*p*-coumaroyl)-*β*-D-fru*f*)

carbon[a]	$\delta_{C\ (DMSO)}$[b]	proton[a]	δ_H (*J* in Hz)
p-coumaroyl moiety at *α*-D-glu*p*		*p*-coumaroyl moiety at *α*-D-glu*p*	
1	125.25		
2	130.50	2	7.26 d-like (7.8)
3	116.34	3	6.76 d-like (8.3)
4	160.00		
5	116.34	5	6.76 d-like (8.3)
6	130.50	6	7.26 d-like (7.8)
7	145.70	7	7.40 d (16.1)
8	114.06	8	6.03 d (16.0)
9	166.09		
p-coumaroyl moiety at *β*-D-fru*f*		*p*-coumaroyl moiety at *β*-D-fru*f*	
1′	125.48		
2′	130.73	2′	7.54 d-like (8.1)
3′	116.24	3′	6.73 d-like (8.5)
4′	160.18		
5′	116.24	5′	6.73 d-like (8.5)
6′	130.73	6′	7.54 d-like (8.1)
7′	145.73	7′	7.61 d (15.9)
8′	114.37	8′	6.38 d (16.0)
9′	166.02		
α-D-glu*p*		*α*-D-glu*p*	
1″	91.57	1″	5.26 d (3.3)
2″	72.33	2″	3.43 bd (10.5)
3″	78.49	3″	3.74 ov
4″	69.10	4″	4.82 bdd (9.6, 9.6)
5″	71.07	5″	4.00−3.94 m
6″	60.55	6″a	3.34 ov
		6″b	3.44 ov
β-D-fru*f*		*β*-D-fru*f*	
1‴	63.5	1‴a	3.40 ov
		1‴b	
2‴	103.9	2‴	
3‴	77.81	3‴	5.34 d (7.5)
4‴	72.83	4‴	4.12 dd (7.4)
5‴	83.50	5‴	3.78 ov, m
6‴	62.02	6‴a	3.63 dd (6.5, 11.6)
		6‴b	3.59 dd (2.6, 11.3)
α-L-rha*p* (1→3)		*α*-L-rha*p* (1→3)	
1⁗	101.71	1⁗	4.81 bs
2⁗	71.08	2⁗	3.65 bs
3⁗	71.15	3⁗	3.43−3.37 m
4⁗	80.02	4⁗	3.18 t-like (9.2)
5⁗	67.45	5⁗	3.32 m
6⁗	18.75	6⁗	0.79 d (6.0)
α-L-rha*p* (1→4)		*α*-L-rha*p* (1→4)	
1⁗′	101.87	1⁗′	4.82 bs
2⁗′	70.99	2⁗′	3.63−3.64 bs
3⁗′	71.148	3⁗′	3.4 ov
4⁗′	77.81	4⁗′	3.27 ov
5⁗′	67.54	5⁗′	3.26 ov
6⁗′	17.7	6⁗′	0.86 d (6.3)
β-D-api*f* (1→4)		*β*-D-api*f* (1→4)	
1⁗″	109.70	1⁗″	5.17 d (2.5)
2⁗″	76.67	2⁗″	3.76 bd (2.5)
3⁗″	79.25		
4⁗″	63.53	4⁗″a	3.85 d (8.5)
		4⁗″b	3.85 ov
5⁗″	73.50	5⁗″	3.36 ov

[a]For numbering, see Figure 3A. [b]Assignments were based on ^{1}H−^{1}H COSY, sel 1D TOCSY, gHSQC, TOCSY, gDQFCOSY, ROESY, and gHMBC experiments.

range correlation with the rhamnosyl H-1⁗ in the gHMBC spectrum, indicating the rha(1 → 3)glu linkage as shown in Figure 3B. The ^{1}H NMR signal of H-1⁗ at *δ* 4.81 (bs) indicated the *α*-configuration of the anomeric rhamnose atom.

The remaining 18 signals in the ^{13}C NMR spectrum were assigned as two *p*-coumaroyl moieties (Table 2; Figure 3). HMBC correlations of the carboxylic C-9 of a *p*-coumaroyl moiety and H-4″ of the glucose revealed the position of the *p*-coumaroyl moiety at C-4″ as shown in Figure 3B. By analogy, a long-range correlation of the fructose H-3‴ and the second *p*-coumaroyl carboxyl C-9′ unveiled the presence of a further *p*-coumaroyl ester (Figure 3B). Both *p*-coumaroyl moieties were in (*E*)-configuration as indicated by the size of the coupling constants, *J* = 15.9−16.1 Hz, of the respective ^{1}H NMR signals (H-7, H-8, H-7′, H-8′; Table 2) as previously reported for (*E*)- and (*Z*)-coumaroyl moieties.[11] According to our GC-MS analyses, the above-mentioned sugars were D-glucose, D-fructose, L-rhamnose, and D-apiose. Therefore, the structure of compound **14** was established to be *β*-D-api*f*-(1→4)-*α*-L-rha*p*-(1→4)-*α*-L-rha*p*-(1→3)-(4-*O*-(*E*)-*p*-coumaroyl)-*α*-D-glu*p*-(1→2)-(3-*O*-(*E*)-*p*-coumaroyl)-*β*-D-fru*f*.

Compound **15** was obtained as a white amorphous powder. Its molecular formula was determined to be $C_{42}H_{54}O_{23}$ according to our HR-FT-ESI-MS measurements (Table 1). Its acidic hydrolysis yielded free *p*-coumaric acid as the only phenolic constituent. Compound **15** gave a pseudomolecular ion $[M - H]^-$ at *m/z* 925, yielding predominant fragments $[M - H - 146]^-$ at *m/z* 779 and $[M - H - 146 - 146]^-$ at *m/z* 633 during CID experiments (Table 1). The consecutive losses of 146 Da indicated the presence of two deoxy-hexose moieties. A fragment ion $[M - H - 164]^-$ at *m/z* 761 was possibly caused by the loss of the above-mentioned *p*-coumaric acid moiety.

In agreement with the proposition of two deoxy-hexose moieties, analysis of the ^{13}C NMR spectrum showed 12 characteristic signals of 2 rhamnosyl moieties, respectively (Table 3). Comparison of the ^{1}H and ^{13}C NMR signals (Table 3) as well as HMBC and ROESY long-range correlations (Figure 4) revealed a highly similar structural identity of compound **14** and **15**, consisting of two *p*-coumaroyl, one glucosyl, one fructosyl, and two rhamnosyl moieties. Glycosidic linkages, anomeric configurations, and (*E*)-configuration of the *p*-coumaroyl double bonds of compound **15** were identical to those of compound **14** as shown by the NMR data in Tables 2 and 3. Likewise, the absolute sugar configurations were identical to those described for compound **14**. In summary, the structure of compound **15** was shown to be a *α*-L-rha*p*-(1→4)-*α*-L-rha*p*-(1→3)-(4-*O*-(*E*)-*p*-coumaroyl)-*α*-D-glu*p*-(1→2)-

DOI: 10.1021/acs.jafc.5b03532
J. Agric. Food Chem. 2015, 63, 8905−8911

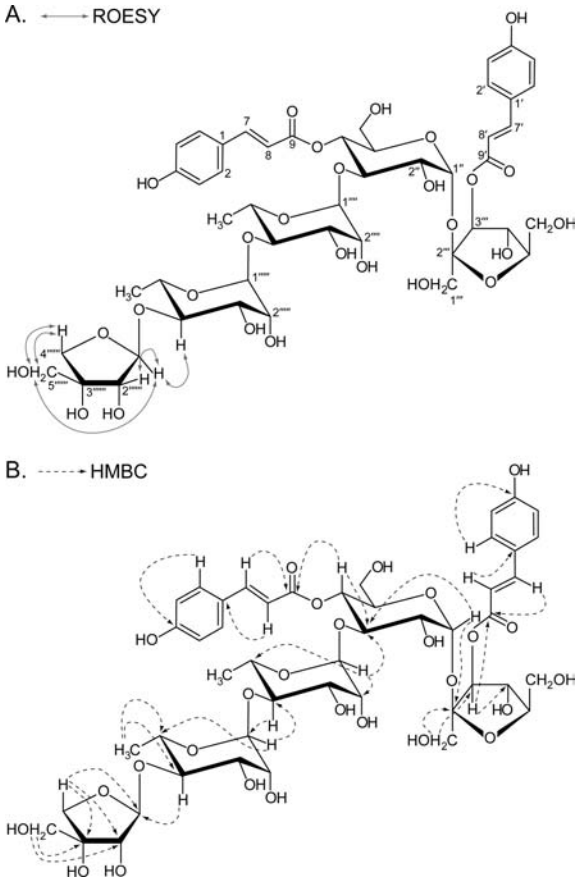

Figure 3. Important (A) ROESY and (B) HMBC long-range correlations between carbon and hydrogen atoms of quillajaside B.

(3-*O*-(*E*)-*p*-coumaroyl)-*β*-D-fruf. Due to the complexity of their systematic names, we proposed to name the smaller compound **15** quillajaside A, whereas the larger compound **14** was named quillajaside B.

Tentative Identification of Further *p*-Coumaroyl Sucrose Esters. A tentative biosynthetic series of precursors and products of quillajasides A and B may be proposed when detected compounds with highly related UV and mass spectra are considered. The most basic detectable *p*-coumaroylated substance was compound **5**, presumably representing a *p*-coumaroylated sucrose ($C_{21}H_{27}O_{13}$) according to its UV spectrum, its $[M - H]^-$ at *m*/*z* 487.1417 (calcd value in Table 1), and several characteristic CID losses and fragment ions (Table 1). A *p*-coumaroyl rhamnosyl sucrose ($C_{27}H_{37}O_{17}$, compound **11**) was tentatively identified by its UV and mass spectra, particularly, its $[M - H]^-$ at *m*/*z* 633.2022 (Table 1). Because rhamnosyl- and *p*-coumaroyl moieties are nominally isobaric, HR-MS was crucial to distinguish the identity of compound **11** clearly from a putative di-*p*-coumaroyl sucrose ($C_{30}H_{33}O_{15}$), which was not detected in the extract.

Possibly representing a direct biosynthetic derivative of the quillajaside A, a *p*-coumaroyl dirhamnosyl sucrose (compound **12**) was found according to our analytical data (Table 1). A total of three di-*p*-coumaroyl dirhamnosyl sucrose esters (compounds **15** (quillajaside A), **18**, and **21**) were identified, whereas di-*p*-coumaroyl (mono)-rhamnosyl sucroses were not detected. Furthermore, two di-*p*-coumaroyl dirhamnosyl apiosyl sucrose esters (i.e., compounds **14** (quillajaside B), **16**, and **17**) were detected. A rhamnosylated derivative of quillajaside B was observed (compound **13**), being tentatively identified as di-*p*-coumaroyl trirhamnosyl apiosyl sucrose ([M

Table 3. ^{1}H (500 MHz) and ^{13}C (125 MHz) NMR Data of Quillajaside A, 15 (*α*-L-rha*p*-(1→4)-*α*-L-rha*p*-(1→3)-(4-*O*-*p*-coumaroyl)-*α*-D-glu*p*-(1→2)-(3-*O*-*p*-coumaroyl)-*β*-D-fru*f*)

carbon[a]	$\delta_{C\ (pyridine)}$[b]	proton[a]	δ_H (*J* in Hz)
p-coumaroyl moiety at *α*-D-glu*p*		*p*-coumaroyl moiety at *α*-D-glu*p*	
1	126.27		
2	130.90	2′	7.58 d-like (8.8)
3	116.96	3′	7.37 d-like (8.7)
4	161.62		
5	116.96	5′	7.37 d-like (8.7)
6	130.90	6′	7.58 d-like (8.8)
7	146.40	7	7.97 d (15.9)
8	114.68	8	6.52 d (16.2)
9	167.39		
p-coumaroyl moiety at *β*-D-fru*f*		*p*-coumaroyl moiety at *β*-D-fru*f*	
1	126.44		
2′	130.97	2′	7.69 d-like (8.4)
3′	116.83	3′	7.25 d-like (8.6)
4′	161.74		
5′	116.83	5′	7.69 d-like (8.4)
6′	130.97	6′	7.25 d-like (8.6)
7′	146.40	7′	8.09 d (15.8)
8′	114.74	8′	6.73 d (16.0)
9′	167.46		
α-D-glu*p*		*α*-D-glu*p*	
1″	92.9	1″	6.14 d (3.7)
2″	73.2	2″	4.14 dd (3.4, 9.5)
3″	80.0	3″	4.79 dt (9.9)
4″	70.4	4″	5.75 t (9.6)
5″	72.4	5″	4.90 ddd (2.5, 5.1, 10.2)
6″	61.8	6″a	4.12 dd (4.9, 12.4)
		6″b	4.30 ov
β-D-fru*f*		*β*-D-fru*f*	
1‴	65.0	1‴a	4.30 ov
		1‴b	4.30 ov
2‴	105.2	2‴	
3‴	79.5	3‴	6.40 d (7.4)
4‴	73.8	4‴	5.30 dd (7.3, 7.4)
5‴	84.7	5‴	4.76 ddd (3.7, 5.5, 7.2)
6‴	62.7	6‴a	4.56 dd (6.3, 12.2)
		6‴b	4.45 dd (3.7, 12.2)
α-L-rha*p* (1→3)		*α*-L-rha*p* (1→3)	
1⁗	103.2	1⁗	5.89 d (1.7)
2⁗	72.5	2⁗	4.70 dd (1.7, 3.2)
3⁗	76.62	3⁗	4.51 dd (3.2, 9.3)
4⁗	80.7	4⁗	4.27 t-like (9.4)
5⁗	68.5	5⁗	4.31 ov
6⁗	19.4	6⁗	1.50 d (6.0)
α-L-rha*p* (1→4)		*α*-L-rha*p* (1→4)	
1⁗′	103.15	1⁗′	6.07 d (1.5)
2⁗′	72.1	2⁗′	4.78 dd (1.6, 3.5)
3⁗′	72.4	3⁗′	4.41 dd (3.3, 9.0)
4⁗′	73.6	4⁗′	4.24 t-like (9.2)
5⁗′	70.1	5⁗′	4.19 m, ov
6⁗′	18.2	6⁗′	1.45 d (6.0)

[a]For numbering, see Figure 4A. [b]Assignments were based on ^{1}H–^{1}H COSY, sel 1D TOCSY, gHSQC, TOCSY, gDQFCOSY, ROESY, and gHMBC experiments.

DOI: 10.1021/acs.jafc.5b03532
J. Agric. Food Chem. 2015, 63, 8905−8911

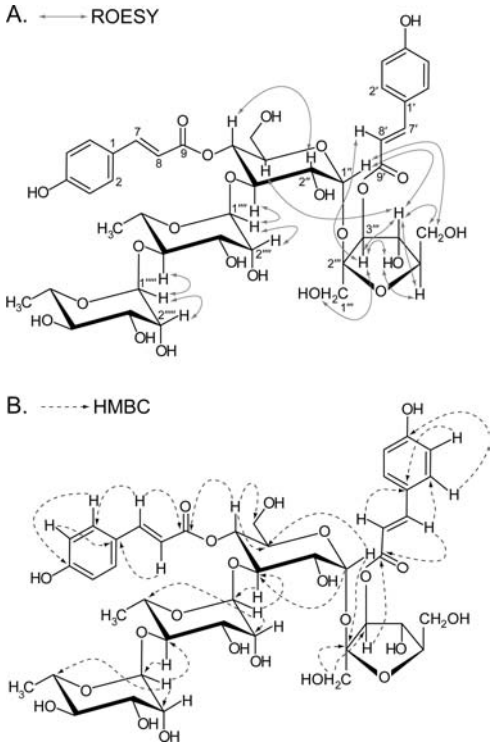

Figure 4. Important (A) ROESY and (B) HMBC long-range correlations between carbon and hydrogen atoms of quillajaside A.

$-$ H]$^-$ at m/z 1203.3957, calcd values in Table 1). Further detected compounds (**22**–**29**) represented sucrose derivatives with three *p*-coumaroyl moieties, at least two rhamnosyl moieties, and eventually an apiosyl moiety (Table 1). The highest molecular weight compounds detected in the aqueous extracts were compounds **22** and **24** with an [M $-$ H]$^-$ at m/z 1349, representing tri-*p*-coumaroyl trirhamnosyl monoapiosyl sucroses (Table 1).

In brief summary, the aqueous extracts of the inner bark of *Q. saponaria* Molina were shown to contain a total of 22 phenylpropanoid sucrose esters, being linked to up to 1 apiosyl, 3 rhamnosyl, and 3 *p*-coumaroyl moieties. Full structural elucidation was only possible for compounds **14** and **15** (quillajasides A and B). Nevertheless, because the occurrence of these unique compounds is highly characteristic of *Quillaja* extracts including the food additive E999, they may represent valuable authenticity markers for the detection of *Quillaja* extracts in food and cosmetic formulations. According to a previous paper,[12] ca. 150 phenylpropanoid sucrose esters have been identified previously, some of which exerted biological activities such as a cancer chemopreventive activity.[13] Moreover, a *p*-coumaroyl sucrose ester from wild buckwheat (*Fagopyrum esculentum* Moench) was recently shown to inhibit α-amylase activity and, thus, proposed to serve as a functional food ingredient for controlling postprandial hyperglycemia by modulating starch degradation during digestion.[14] Further studies on these *p*-coumaroyl sucrose esters, their biofunctionality in the bark of *Q. saponaria*, and their bioactivity in humans should be encouraged, particularly as these compounds are ingested daily by consumers worldwide.

AUTHOR INFORMATION

Corresponding Author

*(R.M.S.) Phone: +49 711 459 22995. Fax: +49 711 459 24110. E-mail: ralf.schweiggert@uni-hohenheim.de.

Notes

The authors declare no competing financial interest.

ACKNOWLEDGMENTS

We are grateful to Dr. Regina Walther from Pera Ingredients (Springe-Eldagsen, Germany) for generously donating the inner bark of *Q. saponaria* Molina. We also acknowlege Dr. Jens Pfannstiel (University of Hohenheim) for conducting the high-resolution mass spectrometric analyses on the isolated compounds **14** and **15**. We thank Joachim Trinkner (University of Stuttgart, Germany) for conducting the HPLC-ESI-HR-MS analyses.

REFERENCES

(1) San Martín, R.; Briones, R. Industrial uses and sustainable supply of *Quillaja saponaria* (Rosaceae) saponins. *Econ. Bot.* **1999**, *53*, 302–311.

(2) Marciani, D. J. Triterpene saponin analogs having adjuvant and immunostimulatory activity. Patent US 5977081 A, 1999.

(3) van Setten, D. C.; van de Werken, G. Molecular structures of saponins from *Quillaja saponaria* Molina. In *Saponins Used in Traditional and Modern Medicine—Adances in Experimental Medicine and Biology*; Waller, G. R., Yamasaki, K., Eds.; Springer: New York, 1996; Vol. 404, pp 185–193.

(4) Oleszek, W.; Hamed, A. Saponin-based surfactants. In *Surfactants from Renewable Resources*; Kjellin, M., Johannson, I., Eds.; Wiley: Hoboken, NJ, USA, 2010; pp 239–249.

(5) Maier, C.; Conrad, J.; Carle, R.; Weiss, J.; Schweiggert, R. M. Phenolic constituents in commercial aqueous quillaja (*Quillaja saponaria* Molina) wood extracts. *J. Agric. Food Chem.* **2015**, *63*, 1756–1762.

(6) da Silva, B. P.; Velozo, L. S. M.; Parente, J. P. Biochanin A triglycoside from *Andira inermis*. *Fitoterapia* **2000**, *71*, 663–667.

(7) Golovchenko, V. V.; Ovodova, R. G.; Shashkov, A. S.; Ovodov, Y. S. Structural studies of the pectic polysaccharide from duckweed *Lemna minor* L. *Phytochemistry* **2002**, *60*, 89–97.

(8) Guo, S.; Kenne, L. Characterization of some *O*-acetylated saponins from *Quillaja saponaria* Molina. *Phytochemistry* **2000**, *54*, 615–623.

(9) Ishii, T.; Yanagisawa, M. Synthesis, separation and NMR spectral analysis of methyl apiofuranosides. *Carbohydr. Res.* **1998**, *313*, 189–192.

(10) Snyder, J. R.; Serianni, A. S. DL-Apiose substituted with stable isotopes: synthesis, NMR-spectral analysis, and furanose anomerization. *Carbohydr. Res.* **1987**, *166*, 85–99.

(11) Lu, Y.; Yeap Foo, L. Flavonoid and phenolic glycosides from *Salvia officinalis*. *Phytochemistry* **2000**, *55*, 263–267.

(12) Zhao, W.; Huang, X.-X.; Yu, L.-H.; Liu, Q.-B.; Li, L.-Z.; Sun, Q.; Song, S.-J. Tomensides A–D, new antiproliferative phenylpropanoid sucrose esters from *Prunus tomentosa* leaves. *Bioorg. Med. Chem. Lett.* **2014**, *24*, 2459–2462.

(13) Takasaki, M.; Konoshima, T.; Kuroki, S.; Tokuda, H.; Nishino, H. Cancer chemopreventive activity of phenylpropanoid esters of sucrose, vanicoside B and lapathoside A, from *Polygonum lapathifolium*. *Cancer Lett.* **2001**, *173*, 133–138.

(14) Liu, T.; Yip, Y. M.; Song, L.; Feng, S.; Liu, Y.; Lai, F.; Zhang, D.; Huang, D. Inhibiting enzymatic starch digestion by the phenolic compound diboside A: a mechanistic and in silico study. *Food Res. Int.* **2013**, *54*, 595–600.

DOI: 10.1021/acs.jafc.5b03532
J. Agric. Food Chem. 2015, 63, 8905–8911

confined water (non-free diffusible) within the aggregate structure.

MATERIALS AND METHODS

Materials. Defatted soy flour was provided by Cargill BV (Amsterdam, Netherlands). Micellar casein isolate was kindly provided by Friesland Campina in a concentration of 14.6% (w/w). Anhydrous magnesium sulfate ($MgSO_4$), anhydrous magnesium chloride ($MgCl_2$), calcium sulfate dihydrate ($CaSO_4{\cdot}2H_2O$), calcium chloride dihydrate ($CaCl_2{\cdot}2H_2O$), and deuterium oxide (D_2O) with a purity of 99.9 atom % D were obtained from Sigma-Aldrich (Steinheim, Germany). Reagents were of analytical grade and used without further purification.

Preparation of (Soy) Protein Solutions. A solution of soy proteins, further denoted as SP, was prepared as described by Urbonaite et al.[1] The protein content of SP was determined by Kjeldahl (calculated using $N \times 6.25$), where the protein isolation yielded typical 11−12% (w/w) stock solutions. The ratio of the predominant proteins glycinin/β-conglycinin was estimated to be 50:50 by gel electrophoresis and reversed-phase high-performance liquid chromatography (HPLC) (results are not shown). The SP solution was stored at 4 °C in the presence of 0.02% sodium azide and used within 1 month after preparation. The enthalpy change, indicative for the protein nativity, was 15.2 J/g of protein as measured by differential scanning calorimetry (DSC, Q1000, TA Instrument, New Castle, DE).

As a reference material, a casein micelle stock solution, depleted of whey proteins, was prepared as described by Nieuwland et al.,[12] diluted to 12% (w/w) and stored at −20 °C until further use. The casein micelle stock solution further denoted as CM was defrosted overnight in the refrigerator and equilibrated at room temperature for 2 h at 20 °C before usage.

Preparation and Characterization of SP Aggregates (0.1%, v/v, Protein). *Preparation of 0.1% (v/v) SP Aggregates.* Stock solutions of SP were diluted to 2% (w/w) protein, and 20 mM salt solutions with $MgSO_4$, $MgCl_2$, $CaSO_4$, and $CaCl_2$ were prepared. A 40 mM 3-(*N*-morpholino)propanesulfonic acid (MOPS) buffer was prepared at pH 7.0. All solutions were filtered with disposable syringe filters (Machery-Nagel Chromafil RC-20/25, with a pore size of 0.45 μm). The protein stock solutions were mixed with salt solutions to a final protein concentration of 0.1% (v/v), a salt concentration of 0.35 mM, and 20 mM MOPS buffer in a total volume of 2 mL. Prepared solutions were heated at 95 °C for 30 min to allow for aggregation of the proteins, and the solution was left to cool to 25 °C. When other protein or salt concentrations were used, it is accordingly indicated in the text.

Characterization of 0.1% (v/v) SP Aggregates. Dynamic Light Scattering (DLS). The size of the protein aggregates prepared as described above was determined using DLS (Zetasizer Nano ZS, Malvern Instruments, Ltd., Worcestershire, U.K.) by 173° angle backward scattering. Measurements were performed at 20 °C and repeated 5 times per sample. The data were analyzed using a non-negative least-square analysis (general purpose model).

Static Light Scattering (SLS). To obtain a structure factor of the protein aggregates, SLS measurements were performed. Samples were prepared at a protein concentration from 0.001 to 0.3% protein (v/v) in a 20 mM MOPS buffer (pH 7.0) in the presence of salt, as described above, while keeping the protein/salt ratio constant. Measurements were performed using an ALV compact goniometer system with four detector units (ALV/CGS-4, Langen, Germany) and two ALV-5000/E multiple tau digital correlators. A Coherent Verdi V2 diode-pumped laser was used, operating with vertically linearly polarized light with a wavelength $\lambda = 532$ nm. The range of scattering wave vectors covered $4.65 \times 10^{-3} < q < 3.09 \times 10^{-2}$ nm^{-1} [$q = 4\pi n_s \sin(\theta/2)/\lambda$, with n_s the refractive index of the solution and θ the angle of observation]. The temperature of the cuvette holder was controlled by a thermostat bath at 20 ± 0.1 °C. If necessary, the solutions were diluted to exclude interparticle interactions.

Asymmetric Flow Field Flow Fractionation (AF4). AF4 was used to fractionate polydisperse SP aggregates, followed by an online multi-angle static laser light scattering (MALLS) detection and concentration measurement using ultraviolet (UV) and refractive index (RI) to determine the particle size and mass. The AF4 instrumentation comprised of a HPLC unit (Ultimate 3000, Dionex/Thermo Fisher Scientific, Sunnyvale, CA), MALLS (Dawn Heleos-II; $\lambda = 658$ nm; 130 mW laser, vertically polarized), and a RI detector (Optilab T-rEX, B, Whyatt Technology, Santa Barbara, CA). A separation channel (HF5 cartridge, Wyatt Technology, Dernbach, Germany) was comprised of a polyethersulfone hollow fiber with a nominal molecular weight cutoff of 10 kDa, corresponding to an average pore size of 5 nm (fiber type FUS 0181, Microdyn-Nadir, Wiesbaden, Germany). Data collection and analysis were performed using Astra-6 software.

Protein aggregates of 0.1% protein (v/v) in a 20 mM MOPS buffer at pH 7.0 in the presence of 0.35 mM divalent salt were measured. The sample injection volume was 20 μL using a 60 μL loop in partial inject mode. The detector flow rate was kept constant at 0.5 mL min^{-1}. The sample was injected at a flow rate of 0.2 mL min^{-1} and focused for 8 min. Elution was performed under varying cross-flow rate (V_x). At the start of elution, V_x was kept constant at 0.5 mL min^{-1} for 10 min, followed by a decay in 3 steps: from 0.5 to 0.35 mL min^{-1} in 1 min, from 0.35 to 0.2 mL min^{-1} in 2 min, and from 0.2 to 0 mL min^{-1} in 8 min. Then, V_x was kept at that zero velocity for 10 min. Light scattering signals from 53° to 100° were used for the data extrapolation using a first-order Zimm plot fit. From the fitted weight-averaged molar masses of the aggregates (M_m) and *Z*-averaged radius of gyration (R_g), the apparent density (ρ_{app}) was calculated using the following equation:

$$\rho_{app} = \frac{M_m}{N_A \frac{4}{3}\pi {R_g}^3} \quad (1)$$

where N_A is Avogadro's number.

Preparation and Characterization of SP Aggregates for Entrapped and Confined Water Measurements (1%, v/v, Protein). *Preparation of 1% (v/v) SP Aggregates.* The prerequisite for aggregates used for measurements for free diffusible water (equal to entrapped minus confined) and non-free diffusible (confined) water is that they need to be large and dense enough to be pelleted upon centrifugation [at 20 000 relative centrifugal force (RCF)]. For this reason, aggregates were prepared at 1% (v/v) protein by keeping the protein/salt ratio the same as for aggregates prepared for the structural characterization, as described above. Protein stock solutions were mixed with salt solutions to a final protein concentration of 1% (v/v) and a salt concentration of 3.5 mM, as described in the Preparation of 0.1% (v/v) SP Aggregates section earlier above. Solutions were heated at 95 °C for 30 min to allow for aggregation of the proteins to occur, and the solution was then left to cool at room temperature to 25 °C. When other protein or salt concentrations were used, it is accordingly indicated in the text.

Characterization of 1% (v/v) SP Aggregates. Scanning Electron Microscopy (SEM). Aggregates prepared at a 1% (v/v) protein concentration at pH 7.0 in the presence of 3.5 mM $MgSO_4$, $MgCl_2$, $CaSO_4$, and $CaCl_2$ salts were imaged by SEM. Circular glass coverslips of 8 mm (Menzel, Brauschweig, Germany) were cleaned by dipping twice in alcohol. The excess of remaining alcohol on the edge of the glass was carefully tipped to a filter paper. A piece of parafilm was spread on the table, using a few droplets of water for better sticking capacity, to obtain a clean hydrophobic surface. Poly-L-lysine of 0.2% (w/v) was pipetted in 100 μL quantities on the parafilm surface to obtain single droplets. Each coverslip was placed on top of the droplet, carefully turned around, and left for 5 min to ensure that both sides were completely covered with poly-L-lysine. Treated coverslips were dipped in Milli-Q water twice, and an excess of remaining water was carefully tipped to a filter paper. Rinsed coverslips were placed in the holder and left to dry overnight at room temperature. Finished coverslips were placed for 30 min in 1 mL Eppendorf tubes filled with the 0.3% (v/v) aggregate dispersions for aggregate attachment. Coverslips with attached aggregates were washed twice in Milli-Q

DOI: 10.1021/acs.jafc.5b03784
J. Agric. Food Chem. 2015, 63, 8912−8920

water, placed in a 2.5% (v/v) glutaraldehyde solution for 30 min for cross-linking of the proteins, and later washed in Milli-Q water again to rinse off the gluteraldehyde. The samples were dehydrated in a series of acetone (10, 30, 50, 70, and 100%) for 10 min per step and critical point dried (CPD) with carbon dioxide (CPD 030, BalTec, Liechtenstein, Germany). The coverslips were fitted on a sample holder by carbon adhesive tabs (Electron Microscopy Sciences, Fort Washington, PA) and subsequently sputter-coated with a 10 nm thick layer of iridium (MED 020, Leica, Vienna, Austria). Samples were analyzed in a field emission scanning electron microscope (Magellan 400, FEI, Eindhoven, Netherlands) at a working distance of approximately 4 mm, with scanning electron (SE) detection at 2 kV and 6.3 pA. The digital images were contrast-optimized with Photoshop CS5.

ImageJ 1.49d was used as a tool to evaluate bead sizes visualized in SEM images at magnifications of 100 000. On average, three images were analyzed per aggregate type. Approximately 10 spots per image were evaluated for the bead sizes. Bead sizes were obtained by direct visual inspection of the aggregate image and averaged.

Pelleting Aggregates Using Centrifugation. Prepared 1% (v/v) protein aggregate solutions at pH 7.0 in the presence of 3.5 mM $MgSO_4$, $MgCl_2$, $CaSO_4$, and $CaCl_2$ were centrifuged at 20 000 RCF for 10 min at 20 °C (centrifuge 5430R, Eppendorf AG, Hamburg, Germany). The protein content in the pellet was determined by measuring the protein content in the supernatant after the addition of 8 M urea as a powder (0.755 g of urea/g of supernatant). To optimize protein solubilization in 8 M urea, the supernatant was heated at 70 °C for 10 min. The protein content was determined by measuring the absorbance at 280 nm with a Cary 50 Bio UV−visible spectrophotometer (Agilent Technologies, Amstelveen, Netherlands). A linear calibration curve for proteins was obtained by measuring the absorbance of 0.005−1% (v/v) SP solutions in the presence of 8 M urea. Using these calibration curves, the protein content (g) in the supernatant was obtained. The difference between the total protein content of the sample and that measured in the supernatant phase was taken as the protein content of the pellet (g) ($m_{protein}$). For all four different salts, approximately 37% non-pelleted aggregates remained in the supernatant, and thus, it was assumed that 63% was present in the pellet.

Alternatively, the non-filtrated and filtrated supernatants (Machery-Nagel Chromafil RC-20/25, with a pore size of 0.45 μm) were analyzed by sodium dodecyl sulfate−polyacrylamide gel electrophoresis (SDS−PAGE) and DLS (results not shown). The results confirmed that non-pelleted proteins were actually small aggregates that did not sediment during centrifugation at 20 000 RFC for 10 min.

Pellet Density by X-ray Computer Tomography (XRT). The pellet volume was measured by XRT. Pelleted 1% (v/v) aggregates in the presence of 3.5 mM $MgSO_4$, $MgCl_2$, $CaSO_4$, and $CaCl_2$ salts were measured non-invasively as a three-dimensional (3D) structure with a spatial resolution of 10 μm by XRT, GE Phoenix v|tomelx m, 180 kV transmission tube (Windstorm, Germany). The transmission of the conical X-ray beam through the sample was recorded by a digital GE DXR detector array with 2024 × 2024 pixels (pixel size of 200 μm). Samples were imaged at the distance of 40.8 mm. Power settings of 100 kV and 135 μA were used. The 3D density map was obtained after tomographical reconstruction of images acquired under 1200 rotations over 360° with a step size of 0.3°. The acquisition time for one projection was 250 ms. Averaging three projections results in a total acquisition and read-out time of about 20 min.

Water Entrapped in the Pellet. The 1% (v/v) protein aggregate solutions prepared in the presence of 3.5 mM $MgSO_4$, $MgCl_2$, $CaSO_4$, and $CaCl_2$ salts were centrifuged at 20 000 RCF for 10 min at 20 °C (centrifuge 5430R, Eppendorf AG, Hamburg, Germany). The supernatant was carefully removed using a pipet, and the remaining serum was drained by leaving the Eppendorf tubes upside down on the filter paper for 15 min. The tubes containing the protein aggregate pellets were weighted. Water entrapped in the pellet (EW) was calculated as the water remaining in the pellet after centrifugation according to eq 2 and expressed as grams of water per gram of protein retained by the pellet.

$$EW = \frac{W_{total} - W_{removed}}{m_{protein}} \quad (2)$$

In this equation, W_{total} is the water present in the sample (g), $W_{removed}$ is the sum of the supernatant and water drained from the tube after centrifugation (g), and $m_{protein}$ is the mass of the pelleted proteins (g). When other salt concentrations were used, it is accordingly indicated in the text. Measurements were performed at least in duplicate.

Free Diffusible Water Determined by Proton Nuclear Magnetic Resonance (^{1}H NMR). Free diffusible water (EW_{FD}) is defined as the sum of water present in between pelleted aggregates and free diffusible water entrapped within aggregates. EW_{FD} was measured by ^{1}H NMR. To confirm that all free diffusible water is accounted for at the first redispersion step, the pellets were subsequently redispersed in 2 mL of D_2O using a 1 mL pipet tip by gentle manipulation with the pipet tip. Dispersions in D_2O were left for 30 min to allow for H_2O present in the aggregates to exchange with D_2O to form HDO, and subsequently, the samples were centrifuged again at 20 000 RCF for 10 min at 20 °C (centrifuge 5430R, Eppendorf AG, Hamburg, Germany). This procedure was repeated 3 times and is further denoted as consecutive washing steps. HDO present in the collected supernatant was quantified by nuclear magnetic resonance (NMR). ^{1}H NMR spectra of D_2O samples containing HDO were recorded at a probe temperature of 300 K on a Bruker AVANCE III 500 spectrometer at the Wageningen NMR Centre (WNMRC), Wageningen, Netherlands. For each spectrum, eight scans were recorded with a relaxation delay of 10 s.

Non-free Diffusible Water Confined within Aggregates. Non-free diffusible water confined within aggregates (grams of water per gram of protein) (CW) was calculated as follows:

$$CW = \frac{EW - EW_{FD}}{m_{protein}} \quad (3)$$

in which EW_{FD} was measured by ^{1}H NMR, as explained above.

To demonstrate if (partial) aggregate dissociation would release an additional amount of water, pellets were dispersed in D_2O containing 8 M deuterated urea. Deutarated urea was obtained by dissolving urea up to 10 M in D_2O and freeze-dried (repeated 3 times). Pellets in the presence of urea were heated at 70 °C for 10 min in the water bath to allow for aggregates to dissociate.

Definitions. From the experimental setup described above, the water entrapped by the aggregates once pelleted is defined as the total amount of entrapped water by the pellet (EW). The sum of water present in between pelleted aggregates and water entrapped within aggregates free to diffuse is defined as free diffusible water (EW_{FD}). Confined water within the aggregate (CW) is defined as water that is hindered in its diffusion because of the physical aggregate structure. This water is non-free diffusible on the time scale of the measurement (15 min).

RESULTS AND DISCUSSION

Aggregate Size. In this study, it was aimed to obtain protein aggregates different in size and density and to show if the acquired structures account for different amounts of entrapped and confined water present within the aggregate. The sizes of the aggregates prepared in a 0.1% (v/v) SP solution in the presence of 0.35 mM $MgSO_4$, $MgCl_2$, $CaSO_4$, and $CaCl_2$ salts were measured using DLS, and the results are shown in Figure 1. The Z-averaged diameter of these aggregates increased in size from 94 to 130 nm, going from the addition of $MgSO_4$ to $MgCl_2$, $CaSO_4$, and $CaCl_2$.

Aggregate Density. Information on the aggregate structure was further obtained using AF4 fractograms yielding a so-called conformation plot (Figure 2A), showing the scaling of the size (R_g) and the averaged molar mass (M_m). Although the conformation plot of SP aggregates shows similar curves for the different salts indicative for comparable aggregate "build-

DOI: 10.1021/acs.jafc.5b03784
J. Agric. Food Chem. 2015, 63, 8912−8920

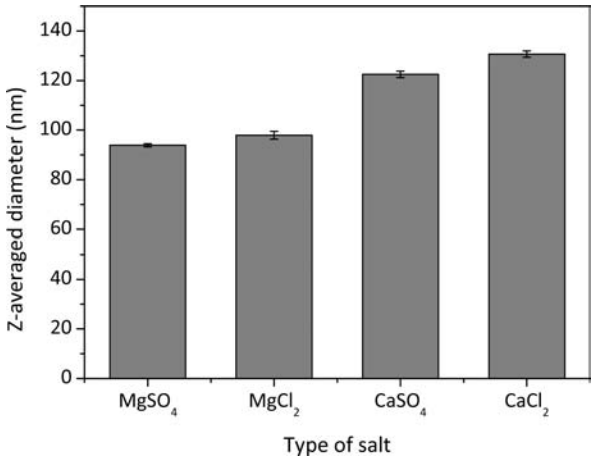

Figure 1. *Z*-averaged diameter of aggregates prepared in 0.1% (v/v) SP solution in 20 mM MOPS buffer at pH 7.0 in the presence of 0.35 mM $MgSO_4$, $MgCl_2$, $CaSO_4$, and $CaCl_2$ salts.

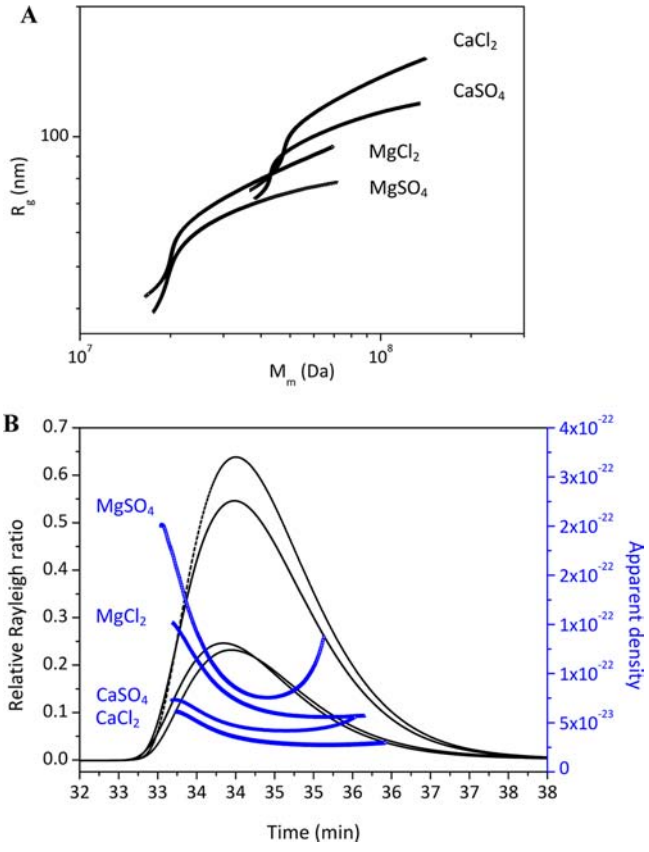

Figure 2. (A) Conformation plot indicating the scaling of size (R_g) to molar mass (M_m). (B) Rayleigh ratio (lower peaks for magnesium salts and higher peaks for calcium salts) and the calculated apparent density using eq 1 of SP aggregates in 20 mM MOPS buffer at pH 7.0 in the presence of 0.35 mM $MgSO_4$, $MgCl_2$, $CaSO_4$, and $CaCl_2$ salts.

up", it can be observed that aggregates formed in the presence of $MgSO_4$ are the smallest and aggregates formed in the presence of $CaCl_2$ are the largest in size, in agreement with DLS data. In agreement with Figure 1, aggregates prepared in the presence of magnesium salts had a lower averaged molar mass compared to aggregates prepared in the presence of calcium salts.

Assuming that R_g and M_m of aggregates have a power law relationship as $R_g \sim M_m^{1/d_f}$, the exponent of such a curve provides a fractal dimension (d_f).[13] On a log−log plot, this relation should yield a straight line, where the slope represents the fractal dimension. The fractal dimension directly relates to the openness of aggregates, where a lower d_f represents a more open aggregate structure.[14−16] From Figure 2A, it can be seen that measured SP aggregates had 1 order of magnitude variation in M_m and the curve of R_g over M_m obtained is not linear. On the basis of these results, the fractal dimension (d_f) could not be obtained for measured SP aggregates, but the results still provide an indication of the internal density of the aggregates. From the curve, two regimes can be distinguished. These curves show that the fractal dimension for smaller sized aggregates is larger (steeper slope) than for larger aggregates. The beginning of the curve indicates a range of aggregates increasing in size but having the same molar mass, and the second part of the curve shows aggregates increased in size and density. Because SPs have an affinity for divalent cations, the addition of these salts cause instantaneous protein clustering (nucleation). A fast initial clustering could yield inefficiently formed aggregates that serve as a nucleus for denatured proteins to form a dense shell during heating. As a result, a more open aggregate structure inside in the aggregate could be formed in comparison to the outer structure.

The densities of above-mentioned aggregates were derived from the aggregate size (R_g) and average mass of the aggregate (M_m) measured using AF4.[13,17] The apparent aggregate density of different SP aggregates was calculated using eq 1 and is shown in Figure 2B, depicting the Rayleigh ratio (scattering light intensity) and the calculated apparent densities. From the figure, it can be observed that aggregates decrease in apparent density following this order $MgSO_4$, $MgCl_2$, $CaSO_4$, and $CaCl_2$. To conclude, SP aggregates increased in size and decreased in density following the salt type order $MgSO_4$, $MgCl_2$, $CaSO_4$, and $CaCl_2$.

Transition from 0.1 to 1% (v/v) Aggregates. To determine the amount of water associated with the aggregate, the aggregates had to be collected as a pellet. Aggregates prepared at 0.1% (v/v) concentration were too small to be pelleted. Aggregates used for the determination of free diffusible water and water confined within the aggregate were prepared at 1% (v/v) protein concentration in the presence of 3.5 mM $MgSO_4$, $MgCl_2$, $CaSO_4$, and $CaCl_2$ salts. To translate the measured aggregate characteristics (differences in size and density) of aggregates prepared at 0.1% (v/v) protein to aggregates prepared at 1% (v/v) protein, SLS experiments were performed to obtain the size of aggregates prepared at concentrations of 0.001−0.3% (v/v) protein in the presence of salts while keeping the protein/salt ratio constant to obtain a structure factor for the different protein aggregates. For all salts, the size of the aggregates increased with increasing protein concentration (results not shown). Because these aggregates were too large at all concentrations prepared, it was not possible to obtain a reliable structure factor.

Aggregate Morphology (1%, v/v). To verify whether differences in size and density are apparent in 1% (v/v) SP aggregates in the presence of the various salts, SEM imaging of these aggregates was performed. Aggregates depicted at different length scales are shown in Figure 3. From images with the lowest magnification, it can be observed that the aggregates differ in size; aggregates prepared in the presence of $MgSO_4$ were the smallest, and aggregates prepared in the

DOI: 10.1021/acs.jafc.5b03784
J. Agric. Food Chem. 2015, 63, 8912−8920

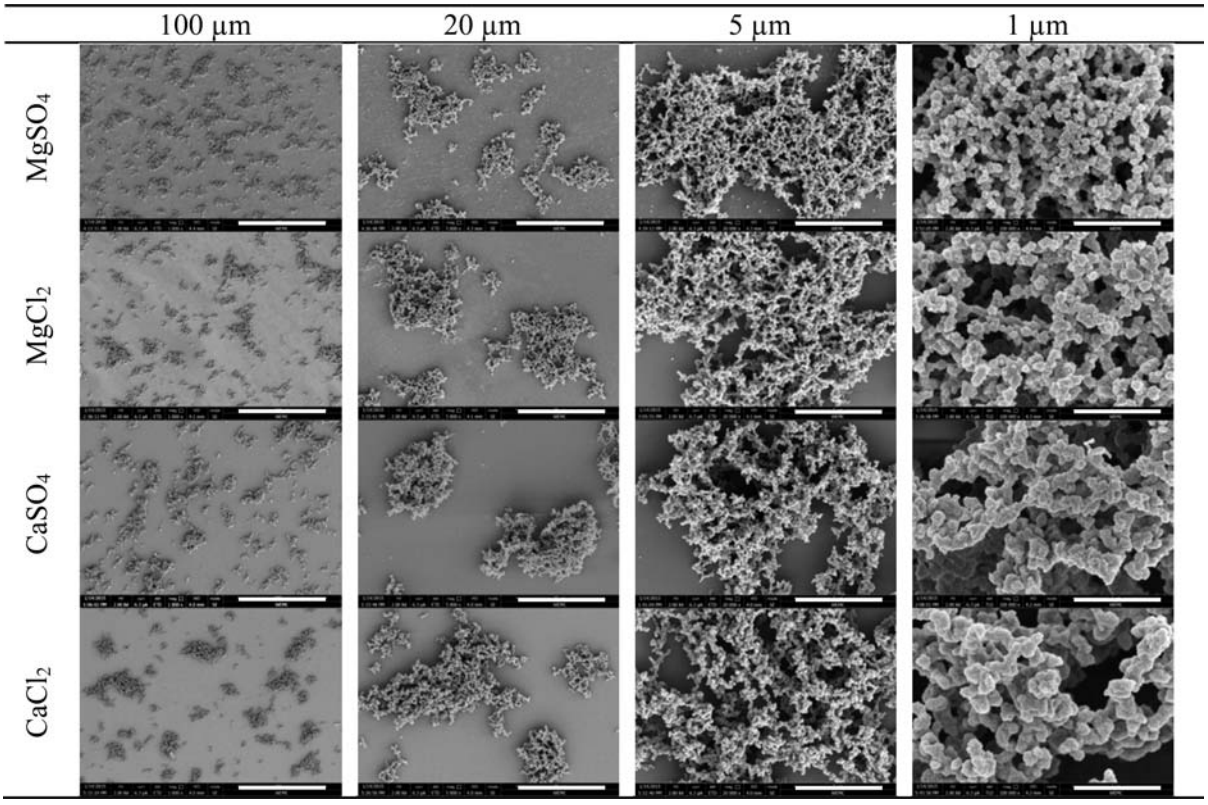

Figure 3. SEM images of 1% (v/v) SP aggregates prepared in 20 mM MOPS buffer at pH 7.0 in the presence of 3.5 mM $MgSO_4$, $MgCl_2$, $CaSO_4$, and $CaCl_2$ salts over different length scales. The indicated length scales correspond to the bar in the image.

presence of $CaCl_2$ were the largest in size, in agreement with the results above. The aggregates formed had an irregular shape and were polydisperse. In the presence of magnesium salts, aggregates varied from approximately 5 to 20 μm. In the presence of $CaSO_4$, the aggregates varied between 5 and 25 μm, and in the presence of $CaCl_2$, aggregates up to 30 μm were found. Differences in the aggregate microstructure in the presence of different salts were seen on 1 μm scale images (images on the right) in the bead size and in thickness of the strands, which were composed from these beads. The beads were fairly regular spherical particles and increased in size as measured by image analysis from 0.1 to 0.3 μm (Figure 4)

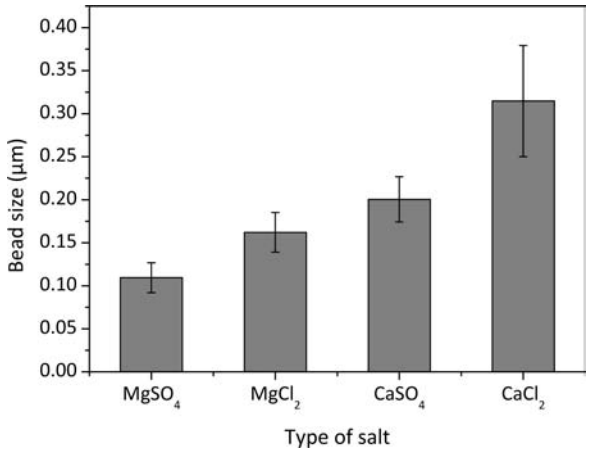

Figure 4. Bead sizes of 1% (v/v) SP aggregates prepared at pH 7.0 in the presence of 3.5 mM $MgSO_4$, $MgCl_2$, $CaSO_4$, and $CaCl_2$ salts imaged by SEM.

following the salt addition in the order of $MgSO_4$, $MgCl_2$, $CaSO_4$, and $CaCl_2$. The increment in size and more open formed structures observed in Figure 3 are in agreement with aggregate size and density results shown in Figures 2 of aggregates prepared at 0.1% (v/v) protein concentration.

Water Entrapped by the Pelleted Aggregates. Protein aggregates prepared at 1% (v/v) in the presence of 3.5 or 8.0 mM $MgSO_4$, $MgCl_2$, $CaSO_4$, and $CaCl_2$ salts were centrifuged at 20 000 RCF for 10 min at 20 °C. The quantity of water entrapped by the pelleted aggregates, *EW* (water in between and within the aggregates), is shown in Figure 5. From the figure, it can be observed that *EW* by the pelleted aggregates prepared in the presence of 3.5 mM salts increased from approximately 8 to 13 g of water/g of protein for salts in the following order of $MgSO_4$, $MgCl_2$, $CaSO_4$, and $CaCl_2$. No significant difference was found between *EW* of aggregates prepared in the presence of $MgSO_4$ and $MgCl_2$ salts (~8 g of water/g of protein). Aggregates prepared in the presence of $CaSO_4$ entrapped slightly more water (~8.5 g of water/g of protein) compared to aggregates prepared in the presence of magnesium salts, while in the presence of $CaCl_2$, this difference became much larger (~13 g of water/g of protein).

Measured pellet densities using XRT (Table 1) increased in the following order of $MgSO_4$, $MgCl_2$, $CaSO_4$, and $CaCl_2$. The protein content in the pellets was comparable for all samples measured (discussed in the Materials and Methods), but the amounts of entrapped water by the different pelleted aggregates differed (Figure 5). Because the protein content of the pellets is comparable, it can be concluded that aggregates prepared differed in size and structure as well as in the amount of entrapped water. Thus, higher pellet density (mass of sum of protein and water over volume) would indicate lower aggregate

DOI: 10.1021/acs.jafc.5b03784
J. Agric. Food Chem. 2015, 63, 8912−8920

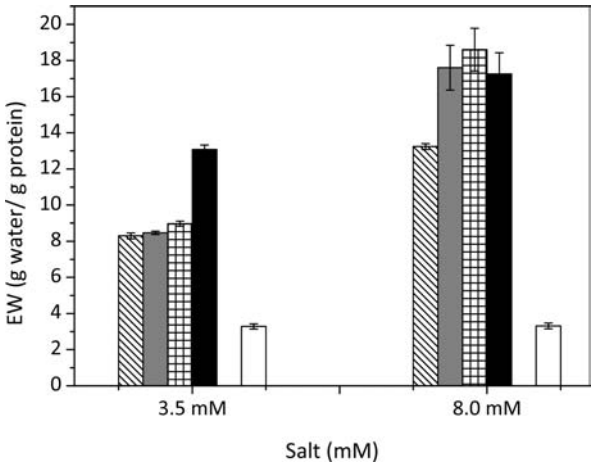

Figure 5. Water entrapped (*EW*) by the pelleted 1% (v/v) SP aggregates prepared in the presence of 3.5 and 8.0 mM $MgSO_4$ (striped columns), $MgCl_2$ (gray columns), $CaSO_4$ (grid columns), and $CaCl_2$ (black columns). White columns stand for a control sample containing 1% (v/v) CM aggregates prepared in the presence of 3.5 and 8.0 mM $CaCl_2$.

Table 1. Densities of Pelleted 1% (v/v) SP Aggregates Prepared in the Presence of 3.5 mM Salts at pH 7.0

	pellet (g)	volume[a] (mm^3)	density (g/cm^3)
$MgSO_4$	0.118 ± 0.002	114	1.035
$MgCl_2$	0.123 ± 0.002	111	1.106
$CaSO_4$	0.134 ± 0.002	121	1.105
$CaCl_2$	0.186 ± 0.002	159	1.171

[a]Single measurement.

density because the protein content in the pellets is comparable. This finding is in agreement with the results reported by Nieuwland and colleagues, where larger and denser egg ovalbumin aggregates in the gel measured on larger length scales by spin-echo small-angle neutron scattering (SESANS) resulted in lower gel WH.[10]

To illustrate whether higher salt concentrations would affect the size of the aggregate and the accompanying amount of *EW*, an additional set of aggregates was prepared from a 1% (v/v) protein solution in the presence of 8.0 mM salt. The pelleted 1% (v/v) aggregates (Figure 5) entrapped approximately double the amount of water ranging from approximately 13 to 19 g of water/g of protein compared to aggregates prepared in the presence of 3.5 mM salts. Obtained results on aggregate size confirmed that pelleted aggregates prepared at a higher salt concentration are larger and can, thereby, entrap more water.

Aggregate Compressibility. To compare the amount of *EW* in pelleted aggregates to water entrapped by the aggregates in solution, the apparent density, ρ_{app} (g/cm^3), of 0.1% (v/v) SP aggregates was calculated using the radius of gyration (R_g) and averaged molar mass (M_m) obtained from AF4 measurements (see eq 1). The quantity of water entrapped by aggregates was calculated as $1/\rho_{app}$ (grams of water per gram of protein) and is presented in Table 2. Values for entrapped water calculated for 0.1% (v/v) aggregates and measured *EW* values for 1% aggregates are shown in Table 2 and are expressed as grams of water per gram of protein. From the calculated values of entrapped water by aggregates in solution, it can be observed that aggregates larger in size and lower in density (for $CaCl_2$) can entrap more water. The difference in water entrapped by the aggregates in the solution and those compressed in a pellet (*EW*) could be explained by aggregate compressibility at the centrifugation force used. The compressibility factor, taken as the ratio between water entrapped by the aggregates in solution and *EW* (Table 2), shows that smaller and denser aggregates, such as those in the presence of magnesium salts, entrap less water and are also less compressible. Larger and more open aggregates, as in the presence of calcium salts, entrap more water and are more compressible. In agreement with our findings, Bell and colleagues suggested that aggregate strength, determined by the structure of the aggregate (on the basis of the density−size relationship), decreases with increasing aggregate size.[18]

Repetitive Forces Applied on Aggregates. To differentiate between entrapped and confined water by aggregates, pellets were redispersed in D_2O, to allow for water between the aggregates to diffuse from the aggregates and exchange with the solvent, giving HDO that is quantified by ^1H NMR (see the paragraph below on free diffusible water EW_{FD}). This step was repeated up to 3 times (further denoted as subsequent washing steps) to ensure that all free diffusible water was taken into account.

Pelleted protein aggregates were consecutively washed 3 times in D_2O. At each washing step, pelleted aggregates were redispersed in the same amount of D_2O. Changes in *EW* by the pelleted aggregates over washing steps are shown in Figure 6A. From the figure, it can be observed that, with each additional washing step, *EW* by the pelleted aggregates decreased by approximately 12−15%. The decreased amount of *EW* for the subsequent redispersion and centrifugation steps is suggested to represent compressibility of the pelleted aggregates, as described above. To verify that the decrease of *EW* is caused by pellet compressibility and not by aggregate disassembly caused by depletion of divalent ions during the washing step, a control experiment was performed where pelleted aggregates were washed in D_2O in the presence of $CaCl_2$. Obtained results did not show any significant effect on *EW* by pelleted aggregates (data not shown).

The change in the amount of *EW* retrieved from the aggregates by the subsequent washing steps was evaluated by taking the slope of entrapped water over 3 washing steps, as shown in Figure 6A and presented in Figure 6B for the different salts. From the figure, it can be seen that $MgCl_2$ and $CaCl_2$

Table 2. Water Entrapped by 0.1% (v/v) Aggregates Prepared in the Presence of 0.35 mM Salts in the Solution (Calculated) versus 1% (v/v) *EW* by the Pelleted Aggregates (Measured) Prepared in the Presence of 3.5 mM Salts

	aggregates in solution (g of water/g of protein)	*EW* (g of water/g of protein)	compresssibility factor
$MgSO_4$	20.78	8.21	2.53
$MgCl_2$	27.58	8.47	3.26
$CaSO_4$	41.26	8.97	4.60
$CaCl_2$	57.56	13.07	4.40

DOI: 10.1021/acs.jafc.5b03784
J. Agric. Food Chem. 2015, 63, 8912−8920

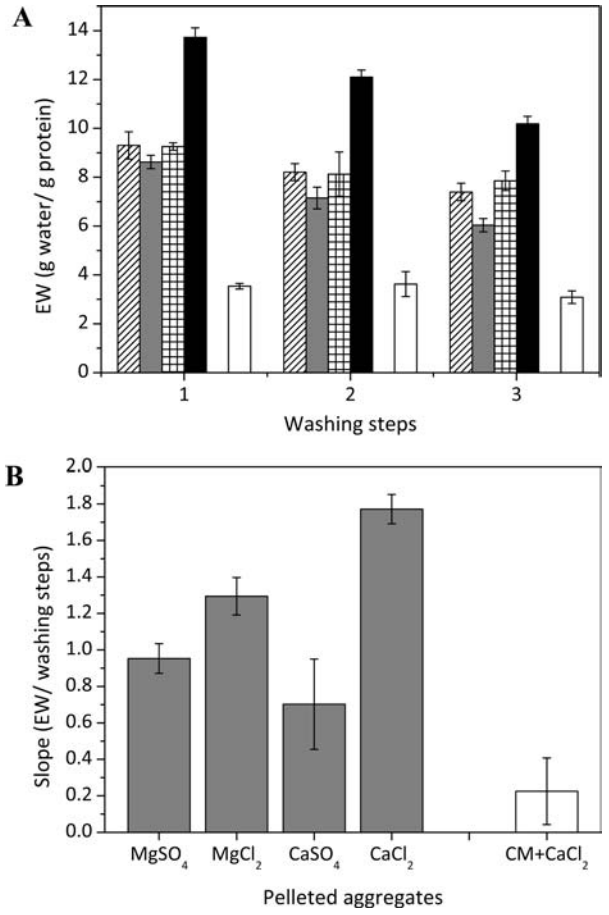

Figure 6. (A) Change in *EW* (D_2O) by 1% (v/v) SP aggregates prepared in the presence of 3.5 mM $MgSO_4$ (striped columns), $MgCl_2$ (gray columns), $CaSO_4$ (grid columns), and $CaCl_2$ (black columns) over washing steps in D_2O. (B) Rate of change in quantity of *EW* (D_2O) by pelleted aggregates prepared in the presence of 3.5 mM salt affected by 3 washing steps. In both panels, white columns stand for a control sample, 1% (v/v) CM aggregates prepared in the presence of $CaCl_2$.

aggregates were more affected by each washing step compared to $MgSO_4$ and $CaSO_4$ aggregates. To conclude, once pelleted aggregates are evaluated, larger and less dense SP aggregates are more compressible compared to smaller and denser aggregates. When reoccurring compression appears (e.g., washing steps), aggregates prepared in the presence of chloride salts (less dense) are compressed more than aggregates prepared in the presence of sulfate salts (more dense).

Free Diffusible Water in between and within Aggregates. The 1% (v/v) SP aggregate pellets were redispersed in D_2O, and free to diffuse water (EW_{FD}) from in between aggregates and from within the aggregates (HDO) was quantified by ^1H NMR. The amount of HDO from the aggregates (in between and within) prepared in the presence of 3.5 mM salt is shown in Figure 7A. More water had diffused from aggregates larger in size and lower in density ($CaSO_4$ and $CaCl_2$). This correlates positively with the results found for *EW* (Figure 5); the more water retained by pelleted aggregates, the more water free to diffuse from these aggregates. A total of 3 consecutive washing steps were performed (Figure 7A), and the results confirmed that almost all EW_{FD} already diffused in the first washing step, because almost no additional water has diffused in the second and third washing steps. This shows that, indifferent to aggregate size or density, all EW_{FD} is exchanged with D_2O on the minutes time scale.

In a parallel experiment, pelleted aggregates were redispersed in D_2O in the presence of 8 M deuterated urea to allow for aggregate dissociation. It was aimed to evaluate if, in the case destabilization of the aggregates would be induced, a larger amount of water, in addition to the regular washing, could be released (Figure 7B). From the figure, it can be seen that the addition of urea released not more than 0.5 g of water/g of protein, independent to the aggregate structure. The amount of additionally released water was marginal compared to the free diffusible water measured.

For comparison, CM aggregates prepared from a 1% (v/v) solution in the presence of 3.5 mM $CaCl_2$ were also analyzed. CMs are known for their loose packing and high porosity.[19] They have a voluminosity in milk of about 3−4 g of water/g of dry casein,[20,21] where only a relatively small proportion, around 0.5 g of H_2O/g of dry casein, is directly bound to the casein.[20] Because of the sponge-like colloidal casein micelle structure, obtained particles were expected to have a high amount of water displaced from the (pelleted) material when force is applied. CM particles visualized by SEM had very coarse open structures up to 50 μm in size (data not shown). *EW* measured of pelleted CM particles was ∼4 times lower compared to *EW* of pelleted SP ($CaCl_2$) aggregates (white columns in Figure 5). Although CM particles were larger in size compared to the soy aggregates, they entrap less water, indicating high aggregate compressibility. The small change in *EW* as affected by reoccurring compression (washing steps) indicates a small

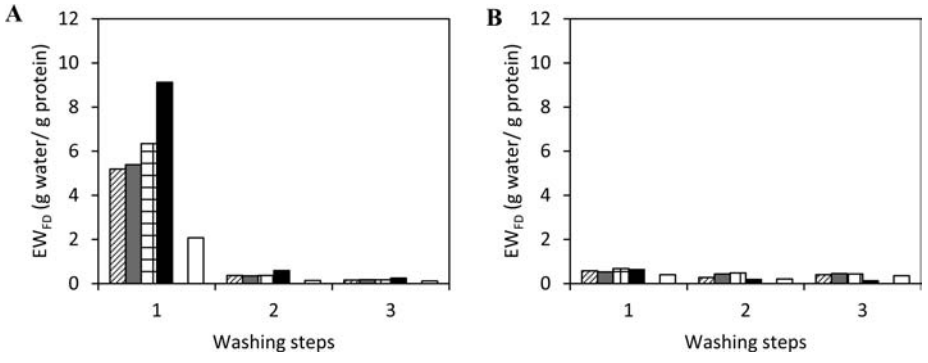

Figure 7. (A) Quantity of measured HDO diffused from aggregates (EW_{FD}) prepared in the presence of 3.5 mM $MgSO_4$ (striped columns), $MgCl_2$ (gray columns), $CaSO_4$ (grid columns), and $CaCl_2$ (black columns) salts. (B) Additionally released non-free diffusible water measured in the presence of 8 M deuterated urea. In both panels, white columns stand for the reference, 1% (v/v) CM aggregates prepared in the presence of $CaCl_2$.

DOI: 10.1021/acs.jafc.5b03784
J. Agric. Food Chem. 2015, 63, 8912−8920

degree of compression at reoccurring forces, because the maximum compression of the structures has already occurred in the first centrifugation step (Figure 6B). In comparison to SP aggregates, as expected, CM particles had the lowest amount of water entrapped. The large size, open structure, and large compressibility of CM particles lead to high water displacement from the aggregate when an external force is applied.

Confined Water within the Aggregate Structure. Confined water within the aggregate (*CW*) is defined as water that is hindered in its diffusion because of the physical aggregate structure. The results for calculated *CW* (eq 3) for different aggregates are shown in Figure 8. From the figure, it

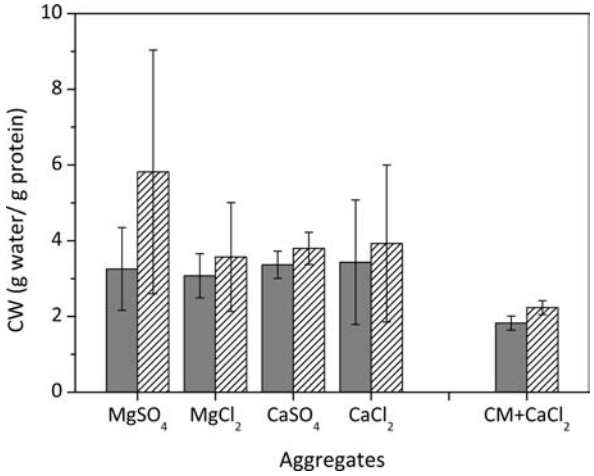

Figure 8. Confined water (*CW*) within aggregates: 3.5 mM (light gray columns) versus 8.0 mM (striped columns).

can be observed that, in case of SP aggregates, the amount of *CW* within aggregates is independent of the aggregate structure (size and density) and accounts for approximately 3.5 g of water/g of protein. The reference material accounted for approximately 2 g of water/g of protein and suggests that this quantity is protein-specific.

From the above results, it can be concluded that *EW* by pelleted aggregates depends upon the aggregate size, density, and compressibility, whereas *CW* within aggregates is aggregate-structure-independent but seems to be protein-specific.

Modulation of Entrapped Water. Above, it was shown that different types of salts can be used to obtain different aggregate structures for SPs. To evaluate to what extent these different aggregates can be tuned for the amount of *EW* and *CW*, different salt concentrations (3.5−10 mM) were tested. The obtained aggregates were measured for *EW* and EW_{FD}. The results for measured *EW* and calculated *CW* are shown in Figure 9. From Figure 9A, a transition-like behavior in *EW* of aggregates prepared at increased salt concentrations can be observed. Aggregates prepared at higher salt concentrations retained more water. The transition from lower *EW* to higher *EW* appeared earlier over the salt concentration range in the order of $CaCl_2$ > $CaSO_4$ > $MgCl_2$ > $MgSO_4$. The varied salt concentration yielded aggregates different in size and density, and as a result, the amount of *EW* in the pellet varied from approximately 10 to 25 g of water/g of protein. The same aggregates measured for *CW* within the aggregates (Figure 9B) resulted in 2−4 g of water/g of protein and confirmed that confined water is aggregate-structure-independent.

In conclusion, from this work, two types of water within SP aggregates have been distinguished: (i) entrapped water and (ii) confined water. Entrapped water is associated with (pelleted) aggregates and is not constrained in the exchangeability with a solvent. Confined water in aggregates is hindered in its diffusion because of physical restrictions. This work aimed to show whether aggregates different in structure differ in these two types of water. Prepared aggregates increased in size and decrease in apparent density following the salt type order $MgSO_4$, $MgCl_2$, $CaSO_4$, and $CaCl_2$. Calculations based on AF4 data of water entrapped by aggregates in solution resulted in 21 g of water/g of protein for $MgSO_4$ aggregates (smallest and most dense) and 58 g of water/g of protein for $CaCl_2$ aggregates (largest and least dense). The amount of water entrapped by the pelleted aggregates was from ∼2 to 4 times lower; the difference in entrapped water by the aggregates in the solution and the pelleted aggregates was accounted for by aggregate compressibility (under centrifugal force). Smaller and denser aggregates prepared in the presence of magnesium salts were about twice less compressible compared to larger and less dense aggregates prepared in the presence of calcium salts. When consecutive compression was applied (e.g., washing steps), aggregates prepared in the presence of sulfate salts (smaller and more dense structures) were less deformable, as reflected by the quantity of entrapped D_2O compared to

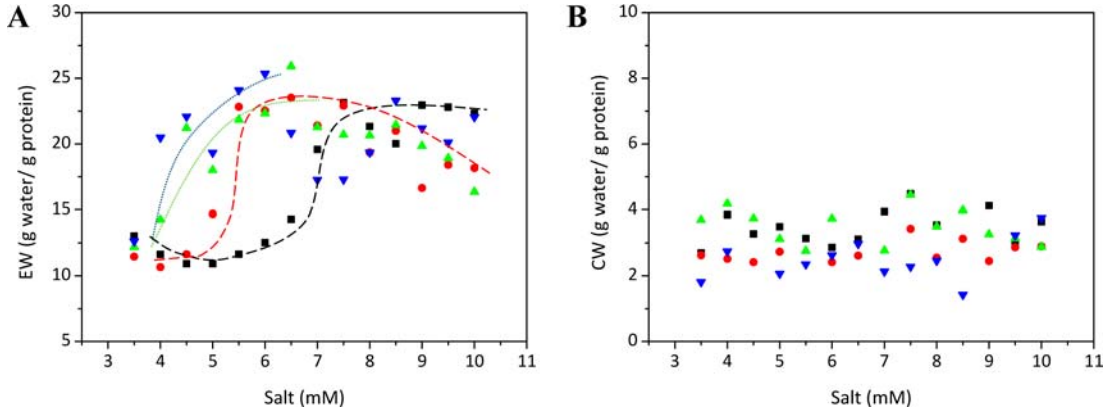

Figure 9. (A) Water entrapped (*EW*) by 1% (v/v) SP aggregates prepared in the presence of 3.5−10 mM $MgSO_4$ (black squares), $MgCl_2$ (red circles), $CaSO_4$ (green upward-facing triangles), and $CaCl_2$ (blue downward-facing triangles). To guide the eye, dashed lines are added for magnesium salts and dotted lines are added for calcium salts. (B) Water confined (*CW*) within aggregate structures.

DOI: 10.1021/acs.jafc.5b03784
J. Agric. Food Chem. 2015, 63, 8912−8920

aggregates prepared in the presence of chloride salts (larger and less dense structures). Diffusible water measurements showed that, irrespective of the aggregate size or density, all diffusible water is instantly exchanged with D_2O. The larger and less dense aggregates entrap more water, and the amount of entrapped water is proportional to the amount of diffusible water. In the case of SP aggregates, the amount of confined water within aggregates is aggregate-structure-independent and approximately 3.5 g of water is confined per gram of protein. Variation in the aggregate structure by varying the salt concentration showed that a broad range of the amount of water entrapped in the pellet can be obtained. However, confined water remained independent of the aggregate structure and varied only between 2 and 4 g of water/g of protein. To conclude, in the case where no forces are applied, larger and less dense aggregates entrap more water. When an external force is applied, more water can be displaced from these aggregates. The aggregate structural aspects do not affect the quantity of confined water within the aggregate structure. Insights in the aggregate size and deformability can be used to better tune WH on the larger length scales.

AUTHOR INFORMATION

Corresponding Author

*Telephone: +31-317-486160. E-mail: laurice.pouvreau@nizo.com.

Notes

The authors declare no competing financial interest.

ACKNOWLEDGMENTS

The authors gratefully acknowledge Pieter de Waard for the help with ^{1}H NMR measurements and Tiny Franssen-Verheijen for the help with SEM imaging.

REFERENCES

(1) Urbonaite, V.; de Jongh, H. H. J.; van der Linden, E.; Pouvreau, L. Origin of water loss from soy protein gels. *J. Agric. Food Chem.* **2014**, *62*, 7550−7558.

(2) Hermansson, A. M.; Lucisano, M. Gel characteristics—water-binding properties of blood plasma gels and methodological aspects on the waterbinding of gel systems. *J. Food Sci.* **1982**, *47*, 1955−1959.

(3) Urbonaite, V.; de Jongh, H. H. J.; van der Linden, E.; Pouvreau, L. Water holding of soy protein gels is set by coarseness, modulated by calcium binding, rather than gel stiffness. *Food Hydrocolloids* **2015**, *46*, 103−111.

(4) Urbonaite, V.; de Jongh, H. H. J.; van der Linden, E.; Pouvreau, L. Permeability of gels is set by the impulse applied on the gel. *Food Hydrocolloids* **2015**, *50*, 7−15.

(5) Ikeda, S.; Morris, V. J. Fine-stranded and particulate aggregates of heat-denatured whey proteins visualized by atomic force microscopy. *Biomacromolecules* **2002**, *3*, 382−389.

(6) Alting, A. C.; Hamer, R. J.; de Kruif, C. G.; Paques, M.; Visschers, R. W. Number of thiol groups rather than the size of the aggregates determines the hardness of cold set whey protein gels. *Food Hydrocolloids* **2003**, *17*, 469−479.

(7) Hermansson, A. M. Gel characteristics—structure as related to texture and waterbinding of blood plasma gels. *J. Food Sci.* **1982**, *47*, 1965−1972.

(8) Hermansson, A. M. Structuring water by gelation. In *Food Materials Science*; Aguilera, J. M., Lillford, P. J., Eds.; Springer: New York, 2008; Chapter 13, pp 255−280, DOI: 10.1007/978-0-387-71947-4_13.

(9) Walstra, P. *Physical Chemistry of Foods*; Marcel Dekker: New York, 2003.

(10) Nieuwland, M.; Bouwman, G. W.; Pouvreau, L.; Martin, A. M.; de Jongh, H. H. J. Relating water holding of ovalbumin gels to aggregate structure. *Food Hydrocolloids* **2016**, *52*, 87−94.

(11) Peters, J. P. C. M.; Luyten, H.; Alting, A. C.; Boom, R. M.; van der Goot, A. J. Effect of crosslink density on the water-binding capacity of whey protein microparticles. *Food Hydrocolloids* **2015**, *44*, 277−284.

(12) Nieuwland, M.; Bouwman, G. W.; Bennink, L. M.; Silletti, E.; de Jongh, H. H. Characterizing length scales that determine the mechanical behavior of gels from crosslinked casein micelles. *Food Biophys.* **2015**, DOI: 10.1007/s11483-015-9399-y.

(13) Aymard, P.; Durand, D.; Nicolai, T.; Gimel, J. C. Fractality of globular protein aggregates: From the molecular to the microscopic level. *Fractals* **1997**, *05*, 23−43.

(14) Pouzot, M.; Nicolai, T.; Durand, D.; Benyahia, L. Structure factor and elasticity of a heat-set globular protein gel. *Macromolecules* **2004**, *37*, 614−620.

(15) Weijers, M.; Visschers, R. W.; Nicolai, T. Influence of the ionic strength on the structure of heat-set globular protein gels at ph 7. Ovalbumin. *Macromolecules* **2004**, *37*, 8709−8714.

(16) Mehalebi, S.; Nicolai, T.; Durand, D. Light scattering study of heat-denatured globular protein aggregates. *Int. J. Biol. Macromol.* **2008**, *43*, 129−135.

(17) Dhayal, S. K.; Gruppen, H.; de Vries, R.; Wierenga, P. A. Controlled formation of protein nanoparticles by enzymatic cross-linking of α-lactalbumin with horseradish peroxidase. *Food Hydrocolloids* **2014**, *36*, 53−59.

(18) Bell, D. J.; Heywood-Waddington, D.; Hoare, M.; Dunnill, P. The density of protein precipitates and its effect on centrifugal sedimentation. *Biotechnol. Bioeng.* **1982**, *24*, 127−141.

(19) Walstra, P. The voluminosity of bovine casein micelles and some of its implications. *J. Dairy Res.* **1979**, *46*, 317−323.

(20) McMahon, D. J.; Brown, R. J. Composition, structure, and integrity of casein micelles: A review1. *J. Dairy Sci.* **1984**, *67*, 499−512.

(21) Dalgleish, D. G. On the structural models of bovine casein micelles-review and possible improvements. *Soft Matter* **2011**, *7*, 2265−2272.

DOI: 10.1021/acs.jafc.5b03784
J. Agric. Food Chem. 2015, 63, 8912−8920

Furthermore, the presence of *a*FAs documented hitherto in food has been attributed to bacterial sources.[3,9,10] This was verified by means of stable carbon isotope analysis in that (the bacterial) *a*FAs in fish and milk fat were more depleted in ^{13}C than conventional fatty acids.[22] Hence, we also studied the bulk $\delta^{13}C$ values (‰) of Brussels sprouts (whole buds and extracted lipids) and the $\delta^{13}C$ values (‰) of *a*17:0 and other fatty acids in Brussels sprouts by compound-specific isotope analysis.

MATERIALS AND METHODS

Chemicals and Standards. Racemic standards of *a*FAs (*a*13:0, *a*14:0, *a*15:0, *a*16:0, *a*17:0, *a*18:0, *a*19:0) and *i*FAs (*i*14:0, *i*15:0, *i*16:0, *i*17:0, *i*18:0) were ordered from Larodan (Malmö, Sweden). Enantiopure (*S*)-enantiomers of *a*15:0 and *a*17:0 as well as 10,11-undecanoic acid and tetradecanoic acid ethyl ester were synthesized by Thurnhofer et al.[23,24] 8-Phenyloctanoic acid (Ph-8:0, purity = 97%) was from Alfa Aesar (Karlsruhe, Germany), whereas myristic acid (14:0) and palmitic acid (16:0) were from Fluka (St. Gallen, Switzerland). A Supelco 37-component FAME mix was ordered from Sigma-Aldrich (Taufkirchen, Germany). Methanol and *n*-hexane (both of HPLC grade, Chem Solute), as well as ethyl acetate and cyclohexane (both purest) were from Th. Geyer (Renningen, Germany). Methanol/ethyl acetate and ethyl acetate/cyclohexane were combined (1:1, v/v) and distilled to obtain the azeotrope (i.e., 44:56 and 54:46, w/w). Tetrahydrofuran (THF) (Fisher Scientific, Schwerte, Germany) was distilled and stored over a molecular filter (3 Å) in the dark until use. Bulk sorbent (isolute-HM-N) was from Biotage (Uppsala, Sweden). Urea (99.5% pure), Na_2SO_4 (99%), NaCl (99.8%), and sulfuric acid (Rotipuran, 98%) were from Carl Roth (Karlsruhe, Germany). PtO_2 was from Sigma-Aldrich (Steinheim, Germany). Hydrogen, helium (both 5.0 quality), and carbon dioxide gas (IRMS reference gas, 4.5 quality) were from Westfalen (Münster, Germany). USGS40 (certified $\delta^{13}C$ value of -26.39 ± 0.04‰ relative to Vienna PeeDee Belemnite (V_{PDB})[25]) was from the U.S. Geological Survey (Reston Stable Isotope Laboratory, Reston, VA, USA). Tin capsules for liquids (Sn purity = 99.9%, 0.04 mL volume, 3.5 × 5.5 mm size) and solids (Sn purity = 97.5%, 0.07 mL volume, 4.0 × 6.0 mm size) were from IVA Analysentechnik (Meerbusch, Germany).

Samples. Four samples of Brussels sprouts (*Brassica oleracea* L. var. *gemmifera*) were obtained from four local farmers close to Stuttgart, Germany (i.e., in Remseck, Bittenfeld, Kernen, and Remstal). The cultivars of the German Brussels sprout samples were the following: Maximus (sample 1), Genius (samples 2 and 3), and Sirius (sample 4). Five additional samples of unknown cultivars were purchased in a local supermarket (three originated from The Netherlands and two from Belgium).

Gas Chromatography with Electron Ionization Mass Spectrometry (GC-MS). FAMEs were analyzed with an HP 5890 series II gas chromatograph in combination with an HP 7673A autosampler and an HP 5971A mass selective detector (Hewlett-Packard/Agilent, Waldbronn, Germany). The temperature of the injection port, operated in splitless mode (1 μL injected), was set to 250 °C. A 60 m length, 0.25 mm internal diameter, fused silica column coated with 0.1 μm film thickness 10% cyanopropylphenyl, 90% bis-cyanopropyl polysiloxane (Rtx-2330, Restek, Bellefonte, PA, USA) was used as the stationary phase. The helium carrier gas was transported with a constant flow of 1 mL/min. The GC oven temperature started at 60 °C, was held for 1 min, and then ramped at 6 °C/min to 150 °C, at 4 °C/min to 190 °C, and finally at 7 °C/min to 250 °C (held for 7 min) (modified from Thurnhofer et al.[26]). Electron ionization was performed at 70 eV. The transfer line and the ion source temperature were set at 280 and 165 °C, respectively. In the full scan mode, *m*/*z* 50−550 was recorded after a solvent delay of 8 min. In the selected ion monitoring (SIM) mode, *m*/*z* 74, 87, 81, 79, 88, and 101 were measured from 8 min until the end of the run.[26] In addition, *m*/*z* values representing the molecular ions of different FAMEs were determined in nine time windows (Table S1, Supporting Information).[26] The time windows were set by measuring the retention times of 49 FAMEs (i.e., a 37-component FAME mix spiked with methyl esters of 7 *a*FAs and 5 *i*FAs).

By GC-MS in the SIM mode, FAMEs were identified on the basis of (i) identical retention times with FAMEs in the reference standard and (ii) the match of the molecular ion and selected fragment ions in the mass spectral data.[26] Co-elutions were observed for the methyl esters of *i*17:0 and 16:1 isomers and well as those of *i*18:0 and 17:1 isomers. Elution of *a*FA methyl esters without interference from methyl esters of unsaturated fatty acids was monitored by means of *m*/*z* 240 (M^+ of 14:1-ME), *m*/*z* 256 (M^+ of *a*15:0-ME), *m*/*z* 268 (M^+ of 16:1-ME), *m*/*z* 284 (M^+ of *a*17:0-ME), *m*/*z* 296 (M^+ of 18:1-ME), and *m*/*z* 312 (M^+ of *a*19:0-ME).

Extraction of Samples. Edible buds of Brussels sprouts (cut into pieces) were freeze-dried for 5 days in a LYOVAC GT 2 system (Leybold-Heraeus, Hürth, Germany) at 0.1 mbar (Figure 2, step 1).

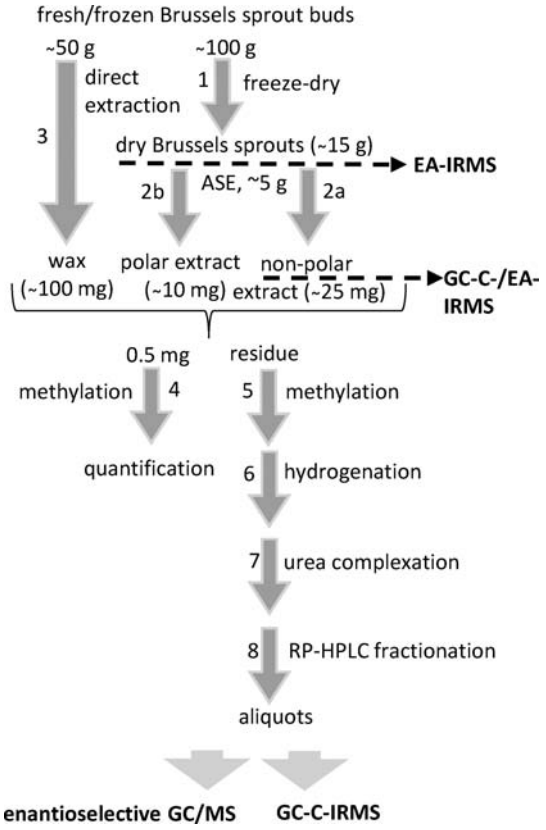

Figure 2. Work flow of the preparation of Brussels sprouts with (1) freeze-drying, (2) accelerated solvent extraction with (a) ethyl acetate/cyclohexane and (b) ethyl acetate/methanol, (3) direct extraction with *n*-hexane, (4) methylation with internal standards,[24] (5) methylation, (6) hydrogenation, (7) urea complexation, and (8) RP-HPLC fractionation.

Lipids were extracted by means of accelerated solvent extraction (ASE 200, Dionex, Idstein, Germany) according to the method of Hauff and Vetter.[27] For this purpose, ~5 g of freeze-dried sample was placed in 22 mL extraction cells and the residual space was made up with ~2 g of bulk isolute sorbent. Each cell was extracted twice with 40 mL of ethyl acetate/cyclohexane (1:1 v/v) (Figure 2, nonpolar extract, step 2a) followed by one portion of 40 mL of methanol/ethyl acetate (1:1 v/v) (Figure 2, polar extract, step 2b) (125 °C, 10 MPa, heating time of 6 min).[27] The nonpolar and polar ASE extracts were individually concentrated in a rotary evaporator (200 mbar, 35 °C bath temperature) and adjusted to exactly 5 mL in a calibrated flask. Aliquots (1 mL) were used for gravimetric determination of the lipid content.

DOI: 10.1021/acs.jafc.5b03877
J. Agric. Food Chem. 2015, 63, 8921−8929

Extraction of the wax layer was based on the method of Cannon et al., which consists of extraction with *n*-hexane followed by cooling and collection of the crystalline wax fraction from the hexane extract by filtration.[28] Initial tests showed that >97% of the extracted substances crystallized and only ~3% was separated in the form of an oily residue. Subsequent analysis of the fatty acid pattern in the hexane extract and the oily and crystalline fractions differed by <5%. Therefore, the crystallization step was omitted, and the neat hexane extract was analyzed for the wax phase. In praxis, the wax layer of edible Brussels sprout buds (50 g) was extracted with 100 mL of *n*-hexane in an ultrasonic bath (2 h, 40 °C) (Figure 2, step 3). The solution was filtered, and the organic solvent was evaporated to dryness on a rotavapor system (200 mbar, 35 °C water bath temperature). The lipid content of the wax was determined gravimetrically.

Preparation of Fatty Acid Methyl Esters. For quantitative analysis (Figure 2, step 4), aliquots (representing ~0.5 mg of fat) of the nonpolar (step 2a) and polar (step 2b) ASE extract as well as the extracted wax (step 3) were methylated with 2 mL of 1% sulfuric acid in methanol in a sand bath (80 °C, 1.5 h) after the addition of 10 μL of a solution of 10,11-dichloroundecanoic acid (internal standard I, 1 mg/mL solvent).[24] The lipid extracts of the samples were cooled on ice, 2 mL of a pure water and saturated aqueous solution of NaCl was added, and FAMEs were extracted with 2 mL of *n*-hexane according to the method of Thurnhofer et al.[24] After the addition of 10 μL of a tetradecanoic acid ethyl ester solution (internal standard II, 0.5 mg/mL),[24] the resulting sample solution was used for FAME quantification by nonchiral GC-MS. All samples were analyzed in duplicates, but only mean values will be presented, because of an excellent agreement of the replicate samples (<1% discrepancy). To calculate the fatty acid composition in the edible part of Brussels sprouts, individual amounts of FAs in the polar ASE extracts and the nonpolar ASE extracts were summed. Fatty acid standards (2.6 mg of Ph-8:0 as well as *a*FAs, *i*FAs, 14:0 and 16:0, ~5 mg per compound) were methylated without the use of internal standards.

For enantioselective and stable isotope analysis, ~20 mg of extracted nonpolar and ~5 mg of polar ASE extracts as well as ~195 mg of wax layer (after solvent removal) were methylated with 1% sulfuric acid in methanol (20 mL per 100 mg fat/extract) by refluxing for 2 h in a 250 mL round-bottom flask (Figure 2, step 5).[29] After cooling on ice, 10 mL of water and 10 mL of a saturated aqueous solution of NaCl were added, and FAMEs were extracted three times with *n*-hexane (10 mL per 100 mg fat, respectively). *n*-Hexane extracts were concentrated to 5 mL in a rotatory evaporator (40 °C bath temperature, 200 mbar) and used for *a*FAME enrichment (Figure 2, steps 6–8).

Enrichment of *anteiso*-Fatty Acid Methyl Esters for Enantioselective and Stable Carbon Isotope Analysis. FAME solutions of Brussels sprout buds (gathered from the wax as well as the nonpolar and polar ASE extracts) were separately hydrogenated to remove unsaturated fatty acids according to the method of Hauff et al. (Figure 2, step 6).[30] Briefly, FAME solutions in *n*-hexane (see above) were evaporated to dryness in a gentle stream of nitrogen (35 °C), redissolved in THF (7 mL per 100 mg FAME), and transferred into a 50 mL round-bottom, two-neck flask. PtO_2 (~3 mg) was added, and the flask was purged with nitrogen for 2 min. A hydrogen-filled balloon was set on one neck, the flask was filled with hydrogen, and the second neck was closed with a stopper. The sample solution with the FAMEs was stirred for 2 h at room temperature. After hydrogenation, the catalyst was separated by membrane filtration (0.45 μm) and the solvent was removed in a nitrogen stream (35 °C) and redissolved in 5 mL of *n*-hexane. An aliquot (about 0.1 mg/mL) was analyzed by GC-MS. The major part of the sample (~95%) was transferred into a preweighed 250 mL round-bottom flask, the solvent was removed by rotary evaporation (40 °C bath temperature and 250 mbar), and the weight of FAMEs was determined gravimetrically. Urea complexation (Figure 2, step 7) was performed by adding urea and methanol to give the ratio FAMEs/urea/methanol of 1:6:20 (w/w/v).[29] After shaking, the sample solutions were heated to 60 °C and then stored for 3 days at room temperature without any vibration.[29] Samples were transferred through a fluted filter into another flask, and the filtrate was mixed with (i) 15 mL of water (bidistilled) and (ii) 15 mL of saturated NaCl solution. Dissolved FAMEs were extracted five times with 10 mL of *n*-hexane. The combined *n*-hexane extracts were evaporated to dryness. After weighing out, the FAMEs were redissolved in 5 mL of *n*-hexane. An aliquot was analyzed by nonchiral GC-MS. The majority of the FAME fraction was fractionated by nonaqueous reversed-phase high-performance liquid chromatography (RP-HPLC) (Figure 2, step 8) using an HPLC system consisting of a 600S controller, a 717 plus autosampler, a 616 pump, and a 996 photodiode array detector operated at 210–400 nm (Waters, Milford, MA, USA). Three serially connected 250 mm length × 4 mm internal diameter C_{18} columns (ET 250/8/4 Nucleosil 7 C_{18}, 7 μm particle size, then ET 250/8/4 Nucleosil 5 C_{18}-AB, 5 μm particle size, and finally again ET 250/8/4 Nucleosil 7 C_{18}) from Macherey-Nagel (Düren, Germany) were used as stationary phase, whereas methanol served as the mobile phase (flow rate of 0.5 mL/min).[1,30] The injector was equipped with a 200 μL sample loop into which solutions of 150 μL of FAME standards or solutions of Brussels sprouts were injected.

The RP-HPLC fractionation scheme was developed by means of the injection of 10 μg of *a*15:0-ME, 10 μg of *a*17:0-ME, 50 μg of 14:0-ME, 50 μg of 16:0-ME, and 20 μg of Ph-8:0-ME (FAME standard solution in methanol). Ninety fractions of 0.5 min (250 μL) were collected between 15 and 60 min. The fractions were evaporated to dryness, redissolved in 200 μL of *n*-hexane, and analyzed by GC-MS. On the basis of these results, FAMEs from Brussels sprout samples (~0.1 mg) and ~20 μg of Ph-8:0-ME in 200 μL of methanol were injected, and the fractionation was started 2.5 min after the detection of the UV signal of the internal standard Ph-8:0-ME (retention time ~ 16.5 min) with one 3 min fraction (~19–22 min, F1), four 1 min fractions (~22–23 min, F2; ~23–24 min, F3; ~24–25 min, F4; ~25–26 min, F5), and finally one 2 min fraction (~26–28 min, F6). The solvent of the six fractions was evaporated in a gentle stream of nitrogen (40 °C) followed by the addition of 150 μL of *n*-hexane. The solutions were screened by nonchiral GC-MS analysis.

Enantioselective GC-MS Analysis. An HP GCD plus GC-MS system equipped with an HP 6890 autosampler (Hewlett-Packard, Waldbronn, Germany) was used in combination with a GC capillary column (60 m, 0.25 mm internal diameter, 0.18 μm film thickness) coated with 66% heptakis(2,3-di-*O*-methyl-6-*O*-*tert*-butyldimethylsilyl)-β-cyclodextrin (β-TBDM) in OV-1701 (custom-made by BGB Analytik, Adliswil, Switzerland). Composition and dimensions were the same as in a prototype previously used by Hauff et al.[1] Sample and standard solutions (1 μL) were injected in splitless mode at 250 °C. The transfer line and the ion source temperatures were set at 280 and 165 °C, respectively. The helium carrier gas was transported with a constant flow rate of 1.0 mL/min. Enantioselective GC-MS-SIM determinations were carried out by monitoring *m*/*z* 74, 87, and 242 (M^+ of 14:0-ME isomers), *m*/*z* 256 (M^+ of 15:0-ME isomers including *a*15:0-ME), *m*/*z* 270 (M^+ of 16:0-ME isomers), and *m*/*z* 284 (M^+ of 17:0-ME isomers including *a*17:0-ME) throughout the run.[1] Low isothermal elution temperatures of *a*FA methyl esters required longer retention times than the maximum run time of our GC-MS data processing software (650 min).[1] Therefore, two runs were programmed consecutively, injecting air in run 2 and setting the column equilibration time between runs 1 and 2 to 0 s as well as starting temperature in run 2 at the final isothermal temperature of run 1 (Figure S1, Supporting Information).[1] Different GC oven programs and carrier gas flows (0.8, 0.9, 1.0, 1.2 mL/min) were investigated, and the best enantiomer resolution was obtained with 1 mL/min under the following conditions. The GC oven temperature program started at 60 °C, which was held for 1 min. This was followed by a ramp of 20 °C/min to 112 °C (temperature held for 455 min) and a ramp of 1 °C/min to 132 °C (temperature held for 171 min) (run time = 650 min).[1] The second run started at 132 °C for 260 min (combined isothermal time at 132 °C = 431 min).[1] Then, the temperature was raised at 30 °C/min to 200 °C (temperature held for 15 min) to elute other compounds in the sample extracts. The total run time was 927 min (Figure S1, Supporting Information). Racemic *a*15:0-ME eluted after 514.3 min ((*R*)-*a*15:0) and 516.2 min ((*S*)-*a*15:0) from the β-TBDM column. The valley between the peaks was 48%. Likewise, the

DOI: 10.1021/acs.jafc.5b03877
J. Agric. Food Chem. 2015, 63, 8921–8929

enantiomers of *a*17:0-ME (868.4 min (*R*)-*a*17:0 and 872.9 min (*S*)-*a*17:0) were partly resolved (the valley between the peaks was 39%). Despite the longer GC oven program and the same carrier gas flow, the new β-TBDM column provided smaller peaks, longer retention times, and a better enantiomer resolution for *a*15:0-ME and *a*17:0-ME compared to the study of Hauff et al. (retention times *a*15:0-ME 450.2 and 456.1 min, valley of 35%, and retention times *a*17:0-ME 730.1 and 739.9 min, valley of 18%).[1] The methyl esters of 14:1n-5, 14:0, *i*15:0, 15:0, 16:1n-7, 16:0, *i*17:0, and 17:0 (t_R 360, 410, 520, 550, 650, 708, 880, and 890 min, respectively) did not interfere with the *a*FAs.

Peaks in the GC-MS-SIM chromatograms (*m*/*z* 74 and 87) of samples were smoothed using the method of Savitzky and Golay.[31] Results were expressed by the enantiomeric excess (ee in %) of the (*S*)-enantiomers according to eq 1:[32]

$$\text{ee} = \frac{[S] - [R]}{[S] + [R]} \times 100\ (\%) \quad (1)$$

with [*S*] and [*R*] being the concentrations of the (*S*)- and (*R*)-enantiomers of the methyl ester of *a*15:0 and *a*17:0, respectively.

On the basis of previous experience, we expected dominance of (*S*)-*a*FAs and possible traces of the (*R*)-enantiomers.[1,2] Evaluation was carried out relative to the following mixtures of racemic and (*S*)-enantiopure *a*15:0-ME and *a*17:0-ME: Four vials containing 100 μL of (*S*)-*a*15:0-ME and (*S*)-*a*17:0-ME (2.5 ng/μL per compound) were prepared, and 2, 5, 10, or 25 μL was removed with a microliter syringe and substituted by the same volume of racemic solution (5 ng/μL of *a*15:0-ME and *a*17:0-ME). These samples corresponded with a share of (*R*)-*a*FAMEs at 2% (ee = 96%), 5% (ee = 90%), 10% (ee = 80%), and 25% (ee = 50%). The fifth reference standard consisted of (*S*)-enantiopure *a*FAMEs. GC-MS-SIM chromatograms (after peak smoothing[31]) of the five reference standards were characterized by increasing shoulder peaks with decreasing ee (Figure 3). In the case of *a*15:0-ME, ee = 96% could be unequivocally distinguished from ee = 100%, and ">98%" was defined to be the maximum value that could be verified under these chromatographic conditions (Figure 3a). The same approach verified that "ee > 96%" was the limit for *a*17:0-ME (Figure 3b).

Samples in which the peak shape of the *a*FA methyl esters showed no noticeable deviation from the one of neat (*S*)-*a*FAME standards were classified enantiopure (ee > 98% for *a*15:0-ME and ee > 96% for *a*17:0-ME). In the case of the detection of (*R*)-enantiomers prior to the first eluting (*S*)-enantiomer in samples, ee was assigned on the basis of the closest match of the abundance of the shoulder peak with the one in the reference standards. This procedure was carried out with both *m*/*z* 74 and 87, and all samples were processed and analyzed at least in duplicate (by individual weighing in and including all enrichment steps). For verification of *a*FA methyl esters, SIM ion traces were superimposed to prove congruent run for both enantiomers (Figure S2, Supporting Information) and thereby excluding coelutions with other compounds.[2] Racemic *a*19:0-ME could not be sufficiently resolved on the β-TBDM column, and its enantioselectivity in Brussels sprout buds could not be explored.

Stable Carbon Isotope Analysis (δ^{13}C Values in ‰). Compound-specific isotope analysis was performed with a Delta plus XP mass spectrometer (Thermo Finnigan MAT, Bremen, Germany) coupled to a 6890 GC (Agilent, Waldbronn, Germany) via a GCC III combustion/reduction interface (GC-C-IRMS). The oxidation reactor (CuO, NiO, Pt) was operated at 940 °C and the reduction reactor (Cu wires) at 650 °C.[22] Removal of water was facilitated by a Nafion tube. Three ion currents (i.e., *m*/*z* 44, 45, and 46 were monitored throughout the run, and standardization of runs was achieved by injecting five times CO_2 gas with a known δ^{13}C value (−28.4‰) directly into the ion source of the mass spectrometer. A 30 m × 0.25 mm internal diameter column coated with a 0.25 μm film of 50% phenyl, 50% dimethylpolysiloxane (CP-Sil 24CB, Varian, Middelburg, The Netherlands), was used in combination with the following GC oven program: 60 °C (hold for 1 min), raised at 10 °C/min to 160 °C, raised at 2 °C/min to 200 °C, and raised at 10 °C/min to 270 °C (hold for 5 min). The injector temperature was set at 260 °C, and the

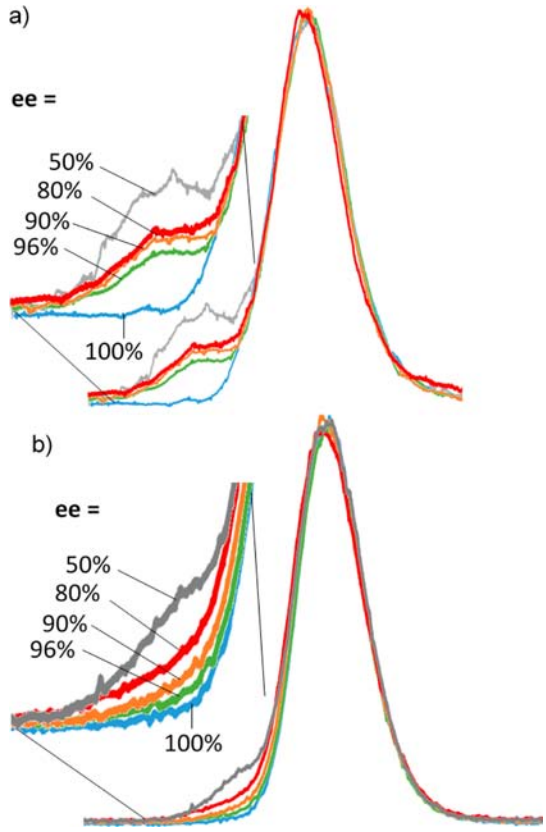

Figure 3. GC-MS-SIM chromatograms (*m*/*z* 74) of the enantioselective determination of a standard solution of (*S*)-*anteiso*-fatty acid methyl esters and admixtures with various amounts of racemic standards on β-TBDM after smoothing according to Savitzky and Golay:[31] (a) *a*15:0-ME and (b) *a*17:0-ME with partial enlargement inserted with lines in blue, ee 100%; green, ee 96%; orange, ee 90%; red, ee 80%; and gray, ee 50%.

helium carrier gas flow rate was 1.6 mL/min. HPLC fractions (step 8) of polar and nonpolar ASE extracts of four samples from Germany, two samples from Belgium, and one sample from The Netherlands (2 μL) that contained both *a*17:0-ME and 16:0-ME were used for the measurements. The HPLC fractions were adjusted to *a*17:0-ME ~ 30 ng/μL, and the solution was measured five times. The second fatty acid, 16:0-ME, was detected in two HPLC fractions. After GC-IRMS measurement of *a*17:0-ME, this and the subsequent HPLC fraction were combined and diluted to give 16:0-ME = 30 ng/μL. The resulting solution was also measured five times in the samples. Two microliters of the samples was injected in splitless mode (split opened after 2 min), and data were processed with Isodat 2.0 software (Thermo Finnigan MAT, Bremen, Germany). Due to a rapid and quantitative derivatization, no kinetic isotope effects were expected in the formation of FAMEs.[33,34] For quality control, selected samples were also analyzed without previous enrichment of *a*17:0-ME and 16:0-ME (injection of 30 ng of the analytes). Only this retention time range was transferred from the GC column to the combustion unit. The resulting δ^{13}C value (in ‰) matched the one in the enriched samples. By this measure it was verified that sample enrichment was not accompanied by isotope discrimination.

Bulk δ^{13}C values (‰) of nonpolar ASE extracts as well as freeze-dried whole edible buds of Brussels sprouts were analyzed with a Euro EA 3000 elemental analyzer (Hekatech, Wegberg, Germany) coupled to the IRMS system mentioned above. The furnace temperatures for oxidation and reduction were set to 650 and 1000 °C, respectively, and the helium carrier gas pressure was set at 70 kPa with a purge flow at 80 mL/min. Each EA-IRMS run started by measuring three times the reference CO_2 gas. For sample measurement about 2 mg of freeze-

DOI: 10.1021/acs.jafc.5b03877
J. Agric. Food Chem. 2015, 63, 8921−8929

Table 1. Country of Origin and $\delta^{13}C$ Values of the Whole Freeze-Dried Plants, Nonpolar Lipid Extracts, Palmitic Acid Methyl Ester (16:0-ME), and *anteiso*-Heptadecanoic Acid Methyl Ester (*a*17:0-ME) as well as Amounts of Individual Fatty Acids in the Wax and Lipids[a] of the Brussels Sprout Samples

	concentration (mg/100 g Brussels sprouts)																	
sample:	1		2		3		4		5		6		7		8		9	
origin:	Germany		Germany		Germany		Germany		Belgium		Belgium		Netherlands		Netherlands		Netherlands	
cultivar:	Maximus		Genius		Genius		Sirius		unknown		unknown		unknown		unknown		unknown	
	wax	lipid	wax	lipid	wax	lipid	wax	lipid	wax	lipid	wax	lipid	wax	lipid	wax	lipid	wax	lipid
short chain, sat.[b]	0.29	0.66	0.45	0.99	0.48	1.18	0.62	0.44	0.43	0.67	0.40	0.98	0.81	0.89	0.84	0.91	0.99	0.83
16:0	0.69	90.8	1.01	86.1	0.82	61.0	1.67	40.3	1.25	77.3	0.66	95.8	1.70	84.8	1.95	85.3	1.65	87.5
long chain, sat.[c]	0.60	7.29	0.86	11.2	1.05	12.8	1.98	8.13	1.12	12.6	0.79	11.3	1.56	9.37	1.62	8.13	1.42	8.54
monoenic	0.09	8.63	0.01	8.66	0.02	8.63	0.11	4.30	0.08	8.15	0.01	11.0	0.05	9.87	0.06	11.0	0.09	9.25
dienoic	0.17	35.7	0.15	28.4	0.10	25.2	0.24	18.3	0.20	31.7	0.09	40.1	0.25	31.5	0.31	34.2	0.25	29.5
trienoic	1.05	94.6	1.54	82.0	0.88	57.5	1.10	33.5	1.22	80.1	0.52	94.1	1.49	75.8	1.51	76.5	1.40	73.5
*a*15:0	0.004	0.04	0.01	0.07[d]	0.01	0.09[d]	0.03[d]	0.02	0.03[d]	0.05	0.01	0.07[d]	0.01	0.03	0.02	0.03	0.01	0.02
*a*17:0[e]	0.15	2.78	0.23	6.98	0.24	6.32	0.26	3.20	0.18	5.74	0.20	7.1	0.31	4.70	0.49	4.35	0.30	3.24
*a*19:0	0.15	0.70	0.25	1.87	0.26	1.92	0.32	1.03	0.19	1.35	0.20	1.65	0.35	1.48	0.47	1.21	0.29	1.12
*a*21:0	0.01	0	0.04	0.17	0.04	0.17	0.04	0.08	0.02	0.07	0.03	0.12	0.04	0.12	0.01	0.09	0.02	0.07
*i*16:0	0.01	0.24	0.02	0.19	0.01	0.14	0.03	0.08	0.02	0.21	0.01	0.20	0.03	0.14	0.04	0.11	0.02	0.14
*i*18:0	0.07	0.49	0.10	0.18	0.08	0.29	0.17	0.2	0.13	0.52	0.07	0.32	0.18	0.31	0.22	0.29	0.16	0.20

	$\delta^{13}C$ values (‰)								
sample:	1	2	3	4	5	6	7	8	9
origin:	Germany	Germany	Germany	Germany	Belgium	Belgium	Netherlands	Netherlands	Netherlands
cultivar:	Maximus	Genius	Genius	Genius	Sirius	unknown	unknown	unknown	unknown
$\delta^{13}C$, plant	−28.4	−28.3	−27.5	−28.6	−29.6	−27.0	−29.1		
$\delta^{13}C$, lipids	−35.2	−34.1	−34.3	−35.6	−37.4	−35.0	−37.0		
$\delta^{13}C$, 16:0-ME	−34.5	−33.5	−33.5	−35.0	−37.1	−34.4	−37.3	−37.5	−37.8
$\delta^{13}C$, *a*17:0-ME	−34.0	−33.1	−32.8	−33.9	−35.8	−34.1	−36.0	−36.0	−36.2

[a]Summed nonpolar and polar ASE extract. [b]Sum of the contribution of 8:0−15:0. [c]Sum of the contribution of >16:0. [d](*S*)-Enantiopure (ee >98%). [e](*S*)-Enantiopure (ee >96%).

J. Agric. Food Chem. 2015, 63, 8921−8929
DOI: 10.1021/acs.jafc.5b03877

dried Brussels sprouts was transferred by means of a spatula/syringe into tin capsules for solids, and an aliquot of the nonpolar ASE extract was placed in preweighed tin capsules for liquids. The capsules were stored overnight at room temperature for total evaporation of the solvent from the lipid samples, and the lipid amount was determined by reweighing of the fat-containing capsules.[35] Each sample was analyzed in duplicate. USGS40 was used as secondary standard to calibrate the system.[25] $\delta^{13}C$ values (‰) were calculated by means of the international internal Standard V_{PDB} (in ‰), where R is the measured isotope ratio $^{13}C/^{12}C$ eq 2:[34]

$$\delta^{13}C\ (‰) = (R_{sample} - R_{standard})/R_{standard} \times 10^3 \quad (2)$$

RESULTS AND DISCUSSION

Fatty Acid Pattern and Share of *anteiso*-Fatty Acids in Brussels Sprout Buds. Fatty acids were determined as methyl esters but will be discussed as fatty acids to keep the text simpler. Both *a*FAs and *i*FAs were detected in all Brussels sprout samples (i.e., the ASE extracts representing the edible part and *n*-hexane extracts representing the wax) (Table 1). Due to the low contribution of the wax to Brussels sprouts, the amount of *a*FAs was on average 10-fold higher in the total lipids (i.e., ~3−7 mg *a*17:0/100 g Brussels sprouts) than in the wax layer (~0.2−0.5 mg *a*17:0/100 g Brussels sprouts; Table 1). This was surprising because the presence of *a*FAs had hitherto been reported only in (surface) wax[17,18] but not in the edible part of Brussels sprouts.[36] In the present samples, the wax layer and the total lipids (sum of nonpolar and polar ASE extracts) were dominated by *a*17:0 and *a*19:0, whereas *a*15:0 and *a*21:0 occurred only as minor components (Table 1; Figure 4). Typically, *a*17:0 and *a*19:0 were on the same level in wax, whereas *a*17:0 was more abundant in the total lipids (Table 1; Figure 4). In addition, the samples also contained *i*16:0 and *i*18:0 (i.e., a total of six BCFAs). The main difference between total lipids and wax layer originated from differences in *a*17:0.

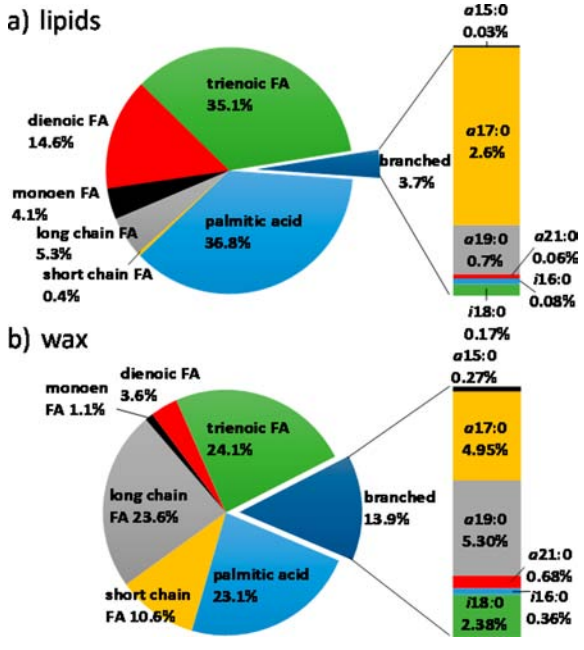

Figure 4. Share of different fatty acids in the fatty acid pattern in lipids (sum of nonpolar and polar ASE extracts) (a) and wax (b) of Brussels sprout buds with short-chain FA defined as the sum of the contribution of 8:0−15:0 and long-chain FA as the sum of the contribution of >16:0.

The BCFA pattern in our wax samples differed from two literature reports in the fact that long-chained BCFAs were more relevant in the previous studies.[17,18] Baker and Holloway additionally detected *a*23:0 (0.6%) and even-numbered, long-chained *i*FAs (up to *i*24:0) in Brussels sprout wax.[17] Even longer homologues (*a*25:0−*a*31:0, dominated by *a*29:0, 29.8%) were detected in the free fatty acid fraction of the wax of a subglaucous mutant of *B. oleracea*.[18] These examples indicate different patterns from sample to sample depending on growing conditions and genotype.[17] The presence of BCFAs has been associated with their role in membrane fluidity.[12,13,15] However, separate investigation of the nonpolar and polar ASE extracts did not reveal higher *a*FA contents in the polar fraction.

The contribution of *a*17:0 to the fatty acid pattern in the total lipids of Brussels sprouts (~2.6% of the fatty acids; Figure 4a) was higher than in the major sources of *a*FAs in food, that is, fish oil (~0.5%)[7,9] and milk fat of ruminants (~1%).[3,8,10] Apart from BCFAs, the fatty acid patterns of the wax[12] and the total lipids of Brussels sprouts[30,31] were similar to those reported in the literature. Short-chain saturated fatty acids (8:0−15:0) as well as the long-chain saturated fatty acids (>16:0) represented less than 10 and 25% of the fatty acid pattern, and 16:0 was the most abundant saturated fatty acid (>20%, Figure 4). The majority of unsaturated fatty acids originated from 18:3n-3 (trienoic acids >20%; Table 1; Figure 4,5a).

The sole presence of odd-numbered *a*FAs in Brussels sprouts agreed with reports in fish[7] and milk from ruminants.[8] By contrast, even-numbered *a*FAs were described in alpine plants (*Oxygraphos glacialis*, *Rhodiola pamiroalaica*, and *Swertia*

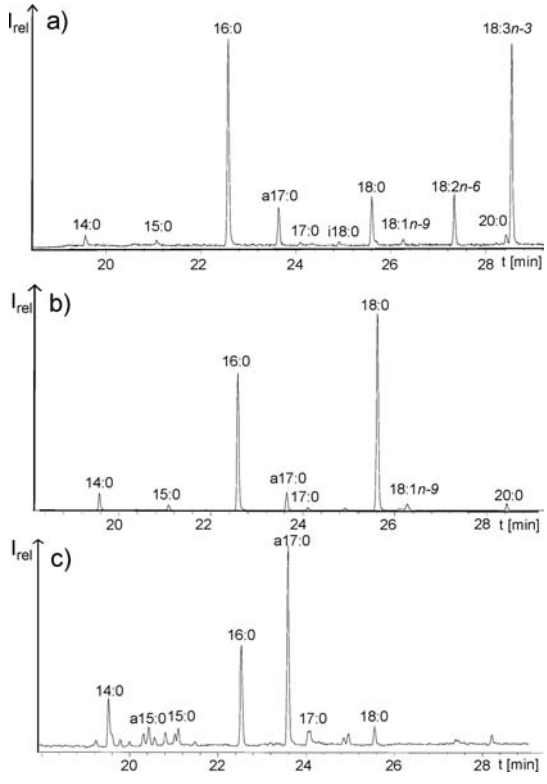

Figure 5. GC-EI-MS-SIM chromatograms (TIC) of the methyl esters from the polar lipid ASE extract of Brussels sprout buds with (a) sample before hydrogenation and urea complexation, (b) sample after hydrogenation, and (c) filtrate of the urea complexation.

DOI: 10.1021/acs.jafc.5b03877
J. Agric. Food Chem. 2015, 63, 8921−8929

marginata)[12] and in the phospholipids from petals and yellow-white leaves from *Antirrhiunum majus* (*a*22:0).[15] Only *a*17:0 was described in Pinaceae and *Ginkgo biloba* seed lipids.[14]

Enrichment of a15:0 and a17:0 from FAME Solutions of the Samples. Partly due to the low contributions of *a*FAs (Table 1) and presumably low contributions of (*R*)-*a*FAs in the samples,[1,2] it was necessary to perform a selective enrichment of the *a*FAs by (i) hydrogenation, (ii) urea complexation, and (iii) RP-HPLC (see Materials and Methods). After hydrogenation, 18:3n-3 and 18:2n-6 (~30−50% of the fatty acids in Brussels sprouts; Figure 4) were no more detected in the solutions (Figure 5a,b; Table S2, Supporting Information). Only low amounts of 18:1n-9 (<2.1% of the total FAs) were still present in the sample solutions (Table S2, Supporting Information). Consequently, the abundance of 18:0 and 16:0 increased, and these were now the most abundant FAMEs (Figure 5b). The relative contribution of *a*FAs remained unchanged (Table S2, Supporting Information). After separation of 18:0 and 16:0 by urea complexation,[29,37,38] *a*17:0 became the dominant FAME in the resulting sample solutions (Figure 5c; Table S2, Supporting Information). Despite the effective enrichment of *a*15:0-ME and *a*17:0-ME up to this point, the varied abundance of both *a*FAs (*a*17:0 ≫ *a*15:0; Table 1) and other FAMEs in the extracts still prevented the direct enantioselective determination of both compounds on the *β*-TBDM column. Hence, a final enrichment step was performed by means of nonaqueous RP-HPLC.[1] *a*15:0-ME eluted into RP-HPLC fraction F2 with a purity of ~80% (additionally <10% 14:0-ME), whereas *a*17:0-ME was collected in RP-HPLC fraction F5 (purity of ~75%, along with aliquots of 16:0-ME). Further fatty acids were not detected by means of *m*/*z* 74 and 87. Both 14:0 and *a*15:0 as well as 16:0 and *a*17:0 were well separated on the *β*-TBDM column. Hence, coelutions were not expected during enantioselective GC analysis.

Enantioselectivity of *anteiso*-Fatty Acids in the Samples. Due to low amounts in the solutions (<0.5 ng/μL sample solution) enantioselective determinations of *a*15:0 were successful in only three enriched nonpolar and polar ASE extracts from Brussels sprouts (samples 2, 3, and 6) as well as in two wax samples (samples 4 and 5). By contrast, *a*17:0 could be measured in wax, polar, and nonpolar ASE extract of all Brussels sprout samples. Without exception, the peaks of *a*15:0-ME and *a*17:0-ME were fully congruent with the peak shape of pure (*S*)-*a*15:0-ME standard (ee > 98%) and (*S*)-*a*17:0-ME standard, respectively (ee > 96%). In either case, even in the polar ASE extract, the (*R*)-enantiomer could not be detected. This contrasts with *a*FAs of dairy products and fish, where the (*R*)-enantiomers represented up to 10% of *a*15:0 and *a*17:0.[1,2] The reasons for the varied presence or absence of (*R*)-*a*FAs are currently unknown.

Stable Carbon Isotope Analysis (δ^{13}C Values in ‰). Fatty acids from bacteria living on the wax surface were a possible source of *a*FAs in this sample matrix. In this context it has been shown that bacteria utilize ^{12}C in preference to ^{13}C.[39] As a consequence, bacterial fatty acids in milk fat, including *a*FAs, were lighter in carbon than conventional fatty acids such as 16:0.[22] However, compound-specific isotope analysis of FAMEs from Brussels sprout samples showed no such difference in the δ^{13}C values between *a*17:0-ME and 16:0-ME (Table 1). Both fatty acids showed δ^{13}C values in the range from −37.7 to −32.8‰ with *a*17:0-ME being lighter in carbon in some samples and 16:0-ME being lighter in carbon in other samples (Table 1). Hammer et al. also found more negative δ^{13}C values for 17:0 isomers than in even-numbered FAs in the lipids of seagrass (*Halodule wrightii*) and redhead ducks, indicating different sources or synthesis via distinct catabolic pathways.[40] This scenario was obviously not valid for Brussels sprouts.

Because both FAMEs were comparably light in carbon, we additionally investigated bulk δ^{13}C values. Freeze-dried total Brussels sprout buds (−29.6 to −27.0‰; median, −28.4‰; Table 1; Figure 6) were in the "lighter" range of C_3-plants

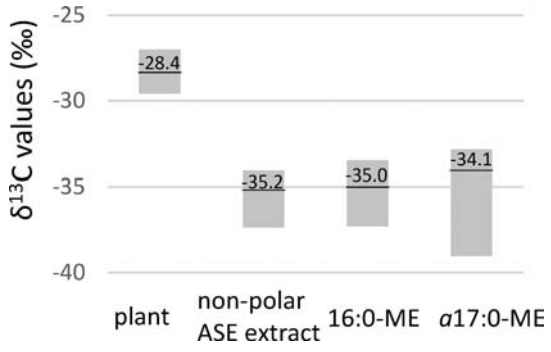

Figure 6. Range and median of the δ^{13}C values of the whole freeze-dried Brussels sprout buds and the nonpolar ASE extract (obtained with cyclohexane/ethyl acetate extraction) measured with EA-IRMS as well as the δ^{13}C values from the palmitoic acid methyl ester (16:0-ME) and the *anteiso* heptadecanoic acid methyl ester (*a*17:0-ME) measured with GC-C-IRMS.

(δ^{13}C values < −24‰).[34,41,42] The comparably wide range ($\Delta\delta^{13}$C = 2.6‰) between individual samples was most likely due to different climatic, geographic, and growing conditions (e.g., in greenhouse or field).[34] Interestingly, the range of δ^{13}C values in the samples from Germany ($\Delta\delta^{13}$C = 1.1‰) was comparably small (Table 1). In accordance with other studies,[42] the nonpolar ASE extract, representing the lipid fraction, was more depleted in ^{13}C than the whole plant (median, −35.2‰; Table 1; Figure 6). The difference (on average, 7.1‰) between the δ^{13}C values of lipids and whole plants was comparable with results from seagrass ($\Delta\delta$ ^{13}C = 6.7‰).[40] The δ^{13}C values of lipids varied by ~3‰, and samples lightest in carbon of lipids were those lightest in carbons of the FAMEs (Table 1). The difference between δ^{13}C values in lipids and the mean value of the two FAMEs was ~1‰, which is partly due to the isotope signature of the methanol used in the methylation step and also due to intrinsic differences between values obtained from EA-IRMS and GC-C-IRMS.[33,34,43] On the basis of stable carbon isotope ratios, we found no evidence that *a*FAs in Brussels sprouts originated from microorganisms but were rather from the plant itself. A possible biosynthesis pathway may include *α*-keto acid elongation without fatty acid synthase-mediated reactions, similar to the biosynthesis postulated in different plants for branched medium-chain fatty acids.[44] Further investigations are required to understand the biochemistry of *a*FAs and possibly other chiral fatty acids. It is evident from our study that such investigations should include the enantioselective determination of the final products, that is, the *a*FAs. The methods described in this work are suited for this purpose and thus justify the great efforts made during sample preparation and enantioselective evaluation.

DOI: 10.1021/acs.jafc.5b03877
J. Agric. Food Chem. 2015, 63, 8921−8929

■ ASSOCIATED CONTENT

Supporting Information

The Supporting Information is available free of charge on the ACS Publications website at DOI: 10.1021/acs.jafc.5b03877

GC-MS-SIM time windows and ions monitored for the analysis of fatty acid methyl esters (Table S1), scheme of the oven temperature program used for the enantioselective GC-MS determination of *anteiso*-fatty acid methyl esters on 66% *β*-TBDM in OV-1701 (Figure S1), a partial GC-MS-SIM chromatogram of *a*17:0-ME of RP-HPLC fraction 5 of the wax of Brussels sprouts (Figure S2), and the contribution (%) of individual fatty acids to the fatty acid pattern of the Brussels sprout samples after enrichment by hydrogenation and urea complexation (Table S2) (PDF)

■ AUTHOR INFORMATION

Corresponding Author

*(W.V.) E-mail: walter.vetter@uni-hohenheim.de. Phone: +49 711 459 24016. Fax: +49 711 459 24377.

Notes

The authors declare no competing financial interest.

■ ACKNOWLEDGMENTS

We are grateful to Georg Hottinger (BGB Analytik, Adliswil, Switzerland) for the preparation of the GC column coated with 66% heptakis(6-*O*-*tert*-butyldimethylsilyl-2,3-di-*O*-methyl)-*β*-cyclodextrin in OV-1701 and to Wolfgang Armbruster (Institute of Food Chemistry at the University of Hohenheim, Stuttgart, Germany) for GC-IRMS measurements. We also thank the Ministry of Science, Research and Art of Baden-Württemberg (Germany) for a stipend grant to D. E.

■ ABBREVIATIONS USED

*a*15:0, 12-methyltetradecanoic acid; *a*17:0, 14-methylhexadecanoic acid; *a*19:0, 16-methyloctadecanoic acid; *a*21:0, 18-methyldecosanoic acid; Ph-8:0, 8-phenyloctanoic acid; *a*FA, *anteiso*-fatty acid; BCFA, branched-chain fatty acid; EA-IRMS, elemental analyzer coupled to isotope ratio mass spectrometry; ee, enantiomeric excess; FAME, fatty acid methyl ester; GC-C-IRMS, gas chromatography−combustion isotope ratio mass spectrometry; GC-MS, gas chromatography with electron ionization mass spectrometry; *i*FA, *iso*-fatty acid; RP-HPLC, reversed-phase high-performance liquid chromatography; SIM, selected ion monitoring mode

■ REFERENCES

(1) Hauff, S.; Hottinger, G.; Vetter, W. Enantioselective analysis of chiral *anteiso* fatty acids in the polar and neutral lipids of food. *Lipids* **2010**, *45*, 357−365.

(2) Thurnhofer, S.; Hottinger, G.; Vetter, W. Enantioselective determination of *anteiso* fatty acids in food samples. *Anal. Chem.* **2007**, *79*, 4696−4701.

(3) Ran-Ressler, R. R.; Bae, S.; Lawrence, P.; Wang, D. H.; Brenna, J. T. Branched-chain fatty acid content of foods and estimated intake in the USA. *Br. J. Nutr.* **2014**, *112*, 565−572.

(4) Kaneda, T. *Iso*- and *anteiso*-fatty acids in bacteria: biosynthesis, function, and taxonomic significance. *Microbiol. Rev.* **1991**, *55*, 288−302.

(5) Suutari, M.; Laakso, S. Microbial fatty acids and thermal adaptation. *Crit. Rev. Microbiol.* **1994**, *20*, 285−328.

(6) Kaneda, T. Fatty acids of the genus *Bacillus*: an example of branched-chain preference. *Bacteriol. Rev.* **1977**, *41*, 391−418.

(7) Ackman, R. G.; Hooper, S. N. Branched-chain fatty acids of four fresh-water fish oils. *Comp. Biochem. Physiol.* **1970**, *32*, 117−125.

(8) Dreiucker, J.; Vetter, W. Fatty acids patterns in camel, moose, cow and human milk as determined with GC/MS after silver ion solid phase extraction. *Food Chem.* **2011**, *126*, 762−771.

(9) Hauff, S.; Vetter, W. Quantification of branched chain fatty acids in polar and neutral lipids of cheese and fish samples. *J. Agric. Food Chem.* **2010**, *58*, 707−712.

(10) Massart-Leën, A. M.; De Pooter, H.; Decloedt, M.; Schamp, N. Composition and variability of the branched-chain fatty acid fraction in the milk of goats and cows. *Lipids* **1981**, *16*, 286−292.

(11) Iverson, J. L.; Harrill, P. G. Fatty acid composition of palm kernel, illipe, and shea nut oils by urea fractionation and programmed temperature gas chromatography. *J. Assoc. Off. Anal. Chem.* **1967**, *5*, 1335−1338.

(12) Tsydendambaev, V. D.; Christie, W. W.; Brechany, E. Y.; Vereshchagin, A. G. Identification of unusual fatty acids of four alpine plant species from the Pamirs. *Phytochemistry* **2004**, *65*, 2695−2703.

(13) Guerreiro, O.; Alves, S. P.; Duarte, M. F.; Bessa, R. J.; Jerónimo, E. *Cistus ladanifer* L. shrub is rich in saturated and branched chain fatty acids and their concentration increases in the Mediterranean dry season. *Lipids* **2015**, *50*, 493−501.

(14) Wolff, R. L.; Christie, W. W.; Coakley, D. The unusual occurrence of 14-methylhexadecanoic acid in Pinaceae seed oils among plants. *Lipids* **1997**, *32*, 971−973.

(15) Radunz, A. On the function of methyl-branched chain fatty acids in phospholipids of cell membranes of higher plants. In *The Metabolism, Structure, and Function of Plant Lipids*; Stumpf, P. K., Mudd, J. B., Nes, W. D., Eds.; Plenum Press: New York, 1987; pp 197−200.

(16) Arrendale, R.; Severson, R.; Chortyk, O.; Stephenson, M. Isolation and identification of the wax esters from the cuticular waxes of green tobacco leaf. *Contr. Tobacco Res.* **1988**, *14*, 67−84.

(17) Baker, E. A.; Holloway, P. J. Branched-chain constituents of Brussels sprout wax. *Phytochemistry* **1975**, *14*, 2463−2467.

(18) Netting, A. G.; Macey, M. J. K.; Barber, H. N. Chemical genetics of a sub-glaucous mutant of *Brassica oleracea*. *Phytochemistry* **1972**, *11*, 579−585.

(19) Ran-Ressler, R. R.; Khailova, L.; Arganbright, K. M.; Adkins-Rieck, C. K.; Jouni, Z. E.; Koren, O.; Ley, R. E.; Brenna, J. T.; Dvorak, B. Branched chain fatty acids reduce the incidence of necrotizing enterocolitis and alter gastrointestinal microbial ecology in a neonatal rat model. *PLoS One* **2011**, *6*, e29032.

(20) Yang, Z.; Liu, S.; Chen, X.; Chen, H.; Huang, M.; Zheng, J. Induction of apoptotic cell death and in vivo growth inhibition of human cancer cells by a saturated branched-chain fatty acid, 13-methyltetradecanoic acid. *Cancer Res.* **2000**, *60*, 505−509.

(21) Wongtangtintharn, S.; Oku, H.; Iwasaki, H.; Toda, T. Effect of branched-chain fatty acids on fatty acid biosynthesis of human breast cancer cells. *J. Nutr. Sci. Vitaminol.* **2004**, *50*, 137−143.

(22) Vetter, W.; Gaul, S.; Thurnhofer, S.; Mayer, K. Stable carbon isotope ratios of methyl-branched fatty acids are different to those of straight-chain fatty acids in dairy products. *Anal. Bioanal. Chem.* **2007**, *389*, 597−604.

(23) Thurnhofer, S.; Vetter, W. Synthesis of (*S*)-(+)-enantiomers of food-relevant (*n*-*S*)-monoenoic and saturated *anteiso*-fatty acids by a Wittig reaction. *Tetrahedron* **2007**, *63*, 1140−1145.

(24) Thurnhofer, S.; Lehnert, K.; Vetter, W. Exclusive quantification of methyl-branched fatty acids and minor 18:1-isomers in foodstuff by GC/MS in the SIM mode using 10,11-dichloroundecanoic acid and fatty acid ethyl esters as internal standards. *Eur. Food Res. Technol.* **2008**, *226*, 975−983.

(25) Coplen, T. B.; Brand, W. A.; Gehre, M.; Gröning, M.; Meijer, H. A.; Toman, B.; Verkouteren, R. M. New guidelines for $\delta^{13}C$ measurements. *Anal. Chem.* **2006**, *78*, 2439−2441.

(26) Thurnhofer, S.; Vetter, W. A gas chromatography/electron ionization-mass spectrometry-selected ion monitoring method for determining the fatty acid pattern in food after formation of fatty acid methyl esters. *J. Agric. Food Chem.* **2005**, *53*, 8896−8903.

DOI: 10.1021/acs.jafc.5b03877
J. Agric. Food Chem. 2015, 63, 8921−8929

(27) Hauff, S.; Vetter, W. Quantification of fatty acids as methyl esters and phospholipids in cheese samples after separation of triacylglycerides and phospholipids. *Anal. Chim. Acta* **2009**, *636*, 229−235.
(28) Cannon, C.; Kummerow, F. A. A comparison of plant and grain wax from two varieties of sorghum. *J. Am. Oil Chem. Soc.* **1957**, *34*, 519−520.
(29) Schröder, M.; Vetter, W. Detection of 430 fatty acid methyl esters from a transesterified butter sample. *J. Am. Oil Chem. Soc.* **2013**, *90*, 771−790.
(30) Hauff, S.; Vetter, W. Exploring the fatty acids of *vernix caseosa* in form of their methyl esters by off-line coupling of non-aqueous reversed phase high performance liquid chromatography and gas chromatography coupled to mass spectrometry. *J. Chromatogr. A* **2010**, *1217*, 8270−8278.
(31) Savitzky, A.; Golay, M. J. Smoothing and differentiation of data by simplified least squares procedures. *Anal. Chem.* **1964**, *36*, 1627−1639.
(32) Vetter, W. Enantioselective fate of chiral chlorinated hydrocarbons and their metabolites in environmental samples. *Food Rev. Int.* **2001**, *17*, 113−182.
(33) Rieley, G. Derivatization of organic compounds prior to gas chromatographic−combustion−isotope ratio mass spectrometric analysis: identification of isotope fractionation processes. *Analyst* **1994**, *119*, 915−919.
(34) Meier-Augenstein, W. Stable isotope analysis of fatty acids by gas chromatography−isotope ratio mass spectrometry. *Anal. Chim. Acta* **2002**, *465*, 63−79.
(35) Kaffarnik, S.; Schröder, M.; Lehnert, K.; Baars, T.; Vetter, W. $\delta^{13}C$ values and phytanic acid diastereomer ratios: combined evaluation of two markers suggested for authentication of organic milk and dairy products. *Eur. Food Res. Technol.* **2014**, *238*, 819−827.
(36) Nasirullah; Werner, G.; Seher, A. Fatty acid composition of lipids from edible parts and seeds of vegetables. *Fette, Seifen, Anstrichm.* **1984**, *86*, 264−268.
(37) Swern, D.; Parker, W. Application of urea complexes in the purification of fatty acids, esters, and alcohols. I. Oleic acid from inedible animal fats. *J. Am. Oil Chem. Soc.* **1952**, *29*, 431−434.
(38) Täufel, K.; Müller, G.; Franzke, C. Über die Adduktbildung langkettiger Fettsäuren mit Harnstoff. *Nahrung* **1958**, *2*, 255−267.
(39) Kaplan, I. R.; Rittenberg, S. C. Carbon isotope fractionation during metabolism of lactate by *Desulfovibrio desulfuricans*. *J. Gen. Microbiol.* **1964**, *34*, 213−217.
(40) Trust Hammer, B.; Fogel, M. L.; Hoering, T. C. Stable carbon isotope ratios of fatty acids in seagrass and redhead ducks. *Chem. Geol.* **1998**, *152*, 29−41.
(41) Meier-Augenstein, W. Applied gas chromatography coupled to isotope ratio mass spectrometry. *J. Chromatogr. A* **1999**, *842*, 351−371.
(42) Deines, P. The isotopic composition of reduced organic carbon. In *Handbook of Environmental Isotope Geochemistry, 1. The Terrestrial Environment, A*; Fritz, P. Fontes, J. Ch., Eds.; Elsevier: Amsterdam, The Netherlands, 1980; Vol. 1, pp 329−406.
(43) Mottram, H. R.; Evershed, R. P. Practical considerations in the gas chromatography/combustion/isotope ratio monitoring mass spectrometry of ^{13}C-enriched compounds: detection limits and carryover effects. *Rapid Commun. Mass Spectrom.* **2003**, *17*, 2669−2674.
(44) Kroumova, A. B.; Xie, Z.; Wagner, G. J. A pathway for the biosynthesis of straight and branched, odd- and even-length, medium-chain fatty acids in plants. *Proc. Natl. Acad. Sci. USA* **1994**, *91*, 11437−11441.

DOI: 10.1021/acs.jafc.5b03877
J. Agric. Food Chem. 2015, 63, 8921−8929

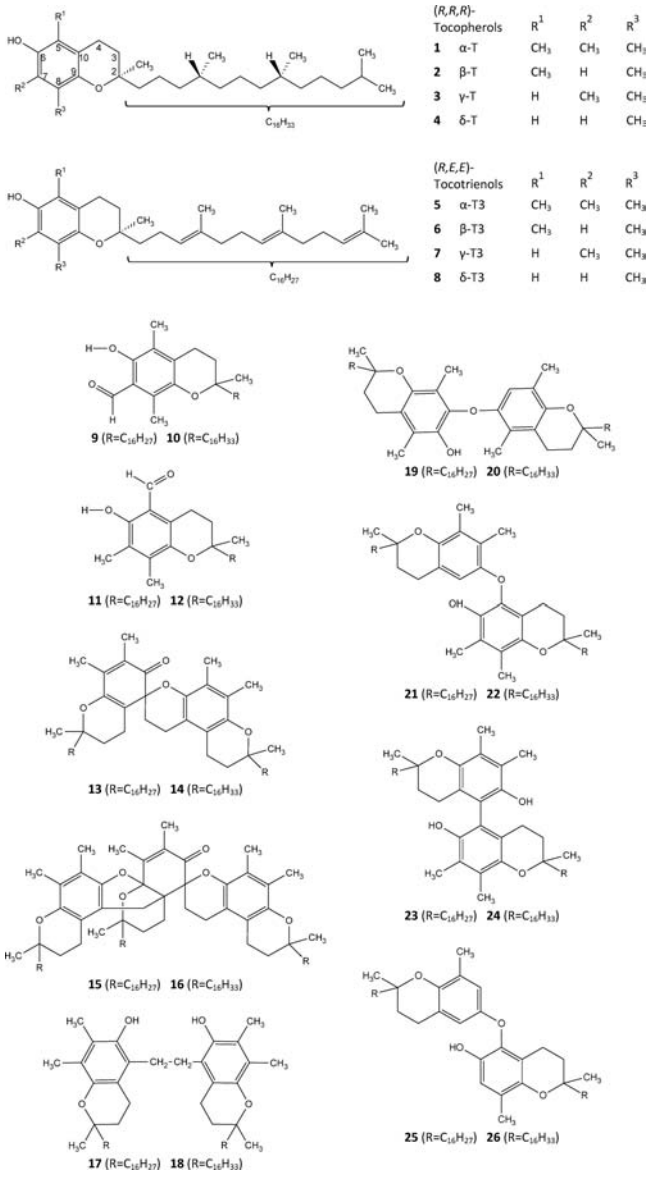

Figure 1. Structures of the vitamin E subgroups tocopherol (T) and tocotrienol (T3) and the most important oxidation products of tocotrienols and tocopherols.

h, 100 °C) of α-T3 (model matrix *n*-hexane) from the eight tocochromanols by HPLC with DAD and fluorescence detection (HPLC-DAD-F), and identified these oxidation products spectroscopically (HPLC-PBI-EIMS, i.e., HPLC-EIMS with particle beam interface (PBI)).[8,13] The predominant oxidation products from α-T3 were α-tocotrienol dihydroxydimer (**17**), 7-formyl-β-tocotrienol (**9**), and 5-formyl-γ-tocotrienol (**11**) (Figure 1). Minor proportions of α-tocotrienol quinone and its dimers were also detected with this method. Data in the literature suggest that non-α-T3 vitamers should form dimers as major oxidation products,[14−17] but there are as yet no reports of HPLC analysis of the oxidation products of β-, γ-, and δ-T3.

The potential role of tocotrienols in the treatment and prevention of breast cancer by inducing growth inhibition and apoptosis was recently reviewed.[6] Viola et al.[18] investigated human SKBR3 breast carcinoma cells and found fast and sustained mitochondrial uptake of δ-T3 followed by oxidative transformation of δ-T3 to its quinone derivative, which possibly contributes to cytotoxicity and apoptotic effects through oxidative damage of mitochondria and functional destabilization in the course of redox-recycling of the quinone. Furthermore, it has been suggested that the anticancer effect of tocotrienols is at least partially caused by targeting multiple intracellular signaling pathways associated with tumor cell viability,[19] independent of the antioxidant activity of tocotrienols.[20]

Knowledge of the in vitro bioactivity may help to design and interpret results obtained in in vivo studies. The majority of in vitro studies on the anticancer effects of γ- and δ-T3 have in common that the effective extracellular concentrations applied in vitro exceed the physiological concentrations.[21] With regard to the oral bioavailability of tocotrienol vitamers, α-T3 is preferentially transferred into the bloodstream when compared to γ- and δ-T3.[5] Strategies are being developed to overcome the limited bioavailability, to enhance the efficacy of therapeutic protocols.[21] Tocotrienols have a comparatively short elimination half-life in vivo due to their high metabolic rate and antioxidant activity. Redox inactivation should stabilize the tocotrienols in vivo. This hypothesis is supported by reports that redox-silent derivatives of tocotrienols such as esters, carbamates, or ethers, which mask the hydroxyl group at the C-6 position critical for antioxidant activity, show potent or even enhanced anticancer properties.[6,18,22]

Numerous studies have shown that tocotrienols[23−28] or palm TRF[29−31] significantly inhibit the growth of estrogen receptor-positive MCF-7 human breast cancer cells in vitro. For example, concentrations that inhibited 50% of cell growth in comparison to the control (i.e., the IC_{50} value) over 72 h were in the range from 8 to 25 μM and decreased in the order α-T3 > δ-T3 ≥ γ-T3 > palm TRF > α-T-free palm TRF, which means that the antiproliferative activities of coexisting tocotrienols from palm TRF and α-T-free palm TRF were found to be higher than those of pure tocotrienols.[32] The growth-inhibiting effect of tocotrienols on MCF-7 cells was shown to occur estrogen-independently.[21] Oxidized tocotrienol preparations have not yet been investigated in regard to their activity against breast cancer cells despite the fact that oxidation products of tocotrienols often are unavoidable during food processing or storage of tocotrienol supplements. Consequently, it was of interest to study the effect of tocotrienol-rich preparations that have undergone controlled oxidation on the viability of human breast cancer cells, in particular, the MCF-7 cell line.

The aims of this study were (i) to apply our previously described HPLC-DAD and HPLC-PBI-EIMS methods for the analysis of α-T3 oxidation products to the separation and evaluation of oxidation products generated from the other vitamers; (ii) to determine the composition of equimolar tocotrienol test compounds (α-T3, γ-T3, and palm TRF) before and after thermal oxidation in the model matrix *n*-hexane; (iii) to compare the effect of the untreated and thermally oxidized tocotrienol test compounds exemplarily on the viability of human MCF-7 breast cancer cells; and (iv) to estimate in a first approach the potential anticancer activity of the tocotrienol oxidation products. This study did not attempt to elucidate cell toxicity mechanisms but to provide first evidence of the importance of tocotrienol oxidation products by testing the effects of nonoxidized and oxidized tocotrienols under the same cell culture conditions. The results are expected to be valuable in the search for tocotrienol derivatives with

DOI: 10.1021/acs.jafc.5b04388
J. Agric. Food Chem. 2015, 63, 8930−8939

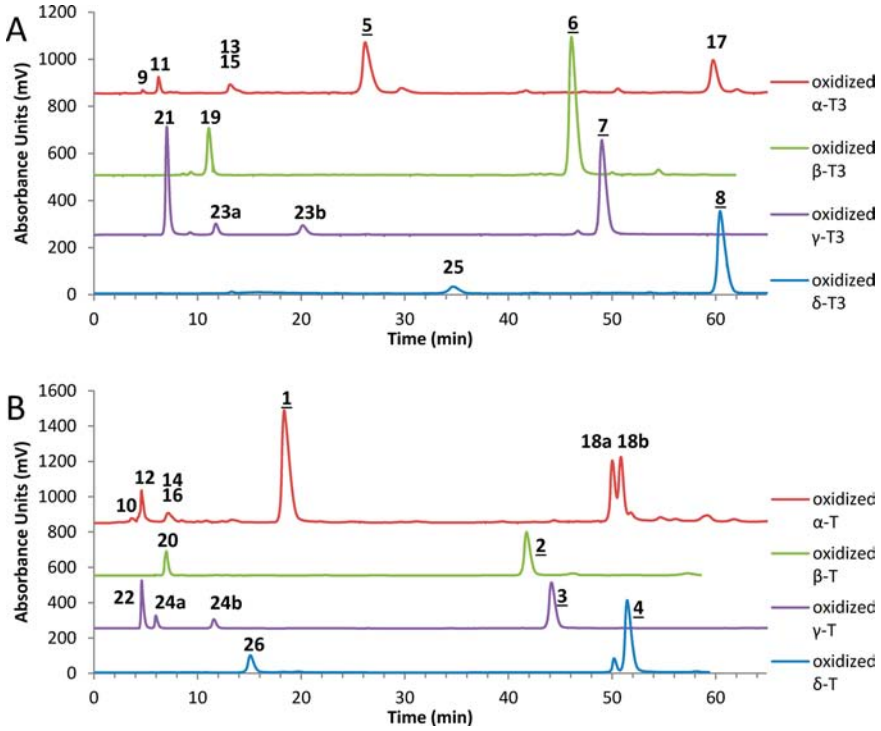

Figure 2. Normal-phase HPLC-UV chromatograms of the eight tocochromanol reference substances after thermal oxidation in *n*-hexane (3 h at 100 °C), recorded at 280 nm. The corresponding parent compounds are marked by underlined numbers. (A) Oxidized tocotrienols: **5**, α-tocotrienol; **6**, β-tocotrienol; **7**, γ-tocotrienol; **8**, δ-tocotrienol; **9**, 7-formyl-β-tocotrienol; **11**, 5-formyl-γ-tocotrienol; **13**, **15**, α-tocotrienol spirodimers/trimers; **17**, α-tocotrienol dihydroxydimer; **19**, 7-(β-tocotrienoxy)-β-tocotrienol; **21**, 5-(γ-tocotrienoxy)-γ-tocotrienol; **23a**, **23b**, 5-(γ-tocotrienyl)-γ-tocotrienol, atropisomers; **25**, 5-(δ-tocotrienoxy)-δ-tocotrienol. (B) Oxidized tocopherols: **1**, α-tocopherol; **2**, β-tocopherol; **3**, γ-tocopherol; **4**, δ-tocopherol; **10**, 7-formyl-β-tocopherol; **12**, 5-formyl-γ-tocopherol; **14**, **16**, α-tocopherol spirodimers/trimers; **18a**, **18b**, α-tocopherol dihydroxydimers; **20**, 7-(β-tocopheryl)-β-tocopherol; **22**, 5-(γ-tocopheroxy)-γ-tocopherol; **24a**, **24b**, 5-(γ-tocopheryl)-γ-tocopherol, atropisomers; **26**, 5-(δ-tocopheroxy)-δ-tocopherol.

enhanced anticancer properties and in future studies on the nature of the observed biological effects. Although it is not possible to draw direct conclusions from tocochromanol oxidation products generated in model systems on the relevance of these oxidation products in food systems, the expected results should nevertheless help in future studies dealing with unwanted oxidative degradation during storage and processing of tocotrienol-rich foods or pharmaceuticals.

MATERIALS AND METHODS

Chemicals and Test Compounds. The following tocotrienols were obtained from Davos Life Science (Singapore): α-, β-, γ-, and δ-T; α-, β-, γ-, and δ-T3 (each >97%); and palm tocotrienol-rich fraction (TRF) (>97%). The HPLC solvents used were ethanol, *n*-hexane, and acetonitrile, from Sigma-Aldrich (Steinheim, Germany); 1,4-dioxane (not stabilized), from Carl Roth (Karlsruhe, Germany); and *tert*-butyl methyl ether (TBME) and chloroform (stabilized), from Acros Organics (Geel, Belgium).

The cell culture medium used was Dulbecco's modified Eagle medium (DMEM) supplemented with 10% fetal bovine serum, 1% 10000 U/mL penicillin, 1% 10000 μg/mL streptomycin, and 1% 200 mM L-glutamine (all from Biochrom, Berlin, Germany). MCF-7 human breast cancer cells were obtained from LGC Standards (Wesel, Germany). The alamarBlue reagent was purchased from AbD Serotec (Puchheim, Germany).

Thermal Oxidation of Vitamers in Model Matrix *n*-Hexane and Preparation of Ethanolic Stock Solutions. To generate tocotrienol oxidation products for use as HPLC reference substances, our previously described method[8] for the thermal oxidation of α-T3 was applied to the test compounds studied here: 100 mg of each vitamer (α-, β-, γ-, and δ-T; α-, β-, γ-, and δ-T3) was dissolved in 100 mL of *n*-hexane; 2 mL samples of the vitamer solutions (each 1000 μg/mL) were transferred into 4 mL brown glass vials and placed in a drying oven for 3 h at 100 °C. The vials were left open during heat treatment. Thereafter, the oxidized, dry samples were brought to room temperature, and the sample volume was adjusted to 500 μL with *n*-hexane. The solutions were used for HPLC-UV and HPLC-PBI-EIMS analysis.

For use in cell viability assays, α-T3, γ-T3, and palm TRF were each dissolved in *n*-hexane at a concentration of 150 mM. Five hundred microliter samples of vitamer solutions were transferred into 1.4 mL brown glass vials and placed in a drying oven at 110 °C for 10 h (α-T3 and palm TRF) or 16 h (γ-T3). The vials were left open during heat treatment, after which the oxidized, dry samples were brought to room temperature, and the volumes were adjusted to 500 μL with ethanol. The composition of these ethanolic stock solutions was determined by HPLC-DAD after appropriate dilution.

HPLC Separation and Spectroscopic Analysis of Tocochromanol Oxidation Products. The separation and identification of the eight reference substances (individually oxidized α-, β-, γ-, and δ-T and α-, β-, γ-, and δ-T3) were performed using our previously established HPLC-PBI-MS method[8] with an additional in-line detection at 280 nm on an 8700 UV detector from Knauer (Berlin, Germany).

The HPLC-DAD analysis (200–400 nm) of the oxidized and nonoxidized test compounds α-T3, γ-T3, and palm TRF was performed using a 250 mm × 4 mm i.d., 3 μm, ProntoSil 120-3 Diol column (Knauer, Berlin, Germany) according to our previously established HPLC-DAD-F method[8] with a smaller sample loop (20 μL) and a modified gradient program for accelerated elution as follows: 0–5 min, 100% A; 20 min, 70% A; 30 min, 100% B; 30–60 min, 100% B, where eluent A was *n*-hexane and eluent B was *n*-hexane/dioxane/TBME (95:3:2, v/v/v).

DOI: 10.1021/acs.jafc.5b04388
J. Agric. Food Chem. 2015, 63, 8930–8939

Table 1. UV and EIMS Spectroscopic Characteristics of the Most Important Tocochromanol Oxidation Products Formed during Individual Thermal Oxidation in the Model Matrix *n*-Hexane

structure no. of oxidation product, chemical name	retention time (min)	UV max (nm)	M^+ (main EIMS fragments)
educt: α-form			
9, 7-formyl-β-tocotrienol	6.2	385, 277, 244	*m/z* 438 (219, 191, 179, 151)
10, 7-formyl-β-tocopherol	3.6	395, 290, 283[33]	*m/z* 444 (219, 205, 203, 179, 151)
11, 5-formyl-γ-tocotrienol	7.6	380, 287, 279, 244	*m/z* 438 (219, 191, 179, 151)
12, 5-formyl-γ-tocopherol	4.2	386, 290, 282, 275[33]	*m/z* 444 (219, 205, 203, 179, 151)
13, α-tocotrienol spirodimers/ **15**, α-tocotrienol spirotrimers	13.0−13.6	300	*m/z* 845/nd (847, 845, 625, 424, 422, 205, 203, 165)
14, α-tocopherol spirodimers/ **16**, α-tocopherol spirotrimers	7.0−7.5	339, 301, 290/292, 290[33]	*m/z* 857/nd (859, 857, 630, 430, 205, 203, 165)
17, α-tocotrienol dihydroxydimer	57	297	*m/z* 847 (424, 422, 205, 203, 165)
18, α-tocopherol dihydroxydimers	49.9, 50.8	300, 290, 275[33]	*m/z* 859 (430, 205, 203, 165)
educt: β-form			
19, 7-(β-tocotrienoxy)-β-tocotrienol	11.1	295	*m/z* 818 (410, 203, 151)
20, 7-(β-tocopheroxy)-β-tocopherol	6.9	295[14]	*m/z* 830 (416, 191, 151)
educt: γ-form			
21, 5-(γ-tocotrienoxy)-γ-tocotrienol	7	296	*m/z* 818 (410, 191, 151)
22, 5-(γ-tocopheroxy)-γ-tocopherol	4.6	297[15]	*m/z* 830 (416, 191, 151)
23, 5-(γ-Tocotrienyl)-γ-tocotrienol, atropisomers	11.8, 20.2	304	*m/z* 818 (410, 191, 151)
24, 5-(γ-tocopheryl)-γ-tocopherol, atropisomers	5.9, 11.5	304, 305[15]	*m/z* 830 (416, 191, 151)
educt: δ-form			
25, 5-(δ-tocotrienoxy)-δ-tocotrienol	34.9	297	*m/z*[a] 790 (396, 191, 161)
26, 5-(δ-tocopheroxy)-δ-tocopherol	15.0	295[15]	*m/z* 802 (402, 191, 161)

[a]Predicted *m/z* values from 5-(δ-tocopheroxy)-δ-tocopherol EIMS results. M^+, molecular ion; nd, not detected.

Molar contents of dimeric oxidation products in oxidized test compounds were approximatively calculated from the corresponding peak area (UV detection), assuming that a dimeric tocotrienol oxidation product has the same molar extinction coefficient (ε, 1 g^{-1} cm^{-1}) as the monomeric parent compound, which results in half the molar concentration of a dimeric compound compared to its monomeric parent compound with the same peak area. This approach is supported by literature data, according to which α-T and its dihydroxydimer have very similar ε values.[33]

Cell Viability Assay. The six ethanolic stock solutions containing either 150 mM nonoxidized α-T3, γ-T3, or palm TRF or 150 mM oxidized α-T3, γ-T3, or palm TRF were diluted with ethanol to prepare 0, 20, 25, 50, and 100 mM solutions. To facilitate the comparison between oxidized and nonoxidized test compounds, the concentration values of dilutions of oxidized test compounds refer to the vitamer concentration prior to oxidation. The ethanolic dilutions were further diluted 1:1000 with complete medium to yield concentrations of 20, 25, 50, and 100 μM for use in the cell viability assays.

MCF-7 cells were grown as monolayer cultures in medium in a humidified atmosphere of 5% CO_2 at 37 °C and passaged twice a week by bringing them in suspension with 0.05% trypsin/0.02% EDTA (w/v) in PBS (Biochrom, Berlin, Germany). For the experiment, cells at passages 7−16 were seeded in 96-well plates at a density of 5×10^3 cells/well and were allowed to adhere for 24 h. Then, the medium was removed and cells were treated with 200 μL of either α-T3 (0−100 μM), γ-T3 (0−100 μM), or TRF (0−100 μM) for 72 h. Ethanol (0.1%) was used as negative control. Culture medium in all wells was then replaced by medium containing 5% (v/v) alamarBlue reagent solution. After a 3 h incubation at 25 °C, fluorescence *F* (λ_{ex} 560 nm, λ_{em} 590 nm) was measured in a plate reader. Experimental results were expressed as viability in percent relative to control (100%). The absolute half-maximal inhibitory concentration (IC_{50}) and the 95% confidence interval (CI) were determined by nonlinear regression curve fit analysis using GraphPad Prism version 6.04 (GraphPad Software, La Jolla, CA, USA).

Statistics. All cell viability experiments were performed four times with independent cell cultures. Data were tested for outliers and homoscedasticity. An analysis of variance (ANOVA) was performed to determine statistically significant differences between the different experimental groups. The selected significance level was $\alpha = 0.001$. All statistical parameters were calculated using Valoo 2.3.[34]

RESULTS AND DISCUSSION

HPLC-UV Analysis of the Eight Reference Substances (Individually Oxidized α-, β-, γ-, and δ-T3 and -T). The chromatograms resulting from HPLC-UV of each of the eight individually oxidized α-, β-, γ-, and δ-T3 and -T are shown in Figure 2. The molecular structures, main EIMS fragments, and UV spectroscopic data of the most important tocotrienol oxidation products are summarized in Figure 1 and Table 1. In all chromatograms (Figure 2), additional peaks appeared along with the recovered tocochromanols. Under the conditions applied in this experiment, both α-vitamers (**1**, **5**) showed the same types of oxidation products, the dihydroxydimer (**17**, **18**) being the most striking for each α-vitamer (Figure 2). There were no indications that quinone or epoxide derivatives were present. Chromatograms of oxidized non-α-tocotrienols (i.e., β-, γ-, and δ-T3, **6**−**8**) (Figure 2A) showed the same peak pattern as the corresponding oxidized non-α-tocopherols (**2**−**4**) (Figure 2B). By means of HPLC-PBI-MS analysis of the tocotrienol and tocopherol oxidation products, we found the same types of oxidation products for the corresponding pairs of vitamers (β-T3 and β-T, etc.) and determined that the non-α-T3 vitamers formed dimers as major oxidation products: β-T3 (**6**) formed 7-(β-tocotrienoxy)-β-tocotrienol (**19**); γ-T3 (**7**) formed 5-(γ-tocotrienoxy)-γ-tocotrienol (**21**) and two mutual atropisomers (peaks **23a** and **23b**) of 5-(γ-tocotrienyl)-γ-tocotrienol (**23**);[12] and δ-T3 (**8**) formed 5-(δ-tocotrienoxy)-δ-

DOI: 10.1021/acs.jafc.5b04388
J. Agric. Food Chem. 2015, 63, 8930−8939

Table 2. Composition of Ethanolic Stock Solutions of T3 Test Compounds Determined by Means of HPLC-DAD

	without thermal oxidation		after thermal oxidation of 150 mM test compound (110 °C, *n*-hexane solution) and redissolution in ethanol	
	mM	percentage of total tocochromanol	mM	%[a]
test compound α-tocotrienol			**after 10 h of thermal oxidation**	
5, α-tocotrienol (α-T3)	150	100	45.6	31
17, α-tocotrienol dihydroxydimer			7.4	10
9, 7-formyl-β-tocotrienol			0.3	0.2
11, 5-formyl-γ-tocotrienol			0.9	0.6
13, 15, α-tocotrienol spirodimers/trimers			nd[c]	n.d.
test compound γ-tocotrienol			**after 16 h of thermal oxidation**	
7, γ-tocotrienol (γ-T3)	150	100	29.8	20
21, 5-(γ-tocotrienoxy)-γ-tocotrienol			8.2	11
23a, 5-(γ-tocotrienyl)-γ-tocotrienol, atropisomer			7.5	10
23b, 5-(γ-tocotrienyl)-γ-tocotrienol, atropisomer			9.7	13
test compound palm tocotrienol-rich fraction (TRF)			**after 10 h of thermal oxidation**	
1, α-tocopherol (α-T)	10.7	7.1	0.3	2.5
5, α-tocotrienol (α-T3)	38.1	25.4	3.4	9
6, β-tocotrienol (β-T3)	4.8	3.2	1.5	32
7, γ-tocotrienol (γ-T3)	69.9	46.6	9.1	13
8, δ-tocotrienol (δ-T3)	26.6	17.7	≤6.7[b]	≤25[b]
sum	150	100	≤21.0	
21, 5-(γ-tocotrienoxy)-γ-tocotrienol			6.3	9
23a, 5-(γ-tocotrienyl)-γ-tocotrienol, atropisomer			9.8	14
23b, 5-(γ-tocotrienyl)-γ-tocotrienol, atropisomer			5.6	8
9, 7-formyl-β-tocotrienol			0.5	1.3
11, 5-formyl-γ-tocotrienol			1.2	3.1

[a]Percentage of peak area of parent vitamer not having been thermally oxidized. [b]This value most probably includes a minor α-T3 oxidation product (α-tocotrienol dihydroxydimer). [c]nd, not detected.

tocotrienol (**25**) (Figures 1 and 2A; Table 1). As the oxidation of tocochromanols takes place at the phenolic chromanol "head" and not at the side chain, the oxidation products of tocochromanols that share the same chromanol "head" are expected to be the same, differing only in the side chain. For α-T3, this has previously been described by us in detail and confirmed by spectroscopic analysis.[8]

Tocochromanoxyl radicals primarily undergo radical−radical coupling reactions in apolar, aprotic solvents such as *n*-hexane, as used in the present study. If other potentially unstable radicals are absent, the tocochromanoxyl radicals react by self-coupling, forming dimers.[12,35] A major product of the α-tocotrienoxyl radical is the α-T3-dihydroxydimer (**17**), which is formed by dimerization through the *ortho* methyl groups at the initial position C-5. The β-, γ-, or δ-tocotrienoxyl radicals, which have free (nonmethylated) *ortho* positions, primarily form dimers through these positions, thereby leading to tocotrienol (diphenol) dimers due to *ortho*−*ortho* couplings, for example, 5-(γ-tocotrienyl)-γ-tocotrienol (**23**);, and to tocotrienol−tocotrienyl ether dimers due to coupling of the tocotrienoxyl oxygen of one tocotrienol with the *ortho* position of the other, for example, 5-(γ-tocotrienoxy)-γ-tocotrienol) (**21**) (Figure 1).

Remarkably, the HPLC-UV chromatogram of oxidized α-T showed the α-T dihydroxydimer (**18**) as a double peak (peak **18a** and **18b**) (Figure 2B). This is in agreement with prior findings.[33,36] The double peak is probably due to the presence of two α-T dihydroxydimer atropisomers (**18**), which differ in the positions of the chromanol rings caused by the rotation of the monomer-connecting ethyl bond; in the case of the α-T3-dihydroxydimer (**17**), there were no indications of the presence of atropisomers (peak **17**) (Figure 2B), thus suggesting that the specific steric structures of the tocopherol or tocotrienol side chains play a role in this phenomenon. The data on oxidized non-α-tocotrienols (Figure 2) are in agreement with previous work on tocotrienol oxidation products.[14−17] The dimeric oxidation product resulting from the β-vitamers was assigned to the ether dimer **19** and not the diphenol dimer by comparison with chromatographic and UV spectroscopic characteristics reported by Nilsson et al.[14] In accordance with data from the literature,[14,15,17] only one type of dimer was found for the δ-vitamers, that is, the ether dimer **25**. This is the first report on the HPLC-UV and -PBI-EIMS characteristics of the oxidation products of all eight tocochromanols resulting from their individual thermal oxidation (100 °C, 3 h) in *n*-hexane. However, it should be kept in mind that all of these oxidation products may decompose further to form decomposition products that cannot be detected with this method.[13]

Composition of Test Compounds before and after Thermal Oxidation. The T3 test compounds, that is, individual α-T3, individual γ-T3, and mixed tocochromanols from palm TRF, were dissolved in *n*-hexane and thermally oxidized at 110 °C for 10−16 h. Table 2 shows the composition and the total content (sum of all vitamers) of tocochromanols of the test compounds before and after thermal oxidation. Figure 3 shows the HPLC-DAD chromatograms of palm TRF before (Figure 3A) and after thermal oxidation (Figure 3B,C). The amounts of tocochromanols and oxidation products in the

DOI: 10.1021/acs.jafc.5b04388
J. Agric. Food Chem. 2015, 63, 8930−8939

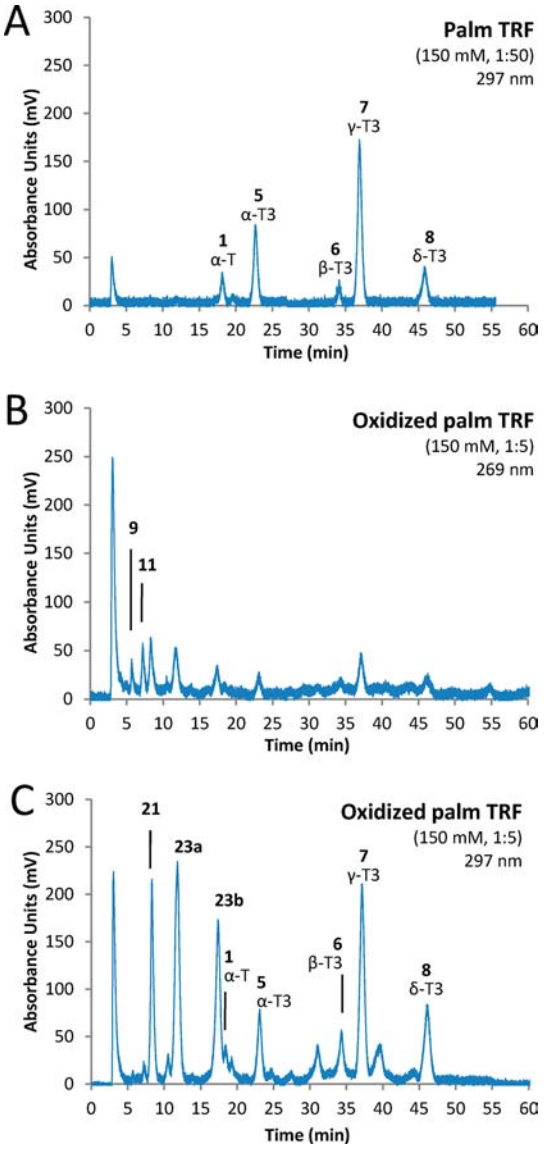

Figure 3. Diol-modified normal-phase HPLC-DAD chromatograms of palm TRF (A) before and (B, C) after thermal oxidation in the model matrix *n*-hexane (10 h at 110 °C), recorded at (A, C) 297 nm or (B) 269 nm. **1**, α-tocopherol (T); **5**–**8**, tocotrienols (T3); **9**, 7-formyl-β-tocotrienol; **11**, 5-formyl-γ-tocotrienol; **23a**, **23b**, 5-(γ-tocotrienyl)-γ-tocotrienol, atropisomers.

test compounds were assessed using a HPLC-DAD method similar to the HPLC-UV method for the oxidized reference substances (Figure 2), but with application of a steeper elution gradient, which is the reason for their overall shorter retention times (Figure 3) in comparison to those of the reference substances.

Thermal oxidation of α-T3, γ-T3, and palm TRF, each containing 150 mM total T3, resulted in a decrease in tocochromanol compounds and the emergence of oxidation products. After a 10 h thermal oxidation of the α-T3 test compound, the percentage of α-T3 recovered was 31%. On the basis of preliminary tests and in analogy with tocopherols, where the redox potential of γ-T is higher (+0.348 V) than that of α-T (+0.273 V),[12] γ-T3 was expected to be a weaker hydrogen donor and to degrade less intensely than α-T3. Therefore, the γ-T3 test compound was treated for a longer time (for 16 h instead of 10 h). The percentage of γ-T3 recovered was 20% (Table 2); assuming linear degradation, the calculated recovery after 10 h is 75%. In the palm TRF sample, the vitamers degraded to different degrees: thermal oxidation led to an extensive loss of α-T (only 2.5% was recovered) followed by α-T3, γ-T3, δ-T3, and β-T3, with residual percentages of 9, 13, ≤25, and 32%, respectively, so that the oxidized palm TRF contained strikingly less total tocochromanols (21.0 mM) than oxidized α-T3 (45.6 mM) and γ-T3 (29.8 mM), even though the γ-T3 test compound was oxidized for a longer time (for 16 h) than the other test compounds (10 h).

The chemistry of oxidation of the tocochromanols is complex and depends largely on the oxidation conditions,[35] for example, concentration, type of solvent or lipid matrix, temperature, and presence of light or oxygen. Because of the complex test systems and the resulting difficulties in evaluating the relative antioxidant activity of tocochromanols in vitro, there is a widespread controversy regarding this topic,[9] and it is difficult to draw any general conclusions.[37] In our hexanoic palm TRF sample, tocochromanols did not compete with lipids or model substances as substrates for oxidation, but different tocochromanols competed with themselves. Clearly, the α-vitamers in the palm TRF degraded most intensely, but apparently without simultaneously protecting γ-T3 from degradation (Table 2). The results suggest that the above-mentioned pro-oxidant property of the α-vitamers may cause a higher overall degradation of the vitamers in the oxidized palm TRF sample than the samples with individual tocotrienols. There are as yet no reports in the literature on the composition of highly concentrated hexanoic solutions of T3-rich mixed tocochromanols after thermal oxidation.

The oxidation products detected in α- and γ-T3 test compounds (Table 2) were found to be the same types of oxidation products as was expected from the results from the corresponding reference substances (Table 1). The oxidation products detected in the test compounds were predominantly dimers (Table 2). All of these dimers (**17**, **21**, **23**) are phenols or diphenols and can still act as antioxidants.[12] It should be noted that HPLC-DAD analysis showed no indications of dimeric oxidation products other than those composed of two γ-T3 or two α-T3 and that at most a minor proportion of an α-T3-dimer was formed, as indicated in the footnote of Table 2. This corresponds to the findings of Ha and Igarashi,[15] who autoxidized α- and γ-T mixtures in methyl linoleate (10 h, 97.8 °C) and detected no mixed dimers, composed of different types of vitamers, among the isolated oxidation products by means of spectroscopic structure determination and found that dimers of γ-T predominated over those of α-T.

Only small amounts of the aldehydic α-T3 oxidation products 5-formyl-γ-tocotrienol (**11**) and 7-formyl-β-tocotrienol (**9**) were also present in the α-T3 and TRF sample after thermal oxidation (Table 2; Figure 3B). These compounds, analogously to the aldehydes of tocopherols,[38] should have negligible antioxidant properties because of the formation of strong intramolecular hydrogen bonds between the hydroxyl group and the corresponding carbonyl group in the *ortho* position.

The conditions of thermal oxidation applied in our study led to an intensive decrease in all tocotrienol vitamers and necessarily to the generation of oxidation products. As suggested by the material balance (Table 2), the tocotrienol oxidation products newly separated, identified, and quantitated in the present study probably coexist with small-molecule products, which have lost the characteristic molecular moieties

DOI: 10.1021/acs.jafc.5b04388
J. Agric. Food Chem. 2015, 63, 8930–8939

of tocotrienols in the course of the oxidation progress and which were not identified by any of the analytical methods applied by us. In summary, the experimental design provided distinctly composed test compounds before and after thermal oxidation and, therefore, allowed the assessment of the importance of tocotrienol oxidation products with respect to anticancer effects of test compounds in an initial in vitro approach.

Effect of Nonoxidized Tocotrienols on the Viability of Human MCF-7 Breast Cancer Cells. Treatment of human MCF-7 breast cancer cells for 72 h with α-T3, γ-T3, and palm TRF reduced the cell viability in a dose-dependent manner in comparison to the control, with no tocochromanols (Figure 4). After treatment with 100 μM α-T3, γ-T3, or palm TRF, significantly ($p < 0.001$) fewer living cells were determined by means of the alamarBlue assay: 58 ± 2, 68 ± 4, and 29 ± 5%, respectively. In accordance with Loganathan et al.,[32] we found individual α- and γ-T3 vitamers to be less potent in reducing the viability of MCF-7 cells than equimolar total concentrations of mixed tocochromanols from palm TRF (Figure 4). This also agrees with the findings of Yu et al.,[39] who found that MCF-7 cells were most sensitive to the δ-T3 vitamer, which was a component of our palm TRF.

The IC_{50} values of α-T3, γ-T3, and palm TRF were greater than 100 μM in the cases of α-T3 and γ-T3 and 59 μM (95% CI = 51−68 μM) for palm TRF (Figure 4); when the MCF-7 breast cancer cells were treated with the γ-T3 vitamer at the lowest concentration (20 μM), there was a slight increase in cell viability (115 ± 4%) (Figure 4B). The IC_{50} values determined in our study are higher than data in the literature on anticancer effects of tocotrienols in MCF-7 cells.[23−27,29−32] One explanation for this difference is that the other research groups conducted the viability tests with MCF-7 cells in media containing inactivated FBS, charcoal-stripped FBS, or a lower percentage of FBS: because FBS contains growth factors, stimulating endogenous hormones,[40] it might attenuate the effects of tocotrienols on cell viability.[24] Moreover, MCF-7 cells from different laboratories have been reported to have different biological properties, most probably due to an inherent genetic variability when cultured and passaged under different conditions.[41]

Furthermore, our observation that nonoxidized γ-T3 (IC_{50} = 134 μM, 95% CI = 92−196 μM) possesses a lower potency than nonoxidized α-T3 (IC_{50} = 125 μM, 95% CI = 107−145 μM) is in contrast to some study results reported in the literature.[21,27] Our observation was made after a treatment period of 72 h. However, after a treatment period of only 24 h, the IC_{50} values of α-T3 (93 μM, 95% CI = 72−121 μM) and γ-T3 (20 μM, 95% CI = 16−25 μM) were much lower than after 72 h, and the IC_{50} value of γ-T3 was lower than that of α-T3, which is in accordance with literature data.[27] After a treatment period of 48 h, the MCF-7 cell viability was considerably stimulated when compared to the 24 h results by nearly every one of the applied concentrations of nonoxidized and oxidized test compounds, but most intensely at the lowest concentrations of each test compound. These obvious hormetic effects were attenuated after a treatment period of 72 h and turned into a dose-dependent decrease of cell viability, except for oxidized palm TRF. Therefore, and to achieve the most conclusive comparison between the effects of nonoxidized and oxidized test compounds, we decided to evaluate the data from the 72 h experiments, as displayed in Figure 4.

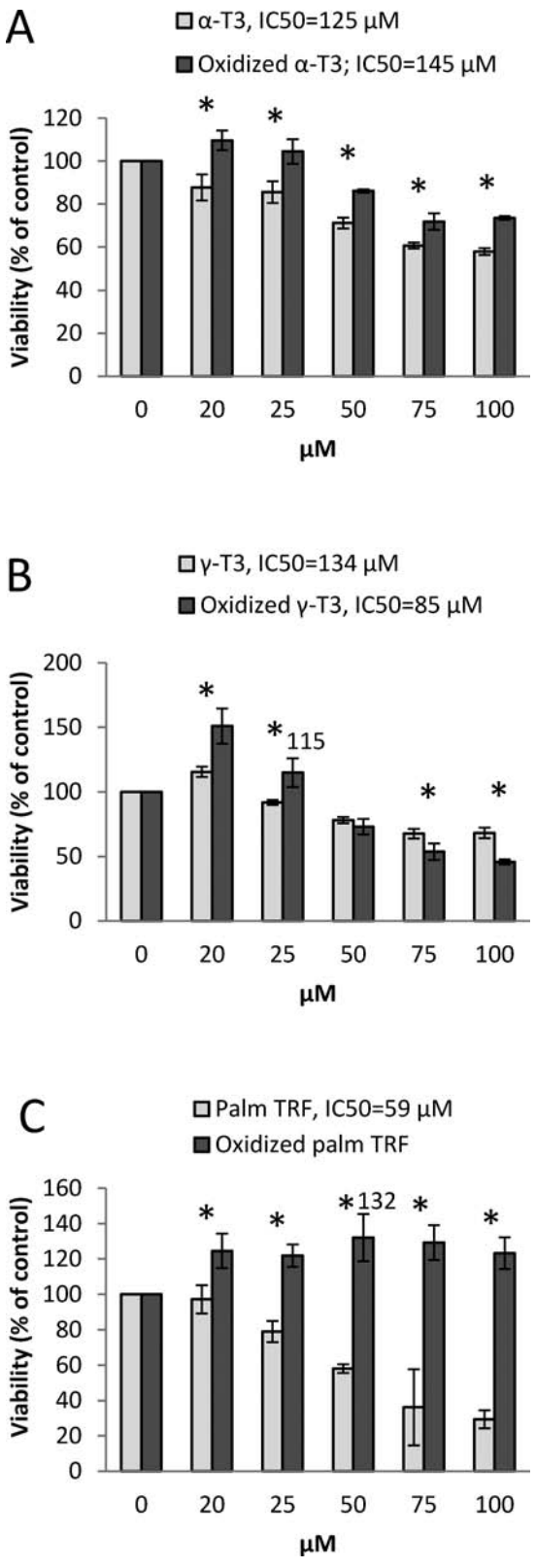

Figure 4. Effect of test compounds before and after thermal oxidation on the viability of MCF-7 human breast cancer cells in medium containing 10% fetal bovine serum after a treatment period of 72 h: (A) α-tocotrienol (α-T3); (B) γ-tocotrienol (γ-T3); (C) palm tocotrienol-rich fraction (palm TRF). Pairs of bars labeled with an asterisk (*) indicate significantly different viabilities caused by equimolar test compounds ($p < 0.001$). Data are representative of four independent experiments.

DOI: 10.1021/acs.jafc.5b04388
J. Agric. Food Chem. 2015, 63, 8930−8939

The increased proliferation caused by tocotrienols described in this study has also been observed by other research groups applying experimental conditions similar to ours in regard to culture medium composition and duration of incubation. For example, Nesaretnam et al.[42] observed that the lowest tested concentration of palm TRF (about 75 μM total tocochromanols) stimulated the proliferation of human MDA-MB-435 breast cancer cells when the cells were incubated in culture medium containing 10% FBS and palm TRF for 48 h, whereas higher concentrations of TRF caused an increasing inhibitory effect. Furthermore, Burdeos et al.[43] recently found an increased cell proliferation rate of about 70% compared to the control after treating mouse hepatocellular carcinoma cells (Hepa 1-6) with culture medium containing 10% FBS and 1−15 μM γ-T3 for 24 h; however, at higher concentrations, γ-T3 inhibited the proliferation of tumor cells. The reason for the increase in viability at lower tocochromanol concentration is still unknown, but it has been speculated that the antioxidative effect of γ-T3 could be responsible for this phenomenon.[43]

Explaining the differences in anticancer activity between the α- and γ-tocotrienols over time, the following literature may be relevant. The in vitro anticancer activity was shown to be a function of the cellular uptake rate and cell content of the different vitamers, as recently summarized by Viola et al.[21] Tocotrienols are more potent in suppressing mouse mammary tumor cell growth and viability than tocopherols due to their preferential uptake, which rapidly provides levels leading to cytotoxic effects, and in this context γ- and δ-tocotrienols show higher uptake rates than α-T3.[21,44] However, once the same intracellular concentration is reached, the difference in the anticancer activity between the vitamers decreases.[21] In accordance with this observation, the testing of a series of tocotrienols in human SKBR3 breast carcinoma cells revealed that δ-T3 clearly was the most potent compound capable of inhibiting cell viability after a 24 h treatment, followed by γ- and α-T3. However, after 48 h, α-T3 showed the highest inhibitory effect, and this effect was also observed in murine TUBO breast carcinoma cells.[18]

Effect of Oxidized Tocotrienols on the Viability of Human MCF-7 Breast Cancer Cells. The α- and γ-T3 test compounds that underwent thermal oxidation affected the viability of MCF-7 cells in a dose-dependent manner (Figure 4A,B), as did the nonoxidized α- and γ-T3 test compounds. The calculated IC_{50} (145 μM, 95% CI = 101−209 μM) of the oxidized α-T3 was higher than that of nonoxidized α-T3, and the viability of cancer cells was in all cases significantly higher than when treated with equimolar nonoxidized α-T3 solutions ($p < 0.001$). This is plausible in consideration of the fact that only 31% of the initial α-T3 content was recovered in the oxidized α-T3 (Table 2). However, oxidized α-T3 decreased the viability of cancer cells to a greater extent than would be expected from the recovered α-T3 content alone, indicating that the oxidation products present in the test compounds also possess some antitumor activity in vitro.

The oxidized γ-T3 compound enhanced cancer cell viability at the lowest tested concentrations (20 and 25 μM). In consideration of the fact that only 20% of the initial γ-T3 content in the oxidized γ-T3 was recovered (Table 2) and that, as mentioned above, low concentrations of tocotrienols in particular were found to stimulate cell viability, it is plausible that the cell viability increased significantly ($p < 0.001$) compared to treatment with the equimolar nonoxidized γ-T3 test compound. However, with higher concentrations of oxidized γ-T3, the viability-inhibiting effect was greater than that of equimolar nonoxidized γ-T3; consequently, the calculated IC_{50} (85 μM, 95% CI = 65−111 μM) was lower than for nonoxidized γ-T3 (Figure 4B). These data suggest that, above a minimum concentration of 25−50 μM γ-T3, the effect on cell viability of the test products containing oxidation products generated from any amount of γ-T3 given, was significantly stronger than that of the equimolar nonoxidized γ-T3 test products. However, it remains unknown whether this enhanced activity was caused by the oxidation products per se or whether the γ-T3 molecule acted more effectively through an interaction with the oxidation products. Nevertheless, our observation that the cell viability decreasing activity of the oxidized γ-T3 test compound was greater than that of equimolar, nonoxidized γ-T3 may be of value in the above-mentioned search for redox-silent tocotrienol derivatives to identify substances with higher effectivity and bioavailability and deserves further investigation. As the in vitro bioactivity greatly depends on the intracellular concentration of tocotrienol forms,[18,21] assessing the cellular uptake of the specific γ-T3 oxidation products should help in the evaluation if these can be associated with the improved activity or if other and, so far, unknown characteristics of oxidized γ-T3 or the tested MCF-7 cell line could explain these results.

Whereas the nonoxidized palm TRF test compound decreased the viability of cancer cells more extensively than the individual α- and γ-T3, the oxidized palm TRF surprisingly did not reduce cell viability; on the contrary, a stimulating effect was observed at all concentrations of oxidized palm TRF (Figure 4C), and oxidation products generated from equimolar palm TRF test compounds clearly did not affect cell viability. This surprising result was predictable neither from the results obtained with the tested oxidized α- or γ-T3 test compounds nor from the decrease of the highly anticancerous δ-T3 vitamer. However, it is likely that the oxidation of palm TRF led to the formation of much less bioactive or bioavailable products, which prevented cell viability from decreasing as was observed for oxidized α- and γ-T3. It is obvious that, particularly in systems containing mixed tocochromanols, the mechanisms leading to changes in tumor cell viability, the interactions between different compounds, and the relationship between structure and effectiveness are complex and merit further investigation. This conclusion is supported by the results of a preliminary experiment in our laboratory, in which oxidized palm TRF (0−100 μM) clearly decreased the cell number of human colon adenocarcinoma HT-29 cells after a treatment period of 96 h in a dose-dependent manner as determined by performing the sulforhodamine B (SRB) assay.

There are few studies available on the activity of oxidation products of tocochromanols in biological systems, and where such products are discussed, in most cases these are quinones, oxidation products primarily formed in polar, protic solvents. Shrader et al.[45] reported that α-tocopherol quinone, an oxidative metabolite of α-T, is a potent cellular protectant against oxidative stress, whereby its biological activity depends upon its ability to undergo reversible two-electron redox cycling. Dolfi et al.[46] observed that γ- and δ-tocopherol quinones had much higher inhibitory effects on human colon cancer HCT-116 and HT-29 cells compared to their parent compounds after a 72 h incubation; however, α-T and its quinone derivative were rather ineffective. Jones et al.[47] found that γ-tocopherol quinone, but not α-tocopherol quinone, induced apoptosis in human ZR-75-1 breast cancer cells. Goh

DOI: 10.1021/acs.jafc.5b04388
J. Agric. Food Chem. 2015, 63, 8930−8939

et al.[48] reported that no oxidative dimeric compounds from γ-T3 exhibited activity against tumor promotion by inhibition of the expression of Epstein−Barr virus early antigen in Raji cells, wheras monomeric γ-T3 did.

In conclusion, this study has shown that individually thermally oxidized non-α-tocotrienols formed certain dimeric oxidation products, as did the corresponding non-α-tocopherols treated in the same way. Furthermore, it was shown that our HPLC-UV method is well applicable for separating the oxidation products from the parent compound, as was the HPLC-DAD method for determining the most important components of test products, even those containing mixed tocotrienols (i.e., palm TRF) that have undergone thermal oxidation in the model matrix *n*-hexane. Moreover, it was shown that equimolar concentrations of tocotrienol test compounds subjected to thermal oxidation had significantly different effects on the viability of human MCF-7 breast cancer cells compared to nonoxidized tocotrienol test compounds after a treatment period of 72 h in culture medium containing 10% FBS. Our findings also indicate that oxidation products of γ-T3 can contribute to the decrease in viability of human MCF-7 breast cancer cells and even enhance the antitumor activity in vitro, but that oxidized tocotrienol mixtures did not behave as expected from the results obtained with the individual vitamers. This is the first approach toward estimating the biological activity of tocotrienol oxidation products against breast cancer cells. These findings should be taken into account not only in the search for tocotrienol derivatives with enhanced anticancer properties but also in dealing with unwanted oxidative degradation during storage and processing of tocotrienol-rich foods or pharmaceuticals. Over all, these results should stimulate further investigations to elucidate the mechanisms responsible for enhancing or attenuating the anticancer properties of tocotrienols through oxidation.

■ ASSOCIATED CONTENT

Supporting Information

The Supporting Information is available free of charge on the ACS Publications website at DOI: 10.1021/acs.jafc.5b04388.

Figure showing the thermal oxidation of tocotrienols over time; figure and tables showing the effects of test compounds on the viability of MCF-7 breast cancer cells after treatment periods of 24, 48, and 72 h, the corresponding IC_{50}data, and statistical evaluation; figure showing the effects of test compounds on the growth of human colon adenocarcinoma HT-29 cells after a treatment period of 96 h (PDF)

■ AUTHOR INFORMATION

Corresponding Author

*(A.M.D.) Phone: +49 511 856 7365. Fax: +49 511 856 827365. E-mail: astrid.drotleff@tiho-hannover.de.

Funding

This work is part of the "Food Network" project funded by the German Ministry for Science and Culture of Lower Saxony through the Research Association of Agricultural and Nutritional Science of Lower Saxony (Forschungsverbund Agrar- und Ernährungswissenschaften Niedersachsen, FAEN).

Notes

The authors declare no competing financial interest.

■ ACKNOWLEDGMENTS

We gratefully acknowledge Nicole Brauer for conducting the cell culture work.

■ ABBREVIATIONS USED

CI, confidence interval; F, fluorescence; IC_{50}, half-maximal inhibitory concentration; PBI, particle beam interface; T, tocopherol; T3, tocotrienol; TBME, *tert*-butyl methyl ether; TRF, tocotrienol-rich fraction

■ REFERENCES

(1) McLaughlin, P. J.; Weihrauch, J. L. Vitamin-E content of foods. *J. Am. Diet. Assoc.* **1979**, *75*, 647−665.

(2) Frega, N.; Mozzon, M.; Bocci, F. Identification and estimation of tocotrienols in the annatto lipid fraction by gas chromatography mass spectrometry. *J. Am. Oil Chem. Soc.* **1998**, *75*, 1723−1727.

(3) Aggarwal, B. B.; Sundaram, C.; Prasad, S.; Kannappan, R. Tocotrienols, the vitamin E of the 21st century: Its potential against cancer and other chronic diseases. *Biochem. Pharmacol.* **2010**, *80*, 1613−1631.

(4) Bohnsack, C.; Ternes, W.; Büsing, A.; Drotleff, A. M. Tocotrienol levels in sieving fraction extracts of brewer's spent grain. *Eur. Food Res. Technol.* **2011**, *232*, 563−573.

(5) Drotleff, A. M.; Bohnsack, C.; Schneider, I.; Hahn, A.; Ternes, W. Human oral bioavailability and pharmacokinetics of tocotrienols from tocotrienol-rich (tocopherol-low) barley oil and palm oil formulations. *J. Funct. Foods* **2014**, *7*, 150−160.

(6) Sylvester, P. W.; Akl, M. R.; Malaviya, A.; Parajuli, P.; Ananthula, S.; Tiwari, R. V.; Ayoub, N. M. Potential role of tocotrienols in the treatment and prevention of breast cancer. *BioFactors* **2014**, *40*, 49−58.

(7) Piironen, V.; Varo, P.; Koivistoinen, P. Stability of tocopherols and tocotrienols during storage of foods. *J. Food Compos. Anal.* **1988**, *1*, 124−129.

(8) Büsing, A.; Ternes, W. Separation of α-tocotrienol oxidation products and eight tocochromanols by HPLC with DAD and fluorescence detection and identification of unknown peaks by DAD, PBI-EIMS, FTIR, and NMR. *Anal. Bioanal. Chem.* **2011**, *401*, 2843−2854.

(9) Ko, S. N.; Kim, C. J.; Kim, C. T.; Kim, Y.; Kim, I. H. Effects of tocopherols and tocotrienols on the inhibition of autoxidation of conjugated linoleic acid. *Eur. J. Lipid Sci. Technol.* **2010**, *112*, 496−501.

(10) Kim, H. J. Effect of α-, β-, γ-, and δ-tocotrienol on the oxidative stability of lard. *J. Am. Oil Chem. Soc.* **2014**, *91*, 777−782.

(11) Seppanen, C. M.; Song, Q. H.; Csallany, A. S. The antioxidant functions of tocopherol and tocotrienol homologues in oils, fats, and food systems. *J. Am. Oil Chem. Soc.* **2010**, *87*, 469−481.

(12) Kamal-Eldin, A.; Appelqvist, L. A. The chemistry and antioxidant properties of tocopherols and tocotrienols. *Lipids* **1996**, *31*, 671−701.

(13) Büsing, A.; Drotleff, A. M.; Ternes, W. Identification of α-tocotrienolquinone epoxides and development of an efficient molecular distillation procedure for quantitation of α-tocotrienol oxidation products in food matrices by high-performance liquid chromatography with diode array and fluorescence detection. *J. Agric. Food Chem.* **2012**, *60*, 8302−8313.

(14) Nilsson, J. L. G.; Daves, G. D., Jr.; Folkers, K. Oxidative dimerization of α-, β-, γ-, and δ-tocopherols. *Acta Chem. Scand.* **1968**, *22*, 207−218.

(15) Ha, K. H.; Igarashi, O. The oxidation products from two kinds of tocopherols coexisting in autoxidation system of methyl linoleate. *J. Nutr. Sci. Vitaminol.* **1990**, *36*, 411−421.

(16) Goh, S. H.; Hew, N. F.; Lee, M. Stereochemistry of bichromanyl dimers from γ-tocopherol and γ-tocotrienol. *Tetrahedron Lett.* **1992**, *33*, 4613−4616.

DOI: 10.1021/acs.jafc.5b04388
J. Agric. Food Chem. 2015, 63, 8930−8939

(17) Goh, S. H.; Hew, N. F.; Ong, A. S. H.; Choo, Y. M.; Brumby, S. Tocotrienols from palm oil − electron-spin-resonance spectra of tocotrienoxyl radicals. *J. Am. Oil Chem. Soc.* **1990**, *67*, 250−254.
(18) Viola, V.; Ciffolilli, S.; Legnaioli, S.; Piroddi, M.; Betti, M.; Mazzini, F.; Pierpaoli, E.; Provinciali, M.; Galli, F. Mitochondrial-dependent anticancer activity of δ-tocotrienol and its synthetic derivatives in HER-2/neu overexpressing breast adenocarcinoma cells. *BioFactors* **2013**, *39*, 485−493.
(19) Kannappan, R.; Gupta, S. C.; Kim, J. H.; Aggarwal, B. B. Tocotrienols fight cancer by targeting multiple cell signaling pathways. *Genes Nutr.* **2012**, *7*, 43−52.
(20) Constantinou, C.; Papas, A.; Constantinou, A. I. Vitamin E and cancer: an insight into the anticancer activities of vitamin E isomers and analogs. *Int. J. Cancer* **2008**, *123*, 739−752.
(21) Viola, V.; Pilolli, F.; Piroddi, M.; Pierpaoli, E.; Orlando, F.; Provinciali, M.; Betti, M.; Mazzini, F.; Galli, F. Why tocotrienols work better: insights into the in vitro anti-cancer mechanism of vitamin E. *Genes Nutr.* **2012**, *7*, 29−41.
(22) Yano, T.; Sato, A.; Sekine, M.; Virgona, N.; Ota, M. Redox-inactive analogue of tocotrienol as a potential anti-cancer agent. *Anti-Cancer Agents Med. Chem.* **2013**, *13*, 496−501.
(23) Pierpaoli, E.; Viola, V.; Pilolli, F.; Piroddi, M.; Galli, F.; Provinciali, M. γ- and δ-tocotrienols exert a more potent anticancer effect than α-tocopheryl succinate on breast cancer cell lines irrespective of HER-2/neu expression. *Life Sci.* **2010**, *86*, 668−675.
(24) Hsieh, T. C.; Wu, J. M. Suppression of cell proliferation and gene expression by combinatorial synergy of EGCG, resveratrol and γ-tocotrienol in estrogen receptor-positive MCF-7 breast cancer cells. *Int. J. Oncol.* **2008**, *33*, 851−859.
(25) Hsieh, T. C.; Elangovan, S.; Wu, J. M. γ-Tocotrienol controls proliferation, modulates expression of cell cycle regulatory proteins and up-regulates quinone reductase NQO2 in MCF-7 breast cancer cells. *Anticancer Res.* **2010**, *30*, 2869−2874.
(26) Gopalan, A.; Yu, W. P.; Jiang, Q.; Jang, Y. M.; Sanders, B. G.; Kline, K. Involvement of de novo ceramide synthesis in γ-tocopherol and γ-tocotrienol-induced apoptosis in human breast cancer cells. *Mol. Nutr. Food Res.* **2012**, *56*, 1803−1811.
(27) Patacsil, D.; Tran, A. T.; Cho, Y. S.; Suy, S.; Saenz, F.; Malyukova, I.; Ressom, H.; Collins, S. P.; Clarke, R.; Kumar, D. Gamma-tocotrienol induced apoptosis is associated with unfolded protein response in human breast cancer cells. *J. Nutr. Biochem.* **2012**, *23*, 93−100.
(28) Parajuli, P.; Tiwari, R. V.; Sylvester, P. W. Anti-proliferative effects of γ-tocotrienol are associated with suppression of c-Myc expression in mammary tumour cells. *Cell Proliferation* **2015**, *48*, 421−435.
(29) Guthrie, N.; Gapor, A.; Chambers, A. F.; Carroll, K. K. Inhibition of proliferation of estrogen receptor-negative MDA-MB-435 and -positive MCF-7 human breast cancer cells by palm oil tocotrienols and tamoxifen, alone and in combination. *J. Nutr.* **1997**, *127*, S544−S548.
(30) Nesaretnam, K.; Stephen, R.; Dils, R.; Darbre, P. Tocotrienols inhibit the growth of human breast cancer cells irrespective of estrogen receptor status. *Lipids* **1998**, *33*, 461−469.
(31) Park, S. K.; Sanders, B. G.; Kline, K. Tocotrienols induce apoptosis in breast cancer cell lines via an endoplasmic reticulum stress-dependent increase in extrinsic death receptor signaling. *Breast Cancer Res. Treat.* **2010**, *124*, 361−375.
(32) Loganathan, R.; Selvaduray, K. R.; Nesaretnam, K.; Radhakrishnan, A. K. Differential and antagonistic effects of palm tocotrienols and other phytonutrients (carotenoids, squalene and coenzyme Q10) on breast cancer cells *in vitro*. *J. Oil Palm Res.* **2013**, *25*, 208−215.
(33) Al-Malaika, S.; Issenhuth, S.; Burdick, D. The antioxidant role of vitamin E in polymers V. Separation of stereoisomers and characterisation of other oxidation products of dl-α-tocopherol formed in polyolefins during melt processing. *Polym. Degrad. Stab.* **2001**, *73*, 491−503.
(34) Nieto-Ernst, S. Valoo 2.3. In *Analytik Software*, Leer, Germany, 2009.
(35) Ouchi, A.; Nagaoka, S.-i.; Suzuki, T.; Izumisawa, K.; Koike, T.; Mukai, K. Finding of synergistic and cancel effects on the aroxyl radical-scavenging rate and suppression of prooxidant effect for coexistence of α-tocopherol with β-, γ-, and δ-tocopherols (or -tocotrienols). *J. Agric. Food Chem.* **2014**, *62*, 8101−8113.
(36) Al-Malaika, S.; Issenhuth, S. The antioxidant role of vitamin E in polymers. IV. Reaction products of DL-α-tocopherol with lead dioxide and with polyolefins. *Polymer* **2001**, *42*, 2915−2939.
(37) Isnardy, B.; Wagner, K. H.; Elmadfa, I. Effects of α-, γ-, and δ-tocopherols on the autoxidation of purified rapeseed oil triacylglycerols in a system containing low oxygen. *J. Agric. Food Chem.* **2003**, *51*, 7775−7780.
(38) Suarna, C.; Southwellkeely, P. T. Antioxidant activity of oxidation-products of α-tocopherol and of its model-compound 2,2,5,7,8-pentamethyl-6-chromanol. *Lipids* **1991**, *26*, 187−190.
(39) Yu, W. P.; Simmons-Menchaca, M.; Gapor, A.; Sanders, B. G.; Kline, K. Induction of apoptosis in human breast cancer cells by tocopherols and tocotrienols. *Nutr. Cancer* **1999**, *33*, 26−32.
(40) Engel, N.; Lisec, J.; Piechulla, B.; Nebe, B. Metabolic profiling reveals sphingosine-1-phosphate kinase 2 and lyase as key targets of (phyto-) estrogen action in the breast cancer cell line MCF-7 and not in MCF-12A. *PLoS One* **2012**, *7*, e47833.
(41) Osborne, C. K.; Hobbs, K.; Trent, J. M. Biological differences among MCF-7 human breast cancer cell lines from different laboratories. *Breast Cancer Res. Treat.* **1987**, *9*, 111−121.
(42) Nesaretnam, K.; Guthrie, N.; Chambers, A. F.; Carroll, K. K. Effect of tocotrienols on the growth of a human breast-cancer cell-line in culture. *Lipids* **1995**, *30*, 1139−1143.
(43) Burdeos, G. C.; Nakagawa, K.; Watanabe, A.; Kimura, F.; Miyazawa, T. γ-Tocotrienol attenuates triglyceride through effect on lipogenic gene expressions in mouse hepatocellular carcinoma Hepa 1-6. *J. Nutr. Sci. Vitaminol.* **2013**, *59*, 148−151.
(44) McIntyre, B. S.; Briski, K. P.; Gapor, A.; Sylvester, P. W. Antiproliferative and apoptotic effects of tocopherols and tocotrienols on preneoplastic and neoplastic mouse mammary epithelial cells. *Proc. Soc. Exp. Biol. Med.* **2000**, *224*, 292−301.
(45) Shrader, W. D.; Amagata, A.; Barnes, A.; Hinman, A.; Jankowski, O.; Lee, E.; Kheifets, V.; Komatsuzaki, R.; Mollard, P.; Murase, K.; Rioux, P.; Wesson, K.; Miller, G. Towards a modern definition of vitamin E-evidence for a quinone hypothesis. *Bioorg. Med. Chem. Lett.* **2012**, *22*, 391−395.
(46) Dolfi, S. C.; Yang, Z. H.; Lee, M. J.; Guan, F.; Hong, J.; Yang, C. S. Inhibitory effects of different forms of tocopherols, tocopherol phosphates, and tocopherol quinones on growth of colon cancer cells. *J. Agric. Food Chem.* **2013**, *61*, 8533−8540.
(47) Jones, K. H.; Liu, J. J.; Roehm, J. S.; Eckel, J. J.; Eckel, T. T.; Stickrath, C. R.; Triola, C. A.; Jiang, Z. C.; Bartoli, G. M.; Cornwell, D. G. γ-Tocopheryl quinone stimulates apoptosis in drug-sensitive and multidrug-resistant cancer cells. *Lipids* **2002**, *37*, 173−184.
(48) Goh, S. H.; Hew, N. F.; Norhanom, A. W.; Yadav, M. Inhibition of tumor promotion by various palm-oil tocotrienols. *Int. J. Cancer* **1994**, *57*, 529−531.

DOI: 10.1021/acs.jafc.5b04388
J. Agric. Food Chem. 2015, 63, 8930−8939

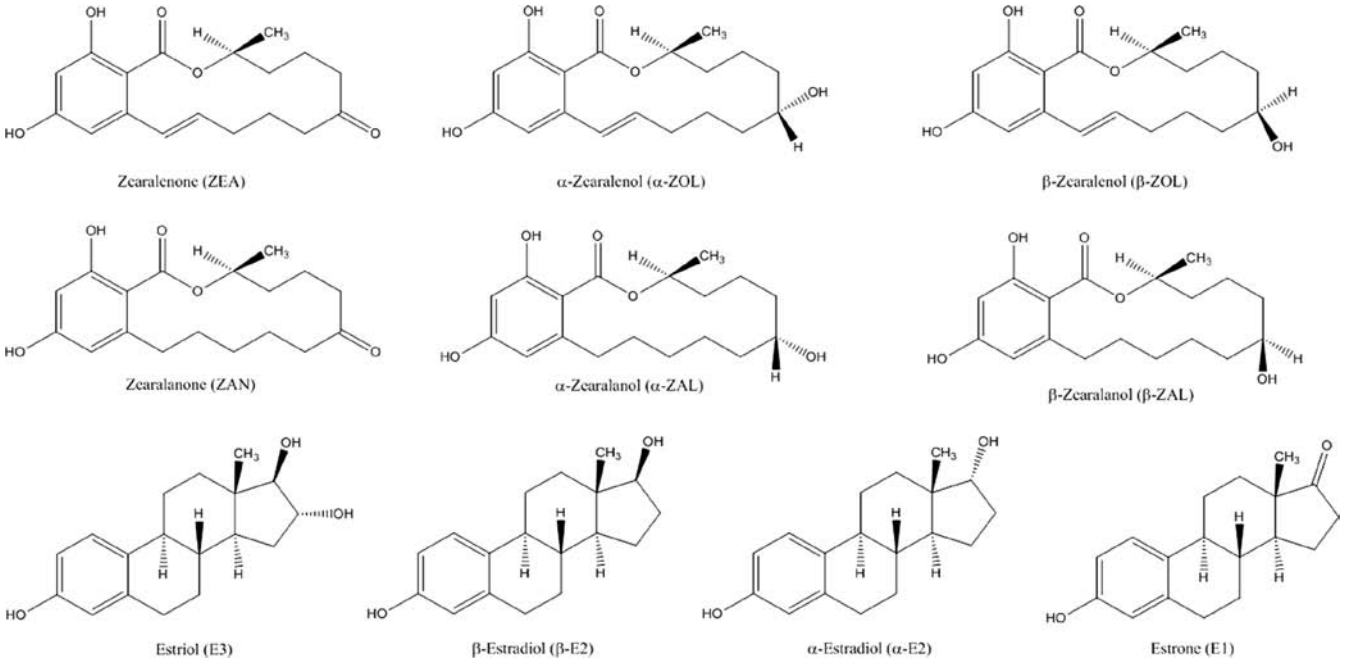

Figure 1. Chemical structure, names, and abbreviation of the free estrogens and resorcyclic acid lactones analyzed.

zearalanol (β-ZAL), which is its primary metabolite in bovine. Therefore, all of these analytes could be found in animals that had consumed feed naturally contaminated with mycoestrogens[9,10] or treated with the growth promoter α-ZAL. Moreover, α-ZAL and its metabolites are also related to the metabolism of ZEA in animals and can occur from its metabolic pathway. In all cases, all of these compounds could reach milk with the same effects of free estrogens; therefore, their presence should be monitored too. To reach this goal, an analytical methodology should be able to simultaneously detect all these compounds, natural estrogens and mycoestrogens, at trace levels despite the lack of maximum residue levels in milk and other dairy products. Because of the complexity of milk, the analysis of estrogens and related compounds is sometimes challenging, and many steps during sample preparation are required. Delipidation and deprotenization are commonly employed procedures in milk analysis, but they are time-consuming and can lead to analyte loss. At the same time, it would be difficult to employ the conventional commercial solid-phase extraction (SPE) cartridges without any sample pretreatments. In addition, the newest and fast extraction methodologies, such as QuEChERS, are rarely used for this type of analytes in milk.

To overcome these challenges, in this work we developed and validated an analytical methodology for fast, simple, and simultaneous determination of mycoestrogens and natural estrogens in different commercial milk samples, without any sample pretreatment. The developed method, based on ultrahigh-performance liquid chromatography coupled to tandem mass spectrometry via electrospray source (UHPLC/ESI-MS/MS), is able to achieve very good recoveries, negligible or very low matrix effect, and lower limits of detection and quantification than previously published methods, without any selectivity loss.

MATERIALS AND METHODS

Chemicals and Reagents. Acetonitrile (ACN), Methanol (MeOH), CH_2Cl_2, NH_3 (30%), HCOOH (>98%), and HCl were supplied by Sigma-Aldrich (Milan, Italy). All reagents were of analytical reagent grade; solvents were LC-MS grade. Ultrapure water (resistivity 18.2 MΩ cm^{-1}) was obtained using an Arium water purification system (Sartorious, Florence, Italy).

Pure standards of all selected compounds, i.e., E1, 17β-estradiol (β-E2), 17α-estradiol (α-E2), E3, ZEA, α-zearalenol (α-ZOL), β-zearalenol (β-ZOL), ZAN, α-ZAL, and β-ZAL, were purchased from Sigma-Aldrich (St. Louis, MO, US). The commercially available deuterated standards 17β-estradiol-16,16,17-d3 (β-E2-d3) and zearalenone-d6 (ZEA-d6) were purchased as pure standards from Wellington Laboratories (Toronto, Ontario, Canada) and were used as internal standards (ISs).

Full names and abbreviations of the selected compounds are reported in Figure 1. Individual stock standard solutions of the analytes were prepared in MeOH at the 1 mg mL^{-1} level. Composite working standard solutions were prepared by suitable dilution of stocks, used for recovery experiments, and renewed weekly.

Extraction and Cleanup Apparatus. A model ST ultrasonic bath at a frequency of 50 ± 3 kHz from Stimin (Milan, Italy) and an ALC (Milan, Italy) multispeed refrigerated centrifuge PK131R were used. Polypropylene tubes, polyethylene frits, and the vacuum manifold were from Supelco (Bellefonte, PA, US). All samples were extracted and cleaned by SPE cartridges packed with Carbograph-4 supplied by LARA (Rome, Italy). Carbograph-4 is a graphitized carbon black (GCB) similar to Carboprep 200 (Restek) and ENVI-carb X (Supelco).[11,12] Acrodisc 13 mm syringe filters with 0.2 μm GHP membrane (used for the filtration of samples prior to the injection into the chromatographic system) were from Pall (Pall Corp., MI, US).

Sample Collection and Preparation. Different types of cow whole milk, ultrahigh-temperature (UHT) pasteurized whole milk (3.6 g of fat, 3.30 g of protein per 100 mL), goat milk (3.9 g of fat, 3.2 g of protein per 100 mL), donkey milk (1.21 g of fat, 1.74 g of protein per 100 mL), and powder milk (0.1 g of fat and 3.3 g of protein per 100 mL of reconstituted milk) were purchased from local markets. The method was developed on whole milk, which is considered to be the worst case in terms of interferent content (such as proteins and fats).

Fortified samples were prepared by spiking 10 mL of milk with suitable amounts of composite working standard solutions and defined concentration of ISs (2 μg/L for β-E2-d3 and 1.5 μg/L for ZEA-d6), diluted to 250 mL with ultrapure water, and passed through the Carbograph-4 cartridges at about 20 mL min^{-1}. Cartridges were prepared by placing 500 mg of the adsorbent inside 6 mL polypropylene tubes between two polyethylene frits. Before the

DOI: 10.1021/acs.jafc.5b02815
J. Agric. Food Chem. 2015, 63, 8940−8946

samples were processed, these cartridges were attached to a vacuum manifold apparatus and washed sequentially with 10 mL of CH_2Cl_2/MeOH (80/20, v/v), 5 mL of MeOH, 20 mL of 10 mmol L^{-1} HCl solution, and 10 mL of ultrapure water. Then, the cartridge was washed sequentially with 50 mL of ultrapure water, 10 mL of MeOH acidified with 50 mmol L^{-1} HCOOH, and 5 mL of MeOH. Acidified MeOH was necessary to elute some compounds that could interfere with the analysis of free estrogens, especially E3.[13] Analytes were then eluted with 15 mL of CH_2Cl_2/MeOH (80/20, v/v). The eluate was evaporated to dryness in a water bath at 37 °C under a gentle stream of nitrogen. The residue was dissolved in 500 μL of water/MeOH (50/50, v/v) and then forced through a 0.2 μm GHP membrane syringe filter. A 5 μL sample of each final solution was analyzed by UHPLC/ESI-MS/MS.

UHPLC/ESI-MS/MS Analysis. Liquid chromatography was performed by using an Ultimate 3000 LC system (Thermo Fisher Scientific, Bremen, Germany) that consisted of a binary four-line pump, equipped with a degasser, a thermostated microwell-plate autosampler, and a thermostated column oven.

A 5 μL aliquot of sample was injected on a Hypersil Gold (50 × 2.1 mm i.d., 1.9 μm particle size) equipped with a Security guard Hypersil Gold (4 × 2.1 mm i.d., 5 μm particle size), both from Thermo Fisher Scientific. The column was maintained in the thermostated column compartment at 40 °C. Mobile phases were water (A) and ACN (B). For separation of the analytes, gradient elution was performed by linearly increasing the amount of B in A at flow rate of 300 μL min^{-1}. The starting mobile phase composition was 15% B. After an isocratic step at 15% B for 1 min, B was linearly increased to 50% within 7 min, brought to 99% in 2 min, and held constant for 5 min. Finally, the B content was lowered to 15% and the column was allowed to re-equilibrate for 5 min, for a total cycle time of 20 min.

A freshly prepared solution of NH_3, 80 mmol L^{-1} in water/MeOH (50/50, v/v), was added to the LC column effluent at a flow rate of 50 μL min^{-1} by means of a PerkinElmer series 200 micropump (Norwalk, CT, US). MS/MS detection was performed with a TSQ Vantage triple-stage quadrupole mass spectrometer (Thermo Fisher Scientific) connected with the LC system via a heated ESI source, operated in negative ionization mode. Spray voltages of 2.6 kV were applied, whereas declustering voltage was maintained to 0 V. The vaporizer temperature was set to 280 °C, and the capillary (ion-transfer tube) temperature to 220 °C. Sheath gas pressure, ion sweep gas pressure, and auxiliary gas pressure were set to 40, 0, and 20 (arbitrary units), respectively. Mass calibrations and resolution adjustments on the resolving lens and quadrupoles were automatically performed using the manufacturer's solution introduced via infusion pump at 5 μL min^{-1} flow rate. To optimize the tuning parameters for each compound, 1 ng μL^{-1} standard solutions in water/MeOH (50/50, v/v) were infused at 10 μL min^{-1}. The negative precursor ions were selected by the first quadrupole and fragmented in the collision cell with the appropriate collision energy. From the MS/MS full-scan spectra, suitable transitions were selected for acquisition in selected reaction monitoring (SRM) mode. The whole LC-MS system was managed by Xcalibur software (v.2.1, Thermo Fisher Scientific).

Method Performance. The method developed was evaluated according to recovery, matrix effect, linearity, precision (intra- and interday precision), and limits of detection (LODs) and limits of quantifications (LOQs) under the optimized conditions.

Recovery. The relative recoveries of the analytes were calculated by comparing the peak area ratio relative to that of the ISs obtained by spiking milk samples containing no detectable analyte quantities with the composite working standard solutions and ISs at four different concentration levels (5, 0.5, 0.2, and 0.05 μg/L) before and after the extraction procedure in triplicate.

Matrix Effect. Signal suppression (or enhancement) on ESI-MS/MS response due to matrix components, i.e., matrix effect (ME), was assessed by comparing the response of each analyte in matrix with respect to their response in solvent via the formula $[1 - (A_{matrix}/A_{standard})]\cdot 100$ where A_{matrix} and $A_{standard}$ are the relative peak area with respect to the ISs area of the analyte in matrix and in solvent, respectively. This was assessed during recovery experiments for each considered concentration.

Linearity. For linearity evaluation, two sets of calibration lines, named "standard" and "matrix-matched", were constructed. The standard calibration curve was constructed by diluting appropriate volumes of the working standard solution in water/MeOH (50/50, v/v), and adding the same amount of ISs at all times. Each point of the matrix-matched calibration curve was prepared following the procedure applied for recovery experiments as described in the previous section. Also in this case the same amount of IS was added at all times. Both standard and matrix-matched solutions were prepared at six concentration levels, ranging from 5 to 0.02 μg/L.

Precision. Precision of the method was assessed by the repeatability and reproducibility studies and expressed as recoveries and the relative standard deviation (RSD, %). The intraday precision (RSDr) was expressed as the standard deviation of the recovery values ($n = 6$) of the spiked samples at three levels measured during the same day. The interday precision (RSD_R) was determined by analyzing the spiked samples ($n = 3$) for six different days at the same levels.

LODs and LOQs. Method sensitivity was evaluated by LODs and LOQs.

The LODs and LOQs can be either instrumental (ILODs and ILOQs) or relative to the applied methodology (MLODs and MLOQs). To calculate LODs, the standard deviation of the response (σ) was divided by the slope of the calibration curve (S), according to the formula LOD = $3\sigma/S$ using the standard calibration curve for ILOD and matrix-matched calibration curve for MLOD.

In the same way, ILOQ and MLOQ were estimated according to the formula LOQs = $10\sigma/S$. These values were calculated employing data generated from regression statistics performed using standard and matrix-matched calibration points in the range of the lower concentrations (0.02−0.2 μg/L). The sum of the ion currents of the SRM transitions was considered to determine LOQs, while the less intense transition was considered to evaluate LODs.

RESULTS AND DISCUSSION

LC-MS/MS Optimization. The ESI-MS/MS fragmentation profile of all considered analytes was investigated by infusion experiments of single standards of approximately 1 ng/μL, prepared in water/MeOH (50/50, v/v).

Mycoestrogens and free estrogens were studied in negative ionization mode, giving in all cases $[M-H]^-$ as precursor ion. The list of precursor and fragment ions is shown in Table 1 together with their optimized S-lens and collision energies (CE).

UHPLC conditions were also investigated to determine the best mobile phases to separate the analytes using C18 stationary phase.

It has been reported[14] that neutral mobile phases, such as water/ACN or water/MeOH, showed great results in term of free estrogens separation; therefore, preliminary experiments were carried out testing these solvents. ACN resulted in the most appropriate organic solvents for chromatographic elution of all analytes in terms of peak separation and signal-to-noise ratio, especially because ACN allowed us to well separate ZAN, α-ZOL, and β-ZOL, which coeluted using MeOH as organic mobile phase.

In addition, to achieve more stable and reproducible signals and enhance the ionization of free estrogens, post column addition of NH_3 was introduced because of the incompatibility of high pH mobile phases with the silica-bonded C18 stationary phase. The addition of the basic modifier can significantly improve the deprotonation of the very weakly acid free estrogens; this resulted in a significant increase in the intensity and stability of the response of the ESI-MS system.

DOI: 10.1021/acs.jafc.5b02815
J. Agric. Food Chem. 2015, 63, 8940−8946

Table 1. Full Name, Abbreviation, Retention Time, Precursor and Product Ions, and MS Parameters of the Analyzed Compounds

compound abbreviation	retention time (min)	precursor ion $[M-H]^-$ (m/z)	product ion (m/z)	CE	S-lens
estriol (E3)	4.87	287.1	143.0	50	160
			145.1	40	
β-zearalanol (*β*-ZAL)	6.71	321.0	277.2	23	126
			161.2	32	
β-zearalenol (*β*-ZOL)	6.80	319.0	275.1	20	150
			160.0	28	
β-Estradiol-d3 (*β-E2-d3*)	7.28	274.0	143.0	60	181
			145.1	60	
α-zearalanol (*α*-ZAL)	7.29	321.0	277.2	23	126
			161.2	32	
β-estradiol (*β*-E2)	7.31	271.1	145.1	40	159
			183.2	40	
α-zearalenol (*α*-ZOL)	7.44	319.0	275.1	23	149
			160.0	36	
α-estradiol (*α*-E2)	7.56	271.1	145.1	40	159
			183.2	40	
estrone (E1)	7.84	269.1	145.1	40	128
			159.1	32	
zearalanone (ZAN)	8.12	319.0	275.2	22	127
			205.1	25	
zearalenone-d6 (*ZEA-d6*)	8.12	323.0	175.1	26	125
			131.1	33	
zearalenone (ZEA)	8.17	317.0	175.1	25	150
			131.1	33	

Concentration of 80 mmol/L of NH_3 in water/MeOH (50/50, v/v) mixture was chosen because of the volatility of the phase. The best conditions in terms of peak area reproducibility were achieved at a flow rate of 50 μL min^{-1}.

The mass-chromatograms of free estrogens and mycoestrogens are shown in panels a and b of Figure 2, respectively. All the examined compounds were analyzed in one chromatographic run. Each peak is relative to the sum of the selected transitions in an analyte-free milk sample spiked at the lowest level considered for recovery experiments (0.05 μg/L) using the composite standard working solution.

Sample Preparation. *Solid-Phase Extraction with GCB.* Milk analysis is very often challenging because many interfering compounds, such as proteins and fats, are present. They can suppress analyte signals, especially for compounds that can be present at a trace level. For this reason, deproteinization and/or defatting are often employed before extraction. This could lead to analyte loss, reduced reproducibility of the method, and long and time-consuming procedures. The use of Carbograph-4 can avoid these limitations because of its sorbent qualities. It is essentially a nonspecific and nonporous sorbent with a surface area of about 200 m^2 g^{-1}. The surface framework of this type of sorbent used in SPE was shown to be contaminated by oxygen complexes. These groups are able to interact so strongly with sufficiently acidic compounds that conventional solvent systems are not able to desorb them.[15,16] Because of the presence of positively charged chemical heterogeneities on their surface, GCB can be considered to be both reversed-phase sorbent and anion exchanger, showing great versatility. Therefore, it exhibits the advantage of being able to simultaneously extract neutral, basic, and acidic compounds.

In our recent work we used Carbograph-4 for the determination of free and conjugated estrogens in milk.[17] In this case, backflush elution mode was necessary because of the excessive retention of the conjugates into the sorbent.

Here we chose to directly focus on the free estrogens and mycoestrogens, present in milk and potentially dangerous for human health; therefore, the methodology was adapted and optimized for this purpose. With the optimized procedure it was possible to elute all the analytes with CH_2Cl_2/MeOH after a simple dilution of milk in water. Recovery experiments were performed at four concentration levels, and the results are shown in Table 2. The employed methodology provided very good recoveries with negligible matrix effect also at the lowest concentration level, demonstrating the effectiveness of this SPE for a very complex matrix, such as whole milk.

Comparison with Other Extraction Methods. Searching the literature for works dealing with endocrine disruptors in milk provides several publications, but only very few methods addressed the determination of resorcyclic acid lactones and endogenous estrogenic compounds in milk. In particular, most works were especially dedicated to the presence of free estrogens in milk and dairy products. On the other hand, methods for the determination of ZEA and its metabolites were developed, but they comprised other mycotoxin compounds as well. In this context only two works described methods for their analysis in milk as estrogenic compounds together with mycoestrogens by LC-MS/MS,[18,19] and in only one work were free estrogens also considered, but they were analyzed with other techniques.[20]

In their work, Xia et al.[18] analyzed the six resorcyclic acid lactones with SPE using the Oasis MAX cartridges in whole milk samples. This polymeric sorbent has properties similar to GCB sorbent because it contains quaternary amine groups on the surface; therefore, it can act as reversed-phase sorbent and anion exchanger. For this reason we decided to verify if the cited procedure could work also for simultaneous extraction of estrogens and mycoestrogens in comparison to our optimized procedure.

For this purpose recovery experiments were carried out using Oasis MAX cartridges at two concentration levels (1 μg/L and 0.05 μg/L) following the procedure reported Xia et al.[18] Results demonstrated that at high spiking levels recoveries range between 70 and 90%, except for E3 (only 13%, data not shown). This can be explained probably because E3, being the most polar analyte, could be lost during cartridge washing with ACN. At lower spiking levels, which is the scenario in milk samples, this methodology was unable to recover free estrogens, and mycoestrogens recoveries decreased significantly. This result was attributed to the low concentration levels, in which case the sample pretreatment (deproteinization step) can become a crucial and limiting step; in fact, the unavoidable analyte loss and the inefficiency of the commercial sorbent to retain and elute the analytes significantly affected sample recoveries. On the other hand, with the optimized method using GCB as sorbent, it was possible to reach lower method detection limits (MDLs) and method quantification limits (MQLs), with negligible or very low matrix effect, which

DOI: 10.1021/acs.jafc.5b02815
J. Agric. Food Chem. 2015, 63, 8940−8946

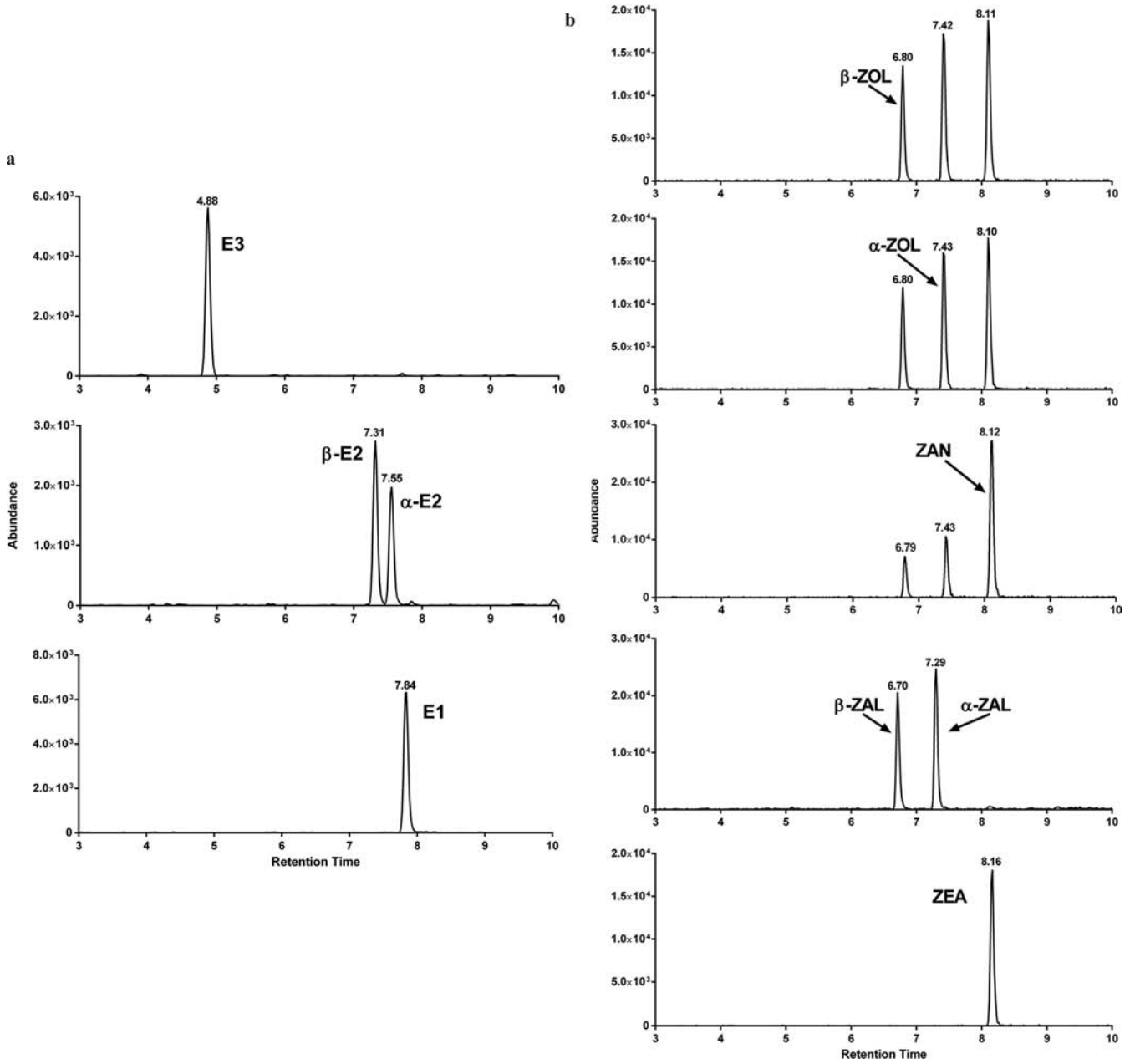

Figure 2. Selected ion chromatograms of MRM of the investigated (a) free estrogens and (b) resorcyclic acid lactones. Each peak is relative to the sum of the selected transitions for each estrogen in a milk sample spiked at 0.05 μg/L with the composite standard working solution.

Table 2. Relative Recoveries (n = 3 for Each Level) and Matrix Effect of Free Estrogens and Resorcyclic Acid Lactones in Milk Samples Spiked at Four Different Concentration Levels

	5 μg/L		0.5 μg/L		0.2 μg/L		0.05 μg/L	
analyte	R% (RSD)	ME%	R% (RSD)	ME%	R% (RSD)	ME%	R% (RSD)	ME%
E3	93.0 (2.5)	2	81.6 (3.4)	−8	94.6 (4.0)	6	107.2 (6.4)	−2
β-ZAL	92.4 (1.4)	6	101.7 (2.0)	2	97.6 (3.3)	4	100.7 (5.2)	5
β-ZOL	85.3 (3.5)	12	90.3 (4.1)	1	100.8 (7.6)	−6	106.4 (9.0)	−4
α-ZAL	91.6 (4.0)	10	95.6 (9.6)	−1	94.4 (2.6)	2	101.1 (3.4)	2
β-E2	90.3 (2.6)	9	83.8 (6.7)	0	89.1 (7.8)	9	71.9 (5.4)	0
α-ZOL	96.8 (5.3)	5	98.2 (3.0)	8	110.2 (6.8)	−1	99.6 (4.6)	−3
α-E2	85.7 (7.1)	6	70.8 (8.2)	7	68.9 (8.1)	8	67.4 (10.2)	7
E1	91.4 (3.7)	4	82.0 (2.3)	7	100.9 (5.0)	2	96.8 (8.1)	8
ZAN	95.2 (2.5)	2	92.1 3(3.5)	0	102.3 (4.3)	10	98.0 (3.0)	6
ZEA	90.0 (2.0)	3	84.9 (4.0)	4	97.9 (3.9)	−9	99.6 (2.3)	−2

DOI: 10.1021/acs.jafc.5b02815
J. Agric. Food Chem. 2015, 63, 8940−8946

Table 3. Validation Parameters of the Proposed LC/ESI-MS/MS Method for the Selected Compounds in Milk

analyte	R^2	R (%); RSDr[a] (%) 0.5 μg/L	R (%); RSDR[b] (%) 0.5 μg/L	R (%); RSDr[a] (%) 0.2 μg/L	R (%); RSDr[a] (%) 0.05 μg/L	R (%); RSD_R[b] (%) 0.2 μg/L	R (%); RSD_R[b] (%) 0.05 μg/L	ILOD (pg inj)	ILOQ (pg inj)	MLOD (μg/L)	MLOQ (μg/L)
E3	0.9999	80.0; 6.4	77.8; 7.9	91.0; 8.5	96.0; 13.2	93.5; 13.4	90.0; 10.0	2.5	3.6	0.06	0.09
β-ZAL	0.9998	95.0; 7.0	92.3; 5.6	84.3; 22.6	78.7; 10.7	90.8; 31.1	94.8; 11.4	1.0	3.5	0.06	0.2
β-ZOL	0.9992	88.4; 6.6	83.3; 8.8	79.5; 15.2	91.0; 16.8	87.9; 18.8	93.2; 14.7	3.5	6.0	0.1	0.1
α-ZAL	0.9999	93.7; 5.3	90.1; 6.1	92.0; 13.6	89.1; 7.7	92.6; 15.7	101.0; 3.2	2.5	4.5	0.06	0.09
β-E2	0.9999	81.3; 10.2	82.8; 15.0	95.6; 7.4	90.3; 11.1	95.0; 6.8	92.0; 16.3	2.0	6.5	0.02	0.06
α-ZOL	0.9999	96.0; 3.5	94.5; 5.0	100.9; 4.8	95.8; 5.2	98.2; 5.7	97.4; 6.8	1.5	3.0	0.03	0.07
α-E2	0.9998	75.1; 9.4	88.0; 10.0	75.8; 9.3	85.7; 14.8	90.3; 14.2	92.6; 12.4	4.0	4.0	0.01	0.02
E1	0.9991	84.1; 6.7	86.0; 9.4	87.0; 8.6	94.1; 8.0	97.6; 5.1	91.0; 7.8	3.5	3.5	0.03	0.06
ZAN	1.0000	95.2; 3.3	93.3; 5.9	93.4; 7.8	88.0; 9.1	85.1; 11.4	95.5; 9.7	0.28	1.5	0.004	0.01
ZEA	1.0000	82.4; 5.1	80.8; 4.7	85.7; 6.8	91.6; 4.8	93.9; 7.2	89.4; 3.9	1.0	3.0	0.02	0.02

[a]Intraday precision, $n = 6$ within the same day. [b]$n = 6$ in 6 different days; $n = 3$ within each day.

did not influence analyte signals also at low concentration, demonstrating the effectiveness of the cleanup for all the considered compounds.

Method Performance. The developed method showed good linearity for all the analytes investigated also in the range of the low concentrations with correlation coefficients ranging between 0.9991 and 1, as shown in Table 3. In the majority of the works previously published, LOD and LOQ values were calculated using the signal-to-noise ratio of the transitions of the analyzed compounds. However, when operating in MS/MS mode with modern triple quadrupole mass spectrometers, the baseline noise is very often quite totally absent; therefore, the extrapolated LOD and LOQ values are notably underestimated and not realistic.

For this reason the detection and quantification limits were assessed considering the standard deviation of the response and the slope, i.e., LOD = $3\sigma/S$, where σ is the standard deviation of the response and S the slope of the calibration curve. For the estimate of σ, the standard deviation of the y-intercept of the regression line was used. In the same way, LOQ was estimated as $10\sigma/S$. For LOQ measurements, for each analyte the sum of the two transitions was considered, whereas for LOD measurements only the response of the second-most intense SRM transition was considered. To assess the reliability of the results we used the standard deviation and the slope of the linear regression generated from the lower calibration points (between 0.02 and 0.2 μg/L, nearer to LOD and LOQ values). Then, to verify the obtained values for the developed method, blank milk samples were spiked at MDL and MQL concentrations. Moreover, as reported in the Commission Decision 2002/657/EC,[21] we decided that the presence of a compound is confirmed if the relative intensities of their selected transitions correspond to those in the calibration standard, under certain set conditions, within set tolerances. For this reason, the relative intensities of the selected transition for all the analytes were checked and compared in each point of the standard and matrix matched calibration curve for their real detection. Finally, the calculated values were confirmed by spiking a blank sample with the found concentrations. As shown in Table 3, with this method it is possible to reach good detection and quantification limits, which are lower than those of other published methods. This result is crucial for this type of analysis, especially because natural contamination of estrogenic compounds is often present at trace levels.

Analysis of Milk Samples. To demonstrate its applicability, the developed method was employed to analyze different whole milk samples: 16 cow milk samples, 2 UHT cow milk samples, 3 powder cow milk samples, 4 goat milk samples, and 5 donkey milk samples. As for the method development, we chose to consider whole milk as the worst case in terms of complexity and because it is also known that free estrogens could be found in larger amounts in samples richer in fats. Results obtained in sample analysis indicated that in 4 of the 16 samples of cow milk E1 was found at concentrations between its MLOD and MLOQ value, and in one of them also ZEA was found between its MLOD and MLOQ value. The other samples did not show any contamination.

AUTHOR INFORMATION

Corresponding Author

*Phone: +39 06 4991 3834. E-mail: chiara.cavaliere@uniroma1.it.

Notes

The authors declare no competing financial interest.

REFERENCES

(1) Malekinejad, H.; Scherpenisse, P.; Bergwerff, A. A. Naturally occurring estrogens in processed milk and in raw milk (from gestated cows). *J. Agric. Food Chem.* **2006**, *54*, 9785−9791.

(2) Johnson, A. C.; Williams, R. J.; Matthiessen, P. The potential steroid hormone contribution of farm animals to freshwaters, the United Kingdom as a case study. *Sci. Total Environ.* **2006**, *362*, 166−178.

(3) Capriotti, A. L.; Cavaliere, C.; Colapicchioni, V.; Piovesana, S.; Samperi, R.; Laganà, A. Analytical strategies based on chromatography-mass spectrometry for the determination of estrogen-mimicking compounds in food. *J. Chromatogr. A* **2013**, *1313*, 62−77.

(4) Socas-Rodríguez, B.; Asensio-Ramos, M.; Hernández-Borges, J.; Herrera-Herrera, A. V.; Rodríguez-Delgado, M. T. Chromatographic analysis of natural and synthetic estrogens in milk and dairy products. *TrAC, Trends Anal. Chem.* **2013**, *44*, 58−77.

(5) Wielogorska, E.; Elliott, C. T.; Danaher, M.; Chevallier, O.; Connolly, L. Validation of an ultra high performance liquid chromatography-tandem mass spectrometry method for detection and quantitation of 19 endocrine disruptors in milk. *Food Control* **2015**, *48*, 48−55.

(6) Fink-Gremmels, J.; Malekinejad, H. Clinical effects and biochemical mechanisms associated with exposure to the mycoestrogen zearalenone. *Anim. Feed Sci. Technol.* **2007**, *137*, 326−341.

(7) Gareis, M.; Wolff, J. Relevance of mycotoxin contaminated feed for farm animals and carryover of mycotoxins to food of animal origin. *Mycoses* **2000**, *43*, 79−83.

DOI: 10.1021/acs.jafc.5b02815
J. Agric. Food Chem. 2015, 63, 8940−8946

(8) Yiannikouris, A.; Jouany, J. P. Mycotoxins in feeds and their fate in animals: a review. *Anim. Res.* **2002**, *51*, 81−99.
(9) Zollner, P.; Jodlbauer, J.; Kleinova, M.; Kahlbacher, H.; Kuhn, T.; Hochsteiner, W.; Lindner, W. Concentration Levels of Zearalenone and Its Metabolites in Urine, Muscle Tissue, and Liver Samples of Pigs Fed with Mycotoxin-Contaminated Oats. *J. Agric. Food Chem.* **2002**, *50*, 2494−2501.
(10) Capriotti, A. L.; Caruso, G.; Cavaliere, C.; Foglia, P.; Samperi, R.; Laganà, A. Multiclass mycotoxin analysis in food, environmental and biological matrices with chromatography/mass spectrometry. *Mass Spectrom. Rev.* **2012**, *31*, 466−503.
(11) Cavaliere, C.; Foglia, P.; Pastorini, E.; Samperi, R.; Laganà, A. Liquid chromatography/tandem mass spectrometric confirmatory method for determining aflatoxin M1 in cow milk: Comparison between electrospray and atmospheric pressure photoionization sources. *J. Chromatogr. A* **2006**, *1101*, 69−78.
(12) Bogialli, S.; D'Ascenzo, G.; Di Corcia, A.; Laganà, A.; Nicolardi, S. A simple and rapid assay based on hot water extraction and liquid chromatography−tandem mass spectrometry for monitoring quinolone residues in bovine milk. *Food Chem.* **2008**, *108*, 354−360.
(13) Laganà, A.; Fago, G.; Marino, A.; Santarelli, D. Liquid chromatography tandem mass spectrometry applied to the analysis of natural and synthetic steroids in environmental waters. *Anal. Lett.* **2001**, *34*, 913−926.
(14) Gentili, A.; Perret, D.; Marchese, S.; Mastropasqua, R.; Curini, R.; Di Corcia, A. Analysis of free estrogens and their conjugates in sewage and river waters by solid-phase extraction then liquid chromatography-electrospray-tandem mass spectrometry. *Chromatographia* **2002**, *56*, 25−32.
(15) Hennion, M. C. Graphitized carbons for solid-phase extraction. *J. Chromatogr. A* **2000**, *885*, 73−95.
(16) Laganà, A.; Fago, G.; Marino, A. Simultaneous Determination of Imidazolinone Herbicides from Soil and Natural Waters Using Soil Column Extraction and Off-Line Solid-Phase Extraction Followed by Liquid Chromatography with UV Detection or Liquid Chromatography/Electrospray Mass Spectroscopy. *Anal. Chem.* **1998**, *70*, 121−130.
(17) Capriotti, A. L.; Cavaliere, C.; Foglia, P.; Samperi, R.; Stampachiacchiere, S.; Ventura, S.; Laganà, A. Ultra-high-performance liquid chromatography-tandem mass spectrometry for the analysis of free and conjugated natural estrogens in cow milk without deconjugation. *Anal. Bioanal. Chem.* **2015**, *407*, 1705−1719.
(18) Xia, X.; Li, X.; Ding, S.; Zhang, S.; Jiang, H.; Li, J.; Shen, J. Ultra-high-pressure liquid chromatography−tandem mass spectrometry for the analysis of six resorcylic acid lactones in bovine milk. *J. Chromatogr. A* **2009**, *1216*, 2587−2591.
(19) Sørensen, L. K.; Elbæk, T. H. Determination of mycotoxins in bovine milk by liquid chromatography tandem mass spectrometry. *J. Chromatogr. B: Anal. Technol. Biomed. Life Sci.* **2005**, *820*, 183−196.
(20) D' Orazio, G.; Asensio-Ramos, M.; Hernandez-Borges, J.; Rodrıguez-Delgado, M. A.; Fanali, S. Evaluation of the combination of a dispersive liquid−liquid microextraction method with micellar electrokinetic chromatography coupled to mass spectrometry for the determination of estrogenic compounds in milk and yogurt. *Electrophoresis* **2015**, *36*, 615−625.
(21) Commission Decision 2002/657/EC of 12 August 2002 implementing Council Directive 96/23/EC concerning the performance of analytical methods and the interpretation of results, as amended by Decision 2003/181/EC (4). *Official Journal of the European Communities*, 8−36.

DOI: 10.1021/acs.jafc.5b02815
J. Agric. Food Chem. 2015, 63, 8940−8946

teristics such as longer emission lifetime and delayed relaxation time, making the lowest background noises from short-lived autofluorescence and scattering light of the analytical system to be achieved; therefore, RTP is favorable for analysis of complex samples as a signal transduction method.[19−31] Recently, the RTP of doped quantum dots (QDs), e.g., Mn-doped ZnS QDs, has attracted growing attention on optosensing.[20−31] Doped QDs have been considered as a novel type of luminescent material and displayed promising applications in fabricating chemosensors, biosensors, and bioimaging based on their intrinsic advantages of conventional QDs.[20] However, most research has been interested in developing QD-based fluorescent chemo/biosensors; the distinguished phosphorescent properties of QDs still have not been used sufficiently for applications in analytical chemistry.[20] As far as we know, such RTP of QDs used to detect OPPs has rarely been reported.[25] On the other hand, colorimetric assays, which can be achieved with naked eyes or UV/vis spectrometry, have shown some advantages in their simpleness such as simple instrumentation and easy operation procedures.[32−37] Typically, colorimetric detections based on gold nanoparticles (AuNPs), which generally display different colors in the visible range resulting from their localized surface plasmon resonance (LSPR) absorption and scattering,[36,37] have been applied for a variety of analytes including biomacromolecules, small molecules, and metal ions.[32−37] We believe that the sensing strategy combining phosphorimetric and colorimetric techniques will provide a novel method with simplicity and high sensitivity for analytical applications.

In this study, we demonstrate a dual-signaling sensing system by taking advantages of both phosphorimetric and colorimetric methods for the first time, which relies on the inner filter effect (IFE) of AuNPs on the phosphorescence of Mn-ZnS QDs. In this IFE system, AuNPs and Mn-ZnS QDs are designed as the absorber−phosphor pair to regulate the phosphorescence emission of Mn-ZnS QDs. The IFE of luminescent species is generally defined as the absorption of the excitation and/or emission of lumiphores by absorbers and therefore leads to the quenching of lumiphores in the IFE systems.[38] More importantly, the linking between the absorbers and the lumiphore is not required in IFE detection systems, making the IFE-based detection considerably flexible and simpler for analytical applications. On the other hand, an improved detection sensitivity may be obtained compared with the absorbance or luminescence intensity alone because the varying absorbance of absorbers results in exponential variance in the luminescence of lumiphores.[38] Recently, a few studies have demonstrated IFE-based applications in developing novel fluorescence assays, although it usually introduces undesired systematic errors to fluorescence measurements and is expected to be avoided.[39−45] However, to the best our knowledge, analytical application that relies on IFE of AuNPs on the phosphorescence of QDs has not been reported so far. In the present study, we describe a colorimetric and phosphorimetric dual-signaling strategy for sensitive assay of OPPs including paraoxon, parathion, omethoate, and dimethyl dichlorovinyl phosphate (DDVP) (Figure 1). The assay principle is attributed to the remarkable quenching of the phosphorescence of Mn-ZnS QDs by AuNPs via IFE and the inhibition of the activity of acetylcholinesterase (AChE) by OPPs. In the presence of OPPs, the production of thiocholine from the hydrolysis of acetylthiocholine catalyzed by AChE is hindered, resulting in the aggregation of AuNPs and thereby the restoration of the IFE-quenched phosphorescence of Mn-ZnS QDs. Consequently, the aggregation of AuNPs and the phosphorescence recovery of Mn-ZnS QDs are dependent on OPP concentration. On the basis of the variations of absorbance and phosphorescence of the analytical system, a dual-readout assay for OPPs has been proposed.

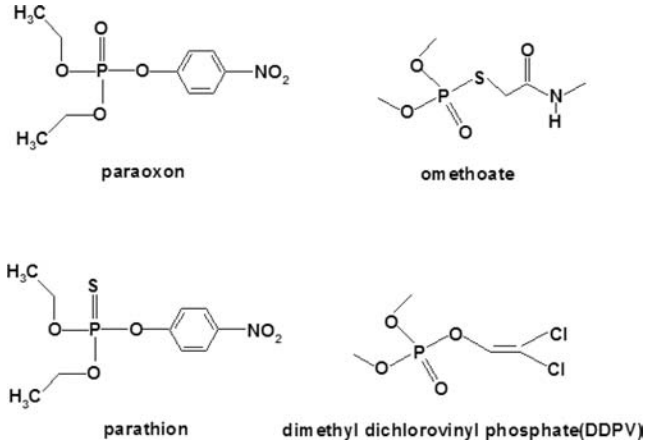

Figure 1. Chemical structures of organophosphorus pesticides tested in this study.

EXPERIMENTAL PROCEDURES

Materials and Apparatus. $ZnSO_4·7H_2O$, $Na_2S·9H_2O$, $MnCl_2·4H_2O$, mercaptopropionic acid (MPA), $HAuCl_4·H_2O$, sodium citrate, acetylcholinesterase (AChE, from *Electrophorus electricus*), and acetylthiocholine iodide were provided by Sigma-Aldrich (Tianjing, China). Paraoxon, dimethyl dichlorovinyl phosphate (DDVP), parathion, and omethoate were obtained from Aladdin-Reagent Co. (Beijing, China). The reagents used in this study are of analytical grade and without further purification. The ultrapure water (Mill-Q, Millipore, 18.2 MΩ resistivity) was used for all the experiments in this study. Mn-Doped ZnS QDs modified with MPA and citrate-modified AuNPs were synthesized with the procedures reported in the literature.[30,31,46]

UV/vis absorption spectra were performed on a UV-3010 spectrophotometer (Hitachi, Japan). Phosphorescence spectra were recorded on an LS-55 fluorescence spectrophotometer (PerkinElmer Company, U.S.A.) using a quartz cell (1 cm × 1 cm) in the phosphorescence mode. Decay curve measurements were carried out on a model FLS920 steady-state and lifetime spectrometer (Edinburgh Instruments Ltd., Livingston, U.K.). Apple juice was prepared with a juice extractor.

The freshly prepared aqueous solution of acetylthiocholine (1.0 mM) was used immediately (not exceeding 3 h) to reduce its hydrolysis. The stock solution of pesticides (4.0 mM) was first prepared with methanol and then was diluted to desired concentrations with ultrapure water. AChE (1.0 U/mL) was prepared with phosphate-buffered solution (pH 8.0, 10 mM) and used immediately for the following experiments.

Experimental Procedures for the Assay of OPPs. Paraoxon, one typical OPP frequently used, was selected as the representative pesticide for carrying out the experiments. AChE (20 μL, 1 U/mL) was first mixed with 0.5 mL of phosphate buffer containing different concentrations of paraoxon at 37 °C for 20 min. Acetylthiocholine (20 μL, 1 mM), AuNPs (0.67 mL, 12 nM), and Mn-ZnS QDs (0.2 mL, 40 mg/L) were introduced into each mixture, respectively, and then the resulting mixtures were scaled to 2.0 mL using phosphate buffer and mixed thoroughly. After incubating in the dark for 10 min, UV/vis absorption and phosphorescence spectra were recorded, respectively, and the phosphorescence emission spectra were measured at 580 nm under the excitation at 290 nm. All measurements were repeated at least five times.

DOI: 10.1021/acs.jafc.5b03096
J. Agric. Food Chem. 2015, 63, 8947−8954

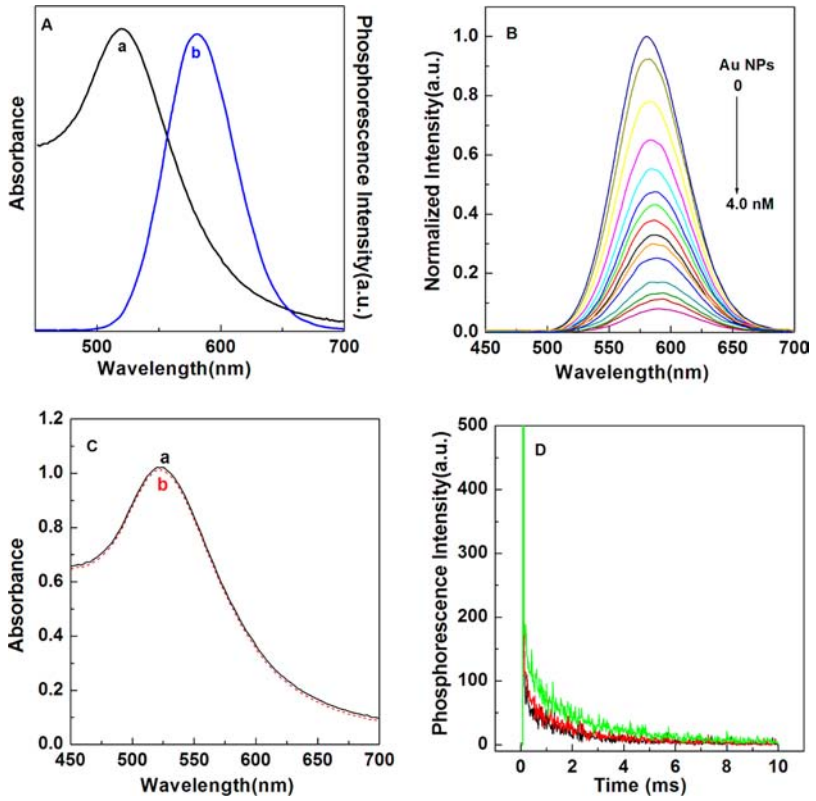

Figure 2. (A) Overlay spectra of absorption spectrum of AuNPs (a) and phosphorescence emission spectrum of Mn-ZnS QDs (b), (B) phosphorescence spectra of Mn-ZnS QDs in the presence of various concentrations of AuNPs (from top to bottom: 0, 0.2, 0.6, 0.8, 1.0, 1.3, 1.5, 1.8, 2.0, 2.5, 2.8, 3.0, 3.2, 3.5, 4.0 nM), (C) absorption spectrum of AuNPs in the absence (a) and presence (b) of Mn-ZnS QDs(C), and (D) the phosphorescence lifetime of Mn-ZnS QDs in the absence (green line) and presence of 1.0 nM (red line) and 2.0 nM (black line) AuNPs. Unless otherwise stated, the concentrations for Mn-ZnS QDs and AuNPs are 4 mg/L and 4.0 nM, respectively. The excitation wavelength for phosphorescence measurements is at 290 nm.

Analysis of Paraoxon in Spiked Samples and Contaminated Samples. In this study, lake water and apple juice made from clean apples (i.e., without sprayed OPPs) were used for spiked experiments, while the apple juice made from apples sprayed with OPPs was used for investigating OPP residues with time. The apples (with or without sprayed OPPs) were smashed into pieces and then squeezed into homogenates with juice squeezer. The obtained homogenates (20 g) were dissolved into 20 mL of methanol, and the resultant dispersion was filtered with a 0.22 μm filter (PES membrane) to get rid of the insoluble matrixes,[12] and then apple juice was collected for further experiments. For spiked experiments, different volumes of paraoxon stock solutions (4.0 mM, i.e., 1.1 g/L) were incubated in the prepared 4.0 mL of real sample (lake water or apple juice) and then scaled to 5.0 mL using buffer, resulting in final concentrations of paraoxon of 5.0 nM, 10.0 nM, and 100.0 mM, respectively. Five μL of the resulting sample was mixed with AChE (20 μL, 1U/mL) and incubated at 37 °C for 20 min, following by the introduce of acetylthiocholine (20 μL, 1 mM), AuNPs (0.67 mL, 12 nM), and Mn-ZnS QDs (0.2 mL, 40 mg/L). The mixture was then scaled to 2.0 mL by phosphate buffer, mixed thoroughly, and incubated for 10 min in the dark, and then UV/vis absorption and phosphorescence were recorded. For the contaminated apple juice, similar analytical procedures were adopted.

RESULTS AND DISCUSSION

IFE of AuNPs on Phosphorescence of Mn-ZnS QDs. Generally, the key point in designing an IFE-based analytical system is to select a suitable absorber/lumiphore pair because the effective IFE could happen under the conditions of sufficient spectral overlapping between the absorber absorption and the excitation and/or emission of the lumiphore.[38,43] However, the conventional absorber generally possesses a small absorption coefficient, which limits the IFE efficiency and therefore reduces the sensitivity of the IFE-based analytical system. Consequently, such luminescent method based on IFE has not been extensively exploited so far.[38,43] Undoubtedly, to get high sensitivity for IFE-based detection, the important thing is to improve the inner filter efficiency and, thus, to achieve a low luminescent background.[38,43] To such an attempt, a practical approach is to expand the spectral overlapping of absorber absorption with lumiphore emission, and/or to select proper absorber with larger absorption coefficient.[38,43] In this study, AuNPs have been chosen as the absorbers, which is based on the fact that AuNPs possess a much larger absorption coefficient (e.g., 2.7×10^8 /M/cm at 520 nm for the particles with a diameter of 13 nm[46]) compared to those of usual chromophores. Figure 2A shows a good overlap of the absorption band of AuNPs (curve a) with the phosphorescence emission band of Mn-ZnS QDs (curve b), which provides a precondition for possible IFE between AuNPs and Mn-ZnS QDs. To confirm the IFE occurred between AuNPs and Mn-ZnS QDs, the phosphorescence spectra of Mn-ZnS QDs were investigated when Mn-ZnS QDs were mixed with various concentrations of AuNPs. We can see from Figure 2B that the phosphorescence emission of Mn-ZnS QDs gradually decreases upon increasing concentrations of AuNPs. In the present system (pH 8.0), the AuNPs obtained with citrate reduction method were capped with citrate and negatively charged, supported by its zeta potential, −36.6 mV, because of the ionization of the −COOH group in citrate.[44] The zeta potential

DOI: 10.1021/acs.jafc.5b03096
J. Agric. Food Chem. 2015, 63, 8947−8954

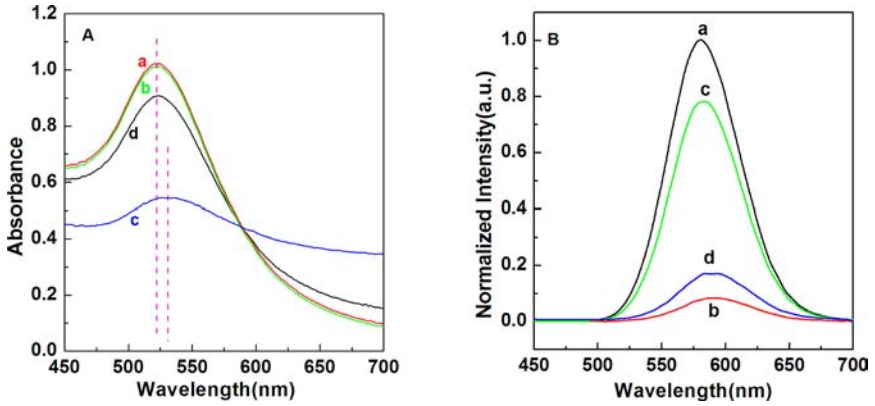

Figure 3. (A) UV/vis absorption spectra of AuNPs (a), Mn-ZnS QD−AuNP mixed solution (b), Mn-ZnS QD−AuNP solution incubated with AChE and acetylthiocholine (c), and Mn-ZnS QD−AuNP solution containing AChE was pretreated with paraoxon, and acetylthiocholine (d); (B) phosphorescence spectra of Mn-ZnS QDs (a), Mn-ZnS QD−AuNP mixed solution (b), Mn-ZnS QD−AuNP mixed solution incubated with AChE and acetylthiocholine (c), and Mn-ZnS QD−AuNP mixed solution containing AChE was pretreated with paraoxon and acetylthiocholine (d). The concentrations for AChE, acetylthiocholine, AuNPs, Mn-ZnS QDs, and paraoxon are 10 mU/mL, 10 μM, 4 nM, 4 mg/L, and 1 μM, respectively.

of the MPA-capped Mn-ZnS QDs was also measured, and the zeta potential was −46 mV in pH 8.0 phosphate buffer because of the ionization of the −COOH group in MPA (pK_{COOH} = 4.32[47]). The electrostatic repulsion interaction causes the formation of a complex, or energy transfer could not happen in the present system because the plasmon absorption band of AuNPs did not show obvious changes in the presence of Mn-ZnS QDs (Figure 2C).[43,48] Moreover, the phosphorescence lifetimes of Mn-ZnS QDs that coexisted with or without AuNPs were compared. From Figure 2D, no obvious changes in the average lifetime of the Mn-ZnS QDs were observed in the presence of AuNPs, suggesting that the complex resulting from Mn-ZnS QDs and AuNPs could not be formed through hydrogen bonding or electrostatic forces.[49] The observation from the studies on phosphorescence lifetime further confirms that there existed an efficient IFE of AuNPs on the phosphorescence of Mn-ZnS QDs, while no energy transfer between Mn-ZnS QDs and AuNPs occurs because nonradiative energy transfer basically changes the excitation lifetime of the energy donor.[49] On the basis of these experimental results, we believed that the decreased phosphorescence emission may be mainly ascribed to the IFE of AuNPs on the phosphorescence of Mn-ZnS QDs rather than other possible processes.

Notably, the quenching efficiency (E_q) of QDs by the IFE of AuNPs can be calculated via the equation:

$$E_q = 1 - P/P_0$$

Herein, P and P_0 are the phosphorescence intensity in the presence and absence of AuNPs, respectively. In this system, the maximum E_q was estimated to be as high as 80.2% in the presence of as low as 4.0 nM Au NPs, which is much greater than the IFE-based fluorescent analytical system.[43] This high quenching efficiency can be ascribed to the large absorption coefficient of AuNPs, and such a low background of the system is highly desirable for sensitive phosphorescence assay.

Dual-Signal Mechanism for OPP Assay through Inhibiting AChE Activity by OPPs. To construct a system for the OPP assay via the modulation of IFE of AuNPs on phosphorescence of Mn-ZnS QDs, a mixed solution containing optimized concentration of 4.0 nM AuNPs and 4.0 mg/L Mn-ZnS QDs was first prepared. It can be seen that the absorbance and color of the as-prepared solution (the solution color is red) (curve b in Figure 3A) remained unchanged and were the same as that of pure AuNPs solution (curve a in Figure 3A), and they displayed the typical characteristic absorption at 520 nm. Upon the addition of both acetylthiocholine and AChE into a Mn-ZnS QD−AuNP mixed solution, the quenched phosphorescence of Mn-ZnS QDs (curve b in Figure 3B) recovered significantly (curve c in Figure 3B), followed by the decreased of absorbance and the slight shift of the absorption band (solution color was changed from red to purple) (curve c in Figure 3A). To investigate the potential application in pesticides determination, AChE (10 mU/mL) was first mixed with paraoxon (1.0 μM) and incubated for 20 min at 37 °C; acetylthiocholine (10 μM), AuNPs (4.0 nM), and Mn-ZnS QDs (4.0 mg/L) were then mixed together in sequence. We found that the absorbance was recovered with a duration of 30 min (curve d in Figure 3A), and phosphorescence recovery of Mn-ZnS QDs was impeded (curve d in Figure 3B), accompanied by the change in the color of the mixed solution from purple to red. These results indicate that paraoxon can surpress the activity of AChE, thus hindering the production of thiolcholine from the hydrolysis of acetylthiocholine catalyzed by AChE. Consequently, the absence of paraoxon can not only lead to absorbance change (also color change) but also can lead to the phosphorescence recovery of Mn-ZnS QD−AuNP solutions. Additionally, we can clearly see the aggregating behavior of AuNPs that resulted from the addition of AChE and acetylthiocholine from the analysis of transmission electron microscopy (TEM). Upon the addition of AChE and acetylthiocholine, the monodispersed AuNPs show a tendency to aggregate together and form AuNPs aggregates, which is agreement with the spectral changes displayed in Figure 3A (curve c). However, AuNP aggregates are prevented while inhibiting AChE with paraoxon. TEM analysis is also in agreement with the transforms in the aggregation states of AuNPs, demonstrating that paraoxon has the ability to prevent and form AuNP aggregates.

Analytical Performances of the AuNPs−Mn-ZnS QDs Dual-Signal Readout System for OPPs Assay. To investigate the analytical performances of the present system for the assay of OPPs, we first investigated one of the most commonly used OPPs, paraoxon, as the representative model pesticide. Prior to detection, paraoxon with different concentrations was introduced to aliquots of AChE solution, respectively, and the mixtures were incubated at 37 °C to

DOI: 10.1021/acs.jafc.5b03096
J. Agric. Food Chem. 2015, 63, 8947−8954

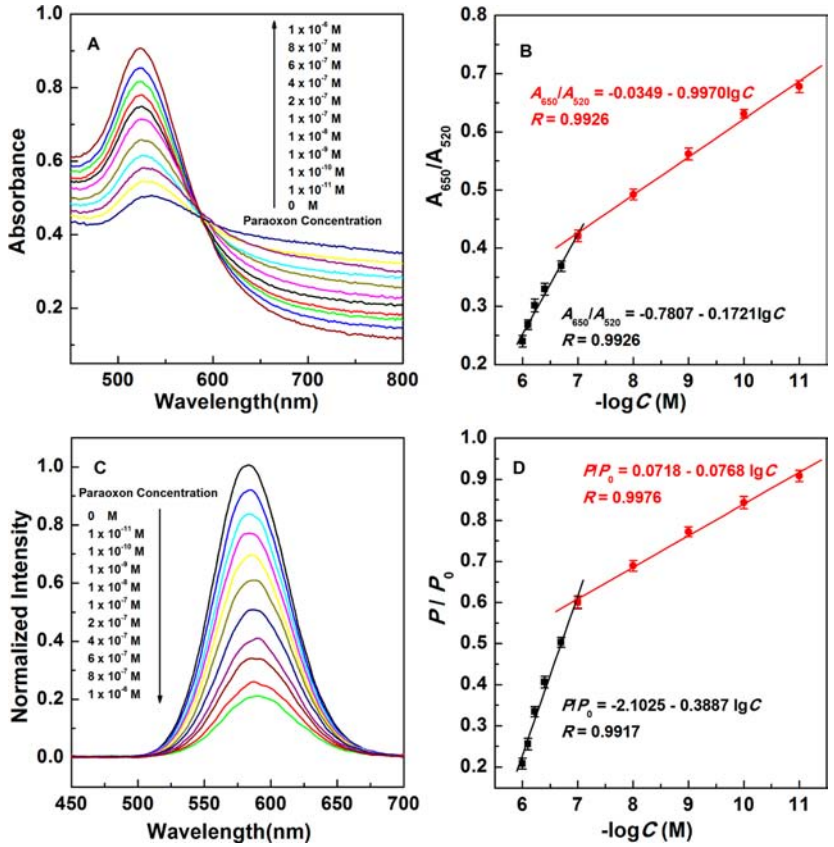

Figure 4. Absorption (A) and phosphorescence (C) spectra of the present system in the presence of increasing concentrations of paraoxon, and the linear calibration of (B) A_{650}/A_{520} and (D) P/P_0 versus the logarithm of paraoxon concentration. The concentrations for AChE, acetylthiocholine, AuNPs, and Mn-ZnS QDs are the same as those in Figure 2.

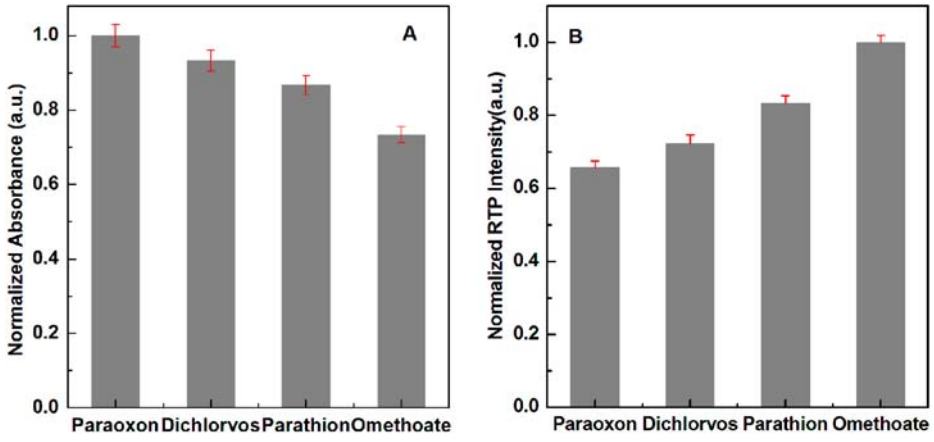

Figure 5. Normalized (A) absorbance and (B) phosphorescence response of different OPPs with the same concentration of 200 nM toward the present system. The concentrations for AChE, acetylthiocholine, AuNPs, and Mn-ZnS QDs are the same as those in Figure 2.

react for 20 min. AuNPs, Mn-ZnS QDs, and acetylthiocholine were then introduced into each mixture in sequence. After incubating for 10 min, it can be seen that the color of the solution transforms gradually from red to purple, which is dependent on paraoxon concentrations. The UV/vis absorption spectra displayed in Figure 4A demonstrated that the absorption band was slightly red-shifted, further confirming the color transforming arising from aggregation of AuNPs. The aggregation and relevant color transforming of AuNPs that resulted from AChE-catalysis hydrolysis could be exploited for fabricating colorimetric (visual) sensor of paraoxon. As shown in Figure 4A, upon increasing the paraoxon concentrations, the absorption peak located at 520 nm increased gradually, accompanied with the gradual decrease of absorption band ranging from 600 to 800 nm. The correlation analysis of A_{650}/A_{520} (the absorbance ratio at 650 and 520 nm) against the concentrations of the paraoxon displayed a linear relationship (Figure 4B), and the larger A_{650}/A_{520} values indicated lower levels in aggregation of AuNPs, consistent with lower paraoxon concentrations. In this study, good linear relationships with different slopes ranging from 10^{-11} to 10^{-7} M (i.e., 2.75 ×

DOI: 10.1021/acs.jafc.5b03096
J. Agric. Food Chem. 2015, 63, 8947−8954

Table 1. Results of the Determination of Paraoxon in Spiked Real Samples[a]

		colorimetric method			RTP method		
sample	spiked/nM	found/nM	recovery/%	RSD[b]/%	found/nM	recovery/%	RSD[b]/%
lake water	0						
	5.0	4.93 ± 0.01	98.6 ± 0.2	1.45	4.95 ± 0.01	99.0 ± 0.2	1.24
	10.0	10.23 ± 0.03	102.3 ± 0.3	1.98	10.09 ± 0.02	100.9 ± 0.2	2.03
	100.0	104.5 ± 0.6	104.5 ± 0.6	2.23	103.8 ± 0.4	103.8 ± 0.4	1.54
apple juice	0						
	5.0	4.84 ± 0.02	96.8 ± 0.4	1.81	4.97 ± 0.02	98.8 ± 0.4	1.11
	10.0	10.32 ± 0.01	103.2 ± 0.1	2.15	10.12 ± 0.02	101.2 ± 0.2	1.95
	100.0	102.8 ± 0.7	102.8 ± 0.7	3.00	101.9 ± 0.3	101.9 ± 0.3	2.97

[a]Average of five repeated measurements. [b]RSD represents relative standard deviation.

10^{-9}–2.75×10^{-5} g/L) and 10^{-7} to 10^{-6} M (i.e., 2.75×10^{-5}–2.75×10^{-4} g/L) were obtained, respectively.

Furthermore, on the basis of the IFE of AuNPs on Mn-ZnS QDs, a phosphorescence method for paraoxon assay was also constructed. It can be seen from Figure 4C that phosphorescence emission of Mn-ZnS QDs decreased gradually upon increasing the paraoxon concentration, corresponding to the increasing of the absorbance of AuNPs at 520 nm. As shown in Figure 4D, the intensities of phosphorescence emission of Mn-ZnS QDs were concentration-dependent, and higher concentrations of paraoxon resulted in less phosphorescence recovery. The linear plots of the relative phosphorescence intensity (P/P_0) against paraoxon concentrations ranging from 10^{-11} to 10^{-7} M (i.e., 2.75×10^{-9}–2.75×10^{-5} g/L) and 10^{-7} to 10^{-6} M (i.e., 2.75×10^{-5}–2.75×10^{-4} g/L) (Figure 4D) were obtained, respectively. The detection limit ($3\sigma/s$) for paraoxon (lower concentration range) was found to be 1.07 pM (0.29 ng/L). This lowest detectable concentration is much lower than the maximum residue limits (MRL) in European Union pesticides database (0.01 mg/L).[50] The low detection limit is also much lower than that of previous assay of paraoxon.[11,13] The repeatability of the present assay was also investigated by measuring 50 nM paraoxon, and the relative standard deviation (RSD) for seven repeated detection was calculated to be 3.73%, suggesting that the response of the present dual-signal system to paraoxon is highly reproducible.

The present dual-readout strategy for the assay of other three usual OPPs including DDVP, parathion, and omethoate was also investigated using the same detection procedures designed for paraoxon. The results show that the inhibition responses of these three OPPs are still dependent on the concentration of pesticides. The inhibition responses of the typical OPPs at the concentration of 200 nM to the system were compared. From the UV/vis absorption and corresponding phosphorescence response, the inhibition efficiency could be evaluated. As shown in Figure 5, the inhibition efficiencies of the four OPPs are different and display an order (from strong to weak) of paraoxon, DDVP, parathion, and omethoate. These results also suggested that the established biosensors could be used for determination of different kinds of OPPs. The limits of detection ($3\sigma/s$) for parathion, omethoate, and DDVP are found to be 2.03 pM (0.59 ng/L), 3.12 pM (0.67 ng/L), and 1.98 pM (0.44 ng/L), respectively. These lowest detectable concentrations are also much lower than MRLs that originated from the European Union pesticides database (MRLs are 0.05 mg/L and 0.02 mg/L for parathion andomethoate, and and not shown for DDVP).[50]

Anti-Interference Capability of the Present System for OPPs. For demonstrating the specificity of the present system for OPP assay, the influences of potential different interfering substances including glucose, sucrose and sodium acetate, histidine, tryptophan, and glycerol were investigated under the same experimental conditions. We choose paraoxon detection as a model, and the selectivity of phosphorescence for paraoxon detection was evaluated by testing a mixture of paraoxon with different interfering substances. The results demonstrate that the phosphorescence responses changed less when the interfering species with identical concentration were present in the present system, indicating that the present system displays high selectivity for assaying paraoxon and, therefore, can be applied for OPP detection in real samples.

Detection of OPP Residues in Spiked Samples and Authentic Contaminated Samples. To demonstrate the real applications of the present method for selective assaying of OPPs, we chose paraoxon as the representative model pesticide and the amounts of paraoxon in local natural lake water and apple juice samples were detected using the standard addition method. Paraoxon with different concentrations including 5.0, 10.0, and 100.0 nM was introduced into lake water and apple juice solutions, respectively, and then detected by the proposed colorimetric and phosphorimetric method. The determinated results are displayed in Table 1, and it can be seen that excellent recoveries ranging from 96.8 ± 0.4% to 104.5 ± 0.6% were obtained and the RSDs were <3.0% for all determinations, indicating that the present method is reliable and applicable for OPP assay in real samples.

The residual pesticides in contaminated apples with the present biosensor were further evaluated. A standard paraoxon solution (4.0 mM, i.e., 1.1 g/L) was sprinkled on the surface of apples with a sprayer and then stored for 24 h at ambient temperature, and the contaminated apples were then processed to get apple juice. We investigated the residual paraoxon concentration of the contaminated apples with the time, and the residual paraoxon in each aliquot sample was measured every 2 days over a duration of 1 week and compared with the results analyzed by high-performance liquid chromatography (HPLC). It can be seen from Table 2 that the obtained detection results using the proposed assay are in agreement with those analyzed with HPLC, suggesting that the present method could be used to detect residual pesticides in authentic contaminated samples accurately.

In conclusion, a colorimetric and phosphorimetric dual-signal strategy, relying on the IFE of AuNPs on phosphorescence of Mn-ZnS QDs, for the assay of OPPs has been demonstrated for the first time. The mechanism for dual-signal transduction has been investigated with different techniques including UV/vis absorption spectra, phosphorescence spectra, and TEM images. The results demonstrate that lowest detectable concentration

DOI: 10.1021/acs.jafc.5b03096
J. Agric. Food Chem. 2015, 63, 8947–8954

Table 2. Results of the Determination of Paraoxon in Contaminated Real Apple Samples[a]

	RTP method		HPLC method	
samples	found/nM	RSD[b]/%	found/nM	RSD[b]/%
blank[c]	-		-	
1st day	5.01 ± 0.02	0.95	4.99 ± 0.01	1.0
3rd day	4.97 ± 0.01	2.35	4.95 ± 0.01	2.01
5th day	4.33 ± 0.07	2.71	4.39 ± 0.02	1.33
7th day	4.34 ± 0.02	2.69	4.38 ± 0.01	2.12

[a]Average of five repeated measurements. [b]RSD represents relative standard deviation. [c]The samples not contaminated with paraoxon are designed as blank.

for each pesticide is much lower than the MRLs originated from the European Union pesticides database, showing potential applications of the present method for assaying OPPs in real settings.

■ ASSOCIATED CONTENT

Supporting Information

The Supporting Information is available free of charge on the ACS Publications website at DOI: 10.1021/acs.jafc.5b03096.

Synthesis and characterization of Mn-ZnS QDs and AuNPs, TEM images of AuNPs aggregating transform, and the experiments of evaluation of anti-interference (PDF)

■ AUTHOR INFORMATION

Corresponding Author

*Tel.: +86-553-3937136; Fax: +86-553-3869302; E-mail: fgao@mail.ahnu.edu.cn.

Funding

The funds from Natural Science Foundation of China (Grant no. 21175002), Program for New Century Excellent Talents in University (NCET-12-0599), and the project sponsored by SRF for ROCS and SEM are deeply acknowledged for financial support.

Notes

The authors declare no competing financial interest.

■ REFERENCES

(1) Fenik, J.; Tankiewicz, M.; Biziuk, M. Properties and determination of pesticides in fruits and vegetables. *TrAC, Trends Anal. Chem.* **2011**, *30*, 814−826.

(2) Pundir, C. S.; Chauhan, N. Acetylcholinesterase inhibition-based biosensors for pesticide determination: A review. *Anal. Biochem.* **2012**, *429*, 19−31.

(3) Meng, X.; Wei, J.; Ren, X.; Ren, J.; Tang, F. A simple and sensitive fluorescence biosensor for detection of organophosphorus pesticides using H_2O_2-sensitive quantum dots/bi-enzyme. *Biosens. Bioelectron.* **2013**, *47*, 402−407.

(4) Quinn, D. M. Acetylcholinesterase: enzyme structure, reaction dynamics, and virtual transition states. *Chem. Rev.* **1987**, *87*, 955−979.

(5) Zhou, T.; Xiao, X.; Li, G. Microwave accelerated selective soxhlet extraction for the determination of organophosphorus and carbamate pesticides in ginseng with gas chromatography/Mass spectrometry. *Anal. Chem.* **2012**, *84*, 5816−5822.

(6) Li, M.; Sheng, E.; Cong, L.; Wang, M. Development of immunoassays for detecting clothianidin residue in agricultural products. *J. Agric. Food Chem.* **2013**, *61*, 3619−3623.

(7) Krepker, M. A.; Segal, E. Dual-functionalized porous Si/hydrogel hybrid for label-Free biosensing of organophosphorus compounds. *Anal. Chem.* **2013**, *85*, 7353−7360.

(8) Yao, G. H.; Liang, R. P.; Huang, C. F.; Wang, Y.; Qiu, J. D. Surface plasmon resonance sensor based on magnetic molecularly imprinted polymers amplification for pesticide recognition. *Anal. Chem.* **2013**, *85*, 11944−11951.

(9) Zhao, Y.; Ma, Y.; Li, H.; Wang, L. Composite QDs@MIP Nanospheres for specific recognition and direct fluorescent quantification of pesticides in aqueous media. *Anal. Chem.* **2012**, *84*, 386−395.

(10) Zhang, K.; Mei, Q.; Guan, G.; Liu, B.; Wang, S.; Zhang, Z. Ligand replacement-induced fluorescence switch of quantum dots for ultrasensitive detection of organophosphorothioate pesticides. *Anal. Chem.* **2010**, *82*, 9579−9586.

(11) Liao, S.; Han, W.; Ding, H.; Xie, D.; Tan, H.; Yang, S.; Wu, C.; Shen, G.; Yu, R. Modulated dye retention for the signal-on fluorometric determination of acetylcholinesterase inhibitor. *Anal. Chem.* **2013**, *85*, 4968−4973.

(12) Liu, D.; Chen, W.; Wei, J.; Li, X.; Wang, Z.; Jiang, X. A highly sensitive, dual-readout assay based on gold nanoparticles for organophosphorus and carbamate pesticides. *Anal. Chem.* **2012**, *84*, 4185−4191.

(13) Liang, M.; Fan, K.; Pan, Y.; Jiang, H.; Wang, F.; Yang, D.; Lu, D.; Feng, J.; Zhao, J.; Yang, L.; Yan, X. Fe_3O_4 magnetic nanoparticle peroxidase mimetic-based colorimetric assay for the rapid detection of organophosphorus pesticide and nerve agent. *Anal. Chem.* **2013**, *85*, 308−312.

(14) Trettnak, W.; Reininger, F.; Zinterl, E.; Wolfbeis, O. S. Fiber-optic remote detection of pesticides and related inhibitors of the enzyme acetylcholine esterase. *Sens. Actuators, B* **1993**, *11*, 87−93.

(15) Guan, G.; Yang, L.; Mei, Q.; Zhang, K.; Zhang, Z.; Han, M. Y. Chemiluminescence switching on peroxidase-like Fe_3O_4 nanoparticles for selective detection and simultaneous determination of various Pesticides. *Anal. Chem.* **2012**, *84*, 9492−9497.

(16) Xie, C.; Li, H.; Li, S.; Wu, J.; Zhang, Z. Surface molecular self-assembly for organophosphate pesticide imprinting in electropolymerized poly(p-aminothiophenol) membranes on a gold nanoparticle modified glassy carbon electrode. *Anal. Chem.* **2010**, *82*, 241−249.

(17) Wu, P.; Miao, L. N.; Wang, H. F.; Shao, X. G.; Yan, X. P. A multidimensional sensing device for the discrimination of proteins based on manganese-doped ZnS quantum dots. *Angew. Chem., Int. Ed.* **2011**, *50*, 8118−8121.

(18) Deng, J.; Ma, W.; Yu, P.; Mao, L. Colorimetric and fluorescent dual mode sensing of alcoholic strength in spirit samples with stimuli-responsive infinite coordination polymers. *Anal. Chem.* **2015**, *87*, 6958−6965.

(19) Sánchez-Barragán, I.; Costa-Fernández, J.; Valledor, M.; Campo, J.; Sanz-Medel, A. Room-temperature phosphorescence (RTP) for optical sensing. *TrAC, Trends Anal. Chem.* **2006**, *25*, 958−967.

(20) Wu, P.; Yan, X. Doped quantum dots for chemo/biosensing and bioimaging. *Chem. Soc. Rev.* **2013**, *42*, 5489−5521.

(21) Shu, X.; Chen, Y.; Yuan, H.; Gao, S.; Xiao, D. H_2O_2 sensor based on the room-temperature phosphorescence of nano TiO_2/SiO_2 composite. *Anal. Chem.* **2007**, *79*, 3695−3702.

(22) Zhou, T.; Wang, N.; Li, C.; Yuan, H.; Xiao, D. Sulfide sensor based on room-temperature phosphorescence of PbO/SiO_2 nanocomposite. *Anal. Chem.* **2010**, *82*, 1705−1711.

(23) Li, J.; Zhou, W.; Ouyang, X.; Yu, H.; Yang, R. H.; Tan, W.; Yuan, J. Design of a room-temperature phosphorescence-based molecular beacon for highly sensitive detection of nucleic acids in biological fluids. *Anal. Chem.* **2011**, *83*, 1356−1362.

(24) He, Y.; Wang, H. F.; Yan, X. P. Exploring Mn-Doped ZnS quantum dots for the room-temperature phosphorescence detection of enoxacin in biological fluids. *Anal. Chem.* **2008**, *80*, 3832−3837.

(25) Wang, H. F.; He, Y.; Ji, T. R.; Yan, X. P. Surface molecular imprinting on Mn-Doped ZnS quantum dots for room-temperature phosphorescence optosensing of pentachlorophenol in water. *Anal. Chem.* **2009**, *81*, 1615−1621.

(26) He, Y.; Wang, H. F.; Yan, X. P. Self-assembly of Mn-Doped ZnS quantum dots/Octa(3-aminopropyl) octasilsequioxane octahydro-

DOI: 10.1021/acs.jafc.5b03096
J. Agric. Food Chem. 2015, 63, 8947−8954

chloride nanohybrids for optosensing DNA. *Chem. - Eur. J.* **2009**, *15*, 5436−5440.
(27) Wu, P.; He, Y.; Wang, H. F.; Yan, X. P. Conjugation of glucose oxidase onto Mn-Doped ZnS quantum dots for phosphorescent sensing of glucose in biological fluids. *Anal. Chem.* **2010**, *82*, 1427−1433.
(28) Wang, H. F.; Li, Y.; Wu, Y. Y.; He, Y.; Yan, X. P. Ascorbic acid induced enhancement of room temperature phosphorescence of sodium tripolyphosphate-capped Mn-Doped ZnS quantum dots: mechanism and bioprobe applications. *Chem. - Eur. J.* **2010**, *16*, 12988−12994.
(29) Yan, H.; Wang, H. F. Turn-on room temperature phosphorescence assay of heparin with tunable sensitivity and detection window based on target-induced self-assembly of polyethyleneimine capped Mn-Doped ZnS quantum dots. *Anal. Chem.* **2011**, *83*, 8589−8595.
(30) Zhang, L.; Zhang, R.; Cui, P.; Cao, W.; Gao, F. An efficient phosphorescence energy transfer between quantum dots and carbon nanotubes for ultrasensitive turn-on detection of DNA. *Chem. Commun.* **2013**, *49*, 8102−8104.
(31) Zhang, L.; Cui, P.; Zhang, B.; Gao, F. Aptamer-based turn-on detection of thrombin in biological fluids based on efficient phosphorescence energy transfer from Mn-Doped ZnS quantum dots to carbon nanodots. *Chem. - Eur. J.* **2013**, *19*, 9242−9250.
(32) Jiang, Y.; Zhao, H.; Lin, Y.; Zhu, N.; Ma, Y.; Mao, L. Colorimetric detection of glucose in rat brain using gold nanoparticles. *Angew. Chem., Int. Ed.* **2010**, *49*, 4800−4804.
(33) Jiang, Y.; Zhao, H.; Zhu, N.; Lin, Y.; Yu, P.; Mao, L. A simple assay for direct colorimetric visualization of trinitrotoluene at picomolar levels using gold nanoparticles. *Angew. Chem., Int. Ed.* **2008**, *47*, 8601−8604.
(34) Vilela, D.; González, M. C.; Escarpa, A. Sensing colorimetric approaches based on gold and silver nanoparticles aggregation: Chemical creativity behind the assay. A review. *Anal. Chim. Acta* **2012**, *751*, 24−43.
(35) Qian, Q.; Deng, J.; Wang, D.; Yang, L.; Yu, P.; Mao, L. Aspartic acid-promoted highly selective and sensitive colorimetric sensing of cysteine in rat brain. *Anal. Chem.* **2012**, *84*, 9579−9584.
(36) Saha, K.; Agasti, S. S.; Kim, C.; Li, X.; Rotello, V. M. Gold nanoparticles in chemical and biological sensing. *Chem. Rev.* **2012**, *112*, 2739−2779.
(37) Deng, J.; Yu, P.; Wang, Y.; Yang, L.; Mao, L. Visualization and quantification of neurochemicals with gold nanoparticles: opportunities and challenges. *Adv. Mater.* **2014**, *26*, 6933−6943.
(38) Yuan, P.; Walt, D. R. Calculation for fluorescence modulation by absorbing species and its application to measurements using optical fibers. *Anal. Chem.* **1987**, *59*, 2391−2394.
(39) Shao, N.; Zhang, Y.; Cheung, S.; Yang, R.; Chan, W.; Mo, T.; Li, K.; Liu, F. Copper ion-selective fluorescent sensor based on the inner filter effect using a spiropyran derivative. *Anal. Chem.* **2005**, *77*, 7294−7303.
(40) He, H.; Li, H.; Mohr, G.; Kovacs, B.; Werner, T.; Wolfbeis, O. S. Novel type of ion-selective fluorosensor based on the inner filter effect: an optrode for potassium. *Anal. Chem.* **1993**, *65*, 123−127.
(41) Gabor, G.; Walt, D. R. Sensitivity enhancement of fluorescent pH indicators by inner filter effects. *Anal. Chem.* **1991**, *63*, 793−796.
(42) Tohda, K.; Lu, H.; Umezawa, Y.; Gratzl, M. Optical detection in microscopic domains. 2. inner filter effects for monitoring non-fluorescent molecules with fluorescence. *Anal. Chem.* **2001**, *73*, 2070−2077.
(43) Shang, L.; Dong, S. Design of fluorescent assays for cyanide and hydrogen peroxide based on the inner filter effect of metal nanoparticles. *Anal. Chem.* **2009**, *81*, 1465−1470.
(44) Xu, L.; Li, B.; Jin, Y. Inner filter effect of gold nanoparticles on the fluorescence of quantum dots and its application to biological aminothiols detection. *Talanta* **2011**, *84*, 558−564.
(45) Zhai, W.; Wang, C.; Yu, P.; Wang, Y.; Mao, L. Single-layer MnO_2 nanosheets suppressed fluorescence of 7-hydroxycoumarin: mechanistic study and application for sensitive sensing of ascorbic acid in vivo. *Anal. Chem.* **2014**, *86*, 12206−12213.
(46) Liu, D. B.; Chen, W. W.; Sun, K.; Deng, K.; Zhang, W.; Wang, Z.; Jiang, X. Y. Resettable, multi-readout logic gates based on controllably reversible aggregation of gold nanoparticles. *Angew. Chem., Int. Ed.* **2011**, *50*, 4103−4107.
(47) Zhang, H.; Zhou, Z.; Yang, B.; Gao, M. The influence of carboxyl groups on the photoluminescence of mercaptocarboxylic acid-stabilized CdTe nanoparticles. *J. Phys. Chem. B* **2003**, *107*, 8−13.
(48) Wang, X.; Guo, X. Ultrasensitive Pb^{2+} detection based on fluorescence resonance energy transfer (FRET) between quantum dots and gold nanoparticles. *Analyst* **2009**, *134*, 1348−1354.
(49) Cui, X.; Liu, M.; Li, B. X. Homogeneous fluorescence-based immunoassay via inner filter effect of gold nanoparticles on fluorescence of CdTe quantum dots. *Analyst* **2012**, *137*, 3293−3299.
(50) http://ec.europa.eu/food/plant/plant_protection_products/pesticides_database/index_en.htm.

DOI: 10.1021/acs.jafc.5b03096
J. Agric. Food Chem. 2015, 63, 8947−8954

Table 1. Ingredient Composition (w/w %) of Sesame-Flavored Oil Samples Used as the Model of Adulterated Sesame Oils in the Present Study

	ingredients							
sample	sesame oil	corn oil	soybean oil	sunflower oil	perilla oil	cottonseed oil	canola oil	others[a]
1	44	53		3				tr[b]
2	42	50	5	3				tr
3	40	50	10					
4	38	32	30					tr
5	36	48	14	2				tr
6	35	52	10	2		1		tr
7	32	40	20		8			
8	30	30	10		29			1
9	27	31	32	2	8			tr
10	24	30	45	1				tr
11	22	76		2				
12	22	56	20	2				
13	20	75	5					
14	14	37	48	1				tr
15	10	89		1				tr
16	10	69	20	1				tr
17	9	90		1				tr
18	8	26	63	1		1		1
19	5	95						tr
20	5	52	43					tr
21	undef[c]	70	28					tr
22		91				7		2
23		90	10					tr
24		80	10				10	tr
25		64	36					

[a]Other ingredients include flavoring agents or imported sesame flavored oil with unknown ingredients. [b]Trace, <0.05 w/w %. [c]Undefined.

profile of the oils. Orthogonal projection to latent structure discriminant analysis (OPLS-DA) was used to select variables that most effectively discriminate between the authentic and adulterated sesame oils. The predictive discrimination power of the selected variables was then evaluated in a blind trial using oil samples consisting of sesame oils, sesame-flavored oils, and sesame oils to which foreign edible oils were added at different concentrations.

MATERIALS AND METHODS

Sample Preparation. Samples of authentic sesame oils (n = 35) were prepared in our laboratory by extraction from 16 samples of Korean sesame seeds and 19 samples of imported sesame seeds obtained from local grocery stores in Korea. The sesame seeds were roasted in a drum roster (model THDR-01, Taehwan Automation Industry Co., Seoul, Korea) at 200 °C for 30 min, and the oil was then extracted from the roasted seeds using an oil press (model Oil Love, National Eng. Co., Goyang, Korea). The extracted oil was centrifuged at 9600g for 10 min to remove precipitated impurities and was completely dried under nitrogen gas. Twenty-five samples of commercial sesame-flavored oils were purchased from local grocery stores in Korea. Table 1 lists the type and amount of ingredients in the commercial sesame-flavored oils, as indicated on the product labels. Four samples of commercial roasted sesame oils in which the α-linolenic acid (18:3n-3) content deviated from the standards of roasted sesame oil in the Korea Food Code[14] (i.e., 18:3n-3 content, > 0.5 w/w %) were obtained from local grocery stores. Samples of adulterated sesame oils (n = 29) consisted of commercial sesame-flavored oils and commercial roasted sesame oils. The above samples of authentic and adulterated sesame oils were used to select variables that best characterize authentic sesame oils using an OPLS-DA technique. Blind samples of sesame oils (n = 70) were provided by the National Institute of Food and Drug Safety Evaluation (NIFDS) of the Ministry of Food and Drug Safety, Korea (http://www.nifds.go.kr). The blind oil samples consisted of 14 samples of commercial sesame oils in which the 18:3n-3 content of 6 samples met the standards of roasted sesame oil in the Korea Food Code and that of the other 8 samples deviated from the standards; 6 samples of commercial sesame-flavored oils; and 50 samples of commercial sesame oils to which commercial corn oils, commercial soybean oils, or commercial sesame-flavored oils were added at concentrations of 3, 5, 10, 15, and 25 v/v%. These blind oil samples were used to examine whether their authenticity could be correctly verified by applying the range of variables found in the authentic sesame oil samples. Samples of corn (n = 5), soybean (n = 5), sunflower (n = 5), perilla (n = 5), cottonseed (n = 3), and canola oils (n = 5) were also obtained from Korea's major food companies.

Stable Isotope Analysis. The carbon stable isotope ratio ($^{13}C/^{12}C$) of the oil samples was analyzed using a Delta V Advantage (Thermo Scientific, Bremen, Germany) isotope ratio mass spectrometer (IRMS) coupled with a Flash 2000 (Thermo Scientific) elemental analyzer (EA). An aliquot of each oil sample (0.2 μL) was placed into a 3.3 × 5 mm tin capsule (IVA Analysentechnik e.K., Meerbusch, Germany) and injected into the EA. The combustion and reduction tubes were maintained at 1000 and 750 °C, respectively, to convert the carbon in the oil samples into CO_2 gas under a stream of helium and oxygen. The resultant CO_2 was diluted with helium by 60 v/v % and was separated in a gas chromatography (GC) column (PTFE, 2 m; 6 × 5 mm, Agilent Technologies, The Netherlands), and its isotopic composition was measured on the IRMS. The analysis of the hydrogen ($^2H/^1H$) and oxygen ($^{18}O/^{16}O$) stable isotope ratios of the oil samples was performed using a Flash 2000 HT (Thermo Scientific) pyrolyzer connected to the Delta V Advantage IRMS. An aliquot of each oil sample (0.2 μL for the measurement of the hydrogen stable isotope ratio and 0.5 μL for the measurement of the oxygen stable isotope ratio) was wrapped in a 3.3 × 5 mm silver capsule (IVA Analysentechnik e.K.), pyrolyzed at 1400 °C under a helium flow, and passed through a column packed with glassy carbon chips to

DOI: 10.1021/acs.jafc.5b04082
J. Agric. Food Chem. 2015, 63, 8955−8965

Table 2. Stable Isotope Ratio Values of Carbon, Hydrogen, snd Oxygen in the Authentic and Adulterated Sesame Oil Samples

variable		authentic sesame oil[a] (n = 35)	adulterated sesame oil[b] (n = 29)
δ^{13}C	range	−32.4 to −28.0	−31.1 to −16.7
(‰ vs VPDB)	mean	−29.8	−27.0[c]
δ^{2}H	range	−205.6 to −137.9	−202.1 to −151.6
(‰ vs VSMOW)	mean	−181.4	−172.5[c]
δ^{18}O	range	14.5−27.6	15.1−22.5
(‰ vs VSMOW)	mean	18.8	19.2

[a]Prepared in the laboratory by extraction from sesame seeds after roasting. [b]Consists of 25 samples of commercial sesame flavored oils and 4 samples of commercial roasted sesame oils in which the 18:3n-3 content deviated from the standards of roasted sesame oil in the Korea Food Code. [c]Significantly different from authentic sesame oil, $P < 0.05$.

convert the hydrogen and oxygen in the oil samples into H_2 and CO gases, respectively. The H_2 and CO were subsequently separated in a GC column (PTFE, 2 m; 6 × 5 mm, Agilent Technologies), and their isotopic compositions were analyzed on the IRMS. The stable isotope ratio was expressed as the delta (δ) value in per mille (‰) deviation from the respective international standard, that is, Vienna Pee Dee Belemnite (VPDB, $CaCO_3$) for carbon (i.e., δ^{13}C) and Vienna Standard Mean Ocean Water (VSMOW, H_2O) for hydrogen (i.e., δ^{2}H) and oxygen (i.e., δ^{18}O), according to the equation

$$\delta\ (‰) = [(R_s - R_{std})/R_{std}] \times 1000 \quad (1,)$$

where R represents the ratio of heavy to light isotopes and R_s and R_{std} are the isotope ratios of the oil sample and the international standard, respectively. The δ^{13}C value of each oil sample was determined from the standard calibration curve of fuel oil NBS 22 (IAEA-International Atomic Energy Agency, Vienna, Austria), cellulose IAEA-CH-3 (IAEA), and sucrose IAEA-CH-6 (IAEA) with certified δ^{13}C values of −30.0, −24.7, and −10.4‰ on the PDB scale, respectively. The δ^{2}H value was calibrated with the standard curve of ice core water USGS46 (U.S. Geological Survey (USGS)), NBS 22 (IAEA), and VSMOW (IAEA) with certified δ^{2}H values of −235.8, −119.6, and 0‰ on the VSMOW scale, respectively. The δ^{18}O value of the oil samples was determined using the standard calibration curves of VSMOW (IAEA), water UC04 (USGS), and benzoic acid IAEA-602 (IAEA), which had certified δ^{18}O values of 0, 38.9, and 71.4‰ on the VSMOW scale, respectively.

^{1}H NMR Analysis. Each oil sample (100 μL) was dissolved in 600 μL of deuterated chloroform (99.8% atom D, with 0.03 v/v % tetramethylsilane (TMS)) from Sigma-Aldrich and injected into 5 mm NMR tubes (Wilmad-Lab Glass, Buena, NJ, USA). The chloroform and TMS provided a field frequency lock and a chemical shift reference, respectively. ^{1}H NMR spectra were obtained using a 600 MHz NMR spectrometer (VNS-600, Varian Inc., Palo Alto, CA, USA). Prior to analysis, a phase correction was applied to all spectra using VnmrJ software (Agilent Technologies Inc., Santa Clara, CA, USA); then, MestReNova software (Mestrelab Research, Santiago de Compostela, Spain) was used as the analytical software for the spectra. The baseline correction of all of the spectra was performed with the Whittaker smoother method, and some dislocated spectra were aligned using the align spectra method. The integration value of each peak was determined and normalized on the basis of the first peak (0.7446−1.0445 ppm), which was derived from the terminal methyl group of fatty acids to avoid dilution effects on the samples.

Fatty Acid Analysis. Each oil sample (20 mg) was saponified with 0.5 M methanolic sodium hydroxide (3 mL) at 85 °C for 10 min, cooled to room temperature, and then methylated with 14% boron trifluoride in methanol (3 mL) at 85 °C for 10 min. After the samples had cooled to room temperature, isooctane (3 mL) and saturated sodium chloride solution (5 mL) were added, and the mixture was vortexed. The upper isooctane layer containing fatty acid methyl esters (FAMEs) was collected and passed through an anhydrous sodium sulfate column. The FAMEs were analyzed using gas−liquid chromatography. An Agilent Technologies 7890 N gas chromatograph (Palo Alto, CA, USA), equipped with a flame ionization detector and a fused silica capillary column (SP-2560, 100 m × 0.25 mm i.d. × 0.2 mm film thickness, Supelco, Bellefonte, PA, USA) was used for the analysis. Each sample (1 μL) was injected in split mode (split ratio of 200:1). The carrier gas was helium at a flow rate of 1.0 mL/min. The injector and detector temperatures were maintained at 225 and 285 °C, respectively. The oven temperature was initially held at 100 °C for 4 min. It was then programmed to increase to 240 °C at a rate of 3 °C/min and held at 240 °C for 17 min. The FAMEs were identified by comparing their retention times with those of reference standards (Supelco 37 component FAME Mix), and their relative contents were calculated as w/w %.

Statistical Analysis. A two-tailed Student's t test was performed to determine the differences between the authentic and adulterated sesame oil samples ($P < 0.05$). The differences among oil samples including corn, soybean, sunflower, perilla, cottonseed, and canola oil samples as well as authentic and adulterated sesame oil samples were determined using one-way ANOVA followed by Duncan's multiple-range test ($P < 0.05$). Pearson's correlation test was performed to determine whether a significant linear relationship existed between the two variables ($P < 0.01$). The above three statistical analyses were conducted using IBM SPSS Statistics (version 20) software (SPSS Inc., Chicago, IL, USA). Using the stable isotope ratio, ^{1}H NMR spectrum, and fatty acid composition data, OPLS-DA was performed in SIMCA-P+ (version 12.0) software (Umetrics, Umeda, Sweden). Pareto scaling was applied to each of the three data sets prior to OPLS-DA. The OPLS-DA model was validated using cross-validated ANOVA. An S-plot from OPLS-DA was used to identify significant variables that effectively discriminated between the authentic and adulterated sesame oil samples.

RESULTS AND DISCUSSION

Stable Isotope Ratio. The carbon, hydrogen, and oxygen stable isotope ratios of adulterated sesame oils were compared to those of authentic sesame oils (Table 2). The δ^{13}C value of adulterated sesame oil samples was significantly ($P < 0.05$) greater than that of authentic sesame oil samples. This arose from the fact that corn oil, the δ^{13}C value of which is known to be greater than that of sesame oil,[5] is most frequently added to adulterated sesame oils. In the present study, we also analyzed the carbon stable isotope ratio of six different kinds of edible oils commonly used for the adulteration of sesame oil, that is, corn, soybean, sunflower, perilla, cottonseed, and canola oils. Our analysis showed that the δ^{13}C value was significantly greater in corn oil samples (range, −16.9 to −15.7‰; mean, −16.2‰) than in authentic sesame oil samples, whereas the δ^{13}C values of the soybean (range, −31.0 to −30.4‰; mean, −30.6‰), sunflower (range, −29.2 to −28.1‰; mean, −28.6‰), perilla (range, −30.0 to −29.1‰; mean, −29.5‰), cottonseed (range, −29.4 to −29.0‰; mean, −29.2‰), and canola oil samples (range, −31.3 to −28.2‰; mean, −29.6‰) were not significantly different from that of the authentic sesame oil samples.

The δ^{2}H value was significantly ($P < 0.05$) greater in adulterated sesame oil samples compared to authentic sesame oil samples. However, the difference in δ^{2}H values between the

DOI: 10.1021/acs.jafc.5b04082
J. Agric. Food Chem. 2015, 63, 8955−8965

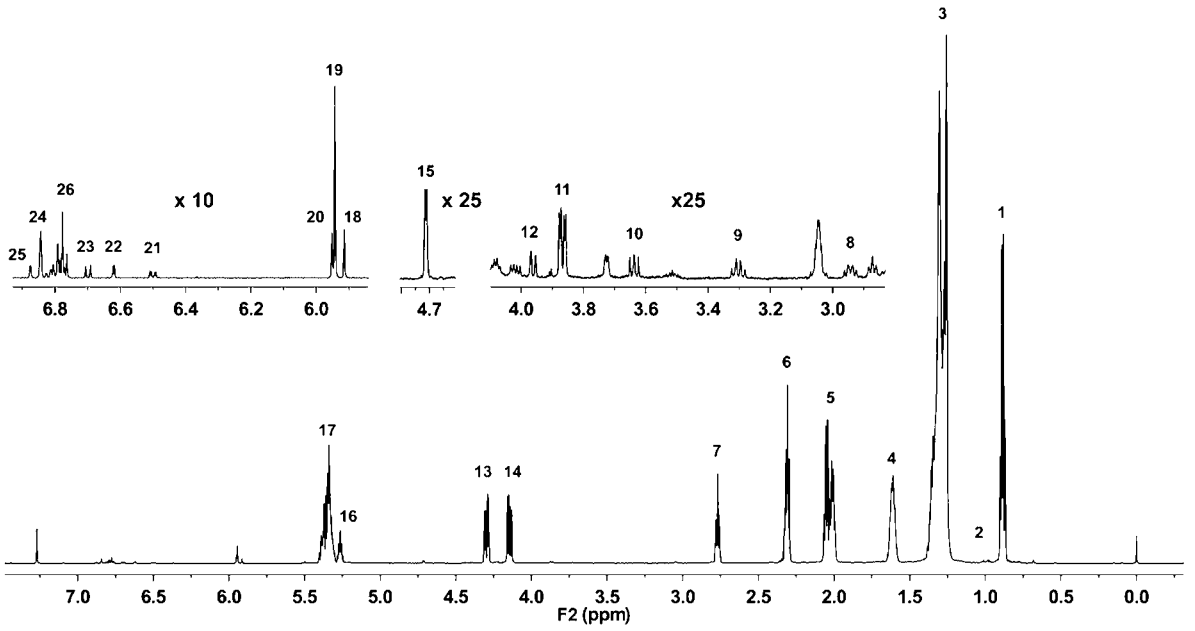

Figure 1. Typical ^{1}H NMR spectra of sesame oil samples used in the present study. Labeled peaks are assigned in Table 3.

Table 3. Chemical Shift and Peak Assignments in the ^{1}H NMR pectra (Figure 3) of Sesame Oil Samples According to Previously Published Studies[15−17]

peak	chemical shift range (ppm)	chemical formula moiety
2	0.9406−1.0030	$CH_3CH_2CH{=}CHCH_2CH{=}CHCH_2CH{=}CH(CH_2)_7COOH$
5	1.9146−2.1659	$-CH_2CH{=}CHCH_2CH{=}CHCH_2-$
7	2.7208−2.8533	$-CH_2CH{=}CHCH_2CH{=}CHCH_2-$
8	2.9811−3.1151	sesamolin H1
9	3.2495−3.3649	sesamolin H5
10	3.5914−3.6819	sesamolin H4a
11	3.8254−3.8970	sesamin H4, H8
12	3.9256−3.9914	sesamolin H8a
15	4.6679−4.7513	sesamin H2, H6
17	5.2904−5.4201	$-CH_2CH{=}CHCH_2CH{=}CHCH_2-$
18	5.9028−5.9244	sesamolin H5′
19	5.9318−5.9471	sesamin H5′, H5″
20	5.9471−5.9625	sesamolin H5″
21	6.4788−6.5214	sesamolin H9″
22	6.6017−6.6369	sesamolin H2″
23	6.6763−6.7230	sesamolin H8″
24	6.8321−6.8598	sesamin H2′, H2″
25	6.8605−6.8910	sesamolin H2′
26	6.7429−6.8997	rest of the aromatic Hs in sesamin and sesamolin

authentic and adulterated sesame oil samples was not pronounced compared to that in the δ^{13}C values. This occurs because, unlike the Student's t test results, the ANOVA results showed that the δ^{2}H value of the authentic sesame oil samples was not significantly different from that of the adulterated sesame oil samples or that of the corn (range, −180.7 to −150.7‰; mean, −170.2‰) soybean (range, −174.7 to −165.3‰; mean, −170.8‰), sunflower (range, −180.6 to −150.2‰; mean, −168.4‰), perilla (range, −192.3 to −187.9‰; mean, −190.2‰), or canola oil samples (range, −230.7 to −137.1‰; mean, −197.5‰). However, the δ^{2}H value of the cottonseed oil samples (range, −143.6 to −139.9‰; mean, −142.1‰) was significantly (P < 0.05) greater than that of the authentic sesame oil samples.

The δ^{18}O value of the adulterated sesame oil samples was not significantly different from that of the authentic sesame oil samples. Our analysis found that the δ^{18}O value of the authentic sesame oil samples was also not significantly different from that of the corn (range, 19.7−23.1‰; mean, 20.6‰) soybean (range, 20.0−21.8‰; mean, 20.7‰), sunflower (range, 20.1−23.4‰; mean, 22.0‰), perilla (range, 16.4−20.3‰; mean, 17.4‰), or cottonseed oil samples (range, 19.8−22.7‰; mean, 20.8‰). However, the δ^{18}O value of the canola oil samples (range, 20.8−40.5‰; mean, 27.0‰) was significantly (P < 0.05) greater than that of the authentic sesame oil samples.

^{1}H NMR Spectrum. Figure 1 shows a typical ^{1}H NMR spectrum of the authentic sesame oils obtained in the present study. The spectrum was composed of 26 main peaks, which have been assigned previously.[15−17] The chemical shift ranges

DOI: 10.1021/acs.jafc.5b04082
J. Agric. Food Chem. 2015, 63, 8955−8965

of the 19 peaks attributed to the unsaturated acyl moieties in the triacylglycerols and lignans present in the sesame oils and their assignments are summarized in Table 3. Peak 2 signifies the terminal methyl group of n-3 fatty acids including 18:3n-3. Peaks 5 and 7 signify a methylene group next to a C=C double bond and a methylene group between two C=C double bonds, respectively. Peak 17 signifies a vinyl proton (i.e., a proton directly attached to a C=C double bond). The other 15 peaks (i.e., peaks 8−12, 15, and 18−26) are attributed to the protons of sesamin and sesamolin, which are two major sesame lignans that are unique phenolic compounds possessing a methylene dioxy fragment (−OCH_2O−), as shown in Figure 2. The carbon numbering system used in this study is also shown in the figure.

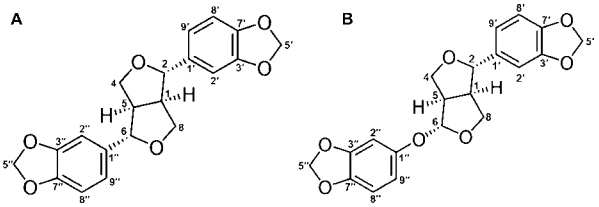

Figure 2. Carbon numbering in sesamin (A) and sesamolin (B).

Table 4 compares the integration values of the 19 peaks mentioned above for authentic and adulterated sesame oils. The integration value of peak 2 (I2 value) was significantly ($P < 0.05$) greater in the adulterated sesame oil samples than in the authentic sesame oil samples. This is attributed to the fact that the edible oils rich in 18:3n-3 such as soybean, perilla, and canola oils are commonly used for the adulteration of sesame oil. Our analysis demonstrated that the I2 value of the soybean (range, 0.0649−0.0752; mean, 0.0712), perilla (range, 0.5699−0.6049; mean, 0.5871), and canola oil samples (range, 0.0865−0.1057; mean, 0.0942) was significantly ($P < 0.05$) greater than that of the authentic sesame oil samples. However, the I2 values of corn (range, 0.0156−0.0203; mean, 0.0177), sunflower (range, 0.0051−0.0136; mean, 0.0098), and cottonseed oil samples (range, 0.0028−0.0150; mean, 0.0109) were not significantly different from that of the authentic sesame oil samples.

The integration value of peak 7 (I7 value) of the adulterated sesame oil samples was significantly ($P < 0.05$) greater than that of the authentic sesame oil samples. This result indicates that adulterated sesame oil contains greater amounts of polyunsaturated fatty acids, such as linoleic acid (18:2n-6), having methylene-interrupted double bonds in their structures. Our fatty acid analysis also demonstrated that the 18:2n-6 content was higher in the adulterated sesame oil samples than in the authentic sesame oil samples, as described below.

Adulterated sesame oil samples had significantly ($P < 0.05$) smaller integration values for all of the peaks derived from sesamin and sesamolin compared to those in the authentic sesame oil samples. For example, the adulterated and authentic sesame oil samples had mean integration values of 0.0027 and 0.0135 for peak 26 (I26 value), respectively. These results were caused by the much higher levels of lignan compounds including sesamolin and sesamin in sesame oil than in most other edible oils. In the present study, peak 26 was not detected in the ^{1}H NMR spectra of corn, soybean, sunflower, perilla, cottonseed, or canola oil.

Table 4. Integration Values of ^{1}H NMR Peaks in Authentic and Adulterated Sesame Oil Samples

variable[a]		authentic sesame oil[b] (n = 35)	adulterated sesame oil[c] (n = 29)
I2	range	0.0061−0.0165	0.0175−0.1517
	mean	0.0122	0.0698[d]
I5	range	1.0543−1.1466	1.0342−1.1133
	mean	1.0901	1.0871
I7	range	0.2517−0.3152	0.2850−0.4492
	mean	0.2806	0.3775[d]
I8	range	0.0012−0.0077	0.0000−0.0038
	mean	0.0033	0.0006[d]
I9	range	0.0002−0.0017	0.0000−0.0015
	mean	0.0010	0.0002[d]
I10	range	0.0002−0.0018	Trace[d]−0.0011
	mean	0.0008	0.0002[d]
I11	range	0.0016−0.0085	0.0000−0.0040
	mean	0.0035	0.0007[d]
I12	range	0.0003−0.0019	0.0000−0.0010
	mean	0.0008	0.0001[d]
I15	range	0.0017−0.0087	0.0000−0.0040
	mean	0.0036	0.0007[d]
I17	range	0.7800−0.8656	0.8174−0.9798
	mean	0.8192	0.9102[d]
I18	range	0.0007−0.0047	0.0000−0.0024
	mean	0.0019	0.0003[d]
I19	range	0.0033−0.0178	Trace−0.0081
	mean	0.0071	0.0016[d]
I20	range	0.0008−0.0044	Trace−0.0024
	mean	0.0019	0.0004[d]
I21	range	0.0004−0.0020	0.0000−0.0012
	mean	0.0010	0.0001[d]
I22	range	0.0004−0.0022	0.0000−0.0012
	mean	0.0009	0.0001[d]
I23	range	0.0003−0.0023	0.0000−0.0012
	mean	0.0009	0.0001[d]
I24	range	0.0015−0.0086	0.000−0.0040
	mean	0.0035	0.0007[d]
I25	range	0.0003−0.0022	0.0000−0.0012
	mean	0.0009	0.0001[d]
I26	range	0.0056−0.0329	0.0000−0.0147
	mean	0.0135	0.0027[d]

[a]Integration values of ^{1}H NMR peaks. Numbers represent the peak numbers shown in Figure 1. [b]Prepared in the laboratory by extraction from sesame seeds after roasting. [c]Consists of 25 samples of commercial sesame flavored oils and 4 samples of commercial roasted sesame oils in which the 18:3n-3 content deviated from the standards of roasted sesame oil in the Korea Food Code. [d]Significantly different from authentic sesame oil, $P < 0.05$.

Fatty Acid Composition. The total fatty acid compositions of the authentic sesame oils were compared to those of the adulterated sesame oils (Table 5). The two major fatty acids of the authentic sesame oil samples were 18:2n-6 and oleic acid (18:1n-9). The adulterated sesame oil samples had significantly ($P < 0.05$) greater 18:2n-6 content than the authentic sesame oil samples. However, the 18:1n-9 content was significantly ($P < 0.05$) lower in the adulterated sesame oil samples than in the authentic sesame oil samples. This is attributed to the fact that most of the edible oils used for adulteration of sesame oil contain more 18:2n-6 and less 18:1n-9 than sesame oil. Our analysis found that the 18:2n-6 contents of corn (range, 48.5−53.8 w/w %; mean, 52.0 w/w %), soybean (range, 51.1−52.9

DOI: 10.1021/acs.jafc.5b04082
J. Agric. Food Chem. 2015, 63, 8955−8965

Table 5. Content Values (w/w %) of Fatty Acids in the Authentic and Adulterated Roasted Sesame Oil Samples

variable		authentic sesame oil[a] (n = 35)	adulterated sesame oil[b] (n = 29)
saturated fatty acid			
16:0	range	8.2−10.1	8.4−11.7
	mean	9.1	10.3[c]
18:0	range	4.3−6.6	2.2−5.9
	mean	5.3	3.9[c]
20:0	range	0.5−0.8	0.4−0.6
	mean	0.6	0.5[c]
unsaturated fatty acid			
16:1	range	0.1−0.2	na[d]
	mean	0.1	0.1
18:1n-9	range	35.3−43.0	23.3−38.5
	mean	39.3	28.4[c]
18:1n-7	range	0.8−1.0	0.6−1.5
	mean	0.9	1.1[c]
18:2n-6	range	38.3−48.7	38.6−52.7
	mean	44.0	47.8[c]
18:3n-3	range	0.3−0.4	0.5−11.4
	mean	0.3	5.1[c]
20:1	range	0.1−0.2	0.2−4.2
	mean	0.2	0.9[c]
trans fatty acid			
18:1*t*	range	<0.05−0.2	0.1−0.5
	mean	0.1	0.1
18:2*t*	range	<0.05−0.3	0.1−3.4
	mean	0.1	1.0[c]
18:3*t*	range	0.0 to <0.05	0.0−2.0
	mean	<0.05	0.7[c]

[a]Prepared in the laboratory by extraction from sesame seeds after roasting. [b]Consists of 25 samples of commercial sesame flavored oils and 4 samples of commercial roasted sesame oils in which the 18:3n-3 content deviated from the standards of roasted sesame oil in the Korea Food Code. [c]Significantly different from authentic sesame oil, $P < 0.05$. [d]na, not available.

w/w %; mean, 51.8 w/w %), sunflower (range, 52.7−61.6 w/w %; mean, 56.9 w/w %), and cottonseed oil samples (range, 55.8−57.5 w/w %; mean, 56.9 w/w %) were significantly greater ($P < 0.05$) than that of the authentic sesame oil samples, whereas the 18:1n-9 content was significantly lower ($P < 0.05$) in corn (range, 30.1−35.2 w/w %; mean, 31.6 w/w %), soybean (range, 22.0−25.0 w/w %; mean, 23.8 w/w %), sunflower (range, 26.5−35.8 w/w %; mean, 31.2 w/w %), perilla (range, 13.9−20.4 w/w %; mean, 17.5 w/w %), and cottonseed oil samples (range, 16.5−18.7 w/w %; mean, 17.3 w/w %) compared to the authentic sesame oil samples.

The adulterated sesame oil samples showed a significant ($P < 0.05$) difference from the authentic sesame oil samples in that they contained a considerable amount of 18:3n-3. This is because edible oils rich in 18:3n-3 are widely used for the adulteration of sesame oil. Our analysis showed that the 18:3n-3 content of soybean (range, 5.4−6.9 w/w %; mean, 6.0 w/w %), perilla (range, 58.9−63.1 w/w %; mean, 60.7 w/w %), and canola oil samples (range, 6.8−8.1 w/w %; mean, 7.6 w/w %) was significantly ($P < 0.05$) greater than that of the authentic sesame oil samples.

Another major difference in the fatty acid composition between the authentic and adulterated sesame oil samples was that the adulterated sesame oil samples had significantly ($P < 0.05$) higher *trans* fatty acid content, such as 18:2*t* and 18:3*t*, than the authentic sesame oil samples. The mean 18:2*t* contents of the authentic and adulterated sesame oil samples were 0.1 and 1.0 w/w %, respectively. The mean 18:3*t* content of the adulterated sesame oil samples was 0.7 w/w %, whereas authentic sesame oil samples contained little 18:3*t*. Our analysis found that the 18:2*t* and 18:3*t* contents of most edible oils (i.e., corn, soybean, sunflower, perilla, and canola oils for 18:2*t* content; corn, soybean, sunflower, perilla, and cottonseed oils for 18:3*t* content) used as the main ingredients in adulterated sesame oils were not significantly different from those of authentic sesame oil (data not shown). These results suggest the possibility that low-quality ingredients containing a considerable amount of *trans* fatty acids were added to the adulterated sesame oil samples (particularly, sesame-flavored oils) used in the present study.

Variables To Verify Sesame Oil Authenticity. OPLS-DA, a supervised multivariate statistical method, was performed to obtain information on differences in the stable isotope ratio, ^{1}H NMR spectrum, and fatty acid composition data between the authentic and adulterated sesame oils. An OPLS-DA model was generated from each of the three data sets, as well as by including all three types of analytical data. The cross-validated ANOVA P value was 4.92×10^{-2} for the model from the stable isotope ratio data; 3.24×10^{-17} for the model from the ^{1}H NMR spectral data; 1.05×10^{-19} for the model from the fatty acid composition data; and 3.79×10^{-16} for the model from all three types of data. The model fit parameters were $R^2Y = 0.316$ and $Q^2Y = 0.193$ for the model from the stable isotope ratio data; $R^2Y = 0.769$ and $Q^2Y = 0.752$ for the model from the ^{1}H NMR spectral data; $R^2Y = 0.854$ and $Q^2Y = 0.823$ for the model from the fatty acid composition data; and $R^2Y = 0.853$ and $Q^2Y = 0.792$ for the model from all three types of data. These results suggest that the model from the stable isotope ratio data had low goodness-of-fit compared to the other three models. However, these models were not employed to verify the authenticity of sesame oils in the present study because they did not clearly discriminate between the authentic and adulterated sesame oil samples when displayed as score plots (data available in Figure S1 of the Supporting Information). Instead, an S-plot constructed by the OPLS-DA model, in which the X-axis and Y-axis represent the contribution and confidence of the variables, respectively, was used to identify statistically significant variables that can be used to discriminate between the authentic and adulterated sesame oil samples (Figure 3). In the S-plot, the closer a variable is to the upper right or lower left corner of the graph, the more strongly the variable contributes to the difference between the two groups and the more significant is its contribution. Accordingly, the δ^{13}C value in the upper right corner in Figure 3A was selected as a variable to effectively discriminate between the authentic and adulterated sesame oil samples. Among the integration values of 19 different ^{1}H NMR peaks, I2 and I7 values in the upper right corner and the I26 value in the lower left corner were selected (Figure 3B). However, the I17 value, which was very close to the I7 value, was not selected as a variable to verify the authenticity of sesame oil samples because it showed strong positive correlation to the I7 value (Pearson's $R = 0.991$). In Figure 3C, among the content values of 12 different fatty acids, the 18:1n-9 content in the upper right corner and the 18:3n-3, 18:2*t*, and 18:3*t* contents in the lower left corner were regarded as the variables that contribute the most to the difference between the authentic and adulterated sesame oil samples.

DOI: 10.1021/acs.jafc.5b04082
J. Agric. Food Chem. 2015, 63, 8955−8965

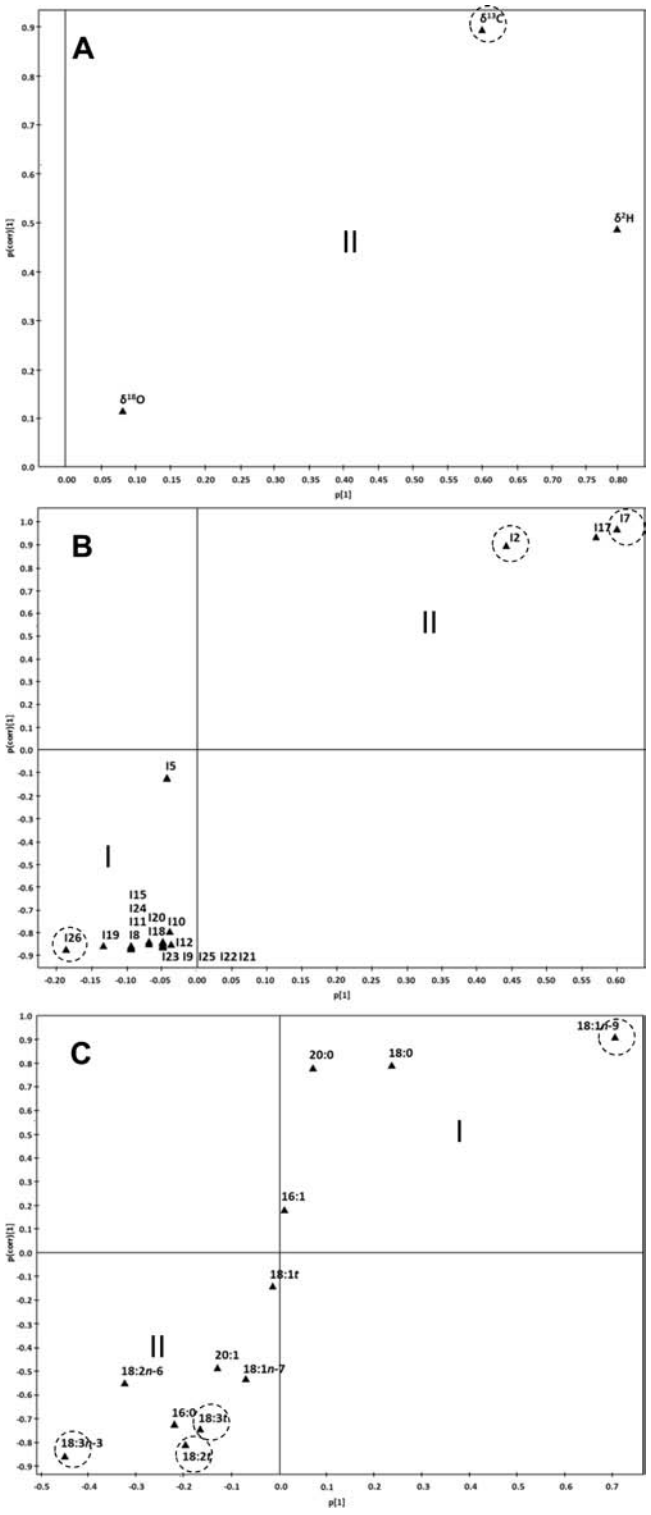

Figure 3. S-plots generated by orthogonal partial least-squares discriminant analysis (OPLS-DA) for (A) stable isotope ratio data, (B) ^{1}H NMR spectrum data, and (C) fatty acid composition data obtained from authentic and adulterated sesame oil samples: (I) authentic sesame oil; (II) adulterated sesame oil.

Table 6 lists the range of the eight selected variables in the authentic sesame oil samples used in this study.

Discrimination of Authenticity of Blind Samples. To evaluate the predictive discrimination power of the eight variables selected above, a blind trial was conducted using 70 oil samples (Table 7). The authenticity of the blind samples was determined by applying the range of variables in the authentic sesame oil samples as follows. If the measured values of the samples are all within the range of the variables, the sample is authentic sesame oil, whereas if any of the measured values is outside the range, the sample may have been adulterated. Among 70 blind samples, 18, 56, and 54 samples were classified correctly using the variables selected from the stable isotope ratio (procedure I), ^{1}H NMR spectrum (procedure II), and fatty acid composition data (procedure III), respectively. The combined use of two different types of variables increased the number of samples classified correctly. That is, procedure IV (procedures I + II), procedure V (procedures I + III), and procedure VI (procedures II + III) correctly verified the authenticity of 63, 60, and 60 samples, respectively. Finally, 65 of 70 blind samples were correctly classified using all eight variables (procedure VII), demonstrating that the combined analysis of the stable isotope ratio, ^{1}H NMR spectrum, and fatty acid profiles of the oils is a useful procedure to verify the authenticity of sesame oil.

Table 6. Range of Variables Selected To Verify Sesame Oil Authenticity in the Authentic Sesame Oil Samples Used in the Present Study

variable[a]	range
δ^{13}C (‰ vs VPDB)	−32.4 to −28.0
I2	0.0061−0.0165
I7[b]	0.2517−0.3152
I26[c]	0.0056−0.0329
18:1n-9 (w/w %)	35.3−43.0
18:3n-3 (w/w %)	0.3−0.4
18:2*t* (w/w %)	0.0−0.5
18:3*t* (w/w %)	0.0−0.1

[a]See Tables 2, 4, and 5

More specifically, all measured values of the blind samples 1−6, which were authentic commercial sesame oils, were within the range of the variables in the authentic sesame oil samples. Blind samples 7−14, which were commercial sesame oils in which the 18:3n-3 content was >0.5 w/w %, had an I2 value outside the range of the authentic sesame oil samples, indicating that the 18:3n-3 content and I2 value were closely correlated. Seven of the eight blind samples also had I7 value and 18:1n-9 content outside the range found in the authentic sesame oil samples. Blind samples 15−20, which were commercial sesame-flavored oils, had measured values of all eight variables that were outside the range found in the authentic sesame oils except for the 16, 18, and 20. These three blind samples had δ^{13}C values within the range found in the authentic sesame oil samples. These samples displayed a relatively high I2 value and 18:3n-3 content compared to blind samples 15, 17, 19, and 20. These results suggest that a possible main ingredient contained within them consists of 18:3n-3-rich edible oils (e.g., soybean, perilla, and canola oils) obtained from C_3 plants, which use the Calvin cycle for fixing atmospheric carbon dioxide. Among 70 blind samples, the 6 samples from the sesame-flavored oils were the only ones that had an I26 value outside the range found in the authentic sesame oil samples, indicating that the variable can be used as an indicator to distinguish adulterated sesame oils prepared in the same way as sesame-flavored oil. Similarly, these six blind samples had relatively high 18:2*t* and 18:3*t* contents compared to the other blind samples, suggesting that these variables can be used to

DOI: 10.1021/acs.jafc.5b04082
J. Agric. Food Chem. 2015, 63, 8955−8965

Table 7. Classification of the Authenticity of Blind Oil Samples

		variable[a]								classification procedure[b]						
	ingredient[c]	δ^{13}C (‰ vs VPDB)	I2	I7	I26	18:1n-9(w/w %)	18:3n-3 (w/w %)	18:2*t* (w/w %)	18:3*t* (w/w %)	I	II	III	IV	V	VI	VII
1	SO 1	−28.9	0.0155	0.2808	0.0100	39.1	0.3	0.3	<0.05	C[d]	C	C	C	C	C	C
2	SO 2	−28.8	0.0061	0.2901	0.0091	38.4	0.3	0.3	0.1	C	C	C	C	C	C	C
3	SO 3	−28.8	0.0163	0.2711	0.0105	39.9	0.3	0.4	<0.05	C	C	C	C	C	C	C
4	SO 4	−29.9	0.0137	0.2826	0.0146	39.7	0.3	0.1	0.1	C	C	C	C	C	C	C
5	SO 5	−32.0	0.0149	0.2936	0.0121	38.9	0.4	0.1	<0.05	C	C	C	C	C	C	C
6	SO 6	−28.2	0.0146	0.2709	0.0065	40.4	0.3	0.1	<0.05	C	C	C	C	C	C	C
7	SO 7	−29.1	**0.0305**[e]	**0.3382**[e]	0.0100	37.2	**0.7**[e]	0.3	0.0	I[f]	C	C	C	C	C	C
8	SO 8	−30.7	**0.0274**	**0.3463**	0.0101	**30.3**[e]	**3.0**	0.5	**0.2**[e]	I	C	C	C	C	C	C
9	SO 9	−30.8	**0.0379**	**0.3555**	0.0101	**31.6**	**2.3**	0.4	**0.2**[e]	I	C	C	C	C	C	C
10	SO 10	−30.8	**0.0281**	**0.3428**	0.0101	**30.7**	**2.7**	0.5	**0.2**[e]	I	C	C	C	C	C	C
11	SO 11	−30.4	**0.0166**	0.3002	0.0137	**32.2**	**1.8**	0.4	0.1	I	C	C	C	C	C	C
12	SO 12	−30.6	**0.0392**	**0.3646**	0.0094	**31.7**	**1.9**	0.5	0.1	I	C	C	C	C	C	C
13	SO 13	−30.7	**0.0340**	**0.3502**	0.0103	**31.0**	**2.6**	0.4	**0.2**[e]	I	C	C	C	C	C	C
14	SO 14	−30.4	**0.0422**	**0.3552**	0.0099	**32.1**	**1.8**	0.5	0.1	I	C	C	C	C	C	C
15	SFO 1	**−23.1**[e]	**0.0612**	**0.3801**	**0.0000**[e]	**26.5**	**4.2**	**1.6**[e]	**0.3**[e]	C	C	C	C	C	C	C
16	SFO 2	−30.6	**0.0696**	**0.4025**	**0.0000**	**24.7**	**5.0**	**0.8**[e]	**0.6**[e]	I	C	C	C	C	C	C
17	SFO 3	**−18.3**[e]	**0.0268**	**0.3477**	**0.0021**	**30.0**	**1.1**	**1.4**[e]	**0.3**[e]	C	C	C	C	C	C	C
18	SFO 4	−28.4	**0.1025**	**0.4296**	**0.0007**	**23.6**	7.7	**1.1**[e]	**1.2**[e]	I	C	C	C	C	C	C
19	SFO 5	**−16.2**[e]	**0.0363**	**0.3383**	**0.0000**	**29.0**	**2.0**	**2.6**[e]	**0.3**[e]	C	C	C	C	C	C	C
20	SFO 6	−30.0	**0.0730**	**0.4020**	**0.0003**	**26.7**	**3.2**	**0.6**[e]	**0.4**[e]	I	C	C	C	C	C	C
21	SO 1 + CO 1 (75:25, v/v)	**−25.6**[e]	0.0150	0.2891	0.0070	37.4	**0.5**	0.3	0.1	C	I	C	C	C	C	C
22	SO 2 + CO 1 (75:25, v/v)	**−25.5**[e]	0.0125	0.2998	0.0058	36.5	**0.5**	0.3	0.1	C	I	C	C	C	C	C
23	SO 3 + CO 1 (75:25, v/v)	**−25.5**[e]	0.0129	0.2863	0.0081	38.0	**0.5**	0.4	<0.05	C	I	C	C	C	C	C
24	SO 1 + CO 1 (85:15, v/v)	**−26.6**[e]	**0.0173**	0.2843	0.0077	37.6	0.4	0.4	0.1	C	C	I	C	C	C	C
25	SO 2 + CO 1 (85:15, v/v)	**−27.0**[e]	0.0054	0.2955	0.0070	37.4	0.4	0.3	0.1	C	I	I	C	C	I	C
26	SO 3 + CO 1 (85:15, v/v)	**−26.7**[e]	0.0131	0.2768	0.0089	40.3	0.4	0.4	<0.05	C	I	I	C	C	I	C
27	SO 4 + CO 2 (90:10, v/v)	−28.5	0.0149	0.2882	0.0133	38.8	0.4	0.1	0.1	I	I	I	I	I	I	I
28	SO 5 + CO 2 (90:10, v/v)	−30.4	**0.0184**	0.2972	0.0109	38.1	0.4	0.2	<0.05	I	C	I	C	I	C	C
29	SO 6 + CO 2 (90:10, v/v)	**−26.9**[e]	0.0158	0.2783	0.0058	39.2	0.4	0.2	<0.05	C	I	I	C	C	I	C
30	SO 4 + CO 2 (95:5, v/v)	−29.2	**0.0174**	0.2844	0.0139	39.3	0.3	0.1	0.1	I	C	I	C	I	C	C
31	SO 5 + CO 2 (95:5, v/v)	−31.2	**0.0177**	0.2955	0.0115	38.3	0.4	0.1	<0.05	I	C	I	C	I	I	C
32	SO 6 + CO 2 (95:5, v/v)	**−27.5**[e]	0.0161	0.2734	0.0061	39.8	0.4	0.1	0.1	C	I	I	C	C	I	C
33	SO 4 + CO 2 (97:3, v/v)	−29.4	**0.0180**	0.2809	0.0141	39.4	0.3	0.1	<0.05	I	C	I	C	I	C	C
34	SO 5 + CO 2 (97:3, v/v)	−31.5	**0.0218**	0.2933	0.0114	38.7	0.4	0.1	0.1	I	C	I	C	I	C	C
35	SO 6 + CO 2 (97:3, v/v)	**−27.8**[e]	**0.0220**	0.2712	0.0061	39.8	0.3	0.1	<0.05	C	C	I	C	C	C	C
36	SO 1 + SBO 1 (75:25, v/v)	−29.2	**0.0305**	0.3140	0.0065	**35.0**	**1.7**	0.3	**0.2**[e]	I	C	C	C	C	C	C
37	SO 2 + SBO 1 (75:25, v/v)	−29.2	**0.0278**	**0.3183**	0.0059	**34.6**	**1.6**	0.4	**0.2**[e]	I	C	C	C	C	C	C
38	SO 3 + SBO 1 (75:25, v/v)	−29.2	**0.0332**	0.3100	0.0075	35.7	**1.7**	0.5	**0.2**[e]	I	C	C	C	C	C	C
39	SO 1 + SBO 1 (85:15, v/v)	−29.0	**0.0274**	0.2972	0.0079	36.6	**1.1**	0.4	0.1	I	C	C	C	C	C	C
40	SO 2 + SBO 1 (85:15, v/v)	−29.1	**0.0264**	0.3033	0.0068	36.0	**1.1**	0.4	**0.2**[e]	I	C	C	C	C	C	C
41	SO 3 + SBO 1 (85:15, v/v)	−29.0	**0.0216**	0.2963	0.0091	37.3	**1.1**	0.4	**0.2**[e]	I	C	C	C	C	C	C
42	SO 4 + SBO 2 (90:10, v/v)	−29.9	**0.0211**	0.2965	0.0132	38.5	**0.8**	0.2	0.1	I	C	C	C	C	C	C

J. Agric. Food Chem. 2015, 63, 8955−8965 DOI: 10.1021/acs.jafc.5b04082

Table 7. continued

		variable[a]								classification procedure[b]						
	ingredient[c]	δ^{13}C (‰ vs VPDB)	I2	I7	I26	18:1n-9(w/w %)	18:3n-3 (w/w %)	18:2*t* (w/w %)	18:3*t* (w/w %)	I	II	III	IV	V	VI	VII
43	SO 5 + SBO 2 (90:10, v/v)	−31.9	**0.0218**	0.3052	0.0108	37.4	**0.9**	0.2	0.1	I	C	C	C	C	C	C
44	SO 6 + SBO 2 (90:10, v/v)	−28.4	**0.0236**	0.2859	0.0057	38.7	**0.9**	0.2	0.1	I	C	C	C	C	C	C
45	SO 4 + SBO 2 (95:5, v/v)	−29.9	**0.0188**	0.2874	0.0139	38.7	**0.6**	0.2	0.1	I	C	C	C	C	C	C
46	SO 5 + SBO 2 (95:5, v/v)	−31.9	**0.0198**	0.2990	0.0113	38.1	**0.6**	0.2	0.1	I	C	C	C	C	C	C
47	SO 6 + SBO 2 (95:5, v/v)	−28.3	**0.0167**	0.2774	0.0061	39.4	**0.6**	0.1	0.1	I	C	C	C	C	C	C
48	SO 4 + SBO 2 (97:3, v/v)	−29.9	**0.0166**	0.2861	0.0143	39.2	**0.5**	0.1	<0.05	I	C	C	C	C	C	C
49	SO 5 + SBO 2 (97:3, v/v)	−32.0	**0.0196**	0.2959	0.0116	38.6	**0.5**	0.1	0.1	I	C	C	C	C	C	C
50	SO 6 + SBO 2 (97:3, v/v)	−28.2	**0.0169**	0.2746	0.0062	39.7	**0.5**	0.1	0.1	I	C	C	C	C	C	C
51	SO 15 + SFO 7 (75:25, v/v)	−29.2	**0.0232**	0.2952	0.0115	38.2	**1.2**	0.3	**0.2**[e]	I	C	C	C	C	C	C
52	SO 16 + SFO 7 (75:25, v/v)	−29.2	**0.0227**	0.2793	0.0084	39.0	**1.2**	0.3	0.1	I	C	C	C	C	C	C
53	SO 15 + SFO 8 (75:25, v/v)	−29.2	**0.0241**	0.2952	0.0116	38.5	**1.3**	0.3	0.1	I	C	C	C	C	C	C
54	SO 16 + SFO 8 (75:25, v/v)	−29.3	**0.0246**	0.2808	0.0084	38.7	**1.3**	0.3	**0.2**[e]	I	C	C	C	C	C	C
55	SO 15 + SFO 7 (85:15, v/v)	−29.4	**0.0194**	0.2841	0.0130	39.7	**0.9**	0.2	0.1	I	C	C	C	C	C	C
56	SO 16 + SFO 7 (85:15, v/v)	−29.3	**0.0200**	**0.2459**[e]	0.0103	40.4	**0.8**	0.2	0.1	I	C	C	C	C	C	C
57	SO 15 + SFO 8 (85:15, v/v)	−29.3	**0.0233**	0.2949	0.0117	39.8	**0.9**	0.2	0.1	I	C	C	C	C	C	C
58	SO 16 + SFO 8 (85:15, v/v)	−29.3	**0.0204**	0.2671	0.0094	40.3	**0.9**	0.2	0.1	I	C	C	C	C	C	C
59	SO 15 + SFO 7 (90:10, v/v)	−29.4	**0.0176**	0.2781	0.0137	40.5	**0.7**	0.2	0.1	I	C	C	C	C	C	C
60	SO 16 + SFO 7 (90:10, v/v)	−29.4	**0.0191**	0.2668	0.0094	41.0	**0.7**	0.3	0.1	I	C	C	C	C	C	C
61	SO 15 + SFO 8 (90:10, v/v)	−29.4	**0.0189**	0.2841	0.0131	40.5	**0.7**	0.2	0.1	I	C	C	C	C	C	C
62	SO 16 + SFO 8 (90:10, v/v)	−29.4	**0.0183**	0.2598	0.0099	41.0	**0.7**	0.2	0.1	I	C	C	C	C	C	C
63	SO 15 + SFO 7 (95:5, v/v)	−29.5	0.0149	0.2727	0.0144	41.2	**0.5**	0.2	0.1	I	I	C	I	C	C	C
64	SO 16 + SFO 7 (95:5, v/v)	−29.5	**0.0180**	0.2608	0.0098	41.9	**0.5**	0.2	0.1	I	C	C	C	C	C	C
65	SO 15 + SFO 8 (95:5, v/v)	−29.5	0.0156	0.2737	0.0145	41.3	**0.5**	0.2	0.1	I	I	C	I	C	C	C
66	SO 16 + SFO 8 (95:5, v/v)	−29.5	**0.0173**	0.2541	0.0103	41.9	**0.5**	0.2	0.1	I	C	C	C	C	C	C
67	SO 15 + SFO 7 (97:3, v/v)	−29.6	0.0128	0.2718	0.0148	41.4	0.4	0.2	<0.05	I	I	I	I	I	I	I
68	SO 16 + SFO 7 (97:3, v/v)	−29.6	0.0153	0.2549	0.0103	42.2	0.4	0.1	0.1	I	I	I	I	I	I	I
69	SO 15 + SFO 8 (97:3, v/v)	−29.5	0.0145	0.2713	0.0148	41.5	0.4	0.2	<0.05	I	I	I	I	I	I	I
70	SO 16 + SFO 8 (97:3, v/v)	−29.5	0.0157	0.2545	0.0103	42.3	0.4	0.1	0.1	I	I	I	I	I	I	I
total no. of samples correctly classified										18	56	54	63	60	60	65

[a]See Tables 2, 4, and 5. [b]If measured values of the samples are all within the range of the variables listed in Table 6, the sample is an authentic sesame oil, whereas for any of the measured values outside the range, the sample may have been adulterated. Procedure I uses the δ^{13}C value; procedure II uses the I2, I7, and I26 values; procedure III uses the 18:1n-9, 18:3n-3, 18:2*t*, and 18:3*t* content values; procedure IV is a combination of procedures I and II; procedure V is a combination of procedures I and III; procedure VI is a combination of procedures II and III; and procedure VII is a combination of procedures I, II, and III. [c]CO, corn oil; SO, sesame oil; SBO, soybean oil; SFO, sesame-flavored oil. Samples 1−6 are samples of sesame oils in which the 18:3n-3 content met the standards of roasted sesame oil in the Korea Food Code; samples 7−14 are samples of sesame oils in which the 18:3n-3 content deviated from the standards. [d]Correctly classified. [e]Entries in boldface type are outside the range of values of the authentic sesame oil samples used in the present study. [f]Incorrectly classified.

J. Agric. Food Chem. 2015, 63, 8955−8965
DOI: 10.1021/acs.jafc.5b04082

effectively characterize adulterated sesame oils containing low-quality ingredients (e.g, extracts from feed sesame cake).

Finally, we evaluated the discrimination limit of using the eight variables as indictors to verify sesame oil authenticity from the results of the blind trial using commercial sesame oils to which commercial corn (samples 21−35), soybean (samples 36−50), or sesame-flavored oils (samples 51−70) were added at different concentrations. All of the samples of sesame oils with corn oils added at concentrations of 15 and 25 v/v% were correctly classified as being adulterated because they had a $\delta^{13}C$ value or 18:3n-3 content outside the range of the variables in the authentic sesame oil samples. It is noteworthy that, in the present study, the upper range limit of the 18:3n-3 content was 0.4 w/w %, although the 18:3n-3 content ≤0.5 w/w % is the standard of roasted sesame oil in the Korea Food Code.[14] However, a sample (no. 27) of sesame oil with corn oil added at a concentration 10 v/v% was incorrectly classified, indicating that it is difficult to distinguish sesame oil adulterated with corn oil at concentrations ≤10 v/v%. Conversely, all of the samples of sesame oils with soybean oils added at concentrations of 3−25 v/v% were correctly distinguished. The samples of sesame oils containing sesame-flavored oils were used to evaluate the discrimination limit of our procedure for sesame oils adulterated with more than one kind of foreign edible oil. All of the samples of sesame oils with sesame-flavored oils added at concentrations of 5−25 v/v% were correctly distinguished because their I2 value, I7 value, 18:3n-3 content, or 18:3*t* content was outside the range of the variables in the authentic sesame oil samples. However, all of the samples (nos. 67−70) of sesame oils containing sesame-flavored oils at a concentration 3 v/v% were incorrectly classified as authentic sesame oils.

In conclusion, this study is the first to report the verification of the authenticity of roasted sesame oils using combined analysis of stable isotope ratio, ^1H NMR spectroscopy, and fatty acid profiles of the oils. Commercial sesame-flavored oils were used as the principal model of adulterated sesame oils considering the fact that many adulterated sesame oils distributed in Korea are manufactured by adding more than one kind of foreign edible oil. We observed statistically significant differences in eight measured values between the authentic and adulterated sesame oils and employed them as variables to verify the authenticity of sesame oils. The variables include the $\delta^{13}C$ value from the stable isotope ratio data; I2, I7, and I26 values from ^1H NMR spectrum data, which were positively associated with the abundance of the methyl group of n-3 fatty acids; methylene between two carbon double bonds present in unsaturated acyl moieties of triacylglycerols; lignans (i.e., sesamin and sesamolin) present in the oils; and 18:1n-9, 18:3n-3, 18:2*t*, and 18:3*t* content values from the fatty acid profile data. Adulterated sesame oils had significantly ($P < 0.05$) greater $\delta^{13}C$, I2, I7, 18:3n-3 content, 18:2*t* content, and 18:3*t* content values than the authentic sesame oils, whereas the I26 and 18:1n-9 content values were significantly ($P < 0.05$) lower in the adulterated sesame oils than in the authentic sesame oils. It was demonstrated that the adulteration of sesame oils could be effectively verified by applying the range of eight variables observed in the authentic sesame oils. Thus, it would be possible to use these eight variables and their ranges as new specifications and standards of sesame oils distributed in Korea. The results of this study also showed that our discrimination procedure distinguished the sesame oils with corn oils added at concentrations ≥15 v/v %, soybean oils added at concentrations ≥3 v/v %, or sesame-flavored oils added at concentrations ≥5 v/v %.

■ ASSOCIATED CONTENT

Supporting Information

The Supporting Information is available free of charge on the ACS Publications website at DOI: 10.1021/acs.jafc.5b04082.

Score plots generated by OPLS-DA for stable isotope ratio data, ^1H NMR spectrum data, fatty acid composition data, and all three types of analytical data obtained from authentic and adulterated sesame oil samples (Figure S1) (PDF)

■ AUTHOR INFORMATION

Corresponding Authors

*(S.A.) Phone: + 82-2-820-5230. Fax: + 82-2-825-4736. E-mail: sangdoo@cau.ac.kr.

*(B.H.K.) Phone: + 82-31-670-3033. Fax: + 82-31-675-4853. E-mail: bhkim@cau.ac.kr.

Author Contributions

[||]J.K. and G.J. contributed to this work equally.

Funding

This research was supported by a grant (14162MFDS971) from the Ministry of Food and Drug Safety, Korea, in 2014.

Notes

The authors declare no competing financial interest.

■ ACKNOWLEDGMENTS

We are grateful to Dr. Dongho Lee from the Division of Earth and Environmental Science Research, Korea Basic Science Institute, for his help with stable isotope analysis.

■ REFERENCES

(1) Kim, B. H.; Akoh, C. C. Characteristics of structured lipid prepared by lipase-catalyzed acidolysis of roasted sesame oil and caprylic acid in a bench-scale continuous packed bed reactor. *J. Agric. Food Chem.* **2006**, *54*, 5132−5141.

(2) Food and Agriculture Organization of the United Nations. Statistics Division Home Page, FAOSTAT; http://faostat3.fao.org/home/E (accessed March 1, 2015).

(3) Korea Ministry of Food and Drug Safety. Imported Foods Information Site; http://www.foodnara.go.kr/importfood/src/main/main_poll.jsp (accessed March 1, 2015).

(4) Lee, W. J.; Su, N. W.; Lee, M. H.; Lin, J. T. Assessment of authenticity of sesame oil by modified Villavecchia test and HPLC-ELSD analysis of triacylglycerol profile. *Food Res. Int.* **2013**, *53*, 195−202.

(5) Seo, H. Y.; Ha, J.; Shin, D. B.; Shim, S. L.; No, K. M.; Kim, K. S.; Lee, K. B.; Han, S. B. Detection of corn oil in adulterated sesame oil by chromatography and carbon isotope analysis. *J. Am. Oil Chem. Soc.* **2010**, *87*, 621−626.

(6) Aued-Pimentol, S.; Takemoto, E.; Antoniassi, R.; Badolato, E. S. G. Composition of tocopherols in sesame seed oil: an indicative of adulteration. *Grasas Aceites* **2006**, *57*, 205−210.

(7) Lee, D. S.; Lee, E. S.; Kim, H. J.; Kim, S. O.; Kim, K. Reversed phase liquid chromatographic determination of triacylglycerol composition in sesame oils and the chemometric detection of adulteration. *Anal. Chim. Acta* **2001**, *429*, 321−330.

(8) Hai, Z.; Wang, J. Electronic nose and data analysis for detection of maize oil adulteration in sesame oil. *Sens. Actuators, B* **2006**, *119*, 449−455.

(9) Hai, Z.; Wang, J. Detection of adulteration in camellia seed oil and sesame oil using an electronic nose. *Eur. J. Lipid Sci. Technol.* **2006**, *108*, 116−124.

DOI: 10.1021/acs.jafc.5b04082
J. Agric. Food Chem. 2015, 63, 8955−8965

(10) Fadzlillah, N. A.; Man, Y. B. C.; Rohman, A. FTIR spectroscopy combined with chemometric for analysis of sesame oil adulterated with corn oil. *Int. J. Food Prop.* **2014**, *17*, 1275−1282.
(11) Fauhl, C.; Reniero, F.; Guillou, C. ^{1}H NMR as a tool for the analysis of mixtures of virgin olive oil with oils of different botanical origin. *Magn. Reson. Chem.* **2000**, *38*, 436−443.
(12) Garcia-Gonzalez, D. L.; Mannia, L.; D'Imperio, M.; Segre, A. L.; Aparicio, R. Using ^{1}H and ^{13}C NMR techniques and artificial neural networks to detect the adulteration of olive. *Eur. Food Res. Technol.* **2004**, *219*, 545−548.
(13) Vigli, G.; Philippidis, A.; Spyros, A.; Dais, P. Classification of edible oils by employing ^{31}P and ^{1}H NMR spectroscopy in combination with multivariate statistical analysis. A proposal for the detection of seed oil adulteration in virgin olive oils. *J. Agric. Food Chem.* **2003**, *51*, 5715−5722.
(14) Korea Ministry of Food and Drug Safety. Food Code, Article 5, Standards and specifications for each food product; http://www.mfds.go.kr/eng/index.do?nMenuCode=63 (accessed March 1, 2015).
(15) Sega, A.; Zanardi, I.; Chiasserini, L.; Gabbrielli, A.; Bocci, V.; Travagli, V. Properties of sesame oil by detailed ^{1}H and ^{13}C NMR assignments before and after ozonation and their correlation with iodine value, peroxide value, and viscosity measurements. *Chem. Phys. Lipids* **2010**, *163*, 148−156.
(16) Dachtler, M.; van de Put, F. H. M.; von Stijn, F.; Beindorff, C. M.; Fritsche, J. On-line LC-NMR-MS characterization of sesame oil extracts and assessment of their antioxidant activity. *Eur. J. Lipid Sci. Technol.* **2003**, *105*, 488−496.
(17) Kang, S. S.; Kim, J. S.; Jung, J. H.; Kim, Y. H. NMR assignments of two furofuran lignans from sesame seeds. *Arch. Pharmacal Res.* **1995**, *18*, 361−363.

DOI: 10.1021/acs.jafc.5b04082
J. Agric. Food Chem. 2015, 63, 8955−8965

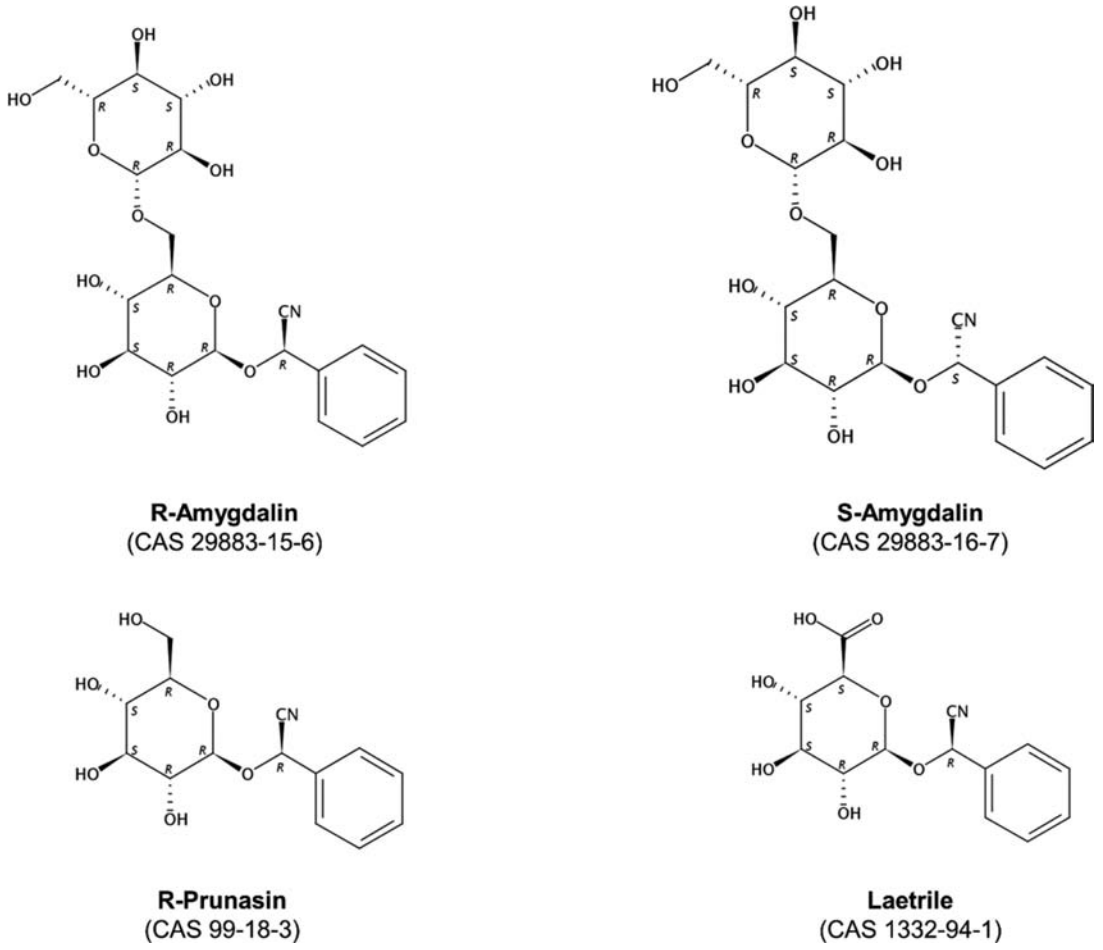

Figure 1. Chemical structures of amygdalin, D-mandelonitrile-β-D-gentiobioside with the *R*-configuration of the labeled carbon, and its *S*-amygdalin (neo-amygdalin) epimer or L-mandelonitrile- β-D-gentiobioside. Prunasin is the D-mandelonitrile-β-D-glucoside, and laetrile is the D-mandelonitrile-β-D-glucuronic acid.

chromatographic methods for the separation and quantification of amygdalin epimers, because the *R*- and *S*-configurations can have significantly different biochemical and physiological properties. Herein we outline the fastest and most reliable approaches for doing such analyses. Subsequently, the developed analytical approaches are used to evaluate the factors affecting amygdalin epimerization.

MATERIALS AND METHODS

Chemicals. Amygdalin, $C_{20}H_{27}NO_{11}$, mol wt 457.4, CAS Registry No. 29883-15-6, was obtained from Sigma-Aldrich (St. Louis, MO, USA) as ≥97% pure (BioXtra) and from Trappsol (from CTD Holdings, Shanghai DND Pharm-Technology Co. Inc., lot 20140103). Both were used as received. *S*-Amygdalin is not commercially available. It was formed by epimerization of *R*-amygdalin. We note that *Sigma-Aldrich also lists incorrectly the laetrile name as a synonym for amygdalin, whereas laetrile is a very different compound* as seen in Figure 1. Additionally, *Beilstein's Handbuch der Organischen Chemie* mentions that the dextro- and laevo- notations were interchangeably used for the naturally occurring amygdalin CAS Registry No. 29883-15-6.[2] Ten sealed ampules of commercial injectable amygdalin were purchased from www.cytopharma.com. The solutions are sold as "vitamin B17" in sealed amber glass ampules.

Methanol and acetonitrile were HPLC grade solvents obtained from Sigma-Aldrich. Ammonium hydroxide was a 29.5% w/v (about 17 M) solution from Fisher Scientific (Fair Lawn, NJ, USA). Water (18.2 MΩ) was produced by a Millipore Synergy 185 system (EMD, Billerica, MS, USA). The following glassware/vials were studied for epimerization of *R*-amygdalin: Wheaton 120 mL (catalog no. 225546, batch 1542790), Restek 20 mL vials (catalog no. 23082), VWR 8 dram glass vials (66011-165, lot 052A06), Supelco vials with a screw cap with septum (~23 mL), a 25 mL Chemglass round-bottom flask (19/22 standard taper) with a reflux condenser, and boiling glass pieces made by crushing 9″ Pasteur pipets (Fisher brand, catalog no. 13-678-6B). Two sets of glassware were studied, one as received, and the other set was soaked in KOH/2-propanol base bath, followed by detergent washing, rinsing with copious amounts of deionized water, and oven-drying before use. As an experimental control, a 250 mL high-density polyethylene bottle (HDPE) from Wheaton was used to boil amygdalin. Plastic syringes with stainless steel needles were used for transferring water and sampling.

Chromatographic Columns and Systems. The following 25 × 0.46 cm i.d. commercial columns packed with fully porous 5 μm particle size were obtained from Supelco (Bellefonte, PA, USA): Chirobiotic V, Cyclobond I 2000 RSP, and Cyclobond I 2000 HP-RSP. Porous graphitic carbon (Hypercarb, Thermo Scientific, 15 × 0.46 cm, 5 μm fully porous particle with 25 nm pore diameter and 170 m^2/g surface area) was a gift from Dionex, Thermo Scientific (Waltham, MA, USA). Additionally, hydroxypropyl-β-cyclodextrin was purchased from Sigma and bonded on 2.7 μm superficially porous silica particles with a surface area of 120 m^2/g and pore size of 120 Å according to a proprietary procedure. The particles were provided by Agilent Technologies (Wilmington, DE, USA). The core is 1.7 μm in diameter, and the surrounding shell thickness is 0.5 μm. The column was slurry packed into a 5 cm × 0.46 cm i.d. column. Two chromatographic systems from Agilent (Santa Clara, CA, USA) were used. The first one was a model Infinity 1260 Quaternary LC system

DOI: 10.1021/acs.jafc.5b03120
J. Agric. Food Chem. 2015, 63, 8966−8973

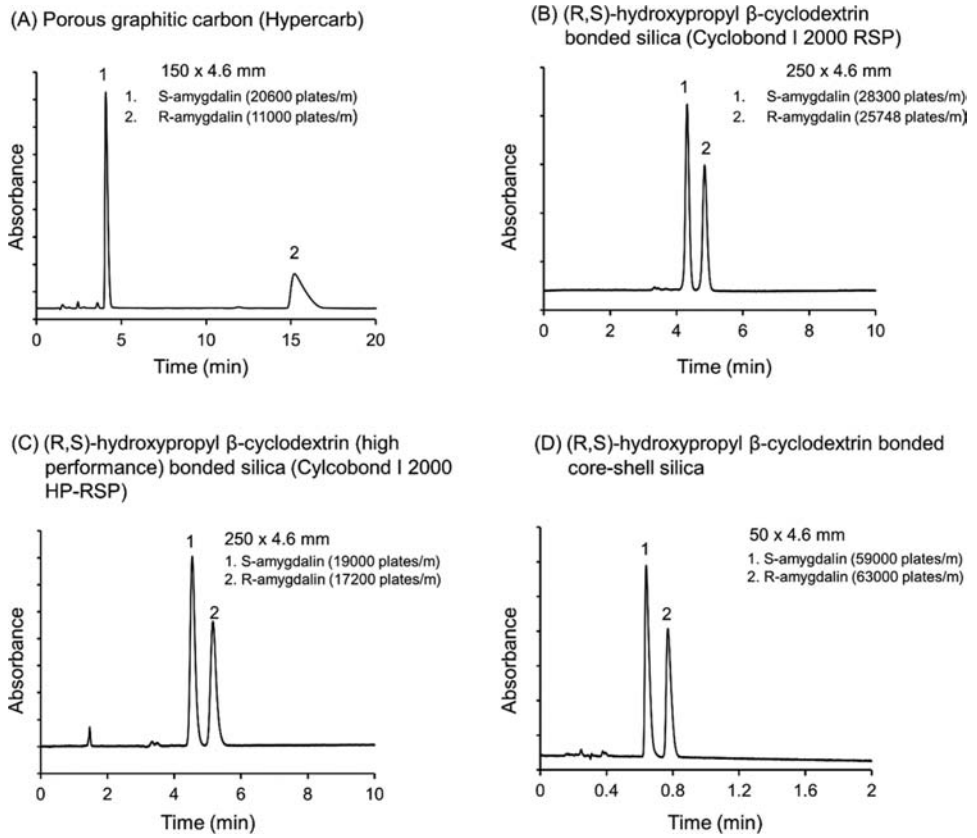

Figure 2. Amygdalin epimer LC analyses: (A) porous graphitic carbon column (15 × 0.46 cm i.d.) with 90:10 MeOH/H_2O at 1.5 mL/min; (B) Cylcobond I 2000 RSP (25 × 0.46 cm i.d.) with 20:80 MeOH/H_2O at 1.0 mL/min; (C) Cyclobond I 2000 HP-RSP (25 × 0.46 cm i.d.) with 30:70 MeOH/H_2O with 1.0 mL/min; (D) the same column chemistry as in (C) bonded on 2.7 μm core−shell particles packed in a 5 cm × 0.46 cm i.d. column 10:90 MeOH/H_2O at 1.8 mL/min. Detection wavelength = 254 nm. All analyses were done at ambient temperature.

with a gradient capable quaternary pump with a maximum pressure of 600 bar (8600 psi), an autosampler, a column oven, and a diode array detector. The second system was a model Infinity 1290 with an ultrahigh-pressure binary pump (UHPLC, maximum pressure of 1200 bar or 17000 psi) with an autosampler with an ultrafast diode array detector. The detector setting on UHPLC was 160 Hz and 0.016 s response time. Amygdalin absorbs at 220 and 254 nm. Both wavelengths can be used for detection. All separations were performed at ambient temperature.

An external calibration curve was constructed by making standards from 76 to 1525 ppm of *R*-amygdalin (Sigma, BioXtra ≥97% pure) in 0.1% aqueous acetic acid solution. The analysis was done in triplicate at 220 nm with an injection volume of 1 μL on a 5 cm × 0.46 cm core−shell hydroxypropyl-β-cylcodextrin column. The mobile phase was 90%H_2O/10% methanol at a flow rate of 1.8 mL/min. Thoroughly washed glass volumetric flasks were used. The curve was linear with a correlation coefficient R^2 value of 0.9995. We note that traces of *S*-amygdalin are present in commercial *R*-amygdalin. The commercial samples were diluted to bring their concentration within the range of the calibration curve.

Procedure for Amygdalin Epimerization. Two approaches were used in the epimerization studies. The first procedure is more efficient and faster (∼15 min), but introduces a very small amount of ammonia. This method was used for chromatographic method development for the separation of the *S*-isomer. For the "ammonia added method", 0.1 g of amygdalin was dissolved by sonication in deionized water (18.2 MΩ) in 10 mL of deionized water, and 10 μL of ACS certified concentrated ammonia (29%) was added via glass syringe. Within 15−20 min, all of the amygdalin epimerized to a ratio of 57% *S*-amygdalin and 43% *R*-amygdalin at room temperature. In the second method, where we show the glassware effect, 0.1 g/10 mL of amygdalin was heated on an oil bath in deionized water in thoroughly cleaned glassware for 60 min. An approximately 0.5 mL aliquot was drawn via stainless steel needle in a plastic syringe and transferred into a 1.8 mL amber VWR glass autosampler vial (catalog no. 82030-974).

RESULTS AND DISCUSSION

Amygdalin has 11 stereogenic centers, 10 of which are contained in the two glucopyranose moieties, and these are not easily isomerized. The remaining stereogenic center (i.e., the carbon atom with the phenyl and nitrile substituents) is susceptible to inversion, which can give rise to the formation of *S*-amygdalin. For extraction and analytical purposes, amygdalin is extracted in polar solvents including ethanol, methanol, ethyl acetate, and water, from seeds or kernels.[12] It was noted recently that polar solvents give low recoveries of amygdalin because of conversion of the natural isomer into the *S*-amygdalin, where 35% of natural amygdalin converted into the isomer upon 24 h of standing.[6] It is therefore critical to know the relative concentrations of the isomers in any study of or with these compounds. We also note that amygdalin starts to degrade even after boiling in pure water for a short period of time (∼1 h). To develop a reliable analytical method and produce *S*-amygdalin (for which there is no known commercial source), we used a small quantity of ammonia to produce the other epimer. This procedure is very efficient in promoting epimerization provided that optimal levels of ammonia are used (10 μL/10 mL). Using higher concentrations of bases can hydrolyze amygdalin into many side products including ammonia and mandelic acid, and often the cyano group is hydrated to the amide.[2,14] Existing separation methods relying

DOI: 10.1021/acs.jafc.5b03120
J. Agric. Food Chem. 2015, 63, 8966−8973

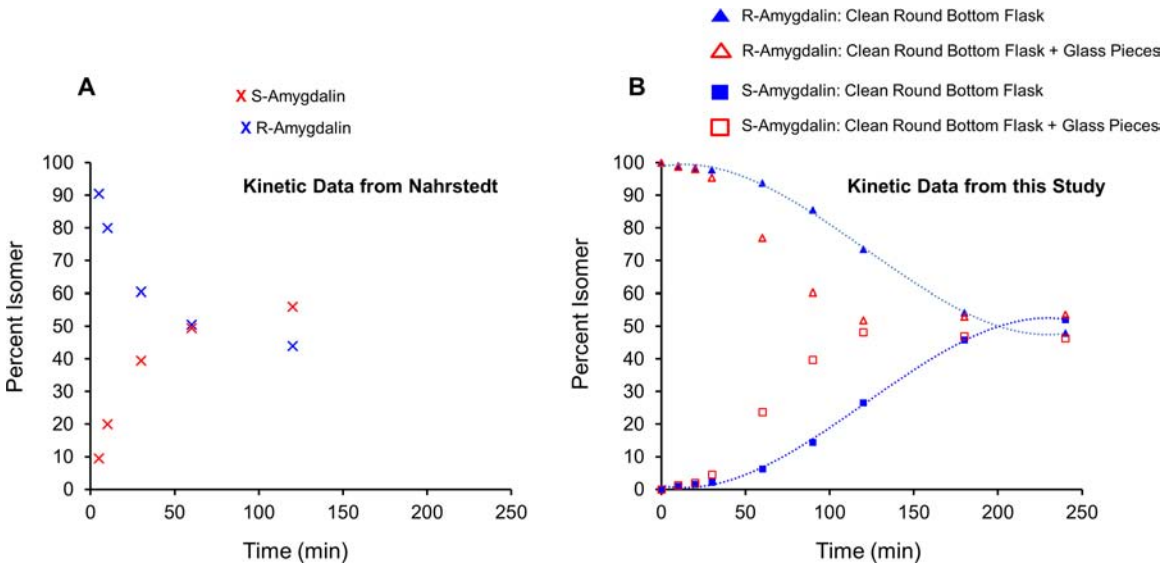

Figure 3. (A) Amygdalin concentration change due to epimerization under the Nahrstedt experiment of boiling amygdalin in water. (B) Heating amygdalin with deionized water in a 25 mL round-bottom flask (19/22 standard taper) with a reflux condenser (blue). Boiling glass pieces were made by crushing 9 in. Pasteur pipets (Fisher brand, catalog no. 13-678-6B) (red). The oil bath was kept at 107−110 °C.

on C_{18} stationary phases or other enzymatic approaches have a very strong potential to miss the *S*-isomer, thereby producing misleading information about the actual quantification of the naturally occurring *R*-amygdalin.[4,6,9−13,15−18] As a result, it is not surprising that many recent publications on amygdalin analysis do not mention/identify the *S*-amygdalin, which is always present to some extent depending on the storage conditions, extraction solvents, and analytical procedures. Although in a few specific cases, using advanced instrumentation such as MS-MS that may allow differentiation of epimers,[19,20] ideally it is desired and usually necessary that the epimers are separated chromatographically. Thus, the separation of the natural and its unwanted isomerized amygdalin is best done chromatographically.

Analytical Scale Separation of *R*- and *S*-Amygdalin. Early on, the separation of amygdalin epimers was accomplished by gas chromatography (GC) of their trifluoroacetylated derivatives on a semipolar capillary column (versilube F-50, a trichlorophenyl polysiloxane GC stationary phase) in 25 min at 180 °C.[7] Later, capillary electrophoresis was used to separate the epimers in 15 min with good selectivity using a cyclodextrin chiral additive to the electrolyte.[21] However, in most studies, liquid chromatography (LC) seems to have been the method of choice with a C_{18} phase, which produces overlapping/shoulder peaks for *R*- and *S*-amygdalin.[6]

In Figure 2, we show the utility of the preferred stationary phases for amygdalin using simple MS friendly mobile phases in the isocratic mode ($MeOH/H_2O$ without any additives). A number of achiral and chiral phases such as porous graphitic carbon, vancomycin, teicoplanin, cyclodextrin-bonded silica, and hydroxypropyl-*β*-cyclodextrin columns were studied. Porous graphitic carbon (PGC) is a very hydrophobic phase made of sheets of graphitized carbon. The flat surface of carbon allows for excellent shape selectivity of adsorbed molecules and, therefore, the *S*- and *R*-isomers have exceptionally high selectivity, which is not seen in any silica-based column. Thus, PGC can be employed when an exceptionally wide separation window is desired between the isomers (such as in preparative work). In Figure 2A, it can be seen that the *S*-amygdalin elutes earlier than the *R*-isomer with an impressive resolution of 12. The peak shapes and efficiencies for the two isomers are very different, showing that naturally occurring *R*-amygdalin has a very strong interaction with the carbon surface (3100 vs 1650 plates for the *S*- and *R*-isomers, respectively). The previous study,[9] which utilized PGC for the separation of amygdalin for the first time and used a methanol/water mobile phase, did not observe the formation of *S*-isomer. Given the very large selectivity, it is easy to miss the formation of *S*-amygdalin during the extraction process from natural products, or any biochemical studies on porous graphitic carbon. In Figure 2B,C, the separation of amygdalin epimers is shown on (*R*,*S*)-hydroxypropyl-modified *β*-cyclodextrin chiral columns. The key difference between the two columns is the nature of bonding to the silica surface. In general, the Cyclobond-I 2000 HP-RSP separates by extended H-bonding capability, offers broad chiral selectivity for chiral screening, and is most beneficial for basic and neutral compounds. Both chiral columns are able to separate the amygdalin epimers with an isocratic methanol/water mobile phase with baseline resolution and narrow symmetrical peaks showing more than 25000 plates/m. The *S*-amygdalin eluted first on both columns. It is interesting to note that *S*-amygdalin also eluted earlier on the PGC despite being a very different material from silica. A similar chiral column Cyclobond I 2000 HP-RSP produced a complete epimer separation in 5 min with 19000 plates/m (Figure 2C) but with higher methanol concentration.

To speed the same analysis, a recently introduced core−shell (*R*,*S*)-hydroxypropyl-modified *β*-cyclodextrin[22] column of 5 cm length was tested with a modern UHPLC chromatographic system. It was able to fully separate the amygdalin epimers under 50 s (Figure 2D) needing only 1.8 mL of 10/90 v/v methanol/water mobile phase. The measured efficiency was as high as 60000 plates/m with a resolution factor >2. Again, amygdalin, with its *R*-mandelonitrile stereogenic center, eluted after the *S*-amygdalin epimer (Figure 1).

Factors Influencing Amygdalin Epimerization. The Cyclobond I 2000 RSP with a 20:80 v/v methanol/water mobile phase was used for all kinetic studies on amygdalin

DOI: 10.1021/acs.jafc.5b03120
J. Agric. Food Chem. 2015, 63, 8966−8973

Table 1. Epimerization Kinetics of Amygdalin in Different Glassware and Solvents

	expt with amygdalin	% *R*-amygdalin remaining[a] 10 min	30 min	60 min	comments and refs[b]
a	distilled water in glass at 100 °C	80.0	60.5	50.5	47% amygdalin remains intact after 2 h[24]
b	pure ethanol at 85 °C	negligible conversion			no conversion to *S*-amygdalin during 2 h of heating[24]
c	methanol/ethyl acetate azeotrope at 105 °C	100	100	100	no conversion to *S*-amygdalin during 2 h of heating[24]
d	distilled water in glass at 100 °C		66.6		45% amygdalin remains intact after 2 h minimum of boiling with a major unknown side product[29]
e	water + 0.05% citric acid at 100 °C		no conversion		negligible conversion to *S*-amygdalin in 2 h[29]
f	heating in dimethyl sulfoxide in glass		no conversion		the authors observed no conversion to the *S*-isomer (temperature and duration not mentioned)[27]
g	boiling water at in Pt vessel		no conversion		the authors observed no conversion to the *S*-isomer (boiling duration not mentioned)[27]
h	heating in deionized water in a VWR glass vial (as received)	44.5	39.7	35.0	ratio of *R*:*S* 47:53 after 1 h; oil bath temperature 109 °C
i	heating in deionized water in a washed VWR vial	93.0	68.3	55.2	ratio of *R*:*S* isomer 56:43 after 1 h; vial cleaned thoroughly before use
j	heating in deionized water in a Wheaton glass vial (as received)	43.3	41.9	35.0	ratio of *R*:*S* isomer 46:54 after 1 h; oil bath temperature 108 °C
k	heating in deionized water in a washed Wheaton glass vial	87.2	44.0	41.1	ratio of *R*:*S* isomer 46:53 after 1 h; oil bath temperature 106 °C
l	heating in deionized water Supelco glass vials (as received)	44.2	40.5	36.3	ratio of *R*:*S* isomer 47:53 after 1 h; oil bath temperature 108 °C
m	heating in deionized water in a washed Supelco glass vials	80.0	51.9	47.2	ratio of *R*:*S* isomer 49:51 after 1 h; oil bath temperature 108 °C
n	heating in deionized water in a Restek vial (as received)	51.9	41.6	40.6	ratio of *R*:*S* isomer 47:53 after 1 h; oil bath temperature 109 °C
o	heating in deionized water in a washed Restek glass vial	76.4	53.7	49.9	ratio of *R*:*S* isomer 52:48 after 1 h; oil bath temperature 109 °C
p	heating in high-density polyethylene (HDPE)	98.4	98.6	97.8	ratio *R*:*S* isomer 82:18 even after 3 h; oil bath at 110 °C

[a]The percentage of *R*-amygdalin remaining is expressed as chromatographic peak area as a function of time (note that in as-received glassware, side products form during boiling). [b]The ratio of *R*:*S* given in the column is expressed without regard for the minor side product that forms on boiling.

epimerization. Two early, very detailed, epimerization studies, which are more than four decades old, exist in the German literature.[23,24] The authors examined some of the factors influencing amygdalin epimerization such as (i) solvent, water, methanol, ethanol, ethyl acetate, and an azeotrope of methanol/ethyl acetate; (ii) temperature; and (iii) pH. The mandelonitrile stereogenic center changes configuration as indicated (Figure 1):

$$R\text{-amygdalin} \underset{k_S}{\overset{k_R}{\rightleftarrows}} S\text{-amygdalin} \tag{1}$$

$$\frac{[S]_{eq}}{[R]_{eq}} = \frac{k_R}{k_S} = K \tag{2}$$

Making measurements at different times in different conditions, Nahrstedt determined that the k_R and k_S kinetic rate constants were greatly affected by pH, solvent, and temperature but that the K thermodynamic equilibrium constant was little affected.[24] Similar observations have been made on the epimerization of lactose, where the equilibrium constant changed by only ∼10% in the temperature range of 25−49 °C.[25] This means that the epimerization equilibrium is reached more or less rapidly depending on the experimental conditions, but eventually produces a mixture of 43% *R*-amygdalin plus 57% *S*-amygdalin. This implies that, by nature, the *S*-isomer will predominate in a mixture.

Nahrstedt established that the amygdalin equilibrium constant was $K = 1.3$ with kinetic constants $k_R = 3.4 \times 10^{-4}$ s^{-1} and $k_S = 2.6 \times 10^{-4}$ s^{-1} in distilled boiling water.[24] Figure 3A shows the amygdalin epimerization data. Unfortunately, the details on water purification procedure, its storage, and glassware history were not provided in this work. In Figure 3B, we show a striking comparison when the glassware is thoroughly cleaned, deionized water (18.2 ΩM) is utilized, and there is minimum contact with other glassware. When amygdalin is heated in deionized water, the initial reaction rate is very slow (cf. Figure 3A), and after a certain period, it tends to proceed more rapidly. This reaction profile does not follow Nahrstedt's first-order kinetics in the beginning but eventually reaches the same equilibration ratio of products. We speculate that the water used by the author was perhaps distilled and stored in glass (which already contained enough "leachates" to accelerate the reaction). If the same *R*-amygdalin starting material solution is heated in the presence of glass pieces, made by crushing Pasteur pipets, the reaction proceeds more quickly with a >60 min difference in equilibration time. The glassware effect was tested using different heating methods in different flasks (direct heating on a mantle vs oil bath heating), and all produced general results; that is, initial conversion is slow and, after a certain period, the epimerization proceeds more rapidly.

We did an extensive study on the nature of the glassware (see Materials and Methods for glassware sources). Table 1 lists the epimerization amounts obtained in different conditions taken from the literature or obtained by our own experiments using the RPLC method with a cyclodextrin chiral stationary phase.[26] The first observation is that a protic solvent such as water is required for epimerization to occur; for instance, freeze-dried amygdalin samples were stable as were dimethyl sulfoxide solutions.[27] The epimerization is also negligible in ethanol at 65 °C; however, Nahrstedt noted that heating amygdalin in ethanol (95 °C oil bath temperature) also converted 14% of the *R*-amygdalin into the *S*-isomer. However, it was not clear whether the ethanol employed was anhydrous or not. In our

DOI: 10.1021/acs.jafc.5b03120
J. Agric. Food Chem. 2015, 63, 8966−8973

initial part of the experimental work, we noted that dry amygdalin remains stable with respect to epimerization.

With the availability of modern columns and instruments, it is now possible to revisit early epimerization studies. The most interesting aspect is that the nature of the container seems to have a significant effect on the epimerization of amygdalin. In Table 1, we show an extensive list of glassware (vials) that was tested for epimerization. It is likely that modern researchers will use vials/containers from one of these major manufacturers for storing/extracting amygdalin samples. *R*-Amygdalin was heated in pure deionized water to assess the glassware effect and evaluate the conversion amounts. Examination of Table 1 will show a trend in epimerization. First, if vials are used as received, the epimerization of *R*-amygdalin is very rapid (e.g., Wheaton/Restek/VWR/Supelco). All vials are considered clean for routine analytical work. However, after thorough washing of the vials in a base bath, detergent, hot water, and deionized water, the reaction rates become slower. Eventually, in most cases, the *S*-isomer dominates. One interesting observation in Table 1 is that epimerization is almost nonexistent after boiling a distilled water amygdalin solution in a platinum vessel. The authors used nuclear magnetic resonance (NMR) for their studies.[27] As seen in Table 1, boiling amygdalin in high-density polyethylene bottles does not promote epimerization like Pt vessels. Even after 3h of heating in plastic, 80% *R*-amygdalin remained intact this work. On the basis of the information included in Table 1, it is clear that glassware plays a role in the epimerization because Pt and plastic vessels significantly slow the epimerization process. It is likely that different forms of glassware leach soluble components in hot deionized water (e.g., silicates), which act as weak bases, thus promoting the epimerization of amygdalin.

Analysis of Commercial Amygdalin Samples. Commercial amygdalin is usually sold as "vitamin B17". One major vendor sells injectable solutions of amygdalin with a label D-mandelonitrile-β-D-glucosido-6-β-glucoside in amber glass vials. We directly injected the commercial amygdalin samples to see the chromatographic profile of the commercial sample on core–shell bonded (*R*,*S*)-hydroxypropyl β-cyclodextrin. Figure 4 shows the chromatograms of the ampule components. It is clear that the major components are indeed amygdalin and its isomer. In each injectable ampule, the *S*:*R* amygdalin ratio is 54:46, which is very close to the equilibrium value of 57:43 reported by Nahrsted and from our own observations.[24] It is interesting to note that the pH of the injectable solution is 6.1. At such a pH the epimerization rate is very slow.[24] We note an additional impurity, which appears to be a side product of amygdalin degradation (see Figure 4). The chromatographic fraction at 0.4 min was analyzed by ESI-mass spectrometry. The m/z ratio of the peaks is 498.25, which corresponds to the sodium adduct of the cyano group in amygdalin being replaced by the amide. Thus, the natural amygdalin being sold as injectable solution is contaminated by >50% of unnatural *S*-isomer and smaller amounts (~5%) of the amide formed by the hydration of the nitrile group in amygdalin.

The *R*-amygdalin content in "vitamin B17" was quantified using an external calibration curve. The typical concentration of *R*-amygdalin was found to be 87245 ppm with a relative standard deviation of 0.2%. The limit of detection, as calculated from 3 times the standard error in the intercept, was calculated to be 14.6 ppm. All amygdalin standards had to be prepared in ~0.1% acetic acid solution to prevent significant epimerization.

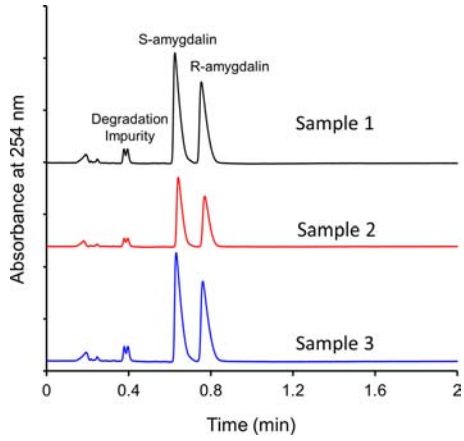

Figure 4. Ultrafast separation of commercial as-received injectable amygdalin solutions sold as vitamin B17 by a vendor. Chromatographic profiles of three separate vials are overlaid. Chromatographic conditions: 5 × 0.46 cm i.d. column containing 2.7 μm core–shell particles bonded with (*R*,*S*)-hydroxypropyl β-cyclodextrin; mobile phase, 10:90 MeOH/H_2O at 1.8 mL/min; injection volume, 0.03 μL; detection at 254 nm.

Standards prepared without acid epimerized by ~30% during the analysis.

Comments on Amygdalin Analysis and Storage. The important point when dealing with an amygdalin sample is to know the chemical nature of the compound considered. The naturally occurring amygdalin can convert into the undesired *S*-amygdalin during extraction, refluxing, and storage in various vials (all of which can be accelerated by pH, glass, and temperature). This trend is very clear in Table 1. Even worse, the amygdalin solution sold as an "alternative cure" to treat various illnesses is also sold in glass ampules. As stated earlier, most of the recent analytical methods have either neglected or missed the signal from *S*-amygdalin from the C_{18} columns. Although C_{18} or reversed phase cyano columns can practically separate the isomers as shown in the published results,[7,14] depending on the conditions, more recent studies do not seem to mention or notice the formation of the *S*-amygdalin.[4,10−12,15,16,18] Additionally, amygdalin is easily hydrolyzed by acids and bases. To reduce amygdalin hydrolysis by the digestive track, injectable solutions were sold (in alternative medicine, no FDA approval) in physiological solution and glass vials.[28] Depending on the nature of the glass making the vial, the storage time, and conservation temperature, it is most likely that epimerization changes the amygdalin content of such vials to 43% of the nominal label concentration with 57% of this concentration being *S*-amygdalin. Because both epimers can potentially release hydrogen cyanide, both are toxic.

In a recently published work, the ELISA method was proposed for amygdalin analysis. The problem is that the hapten–protein conjugate, needed to trigger the antibody formation by rabbits, was prepared in glassware at pH 9.4 using a carbonate–bicarbonate buffer for >6 h.[11] To see the effect of carbonate–bicarbonate buffer on amygdalin, we tested amygdalin epimerization in the same system at room temperature in a HPLC vial (which is certified to be clean from VWR, and at room temperature epimerization was negligible). The amygdalin–carbonate bicarbonate system was sampled after 10 min. Starting from 97% *R*-isomer, in just 30 min, 88% of the *R*-isomer remained. Within 2 h, only 68% of the *R*-amygdalin remained. After 3 h, 60% *R*-amygdalin

DOI: 10.1021/acs.jafc.5b03120
J. Agric. Food Chem. 2015, 63, 8966−8973

remained, and the rest was converted into the *S*-isomer. Note that this isomerization is slower as compared to the ammonia method (complete epimerization is within 20 min). Hence, the ELISA-reported results are likely the global epimer concentration fitting the simultaneous HPLC analyses obtained with an achiral C_{18} column that was perhaps unable to separate the epimers and therefore gave a combined peak for the two forms.[11]

Amygdalin tablets and pills are still proposed commercially today as a natural dietary supplement under the wrong name of laetrile or the questionable name of "vitamin B17". There are scientifically unsupported blog comments suggesting health benefits and possible cancer remissions.[28] Dry products may contain pure amygdalin found in apricot seeds; however, vials of liquids (for intravenous injection) upon long-standing contain only 43% amygdalin and 57% of its epimerized form. Considering that 1 g of amygdalin can release 59 mg of HCN and that the lethal dose for human cyanide poisoning is about 2.5 mg/kg body weight, six tablets containing 500 mg of amygdalin each could theoretically kill an adult if the molecule is completely hydrolyzed, releasing 180 mg of HCN. Children have been reported to have been subjected to such poisoning.[17] From an analytical point of view, it is important to know that the epimerization of amygdalin can be fast in aqueous solutions depending on the temperature and pH. Furthermore, the containers of amygdalin aqueous solutions can accelerate epimerization as seen in Figure 4.

Because the separation of the two epimers is rapid and selective when cyclodextrin chiral columns or porous graphitic carbon columns are used in liquid chromatography, these approaches are recommended for all such assays. We suggest better practices for amygdalin storage. If glassware is being used for extraction, it should be thoroughly washed (as detailed under Materials and Methods) before use. Ideally, solution or extracts of amygdalin should be stored in inert containers such as high-density polyethylene (HDPE) and the solutions should be mildly acidic (e.g., 0.1% acetic acid). Some authors recommend using citric acid/ascorbic acid to prevent epimerization for long-term storage of amygdalin solutions.[29] We also suggest that the amygdalin solutions be refrigerated to slow the kinetics of epimerization. We also note that dry amygdalin is sold and stable in glass containers with respect to epimerization.

In this work, our aim was to set good guidelines for the analysis of amygdalin and potentially other molecules, which can easily epimerize during storage. In the case of amygdalin, the importance of using chromatographic columns with different selectivity than a typical C_{18} column is essential when a given analyte can epimerize easily during storage. Using the same unique selectivity columns on superficially porous particles, the analysis time can be reduced to sub-minute separations for the first time. We showed an important result that the epimerization of amygdalin is heavily glassware dependent; its treatment history and even "clean" vials from various vendors can show drastically different reaction rates of the conversion to the optical isomer (*S*-amygdalin). We explicitly show that even clean *as-received* glassware from various vendors can also significantly alter the rate of epimerization reactions.

AUTHOR INFORMATION

Corresponding Author

*(D.W.A.) Fax: (817) 272-0619. Phone: (817) 272-0632. E-mail: sec4dwa@uta.edu.

Funding

D.W.A. thanks the CTD Holding Co. for financial support. A.B. thanks the French Centre National pour la Recherche Scientifique for support through ISA CNRS UMR5280.

Notes

The authors declare no competing financial interest.

ACKNOWLEDGMENTS

M.F.W. thanks Christopher A. Pohl and Jamieson Doug (Dionex, Thermo Fisher) for the gift of a porous graphitic carbon column.

REFERENCES

(1) Ganjewala, D.; Kumar, S.; Asha, D.; Ambika, K. Advances in cyanogenic glycosides biosynthesis and analyses in plant: a review. *Acta Biol. Szeged.* **2010**, *54*, 1−14.

(2) *Beilsteins Handbuch der Organischen Chemie*, 4, Auflage, Bd. 31; Springer Verlag: Berlin, Germany, 1938.

(3) Chassagne, D.; Crouzet, J. C.; Bayonove, C. L.; Baumes, R. L. Identification and quantification of passion fruit cyanogenic glycosides. *J. Agric. Food Chem.* **1996**, *44*, 3817−3820.

(4) Bolarinwa, I. F.; Orfila, C.; Morgan, M. R. A. Determination of amygdalin in apple seeds, fresh apples and processed apple juices. *Food Chem.* **2015**, *170*, 437−442.

(5) Wirthensohn, M. G.; Chin, W. L.; Franks, T. K.; Baldock, G.; Ford, C. M.; Sedglev, M. Characterising the flavour phenotypes of almond (*Prunus dulcis* Mill.) kernels. *J. Hortic. Sci. Biotechnol.* **2008**, *83*, 462−468.

(6) Lee, J.; Zhang, G.; Wood, E.; Castillo, C. R.; Mitchell, A. E. Quantification of amygdalin in nonbitter, semibitter, and bitter almonds (*Prunus dulcis*) by UHPLC-(ESI)QqQ MS/MS. *J. Agric. Food Chem.* **2013**, *61*, 7754−7759.

(7) Cairns, T.; Froberg, J. E.; Gonzales, S.; Langham, W. S.; Stamp, J. J.; Howie, J. K.; Sawyer, D. T. Analytical-chemistry of amygdalin. *Anal. Chem.* **1978**, *50*, 317−322.

(8) Krieble, V. K. The amygdalins and their inter-reactions with emulsin. *J. Am. Chem. Soc.* **1912**, *34*, 716−735.

(9) Berenguer-Navarro, V.; Giner-Galvan, R. M.; Grane-Teruel, N.; Arrazola-Paternina, G. Chromatographic determination of cyanoglycosides prunasin and amygdalin in plant extracts using a porous graphitic carbon column. *J. Agric. Food Chem.* **2002**, *50*, 6960−6963.

(10) Bolarinwa, I. F.; Orfila, C.; Morgan, R. A. Amygdalin content of seeds, kernels and food products commercially-available in the UK. *Food Chem.* **2014**, *152*, 133−139.

(11) Bolarinwa, I. F.; Orfila, C.; Morgan, M. R. A. Development and application of an enzyme-linked immunosorbent assay (ELISA) for the quantification of amygdalin, a cyanogenic glycoside, in food. *J. Agric. Food Chem.* **2014**, *62*, 6299−6305.

(12) Hosseini, M.; Heydari, R.; Alimoradi, M. Reversed-phase vortex-assisted liquid−liquid microextraction: a new sample preparation method for the determination of amygdalin in oil and kernel samples. *J. Sep. Sci.* **2015**, *38*, 663−669.

(13) Lin, W.-C.; Lin, J.-Y. Five bitter compounds display different anti-inflammatory effects through modulating cytokine secretion using mouse primary splenocytes in vitro. *J. Agric. Food Chem.* **2011**, *59*, 184−192.

(14) Smith, D. J.; Weber, J. D. Preparative and analytical separation of amygdalin and related-compounds in injectables and tablets by reversed-phase hplc and the effect of temperature on the separation. *J. Chromatogr. Sci.* **1984**, *22*, 94−98.

(15) Li, X.-b.; Liu, C.-h.; Zhang, R.; Huang, X.-t.; Li, Y.-y.; Han, L.; Xu, M.-l.; Mi, S.-q.; Wang, N.-s. Determination and pharmacokinetics

DOI: 10.1021/acs.jafc.5b03120
J. Agric. Food Chem. 2015, 63, 8966−8973

of amygdalin in rats by LC−MS-MS. *J. Chromatogr. Sci.* **2014**, *52*, 476−481.
(16) Wang, T.; Lu, S.; Xia, Q.; Fang, Z.; Johnson, S. Separation and purification of amygdalin from thinned bayberry kernels by macroporous adsorption resins. *J. Chromatogr. B: Anal. Technol. Biomed. Life Sci.* **2015**, *975*, 52−58.
(17) Sahin, S. Cyanide poisoning in children caused by apricot seeds. *J. Health Med. Inf.* **2011**, *2*, 106−111.
(18) Lv, W.-F.; Ding, M.-Y.; Zheng, R. Isolation and quantitation of amygdalin in apricot-kernel and *Prunus tomentosa* Thunb. by HPLC with solid-phase extraction. *J. Chromatogr. Sci.* **2005**, *43*, 383−387.
(19) Tao, Y.; Julian, R. R. Identification of amino acid epimerization and isomerization in crystallin proteins by tandem LC-MS. *Anal. Chem.* **2014**, *86*, 9733−9741.
(20) Troć, A.; Zimnicka, M.; Danikiewicz, W. Separation of catechin epimers by complexation using ion mobility mass spectrometry. *J. Mass Spectrom.* **2015**, *50*, 542−548.
(21) Isozaki, T.; Matano, Y.; Yamamoto, K.; Kosaka, N.; Tani, T. Quantitative determination of amygdalin epimers by cyclodextrin-modified micellar electrokinetic chromatography. *J. Chromatogr. A* **2001**, *923*, 249−254.
(22) Patel, D. C.; Breitbach, Z. S.; Wahab, M. F.; Barhate, C. L.; Armstrong, D. W. Gone in seconds: praxis, performance, and peculiarities of ultrafast chiral liquid chromatography with superficially porous particles. *Anal. Chem.* **2015**, *87*, 9137−9148.
(23) Smith, I. A. Über den Mechanismus der asymmetrischen katalytischen Racemisation des Amygdalins. *Ber. Deutsch Chem. Ges. B* **1934**, *67*, 1307−1317.
(24) Nahrstedt, A. Die Isomerisierung von Amygdalin und Homologen. *Arch. Pharm. (Weinheim, Ger.)* **1975**, *308*, 903−910.
(25) Jawad, R.; Drake, A. F.; Elleman, C.; Martin, G. P.; Warren, F. J.; Perston, B. B.; Ellis, P. R.; Hassoun, M. A.; Royall, P. G. Stability of sugar solutions: a novel study of the epimerization kinetics of lactose in water. *Mol. Pharmaceutics* **2014**, *11*, 2224−2238.
(26) Stalcup, A. M.; Chang, S.-C.; Armstrong, D. W.; Pitha, J. (*S*)-2-Hydroxyprophyl-*β*-cyclodextrin, a new chiral stationary phase for reversed-phase liquid chromatography. *J. Chromatogr. A* **1990**, *513*, 181−194.
(27) Turczan, J. W.; Medwick, T. Nuclear magnetic-resonance studies of cyanogenic glycosides − spectra of amygdalin and neoamygdalin in DMSO-d_6 and D_2O − epimerization studies − predicted laetrile spectrum. *J. Assoc. Off. Anal. Chem.* **1979**, *62*, 190−196.
(28) http://www.tjsupply.com/amygdalin-b17-products.html (accessed June 22, 2015).
(29) Hwang, E. Y.; Lee, J. H.; Lee, Y. M.; Hong, S. P. Reverse-phase HPLC separation of D-amygdalin and neoamygdalin and optimum conditions for inhibition of racemization of amygdalin. *Chem. Pharm. Bull.* **2002**, *50*, 1373−1375.

DOI: 10.1021/acs.jafc.5b03120
J. Agric. Food Chem. 2015, 63, 8966−8973

MATERIALS AND METHODS

General Experimental Instruments and Procedures. ^{1}H and ^{13}C NMR spectra were performed on a Bruker AM-400BB instrument (Bruker, Karlsruhe, Germany) with TMS as internal standard, operating at 400 and 100 MHz, respectively. EI-MS was measured with a VG ZAB-HS instrument (VG, East Sussex, UK), and ESI-ION trap was measured with an Esquire 6000 instrument (Bruker Daltonics, Billerica, MA, USA). Column chromatography (CC) used Sephadex LH-20 (25−100 mm) (Pharmacia Fine Chemical Co., Ltd., Berlin, Germany), silica gel 60 RP-18 (230−400 mesh) (Merck, Rahway, NJ, USA), and silica gel (200−300 mesh) (Qingdao Haiyang Chemical Co., Ltd., Qingdao, China). TLC was performed on precoated silica gel 60 F254 plates (Qingdao Haiyang Chemical Co., Ltd.), and spots were detected by ultraviolet (UV) illumination and sprayed with 5% H_2SO_4 in C_2H_5OH (v/v).

HPLC Analysis. The HPLC analysis was carried out on a HP1100 system (Agilent, Santa Clara, CA, USA) with a model G1315D diode array, and the column used was a 150 mm × 4.6 mm, 5 μm, GraceSmart Rp C18 (Grace Corp., Deerfield, IL, USA). The solvent of methanol for HPLC analysis was of HPLC gradient grade (Anhui Fulltime Co., Ltd., Hefei, China). Compounds were monitored at 211 and 254 nm, and UV spectra were recorded between 200 and 400 nm. The mobile phase, which was composed of methanol (A) and water (B), was programmed as follows: 0−30 min, A 80%. The flow rate with an injection volume of 20 μL was 0.8 mL/min at a column temperature of 35 °C.

Plant Material. The plants were collected from Mengtong of Shandong province, China, in 2014. The tobacco seeds are of Zhongyan 100 and were kindly provided by Tobacco Research Institute of Chinese Academy of Agricultural Sciences (CAAS). The seeds of *L. sativa* were purchased from a seed company in Shandong.

Soil Sample. Soil samples surrounding the root of flue-cured tobacco were collected from Mengtong (the same location where flue-cured tobacco was collected) of Shandong province, China, in 2014. Five different soil samples were collected about 15 cm deep around the root of flue-cured tobacco. The collected samples were dried in the dark at room temperature and then stored at 4 °C until they were extracted and analyzed. Soil samples were crushed and then passed through a 1 mm screen sieve to remove root contaminants, with visible root fibers picked out by hand. A sieved sample (100 g) was extracted ultrasonically with methanol three times (30 min each). The filtrate was concentrated in a vacuum to near dryness on a rotary evaporator. Then, the dry residue from the evaporation was redissolved in 100% MeOH and passed through a 0.45 μm nylon membrane filter prior to HPLC analysis.

Extraction and Isolation of Allelochemicals from Rhizosphere Soils. The tobacco plants were carefully uprooted, and clump soil was shaken off. The roots with rhizosphere soil were quickly washed in a container with distilled water, and 10 L of filtrate was collected. After clarification filtration, the resultant filtrate was adsorbed by macroporous adsorptive resin (XAD-4), eluting with ethanol. Then the desorbed solution was concentrated in a vacuum to near dryness on a rotary evaporator, yielding the exudates (1.8 g).

The exudates was submitted to silica gel CC (25 × 125 cm) with chloroform/EtOAc [1:0 (2 L), 10:1 (3 L), 5:1 (2.5 L), 2:1 (3 L), 1:1 (1 L), 0:1 (2 L)]−methanol to give fractions A−F by means of TLC analysis. Fractions A, D, and E showed significant inhibitory activities in the bioassays against lettuce seedlings. Fraction A was separated by Sephadex LH-20 column (2.5 × 160 cm, 20 mg) (1:1 $CHCl_3$/CH_3OH), then passed through silica gel CC (1.2 × 60 cm, 10 mg), and eluted with petroleum/acetone (60:1, v/v) to produce compound **3**. Fraction D was separated by Sephadex LH-20 column (2.5 × 160 cm, 20 mg) (1:1, $CHCl_3$/CH_3OH) to produce compound **4**, then passed through silica gel CC (1.2 × 60 cm,10 mg), and eluted with petroleum/EtOAc (3:1, v/v) to produce compounds **2** and **5**. Fraction E was separated by Sephadex LH-20 column (2.5 × 160 cm, 10 mg) (1:1 $CHCl_3$/CH_3OH), then passed through silica gel CC (1.2 × 60 cm, 10 mg), and eluted with petroleum/EtOAc (3:1, v/v) to produce compound **1**.

Bioassays. Inhibitory activities on the growth of tobacco and *L. sativa* seedlings were evaluated using the plate-culture method. The seeds of tobacco and *L. sativa* were soaked in 10% hypochlorite for 7 min, washed five times by distilled sterile water, and then germinated on filter paper with a photoperiod condition of 16/8 h day/night at 22 °C for 7 and 3 days, respectively. Then, the tested seedlings were transferred to 6-well plates (VWR Scientific, Inc., Shanghai, China), and the extracts of tobacco rhizospheric soil chemicals isolated were diluted with dimethyl sulfoxide (DMSO) with aliquots (10 μL) added to each of the treated wells (10 μL of DMSO was added as control). Then, the plants were incubated in a constant-temperature humidity chamber at 22 °C, under a 16 h light/8 h dark photoperiod (*L. sativa* seeds for 3 days, tobacco seeds for 7 days). The extracts of tobacco rhizospheric soil were prepared at final concentrations of 400, 200, and 100 μg/mL, and compounds **1**−**6** were prepared for 200, 100, 50, and 25 μg/mL. Three replicates were performed per treatment. The root length and stem length were measured at the end of the experiment. Inhibitory ratios (%) were determined by the formula [(control length − plant length treated)/control length] × 100.

Statistical Analysis. All data were subject to an analysis of variance using SPSS Statistics 18. Each value was expressed as the mean ± standard error (SE). The significant differences in seedling growth between the treatments and control were calculated using a one-way analysis of variance (ANOVA) followed by a Fisher's least significant difference (LSD) test.

Identification and Quantitation of Allelochemicals in the Soil. Identifications of the compounds in the soil of flue-cured tobacco were completed by comparing the retention times to the standards of compounds **1**−**3**. The quantitation of compound **1** in the soil was also done. The standard curves were performed using the linear regression method, and peak areas at 210 nm were plotted versus concentrations. The regression equation of compound **1** was $y = 14780525x + 58587$ ($r^2 = 0.9989$).

RESULTS

Isolation of Phytotoxic Chemicals from Rhizosphere Soil of Flue-Cured Tobacco. The isolation of compounds from rhizosphere soil of flue-cured tobacco was conducted by a bioassay-directed fractionation approach. The results showed that the crude root exudates from the rhizosphere soil of flue-cured tobacco had significant inhibitory effects on seedling growth of tobacco and *L. sativa* (Figure 1), indicating that there are potential inhibitors in the extracts of rhizosphere soil that affect the growth of tobacco plants themselves and other plant seedlings. The allelopathic effects of rhizosphere soil extracts

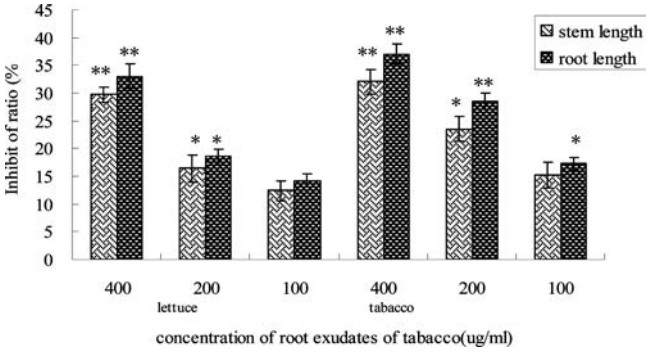

Figure 1. Phytotoxic effects of flue-cured tobacco root exudates against lettuce and tobacco seedlings at concentrations of 100, 200, and 400 μg/mL, respectively. Values are presented as a percentage of the mean compared to the control. Means significantly lower than the DMSO controls are indicated with one asterisk (*) (Dunnett's one-sided *t* test; $p < 0.05$) or two asterisks (**) ($p < 0.01$). Error bars are one standard error of the mean. $N = 3$.

DOI: 10.1021/acs.jafc.5b03086
J. Agric. Food Chem. 2015, 63, 8975−8980

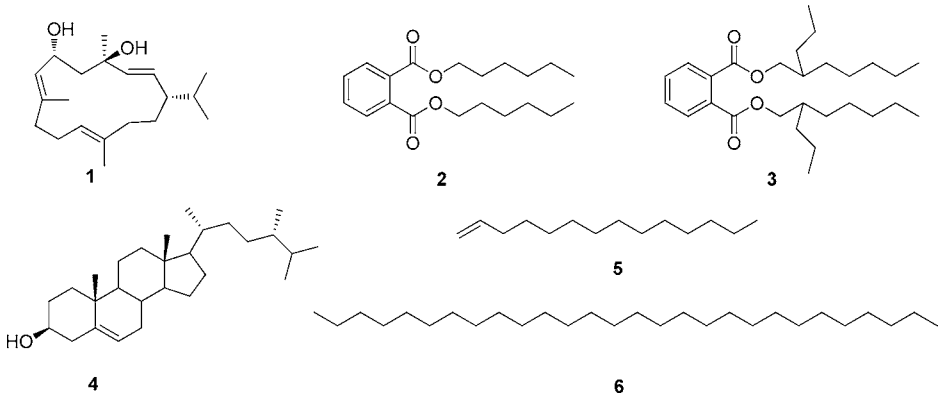

Figure 2. Structures of the compounds isolated from rhizosphere soil of flue-cured tobacco.

showed dose-dependent alterations. This was in accordance with previous studies.[18] It was also found that the extracts showed a stronger inhibitory effect on tobacco than *L. sativa* and implied remarkable autotoxicity.

Six compounds (Figure 2), including *β*-cembrenediol (**1**),[21] di-*n*-hexyl phthalate (**2**),[22] bis(2-propylheptyl) phthalate (**3**),[23] ergosta-5-en-3-ol (**4**),[24] 1-tetradecene (**5**),[25] and octacosane (**6**),[26] were isolated from rhizosphere soil and characterized by spectroscopic methods.

Phytotoxic Activities of the Purified Compounds on *L. sativa* Seedlings. The bioassay technique is commonly used to identify whether isolated compounds have allelopathic behavior. Compounds **1**–**6**, isolated and purified from the rhizosphere soil of flue-cured tobacco, were evaluated for phytotoxic activities against the seedling growth of *L. sativa*. Results indicated that compounds **1**, **2**, and **3** decreased the growth of the tested seedlings at different degrees, and the inhibitory effects of the three compounds showed dose-dependent alterations, whereas compounds **4**, **5**, and **6** had only a slight inhibitory activity (Figure 3). Compound **1** showed a significantly stronger inhibitory activity than the other two compounds at higher concentrations (≤100 μg/mL). Compounds **2** and **3** showed weaker activity than that of compound **1** at low concentrations (≤50 μg/mL), whereas all three compounds were much more effective at high concentrations (≥100 μg/mL). At higher concentrations, the inhibitory effects on the root growth of *L. sativa* are more significant than those on stem length. The root length of *L. sativa* seedlings treated with compound **1** at 200 μg/mL was reduced by 88.09% compared to the control, the seedlings showed wilting symptoms, and the roots turned yellow. Compound **1** arrested the growth of the treated plants at higher concentrations, but did not kill them.

Identification of Allelochemicals in Soil Samples. To achieve verification of the allelochemicals released from the flue-cured tobacco plant into soil during its growth, HPLC was used to confirm the existence of the allelochemicals in the zone soil by comparing their retention times with those of the standards of compounds **1**–**3** (Figure 4). With comparison to the chromatogram of the rhizosphere soil, compounds **1**, **2**, and **3** appeared in the chromatogram of soil samples. It was then verified that compounds **1**, **2**, and **3** should be released into the soil environment and act as allelochemicals by the plant in the course of its growth and development.

The standard curves were obtained by use of the linear regression method, and peak areas at 210 nm were plotted to

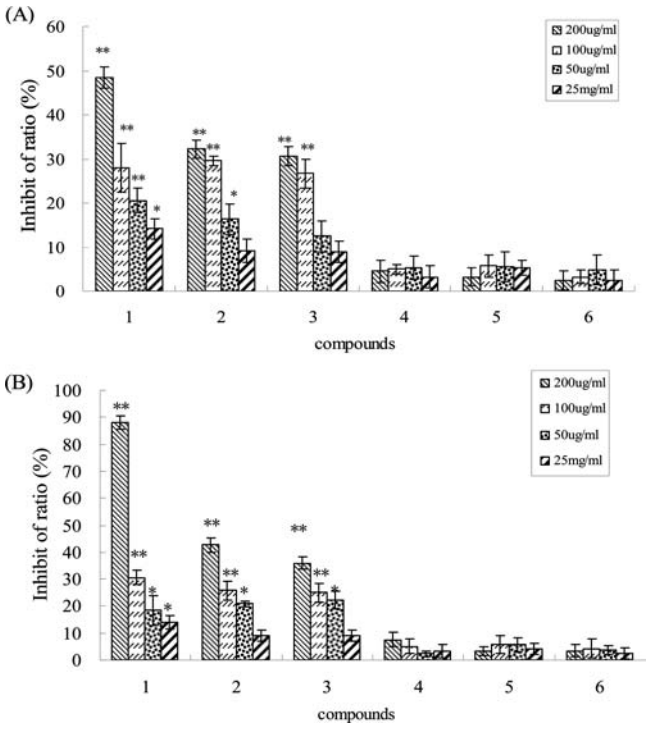

Figure 3. Phytotoxic effects of compounds **1**–**6** on lettuce seedling stem length (A) and root length (B) at concentrations of 25, 50, 100, and 200 μg/mL, respectively. Values are presented as a percentage of the mean compared to the control. Means significantly lower than the DMSO controls are indicated with one asterisk (*) (Dunnett's one-sided *t* test; $p < 0.05$) or two asterisks (**) ($p < 0.01$). Error bars are one standard error of the mean. $N = 3$.

calculate concentrations; thus, the concentration of compound **1** in the soil was determined as 2.23 μg/g.

Autotoxicity of the Allelochemicals on Flue-Cured Tobacco Seedlings. Results showed that compounds **1**, **2**, and **3** isolated as the allelochemicals of flue-cured tobacco had remarkable phytotoxicity against tobacco seedlings (Table 1). When tobacco seedlings were treated with compounds **1** and **2** at 200 μg/mL, their root and stem lengths were significantly reduced by 60.26 and 42.31% and by 45.45 and 39.80%, respectively. This indicated that tobacco can release some organic compounds into the surrounding environment with autotoxic allelopathy to the plant itself.

Allelochemicals are low-molecular-weight compounds released from living or decomposed plant tissues during growth.

DOI: 10.1021/acs.jafc.5b03086
J. Agric. Food Chem. 2015, 63, 8975−8980

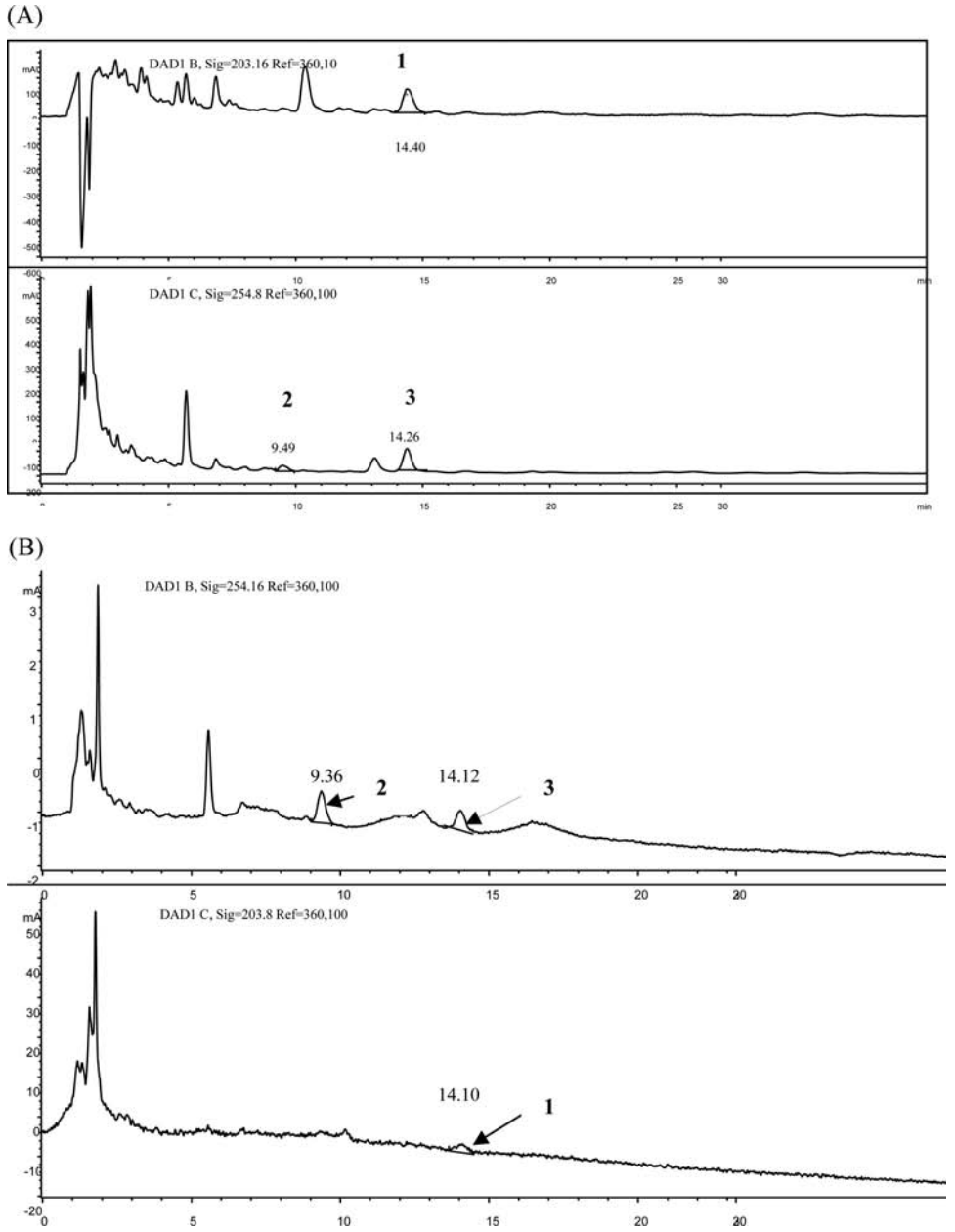

Figure 4. HPLC analysis of the rhizosphere soil and zone soil of flue-cured tobacco. (A) Compounds **1**, **2**, and **3** were confirmed in the HPLC chromatogram of the rhizosphere soil and had LC retention times of 14.40, 9.49, and 14.26 min, respectively. (B) Compounds **1**, and **2**, and **3** are shown in the HPLC chromatogram of the zone soil and had LC retention times of 14.10, 9.36, and 14.10 min, respectively.

Many plants could produce various allelochemicals such as phenols, terpenoids, and alkaloids and inhibit the growth of others. Compound **1** belongs to the terpenoids, which are the second type of allelochemicals, mostly released through volatilization and root exudation into soil to influence the growth of neighboring plant or themselves. Compound **1** is an important surface exudate of tobacco leaf, which had been reported to exhibit various activities, such as antifungal activity[27,28] and insecticide activity,[29] and might be leached into the soil, so that it is detected in soil samples. Compounds **2** and **3** are phthalate derivatives, which had been detected in root exudates of many crops and inhibit germination and seedling growth.[30,31] A prior study had found that esters and terpenoids have strong allelopathic potential in low concentration.[32] These two types of allelochemicals might be released into the soil environment through root and/or leaf exudates by flue-cured tobacco. It had been found that some of the terpenoids and esters secreted from plants exhibit strong allelopathic potential at low concentrations.[33] Our results are in good accordance with the reports in the literature, but the isolation and determination of these two types of allelochemicals of flue-cured tobacco are reported for the first time.

Autotoxicity, which is defined as a deleterious allelopathic effect among individuals of the same species, has been documented in various crops.[34,35] Autotoxicities in eggplant and peanut had been reported as one possible factor that contributes to replant failure.[36,37] Tobacco synthesizes various secondary metabolites during its growth and development; it is known that the natural products are one of the most important factors to evaluate the qualities of tobacco leaf and cigarette. The culture of flue-cured tobacco has often been hampered by replant failure exhibiting autotoxic effects on the seedlings of

DOI: 10.1021/acs.jafc.5b03086
J. Agric. Food Chem. 2015, 63, 8975−8980

Table 1. Autotoxic Effect of Compounds from Root Exudates of Flue-Cured Tobacco on Tobacco Seedling[a]

compd	stem length (cm, mean ± SE)					root length (cm, mean ± SE)				
	control	25 μg/mL	50 μg/mL	100 μg/mL	200 μg/mL	control	25 μg/mL	50 μg/mL	100 μg/mL	200 μg/mL
1	1.41 ± 0.04a	1.24 ± 0.03b	1.12 ± 0.03c	0.99 ± 0.04c	0.77 ± 0.04d	0.56 ± 0.01a	0.48 ± 0.05b	0.42 ± 0.03c	0.37 ± 0.07d	0.22 ± 0.06e
2	1.41 ± 0.04a	1.32 ± 0.02b	1.29 ± 0.04b	1.04 ± 0.02c	0.84 ± 0.07d	0.56 ± 0.01a	0.52 ± 0.02a	0.45 ± 0.08b	0.41 ± 0.06c	0.31 ± 0.04d
3	1.41 ± 0.04a	1.35 ± 0.05a	1.21 ± 0.09b	1.03 ± 0.01c	0.85 ± 0.01d	0.56 ± 0.01a	0.53 ± 0.02a	0.48 ± 0.03b	0.42 ± 0.05b	0.32 ± 0.03c

[a]Different letters in the same row refer to the Duncan test, $p < 0.05$.

this plant itself. It is considered that the homogeneity of both allelochemical and chemical compositions of tobacco accumulated in the soil environment is the major reason for allelopathic autotoxicity in the continuous cropping systems, but the specific allelochemicals released into the soil environment responsible for the autotoxic allelopathy have not been clarified until now. In this study, compounds **1**−**3** isolated from the root exudates of flue-cured tobacco showed observably phytotoxic activities against *L. sativa* and tobacco plant itself. With the results of bioassay and verification in the root zone soil by HPLC, the three compounds were determined as allelochemicals released into the soil environment by flue-cured tobacco and inhibiting its own growth. The results suggest that flue-cured tobacco exploits allelopathy as one main factor in replant failure. It is interesting to note that compound **1** has a strong inhibitory effect on *L. sativa* as well, and the treated *Lactuca* seedlings showed wilting symptoms at a concentration of 200 μg/mL. Even though the potential mechanism of action needs further study to be elucidated, our findings suggest that the high levels of compound **1** in tobacco may be utilized in many applications.

AUTHOR INFORMATION

Corresponding Author

*(B.Q.) Phone: +86-931-4968372. Fax: +86-931-8277088. E-mail: bqin@licp.cas.cn.

Funding

This work was supported by the National Natural Science Foundation of China (No. 31070386, 21302195, and 31300290), 135 key cultivation program of the Chinese Academy of Sciences, and the open project of Key Laboratory of Tobacco Diseases and Insect Pests Monitoring Controlling and Integrated Management, Institute of Tobacco Research, Chinese Academy of Agricultural Sciences (IPM 201404).

Notes

The authors declare no competing financial interest.

REFERENCES

(1) Xiao, X.; Cheng, Z.; Meng, H.; Khan, M. A.; Li, H. Intercropping with garlic alleviated continuous cropping obstacle of cucumber in plastic tunnel. *Acta Agric. Scand., Sect. B* **2012**, *62*, 696−705.

(2) Deng, Y. C.; Huang, J. G. Effect of long continuous cropping on the yields of flue-cured tobacco and nutrients in soils. *Plant Nutr. Fertil. Sci.* **2010**, *16*, 840−845.

(3) Jia, Z. H.; Yi, J. H.; Su, Y. R.; Shen, H. Autotoxic substances in the root exudates from continuous tobacco cropping. *Allelopathy J.* **2011**, *27*, 87−96.

(4) Ogweno, J.; Yu, J. Autotoxic potential in soil sickness: a re-examination. *Allelopathy J.* **2006**, *18*, 93.

(5) Wu, L. J.; Zhao, Y. H.; Guan, Y. M.; Pang, S. F. A review on studies of the reason and control methods of succession cropping obstacle of *Panax ginseng* CA Mey. *Special Wild Econ. Anim. Plant Res.* **2008**, *2*, 68−72.

(6) Kong, C. H.; Chen, L. C.; Xu, X. H.; Wang, P.; Wang, S. L. Allelochemicals and activities in a replanted Chinese fir (*Cunninghamia lanceolata* (Lamb.) Hook) tree ecosystem. *J. Agric. Food Chem.* **2008**, *56*, 11734−11739.

(7) Rice, E. L. *Allelopathy*; Academic Press: New York, 1984.

(8) Rial, C.; Novaes, P.; Varela, R. M.; G. Molinillo, J. M.; Macias, F. A. Phytotoxicity of Cardoon (*Cynara cardunculus*) Allelochemicals on Standard Target Species and Weeds. *J. Agric. Food Chem.* **2014**, *62*, 6699−6706.

(9) Wu, H.; Pratley, J.; Lemerle, D.; An, M.; Li Liu, D. Autotoxicity of wheat (*Triticum aestivum* L.) as determined by laboratory bioassays. *Plant Soil* **2007**, *296*, 85−93.

DOI: 10.1021/acs.jafc.5b03086
J. Agric. Food Chem. 2015, 63, 8975−8980

(10) Bi, X. B.; Yang, J. X.; Gao, W. W. Autotoxicity of phenolic compounds from the soil of American ginseng (*Panax quinquefolium* L.). *Allelopathy J.* **2010**, *25*, 115−122.
(11) Yang, M.; Zhang, X.; Xu, Y.; Mei, X.; Jiang, B.; Liao, J.; Zhu, S. Autotoxic ginsenosides in the rhizosphere contribute to the replant failure of *Panax notoginseng*. *PLoS One* **2015**, *10*, e0118555.
(12) Bais, H. P.; Park, S. W.; Weir, T. L.; Callaway, R. M.; Vivanco, J. M. How plants communicate using the underground information superhighway. *Trends Plant Sci.* **2004**, *9*, 26−32.
(13) Asao, T.; Hasegawa, K.; Sueda, Y.; Tomita, K.; Taniguchi, K.; Hosoki, T.; Matsui, Y. Autotoxicity of root exudates from taro. *Sci. Hortic.* **2003**, *97*, 389−396.
(14) Li, X. G.; Ding, C. F.; Hua, K.; Zhang, T. L.; Zhang, Y. N.; Zhao, L.; Wang, X. X. Soil sickness of peanuts is attributable to modifications in soil microbes induced by peanut root exudates rather than to direct allelopathy. *Soil Biol. Biochem.* **2014**, *78*, 149−159.
(15) Bertin, C.; Yang, X. H.; Weston, L. A. The role of root exudates and allelochemicals in the rhizosphere. *Plant Soil* **2003**, *256*, 67−83.
(16) Hao, W. Y.; Ren, L. X.; Ran, W.; Shen, Q. R. Allelopathic effects of root exudates from watermelon and rice plants on *Fusarium oxysporum* f. *sp. niveum*. *Plant Soil* **2010**, *336*, 485−497.
(17) Huang, L. F.; Song, L. X.; Xia, X. J.; Mao, W. H.; Shi, K.; Zhou, Y. H.; Yu, J. Q. Plant soil feedbacks and soil sickness: from mechanisms to application in agriculture. *J. Chem. Ecol.* **2013**, *39*, 232−242.
(18) Chen, D. M.; Huang, J. W.; Ke, W. H.; Wang, H. B.; He, H. B.; Zhang, Z. Y.; Lin, W. X. Allelopathic evaluation of continuous cropping tobacco rhizospheric soil and allelochemical identification. *J. Chinese Tobacco Sci.* **2012**, *18*, 46−52.
(19) Jianhua, Y. I.; Jia, Z.; Lin, Q.; Huizhen, L. V.; Shen, H. Allelopathic effects of decaying tobacco leaves on tobacco seedlings. *Allelopathy J.* **2012**, *29*, 51−62.
(20) Hui, Y. Y.; Hong, B. L.; Guo, M. S.; Sampietro, D. A.; Xin, X. G. Effects of allelochemicals from tobacco root exudates on seed germination and seedling growth of tobacco. *Allelopathy J.* **2014**, *33*, 107−119.
(21) Begley, M. J.; Crombie, L.; McNamara, D.; Firth, D. F.; Smith, S.; Bevan, P. C. Cembrenediols in the curing of tobacco. X-ray crystal structures of β-cembrenediol and α-cembreneketol. *Phytochemistry* **1988**, *27*, 1695−1703.
(22) Kim, Y. J.; Jonas, J. Dynamics of complex phthalate liquids. 2. Structural effects of side chains. *J. Phys. Chem. A* **1998**, *102*, 2778−2784.
(23) Yang, G. Q.; Qiu, W. R.; Jin, Y. N.; Wan, F. H. Potential allelochemicals from root exudates of invasive *Ageratina adenophora*. *Allelopathy J.* **2013**, *32*, 233.
(24) Thompson, M. J.; Dutky, S. R.; Patterson, G. W.; Gooden, E. L. NMR spectra of C-24 isomeric sterols. *Phytochemistry* **1972**, *11*, 1781−1790.
(25) Lv, C. S.; Li, Y. C.; Yang, Y.; Yan, Z. L.; Zhou, X. G. Oligomerization of 1-tetradecene to synthesize high performance lubricating base oil. *Appl. Chem. Ind.* **2015**, *44*, 76−80.
(26) Jing, L. L.; He, L.; Fan, P. C.; Jia, Z. P.; Ma, H. P. Chemical constituents with anti-hypoxia activity from *Saussurea involucrate*. *J. Chinese Med. Mater.* **2015**, *38*, 89−92.
(27) Menetrez, M. L.; Spurr, H. W., Jr; Danehower, D. A.; Lawson, D. R. Influence of tobacco leaf surface chemicals on germination of *Peronospora tabacina* adam sporangia. *J. Chem. Ecol.* **1990**, *16*, 1565−1576.
(28) Kennedy, B. S.; Nielsen, M. T.; Severson, R. F. Biorationals from *Nicotiana* protect cucumbers against *Colletotrichum lagenarium* (Pass.) ell. & halst disease development. *J. Chem. Ecol.* **1995**, *21*, 221−231.
(29) Lin, Y.; Wagner, G. J. Surface disposition and stability of pest-interactive, trichome-exuded diterpenes and sucrose esters of tobacco. *J. Chem. Ecol.* **1994**, *20*, 1907−1921.
(30) Yang, G. Q.; Wan, F. H.; Liu, W. X.; Zhang, X. W. Physiological effects of allelochemicals from leachates of *Ageratina adenophora* (Spreng.) on rice seedlings. *Allelopathy J.* **2006**, *18*, 237−245.
(31) Yang, G. Q.; Wan, F. H.; Liu, W. X.; Guo, J. Influence of two allelochemicals from *Ageratina adenophora Sprengel* on ABA, IAA and ZR contents in roots of upland rice seedlings. *Allelopathy J.* **2008**, *21*, 253−262.
(32) Macías, F. A.; Castellano, D.; Molinillo, J. M. Search for a standard phytotoxic bioassay for allelochemicals. Selection of standard target species. *J. Agric. Food Chem.* **2000**, *48*, 2512−2521.
(33) Zhang, Z. Y.; Xie, X. B.; Chen, D. M.; Xi, X. Y. Study on allelopathic autotoxicity and continuous cropping obstacles of tobacco. *J. Chinese Tobacco Sci.* **2011**, *8*, 88−92.
(34) Chou, C. H.; Lin, H. J. Autointoxication mechanisms of *Oryza sativa*. *J. Chem. Ecol.* **1976**, *2*, 353−367.
(35) Wu, H. W.; Pratley, J.; Lemerle, D.; An, M.; Liu, D. L. Autotoxicity of wheat (*Triticum aestivum* L.) as determined by laboratory bioassays. *Plant Soil* **2007**, *296*, 85−93.
(36) Chen, S. L.; Zhou, B. L.; Lin, S. S. Effects of cinnamic acid and vanillin on grafted eggplant root growth and physiological characteristics. *J. Appl. Ecol.* **2010**, *21*, 1446−1452.
(37) Huang, Y. Q.; Han, X. R.; Yang, J. F. Autotoxicity of peanut and identification of phytotoxic substances in rhizosphere soil. *Allelopathy J.* **2013**, *31*, 297.

DOI: 10.1021/acs.jafc.5b03086
J. Agric. Food Chem. 2015, 63, 8975−8980

S. bicolor were obtained from LG Sementes (Goianésia, GO, Brazil), and seeds of *L. sativa* from Feltrin Sementes (Farroupilhas, RS, Brazil).

Plant Material Samples. Leaves of *P. amboinicus* were collected during the morning in Alegre (ES, Brazil). The exsiccation (n. 21590) was deposited in the herbarium (VIES) at the Federal University of Espírito Santo (UFES). Plants were classified by the botanist A.C. Tuler.

Essential Oil. Essential oil was extracted using 500 g of fresh leaves from *P. amboinicus*, cut into small pieces and placed in a round-bottom 5 L flask coupled to a Clevenger (modified). The flask was half filled with distilled water, and hydrodistillation was performed for 3 h after the water was boiled. During this time, the hydrolate (150 mL) was collected and subsequently subjected to liquid−liquid extraction using pentane (3 × 40 mL). The organic phase was dried with anhydrous sodium sulfate and filtered. The filtrate was concentrated under reduced pressure in a rotatory evaporator to obtain the essential oil.

To determine the composition of the *P. amboinicus* essential oil, gas chromatography coupled to mass spectrometry (GC-MS) was used. A capillary column of fused silica Rtx-5MS (30 m long, 0.25 mm internal diameter) was used with helium as the carrier gas. The temperatures were 220 °C for the injector and 300 °C for the detector. The initial column temperature was 60 °C, programmed for an increase of 3 °C per minute until reaching the maximum temperature of 240 °C. To determine the chemical constituents of the *P. amboinicus* essential oil, the obtained mass spectra was compared with reference data from the equipment database, using data from other sources and the Kovats index (KI).[15] To determine the KI, a mixture of linear alkanes (C_9 and C_{26}) was injected into the chromatograph, under the same conditions used in the referenced essential oil analysis. Retention indices (KI) were calculated using eq 1.

$$KI = 100Z + \frac{100[(\log t'_R X) - (\log t'_R Z)]}{(\log t'_R Z + 1) - (\log t'_R Z)} \quad (1)$$

where X is the analyzed compound, Z the number of carbon atoms of the hydrocarbon with retention time immediately preceding the retention time of X, $t'_R X$ the adjusted retention time of X, $t'_R Z$ the adjusted retention time of Z, and $t'_R Z + 1$ the adjusted retention time of the hydrocarbon with retention time immediately preceding the retention time of X.

For component quantification, *P. amboinicus* essential oil was analyzed on a gas chromatograph equipped with a flame ionization detector. The stationary phase was the capillary column Rtx-5MS (30 m long and 0.25 mm internal diameter). Nitrogen was used as carrier gas. Temperature programming was the same as previously reported for GC-MS analysis. The temperatures of the injector and the detector were 240 and 250 °C, respectively. A 10 mg sample of essential oil was diluted in 1 mL of dichloromethane, and 1 μL of the mixture was injected.[16]

Biological Assay. To perform the biological tests, solutions of essential oil from *P. amboinicus* leaves were prepared in dichloromethane at the concentrations of 0% (dichloromethane), 0.015%, 0.030%, 0.060%, and 0.120% (w v^{-1}). The compounds carvacrol and thymol were applied at the same concentrations as the essential oil. The herbicides glyphosate and boral were used as positive controls. Seeds of *Sorghum bicolor* (monocot) and of *L. sativa* (dicot) were used as plant models. For the germination tests, 2 mL of each solution were added to Petri dishes with 9 cm diameter containing filter paper. Twenty-five seeds of *S. bicolor* and of *L. sativa* were used for each treatment, with five repetitions. The dishes were sealed with plastic foil and placed in the germination chamber (BOD) at 24 ± 2 °C, where they were kept for the duration of the experiment.

Phytotoxicity. The number of germinated seeds was evaluated from 8 to 48 h, at 8 h intervals. The germination speed index (GSI) was obtained according to the formula:

$$(N_1)\cdot 1 + (N_2 - N_1)\cdot 1/2 + (N_3 - N_2)\cdot 1/3 + \ldots(N_y - (N_{y-1}))\cdot 1/y$$

where N_y represents the number of seeds germinated in a given period and y represents the total number of time intervals. The percentage of

Table 1. Chemical Constituents of Essential Oil from Leaves of *P. amboinicus*[a]

no.	compound	IR	GC peak area (%)
1	NI	—	2.74
2	NI	—	1.62
3	oct-1-en-3-ol	909	1.79
4	carvacrol	1306	88.61
5	eugenol	1360	1.59
6	Z-caryophyllene	1399	2.39
7	NI	1496	1.26

[a]The compounds are listed in order of elution in the Rtx-5MScolumn. RI: retention index compared to linear alkanes (C_9 and C_{26}). Peak area percentages are calculated in GC (gas chromatography) Rtx-5MScolumn. NI, not identified.

Table 2. Germination Parameters for *L. sativa* and *S. bicolor* Treated with Different Concentrations of *P. amboinicus* Essential (EO), Thymol, and Carvacrol[a,b]

		L. sativa		*S. bicolor*	
solution	concentration (% m v^{-1})	GR	GSI	GR	GSI
EO	0.120	0	0	23.2	1
	0.060	85.6abcd	6.63c	80bcd	4.22
	0.030	88abd	6.88c	83.2abcd	5.28d
	0.015	88.8abd	8.37	93.6abcd	5.7cd
thymol	0.120	0	0	54.4	2.98
	0.060	70.4bcd	4.97c	86.4abcd	5.25d
	0.030	82.4abcd	6.48c	90.4abcd	5.25d
	0.015	89.6abcd	9.53abd	89.6abcd	5.44d
carvacrol	0.120	0.8	0.4	21.6	1.19
	0.060	10.4	0.8	68.8d	4.76
	0.030	81.6abcd	6.75c	84.8abcd	5.69abcd
	0.015	89.6abd	9.53abd	89.6abcd	6.3abcd
	water	91.2a	10.48a	96.8a	6.81a
	glyphosate	88.8b	10.4b	94.4b	6.84b
	boral	72.0c	6.48c	93.6c	6.57c
	dichloromethane	89.6d	10.41d	84.0d	6.14d

[a]GR, percentage of germination; GSI, germination speed index. [b]Means followed by the same letter in the column do not differ by Dunnett's test ($P > 0.05$).

DOI: 10.1021/acs.jafc.5b03049
J. Agric. Food Chem. 2015, 63, 8981−8990

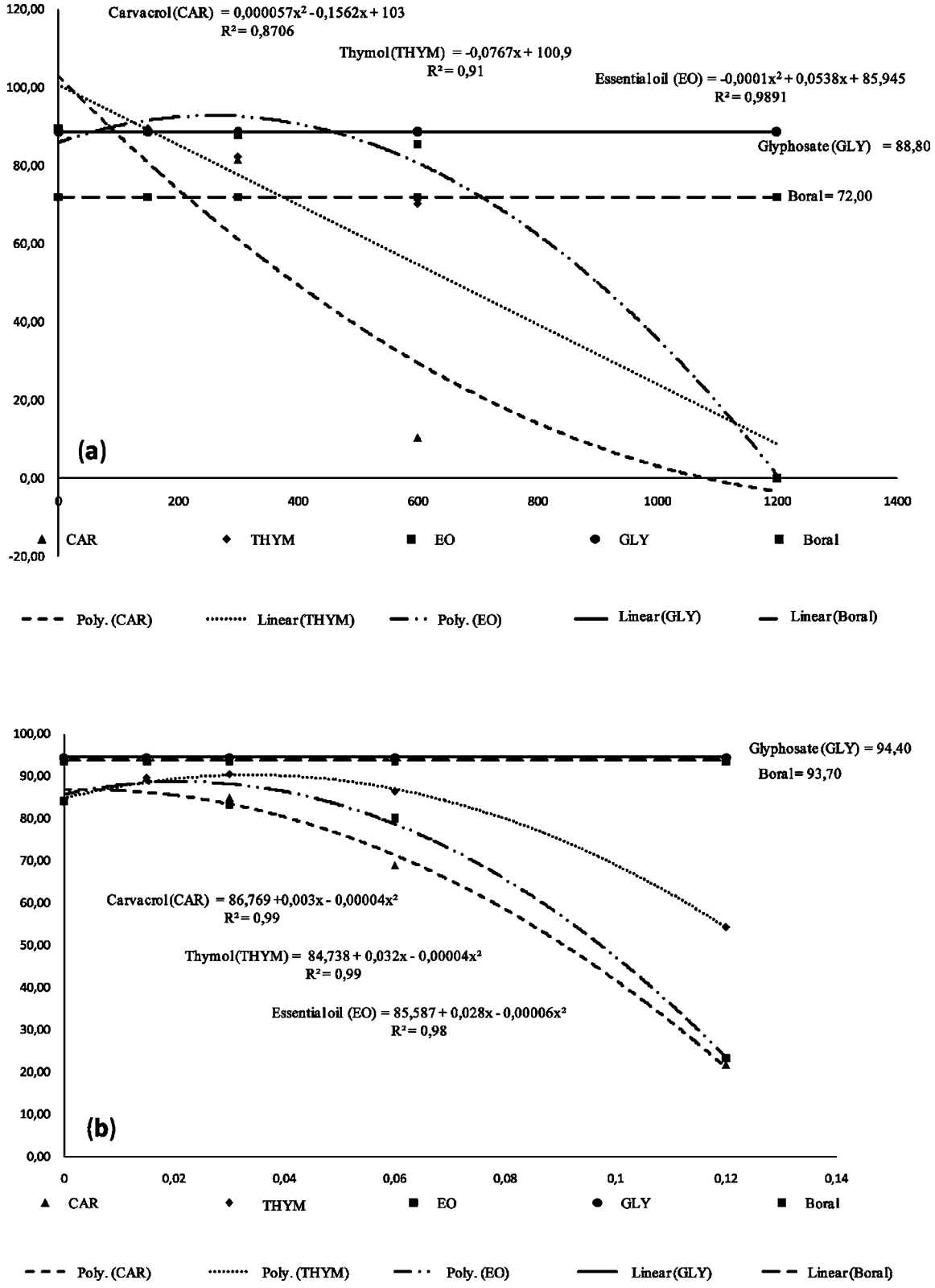

Figure 1. Graphs of GR (percentage of germination) for *L. sativa* (a) and *S. bicolor* (b) treated with solutions of *P. amboinicus* essential oil, thymol, and carvacrol.

germinated seeds (GR) and the root length (RL) were obtained after 48 h. The aerial parts of the plantlets were measured after 120 h to determine the aerial growth (AG). All measurements were taken with a digital caliper.

Cytotoxicity. After 48 h of exposure, 10 roots from each dish were collected and fixed in an ethanol: acetic acid solution (3:1/v v^{-1}), and stored at −4 °C for at least 24 h. For cytogenetic analysis, the slides were prepared using the squash technique and stained with 2% acetic orcein.[3] Approximately 5000 meristematic cells were evaluated per treatment, observing and quantifying the different stages of mitotic division. The mitotic index (MI) was obtained by dividing the number of cells in the process of division (prophase, metaphase, anaphase, and telophase) by

DOI: 10.1021/acs.jafc.5b03049
J. Agric. Food Chem. 2015, 63, 8981−8990

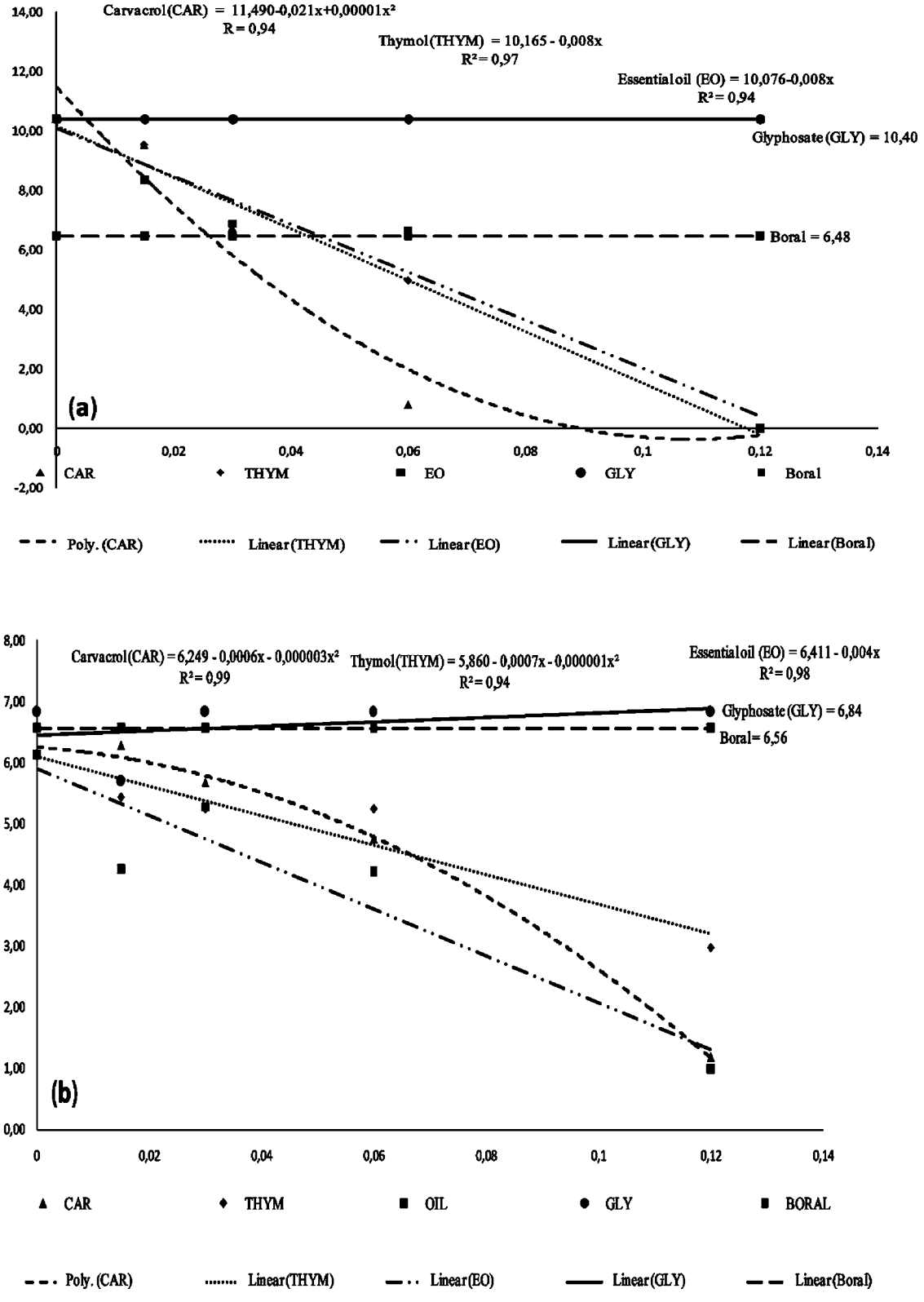

Figure 2. Graphs of GSI (germination speed index) for *L. sativa* (a) and *S. bicolor* (b) treated with solutions of *P. amboinicus* essential oil, thymol, and carvacrol.

the total number of cells evaluated in each treatment. The frequencies of chromosome and nuclear alterations were calculated by dividing the number of alterations (chromosomal or nuclear, respectively) by the total number of cells analyzed.[17]

Statistical Analysis. The experiment was done in a completely randomized design (CRD) using a 3 × 5 + 2 factorial scheme with 3 treatments (carvacrol, thymol, and essential oil), 5 concentrations (0.120%, 0.060%, 0.030%, 0.015% w v^{-1} and 0%), and 2 additional treatments (boral and glyphosate). When significant, the obtained cytotoxicity data were subjected to analysis of variance, and the means were compared by the Dunnett's test at 5% significance. The phytotoxicity data when significant were the quantitative factors (concentrations of

DOI: 10.1021/acs.jafc.5b03049
J. Agric. Food Chem. 2015, 63, 8981−8990

the solutions used) applied to analysis of regression, with the models to be chosen based on the significance of the regression coefficients, using Student's t test at 5% probability and the coefficient of determination (R^2). For the significant qualitative factors related to the "solutions" variables, Dunnett's test was used at 5% significance to compare the treatments. For statistical analysis of qualitative factors (Dunnett, 5% significance) used the Genes program,[18] and quantitative factors (regression) used the Sisvar program.[19]

RESULTS AND DISCUSSION

Essential Oil. The yield of essential oil from the leaves of *P. amboinicus* was 0.12% (w w^{-1}) compared to plant dry mass. Bandeira et al. found a 0.43% essential oil content in the leaves of this species.[20] Four compounds were identified in the essential oil (Table 1). Two chemotypes have been reported for this species, one rich in thymol and the other in carvacrol. Here, carvacrol was found to be the main constituent (88.61%). These compounds are isomers and belong to the class of aromatic monoterpenes.[12]

Carvacrol was also identified as the main constituent (77.16%) in the essential oil of *P. amboinicus* leaves by Joshi et al., while Oliveira et al. found thymol to be the main component of this oil (75.54%).[21,22]

Genetic factors are responsible for determining the chemical composition of essential oils. However, other factors may also generate changes in secondary metabolite production.[23] Biotic and abiotic factors may interfere with the quality and quantity of the secondary products resulting from the plant metabolism at a given time. The main biotic factors are plant−microorganism, plant−insect, and plant−plant interactions, as well as age and development stage. Abiotic factors include luminosity, temperature, rainfall, nutrition, season and time of collection, and harvest and postharvest techniques. These factors may present correlations among themselves and do not act in isolation. In a study with *Acorus calamus* L., Kumari et al. observed that the addition of UV−B complementary indices caused a significant carvacrol increase in the plant's essential oil composition.[24]

Biological Assay. *Plectranthus amboinicus* essential oil and its chemotypes in pure form, thymol and carvacrol, in dichloromethane solution at concentrations of 0.120%, 0.060%, 0.030%, and 0.015% (w v^{-1}) and the negative control (0.000%) were tested with respect to germination and growth of *L. sativa* root (dicot) and *S. bicolor* (monocots). In all treatments, the solutions with higher concentrations had the most significant effects in the referenced tests.

The data regarding GR (percentage of germination) and GSI (germination speed index) for *L. sativa* and *S. bicolor* are described in Table 2. For all the different solutions tested in *L. sativa* at the concentration of 0.120%, the values of GR presented a significant difference compared to the positive controls (Figure 1a). The solution of carvacrol at 0.060% presented a significant difference compared to the positive controls. For GSI, only the thymol and carvacrol solutions at 0.015% did not differ from the negative control treatment (0.000%), while the essential oil presented differences at all tested concentrations. This way, germination was retarded but did not cease (Figure 2a).

The GR values for *S. bicolor* in all treatments at the concentrations of 0.120% and 0.060% were lower than the negative control, although germination occurred in all tests (Figure 1b). The GSI data for all treatments at all concentrations were different from the positive and negative controls, with only the *P. amboinicus* essential oil at 0.015% not differing from the boral herbicide (Figure 2b).

The allelopathic effects may be less intense on the final germination percentage and more intense on the germination speed, as shown by Oliveira et al. when considering the allelopathic potential of aqueous extracts from mulungu bark (*Erythrina velutina* Willd. − Leguminosae) on *L. sativa*.[25]

The results obtained referring to germination and GSI can be explained by the fact that the allelopathic effect in plants is most often expressed not by the amount of germinated seeds, but rather by the retardation of their germination.[26] Monoterpenoids may have allelopathic activity, which interferes with germination and plant development. Moreover, these substances are able to affect physiological processes, such as photosynthesis, chlorophyll synthesis, lipid accumulation in the cytoplasm, and reduction of organelles because of ruptured membranes.[27]

In a study by Romero et al. on the effect of natural monoterpenes on mycelium growth and conidium germination in *Corynespora cassiicola*, the authors found that thymol and carvacrol present the highest effects on the reduction of germination.[28]

According to Yamagushi et al., eucalyptus and guacatonga (*Casearia sylvestris*), which contain monoterpenes in their composition, may be considered potentially allelopathic by reducing and inhibiting germination and GSI in various vegetables (mustard, cabbage, broccoli, kale, turnip, rocket, lettuce, tomato, and radish).[29]

The values for root length (RL) and aerial length (AL) after germination of *L. sativa* and *S. bicolor* treated with different concentrations of *P. amboinicus* essential oil, thymol and carvacrol, are presented in Table 3. The RL of *L. sativa* decreased progressively with increased concentrations of all tested solutions (Figure 3a). RL was not reduced when using *P. amboinicus* essential oil or carvacrol at 0.015%.

Table 3. Parameters for Root and Aerial Growth of *L. sativa* and *S. bicolor* Treated with Different Concentrations of *P. amboinicus* Essential Oil (EO), Thymol, and Carvacrol[a,b]

		L. sativa		*S. bicolor*	
solution	concentration (% m v^{-1})	RG (cm)	AG (cm)	RG (cm)	AG (cm)
EO	0.120	0	0 bc	1.3bc	2.78ad
	0.060	0	0 bc	2.41b	2.59ad
	0.030	4.81	1.63bc	2.68b	3.09ad
	0.015	5.71	2.31bcd	3.08	4.26ad
thymol	0.120	7.7ad	2.69bd	1.49bc	1.06bc
	0.060	0	0 bc	2.05bc	2.87a
	0.030	2.68bc	0.18bc	2.57b	2.94ad
	0.015	3.78b	0.34bc	3.01	2.64
carvacrol	0.120	7.04d	2.36bcd	0.7bc	0.52bc
	0.060	0.02	0bc	3.33	4.07ad
	0.030	0.42	0bc	5.05	5.67ad
	0.015	4.44b	2.13bcd	5.22	5.63ad
	water	91.2a	7.87ad	7.38a	4.91a
	glyphosate	88.8b	8.71a	1.78b	0b
	boral	72.0c	3.28b	1.26c	0c
	dichloromethane	89.6d	2.15c	7.26d	4.97d

[a]RG, root growth; AG, aerial growth. [b]Means followed by the same letter in the column do not differ by Dunnett's test ($P > 0.05$).

All solutions tested at 0.120% were more effective at reducing root growth in *L. sativa* than the herbicides glyphosate and boral. Moreover, a decrease in aerial growth was observed in all treatments as concentrations increased (Figure 4a).

For *S. bicolor*, all treatments at all tested concentrations showed significant reductions in growth compared to the negative control

DOI: 10.1021/acs.jafc.5b03049
J. Agric. Food Chem. 2015, 63, 8981−8990

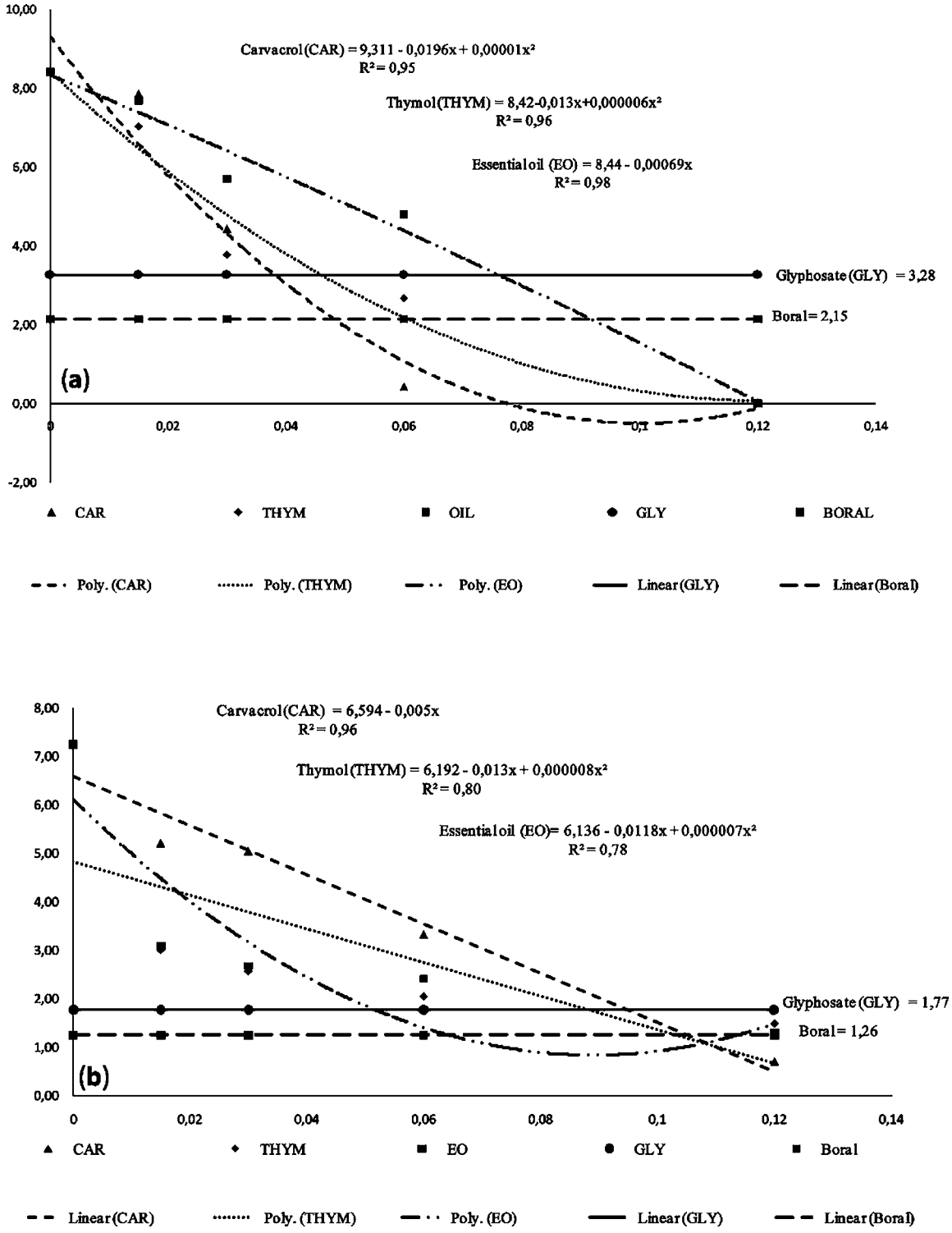

Figure 3. Graphs of RG (root growth) for *L. sativa* (a) and *S. bicolor* (b) treated with solutions of *P. amboinicus* essential oil, thymol, and carvacrol.

(Table 3). Figures 3b and 4b represent root and aerial growth, respectively. These aspects were not significant for any essential oil concentration or for thymol at 0.030%.

Alves et al. tested *Lippia sidoides* essential oil on *L. sativa* seeds and noted there was a phytotoxic effect, with thymol being the main component present in this oil.[30] Monoterpenes may show allelopathic effects; the vapors of these substances can cause anatomical and physiological alterations in plantlets.[31] According to Formagio et al., inhibiting root growth is an important ecological aspect, as it reduces the competitive pressure of the plant, enabling the neighboring species to establish dominance features.[32] The inhibitory effect of germination and of the root and aerial growth characteristic of the allelopathic agents may be related to their interference with cell division, membrane permeability, and enzyme activation.[33,34]

The cytogenetic study was used to analyze the alterations caused by *P. amboinicus* essential oil, thymol, and carvacrol on the *L. sativa* cell cycle. The same concentrations were used as in the

DOI: 10.1021/acs.jafc.5b03049
J. Agric. Food Chem. 2015, 63, 8981−8990

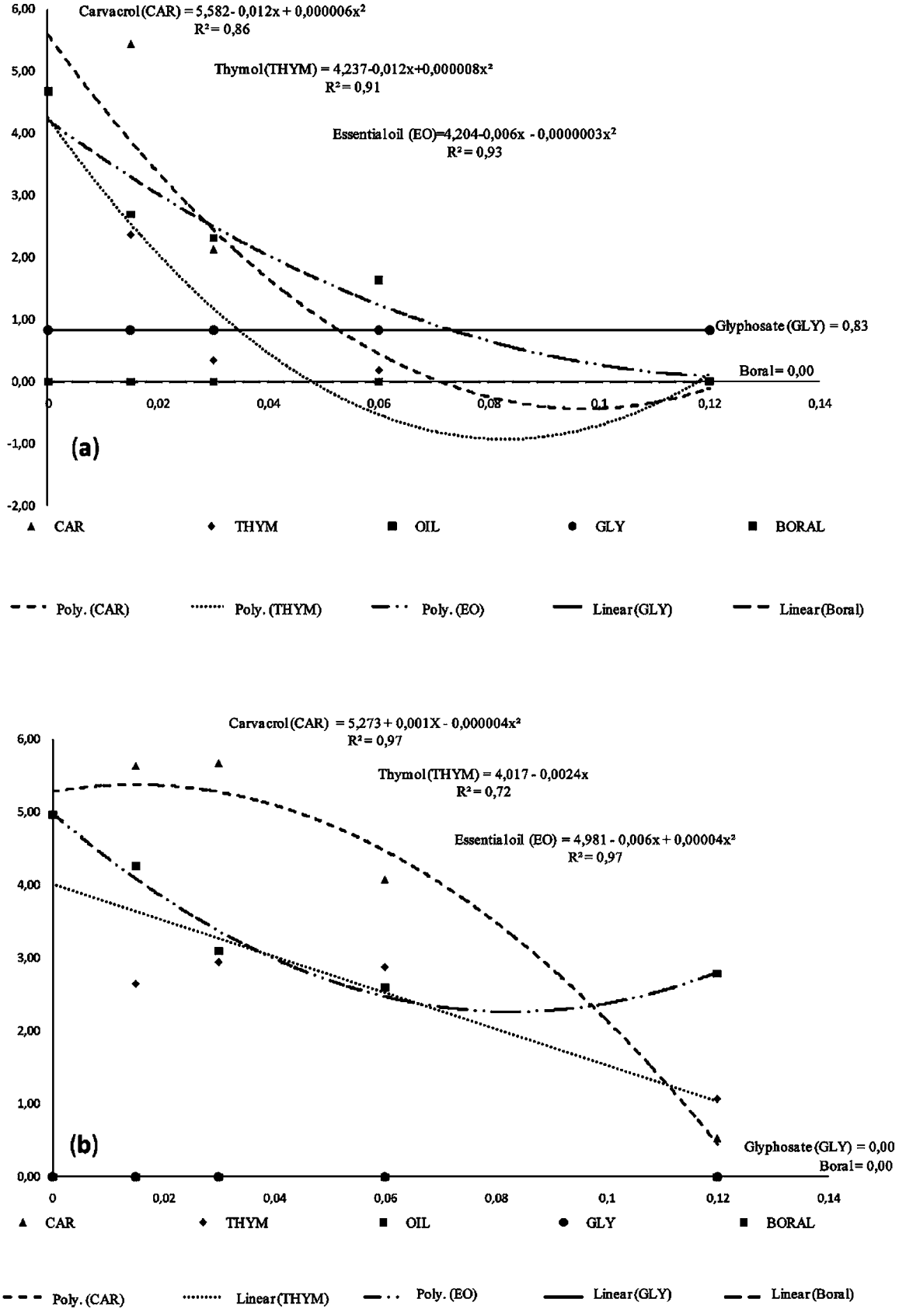

Figure 4. Graphs of AG (aerial growth) for *L. sativa* (a) and *S. bicolor* (b) treated with solutions of *P. amboinicus* essential oil, thymol, and carvacrol.

phytotoxic test, except for 0.120% because it totally inhibited seed germination in all tested solutions. The results of the cell divisions are shown in Tables 4 and 5.

The percentage of interphases was identical to the negative controlin the treatments with carvacrol at all tested concentrations. On the contrary, a decrease occurred using the thymol

DOI: 10.1021/acs.jafc.5b03049
J. Agric. Food Chem. 2015, 63, 8981−8990

Table 4. Normal Cell Division Parameters from Cytogenetics of *L. sativa* Treated with Different Concentrations of *P. amboinicus* Essential Oil (EO), Thymol, and Carvacrol[a,b]

solution	concentration (% w v^{-1})	I%	P%	M%	A%	T%	MI%
EO	0.060	85.52	49.08abcd	22.89ad	11.42	18.36ad	8.08ad
	0.030	83.1	45.13abcd	24.5ad	13.2	19.73ad	8.54d
	0.015	82.72	45.51abcd	23.79ad	11.81	23.83d	9.22
thymol	0.060	85.24	51.37abcd	23.03ad	8.88	19.73ad	8.7
	0.030	86.16	50.28abcd	23.19ad	10.6	19.45ad	8.86d
	0.015	86.38	45.36abcd	23.17ad	12.62ad	24.11ad	9.38d
carvacrol	0.060	93.96ab	53.29ad	21.51ad	10.99	8.49b	4.36
	0.030	93.24a	45.72ad	22.84ad	14.04ad	14.52ad	5.82
	0.015	92.5ad	41.8ad	26.05ad	18.66ad	11.51ad	6.12
	water	92.6a	41.44a	23.71a	17.39a	17.81a	7.36a
	glyphosato	95.06b	80.8b	8.98b	3.43b	2.46b	2.64b
	boral	69.62c	40c	0c	0c	0c	0.04c
	dichloromethane	91.76d	44.45d	21.98d	16.78d	18.63d	8.1d

[a]I%, percentage of interphases; P%, percentage of prophases; M%, percentage of metaphases; A%, percentage of anaphases; T%, percentage of telophases; MI%, percentage values of MI. [b]Means followed by different letters differed significantly according to Dunnett's test ($P > 0.05$); means followed by the same letter were similar according to the same test.

Table 5. Chromosome and Nuclear Alterations Observed in Root Meristems of *L. sativa* Treated with Different Concentrations of *P. amboinicus* Essential Oil (EO), Thymol, and Carvacrol[a,b]

solution	concentration (% w v^{-1})	CA%	NA%	Lost%	Sticky%	C-metaphase%	Bridge%	C-Poly%
EO	0.060	1.28	6.4	0.2abcd	0.32d	0.48	0.08abcd	0.2
	0.030	1.54	8.36	0.28	0.46	0.26abd	0.24d	0.3
	0.015	1.48	8.06	0.26b	0.62	0.22abcd	0.16ad	0.22
thymol	0.060	1.52	6.06	0.18abc	0.7	0.36bd	0.14ad	0.14
	0.030	1.44	4.98	0.16abcd	0.76	0.28abd	0.14ad	0.08abcd
	0.015	1.14	4.24	0.1abcd	0.82	0.08abcd	0.12abcd	0.02abcd
carvacrol	0.060	0.56abd	1.68b	0.02abcd	0.12abcd	0.4bd	0.02abcd	0abcd
	0.030	0.7d	0.94abd	0.02abcd	0.18abd	0.34abd	0.1abcd	0.06abcd
	0.015	0.84d	1.38abd	0.1abcd	0.2acd	0.34abd	0.12abcd	0.08abcd
	water	0.22a	0.04a	0.02a	0.08a	0.1a	0.02a	0a
	glyphosato	0.22b	2.3b	0.04b	0.02b	0.16b	0b	0b
	boral	0c	30.34c	0c	0c	0c	0c	0c
	dichloromethane	0.48d	0.14d	0d	0.22d	0.16d	0.1d	0d

[a]CA%, percentage of chromosome alterations; NA%, percentage of nuclear alterations; Lost%, percentage of lost chromosomes; Sticky%, percentage of sticky chromosomes; C-metaphase%, percentage of c-metaphases; Bridge%, percentage of bridges; C-Poly%, percentage of chromosome polyploidization. [b]Means followed by different letters present significant difference according to Dunnett's test ($P > 0.05$); means followed by the same letter present similarity according to the same test.

and *P. amboinicus* essential oil solutions (Table 4). This result is directly related to the MI, where all treatments differed from the negative control. The carvacrol solutions caused MI to decrease, however, while the other treatments (thymol and essential oil) caused this index to increase.

In the treatment of *L. sativa* with the herbicide boral, a very high index of condensed nuclei and a very low MI were observed (Table 5). The MI is used to evaluate the cytotoxicity of allelopathic agents. MI values significantly lower than the control indicate that the alterations are caused by the action of chemical components on the growth and development of the exposed organisms. On the other hand, if the MI presents values higher than the control because of increased cell division, this may be harmful to the organism as it may lead to disordered cell proliferation and eventually chromosome abnormalities.[35]

The presence of chromosome abnormalities was greater in all treatments compared to the controls, whereas nuclear alterations only differed from the controls in the treatments with *P. amboinicus* essential oil and thymol (Table 5). The detected alterations were lost chromosome, sticky chromosome, C-metaphase, and chromosome polyploidization (Figure 5).

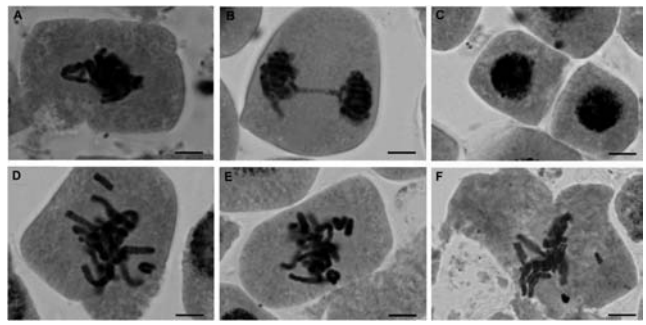

Figure 5. Abnormally dividing cells of *L. sativa* after exposure to carvacrol solution (0.060%, w v^{-1}): (A) stickiness metaphase, (B) anaphase bridge, (C) condensed nucleus, (D, E) laggard chromosomes, and (F) micro-c-metaphase. Scale bar is 5 μm.

Compared to the chromosomal alterations found, what most differentiated the controls was the percentage of sticky chromosomes (Table 5) that found significant differences between the controls and all treatments except the carvacrol.

DOI: 10.1021/acs.jafc.5b03049
J. Agric. Food Chem. 2015, 63, 8981−8990

The presence of sticky chromosomes is generally attributed to the toxic effects of chemical agents on the organization of chromatin. Because chromatin organization is affected, chromosome bridges may arise, as observed in this work (Table 5).

In view of these results, it is suggested that the essential oil of *P. amboinicus*, carvacrol, and thymol have potential for use as bioherbicides and may help to minimize the damage to biodiversity and human health caused by intensive herbicide use.

AUTHOR INFORMATION

Corresponding Author

*Phone: (55) 028 35528661. Fax: (55) 028 35528655. E-mail: patriciafontespinheiro@yahoo.com.br.

Notes

The authors declare no competing financial interest.

ACKNOWLEDGMENTS

We thank the National Council for Scientific and Technological Development (CNPq) for financial support (484183/2013-3).

REFERENCES

(1) Vieira-Filho, J. E. R.; Campos, A. C.; Ferreira, C. M. Abordagem alternativa do crescimento agrícola: um modelo de dinâmica evolucionária. *Rev. Bras. Inov.* **2009**, 425−476.

(2) Yang, D. T.; Zhu, X. Modernization of agriculture and long-term growth. *J. Monet. Econ.* **2013**, *60* (3), 367−382.

(3) Tavella, L. B.; Silva, Í. N.; Fontes, L. D. O.; Dias, J. R. M.; Silva, M. I. D. L. O uso de agrotóxicos na agricultura e suas consequências toxicológicas e ambientais. *Agrop. Cient. Sem.* **2012**, *7* (2), 6−12.

(4) Fagundes, M. Z.; Gonçalves, M. A.; Soares, M. P.; Martins, M. L.; Zanella, R.; Riet-Correa, F.; Anjos, B. L. Clinicopathological and toxicological aspects of poisoning by the clomazone herbicide in sheep. *Small Ruminant Res.* **2015**, *124*, 120−126.

(5) de, M. M.; Boccolini, P.; Boccolini, C. S.; de Rezende Chrisman, J.; Markowitz, S. B.; Koifman, S.; Koifman, R. J.; Meyer, A. Pesticide use and non-Hodgkin's lymphoma mortality in Brazil. *Int. J. Hyg. Environ. Health* **2013**, *216* (4), 461−466.

(6) IARC. Monographs Volume 112: Evaluation of Five Organophosphate Insecticides and Herbicides. March 20, 2015. Available at: http://www.iarc.fr/en/media-centre/iarcnews/pdf/MonographVolume112.pdf.

(7) INCA. Posicionamento do Instituto Nacional de Câncer José Alencar Gomes da Silva. Acercados Agrotóxicos. 2015 Available at: http://www1.inca.gov.br/inca/Arquivos/comunicacao/posicionamento_do_inca_sobre_os_agrotoxicos_06_abr_15.pdf.

(8) Ribeiro, J. P. N.; Lima, M. I. S. Potencial alelopático de *Crinum americanum* L. sob diferentes condições de extração. *Semina: Cienc. Agrar.* **2011**, *32* (2), 465−472.

(9) Pannacci, E.; Tei, F. Effects of mechanical and chemical methods on weed control, weed seed rain and crop yield in maize, sunflower and soyabean. *Crop Prot.* **2014**, *64*, 51−59.

(10) Li, J.; Liu, X.; Dong, F.; Xu, J.; Li, Y.; Shan, W.; Zheng, Y. Potential allelopathic effects of volatile oils from *Descurainia sophia* (L.) Webb ex Prantl on wheat. *Biochem. Syst. Ecol.* **2011**, *39* (1), 56−63.

(11) Rowshan, V.; Farhadi, F.; Najafian, S. The essential oil of *Dodonaea viscosa* leaves is allelopathic to rosemary (*Rosmarinus officinalis* L.). *Ind. Crops Prod.* **2014**, *56*, 241−245.

(12) Murthy, P. S.; Ramalakshmi, K.; Srinivas, P. Fungitoxic activity of Indian borage (*Plectranthus amboinicus*) volatiles. *Food Chem.* **2009**, *114* (3), 1014−1018.

(13) Kordali, S.; Cakir, A.; Ozer, H.; Cakmakci, R.; Kesdek, M.; Mete, E. Antifungal, phytotoxic and insecticidal properties of essential oil isolated from Turkish *Origanum acutidens* and its three components, carvacrol, thymol and p-cymene. *Bioresour. Technol.* **2008**, *99* (18), 8788−8795.

(14) Marco, C. A.; Teixeira, E.; Simplício, A.; Oliveira, C.; Costa, J.; Feitosa, J. Chemical composition and allelopathyc activity of essential oil of *Lippia sidoides* Cham. *Chil. J. Agric.Res.* **2012**, *72* (1), 157−160.

(15) Adams, R. P. *Identification of essential oil components by gas chromatography/mass spectrometry*, 4th ed.; Allured Publishing Corporation: Carol Stream, IL, 2007.

(16) Pinheiro, P. F.; Queiroz, V. T.; Rondelli, V. M.; Costa, A. V.; Marcelino, T. P.; Pratissoli, D. Chemical characterization and toxicity of citronella grass essential oil on *Frankliniella schultzei* and *Myzus persicae*. *Cienc. Agrotecnol.* **2013**, *37*, 138−144.

(17) Andrade-Vieira, L. F.; Botelho, C. M.; Palmieri, M. J.; Laviola, B. G.; Praça-Fontes, M. M. Effects of *Jatropha curcas* oil in *Lactuca sativa* root tip bioassays. *An. Acad. Bras. Cienc.* **2014**, *86*, 373−382.

(18) Cruz, C. D. *Programa Genes - Diversidade Genética*. UFV: Viçosa, Brazil, 2008; Vol. *1*, p 278.

(19) Ferreira, D. F. SisVar: Sistema de análise de variância para dados balanceados, versão 4.0. DEX/UFLA: Lavras, 2000. (Software estatístico.)

(20) Bandeira, J. M.; Barbosa, F. F.; Barbosa, L. M. P.; Rodrigues, I. C. S.; Bacarin, M. A.; Peters, J. A.; Braga, E. J. B. Composição do óleo essencial de quatro espécies do gênero. *Plectranthus. Rev. Bras. Plantas Med.* **2011**, *13* (2), 157−164.

(21) Joshi, R. K.; Badakar, V.; Kholkute, S. D. Carvacrol rich essential oils of *Coleus aromaticus* (Benth.) from Western Ghats Region of North West Karnataka, India. *Adv. Environ. Biol.* **2011**, *5* (6), 1307−1310.

(22) Oliveira, R. A.; Sá, I. C.; Duarte, L. P.; Oliveira, F. F. Constituintes voláteis de *Mentha pulegium* L. e *Plectranthus amboinicus* (Lour.) Spreng; [Volatile constituents of *Mentha pulegium* L. and *Plectranthus amboinicus* (Lour.) Spreng]. *Rev. Bras. Plantas Med.* **2011**, *13* (2), 165−169.

(23) Morais, L. A. S. Influência dos fatores abióticos na composição química dos óleos essenciais. *Hortic. Bras.* **2009**, *27* (2), S4050−S4063 (Supplemental CD ROM).

(24) Kumari, R.; Agrawal, S. B.; Singh, S.; Dubey, N. K. Supplemental ultraviolet-B induced changes in essential oil composition and total phenolics of *Acorus calamus* L. (sweet flag). *Ecotoxicol. Environ. Saf.* **2009**, *72*, 2013−2019.

(25) Oliveira, A. K.; Coelho, M. F. B.; Maia, S. S. S.; Diógenes, F. E. P.; Medeiros-Filho, F. M. Alelopatia de extratos de diferentes órgãos de mulungu na germinação de alface. *Hort. Bras.* **2012**, *30*, 480−483.

(26) Iganci, J. R. V.; Bobrowski, V. L.; Heiden, G.; Stein, V. C.; Rocha, B. H. G.; Efeito do Extrato; Aquoso de Diferentes. Espécies de Boldo sobre a Germinação e Indice Mitótico de *Allium cepa* L. *Arq. Inst. Biol., São Paulo* **2006**, *73* (1), 79−82, http://200.144.6.109/docs/arq/V73_1/iganci.PDF.

(27) Grosso, C.; Coelho, J. A.; Urieta, J. S.; Palavra, A. M. F.; Barroso, J. G. Herbicidal activity of volatiles from coriander, winter savory, cotton lavender, and thyme isolated by hydrodistillation and supercritical fluid extraction. *J. Agric. Food Chem.* **2010**, *58* (20), 11007−11013.

(28) Romero, A. L.; Oliveira, R. R.; Romero, R. B. Efeito de monoterpenos naturais no crescimento micelial e germinação de conídios de. *Pesqui. Agropecu. Pernambucana* **2013**, *18* (1), 3−7.

(29) Yamagushi, M. Q.; Gusman, G. S.; Vestena, S. Efeito alelopático de extratos aquosos de *Eucalyptus globulus* Labill. e de *Casearia sylvestris* Sw. sobre espécies cultivadas. *Semina: Cienc. Agrar.* **2011**, *32* (4), 1361−1374.

(30) Alves, M. C. S.; Medeiros-Filho, S.; Innecco, R.; Torres, S. B. Alelopatia de extratos voláteis na germinação de sementes e no comprimento da raiz de alface. *Pesqui. Agropecu. Bras.* **2004**, *39* (11), 1083−1086.

(31) von Poser, G. L.; Menut, C.; Toffoli, M. E.; Sobral, M.; Bessiere, J. M.; Lamaty, G.; Henriques, A. T.; Verin, P. Aromatic plants from Brazil: 4. Essential oil composition and allelopathic effect of the Brazilian Lamiaceae Hesperozygis ringens (Benth.) Epling and Hesperozygis rhododon Epling. *J. Agric. Food Chem.* **1996**, *44*, 1829−1832.

(32) Formagio, A. S. N.; Masetto, T. E.; Vieira, M. C.; Zárate, N. A. H; Matos, A. I. N. Potencial alelopático e antioxidante de extratos vegetais. *Biosci. J.* **2014**, *30* (s2), 629−638.

(33) Rodrigues, L. R. A.; Rodrigues, T. J. D.; Reis, R. A. Alelopatia em plantas forrageiras. FUNEP: Jaboticabal, 1999; p 18.

DOI: 10.1021/acs.jafc.5b03049
J. Agric. Food Chem. 2015, 63, 8981−8990

(34) Rosado, L. D. S.; Rodrigues, H. C. A.; Pinto, J.E.B. P.; Custódio, T. N.; Pinto, L. B. B.; Bertolucci, S. K. V. Alelopatia do extrato aquoso e do óleo essencial de folhas do manjericão "Maria Bonita" na germinação de alface, tomate e melissa. *Rev. Bras. Pl. Med.* **2009**, *11* (4), 422−428.
(35) Leme, D. M.; Marin-Morales, M. A. *Allium cepa* test in environmental monitoring: A review on its application. *Mutat. Res., Rev. Mutat. Res.* **2009**, *682* (1), 71−81.

DOI: 10.1021/acs.jafc.5b03049
J. Agric. Food Chem. 2015, 63, 8981−8990

complex intestinal microflora. Moreover, current data on the change of the bioactivity of procyanidin dimers after degradation by the intestinal microflora are limited, and some results are inconsistent or contrary. For example, Li et al.[14] reported that the total antioxidant capability of litchi pericarp procyanidins was significantly enhanced after microbial incubation. However, ellagitannins from pomegranate juice that possess potent in vitro antioxidant were reported to be metabolized into poor antioxidant derivatives by the colonic microflora.[15] To the best of our knowledge, studies directly comparing the catabolites of A-type and B-type dimers, as well as the change in the antioxidant activity after bioconversions in the same system, are unavailable. Therefore, one aim of the present study was to compare the intestinal metabolism of four proanthocyanidins, namely, B-type EC dimer, A-type EC dimer, A-type ECG dimer, A-type EGCG dimer, by rat intestinal flora, and the other was to investigate how the antioxidant activities of the dimers will change after the metabolism. We believed that our results will serve as the basis for a better understanding of the chemical structure−activity relationships of A-type and B-type procyanidin dimers in vivo.

MATERIALS AND METHODS

Chemicals. High-performance liquid chromatography grade acetonitrile, methanol, and formic acid were obtained from Fisher Scientific International Inc. (Waltham, MA, USA). Commercial standards of procyanidin B1, procyanidin A2, 4′-hydroxyphenylacetic acid and 3′-hydroxyphenylacetic acid (HPLC ≥ 98%) were purchased from Shanghai yuanye Bio-Technology Co., Ltd. (Shanghai, China). Other chemicals were purchased from Sinopharm Chemical Reagent Co., Ltd. (Shanghai, China) and were of analytical grade. Ultrapure water was acquired from a Milli-Q water purification system (Millipore Corp., Bedford, MA, USA). A commercial kit for the determination of T-AOC was purchased from Nanjing Jiancheng Bioengineering Institute (Nanjing, China).

Sample Preparation. A-type ECG dimer and A-type EGCG dimer were prepared from persimmon (*Diospyros kaki*) according to the method we previously reported[16] and further purified by preparative HPLC. B-type EC dimer was isolated from Granny Smith apples (*Malus domestica*) and characterized by HPLC-MS/MS as previously reported.[17] A-type EC dimer was prepared from peanut (*Arachis hypogaea*) red skins according to the method we previously reported.[16] The purity of B-type EC dimer was analyzed by HPLC to be 87.57% with commercial procyanidin B1 as the standard, the purities of A-type EC dimer, A-type ECG dimer, and A-type EGCG dimer were confirmed by HPLC to be 88.72, 82.56, and 93.28%, respectively, using procyanidin A2 as the standard. Stock solutions (2.5 mg/mL) of the analytes were dissolved in methanol and stored at 4 °C before the incubation experiments.

Animals. Male Sprague−Dawley rats, weighing 200 ± 15 g, were purchased from the Experimental Animal Center of Wuhan University (Wuhan, China) and housed in a room at 25 °C and 50 ± 10% relative humidity. After 1 week of acclimation, the rats were anesthetized and dissected. All experimental procedures were in accordance with Chinese legislation on the use and care of laboratory animals and were authorized by the Huazhong Agricultural University of Science and Technology Committee on animal care and use.

Preparation of Inoculum. The method of Engemann et al.[13] was employed. Briefly, the feces obtained from five rats were weighed during slaughtering and then transferred to an anaerobic chamber, which was set at 37 °C. All preparations were performed in the anaerobic chamber flushed with N_2 to maintain the strict anaerobic atmosphere. In addition, all of the solutions, buffers, and glass vessels were reserved through the high-pressure steam sterilization at 121 °C for 30 min before use. The cecum was diluted with 0.15 M PBS (pH 6.2) (1:8; m/v) containing an 11.1% Na_2S solution (575.9 mg/100 mL of 0.037 M NaOH) and a 0.0125% trace element solution (13.2 g/100 mL $CaCl_2{\cdot}2H_2O$, 10.0 g/100 mL $MnCl_2{\cdot}4H_2O$, 1.0 g/100 mL $CoCl_2{\cdot}6H_2O$, and 8.0 g/100 mL $FeCl_3{\cdot}6H_2O$).[18] The inoculum suspensions were filtered through a coarsely meshed net to remove larger particles and then used for the incubation experiments. Stock solutions of four procyanidin dimers (2.5 mg/mL in methanol) were diluted 1:10 (v/v) with the active or inactivated fecal solution. The samples were fermented at 37 °C in the anaerobic chamber and were taken after incubation for 0, 6, 12, and 24 h. The metabolism of the flora was stopped after incubation by storage at −80 °C until the chromatographic analysis of the metabolites. An aliquot of the sterilized fecal suspensions with stock solutions was used as control for chemical degradation and matrix effects, and the sterilized inoculum suspensions without the stock solutions of the analytes were used as blank. All incubation experiments were performed in triplicate.

HPLC Analysis. The frozen samples were thawed quickly and extracted with an equal volume of ethyl acetate three times. Subsequently, the ethyl acetate extracts were evaporated under N_2. Each residue obtained was dissolved in 1 mL of methanol. The separation was performed on a Waters e2695 HPLC system (Milford, MA, USA) with an Agilent TC-C18 column (150 × 4.6 mm i.d., 5 μm). The solution was filtered through a 0.22 μm cellulose acetate spin filter before 10 μL was injected into the HPLC with detection at 280 nm. Separation was accomplished at 30 °C with 0.13% formic acid in water (solvent A) and acetonitrile (solvent B) using the gradient 0−10 min, 10% solvent B; 10−15 min, 20% solvent B; 15−20 min, 40% solvent B; 20−25 min, 55% solvent B; 25−35 min, 55% solvent B, and re-equilibrated at 10% solvent B for 10 min. The flow rate was 0.8 mL/min, and the eluate was monitored at 280 nm.

LC-ESI-MS Analysis. LC-MS/MS analysis was performed by an Agilent 1100 liquid chromatograph system with an Agilent TC-C18 column (150 × 4.6 mm i.d., 5 μm) and an Agilent 1100 LC-MS spectrometer equipped with a diode array UV detector and an ESI interface (Agilent Technologies Co., Ltd., Santa Clara, CA, USA). The mobile phase and gradient were the same as for the HPLC analysis mentioned above. The negative ion polarity mode was carried out, and the spray needle voltage and the heated capillary temperature were 3500 V and 325 °C, respectively. The drying gas (N_2) flow rate was set at 10 L/min. The analysis was implemented using full scan, and the mass spectra scale ranged from m/z 50 to 2000.

Assays of the Antioxidant Activity. *Total Antioxidant Capability (T-AOC).* The T-AOC of metabolites after the microbial metabolism was estimated by the total antioxidant capability assay kit (Nanjing, China) according to the method of Li et al.[14] The T-AOC value of solutions of each dimer diluted with inactivated fecal solution was set as relative level of 100%.

ABTS Radical Cation Scavenging Capability. The $ABTS^{\bullet+}$ scavenging capacity of the metabolites was examined with 7 mM ABTS stock solution containing 2.45 mM potassium persulfate, which was stored in the dark at room temperature overnight. The $ABTS^{\bullet+}$ solution was diluted with ethanol to an absorbance of 0.70 ± 0.02 at 734 nm and equilibrated at 30 °C before use.[19] The metabolites were diluted with methanol 100-fold and mixed with $ABTS^{\bullet+}$ solution (v/v, 1:20). The $ABTS^{\bullet+}$ scavenging activity was evaluated as the percentage inhibition with regard to the following equation: inhibition (%) = $[A_0 - (A_1 - A_2)]/A_0 \times 100$, where A_0, A_1, and A_2 are the absorbance of the control, sample, and blank, respectively. The inhibition of solutions of each dimer diluted with inactivated fecal solution was set as relative level of 100%.

Statistical Analysis. All of the determinations are presented as the mean ± standard deviation (SD) and performed in triplicate. Data were calculated using one-way ANOVA of SPSS 17.0 followed by Tukey's multiple-range test. Differences were considered significant at a p value <0.05.

RESULTS AND DISCUSSION

Stability of Four Dimers in Rat Intestinal Flora Model. Four PA dimers at the concentration of 2.5 mg/mL did not show inhibition on the growth of rat intestinal flora. PA dimers with different chemical structures varied significantly in the

DOI: 10.1021/acs.jafc.5b03657
J. Agric. Food Chem. 2015, 63, 8991−8998

stability after incubation with rat intestinal flora. Among the four dimers tested, A-type EC dimer was the most stable, whereas A-type ECG dimer and A-type EGCG dimer were the least stable (Figure 1). The half-lives were 24.04, 14.70, 6.23, and 7.46 h for A-type EC dimer, B-type EC dimer, A-type ECG dimer, and A-type EGCG dimer, respectively, under the current incubation condition. Our results were inconsistent with those of Engemann et al.,[13] who reported that procyanidin A2 degraded by nearly 80% after incubation with pig cecum flora. The difference was probably due to the diversity between the pig cecum microbiota and the rat intestinal microbiota. An additional C2−O−C7 ether linkage in A-type EC dimer could explain its greater stability relative to the B-type EC dimer.[3] Compared to A-type EC dimer and B-type EC dimer, A-type ECG and EGCG dimer degraded more quickly. The additional galloyl groups, which were very susceptible to be hydrolyzed, gave a possible explanation for the greater instability of A-type (E)CG dimer and A-type (E)GCG dimer against microbial degradation.[20]

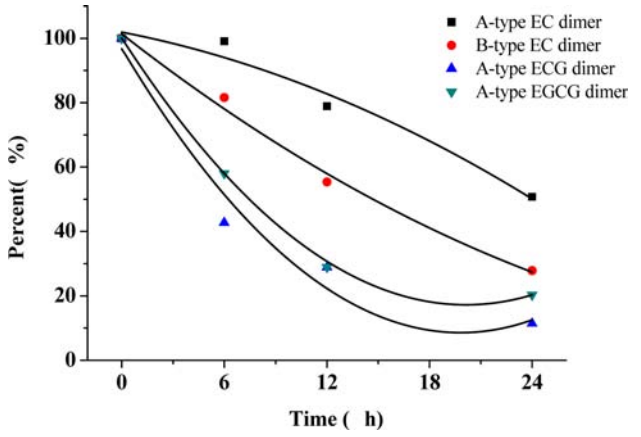

Figure 1. Stability of four dimers in rat intestinal flora model. The concentration of each dimer was 2.5 mg/mL.

Metabolites Derived from Bioconversion of Four PA Dimers. The HPLC profiles of the metabolites of four PA dimers decomposed by rat intestinal microbiota at different times are shown in Figure 2. Four new peaks (peaks 1−4 in Figure 2a) appeared after B-type EC dimer was incubated with rat intestinal microbiota. Compared to incubation for 6 h, the intensities of peaks 2 and 4 at 24 h doubled, whereas the intensities of peaks 1 and 3 did not change obviously. We excluded the possibility that these new peaks were derived from purely chemical transformation by using the control group

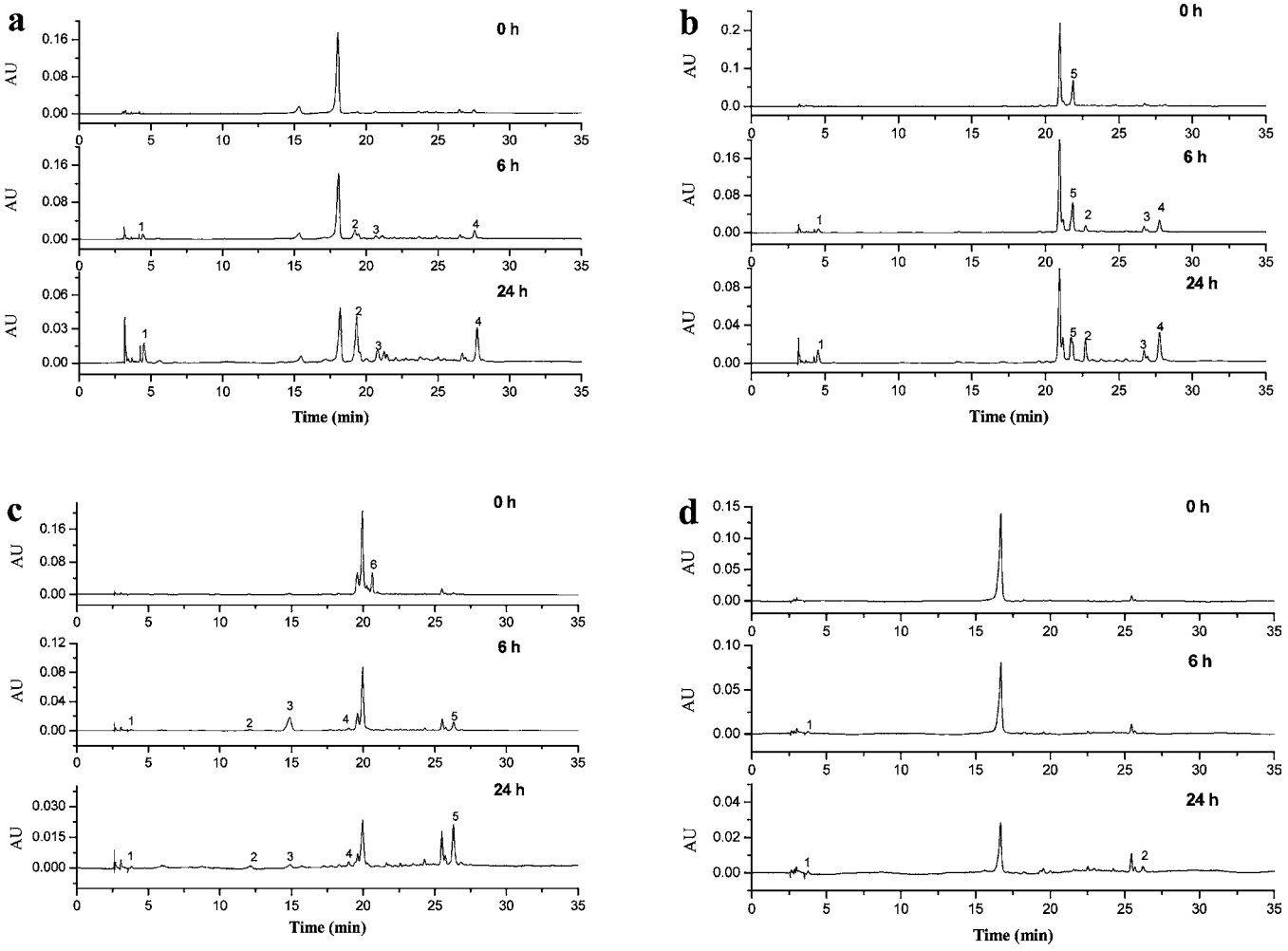

Figure 2. HPLC analysis of B-type EC dimer (a), A-type EC dimer (b), A-type ECG dimer (c), and A-type EGCG dimer (d) at different incubation times (0, 6, 24 h) with rat intestinal microbiota. Peaks 1−5 indicate newly formed metabolites.

DOI: 10.1021/acs.jafc.5b03657
J. Agric. Food Chem. 2015, 63, 8991−8998

Table 1. LC-MS/MS Data of Proanthocyanidin Metabolites

dimer	peak	$[M - H]^-$ (m/z)	MS^2 ions (m/z)	compound
B-type EC dimer	1	151.2	107.5	4′-hydroxyphenylacetic acid
	2	291.1	272.9, 247.0, 205.1, 167.1, 123.2	1-(3′,4′-dihydroxyphenyl)-3-(2″,4″,6″-trihydroxyphenyl)propan-2-ol
	3	670.9	589.0	unknown
	4	815.6	407.3	polymer
A-type EC dimer	1	151.3	107.2	4′-hydroxyphenylacetic acid
		195.5	176.2, 158.3	derivative of hydroxyphenylvaleric acid
		177.2	159.1, 77.7	5-phenylvaleric acid
	2	577.2	541.1, 409.5, 291.5	catabolite C1[a]
	3	407.3	387.9, 371.3	unknown
	4	815.7	407.3	polymer
A-type ECG dimer	1	209.1	163.9, 147.9, 121.0	5-(3′,4′-dihydroxyphenyl)valeric acid or 5-(4-hydroxy)-(3′-hydroxyphenyl)valeric acid
		439.3	312.7, 288.8, 168.7	structural unit of A-type ECG dimer
	5	815.7	407.3	polymer
A-type EGCG dimer	1	455.1	329.0, 302.6, 260.6	structural unit of A-type EGCG dimer
	2	815.7	407.3	polymer

[a]Reference 13 reported by Engemann et al., 2011.

consisting of the test substance in sterilized fecal culture medium. Besides, there had little change for the peaks of these impurities. The structures of the new peaks were analyzed by LC-MS/MS (Table 1). The molecular ion of peak 1 was observed at m/z 151.2 with a characteristic fragment at m/z 107.5, which resulted from the elimination of CO_2 from the molecular ion. The MS fragmentation pattern of peak 1 was identical to that of hydroxyphenylacetic acid as previously reported.[21] Peak 1 (m/z 151.2) was identified as 4′-hydroxyphenylacetic acid by comparison of its retention time, UV−vis spectra, and mass spectra with those of the authentic standards 4′-hydroxyphenylacetic acid and 3′-hydroxyphenylacetic acid. Stoupi et al.[21] identified 3′-hydroxyphenylacetic acid from catabolites of procyanidin B2 by human fecal microbiota. Peak 2 showed an $[M - H]^-$ ion peak at m/z 291.1, suggesting the presence of a C-ring-opened diaryl-propan-2-ol unit or a flavanol unit containing a reduced A-ring,[22] which resulted from the quinine methide (QM) pathway of the dimer. The characteristic fragment ions were found at m/z 272.9 and 247.0 in the MS^2 spectrum of m/z 291.1 (Table 1), suggesting the loss of H_2O and CO_2. These fragments were in agreement with previous studies,[23,24] so the ion at m/z 291.1 was identified as 1-(3′,4′-dihydroxyphenyl)-3-(2″,4″,6″-trihydroxyphenyl)propan-2-ol. Wang et al.[25] also demonstrated that anaerobic incubation of (+)-catechin with *Eubacterium* sp. strain SDG-2 resulted in the formation of 1-(3′,4′-dihydroxyphenyl)-3-(2″,4″,6″-trihydroxyphenyl)propan-2-ol. Peak 3 was heterogeneous with a main ion at m/z 670.9 and several minor ions at m/z 689.1, 660.9, 665.3, and 693.2, respectively, indicating a mixture. Among these molecular ions, a MS^2 fragment ion of m/z 670.9 was found at m/z 589.0, which resulted from the loss of 81 amu from the molecular ion. Although methylated form of B-type EC dimer showed a molecular ion at m/z 589.0 and Shoji et al.[26] illustrated that methylated procyanidin dimers B1 and B2 (m/z 589) were detected in rat plasma 2 h after administration of these procyanidins, it was unlikely that the methylation would occur in the in vitro model. Therefore, further work is needed to verify the structure of this compound. Peak 4 showed a $[M - H]^-$ ion at m/z 815.6 with a MS^2 fragment ion at m/z 407.3. Characteristic fragment ion at m/z 425 corresponded to the loss of 152 aum upon C-ring cleavage of the terminal unit of procyanidin B2 (m/z 577), and the ion at m/z 407 was produced by a further loss of a water molecule.[21] The characteristic MS^3 fragment ions of m/z 407.3 were seen at m/z 389.3 and 371.4, separately, suggesting the loss of one and two H_2O molecules, separately. We speculated that the fragment ion at m/z 407.3 was derived from the retro-Diels−Alder (RDA) fragmentation of the B-type EC dimer, followed by a further loss of H_2O, and then peak 4 might be formed through polymerization of two molecules of m/z 407.3. The detailed structure of peak 4 needed further confirmation.

HPLC-MS analysis indicated that the A-type EC dimer we obtained contained a main component with the retention time of 20.97 min and a minor component (peak 5) with the retention time of 21.86 min. These two peaks were approved to be a pair of isomers of A-type EC dimer, as evidenced by their molecular mass and fragmentation patterns shown in Supporting Information Figure S1-a. As shown in Figure 2b, four new peaks (1, 2, 3, 4) were detected after the incubation of A-type EC dimer with rat intestinal microbiota, and the peak intensities increased as the incubation time extended, whereas the intensity of peak 5 attenuated with time. Peak 1 was heterogeneous with three main ions at m/z 151.3, 195.5, and 177.2, respectively. The molecular ion $[M - H]^-$ at m/z 151.3 was quite similar to peak 1 of B-type EC dimer, with a MS^2 fragmentation at m/z 107.2. Similar to peak 1 in Figure 2a, based on the same retention time, UV−vis spectra and mass data with the authentic 4′-hydroxyphenylacetic acid, this compound (m/z 151.3) was identified as 4′-hydroxyphenylacetic acid.[21] The MS^2 fragments of the m/z 195.5 were at m/z 176.2 and 158.3 (Table 1), which showed a similar fragmentation pathway of hydroxyphenylvaleric acid but 2 Da higher than hydroxyphenylvaleric acid as a metabolite of procyanidin dimer by human fecal microbiota reported by Stoupi et al.[21] We deduced that it might be a derivative of

DOI: 10.1021/acs.jafc.5b03657
J. Agric. Food Chem. 2015, 63, 8991−8998

hydroxyphenylvaleric acid. The MS^2 fragment ions of m/z 177.2 were found at m/z 159.1 and 77.7. The molecular ion and MS^2 fragment ions of m/z 177.2 were identical to those of 5-phenylvaleric acid standards.[21] Therefore, 5-phenylvaleric acid was identified as a metabolite of A-type EC dimer by rat intestinal microbiota. These phenolic acids were also detected in catabolites of procyanidin A2 by human gut microbiota or pig cecum microbiota.[13,27] Peak 2 showed an $[M - H]^-$ ion at m/z 577.2, and four characteristic fragment ions found at m/z 541.1, 451.3, 409.5, and 291.5 (Table 1) respectively. This peak showed a dimeric character instead of monomeric. It showed the MS fragmentation pattern identical to that of catabolite C1, which was reported by Engemann et al.[13] as a metabolite of procyanidin A2 in the pig cecum model generated by the microbiota by cleaving the ether linkage at C′-ring with the newly formed hydroxy group positioned at the A′-ring.[28] Therefore, peak 2 was identified as catabolite C1. The molecular ion of peak 3 was at m/z 407.3 with high intensity, with MS^2 fragment at m/z 387.9 and 371.3. The metabolite (m/z 407.3) may be the product from RDA fission. The fragment ion at m/z 387.9 might be derived from the elimination of water and a reductive cleavage of the C2−O−C7 ether linkage from the molecular ion (m/z 407.3), but there is no report about the metabolite of m/z 407.3, which just appeared as the MS^2 secondary ion.[21,22] Therefore, the detailed structure of peak 3 needs further confirmation. Meanwhile, peak 4 showed the same MS fragmentation patterns as peak 4 in Figure 2a, indicating the same proposed structure.

Similar to the A-type EC dimer, the A-type ECG dimer we obtained contained two isomers, with the retention times of 19.95 and 21.01 min, separately, in the HPLC-MS chromatogram of Figure 2c (0 h). The MS and MS^2 spectrum of peak 6 with the retention time at 21.01 min is provided in Figure.S1-b. After incubation with rat intestinal microbiota for 6 h, A-type ECG dimer decreased by 48%. As shown in Figure 2c, five new peaks were observed after the incubation. The intensity of peak 3 increased after 6 h of incubation, but decreased as the incubation time was extended to 24 h, whereas intensities of other peaks changed little over time. Peak 1 was heterogeneous with several ions at m/z 209.1, 335.1, 439.3, and 479.2, respectively, indicating a mixture. The MS^2 fragment ions of m/z 209.1 were m/z 163.9, 147.9, and 121.0, separately. Similar MS fragmentation patterns were reported in the metabolites of ECG by human intestinal bacteria.[29,30] Therefore, the ion at m/z 209.1 might be 5-(3′,4′-dihydroxyphenyl)valeric acid or 5-(4-hydroxy)-(3′-hydroxyphenyl)valeric acid, but the lack of the commercial standards hindered the further confirmation of the exact structure of m/z 209.1. Additionally, the cleavage of the C-ring at the lower unit or the breakage at C4−C8 and C2−O−C7 bonds can contribute to the formation of small molecular weight phenolic acids.[12,21,30] The $[M - H]^-$ ion at m/z 439.3 might be the structural unit of the A-type ECG dimer, indicating interflavan bond breakage of the dimer might have happened. Various molecular ions were detected in peaks 2 and 3 (Table 1), but we failed to get the MS^2 fragments. We also failed to obtain the MS signals of peak 4, so the identities of these three peaks are not clear. Peak 5 showed identical MS ion and MS^2 fragment ions with those of peak 4 in Figure 2a,b, indicating the same proposed compound.

Although the A-type EGCG dimer is the most unstable and degraded quickly, only two small new peaks were detected in the catabolites of A-type EGCG dimer, after incubation with rat intestinal microbiota for 24 h (Figure 2d, peaks 1 and 2). We failed to detect other new peaks in the products, which might be because the minor decomposed products could not be detected under our current analytical conditions. Little change in the intensity of peaks 1 and 2 was observed with increasing incubation time. Peak 1 showed a molecular ion $[M - H]^-$ at m/z 455.1 with the MS^2 fragment ion at m/z 329.0, which corresponded to the loss of 126 aum of phloroglucinol ($[M - H - C_6O_3H_6]^-$) from the molecular ion m/z 455.1. Therefore, peak 1 (m/z 455.1) was the structural unit of the A-type EGCG dimer. This result also gave evidence that interflavan bond breakage of the A-type EGCG dimer happened in the current conditions. It has been reported that procyanidin dimers could be degraded into monomers by the intestinal microbiota or other derivatives of benzonic acid, phenylacetic acid, and phenylpropionic acid.[31] Similarly, the molecular ion $[M - H]^-$ of peak 2 was also found at m/z 815.7, with the same MS^2 fragment ions with that of peak 4 in Figure 2a,b and peak 5 in Figure 2c, indicating the same structure.

This study is the first direct comparison of the catabolism of four structurally different PA dimers by rat intestinal microbiota. We detected some metabolites such as 4′-hydroxyphenylacetic acid, 5-phenylvaleric acid, dihydroxyphenylvaleric acid, and 1-(3′,4′-dihydroxyphenyl)-3-(2″,4″,6″-trihydroxyphenyl)-propan-2-ol, which were reported previously in other studies.[21,24] Although the exact catabolism route of the dimers was not clear, our current data suggested that the early cleavage of C4−C8 interflavan bond could happen. Because we detected the structural units of both A-type ECG and EGCG dimers in the metabolites, the presence of 4′-hydroxyphenylacetic acid in both B-type and A-type EC dimers gave indirect evidence for the cleavage of the C4−C8 interflavan bond.[13,21] It was assumed that this metabolic pathway depended on the competence of the flora, which occurred during the incubation of B-type procyanidin dimers with human fecal microbiota reported by Stoupi et al.[21] and Appeldoorn et al.[12] Our results and previous results suggested that human fecal microbiota and rat intestinal microbiota had some similar competence in studying the intestinal metabolism of PA dimers. However, the amount of the monomers was trace, which might be due to the slow and low conversion of dimers into monomers followed by a rapid conversion into phenolic acids.[12,37] Previous study revealed that EGCG could be hydrolyzed into (−)-epigallocatechin (EGC) by rat intestinal bacteria and then converted to the main metabolite, 5-(4-hydroxy)-(3′,5′-dihydroxy)-phenylvaleric acid, by decomposition of the phloroglucinol ring.[24] Nevertheless, we did not detect this compound in metabolites of A-type EGCG dimer, and it might be that the amount of EGCG monomer generated was trace and this metabolite could not be detected. In addition, 1-(3′,4′-dihydroxyphenyl)-3-(2″,4″,6″-trihydroxyphenyl)propan-2-ol and the dimeric catabolite[13] were detected in the metabolites of B-type EC dimer and A-type EC dimer, respectively, which suggested that reductive cleavage of the C-ring and cleavage of the A-ring occurred.[3] A metabolite (m/z 670.9) detected only in the metabolites of B-type EC dimer demonstrated that the degradation route of B- and A-type dimers might somewhat differ. However, Stoupi et al.[21] observed dimeric intermediates in procyanidin B2 catabolites by human fecal microflora, suggesting the catabolites may vary significantly depending on the composition of the intestinal microflora. In addition, the metabolism of the A-type ECG dimer was more complex than those of B-type and A-type EC dimer, but we failed to obtain more information on the structure of the metabolites. More

DOI: 10.1021/acs.jafc.5b03657
J. Agric. Food Chem. 2015, 63, 8991−8998

surprisingly, although the A-type EGCG dimer was the most unstable, few metabolites were detected. This might be explained by the very complex and small amount of decomposed products that could not be detected under our current analytical conditions. Moreover, a compound with a molecular ion at m/z 815.6 was found in all four procyanidin dimers. We checked the MS spectrum of the control and confirmed this product was a catabolite of these dimers, but its exact structure needs further confirmation. Stoupi et al.[22] also identified some "dimeric " intermediate from procyanidin B2 catabolism by human fecal microflora.

However, some small phenolic compounds, including hydroxyphenylpropionic acid, 3,4-dihydroxyphenylpropionic acid,[32] 5-(3′,4′-dihydroxylphenyl)-γ-valerolactone, 5-(3′-hydroxyphenyl)valeric acid,[21] 3-(3′,4′-dihydroxyphenyl)-propionic acid, and 3-(4′-hydroxyphenyl)propionic acid, which were often reported as key metabolites of PAs, were not detected in our experiments. In addition, we detected fewer metabolites in the current study than were found in similar studies. The different experimental conditions might explain the different results between our experiments and those from other groups. First, we used rat microbiota flora instead of human fecal microbiota or pig cecum microbiota in other studies, and the different microbiota flora compositions might lead to different metabolites. Second, we used pure PA dimers in our study, but some studies used grape seed extracts[33,34] as the parent compounds, which might bring out different results. Third, only peaks detected by HPLC were analyzed by HPLC-MS in our study. Considering MS experiments may allow the detection of compounds not detected by HPLC, we screened the whole MS spectra but detected only m/z 191 in the spectra with an extremely low intensity, and we failed to obtain the MS^2 fragment ions. Therefore, Fourier transform mass spectrometry (FTMS),[13] UPLC/DAD-ESI-Q-TOF-MS,[35,36] or some more sensitive detection experiments that were used by other authors to detect the trace metabolites are needed to further confirm the exact structures of the metabolites in future work.

Change in the Antioxidant Activity of the Four Dimers after Bioconversion by Rat Intestinal Microbiota. It is well-known that proanthocyanidins have potent antioxidant activities in vitro.[38,39] However, the bioactivity of proanthocyanidins is affected by their bioavailability and biotransformation in vivo. Because the procyanidins are poorly absorbed during passage through the gastrointestinal tract, either a decrease or an increase in the antioxidant potential caused by the bacterial metabolism is possible. However, current data concerning the change in antioxidant potential of procyanidins after metabolism is scarce. Therefore, the T-AOC and ABTS assays were used to evaluate the antioxidant activity change of the four dimers after incubation with rat intestinal microbiota.

Figure 3 shows the T-AOC of four dimers at different incubation times. It was obvious that the T-AOC values of the A-type dimers were enhanced significantly after incubation with the rat intestinal microbiota for 6 h, but attenuated as the incubation time was prolonged to 24 h. After incubation for 6 h, the T-AOC of the metabolites of A-type EC, ECG, and EGCG dimers increased by 45, 7, and 41%, compared to the original dimers without conversion, respectively. However, the T-AOC of the B-type EC dimer decreased over time after incubation. Similar results were observed in the $ABTS^{\bullet+}$ assay. The scavenging capacity of the A-type dimers on $ABTS^{\bullet+}$ was

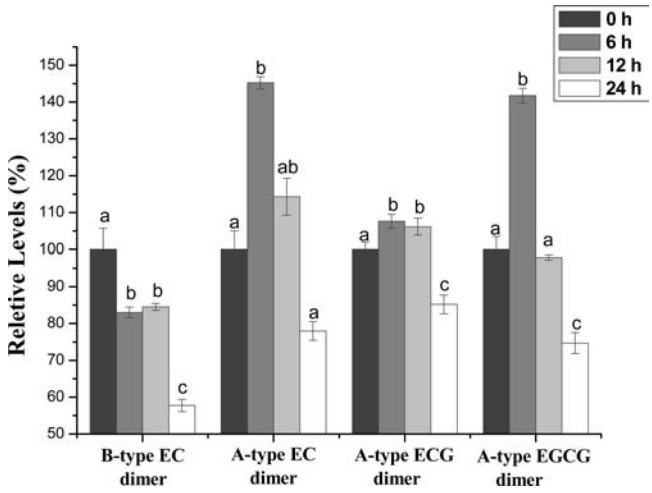

Figure 3. Changes of T-AOC of four different dimers before and after incubation with rat intestinal microbiota. Results are expressed as the mean ± SD of three independent experiments. Different letters among groups indicate significant difference ($p < 0.05$) by Tukey's test.

enhanced after incubation for 6 h but attenuated after 12 h of incubation (Figure 4). However, the $ABTS^{\bullet+}$ scavenging

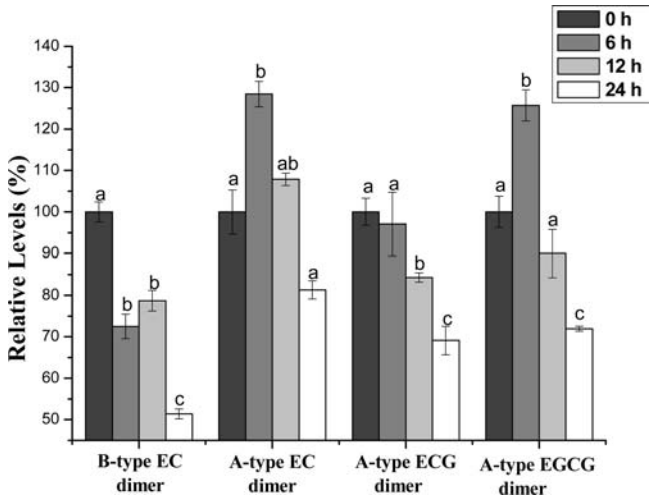

Figure 4. Changes of $ABTS^{\bullet+}$ radical scavenging activities of four different dimers before and after incubation with rat intestinal microbiota. Results are expressed as the mean ± SD of three independent experiments. Different letters among groups indicate significant difference ($p < 0.05$) by Tukey's test.

capacity of the B-type EC dimer decreased over time. Li et al.[14] concluded that *Streptococcus thermophilus* and *Lactobacillus casei*-01 could convert litchi pericarp procyanidins to a more effective antioxidant agent. However, they compared only the T-AOC of litchi pericarp oligomeric procyanidins before and after microbial incubation for 30 h. Our present study suggested the antioxidant capability of procyanidin dimers after bioconversion by rat intestinal microbiota differed significantly with incubation time, probably due to the different metabolite compositions at different incubation times. Therefore, for the change in antioxidant potential of procyanidins after metabolism, both microbiota and incubation conditions should be taken into consideration.

In summary, the present study indicated that after incubation with rat intestinal flora, structurally different PA dimers differed

DOI: 10.1021/acs.jafc.5b03657
J. Agric. Food Chem. 2015, 63, 8991−8998

significantly not only in stability but also in catabolism routes and catabolites. The stability of four proanthocyanidins incubated with rat intestinal microbiota was in the order A-type EC dimer > B-type EC dimer > A-type ECG dimer > A-type EGCG dimer under anaerobic condition. Although the early cleavage of the C4−C8 interflavan bond as well as the reductive cleavage of the C-ring and cleavage of A-ring occurred in both B-type and A-type dimers, the degradation routes of B-type EC dimer and A-type EC dimer might somewhat differ, as evidenced by different metabolites derived from different dimers. The antioxidant capabilities of the A-type dimers were enhanced significantly after incubation with the rat intestinal microbiota for 6 h, but attenuated as the incubation time was prolonged to 24 h. In contrast, the antioxidant capacity of the B-type EC dimer decreased during the incubation. Our results suggested the change of antioxidant capability of procyanidin dimers after bioconversion by rat intestinal microbiota was not only structure dependent but also incubation conditions dependent. To better understand the health benefits of procyanidin dimers, further work on the catabolism route as well as the bioactivity activities of the microbial metabolites is needed.

■ ASSOCIATED CONTENT

Supporting Information

The Supporting Information is available free of charge on the ACS Publications website at DOI: 10.1021/acs.jafc.5b03657.

ESI spectra of the main impurities of A-type EC and ECG dimers (PDF)

■ AUTHOR INFORMATION

Corresponding Author

*(C.L.) Phone: 86-27-87282966. Fax: 86-27-87282966. E-mail: lichmyl@mail.hzau.edu.cn.

Funding

This study was supported by the National Natural Science Foundation of China (No. 31271833), the Chinese Ministry Program for New Century Excellent Talents in University (NCET-12-0865), the Special Fund for Agro-scientific Research in the Public Interest (No. 201203047), and Fundamental Research Funds for the Central Universities (2013PY022).

Notes

The authors declare no competing financial interest.

■ ABBREVIATIONS USED

PA, proanthocyanidin; EC, (−)-epicatechin; ECG, (−)-epicatechin-3-gallate; EGCG, (−)-epigallocatechin gallate; B-type EC dimer, epicatechin-(4β→8)-epicatechin; A-type EC dimer, epicatechin-(4β→8,2β→O→7)-epicatechin; A-type ECG dimer, epicatechin-3-gallate-(4β→8,2β→O→7)-epicatechin-3-gallate; A-type EGCG dimer, epigallocatechin-3-gallate-(4β→8,2β→O→7)-epigallocatechin-3-gallate; PAs, proanthocyanidins; RDA, retro-Diels−Alder; QM, quinine methide; FRAP, ferric reducing antioxidant power; DPPH, 2,2-diphenyl-1-picrylhydrazyl; ABTS, 2,2-azinobis(3-ethylbenzothiazoline-6-sulfonic acid)

■ REFERENCES

(1) Gu, L. W.; Kelm, M. A.; Hammerstone, J. F.; Beecher, G.; Holden, J.; Haytowitz, D.; Gebhardt, S.; Prior, R. L. Concentrations of proanthocyanidins in common foods and estimations of normal consumption. *J. Nutr.* **2004**, *134*, 613−617.

(2) Gu, L. W.; Kelm, M. A.; Hammerstone, J. F.; Beecher, G.; Holden, J.; Haytowitz, D.; Prior, R. L. Screening of foods containing proanthocyanidins and their structural characterization using LC-MS/MS and thiolytic degradation. *J. Agric. Food Chem.* **2003**, *51*, 7513−7521.

(3) Ou, K.; Gu, L. Absorption and metabolism of proanthocyanidins. *J. Funct. Foods* **2014**, *7*, 43−53.

(4) Williamson, G.; Manach, C. Bioavailability and bioefficacy of polyphenols in humans. II. Review of 93 intervention studies. *Am. J. Clin. Nutr.* **2005**, *81*, 243S−255S.

(5) Koleckar, V.; Rehakova, Z.; Brojerova, E.; Kuca, K.; Jun, D.; Macakova, K.; Opletal, L.; Drasar, P.; Jahodar, L.; Chilebek, J.; Cahlikova, L. Proanthocyanidins and their antioxidation activity. *Chem. Listy* **2012**, *106*, 113−121.

(6) Schroeter, H.; Heiss, C.; Spencer, J. P. E.; Keen, C. L.; Lupton, J. R.; Schmitz, H. H. Recommending flavanols and procyanidins for cardiovascular health: current knowledge and future needs. *Mol. Aspects Med.* **2010**, *31*, 546−557.

(7) Tsang, C.; Auger, C.; Mullen, W.; Bornet, A.; Rouanet, J. M.; Crozier, A.; Teissedre, P. L. The absorption, metabolism and excretion of flavan-3-ols and procyanidins following the ingestion of a grape seed extract by rats. *Br. J. Nutr.* **2005**, *94*, 170−181.

(8) Appeldoorn, M. M.; Vincken, J.-P.; Gruppen, H.; Hollman, P. C. H. Procyanidin fimers A1, A2, and B2 are absorbed without conjugation or methylation from the small intestine of rats. *J. Nutr.* **2009**, *139*, 1469−1473.

(9) Kahle, K.; Kempf, M.; Schreier, P.; Scheppach, W.; Schrenk, D.; Kautenburger, T.; Hecker, D.; Huemmer, W.; Ackermann, M.; Richling, E. Intestinal transit and systemic metabolism of apple polyphenols. *Eur. J. Nutr.* **2011**, *50*, 507−522.

(10) Lu, W.-C.; Huang, W.-T.; Kumaran, A.; Ho, C.-T.; Hwang, L. S. Transformation of proanthocyanidin A2 to its isomers under different physiological pH conditions and common cell culture medium. *J. Agric. Food Chem.* **2011**, *59*, 6214−6220.

(11) Xu, Z.; Wei, L.; Ge, Z.; Zhu, W.; Li, C. Comparison of the degradation kinetics of A-type and B-type proanthocyanidins dimers as a function of pH and temperature. *Eur. Food Res. Technol.* **2015**, *240*, 707−717.

(12) Appeldoorn, M. M.; Vincken, J.-P.; Aura, A.-M.; Hollman, P. C. H.; Gruppen, H. Procyanidin dimers are metabolized by human microbiota with 2-(3,4-dihydroxyphenyl)acetic acid and 5-(3,4-dihydroxyphenyl)-γ-valerolactone as the major metabolites. *J. Agric. Food Chem.* **2009**, *57*, 1084−1092.

(13) Engemann, A.; Hübner, F.; Rzeppa, S.; Humpf, H.-U. Intestinal metabolism of two A-type procyanidins using the pig cecum model: detailed structure elucidation of unknown catabolites with fourier transform mass spectrometry (FTMS). *J. Agric. Food Chem.* **2012**, *60*, 749−757.

(14) Li, S.; Chen, L.; Yang, T.; Wu, Q.; Lv, Z.; Xie, B.; Sun, Z. Increasing antioxidant activity of procyanidin extracts from the pericarp of *Litchi chinensis* processing waste by two probiotic bacteria bioconversions. *J. Agric. Food Chem.* **2013**, *61*, 2506−2512.

(15) Cerda, B.; Espin, J. C.; Parra, S.; Martinez, P.; Tomas-Barberan, F. A. The potent in vitro antioxidant ellagitannins from pomegranate juice are metabolised into bioavailable but poor antioxidant hydroxy-6*H*-dibenzopyran-6-one derivatives by the colonic microflora of healthy humans. *Eur. J. Nutr.* **2004**, *43*, 205−220.

(16) Dong, X.; Zou, B.; Zhang, Y.; Ge, Z.; Du, J.; Li, C. Preparation of A-type proanthocyanidin dimers from peanut skins and persimmon pulp and comparison of the antioxidant activity of A-type and B-type dimers. *Fitoterapia* **2013**, *91*, 128−139.

(17) Li, C.; Trombley, J. D.; Schmidt, M. A.; Hagerman, A. E. Preparation of an acid butanol standard from fresh apples. *J. Chem. Ecol.* **2010**, *36*, 453−460.

(18) Seefelder, W. Fumonisins and their reaction products in food: occurence, biological activity and metabolism. PhD Thesis; University of Wuerzburg: Germany, 2003

DOI: 10.1021/acs.jafc.5b03657
J. Agric. Food Chem. 2015, 63, 8991−8998

(19) Re, R.; Pellegrini, N.; Proteggente, A.; Pannala, A.; Yang, M.; Rice-Evans, C. Antioxidant activity applying an improved ABTS radical cation decolorization assay. *Free Radical Biol. Med.* **1999**, *26*, 1231−1237.
(20) van't Slot, G.; Humpf, H.-U. Degradation and metabolism of catechin, epigallocatechin-3-gallate (EGCG), and related compounds by the intestinal microbiota in the pig cecum model. *J. Agric. Food Chem.* **2009**, *57*, 8041−8048.
(21) Stoupi, S.; Williamson, G.; Drynan, J. W.; Barron, D.; Clifford, M. N. A comparison of the in vitro biotransformation of (−)-epicatechin and procyanidin B2 by human faecal microbiota. *Mol. Nutr. Food Res.* **2010**, *54*, 747−759.
(22) Stoupi, S.; Williamson, G.; Drynan, J. W.; Barron, D.; Clifford, M. N. Procyanidin B2 catabolism by human fecal microflora: partial characterization of 'dimeric' intermediates. *Arch. Biochem. Biophys.* **2010**, *501*, 73−78.
(23) Guoqiang, L.; Jing, D.; Hong, W.; Leren, W.; Yuki, H.; ShiZhong, C. ESI fragmentation studies of four tea catechins. *Chem. J. Chinese Univ.* **2009**, *30*, 1566−1570.
(24) Takagaki, A.; Nanjo, F. Metabolism of (−)-epigallocatechin gallate by rat intestinal flora. *J. Agric. Food Chem.* **2010**, *58*, 1313−1321.
(25) Wang, L. Q.; Meselhy, M. R.; Li, Y.; Nakamura, N.; Min, B. S.; Qin, G. W.; Hattori, M. The heterocyclic ring fission and dehydroxylation of catechins and related compounds by *Eubacterium* sp. strain SDG-2, a human intestinal bacterium. *Chem. Pharm. Bull.* **2001**, *49*, 1640−1643.
(26) Shoji, T.; Masumoto, S.; Moriichi, N.; Akiyama, H.; Kanda, T.; Ohtake, Y.; Goda, Y. Apple procyanidin oligomers absorption in rats after oral administration: analysis of procyanidins in plasma using the porter method and high-performance liquid chromatography/tandem mass spectrometry. *J. Agric. Food Chem.* **2006**, *54*, 884−892.
(27) Ou, K.; Sarnoski, P.; Schneider, K. R.; Song, K.; Khoo, C.; Gu, L. Microbial catabolism of procyanidins by human gut microbiota. *Mol. Nutr. Food Res.* **2014**, *58*, 2196−2205.
(28) van't Slot, G.; Mattern, W.; Rzeppa, S.; Grewe, D.; Humpf, H.-U. Complex flavonoids in cocoa: synthesis and degradation by intestinal microbiota. *J. Agric. Food Chem.* **2010**, *58*, 8879−8886.
(29) Takagaki, A.; Nanjo, F. Catabolism of (+)-catechin and (−)-epicatechin by rat intestinal microbiota. *J. Agric. Food Chem.* **2013**, *61*, 4927−4935.
(30) Meselhy, M. R.; Nakamura, N.; Hattori, M. Biotransformation of (−)-epicatecbin 3-*O*-gallate by human intestinal bacteria. *Chem. Pharm. Bull.* **1997**, *45*, 888−893.
(31) Groenewoud, G.; Hundt, H. K. L. The microbial metabolism of condensed (+)-catechins by rat-caecal microflora. *Xenobiotica* **1986**, *16*, 99−107.
(32) Mateos-Martin, M. L.; Perez-Jimenez, J.; Fuguet, E.; Lluis Torres, J. Profile of urinary and fecal proanthocyanidin metabolites from common cinnamon (*Cinnamomum zeylanicum* L.) in rats. *Mol. Nutr. Food Res.* **2012**, *56*, 671−675.
(33) Cueva, C.; Sanchez-Patan, F.; Monagas, M.; Walton, G. E.; Gibson, G. R.; Martin-Alvarez, P. J.; Bartolome, B.; Victoria Moreno-Arribas, M. In vitro fermentation of grape seed flavan-3-ol fractions by human faecal microbiota: changes in microbial groups and phenolic metabolites. *FEMS Microbiol. Ecol.* **2013**, *83*, 792−805.
(34) Sanchez-Patan, F.; Cueva, C.; Monagas, M.; Walton, G. E.; Gibson, G. R.; Martin-Alvarez, P. J.; Victoria Moreno-Arribas, M.; Bartolome, B. Gut microbial catabolism of grape seed flavan-3-ols by human faecal microbiota. Targetted analysis of precursor compounds, intermediate metabolites and end-products. *Food Chem.* **2012**, *131*, 337−347.
(35) Liang, N. N.; He, F.; Pan, Q. H.; Wang, J.; Reeves, M. J.; Duan, C. Q. Optimization of sample preparation and phloroglucinol analysis of Marselan grape skin proanthocyanidins using HPLC-DAD-ESI-MS/MS. *S. Afr. J. Enol. Vitic.* **2012**, *33*, 122−131.
(36) Goodrich, K. M.; Neilson, A. P. Simultaneous UPLC-MS/MS analysis of native catechins and procyanidins and their microbial metabolites in intestinal contents and tissues of male Wistar Furth inbred rats. *J. Chromatogr. B: Anal. Technol. Biomed. Life Sci.* **2014**, *958*, 63−74.
(37) Aura, A.-M.; Mattila, I.; Seppanen-Laakso, T.; Miettinen, J.; Oksman-Caldentey, K.-M.; Oresic, M. Microbial metabolism of catechin stereoisomers by human faecal microbiota: comparison of targeted analysis and a non-targeted metabolomics method. *Phytochem. Lett.* **2008**, *1*, 18−22.
(38) Maldonado, P. D.; Rivero-Cruz, I.; Mata, R.; Pedraza-Chaverri, J. Antioxidant activity of A-type proanthocyanidins from *Geranium niveum* (Geraniaceae). *J. Agric. Food Chem.* **2005**, *53*, 1996−2001.
(39) Zhang, H.; Yerigui; Yang, Y.; Ma, C. Structures and antioxidant and intestinal disaccharidase inhibitory activities of A-type proanthocyanidins from peanut skin. *J. Agric. Food Chem.* **2013**, *61*, 8814−8820.

DOI: 10.1021/acs.jafc.5b03657
J. Agric. Food Chem. 2015, 63, 8991−8998

urine. The chemical structures were characterized on the basis of their MS and MS^2 data. The principal metabolic pathways of salidroside were proposed as well.

MATERIALS AND METHODS

Chemicals. Salidroside was purchased from the National Institutes for Food and Drug Control (Beijing, China). *p*-Tyrosol was purchased from Sigma (St. Louis, MO, USA). HPLC grade acetonitrile and methanol were obtained from Fisher Scientific (Pittsburgh, PA, USA). HPLC grade water was purified by a Millipore Milli-Q purification system via deionized water (Billerica, MA, USA). All other reagents were of reagent grade.

Animals and Drug Administration. Male Wistar rats (200 ± 20 g of body weight) were purchased from the Laboratory Animal Center of Jilin University (Changchun, Jilin Province, China). Animals were handled according to the standard procedures approved by the institutional animal care and use committee. All rats experienced an overnight fasting with free access to water before oral administration. Rats were acclimatized for 1 week before experiments. The rats were divided into three groups: salidroside administration groups (low and high doses) and control group; each group contained three rats. Salidroside dissolved in saline was orally administered to the rats at a single dose of 100 mg/kg of body weight for the Q-TOF-MS detection or at a single dose of 500 mg/kg of body weight for the Q-trap-MS detection. The rats in the control group were administered the solvent saline orally at the same volume as the treatment group.

Sample Collection. Rats were housed in metabolic cages for 3 days. Urine samples were collected at intervals of 0−12, 12−24, 24−48, and 48−72 h after salidroside administration. All samples were stored at −40 °C until further use.

Sample Preparation. Briefly, 600 μL of methanol was added to 200 μL of urine followed by vortexing for 5 min and centrifugation at 15000*g* for 10 min. The supernatant of the sample was transferred to a clean test tube and evaporated to dryness under nitrogen. The residue was redissolved in 200 μL of water, and the supernatant was ready for the injection after centrifugation at 15000*g* for 10 min.

UPLC/Q-TOF-MS Analysis. The analysis was performed on a Waters ACQUITY ultraperformance liquid chromatographic system (Waters Corp., Milford, MA, USA) coupled with a Waters ACQUITY Synapt G2 quadrupole time-of-flight (Q-TOF) tandem mass spectrometer (Waters Corp., Manchester, UK). System control and data acquisition were performed using MassLynx V4.1 software.

Chromatographic separation was achieved on an ACQUITY UPLC HSS T3 column (1.7 μm, 50 mm × 2.1 mm; Waters Corp., Milford, MA, USA). The mobile phase system consisted of acetonitrile (A) and water (B) at a flow rate of 0.25 mL/min. The time program of the gradient was 0−2 min, 0% A; 2−5 min, 0−5% A; 5−10 min, 5−10% A; 10−15 min, 10−80% A; 15−18 min, 80−0% A; 18−20 min, 0% A for equilibration of the column. The column and autosampler temperatures were maintained at 40 and 4 °C, respectively.

Metabolites were detected in negative ionization mode. The optimized MS conditions were as follows: capillary voltage, 2.5 kV; sample cone voltage, 40 V; extraction cone voltage, 4.0 V; source temperature, 120 °C; desolvation temperature, 400 °C; desolvation gas, 800 L/h nitrogen; and cone gas, 50 L/h nitrogen. Argon was used as collision gas. For accurate mass measurement, data were collected in centroid mode, and an external reference (LockSpray) at a concentration of 200 pg/mL in 50% acetonitrile−water solution (including 0.1% formic acid) was employed to generate $[M - H]^-$ ion in negative mode at m/z 554.2615 via a lock spray interface at a flow rate of 5 μL/min to acquire accurate mass during the analysis. MS^E analysis was performed in two scan functions: 5 eV for the low collision energy scan and a collision energy ramp of 10−30 eV for the high-collision energy scan. To get more clean and accurate fragments for each metabolite, MS/MS analysis was performed with a collision energy ramp of 10−25 eV.

HPLC/Q-Trap-MS Analysis. The analysis was performed on a Shimadzu LC 20AD system (Shimadzu, Kyoto, Japan) coupled with an Applied Biosystem Sciex API 4000 Q-trap mass spectrometer (Foster City, CA, USA). The Analyst software package (version 1.6) was used for system control, data acquisition, and processing.

The separation was performed on an Aglient Proshell 120 column (2.7 μm, 100 mm × 2.1 mm; Palo Alto, CA, USA), with mobile phases of water (A) and acetonitrile (B) eluting in the following program: 0−2 min, 2% B; 2−7 min, 5% B; 7−12 min, 5−10% B; 12−13 min, 10−80% B; 13.0−13.1 min, 80−2% B; 13.1−16 min, 2% B. The flow rate was 0.3 mL/min, and the injection volume was 2 μL.

The detection was performed under negative mode with a Turbo VTM Ion Source. Polypropylene glycol dilution solvent was used to turn the ion optics. The optimized MS conditions were as follows: nitrogen as the nebulizer, heater, curtain, and collision gas with nebulizer (GS1), heater (GS2), and curtain gas flow rates of 45, 45, and 25 psi, respectively; ion-spray needle voltage, −4500 V; and heater gas temperature, 550 °C.

Multiple ion monitoring (MIM) mode was utilized to analyze the biological samples. A set of MIM ion transitions of the metabolites detected in Q-TOF-MS were introduced for the detection of potential metabolites of salidroside. The parameters were used as follows: The dwell time, declustering potential, and collision energy of each MIM ion transition were fixed at 30 ms, −40 V, and −10 eV, respectively; CE and collision energy spread (CES) of EPI were fixed at −40 and ±20 eV.

RESULTS AND DISCUSSION

Fragmentation of Salidroside Standard. Because metabolites can retain the base substructure of the parent compound, the first important step in the analysis of metabolites of salidroside in rat urine is to obtain its chromatogram and mass spectrum characterization. All of these data were the substructural "template" for interpreting the structures of the metabolites.

The chromatographic and mass spectrometric conditions were optimized using salidroside. Under negative electrospray ionization mode, the salidroside molecule ($C_{14}H_{20}O_7$, MW = 300.12 Da) could easily form a molecular ion of m/z 299.1127 ($[M - H]^-$). The product ion spectrum of the molecular ion of salidroside and its predominant fragmentation patterns are illustrated in Figure 2. Fragmentation of the molecular ion of salidroside led to four major product ions at m/z 179.0562, 137.0599, 119.0496, and 113.0230. The product ions at m/z 179.0562 ($C_6H_{11}O_6$) and m/z 137.0599 ($C_8H_9O_2$) were ions of glucose and the aglycone *p*-tyrosol produced by the salidroside molecular ion. The product ion at m/z 119.0496 (C_8H_7O) was formed by the loss of a molecule of hydrone from the ion at m/z 137.0599. The product ion at m/z 113.0230 ($C_5H_5O_3$) was inferred to be produced by the loss of one molecule of formaldehyde and two molecules of hydrone from the ion at m/z 179.05629, so it can be concluded that the ions at m/z 179.0562, 137.0599, 119.0496, and 113.0230 were the characteristic product ions of salidroside.

In Vivo Metabolites of Salidroside. Metabolites of salidroside in rat urine were achieved by comparing the data of blank and salidroside-dosed samples. Unique precursor ions found in salidroside-dosed samples were considered as potential metabolites for MS^2 analysis. Eight metabolites were thus identified (M1−M8). The retention times, measured and calculated masses, accurate masses, mass errors, and MS/MS product ions of salidroside (M0) and its speculated metabolites (M1−M8) are summarized in Table 1. The mass errors between the measured and the calculated values were < 6 ppm, which displays a high level of confidence in the compositions of the speculated metabolites. The chemical structures were proposed using MS and MS^2 data.

DOI: 10.1021/acs.jafc.5b04510
J. Agric. Food Chem. 2015, 63, 8999−9005

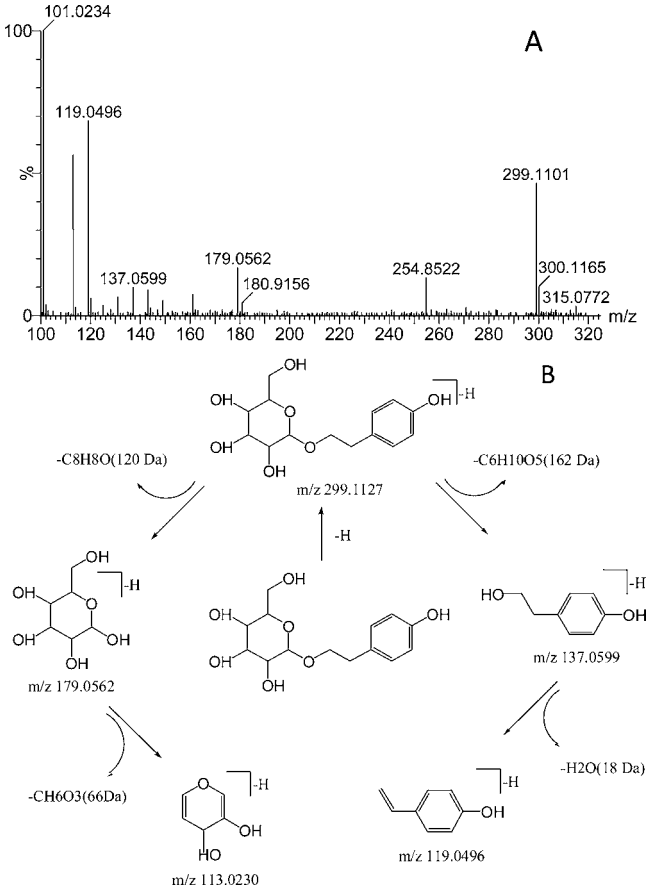

Figure 2. (A) MS^2 spectrum of salidroside; (B) its proposed fragmentation pathways in negative ion mode with m/z 299.11 as the precursor ion.

Parent Drug M0. M0 was identified with an accurate $[M - H]^-$ ion of m/z 299.1127 (−1.3 ppm, $C_{14}H_{19}O_7$). The productions of M0 were identical to those of salidroside standard. Therefore, M0 was designated salidroside.

Metabolite M1. The Q-TOF MS spectrum of M1 provided an accurate $[M - H]^-$ ion at m/z 475.1456 (0.8 ppm, $C_{20}H_{27}O_{13}$), which was 176 Da higher than that of M0. Further Q-TOF MS^2 fragmentation (Figure 3A) showed fragment ions at m/z 175.0741, 137.0607, 113.0231, and 85.0297. The diagnostic ion at m/z 175.0741 was the $[M - H]^-$ ion of glucuronic acid. The product ion at m/z 113.0231 ($C_5H_5O_3$) could be fragmentized from the salidroside fragment ion as well as glucuronic acid molecular ion, displaying a strengthened abundance. The product ion at m/z 85.0297 was the loss of 18 Da (hydrone group) from the ion at m/z 113.0231. Furthermore, another diagnostic fragment ion at m/z 137.0607 was the aglycone *p*-tyrosol, the same as the product ion of parent drug M0. M1 was assessed as the glucuronidated product of M0. The MS^2 fragmentation (Figure 4A) of M1 showed product ions at m/z 313.3 and 299.4 by Q-trap-MS, demonstrating the glucuronidation occurred at the hydroxyl group on the phenyl ring.

Metabolite M2. M2 was detected by Q-TOF-MS with an $[M - H]^-$ ion at m/z 379.0710 (2.9 ppm, $C_{14}H_{19}O_{10}S$), which was 80 Da higher than that of M0, implying sulfation of M0. Q-TOF MS^2 fragmentation (Figure 3B) showed fragment ions at m/z 137.0583, 119.0498, 113.0235, and 79.9576. The diagnostic ion at m/z 79.9576 was the sulfuric acid group; the other product ions were identical with the fragment ions of M0. Accordingly, M2 was structurally identified as the sulfated conjugate of M0. The product ion at m/z 217.0 (Figure 4B) found by Q-trap-MS detection indicated the sulfation at the hydroxyl group on the phenyl ring.

Metabolite M3. Metabolite M3 was detected with an accurate $[M - H]^-$ ion at m/z 137.0607 (2.9 ppm, elemental composition of $C_8H_9O_2$). It was similar to the product ion at m/z 137.0599 of parent drug M0. The product ion at m/z 137.0599 was assigned as the aglycone, according to the structure of salidroside. The Q-TOF MS^2 fragmentations of M3, shown in Figure 3C, were observed at m/z 119.0476, 106.0411, and 93.0329. These two characteristic fragment ions at m/z 119.0476 and 93.0329 were formed by the loss of 18 Da (hydrone group) and 44 Da (vinyl alcohol group) from the $[M - H]^-$ ion at m/z 137.0599, respectively. The MS^2 product ion at m/z 106.0411 was formed by the loss of 13 Da (methenyl group) from the fragment ion at m/z 119.0476. According to our previous study, we also found the product ion at m/z 106.0411 from the aglycone standard.[18] Hence, M3 was identified as *p*-tyrosol, the aglycone of M0.

Metabolite M4. The Q-TOF MS spectrum of M4 (Figure 3D) provided an accurate $[M - H]^-$ ion at m/z 313.0927 (1.3 ppm, $C_{14}H_{17}O_8$), which was 176 Da (glucuronic acid group) higher than that of M3. Three major fragment ions were found at m/z 175.0241 (the $[M - H]^-$ ion of glucuronic acid), 137.0607 ($[M - H]^-$ ion of the aglycone *p*-tyrosol), and 113.0231 ($C_5H_5O_3$). According to the Q-trap MS^2 spectrum of M4 (Figure 4C), the product ion at m/z 295.1 indicated the glucuronidation was at the hydroxyl group on the phenyl ring.

Table 1. Retention Times, Measured and Calculated Masses, Accurate Masses, and MS/MS Product Ions of Salidroside (M0) and Its Metabolites (M1−M8)

metabolite	retention time (min)	elemental composition	measured mass $[M - H]^-$ (m/z)	predicted mass $[M - H]^-$ (m/z)	error (ppm)	fragment ions (m/z)	metabolite description
M0	7.23	$C_{14}H_{20}O_7$	299.1127	299.1131	−1.3	179.0562, 137.0599, 119.0496, 113.0230	null
M1	1.90	$C_{20}H_{28}O_{13}$	475.1456	475.1452	+0.8	175.0741, 137.0607, 113.0231	+ GlcA
M2	3.18	$C_{14}H_{20}O_{10}S$	379.0710	379.0699	+2.9	137.0583, 119.0498, 113.0235, 101.0231, 79.9576	+ SO_3
M3	6.87	$C_8H_{10}O_2$	137.0607	137.0603	+2.9	119.0476, 106.0411	− Glc
M4	0.97	$C_{14}H_{18}O_8$	313.0927	313.0923	+1.3	175.0241, 137.0607, 113.0231	− Glc + GlcA
M5	2.17	$C_8H_{10}O_5S$	217.0161	217.0171	−4.6	137.0607, 79.9576	− Glc + SO_3
M6	4.37	$C_8H_{10}O_6S$	233.0107	233.0120	−5.6	153.0551, 123.0433, 79.9558	− Glc + SO_3 + OH
M7	4.21	$C_9H_{12}O_5S$	231.0336	231.0327	+3.9	151.0757, 79.9576	− Glc + SO_3 + CH_3
M8	4.54	$C_{14}H_{18}0_7$	297.0985	297.0974	+3.7	175.0241, 121.0642, 113.0231	− Glc + GlcA − OH

DOI: 10.1021/acs.jafc.5b04510
J. Agric. Food Chem. 2015, 63, 8999−9005

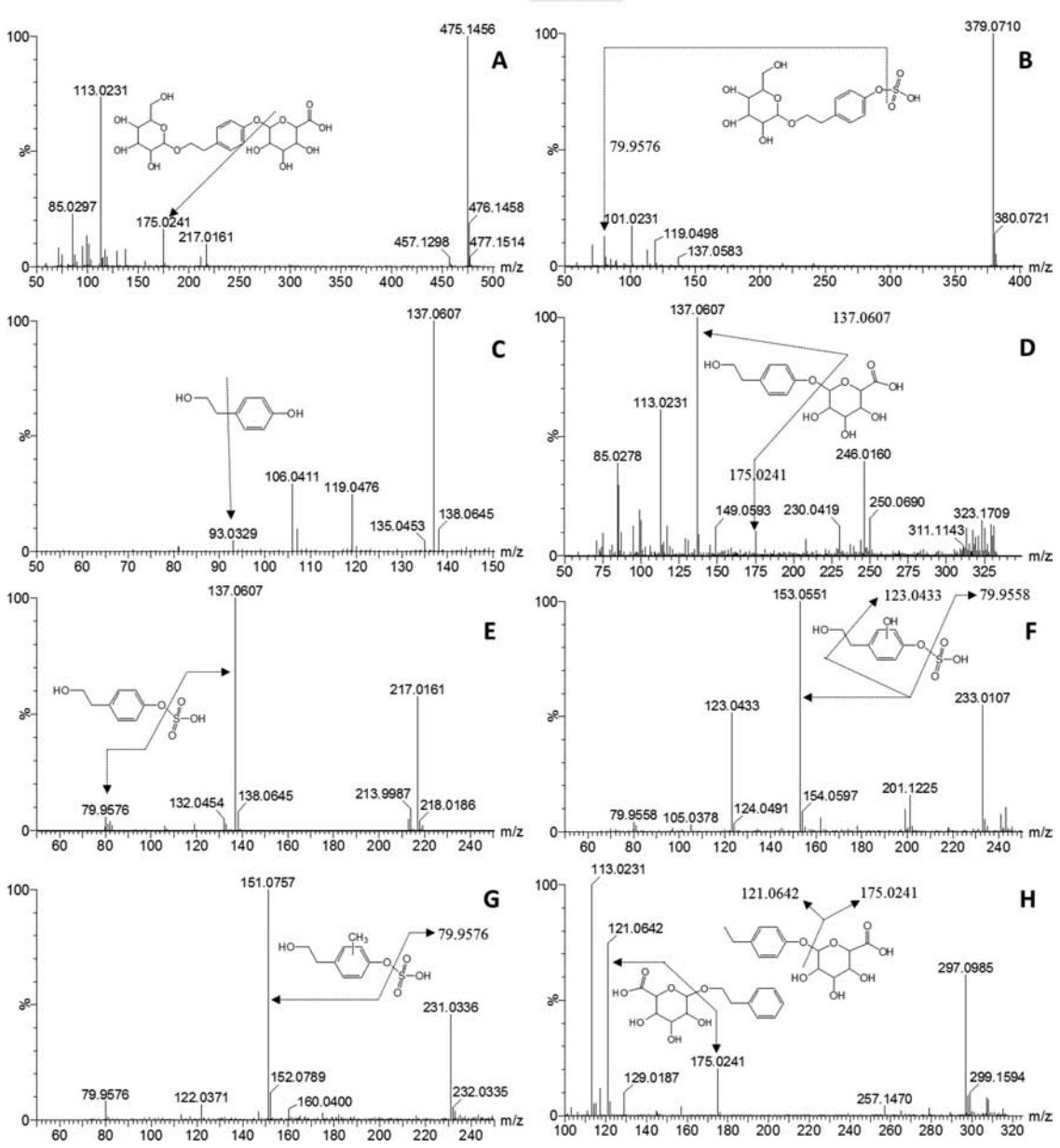

Figure 3. MS^2 spectra of metabolites M1 (A), M2 (B), M3 (C), M4 (D), M5 (E), M6 (F), M7 (G), and M8 (H) by UPLC/Q-TOF-MS. The MS^2 data were obtained with $[M - H]^-$ as the precursor ion.

M4 was identified as the glucuronidated product of M3 or the deglycosylation product of M1.

Metabolite M5. Metabolite M5 (Figure 3E) was detected with an accurate $[M - H]^-$ ion at m/z 217.0161 (−4.6 ppm, $C_8H_9O_5S$), which was 80 Da higher than that of M3, suggesting a sulfuric acid group was conjugated to M3. Fragment ions at m/z 137.0583 and 79.9576 of the Q-TOF MS^2 fragmentation also proved the existence of the aglycone and sulfate. The product ion at m/z 173.1 (Q-trap MS^2 spectrum, Figure 4D) of M5 indicated the sulfation was at the hydroxyl group on the phenyl ring. Therefore, M5 was the product from the sulfation of M3 or the deglycosylation of M2.

Metabolite M6. M6 (Figure 3F) was detected with an accurate $[M - H]^-$ ion at m/z 233.0107 (−5.6 ppm, $C_8H_9O_6S$). The molecular ion at m/z 233.0107 was 16 Da more than m/z 217.0161(M5), which suggested that M6 was a hydroxylation metabolite of M5. The fragment ion of M6 at m/z 153.0551 was also 16 Da more than the product ion at m/z 137.0583, and the ion at m/z 123.0433 was a further loss of hydroxymethyl (OCH_2) from the side chain of the ion at m/z 153.0551. The existence of 123.0433 proved that the hydroxylation occurred on the phenyl ring. The product ion at m/z 189.1 (Q-trap MS^2 spectrum, Figure 4E) of M6 further confirmed the sulfation position, the same as M5, was at the hydroxyl group on the phenyl ring. Hence, M6 was characterized as the hydroxylation product of M5.

Metabolite M7. The Q-TOF MS spectrum of M7 provided an accurate $[M - H]^-$ ion at m/z 231.0336 (3.9 ppm, $C_9H_{11}O_5S$). MS^2 fragmentation (Figure 3G) showed fragment ions at m/z 151.0757 and 79.9576. The molecular ion at m/z 231.0336 and its MS^2 fragment ion at m/z 151.0757 were 14 Da more than m/z 217.0161 (M5) and its product ion at m/z 137.0583. According to product ions at m/z 187.0 and 213.2 of M7 (Q-trap MS^2 spectrum Figure 4F), the position of

DOI: 10.1021/acs.jafc.5b04510
J. Agric. Food Chem. 2015, 63, 8999−9005

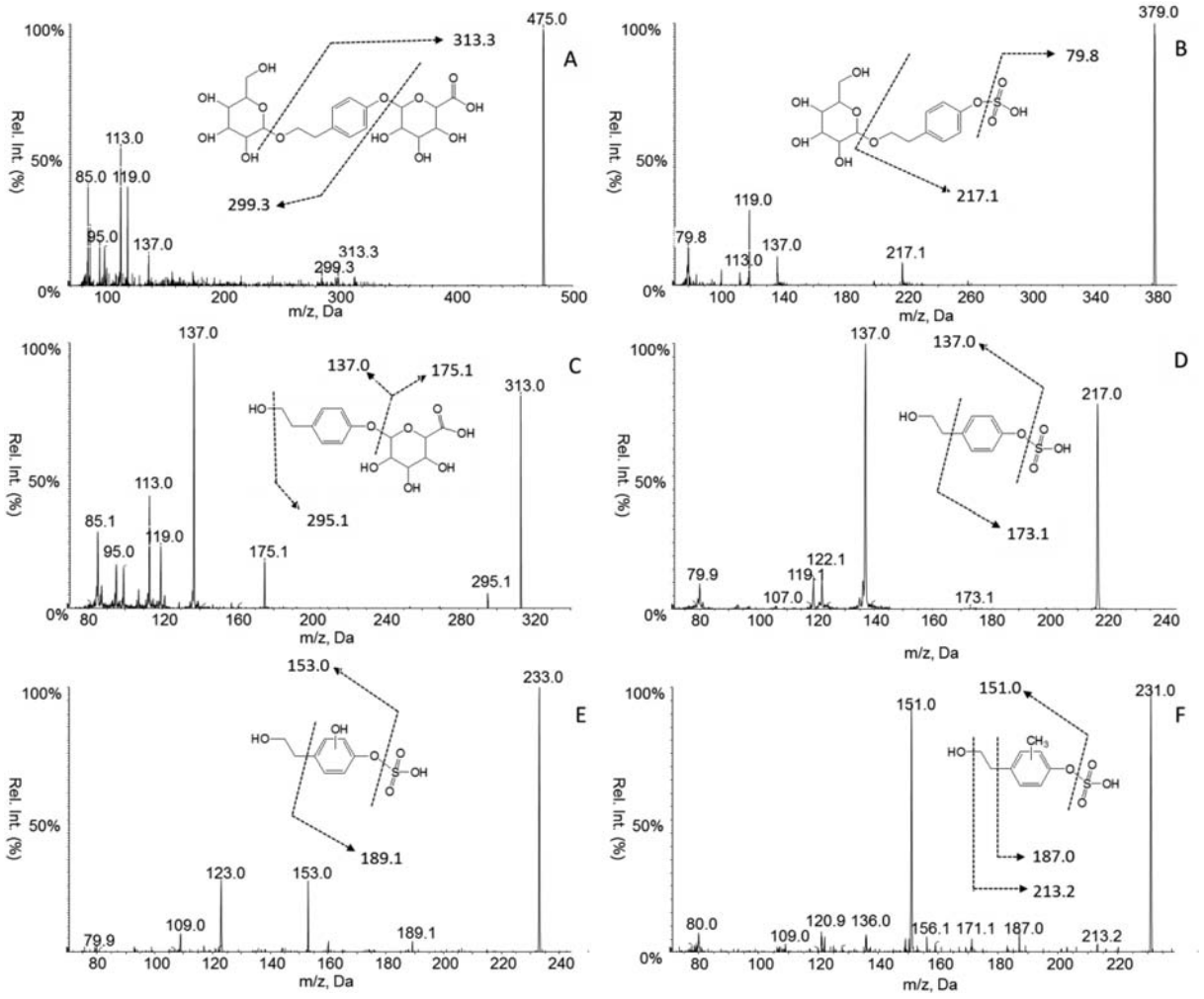

Figure 4. MS^2 spectra of metabolites M1 (A), M2 (B), M4 (C), M5 (D), M6 (E), and M7 (F) by HPLC/Q-trap-MS.

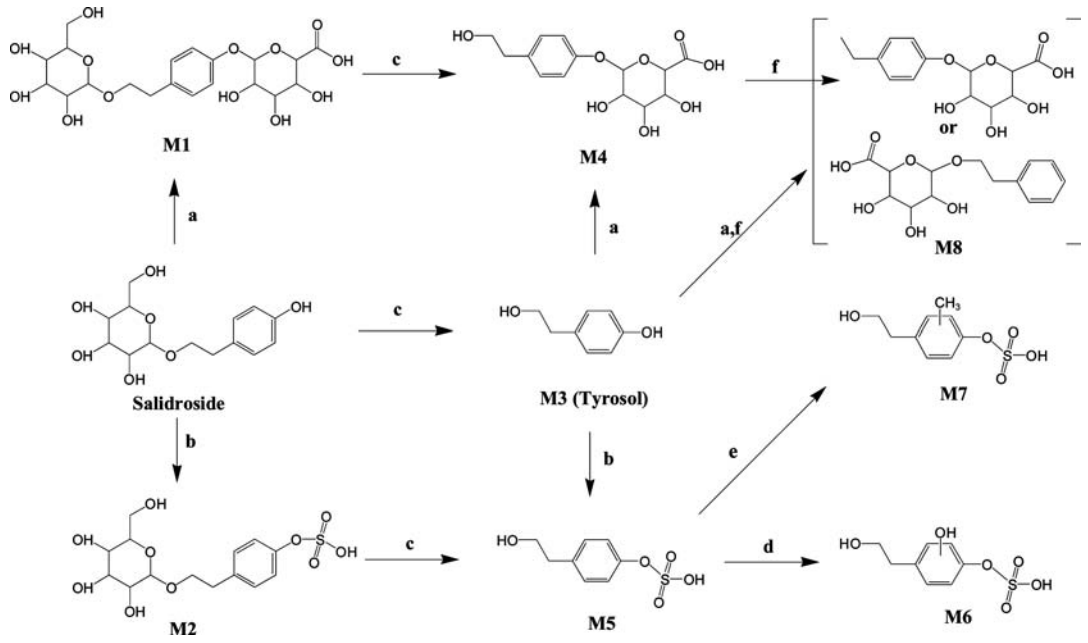

Figure 5. Proposed metabolite structures and predicted salidroside metabolic pathway: (a) glucuronidation; (b) sulfation; (c) deglycosylation; (d) hydroxylation; (e) methylation; (f) dehydroxylation.

DOI: 10.1021/acs.jafc.5b04510
J. Agric. Food Chem. 2015, 63, 8999−9005

methylation can only be asserted on the phenyl ring, and the sulfation occurred at the hydroxyl group on the phenyl ring. Hence, M7 was characterized as the methylation product of M5.

Metabolite M8. M8 (Figure 3H) was detected at 4.54 min and with an accurate $[M - H]^-$ ion at m/z 297.0985 (3.7 ppm, $C_{14}H_{17}O_7$), Further MS^2 fragmentation (Figure 3H) showed fragment ions at m/z 175.0241, 121.0642, and 113.0231. The molecular ion at m/z 297.0985 and its MS^2 fragment ion at m/z 121.0642 were 16 Da less than m/z 313.0923 (M4) and its product ion at m/z 137.0583, suggesting M8 was the dehydroxylation product of metabolite M4. The diagnostic ions of glucuronic acid at m/z 175.0741 and 113.0231 were detected, further proving the glucuronidation. We failed to get the signals of M8 by Q-trap MS detection. We could not identify the exact position of dehydroxylation.

Metabolic Pathways of Salidroside in Rats. In the present study, metabolites in rat urine samples after oral administration of salidroside were detected and identified through UPLC/Q-TOF-MS and HPLC/Q-trap-MS. Eight metabolites have been characterized in the urine samples within 12 h after oral administration; most of these metabolites could not be detected after 12 h. *p*-Tyrosol (M3) was the only phase I metabolite detected, formed by deglycosylation of salidroside. Two phase II metabolites of salidroside were derived from glucuronidation (M1) and sulfation (M2). The other metabolites were phase II metabolites of *p*-tyrosol, including the direct glucuronidation (M4) and sulfation (M5) products. Puzzlingly, the sulfation of hydroxylated (M6) and methylated (M7) *p*-tyrosol and the glucuronidation of dehydroxylated *p*-tyrosol (M8) were identified, whereas the corresponding phase I metabolites were not detected. A possible explanation is that salidroside metabolizes to *p*-tyrosol, which probably experienced hydroxylation, methylation, and dehydroxylation in vivo and the phase I products readily converted to phase II metabolites M6, M7, and M8. We also tested the feces samples, but no metabolite was found. In our previous study, *p*-tyrosol was found in urine samples but not in plasma and feces samples after oral administration, which is consistent with our present results.[18,26] The possible structures of metabolites and predicted metabolic pathway are speculated in Figure 5.

In summary, salidroside and its deglycosylation phase I metabolite *p*-tyrosol were further metabolized to glucuronidation and sulfation products and mainly excreted through the urine excretion pathway.

AUTHOR INFORMATION

Corresponding Author

*(Y.W.) Phone/fax: +86-451-82190052. E-mail: ywang1971@hotmail.com.

Funding

This research was financially supported by the Fundamental Research Funds for the Central Universities (DL13EA02) and Heilongjiang Provincial Natural Science Foundation of China (C201139).

Notes

The authors declare no competing financial interest.

ACKNOWLEDGMENTS

We are grateful to Ting Liu and Zhimin Long from SCIEX Shanghai Application Support Center for performing the Q-trap MS analysis.

REFERENCES

(1) Khanum, F.; Bawa, A. S.; Singh, B. *Rhodiola rosea*: a versatile adaptogen. *Compr. Rev. Food Sci. Food Saf.* **2005**, *4*, 55−62.

(2) Platikanov, S.; Evstatieva, L. Introduction of wild golden root (*Rhodiola rosea* L.) as a potential economic crop in Bulgaria. *Econ Bot.* **2008**, *62*, 621−627.

(3) Furmanowa, M.; Kedzia, B.; Hartwich, M.; Kozlowski, J.; Krajewska-Patan, A.; Mscisz, A.; Jankowiak, J. Phytochemical and pharmacological properties of *Rhodiola rosea* L. *Herba Pol.* **1999**, *45*, 108−113.

(4) Ye, Y. C.; Chen, Q. M.; Jin, K. P.; Zhou, S. X.; Chai, F. L.; Hai, P. Effect of salidroside on cultured myocardial cells anoxia/reoxygenation injuries. *Acta Pharmacol. Sin.* **1993**, *14*, 424−426.

(5) Hu, X. L.; Lin, S. X.; Yu, D. H.; Qiu, S. F.; Zhang, X. Q.; Mei, R. H. A preliminary study: the anti-proliferation effect of salidroside on different human cancer cell lines. *Cell Biol. Toxicol.* **2010**, *26*, 499−507.

(6) Fang, D. L.; Chen, Y.; Xu, B.; Ren, K.; He, Z. Y.; He, L. L.; Lei, Y.; Fan, C. M.; Song, X. R. Development of lipid-shell and polymer core nanoparticles with water-soluble salidroside for anti-cancer. *Int. J. Mol. Sci.* **2014**, *15*, 3373−3388.

(7) Wang, J.; Li, J. Z.; Lu, A. X.; Zhang, K. F.; Li, B. J. Anticancer effect of salidroside on A549 lung cancer cells through inhibition of oxidative stress and phospho-p38 expression. *Oncol. Lett.* **2014**, *7*, 1159−1164.

(8) Lanza, A. M. D.; Martinez, M. J. A.; Matellano, L. F.; Carretero, C. R.; Castillo, L. V.; Sen, A. M. S.; Benito, P. B. Lignan and phenylpropanoid glycosides from *Phillyrea latifolia* and their *in vitro* anti-inflammatory activity. *Planta Med.* **2001**, *67*, 219−223.

(9) Qian, E. W.; Ge, D. T.; Kong, S. K. Salidroside protects human erythrocytes against hydrogen peroxide-induced apoptosis. *J. Ethnopharmacol.* **2011**, *133*, 308−314.

(10) Zhang, L.; Yu, H. X.; Sun, Y.; Lin, X. F.; Chen, B.; Tan, C.; Cao, G. X.; Wang, Z. W. Protective effects of salidroside on hydrogen peroxide-induced apoptosis in SH-SY5Y human neuroblastoma cells. *Eur. J. Pharmacol.* **2007**, *564*, 18−25.

(11) Wu, Y. L.; Piao, D. M.; Han, X. H.; Nan, J. X. Protective effects of salidroside against acetaminophen-induced toxicity in mice. *Biol. Pharm. Bull.* **2008**, *31*, 1523−1529.

(12) Mao, G. X.; Deng, H. B.; Yuan, L. G.; Li, D. D.; Yvonne Li, Y. Y.; Wang, Z. Protective role of salidroside against aging in a mouse model induced by D-galactose. *Biomed. Environ. Sci.* **2010**, *23*, 161−166.

(13) Wang, H. B.; Ding, Y. Y.; Zhou, J.; Sun, X. L.; Wang, S. W. The *in vitro* and *in vivo* antiviral effects of salidroside from *Rhodiola rosea* L. against coxsackievirus B3. *Phytomedicine* **2009**, *16*, 146−155.

(14) Li, T. L.; Xu, G. H.; Wu, L. L.; Sun, C. Y. Pharmacological studies on the sedative and hypnotic effect of salidroside from the Chinese medicinal plant *Rhodiola sachalinensis*. *Phytomedicine* **2007**, *14*, 601−604.

(15) Mao, Y.; Zhang, X. R.; Zhang, X. D.; Lu, G. C. Development of an HPLC method for the determination of salidroside in beagle dog plasma after administration of salidroside injection: application to a pharmacokinetics study. *J. Sep. Sci.* **2007**, *30*, 3218−3222.

(16) Chang, Y. W.; Yao, H. T.; Hsieh, S. H.; Lu, T. J.; Ye, T. K. Quantitative determination of salidroside in rat plasma by on-line solid-phase extraction integrated with high-performance liquid chromatography/electrospray ionization tandem mass spectrometry. *J. Chromatogr. B: Anal. Technol. Biomed. Life Sci.* **2007**, *857*, 164−169.

(17) Yu, S.; Liu, L.; Wen, T.; Liu, Y. C.; Wang, D. L.; He, Y. X.; Liang, Y.; Liu, X. D.; Xie, L.; Wang, G. J.; Wei, W. Z. Development and validation of a liquid chromatographic/electrospray ionization mass spectrometric method for the determination of salidroside in rat

DOI: 10.1021/acs.jafc.5b04510
J. Agric. Food Chem. 2015, 63, 8999−9005

plasma: application to the pharmacokinetics study. *J. Chromatogr. B: Anal. Technol. Biomed. Life Sci.* **2008**, *861*, 10−15.
(18) Guo, N.; Hu, Z. W.; Fan, X. X.; Zheng, J.; Zhang, D. H.; Xu, T.; Yu, T.; Wang, Y.; Li, H. Y. Simultaneous determination of salidroside and its aglycone metabolite *p*-tyrosol in rat plasma by liquid chromatography-tandem mass spectrometry. *Molecules* **2012**, *17*, 4733−4754.
(19) Zhang, Y.; Li, L. Q.; Lin, L.; Liu, J. X.; Zhang, Z. H.; Xu, D. J.; Xiang, F. J. Pharmacokinetics, tissue distribution, and excretion of salidroside in rats. *Planta Med.* **2013**, *79*, 1429−1433.
(20) Vissers, M. N.; Zock, P. L.; Roodenburg, A. J.; Leenen, R.; Katan, M. B. Olive oil phenols are absorbed in humans. *J. Nutr.* **2002**, *132*, 409−417.
(21) Corona, G.; Tzounis, X.; Assunta, D. M.; Deiana, M.; Debnam, E. S.; Visioli, F.; Spencer, J. P. The fate of olive oil polyphenols in the gastrointestinal tract: implications of gastric and colonic microflora-dependent biotransformation. *Free Radical Res.* **2006**, *40*, 647−658.
(22) Mateos, R.; Goya, L.; Bravo, L. Metabolism of the olive oil phenols hydroxytyrosol, tyrosol, and hydroxytyrosyl acetate by human hepatoma HepG2 cells. *J. Agric. Food Chem.* **2005**, *53*, 9897−9905.
(23) Guo, J. M.; Xue, C. F.; Shang, E. X.; Duan, J. A.; Tang, Y. P.; Qian, D. W. Identification of hyperoside metabolites in rat using ultra performance liquid chromatography/quadrupole-time-of-flight mass spectrometry. *J. Chromatogr. B: Anal. Technol. Biomed. Life Sci.* **2011**, *879*, 1987−1992.
(24) Cui, L.; Sun, E.; Zhang, Z. H.; Qian, Q.; Tan, X. B.; Xu, F. J.; Jia, X. B. Metabolite profiles of epimedin B in rats by ultra performance liquid chromatography/ quadrupole-time-of-flight mass spectrometry. *J. Agric. Food Chem.* **2013**, *61*, 3589−3599.
(25) Xia, Y. Q.; Miller, J. D.; Bakhtiar, R.; Franklin, R. B.; Liu, D. Q. Use of a quadrupole linear ion trap mass spectrometer in metabolite identification and bioanalysis. *Rapid Commun. Mass Spectrom.* **2003**, *17*, 1137−1145.
(26) Guo, N.; Zhu, M. X.; Han, X. J.; Sui, D.; Wang, Y.; Yang, Q. The metabolism of salidroside to its aglycone *p*-tyrosol in rats following the administration of salidroside. *PLoS One* **2014**, *9*, e103648.

DOI: 10.1021/acs.jafc.5b04510
J. Agric. Food Chem. 2015, 63, 8999−9005

Table 1. ^{1}H (400 MHz) and ^{13}C NMR (100 MHz) Spectroscopic Data for Compounds 1 and 2 (δ ppm in $CDCl_3$ and J in Hz)[a]

	1			2		
position	δ_H	δ_C		δ_H	δ_C	
1	3.93 m	64.0	CH_2	3.93 m	64.2	CH_2
2	1.25 m, 1.43 m	26.5	CH_2	1.25 m, 1.42 m	26.5	CH_2
3	1.01 m, 1.29 m	31.0	CH_2	1.02 m, 1.26 m	31.1	CH_2
4	2.69 m	33.0	CH	2.69 m	33.0	CH
5		132.2	C		132.0	C
6	5.19 d (1.8)	69.1	CH	5.22 d (1.8)	68.9	CH
7	3.46 m	42.9	CH	3.48 m	42.8	CH
8	4.94 ddd (7.8, 3.9, 2.1)	74.9	CH	4.94 ddd (7.8, 3.8, 2.1)	75.0	CH
9	2.47 m, 2.68 m	34.6	CH_2	2.48 m, 2.72 m	34.6	CH_2
10		133.6	C		133.7	C
11		136.3	C		136.3	C
12		169.5	C		169.5	C
13	5.94 d (2.4), 6.37 d (2.7)	124.9	CH_2	5.95 d (2.3), 6.37 d (2.7)	124.9	CH_2
14	1.81 s	20.5	CH_3	1.81 s	20.5	CH_3
15	0.86 d (6.9)	18.6	CH_3	0.88 d (6.8)	18.5	CH_3
1′		177.0	C		173.2	C
2′	2.47 m	34.0	CH	2.09 m, 2.30 m	41.6	CH_2
3′	1.14 d (6.8)	18.8	CH_3	1.86 m	31.9	CH
4′	1.16 d (6.8)	18.9	CH_3	1.21 m, 1.37 m	29.2	CH_2
5′				0.89 t (6.8)	11.2	CH_3
6′				0.88 d (6.8)	19.2	CH_3
1″		177.3	C		171.2	C
2″	2.47 m	34.2	CH	2.04 s	20.9	CH_3
3″	1.14 d (6.8)	19.0	CH_3			
4″	1.16 d (6.8)	19.0	CH_3			

[a]The assignments were based on DEPT and 2D NMR experiments.

(ODS) (MeOH in H_2O, from 81 to 92%) to yield three subfractions ($F_{2\text{-}1}$–$F_{2\text{-}3}$). $F_{2\text{-}1}$ was purified by HPLC (80% MeOH in H_2O) to obtain compound **1** (t_R = 42 min, 5.9 mg). Fraction F_3 afforded seven subfractions $F_{3\text{-}1}$–$F_{3\text{-}7}$ through the same MPLC (MeOH in H_2O, 78–94%). The further purification of $F_{3\text{-}2}$ afforded compounds **2** (t_R = 29 min, 69.4 mg) and **5** (t_R = 19 min, 7.6 mg) using the above HPLC system (84% MeOH in H_2O). Fraction F_4 (7 g) was fractioned on the same MPLC (76–92% MeOH in H_2O) to afford four subfractions $F_{4\text{-}1}$–$F_{4\text{-}4}$, and $F_{4\text{-}1}$ purified by the HPLC system (65% MeOH in H_2O) afforded compound **6** (t_R = 53 min, 14.2 mg). Fraction F_5 was chromatographed on MPLC (74–93% MeOH in H_2O) to give five subfractions $F_{5\text{-}1}$–$F_{5\text{-}5}$. The further purification of $F_{5\text{-}3}$ by HPLC (83% MeOH in H_2O) gave compound **7** (t_R = 23 min, 13.3 mg), while $F_{5\text{-}4}$ purified using HPLC (89% MeOH in H_2O) yielded compounds **3** (t_R = 22 min, 23.9 mg) and **4** (t_R = 35 min, 24.1 mg). On the basis of a similar procedure, fraction F_6 afforded seven subfractions $F_{6\text{-}1}$–$F_{6\text{-}7}$, and compound **8** (t_R = 16 min, 12.9 mg) was isolated from $F_{6\text{-}3}$ (84% MeOH in H_2O); fraction F_8 afforded eight subfractions $F_{8\text{-}1}$–$F_{8\text{-}8}$, and compounds **9** (t_R = 14 min, 17.8 mg) and **10** (t_R = 25 min, 20.8 mg) were isolated from $F_{8\text{-}4}$ (75% MeOH in H_2O).

(4*S*,6*S*,7*S*,8*R*)-1,6-*O*,*O*-Diisobutyrylbritannilactone (1). Yellow oil. $[\alpha]_D^{23}$: −18.8 (*c* 0.11, CH_2Cl_2). ECD (CH_3CN): 193 ($\Delta\varepsilon$ 1.50), 213 ($\Delta\varepsilon$ −5.64). IR (KBr) ν_{max}: 3423, 2957, 2924, 2871, 2851, 1766, 1731, 1662, 1464, 1403, 1378, 1347, 1320, 1274, 1191, 1154, 1038, 975, 946, 892, 853, 817, 760, 722, 638 cm^{-1}. ^{1}H NMR (400 MHz, $CDCl_3$) and ^{13}C NMR (100 MHz, $CDCl_3$) data: see Table 1. ESIMS *m*/*z*: 407 $[M + H]^+$. HR-ESIMS *m*/*z*: 407.2431 $[M + H]^+$, calcd for $C_{23}H_{35}O_6$ 407.2434.

(4*S*,6*S*,7*S*,8*R*)-1-*O*-Acetyl-6-*O*-(3-methylvaleryloxy)-britannilactone (2). Yellow oil. $[\alpha]_D^{23}$: −20.2 (*c* 0.16, CH_2Cl_2). ECD (CH_3CN): 193 ($\Delta\varepsilon$ 3.59), 212 ($\Delta\varepsilon$ −17.59). IR (KBr) ν_{max}: 3446, 2959, 2925, 2874, 2852, 1766, 1732, 1663, 1463, 1402, 1380, 1366, 1318, 1243, 1179, 1153, 1034, 976, 949, 893, 818, 637, 607 cm^{-1}. ^{1}H NMR (400 MHz, $CDCl_3$) and ^{13}C NMR (100 MHz, $CDCl_3$) data: see Table 1. ESIMS *m*/*z*: 429 $[M + Na]^+$. HR-ESIMS *m*/*z*: 429.2245 $[M + Na]^+$, calcd for $C_{23}H_{34}NaO_6$ 429.2253.

Japonicone U (3). Yellow oil. $[\alpha]_D^{23}$: +10.6 (*c* 0.23, CH_2Cl_2). ECD (CH_3CN): 212 ($\Delta\varepsilon$ −18.74), 238 ($\Delta\varepsilon$ 3.03). IR (KBr) ν_{max}: 3441, 2956, 2924, 2869, 2852, 1770, 1732, 1683, 1462, 1377, 1235, 1164, 1029, 984, 953, 916, 850, 816, 752, 633 cm^{-1}. ^{1}H NMR (400 MHz, $CDCl_3$) and ^{13}C NMR (100 MHz, $CDCl_3$) data: see Table 2. ESIMS *m*/*z*: 689 $[M + Na]^+$. HR-ESIMS *m*/*z*: 689.3299 $[M + Na]^+$, calcd for $C_{38}H_{50}NaO_{10}$ 689.3302.

Japonicone V (4). Yellow oil. $[\alpha]_D^{23}$: +13.0 (*c* 0.19, CH_2Cl_2). ECD (CH_3CN): 211 ($\Delta\varepsilon$ −20.36), 237 ($\Delta\varepsilon$ 3.10). IR (KBr) ν_{max}: 3443, 2956, 2924, 2869, 2852, 1770, 1732, 1670, 1463, 1377, 1236, 1166, 1126, 1085, 1030, 984, 919, 903, 815, 723, 701, 675, 633 cm^{-1}. ^{1}H NMR (400 MHz, $CDCl_3$) and ^{13}C NMR (100 MHz, $CDCl_3$) data: see Table 2. ESIMS *m*/*z*: 717 $[M + Na]^+$. HR-ESIMS *m*/*z*: 717.3613 $[M + Na]^+$, calcd for $C_{40}H_{54}NaO_{10}$ 717.3615.

Computational Methods. The calculated ECD spectra were obtained according to the published methods previously.[12,15,16]

Antiproliferative Activities. The antiproliferative activities of compounds **1**–**10** were evaluated by the 3-(4,5-dimethylthiazol-2-yl)-2,5-diphenyltetrazolium bromide (MTT) assay. Cells (1×10^4/well) were incubated for 48 h in the absence or presence of the tested compounds. Then, cells were incubated for another 4 h after adding MTT solution [5 mg/mL in phosphate-buffered saline (PBS)], and the formazan crystals were solubilized with dimethyl sulfoxide (DMSO). The absorbance was determined at 490 nm using a microplate reader (Thermo Fisher Scientific, Inc., Waltham, MA). Etoposide was used as a positive control. The experiments were performed in triplicate.

RESULTS AND DISCUSSION

Column chromatography (silica gel, MPLC, and HPLC) separation of the ethyl acetate layer from the methanol extract of the flowers of *I. japonica* afforded two new 1,10-*seco*-

DOI: 10.1021/acs.jafc.5b03075
J. Agric. Food Chem. 2015, 63, 9006–9011

Table 2. ^{1}H (400 MHz) and ^{13}C NMR (100 MHz) Spectroscopic Data for Compounds 3 and 4 (δ ppm in $CDCl_3$ and J in Hz)[a]

	3			4		
position	δ_H	δ_C		δ_H	δ_C	
1	3.95 m, 4.05 m	64.1	CH_2	3.95 m, 4.05 m	64.1	CH_2
2	1.38 m, 1.52 m	26.8	CH_2	1.38 m, 1.52 m	26.8	CH_2
3	1.26 m	31.8	CH_2	1.26 m	31.9	CH_2
4	2.64 m	33.8	CH	2.65 m	33.9	CH
5		133.1	C		133.0	C
6	5.56 s	65.9	CH	5.58 s	65.8	CH
7	2.51 m	49.4	CH	2.51 m	49.5	CH
8	4.98 m	75.5	CH	4.98 m	75.6	CH
9	2.33 m, 2.62 m	34.8	CH_2	2.33 m, 2.63 m	34.7	CH_2
10		134.0	C		134.0	C
11		55.2	C		55.2	C
12		177.4	C		177.4	C
13	2.05 m, 2.40 m	35.1	CH_2	2.05 m, 2.40 m	35.1	CH_2
14	1.80 s	20.8	CH_3	1.80 s	20.8	CH_3
15	0.86 d (6.9)	18.9	CH_3	0.89 d (7.0)	19.4	CH_3
1′		63.1	C		63.1	C
2′	4.57 s	81.3	CH	4.56 s	81.3	CH
3′	2.77 m	57.7	CH	2.78 m	57.6	CH
4′		134.2	C		134.1	C
5′		136.9	C		136.9	C
6′	2.05 m, 2.98 m	26.0	CH_2	2.05 m, 2.98 m	26.0	CH_2
7′	2.85 m	45.0	CH	2.85 m	45.0	CH
8′	4.21 m	82.6	CH	4.21 m	82.6	CH
9′	2.35 m, 2.05 m	36.0	CH_2	2.35 m, 2.05 m	36.0	CH_2
10′	2.23 m	29.7	CH	2.23 m	29.7	CH
11′		139.7	C		139.7	C
12′		170.2	C		170.2	C
13′	6.21 d (3.3), 5.52 d (3.0)	119.2	CH_2	6.21 d (3.2), 5.52 d (3.0)	119.2	CH_2
14′	1.03 d (7.2)	17.0	CH_3	1.03 d (7.2)	17.0	CH_3
15′	1.63 s	14.3	CH_3	1.63 s	14.3	CH_3
1″		171.1	C		171.1	C
2″	1.97 s	20.9	CH_3	1.98 s	20.9	CH_3
1‴		175.7	C		172.1	C
2‴	2.33 m	34.1	CH	2.18 m, 2.22 m	41.6	CH_2
3‴	1.11 d (6.9)	18.7	CH_3	1.31 m	31.6	CH
4‴	1.11 d (6.9)	18.5	CH_3	1.23 m, 1.31 m	29.2	CH_2
5‴				0.86 t (7.4)	11.2	CH_3
6‴				0.88 d (7.0)	18.5	CH_3
1⁗		170.8	C		170.8	C
2⁗	2.03 s	21.1	CH_3	2.03 s	20.9	CH_3

[a]The assignments were based on DEPT and 2D NMR experiments.

eudesmanolide derivatives **1** and **2**, two new sesquiterpene lactone dimers **3** and **4**, and six known analogues **5**−**10** (Figure 1). The known compounds were identified as 1-*O*-acetyl-6-*O*-isobutyrylbritannilactone (**5**),[17] 1,6-*O*,*O*-diacetylbritannilactone (**6**),[17] 6-*O*-(3-methylvaleryloxy)britannilactone (**7**),[4] 6-*O*-isobutyryl britannilactone (**8**),[4] 1-*O*-acetyl-britannilactone (**9**),[17] and inulanolide A (**10**).[18]

Compound **1** was obtained as yellow oil, and its molecular formula was deduced to be $C_{23}H_{34}O_6$ by HR-ESIMS (HR-ESIMS m/z 407.2431 $[M + H]^+$, calcd for $C_{23}H_{35}O_6$ 407.2434), suggesting seven unsaturation degrees. The IR spectrum of compound **1** showed strong absorption bands of olefinic (1662 cm^{-1}), carbonyl (1731 cm^{-1}), γ-lactone (1766 cm^{-1}), and hydroxy (3423 cm^{-1}) groups. The ^{1}H NMR spectrum (Table 1) showed the presence of an *exo*-methylene at δ_H 5.94 (d 2.4) and 6.37 (d 2.7), two oxygenated methine protons at δ_H 5.19 (d 1.8) and 4.94 (ddd 7.8, 3.9, and 2.1), an oxygenated methylene proton at δ_H 3.93 (m), and six methyl protons at δ_H 0.86 (3H, d, 6.9), 1.14 (6H, d, 6.8), 1.16 (6H, d, 6.8), and 1.81 (3H, s). The ^{13}C NMR spectrum (Table 1) of compound **1** showed 23 carbon resonances. On the basis of the one-dimenisonal (1D) NMR spectra, two isobutyryl groups were obvious [δ_H 2.47 (m, H-2′), 1.14 (d, 6.8, H-3′), 1.16 (d, 6.8, H-4′) and 2.47 (m, H-2″), 1.14 (d, 6.8, H-3″), 1.16 (d, 6.8, H-4″); δ_C 177.0 (C-1′), 34.0 (C-2′), 18.8 (C-3′), 18.9 (C-4′) and 177.3 (C-1″), 34.2 (C-2″), 19.0 (C-3″), 19.0 (C-4″)]. The additional 15 resonances included two methyls, five methylenes (including an *exo*-methylene and one oxygenated methylene), four methines (including two oxygenated methines), and four quaternary carbons on the basis of distortionless enhancement by polarization transfer (DEPT) and heteronuclear multiple-quantum coherence (HMQC) spectra. According to the aforementioned spectroscopic evidence, the unsaturation degrees, and the *Inula* sesquiterpenes,[4,19,20] compound **1**

DOI: 10.1021/acs.jafc.5b03075
J. Agric. Food Chem. 2015, 63, 9006−9011

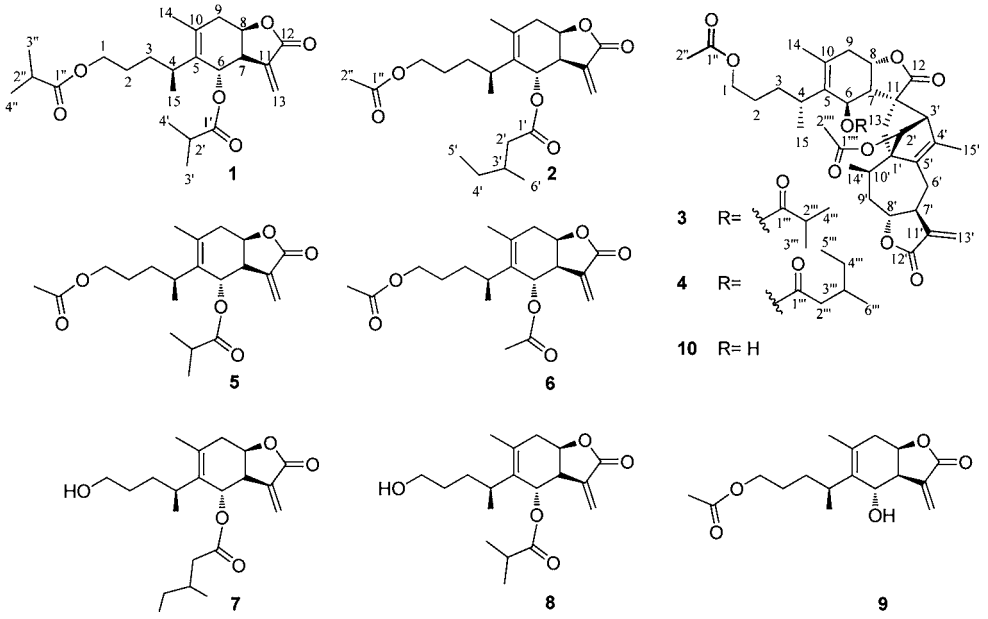

Figure 1. Structures of compounds **1**−**10** from the flowers of *I. japonica*.

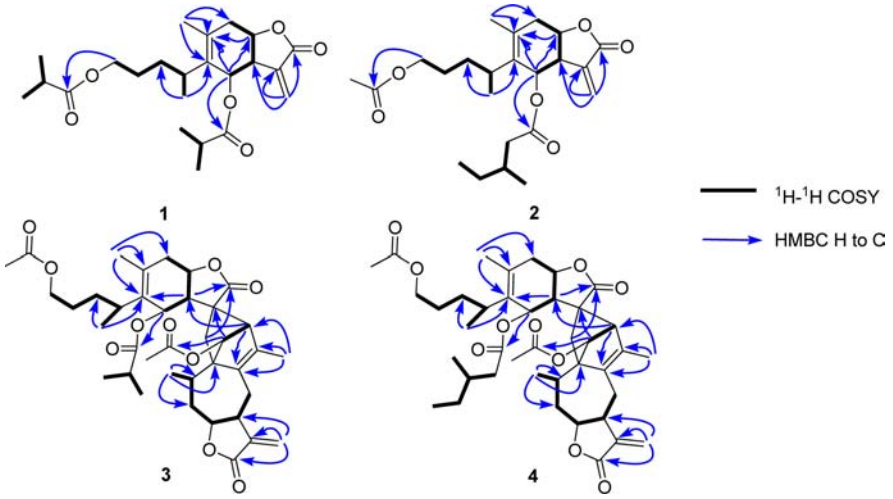

Figure 2. Selected HMBC and ^{1}H−^{1}H COSY correlations of compounds **1**−**4**.

might possess a 1,10-*seco*-eudesmanolide skeleton, which was confirmed by HMBC and ^{1}H−^{1}H correlation spectroscopy (COSY) experiments (Figure 2). HMBC correlations of H-1 (δ_H 3.93) with δ_C 177.3 and of H-6 (δ_H 5.19) with δ_C 177.0 placed two isobutyryl groups at C-1 and C-6, respectively. Further analyses of the two-dimensional (2D) NMR spectra led to the assignment of all of the proton and carbon signals, and the planar structure for compound **1** was thus established.

The relative configuration of compound **1** was determined on the basis of nuclear Overhauser effect spectroscopy (NOESY) experiment and coupling constants. The small coupling constants of H-6 with H-7 (d, 1.8 Hz) as well as NOESY correlations of H-7/H-8 and H-6/H$_3$-15 (Figure 3) suggested a *cis* configuration for the bicyclic ring and an α orientation of the 6-isobutyryl group. Through comparing the calculated and experimental ECD spectra, as shown in Figure 4, the absolute configurations of C-4, C-6, C-7, and C-8 in compound **1** were determined as 4*S*, 6*S*, 7*S*, and 8*R*, respectively. The structure of compound **1** was thus elucidated as (4*S*,6*S*,7*S*,8*R*)-1,6-*O*,*O*-diisobutyrylbritannilactone. The absolute configuration of compound **1** was consistent with the 1,10-*seco*-eudesmanolide derivative 1-*O*-acetylbritannilactone from *Inula britannica*, whose absolute configuration was

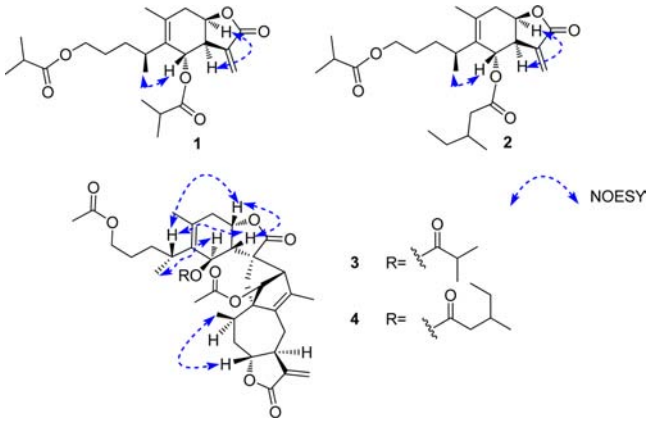

Figure 3. Selected NOESY correlations of compounds **1**−**4**.

DOI: 10.1021/acs.jafc.5b03075
J. Agric. Food Chem. 2015, 63, 9006−9011

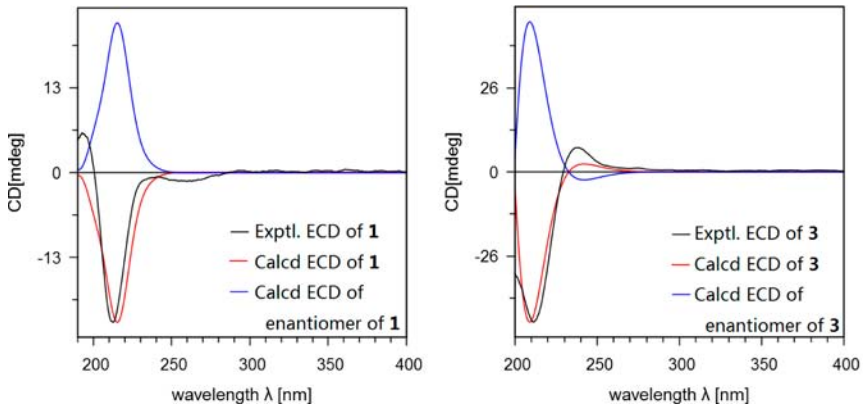

Figure 4. Calculated and experimental ECD spectra for compounds **1** (left) and **3** (right) in acetonitrile.

determined by single-crystal X-ray crystallography with Cu Kα radiation.[17]

Compound **2** possessed a molecular formula $C_{23}H_{34}O_6$ according to HR-ESIMS (HR-ESIMS *m/z* 429.2245 [M + Na]$^+$, calcd for $C_{23}H_{34}NaO_6$ 429.2253). The NMR data (Table 1) were comparable to those of compound **9**.[17] The only difference was that the hydroxy group at C-6 in compound **9** was replaced by the 3-methylvaleryloxy group in compound **2**. On the basis of confirmations with ^{1}H−^{1}H COSY, HMBC, and NOESY spectra (Figures 2 and 3), compound **2** was assigned to be 1-*O*-acetyl-6-*O*-(3-methylvaleryloxy)britannilactone. The ECD spectrum of compound **2** (Figure S24 of the Supporting Information) resembled that of compound **1** with the Cotton effects at 193 nm (positive) and 212 nm (negative), and the absolute configuration was thus defined as 4*S*, 6*S*, 7*S*, and 8*R*.

Compound **3** gave a molecular formula $C_{38}H_{50}O_{10}$ deduced from HR-ESIMS (*m/z* 689.3299 [M + Na]$^+$, calcd for $C_{38}H_{50}NaO_{10}$ 689.3302), indicating 14 unsaturation degrees. The ^{13}C and DEPT NMR spectra of compound **3** revealed 38 carbon signals, including 8 methyls, 8 methylenes, 10 methines, and 12 quarternary carbons, which was confirmed by HMQC (Table 2). It was obvious that two acetyl groups and one isobutyryl group (δ_C 171.1 and 20.9, δ_H 1.97; δ_C 170.8 and 21.1, δ_H 2.03; δ_C 175.7, 34.1, 18.7, and 18.5, δ_H 2.33 and 1.11) were present from the NMR spectra, including ^{1}H−^{1}H COSY and HMBC correlations (Table 2). On the basis of the spectroscopic data and the molecular formula, compound **3** might be a sesquiterpene dimer consisting of eudesmane and guaiane sesquiterpenoids.[6−10] A detailed comparison to known sesquiterpene dimer **10** revealed that the ^{13}C and ^{1}H NMR spectroscopic data of compound **3** resembled those of compound **10**, except for an isobutyryloxy group in compound **3** instead of the hydroxy group attached to C-6 in compound **10**. The locations of two acetoxy groups and one isobutyryloxy group were established by a HMBC experiment, revealing correlations of the proton signals at δ_H 3.95, 4.57, and 5.56 with δ_C 171.1 (C-1″), 170.8 (C-1‴″), and 175.7 (C-1‴), respectively (Figure 2). The further analysis of ^{1}H−^{1}H COSY and HMBC correlations confirmed it. The NOESY correlations of H-4/H-7, H-4/H-8, and H_3-15/H-6 were observed (Figure 3). The absolute configuration of compound **3** was also determined through the time-dependent density functional theory (TDDFT) ECD calculations. As shown in Figure 4, the calculated ECD spectrum of compound **3** matched the experimental result well (Figure 4), suggesting an absolute configuration of 4*R*, 6*R*, 7*R*, 8*S*, 11*S*, 1′*R*, 2′*R*, 3′*S*, 7′*S*, 8′*R*, and 10′*R* in compound **3**. The structure of compound **3** was therefore elucidated, and the compound was named japonicone U.

The molecular formula of compound **4** was deduced to be $C_{40}H_{54}O_{10}$ according to HR-ESIMS (*m/z* 717.3613 [M + Na]$^+$, calcd for $C_{40}H_{54}NaO_{10}$ 717.3615). The ^{13}C and ^{1}H NMR spectroscopic data of compound **4** (Table 2) resembled the sesquiterpene dimer japonicone Q,[9] except for an acetoxy group in compound **4** instead of the hydroxy group of C-1 in japonicone Q. Furthermore, the HMBC correlation from H-1 to C-1″ confirmed that the acetoxy group was located at C-1 (Figure 2). According to the above analysis, the structure of compound **4** was elucidated as shown (Figure 1). In the ECD spectrum (Figure S25 of the Supporting Information) of compound **4**, a negative Cotton effect appeared at 211 nm, while a positive Cotton effect was observed at 237 nm. The ECD features in compound **4** were identical with those of compound **3**, indicating that both compounds possessed the same configuration. The absolute configuration of compound **4** was therefore assigned to be 4*R*, 6*R*, 7*R*, 8*S*, 11*S*, 1′*R*, 2′*R*, 3′*S*, 7′*S*, 8′*R*, and 10′*R*, and the compound was named japonicone V.

The flowers of *I. japonica* have been employed for patients suffering from cancers.[3] Compounds **1**−**10** were therefore assayed *in vitro* for their antiproliferative activities against MCF-7 and MDA-MB-231 cells through the MTT method (Table 3). All of the isolated compounds displayed the antiproliferative

Table 3. Antiproliferative Activities of Compounds 1−10 against Two Human Breast Cancer Cell Lines

	IC$_{50}$ (μM)[a]	
compound	MCF-7	MDA-MB-231
1	>100	93.60 ± 6.10
2	15.56 ± 1.16	15.55 ± 1.93
3	29.64 ± 5.05	27.46 ± 3.54
4	0.20 ± 0.04	6.22 ± 1.30
5	32.30 ± 6.28	70.97 ± 3.42
6	68.00 ± 3.70	79.46 ± 8.59
7	26.34 ± 4.97	36.32 ± 3.91
8	23.64 ± 3.43	76.52 ± 4.78
9	>100	>100
10	6.69 ± 1.86	39.96 ± 2.31
etoposide[b]	21.78 ± 1.86	57.43 ± 0.56

[a]The data were expressed as means ± standard deviation. [b]Etoposide was used as a positive control.

DOI: 10.1021/acs.jafc.5b03075
J. Agric. Food Chem. 2015, 63, 9006−9011

effects. Compound **4** exhibited the most potent effect, with an IC_{50} value of 0.20 ± 0.04 μM against MCF-7 cells, followed by compounds **10** (6.69 ± 1.86 μM) and **2** (15.56 ± 1.16 μM). For the MDA-MB-231 cell line, all of the isolates, except compound **9**, showed significant cytotoxicity, with the IC_{50} values ranging from 6.22 ± 1.30 to 93.60 ± 6.10 μM. Compound **4** still displayed the highest antiproliferative activity (IC_{50} value of 6.22 ± 1.30 μM) against MDA-MB-231 cells, which was much more active than the positive control, etoposide.

In summary, ten 1,10-*seco*-eudesmanolide derivatives, including four new compounds, were isolated from the flowers of *I. japonica*. The antiproliferative potencies of these compounds were investigated through the MTT assay. The results revealed that some of them, especially the new compound **4**, showed strong antiproliferative effects on the human breast cancer cells and might be used as potential antitumor chemotherapy agent candidates.

■ ASSOCIATED CONTENT

Supporting Information

The Supporting Information is available free of charge on the ACS Publications website at DOI: 10.1021/acs.jafc.5b03075.

1D and 2D NMR, HR-ESIMS, and ECD spectra of compounds **1**−**4** (PDF)

■ AUTHOR INFORMATION

Corresponding Author

*Telephone/Fax: +86-22-23502595. E-mail: victgyq@nankai.edu.cn.

Notes

The authors declare no competing financial interest.

■ ACKNOWLEDGMENTS

This work was supported by the Ministry of Science and Technology 973 Project (2014CB560709), the Tianjin Science and Technology Program (13JCQNJC13600), the Specialized Research Fund for the Doctoral Program of Higher Education of China (20120031120048), and the Fundamental Research Funds for the Central Universities of China (65011201).

■ REFERENCES

(1) Editorial Committee of Administration Bureau of Chinese Plant Medicine. *Chinese Flora*; Science Press: Beijing, China, 1979; p 263.

(2) Shi, X.; Zhang, K.; Xue, N.; Su, L.; Ma, G.; Qi, J.; Wu, Y.; Wang, Q.; Shi, Q. Differentiation of genuine *Inula britannica* L. and substitute specimens based on the determination of 15 components using LC−MS/MS and principal components analysis. *Food Chem.* **2013**, *141*, 4019−4025.

(3) Seca, A. M.; Grigore, A.; Pinto, D. C.; Silva, A. M. The genus *Inula* and their metabolites: from ethnopharmacological to medicinal uses. *J. Ethnopharmacol.* **2014**, *154*, 286−310.

(4) Qin, J. J.; Jin, H. Z.; Zhu, J. X.; Fu, J. J.; Zeng, Q.; Cheng, X. R.; Zhu, Y.; Shan, L.; Zhang, S. D.; Pan, Y. X.; Zhang, W. D. New sesquiterpenes from *Inula japonica* Thunb. with their inhibitory activities against LPS−induced NO production in RAW264.7 macrophages. *Tetrahedron* **2010**, *66*, 9379−9388.

(5) Tang, S. A.; Zhu, H.; Qin, N.; Zhou, J. Y.; Lee, E.; Kong, D. X.; Jin, M. H.; Duan, H. Q. Anti−inflammatory terpenes from flowers of *Inula japonica*. *Planta Med.* **2014**, *80*, 583−589.

(6) Qin, J. J.; Jin, H. Z.; Fu, J. J.; Hu, X. J.; Wang, Y.; Yan, S. K.; Zhang, W. D. Japonicones A−D, bioactive dimeric sesquiterpenes from *Inula japonica* Thunb. *Bioorg. Med. Chem. Lett.* **2009**, *19*, 710−713.

(7) Qin, J. J.; Jin, H. Z.; Zhu, J. X.; Fu, J. J.; Hu, X. J.; Liu, X. H.; Zhu, Y.; Yan, S. K.; Zhang, W. D. Japonicones E−L, dimeric sesquiterpene lactones from *Inula japonica* Thunb. *Planta Med.* **2010**, *76*, 278−283.

(8) Qin, J. J.; Wang, L. Y.; Zhu, J. X.; Jin, H. Z.; Fu, J. J.; Liu, X. F.; Li, H. L.; Zhang, W. D. Neojaponicone A, a bioactive sesquiterpene lactone dimer with an unprecedented carbon skeleton from *Inula japonica*. *Chem. Commun.* **2011**, *47*, 1222−1224.

(9) Zhu, J. X.; Qin, J. J.; Jin, H. Z.; Zhang, W. D. Japonicones Q−T, four new dimeric sesquiterpene lactones from *Inula japonica* Thunb. *Fitoterapia* **2013**, *84*, 40−46.

(10) Xu, X. Y.; Sun, P.; Guo, D. A.; Liu, X.; Liu, J. H.; Hu, L. H. Cytotoxic sesquiterpene lactone dimers isolated from *Inula japonica*. *Fitoterapia* **2015**, *101*, 218−223.

(11) Wang, G. W.; Qin, J. J.; Cheng, X. R.; Shen, Y. H.; Shan, L.; Jin, H. Z.; Zhang, W. D. *Inula* sesquiterpenoids: structural diversity, cytotoxicity and anti−tumor activity. *Expert Opin. Invest. Drugs* **2014**, *23*, 317−345.

(12) Xu, J.; Ji, F.; Kang, J.; Wang, H.; Li, S.; Jin, D. Q.; Zhang, Q.; Sun, H.; Guo, Y. Absolute Configurations and NO Inhibitory Activities of Terpenoids from *Curcuma longa*. *J. Agric. Food Chem.* **2015**, *63*, 5805−5812.

(13) Chen, H.; Xie, C.; Wang, H.; Jin, D. Q.; Li, S.; Wang, M.; Ren, Q.; Xu, J.; Ohizumi, Y.; Guo, Y. Sesquiterpenes inhibiting the microglial activation from *Laurus nobilis*. *J. Agric. Food Chem.* **2014**, *62*, 4784−4788.

(14) Wang, M.; Zhang, Q.; Wang, H.; Ren, Q.; Sun, Y.; Xie, C.; Xu, J.; Jin, D. Q.; Ohizumi, Y.; Guo, Y. Characterization and NO inhibitory activities of chemical constituents from an edible plant *Petasites tatewakianus*. *J. Agric. Food Chem.* **2014**, *62*, 9362−9367.

(15) Xu, J.; Kang, J.; Cao, X.; Sun, X.; Yu, S.; Zhang, X.; Sun, H.; Guo, Y. Characterization of diterpenes from *Euphorbia prolifera* and their antifungal activities against phytopathogenic fungi. *J. Agric. Food Chem.* **2015**, *63*, 5902−5910.

(16) Zhang, Q.; Xiao, J.; Sun, Q. Q.; Qin, J. C.; Pescitelli, G.; Gao, J. M. Characterization of cytochalasins from the endophytic *Xylaria* sp. and their biological functions. *J. Agric. Food Chem.* **2014**, *62*, 10962−10969.

(17) Dong, S.; Tang, J. J.; Zhang, C. C.; Tian, J. M.; Guo, J. T.; Zhang, Q.; Li, H.; Gao, J. M. Semisynthesis and in vitro cytotoxic evaluation of new analogues of 1−*O*−acetylbritannilactone, a sesquiterpene from *Inula britannica*. *Eur. J. Med. Chem.* **2014**, *80*, 71−82.

(18) Jin, H. Z.; Lee, D.; Lee, J. H.; Lee, K.; Hong, Y. S.; Choung, D. H.; Kim, Y. H.; Lee, J. J. New sesquiterpene dimers from *Inula britannica* inhibit NF−kappaB activation and NO and TNF−alpha production in LPS−stimulated RAW264.7 cells. *Planta Med.* **2006**, *72*, 40−45.

(19) Zhang, X. F.; Du, J. L.; Ren, J.; Ye, F. M.; Xie, Y. G.; Cheng, X. R.; Yan, S. K.; Jin, H. Z. Three new sesquiterpene lactones from *Inula britannica*. *Arch. Pharmacal Res.* **2015**, *38*, 666−672.

(20) Bai, N.; Lai, C. S.; He, K.; Zhou, Z.; Zhang, L.; Quan, Z.; Zhu, N.; Zheng, Q. Y.; Pan, M. H.; Ho, C. T. Sesquiterpene lactones from *Inula britannica* and their cytotoxic and apoptotic effects on human cancer cell lines. *J. Nat. Prod.* **2006**, *69*, 531−535.

DOI: 10.1021/acs.jafc.5b03075
J. Agric. Food Chem. 2015, 63, 9006−9011

Figure 1. Tuber appearance of the 12 iron biofortified potato clones under investigation.

or ferric iron (Fe(III)). Ferric iron, the likely predominant form of iron in potato tubers,[19] must be first reduced to Fe(II) to be taken up by the divalent metal ion transporters of the intestinal epithelial cells.[20] Intracellular iron concentration, storage, and detoxification are further under the control of the ferritin protein. Non-heme iron absorption may be enhanced by simultaneous intake of vitamin C, citric acid, and animal proteins, whereas phytates, calcium, and phenolic compounds may inhibit the absorption. Potato tubers contain significant amounts of vitamin C, which is a potent enhancer of iron uptake in humans. Phenolic compounds, also present in potato, may, on the other hand, reduce in general iron uptake, through the formation of insoluble complexes with ferric iron in the gastrointestinal tract.[21] A recent study showed however that some phenolic compounds may promote iron absorption, stressing the complexity of the interactions of this large family of compounds.[22]

Given the time and expense required for in vivo trials, in vitro models have been developed to estimate iron bioavailability from food.[23] In combination with simulated human gastrointestinal digestion, the Caco-2 cell model has been demonstrated to be effective in comparing iron bioavailability from diverse bean, rice, and maize genotypes.[24−26] The Caco-2 cell line is derived from a human colorectal adenocarcinoma. These cells may undergo differentiation and polarization to form monolayers of intestinal epithelial cells. Ferritin level in cells is a sensitive marker of iron uptake and enables measurement of iron availability in vitro.[24]

The purpose of this study was to compare the in vitro iron availability from diverse iron biofortified International Potato Center (CIP) potato clones grown in the Peruvian Andes and, thereby, to provide key information to breeders seeking to increase bioavailable iron from potato. Caco-2 cells were used as a model of human intestine, with ferritin formation as a marker of iron absorption.[27] The bioaccessibility of iron, vitamin C, phenolic compounds, and carotenoids were first measured following an in vitro gastrointestinal digestion procedure[28] in order to get a better picture of the potential interactions that could explain the observed variations in the bioavailability of iron from potato tubers.

MATERIALS AND METHODS

Chemicals. Solvents [of analytical or high-performance liquid chromatography (HPLC) grade as required] were obtained from VWR International (Leuven, Belgium). Carotenoid standards (lutein, neoxanthin, violaxanthin, zeaxanthin, antheraxanthin, β-cryptoxanthin, β-carotene, and lutein-5,6-epoxide) were purchased from Carotenature (Lupsingen, Switzerland). Phenolic compounds (chlorogenic acid, neochlorogenic acid, cryptochlorogenic acid, caffeic acid, gallic acid, and rutin) were purchased from Sigma-Aldrich (St. Louis, MO). Kaempferol-3-rutinoside and petanine were obtained from Extrasynthese (Genay, France). All digestive enzymes were purchased from Sigma-Aldrich (St. Louis, MO). Nitric acid (HNO_3) and H_2O_2 for the mineral analyses were obtained from LGC Standards (Molsheim, France) and Fisher Scientific (Tournai, Belgium), respectively. Cell culture media, unless otherwise specified, were purchased from Invitrogen (Groningen, The Netherlands).

Plant Materials. Twelve diploid ($2n = 2x = 24$) potato clones, from the biofortified potato population developed at the International Potato Center (CIP), were used for this study (Figure 1). Samples of the 12 clones were obtained from a field trial planted in April 2013 at CIP's experimental station in Huancayo (Peru, 3280 m above sea level) and harvested in September 2013. Recommended agronomical practices were applied. Five to ten representative mature tubers were collected at harvest, washed, and shipped to the Luxembourg Institute of Science and Technology (LIST), where they were stored in incubators at 10 °C prior to sampling and analysis. Tubers were washed thoroughly with acidified water (pH 3) in order to remove any soil residues and avoid mineral contamination of the samples. They were further rinsed with demineralized water. For cooking, demineralized water was added in stainless steel pots and brought to boiling on induction plates. Unpeeled tubers were cooked for 10−15 min. Once cooked, tubers were peeled using ceramic knives to avoid

DOI: 10.1021/acs.jafc.5b02904
J. Agric. Food Chem. 2015, 63, 9012−9021

metal contamination and pureed in a mortar and pestle. Homogenized samples were further submitted to the in vitro digestion protocol, while representative samples were frozen in liquid nitrogen, and kept at −80 °C until chemical analysis.

In Vitro Digestion. The in vitro digestion protocol was performed as described by Miranda et al.[28] Approximately 10 g of boiled potato flesh underwent in vitro digestion. The digestions were performed in triplicate. Salivary digestion was first simulated by adding 5 mL of α-amylase in NaCl 0.9% (450 U/g of potato flesh) at pH 6.9 and shaking for 10 min at room temperature. For the gastric step, pepsin (6500 U/g of potato flesh) and 25 mL of NaCl 0.9% were added. The pH was decreased to 2 with HCl. The mixture was then shaken for 1 h at 37 °C. For the duodenal step, the pH was increased to 5.5 using $NaHCO_3$ 1 M. Bile extract (11 mg/g of potato flesh) and pancreatin (1.8 mg/g of potato flesh) were then added and the incubation volume was set to 50 mL. The digestion mixture (pH 7) was then further shaken for 2 h at 37 °C. The final digestion extract was centrifuged (5000*g* for 20 min at 4 °C) and the supernatant was filtered (PVDF, 0.2 μm). Digests were then flash frozen in liquid nitrogen and kept at −80 °C until further analysis. A control was made using the digestive enzymes in the same conditions without plant material. For cytotoxicity and iron uptake experiments, the potato digests were quickly thawed by mixing in a water bath at 37 °C, directly appropriately diluted, and added onto the Caco-2 cells.

Vitamin C Analysis. *Extraction.* The extraction of vitamin C was conducted as described previously by Andre et al.[9] Briefly, approximately 750 mg of boiled material was weighed in a 15 mL Falcon tube and 4 mL of an aqueous solution containing 5% metaphosphoric acid and 1% dithiothreitol were added. The dithiothreitol allows the reduction of dehydroascorbic to ascorbic acid and thereby quantifying ascorbic acid as total vitamin C content. Therefore, we quantified the total vitamin C, which includes both molecules. After shaking the samples for 1 h at 4 °C, the samples were centrifuged (5000*g*, 15 min, 4 °C). The supernatant was collected and the extraction was repeated. The pooled supernatants were filtered (0.2 μm) and analyzed by high-performance liquid chromatography coupled with a diode array detector (UPLC-DAD). The extraction was done in triplicate. For the analysis of potato digests, 0.5 mL of digest was mixed with 0.5 mL of an aqueous solution containing 10% metaphosphoric acid and 2% dithiothreitol, shaken for 30 s at 4 °C, centrifuged (5000*g*, 5 min, 4 °C), and filtered (0.2 μm) prior to analysis.

UPLC-DAD Analysis. The quantification was carried out using a Waters Acquity UPLC system (Milford, MA) equipped with a photodiode array detector. An aliquot of 5 μL was injected onto an Acquity UPLC HSS T3 column (2.1 × 100 mm, 1.8 μm particle size, Waters, Milford, MA) at 40 °C and a flow rate of 0.5 mL/min. The eluents were 0.1% formic acid in water (A) and 0.1% formic acid in acetonitrile (B). The gradient was as follows: 0 min, 0% B; 1.5 min, 0% B; 2 min, 100% B; 5 min, 100% B; 5.5 min, 0% B; 7 min, 0% B. Ascorbic acid was detected at 243 nm according to its absorption maximum and quantified using a six-point calibration curve. Furthermore, a validation standard was injected after every tenth sample injection.

Phenolic Compound Analysis. *Extraction.* The extraction of phenolic compound was conducted as described previously by Andre et al.[8] Briefly, approximately 750 mg of fresh or boiled material was weighed in a 15 mL Falcon tube and 10 mL of methanol/water/acetic acid (80:19.5:0.5, v/v/v). This mixture was homogenized using a vortex for 30 s and shaken for 2 h at room temperature. After centrifugation at 5000*g* for 15 min at 4 °C, the supernatant was collected and evaporated to dryness in a SpeedVac concentrator (Heto, Thermo Electron Corp., Waltham, MA). Polyphenols were resuspended in 1 mL of an aqueous solution containing 5% methanol and filtered through a 0.2 μm PVDF syringe filter prior to UPLC-DAD injection. For the analysis of potato digests, 1 mL of filtered digest was kept in an amber HPLC vial prior to analysis.

UPLC-DAD Analysis. The quantification was carried out as reported by Deußer et al.,[29] using the same equipment and column described for the vitamin C analysis. The injection volume was 10 μL, the column temperature was 50 °C, and the flow rate was 0.75 mL/min. The eluents were 0.1% trifluoroacetic acid in water (A) and 0.1% trifluoroacetic acid in acetonitrile (B). The gradient was as follows: 0 min, 5% B; 9.27 min, 5% B; 13.53 min, 14% B; 22.60 min, 35% B; 23 min, 95% B; 25 min, 95% B; 26 min, 5% B. Phenolic compounds were detected at 280, 320, 360, or 520 nm according to their absorption maximum. For quantification, a six-point calibration curve was used. Furthermore, a validation standard was injected after every tenth injection. Anthocyanins were quantified as petanin equivalents.

Carotenoid Analysis. *Extraction.* Approximately 0.75 g of material was mixed with 5 mL of acetone. This mixture was homogenized using a vortex for 30 s and shaken on ice for 30 min to allow extraction of the lipophilic compounds. After centrifugation at 5000*g* for 15 min, the supernatant was collected. The extraction was repeated on the pellet using the same extraction solvent. Both supernatants were combined, evaporated to dryness under a gentle stream of nitrogen, and resuspended in 1 mL of MTBE:MeOH (1:1). The samples were filtered (0.2 μM) into an HPLC amber vial and stored at −80 °C prior to analysis. For the intestinal filtrates, a 4 mL aliquot was first mixed with 1 mL of 30% methanolic KOH and incubated for 30 min on ice. Carotenoids were extracted by addition of 4 mL of hexane:acetone (1:1, v/v), shaken for 1 min, and centrifuged for 2 min at 5000*g* at 4 °C to hasten phase separation. The hexane phase was collected and transferred into a second tube. The extraction process was repeated with 4 mL of hexane and the combined hexane phases were dried under a stream of nitrogen using a TurboVapLV apparatus (Biotage, Sweden). The residue was redissolved in 500 μL of MTBE/MeOH (1:1/v:v), filtered through a 0.2 μm PVDF syringe filter and stored at −80 °C until analysis.

UPLC-DAD Analysis. For the carotenoid quantification, an Acquity UPLC BEH C18 column (2.1 × 100 mm, 1.7 μm particle size, Waters) was used as described by Kaulmann et al.[30] The eluents were (A) ammonium acetate (50 mM):methanol (60:40, v/v) and (B) acetonitrile:dichloromethane (80:20, v/v), and the gradient was as follows: 0 min, 42% B, flow rate 0.35 mL/min; 4 min, 47% B; 11 min, 47% B; 13 min, 80% B, flow rate 0.40 mL/min; 18 min, 85% B; 29 min, 85% B, flow rate 0.35 mL/min; 30 min 42% B. The injection volume was 2.5 μL. Carotenoids were detected and quantified at 442 nm (violaxanthin, neoxanthin), 447 nm (lutein, antheraxanthin), and 453 nm (zeaxanthin, β-carotene) using six-point calibration curves.

Determination of Iron Content. Raw and cooked samples (about 1 g of fresh weight) were mineralized in 7 mL of nitric acid (HNO_3 for trace analysis minimum 67%) and 3 mL of H_2O_2 (30% w/w). For the mineralization of intestinal filtrates (3 mL), a mixture of 1.75 mL of HNO_3 and 0.75 mL of H_2O_2 was used. Acid mineralization was then performed in PFA tubes in a microwave oven (Anton Paar Multiwave Pro, Graz, Austria) by increasing temperature and pressure until 200 °C and 30 bar. At the end of the procedure, samples were diluted with demineralized water up to 25 mL for potatoes and up to 10 mL for filtrates, and kept at 4 °C prior to analysis. Blanks for all samples and a certified reference material for potatoes (spinach, NCS ZC 73013, LGC standards, France) were included at each mineralization cycle for quality control. The extraction was performed in triplicate for each clone on boiled and digestion materials. Samples were analyzed by inductively coupled plasma mass spectrometry (ICP-MS, PerkinElmer Elan DRC-e,Waltham, MA) as described by Lefèvre et al.[31] The concentrations in aluminum and chrome were also determined to detect any potential contamination and were below 2 and 0.04 ppm, respectively.

Cell Viability. Cytotoxicity of the potato digestion mixtures was determined using the resazurin/Alamar Blue assay. Cells were first seeded into 96-well plates at 1×10^4 cells per well and allowed to attach at 37 °C for 18 h. Cells were then exposed to digests for 24 h. Culture medium was then removed and 100 μL of cell culture medium containing 500 μM resazurin was added to each well. After 2−3 h, the formation of resorufin by cellular metabolic activity was recorded using a microplate fluorometer (excitation wavelength 530 nm, emission at 590 nm, 37 °C). A negative control with no cells was used for background subtraction. The percentage of cell viability was calculated using the nontreated cells as positive control (100% cell viability). The

DOI: 10.1021/acs.jafc.5b02904
J. Agric. Food Chem. 2015, 63, 9012−9021

toxicity of the 12 potato tubers digests has been evaluated. As a conclusion, the digests will be diluted 5 times before our iron absorption experiments. At this concentration, there was no significant difference with the negative control (100% cell viability) for any potato clones.

Cell Culture and Ferritin Measurement. The TC-7 Caco-2 subclone cells (ATCC No. HTB-37) were a generous gift from Monique Rousset (INSERM, Paris, France). Cells were seeded (50 000 cells/cm^2) into six well plates (VWR) and grown in Dulbecco's modified Eagle's medium + GlutaMAX (DMEM, Invitrogen, Halle, Belgium) with 10% fetal bovine serum (FBS, Gibco, Halle, Belgium), 1% penicillin/streptomycin (Gibco), and 1% nonessential amino acids (Sigma-Aldrich, St. Louis, MO). Cells were maintained in FBS at 37 °C in an incubator with 10% CO_2/90% O_2 under constant humidity.

Protocol 1. Cells were maintained in DMEM supplemented with 10% FBS, which was changed every couple of days. Cells were used for experiments 14 days after seeding. The integrity of the monolayer was verified by optical microscopy. At 48 h prior to the experiment, the growth medium was removed from culture wells, the cell layer was washed with phosphate buffered saline (PBS), and the growth medium was replaced with minimum essential medium (MEM) at pH 7.0. The MEM was supplemented with 10 mmol/L PIPES, 1% antibiotic/antimycotic solution, 4 mg/L hydrocortisone, 5 mg/L insulin, 5 μg/L selenium, 34 μg/L triiodothyronine, and 20 μg/L epidermal growth factor, as described by Glahn et al.[24] Caco-2 cells were treated with or without 20 μM $FeCl_3$ and 1 mM ascorbic acid to induce ferritin synthesis, as well as with or without solutions containing 20% intestinal filtrate diluted in MEM (v/v). Incubation was done for 4 h. The treatment was then removed and replaced by MEM for 20 h.

Protocol 2. After seeding, cells were maintained in DMEM supplemented with 2% FBS, which was changed every couple of days. Cells were used for experiments 14 days after seeding as described in protocol 1. At 48 h prior to the experiment, the growth medium was replaced with supplemented MEM. Caco-2 cells were treated with or without 4 μM $FeCl_3$ and 1 mM ascorbic acid to induce ferritin synthesis, with or without 100 μM $FeSO_4$, as well as with or without solutions containing 10 or 20% intestinal filtrate diluted in MEM (v/v). Incubation was done for 24 h.

Cell Harvest and Ferritin Analysis. Cells were lysed in ice-cold extraction buffer: 50 mM HEPES pH 7.6, 50 mM KCl, 50 mM NaF, 5 mM NaPPi, 5 mM EDTA, 5 mM EGTA. Inhibitor cocktail (P-8340, Sigma-Aldrich, St. Louis, MO) and Triton X-100 (1%) were added extemporaneously. The lysate was centrifuged (20 min/16000g/4 °C). Ferritin levels were determined using the human ferritin enzyme-linked immunosorbent assay (ELISA) kit provided by Biovendor (Brno, Czech Republic). The plates were read at 450 nm with a luminometer (Synergy 2, Biotek Instruments, Inc.; Drongenbos, Belgium). Results were normalized by total protein concentration measured by spectrophotometry using a Bradford kit (Biorad) and bovine serum albumin (BSA) as a standard.

Statistical Analyses. Pearson and Spearman Rank correlation coefficients were determined on (log-transformed, when necessary) data to evaluate relationships between variables. ANOVA and Tuckey tests were carried out on the bioavailable iron (ferritin) values. Principal component analysis (PCA) was performed on standardized data to evaluate the contribution of the different variables (iron, bioactives) to iron bioavailability. For these purposes, the statistical software R (www.r-project.org, version 2014) and SigmaPlot 12.5 (Systat Software Inc., San Jose, CA) were used.

RESULTS AND DISCUSSION

Concentration and Bioaccessibility of Iron, Vitamin C, Carotenoids, and Phenolics in Boiled Potatoes. The total iron concentrations in boiled peeled potato tubers ranged from 21.29 μg/g dry weight (DW) for the clone CIP_311200.003 to 39.47 μg/g DW for the clone CIP_311422.019, with an average value of 29.9 μg/g DW (Table 1). Five of the biofortified clones evaluated showed iron concentrations above 30 μg/g, a concentration that is similar to the unique highest value reported for the native Andean landrace CIP_703274.[1] The percentage of iron bioaccessibility, i.e. the amount of iron that is released during digestion, was genotype-dependent and varied from 63.7 to 79.0%, with an average value of 70.6% (Table 1). There was a strong positive relationship between the iron concentrations in the boiled tuber and the iron recovered after in vitro digestion ($r = 0.93$, $p < 0.01$), suggesting that tuber iron values are good indicators of the bioaccessible fraction. To our knowledge, this is the first report on the bioaccessibility of iron from potato. In vitro bioaccessibility of iron has been evaluated in various cereals and legumes, showing values, in general, that are lower than the ones presented here for potato. Lestienne et al.[32] reported iron bioaccessibility of about 10% from whole pearl millet flour, which increased to 24% after dephytinization. The bioaccessibility of iron from fava bean, soybean, and rice has also been shown to increase from 6.3 to 31.5%, from 6.2 to 30.7%, and from 5.6 to 19%, respectively, after phytate degradation through germination.[33] Wheat iron bioaccessibility was low (4.6%), with no improvement seen after dephytinization.[33] It is worth stressing that our study was performed on cooked and pureed material, which may not be the case for the above-mentioned studies.

Table 1. Concentration of Iron in Boiled Tubers, Bioaccessible Iron, and Percentage of Iron Released during in Vitro Digestion of 12 Experimental Potato Clones[a]

accession no.	skin and flesh color[b]	total iron in boiled tissue (μg/g DW)	bioaccessible iron (μg/g DW)	% release
CIP_311200.003	P/Cp	21.29 ± 0.48	15.83 ± 1.45	74.33
CIP_311575.003	Y/Y	25.64 ± 1.16	20.25 ± 2.61	79.00
CIP_311575.013	Y/Y	23.44 ± 1.86	15.95 ± 1.02	68.05
CIP_311422.014	P/Cr	27.96 ± 0.96	21.62 ± 0.49	77.33
CIP_311422.016	P/Cp	31.03 ± 2.80	19.78 ± 2.73	63.73
CIP_311422.019	P/Cp	39.47 ± 3.69	28.53 ± 0.39	72.29
CIP_311624.021	R/Y	26.87 ± 1.02	17.81 ± 1.97	66.29
CIP_311097.055	C/Cp	31.95 ± 3.64	20.45 ± 2.43	64.01
CIP_311420.074	C/Cp	33.64 ± 0.51	23.59 ± 0.93	70.14
CIP_311611.079	C/Cr	23.75 ± 1.17	17.12 ± 1.25	72.06
CIP_311623.105	R/Yr	36.96 ± 0.71	27.91 ± 1.31	75.51
CIP_311623.123	C/C	35.50 ± 5.79	22.89 ± 2.46	64.49

[a]Data are expressed on a dry weight basis and represent mean ± SD ($n = 3$). [b]Primary (in uppercase) and secondary skin color/primary (in uppercase) and secondary flesh colors: P, purple; R, red; Y, yellow; C, cream.

Our in vitro digestion procedure allowed us to estimate that the consumption of 200 g of potato tubers triggers mean iron concentrations of 20 μM at the intestinal level (considering that potato is diluted in 1 L of gastrointestinal fluids). It is worth noting that these values represent the total bioaccessible iron content and do not reflect the bioavailable iron. Also, this measurement does not give any information about iron species. On top of this, potato is a complex matrix containing numerous components that may improve or inhibit iron absorption.[6] Absorption of non-heme iron can be improved or impeded by the binding of iron to compounds such as chelators and ligands that create complexes. Vitamin C, along with citric acid, has been described as a potent enhancer of iron uptake.[34] On the other hand, oxalic acid, phytates (as described earlier), calcium, and zinc, as well as some phenolic compounds, may reduce iron absorption.[28] Although less well-documented, carotenoids may interact with minerals including iron and form precipitates that

DOI: 10.1021/acs.jafc.5b02904
J. Agric. Food Chem. 2015, 63, 9012−9021

could potentially reduce their absorption.[35] In this study, we focused on the predominant potato phytochemicals, i.e. vitamin C, phenolic compounds, and carotenoid compounds. As was done for iron, we determined the levels of these compounds in boiled material tubers well as in intestinal digests.

The average total vitamin C concentration in boiled potato tubers was 526 μg/g DW (Table 2). About 32% of this content remained in the intestinal digest. This reduction is likely due to the instability of the compound at the pH and temperature conditions of the in vitro digestion procedure and/or the reduced extent of release from the potato matrix. To our knowledge, this is the first report on vitamin C bioaccessibility from potato tubers. Higher levels of degradation have been observed in tomatoes,[36] broccoli,[37] and blended fruit juice,[38] showing bioaccessibility values of 0, 9, and 15%, respectively, which could be due to differences in the matrix composition but also in the gastrointestinal digestion protocol.

Table 2. Concentration of Vitamin C in Boiled Potato Tubers and Bioaccesible Vitamin C of 12 Experimental Potato Clones[a]

accession no.	vitamin C in boiled tissue (μg/g DW)	bioaccessible vitamin C (μg/g DW)
CIP_311200.003	754.43 ± 33.25	281.80 ± 29.63
CIP_311575.003	873.46 ± 37.70	402.52 ± 67.88
CIP_311575.013	413.02 ± 17.71	179.18 ± 4.72
CIP_311422.014	335.58 ± 27.57	106.00 ± 4.19
CIP_311422.016	411.30 ± 55.50	156.16 ± 19.10
CIP_311422.019	369.26 ± 19.73	132.71 ± 7.28
CIP_311624.021	333.80 ± 23.32	112.38 ± 20.60
CIP_311097.055	496.21 ± 16.98	80.48 ± 5.63
CIP_311420.074	532.16 ± 35.80	89.22 ± 2.70
CIP_311611.079	656.35 ± 13.45	138.18 ± 14.02
CIP_311623.105	412.52 ± 51.27	156.81 ± 11.31
CIP_311623.123	718.05 ± 73.56	166.15 ± 1.49

[a]Data are expressed on a dry weight basis ± SD (n = 3).

The potato carotenoid pattern was dominated by lutein and zeaxanthin, followed by antheraxanthin, violaxanthin, neoxanthin, and β-carotene (Table 3). Their identification was confirmed by comparison of their retention times and UV spectra with those of authentic standards. The clones CIP_311575.003, CIP_311575.013, and CIP_311623.105 presented the highest total carotenoid contents and the highest zeaxanthin concentrations in particular. The bioaccessibility of lutein and zeaxanthin in the 12 biofortified clones ranged from 53 to 160% and from 24 to 388%, respectively. The bioaccessibility of lutein and zeaxanthin in the yellow clones (CIP_311575.003, CIP_311575.013, and CIP_311623.123) ranged from 76 to 82% for lutein and from 24 to 55% for zeaxanthin. In a recent study, Burgos et al.[39] estimated that the bioaccessibility of lutein and zeaxanthin in yellow fleshed potatoes ranged from 33 to 71% and from 51 to 71%, respectively. Interestingly, the gastrointestinal digestion process allowed release of zeaxanthin from the potato matrix of five clones to a greater extent than that observed in the respective boiled samples. Chemical extraction from boiled material may therefore underestimate carotenoid amounts that can be released during digestion and that are actually bioaccessible. On the other hand, the efficiency of micellarization or bioaccessibility of the other carotenoids could not be determined, as they were below the detection limit in the intestinal digest. This is likely due to the in vitro digestion method we used, which created favorable conditions for water-soluble compounds and limiting ones for the production of mixed micelles, essential for lipophilic compounds such as carotenoids. The bioaccessibility of carotenoids (micellarization) is largely enhanced when dietary fat is consumed together with carotenoids. In addition, the concentrations in β-carotene were already low in boiled potatoes. Indeed, the β-carotene level is usually negligible in the tubers of commercial potato varieties whereas it is detected in low but quantifiable amounts in some native Andean cultivars.[8]

The phenolic profile of potato extracts was dominated by chlorogenic acid, neochlorogenic acid, cryptochlorogenic acid, caffeic acid, rutin, kaempferol-3-rutinoside, and ferulic acid as a minor component (Table 4). The presence of anthocyanins was also detected in purple-fleshed clones. The mean bioaccessibility value for total chlorogenic acids (sum of the three chlorogenic acid isomers) was 24.5%, with clones CIP_311623.123 and CIP_311611.079 showing the highest bioaccessibility values (82 and 65%, respectively). Similarly, the bioaccessibility of total chlorogenic acids evaluated in another study on apple cultivars ranged from 32 to 57%.[40] Using two Luxembourg-grown potato varieties, Miranda et al.[28] showed however higher concentrations of chlorogenic acids in the intestinal filtrate than in boiled potatoes. It is worth noting that some components such as rutin and kaempferol-3-rutinoside were not detectable in boiled tubers of some genotypes under investigation but were released during digestion, suggesting that a traditional solvent extraction on boiled material may also underestimate the presence of phenolic compounds that are actually bioaccessible. The bioaccessibility of anthocyanins across the purple-fleshed clones ranged from 40 to 81%, which is similar to the recovery rate observed in chokeberries.[41] Much lower bioaccessibility values have however been reported in the literature with regard to anthocyanins, due to their high instability in the mild alkaline intestinal environment.[40] Discrepancies could be explained by the variability of the in vitro digestion protocols and also by the type of anthocyanins present in the plant matrix. Interestingly, most anthocyanins present in purple-fleshed potato tubers are acylated with hydroxycinnamic acids, which are known to increase the stability of the compounds.[8]

No significant overall correlation was evident between iron bioaccessibility and vitamin C, carotenoid, and phenolic concentrations. However, the highest iron bioaccessibility was observed in the clone CIP_311575.003 that also presented the highest vitamin C concentration, while the lowest bioaccessibility values were observed in three purple-fleshed clones with high levels of anthocyanins and chlorogenic acid (CIP_311422.016, CIP_311097.055, and CIP_311420.074).

Evaluation of the in Vitro Bioavailability of Iron from Boiled Potatoes. We used an in vitro Caco-2 cell culture model to evaluate iron bioavailability from potato tubers by measuring ferritin formation in the cells (i.e., a measure of cell iron uptake) following exposure to digests of the samples. The toxicity of the digests of the 12 genotypes was first evaluated and the cell viability was above 70% for all accessions when used at 20% on the cells. Following classical culture conditions (protocol 1), ferritin values for the control (MEM only) were about 9 ng/mg of protein. As expected, ferritin synthesis was induced up to 190 ng/mg of protein in Caco-2 cells supplemented with 20 μM $FeCl_3$ and 1 mM vitamin C. These values are in agreement with those described in the

DOI: 10.1021/acs.jafc.5b02904
J. Agric. Food Chem. 2015, 63, 9012−9021

Table 3. Concentration of Carotenoid in Boiled Potato Tubers and Bioaccessible Carotenoids of 12 Experimental Potato Clones[a]

accession no.	DM (%)	lutein (μg/g DW)	zeaxanthin (μg/g DW)	violaxanthin (μg/g DW)	antheraxanthin (μg/g DW)	β-carotene (μg/g DW)	neoxanthin (μg/g DW)
CIP_311200.003							
boiled	26.2	3.84 ± 0.21	1.97 ± 0.12	nd[b]	0.56 ± 0.02	0.34 ± 0.04	0.33 ± 0.08
bioaccessible		2.80 ± 0.29	2.32 ± 0.41	nd	nd	nd	nd
CIP_311575.003							
boiled	21.4	6.43 ± 0.21	19.62 ± 1.86	0.40 ± 0.04	5.83 ± 0.70	0.61 ± 0.08	2.09 ± 0.26
bioaccessible		5.31 ± 0.90	10.90 ± 5.61	nd	nd	nd	nd
CIP_311575.013							
boiled	30.9	2.57 ± 0.13	23.65 ± 2.09	nd	1.41 ± 0.16	0.36 ± 0.01	0.67 ± 0.05
bioaccessible		2.06 ± 0.42	5.70 ± 5.81	nd	nd	nd	nd
CIP_311422.014							
boiled	36.9	4.10 ± 0.13	1.74 ± 0.19	0.29 ± 0.02	nd	0.32 ± 0.02	0.30 ± 0.05
bioaccessible		2.16 ± 0.29	1.50 ± 0.53	nd	nd	nd	nd
CIP_311422.016							
boiled	25.8	6.56 ± 0.17	nd	nd	nd	nd	nd
bioaccessible		5.61 ± 0.44	4.39 ± 0.55	nd	nd	nd	nd
CIP_311422.019							
boiled	24.8	5.08 ± 0.23	0.90 ± 0.08	0.47 ± 0.04	nd	0.52 ± 0.05	0.67 ± 0.12
bioaccessible		4.10 ± 1.71	3.51 ± 1.50	nd	nd	nd	nd
CIP_311624.021							
boiled	24.7	4.22 ± 0.61	2.62 ± 0.13	0.31 ± 0.05	nd	0.39 ± 0.09	0.27 ± 0.08
bioaccessible		6.77 ± 0.72	5.11 ± 1.64	nd	nd	nd	nd
CIP_311097.055							
boiled	29.1	4.10 ± 0.51	2.65 ± 0.52	nd	0.77 ± 0.06	0.34 ± 0.03	0.00 ± 0.00
bioaccessible		3.78 ± 0.42	2.73 ± 0.27	nd	nd	nd	nd
CIP_311420.074							
boiled	22.8	5.62 ± 0.39	nd	nd	nd	0.48 ± 0.02	0.63 ± 0.14
bioaccessible		4.41 ± 0.24	2.63 ± 0.66	nd	nd	nd	nd
CIP_311611.079							
boiled	24.9	3.37 ± 0.97	6.58 ± 1.19	0.41 ± 0.09	nd	nd	nd
bioaccessible		3.01 ± 0.81	6.30 ± 1.15	nd	nd	nd	nd
CIP_311623.105							
boiled	25.4	2.35 ± 0.27	41.50 ± 2.23	0.38 ± 0.13	0.67 ± 0.05	nd	0.43 ± 0.03
bioaccessible		1.94 ± 0.99	11.87 ± 4.71	nd	nd	nd	nd
CIP_311623.123							
boiled	22.7	3.98 ± 0.25	14.05 ± 2.62	0.54 ± 0.04	nd	nd	0.43 ± 0.04
bioaccessible		3.03 ± 0.70	7.44 ± 1.30	nd	nd	nd	nd

[a]Data are expressed on a dry weight basis ± SD (n = 3). The dry matter content (DM) is also presented. [b]nd, compound not detected.

literature.[28] There were no significant changes in ferritin concentrations when the cells were exposed to an in vitro digestion blank as compared to the control values, indicating that the variations in ferritin levels observed from potato digests are due to their constituents and not to the digestion enzyme mixture. Intrinsic iron bioavailability from the digests of the 12 genotypes was first evaluated. Ferritin concentrations were not significantly different from the baseline (control exposed to MEM only, data not shown). Similar results have previously been reported with this Caco-2 in vitro model and high phenolic-containing food such as beans.[25,42] The influence of potato components on the uptake of extrinsic iron was then investigated. The data for the Caco-2 cell ferritin formation following exposure to the digests of the 12 genotypes are summarized in Figure 2. The data are presented as the percentage of the response of the positive control (exposure to digest blank containing 20 μM $FeCl_3$ and 1 mM vitamin C). In the presence of 20% potato digest, the iron absorption ranged from 1.8% for the clone CIP_311422.016 to 8% for CIP_311624.021 as compared to the reference control. It appears therefore that potato digests host components that may interact with iron and reduce its absorption. Significant differences were found between the genotypes, with CIP_311200.003 and CIP_311624.021 exhibiting higher in vitro iron bioavailability when compared with the remaining genotypes. On the other hand, the purple-fleshed clones with the highest levels of total anthocyanins and chlorogenic acid (CIP_311422.016, CIP_311097.055, CIP_311420.074, and CIP_311422.014) showed the lowest iron bioavailability. In order to identify the major contributors or inhibitors of the in vitro iron bioavailability, a principal component analysis (PCA) was performed on the total iron content, bioactive composition, and ferritin values (Figure 3). The first two principal components (PC) accounted for 51.37% of the total variance. There was no association between variation for cell ferritin and total iron content. Interestingly, cell ferritin formation was associated with total vitamin C content and was inversely related to the phenolic compound levels, in particular total anthocyanins, caffeic acid, rutin, and kaempferol-3-rutinoside, as well as to chlorogenic acid.

DOI: 10.1021/acs.jafc.5b02904
J. Agric. Food Chem. 2015, 63, 9012−9021

Table 4. Concentration of Phenolics in Boiled Potato Tubers and Bioccessible Phenolics in 12 Experimental Potato Clones[a]

accession no.	total anthocyanins (μg/g DW)	chlorogenic acid (μg/g DW)	neochlorogenic acid (μg/g DW)	cryptochlorogenic acid (μg/g DW)	caffeic acid (μg/g DW)	ferulic acid (μg/g DW)	rutin (μg/g DW)	kaempferol-3-rutinoside (μg/g DW)
CIP_311200.003								
boiled	206.9 ± 168.6	835.5 ± 207.3	133.5 ± 61.9	433.8 ± 162.3	22.4 ± 9.9	3.3 ± 1.9	7.0 ± 1.6	10.5 ± 3.8
bioaccessible	167.0 ± 23.2	139.9 ± 17.9	8.7 ± 8.2	5.7 ± 3.2	5.6 ± 0.7	1.0 ± 0.3	5.9 ± 0.7	9.7 ± 0.3
CIP_311575.003								
boiled	nd[b]	925.9 ± 102.8	148.5 ± 4.2	495.4 ± 37.2	nd	4.7 ± 2.3	0.0 ± 0.0	nd
bioaccessible	nd	190.9 ± 94.2	4.8 ± 2.1	53.2 ± 9.9	9.9 ± 1.1	1.0 ± 0.1	3.0 ± 0.1	4.3 ± 0.2
CIP_311575.013								
boiled	nd	474.1 ± 163.8	116.9 ± 38.2	326.5 ± 112.3	19.0 ± 5.2	2.1 ± 0.6	nd	nd
bioaccessible	nd	76.0 ± 7.3	4.8 ± 1.7	50.3 ± 21.9	4.3 ± 0.4	0.9 ± 0.0	1.9 ± 0.0	3.1 ± 0.1
CIP_311422.014								
boiled	637.24 ± 35.4	2290.4 ± 338.5	401.5 ± 60.2	1254.9 ± 185.9	32.8 ± 4.1	1.7 ± 0.3	3.8 ± 0.1	44.1 ± 5.2
bioaccessible	393.4 ± 26.8	756.61 ± 33.15	102.5 ± 4.5	78.6 ± 13.8	7.5 ± 0.5	0.6 ± 0.1	4.5 ± 0.3	33.5 ± 3.8
CIP_311422.016								
boiled	744.5 ± 76.6	2413.8 ± 104.7	520.1 ± 26.2	1552.1 ± 79.7	47.5 ± 2.1	2.6 ± 0.9	11.4 ± 5.7	33.0 ± 1.2
bioaccessible	463.0 ± 74.9	448.4 ± 68.4	8.1 ± 8.5	3.7 ± 0.2	11.4 ± 1.3	1.1 ± 0.6	3.6 ± 1.6	29.6 ± 5.1
CIP_311422.019								
boiled	310.2 ± 42.5	1030.1 ± 109.8	157.3 ± 21.4	515.1 ± 62.0	61.2 ± 1.3	2.1 ± 0.1	10.0 ± 1.3	30.5 ± 4.7
bioaccessible	224.9 ± 13.8	167.3 ± 17.9	18.7 ± 1.1	5.5 ± 0.3	10.5 ± 2.2	1.6 ± 0.1	7.0 ± 4.3	23.7 ± 2.7
CIP_311624.021								
boiled	nd	663.2 ± 273.3	131.1 ± 28.3	382.7 ± 109.6	8.6 ± 4.3	2.2 ± 0.5	8.1 ± 2.9	13.0 ± 2.4
bioaccessible	nd	81.0 ± 24.0	14.6 ± 2.2	4.2 ± 0.2	3.0 ± 1.1	0.9 ± 0.2	5.1 ± 1.8	8.9 ± 2.2
CIP_311097.055								
boiled	728.7 ± 50.7	3364.3 ± 402.7	575.6 ± 55.5	1828.8 ± 194.2	68.2 ± 12.8	3.5 ± 1.8	9.1 ± 4.9	7.0 ± 0.8
bioaccessible	432.5 ± 51.06	660.1 ± 49.9	71.0 ± 16.4	3.6 ± 0.3	200.8 ± 18.9	1.6 ± 0.2	15.9 ± 1.9	22.0 ± 2.1
CIP_311420.074								
boiled	1440.5 ± 302.7	3027.8 ± 185.0	324.1 ± 24.9	1189.2 ± 73.7	50.1 ± 10.0	4.1 ± 0.2	6.9 ± 0.3	40.9 ± 0.9
bioaccessible	578.3 ± 89.7	450.0 ± 10.2	35.3 ± 10.5	8.3 ± 3.7	9.5 ± 4.8	1.4 ± 0.4	4.8 ± 1.1	29.0 ± 7.6
CIP_311611.079								
boiled	nd	828.2 ± 58.2	61.1 ± 6.5	257.1 ± 127.3	19.8 ± 6.5	4.6 ± 3.4	nd	nd
bioaccessible	nd	667.6 ± 17.4	74.4 ± 9.9	4.1 ± 0.3	10.3 ± 2.3	1.6 ± 0.3	2.2 ± 0.1	4.2 ± 0.3
CIP_311623.105								
boiled	nd	317.9 ± 63.2	88.8 ± 4.8	35.5 ± 37.7	7.1 ± 0.9	2.1 ± 0.1	7.5 ± 0.4	nd
bioaccessible	nd	283.6 ± 10.9	31.5 ± 1.2	2.8 ± 0.2	9.1 ± 1.0	1.1 ± 0.0	4.1 ± 0.1	10.8 ± 1.1
CIP_311623.123								
boiled	nd	507.5 ± 32.3	83.3 ± 8.2	268.6 ± 26.6	45.6 ± 6.9	6.2 ± 7.3	nd	nd
bioaccessible	nd	426.8 ± 61.0	65.0 ± 14.3	212.6 ± 47.8	9.7 ± 0.8	6.4 ± 6.5	2.4 ± 0.1	4.3 ± 0.2

[a]Data are expressed on a dry weight basis ± SD, respectively (n = 3). [b]nd, compound not detected.

Effect of Potato Digests on Iron Uptake Using Iron-Deprived Caco-2 Cells. In order to mimic anemic conditions and thereby increase the reactivity of the cells when exposed to iron, Caco-2 cells were cultured in low-iron media postseeding (see Protocol 2 under Material and Methods). The basal ferritin level was successfully reduced from 9 to 3 ng/mg of protein. Cells appeared much more reactive, showing an increase of ferritin expression up to 174 ng/mg of protein when exposed to 4 μM $FeCl_3$ (+1 mM vitamin C), an induction similar to the one we previously obtained with 20 μM $FeCl_3$ (and 1 mM vitamin C) following protocol 1. The value of 4 μM $FeCl_3$ is also the average iron concentration found in potato digests after a 5-fold dilution as used in our Caco-2 experiments. Using four contrasting genotypes in terms of iron and bioactive composition (Figure 3, genotypes in bold), the intrinsic iron bioavailability from 20% potato digest was evaluated, with no significant induction of ferritin (data not shown), as previously described with protocol 1. It appears that even with iron-deprived cells the inhibition of iron uptake is strong. The addition of 4 μM FeCl3 and 1 mM ascorbic acid induced ferritin expression, with iron uptake ranging from 4% for the clone CIP_311422.014 to 6.2% for CIP_311624.021 (Figure 4). Ferritin synthesis was further increased when the potato digests were diluted down to 10% of the media, confirming the inhibitory role of potato constituents. It is noteworthy that the yellow-fleshed clone CIP_311624.021 triggered consistently higher in vitro iron bioavailability as compared to its counterparts, suggesting a reduced level of inhibitors (including phenolic compounds) in that cultivar.

Conclusions. We showed that more than 50% of the potato iron is released from the matrix during the in vitro digestion and is therefore available at the intestinal level. Hydrophilic bioactive components such as vitamin C and phenolic compounds in potato tubers are also bioaccessible to a large extent. The intestinal absorption of intrinsic iron from potato tubers could however not be detected using our in vitro Caco-2 cell model. Inhibition of iron uptake is typically reported for foods containing high levels of phenolic compounds, which could partly explain our results. Only human studies will provide a clear and valid percentage of iron absorption from potatoes. Indeed, a recent human study showed significant iron absorption from test meals based on pearl millet (7.5%),[43]

DOI: 10.1021/acs.jafc.5b02904
J. Agric. Food Chem. 2015, 63, 9012−9021

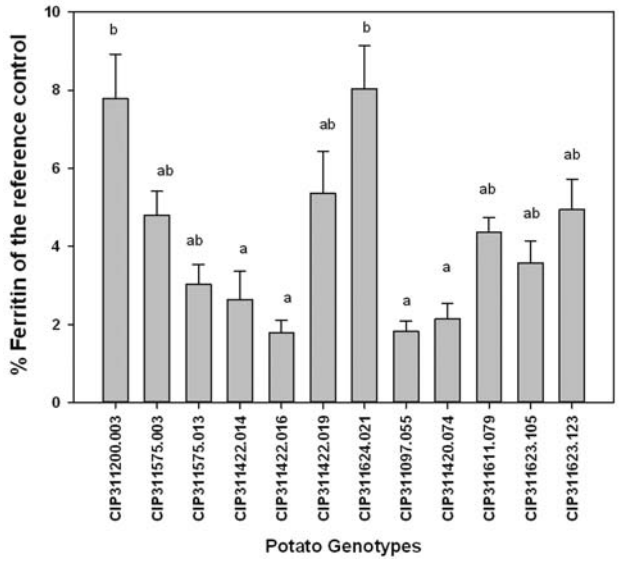

Figure 2. Iron bioavailability from 12 potato clones as measured by ferritin expression in Caco-2 cells. Ferritin expression was evaluated by an ELISA assay and normalized by total protein concentration. Caco-2 cells were exposed to potato digest supplemented with iron (20 μM $FeCl_3$) and ascorbate (1 mM). The data are presented as percentage of the positive control (exposure to digest blank containing 20 μM $FeCl_3$ and 1 mM vitamin C). Values are means ± SEM (n = 9, resulting from three independent experiments). Bar values with no letter in common are significantly different ($p < 0.05$).

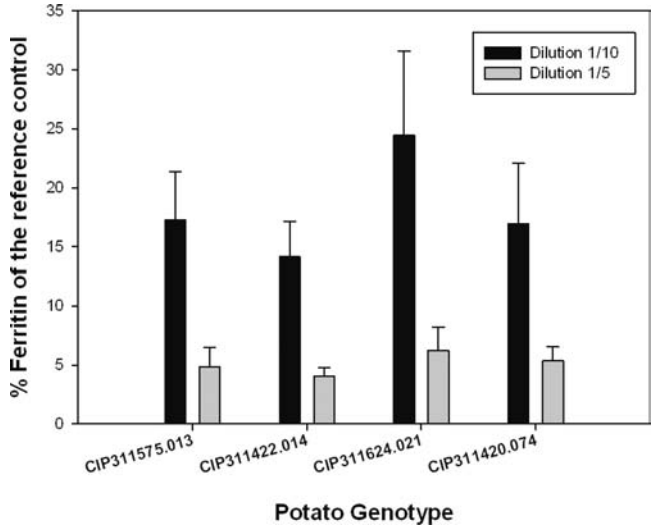

Figure 4. Iron bioavailability from four potato clones as measured by ferritin expression in Caco-2 cells grown under low iron conditions. Ferritin expression was evaluated by an ELISA assay and normalized by total protein concentrations. Caco-2 cells were exposed to 10 or 20% potato digest supplemented with iron (4 μM $FeCl_3$) and ascorbate (1 mM). The data are presented as percentages of the positive control (exposure to digest blank containing 4 μM $FeCl_3$ and 1 mM vitamin C). Values are means ± SEM (n = 9, resulting from three independent experiments). There was no significant difference between the genotypes.

whereas this food matrix is known to contain high levels of iron absorption inhibitors such as phytates and phenolic compounds. Tako et al.[42,44] also showed that the Caco-2 model predicted well animal iron absorption results for bean and pearl millet meals. The Caco-2 cell model is an advantageous preliminary in vitro screening method to efficiently identify promising clones in terms of iron bioavailability. Indeed, when an extrinsic source of iron was added ($FeCl_3$) to the digestion mixture, ferritin synthesis (marker of iron uptake) was noticed to an extent depending on the genotype. Nonsupervised multivariate analyses revealed opposing relationships between the bioavailable iron values (as determined by cell ferritin formation) and the phenolic concentrations. In our assay procedure, carotenoid concentrations did not influence iron bioavailability, whereas the potato vitamin C was positively correlated with the ferritin values. The determination of the iron content in cooked potato tubers was not a good indicator of iron bioavailability, as evaluated by our Caco-2 cell-based model. Indeed, the values of bioavailable iron are the result of various and complex interactions that could be attributed to endogenous iron, to phenolic compounds, to other non-

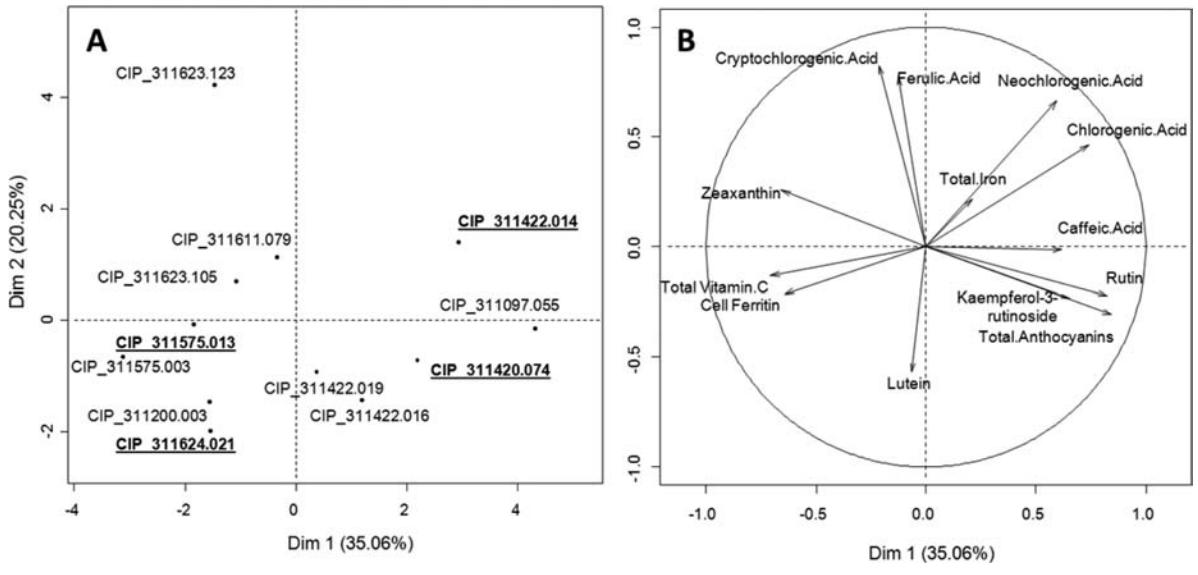

Figure 3. Principal component analysis (PCA) resulting from the in vitro iron bioavailability evaluation of 12 potato clones. (A) Score plots of the 12 potato genotypes. (B) Loading plot showing the relationships between the 13 variables.

DOI: 10.1021/acs.jafc.5b02904
J. Agric. Food Chem. 2015, 63, 9012−9021

identified molecules, and to synergistic as well as antagonistic effects among all these components. Such models may help plant breeders interested in increasing the bioavailable levels of iron and/or reducing the amount and type of iron uptake inhibitors in staple food crops such as potato. Deeper metabolite profiling studies on potato tubers, including phytate measurements, should also be performed to better identify other potential iron absorption inhibitors. Controlled human intervention or animal trials will however be needed to improve our knowledge on iron absorption from potato.

AUTHOR INFORMATION

Corresponding Author

*E-mail: christelle.andre@list.lu.

Funding

This study was partly supported by the CGIAR Research Program on Agriculture for Nutrition and Health (CRP-A4NH).

Notes

The authors declare no competing financial interest.

ACKNOWLEDGMENTS

We thank Aude Corvisy for her help in in vitro digestion and cell culture analyses, Boris Untereiner for his help in phytochemical extractions, and Walter Amoros for providing the biofortified potato clones in Peru.

ABBREVIATIONS USED

DW, dry weight; PCA, principal component analysis; MEM, minimum essential medium; SD, standard deviation; SEM, standard error of the mean; P, purple; R, red; Y, yellow; C, cream; nd, compound not detected; DM, dry matter

REFERENCES

(1) Burgos, G.; Amoros, W.; Morote, M.; Stangoulis, J.; Bonierbale, M. Iron and zinc concentration of native Andean potato cultivars from a human nutrition perspective. *J. Sci. Food Agric.* **2007**, *87*, 668−675.

(2) Anderson, K. A.; Magnuson, B. A.; Tschirgi, M. L.; Smith, B. Determining the geographic origin of potatoes with trace metal analysis using statistical and neural network classifiers. *J. Agric. Food Chem.* **1999**, *47*, 1568−1575.

(3) Haynes, K.; Yencho, G.; Clough, M.; Henninger, M.; Sterrett, S. Genetic variation for potato tuber micronutrient content and implications for biofortification of potatoes to reduce micronutrient malnutrition. *Am. J. Potato Res.* **2012**, *89*, 192−198.

(4) Paget, M.; Amoros, W.; Salas, E.; Eyzaguirre, R.; Alspach, P.; Apiolaza, L.; Noble, A.; Bonierbale, M. Genetic evaluation of micronutrient traits in diploid potato from a base population of Andean Landrace Cultivars. *Crop Science* **2014**, *54*, 1949−1959.

(5) Burlingame, B.; Mouillé, B.; Charrondière, R. Nutrients, bioactive non-nutrients and anti-nutrients in potatoes. *J. Food Compos. Anal.* **2009**, *22*, 494−502.

(6) Andre, C. M.; Legay, S.; Iammarino, C.; Ziebel, J.; Guignard, C.; Larondelle, Y.; Hausman, J.-F.; Evers, D.; Miranda, L. M. The Potato in the Human Diet: a Complex Matrix with Potential Health Benefits. *Potato Res.* **2014**, *57*, 201−214.

(7) Miller, P. E.; Snyder, D. C. Phytochemicals and cancer risk: a review of the epidemiological evidence. *Nutr. Clin. Pract.* **2012**, *27*, 599.

(8) Andre, C. M.; Oufir, M.; Guignard, C.; Hoffmann, L.; Hausman, J.-F.; Evers, D.; Larondelle, Y. Antioxidant profiling of native Andean potato tubers (Solanum tuberosum L.) reveals cultivars with high levels of β-carotene, α-tocopherol, chlorogenic acid, and petanin. *J. Agric. Food Chem.* **2007**, *55*, 10839−10849.

(9) Andre, C. M.; Ghislain, M.; Bertin, P.; Oufir, M.; del Rosario Herrera, M.; Hoffmann, L.; Hausman, J.-F.; Larondelle, Y.; Evers, D. Andean potato cultivars (Solanum tuberosum L.) as a source of antioxidant and mineral micronutrients. *J. Agric. Food Chem.* **2007**, *55*, 366−378.

(10) Burgos, G.; Salas, E.; Amoros, W.; Auqui, M.; Muñoa, L.; Kimura, M.; Bonierbale, M. Total and individual carotenoid profiles in Solanum phureja of cultivated potatoes: I. Concentrations and relationships as determined by spectrophotometry and HPLC. *J. Food Compos. Anal.* **2009**, *22*, 503−508.

(11) Fernandez-Orozco, R.; Gallardo-Guerrero, L.; Hornero-Méndez, D. Carotenoid profiling in tubers of different potato (*Solanum* sp) cultivars: Accumulation of carotenoids mediated by xanthophyll esterification. *Food Chem.* **2013**, *141*, 2864−2872.

(12) Carillo, P.; Cacace, D.; De Pascale, S.; Rapacciuolo, M.; Fuggi, A. Organic vs. traditional potato powder. *Food Chem.* **2012**, *133*, 1264−1273.

(13) Maggio, A.; Carillo, P.; Bulmetti, G. S.; Fuggi, A.; Barbieri, G.; De Pascale, S. Potato yield and metabolic profiling under conventional and organic farming. *Eur. J. Agron.* **2008**, *28*, 343−350.

(14) Thompson, B. Food-based approaches for combating iron deficiency. *Nutritional Anemia*; Kraemer, K., Zimmermann, M. B., Eds.; Sight and Life Press: Basel, Switzerland, 2007; p 337.

(15) Scholl, T. O. Iron status during pregnancy: setting the stage for mother and infant. *Am. J. Clin. Nutr.* **2005**, *81*, 1218S−1222S.

(16) White, P. J.; Broadley, M. R. Biofortifying crops with essential mineral elements. *Trends Plant Sci.* **2005**, *10*, 586−593.

(17) Brown, C. Breeding for phytonutrient enhancement of potato. *Am. J. Potato Res.* **2008**, *85*, 298−307.

(18) Brown, C. R.; Haynes, K. G.; Moore, M.; Pavek, M. J.; Hane, D. C.; Love, S. L.; Novy, R. G.; Miller, J., Jr Stability and broad-sense heritability of mineral content in potato: Iron. *Am. J. Potato Res.* **2010**, *87*, 390−396.

(19) Cámara, F.; Amaro, M.; Barberá, R.; Lagarda, M. Speciation of bioaccessible (heme, ferrous and ferric) iron from school menus. *Eur. Food Res. Technol.* **2005**, *221*, 768−773.

(20) Gunshin, H.; Mackenzie, B.; Berger, U. V.; Gunshin, Y.; Romero, M. F.; Boron, W. F.; Nussberger, S.; Gollan, J. L.; Hediger, M. A. Cloning and characterization of a mammalian proton-coupled metal-ion transporter. *Nature* **1997**, *388*, 482−488.

(21) Brune, M.; Rossander, L.; Hallberg, L. Iron absorption and phenolic compounds: importance of different phenolic structures. *Eur. J. Clin. Nutr.* **1989**, *43*, 547−557.

(22) Hart, J. J.; Tako, E.; Kochian, L. V.; Glahn, R. P. Identification of Black Bean (Phaseolus vulgaris L.) Polyphenols That Inhibit and Promote Iron Uptake by Caco-2 Cells. *J. Agric. Food Chem.* **2015**, *63*, 5950−5956.

(23) Etcheverry, P.; Grusak, M. A.; Fleige, L. E. Application of in vitro bioaccessibility and bioavailability methods for calcium, carotenoids, folate, iron, magnesium, polyphenols, zinc, and vitamins B (6), B (12), D, and E. *Front. Physiol.* **2012**, *3*, 317.

(24) Glahn, R. P.; Lee, O. A.; Yeung, A.; Goldman, M. I.; Miller, D. D. Caco-2 cell ferritin formation predicts nonradiolabeled food iron availability in an in vitro digestion/Caco-2 cell culture model. *J. Nutr.* **1998**, *128*, 1555−1561.

(25) Ariza-Nieto, M.; Blair, M. W.; Welch, R. M.; Glahn, R. P. Screening of iron bioavailability patterns in eight bean (Phaseolus vulgaris L.) genotypes using the Caco-2 cell in vitro model. *J. Agric. Food Chem.* **2007**, *55*, 7950−7956.

(26) Glahn, R. P.; Cheng, Z.; Welch, R. M.; Gregorio, G. B. Comparison of Iron Bioavailability from 15 Rice Genotypes: Studies Using an in Vitro Digestion/Caco-2 Cell Culture Model. *J. Agric. Food Chem.* **2002**, *50*, 3586−3591.

(27) Glahn, R. P.; Wien, E. M.; Van Campen, D. R.; Miller, D. D. Caco-2 cell iron uptake from meat and casein digests parallels in vivo studies: use of a novel in vitro method for rapid estimation of iron bioavailability. *J. Nutr.* **1996**, *126*, 332−339.

(28) Miranda, L.; Deußer, H.; Evers, D. The impact of in vitro digestion on bioaccessibility of polyphenols from potatoes and sweet

DOI: 10.1021/acs.jafc.5b02904
J. Agric. Food Chem. 2015, 63, 9012−9021

potatoes and their influence on iron absorption by human intestinal cells. *Food Funct.* **2013**, *4*, 1595−1601.
(29) Deußer, H.; Guignard, C.; Hoffmann, L.; Evers, D. Polyphenol and glycoalkaloid contents in potato cultivars grown in Luxembourg. *Food Chem.* **2012**, *135*, 2814−2824.
(30) Kaulmann, A.; Jonville, M.-C.; Schneider, Y.-J.; Hoffmann, L.; Bohn, T. Carotenoids, polyphenols and micronutrient profiles of Brassica oleraceae and plum varieties and their contribution to measures of total antioxidant capacity. *Food Chem.* **2014**, *155*, 240−250.
(31) Lefèvre, I.; Ziebel, J.; Guignard, C.; Hausman, J.-F.; Gutiérrez Rosales, R. O.; Bonierbale, M.; Hoffmann, L.; Schafleitner, R.; Evers, D. Drought impacts mineral contents in Andean potato cultivars. *J. Agron. Crop Sci.* **2012**, *198*, 196−206.
(32) Lestienne, I.; Besançon, P.; Caporiccio, B.; Lullien-Péllerin, V.; Tréche, S. Iron and zinc in vitro availability in pearl millet flours (Pennisetum glaucum) with varying phytate, tannin, and fiber contents. *J. Agric. Food Chem.* **2005**, *53*, 3240−3247.
(33) Luo, Y.-W.; Xie, W.-H.; Jin, X.-X.; Wang, Q.; He, Y.-J. Effects of germination on iron, zinc, calcium, manganese, and copper availability from cereals and legumes. *CyTA–J. Food* **2014**, *12*, 22−26.
(34) Yun, S.; Habicht, J.-P.; Miller, D. D.; Glahn, R. P. An In Vitro Digestion/Caco-2 Cell Culture System Accurately Predicts the Effects of Ascorbic Acid and Polyphenolic Compounds on Iron Bioavailability in Humans. *J. Nutr.* **2004**, *134*, 2717−2721.
(35) Biehler, E.; Hoffmann, L.; Krause, E.; Bohn, T. Divalent Minerals Decrease Micellarization and Uptake of Carotenoids and Digestion Products into Caco-2 Cells. *J. Nutr.* **2011**, *141*, 1769−1776.
(36) Toor, R. K.; Savage, G. P.; Lister, C. E. Release of antioxidant components from tomatoes determined by an in vitro digestion method. *Int. J. Food Sci. Nutr.* **2009**, *60*, 119−129.
(37) Vallejo, F.; Gil-Izquierdo, A.; Pérez-Vicente, A.; García-Viguera, C. In vitro gastrointestinal digestion study of broccoli inflorescence phenolic compounds, glucosinolates, and vitamin C. *J. Agric. Food Chem.* **2004**, *52*, 135−138.
(38) Rodríguez-Roque, M. J.; Rojas-Graü, M. A.; Elez-Martínez, P.; Martín-Belloso, O. Changes in vitamin C, phenolic, and carotenoid profiles throughout in vitro gastrointestinal digestion of a blended fruit juice. *J. Agric. Food Chem.* **2013**, *61*, 1859−1867.
(39) Burgos, G.; Muñoa, L.; Sosa, P.; Bonierbale, M.; zum Felde, T.; Díaz, C. In vitro Bioaccessibility of Lutein and Zeaxanthin of Yellow Fleshed Boiled Potatoes. *Plant Foods Hum. Nutr.* **2013**, *68*, 385−390.
(40) Bouayed, J.; Deußer, H.; Hoffmann, L.; Bohn, T. Bioaccessible and dialysable polyphenols in selected apple varieties following in vitro digestion vs. their native patterns. *Food Chem.* **2012**, *131*, 1466−1472.
(41) Bermúdez-Soto, M.-J.; Tomás-Barberán, F.-A.; García-Conesa, M.-T. Stability of polyphenols in chokeberry (Aronia melanocarpa) subjected to in vitro gastric and pancreatic digestion. *Food Chem.* **2007**, *102*, 865−874.
(42) Tako, E.; Beebe, S. E.; Reed, S.; Hart, J. J.; Glahn, R. P. Polyphenolic compounds appear to limit the nutritional benefit of biofortified higher iron black bean (Phaseolus vulgaris L.). *Nutr. J.* **2014**, *13*, 28.
(43) Cercamondi, C. I.; Egli, I. M.; Mitchikpe, E.; Tossou, F.; Zeder, C.; Hounhouigan, J. D.; Hurrell, R. F. Total iron absorption by young women from iron-biofortified pearl millet composite meals is double that from regular millet meals but less than that from post-harvest iron-fortified millet meals. *J. Nutr.* **2013**, *143*, 1376−1382.
(44) Tako, E.; Reed, S.; Budiman, J.; Hart, J.; Glahn, R. Higher iron pearl millet (Pennisetum glaucum L.) provides more absorbable iron that is limited by increased polyphenolic content. *Nutr. J.* **2015**, *14*, 11.

DOI: 10.1021/acs.jafc.5b02904
J. Agric. Food Chem. 2015, 63, 9012−9021

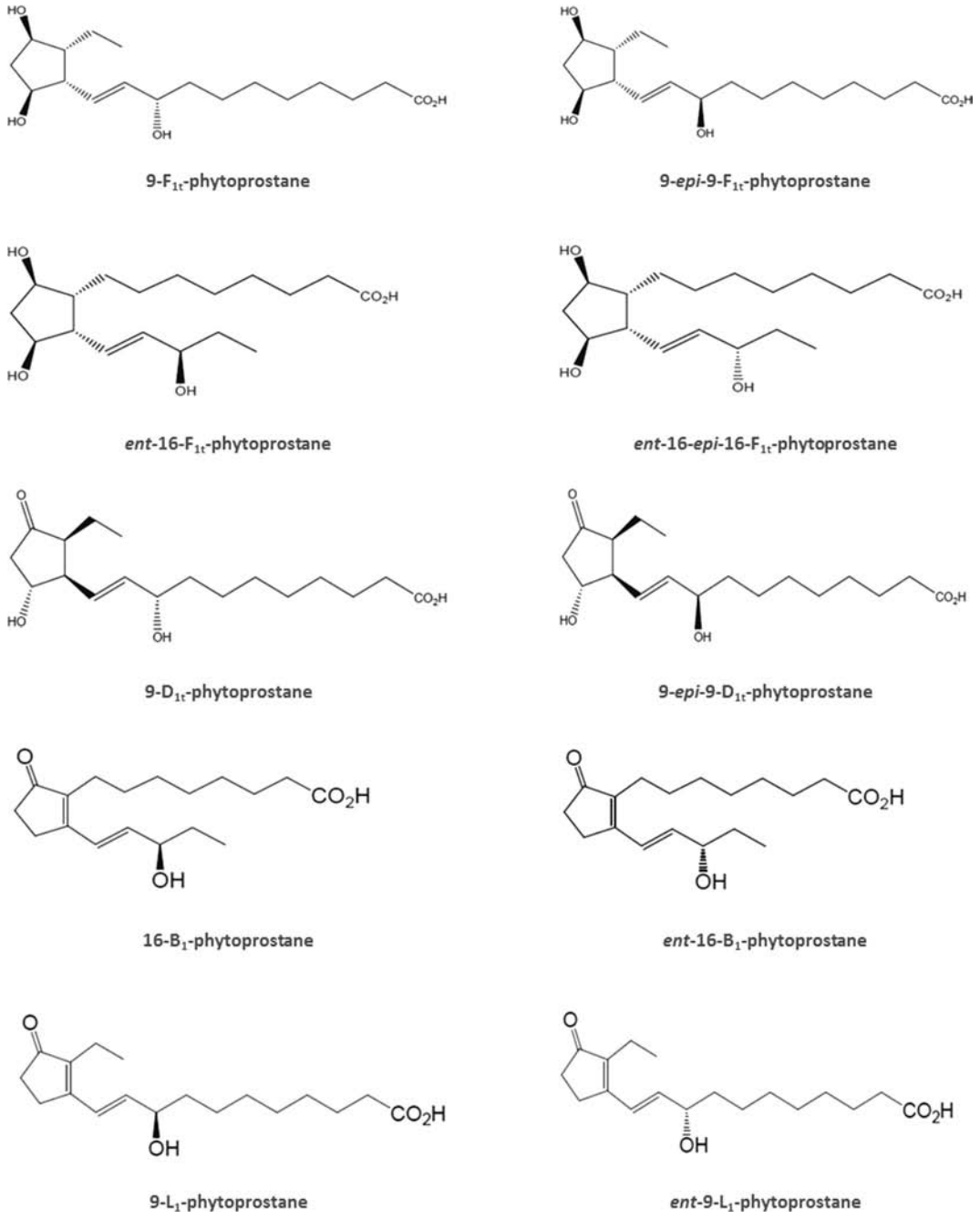

Figure 1. Metabolites of the different families of phytoprostanes.

procedure, in relation to changes in the phytoprostane content of wine or must, is a wide field to explore. It is made even more important by taking into account that the scientific literature has highlighted phytoprostanes as a representative tool for measuring in vivo stress in plants.[4,6] Phytoprostanes could also be of interest to wineries, to determine the oxidative status of their products and as a quality control in the winemaking process.

MATERIALS AND METHODS

Standards and Reagents. Phytoprostanes are very stable in their frozen form, they can remain unaltered for several years. Phytoprostane standards (9-F_{1t}-phytoprostane (Phyto1), *ent*-16-*epi*-16-F_{1t}-phytoprostane + *ent*-16-F_{1t}-phytoprostane (Phyto2+3), 9-*epi*-9-D_{1t}-phytoprostane (Phyto4), 9-D_{1t}-phytoprostane (Phyto5), 16-B_1-phytoprostane + *ent*-16-B_1-phytoprostane (Phyto6+7), 9-L_1-phytoprostane + *ent*-9-L_1-phytoprostane (Phyto8+9)) were synthesized according to previous procedures.[13−16]

Solid-phase extraction (SPE) cartridge was Strata X-AW (100 mg/3 mL) from Phenomenex (Torrance, CA, USA). Both butylated hydroxyanisole (BHA) and bis(2-hydroxyethyl)aminotris-(hydroxymethyl)methane (BIS-TRIS) were purchased from Sigma-Aldrich (St. Louis, MO, USA). Methanol (MeOH) was acquired from VWR (Fontenay-sous-Bois, France), acetonitrile was obtained from Merck (Darmstadt, Germany), and *n*-hexane was purchased from Panreac (Barcelona, Spain). All LC-MS grade solvents were obtained from J. T. Baker (Phillipsburg, NJ, USA). Water was treated in a Milli-Q water purification system (Millipore, Bedford, MA, USA).

Red Wine Samples. Red wines were provided by Baigorri winery (Bodegas Baigorri S.A.U, Samaniego, Álava, Spain). Three different wines were selected to study different vinification and aging

DOI: 10.1021/acs.jafc.5b03365
J. Agric. Food Chem. 2015, 63, 9022−9028

procedures. For correct maintenance, they were stored between 12 and 14 °C after bottling.

"Baigorri carbonic maceration 2010" wine (CMW) was made with a combination of tips of bunches from hand-harvested Tempranillo grapes. Before being fermented, the grapes were macerated for a long time. Short fermentations in stainless steel tanks were performed. No aging procedure was employed.

"Baigorri aged 2007" wine (AW) was manufactured using the tips of bunches of hand-harvested Tempranillo (90%), Garnacha (5%), and other native grape varieties (5%). Long macerations and intracellular fermentations in stainless steel tanks were employed. Large oak barrels were employed during the 14 months of aging.

"Baigorri high expression 2010" wine (HEW) was made from hand-harvested Tempranillo grapes selected from very old (>50 years) and low-yielding vineyards. For its long maceration and fermentation times, stainless steel tanks were used throughout the process. Large oak barrels were also employed during the 22 months of aging.

The alcoholic grades of CMW and AW were similar (13.5°), but that of HEW was slightly higher (14°).

Must Samples. The musts analyzed during the current study were stored at −20 °C for 7 months after the harvest of the grapes, so that the fermentation process did not begin. They were the original grape juices used for the winemaking procedure of each wine. This allows elucidation of the effect of the winemaking process, by direct comparison of each must with its respective wine.

The must samples are referred to in the text as follows: CMM for the initial must of "Baigorri carbonic maceration" wine, AM for the initial must of "Baigorri aged 2010" wine, and HEM for the initial must of "Baigorri high expression 2010" wine.

The chemical compositions of the samples were quite similar. Total acidity values of must samples were 4.44, 5.81, and 6.58 g/L for CMM, AM, and HEM, respectively. Finally, density values were 1102, 1099, and 1100, whereas pH values were 3.65, 3.42, and 3.52 for CMM, AM, and HEM, respectively.

Extraction of Phytoprostanes. For the analysis of phytoprostanes, their extraction from wines and musts was performed following the SPE method developed by Medina et al.[17] and Collado-González et al.,[12] slightly modified for the wine matrix. A mixture of three different bottles of each wine was employed for the extraction. Strata X-AW cartridges were employed for the SPE and were conditioned with 2 mL of methanol followed by 2 mL of Milli-Q water. After that, the cartridges were washed with 2 mL of water, 2 mL of methanol/water (1:3, v/v), and 2 mL of acetonitrile. Finally, the samples were eluted with 1 mL of methanol. The samples were brought to dryness under vacuum, reconstituted with 200 μL of elution phases A:B (90:10, v/v), and filtered through a Millex HV13 0.45 μm membrane filter (Millipore, Bedford, MA, USA).

UHPLC-QqQ-MS/MS Analyses. Separation of the phytoprostanes present in the samples was performed using a UHPLC coupled to a 6460 QqQ-MS/MS (Agilent Technologies, Waldbronn, Germany), as previously described.[12] Each sample was analyzed in triplicate. Chromatographic separation was carried out on a BEH 156 2.1 × 50 mm, 1.7 μm, C_{18} column (Waters, Milford, MA, USA). The column temperatures were 6 °C (left side) and 6 °C (right side). The mobile phases employed were solvent A (water/acetic acid (99.99:0.01, v/v)) and solvent B (methanol/acetic acid (99.99:0.01, v/v)). The elution was performed at a flow rate of 0.2 mL/min, using the following gradient profile: 60% B at 0 min, 62% B at 2 min, 62.5% B at 4 min, reaching 65% B at 8 min, and returning to the initial conditions at 8.01 min.

The MS analysis was applied in the multiple reaction monitoring (MRM) negative ESI mode. The ESI conditions and ion optics were as previously described.[12] Data acquisition and processing were performed using MassHunter software, version B.04.00 (Agilent Technologies). The quantitation of phytoprostanes detected in the wines and musts was performed using authentic standards of 9-F_{1t}-phytoprostane, *ent*-16-*epi*-16-F_{1t}-phytoprostane, *ent*-16-F_{1t}-phytoprostane, 9-*epi*-9-D_{1t}-phytoprostane, 9-D_{1t}-phytoprostane, 16-B_1-phytoprostane, *ent*-16-B_1-phytoprostane, 9-L_1-phytoprostane, and *ent*-9-L_1-phytoprostane. The synthetic isoprostane d_4-15-F_{2t}-IsoP (8-isoPGF$_{2\alpha}$-d_4) was used as the internal standard.

Statistical Analysis. An analysis of variance (ANOVA; Duncan) was applied to establish significant differences between the means obtained for the different samples of wine and must. A probability value of $p < 0.05$ was adopted as the criterion for significant differences. These analyses were performed with SPSS version 15 software (SPSS Inc., Chicago, IL, USA).

RESULTS AND DISCUSSION

Qualitative Analysis of Phytoprostanes. The individual phytoprostanes found in wines and musts are shown in Figure 2. Their identification was confirmed according to their molecular masses, the precursor ions (m/z 327.2 and 307.2), the characteristic MS/MS fragmentation product ions, and the corresponding retention times. In contrast to prostaglandins, phytoprostanes are formed nonenzymatically as regio- and stereoisomeric mixtures.[12] The phytoprostane profiles of the

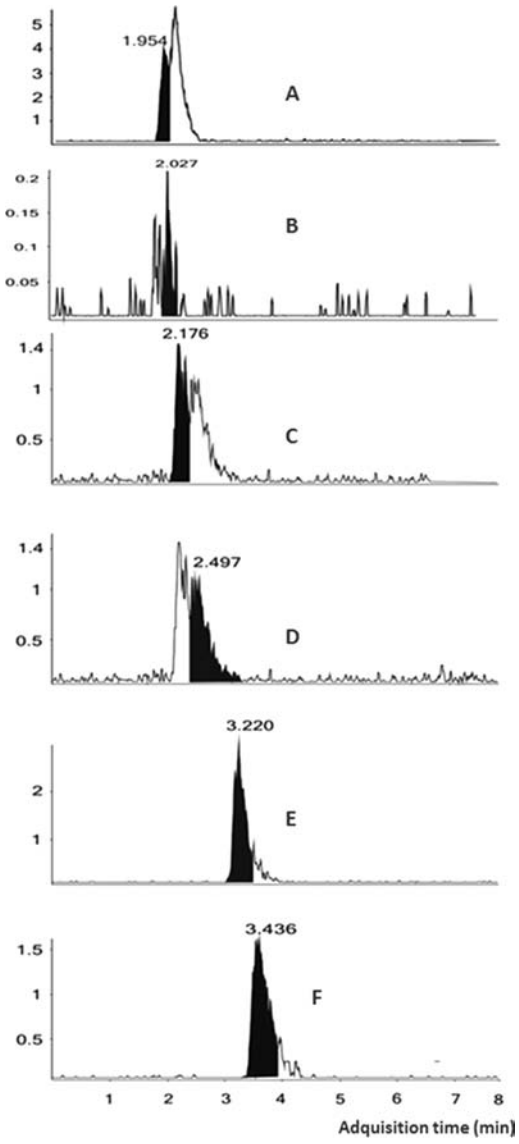

Figure 2. Phytoprostane chromatograms for CMW, measured by UPLC-MS/MS: (A) 9-F_{1t}-phytoprostane; (B) *ent*-16-*epi*-16-F_{1t}-phytoprostane + *ent*-16-F_{1t}-phytoprostane; (C) 9-*epi*-9-D_{1t}-phytoprostane; (D) 9-D_{1t}-phytoprostane; (E) 16-B_1-phytoprostane + *ent*-16-B_1-phytoprostane; (F) 9-L_1-phytoprostane + *ent*-9-L_1-phytoprostane.

DOI: 10.1021/acs.jafc.5b03365
J. Agric. Food Chem. 2015, 63, 9022−9028

analyzed beverage samples indicate the presence in all samples of the 9 and 16 series of the F_1- and D_1-classes of phytoprostanes. The B-series and L-series did not present a well standardized distribution among the different samples. In addition, only one wine (CMW) and one must (HEM) contained enantiomers of the racemic mixtures of 16-B_1- and 9-L_1-phytoprostane (Phyto6+7 and Phyto8+9). It is important to emphasize that the analytical conditions employed in this study did not allow separation of the enantiomers of the racemic mixtures of 16-B_1-phytoprostane + *ent*-16-B_1-phytoprostane and 9-L_1-phytoprostane + *ent*-9-L_1-phytoprostane. Therefore, both enantiomers of L- and B-series were quantitated together.

Four phytoprostanes were identified in all of the samples (the three wines and the three musts): Phyto1, Phyto2+3, Phyto4, and Phyto5.

Quantitative Analysis of Phytoprostanes. The concentrations of total free phytoprostanes are represented in Figure 3.

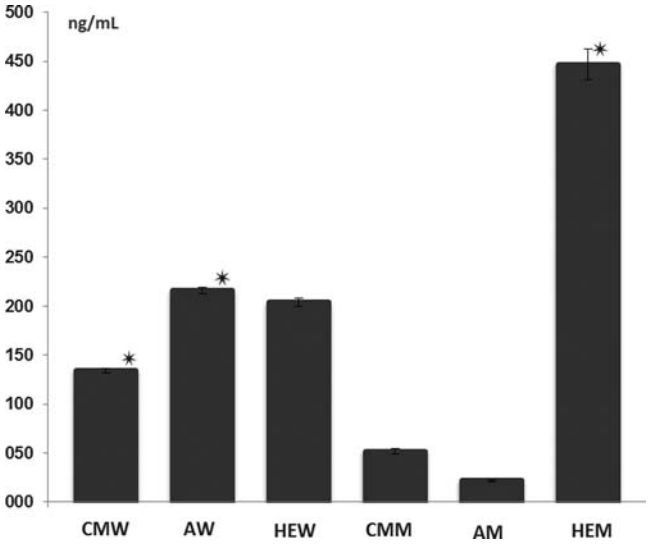

Figure 3. Concentrations of total phytoprostanes. CMW/CMM, wine/must with carbonic maceration; AW/AM, aged wine/must; HEW/HEM, high-expression wine/must.

This concentration varied widely among the three primary musts. In fact, no significant difference ($p > 0.05$) in the final concentration of total phytoprostanes was found when the primary must corresponding to carbonic maceration wine (CMM) (48.9 ± 2.6 ng/mL) and the primary must of aged wine (AM) (20.5 ± 0.8 ng/mL) were compared. However, the primary must of high-expression wine (HEM) had a significantly higher level ($p < 0.01$) of total phytoprostanes (430.9 ± 15.7 ng/mL) than CMM or AM. As commented on above, HEM came from very old and low-yielding vineyards (>50 years old), which are exposed to more stress factors than newer vineyards.[18] This would probably lead to an increase in pro-oxidant reactive species and to the subsequent formation of phytoprostanes by lipid peroxidation of ALA. Consequently, differences in agronomic factors (vineyard age) could have contributed to the different concentrations of total phytoprostanes, compared to HEM, in the must from grapes grown in the new vineyards (CMM and AM).

In the three wine samples studied, the total phytoprostane concentration did not present a standardized range. Actually, the values did not vary ($p > 0.05$) between aged wine (AW) (213.2 ± 3.1 ng/mL) and high-expression wine (HEW) (199.8 ± 4.2 ng/mL), but the total phytoprostane concentration of carbonic maceration wine (CMW) (131.7 ± 2.3 ng/mL) was significantly lower ($p > 0.05$).

The levels of individual phytoprostanes varied consistently among the different classes of phytoprostanes (Table 1). The F_1-phytoprostane series class was generally the most abundant class ($p < 0.05$) found in all of the samples, Phyto1 being the most abundant compound (436.6 ± 7.9 ng/mL). Likewise, a change in the proportion of the F_1-phytoprostane series was observed in both aged wines (AW and HEW). In CMM, AM, HEM, and CMW, Phyto1 was found at a higher concentration ($p < 0.05$) (32.7 ± 1.8, 13.5 ± 0.1, 149.8 ± 1.8, and 90 ± 0.9 ng/mL, respectively) than the sum of Phyto2+3 (6.8 ± 0.3, 4.5 ± 0.1, 50.1 ± 0.1, and 19.9 ± 0.4 ng/mL, respectively). However, in AW and HEW the opposite relationship was found: the sum of Phyto2+3 (133.8 ± 2.2 and 124.9 ± 1.7 ng/mL, respectively) exceeded the level of Phyto1 (76.9 ± 0.7 and 73.6 ± 2.4 ng/mL, respectively). Therefore, transformations of the stereoisomers during the aging of wines could change the proportion of the F_1-phytoprostane series.

The D_1-phytoprostane series class was found primarily in HEM. Two epimeric compounds (Phyto4 (25.1 ± 2.1 ng/mL) and Phyto5 (200.4 ± 11.1 ng/mL)) were abundant in HEM. However, the level of Phyto4 in the rest of the samples did not exceed 0.6 ng/mL, whereas Phyto5 was also plentiful in CMW (17.1 ± 0.7 ng/mL). Minor amounts were found in CMM and AM (8.7 ± 0.4 and 2.3 ± 0.5 ng/mL, respectively), with even lower values in the rest of the samples.

As commented above, the analytical conditions employed in the present study did not allow the separation of the different enantiomers. Therefore, enantiomers of both the 9-L- and 16-B-phytoprostanes series of B_1- and L_1- phytoprostanes were quantitated together. Consequently, these two classes were

Table 1. Content of Individual Phytoprostanes Analyzed in Three Types of Musts and Wines[a]

structure	phytoprostane	CMW	AW	HEW	CMM	AM	HEM
Phyto1	9-F_{1t}-phytoprostane	90.04 ± 0.9	76.9 ± 0.7	73.5 ± 2.4	32.7 ± 1.8	13.5 ± 0.1	149.8 ± 1.8
Phyto2+3	*ent*-16-*epi*-16-F_{1t}-phytoprostane + *ent*-16-F_{1t}-phytoprostane	19.9 ± 0.3	133.8 ± 2.2	124.9 ± 1.7	6.7 ± 0.2	4.5 ± 0.08	50.1 ± 0.08
Phyto4	9-*epi*-9-D_{1t}-phytoprostane	0.4 ± 0.02	0.1 ± 0.02	0.09 ± 0.005	0.6 ± 0.03	0.1 ± 0.06	21.5 ± 2.1
Phyto5	9-D_{1t}-phytoprostane	17.1 ± 0.7	2.2 ± 0.01	1.2 ± 0.01	8.7 ± 0.4	2.3 ± 0.5	200.4 ± 11.1
Phyto6+7	16-B_1-phytoprostane + *ent*-16-B_1-phytoprostane	0.3 ± 0.001	ND	ND	ND	ND	2.5 ± 0.1
Phyto8+9	9-L_1-phytoprostane + *ent*-9-L_1-phytoprostane	3.8 ± 0.2	ND	ND	ND	ND	6.4 ± 0.3

[a]Results are expressed in ng/mL ± SD. CMW/CMM, carbonic maceration wine/must; AW/AM, aged wine/must; HEW/HEM, high expression wine/must; ND, not detected.

DOI: 10.1021/acs.jafc.5b03365
J. Agric. Food Chem. 2015, 63, 9022−9028

identified and quantitated as the sum of 9-L_1- + 9-L_1-*ent*-16-B_1-phytoprostane and the sum of 16-B_1- + *ent*-16-$B_1$9-L_1-phytoprostane, respectively. Finally, compounds from the B_1- and L_1-phytoprostane classes (Phyto6+7 and Phyto8+9) were found in very low amounts. Only in CMW and HEM they were abundant enough to be quantitated, according to the limit of quantitation of the method developed by Collado-González et al.[12] In fact, in these two samples, the sums of the concentrations of Phyto6+7 (2.8 ± 0.1 ng/mL) and Phyto8+9 (10.3 ± 0.5 ng/mL) were not significant compared to the quantities found in the other phytoprostane classes ($p > 0.05$).

The vinification process seems to modify the initial content of phytoprostanes in the must, because wines CMW and AW showed higher total phytoprostane concentrations than CMM and AM (their corresponding primary musts). The musts CMM (48.7 ± 2.4 ng/mL) and AM (20.4 ± 0.7 ng/mL) had lower concentrations ($p < 0.05$) of total phytoprostanes than their respective finished wines (131.8 ± 2.1 and 213 ± 2.9 ng/mL for CMW and AW, respectively). The wine aging process may be an important factor in the formation of phytoprostanes. The musts CMM and AM exhibited similar ($p > 0.05$) phytoprostane levels. Nevertheless, after the vinification process, the total phytoprostane concentration in CMW was lower than in AW. In the case of CMW, this concentration could have been a consequence of the carbonic maceration process (extraction) applied to the grapes and the consequent alcoholic and malolactic fermentation in stainless steel tanks.[19] However, the vinification of AW could have been more oxidative, owing to the use of oak wood barrels for the aging procedure employed in the vinification. This could have released pro-oxidant compounds into the medium, in addition to promoting greater contact with oxygen.[20] In wine, ROS can be produced by reduced transition metals ions such as copper or iron. Superoxide radical anions, hydroperoxyl radicals, or hydrogen peroxide could be responsible of the oxidation of ALA.[21] The vinification of AW included an aging process that was not included in the production of CMW. The oxidation processes during this vinification, besides the aging of the red wine, could have led to the production of reactive pro-oxidant molecules that oxidize ALA to phytoprostanes, explaining the difference in the final level of total phytoprostanes between CMW and AW.

By contrast, in the vinification process that yielded HEW from HEM, the primary must showed a total phytoprostane concentration that was >2-fold higher (430.9 ± 15.7 ng/mL) than that of the finished wine (199.8 ± 4.2 ng/mL). This reduction could be mainly attributable to the great loss of the 9-series of the D_1-phytoprostane class. It is important to highlight that the D_1-phytoprostane class is the only one studied that is not a terminal compound (end product) in the nonenzymatic lipid peroxidation. In this sense, the decline of the total phytoprostane content may be explained by the rearrangement into J_1- and dJ_1-phytoprostanes, by a dehydration reaction, of the Phyto5, present in large amounts in HEM (200.4 ± 11.2 ng/mL). This probably occurred during the vinification process of HEW. Because pro-oxidant compounds are present during the vinification process, the stability of intermediate phytoprostanes is uncertain.[3,22] The oxidizing conditions during the vinification process probably led to the oxidation of ALA and, thus, the formation of D_1-phytoprostanes. The D_1-phytoprostanes may have been oxidized to J_1- and dJ_1-phytoprostanes, but this could not be investigated as there are no authentic markers available for these compounds.

To our knowledge, no papers that describe the phytoprostane content in wine or must have been published. Nevertheless, a few plant matrices have been investigated to report the phytoprostane occurrence.[3] Tobacco, *Arabidopsis thaliana*, *Crotalaria cobalticola*, *Eschscholzia californica*, and birch pollen have shown the presence of phytoprostanes. Birch pollen had the highest phytoprostane concentration of all these matrices (32 μg/g).[23] Consequently, the selection of the plant tissue analyzed is very important, because ROS are not produced equally throughout all of the structures of the plant. In fact, green tissues are the most likely producers of ROS, because of the singlet oxygen formed in the chloroplast during photosynthesis, leading to an increase in the number of peroxidation products.[22] Savchenko et al.[24] reported that the total amount of phytoprostanes in photosynthetic tissue is 10 times higher than in roots. In this sense, depending on the tissue studied, phytoprostane levels might vary extensively. Few researchers have reported phytoprostane contents in foods. Durand et al.[22] described high amounts of phytoprostanes in tomato leaves, F_1-, E_1-, and d-J_1-phytoprostanes being the most abundant. The level of phytoprostanes in almonds and olive/sunflower oil has been reported to range from 4.0 to 23.8 ng/100 g.[12,25,26]

Researchers have highlighted the importance of phytoprostanes as bioactive lipid derivatives, not only in plant matrices but also in mammalian systems.[27] Phytoprostanes, derived from a nonenzymatic oxidation reaction, are believed to exert beneficial effects in the organism.[3,5,27] Due to their similarities to different prostaglandins, they could mimic the effects of the latter on the organism.[4,22,28] In the present survey, F_1-phytoprostanes were the most abundant class of phytoprostanes in all of the samples studied (436.6 ± 7.9 ng/mL for 9-F_{1t}-phytoprostane and 340.1 ± 4.8 ng/mL for *ent*-16-*epi*-16-F_{1t}-phytoprostane). These phytoprostanes can regulate inflammatory responses in dendritic cells.[23] Karg et al.[5] reported that A_1- and B_1-phytoprostanes inhibited the release of nitric oxide in lipopolysaccharide-stimulated RAW264.7 macrophages. Thus, cardiovascular diseases could be ameliorated by the effects of phytoprostanes. In fact, Barden et al.[28] related the intake of F_1-phytoprostanes to protective effects on the cardiovascular system.

The importance of the intake of phytoprostanes could be related to neuroprotective effects, too. Minghetti et al.[27] showed that B_1-phytoprostanes were biologically active in experimental models of immature cells of the central nervous system, exhibiting neuroprotective effects against oxidant injury induced by hydrogen peroxide and promoting myelination through mechanisms that involve activation of the peroxisome proliferator-activated receptor (PPAR)-γ.

Bioavailability of phytoprostanes has also been demonstrated in vivo with healthy humans. Barden et al.[28] examined the effect of flaxseed oil, containing arachidonic acid; they examined the effect of a diet supplemented with flaxseed oil on F_1-phytoprostane and F_2-isoprostane concentrations in the urine and plasma of healthy men. Both the plasma and urine analyses confirmed the absorption of phytoprostanes by the intestinal tract. The esterified and nonesterified phytoprostane levels before intake of flaxseed oil were higher in plasma than in urine. Not only oil has been demonstrated to contain phytoprostanes, parenteral nutrition[5] has also shown a significant content of these metabolites (0.09−99 mg/L).

DOI: 10.1021/acs.jafc.5b03365
J. Agric. Food Chem. 2015, 63, 9022−9028

Assuming these possible beneficial effects, phytoprostanes would have an important impact on the Mediterranean diet, due to the wide consumption of wine around the world. The F_1-phytoprostane concentrations found in the red wines and musts and the suggested beneficial effects on the organism make their contribution relevant in the beneficial effects of the Mediterranean diet. However, further studies seem to be necessary to understand the physiological relevance of phytoprostanes in general and of F_1-phytoprostanes in particular, for example, their role in preventing myocardial infarction or heart disease.

To the best of our knowledge, this is the first paper describing the presence of phytoprostanes in wine or must. The results showed the F_1-phytoprostanes as the most abundant class for all samples. Likewise, D_1-phytoprostanes were present in musts in large quantities, especially in HEM. Vinification and aging procedures may influence and change the initial phytoprostane profile, favoring the formation of pro-oxidant species. Further studies are needed to elucidate the development of phytoprostanes during wine production.

With the possible beneficial effects of phytoprostanes in the cardiovascular system and the high concentrations observed in wines and musts taken into account, phytoprostanes could be an important factor in the cardioprotective or cerebrovascular effects of red wine and the Mediterranean diet, due to their possible anti-inflammatory effects. However, further clinical trials with humans and with animal models are necessary to elucidate how phytoprostanes could improve the cardiovascular system or exert neuroprotective effects.

AUTHOR INFORMATION

Corresponding Author

*(A.G.-I.) Phone: +34 968396363. Fax: +34 968396213. E-mail: angelgil@cebas.csic.es.

Funding

We are grateful to the UCAM for its support during the development of the assay for the study. The study received financial support from national funding agencies through Project AGL2011-23690 (CICYT). S.M. is grateful to the CICYT for a research contract (AGL2011-23690).

Notes

The authors declare no competing financial interest.

ACKNOWLEDGMENTS

We thank Pablo Rodríguez and David Walker, expert reviewers of the written English.

REFERENCES

(1) Guerrero, R. F.; García-Parrilla, M. C.; Puertas, B.; Cantos-Villar, E. Wine; resveratrol and health: a review. *Nat. Prod. Commun.* **2009**, *4* (5), 635−658.

(2) Magder, S. Reactive oxygen species: toxic molecules or spark of life? *Crit. Care* **2006**, *10* (1), 208.

(3) Durand, T.; Bultel-Poncé, V.; Guy, A.; El Fangour, S.; Rossi, J. C.; Galano, J. M. Isoprostanes and phytoprostanes: bioactive lipids. *Biochimie* **2011**, *93* (1), 52−60.

(4) Imbusch, R.; Mueller, M. J. Formation of isoprostane f2-like compounds (phytoprostanes f1) from α-linolenic acid in plants. *Free Radical Biol. Med.* **2000**, *28* (5), 720−726.

(5) Karg, K.; Dirsch, V. M.; Vollmar, A. M.; Cracowski, J. L.; Laporte, F.; Mueller, M. J. Biologically active oxidized lipids (phytoprostanes) in the plant diet and parenteral lipid nutrition. *Free Radical Res.* **2007**, *41* (1), 25−37.

(6) Thoma, I.; Loeffler, C.; Sinha, A. K.; Gupta, M.; Krischke, M.; Steffan, B.; Roitsch, T.; Mueller, M. J. Cyclopentenone isoprostanes induced by reactive oxygen species trigger defense gene activation and phytoalexin accumulation in plants. *Plant J.* **2003**, *34* (3), 363−375.

(7) Loeffler, C.; Berger, S.; Guy, A.; Durand, T.; Bringmann, G.; Dreyer, M.; Von Rad, U.; Durner, J.; Mueller, M. J. B_1-phytoprostanes trigger plant defense and detoxification responses. *Plant Physiol.* **2005**, *137* (1), 328−340.

(8) Mueller, S.; Hilbert, B.; Dueckershoff, K.; Roitsch, T.; Krischke, M.; Mueller, M. J.; Berger, S. General detoxification and stress responses are mediated by oxidized lipids through tga transcription factors in arabidopsis. *Plant Cell* **2008**, *20* (3), 768−785.

(9) Traidl-Hoffmann, C.; Mariani, V.; Hochrein, H.; Karg, K.; Wagner, H.; Ring, J.; Mueller, M. J.; Jakob, T.; Behrendt, H. Pollen-associated phytoprostanes inhibit dendritic cell interleukin-12 production and augment t helper type 2 cell polarization. *J. Exp. Med.* **2005**, *201* (4), 627−636.

(10) Mariani, V.; Gilles, S.; Jakob, T.; Thiel, M.; Mueller, M. J.; Ring, J.; Behrendt, H.; Traidl-Hoffmann, C. Immunomodulatory mediators from pollen enhance the migratory capacity of dendritic cells and license them for th2 attraction. *J. Immunol.* **2007**, *178* (12), 7623−7631.

(11) Gutermuth, J.; Bewersdorff, M.; Traidl-Hoffmann, C.; Ring, J.; Mueller, M. J.; Behrendt, H.; Jakob, T. Immunomodulatory effects of aqueous birch pollen extracts and phytoprostanes on primary immune responses in vivo. *J. Allergy Clin. Immunol.* **2007**, *120* (2), 293−299.

(12) Collado-González, J.; Pérez-López, D.; Memmi, H.; Gijón, M. C.; Medina, S.; Durand, T.; Guy, A.; Galano, J. M.; Ferreres, F.; Torrecillas, A.; Gil-Izquierdo, A. Water deficit during pit hardening enhances phytoprostanes content; a plant biomarker of oxidative stress; in extra virgin olive oil. *J. Agric. Food Chem.* **2015**, *63* (14), 3784−3792.

(13) El Fangour, S.; Guy, A.; Vidal, J. P.; Rossi, J. C.; Durand, T. A flexible synthesis of the phytoprostanes B_1 types I and II. *J. Org. Chem.* **2005**, *70* (3), 989−997.

(14) El Fangour, S.; Guy, A.; Despres, V.; Vidal, J. P.; Rossi, J. C.; Durand, T. Total synthesis of the eight diastereomers of the syn-anti-syn phytoprostanes F_1 types I and II. *J. Org. Chem.* **2004**, *69* (7), 2498−2503.

(15) Durand, T.; Guy, A.; Henry, O.; Roland, A.; Bernad, S.; El Fangour, S.; Vidal, J. P.; Rossi, J. C. Total syntheses of iso-; neuro- and phytoprostanes: new insight in lipid chemistry. *Chem. Phys. Lipids* **2004**, *128* (1−2), 15−33.

(16) Pinot, E.; Guy, A.; Fournial, A.; Balas, L.; Rossi, J. C.; Durand, T. Total synthesis of the four enantiomerically pure diasteroisomers of the phytoprostanes E_1 type II and of the 15-E_{2t}-isoprostanes. *J. Org. Chem.* **2008**, *73* (8), 3063−3069.

(17) Medina, S.; Domínguez-Perles, R.; Gil, J. I.; Ferreres, F.; García-Viguera, C.; Martínez-Sanz, J. M.; Gil-Izquierdo, A. A ultra-pressure liquid chromatography/triple quadrupole tandem mass spectrometry method for the analysis of 13 eicosanoids in human urine and quantitative 24 h values in healthy volunteers in a controlled constant diet. *Rapid Commun. Mass Spectrom.* **2012**, *26* (10), 1249−1257.

(18) Soleas, G. J.; Diamandis, E. P.; Goldberg, D. M. Wine as a biological fluid: history; production; and role in disease prevention. *J. Clin. Lab. Anal.* **1997**, *11* (5), 287−313.

(19) Tesniere, C.; Flanzy, C. *Adv. Food Nutr. Res.* **2011**, *63*, 1−15.

(20) Jackson, R. *Wine Science*, 3rd ed.; Academic Press: Burlington, MA, USA, 200810.1016/B987-0-12-373646-8.50020-2.

(21) Oliveira, C. M.; Ferreira, A. C. S.; De Freitas, V.; Silva, A. M. S. Oxidation mechanisms occurring in wines. *Food Res. Int.* **2011**, *44* (5), 1115−1126.

(22) Durand, T.; Bultel-Poncé, V.; Guy, A.; Berger, S.; Mueller, M. J.; Galano, J. M. New bioactive oxylipins formed by non-enzymatic free-radical-catalyzed pathways: the phytoprostanes. *Lipids* **2009**, *44* (10), 875−888.

(23) Gilles, S.; Mariani, V.; Bryce, M.; Mueller, M. J.; Ring, J.; Jakob, T.; Pastore, S.; Behrendt, H.; Traidl-Hoffmann, C. Pollen-drived E_1-

DOI: 10.1021/acs.jafc.5b03365
J. Agric. Food Chem. 2015, 63, 9022−9028

Pytoprostanes signal via PPAR-γ and NF-κB-dependent mechanisms. *J. Immunol.* **2009**, *182* (11), 6653−6658.
(24) Savchenko, T. V.; Zastrijnaja, O. M.; Klimov, V. V. Oxylipins and plant abiotic stress resistance. *Biochemistry (Moscow)* **2014**, *79* (4), 362−375.
(25) Collado-González, J.; Durand, T.; Ferreres, F.; Medina, S.; Torrecillas, A.; Gil-Izquierdo, A. Phytoprostanes. *Lipid Technol.* **2015**, *27* (6), 127−130.
(26) Carrasco-Del Amor, A. M.; Collado-Gonzalez, J.; Aguayo, E.; Guy, A.; Galano, J. M.; Durand, T.; Gil-Izquierdo, A. Phytoprostanes in almonds: Identification; quantitation; and impact of cultivar and type of cultivation. *RSC Adv.* **2015**, *5* (63), 51233−51241.
(27) Minghetti, L.; Salvi, R.; Lavinia Salvatori, M.; Antonietta Ajmone-Cat, M.; De Nuccio, C.; Visentin, S.; Bultel-Poncé, V.; Oger, C.; Guy, A.; Galano, J. M.; Greco, A.; Bernardo, A.; Durand, T. Nonenzymatic oxygenated metabolites of α-linolenic acid B_1- and L_1-phytoprostanes protect immature neurons from oxidant injury and promote differentiation of oligodendrocyte progenitors through ppar-γ activation. *Free Radical Biol. Med.* **2014**, *73*, 41−50.
(28) Barden, A. E.; Croft, K. D.; Durand, T.; Guy, A.; Mueller, M. J.; Mori, T. A. Flaxseed oil supplementation increases plasma F_1-phytoprostanes in healthy men. *J. Nutr.* **2009**, *139* (10), 1890−1895.

DOI: 10.1021/acs.jafc.5b03365
J. Agric. Food Chem. 2015, 63, 9022−9028

activity of 2.4 Anson units (AU) per gram. One AU is the amount of enzyme that under standard conditions digests hemoglobin at an initial rate that produces an amount of trichloroacetic acid-soluble product which gives the same color with the Folin reagent as 1 mequiv of tyrosine released per minute. Optimal endoprotease activity was obtained by application trials to pH 8.0. Flavourzyme 1000 MG is an exopeptidase and endoprotease complex with an activity of 1.0 leucine aminopeptidase unit (LAPU) per gram. One LAPU is the amount of enzyme that hydrolyzes 1 mmol of leucine−*p*-nitroanilide per minute. Optimal exopeptidase activity was obtained by application trials at pH 7.0.

Preparation of DRB. RB mixed varieties were obtained from Padiberas National Berhad (BERNAS) rice milling factory, Tiram Jaya, Kuala Selangor, Malaysia. Freshly milled rice bran was stabilized and dried to constant weight at 100−105 °C in a custom-fabricated commercial stabilizer (Ansa Technology Sdn. Bhd, Johor, Malaysia). In brief, the rice bran powder was poured evenly into heat-resistant glass cookware and heated under high power (1000 W) in the stabilizer for approximately 180−220 s. After drying, RB was passed through a sieve (≤0.5 mm) and stored at 4 °C in a freezer prior to extractions. RB was then subjected to supercritical fluid carbon dioxide extraction (SFE; Thar 1000 F, Thar Technologies, Inc., Pitttsburgh, PA, USA) to obtain the DRB.

Preparation of DRB Protein Concentrate. DRB was mixed with deionized water in the ratio of 1:10 (w/v) and then 3 M NaOH was added until the final pH of the mixture was 10.5. The mixture was stirred for 1 h at room temperature and then centrifuged at 4000*g* for 10 min. An additional extraction was carried out with the same volume of alkaline solution. Supernatants were pooled and the pH was adjusted to the isoelectric point (pH 4.5). The precipitate was then recovered by centrifugation at 4000g for 10 min, and washed with distilled water adjusted to the isoelectric point, after which it was freeze-dried until further use.

Characterization of DRB Protein Concentrate. *Determination of Yield and Protein Content of DRB Protein Concentrate.* The Lowry assay was performed to obtain the protein content of DRB protein fractions.[19] The absorbance of the sample or standard was measured at 630 nm using a microplate reader (Opsys MR, Thermo Labsystems, Franklin, MA, USA). The results were interpreted as milligrams of bovine serum albumin equivalents per gram of dried weight of sample (mg BSA/g).

Amino Acid Analysis of DRB Protein Concentrate. The amino acid analysis of DRB protein fractions was carried out according to the method of Kwanyuen and Burton[20] with some minor modifications. Briefly, sample with at least 16% protein content was placed in a sealable test tube. The test tube was acid-washed with 6 N hydrochloric acid (HCl) and dried prior to use. Then, the lyophilized protein was hydrolyzed with 6 N HCl at 110 °C for 24 h. After hydrolysis, L-2-aminobutyric acid (AABA; 0.2578 g of AABA was made up to 1 L of 0.1 N HCl solution) was added into the hydrolysate in a ratio of 10 ml per 15 ml of the hydrolysate. The hydrolysate was then filtered using Whatman filter paper, grade 1 (Sigma-Aldrich Co.), and the supernatant was topped up to 50 mL using deionized water. The hydrolyzed sample was stored at −20 °C.

To prepare the derivatized solution, 10 μL of the hydrolyzed sample was dried under vacuum. The hydrolyzed sample was neutralized by adding 20 μL of a 2:2:1 mixture of methanol/water/TEA (v/v). The mixture was vortexed and fully dried under vacuum. Then, precolumn derivatization was performed by adding 20 μL of a mixture of 7:1:1:1 methanol/water/TEA/PITC (v/v) and mixing well with a vortex stirrer. The mixture was allowed to stand at room temperature for 20 min. Then, the sample was completely dried under vacuum. The sample was finally stored in a freezer prior to HPLC analysis.

The dried samples were redissolved in 100 μL of buffer A containing 0.1 M ammonium acetate (pH 6.5) and filtered through a Millipore membrane (0.22 μm). Then, 20 μL of the sample was injected and analyzed with an HPLC system equipped with a column heater, autosampler, variable wavelength detector, and data acquisition software controller. The reverse-phase column used was a Pico-Tag (3.9 × 150 mm), dimethyloctadecylsilyl-bonded amorphous silica, with an inline column filter. The column temperature was maintained at 43 °C. The samples were separated and eluted by a gradient resulting from mixing mobile phases A and B. Mobile phase A consisted of 0.1 M ammonium acetate, pH 6.5, whereas mobile phase B consisted of 44:46:10 0.1 M ammonium acetate/acetonitrile/methanol (v/v), pH 6.5. The flow rate was 1 mL/min throughout, and the gradient consisted of the following profiles: 100% A at start, 90% A and 10% B at 15 min, 60% A and 40% B at 30 min, 50% A and 50% B at 40 min, 100% B at 50 min, 100% A at 57−60 min. The samples eluted from the column were detected at 254 nm and recorded. The results were analyzed and compared with amino acid standards (AAS18, Sigma). The amino acid score (AAS) for the essential amino acid was calculated according to the formula

$$\text{amino acid ratio} = \frac{\text{mg of an essential amino acid in 1 g of sample}}{\text{mg of the same essential amino acid in 1 g of a reference pattern}}$$

The AAS was determined based on the lowest amino acid ratio. The scoring patterns suggested by the FAO/WHO/UHU[21] for adults were used in the present study.

Preparation of DRB Protein Hydrolysates. DRB was treated batchwise with Alcalase and Flavourzyme by individual, combination, or sequential treatment. Table 1 shows the experimental conditions of hydrolysis for different enzyme systems. Individual hydrolyses were developed over 4 h, whereas combination treatment was carried out by combining the two proteases for 4 h, and sequential treatment was carried out with an initial hydrolysis (1 h) using Alcalase and a second one (3 h) using Flavourzyme. The hydrolysis were carried out using the following parameters: (A) Alcalase hydrolysis, substrate concentration (*S*) = 10%; enzyme−substrate ratio (E/S) = 0.4 AU/g of protein; temperature *T* = 50 °C; pH 8.0; (F) Flavourzyme hydrolysis, *S* = 10%; E/S = 100 LAPU/g of protein, *T* = 50 °C, pH 7.0.

Table 1. Experimental Conditions of Hydrolysis for the Different Enzyme Systems

enzyme system[a]	detail	pH	temperature (°C)
DRB_A	partial hydrolysis using Alcalase	8.0	50
DRB_F	partial hydrolysis using Flavourzyme	7.0	50
DRB_A+F	partial hydrolysis with a combination of Alcalase and Flavourzyme	8.0	50
DRB_A●F	sequential hydrolysis using Alcalase and Flavourzyme	8.0 for Alcalase 7.0 for Flavourzyme	50

[a]DRB_A+F corresponds to simultaneous hydrolysis with Alcalase and Flavourzyme. DRB_A●F represents sequential hydrolysis using Alcalase first for 1 h followed by Flavourzyme with intermediate pH adjustment.

Briefly, the suspension was adjusted initially to the appropriate temperature and pH before the proteases, Alcalase and Flavourzyme, were added individually or in combination. Once the enzymes were added, the pH of the reaction was monitored constantly and adjusted to the optimal level by adding 0.5 N NaOH every time it decreased 0.1 unit from the optimal pH. The amount of added NaOH was recorded and later used for the calculation of degree of hydrolysis (DH). The enzymes were subsequently deactivated by heating the mixture to 95 °C for 15 min. The resulting hydrolysates were centrifuged at 3000*g* for 30 min at 4 °C to separate the soluble hydrolyzed material from the insoluble residue.

Determination of DH and Protein Content of DRB Protein Hydrolysates. The DH of DRB protein hydrolysates, defined as the percentage of peptide bonds cleaved, was calculated as

DOI: 10.1021/acs.jafc.5b03420
J. Agric. Food Chem. 2015, 63, 9029−9036

$$\mathrm{DH}\ (\%) = (BN_b)/(M_p \propto h_{total})$$

where B is the amount of alkali consumed (mL), N_b is the normality of alkali, M_p is the mass of the substrate (protein in grams, % N × 6.25), $1/\alpha$ is the calibration factor for pH-stat, and h_{total} is the content of peptide bonds.[22] The protein content was determined by using the Lowry method.[19]

Determination of Iron-Binding Capacity of DRB Protein Hydrolysates. The iron-binding capacity of DRB protein hydrolysates was determined according to the method of Decker and Welch[23] with some modifications. Briefly, 1 mL of sample solution was mixed with 3.0 mL of distilled water. The mixture was then reacted with 0.1 mL of 1 mM $FeSO_4$ and 0.2 mL of 5 mM 3-(2-pyridyl)-5,6-bis(4-phenylsulfonic acid)-1,2,4-triazine (Ferrozine) for 20 min at room temperature. The absorbance was read at 562 nm. The control was prepared in the same manner except that distilled water was used instead of the sample. EDTA was used as positive control. Iron-binding capacity was expressed as a percentage of the total iron ion content and was calculated as

$$[\text{iron solubility}]\% = [\text{iron ion}]_{\text{supernatant}}/[\text{iron ion}]_{\text{total}} \times 100$$

where $[\text{iron ion}]_{\text{supernatant}}$ is the supernatant iron ion content from the suspension and $[\text{iron ion}]_{\text{total}}$ is the total iron ion content of the suspension.

Cell Culture. Caco-2 cells originating from human colorectal carcinoma (courtesy of Chan Kim Wei from Universiti Putra Malaysia) were thawed and cultured at passage 22. The passage of the cells used in the experiments was between 25 and 33. Cells were cultivated in a 25 cm^2 tissue culture flask and grown in Dulbecco's modified Eagle medium (DMEM) supplemented with 20% (v/v) fetal bovine serum, 1% (v/v) nonessential amino acids, 1% (v/v) penicillin−streptomycin solution, and 0.1% (v/v) fungizone. The flask was incubated in a 5% CO_2 incubator at 37 °C and 95% relative humidity.

Collagen Coating and Cell Culture on the Insert of the 6-Well Transwell Plate. A 2 mg/mL stock solution of the rat tail collagen type I was prepared by adding an appropriate amount of 0.02 M acetic acid. The solution was allowed to stir at room temperature for 1 h until fully dissolved. The working collagen solution was diluted to 10 $\mu g/cm^2$ from the stock solution. Each of the inserts in the 6-well transwell plate was coated with 0.6 mL of working collagen solution. The collagen was allowed to bind for 4 h at 37 °C. The excess fluid was removed from the coated surface, and the inset was allowed to dry in a biological safety cabinet. The sterile insert was rinsed with PBS twice prior to cell seeding.

Then, 1.5 mL of the cell suspension was seeded into apical wells for each insert and incubated in the 5% CO_2 incubator at 37 °C and 95% relative humidity. The basolateral wells of the transwell were filled with 2.6 mL of fresh medium. The medium in the insert was changed every 2 days, whereas the medium in the basolateral wells was changed every 4−5 days. The sequence of medium changing was removal of medium from basolateral and then apical wells. The medium was added into apical wells and then only basolateral wells. The sequence of medium changing was chosen to avoid hydrostatic break of the cell monolayer. The cells were allowed to grow and differentiate for 18−21 days with monitoring of the TEER value, phenol red diffusion, and transmission electron microscopy (TEM) study.

Cell Viability Assay of DRB Protein Hydrolysates. Cell viability was determined by using the MTT assay. Cells were cultured in DMEM containing 10% FBS and seeded in 96-well plates (1×10^5 cells/mL) until the cells reached confluence. The cells were then treated with culture medium (control) and different concentrations of the sample (0−1000 ppm) for 24 h. The cells were subsequently incubated with MTT solution (Sigma, St. Louis, MO, USA) for another 4 h at 37 °C. The medium was then removed, and the blue formazan crystal was solubilized in 150 μL of dimethyl sulfoxide (DMSO; Sigma). Absorbance was measured at 570 nm on Opsis MR microplate reader (Dynex Technologies, Chantilly, VA, USA).

In Vitro Gastrointestinal Digestion of DRB Peptide Hydrolysates. Gastrointestinal digestion was applied to DRB using the in vitro methods described by Vattem et al.[13] and Miller et al.[24] with some modifications. Briefly, DRB peptide hydrolysates (5 g) were incubated for 1 h at 37 °C in a 0.32% (w/v) pepsin solution containing 30 mM NaCl and 0.7% (v/v) of 0.2 N HCl, pH 1.2, in a 1/20 (w/w) enzyme/protein hydrolysate relation to mimic the gastric fluid digestion condition. Then, 5 mg of $FeSO_4$ (37.5 μmol)[13] was added and followed by sufficient water to top up the solution to 50 mL.

To further simulate the intestinal fluid digestion, the pH of the pepsin digests was adjusted to 5.0 by dropwise addition of 0.05 M $NaHCO_3$. Subsequently, the mixture was incubated for 3 h at 37 °C in a pancreatin−bile solution containing 0.005 g of pancreatin and 0.03 g of bile salts/g of sample. When the intestinal digestion was completed, the samples were kept for 10 min in an ice bath. The pH of the samples was then raised to 7.2 using 0.5 M NaOH. The digests were subjected to centrifugation (4000g, 25 min, and 4 °C). The supernatants were collected and filtered through a dialysis tubing cellulose membrane (D9777 Sigma, average flat width = 25 mm, typical molecular weight cutoff = 14000) using the method of Jovani et al.[25] prior to iron uptake experiments.

Iron Uptake by Caco-2 Cells. Cells were seeded at a density of $(1-1.5) \times 10^5$ cells/cm^2 in a collagen-coated 6-well transwell plates (Costar, High Wycombe, UK). The iron uptake experiment was conducted when the percent of phenol red diffusion was <2.5% and the transmonolayer electrical resistance was >500 Ω cm^2. Briefly, growth medium was removed from the transwell by aspiration, and the upper and lower chambers were rinsed twice with phosphate-buffered saline (PBS) solution. This was followed by adding 1.5 mL of DMEM in the lower chamber and 0.5 mL of in vitro digested sample to the upper chamber. The apical samples and basal solutions were then collected after 4 h of incubation. The cells in the inset were lysed and harvested by adding 0.5 mL of 1 M NaOH. Total mineral content was measured in the apical solutions, cell monolayer, and basal solutions by using the formulas as provided in the following section.

Iron contents in DRB hydrolysates and Caco-2 cell absorption were measured by inductively coupled plasma atomic emission spectrometry (ICP-AES; ELAN DRC-e, PerkinElmer). Iron standards were prepared by diluting the $FeSO_4$ solution into series of concentrations (3.125−100.00 $\mu g/L$) with the same mixture used for the samples. The detection limit of iron analysis using ICP-MS was <0.010 $\mu g/L$. The solubility, retention, transport efficiency, and uptake efficiency percentage were determined according to the methods of Frontela et al.[26]

The experiment was conducted in a two-phases. In the first phase, rice bran protein hydrolysates with different enzymatic treatments were investigated. The best enzymatic system to obtain the optimal iron uptake in the cell model was chosen and allocated to the second phase. In the second phase, a variety of rice bran protein hydrolysates were prepared by incubation with combination of Alcalase and Flavourzyme for different periods of time, which allowed investigation of the best period of time to obtain the DRB protein hydrolysate with the highest iron-uptake capacity.

Statistical Analysis. All of the values are the mean of at least two replicates, and data are reported as the mean ± standard deviation (SD). The data were analyzed by Univariate analysis of variance (ANOVA) and Pearson's correlation coefficient. Duncan's multiple-range test (DMRT) was used to determine the differences among the samples. All of the analyses were conducted using GraphPad Prism 6 for Windows version 6.01 (GraphPad Software Inc., San Diego, CA, USA). Significant levels were defined as probabilities of ≤0.05.

RESULTS

Yield, Protein Content, and Amino Acid Content of DRB Protein Concentrate. The average yield and protein content of DRB protein concentrate were 11.85% (or 11.85 g/100 g DRB) and 82.61 mg BSA/g, respectively. The result of amino acid analysis for DRB protein concentrate and DRB protein fractions is presented in Table 2. Most of the essential amino acids in DRB protein concentrate, except phenylalanine

DOI: 10.1021/acs.jafc.5b03420
J. Agric. Food Chem. 2015, 63, 9029−9036

Table 2. Amino Acid Composition of DRB and DRB Protein Fractions and Their Amino Acid Scores Calculated on the Basis of FAO and NRC Reference Proteins[a]

	amino acid composition		
essential amino acid	defatted rice bran protein (mg/g crude protein, dry basis)	reference protein[b]	amino acid ratio[c]
lysine	3.51 ± 0.01	1.60	2.19 ± 0.01
leucine	5.63 ± 0.20	1.90	2.96 ± 0.20
isoleucine	3.03 ± 0.11	1.30	2.33 ± 0.11
valine	4.21 ± 0.17	1.30	3.24 ± 0.17
threonine	2.20 ± 0.09	0.90	2.44 ± 0.09
histidine	1.85 ± 0.09	1.60	1.16 ± 0.09
phenylalanine + tyrosine	4.23 ± 0.23	1.90	2.23 ± 0.23
methionine + cysteine	1.47 ± 0.15	1.70	0.86 ± 0.15
amino acid score for DRB protein concentrate			86

[a]Defatted rice bran protein was prepared by isoelectric point precipitation, as stated under Materials and Methods. [b]Reference protein: essential amino acid requirement for adults according to FAO/WHO/UNU (1985) (mg/g crude protein, dry basis). The protein quality of DRB was analyzed by applying the amino acid score based on the reference protein of FAO/WHO/UHU (1985). [c]Amino acid ratio referred to the ratio of a gram of the limiting amino acid (methionine + cysteine in the DRB protein concentrate) to the same amount of the corresponding amino acid in the reference protein multiplied by 100.

and methionine, exceeded the requirements of the reference protein for adults according to the FAO/WHO/UHU.[21]

Enzymatic Hydrolysis of DRB. Figure 1 shows the extracted peptide from DRB after treatment with different

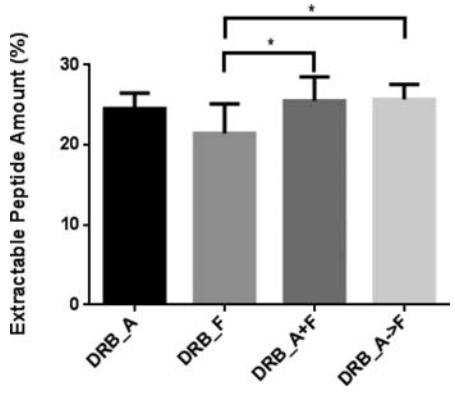

Figure 1. Extractable peptide amount (%) from DRB protein isolated by different enzyme hydrolysis treatments: treated with Alcalase (DRB_A), treated with Flavourzyme (DRB_F), treated with a combination of Alcalase and Flavourzyme (DRB_A+F), and sequentially treated with Alcalase and Flavourzyme (DRB_A•F). (*) Means were significantly different at $p \leq 0.05$ ($n = 3$).

enzymes. The peptide amounts of Alcalase-treated and Flavourzyme-treated DRB samples were 24.54 and 21.46%, respectively. DRB treated with Alcalase and Flavourzyme, either in combination (25.51%) or sequentially (25.70%), had significantly higher protein contents than the Flavourzyme-treated DRB sample, but not the Alcalase-treated DRB sample.

The added enzymes affected the DH in a time-dependent manner as shown in Figure 2. For all of the enzymatic

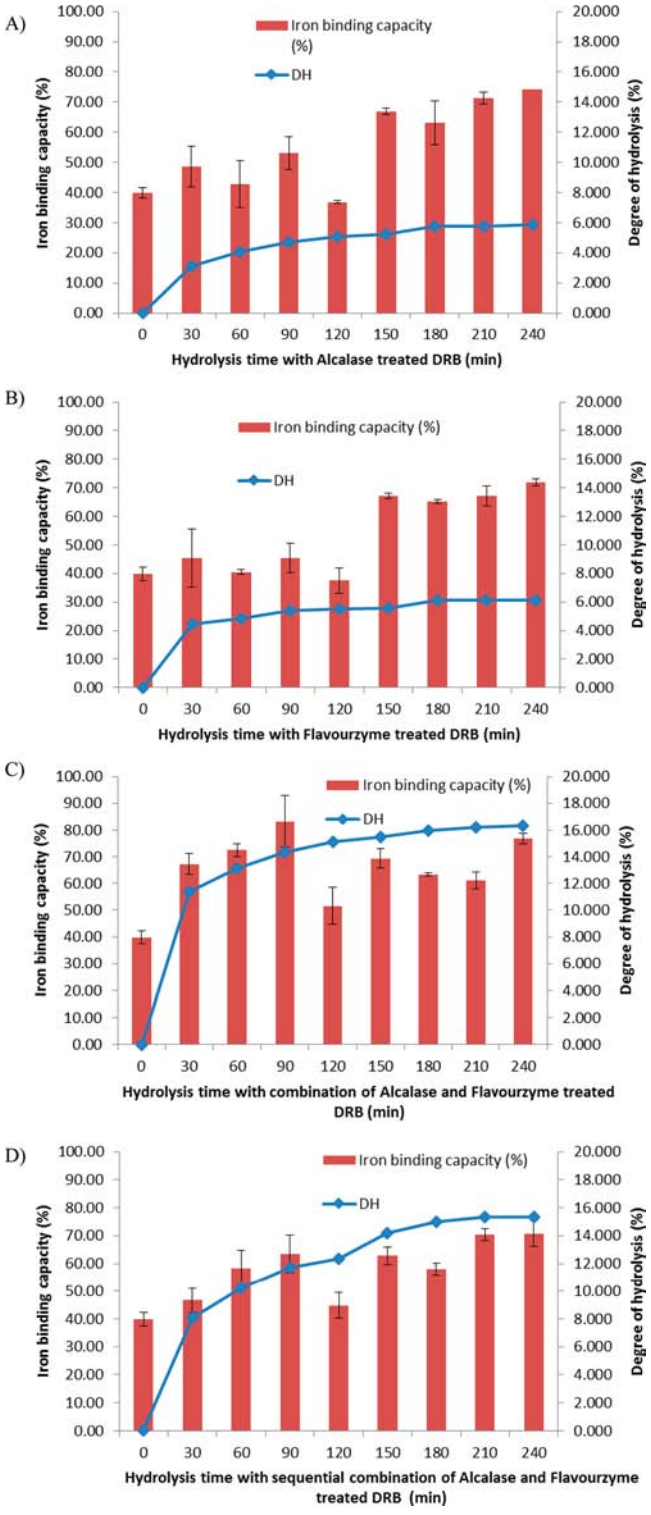

Figure 2. Effects of different hydrolysis times on the iron-binding capacities of DRB hydrolysates isolated by different enzyme hydrolysis treatments: Alcalase (A); Flavourzyme (B); combination of Alcalase and Flavourzyme (C); sequential treatment with Alcalase and Flavourzyme (D). All measurements are expressed as means ± SD of three independent experiments.

treatments, DH values increased dramatically in the primary hydrolysis stage, followed by slow increases in hydrolyses with increasing treatment times. The combination of Alcalase and Flavourzyme treatment exhibited higher DH for the DRB

DOI: 10.1021/acs.jafc.5b03420
J. Agric. Food Chem. 2015, 63, 9029−9036

hydrolysates compared with the individual enzyme treatments at all sampling times. Thus, with Alcalase, DH was 5.87%, whereas 6.12% of DH was obtained for Flavourzyme after 4 h of reaction. The DH of DRB hydrolysates with combination of Alcalase and Flavourzyme at 4 h of treatment was 16.35%. These values represent 10.48% more hydrolysis than with Alcalase and 10.23% more than with Alcalase.

Furthermore, protein hydrolysis was carried out using sequential treatment with the proteases Alcalase and Flavourzyme. After 60 min of Alcalase addition, a protein hydrolysate with a 10.22% DH was obtained (Figure 2D). Subsequent to the addition of Flavourzyme, an extensive hydrolysate with a higher DH (15.34% after 4 h of treatment) was obtained. However, it was slightly lower than that of the combination treatment set.

Iron-Binding Capacity of DRB. The iron-binding capacities of the DRB protein and its hydrolysates obtained at different hydrolysis times are shown in Figure 2. DRB protein hydrolysates taken at various hydrolysis periods (30, 60, 90, 120, 150, and 180 min) showed different iron-binding capacities. The effects of all hydrolysates obtained at different hydrolysis times were significantly higher than that of DRB itself. The peptide hydrolysate after treatment with a combination of Alcalase and Flavourzyme exhibited optimal iron-binding capacity (83%) at 90 min. Increasing the hydrolysis time after 90 min did not significantly increase the iron-binding activity of peptide hydrolysate.

Iron Uptake by Caco-2 Cells. The confluence and the confirmation of the Caco-2 differentiation were monitored by TEER and phenol red diffusion assay. These assays were also conducted during the iron uptake assay to ensure the monolayer integrity. These values were kept constant before and after the experiment (data not shown), indicating the Caco-2 cell monolayers remained intact for use in the studies. Besides that, changes of the morphology in Caco-2 cells were observed under TEM. The expression of microvilli and tight junctions were assessed by examining the cell morphology after day 20. The TEM images (data not shown) showed that the Caco-2 cells demonstrated morphologic differentiation with the presence of numerous microvilli. The integrity of the monolayer was confirmed by the presence of tight junctions in the apical zone. Therefore, the formation of these features highly indicated the validity of the Caco-2 cells as intestine-like cell model for the study of bioavailability.

To evaluate whether the DRB peptide hydrolysates were cytotoxic to cells, Caco-2 cells were treated with increasing concentrations of the DRB peptide hydrolysates from 0 to 1000 ppm. All four DRB hydrolysates showed good effects on cell viability even at a concentration of 1000 ppm (data not shown).

The results obtained in the iron retention, transport, and uptake assays by Caco-2 from DRB hydrolysates are summarized in Table 3. Hydrolysis caused an increase in retention percentage, transport, and uptake efficiencies of iron in all of the DRB hydrolysates. Significant differences ($P < 0.05$) in the iron retention percentage and transport and uptake efficiencies were observed for DRB_A+B hydrolysate compared to the DRB protein without hydrolysis treatment. In addition, the iron solubility percentages of DRB_F and DRB_A+B were increased significantly as well. Therefore, we selected the DRB hydrolysate obtained using combined treatment of Alcalase and Flavourzyme to further investigate the optimal hydrolysis time of DRB hydrolysate−iron complex.

Table 3. Iron Retention, Transport, and Uptake by DRB following Treatments with Alcalase and Flavourzyme[a]

	solubility (%)	retention (μg/L)	retention (%)	transport (μg)	transport (%)	transport efficiency (%)	uptake (μg)	uptake (%)	uptake efficiency (%)
DRB_A	18.60 ± 5.87ab	2.40 ± 0.64a	4.80 ± 1.27a	5.40 ± 2.62a	10.80 ± 5.23a	2.01 ± 0.97ab	7.80 ± 3.25a	15.60 ± 6.51a	2.90 ± 1.21a
DRB_F	26.63 ± 3.92a	7.43 ± 2.23ab	14.85 ± 4.45ab	6.40 ± 0.85a	12.80 ± 1.70a	3.41 ± 0.45b	13.83 ± 3.08ab	27.65 ± 6.15ab	7.36 ± 1.64bc
DRB_A+F	27.68 ± 4.84a	11.70 ± 3.64b	23.40 ± 7.28b	5.33 ± 0.60a	10.65 ± 1.20a	2.95 ± 0.33b	17.03 ± 4.24b	34.05 ± 8.49b	9.42 ± 2.35c
DRB_A→F	19.40 ± 6.01ab	5.15 ± 0.49a	10.30 ± 0.99a	4.75 ± 2.76a	9.50 ± 5.52a	1.84 ± 1.07ab	9.90 ± 3.25ab	19.80 ± 6.51ab	3.84 ± 1.26ab
DRBP	10.30 ± 0.49b	3.10 ± 0.49a	6.20 ± 0.99a	2.40 ± 0.49a	4.80 ± 0.99a	0.49 ± 0.10a	5.50 ± 0.00a	11.00 ± 0.00a	1.13 ± 0.00a

[a]Mean values ± standard deviation ($n = 3$). Different letters (a−c) denote significant differences ($P < 0.05$) between values in the same column. DRB_A, Alcalase-treated DRB protein hydrolysate; DRB_F, Flavourzyme-treated DRB protein hydrolysate; DRB_A+F, combination of Alcalase and Flavourzyme treatment of DRB protein hydrolysate; DRB_A→F, sequential treatment of Alcalase and Flavourzyme-treated DRB protein hydrolysate; DRBP, DRB protein without hydrolysis treatment.

DOI: 10.1021/acs.jafc.5b03420
J. Agric. Food Chem. 2015, 63, 9029−9036

To select the DRB hydrolysate with the highest iron-uptake capacity, a variety of hydrolysates were prepared by incubation with Alcalase and Flavourzyme for different periods of time in the present work. Depending on the hydrolysis treatment period, DRB hydrolysate exhibited improved or inhibitory effects on iron uptake by Caco-2 cells. As shown in Table 4, DRB treated with both Alcalase and Flavourzyme significantly improved ($P < 0.05$) iron solubility percentage and retention percentage as well as transport and uptake efficiencies compared with the unhydrolyzed DRB sample (DRB_A+F 0). DRB treated with Alcalase and Flavourzyme at a hydrolysis time of 180 min was found to have the highest improvement of the overall iron uptake in Caco-2 cells, with an uptake efficiency of up to 9.61% compared to that of DRB without treatment, that is, when the hydrolysis time was 0 h (1.70%). When the hydrolysis treatment was prolonged to 240 min, the iron solubility, retention percentage, and transport and uptake efficiencies decreased significantly.

DISCUSSION

The protein quality of DRB protein concentrate was analyzed by applying the amino acid score based on the reference protein for adults according to FAO/WHO/UHU.[21] The amino acid score of DRB protein concentrate was 86 (as seen in Table 3), indicating that all of the amino acids in DRB protein concentrate were in sufficient quantity required for an adult, except for methionine and cysteine. Cysteine is a semiessential amino acid that can be synthesized in the human body. Therefore, methionine, which is not synthesized in the human body, is the limiting amino acid in DRB. It is commonly depleted in plant proteins and could be supplemented easily from other diets.

Amino acids in the form of peptides are more favorably absorbed in the body compared with the whole protein or the free amino acid mixtures. The reduced hypertonicity in the presence of the peptides enhances their absorption efficiency and reduces the osmotic problems during the digestion process.[27] Besides that, chemical solvent extraction could cause undesirable denaturation and side reactions such as the Maillard reaction to the protein products, as well as reduce the purity of protein products by extracting nonprotein components that coprecipitate with protein and thus lower the protein quality.[28] As a result of these considerations, DRB in the present study was subjected to enzymatic hydrolysis to further enhance protein quality and peptide solubility as well as its functionality as an iron-binding peptide and to increase the bioavailability.

Two proteases, Alcalase and Flavourzyme, with different catalytic activities were used. Alcalase is a protease with endoprotease activity and has been widely used for the generation of protein hydrolysates.[22] Flavourzyme, on the other hand, is a mixture of endoprotease and exoprotease used for debittering and generation of extensive hydrolysate. The extractable peptide hydrolysates were significantly increased at $p \leq 0.05$ when both enzymes were used in the treatment, as compared to those of the Flavourzyme hydrolysis treatment. This might due to the synergetic effects of both enzymes to digest a broader specification of hydrolysis sites. The sequential enzymatic hydrolysis was carried out by using Alcalase as the initial digestion enzyme, followed by Flavourzyme after 60 min. With the predigestion with Alcalase, it was assumed that an increasing exposure of both terminal sites of the peptide possibly facilitates the exoprotease activity of Flavourzyme.

Table 4. Iron Retention, Transport, and Uptake from DRB Hydrolysates by Caco-2 Cells at Different Times[a]

	solubility (%)	retention (μg)	retention (%)	transport (μg)	transport (%)	transport efficiency (%)	uptake (μg)	uptake (%)	uptake efficiency (%)
DRB_A+F 0	13.76 ± 2.523a	2.38 ± 0.102a	4.77 ± 0.204a	3.79 ± 1.312a	7.58 ± 2.625a	1.04 ± 0.361a	6.18 ± 1.211a	12.35 ± 2.421a	1.70 ± 0.333a
DRB_A+F 60	23.18 ± 0.407bc	7.87 ± 0.407b	15.74 ± 0.815b	5.10 ± 0.000a	10.21 ± 0.000a	2.37 ± 0.000bc	12.98 ± 0.407b	25.95 ± 0.815b	6.02 ± 0.042b
DRB_A+F 120	25.10 ± 0.339b	10.08 ± 0.611c	20.16 ± 1.222c	5.01 ± 0.136a	10.02 ± 0.272a	2.52 ± 0.019bc	15.09 ± 0.475c	30.18 ± 0.950c	7.58 ± 0.068c
DRB_A+F 180	27.48 ± 0.373c	12.53 ± 0.679d	25.06 ± 1.358d	4.96 ± 0.475a	9.92 ± 0.950a	2.73 ± 0.090c	17.49 ± 0.204d	34.98 ± 0.407d	9.61 ± 0.039d
DRB_A+F 240	23.88 ± 0.238b	9.72 ± 0.509c	19.44 ± 1.018c	4.72 ± 0.136a	9.44 ± 0.272a	2.26 ± 0.016b	14.44 ± 0.373bc	28.88 ± 0.747bc	6.90 ± 0.044bc

[a]Mean values ± standard deviation ($n = 3$). Different letters (a−c) denotes significant differences ($P < 0.05$) between values in the same column. DRB_A+F 0, combination of Alcalase and Flavourzyme treatment of DRB protein hydrolysate at 0 min; DRB_A+F 60, combination of Alcalase and Flavourzyme treatment of DRB protein hydrolysate at 60 min; DRB_A+F 120, combination of Alcalase and Flavourzyme treatment of DRB protein hydrolysate at 120 min; DRB_A+F 180, combination of Alcalase and Flavourzyme treatment of DRB protein hydrolysate at 180 min; DRB_A+F 240, combination of Alcalase and Flavourzyme treatment of DRB protein hydrolysate at 240 min.

DOI: 10.1021/acs.jafc.5b03420
J. Agric. Food Chem. 2015, 63, 9029−9036

However, the results revealed that there is no significant enhancement of the extractable peptide amount in sequential enzymatic treatment when compared to those of combination enzymatic treatment, indicating the sequence of adding the enzymes in the hydrolysis process is less important.

Hydrolysates produced by combination treatment of Alcalase and Flavourzyme showed the best iron-binding capacity. The peptide hydrolysate after being treated by Alcalase and Flavourzyme exhibits optimal iron-binding capacity (83%) at the 90 min time of hydrolysis. Further increasing the hydrolysis time did not significantly increase the iron-binding activity of the peptide hydrolysate. This might be due to several factors, such as inhibitory effects of end products, enzyme inhibitors in the substrate, or the structural limitation of the enzymes to further digestion.[8]

Mineral binding and release in the human body is a dynamic process involving the absorption of the mineral in the digestive tract such as duodenum and intestine.[8] The solubility of iron, especially in the basic conditions of the duodenum and proximal jejunum, is of great importance for its in vivo absorption and bioavailability.[8,29] Iron solubility, iron retention, transport efficiency, and uptake efficiency percentages can be used as predictors for the iron intestinal bioavailability.[27,30] In this study, an in vitro digestion/human colonic adenocarcinoma (Caco-2) cell model system invented by R. P. Glahn, which mimics the gastric and intestinal digestion of humans, was used for iron bioavailability studies. The study was conducted in two parts; the iron uptake of the four DRB peptide hydrolysates was determined, and then the peptide hydrolysate with the highest iron uptake was chosen and further investigated in a time-dependent manner for its iron uptake efficiency. The iron contents were determined using ICP-MS, which is a sensitive detector for iron detection with the detection limit of 1 ppb.

When the results are expressed in percentages in relation to the soluble content, significant differences are observed among the samples. Iron solubility of the nonhydrolyzed DRB in this study was lower than those of hydrolyzed samples as well as those reported in a previous study.[25,26] This could have been due to the fiber components from the nonhydrolyzed DRB. Moreover, it is reported that some dietary fiber components decrease the mineral bioavailability by binding to the mineral ions.[31] The effect of hydrolysis caused an increase in retention percentage, transport, and uptake efficiencies of iron in all of the DRB protein hydrolysates. This indicated that the hydrolysis degree, that is, peptide length and size, is one of the important factors which influence the iron uptake efficiency of DRB protein hydrolysate in Caco-2 cells. Significant differences ($P < 0.05$) on the iron retention percentage and transport and uptake efficiencies were observed for DRB_A+B hydrolysate when compared to that of other samples. Therefore, we selected DRB_A+F, which is the DRB protein hydrolysate obtained using combined treatment of Alcalase and Flavourzyme, to further investigate the optimal hydrolysis time of the DRB protein hydrolysate−iron complex.

Furthermore, as can be recalled, although the iron-binding capacity was highest for the DRB_A+F at 90 min, the optimal cellular iron uptake was at 180 min probably indicating that at 90 min, the chemical properties of the DRB_A+F tended toward stronger bonding between the DRB constituents and the iron, which may have been weakened with the passage of time and hence the enhanced release of the iron when hydrolysis lasted for 180 min. Moreover, there was a progressive increase in cellular iron uptake with time until 180 min, when it dropped, suggesting that the bonding between the iron and DRB was weakened with increasing hydrolysis time. This hypothesis is supported by the lack of a parallel relationship between solubility and bioavailability of iron and other minerals in Caco-2 cells.[32,33]

The present study demonstrated that DRB hydrolysates produced by combination hydrolysis using Alcalase and Flavourzyme had potent iron-binding capacities. Additionally, using an in vitro digestion and absorption model (Caco-2 cell model), iron transport and uptake efficiencies of the combination Alcalase and Flavourzyme-treated DRB samples were found to be significantly higher than those of the nonhydrolyzed samples. The implications of these results are that DRB protein hydrolysates can be used as iron-fortified supplements and hence need to be studied further.

AUTHOR INFORMATION

Corresponding Authors

*(M.U.I.) E-mail: mustyimam@gmail.com. Phone: +603-8947-2115. Fax: +603-8947-2116.

*(M.I.) E-mail: maznahis@upm.edu.my. Phone: +603-8947-2115. Fax: +603-8947-2116.

Funding

This study was funded by Universiti Putra Malaysia.

Notes

The authors declare no competing financial interest.

REFERENCES

(1) Kassebaum, N. J.; Jasrasaria, R.; Naghavi, M.; Wulf, S. K.; Johns, N.; Lozano, R.; et al. A systematic analysis of global anemia burden from 1990 to 2010. *Blood* **2014**, *123* (5), 615−624.

(2) McLean, E.; Cogswell, M.; Egli, I.; Wojdyla, D.; De Benoist, B. Worldwide prevalence of anaemia, WHO vitamin and mineral nutrition information system, 1993−2005. *Public Health Nutr.* **2009**, *12* (04), 444−454.

(3) Ngui, R.; Lim, Y. A. L.; Chong Kin, L.; Sek Chuen, C.; Jaffar, S. Association between anaemia, iron deficiency anaemia, neglected parasitic infections and socioeconomic factors in rural children of West Malaysia. *PLoS Neglected Trop. Dis.* **2012**, *6* (3), e1550.

(4) Haniff, J.; Das, A.; Onn, L. T.; Sun, C. W.; Nordin, N. M.; Rampal, S.; Bahrin, S.; Ganeslingam, M.; Kularatnam, K. I.; Zaher, Z. M. Anemia in pregnancy in Malaysia: a cross-sectional survey. *Asia Pac. J. Clin. Nutr.* **2007**, *16* (3), 527−536.

(5) Foo, L. H.; Khor, G. L.; Tee, E. S.; Prabakaran, D. Iron status and dietary iron intake of adolescents from a rural community in Sabah, Malaysia. *Asia Pac. J. Clin. Nutr.* **2004**, *13* (1), 48−55.

(6) Martinez-Navarrete, N.; Camacho, M. M.; Martinez-Lahuerta, J.; Martinez-Monzo, J.; Fito, P. Iron deficiency and iron fortified foods-review. *Food Res. Int.* **2002**, *35* (2), 225−231.

(7) Beard, J. L.; Dawson, H.; Pinero, D. J. Iron metabolism: a comprehensive review. *Nutr. Rev.* **1996**, *54* (10), 295−317.

(8) Wang, X.; Li, M.; Li, M.; Mao, X.; Zhou, J.; Ren, F. Preparation and characteristics of yak casein hydrolysate−iron complex. *Int. J. Food Sci. Technol.* **2011**, *46* (8), 1705−1710.

(9) Huang, G.; Ren, Z.; Jiang, J. Separation of Iron-Binding Peptides from Shrimp Processing By-products Hydrolysates. *Food Bioprocess Technol.* **2011**, *4* (8), 1527−1532.

(10) Zhang, M.-N.; Huang, G.-R.; Jiang, J.-X. Iron binding capacity of dephytinised soy protein isolate hydrolysate as influenced by the degree of hydrolysis and enzyme type. *J. Food Sci. Technol.* **2014**, *51*, 994−999.

(11) Lee, S.-H; Song, K. B. Purification of an iron-binding nona-peptide from hydrolysates of porcine blood plasma protein. *Process Biochem.* **2009**, *44* (3), 378−381.

DOI: 10.1021/acs.jafc.5b03420
J. Agric. Food Chem. 2015, 63, 9029−9036

(12) Kim, S. B.; Seo, I. S.; Khan, M. A.; Ki, K. S.; Nam, M. S.; Kim, H. S. Separation of iron-binding protein from whey through enzymatic hydrolysis. *Int. Dairy J.* **2007**, *17* (6), 625−631.
(13) Vattem, D. A.; Mahoney, R. R. Production of dialysable iron by in vitro digestion of chicken muscle protein fractions: the size of the dialysable iron. *J. Sci. Food Agric.* **2005**, *85* (9), 1537−1542.
(14) Yeung, A.; Glahn, R.; Miller, D. Effects of iron source on iron availability from casein and casein phosphopeptides. *J. Food Sci.* **2002**, *67* (3), 1271−1275.
(15) Adebiyi, A. P.; Adebiyi, A. O.; Yamashita, J.; Ogawa, T.; Muramoto, K. Purification and characterization of antioxidative peptides derived from rice bran protein hydrolysates. *Eur. Food Res. Technol.* **2009**, *228* (4), 553−563.
(16) Ohara, I.; Tabuchi, R.; Onai, K. Effects of modified rice bran on serum lipids and taste preference in streptozotocin-induced diabetic rats. *Nutr. Res. (N. Y., NY, U. S.)* **2000**, *20* (1), 59−68.
(17) Zhang, H.; Yokoyama, W. H.; Zhang, H. Concentration-dependent displacement of cholesterol in micelles by hydrophobic rice bran protein hydrolysates. *J. Sci. Food Agric.* **2012**, *92* (7), 1395−1401.
(18) Kannan, A.; Hettiarachchy, N.; Narayan, S. Colon and breast anti-cancer effects of peptide hydrolysates derived from rice bran. *Open Bioact. Compd. J.* **2009**, *2* (1), 17−20.
(19) Lowry, O. H.; Rosebrough, N. J.; Farr, A. L.; Randall, R. J. Protein measurement with the Folin phenol reagent. *J. Biol. Chem.* **1951**, *193* (1), 265−275.
(20) Kwanyuen, P.; Burton, J. A Modified Amino Acid Analysis Using PITC Derivatization for Soybeans with Accurate Determination of Cysteine and Half-Cystine. *J. Am. Oil Chem. Soc.* **2010**, *87* (2), 127−132.
(21) FAO/WHO/UNU. *Energy and protein Requirements*; report of the joint FAO/WHO/UNU expert consultation, WHO Technical Report Series; FAO, WHO and the United Nations University: Geneva, Switzerland, 1985; pp 1−206.
(22) Adler-Nissen, J. Determination of the degree of hydrolysis of food protein hydrolysates by trinitrobenzenesulfonic acid. *J. Agric. Food Chem.* **1979**, *27* (6), 1256−1262.
(23) Decker, E. A.; Welch, B. Role of ferritin as a lipid oxidation catalyst in muscle food. *J. Agric. Food Chem.* **1990**, *38* (3), 674−677.
(24) Miller, D. D.; Schricker, B. R.; Rasmussen, R. R.; Van Campen, D. An in vitro method for estimation of iron availability from meals. *Am. J. Clin. Nutr.* **1981**, *34* (10), 2248−2256.
(25) Jovaní, M.; Barberá, R.; Farré, R.; Martín de Aguilera, E. Calcium, iron, and zinc uptake from digests of infant formulas by Caco-2 cells. *J. Agric. Food Chem.* **2001**, *49* (7), 3480−3485.
(26) Frontela, C.; Scarino, M. L.; Ferruzza, S.; Ros, G.; Martínez, C. Effect of dephytinization on bioavailability of iron, calcium and zinc from infant cereals assessed in the Caco-2 cell model. *World J. Gastroenterol.* **2009**, *15* (16), 1977.
(27) Clemente, A. Enzymatic protein hydrolysates in human nutrition. *Trends Food Sci. Technol.* **2000**, *11* (7), 254−262.
(28) Kolar, C. W.; Richert, S. H.; Decker, C. D.; Steinke, F. H.; Vander Zanden, R. J. Isolated soy protein. In *New Protein Foods*; Altschul, A. M., Wilcke, H. L., Eds.; Academic Press: New York, 1985; Vol. 5.
(29) Vegarud, G. E.; Langsrud, T.; Svenning, C. Mineral-binding milk proteins and peptides; occurrence, biochemical and technological characteristics. *Br. J. Nutr.* **2000**, *84* (S1), 91−98.
(30) Proulx, A. K.; Reddy, M. B. Fermentation and lactic acid addition enhance iron bioavailability of maize. *J. Agric. Food Chem.* **2007**, *55* (7), 2749−2754.
(31) Bosscher, D.; Van Caillie-Bertrand, M.; Van Cauwenbergh, R.; Deelstra, H. Availabilities of calcium, iron, and zinc from dairy infant formulas is affected by soluble dietary fibers and modified starch fractions. *Nutrition* **2003**, *19* (7), 641−645.
(32) Pynaert, I.; Armah, C.; Fairweather-Tait, S.; Kolsteren, P.; Van Camp, J.; Henauw, S. D. Iron solubility compared with in vitro digestion−Caco-2 cell culture method for the assessment of iron bioavailability in a processed and unprocessed complementary food for Tanzanian infants (6−12 months). *Br. J. Nutr.* **2006**, *95* (04), 721−726.
(33) Camara, F.; Amaro, M. A.; Barbera, R.; Clemente, G. Bioaccessibility of minerals in school meals: comparison between dialysis and solubility methods. *Food Chem.* **2005**, *92* (3), 481−489.

DOI: 10.1021/acs.jafc.5b03420
J. Agric. Food Chem. 2015, 63, 9029−9036

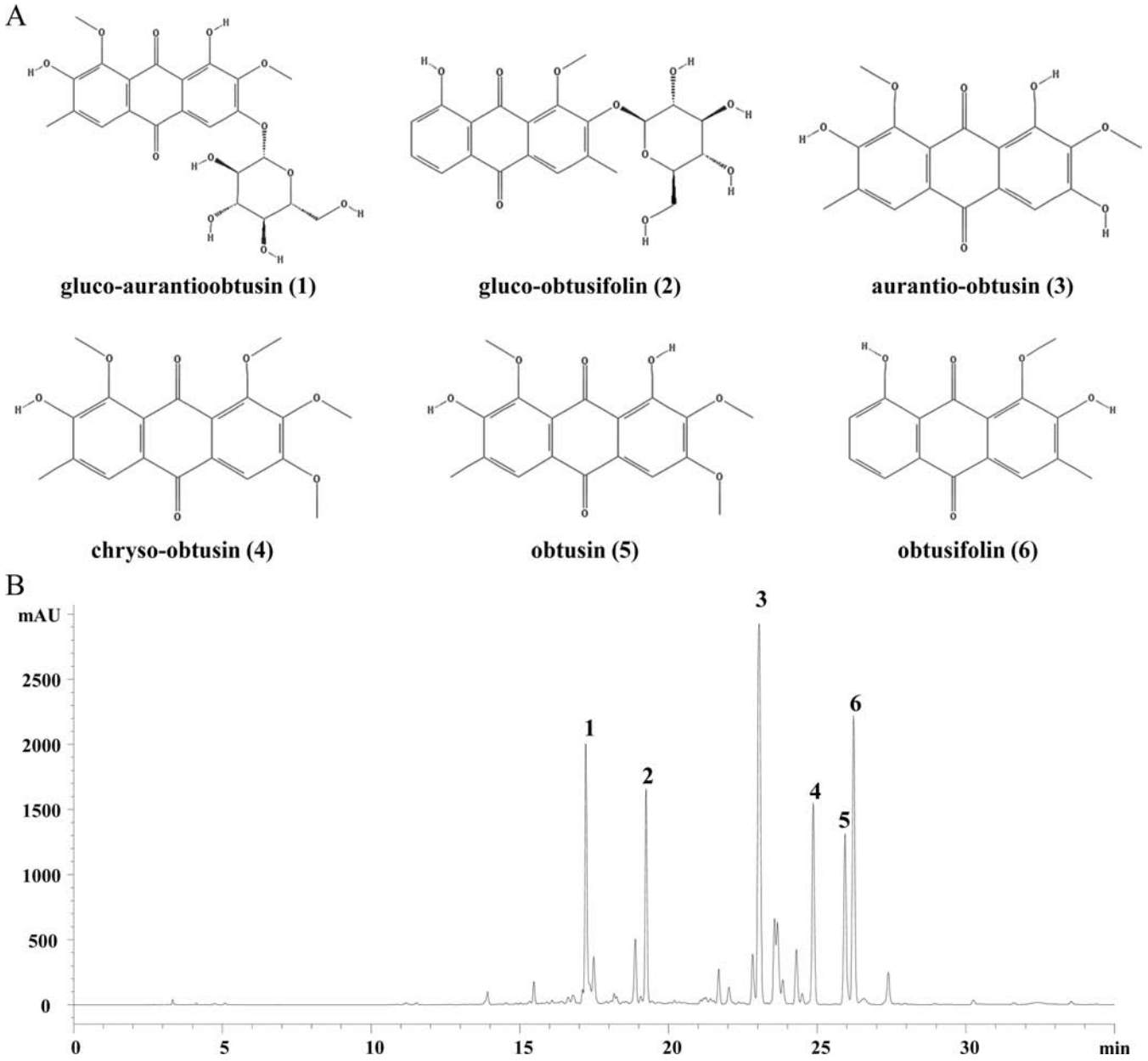

Figure 1. (A) Chemical structure of anthraquinones and (B) HPLC chromatogram from *C. tora* seed extract (CTE).

serum (FBS; Hyclone, South Logan, UT, USA), penicillin (Invitrogen, Carlsbad, CA, USA), Dulbecco's modified Eagle's medium (DMEM; Hyclone, South Logan, UT, USA), and phospho-Syk (Tyr525/526) antibody, phospho-phospholipase C (PLC)γ (Tyr783) antibody, phospho-PKD/PKCμ (Ser916) antibody, phosphor-SAPK/JNK (Thr183/Tyr185) antibody, SAPK/JNK (Thr183/Tyr185) antibody, phospho-p44/42 MAPK antibody (Erk1/2), p44/42 MAPK (Erk1/2) antibody, phospho-p38 antibody, p38 antibody, and β-actin antibody (all from Cell Signaling Technology Inc., Danvers, MA, USA).

Plant Material. Seeds of *C. tora*, collected in Yeongcheon, Gyeongsang Province, Korea, were purchased from a commercial supplier in Gyeongdong market, Seoul, Korea, in August 2013 and were identified by one of the authors (H.-J.L.). A voucher specimen was deposited at the Korea Institute of Science and Technology (KIST), Gangneung Institute. Extraction was performed by sonication using an RK158S ultrasonic bath (Bandelin, Germany).

Extraction and Isolation of Anthraquinones from *C. tora* Seeds. One kilogram of the dried seeds of *C. tora* was extracted with 1 L of 95% ethanol at room temperature and filtered through Whatman No. 1 filter paper (GE Healthcare Life Sciences, PA, USA). The filtrate was concentrated under reduced pessure by rotary evaporation at 40 °C, and 95 g of EtOH extract (CTE) was obtained. Isolation of anthraquinones (Figure 1) from *C. tora* was done as previously described.[16]

Cell Culture. RBL-2H3 cells were obtained from the American Type Culture Collection (ATCC, Manassas, VA, USA) via the Korean Cell Line Bank (KCLB No. 22256, Seoul, Korea). Cells were cultured in DMEM supplemented with 10% FBS and 100 U/mL penicillin. Cells were grown in 75 cm^2 culture flasks at 37 °C with 5% CO_2 in a humidified atmosphere.

Cell Viability Assay. Cell viability was checked using a 3-[4,5-dimethylthiazol-2-yl]-2,5-diphenyltetrazolium bromide (MTT) colorimetric assay (Sigma-Aldrich, St Louis, MO, USA). RBL-2H3 cells were grown in 24-well plates (2×10^5 cells/mL) for 24 h. After treatment of the cells with various concentrations of CTE and aurantio-obtusin for 6 h, the cells were washed and then treated with 200 μL of MTT (0.5 mg/mL) and cells were incubated for an additional 4 h. Cells were then washed, and the insoluble formazan products were dissolved in 200 μL of DMSO. Absorbance was measured by spectrophotometry at

DOI: 10.1021/acs.jafc.5b03836
J. Agric. Food Chem. 2015, 63, 9037−9046

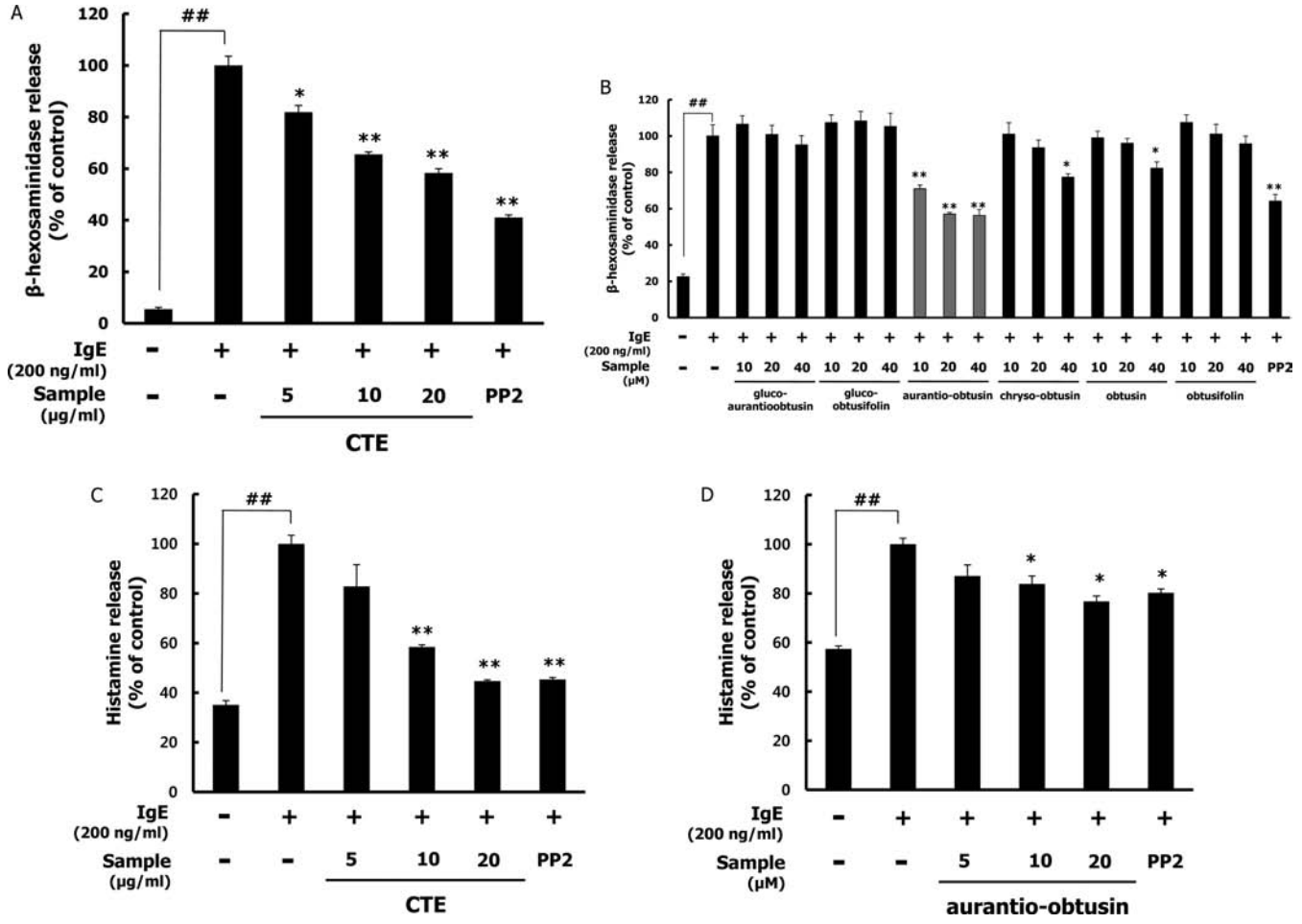

Figure 2. Effects of CTE and aurantio-obtusin on β-hexosaminidase and histamine release. (A) The degranulation was determined by measuring β-hexosaminidase release in DNP-IgE-sensitized RBL-2H3 cells. The RBL-2H3 cells were treated in the presence or absence of CTE (5, 10, or 20 μg/mL) for 1 h and then stimulated for 1 h with DNP-BSA. (B) The RBL-2H3 cells were treated in the presence or absence of gluco-aurantioobtusin (1), gluco-obtusifolin (2), aurantio-obtusin (3), chryso-obtusin (4), obtusin (5), or obtusifolin (6) (10, 20, or 40 μM) for 1 h and then stimulated for 1 h with antigen. (C, D) Histamine release was determined with enzyme-linked immunosorbent assay kit. The RBL-2H3 cells were treated in the presence or absence of CTE (5, 10, or 20 μg/mL) and aurantio-obtusin (5, 10, or 20 μM) for 1 h and then stimulated for 1 h with antigen. PP2 (10 μM) is a general Src-family kinase inhibitor. Results are expressed as the mean ± SD of three independent experiments ($^{\#\#}p < 0.01$, $^{*}p < 0.05$, and $^{**}p < 0.01$).

550 nm using a microplate reader (Bio-Tek Instruments, Winooski, VT).

Measurement of Histamine and β-Hexosaminidase Release. RBL-2H3 cells were sensitized with 0.2 μg/mL monoclonal DNP-IgE. Cells were washed with modified PIPES buffer (25 mM PIPES, pH 7.2, 119 mM NaCl, 5 mM KCl, 0.4 mM $MgCl_2 \cdot 6H_2O$, 1 mM $CaCl_2$, 5.6 mM glucose, 40 mM NaOH, and 0.1% BSA). Cells were treated with CTE or compounds **1**−**6** at the indicated concentrations for 1 h at 37 °C. After incubation, cells were challenged with 0.2 μg/mL DNP-BSA for 1 h at 37 °C. Histamine was then detected using an enzyme immunoassay kit (Oxford Biomedical Research, Rochester Hills, MI). Histamine release was expressed as a percentage of the total histamine produced by unstimulated cells. To determine β-hexosaminidase release, supernatants and lysed pellets were aliquoted into 96-well plates. Samples were mixed with substrate solution (1 mM *p*-nitrophenyl *N*-acetyl-β-D-glucosamine in 0.05 M citrate buffer, pH 4.5) and incubated for 1 h at 37 °C. Reactions were terminated by the addition of 0.05 M sodium carbonate buffer, pH 10. Absorbance was measured by spectrophotometry at 405 nm.

Measurement of Prostaglandin E_2. Cell culture medium was collected, and the secretion of prostaglandin E_2 (PGE_2) was determined using competitive radioimmunoassay kits (R&D Systems, MN, USA, and Cayman Chemical, MI, USA, respectively) according to the manufacturers' protocol.

Measurement of Cytokine Release. IgE-sensitized RBL-2H3 cells were incubated with CTE and aurantio-obtusin (various concentrations) for 1 h and stimulated with DNP-BSA for 4 h. Interleukin (IL)-4 and tumor necrosis factor (TNF)-α concentrations in cell culture supernatants were measured using enzyme-linked immunosorbent assay kits (Abcam, U.K.).

Measurement of Reactive Oxygen Species (ROS) Production. RBL-2H3 cells were pretreated with CTE and aurantio-obtusin for 1 h before being sensitized overnight with 0.2 μg/mL of DNP-specific IgE antibody. The cells were washed with PBS, and stained with 40 μM DCFH-DA for 30 min. For fluorescence staining assay, cells were then stimulated with 1 μg/mL of DNP-BSA for 30 min, and changes in fluorescence intensity were measured using a microplate reader (Bio-Tek Instruments, Winooski, VT) at excitation and emission wavelengths of 485 and 530 nm, respectively.

Reverse Transcription-Polymerase Chain Reaction. (RT-PCR). RNA was extracted with TRIzol reagent (Invitrogen) according to the manufacturer's protocol and quantified by spectrophotometry at 260 nm. The cDNA was synthesized in a 20 μL reaction containing 1 μg of total RNA, oligo (dT), and reverse transcriptase premix (Elpis-Biotech., Inc., Taejeon, Korea). Reverse transcription (RT) was initiated at 70 °C for 5 min, followed by incubation at 42 °C for 60 min, and was terminated at 94 °C for 5 min. Amplification of the cDNA products (5 μL) by PCR was performed with a PCR premix

DOI: 10.1021/acs.jafc.5b03836
J. Agric. Food Chem. 2015, 63, 9037−9046

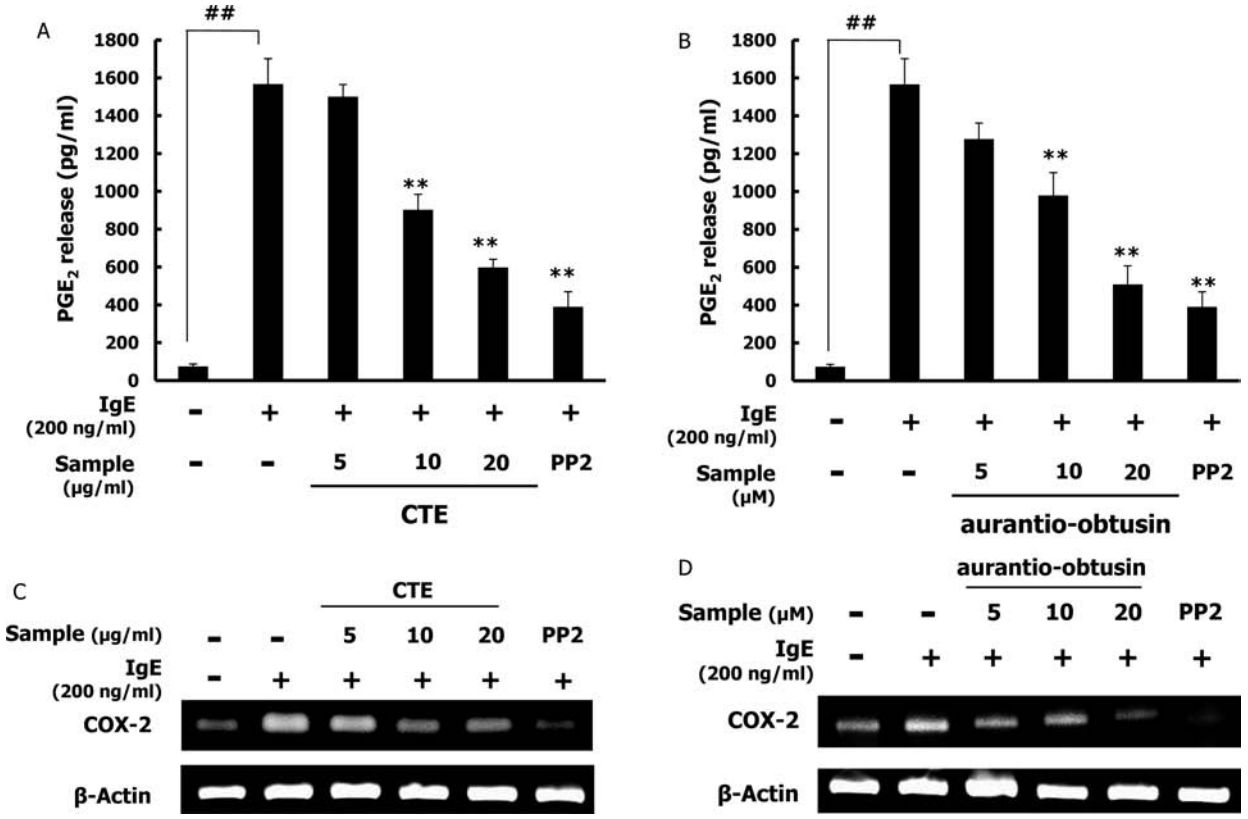

Figure 3. Effects of CTE and aurantio-obtusin on PGE_2 secretion and COX-2 mRNA expression. RBL-2H3 cells were treated with CTE (5, 10, or 20 μg/mL) and aurantio-obtusin (5, 10, or 20 μM) for 1 h and then stimulated for 4 h with antigen. (A, B) PGE_2 secretion was determined by enzyme-linked immunosorbent assay kit. (C, D) COX-2 mRNA level was determined with RT-PCR. PP2 (10 μM) is a general Src-family kinase inhibitor. Results are expressed as the mean ± SD of three independent experiments ($^{\#\#}p < 0.01$, $^{*}p < 0.05$, and $^{**}p < 0.01$).

(Elpis-Biotech) and the following primer pairs: TNF-α forward, 5′-CAA GGA GCA GAA GTT CCC AA-3′, and TNF-α reverse, 5′-CGG ACT CCG TGA TGT CTA AG-3′ (500 bp); IL-4 forward, 5′-ACC TTG CTG TCA CCC TGT TC-3′, and IL-4 reverse, 5′-TTG TGA GCG TGG ACT CAT TC-3′ (351 bp); COX-2 forward, 5′- TGA CTG TAC CCG GAC TGG AT-3′, and COX-2 reverse, 5′-CAT GGG AGT TGG GCA GTC AT-3′ (322 bp); β-actin forward, 5′-AGC CAT GTA CGT AGC CAT CC-3′, and β-actin reverse, 5′-TCT CAG CTG TGG TGG TGA AG-3′ (227 bp). Before PCR amplification, primers for cytokines and β-actin were denatured at 94 °C for 5 min. Amplification consisted of 28 cycles of denaturation at 94 °C for 30 s, annealing for 1 min, and extension at 72 °C for 1 min, followed by a final 5 min extension at 72 °C. PCR was performed using a GeneAmp PCR System 9700 (Applied Biosystems, Foster City, CA, USA). PCR products were separated by 1.5% agarose gel electrophoresis and visualized by ethidium bromide staining and UV illumination. Densitometry was performed using DIG chemiluminescent film (volume of all markers/volume of β-actin).

Passive Cutaneous Anaphylaxis (PCA) in Mice. DNP-IgE (0.5 mg) was subcutaneously injected onto the ears of BALB/c mice (4-week-old male). After 24 h, the mice were orally administered with CTE (200 mg/kg), aurantio-obtusin (50 mg/kg), or cetirizine (20 mg/kg). After 1 h, the mice were injected intravenously with DNP-BSA (250 μg) in PBS containing Evans Blue (5 mg/mL). After 60 min, the ear tissue was removed and absorbed dye was extracted overnight in formamide (700 μL) at 63 °C. The absorbance was measured at 620 nm. Animal experimental procedures were approved by the Animal Care and Use Committee of KIST.

Western Blot Analysis. RBL-2H3 cells were lysed in RIPA buffer (containing 150 mM NaCl, 1.0% IGEPAL CA-630, 0.5% sodium deoxycholate, 0.1% SDS, 50 mM Tris, pH 8.0) containing protease inhibitors and then placed on ice for 10 min. Lysate protein concentrations were determined by Bradford protein assay (Bio-Rad Laboratories, Hercules, CA, USA). Equal amounts of protein (30 μg) were loaded in each sample, separated by 10% sodium dodecyl sulfate−polyacrylamide gel electrophoresis, and transferred to nitrocellulose membranes (Whatman GmbH, Dassel, Germany). Blotted membranes were blocked with 5% skimmed milk in Tris-buffered saline containing 0.1% Tween 20 for 1 h, and then incubated with primary antibodies for 16 h at 4 °C. After three washes in Tris-buffered saline containing 0.1% Tween 20, the membranes were incubated with horseradish peroxidase-linked secondary antibodies (Santa Cruz Biotechnology, Santa Cruz, CA, USA) for 2 h. Proteins were detected with enhanced chemoluminescence (Amersham Biosciences, Little Chalfont, U.K.) and visualized using an ECL Advanced system (GE Healthcare, Hatfield, U.K.).

Statistical Analysis. Each experiment was performed at least three times. Results are expressed as the mean ± standard deviation (SD). Vehicle (DMSO) and treated groups were compared by one-way analysis of variance followed by Scheffe's test (SPSS 17.0, Chicago, IL, USA). $^{\#\#}p < 0.01$, $^{*}p < 0.05$, and $^{**}p < 0.01$ were considered statistically significant. $^{\#\#}p < 0.01$ compared with the control group (DNP-IgE treatment alone); $^{*}p < 0.05$ and $^{**}p < 0.01$ compared with the DNP-IgE and DNP-BSA stimulated group.

RESULTS

Identification of Anthraquinones in *C. tora* Seeds. Six anthraquinones were identified in *C. tora* using liquid chromatography−mass spectrometry, namely, gluco-aurantioobtusin, gluco-obtusifolin, aurantio-obtusin, chryso-obtusin, obtusin, and obtusifolin (Figure 1).

Effects of CTE and Aurantio-obtusin on Degranulation and Histamine Release in IgE-Sensitized RBL-2H3 Cells. The effects of CTE and aurantio-obtusin on cell cytotoxicity were assessed by the colorimetric MTT assay.

DOI: 10.1021/acs.jafc.5b03836
J. Agric. Food Chem. 2015, 63, 9037−9046

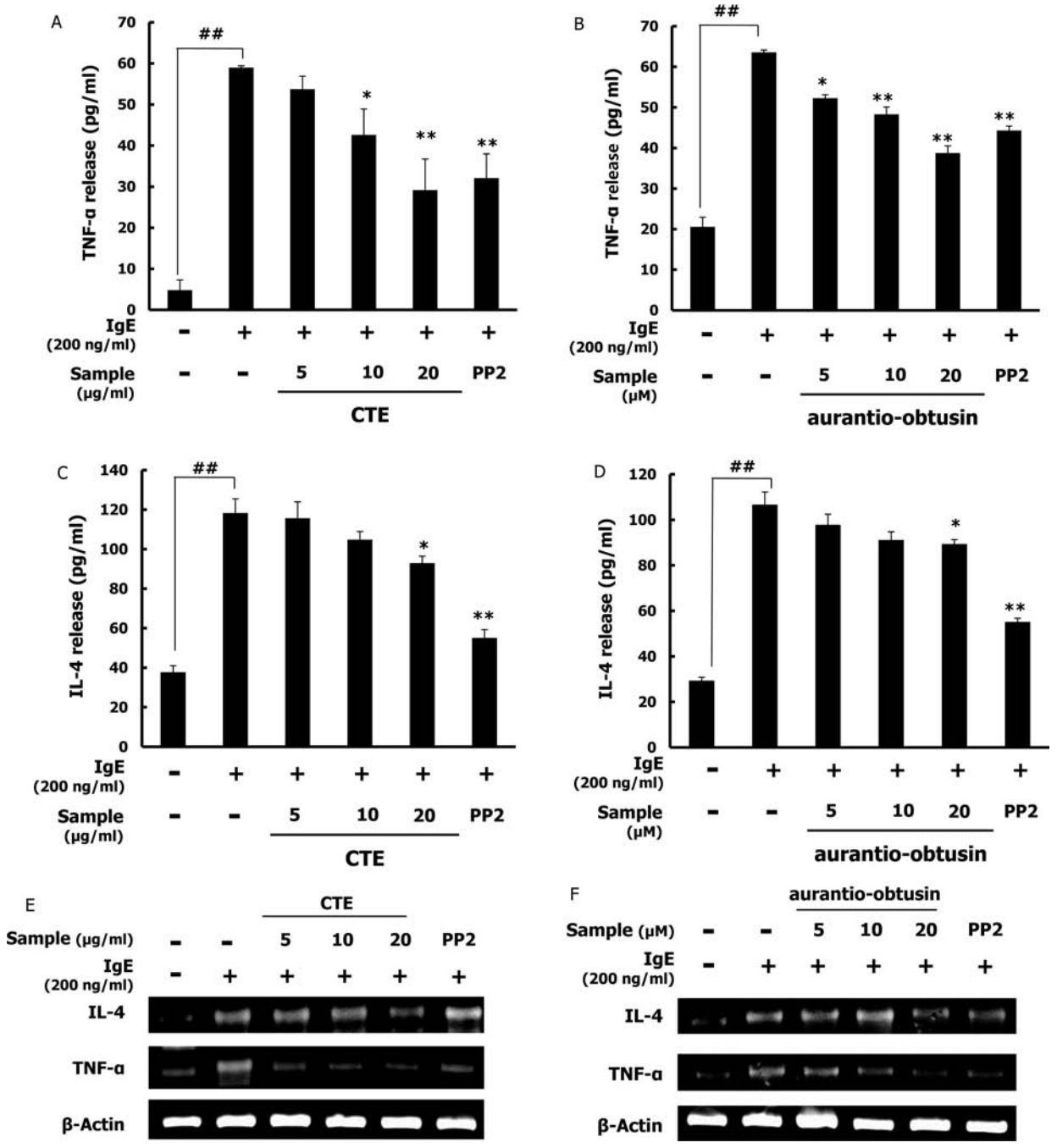

Figure 4. Effects of CTE and aurantio-obtusin on TNF-α and IL-4 production and mRNA expression. RBL-2H3 cells were treated with CTE and aurantio-obtusin for 1 h and then stimulated with DNP-BSA for 4 h. (A–D) TNF-α and IL-4 production was determined by enzyme-linked immunosorbent assay kit. (E, F) mRNA levels of TNF-α and IL-4 were determined with RT-PCR. PP2 (10 μM) is a general Src-family kinase inhibitor. Results are expressed as the mean ± SD of three independent experiments ($^{\#\#}p < 0.01$, $^{*}p < 0.05$, and $^{**}p < 0.01$).

CTE (up to 20 μg/mL) or aurantio-obtusin (up to 20 μM) had no effect on RBL-2H3 cell viability (Figures S1 and S2). To verify the effects of CTE and its isolated compounds on degranulation of mast cell, we examined their potential to suppress the β-hexosaminidase release. CTE suppressed β-hexosaminidase release in IgE-sensitized mast cells in a dose-dependent manner (Figure 2A). In addition, aurantio-obtusin inhibited β-hexosaminidase release more than gluco-aurantioobtusin, gluco-obtusifolin, chryso-obtusin, obtusin, and obtusifolin in IgE-sensitized mast cells (Figure 2B). Thus, additional experiments were carried out using aurantio-obtusin. The effects of CTE and aurantio-obtusin on histamine release were also assessed to investigate potential antiallergic activities. CTE and aurantio-obtusin repressed histamine release in IgE-sensitized mast cells (Figures 2C and 2D).

Inhibitory Effects of CTE and Aurantio-obtusin on PGE_2 Production and Cyclooxygenase 2 (COX-2) Expression in IgE-Sensitized RBL-2H3 Cells. In antigen-stimulated mast cells, the arachidonate cascade is initiated via the FcεRI receptor and recruits inflammatory cells, such as neutrophils, Th2 cells, eosinophils, and basophils.[17] Therefore, these arachidonic acid metabolites contribute to inflammation

DOI: 10.1021/acs.jafc.5b03836
J. Agric. Food Chem. 2015, 63, 9037–9046

in allergic diseases, and suppression of their production is essential to prevent or treat allergic diseases. To investigate the effects of CTE and aurantio-obtusin on the production of PGE_2, RBL-2H3 cells were sensitized with 200 ng/mL DNP-IgE overnight and treated with CTE and aurantio-obtusin for 1 h followed by the treatment with DNP-BSA for 24 h. CTE and aurantio-obtusin significantly inhibited PGE_2 production in a dose-dependent manner in IgE-stimulated RBL-2H3 cells (Figures 3A and 3B). The effects of CTE and aurantio-obtusin on COX-2 expression were confirmed by RT-PCR. DNP-BSA increased COX-2 mRNA expression in IgE-sensitized mast cells. However, treatment with CTE and aurantio-obtusin reduced IgE-mediated upregulation of COX-2 expression (Figures 3C and 3D). These results indicated that CTE and aurantio-obtusin inhibit the release of pro-inflammatory lipid mediators from activated mast cells and suggest that they may have an antiallergic effect.

Inhibitory Effects of CTE and Aurantio-obtusin on the Production and mRNA Expression of Tumor Necrosis Factor (TNF)-α and Interleukin (IL)-4 in IgE-Sensitized RBL-2H3 Cells. Allergic inflammatory responses are induced by proinflammatory cytokines from activated mast cells. TNF-α and IL-4, which are proinflammatory cytokines, are essential in allergy-related diseases.[18] We therefore determined whether CTE and aurantio-obtusin inhibited the production and mRNA expression of TNF-α and IL-4 in IgE-stimulated RBL-2H3 cells. Consistently with the previous report,[19] the increase of the production and expression of TNF-α and IL-4 was obvious by DNP-BSA stimulation in mast cells. CTE and aurantio-obtusin decreased both the production (Figures 4A–D) and mRNA expression (Figures 4E and 4F) of TNF-α and IL-4. These results showed that CTE and aurantio-obtusin have an inhibitory effect on the production and expression of proinflammatory cytokines in mast cells.

Effects of CTE and Aurantio-obtusin on Reactive Oxygen Species (ROS) Production in IgE-Sensitized RBL-2H3 Cells. Several reports suggested that activated mast cells have increased intracellular ROS levels.[20] Moreover, ROS augments histamine release in mast cells,[21] and H_2O_2 can regulate phosphorylation of PLCγ.[22] We next examined to investigate whether CTE and aurantio-obtusin attenuate ROS production following IgE-mediated mast cell activation using the DCFH-DA fluorescent indicator. Fluorometer analysis showed that the level of ROS increased from 10.60% in nonstimulated cells to 58.62% in antigen-sensitized cells. However, ROS production was significantly reduced by CTE or aurantio-obtusin treatment in a dose-dependent manner (Figures 5A and 5B).

Effects of CTE and Aurantio-obtusin on FcεRI Signaling in IgE-Sensitized RBL-2H3 Cells. Aggregation of FcεRI consecutively initiates IgE-mediated phosphorylation of tyrosine kinases such as Syk and Lyn, and subsequently tyrosine phosphorylation of cellular proteins such as PLCγ and PKC.[19] PP2, a general Scr-family kinase inhibitor, significantly suppresses Syk phosphorylation.[19] To determine the mechanisms underlying CTE- and aurantio-obtusin-mediated inhibition of allergic responses, we examined several intracellular signals. Phosphorylation of Syk, PKD/PKCμ, and PLCγ was induced in antigen-stimulated RBL-2H3 cells, and this phosphorylation was inhibited by treatment with CTE and aurantio-obtusin (Figures 6A and 6B). We also examined the effects of CTE and aurantio-obtusin on MAPKs because of their role in the production of TNF-α and IL-4.[23] Among

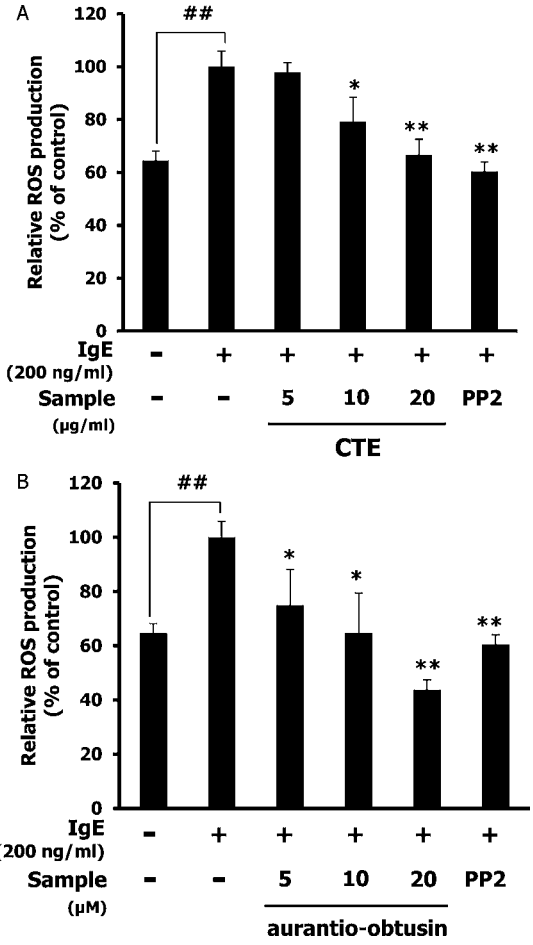

Figure 5. Effect of CTE and aurantio-obtusin on intracellular ROS production. (A, B) RBL-2H3 cells were treated with CTE and aurantio-obtusin for 1 h and then stained with 40 μM 2′7′-dichlorofluorescein diacetate (DCFH-DA; Sigma-Aldrich) for 30 min. The stained cells were then stimulated with DNP-BSA for 10 min. After 30 min, ROS levels were analyzed by flow cytometry. PP2 (10 μM) is a general Src-family kinase inhibitor. Results are expressed as the mean ± SD of three independent experiments ($^{\#\#}p < 0.01$, $^{*}p < 0.05$, and $^{**}p < 0.01$).

phosphorylation of ERK, JNK, and p38 induced by antigen stimulation, phosphorylation of ERK was only suppressed by treatment with CTE and aurantio-obtusin (Figures 6C and 6D). These results suggest that CTE and aurantio-obtusin suppresses mast cell activation by inactivation of FcεRI signaling and ERK in mast cells.

Effect of CTE and Aurantio-obtusin on IgE-Mediated PCA in Mice. PCA is generally used to measure local allergic responses in vivo.[24] To examine whether CTE and aurantio-obtusin repressed allergic reactions, we introduced a IgE-mediated PCA model. IgE was subcutaneously injected onto the left ear tissue of mouse, followed by injection of DNP-BSA containing 5% Evans Blue. CTE and aurantio-obtusin suppressed the IgE-sensitized PCA response (Figures 7A and 7B). Cetrazine, a typical antihistamine drug, was used as a positive control.[25]

DISCUSSION

Type I hypersensitivity is triggered by inflammatory chemical mediators (cytokines, ILs, LTs, and PGs) secreted from immune cells such as eosinophils, basophils, and mast cells.

DOI: 10.1021/acs.jafc.5b03836
J. Agric. Food Chem. 2015, 63, 9037–9046

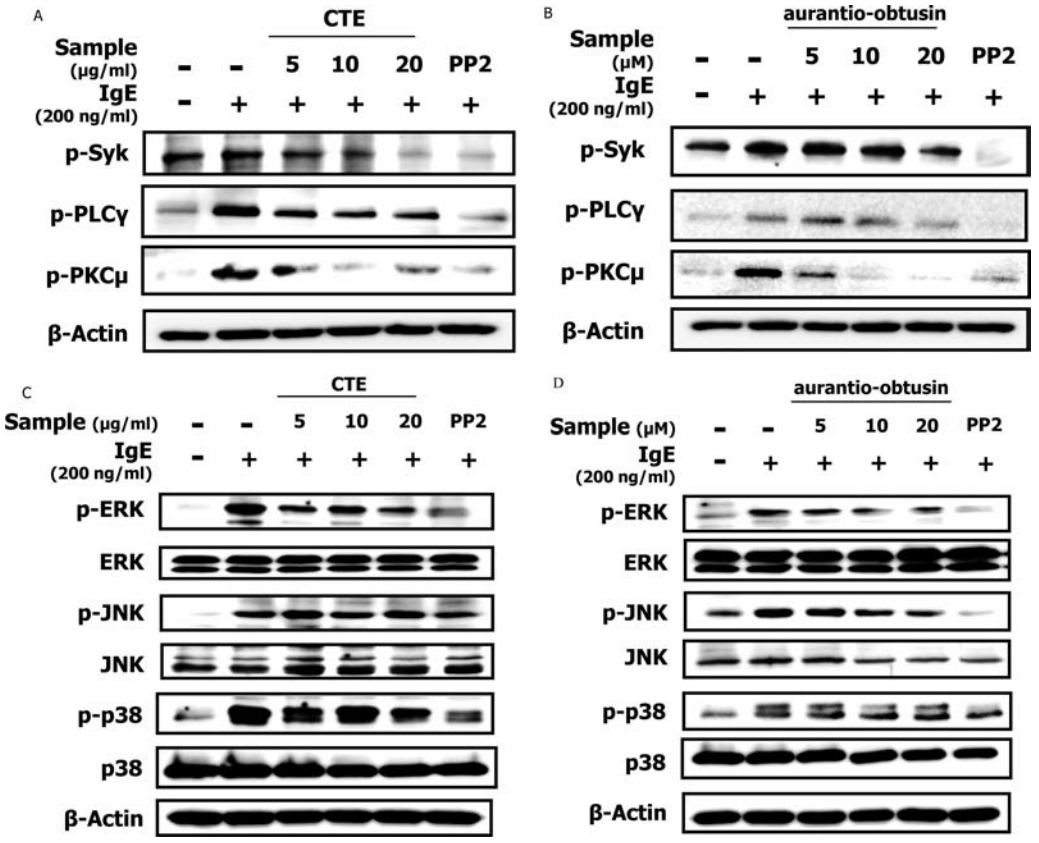

Figure 6. Effect of CTE and aurantio-obtusin on FcεRI Signaling. (A, B) RBL-2H3 cells were treated with CTE and aurantio-obtusin for 1 h and then stimulated with DNP-BSA for 10 min. Phosphorylation of Syk, PLCγ, and PKD/PKCμ was determined with Western blot analysis. (C, D) RBL-2H3 cells were treated with CTE and aurantio-obtusin for 1 h and then stimulated with DNP-BSA for 30 min. Phosphorylation of JNK, ERK, and p38 was determined with Western blot analysis. PP2 (10 μM) is a general Src-family kinase inhibitor.

Particularly, mast cells are key players in the control of allergic related reactions.[26] A recent study revealed that mast cell-released chemical mediators (histamines, cytokines, and proteases) play a crucial role during allergic mediated inflammation in mast cell-deficient mice.[27] Therefore, several studies have reported specific mediators of mast cell activation and identified novel compounds that inhibit these allergic mediators.[3,28,29]

Anthraquinones are predominantly reported in and isolated from the seeds of *Cassia tora* L. (syn. Senna tora) and *Cassia obtusifolia* L. (syn. Senna obtusifolia),[30,31] and may possess anti-inflammation, antioxidant, and anticancer properties.[32−34] Moreover, anthraquinones inhibit chemical mediators of mast cell activation. For instance, emodin, rhein, and citreorosein, three naturally occurring anthraquinone derivatives, suppress the IgE-mediated anaphylactic reaction, mast cell activation, and LT generation.[35−37] Among anthraquinone derivatives isolated from *C. tora*, aurantio-obtusin is the major compound. It is also used as a quality control marker of *C. tora* and reportedly has antihypertensive, hepatoprotective, antimutagenic, osteogenic, and estrogenic activities.[38−42] However, the effects of *C. tora* seed and aurantio-obtusin on allergic diseases have not been studied. In this study, we assessed the inhibitory effects of CTE and its active compound aurantio-obtusin on allergic inflammation in mast cells.

Activation of FcεRI receptors by the high-affinity binding and aggregation of IgE triggers a signaling cascade that led to degranulation and production of inflammatory mediators, such as inflammatory cytokines, lipid-derived mediators, and histamine.[43] CTE and aurantio-obtusin suppressed the secretion of β-hexosaminidase (Figures 2A and 2B) and histamine (Figures 2C and 2D). These results suggest that the antiallergic activities of CTE and aurantio-obtusin are caused by the inhibition of histamine release, which causes smooth muscle contraction, vascular permeability, and inflammation.

The FcεRI receptor signals through Syk, Lyn, and PLCγ to regulate mast cell activation.[17] The FcεRI receptor aggregates to IgE and starts intracellular signal cascade to derive allergic reactions. Stimulated FcεRI initiates phosphorylation of Syk, which binds to immunoreceptor tyrosine-based activation motifs present on the β and γ chains of FcεRI. Consecutively, Syk derives phosphorylation of PKC and PLCγ.[44] Remarkably, CTE and aurantio-obtusin declined the phosphorylation of Syk, PLCγ, and PKD/PKCμ (Figures 6A and 6B). These results suggest that CTE and aurantio-obtusin have antiallergic effects in IgE-sensitized mast cells by inhibiting the phosphorylation of Syk, PKC, and PLCγ, and consequently inhibiting mast cell degranulation.

CTE and aurantio-obtusin also decreased production of the inflammatory mediator PGE_2, which is an arachidonic acid metabolite, via suppression of the COX pathways (Figures 3A and 3B).[45] Furthermore, CTE and aurantio-obtusin inhibited mRNA COX-2 expression, a key enzyme in these pathways (Figures 3C and 3D). These results indicate that CTE and aurantio-obtusin inhibit generation of inflammatory lipid mediators by inhibiting the COX pathways.

DOI: 10.1021/acs.jafc.5b03836
J. Agric. Food Chem. 2015, 63, 9037−9046

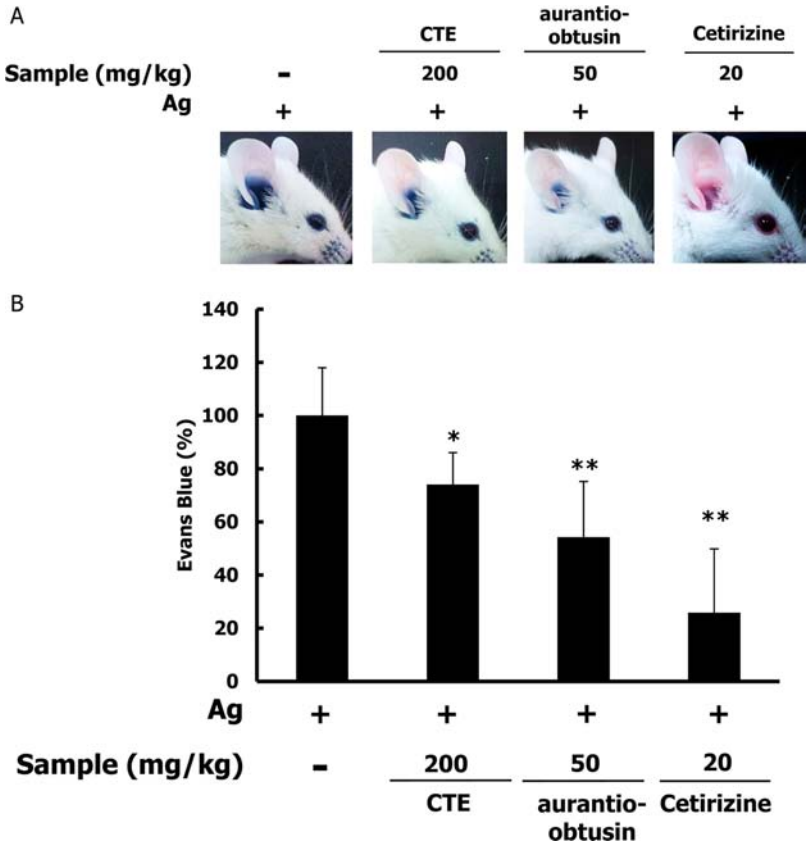

Figure 7. Effect of CTE and aurantio-obtusin on IgE-mediated passive cutaneous anaphylaxis (PCA). (A) Mice were sensitized with IgE for 1 h and then orally administered with CTE (200 mg/kg), aurantio-obtusin (50 mg/kg), or cetrizine (20 mg/kg) for 1 h. The ears of mice absorbed with Evans Blue were photographed. (B) The ear absorbed dye was extracted with formamide. The quantification data is presented as % of IgE- sensitized control. Cetrizine (20 mg/kg) is an antihistamine reference drug. Data are expressed as the mean ± SD ($n \geq 6$) (*$p < 0.05$ and **$p < 0.01$).

CTE and aurantio-obtusin inhibited both the production and mRNA expression of the proinflammatory mediators TNF-α and IL-4 (Figure 4). TNF-α and IL-4 play an essential role in activating and continuing allergic responses in mast cells. IL-4 derives T-cell development and switches B-cells to the IgE isotype. TNF-α also induces physiological immune reactions by stimulating tissue fibrosis and leukocyte infiltration, and initiates cytokine-mediated inflammatory states by promoting cytokine production.[46] Even though inflammation is a physiological defense system against pathogens, overexpression of cytokines can also cause serious inflammatory disorders such as asthma and atopic dermatitis. Our results indicate that these compounds are beneficial for the treatment of allergic disorders.

Furthermore, the function of ROS as an inducer of degranulation and Ca^{2+} increase was revealed in recent studies.[47,48] In the meantime, prevention of ROS production reportedly suppresses IgE-mediated histamine secretion.[25] Thus, blockade of ROS production is regarded to be significant for inhibition of mast cell activation. CTE and aurantio-obtusin effectively reduced ROS production in IgE-sensitized RBL-2H3 cells. Several studies reported that CTE and aurantio-obtusin have an antioxidant property,[49,50] which may result from their high ROS-elimination activity. These results suggest that the antioxidant property of CTE and aurantio-obtusin results in the inhibition of mast cell activation.

MAPK signaling is a key therapeutic target in allergic diseases.[51] Consequently, to examine the mechanism by which CTE and aurantio-obtusin suppress mast cell activation, phosphorylation of ERK, JNK, and p38 was assessed. CTE and aurantio-obtusin suppressed IgE-mediated phosphorylation of ERK, indicating that these compounds mitigate mast cell activation by inhibiting MAPK pathway (Figures 6C and 6D).

In conclusion, CTE and its active compound aurantio-obtusin suppressed degranulation, the generation of histamine, inflammatory lipid mediators, and proinflammatory cytokines, and intracellular ROS production in IgE-sensitized mast cells. CTE and aurantio-obtusin also decreased signaling cascade from the FcεRI receptor by inhibiting the activation of Syk, PLCγ, PKC, and MAPK, all of which intermediate allergic reactions in IgE-sensitized mast cells. Our results suggest that CTE and aurantio-obtusin are beneficial therapeutic agents to prevent or treat IgE-sensitized allergic disorders.

■ ASSOCIATED CONTENT

Supporting Information

The Supporting Information is available free of charge on the ACS Publications website at DOI: 10.1021/acs.jafc.5b03836.

Cell viability of CTE and aurantio-obtusin (PDF)

■ AUTHOR INFORMATION

Corresponding Author

*Natural Products Research Center, Korea Institute of Science and Technology Gangneung Institute, 679 Saimdang-ro, Gangneung, Gangwon-do, Republic of Korea. Phone: 82-33-650-3651. Fax: 82-33-650-3679. E-mail: cwnho@kist.re.kr.

DOI: 10.1021/acs.jafc.5b03836
J. Agric. Food Chem. 2015, 63, 9037−9046

Funding

This work was supported by an intramural grant (2Z04381) from Korea Institute of Science and Technology, Gangneung Institute.

Notes

The authors declare no competing financial interest.

■ ABBREVIATIONS USED

DMSO, dimethyl sulfoxide; FcεRI, Fc receptor for IgE; IL, interleukin; MAPK, mitogen-activated protein kinases; RBL, rat basophilic leukemia; TNF, tumor necrosis factor; IgE, immunoglobulin E; PLC, phospholipase; PKC, protein kinase C; ERK, extracellular signal-regulated kinase; JNK, c-Jun N-terminal kinase; PGs, prostaglandins; COX-2, cyclooxygenase 2

■ REFERENCES

(1) Galli, S. J.; Tsai, M.; Piliponsky, A. M. The development of allergic inflammation. *Nature* **2008**, *454*, 445−454.

(2) Simons, F. E. R. Anaphylaxis. *J. Allergy Clin. Immunol.* **2010**, *125*, S161−S181.

(3) Rosenwasser, L. J. Mechanisms of IgE inflammation. *Curr. Allergy Asthma Rep.* **2011**, *11*, 178−183.

(4) Gilfillan, A. M.; Tkaczyk, C. Integrated signaling pathways for mast-cell activation. *Nat. Rev. Immunol.* **2006**, *6*, 218−230.

(5) Itoh, T.; Ohguchi, K.; Iinuma, M.; Nozawa, Y.; Akao, Y. Inhibitory effects of polymethoxy flavones isolated from *Citrus reticulate* on degranulation in rat basophilic leukemia RBL-2H3: enhanced inhibition by their combination. *Bioorg. Med. Chem.* **2008**, *16*, 7592−7598.

(6) Suzuki, Y.; Yoshimaru, T.; Yamashita, K.; Matsui, T.; Yamaki, M.; Shimizu, K. Exposure of RBL-2H3 mast cells to Ag(+) induces cell degranulation and mediator release. *Biochem. Biophys. Res. Commun.* **2001**, *283*, 707−714.

(7) Qu, X.; Miah, S. M.; Hatani, T.; Okazaki, M.; Hori-Tamura, N.; Yamamura, H.; Hotta, H.; Sada, K. Selective inhibition of FcepsilonRI-mediated mast cell activation by a truncated variant of Cbl-b related to the rat model of type 1 diabetes mellitus. *J. Biochem.* **2005**, *137*, 711−720.

(8) Zhao, X.; Wang, Q.; Qian, Y.; Pang, L. *Cassia tora* L. (Jue-ming-zi) has anticancer activity in TCA8113 cells *in vitro* and exerts anti-metastatic effects *in vivo*. *Oncol. Lett.* **2013**, *5*, 1036−1042.

(9) Cho, S. H.; Kim, T. H.; Lee, N. H.; Son, H. S.; Cho, I. J.; Ha, T. Y. Effects of *Cassia tora* fiber supplement on serum lipids in Korean diabetic patients. *J. Med. Food* **2005**, *8*, 311−318.

(10) Guan, Y.; Zhao, S. Yishou jiangzhi (de-blood-lipid) tablets in the treatment of hyperlipemia. *J. Tradit. Chin. Med.* **1995**, *15*, 178−179.

(11) Kim, D. H.; Kim, S.; Jung, W. Y.; Park, S. J.; Park, D. H.; Kim, J. M.; Cheong, J. H.; Ryu, J. H. The neuroprotective effects of the seeds of *Cassia obtusifolia* on transient cerebral global ischemia in mice. *Food Chem. Toxicol.* **2009**, *47*, 1473−1479.

(12) Kim, Y. M.; Lee, C. H.; Kim, H. G.; Lee, H. S. Anthraquinones isolated from *Cassia tora* (Leguminosae) seed show an antifungal property against phytopathogenic fungi. *J. Agric. Food Chem.* **2004**, *52*, 6096−6100.

(13) Yen, G. C.; Chung, D. Y. Antioxidant effects of extracts from *Cassia tora* L. prepared under different degrees of roasting on the oxidative damage to biomolecules. *J. Agric. Food Chem.* **1999**, *47*, 1326−1332.

(14) Wong, S. M.; Wong, M. M.; Seligmann, O.; Wagner, H. New antihepatotoxic naphtho-pyrone glycosides from the seeds of *Cassia tora*. *Planta Med.* **1989**, *55*, 276−280.

(15) Patil, U. K.; Saraf, S.; Dixit, V. K. Hypolipidemic activity of seeds of *Cassia tora* Linn. *J. Ethnopharmacol.* **2004**, *90*, 249−252.

(16) Jang, D. S.; Lee, G. Y.; Kim, Y. S.; Lee, Y. M.; Kim, C. S.; Yoo, J. L.; Kim, J. S. Anthraquinones from the seeds of *Cassia tora* with inhibitory activity on protein glycation and aldose reductase. *Biol. Pharm. Bull.* **2007**, *30*, 2207−2210.

(17) Roth, K.; Chen, W. M.; Lin, T. J. Positive and negative regulatory mechanisms in high-affinity IgE receptor-mediated mast cell activation. *Arch. Immunol. Ther. Exp.* **2008**, *56*, 385−399.

(18) Theoharides, T. C.; Kalogeromitros, D. The critical role of mast cells in allergy and inflammation. *Ann. N. Y. Acad. Sci.* **2006**, *1088*, 78−99.

(19) Lee, J. H.; Kim, J. W.; Ko, N. Y.; Mun, S. H.; Her, E.; Kim, B. K.; Han, J. W.; Lee, H. Y.; Beaven, M. A.; Kim, Y. M.; Choi, W. S. Curcumin, a constituent of curry, suppresses IgE-mediated allergic response and mast cell activation at the level of Syk. *J. Allergy Clin. Immunol.* **2008**, *121*, 1225−1231.

(20) Wolfreys, K.; Oliveira, D. B. Alterations in intracellular reactive oxygen species generation and redox potential modulate mast cell function. *Eur. J. Immunol.* **1997**, *27*, 297−306.

(21) Niu, X. F.; Ibbotson, G.; Kubes, P. A. balance between nitric oxide and oxidants regulates mast cell-dependent neutrophil-endothelial cell interactions. *Circ. Res.* **1996**, *79*, 992−999.

(22) Suzuki, Y.; Yoshimaru, T.; Matsui, T.; Inoue, T.; Niide, O.; Nunomura, S.; Ra, C. Fc epsilon RI signaling of mast cells activates intracellular production of hydrogen peroxide: role in the regulation of calcium signals. *J. Immunol.* **2003**, *171*, 6119−6127.

(23) Zhang, C.; Baumgartner, R. A.; Yamada, K.; Beaven, M. A. Mitogen-activated protein (MAP) kinase regulates production of tumor necrosis factor-α and release of arachidonic acid in mast cells: indications of communication between p38 and p42 MAP kinases. *J. Biol. Chem.* **1997**, *272*, 13397−13402.

(24) Levy, L. Simultaneous passive cutaneous anaphylaxis and arthus reactions in mouse, rat and guinea-pig. *Immunology* **1964**, *7*, 91−96.

(25) Chodaczek, G.; Bacsi, A.; Dharajiya, N.; Sur, S.; Hazra, T. K.; Boldogh, I. Ragweed pollen-mediated IgE-independent release of biogenic amines from mast cells via induction of mitochondrial dysfunction. *Mol. Immunol.* **2009**, *46*, 2505−2514.

(26) Galli, S. J.; Kalesnikoff, J.; Grimbaldeston, M. A.; Piliponsky, A. M.; Williams, C. M.; Tsai, M. Mast cells as "tunable" effector and immunoregulatory cells: recent advances. *Annu. Rev. Immunol.* **2005**, *23*, 749−786.

(27) Wershil, B. K. Mast cell-deficient mice and intestinal biology. *Am. J. Physiol.: Gastrointest. Liver Physiol.* **2000**, *278*, G343−G348.

(28) Tanifuji, S.; Aizu-Yokota, E.; Funakoshi-Tago, M.; Sonoda, Y.; Inoue, H.; Kasahara, T. Licochalcones suppress degranulation by decreasing the intracellular Ca^{2+} level and tyrosine phosphorylation of ERK in RBL-2H3 cells. *Int. Immunopharmacol.* **2010**, *10*, 769−776.

(29) Westcott, J. Y.; Wenzel, S. E.; Dreskin, S. C. Arachidonate-induced eicosanoid synthesis in RBL-2H3 cells: stimulation with antigen or A23187 induces prolonged activation of 5-lipoxygenase. *Biochim. Biophys. Acta, Lipids Lipid Metab.* **1996**, *1303*, 74−81.

(30) Xu, L.; Chan, C. O.; Lau, C. C.; Yu, Z.; Mok, D. K.; Chen, S. Simultaneous determination of eight anthraquinones in Semen Cassiae by HPLC-DAD. *Phytochem. Anal.* **2012**, *23*, 110−116.

(31) Zhang, C.; Wang, R.; Liu, B.; Tu, G. Structure elucidation of a sodium salified anthraquinone from the seeds of *Cassia obtusifolia* by NMR technique assisted with acid-alkali titration. *Magn. Reson. Chem.* **2011**, *49*, 529−532.

(32) Aviello, G.; Rowland, I.; Gill, C. I.; Acquaviva, A. M.; Capasso, F.; McCann, M.; Capasso, R.; Izzo, A. A.; Borrelli, F. T Anti-proliferative effect of rhein, an anthraquinone isolated from Cassia species, on Caco-2 human adenocarcinoma cells. *J. Cell. Mol. Med.* **2010**, *14*, 2006−2014.

(33) Jung, H. A.; Chung, H. Y.; Yokozawa, T.; Kim, Y. C.; Hyun, S. K.; Choi, J. S. Alaternin and emodin with hydroxyl radical inhibitory and/or scavenging activities and hepatoprotective activity on tacrine-induced cytotoxicity in HepG2 cells. *Arch. Pharmacal Res.* **2004**, *27*, 947−953.

(34) He, Z. W.; Wei, W.; Li, S. P.; Ling, Q.; Liao, K. J.; Wang, X. Anti-allodynic effects of obtusifolin and gluco-obtusifolin against inflammatory and neuropathic pain. *Biol. Pharm. Bull.* **2014**, *37*, 1606−1616.

(35) Lu, Y.; Yang, J. H.; Li, X.; Hwangbo, K.; Hwang, S. L.; Taketomi, Y.; Murakami, M.; Chang, Y. C.; Kim, C. H.; Son, J. K.;

DOI: 10.1021/acs.jafc.5b03836
J. Agric. Food Chem. 2015, 63, 9037−9046

Chang, H. W. Emodin, a naturally occurring anthraquinone derivative, suppresses IgE-mediated anaphylactic reaction and mast cell activation. *Biochem. Pharmacol.* **2011**, *82*, 1700−1708.
(36) Singh, B.; Nadkarni, J. R.; Vishwakarma, R. A.; Bharate, S. B.; Nivsarkar, M.; Anandjiwala, S. The hydroalcoholic extract of *Cassia alata* (Linn.) leaves and its major compound rhein exhibits antiallergic activity via mast cell stabilization and lipoxygenase inhibition. *J. Ethnopharmacol.* **2012**, *141*, 469−473.
(37) Lu, Y.; Li, Y.; Jahng, Y.; Son, J. K.; Chang, H. W. Citreorosein inhibits degranulation and leukotriene C(4) generation through suppression of Syk pathway in mast cells. *Mol. Cell. Biochem.* **2012**, *365*, 333−341.
(38) Vishnuprasad, C. N.; Tsuchiya, T.; Kanegasaki, S.; Kim, J. H.; Han, S. S. Aurantio-obtusin stimulates chemotactic migration and differentiation of MC3T3-E1 osteoblast cells. *Planta Med.* **2014**, *80*, 544−549.
(39) Hyun, S. K.; Lee, H.; Kang, S. S.; Chung, H. Y.; Choi, J. S. Inhibitory activities of *Cassia tora* and its anthraquinone constituents on angiotensin-converting enzyme. *Phytother. Res.* **2009**, *23*, 178−184.
(40) Byun, E.; Jeong, G. S.; An, R. B.; Li, B.; Lee, D. S.; Ko, E. K.; Yoon, K. H.; Kim, Y. C. Hepatoprotective compounds of Cassiae Semen on tacrine-induced cytotoxicity in Hep G2 cells. *Korean J. Pharmacogn.* **2007**, *38*, 400−402.
(41) Choi, J. S.; Lee, H. J.; Park, K. Y.; Ha, J. O.; Kang, S. S. In vitro antimutagenic effects of anthraquinone aglycones and naphthopyrone glycosides from *Cassia tora*. *Planta Med.* **1997**, *63*, 11−14.
(42) El-Halawany, A. M.; Chung, M. H.; Nakamura, N.; Ma, C. M.; Nishihara, T.; Hattori, M. Estrogenic and anti-estrogenic activities of *Cassia tora* phenolic constituents. *Chem. Pharm. Bull.* **2007**, *55*, 1476−1482.
(43) Beaven, M. A.; Metzger, H. Signal transduction by Fc receptors: the Fc epsilon RI case. *Immunol. Today* **1993**, *14*, 222−226.
(44) Siraganian, R. P.; de Castro, R. O.; Barbu, E. A.; Zhang, J. Mast cell signaling: the role of protein tyrosine kinase Syk, its activation and screening methods for new pathway participants. *FEBS Lett.* **2010**, *584*, 4933−4940.
(45) Gonzalez-Periz, A.; Claria, J. New approaches to the modulation of the cyclooxygenase-2 and 5-lipoxygenase pathways. *Curr. Top. Med. Chem.* **2007**, *7*, 297−309.
(46) Hanada, T.; Yoshimura, A. Regulation of cytokine signaling and inflammation. *Cytokine Growth Factor Rev.* **2002**, *13*, 413−421.
(47) Suzuki, Y.; Yoshimaru, T.; Inoue, T.; Niide, O.; Ra, C. Role of oxidants in mast cell activation. *Chem. Immunol. Allergy* **2005**, *87*, 32−42.
(48) Camello-Almaraz, C.; Gomez-Pinilla, P. J.; Pozo, M. J.; Camello, P. J. Mitochondrial reactive oxygen species and Ca^{2+} signaling. *Am. J. Physiol. Cell Physiol.* **2006**, *291*, C1082−C1088.
(49) Yen, G. C.; Chuang, D. Y. Antioxidant properties of water extracts from Cassia tora L. in relation to the degree of roasting. *J. Agric. Food Chem.* **2000**, *48*, 2760−2765.
(50) Xu, S. C.; Ren, Y.; Wan, L.; Li, W. K.; Wong, N. B.; Zhang, J. X.; Liao, Q.; Ji, L. DFT insight into the UV-Vis spectra and radical scavenging activity of aurantio-obtusin. *J. Theor. Comput. Chem.* **2013**, *12*, 1350024.
(51) Abdel-Raheem, I. T.; Hide, I.; Yanase, Y.; Shigemoto-Mogami, Y.; Sakai, N.; Shirai, Y. Protein kinase C-alpha mediates TNF release process in RBL-2H3 mast cells. *Br. J. Pharmacol.* **2005**, *145*, 415−23.

DOI: 10.1021/acs.jafc.5b03836
J. Agric. Food Chem. 2015, 63, 9037−9046

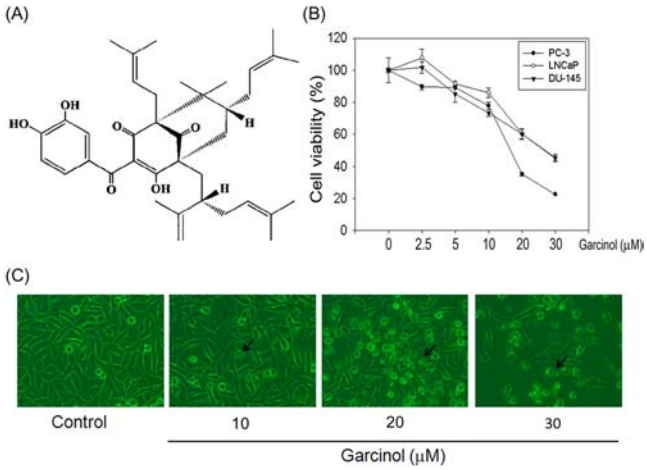

Figure 1. Effect of garcinol on the viability of human prostate cancer cells. (A) Chemical structure of garcinol. (B) The viability of DU-145, PC-3, and LNCaP cell lines was examined by MTT assay. $*p < 0.05$ compared to the control group. (C) Morphological changes of PC-3 cell after 12 h treatment with garcinol 10 μM, 20 μM, and 30 μM.

it has showed a better efficacy to induce apoptosis.[10] The mechanism of garcinol inducing apoptosis has implied that the release of cytochrome *c* into the cytosol can trigger procaspase-9 processing, activation of caspase-3 and caspase-2, and degradation of poly(ADP-ribose) polymerase (PARP). DNA fragmentation has also been observed, indicating the digestion of DNA fragmentation factor-45 (DFF-45) through the caspase-activated deoxyribonuclease.[10]

Cancer cells can be resistant through deregulation of apoptosis even though they are initially sensitive to apoptotic induction. Agents that kill cancer cells through nonapoptotic pathways or re-enhancing the apoptosis may circumvent this drug resistance. Therefore, looking for a new agent either to induce autophagy or increase the cell apoptosis has attracted attention. Systematic study of garcinol to induce cell death through both ways was applied in this study.

MATERIALS AND METHODS

Material. Garcinol was isolated from the dried rind of *G. indica* to 98% purity. The extraction procedure was adapted from the previous study.[11] Ethanol was used to extract *G. indica*, and the ethanol extract was fractionated using a silica gel column. Hexane−ethyl acetate solvent was used to elute garcinol fraction, which was redissolved in hexane after being dried. Hexane solution was kept in the freezer for 24 h, and the yellow amorphous powder precipitated. The yellow powder was dissolved in hot acetonitrile and recrystallized. The purity of garcinol was determined using 1D and 2D NMR (Varian AM-600) and APCI-MS (Fisons VG platform II) (NMR and MS data shown in the previous study[11]). The purified garcinol was dissolved in dimethyl sulfoxide (DMSO).

Cell Culture. The human prostate cancer cell lines DU-145, PC-3, and LNCaP were bought from American Type Culture Collection (ATCC, Manassas, VA). The culture media contained RPMI-1640 medium supplemented with 10% endotoxin-free, heat-inactivated fetal calf serum (GIBCO, Grand Island, NY), 100 mg/mL of streptomycin, and 100 units/mL of penicillin.

Determination of Cell Viability. Cell viability was tested using 3-(4,5-dimethylthiazol-2-yl)-2,5-diphenyl tetrazolium bromide (MTT). The method was adapted from the previous paper.[10] DU-145, PC-3, and LNCaP cells were treated with a series of concentrations of garcinol, and cell viability was obtained using an enzyme-linked immunosorbent assay.

DNA Extraction and Electrophoretic Analysis. The PC-3 cells were harvested and washed with phosphate-buffered saline (PBS). The extraction method followed the previous procedure.[10] The DNA was extracted using phenol/chloroform/isoamyl alcohol (25:24:1) and was analyzed by 2% agarose gel electrophoresis. DNA was stained with ethidium bromide before being visualized under UV light and photographed.

Flow Cytometry. PC-3 cells (2×10^5) were cultured in 60 mm Petri dishes in RPMI-1640 medium and incubated for 24 h. The details of the flow cytometry methodology followed the previous experiment design.[10] The propidium iodide−DNA complex was quantitated using FACScan cytometry (Becton Dickinson, San Jose, CA). ModFit LT for Mac 3.0 software (Becton Dickinson) was used to quantify the fraction of each cell cycle stage.

Analysis of the Mitochondrial Trans-Membrane Potential. Flow cytometry was used to measure the potential change of the mitochondrial trans-membrane. PC-3 cells were treated with garcinol (30 μM) for different time periods, and the potential of mitochondrial trans-membrane was measured with the direct application of 40 nM 3,3′-dihexyloxacarbocyanine [DiOC6(3)] (Molecular Probes, Eugene, OR). The fluorescence intensity was quantified by flow cytometry after the cells were stained for 30 min at 37 °C. Histograms were analyzed using Cell Quest software. Histograms from treated cells were compared with those from untreated, control cells.

Western Blot Analysis. The basic procedure of Western blot analysis was the same as the previous study.[10] The primary antibodies used included anticaspase-3, -9 (PharMingen, San Diego, CA), anti-Bcl-2, anti-Bcl-X_L, anti-Bax, anti-Bad (Santa Cruz Biotechnology, Santa Cruz, CA), antipoly(ADP-ribose) polymerase (PARP), LC3 I/II, Beclin-1, Atg 12, Atg 5, ERK1/2, phosphoERK1/2, JNK1/2, phospho-1/2, p38, phosphor-p38, PI3K, phospho-PI3K, PDK1, phosphor-PDK1, Akt, phospho-Akt, GSK3β, phosphor-GSK3β, mTOR, phosphor-mTOR (UBI Inc., Lake Placid, NY, USA), anti-Bag-1, anti-Mcl-1 (R and D System Inc., Minneapolis, MN, USA), anti-β-actin (Transduction Laboratory, Lexington, KY, USA), and anti-DFF45/inhibitor of caspase activated DNase (ICAD) (MBL, Naka-Ku, Nagoya, Japan) antibodies.

Human Prostate Tumor Xenograft Mouse Model. Each nude mouse was injected with prostate cancer PC-3 cells (3×10^6) in 200 μL of a PBS solution between the scapulae. The tumor size was measured using a caliper, and the tumor volume was estimated via the following formula: tumor volume (mm^3) = $L \times W^2/2$, where L was the length and W was the width. When the tumor size reached the average of 50−100 mm^3, the mice were randomly divided into six groups (6−8 animals/group). In the groups with intraperitoneal treatment, the mice were injected with garcinol (50 mg/kg/d) in 200 μL of coil oil for 5 days per week, while the control group received just corn oil injections. In the groups with oral treatment, the animals were orally administered with either 200 μL of corn oil or garcinol in corn oil (50 mg/kg/d) for 5 days per week. The dietary intake and the body weight of each animal (average weight = 17 g) were monitored every day. The tumor volume was calculated twice per week. After 40−50 days, the mice were sacrificed by CO_2 asphyxiation. The livers, kidneys, spleens, and solid tumors were excised immediately and weighed. The average tumor volumes and weights of each group were represented as the means ± standard deviation (SD). The tumor tissue was cut into small portions for Western blot analysis.

Statistical Analysis. All results were obtained through three independent experiments and presented as means ± standard error of the mean (SE). The differences between the control group and the different concentrations of garcinol were analyzed by Student's *t* test. The data was considered statistically significant at a *P*-value of <0.05.

RESULTS

Cytotoxic Effects of Garcinol in DU-145, PC-3, and LNCaP Cells. To investigate the cytotoxic effect of garcinol on cells, various concentrations of garcinol were applied to three different cell lines (DU-145, PC-3, and LNCaP cells). The cell viability was verified using the MTT assay. Figure 1B showed a

DOI: 10.1021/acs.jafc.5b03851
J. Agric. Food Chem. 2015, 63, 9047−9052

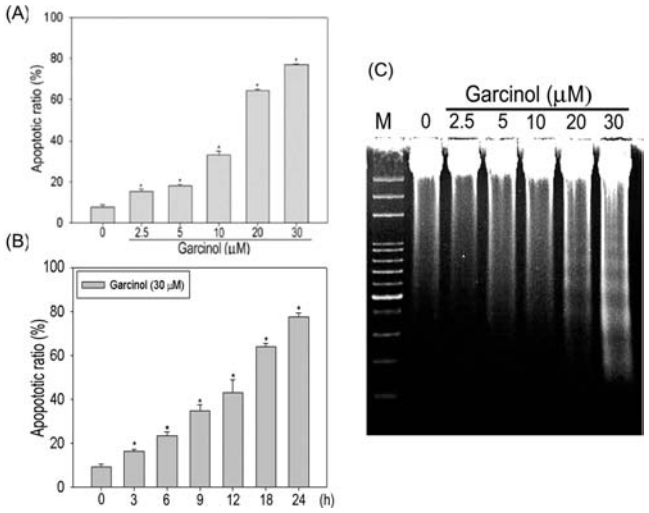

Figure 2. Effect of garcinol on induction of apoptosis and DNA fragmentation in PC-3. (A, B) PC-3 cells treated with increasing doses of garcinol for 24 h or treated with 30 μM garcinol for the indicated time and then determination of sub-G1 cells by flow cytometry. Comparisons were subjected to Student's t test. Significantly different at $^*P < 0.05$. (C) PC-3 cell were treated with 0, 2.5, 5, 10, 20, and 30 μM for 24 h. DNA fragmentation was analyzed by 2% agarose electrophoresis. Data are representative of three independent experiments.

concentration-dependent manner of cytotoxic effects, and PC-3 exhibited the highest ratio of cell death when 30 μM garcinol was applied. Therefore, PC-3 cells were used for the subsequent studies.

Sub-G1 cells and apoptotic ratio were quantified using flow cytometry. The apoptotic ratio was shown in a concentration-dependent manner with garcinol treatment at different concentrations (Figure 2A), and the highest apoptotic ratio was obtained at a concentration of 30 μM garcinol. Moreover, treated with 30 μM of garcinol in a time-course study, PC-3 cells started apoptosis after 3 h, and continued up to 24 h (Figure 2B).

Induction of DNA Fragmentation in PC-3 Cells by Garcinol. Apoptosis induces morphological changes such as cell shrinkage and DNA fragmentation. PC-3 cells were treated with garcinol at different concentrations for 24 h, and DNA fragmentation was studied. The DNA fragmentation also followed a dose-dependent pattern (Figure 2C). The emergence of DNA ladders was shown at the 5 μM of garcinol treatment. Light microscopy can be used to observe the morphological changes in PC-3 cells which were induced by garcinol treatment. As shown in Figure 1C, apoptotic bodies were obtained in PC-3 cells after treatment with garcinol in a dose-dependent manner.

Induction of Mitochondrial Dysfunction by Garcinol. Mitochondria are specialized organelles containing an outer membrane and an inner membrane separated by an intermembrane space that contains many proapoptotic proteins. Induction of apoptosis causes the changes of mitochondrial membrane potential which can be analyzed by measuring log fluorescence intensity with flow cytometry. The potential of mitochondrial membrane was reduced by the treatment of garcinol at a certain time. For example, PC-3 cells were incubated with garcinol for 60

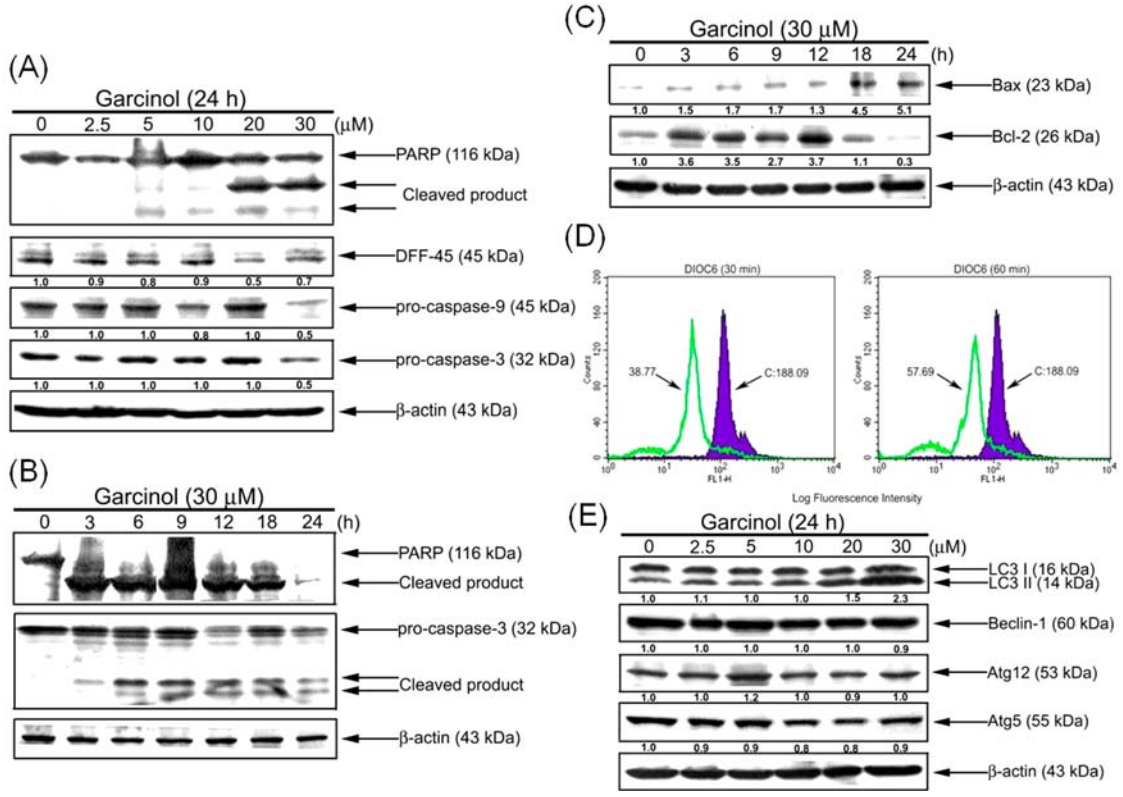

Figure 3. Intracellular response of caspase activation, mitochondrial dysfunction, and Bcl-2 protein expression in garcinol-treated PC-3 cells. (A–C, E) PC-3 cells treated with increasing doses of garcinol for 24 h or treated with 30 μM garcinol for various times. Proteins (50 μg/lane) were separated by SDS–PAGE, immunoblotted with anticaspases-9, -3, PARP, DFF-45, LC3, Beclin-1, Atg5, and Atg12 antibody. (D) PC-3 cells were treated with 30 μM garcinol for indicated times and were then incubated with 40 nM 3,3′-dihexyloxacarbocyanine iodide and analyzed by flow cytometry. Data are representative of three independent experiments.

DOI: 10.1021/acs.jafc.5b03851
J. Agric. Food Chem. 2015, 63, 9047–9052

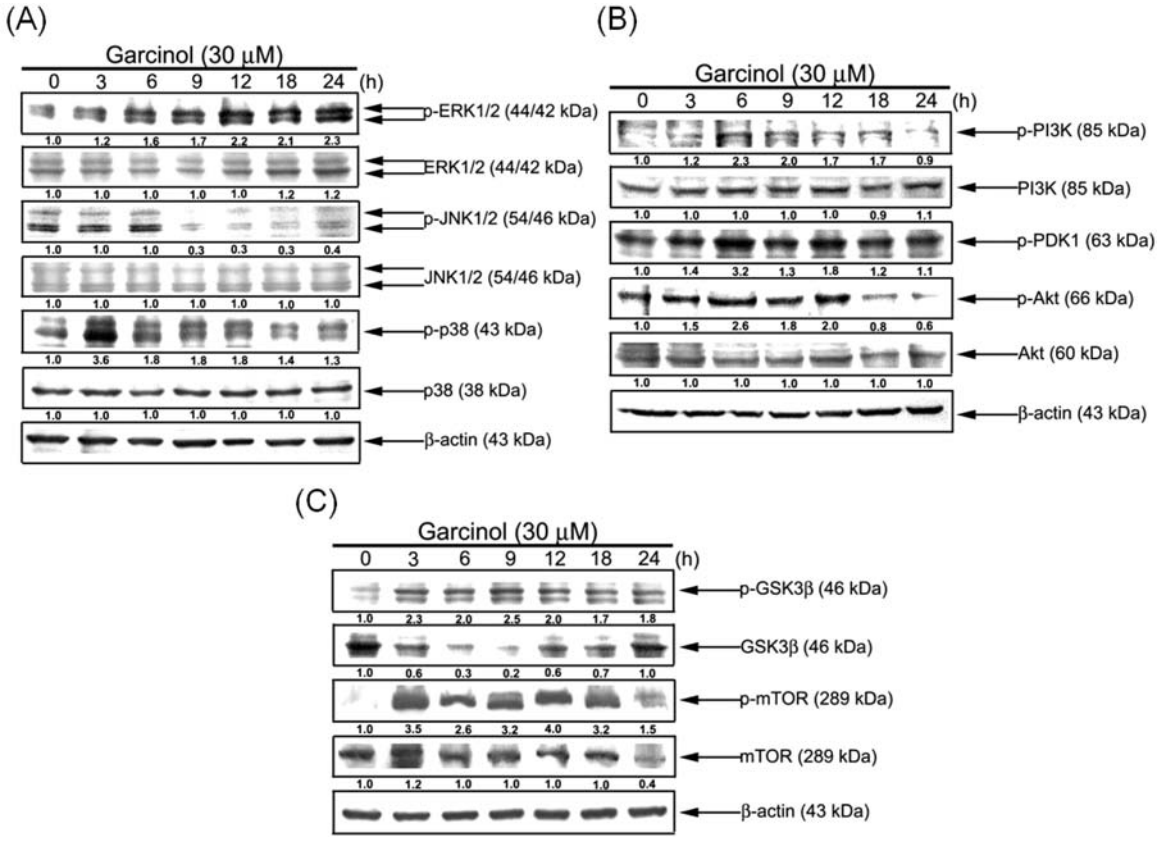

Figure 4. Effect of the expression of MAPKs, PI3k/Akt, and downstream target proteins in garcinol-treated PC-3 cells. PC-3 cells were treated with 30 μM garcinol for 0, 3, 6, 9, 12, 18, and 24 h, and the expression of MAPKs (A), PI3k/PDK1/Akt (B), GSK3β and mTOR (C) protein was analyzed by immunoblotting. The levels of β-actin, total-p38, -JNK1/2, -ERK1/2, -PI3K, -Akt, -GSK3β, and -mTOR protein were used as controls for equal loading of protein in different lanes. Data are representative of three independent experiments.

min, and the mitochondrial membrane potential reduced to 57.69, compared to the control of 168.09, indicating that garcinol induces apoptosis in PC-3 cells via the mitochondrial pathway (Figure 3D). In addition, the level of Bax and Bcl-2 was evaluated at different time points. An apparent increase of Bax was shown, while the level of Bcl-2 increased from 0 to 12 h and decreased significantly after 12 h (Figure 3C). The increase of the Bax/Bcl-2 ratio resulted in an enhancement of apoptosis.

Induction of Caspase Activity, PARP Cleavage, and DFF-45 Degradation by Garcinol. The levels of procaspases-3 and -9 in PC-3 cells were changed with the treatment of garcinol in a concentration-dependent manner indicating the effect of garcinol in the activation of caspases. Garcinol (30 μM) reduced the level of procaspases-3 and -9, indicating an increase of activity of caspase-3 and -9. Meanwhile, cleavage of PARP and DFF-45 was induced by garcinol in a dose-dependent manner (Figure 3A). As shown in Figure 3B, protein cleavage of procaspase-3 occurred after 3 h exposure to garcinol. To detect PARP cleavage as a result of caspase-3 activation, PC-3 cells were treated with 30 μM garcinol for various durations. Garcinol induced time dependent proteolytic cleavage of PARP is shown in Figure 5C.

Induction of p-mTOR and p-GSK-3β Pathways in PC-3 Cells. To clarify the occurrence of autophagy induced by garcinol, expressions of LC3B and beclin-1, which are hallmarks of autophagy, were studied in PC-3 cells treated with/without garcinol using immunoblot. As shown in Figure 3E, the amounts of LC3B I/II proteins increased after treatment with garcinol in a dose-dependent manner. However, garcinol did not cause significant changes in the expression of beclin-1, Atg 12, and Atg 5, suggesting that garcinol induced little autophagy, and apoptosis could be the major pathway inducing cell death. In addition, phosphorylation of mTOR increased from the very beginning of the garcinol treatment and so did of mTOR (Figure 4C). As shown in Figure 4C, treatment with garcinol also increased phosphorylated GSK-3β gradually, and then it decreased a little bit, but the total level still slightly increased. These results indicated that garcinol inhibited autophagy which may enhance the apoptotic cell death. Therefore, these findings suggested that garcinol may switch between autophagy and apoptosis though controlling p-mTOR/mTOR and GSK-3β signaling pathways in PC-3 cells.

PI3K/Akt and MAPK Signaling Pathways Are Involved in Garcinol Inhibiting Autophagy in PC-3 Cells. Studies showed that PI3K/Akt and ERK1/2 pathways were involved in regulating autophagy.[12,13] However, the function of p38 and JNK1/2 MAPKs is still unclear. Therefore, we investigated how these signaling pathways functioned in inhibiting autophagy by garcinol in PC-3 cells. As shown in Figure 4B, phosphorylation of PI3K, Akt, and PDK1 increased after garcinol treatment (0−12 h) and then decreased in cells. However, p-ERK1/2 was quite low, and after 6 h treatment with garcinol the level of p-ERK1/2 gradually increased, while phosphorylated JNK1/2 decreased, and p-38 increased effectively for a period of 0−3 h, respectively, and then decreased (Figure 4A). Taken together, these results indicated that garcinol activated the PI3K/Akt/mTOR and GSK-3β pathways and inhibited the ERK1/2 pathway for 0−6 h

DOI: 10.1021/acs.jafc.5b03851
J. Agric. Food Chem. 2015, 63, 9047−9052

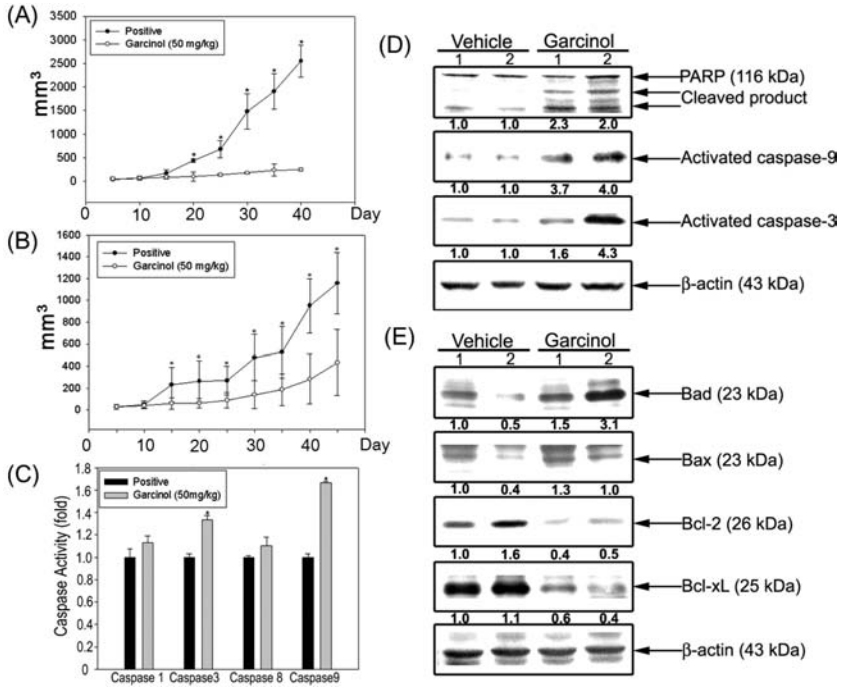

Figure 5. Apoptosis-related protein expression of PC-3 tumor xenograft in nude mice. PC-3 cells were injected subcutaneously between the scapulas of nude mice. Once tumor volume reached approximately 50 mm^3, the animal received an ip (A) or oral gavage (B) of 50 mg/kg garcinol or corn oil five times per week for 40−50 days. Average tumor volume of corn oil-treated versus garcinol-treated nude mice ($n = 5$). Five samples were analyzed in each group, and values represent the mean ± SE. Comparisons were subjected to Student's t test. Significantly different at $^*P < 0.05$. When the animal received ip dose, (C) enzymatic activity of caspase-1, caspase-3, caspase-8, caspase-9 was examined by spectrofluorimetry (excitation = 360 nm; emission = 460). With ip dose, (D, E) apoptosis-related protein expression was examined by Western blot.

treatment, suggesting that these changes mediated garcinol-inhibited autophagy in PC-3 cells.

Apoptosis-Related Protein Expression of PC-3 Tumor Xenograft in Nude Mice. Apoptosis-related protein expression was studied by using PC-3 xenograft prostate cancer mice. Those mice were accepted either an ip or oral gavage of 50 mg/kg garcinol five times per week for 40−50 days. Compared to the positive control, admission of garcinol in either way could significantly decrease the tumor volume. As shown in Figure 5C, caspase-3 and -9 were all activated by garcinol, indicating the activation of apoptosis. More expressions of caspase-3 and -9 were obtained, and the cleavage of PARP was also observed (Figure 5D). The antiapoptotic proteins such as Bcl-2 and Bcl-xL have been shown to decrease with the treatment of garcinol, while the proapoptotic proteins (Bax and Bad) have been expressed more because of the addition of garcinol. The tumor size was reduced 80 percent due to garcinol treatment. Those results suggested that garcinol could be one of the potential chemotherapy agents for human prostate cancer.

DISCUSSION

According to previous studies, the mechanisms of antitumor of garcinol mainly focus on the induction of apoptosis. Of note, the majority of cancer chemopreventive agents inhibit cancer growth by activating the mechanisms of programmed cell death such as apoptosis and autophagy. Garcinol could induce apoptosis in MCF-7 cells by downregulating NF-κB.[14] Activation of caspase-3 is a major way to induce apoptosis by treating with garcinol,[10] and downregulation of MAPK/ERK and PI3K/Akt could also induce apoptosis when HT-29 cells were incubated with garcinol.[15] However, besides apoptosis, autophagy is also an important pathway for cell death in cancer therapy. The relationship between apoptosis and autophagy is complex and depends on types of cels and stress. Tumor cells with defects in apoptosis pathways undergo autophagy.[16] It has also been suggested that autophagy may provide an alternative way to prevent cancer development, slow down tumor progression, and enhance the efficacy of cancer treatments.[8]

In this study, we systematically investigated the antitumor effect of garcinol in PC-3 cell lines and the relationship between apoptosis and autophagy. Garcinol treatment decreased cell viability and strongly induced apoptosis in PC-3 cells. Garcinol contains a phenolic, a β-diketone, and an α,β-unsaturated ketone moiety. The α,β-unsaturated carbonyls are easily bound with thiols such as glutathione, which is the most abundant non-protein thiol in vivo. Binding with glutathione, which would cause intracellular glutathione depletion, could induce mitochondrial dysfunction. As the results show, the mitochondrial membrane potential was reduced by the treatment of garcinol. Morphological changes are caused by caspase. Once the "initiator" or "effector" caspases activated (caspase-9 or -3), they would cause the release of mitochondrial proteins to trigger apoptosis pathways. Those mitochondrial proteins include pro- and antiapoptotic proteins which, for example, are Bax and Bcl-2, respectively. Meanwhile, activation of caspase-3 would also cause the cleavage of PARP and DFF-45, whose cleavage products have been observed in our results. Consider all, garcinol induced apoptosis in PC-3 by increasing the ratio of Bax/Bcl-2 ratio, reducing mitochondrial membrane potential, and suppressing procaspase-9, procaspase-3, PARP, and DFF-45.

In autophagy, caspases are not activated, and DNA fragmentation is not apparent. Most cellular systems where autophagy has been involved have defects in the apoptosis signaling pathway.[17] However, the interesting question is if any

DOI: 10.1021/acs.jafc.5b03851
J. Agric. Food Chem. 2015, 63, 9047−9052

molecular correlation between autophagy and apoptosis exists. Apoptosis can happen due to inhibition of autophagy while autophagy can be activated due to inhibition of apoptosis. In order to promote autophagy and limit tumor progression, mTOR pathway can be inhibited, because autophagy is required for the effective management of metabolic stress.[18] A large number of stimuli modulate autophagy, and numerous signaling pathways such as PI3 Kinase/AKt, MAP kinases, and AMP dependent protein Kinase regulate this process. Most of them work through the mTOR pathway.[8] Natural products have been shown to induce autophagy through inhibiting the PI3 Kinase/AKT and mTOR, and activating the MAP kinase, but garcinol inhibited autophagy through activating the PI3K/AKT and the mTOR, of which the mechanism pathways are still consistent with other studies.[19,20] Suppression of the mTOR increases the levels of activated LC-3 and beclin-1.[20,21] Garcinol inhibited autophagy, which may enhance cell apoptosis. The mechanism pathways will be discussed in a future study.

In order to verify the anticancer effect of garcinol, we also fed mice either by intraperitoneal injection or oral administration. After 40−50 days of treatment, the cancer volume was significantly reduced by treatment of garcinol, and all parameters related to apoptosis showed that apoptosis was induced by garcinol administration. Many cancer cells are resistant to some agents if the treatment proceeds for a long time. Searching for novel compounds of chemoprevention becomes a growing interest in the anticancer therapy field. The optimal antiproliferative effects of garcinol have been demonstrated in PC-3 human prostate cancer cells and nude mice. The anticancer effects of garcinol are regulated by inhibiting autophagy and re-enhancing apoptosis. The signaling pathways mediating garcinol-induced apoptosis and -inhibited autophagy have been identified. To the best of our knowledge, this study first showed that garcinol could induce apoptosis and inhibit autophagy in prostate cancer cells. In conclusion, garcinol possesses a potential property of chemoprevention.

AUTHOR INFORMATION

Corresponding Author

*Institute of Food Science and Technology, National Taiwan University, No. 1, Section 4, Roosevelt Road, Taipei 10617, Taiwan. Tel.: +886 2 33664133. Fax: +886-2-33661771. E-mail: mhpan@ntu.edu.tw.

Funding

This study was supported by the National Taiwan University NTU-104R7777; Ministry of Science and Technology 101-2628-B-022-001-MY4, 102-2628-B-002-053-MY3.

Notes

The authors declare no competing financial interest.

REFERENCES

(1) Carlsson, S.; Vickers, A. J.; Roobol, M.; Eastham, J.; Scardino, P.; Lilja, H.; Hugosson, J. Prostate cancer screening: facts, statistics, and interpretation in response to the US preventive services task force review. *J. Clin. Oncol.* **2012**, *30*, 2581−2584.

(2) Syed, D. N.; Khan, N.; Afaq, F.; Mukhtar, H. Chemoprevention of prostate cancer through dietary agents: progress and promise. *Cancer Epidemiol., Biomarkers Prev.* **2007**, *16*, 2193−2203.

(3) Boise, L. H.; Gonzalez-Garcia, M.; Postema, C. E.; Ding, L.; Lindsten, T.; Turka, L. A.; Mao, X.; Nunez, G.; Thompson, C. B. *bcl-x*, a *bcl-2*-related gene that functions as a dominant regulator of apoptotic cell death. *Cell* **1993**, *74*, 597−608.

(4) Earnshaw, W. C.; Martins, L. M.; Kaufmann, S. H. Mammalian caspases: structure, activation, substrates and functions during apoptosis. *Annu. Rev. Biochem.* **1999**, *68*, 383−424.

(5) Salvesen, G. S.; Dixit, V. M. Caspases: intracellular signalling by proteolysis. *Cell* **1997**, *91*, 443−446.

(6) Kroemer, G.; Jaattela, M. Lysosomes and autophagy in cell death control. *Nat. Rev. Cancer* **2005**, *5*, 886−897.

(7) Kabeya, Y.; Mizushima, N.; Ueno, T.; Yamamoto, A.; Kirisako, T.; Noda, T.; Kominami, T.; Ohsumi, T.; Yoshimori, T. LC3, a mammalian homologue of yeast Apg8p, is localized in autophagosome membranes after processing. *EMBO J.* **2000**, *19*, 5720−5728.

(8) Thorburn, A. Apoptosis and autophagy: regulatory connections between two supposedly different processes. *Apoptosis* **2008**, *13*, 1−9.

(9) Tang, W.; Pan, M. H.; Sang, S.; Li, S.; Ho, C. T. Garcinol from Garcinia indica: chemistry and health beneficial effects. In *Tropical and Subtropical Fruits: Flavors, Color, and Health Benefits*; Patil, B. S., Jayaprakasha, G. K., Roa, C. O., Mahattanatawee, K., Eds.; American Chemical Society: Washington, DC, 2013; Vol. *1129*, pp 133−145.

(10) Pan, M. H.; Chang, W. L.; Lin-Shiau, S. Y.; Ho, C. T.; Lin, J. K. Induction of apoptosis by garcinol and curcumin through cytochrome c release and activation of caspases in human leukemia HL-60 cells. *J. Agric. Food Chem.* **2001**, *49*, 1464−1474.

(11) Sang, S.; Pan, M. H.; Cheng, X.; Bai, N.; Stark, R. E.; Rosen, R. T.; Lin-Shiau, S. Y.; Lin, J. K.; Ho, C. T. Chemical studies on antioxidant mechanism of garcinol: analysis of radical reaction products if garcinol and their antitumor activities. *Tetrahedron* **2001**, *57*, 9931−9938.

(12) Yap, T. A.; Garrett, M. D.; Walton, M. I.; Raynaud, F.; de Bono, J. S.; Workman, P. Targeting the PI3K-AKT-mTOR pathway: progress, pitfalls, and promises. *Curr. Opin. Pharmacol.* **2008**, *8*, 393−412.

(13) Cui, Q.; Tashiro, S.; Onodera, S.; Minami, M.; Ikejima, T. Oridonin induced autophagy in human cervical carcinoma HeLa cells through Ras, JNK, and P38 regulation. *J. Pharmacol. Sci.* **2007**, *105*, 317−325.

(14) Ahmad, A.; Wang, Z.; Ali, R.; Maitah, M. Y.; Kong, D.; Banerjee, S.; Padhye, S.; Sarkar, F. H. Apoptosis-inducing effect of garcinol is mediated by NF-κB signaling in breast cancer cells. *J. Cell. Biochem.* **2010**, *109*, 1134−1141.

(15) Liao, C. H.; Sang, S.; Ho, C. T.; Lin, J. K. Garcinol modulates tyrosine phosphorylation of FAK and subsequently induces apoptosis through down regulation of Src, ERK, and Akt survival signaling in human colon cancer cells. *J. Cell. Biochem.* **2005**, *96*, 155−169.

(16) Degenhardt, K.; Mathew, R.; Beaudoin, B.; Bray, K.; Anderson, D.; Chen, G.; Mukherjee, C.; Shi, Y.; Gelinas, C.; Fan, Y.; Nelson, D. A.; Jin, S.; White, E. Autophagy promotes tumor cell survival and restricts necrosis, inflammation, and tumorigenesis. *Cancer Cell* **2006**, *10*, 51−64.

(17) Yu, L.; Wan, F.; Dutta, S.; Welsh, S.; Liu, Z. H.; Freundt, E.; Baehrecke, E. H.; Lenardo, M. Autophagic programmed cell death by selective catalase degradation. *Proc. Natl. Acad. Sci. U. S. A.* **2006**, *103*, 4952−4957.

(18) Mathew, R.; Karantza-Wadsworth, V.; White, E. Role of autophagy in cancer. *Nat. Rev. Cancer* **2007**, *7*, 961−967.

(19) Chiu, H. W.; Ho, S. Y.; Guo, H. R.; Wang, Y. J. Combination treatment with arsenic trioxide and irradiation enhances autophagic effects in U118-MG cells through increased mitotic arrest and regulation of PI3K/Akt and ERK1/2 signaling pathways. *Autophagy* **2009**, *5*, 472−483.

(20) Chen, R. J.; Ho, C. T.; Wang, Y. J. Pterostilbene induces autophagy and apoptosis in both sensitive and chemoresistant human bladder cancer cells. *Mol. Nutr. Food Res.* **2010**, *54*, 1819−1832.

(21) Levine, B.; Kroemer, G. Autophagy in the pathogenesis of disease. *Cell* **2008**, *132*, 27−42.

DOI: 10.1021/acs.jafc.5b03851
J. Agric. Food Chem. 2015, 63, 9047−9052

HUVECs, the production of adhesion molecules and chemokines, and the activation of NF-κB in HUVECs.

MATERIALS AND METHODS

Materials. Endothelial cell growth medium (EGM-2) and primary cultured HUVECs were obtained from Lonza (Walkersville, MD, USA). CellTiter^{96} AQ_{ueous} One Solution Cell Proliferation assay kit and reverse transcriptase were purchased from Promega (Madison, WI, USA). Primary and secondary antibodies were obtained from Santa Cruz Biotechnology (Santa Cruz, CA, USA) and Abcam (Danvers, MA, USA). An enhanced chemiluminescence (ECL) detection system was purchased from GE Healthcare Bio-Science (Piscataway, NJ, USA). QIAzol lysis reagent was purchased from Quiagen (Valencia, CA, USA). 2′,7′-Bis(2-carboxyethyl)-5(6)-carboxyfluorescein acetoxy-methylester (BCECF-AM), Alexa Fluor 488-conjugated secondary antibody, and 4′,6-diamidino-2-phenylindole (DAPI) were purchased from Invitrogen (Carlsbad, CA, USA). 2′,7′-Dichlorofluorescin diacetate (DCFH-DA), dimethyl sulfoxide (DMSO), and phenylmethanesulfonyl fluoride (PMSF) were obtained from Sigma-Aldrich Corp. (St. Louis, MO, USA).

Isolation of SQA. *S. serratifolium* was collected along the coast of Busan, South Korea, in April 2014. Specimen identity was confirmed by an agal biologist (N. G. Kim) at the Department of Marine Biology and Aquaculture, Gyeongsang National University, South Korea. Dried seaweed (1.5 kg) was extracted twice with 95% (v/v) ethanol (6 L/each) at 70 °C for 3 h. The ethanolic extract (150.7 g) was obtained by concentration under reduced pressure. To obtain the *n*-hexane-soluble fraction, the extract was suspended in water/ethanol (9:1, v/v) and then partitioned with *n*-hexane to produce 121 g of *n*-hexane-soluble fraction. An aliquot of *n*-hexane fraction was separated by a recycled HPLC system with a Phenomenex Luna RP-18(2) column (250 × 21.2 mm, 15 μm, Phenomenex, Torrence, CA, USA). The elution profile was composed of a linear gradient from methanol (A)/water (B) (90:10) to A/B (94:6) for 35 min, A/B (94:6) to A/B (100:0) for 2 min, and re-equilibrated with A/B (90:10) for 10 min after a 10 min hold with A/B (100:0). Peaks were monitored at 270 nm, and the flow rate was 7 mL/min. The purity of a fraction exhibiting strong anti-inflammatory activity based on the inhibition of ICAM-1 production in TNF-α-stimulated HUVECs was improved by the same HPLC system with Luna RP-18 [Luna C18(2), 250 × 10 mm, 5 μm] at a flow rate of 3.0 mL/min. The fraction was eluted with a linear gradient from methanol A/B (93.4:6.6) to A/B (93.8:6.2) for 20 min, A/B (93.8:6.2) to A/B (100:0) for 2 min, and re-equilibrated with A/B (93.8:6.2) for 10 min after a 10 min hold with A/B (100:0). The purity of the separated compound was >98.0%, as evaluated by the same HPLC system with the Luna RP-18 column [Luna C18(2), 3 μm, 150 × 3.0 mm]. The content of the compound was estimated to be 0.62 ± 0.07 g per 100 g of dried *S. serratifolium*.

Spectrometry. A JNM ECP-400 spectrometer (JEOL, Japan) was used to resolve ^{1}H and ^{13}C NMR spectra. CD_3OD with tetramethylsilane was used as an internal standard. Heteronuclear multiple-bond correlation and heteronuclear multiple-quantum correlation spectra were monitored using pulsed field gradients. The structure of SQA is shown in Supporting Information Figure S1.

Structural Elucidation of SQA. $C_{27}H_{36}O_4$ (MW = 424); ^{1}H NMR (CD_3OD, 400 MHz) δ 3.12 (2H, d, *J* = 6.9 Hz, H-1), 5.17 (1H, t, *J* = 7.4 Hz, H-2), 2.08 (2H, m, H-4), 2.09 (2H, m, H-5), 5.10 (1H, m, H-6), 2.09 (2H, m, H-8), 2.59 (2H, dt, *J* = 7.2 and 7.2 Hz, H-9), 5.84 (1H, t, *J* = 7.3 Hz, H-10), 2.19 (2H, t, *J* = 7.2 Hz, H-12), 2.12 (2H, m, H-13), 5.06 (1H, tt, *J* = 7.3 and 1.4 Hz, H-14), 1.65 (3H, s, CH_3-16), 1.58 (3H, s, CH_3-17), 1.60 (3H, s, CH_3-19), 1.62 (3H, s, H-20), 6.42 (1H, m, H-3′), 6.56 (1H, quin, *J* = 1.4 Hz, H-5′), 2.12 (3H, d, *J* = 1.5 Hz, aromatic-CH_3); ^{13}C NMR (CD_3OD, 100 MHz) δ 28.5 (C-1), 120.1 (C-2), 140.4 (C-3), 40.7 (C-4), 27.3 (C-5), 125.7 (C-6), 135.8 (C-7), 40.3 (C-8), 29.0 (C-9), 142.6 (C-10), 132.9 (C-11), 36.1 (C-12), 28.9 (C-13), 124.8 (C-14), 133.4 (C-15), 25.9 (C-16), 17.8 (C-17), 171.6 (C-18), 15.97 (C-19), 16.0 (C-20), 189.4 (C-1′), 150.0 (C-2′), 133.0 (C-3′), 188.9 (C-4′), 133.96 (C-5′), 147.6 (C-6′), 16.1 (aromatic-CH_3). .

Mass Spectrometry Analysis. The molecular weight of SQA was confirmed by mass spectrometry. The mass spectrometry analysis was performed with a Shimadzu GCMS-QP2010 Ultra instrument with a direct sample inlet device (DI-2010, Kyoto, Japan). The initial probe temperature was 40 °C/min; it was ramped to 350 °C and held for 2 min. The ion source temperature was 200 °C, and the injection volume was 0.5 μL. The mass spectrum is shown in Supporting Information Figure S1.

Cell Culture and Viability Assay. 3-(4,5-Dimethylthiazol-2-yl)-5-(3-carboxymethoxyphenyl)-2-(4-sulfophenyl)-2*H*-tetrazolium (MTS) was used to assess the cytotoxicity of SQA. Briefly, cells were seeded in a 96-well plate at a density of 5 × 10^3 cells/well. The cells were treated with a serial dilution of SQA indicated in the figure legend. MTS solution was added with fresh medium for 1 h based on the manufacturer's instruction followed by measurement of the absorbance at 490 nm using a microplate reader (Glomax Multi Detection System, Promega).

Cell-Based Enzyme-Linked Immunsorbent Assay (ELISA). The expression of ICAM-1 and VCAM-1 in HUVECs was determined by cell-based ELISA as described by Manduteanu et al.[17] Briefly, HUVECs were placed in a 24-well plate at a density of 5 × 10^4 cells/well. After 24 h of incubation, cells were exposed to diverse concentrations of SQA for 1 h. After removal of culture medium, the cells were stimulated with TNF-α (10 ng/mL) for 6 h. The cells fixed by 1% paraformaldehyde were blocked with 2% BSA. After exposure to mouse anti-human ICAM-1 or VCAM-1 antibodies for 1 h followed by washing, cells were incubated with the horseradish peroxidase-conjugated secondary antibody for 1 h. Expression levels of ICAM-1 and VCAM-1 were quantified by the addition of peroxidase substrate solution, and the absorbance was measured at 490 nm with a microplate reader (Glomax Multi Detection System, Promega).

Monocyte Adhesion Assay. Confluent HUVECs pretreated with SQA for 1 h were stimulated with TNF-α (10 ng/mL) for 6 h. THP-1 monocytes (KCLB, Seoul, Korea) were tagged with the compound BCECF-AM (10 μM). The tagged THP-1 monocytes (2.5 × 10^5) were gently added to the HUVEC monolayer and incubated for 1 h. Unbound THP-1 cells were discarded by PBS washing. HUVEC-attached THP-1 cells were observed with an LSM700 laser scanning confocal microscope (Carl Zeiss, Oberkochen, Germany). In parallel, HUVEC-adherent monocytes were harvested with cell lysis solution (50 mM Tris-HCl, containing 0.1% SDS, pH 8.0), and the fluorescence intensity was determined using a fluorescence microplate reader (Dual Scanning SPECTRAmax, Molecular Devices Co., Sunnyvale, CA, USA) at 485 nm (excitation wavelength) and 535 nm (emission wavelength). The results were shown as relative monocyte adhesion levels compared with the control group.

Reverse Transcription-Polymerase Chain Reaction (RT-PCR). SQA-pretreated HUVECs were stimulated with TNF-α for 6 h. RNA was isolated using the QIAzol reagent. cDNA was synthesized with oligo-dT primer and superscript reverse transcriptase using total RNA (5 μg). PCR was conducted with corresponding primers (Supporting Information Table 1). Densitometric analysis was performed using EZ-Capture II (ATTO & Rise Co., Tokyo, Japan) and CS analyzer (ver. 3.00 software, ATTO).

Intracellular ROS Measurement. ROS scavenging activity of SQA was determined with fluorescent probe DCFH-DA. Confluent HUVECs in black 96-well plates were pretreated with 5, 10, and 15 μM SQA for 1 h. After the wells had been washed with PBS, the cells were treated with 20 μM DCFH-DA for 30 min at 37 °C and then stimulated with TNF-α (10 ng/mL) for 1 h. The fluorescence level was determined using a fluorescence microplate reader (Dual Scanning SPECTRAmax) at 485 nm (excitation wavelength) and 528 nm (emission wavelength).

Preparation of Cytosolic and Nucleus Extracts. HUVECs were seeded in a culture dishes at a density of 6 × 10^5 cells/dish and cultured for 24 h. Cultured cells were pretreated with 0, 5, 10, and 15 μM of SQA for 1 h and stimulated with TNF-α for 30 min. Separation of cytosolic and nucleus extracts was performed as previously described.[18]

DOI: 10.1021/acs.jafc.5b04050
J. Agric. Food Chem. 2015, 63, 9053−9061

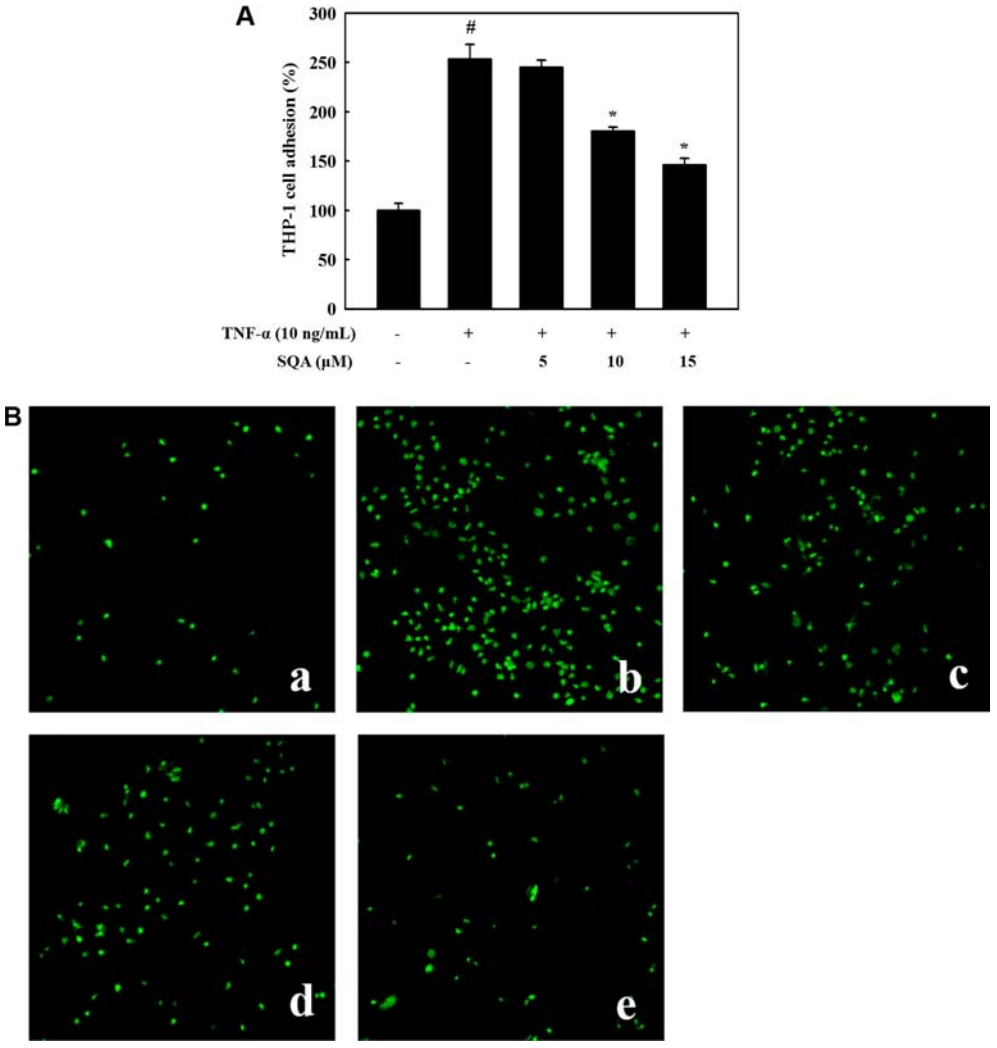

Figure 1. Effect of SQA on the adhesion of THP-1 monocytes to TNF-α-stimulated HUVECs. Cells were treated with the indicated concentrations of SQA for 1 h and then stimulated with TNF-α for 6 h. Fluorescence-labeled THP-1 was added to the HUVECs and allowed to adhere for 1 h, and adhesion was determined using a fluorescence microplate reader at excitation and emission wavelengths of 485 and 535 nm (A). Pictures are representative fields captured by fluorescence microscope (B): (a) control; (b) TNF-α; (c) cotreated with TNF-α and SQA (5 μM); (d) cotreated with TNF-α and SQA (10 μM); (e) cotreated with TNF-α and SQA (15 μM). The values are shown as the means ± SDs from three independent experiments. (#) $P < 0.05$ represents significant differences versus the control group; (*) $P < 0.05$ represents significant differences versus the TNF-α-only group.

Western Blotting Analysis. HUVECs pretreated with 0, 5, 10, and 15 μM SQA for 1 h were stimulated with TNF-α (10 ng/mL) at times indicated in the figure legends. The specific procedure for Western blotting is described in our previous paper.[18]

Immunofluorescence Analysis. HUVECs were cultured on glass coverslips (SPL Life Sciences Co., Gyeonggi-do, Korea) for 24 h. After treatment of cells with SQA for 1 h, cells were stimulated with TNF-α (10 ng/mL) for 30 min. The specific procedure for immunofluorescence analysis of NF-κB is described in our previous paper.[19]

Statistical Analysis. Data are expressed as the means ± standard deviations (SDs). Data analysis was performed using ANOVA followed by Bonferroni test. P values <0.05 were considered statistically significant. SPSS for Windows, version 10.07 (SPSS Inc., Chicago, IL, USA), was used for all analyses.

RESULTS

SQA Inhibits TNF-α-Induced Binding of Monocytes to HUVECs. To examine the cytotoxicity of SQA, the viability of HUVECs was measured by the MTS cell proliferation assay kit. HUVECs were cultured in 96-well microplates for 24 h and pretreated with various final concentrations of SQA (5, 10, and 15 μM) in TNF-α-stimulated HUVECs. The viability was not influenced up to 15 μM SQA in HUVECs (Supporting Information Figure S2). Thus, the HUVECs were treated with SQA in the concentration range of 5, 10, and 15 μM for further experiments. Because inflammation-derived monocyte adhesion to HUVECs is an essential step in atherosclerosis development, we investigated whether SQA inhibits the adhesion of THP-1 monocytes to TNF-α-treated HUVECs. Stimulation of the HUVECs with TNF-α for 6 h markedly increased cell adhesion. However, SQA dose-dependently inhibited TNF-α-induced binding of monocytes to HUVECs (Figure 1A). To verify the inhibition of SQA on the monocyte recruitment to the TNF-α-stimulated vascular endothelium, microscopic observation was performed using BCECF-AM staining assay. As shown in Figure 1B, heavy fluorescent staining was shown on the HUV treated with TNF-α alone for 6 h, indicating marked adhesion of THP-1 to the stimulated HUVECs. However, SQA

DOI: 10.1021/acs.jafc.5b04050
J. Agric. Food Chem. 2015, 63, 9053−9061

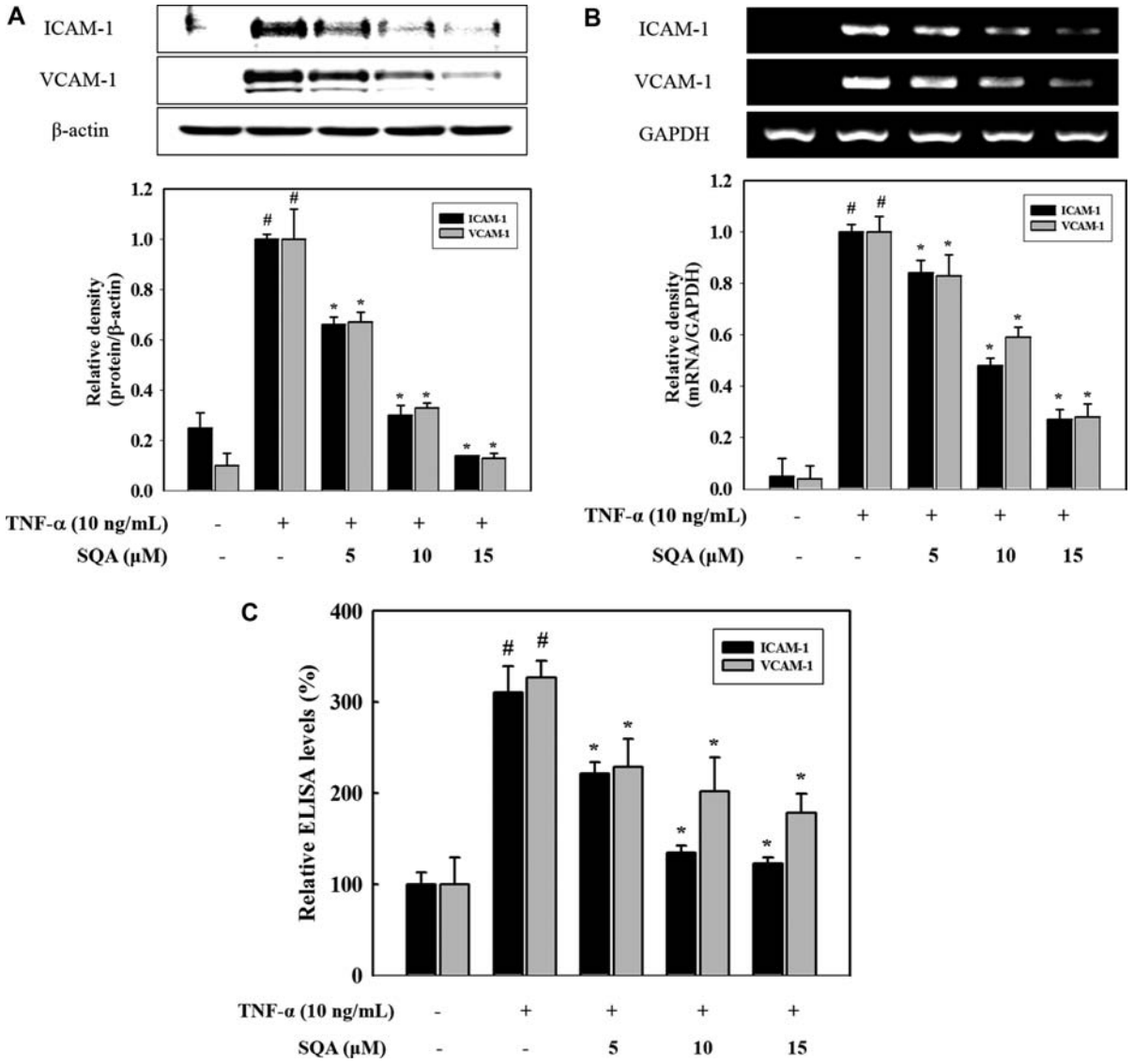

Figure 2. Effect of SQA on the production of TNF-α-induced ICAM-1 and VCAM-1 expression in HUVECs. Cells pretreated with the indicated concentration of SQA for 1 h were stimulated with TNF-α for 6 h. Equal amounts of total protein were separated by 10% SDS-PAGE. The expression of ICAM-1, VCAM-1, and β-actin protein was examined by Western blotting using corresponding antibodies (A). Cells pretreated with the indicated concentration of SQA for 1 h were stimulated with TNF-α for 6 h, and total RNA was prepared for RT-PCR (B). Fixed cells with 1% paraformaldehyde were analyzed by ELISA for the cell surface expression of ICAM-1 (black) and VCAM-1 (gray) (C). The values are shown as the means ± SDs from three independent experiments. (#) $P < 0.05$ represents significant differences versus the nontreated group; (*) $P < 0.05$ represents significant differences versus the TNF-α-only group.

decreased adhesion of THP-1 to TNF-α-treated HUVECs in a dose-dependent manner.

SQA Inhibits the Production of TNF-α-Induced Adhesion Molecules. Monocyte adhesion to HUVECs is critically regulated by ICAM-1 and VCAM-1. To further study the inhibition of adhesion molecule expression by SQA, we assessed the production of VCAM-1 and ICAM-1 proteins using Western blotting. The expression levels of both adhesion molecules were remarkably elevated in TNF-α-treated HUVECs (Figure 2A). SQA pretreatment markedly prevented the production of both VCAM-1 and ICAM-1 dose-dependently. To further investigate the effect of SQA on VCAM-1 and ICAM-1 gene expression, RT-PCR was performed. Our data showed that SQA dose-dependently suppressed the mRNA expression of both adhesion genes in TNF-α-treated HUVECs (Figure 2B). Furthermore, the result of cell-based ELISA showed that SQA dose-dependently suppressed the expression of VCAM-1 and ICAM-1 in TNF-α-treated HUVECs (Figure 2C). These data indicate that the SQA-mediated down-regulation of adhesion molecules in TNF-α-treated endothelium is primarily attributable to their transcriptional repression.

SQA Inhibits TNF-α-Induced Chemokine Production. Recruitment of monocytes to endothelium is regulated by chemokines, including IL-8 and MCP-1. As shown in Figure 3, exposure of HUVECs to TNF-α for 6 h enhanced the protein (Figure 3A) and mRNA (Figure 3B) expression of MCP-1 and IL-8. SQA concentration as low as 15 μM inhibited TNF-α-induced overexpression of both chemokines. Therefore, SQA efficiently suppressed the vascular inflammation related to the development of atherosclerosis.

SQA Inhibits TNF-α-Induced NF-κB Activation in HUVECs. To assess whether SQA inhibits the translocation

DOI: 10.1021/acs.jafc.5b04050
J. Agric. Food Chem. 2015, 63, 9053−9061

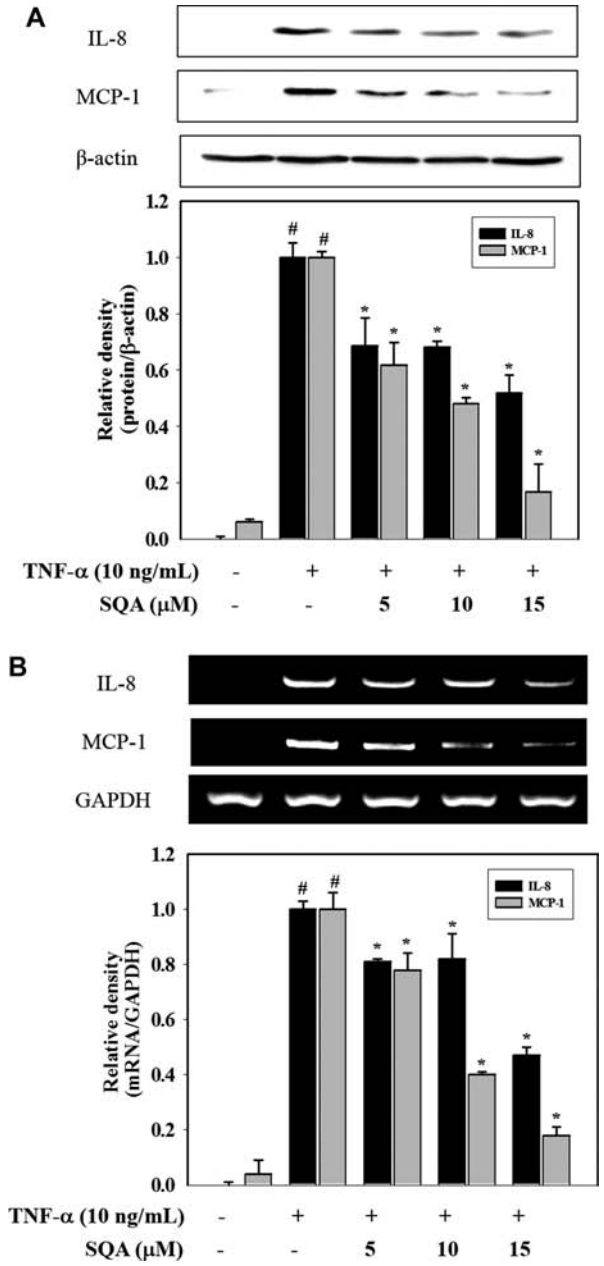

Figure 3. Effect of SQA on TNF-α-induced IL-8 and MCP-1 protein and mRNA expression. Cells pretreated with the indicated concentration of SQA for 1 h were stimulated with TNF-α for 24 h. IL-8 and MCP-1 protein expression was examined by Western blot (A). Cells pretreated with SQA for 1 h were stimulated with TNF-α for 6 h. IL-8 and MCP-1 mRNA expression was determined by RT-PCR (B). The values are shown as the means ± SDs from three independent experiments. (#) $P < 0.05$ represents significant differences versus the control group; (*) $P < 0.05$ represents significant differences versus the TNF-α-only group.

of NF-κB into the nucleus, microscopic analysis was performed. Confocal observation indicated that NF-κB/p65 was mostly located in the cytoplasmic region under unstimulated condition. With TNF-α treatment, most of the cytoplasmic NF-κB/p65 translocated to the nucleus (Figure 4A). However, SQA treatment at 15 μM markedly inhibited the NF-κB/p65 translocation. For further investigating the molecular mechanism underlying SQA-mediated inhibition of NF-κB/p65 translocation in TNF-α-stimulated cells, we examined the phosphorylation of inhibitor κB kinase (IKK)-β and inhibitor κB (IκB)-α that are associated with the NF-κB activation. TNF-α markedly caused the phosphorylation of IKK-β and led to IκB-α phosphorylation, whereas SQA inhibited the phosphorylation of both proteins dose-dependently (Figure 4B). The protein level of cytosolic IκB-α at 15 μM SQA was comparable to that of the control group possibly due to the inhibitory effect of SQA on the phosphorylation IκB-α via of IKK-β activation (Figure 4B). In addition, TNF-α-mediated increase in NF-κB protein level in the nucleus was dose-dependently decreased by SQA treatment (Figure 4C). These results suggest that the SQA-mediated inhibition of the production of adhesion molecules and pro-inflammatory chemokines was regulated through the NF-κB pathway in the TNF-α-stimulated cells.

SQA Inhibits TNF-α-Induced ROS Production. TNF-α activates the membrane-bound NADPH oxidase in endothelium and promotes ROS production, a second messenger for NF-κB activation.[20] We assessed the inhibitory effects of the SQA on intracellular ROS accumulation in HUVECs by TNF-α treatment. TNF-α-induced ROS was markedly reduced by SQA pretreatment (Figure 5, $P < 0.05$), indicating that intrinsic antioxidant activity of SQA might suppress NF-κB activation through scavenging TNF-α-induced ROS.

SQA Inhibits TNF-α-Induced MMP-9 Secretion. Matrix metalloproteinase (MMP)-9 is involved in the process of monocyte transmigration by its ability to impair the major components of basement membrane.[21] During vascular inflammation, MMP-9 is particularly essential for arterial lesion development through its regulation of migration, extravasation, and infiltration of immune cells. For this, TNF-α-treated HUVECs were cultured under serum-free conditions for 24 h, and the released MMP-9 in culture media was determined by Western blotting. TNF-α-induced MMP-9 was dose-dependently suppressed by SQA treatment (Figure 6, $P < 0.05$).

DISCUSSION

In the present study, we isolated SQA from *S. serratifolium*, and its antioxidant and anti-inflammatory activities were investigated using TNF-α-treated HUVECs. Our major findings showed that SQA blocked the adhesion of THP-1 monocytes to TNF-α-treated HUVECs by suppressing expression of adhesion molecules and pro-inflammatory chemokines; suppressed the TNF-α-induced NF-κB activation by blocking IκB-α degradation via the regulation of IKK-β phosphorylation; and suppressed TNF-α-induced MMP-9 production in HUVECs. To our knowledge, this is the first in vitro evidence that SQA is an efficient anti-inflammatory reagent to alleviate vascular inflammation and to improve endothelial dysfunction.

Attachment of monocytes to vascular endothelium is an early step in inflammatory mechanisms of atherosclerosis.[2] Pro-inflammatory stimuli, such as TNF-α exposure, initiate the endothelial expression of adhesion molecules that stimulates the attachment of circulating lymphocytes and monocytes to endothelium.[1] In this stage, the adhesion molecules such as VCAM-1 and ICAM-1 are well-known inflammatory markers, which are related to tight adhesion of monocytes in atherosclerosis-prone sites of the endothelium.[1] Both adhesion molecules are primarily produced in advanced human coronary atherosclerotic plaque and in experimental atherosclerosis animals.[9,22] Our results indicate that SQA prevented the TNF-α-induced endothelial production of VCAM-1 and ICAM-1in HUVECs as well as attachment of THP-1 cells to HUVECs. These data indicate that the anti-inflammatory effect

DOI: 10.1021/acs.jafc.5b04050
J. Agric. Food Chem. 2015, 63, 9053−9061

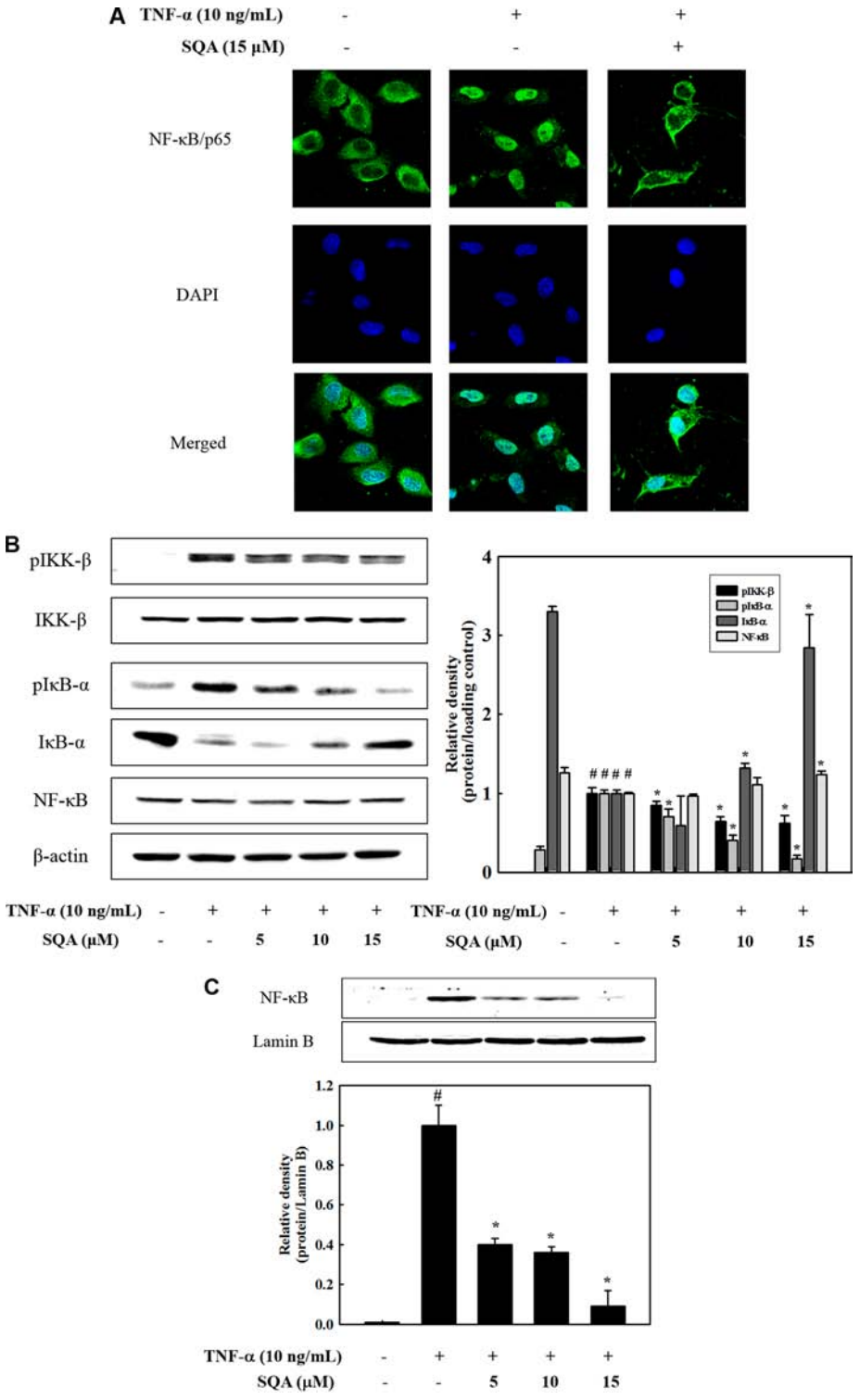

Figure 4. Effect of SQA on the NF-κB translocation in TNF-α-treated HUVECs. Cells were pretreated with or without SQA for 1 h followed by TNF-α treatment for 30 min. The subunits of NF-κB/p65 were detected by using anti-NF-κB polyclonal antibody and Alexa Fluor 488-conjugated secondary antibody. The nuclei were detected by DAPI staining, and confocal microscopy was used to capture the images (A). Cells were incubated with the indicated concentration of SQA for 1 h and then exposed to TNF-α (10 ng/mL) for 30 min. Cytosolic (B) and nucleus (C) fractions were analyzed by Western blotting. The values are shown as the means ± SDs from three independent experiments. (#) $P < 0.05$ represents significant differences versus the control group; (∗) $P < 0.05$ represents significant differences versus the TNF-α-only group.

of SQA on TNF-α-treated cells is mediated at least partially by suppressing the adhesion molecules. Importantly, the current findings suggest that the SQA-mediated reduction of adhesion molecules is closely related to transcriptional regulation of both ICAM-1 and VCAM-1 mRNA expression in TNF-α-treated HUVECs. This study appears to be the first finding to show the action of SQA on the transcriptional regulations of adhesion molecules in TNF-α-treated HUVECs.

Monocyte recruitment followed by endothelial inflammation is closely associated with inflammatory mechanisms of

DOI: 10.1021/acs.jafc.5b04050
J. Agric. Food Chem. 2015, 63, 9053−9061

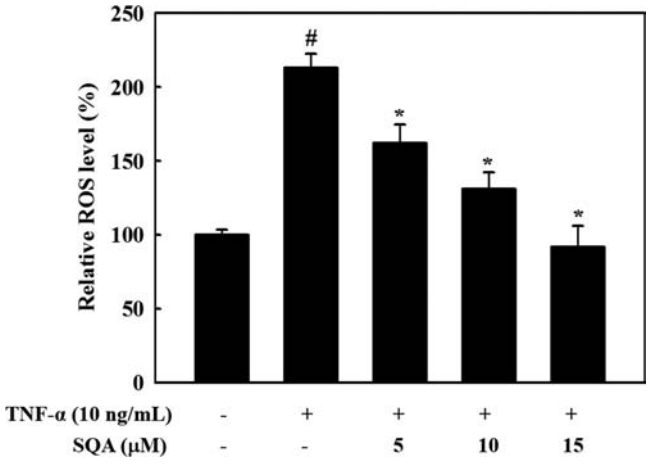

Figure 5. Effect of SQA on the TNF-α-induced ROS production. Cells pretreated with the indicated concentrations of SQA for 1 h were stimulated with TNF-α (10 ng/mL) for 30 min. ROS was determined by DCFH-DA with fluorescent analysis. The values are shown as the means ± SDs from three independent experiments. (#) $P < 0.05$ represents significant differences versus the control group; (*) $P < 0.05$ represents significant differences versus the TNF-α-only group.

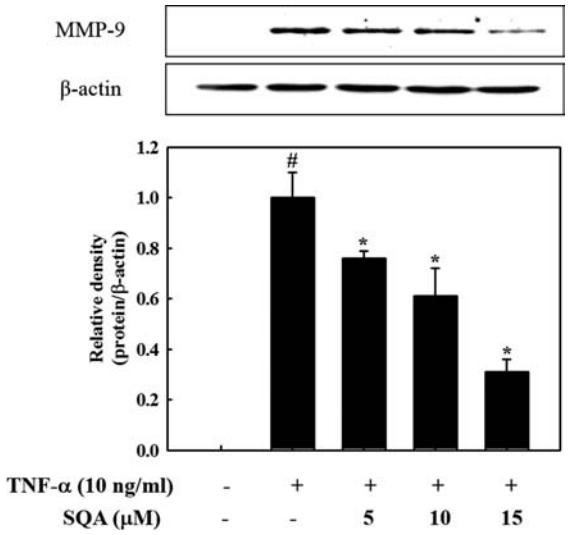

Figure 6. Effect of SQA on TNF-α-induced MMP-9 secretion. Cells pretreated with the indicated concentration of SQA for 1 h were stimulated with TNF-α for 24 h. The collected culture medium was analyzed by Western blotting using MMP-9 antibody. The values are shown as the means ± SDs from three independent experiments. (#) $P < 0.05$ represents significant differences versus the control group; (*) $P < 0.05$ represents significant differences versus the TNF-α-only group.

atherosclerosis. Various studies demonstrated important roles of pro-inflammatory chemokines, such as IL-8 and MCP-1, in the development and progression of atherosclerosis.[3,5,9] MCP-1 is mainly involved in the recruitment of monocytes to atheroma. The recruited monocytes differentiate into macrophages in the atherosclerotic lesion.[23,24] IL-8 is an important factor for adhesion, transmigration, and retention of monocyte/macrophages in the atherosclerotic lesion. IL-8 is associated with activating intimal macrophages due to overexpression of chemokine receptors on the intimal macrophage.[23] Thus, inhibiting IL-8 and MCP-1 would block adhesion and migration of monocytes to endothelium. Therefore, blocking these chemokines may be an appropriate strategy for preventing or treating atherosclerosis. In this study, SQA inhibited the TNF-α-induced production of IL-8 and MCP-1 from endothelial cells. These data suggest that the anti-inflammatory action of SQA on TNF-α-induced endothelium is mediated at least partially by inhibition of chemokines.

The ROS-dependent NF-κB activation is an essential signaling for regulating inflammatory responses, which are closely related to vascular diseases by induction of endothelial cell adhesion molecules.[25] NF-κB is an important transcription factor that is associated with the expression of adhesion molecules and chemokines.[26] As discussed above, attachment of monocyte to endothelium is induced and stimulated through pro-inflammatory chemokines and adhesion molecules, including ICAM-1, VCAM-1, IL-8, and MCP-1 in endothelial cells.[26,27] The gene expression of these molecules is increased by NF-κB activation. In unstimulated conditions, NF-κB is primarily distributed in the cytoplasm as an inactive complex binding to IκB-α. Excess ROS production stimulated by TNF-α involves the phosphorylation of IKK complex, which phosphorylates IκB-α, thereby leading to the degradation of IκB-α and translocation of NF-κB into the nucleus.[2,28] Thus, NF-κB is an attractive target for the development of pharmaceutical agents for interfering with the development and progression of atherosclerosis. Although mechanisms underlying SQA-mediated NF-κB regulation remain unknown, the current study showed that SQA suppresses NF-κB activation by inhibiting proteolytic degradation of IκB-α induced by TNF-α in HUVECs. The confocal microscopic analysis suggests that SQA inhibited NF-κB translocation into the nucleus induced by TNF-α in HUVECs. Therefore, these results showed the ability of SQA to suppress TNF-α-mediated NF-κB activation in HUVECs. In the current study, SQA treatment significantly decreased the TNF-α-induced ROS production in HUVECs, suggesting that SQA has antioxidant activity. It was shown that ROS stimulate activation of diverse transcription factors including NF-κB in cultured HUVECs, contributing to induction of chemokines and adhesion molecules.[10,29] We found that SQA notably inhibited the TNF-α-induced NF-κB activation. On the basis of these data, the inhibitory effect of SQA on the production of adhesion molecules and chemokines is regulated by the NF-κB signaling pathway via blockade of ROS production with SQA's intrinsic antioxidant activity. Hence, it is likely that the reductions of ICAM-1, VCAM-1, IL-8, and MCP-1 expression in HUVECs are mainly related to the regulation of NF-κB pathway through the removal of ROS by SQA's antioxidant activity.

MMPs catalyze removal of the basement membrane around vascular smooth muscle cells and facilitate contacts with the interstitial matrix.[30] During the progression of atherosclerosis, endothelial cells degrade the basement membrane to recruit smooth muscle cells into intima, where type IV collagen is the major component. Among MMPs, MMP-9 has been emphasized in vascular inflammation, because the collagenolytic activity of MMP-9 makes endothelial cells intrude into the basement membrane of vascular structure.[31] Therefore, endothelial cell-secreted MMP-9 may play a mandatory role in degrading the basement membrane through its type IV collagenase activity.[32] MMP-9, expressed by TNF-α-induced NF-κB activation, is shown to enhance the infiltration of smooth muscle cells to intima by mediating the digestion of extracellular matrix.[33,34] Thus, TNF-α-induced MMP-9 expression plays an essential function during atherosclerotic

DOI: 10.1021/acs.jafc.5b04050
J. Agric. Food Chem. 2015, 63, 9053−9061

progression. In this study, we found that SQA notably suppressed the TNF-α-induced MMP-9 production. These data suggest that the progression of atherosclerosis by TNF-α may be alleviated by SQA's inhibitory action of MMP-9 production via NF-κB activation.

In summary, we have shown that SQA inhibits the mRNA and protein expression of adhesion molecules including ICAM-1 and VCAM-1 in TNF-α-stimulated HUVECs. Furthermore, the anti-inflammatory roles of SQA in TNF-α-treated cells appear to be closely related to the inactivation of the NF-κB pathway. Further confirmation of anti-inflammatory effects of SQA and underlying mechanisms in animal models will be important for therapeutic application of SQA for treating vascular inflammation-associated diseases such as atherosclerosis.

■ ASSOCIATED CONTENT

Supporting Information

The Supporting Information is available free of charge on the ACS Publications website at DOI: 10.1021/acs.jafc.5b04050.

Supplementary table (oligonucleotide primers used for RT-PCR) and figures (mass spectrometry analysis of SQA; effect of SQA on cell viability in HUVECs) (PDF)

■ AUTHOR INFORMATION

Corresponding Author

*(H.-R.K.) Mail: Department of Food Science and Nutrition, Pukyong National University, 599-1 Daeyeon-3-dong, Nam-gu, Busan 608-737, South Korea. Phone: +82-51-629-5847. Fax: +82-51-629-5842. E-mail: hrkim@pknu.ac.kr.

Author Contributions

‖W.-G.G. and B.L. contributed equally to this work.

Funding

This research was supported by the project "Development of neutraceuticals from *Sargassium serratifolium*" funded by the Ministry of Oceans and Fisheries, Korea, and by the Basic Science Research Program through the National Research Foundation of Korea (NRF) funded by the Ministry of Science, ICT & Future Planning (2015R1A2A2A01006143).

Notes

The authors declare no competing financial interest.

■ ABBREVIATIONS USED

BCECF-AM, 2′,7′-bis(2-carboxyethyl)-5(6)-carboxyfluorescein acetoxy-methylester; BSA, bovine serum albumin; DAPI, 4′,6-diamidino-2-phenylindole; DCFH-DA, 2′,7′-dichlorofluorescin diacetate 4′,6-diamidino-2-phenylindole; DMSO, dimethyl sulfoxide; ECL, enhanced chemiluminescence; EGM-2, endothelial cell growth medium; HUVEC, human umbilical vein endothelial cell; GAPDH, glyceraldehyde-3-phosphate dehydrogenase; ICAM-1, intracellular adhesion molecule-1; IκB-α, inhibitor κB-α; IKK-β, inhibitor κB kinase-β; IL-8, interleukin-8; MCP-1, monocyte chemoattractant protein-1; MMP, matrix metalloproteinase; MTS, 3-(4,5-dimethylthiazol-2-yl)-5-(3-carboxymethoxyphenyl)-2-(4-sulfophenyl)-2*H*-tetrazolium; NF-κB, nuclear factor kappa B; PMSF, phenylmethanesulfonyl fluoride; ROS, reactive oxygen species; SQA, sargaquinoic acid; VCAM-1, vascular cell adhesion molecule-1

■ REFERENCES

(1) Packard, R. R.; Libby, P. Inflammation in atherosclerosis: from vascular biology to biomarker discovery and risk prediction. *Clin. Chem.* **2008**, *54*, 24−38.

(2) Madge, L. A.; Pober, J. S. TNF signaling in vascular endothelial cells. *Exp. Mol. Pathol.* **2001**, *70*, 317−325.

(3) Rao, R. M.; Yang, L.; Garcia-Cardena, G.; Luscinskas, F. W. Endothelial-dependent mechanisms of leukocyte recruitment to the vascular wall. *Circ. Res.* **2007**, *101*, 234−247.

(4) Sprague, A. H.; Khalil, R. A. Inflammatory cytokines in vascular dysfunction and vascular disease. *Biochem. Pharmacol.* **2009**, *78*, 539−552.

(5) Yang, Y. Y.; Hu, C. J.; Chang, S. M.; Tai, T. Y.; Leu, S. J. Aspirin inhibits monocyte chemoattractant protein-1 and interleukin-8 expression in TNF-α stimulated human umbilical vein endothelial cells. *Atherosclerosis* **2004**, *174*, 207−213.

(6) Kleinbongard, P.; Heusch, G.; Schulz, R. TNFα in atherosclerosis, myocardial ischemia/reperfusion and heart failure. *Pharmacol. Ther.* **2010**, *127*, 295−314.

(7) Pober, J. S.; Min, W.; Bradley, J. R. Mechanisms of endothelial dysfunction, injury, and death. *Annu. Rev. Pathol.: Mech. Dis.* **2009**, *4*, 71−95.

(8) Boyle, E. M., Jr.; Kovacich, J. C.; Canty, T. G., Jr.; Morgan, E. N.; Chi, E.; Verrier, E. D.; Pohlman, T. H. Inhibition of nuclear factor-κB nuclear localization reduces human E-selectin expression and the systemic inflammatory response. *Circulation* **1998**, *98*, II282−288.

(9) Nallasamy, P.; Si, H.; Babu, P. V.; Pan, D.; Fu, Y.; Brooke, E. A.; Shah, H.; Zhen, W.; Zhu, H.; Liu, D.; Li, Y.; Jia, Z. Sulforaphane reduces vascular inflammation in mice and prevents TNF-α-induced monocyte adhesion to primary endothelial cells through interfering with the NF-κB pathway. *J. Nutr. Biochem.* **2014**, *25*, 824−833.

(10) Pennathur, S.; Heinecke, J. W. Oxidative stress and endothelial dysfunction in vascular disease. *Curr. Diabetes Rep.* **2007**, *7*, 257−264.

(11) Rahman, I.; Gilmour, P. S.; Jimenez, L. A.; MacNee, W. Oxidative stress and TNF-α induce histone acetylation and NF-κB/AP-1 activation in alveolar epithelial cells: potential mechanism in gene transcription in lung inflammation. *Mol. Cell. Biochem.* **2002**, *234*, 239−248.

(12) Guzik, T. J.; Harrison, D. G. Vascular NADPH oxidases as drug targets for novel antioxidant strategies. *Drug Discovery Today* **2006**, *11*, 524−533.

(13) Tsang, C. K.; Kamei, Y. Sargaquinoic acid supports the survival of neuronal PC12D cells in a nerve growth factor-independent manner. *Eur. J. Pharmacol.* **2004**, *488*, 11−18.

(14) Kang, G. J.; Han, S. C.; Yoon, W. J.; Koh, Y. S.; Hyun, J. W.; Kang, H. K.; Youl Cho, J.; Yoo, E. S. Sargaquinoic acid isolated from *Sargassum siliquastrum* inhibits lipopolysaccharide-induced nitric oxide production in macrophages via modulation of nuclear factor-κB and c-Jun N-terminal kinase pathways. *Immunopharmacol. Immunotoxicol.* **2013**, *35*, 80−87.

(15) Kim, S. N.; Choi, H. Y.; Lee, W.; Park, G. M.; Shin, W. S.; Kim, Y. K. Sargaquinoic acid and sargahydroquinoic acid from *Sargassum yezoense* stimulate adipocyte differentiation through PPARα/γ activation in 3T3-L1 cells. *FEBS Lett.* **2008**, *582*, 3465−3472.

(16) de la Mare, J. A.; Lawson, J. C.; Chiwakata, M. T.; Beukes, D. R.; Edkins, A. L.; Blatch, G. L. Quinones and halogenated monoterpenes of algal origin show anti-proliferative effects against breast cancer cells in vitro. *Invest. New Drugs* **2012**, *30*, 2187−2200.

(17) Manduteanu, I.; Voinea, M.; Antohe, F.; Dragomir, E.; Capraru, M.; Radulescu, L.; Simionescu, M. Effect of enoxaparin on high glucose-induced activation of endothelial cells. *Eur. J. Pharmacol.* **2003**, *477*, 269−276.

(18) Gwon, W. G.; Lee, M. S.; Kim, J. S.; Kim, J. I.; Lim, C. W.; Kim, N. G.; Kim, H. R. Hexane fraction from *Sargassum fulvellum* inhibits lipopolysaccharide-induced inducible nitric oxide synthase expression in RAW 264.7 cells via NF-κB pathways. *Am. J. Chin. Med.* **2013**, *41*, 565−584.

(19) Lee, M. S.; Kwon, M. S.; Choi, J. W.; Shin, T.; No, H. K.; Choi, J. S.; Byun, D. S.; Kim, J. I.; Kim, H. R. Anti-inflammatory activities of

DOI: 10.1021/acs.jafc.5b04050
J. Agric. Food Chem. 2015, 63, 9053−9061

an ethanol extract of *Ecklonia stolonifera* in lipopolysaccharide-stimulated RAW 264.7 murine macrophage cells. *J. Agric. Food Chem.* **2012**, *60*, 9120−9129.
(20) Kim, J. H.; Na, H. J.; Kim, C. K.; Kim, J. Y.; Ha, K. S.; Lee, H.; Chung, H. T.; Kwon, H. J.; Kwon, Y. G.; Kim, Y. M. The non-provitamin A carotenoid, lutein, inhibits NF-κB-dependent gene expression through redox-based regulation of the phosphatidylinositol 3-kinase/PTEN/Akt and NF-κB-inducing kinase pathways: role of H_2O_2 in NF-κB activation. *Free Radical Biol. Med.* **2008**, *45*, 885−896.
(21) Nagaoka, I.; Hirota, S. Increased expression of matrix metalloproteinase-9 in neutrophils in glycogen-induced peritoneal inflammation of guinea pigs. *Inflammation Res.* **2000**, *49*, 55−62.
(22) O'Brien, K. D.; Allen, M. D.; McDonald, T. O.; Chait, A.; Harlan, J. M.; Fishbein, D.; McCarty, J.; Ferguson, M.; Hudkins, K.; Benjamin, C. D.; et al. Vascular cell adhesion molecule-1 is expressed in human coronary atherosclerotic plaques. Implications for the mode of progression of advanced coronary atherosclerosis. *J. Clin. Invest.* **1993**, *92*, 945−951.
(23) Boisvert, W. A. Modulation of atherogenesis by chemokines. *Trends Cardiovasc. Med.* **2004**, *14*, 161−165.
(24) Lin, J.; Kakkar, V.; Lu, X. Impact of MCP-1 in atherosclerosis. *Curr. Pharm. Des.* **2014**, *20*, 4580−4588.
(25) Chen, J. W.; Chen, Y. H.; Lin, F. Y.; Chen, Y. L.; Lin, S. J. *Ginkgo biloba* extract inhibits tumor necrosis factor-α-induced reactive oxygen species generation, transcription factor activation, and cell adhesion molecule expression in human aortic endothelial cells. *Arterioscler., Thromb., Vasc. Biol.* **2003**, *23*, 1559−1566.
(26) Liang, Y.; Zhou, Y.; Shen, P. NF-κB and its regulation on the immune system. *Cell. Mol. Immunol.* **2004**, *1*, 343−350.
(27) de Winther, M. P.; Kanters, E.; Kraal, G.; Hofker, M. H. Nuclear factor κB signaling in atherogenesis. *Arterioscler., Thromb., Vasc. Biol.* **2005**, *25*, 904−914.
(28) Zhang, H.; Park, Y.; Wu, J.; Chen, X.; Lee, S.; Yang, J.; Dellsperger, K. C.; Zhang, C. Role of TNF-α in vascular dysfunction. *Clin. Sci.* **2009**, *116*, 219−230.
(29) Jia, Z.; Nallasamy, P.; Liu, D.; Shah, H.; Li, J. Z.; Chitrakar, R.; Si, H.; McCormick, J.; Zhu, H.; Zhen, W.; Li, Y. Luteolin protects against vascular inflammation in mice and TNF-α-induced monocyte adhesion to endothelial cells via suppressing IKBα/NF-κB signaling pathway. *J. Nutr. Biochem.* **2015**, *26*, 293−302.
(30) Newby, A. C. Dual role of matrix metalloproteinases (matrixins) in intimal thickening and atherosclerotic plaque rupture. *Physiol. Rev.* **2005**, *85*, 1−31.
(31) Berg, G.; Miksztowicz, V.; Schreier, L. Metalloproteinases in metabolic syndrome. *Clin. Chim. Acta* **2011**, *412*, 1731−1739.
(32) Jin, Y. J.; Park, I.; Hong, I. K.; Byun, H. J.; Choi, J.; Kim, Y. M.; Lee, H. Fibronectin and vitronectin induce AP-1-mediated matrix metalloproteinase-9 expression through integrin $\alpha_5\beta_1/\alpha_v\beta_3$-dependent Akt, ERK and JNK signaling pathways in human umbilical vein endothelial cells. *Cell. Signalling* **2011**, *23*, 125−134.
(33) Gerthoffer, W. T. Mechanisms of vascular smooth muscle cell migration. *Circ. Res.* **2007**, *100*, 607−621.
(34) Tan, C.; Liu, Y.; Li, W.; Deng, F.; Liu, X.; Wang, X.; Gui, Y.; Qin, L.; Hu, C.; Chen, L. Associations of matrix metalloproteinase-9 and monocyte chemoattractant protein-1 concentrations with carotid atherosclerosis, based on measurements of plaque and intima-media thickness. *Atherosclerosis* **2014**, *232*, 199−203.

DOI: 10.1021/acs.jafc.5b04050
J. Agric. Food Chem. 2015, 63, 9053−9061

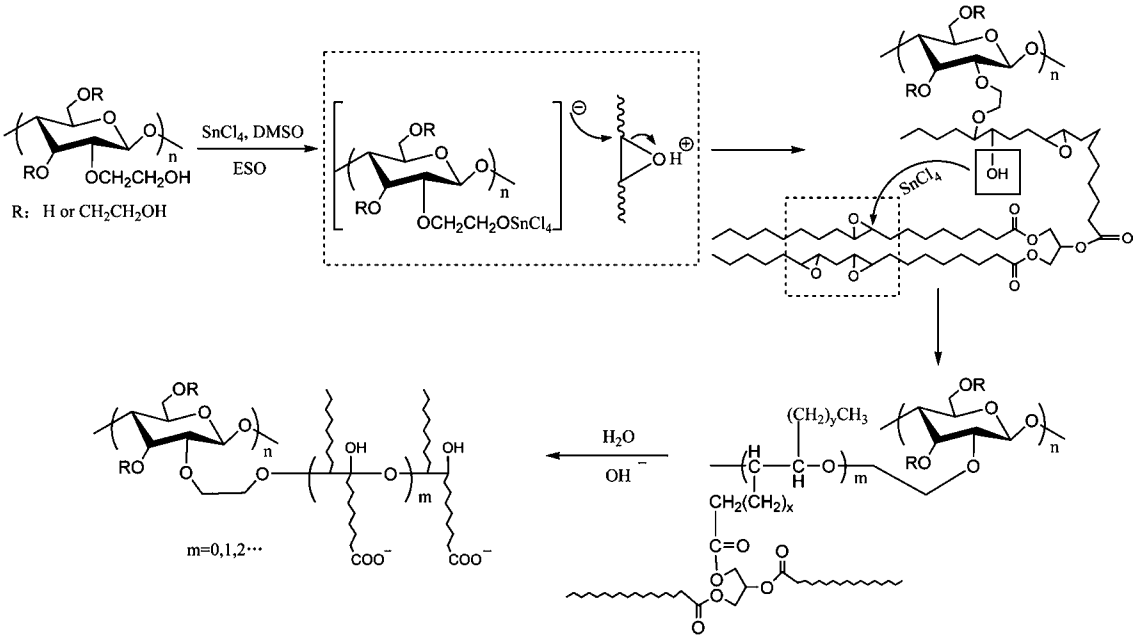

Figure 1. Synthetic route of H-ESO-HEC polymeric surfactants.

grafted cellulose surfactants formed via cellulose derivatives as backbones are polymerized saponified fatty acid surfactants. Therefore, cellulose chains grafting saponified fatty acid esters to form ionic surfactants—instead of fatty acid-esterified cellulose surfactants—may become an effective method for synthesis of cellulose-based surfactants with highly surface-active properties. Fortunately, the chemical reactivities of some fatty acids isolated from vegetable oils can achieve this vision.

Soybean oil is one of the most abundant renewable vegetable oils in the world.[23] It possesses three unsaturated fatty acids, oleic (23%), linoleic (54%), and linolenic (8%). It contains 1, 2, and 3 double bonds, respectively.[24] The double bonds can be used in many reactions including addition reaction,[25] oxidation reaction,[26] and polymerization reaction.[27] More significantly, the expoxidation reaction makes the soybean oil become epoxidized soybean oil (ESO). A ring-opening reaction of ESO with different alcohols was carried out in the presence of Amberlyst 15 (Dry) as a catalyst.[28] Furthermore, the ring-opening polymerization of ESO can be catalyzed by boron trifluoride diethyl etherate ($BF_3{\cdot}OEt_2$) in liquid carbon dioxide and methylene chloride.[26,29] The ESO-based polymeric surfactants in particular were prepared by hydrolysis of polymerized ESO with a base.[22] These interesting works suggest that hydroxyl groups of cellulose can initiate ring-opening polymerization of ESO in the presence of catalysts. Moreover, novel saponified fatty acid-modified cellulose-based polymeric surfactants are obtained by saponification of the ESO-grafted cellulose products in which fatty acid chains are combined with cellulose by an ether linkage at the middle site of a fatty acid molecular chain.

To prove this assumption, modification of HEC by grafting ESO was investigated and hydrolysis of ESO-grafted HEC (ESO-HEC) was performed with sodium hydroxide (Figure 1). The hydrolyzed ESO-HEC (H-ESO-HEC) products were characterized with Fourier transform infrared (FT-IR) and ^1H and ^{13}C nuclear magnetic resonance (NMR) spectroscopies, high-temperature gel permeation chromatography (HT-GPC), and differential scanning calorimetry (DSC). After neutralizing the carboxylic acid of H-ESO-HEC with sodium hydroxide, novel polymeric surfactants (H-ESO-HEC-Na) were obtained, and the effects of polymeric surfactants on the surface tension of water were investigated as a function of the concentration of H-ESO-HEC-Na. In addition, the rheological behaviors of the H-ESO-HEC were investigated.

MATERIALS AND METHODS

Materials. Hydroxyethyl cellulose (HEC), epoxidized soybean oil (ESO), and stannic chloride ($SnCl_4$) were purchased from Aladdin Industrial Co., Ltd. Dimethyl sulfoxide (DMSO) was purchased from Sinopharm Chemical Reagent Co., Ltd. Sodium hydroxide (NaOH), hydrochloric acid (HCl), and ethyl acetate were obtained from Nanjing Chemical Reagent Co., Ltd. Deionized water was purified to a conductivity of 18.3 MΩ·cm on a Hitech-Sciencetool Master-Q laboratory water purification system (Shanghai Hetai Reagent Co., Ltd.). All chemicals were used without further purification.

Synthesis of ESO-Grafted HEC Derivatives (ESO-HEC). HEC (1.0 g) was dissolved in 40 mL of DMSO under stirring at room temperature for 2 h and then transferred into a three-necked round-bottomed flask. ESO (1.0 g) was added to the HEC solution. The mixture was stirred by mechanical agitation at room temperature. A mixture of 10 μL of $SnCl_4$ and 10 mL of DMSO was then added dropwise into the reactor, and the reaction was maintained for 30 min. The resulting products were washed sequentially with deionized water to remove DMSO and dried under vacuum at 50 °C. Finally, the ESO-grafted HEC derivatives (ESO-HEC) were obtained.

Hydrolysis of ESO-HEC (H-ESO-HEC). The ESO-HEC (2.0 g) was added to a flask with 50 mL of 0.6 M NaOH solution. The reactor was heated to 100 °C with agitation for 12 h under a condensing condition. After reaction, the solution was separated by filtration and the aqueous solution was removed by reduced pressure distillation. The solid product was washed with ethyl acetate three times to remove the glycerin. The solid product was then redispersed in aqueous solution, and the solution was adjusted to pH 5−6 by 0.1 M HCl. The solution became turbid, and the product appeared as a floating oil. The product was extracted by ethyl acetate, and the organic phase was washed with hot distilled water three times. Finally, the H-ESO-HEC product was purified by reduced pressure distillation. The H-ESO-HEC-Na was obtained by neutralizing the carboxylic acid of H-ESO-HEC with sodium hydroxide.

FT-IR. Fourier transform infrared (FT-IR) spectra were used to confirm the structure of the H-ESO-HEC. These spectra were

DOI: 10.1021/acs.jafc.5b03765
J. Agric. Food Chem. 2015, 63, 9062−9068

Table 1. Effect of Reaction Condition on Yield and Carboxyl Content and the HT-GPC Data of H-ESO-HEC

samples	HEC:ESO (mass ratio)	yield[a] (g/g)	carboxyl content[b] (mmol/g)	HT-GPC data		
				$M_n \times 10^5$ (Daltons)	$M_w \times 10^5$ (Daltons)	PDI[c]
HEC			0	0.7	2.28	3.20
H-ESO-HEC-I	1:1	1.2	1.89 ± 0.13	1.48	2.71	1.80
H-ESO-HEC-II	1:2	1.6	2.12 ± 0.06	1.55	3.31	2.10
H-ESO-HEC-III	1:3	1.9	2.35 ± 0.10	3.77	5.50	1.46
H-ESO-HEC-IV	1:4	2.1	2.72 ± 0.03	4.19	6.61	1.57
H-ESO-HEC-V	1:5	2.7	2.80 ± 0.11	4.58	8.28	1.80

[a]Expressed as grams of the H-ESO-HEC per gram of HEC (on dry mass basis). [b]Expressed as millimoles of carboxyl per gram of H-ESO-HEC (on dry mass basis). [c]Determined by M_w/M_n.

obtained on a Thermo Scientific Nicolet IS10 spectrometer with the attenuated total reflectance (ATR) method. The spectra were recorded over the range 4000−500 cm^{-1} at 4 cm^{-1} resolution and averaged over 16 scans per sample.

NMR. ^1H NMR and ^{13}C NMR spectra for H-ESO-HEC were recorded at 40 °C on a BRUKER AV400 spectrometer (Bruker, Rheinstetten, Germany) operating at frequencies of 400.13 and 100.61 MHz, respectively. Deuterated dimethyl sulfoxide (DMSO-d_6) and tetramethylsilicane (TMS) were used as the solvent and the internal standard, respectively. The chemical shift values were referenced to the signals of DMSO-d_6 and TMS.

HT-GPC. Molecular weight distribution curves and relative values of number-average (M_n) and weight-average (M_w) molecular weight of H-ESO-HEC were determined by HT-GPC (HT-GPC Module 350A, Viscotek; GPC equipped with I-MBHMW-3078 HT-GPC column) at 60 °C. The HT-GPC instrument was equipped with a refractive index detector, viscosity detector, and small-angle light scattering detector. The flow rate of the carrier solvent (HPLC-grade DMSO) was 1.0 mL/min. Samples were filtered over microfilters with a pore size of 0.2 μm (Nylon, Millex-HN 13 mm Syringes Filters, Millipore). The results were obtained from OmniSEC software.

Conductimetry. The carboxyl content of H-ESO-HEC was determined by conductometric titrations.[30] The H-ESO-HEC (30−40 mg) was suspended into 15 mL of 0.01 M hydrochloric acid solution. After 2 h of stirring, the suspensions were titrated with 0.01 M NaOH. The carboxyl content of the sample was determined from the conductivity and V_{NaOH} curve. The carboxyl content is calculated by the following equation

$$\text{carboxyl content(mmol/g)} = \frac{c(V_2 - V_1)}{m} \quad (1)$$

Here, V_1 and V_2 are the volumes of NaOH (mL) in the first and second inflection points of titration curves, respectively. c is the concentration of NaOH (mmol/L), and m is the weight of oven-dried sample (mg). To minimize errors, titrations were duplicated at least three times, and the average value was retained for the discussion.

DSC. To determine the ring-opening polymerization of ESO, the DSC measurements of the H-ESO-HEC were performed on a Diamond DSC at 40 mL/min dry nitrogen as the purge gas. Typically, ∼4 mg of the H-ESO-HEC was accurately weighed in an aluminum pan and sealed with pin-perforated lids. The sample was cooled to −50 °C at a rate of 10 °C/min, and a refrigerated cooling system was used to equilibrate the sample at −50 °C for 5 min. Data were recorded while the oven temperature was raised from −50 to 0 °C at 10 °C/min.

Surface Tension. The surface tension of H-ESO-HEC-Na was measured at 25 °C using the Wilhelmy plate T107 (width, 19.44 mm; thickness, 0.1 mm; height, 65 mm; circumference, 39.08) on a Sigma 701 Automatic Surface Tensiometer. The instrument was calibrated against pure water before measurements were made. The concentration of H-ESO-HEC-Na surfactant was gradually increased by dispersing stock solution into the measurement cell. The software automatically determined the surface tension as a function of the bulk concentration. The surface tension data were plotted against the H-ESO-HEC-Na concentration in water from 0.0003 to 2.0 g/L. Each concentration of aqueous H-ESO-HEC-Na solution was tested in triplicate—this was done automatically by the instrument. The concentration at which the equilibrium surface tension of the polymeric surfactants stopped decreasing with concentration and plateaued is the critical micelle concentration (CMC).[22] From the inflection point of the plot, the critical micelle concentration (CMC) and minimum surface tension (γ_{cmc}) were derived. All data were obtained from the OneAttention software.

Krafft Point (KP). A 20 mL amount of 0.5 wt % surfactant aqueous solution (at least quintuplicate the CMC of studied surfactant) was prepared in an alkaline solution and added to a beaker. The beaker was then heated, and the particular temperature was recorded as KP when the solution transformed from turbid to pellucid.[31]

Hydrophile Lipophile Balance (HLB) Value. The emulsions were prepared using a mixture of the nonionic surfactants Tween 60 and Span 80 to satisfy the proper HLB values for optimum emulsification conditions. The mixed HLB values were calculated with the following equation

$$HLB_{mix} = HLB_T \times T\% + HLB_S \times S\% \quad (2)$$

Here, HLB_{mix}, HLB_T, and HLB_S are the HLB values of the mixed surfactants, Tween 60 (14.9), and Span 80 (4.3), respectively. The T% and S% are the mass percentages of Tween 60 and Span 80 in the mixed surfactants, respectively.[32] All HLB values used were measured at 25 °C.

Rheology. Rheological measurements were performed at a rotational rheometer HAAKE MARS II equipped with a measuring geometry named PP60 Ti (diameter, d = 50 mm). The H-ESO-HEC-Na-III was selected to evaluate the rheological properties. H-ESO-HEC-Na-III solutions at three different concentrations (0.1, 1, and 5 g/L) were prepared to measure the shear viscosity that changed with the shear rate ranging from 0.01 to 100 s^{-1}.[15] The rheological measurements were carried out at 40 °C. All data were obtained using the HAKKE RheoWin data manager software.

Statistical Method. Origin Pro 9.0 was used to calculate the standard deviation of carboxyl content and the surface tension of H-ESO-HEC. The standard deviation was calculated with the following equation

$$S = \sqrt{\frac{\sum_{i=1}^{n}(X_i - \bar{X})^2}{n-1}} \quad (3)$$

Here, S is the standard deviation of a sample, X_i is the ith value in a sample, $\bar{X}$ is the average number of a sample, and n is the total number of a sample.

RESULTS AND DISCUSSION

Figure 1 outlines a simplified mechanism for the entire reaction. The ESO-HEC was prepared via ring-opening polymerization, in which the hydroxyl groups of HEC acted as initiators. In addition, the ring-opening polymerization generated new hydroxyl groups that can also act as initiators via the $SnCl_4$ catalyst. The polymeric ESO were covalently bound to the HEC, and hydrolysis of ESO-HEC (H-ESO-HEC) was

DOI: 10.1021/acs.jafc.5b03765
J. Agric. Food Chem. 2015, 63, 9062−9068

obtained with sodium hydroxide. As shown in Table 1, H-ESO-HEC products with different molecular weights were obtained by adjusting the mass ratio of HEC and ESO in graft reaction. The graft reaction occurred at room temperature with a short reaction time because of the high activity of the $SnCl_4$ catalyst. The yields of the H-ESO-HEC were measured and ranged from 1.2 to 2.7 g per gram of HEC as the amount of ESO increased in the graft polymerization reaction. In addition, H-ESO-HEC-Na samples with different molecular weights were obtained by neutralizing carboxylic acid of H-ESO-HEC with sodium hydroxide.

Spectroscopic Identification of the Structures of H-ESO-HEC. In Figure 2, the FT-IR spectrum of H-ESO-HEC-III

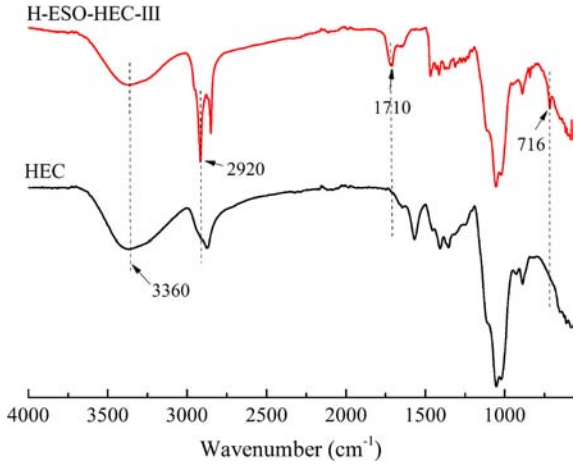

Figure 2. FT-IR spectra of HEC and H-ESO-HEC-III.

attested to the presence of ESO chains onto the HEC by appearance of the characteristic absorption bands assigned to the carbonyl functions at 1710 cm^{-1} versus the HEC. The spectral peak at 2920 cm^{-1} was attributed to the $-CH_3$ group of the alkane chains of ESO. Also, peaks at 716 cm^{-1} indicate the vibration of $-(CH_2)_n-$ ($n \geq 4$).[33] No significant change in hydroxyl group signal at 3360 cm^{-1} was noticed because the hydroxyl groups of the HEC acted as initiators and were consumed in the grafting reaction. The ring-opening polymerization generated new hydroxyl groups simultaneously—these are obvious from Figure 1. These results indicated that the H-ESO-HEC was prepared successfully.

The introduction of the ESO on HEC chains is further confirmed by the ^1H and ^{13}C NMR spectra of the H-ESO-HEC-III in Figure 3. In ^1H NMR spectrum, the clusters of signal peaks ranged from δ 0.8 to 1.6. These were related to the protons of the alkane chains of ESO on HEC. The peaks at δ 2.1 corresponded to the side groups −OH of the HEC. The alkane chains were produced by the ring-open reaction. The clusters of signal peaks in the range from δ 3.2 to 5.0 were attributed to the chemical shifts of anhydroglucose unit (AGU) protons. In the ^{13}C NMR spectrum, the possible assignments of the peaks were found according to the previous literature.[34,35] The inserted region at δ 176 correspond to carbonyl signals of the carboxylate groups.[36] The C-1 carbon resonance in AGU was poor at δ 101. The clusters of signal peaks in the range from δ 62 to 76 contributed to the chemical shifts of AGU carbons. Table 2 offers detailed information. Distinct peaks were observed at δ 62. There are attributed to the C-6 substituted by the hydroxyethylation and connected to the

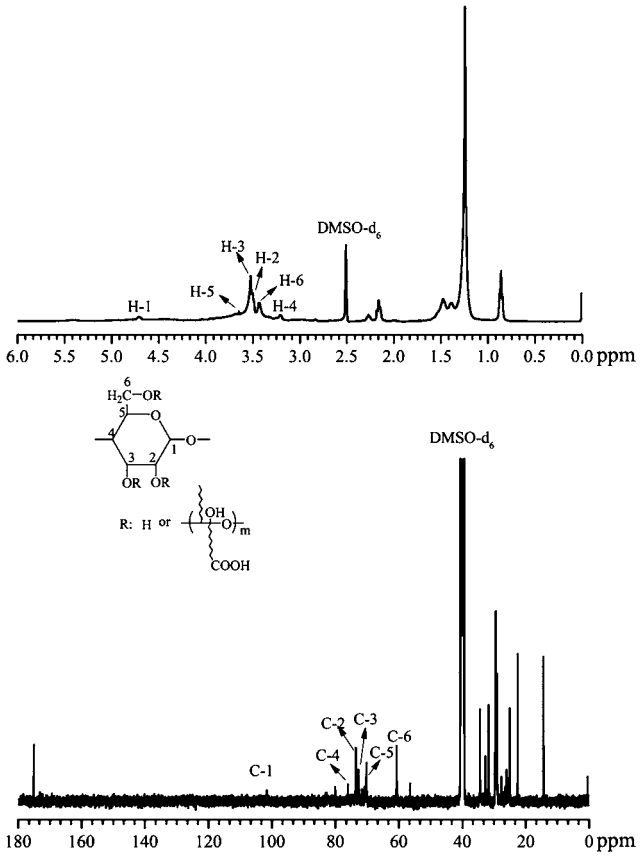

Figure 3. ^1H NMR and ^{13}C NMR spectrum of H-ESO-HEC-III sample in DMSO-d_6.

Table 2. ^1H and ^{13}C NMR Signals of H-ESO-HEC

^1H NMR		^{13}C NMR	
signal	δ (ppm)	signal	δ (ppm)
−**OH**	2.10	−**COOH**	176
$-(CH_2)_n-CH_3$	0.90	$-CH_3$	15
$-(CH_2)_n-CH_3$	1.30−1.50	$-CH_2-$	27−35
CH_2-O-CH_2	2.80	CH_2-O-CH_2	83
CH−OH	3.20	CH−OH	80
AGU−H_1	4.75	AGU−C_1	101
AGU−H_2	3.50	AGU−C_2	74
AGU−H_3	3.55	AGU−C_3	70
AGU−H_4	3.30	AGU−C_4	76
AGU−H_5	3.65	AGU−C_5	73
AGU−H_6	3.45	AGU−C_6	62

ether bond that is obtained by graft polymerization. The clusters of peaks in the range from δ 10 to 35 corresponding to the carbon signals of ESO chains demonstrated that the graft reaction was successful. ^1H NMR and ^{13}C NMR spectroscopy confirmed the characteristic groups of H-ESO-HEC-III.

Molecular Weight and Carboxyl Content of H-ESO-HEC. The molecular weight value of H-ESO-HEC was determined by HT-GPC. The HT-GPC profile signals of the refractive index detector are shown in Figure 4. This shows that the H-ESO-HEC with different molecular weights had a similar tendency of distribution and moved toward the higher molecular weight regions as the amount of ESO increased in the graft reaction. As listed in Table 1, the M_n of H-ESO-HEC (I−V) ranged from 1.48×10^5 to 4.58×10^5 Da and the M_w of

DOI: 10.1021/acs.jafc.5b03765
J. Agric. Food Chem. 2015, 63, 9062−9068

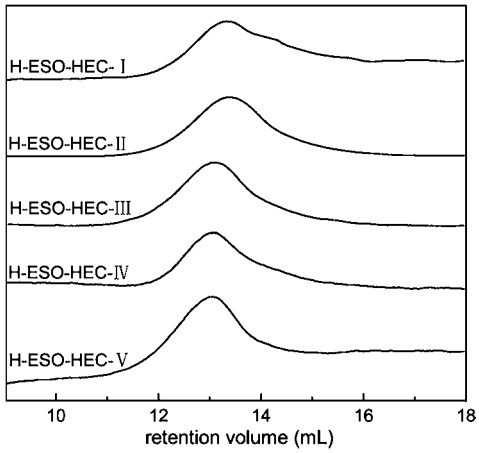

Figure 4. GPC profile signal of the refractive index of H-ESO-HEC samples.

H-ESO-HEC (I–V) ranged from 2.71×10^5 to 8.28×10^5 Da along with the mass ratio of HEC and ESO ranged from 1:1 to 1:5, respectively. The conductometric titration curve to determine the carboxyl content of H-ESO-HEC-III was divided into three parts in Figure 5. The first part showed the presence

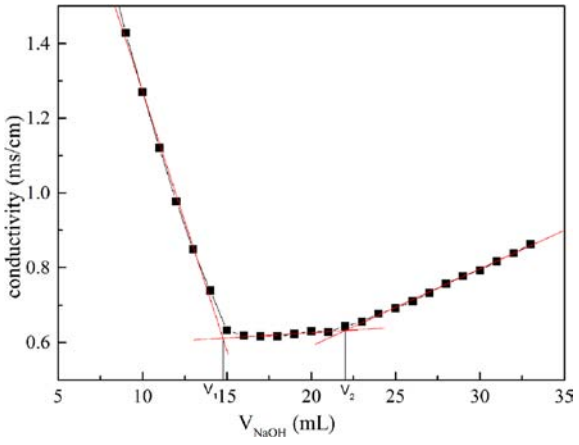

Figure 5. Conductometric titration curve of H-ESO-HEC-III.

of a strong acid corresponding to excess HCl. The second part where the conductivity remains constant showed a weak acid corresponding to the carboxyl content. The last part showed that strong base corresponded to an excess of sodium hydroxide. V_1 and V_2 are volumes of NaOH (mL) in the first and second inflection points of the titration curves, respectively. Finally, the carboxyl content can be calculated by eq 1. The carboxyl contents of H-ESO-HEC (I–V) were 1.89–2.80 mmol/g (Table 1). We concluded that the carboxyl content was closely associated with the molecular weight. As the amount of ESO increased in graft reaction, the carboxyl content increased according to the M_n of H-ESO-HEC. In addition, the polydispersity indexes (PDI) of H-ESO-HEC (I–V) ranged from 1.46 to 2.1. This indicates that the H-ESO-HEC samples had a wide distribution (Figure 4).

DSC Analysis. The ring-opening polymerization of ESO grafting on HEC was confirmed by DSC in which the glass transition temperature (T_g) was determined to be the temperature at the inflection point. Figure 6 clearly illustrates that there was no T_g in HEC and H-ESO-HEC-I because the

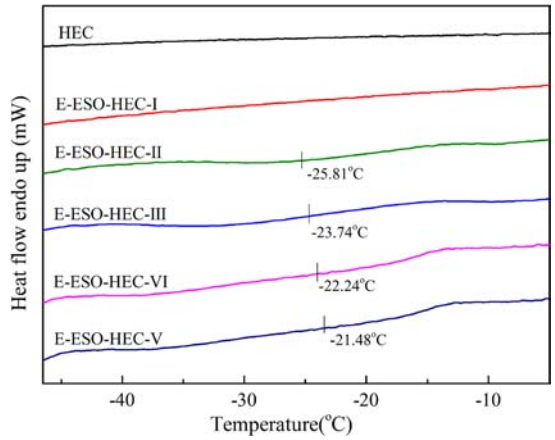

Figure 6. DSC curves of HEC and H-ESO-HEC samples.

HEC did not exhibit glass transition, and there was no polymerization of ESO on HEC in H-ESO-HEC-I. Previous literature reported that the products obtained by ring-opening polymerization of ESO had T_g.[26] The T_g values of H-ESO-HEC-II, H-ESO-HEC-III, H-ESO-HEC-IV, and H-ESO-HEC-V were −25.81, −23.74, −22.24, and −21.48 °C, respectively. As expected, increasing the amount of ESO in the graft reaction resulted in more ESO being grafted on HEC. The ring-opening polymerization reaction took place in the graft reaction—this was consistent with the GPC results. Furthermore, the T_g of H-ESO-HEC samples became higher as the molecular weights of H-ESO-HEC increased.

Surface Tension of Aqueous H-ESO-HEC Polymeric Surfactants. The H-ESO-HEC products were added to a beaker containing the required amount of NaOH to neutralize all of the acidic protons from carboxylic acid groups. This was then placed in a 60 °C water bath and stirred with a glass rod until the samples were dissolved.[28,29] A series of aqueous solutions of the H-ESO-HEC-Na were prepared, and their surface tensions were investigated at room temperature. It is well known that amphiphilic polymers with a suitable hydrophilic–hydrophobic balance can form a micelle structure when exposed to a selective solvent.[37] As shown in Figure 7, the surface tension of H-ESO-HEC-Na in water decreased markedly at low concentration at first. When the concentration was higher, the surface tension reduced slightly. Finally, the

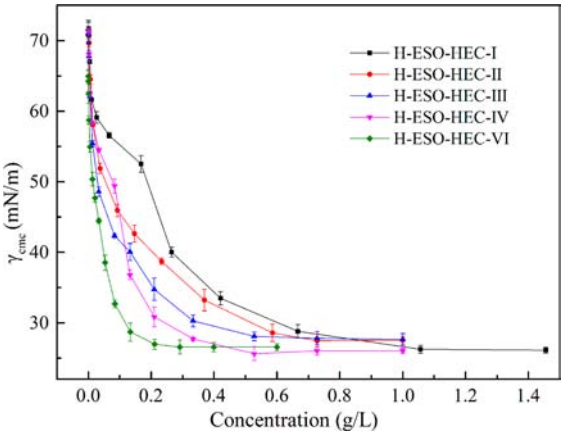

Figure 7. Effect of H-ESO-HEC-Na concentration in water on equilibrium surface tension of water.

DOI: 10.1021/acs.jafc.5b03765
J. Agric. Food Chem. 2015, 63, 9062–9068

surface tension was held nearly constant because its concentration was sufficiently high.

As shown in Table 3, the minimum surface tensions of H-ESO-HEC-Na (I–V) were almost the same and ranged from 26.33 to 28.88 mN/m. The H-ESO-HEC-Na displayed efficient surface properties versus HEC and the hydrolyzed ESO at 54.68 and 34.28 mN/m, respectively. In addition, the previous studies reported that the surface tension of fatty acid-esterified cellulose derivatives ranged between 46 and 65 mN/m.[17,18] Different efficiency of these fatty acid-modified cellulose polymeric surfactants in lowering surface tensions of water was attributed to the status of fatty acid in polymeric surfactants. In our study, hydroxyl groups of HEC acted as initiators for ring-opening polymerization of ESO. The fatty acid chains were combined with HEC by ether linkage at the middle site of the fatty acid molecular chain. In this structure, both the hydrophobic alkanes and the hydrophilic carboxyl were introduced into HEC. The simultaneous introduction of hydrophobic alkanes and hydrophilic carboxyl groups improved the hydrophilic–hydrophobic balance of HEC and provided an opportunity to form micelles in water. The CMC values of H-ESO-HEC-Na were decreased from 1.053 to 0.157 g/L along with the obviously increasing molecular weight of H-ESO-HEC-Na. As the molecular weights increased, the H-ESO-HEC-Na displayed greater propensity to form micelles because of the flexible molecular chains. This indicated that the efficiency in reducing surface tension was significantly enhanced when the molecular weight of H-ESO-HEC-Na increased. The KP of the H-ESO-HEC-Na ranged from 39 to 68 °C. It increased as a function of molecular weight accordingly. The HLB values of the samples ranged from 9.6 to 10.6.

Table 3. CMC, γ_{cmc}, KP, and HLB Values of Samples

samples	CMC (g/L)	γ_{cmc} (mN/m)	KP (°C)	HLB value
HEC		54.68 ± 1.20		
H-ESO-Na	1.105	34.28 ± 0.93	18	9.6–10.6
H-ESO-HEC-Na-I	1.053	26.33 ± 0.56	39	9.6–10.6
H-ESO-HEC-Na-II	0.702	28.88 ± 0.99	42	9.6–10.6
H-ESO-HEC-Na-III	0.514	27.83 ± 0.61	45	9.6–10.6
H-ESO-HEC-Na-IV	0.402	26.37 ± 0.50	52	9.6–10.6
H-ESO-HEC-Na-V	0.157	26.94 ± 1.26	68	9.6–10.6

Surface Rheological Properties. The apparent viscosities of the H-ESO-HEC-Na aqueous solution as a function of shear rate at different concentrations were investigated. The results of H-ESO-HEC-Na-III displayed the same properties as the other products (Figure 8). The curves were not smooth at the low-shear rate because of instrument error and the complete minor viscosity. Therefore, the curve of the 0.1 g/L H-ESO-HEC-Na-III can largely be considered a straight line. The curve of the 0.1 g/L H-ESO-HEC-Na-III below the CMC demonstrated that the solution behaved like water due to the low number of species H-ESO-HEC-Na-III in solution. The curves of the 1.0 and 5.0 g/L H-ESO-HEC-Na-III above the CMC that formed micelles in aqueous solution can be divided into two parts. First, the viscosity of the H-ESO-HEC-Na-III solution decreased as the shear rate increased, and the H-ESO-HEC-Na-III solution exhibited a pseudoplastic property at the low-shear rate.[38] This was because micelles in aqueous solution were damaged, and the macromolecules experienced conformational change.[39] Its winding structure was separated under the action of shearing force and arranged along the flow direction along with the increasing shear rate.[40] Sequentially, the viscosity remained constant when the shear rate reached a certain level. It behaved like a Newtonian property.[41] This is because the winding structure was completely destroyed, and the molecular orientation reached a limiting condition.

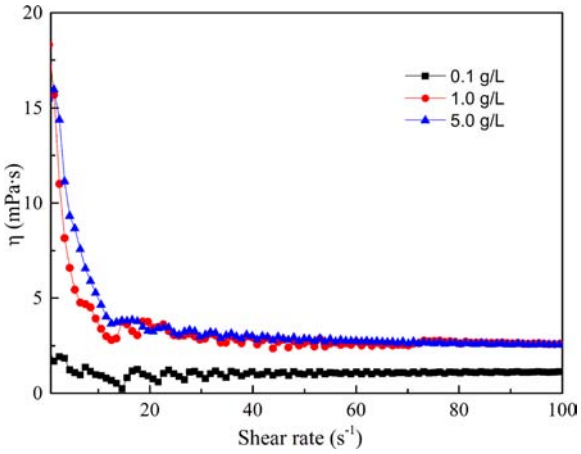

Figure 8. Apparent viscosity of the H-ESO-HEC-Na-III solution as a function of shear rate.

In summary, ESO-grafted HECs were prepared via ring-opening polymerization, and five novel polymeric surfactants H-ESO-HEC-Na (I–V) were obtained by neutralization of H-ESO-HEC with sodium hydroxide. The molecular weights of H-ESO-HEC products were varied by adjusting the mass ratio of HEC and ESO in the grafting reaction. The synthesized polymeric surfactants H-ESO-HEC-Na exhibited higher activities in reducing water surface tension. These ranged from 26.33 to 28.88 mN/m in comparison to 34.28 mN/m for hydrolyzed ESO and 54.68 mN/m for HEC. In addition, the efficiency in reducing water surface tension was definitely enhanced when the molecular weights of H-ESO-HEC increased. Rheological measurements indicated that the H-ESO-HEC-Na solutions changed from a pseudoplastic state to Newtonian with increasing shear rate. This study may facilitate an increase in the use of renewable and biodegradable materials with improved properties as polymeric surfactants.

AUTHOR INFORMATION

Corresponding Authors

*E-mail: liuheicifp@hotmail.com.

*E-mail: shangsb@hotmail.com.

Funding

The authors express their gratitude for the financial support from the Natural Science Foundation of Jiangsu Province of China (BK2012063 and BK20140973), Special Fund for Basic Scientific Research Business of Central Public Research Institutes (CAFINT2012C05), and National Natural Science Foundation of China (31200446).

Notes

The authors declare no competing financial interest.

REFERENCES

(1) Tomanova, V.; Srokova, I.; Ebringerova, A.; Sasinkova, V. Surface-Active and Associative Properties of Ionic Polymeric Surfactants Based on Carboxymethylcellulose. *Polym. Eng. Sci.* **2011**, *51*, 1476–1483.

DOI: 10.1021/acs.jafc.5b03765
J. Agric. Food Chem. 2015, 63, 9062–9068

(2) Nikfarjam, N.; Qazvini, N. T.; Deng, Y. L. Surfactant free Pickering emulsion polymerization of styrene in w/o/w system using cellulose nanofibrils. *Eur. Polym. J.* **2015**, *64*, 179−188.
(3) Hu, Z.; Ballinger, S.; Pelton, R.; Cranston, E. D. Surfactant-enhanced cellulose nanocrystal Pickering emulsions. *J. Colloid Interface Sci.* **2015**, *439*, 139−148.
(4) Khuman, P.; Singh, W. B. K.; Devi, S. D.; Naorem, H. Viscosity-Temperature Behavior of Hydroxypropyl Cellulose Solution in Presence of an Electrolyte or a Surfactant: A Convenient Method to Determine the Cloud Point of Polymer Solutions. *J. Macromol. Sci., Part A: Pure Appl.Chem.* **2014**, *51*, 924−930.
(5) Durand, A. Synthesis of amphiphilic polysaccharides by micellar catalysis. *J. Mol. Catal. A: Chem.* **2006**, *256*, 284−289.
(6) Zhang, L. M. Cellulosic associative thickeners. *Carbohydr. Polym.* **2001**, *45*, 1−10.
(7) Karlberg, M.; Thuresson, K.; Lindman, B. Hydrophobically modified ethyl (hydroxyethyl) cellulose as stabilizer and emulsifying agent in macroemulsions. *Colloids Surf., A* **2005**, *262*, 158−167.
(8) Landoll, M. L. U.S. Patent No. 4,228,277, 1980.
(9) Landoll, L. M. Nonionic polymer surfactants. *J. Polym. Sci., Polym. Chem. Ed.* **1982**, *20*, 443−455.
(10) Yang, F.; Liu, Y. N.; Yu, J. L.; Li, H. P.; Li, G. Synthesis, micellization behavior and alcohol induced amphipathic cellulose film of cellulose-based amphiphilic surfactant. *Appl. Surf. Sci.* **2015**, *345*, 187−193.
(11) Evani, S. U.S. Patent No. 4,432,881, 1984.
(12) Li, Z. X.; Wang, L. G.; Huang, Y. Photoinduced graft copolymerization of polymer surfactants based on hydroxyethyl cellulose. *J. Photochem. Photobiol., A* **2007**, *190*, 9−14.
(13) Sardar, N.; Ali, M. S.; Kamil, M.; Kabir-ud-Din. Phase Behavior of Nonionic Polymer Hydroxypropylmethyl Cellulose: Effect of Gemini and Single-Chain Surfactants on the Energetics at the Cloud Point. *J. Chem. Eng. Data* **2010**, *55*, 4990−4994.
(14) Thongngam, M.; McClements, D. J. Characterization of interactions between chitosan and an anionic surfactant. *J. Agric. Food Chem.* **2004**, *52*, 987−991.
(15) Wei, Y. P.; Cheng, F.; Hou, G.; Sun, S. F. Amphiphilic cellulose: Surface activity and aqueous self-assembly into nano-sized polymeric micelles. *React. Funct. Polym.* **2008**, *68*, 981−989.
(16) Srokova, I.; Talaba, P.; Hodul, P.; Balazova, A. Emulsifying agents based on O-(carboxymethyl)cellulose. *Tenside, Surfactants, Deterg.* **1998**, *35*, 342−344.
(17) Yu, J. L.; Yang, F.; Liu, Z. H.; Liu, Y. N.; Li, G. Preparation and Characterization of C-10-C-14 Alkyl Cellulose Ester Sulfate Surfactant. *J. Surfactants Deterg.* **2014**, *17*, 647−653.
(18) Tomanova, V.; Pielichowski, K.; Srokova, I.; Zoldakova, A.; Sasinkova, V.; Ebringerova, A. Microwave-assisted synthesis of carboxymethylcellulose based polymeric surfactants. *Polym. Bull.* **2008**, *60*, 15−25.
(19) Peydecastaing, J.; Girardeau, S.; Vaca-Garcia, C.; Borredon, M. E. Long chain cellulose esters with very low DS obtained with non-acidic catalysts. *Cellulose* **2006**, *13*, 95−103.
(20) Chumpitaz, L. D. A.; Coutinho, L. F.; Meirelles, A. J. A. Surface tension of fatty acids and triglycerides. *J. Am. Oil Chem. Soc.* **1999**, *76*, 379−382.
(21) Osipow, L.; Snell, F. D.; Marra, D.; York, W. C. Surface Activity of Monoesters - Fatty Acid Esters of Sucrose. *Ind. Eng. Chem.* **1956**, *48*, 1462−1464.
(22) Liu, Z. S.; Biresaw, G. Synthesis of Soybean Oil-Based Polymeric Surfactants in Supercritical Carbon Dioxide and Investigation of Their Surface Properties. *J. Agric. Food Chem.* **2011**, *59*, 1909−1917.
(23) Biermann, U.; Bornscheuer, U.; Meier, M. A. R.; Metzger, J. O.; Schäfer, H. J. Oils and Fats as Renewable Raw Materials in Chemistry. *Angew. Chem., Int. Ed.* **2011**, *50*, 3854−3871.
(24) Lawate, S. S.; Lal, K.; Huang, C. *Vegetable oils-structure and performance*; CRC Press: New York, 1997; p 103.
(25) Bantchev, G. B.; Kenar, J. A.; Biresaw, G.; Han, M. G. Free Radical Addition of Butanethiol to Vegetable Oil Double Bonds. *J. Agric. Food Chem.* **2009**, *57*, 1282−1290.
(26) Lowe, A. B. Thiol-ene "click" reactions and recent applications in polymer and materials synthesis: a first update. *Polym. Chem.* **2014**, *5*, 4820−4870.
(27) Liu, Z. S.; Doll, K. M.; Holser, R. A. Boron trifluoride catalyzed ring-opening polymerization of epoxidized soybean oil in liquid carbon dioxide. *Green Chem.* **2009**, *11*, 1774−1780.
(28) Lathi, P. S.; Mattiasson, B. Green approach for the preparation of biodegradable lubricant base stock from epoxidized vegetable oil. *Appl. Catal., B* **2007**, *69*, 207−212.
(29) Biresaw, G.; Liu, Z. S.; Erhan, S. Z. Investigation of the surface properties of polymeric soaps obtained by ring-opening polymerization of epoxidized soybean oil. *J. Appl. Polym. Sci.* **2008**, *108*, 1976−1985.
(30) da Silva Perez, D.; Montanari, S.; Vignon, M. R. TEMPO-mediated oxidation of cellulose III. *Biomacromolecules* **2003**, *4*, 1417−1425.
(31) Wang, X. G.; Yan, F.; Li, Z. Q.; Zhang, L.; Zhao, S.; An, J. Y.; Yu, J. Y. Synthesis and surface properties of several nonionic-anionic surfactants with straight chain alkyl-benzyl hydrophobic group. *Colloids Surf., A* **2007**, *302*, 532−539.
(32) Liu, W. R.; Sun, D. J.; Li, C. F.; Liu, Q.; Xu, H. Formation and stability of paraffin oil-in-water nano-emulsions prepared by the emulsion inversion point method. *J. Colloid Interface Sci.* **2006**, *303*, 557−563.
(33) Wei, Y. P.; Cheng, F.; Zheng, H. Synthesis and flocculating properties of cationic starch derivatives. *Carbohydr. Polym.* **2008**, *74*, 673−679.
(34) Zhou, J. P.; Xu, Y. L.; Wang, X. L.; Qin, Y.; Zhang, L. N. Microstructure and aggregation behavior of methylcelluloses prepared in NaOH/urea aqueous solutions. *Carbohydr. Polym.* **2008**, *74*, 901−906.
(35) Tezuka, Y.; Imai, K.; Oshima, M.; Chiba, T. Determination of Substituent Distribution in Cellulose Ethers by Means of a C-13 Nmr-Study on Their Acetylated Derivatives 0.4. O-Methyl-O-Hydroxyalkylcelluloses. *Makromol. Chem.* **1990**, *191*, 681−690.
(36) Reuben, J.; Conner, H. Analysis of the carbon-13 NMR spectrum of hydrolyzed O-(carboxymethyl) cellulose: Monomer composition and substitution patterns. *Carbohydr. Res.* **1983**, *115*, 1−13.
(37) Eastoe, J.; Dalton, J. S. Dynamic surface tension and adsorption mechanisms of surfactants at the air-water interface. *Adv. Colloid Interface Sci.* **2000**, *85*, 103−144.
(38) Hong, P.; Fa, C.; Wei, Y. P.; Sen, Z. Surface properties and synthesis of the cellulose-based amphoteric polymeric surfactant. *Carbohydr. Polym.* **2007**, *69*, 625−630.
(39) Tam, K. C.; Jenkins, R. D.; Winnik, M. A.; Bassett, D. R. A structural model of hydrophobically modified urethane-ethoxylate (HEUR) associative polymers in shear flows. *Macromolecules* **1998**, *31*, 4149−4159.
(40) Ji, Y. Q.; Wang, W. S.; Li, G. Z.; Zheng, L. Q. Rheological properties of wormlike micelles formed in the sodium oleate/trisodium phosphate aqueous solution. *Chin. Chem. Lett.* **2008**, *19*, 483−487.
(41) Kastner, U.; Hoffmann, H.; Dönges, R.; Ehrler, R. Interactions between modified hydroxyethyl cellulose (HEC) and surfactants. *Colloids Surf., A* **1996**, *112*, 209−225.

DOI: 10.1021/acs.jafc.5b03765
J. Agric. Food Chem. 2015, 63, 9062−9068

guaiacol, and canolol (4-vinyl syringol), are natural compounds widespread in the plant kingdom.[20,21] In industry, these substances are treated as food additives and are approved as flavouring agents by regulatory agencies.[22] They are also involved in resin, elastomer, and adhesive production.[23] However, no study has examined the possibility to produce lipophilic antioxydants from vinylphenols.

In the present work, the strong nucleophilic character of vinylphenols has been exploited to propose an original way for lipophilization by means of peracids. As a vinylphenol representative, 4-vinyl guaiacol (**2**) was selected to undergo this transformation.

Thus, the perhydrolysis activity of CAL-B[24] contributed to produce a set of peracids, with different alkyl chain lengths, which were grafted by electrophilic addition to the 4-vinyl guaiacol double bond. Subsequently, the antioxidant activity of 4-vinyl guaiacol and its resulting hydroxyesters was evaluated using the conjugated autoxidizable triene (CAT) assay. The synthesized hydroxyesters can be used as effective antioxidants in multiphase food products and pharmaceuticals.

MATERIALS AND METHODS

Chemicals. Vanillin (99%), malonic acid (99%), piperidine (≥99.5%), butanoic acid (≥99%), hexanoic acid (≥98%), octanoic acid (≥98%), decanoic acid (≥98%), dodecanoic acid (≥98%), octadecanoic acid (≥95%), *tert*-butyldimethysilyl chloride (97%), imidazole (≥99%), immobilized CAL-B (Novozym 435), hydrogen peroxide (30 wt % in H_2O), tung oil from *Aleurites fordii* seeds [average molecular weight (MW) = 872 g mol^{-1}], phosphate buffered saline (PBS) at pH 7.2, polyoxyethylene(23)lauryl ether [Brij 35, estimated molar mass (MM) = 1198 g mol^{-1}], and (±)-6-hydroxy-2,5,7,8-tetramethylchromane-2-carboxylic acid (Trolox) were purchased from Sigma-Aldrich France. 2,2′-Azobis(2-methylpropionamidine) dihydrochloride (AAPH) was obtained from Wako Chemical (Neuss, Germany). Glacial acetic acid was purchased from Merck France. Hexadecanoic acid was supplied by SEPPIC France. All solvents were analytical- or high-performance liquid chromatography (HPLC)-grade (Sigma-Aldrich France) and were used as received.

All of the reactions were monitored by thin-layer chromatography (TLC) performed on silica gel 60 F254 (provided by Merck). All compounds were dissolved in $CDCl_3$ and analyzed using a Bruker 400 MHz spectrometer, operating at 400 MHz for ^1H and 100 MHz for ^{13}C. Chemical shifts were referenced using residual internal CH_3Cl signals at 7.26 and 77.0 ppm for ^1H and ^{13}C, respectively. Assignments of both proton and carbon resonances, identification, and structure characterization of products were performed using both one-dimensional (1D) and two-dimensional (2D) nuclear magnetic resonance (NMR) spectrum analysis and homonucluear ^1H and heteronuclear $^1H/^{13}C$ experiments. Elemental analyses were performed by combustion on Flash EA 1112 (ThermoFinnigan 2003). High-resolution mass spectrometry (HRMS) analyses were performed by a Xevo-G2-XS Q-Tof (from Waters). Statistical analysis [one-way analysis of variation (ANOVA)] of CAT values was performed using JMP software, version 12 (SAS Institute, Cary, NC). The means were then compared using Student's *t* test. The significance level α was set to 0.05.

Protection of the Phenolic Hydroxyl of 4-Vinyl Guaiacol (2). Under argon, a solution of *tert*-buthyldimethylsilyl chloride (1.2 mmol, 0.18 g) in *N*,*N*-dimethylformamide (DMF) (2 mL) was added dropwise to a stirred solution of 4-vinyl guaiacol (**2**) (1 mmol, 0.15 g) and imidazole (2.5 mmol, 0.17 g) in DMF (3 mL). Stirring was maintained 26 h at room temperature, and then water (25 mL) and ethyl acetate (25 mL) were added. The aqueous layer was separated and extracted with ethyl acetate (2 × 25 mL). The combined organic layers were washed with brine (30 mL), dried over anhydrous $MgSO_4$, and concentrated under reduced pressure. Flash chromatography purification (90:10 petroleum ether/ethyl acetate) afforded the following.

*tert-Butyl(2-methoxy-4-vinylphenoxy)dimethylsilane (**3**).* Colorless oil, 85% yield (0.83 mmol). ^1H NMR (400 MHz, $CDCl_3$) δ: 0.18 (s, 6H, H12), 1.02 (s, 9H, H10), 3.84 (s, 3H, H9), 5.14 (dd, *J* = 10.8 and 0.91 Hz, 1H, H8), 5.61 (dd, *J* = 17.6 and 0.91 Hz, 1H, H8), 6.65 (dd, *J* = 17.6 and 10.9 Hz, 1H, H7), 6.81 (d, *J* = 8.1 Hz, 1H, H6), 6.88 (dd, *J* = 8.2 and 1.9 Hz, 1H, H5), 6.94 (s, 1H, H2) ppm. ^{13}C NMR (100 MHz, $CDCl_3$) δ: 4.6 (C12), 18.4 (C11), 25.7 (C10), 55.4 (C9), 109.6 (C2), 111.7 (C8), 119.4 (C6), 120.4 (C5), 131.7 (C1), 136.7 (C7), 145.1 (C4), 151.0 (C3) ppm. [M + H^+] calcd, 265.1504; found, 265.1510. $C_{15}H_{24}O_2Si$ calcd C, 68.13; H, 9.15; Si, 10.62; found C, 70.02; H, 8.89; Si, 11.31.

Lipophilization of the Silylated Vinylphenol (3). In a 50 mL round-bottom flask equipped with a magnetic stirrer, 2 mmol of carboxylic acid, 3 mmol of 30% hydrogen peroxide (0.34 mL), and Novozym 435 (10 wt % relative to the weight of the silylated vinylphenol, 0.026 g) were mixed in 2 mL of toluene. After 30 min at 40 °C, a solution of compound **3** (1 mmol, 0.26 g) in toluene (1 mL) was added to the reaction medium over 2 h. The reaction was monitored by TLC. After the complete consumption of the peracid, catalyst beads were removed from the reaction mixture by filtration and 30 mL of water and 30 mL of ethyl acetate were added to the filtered reaction mixture. The aqueous layer was separated and extracted with ethyl acetate (2 × 30 mL). The combined organic layers were washed with brine (40 mL), dried over anhydrous $MgSO_4$, and concentrated under reduced pressure. The phenolic group deprotection was performed on the crude products.

Deprotection of the Phenolic Hydroxyl. The crude product formed from the reaction of compound **3** with peracids (1 mmol) was diluted in 2 mL of dry tetrahydrofuran (THF), and the solution was cooled to 0 °C. Under argon, a solution of tetra-*N*-butylammonium fluoride (TBAF) (1.2 mmol) in 2 mL of dry THF was added dropwise to the previous solution. After 3 h at 0 °C, water (25 mL) and ethyl acetate (25 mL) were added. The aqueous layer was separated and extracted with ethyl acetate (2 × 25 mL). The combined organic layers were washed with brine (30 mL), dried over anhydrous $MgSO_4$, and concentrated under reduced pressure. Flash chromatography purification (from 90:10 to 60:40 petroleum ether/ethyl acetate) afforded β-hydroxyesters **4a**−**4h** and α-hydroxyesters **5b**−**5e**. For example, the electrophilic addition of octanoic peracid to compound **3** gave rise to the following.

*2-Hydroxy-1-(4-hydroxy-3-methoxyphenyl)ethyl Octanoate (**4d**).* Yellow oil, 46% yield (0.45 mmol). ^1H NMR (400 MHz, $CDCl_3$) δ: 0.88 (t, *J* = 6.9 Hz, 3H, H17), 1.26−1.1.29 (m, 8H, H16−H13), 1.62−1.66 (m, 2H, H12), 2.38 (t, *J* = 7.40 Hz, 2H, H11), 3.78 (dd, *J* = 11.90 and 4.30 Hz, 1H, H9α), 3.86 (m, 1H, H9β), 3.90 (s, 3H, H7), 5.65 (s, 1H, OH aliphatic), 5.79 (dd, *J* = 7.60 and 4.30 Hz, 1H, H8), 6.86 (d, *J* = 8.46 Hz, 1H, H6), 6.89 (d, *J* = 7.80 Hz, 1H, H5), 6.91 (s, 1H, H2) ppm. ^{13}C NMR (100 MHz, $CDCl_3$) δ: 14.0 (C17), 22.5 (C16), 25.0 (C12), 28.8 (C15), 29.0 (C14), 31.6 (C13), 34.5 (C11), 55.9 (C7), 66.0 (C9), 76.5 (C8), 109.5 (C2), 114.5 (C5), 119.8 (C6), 129.0 (C1), 145.8 (C4), 146.5 (C3), 173.5 (C10) ppm. [M + H^+] calcd, 311.1821; found, 311.1835. $C_{17}H_{26}O_5$ calcd C, 65.78; H, 8.44; found C, 65.67; H, 8.51.

*2-Hydroxy-2-(4-hydroxy-3-methoxyphenyl)ethyl Octanoate (**5d**).* Yellow oil, 30% yield (0.29 mmol). ^1H NMR (400 MHz, $CDCl_3$) δ: 0.89 (t, *J* = 6.9 Hz, 3H, H17), 1.28−1.33 (m, 8H, H16−H13), 1.64 (m, 2H, H12), 2.36 (t, *J* = 7.50 Hz, 2H, H11), 3.90 (s, 3H, H7), 4.16 (dd, *J* = 11.50 and 3.58 Hz, 1H, H9α), 4.25 (dd, *J* = 11.50 and 3.50 Hz, 1H, H9β), 4.89 (dd, *J* = 8.40 and 3.40 Hz, 1H, H8), 5.66 (s, 1H, OH aliphatic), 6.86 (dd, *J* = 8.50 and 1.80 Hz, 1H, H6), 6.89 (d, *J* = 8.10 Hz, 1H, H5), 6.94 (s, 1H, H2) ppm. ^{13}C NMR (100 MHz, $CDCl_3$) δ: 14.0 (C17), 22.35 (C16), 24.9 (C12), 28.8 (C15), 29.0 (C14), 31.6 (C13), 34.2 (C11), 55.9 (C7), 69.2 (C9), 73.3 (C8), 108.5 (C2), 114.3 (C5), 119.2 (C6), 131.8 (C1), 145.6 (C4), 146.7 (C3), 174.0 (C10) ppm. [M + H^+] calcd, 311.1821; found, 311.1817. $C_{17}H_{26}O_5$ calcd C, 65.78; H, 8.44; found C, 65.91; H, 8.36.

The other NMR data are displayed in the Supporting Information.

DOI: 10.1021/acs.jafc.5b03551
J. Agric. Food Chem. 2015, 63, 9069−9075

Determination of the Antioxidant Capacity Using the CAT Assay. Prior to use, commercial tung oil was stripped (removal of polar compounds, including tocopherols) as follows. In a glass column packed with 25 g of alumina, 25 mL of a tung oil solution in *n*-hexane (200 mg mL^{-1}) was eluted followed by 25 mL of hexane. Then, hexane was evaporated under vacuum, and the stripped tung oil was aliquoted into brown glass tubes, inerted under nitrogen stream, and stored at −18 °C until use. All experiments were performed under shelter from light, as much as possible.

Fresh solutions of Trolox and phenolics at concentrations ranging from 0.4 to 4.0 mmol L^{-1} were prepared in chloroform/methanol (2:1), then diluted in methanol to obtain a concentration range of 0.1−1.0 μmol L^{-1}, and stored in amber vials. A total of 50 μL of these solutions was transferred to a 96-well microplate (Greiner, Frickenhausen, Germany), which was then preheated to 37 °C and shook in a thermostated shaker (PHMT Grant Instruments, Ltd., Shepreth, U.K.) for 5 min at 1200 rpm.

A total of 25 mL of PBS containing Brij 35 (34 μmol L^{-1}) was added to 5 mg of stripped tung oil into an amber glass vial. Thereafter, this premixture was vortexed for 10 s prior to homogenization in an Ultra Turrax homogenizer (Janke and Kunkel, Staufen, Germany) at 2400 rpm for 90 s. Each well of the microplate was supplemented with 100 μL of this emulsion. To enhance repeatability, the microplate was immediately preheated and maintained under stirring in a thermostated shaker (PHMT Grant Instruments, Ltd.) at 37 °C for 1 min at 1200 rpm.

A total of 50 μL of a solution of AAPH in PBS (4 mmol L^{-1}), prepared immediately before reading, was added to wells. Finally, each well contained a final volume of 200 μL, with 115 μmol L^{-1} tung oil, 17 μmol L^{-1} Brij 35, 1 mmol L^{-1} of AAPH, and antioxidants at various concentrations (0.25−1.0 μmol L^{-1}). The kinetics of the reaction were immediately assessed by monitoring absorbance decay at 273 nm. Measurements were taken every minute within 6 h at 37 ± 0.5 °C with shaking the plate 5 s before each reading, using a microplate reader model M1000 (Tecan, Groedig, Austria) equipped with software Magellan.

All measurements were performed in triplicate and reported as the average ± standard deviation (SD). To normalize data, the raw absorbance values were expressed in relative absorbance according to eq 1

$$\text{relative absorbance} = \frac{A_t}{A_0} \quad (1)$$

where A_t and A_0 are the absorbances read at times t and 0 min, respectively. The area under the curve (AUC) corresponding to the decay of relative absorbance was calculated thanks to eq 2.

$$\text{AUC} = 1 + \frac{A_1}{A_0} + \frac{A_2}{A_0} + \ldots + \frac{A_{359}}{A_0} + \frac{A_{360}}{A_0} \quad (2)$$

The chart area provided by an antioxidant sample was then calculated using the difference between AUC in the presence of a sample of antioxidant (AUC_{sample}) and the blank (AUC_{blank}) corresponding to a solution without antioxidant. Trolox was used as an internal calibration standard. Thus, the antioxidant capacity (CAT value) of a sample was given in Trolox equivalents and calculated by eq 3

$$\text{CAT value} = \frac{(\text{AUC sample} - \text{AUC blank})}{(\text{AUC Trolox} - \text{AUC blank})} \frac{(\text{moles of Trolox})}{(\text{moles of sample})} \quad (3)$$

where AUC_{sample}, AUC_{blank}, and AUC_{Trolox} are the areas in the graph where the protection of tung oil occurs in the presence of a sample, the antioxidant-free solution, and the solution containing Trolox, respectively. The CAT value is expressed in moles of Trolox per moles of the tested compound, i.e., in Trolox equivalents.

RESULTS AND DISCUSSION

To produce antioxidant 4-vinyl guaiacol derivatives with increased lipophilicity, the following four-step synthesis route was adopted: (i) 4-vinyl guaiacol (**2**) production from vanillin, (ii) protection of the compound **2** phenolic hydroxyl by silyl etherification (to avoid the undesirable oxidation or polymerization side reactions), (iii) electrophilic addition of the *in situ*-generated peracids (with different chain lengths) to protected 4-vinyl guaiacol (**3**), and (iv) phenolic hydroxyl deprotection.

Synthesis of 4-Vinyl Guaiacol (2) and Protection of Its Hydroxyl Group. Generally, the availability of vinylphenols in natural sources does not meet the industrial requirements. Hence, several chemical syntheses of these phenolic compounds, including catalytic dehydrogenation of ethylphenols, Wittig reaction, or hydroxycinnamic acid decarboxylation, have been described.[25] However, a majority of these procedures required expensive reagents and harsh conditions to eventually give rise to the products in low yields. Recently, an efficient synthesis of these compounds by the Knoevenagel−Doebner[25] reaction in mild conditions was described by Sinha et al. Hence, this synthetic pathway was adopted to produce 4-vinyl guaiacol (**2**) from vanillin (**1**).

Subsequently, the 4-vinyl guaiacol hydroxyl group was temporary masked to avoid the competitive oxidation and polymerization side reactions. Among several protecting groups, *tert*-butyldimethylsilyl (TBDMS) was selected because of its stability in a variety of organic reactions and the facility by which it can be introduced and removed under mild conditions.[26,27] The treatment of compound **2** with *tert*-butyldimethylsilyl chloride and imidazole at room temperature led to the silyl ether derivative **3** with 85% yield (Figure 1).

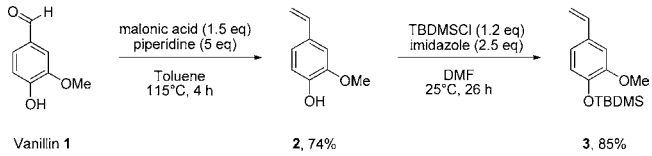

Figure 1. 4-Vinyl guaiacol synthesis and its phenolic hydroxyl etherification.

Lipophilization of Compound 3 by Electrophilic Esterification. As reported in the literature, various reaction parameters can influence the lipase activity and, thus, the peracid formation. Among several organic solvents tested, the highest yields of peracids were observed using toluene or hexane.[28] Törnvall et al.[29] and Orellana-Coca et al.[24] investigations have demonstrated that elevated temperatures (above 60 °C) together with hydrogen peroxide at high concentrations (6−12 M) resulted in a rapid loss of enzyme activity. When these different data are taken into account, the vinylic derivative **3** was reacted with caprylic peracid (octanoic peracid) in a two-phase reaction. First, the CAL-B-catalyzed perhydrolysis of caprylic acid was initiated at 40 °C during 30 min in toluene. Then, the solution of compound **3**, in the same solvent, was added to the previous mixture over 2 h. During the whole reaction, the hydrogen peroxide concentration did not exceed 1 M.

After 6 h of reaction and the usual work up (described in the Materials and Methods), the crude product was treated with TBAF in THF at 0 °C, allowing for the silyl ether cleavage and the hydroxyl group recovery within 3 h.

Instead of the expected epoxidized products, hydroxyester derivatives **4d** and **5d** were produced in 76% overall yield (Figure 2).

DOI: 10.1021/acs.jafc.5b03551
J. Agric. Food Chem. 2015, 63, 9069−9075

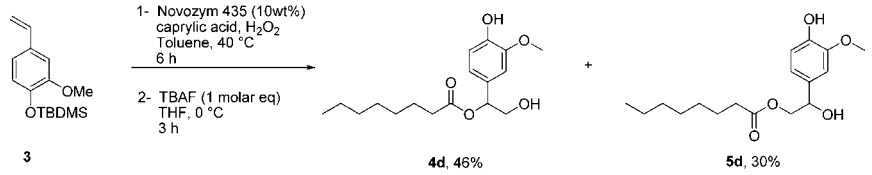

Figure 2. Electrophilic esterification of compound **3**, followed by hydroxyl group deprotection.

The addition of decanoic peracid to compound **3** was proven by NMR. Indeed, the characteristic proton signals of the vinylic double bond at 5.07, 5.64, and 6.67 ppm disappeared and were replaced by α-hydroxyl (3.78−3.86 ppm for compound **4d** and 4.89 ppm for compound **5d**) and α-ester (5.79 ppm for compound **4d** and 4.16−4.25 ppm for compound **5d**) proton signals. The appearance of shielded aliphatic proton signals on the ^{1}H NMR spectrum and the ester carboxyl signal on the ^{13}C NMR spectrum indicated the grafting of the carboxylic acid moiety on compound **3**.

On the basis of these results, other carboxylic acids (ranging from C2 to C18) were used to assess the reactivity of compound **3** with the *in situ*-generated corresponding peracids and to produce phenolic hydroxyesters with different side-chain lengths. The reaction products are depicted in both Figure 3 and Table 1.

Considering the results displayed in Table 1, two main aspects should be discussed: (i) the peracid addition to the vinylic double bond instead of its epoxidation and (ii) the arising of two addition isomers with the predominance of the derivatives bearing a primary alcohol function (**4a**−**4h** derivatives).

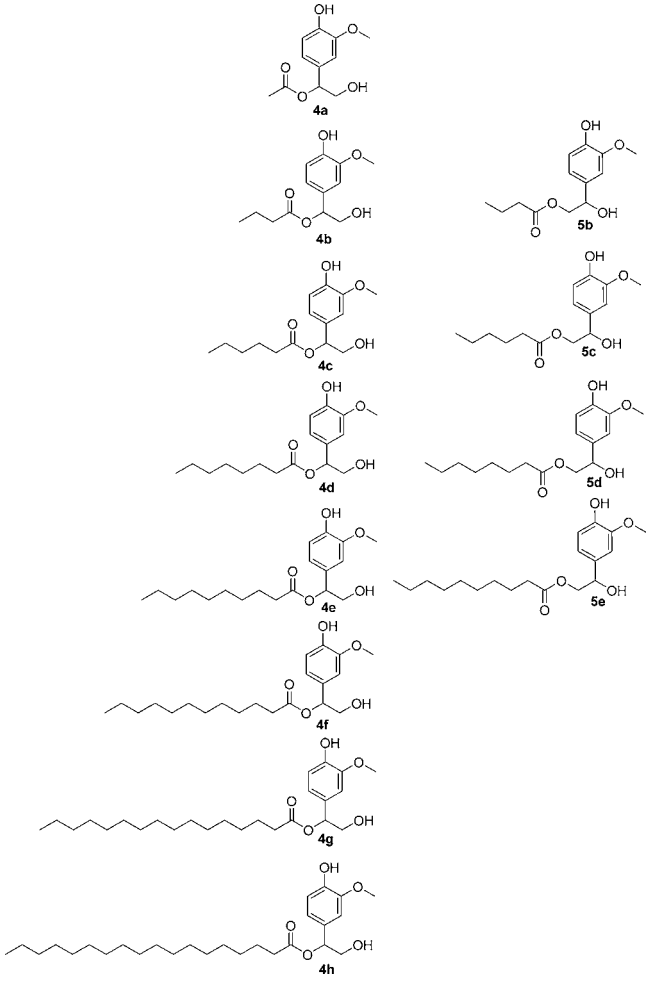

Figure 3. Chemical structures of hydroxyesters **4a**−**4h** and **5b**−**5e**.

Table 1. Electrophilic Addition Products (after the Phenolic Hydroxyl Deprotection) of Peracids on Compound 3

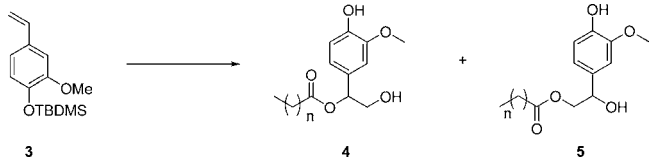

entry	acid	reaction time (h)[a]	product	product yield (%)	CAT value[b]
1	ethanoic acid (n = 0)[c]	126	**4a**	33	0.46 ± 0.05
			5a		
2	butanoic acid (n = 2)[c]	102	**4b**	26	0.80 ± 0.04
			5b	22	0.49 ± 0.01
3	hexanoic acid (n = 4)	4	**4c**	43	0.55 ± 0.01
			5c	32	0.19 ± 0.05
4	octanoic acid (n = 6)	6	**4d**	46	0.57 ± 0.03
			5d	30	0.24 ± 0.02
5	decanoic acid (n = 8)	7	**4e**	43	0.24 ± 0.04
			5e	31	0.22 ± 0.07
6	dodecanoic acid (n = 10)	6.5	**4f**	77	0.19 ± 0.04
			5f		
7	hexadecanoic acid (n = 14)	24	**4g**	68	0.19 ± 0.02
			5g		
8	octadecanoic acid (n = 16)	20	**4h**	72	0.12 ± 0.02
			5h		

[a]Reactions were monitored by TLC and stopped after the complete conversion of compound **3**. [b]The CAT value of 4-vinyl guaiacol is 0.40 ± 0.03. [c]Reactions of compound **3** with hexanoic to octadecanoic acids were performed by loading 10 wt % of enzyme (relative to the compound **3** weight). However, the addition of both ethanoic and butanoic peracids to the compound **3** double bond required 30 and 20 wt % of enzyme, respectively.

Peracid Addition to the Double Bond of Compound 3. Generally, in the chemo-enzymatic oxidation of olefins, lipase catalyzes the formation of peracids, from the perhydrolysis reaction between carboxylic acids and an oxidizing agent, such as H_2O_2, which then donates an oxygen atom to the double bond, affording the corresponding epoxide and regenerating the carboxylic acids. The epoxidation step occurs through a concerted transition state, also known as a symmetry butterfly transition state. The bond between oxygen and alkene is being formed at the same time that the peroxy bond is breaking and the peracid proton is transferred from the hydroxyl group to carbonyl oxygen.

However, in the present instance, the generated peracids did not achieve their expected task as an oxygen carrier but an electrophilic addition rather occurred to the vinyl double bond of compound **3**. As previously mentioned, the presence of the electron-releasing groups *O*-TBDMS and *O*-methyl on the

DOI: 10.1021/acs.jafc.5b03551
J. Agric. Food Chem. 2015, 63, 9069−9075

aromatic ring of compound **3** contribute, by a mesomeric effect to enhance the electron density on the vinylic double bond. The electrophilic peroxide oxygen of peracid attacks the double bond and forms a three-membered cyclic transition state (**I**)[19] (Figure 4). Then, the electron-rich carboxylate group of peracid

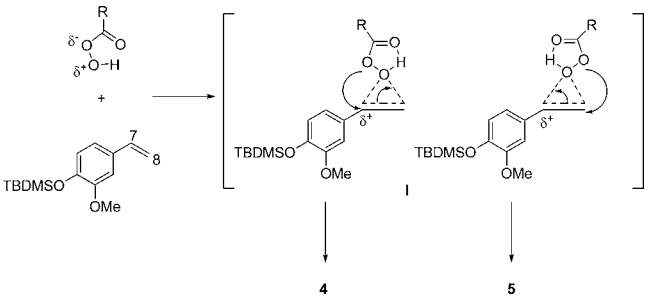

Figure 4. 1,2-Addition mechanism of compound **3** with peracids.

attacks either C7 or C8 carbons, leading to the simultaneous cleavage of the bonds between these carbons and the peroxide oxygen and the formation of compounds **4** and **5**. The intervention of the electron-releasing groups to orientate the reaction mechanism toward peracid addition is confirmed by Sarma et al.,[30] who demonstrated that styrene derivatives, with electron-withdrawing substituents, are rather epoxidized in the presence of peracids.

Peracid Addition Products. As displayed in Table 1, excluding compounds **4a**, **4b**, and **5b**, the addition products of peracids on the vinylic double bond of compound **3** after hydroxyl deprotection were obtained with fair yields ranging from 68 to 77%. The reaction of both ethanoic and butanoic peracids with compound **3** required a longer time and a higher amount of enzyme to afford addition products with relatively lower yields (entries 1 and 2). This is likely due to the peracid stability, which is highly dependent upon their molecular weight. Indeed, the smaller the peracids, the faster their decomposition; in particular, methanoic and ethanoic peracids are highly unstable.[31]

Despite the lower reaction yield of butanoic peracid, this latter led to the formation of two addition products **4b** and **5b**, with a slight predominance of the derivative bearing a primary alcohol function (**4b**). The same trend was observed for hexanoic, octanoic, and decanoic peracids, indicating that, from C4 to C8, peracids exhibit the same reactivity toward compound **3**. Although the predominance of **4**-type products is not very significant, it results from the addition of the peracid electrophilic oxygen on the most nucleophilic double bond carbon.

From dodecanoic to octadecanoic peracids (entries 6−8), only the **4**-type products were formed. The presence of a long alkyl chain in the reaction intermediate **I** seems to further polarize the C7−C8 bond, localizing the negative charge on C8. Hence, only electron-deficient C7 was attacked by the carboxylate group.

Owing to the good enzyme affinity to dodecanoic acid,[28] its corresponding peracid afforded the addition product (**4f**) with the highest yield (77%) in a relatively short time (entry 6).

This particular reactivity of peracids allowed for the production of a set of phenolic hydroxyesters with side-chain lengths ranging from C2 to C18. To obtain equivalent reaction yields, the other strategies based on the lipase-B-catalyzed esterification and transesterification generally require harsher operational conditions, such as a longer reaction time (7−30 days) and higher temperatures (50−60 °C).[32]

After synthesis, the antioxidant potency of these lipophilized phenolics was assessed by the CAT assay.

Determination of the Antioxidant Capacity of Lipophilized Derivatives of 4-Vinyl Guaiacol. In this study, the CAT assay was used to evaluate the antioxidant capacity of the synthesized phenolic hydroxyesters. The triacylglycerols of tung oil are mainly (ca. 85%) comprised of α-eleostearic acid [(9*Z*,11*E*,13*E*)-9,11,13-octadecatrienoic acid]. Owing to the presence of a conjugated triene, this fatty acid strongly absorbs at 273 nm and is highly prone to oxidation. Consequently, under oxidizing conditions, a degradation of conjugated triene may be simply observed upon the signal loss at 273 nm. These properties allow for an efficient, easy, rapid, and direct assessment of lipid oxidation in the heterophasic system. Thus, the CAT assay provides relevant screening of antioxidant abilities of molecules, because it is representative of unsaturated fatty acid oxidation pathways that occur in foods and biological systems.[33] As depicted in both Table 1 and Figure 5, the

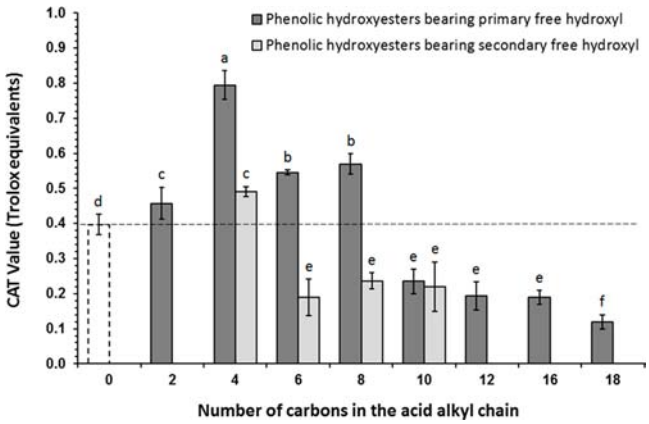

Figure 5. CAT values of 4-vinyl guaiacol (white bar) and the lypophilized molecules: phenolic hydroxyesters bearing primary free hydroxyl (dark gray bars) and phenolic hydroxyl esters bearing secondary free hydroxyl (light gray bars). Values followed by the same letter are not significantly different ($p \leq 0.05$). Values are mean ± SD ($n = 3$).

antioxidant ability of 4-vinyl guaiacol was significantly affected by the grafting of the lipophilic moiety (alkyl chain of variable length). Moreover, the isomer nature (phenolic ester bearing a primary or secondary hydroxyl) may significantly affect the antioxidant activities in such a heterogeneous medium. Indeed, isomers exhibiting the secondary alcohol function presented lower antioxidant activities, with only a slight enhancement for the butyl ester (CAT value = 0.49 ± 0.01) in comparison to 4-vinyl guaiacol (CAT value = 0.40 ± 0.03). One may argue that the difference between the two regioisomers might be explained by the negative inductive effect (−I) of the free aliphatic hydroxyl group. Thus, the one closest to the benzene ring would disrupt the resonance stabilization of the phenoxyl radicals more, resulting in a lower antioxidant ability and CAT value. As far as the phenolic esters with primary free hydroxyl (obtained with higher yields), significant improvement in the antioxidant activity was observed with the addition of 2, 4, 6, and 8 carbons in the ester alkyl chain (**4a**, **4b**, **4c**, and **4d**, respectively) when compared to 4-vinyl guaiacol. The non-lipophilized molecule **2** presented a CAT value of 0.40 ± 0.03,

DOI: 10.1021/acs.jafc.5b03551
J. Agric. Food Chem. 2015, 63, 9069−9075

while compounds **4a**−**4d** had CAT values of 0.80 ± 0.05, 0.49 ± 0.04, 0.55 ± 0.01, and 0.57 ± 0.03, respectively. Conversely, their counterparts with 10, 12, 16, and 18 carbons in the alkyl chain (**4f**, **4g**, and **4h**, respectively) showed a lower antioxidant ability in comparison to 4-vinyl guaiacol. The order of antioxidant capacity was C4 > C8 ≈ C6 > C2 ≫ C10 ≥ C12 ≈ C16 > C18, and a clear pattern with respect to the effect of the alkyl chain length on the antioxidant ability was observed. Indeed, the effectiveness of antioxidants has been shown to increase as a function of the increasing alkyl chain length to a critical point (4 carbons), followed by a steady decrease beyond that point when more hydrophobic moieties are linked. This nonlinear effect named "cut-off effect" has already been reported in the literature with similar experiments performed with a series of alkyl chlorogenates, rosmarinates, ferulates, and coumarates.[34−37] In these studies, the antioxidant activities were drastically improved with increasing alkyl chain lengths until an optimized activity ranging between 8 and 12 carbon atoms. In both series of esters synthesized from 4-vinyl guaiacol, the highest antioxidant capacity was obtained with an alkyl chain of 4 carbons.

As previously observed,[38,39] the intrinsic chemical reactivity of an antioxidant toward oxidizing species is not the only factor that governs its activity, with this feature being in fact multifactorial. A suitable location, position, mobility, and concentration of antioxidant at the interface but also its reactivity toward free radical can drastically change antioxidant efficiency. It is now accepted that lipophilization mostly affects antioxidant properties by changing the partitioning of the molecule. In such lipid-based dispersions, the antioxidant molecule may distribute in the aqueous or lipid phase as well as in the intermediate pseudo-phase (interface) as monomer, micelle, or aggregate forms, which results in a different reactivity. Thus, the antioxidant activity of the lipophilized molecules synthesized from 4-vinyl guaiacol can be explained by their polymorphism and partitioning in the present environment. The first group, composed of ethyl ester (**4a**), tends to partition within the aqueous phase with limited interaction with the interface of the lipid droplets where oxidation occurs. Consequently, it displays a CAT value equal to that of the native molecule because of their equivalent polarity (Table 1). The second group formed by butyl ester (**4b**) showed the highest CAT values. This may be explained by a better location of this molecule at the oil/water interface, promoting oil protection against the oxidizing species (R−C$^{\bullet}$, R−COO$^{\bullet}$, etc.) generated by the azo initiator. When the chain length was increased beyond this limit, the amount of esters in the intermediate phase is expected to decrease, while the amount in the lipid phase is supposed to increase, which partly explains the diminution in the CAT values in the third group composed of medium alkyl chains (C6 and C8). Also, these molecules could be found in different polymorphisms: monomers, which may protect oil droplets against oxidation when located at the interface and micelles, which will be only sparsely involved against the lipid droplet oxidation. Finally, the last group composed of esters with 10 or more carbons in the alkyl chain, exhibited very low antioxidant activities because of their high lipophilic character. These compounds are mainly located within the lipid phase, with a limited activity at the interface. Moreover, they might also be physically isolated from the emulsion interface through the formation of aggregates (micelles or precipitates) that reduce their concentration in the reactive interphase.

Generally, phenolic compound lipophilization catalyzed by CAL-B is performed through esterification or transesterification reactions. However, it has been shown in this study that the perhydrolysis activity of lipase B was an efficient way to graft alkyl chains with different lengths on 4-vinyl guaiacol. The chemical structure of this vinylphenol derivative and, particularly, its nucleophilic vinylic double bond contributed to modify the usual reactivity of peracids, leading to the one-pot production of different hydroxyesters by electrophilic addition. Within this addition, the formation of hydroxyesters bearing primary hydroxyl groups was promoted, especially when the chain length of the peracid exceeded eight carbons. The assessment of the antioxidant potency of the resulting hydroxyesters demonstrated that the 4-vinyl guaiacol antioxidant activity was enhanced by the grafting of alkyl chains with 2−8 carbons. Therefore, this new route of phenolipid synthesis through lipophilization of vinylphenols represents a good strategy to promote and optimize the effectiveness of their natural antioxidant activity in the heterophasic system encountered in food emulsions, cosmetics, and biological systems.

■ ASSOCIATED CONTENT

Supporting Information

The Supporting Information is available free of charge on the ACS Publications website at DOI: 10.1021/acs.jafc.5b03551.

NMR spectra and HRMS data of the synthesized products as well as the statistical analysis of CAT values (PDF)

■ AUTHOR INFORMATION

Corresponding Author

*Telephone: +33-4-99-61-24-54. E-mail: aouf@supagro.inra.fr.

Notes

The authors declare no competing financial interest.

■ ACKNOWLEDGMENTS

This work was possible thanks to the support of TERRES INOVIA/France. The authors would like to thank the CNPq/Brazil (Ciência sem Fronteiras) for Erika Zago scholarship.

■ REFERENCES

(1) Balasundram, N.; Sundram, K.; Samman, S. Phenolic compounds in plants and agri-industrial by-products: Antioxidant activity, occurrence, and potential uses. *Food Chem.* **2006**, *99*, 191−203.

(2) Mazandarani, M.; Moghaddam, P. Z.; Zolfaghari, M. R.; Ghaemi, E. A.; Bayat, H. Effects of solvent type on phenolics and flavonoids content and antioxidant activities in Onosma dichroanthum Boiss. *J. Med. Plants Res.* **2012**, *6*, 4481−4488.

(3) Yin, J.; Si, C.-L.; Wang, M.-H. Antioxidant Activity of Flavonoids and Their Glucosidesfrom Sonchus oleraceus L. *J. Appl. Biol. Chem.* **2008**, *51*, 57−60.

(4) Frankel, E. N.; Meyer, A. S. The problems of using one-dimensional methods to evaluate multifunctional food and biological antioxidants. *J. Sci. Food Agric.* **2000**, *80*, 1925−1941.

(5) Kahkonen, M. P.; Hopia, A. I.; Vuorela, H. J.; Rauha, J. P.; Pihlaja, K.; Kujala, T. S.; Heinonen, M. Antioxidant activity of plant extracts containing phenolic compounds. *J. Agric. Food Chem.* **1999**, *47*, 3954−3962.

(6) El-Seedi, H. R.; El-Said, A. M. A.; Khalifa, S. A. M.; Goransson, U.; Bohlin, L.; Borg-Karlson, A.-K.; Verpoorte, R. Biosynthesis, Natural Sources, Dietary Intake, Pharmacokinetic Properties, and Biological Activities of Hydroxycinnamic Acids. *J. Agric. Food Chem.* **2012**, *60*, 10877−10895.

DOI: 10.1021/acs.jafc.5b03551
J. Agric. Food Chem. 2015, 63, 9069−9075

(7) Pratt, D. E.; Hudson, B. J. F. *Natural Antioxidant Not Exploited Commercially*; Hudson, B. J. F., Ed.; Elsevier Science Publishers: London, U.K., 1990; pp 171−191.
(8) Stamatis, H.; Sereti, V.; Kolisis, F. N. Studies on the enzymatic synthesis of lipophilic derivatives of natural antioxidants. *J. Am. Oil Chem. Soc.* **1999**, *76*, 1505−1510.
(9) Cassani, J.; Luna, H.; Navarro, A.; Castillo, E. Comparative esterification of phenylpropanoids versus hydrophenylpropanoids acids catalyzed by lipase in organic solvent media. *Electron. J. Biotechnol.* **2007**, *10*, 508−513.
(10) Compton, D. L.; Laszlo, J. A.; Berhow, M. A. Lipase-catalyzed synthesis of ferulate esters. *J. Am. Oil Chem. Soc.* **2000**, *77*, 513−519.
(11) Topakas, E.; Stamatis, H.; Biely, P.; Kekos, D.; Macris, B. J.; Christakopoulos, P. Purification and characterization of a feruloyl esterase from Fusarium oxysporum catalyzing esterification of phenolic acids in ternary water-organic solvent mixtures. *J. Biotechnol.* **2003**, *102*, 33−44.
(12) Guyot, B.; Bosquette, B.; Pina, M.; Graille, J. Esterification of phenolic acids from green coffee with an immobilized lipase from Candida antarctica in solvent-free medium. *Biotechnol. Lett.* **1997**, *19*, 529−532.
(13) Vosmann, K.; Weitkamp, P.; Weber, N. Solvent-free lipase-catalyzed preparation of long-chain alkyl phenylpropanoates and phenylpropyl alkanoates. *J. Agric. Food Chem.* **2006**, *54*, 2969−2976.
(14) Weitkamp, P.; Vosmann, K.; Weber, N. Highly efficient preparation of lipophilic hydroxycinnamates by solvent-free lipase-catalyzed transesterification. *J. Agric. Food Chem.* **2006**, *54*, 7062−7068.
(15) Cabrera, Z.; Gutarra, M. L. E.; Guisan, J. M.; Palomo, J. M. Highly enantioselective biocatalysts by coating immobilized lipases with polyethyleneimine. *Catal. Commun.* **2010**, *11*, 964−967.
(16) Garcia-Urdiales, E.; Alfonso, I.; Gotor, V. Enantioselective enzymatic desymmetrizations in organic synthesis. *Chem. Rev.* **2005**, *105*, 313−354.
(17) Paal, T. A.; Forro, E.; Liljeblad, A.; Kanerva, L. T.; Fulop, F. Lipase-catalyzed kinetic and dynamic kinetic resolution of 1,2,3,4-tetrahydroisoquinoline-1-carboxylic acid. *Tetrahedron: Asymmetry* **2007**, *18*, 1428−1433.
(18) Bernhardt, P.; Hult, K.; Kazlauskas, R. J. Molecular basis of perhydrolase activity in serine hydrolases. *Angew. Chem., Int. Ed.* **2005**, *44*, 2742−2746.
(19) Chen, X. C.; Gu, W. X.; Jing, X. B.; Pan, X. F. A new approach for synthesis of erythro 8-O-4 ′ neolignans. *Synth. Commun.* **2002**, *32*, 557−564.
(20) Das, B.; Kashinatham, A.; Srinivas, K. V. Alkamides and other constituents of Piper longum. *Planta Med.* **1996**, *62*, 582−582.
(21) Lasekan, O. O.; Feijao Teixeira, J. P.; Salva, T. J. G. Volatile flavour compounds of cooked acha (Digitaria exilis Stapf). *Food Chem.* **2001**, *75*, 333−337.
(22) Joint FAO/WHO Expert Committee on Food Additives (JECFA). *Evaluation of Certain Food Additives and Contaminants*; World Health Organization (WHO): Geneva, Switzerland, 2001; WHO Rechnical Report Series 901.
(23) Lee, S. M.; Frechet, J. M. J.; Willson, C. G. Photo-cross-linking of poly(4-hydroxystyrene) via electrophilic aromatic-substitution - use of polyfunctional benzylic alcohols in the design of chemically amplified resist materials with tunable sensitivities. *Macromolecules* **1994**, *27*, 5154−5159.
(24) Orellana-Coca, C.; Adlercreutz, D.; Andersson, M. M.; Mattiasson, B.; Hatti-Kaul, R. Analysis of fatty acid epoxidation by high performance liquid chromatography coupled with evaporative light scattering detection and mass spectrometry. *Chem. Phys. Lipids* **2005**, *135*, 189−199.
(25) Sinha, A. K.; Sharma, A.; Joshi, B. P. One-pot two-step synthesis of 4-vinylphenols from 4-hydroxy substituted benzaldehydes under microwave irradiation: a new perspective on the classical Knoevenagel−Doebner reaction. *Tetrahedron* **2007**, *63*, 960−965.
(26) Mancilla, G.; Femenia-Rios, M.; Grande, M.; Hernandez-Galan, R.; Macias-Sanchez, A. J.; Collado, I. G. Enantioselective, chemoenzymatic synthesis, and absolute configuration of the antioxidant (−)-gloeosporiol. *Tetrahedron* **2010**, *66*, 8068−8075.
(27) Runarsson, O. V.; Malainer, C.; Holappa, J.; Sigurdsson, S. T.; Masson, M. *tert*-Butyldimethylsilyl O-protected chitosan and chitooligosaccharides: useful precursors for N-modifications in common organic solvents. *Carbohydr. Res.* **2008**, *343*, 2576−2582.
(28) Björkling, F.; Godtfredsen, S. E.; Kirk, O. Lipase-mediated formation of peroxycarboxylic acids used in catalytic epoxidation of alkenes. *J. Chem. Soc., Chem. Commun.* **1990**, 1301−1303.
(29) Tornvall, U.; Orellana-Coca, C.; Hatti-Kaul, R.; Adlercreutz, D. Stability of immobilized Candida antarctica lipase B during chemoenzymatic epoxidation of fatty acids. *Enzyme Microb. Technol.* **2007**, *40*, 447−451.
(30) Sarma, K.; Bhati, N.; Borthakur, N.; Goswami, A. A novel method for the synthesis of chiral epoxides from styrene derivatives using chiral acids in presence of Pseudomonas lipase G6 PSL G6 and hydrogen peroxide. *Tetrahedron* **2007**, *63*, 8735−8741.
(31) Lefort, D.; Fossey, J.; Gruselle, M.; Nedelec, J. Y.; Sorba, J. Reactivity and selectivity of homolytic substitution-reactions on the peroxyacid group. *Tetrahedron* **1985**, *41*, 4237−4252.
(32) Figueroa-Espinoza, M. C.; Villeneuve, P. Phenolic acids enzymatic lipophilization. *J. Agric. Food Chem.* **2005**, *53*, 2779−2787.
(33) Laguerre, M.; Lopez-Giraldo, L. J.; Lecomte, J.; Barea, B.; Cambon, E.; Tchobo, P. F.; Barouh, N.; Villeneuve, P. Conjugated autoxidizable triene (CAT) assay: A novel spectrophotometric method for determination of antioxidant capacity using triacylglycerol as ultraviolet probe. *Anal. Biochem.* **2008**, *380*, 282−290.
(34) Bayrasy, C.; Chabi, B.; Laguerre, M.; Lecomte, J.; Jublanc, E.; Villeneuve, P.; Wrutniak-Cabello, C.; Cabello, G. Boosting Antioxidants by Lipophilization: A Strategy to Increase Cell Uptake and Target Mitochondria. *Pharm. Res.* **2013**, *30*, 1979−1989.
(35) Laguerre, M.; López Giraldo, L. J.; Lecomte, J.; Figueroa-Espinoza, M.-C.; Barea, B.; Weiss, J.; Decker, E. A.; Villeneuve, P. Chain Length Affects Antioxidant Properties of Chlorogenate Esters in Emulsion: The Cutoff Theory Behind the Polar Paradox. *J. Agric. Food Chem.* **2009**, *57*, 11335−11342.
(36) López-Giraldo, L. J. *Lipophilisation Enzymatique de Composés Phénoliques et Évaluation de Leurs Propriétés Antioxydantes (Enzymatic Lipophilization of Phenolic Compounds and Evaluation of Their Antioxidant Properties)*; Montpellier SupAgro: Montpellier, France, 2008.
(37) Sørensen, A.-D. M.; Durand, E.; Laguerre, M.; Bayrasy, C.; Lecomte, J.; Villeneuve, P.; Jacobsen, C. Antioxidant Properties and Efficacies of Synthesized Alkyl Caffeates, Ferulates, and Coumarates. *J. Agric. Food Chem.* **2014**, *62*, 12553−12562.
(38) Panya, A.; Laguerre, M.; Bayrasy, C.; Lecomte, J.; Villeneuve, P.; McClements, D. J.; Decker, E. A. An Investigation of the Versatile Antioxidant Mechanisms of Action of Rosmarinate Alkyl Esters in Oil-in-Water Emulsions. *J. Agric. Food Chem.* **2012**, *60*, 2692−2700.
(39) Laguerre, M.; Bayrasy, C.; Panya, A.; Weiss, J.; McClements, D. J.; Lecomte, J.; Decker, E. A.; Villeneuve, P. What Makes Good Antioxidants in Lipid-Based Systems? The Next Theories Beyond the Polar Paradox. *Crit. Rev. Food Sci. Nutr.* **2015**, *55*, 183−201.

DOI: 10.1021/acs.jafc.5b03551
J. Agric. Food Chem. 2015, 63, 9069−9075

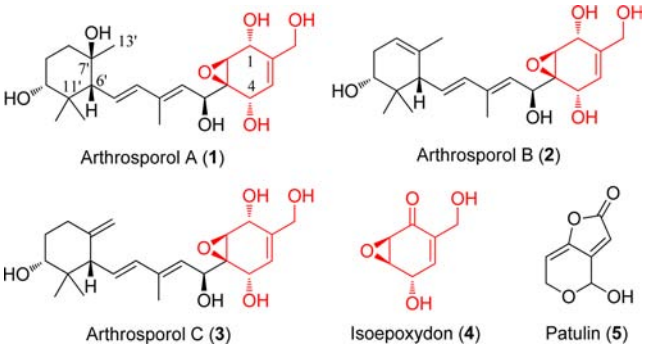

Figure 1. Arthrosporols A–C (**1**–**3**) from nematode-trapping fungus *A. oligospora*, isoepoxydon (**4**), and patulin (**5**).

been evoking our great interest in the biosynthesis of this class of naturally occurring metabolites from *A. oligospora*.

We now report the identification of the polyketide synthase (PKS) gene encoding 6-methylsalicylic acid synthase involved in the biosynthesis of the arthrosporol metabolites in *A. oligospora*. The effect of disruption of the PKS gene on the production of arthrosporol metabolites was investigated. The formation of adhesive trapping networks and capture of nematodes by the mutant strain were also studied. Our results suggested that the PKS gene might play an important role in regulating the trap formation and the lifestyle switching of this fungus.

MATERIALS AND METHODS

Sequence and Phylogenetic Analysis of *AOL_s00215g283* in *A. oligospora*. Predicted *AOL_s00215g283* in *A. oligospora* was annotated by BLAST searches against protein databases and InterProScan searches against protein domain databases. The amino acid sequence of AOL_s00215g283 in *A. oligospora* was downloaded from GenBank, and the sequences from different fungi were downloaded from GenBank. The amino acid sequences from different fungi were analyzed using the DNAman software package, version 5.2.2 (Lynnon Biosoft, Vaudreuil, Quebec, Canada). A neighbor-joining tree was constructed using the Mega 5.1 software package. A web-based analysis platform antiSMASH 2.0[15] was applied to perform genome mining of the biosynthetic gene clusters. The conserved functional domains were analyzed using InterProScan 4.8 with default parameter settings.

Fungal Material. The strain *A. oligospora* YMF 1.3170 was isolated from Jiuquan, Gansu, People's Republic of China,[14] and identified as *A. oligospora* by morphological features. The isolate was deposited in the strain collection of the Laboratory for Conservation and Utilization of Bio-Resources and Key Laboratory for Microbial Resources of the Ministry of Education, Yunnan University. After the conidia of *A. oligospora* YMF 1.3170 had developed on potato dextrose agar (PDA) slants in test tubes at 25 °C, the strain was kept at −30 °C as stock cultures. DNA extraction of *A. oligospora* YMF 1.3170 and polymerase chain reaction (PCR) amplification of the internal transcribed spacer (ITS) rRNA gene were carried out according to the literature. A characteristic fragment (GenBank accession number JX244893) was amplified by PCR using the species-specific primers ITS4 and ITS5 and the genome DNA of *A. oligospora* YMF 1.3170 as the template. The BLAST searches in the GenBank showed that the DNA fragment was most similar to the published ITS sequences of *A. oligospora*, consistent with morphological identifications.

Disruption Vector Construction. The plasmid pAg1-H3,[16] which was used for gene disruption vector construction and transformation, was maintained in *Escherichia coli* strain DH5a (Takara, Shiga, Japan). The strain *A. oligospora* YMF 1.3170 used in this study was maintained on PDA at 28 °C. Genomic DNA of *A. oligospora* YMF 1.3170 was extracted as previously described.[17] Restriction endonucleases and DNA-modifying enzymes were from New England Biolabs (Beverly, MA). In-Fusion HD Cloning Kits were from Clontech Laboratories (Mountain View, CA). The left and right DNA fragments flanking the hygromycin-resistant gene (hygR) in pAg1-H3 vector were PCR-amplified from the genomic DNA of *A. oligospora* YMF 1.3170 by GXL high-fidelity DNA polymerase (Takara, Shiga, Japan), using primer sets 283-5f, GAGCTCGGTACCAAGGCCCGGGGGAGCCGCAGAGGACAACA; 283-5r, AGGCCTGATCATCGATGGGCCCCGACATGCCATGCCGATT; 283-3f, TCTAGAGGATCCCCCGACTAGTATTATCGGTAGCCTTTGTC; and 283-3r, CACGAAGCTTGCATGCCTGCAGGAGGATTCGGTATTGTTGTT. The DNA fragments (5′ flank and 3′ flank) were purified using NucleoSpin Gel and PCR Clean-up Kit (Macherey-Nagel, Düren, Germany). The purified 5′ flank DNA fragment was inserted into the *Sma*I- and *Apa*I-digested pAg1-H3 vector by the in-fusion method to produce pAg1-H3-283-5′. Similarly, the 3′ flank DNA fragment was inserted into the *Spe*I and *Sbf*I sites of pAg1-H3-283-5′ to generate the completed disruption vector pAg1-H3-283-5′-3′.

The homologous fragment amplifications were carried out as follows. A total of 1 μL of the prepared genomic DNA template from *A. oligospora* YMF 1.3170 was added to a 50 μL PCR amplification system using GXL high-fidelity DNA polymerase following the instructions of the manufacturer (Takara). All PCRs were carried out in a Veriti 96-well thermal cycler (PE Applied Biosystems). The amplification program consisted of predenaturation at 95 °C for 3 min, followed by 30 cycles of denaturation at 98 °C for 10 s, annealing at 57 °C for 15 s, and elongation at 68 °C for 2 min, with a final extension step at 68 °C for 10 min.

Preparation of Fungal Protoplasts. Regeneration medium PDASS (PDA supplied with 0.6 M sucrose, 0.3 g/L yeast extract, 0.3 g/L tryptone, and 0.3 g/L peptone) was used for protoplast regeneration,[18] and PDASS supplemented with 200 μg/mL hygromycin B (Amresco, Solon, OH) was used for selecting transformants. In the initial transformation for the disruption of the PKS gene, four 1 cm diameter mycelia plugs from YMA medium (2 g/L yeast extract, 10 g/L malt extract, and 18 g/L agar) for 7 days at 28 °C were inoculated into 100 mL of TG medium consisting of 1% tryptone (Oxoid, Basingstoke, U.K.) and 1% glucose and cultures at 30 °C and 180 rpm for 36 h. The mycelia were harvested and resuspended in 20 mL of a filter-sterilized enzyme solution that contained 120 mg of lysing enzymes (Sigma, St. Louis, MO), 0.4 mL of cellulase (Sigma, St. Louis, MO), and 100 mg of snailase (Solarbio, Beijing, China) in 0.6 M $MgSO_4$ at pH 6.0. Snailase, extracted from the crop and digestive tract of snails, consists of more than 30 enzymes, including cellulase, hemicellulase, β-glucuronidase, etc. The suspension was incubated for 4 h at 28 °C on a rotary shaker at 180 rpm. Protoplasts were collected by filtering through six layers of sterile lens-cleaning tissue and centrifuged at 1000*g*. The protoplasts were washed twice with KTC (1.2 M KCl, 10 mM Tris-HCl, and 50 mM $CaCl_2$) solution and finally resuspended in the same solution.

Transformation of Fungus *A. oligospora*. The protoplast-based protocol for the gene disruption in *A. oligospora* YMF 1.3170 was performed as described in a previous report,[18] with modifications. A total of 100 μL of protoplasts (ca. 8.0×10^7 mL^{-1}) were mixed with 10 μg of linear DNA in a 1.5 mL centrifuge tube. After 30 min of incubation on ice, 600 μL of PTC (50% polyethylene glycol 6000, 20 mM Tris–HCl at pH 7.5, and 50 mM $CaCl_2$) was added to the mixture and mixed gently. After incubation at 28 °C for 1 h and regeneration for 12 h, the putatively transformed protoplasts were plated onto PDAS medium (PDA supplemented with 5 g/L molasses, 0.6 M saccharose, 0.3 g/L yeast extract, 0.3 g/L tryptone, and 0.3 g/L casein peptone) containing 200 μg/mL hygromycin B (Roche Corporation, Germany). The transformation colonies were selected after incubation at 28 °C for 6–7 days. After single-spore isolation, the putative transformants were transferred onto TYGA medium alone (10 g/L tryptone, 10 g/L glucose, 5 g/L yeast extract, 5 g/L molasses, and 18 g/L agar) containing 200 μg/mL hygromycin B and incubated for 5 days at 28 °C. Genomic DNA of putative transformants were extracted and verified by PCR to check for the integration of genes in

DOI: 10.1021/acs.jafc.5b04244
J. Agric. Food Chem. 2015, 63, 9076–9082

the genome. The positive transformants were further confirmed by Southern blot analyses. Southern analysis was carried out according to the instructions provided by the North2South chemiluminescent hybridization and detection kit (Pierce, Rockford, IL). The primer pair 283-S1 (TTGGAGAAACCGAACAACCT) and 283-S2 (TTGGTGAGGAGTGAATAGCG) were used as Southern hybridization probes, and restriction enzyme *Ssp*I was used to digest the genomic DNA of the wild-type *A. oligospora* and the mutant strains for Southern analysis.

Vegetative Growth and Conidia Yield Comparisons. The 9 mm diameter mycelia plugs from 7-day-old fungal colonies of the wild-type and mutant strains were inoculated onto 9 cm plates with different media (6 replicates/strain). The mycelia plugs of the same size and age were incubated at 28 °C at both light and dark conditions for 6−10 days, respectively. Radial colony growth rates and colony morphology were recorded at a 24 h interval for 1 week, and the growth rate was calculated as millimeters per hour each day. The growth rates and colony morphology of the wild-type and mutant strains were compared in PDA, YMA (2 g/L yeast extract, 10 g/L malt extract, and 18 g/L agar), and TYGA (10 g/L tryptone, 10 g/L glucose, 5 g/L yeast extract, 5 g/L molasses, and 18 g/L agar) media. Similarly, to test the adaptive abilities, the growth rates were compared in TGA medium supplemented with stress-related compounds, including 0.1−0.3 mol/L NaCl, 5−15 mmol/L H_2O_2, and 0.01−0.03% sodium dodecyl sulfate (SDS).

To assess sporulation capacities of the wild-type and mutant strains, 100 μL aliquots of conidial suspension were spread on 9 cm plates with YMA medium and incubated for 10 days at 28 °C and the conidia were washed in 10 mL of sterile water, followed by filtration through four layers of lens tissues to remove mycelial debris. The concentrations of the conidial suspension were determined with microscopic counts on a hemocytometer.[18]

Induction of Trap Formation and Virulence Assays. *Caenorhabditis elegans* (strain N2) was cultured in oatmeal medium at 22 °C for 6−7 days. The wild-type and mutant strains were cultivated on agar plates by spreading approximately 10^6 conidia per plate. After 3 days of incubation at 28 °C, 300 adult nematodes were added to the middle of the plate. Fungal mycelia and traps were observed, and the numbers of captured nematodes were recorded after 12 and 24 h, respectively, under light microscopy (Olympus, Tokyo, Japan). The experiments were performed in triplicate.

Fermentation and Extraction Procedures. The wild-type *A. oligospora* and the Δ*AOL_s00215g283* mutant strains cultured on PDA medium at 28 °C for 7 days were inoculated into 500 mL flasks containing 250 mL of production PD medium (200 g/L potato and 20 g/L dextrose). The culture broths of the 14-day-old liquid fermentations (1.5 L each strain) were filtered to separate the mycelia from the cultures. The culture filtrates were concentrated *in vacuo* to 50 mL and were exhaustively extracted overnight with ethyl acetate (1:1, v/v). The organic fractions were evaporated to dryness to give residues. The dried organic residues were then dissolved in 500 μL of methanol, filtered through 0.22 μm membranes, and further analyzed using high-performance liquid chromatography with photodiode array detection (HPLC−DAD) and gas chromatography−mass spectrometry (GC−MS).

HPLC Analysis. HPLC analysis was carried out using a HPLC-1200 series (Agilent, Waldbronn, Germany) system equipped with a G1311A binary pump and G1315A photodiode array ultraviolet/visible (UV/vis) detector, employing the following instrumental conditions: column, CAPCELL PAK C18, 5 μm, 4.6 × 250 mm (Shiseido). The total flow rate was 1 mL/min; mobile phase A was 0.1% formic acid in water; and mobile phase B was 0.1% formic acid in acetonitrile. The column temperature was maintained at 40 °C. The injection volume for the extracts was 25 μL. The liquid chromatography (LC) conditions were manually optimized on the basis of separation patterns with the following gradient: 0−2 min, 10% B; 10 min, 25% B; 30 min, 35% B; 35 min, 50% B; 45 min, 90% B; 47 min, 10% B; and 49 min, 10% B. UV spectra were recorded at 220−400 nm. The standard sample arthrosporol A was isolated from wild-type *A. oligospora* according to the modified method described in the literature.[14] A 14-day-old fermentation broth of strain *A. oligospora* YMF 1.3170 cultured on PDA medium was filtered to separate the mycelia from the culture. The culture filtrate was concentrated *in vacuo* and partitioned with acetyl acetate, and the organic part was evaporated to dryness to give an oily residue. The residue was loaded onto a macroporous resin column (7 × 80 cm) and eluted with H_2O−MeOH (0, 25, 50, and 90%, each in 3 L) to yield four fractions (A−D) based on thin-layer chromatography (TLC) behavior. Fraction C obtained on elution with 50−90% MeOH−H_2O was further subjected to a Sephadex LH-20 gel column (4 × 150 cm) eluting with MeOH (2.5 L) to yield six subfractions. Subfraction 3 was repeatedly subjected to a Sephadex LH-20 gel column (3 × 100 cm) eluting with acetone (2.3 L), a C18 column (3 × 50 cm) eluting with H_2O−MeOH (35, 37, and 39%, each in 1.8 L), and a silica gel column (2 × 40 cm) eluting with $CHCl_3$−MeOH (35:1 and 20:1, each in 1.5 L) to obtain arthrosporol A. The purified sample arthrosporol A was elucidated and confirmed with nuclear magnetic resonance (NMR) data.[14]

GC−MS Analysis, Metabolite Identification, and Semi-quantitation. The GC−MS analysis was performed with a 5890 series II Plus gas chromatograph interfaced with a model 5972 mass spectrometric detector (Hewlett-Packard, Avondale, PA) equipped with a 30 m long, 0.25 mm inner diameter, and 0.5 μm film thickness HP5-MS capillary column. The temperature was programmed from 100 to 300 °C at a rate of 5 °C/min. Helium was used as a carrier gas at a flow rate of 0.7 mL/min. The split ratio was 1:20; the injector temperature was 280 °C; the interface temperature was 300 °C; and the ionization voltage was 70 eV.

Identification of these peaks was performed through retention time index and mass spectrum.[19] Compounds were designated as metabolites if they were identified with a match 900 on a scale of 0−1000 and retention index (RI) deviation of 3.0. The semi-quantitative analysis of the main compounds was carried out by internal normalization with the area of each compound. The addition of each area of the compounds corresponds to 100% area.[20]

Statistical Analysis. Statistical analysis were performed using the SPSS package, version 17.0 for Windows (Chicago, IL). Differences with $p < 0.05$ were regarded as statistically significant, and differences with $p < 0.01$ were regarded as highly statistically significant.

RESULTS AND DISCUSSION

The arthrosporol metabolites possess a novel hybrid carbon skeleton consisting of a polyketide-derived epoxycyclohexenol combined with a terpenoid-derived monocyclic sesquiterpenol substructure. Arthrosporols B (**2**) and C (**3**) were assumed to be two dehydration derivatives of arthrosporol A (**1**).[14] All of the arthrosporols shared the same epoxycyclohexenol moiety, and the difference among them only occurred in the monocyclic sesquiterpenol substructure. From the biosynthetic point of view, a PKS gene should be involved in the production of arthrosporols in nematode-trapping fungus *A. oligospora*.

A search for the epoxycyclohexenol moiety in the SciFinder database found that the epoxycyclohexenol moiety of arthrosporols was quite similar to a known compound isoepoxydon (**4**) (Figure 1).[21] They even shared the same stereochemistry for the epoxy ring and the hydroxyl group at C-4. The only difference between them was that the hydroxyl group at C-1 in the epoxycyclohexenol moiety of arthrosporols was replaced by a ketone at C-1 in isoepoxydon.

Isoepoxydon is an important intermediate metabolite for the biosynthesis of a well-studied antibiotic and mycotoxin, patulin (**5**). Patulin a toxic chemical contaminant produced by *Aspergillus*, *Penicillium*, and *Byssochlamys* spp.[22] It is the most common mycotoxin found in apples and apple-derived products, such as juice, cider, compotes, and other food, intended for young children. The fact that exposure to this mycotoxin is associated with immunological, neurological, and gastrointestinal outcomes has led to patulin being included

DOI: 10.1021/acs.jafc.5b04244
J. Agric. Food Chem. 2015, 63, 9076−9082

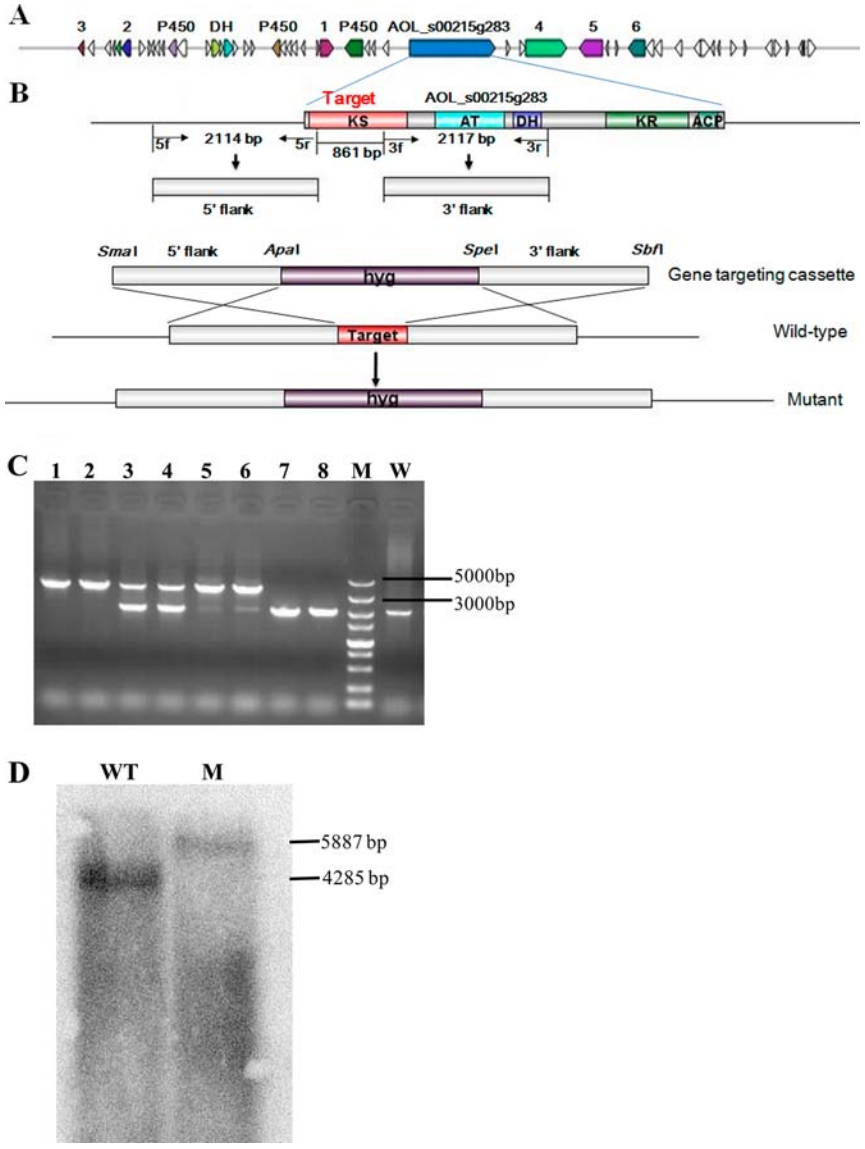

Figure 2. *AOL_s00215g283* gene cluster and schematic diagram of gene disruption. (A) *AOL_s00215g283* gene cluster spanning 51.843 kb and consisting of 11 genes with their predicted functions color-coded: 1, amidohydrolase (AOL_s00215g281); 2, mannose-6-phosphate isomerase (AOL_s00215g277); 3, polyprenyltransferase (AOL_s00215g276); 4, DNA translocase (AOL_s00215g284); 5, Gcd10p family (AOL_s00215g285); 6, single-stranded nucleic-acid-binding domain (AOL_s00215g286); P450, cytochrome P450s (AOL_s00215g282, AOL_s00215g280, and AOL_s00215g278); and DH, dehydrogenase (AOL_s00215g279). (B) Sketch map of the replacement of the targeting gene using a homologous recombination method. (C) Transformants confirmed by the PCR method: W, wild-type strain; lanes 1 and 2, two Δ*AOL_s00215g283* mutants; M, marker (DL5000). (D) Southern analysis of the wild-type strain (WT) and the Δ*AOL_s00215g283* mutant (M). The genomic DNA was digested using *Ssp*I.

among mycotoxins whose level in food is regulated in many countries around the world.[23] Similar to several other major mycotoxins, including aflatoxins, fumonisins, zearalenone, and ochratoxins, patulin is a polyketide metabolite.[24] The first step in the biosynthesis of patulin needs the involvement of a PKS, identified as 6-methylsalicylic acid synthase.[25] The most recent study revealed that 6-methylsalicylic acid synthase is also involved in the production of a meroterpenoid antibiotic yanuthone D in *Aspergillus niger*.[26]

Bioinformatic analysis of the *A. oligospora* genome identified five putative PKS genes. Among these genes, the gene *AOL_s00215g283* was annotated for type I PKS synthase.[17] Sequence analysis and a database search using the BLASTP program revealed that the amino acid sequence of AOL_s00215g283 shared 53% similarity to 6-methylsalicyclic acid synthases from *Endocarpon pusillum* (XP_007785679.1), *Byssochlamys nivea* (AAK48943.1), and *Aspergillus terreus* (BAA20102.2 and XP_001215453.1). A total of 42 homologues of AOL_s00215g283 were retrieved, and a neighbor-joining phylogenetic tree was built using these amino acid sequences of these proteins. From this tree, we found that AOL_s00215g283 was clustered within the fungal polyketide synthases and formed a distinct monophyletic branch with no other closely related PKS as of yet. Strangely, no homologues identified from other nematode-trapping fungi, such as *Dactylellina haptotyla* and *Drechslerella stenobrocha*,[17] clustered with the amino acid sequence of AOL_s00215g283.

A previous study revealed that the genes involved in the patulin biosynthesis pathway have been found to be located in a cluster on one chromosome as is the case for a large number of

DOI: 10.1021/acs.jafc.5b04244
J. Agric. Food Chem. 2015, 63, 9076−9082

mycotoxin pathways.[24] Five genes in the early portion of the patulin biosynthesis pathway up to the production of isoepoxydon have been identified as *PatK*, *PatG*, *PatH*, *PatI*, and *PatN*, encoding 6-methylsalicylic acid synthase, 6-methylsalicylic acid decarboxylase, and three cytochrome P450s, including *m*-cresol hydroxylase (P450), *m*-hydroxybenzyl alcohol hydroxylase (P450), and isoepoxydon dehydrogenase (P450), respectively.[22]

The analysis of the similar cluster involved in the biosynthesis of isoepoxydon in the *A. oligospora* genome was carried out. Through antiSMASH 2.0, a cluster containing the predicted PKS gene *AOL_s00215g283* was identified (Figure 2A). Most notably, the upstream flanking region of the gene *AOL_s00215g283* encodes an amidohydrolase (AOL_s00215g281), a dehydrogenase (AOL_s00215g279), a mannose-6-phosphate isomerase (AOL_s00215g277), a polyprenyltransferase (AOL_s00215g276), and three cytochrome P450s (AOL_s00215g278, AOL_s00215g280, and AOL_s00215g282). Interestingly, the downstream flank of the cluster encodes a DNA translocase (AOL_s00215g284), a member of the Gcd10p family (AOL_s00215g285), and a single-stranded nucleic-acid-binding domain (AOL_s00215g286). The amino acid sequence of AOL_s00215g281 shares 55% similarity to the 6-methylsalicylic acid decarboxylase (PatG). The amino acid sequence of AOL_s00215g282 shares 48 and 44% similarity to cytochrome P450s, PatH and PatI, respectively.

All of the above indicated that the gene cluster with the gene *AOL_s00215g283* was likely involved in the production of 6-methylsalicylic acid, which was predicted to be the first precursor for the biosynthesis of the polyketide-derived epoxycyclohexenol in arthrosporols.

To investigate the biological function of the gene *AOL_s00215g283*, the target fragment of this gene was knocked out by homologous recombination. Conserved domain analysis demonstrated that the gene *AOL_s00215g283* encoded five typical catalytic domains, including ketide synthase (KS), acyltransferase (AT), dehydratase (DH), *β*-ketoacylreductase domain (KR), and acyl carrier protein (ACP) for the PKS (Figure 2A). The fragment in the sequence encoding the KS domain was chosen to be the target. A modified method for genetic disruption of the gene *AOL_s00215g283* was developed using double-crossover recombination with the hygromycin-resistance gene (hyg) as a selection marker. The two homologous regions were amplified from *A. oligospora* genomic DNA using primers containing overlapping regions with the vector and the hyg-resistance cassette (Figure 2B). The disruption vector was transformed into the protoplasts of *A. oligospora* and yielded 20 transformants. Genomic DNAs of these transformants were isolated, and the site-specific insertion were confirmed using diagnostic PCR. In comparison to a 2035 bp fragment from the wild-type strain of *A. oligospora*, a 3637 bp fragment was amplified from the transformants using the primers 283yz-5f/283yz-3r (Figure 2C). In addition, these transformants were further confirmed using Southern blot analysis; the single band hybridizing the Δ*AOL_s00215g283* gene probe was observed in the wild-type strains and transformants (Figure 2D); and the sizes of the hybridized bands were consistent with expectation, indicating that the sequence encoding for the KS domain in the gene *AOL_s00215g283* in the mutant Δ*AOL_s00215g283* strain was disrupted. In comparison to the wild-type strain, the mutant Δ*AOL_s00215g283* strain showed similar growth rates and conditions on YMA, PDA, and TYGA media (Figure 3) and displayed a slight reduction in conidiation on the YMA

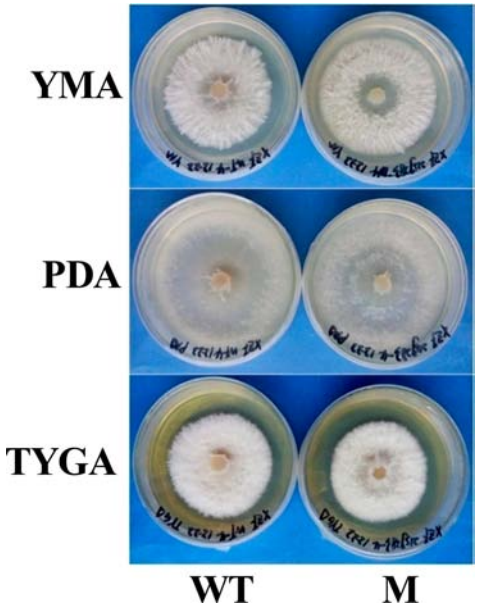

Figure 3. Comparison of the mycelia growths of the wild-type and mutant Δ*AOL_s00215g283* strains on YMA, PDA, or TYGA for 6 days at 28 °C.

medium. Similarly, both the mutant Δ*AOL_s00215g283* and wild-type strains exhibited the same growths in the presence of stress-related compounds. However, the mutant Δ*AOL_s00215g283* strain formed more adhesive networks than the wild-type strain after the nematodes were added on the 4 day cultures (Figure 4). After 12 h, the number of adhesive networks formed by the mutant Δ*AOL_s00215g283* was 318 cm^{-2} (Figure 4B), 10 times more than that of the wild-type strain (27 cm^{-2}). At the same time, the number of captured nematodes by the mutant Δ*AOL_s00215g283* was more than twice that of the wild-type strain (Figure 4C).

It was obvious that the mutant Δ*AOL_s00215g283* strain cultivated in liquid PDB for 14 days yielded light-colored culture compared to the wild-type strain. Both cultures were extracted, and the extracting organic portions were dried under *vacuo* to give a 276 mg extract for the wild-type strain and 54 mg for the mutant Δ*AOL_s00215g283*. The weight of the extract from the mutant Δ*AOL_s00215g283* strain was less than one-fifth of that from the wild-type strain. To investigate the involvement of the gene *AOL_s00215g283* in the biosynthesis of arthrosporols, both the extracts were then analyzed with the HPLC−DAD method (Figure 5). It is noteworthy that the HPLC metabolite profile of the mutant Δ*AOL_s00215g283* strain showed a significant difference from that of the wild-type strain. In comparison to the wild-type strain, the mutant Δ*AOL_s00215g283* strain lacked almost most of the peaks during the retention times ranging between 21 and 40 min in the HPLC chromatogram (Figure 5A). This was consistent with the above result that much less extract was obtained from the mutant Δ*AOL_s00215g283* strain. Further detailed analysis showed that no arthrosporol A was detected in the cultural broth of the mutant Δ*AOL_s00215g283* strain (Figure 5B), indicating that the disruption of the *AOL_s00215g283* gene led to a total loss of arthrosporol A

DOI: 10.1021/acs.jafc.5b04244
J. Agric. Food Chem. 2015, 63, 9076−9082

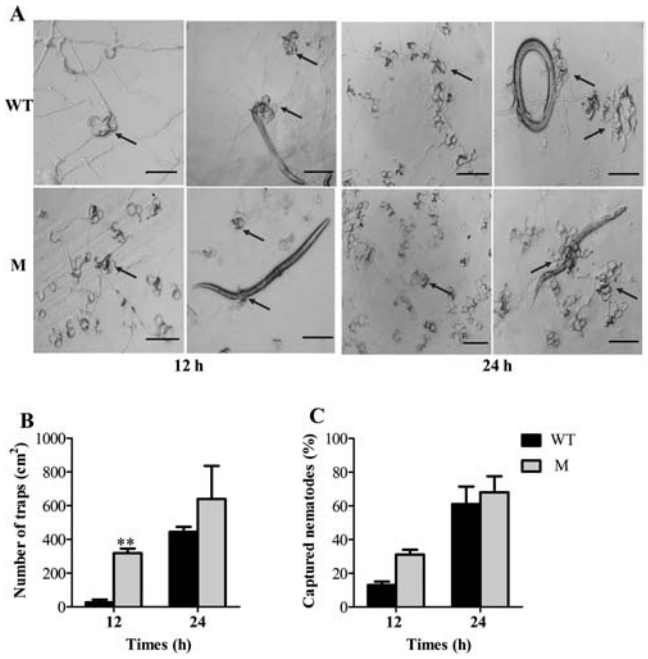

Figure 4. Comparison of trap formations and captured nematodes between the wild-type and mutant Δ*AOL_s00215g283* strains. (A) Formation of traps of the wild-type and mutant Δ*AOL_s00215g283* strains at 12 and 24 h: WT, wild-type strain; M, mutant Δ*AOL_s00215g283*. Scale bar = 50 μm. (B) Comparison of the trap formations. (**) $p < 0.01$ versus the wild-type strain. (C) Comparison of the fungal nematicidal activity against *C. elegans*.

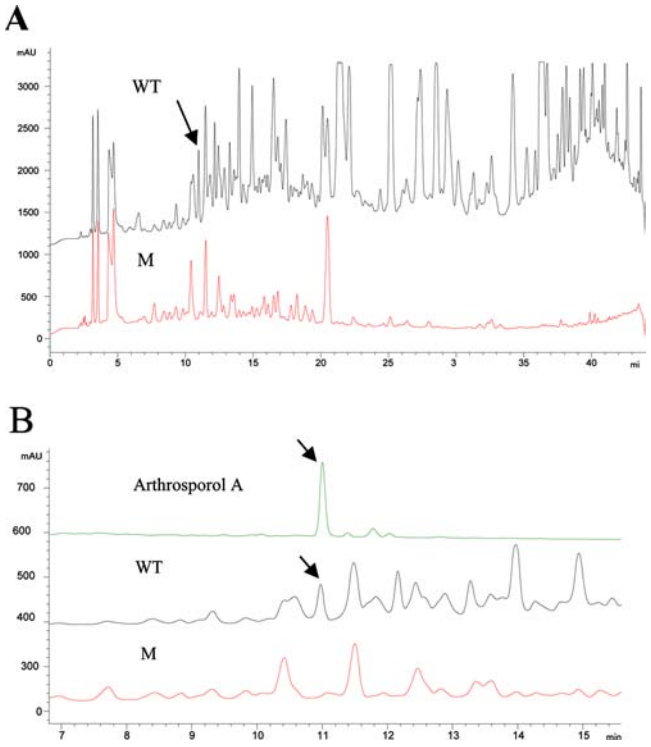

Figure 5. (A) HPLC analysis of the methanol extracts of the cultural broths from the wild-type strain (black line) and Δ*AOL_s00215g283* mutant (red line). (B) Amplified portion of the HPLC spectrum of the methanol extracts of the cultural broths from the wild-type strain (black line), mutant Δ*AOL_s00215g283* (red line), and arthrosporol A (green line). Black arrows indicate the peak of arthrosporol A at around 11 min.

and the gene *AOL_s00215g283* played a key role in the biosynthetic pathway for arthrosporol A.

Considering the possibility that the lack of the epoxycyclohexenol moiety caused by the disruption of the *AOL_s00215g283* gene might lead to the accumulation of the terpenoid-derived sesquiterpenol substructure, together with the fact that most sesquiterpenoids are volatile compounds, the culture broth of the wild-type and mutant Δ*AOL_s00215g283* strains were further analyzed by the GC−MS method. Surprisingly, two linear sesquiterpenoids, sesquirosefuran and 3,7,11-trimethyl-2,6,10-dodecatrienal, were found only in the wild-type strain. It is likely that the disruption of the *AOL_s00215g283* gene might also affect the production of the farnesol derivatives in *A. oligospora*.

A previous study displayed that farnesol secreted by *Candida albicans* could block the transition from yeast to hypha.[27] Reports of farnesol production by ascomycetes other than yeasts are rare, although some studies reported that farnesol blocked conidiation of *A. niger*,[28] inhibited cell wall integrity signaling and caused mislocalization of regulatory Rho proteins in *Aspergillus fumigatus*,[29] and also inhibited growth of other ascomycetes, for example, that of *Fusarium graminearum*.[30] In addition, farnesol displayed an intriguing effect on the *Neurospora crassa* circadian clock, which coordinated rhythmic asexual reproduction during vegetative growth.[31] Whether the lack of farnesol derivatives or terpenoid-derived arthrosporols in nematode-trapping fungus *A. oligospora* induced higher trap formation and less metabolite production need further detailed study.

In conclusion, by gene engineering and chemical metabolite profiling, we have identified the PKS gene *AOL_s00215g283* in nematode-trapping fungus *A. oligospora*. Our result revealed that the PKS gene played significant roles in not only the biosynthesis for the arthrosporols but also the fungal ability for predatory trap formation.

■ ASSOCIATED CONTENT

Supporting Information

The Supporting Information is available free of charge on the ACS Publications website at DOI: 10.1021/acs.jafc.5b04244.

Unrooted neighbor-joining tree of fungal PKS synthase homologues (Figure S1), comparison of the growths and sporulations of the wild-type and mutant Δ*AOL_s00215g283* strains (Figure S2), 10 day culture broths of the Δ*AOL_s00215g283* mutant and wild-type strains (Figure S3), list of predicted functions of genes in the *AOL_s00215g283* gene cluster (Table S1), compounds detected by GC−MS analysis in the wild-type strain (Table S2), and compounds detected by GC−MS analysis only in the mutant Δ*AOL_s00215g283* (Table S3) (PDF)

■ AUTHOR INFORMATION

Corresponding Author

*Telephone: 86-871-65032538. Fax: 86-871-65034838. E-mail: xmniu@ynu.edu.cn.

Funding

This work was sponsored by projects from the National Natural Science Foundation of China (31070051), the National Basic Research Program of China (973 Program) on Biological Control of Key Crop Pathogenic Nematodes

DOI: 10.1021/acs.jafc.5b04244
J. Agric. Food Chem. 2015, 63, 9076−9082

(2013CB127505), the National High Technology Research and Development Program of China (2011AA10A205), and the Yunnan University Program for Excellent Young Talents awarded to Xue-Mei Niu (XT412003).

Notes

The authors declare no competing financial interest.

■ ACKNOWLEDGMENTS

The authors thank Prof. Ze-Fen Yu and Dr. Ying Zhang for fungal identification and Prof. Zhiqiang An for the plasmid pAg1-H3.

■ REFERENCES

(1) Abad, P.; Gouzy, J.; Aury, J.-M.; Castagnone-Sereno, P.; Danchin, E. G. J.; Deleury, E.; Perfus-Barbeoch, L.; Anthouard, V.; Artiguenave, F.; Blok, V. C.; Caillaud, M.-C.; Coutinho, P. M.; Dasilva, C.; De Luca, F.; Deau, F.; Esquibet, M.; Flutre, T.; Goldstone, J. V.; Hamamouch, N.; Hewezi, T.; Jaillon, O.; Jubin, C.; Leonetti, P.; Magliano, M.; Maier, T. R.; Markov, G. V.; McVeigh, P.; Pesole, G.; Poulain, J.; Robinson-Rechavi, M.; Sallet, E.; Ségurens, B.; Steinbach, D.; Tytgat, T.; Ugarte, E.; van Ghelder, C.; Veronico, P.; Baum, T. J.; Blaxter, M.; Bleve-Zacheo, T.; Davis, E. L.; Ewbank, J. J.; Favery, B.; Grenier, E.; Henrissat, B.; Jones, J. T.; Laudet, V.; Maule, A. G.; Quesneville, H.; Rosso, M.-N.; Schiex, T.; Smant, G.; Weissenbach, J.; Wincker, P. Genome sequence of the metazoan plant-parasitic nematode *Meloidogyne incognita*. *Nat. Biotechnol.* **2008**, *26*, 909−915.

(2) Castagnone-Sereno, P.; Danchin, E. G.; Perfus-Barbeoch, L.; Abad, P. Diversity and evolution of root-knot nematodes, genus *Meloidogyne*: new insights from the genomic era. *Annu. Rev. Phytopathol.* **2013**, *51*, 203−20.

(3) Stirling, G. R. Biological control of plant-parasitic nematodes. In *Diseases of Nematodes*; Poinar, G. O., Jansson, H.-B., Eds.; CRC Press: Boca Raton, FL, 1988; Vol. *2*, pp 93−139.

(4) Nordbring-Hertz, B. Nematophagous fungi: Strategies for nematode exploitation and for survival. *Microbiol. Sci.* **1988**, *5*, 108−116.

(5) Yang, Y.; Yang, E. C.; An, Z. Q.; Liu, X. Z. Evolution of nematode-trapping cells of predatory fungi of the Orbiliaceae based on evidence from rRNA-encoding DNA and multiprotein sequences. *Proc. Natl. Acad. Sci. U. S. A.* **2007**, *104*, 8379−8384.

(6) Pramer, D. Nematode-trapping fungi. *Science* **1964**, *144*, 382−388.

(7) Mo, M. H.; Chen, W. M.; Su, H. Y.; Zhang, K. Q.; Duan, C. Q.; He, D. M. Heavy metal tolerance of nematode-trapping fungi in lead polluted soils. *Appl. Soil Ecol.* **2006**, *31*, 11−19.

(8) Schmidt, A. R.; Dorfelt, H.; Perrichot, V. Carnivorous fungi from Cretaceous amber. *Science* **2007**, *318*, 1743−1743.

(9) Nordbring-Hertz, B. Morphogenesis in the nematode-trapping fungus *Arthrobotrys oligospora*-an extensive plasticity of infection structures. *Mycologist.* **1999**, *18*, 125−133.

(10) Niu, X.-M.; Zhang, K.-Q. *Arthrobotrys oligospora*: a model organism for understanding the interaction between fungi and nematodes. *Mycology* **2011**, *2*, 59−78.

(11) Stadler, M.; Sterner, O.; Anke, H. New biologically active compounds from the nematode-trapping fungus *Arthrobotrys oligospora* Fresen. *Z. Naturforsch.* **1993**, *48c*, 843−850.

(12) Anderson, M. G.; Jarman, T. B.; Rickards, R. W. Structures and absolute configurations of antibiotics of the oligosporon group from the nematode-trapping fungus *Arthrobotrys oligospora*. *J. Antibiot.* **1995**, *48*, 391−398.

(13) Wei, L. X.; Zhang, H. X.; Tan, J. L.; Chu, Y. S.; Li, N.; Xue, H. X.; Wang, Y. L.; Niu, X. M.; Zhang, Y.; Zhang, K. Q. Arthrobotrisins A-C, oligosporons from the nematode-trapping fungus *Arthrobotrys oligospora*. *J. Nat. Prod.* **2011**, *74*, 1526−1530.

(14) Zhang, H. X.; Tan, J. L.; Wei, L. X.; Wang, Y. L.; Zhang, C. P.; Wu, D. K.; Zhu, C. Y.; Zhang, Y.; Zhang, K. Q.; Niu, X. M. Morphology regulatory metabolites from *Arthrobotrys oligospora*. *J. Nat. Prod.* **2012**, *75*, 1419−1423.

(15) Weber, T.; Blin, K.; Duddela, S.; Krug, D.; Kim, H. U.; Bruccoleri, R.; Lee, S. Y.; Fischbach, M. A.; Müller, R.; Wohlleben, W.; Breitling, R.; Takano, E.; Medema, M. H. antiSMASH 3.0—A comprehensive resource for the genome mining of biosynthetic gene clusters. *Nucleic Acids Res.* **2015**, *43*, W237−W243.

(16) Niu, X. M.; Chen, L.; Yue, Q.; Wang, B. L.; Zhang, J. X.; Zhu, C. Y.; Zhang, K. Q.; Bills, G. F.; An, Z. Q. Characterization of thermolide biosynthetic genes and a new thermolide from sister thermophilic fungi. *Org. Lett.* **2014**, *16*, 3744−3747.

(17) Yang, J. K.; Wang, L.; Ji, X. L.; Feng, Y.; Li, X. M.; Zou, C. G.; Xu, J. P.; Ren, Y.; Mi, Q. L.; Wu, J. L. Genomic and proteomic analyses of the fungus *Arthrobotrys oligospora* provide insights into nematode-trap formation. *PLoS Pathog.* **2011**, *7*, e1002179.

(18) Zhao, X. Y.; Wang, Y. C.; Zhao, Y.; Huang, Y.; Zhang, K. Q.; Yang, J. K. Malate synthase gene AoMls in the nematode-trapping fungus *Arthrobotrys oligospora* contributes to conidiation, trap formation, and pathogenicity. *Appl. Microbiol. Biotechnol.* **2014**, *98*, 2555−2563.

(19) Molyneux, R. J.; Schieberle, P. Compound identification: a journal of agricultural and food chemistry perspective. *J. Agric. Food Chem.* **2007**, *55*, 4625−4629.

(20) Schieberle, P.; Molyneux, R. J. Quantitation of sensory-active and bioactive constituents of food: a journal of agricultural and food chemistry perspective. *J. Agric. Food Chem.* **2012**, *60*, 2404−2408.

(21) Sekiguchi, J.; Gaucher, G. M. Isoepoxydon, a new metabolite of the patulin pathway in *Penicillium urticae*. *Biochem. J.* **1979**, *182*, 445−453.

(22) Puel, O.; Galtier, P.; Oswald, I. P. Biosynthesis and toxicological effects of patulin. *Toxins* **2010**, *2*, 613−631.

(23) Desmarchelier, A.; Mujahid, C.; Racault, L.; Perring, L.; Lancova, K. Analysis of patulin in pear- and apple-based foodstuffs by liquid chromatography electrospray ionization tandem mass spectrometry. *J. Agric. Food Chem.* **2011**, *59*, 7659−7665.

(24) Huffman, J.; Gerber, R.; Du, L. Recent advancements in the biosynthetic mechanisms for polyketide-derived mycotoxins. *Biopolymers* **2010**, *93*, 764−776.

(25) Tannous, J.; El Khoury, R.; Snini, S. P.; Lippi, Y.; El Khoury, A.; Atoui, A.; Lteif, R.; Oswald, I. P.; Puel, O. Sequencing, physical organization and kinetic expression of the patulin biosynthetic gene cluster from *Penicillium expansum*. *Int. J. Food Microbiol.* **2014**, *189*, 51−60.

(26) Holm, D. K.; Petersen, L. M.; Klitgaard, A.; Knudsen, P. B.; Jarczynska, Z. D.; Nielsen, K. F.; Gotfredsen, C. H.; Larsen, T. O.; Mortensen, U. H. Molecular and chemical characterization of the biosynthesis of the 6-MSA-derived meroterpenoid yanuthone D in *Aspergillus niger*. *Chem. Biol.* **2014**, *21*, 519−29.

(27) Mosel, D. D.; Dumitru, R.; Hornby, J. M.; Atkin, A. L.; Nickerson, K. W. Farnesol concentrations required to block germ tube formation in *Candida albicans* in the presence and absence of serum. *Appl. Environ. Microbiol.* **2005**, *71*, 4938−4940.

(28) Lorek, J.; Poggeler, S.; Weide, M. R.; Breves, R.; Bockmuhl, D. P. Influence of farnesol on the morphogenesis of *Aspergillus niger*. *J. Basic Microbiol.* **2008**, *48*, 99−103.

(29) Dichtl, K.; Ebel, F.; Dirr, F.; Routier, F. H.; Heesemann, J.; Wagener, J. Farnesol misplaces tip-localized Rho proteins and inhibits cell wall integrity signalling in *Aspergillus fumigatus*. *Mol. Microbiol.* **2010**, *76*, 1191−1204.

(30) Semighini, C. P.; Murray, N.; Harris, S. D. Inhibition of *Fusarium graminearum* growth and development by farnesol. *FEMS Microbiol. Lett.* **2008**, *279*, 259−264.

(31) Granshaw, T.; Tsukamoto, M.; Brody, S. Circadian rhythms in *Neurospora crassa*: farnesol or geraniol allow expression of rhythmicity in the otherwise arrhythmic strains frq10, wc-1, and wc-2. *J. Biol. Rhythms* **2003**, *18*, 287−296.

DOI: 10.1021/acs.jafc.5b04244
J. Agric. Food Chem. 2015, 63, 9076−9082

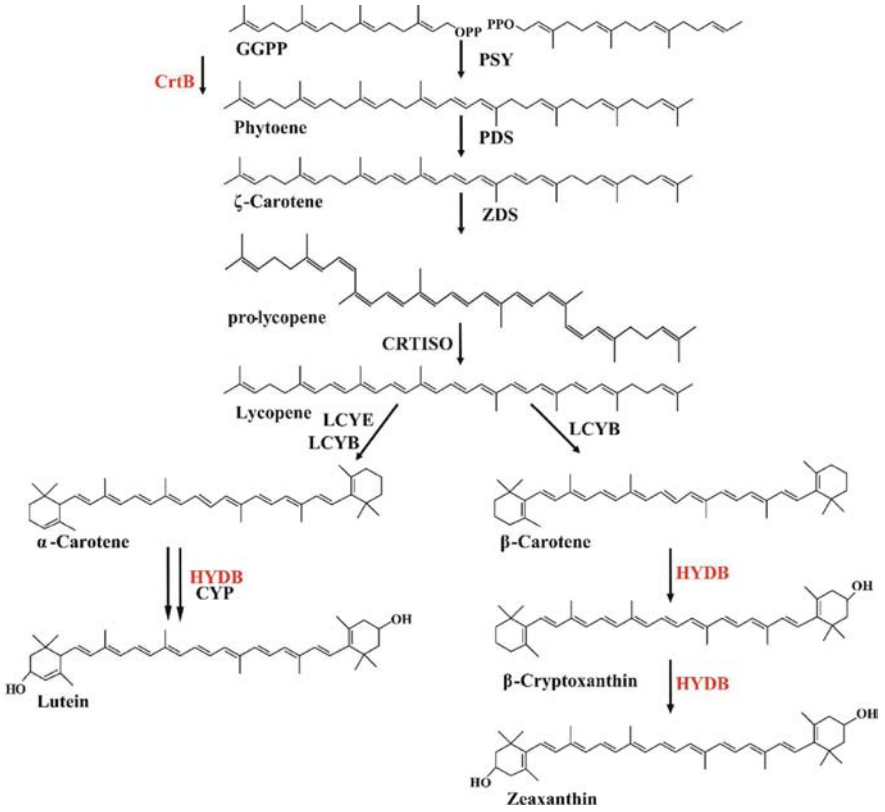

Figure 1. Carotenoid biosynthetic pathway. Enzymatic conversions are indicated with arrows, with the enzymes in bold. PSY/CrtB, phytoene synthase; PDS, phytoene desaturase; ZDS, ζ-carotene desaturase; CRTISO, carotenoid isomerases; LCYB, lycopene β-cyclase; LCYE, lycopene ε-cyclase; HYDB, β-carotene hydroxylase; CYP, carotenoid ε-hydroxylase (cytochrome P450 type).

hydroxylase expression was implemented and accumulated a high ratio of β-carotene in total carotenoid content, indicating that it is a practicable and effective approach to improve provitamin A.[25,26]

Up to now, there are two strategies to accumulate carotenoids in plant metabolic engineering. The first strategies are "push strategies", which are dependent on the overexpression of a rate-limiting enzyme in the pathway, such as successful reports in rice and maize with overexpression of *PSY* or bacterial phytoene synthase gene (*CrtB*).[27−31] The second strategies are "block strategies", which rely on the silencing of a downstream biosynthetic step. Besides the examples of potato and orange, other researches of "block strategies" include the silencing of lycopene β-cyclases to increase lycopene in tomato fruits or the silencing of zeaxanthin epoxidase to accumulate zeaxanthin in potato tubers.[32,33] Although carotenoid is one of the major pigments and determines the nutritional value of wheat,[34] wheat grains have very low carotenoid content and mainly accumulate lutein, which lacks provitamin A activity. In our previous study, the β-carotene content was increased by introducing *CrtB* and *CrtI* genes, whereas the high ratio of β-carotene accumulation could not be previously estimated, which also unveiled three important regulation nodes to be regulated in the carotenoid biosynthetic pathway of hexaploid wheat: (i) phytoene biosynthesis; (ii) lycopene cyclization; and (iii) carotene hydroxylation.[9] There are two types of *HYD* genes (*TaHYD1* and *TaHYD2*) in common wheat, which encode proteins that are 72% identical to each other over 90% of the protein length.[35] In this work, the expression of an endogenous *TaHYD* was blocked by RNA interference (RNAi) in transgenic wheat. To specifically and quantitatively increase the provitamin A content in the wheat endosperm, "push strategies" and "block strategies" were combined in wheat metabolic engineering. The expected result of this engineering was that the content of β-carotene would increase in the endosperm of transgenic wheat compared with that in the wild type.

MATERIALS AND METHODS

Plant Materials and Treatments. Wheat plants (*Triticum aestivum* L. cv. Bobwhite) were grown in the experimental field of Huazhong University of Science and Technology in Wuhan, China. To more favorably accumulate carotenoid, a yellow-kernel cultivar was chosen.

RNA and Genomic DNA Isolation. Total RNA was extracted from different wheat tissues using TRIzol reagent (Invitrogen, Carlsbad, CA, USA) according to the manufacturer's instructions. The RNA concentration and purity were analyzed using a NanoDrop ND-2000 spectrophotometer (Thermo Scientific, Wilmington, DE, USA). The integrity of the RNA sample was assessed by nondenaturing agarose gel analysis. Genomic DNA was isolated from the wheat leaves using the cetyltrimethylammonium bromide (CTAB) extraction method.[36]

Plasmid Constructs. The pLRPT vector containing the endosperm-specific promoter *1Dx5* and *35S* terminator was used to construct the overexpression (OE) and RNAi vector. Fragments of 225 bp corresponding to *TaHYD1* and *TaHYD2* were isolated by RT-PCR using specific primers with incorporated restriction sites (Supporting Information Table S1). The selected fragments followed the selection strategies for RNAi in wheat, and the highly conserved fragment was chosen as the silencing target.[37] The RNAi construct contained a cDNA fragment derived from *TaHYD* and was oriented in the sense and antisense directions at the ends of the construct, respectively, separated by an intron sequence, and the resulting

DOI: 10.1021/acs.jafc.5b04279
J. Agric. Food Chem. 2015, 63, 9083−9092

plasmid was named pLRPT-HYD-RNAi (Figure 2). The intron was derived from the wheat *TAK14* gene (AF325198). pLRPT-CrtB

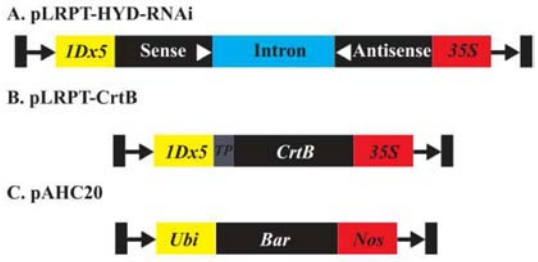

Figure 2. Structures of the three transformation plasmids (pLRPT-HYD-RNAi, pLRPT-CrtB, and pAHC20) used in this study. *1Dx5*, endosperm-specific promoter of the high-molecular-mass glutenin subunit gene *1Dx5* from wheat; *CaMV35S*, cauliflower mosaic virus (*CaMV*) *35S* terminator; *Ubi*, constitutive maize ubiquitin-1 promoter; *TP*, transit peptide from pea Rubisco small subunit (rbcS); CrtB, phytoene synthase gene from *E. uredovora*; *Bar*, bialaphos resistance gene; *NOS*, *Agrobacterium tumefaciens* nopaline synthase (*NOS*) terminator.

carries the bacterial phytoene synthase gene under the control of *1Dx5* promoter, which had been used in previous research and was stored in our laboratory.[9] A sequence encoding a transit peptide from the pea Rubisco small subunit (*rbcS*) was fused to the *1Dx5* promoter in the plasmid pLRPT-CrtB. Plasmid pAHC20 carrying a selectable *bar* gene, which confers resistance to the herbicide phosphinothricin, was also used.

Wheat Transformation and Regeneration. Transgenic wheat lines were generated according to the bombardment method as reported by Sparks et al.[38] Wheat immature scutella (14 days after pollination, DAP) from the Bobwhite cultivar were transformed with the plasmids of pLRPT-HYD-RNAi/pLRPT-CrtB/pAHC20 at a 2:2:1 molar ratio, pLRPT-HYD-RNAi/pAHC20 at a 3:1 molar ratio, and pLRPT-CrtB/pAHC20 at a 3:1 molar ratio. The regenerated plants were screened using the herbicide phosphinotricin (3 mg L^{-1}). The surviving plants were transferred to soil and grown to maturity under growth chamber conditions (22/16 °C day/night, 16/8 h light/dark cycle, and 300 μmol m^{-2} s^{-1} photosynthetic photon flux density). The regenerated plants were confirmed by PCR amplification using gene-specific primers, and then the products were sequenced (Supporting Information Tables S1 and S2). The immature seed from PCR-positive transgenic plants was also confirmed by Western blotting. Then, the transgenic plants were self-pollinated, and the nonsegregant lines were selected for analyses of the carotenoid composition and carotenoid biosynthetic gene expression levels.

Western Blotting. The bacterial expression vectors pET-32a and pET-28 were used to express CrtB and HYD proteins in *Escherichia coli*, respectively. The primers were designed to amplify only the coding regions (*CrtB* and *HYD*) (Supporting Information Table S1). The construction of the expression vector pET-32a-CrtB and pET-28-HYD and the expression and purification of the recombinant proteins were performed as described by Miao et al.[39] The CrtB and HYD proteins were purified from a heterologous system. Polyclonal antibodies against the CrtB and HYD proteins were generated by immunizing Japanese white rabbits with CrtB and HYD proteins.

Total wheat seed proteins were extracted from the transgenic and control lines according to the method of He et al.[40] Western blotting was performed following the method of Ma et al.[41] An antibody against the plant housekeeping protein actin was used to normalize for equal amounts of proteins and to calculate the relative loading volume for each sample. The amounts of CrtB and HYD proteins were determined by a densitometry analysis of the Western blotting results in three biological replicates using Bio-Rad Quantity One 1-D software version 4.6.2 (Bio-Rad, Hercules, CA, USA).

Analysis of Carotenoid Composition by HPLC. Carotenoid extracts from mature grain were prepared according to the method of Rodríguez-Suárez et al. with modifications.[42] Seed samples were ground into fine powder and placed in a 50 mL volumetric centrifuge tube. Pigments were extracted with 4 mL of acetone (containing 0.1% BHT) during 2 min by vortexing, following sonication for 1 min. The mixture was centrifuged at 5000 rpm for 5 min at 4 °C, and the extracted carotenoids in the acetone phase were collected. The extraction operation was repeated three times, and the acetone fractions were pooled. The solvent was evaporated under a nitrogen stream, and the pigments were dissolved in 0.3 mL of methyl *tert*-butyl ether containing 0.01% (w/v) BHT. After centrifuging at 12000 rpm at 4 °C for 30 min, the sample was filtered through a 0.22 μm filter before high-performance liquid chromatography (HPLC) analysis. For quantitative purposes, β-apo-8′-carotenal was added to each sample as an internal standard prior to extraction (10 μg g^{-1} of freeze-dried sample). Analyses were performed in quadruplicate. All of the operations were performed under dimmed light to prevent the isomerization and photodegradation of carotenoids.

The sample was injected into the HPLC system. The HPLC system included a model 2996 photodiode array detection (DAD) system, a 1525 solvent delivery system, and a Breeze2 Chromatography Manager (Waters Corp., Milford, MA, USA). The carotenoids were separated on a YMC C30 carotenoid column (150 × 4.6 mm, packing 3 μm) (Wilmington, NC, USA) at 25 °C. All of the eluate was under 200−700 nm monitoring. Solvent A was acetonitrile/methanol (3:1, v/v), containing 0.01% BHT and 0.05% triethylamine (TEA, Sigma, Shanghai, China), and solvent B was 100% MTBE, containing 0.01% BHT. The parameters of mobile phase gradient were programmed as follows: 0−10 min, A/B (95:5); 10−19 min, A/B (86:14); 19−29 min, A/B (75:25); 29−54 min, A/B (50:50); 54−66 min, A/B (26:74), and back to the initial condition for re-equilibration. All of the solvents were of HPLC grade (J. T. Baker, Phillipsburg, NJ, USA). Carotenoid standards for lutein, zeaxanthin, β-cryptoxanthin, α-carotene, *trans*-β-carotene, β-apo-8′-carotenal, and *trans*-lycopene calibration were purchased from Sigma-Aldrich (Shanghai, China); 9-*cis*-β-carotene was purchased from Carotenature (Lupsingen, Switzerland) (Supporting Information Figure S1). These standards and the β-apo-8′-carotenal internal standard were used to generate standard calibration curves.[43−46]

Quantitative PCR (qPCR) Analysis. The qPCR analysis was performed with a Real-Time PCR Detection System (CFX Connect Optics Module, Bio-Rad, Hercules, CA, USA) using SuperReal PreMix Plus (SYBR Green) (FP205, Tiangen, Beijing, China). The amplification was performed with the following program: 40 cycles of 95 °C for 15 s and 60 °C for 60 s. Fluorescence was acquired at 60 °C. The specificity of the unique amplification product was determined by a melt curve analysis from 55 to 99 °C. The data were analyzed using Lightcycler software version 4 and were normalized to the expression of the wheat *β-actin* gene due to its relatively constitutive expression level throughout the wheat developmental process. The quality of the cDNA templates and PCR amplifications was verified by an analysis of negative controls without template and no-reverse transcription for each primer pair. A dissociation curve analysis was performed following qPCR, and a single peak was observed for each primer pair. Some of the qPCR products were separated on agarose gels, and single bands at expected sizes were detected.

RESULTS

Different Metabolic Strategies Generate Different Effects with Distinct Carotenoid Profiles. The immature scutella from the Bobwhite cultivar were transformed with three constructs containing unlinked transgenes. The pLRPT-HYD-RNAi and pLRPT-CrtB were controlled by the endosperm-specific *1Dx5* promoter. The selectable marker bialaphos resistance gene (*bar*) gene was expressed constitutively (Figure 2). The hypothesis is that the successful transformations would

DOI: 10.1021/acs.jafc.5b04279
J. Agric. Food Chem. 2015, 63, 9083−9092

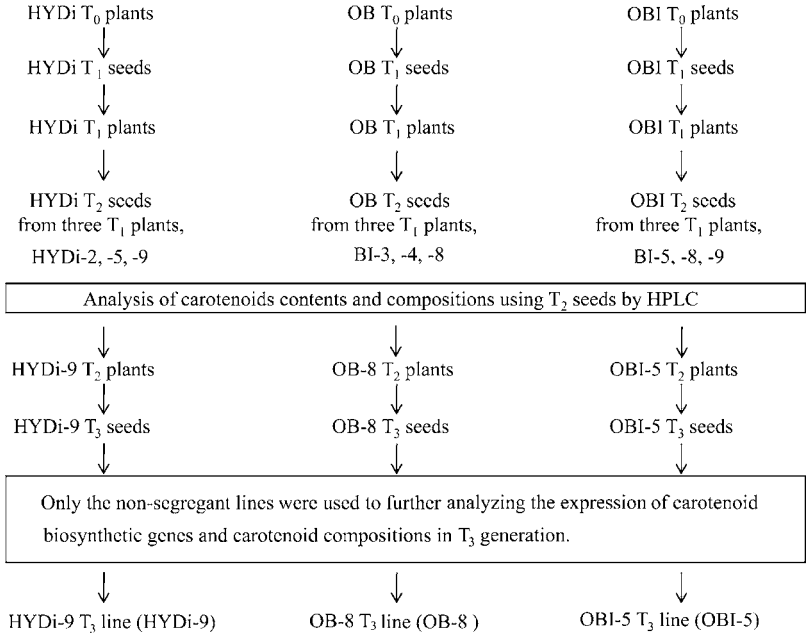

Figure 3. Propagation of transgenic wheat and selection of nonsegregant lines. OB is the line with expression of *CrtB*; HYDi is the line with silencing of *HYD*; OBI is the line with expression of *CrtB* and silencing of *HYD*.

result in a yellower kernel appearance in transgenic lines. The differences in the external coloration of the grains were confirmed by measuring the color index by Chroma Meter.[47] Colorimetric results of grains demonstrated that transgenic lines had higher values of b^* (yellowness), which showed significant correlation with lutein and β-carotene content, in contrast to two controls (Supporting Information Figure S2). The differences of the color index indicate that different transgenic lines accumulated different levels of carotenoid in grains. The most intense red/yellow grains from the positive lines were chosen to generate the transgenic progeny by self-pollination for further analyses (Figure 3).

To examine carotenoid accumulation in the seeds of different transgenic lines, a HPLC analysis was conducted to compare the profiles of carotenoid content and composition in wheat seeds. There were no significant differences in carotenoid composition between the wild type and vector control (VC). The carotenoid profiles of the mature seeds from three T_2 transgenic lines were different from those of the wild-type controls. Several novel carotenes were detected in the transgenic wheat lines including lycopene, β-cryptoxanthin, α-carotene, and phytoene (Supporting Information Table S3). Meanwhile, the HPLC results revealed that, consistent with the silencing of the *HYD* gene, the levels of β-carotene were significantly increased in seeds from the *HYD* RNAi (HYDi) lines compared with that of the VC lines.

Detailed HPLC analyses were conducted to determine the carotenoid content and composition of seeds from different transgenic lines of the T_3 generation (Figure 4). Total carotenoid and provitamin A contents in three T_3 transgenic lines were significantly improved, and the content also showed the difference between the same generation from the same T_2 transgenic lines (Figure 5A). The total carotenoid content increased to 3.7 μg g^{-1} dry weight (DW) in the HYDi-9 plants, to 7.35 μg g^{-1} DW in the OB-8 plants, and to 9.3 μg g^{-1} DW in the OBI-5 plants compared with the wild type (1.22 μg g^{-1} DW). Furthermore, the provitamin A content significantly increased in all three of the transgenic wheat lines, ranging from 2.24 μg g^{-1} DW (HYDi) to 5.55 μg g^{-1} DW (OBI). The β-carotene contents of the HYDi-9, OB-8, and OBI-5 lines significantly increased by 10.5-, 14.6-, and 31-fold, respectively (Figure 5B). Thus, the significantly increased carotenoid and provitamin A contents in the transgenic lines were due primarily to the increased β-carotene levels.

The different transgenic lines showed diverse changes under the effects of different transgenes. The content of β-carotene in the transgenic line HYDi-9 increased 10.5-fold (1.76 μg g^{-1} DW) by silencing *HYD* compared with the wild-type (0.167 μg g^{-1} DW), accompanied by decreased lutein and zeaxanthin contents. The overexpression of *CrtB* in the wheat endosperm, introducing more flux into the carotenoid biosynthetic pathway, increased the total carotenoid content, particularly the content of lutein and β-carotene. The combination of overexpressing *CrtB* and silencing *HYD* resulted in the highest accumulation of β-carotene, with levels up to 31-fold (5.06 μg g^{-1} DW) higher than that of the wild type. The contents of lutein and zeaxanthin in the OBI lines were lower than those in the OB lines but higher than those in the HYDi lines. Notably, lycopene appeared and accumulated in all three of the transgenic lines. By contrast, the first committed carotenoid product, phytoene, appeared only in the transgenic lines that expressed *CrtB*. Different geometric isomers of carotenoid were also detected in the three classes of transgenic lines (Figure 4). 9-*cis*-β-carotene was the major component of β-carotene isomers. In addition, *trans*-lycopene and *cis*-lycopene were also detected in the three transgenic lines. An undefined carotenoid appeared in the carotenoid profiles of three transgenic lines, the absorbance spectrum of which was similar to that of a lycopene isomer (Figure 4). The phenotype of the transgenic lines was stably inherited (Supporting Information Table S4).

Profiles of Endogenous Carotenoid Biosynthetic Genes in Different Transgenic Wheat Lines. Expression of both transgenes, *CrtB* and *HYD*, was determined by qRT-PCR in the endosperms of transgenic and control wheat lines (Table 1). As anticipated, transcript levels of *CrtB* and *HYD*

DOI: 10.1021/acs.jafc.5b04279
J. Agric. Food Chem. 2015, 63, 9083−9092

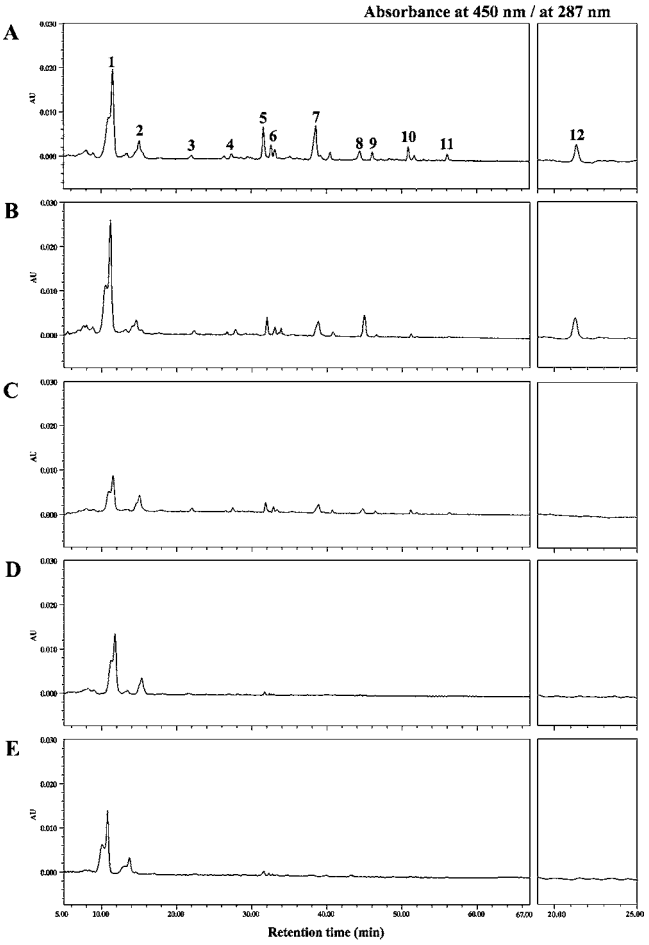

Figure 4. HPLC characterization of carotenoids that were extracted from the grains of T_3 transgenic and control wheat: (A) OBI-5; (B) OB-8; (C) HYDi-9; (D) VC-10 (transgenic vector control); (E) Bobwhite (wild-type). Peaks: 1, lutein; 2, zeaxanthin; 3, β-cryptoxanthin; 4, α-carotene; 5, *trans*-β-carotene; 6, 9-*cis*-β-carotene; 7, undefined carotene; 8,9, *cis*-lycopene; 10, *trans*-lycopene; 11, isomer of lycopene; 12, phytoene.

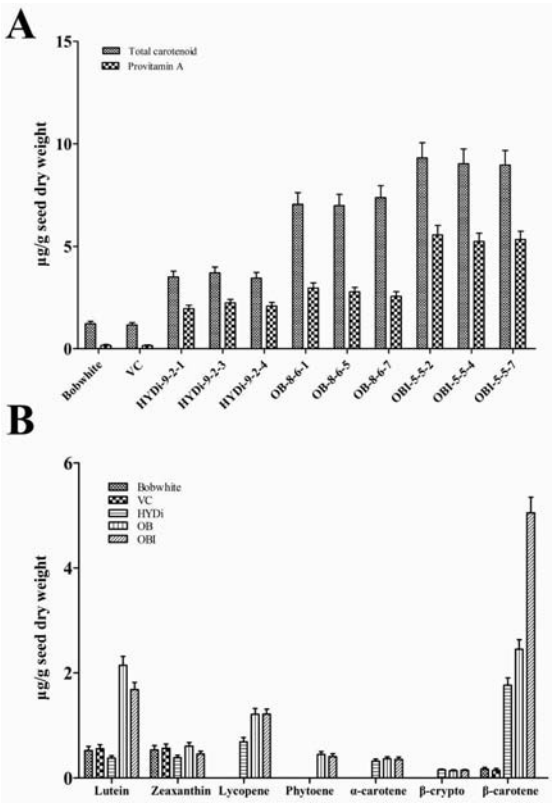

Figure 5. Carotenoid and provitamin A contents in the grains from transgenic wheat. (A) Total carotenoid and provitamin A contents in the wheat whole grains of T_3 transgenic lines (OBI-5, HYDi-9, and OB-8) and their untransformed control, Bobwhite. The amount of total carotenoid is equal to the sum of all of the carotenoids, and the provitamin A carotenoids were calculated as the sum of α-carotene, β-cryptoxanthin, and β-carotene contents in the extracted samples. (B) Carotenoid compositions in the wheat grains from transgenic and control lines in the T_3 generation. The average of each carotenoid species was determined from five individual plant heads per line. The data are presented as the means ± SD.

were detected only in the corresponding transgenic lines. Then, the expression of CrtB and HYD proteins in the transgenic and control lines was also analyzed by Western blot. The levels of CrtB and HYD proteins in the transgenic and control lines are shown in Figure 6, in which a clear band of CrtB with expected molecular weight was detected only in the transgenic OB and OBI lines. HYD expression was detected in the transgenic, wild-type, and VC lines. However, significant differences were observed between the transgenic and control lines, and all of the transgenic lines exhibited decreased levels of HYD in comparison with wild type, which meant that the translational level of HYD was down-regulated by RNAi.

To further understand changes of carotenoid content in the transgenic wheat lines, the expression of endogenous carotenoid biosynthetic genes was analyzed to determine whether they were regulated in response to transgene expressing. In the present study, the *1Dx5* endosperm-specific promoter was employed to avoid influencing the expression levels in other tissues. As shown in Figure 6, the expression of *CrtB* was only detected in the OB and OBI lines and most of the lines showed similar expression, indicating the stability driven by the *1Dx5* promoter. To further examine the effect of the transgenes on the expression of carotenogenic genes in the transgenic plants, expression of the endogenous carotenogenic gene was measured by qRT-PCR. As shown in Figure 7, the expression of the endogenous carotenogenic genes was different in the transgenic, VC, and wild-type lines, whereas that in the VC and wild-type lines showed no difference in the wheat endosperm. In the transgenic line OB with the exogenous gene *CrtB*, the expression levels of Phytoene desaturase (*PDS*), ζ-carotene desaturase (*ZDS*), *LCYE*, and *LCYB* were up-regulated, whereas in the HYDi and OBI lines, *PSY* was up-regulated. Because of the down-regulation of *HYD* in the transgenic line HYDi, the transcript levels of *PDS*, *LCYE*, and *LCYB* showed the same tendencies and presented greater changes, except for *ZDS* expression. The combination of overexpressing *CrtB* and silencing *HYD* efficiently improved provitamin A levels by increasing the β-carotene content in the transgenic line OBI. Thus, *PDS*, *ZDS*, *LCYE*, and *LCYB* expression levels had superimposed effects accompanied by the highest expression levels in the three classes of transgenic lines.

DISCUSSION

Vitamin A deficiency is a global health problem and accounts for increased childhood mortality and disease.[7,48−50] Due to the widespread effects of vitamin A deficiency and effective benefits of carotenoid, there are attempts to improve carotenoid content

DOI: 10.1021/acs.jafc.5b04279
J. Agric. Food Chem. 2015, 63, 9083−9092

Table 1. Transgene Expression Level and Carotenoid Content in Transgenic Lines[a]

transgenic line (T_3 generation)	relative transcript levels[b] *crtB*	relative transcript levels[b] *HYDi*	total carotenoids[c] ($\mu g\ g^{-1}$ dry seed wt)	provitamin A[c] ($\mu g\ g^{-1}$ dry seed wt)
Bobwhite	0	0	1.22 ± 0.12	0.16 ± 0.04
OB-8	0.124 ± 0.005	0	7.37 ± 0.59	2.56 ± 0.23
HYDi-9	0	0.046 ± 0.003	3.70 ± 0.29	2.25 ± 0.17
OBI-5	0.098 ± 0.004	0.062 ± 0.004	9.31 ± 0.74	5.55 ± 0.46

[a]The data represent mean values ± SD and are derived from at least three independent plants per line. [b]Relative transpcript levels (normalized with respect to the *β-actin* transcript) were determined by qRT-PCR. [c]Total carotenoids (sum of all carotenoid content measured) and provitamin A content (sum of *α*-carotene, *β*-cryptoxanthin, *β*-carotene) were determined by HPLC analysis.

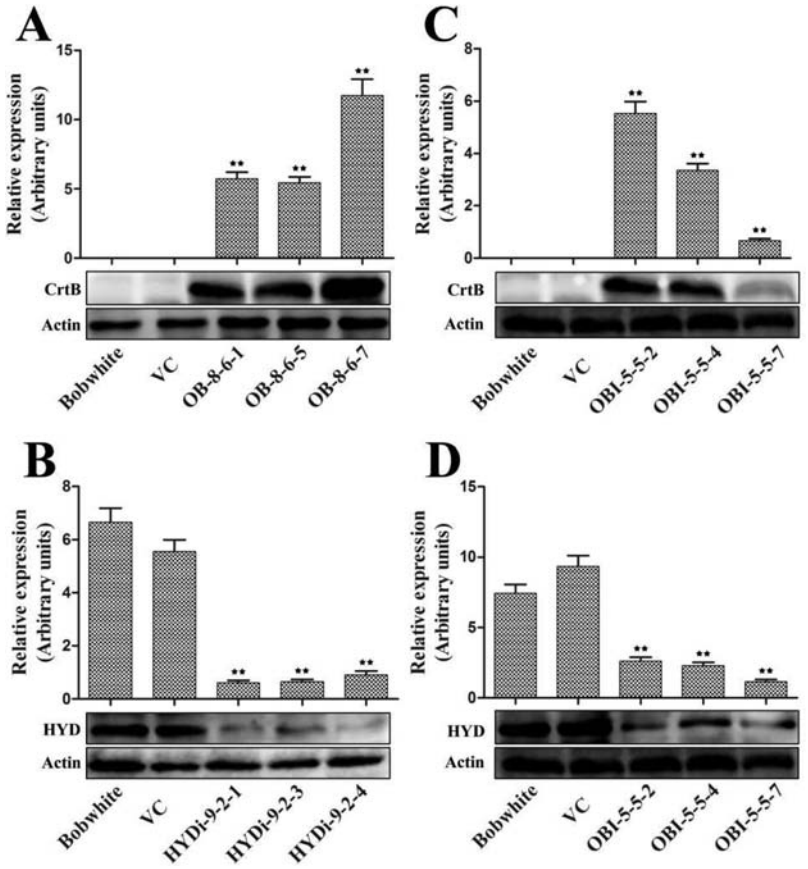

Figure 6. Levels of CrtB and HYD proteins in the endosperms from transgenic and control wheat lines as indicated by Western blotting: (A) CrtB proteins in the OB-8 and control lines; (B) HYD proteins in the HYDi-9 and control lines; (C) CrtB proteins in the OBI-5 and control lines; (D) HYD proteins in the OBI-5 and control lines. The double asterisk indicates significant differences between the control Bobwhite and transgenic lines at a $P = 0.01$ probability level. The relative amounts of the CrtB and HYD proteins in the transgenic lines were densitometrically quantified with respect to the nontransformed control line (cv. Bobwhite).

in staple crops by metabolic engineering, especially improving *β*-carotene content.[27,28] In our study, improving the content of *β*-carotene was the first goal. A combination of "push strategy" and "block strategy" holds good prospect to further increase of the provitamin A content in wheat.

Endosperm-Specific Expression of CrtB Introduces More Substrate Flux into Carotenoid Biosynthetic Pathway. In this study, our results demonstrate that *CrtB* expression in the wheat endosperm significantly increased the carotenoid content, suggesting that the expression of *CrtB* can provide an additional carotenoid flux into carotenoid biosynthesis. The results of Western blotting detected only the expression of *CrtB* in transgenic lines (Figure 6), which was also consolidated this conclusion. The total carotenoid and provitamin A contents were significant improved, up to 6.5-fold (7.37 $\mu g\ g^{-1}$ DW) and 14.6-fold (2.45 $\mu g\ g^{-1}$ DW) in transgenic lines OB as compared with wild type (Figure 5). Although CrtB expression varied, the carotenoid contents in the different transgenic lines were not significantly different, suggesting that the enzyme activity of CrtB was sufficient for product synthesis. This may be due to the limitation of isoprenoid precursors in the carotenoid pathway.[28,30] Meanwhile, it is interesting to note that when the *CrtB* gene was overexpressed in a low-carotenoid wheat phenotype, of which the kernel was light yellow, the accumulations of total carotenoid and *β*-carotene were less than those in the present study with a yellow kernel.[9] This phenomenon might be explained by the observation that storage capacity also appears to be responsible for the enhanced accumulation of carotenoids, such as *high-pigment* (*hp*) mutants of tomato

DOI: 10.1021/acs.jafc.5b04279
J. Agric. Food Chem. 2015, 63, 9083−9092

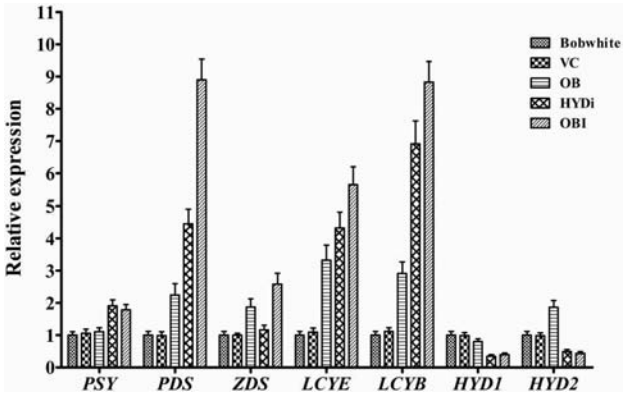

Figure 7. Expression levels of the endogenous carotenoid biosynthetic genes in the endosperm from transgenic and control wheat lines. The gene expression levels were measured by quantitative reverse transcription PCR and are determined relative to the transcript levels of the constitutively expressed *β-actin* gene in the same samples. The expression levels of these genes for the transformed lines are given as the expression levels relative to the values for the nontransformed control line Bobwhite. The qRT-PCR results for each gene were generated from three biological replicates with three technical replicates each, and the data are shown as the means ± SD.

accumulated more carotenoid due to the increased plastid volume per cell.[51,52] This result indicates that storage capacity for carotenoid accumulation is a potential target to improve carotenoid content in metabolic engineering.[53] In wheat grain, lutein existed in whole grains, not just in the seed endosperm. Experimental evidence from Qin showed that the content of zeaxanthin and lutein in mature wheat embryos was very low, and other compounds were hardly detected.[35] This implies that most of the carotenoid content is stored in wheat endosperm, including β-carotene. In addition, the up-regulation of carotenogenic gene expression levels explains the lutein and β-carotene increase, and the phytoene accumulation suggests that desaturation enzymes are insufficient in carotenoid biosynthesis, indicating that the carotenoid pathway can be further manipulated at the levels of PDS and ZDS in these transgenic lines.

HYD enzymes play a significant role in the downstream carotenoid pathway, which influences the accumulation of provitamin A in plants. In *Arabidopsis chy1chy2lut2* mutants, β-carotene is the main carotenoid in leaves due to the loss of hydroxylase function.[54] In potato carotenoid metabolic engineering, the accumulation of β-carotene was enhanced by silencing of β-carotene hydroxylases (*CHY1* and *CHY2*) in potato tuber.[26] The transcriptional and translational levels of carotene hydroxylase were simultaneously down-regulated by *HYD* silencing, accompanied by the β-carotene content increasing 10-fold and the lutein and zeaxanthin decreasing in the HYDi-9 transgenic line compared with that of the wild type, suggesting that silencing of *HYD* prevented a part of β-carotene from hydroxylating into lutein or zeaxanthin. Furthermore, although *LCYE* and *LCYB* expression levels were up-regulated in HYDi-9, lycopene accumulation revealed insufficient cyclases in carotene biosynthesis. However, lycopene was not detected in wild-type, suggesting that the activity of cyclases is enough for carotene biosynthesis. One of the possible reasons for this observed phenotype could be that the down-regulation of HYD might lead to a feedback regulation to up-regulate *PSY* expression and add more flux into the pathway. This phenomenon was also reported in other studies, which showed that tuber-specific silencing of *LCYE* and *HYD* in potato resulted in the up-regulation of *PSY*.[26,55] It also suggested that the feedback induction of endogeneous genes was correlated with increased levels of carotenoids or intermediates.[56] In the transgenic line OB-8, the additional carotenoid flux that was added into metabolic flux in the pathway coincided with the up-regulation of genes encoding downstream enzymes, whereas HYD down-regulation led to β-carotene accumulation accompanied by the up-regulation of upstream genes. These results suggest that carotenoid biosynthesis is a complicated system and that metabolic feedback regulation generally exists in the carotenoid biosynthetic pathway.

Combination of "Push Strategy" and "Block Strategy" Significantly Enhances Provitamin A Content in Wheat Endosperm. From the results of transgenic line HYDi-9, β-carotene content was significantly improved compared with wild type. However, wheat grains have a very low carotenoid content, which does not have sufficient flux to accumulate abundant specific products by blocking downstream genes; therefore, the possibility thus exists to further improve β-carotene content by adding upstream flux. In our transgenic line OB-8, the carotenoid content significantly increased, indicating that the additional flux could be introduced by *CrtB* expression. The highest levels of β-carotene accumulation to date were obtained using a combination of "push" and "block" strategies in wheat. Several carotenoid isomers were not calculated into the total carotenoid content; thus, the actual total carotenoid content was even higher than the calculated content. The most famous and successful exploitation case of carotenoid metabolic engineering is "Golden Rice", which can supply sufficient provitamin A through the daily diet. The U.S. recommended dietary allowance (RDA) for 1−3-year-old children is 300 μg of vitamin A.[57] Transgenic staple crops such as maize and potato also reached this RDA standard.[28,58] Although the best wheat transgenic lines were not yet up to the standard, phytoene and lycopene accumulation also showed that there still existed huge potentials for more β-carotene accumulation. Although desaturation and cyclase gene expression levels were highest in the OBI transgenic lines, phytoene and lycopene accumulation showed that changing the expression levels of other carotenogenic genes would shift the rate-limiting action to another step in the wheat carotenoid pathway. These results also showed that integration of another gene, the carotene desaturase gene (*CrtI*), could further improve the content of β-carotene and other carotenoids by increasing the desaturation activity in wheat carotenoid biosynthetic pathway. For instance, in the transgenic wheat with introduced *CrtB* and *CrtI*, the accumulation of β-carotene and total carotenoid was more abundant than sole expression of *CrtB* in transgenic wheat.[9]

In the transgenic line OBI-5, the contents of lutein and zeaxanthin showed a decrease compared with the OB-8 lines, which suggests that the HYDi could exert the effect simultaneously on both β,ε-carotenoid and β,β-carotenoid to accumulate β-carotene. Meanwhile, the higher accumulation of lutein than zeaxanthin in the OB and OBI transgenic lines suggests that the transgenic lines also exhibited a preference for carotenoid metabolic flux toward the β,ε-carotene branch when additional flux was added into the pathway, similar to the wild-type accumulation of lutein.

CrtB and HYDi Regulate β-Carotene Accumulation in Wheat Endosperm through Different Mechanisms. In the present study, overexpression of *CrtB* and silencing of *HYD*

DOI: 10.1021/acs.jafc.5b04279
J. Agric. Food Chem. 2015, 63, 9083−9092

regulate different endogenous carotenoid biosynthesis genes with different variation, suggesting the accumulation of β-carotene through different mechanisms. In OB lines, the expressions of *PDS*, *ZDS*, *LCYE*, *LCYB*, and *HYD2* were up-regulated, and only *PSY* and *HYD1* were unaffected (Figure 7). In contrast, in HYDi lines, the expression of *PSY* was up-regulated, but *ZDS* was unaffected. In both transgenic lines, β-carotene and total carotenoid were enriched by the transgenes. In transgenic line OB expressing *CrtB*, the greater upstream flux introduced into the pathway forward the corresponding downstream gene up-regulation. In contrast, in the HYDi line silencing *HYD*, the accumulation of β-carotene resulted in feedback regulation accompanied by the up-regulation of upstream genes. In addition, the up-regulation levels in HYDi lines were higher than in OB lines. These results suggest that the flux added into OB and HYDi lines may be through different mechanisms, in one case due to the additional flux introduced and in another through the feedback regulation to up-regulate *PSY*.

The presented results indicate that the block strategy to silence *HYD* in the wheat carotenoid pathway seems to be feasible to accumulate β-carotene content specifically. Indeed, the combination of these two strategies is effective in accumulating β-carotene in the wheat endosperm. Our results show that this strategy leads to the highest accumulation of β-carotene in the wheat endosperm; the results also demonstrate the feasibility of utilizing this strategy in carotenoid metabolic engineering and reveal the different mechanisms of β-carotene accumulation.

■ ASSOCIATED CONTENT

Supporting Information

The Supporting Information is available free of charge on the ACS Publications website at DOI: 10.1021/acs.jafc.5b04279.

Primer sequences used in this study; generation of transgenic wheat plants; carotenoid content and composition in T_2 and T_3 seeds from transgenic and control wheat plants; absorption spectra of carotenoids; color characteristics of grains from transgenic and control lines of wheat, CIE *b** values (PDF)

■ AUTHOR INFORMATION

Corresponding Authors

*(G.Y.) E-mail: ygx@hust.edu.cn. Phone: 0086-(0)27-87792271. Fax: 0086-(0)27-87792272.

*(G.H.) E-mail: hegy@hust.edu.cn. Phone: 0086-(0)27-87792271. Fax: 0086-(0)27-87792272.

Present Address

‡Department of Food Science and Engineering, School of Marine Science, Ningbo University, No. 818 Fenghua Road, Ningbo 315211, Zhejiang Province, China.

Author Contributions

†J.Z., X.W., and Y.M. contributed equally to this work.

Funding

This work was supported by the International S&T Cooperation Key Projects of the Chinese Ministry of Science and Technology (Grant 2009DFB30340), the National Genetically Modified New Varieties of Major Projects of China (Grant 2015ZX08002004-007 and 2015ZX08010004), the National Natural Science Foundation of China (No. 31071403 and 31371614), and the Research Fund for the Doctoral Program of Higher Education of China (Grant 20120142110075).

Notes

The authors declare no competing financial interest.

■ ACKNOWLEDGMENTS

We acknowledge Dr. Sandmann from the Institute of Molecular Bioscience, J. W. Goethe University, Frankfurt am Main, Germany, for providing the plasmid pACCRT-EB. We thank Dandan Li for editorial assistance and helpful discussions.

■ ABBREVIATIONS USED

CrtB, bacterial phytoene synthase gene; CYP, ε-ring hydroxylase; DAP, days after pollination; HPLC, high-performance liquid chromatography; HYD, carotenoid hydroxylase; LCYB, lycopene β-cyclase; LCYE, lycopene ε-cyclase; OE, overexpression; PDS, phytoene desaturase; PSY, phytoene synthase; QTL, quantitative trait locus; RNAi, RNA interference; VAD, vitamin A deficiency; ZDS, ζ-carotene desaturase

■ REFERENCES

(1) Tanaka, Y.; Sasaki, N.; Ohmiya, A. Biosynthesis of plant pigments: anthocyanins, betalains and carotenoids. *Plant J.* **2008**, *54*, 733−749.

(2) DellaPenna, D.; Pogson, B. J. Vitamin synthesis in plants: tocopherols and carotenoids. *Annu. Rev. Plant Biol.* **2006**, *57*, 711−738.

(3) Zhu, C.; Bai, C.; Sanahuja, G.; Yuan, D.; Farre, G.; Naqvi, S.; Shi, L.; Capell, T.; Christou, P. The regulation of carotenoid pigmentation in flowers. *Arch. Biochem. Biophys.* **2010**, *504*, 132−141.

(4) Fraser, P. D.; Bramley, P. M. The biosynthesis and nutritional uses of carotenoids. *Prog. Lipid Res.* **2004**, *43*, 228−265.

(5) Zhu, C.; Sanahuja, G.; Yuan, D.; Farré, G.; Arjó, G.; Berman, J.; Zorrilla-López, U.; Banakar, R.; Bai, C.; Pérez-Massot, E. Biofortification of plants with altered antioxidant content and composition: genetic engineering strategies. *Plant Biotechnol. J.* **2013**, *11*, 129−141.

(6) Farré, G.; Bai, C.; Twyman, R. M.; Capell, T.; Christou, P.; Zhu, C. Nutritious crops producing multiple carotenoids−a metabolic balancing act. *Trends Plant Sci.* **2011**, *16*, 532−540.

(7) Pérez-Massot, E.; Banakar, R.; Gómez-Galera, S.; Zorrilla-López, U.; Sanahuja, G.; Arjó, G.; Miralpeix, B.; Vamvaka, E.; Farré, G.; Rivera, S. M. The contribution of transgenic plants to better health through improved nutrition: opportunities and constraints. *Genes Nutr.* **2013**, *8*, 29−41.

(8) Shewry, P. Wheat. *J. Exp. Bot.* **2009**, *60*, 1537−1553.

(9) Wang, C.; Zeng, J.; Li, Y.; Hu, W.; Chen, L.; Miao, Y.; Deng, P.; Yuan, C.; Ma, C.; Chen, X.; Zang, M.; Wang, Q.; Li, K.; Chang, J.; Wang, Y.; Yang, G.; He, G. Enrichment of provitamin A content in wheat (*Triticum aestivum* L.) by introduction of the bacterial carotenoid biosynthetic genes *CrtB* and *CrtI*. *J. Exp. Bot.* **2014**, *65*, 2545−56.

(10) Cong, L.; Wang, C.; Chen, L.; Liu, H. J.; Yang, G. X.; He, G. Y. Expression of phytoene synthase1 and carotene desaturase crtl genes result in an increase in the total carotenoids content in transgenic elite wheat (*Triticum aestivum* L.). *J. Agric. Food Chem.* **2009**, *57*, 8652−8660.

(11) Ruiz-Sola, M. A.; Rodriguez-Concepcion, M. Carotenoid biosynthesis in *Arabidopsis*: a colorful pathway. *Arabidopsis Book* **2012**, *10*, e0158.

(12) Cunningham, F. X.; Sun, Z.; Chamovitz, D.; Hirschberg, J.; Gantt, E. Molecular structure and enzymatic function of lycopene cyclase from the cyanobacterium *Synechococcus* sp. strain PCC7942. *Plant Cell* **1994**, *6*, 1107−1121.

(13) Park, H.; Kreunen, S. S.; Cuttriss, A. J.; DellaPenna, D.; Pogson, B. J. Identification of the carotenoid isomerase provides insight into carotenoid biosynthesis, prolamellar body formation, and photomorphogenesis. *Plant Cell* **2002**, *14*, 321−332.

DOI: 10.1021/acs.jafc.5b04279
J. Agric. Food Chem. 2015, 63, 9083−9092

(14) Farré, G.; Blancquaert, D.; Capell, T.; Van Der Straeten, D.; Christou, P.; Zhu, C. Engineering complex metabolic pathways in plants. *Annu. Rev. Plant Biol.* **2014**, *65*, 187−223.
(15) Farré, G.; Sanahuja, G.; Naqvi, S.; Bai, C.; Capell, T.; Zhu, C.; Christou, P. Travel advice on the road to carotenoids in plants. *Plant Sci.* **2010**, *179*, 28−48.
(16) Pozniak, C.; Knox, R.; Clarke, F.; Clarke, J. Identification of QTL and association of a phytoene synthase gene with endosperm colour in durum wheat. *Theor. Appl. Genet.* **2007**, *114*, 525−537.
(17) Li, F. Q.; Vallabhaneni, R.; Yu, J.; Rocheford, T.; Wurtzel, E. T. The maize phytoene synthase gene family: overlapping roles for carotenogenesis in endosperm, photomorphogenesis, and thermal stress tolerance. *Plant Physiol.* **2008**, *147*, 1334−1346.
(18) Li, F.; Vallabhaneni, R.; Wurtzel, E. T. PSY3, a new member of the phytoene synthase gene family conserved in the Poaceae and regulator of abiotic stress-induced root carotenogenesis. *Plant Physiol.* **2008**, *146*, 1333−1345.
(19) Gallagher, C. E.; Matthews, P. D.; Li, F.; Wurtzel, E. T. Gene duplication in the carotenoid biosynthetic pathway preceded evolution of the grasses. *Plant Physiol.* **2004**, *135*, 1776−1783.
(20) Zeng, J.; Wang, C.; Chen, X.; Zang, M.; Yuan, C.; Wang, X.; Wang, Q.; Li, M.; Li, X.; Chen, L. The lycopene β-cyclase plays a significant role in provitamin A biosynthesis in wheat endosperm. *BMC Plant Biol.* **2015**, *15*, 112.
(21) Hirschberg, J. Carotenoid biosynthesis in flowering plants. *Curr. Opin. Plant Biol.* **2001**, *4*, 210−8.
(22) Matthews, P. D.; Wurtzel, E. T. 5.3 Biotechnology of food colorant production. In *Food Colorants: Chemical and Functional Properties*; CRC: Boca Raton, FL, USA, 2007; p 34810.1201/9781420009286.sec5b.
(23) Yan, J.; Kandianis, C. B.; Harjes, C. E.; Bai, L.; Kim, E.-H.; Yang, X.; Skinner, D. J.; Fu, Z.; Mitchell, S.; Li, Q. Rare genetic variation at *Zea mays* crtRB1 increases β-carotene in maize grain. *Nat. Genet.* **2010**, *42*, 322−327.
(24) Arango, J.; Jourdan, M.; Geoffriau, E.; Beyer, P.; Welsch, R. Carotene hydroxylase activity determines the levels of both α-carotene and total carotenoids in orange carrots. *Plant Cell* **2014**, *26*, 2223−2233.
(25) Pons, E.; Alquézar, B.; Rodríguez, A.; Martorell, P.; Genovés, S.; Ramón, D.; Rodrigo, M. J.; Zacarías, L.; Peña, L. Metabolic engineering of β-carotene in orange fruit increases its in vivo antioxidant properties. *Plant Biotechnol. J.* **2014**, *12*, 17−27.
(26) Diretto, G.; Welsch, R.; Tavazza, R.; Mourgues, F.; Pizzichini, D.; Beyer, P.; Giuliano, G. Silencing of beta-carotene hydroxylase increases total carotenoid and β-carotene levels in potato tubers. *BMC Plant Biol.* **2007**, *7*, 11.
(27) Paine, J. A.; Shipton, C. A.; Chaggar, S.; Howells, R. M.; Kennedy, M. J.; Vernon, G.; Wright, S. Y.; Hinchliffe, E.; Adams, J. L.; Silverstone, A. L.; Drake, R. Improving the nutritional value of Golden Rice through increased pro-vitamin A content. *Nat. Biotechnol.* **2005**, *23*, 482−487.
(28) Aluru, M.; Xu, Y.; Guo, R.; Wang, Z. G.; Li, S. S.; White, W.; Wang, K.; Rodermel, S. Generation of transgenic maize with enhanced provitamin A content. *J. Exp. Bot.* **2008**, *59*, 3551−3562.
(29) Ravanello, M. P.; Ke, D. Y.; Alvarez, J.; Huang, B. H.; Shewmaker, C. K. Coordinate expression of multiple bacterial carotenoid genes in canola leading to altered carotenoid production. *Metab. Eng.* **2003**, *5*, 255−263.
(30) Fraser, P. D.; Romer, S.; Shipton, C. A.; Mills, P. B.; Kiano, J. W.; Misawa, N.; Drake, R. G.; Schuch, W.; Bramley, P. M. Evaluation of transgenic tomato plants expressing an additional phytoene synthase in a fruit-specific manner. *Proc. Natl. Acad. Sci. U. S. A.* **2002**, *99*, 1092−1097.
(31) Zhu, C. F.; Naqvi, S.; Breitenbach, J.; Sandmann, G.; Christou, P.; Capell, T. Combinatorial genetic transformation generates a library of metabolic phenotypes for the carotenoid pathway in maize. *Proc. Natl. Acad. Sci. U. S. A.* **2008**, *105*, 18232−18237.
(32) Rosati, C.; Aquilani, R.; Dharmapuri, S.; Pallara, P.; Marusic, C.; Tavazza, R.; Bouvier, F.; Camara, B.; Giuliano, G. Metabolic engineering of β-carotene and lycopene content in tomato fruit. *Plant J.* **2000**, *24*, 413−419.
(33) Romer, S.; Lubeck, J.; Kauder, F.; Steiger, S.; Adomat, C.; Sandmann, G. Genetic engineering of a zeaxanthin-rich potato by antisense inactivation and co-suppression of carotenoid epoxidation. *Metab. Eng.* **2002**, *4*, 263−272.
(34) Mares, D. J.; Campbell, A. Mapping components of flour and noodle colour in Australian wheat. *Aust. J. Agric. Res.* **2001**, *52*, 1297−1309.
(35) Qin, X.; Zhang, W.; Dubcovsky, J.; Tian, L. Cloning and comparative analysis of carotenoid β-hydroxylase genes provides new insights into carotenoid metabolism in tetraploid (*Triticum turgidum* ssp. *durum*) and hexaploid (*Triticum aestivum*) wheat grains. *Plant Mol. Biol.* **2012**, *80*, 631−646.
(36) Sambrook, J.; Fritsch, E. F.; Maniatis, T. *Molecular Cloning: A Laboratory Manual*, 2nd ed.; Cold Spring Harbor Laboratory: Cold Spring Harbor, NY, USA, 1989.
(37) Fu, D.; Uauy, C.; Blechl, A.; Dubcovsky, J. RNA interference for wheat functional gene analysis. *Transgenic Res.* **2007**, *16*, 689−701.
(38) Sparks, C.; Jones, H. Transformation of wheat by biolistics. In *Transgenic Crops of the World*; Springer: New York, 2004; pp 19−34.
(39) Miao, Y.; Chen, L.; Wang, C.; Wang, Y.; Zheng, Q.; Gao, C.; Yang, G.; He, G. Expression, purification and antimicrobial activity of puroindoline A protein and its mutants. *Amino Acids* **2012**, *43*, 1689−1696.
(40) He, G.; Rooke, L.; Steele, S.; Békés, F.; Gras, P.; Tatham, A.; Fido, R.; Barcelo, P.; Shewry, P.; Lazzeri, P. Transformation of pasta wheat with high-molecular-weight glutenin subunit genes and modification of dough functionality. *Mol. Breed.* **1999**, *5*, 377−386.
(41) Ma, F.; Li, M.; Li, T.; Liu, W.; Liu, Y.; Li, Y.; Hu, W.; Zheng, Q.; Wang, Y.; Li, K. Overexpression of avenin-like b proteins in bread wheat (*Triticum aestivum* L.) improves dough mixing properties by their incorporation into glutenin polymers. *PLoS One* **2013**, *8*, e66758.
(42) Rodríguez-Suárez, C.; Mellado-Ortega, E.; Hornero-Méndez, D.; Atienza, S. G. Increase in transcript accumulation of Psy1 and e-Lcy genes in grain development is associated with differences in seed carotenoid content between durum wheat and tritordeum. *Plant Mol. Biol.* **2014**, *84*, 659−673.
(43) Sander, L. C.; Sharpless, K. E.; Pursch, M. C_{30} Stationary phases for the analysis of food by liquid chromatography. *J. Chromatogr. A* **2000**, *880*, 189−202.
(44) Fraser, P. D.; Pinto, M. E. S.; Holloway, D. E.; Bramley, P. M. Application of high-performance liquid chromatography with photodiode array detection to the metabolic profiling of plant isoprenoids. *Plant J.* **2000**, *24*, 551−558.
(45) Rodriguez-Amaya, D.; Kimura, M. *Harvest Plus Handbook for Carotenoid Analysis*; International Food Policy Research Institute and International Center for Tropical Agriculture: Washington, DC, USA, 2004.
(46) Liu, Q.; Xu, J.; Liu, Y.; Zhao, X.; Deng, X.; Guo, L.; Gu, J. A novel bud mutation that confers abnormal patterns of lycopene accumulation in sweet orange fruit (*Citrus sinensis* L. Osbeck). *J. Exp. Bot.* **2007**, *58*, 4161−4171.
(47) Humphries, J. M.; Graham, R. D.; Mares, D. J. Application of reflectance colour measurement to the estimation of carotene and lutein content in wheat and triticale. *J. Cereal Sci.* **2004**, *40*, 151−159.
(48) Black, R. E.; Allen, L. H.; Bhutta, Z. A.; Caulfield, L. E.; De Onis, M.; Ezzati, M.; Mathers, C.; Rivera, J. Maternal and child undernutrition: global and regional exposures and health consequences. *Lancet* **2008**, *371*, 243−260.
(49) Underwood, B. A. Vitamin A deficiency disorders: international efforts to control a preventable "pox". *J. Nutr.* **2004**, *134*, 231S−236S.
(50) WHO. *Global Prevalence of Vitamin A Deficiency in Populations at Risk 1995−2005: WHO Global Database on Vitamin A Deficiency*; Geneva, Switzerland, 2009.
(51) Galpaz, N.; Wang, Q.; Menda, N.; Zamir, D.; Hirschberg, J. Abscisic acid deficiency in the tomato mutant high-pigment 3 leading to increased plastid number and higher fruit lycopene content. *Plant J.* **2008**, *53*, 717−730.

DOI: 10.1021/acs.jafc.5b04279
J. Agric. Food Chem. 2015, 63, 9083−9092

(52) Kolotilin, I.; Koltai, H.; Tadmor, Y.; Bar-Or, C.; Reuveni, M.; Meir, A.; Nahon, S.; Shlomo, H.; Chen, L.; Levin, I. Transcriptional profiling of high pigment-2dg tomato mutant links early fruit plastid biogenesis with its overproduction of phytonutrients. *Plant Physiol.* **2007**, *145*, 389−401.
(53) Bai, C.; Capell, T.; Berman, J.; Medina, V.; Sandmann, G.; Christou, P.; Zhu, C. Bottlenecks in carotenoid biosynthesis and accumulation in rice endosperm are influenced by the precursor−product balance. *Plant Biotechnol. J.* **2015**, n/a.
(54) Fiore, A.; Dall'Osto, L.; Fraser, P. D.; Bassi, R.; Giuliano, G. Elucidation of the *β*-carotene hydroxylation pathway in *Arabidopsis thaliana*. *FEBS Lett.* **2006**, *580*, 4718−4722.
(55) Diretto, G.; Tavazza, R.; Welsch, R.; Pizzichini, D.; Mourgues, F.; Papacchioli, V.; Beyer, P.; Giuliano, G. Metabolic engineering of potato tuber carotenoids through tuber-specific silencing of lycopene epsilon cyclase. *BMC Plant Biol.* **2006**, *6*, 13.
(56) Avendaño-Vázquez, A.-O.; Cordoba, E.; Llamas, E.; San Román, C.; Nisar, N.; De la Torre, S.; Ramos-Vega, M.; de la Luz Gutiérrez-Nava, M.; Cazzonelli, C. I.; Pogson, B. J. An uncharacterized apocarotenoid-derived signal generated in *ζ*-carotene desaturase mutants regulates leaf development and the expression of chloroplast and nuclear genes in *Arabidopsis*. *Plant Cell* **2014**, *26*, 2524−2537.
(57) Trumbo, P.; Yates, A. A.; Schlicker, S.; Poos, M. Dietary reference intakes: vitamin A, vitamin K, arsenic, boron, chromium, copper, iodine, iron, manganese, molybdenum, nickel, silicon, vanadium, and zinc. *J. Am. Diet. Assoc.* **2001**, *101*, 294−301.
(58) Diretto, G.; Al-Babili, S.; Tavazza, R.; Papacchioli, V.; Beyer, P.; Giuliano, G. Metabolic engineering of potato carotenoid content through tuber-specific overexpression of a bacterial mini-pathway. *PLoS One* **2007**, *2*, e350.

DOI: 10.1021/acs.jafc.5b04279
J. Agric. Food Chem. 2015, 63, 9083−9092

Table 1. Summary of Reported Findings from Previous in Vivo Investigations into the Effect of Gel Strength on Volatile Release

study system	ref	volatile release with chewing	perception	conclusion
whey protein gels 4−11% APCI-MS	16	no difference in nose-space concentrations as gel strength increased for diacetyl or ethyl butanoate	decrease in time intensity flavor perception as gel strength increased	differences in perceived flavor were psychophysical rather than based on differences in in vivo release
HPMC gels 0−2% APCI-MS	17	no differences in in-nose release of ethyl butanoate	decrease in perceived strawberry flavor with greater viscosity	cross-modal perceptual or receptor level influence of viscosity on perceived flavor, i.e., not physicochemical
gelatin gels 2−10% APCI-MS	14	ethyl hexanoate, AUC ↓ with ↑ firmness, increase T_{max}	no sensory data reported	decrease in release with increased gel thickness
pectin 1.5−2.0% PTR-MS	36	some differences in release depending on the mastication rates	no sensory data reported	
pectin 0.75−1% PTR-MS	15	increase in AUC, I_{max}, or T_{max} for range of volatiles with increased rigidity	decrease in perceived strawberry odor and flavor	in contrast to static headspace data, where release ↓ with increased pectin
gelatin 1.3−1.8% PTR-MS	15	no increase in AUC, I_{max} or T_{max} for range of volatiles	decrease in perceived strawberry odor and flavor	in contrast to static headspace data, where release ↓ with increased gelatin
whey protein gels 4−10%	12, 13	no differences in total AUC or I_{max} for ethyl butanoate, but increased preswallow T_{max}; significantly greater release from 4% gel in the first 10 s of chewing	lower sensory ratings for harder gels	faster volatile release from softer gels, however total release similar in hard and soft gels
casein gels of different hardness	37	release of a range of volatiles was greater and faster from harder gels in vivo; no differences in the in vitro model systems.	no sensory information measured	key parameter for release differences was the interaction of the gels of different hardness with the human masticatory apparatus
gelatin 5−15% PTR-MS	18	few differences in release patterns between 5 and 15% gelatin with chewing; large differences with melting (nonchewing) protocol	mean temporal dominance of sensation data increased with gel strength	decrease in release of ethyl hexanoate with increased gel strength; timing of release different with the in mouth melting
cheese model system APCI-MS	38	ethyl propanoate release, ↑ firmness, ↑ fat 2-nonanone release ≠ firmness 2-nonanone ↓ fat		despite large differences in individual release, overall observations valid

grade aroma compounds were donated by Givaudan (Baulkam Hills, Australia), namely, a homologous series of methyl ketones (2-butanone, 2-pentanone, 2-heptanone, 2-octanone, and 2-nonanone), ethyl butanoate, and ethyl hexanoate (Table 2). A stock solution of the volatile mix was prepared at 5% (v/v) of each compound in ethanol. Sodium chloride was purchased from Sigma-Aldrich (USP grade; Castle Hill, Australia). A soy-based stable lipid emulsion, IVELIP (20% fat), was supplied by Baxter Health (Toongabbie, Australia).

Gel Preparation. The stock solution of volatiles was used for aromatization of the gels. Most of the volatiles are present in blue cheese flavor and have been used previously by our group.[4,11,24] Characteristic odor qualities and fat solubility ($K_{o/w}$) are listed in Table 2. Sodium chloride was added to all gels at a concentration of 0.8% w/w sodium. This concentration was chosen to represent the average salt present in cheese (NUTTAB 2010 food nutrient database, Food Standards Australia New Zealand). It should be noted that the IVELIP was very low in sodium (0.03% w/v). Deionized (reverse osmosis) water was used to prepare the gels. Gels of increasing rigidity were made by adding agar according to a logarithmic concentration series: 1.0, 1.7, 2.9, and 5.0% (w/v). The total amount of fat in gels (2, 5, and 10% w/v) was adjusted by addition of appropriate amounts IVELIP. Two drops of red food coloring were added to allow easy visual inspection of the homogeneity of mixing.

Dry ingredients and fat emulsion (if used) were weighed into Schott bottles (500 mL) placed in a boiling water bath for 30 min with vigorous shaking at 5 min intervals. Hot samples were poured into graduated cylindrical screw-top plastic containers (~120 mL volume) to the 100 mL mark. After cooling to ~50 °C, a volume of the volatile mix stock solution (50 μL; 5% each compound) was quickly added under the surface of the liquid to obtain a final concentration of ~25 ppm (Table 2). Containers were immediately sealed and agitated to ensure homogeneous mixing and then placed in an ice bath to set. Samples were stored at 4 °C overnight to fully set. Prior to evaluation, samples were unmolded, sliced into cylinders (19 mm radius × 15 mm thickness), and then cut into quarters of ~5 g (total sample weight ~ 20 g).

Gel Rheology. Agar gel cylinders (14 mm × 14 mm height) were prepared for large deformation analysis. Dodecane (99%, Sigma-Aldrich) was used as lubricant on the interactive surfaces between the cylinder and the instrument. Compression tests were performed in duplicate using an Instron 5564 instrument (Instron Pty. Ltd., Melbourne, Australia) loaded with a 500N cell and a 35 mm aluminum cylinder probe at a crosshead speed of 60 mm/min. The sample was compressed to 50% of its original height (7 mm). Once the set height was reached, the probe was automatically lifted back to the starting position. The true stress (σ_e) and true strain (ε_e) of the first compression were calculated using the following equations: $\sigma_e = FH/(A_0H_0)$ and $\varepsilon_e = \ln(H/H_0)$, where F is the force measured during compression, A_0 is the initial cross-sectional area of the sample, H_0 is the initial sample height, and H is the deformed sample height. Young's modulus was calculated as $E = \sigma_e/\varepsilon_e$, where E is a measure of the rigidity or brittleness of a gel. E was determined in duplicate for the pure agar gels series and also for the 5% agar gels with the addition of different fat levels (0, 2, 5, and 10% fat).

Time−Intensity Sensory Evaluation and Oral Breakdown Studies. Approval to conduct the sensory studies with human subjects was obtained from the CSIRO low risk ethics committee (LR06-2011). A discrete interval time−intensity method was used to measure dynamic sensory perception anchored by chew number, similar to a progressive profiling method.[25] This method was developed to enable comparisons between measurements of sensory perception with aroma release data at the same point during mastication.

An experienced trained sensory panel (n = 10) participated in two training sessions prior to evaluation. Assessors were familiarized with the samples, and the assessment technique was standardized. The sensory characteristics of the gels and changes over the course of the eating event were defined by a consensus descriptive vocabulary that included five attributes: *resistance to chewing* (force required to bite down on the sample), *particle size* (perceived particle size assessed by moving the sample between the tongue and the palate), *blue cheese flavor* (the dominant integrated flavor percept in the volatile mix), *overall flavor*

DOI: 10.1021/acs.jafc.5b03441
J. Agric. Food Chem. 2015, 63, 9093−9102

Table 2. Volatile Compounds Spiked into the Agar Gels, Corresponding Ions (m/z) Measured by the PTR-MS, Lipophilicity ($K_{o/w}$), Concentration in Gel, and Aroma Character

aroma compound	ion m/z ($M + H^+$)	$K_{o/w}$[a]	concn in gel (mg/kg)	concn in gel (mM)	aroma perception[b]
2-butanone	73	1.9	20.02	0.28	chemical, slight fruity green
2-pentanone	87	8.1	20.02	0.23	sweet, fruity, banana-like
2-heptanone	115	95.5	20.32	0.18	fruity, spicy, banana
2-octanone	129	234.4	20.32	0.19	dairy, waxy, cheese, woody, mushroom
2-nonanone	143	1380	20.42	0.17	cheesy, green, fruity, dairy, dirty, buttery
ethyl butanoate	117	70.8	21.75	0.18	fruity, sweet, tutti-frutti
ethyl hexanoate	145	676	21.67	0.15	fruity, pineapple, banana, winey

[a] $K_{o/w}$ values were obtained from the ChemSpider database (http://www.chemspider.com/), Royal Society of Chemistry. [b] From ref 39.

intensity (the sum of all flavor sensations in the mouth, including taste and aroma), and *salty taste* (the saltiness intensity defined by reference sodium chloride solutions). The panel proceeded to the evaluation of the attributes at four time points, 2, 5, and 10 chews, and finally when subjects naturally wanted to swallow. Subjects were instructed to spit out the masticated samples into a provided spittoon.

Samples were presented in triplicate in randomized order in 2 h sessions over two consecutive days. The perceived intensity of attributes was measured using 100 mm unstructured line scales scale anchored at 5 and 95%. For a given day, assessors evaluated only three attributes to minimize sensory fatigue (resistance to chewing/particle size/overall flavor intensity or resistance to chewing/blue cheese flavor/salty taste). Data were collected using Compusense *five* (release 4.6, Guelph, ON, Canada). Hence, a total of 30 replicate assessments were available for each sensory attribute (10 assessors × 3) per sample at each time point.

On separate days, panelists evaluated the oral processing parameters. Evaluation was conducted in triplicate, and samples were presented in a randomized order. The number of chews to swallow (NCS) as well as the time to reach the need to swallow (TTS) measured with a stopwatch was recorded. Subjects were instructed to continue chewing each sample until there was no further reduction in the perceived size of particles (size of the pieces sensed with the tongue and palate). This was measured as the number of chews to fine particles (NCF) and time to form fine particles (TTF). A total of 32 replicate assessments (16 subjects × 2) were used in statistical analyses.

In Vivo Aroma Release Using Proton Transfer Reaction Mass Spectrometry (PTR-MS). Aroma release during mastication of agar gels was measured using human subjects ($n = 6$) interfaced with a high-sensitivity quadrupole PTR-MS (Ionicon Analytik GmbH, Innsbruck, Austria) using a controlled breathing and chewing protocol.[5] The selected subjects had participated in the descriptive profiling of the gels and had previous experience performing in vivo PTR-MS experiments. During initial piloting experiments, the absence of interfering ions from the pure lipid emulsion was confirmed (Table 2).

Subjects introduced one 5 g cube of gel sample into their mouth after five background breaths. After sample introduction (on breath 6), subjects were required to chew once only during each inhalation for the first five breath cycles for maximum resolution in the early stages of mastication. For the subsequent breath cycles (11−25) subjects were trained to chew twice during the in-breath and twice during the out-breath (4 chews per breath cycle); full breath cycle duration was 3 s. Previous testing determined that this was a sufficient number of chews to process the hardest gel (5% agar) to the point of swallow for all subjects. Regardless of the gel hardness and swallow time, subjects were required to continue chewing each sample for the full 25 breath cycles (65 chews) to obtain a complete data set for each sample. Each subject assessed samples in quadruplicate (i.e., 6 samples × 6 subjects × 4 replicates × 7 ions = 1008 release data). Hence, for each sample there were a total of 24 replicates (6 panelists × 4 replicates).

Volatiles were measured by the PTR-MS using multiple ion detection mode. Subjects breathed through a soft plastic disposable cannula, and the exhaled breath was drawn into the reaction chamber of the PTR-MS.[4] The parameters of the drift tube were as follows: drift voltage, 550 V; pressure, 2.2 mbar; temperature, 70 °C. Exhaled nostril breath was drawn through the inlet tubing at a rate of 400 mL min^{-1} and at a rate of 15 mL min^{-1} into the reaction chamber. Data were acquired at a rate of 2 Hz.

In Vitro Volatile Release. To help clarify the in vivo data, a simple in vitro system was developed using a commercial coffee grinder (Breville, Australia; model-BCG 300/A). Gas-tight inlet and outlet Luer-lock fittings were engineered into the grinder lid and connected directly to the inlet tube of PTR-MS via an automated solenoid switching relay. Agar gel samples, prepared identically as for in vivo studies, were sliced (∼20 g) into four equal portions of ∼5g and placed inside the grinder, between the four cutting blades. The headspace was allowed to equilibrate for 5 min before the solenoid valve was opened to sample the headspace concentrations. After 100 s of volatile measurement, the blender was turned on for 20 s to break the gel into fine particles and then turned off, and the PTR-MS analysis was continued for ∼100 s. Data from the first 30 s of turning on the blender were used in the statistical analyses. The same PTR-MS conditions, protocols, and gels were used as in vivo experiments. Four replicates were obtained for each sample.

Data Processing and Data Analysis. The quantitative ratings for each sensory attribute were collated and analyzed at each time point (after 2, 5, and 10 chews and final) using analysis of variance (ANOVA) with agar, fat (when relevant), and assessor as main fixed treatment factors and attributes as dependent variables.

PTR-MS concentration data files were imported into Excel (Microsoft) and processed in a manner similar to that described in previous work.[5] Data from the initial five breath cycles were removed from files before calculation of the area under the volatile release curve (AUC) and maximum intensity (I_{max}) using the replicate raw release curves for statistical analysis by multivariate analysis of variance (MANOVA) using the GenStat statistical software package (16th edition, VSN International, Hemel Hempstead, UK). Initial rate of flavor release was expressed as average AUC per chew for the first nine chews only. Fixed effects of agar strength, fat level, volatile ion, and subject on the release curve parameters were determined. Panel-averaged AUC per chew data were used to model volatile release curves for each volatile ion using the data modeling software IGOR-Pro (Wavemetrics Inc., Lake Oswego, OR, USA). Panel-averaged raw volatile release curves were imported into IGOR-PRO, and the curves were smoothed twice using a moving box average function (20 data points). A similar approach was used to analyze the in vitro release data. To assess agar effects, the raw data from the pure agar series were analyzed. For the effect of fat, data from 1 and 5% gar gels, with either no added fat (0%) or 10% fat, were analyzed.

RESULTS AND DISCUSSION

Gel Rheological Parameters. As expected, E increased with increasing gel strength, which was more or less linear at lower gels strengths (Table 3). A strong increase in the value of E in the transition from 2.9 to 5% agar was measured; the 5% gel was >3 times more rigid than the 2.9% agar gel. Similar nonlinear or exponential relationships between agar concentration and gel hardness were reported previously and possibly reflected a corresponding abrupt increase in the agarose network density.[22,26] The introduction of fat (2%) into the 5% agar gel

DOI: 10.1021/acs.jafc.5b03441
J. Agric. Food Chem. 2015, 63, 9093−9102

Table 3. Mean Values (n = 2) of Young's Modulus (E) ± Standard Deviation for Pure Agar Gels and 5% Agar Gels with Added Fat

pure agar series		5% agar with fat	
agar (%)	E (N m^{-2})	fat (%)	E (N m^{-2})
1.0	46 ± 6	0	635 ± 6
1.7	83 ± 2	2	175 ± 12
2.9	186 ± 5	5	156 ± 3
5.0	635 ± 6	10	145 ± 9

profoundly decreased the gel rigidity; a >3-fold reduction in E was measured. Fat droplets disrupt the agarose gel network and introduce stress points, which fail more easily. Further addition of fat resulted in smaller incremental decreases in E, indicating softer gels.

Effect of Agar and Fat on Oral Processing Parameters. Both the gel strength and fat content had highly significant effects on the oral processing parameters measured (Table 4). As expected, both the NCS and the TTS increased as the agar strength increased, signifying that a greater amount of oral processing was required to reduce the gel into particles and form a bolus ready for swallowing. The largest incremental increase in NCS and TTS was measured when the gel strength increased from 1.7 to 2.9% agar content, suggesting a significant change in the gel structure affecting oral processing. A smaller increase in the parameters was measured in the transition from 2.9 to 5% agar, somewhat different from the rheological data (E). It should be noted that we did not measure the peak force of each chew; this parameter may have corresponded more closely to the rheological data. Fat (10%) decreased both NCS and TTS for each agar gel strength; this is thought to be due to the softening effect of the oil as it disrupts the agar network and provides areas of structural weakness. The greatest impact of fat was in the 2.9% agar gel, indicated by the largest drop in E, resulting in less oral breakdown work (Table 3). The added fat would have also resulted in greater lubrication, a more cohesive bolus formation, and subsequent shorter swallowing times.[8] These data clearly show that the preswallow residence time in the oral cavity increased with increased agar gel strength because more chews were required before a bolus for swallowing could be produced.

Effect of Agar on Gel Sensory Properties. The perceived resistance to chewing of the gel was directly proportional to the agar gel strength (Figure 1, top row). Significant differences (P < 0.001) in gel resistance were measured at each time point during chewing for the pure agar gels, except at the point of swallow (final chew), where only small differences were measured. Perceived particle size was also proportional to the gel strength, with only small differences at final chew. The overall effect of agar on perceived saltiness was significant (P < 0.001). Perceived saltiness increased with chew number (up to 10 chews) for all samples. Agar concentration also affected saltiness perception with no difference measured between the 1 and 1.7% agar gels but large decreases in the transition to the 2.9 and 5% agar gels. Even after reduction of gels to fine particles, differences in perceived saltiness persisted, suggesting residual physical entrapment of sodium ions. Decreasing perceived saltiness with increasing gel strength has been described previously.[27] Although blue cheese flavor perception decreased with increased gel strength, the difference reached significance only at the final chew in the 5% agar gel. Overall flavor intensity decreased proportionally to gel strength. In summary, the sensory data clearly indicated that the flavor perception decreased as the agar gel strength increased, in agreement with most other studies (Table 1).

Effect of Fat on Gel Sensory Properties. Addition of 10% fat to 1 and 5% agar gels decreased the perceived resistance to chewing and perceived particle size compared to the pure agar gels (Figure 1, bottom row). This effect was mainly apparent for the harder 5% agar gels, probably because at 1% agar, the gel is already soft and the oil droplets easily fit within the agar structure, affecting only slightly the agar biopolymer network. Blue cheese flavor decreased with the addition of fat, especially in the softer 1% agar gel systems. Lipophilic volatiles would have partitioned into the fat droplets within the gels. In the softer gel, the relative effect of fat on blue cheese flavor suppression was greater than at 5%. At the higher agar concentration, structural impedance of diffusion within the agarose biopolymer was also expected to be a significant mechanism in release suppression.

Unexpectedly, the effect of fat on saltiness perception was not significant at any time point, in contrast to other studies.[28] Interestingly, the perceived overall flavor intensity decreased with fat addition at 1% agar gel strength, but increased significantly with fat addition at 5% gel strength. Although blue cheese flavor decreased with added fat, the effect was significant only after 10 chews and at the final chew for the 5% agar gel. Perceived overall flavor intensity was suppressed by fat in the softer 1% gel, but increased in the 5% gel. These differences in overall flavor perception appeared to be independent of the differences in perceived saltiness. A possible explanation was that the 1% agar gel (with and without added fat) had the same perceived resistance to chew, suggesting a similar rate of gel breakdown. Once the gel structure was fully broken down, partitioning of volatiles into the fat phase was expected to significantly affect release. In the 5% agar gels the addition of fat decreased resistance to chewing, facilitating more rapid gel breakdown, an increase in surface area, and faster release.

Agar Effect on in Vivo Volatile Release. Smoothed average agar curves for 2-butanone (low fat solubility), 2-heptanone (intermediate fat solubility), 2-nonanone (high fat solubility), ethyl butanoate (intermediate fat solubility), and ethyl hexanoate (high fat solubility) are shown in Figure 2 (top

Table 4. Mean (n = 32[b]) Oral Breakdown Parameters Measured for the Pure Agar Gels and Agar Gels with 10% Added Fat (IVELIP)

	pure agar				agar + 10% fat				agar		fat	
agar concn	1.0%	1.7%	2.9%	5.0%	1.0%	1.7%	2.9%	5.0%	LSD	P	LSD[a]	P
no. of chews to swallow (NCS)	18.3	26.3	37.3	41.9	16.5	23.2	29.9	40.8	2.4	<0.001	1.6	<0.001
time to swallow (s) (TTS)	11.1	16.3	22.4	26	10.6	14.3	17.9	23	1.5	<0.001	1.2	<0.001
no. of chews to fine particles (NCF)	37.3	50.6	63.2	71.7	32.9	41.5	52.4	67.8	3.4	<0.001	2.4	<0.001
time to fine particles (s) (TTF)	24.7	32.2	41	44.8	22.6	27.9	33.3	42.7	2.6	<0.001	1.8	<0.001

[a]LSD, least significant difference calculated for the effects of agar and fat. [b]16 subjects × 2 replicates.

DOI: 10.1021/acs.jafc.5b03441
J. Agric. Food Chem. 2015, 63, 9093−9102

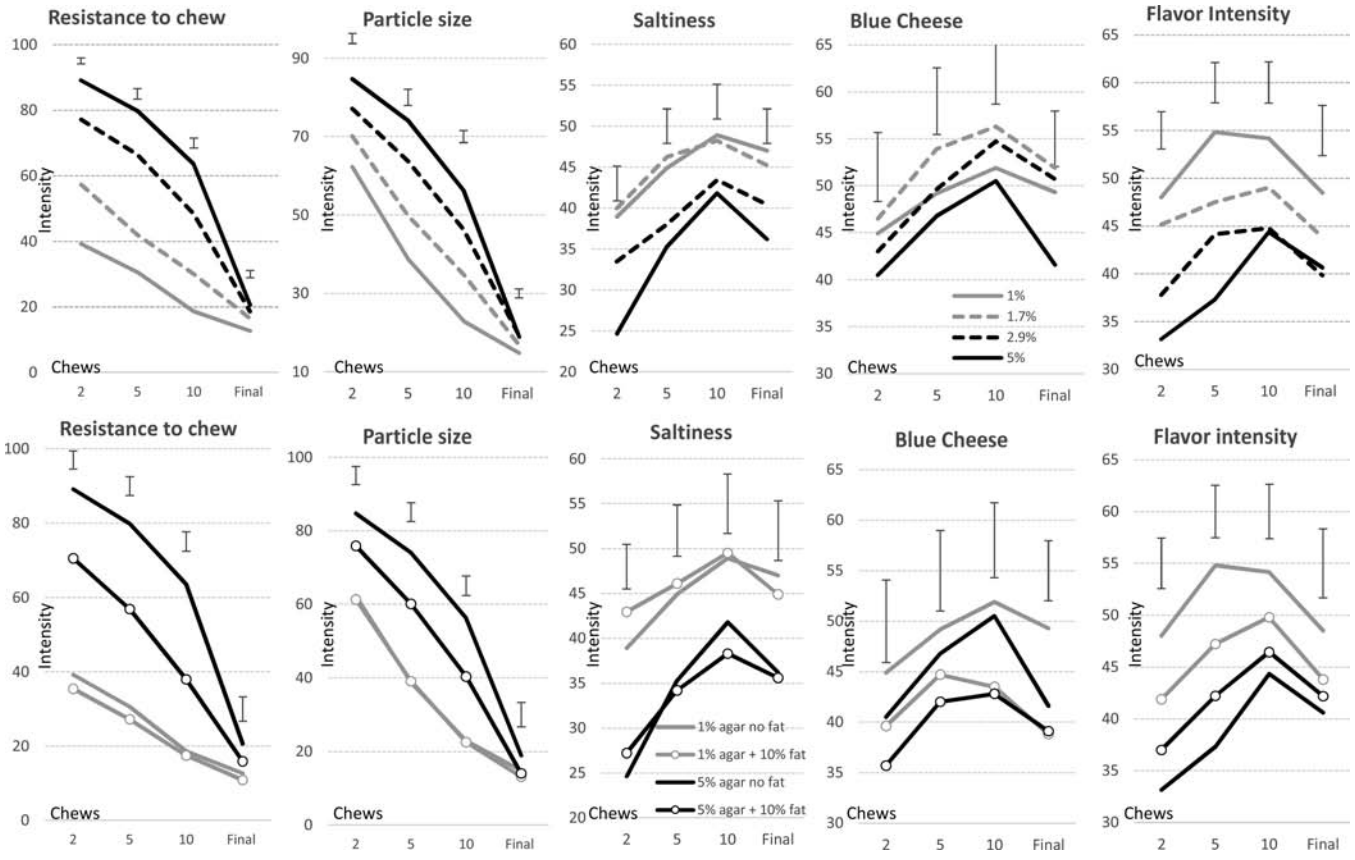

Figure 1. (Top row) Mean (n = 30) sensory properties of pure agar gels (1.0, 1.7, 2.9, and 5.0% agar) after 2, 5, and 10 chews and at the point of swallow (final). (Bottom row) Mean (n = 30) sensory properties of pure agar gels (1 and 5% agar) and corresponding agar gels with 10% fat added after 2, 5, and 10 chews and at the point of swallow (final). Error bars represent the least significant difference (LSD) at a specific chew number.

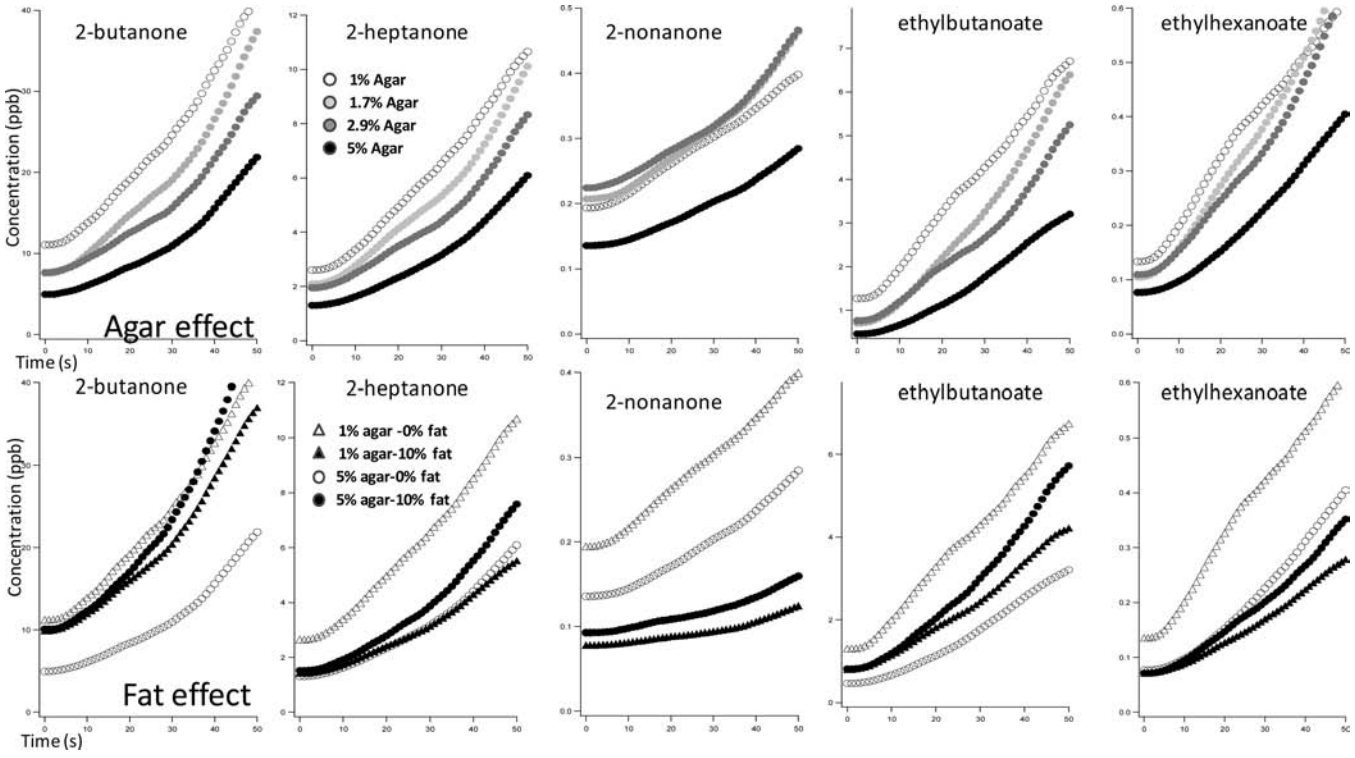

Figure 2. Smoothed average (n = 24) in vivo volatile release curves for selected volatiles in pure agar gels (top row) and in agar gels with fat (bottom row).

DOI: 10.1021/acs.jafc.5b03441
J. Agric. Food Chem. 2015, 63, 9093−9102

Table 5. Effect of Agar Concentration on Mean (n = 24) in Vivo Release Parameters AUC, I_{max}, and Initial Release Rate

	pure agar effects								
agar (%)	m/z 73.00	m/z 87.00	m/z 115.00	m/z 129.00	m/z 143.00	m/z 117.00	m/z 145.00	effect	P
					AUC				
1.0	3123	1684	818	265	36	466	46	agar	<0.001
1.7	2888	1531	804	293	44	429	50	ion	<0.001
2.9	2361	1219	664	256	45	350	47	agar−ion	<0.001
5.0	1694	877	490	178	28	228	31		
LSD_{agar}[a]	260	144	96	34	5.8	70	8		
					I_{max}				
1.0	211	107	36	9	1	38	2	agar	<0.001
1.7	197	101	39	11	2	34	3	ion	<0.001
2.9	156	84	33	10	3	29	3.4	agar−ion	<0.001
5.0	114	59	25	8	5	19	5.05		
LSD_{agar}[a]	25	13	7	16	0.1	6.6	0.4		
					Release Rate				
1.0	47.64	25.71	12.27	4.3	0.69	7.56	0.78	agar	<0.001
1.7	36.59	19.46	10.1	4.02	0.73	5.3	0.67	ion	<0.001
2.9	31.67	16.03	8.55	3.57	0.68	4.45	0.54	agar−ion	<0.001
5.0	21.08	10.74	5.88	2.41	0.47	2.79	0.40		
LSD_{agar}[a]	5.5	2.8	1.6	0.7	0.14	1	0.13		

[a]LSD_{agar}, least significant difference for comparing the effect of agar on individual volatiles within columns (P < 0.05).

Table 6. Effect of Agar and Fat Concentration on in Vivo Release Parameters AUC, I_{max}, and Initial Release Rate

		agar and fat effects								
agar (%)	fat (%)	m/z 73.00	m/z87.00	m/z115.00	m/z129.00	m/z 143.00	m/z 117.00	m/z 145.00	effect	P
						AUC				
1	0	3123	1684	819	265	36	466	46	agar	0.04
	10	2684	1344	402	99	12	267	20	fat	0.06
5	0	1694	877	490	178	28	228	31	ion	<0.001
	10	3428	1794	573	134	16	399	27	agar−ion	NS
									agar−fat	<0.001
$LSD_{agar×fat}$[a]		750	420	165	37	4	139	8.7	fat−ion	<0.001
						I_{max}				
1	0	211	107	36	9.1	1.4	38	2.5	agar	0.008
	10	194	98	18	3.2	0.5	21	1.2	fat	0.035
5	0	114	59	25	6.8	1.1	18	2	ion	<0.001
	10	215	112	26	4.8	0.7	31	1.4	agar−fat	<0.001
		54	29	9.4	1.9	0.17	11.2	0.56	agar−ion	0.015
$LSD_{agar×fat}$[a]									fat−ion	<0.001
						Release Rate				
1	0	47.62	25.69	12.25	4.28	0.67	7.55	0.76	agar	<0.001
	10	39.83	20.73	5.89	1.49	0.23	4.24	0.31	fat	NS
5	0	21.06	10.72	5.86	2.39	0.45	2.77	0.38	ion	<0.001
	10	43.03	21.73	6.93	1.93	0.28	4.89	0.36	agar−fat	<0.001
									agar−ion	<0.001
$LSD_{agar×fat}$[a]		10.5	5.26	1.78	0.53	0.09	1.8	0.11	fat−ion	<0.001

[a]$LSD_{agar×fat}$, least significant difference for comparing the agar × fat interaction effect on individual volatiles within columns (P < 0.05).

row). The initial (zero-time) concentration (before chewing) generally mirrored gel strength, regardless of the lipophilicity of volatiles, suggesting slower diffusion from the gels. During mastication, release increased for the entire chewing period (50 s). This release pattern was consistent with continuous breakdown of the agar structure and concomitant increase in surface area being the main rate-limiting factor. It can be seen from the release curves that overall the greatest release (AUC) per unit time was measured for the weakest gel (1% agar). As the gel strength increased, total AUC decreased; this was most apparent between the 2.9 and 5% gel transition. The release curve patterns were similar regardless of volatile lipophilicity, suggesting that release impedance was predominantly related to diffusion phenomena and the available surface area. The effect of agar strength on AUC, I_{max}, and initial release rate is summarized in Table 5. Both agar and volatile type had highly significant effects on release, as did the agar−volatile ion interaction. Incremental decreases were larger for the more hydrophilic compounds, for example, 2-butanone and 2-pentanone, compared to the more lipophilic compounds, fore example, 2-nonanone and ethyl hexanoate, as the agar strength increased. This suggests that some positive electrostatic forces resulting in agar−volatile interactions were likely to be in operation as well as pure structural impedance effects.[29,30] The in

DOI: 10.1021/acs.jafc.5b03441
J. Agric. Food Chem. 2015, 63, 9093−9102

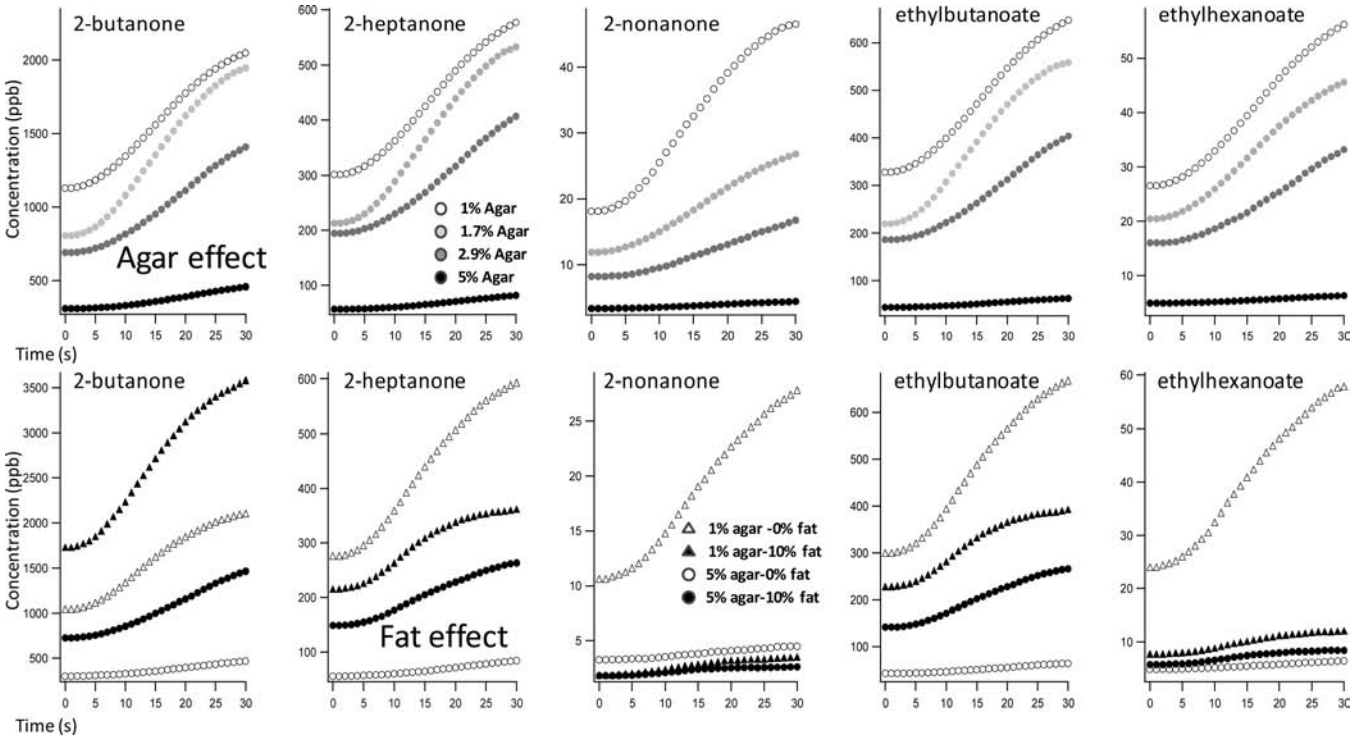

Figure 3. Smoothed average ($n = 4$) in vitro volatile release curves for selected volatiles in pure agar gels (top row) and in agar gels with fat (bottom row).

vivo data for the pure agar gels clearly showed that the release of all volatiles, irrespective of $K_{o/w}$, was impeded with increased gel rigidity, therefore supporting the sensory data. It is important to note that softer gels will be swallowed earlier compared to more rigid gels, having a shorter average residence time in the oral cavity.

Fat Effect on in Vivo Volatile Release. The combined effect of fat and agar together on in vivo release was more complex than pure agar effects. In the combined experiment, the effect of agar on volatile release (AUC) was overall significant, and the effect of fat approached significance (Table 6). The interactions of agar−volatile ion and fat−volatile ion were, however, both highly significant ($P < 0.001$), indicating that the effects differed depending on the lipophilicity of the volatile compounds. Similar effects were measured for I_{max} and the initial release rate (Table 6). The effect of fat addition to release curves is shown for 1 and 5% agar gels with either 0 or 10% added lipid (Figure 2, bottom row). Curves for 2-butanone (low fat solubility, $K_{o/w} = 1.9$), 2-heptanone (intermediate fat solubility, $K_{o/w} = 95.5$), and 2-nonanone (high fat solubility, $K_{o/w} = 1380$), ethyl butanoate (intermediate fat solubility, $K_{o/w} = 70.8$), and ethyl hexanoate (high fat solubility $K_{o/w} = 676$) are shown. Theory predicts that 2-butanone, the least fat-soluble volatile, would be minimally affected by the presence of lipid.[11] Although fat had a negligible effect on the release of 2-butanone from the 1% gel, in the 5% gel, a significant increase was measured. Given that the release of more lipophilic compounds (2-octanone, 2-nonanone) decreased, this observation suggested that a repulsive or lipophobic interaction between the fat and 2-butanone pushed the water-soluble volatile more rapidly out of the matrix. In a previous study, 2-butanone was released more rapidly when lipid emulsion was present in a dynamic in vitro system.[4] For 2-heptanone, the presence of fat profoundly decreased release in 1% agar; however, a slight increase in release was measured at 5% gel strength with the addition of fat. For 2-nonanone, the most fat soluble volatile, the suppressive effect of fat was apparent at both gel strengths. For ethyl butanoate, fat decreased release at 1% agar strength, but the opposite was observed at the higher gel strength, similar to 2-heptanone (Figure 2, bottom row).

The oral breakdown data indicated that the resistance to chewing was similar for the 1% agar gel with and without fat, implying that the structure broke down at a similar rate and the differences in release were likely due to fat effects rather than differences in surface area and diffusion. In contrast, at 5% gel strength, the softening effect of fat was apparent by the reduced modulus (Table 3) and lower resistance to chewing, implying a faster breakdown of the gel and greater surface area exposure, increasing the rate of release of the flavor compound. The harder particles formed from the 5% gel (with 10% fat) were more rubbery and rigid. It is hypothesized that particles coalesced in the mouth more slowly than the softer 1% agar (with 10% fat) particles, contributing to the observed greater release of some compounds, such as 2-butanone and ethyl butanoate in the harder gels. Another hypothesis was that lipophobic forces were acting on these two volatiles of low or intermediate fat solubility.

In Vitro System Data: Agar Effects. Although the in vivo data demonstrated a strong agar gel effect, it was not clear whether this was mainly due to differences in the rate of structure breakdown and corresponding increased surface area or other electrostatic (positive or negative) interactions between the agarose material and volatile compounds or both. In the in vitro system, the agar gels were broken into small particles only to form a large increase in surface area. No process to mimic bolus formation was present. It should also be noted that no saliva was present in the in vitro cell. The mean ($n = 4$) smoothed in vitro release curves for the pure agar gels are shown in Figure 3. As expected, the in vitro release showed lower variability compared to the data obtained from human subjects. The initial equilibrium concentration of volatiles above the gels (before the structure was broken) mirrored the gel strength (Figure 3). The release

DOI: 10.1021/acs.jafc.5b03441
J. Agric. Food Chem. 2015, 63, 9093−9102

Table 7. Effect of Increasing Agar Strength on in Vitro Release Parameters AUC and I_{max} [a]

agar (%)	fat (%)	*m/z* 73.00	*m/z* 87.00	*m/z* 115.00	*m/z* 129.00	*m/z* 143.00	*m/z* 117.00	*m/z* 145.00	effect	*P*
					AUC					
1.0		243315	120112	65775	23612	3077	68384	5914	agar	<0.001
1.7		248622	127253	66025	22276	2872	63898	5338	ion	<0.001
2.9		180738	92329	48346	16150	2017	43765	3662	agar−ion	<0.001
5.0		62281	25113	10263	3913	552	7042	708		
LSD_{agar} [b]		28982	16568	6166	3460	266	12262	466		
					I_{max}					
1.0		2374	1187	681.3	250.2	34.3	760.7	70.7	agar	<0.001
1.7		2545	1308	667.1	227.6	32	638.8	56.7	ion	<0.001
2.9		1869	939	499.7	163.4	23	477.8	41.7	agar−ion	<0.001
5.0		593	236	97.9	40.6	6.6	74	8.4		
LSD_{agar} [b]		310	176	62	37	5	132	5		
					AUC					
1	0	243315	120112	65775	23612	3077	68384	5914	agar	<0.001
	10	430565	207912	45525	7217	451	48208	1465	fat	<0.001
5	0	62281	25113	10263	3913	552	7042	708	ion	<0.001
	10	175242	91699	29547	5063	329	28005	965	agar−fat	NS
$LSD_{agar\times fat}$ [c]		37240	26586	9480	3280	350	13762	1244	agar−ion	<0.001
									fat−ion	<0.001
					I_{max}					
1	0	2374	1187	681	250	34	761	71	agar	<0.001
	10	4349	2125	447	72	6	489	17	fat	<0.001
5	0	593	236	98	41	7	74	8	ion	<0.001
	10	1732	941	302	50	4	301	11	agar−fat	NS
$LSD_{agar\times fat}$ [c]		422	296	99	34	4	149	15	agar−ion	<0.001
									fat−ion	<0.001

[a]Data are the mean of four replicates. [b]LSD_{agar}, least significant difference for comparing the effect of agar on individual volatiles within column ($P < 0.05$). [c] $LSD_{agar\times fat}$, least significant difference for comparing the effect of agar×fat interaction on individual volatiles within column ($P < 0.05$).

from the gels increased rapidly during the initial shear period (10 s) to a maximum value within ∼50 s. As the agar concentration increased, the rate of release decreased, regardless of the volatile $K_{o/w}$. Even after reduction to fine particles, the release remained proportional to the agar gel strength (even after a further 15 min of monitoring, data not shown). In agreement with the in vivo data, the in vitro release rate decreased with increased gel strength regardless of the volatile lipophilicity. The main effects of agar strength and volatile type were significant ($P < 0.001$) (Table 7). The in vitro data clearly showed that the greatest impedance of release occurred in the transition from 2.9 to 5% agar gel strength, which was also supported by the rheological data. The agar−ion interaction term was significant ($P < 0.001$), where the relative decreases in the release of 2-nonanone were greater with increased agar strength compared to less lipophilic compounds, for example, 2-butanone.

In Vitro System Data: Fat Effects. As samples were rapidly sheared under in vitro conditions, differences in the rate of structural breakdown were not expected to be important, but rather true physicochemical effects. Once small particles were formed in the in vitro cell, they were not forced to recoalesce into a bolus, as would be the case in the mouth during mastication. Although the in vitro system was only a crude approximation of the masticatory apparatus, the main effects of agar and fat on release could be separated from other physiological effects. In vitro release curves for 2-butanone, 2-heptanone, 2-nonanone, ethyl butanoate, and ethyl hexanoate in agar gels with and without fat (10%) are shown (Figure 3, bottom row). For 2-butanone, the rate of release was greater with 10% fat at both gel strengths, supporting the hypothesis that a hydrophobic interaction may have occurred. The release of 2-butanone from the 1% gel release was different from the in vivo data, where no increase in release was measured with the addition of fat. It is hypothesized that the soft gel particles more easily recombined or recoalesced under in vivo conditions than in the in vitro system.

For 2-heptanone, the suppressive effect of fat was clear at 1%, but reversed at 5% strength. This result was similar to the in vivo data, where a similar trend was measured. For the more fat soluble volatiles 2-octanone and 2-nonanone, the inhibitory effect of fat on release was profound, regardless of gel strength. The release pattern of ethyl butanoate was similar to that of 2-heptanone (similar $K_{o/w}$) and also similar to the in vivo data. There are few published studies in which both gel strength and fat effects are simultaneously measured.[14,23] Whereas the strong suppressive effect of fat on the release of lipophilic volatiles is well-known,[4,11,31,32] the potential for lipophobic interactions, increasing the rate of release of molecules with low fat solubility, is barely described in the literature. For example, the release of volatiles with low fat solubility (e.g., 2-butanone[4,11] and 2,3-butanedione[33]) was slightly higher in emulsions under dynamic conditions in the presence of fat. It was of interest that the sensory panel rated the 5% agar with 10% fat sample higher in overall flavor intensity than the pure agar 5% gel. The in vivo and in vitro data clearly showed higher release for a number of volatiles, for example, 2-butanone and 2-pentanone, thus supporting the sensory data.

Both the in vivo and in vitro data showed unambiguously that volatile release decreased as the agar strength or gel rigidity increased, although the magnitude of the measured agar effect was relatively larger in the in vitro system. Previous studies have demonstrated a significant decrease in release with increased gel

DOI: 10.1021/acs.jafc.5b03441
J. Agric. Food Chem. 2015, 63, 9093−9102

strength,[14,23] but not others,[16,34] whereas various effects were reported in one study.[15] The in vitro cell only decreased the particle size and increased the surface area; it did not replicate the complex process of saliva mixing and bolus formation that occurs during mastication. The in vitro data were more reproducible and easier to interpret than the in vivo data, with high inter- and intraindividual variation in oral behavior being well-known. Regardless, both data sets showed similar directional trends. The effect of agar concentration on volatile release was relatively stronger for the more hydrophilic compounds, for example, 2-butanone and 2-pentanone, suggesting an electrostatic attractive force was in operation as well as other effects, for example, diffusion through structural hindrance. Overall, the findings strongly indicated that physicochemical mechanisms were mainly responsible for perceived flavor differences in agar gels rather than cross-modal interactions between texture and flavor perception.[16,17] It should be emphasized that gels made from gelatin and other hydrocolloids may have different release properties due to melting behavior or other physicochemical properties.

The release curve information generated here may be used as data input into future computational models of human oral processing and flavor release with some adaptation, for example, release per chew data, to better understand flavor release and sensory perception.[7,35] Using similar approaches, it may be possible to better understand the effects of the food matrix and fat in real food systems and also contribute to the development of reformulated manufactured food products.

AUTHOR INFORMATION

Corresponding Author

*(D.F.) Phone: +61 (2) 9490 8584. E-mail: damian.frank@csiro.au.

Present Address

†(G.T.E.) Department of Food Science, University of Otago, P.O. Box 56, Dunedin 9054, New Zealand.

Notes

The authors declare no competing financial interest.

ACKNOWLEDGMENTS

We acknowledge Mi Xu for performing the rheological experiments. We thank Mahshid Roohani for her assistance in manufacturing the gels used in the study.

REFERENCES

(1) Gierczynski, I.; Guichard, E.; Laboure, H. Aroma perception in dairy products: the roles of texture, aroma release and consumer physiology. A review. *Flavour Fragrance J.* **2011**, *26*, 141−152.

(2) Foster, K. D.; Grigor, J. M. V.; Cheong, J. N.; Yoo, M. J. Y.; Bronlund, J. E.; Morgenstern, M. P. The role of oral processing in dynamic sensory perception. *J. Food Sci.* **2011**, *76*, R49−R61.

(3) Salles, C.; Chagnon, M. C.; Feron, G.; Guichard, E.; Laboure, H.; Morzel, M.; Semon, E.; Tarrega, A.; Yven, C. In-mouth mechanisms leading to flavor release and perception. *Crit. Rev. Food Sci. Nutr.* **2010**, *51*, 67−90.

(4) Frank, D.; Appelqvist, I.; Piyasiri, U.; Delahunty, C. In vitro measurement of volatile release in model lipid emulsions using proton transfer reaction mass spectrometry. *J. Agric. Food Chem.* **2012**, *60*, 2264−2273.

(5) Frank, D. C.; Eyres, G. T.; Piyasiri, U.; Delahunty, C. M. Effect of food matrix structure and composition on aroma release during oral processing using in vivo monitoring. *Flavour Fragrance J.* **2012**, *27*, 433−444.

(6) Harrison, S. M.; Cleary, P. W. Towards modelling of fluid flow and food breakage by the teeth in the oral cavity using smoothed particle hydrodynamics (SPH). *Eur. Food Res. Technol.* **2014**, *238*, 185−215.

(7) Harrison, S. M.; Cleary, P. W.; Eyres, G.; Sinnott, M. D.; Lundin, L. Challenges in computational modelling of food breakdown and flavour release. *Food Funct.* **2014**, *5*, 2792−2805.

(8) Engelen, L.; Fontijn-Tekamp, A.; van der Bilt, A. The influence of product and oral characteristics on swallowing. *Arch. Oral Biol.* **2005**, *50*, 739−746.

(9) de Roos, K. B.; Graf, E. Nonequilibrium partition model for predicting flavor retention in microwave and convection heated foods. *J. Agric. Food Chem.* **1995**, *43*, 2204−2211.

(10) Seuvre, A. M.; Diaz, M. A. E.; Voilley, A. Influence of the food matrix structure on the retention of aroma compounds. *J. Agric. Food Chem.* **2000**, *48*, 4296−4300.

(11) Frank, D.; Appelqvist, I.; Piyasiri, U.; Wooster, T. J.; Delahunty, C. Proton transfer reaction mass spectrometry and time intensity perceptual measurement of flavor release from lipid emulsions using trained human subjects. *J. Agric. Food Chem.* **2011**, *59*, 4891−4903.

(12) Mestres, M.; Kieffer, R.; Buettner, A. Release and perception of ethyl butanoate during and after consumption of whey protein gels: relation between textural and physiological parameters. *J. Agric. Food Chem.* **2006**, *54*, 1814−1821.

(13) Mestres, M.; Moran, N.; Jordan, A.; Buettner, A. Aroma release and retronasal perception during and after consumption of flavored whey protein gels with different textures. 1. In vivo release analysis. *J. Agric. Food Chem.* **2005**, *53*, 403−409.

(14) Malone, M. E.; Appelqvist, I. A. M. Gelled emulsion particles for the controlled release of lipophilic volatiles during eating. *J. Controlled Release* **2003**, *90*, 227−241.

(15) Boland, A. B.; Delahunty, C. M.; van Ruth, S. M. Influence of the texture of gelatin gels and pectin gels on strawberry flavour release and perception. *Food Chem.* **2006**, *96*, 452−460.

(16) Weel, K. G. C.; Boelrijk, A. E. M.; Alting, A. C.; van Mil, P. J. J. M.; Burger, J. J.; Gruppen, H.; Voragen, A. G. J.; Smit, G. Flavor release and perception of flavored whey protein gels: perception is determined by texture rather than by release. *J. Agric. Food Chem.* **2002**, *50*, 5149−5155.

(17) Hollowood, T. A.; Davidson, J. M.; DeGroot, L.; Linforth, R. S. T.; Taylor, A. J. Taste release and its effect on overall flavor perception. In *Chemistry of Taste: Mechanisms, Behaviors and Mimics*; Given, P., Paredes, D., Eds.; ACS Symposium Series 825; American Chemical Society: Washington DC, USA, 2002l pp 166−178.

(18) Deleris, I.; Saint-Eve, A.; Dakowski, F.; Semon, E.; Le Quere, J. L.; Guillemin, H.; Souchon, I. The dynamics of aroma release during consumption of candies of different structures, and relationship with temporal perception. *Food Chem.* **2011**, *127*, 1615−1624.

(19) Labropoulos, K. C.; Niesz, D. E.; Danforth, S. C.; Kevrekidis, P. G. Dynamic rheology of agar gels: theory and experiments. Part I. Development of a rheological model. *Carbohydr. Polym.* **2002**, *50*, 393−406.

(20) Labropoulos, K. C.; Niesz, D. E.; Danforth, S. C.; Kevrekidis, P. G. Dynamic rheology of agar gels: theory and experiments. Part II: gelation behavior of agar sols and fitting of a theoretical rheological model. *Carbohydr. Polym.* **2002**, *50*, 407−415.

(21) Arnott, S.; Fulmer, A.; Scott, W. E.; Dea, I. C. M.; Moorhouse, R.; Rees, D. A. Agarose double helix and its function in agarose-gel structure. *J. Mol. Biol.* **1974**, *90*, 269−284.

(22) Nayar, V. T.; Weiland, J. D.; Nelson, C. S.; Hodge, A. M. Elastic and viscoelastic characterization of agar. *J. Mech. Behav. Biomed. Mater.* **2012**, *7*, 60−68.

(23) Malone, M. E.; Appelqvist, I. A. M.; Norton, I. T. Oral behaviour of food hydrocolloids and emulsions. Part 2. Taste and aroma release. *Food Hydrocolloids* **2003**, *17*, 775−784.

(24) Frank, D.; Owen, C.; Patterson, J. Solid phase microextraction (SPME) combined with gas-chromatography and olfactometry-mass spectrometry for characterization of cheese aroma compounds. *Lebensm. Wiss. Technol.* **2004**, *37*, 139−154.

DOI: 10.1021/acs.jafc.5b03441
J. Agric. Food Chem. 2015, 63, 9093−9102

(25) Jack, F. R.; Piggott, J. R.; Paterson, A. Analysis of textural changes in hard cheese during mastication by progressive profiling. *J. Food Sci.* **1994**, *59*, 539−543.
(26) Piazza, L.; Benedetti, S. Investigation on the rheological properties of agar gels and their role on aroma release in agar/limonene solid emulsions. *Food Res. Int.* **2010**, *43*, 269−276.
(27) Costell, E.; Peyrolon, M.; Duran, L. Note. Influence of texture and type of hydrocolloid on perception of basic tastes in carrageenan and gellan gels. *Food Sci. Technol. Int.* **2000**, *6*, 495−498.
(28) Lawrence, G.; Buchin, S.; Achilleos, C.; Berodier, F.; Septier, C.; Courcoux, P.; Salles, C. In vivo sodium release and saltiness perception in solid lipoprotein matrices. 1. Effect of composition and texture. *J. Agric. Food Chem.* **2012**, *60*, 5287−5298.
(29) Arvisenet, G.; Le Bail, P.; Voilley, A.; Cayot, N. Influence of physicochemical interactions between amylose and aroma compounds on the retention of aroma in food-like matrices. *J. Agric. Food Chem.* **2002**, *50*, 7088−7093.
(30) Arvisenet, G.; Voilley, A.; Cayot, N. Retention of aroma compounds in starch matrices: competitions between aroma compounds toward amylose and amylopectin. *J. Agric. Food Chem.* **2002**, *50*, 7345−7349.
(31) Martuscelli, M.; Savary, G.; Pittia, P.; Cayot, N. Vapour partition of aroma compounds in strawberry flavoured custard cream and effect of fat content. *Food Chem.* **2008**, *108*, 1200−1207.
(32) Roberts, D. D.; Acree, T. E. Effects of heating and cream addition fresh raspberry aroma using a retronasal aroma simulator and gas chromatography olfactometry. *J. Agric. Food Chem.* **1996**, *44*, 3919−3925.
(33) Roberts, D. D.; Pollien, P.; Watzke, B. Experimental and modeling studies showing the effect of lipid type and level on flavor release from milk-based liquid emulsions. *J. Agric. Food Chem.* **2003**, *51*, 189−195.
(34) Lethuaut, L.; Weel, K. G. C.; Boelrijk, A. E. M.; Brossard, C. D. Flavor perception and aroma release from model dairy desserts. *J. Agric. Food Chem.* **2004**, *52*, 3478−3485.
(35) Harrison, S. M.; Eyres, G.; Cleary, P. W.; Sinnott, M. D.; Delahunty, C.; Lundin, L. Computational modelling of food oral breakdown using smoothed particle hydrodynamics. *J. Texture Stud.* **2014**, *45*, 97−109.
(36) Hansson, A.; Giannouli, P.; Van Ruth, S. The influence of gel strength on aroma release from pectin gels in a model mouth and in vivo, monitored with proton-transfer-reaction mass spectrometry. *J. Agric. Food Chem.* **2003**, *51*, 4732−4740.
(37) Gierczynski, I.; Laboure, H.; Semon, E.; Guichard, E. Impact of hardness of model fresh cheese on aroma release: in vivo and in vitro study. *J. Agric. Food Chem.* **2007**, *55*, 3066−3073.
(38) Laboure, H.; Repoux, M.; Courcoux, P.; Feron, G.; Guichard, E. Inter-individual retronasal aroma release variability during cheese consumption: Role of food oral processing. *Food Res. Int.* **2014**, *64*, 692−700.
(39) Burdock, G. A. *Fenaroli's Handbook of Flavor Ingredients*, 5th ed.; CRC Press: Boca Raton, FL, USA, 2005.

DOI: 10.1021/acs.jafc.5b03441
J. Agric. Food Chem. 2015, 63, 9093−9102

Table 1. Validation Parameters of the Method Developed To Quantitate 1,4-Cineole and 1,8-Cineole in Red Wines

compound	RI[a] DB-wax/HP-5	quant. ion (m/z)[b]	linearity range (μg/L)	mean r^2 [c] (n = 3)	slope reproducibility (%) (n = 3)	LOD[d] (μg/L)	LOQ[d] (μg/L)	repeatability (%) (n = 10) low[e]	repeatability (%) (n = 10) medium[e]	reproducibility (%) (n = 5)	average recovery (%) (n = 3)
1,4-cineole	1185/1014	111	0.025−2.5	0.9993 ± 0.0007	1.7	0.001	0.004	6.3	4.4	4.7	98 ± 9
1,8-cineole	1210/1030	108	0.1−10	0.9997 ± 0.0002	4.5	0.003	0.01	3.7	3.9	2.9	93 ± 2

[a]RI for Kovats retention index on polar (DB-Wax) and apolar (HP-5) columns. [b]Quant. ion = ions used for quantitation. [c]r^2 = coefficient of determination. [d]The limits of detection (LODs) (concentration for signal/noise = 3) and the limits of quantitation (LOQs) (concentration for signal/noise = 10) were manually calculated from the ratio of the peak heights to the average noise before and after each peak. [e]Repeatability was assessed for low concentrations at 0.05 and 0.4 μg/L for 1,4-cineole and 1,8-cineole, respectively, and for medium concentrations at 0.5 and 2 μg/L, respectively.

as "minty", "cooling piney", "camphoraceous", and "eucalyptol-like",[18] but no detection threshold of this compound has been reported in the literature.

Because of the comparable natural occurrence of 1,4-cineole and 1,8-cineole, their olfactory similarity, and the importance of 1,8-cineole in Australian red wines, this study aimed to investigate the occurrence and potential contribution of 1,4-cineole to red wine aroma. A headspace−solid-phase microextraction−gas chromatography−mass spectrometry (HS−SPME−GC−MS) method was developed and validated to quantitate 1,4-cineole and 1,8-cineole in Australian red wines. Discriminative and descriptive sensory methods were used to characterize the contribution of 1,4-cineole, both independently and in combination with 1,8-cineole, upon Cabernet Sauvignon wine aroma.

MATERIALS AND METHODS

Material. Standards including 1,4-cineole (98.5%), 1,8-cineole (99%), octan-2-ol (97%), 3-isobutyl-2-methoxypyrazine (IBMP, 99%), and menthol (99%) were purchased from Sigma-Aldrich (Castle Hill, New South Wales, Australia). Stock and working solutions of standards were prepared volumetrically in ethanol (AnalaR NORMAPUR, VWR, Fontenay-sous-Bois, France) and stored at −20 °C. Water was obtained from a Milli-Q purification system (Millipore, North Ryde, New South Wales, Australia). Sodium chloride (NaCl) was purchased from Merck (Darmstadt, Germany). Deionized water was obtained from a Milli-Q mixed bed resin system (18 MΩ/cm and 25 °C).

Wines. A range of commercial Australian red wines (104 in total) comprising of 51 Cabernet Sauvignon, 4 Cabernet Sauvignon/Merlot blends (60−80% Cabernet Sauvignon), 27 Shiraz, and 22 Pinot Noir wines were purchased. The wines originated from important regions for Cabernet Sauvignon, Shiraz, and Pinot Noir wine production. Cabernet Sauvignon wines (varietal and blends) were from Coonawarra (31%), Margaret River (27%), Barossa and McLaren Vale (25%), and other regions located in South Australia, Victoria, and New South Wales (17%). Shiraz wines were from Barossa and McLaren Vale (37%), Coonawarra (19%), Margaret River (11%), and other regions located in South Australia, Victoria, and New South Wales (33%). Pinot Noir wines were from Victoria (50%), Orange (36%), other regions located in South Australia and Tasmania (14%). Cabernet Sauvignon and Shiraz wines were mainly from 2012, 2011, 2010, and 2009 (mean age of 3.5 years). Pinot Noir wines were from 2013, 2012, and 2011 (mean age of 2 years).

Cineole Isomer Analysis. The method for quantitating 1,4-cineole and 1,8-cineole by HS−SPME−GC−MS was developed in combination of previously published methods for wine volatiles.[8,19]

Spiking and Sample Preparation. The development and the validation of the method were carried out using Australian red wines from the 2013 vintage. The method consisted of adding 20 μL of a stock solution of octan-2-ol (internal standard) at 5 mg/L in absolute ethanol to 10 mL of wine. To a 20 mL headspace vial 3 g of NaCl, 5 mL of wine spiked with internal standard, and 5 mL of deionized water were added. The vial was then tightly sealed with a polytetrafluoroethylene (PTFE)-lined cap, and contents were homogenized.

Instrumentation. An Agilent 7890A gas chromatograph, equipped with a Gerstel multipurpose sampler with automated SPME capability, interfaced to an Agilent 5975C triple-axis mass detector was used. A MSD Chemstation E.02.00.493 (Agilent Technologies, Ltd.) and National Institute of Standards and Technology (NIST) MS Search 2.0 version 2008 were used to control the instrument and for mass spectra assessment. Prepared samples were placed in the tray until analysis, whereupon vials were transferred to a heater block. The extraction consisted of preincubating the vial for 10 min at 40 °C with swirling at 500 rpm, inserting a 1 cm divinylbenzene/carboxen/polydimethylsiloxane (DVB/CAR/PDMS) 50/30 μm fiber (Supelco, Bellefonte, PA) into the headspace for 30 min at 40 °C while the solution was swirled again. The fiber was then transferred to the injector for desorption at 250 °C for 1 min, withdrawn, and injected into a second injector set at 270 °C with a 50:1 split for 10 min with a 10 mL/min purge flow to clean the fiber, prior to the next sample analysis. A fused silica capillary column (DB-Waxetr, 60 m × 0.25 mm inner diameter, 0.25 μm film thickness, Agilent Technologies, Santa Clara, CA) was used for compound separation by gas chromatography. The injector block was fitted with a 1 mm internal diameter borosilicate liner (SGE), and the injector temperature set to 260 °C in splitless mode. The oven temperature program commenced at 40 °C for 5 min, increased to 120 °C at a rate of 3 °C/min, with a final increase to 220 °C at a rate of 15 °C/min, and held for 15 min. The total run time was 53.3 min. The flow rate of ultrahigh-purity helium gas was constant at 3 mL/min. The MS source, quadrupole, and transfer line temperatures were set to 230, 150, and 275 °C, respectively.

Compound Identification and Quantitative Analysis. The identification of 1,4-cineole and 1,8-cineole (Figure 1) in wines was performed by comparing retention times and mass spectra (scan mode) to those of pure standards at 20 μg/L in water and red wine. Kovats retention indices (RIs) were checked for each compound using a commercial mixture of n-alkanes (Sigma, Steinheim, Germany), with an identical oven ramp profile and gas flow rates as used for the final analyzes on DB-Waxetr (60 m × 0.25 mm inner diameter, 0.25 μm film thickness) and HP-5MS (30 m × 0.25 mm inner diameter, 0.25 μm film thickness) columns. Mass spectral data were collected in both selective ion monitoring (SIM) and scan mode (m/z 35−350) at an ionization voltage of 70 eV. The mass spectra of both cineole isomers are available in the NIST 08 MS database. Quantifier and qualifier ions were selected as described in the literature for 1,8-cineole[8] and based on the best signal/noise ratio measured in red wines for 1,4-cineole. The ions monitored in SIM runs were m/z 71, 81, 93, 108, 111, 125, 139, and 154 for the cineole isomers and m/z 45 and 55 for octan-2-ol. The quantitation ions used for the cineole isomers are listed in Table 1, while m/z 45 was used for octan-2-ol. The other ions were used as qualifiers.

DOI: 10.1021/acs.jafc.5b03847
J. Agric. Food Chem. 2015, 63, 9103−9111

Table 2. Code of Samples Used for Sensory Analysis

code	description	concentration
wat	water	
CS	Cabernet Sauvignon wine	3.4 ng/L IBMP
		0.09 μg/L 1,4-cineole
CSi	CS wine spiked with IBMP	10 ng/L IBMP
wat + 1,4c-0.13	1,4-cineole in water	0.13 μg/L 1,4-cineole
wat + 1,4c-0.27	1,4-cineole in water	0.27 μg/L 1,4-cineole
CS + 1,4c-0.13	1,4-cineole in CS wine	0.22 μg/L 1,4-cineole
CS + 1,4c-0.27	1,4-cineole in CS wine	0.36 μg/L 1,4-cineole
CS + 1,4c-0.54	1,4-cineole in CS wine	0.63 μg/L 1,4-cineole
CS + 1,8c	1,8-cineole in CS wine	2.5 μg/L 1,8-cineole
CSi + 1,4c	1,4-cineole in CSi wine	1.6 μg/L 1,4-cineole
CSi + 1,8c	1,8-cineole in CSi wine	2.5 μg/L 1,8-cineole
CSi + 1,8c-10	1,8-cineole in CSi wine	10 μg/L 1,8-cineole
CSi + 1,4c + 1,8c	1,4-cineole + 1,8-cineole in CSi wine	1.6 μg/L 1,4-cineole
		2.5 μg/L 1,8-cineole
CSi + 1,4c + 1,8c-10	1,4-cineole + 1,8-cineole in CSi wine	1.6 μg/L 1,4-cineole
		10 μg/L 1,8-cineole

Method Validation. Linearity was validated by a series of seven standard additions of 1,4-cineole and 1,8-cineole in three different commercial red wines (Shiraz, Cabernet Sauvignon, and Merlot). The initial concentrations of 1,4-cineole and 1,8-cineole in the wines used for validation were below 0.1 and 0.5 μg/L, respectively. The calibration ranges are displayed in Table 1. The precision of the method was assessed by analyzing 10 replicates of a commercial Shiraz with 1,4-cineole and 1,8-cineole at 0.05 and 0.4 μg/L, respectively, which covered the low range of concentrations. A second trial for the assessment of precision was made at a medium range of the concentration for both 1,4-cineole and 1,8-cineole, with the same wine spiked at 0.5 and 2 μg/L, respectively. The robustness of the method was determined by analyzing five replicates of the same spiked wine over a period of 2 weeks. For the accuracy study (recovery), three different varietal red wines (Cabernet Sauvignon, Shiraz, and Pinot Noir) were spiked with 1,4-cineole and 1,8-cineole at the same concentrations as used for repeatability. To ensure that the accuracy of the method was maintained, a control red wine sample spiked with cineole isomers as previously indicated was regularly included in the set of samples to be quantitated.

Sensory Analyses. *General Conditions.* Sensory analyses were performed with samples prepared in water and wine as previously described.[20] Sample assessments were undertaken in a temperature-controlled room, in individual booths (ISO 8589:2007), using covered, white ISO glasses (ISO 3591:1977) containing about 30 mL of liquid, coded with random three-digit numbers. Sessions lasted approximately 10 min. All sensory samples underwent orthonasal evaluation. The wine used for the discriminative and descriptive analyses was a 2012 Cabernet Sauvignon wine from the south of France (CS) with the following parameters measured by Fourier transform mid-infrared spectroscopy (WineScan Instrument, Foss Analytical, Hillerød, Denmark): alcohol, 12.9% (v/v); pH, 3.6; titratable acidity, 4.6 g/L as tartaric acid; and volatile acidity, 0.43 g/L. The initial concentrations of IBMP measured as described[21] and 1,4-cineole were 3.8 ng/L and 0.09 μg/L, respectively. The concentration of 1,8-cineole was below the limit of quantitation. Coded samples (Table 2) were prepared approximately 15 h prior to the session and kept at 18 °C in sealed vials to ensure chemical and sensory equilibrium. Analyses were also performed to check the solution stability between the sensory sessions. No significant loss of cineoles or IBMP was observed in either the water or wine solutions.

Sensory Panel. Judges were selected on the basis of availability and interest. A total of 16−33 volunteers participated in the various sensory panels. All panelists were research laboratory staff at the Institute of the Sciences of Vines and Wines (ISVV), Bordeaux University, and showed different levels of expertise in sensory analysis. The ages of the panelists ranged from 21 to 53 years, and the panel was comprised of between 55 and 65% females depending upon the panel.

Discriminative Analysis. Triangle tests were performed for 1,4-cineole solution samples in deionized water and CS wine. Each solution of 1,4-cineole, present at the concentrations listed in Table 2, was compared to either deionized water or the base CS wine. For each triangle test, three numbered samples (two identical and one different) were presented in a random order. Each judge used direct olfaction to identify the sample perceived as different in each test and was instructed to provide a response, even if they were uncertain of the correctness of their answer. Each triangle test was performed in duplicate.

Descriptive Analysis. The descriptive analysis focused on the impact of 1,4-cineole, in both isolation and combination with 1,8-cineole on the aromatic profile of Cabernet Sauvignon wines using an adapted version of the Deviation from Reference Method.[22] CS wine was spiked with IBMP to reach a final concentration of 10 ng/L (CSi in Table 2). This reflected the IBMP levels measured[21] in 14 wines from Margaret River and Coonawarra regions in a preliminary survey (data not shown). Additions of 1,4-cineole and 1,8-cineole were performed in the CSi wine at concentrations comparable to that found in Australian Cabernet Sauvignon wines (Table 2) and perceptible by the panel (Table 3). The tests were performed by comparing the aromatic perception of the hay, bay leaf, and blackcurrant reference

Table 3. Proportion of Positive Answers for Triangle Tests Performed in Water (Wat) and Cabernet Sauvignon Wine (CS) for 1,4-Cineole[a]

test	proportion of positive answer (%) (number of responses)	level of significance
wat + 1,4c-0.13 versus wat	38 (16)	NS[b]
wat + 1,4c-0.27 versus wat	56 (32)	$p = 0.01$
CS + 1,4c-0.13 versus CS	31 (36)	NS
CS + 1,4c-0.27 versus CS	28 (36)	NS
CS + 1,4c-0.54 versus CS	53 (34)	$p = 0.05$
CS + 1,8c versus CS	53 (36)	$p = 0.05$

[a]Sample codes are shown in Table 2. For each comparison, results were calculated by adding one and two positive sample tests. [b]NS = non-significant.

DOI: 10.1021/acs.jafc.5b03847
J. Agric. Food Chem. 2015, 63, 9103−9111

standards (Table 4) to CSi wine that has been spiked with 1,4-cineole and 1,8-cineole (Table 2). For each test, the panel assessed the olfactory similarity of spiked CSi wine samples compared to the standard presented. A previous series of triangle tests had shown that a similar range of 1,4-cineole and 1,8-cineole concentrations was able to be detected by the panel (Table 3). Panelists scored the similarity between spiked wine and standard using a 10 cm scale, with the highest scores plotted on the right side of the scale (0, low; 10, high). The samples with the highest scores were perceived as most similar to the corresponding reference standard.

Table 4. Descriptors and Corresponding Reference Standards Used for Descriptive Analysis

attribute	composition of the reference
bay leaf	maceration of 50 mg of commercial crumbled bay leaves for 2 min in water/wine
capsicum	solution of IBMP at 100 μg/L in water
eucalyptus	solution of 1,8-cineole at 100 μg/L in water
forest floor	maceration of 3 g of a mix of forest humus and oak leaves for 10 min in water
fresh	solution of menthol at 100 μg/L in water
hay	diluted macerate (1:3) of 500 mg of commercial hay in 100 mL in water/wine for 2 min
licorice	one licorice candy (Ricola) dissolved in 100 mL of water
spicy	500 mg of a commercial mix of ground black, red, and green pepper corns in 100 mL of water
blackcurrant	maceration of 40 g of commercial blackcurrant jam in 100 mL of water/wine for 1 min
black cherry	maceration of 40 g of commercial black cherry jam in 100 mL of water/wine for 1 min
dark fruit	maceration of 20 g of commercial blackberry jam and 20 g of blueberry jam in 100 mL of water for 10 min
red fruit	maceration of 40 g of commercial red berry fruit jam (strawberry, red cherry, and raspberry) in 100 mL of water

Multidimensional Scaling. A descriptive sorting task was used to characterize the aromatic differences between 10 Cabernet Sauvignon wines originating from the Coonawarra (n = 5) and Margaret River (n = 5) regions. Coonawarra wines were from 2010 (n = 3), 2011, and 2012 vintages, and Margaret River wines were from 2011 (n = 3), 2010, and 2012 vintages. The protocol of the sorting focused on orthonasal evaluation was as recently described.[23] The sensory description of the wine groups during the sorting task was based on 12 descriptors with appropriate reference standards that are commonly used by wine experts to describe the aroma of Australian Cabernet Sauvignon wines (Table 4). The panelists were asked to choose the most relevant terms from this list to define each group and were instructed to form between two and nine groups, with a maximum of five descriptors per group. During the session, participants had the opportunity to refresh their aroma memory by reassessing the reference standards.

Statistical Analysis. *Chemical Analysis.* The significance was examined using one-way analysis of variance (ANOVA), and the means were separated using Fisher's least significant difference (LSD) test (different letters account for significant differences at $p \leq 0.05$). ANOVA was performed using Excel software (Microsoft Corporation, Redmond, WA).

Sensory Analysis. The results of all of the triangle tests were statistically analyzed on the basis of the binomial law corresponding to the distribution of answers in this type of test (NF EN ISO 4120, 2007).

Descriptive data were analyzed using a one-way ANOVA (XLSTAT software). When more than two samples were compared, all descriptors were mean-centered per panelist and scaled to unit variance. Samples were considered as significant at $p < 0.05$. The data from multiple comparison tests were processed with a Duncan post-hoc test.

For the sorting task, dissimilarities between samples were analyzed using non-metric multidimensional scaling (MDS) as described elsewhere.[23] The analysis of 1,4-cineole, 1,8-cineole, and IBMP of the wines aimed to identify potential relationships between wine composition and the effect of regionality on aroma. The correlations between wines, attributes, and chemical compounds were plotted on a MDS map.

RESULTS AND DISCUSSION

Development and Validation of a Quantitation Method of 1,4-Cineole and 1,8-Cineole in Red Wines. Cineole isomers are symmetrical monoterpenic cyclic ethers exhibiting an epoxy-*p*-menthane structure, differing only by the position of the epoxy group (Figure 1). While 1,8-cineole has been previously quantitated in Australian red wines,[8] quantitative data for 1,4-cineole in wine have not been previously reported. However, 1,4-cineole has already been identified in red wines.[15,16] The identification of 1,4-cineole in red wines has been confirmed in the present study by the presence of peaks that displayed the identical mass spectrum of 1,4-cineole at the retention time that matched the 1,4-cineole retention index on two types of columns. The GC−MS parameters were adapted to cineole isomer analysis from a published method developed for wine volatile analysis.[19] Quantitation method validation was carried out assessing linearity, repeatability, reproducibility, limits of detection and quantitation, and recoveries in different red wines (Table 1). The standard curves obtained were linear and repeatable throughout the concentration range. The calculated limits of quantitation (LOQs) were 4 and 10 ng/L for 1,4-cineole and 1,8-cineole, respectively, and the calculated limits of detection (LODs) were 1 and 3 ng/L for 1,4-cineole and 1,8-cineole, respectively. The precision, robustness, and accuracy of the method were satisfactory for both compounds. The relative standard deviations for repeatability and reproducibility were below 7%, and recovery rates were measured at between 90 and 106% (Table 1). Interestingly, the method validation data revealed that the use of deuterated analogues was not necessary and octan-2-ol was well-adapted to HS−SPME−GC−MS analysis of 1,4-cineole and 1,8-cineole in red wines.

Survey of Cineole Isomers in Red Wines. The method was applied to analyze 1,4-cineole and 1,8-cineole in 104 commercial Australian Cabernet Sauvignon, Shiraz, and Pinot Noir wines from different regions and vintages. The results of this quantitative investigation are summarized in Table 5.

Table 5. Mean Concentrations ± Standard Deviation (SD) of 1,4-Cineole and 1,8-Cineole in Australian Cabernet Sauvignon, Shiraz, Pinot Noir Wines[a]

	Cabernet Sauvignon (n = 51)	Shiraz (n = 27)	Pinot Noir (n = 22)
1,4-cineole	0.59 ± 0.33 a	0.07 ± 0.04 c	0.22 ± 0.2 b
1,8-cineole	2.82 ± 3.26 a	1.75 ± 1.42 a	0.99 ± 0.33 b

[a]One-way ANOVA was used to compare data. Means followed by different letters in a row are significant at $p \leq 0.05$ (Fischer's LSD). All quoted uncertainty is the standard deviation of each group of wines.

Varietal Differences. 1,4-Cineole was detected in all of the wines analyzed with concentrations ranging from 0.023 to 1.6 μg/L. An important varietal effect was observed with an average concentration of 8.4- and 2.7-fold higher in Cabernet Sauvignon than in Shiraz and Pinot Noir wines, respectively (Table 5). All of the Shiraz wines exhibited concentrations below 0.2 μg/L, and 87% of Pinot Noir wines showed

DOI: 10.1021/acs.jafc.5b03847
J. Agric. Food Chem. 2015, 63, 9103−9111

concentrations below 0.4 μg/L. Conversely, 1,4-cineole concentrations were above 0.4 μg/L in 68% of the Cabernet Sauvignon wines analyzed, including seven wines with concentrations above 1 μg/L (Figure 2). The varietal differences measured in this study between Pinot Noir and Cabernet Sauvignon will require further investigations because Pinot Noir wines originated from different regions compared to Cabernet Sauvignon wines. The 1,4-cineole/1,8-cineole concentration ratios in Cabernet Sauvignon wines ranged from 0.015 to 1.24 (Supplementary Figure 1 of the Supporting Information). The distribution of 1,4-cineole in Australian red wines was therefore very different in comparison to 1,8-cineole. These results indicate that 1,4-cineole and 1,8-cineole in wines might have different origins and suggest that the occurrence of 1,4-cineole in wine is probably not due to the presence of eucalyptus trees in the vicinity of the vineyard, as has been reported for 1,8-cineole.[9] Further studies investigating the origin of 1,4-cineole in wine are warranted.

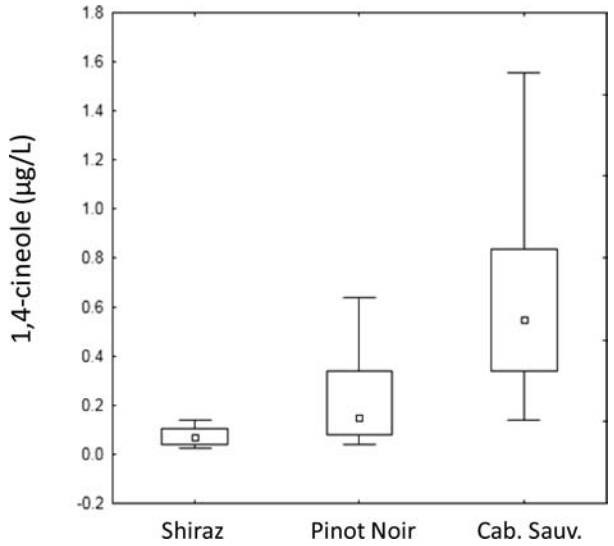

Figure 2. Distribution of 1,4-cineole concentrations in Australian red wines represented as box plots with the minimum, maximum, median, and quartiles. Cab. Sauv. = Cabernet Sauvignon.

The concentrations of 1,8-cineole were also cultivar-dependent, with higher concentrations in Australian Cabernet Sauvignon and Shiraz than Pinot Noir wines (Table 4). However, one Pinot Noir wine contained 23 μg/L 1,8-cineole. Both this wine and two Cabernet Sauvignon wines containing 19 and 66 μg/L, respectively, were considered as outliers and were not taken into account for the varietal comparison. These findings add to the uncertainty regarding the origin of 1,8-cineole in red wines and suggest that, as previously hypothesized,[5,11] factors other than proximity to eucalyptus trees may be important in determining the final concentration of this compound in wines.

Influence of the Wine Geographic Origin. Significant variations in 1,4-cineole and 1,8-cineole concentrations were measured between wines originating from different regions of Australia (Figure 3A). The Cabernet Sauvignon wines originating from Margaret River exhibited higher concentrations of 1,4-cineole than wines from Barossa and McLaren Vale ($p < 0.05$) and to a lesser extent Coonawarra ($p = 0.08$). Conversely, higher concentrations of 1,8-cineole were found in Cabernet Sauvignon and Shiraz wines produced from Coonawarra compared to Barossa and McLaren Vale ($p < 0.05$) and Margaret River to a lesser extent ($p = 0.13$) (Figure 3B). Regional variations of 1,8-cineole in Australian Cabernet Sauvignon have been previously reported.[5] The higher levels of 1,8-cineole found in the Coonawarra Cabernet Sauvignon wines are in agreement with anecdotal sensory descriptions, which include "eucalyptus" and "minty"[6] aromas, which are reminiscent of 1,8-cineole.

These results suggest that 1,4-cineole and 1,8-cineole concentrations in wine could be related to abiotic factors that characterize a terroir unit[24] (climate × soil moisture) and influence grape composition. Appropriate studies to investigate the effect of the temperature and water availability on the grape

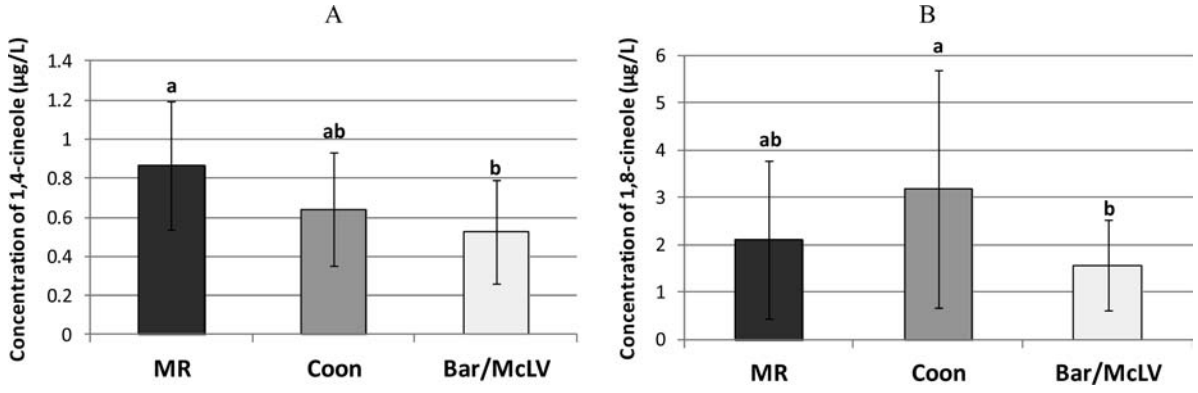

Figure 3. Effect of the geographic origin on the (A) 1,4-cineole concentration in Australian Cabernet Sauvignon wines and (B) 1,8-cineole concentration in Australian Cabernet Sauvignon and Shiraz wines. One-way ANOVA was used to compare data. Different letters on a column represent significantly ($p \leq 0.05$) different concentrations expressed in micrograms per liter. Standard errors were used for the error bars. MR, Margaret River; Bar/McLV, Barossa and McLaren Vale; and Coon, Coonawarra. The wine distribution for Figure 5A is as follows: for Margaret River, $n = 13$ with vintages as follows: 2011, $n = 9$; 2010, $n = 3$; and 2009, $n = 1$; for Coonawarra, $n = 12$ with vintages as follows: 2011, $n = 3$; 2010, $n = 7$; and 2009, $n = 2$; and for Barossa and McLaren Vale, $n = 13$ with vintages as follows: 2011, $n = 8$; 2010, $n = 4$; and 2009, $n = 1$. The wine distribution for Figure 5B is as follows: for Margaret River, $n = 17$ as follows: Cabernet Sauvignon/Shiraz, $n = 14/n = 3$ with vintages as follows: 2012, $n = 1$; 2011, $n = 11$; 2010, $n = 4$; and 2009, $n = 1$; for Coonawarra, $n = 21$ as follows: Cabernet Sauvignon/Shiraz, $n = 16/n = 5$ with vintages as follows: 2012, $n = 3$; 2011, $n = 5$; 2010, $n = 10$; 2009, $n = 2$; and 2005, $n = 1$; and for Barossa and McLaren Vale, $n = 22$ as follows: Cabernet Sauvignon/Shiraz, $n = 13/n = 9$ with vintages as follows: 2012, $n = 1$; 2011, $n = 14$; 2010, $n = 6$; and 2009, $n = 1$.

DOI: 10.1021/acs.jafc.5b03847
J. Agric. Food Chem. 2015, 63, 9103−9111

metabolites that influence 1,4-cineole and 1,8-cineole concentrations in wines should be considered.

Sensory Characterization of Cineoles in Red Wine. *Impact Level of 1,4-Cineole in Red Wine.* The measurement of the perception threshold, performed with the ascending three-alternative forced choice (3AFC) task method, is one of the most common techniques used to evaluate quantitatively the aromatic potency of wine odorants.[25] However, recent works on perceptive interactions demonstrated, using single triangle tests, that aromatic compounds could potentially contribute to wine aromas through synergistic effects when their levels were below reported perception thresholds.[26−28] The method of single triangle tests was therefore used in the present study to check if levels of 1,4-cineole measured in Australian red wines were perceivable in water and red wines. Comparisons presented in Table 3 show that 1,4-cineole was perceived in water at 0.27 μg/L and that an addition of 0.54 μg/L in Cabernet Sauvignon wine, to produce a final concentration of 0.63 μg/L, was required before panelist perception. In comparison to the concentrations of 1,4-cineole found in the Cabernet Sauvignon wines, this suggests that 60% of the Australian Cabernet Sauvignon wines in this study had concentrations of 1,4-cineole potentially perceivable. In contrast, the average concentration of 1,4-cineole in Shiraz and Pinot Noir wines was 7- and 2.5-fold lower, respectively, than the range of concentrations potentially detectable in Cabernet Sauvignon wines. These findings suggest that 1,4-cineole has an influence on the aromatic profile of Australian Cabernet Sauvignon wines.

Sensory Characterization of 1,4-Cineole and 1,8-Cineole in Cabernet Sauvignon Wines. Descriptive analysis was undertaken to characterize the impact of 1,4-cineole in the presence and absence of 1,8-cineole on the aroma of Australian Cabernet Sauvignon wines. The presence of IBMP was also considered because this compound contributes highly to the herbaceous aroma of Cabernet Sauvignon wines investigated in this study.[2] Preliminary sensory evaluation of Cabernet Sauvignon wines with concentrations of IBMP, 1,4-cineole, and 1,8-cineole at 10 ng/L, 1.6 μg/L, and 2.5 μg/L respectively (Table 2), was performed by a small panel of five experts with extensive experience in wine aroma evaluation to generate relevant descriptors. The main sensory attributes used to describe the wines spiked with 1,4-cineole and 1,8-cineole were "hay", "dried herbs", "fresh", "mint", and "blackcurrant". The "fresh" and "minty" aromas are common characteristics of numerous Australian Cabernet Sauvignon wines to which 1,8-cineole has been previously associated.[4] Therefore, the descriptive analysis focused on the investigation of the "hay", "bay leaf", and "blackcurrant" attributes using an adapted version of the Deviation from Reference Method.[22] The ANOVA and Duncan post-hoc test showed that the addition of 1,4-cineole, both independently and in combination with 1,8-cineole, enhanced hay aromas compared to the control wine ($p < 0.05$) (Figure 4A). The intensity of bay leaf notes was significantly enhanced by the association of 1,4-cineole and 1,8-cineole ($p < 0.05$) (Figure 4B). An additional comparison showed that raising the concentrations of 1,8-cineole (10 μg/L) in this combination led to an increase in the intensity of bay leaf aromas ($p < 0.05$) (Figure 4C). In contrast, the panel was not able to significantly separate the different wines according to blackcurrant aromas, even though the addition of only 1,8-cineole tended to be perceived with more pronounced notes of blackcurrant (Supplementary Figure 2 of the Supporting Information). To check the veracity of these observations, a final comparison between the control wine and the same wine spiked with high concentrations of 1,8-cineole (10 μg/L) was

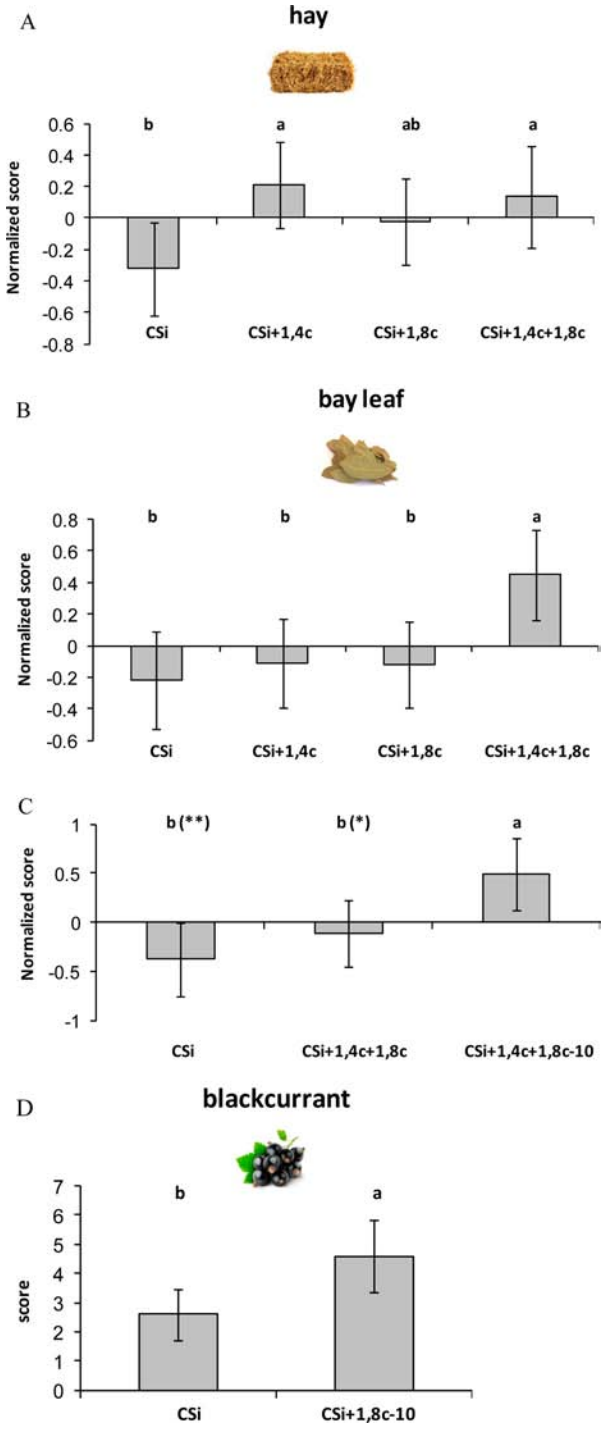

Figure 4. Descriptive analysis: evaluation of the contribution of 1,4-cineole and 1,8-cineole to (A) hay, (B and C) bay leaf, and (D) blackcurrant aromas in Cabernet Sauvignon wines using the Deviation from Reference Method (test of similarity). Sample codes are shown in Table 2. Wines and reference standards were prepared as indicated in Tables 2 and 4, respectively. The number of panelists was 33 for trials A and B and 17 for trials C and D. Results were expressed in normalized score for trials A−C and in absolute score for trial D. Standard errors measured on normalized score (A−C) and absolute score (D) were used for the error bars.

DOI: 10.1021/acs.jafc.5b03847
J. Agric. Food Chem. 2015, 63, 9103−9111

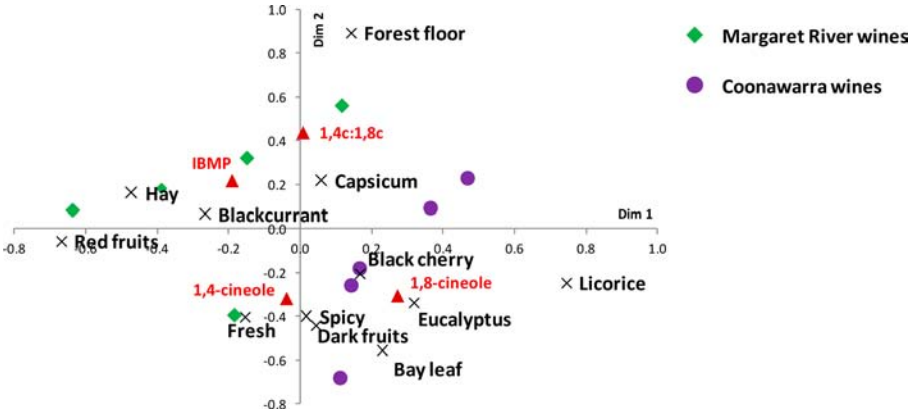

Figure 5. Two-dimensional MDS configuration of the 10 sorted Australian Cabernet Sauvignon wines from Margaret River (diamonds) and Coonawarra (circles) and correlations of the sensory terms (crosses) and chemical compounds (triangles) with the dimensions.

undertaken. The wine spiked with 1,8-cineole was perceived significantly higher for blackcurrant aromas than the control wine, confirming the previous trend ($p < 0.05$) (Figure 4D).

These findings indicate that 1,4-cineole, in both isolation and combination with 1,8-cineole, may contribute to the hay and dried herbs aromas that have been reported in Australian Cabernet Sauvignon wines. These compounds have both been reported in different aromatic herbs, such as thyme,[29] sage,[30] and bay leaf,[31] and the contribution of 1,8-cineole to the sensory perception of aromatic herbs has been reported in bay leaf and rosemary essential oils.[32,33]

While several studies have identified 1,8-cineole as a potent aroma of blackcurrant,[34,35] the current study suggests a relationship between 1,8-cineole and blackcurrant aroma in red wines. In particular, a contribution to the pronounced blackcurrant aroma in some Australian Cabernet Sauvignon wines, possibly in combination with other compounds, such as dimethyl sulfide,[36] is plausible.

Contribution of Cineole Isomers to Regional Aromas of Australian Cabernet Sauvignon Wines. The potential contribution of 1,4-cineole and 1,8-cineole to the regional typicity of Australian Cabernet Sauvignon wine aroma was investigated by comparison of Coonawarra and Margaret River wines using a sorting method. Wines were grouped according to their geographic origin (Figure 5), with Coonawarra wines associated with 1,8-cineole and attributes such as "eucalyptus", "bay leaf", "licorice", and "black cherry". These results indicate that 1,8-cineole might be an important marker of Coonawarra Cabernet Sauvignon and contribute to the eucalyptus, bay leaf, and fresh licorice aromas that are often empirically reported in these wines.[6,37] Margaret River wines were more associated with the 1,4-cineole/1,8-cineole ratio, IBMP, and descriptors such as "hay", "forest floor", "capsicum", "red fruit", and "blackcurrant". This region is generally known to produce wines with some elegant herbaceous aromas.[6,37] IBMP has been reported to contribute to green aromas perceived in Cabernet Sauvignon wines from Margaret River.[38] Even though IBMP was more correlated to Margaret River than Coonawarra wines, the concentrations measured in the present study were considerably lower (<13 ng/L) than reported in a previous work.[38] This suggests that compounds other than IBMP might contribute to Margaret River Cabernet Sauvignon typicality. The average concentrations of 1,4-cineole in Margaret River and Coonawarra wines selected for the sorting task were in the same range (0.74 and 0.69 μg/L, respectively). However, the 1,4-cineole/1,8-cineole ratios were higher in Margaret River wines and more correlated with the herbaceous attributes perceived in these wines (Figure 5).

Contrary to the descriptive analysis results, no relationship between 1,8-cineole and blackcurrant aromas was identified when the Coonawarra and Margaret River wines were compared. This lack of consistency confirms that the perception of blackcurrant aromas in red wines is complex and probably not due to only one or two compounds.[36]

The descriptors used for the sorting task were selected because they closely aligned to cineole isomers and IBMP aromas reported in the literature.[2,8] Some relationships between the sorting task and cineole isomer composition were also supported by the previously described descriptive analysis. These findings suggest that 1,4-cineole might contribute to the aromatic typicality of Margaret River Cabernet Sauvignon, when it is associated with moderate levels of IBMP and 1,8-cineole. In contrast, high concentrations of 1,8-cineole in combination with 1,4-cineole and IBMP seem to favor the expression of bay leaf aromas. A bay leaf aroma was found to be a more important descriptor for Coonawarra wines with an average concentration of 1,8-cineole of 7.7 μg/L, which was 2.9-fold higher than in the Margaret River wines. It appears that the relative concentrations of 1,4-cineole and 1,8-cineole contribute, probably with other compounds, to the regional differentiation found between Margaret River and Coonawarra Cabernet Sauvignon wines.

These results demonstrate that cineole isomers may be valuable aromatic markers for Australian Cabernet Sauvignon wines and to a lesser regional typicality. Further studies to investigate the occurrence of cineole isomers in other cultivars and wines from other important regions in the world are warranted.

■ ASSOCIATED CONTENT

Supporting Information

The Supporting Information is available free of charge on the ACS Publications website at DOI: 10.1021/acs.jafc.5b03847.

Distribution of 1,4-cineole/1,8-cineole concentration ratios in Australian Cabernet Sauvignon wines (Supplementary Figure 1) and descriptive analysis: evaluation of the contribution of 1,4-cineole and 1,8-cineole to blackcurrant aroma in Cabernet Sauvignon wines using the Deviation from Reference Method (test of similarity) and expressed in normalized score (33 panelists), with

DOI: 10.1021/acs.jafc.5b03847
J. Agric. Food Chem. 2015, 63, 9103−9111

the sample codes shown in Table 2 and standard errors measured on normalized score used for the error bars (Supplementary Figure 2) (PDF)

AUTHOR INFORMATION

Corresponding Author

*Telephone: +61-2-6933-4821. Fax: +61-2-6933-2940. E-mail: gantalick@csu.edu.au.

Funding

The authors thank the grape growers and wine makers of Australia through their investment body the Australian Grape and Wine Authority (AGWA) and the Australian federal government for their financial support.

Notes

The authors declare no competing financial interest.

ACKNOWLEDGMENTS

The authors are grateful to all of the sensory panelists of Bordeaux University who contributed to this study. The National Wine and Grape Industry Centre is an alliance between Charles Sturt University, New South Wales Department of Primary Industry, and New South Wales Wine Industry Association.

REFERENCES

(1) Anderson, K.; Arial, N. R. *Which Winegrape Varieties Are Grown Where? A Global Empirical Picture*; Adelaide University: Adelaide, South Australia, Australia, 2013.

(2) Allen, M. S.; Lacey, M. J.; Boyd, S. J. Determination of methoxypyrazines in red wines by stable isotope dilution gas chromatography-mass spectrometry. *J. Agric. Food Chem.* **1994**, *42*, 1734−1738.

(3) Peynaud, E.; Blouin, J. Nature et origine des sensations. In *Le Goût du Vin*, 4th ed.; Dunod: Paris, France, 2006; pp 115−116.

(4) Robinson, A. L.; Adams, D. O.; Boss, P. K.; Heymann, H.; Solomon, P. S.; Trengove, R. D. The relationship between sensory attributes and wine composition for Australian Cabernet Sauvignon wines. *Aust. J. Grape Wine Res.* **2011**, *17*, 327−340.

(5) Robinson, A. L.; Adams, D. O.; Boss, P. K.; Heymann, H.; Solomon, P. S.; Trengove, R. D. Influence of geographic origin on the sensory characteristics and wine composition of *Vitis vinifera* cv. Cabernet Sauvignon wines from Australia. *Am. J. Enol. Vitic.* **2012**, *63*, 467−476.

(6) Halliday, J. *Australian Wine Companion*; Hardie Grant Books: Richmond, Victoria, Australia, 2011.

(7) Hervé, E.; Price, S.; Burns, G. Eucalyptol in wines showing a "eucalyptus" aroma. In *Proceedings of VIIème Symposium International d'Oenologie*; Lonvaud, A., de Revel, G., Darriet, P., Eds.; Tec & Doc Lavoisier: Paris, France, 2003.

(8) Capone, D. L.; Van Leeuwen, K.; Taylor, D. K.; Jeffery, D. W.; Pardon, K. H.; Elsey, G. M.; Sefton, M. A. Evolution and occurrence of 1,8-cineole (eucalyptol) in Australian wine. *J. Agric. Food Chem.* **2011**, *59*, 953−959.

(9) Capone, D. L.; Jeffery, D. W.; Sefton, M. A. Vineyard and fermentation studies to elucidate the origin of 1,8-cineole in Australian red wine. *J. Agric. Food Chem.* **2012**, *60*, 2281−2287.

(10) Kalua, C. M.; Boss, P. K. Evolution of volatile compounds during the development of Cabernet Sauvignon grapes (*Vitis vinifera* L.). *J. Agric. Food Chem.* **2009**, *57*, 3818−3830.

(11) Kalua, C. M.; Boss, P. K. Comparison of major volatile compounds from Riesling and Cabernet Sauvignon grapes (*Vitis vinifera* L.) from fruitset to harvest. *Aust. J. Grape Wine Res.* **2010**, *16*, 337−348.

(12) Romagni, J. G.; Allen, S. T.; Dayan, F. E. Allelopathic effects of volatile cineoles on two weedy plant species. *J. Chem. Ecol.* **2000**, *26*, 303−313.

(13) Leão Lana, E. J.; da Silva Rocha, K. A.; Kozhevnikov, I. V.; Gusevskaya, E. V. Synthesis of 1,8-cineole and 1,4-cineole by isomerization of α-terpineol catalysed by heteropoly acid. *J. Mol. Catal. A: Chem.* **2006**, *259*, 99−102.

(14) Takaishi, M.; Fujita, F.; Uchida, K.; Yamamoto, S.; Sawada, M.; Chihiro, H.; Shimizu, M.; Tominaga, M. 1,8-cineole, a TRPM8 agonist, is a novel natural antagonist of human TRPA1. *Mol. Pain* **2012**, *8*, 86−97.

(15) Robinson, A. L.; Boss, P. K.; Heymann, H.; Solomon, P. S.; Trengove, R. D. Development of a sensitive non-targeted method for characterizing the wine volatile profile using headspace solid-phase microextraction comprehensive two-dimensional gas-chromatography time-of-flight mass spectrometry. *J. Chrom. A* **2011**, *1218*, 504−517.

(16) Weldegergis, B. T.; de Villiers, A.; McNeish, C.; Seethapathy, S.; Mostafa, A.; Górecki, T.; Crouch, A. M. Characterisation of volatile components of Pinotage wines using comprehensive two-dimensional gas chromatography coupled to time-of-flight mass spectrometry (GC x GC-TOFMS). *Food Chem.* **2011**, *129*, 188−199.

(17) Bignell, C. M.; Dunlop, P. J.; Brophy, J. J.; Jackson, J. F. Volatile leaf oils of some Queensland and Northern Australian species of the genus *Eucalyptus*. (Series II). Part I. Subgenus Symphyomyrtus, section Adnataria: (a) series Oliganthae, *(b) se*ries Ochrophloiae, (c) series Moluccanae, (d) series Polyanthemae, (e) series Paniculatae, (f) series Melliodorae and (g) series Porantheroideae. *Flavour Fragrance J.* **1997**, *12*, 19−27.

(18) Mosciano, G. Organoleptic characteristics of flavor material. *Perfum. Flavor.* **1992**, *17* (3), 54.

(19) Antalick, G.; Šuklje, K.; Blackman, J. W.; Meeks, M.; Deloire, A.; Schmidtke, L. M. Influence of grape composition on red wine ester profile: comparison between Cabernet Sauvignon and Shiraz cultivars from Australian warm climate. *J. Agric. Food Chem.* **2015**, *63*, 4664−4672.

(20) Martin, N.; de Revel, G. Sensory evaluation: Scientific bases and oenological applications. *J. Int. Sci. Vigne Vin* **1999**, 81−93.

(21) Franc, C.; David, F.; de Revel, G. Multi-residue off-flavour profiling in wine using stir bar sorptive extraction-thermal desorption-gas-chromatography-mass-spectrometry. *J. Chrom. A* **2009**, *1216*, 3318−3327.

(22) Larson-Powers, N.; Pangborn, R. M. Descriptive analysis of the sensory properties of beverages and gelatins containing sucrose or synthetic sweeteners. *J. Food Sci.* **1978**, *43*, 47−51.

(23) Šuklje, K.; Antalick, G.; Buica, A.; Langlois, J.; Coetzee, Z. A.; Gouot, J.; Schmidtke, L. M.; Deloire, A. Clonal differences and impact of defoliation on Sauvignon blanc (*Vitis vinifera* L.) wines: a chemical and sensory investigation. *J. Sci. Food Agric.* **2015**, DOI: 10.1002/jsfa.7165.

(24) Deloire, A.; Vaudour, E.; Carey, V.; Bonnardot, V.; Van Leeuwen, C. Grapevine responses to terroir, a global approach. *J. Int. Sci. Vigne Vin* **2005**, *39*, 149−162.

(25) Lawless, H. T.; Heymann, H. S. Measurement of sensory threshold. In *Sensory Evaluation of Food*, 2nd ed.; Heldman, D. R., Ed.; Springer: New York, 2010; pp 125−145.

(26) Escudero, A.; Campo, E.; Farina, L.; Cacho, J.; Ferreira, V. Analytical characterization of the aroma of five premium red wines. Insights into the role of odor families and the concept of fruitiness of wines. *J. Agric. Food Chem.* **2007**, *55*, 4501−4510.

(27) Pineau, B.; Barbe, J. C.; Van Leeuwen, C.; Dubourdieu, D. Examples of perceptive interactions involved in specific "red-and-black-berry" aromas in red wines. *J. Agric. Food Chem.* **2009**, *57*, 3702−3708.

(28) Lytra, G.; Tempere, S.; de Revel, G.; Barbe, J. C. Impact of perceptive interactions on red wines fruity aroma. *J. Agric. Food Chem.* **2012**, *60*, 12260−12269.

(29) Amarti, F.; El Ajjouri, M.; Ghanmi, M.; Satrani, B.; Aafi, A.; Farah, A.; Khia, A.; Guedira, A.; Rahouti, M.; Chaouch, A. Composition chimique, activité antimicrobienne et antioxydante de

DOI: 10.1021/acs.jafc.5b03847
J. Agric. Food Chem. 2015, 63, 9103−9111

l'huile essentielle de *Thymus zygis* du Maroc. *Phytotherapie* **2011**, *9*, 149−157.
(30) Muller, W. H.; Muller, C. H. Volatile growth inhibitors produced by Salvia species. *Bull. Torrey Bot. Club* **1964**, *91*, 327−330.
(31) Hogg, J. W.; Terhune, S. J.; Lawrence, B. M. Dehydro-1,8-cineole: A new monoterpeneoxide in *Laurus noblis* oil. *Phytochemistry* **1974**, *13*, 868−869.
(32) Marzouki, H.; Piras, A.; Bel Haj Salah, K.; Medini, H.; Pivetta, T.; Bouzid, S.; Marongiu, B.; Falconieri, D. Essential oil composition and variability of Laurus nobilis L. growing in Tunisia, comparison and chemometric investigation of different plant organs. *Nat. Prod. Res.* **2009**, *23*, 343−354.
(33) Moss, M.; Oliver, L. Plasma 1,8-cineole correlates with cognitive performance following exposure to rosemary essential oil aroma. *Ther. Adv. Psychopharmacol.* **2012**, *2*, 103−113.
(34) Latrasse, A.; Rigaud, J.; Sarris, J. L'arôme du cassis (*Ribes nigrum* L.), odeur principale et notes secondaires. *Sci. Aliments* **1982**, *2*, 145−162.
(35) Mikkelsen, B. B.; Poll, L. Decomposition and transformation of aroma compounds and anthocyanins during black currant (*Ribes nigrum* L.) juice processing. *J. Food Sci.* **2002**, *67*, 3447−3455.
(36) Lytra, G.; Tempere, S.; Zhang, S.; Marchand, S.; de Revel, G.; Barbe, J. C. Olfactory impact of dimethyl sulfide on red wine fruity esters aroma expression in model solution. *J. Int. Sci. Vigne Vin* **2014**, *48*, 75−85.
(37) Time Inc. (UK) Ltd.. Panel Tasting: Coonawarra and Margaret River Cabernet Sauvignon. *Decanter* **2012**, 97−108.
(38) Wilkinson, K.; Kennedy, U.; Gibberd, M. Green characters in Cabernet Sauvignon. In *Australian Society of Viticulture and Oenology Seminar*; Oag, D., DeGaris, K., Partridge, S., Dundon, C., Francis, M., Johnstone, R., Hamilton, R., Eds.; Australian Society of Viticulture and Oenology (ASVO): Mildura, Victoria, Australia, 2006; pp 60−64.

DOI: 10.1021/acs.jafc.5b03847
J. Agric. Food Chem. 2015, 63, 9103−9111

chosen as the treatment method because it represents the maximum temperature for cooking in water under atmospheric pressure. The meat and cooking water were separated and analyzed using sodium dodecyl sulfate−polyacrylamide gel electrophoresis (SDS−PAGE) in conjunction with LC−MS/MS (GeLC) and 1D LC−MS/MS, respectively.

MATERIALS AND METHODS

Porcine trypsin used for proteomic sample preparation was of sequencing grade and was purchased from Promega (Madison, WI).

Experimental Design. Lamb longissimus thoracis et lumborum, pooled from five animals and carefully blended to minimize tissue inhomogeneity and animal-to-animal variation between replicates, was used for the study. Each cooking control/treatment was performed in triplicate. The experimental workflows, GeLC of meat, cooking water (including water from control, which is described later in the Materials and Methods section) peptidomics, and cooking water and meat homogenate residue proteomics, are briefly summarized in Figure 1. Each experimental workflow was subjected to one LC−MS/MS analysis.

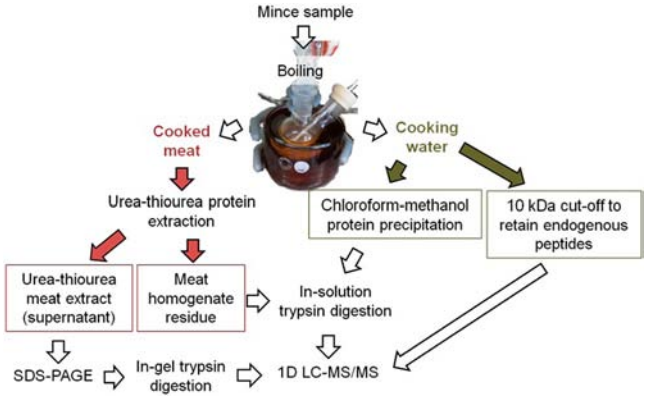

Figure 1. A schematic representation of the experimental workflows.

Lamb Meat. Five 11-month-old Coopworth ram lambs were slaughtered on August 29, 2013, at a local processing plant. The average carcass weight was 22.3 ± 4 kg. After hanging in the chiller of the processing plant for 24 ± 2 h, the backstrap [longissimus thoracis et lumborum (LTL)] was removed from each animal and the bulk of connective tissue was removed. The meat was vacuum-packed and transported to AgResearch (Lincoln campus) on crushed ice in an ice box. After additional aging at −1 °C to 48 ± 1 h post-mortem, meat was subsampled and stored at −80 °C until use. Meat subsamples from each animal (average 17.7 ± 0.5 g) were thawed in a fridge for about 4 h, diced into ∼1 cm^3 cubes, pooled with gentle stirring and minced using the chopper accessory of a Braun MR 4050 CA blender (Kronberg, Germany) according to the manufacturer's instruction for 12 × 2 s (<1 s pause in between). Ground meat was aliquoted, snap-frozen in liquid nitrogen to minimize freezing damage, and stored at −80 °C until use. The pH of the aged mince was 6.05, as measured directly by a HI 99163 meat pH meter (Hannah Instruments, Woonsocket, RI).

Meat Boiling. The design of the cooking method was based on the work of Deb-Choudhury et al.[6] with modifications. An aliquot of lamb meat mince was thawed at room temperature for 30 min, and then 0.6 ± 0.09 g (wet weight) of meat was transferred into a round-bottom flask and boiled at a meat to water ratio of 1:8 (w/v) for 10 or 240 min under reflux. The detailed method and the images of the cooking setup are shown in Supporting Information 1. For the control (raw meat without boiling), the setup was the same as described above except a room temperature oil bath was used and the "total heating" time (i.e., the period of time when the flask was in the oil bath) was 15 min. This 15 min period is roughly equal to the time meat and water spent in the heating source during the 10 min boiling, as it took around 1.9−2.9 min to raise water from room temperature to 100 °C in this study. Once the boiling time was reached, the flask was immediately placed in an ice−water bath for 10 min. After cooling, the bulk of meat surrounded by water during cooking and cooking water were carefully transferred to a glass centrifuge tube and centrifuged for 40 min at 10 840*g* at 4 °C. The supernatant (i.e., cooking water) was aliquoted and stored at −80 °C while the meat was subjected to protein extraction as described below. The control was treated with the same procedure as cooked samples.

Protein Extraction. Cooked meat was weighed, followed by soaking in urea−thiourea solution [7 M urea, 2 M thiourea, and 2% freshly added dithiothreitol (DTT)] at 1:16 ratio (w/v based on wet weight after cooking) for 5 min followed by homogenization in a hand-held, serrated pestle homogenizer over ice for four cycles of 1 min grinding and 10 s pause. The homogenates were shaken vigorously using a reciprocal shaker at room temperature for 1 h and then aliquoted and stored at −80 °C. For SDS−PAGE, the homogenate was centrifuged at 17 810*g* for 20 min at 15 °C and the supernatant (hereinafter termed "urea−thiourea extract") was used. Residues from meat homogenate (hereinafter termed "meat homogenate residue") were also obtained for proteomic analysis: 100 μL of the meat homogenate sample was centrifuged at 17 810*g* for 20 min at 15 °C. Supernatants were removed by aspiration. The remaining pellets were washed by vortexing in double deionized water twice, followed by one wash with methanol, and defatted with one wash of chloroform−methanol (2:1, v/v), based on the method of Kannamkumarath et al.,[12] and one wash with methanol. Pellets were dried in a vacuum centrifuge at 30 °C and then subjected to in-solution digestion with trypsin.

Protein was extracted from cooking water using a chloroform−methanol precipitation method based on the work of Wessel and Flügge.[13] The pellet was dried in a vacuum centrifuge at 30 °C and stored at −80 °C. Protein concentrations of cooking water samples and urea−thiourea extracts were estimated using a 2D-Quant kit (GE Healthcare Bio-Sciences AB, Uppsala, Sweden) according to the manufacturer's instruction. Protein from the cooking water of samples boiled 10 min was preconcentrated by the protein precipitation method before doing the assay to ensure a protein concentration above the detection limit of the kit.

SDS−PAGE. Urea−thiourea extract was mixed with SDS−sample buffer (93.8 mM Tris-HCl, 25% glycerol, 5% SDS, 0.01% bromophenol blue, pH 6.8, and freshly added 350 mM DTT) in 1:1.5 ratio (v/v) and shaken gently at 30 °C for 1 h. Samples were run on a 4−20% T precast gel (Bio-Rad, 133 × 87 × 1 mm) at a constant voltage of 200 V with current and power limits set to 80 mA (160 mA for two gels) and 15 W, respectively for 42 min. Each set of replicates was run on a separate gel. For preparative gel lanes used for GeLC, 100 μg of protein per meat sample was loaded in a well. For analytical gel lanes, 25 μg of protein per meat sample was loaded in a well. Protein fixation and gel staining and destaining procedures are described in Supporting Information 1. Gel images were taken using a Nikon D100 digital camera over a light box. Relative stain intensity across each analytical lane was estimated using ImageJ v1.45s (Rasband, National Institutes of Health).

Protein Digestion for LC−MS/MS Analysis. Each preparative lane was divided into nine sections of approximately equal length (Figures 2 and S1-5). Each gel section was split perpendicularly into two slices; one slice was used for a LC−MS/MS analysis, while the other was stored at −80 °C as a back-up. In-gel digestion was based on the method of Deb-Choudhury et al.[8] with modifications. The procedure is provided in Supporting Information 1.

For cooking water samples, protein (11 μg) extracted from a sample was sonicated in 10 mM of tris(2-carboxyethyl)phosphine hydrochloride (TCEP), 60 mM ammonium bicarbonate at a temperature below 25 °C (achieved by adding ice slurry in the sonication bath) for 10 min and then vortexed for 45 min at 37 °C to reduce the disulfide bonds. After returning to room temperature, the samples were alkylated in 25 mM (final concentration) iodoacetamide for 30 min at 25 °C under shaking. Alkylation was followed by incubation in 10 mM TCEP (final concentration) for 1 h at 25 °C under gentle shaking.

DOI: 10.1021/acs.jafc.5b03324
J. Agric. Food Chem. 2015, 63, 9112−9123

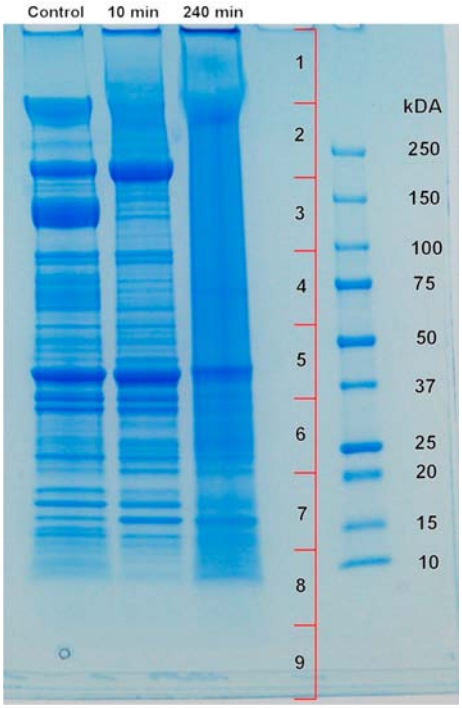

Figure 2. Representative analytical SDS−PAGE gel lanes of lamb meat protein extracts (from cooking replicate 1; refer to Supporting Information 2). Red marks on the right-hand side of the image indicate the approximate position of the gel sections from the preparative lanes sliced for proteomic analysis.

Samples were diluted by adding one volume of 50 mM ammonium bicarbonate, following by addition of 0.22 μg of trypsin. Acetonitrile was added to each sample to a final concentration of 10% (v/v). Digestion was performed at 37 °C with shaking overnight. Digests were centrifuged at 17 810*g* for 10 min at 15 °C. Around 200 μL of supernatant from each sample was dried in a vacuum centrifuge at 30 °C and stored at −80 °C until analysis. For meat homogenate residue samples, the dried pellet was sonicated in 10 mM of TCEP in 60 mM ammonium bicarbonate at a temperature below 25 °C for 10 min and then vortexed for 45 min at 37 °C. The rest of the in-solution digestion steps were as described above for the cooking water samples, except 1.25 μg of trypsin was used for digesting each pellet sample. The supernatant from each sample was dried in a vacuum centrifuge at 30 °C and stored at −80 °C until analysis.

Cooking Water Peptidomic (Undigested) Samples. To determine endogenous peptides from cooking water by LC−MS/MS analysis, 396 μL of each sample was acidified with 4 μL of formic acid (1% final concentration) and centrifuged in a 10 kDa MW cutoff spin column (Merck Millipore) at 13 800*g* at 4 °C. For the control and 10 and 240 min cooking samples, centrifugation was performed for 61−72, 38−44, and 56−68 min, respectively, to collect the bulk of the liquid phase. These different times were used because the filtering speed varied between the samples. The filtrate was dried down in the vacuum centrifuge at 30 °C and stored at −80 °C until analysis.

LC−MS/MS Sample Preparation and Conditions. For gel samples, the tryptic digest of each slice was resuspended in 50 μL of 2% acetonitrile/0.5% formic acid. The reconstituted samples were spun at 17 810*g* for 10 min at 4 °C. The supernatant was used for LC−MS/MS. Dilution was performed on the basis of stain intensity with 2% acetonitrile/0.5% formic acid as specified in Tables S1−2 and S1−3. For nongel samples, dried tryptic digests or cooking water peptidomic (undigested) samples were reconstituted in 2% acetonitrile/5% formic acid in a sonication bath kept below 25 °C for 5 min prior to vortexing. Reconstituted samples were centrifuged for 10 min at 4 °C at 17 810*g*. The supernatant was cleaned using a C18 material StageTip (Thermo Scientific) according to the established protocol,[14] except that more washing with 0.5% formic acid was applied. After drying in a vacuum centrifuge, the samples were reconstituted in 50 μL of 2% acetonitrile/0.5% formic acid using sonication and vortexing as described above. After 5 min of centrifugation at 4 °C and 17 810*g*, the supernatant was diluted with 2% acetonitrile/0.5% formic acid (1 in 4 for cooking water digested and undigested samples; 1 in 2 for meat homogenate residue sample) for LC−MS/MS.

LC−MS/MS was carried out as described by Yu et al.[15] with modifications. For a single LC−MS/MS run of each sample, 5 μL (out of 50 μL) was loaded on a C18 trap column (UHPLC Nanopeptide Trap Magic C18AQ, particle size 5 μm, pore size 200 Å, Bruker Michrom) at a flow rate of 5 μL/min. The trap column was switched in line with a reversed-phase analytical column (Intensity C18P UHPLC Nano Column, particle size 1.8 μm, pore size 100 Å, i.d. 0.1 mm, length 300 mm, Bruker Michrom). The loading and desalting solvent used was the same as mobile phase A (0.1% formic acid). The reverse-phase elution gradient was 2−45% mobile phase B (98% acetonitrile/0.1% formic acid) in 60 min at a flow rate of 400 nL/min at a column oven temperature of 60 °C. Between runs, the column was reconditioned by increasing mobile phase B to 95% in 2 min, holding for 3 min, and then bringing it down to 0% solvent B in 1 min. The column was equilibrated in 100% mobile phase A for 4 min.

Data Analysis. MS/MS spectra of each LC−MS/MS run were converted into a peak list in mgf format using DataAnalysis v4.1 software (Bruker).

Creation of a Small Sequence Database. Peak lists were searched against the combined *Ovis aries* sequence database[15] using a local Mascot server (Matrix Science) version 2.4. The search parameters, the peptide and protein score thresholds, are described in Supporting Information 1. All Mascot search results were compiled into a minimal protein list using the ProteinExtractor algorithm (Bruker Daltonics). All protein sequences (396 sequences, including keratins) from this list were retrieved to create a separate, shortlist database adapted for subsequent Mascot searches involving a higher number of variable modifications or no enzyme specificity.

Protein Identification. Briefly, two types of Mascot searches against the shortlist database were performed. One is the Percolator[16] (v1.14) postprocessed search, and the other is the standard Mascot search. Only a protein that was identified in a Percolator postprocessed search, as well as in the standard Mascot search of a single LC−MS/MS run, was accepted as identified. All entries with a name containing keratin were rejected. The two Mascot search approaches are described in Supporting Information 1. The accepted protein identifications and the number of their corresponding peptide identifications (peptide IDs), according to the standard Mascot search results, in each LC−MS/MS run are summarized in Tables S2-10−S2-13. The raw protein identification reports from which Tables S2-10−S2-13 were compiled are provided in Tables S2-14−S2-25.

Protein Modifications. Original, unmerged peak lists were searched against the shortlist database using the Mascot search approach for creating the shortlist database as mentioned above, but with the following changes: searches were performed against the shortlist database, and the MS/MS error tolerance was set to 0.4 Da. Furthermore, additional variable modifications (Table S1-4) divided into 16 groups (each group for one Mascot search) were included. These additional modifications are known potential heating and/or reactive oxygen species induced modifications. Not all of them may be well-suited for the MS/MS data acquisition setup used in the present study according to the literature, for example, Hex (K)[17] and the −1 Da allysine (K).[18] Peptide IDs carrying a modification of interest were manually evaluated as specified in Supporting Information 1. ProteinScape (Bruker Daltonics) annotated MS/MS spectra of the qualified peptides and their unmodified counterparts (defined in Supporting Information 1) are given in Supporting Information 3.

Estimation of Percent Non/Semitryptic Peptides. Peak lists corresponding to all the sections of a single gel lane were merged into one file. Peak lists were searched against the shortlist database using the standard Mascot search approach employed for protein identification. Estimation was based on a minimal list of accepted

DOI: 10.1021/acs.jafc.5b03324
J. Agric. Food Chem. 2015, 63, 9112−9123

Table 1. Number of Proteins Identified in the GeLC, Cooking Water Proteomics, Cooking Water Peptidomics, and Meat Homogenate Residue

		number of proteins identified (mean ± SD)				proteins exclusive to control or a treatment			
treatment	*n*	GeLC[a]	in solu cw[b]	PepT cw[c]	in solu resiD[d]	GeLC	in solu cw	PepT cw	in solu resiD
control	3	142 ± 2	27 ± 3	6 ± 2	54 ± 10	19	21	6	9
10 min boiling	3	156 ± 14	36 ± 3	3 ± 1	56 ± 7	37	22	1	6
240 min boiling	3	91 ± 13	23 ± 4	8 ± 2	51 ± 3	2	9	11	8

[a]GeLC experiments of urea−thiourea extracts. [b]Cooking water in-solution digested proteomic experiments. [c]Cooking water peptidomic experiments. [d]Meat homogenate residue in-solution digested proteomic experiments.

peptide IDs compiled by ProteinScape, and the results are given in Tables S1-6 and S1-7.

Statistical Analysis. Paired *t* test (Analysis ToolPak on Microsoft Excel 2007) was used to support discussion of differences in numbers of protein identifications between control and a treatment. The statistical significance was set at $p < 0.05$.

RESULTS AND DISCUSSION

This study aims to improve the understanding of the effect of boiling, a commonly practiced cooking method, on the primary structure of lamb meat proteins using a shotgun proteomic approach. Meat and cooking water were separated after cooking. The meat was extracted in a urea−thiourea solution for the GeLC analysis, while the residue was washed with water and organic solvents for the direct LC−MS/MS analysis. The denaturing character of the urea−thiourea solution should solubilize most myofibrillar and sarcoplasmic proteins from raw meat. This was validated by the presence of the major sarcoplasmic and myofibrillar proteins, e.g., pyruvate kinase isozymes M1/M2 and myosin heavy chains, in the control urea−thiourea extract (Table S2−10). A GeLC approach has previously been utilized to characterize the lamb meat proteome from longissimus lumborum muscle.[15] The proteins and endogenous peptides from the cooking water were separately analyzed by direct LC−MS/MS. Peptide and protein identification was initially carried out by Mascot, a very widely used MS/MS data searching software, followed by stringent evaluation as described in the Materials and Methods and in the Data Analysis section of Supporting Information 1. The results are presented and discussed in terms of (1) change in proteomic profile and (2) protein primary level modifications characterized.

Proteomic Profile Change in Response to Boiling. *GeLC of the Meat Protein Extract.* The results showed that meat samples boiled for 10 min had the highest number of protein identifications, while boiling for 240 min resulted in the least, with an average difference of 65 proteins between the two treatments (Table 1). In total, 232 proteins were identified from the control and cooked samples under this experimental workflow (Table S2-10). The average number of protein identifications at 10 min boiling was significantly higher than that of 240 min ($p = 0.037$), but there was no difference with the control ($p = 0.225$). It is not surprising that the samples that underwent the harshest treatment had the lowest number of protein identifications, as also observed by Arena et al.[19] and Deb-Choudhury et al.[6] This is consistent with proteins becoming more resistant to trypsin digestion, due to arginine/lysine modifications or cross-linking/aggregation, and/or too modified or fragmented to be detected by an automatic MS/MS database search approach.

The SDS−PAGE profiles showed alteration in banding pattern between the short (10 min) and long (240 min) boiling times and the control (Figure 2; gel images for the other two cooking replicates are given in Figure S1-5). The overall banding patterns between replicates looked similar, although the protein mobility varied between the 42 min electrophoresis runs. The control and 10 min samples showed defined but somewhat different banding patterns, while the 240 min sample exhibited almost a smear above the 50 kDa marker. Five regions across the gel lanes (specified in Table S1-8) showed distinct changes in banding patterns in response to boiling. These changes, along with the potentially related GeLC results, are summarized in Table S1-8. Several water-soluble proteins, e.g., adenylate kinase 1 and β-enolase, were released into water during the control soaking, because many fewer peptide IDs from these proteins were found in the control as opposed to the 10 min boiling (Table S2-10). The reason is likely to be protein denaturation upon boiling resulting in reduced water solubility.

The overall results showed that the 240 min boiling potentially aggregates, polymerizes, and/or fragments several proteins, including the sarcoplasmic proteins L-lactate dehydrogenase A chain isoform 1 and glycogen myophosphorylase and the myofibrillar proteins TPM1, tropomyosin β-chain isoform 1, and α-actinin-2 and -3, as a greater number of peptides derived from these proteins were identified in the higher and/or lower molecular weight gel sections relative to their theoretical M_r (M_{rt}) than the control and 10 min samples (Table S2-10).

The giant myofibrillar protein titin was highly abundant in the control and 10 min samples according to the number of peptide IDs. The number greatly declined at 240 min boiling. The myosin light chain 1/3 (one of the myosin light chain isoforms) showed signs of truncation, whereas fast skeletal myosin light chain 2 exhibited signs of aggregation at 10 min of boiling, but at 240 min, both protein aggregation and fragmentation were observed (Table S2-10). Meat protein aggregation induced by cooking can involve both noncovalent and covalent binding. An increase in protein surface hydrophobicity due to thermal denaturation has been shown to play an important role in cooking-induced protein aggregation in meat.[3,20] Several types of cross-links have been shown to be implicated in aggregation of meat protein upon heating, including dityrosine, Schiff bases,[20] disulfide bridges,[3] and protein carbonylation.[21]

At 240 min of boiling, several bands remained relatively more defined. They were all found below the 50 kDa marker (Figures 2 and S1-5). Two of them are particularly distinguished: one had an M_r around 40 kDa and the other had an M_r of approximately 16 kDa. The results here as well as previous findings[15] suggest that one band is mainly creatine kinase M-type, skeletal muscle α-actin, and fructose-bisphosphate aldolase A isoform 1, whereas the other is myoglobin. Creatine kinase M-type and fructose-bisphosphate aldolase A isoform 1

DOI: 10.1021/acs.jafc.5b03324
J. Agric. Food Chem. 2015, 63, 9112−9123

seemed to be involved in the cooking-induced protein aggregation on account of their appearance in the higher molecular weight gel sections of the boiled samples. Actin and myoglobin appeared to be involved in both protein aggregation/polymerization and fragmentation at 240 min of boiling according to the GeLC results (Tables S2-10). There were also actin peptides identified in multiple gel sections in the control both above and below its M_{rt}, although to a noticeably lesser extent compared to the 240 min samples. This was probably associated with post-mortem actomyosin complex formation and proteolysis.[22] Wen et al.[23] found myosin light chain 3 and triosephosphate isomerase were more tolerant to cooking (up to 100 °C) than several other major meat proteins. While the former was not detected in the present study, the latter also seemed to exhibit relatively higher heat stability, because at 240 min the gel section(s) from the M_{rt} range of the intact protein contained similar numbers of the peptide IDs to those of the 10 min samples.

With regard to myosin heavy chains (M_{rt} ranging from 221 to 223 kDa), one of the most abundant meat proteins, the extent of involvement from boiling on their aggregation remains to be uncovered, because quite a few of their peptides were identified in the top gel sections, regardless of treatment (Table S2-10). It was recently shown that even in raw, fresh bovine LTL, four myosin heavy chain isoforms have been identified in a band above 600 kDa.[24] It is worth noting that the number of peptide IDs among control/cooked samples for some myosin heavy chain isoforms, e.g., myosin-8, varied greatly between replicates (Table S2-10). This may be caused by the protein inference issue in shotgun proteomics[25] due to the high amino acid sequence similarity among these proteins.

Protein aggregation has important implications for the food industry and the consumer. It has been shown to interfere with protein and peptide extraction processes and to reduce the sensitivity of meat protein to enzymatic proteolysis in some model studies.[26] The former can increase the production cost, whereas the latter might be related to retardation of protein absorption. On the other hand, aggregation can be manipulated to modulate gel formation and textural properties, which is essential in the making of comminuted meat products.[2] Identification of the protein species and modifications involved in aggregation via proteomic techniques can help better inform the control of such process-induced protein aggregation.

Cooking Water. Meat soup and stock are widely consumed globally. Hence, proteomic and peptidomic evaluation of the meat cooking water are of particular interest. The numbers of protein and peptide identifications in the proteomic (digested) samples were clearly higher than those in their corresponding peptidomic (undigested) samples (Tables 1 and S2-11 and S2-12). Boiling for 10 min gave the highest number of protein identifications in the digested samples but the least in the undigested samples, while the converse was true for the 240 min samples.

The proteomic (digested) results showed distinctly different protein profiles between the control and boiled samples (Tables 1 and S2-11). In the 10 min digested samples, the numbers of the identified sarcoplasmic proteins were clearly reduced compared to the control value. Type I collagen was the most abundant protein in terms of the number of peptide IDs, while type III collagen was not detected. The findings here agree with those of Burson and Hunt.[27] Although protocollagen strands are long, they are not known to aggregate.[28] This special characteristic is very likely attributed to the prevalence of proline and glysine residues in protocollagen, the two residues with the lowest propensity to form a β-sheet.[28] A number of cytoskeletal proteins, e.g., nebulin, titin, and myosin light chain isoforms but not myosin heavy chains and actin, also emerged at 10 min boiling. In the 240 min digested samples, myosin heavy chains appeared and became the most abundant protein. Actin also appeared at this time point. TPM1 and tropomyosin β-chain isoform 1 seemed to become more abundant in this fraction. The number of peptide IDs for myosin light chain isoforms did not vary much between 10 and 240 min of boiling. The undigested results strongly suggest that the backbones of six proteins consisting of sarcoplasmic, myofibrillar, and mitochondrial proteins have been cleaved upon prolonged boiling, because they were found in at least two replicates of the 240 min samples but not in those from control or 10 min samples (Table S2-12).

The protein concentrations in the control cooking water were much higher than those of the boiled samples (Table 2).

Table 2. Estimated Protein Concentrations of Cooking Water and Urea−Thiourea Extracts

		mean protein concentration (μg/μL, ±SD)	
treatment	n	cooking water	urea−thiourea extract
control	3	3.42 ± 0.39	8.67 ± 0.50
10 min boiling	3	0.07 ± 0.01	12.95 ± 0.49
240 min boiling	3	0.64 ± 0.11	10.97 ± 0.61

At 240 min the protein concentrations increased by about 7-fold of those in the 10 min samples. A similar trend was also found by Deb-Choudhury et al.[6] The higher protein concentrations observed in the control cooking water should arise from the water-soluble proteins (Table S2-11) extracted during the control cooking (see the Materials and Methods), where the raw mince was stirred in water at room temperature. The initial drop in protein content at short boiling time may be explained by the aggregation of water-soluble proteins according to the digested results. Curiously, the marked increase of peptide IDs derived from the myofibrillar proteins observed in the cooking water digested results of the boiling samples (especially at 240 min), but not the corresponding cooking water undigested results, might be explained by the peptide aggregation hypothesis proposed by Deb-Choudhury et al.[6] Taking myosin heavy chains as an example (Tables S2-11 and S2-12), myosin heavy chains are normally not water-soluble unless cleaved into peptides. If their heat-hydrolysis products were part of large soluble peptide aggregates, then they might suit the proteomic, rather than the peptidomic (undigested), approach better.

These cooking water results suggest that meat soups, broths, and sauces prepared by sustained periods of boiling will likely contain several major myofibrillar and connective tissue proteins as the main proteinaceous component and have a higher protein content than those prepared by short periods of boiling.

Meat Homogenate Residue. In this fraction, the total number of peptide IDs for the major meat connective tissue collagens, collagen α-1(I) chain, collagen α-2(I) chain, and collagen α-1(III) chain (Table S2-13), were noticeably higher than those found in the urea−thiourea extract (Table S2-10). These collagens were found in all replicates of control and 10 min samples but not in any of the 240 min samples. It is speculated that after 240 min of boiling, both type I and III

DOI: 10.1021/acs.jafc.5b03324
J. Agric. Food Chem. 2015, 63, 9112−9123

Table 3. Peptides with Heat-Induced Modification Found in the Boiled Samples Only (Oxidative modifications are indicated in bold font. The "unmodified" peptide counterpart is indicated in italic font with gray shading.)

Treatment[a]	Replicate #[b]	Position[c]	m/z[d]	z[e]	RT[f] (min)	R_{fN}[g]	Peptide sequence and protein of origin	R_{fC}[h]	Modification(s)[i]
GeLC of meat (urea-thiourea extract)									
10 min; 4	2	163 - 179	957.0	2	44.4	K	LAMQEFMILPVGASSFR PREDICTED: beta-enolase [Ovis aries]	E	**F6: Oxidation**
10 min; 4	*2*	*163 - 179*	*957.0*	*2*	*43.0*	*K*	*LAMQEFMILPVGASSFR* *PREDICTED: beta-enolase [Ovis aries]*	*E*	***M7: Oxidation*** *(Counterpart)*
			949.0		*46.0*		*LAMQEFMILPVGASSFR* *PREDICTED: beta-enolase [Ovis aries]*		*(Counterpart)*
10 min; 6	3	161 - 175	809.8	2	38.0	K	VVLAYEPVWAIGTGK Triosephosphate isomerase 1 (tentative) cs39 [Ovis aries]	T	**W9: Oxidation**
10 min; 6	*3*	*161 - 175*	*801.9*	*2*	*40.1*	*K*	*VVLAYEPVWAIGTGK* *Triosephosphate isomerase 1 (tentative) cs39 [Ovis aries]*	*T*	*(Counterpart)*
240 min; 8	1	299 - 314	851.3	2	26.8	N	NVMSGGTTMYPGIADR PREDICTED: actin, alpha skeletal muscle isoform 1 [Ovis aries]	M	**M3: Oxidation;** **Y10: Oxidation**
240 min; 8	*1*	*299 - 314*	*851.4*	*2*	*25.0*	*N*	*NVMSGGTTMYPGIADR* *PREDICTED: actin, alpha skeletal muscle isoform 1 [Ovis aries]*	*M*	***M3: Oxidation;*** ***M9: Oxidation*** *(Counterpart)*
			843.4		*27.9*		*NVMSGGTTMYPGIADR* *PREDICTED: actin, alpha skeletal muscle isoform 1 [Ovis aries]*		***M3: Oxidation*** *(Counterpart)*
10 min; 3	1	1864 - 1874	656.9	2	31.3	R	LQDLVDKLQAK PREDICTED: myosin-1 [Ovis aries]	V	K7: Acetyl
10 min; 3	*1*	*1864 - 1874*	*635.8*	*2*	*26.7*	*R*	*LQDLVDKLQAK* *PREDICTED: myosin-1 [Ovis aries]*	V	*(Counterpart)*
10 min; 6	2	101 - 117	952.5	2	36.4	K	SVMLQIAATELEKGEGR PREDICTED: troponin I, fast skeletal muscle [Ovis aries]	R	K13: Carboxyethyl
10 min; 6	*2*	*101 - 113*	*716.9*	*2*	*37.3*	*K*	*SVMLQIAATELEK* PREDICTED: troponin I, fast skeletal muscle [Ovis aries]	*G*	*(Counterpart)*
240 min; 4	2	186 - 198	841.8	2	52.6	R	DLTDYLMKILTER PREDICTED: actin, alpha skeletal muscle isoform 1 [Ovis aries]	G	K8: Carboxyethyl
240 min; 4	*2*	*186 - 193*	*499.7*	*2*	*32.4*	*R*	*DLTDYLMK* *PREDICTED: actin, alpha skeletal muscle isoform 1 [Ovis aries]*	*I*	***M7: Oxidation*** *(Counterpart)*
240 min; 7	1	4 - 17	792.9	2	48.4	L	SDGEWQLVLNAWGK	V	S1: Dehydration
240 min; 6	2				47.2		RecName: Full=Myoglobin		
240 min; 7	*1*	*4 - 17*	*801.9*	*2*	*44.5*	*L*	*SDGEWQLVLNAWGK* *RecName: Full=Myoglobin*	*V*	*(Counterpart)*
240 min; 7	*1*	*2 - 17*	*886.9*	*2*	*46.1*	*M*	*GLSDGEWQLVLNAWGK*	*V*	*(Counterpart)*
240 min; 6	*2*				*45.3*		*RecName: Full=Myoglobin*		
240 min; 7	*1*		*907.9*	*2*	*51.5*		*GLSDGEWQLVLNAWGK*		*G1: Acetyl*
240 min; 6	*2*				*51.0*		*RecName: Full=Myoglobin*		*(Counterpart)*
10 min; 1	3	3666 - 3679	766.9	2	38.7	K	FTSITDTPEIVLAK PREDICTED: nebulin [Ovis aries]	V	T5: Didehydro
10 min; meat residue	*1*	*3666 - 3679*	*767.9*	*2*	*37.4*	*K*	*FTSITDTPEIVLAK* *PREDICTED: nebulin [Ovis aries]*	*V*	*(Counterpart)*
240 min; 1	1	222 - 237	834.9	2	49.6	D	QIISANPLLEAFGNAK	T	Q1: Gln->pyro-Glu
240 min; 8	1		834.9		50.2		PREDICTED: myosin-1 [Ovis aries]		
240 min; 2	2		834.9		49.9				
240 min; 3	2		834.9		50.0				
240 min; 6	2		834.9		50.0				
240 min; 7	2		834.9		50.1				
240 min; 1	3		834.9		50.1				
240 min; 3	3		834.9		50.0				
240 min; 7	3		835.0		49.9				
240 min; 1	*1*	*215 - 237*	*826.1*	*3*	*46.9*	*K*	*MQGTLEDQIISANPLLEAFGNAK*	*T*	***M1: Oxidation***
240 min; 3	*2*		*826.1*		*46.5*		*PREDICTED: myosin-1 [Ovis aries]*		*(Counterpart)*
240 min; 1	*3*		*826.1*		*46.8*				
240 min; 4	*3*		*826.1*		*46.3*				
240 min; 1	*1*		*820.8*		*47.4*		*MQGTLEDQIISANPLLEAFGNAK*		*(Counterpart)*
240 min; 2	*2*		*820.7*		*47.3*		*PREDICTED: myosin-1 [Ovis aries]*		
240 min; 3	*2*		*820.7*		*47.3*				
240 min; 1	*3*		*820.7*		*47.3*				
240 min; 4	*3*		*820.7*		*47.0*				
240 min; 4	2	219 - 234	834.8	2	50.3	D	QIIQANPALEAFGNAK PREDICTED: myosin-7 [Ovis aries]	T	Q1: Gln->pyro-Glu; N6: Deamidated
Control; 4	*2*	*214 - 234*	*1100.5*	*2*	*41.2*	*K*	*GTLEDQIIQANPALEAFGNAK* *PREDICTED: myosin-7 [Ovis aries]*	*T*	*(Counterpart)*
240 min; 8	1	124 – 135	698.8	2	40.4	D	QGTYEDFVEGLR	V	Q1: Gln->pyro-Glu
10 min; 7	2		698.9		40.1		PREDICTED: myosin light chain 1/3, skeletal muscle		
240 min; 7	2		698.8		39.7		isoform isoform 1 [Ovis aries]		
10 min; 6	*3*	*123 - 135*	*764.8*	*2*		*K*	*DQGTYEDFVEGLR* *PREDICTED: myosin light chain 1/3, skeletal muscle isoform isoform 1 [Ovis aries]*	*V*	*(Counterpart)*

DOI: 10.1021/acs.jafc.5b03324
J. Agric. Food Chem. 2015, 63, 9112−9123

Table 3. continued

Treatment[a]	Replicate #[b]	Position[c]	m/z[d]	z[e]	RT[f] (min)	R_{fN}[g]	Peptide sequence and protein of origin	R_{fC}[h]	Modification(s)[i]
GeLC of meat (urea-thiourea extract)									
240 min; 8	1	316 - 328	708.9	2	27.7	M	QKEITALAPSTMK PREDICTED: actin, alpha skeletal muscle isoform 1 [Ovis aries]	I	Q1: Gln->pyro-Glu; **M12: Oxidation**
240 min; 8	1		700.9		30.4		QKEITALAPSTMK		Q1: Gln->pyro-Glu
240 min; 7	2		700.8		30.6		PREDICTED: actin, alpha skeletal muscle isoform 1 [Ovis aries]		
240 min; 8	*1*	*317 - 328*	*645.3*	*2*	*24.6*	*Q*	*KEITALAPSTMK* *PREDICTED: actin, alpha skeletal muscle isoform 1 [Ovis aries]*	*I*	*(Counterpart)*
240 min; 4	*2*	*318 - 328*	*581.3*	*2*	*29.8*	*K*	*EITALAPSTMK*	*I*	*(Counterpart)*
240 min; 7	*2*				*28.9*		*PREDICTED: actin, alpha skeletal muscle isoform 1 [Ovis aries]*		
Cooking water proteomics									
10 min	2	66 - 78	710.4	2	43.2	H	GNTVLTALGGILK	K	G1: Hex;
10 min	3		710.3		42.9		RecName: Full=Myoglobin		N2: Deamidated
10 min	*2*	*65 - 78*	*697.4*	*2*	*38.6*	*K*	*HGNTVLTALGGILK*	*K*	*(Counterpart)*
10 min	*3*				*38.1*		*RecName: Full=Myoglobin*		
10 min	*2*		*725.9*		*39.4*		*HGNTVLTALGGILK* *RecName: Full=Myoglobin*		*H1: Carbamidomethyl (Counterpart)*
Cooking water peptidomics									
Control	*1*	*141 - 154*	*771.4*	*2*	*35.4*	*R*	*NDMAAQYKVLGFQG*	-	*(Counterpart)*
Control	*2*				*34.8*		*myoglobin [Ovis aries]*		
Control	*3*				*34.2*				
10 min	1	142 - 154	714.4	2	36.7	N	DMAAQYKVLGFQG	-	
10 min	2		714.3		36.1		myoglobin [Ovis aries]		
10 min	3				35.4				
240 min	1		714.3		38.6				
240 min	2				35.3				
240 min	3				37.7				
240 min	3		714.9		35.8		DMAAQYKVLGFQG myoglobin [Ovis aries]	-	Q12: Deamidated
240 min	1	142 - 154	722.3	2	35.9	N	DMAAQYKVLGFQG	-	**M2: Oxidation**
240 min	2		722.4		34.4		myoglobin [Ovis aries]		
240 min	3		722.3		34.9				
240 min	1		722.9		35.7		DMAAQYKVLGFQG myoglobin [Ovis aries]		**M2: Oxidation**; Q12: Deamidated
10 min	1	143 - 154	656.8	2	34.0	D	MAAQYKVLGFQG	-	
240 min	2				32.7		myoglobin [Ovis aries]		
240 min	3				33.1				
240 min	2	143 - 154	664.8	2	31.9	D	MAAQYKVLGFQG	-	**M1: Oxidation**
240 min	3				32.5		myoglobin [Ovis aries]		
240 min	3	372 - 381	567.2	2	26.9	Q	SIDDMIPAQK creatine kinase M-type [Ovis aries]	-	**M5: Oxidation**
Control	*1*	*370 - 381*	*651.8*	*2*	*27.3*	*K*	*GQSIDDMIPAQK*	-	*(Counterpart)*
Control	*2*				*30.0*		*creatine kinase M-type [Ovis aries]* *(this peptide ID came from the cooking water proteomic (digested) samples because none was identified in the peptidomic (undigested) samples)*		
240 min	1	222 - 235	735.4	2	58.9	D	QIISANPLLEAFGN	A	Q1: Gln->pyro-Glu
240 min	2		735.3		57.5		PREDICTED: LOW QUALITY PROTEIN: myosin-8 [Ovis aries] *For an unmodified Counterpart, refer to the GeLC results in this table because none was identified in the undigested samples.*		
Meat homogenate residue proteomics									
240 min	3	222 - 237	834.8	2	50.2	D	QIISANPLLEAFGNAK PREDICTED: myosin-1 [Ovis aries]	T	Q1: Gln->pyro-Glu
240 min	*3*	*215 - 237*	*826.0*	*3*	*46.7*	*K*	*MQGTLEDQIISANPLLEAFGNAK* *PREDICTED: myosin-1 [Ovis aries]*	*T*	***M1: Oxidation*** *(Counterpart)*

[a]Control or boiling time (min); the corresponding gel section/in-solution-digested sample (if applicable). [b]Each replicate # corresponds to a single specific cooking experiment replicate (refer to Tables S2-1−S2-9 of Supporting Information 2). [c]Position of the peptide in the protein sequence. [d]Rounded to the first decimal place. [e]Charge. [f]Retention time. [g]Amino acid residue preceding the peptide sequence. [h]Amino acid residue following the peptide sequence. [i]"Counterpart" refers to an "unmodified" version of the modified peptide. Refer to the Data Analysis section of Supporting Information 1 for details.

collagens may have been severely hydrolyzed and/or modified. Curiously, more nebulin-derived peptides were found in the meat homogenate residue of the control and 10 min samples than in the corresponding urea−thiourea extracts. This did not happen to the highly abundant myofibrillar proteins, including myosin heavy chains, actin, and titin. The observation implies that the urea−thiourea solution is perhaps less effective in solubilizing nebulin.

All the proteins identified here can also be found in the urea−thiourea extract except three histones, 60S ribosomal protein, fibrillin-1, and pyruvate dehydrogenase E1 component subunit α (somatic form, mitochondrial). The peptide IDs of

DOI: 10.1021/acs.jafc.5b03324
J. Agric. Food Chem. 2015, 63, 9112−9123

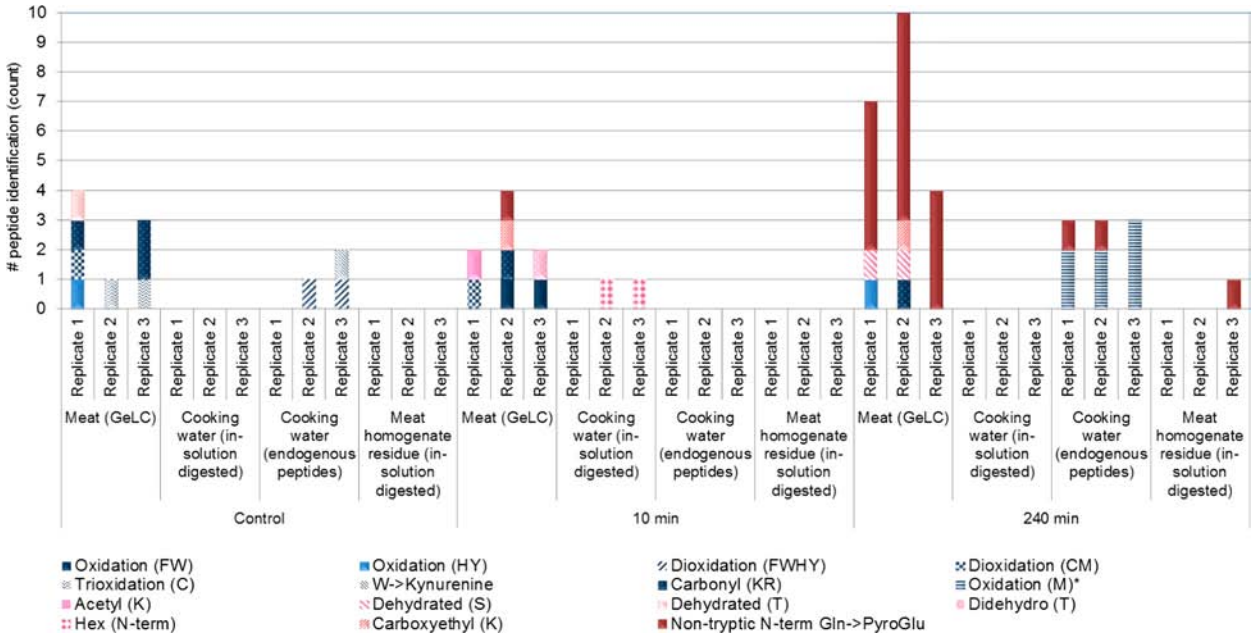

Figure 3. Relative numbers of observed modified peptides. *This modification was only investigated in the cooking water peptidomic (undigested) samples; the rationale is given in the Results and Discussion of the text.

many sarcoplasmic and myofibrillar proteins found in this fraction may originate from the proteins precipitated from the residue urea−thiourea extract during the pellet washing with water. This protein precipitation process might somewhat resemble the effect of thermal denaturation on the protein aggregation in cooked meat. Urea, as a chemical denaturant, disrupts hydrogen bonds, unfolds a protein's hydrophobic cores, and reduces ionic bonds between proteins,[29] but it generally binds weakly to proteins.[30] Therefore, the pellet washing step probably caused the partially folded intermediates to interact, similar to the process that results in formation of inclusion bodies during expression of recombinant proteins.[31] Thermal denaturation in proteins is generally linked to rupture of hydrogen bonds or electrostatic bonds, as well as an increase in protein surface hydrophobicity.[20] Exposure to the protein surface of hydrophobic amino acids may promote formation of noncovalently linked aggregates, as proteins can now stick together more easily.[26]

Heat-Induced Modifications. A summary of peptides observed with hydrothermally induced side-chain modifications (and detected only in the cooked samples) are presented in Table 3. The rest of the observed non-native peptides, including those observed in the control uncooked samples, are presented in Tables S2-26−S2-27. The relative numbers of observed modified peptides found are summarized in Figure 3.

GeLC of the Meat Protein Extract. Three peptides were identified with oxidative modification to aromatic residues resulting from heat treatment (Table 3). Two of these, with either a phenylalanine oxidation or a tryptophan oxidation (hydroxytryptophan), appeared to come from truncated proteins based on their observed positions of the gel sections.

The oxidation of aromatic residues has been shown to be associated with reactive oxygen species (ROS) attack.[10] Oxidation of phenylalanine has previously been reported in beef mince boiled in water,[6] while hydroxytryptophan and dihydroxyphenylalanine (DOPA) have both been identified in hydrothermally treated wool proteins.[10] Indeed, hydrothermal treatment has been found to be capable of inducing formation of certain ROS, such as the hydroxyl radical.[10] In addition, heating of ground meat in boiling water can cause the nonheme iron level to rise[32] and the nonheme iron can catalyze oxidative reactions.[33] Site-specific hydroxytryptophan formation has also been found previously to increase with heating in milk, another important dietary protein source.[34] Further, this study on milk suggested that this modification product can be unstable upon prolonged heating. The extent of tryptophan modification has been observed in some cases to depend on the amino acid microenvironment.[35] Oxidation of methionine (methionine sulfoxide) can sometimes occur during sample handling such as during in-gel trypsin digestion.[36] Therefore, in this study methionine sulfoxide was only considered as a modification of interest in the cooking water peptidomic analysis, in which the samples were handled at much lower temperature overall without the 37 °C incubation in ammonium bicarbonate, as performed in the proteomic analysis.

There were also oxidative modifications observed on other nonaromatic amino acid residues. Notably, cysteine trioxidation (sulfonic acid) was identified in two of the control replicates, whereas methionine double oxidation (methionine sulfone) was identified in one of the control replicates (Table S2-26). The latter was also found in one of the 10 min cooking replicates. Meltretter et al.[34] have detected the site-specific cysteine-derived sulfonic acid formation in raw, defatted milk, but its level was found to increase significantly when the samples were heated at 99 °C. The authors also detected methionine sulfone at a specific methionine residue in the raw milk, and its level was found to remain stable during the heating (at 99 °C up to 23 min).[34] Indeed, meat mincing,[37] freeze−thaw,[38] and the subsequent sample handling may all expose the meat protein to oxidation.

Carbonylation of lysine[39] was observed in both the control and boiled samples. Curiously, it did not seem to prevent trypsin cleavage (Table S2-26). A background level of oxidized protein has been previously observed in raw meat.[3,21] Formation of 2-amino-3-ketobutyric acid from a threonine residue[40] (didehydro of threonine) was also here identified in

DOI: 10.1021/acs.jafc.5b03324
J. Agric. Food Chem. 2015, 63, 9112−9123

one of the 10 min samples. Notably, N^{ϵ}-carboxyethyllysine (CEL) was detected at 10 min heating and also at 240 min heating. CEL and N^{ϵ}-carboxymethyllysine (CML) are common AGEs that have been found to increase steadily with heating time and heating temperature in ground beef under pasteurization conditions.[7] However, CML was not identified in the present study.

One semitryptic peptide (a "semi-tryptic" peptide is a peptide that was cleaved at the C-terminal side of arginine or lysine at one end but not the other), L.SDGEWQLVLNAWGK.V, with a nontryptic cleavage at the N-terminus and a dehydrated serine (serine-derived dehydroalanine) at the N-terminal residue was identified exclusively at 240 min cooking time. Protein and peptide backbone hydrolysis have been observed in hydrothermally aged wool fabric[41] and dry-heat-stressed buserelin peptide,[42] respectively, whereas the formation of serine-derived dehydroalanine has been detected in heated β-casein solutions.[43]

Cyclization of N-terminal glutamine to pyroglutamic acid (N-terminal Gln → pyro-Glu) tryptic peptides was observed (Tables S2-14−S2-16 and S2-23−S2-25). This is not unexpected, since the conditions of trypsin digestion have been shown to promote this cyclization process.[44] However, semitryptic peptides and cooking water endogenous peptides containing this modification were also found in the cooked samples, primarily at 240 min boiling (Figure 3). In addition, the majority of these peptides were cleaved at the C-terminal side of aspartic acid residue (Table 3). Heating alone has been found to cause N-terminal pyroglutamic acid formation in the tripeptide Gln-Leu-ProNH_2 in 50 mM Tris-HCl buffer (pH 7).[45] Site-specific cleavage at the C-terminal side of aspartic residue has been shown to occur when heating the solid sample of the peptides/lysozyme for 10 s to a final temperature of 220−250 °C under atmospheric condition, and a hydrolysis mechanism via a cyclic intermediate was proposed.[46] Taken together, the results suggested that prolonged boiling is capable of introducing protein cleavage and probably also causing N-terminal Gln → pyro-Glu.

Cyclization of N-terminal glutamic acid to pyroglutamic acid (N-terminal Glu → pyro-Glu) has been detected in one of the control replicates (Table S2-28). Chelius et al.[47] have reported that N-terminal Glu → pyro-Glu can take place in vitro at fairly mild temperatures and is pH-dependent. By contrasting with the study of Dick et al.[44] on N-terminal Gln → pyro-Glu formation, it appears that N-terminal Glu → pyro-Glu occurs much more slowly at similar temperature and pH. This likely explains why much fewer tryptic peptides with an N-terminal Glu → pyro-Glu were detected in the present study.

With regard to the levels of semitryptic peptides, which can be used to reflect the extent of hydrothermal protein backbone hydrolysis,[41] the 240 min samples had a higher average figure compared to the control and the 10 min samples (Figure 4). Fully nontryptic peptides, in comparison, were scarce in number (three or less per cooking replicate) regardless of treatment (Table S1-6), with no clear trend observed among the samples.

Cooking Water. In the cooking water digested samples, one peptide with both a deamidated asparagine residue and a +162 Da modification at the nontryptic N-terminal residue was exclusively identified in the 10 min boiling samples (Table 3). The annotated MS/MS spectrum for this peptide is shown in Figure 5. This mass increase is consistent with the heat-induced

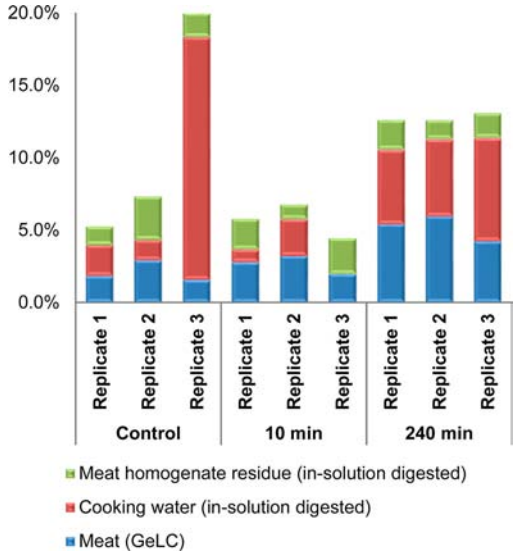

Figure 4. Percentage of semitryptic peptide identification in the proteomic (digested) samples. Please note that the values obtained from different experimental workflows for each cooking replicate are independent of each other and do not necessarily add up to 100%.

formation of glucose-derived Amadori compound, an early-stage Maillard glycation adduct.

The level of semitryptic peptides is shown in Figure 4. No marked difference in proteomic profiles was found between the control replicates (Table S2-11). The proportion of semitryptic peptides in the control and 10 min boiling samples were similar (except one outlier in the controls; its higher level of nontryptic cleavages might be associated with certain endogenous proteolytic system(s) in meat[48,49] that could be at work during the "control cooking" process and the subsequent centrifugation) while the 240 min boiling appeared to generate a distinctly higher proportion of semitryptic peptides.

One particular peptide from myoglobin was observed to undergo progressive truncation in the course of boiling (Table 3):

R.NDMAAQYKVLGFQG.- (exclusively in controls) →
N.DMAAQYKVLGFQG.- (10 and 240 min samples) →
D.MAAQYKVLGFQG.- (10 and 240 min samples).

Protein cleavage occurred at the C-terminal side of aspartic acid and asparagine. C-terminal side cleavage at aspartic acid was also found in the urea−thiourea extracts of the cooked meat, as already discussed. Methionine sulfoxide and modification of the N-terminal Gln → pyro-Glu were observed after 240 min boiling (Table 3).

Physical properties (e.g., texture, color, and flavor) as well as the nutritional value of meat can be affected when the primary structure of meat proteins is altered.[50] For example, an increase in meat protein oxidation has been associated with lower water-holding capacity and a decrease in protein solubility, whereas some studies showed that protein oxidation contributes to the increased gel-forming ability.[4] Modification of the essential amino acid residues (tryptophan, phenylalanine, threonine, lysine, and methoinine) observed in this study after cooking will affect the nutritional value of the meat. This issue is particularly important for amino acids that are already present in relative lower abundance in meat, e.g., tryptophan. In addition, certain modifications of the residues used by a pancreatic protease as cleavage sites, e.g., the lysine → CEL characterized here, result in miscleavage of the proteins and

DOI: 10.1021/acs.jafc.5b03324
J. Agric. Food Chem. 2015, 63, 9112−9123

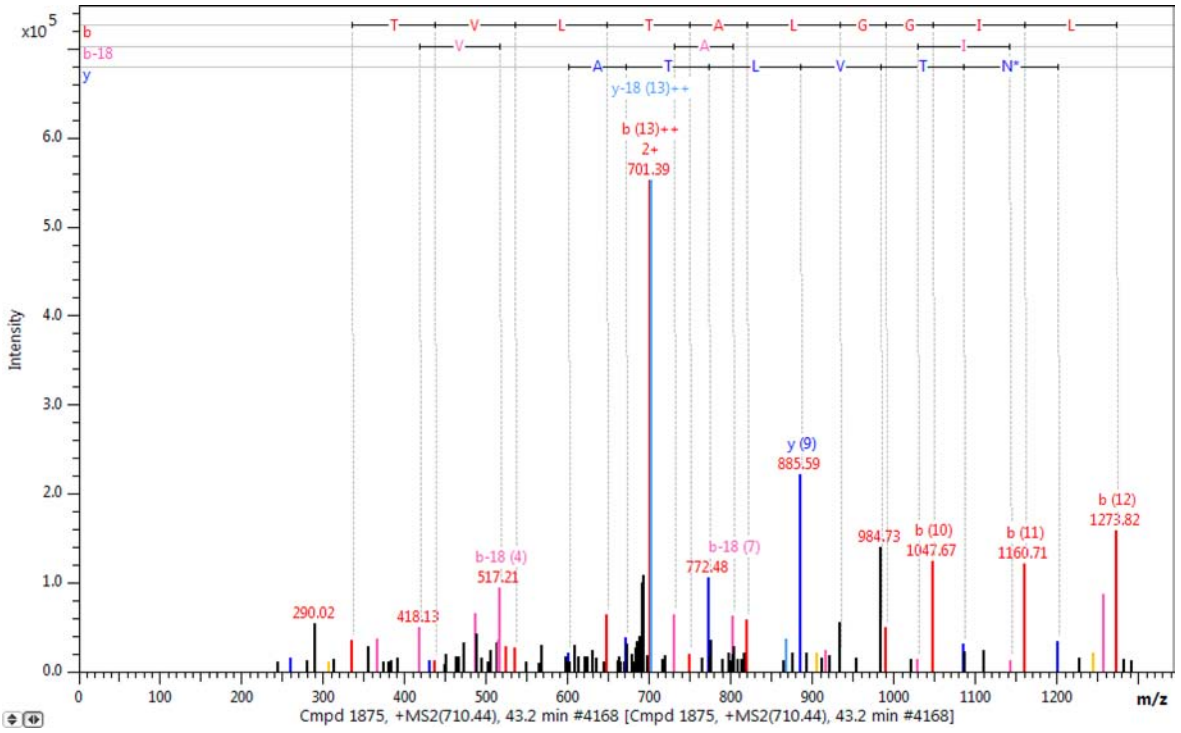

Figure 5. ProteinScape annotated MS/MS spectrum showing a hexose glycated N-terminus from one of the two 10 min boiling samples where the peptide was detected.

may compromise their bioavailability. On the other hand, in a competing process, production of smaller peptides through heat-induced backbone cleavage may facilitate the absorption of proteins.

Meat Homogenate Residue. Fewer potential heat-modified peptides were detected in this fraction compared to the urea–thiourea extract and the cooking water (Table 3). This may imply the presence of higher levels of protein cross-links and/or arginine and lysine modifications. In one of the control replicates, a tryptic peptide with N-terminal Glu → pyro-Glu was identified (Table S2-28). In the boiled samples, the modification Gln → pyro-Glu at a nontryptic N-terminus was observed after 240 min boiling.

Future work utilizing alternative sample preparation (e.g., employing Glu-C for protein digestion) and MS/MS approaches (e.g., electron transfer dissociation or using a high-resolution instrument) could help identify more modified peptides. In addition, technical replicates can be implemented to further increase the certainty on the identification of the amino acid residue level modifications that have not been observed in all the control or boiling replicates (Figure 3).

In summary, this study has generated new knowledge and insights into the molecular-level modifications occurring in lamb meat proteins during boiling, through a detailed proteomic and peptidomic evaluation. The modifications characterized provide a good basis for better understanding the effect of this common food processing and preparation method on the nutritional and functional properties of red-meat-based foods.

■ ASSOCIATED CONTENT

Supporting Information

The Supporting Information is available free of charge on the ACS Publications website at DOI: 10.1021/acs.jafc.5b03324.

Supplementary Experimental Section for the Material and Methods and Tables S1-1–S1-8 and Figures S1-1–S1-5 (Supporting Information 1) (PDF)

Tables S2-1–S2-28 (Supporting Information 2) (ZIP)

ProteinScape annotated MS/MS spectra of peptides with a modification of interest and their unmodified counterparts (Supporting Information 3) (PDF)

■ AUTHOR INFORMATION

Corresponding Author

*Tel: +64-3-321-8814. E-mail: Robert.Yu@agresearch.co.nz.

Funding

The authors gratefully acknowledge the financial support from AgResearch Core Funding, Lincoln University, and the Biomolecular Interaction Centre as part of the Red Meat CombiFoods Programme (MBIE reference # C10X1005; AgResearch Contract # A19119(A)).

Notes

The authors declare no competing financial interest.

■ ACKNOWLEDGMENTS

The authors would like to thank Santanu Deb-Choudhury, Anita Grosvenor, Stephen Haines, and Ian McNaughton, for their technical advice, and Brendan Haigh and Linda Samuelsson, for critical review of the manuscript.

■ REFERENCES

(1) Lawrie, R. A.; Ledward, D. A. Meat and human nutrition. In *Lawrie's Meat Science*, 7th ed.; Ledward, R. A. L. A., Ed.; Woodhead Publishing: Cambridge, UK, 2006; Chapter 11, pp 342–357.

(2) Tornberg, E. Effects of heat on meat proteins – Implications on structure and quality of meat products. *Meat Sci.* **2005**, *70*, 493–508.

(3) Santé-Lhoutellier, V.; Astruc, T.; Marinova, P.; Greve, E.; Gatellier, P. Effect of Meat Cooking on Physicochemical State and in

DOI: 10.1021/acs.jafc.5b03324
J. Agric. Food Chem. 2015, 63, 9112–9123

Vitro Digestibility of Myofibrillar Proteins. *J. Agric. Food Chem.* **2008**, *56*, 1488−1494.
(4) Zhang, W.; Xiao, S.; Ahn, D. U. Protein Oxidation: Basic Principles and Implications for Meat Quality. *Crit. Rev. Food Sci. Nutr.* **2013**, *53*, 1191−1201.
(5) Gatellier, P.; Kondjoyan, A.; Portanguen, S.; Grève, E.; Yoon, K.; Santé-Lhoutellier, V. Determination of aromatic amino acid content in cooked meat by derivative spectrophotometry: Implications for nutritional quality of meat. *Food Chem.* **2009**, *114*, 1074−1078.
(6) Deb-Choudhury, S.; Haines, S.; Harland, D.; Clerens, S.; van Koten, C.; Dyer, J. Effect of Cooking on Meat Proteins: Mapping Hydrothermal Protein Modification as a Potential Indicator of Bioavailability. *J. Agric. Food Chem.* **2014**, *62*, 8187−8196.
(7) Sun, X.; Tang, J.; Wang, J.; Rasco, B. A.; Lai, K.; Huang, Y. Formation of advanced glycation endproducts in ground beef under pasteurisation conditions. *Food Chem.* **2015**, *172*, 802−807.
(8) Deb-Choudhury, S.; Plowman, J. E.; Thomas, A.; Krsinic, G. L.; Dyer, J. M.; Clerens, S. Electrophoretic mapping of highly homologous keratins: A novel marker peptide approach. *Electrophoresis* **2010**, *31*, 2894−2902.
(9) Huang, L.; Kong, B.; Zhao, J.; Liu, Q.; Diao, X. Contributions of Fat Content and Oxidation to the Changes in Physicochemical and Sensory Attributes of Pork Dumpling Filler during Frozen Storage. *J. Agric. Food Chem.* **2014**, *62*, 6390−6399.
(10) Grosvenor, A. J.; Morton, J. D.; Dyer, J. M. Proteomic characterisation of hydrothermal redox damage. *J. Sci. Food Agric.* **2011**, *91*, 2806−2813.
(11) Hebling, C. M.; McFarland, M. A.; Callahan, J. H.; Ross, M. M. Global Proteomic Screening of Protein Allergens and Advanced Glycation Endproducts in Thermally Processed Peanuts. *J. Agric. Food Chem.* **2013**, *61*, 5638−5648.
(12) Kannamkumarath, S.; Wrobel, K.; Wrobel, K.; Vonderheide, A.; Caruso, J. HPLC−ICP−MS determination of selenium distribution and speciation in different types of nut. *Anal. Bioanal. Chem.* **2002**, *373*, 454−460.
(13) Wessel, D.; Flügge, U. I. A method for the quantitative recovery of protein in dilute solution in the presence of detergents and lipids. *Anal. Biochem.* **1984**, *138*, 141−143.
(14) Rappsilber, J.; Mann, M.; Ishihama, Y. Protocol for micro-purification, enrichment, pre-fractionation and storage of peptides for proteomics using StageTips. *Nat. Protoc.* **2007**, *2*, 1896−1906.
(15) Yu, T.-Y.; Morton, J. D.; Clerens, S.; Dyer, J. M. In-depth characterisation of the lamb meat proteome from longissimus lumborum. *EuPa Open Proteomics* **2015**, *6*, 28−41.
(16) Brosch, M.; Yu, L.; Hubbard, T.; Choudhary, J. Accurate and Sensitive Peptide Identification with Mascot Percolator. *J. Proteome Res.* **2009**, *8*, 3176−3181.
(17) Zhang, Q.; Frolov, A.; Tang, N.; Hoffmann, R.; van de Goor, T.; Metz, T. O.; Smith, R. D. Application of electron transfer dissociation mass spectrometry in analyses of non-enzymatically glycated peptides. *Rapid Commun. Mass Spectrom.* **2007**, *21*, 661−666.
(18) Chen, Y.; Zhang, J.; Xing, G.; Zhao, Y. Mascot-Derived False Positive Peptide Identifications Revealed by Manual Analysis of Tandem Mass Spectra. *J. Proteome Res.* **2009**, *8*, 3141−3147.
(19) Arena, S.; Renzone, G.; Novi, G.; Scaloni, A. Redox proteomics of fat globules unveils broad protein lactosylation and compositional changes in milk samples subjected to various technological procedures. *J. Proteomics* **2011**, *74*, 2453−2475.
(20) Promeyrat, A.; Gatellier, P.; Lebret, B.; Kajak-Siemaszko, K.; Aubry, L.; Santé-Lhoutellier, V. Evaluation of protein aggregation in cooked meat. *Food Chem.* **2010**, *121*, 412−417.
(21) Traore, S.; Aubry, L.; Gatellier, P.; Przybylski, W.; Jaworska, D.; Kajak-Siemaszko, K.; Santé-Lhoutellier, V. Effect of heat treatment on protein oxidation in pig meat. *Meat Sci.* **2012**, *91*, 14−21.
(22) Becila, S.; Herrera-Mendez, C.; Coulis, G.; Labas, R.; Astruc, T.; Picard, B.; Boudjellal, A.; Pelissier, P.; Bremaud, L.; Ouali, A. Postmortem muscle cells die through apoptosis. *Eur. Food Res. Technol.* **2010**, *231*, 485−493.
(23) Wen, S.; Zhou, G.; Li, L.; Xu, X.; Yu, X.; Bai, Y.; Li, C. Effect of Cooking on in Vitro Digestion of Pork Proteins: A Peptidomic Perspective. *J. Agric. Food Chem.* **2015**, *63*, 250−261.
(24) Wu, G.; Clerens, S.; Farouk, M. M. LC MS/MS identification of large structural proteins from bull muscle and their degradation products during post mortem storage. *Food Chem.* **2014**, *150*, 137−144.
(25) Nesvizhskii, A. I.; Aebersold, R. Interpretation of Shotgun Proteomic Data: The Protein Inference Problem. *Mol. Cell. Proteomics* **2005**, *4*, 1419−1440.
(26) Promeyrat, A.; Bax, M. L.; Traoré, S.; Aubry, L.; Santé-Lhoutellier, V.; Gatellier, P. Changed dynamics in myofibrillar protein aggregation as a consequence of heating time and temperature. *Meat Sci.* **2010**, *85*, 625−631.
(27) Burson, D. E.; Hunt, M. C. Heat-induced changes in the proportion of types I and III collagen in bovine Longissimus dorsi. *Meat Sci.* **1986**, *17*, 153−160.
(28) Shoulders, M. D.; Raines, R. T. Collagen Structure and Stability. *Annu. Rev. Biochem.* **2009**, *78*, 929−958.
(29) Rabilloud, T. Solubilization of proteins in 2DE: an outline. *Methods Mol. Biol. (N. Y., NY, U. S.)* **2009**, *519*, 19−30.
(30) Otzen, D. Protein-surfactant interactions: A tale of many states. *Biochim. Biophys. Acta, Proteins Proteomics* **2011**, *1814*, 562−591.
(31) Burgess, R. R. Refolding Solubilized Inclusion Body Proteins. In *Methods in Enzymology*; Richard, R. B., Murray, P. D., Eds.; Academic Press: New York, 2009; Vol. *463*, Chapter 17, pp 259−282.
(32) Schricker, B. R.; Miller, D. D.; Stouffer, J. R. Measurement and Content of Nonheme and Total Iron in Muscle. *J. Food Sci.* **1982**, *47*, 740−743.
(33) Rhee, K. S.; Ziprin, Y. A.; Ordonez, G. Catalysis of lipid oxidation in raw and cooked beef by metmyoglobin-hydrogen peroxide, nonheme iron, and enzyme systems. *J. Agric. Food Chem.* **1987**, *35*, 1013−1017.
(34) Meltretter, J.; Wüst, J.; Pischetsrieder, M. Modified Peptides as Indicators for Thermal and Nonthermal Reactions in Processed Milk. *J. Agric. Food Chem.* **2014**, *62*, 10903−10915.
(35) Perdivara, I.; Deterding, L.; Przybylski, M.; Tomer, K. Mass spectrometric identification of oxidative modifications of tryptophan residues in proteins: Chemical artifact or post-translational modification? *J. Am. Soc. Mass Spectrom.* **2010**, *21*, 1114−1117.
(36) Froelich, J. M.; Reid, G. E. The origin and control of ex vivo oxidative peptide modifications prior to mass spectrometry analysis. *Proteomics* **2008**, *8*, 1334−1345.
(37) Estévez, M.; Ventanas, S.; Heinonen, M.; Puolanne, E. Protein Carbonylation and Water-Holding Capacity of Pork Subjected to Frozen Storage: Effect of Muscle Type, Premincing, and Packaging. *J. Agric. Food Chem.* **2011**, *59*, 5435−5443.
(38) Xia, X.; Kong, B.; Liu, Q.; Liu, J. Physicochemical change and protein oxidation in porcine longissimus dorsi as influenced by different freeze−thaw cycles. *Meat Sci.* **2009**, *83*, 239−245.
(39) Xu, G.; Chance, M. R. Hydroxyl Radical-Mediated Modification of Proteins as Probes for Structural Proteomics. *Chem. Rev.* **2007**, *107*, 3514−3543.
(40) Stadtman, E. R.; Levine, R. L. Free radical-mediated oxidation of free amino acids and amino acid residues in proteins. *Amino Acids* **2003**, *25*, 207−218.
(41) Solazzo, C.; Wilson, J.; Dyer, J. M.; Clerens, S.; Plowman, J. E.; von Holstein, I.; Walton Rogers, P.; Peacock, E. E.; Collins, M. J. Modeling Deamidation in Sheep α-Keratin Peptides and Application to Archeological Wool Textiles. *Anal. Chem.* **2014**, *86*, 567−575.
(42) D'Hondt, M.; Fedorova, M.; Peng, C.-Y.; Gevaert, B.; Taevernier, L.; Hoffmann, R.; De Spiegeleer, B. Dry heat forced degradation of buserelin peptide: Kinetics and degradant profiling. *Int. J. Pharm.* **2014**, *467*, 48−59.
(43) van Boekel, M. A. J. S. Heat-induced deamidation, dephosphorylation and breakdown of caseinate. *Int. Dairy J.* **1999**, *9*, 237−241.
(44) Dick, L. W.; Kim, C.; Qiu, D.; Cheng, K.-C. Determination of the origin of the N-terminal pyro-glutamate variation in monoclonal

DOI: 10.1021/acs.jafc.5b03324
J. Agric. Food Chem. 2015, 63, 9112−9123

antibodies using model peptides. *Biotechnol. Bioeng.* **2007**, *97*, 544−553.
(45) Fernández García, A.; Butz, P.; Trierweiler, B.; Zöller, H.; Stärke, J.; Pfaff, E.; Tauscher, B. Pressure/Temperature Combined Treatments of Precursors Yield Hormone-like Peptides with Pyroglutamate at the N Terminus. *J. Agric. Food Chem.* **2003**, *51*, 8093−8097.
(46) Zhang, S.; Basile, F. Site-Specific Pyrolysis-Induced Cleavage at Aspartic Acid Residue in Peptides and Proteins. *J. Proteome Res.* **2007**, *6*, 1700−1704.
(47) Chelius, D.; Jing, K.; Lueras, A.; Rehder, D. S.; Dillon, T. M.; Vizel, A.; Rajan, R. S.; Li, T.; Treuheit, M. J.; Bondarenko, P. V. Formation of Pyroglutamic Acid from N-Terminal Glutamic Acid in Immunoglobulin Gamma Antibodies. *Anal. Chem.* **2006**, *78*, 2370−2376.
(48) Sentandreu, M. A.; Coulis, G.; Ouali, A. Role of muscle endopeptidases and their inhibitors in meat tenderness. *Trends Food Sci. Technol.* **2002**, *13*, 400−421.
(49) Houbak, M. B.; Ertbjerg, P.; Therkildsen, M. In vitro study to evaluate the degradation of bovine muscle proteins post-mortem by proteasome and μ-calpain. *Meat Sci.* **2008**, *79*, 77−85.
(50) Clerens, S.; Plowman, J. E.; Dyer, J. M. Food Proteomics: Mapping Modifications. In *Proteomic Applications in Biology*; Heazlewood, J., Petzold, C. J., Eds.; InTech: Rijeka, Croatia, 2012; pp 3−32.

■ NOTE ADDED AFTER ASAP PUBLICATION

This article published September 18, 2015 with errors in Table 3. The corrected version published September 23, 2015.

DOI: 10.1021/acs.jafc.5b03324
J. Agric. Food Chem. 2015, 63, 9112−9123

Scheme 1. Molecular Structures of (a) Predominant Species of Soybean PC, (b) Chl *a*, (c) Lyc, (d) *β*-Car, (e) Ast, and (f) Zea

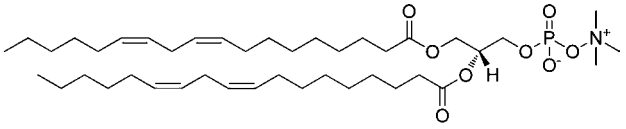

(a) Soybean Phosphatidylcholine

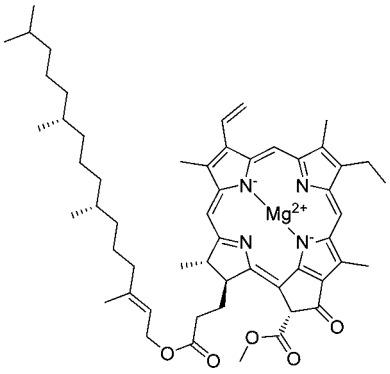

(b) Chlorophyll *a* (Chl *a*)

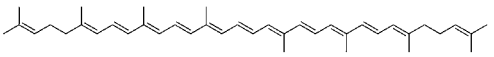

(c) Lycopene (Lyc)

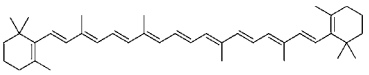

(d) *β*-Carotene (*β*-Car)

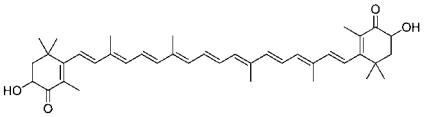

(e) Astaxanthin (Ast)

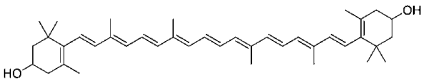

(f) Zeaxanthin (Zea)

(Beijing, China). Purified water was prepared using a Milli-Q Academic Water Purification System (Millipore Corp., Billerica, MA).

Electroformation of GUVs. GUVs were prepared using an electroformation method with certain modifications.[17] Briefly, the cell used for GUV preparation consisted of two indium tin oxide (ITO) glass substrates separated by a Teflon spacer with a thickness of ~3 mm. The PC reagent was dissolved in chloroform at a concentration of 4 mg/mL. Chl *a* was predissolved in methanol and used as the photosensitizer. *β*-Car and Lyc predissolved in chloroform and Zea and Ast predissolved in methanol were used as antioxidants. The final molar ratio of PC reagent and Chl *a* was 100:1, and the final molar ratio of PC reagent and each individual carotenoid was 200:1. The solutions were deposited on one of the conductive surfaces of ITO glass substrates and then dried in vacuum for 2 h. About 2.5 mL of 100 mM sucrose solution was injected into the cell, which was afterward sealed using silicone grease. Alternative electrical fields from a Rigol DG1022U function generator (Rigol Technologies, Beijing, China) were applied to the cell to generate a turbid GUV suspension with a volume of approximately 2.5 mL.

Optical Microscopy and Digital Image Processing. The experimental setup for fluorescence microscopy was described elsewhere.[13] Briefly, 200 *μ*L of liposome suspension was added to a Costar 24-well cell culturing cluster (Corning Incorporated, Corning, NY), which was fixed on the translational stage. Light radiation in 400−440 nm from an ultrahigh-pressure mercury lamp was used for excitation with a power of 0.81 mW and was focused on an area with a diameter of 80 *μ*m. A band-pass filter (500−570 nm) was used to minimize the fluorescence emission from Chl *a*. Liposome images were collected every 1 s, and each GUV preparation was measured independently for at least 30 times. GUVs unsensitized with Chl *a* were used as a blank, whereas sensitized GUVs without antioxidant added were used as a control. Evaluation of the liposome physical integrity was performed using digital image processing on the basis of heterogeneity.[18,19] Briefly, raw images were digitized into 16-bit grayscale format with an area of 100 × 100 pixels selected as region of interest (ROI). The 16-bit grayscale intensity interval was divided into 256 subintervals by default. Histogram counts (p) over these subintervals were used to calculate the entropy, defined as $E = -\sum p \log_2 p$, which was used as a statistical scalar for measuring the heterogeneity.[19] The budding process of GUVs was characterized by entropy change (ΔE) with reference to the average entropy at minus delay time, i.e., before light irradiation.[13]

RESULTS AND DISCUSSION

The blank soybean PC GUVs used as a membrane model were found resistant to light exposure (400−440 nm) because no change in GUV morphology was observed. Incorporating Chl *a* (Scheme 1) as a photosensitizer made them sensitive to light exposure as evidenced by the fast increase in entropy and budding (Figures 1−3), which could be quantified using the entropy change ΔE defined in the Materials and Methods.[13] It is seen in Figures 1 and 2 that ΔE increased immediately upon light exposure for control and Chl *a*-sensitized GUVs with *β*-Car. In contrast, Lyc, Zea, and Ast, each added separately, induced a significant lag phase for the increase of ΔE. The spatial arrangement of the GUVs as a model for membranes is depicted in Scheme 2. In this scheme, Chl *a* as a hydrophobic molecule lies in the interior of the lipid bilayer together with hydrophobic Lyc (or *β*-Car), while Ast (or Zea) with polar substituents to ending rings anchors in the water/lipid interfaces.

Three effects on the budding process resulting from photosensitization may be identified from the temporal evolution of ΔE during light exposure, as results from the addition of each individual carotenoid investigated (Figures 2 and 3): (i) Lyc, Zea, and Ast each, in contrast to *β*-Car, resulted in a significant lag phase, during which ΔE was essentially unchanged. (ii) The ΔE increasing rate after the lag phase decreased upon incorporation of each individual carotenoid, especially for the case of Ast. (iii) The final level of heterogeneity was found similar for Ast and Zea, both similar to the control, but for *β*-Car and Lyc, the levels were found to be comparable and significantly lower.

The length of the lag phase increased in the order of control < *β*-Car < Lyc < Zea < Ast as most clearly seen from Figure 3. Notably, Zea and Ast are both xanthophylls with hydrophilic groups (Scheme 1). Xanthophylls are known to be anchored in the water/lipid interfaces of membranes resulting in the decrease of the membrane fluidity,[12,20] and such effects may be important in the initial protection against photosensitized oxidation and result in a lag phase (*vide infra*).

The rate of ΔE increase following the initial lag phase obeys another ordering than the length of the lag phase: Ast < Lyc < *β*-Car < Zea < control (Table 1). Ast accordingly

DOI: 10.1021/acs.jafc.5b03658
J. Agric. Food Chem. 2015, 63, 9124−9130

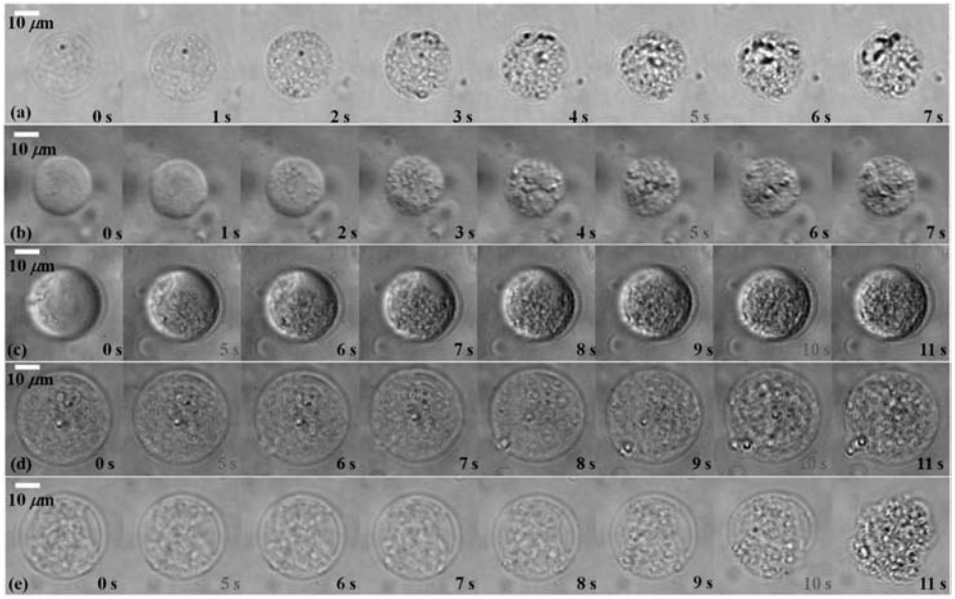

Figure 1. Images of Chl *a*-sensitized GUV samples exposed to light (400−440 nm, 160 mW/mm^2) for an indicated time at room temperature: (a) control, (b) *β*-Car, (c) Lyc, (d) Zea, and (e) Ast added.

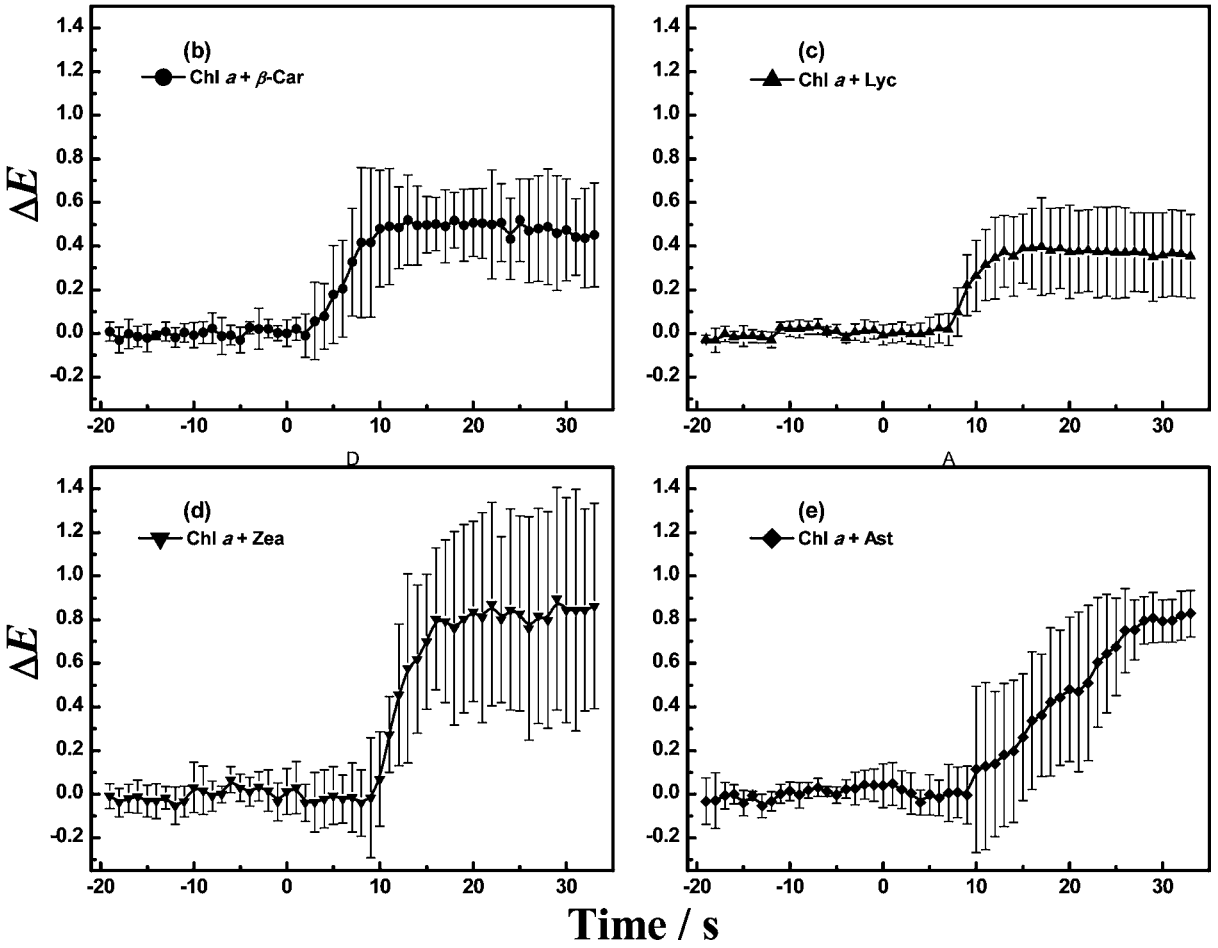

Figure 2. Δ*E* as a metric of image heterogeneity versus time for budding of Chl *a*-sensitized GUVs with the addition of individual carotenoid exposed to light (400−440 nm, 160 mW/mm^2). For control, see Figure 3. Statistics: mean ± standard deviation (SD) (n = 6).

both induces the longest lag phase and results in the slowest Δ*E* increasing rate, while Zea, which also induces a long lag phase as a xanthophyll, yields little protection during the subsequent development of Δ*E* (Table 1). Notably, the two carotenes, Lyc and *β*-Car, have comparable Δ*E* increasing rates.

DOI: 10.1021/acs.jafc.5b03658
J. Agric. Food Chem. 2015, 63, 9124−9130

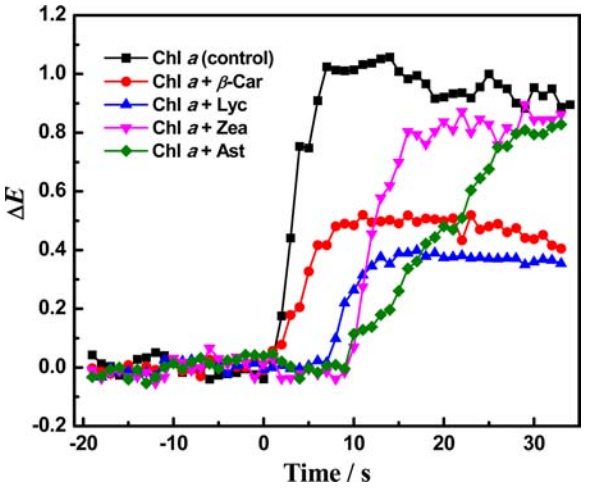

Figure 3. Comparison of temporal evolution profiles of ΔE for budding of Chl *a*-sensitized GUVs with individual carotenoid added. The time evolutions are from Figure 2. For clarity, error bars are not shown.

Scheme 2. Ast and Lyc in a Liposomal Membrane[a]

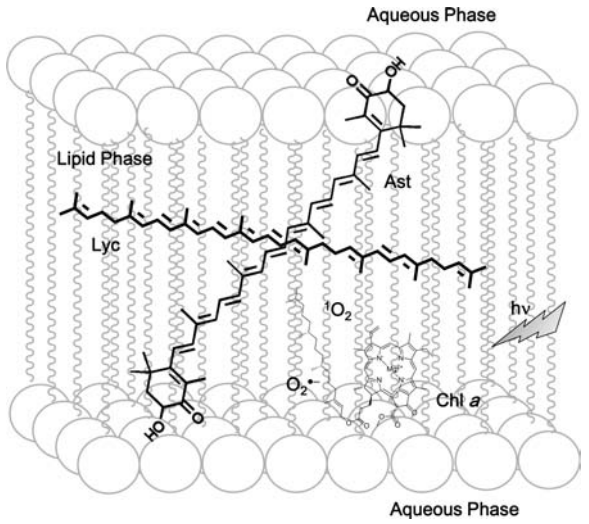

[a]Membrane thickness is approximately 4 nm.

Table 1. Lag Phases, Initial Rates, Final Levels (ΔE_∞), and Area under Curve (AUC) of $\Delta E/t$ Evolutions for Each GUV Preparation[a]

sample (n = 6)	lag phase (s)	initial rate (s^{-1})	ΔE_∞	AUC (au)
control	0.15	$(165 \pm 13) \times 10^{-3}$	0.90	29
β-Car	1.8	$(75 \pm 5) \times 10^{-3}$	0.46	14
Lyc	7.3	$(65 \pm 6) \times 10^{-3}$	0.37	8.9
Zea	7.8	$(121 \pm 9) \times 10^{-3}$	0.82	17
Ast	8.9	$(40.4 \pm 1.3) \times 10^{-3}$	0.80	12
Ast + β-Car	14	$(18.3 \pm 0.9) \times 10^{-3}$	0.32	6.7
Ast + Zea	17	$(10.3 \pm 1.7) \times 10^{-3}$	0.24	3.2
Ast + Lyc	26	$(52 \pm 4) \times 10^{-3}$	0.30	2.2

[a]AUCs were calculated from the end of lag phases until 31 s for GUV preparations with incorporating single carotenoids or until 40 s for those with combined carotenoids added.

The final level of heterogeneity was quantified as both the final value for ΔE and the area under the $\Delta E-t$ curve in arbitrary units after the lag phase, which are compared in Figure 3 and Table 1. The GUVs with Lyc and β-Car are seen to yield the best protection as evaluated by the final level of heterogeneity. GUVs with Ast and Zea both reach approximately the same final levels of heterogeneity as the control.

Two factors seem to control the pattern of protection of GUVs against budding. One could be related to the decreased fluidity of membranes of GUVs as resulting from incorporation of Ast or Zea. Chl *a*, as a photosensitizer, may operate through two mechanisms as outlined in Figure 4.[21] Type II

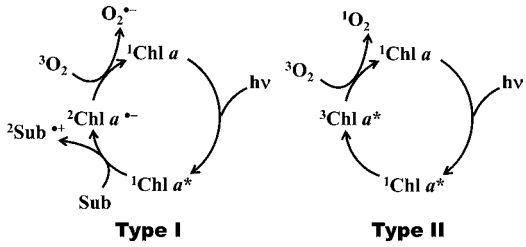

Figure 4. Type I and type II photosensitization by Chl *a*.[16]

photosensitization will yield singlet oxygen $^1O_2$, which will diffuse from Chl *a* with a rate depending upon the fluidity of the membrane in competition with quenching. The $^1O_2$ quenching rates are comparable for the four carotenoids in homogeneous solutions (Table 2), and hence, the other factor

Table 2. Second-Order Rate Constant, k_2, for Quenching of Singlet Oxygen by Carotenoids in Benzene and in Unilamellar Liposomes, Standard Reduction Potential for Carotenoid Radical Cation versus NHE, $E°$, in Dichloromethane, Electron Acceptor Capacities, R_a, and Electron Donor Capabilities, R_d, All at Room Temperature

	k_2 (L mol^{-1} s^{-1})				
carotenoid	benzene[a]	liposomes[a]	$E°$ (V)[b]	R_a[c]	R_d[c]
β-Car	1.3×10^{10}	2.3×10^{10}	0.84	0.46	1.40
Lyc	1.7×10^{10}	2.4×10^{10}	0.81		
Zea	1.6×10^{10}	2.3×10^{10}	0.85	0.49	1.44
Ast	1.1×10^{10}	5.9×10^{9}	0.97	0.94	2.10

[a]From ref 22. [b]From refs 25 and 26. [c]From ref 24.

may be important in controlling the oxidation of the phospholipids by $^1O_2$.[22] Tentatively, the longer lag phases seen for Ast and Zea relative to Lyc and β-Car may be assigned to a decrease in the rate of diffusion as a result of the decreased fluidity of the membrane by anchoring of Ast and Zea in the membrane surface. A lower diffusion rate will delay the oxidation of the phospholipids at the lipid/water interface but will not prevent the formation of the hydroperoxides that result in a final increase in ΔE and budding. The second factor could be related to the electron-accepting capability of Ast. Ast is the least reducing among the four carotenoids (Table 2). It has a high electron-accepting capability, as provided by quantum chemical calculations, and has been suggested to oxidize the superoxide radical anion

$$\text{Ast} + O_2^{\bullet-} \rightarrow \text{Ast}^{\bullet-} + O_2$$

in contrary to most other carotenoids.[6,23] Chl *a* may operate partly through a type I mechanism for photosensitization, resulting in the formation of radicals (Figure 4). $O_2^{\bullet-}$, when produced in the membrane, many react with Ast but not Zea or the carotenes like β-Car and Lyc. This could explain

DOI: 10.1021/acs.jafc.5b03658
J. Agric. Food Chem. 2015, 63, 9124−9130

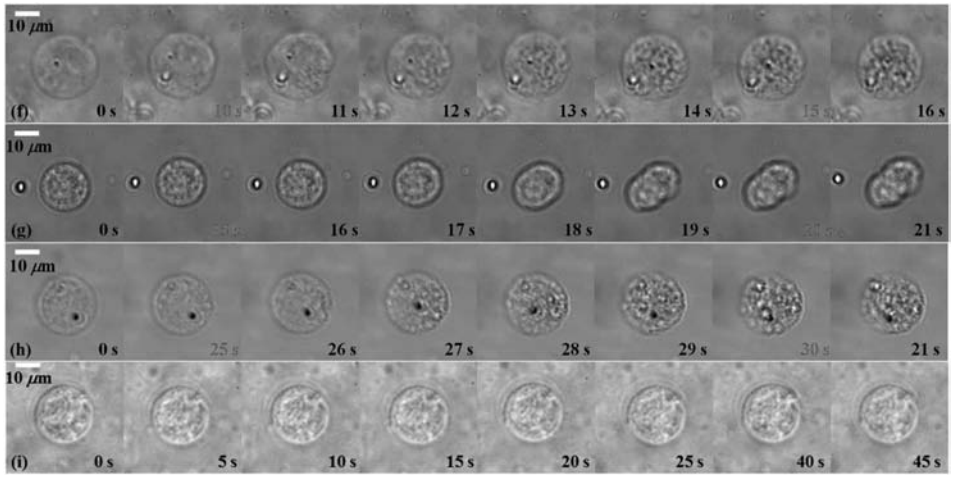

Figure 5. Images of Chl *a*-sensitized GUV samples exposed to light (400−440 nm, 160 mW/mm^2) at the indicated time at room temperature: (f) *β*-Car and Ast, (g) Zea and Ast, (h) Lyc and Ast, and (i) unsensitized blank GUVs.

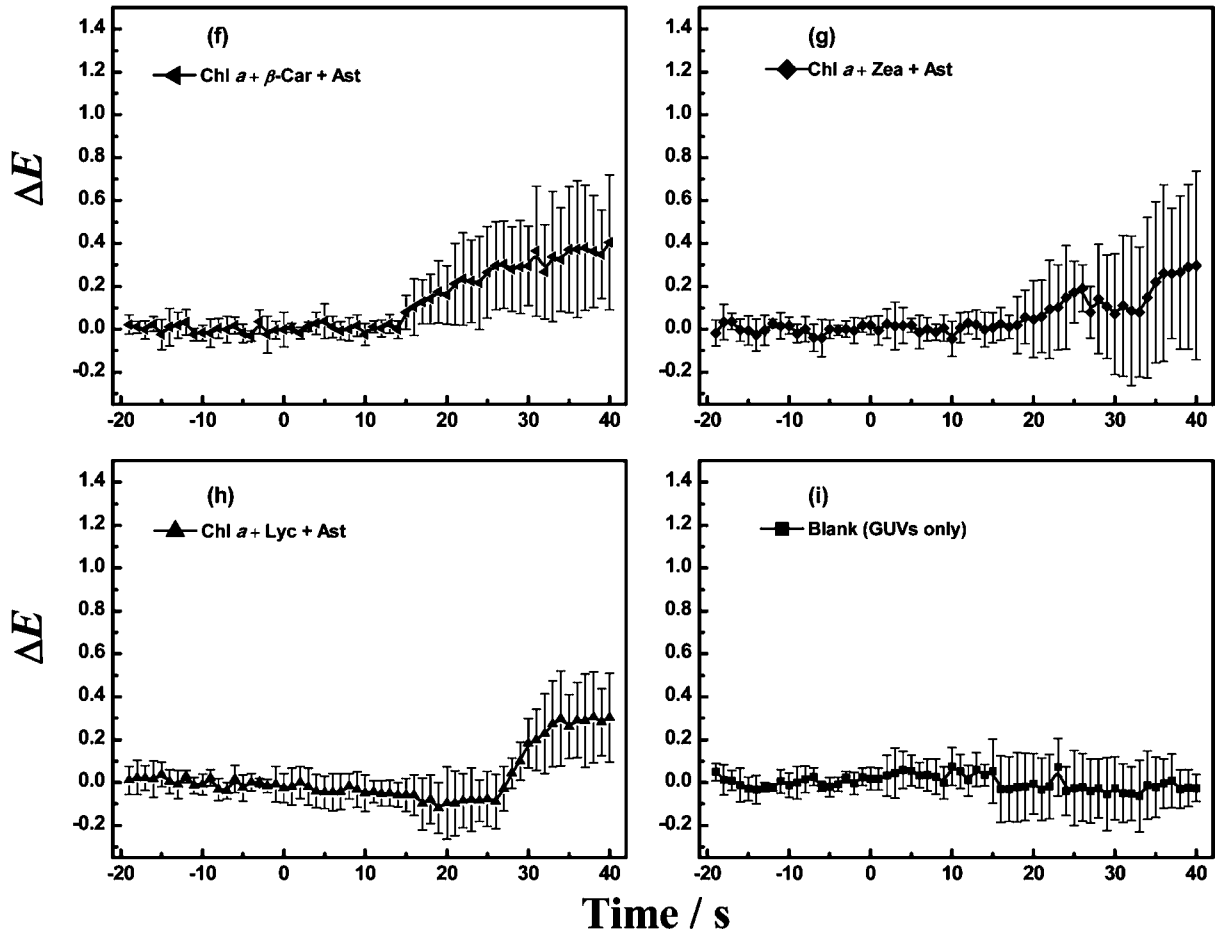

Figure 6. Δ*E* as a metric of image heterogeneity versus time for budding of Chl *a*-sensitized GUVs with the addition of combined carotenoids and blank GUVs exposed to light (400−440 nm, 160 mW/mm^2). Statistics: mean ± SD (n = 6).

the decreased rate in the development of Δ*E* following the lag phase as seen for Ast but not for the other three carotenoids. What still remains to be explained is, however, the higher final level of Δ*E* for Zea and Ast compared to *β*-Car and Lyc. It may be the result of another type of process not directly related to the type I and type II photosensitized oxidation but involving reduction of an initially formed radical precursor to peroxides by the more reducing Lyc and *β*-Car but not by Ast and Zea to give the lowest values for final Δ*E*

$$\text{Lyc} + \text{R}^{\bullet} + \text{H}^{+} \rightarrow \text{Lyc}^{\bullet +} + \text{RH}$$

The combination of Ast with each of the three other carotenoids clearly showed synergetic effects, which may help to explain in more details the complex pattern of reactions Figures 5 and 6. Ast combined with Lyc resulted in the longest

DOI: 10.1021/acs.jafc.5b03658
J. Agric. Food Chem. 2015, 63, 9124−9130

lag phase and also the lowest level for the final heterogeneity. The combination of the most reducing and the most oxidizing carotenoid seems optimal for protection of the membrane against photosensitized budding and disintegration. Apparently, the longer lag phase is the result of a decrease in the rate of $^1O_2$ diffusion from type II photosensitization by Chl *a* via anchoring of Ast, while the lower level for final heterogeneity is the result of reduction of hydroperoxides by the strongly reducing Lyc. The combination of Ast and *β*-Car shows a similar protective effect, confirming that a carotenoid with a high electron-accepting capability together with another carotenoid with a strong electron-donating capability results in prominent synergistic effects (Figure 7). Carotenoids have

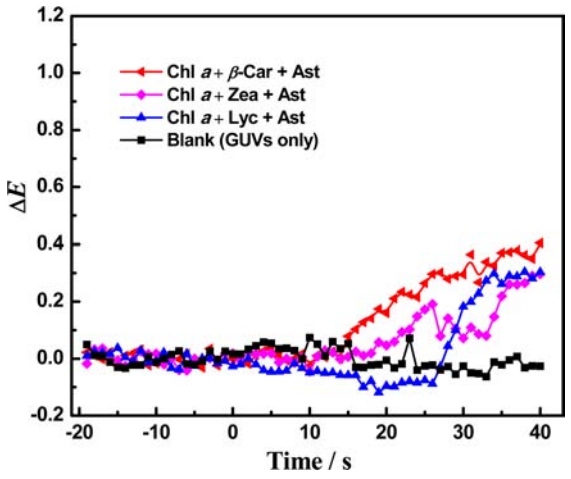

Figure 7. Comparison of time evolution of Δ*E* as a metric of heterogeneity for budding of Chl *a*-sensitized GUVs with combined carotenoids and blank GUVs. The time evolutions are from Figure 6. For clarity, error bars are not shown.

both the capability for electron donation and for electron acceptance depending upon their structures.[24−26] Most carotenoids are good electron donors, but the conclusion from the present study seems to be that combination of carotenoids being good electron donors with those being good electron acceptors like Ast may yield the optimal protection against photosensitized degradation of membranes. The use of GUVs for the study of oxidative processes in membranes is promising because spatial aspects of oxidation may be understood on the basis of the distribution of Chl *a* as a photosensitizer located in the lipophilic interior and potential antioxidants with distribution depending upon their hydrophilic/lipophilic balance (Scheme 2).

AUTHOR INFORMATION

Corresponding Authors

*Telephone: +86-10-62516604. E-mail: jpzhang@chem.ruc.edu.cn.

*Telephone: +45-3533-3221. E-mail: ls@food.ku.dk.

Funding

This work has been supported by the Natural Science Foundation of China (Grant 21173265), the Fundamental Research Funds for the Central Universities, and the Research Funds of Renmin University of China (RUC; 10XNI007, 14XNLQ04, and 14XNH058).

Notes

The authors declare no competing financial interest.

ACKNOWLEDGMENTS

The authors are indebted to Professor Peng Yang at the School of Chemistry and Chemical Engineering, Shaanxi Normal University, for his help in GUV preparation.

ABBREVIATIONS USED

Ast, astaxanthin; Lyc, all-*trans*-lycopene; Zea, zeaxanthin; *β*-Car, all-*trans*-*β*-carotene; Chl *a*, chlorophyll *a*; PC, L-*α*-phosphatidylcholine; GUV, giant unilamellar vesicle; $^1O_2$, singlet oxygen; $O_2^{\bullet -}$, superoxide radical anion; $HO^{\bullet}$, hydroxyl radical; ROI, region of interest; AUC, area under curve

REFERENCES

(1) Kispert, L. D.; Polyakov, N. E. Carotenoid radicals: cryptochemistry or natural colorants. *Chem. Lett.* **2010**, *39*, 148−155.
(2) Skibsted, L. H. Carotenoids in antioxidant networks. Colorants or radical scavengers. *J. Agric. Food Chem.* **2012**, *60*, 2409−2417.
(3) Naguib, Y. M. A. Antioxidant activities of astaxanthin and related carotenoids. *J. Agric. Food Chem.* **2000**, *48*, 1150−1154.
(4) Bolin, A. P.; Macedo, R. C.; Marin, D. P.; Barros, M. P.; Otton, R. Astaxanthin prevents in vitro auto-oxidative injury in human lymphocytes. *Cell Biol. Toxicol.* **2010**, *26*, 457−467.
(5) Galano, A. Relative antioxidative efficiency of a large series of carotenoids in term of one electron transfer reactions. *J. Phys. Chem. B* **2007**, *111*, 12898−12908.
(6) Galano, A.; Vargas, R.; Martínez, A. Carotenoids can act as antioxidants by oxidizing the superoxide radical anion. *Phys. Chem. Chem. Phys.* **2010**, *12*, 193−200.
(7) Jensen, C.; Birk, E.; Jokumsen, A.; Skibsted, L. H.; Bertelsen, G. Effect of dietary levels of fat, *α*-tocopherol and astaxanthin on colour and lipid oxidation during storage of frozen rainbow trout (Oncorhynchus mykiss) and during chill storage of smoked trout. *Z. Lebensm. Unters. Forsch.* **1998**, *207*, 189−196.
(8) Miyawaki, H.; Takahashi, J.; Tsukahara, H.; Takehara, I. Effects of astaxanthin on human blood rheology. *J. Clin. Biochem. Nutr.* **2008**, *43*, 69−74.
(9) Hussein, G.; Sankawa, U.; Goto, H.; Matsumoto, K.; Watanabe, H. Astaxanthin, a carotenoids with potential in human health and nutrition. *J. Nat. Prod.* **2006**, *69*, 443−449.
(10) Hussein, G.; Nakamura, M.; Zhao, Q.; Iguchi, T.; Goto, H.; Sankawa, U.; Watanabe, H. Antihypertensive and neuroprotective effects of astaxanthin in experimental animals. *Biol. Pharm. Bull.* **2005**, *28*, 47−52.
(11) Sliwka, H. R.; Melø, T. B.; Foss, B. J.; Abdel-Hafez, S. A.; Partali, V.; Nadolski, G.; Jackson, H.; Lockwood, S. E. Electron- and energy-transfer properties of hydrophilic carotenoids. *Chem. - Eur. J.* **2007**, *13*, 4458−4466.
(12) Liang, J.; Tian, Y.-X.; Yang, F.; Zhang, J.-P.; Skibsted, L. H. Antioxidant synergism between carotenoids in membranes. Astaxanthin as a radical transfer bridge. *Food Chem.* **2009**, *115*, 1437−1442.
(13) Liang, R.; Liu, Y.; Fu, L.-M.; Ai, X.-C.; Zhang, J.-P.; Skibsted, L. H. Antioxidants and physical integrity of lipid bilayers underoxidative stress. *J. Agric. Food Chem.* **2012**, *60*, 10331−10336.
(14) Wang, H.-J.; Liang, R.; Fu, L.-M.; Han, R.-M.; Zhang, J.-P.; Skibsted, L. H. Nutritional aspects of *β*-carotene and resveratrol antioxidant synergism in giant unilamellar vesicles. *Food Funct.* **2014**, *5*, 1573.
(15) Zhang, J.-P.; Chen, C.-H.; Koyama, Y.; Nagae, H. Vibrational relaxation and redistribution in the $2A_g^-$ state of all-*trans*-lycopene as revealed by picosecond time-resolved absorption spectroscopy. *J. Phys. Chem. B* **1998**, *102*, 1632−1640.
(16) Shioi, Y.; Fukae, R.; Sasa, T. Chlorophyll analysis by high performance liquid chromatography. *Biochim. Biophys. Acta, Bioenerg.* **1983**, *722*, 72−79.
(17) Angelova, M. I.; Soléau, S.; Méléard, Ph.; Faucon, J. F.; Bothorel, P. Preparation of giant vesicles by external AC electric fields. Kinetics and applications. In *Trends in Colloid and Interface Science VI*; Helm,

DOI: 10.1021/acs.jafc.5b03658
J. Agric. Food Chem. 2015, 63, 9124−9130

C., Lösche, M., Möhwald, H., Eds.; Steinkopff: Darmstadt, Germany, 1992; Progress in Colloid and Polymer Science, Vol. *89*, pp 127−131, DOI: 10.1007/BFb0116295.

(18) Liang, R.; Zhang, J. P.; Skibsted, L. H. Evaluation of physical integrity of lipid bilayer under oxidative stress: Application of fluorescence microscopy and digital image processing. In *Advanced Protocols in Oxidative Stress III*; Armstrong, D., Eds.; Springer: New York, 2015; Methods in Molecular Biology, Vol. *1208*, Chapter 9, pp 111−121, DOI: 10.1007/978-1-4939-1441-8_9.

(19) Gonzalez, R. C.; Woods, R. E.; Eddins, S. L. *Digital Image Progressing Using MATLAB*, 2nd ed.; Prentice-Hall: Upper Saddle River, NJ, 2009; Chapter 12, pp 597−673.

(20) Stahl, W.; Junghans, A.; de Boer, B.; Driomina, E. S.; Briviba, K.; Sies, H. Carotenoid mixtures protect multilamellar liposomes against oxidative damage: synergistic effects of lycopene and lutein. *FEBS Lett.* **1998**, *427*, 305−308.

(21) Stratton, S. P.; Schaefer, W. H.; Liebler, D. C. Isolation and identification of singlet oxygen oxidation products of β-carotene. *Chem. Res. Toxicol.* **1993**, *6*, 542−547.

(22) Cantrell, A.; McGarvey, D. J.; George Truscott, T.; Rancan, F.; Böhm, F. Singlet oxygen quenching by dietary carotenoids in a model membrane environment. *Arch. Biochem. Biophys.* **2003**, *412*, 47−54.

(23) Han, R.-M.; Chen, C.-H.; Tian, Y.-X.; Zhang, J.-P.; Skibsted, L. H. Fast regeneration of carotenoids from radical cations by isoflavonoid dianions: importance of the carotenoid keto group for electron transfer. *J. Phys. Chem. A* **2010**, *114*, 126−132.

(24) Martínez, A.; Rodríguez-Gironés, A.; Barbosa, A.; Costas, M. Donator acceptor map for carotenoids, melantonin and vitamin. *J. Phys. Chem. A* **2008**, *112*, 9037−9042.

(25) Han, R.-M.; Tian, Y.-X.; Wu, Y.-S.; Wang, P.; Ai, X.-C.; Zhang, J.-P.; Skibsted, L.-H. Mechanism of radical cation formation from the excited states of zeaxanthin and astaxanthin in chloroform. *Photochem. Photobiol.* **2006**, *82*, 538−546.

(26) Liu, D.; Gao, Y.; Kispert, L. D. J. Electrochemical properties of natural carotenoids. *J. Electroanal. Chem.* **2000**, *488*, 140−150.

DOI: 10.1021/acs.jafc.5b03658
J. Agric. Food Chem. 2015, 63, 9124−9130

has been reported in tobacco products such as cigarettes[10] and chewable tobacco mixtures including other plant material such as betel leaf.[11] Exposure to aflatoxins in cigarettes may be mitigated by their potential destruction in the combustion process;[12] however, aflatoxins present in a smokeless product are likely to be introduced into the body via ingestion.[13]

AFB_1 has traditionally been detected in commodities by use of HPLC with fluorescence detection,[14] with HPLC-MS/MS and UHPLC-MS/MS methods becoming more common.[15−17] The use of mass spectrometry for AFB_1 detection is not new,[18] but advances in these technologies have resulted in methods for AFB_1 with limits of detection (LOD) in the low parts per trillion (ppt) range.[15] In this study, we have developed and validated a method for the determination of AFB_1 in smokeless tobacco products and applied it to the analysis of a selection of smokeless tobacco products commercially available in the United States. Although our method was optimized for AFB_1 detection and quantitation, we have also validated it for detecting and quantifying aflatoxins B_2 (AFB_2), G_1 (AFG_1), and G_2 (AFG_2). To ensure the highest possible degree of specificity and sensitivity toward AFB_1 measurement, we employed immunoaffinity chromatography (IAC) to selectively bind AFB_1 from product sample extracts and UHPLC-MS/MS with $^{13}C_{17}$-labeled internal standards for detection.

MATERIALS AND METHODS

Samples, Standards, and Reagents. Reverse osmosis deionized water, HPLC grade solvents, and high-purity reagents were used throughout. Stock solutions of AFB_1 (2.0 ng/μL) as well as the internal standard $^{13}C_{17}$-AFB_1 (0.5 ng/μL) in acetonitrile were purchased (Romer Laboratories, Union, MO, USA) and stored at −20 °C, from which calibrators were made as needed. Internal standard (100 μL) was diluted into 1900 μL of acetonitrile to generate a solution of 12.5 pg/μL. 2S3 Kentucky Reference Moist Snuff (University of Kentucky, College of Agriculture, Lexington, KY, USA) was used as a matrix for blanks, calibrators, and quality control (QC) samples. A convenience sample of 32 commercially available smokeless tobacco products was acquired by purchasing products at the retail point-of-sale in the Washington, DC, USA, and Atlanta, GA, USA, metropolitan areas in 2013. The convenience sample consisted of 12 loose moist snuffs, 4 pouched moist snuffs, 6 dry snuffs, 7 chewing tobaccos, and 3 snus. A total of 17 product brands produced by 8 manufacturers were sampled. Tobacco products purchased in the Washington, DC, area were shipped to CDC at room temperature, arriving within 48 h following shipment. Products were inventoried and then stored at −70 °C until further use.

Sample Preparation. Tobacco products stored at −70 °C were first transferred to a −20 °C freezer for 1 h and then allowed to acclimate to room temperature. Once at room temperature, an entire retail package (i.e., tin, pouch, etc.) of each product was weighed to determine its fresh weight. Products were then dried for at least 10 h at 55 °C. After drying, the products were reweighed to obtain a dry weight. The difference between the two values was then used to determine the relative moisture (i.e., oven volatiles) content (%) of the products. The dried products were next milled to a fine powder under liquid nitrogen by use of a model 6770 cryomill (SPEX Sample Prep, Metuchen, NJ, USA). The resulting powder was then thoroughly mixed to ensure uniform distribution, and 2 g aliquots (± ≤0.0015 g) were weighed out in 15 mL polypropylene centrifuge tubes (Becton Dickinson, Franklin Lakes, NJ, USA). This process was also performed on the reference smokeless tobacco product used as the matrix for blanks, calibrators, and QC samples. Aliquots of the reference smokeless tobacco product were then amended with 40 μL of the $^{13}C_{17}$-AFB_1 and AFB_1 to generate 10 calibrators (0.005, 0.010, 0.020, 0.050, 0.100, 0.200, 0.500, 1.000, 2.000, and 5.000 ppb), and 3 QC samples (0.07 ppb (low), 0.21 ppb (medium), and 0.7 ppb (high)). Test samples were also amended with 40 μL of the $^{13}C_{17}$-AFB_1 internal standards. Ten milliliters of 80:20 methanol/water solution and 0.2% Tween 20 (Fisher, Fair Lawn, NJ, USA) was then added to the blank, calibrator standards, and samples, and they were capped and sealed with parafilm and extracted for 4 h on a rotary mixer set at a 45° angle at 30 rpm. After extraction, the tubes were transferred to a centrifuge equipped with a swing-bucket rotor and centrifuged at 3700 rpm for 10 min to separate the tobacco samples from their respective extraction solutions. The clarified sample extracts were then transferred to new 15 mL polypropylene centrifuge tubes and stored overnight at 4 °C.

IAC Column Cleanup. Samples were first allowed to come to room temperature if previously refrigerated. The samples were diluted (1 mL of sample in 4 mL of water, 0.2% Tween 20), loaded onto an Aflatest WB immunoaffinity column (Vicam, Milford, MA, USA) and allowed to elute via gravity. The IAC column was then washed once with 10 mL of methanol/water (20:80, v/v) and 0.2% Tween 20, followed by 10 mL of methanol/water (20:80, v/v). Analytes were finally eluted with 1.0 mL of acetonitrile into 13 × 100 mm level 2 borosilicate silanized glass collection tubes (Kimble Chase, Vineland, NJ, USA). The collection tubes were then transferred to a Savant SpeedVac Plus SC210A rotary vacuum concentrator (Thermo Fisher, Asheville, NC, USA) and evaporated to dryness under gentle conditions (drying rate set to low). The samples were next reconstituted with 400 μL of methanol/water (60:40, v/v) and transferred to 2 mL autosampler vials with a PTFE/silicone septa for UHPLC-MS/MS analysis.

UHPLC-MS/MS Analysis. Our UHPLC-MS/MS system consisted of an Acquity I-Class Binary Solvent Manager, an Acquity I-Class Sample Manager, and an Acquity I-Class Column Compartment coupled to a Waters Xevo TQ-S tandem quadrupole mass spectrometer (Waters, Milford MA, USA). The UHPLC-MS/MS was controlled by Acquity UPLC Console Software 1.51.3347 and MassLynx Software 4.1 (Waters). Analytes of interest were separated using a 100 × 3 mm, 2.7 μm particle Supelco Ascentis Express C_{18} column (Supelco Analytical, Bellefonte, PA, USA) with a 0.5 μm × 0.004 in. i.d. KrudKatcher Ultra HPLC in-line filter (Phenomenex, Torrance, CA, USA). A gradient consisting of water with 0.1 mM ammonium formate (solvent A) and 99:1 methanol/water with 0.1 mM ammonium formate (solvent B) at a constant flow rate of 1.0 mL/min was used. The solvent gradient program was as follows: 0 min, 40% B; 1.0 min, 55% B; 1.25 min, 100% B; 1.75 min, 100% B; 2.0 min, 40% B; 2.5 min, 40% B. The injection volume used was 10 μL. The column temperature was maintained at 70 °C. MS/MS transitions (m/z) for AFB_1 were as follows: 313.32 → 241.22 (quantitation); 313.32 → 285.08 (confirmation); 330.37 → 301.09 ($^{13}C_{17}$-labeled internal standard). Global mass spectrometer settings were as follows: capillary voltage, 3.5 kV; cone voltage, 75 V; source offset voltage, 50 V; source temperature, 150 °C; desolvation temperature, 650 °C; cone gas, nitrogen (600 L/h); desolvation gas, nitrogen (600 L/h); collision gas, argon (0.20 mL/min); nebulizer gas, nitrogen (6.00 bar). Analytes were quantified by interpolation of peak area ratios of the analyte over its $^{13}C_{17}$-labeled internal standard for MS/MS transitions against a 10-point calibration curve ($1/x$ weighting).

Validation. QC samples were prepared at three distinct concentrations levels across the calibration range. QC samples were generated for each run via direct spiking of blank reference tobacco. All QC samples were run at the beginning and end of each analysis batch. Data from the first 20 independent runs (days) were used to establish the QC limits as part of a multirule procedure for determining whether instrument runs were in or out of control.[19] QC samples were also used for determining the recovery of the method, extraction efficiency, and other validation tests as indicated. The within-run and between-run coefficients of variation from the 20 day duplicate analysis of the three QC samples were also used to assess within-run and between-run imprecision, respectively.

Method robustness was tested by varying the solvent extraction conditions from the proposed method to different percentages of water and methanol (30:70 and 10:90, v/v) as well as by varying the mass of tobacco extracted from the method from 2 to 1 or 3 g. The robustness of the IAC step was also tested by varying the volume of

DOI: 10.1021/acs.jafc.5b02622
J. Agric. Food Chem. 2015, 63, 9131−9138

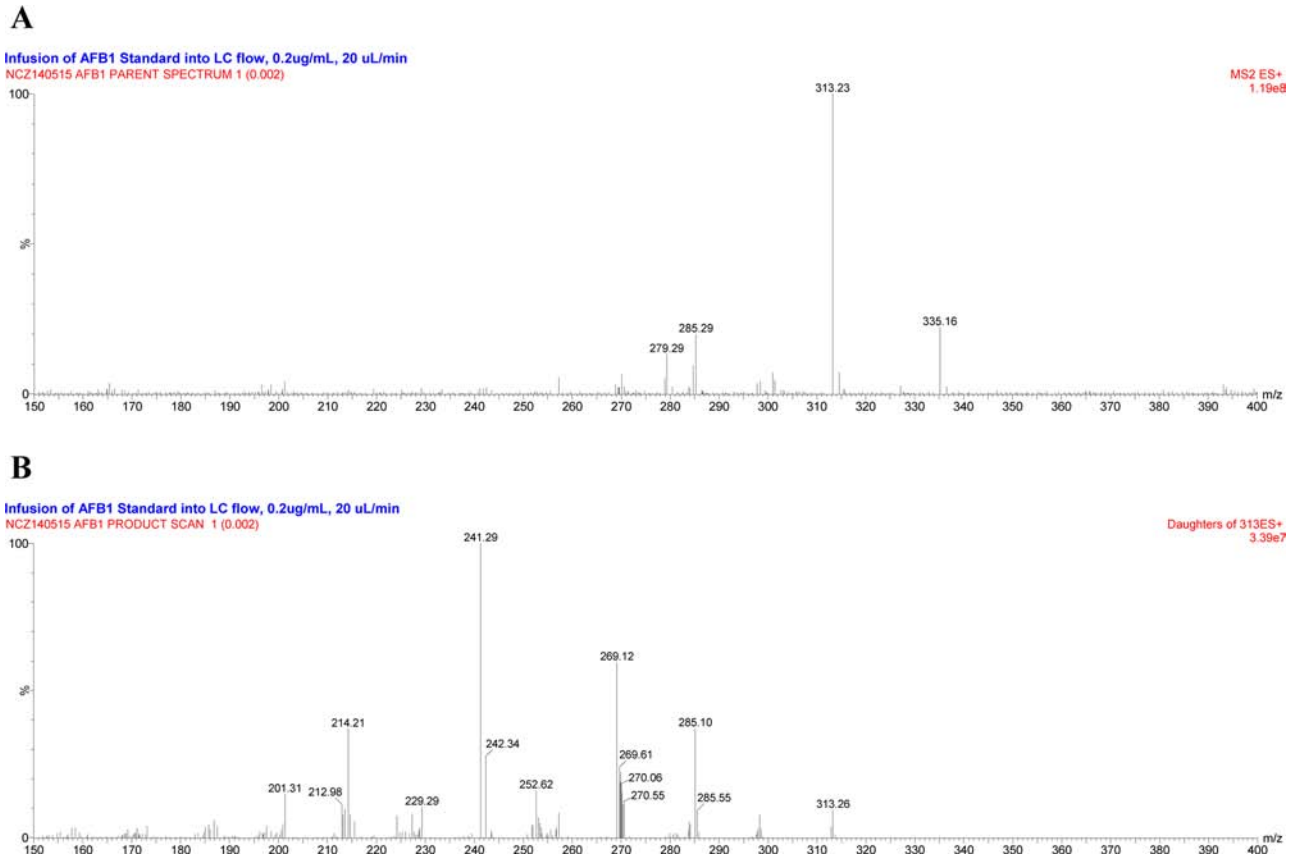

Figure 2. (A) Precursor and (B) product ion scans for AFB_1 (**1**).

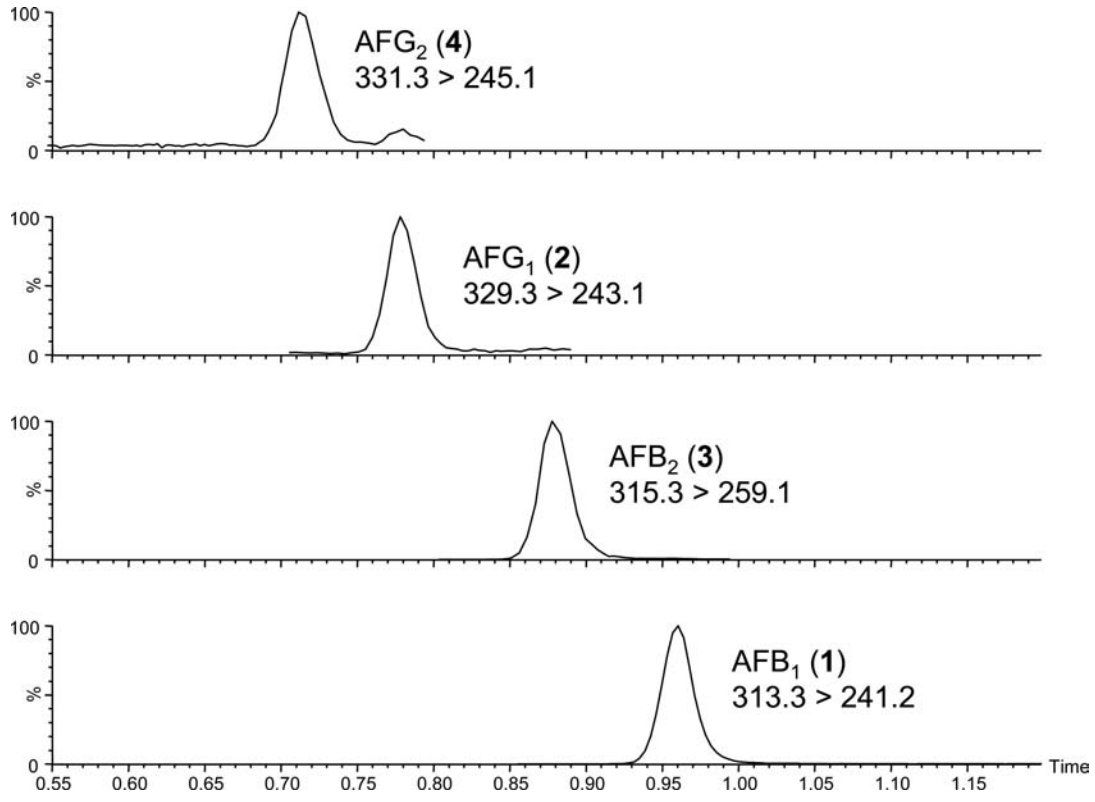

Figure 3. MS/MS chromatograms of aflatoxins (**1**–**4**).

sample extract loaded on the IAC column and the volume of solvent used to elute the analytes as well as substitution of the IAC column specified in the method with similar IAC column products. In all cases seven replicates of the test condition were performed on a single day.

DOI: 10.1021/acs.jafc.5b02622
J. Agric. Food Chem. 2015, 63, 9131−9138

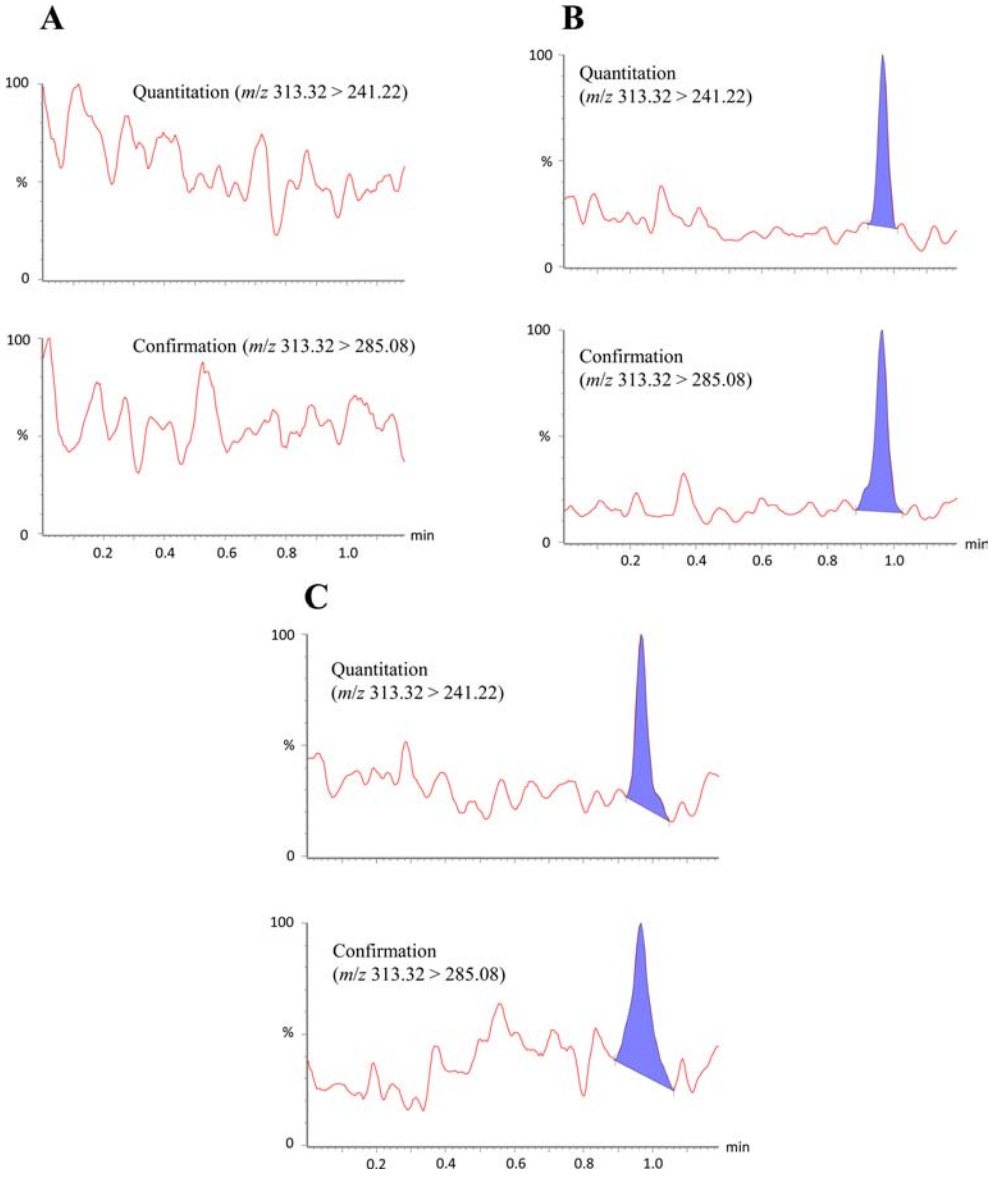

Figure 4. Sample MS/MS AFB_1 (**1**) chromatograms: (A) reference tobacco blank (2S3 Kentucky Reference Moist Snuff); (B) low QC sample (2S3 Kentucky Reference Moist Snuff spiked with 0.07 ppb of AFB_1); (C) commercial smokeless tobacco product (endogenous concentration of 0.007 ppb AFB_1).

LODs were determined by performing repeat measurements in samples spiked with concentrations near the LOD. By plotting the standard deviation of these samples as a function of concentration, an estimate of the standard deviation at a concentration of zero (σ_0) was obtained by extrapolation, and the LOD was calculated as $3\sigma_0$.[20]

Product Analysis. A minimum of seven replicate measurements were made on each commercial product tested. Each replicate consisted of an independent sample that was prepared and run on a different day. QC samples and calibrators were prepared and analyzed in duplicate, bracketing the product samples in the analysis sequence. Calibrations were determined as the average from these duplicate injections. Run performance was determined by comparing QC values from each run versus acceptance rules determined from QC limits.[19]

RESULTS AND DISCUSSION

Method Development and Optimization. We infused a standard of AFB_1 and were able to generate a mass spectrum dominated by a $[M + H]^+$ molecular ion of m/z 313.2, with evidence of a $[M + Na]^+$ adduct at m/z 335.16. Similarly, we found a $[M + H]^+$ molecular ion of m/z 330.21 and a $[M + Na]^+$ adduct at m/z 352.19 when infusing the $^{13}C_{17}$-AFB_1 internal standard (Figure 2). Using the $[M + H]^+$ molecular ion as our precursor ion for both the standard and internal standard, we observed predominant MS/MS fragment product ions at m/z 241.29, 269.12, and 285.10 for AFB_1 and at m/z 255.32, 284.50, and 301.15 for $^{13}C_{17}$-AFB_1. After optimizing the MS/MS parameters for each of the fragments, we selected m/z 313.32 → 241.22 for AFB_1 quantitation, m/z 313.32 → 285.08 for AFB_1 confirmation, and m/z 330.37 → 301.09 for internal standardization with $^{13}C_{17}$-AFB_1. These transitions were selected because they represented the best available choices in terms of signal intensity, signal-to-noise ratio, and blank baseline in the chromatographic method, and the product ions did not appear to be the product of nonspecific losses (e.g., H_2O, NH_3). Our selection of the m/z 313.32 → 241.22 transition for AFB_1 quantitation is consistent with its use in other LC-MS/MS methods.[16,21,22] Using an analogous approach we also identified quantitation and confirmation

DOI: 10.1021/acs.jafc.5b02622
J. Agric. Food Chem. 2015, 63, 9131−9138

Table 1. Analytical Performance

MS/MS transition (m/z)	LOD[b] (ppb)	QC samples		characterization mean and standard deviation (SD)[a]			recovery of target concentration[a] (%)
		level	target (ppb)	mean (ppb)	SD (ppb)	CV (%)	
quantitation: 313.32 → 241.22	0.007	low	0.07	0.078	0.007	9.4	111
		medium	0.21	0.220	0.014	6.5	105
		high	0.70	0.738	0.041	5.5	105
confirmation: 313.32 → 285.08	0.009	low	0.07	0.079	0.009	10.9	113
		medium	0.21	0.220	0.014	6.2	105
		high	0.70	0.730	0.040	5.5	104

[a]Measured over 20 days (2 replicates/day). [b]Measured over 15 days (1 replicate/day).

MS/MS transitions for AFB_2, AFG_1, and AFG_2, as well as internal standardization MS/MS transitions for their respective $^{13}C_{17}$-labeled analogues.

Chromatographic separations based on C_{18} stationary phases have frequently been used in LC-MS/MS methods for aflatoxins.[16,23] After testing a sampling of C_{18} columns as well as other stationary phases, we decided upon a fused-core C_{18} column for our method. Using this column and a methanol/water gradient with 0.1 M ammonium formate, we were able to develop a separation that resolved AFB_1, AFB_2, AFG_1, and AFG_2 in <1 min (Figure 3) with performance optimized for AFB_1 quantitation and confirmation (Figure 4). Using our QC sample data, we found that the average retention time for AFB_1 was 0.94 min and varied by <2% CV over 15 days. Our selection of a fused-core particle stationary phase over traditional porous particles proved to be advantageous in that it allowed us to perform the chromatographic separation at a relatively high flow rate (1 mL/min) with very high peak resolution while still operating at the lower end of LC pressures (~450 bar). This relatively low operating pressure permits the possible adaptation of our method beyond UHPLC systems to midpressure HPLC systems capable of operating pressures of up to 600 bar.

Because smokeless tobacco products can occur in a variety of heterogeneous forms, we dried and cryogenically milled all products prior to analysis to generate homogeneous, powdered samples that were of similar consistency across all product types. The drying step also enabled us to determine the moisture content (i.e., oven volatiles) of the products as part of the sample preparation process as opposed to performing a separate moisture determination. Our drying conditions for the smokeless tobacco products (55 °C, >10 h) differed from those typically used for determining moisture content (100 °C, 3 h).[24,25] We evaluated our drying step for possible aflatoxin losses by calculating analyte recoveries based on the addition of the internal standard both before and after the drying step. We observed quantitative recovery in replicate analyses (n = 5) of a dry snuff product with ~0.3 ppb of endogenous AFB_1 present, as well as samples of 2S3 Kentucky Reference Moist Snuff to which a net concentration of 0.7 ppb of AFB_1 was added. Although our testing of a selection of smokeless tobacco products dried at 100 °C did not show any noticeable aflatoxin losses, we decided to dry products at 55 °C as a more conservative approach. We also observed no differences in the moisture content determinations of several smokeless tobacco products performed under both drying conditions.

We used a methanol/water extraction followed by IAC column cleanup to isolate aflatoxins from smokeless tobacco samples. Our extraction methodology is similar to that developed for analyses of aflatoxins from corn, peanuts, and peanut butter (AOAC Method 991.31).[26] In optimizing the extraction step we found that acetonitrile/water mixtures[14] were as effective as methanol/water mixtures in terms of analyte recovery; however, we decided to use a methanol/water extraction as it was consistent with the IAC column manufacturer recommendations as well as other published methods.[26] The use of IAC, or a comparable postextraction cleanup technique such as SPE, was necessary to analyze the tobacco extracts for AFB_1. Attempts that we made to perform direct analyses on the tobacco extracts without a postextraction cleanup step resulted in complete suppression of all analyte and internal standard signals. We also found that the use of a surfactant was essential to the IAC process to mitigate nonspecific binding. When we omitted the surfactant from the IAC process, we frequently encountered discoloration and clogging of the IAC column bed. In addition to IAC, SPE has been used for postcolumn cleanup of aflatoxin extracts.[15,27] We tested an SPE substrate used for determining aflatoxins, but in our application we were unable to attain SPE recoveries as high as those we observed with IAC (~70% recovery for SPE vs ~100% for the IAC). In light of the apparently better analyte recovery and the specificity and selectivity inherent to the immunoaffinity process, we decided to use IAC over SPE in our method.

Through the course of method development, we noted steps in the sample preparation process that were particularly susceptible to analyte losses with the potential to greatly affect analyte recovery and overall method performance. First, we observed that aflatoxins were susceptible to apparent binding during the dry-down and reconstitution step if untreated borosilicate glass was used versus silanized glass. When using untreated borosilicate glass tubes, we found that analyte recoveries were ~5% lower in acetonitrile samples and ~70% lower in methanol samples than when silanized glass was used with either solvent type. Consequently, we used acetonitrile and silanized glass for all dry-down steps. Second, we observed that prolonged exposure to air during the dry-down step resulted in analyte losses, presumably to oxidation. In dried samples that were exposed to air, we found that ~95% of aflatoxins were lost after 8 h, with complete loss occurring after 72 h. By comparison, we observed no analyte losses in dried samples that were purged with nitrogen and capped for the same time frame. For this reason, care had to be taken to perform the dry-down step under gentle conditions and promptly reconstitute the dried samples to minimize analyte losses due to oxidation.

Method Validation. We prepared QC samples for each run at three levels (low, medium, and high) to track instrument run

DOI: 10.1021/acs.jafc.5b02622
J. Agric. Food Chem. 2015, 63, 9131−9138

Table 2. Aflatoxin B_1 in Commercially Available Smokeless Tobacco Products

			aflatoxin B_1 (AFB_1) analysis		
category	ID	moisture content (%)	replicates (n)	AFB_1 concentration[a] ± SD (ppb)	CV (%)
chew[b]	chew 1a	21.3	7	0.029 ± 0.002	6
	chew 1b	23.6	7	0.013 ± 0.002	16
	chew 2a	20.7	7	0.015 ± 0.003	17
	chew 2b	23.2	9	0.016 ± 0.002	10
	chew 3	22.0	9	<LOD	N/A
	chew 4	22.1	9	<LOD	N/A
	chew 5	21.3	8	<LOD	N/A
dry snuff	dry snuff 1	2.0	9	0.032 ± 0.009	27
	dry snuff 2	5.1	8	0.050 ± 0.006	11
	dry snuff 3	4.4	8	0.026 ± 0.007	27
	dry snuff 4	4.0	9	0.271 ± 0.051	19
	dry snuff 5	3.7	9	0.013 ± 0.005	38
	dry snuff 6	4.6	9	0.153 ± 0.024	16
moist snuff (loose)	all products tested (n = 12)	51–56	7–8	<LOD	N/A
moist snuff (pouched)	all products tested (n = 4)	46–54	7–8	<LOD	N/A
snus	all products tested (n = 4)	26–32	8	<LOD	N/A

[a]Concentration is based on dry mass of product. [b]Chew 1a and chew 1b were different lots from the same brand. Chew 2a and chew 2b were different lots from the same brand.

control as well as to perform certain aspects of method validation. The QC pools were assigned target values and uncertainty limits by duplicate analysis over 20 days. These data were also used to determine method imprecision for AFB_1 (Table 1). Between-run imprecision for AFB_1 was 4.5–8.4% and within run imprecision was 4.4–6.0%, depending on the QC level. Overall imprecision of the method was 5.5–9.4%. Recovery of the target amount in our QC samples was generally within 10% of being quantitative (100%), ranging from 105 to 111%.

The LOD of our method is estimated to be 0.007 ppb for AFB_1. Although direct comparison of LODs among different methods is not straightforward because of differences and/or missing details in how LODs were calculated, we believe that our detection limit of 0.007 ppb for AFB_1 is among the lowest of comparable LC-MS/MS methods. For instance, Huang et al.[15] demonstrated a LOD of 0.009 ppb for AFB_1 in peanuts by LC-MS/MS. An LOD in the low parts per trillion range is beneficial, as our method can be used not only for potential regulatory level investigation work, which is typically in the parts per billion range, but also for characterization of products at much lower AFB_1 concentrations.

We examined the confirmation ratio, that is, the peak area of the confirmation MS/MS transition divided by the area of the quantitation MS/MS transition, for AFB_1 across all calibrators and QC samples during the 20 day characterization period. The confirmation ratio was 1.03–1.04 with a CV of <10% at concentrations ≥0.07 ppb (the target concentration of the low QC). At concentrations of <0.07 ppb the CV of the ratio gradually increased to ∼20% at 0.02 ppb and to ∼30% at 0.01 ppb.

We investigated method robustness by identifying five critical method parameters and evaluating the effect of intentionally varying these parameters on QC sample results. The variables we investigated were the volume of sample extract loaded onto the IAC, elution volume from the IAC, extraction solvent composition, mass of tobacco extracted, and IAC type. We performed seven replicates of each test condition on a single day and compared these results with those obtained from the 20 day characterization. When we increased the volume of sample extract loaded on the IAC column from 1 to 2 mL, the accuracy and precision of the AFB_1 and AFB_2 results appeared to be unaffected; however, AFG_1 and AFG_2 recoveries in the low pool appeared to be slightly lower. We found that decreasing the volume of extract loaded on the IAC column to 0.5 mL resulted in apparent higher imprecision for all aflatoxins, and in some cases a spurious effect on recovery of the pool target value was observed. Changing the extraction composition or the IAC products did not appear to have an appreciable effect on the accuracy or precision of the QC analyses. We observed that reducing the amount of tobacco in the extraction from 2 to 1 g did not seem to affect AFB_1 but resulted in lower recoveries for AFG_2. Increasing the amount of tobacco to 3 g frequently resulted in the extraction tubes cracking during the centrifugation step. Altering the volume of elution solvent used, as well as substituting different IAC products, did not appear to have much effect on the QC values.

Product Analyses. We first determined the moisture content of the loose moist snuff, pouched moist snuff, dry snuff, snus, and chewing tobacco products selected for our analyses. We observed that dry snuffs were generally <5% moisture by weight, chews were ∼20% moisture, snus were ∼30% moisture, and moist snuffs were ∼50% moisture (Table 2). Our moisture determinations were generally consistent with the expected values for these product classes reported in the literature.[5,28]

Using our LC-MS/MS method, we then analyzed samples of the selected smokeless tobacco products for AFB_1 and reported these data as the mean concentration found in the dry product (n = 7–9, depending on the product) (Table 2). We observed that AFB_1 concentrations were less than our method LOD of 0.007 ppb in all of the loose moist snuff, pouched moist snuff, and snus products we tested. All of the dry snuff products and a majority of the chew products (5 of 7) we tested had detectable concentrations of AFB_1. The dry snuffs had the highest AFB_1 concentrations among all product types we tested, with the

DOI: 10.1021/acs.jafc.5b02622
J. Agric. Food Chem. 2015, 63, 9131–9138

highest mean AFB_1 concentration among the dry snuffs tested being 0.271 ± 0.051 ppb. By comparison, the highest concentration of AFB_1 we observed among the chew products tested was approximately an order of magnitude lower (0.029 ± 0.002 ppb). For two chew products we tested different lot numbers of the same product to gain insight into within-product variability (Table 2). We observed a high degree of variability among the two lots tested for one of the chew products (chew 1, 0.029 ± 0.002 vs 0.013 ± 0.002 ppb), whereas the other product (chew 2) showed much closer agreement among tested lots (0.015 ± 0.003 vs 0.016 ± 0.002 ppb).

Overall, the concentrations of AFB_1 we found in the smokeless tobacco products we surveyed were much lower than the 20 ppb regulatory limit typical for foods and feeds.[1] We did not detect AFB_2, AFG_1, or AFG_2 in any of the smokeless tobacco products we tested. AFB_1 concentrations tend to be higher than other aflatoxins when contamination is present, and given the AFB_1 concentrations we detected were already in the parts per trillion range, it is not surprising that we did not detect any other aflatoxins. Furthermore, the LODs for AFB_2 (0.01 ppb), AFG_1 (0.02 ppb), and AFG_2 (0.1 ppb) with our method were higher than that of AFB_1 (0.007 ppb).

Interpretation of our findings is not straightforward. First, although we were able to confirm the presence of AFB_1 in several smokeless tobacco products, we have no way to identify the source of the AFB_1 contamination. Although AFB_1 contamination can occur directly in tobacco leaves,[8,9] it is also possible that AFB_1 contamination found in a smokeless tobacco product may result from an additive. For example, heavy casings, such as molasses, licorice, and fruit extracts, that are added during processing are potential sources of AFB_1 contamination. The amounts of these additives can be significant, such as in chewing tobacco, where added sugar content is typically 35%.[5] Conversely, the absence of AFB_1 in many of the smokeless tobacco products we tested may also be due to additives introduced during processing, such as the addition of sodium propionate as a fungicide. Additives raising the pH of smokeless tobacco products as a means of increasing nicotine potency may also affect AFB_1 concentrations.[5] Second, we noted with interest that the smokeless tobacco products with the lowest moisture content (dry snuffs) had the highest AFB_1 concentrations, whereas we were unable to detect AFB_1 in any of the products with the highest moisture content (moist snuff). This seems counterintuitive, as from a simplistic standpoint we would expect moisture encountered in storage to contribute to higher aflatoxin concentrations, and suggests to us that the mechanism by which AFB_1 contamination is introduced into smokeless tobacco products is much more complex. Finally, the potential health effects of AFB_1 in a smokeless tobacco depend not only upon the amount of AFB_1 present but also on the different ways in which a smokeless tobacco product can be used. This may be particularly important in the case of dry snuffs, as not only did we observe the highest AFB_1 concentrations in these products, but it is also the only class of smokeless tobacco product we tested that is used both orally and nasally. Even among smokeless tobacco products that are strictly used orally, product class and cultural practices can determine whether a product is used for minutes versus hours and consequently influence potential AFB_1 exposure.[5]

We believe that our work has two key strengths: we believe it to be the first published report of an LC-MS/MS method specifically designed for determining aflatoxin concentrations in tobacco products and that the data we present are also the first published survey of AFB_1 concentrations in a subset of smokeless tobacco products commercially available in the United States. We do acknowledge, however, that there are limitations to our work that warrant further investigation. Although we were able to apply our method to a variety of smokeless tobacco products (moist and dry snuffs, snus, chews), there exist other product classes that we did not test (e.g., dissolvables, "sticks"), and these products may not be amenable to our procedure without modification and additional validation. We were able to identify a reference smokeless tobacco product (2S3 Kentucky Reference Moist Snuff) that was free of detectable aflatoxin and successfully used it as a matrix for blanks, calibrators, and QC samples. The availability, however, of a reference material with a detectable endogenous concentration of AFB_1 would be beneficial as it could potentially be used as a QC material without the need for analyte spiking and could possibly be developed as a positive AFB_1 reference material. We were successful in using the IAC process to isolate AFB_1 from the complex sample extracts with a great degree of specificity; however, this process was performed manually in our study and was time-consuming. Automating the IAC process as well as other steps in the sample extraction process should be investigated in the future as a means of improving sample throughput.

■ ASSOCIATED CONTENT

Supporting Information

The Supporting Information is available free of charge on the ACS Publications website at DOI: 10.1021/acs.jafc.5b02622.

Supplemental Table 1, UHPLC-MS/MS Analysis Parameters for AFB_2, AFG_1, and AFG_2; Supplemental Table 2, Analytical Performance for AFB_1, AFB_2, AFG_1, and AFG_2; Supplemental Table 3, Robustness Testing: Volume of Sample Extract Loaded on IAC Column; Supplemental Table 4, Robustness Testing: Extraction Composition; Supplemental Table 5, Robustness Testing: Mass of Tobacco Extracted; Supplemental Table 6, Robustness Testing: Volume of Elution Solvent Used in IAC Step; Supplemental Table 7, Robustness Testing: Substituting IAC Products (PDF)

■ AUTHOR INFORMATION

Corresponding Author

*(M.E.R.) Phone: (770) 488-7394. Fax: (404) 638-5431. E-mail: MRybak@cdc.gov.

Funding

This study was funded by the U.S. Food and Drug Administration, Center for Tobacco Products.

Notes

The findings and conclusions in this report are those of the authors and do not necessarily represent the official views or positions of the CDC/Agency for Toxic Substances and Disease Registry, the FDA, or the Department of Health and Human Services.

The authors declare no competing financial interest.

■ ACKNOWLEDGMENTS

We thank Stephen Stanfill, Dr. Clifford Watson, and Tameka Lawler, of the Centers for Disease Control and Prevention, National Center for Environmental Health, and Jeannie Jeong-

DOI: 10.1021/acs.jafc.5b02622
J. Agric. Food Chem. 2015, 63, 9131−9138

Im of the Food and Drug Administration, Center for Tobacco Products, for their collegial input on this project.

ABBREVIATIONS USED

AFB_1, aflatoxin B_1; AFB_2, aflatoxin B_2; AFG_1, aflatoxin G_1; AFG_2, aflatoxin G_2; CV, coefficient of variation; HPHCs, Harmful and Potentially Harmful Constituents; IAC, immunoaffinity chromatography; LC, liquid chromatography; SPE, solid phase extraction

REFERENCES

(1) U.S. DHHS. *Chemical Contaminants, Metals, Natural Toxins & Pesticides > Guidance for Industry: Action Levels for Poisonous or Deleterious Substances in Human Food and Animal Feed*; U.S. Food and Drug Administration: Washington, DC, USA, 2000; http://www.fda.gov/Food/GuidanceRegulation/GuidanceDocumentsRegulatoryInformation/ChemicalContaminantsMetalsNaturalToxinsPesticides/ucm077969.htm (accessed Sept 8, 2015).

(2) *Mycotoxins: Risks in Plant, Animal and Human Systems. Task Force Report 139*; Council for Agricultural Science and Technology (CAST): Ames, IA, USA, 2003.

(3) U.S. DHHS. *Harmful and Potentially Harmful Constituents in Tobacco Products and Tobacco Smoke; Established List*; U.S. Food and Drug Administration: Washington, DC, USA, 2012; http://www.fda.gov/downloads/TobaccoProducts/GuidanceComplianceRegulatoryInformation/UCM297981.pdf (accessed Sept 8, 2015).

(4) Rodu, B.; Jansson, C. Smokeless tobacco and oral cancer: a review of the risks and determinants. *Crit. Rev. Oral Biol. Med.* **2004**, *15*, 252−263.

(5) IARC. working group on the evaluation of carcinogenic risks to humans. Smokeless tobacco and some tobacco-specific N-nitrosamines. *IARC Monogr. Eval. Carcinog. Risks Hum.* **2007**, *89*, 1−592.

(6) Stepanov, I.; Jensen, J.; Hatsukami, D.; Hecht, S. S. New and traditional smokeless tobacco: comparison of toxicant and carcinogen levels. *Nicotine Tob. Res.* **2008**, *10*, 1773−1782.

(7) Hatsukami, D. K.; Ebbert, J. O.; Feuer, R. M.; Stepanov, I.; Hecht, S. S. Changing smokeless tobacco products. *Am. J. Prev. Med.* **2007**, *33*, S368−S378.

(8) Pattee, H. E. Production of aflatoxins by *Aspergillus flavus* cultured on flue-cured tobacco. *Appl. Microbiol.* **1969**, *18*, 952−953.

(9) Varma, S. K.; Verma, R.A.; Jha, A. K. Ecotoxicological aspects of *Aspergilli* present in the phylloplane of stored leaves of chewing tobacco (*Nicotiana tobaccum*). *Mycopathologia* **1991**, *113*, 19−23.

(10) Edinboro, L. E.; Karnes, H. T. Determination of aflatoxin B1 in sidestream cigarette smoke by immunoaffinity column extraction coupled with liquid chromatography/mass spectrometry. *J. Chromatogr. A* **2005**, *1083*, 127−132.

(11) Verma, R. J.; Kolhe, A. S.; Dube, H. C. Aflatoxin contamination in chewing products. *Proc. Natl. Acad. Sci., India, Sect. B* **1995**, *65*, 167−170.

(12) Tso, T. C.; Sorokin, T. Examination of aflatoxin B1 in leaf tobacco and in cigarette smoke condensate. *Beitr. Tabakforsch.* **1967**, *4*, 18−20.

(13) Kensler, T. W.; Roebuck, B. D.; Wogan, G. N.; Groopman, J. D. Aflatoxin: a 50-year odyssey of mechanistic and translational toxicology. *Toxicol. Sci.* **2011**, *120*, S28−S48.

(14) Trucksess, M. W.; Weaver, C. M.; Oles, C. J.; Fry, F. S., Jr.; Noonan, G. O. Determination of aflatoxins B1, B2, G1, and G2 and ochratoxin A in ginseng and ginger by multitoxin immunoaffinity column cleanup and liquid chromatographic quantitation: collaborative study. *J. AOAC Int.* **2008**, *91*, 511−523.

(15) Huang, B.; Han, Z.; Cai, Z.; Wu, Y.; Ren, Y. Simultaneous determination of aflatoxins B1, B2, G1, G2, M1, and M2 in peanuts and their derivative products by ultra-high-performance liquid chromatography-tandem mass spectrometry. *Anal. Chim. Acta* **2010**, *662*, 62−68.

(16) Li, W.; Herrman, T. J.; Dai, S. Y. Determination of aflatoxins in animal feeds by liquid chromatography/tandem mass spectrometry with isotope dilution. *Rapid Commun. Mass Spectrom.* **2011**, *25*, 1222−1230.

(17) Cervino, C.; Asam, S.; Knopp, D.; Rychlik, M.; Niessner, R. Use of isotope-labeled aflatoxins for LC-MS/MS stable isotope dilution analysis of foods. *J. Agric. Food Chem.* **2008**, *56*, 1873−1879.

(18) Plattner, R. D.; Bennett, G. A.; Stubblefield, R. D. Identification of aflatoxins by quadruple mass spectrometry/mass spectrometry. *J.−Assoc. Off. Anal. Chem.* **1984**, *67*, 734−738.

(19) Caudill, S. P.; Schleicher, R. L.; Pirkle, J. L. Multi-rule quality control for the age-related eye disease study. *Stat. Med.* **2008**, *27*, 4094−4106.

(20) Taylor, J. K. *Quality Assurance of Chemical Measurements*; Lewis Publishers: Boca Raton, FL, USA, 1987; pp 79−82.

(21) Alcaide-Molina, M.; Ruiz-Jiménez, J.; Mata-Granados, J. M.; Luque de Castro, M. D. High through-put aflatoxin determination in plant material by automated solid-phase extraction on-line coupled to laser-induced fluorescence screening and determination by liquid chromatography-triple quadrupole mass spectrometry. *J. Chromatogr. A* **2009**, *1216*, 1115−1125.

(22) Delmulle, B.; De Saeger, S.; Adams, A.; De Kimpe, N.; Van Peteghem, C. Development of a liquid chromatography/tandem mass spectrometry method for the simultaneous determination of 16 mycotoxins on cellulose filters and in fungal cultures. *Rapid Commun. Mass Spectrom.* **2006**, *20*, 771−776.

(23) Liu, R.; Jin, Q.; Tao, G.; Shan, L.; Liu, Y.; Wang, X. LC-MS and UPLC-quadrupole time-of-flight MS for identification of photodegradation products of aflatoxin B1. *Chromatographia* **2010**, *71*, 107−112.

(24) AOAC Official Method 966.02-1968 Loss on Drying (Moisture) in Tobacco; AOAC International: Gaithersburg, MD, USA, 1968.

(25) CORESTA Recommended Method 76 Determination of Moisture Content (Oven Volatiles of Smokeless Tobacco Products; Cooperation Centre for Scientific Research Relative to Tobacco (CORESTA): Paris, France, 2014.

(26) AOAC Official Method 991.31-1994 (2002) Aflatoxins in Corn, Raw Peanuts and Peanut Butter; AOAC International: Gaithersburg, MD, USA, 2002.

(27) Kussak, A.; Andersson, B.; Andersson, K. Automated ample clean-up with solid-phase extraction for the determination of aflatoxins in urine by liquid chromatography. *J. Chromatogr., Biomed. Appl.* **1993**, *616*, 235−241.

(28) Richter, P.; Spierto, F. W. Surveillance of smokeless tobacco nicotine, pH, moisture, and unprotonated nicotine content. *Nicotine Tob. Res.* **2003**, *5*, 885−889.

DOI: 10.1021/acs.jafc.5b02622
J. Agric. Food Chem. 2015, 63, 9131−9138

introduced into the market by BioFront Technologies (Tallahassee, FL, USA). The kit claims include targeting a thermally stable antigen, assay specificity, 0.3 ppm sensitivity, and good recovery (>85%) from spiked samples. We were interested in assessing the kit specificity, sensitivity, and robustness. Included in these investigations were (a) laboratory-prepared ingredients and foods, (b) commercially processed and sold foods with declared and undeclared pistachio presence, (c) pistachio seed/flour and pistachio-containing foods/matrices exposed to select food-processing methods in the laboratory, and (d) commercial and laboratory-prepared foods spiked with known amounts of pistachio proteins.

MATERIALS AND METHODS

Materials. Dehulled raw pistachio seeds, food ingredients, and commercially processed foods were purchased from local grocery stores and restaurants and were processed as needed as earlier described in detail by Tiwari et al.[18] The MonoTrace pistachio ELISA kits were purchased from BioFront Technologies (Tallahassee, FL, USA). Sources of chemicals, reagents, supplies, and instruments have been reported earlier.[20]

Methods. *Pistachio Seed Processing.* Dehulled whole pistachio raw seeds were processed as follows.[21]

1. Pressure cooking in a SterileMax benchtop autoclave (Barnstead International, Inc., Dubuque, IA, USA) at 121 °C, 15 psi, for 15 and 30 min. Autoclaved samples were air-dried at room temperature (~25 °C) in a fume hood until constant weight.

2. Blanching in boiling water (94 °C) for 5 and 10 min. The ratio of nut seeds to water was 1:10 w/v. Samples were patted dry on paper towels and further air-dried at room temperature in a fume hood until constant weight.

3. Frying in Crisco vegetable oil at 191 °C for 1 min. Excess oil was allowed to drain completely on paper towels prior to further handling.

4. Microwave heating in a Panasonic microwave oven (Sears, Roebuck and Co., Hoffman Estates, IL, USA) at 50% (500 W) and 100% power (1000 W) for 3 min.

5. Dry roasting at 140 °C for 30 min and at 168 °C for 12 min. Samples were placed in aluminum pans and subjected to roasting in a TempCon oven (American Scientific Products, McGaw Park, IL, USA) previously heated to the desired temperatures and monitored using a thermometer.

Kaju Roll. Kaju roll is a sweet, popular in India, made by rolling a cashew dough sheet around a pistachio dough log. Cashew and pistachio doughs were each prepared separately using two different recipes: (1) Nestlé recipe[22] and (2) laboratory recipe. Doughs were prepared as described below.

1. Nestlé Recipe. For the cashew dough, 60 g of full-fat cashew nut seed flour, 40 g of Nestlé sweetened condensed milk, 1 g of Ziyad ghee (Indian clarified butter), and 1 g of Dabur rose water were manually mixed in a pan with a spatula and heated at medium-low heat [stove temperature = 130 °C, dough temperature = 77 °C, monitored by a Traceable infrared thermometer (VWR International, LLC, Radnor, PA, USA)] for 10 min to form the dough. Subsequently, 3 g of Nestlé nonfat dry milk powder was added to the dough and the dough was allowed to cool to room temperature.

For the pistachio dough, 60 g of full-fat pistachio seed flour, 40 g of Nestlé sweetened condensed milk, 1 g of Ziyad ghee, 1 g of McCormick cardamom, and 0.5 g of McCormick green food coloring (FD&C Yellow 5 and Blue 1) were manually mixed in a pan with a spatula and heated at medium-low heat for 10 min to form the dough. Subsequently, 3 g of Nestlé nonfat dry milk was added to the dough and the dough was allowed to cool to room temperature.

2. Laboratory Recipe. For the cashew dough, 50 g of cashew full-fat flour and 60 g of Publix confectionery sugar were ground in an Osterizer blender (speed setting "grind"; Galaxy model 869-18R, Jaden Consumer Solutions, Boca Raton, FL, USA) for 1 min followed by the addition of 1 g of Dabur rose water and 8 g of water. The mixture was manually kneaded into dough.

For the pistachio dough, 50 g of pistachio full-fat flour, 60 g of Publix confectionery sugar, and 1 g of McCormick cardamom were ground in an Osterizer blender (speed setting "grind") for 1 min followed by the addition of 0.5 g of McCormick green food coloring and 8 g of water. The mixture was manually kneaded into dough.

To prepare the rolls, 10 g of cashew dough was rolled into a flat sheet (~3 mm thick) and cut into a rectangular shape, whereas pistachio dough (0.1, 0.6, and 1.2 g) was formed into log shapes (2−10 mm diameter) and placed in the center of the cashew sheets. The cashew sheets were tightly rolled around the pistachio logs to form the kaju rolls. Pistachio contents in rolls prepared according to recipe 1 (Nestlé recipe) were 0, 0.6, 3.4, and 6.3% (w/w) and in rolls prepared according to recipe 2 (laboratory recipe) were 0, 0.4, 2.4, and 4.5% (w/w).

Corn Flakes. Forty-five grams of Publix sweet corn kernels were ground in an Osterizer blender (speed setting "grind") for 1 min with 50 mL of distilled water and baked at 120 °C in a KitchenAid Architect II oven (KitchenAid, Benton Harbor, MI, USA) until dry. The moisture content of the sweet corn was 78% as determined according to AOAC Official Method 925.40.[23] The final yield of the corn flakes was approximately 10 g. Pistachio full-fat flour was incurred at 10, 50, 100, 5000, 10000, 20000, and 50000 ppm levels prior to baking.

Sponge Cakes. Seventeen grams of egg was beaten by a KitchenAid hand mixer (speed setting "1") for 4 min. Thirty-four grams of Publix sugar was added, and the mixture was beaten for another 4−5 min until light and fluffy. Twenty-three grams of Publix all-purpose flour, 0.7 g of Argo baking powder, and 0.2 g of Publix salt were sifted into the mixture, and 0.4 g of McCormick vanilla extract was added. In a sauce pan, 20 g of Publix whole milk and 4.7 g of Publix butter were heated on low heat until the butter was melted. The milk and butter were combined with the batter and baked in greased cake pans at 163 °C in a KitchenAid Architect II oven for 30 min. Pistachio full-fat flour was incurred at 10, 50, 100, 5000, 10000, 20000, and 50000 ppm levels prior to baking.

Sugar Cookies. Twenty-three grams of Publix butter was creamed with 30 g of Publix sugar using a KitchenAid hand mixer (speed setting "1") and were then mixed with 6 g of egg and 0.3 g of McCormick vanilla extract. Subsequently, 40 g of Publix all-purpose flour, 0.5 g of Arm & Hammer baking soda, and 0.2 g of Argo baking powder were sifted into the batter and blended to form the dough. The dough was rolled to 0.69 cm thickness and baked at 190 °C in a KitchenAid Architect II oven for 12 min. Pistachio full-fat flour was incurred at 10, 50, 100, 5000, 10000, 20000, and 50000 ppm levels prior to baking.

Flour Preparation. All high moisture content ingredients and foods were dried as described earlier.[17,18] Specifically, heat-sensitive foods (e.g., ice cream, cheese) were freeze-dried (VirTis BenchTop K freeze-dryer, SP Scientific, Warminster, PA, USA), whereas fresh produce (e.g., fruits and vegetables) and high-sugar dried fruit (e.g., raisins, dates) were oven-dried for 24 h at 50−60 °C. All seeds, food ingredients, and processed foods, in their dried from, were ground in an Osterizer blender (speed setting "grind"; Galaxy model 869-18R, Jaden Consumer Solutions, Boca Raton, FL, USA) to obtain uniform flours. As needed, the flours were defatted for 8 h using a Soxhlet apparatus (Thermo Fisher Scientific Inc., Waltham, MA, USA) with petroleum ether (boiling point range of 38.2−54.3 °C) as the solvent (flour-to-solvent ratio of 1:10 w/v). After overnight drying in a fume hood at room temperature, the powders were passed through a 40 mesh sieve and then stored in screw-capped plastic bottles at −20 °C until further use.

Protein Extract Preparation. Protein extracts were prepared as per the ELISA kit instructions. Briefly, sample flours (100 mg each for pistachio and other food ingredients, 1 g each for commercially prepared foods, pistachio-spiked samples, and samples incurred with ≥5000 ppm of pistachio) were extracted in extraction buffer (provided with the ELISA kit; flour-to-solvent ratio of 1:10 w/v) at 60 °C for 10 min with vigorous manual vortex mixing every 2 min. For corn flakes, sponge cakes, and sugar cookies incurred with ≤100 ppm of pistachio, the entire batch of each sample was blended in an Osterizer blender (speed setting "grind") with borate saline buffer (BSB, 0.1 M boric acid, 0.025 M sodium borate, 0.075 M sodium chloride, pH 8.45; sample-to-solvent ratio of 1:10 w/v) at room temperature for 1 min and then magnetically stirred at room temperature for 1 h. The extracts were subsequently centrifuged at 2000*g* (Centrific 225 centrifuge, Thermo Fisher Scientific

DOI: 10.1021/acs.jafc.5b03066
J. Agric. Food Chem. 2015, 63, 9139−9149

Table 1. Food Ingredients (100000 ppm) Tested for Assessing Cross-Reactivity of the MonoTrace Pistachio ELISA Kit[a]

food additives	mustard	lupine	tomato	oat	dairy products
natural pigment	nutmeg	moth bean	turnip green	quinoa	cheese
annatto	onion powder	mung bean	fruits	rice	American cheese
grape seed tannin	oregano	navy bean	apple	rye	cottage cheese
grape skin tannin	parsley	pea	apricot	sorghum	mozzarella cheese
synthetic colorant	poppy seed	pinto bean	banana	wild rice	Parmesan cheese
blue No. 1	table salt	tepary bean	blueberry	breakfast cereal	Romano cheese
green No. 3	turmeric	toor bean	cherry	raisin bran mix	Swiss cheese
red No. 40	vanilla	val bean	coconut	corn flakes	milk product
yellow No. 5	plant foods	oilseeds	cranberry	multigrain cereal	non fat dry milk
thickeners	tree nut	flax seed	date	flour	vanilla ice cream
corn starch	almond	Inca peanut	fig	all purpose flour	yogurt
gum Arabic	Brazil nut	pumpkin seed	kiwifruit	whole wheat flour	animal based foods
gum xanthan	cashew	Spanish peanut	mango peel	fungi	poultry
pectin	charoli	Virginia peanut	mango pulp	mushroom	chicken
spices/seasonings	hazelnut	sesame seed	mango seed	confectionery/bakery	egg white
allspices	macadamia	soybean	orange	dark chocolate	egg yolk
anise seed	pecan	sunflower seed	papaya	milk chocolate	turkey
bay leaf	pine nut	vegetables	peach	white chocolate	meat
black pepper	walnut	asparagus	pear	baking powder	beef
black salt	dry beans	broccoli	pineapple	baking soda	lamb
cardamom	black bean	brussel sprout	plum	brown sugar	pork
cayenne pepper	black-eyed pea	cabbage	raisin	sugar	seafood
cinnamon	black gram	carrot	strawberry	corn syrup	crab
clove	chickpea	cauliflower	grains	honey	flounder
coriander	red kidney bean	collard green	amaranth	jaggery	oyster
cumin	fava bean	green pepper	barley	beverages	salmon
dill seed	garbanzo bean	green salad mix	buckwheat	black tea	scallop
garlic powder	large lima bean	potato	corn	green tea	shrimp
ginger	lentil	spinach	millet	cocoa	tuna

[a]Food matrix from a single batch was weighed in triplicate, and each sample was extracted using buffer provided in the kit. No cross-reactivity was detected (i.e., signal equivalent to <0.09 ppm pistachio).

Inc., Waltham, MA, USA) for 10 min at room temperature. Aliquots of the supernatant were analyzed (supernatants were stored at 4 °C prior to analysis) within 48 h of preparation, and the remainder was stored in plastic microcentrifuge tubes (1.5 mL capacity) at −20 °C until further use.

To compare the antigen extraction efficiency of different buffers under different conditions, full-fat pistachio flours were extracted (flour-to-solvent ratio of 1:10 w/v) in BioFront extraction buffer (EXB; containing 4.51 ± 0.37 mg protein/mL, pH 8.52 ± 0.01), borate saline buffer (BSB; 0.1 M boric acid, 0.025 M sodium borate, 0.075 M sodium chloride, pH 8.45), phosphate-buffered saline (PBS; 0.1 M sodium phosphate, 0.9% w/v sodium chloride, pH 7.20), and sodium bicarbonate buffer (SBC; 0.1 M sodium bicarbonate, 0.9% w/v sodium chloride, pH 9.60) at two different conditions: (1) at room temperature for 1 h with constant vortex mixing or (2) at 60 °C for 10 min with vigorous manual vortex mixing every 2 min. The extracts were centrifuged at 2000*g* for 10 min at room temperature, and the supernatants were collected for soluble protein determination and ELISA.

Osborne Fractionation. Pistachio protein fractions were prepared according to the Osborne method[24] as described in detail by Sze-Tao and Sathe.[25] Briefly, 5 g of defatted pistachio flour was extracted sequentially with 100 mL of 1.0 M NaCl (albumin and globulin), 70% aqueous ethanol (prolamin), and 0.1 M NaOH (alkaline glutelin) for 1 h at room temperature with constant magnetic stirring. The slurry was centrifuged at 12600*g* (J2-21 centrifuge, Beckman Coulter, Inc., Brea, CA, USA) and 4 °C for 15 min following each extraction, and the supernatant was vacuum filtered using Whatman no. 4 filter paper. Residues from centrifugation and filtration were used for the next extraction, whereas filtrates were dialyzed against distilled water for 24 h with six water changes (4 L each). After dialysis, the albumin and globulin fraction (1 M NaCl extract) was centrifuged (12600*g*, 4 °C, 15 min), and the precipitate (globulin) and supernatant (albumin) were separately freeze-dried. Prolamin and glutelin fractions were lyophilized directly after dialysis. All freeze-dried protein fractions were stored in airtight plastic bottles at −20 °C until further analysis.

Protein Determination. The Bradford method[26] using bovine serum albumin (BSA) fraction V (Sigma Chemical Co., St. Louis, MO, USA) as the standard protein (0−600 μg/mL) was used for soluble protein determination.

ELISA Procedure. Ninety-six-well microtiter plates (coated with murine antipistachio mAb and blocked), sample diluent, ready-to-use pistachio standards (0, 0.5, 2, 6, 18, and 36 ppm pistachio), washing buffer, murine anti-pistachio mAb conjugated with horseradish peroxidase (HRP), 3,3′,5,5′-tetramethylbenzidine (TMB) substrate solution, and HRP quench solution were provided in the ELISA kits. Sample extracts were suitably diluted in sample diluent. Two hundred microliters of diluted samples and ready-to-use standards were added to each well and incubated at room temperature for 30 min. The plates were washed three times with washing buffer and blot dried. After washing, 100 μL of HRP-conjugated detection mAb was added to each well, incubated in the dark at room temperature for 30 min, and again washed three times with washing buffer. Subsequently, 100 μL of TMB substrate solution was added and incubated in the dark at room temperature for 10 min. The reaction was stopped by adding 100 μL of quench solution to each well and mixed by gentle pipetting. The absorbance was read at 450 nm by a BioTek PowerWave 200 microplate scanning spectrophotometer (Winooski, VT, USA).

ELISA Validation. 1. Limit of Detection (LOD). The LOD is defined as the minimum concentration of analyte that can be reliably distinguished from background. The LOD of the ELISA was calculated using the following two commonly applied methods. $LOD_1 = 3\sigma/S$, where σ is the standard deviation of the blank (mean) and S is the slope of the standard curve.[27] $LOD_2 = M + 3\sigma$, where M is the mean absorbance of the blank and σ is the standard deviation of the blank.[28] The resulting absorbance of LOD_2 was converted to concentration using the standard curve.

2. Limit of Quantification (LOQ). The LOQ is defined as the minimum concentration of analyte that can be quantitatively

DOI: 10.1021/acs.jafc.5b03066
J. Agric. Food Chem. 2015, 63, 9139−9149

determined with suitable precision and accuracy. The LOQ of the ELISA was calculated using the following formulas. $LOQ_1 = 10\sigma/S$, where σ is the standard deviation of the blank (mean) and S is the slope of the regression line for the linear range.[27] $LOQ_2 = M + 10\sigma$, where M is the mean absorbance of the blank and σ is the standard deviation of the blank.[29] The resulting absorbance of LOQ_2 was converted to concentration using the standard curve.

3. Linear Detection Range. Two hundred microliters of pistachio full-fat flour protein extract (8000 ng pistachio protein/mL diluent) was added to the top row of the horizontally oriented (i.e., 8 rows ×12 columns/row) 96-well microtiter plate, and three times serially diluted samples were processed down the plate. The ELISA was performed as described earlier. A four-parameter curve was generated by KC4 software (version 2.0, Bio-Tek Instruments, Inc., Winooski, VT, USA) to determine the linear detection range and the concentration for 50% maximum signal in the assay.

4. Specificity and Cross-Reactivity. Assay specificity is defined as the ability of an antibody to produce a measurable response only for the analyte of interest (i.e., pistachio protein). Cross-reactivity is a measurement of antibody response to substances other than the analyte.[30] A total of 156 commonly used foods and food ingredients at 100,000 ppm each were tested for cross-reactivity (Table 1). Samples with signal equivalent to <0.09 ppm of pistachio were not considered cross-reactive.

5. Reproducibility. Reproducibility, also called precision, describes the ability of the assay to duplicate results in repeat determinations. Reproducibility was determined by the percent coefficient of variation (%CV) between replicates determined in the same assay (intra-assay variability) and in different assays (inter-assay variability). Variation of six pistachio standards was measured, each with 3 replicates within the plate for intra-assay variability and 12 replicates in different plates for inter-assay variability. The %CV was calculated by using the formula

$$\mathrm{CV}\ (\%) = (\sigma/X) \times 100\%$$

where σ is the standard deviation and X is the mean of the replicate determinations.[20]

6. Uncertainty Estimation. Measurement uncertainty of the validated BioFront MonoTrace pistachio ELISA was estimated at each concentration level of the pistachio standards. The bias uncertainty (u_δ), the combined uncertainty (u_c) of bias and intralaboratory reproducibility, the expanded uncertainty (U), and the relative uncertainty (u_r) were calculated using the following formulas.[31,32]

$$S_R^2 = S_W^2 + S_B^2$$

where S_R^2, S_W^2, and S_B^2 are the intralaboratory reproducibility variance, intra-assay variance, and inter-assay variance, respectively.

$$S_W^2 = \frac{\sum_{i=1}^{p}\sum_{j=1}^{n}(x_{ij} - \overline{x}_i)^2}{p(n-1)} \text{ with } \overline{x}_i = \frac{\sum_{j=1}^{n} x_{ij}}{n}$$

$$S_B^2 = \frac{\sum_{i=1}^{p}(\overline{x}_i - \overline{x})^2}{p-1} - \frac{S_W^2}{n} \text{ with } \overline{x} = \frac{\sum_{i=1}^{p}\sum_{j=1}^{n} x_{ij}}{pn}$$

where x is the analytical result (ppm pistachio), p is the number of kits analyzed, and n is the number of replications within a kit.

$$u_\delta = \sqrt{\frac{S_R^2\left(1 - \gamma + \frac{\gamma}{n}\right)}{p}} \text{ with } \gamma = \frac{S_W^2}{S_R^2} \qquad u_c = \sqrt{S_R^2 + u_\delta^2}$$

$$U = k \times u_c \qquad u_r = \frac{U}{\text{tested concentration}} \times 100\%$$

A coverage factor of $k = 2$ was used to define a 95% confidence interval (assuming the values are normally distributed) where the unknown true value is believed to lie.[31]

7. Recovery. Diluted pistachio soluble protein extracts were spiked to finely ground cereal, corn flake, cookie, dark chocolate, milk chocolate, white chocolate, ice cream, and sponge cake matrices to reach a spiking level equivalent to 10 ppm of pistachio flour.

Pistachio-incurred corn flakes, sponge cakes, and sugar cookies were prepared as described earlier. Pistachio full-fat flours were incurred at 10, 50, 100, 5000, 10000, 20000, and 50000 ppm levels prior to food processing and were processed along with the other ingredients.

The spiked and incurred matrices were then subjected to protein extraction as described under Protein Extract Preparation. The pistachio content was measured and the percent recovery was determined using the following formula:

$$\text{recovery}\ (\%) = (\text{measured pistachio concentration} / \text{predicted pistachio concentration}) \times 100\%$$

8. Assay Applicability and Robustness. Thermally processed pistachio samples (described earlier), commercially sold, matched samples (with and without pistachio), and laboratory-prepared samples were analyzed to determine if the assay can detect processed pistachios and if food matrices interfere with the assay. Each commercial food analyzed was obtained in a single batch to ensure sample homogeneity. Protein extracts of processed pistachios were normalized to 125 ng pistachio protein/mL extraction buffer. The absorbance of the processed samples was compared with the absorbance of the reference. The relative immunoreactivity was calculated as follows:

$$\text{relative immunoreactivity}\ (\%) = [(\mathrm{OD}_{\mathrm{sample}} - \mathrm{OD}_{\mathrm{blank}})/(\mathrm{OD}_{\mathrm{reference}} - \mathrm{OD}_{\mathrm{blank}})] \times 100\%$$

where $\mathrm{OD}_{\mathrm{reference}}$ = OD generated by 25 ng of unprocessed pistachio protein used as the reference and $\mathrm{OD}_{\mathrm{sample}}$ = OD generated by 25 ng of protein from the sample assayed.

Sodium Dodecyl Sulfate–Polyacrylamide Gel Electrophoresis (SDS-PAGE). SDS-PAGE was performed as described by Fling and Gregerson.[33] BSB-solubilized tree nut and legume seed proteins as well as pistachio protein fractions were heat denatured in SDS-PAGE sample buffer (50 mM Tris-HCl, 1% w/v SDS, 0.01% w/v bromophenol blue, and 30% v/v glycerol, pH 6.8) with and without 2% v/v β-mercaptoethanol for 10 min by placing the microcentrifuge tubes containing these samples in a boiling water bath (100 °C). A 4% stacking gel with either a 12% separating gel (6 μg protein/lane) or an 8–25% gradient gel (20 μg protein/lane) was used. Protein samples and molecular mass markers were loaded on the stacking gel and electrophoresed at a constant current of 8 mA/gel (12 h) followed by 30 mA/gel (4–5 h) until the tracking dye reached the separating gel edge.

Western Blot. Following SDS-PAGE, the proteins were transferred onto a 0.22 μm nitrocellulose membrane as described by Towbin et al.[34] The transferred polypeptides were visualized by staining with (0.1% w/v) Ponceau S solution prepared using distilled deionized water. The unbound sites on the nitrocellulose membrane were blocked with 5% (w/v) nonfat dry milk in Tris-buffered saline–Tween 20 (TBS-T, 10 mM Tris, 0.9% w/v sodium chloride, 0.05% v/v Tween 20, pH 7.6) at room temperature for 1 h. The membranes were subsequently washed with three changes of TBS-T, 5 min each. The membranes were then incubated with the HRP-conjugated detection antibody provided in the MonoTrace pistachio ELISA kit (1:10 or 1:50 v/v dilution in TBS-T) overnight at 4 °C on a Lab-line thermal rocker (speed 2; Thermo Fisher Scientific Inc., Waltham, MA, USA). After three washings with TBS-T for 15 min each, the membranes were incubated with HRP-labeled goat anti-mouse IgG polyclonal antibody (pAb, 1:10000 v/v dilution in TBS-T) for 1 h at room temperature on a rocker. The membranes were washed again as described above and incubated with 1.3 mM luminol, 0.2 mM *p*-coumaric acid, and 0.01% (v/v) hydrogen peroxide in 0.1 M Tris-HCl buffer (pH 8.5) for 5 min. The membranes were then exposed (60 s) to an X-ray film for autoradiographic visualization. The molecular mass of recognized polypeptide was determined by the ChemiDoc XRS + Image System (Bio-Rad Laboratories, Inc., Hercules, CA, USA).

Statistics. All ELISA experiments were performed at least in triplicate on a single sample, and data are reported as the mean ± standard deviation of the mean. One-way ANOVA was performed with SPSS software (19.0, SPSS Inc., Chicago, IL, USA) to compare means for

DOI: 10.1021/acs.jafc.5b03066
J. Agric. Food Chem. 2015, 63, 9139–9149

difference. Post hoc analysis was performed using Fisher's least significant difference (LSD) at $P \leq 0.05$.

RESULTS AND DISCUSSION

Assay Sensitivity. The MonoTrace pistachio ELISA kit registered a low background absorbance (0.073 ± 0.009). The LOD_1 (0.09 ppm) and LOD_2 (0.19 ppm) for soluble pistachio proteins suggested the assay is sensitive (Table 2). The assay sensitivity is comparable to the reported sensitivity by Romer (0.13 ppm) and Bio-Check (0.2 ppm) ELISA kits and the recently reported real-time PCR assay sensitivity (0.1 ppm).[13] Compared to the Genon ELISA kit (10 ppm) and the PCR methods reported by Brežná et al.[35] (4 ppm) and Barbieri and Frigeri[36] (100 ppm), the MonoTrace pistachio ELISA kit assay exhibited better sensitivity. The LOQ_1 (0.30 ppm) and LOQ_2 (0.38 ppm) of the MonoTrace pistachio kit are comparable with the LOQ of a previously reported pistachio ELISA (<1 ppm).[37] The kit linear detection range of 0.5−36 ppm (linear regression $R > 0.99$) is similar to the linear range (1−40 ppm) for the Romer kit. The concentration of pistachio soluble protein that registered 50% of the maximum signal is 152 ng/mL (7.9 ppm) (Figure 1), comparable to the value (~137 ng/mL) reported by Lim.[37]

The sensitivity of an assay is considered sufficient when it can reliably detect the minimum dose of an allergen capable of eliciting a clinically measurable response. Many attempts have been made to determine the allergen threshold that causes an adverse reaction. The U.S. Food and Drug Administration established a Threshold Working Group in 2005 but failed to establish the threshold for the major food allergens due to insufficient data at the time.[38] In 2010, the Australian Allergen Bureau first introduced defined allergen threshold levels for precautionary labeling. In their most recent update, the eliciting doses (EDp, dose of allergen at which p% of the allergic population would react) for an allergic reaction in 1% of the population estimated for hazelnut and peanut were 0.2 and 0.1 mg of protein, respectively, and the reference dose for cashew (lower 95% confidence interval of ED_{05}) was 2.0 mg of protein.[39,40] The reference dose for most allergenic foods ranged from 0.03 mg of protein (ED_{01} for egg) to 10 mg of protein (lower 95% confidence interval of ED_{05} for shrimp). Currently, no threshold data are available for pistachio and other tree nuts, and thus the tested kit detection range 0.5−36 ppm must be interpreted with caution.

Table 2. Summary of the MonoTrace Pistachio ELISA Kit for 50% Maximum Signal Concentration, Linear Detection Range, Limit of Detection (LOD), and Limit of Quantification (LOQ)[a]

	ppm pistacho full fat flour	ng pistachio protein/mL
50% max signal concentration (n = 3)	7.9 ± 0.7	151.9 ± 14.7
linear detection range (n = 3)	0.5−36 (R > 0.99)	9.5−684 (R > 0.99)
LOD_1[b] (n = 3)	0.09 ± 0.02	1.73 ± 0.32
LOD_2[c] (n = 3)	0.19 ± 0.07	5.76 ± 1.07
LOQ_1[d] (n = 3)	0.30 ± 0.06	3.64 ± 1.36
LOQ_2[e] (n = 3)	0.38 ± 0.13	7.20 ± 2.40

[a]Data are expressed as mean ± SD. The 50% maximum signal concentration and linear detection range were determined using protein extracts from three different batches of pistachios and repeated in two different kits. The limits of detection and quantification were determined in three different kits using pistachio standards provided in those kits. [b]Limit of detection 1 (LOD_1) was determined on the basis of the standard deviation of the blank (σ) and the slope of the standard curve (S) according to the formula $LOD_1 = 3\sigma/S$. [c]Limit of detection 2 (LOD_2) was determined on the basis of the mean absorbance (M) and standard deviation of the blank (σ) according to the formula $LOD_2 = M + 3\sigma$. [d]Limit of quantification 1 (LOQ_1) was determined on the basis of the standard deviation of the blank (σ) and the slope of the standard curve (S) according to the formula $LOQ_1 = 10\sigma/S$. [e]Limit of quantification 2 (LOQ_2) was determined based on the mean absorbance (M) and standard deviation of the blank (σ) according to the formula $LOQ_2 = M + 10\sigma$.

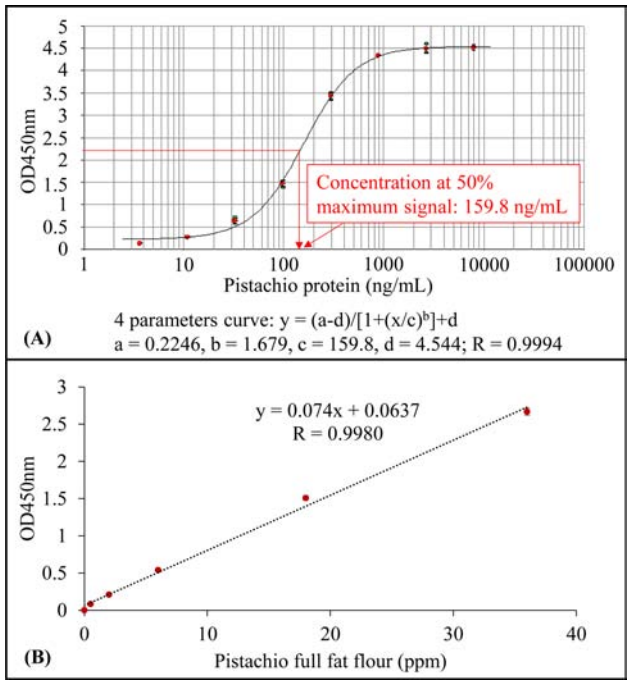

Figure 1. Typical MonoTrace pistachio ELISA kit four-parameter curve (A) and linear standard curve using pistachio protein standards (0, 0.5, 2, 6, 18, and 36 ppm pistachio) provided within the kit (B). The standard curves were repeated three times within a kit.

Assay Efficiency. The MonoTrace pistachio ELISA was rapid with an assay time of approximately 1.5 h (extraction, 10 min; incubation with antigen, 30 min; incubation with detection antibody, 30 min; and color development, 10 min). The updated version of the MonoTrace Pistachio ELISA claims improvement in the assay efficiency and short incubations with antigen/food sample extract, detection antibody, and substrate (10 min each). To determine if the antigen extraction was sufficient, pistachio full-fat flours were extracted in four different buffers (EXB, BSB, PBS, and SBC) under two separate conditions (60 °C, 10 min and room temperature, 1 h). Under both conditions, the kit-provided buffer, EXB, yielded the highest soluble protein extractability and antigen recovery (Table 3). Protein extractions by EXB at 60 °C for 10 min and at room temperature for 1 h were equivalent (P > 0.05).

Assay Specificity. Individuals allergic to one tree nut often exhibit IgE reactivity to other edible nut seed proteins.[41] Cross-reactive tree nuts are usually found in the same botanical family. Strong cross-reactivities have been documented in nut seed proteins of (a) pecan and walnut species of the Juglandaceae family[42−46] and (b) cashew and pistachio of the Anacardiaceae family.[5,43,44,47−53] Cross-reactivity is likely due to the homologous linear amino acid sequence, three-dimensional structural similarity, or both, of different nut seed proteins. Several murine

DOI: 10.1021/acs.jafc.5b03066
J. Agric. Food Chem. 2015, 63, 9139−9149

Table 3. Antigen Extraction Efficiency of Select Buffers under Different Extraction Conditions[a]

condition	extraction buffer	soluble protein (mg/100 mg pistachio full-fat flour)	antigen recovery (%)
60 °C, 10 min	EXB (pH 8.52)[b]	19.0 ± 2.0	101.3 ± 1.8
	BSB (pH 8.45)[c]	15.8 ± 2.1	88.4 ± 2.5
	PBS (pH 7.20)[d]	15.4 ± 1.0	84.1 ± 2.7
	SBC (pH 9.60)[e]	20.4 ± 1.1	98.4 ± 2.1
room temperautre, 1 h	EXB (pH 8.52)	19.2 ± 1.9	104.5 ± 8.6
	BSB (pH 8.45)	17.0 ± 1.2	92.2 ± 2.6
	PBS (pH 7.20)	14.3 ± 1.5	83.0 ± 1.5
	SBC (pH 9.60)	17.2 ± 0.5	95.3 ± 4.0
LSD ($P \leq 0.05$, $n = 3$)		2.61	6.70

[a]Samples were extracted from three different batches of pistachios and tested using a single kit. Data are expressed as mean ± SD ($n = 3$). [b]EXB, BioFront MonoTrace pistachio ELISA kit extraction buffer (pH 8.52 ± 0.01). [c]BSB, borate saline buffer (0.1 M boric acid, 0.025 M sodium borate, 0.075 M NaCl, pH 8.45). [d]PBS, phosphate-buffered saline (0.1 M sodium phosphate, 0.9% w/v NaCl, pH 7.20). [e]SBC, sodium bicarbonate buffer (0.1 M sodium bicarbonate, 0.9% w/v NaCl, pH 9.60).

mAbs raised against cashew Ana o 1 have been reported to recognize the recombinant Pis v 3 in a dot blot assay, indicating that the antibodies are likely targeting the conserved regions of the Anacardiaceae seed proteins.[52] Pistachio seed proteins are also found to be cross-reactive with protein(s) from mango seeds[48] and with proteins from seeds of taxonomically unrelated botanical families such as sunflower, peanut, and walnut.[47] A previously observed cross-reactivity of pistachio ELISA (at 4 ppm level) using sheep antisera as the capture reagent and rabbit antisera as detection reagent with cashew nut seed proteins was therefore not unexpected.[37] Recently, in a multiplex ELISA simultaneously detecting 14 different food allergens and gluten, cross-reactivity of pistachio detection assay with Brazil nut, cashew, and hazelnut seed proteins has also been reported.[54] The MonoTrace pistachio ELISA kit, under the test conditions, is specific and did not display cross-reactivity (signal equivalent to <0.09 ppm of pistachio) with 156 tested commonly used food ingredients at 100,000 ppm including certain Anacardiaceae seeds such as cashew (*Anacardium occidentale*), charoli (*Buchanania lanzan*), and mango (*Mangifera indica*) peel, pulp, and seed (Table 1). The specificity of the kit is likely due to the use of mAbs.

To partially test the aforementioned assumption, the cross-reactivity of the kit detection murine mAb with select tree nut and legume seed proteins was assessed using Western blot. The detection mAb (1:10 v/v dilution in TBS-T) was found to be reactive with the 51 kDa polypeptide of cashew and the 55 kDa polypeptide of charoli in the absence of β-mercaptoethanol (Figure 2). In the presence of β-mercaptoethanol, the detection mAb recognized the 19 and 21 kDa polypeptides in cashew and the 23 kDa polypeptide in charoli. The discrepancy between the ELISA kit results (no cross-reactivity with cashew and charoli)

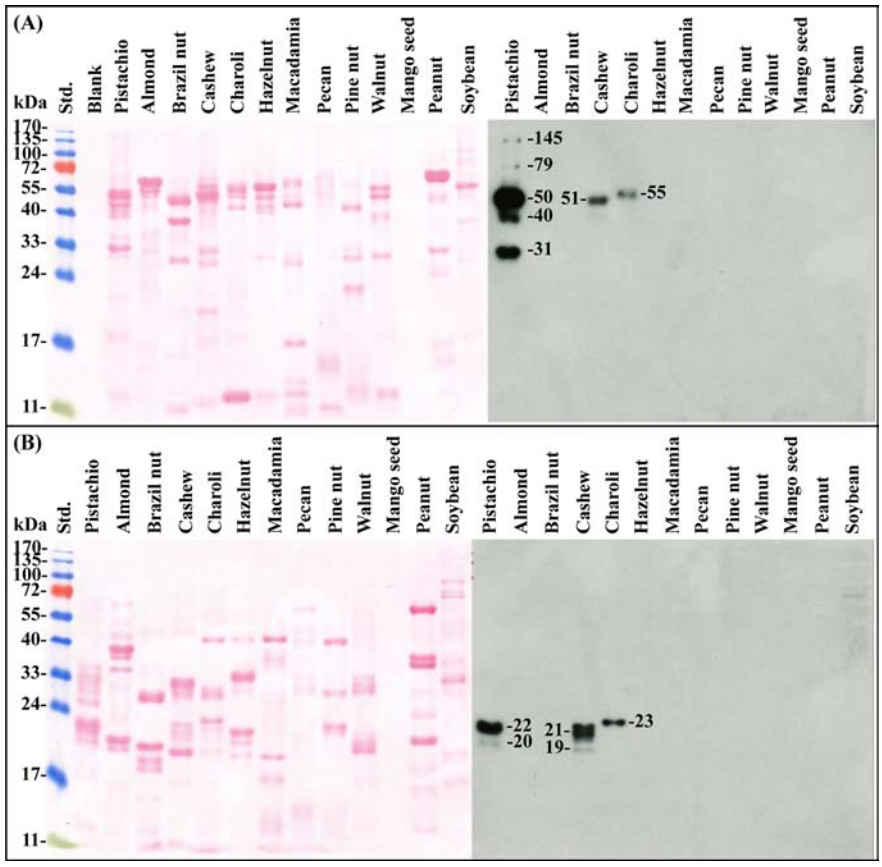

Figure 2. SDS-PAGE pattern (Ponceau S staining) and Western blot of the soluble protein extracts (6 μg/lane) from select tree nut and legume seeds in the absence (A) and presence (B) of 2% (v/v) β-mercaptoethanol. MonoTrace murine anti-pistachio mAb (1:10 v/v dilution in TBS-T) was used as the detection antibody, and goat anti-mouse IgG pAb−HRP (1:10000 v/v dilution in TBS-T) was used as the secondary antibody in the Western blot.

DOI: 10.1021/acs.jafc.5b03066
J. Agric. Food Chem. 2015, 63, 9139−9149

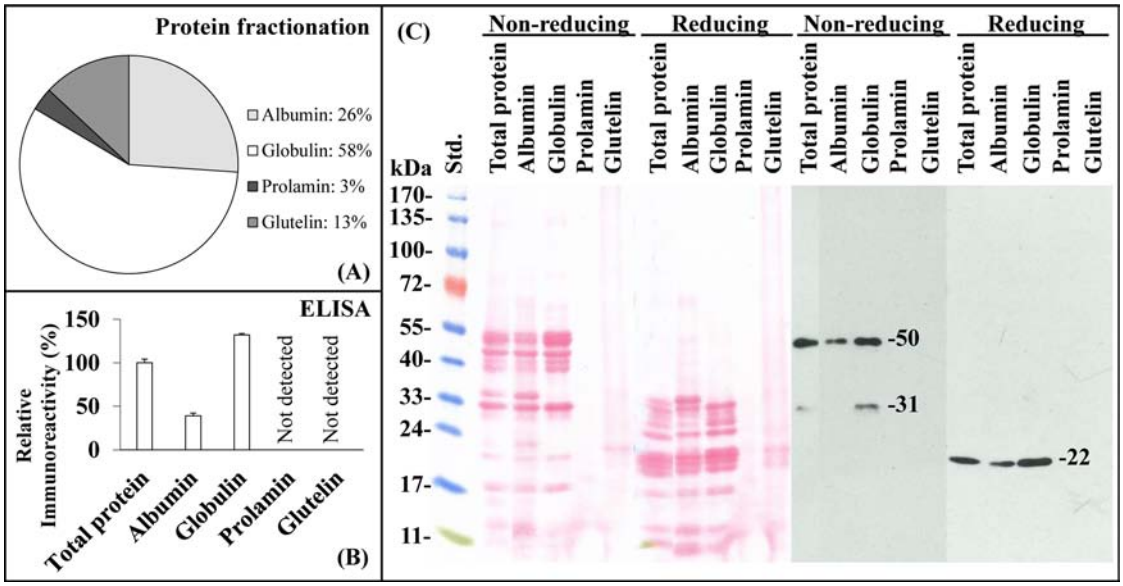

Figure 3. Pistachio protein fractionations (A) and their immunoreactivity assessed by MonoTrace pistachio ELISA kit (B) and Western blot (C). Protein content in ELISA and Western blot was 30 ng/well and 20 μg/lane, respectively. MonoTrace murine anti-pistachio mAb (1:50 v/v dilution in TBS-T) was used as the detection antibody, and goat anti-mouse IgG pAb-HRP (1:10000 v/v dilution in TBS-T) was used as the secondary antibody in the Western blot. Pistachio protein fractions were prepared using three different batches of pistachios. Fractions from all three batches were tested by ELISA, and one batch was tested by Western blot.

Table 4. Intra- and Inter-assay Variability and Uncertainty Estimation for the MonoTrace Pistachio ELISA Kit Using the 0.5−36 ppm Pistachio Standards[a]

					uncertainty[b]			
ppm	intra-assay %CV	inter-assay %CV	back-calculated concentration (ppm)	recovery (%)	u_δ (ppm)	u_c (ppm)	U (ppm)	u_r (%)
0.5	1.3−3.7	24.0	0.4	79.9	0.09	0.22	0.43	87
2	1.4−8.4	15.9	2.1	102.6	0.13	0.32	0.64	32
6	1.2−3.9	19.5	6.6	110.4	0.20	0.48	0.95	16
18	1.2−3.5	14.9	18.7	103.9	0.57	1.35	2.70	15
36	0.5−1.7	12.3	34.8	96.7	0.18	0.50	1.00	3

[a]Pistachio standards from four different kits were tested three times in each kit. [b]u_δ = bias uncertainty, u_c = combined uncertainty, U = expanded uncertainty, and u_r = relative uncertainty.

and Western blot results was likely due to (1) the *capture* antibody not being reactive to cashew and charoli and/or (2) SDS-induced protein unfolding in the Western blot exposing buried epitopes that were inaccessible to the ELISA detection antibody in cashew and charoli native proteins.

Identification of the Target Antigen. As observed in Western blot (Figure 2), the detection mAb (1:10 v/v dilution in TBS-T) of the MonoTrace pistachio ELISA kit recognized three pistachio polypeptides (50, 40, and 31 kDa) in the absence of β-mercaptoethanol. Two polypeptides, molecular masses of 79 and 145 kDa, were weakly recognized. Under reducing condition, the detection mAb exhibited a strong reactivity to a 22 kDa polypeptide and a weaker reaction to a 20 kDa polypeptide.

At 1:50 v/v dilution, the detection mAb recognized the 50 and 31 kDa polypeptides under nonreducing conditions and the 22 kDa polypeptide under reducing conditions (Figure 3). The globulin protein fraction had more intense bands than the total protein extract, indicating the globulins were mainly responsible for the reaction. The detection mAb recognized the albumin protein fraction, suggesting the target antigen was partially soluble in water. Shokraii and Esen have noted the presence of common pistachio globulin polypeptide(s) in the albumin fraction.[55] No polypeptide was recognized by the detection mAb in the prolamin and glutelin fractions under both reducing and nonreducing conditions. The ELISA and Western blot results were consistent. Compared to the total protein extract immunoreactivity designated 100%, the albumins, globulins, prolamins, and glutelins, respectively, registered 39.0, 132, 0, and 0% immunoreactivity.

On the basis of the solubility profile and Western blot, the target antigen of the detection antibody is likely to be the small/basic subunit of the pistachio 11S globulin. The electrophoretic pattern of the recognized pistachio polypeptides under non-reducing conditions was similar to those of purified soybean 11S glycinin, namely, two major bands at 57 and 28 kDa and two light bands at 85 and >100 kDa.[56] So far, four distinct pistachio 11S globulin protein sequences have been reported with predicted molecular masses ranging from 53.2 to 56.5 kDa.[57−59] Among pistachio 11S acidic (35−40 kDa) and basic (22−27 kDa) subunits, the latter have been reported to exhibit a stronger reactivity, compared to the 11S acidic subunit and 2S albumin polypeptides, tested with pooled tree nut-allergic human sera.[51] Therefore, pistachio 11S globulin basic subunit may serve as a good antigen for producing antibodies targeting human allergy relevant epitopes.

Assay Reproducibility, Uncertainty, and Recovery. The intra- and inter-assay variability of the MonoTrace pistachio ELISA kit was <24% CV, demonstrating that the assay is

DOI: 10.1021/acs.jafc.5b03066
J. Agric. Food Chem. 2015, 63, 9139−9149

reproducible (Table 4). Measurement uncertainties of the assay were estimated using the pistachio standards (Table 4). Among the uncertainties, u_δ estimates the uncertainty of the bias (the difference between the ELISA result and the true pistachio concentration), u_c combines the uncertainties of the bias and the reproducibility, U defines an interval about the ELISA result where the true value is confidently believed to lie, and u_r describes the expanded uncertainty in proportion to the corresponding concentration. The relative uncertainty (u_r) had a range of 3−87%, which decreased with increasing concentration. For the 36 ppm of pistachio standard, the unknown true value is located between 35 and 37 ppm with a confidence level of 95%.

Food matrices that may come in contact with pistachio during food manufacturing and processing were tested for their possible assay interference. Previous studies have indicated that certain food matrices may result in over- or under-estimation of the target antigen.[17,18,20] In the current investigation, a spiking level of 10 ppm of pistachio was used. The pistachio recovery range for spiked cereal, corn flake, cookie, dark chocolate, milk chocolate, white chocolate, ice cream, and sponge cake was 81−125% (Table 5). The highest pistachio recovery was observed in spiked

Table 5. Pistachio Recovery from Foods Spiked with Pistachio Soluble Protein Extract As Determined by the MonoTrace Pistachio ELISA Kit

food	manufacturer[a]	spike level (ppm)	recovery[b] (%)
ice cream	Häagen-Dazs	0	ND[c]
		10	92.6 ± 2.3
dark chocolate	Hershey's	0	ND
		10	81.8 ± 1.8
dark chocolate with 5% NFDM		10	93.1 ± 1.1
milk chocolate		0	ND
		10	112.8 ± 3.7
white chocolate		0	ND
		10	110.6 ± 8.3
cereal	Post	0	ND
		10	117.4 ± 5.1
corn flakes	laboratory made	0	ND
		10	125.6 ± 1.7
sponge cake		0	ND
		10	113.8 ± 2.2
cookie		0	ND
		10	122.5 ± 6.2
LSD ($P \leq 0.05$,$n = 3$)			8.53

[a]Commercial sample brands were used for comparison, not for endorsement. [b]Laboratory samples were prepared in triplicate. Commercial foods were obtained in a single batch. All samples were analyzed in triplicate using a kit. Data are expressed as mean ± SD. [c]ND, not detected (signal equivalent to <0.09 ppm pistachio).

corn flakes, whereas the lowest was in dark chocolate. ELISA recovery of 183% for 11S globulin (amandin) for almond-spiked corn flakes has also been reported.[18] The reduced recovery in dark chocolate was consistent with previous observations and was likely induced by the formation of pistachio protein−chocolate polyphenol insoluble complexes.[17,18,20] For foods containing dark chocolate, the addition of 5% w/v nonfat dry milk (NFDM) to the extraction buffer was suggested in the latest version of the kit user's manual. To test this, we added 5% NFDM to the extraction buffer and repeated the assay. This modification in the extraction step significantly improved pistachio recovery from dark chocolate to 93% (from 82%). NFDM proteins may possibly interact with the chocolate polyphenols and acids, thereby improving target antigen solubilization.

To demonstrate how food processing along with the food matrix affects the allergen detection and quantification, laboratory-prepared corn flakes, sponge cakes, and sugar cookies were incurred with full-fat pistachio flour and subjected to thermal processing. Samples were incurred with 10, 50, and 100 ppm of pistachio to mimic the case of inadvertent contamination with pistachio during food processing and with 5000 ppm (0.5% w/w), 10000 ppm (1% w/w), 20000 ppm (2% w/w), and 50000 ppm (5% w/w) pistachio to simulate the case of intentional use of pistachio as an ingredient in food processing. The pistachio recovery ranges for corn flakes, sponge cakes, and sugar cookies were, respectively, 37.3−44.8, 50.3−67.1, and 68.9−82.6% at 10−100 ppm incurring level, and 35.7−49.1, 71.2−99.2, and 78.6−112.2% at 5000−50000 ppm incurring level (Table 6). The

Table 6. Pistachio Recovery from Foods Incurred with Pistachio Full-Fat Flour As Determined by the MonoTrace Pistachio ELISA Kit

	recovery[a] (%)		
pistachio incurred level (ppm)	corn flake	sponge cake	sugar cookie
10	37.3 ± 3.9	50.3 ± 5.1	68.9 ± 15.5
50	45.8 ± 3.5	78.6 ± 3.6	89.2 ± 13.4
100	44.8 ± 6.2	67.1 ± 3.0	82.6 ± 13.0
5000	43.6 ± 6.2	71.2 ± 6.1	91.4 ± 19.7
10000	35.7 ± 4.4	77.9 ± 18.9	78.6 ± 4.9
20000	48.3 ± 5.1	88.2 ± 19.3	108.2 ± 13.8
50000	49.1 ± 2.0	99.2 ± 16.8	112.2 ± 10.4
LSD ($P \leq 0.05$, $n = 3$)	8.20	21.96	23.88
LSD ($P \leq 0.05$, $n = 3$)		9.55	

[a]Samples were prepared and analyzed in triplicate. Data are expressed as mean ± SD.

decreased pistachio recovery from certain incurred samples was in agreement with decreased antigen recovery from gluten-incurred corn bread and milk-incurred cookies and was likely due to (1) interference from other food ingredients, (2) thermally induced antigen denaturation, (3) chemical modification (e.g., Maillard reaction) of the antigen, and/or (4) hindered antigen solubility/extractability.[60,61]

Assay Robustness and Applicability. The assay kit detected pistachio traces when protein extracts prepared from thermally processed pistachio seeds were tested (Table 7). Relative immunoreactivity of the processed pistachio samples ranged from 86% (dry roasting, 168 °C, 12 min) to 182% (blanching, 94 °C, 10 min). The elevated immunoreactivity under certain processing conditions may be due to improved accessibility of a possibly buried epitope.[15] The target antigen, possibly pistachio 11S globulin, is thermally stable, a finding consistent with our previous observations for tree nut 11S globulins including almond amandin[21,62,63] and cashew anacardein.[15,21,64] To test whether the MonoTrace kit targeted antigen is a reliable marker or not, selected 20 paired commercial samples, with and without declared pistachio, were examined. No false-positive or false-negative results were observed for the tested samples except for kaju roll (Table 8). No pistachio was detected in commercially sold kaju roll that was declared to contain pistachio. Kaju roll is a dessert made by rolling rectangular-shaped cashew dough around a log-shaped pistachio

DOI: 10.1021/acs.jafc.5b03066
J. Agric. Food Chem. 2015, 63, 9139−9149

Table 7. Effects of Thermal Processing on Immunoreactivity of Whole Pistachio Seeds As Determined by the MonoTrace ELISA kit

processing	condition	relative immunoreactivity[a] (%)
unprocessed (control)	NA	100.0 ± 1.5
autoclaving	121 °C, 15 psi, 15 min	129.4 ± 38.3
	121 °C, 15 psi, 30 min	134.4 ± 23.3
blanching	94 °C, 5 min	172.7 ± 25.0
	94 °C, 10 min	182.5 ± 23.5
frying	191 °C, 1 min	144.8 ± 29.6
microwaving	500 W, 3 min	161.4 ± 17.9
	1000 W, 3 min	104.8 ± 30.5
roasting	140 °C, 30 min	95.2 ± 3.7
	168 °C, 12 min	86.2 ± 1.2
LSD ($P \leq 0.05$, $n = 3$)		40.75

[a]Pistachios were processed in triplicate using the same batch of seeds and analyzed using one kit. Data are expressed as mean ± SD.

Table 8. Pistachio Detection in Commercially Prepared Foods Using the MonoTrace Pistachio ELISA Kit

food	manufacturer[a]	mg full fat pistachio detected/g sample[b]
vanilla ice cream (−)[c]	Häagen-Dazs	ND
pistachio ice cream (+)		76.2 ± 2.9
Tahitian vanilla bean gelato (−)	Talenti	ND
Sicilian pistachio gelato (+)		175.0 ± 9.6
malai kulfli (−)	Reena's	ND
pista kulfli (+)		166.6 ± 1.5
kaju katli (−)	Rangoli	ND
kaju roll (+)		ND
plain halawa (−)	Mounir Bissat	ND
pistachio halawa (+)		298.6 ± 5.0
rose Turkish delight (−)	Haci Bekir	ND
pistachio Turkish delight (+)		147.0 ± 3.5
vanilla instant pudding and pie filling (−)	Jell-o	ND
pistachio instant pudding and pie filling (+)		0.1 ± 0.0
soledad almond nut blend (−)	Sahale Snacks	ND
pomegranate pistachio almond blend (+)		369.2 ± 9.1
walnut baklava (−)	Little Athens Gyro	ND
pistachio baklava (+)	Pitaria	138.0 ± 17.8
milk chocolate (−)	Hershey's	ND
milk chocolate pistachio (+)	Flicks	685.3 ± 17.1
LSD ($P \leq 0.05$, $n = 3$)		10.66

[a]Commercial sample brands were used for comparison, not for endorsement. [b]Commercial samples from a single batch were weighed into three subsamples, each extracted in extraction buffer and analyzed in a kit. Data are expressed as mean ± SD. ND = not detected (signal equivalent to <0.09 ppm pistachio). [c](−) = without declared pistachio; (+) = with declared pistachio.

dough, into a cylinder. We were unable to detect pistachio presence in tested commercial kaju roll batches (purchased in 2011, 2013, and 2014) using the MonoTrace kits. This "false negative" result was not caused by the interference from the kaju roll matrix as when pistachio full-fat flour was spiked (10 ppm) into the same commercial kaju roll samples, 102.5% of the pistachio protein could be recovered using the kit. It was unclear whether commercial kaju rolls contained pistachio or perhaps just green food colorant. Therefore, we prepared kaju rolls with different pistachio contents (0.6−6.3% w/w for recipe 1, 0.4−4.5% w/w for recipe 2) in our laboratory using two separate recipes. The MonoTrace pistachio kit was able to detect pistachio in all laboratory-prepared kaju rolls. The pistachio recovery ranged from 83 to 89% for recipe 1 kaju rolls and 93−127% for recipe 2 kaju rolls (Table 9). These results suggest that the

Table 9. Pistachio Detection in Laboratory Prepared Kaju Rolls Using the MonoTrace Pistachio ELISA Kit

recipe 1 (Nestlé)		recipe 2 (laboratory developed)	
pistachio % (w/w)	recovery (%)	pistachio % (w/w)	recovery (%)
0	ND[a]	0	ND
0.001 (spiking)	97.7 ± 17.3	0.001 (spiking)	109.4 ± 15.0
0.6	82.5 ± 2.0	0.4	93.0 ± 27.0
3.4	87.1 ± 2.6	2.4	98.3 ± 10.6
6.3	88.6 ± 0.9	4.5	127.1 ± 10.9
LSD ($P \leq 0.05$, $n = 3$)	16.54	LSD ($P \leq 0.05$, $n = 3$)	32.40
LSD ($P \leq 0.05$, $n = 3$)		23.65	

[a]Kaju rolls were prepared using two different recipes, each in triplicate. ND = not detected (signal equivalent to <0.09 ppm pistachio).

negative results obtained on the tested commercial kaju rolls may represent (a) the presence of pistachio below the detection limit of the test kit, (b) the use of a pistachio variety in the tested kaju roll not amenable for detection by the test kit, or (c) a possible example of intentional misbranding.

In conclusion, the results of investigations in this paper indicate that under the test conditions the BioFront MonoTrace pistachio ELISA kit was sensitive, robust, and specific for pistachio detection and quantification.

AUTHOR INFORMATION

Corresponding Author

*(S.K.S.) Phone: (850) 644-5837. Fax: (850) 645-5000. E-mail: ssathe@fsu.edu.

Funding

We gratefully acknowledge financial support from the Department of Nutrition, Food and Exercise Sciences, Florida State University, and the USDA-NIFA 2009-65503-05797, 2011-67017-20079.

Notes

The authors declare no competing financial interest.

ACKNOWLEDGMENTS

We thank Prof. K. H. Roux for his help in designing certain experiments.

REFERENCES

(1) Venkatachalam, M.; Sathe, S. K. Chemical composition of selected edible nut seeds. *J. Agric. Food Chem.* **2006**, *54*, 4705−4714.

(2) *The Fruit and Tree Nuts Yearbook 2014*; U.S. Department of Agriculture, U.S. Government Printing Office: Washington, DC, USA, 2014.

(3) FAOSTAT. http://faostat.fao.org (accessed June 16, 2015).

(4) Sicherer, S. H.; Muñoz-Furlong, A.; Godbold, J. H.; Sampson, H. A. US prevalence of self-reported peanut, tree nut, and sesame allergy: 11-year follow-up. *J. Allergy Clin. Immunol.* **2010**, *125*, 1322−1326.

DOI: 10.1021/acs.jafc.5b03066
J. Agric. Food Chem. 2015, 63, 9139−9149

(5) Noorbakhsh, R.; Mortazavi, S. A.; Shahidi, F. Pistachio allergy-prevalence and in vitro cross-reactivity with other nuts. *Allergol. Int.* **2011**, *60*, 425−432.
(6) Porcel, S.; Sanchez, A.; Rodriguez, E.; Fletes, C.; Alvarado, M.; Jimenez, S.; Hernandez, J. Food-dependent exercise-induced anaphylaxis to pistachio. *J. Invest. Allergol. Clin. Immunol.* **2006**, *16*, 71−73.
(7) Bock, S. A.; Muñoz-Furlong, A.; Sampson, H. A. Fatalities due to anaphylactic reactions to foods. *J. Allergy Clin. Immunol.* **2001**, *107*, 191−193.
(8) Ando, K.; Watanabe, D.; Tamada, Y.; Matsumoto, Y. Oral allergy syndrome with severe anaphylaxis induced by pistachio. *Int. J. Dermatol.* **2011**, *50*, 632−633.
(9) Boyce, J. A.; Assa'ad, A.; Burks, A. W.; Jones, S. M.; Sampson, H. A.; Wood, R. A.; Plaut, M.; Cooper, S. F.; Fenton, M. J.; Arshad, S. H. Guidelines for the diagnosis and management of food allergy in the United States: report of the NIAID-sponsored expert panel. *J. Allergy Clin. Immunol.* **2010**, *126*, S1−S58.
(10) FDA recalls. http://www.fda.gov/Safety/Recalls/ArchiveRecalls/2014 (accessed June 13, 2015).
(11) FDA Food Allergen Labeling and Consumer Protection Act. http://www.fda.gov/downloads/Food/GuidanceRegulation/UCM179394.pdf (accessed October 16, 2014).
(12) Gendel, S. M.; Zhu, J. Analysis of US Food and Drug Administration food allergen recalls after implementation of the food allergen labeling and consumer protection act. *J. Food Prot.* **2013**, *76*, 1933−1938.
(13) López-Calleja, I. M.; de la Cruz, S.; González, I.; García, T.; Martín, R. Survey of undeclared allergenic pistachio (*Pistacia vera*) in commercial foods by hydrolysis probe real-time PCR. *Food Control* **2014**, *39*, 49−55.
(14) Acosta, M. R.; Roux, K. H.; Teuber, S. S.; Sathe, S. K. Production and characterization of rabbit polyclonal antibodies to almond (*Prunus dulcis* L.) major storage protein. *J. Agric. Food Chem.* **1999**, *47*, 4053−4059.
(15) Venkatachalam, M.; Monaghan, E. K.; Kshirsagar, H. H.; Robotham, J. M.; O'Donnell, S. E.; Gerber, M. S.; Roux, K. H.; Sathe, S. K. Effects of processing on immunoreactivity of cashew nut (*Anacardium occidentale* L.) seed flour proteins. *J. Agric. Food Chem.* **2008**, *56*, 8998−9005.
(16) Röder, M.; Vieths, S.; Holzhauser, T. Commercial lateral flow devices for rapid detection of peanut (*Arachis hypogaea*) and hazelnut (*Corylus avellana*) cross-contamination in the industrial production of cookies. *Anal. Bioanal. Chem.* **2009**, *395*, 103−109.
(17) Sharma, G. M.; Roux, K. H.; Sathe, S. K. A sensitive and robust competitive enzyme-linked immunosorbent assay for Brazil nut (*Bertholletia excelsa* L.) detection. *J. Agric. Food Chem.* **2009**, *57*, 769−776.
(18) Tiwari, R. S.; Venkatachalam, M.; Sharma, G. M.; Su, M.; Roux, K. H.; Sathe, S. K. Effect of food matrix on amandin, almond (*Prunus dulcis* L.) major protein, immunorecognition and recovery. *LWT−Food Sci. Technol.* **2010**, *43*, 675−683.
(19) Röder, M.; Vieths, S.; Holzhauser, T. Sensitive and specific detection of potentially allergenic almond (*Prunus dulcis*) in complex food matrices by Taqman® real-time polymerase chain reaction in comparison to commercially available protein-based enzyme-linked immunosorbent assay. *Anal. Chim. Acta* **2011**, *685*, 74−83.
(20) Su, M.; Venkatachalam, M.; Liu, C.; Zhang, Y.; Roux, K. H.; Sathe, S. K. A murine monoclonal antibody based enzyme-linked immunosorbent assay for almond (*Prunus dulcis* L.) detection. *J. Agric. Food Chem.* **2013**, *61*, 10823−10833.
(21) Su, M.; Venkatachalam, M.; Teuber, S. S.; Roux, K. H.; Sathe, S. K. Impact of γ-irradiation and thermal processing on the antigenicity of almond, cashew nut and walnut proteins. *J. Sci. Food Agric.* **2004**, *84*, 1119−1125.
(22) Nestlé Recipes. http://www.nestle-family.com/recipes/english/by-course-or-type-desserts-other-desserts_Kaju-Pista-Rolls-Cashew-and-Pistachio-Rolls_47487.aspx (accessed October 16, 2014).
(23) *Official Methods of Analysis of AOAC International*, 16th ed.; Association of Official Analytical Chemists (AOAC): Arlington, VA, USA, 1995.
(24) Osborne, T. B. *The Vegetable Proteins*, 2nd ed.; Longmans, Green and Co.: London, UK, 1924.
(25) Sze-Tao, K. W. C.; Sathe, S. K. Walnuts (*Juglans regia* L.): proximate composition, protein solubility, protein amino acid composition and protein in vitro digestibility. *J. Sci. Food Agric.* **2000**, *80*, 1393−1401.
(26) Bradford, M. M. A rapid and sensitive method for the quantitation of microgram quantities of protein utilizing the principle of protein-dye binding. *Anal. Biochem.* **1976**, *72*, 248−254.
(27) FDA. Validation of analytical procedures: methodology. *Fed. Regist.* **1997**, *62*, 27463−27467.
(28) Compendium of analytical nomenclature. In *IUPAC Chemical Nomenclature Series*; Inczédy, J., Lengyel, T., Ure, A. M., Freiser, H., Eds.; Blackwell Science: Oxford, UK, 1998.
(29) MacDougall, D.; Crummett, W. B. Guidelines for data acquisition and data quality evaluation in environmental chemistry. *Anal. Chem.* **1980**, *52*, 2242−2249.
(30) Wild, D. *The Immunoassay Handbook*, 4th ed.; Elsevier: Oxford, UK, 2013; p 1036.
(31) Taylor, B. N.; Kuyatt, C. E. *Guidelines for Evaluating and Expressing the Uncertainty of NIST Measurement Results*; NIST Technical Note 1297; U.S. Government Printing Office: Washington, DC, USA, 1994; p 24.
(32) González, A. G.; Herrador, M. Á. A practical guide to analytical method validation, including measurement uncertainty and accuracy profiles. *TrAC, Trends Anal. Chem.* **2007**, *26*, 227−238.
(33) Fling, S. P.; Gregerson, D. S. Peptide and protein molecular weight determination by electrophoresis using a high-molarity tris buffer system without urea. *Anal. Biochem.* **1986**, *155*, 83−88.
(34) Towbin, H.; Staehelin, T.; Gordon, J. Electrophoretic transfer of proteins from polyacrylamide gels to nitrocellulose sheets: procedure and some applications. *Proc. Natl. Acad. Sci. U. S. A.* **1979**, *76*, 4350−4354.
(35) Brežná, B.; Dudášová, H.; Kuchta, T. A novel real-time polymerase chain reaction method for the qualitative detection of pistachio in food. *Eur. Food Res. Technol.* **2008**, *228*, 197−203.
(36) Barbieri, G.; Frigeri, G. Identification of hidden allergens: detection of pistachio traces in mortadella. *Food Addit. Contam.* **2006**, *23*, 1260−1264.
(37) Lim, P. W. *Development of an Enzyme-Linked Immunosorbent Assay (ELISA) for the Detection of Pistachio Residues in Processed Foods*. M.S. Thesis, University of Nebraska, Lincoln, NE, USA, 2010.
(38) Buchanan, R.; Dennis, S.; Gendel, S.; Acheson, D.; Assimon, S. A.; Beru, N.; Bolger, P.; Carlson, D.; Carvajal, R.; Copp, C. Approaches to establish thresholds for major food allergens and for gluten in food. *J. Food Prot.* **2008**, *71*, 1043−1088.
(39) Taylor, S. L.; Baumert, J. L.; Kruizinga, A. G.; Remington, B. C.; Crevel, R. W.; Brooke-Taylor, S.; Allen, K. J.; Houben, G. Establishment of reference doses for residues of allergenic foods: report of the VITAL expert panel. *Food Chem. Toxicol.* **2014**, *63*, 9−17.
(40) Allen, K. J.; Remington, B. C.; Baumert, J. L.; Crevel, R. W.; Houben, G. F.; Brooke-Taylor, S.; Kruizinga, A. G.; Taylor, S. L. Allergen reference doses for precautionary labeling (VITAL 2.0): clinical implications. *J. Allergy Clin. Immunol.* **2014**, *133*, 156−164.
(41) Sicherer, S. H. Clinical implications of cross-reactive food allergens. *J. Allergy Clin. Immunol.* **2001**, *108*, 881−890.
(42) Comstock, S.; McGranahan, G.; Peterson, W.; Teuber, S. Extensive in vitro cross-reactivity to seed storage proteins is present among walnut (*Juglans*) cultivars and species. *Clin. Exp. Allergy* **2004**, *34*, 1583−1590.
(43) Goetz, D. W.; Whisman, B. A.; Goetz, A. D. Cross-reactivity among edible nuts: double immunodiffusion, crossed immunoelectrophoresis, and human specific IgE serologic surveys. *Ann. Allergy, Asthma, Immunol.* **2005**, *95*, 45−52.
(44) Maloney, J. M.; Rudengren, M.; Ahlstedt, S.; Bock, S.; Sampson, H. A. The use of serum-specific IgE measurements for the diagnosis of

DOI: 10.1021/acs.jafc.5b03066
J. Agric. Food Chem. 2015, 63, 9139−9149

peanut, tree nut, and seed allergy. *J. Allergy Clin. Immunol.* **2008**, *122*, 145−151.
(45) Sharma, G. M.; Irsigler, A.; Dhanarajan, P.; Ayuso, R.; Bardina, L.; Sampson, H. A.; Roux, K. H.; Sathe, S. K. Cloning and characterization of 2S albumin, Car i 1, a major allergen in pecan. *J. Agric. Food Chem.* **2011**, *59*, 4130−4139.
(46) Sharma, G. M.; Irsigler, A.; Dhanarajan, P.; Ayuso, R.; Bardina, L.; Sampson, H. A.; Roux, K. H.; Sathe, S. K. Cloning and characterization of an 11S legumin, Car i 4, a major allergen in pecan. *J. Agric. Food Chem.* **2011**, *59*, 9542−9552.
(47) Parra, F.; Cuevas, M.; Lezaun, A.; Alonso, M.; Beristain, A.; Losada, E. Pistachio nut hypersensitivity: identification of pistachio nut allergens. *Clin. Exp. Allergy* **1993**, *23*, 996−1001.
(48) Fernandez, C.; Fiandor, A.; Martinez-Garate, A.; Quesada, J. Allergy to pistachio: crossre activity between pistachio nut and other Anacardiaceae. *Clin. Exp. Allergy* **1995**, *25*, 1254−1259.
(49) Garcia, F.; Moneo, I.; Fernandez, B.; Garcia-Menaya, J.; Blanco, J.; Juste, S. Allergy to Anacardiaceae: description of cashew and pistachio nut allergens. *J. Invest. Allergol. Clin. Immunol.* **1999**, *10*, 173−177.
(50) Rancé, F.; Bidat, E.; Bourrier, T.; Sabouraud, D. Cashew allergy: observations of 42 children without associated peanut allergy. *Allergy* **2003**, *58*, 1311−1314.
(51) Tawde, P. D. *Allergenic Cross-Reactivity between Cashew and Pistachio Nuts*. M.S. Thesis, Florida State University, Tallahassee, FL, USA, 2004.
(52) Willison, L.; Tawde, P.; Robotham, J.; Penney, R. t.; Teuber, S.; Sathe, S.; Roux, K. Pistachio vicilin, Pis v 3, is immunoglobulin E-reactive and cross-reacts with the homologous cashew allergen, Ana o 1. *Clin. Exp. Allergy* **2008**, *38*, 1229−1238.
(53) Hasegawa, M.; Inomata, N.; Yamazaki, H.; Morita, A.; Kirino, M.; Ikezawa, Z. Clinical features of four cases with cashew nut allergy and cross-reactivity between cashew nut and pistachio. *Allergol. Int.* **2009**, *58*, 209−215.
(54) Cho, C. Y.; Nowatzke, W.; Oliver, K.; Garber, E. A. Multiplex detection of food allergens and gluten. *Anal. Bioanal. Chem.* **2015**, *407*, 4195−4206.
(55) Shokraii, E. H.; Esen, A. Composition, solubility and electrophoretic patterns of proteins isolated from Kerman pistachio nuts (*Pistacia vera* L.). *J. Agric. Food Chem.* **1988**, *36*, 425−429.
(56) Wolf, W. J. Sulfhydryl content of glycinin: effect of reducing agents. *J. Agric. Food Chem.* **1993**, *41*, 168−176.
(57) Tawde, P. D.; Robotham, J. M.; Penney, R.; Roux, K. H. *Identification of 11S globulin from pistachio, a cross-reactive allergen*. Submitted (April 17, 2007) to the INSDC, UniProtKB accession no. B2KN55.
(58) Beyer, K.; Grishina, G.; Bardina, L.; Stalcup, D.; Sampson, H. *Identification and cloning of 11S globulin, a new minor allergen from pistachio nut*. Submitted (January 17, 2008) to the INSDC, UniProtKB accession no. B7SLJ1.
(59) Ahn, K.; Bardina, L.; Grishina, G.; Beyer, K.; Sampson, H. Identification of two pistachio allergens, Pis v 1 and Pis v 2, belonging to the 2S albumin and 11S globulin family. *Clin. Exp. Allergy* **2009**, *39*, 926−934.
(60) Sharma, G. M.; Khuda, S. E.; Pereira, M.; Slate, A.; Jackson, L. S.; Pardo, C.; Williams, K. M.; Whitaker, T. B. Development of an incurred cornbread model for gluten detection by immunoassays. *J. Agric. Food Chem.* **2013**, *61*, 12146−12154.
(61) Monaci, L.; Brohée, M.; Tregoat, V.; van Hengel, A. Influence of baking time and matrix effects on the detection of milk allergens in cookie model food system by ELISA. *Food Chem.* **2011**, *127*, 669−675.
(62) Roux, K. H.; Teuber, S. S.; Robotham, J. M.; Sathe, S. K. Detection and stability of the major almond allergen in foods. *J. Agric. Food Chem.* **2001**, *49*, 2131−2136.
(63) Venkatachalam, M.; Teuber, S.; Roux, K.; Sathe, S. Effects of roasting, blanching, autoclaving, and microwave heating on antigenicity of almond (*Prunus dulcis* L.) proteins. *J. Agric. Food Chem.* **2002**, *50*, 3544−3548.
(64) Wei, Y.; Sathe, S. K.; Teuber, S. S.; Roux, K. H. A sensitive sandwich ELISA for the detection of trace amounts of cashew (*Anacardium occidentale* L.) nut in foods. *J. Agric. Food Chem.* **2003**, *51*, 3215−3221.

DOI: 10.1021/acs.jafc.5b03066
J. Agric. Food Chem. 2015, 63, 9139−9149

first hazelnut allergen with a resolved three-dimensional structure.

MATERIALS AND METHODS

Protein Purification. Shelled, raw hazelnuts were frozen, ground in a blender, and defatted by extraction with hexane. Proteins from dried hazelnut flour were extracted with 10 volumes of extraction buffer (20 mM sodium acetate, pH 4.5, containing 0.5 M NaCl and 3% polyvinyl polypyrrolidone). Globulins were removed by precipitation with cold methanol (60%, v/v), and prolamins were precipitated with acetone. After removal of the 2S albumin fraction by anion exchange chromatography (10 mL of Q sepharose; GE Healthcare, Little Chalfont, UK), Cor a 8 was purified from the flow-through by cation exchange chromatography. The flow-through was dialyzed against 20 mM sodium acetate, pH 7.6, and loaded onto a prepacked 1 mL Mono S column (GE Healthcare). Proteins bound to the column were eluted by a linear gradient of increasing concentrations (0−20%) of 1 M NaCl with a flow rate of 1 mL/min. Both columns were attached to a GE ÄKTA FPLC system (GE Healthcare). Fractions were analyzed by Coomassie-stained 15% SDS-PAGE.

Circular Dichroism (CD) Spectroscopy. CD spectra of native Cor a 8 (0.2 μg/μL in 10 mM sodium phosphate buffer, pH 2.5 or 7.5) were measured from 190 to 260 nm on a Jasco J-810 spectropolarimeter (Jasco International Co., Tokyo, Japan) at 20 °C using a 1 mm path length quartz cell. The effect of heating (2 °C/min) was measured at 222 nm. Spectra represent the average of four accumulations collected at 100 nm/min with a 2 s time constant, 0.5 nm resolution, and sensitivity of ±100 mdeg.

N-Terminal Sequencing by Edman Degradation. The N-terminal sequence was determined using an Applied Biosystems Procise 491 sequencer (Applied Biosystems, Foster City, CA, USA). Cor a 8 (100 pmol) was adsorbed onto a Prosorb cartridge and subjected to sequence analysis.

MALDI-TOF-MS. For mass determination nonreduced Cor a 8 was spotted with α-cyano-4-hydroxycinnamic acid onto a ground steel MALDI target plate and measured in linear mode on a MALDI-TOF mass spectrometer (Microflex, Bruker Daltonics, Bremen, Germany).

Crystallization, Data Collection, and Processing. Crystallization experiments were performed at room temperature using the hanging-drop vapor diffusion method and screw-top hanging drop plates (Molecular Dimensions, Altamonte Springs, FL, USA). Purified, natural Cor a 8 in 20 mM Tris, pH 7.5, was mixed with well solution (0.49 M sodium phosphate monobasic monohydrate, 0.91 M potassium phosphate dibasic, pH 6.9) in a 1:1 ratio. Crystals were cryo-protected with well solution and cooled in liquid N_2. Data were collected from single crystals at 100 K at SER-CAT 22BM beamline at the Advanced Photon Source (APS), Argonne National Laboratory (ANL). Crystals belonged to the $P2_1$ spacegroup, and the protein crystallized with two molecules per asymmetric unit (AU). Data were processed with the HKL-2000 software package.[25] Data collection statistics are reported in Table 1.

Structure Determination and Refinement. The structure of Cor a 8 was solved by molecular replacement using nsLTPs Pru p 3 from peach (PDB ID 2ALG) as the start model. Molecular replacement was performed with HKL-3000[26] integrated with MOLREP[27] and selected programs from the CCP4 package.[28] Models were rebuilt using COOT,[29] Buccaneer,[30] and ARP/wARP[31] and refined with REFMAC.[32] MOLPROBITY[33] and ADIT[34] were used for structure validation. Refinement statistics are summarized in Table 1.

Molecular Dynamics Simulations. Molecular force fields of lauric acid anion and *n*-heptane were described with the general amber force field (GAFF), whereas for the proteins, the amber force field ff03.r1 was employed. *n*-Heptane molecule and laureate anion were first optimized in extended conformations in vacuum at the B3LYP/6-31G(d,p) level, and then the electrostatic potential around them was computed at the level that is consistent with the GAFF, that is, HF/6-31G(d). Quantum chemical computations were performed with the Gaussian 09 suite of programs.[35] From the electrostatic potential RESP atomic charges were fitted with the use of antechamber and resp programs from the AmberTools package.[36]

The ionization state of individual protein residues was tested with PROPKA 3.1 software.[37] For pH 7 all residues were predicted to be in their standard ionization state (N- and C-termini all LYS, ARG, and ASP charged).

Initial coordinates of the proteins were taken from PDB 2B5S for Pru p 3 and from PDB 4XUW for Cor a 8, respectively (chains A). The N-terminal Met residue of the Pru p 3 structure was removed, as it was added to the protein due to its heterologous expression in a bacterial host. Protein molecules were subsequently placed in a periodic box filled with explicit water molecules described with the TIP3P model[38] and the appropriate number of chloride anions to compensate the charge of the protein or protein/laureate complex. The box was chosen such that its edge was 10 Å away from the protein surface in either direction. The system was first minimized in three steps: 5000 steps with protein atoms restrained with 500 kcal/mol Å^2 harmonic constant, 5000 steps with 10 kcal/mol Å^2 harmonic restraint on protein, and then 10000 steps of an unrestrained minimization. The minimized system was heated from 0 to 300 K during a 50 ps NV dynamics, and then its density was equilibrated in a 0.5 ns NPT dynamics; in both steps protein backbone atoms were restrained with 1 kcal/mol Å^2. Subsequent unrestrained NPT (T = 300 K, p = 1 atm) dynamics simulation spanned 150 ns for each system, with a snapshot saved every 10 ps. Integration time step was 2 fs, SHAKE algorithm was used to constrain bonds of hydrogen atoms, and temperature and pressure were controlled with the Langevin dynamics and isotropic position scaling algorithm, respectively. MD simulations were conducted with the Amber12 suite with a GPU version of the PMEMD program.[39,40] Snapshots of the last 10 ns of simulations were clustered with the average linkage algorithm applied to Ca carbons of the protein backbone. Representative structures of dominating clusters were used for structure comparisons.

Other Computational Calculations. Protein anisotropic refinement validation and analysis tool (PARVATI) was used to validate anisotropic displacement parameters.[41,42] The SSM algorithm[43] in COOT was used to superpose protein models. All figures containing

Table 1. Crystallographic Data and Refinement Statistics for Cor a 8[a]

PDB code	4XUW
Data collection	
wavelength (Å)	1.00
unit cell (a, b, c; β) (Å; deg)	39.7, 30.8, 56.2; 108.9
space group	$P2_1$
solvent content (%)	28
protein chains in AU	2
resolution range (Å)	50.0−1.10
highest resolution shell (Å)	1.12−1.10
unique reflections	47711 (1266)
redundancy	7.0 (4.1)
completeness (%)	90.7 (49.1)
R_{merge} (%)	5.2 (15.7)
av $I/\sigma(I)$	37.4 (8.5)
Refinement	
R (%)	14.2
R_{free} (%)	17.7
mean B value (Å^2)	20.2
B from Wilson plot (Å^2)	14.4
RMS deviation bond lengths (Å)	0.02
RMS deviation bond angles (deg)	2.3
no. of amino acid residues	184
no. of water molecules	308
Ramachandran plot	
most favored regions (%)	98
additional allowed regions (%)	2

[a]Values in parentheses refer to the highest resolution shell.

DOI: 10.1021/acs.jafc.5b03534
J. Agric. Food Chem. 2015, 63, 9150−9158

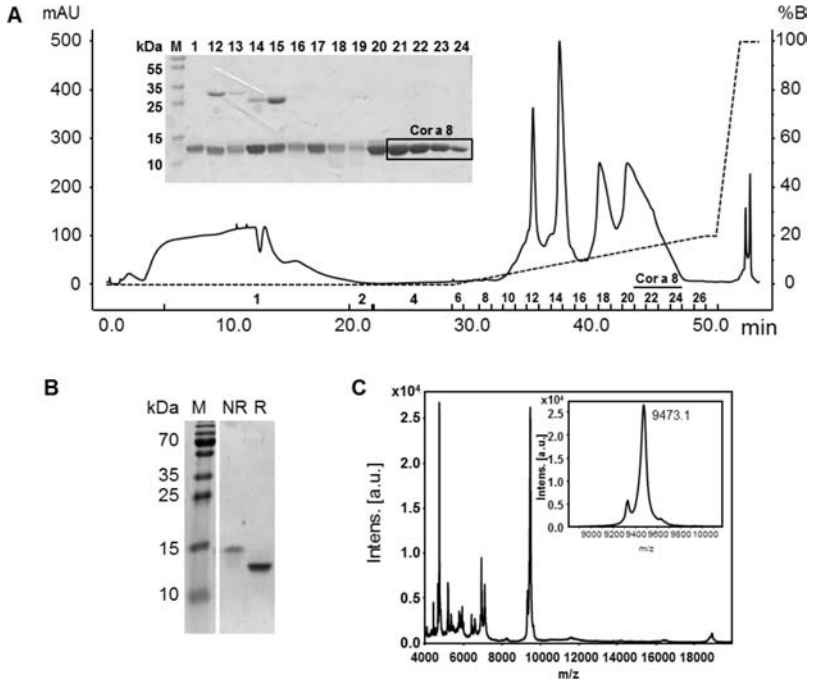

Figure 1. Purification of Cor a 8: (A) cation exchange chromatography of the hazelnut prolamin extract and Coomassie-stained 15% SDS-PAGE of Cor a 8-containing fractions; (B) 15% SDS-PAGE of purified Cor a 8 under nonreducing (NR) and reducing (R) conditions; (C) mass spectrum of Cor a 8.

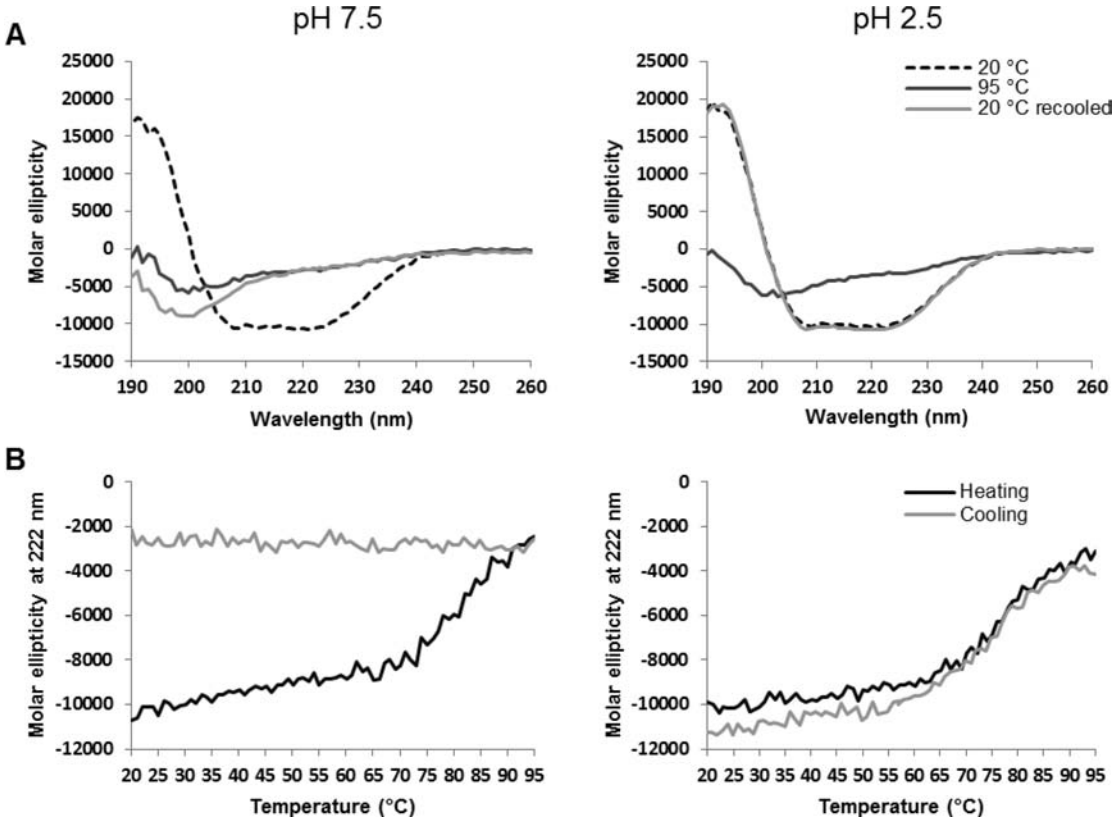

Figure 2. Far-UV CD spectra of Cor a 8: (A) spectra of Cor a 8 at room temperature (dotted line), after heating to 95 °C (dark gray line), and after recooling to room temperature (light gray line) at pH 2.5 and 7.5, respectively; (B) change in molar ellipticity at 222 nm during heating and cooling.

protein structures were prepared with PyMOL[44] or Chimera.[45] PDBePISA was used to calculate the probability of quaternary structure.[46] The Dali server[47] was used to identify structurally similar proteins. The ConSurf server was used to map sequence conservation on the structure of Cor a 8.[48]

RESULTS

Purification and Characterization of Natural Cor a 8.

Cor a 8 was separated from the prolamin fraction of hazelnut extract by using ion exchange chromatography techniques. SDS-

DOI: 10.1021/acs.jafc.5b03534
J. Agric. Food Chem. 2015, 63, 9150−9158

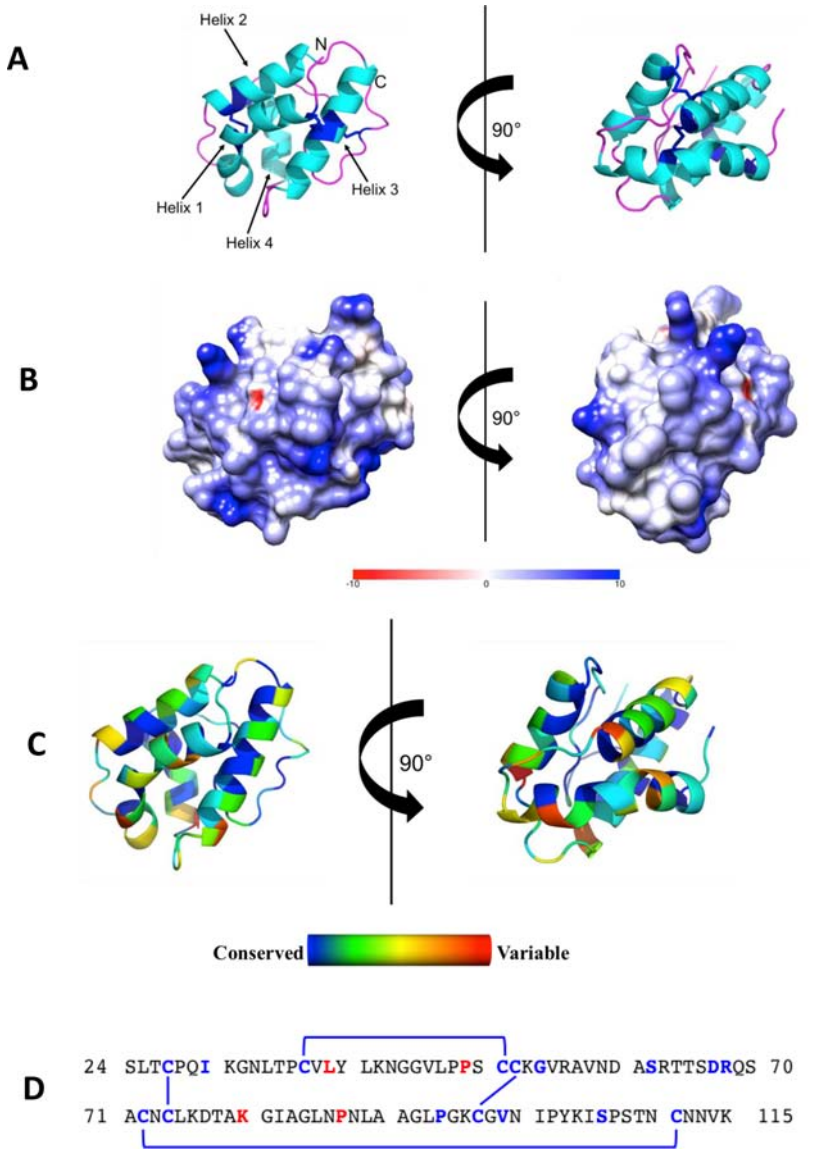

Figure 3. (A) Overall structure of Cor a 8. Secondary structural elements are colored separately where α-helices are cyan, β-sheets are red, loops are magenta, and disulfide bonds are blue. (B) Surface representation of Cor a 8 with electrostatic potentials where blue indicates positive charge and red indicates negative charge in units of kcal/(mol·e). (C) Ribbon representation of Cor a 8 showing conserved residues derived from an alignment of 150 Cor a 8-related protein sequences selected by ConSurf. The most conserved residues are shown in blue, whereas the most variable residues are shown in red. (D) Sequence of Cor a 8, in which the most conserved residues are blue and the most variable residues are red. The cysteine residues participating in disulfide linkages are bracketed.

PAGE analysis revealed that fractions F21−F24 were highly enriched in a protein with a molecular mass of ∼14000 Da (Figure 1A). Upon reduction, a band of about 12000 Da became visible (Figure 1B). This higher apparent molecular weight in SDS-PAGE seems to be characteristic for nsLTPs, as it was also shown for other members of this protein family.[22,49] MALDI-TOF-MS analysis yielded a mass of 9473.1 Da ($[M + H]^+$ = 9475.8; $[M + 2H]^{2+}$ = 4736.7) (Figure 1C), which is in good correlation with the theoretical mass of 9468.0 Da (Uniprot Q9ATH2, aa 24−115). Further evidence came from the N-terminal sequencing, which confirmed the first six N-terminal amino acid residues (SLTCPQ).

Secondary Structure and Thermostability. The overall secondary structural composition and heat stability were investigated using CD spectroscopy (Figure 2). CD spectra of the native protein at room temperature showed the typical characteristics of nsLTPs with high α-helical content. At room temperature, differences in pH did not change the secondary structure. However, the spectra of Cor a 8 prior to and after heating at pH 7.5 were different, showing that thermal unfolding was irreversible, whereas at pH 2.5 the overall protein fold was partially recovered. This demonstrates that Cor a 8 is more stable at acidic than at neutral conditions.

Structural Analysis of Cor a 8. The full-length, immature, Cor a 8 molecule is composed of 115 residues; residues 1−23 correspond to the signal peptide, which is cleaved upon maturation. All residues that comprise the mature protein, 24−115, are visible in the electron density map in both chains A and B. Overall, the mature Cor a 8 molecule is composed of four α-helices connected by loop regions. Eight cysteine residues are present in the mature protein, all of which participate in disulfide bonds: residues 27 and 74, 37 and 51, 52 and 97, and 72 and 111

DOI: 10.1021/acs.jafc.5b03534
J. Agric. Food Chem. 2015, 63, 9150−9158

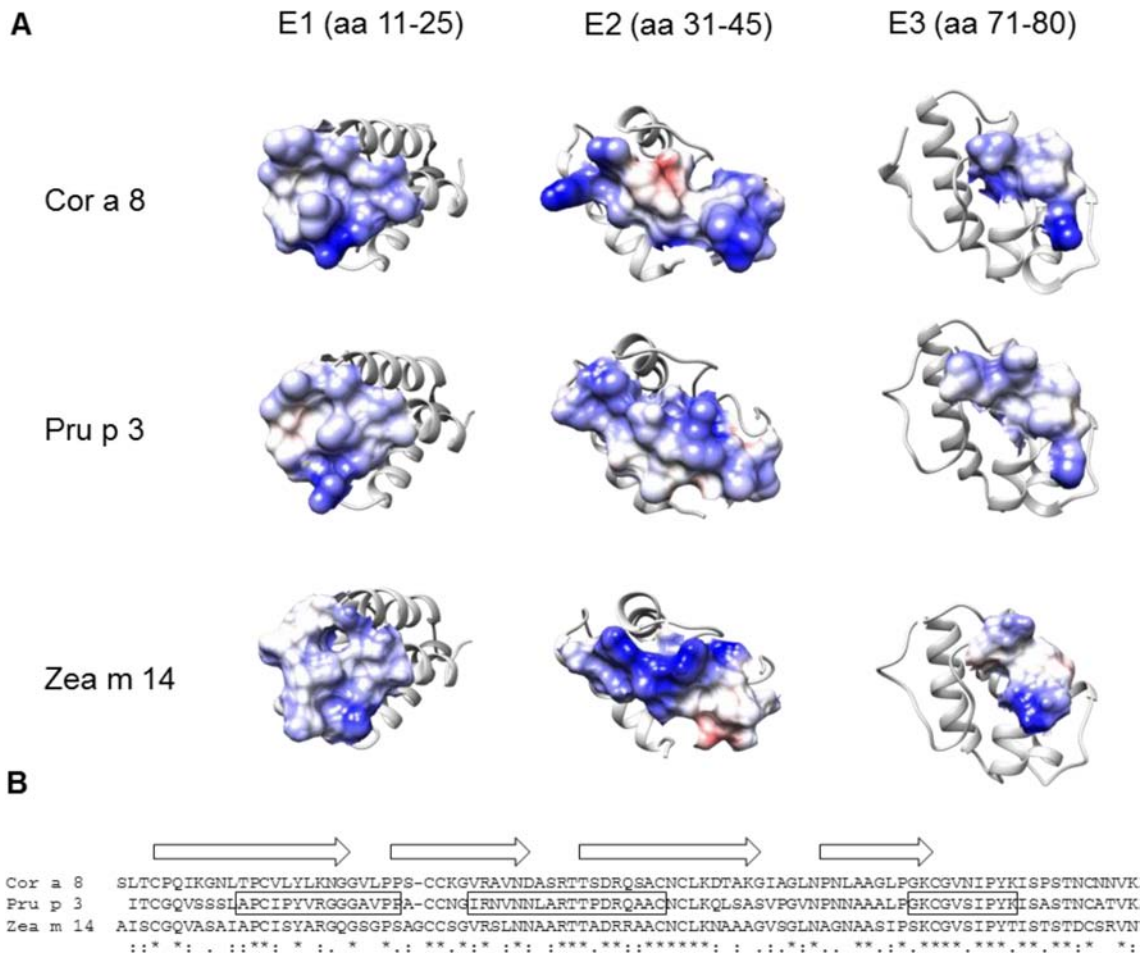

Figure 4. (A) Comparison of known epitope surface regions between Cor a 8, Pru p 3, and Zea m 14 (maize nsLTP); surface representation with electrostatic potentials where blue indicates positive charge and red indicates negative charge in units of kcal/(mol·e). (B) Primary sequence alignment of the mature protein sequences of Cor a 8, Pru p 3, and Zea m 14. Arrows indicate α-helices, and previously identified IgE-binding epitopes of Pru p 3 are marked with boxes.

(Figure 3). A comparison of chains A and B reveals very slight differences between the two, namely, at residues 64−68, 86−89, and 112−115. Chains A and B superpose with a root-mean-square deviation (RMSD) of 0.4 Å over 92 aligned Cα atoms. Although Cor a 8 crystallized with two subunits per asymmetric unit, PDBePISA suggests that this protein is monomeric. Electrostatic potentials were calculated using Chimera and are mapped out on the surface of Cor a 8, shown in Figure 3B.

Structural Comparison of Cor a 8 with Other Members of the nsLTP-family. Upon performing a search to find structurally similar proteins to Cor a 8, the Dali server identified the nsLTP Pru p 3 from peach (PDB ID 2B5S) as the most closely related structure. A superposition of 2B5S on our structure results in a RMSD of 1.4 Å over 91 aligned Cα atoms and a sequence identity of 57%. The peach allergen Pru p 3 (PDB ID 2B5S) has lauric acid bound in both subunits. A comparison of subunit A from Cor a 8 with subunit A of 2B5S reveals large structural differences at the C-terminus, residues 99−115 according to Cor a 8's numbering. Pru p 3's C-terminal loop is moved out toward the surface of the molecule, whereas the same region on Cor a 8 is closer to the core of the molecule. These changes are due to the binding of lauric acid between the third α-helix and the C-terminal loop of Pru p 3. Interestingly, a superposition of the two reveals that the pocket, where lauric acid is bound in the Pru p 3 structure, is occupied by Tyr103 of Cor a 8 (corresponding to Tyr79 of Pru p 3). The corresponding Tyr from Pru p 3 (Tyr79) is flipped outward, allowing for lauric acid to bind.

Dali also identified several nsLTPs from a variety of sources as structurally similar to Cor a 8. Aside from peach, an nsLTP from *Oryza sativa*, rice (for example, PDB ID 1UVC, RMSD value 1.2 Å over 90 aligned Cα atoms, sequence identity of 48%), was identified as the second most structurally similar nsLTP to Cor a 8. 1UVC crystallized with two subunits per asymmetric unit. Each subunit has stearic acid bound, and it is bound to the core of the protein between all four α-helices. A comparison of subunit A from Cor a 8 with subunit A of 1UVC reveals no drastic structural changes between the two structures. There are slight conformational shifts in the α-helices, and the largest structural change is seen at the C-terminal loop, namely, residues 100−115 of Cor a 8 (which correspond to residues 76−91 of 1UVC).

Additionally, Dali identified nsLTPs from barley (for example, PDB ID 3GSH, RMSD value 1.2 Å over 90 aligned Cα atoms, sequence identity of 43%) and maize nsLTP (Zea m 14; PDB ID 1MZL, RMSD value 1.4 Å over 92 aligned Cα atoms, sequence identity of 48%) as structurally similar to Cor a 8. Barley nsLTP (3GSH) has an oxylipin adduct (PDB Ligand ID ASY) bound in both subunits. The adduct splits into two branches, where one branch is buried in the core of the protein between the first and third α-helix and the second branch interacts with the surface of

DOI: 10.1021/acs.jafc.5b03534
J. Agric. Food Chem. 2015, 63, 9150−9158

the protein at the third α-helix. This ligand's mode of binding is very different from that seen in both 2B5S and 1UVC. A superposition of Cor a 8 and 3GSH reveals slight structural differences with the largest conformational change located at the loop that connects helix 1 and helix 2. These differences, however, do not appear to be attributed to bound ligand. Zea m 14 (1MZL) is an apo nsLTP, like that of Cor a 8. A superposition of the two reveals differences in the loop region that connects helix 1 and helix 2, as well as differences in the loop that connects helix 3 and helix 4, and the differences continue on through the C-terminal loop. Furthermore, Dali identified nsLTPs from tobacco (PDB ID 1T12), mung bean (PDB ID 1SIY), and lentil (PDB ID 2MAL) as Cor a 8 related structures that have lower structural similarity than those listed above, but higher sequence identity, at >50% for all three. Figure 3C shows a ribbon representation of the Cor a 8 molecule, indicating conservation among 150 Cor a 8-related protein sequences selected by ConSurf. Furthermore, Figure 3D includes Cor a 8's sequence, where the most and least conserved residues are shown and disulfide linkages are indicated.

Figure 4 shows a comparison of the surface topology of relevant epitope regions of Pru p 3 (E1, aa 11−25; E2, aa 31−45; and E3, aa 71−80)[23] with that of Cor a 8 and Zea m 14. Despite a common backbone structure, differences in the surface topology, defined by the different side chains, are obvious. When E1 from Pru p 3 is compared to the respective areas of Cor a 8 and Zea m 14, the electrostatic potentials seem to be similar. In contrast, E2 from Pru p 3 lacks the negative charges present in Cor a 8 and Zea m 14. Epitope 3 seems to be predominantly neutral in Pru p 3 and Zea m 14, whereas Cor a 8 presents more positive charges in this area.

MD Simulations for Cor a 8. Overall, the structure of the MD relaxed model of the apo form of Cor a 8 is very similar to that seen in the crystal structure. RMSD calculated for all backbone atoms between the crystal structure and a representative snapshot amounts to 2.2 Å, with somewhat larger displacements for fragments 59−63 (2.6 Å), 77−87 (3.0 Å), and the C-terminal fragment 89−92 (3.2 Å). Conformations of the disulfide bridges are preserved throughout the simulated trajectory. For Tyr79, the same rotamer (CG−CB−CA−C ca. −80°) that is observed in the crystal structure prevails (88% of snapshots) during the 150 ns long trajectory. The side chain of Tyr79 remains mostly in hydrophobic regions of the interior of the protein with nearest neighbors Val35, Ser39, Ala48, Cys49, Leu52, and Ile78. Another rotamer of Tyr79 observed in the MD trajectory (12%; CG−CB−CA−C ca. 45°) also features the side chain buried in the hydrophobic interior of the protein.

To model the structure of a Cor a 8 with laureate bound, coordinates of laureate from the stable structure of the Pru p 3/laureate complex (vide infra) were merged with those for the protein from the crystal structure 4XUW. Throughout the whole trajectory laureate remained in this binding site, that is, in the middle of the protein between the four helices, whereas Tyr79 changed its conformation at the eighth ns of the simulation. More specifically, the dihedral angle CG−CB−CA−C changed its value from ca. −63° to ca. +45° (this is a minor (12%) rotamer of Tyr79 observed for the apo form of Cor a 8), which results in placing the phenolic ring of Tyr79 in contact with the aliphatic tail of laureate. Once this configuration was attained, it remained stable until the end of the simulated trajectory. RMSD calculated for all backbone atoms amounts to 1.7 Å, and a larger displacement with respect to the crystal structure was observed for the 76−87 fragment (3.2 Å). As in other simulations, conformation of the disulfide bonds remains the same as in the crystal structure.

MD Simulations for Pru p 3. *Pru p 3/Laureate/n-Heptane Complex.* Simulation for Pru p 3 with laureate and *n*-heptane bound revealed the structure of the complex remains almost unchanged throughout the initial fragment (0−40 ns) of the simulated trajectory. Both ligands occupy the same sites as in the crystal structure, and Tyr79 is exposed at the protein surface. RMSD for the protein backbone calculated with respect to the crystal structure amounts to only 1.2 Å.

A clearly visible conformational change takes place between te 40th and 50th ns of the simulated trajectory, and it consists of movement of the 60−69 fragment (loop and helix) toward the 40−58 helix and simultaneous displacement of the *n*-heptane ligand from its original binding site toward the site originally occupied by laureate. Concertedly, Tyr79 moves into the protein's interior via changing its CG−CB−CA−C dihedral angle from around 180° to around −80°. RMSD for the backbone atoms is 1.85 Å with respect to the crystal structure, and larger differences are observed for fragment 60−69 (3.5 Å), which has moved during the conformational transition, and the C-terminal region 74−91 (2.4 Å). Laureate forms a salt bridge with Arg32, whereas its aliphatic tail takes the place occupied by *n*-heptane in the crystal structure.

Pru p 3/Laureate Complex. The initial geometry of the Pru p 3/laureate complex was obtained by removal of *n*-heptane from the crystal structure (2B5S). After simulations, the overall structure of the protein is very similar to that observed in the crystal; RMSD for all backbone atoms amounts to 1.3 Å, and it is slightly larger for the loop 19−23 (1.7 Å) and fragments 75−86 (2.0 Å) and 86−92 (2.0 Å). Notably, at a fairly early stage of the MD simulation (around 37 ns), the laureate moved from its initial binding site to the site in the middle of the protein, that is, between the four helices, which was previously occupied by *n*-heptane, and it remained in this pocket until the end of the trajectory (150 ns). Once the laureate moved deeper into the protein's interior, Tyr79 followed, finally attaining the same rotamer state as observed for a corresponding residue of Cor a 8.

Apo Pru p 3. Simulations for the apo form of Pru p 3 revealed the side chain of Tyr79 enters the hydrophobic interior of the protein within the first 2 ns of the simulation and later on this residue remains in the same rotamer state as observed for the Pru p 3/laureate complex. RMSD calculated for all backbone atoms with respect to the crystal structure is 2.7 Å; larger displacements are observed for fragments 60−69 (4.3 Å) and 74−91 (4.5 Å).

DISCUSSION

Nonspecific lipid transfer proteins are ubiquitously expressed throughout the plant kingdom, and a number of those have been identified to be important food allergens, such as Pru p 3 from peach, Mal d 3 from apple, and Act d 10 from kiwifruit. Immunological cross-reactivity is primarily due to shared 3D structures, accessible for IgE antibody recognition. However, despite their common structure, nsLTPs display low sequence identities and thus surface-exposed areas. Consequently, it was shown that members from distantly related species do not cross-react to the same extent as members within the same plant family.[50,51] Therefore, structural analysis of individual nsLTPs provides detailed information for allergenic risk assessment.

Purified natural Cor a 8 crystallized in a monoclinic crystal form with an extremely low solvent content of 28% and a Matthews coefficient of 1.71 $Å^3\ Da^{-1}$. These circumstances may contribute to how well the crystal diffracted, because crystals with

DOI: 10.1021/acs.jafc.5b03534
J. Agric. Food Chem. 2015, 63, 9150−9158

lower solvent content tend to diffract better.[52] Notably, the structure of Cor a 8 reported here (PDB ID 4XUW) is one of the most tightly packed structures reported to the PDB.[53] Cor a 8 is the first hazelnut allergen with its structure determined, and the high-resolution model that was obtained provides a very accurate template for in silico analysis of IgE cross-reactivity among Cor a 8 and other nsLTPs.

Moreover, it was shown that the allergen is more stable in an acidic environment, enabling proper refolding post thermal denaturation. These results are in good correlation with a study from Gaier et al., who showed that natural Pru p 3 is more stable under acidic conditions as compared to neutral ones.[54] The authors discuss that cleavage of disulfide bonds at neutral pH and high temperature is due to β-elimination, a reaction in which a base-catalyzed subtraction of a β-proton from a cysteine results in cleavage of disulfide bonds, which was shown for thaumatin.

Molecular dynamics simulations performed for apo- and laureate-bound forms of Cor a 8 and Pru p 3 and the laureate/*n*-heptane double complex of Pru p 3 revealed several structural features of these proteins. First, the preferred site for binding a hydrophobic ligand is located in the center of the protein's core. Second, only when two ligands are bound simultaneously, as in the 2B5S crystal structure of Pru p 3, can the Tyr79 side chain be exposed at the surface of the protein as it can be expelled from the hydrophobic interior by the second ligand. Extended MD simulation for Pru p 3/laureate/*n*-heptane complex indicates, however, that binding of two ligands is not enough to force Tyr79 out, as with binding the two ligands differently (laureate and *n*-heptane swapped and laureate bound more shallowly) Tyr79 attains a rotameric state with its side chain pointing toward the protein's core. In apo forms of the proteins and in complexes with one (laureate) ligand, the Tyr79 side chain is buried in the interior of the protein, where it lines up a substrate pocket.

Two distinctive conformational states have been observed for Pru p 3, an open conformation, which is stable when a hydrophobic ligand occupies a bottom of the substrate pocket in the center of the protein (lined up by Leu10, Cys13-Cys27, Ile14, Val17, Ala66, and Leu69 side chains). This conformation is observed in the crystal structure 2B5S, as well as in the MD simulation for the Pru p 3/laureate complex. When a ligand binds more shallowly, or it is missing completely, the 62−74 helix moves toward the 40−58 helix and a closed conformation forms. No such easily noticeable conformational changes take place upon laureate binding to Cor a 8.

Although the overall structure of nsLTPs is highly conserved, sequence identities among nsLTPs are rather low, showing different degrees of identity among different sources. Members from the Rosaceae family (peach, apple, and almond), for example, show closely related primary structures (88−97% identity), whereas nsLTPs from more distantly related plant species such as seeds, cereals, or pollens are clearly less similar to the Rosaceae allergens, as well as to each other. Borges et al. showed that, on the basis of their relatively high sequence identities, nsLTPs from Rosaceae share consensus epitopes responsible for their IgE-binding cross-reactivity.[55] However, despite their high structural conservation, it seems that nsLTPs from distantly related species do not cross-react to the same extent as members belonging to the Rosaceae family.[22,24] Cross-inhibition experiments indicate that Pru p 3 was able to at least diminish binding to other members of the nsLTP family.[24]

To get a better understanding of the structural determinants relevant for IgE cross-reactivity, we compared the obtained three-dimensional structure of Cor a 8 with known structures of other nsLTPs. Figure 4 shows a comparison of already defined Pru p 3 epitope regions[23] with the corresponding regions from Cor a 8 and Zea m 14. Differences observed in the surface topology, defined by the different side chains, became obvious (Figure 4). Focusing on the electrostatic potentials, these areas demonstrated that differences between Cor a 8 and Pru p 3 were lower as compared to differences between Pru p 3 and maize LTP. Thus, it seems that the occurrence of IgE cross-reactive epitopes is based on the degree of surface topology, dependent on side chains, which are determinants of the allergen−antibody interaction. Since the exposed residues are based on the primary sequence, one could conclude that the degree of IgE cross-reactivity between different members of the nsLTP family depends on similarities of the respective epitope region, defining the molecular surface. This finding correlates with data from a recent study by Morales et al.,[24] who demonstrated that Pru p 3 shares some common epitopes with other nsLTPs, such as Cor a 8, Mal d 3, and Zea m 14. However, no complete inhibition was observed in cross-reactivity studies. This is in accordance with data from Hartz et al., who identified patients with allergic reactions to hazelnut but tolerant for peach.[23]

Currently, only a small fraction of food allergens have their structures determined experimentally. However, it is evident that only "real" structures help us to identify relevant surface-exposed areas, which are important for antibody binding and recognition. Furthermore, obtaining structural data from distantly related members of a protein family allow for more refined/reliable predictions for the range of cross-reactivities, with and without clinical implications. In addition, this information will contribute to the development of molecules with a reduced allergenic activity that would allow for a safer immunotherapeutic approach. As a first step we think that this newly identified Cor a 8 structure will help to elucidate the range of cross-reactivity and major IgE epitopes within the nsLTP family.

■ ASSOCIATED CONTENT

Accession Codes

Coordinates and structure factors have been deposited to the PDB with the following accession code: 4XUW.

■ AUTHOR INFORMATION

Corresponding Authors

*(M.C.) Phone: (803) 777-7399. Fax: (803) 777-9521. E-mail: chruszcz@mailbox.sc.edu.

*(K.H.-S.) Phone: +43 1 40400 51040. Fax: +43 1 40400 51300. E-mail: karin.hoffmann@meduniwien.ac.at.

Funding

This work is partially supported by an ASPIRE grant from the Office of the Vice President of Research at the University of South Carolina. Further support came from the Austrian Science Fund (FWF: SFB F4603 and W1248). This research was additionally supported in part by PL-Grid Infrastructure.

Notes

The authors declare no competing financial interest.

■ ACKNOWLEDGMENTS

Data were collected at Southeast Regional Collaborative Access Team (SER-CAT) 22-BM beamline at the Advanced Photon Source, Argonne National Laboratory. Supporting institutions may be found at www.ser-cat.org/members.html. Use of the Advanced Photon Source was supported by the U.S. Department

DOI: 10.1021/acs.jafc.5b03534
J. Agric. Food Chem. 2015, 63, 9150−9158

of Energy, Office of Science, Office of Basic Energy Sciences, under Contract W-31-109-Eng-38.

ABBREVIATIONS USED

ANL, Argonne National Laboratory; APS, Advanced Photon Source; AU, asymmetric unit cell; CD, circular dichroism; MALDI-TOF-MS, matrix-assisted laser desorption ionization−time of flight−mass spectrometry; nsLTP, nonspecific lipid transfer protein; PDB, Protein Data Bank; RMSD, root-mean-square deviation; SDS, sodium dodecyl sulfate

REFERENCES

(1) Muraro, A.; Werfel, T.; Hoffmann-Sommergruber, K.; Roberts, G.; Beyer, K.; Bindslev-Jensen, C.; Cardona, V.; Dubois, A.; duToit, G.; Eigenmann, P.; Fernandez Rivas, M.; Halken, S.; Hickstein, L.; Host, A.; Knol, E.; Lack, G.; Marchisotto, M. J.; Niggemann, B.; Nwaru, B. I.; Papadopoulos, N. G.; Poulsen, L. K.; Santos, A. F.; Skypala, I.; Schoepfer, A.; Van Ree, R.; Venter, C.; Worm, M.; Vlieg-Boerstra, B.; Panesar, S.; de Silva, D.; Soares-Weiser, K.; Sheikh, A.; Ballmer-Weber, B. K.; Nilsson, C.; de Jong, N. W.; Akdis, C. A. EAACI food allergy and anaphylaxis guidelines: diagnosis and management of food allergy. *Allergy* **2014**, *69*, 1008−1025.

(2) Nwaru, B. I.; Hickstein, L.; Panesar, S. S.; Roberts, G.; Muraro, A.; Sheikh, A. Prevalence of common food allergies in Europe: a systematic review and meta-analysis. *Allergy* **2014**, *69*, 992−1007.

(3) De Knop, K. J.; Verweij, M. M.; Grimmelikhuijsen, M.; Philipse, E.; Hagendorens, M. M.; Bridts, C. H.; De Clerck, L. S.; Stevens, W. J.; Ebo, D. G. Age-related sensitization profiles for hazelnut (*Corylus avellana*) in a birch-endemic region. *Ped. Allergy Immunol.* **2011**, *22*, e139−149.

(4) Hansen, K. S.; Ballmer-Weber, B. K.; Sastre, J.; Lidholm, J.; Andersson, K.; Oberhofer, H.; Lluch-Bernal, M.; Ostling, J.; Mattsson, L.; Schocker, F.; Vieths, S.; Poulsen, L. K. Component-resolved in vitro diagnosis of hazelnut allergy in Europe. *J. Allergy Clin. Immunol.* **2009**, *123*, 1134−1141.

(5) Sicherer, S. H.; Munoz-Furlong, A.; Godbold, J. H.; Sampson, H. A. US prevalence of self-reported peanut, tree nut, and sesame allergy: 11-year follow-up. *J. Allergy Clin. Immunol.* **2010**, *125*, 1322−1326.

(6) Burney, P. G.; Potts, J.; Kummeling, I.; Mills, E. N.; Clausen, M.; Dubakiene, R.; Barreales, L.; Fernandez-Perez, C.; Fernandez-Rivas, M.; Le, T. M.; Knulst, A. C.; Kowalski, M. L.; Lidholm, J.; Ballmer-Weber, B. K.; Braun-Fahlander, C.; Mustakov, T.; Kralimarkova, T.; Popov, T.; Sakellariou, A.; Papadopoulos, N. G.; Versteeg, S. A.; Zuidmeer, L.; Akkerdaas, J. H.; Hoffmann-Sommergruber, K.; van Ree, R. The prevalence and distribution of food sensitization in European adults. *Allergy* **2014**, *69*, 365−371.

(7) Radauer, C.; Nandy, A.; Ferreira, F.; Goodman, R. E.; Larsen, J. N.; Lidholm, J.; Pomes, A.; Raulf-Heimsoth, M.; Rozynek, P.; Thomas, W. R.; Breiteneder, H. Update of the WHO/IUIS Allergen Nomenclature Database based on analysis of allergen sequences. *Allergy* **2014**, *69*, 413−419.

(8) Luttkopf, D.; Muller, U.; Skov, P. S.; Ballmer-Weber, B. K.; Wuthrich, B.; Skamstrup Hansen, K.; Poulsen, L. K.; Kastner, M.; Haustein, D.; Vieths, S. Comparison of four variants of a major allergen in hazelnut (*Corylus avellana*) Cor a 1.04 with the major hazel pollen allergen Cor a 1.01. *Mol. Immunol.* **2002**, *38*, 515−525.

(9) Pastorello, E. A.; Vieths, S.; Pravettoni, V.; Farioli, L.; Trambaioli, C.; Fortunato, D.; Luttkopf, D.; Calamari, M.; Ansaloni, R.; Scibilia, J.; Ballmer-Weber, B. K.; Poulsen, L. K.; Wutrich, B.; Hansen, K. S.; Robino, A. M.; Ortolani, C.; Conti, A. Identification of hazelnut major allergens in sensitive patients with positive double-blind, placebo-controlled food challenge results. *J. Allergy Clin. Immunol.* **2002**, *109*, 563−570.

(10) Faber, M. A.; De Graag, M.; Van Der Heijden, C.; Sabato, V.; Hagendorens, M. M.; Bridts, C. H.; De Clerck, L. S.; Ebo, D. G. Cor a 14: missing link in the molecular diagnosis of hazelnut allergy? *Int. Arch. Allergy Immunol.* **2014**, *164*, 200−206.

(11) Verweij, M. M.; Hagendorens, M. M.; Trashin, S.; Cucu, T.; De Meulenaer, B.; Devreese, B.; Bridts, C. H.; De Clerck, L. S.; Ebo, D. G. Age-dependent sensitization to the 7S-vicilin-like protein Cor a 11 from hazelnut (*Corylus avellana*) in a birch-endemic region. *J. Invest. Allerg. Clin. Immunol.* **2012**, *22*, 245−251.

(12) Masthoff, L. J.; Mattsson, L.; Zuidmeer-Jongejan, L.; Lidholm, J.; Andersson, K.; Akkerdaas, J. H.; Versteeg, S. A.; Garino, C.; Meijer, Y.; Kentie, P.; Versluis, A.; den Hartog Jager, C. F.; Bruijnzeel-Koomen, C. A.; Knulst, A. C.; van Ree, R.; van Hoffen, E.; Pasmans, S. G. Sensitization to Cor a 9 and Cor a 14 is highly specific for a hazelnut allergy with objective symptoms in Dutch children and adults. *J. Allergy Clin. Immunol.* **2013**, *132*, 393−399.

(13) Schocker, F.; Luttkopf, D.; Scheurer, S.; Petersen, A.; Cistero-Bahima, A.; Enrique, E.; San Miguel-Moncin, M.; Akkerdaas, J.; van Ree, R.; Vieths, S.; Becker, W. M. Recombinant lipid transfer protein Cor a 8 from hazelnut: a new tool for in vitro diagnosis of potentially severe hazelnut allergy. *J. Allergy Clin. Immunol.* **2004**, *113*, 141−147.

(14) Flinterman, A. E.; Akkerdaas, J. H.; den Hartog Jager, C. F.; Rigby, N. M.; Fernandez-Rivas, M.; Hoekstra, M. O.; Bruijnzeel-Koomen, C. A.; Knulst, A. C.; van Ree, R.; Pasmans, S. G. Lipid transfer protein-linked hazelnut allergy in children from a non-Mediterranean birch-endemic area. *J. Allergy Clin. Immunol.* **2008**, *121*, 423−428.

(15) Yeats, T. H.; Rose, J. K. The biochemistry and biology of extracellular plant lipid-transfer proteins (LTPs). *Protein Sci.* **2008**, *17*, 191−198.

(16) Salcedo, G.; Sanchez-Monge, R.; Barber, D.; Diaz-Perales, A. Plant non-specific lipid transfer proteins: an interface between plant defence and human allergy. *Biochim. Biophys. Acta, Mol. Cell Biol. Lipids* **2007**, *1771*, 781−791.

(17) Douliez, J. P.; Michon, T.; Elmorjani, K.; Marion, D. Structure, biological and technological functions of lipid transfer proteins and indolines, the major lipid binding proteins from cereal kernels. *J. Cereal Sci.* **2000**, *32*, 1−20.

(18) Kader, J. C.; Julienne, M.; Vergnolle, C. Purification and characterization of a spinach-leaf protein capable of transferring phospholipids from liposomes to mitochondria or chloroplasts. *Eur. J. Biochem.* **1984**, *139*, 411−416.

(19) Sy, D.; Le Gravier, Y.; Goodfellow, J.; Vovelle, F. Protein stability and plasticity of the hydrophobic cavity in wheat ns-LTP. *J. Biomol. Struct. Dyn.* **2003**, *21*, 15−29.

(20) Asero, R.; Mistrello, G.; Roncarolo, D.; de Vries, S. C.; Gautier, M. F.; Ciurana, C. L.; Verbeek, E.; Mohammadi, T.; Knul-Brettlova, V.; Akkerdaas, J. H.; Bulder, I.; Aalberse, R. C.; van Ree, R. Lipid transfer protein: a pan-allergen in plant-derived foods that is highly resistant to pepsin digestion. *Int. Arch. Allergy Immunol.* **2000**, *122*, 20−32.

(21) Lindorff-Larsen, K.; Winther, J. R. Surprisingly high stability of barley lipid transfer protein, LTP1, towards denaturant, heat and proteases. *FEBS Lett.* **2001**, *488*, 145−148.

(22) Diaz-Perales, A.; Lombardero, M.; Sanchez-Monge, R.; Garcia-Selles, F. J.; Pernas, M.; Fernandez-Rivas, M.; Barber, D.; Salcedo, G. Lipid-transfer proteins as potential plant panallergens: cross-reactivity among proteins of *Artemisia* pollen, *Castanea* nut and Rosaceae fruits, with different IgE-binding capacities. *Clin. Exp. Allergy* **2000**, *30*, 1403−1410.

(23) Hartz, C.; Lauer, I.; del Mar San Miguel Moncin, M.; Cistero-Bahima, A.; Foetisch, K.; Lidholm, J.; Vieths, S.; Scheurer, S. Comparison of IgE-binding capacity, cross-reactivity and biological potency of allergenic non-specific lipid transfer proteins from peach, cherry and hazelnut. *Int. Arch. Allergy Immunol.* **2010**, *153*, 335−346.

(24) Morales, M.; Lopez-Matas, M. A.; Moya, R.; Carnes, J. Cross-reactivity among non-specific lipid-transfer proteins from food and pollen allergenic sources. *Food Chem.* **2014**, *165*, 397−402.

(25) Otwinowski, Z.; Minor, W. Processing of X-ray diffraction data collected in oscillation mode. *Methods Enzymol.* **1997**, *276*, 307−326.

(26) Minor, W.; Cymborowski, M.; Otwinowski, Z.; Chruszcz, M. HKL-3000: the integration of data reduction and structure solution − from diffraction images to an initial model in minutes. *Acta Crystallogr., Sect. D: Biol. Crystallogr.* **2006**, *62*, 859−866.

(27) Vagin, A.; Teplyakov, A. MOLREP: an automated program for molecular replacement. *J. Appl. Crystallogr.* **1997**, *30*, 1022−1025.

DOI: 10.1021/acs.jafc.5b03534
J. Agric. Food Chem. 2015, 63, 9150−9158

(28) Winn, M. D.; Ballard, C. C.; Cowtan, K. D.; Dodson, E. J.; Emsley, P.; Evans, P. R.; Keegan, R. M.; Krissinel, E. B.; Leslie, A. G.; McCoy, A.; McNicholas, S. J.; Murshudov, G. N.; Pannu, N. S.; Potterton, E. A.; Powell, H. R.; Read, R. J.; Vagin, A.; Wilson, K. S. Overview of the CCP4 suite and current developments. *Acta Crystallogr., Sect. D: Biol. Crystallogr.* **2011**, *67*, 235−242.
(29) Emsley, P.; Cowtan, K. Coot: model-building tools for molecular graphics. *Acta Crystallogr., Sect. D: Biol. Crystallogr.* **2004**, *60*, 2126−2132.
(30) Cowtan, K. The Buccaneer software for automated model building. 1. Tracing protein chains. *Acta Crystallogr., Sect. D: Biol. Crystallogr.* **2006**, *62*, 1002−1011.
(31) Perrakis, A.; Morris, R.; Lamzin, V. S. Automated protein model building combined with iterative structure refinement. *Nat. Struct. Biol.* **1999**, *6*, 458−463.
(32) Murshudov, G. N.; Skubak, P.; Lebedev, A. A.; Pannu, N. S.; Steiner, R. A.; Nicholls, R. A.; Winn, M. D.; Long, F.; Vagin, A. A. REFMAC5 for the refinement of macromolecular crystal structures. *Acta Crystallogr., Sect. D: Biol. Crystallogr.* **2011**, *67*, 355−367.
(33) Davis, I. W.; Leaver-Fay, A.; Chen, V. B.; Block, J. N.; Kapral, G. J.; Wang, X.; Murray, L. W.; Arendall, W. B., 3rd; Snoeyink, J.; Richardson, J. S.; Richardson, D. C. MolProbity: all-atom contacts and structure validation for proteins and nucleic acids. *Nucleic Acids Res.* **2007**, *35*, W375−383.
(34) Yang, H.; Guranovic, V.; Dutta, S.; Feng, Z.; Berman, H. M.; Westbrook, J. D. Automated and accurate deposition of structures solved by X-ray diffraction to the Protein Data Bank. *Acta Crystallogr., Sect. D: Biol. Crystallogr.* **2004**, *60*, 1833−1839.
(35) Frisch, M. J.; Trucks, G. W.; Schlegel, H. B.; Scuseria, G. E.; Robb, M. A.; Cheeseman, J. R.; Scalmani, G.; Barone, V.; Mennucci, B.; Petersson, G. A.; Nakatsuji, H.; Caricato, M.; Li, X.; Hratchian, H. P.; Izmaylov, A. F.; Bloino, J.; Zheng, G.; Sonnenberg, J. L.; Hada, M.; Ehara, M.; Toyota, K.; Fukuda, R.; Hasegawa, J.; Ishida, M.; Nakajima, T.; Honda, Y.; Kitao, O.; Nakai, H.; Vreven, T.; Montgomery, J. A., Jr.; Peralta, J. E.; Ogliaro, F.; Bearpark, M. J.; Heyd, J.; Brothers, E. N.; Kudin, K. N.; Staroverov, V. N.; Kobayashi, R.; Normand, J.; Raghavachari, K.; Rendell, A. P.; Burant, J. C.; Iyengar, S. S.; Tomasi, J.; Cossi, M.; Rega, N.; Millam, N. J.; Klene, M.; Knox, J. E.; Cross, J. B.; Bakken, V.; Adamo, C.; Jaramillo, J.; Gomperts, R.; Stratmann, R. E.; Yazyev, O.; Austin, A. J.; Cammi, R.; Pomelli, C.; Ochterski, J. W.; Martin, R. L.; Morokuma, K.; Zakrzewski, V. G.; Voth, G. A.; Salvador, P.; Dannenberg, J. J.; Dapprich, S.; Daniels, A. D.; Farkas, Ö.; Foresman, J. B.; Ortiz, J. V.; Cioslowski, J.; Fox, D. J. *Gaussian 09*; Gaussian, Inc.: Wallingford, CT, USA, 2009.
(36) Case, D. A.; Cheatham, T. E., 3rd; Darden, T.; Gohlke, H.; Luo, R.; Merz, K. M., Jr.; Onufriev, A.; Simmerling, C.; Wang, B.; Woods, R. J. The Amber biomolecular simulation programs. *J. Comput. Chem.* **2005**, *26*, 1668−1688.
(37) Olsson, M. H. M.; Sondergaard, C. R.; Rostkowski, M.; Jensen, J. H. PROPKA3: consistent treatment of internal and surface residues in empirical pK(a) predictions. *J. Chem. Theory Comput.* **2011**, *7*, 525−537.
(38) Jorgensen, W. L.; Chandrasekhar, J.; Madura, J. D.; Impey, R. W.; Klein, M. L. Comparison of simple potential functions for simulating liquid water. *J. Chem. Phys.* **1983**, *79*, 926−935.
(39) Case, D. A.; Darden, T. A.; Cheatham, T. E.; Simmerling, C. L.; Wang, J.; Duke, R. E.; Luo, R.; Walker, R. C.; Zhang, W.; Merz, K. M.; Roberts, B.; Hayik, S.; Roitberg, A.; Seabra, G.; Swails, J.; Goetz, A. W.; Kolossváry, I.; Wong, K. F.; Paesani, F.; Vanicek, J.; Wolf, R. M.; Liu, J.; Wu, X.; Brozell, S. R.; Steinbrecher, T.; Gohlke, H.; Cai, Q.; Ye, X.; Wang, J.; Hsieh, M. J.; Cui, G.; Roe, D. R.; Mathews, D. H.; Seetin, M. G.; Salomon-Ferrer, R.; Sagui, C.; Babin, V.; Luchko, T.; Gusarov, S.; Kovalenko, A.; Kollman, P. A. *AMBER 12*; University of California, San Francisco, CA, USA, 2012.
(40) Salomon-Ferrer, R.; Gotz, A. W.; Poole, D.; Le Grand, S.; Walker, R. C. Routine microsecond molecular dynamics simulations with AMBER on GPUs. 2. Explicit solvent particle mesh Ewald. *J. Chem. Theory Comput.* **2013**, *9*, 3878−3888.
(41) Painter, J.; Merritt, E. A. mmLib Python toolkit for manipulating annotated structural models of biological macromolecules. *J. Appl. Crystallogr.* **2004**, *37*, 174−178.
(42) Painter, J.; Merritt, E. A. A molecular viewer for the analysis of TLS rigid-body motion in macromolecules. *Acta Crystallogr., Sect. D: Biol. Crystallogr.* **2005**, *61*, 465−471.
(43) Krissinel, E.; Henrick, K. Secondary-structure matching (SSM), a new tool for fast protein structure alignment in three dimensions. *Acta Crystallogr., Sect. D: Biol. Crystallogr.* **2004**, *60*, 2256−2268.
(44) DeLano, W. L. *PyMOL Molecular Graphics System*, 2010
(45) Pettersen, E. F.; Goddard, T. D.; Huang, C. C.; Couch, G. S.; Greenblatt, D. M.; Meng, E. C.; Ferrin, T. E. UCSF Chimera −a visualization system for exploratory research and analysis. *J. Comput. Chem.* **2004**, *25*, 1605−1612.
(46) Krissinel, E.; Henrick, K. Inference of macromolecular assemblies from crystalline state. *J. Mol. Biol.* **2007**, *372*, 774−797.
(47) Holm, L.; Rosenstrom, P. Dali server: conservation mapping in 3D. *Nucleic Acids Res.* **2010**, *38*, W545−549.
(48) Ashkenazy, H.; Erez, E.; Martz, E.; Pupko, T.; Ben-Tal, N. ConSurf 2010: calculating evolutionary conservation in sequence and structure of proteins and nucleic acids. *Nucleic Acids Res.* **2010**, *38*, W529−533.
(49) Sanchez-Monge, R.; Lombardero, M.; Garcia-Selles, F. J.; Barber, D.; Salcedo, G. Lipid-transfer proteins are relevant allergens in fruit allergy. *J. Allergy Clin. Immunol.* **1999**, *103*, 514−519.
(50) Hartz, C.; Lauer, I.; del Mar San Miguel Moncin, M.; Cistero-Bahima, A.; Foetisch, K.; Lidholm, J.; Vieths, S.; Scheurer, S. Comparison of IgE-binding capacity, cross-reactivity and biological potency of allergenic non-specific lipid transfer proteins from peach, cherry and hazelnut. *Int. Arch. Allergy Immunol.* **2010**, *153*, 335−346.
(51) Morales, M.; Lopez-Matas, M. A.; Moya, R.; Carnes, J. Cross-reactivity among non-specific lipid-transfer proteins from food and pollen allergenic sources. *Food Chem.* **2014**, *165*, 397−402.
(52) Kantardjieff, K. A.; Rupp, B. Matthews coefficient probabilities: Improved estimates for unit cell contents of proteins, DNA, and protein-nucleic acid complex crystals. *Protein Sci.* **2003**, *12*, 1865−1871.
(53) Trillo-Muyo, S.; Jasilionis, A.; Domagalski, M. J.; Chruszcz, M.; Minor, W.; Kuisiene, N.; Arolas, J. L.; Sola, M.; Gomis-Ruth, F. X. Ultratight crystal packing of a 10 kDa protein. *Acta Crystallogr., Sect. D: Biol. Crystallogr.* **2013**, *69*, 464−470.
(54) Gaier, S.; Marsh, J.; Oberhuber, C.; Rigby, N. M.; Lovegrove, A.; Alessandri, S.; Briza, P.; Radauer, C.; Zuidmeer, L.; van Ree, R.; Hemmer, W.; Sancho, A. I.; Mills, C.; Hoffmann-Sommergruber, K.; Shewry, P. R. Purification and structural stability of the peach allergens Pru p 1 and Pru p 3. *Mol. Nutr. Food Res.* **2008**, *52* (Suppl. 2), S220−S229.
(55) Borges, J. P.; Barre, A.; Culerrier, R.; Granier, C.; Didier, A.; Rouge, P. Lipid transfer proteins from Rosaceae fruits share consensus epitopes responsible for their IgE-binding cross-reactivity. *Biochem. Biophys. Res. Commun.* **2008**, *365*, 685−690.

DOI: 10.1021/acs.jafc.5b03534
J. Agric. Food Chem. 2015, 63, 9150−9158

to its immiscibility in water, its low concentration, and the complexity of milk matrices. The determination of milk 17β-estradiol has been carried out by immunological[18] techniques, which offer several advantages compared to conventional analysis (i.e., low cost per sample, high selectivity, and high sensitivity) but are time-consuming. A really valid alternative to detect hormonal contaminants in foods, even 17β-estradiol levels in milk, is biosensors. It has recently been acknowledged that biosensor technologies represent a greatly versatile approach for their capability to solve a large number of analytical problems related to agriculture and food safety as well as environmental security, pharmacology, and medicine.[19] Recently, our laboratory has increased the knowledge about this topic and developed fluorescence polarization assays for the detection of penicillin G directly in milk[20] and of patulin in fruit juices.[21] In the present work, we describe a similar fluorescence polarization approach to measure traces of 17β-estradiol in milk. This assay is based on the use of an ad hoc synthesized 17β-estradiol hemisuccinate−glutamine-binding protein (GlnBP) conjugate labeled with fluorescent probe (Biotium CF647) and of polyclonal monospecific anti-17β-estradiol antibodies. Then, a competitive immunoassay has been performed with the aim to detect 17β-estradiol in milk sample without pretreatment steps. This method is rapid and innovative, and the analysis can be conducted directly in the real matrix with no interference due to different milk compounds, using an infrared emitting probe.

In conclusion, this technique represents a novel approach that allows the detection of any contaminant in a food matrix only by changing fluorescent conjugate molecules and specific antibodies; thus, it is a promising analytical tool in food quality and safety control.

MATERIALS AND METHODS

Reagents. All commercially available reagents were chosen for the highest quality. 1-[3-(Dimethylamino)propyl]-3-ethylcarbodiimide (EDC), bovine serum albumin (BSA; fraction V), 17β-estradiol, ovalbumin (OVA), and 3,5-tetramethylbenzidine (TMB) were purchased from Sigma-Aldrich (St. Louis, MO, USA). A PURE1A Protein A Antibody Purification Kit was purchased from Sigma. Goat polyclonal to rabbit IgG−HRP conjugate (secondary antibody) was from Abcam (Cambridge, UK). Affinity resin EAH Sepharose 4B and ECL detection reagents used in Western blot experiments were purchased from Amersham Biosciences (GE Healthcare Switzerland). Protran nitrocellulose transfer membranes were purchased from Schleicher & Schuell (Dassel, Germany). Microplates (96-well), Nunc LockWell MaxiSorp form, and a microplate reader, Multiskan EX from Thermo Scientific, were used for ELISA experiments. UV measurements were carried out on a Varian Cary 50 Bio spectrophotometer (Agilent Technologies, Santa Clara CA, USA). The fluorescent probe CF647 was purchased from Biotium (Hayward, CA, USA). Fluorescence experiments were performed with an FP-8600 fluorescence spectrometer (Jasco, Japan).

Synthesis of 17β-Estradiol-hemisuccinate. The 17β-estradiol-hemisuccinate (Figure 1B) was synthesized from 17β-estradiol (Figure 1A) following the previously reported procedure[22] but with minor modifications. Briefly, the 17β-estradiol (270 mg, 1.0 mmol) was dissolved in 12 mL of a mixture of benzene/pyridine (8:2, v/v) and refluxed with a succinic anhydride solution (600 mg, 6 mmol) for 24 h. TLC analysis showed the disappearance of the 17β-estradiol and the formation of two bands with a R_f lower than that of 17β-estradiol. The reaction mixture was dried under reduced pressure, and the residue was dissolved in acetone/ethanol (3 mL, 1:1, v/v) and purified by silica gel chromatography. For this purpose, the solution was absorbed on a small amount of silica gel (5.0 g) and, after evaporation of the solvent, the silica was applied on the top of a silica gel column, which

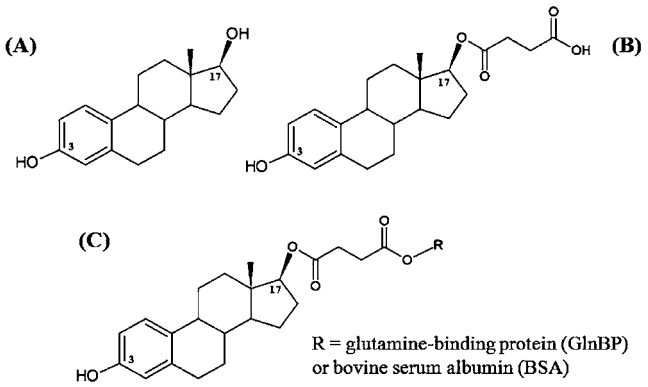

Figure 1. Chemical structure of the 17β-estradiol (A), 17β-estradiol-hemisuccinate derivative (B), and the GlnBP conjugate used for the production of the rabbit anti-17β-estradiol antibodies (C).

was eluted with an increasing amount of methanol in dichloromethane (DCM) (from 0 to 5% of MeOH). The purification furnished the estradiol-3,17β-bis-succinate (70% yield, lower R_f) and a product (at higher R_f), which was identified as a mixture of β-estradiol-3-hemisuccinate (15% yield) and β-estradiol-17-hemisuccinate (15% yield). The estradiol-3,17β-bis-succinate (300 mg), suspended in 10 mL of MeOH, was then treated with 10 mL of a 1.2 M solution of $NaHCO_3$, and the mixture was kept at room temperature under stirring for 15 h. The selective hydrolysis of phenolic ester furnished, as expected, a mixture of estradiol-3β and estradiol-17β-hemisuccinate. The latter (95% yield from bis-succinate) was further purified on a silica gel column (as previously described) eluted with an increasing amount of MeOH in DCM (from 0 to 20%, v/v). ^{1}H NMR and MS results were in agreement with those reported previously.[22]

Preparation of the 17β-Estradiol-hemisuccinate−BSA Conjugate for the Immunization Procedure. The 17β-estradiol-hemisuccinate−BSA conjugate (Figure 1C) was prepared by adding a solution of 17β-estradiol-hemisuccinate (2 mg) in 1 mL of 0.1 M MES buffer, pH 6.0, to a BSA solution (2 mg/mL) in 0.5 mL of the same buffer and 0.1 mL of an EDC solution in H_2O (10 mg/mL). The reaction mixture was incubated for 16 h at 4 °C and then extensively dialyzed for 3 days, against potassium phosphate buffer (20 mM), pH 7.4. The obtained conjugate was spectrophotometrically analyzed at λ = 278 nm (2 mg/mL), but the efficiency of conjugation could not be determined because the maximum absorptions at 278 nm of estradiol (275 nm) and BSA are overlapped.

Antibody Production and Purification. Two rabbits were immunized following a standard protocol by intradermal inoculation of an antigen (0.5 mg per rabbit). After the immunization period, the rabbits were sacrificed, and their blood was recovered and centrifuged to separate blood cells from serum. A 1.5 mL sample of rabbit serum diluted with 1.5 mL of binding buffer Tris (50 mM), pH 7.0, was applied to a protein A column of the PURE 1A Protein A Antibody Purification Kit, Sigma, and the IgG fraction was purified in agreement with the manufacturer's instructions. The IgG fraction was eluted with glycine (0.1 M) at pH 3.0, and immediately buffered in Tris-HCl (1.0 M), at pH 9.0, and its concentration and purity were checked by absorbance measurement at λ = 278 nm and sodium dodecyl sulfate−polyacrylamide gel electrophoresis (SDS-PAGE) analysis, respectively.

Affinity Column Preparation of 17β-Estradiol-hemisuccinate−EAH Sepharose 4B. The affinity column was obtained by conjugating 17β-estradiol-hemisuccinate to EAH Sepharose 4B. Briefly, Sepharose resin (0.6 mL) was washed with distilled water adjusted to pH 4.5 (20 mL) and with HCl, followed by 0.5 M NaCl (80 mL), and then added to a solution of 17β-estradiol-hemisuccinate (2 mg in 0.5 mL of H_2O), and the resulting suspension was gently shaken. The slurry was cooled to 0 °C, and EDC was added to a final concentration of 0.1 M. The reaction mixture was incubated overnight at 4 °C and then it was taken to room temperature. The suspension was washed with H_2O at pH 4.5, 0.1 M acetate buffer containing 0.5 M

DOI: 10.1021/acs.jafc.5b03689
J. Agric. Food Chem. 2015, 63, 9159−9164

NaCl (20 mL), pH 4.0, and 0.1 M PBS containing 0.3 M NaCl, pH 7.4, and finally packed into a polystyrene column (2 mL, Bio-Rad). For the affinity chromatography purification, a solution of IgG (8.0 mg/mL), obtained from protein A purification, was applied dropwise to the previously prepared affinity column. Before elution of the monospecific IgG, three high-salt buffers at pH 7, all containing 10 mM PBS but increasing concentrations of NaCl (0.1, 0.5, amd 1.0 M, respectively), were used to wash away antibodies weakly and unspecifically bound to the column. Instead, monospecific IgG was eluted with 0.1 M glycine, at pH 3.0, and appropriately monitored by absorbance measurements at 278 nm and SDS-PAGE. The fractions containing the antibodies were collected and dialyzed against a buffer containing 0.01 M PBS and 0.1 M NaCl, pH 7.4. The concentration of the monospecific antibodies, spectrophotometrically determined at λ = 278 nm, was 1.3 mg/mL

Preparation of 17β-Estradiol-hemisuccinate−GlnBP Conjugate. The 17β-estradiol-hemisuccinate was conjugated to *Escherichia coli* GlnBP, a protein different from that used for the immunization process, with the aim of avoiding interferences due to BSA during the polyclonal antibody detection. The synthesis of 17β-estradiol-hemisuccinate−GlnBP conjugate (Figure 1C) was carried out following the same procedure previously described for the 17β-estradiol-hemisuccinate−BSA conjugate.

Antibody Titration Experiments. The antibody titer was determined by an indirect ELISA. The antigen (17β-estradiol-hemisuccinate−GlnBP), dissolved in 0.1 M PBS, pH 7.4, was used to coat 96-well microplates, at increasing concentrations from 125 to 5000 ng/mL, and incubated overnight at 4 °C. Control wells were incubated for the same period with GlnBP dissolved in the same buffer. The wells were flushed three times with TBS 1× containing 0.05% Tween (TBST), pH 7.4, and blocked by incubation for 1 h at room temperature with TBST containing OVA (1%). After two washings with TBST, polyclonal and polyclonal monospecific anti-estradiol antibodies were serially diluted in blocking buffer, added to the wells, incubated at room temperature for 1 h, and then washed twice with TBST. Horseradish peroxidase-conjugated anti-rabbit IgG antibodies, diluted 1:12000 in blocking buffer, were added to the wells and incubated at room temperature for 1 h. After two washings with TBST, the enzyme substrate TMB was added, and the color reaction was quenched by adding 2 M HCl, for 5 min. The absorbance measurements were recorded at 450 nm.

Western Blot Experiments. Proteins (BSA, GlnBP, and 17β-estradiol-hemisuccinate−GlnBP, 20 μg for each lane) were separated by 12% SDS-PAGE and then transferred overnight at 4 °C onto a nitrocellulose membrane. Membranes were blocked for 30 min at room temperature in 50 mL of the blocking buffer (TBS containing 5% of milk), washed with TBST (10 min for each washing), and incubated with purified monospecific IgG (1:100000 in the blocking buffer containing Tween 0.05%) for 1 h at room temperature. After three washings with TBST, the filters were incubated with secondary antibody (goat anti-rabbit HRP conjugate, 1:6000 in the blocking buffer containing Tween 0.05%) for 1 h at room temperature and washed three times as described above. Finally, proteins were visualized by chemoluminescence using the Amersham ECL plus and X-ray films developed on the Compact X4, Xograph Imaging systems.

Fluorescence Labeling of 17β-Estradiol-hemisuccinate−GlnBP and Steady-State Fluorescence Measurements. A solution of 17β-estradiol-hemisuccinate−GlnBP (2.0 mg/mL) was concentrated by nitrogen flow and diluted with 0.1 M sodium bicarbonate buffer, pH 7.0, at a final concentration of 4.0 mg/mL. This solution was mixed with the CF647 dye (Biotium) at a protein/dye molar ratio of 1:10 and incubated for 1 h at 37 °C. The labeled molecules were separated from unreacted probe by gel filtration and extensive dialysis in PBS buffer at pH 7.0. Steady-state fluorescence experiments were performed by using an FP-8600 fluorescence spectrometer, equipped with a thermostatic cell holder. The excitation wavelength was fixed at 630 nm, and emission spectra were recorded between 650 and 800 nm with excitation and emission slit widths of 5 and 2.5 nm, respectively. The fluorescence measurements were performed at 25 °C on five times diluted solutions of milk with PBS at pH 7.4. 17β-Estradiol-hemisuccinate−GlnBP-CF647 was incubated with a range of concentrations of antibodies against 17β-estradiol from 0.0 to 2.2 pmol for 10 min, and polarization fluorescence measurements were acquired by inserting a Glan polarizer between the excitation source and the sample, with a vertical (0°) excitation and emission polarized filter.

17β-Estradiol Competitive Assay. A competitive polarization assay was performed at a fixed concentration of antibody against 17β-estradiol (2.2 pmol) in the presence of increasing concentrations of unlabeled 17β-estradiol contaminating the milk (five times diluted with PBS at pH 7.4) at a range of concentration from 0.0 to 47 pmol. The incubation was performed at 25 °C for 10 min. After this pre-incubation in the presence of unlabeled 17β-estradiol, polarization fluorescence measurements were carried out with an FP-8600 fluorescence spectrometer with an excitation and an emission polarized filter set at 0°. The temperature of samples was measured directly in the cuvette with an accuracy of ±0.2 °C.

RESULTS AND DISCUSSION

Steroids have been widely used as growth-promoting agents in livestock with the principal aim to reduce the FCE and increase the animal weight gain and the milk yield in breeding of meat and milk animals. The administration of naturally and synthetic anabolic growth promoters in food-producing animals is now prohibited by the EU because of their potential risk to consumer's health. Nevertheless, illegal use or abuse of 17β-estradiol as an additive in animal feed or as subcutaneous injections, in hormonal treatments, implies a contamination of produced milk with several consequences for human health.[23] In the absence of a precise regulation that sets the maximum limit of such substances in milk and official methods of analysis, the development of procedures addressed at this aim is of great importance. A rapid and simple method to detect the concentration of 17β-estradiol in milk is urgently needed to control all phases of milk production, from the cattle shed to the consumers' table.

Antibody Fluorescence Polarization-Based Sensor for 17β-Estradiol Sensing. In the context of high competence in the biosensor field, we propose a new method of 17β-estradiol detection that combines fluorescence polarization assays and a strategy well-established by our research group (Figure 2), starting from the functionalization of the 17β-estradiol to a more reactive carboxylic derivative with a significantly higher antibody response. Actually, in this context, the 17β-estradiol derivatization process is markedly necessary to obtain a derivate exhibiting a higher stability and a short arm to be conjugated to the protein carrier while maintaining the original skeleton of estradiol. 17β-Estradiol binding to a carrier protein through a spacer such as a hemisuccinic arm is necessary to distance the antigen from the same protein. On the other hand, the presence of a carrier protein conjugated to the hormone was then strongly required for amplifying the immunological response of antibodies against 17β-estradiol that would otherwise be too small because of its very low molecular weight. Then, the synthesis of 17β-estradiol-hemisuccinate was preliminarily carried out with the aim of preparing the antigen 17β-estradiol-hemisuccinate−BSA conjugate (BSA was chosen as carrier protein) to be used in the standard protocols of immunization on two different rabbits (Figure 2). At the end of the immunization period, a protein A antibody chromatograph was used to separate the IgG fraction from the complex pool of serum protein, whereas a further affinity chromatography by EAH Sepharose 4B resin was carried out to isolate specifically

DOI: 10.1021/acs.jafc.5b03689
J. Agric. Food Chem. 2015, 63, 9159−9164

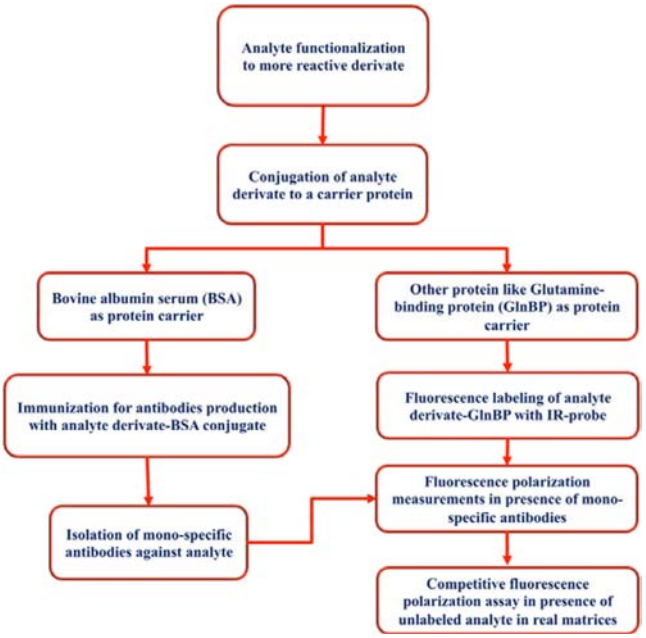

Figure 2. Flowchart of strategy for antibody fluorescence polarization-based sensor.

the monospecific antibodies against 17β-estradiol from total IgG fraction. To verify the specificity and titer of produced antibodies, the 17β-estradiol-hemisuccinate−GlnBP conjugate instead of the 17β-estradiol-hemisuccinate−BSA conjugate was used for the further analysis because of interference problems due to the presence of BSA during the polyclonal antibody detection.

Specificity and Titer of Produced Monospecific Antibodies. The preliminary SDS-PAGE analysis (Figure 3A) of BSA, GlnBP, and 17β-estradiol-hemisuccinate−GlnBP

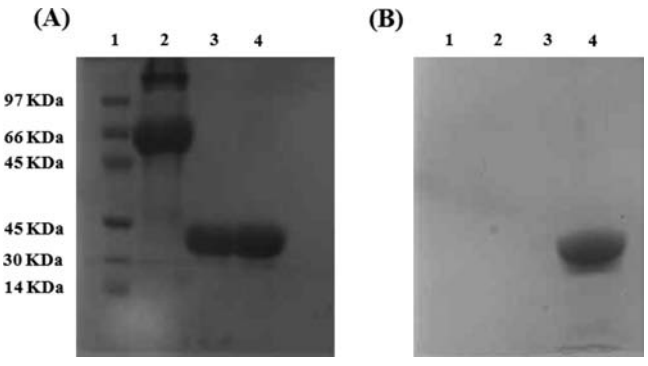

Figure 3. SDS-PAGE (A) and nitrocellulose filter (B) after incubation with 17β-estradiol antibodies. Lanes: 1, molecular weight standards; 2, BSA; 3, GlnBP; 4, 17β-estradiol-hemisuccinate−GlnBP.

demonstrated the purity of the preparations, used in the Western blotting experiments (Figure 3B) to verify the specificity of the produced antibodies. The response to antibody binding was observed only for the conjugate 17β-estradiol-hemisuccinate−GlnBP, and a negative response was registered for BSA and GlnBP (Figure 3B). This confirms the specificity of antibodies versus the only estradiol. In addition, an indirect ELISA test was performed to evaluate the titer of polyclonal monospecific purified antibodies. The results have shown that no signal was registered as a consequence of incubation with different diluted samples of IgG for noncoated wells, whereas an increase of the absorbance was registered as a function of decreasing the dilution factor of polyclonal monospecific antibodies against 17β-estradiol (data not shown). The titer was considered as the maximum antibody dilution able to give a reading of 0.1 absorbance unit. The experiment, performed in triplicate, showed that the titer of anti-17β-estradiol antibodies was excellent. In fact, it was possible to perform the ELISA test with mono-specific IgG dilutions up to 1 to 100000.

Fluorescence Steady-State Measurements of 17β-Estradiol-hemisuccinate−GlnBP-CF 647 Conjugate and Competitive Immunoassay. 17β-Estradiol-hemisuccinate−GlnBP was labeled with a fluorescence probe (CF647 dye), possessing near-infrared emission, to record changes in the emission processes on the basis of specific binding to anti-estradiol antibodies. The polarized emission spectra of 17β-estradiol-hemisuccinate−GlnBP-CF647 fluorescent conjugate were acquired in the absence and in the presence of increasing concentrations of antibodies against estradiol ranging from 0.0 to 2.2 pmol (Figure 4). The fluorescence polarization spectrum

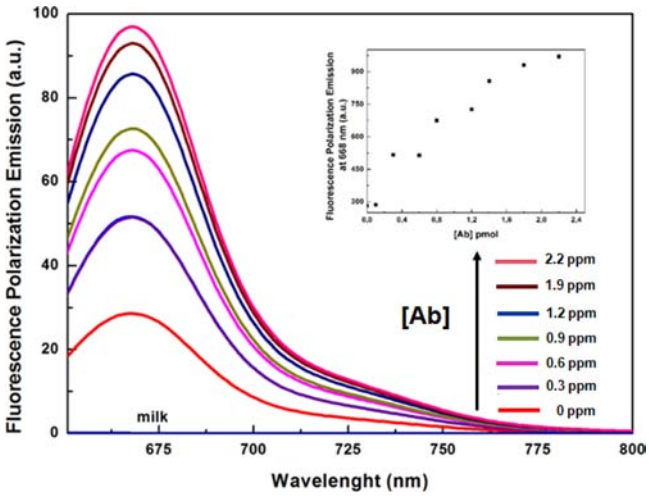

Figure 4. Polarization emission spectra of 17β-estradiol-hemisuccinate−GlnBP-CF647 in the absence and in the presence of increasing concentration of antibodies against 17β-estradiol.

of milk samples showed a maximum of fluorescence emission, centered at 668 nm, and revealed an increase of 17β-estradiol-hemisuccinate−GlnBP-CF647 fluorescence polarization emission as a consequence of binding with anti-17β-estradiol antibody, present in solution. Subsequently, a fluorescence polarization competitive immunoassay was used to measure unlabeled 17β-estradiol in solution. To evaluate the competition between 17β-estradiol-hemisuccinate−GlnBP-CF647 and unlabeled 17β-estradiol for binding with monospecific antibodies against 17β-estradiol, different samples at a fixed concentration of antibody (2.2 pmol) were incubated in the presence of increasing concentrations of unlabeled 17β-estradiol in a range between 0.0 and 47 pmol, before the fluorescence polarization measurements were performed. The polarized fluorescence spectrum in the presence of increasing concentrations of unlabeled 17β-estradiol showed a reduction of fluorescence emission following increasing concentrations of unlabeled 17β-estradiol (Figure 5). The presence of increasing concentrations of the analyte in the milk samples allowed return to the minimum measurable value of the analyte. The

DOI: 10.1021/acs.jafc.5b03689
J. Agric. Food Chem. 2015, 63, 9159−9164

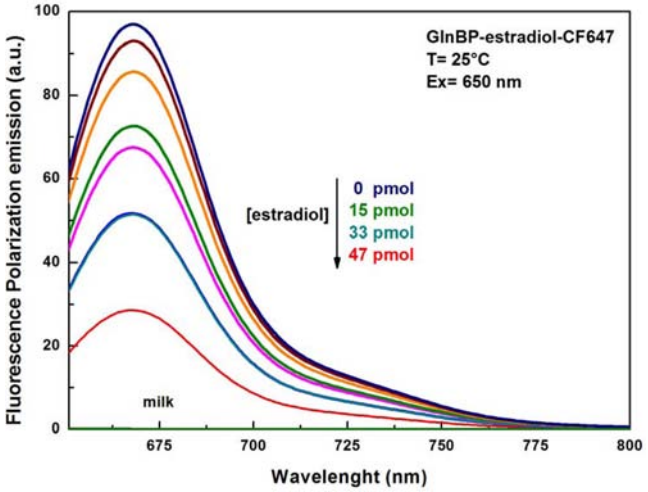

Figure 5. Polarization fluorescence emission spectra of 17β-estradiol-hemisuccinate−GlnBP-CF647.

dose response curve for 17β-estradiol detection in diluted milk reported the polarization fluorescence variations (at 668 nm) as a function of 17β-estradiol concentration (Figure 6). The results demonstrated that 17β-estradiol concentration was easily calculable in milk with a limit of detection (LOD)[24] of <10 pmol, lower than the EU limit.

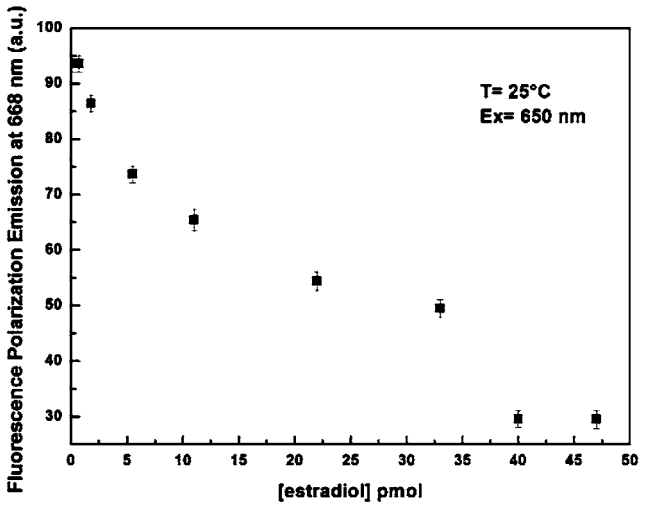

Figure 6. Titration of fluorescence polarization immunoassay with increasing concentration of unlabeled 17β-estradiol.

During the past decade, different efforts have been made by other groups to identify and quantify the presence of 17β-estradiol in food. In the field of biosensor, several assays based on the use of human estrogen receptor have been developed for the determination of 17β-estradiol. These biosensors are highly sensitive but unfortunately not suitably specific due to the wide range of affinity of estrogen receptor to other xenoendocrines.[25,26] Recently, immunosensors and nanobiosensors have also been developed for sensitive and rapid detection of 17β-estradiol by utilizing antibodies or functional polymers,[27,28] ane a DNA-Aptamer optical biosensor has been realized for the detection of 17β-estradiol in water.[29] The present paper shows a fluorescence polarization competitive immunoassay for detecting 17β-estradiol up to a concentration of <10 pmol. This assay can be carried out directly in a real matrix, without any sample pretreatment, providing great advantages in time and cost terms. In addition, the simplicity and quickness of 17β-estradiol quantification, performable during every step of milk production from milking to the commercial product, offer further reasons why our procedure could be preferred to others. Actually, it is not the first time that we have developed a fluorescence polarization-based method to measure a contaminant analyte in a food matrix. During past years, several papers from our laboratory have demonstrated the possibility of detecting other contaminants such as penicillin G[20] and patulin,[21] in milk and in juice, respectively, by using a very similar strategy (Figure 2), even at concentrations much lower than the established EU limit. Our expertise in this field gives us great confidence that this approach can be extended to any contaminant and to any food by carrying out minor modifications, thanks to the high flexibility of the developed method. Therefore, it is our opinion that the fluorescence immunoassay is a valid alternative to the analytical techniques, currently in use, and it can become a promising tool in the control of food quality and safety.

AUTHOR INFORMATION

Corresponding Author

*(S.D'A.) Phone: +39-0825 299101. Fax: +39-0825 78158. E-mail: sabato.dauria@cnr.it.

Funding

This project was realized within the framework of the CNR Commessa "Progettazione e Sviluppo di Biochip per la Sicurezza Alimentare e Salute Umana (SD; MS; AV)" and partially funded by the "SAFE &SMART" project − Nuove tecnologie abilitanti per la food safety e l'integrità delle filiere agro-alimentari in uno scenario globale" (CTN01_00230_240864).

Notes

The authors declare no competing financial interest.

ABBREVIATIONS USED

FCE, feed conversion efficiency; ELISA, enzyme-linked immunosorbent assay; GlnBP, glutamine-binding protein; EDC, 1-[3-(dimethylamino)propyl]-3-ethylcarbodiimide; BSA, bovine serum albumin; OVA, ovalbumin; TMB, 3,5-tetramethylbenzidine; DCM, dichloromethane; SDS-PAGE, sodium dodecyl sulfate−polyacrylamide gel electrophoresis; TBST, Tris-buffer saline Tween

REFERENCES

(1) Schams, D.; Karg, H. Hormones in milk. *Ann. N. Y. Acad. Sci.* **1986**, *464*, 75−86.

(2) Lopez, H.; Bunch, T. D.; Shipka, M. P. Estrogen concentrations in milk at estrus and ovulation in dairy cows. *Anim. Reprod. Sci.* **2002**, *72*, 37−46.

(3) Council Directive 96/22 EC. *Off. J. Eur. Communities* **1996**, *L125*, 3.

(4) Spearow, J. L.; Barkley, M. Genetic control of hormone-induced ovulation rate in mice. *Biol. Reprod.* **1999**, *61*, 851−856.

(5) MacDonald, P. C.; Madden, J. D.; Brenner, P. F.; Wilson, J. D.; Siiteri, P. K. Origin of estrogen in normal men and women with testicular feminization. *J. Clin. Endocrinol. Metab.* **1979**, *49*, 905−916.

(6) Henderson, B. E.; Ross, R.; Bernstein, L. Estrogens as a cause of human cancer: the Richard and Hinda Rosenthal Foundation award lecture. *Cancer Res.* **1988**, *48*, 246−253.

(7) Key, T. J.; Pike, M. C. The dose−effect relationship between 'unopposed' oestrogens and endometrial mitotic rate: its central role in

DOI: 10.1021/acs.jafc.5b03689
J. Agric. Food Chem. 2015, 63, 9159−9164

explaining and predicting endometrial cancer risk. *Br. J. Cancer* **1988**, *57*, 205−212.
(8) Council Directive 96/23 EC. *Off. J. Eur. Communities* **1996**, *L125*, 10−32.
(9) Scortichini, G.; Annunziata, L.; Haouet, M. N.; Benedetti, F.; Krusteva, I.; Galarini, R. ELISA qualitative screening of chloramphenicol in muscle, eggs, honey and milk: method validation according to the Commission Decision 2002/657/EC criteria. *Anal. Chim. Acta* **2005**, *535*, 43−48.
(10) McDonald, J. G.; Matthew, S.; Auchus, R. J. Steroid profiling by gas chromatography-mass spectrometry and high performance liquid chromatography-mass spectrometry for adrenal diseases. *Horm. Cancer* **2011**, *2*, 324−332.
(11) Anizan, S.; Bichon, E.; Monteau, F.; Cesbron, N.; Antignac, J. P.; Le Bizec, B. A new reliable sample preparation for high throughput focused steroid profiling by gas chromatography-mass spectrometry. *J. Chromatogr. A* **2010**, *1217*, 6652−6660.
(12) Courant, F.; Antignac, J. P.; Maume, D.; Monteau, F.; Andre, F.; Le Bizec, B. Determination of naturally occurring oestrogens and androgens in retail samples of milk and eggs. *Food Addit. Contam.* **2007**, *24*, 1358−1366.
(13) Perez, N.; Gutierrez, R.; Noa, M.; Diaz, G.; Luna, H.; Escobar, J.; Munire, Z. Liquid chromatographic determination of multiple sulfonamides, nitrofurans, and chloramphenicol residues in pasteurized milk. *J. AOAC. Int.* **2002**, *85*, 20−24.
(14) D'Orazio, G.; Asensio-Ramos, M.; Hernández-Borges, J.; Rodríguez-Delgado, M. Á.; Fanali, S. Evaluation of the combination of a dispersive liquid-liquid microextraction method with micellar electrokinetic chromatography coupled to mass spectrometry for the determination of estrogenic compounds in milk and yogurt. *Electrophoresis* **2015**, *36*, 615−625.
(15) Yan, W.; Li, Y.; Zhao, L.; Lin, J. M. Determination of estrogens and bisphenol A in bovine milk by automated on-line C30 solid-phase extraction coupled with high-performance liquid chromatography−mass spectrometry. *J. Chromatogr. A* **2009**, *1216*, 7539−7545.
(16) Zhu, Q.; Wang, L.; Wu, S.; Joseph, W.; Gu, X.; Tang, J. Selectivity of molecuarly imprinted solid phase extraction for sterol compounds. *Food Chem.* **2009**, *113*, 608−615.
(17) Shao, B.; Zhao, R.; Meng, J.; Xu, Y.; Wu, G.; Hu, J.; Tu, X. Simultaneous determination of residual hormonal chemicals in meat, kidney, liver tissues and milk by liquid chromatography-tandem mass spectrometry. *Anal. Chim. Acta* **2005**, *548*, 41−50.
(18) Scippo, M. L.; Van De Weerdt, C.; Willemsen, P.; François, J. M.; Rentier-Delrue, F.; Muller, M.; Martial, J. A.; Maghuin-Rogister, G. Detection of illegal growth promoters in biological samples using receptor binding assays. *Anal. Chim. Acta* **2002**, *473*, 135−141.
(19) Kirsch, J.; Siltanen, C.; Zhou, Q.; Revzin, A.; Simonian, A. Biosensor technology: recent advances in threat agent detection and medicine. *Chem. Soc. Rev.* **2013**, *42*, 8733−8768.
(20) Pennacchio, A.; Varriale, A.; Scala, A.; Marzullo, V. M.; Staiano, M.; D'Auria, S. A novel fluorescence polarization assay for determination of penicillin G in milk. *Food Chem.* **2016**, *190*, 381−385.
(21) Pennacchio, A.; Varriale, A.; Esposito, M. G.; Staiano, M.; D'Auria, S. A near-infrared fluorescence assay method to detect patulin in food. *Anal. Biochem.* **2015**, *481*, 55−59.
(22) Das, M.; Singh, R. P.; Datir, S. R.; Jain, S. Intranuclear drug delivery and effective in vivo cancer therapy via estradiol−PEG-appended multiwalled carbon nanotubes. *Mol. Pharmaceutics* **2013**, *10*, 3404−3416.
(23) Travis, R. C.; Key, T. J. Oestrogen exposure and breast cancer risk. *Breast Cancer Res.* **2003**, *5*, 239−247.
(24) Armbruster, D. A.; Pry, T. Limit of blank, limit of detection and limit of quantitation. *Clin. Biochem. Rev.* **2008**, *29*, 49−52.
(25) Miyashita, M.; Shimada, T.; Miyagawa, H.; Akamatsu, M. Surface plasmon resonance-based immunoassay for 17β-estradiol and its application to the measurement of estrogen receptor-binding activity. *Anal. Bioanal. Chem.* **2005**, *381*, 667−673.
(26) Liss, M.; Petersen, B.; Wolf, H.; Prohaska, E. An aptamer-based quartz crystal protein biosensor. *Anal. Chem.* **2002**, *74*, 4488−4495.
(27) Wozei, E.; Hermanowicz, S. W.; Holman, H. Y. N. Developing a biosensor for estrogens in water samples: Study of the real-time response of live cells of the estrogen-sensitive yeast strain RMY/ERERE using fluorescence microscopy. *Biosens. Bioelectron.* **2006**, *21*, 1654−1658.
(28) Pemberton, R. M.; Mottram, T. T.; Hart, J. P. Development of screen-printed carbon electrochemical immunosensor for picomolar concentrations of estradiol in human serum extracts. *J. Biochem. Biophys. Methods* **2005**, *63*, 201−212.
(29) Yildirim, N.; Long, F.; Gao, C.; He, M.; Shi, H. C.; Gu, A. Z. Aptamer-based optical biosensor for rapid and sensitive detection of 17β-estradiol in water samples. *Environ. Sci. Technol.* **2012**, *46*, 3288−3294.

DOI: 10.1021/acs.jafc.5b03689
J. Agric. Food Chem. 2015, 63, 9159−9164

regulated at the transcriptional level by regulatory genes, and thus plant pigmentation patterns are mainly controlled by the expression profiles of regulatory genes.[15−17] The anthocyanin biosynthetic pathway includes genes encoding the enzymes chalcone synthase (*CHS*), chalcone isomerase (*CHI*), flavanone 3′-hydroxylase (*F3H*), dihydroflavonol reductase (*DFR*), leucoanthocyanidin dioxygenase (*LDOX*), and UDP-glucose:-flavonoid 3-*O*-glucosyltransferase (*UFGT*), which were partially cloned in grapevine by Sparvoli et al.[18] The *CHI* (X75963) and *UFGT* (AF000372) genes have been identified in *V. vinifera* and are located in chromosomes 13 and 16, respectively. Despite their localization in the anthocyanin pathway, UFGT and CHI are considered key enzymes.[19] CHI leads to the formation of flavanones in a central branching point of the flavonoid pathway;[16] on the other hand, UFGT is located in a final position of the anthocyanin pathway and is associated with the accumulation of anthocyanins in the berries' skin.[20−22] The *CHI* gene and the remaining genes (*PAL*, *CHS*, *F3H*, *DFR*, *LDOX*) are expressed in both white and red grapevine varieties. *UFGT* is expressed only in red grapevine varieties, and its expression is crucial for anthocyanin biosynthesis.[14,20]

The aim of this study was to develop a new HRM assay for grapevine varietal identification based on the detection of SNPs, insertions, and/or deletions (IN/DELs) in two genes involved in the anthocyanin pathway.

Table 1. Grapevine Varieties Used for SNP Identification, Corresponding Code, and Berry Color

grapevine variety name	code	berry color
Alicante Bouschet	AB	red
Cabernet Sauvignon	CS	red
Chardonnay	Ch	white
Côdega de Larinho	CL	white
Donzelinho tinto	DT	red
Fernão Pires	FP	white
Gouveio	Gou	white
Merlot	M	red
Malvasia Fina	MF	white
Moscatel Galego	MG	white
Pinot Noir	PN	red
Rufete	Ruf	red
Sousão	Sou	red
Tinta Amarela	TA	red
Tinta Barroca	TB	red
Touriga Brasileira	TBr	red
Tinto Cão	TC	red
Touriga Franca	TF	red
Tinta Francisca	TFi	red
Touriga Nacional	TN	red
Tinta Roriz	TR	red
Viosinho	Vio	white

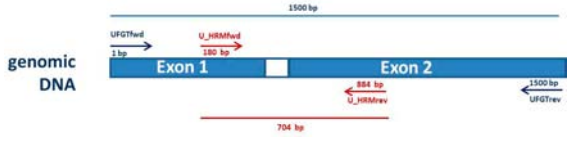

Figure 1. Schematic representation of the primer set used in the *UFGT* gene. The empty space corresponds to the intron.

Table 2. Single-Nucleotide Polymorphisms Identified in *UFGT* Gene with Information on the Genotypes Composition Found across the 22 Grapevine Varieties (*Vitis vinifera* L.)[a]

sample	nucleotide position: 90	98	139	205	207	220	238	240	257	264	265	272	309	366	375	424	425	442	459	483	525	555	560	562	598	600	617	619	636	663	685	762	789	816	841	843
UFGT	C	C	C	G	G	G	G	C	A	G	C	T	G	T	T	-	G	C	C	G	A	A	A	G	A	T	C	A	C	C	A	C	C	T	A	A
TBr	·	·	·	·	·	·	·	·	·	·	·	·	·	·	·	-	·	·	·	·	·	·	·	·	·	·	·	·	·	·	·	·	·	·	·	·
Ch	S	·	·	R	S	S	·	·	·	·	·	·	·	·	Y	-	·	·	·	·	·	M	·	·	·	·	·	·	·	·	·	·	·	·	R	·
MG	S	·	·	R	S	S	·	·	·	·	·	Y	R	·	Y	-	·	·	Y	S	W	M	·	·	·	·	·	·	·	·	·	·	·	·	R	·
GOU	·	·	·	·	·	S	·	M	·	·	·	·	·	·	Y	-	·	·	·	S	W	M	R	·	·	Y	·	·	Y	Y	·	·	·	·	G	·
CS	S	·	·	R	S	S	·	·	·	·	M	Y	A	·	C	T	·	·	Y	S	W	C	·	·	·	·	·	·	·	·	·	·	Y	·	G	W
Sou	S	·	·	R	S	S	·	·	·	·	M	Y	A	·	C	T	·	·	T	S	W	C	·	·	·	·	·	·	·	·	·	·	Y	·	G	W
Vio	S	·	·	R	S	S	·	·	·	·	A	Y	A	·	C	-	·	·	Y	S	W	C	·	·	·	·	·	·	·	·	·	·	Y	·	G	W
FP	G	·	·	A	C	C	·	·	·	·	M	C	A	·	C	-	·	M	T	·	T	C	·	·	T	·	·	·	·	·	·	·	Y	·	G	·
TR	G	·	·	A	C	C	·	·	·	·	M	C	A	·	C	-	·	·	T	·	T	C	·	·	W	·	·	·	·	·	·	·	Y	·	G	·
MF	G	·	·	A	C	C	·	·	·	·	A	C	A	·	C	-	·	·	T	·	T	C	·	·	W	·	·	·	·	·	·	·	Y	·	G	·
Ruf	G	·	·	R	S	C	R	·	·	·	M	C	A	·	C	-	K	M	Y	·	W	C	·	·	W	·	·	·	·	·	·	·	·	·	G	·
M	·	·	·	·	·	·	·	·	·	·	·	·	W	W	C	·	K	C	·	C	·	C	·	·	·	·	·	·	·	·	·	·	·	·	G	T
TB	·	·	·	·	·	·	·	·	·	·	·	·	A	·	C	·	K	·	·	C	·	C	·	·	·	·	·	·	·	·	·	·	·	·	G	T
TN	·	·	·	·	·	·	·	·	·	·	·	·	R	·	Y	·	K	·	·	S	·	M	·	·	·	·	·	·	·	·	·	·	·	·	R	W
TF	·	Y	S	·	·	S	R	·	R	K	·	·	R	·	Y	·	K	·	·	S	·	C	R	R	·	·	M	R	Y	Y	·	Y	M	Y	G	W
TFi	·	Y	S	·	·	S	R	·	R	K	·	·	R	·	Y	·	·	·	·	S	·	C	R	R	·	·	M	R	Y	Y	·	Y	M	Y	G	W

DOI: 10.1021/acs.jafc.5b03463
J. Agric. Food Chem. 2015, 63, 9165−9174

Table 2. continued

	nucleotide position																																		
sample	90	98	139	205	207	220	238	240	257	264	265	272	309	366	375	424	425	442	459	483	525	555	560	562	598	600	617	619	636	663	685	762	789	816	841	843
AB	.	Y	S	.	.	S	R	.	R	K	.	.	R	.	Y	-	.	.	.	S	.	C	R	R	.	.	M	R	Y	Y	.	Y	M	Y	G	W
TA	.	Y	S	.	.	S	R	.	R	K	.	.	R	.	Y	-	.	.	.	S	.	C	R	R	.	.	M	R	Y	Y	.	Y	M	Y	G	W
CL	.	Y	S	.	.	S	R	.	R	K	.	.	R	.	Y	-	.	.	.	S	.	C	R	R	.	.	M	R	Y	Y	.	Y	M	Y	G	W
TC	S	Y	S	R	S	C	R	.	R	K	.	Y	R	.	Y	-	.	.	Y	.	W	C	R	R	.	.	M	R	Y	Y	.	Y	M	C	G	.
DT	.	Y	S	.	.	C	R	M	R	K	.	.	.	.	Y	-	.	.	.	.	.	C	G	R	.	Y	A	G	T	T	.	Y	M	Y	G	.
PN	.	Y	S	.	.	S	S	.	R	K	.	.	.	.	.	-	.	.	Y	.	W	M	.	.	.	.	.	.	.	.	W	.	.	.	S	W

	nucleotide position																							
sample	850	943	955	1014	1054	1083	1122	1131	1134	1144	1146	1160	1165	1193	1232	1245	1273	1345	1404	1405	1409	1459	1481
UFGT	A	C	G	G	T	G	A	T	A	T	G	C	G	A	C	A	G	G	T	T	A	T	A
TBr	.	.	.	.	.	.	.	.	.	.	.	.	.	.	.	.	.	.	.	.	.	.	.
Ch	.	.	.	K	.	.	.	.	.	.	.	.	.	W	Y	.	R	R	.	.	.	.	.
MG	.	.	.	.	.	.	.	.	.	.	.	.	.	W	.	.	.	R	.	.	.	.	.
GOU	.	.	.	.	.	.	.	.	.	K	.	.	.	W	.	.	.	R	.	.	.	.	.
CS	.	S	K	.	Y	.	M	Y	T	.	.	.	.	T	Y	M	A	A	.	.	W	.	.
Sou	.	S	K	.	Y	.	M	Y	T	.	.	.	.	T	Y	M	A	A	.	.	W	.	.
Vio	.	S	K	.	Y	.	M	Y	T	.	.	.	.	T	Y	M	A	A	.	.	W	.	.
FP	.	S	K	.	Y	.	M	Y	T	.	.	.	.	T	T	M	A	A	.	.	W	Y	.
TR	.	S	K	.	Y	.	M	Y	T	.	.	.	.	T	T	M	A	A	.	W	W	Y	R
MF	.	S	K	.	Y	.	M	Y	T	.	.	.	.	T	T	.	A	A	.	.	W	.	.
Ruf	.	.	.	.	Y	.	.	.	T	.	.	.	K	T	T	M	A	A	.	.	.	Y	R
M	.	.	.	.	C	.	.	.	T	.	.	.	.	T	.	.	A	A	.	.	.	.	.
TB	.	.	.	.	C	.	.	.	T	.	.	.	.	T	.	.	A	A	.	.	.	.	.
TN	.	.	.	.	Y	.	.	.	W	.	.	.	.	W	.	.	R	R	.	.	.	.	.
TF	W	.	.	.	Y	.	.	.	T	.	R	S	.	T	Y	.	A	A	.	.	.	.	.
TFi	W	.	.	.	Y	.	.	.	T	.	R	S	.	T	Y	.	A	A	.	.	.	.	.
AB	W	.	.	.	Y	.	.	.	T	.	R	S	.	T	Y	.	A	A	.	.	.	.	.
TA	W	.	.	.	Y	.	.	.	T	.	R	S	.	T	Y	.	A	A	.	.	.	.	.
CL	W	.	.	.	Y	.	.	.	T	.	R	S	.	T	Y	.	A	A	.	.	.	.	.
TC	W	S	K	.	.	.	M	Y	T	.	R	S	.	T	T	M	A	A	.	.	W	.	.
DT	W	.	.	.	.	.	.	.	W	K	R	S	.	T	Y	.	R	A	.	.	.	.	.
PN	.	.	.	.	Y	R	.	.	W	.	.	.	.	W	Y	.	R	R	Y	.	.	.	.

[a]Numbering starts with A of the start codon. Nucleotide code: A, adenine; C, cytosine; T, thymine; G, guanine; M, A or C; R, A or G; W, A or T; S, C or G; Y, C or T; and K, G or T.

DOI: 10.1021/acs.jafc.5b03463
J. Agric. Food Chem. 2015, 63, 9165−9174

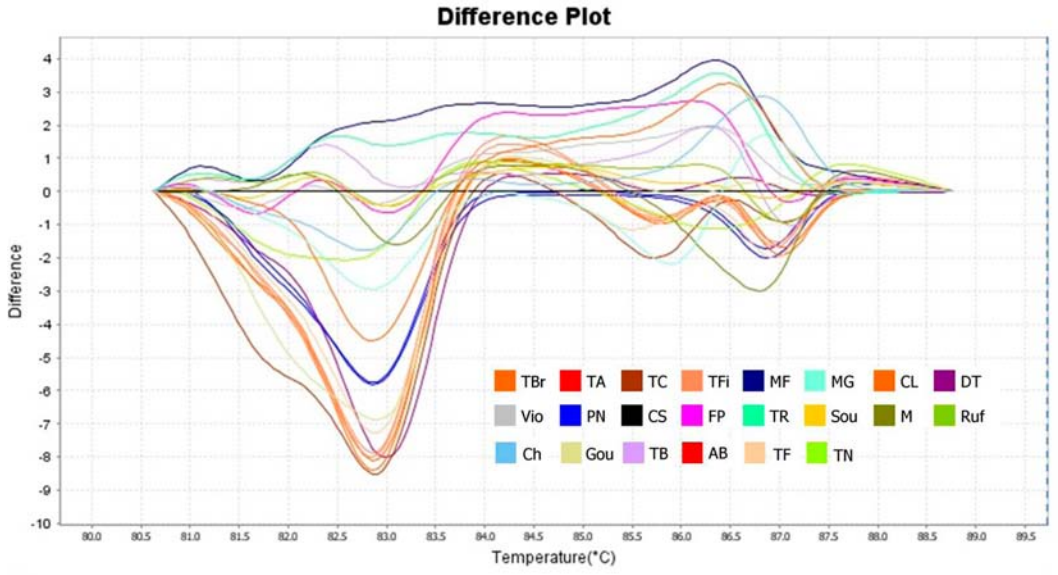

Figure 2. HRM difference plot of 22 grapevine varieties for UFGT fragment showing 18 different genotypes.

MATERIALS AND METHODS

***Vitis vinifera* L. Samples.** Twenty-two *V. vinifera* grapevine varieties (red and white) considered as the most representative genotypes used in wine production in Portugal, including both national and international accessions, were used. Young leaves of each grapevine variety (Table 1) were collected from the Sogrape Vinhos S.A. and Real Companhia Velha vineyards located in the Douro region and immediately frozen in liquid nitrogen.

Young leaves belonging to the clones of each grapevine variety were collected and immediately frozen in liquid nitrogen, from clonal fields belonging to the Sogrape enterprise, to the Sociedade Borges S.A., the Direção Regional de Agricultura e Pescas do Norte, and to the National Ampelographic Collection (CAN), located at Dois Portos in the National Vitivinicultural Research Station (EVN-INIAV).

Genomic DNA Extraction. Total genomic DNA was extracted from frozen young leaves using the CTAB method.[23] Each DNA sample was eluted in 100 μL of 0.1× TE buffer (100 mM Tris-HCl, 0.1 mM EDTA, pH 8), and the purity, integrity, and quantity of all DNA samples were estimated on Nanodrop 1000 spectrophotometer (Thermo Fisher Scientific, Wilmington, DE, USA) measurements and by electrophoresis on 0.8% agarose in 1×Tris−acetate−EDTA (TAE).

SNP Detection: Primer Design, PCR Assays, and PCR Product Sequencing. For SNP detection, single-copy genes are preferred over multicopy to avoid problems associated with paralog genes. In *Vitis*, both *UFGT* and *CHI* genes are single-copy genes; however, the number of *CHI* genes is dependent on the species.[17,24,25] The National Center for Biotechnology Information database (NCBI) was used to find sequences related to these genes using *V. vinifera* genome database (VvGDB). The *UFGT* and *CHI* genes were amplified using primers UFGTfwd (5′-ATGTCTCAAACCACCACCAAC-3′) and UFGTrev (5′-CCGGGAAACCTTTATTTTCA-3′) (Figure 1) and CHIfwd (5′-TATCCCCGAAGATGTCTCCA-3′) and CHIrev (5′-AAAGTG-TCCCGGATGTTAC-3′). generating 1500 and 1725 bp amplicons, respectively. Primers were designed in Primer3 software, considering the following parameters: size (between 18 and 22 bases in length), melting temperature (T_m) in the range of 50−60 °C; a %GC between 40 and 60, and absence of dimerization capability and of significant hairpin formation (>3 bp). The PCR reactions were performed in a 20 μL volume, containing 20 ng of genomic DNA, 1× PCR buffer, 25 mM $MgCl_2$, 0.2 mM dNTPs, 0.2 μM of each primer, and 0.3 U of *Taq* DNA polymerase (Roche). The reactions were incubated at 94 °C for 3 min, followed by 30 cycles of 94 °C/1 min, 58 °C/1 min, 72 °C/2 min, and a final step of 72 °C for 10 min.

PCR amplicons resulting from the amplification of *UFGT* and *CHI* genes were directly sequenced (STAB VIDA; http://www.stabvida.com), and the genotypes of the 22 grapevine varieties were obtained. Sequence alignment was performed using the BioEdit program (http://www.mbio.ncsu.edu/BioEdit/BioEdit.html). The alignments of reverse and forward sequences were applied to produce consensus sequences. The sequences of each individual DNA fragments were aligned with the original sequence to identify the SNP presence.

High-Resolution Melting Assay Design. HRM analysis was performed in a specific 704 bp fragment of the *UFGT* gene using primers U_HRMfwd (5′-GCAATGTAATATCAAGTCC-3′) (starting at 180 bp) and U_HRMrev (5′-TTTCTTTCTTTGAGCCATT-3′) (ending at 884 bp) (Figure 1).

PCR and HRM analyses were performed in a StepOne Real-Time PCR System (Applied Biosystems, Foster City, CA, USA) in a final volume of 20 μL containing the respective primer pair (5 pmol of each primer), 20 ng of gDNA, and the MeltDoctor HRM Master Mix (Applied Biosystems). PCR/HRM included an initial step of 10 min at 95 °C and 40 cycles of 30 s at 95 °C, 30 s at 58 °C, and 30 s at 72 °C. The melting curve was obtained continuously, performed as follows: 30 s at 95 °C, 1 min at 65 °C, 15 s at 95 °C, rising 0.3 °C/s, and 15 s at 65 °C. All reactions were performed in triplicate. High Resolution Melt Software v3.0.1 (Applied Biosystems) was used to analyze the data. After normalization and determination of the temperature shift, the different melting curves of the several plots were generated.

To validate the reference HRM profile for each grapevine variety, DNA from the clones was analyzed using the developed HRM assay, using the previously described conditions.

Phylogenetic Analysis. Predicted amino acid sequences were used for phylogenetic analysis using the COBALT multiple-sequence alignment tool, which takes into consideration the conserved domain database, protein motif database, and sequence similarity (http://www.st-va.ncbi.nlm.nih.gov/tools/cobalt/re_cobalt.cgi).[26]

RESULTS AND DISCUSSION

SNP Identification. The *CHI* gene is located in a central position in the anthocyanin pathway. This gene was sequenced in 22 grapevine varieties (14 Portuguese and 8 international), revealing the existence of only 5 SNPs among all of these varieties (data not shown). The low number of SNPs detected within this gene is in accordance with previous studies, making it a noninteresting marker for varietal identification purposes.[11,27]

DOI: 10.1021/acs.jafc.5b03463
J. Agric. Food Chem. 2015, 63, 9165−9174

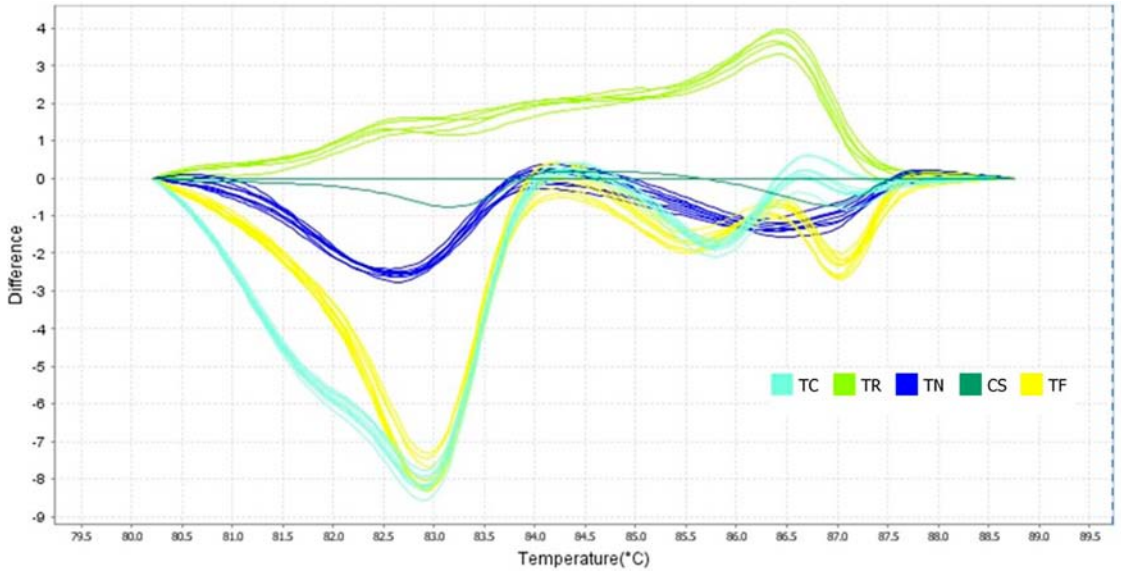

Figure 3. HRM different curves of the most representative grapevine varieties used in wine production in Portugal and corresponding clones for UFGT fragment.

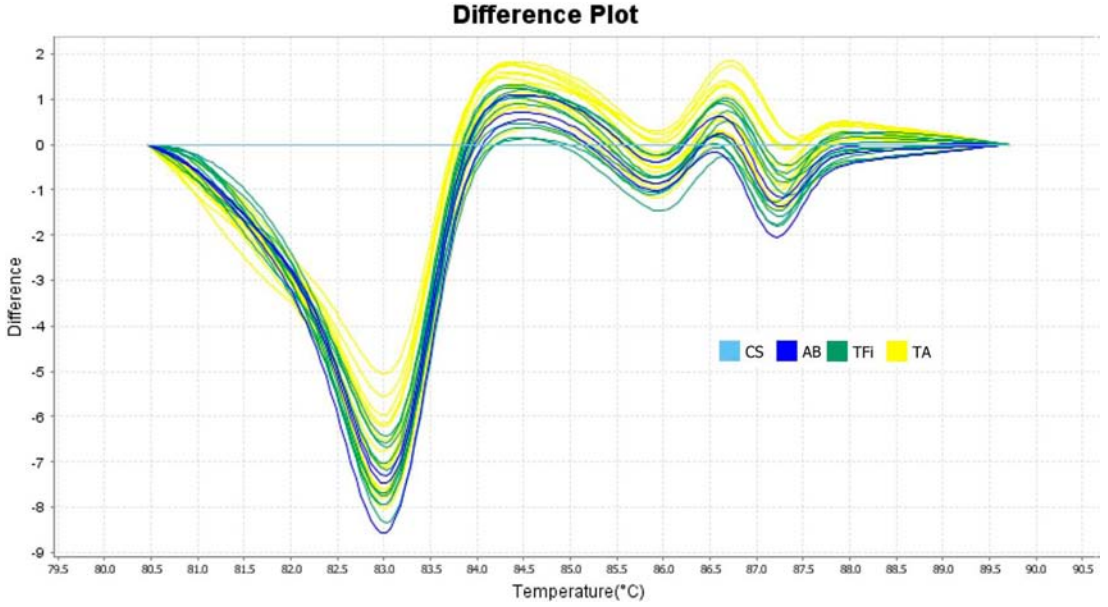

Figure 4. Difference plot of the grapevine varieties and corresponding clones presenting the same genotype for UFGT fragment.

On the contrary, the *UFGT* gene was revealed to be highly polymorphic, presenting a high number of SNPs among the grapevine varieties studied. The *UFGT* gene length covered 1500 bp, and within this region a total of 58 SNPs and an insertion were detected (Table 2). Eighteen SNPs and the insertion were found within the exon 1 region (493 bp) with an average frequency of 1 SNP/25.9 nucleotides. Four SNPs were found in the intron (74 bp) with an average frequency of 1 SNP/18.5 nucleotides. The remaining 36 SNPs were positioned within the exon 2 region (881 bp) with an average frequency of 1 SNP/24.5 nucleotides. These results are interesting because the number of SNPs detected within the coding region is high, contrary to previous studies (sunflower,[28] cotton,[29] and grapevine[30]) where the majority of the SNPs were located in the noncoding region of the genes. The high SNP frequency found within this gene is particularly interesting because *UFGT* has been previously associated with several different types of anthocyanins,[11] which are directly involved in berry skin color and grape organoleptic characteristics.

High-Resolution Melting Curve PCR Analysis. The *CHI* gene was not considered for the HRM approach because the number of SNPs found did not allow the discrimination of the varieties under study.

The HRM assay was designed for *UFGT* gene considering a fragment size of 704 bp. The UFGT HRM fragment included 32 of the 58 SNPs present and the detected insertion, considering the 22 grapevine varieties under study, with an average frequency of 1 SNP/22 nucleotides. Considering the same fragment length, Nicolè et al.[31] reported a frequency of 1 SNP/31.69 nucleotides, revealing that this gene is highly polymorphic and, therefore, interesting for varietal identification.

DOI: 10.1021/acs.jafc.5b03463
J. Agric. Food Chem. 2015, 63, 9165−9174

Table 3. Predicted Amino Acid Sequence Variations in UFGT, Using the Reference Genome, Based on the SNPs Found across the 22 Grapevine Varieties (*Vitis vinifera* L.)[a]

	amino acid position																														
sample	33	47	69	74	80	86	88	89	91	142	153	161	174	181	182	204	256	259	290	293	312	327	357	362	364	373	386	400	424	444	445
UFGT	A	Q	V	A	A	D	E	L	M	A	T	G	N	S	K	M	I	T	L	A	R	Y	L	A	G	Y	A	E	G	F	K
CS	.	.	I	P	.	.	.	.	T	.	I	A	.	.	.	.	V	.	V	S	.	H	.	.	.	F	V	K	R	.	I
Sou	.	.	I	P	.	.	.	.	T	.	I	A	.	.	.	.	V	.	V	S	.	H	.	.	.	F	V	K	R	.	I
Vio	.	.	I	P	.	.	.	.	T	.	I	A	.	.	.	.	V	.	V	S	.	H	.	.	.	F	V	K	R	.	I
FP	.	.	I	P	.	.	.	M	T	.	I	.	Y	.	.	.	V	.	V	S	.	H	.	.	.	F	V	K	R	.	I
MF	.	.	I	P	.	.	.	M	T	.	I	.	Y	.	.	.	V	.	V	S	.	H	.	.	.	F	V	K	R	.	I
TR	.	.	.	P	.	.	.	M	T	.	I	.	Y	.	.	.	V	.	.	S	.	H	.	.	.	F	V	K	R	I	I
Ruf	.	.	.	P	T	.	.	M	T	.	I	.	Y	.	.	.	V	.	.	.	.	H	.	.	W	F	V	K	R	.	.
Ch	.	.	.	P	.	.	.	.	.	.	.	.	.	.	.	.	.	.	.	.	S	.	.	.	.	.	V	.	.	.	.
MG	.	.	.	P	.	.	.	.	T	.	I	.	.	.	.	.	.	.	.	.	.	.	.	.	.	.	.	.	.	.	.
TBr	.	.	.	.	.	.	.	.	.	.	.	.	.	.	.	.	.	.	.	.	.	.	.	.	.	.	.	.	.	.	.
GOU	.	.	.	P	.	.	.	.	.	.	.	.	.	Y	E	.		.	.	.	.	.	V	.	.	.	.	.	.	.	.
M	.	.	.	.	.	.	.	.	.	S	.	A	.	.	.	.	V	.	.	.	.	H	.	.	.	F	.	K	R	.	.
TB	.	.	.	.	.	.	.	.	.	S	.	A	.	.	.	.	V	.	.	.	.	H	.	.	.	F	.	K	R	.	.
TN	.	.	.	.	.	.	.	.	.	S	.	A	.	.	.	.	.	.	.	.	.	H	.	.	.	.	.	.	.	.	.
PN	V	E	.	P	P	G	D	.	.	.	I	.	.	.	.	L	L	.	.	.	.	H	.	.	.	.	V	.	.	.	.
TFi	V	E	.	P	T	G	D	.	.	.	.	A	.	Y	E	.	V	S	.	.	.	H	.	G	.	F	V	K	R	.	.
AB	V	E	.	P	T	G	D	.	.	.	.	A	.	Y	E	.	V	S	.	.	.	H	.	G	.	F	V	K	R	.	.
CL	V	E	.	P	T	G	D	.	.	.	.	A	.	Y	E	.	V	S	.	.	.	H	.	G	.	F	V	K	R	.	.
TA	V	E	.	P	T	G	D	.	.	.	.	A	.	Y	E	.	V	S	.	.	.	H	.	G	.	F	V	K	R	.	.
TF	V	E	.	P	T	G	D	.	.	S	.	A	.	Y	E	.	V	S	.	.	.	H	.	G	.	F	V	K	R	.	.
DT	V	E	.	P	T	G	D	.	.	.	.	.	.	Y	E	.	V	S	.	.	.	.	V	G	.	F	V		R	.	.
TC	V	E	I	P	T	G	D	.	T	.	I.	.	.	Y	E	.	V	S	V	S	.	.	.	G	.	F	V	K	R	.	I

[a]Amino acid code: A, alanine; D, aspartic acid; E, glutamic acid; F, phenylalanine; G, glycine; H, histidine; I, isoleucine; K, lysine; L, leucine; M, methionine; N, asparagine; P, proline; Q, glutamine; R, arginine; S, serine; T, threonine; V, valine; W, tryptophan; Y, tyrosine.

DOI: 10.1021/acs.jafc.5b03463
J. Agric. Food Chem. 2015, 63, 9165−9174

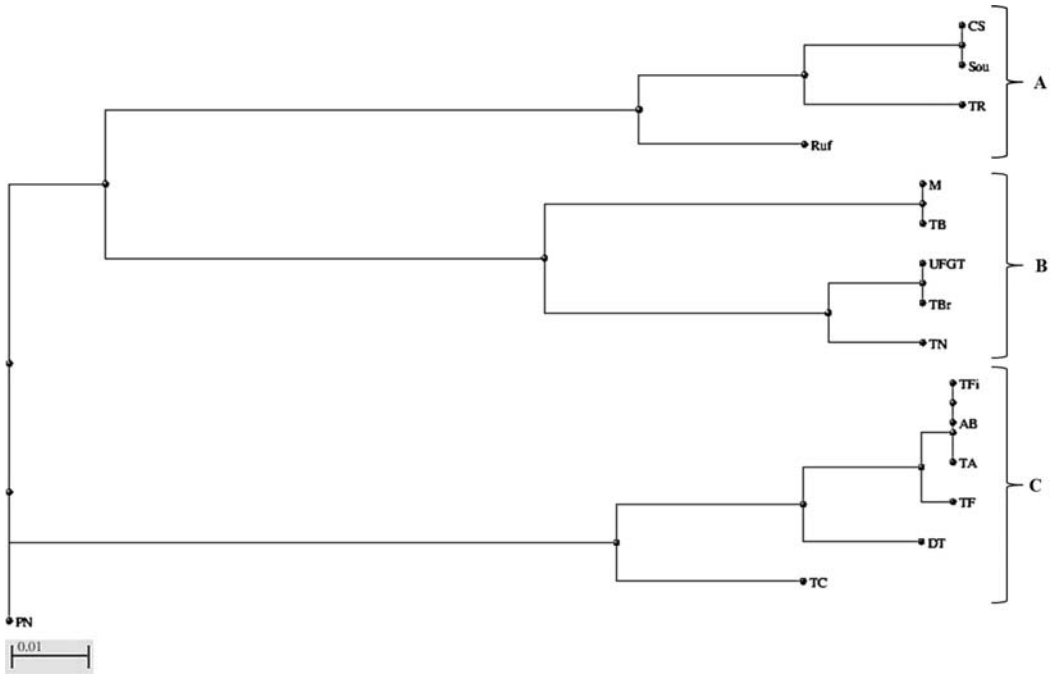

Figure 5. Phylogenetic tree based on deduced amino acid sequence variations of UFGT from the red grapevine varieties using the Cobalt multiple-sequence alignment tool.

Fragment size influences the sensitivity of subsequent HRM analysis, and it is usually advisible that the size does not exceed 300 bp length.[32] In addition, long amplicons may contain several melting domains, resulting in complex melting profiles, meaning that longer amplicons represent small differences in the melting curve caused by small sequence variation. In plants, the studies using HRM report a PCR amplicon range of 50−260 bp.[8,33−35] To our knowledge this is the first paper considering such a large fragment size (704 bp). Therefore, this method is quite promising as it broadens the genotyping potential using HRM analysis. The UFGT targeted sequence generated 18 different melting curve profiles (Figure 2). The T_m values found within all of the samples were similar (T_{m1} = 82.7−83.0 °C; T_{m2} = 86.6−86.9 °C), which did not distinguish the different haplotypes. However, the shapes of the melting curves were very informative, and even when the grapevine variety sequence differed by only a single SNP, this variation was detectable for (a) CS, Sou, and Vio and (b) FP, TR, and MF grapevine varieties (Table 2). Additionally, all of these SNPs belong to class 4, A/T, which is the most challenging genotype variation mainly due to the difficulty associated with the difference in T_m.[7]

These results demonstrate the power, sensitivity, and specificity of this particular HRM assay that allows the identification of several complex genotypes and subsequently the detection of different melting curves (Figure 2). The assay was successful in the definition of the several haplotypes once it was based on the combination of a high number of SNPs within the amplified fragment.

Even though the assay is based on a long fragment, this HRM assay proved to be highly sensitive and was able to distinguish 18 haplotypes based on a combination of 33 nucleotide differences in a unique assay. Previous studies reported the detection of several SNPs and INDELs but always considering simple events,[33,36−39] and not a combination of nucleotide differences. Never, until now, has it been reported that by using a unique assay was it possible to detect such a high number of events in one reaction. The designed HRM assay proved to be powerful and specific.

The shape of the HRM curve for each grapevine variety needed to be further validated in relation to their varietal specification, once there are a high number of clones available within each grapevine variety.[40] Therefore, DNA samples from different clones of each grapevine variety were used and tested for reproducibility. The plants were sampled in established clonal field collections, maintained jointly in private and public institutions, including samples of different regions of the country. The melting curve profiles obtained for each variety were coincident among clones of the same haplotype, indicating that such an assay can be used in the genotype identification of these particular grapevine varieties (Figure 3). The shapes of the melting curve profiles of five red grapevine varieties used in the Douro region are presented as an example in Figure 3. Among them, Cabernet Sauvignon (CS) is used as an international grapevine reference variety. The clones of each grapevine variety present the same genetic profile, reinforcing the assay's robustness.

Four of the 22 grapevine varieties studied (Tinta Francisca, Alicante Bouschet, Côdega de Larinho, and Tinta Amarela) could not be distinguished using this particular HRM assay (Figure 4), once they presented the same sequence for this particular region (Table 2). The sequences of these grapevine varieties differ only from Touriga Franca (TF) in a unique SNP at the 425 bp position (Table 2), which is discriminated using this particular assay.

The robustness of the HRM assay could also be confirmed by the profiles obtained in the clones of the undistinguishable grapevine varieties herein tested (Figure 4), once all of the samples tested presented the same shape HRM melting curve, as expected.

With all of the nucleotide sequences taken into consideration, in particular, the SNPs found in the 22 grapevine

DOI: 10.1021/acs.jafc.5b03463
J. Agric. Food Chem. 2015, 63, 9165−9174

varieties, the amino acid sequences were deduced and aligned. A total of 31 amino acid residue variations were found within the grapevine varieties studied (Table 3).

UFGT gene expression is correlated with the grapevine phenotype, and its transcription is needed for berry pigmentation (no color/red color).[41,42] The anthocyanin profile and content can deeply influence the final wine quality.[43] With the variation of the red grapevine variety amino acid sequences studied taken into consideration, a Cobalt tree was constructed, giving rise to three major groups (Figure 5). Group A included CS, Sou, TR, and Ruf; group B incorporated M, TB, TBr, and TN; and group C comprised TFi, AB, TA, TF, DT, and TC. The Pinot Noir clones analyzed were completely distinguished from all of the grapevine varieties, and therefore they generated an independent branch. The differences found between the amino acid sequence of Pinot Noir and the sequence of the NCBI database were expected, becaue the NCBI reference genome is a hybrid of Pinot Noir.[4] Touriga Brasileira presented the same amino acid sequence as reported in the NCBI database relative to the *UFGT* locus.

Although the *UFGT* gene expression is related to the anthocyanin profile of the grapes,[41] there is a lack of information on the specific profile of each grapevine variety. Some of the most widely used grapevine varieties have been characterized, among them Pinot Noir, Merlot, and Cabernet Sauvignon.

Pinot Noir grapes have a differentiated anthocyanin profile, with only monoglucoside anthocyanins, in contrast with other grapevine varieties (Merlot, Cabernet Sauvignon, Touriga Franca, Tinta Roriz, Touriga Nacional, Sousão, Rufete, Tinta Amarela, Tinta Barroca, Tinto Cão) that present all three types of anthocyanin (monoglucosides, acetates, and coumarates).[44−47] This may justify the outstanding position of Pinot Noir in relation to the other grapevine varieties studied. However, the amino acid variation present within the UFGT sequence has a direct implication on the protein composition, which may or not influence the protein function.

The results obtained through this work represent a good landmark in this particular area and should be considered as a suitable platform for further studies. The deduced amino acid sequences set the bases for a better understanding of the correlation between anthocyanin content and the amino acid profiles.

The present work confirmed the low level of polymorphism of the *CHI* gene and revealed a high level of polymorphism present within the *UFGT* gene of grapevine. The *UFGT* gene allowed the discrimination of 18 different grapevine genotypes among 22 grapevine varieties. From the 58 SNPs and 1 INDEL were predicted a total of 31 amino acid residual changes, enhancing the potential effect on the anthocyanin profile of each variety, which opens doors for further omic studies considering this particular gene.

This study provides the first report on the use of a large fragment in HRM assays, thereby allowing the detection of multiple events (SNP and INDEL) in a unique assay, which can be adapted for large-scale genotyping and mapping in *Vitis*. This assay can be extended for grapevine varietal certification procedures, which are imperative throughout the entire wine chain (plant nursery to wine), because it allows varietal identification.

■ ASSOCIATED CONTENT

Accession Codes

Sequence data from this paper can be found in the GenBank database under accession numbers 1868281767, 1868281812, 1868281815, 1868281817, 1868281828, 1868281830, 1868281834, 1868281836, 1868281838, 1868281843, 1868281845, 1868281852, 1868281855, 1868281862, 1868281865, 1868281867, 1868281870, 1868281872, 1868281874, 1868281876, 1868281878, 1868281881, 1868281883, 1868281885, 1868281887, 1868281892, 1868281894, 1868281897, 1868281899, 1868281901, 1868281903, 1868281905, 1868281907, 1868281909, 1868281911, 1868281913, 1868281915, 1868281917, 1868281919, 1868281921, 1868281924, 1868281926, 1868281928, 1868281930, 1868281933, 1868281935, 1868281937, 1868281939, 1868281941, 1868281943, 1868281945, 1868281947, 1868281949, 1868281951, 1868281953, 1868281955, 1868281957, 1868281960, and 1868281963.

■ AUTHOR INFORMATION

Corresponding Author

*(P.M.-L.) Phone: ++351 259 350 936. Fax: + + 351 259 350 572. E-mail: plopes@utad.pt.

Funding

This research was supported by the Portuguese Foundation for Science and Technology (FCT) within the project Biosensor Development for Wine Traceability in the Douro Region − WineBioCode PTDC/AGR-ALI/117341/2010-FCOMP-01-0124-FEDER-019439 and by a Ph.D. grant (SFRH/BD/44781/2008).

Notes

The authors declare no competing financial interest.

■ ACKNOWLEDGMENTS

We are grateful to Prof. Ântero Martins, Doctor José Eiras-Dias (INIAV), and Dr. Paulo Costa (ADVID) for helping us in the clonal leaf collection and to Sogrape Vinhos S.A., Real Companhia Velha, Sociedade Borges S.A., and Direção Regional de Agricultura e Pescas do Norte for allowing us to collect the samples in their fields.

■ REFERENCES

(1) Dal Santo, S.; Tornielli, G. B.; Zenoni, S.; Fasoli, M.; Farina, L.; Anesi, A.; Guzzo, F.; Delledonne, M.; Pezzotti, M. The plasticity of the grapevine berry transcriptome. *Genome Biol.* **2013**, *14*, R54.

(2) Pereira, L.; Guedes-Pinto, H.; Martins-Lopes, P. An enhanced method for *Vitis vinifera* L., DNA extraction from wines. *Am. J. Enol. Vitic.* **2011**, *62*, 547−552.

(3) Organisation Internationale de la Vigne et du Vin (OIV). *Liste des Descripteurs OIV pour les Variétés et Espèces de Vitid*, 2nd ed.; OIV: Paris, France, 2009.

(4) Jaillon, O.; Aury, J.-M.; Noel, B.; Policriti, A.; Clepet, C. The grapevine genome sequence suggests ancestral hexaploidization in major angiosperm phyla. *Nature* **2007**, *449*, 463−467.

(5) Cabezas, J. A.; Ibáñez, J.; Lijavetzky, D.; Vélez, D.; Bravo, G.; et al. A 48 SNP set for grapevine cultivar identification. *BMC Plant Biol.* **2011**, *11*, 153.

(6) Liew, M.; Pryor, R.; Palais, R.; Meadows, C.; Erali, M.; Lyon, E.; Wittwer, C. Genotyping of single-nucleotide polymorphisms by high-resolution melting of small amplicons. *Clin. Chem.* **2004**, *50*, 1156−1164.

(7) Pietzka, A. T.; Indra, A.; Stöger, A.; Zeinzinger, J.; Konrad, M.; Hasenberger, P.; Allerberger, F.; Ruppitsch, W. Rapid identification of multidrug-resistant *Mycobacterium tuberculosis* isolates by *rpoB* gene scanning using high-resolution melting curve PCR analysis. *J. Antimicrob. Chemother.* **2009**, *63*, 1121−1127.

DOI: 10.1021/acs.jafc.5b03463
J. Agric. Food Chem. 2015, 63, 9165−9174

(8) Han, Y.; Khu, D.-M.; Monteros, M. J. High-resolution melting analysis for SNP genotyping and mapping in tetraploid alfalfa (*Medicago sativa* L.). *Mol. Breed.* **2012**, *29*, 489−501.
(9) Erali, M.; Wittwer, C. T. High resolution melting analysis for gene scanning. *Methods* **2010**, *50*, 250−261.
(10) Mackay, J. F.; Wright, C. D.; Bonfiglioli, R. G. A new approach to varietal identification in plants by microsatellite high resolution melting analysis: application to the verification of grapevine and olive cultivars. *Plant Methods* **2008**, *4*, 8.
(11) Cardoso, S.; Lau, W.; Eiras-Dias, J. E.; Fevereiro, P.; Maniatis, N. A candidate-gene association study for berry colour and anthocyanin content in *Vitis vinifera* L. *PLoS One* **2012**, *7*, e46021.
(12) Castellarin, S. D.; Di Gaspero, G. Transcriptional control of anthocyanin biosynthetic genes in extreme phenotypes for berry pigmentation of naturally occurring grapevines. *BMC Plant Biol.* **2007**, *7*, 46.
(13) Mattivi, F.; Guzzon, R.; Vrhovsek, U.; Stefanini, M.; Velasco, R. Metabolite profiling of grape: flavonols and anthocyanins. *J. Agric. Food Chem.* **2006**, *54*, 7692−7702.
(14) Boss, P.; Davies, C.; Robinson, S. Analysis of the expression of anthocyanin pathway genes in developing *Vitis vinifera* L. cv Shiraz grape berries and the implications for pathway regulation. *Plant Physiol.* **1996**, *111*, 1059−1066.
(15) Holton, T. A.; Cornish, E. C. Genetics and biochemistry of anthocyanin biosynthesis. *Plant Cell* **1995**, *7*, 1071−1083.
(16) Grotewold, E. The genetics and biochemistry of floral pigments. *Annu. Rev. Plant Biol.* **2006**, *57*, 761−780.
(17) Velasco, R.; Zharkikh, A.; Troggio, M.; Cartwright, D. A.; Cestaro, A.; et al. A high quality draft consensus sequence of the genome of a heterozygous grapevine variety. *PLoS One* **2007**, *2*, e1326.
(18) Sparvoli, F.; Martin, C.; Scienza, A.; Gavazzi, G.; Tonelli, C. Cloning and molecular analysis of structural genes involved in flavonoid and stilbene biosynthesis in grape (*Vitis vinifera* L.). *Plant Mol. Biol.* **1994**, *24*, 743−755.
(19) Kuhn, N.; Guan, L.; Dai, Z. W.; Wu, B.-H.; Lauvergeat, V.; Gomès, E.; Li, S.-H.; Godoy, F.; Arce-Johnson, P.; Delrot, S. Berry ripening: recently heard through the grapevine. *J. Exp. Bot.* **2014**, *65*, 4543−4559.
(20) Zheng, Y.; Li, J. H.; Xin, H. P.; Wang, N.; Guan, L.; Wu, B. H.; Li, S. H. Anthocyanin profile and gene expression in berry skin of two red *Vitis vinifera* grape cultivars that are sunlight dependent versus sunlight independent. *Aust. J. Grape Wine Res.* **2013**, *19*, 238−248.
(21) Kobayashi, S.; Ishimaru, M.; Ding, C. K.; Yakushiji, H.; Goto, N. Comparison of UDP-glucose: flavonoid 3-*O*-glucosyltransferase (UFGT) gene sequences between white grapes (*Vitis vinifera*) and their sports with red skin. *Plant Sci.* **2001**, *160*, 543−550.
(22) Cutanda-Perez, M.-C.; Ageorges, A.; Gomez, C.; Vialet, S.; Terrier, N.; Romieu, C.; Torregrosa, L. Ectopic expression of *VlmybA1* in grapevine activates a narrow set of genes involved in anthocyanin synthesis and transport. *Plant Mol. Biol.* **2009**, *69*, 633−648.
(23) Doyle, J. J.; Doyle, J. L. Isolation of plant DNA from fresh tissue. *Focus* **1990**, *12*, 13−15.
(24) Shimada, N.; Aoki, T.; Sato, S.; Nakamura, Y.; Tabata, S.; Ayabe, S. A cluster of genes encodes the two types of chalcone isomerase involved in the biosynthesis of general flavonoids and legume-specific 5-deoxy(iso)flavonoids in *Lotus japonicas*. *Plant Physiol.* **2003**, *131*, 941−951.
(25) Przysiecka, Ł.; Książkiewicz, M.; Wolko, B.; Naganowska, B. Structure, expression profile and phylogenetic inference of chalcone isomerase-like genes from the narrow-leafed lupin (*Lupinus angustifolius* L.) genome. *Front. Plant Sci.* **2015**, *6*, 268.
(26) Papadopoulos, J. S.; Agarwala, R. COBALT: constraint-based alignment tool for multiple protein sequences. *Bioinformatics* **2007**, *23*, 1073−1079.
(27) Salmaso, M.; Faes, G.; Segala, C.; Stefanini, M.; Salakhutdinov, I.; Zyprian, E.; Toepfer, R.; Grando, M. S.; Velasco, R. Genome diversity and gene haplotypes in the grapevine (*Vitis vinifera* L.), as revealed by single nucleotide polymorphisms. *Mol. Breed.* **2005**, *14*, 385−395.
(28) Kolkman, J. M.; Berry, S. T.; Leon, A. J.; Slabaugh, M. B.; Tang, S.; Gao, W.; Shintani, D. K.; Burke, J. M.; Knapp, S. J. Single nucleotide polymorphisms and linkage disequilibrium in sunflower. *Genetics* **2007**, *177*, 457−468.
(29) An, C.; Saha, S.; Jenkins, J. N.; Ma, D. P.; Scheffler, B. E.; Kohel, R. J.; Yu, J. Z.; Stelly, D. M. Cotton (*Gossypium* spp.) R2R3-MYB transcription factors SNP identification phylogenomic characterization, chromosome localization and linkage mapping. *Theor. Appl. Genet.* **2008**, *116*, 1015−1026.
(30) Riahi, L.; Zoghlami, N.; Dereeper, A.; Laucou, V.; Mliki, A.; This, P. Single nucleotide polymorphism and haplotype diversity of the gene NAC4 in grapevine. *Ind. Crops Prod.* **2013**, *43*, 718−724.
(31) Nicolè, S.; Barcaccia, G.; Erickson, D. L.; Kress, J. W.; Lucchin, M. The coding region of the UFGT gene is a source of diagnostic SNP markers that allow single-locus DNA genotyping for the assessment of cultivar identity and ancestry in grapevine (*Vitis vinifera* L.). *BMC Res. Notes* **2013**, *6*, 502.
(32) Druml, B.; Cichna-Markl, M. High resolution melting (HRM) analysis of DNA − its role and potential in food analysis. *Food Chem.* **2014**, *158*, 245−254.
(33) De Koeyer, D.; Douglass, K.; Murphy, A.; Whitney, S.; Nolan, L.; Song, Y.; De Jong, W. Application of high-resolution DNA melting for genotyping and variant scanning of diploid and autotetraploid potato. *Mol. Breed.* **2010**, *25*, 67−90.
(34) Ó Lochlainn, S.; Amoah, S.; Graham, N. S.; Alamer, K.; Rios, J. J.; et al. High resolution melt (HRM) analysis is an efficient tool to genotype EMS mutants in complex crop genomes. *Plant Methods* **2011**, *7*, 43.
(35) Xanthopoulou, A.; Ganopoulos, I.; Tsaballa, A.; Nianiou-Obeidat, I.; Kalivas, A.; Tsaftaris, A.; Madesis, P. Summer squash identification by high-resolution-melting (HRM) analysis using gene-based EST−SSR molecular marker. *Plant Mol. Biol. Rep.* **2014**, *32*, 395−405.
(36) Li, Y.-D.; Chu, Z.-Z.; Liu, X.-G.; Jing, H.-C.; Liu, Y.-G.; Hao, D.-Y. A cost-effective high-resolution melting approach using the EvaGreen dye for DNA polymorphism detection and genotyping in plants. *J. Integr. Plant Biol.* **2010**, *52*, 1036−1042.
(37) Yan, G.-X.; Wu, X.-M.; Li, D.; Zeng, C.-L.; Lv, P.-J.; Gao, G.-Z.; Chen, B.-Y.; Xua, K.; Lv, X.-D. Assessing high-resolution melt curve analysis for accurate detection of DNA polymorphisms in the chloroplast gene accD of Crucifer species. *Biochem. Syst. Ecol.* **2012**, *44*, 352−360.
(38) Han, Y.; Khu, D.-M.; Monteros, M. J. High-resolution melting analysis for SNP genotyping and mapping in tetraploid alfalfa (*Medicago sativa* L.). *Mol. Breed.* **2012**, *29*, 489−501.
(39) Emanuelli, F.; Sordo, M.; Lorenzi, S.; Battilana, J.; Grando, M. S. Development of user-friendly functional molecular markers for VvDXS gene conferring muscat flavor in grapevine. *Mol. Breed.* **2014**, *33*, 235−241.
(40) Ocana, J.; Walter, B.; Schellenbaum, P. Stable MSAP markers for the distinction of *Vitis vinifera* cv Pinot Noir clones. *Mol. Biotechnol.* **2013**, *55*, 236−248.
(41) Lijavetzky, D.; Ruiz-Garcia, L.; Cabezas, J. A.; De Andres, M. T.; Bravo, G.; Ibáñez, A.; Carreño, J.; Cabello, F.; Martínez-Zapater, J. M. Molecular genetics of berry colour variation in table grape. *Mol. Genet. Genomics* **2006**, *276*, 427−435.
(42) Pelsy, F.; Dumas, V.; Bévilacqua, L.; Hocquigny, S.; Merdinoglu, D. Chromosome replacement and deletion lead to clonal polymorphism of berry color in grapevine. *PLoS Genet.* **2015**, *11*, e1005081.
(43) Bindon, K. A.; McCarthy, M. G.; Smith, P. A. Development of wine colour and non-bleachable pigments during the fermentation and ageing of (*Vitis vinifera* L. cv.) Cabernet Sauvignon wines differing in anthocyanin and tannin concentration. *LWT - Food Sci. Technol.* **2014**, *59*, 923−932.
(44) Dimitrovska, M.; Bocevska, M.; Dimitrovski, D.; Doneva-Sapceska, D. Evolution of anthocyanins during vinification of Merlot and Pinot Noir grapes to wines. *Acta Aliment.* **2015**, *44*, 259−267.

DOI: 10.1021/acs.jafc.5b03463
J. Agric. Food Chem. 2015, 63, 9165−9174

(45) Costa, E.; Cosme, F.; Jordão, A. M.; Mendes-Faia, A. Anthocyanin profile and antioxidant activity from 24 grape varieties cultivated in two Portuguese wine regions. *J. Int. Sci. Vigne Vin* **2014**, *48*, 51−62.
(46) Jordão, A. M.; Simão, S.; Correia, A. C.; Gonçalves, F. J. Antioxidant activity evolution during Portuguese red wine vinification and their relation with the proanthocyanidin and anthocyanin composition. *J. Food Process. Preserv.* **2012**, *36*, 298−309.
(47) Jordão, A. M.; Ricardo da Silva, J. M.; Laureano, O. Evolution of anthocyanins during grape maturation of two varieties (*Vitis vinifera* L.), Castelão Francês and Touriga Francesa. *Vitis* **1998**, *37*, 93−94.

DOI: 10.1021/acs.jafc.5b03463
J. Agric. Food Chem. 2015, 63, 9165−9174

Table 1. Antibiotics, Exact Mass, and UHPLC Retention Time for Data Processing and Quantification, and UHPLC/ESI Q-Orbitrap MS Method Performance Results

Antibiotics	Class	Total number	Molecular formula	Retention Time, min	Exact mass[a]				Overall recovery[b,e] (%)	Intermediate precision[c,e] (%)	Measurement uncertainty[d,e] (%)	Peak height at LCL[f] (μg/kg)	Canadian MRLs[k] (μg/kg)
					[M + H]$^+$	[M + NH_4]$^+$	[M + Na]$^+$	[M + 2H]$^{++}$					
1[g]	2	3	4	5	6	7	8	9	10	11	12	13	14
Section A: Compounds with Full validation		**89**											
Abamectin B1a	Endectocides	7	C48H72O14	9.99	873.49948	890.52603	**895.48143**	437.25338	**120.1**	8.9	18.7	438000 (5)	
Doramectin	Endectocides		C50H74O14	10.26	899.51513	916.54168	**921.49708**	450.26121	118.5	9.6	19.2	78600 (1)	
Emamectin B1a	Endectocides		C49H75NO13	9.31	**886.53112**	903.55767	908.51306	443.76920	117.1	7.5	15.4	381000 (1)	
Eprinomectin B1a	Endectocides		C50H75NO14	9.86	914.52603	931.55258	**936.50798**	457.76665	**120.8**	5.9	13.5	195000 (1)	20
Ivermectin	Endectocides		C48H74O14	10.57	875.51513	892.54168	**897.49708**	438.26121	117.3	12.0	24.8	524000 (5)	
Moxidectin	Endectocides		C37H53NO8	10.41	640.38439	657.41094	**662.36634**	320.69584	112.7	**21.8**	43.8	494000 (1)	40
Selamectin	Endectocides		C43H63NO11	10.63	**770.44739**	787.47394	792.42933	385.72733	110.5	**22.2**	48.1	74700 (5)	
Cinoxacin	Fluoroquinolones	17	C12H10N2O5	4.90	**263.06625**	280.09280	285.04819	132.03676	115.9	3.9	8.6	475000 (1)	
Ciprofloxacin	Fluoroquinolones		C17H18FN3O3	3.74	**332.14050**	349.16705	354.12244	166.57389	**38.9**	7.9	16.1	283000 (1)	
Danofloxacin	Fluoroquinolones		C19H20FN3O3	3.78	**358.15615**	375.18270	380.13809	179.58171	**48.0**	12.6	25.2	448000 (1)	
Difloxacin	Fluoroquinolones		C21H19F2N3O3	4.12	**400.14672**	417.17327	422.12867	200.57700	82.5	10.5	22.1	228000 (1)	
Enoxacin	Fluoroquinolones		C15H17FN4O3	3.49	**321.13575**	338.16229	343.11769	161.07151	**30.8**	7.5	15.8	329000 (1)	
Enrofloxacin	Fluoroquinolones		C19H22FN3O3	3.83	**360.17180**	377.19835	382.15374	180.58954	**62.5**	9.8	20.4	427000 (1)	
Flumequine	Fluoroquinolones		C14H12FNO3	6.35	**262.08740**	279.11395	284.06934	131.54734	119.4	4.4	11.8	425000 (1)	
Lomefloxacin	Fluoroquinolones		C17H19F2N3O3	3.93	**352.14672**	369.17327	374.12867	176.57700	**53.1**	6.7	14.1	371000 (1)	
Marbofloxacin	Fluoroquinolones		C17H19FN4O4	3.23	**363.14631**	380.17286	385.12825	182.07679	**44.7**	8.3	18.3	147000 (1)	
Nalidixic Acid	Fluoroquinolones		C12H12N2O3	6.12	**233.09207**	250.11862	255.07401	117.04967	**120.9**	4.7	12.8	422000 (1)	
Norfloxacin	Fluoroquinolones		C16H18FN3O3	3.62	**320.14050**	337.16705	342.12244	160.57389	**34.0**	8.5	17.0	318000 (1)	
Ofloxacin	Fluoroquinolones		C18H20FN3O4	3.49	**362.15106**	379.17761	384.13301	181.57917	**47.4**	8.5	17.7	438000 (1)	
Orbifloxacin	Fluoroquinolones		C19H20F3N3O3	3.94	**396.15295**	413.17950	418.13490	198.58011	74.0	5.9	12.8	777000 (1)	
Oxolinic Acid	Fluoroquinolones		C13H11NO5	5.18	**262.07100**	279.09755	284.05294	131.53914	118.6	4.2	9.1	419000 (1)	
Pipemidic Acid	Fluoroquinolones		C14H17N5O3	3.02	**304.14042**	321.16697	326.12236	152.57385	**24.6**	10.4	21.4	122000 (1)	
Sarafloxacin	Fluoroquinolones		C20H17F2N3O3	4.26	**386.13107**	403.15762	408.11302	193.56918	73.5	6.2	13.3	172000 (1)	
Sparfloxacin	Fluoroquinolones		C19H22F2N4O3	4.55	**393.17327**	410.19982	415.15522	197.09028	80.4	5.7	12.1	740000 (1)	
Lasalocid	Ionophores	5	C34H54O8	10.06	591.38915	**608.41569**	613.37109	296.19821	102.1	12.8	25.7	710000 (1)	
Monensin	Ionophores		C36H62O11	10.09	671.43649	**688.46304**	693.41843	336.22188	111.4	7.7	18.0	409000 (1)	10
Narasin	Ionophores		C43H72O11	10.68	765.51474	**782.54129**	787.49668	383.26101	104.3	18.6	37.4	2120000 (5)	
Nigericin	Ionophores		C40H68O11	10.61	725.48344	**742.50999**	747.46538	363.24536	100.8	**30.6**	**61.7**	1280000 (1)	
Salinomycin	Ionophores		C42H70O11	10.46	751.49909	**768.52564**	773.48103	376.25318	107.5	7.6	15.2	426000 (1)	
Erythromycin	Macrolides	7	C37H67NO13	6.86	**734.46852**	751.49507	756.45046	367.73790	**55.0**	**26.7**	**66.3**	249000 (1)	50
Neospiramycin I	Macrolides		C36H62N2O11	4.92	699.44264	716.46919	721.42458	**350.22496**	**12.4**	14.5	32.7	379000 (1)	
Oleandomycin	Macrolides		C35H61NO12	6.27	**688.42665**	705.45320	710.40860	344.71696	97.6	5.4	11.1	546000 (1)	
Roxithromycin	Macrolides		C41H76N2O15	7.56	837.53185	854.55840	859.51379	**419.26956**	115.9	13.5	27.1	781000 (1)	
Spiramycin I	Macrolides		C43H74N2O14	5.24	843.52128	860.54783	865.50323	**422.26428**	**29.7**	11.5	26.8	228000 (1)	
Tilmicosin	Macrolides		C46H80N2O13	6.06	869.57332	886.59987	891.55526	**435.29030**	**68.8**	9.2	19.5	1080000 (1)	
Tylosin A	Macrolides		C46H77NO17	6.75	**916.52643**	933.55298	938.50837	458.76685	104.9	5.4	11.8	96700 (1)	
2-methyl-4(5)-nitroimidazole	Nitroimidazoles	13	C4H5N3O2	1.68	**128.04545**	145.07200	150.02740	64.52636	95.7	4.3	9.1	252000 (1)	
Dimetridazole	Nitroimidazoles		C5H7N3O2	2.72	**142.06110**	159.08765	164.04305	71.53419	100.8	3.1	6.5	134000 (1)	
Dimetridazole-d3[l]	Nitroimidazoles		C5H4N3O2D3	2.72	**145.07963**	162.10618	167.06157	73.04345					
Etanidazole	Nitroimidazoles		C7H10N4O4	1.11	**215.07748**	232.10403	237.05943	108.04238	**66.4**	12.1	26.5	217000 (1)	
HMMNI	Nitroimidazoles		C5H7N3O3	1.99	**158.05602**	175.08257	180.03796	79.53165	101.1	3.4	7.0	278000 (5)	
HMMNI-d3	Nitroimidazoles		C5H4N3O3D3	2.01	**161.07454**	178.10109	183.05649	81.04091					
Ipronidazole	Nitroimidazoles		C7H11N3O2	4.64	**170.09240**	187.11895	192.07435	85.54984	100.6	2.3	5.4	536000 (1)	
Ipronidazole-d3	Nitroimidazoles		C7H8N3O2D3	4.62	**173.11093**	190.13748	195.09287	87.05910					
Ipronidazole-OH	Nitroimidazoles		C7H11N3O3	3.91	**186.08732**	203.11387	208.06926	93.54730	101.4	2.8	6.4	283000 (1)	
Ipronidazole-OH-d3	Nitroimidazoles		C7H8N3O3D3	3.88	**189.10584**	206.13239	211.08779	95.05656					
Metronidazole	Nitroimidazoles		C6H9N3O3	2.24	**172.07167**	189.09822	194.05361	86.53947	102.5	6.7	13.6	213000 (1)	
Metronidazole-OH	Nitroimidazoles		C6H9N3O4	1.65	**188.06658**	205.09313	210.04853	94.53693	76.9	**24.5**	49.1	131000 (1)	
Nimorazole	Nitroimidazoles		C9H14N4O3	1.28	**227.11387**	244.14042	249.09581	114.06057	**54.3**	9.7	25.2	146000 (1)	
Ornidazole	Nitroimidazoles		C7H10N3O3Cl	3.77	**220.04835**	237.07489	242.03029	110.52781	114.9	3.7	7.9	166000 (1)	
Ronidazole	Nitroimidazoles		C6H8N4O4	2.19	**201.06183**	218.08838	223.04378	101.03455	102.0	3.0	5.9	82400 (1)	
Ronidazole-d3	Nitroimidazoles		C6H5N4O4D3	2.19	**204.08036**	221.10691	226.06230	102.54382					
Ternidazole	Nitroimidazoles		C7H11N3O3	2.94	**186.08732**	203.11387	208.06926	93.5473	103.9	5.6	12.2	267000 (1)	
Tinidazole	Nitroimidazoles		C8H13N3O4S	2.83	**248.06995**	265.09650	270.05190	124.53861	114.1	4.2	9.1	359000 (1)	
5-hydroxyflunixin	NSAIDS	3	C14H11F3N2O3	7.57	**313.07945**	330.10600	335.06140	157.04337	**67.3**	**35.3**	**74.0**	71500 (1)	6
Flunixin	NSAIDS		C14H11F3N2O2	7.88	**297.08454**	314.11109	319.06648	149.04591	119.8	16.0	34.0	1570000 (1)	
Phenylbutazone	NSAIDS		C19H20N2O2	7.97	**309.15975**	326.18630	331.14170	155.08352	**57.8**	**34.7**	**71.0**	280000 (1)	
Penicillin G	Penicillins	2	C16H18N2O4S	6.13	**335.10600**	352.13255	357.08795	168.05664	74.5	**20.6**	**73.9**	304000 (20)	6 (0.01 IU/mL)[j]
Penicillin V	Penicillins		C16H18N2O5S	6.50	**351.10092**	368.12747	373.08286	176.05410	96.0	13.9	31.3	117000 (20)	
Florfenicol	Phenicols	2	C12H14Cl2FNO4S	3.92	358.00774	**375.03429**	379.98968	179.50751	119.7	3.8	9.0	100000 (1)	
Thiamphenicol	Phenicols		C12H15Cl2NO5S	3.13	356.01208	373.03862	**377.99402**	178.50968	111.1	9.7	19.9	55000 (1)	
Dapsone	Sulfonamides	26	C12H12N2O2S	3.21	**249.06922**	266.09577	271.05117	125.03825	107.8	4.2	9.1	1220000 (1)	
Sulfabenzamide	Sulfonamides		C13H12N2O3S	4.33	**277.06414**	294.09069	299.04608	139.03571	113.3	4.9	10.6	329000 (1)	10
Sulfacetamide	Sulfonamides		C8H10N2O3S	1.77	**215.04849**	232.07504	237.03043	108.02788	104.3	10.4	21.2	149000 (1)	10
Sulfachloropyridazine	Sulfonamides		C10H9ClN4O2S	3.71	**285.02075**	302.04730	307.00270	143.01401	105.9	3.7	8.7	215000 (1)	
Sulfadiazine	Sulfonamides		C10H10N4O2S	1.98	**251.05972**	268.08627	273.04167	126.03350	101.8	6.2	12.6	253000 (1)	
Sulfadimethoxine	Sulfonamides		C12H14N4O4S	4.90	**311.08085**	328.10740	333.06280	156.04406	114.3	4.0	8.5	814000 (1)	10
Sulfadoxine	Sulfonamides		C12H14N4O4S	4.09	**311.08085**	328.10740	333.06280	156.04406	110.7	3.9	8.6	1120000 (1)	10
Sulfaethoxypyridazine	Sulfonamides		C12H14N4O3S	4.52	**295.08594**	312.11249	317.06788	148.04661	105.7	3.6	8.5	747000 (1)	10
Sulfaguanidine	Sulfonamides		C7H10N4O2S	1.05	**215.05972**	232.08627	237.04167	108.03350	72.4	14.3	28.8	976000 (1)	10
Sulfamerazine	Sulfonamides		C11H12N4O2S	2.91	**265.07537**	282.10192	287.05732	133.04132	102.0	9.3	20.1	657000 (1)	
Sulfameter	Sulfonamides		C11H12N4O3S	3.22	**281.07029**	298.09684	303.05223	141.03878	108.6	4.0	8.8	556000 (1)	
Sulfamethazine	Sulfonamides		C12H14N4O2S	3.46	**279.09102**	296.11757	301.07297	140.04915	104.4	5.2	10.9	822000 (1)	10
Sulfamethizole	Sulfonamides		C9H10N4O2S2	3.30	**271.03179**	288.05834	293.01374	136.01954	107.2	4.5	9.2	174000 (1)	
Sulfamethoxazole	Sulfonamides		C10H11N3O3S	3.82	**254.05939**	271.08594	276.04133	127.53333	112.3	3.8	8.3	612000 (1)	
Sulfamethoxypyridazine	Sulfonamides		C11H12N4O3S	3.53	**281.07029**	298.09684	303.05223	141.03878	104.6	4.5	9.9	865000 (1)	
Sulfamonomethoxine	Sulfonamides		C11H12N4O3S	3.89	**281.07029**	298.09684	303.05223	141.03878	106.9	3.8	8.5	303000 (1)	
Sulfamoxole	Sulfonamides		C11H13N3O3S	3.28	**268.07504**	285.10159	290.05698	134.54116	89.8	6.7	13.5	494000 (1)	
Sulfanilamide	Sulfonamides		C6H8N2O2S	1.25	**173.03792**	190.06447	195.01987	87.02260	97.1	16.9	36.4	52900 (5)	10
Sulfanitran	Sulfonamides		C14H13N3O5S	6.06	**336.06487**	353.09142	358.04681	168.53607	117.8	4.9	11.1	179000 (5)	
Sulfaphenazole	Sulfonamides		C15H14N4O2S	4.61	**315.09102**	332.11757	337.07297	158.04915	113.4	3.9	8.6	652000 (1)	
Sulfapyridine	Sulfonamides		C11H11N3O2S	2.71	**250.06447**	267.09102	272.04642	125.53588	98.1	4.6	9.3	436000 (1)	10
Sulfaquinoxaline	Sulfonamides		C14H12N4O2S	5.11	**301.07537**	318.10192	323.05732	151.04132	109.5	4.2	9.3	311000 (1)	10
Sulfathiazole	Sulfonamides		C9H9N3O2S2	2.50	**256.02089**	273.04744	278.00284	128.51409	98.1	5.6	11.7	186000 (1)	10
Sulfisomidine	Sulfonamides		C12H14N4O2S	2.33	**279.09102**	296.11757	301.07297	140.04915	83.5	3.3	7.6	345000 (1)	
Sulfisoxazole	Sulfonamides		C11H13N3O3S	4.06	**268.07504**	285.10159	290.05698	134.54116	109.7	3.7	8.5	460000 (1)	
Trimethoprim	Sulfonamides		C14H18N4O3	3.33	**291.14517**	308.17172	313.12711	146.07622	**47.6**	6.7	13.4	1360000 (1)	
4-epitetracycline	Tetracyclines	5	C22H24N2O8	3.09	**445.16054**	462.18709	467.14249	223.08391	96.8	10.5	29.0	288000 (40)	
Chlortetracycline	Tetracyclines		C22H23ClN2O8	4.86	**479.12157**	496.14812	501.10351	240.06442	**53.7**	13.2	31.2	173000 (40)	100
Doxycycline	Tetracyclines		C22H24N2O8	5.58	**445.16054**	462.18709	467.14249	223.08391	**59.8**	12.2	30.1	198000 (40)	
Oxytetracycline	Tetracyclines		C22H24N2O9	3.80	**461.15546**	478.18201	483.13740	231.08137	**30.7**	**20.6**	41.5	158000 (20)	100
Tetracycline	Tetracyclines		C22H24N2O8	3.74	**445.16054**	462.18709	467.14249	223.08391	**43.6**	9.6	22.7	151000 (5)	100
Cefoxitin	β-Lactams	2	C16H17N3O7S2	3.84	428.05807	**445.08462**	450.04001	214.53267	100.5	7.5	16.5	437000 (40)	
Desacetyl cephapirin	β-Lactams		C15H15N3O5S2	1.10	**382.05259**	399.07914	404.03453	191.52993	**15.0**	**54.8**	**110.3**	2600000 (20)	

DOI: 10.1021/acs.jafc.5b04096
J. Agric. Food Chem. 2015, 63, 9175−9187

Table 1. continued

Antibiotics	Class	Total number	Molecular formula	Retention Time, min	Exact mass[a] [M + H]+	[M + NH4]+	[M + Na]+	[M + 2H]++	Overall recovery[b,e] (%)	Intermediate precision[c,e] (%)	Measurement uncertainty[d,e] (%)	Peak height at LCL[f] (μg/kg)	Canadian MRLs[k] (μg/kg)
1[g]	2	3	4	5	6	7	8	9	10	11	12	13	14
Section B: Compounds of Unstable but quantifiable[h]		**13**							Concentration (μg/kg)	Recovery[b] (%)	RSD[c] (%)		
Cloxacillin	Penicillins	3	C19H18ClN3O5S	6.77	**436.07285**	453.09939	458.05479	218.54006	10.0	112.2	7.1	82400 (5)	
									25.0	**122.2**	2.3		
									50.0	101.9	5.5		
									80.0	102.0	6.7		
Dicloxacillin	Penicillins		C19H17Cl2N3O5S	7.00	**470.03387**	487.06042	492.01582	235.52057	50.0	**146.2**	0.9	271000 (40)	
									80.0	79.3	11.0		
Oxacillin	Penicillins		C19H19N3O5S	6.56	**402.11182**	419.13837	424.09376	201.55955	10.0	119.7	7.0	69600 (5)	
									25.0	115.7	4.8		
									50.0	91.0	7.9		
									80.0	101.2	2.3		
Cefamandole	β-Lactams	10	C18H18N6O5S2	4.27	**463.08529**	480.11183	485.06723	232.04628	80.0	**136.6**	3.0	41900 (60)	
Cefapirin	β-Lactams		C17H17N3O6S2	2.42	**424.06315**	441.08970	446.04510	212.53521	25.0	**56.7**	**23.7**	113000 (20)	20
									50.0	**50.0**	9.5		
									80.0	**55.1**	8.4		
Cefazolin	β-Lactams		C14H14N8O4S3	3.30	**455.03729**	472.06384	477.01923	228.02228	80.0	**134.3**	2.3	48800 (60)	
Cefoperazone	β-Lactams		C25H27N9O8S2	3.76	**646.14968**	663.17623	668.13162	323.57848	50.0	**134.3**	5.6	166000 (40)	
									80.0	**122.9**	2.2		
Cefotaxime	β-Lactams		C16H17N5O7S2	3.49	**456.06422**	473.09077	478.04616	228.53575	25.0	94.6	2.9	166000 (20)	
									50.0	88.2	6.7		
									80.0	92.0	2.0		
Cefquinome	β-Lactams		C23H24N6O5S2	2.78	**529.13224**	546.15879	551.11418	265.06976	80.0	99.8	0.5	206000 (60)	
Ceftiofur	β-Lactams		C19H17N5O7S3	5.10	**524.03629**	541.06284	546.01823	262.52178	10.0	**121.5**	2.1	118000 (5)	100
									25.0	**130.6**	6.5		
									50.0	**121.1**	4.1		
									80.0	**124.6**	4.8		
Cefuroxime	β-Lactams		C16H16N4O8S	3.36	425.07616	**442.10271**	447.05811	213.04172	25.0	116.9	4.4	38200 (20)	
									50.0	94.7	5.7		
									80.0	100.7	4.3		
Cephacetrile	β-Lactams		C13H13N3O6S	2.46	340.05978	**357.08633**	362.04173	170.53353	80.0	106.5	3.4	101000 (60)	
Cephalothin[i]	β-Lactams		C16H16N2O6S2	5.00	397.05225	414.07880	419.03420	199.02977	10.0	109.8	5.4	42600 (5)	
									25.0	**122.2**	4.7		
									50.0	113.5	5.3		
									80.0	113.0	1.4		
Section C: Compounds for Screening		**3**											
Tylosin B	Macrolides	1	C39H65NO14	6.42	**772.44778**	789.47433	794.42973	386.72753	no standard but screening				
Ampicillin	Penicillins	1	C16H19N3O4S	3.92	**350.11690**	367.14345	372.09885	175.56209	co-elute with cephradine but screening at 80 μg/kg.				10
Cephradine	β-Lactams	1	C16H19N3O4S	3.92	**350.11690**	367.14345	372.09885	175.56209	co-elute with ampicillin but screening at 80 μg/kg.				
Section D: Compounds Excluded from the Method		**20**											
Amikacin	Aminoglycosides	15	C22H43N5O13	0.92	586.29301	603.31956	**608.27496**	293.65014	not chromatographically retained				
Apramycin	Aminoglycosides		C21H41N5O11	0.91	540.28753	557.31408	**562.26948**	270.64741	not chromatographically retained				
Dihydrostreptomycin	Aminoglycosides		C21H41N7O12	0.92	**584.28860**	601.31515	606.27054	292.64794	not chromatographically retained				125
G418	Aminoglycosides		C20H40N4O10	0.91	497.28172	514.30827	**519.26366**	249.1445	not chromatographically retained				
Gentamycin C1	Aminoglycosides		C21H43N5O7	0.91	**478.32353**	495.35007	500.30547	239.6654	not chromatographically retained				
Gentamycin C1A	Aminoglycosides		C19H39N5O7	0.90	450.29223	467.31877	**472.27417**	225.64975	not chromatographically retained				
Gentamycin C2	Aminoglycosides		C20H41N5O7	0.91	464.30788	481.33442	**486.28982**	232.65758	not chromatographically retained				
Hygromycin B	Aminoglycosides		C20H37N3O13	0.91	528.23991	545.26646	**550.22186**	264.6236	not chromatographically retained				
Kanamycin A	Aminoglycosides		C18H36N4O11	0.92	485.24533	502.27188	**507.22728**	243.12631	not chromatographically retained				
Kanamycin B	Aminoglycosides		C18H37N5O10	0.91	484.26132	501.28787	**506.24326**	242.6343	not chromatographically retained				
Neomycin	Aminoglycosides		C23H46N6O13	0.92	615.31956	632.34611	**637.30151**	308.16342	not chromatographically retained				1500
Paromomycin	Aminoglycosides		C23H45N5O14	0.92	616.30358	633.33013	**638.28552**	308.65543	not chromatographically retained				
Spectinomycin	Aminoglycosides		C14H24N2O7	0.97	**333.16563**	350.19218	355.14757	167.08645	not chromatographically retained				
Streptomycin	Aminoglycosides		C21H39N7O12	0.91	**582.27295**	599.2995	604.25489	291.64011	not chromatographically retained				125
Tobramycin	Aminoglycosides		C18H37N5O9	0.92	468.26640	485.29295	**490.24835**	234.63684	not chromatographically retained				
Amoxicillin	Penicillins	1	C16H19N3O5S	1.03	**366.11182**	383.13837	388.09376	183.55955	low sensitivity or not recovered				
Cefadroxil	β-Lactams	4	C16H17N3O5S	1.05	**364.09617**	381.12272	386.07811	182.55172	low sensitivity or not recovered				
Cefalonium	β-Lactams		C20H18N4O5S2	2.86	**459.07914**	476.10569	481.06108	230.04321	low sensitivity or not recovered				
Cephalexin	β-Lactams		C16H17N3O4S	3.94	**348.10125**	365.12780	370.08320	174.55426	low sensitivity or not recovered				
Cephalosporin C	β-Lactams		C16H21N3O8S	1.10	**416.11221**	433.13876	438.09416	208.55974	low sensitivity or not recovered				

[a]Number in bold font style and underlined indicates ionization form or charge state for data processing or quantification. [b]Bold and underlined are antibiotics with recoveries not in the range of 71 to 120%. [c]Bold and underlined are antibiotics with intermediate precision >20%. [d]Bold and underlined are antibiotics with MU > 50%. [e]For data in red color font, the method performance was based on three spike levels, i.e. 25.0, 50.0, and 80.0 μg/kg, due to its poor sensitivity. For data in sky blue color font, the method performance was based on two spike levels, i.e. 50.0 and 80.0 μg/kg, due to its poor sensitivity. [f]LCL: lowest concentration level of the matrix-matched calibration curve. [g]Column number. [h]The method performance of unstable antibiotics was estimated from one experiment when working solution was prepared fresh. [i]Dimetridazole-d_3 was used as an internal standard for compounds that have no isotopically labeled standards for quantification. [j]Data was processed according to the mass of a fragment m/z 337.03170. [k]Canadian Maximum Residue Limits (MRLs) for Veterinary Drugs in Foods (http://www.hc-sc.gc.ca/dhp-mps/vet/mrl-lmr/mrl-lmr_versus_new-nouveau-eng.php). [l]IU = international unit. 0.006 μg of penicillin G is equivalent to 0.01 IU.

to extract both polar and relatively nonpolar veterinary drugs in a single sample preparation procedure.[4]

In our current study, we further explored the applications of QuEChERS and SOSLE for a single analysis of 125 veterinary drugs from 12 different classes in milk, which were monitored under the Canadian National Chemical Residue Monitoring Program. This paper discusses the respective advantages of either QuEChERS or SOSLE in terms of method simplicity or inclusive coverage of veterinary drugs for quantification or screening in a single analysis. SOSLE was further modified and was adopted as the final extraction method for validation. Furthermore, we employed the same UHPLC/ESI Q-Orbitrap instrument parameters that we used for the determination of 451 pesticides in fruits and vegetables[12] for the analysis of the veterinary drugs in milk. The whole idea was to simplify the routine practice of instrument operations. The same Q-Orbitrap parameters, LC column, LC mobile phases, and LC gradient profile could be used to analyze either pesticides or veterinary drugs in various matrices for different monitoring programs.

Finally, this paper presents a multiclass method using UHPLC/ESI Q-Orbitrap MS along with SOSLE to quantify or screen up to 105 veterinary drug residues from 11 different classes (except aminoglycosides) in milk at low parts-per-billion (ppb) concentration levels. Based on the method performance, the UHPLC/ESI Q-Orbitrap MS method proved to be robust

DOI: 10.1021/acs.jafc.5b04096
J. Agric. Food Chem. 2015, 63, 9175−9187

and sensitive enough to determine over 100 veterinary drug residues of interest from 1.0 to 100.0 μg/kg in milk. The method allows for high throughput testing of routine samples, which greatly benefits monitoring programs, while satisfying regulatory purposes for analysis of a number large of veterinary drugs in a single analysis.

MATERIALS AND METHODS

Materials and Reagents. Five batches of whole milk were collected from five different local farms. All milk samples, which were tested free of the veterinary drug residues using the developed UHPLC/ESI Q-Orbitrap method in the current study, were kept at −20 °C. The Pierce LTQ ESI positive ion calibration solution (10 mL) was purchased from ThermoFisher Scientific (Rockford, IL, USA). The calibration solution, which includes *n*-butylamine (*m*/*z* 74), caffeine (*m*/*z* 195 and its fragment *m*/*z* 138), Ultramark 1621 (*m*/*z* 1022, 1122, 1222, 1322, 1422, 1522, 1622, 1722, 1822), and MRFA (*m*/*z* 524), was used to tune and calibrate the Q-Orbitrap. Ammonium acetate (reagent grade), ammonium sulfate (reagent plus, >99.0%), formic acid (LC-MS grade, ~98%), ammonium formate (for mass spectrometry, >99.0%), oxalic acid (reagent plus, >99.0%), ammonium hydroxide (28−30%), and LC-MS acetonitrile (Chromasolv, 2.5 L) were purchased from Sigma-Aldrich Corp (MO, USA). Acetic acid (glacial acetic acid, reagent grade, 99.7%), acetonitrile (distilled in glass), methanol (distilled in glass), and EDTA disodium salt were obtained from Caledon Laboratories Ltd. (Ont, Canada). Water (18.2 MΩ·cm) used for reagent and sample preparation was obtained from a Barnstead Nanopure system (Thermo Scientific, OH, USA). Veterinary drug standards (Table 1, column 1) were obtained from Sigma-Aldrich Corp or Toronto Research Chemicals (Ont, Canada). Internal standards dimetridazole-d_3, HMMNI-d_3, ipronidazole-d_3, ipronidazole-OH-d_3, and ronidazole-d_3 were purchased from Sigma-Aldrich Corp. A LC vial was a 0.45 μm PVDF Syringeless Filter Device Mini-UniPrep with polypropylene housing (GE Healthcare UK Limited, UK). ENVIRO-CLEAN QuEChERS Mylar pouches that contain 6 g of $MgSO_4$ and 1.5 g of sodium acetate were purchased from UCT Inc. (PA, USA). OASIS HLB Plus 225 mg cartridges were purchased from Waters Corp (MA, USA).

Preparation of Standard Solutions. Individual veterinary drug standard stock solutions were generally prepared at a concentration of 1000 or 2000 μg/mL in methanol, acetonitrile, or water. Intermediate veterinary drug working solutions were prepared at 5.0 μg/mL in methanol from stock solutions. Stock and intermediate solutions were stored at −20 °C. A six-level veterinary drug standard mix working solution was prepared by transferring 0.1, 0.5, 2.0, 4.0, 6.0, and 10.0 mL of 5.0 μg/mL into six separate 50 mL volumetric flasks for their respective concentration levels, and then making up to volume with acetonitrile. The resulting concentrations were 0.010, 0.050, 0.200, 0.400, 0.600, and 1.000 μg/mL, which were used to construct the matrix-matched standard calibration curves. Four-level sample spike veterinary drug standard working solutions were prepared by transferring 4.0, 10.0, 20.0, and 32.0 mL of 5.0 μg/mL into four separate 100 mL volumetric flasks and making up to volume with acetonitrile for their respective concentration levels. The resulting concentrations were 0.200, 0.500, 1.000, and 1.600 μg/mL, which were used for sample fortification. Internal standard working solutions (5.0 μg/mL and 0.5 μg/mL) including dimetridazole-d_3, HMMNI-d_3, ipronidazole-d_3, ipronidazole-OH-d_3, and ronidazole-d_3 were prepared in acetonitrile. All working solutions were stored at 4 °C.

UHPLC/ESI Q-Orbitrap Parameters. The UHPLC/ESI Q-Orbitrap system consisted of an Accela 1250 LC pump and an Accela open autosampler coupled with a Q-Exactive mass spectrometer (ThermoFisher Scientific, Germany). The system was controlled by Xcalibur 2.2 software. The UHPLC/ESI Q-Orbitrap instrument parameters were the same as those we used for the determination of 451 pesticides in fruits and vegetables.[12]

(a). Ultrahigh Pressure Liquid Chromatography. UHPLC mobile phases A and B consisted of 4 mM ammonium formate and 0.10% formic acid in water and methanol, respectively. The UHPLC column utilized was a Hypersil Gold, 100 mm × 2.1 mm, 1.9 μm column (Thermo Scientific, USA). The UHPLC guard column was an Accucore aQ 10 × 2.1 mm, 2.6 μm Defender cartridge (Thermo Scientific, USA). The UHPLC gradient profile and flow rate are shown in Figure 1. The column oven temperature was set at 45 °C, and the autosampler temperature was set at 5 °C. The injection volume was 5 μL, and the total run-time was 14 min.

A

UHPLC Gradient Profile

	Time	A%	B%	μL/min
0	0.00	88.0	12.0	300
1	8.00	5.0	95.0	300
2	9.00	0.0	100.0	300
3	11.00	0.0	100.0	300
4	11.10	88.0	12.0	300
5	14.00	88.0	12.0	300

B

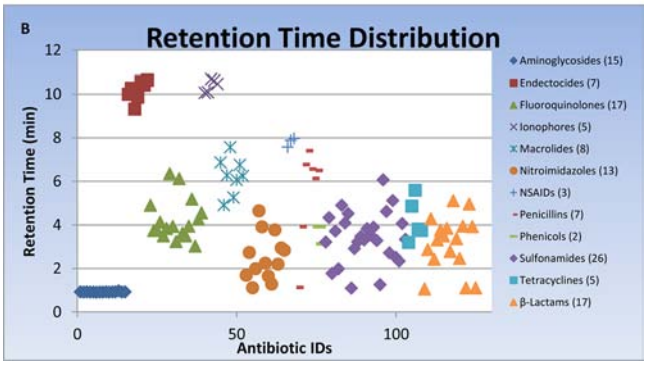

Figure 1. UHPLC gradient profile and liquid chromatographic elution distribution profile for 125 veterinary drugs. Q-Orbitrap was operated in Full MS-SIM mode.

(b). Q-Orbitrap Parameters. The Q-Exactive ion source was equipped with a heated electrospray ionization (HESI) probe, and the Q-Orbitrap was tuned and calibrated using a positive LTQ calibration solution once a week. The Q-Exactive was operated in either Full MS-SIM or Full MS/dd-MS^2 in positive mode. In Full MS-SIM, the Q-Orbitrap performed a full MS scan without HCD (high energy collision dissociation) fragmentation for quantification. The full MS scan range was set from *m*/*z* 80 to 1100 (0 to 12.0 min). The mass resolution was set to 70,000 FWHM at *m*/*z* 200, and the instrument was tuned for maximum ion throughput. The AGC (automatic gain control) target or the number of ions to fill the C-Trap was set at 1.0E6 with a maximum injection time (IT) of 250 ms. All quantitative data in this study were acquired using Full MS-SIM mode. Q-Orbitrap MS means the Q-Exactive that was operated in Full MS-SIM mode for quantification throughout the text.

Targeted identification was achieved by full scan MS, and if a targeted veterinary drug was present, its precursor ion scan, provided by an inclusion list, triggered a data-dependent MS^2 (dd-MS^2) scan. During full MS scan, the mass resolution was set at 70,000 FWHM, AGC target at 1.0E6, maximum IT 250 ms, and scan range from *m*/*z* 80 to 1100. If the targeted compound was detected within the 10 ppm mass error window and achieved by a designated intensity threshold (i.e., setting of 1.7E5), the precursor ions in the inclusion list were then isolated by the quadrupole, and sent to the HCD collision cell for fragmentation via the C-trap. The inclusion list consists of precursor ions that are of interest for targeted identification, and is provided in Table 1 (columns 6−9). The precursor ions were fragmented with stepped normalized collision energy (NCE) to generate the resulting dd-MS^2 product-ion spectra. At this stage, the mass resolution of the Orbitrap analyzer was set at 35,000 FWHM, AGC target at 2E5, maximum IT 120 ms, isolation window 1.0 *m*/*z*, NCE 40 ± 50%, underfill ratio 10%, intensity threshold 1.7E5, apex trigger 2 to 4 s, and dynamic exclusion 10.0 s.

DOI: 10.1021/acs.jafc.5b04096
J. Agric. Food Chem. 2015, 63, 9175−9187

Other Q-Exactive generic parameters were sheath gas flow rate set at 60, Aux gas flow rate 30, sweep gas flow rate 2, spray voltage 3.50 kV, capillary temp 350 °C, S-lens level 55.0, and heater temp 350 °C.

During the initial method development stage, 125 veterinary drugs and 5 isotopically labeled standards (Table 1, column 1) were injected individually onto the UHPLC column (Hypersil Gold, 100 mm × 2.1 mm, 1.9 μm) and the Q-Orbitrap was operated in Full MS/dd-MS^2 positive mode to determine the retention time and identity of each veterinary drug.

Method Development on Sample Extraction. *Method A.* This is the conventional QuEChERS method after slight modification of a published method for the determination of 59 veterinary drug residues in milk[11] with references to other methods.[13,14] QuEChERS performed in this study means a procedure that consists of two steps throughout the text: i.e. Step 1 salting-out acetonitrile/water extraction, and Step 2 dispersive solid-phase extraction (*d-SPE*) cleanup.

Step 1 Extraction. Triplicate milk samples (10 g/sample) were weighed into 50 mL centrifuge tubes (VWR International, Canada). Five hundred μL of 1 ppm working solution was spiked to each sample, which was 50.0 μg/kg of veterinary drugs equivalent in sample. After 15 min, 10 mL of a mixture of acetonitrile and acetic acid (99 + 1, v/v) was added to the sample. The centrifuge tube was capped and vortexed to mix for 45 s, and then 6 g of $MgSO_4$ and 1.5 g of sodium acetate (ENVIRO-CLEAN QuEChERS Mylar pouch) were added to the sample. The sample mixture was capped and shaken at 1500 rpm for 1 min using a 2010 Geno/Grinder (SPEX SamplePrep, Metuchen, NJ, USA) and then centrifuged at 3000 rpm (~2100*g*) for 3 min using a centrifuge (Allegra X-15R Centrifuge, Beckman Coulter Inc., CA, USA).

Step 2 d-SPE Clean-up. Seven mL of supernatant from Step 1 was transferred to a 15 mL centrifuge tube that contained 500 mg of end-capped C_{18} (obtained from the Sep-Pak tC18, Waters Corp.). Five mL of hexane (presaturated with acetonitrile) was added to the supernatant, which was shaken for 30 s by hand. The mixture was centrifuged at 3000 rpm (~2100*g*) for 3 min. The top hexane layer was aspirated to waste. Three mL of sample extracts were transferred into individual 5 mL PYREX brand centrifuge tubes, which were precalibrated with 1 mL volume accuracy (VWR International, Edmonton, AB, Canada). The sample extracts were evaporated to 0.1−0.2 mL, which took approximately 20 min, using an N-EVAP nitrogen evaporator (Organomation Associates Inc., Berlin, MA, USA) at 50 °C under a stream of nitrogen. The extracts were reconstituted up to 0.5 mL with acetonitrile and then to 1.0 mL with 0.1 M ammonium acetate. The extracts were vortexed for 30 s. Five hundred μL of sample extracts was transferred into a 0.45 μm PVDF Syringeless Filter Device Mini-UniPrep vial (Whatman, GE Healthcare Life Science, UK) and pressed to filter. Sample extracts were ready to be injected into an UHPLC/ESI Q-Orbitrap MS for analysis.

Method B. This is a procedure that combines salting-out acetonitrile/water extraction and SPE cleanup, which is known as salting-out supported liquid extraction (SOSLE).[4] SOSLE performed in this study means a procedure that consists of two steps: i.e. Step 1 salting-out acetonitrile/water extraction, and Step 2 solid-phase extraction (SPE) cleanup throughout the text.

Step 1 Extraction. The extraction step of this method was based on SOSLE[4] with a slight modification. Triplicate milk samples (5 g/sample) were weighed into 50 mL centrifuge tubes (VWR International, Canada). Two hundred fifty μL of 1 ppm working solution was spiked to each sample, equivalent to 50.0 μg/kg of veterinary drugs in sample. After 15 min, 5 mL of extraction buffer and 10 mL of acetonitrile were added to the sample. The extraction buffer contained 0.86% oxalic acid and 0.74% EDTA disodium salt, and its pH was adjusted to 3.0 using ammonium hydroxide. The sample mixture was capped and shaken for 30 s by hand and then centrifuged at 3000 rpm (~2100*g*) for 5 min using a centrifuge. The supernatant was transferred into another 50 mL centrifuge tube, to which 1 g of ammonium sulfate was added. The sample mixture was mixed for 2 min by hand, and then was left to stand for 2 min. A phase separation was observed from the mixture, and two layers were obtained.

Step 2 SPE Clean-up. Instead of diatomaceous earth cartridges as in the original SOSLE,[4] polymeric reversed-phase sorbent such as OASIS HLB Plus cartridges was used for SPE cleanup. OASIS HLB Plus 225 mg cartridges, which were paired with 25 mL of syringe barrels, were set up for solid-phase extraction using a Visiprep 24-port SPE Vacuum Manifold (Sigma-Aldrich Corp). The cartridges were preconditioned sequentially with 10 mL of methanol, 10 mL of water, and 2 mL of extraction buffer. The sample extracts from Step 1 were separated into three layers after centrifugation (3000 rpm or ~2100*g*, 3 min). The top acetonitrile layer (~10 mL) was transferred to a 16 × 125 mm disposable test tube and set aside for later to be loaded onto OASIS HLB cartridges. The lower aqueous layer was transferred onto the preconditioned Oasis HLB cartridges under vacuum at −2 to −3 inHg with a flow rate of ~1 mL/min. The very thin middle white layer (~1 or 2 mm), which was supposed to be fat from the sample, was discarded and should be avoided from being transferred onto the cartridges. Oasis HLB cartridges were rinsed further with 2 mL of extraction buffer and allowed to run dry. Finally, the top acetonitrile layer, which served as eluting solvent as well, was dispensed onto the OASIS HLB cartridges. The flow (~1 mL/min) of the eluting solvent was maintained under vacuum at −2 to −3 in Hg, and the eluent was collected into a 16 × 125 mm disposable glass test tube. The OASIS HLB cartridges were run dry under vacuum. The eluent was capped and inverted to mix a few times by hand. Two hundred fifty μL of sample extracts was transferred to a 0.45 μm PVDF Syringeless Filter Device Mini-UniPrep vial, and then 250 μL of 0.1 M ammonium acetate was added. The Mini-UniPrep unit was capped, mixed, and pressed to filter. Sample extracts were ready to be injected to UHPLC/ESI Q-Orbitrap MS for analysis.

Method C. This is a SOSLE method, which is modified from Method B. It consisted of two steps: i.e. Step 1 salting-out acetonitrile/water extraction, and Step 2 SPE cleanup.

Step 1 Extraction. This step is the same as that of Method B.

Step 2 SPE Clean-up. All procedures were the same as Step 2 of Method B until the last step. After the top acetonitrile layer was loaded onto the OASIS HLB cartridges and the eluent was collected into a 16 × 125 mm disposable glass test tube, an additional 5 mL of methanol was dispensed onto the cartridges to elute further. The eluent was collected into the same test tube. The OASIS HLB cartridges were run dry under vacuum. The eluent (~15 mL) was capped and inverted to mix a few times. Two hundred fifty μL of sample extracts was transferred to a 0.45 μm PVDF Syringeless Filter Device Mini-UniPrep vial, and then 250 μL of 0.1 M ammonium acetate was added. The Mini-UniPrep unit was capped, mixed, and pressed to filter. Sample extracts were ready to be injected to UHPLC/ESI Q-Orbitrap MS for analysis.

Method D. This is a SOSLE method, which is modified from Method C. It consisted of two steps: i.e. Step 1 salting-out acetonitrile/water extraction, and Step 2 SPE cleanup.

Step 1 Extraction. This step is the same as that of Method B or C.

Step 2 SPE Clean-up. The procedure was the same as Step 2 of Method C, except the final extracts were concentrated three times. Right after the SPE step, 3 mL of eluent was transferred into individual 5 mL PYREX brand centrifuge tubes, which were precalibrated with 1 mL volume accuracy (VWR International, Canada). The sample extracts was evaporated to 0.1−0.2 mL, which took approximately 20 min, using an N-EVAP nitrogen evaporator (Organomation Associates Inc., USA) at 50 °C under a stream of nitrogen. Then the extracts were reconstituted up to 0.5 mL with acetonitrile and then to 1.0 mL with 0.1 M ammonium acetate. The extracts were vortexed for 30 s. Five hundred μL of sample extracts was transferred into a 0.45 μm PVDF Syringeless Filter Device Mini-UniPrep vial and pressed to filter. Sample extracts were ready to be injected to an UHPLC/ESI Q-Orbitrap MS for analysis.

To calculate an absolute recovery (%) or extraction efficiency of veterinary drugs from each individual method A to D, the UHPLC/ESI Q-Orbitrap MS response (peak area spiked before sample extraction) of a veterinary drug extracted from a sample was compared to that (peak area spiked after sample extraction and cleanup) of a

DOI: 10.1021/acs.jafc.5b04096
J. Agric. Food Chem. 2015, 63, 9175−9187

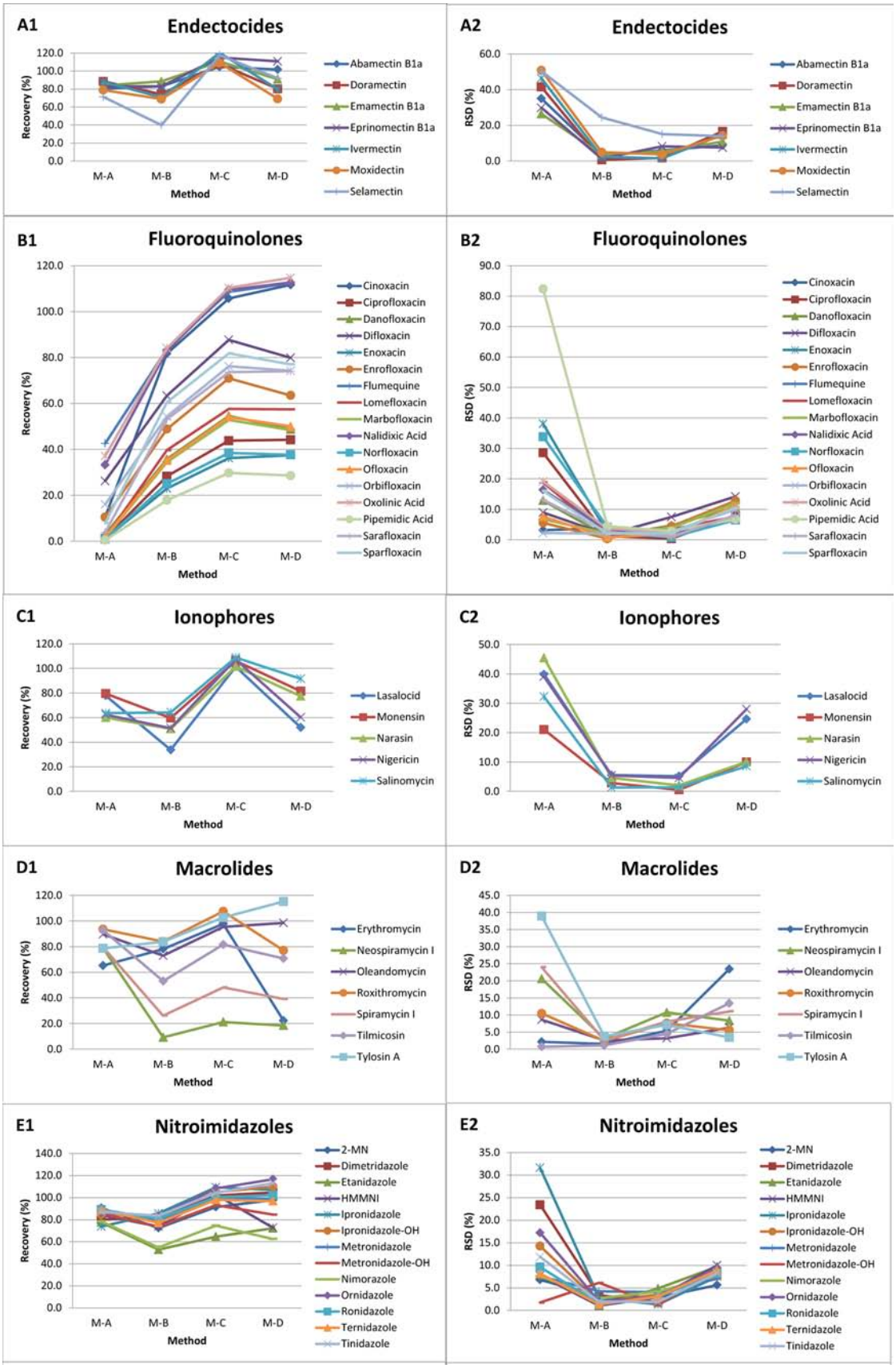

Figure 2. continued

DOI: 10.1021/acs.jafc.5b04096
J. Agric. Food Chem. 2015, 63, 9175−9187

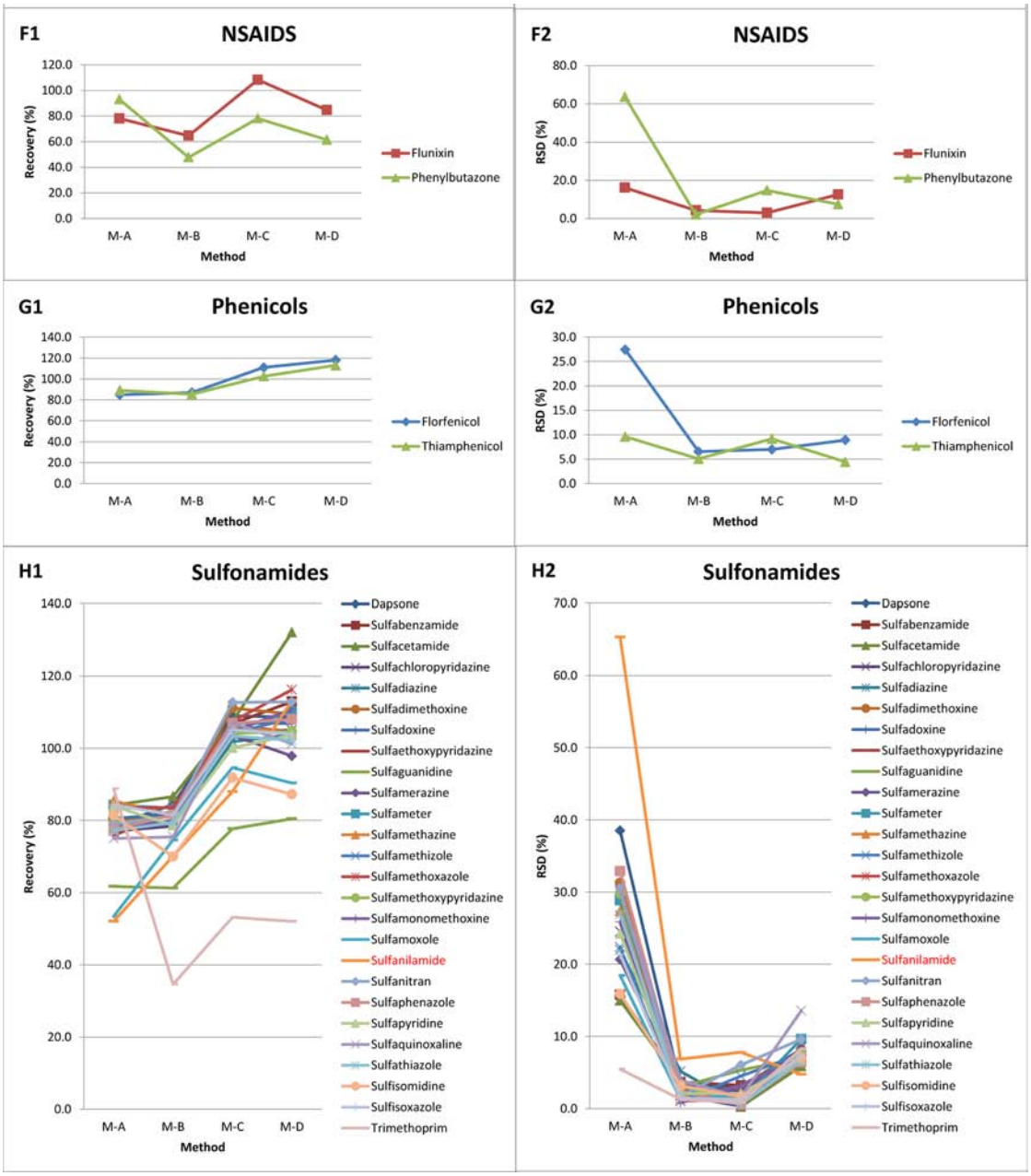

Figure 2. Comparisons of absolute recoveries of different extraction methods for 8 groups of veterinary drugs. Left: absolute recovery. Right: relative standard deviation (RSD, %). M-A: Method A. M-B: Method B. M-C: Method C. M-D: Method D.

veterinary drug prepared in a blank sample extract at 50 μg/kg equivalent in sample. That is

$$\text{Absolute Recovery (\%)} = \frac{\textit{Peak area spiked before}}{\textit{Peak area spiked after}} \times 100$$

Nested Experimental Design and Method Validation. Method D was adopted as the final method for validation in this study.

Fortification Experiment. Milk samples (5.0 g/sample) were weighed into individual 50 mL polypropylene centrifuge tubes (VWR International, Canada). Two hundred fifty μL per four-level sample spike veterinary drug standard working solution(s) were added into four centrifuge tubes to provide 10.0, 25.0, 50.0, and 80.0 μg/kg of veterinary drugs equivalent in sample, followed by the addition of 25 μL of 5.0 μg/mL internal calibration standard working solution (25.0 μg/kg equivalent in sample). Then the samples proceeded to extraction and cleanup.

Preparation of Matrix-Matched Calibration Standards and Calculation. Matrix-matched calibration standards were prepared by adding standards and internal standards to blank sample extracts that were processed through extraction and cleanup. A blank milk sample (5.0 g) was weighed into a 50 mL centrifuge tube, and the sample was processed through the extraction and cleanup as described in Method D. Before reconstitution, 100 μL of each six-level veterinary drug standard mix working solution and 50 μL of 0.50 μg/mL internal calibration working solution were added to the individual sample extracts to provide 1.0, 5.0, 20.0, 40.0, 60.0, and 100.0 μg/kg per standard and 25.0 μg/kg per internal standard equivalent in sample. The rest of the preparation was the same as in Method D.

Matrix-matched standard calibration curves for each individual veterinary drug were constructed using TraceFinder 3.2 (optimized for Environmental and Food Safety) software. Concentration, μg/kg (ppb), versus the ratio (analyte area/IS area) of each individual veterinary drug was plotted. Five commercially available deuterium labeled standards, i.e. dimetridazole-d_3, HMMNI-d_3, ipronidazole-d_3,

DOI: 10.1021/acs.jafc.5b04096
J. Agric. Food Chem. 2015, 63, 9175−9187

ipronidazole-OH-d_3, and ronidazole-d_3, were used as internal standards for quantifying their respective native compounds, and dimetridazole-d_3 was utilized for all other veterinary drugs that had no isotopically labeled standards available. In general, a quadratic function was applied to the calibration curves based on the line of best fit. Occasionally, linear regression may be used for quantification. The $1/x$ weighting was used to improve the accuracy for the quantification of veterinary drugs at low concentrations. Responses for the unknown concentration or fortified samples were compared to the standard curves to calculate the amount of veterinary drug residues, μg/kg (ppb), in samples. Matrix-matched calibration standards were prepared fresh for each batch of samples.

The method was validated according to the nested experimental design, which was described elsewhere.[15] The main factors of variances associated with the method performance or measurement uncertainty of an in-house validated method were concentrations or spiked levels of analytes, matrix effects, day-to-day variation, and within day variation of the method. The last two factors were designated as the intermediate precision. In this study, there were a total of 5 batches of milk samples from 5 different local farms. For each matrix, samples were spiked at 10.0, 25.0, 50.0, and 80.0 μg/kg, in triplicate. Spike experiments were repeated on two different days or by two analysts. Overall recovery, intermediate precision, and measurement uncertainty were calculated using a combined computer program that consisted of SAS codes (SAS Software Release 9.3, SAS Institute Inc., USA) along with a Microsoft Excel (Microsoft Office 2010) workbook.

RESULTS AND DISCUSSION

Ultrahigh Performance Liquid Chromatography. For practical reasons, the same UHPLC/ESI Q-Orbitrap instrument parameters used for the determination of 451 pesticides in fruits and vegetables[12] were utilized for the analysis of veterinary drugs in milk. This includes the same Q-Orbitrap parameters, LC column, LC mobile phases, and LC gradient profile. During the method development stage, 125 veterinary drugs and 5 isotopically labeled standards (Table 1, column 1) were injected individually onto the UHPLC column (Hypersil Gold, 100 mm × 2.1 mm, 1.9 μm), and the Q-Orbitrap was operated in Full MS/dd-MS^2 positive mode. These data ensured that the correct retention times were assigned to the respective compounds, and to determine the identities of veterinary drugs in a mixture of standards. Full MS/dd-MS^2 data were critical to differentiate isobaric compounds. The mobile phases were methanol and water, each containing 4 mM ammonium formate and 0.10% formic acid, and the gradient profile is shown in Figure 1A. Veterinary drugs from a particular class or group demonstrated a similar chemical property in terms of liquid chromatographic retention (Figure 1B). For example, the very polar aminoglycosides were hardly retained on the column, and all were eluted as a group around 0.91 min. Endectocides and ionophores, which are relatively nonpolar, were well retained on the column, and all were eluded between 9.31 and 10.68 min. The elution pattern of the 125 veterinary drugs showed up as clusters of individual classes as depicted in Figure 1B. Aminoglycosides were excluded from the method due to their poor chromatographic retention.

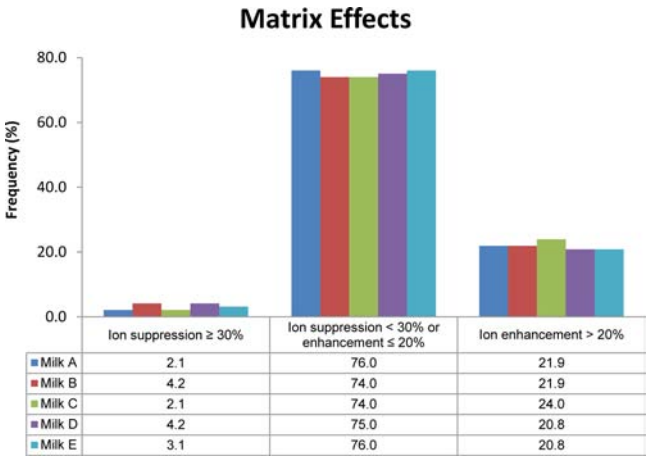

Figure 3. UHPLC/ESI Q-Orbitrap MS matrix effects. The veterinary drugs (Table 1, Section A and B) were prepared in milk sample extracts (a total of 5 matrices) and solvent buffer at a concentration of 50 μg/kg equivalent in sample.

The elution pattern on the reversed-phase column may possibly be perceived as an indication of the extraction efficiency of the method for a class of veterinary drugs. In other words, the retention time (RT) of a veterinary drug may be correlated to the method extraction efficiency. For example when using Method D described in the Materials and Methods, the polar compounds with poor chromatographic retention (<1.28 min), remained as challenges to be extracted from milk samples. Amoxicillin, cefadroxil, and cephalosporin C (Table 1, Section D), which were eluded between 1.03 and 1.10 min, were likely not recovered by the method. Desacetyl cephapirin, etanidazole, nimorazole, and sulfaguanidine (Table 1, Section A), which were eluded between 1.05 and 1.28 min, had recoveries from 15.0 to 72.4%. Sulfanilamide (RT: 1.25 min and recovery: 97.1%) was the only one exception from this observation. In general, the well-retained compounds (RT > 1.5 min) showed good recoveries (Table 1, Section A and B). This is to assume that the chromatographic retention of a veterinary drug as a result of its polarity may serve as an indicator of the extraction efficiency of a method. However, this assumption may not be necessarily true in reverse, since there are many other factors, such as matrix effects, solvent, and solid-phase extract sorbent used that contribute to the extraction efficiency.

Under most circumstances, an extracted ion of a veterinary drug was presented as a single LC peak. Most veterinary drugs had baseline separation from others, resulting from the superior resolving power of both UHPLC and Q-Orbitrap MS. Some were coeluted because they were isobaric compounds such as ampicillin and cephradine (Table 1, Section C). Veterinary drugs were eluted between 1.0 and 11.0 min, and their peak shapes were of Gaussian distribution with a baseline peak-width of 5 to 10 s. The retention times were reproducible under ±0.2 min within- and between-batches for most of the veterinary drugs. With the scan rate of 3 Hz for the resolution of 70,000 FWHM at m/z 200, the Q-Orbitrap provided sufficient data points for quantification. For example, at least 18 data points across the chromatographic peak were generated with a 6 s (0.1 min) baseline peak-width.

Q-Orbitrap Mass Spectrometry. When operated in Full MS-SIM mode with a range from m/z 80.0 to 1100.0 and 70,000 FWHM resolution at m/z 200, the Q-Orbitrap acquired full MS scan data for the quantitation of veterinary drugs. The quantitative results are provided in Table 1 (columns 10−12). When operated in Full MS/dd-MS^2 mode, the Q-Orbitrap acquired product-ion spectra with accurate mass measurements for identification according to a list of targeted exact masses (Table 1, columns 6−9). A three-step normalized collision energy (NCE) of 40 ± 50% (i.e., the center energy 40 NCE; plus one above, 60 NCE; and one below, 20 NCE) was used for the fragmentation of precursor ions in the high-energy collision

DOI: 10.1021/acs.jafc.5b04096
J. Agric. Food Chem. 2015, 63, 9175−9187

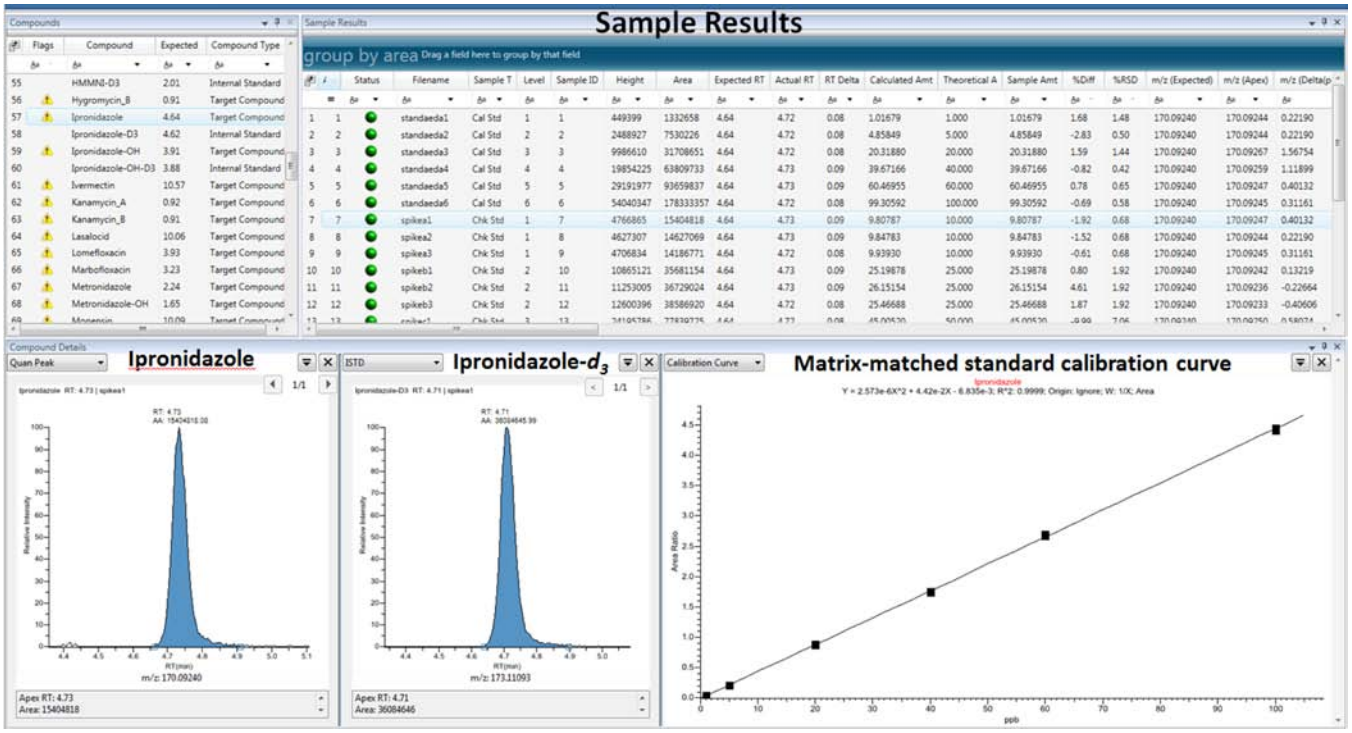

Figure 4. Example of a matrix-matched standard calibration curve along with its isotopically labeled standard (ipronidazole and ipronidazole-d_3).

dissociation (HCD) cell to produce product ions for identification. The product ions created in the three-step NCE were collected sequentially in the HCD and transferred together to the Orbitrap mass analyzer for a single scan detection. Stepped NCE did not work for all of the veterinary drugs because not all were optimally fragmented in the 40 ± 50% NCE range. As a routine practice from our previous experience,[12] the Full MS/dd-MS^2 data of individual veterinary drugs were acquired to determine their identities in a mixture. The data set was also intentionally collected to build a "Compound Database" or automated searchable exact mass spectral library for identification or screening purposes. However, in the current study, we focused on the quantitative aspect of UHPLC/ESI Q-Orbitrap applications for veterinary drugs.

Method Development on Sample Extraction. We began with a list of 125 veterinary drugs, which were included under the CFIA routine monitoring program for determination of veterinary drug residues in milk. The plan was to develop a generic extraction method to include 125 compounds in a single analysis, which previously was achieved using multiple separate single-class methods, and to improve the monitoring program efficiency. Method development was initiated with a conventional QuEChERS but was gradually evolved into SOSLE, to include as many analytes as possible. Because β-lactams, penicillins, and tetracyclines are not stable molecules, their data for absolute recovery comparisons during the method development are not included.

Method A was based on the conventional QuEChERS, which was slightly modified from a published method for the determination of 59 veterinary drug residues in milk[11] with references[13,14] therein. Step 1 utilized the typical salting-out acetonitrile/water extraction, while Step 2 invoked the use of dispersive solid-phase extraction (*d-SPE*) for cleanup to remove nonpolar compounds such as fat in milk. The method was very simple and fast. It worked well for endectocides, ionophores, macrolides, nitroimidazole, NSAIDS, and sulfonamides with absolute recoveries over 70% (Figure 2, left), but the method showed poor repeatability for quantification with relative standard deviations as high as 40−50% (Figure 2, right). Fluoroquinolones (Figure 2-B1) had recoveries ranging from 0.5 to 43.5%, while β-lactams, penicillins, and tetracyclines were not recovered at all (data not shown), as similar observations have been reported elsewhere.[11]

In order to recover β-lactams, penicillins, and tetracyclines, and to improve the recoveries of fluoroquinolones, we looked into other methodologies. Kaufmann et al. developed a procedure known as salting-out supported liquid extraction (SOSLE), which combines the salting-out acetonitrile/water extraction (Step 1) and solid-phase extraction (SPE) cleanup (Step 2) to extract the veterinary drugs in milk.[4] In SOSLE, both acetonitrile and water, from which a phase separation was induced afterward by salting-out using ammonium sulfate, were used to ensure the quantitative extraction of analytes that were distributed in either the aqueous or acetonitrile layer. The mixture of acetonitrile and water was capable of extracting a wide range of analytes from the matrix because it provided significantly higher extraction efficiency for both polar analytes as well as nonpolar compounds.[4] The recoveries of tetracyclines and fluoroquinolones were significantly increased as a result of the addition of complexing agents like EDTA and the use of ammonium sulfate rather than magnesium sulfate to prevent chelation to inorganic salts and to induce a phase separation of the acetonitrile and water mixture. The resulting heavier aqueous phase was loaded onto SPE cartridges which contained coarse-grained kieselguhr (also known as diatomaceous earth). The compounds retained on the cartridges were eluted with the supernatant organic phase (acetonitrile). Final extraction and elution of the analytes was achieved through additional volumes

DOI: 10.1021/acs.jafc.5b04096
J. Agric. Food Chem. 2015, 63, 9175−9187

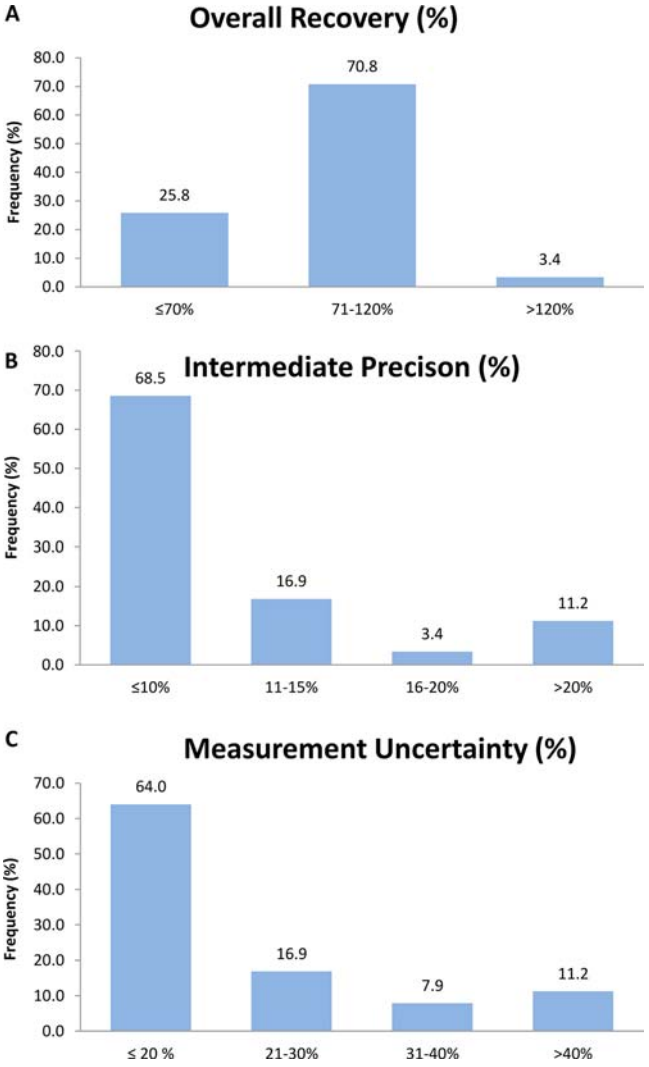

Figure 5. UHPLC/ESI Q-Orbitrap MS method performance for analysis of veterinary drug residues (Table 1, Section A) in milk. A: Overall recovery. B: Intermediate precision. C: Measurement uncertainty.

of acetonitrile. The combined eluents were evaporated to produce the injection-ready extracts.[4]

Due to the relatively large volume of the final extracts (25 mL) resulting from the 45 mL/8.3 g bed size of CHROMABOND XTR columns (diatomaceous earth cartridges, MACHEREY-NAGEL GmbH & Co. KG, Düren,Germany) in the original method[4] and poor repeatability of recoveries from these cartridges in our experiments (data not shown), we modified the method for a more practical application. By switching to polymeric reversed-phase sorbent SPE cartridges (i.e., OASIS HLB Plus 225 mg cartridges), the cleanup process required a significantly smaller volume of organic solvent to elute and the results showed improved repeatability. The polymeric reversed-phase sorbent cartridges have been found to be efficient in extracting both polar and relatively nonpolar veterinary drugs in milk, eggs, and honey.[16,17] As described in the Materials and Methods, in Step 1, Method B used an extraction buffer (0.86% oxalic acid and 0.74% EDTA, pH 3) and acetonitrile to precipitate proteins in milk. After removal of protein by centrifugation, ammonium sulfate was added to the supernatant to induce a phase separation of the sample mixture. In Step 2, the resulting heavier aqueous phase was loaded onto the SPE cartridges to retain polar compounds (such as β-lactams, penicillins, tetracyclines, etc.), followed by the top acetonitrile layer, which contained relatively nonpolar compounds (such as endectocides, ionophores, etc.), to serve as the eluting solvent to elute veterinary drugs on the cartridges. Figure 2 (A2-H2) illustrates that Method B significantly improved the repeatability of recoveries for all veterinary drugs. Figure 2 (A1-H1) also demonstrates that Method B increases the recoveries of fluoroquinolones but decreases recoveries for the ionophores, macrolides, and NSAIDS, while the recoveries of endectocides, nitroimidozles, phenicols, and sulfonamides remained unchanged. It was observed that the recoveries of some macrolides, such as neospiramycin I and spiramycin I, decreased significantly, which might be as a result of their degradation under acid conditions (pH 3).[18]

To improve the recoveries, Method C was modified from Method B by increasing the amount of the eluting solvent in Step 2. Besides the ~10 mL of acetonitrile (top layer after the phase separation) as the eluting solvent, an additional 5 mL of methanol was added to elute any strongly retained veterinary drug residues on the cartridges. Figure 2 (A1-H1) reveals that the recoveries of all veterinary drugs from Method C were increased as compared to Method B. Most of the recoveries increased from 60 or 80% to ~100%, and RSDs were less than 10%, with the exception of a few fluoroquinolones and macrolides. The results indicated that the additional 5 mL of methanol was critical to improve the recoveries in SOSLE when polymeric reversed-phase sorbent cartridges were used for cleanup.

In both Methods B and C, the final extracts were diluted 1:1 rather than being concentrated. These methods may not be applicable to detect low concentration levels of veterinary drugs in milk samples. To lower the detection limits into low parts-per-billion levels (such as 1 ppb), in Step 2, additional concentration and reconstitution steps were implemented in the development of Method D from Method C. As observed from Figure 2, the recoveries of some veterinary drugs from Method D were slightly lower and RSDs higher than the results provided by Method C. Method D proved to be well suited for analyzing milk samples fortified at the 1 ppb concentration level (Table 1, column 13). The final concentrations of veterinary drugs in vials (prior to UHPLC/ESI Q-Orbitrap MS injection) from Method A to D were 150, 12.5, 8.33, and 50 ppb (or ng/mL), respectively. Method D resulted in 6 times concentrated sample extracts compared to Method C. Apparently, the concentration and reconstitution steps caused losses of some compounds and led to slightly increased variation. Overall, in terms of recoveries and RSDs, Method C provided the best performance among the four methods. However, in order to detect veterinary drugs at low concentration levels, especially at the 1 ppb level, Method D was chosen to be validated for the determination of veterinary drugs in milk. It is worth noting that Method D is also able to recover β-lactams, penicillins, and tetracyclines as shown in Table 1.

In summary, as shown in Figure 2, Method A (except for β-lactams, penicillins, and tetracyclines), C, or D can serve as independent methods to be validated for various applications depending on testing scopes and instrument sensitivity. For example, Method A (i.e., QuEChERS) can potentially be validated and used for analysis of endectocides, ionophores, macroldies, nitromidazole, NSAIDS, phenicols, and sulfona-

DOI: 10.1021/acs.jafc.5b04096
J. Agric. Food Chem. 2015, 63, 9175−9187

mides in milk or other matrices because it is simple and fast. For highly sensitive LC-MS systems, Method C (i.e., SOSLE) is the best choice for all veterinary drugs due to its method performance in terms of recovery and repeatability. Method D (i.e., SOSLE) proves to be the most sensitive among all, and it was found it fit for the needs of using UHPLC/ESI Q-Orbitrap MS to quantify veterinary drug residues in milk at low ppb concentration levels.

Matrix Effects. The sample matrix can either enhance or suppress the ionization of veterinary drugs, and its effects can vary from sample-to-sample, which ultimately affects the UHPLC/ESI Q-Orbitrap MS quantitative results. To evaluate matrix effects, the responses (peak areas) of veterinary drugs in sample extracts were compared to those of veterinary drug standards prepared in solvent buffer at 50 μg/kg equivalent in sample. In general, about 74.0−76.0% veterinary drugs had ion suppression <30% or ion enhancement ≤20%, 2.1−4.2% were subjected to ion suppression ≥30%, and 20.8−24.0% were subjected to ion enhancement >20% in milk (Figure 3). Veterinary drugs that were suppressed ≥30% included flunixin, roxithromycin, and thiamphenicol. Veterinary drugs that were enhanced >20% included doramectin, eprinomectin B_{1a}, ivermectin, HMMNI, metronidazole, metronidazole-OH, nimorazole, ternidazole, sulfacetamide, sulfadiazine, sulfaguanidine, sulfamerazine, sulfamethoxypyridazine, sulfathiazole, sulfisomidine, sulfanilamide, 4-epitetracycline, chlortetracycline, oxytetracycline, cefapirin, and desacetyl cephapirin. Therefore, matrix-matched standard calibration curves along with isotopically labeled standards (Figure 4) were used to minimize or compensate for matrix effects to improve the accuracy of the UPLC/ESI Q-Orbitrap MS quantification. Five commercially available deuterium labeled standards, i.e. dimetridazole-d_3, HMMNI-d_3, ipronidazole-d_3, ipronidazole-OH-d_3, and ronidazole-d_3, were used as internal standards for quantifying their respective native compounds, and dimetridazole-d_3 was utilized for all other veterinary drugs. The calibration curves were observed to be linear or quadratic, with coefficient of determinations (R^2) ≥ 0.97. Because of matrix effects, ion source contamination, or other unidentified factors, the responses of some veterinary drugs either decreased or increased slightly over time. To average out the response changes during the course, matrix-matched standard calibration curves were constructed based on the two injections, i.e. before and after spike samples, so as to improve the method performance (Figure 4).

Quantification and Method Performance. The UHPLC/ESI Q-Orbitrap MS method was validated according to a nested design, reported elsewhere. To evaluate the method performance characteristics, including accuracy, expressed as overall recovery, intermediate precision, and measurement uncertainty (MU),[15] four factors, such as concentrations or spiked levels of veterinary drugs, matrix effects, day-to-day variation, and within-day variation (described in the Materials and Methods), were considered. For the 89 veterinary drugs that were chemically stable and were evaluated through the fully nested experimental design, their method performance results are summarized in Tables 1 Section A, and are illustrated in Figure 5. About 70.8% of the veterinary drugs in milk had recoveries between 71% and 120%; 88.8% had intermediate precision ≤20%; and 93.3% showed measurement uncertainty ≤50%. The Codex CAC/GL 71-2009[19] recommended method performance criteria such as recovery of 70−120% and repeatability ≤20% for quantitative analytical methods to support the maximum residue limit for veterinary drug residues in foods. Therefore, Method D demonstrated the optimized performance to quantify a majority of veterinary drugs listed in Table 1 Section A.

For the 13 veterinary drugs, primarily penicillins and β-lactams that were not chemically stable and not able to go through the fully nested experimental design but were still quantifiable, their method performance was summarized according to a one-day experiment and the results are listed in Table 1 Section B. In general, the method for those veterinary drugs demonstrated a good repeatability with the exception of cefapirin and some additional compounds that had a recovery <70% or >120% (Table 1, Section B).

Table 1 Section C lists three veterinary drugs, ampicillin, cephradine, and tylosin B, that can be screened but not quantified. This is becasue ampicillin and cephradine are isobaric compounds and cannot be chromatographically separated, and tylosin B has no standard commercially available to prepare calibration curves for quantification.

Aminoglycosides (a total of 15, Table 1 Section D) were poorly retained due to their polarity on the reversed-phase C_{18} column with retention times ∼0.91 min. Amoxicillin, cefadroxil, cefalonium, cephalexin, and cephalosporin C (a total of 5, Table 1 Section D) showed low sensitivity or were not recovered during the extraction procedure. Therefore, those veterinary drugs (a total of 20) were not included in the final method.

Overall, the UHPLC/ESI Q-Orbitrap MS along with SOSLE can serve as a reliable and practical method for quantifying or screening a total of 105 veterinary drugs in a single extraction process and within a 14 min analytical runtime.

Veterinary Drug Identification. According to Codex CAC/GL 71−2009[19] for veterinary drug analysis and identification, when high resolution mass spectrometers are used in a confirmatory method, the high resolution provides more reliable identification of the mass and may be used to predict the elemental composition of each fragment. For a single stage high resolution mass spectrometer, each structurally significant fragment detected is assigned a value of two identification points, while each product ion generated in a tandem high resolution mass spectrometer is assigned an identification point value of 2.5. In addition, at least one ion ratio must also be measured to eliminate the potential for product ions of the same mass arising from isobaric compounds of similar structure. SANCO/12495/2013[20] required ≥2 diagnostic ions (preferably the precursor ion and its product ion) with mass accuracy <5 ppm along with retention time tolerance of ±0.2 min for identification of pesticides. The UHPLC/ESI Q-Orbitrap provided a measured mass accuracy <5 ppm and a retention time tolerance within ±0.2 min. Full MS/dd-MS^2 was able to obtain product-ion spectra that included both precursor and product ions with accurate masses. Currently, identification was achieved using the Thermo Xcalibur Qual Browser by comparing to the Full MS/dd-MS^2 data of individual veterinary drugs. Studies are in progress to develop "Compound Database" or a searchable exact mass spectral library that can be used for efficient screening and identification including calculating ion ratios using the system software.

Method Sensitivity. The lowest concentration levels (LCL) of individual veterinary drugs, which indicated the method sensitivity, were determined according to the recommended default LC peak height value, i.e. 1.0×10^4, reported elsewhere for the Orbitrap.[21,22] Among 102

DOI: 10.1021/acs.jafc.5b04096
J. Agric. Food Chem. 2015, 63, 9175−9187

quantifiable veterinary drugs (Table 1, Section A and B), 71.6% could be detected and quantified at a concentration level ≤1.0 μg/kg, and 83.3% ≤ 5.0 μg/kg. The method appeared to be less sensitive to tetracyclines, penicillins, and β-lactams, which had LCLs ranging from 20.0 to 60.0 μg/kg. Table 1 lists the Canadian Maximum Residue Limits (MRLs) for veterinary drugs in milk.[23] Except for penicillin G, LCLs were all below their respective MRLs of individual veterinary drugs, demonstrating that the method could be fit for the regulatory purposes of monitoring veterinary drug residues in milk in Canada.

In conclusion, UHPLC/ESI Q-Orbitrap along with SOSLE proved to be a reliable and practical multiclass method for the determination of up to 105 veterinary drug residues from 11 different classes (except aminoglycosides) in milk. The UHPLC/ESI Q-Orbitrap MS, i.e. full MS scan, provided good method accuracy, repeatability, and sensitivity for quantification. Generally, about 70.8% of the 89 veterinary drug residues in milk, which went through the full method validation, had recoveries between 71% and 120%; 88.8% had intermediate precision ≤20%; and 93.3% showed measurement uncertainty ≤50%. UHPLC/ESI Q-Orbitrap dd-MS^2 provided product-ion spectra with accurate mass measurements that allowed for the identification of veterinary drugs. Overall, UHPLC/ESI Q-Orbitrap offers a practical tool for the analysis of a large number of veterinary drug residues in milk for monitoring programs, all with a single extraction in a 14 min analytical runtime.

AUTHOR INFORMATION

Corresponding Author

*Phone: (403) 338-5273; fax: (403) 338-5299; e-mail: jian.wang@inspection.gc.ca.

Notes

The authors declare no competing financial interest.

ACKNOWLEDGMENTS

The authors are grateful to Wendy Cheung and Darcy Dean, Calgary Laboratory, Canadian Food Inspection Agency, for purchasing or preparation of veterinary drug standards for the study.

REFERENCES

(1) Florea, N. F.; Nightingale, C. H. Review of the pharmacodynamics of antibiotic use in animal food production. *Diagn. Microbiol. Infect. Dis.* **2004**, *49*, 105−8.

(2) Mathur, S.; Singh, R. Antibiotic resistance in food lactic acid bacteria–a review. *Int. J. Food Microbiol.* **2005**, *105*, 281−95.

(3) Stolker, A. A. M.; Brinkman, U. A. T. Analytical strategies for residue analysis of veterinary drugs and growth-promoting agents in food-producing animals—a review. *J. Chromatogr. A* **2005**, *1067*, 15−53.

(4) Kaufmann, A.; Butcher, P.; Maden, K.; Walker, S.; Widmer, M. Multi-residue quantification of veterinary drugs in milk with a novel extraction and cleanup technique: Salting out supported liquid extraction (SOSLE). *Anal. Chim. Acta* **2014**, *820*, 56−68.

(5) Ortelli, D.; Cognard, E.; Jan, P.; Edder, P. Comprehensive fast multiresidue screening of 150 veterinary drugs in milk by ultra-performance liquid chromatography coupled to time of flight mass spectrometry. *J. Chromatogr. B: Anal. Technol. Biomed. Life Sci.* **2009**, *877*, 2363−2374.

(6) Hammel, Y. A.; Mohamed, R.; Gremaud, E.; Lebreton, M. H.; Guy, P. A. Multi-screening approach to monitor and quantify 42 antibiotic residues in honey by liquid chromatography-tandem mass spectrometry. *J. Chromatogr. A* **2008**, *1177*, 58−76.

(7) Stolker, A. A.; Rutgers, P.; Oosterink, E.; Lasaroms, J. J.; Peters, R. J.; van Rhijn, J. A.; Nielen, M. W. Comprehensive screening and quantification of veterinary drugs in milk using UPLC-ToF-MS. *Anal. Bioanal. Chem.* **2008**, *391*, 2309−22.

(8) Peters, R. J. B.; Bolck, Y. J. C.; Rutgers, P.; Stolker, A. A. M.; Nielen, M. W. F. Multi-residue screening of veterinary drugs in egg, fish and meat using high-resolution liquid chromatography accurate mass time-of-flight mass spectrometry. *J. Chromatogr. A* **2009**, *1216*, 8206−8216.

(9) Stubbings, G.; Bigwood, T. The development and validation of a multiclass liquid chromatography tandem mass spectrometry (LC−MS/MS) procedure for the determination of veterinary drug residues in animal tissue using a QuEChERS (Quick, Easy, Cheap, Effective, Rugged and Safe) approach. *Anal. Chim. Acta* **2009**, *637*, 68−78.

(10) Martinez Vidal, J. L.; Frenich, A. G.; Aguilera-Luiz, M. M.; Romero-Gonzaez, R. Development of fast screening methods for the analysis of veterinary drug residues in milk by liquid chromatography-triple quadrupole mass spectrometry. *Anal. Bioanal. Chem.* **2010**, *397*, 2777−2790.

(11) Wang, J.; Leung, D. The challenges of developing a generic extraction procedure to analyze multi-class veterinary drug residues in milk and honey using ultra-high pressure liquid chromatography quadrupole time-of-flight mass spectrometry. *Drug Test. Anal.* **2012**, *4* (Suppl 1), 103−111.

(12) Wang, J.; Chow, W.; Chang, J.; Wong, J. W. Ultra-high performance liquid chromatography electrospray ionization Q-Orbitrap mass spectrometry for the analysis of 451 pesticide residues in fruits and vegetables: method development and validation. *J. Agric. Food Chem.* **2014**, *62*, 10375−10391.

(13) Geis-Asteggiante, L.; Lehotay, S. J.; Lightfield, A. R.; Dutko, T.; Ng, C.; Bluhm, L. Ruggedness testing and validation of a practical analytical method for > 100 veterinary drug residues in bovine muscle by ultrahigh performance liquid chromatography-tandem mass spectrometry. *J. Chromatogr. A* **2012**, *1258*, 43−54.

(14) Lehotay, S. J.; Lightfield, A. R.; Geis-Asteggiante, L.; Schneider, M. J.; Dutko, T.; Ng, C.; Bluhm, L.; Mastovska, K. Development and validation of a streamlined method designed to detect residues of 62 veterinary drugs in bovine kidney using ultra-high performance liquid chromatography–tandem mass spectrometry. *Drug Test. Anal.* **2012**, *4* (Suppl 1), 75−90.

(15) Wang, J.; Wotherspoon, D. Determination of pesticides in apples by liquid chromatography with electrospray ionization tandem mass spectrometry and estimation of measurement uncertainty. *J. AOAC Int.* **2007**, *90*, 550−567.

(16) Wang, J.; Leung, D. Analyses of macrolide antibiotic residues in eggs, raw milk, and honey using both ultra-performance liquid chromatography/quadrupole time-of-flight mass spectrometry and high-performance liquid chromatography/tandem mass spectrometry. *Rapid Commun. Mass Spectrom.* **2007**, *21*, 3213−3222.

(17) Wang, J. Confirmatory determination of six penicillins in honey by liquid chromatography/electrospray ionization-tandem mass spectrometry. *J. AOAC Int.* **2004**, *87*, 45−55.

(18) Wang, J. Analysis of macrolide antibiotics, using liquid chromatography-mass spectrometry, in food, biological and environmental matrices. *Mass Spectrom. Rev.* **2009**, *28*, 50−92.

(19) CAC/GL 71-2009. Guidelines for the design and implementation of national regulatory food safety assurance programme associated with the use of veterinary drugs in food producing animals. Adopted 2009. Revision 2012, 2014. *FAO/WHO Codex Alimentarius International Food Standards.* http://www.codexalimentarius.org/standards/list-of-standards/. Accessed on July 30, 2015.

(20) Method validation and quality control procedures for pesticide residues analysis in food and feed. *Document No. SANCO/12571/2013 Supersedes Document No. SANCO/12495/2011 Implemented by 01/01/2014.* http://www.eurl-pesticides.eu/library/docs/allcrl/AqcGuidance_Sanco_2013_12571.pdf. Accessed on July 30, 2015.

DOI: 10.1021/acs.jafc.5b04096
J. Agric. Food Chem. 2015, 63, 9175−9187

(21) Thomas, A.; Geyer, H.; Schänzer, W.; Crone, C.; Kellmann, M.; Moehring, T.; Thevis, M. Sensitive determination of prohibited drugs in dried blood spots (DBS) for doping controls by means of a benchtop quadrupole/Orbitrap mass spectrometer. *Anal. Bioanal. Chem.* **2012**, *403*, 1279−1289.
(22) Hurtaud-Pessel, D.; Jagadeshwar-Reddy, T.; Verdon, E. Development of a new screening method for the detection of antibiotic residues in muscle tissues using liquid chromatography and high resolution mass spectrometry with a LC-LTQ-Orbitrap instrument. *Food Addit. Contam., Part A* **2011**, *28*, 1340−1351.
(23) Canadian Maximum Residue Limits (MRLs) for Veterinary Drugs in Foods. http://www.hc-sc.gc.ca/dhp-mps/vet/mrl-lmr/mrl-lmr_versus_new-nouveau-eng.php. *Accessed on July 30,* 2015.

DOI: 10.1021/acs.jafc.5b04096
J. Agric. Food Chem. 2015, 63, 9175−9187

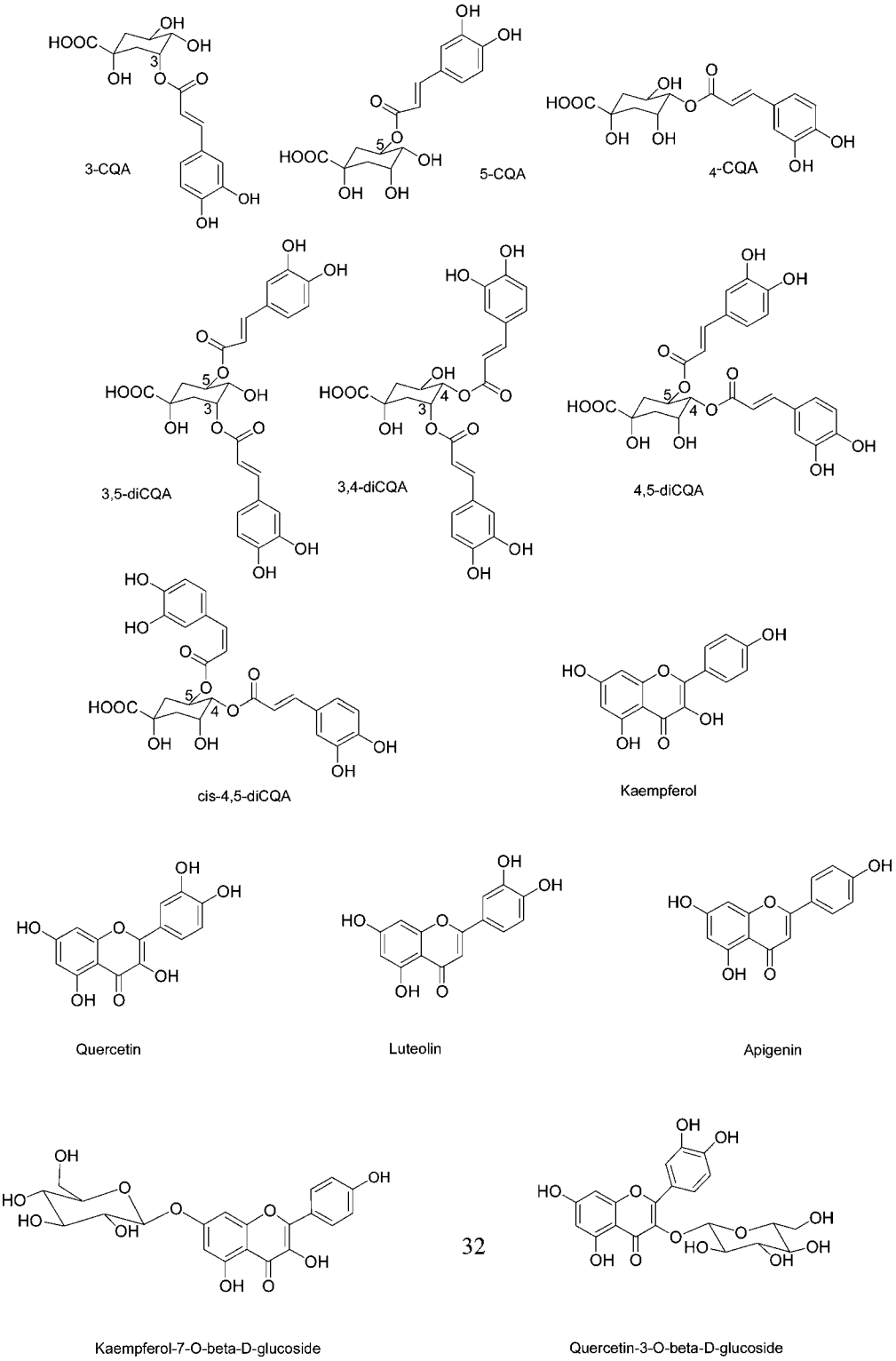

Figure 1. Structures of caffeoylquinic acids and flavonoid glycosides.

and sugar components at different positions attaching on the aglycone ring.[7]

S. rebaudiana belongs to the Asteraceae family of plants, and it is native to Paraguay. The high content of natural sweeteners, the steviol glycosides of the ent-kaurene class of compounds, contained in its leaves makes *S. rebaudiana* of a significant economic value in food industry in many applications as a zero-calorie sweetener. Purified steviol glycosides have only recently been approved as food additives by European and United States legislative authorities, leading to a dramatic increase in its global use and scientific interest in the crop.

MATERIALS AND METHODS

Chemicals. IUPAC numbering has been used for chlorogenic acids and the chlorogenic acids of 3-caffeoylquinic acid (3-CQA), 4-caffeoylquinic acid (4-CQA), 5-caffeoylquinic acid (chlorogenic acid),

DOI: 10.1021/acs.jafc.5b01944
J. Agric. Food Chem. 2015, 63, 9188−9198

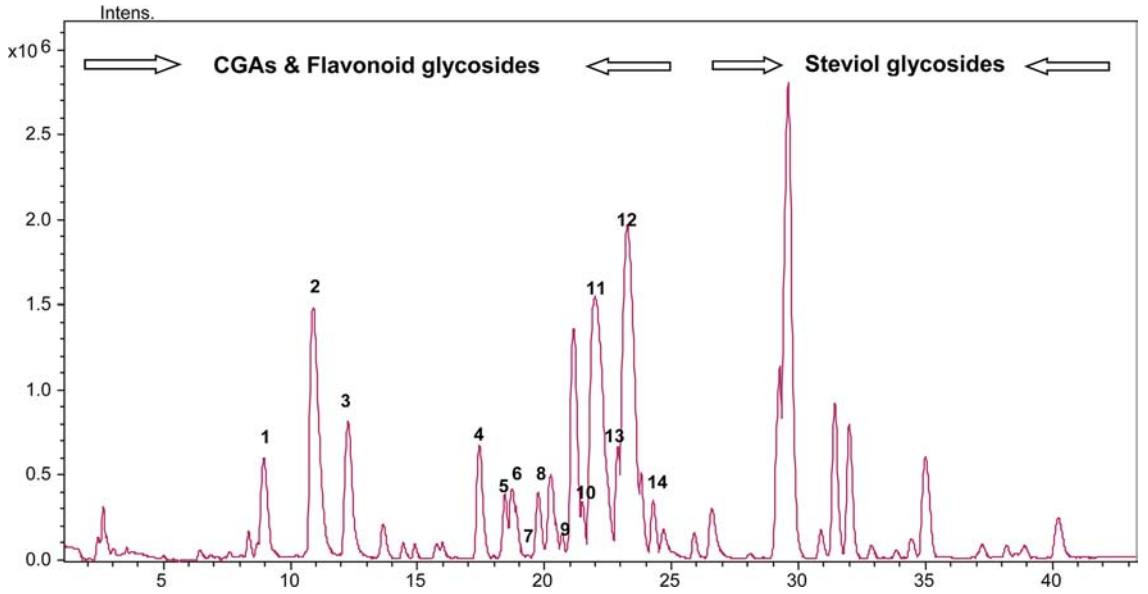

Figure 2. Base-peak chromatogram in negative ion mode using a C-18 column of methanolic *S. rebaudiana* extract showing phenolics (chlorogenic acids, flavonoids, and steviol glycosides).

Table 1. Chromatographic and MS Data on Flavonoid Glycosides and CGAs Present in *S. rebaudiana* Leaves

compound number	compound[a]	m/z ($[M - H^+]^-$)	retention time
1	3-caffeoylquinic acid (3-CQA)	353	8.8
2	5-caffeoylquinic acid (5-CQA)	353	10.9
3	4-caffeoylquinic acid (4-CQA)	353	12.1
4	rutin	609	17.4
5	quercetin-galactoside	463	18.4
6	kaempferol-glucopyranoside	447	18.8
	quercetin-rhamnoside		21.1
7	quercetin-fructoside; luteolin-glucuronide	461	19.3
8	quercetin-pentoside	433	20.2
9	kaempferolxylosylglucoside	579	20.5
10	apigenin-galactoside	431	21.5
11	3,5-dicaffeoylquinic acid (3,5diCQA)	515	22.0
12	4,5-dicaffeoylquinic acid (4,5di-CQA)	515	23.3
13	quercetin-diglucoside-rhamnoside	771	22.9
14	kaempferol-glucosylrhamnosyl-glucoside/galactoside	755	24.2
	kaempferol-rhamnopyranosyl-glucopyranoside (rutinoside) isomers		18.8
15	quercetin-dirhamnoside	593	19.5
	apigenin-diglucoside/galactoside		20.0
16	quercetin-trisaccharide	741	12.7
17	kaempferol 3-rhamnopyranosyl-rhamnopyranosyl-glucopyranoside	739	16.0

[a]Compounds named for flavonoid glycosides are only possible structures, which were not identified or confirmed.

3,4-dicaffeoylquinic acid (3,4-diCQA), 3,5-dicaffeoylquinic acid (3,5-diCQA), and 4,5-dicaffeoylquinic acid (4,5-diCQA); the compounds were purchased from PhytoLab (Vestenbergsgreuth, Germany). Flavonoid glycoside standards were obtained from Sigma-Aldrich; HPLC-grade acetonitrile, methanol, and chloroform were obtained from Carl-Roth GmbH, Karlsruhe.

S. rebaudiana leaves were obtained from Universität Hohenheim who led the trial cultivation in eight different E.U. regions.

Sample Preparation. A 2 g sample of *S. rebaudiana* leaves was immersed in liquid nitrogen, ground in a hammer mill, and extracted first with 150 mL of chloroform in a Soxhlet apparatus (Buchi B-811 extraction system) for 2 h and then with 150 mL of methanol for another 2 h. Solvents were removed from the methanolic extract in vacuo, and extracts were stored at −20 °C until required.

LC-TOF MS. The LC equipment (Agilent 1100 series, Bremen, Germany) comprised a binary pump, an autosampler with a 100 μL loop, and a diode array detector with a light-pipe flow cell (recording at 254 nm and scanning from 200 to 600 nm). This was interfaced with a MicroTOF Focus mass spectrometer (Bruker Daltonics) fitted with an ESI source. The MS parameters were as follows: nebulizer 1.6 bar, dry gas 12.0 L/min, dry temperature 220 °C. The MicroTOF was operated in negative ion mode, and the mass range was 150−1200 m/z. Internal calibration was achieved with 10 mL of 0.1 mol/L sodium formate solution injected through a six-port valve prior to each chromatographic run. Calibration was carried out using the enhanced quadratic calibration mode.

LC-MS^n. The LC equipment (Agilent 1100 series, Bremen, Germany) comprised a binary pump, an autosampler with a 100 μL loop, and a diode array detector with a light-pipe flow cell (recording at 254 nm and scanning from 200 to 600 nm). This was interfaced with an ion-trap mass spectrometer fitted with an ESI source (Bruker Daltonics HCT Ultra, Bremen, Germany) operating in Auto-MS^n mode to obtain

DOI: 10.1021/acs.jafc.5b01944
J. Agric. Food Chem. 2015, 63, 9188−9198

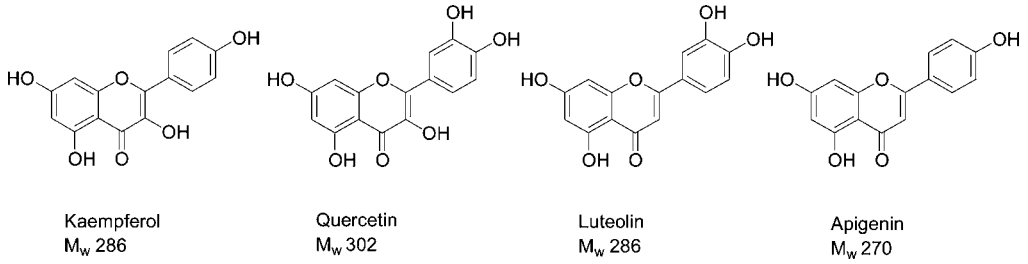

Figure 3. Chemical structure of four flavonoid aglycones identified in *S. rebaudiana* leaves.

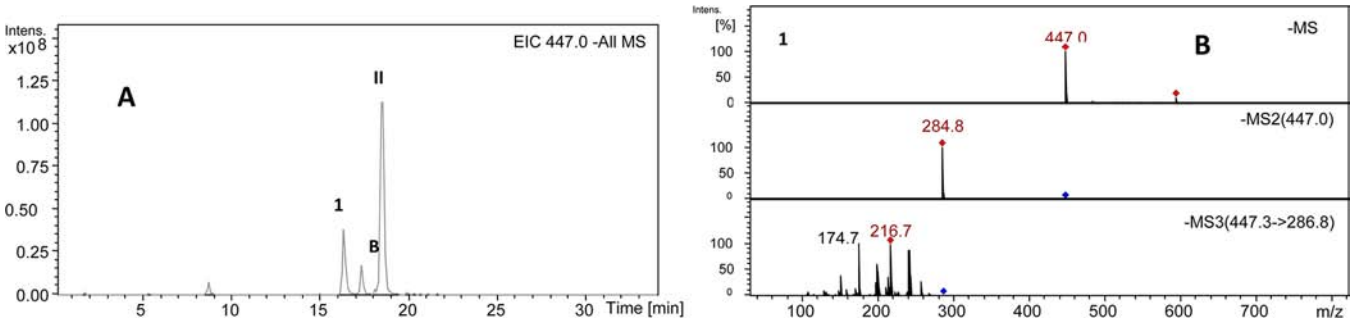

Figure 4. (A) Extracted ion chromatogram of *m/z* 447.0 in negative ion mode and (B) representative tandem MS spectra for compound labeled A in chromatogram, revealing its identity as kaempferolglucopyranoside **1**.

fragment ions *m/z*. Tandem mass spectra were acquired in Auto-MS^n mode (smart fragmentation) using a ramping of the collision energy. Maximum fragmentation amplitude was set to 1 V, starting at 30% and ending at 200%. MS operating conditions (negative mode) were as follows: capillary temperature 365 °C, dry gas flow rate 10 L/min, and nebulizer pressure 50 psi.

HPLC. Separation was achieved on a 250 × 3 mm^2 C18 column (Varian Pursuit XRS) with 5 μm particle size. Solvent A was water/formic acid (1000 + 0.005% v/v), and solvent B was acetonitrile (ACN). Solvents were delivered at a total flow rate of 0.5 mL/min, and the column temperature was set to 25 °C. A 5 μL aliquot of each sample was injected into the LC-MS system unless stated otherwise. The gradient profile was 10−80% B in 60 min and a return to 10% B at 65 and 5 min isocratic to re-equilibrate.

Calibration Curve of Standard Compounds. The most abundant chlorogenic acid derivatives (3-CQA, 4-CQA, 5-CQA, 3,5-diCQA, and 4,5 diCQA) and two flavonoid glycosides (quercetin-3-glycoside and kaempferol-7-glycoside) were chosen for calibration curves.

Stock solutions of the standard compounds were prepared in 80% ACN/water. A series of standard solutions were injected (5 μL) into the LC-MS system. The areas of the peaks of each standard from extracted ion chromatograms (EIC) were used to make the respective standard curves.

Statistical Analyses. Statistical analyses of the data were performed using IBM SPSS 20. The distributions of the variables were tested for normality using the Kolmogorov−Smirnov test. Associations between the variables were investigated using both parametric (Pearson's correlation) and nonparametric (Spearman's correlation) techniques. Results were interpreted using the widely accepted 5% level of significance.

To test whether there were differences on each chlorogenic acid with respect to its origin or variety, separate one-way ANOVA analyses were employed, followed by two posthoc tests: Fisher's least significant difference (LSD) as the least conservative test where equal variances are assumed and Games-Howell test where nonequal variances are assumed for the multiple pair wise comparison tests. All empirical results were interpreted using the widely accepted 5% level of significance ($p < 0.05$).

Principle component analyses (PCA) were carried out on the basis of the LC-MS data set of stevia phenols using Profile Analysis 1.1 (Bruker Daltonics), with kernelizing prior to bucketing and normalization to sum of peaks to allow differentiation between different stevia varieties and geographic origins.

RESULTS AND DISCUSSION

Within a large agricultural trial, *S. rebaudiana* was cultivated in nine southern European locations from 2010 to 2011. Up to three times a year, leaves were harvested from July to September. In total, seven different botanical varieties of *S. rebaudiana* were cultivated. Following harvesting, leaves were dried and analyzed at least three months after harvesting. The European *S. rebaudiana* samples were complemented by commercial *S. rebaudiana* samples cultivated in South America and Asia, resulting in a total of 166 samples.

Table 2. Linearity and Equations of Calibration Curves Obtained by the Least Square Methods

reference compound	linearity (μg/mL)	equation	R^2
3-CQA	1−100	82912*x* + 346549	0.99
5-CQA	5−500	49062*x* + 907693	0.99
4-CQA	1−150	129889*x* + 395550	0.99
3,5-diCQA	10−200	138064*x* + 7000000	0.98
4,5-diCQA	10−400	138243*x* + 4000000	0.98
kaempferol-7-glucoside	50−1000	26105*x* + 6000000	0.98
quercetin-3-glucoside	2−150	97003*x* + 2000000	0.98

Compound Identification. Methanolic *S. rebaudiana* extracts were analyzed by LC-MS^n in the negative ion mode using an ESI ion-trap mass spectrometer, allowing assignments of compounds to regio-isomeric level, and additionally by high-resolution mass spectrometry using LC-ESI-TOF MS in negative ion mode, allowing determination of molecular formulae on the basis of the accurate mass measurements (Supporting Information). Molecular formulas were, in general, accepted if an error below 5 ppm was experimentally observed. The *S. rebaudiana* samples under investigation contained up to 29

DOI: 10.1021/acs.jafc.5b01944
J. Agric. Food Chem. 2015, 63, 9188−9198

Table 3. Statistical Analyses Data of Chlorogenic Acids

	statistics						
	3-CQA	5-CQA	4-CQA	3,5-diCQA	4,5-diCQA	total diCQA	total monoCQA
mean	0.295	2.488	0.124	1.201	1.237	2.435	2.907
std. deviation	0.144	0.852	0.426	0.512	0.485	0.937	1.009
skewness	0.411	0.151	0.151	0.049	0.476	0.111	0.137
kurtosis	−0.217	0.365	0.372	−0.848	0.170	−0.513	0.212
minimum	0.002	0.193	0.010	0.173	0.210	0.311	0.205
maximum	0.719	4.986	0.249	2.476	2.609	4.575	5.608
KS test, asymp sig. (two-tailed)	0.521	0.951	0.916	0.468	0.746	0.584	0.817

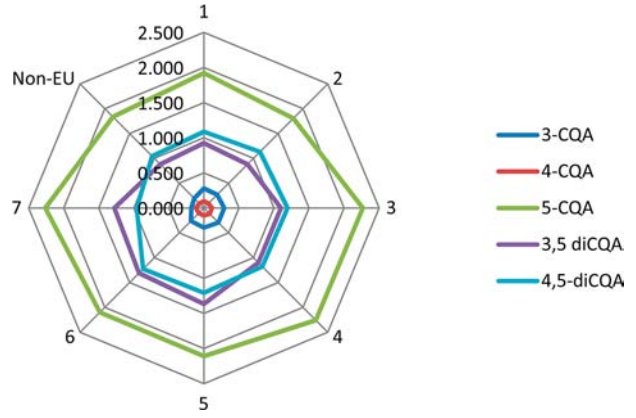

Figure 5. Radar plot of individual chlorogenic acid concentrations varying between seven varieties (average values taken within ±3 σ) and in comparison to non-E.U. samples. Concentrations are given on radial axis in gram per 100 g of dry leaf material.

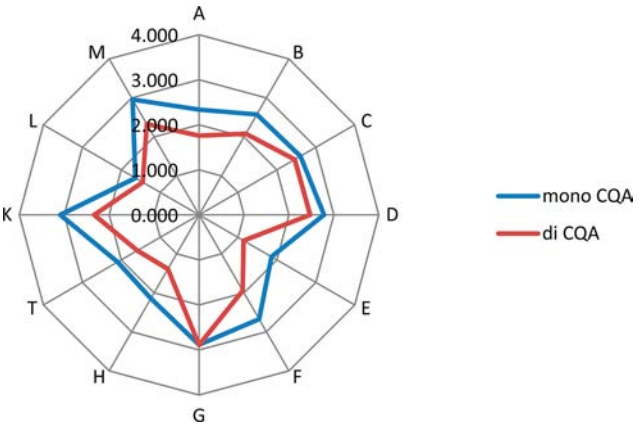

Figure 6. Radar plot of total mono- and diacyl quinic acids (chlorogenic acids) concentrations varying between all origins (average values taken within ±3 σ) and in comparison to non-European Union samples. Concentrations are given on radial axis in grams per 100 g of dry leaf material.

chlorogenic acid derivatives, as published by our group previously.[8] Furthermore, the samples contained a series of flavonoid glycosides. No new additional compounds were identified in any of the samples. Structures are presented in Figure 1.

All analytes showed baseline separation with the exception of the pair of 3,4- and 4,5 dicaffeoylquinic acid. Peak assignments of CGAs have been made on the basis of structure diagnostic hierarchical keys previously developed,[12−15] supported by means of their parent-ion high-resolution mass, UV spectra, and retention times relative to 5-CQA using validated methods in our laboratory.[5] The base-peak chromatogram of *S. rebaudiana* extract is shown in Figure 2. Within the chromatogram, CGAs and flavonoid glycosides elute between 8 and 25 min, whereas steviol glycosides elute at later retention times, between 28 and 40 min.

Four peaks were detected at m/z 353.1 and assigned using the hierarchial keys previously developed as well-known 3-CQA, 5-CQA, 4-CQA, and *cis*-5CQA.[12] Three dicaffeoylquinic acid isomers were identified by their parent ion m/z 515.2 and were assigned as 3,5-diCQA, 3,4-diCQA, and 4,5-diCQA using the hierarchial key.[13] Two further peaks present as minor components showed fragmentation patterns, similar to that of 4,5-diCQA, which are identified as *cis*-isomers of 4,5-diCQA.[16] Tricaffeoylquinic acids and caffeoylshikimates were present as minor compounds, and their regiochemistry assigned using published tandem MS methods.[14,15]

A total of 15 peaks in the chromatogram correspond to flavonoid glycosides with their characteristic fragmentation patterns in tandem MS showing neutral losses of sugar moieties of 162 Da ($C_6H_{10}O_5$) followed by characteristic fragment spectra of the aglycones quercetin (m/z 300), kaempferol (m/z 285), luteolin (m/z 285), and apigenin (m/z 269) in MS^3 (Table 1 and Figure 3). For example, three peaks were located with an m/z value of 447.1 (Figure 4), showing after a neutral loss of 162 Da, a base peak at m/z 285 in MS^2. Further fragmentation in MS^3 with the ion at 285.1 as a precursor ion revealed two fragment ions characteristic for kaempferol and one fragment ion characteristic for luteolin. Additional hydrolysis experiments followed by LC-MS analyses confirmed the presence of aglycones of kaempferol, quercetin, luteolin, and apigenin by comparison of retention times, high-resolution MS data, and tandem MS data compared to those of reference substances in *S. rebaudiana* leaves. Therefore, we tentatively assigned the flavonoid glycosides as hexose conjugates of kaempferol, quercetin, luteolin, and apigenin.

Comparison of the 15 flavonoid glycosides present in *S. rebaudiana* leaves with reference standards, either commercial or obtained through preparative HPLC purification in previous work, showed that all compounds, with the exception of rutin and naringenin, were not identical to the reference compounds available (all 8 glucosides reported in dietary plants and 2 galactosides), as judged by their retention times and fragment spectra. We suggest that the flavonoids present in *S. rebaudiana* are presumably based on fructose, galactose, or mannose. For other plants of the Asteraceae family, it was shown by Harrison et al.[17] that polyfructans are present and by the group of Goffner[18] that additionally galactomannans form the most abundant polymeric carbohydrate structures in this plant family.[18] Hence, it can be speculated that these C6 sugars are present in *S. rebaudiana* leaf flavonoids for which no reference materials are available.

DOI: 10.1021/acs.jafc.5b01944
J. Agric. Food Chem. 2015, 63, 9188−9198

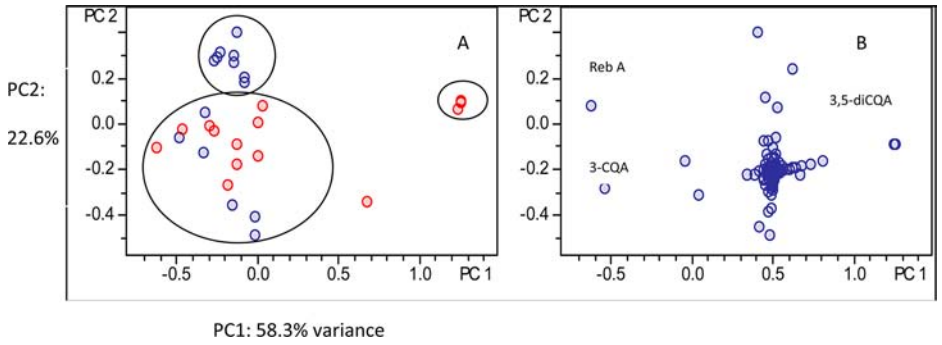

Figure 7. PCA analyses of phenol profiles of 40 *S. rebaudiana* leaf LC-MS data sets (red points, non-E.U. samples; blue points, E.U. samples). (A) Score plot with each color representing a different *S. rebaudiana* variety. (B) Loading plot with each data point corresponding to individual compounds allowing differentiation. Variation explained in PC 1 is 58.3%, and that in PC 2 is 22.6%.

Table 4. ANOVA Results for Effect of Variety on *S. rebaudiana* CGA Content

compound	*F*	sig. (*p*)
One-Way ANOVA		
3-CQA	0.849	0.549
5-CQA	0.459	0.862
4-CQA	0.464	0.859
total mono-CQA	0.463	0.860
3,5-diCQA	1.901	0.075
4,5-diCQA	1.446	0.194
Total-diCQA	1.577	0.149
Robust Test of Equality of Means		
3-CQA Welch	0.926	0.500
5-CQA Welch	0.428	0.878
4-CQA Welch	0.433	0.874
total mono-CQA Welch	0.373	0.911
3,5-diCQA Welch	1.637	0.161
4,5-diCQA Welch	1.250	0.305
total-diCQA Welch	1.402	0.238

Quantification of Chlorogenic Acids and Flavonoids. Quantitation was carried out using eight-point calibration curves. Chlorogenic acids were quantified by LC-UV at 320 nm and by LC-MS using EICs of the pseudomolecular ions at *m*/*z* 353.1 and 515.2 in negative ion mode using an ESI-TOF MS spectrometer. Additionally, flavonoids were quantified by LC-UV using kaempferol-7-glucoside and quercetin-3-glucoside as reference standards, resulting in relative rather than absolute values for flavonoids. All values obtained are quoted in grams per 100 g of dried leaf material (g/100 g).

Chlorogenic acid standard solutions were analyzed by LC-MS using the same chromatographic method as those used for *S. rebaudiana* leaf extracts. Calibration curves for monocaffeoyl derivatives 3-CQA, 4-CQA, and 5-CQA and for dicaffeoyl derivatives 3,4-diCQA, 3,5-diCQA, and 4,5 diCQA were obtained using EICs (Table 2). Pearson correlation coefficients of the calibration curves using LC-MS quantifications are given in Table 2. All calibration curves were linear within the quantification range. Values obtained from LC-UV and LC-MS quantification gave the same absolute concentration values with an error of less than ±5%, showing validity of the method. All quantitative CGA values for all 166 samples are given in the Supporting Information. The quantitative values obtained for all chlorogenic acid derivatives were found to be a factor of 3−5 higher than values previously reported by our group.[8] On occasions, the data showed a 10-fold increase of CGA concentrations. It must be concluded that the material previously investigated which was obtained from commercial sources was of unknown age and origin. Fresh leaves of *S. rebaudiana* contain

Table 5. Correlation Coefficients of Mono and Di-CQAs

		correlations				
		3-CQA	5-CQA	4-CQA	3,5-diCQA	4,5-diCQA
3-CQA	Pearson correlation (*r*)	1	0.762[a]	0.762[a]	0.416[a]	0.514[a]
	sig. (two-tailed)		0.000	0.000	0.000	0.005
	R^2		0.581	0.581	0.173	0.264
5-CQA	Pearson correlation (*r*)	0.762[a]	1	1.000[a]	0.532[a]	0.573[a]
	sig. (two-tailed)	0.000		0.000	0.000	0.000
	R^2	0.581		1	0.283	0.328
4-CQA	Pearson correlation (*r*)	0.762[a]	1.000[a]	1 0.532[a]	0.572[a]	
	sig. (two-tailed)	0.000	0.000		0.000	0.000
	R^2	0.581	1		0.283	0.327
3,5-diCQA	Pearson correlation (*r*)	0.416[a]	0.532[a]	0.532[a]	1	0.791[a]
	sig. (two-tailed)	0.000	0.000	0.000		0.000
	R^2	0.173	0.283	0.283		0.625
4,5-diCQA	Pearson correlation (*r*)	0.514[a]	0.573[a]	0.572[a]	0.791[a]	1
	sig. (two-tailed)	0.000	0.000	0.000	0.000	
	R^2	0.264	0.328	0.327	0.625	

[a]Correlation is significant at the 0.01 level (two-tailed).

DOI: 10.1021/acs.jafc.5b01944
J. Agric. Food Chem. 2015, 63, 9188−9198

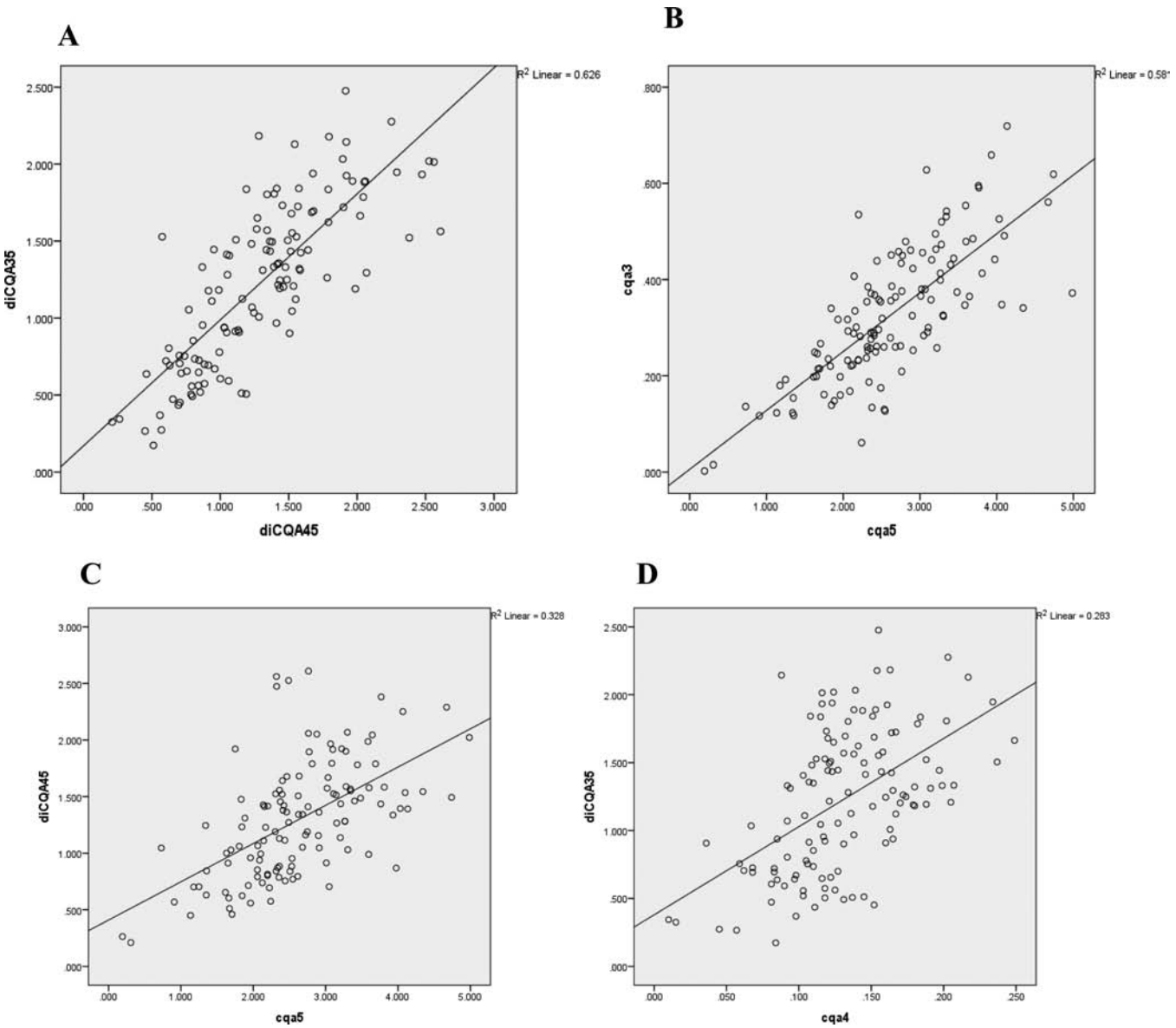

Figure 8. Graph showing the correlation between (A) 3,5-diCQA and 4,5-diCQA, (B) 3-CQA and 5-CQA, (C) 5-CQA and 4,5-diCQA, and (D) 4-CQA and 3,5-diCQA.

significant quantities of CGAs, much higher than previously determined. In terms of absolute quantities, *S. rebaudiana* shows, following green coffee beans and mate leaves, the third highest concentration of CGAs among all dietary materials.

The four flavonoid aglycones quercetin, kaempferol, luteolin, and apigenin were quantified using a LC-UV method monitoring absorption at 280 nm for selected *S. rebaudiana* samples following hydrolysis of the sugar moiety in dilute acid. It is well-established that the molar extinction coefficient of flavonoid glycosides varies only to a small degree if structural variation of the sugar moiety occurs.[19,20] Quantitative values for the four glycones are given in the Supporting Information. All flavonoid glycosides were quantified using a LC-MS method with quercetin-3-glucoside and kaempferol-7-glucoside as reference compounds, complementing the aglycone structure of the flavonoid glycosides.

Analyses of Data. With the quantitation carried out we have obtained a unique data set of the phenolic metabolome of *S. rebaudiana*. This data set requires statistical evaluation, allowing interesting observations and conclusions. We decided to address the following questions in this contribution.

- What is the statistical distribution of quantitative data? Little data is available in the literature that allows for a definite answer to this question.
- How do phenolic quantities vary with variation of origin, harvest, and plant variety?
- Does the data set allow distinction between varieties or origin in a predictive manner by using quantitative phenol concentrations?
- Do quantities of a set of distinct secondary metabolites correlate with one another?

Further questions addressing the influence of the phenolic metabolome on sensory properties or the influence of agricultural parameters on the phenolic metabolome are outside the scope of this contribution and will be commented on at a later stage.

Statistical Spread of Data. The distribution of the data set is an essential step for examination of data in statistical analyses.

DOI: 10.1021/acs.jafc.5b01944
J. Agric. Food Chem. 2015, 63, 9188−9198

Table 6. Pearson Correlation R^2 between CGAs and Flavonoid Glycosides[a,b]

	3-CQA	5-CQA	4-CQA	3,5-diCQA	4,5-diCQA	K7G	Q3G
3-CQA	-	0.762	0.762	0.416	0.514	0.330	0.096
5-CQA	0.762	-	0.991	0.532	0.573	0.298	0.096
4-CQA	0.762	0.976	-	0.532	0.572	0.297	0.095
3,5-diCQA	0.416	0.532	0.532	-	0.791	0.425	0.188
4,5-diCQA	0.514	0.573	0.572	0.791	-	0.351	0.236
K7G	0.330	0.298	0.297	0.425	0.351	-	0.029
Q3G	0.096	0.096	0.095	0.188	0.236	0.029	-

[a]k7g: kaempferol-7-glucoside; q3g: quercetin-3-glucoside. [b]

$1.0 < R^2 < 0.9$

$0.9 < R^2 < 0.7$

$0.4 < R^2 < 0.7$

$R^2 < 0.4$

The most frequent distribution of data is the Gaussian or normal distribution. A normal distribution can be easily characterized by observing its symmetrical bell shaped curve on a histogram (Figure S1). Skewness and Kurtosis values below 1 also show that the data is normally distributed. The Kolmogorov−Smirnov (KS) test was used for the analyses of data distribution. The significance value above 0.05 means that the data is normally distributed.

The quantity of each mono- and di-CQA as well as the total mono- and di-CQAs quantities obtained from 166 *S. rebaudiana* samples showed normal distribution. The KS test result, mean values, standard deviations, skewness, and kurtosis of the curve for each CGA is represented in Table 3. A histogram of 5-CQA is presented as an example in the Supporting Information. The observation of an almost perfect Gaussian distribution in all quantitative data came as a surprise. Normally, phenolic metabolites are assumed to act as defense compounds produced by the plant in various stress situations, in particular, stress induced by pathogens. Hence, a bimodial-shaped distribution of CGA concentrations could be expected with two maxima, whereby the higher concentration maximum corresponds to compound production under stress. The experimental data clearly show that this is not the case. It can be speculated that none of the 166 *S. rebaudiana* samples were under stress. A more reasonable scenario would suggest that CGA quantities right of the maximum of the Gaussian curve, shifted to higher concentrations, constitute a situation of a plant under stress; hence, CGA concentrations are only gradually increased by the plant.

Sample Variation. *Variation between Varieties.* Seven defined botanical varieties of *S. rebaudiana* were cultivated, and their phenolic profile was determined. Average values determined for the seven botanical varieties are presented in a radar plot in Figure 5. From the data, it can be seen that the average concentration of all monocaffeoylquinic acids remains rather constant over all seven varieties (2.123−2.686 g/100 g), whereas a larger spread of data is observed for dicaffeoylquinic acids (1.484−2.432 g/100 g). Varieties 3, 5, 6 ,and 7 show on average increased levels of chlorogenic acids compared to those of variety 2 (Figure 5).

Variation between Origins. *S. rebaudiana* cultivated in nine different locations within the European Union and additional samples from outside the European Union (Supporting Information) were available for comparison. According to the literature, polyphenol concentrations are due to their physiological function as UV protection agents, which are a direct function of growth altitude and climatic conditions, particularly sunshine hours. Accordingly, variations of chlorogenic acid concentrations between different origins should be expected. Indeed, the data reveal significant variations in average CGA concentrations varying from 3.090−1.637 g/100 g for total monocaffeoylquinic acids and 2.890−1.144 g/100 g for dicaffeoylquinic acids. (See the Supporting Information for average values of all origins.) E.U.-cultivated *S. rebaudiana* shows

DOI: 10.1021/acs.jafc.5b01944
J. Agric. Food Chem. 2015, 63, 9188−9198

concentrations of CGAs sandwiched between extreme values at both ends observed in samples from outside the European Union (e.g., highest for origin G samples with an average value of 2.890 g/100 g dicaffeoylquinic acids and trial location L and E samples with a lowest average value of 1.448 and 1.144 g/100 g, respectively). A radar plot shown in Figure 6 was used to display variations between different origins.

The data allow insight into variations between minimum and maximum values of phenolics. Our data show that depending on the compound in question an average factor of 5−8 is observed between minimum and maximum values encountered in plants from an individual harvest, indicating a large statistical spread of phenol concentrations.

Principal Component Analyses. To allow differentiation between different *S. rebaudiana* varieties and geographic origins, a principal component analysis (PCA) was carried out on the basis of the LC-MS data set of *S. rebaudiana* phenols. PCA analysis was carried out with an aim to distinguish E.U.-cultivated samples from non-E.U.-cultivated samples. For this purpose, 20 E.U. and 20 non-E.U. samples were subjected to a PCA analysis. Score and loading plots are shown in Figure 7. From the score plot, it can be seen that the samples fall in three groupings. Group A, from South American samples, can clearly be distinguished from all other samples on the basis of their high diCQA content (from loading plot).

Group B contains exclusively European samples from the a single Southern European cooperative. Finally, group C contains both E.U. and non-E.U. samples, e.g., from Turkey, Ukraine and India, that group together. The sample distinction information from the loading plot suggests that a combination of rebaudioside A concentrations and diCQA concentrations allows distinction here.

A second PCA analysis was carried out to compare variations between different botanical varieties. For this purpose, data from four different botanical varieties were chosen, and a PCA analysis of the full LC-MS data set was carried out. Score plot of PC1 versus PC2 shows little differentiation between sample varieties (Figure S2). However, when looking at higher-order principle components, e.g., PC2 versus PC4, three of the varieties group in the score plot, with two varieties grouping together in the same area of the plot. The loading plot reveals that the compounds responsible for the variations include dicaffeoylquinic acids along with rutin.

Statistical Evaluation of Data. From the obtained data, a series of statistical analyses was carried out. For each variety, origin, or harvest, average values and standard deviations were determined. Additionally, the statistical pattern and type of statistical distribution of the data was analyzed for each subgroup. The correlation studies were performed by Pearson's correlation, with the significance value of $p < 0.05$. Significant differences among *S. rebaudiana* leaves for each variable were assessed with analyses of variance (ANOVA). In contrast to PCA, which provides a more global picture on variances in the sample set, ANOVA allows for identification of more subtle differences, e.g., between two or more sample sets that differs only in a single or a few parameters.

Analyses of Variance. One-way ANOVA was performed to study the influence of origin and, in another test, variety on the mono- and di-CQA content of *S. rebaudiana* leaves cultivated in various regions of European Union with different soil and climatic conditions. A posthoc test was applied to find out which origin destinations or varieties differ, if any.

Influence of Origin. Levene's test was performed to assess whether the assumption of homogeneity of variance between groups is met within the data.

Test of homogeneity results revealed that for dependent variable 3-CQA and 4,5-diCQA Levene's test is not significant ($F_{8/116} = 1.783$, $p = 0.087$ and $F_{8/116} = 1.430$, $p = 0.191$, respectively). However, for 5-CQA, 4CQA, and 3,5-diCQA, Levene's test was significant at the level of 0.05 (Table S4), which indicates that the variances in the different groups of origins are different. (The groups do not have equal variance on the dependent variable, in this case, origin.) Therefore, a modified procedure that does not assume equality of variance (Welch statistic) was also applied to these data along with ANOVA.

ANOVA results (Table S5) did not reveal significant differences between the average CGA content of *S. rebaudiana* leaves of different origins. The data only hints at some differences in the average content of *S. rebaudiana* leaves from different origin destinations. These, however, can be considered only marginally significant at the 5% level ($p = 0.054$ for 4-CQA). Moreover, from the ANOVA output, a robust test of equality of means (Welch test) is considered for the CQAs that do not meet the assumption of homogeneity of variance. Similar to the ANOVA test, if the significance value is less than 0.05 in Welch test, then it means there are statistically significant differences between the groups.

From the results of Welch test and one-way ANOVA, the conclusion is that at least two of the group means are significantly different from the other. Beyond this, it is necessary to conduct a posthoc comparison test to determine exactly which pairs of groups are significantly different. There are varieties of posthoc tests available. A commonly used LSD test is applied for CQAs (3CQA and 4,5-diCQA), which met the assumption of homogeneity of variance. The Games-Howell posthoc test is applied for the CQAs 5CQA, 4CQA, and 3,5diCQA), violating the assumption of homogeneity of variance (equal variances not assumed).

Multiple comparison (post hoc) results obtained from LSD test (Fisher's least significant difference) revealed that the 3-CQA amounts are significantly different at the 0.05 level between the trial locations of C/H, H/A, H/B, and H/N origins. 4,5-diCQAs were significantly different at the 0.05 level for origin H and all the other origins except E.

Multiple comparison (post hoc) results obtained from Games-Howell test revealed that there is no significant difference at the 0.05 level between origins for 5-CQA and 4-CQA. However, a significant difference was observed for 3,5-diCQA between origins F and D with a significance value of 0.008.

Influence of Variety. Test of homogeneity results revealed that for dependent variable 3-CQA ($F_{7/117} = 1.207$, $p = 0.304$), 3,5-diCQA ($F_{7/117} = 0.545$, $p = 0.799$), and 4,5-diCQA ($F_{7/117} = 1.193$, $p = 0.312$) Levene's test was not significant. However, for 5-CQA and 4-CQA, Levene's test was significant at the level of 0.05 ($p = 0.018$; Table S6). As in the analyses of origins, the Welch test was also applied to data for the cases of violation of homogeneity of variances.

ANOVA results did not reveal significant differences between the average CGA content of *S. rebaudiana* leaves of different varieties. Moreover, the Welch test did not reveal any significant difference at the level of 0.05. The results of ANOVA test and Welch test are presented in Table 4.

Posthoc tests with Games-Howell method resulted in no pairwise differences for 5-CQA and 4-CQA for each variety. However, for 3-CQA with the LSD test, the mean difference

DOI: 10.1021/acs.jafc.5b01944
J. Agric. Food Chem. 2015, 63, 9188−9198

between varieties 1 and 5 and between varieties 3 and 5 was significant at the 0.05 level ($p = 0.04$). The varietiey pairs 4−6, 5−7, and 6−7 had a significant difference ($p = 0.04$) when 4,5-diCQA quantity in *S. rebaudiana* leaves was taken as a dependent variable. Variety 6 showed significant difference with varieties 2, 3, 4, and 7 for 3,5-diCQA quantity in *S. rebaudiana* leaves.

With the obtained data set, differences between *S. rebaudiana* leaves and influence of the origin of cultivation and the botanical varieties on the CQAs profile were studied with the most common used statistical method, ANOVA. Pair-wise comparisons of varieties and origins for each CQA were achieved by less conservative statistical post hoc test (LSD) and Games-Howell post hoc test to determine the exact pair of variety/origin that are different from each other.

Correlations: Pearson Parametric Test. The correlation analyses were performed to measure the degree of relation between two chosen CGAs. Correlations of CGAs grouped as mono-CQA to mono-CQA, di-CQA to di-CQA, and mono-CQA to di-CQAs were tested according to Pearson's correlation. Overall, correlation was observed for all CGAs with each other (Table 5). However, a strong correlation was observed between the mono-CQAs and 3,5-diCQA with 4,5-diCQA (Pearson correlation of 0.762 and 0.791, respectively) and 5-CQA with 4,5-diCQA as well as 4-CQA with 4,5-diCQA (Pearson correlation of 0.573 for both cases). The remaining correlations were slightly weaker. All correlation coefficients closer to +1, indicating, for example, that increasing quantity of 5-CQA leads to a quantitative increase of 4,5-diCQA. The square of the correlation coefficient (R^2) is the percent of the variation in one variable that is related to the variation in the other. In the case of correlation of 3,5-diCQA with 4,5-diCQA, 62% of the variance is related (or is correlated) (Figure 8). We have recently shown that concentrations of various *cis*-CGA derivatives produced photochemically by UV irradiation in *S. rebaudiana* leaves show a linear concentration correlation.[21]

Table 6 provides an overview of correlations between 10 selected phenolic metabolites with Pearson R^2 values given. The data can be divided into three subgroups. We assume that an R^2 value between 1 and 0.7 corresponds to a positive correlation, that R^2 values between 0.7 and 0.4 correspond to unclear cases, and that R^2 values lower than 0.4 are evidence of no correlation at all. The presence or absence of positive correlations between the concentrations for several phenolic metabolites deserves some attention and comments. First, the data clearly show that all six CGAs analyzed show a correlation between individual compound concentrations. Therefore, no single compound is biosynthesized at an elevated level. In all 166 samples, an increase of the concentration of a single CGA is accompanied by a concentration increase of all other CGAs. Following an environmental or biochemical stimulus, the biosynthesis of the complete set of CGAs is turned on. We name this phenomenon the "better safe than sorry principle". This observation has been made for the first time for a class of natural products and is not expected. On the basis of the observation that most plants produce a rather large set of CGA isomers, we have argued previously that isomerism in CGA chemistry might be a cunning strategy of gaining evolutionary advantage by covering a large pharmacophoric space through multiple compounds.[13]

In contrast to the class of the CGAs, individual flavonoid glycoside concentrations show no correlation. This indicates that individual flavonoid glycosides are biosynthesized selectively with a specific function for each individual compound.

Interestingly, neither the concentrations of individual flavonoid glycosides and individual chlorogenic acids nor the total CGA and total flavonoid concentrations correlate. This observation is surprising because both classes of compounds are believed to serve plants primarily as UV protecting agents; hence, their concentrations are expected to increase simultaneously. Accordingly, these findings do not confer with the hypothesis that both classes of compounds serve as UV protection agents. However, drawing such a conclusion from statistical data should be done with caution because regulatory feedback mechanisms might be operational that modulate the biosynthesis of compounds which could be cytotoxic to the biosynthesizing organism.

■ ASSOCIATED CONTENT

Supporting Information

The Supporting Information is available free of charge on the ACS Publications website at DOI: 10.1021/acs.jafc.5b01944.

Tables with quantitative data on flavonoids, chlorogenic acids, high-resolution MS data, homogeneity of data, variances including ANOVA analysis, and a PCA plot on phenolic variations. (PDF)

■ AUTHOR INFORMATION

Corresponding Author

*Tel.: 49 421 200 3120. Fax: 49 421 200 3229. E-mail: n.kuhnert@jacobs-university.de.

Notes

The authors declare no competing financial interest.

■ ACKNOWLEDGMENTS

The research leading to these results received funding from the European Union's Seventh Framework Programme managed by Research Executive Agency (http://ec.europa.eu/research/rea(FP7/2007-2013)) under grant agreement no. 232250". We thank Dr. Udo Kienle for fruitful and valuable discussions on the science of *S. rebaudiana* and Dr. R. d'Souza and Mr. A. Shresta for proofreading of the manuscript.

■ REFERENCES

(1) Crozier, A.; Jaganath, I. B.; Clifford, M. N. Dietary phenolics: chemistry, bioavailability and effects on health. *Nat. Prod. Rep.* **2009**, *26*, 1001−1043.

(2) Kroon, P. A.; Clifford, M. N.; Crozier, A.; Day, A. J.; Donovan, J. L.; Manach, C.; Williamson, G. How should we assess the effects of exposure to dietary polyphenols in vitro? *Am. J. Clin. Nutr.* **2004**, *80*, 15−21.

(3) Del Rio, D.; Costa, L. G.; Lean, M. E. J.; Crozier, A. Polyphenols and health: what compounds are involved? *Nutr., Metab. Cardiovasc. Dis.* **2010**, *20*, 1−6.

(4) Hertog, M. G. L.; Feskens, E. J. M.; Kromhout, D.; Hertog, M. G. L.; Hollman, P. C. H.; Hertog, M. G. L.; Katan, M. B. Dietary antioxidant flavonoids and risk of coronary heart disease - The Zutphen elderly study. *Lancet* **1993**, *342*, 1007−1011.

(5) Jaiswal, R.; Patras, M. A.; Eravuchira, P. J.; Kuhnert, N. Profile and Characterization of the Chlorogenic Acids in Green Robusta Coffee Beans by LC-MSn: Identification of Seven New Classes of Compounds. *J. Agric. Food Chem.* **2010**, *58*, 8722−8737.

(6) Clifford, M. N. Chlorogenic acids and other cinnamates - nature, occurrence and dietary burden. *J. Sci. Food Agric.* **1999**, *79*, 362−372.

(7) Hollman, P. C. H.; Arts, I. C. W. Flavonols, flavones and flavanols - nature, occurrence and dietary burden. *J. Sci. Food Agric.* **2000**, *80*, 1081−1093.

DOI: 10.1021/acs.jafc.5b01944
J. Agric. Food Chem. 2015, 63, 9188−9198

(8) Karaköese, H.; Jaiswal, R.; Kuhnert, N. Characterization and Quantification of Hydroxycinnamate Derivatives in Stevia rebaudiana-Leaves by LC-MS(n). *J. Agric. Food Chem.* **2011**, *59*, 10143−10150.
(9) Tadhani, M. B.; Patel, V. H.; Subhash, R. In vitro antioxidant activities of Stevia rebaudianaleaves and callus. *J. Food Compos. Anal.* **2007**, *20*, 323−329.
(10) Rajbhandari, A.; Roberts, M. F. The Flavonoids of Stevia rebaudiana. *J. Nat. Prod.* **1983**, *46*, 194−195.
(11) Wöelwer-Rieck, U. The Leaves of Stevia rebaudiana(Bertoni), Their Constituents and the Analyses Thereof: A Review. *J. Agric. Food Chem.* **2012**, *60*, 886−895.
(12) Clifford, M. N.; Johnston, K. L.; Knight, S.; Kuhnert, N. Hierarchical scheme for LC-MSn identification of chlorogenic acids. *J. Agric. Food Chem.* **2003**, *51*, 2900−2911.
(13) Clifford, M. N.; Knight, S.; Kuhnert, N. Discriminating between the six isomers of dicaffeoylquinic acid by LC-MSn. *J. Agric. Food Chem.* **2005**, *53*, 3821−3832.
(14) Jaiswal, R.; Sovdat, T.; Vivan, F.; Kuhnert, N. Profiling and Characterization by LC-MSn of the Chlorogenic Acids and Hydroxycinnamoylshikimate Esters in Mate (Ilex paraguariensis). *J. Agric. Food Chem.* **2010**, *58*, 5471−5484.
(15) Jaiswal, R.; Kuhnert, N. Hierarchical scheme for liquid chromatography/multi-stage spectrometric identification of 3,4,5-triacyl chlorogenic acids in green Robusta coffee beans. *Rapid Commun. Mass Spectrom.* **2010**, *24*, 2283−2294.
(16) Clifford, M. N.; Kirkpatrick, J.; Kuhnert, N.; Roozendaal, H.; Salgado, P. R. LC-MSn analyses of the cis isomers of chlorogenic acids. *Food Chem.* **2008**, *106*, 379−385.
(17) Ernst, M.; Chatterton, J.; Harrison, P. A. Purification and characterization of a new fructan series from species of Asteraceae. *New Phytol.* **1996**, *132*, 63−66.
(18) Benova-Kakosova, A.; Digonnet, C.; Goubet, F.; Ranocha, P.; Jauneau, A.; Pesquet, E.; Barbier, O.; Zhang, Z. N.; Capek, P.; Dupree, P.; Liskova, D.; Goffner, D. Galactoglucomannans increase cell population density and alter the protoxylem/metaxylem tracheary element ratio in xylogenic cultures of zinnia. *Plant Physiol.* **2006**, *142*, 696−709.
(19) Mattila, P.; Astola, J.; Kumpulainen, J. Determination of flavonoids in plant material by HPLC with diode-array and electro-array detections. *J. Agric. Food Chem.* **2000**, *48*, 5834−5841.
(20) Saracini, E.; Tattini, M.; Traversi, M. L.; Vincieri, F. F.; Pinelli, P. Simultaneous LC-DAD and LC-MS determination of ellagitannins, flavonoid glycosides, and acyl-glycosyl flavonoids in Cistus salvifolius L. leaves. *Chromatographia* **2005**, *62*, 245−249.
(21) Karakose, H.; Jaiswal, R.; Deshpande, S.; Kuhnert, N. Investigation of the Photochemical Changes of Chlorogenic Acids Induced by Ultraviolet Light in Model Systems and in Agricultural Practice with Stevia rebaudianaCultivation as an Example. *J. Agric. Food Chem.* **2015**, *63*, 3338−47.

DOI: 10.1021/acs.jafc.5b01944
J. Agric. Food Chem. 2015, 63, 9188−9198

In plants, under stressful conditions, accumulation and depletion of several primary metabolites are commonly observed.[14,15] Therefore, monitoring the changes in metabolic levels can provide clues to their roles in stress responses and regulation. A key metabolic pathway in plants is the shikimate pathway that links carbon and nitrogen metabolism.[16] Apart from its role in aromatic amino acid synthesis, the shikimate pathway also serves as a major sink for intermediate metabolites from the central carbon metabolism pathways (glycolytic and pentose phosphate pathways). Any perturbations in the shikimate pathway will lead to a disruption in aromatic amino acid synthesis, as well as alter the metabolic stoichiometry of other carbon intermediates, resulting in system-wide perturbations. Metabolomics would therefore be an ideal approach not only to map the glyphosate-induced disruption of plant metabolism, but also to illuminate the physiology that confers resistance to some biotypes.

The glyphosate-mediated disruption of the shikimate pathway could have potential adverse effects on other cellular processes, resulting in secondary effects such as creation of reactive radicals. Earlier studies reported that, in addition to site-specific action, glyphosate also disrupts the photosynthetic machinery by reducing ribulose-1,5-bisphosphate carboxylase/oxygenase (RuBisCO) activity and 3-phosphoglyceric acid (3-PGA) levels,[17] which can result in the generation of reactive oxygen species (ROS), causing a several-fold increase in lipid peroxidation.[18,19] This ROS-mediated glyphosate damage is further supported by the proteomic analysis, which shows glyphosate-treated rice plants have a compositionally similar, but quantitatively lower, proteomic profile compared to that of rice plants treated with paraquat,[20] a free-radical-producing herbicide. Thus, inhibition of EPSPS could result in secondary toxic effects mediated through the production of ROS. Such an effect might be enhanced in glyphosate-resistant *A. palmeri* if some tissues have inadequate protection by *EPSPS* gene amplification as there is evidence that *EPSPS* gene expression is not equal in all tissue types in these plants.[21]

Previous application of metabolomics in understanding the effect of glyphosate on the physiology of plants was limited to the model plant species *Arabidopsis thaliana* and transgenic crop plants.[22−24] Also the metabolomics approach has been recently adopted to understand the effect of chemical stresses on *Lolium perenne* upon exposure to a nonlethal dose of glyphosate.[25] However, to date no studies have employed metabolomics to characterize the physiology of herbicide resistance in weeds. The objective of the present study is to use nontargeted metabolite profiling to elucidate the differential metabolite-level responses to glyphosate in resistant and susceptible biotypes of *A. palmeri*, and to assess the potential role of antioxidant machinery in complementing glyphosate resistance.

MATERIALS AND METHODS

Plant Biotypes. Glyphosate-susceptible (S-biotype) and glyphosate-resistant (T4B1, R-biotype) *A. palmeri* seeds were obtained from Stoneville, MS (Crop Production Systems Research Unit, U.S. Department of Agriculture, Agricultural Research Service (USDA-ARS)). These biotypes have been well characterized, and GR_{50} values for the R-biotype and S-biotype were previously calculated as 1.3 and 0.09 kg ha^{-1}, respectively (∼15-fold resistance).[11] The S-biotype had a single *EPSPS* gene copy, whereas T4B1 had 33 *EPSPS* gene copies.[11] T4B1 was grown from field collected seeds and the resistance was verified by spraying with glyphosate at 0.42 kg ae ha^{-1}. Only those plants that survived this treatment were classified to be glyphosate resistant (first-generation resistant, F-1) and represented that population. Second-generation (F-2) resistant biotypes were obtained by physically spreading the pollen (generated from the greenhouse-grown glyphosate-resistant F-1 generations) from male plants on the female plants (greenhouse-grown glyphosate-resistant F-1 generations) every morning over a period of 2 weeks. Each female plant that produced viable seeds was considered a unique F-2 biotype within a population, with all biotypes within the population having the same male parent. Biotypes raised from the F-2 seeds were confirmed to be resistant to glyphosate following screening with glyphosate at a rate of 0.42 kg ae ha^{-1}. F-2 generated seeds were planted in germination trays containing a commercial germination mixture and then were transplanted to individual pots (10 cm diameter × 9 cm deep) containing the germination mixture upon germination. The plants were grown in a greenhouse at 30 °C/20 °C day/night temperatures with a 14 h photoperiod. The rationale for conducting the experiment in a greenhouse rather than a growth chamber was that the fluorescent lighting routinely used in growth chamber is relatively high in longer wavelength (red region), than shorter wavelengths (blue region). As antioxidant capacity is greatly related to the intensity and the wavelength spectrum of the solar radiation, the spectral energy distribution differences between greenhouse and growth chamber was taken into account in deciding to conduct the study under ambient natural light. The pots were fertilized 5 days after transplantation with 50 mL of 4 g L^{-1} fertilizer (MiracleGrow, 24%−8%−16% [N−P−K], Scotts Miracle-Gro Products, Inc., Marysville, OH) and subirrigated every alternate day until harvest.

Experimental Design and Glyphosate Application. Two weeks after transplanting, the S- and R-biotypes were randomly assigned to two treatment groups, control and glyphosate (Roundup ProMax, Monsanto Co, St. Louis, MO), and sprayed at a rate of 0.4 kg ae ha^{-1}, which corresponds to approximately half the recommended field application rate of glyphosate. Roundup ProMax has about 49% glyphosate potassium salt. We were not able to obtain the other proprietary ingredients that make up 51.2% of this formulation that could be used to treat the control plants; hence, the control plants were treated with water. The respective treatments (water or glyphosate) were applied to 12 plants per biotype using an enclosed spray chamber (DeVries Manufacturing, Hollandale, MN) calibrated to deliver 374 L ha^{-1} through an 8001E flat fan nozzle (Tee Jet Spraying Systems Co., Wheaton, IL). Both R- and S-biotypes were morphologically similar (plant height ∼20 cm) at the time of treatment application. Three youngest apical leaves along with the meristem were harvested from each treatment replicate (six plants per glyphosate and control treatment) at 8 h after treatment (HAT) and 80 HAT, immediately frozen in dry ice, and stored at −80 °C. Six independent treatment replicates were maintained for all subsequent analyses. At 8 HAT, no visible injuries were observed on the glyphosate-treated S- and R-biotypes. At 80 HAT, the glyphosate-treated S-biotype displayed visible leaf necrosis, while the glyphosate-treated R-biotype and the water-treated S- and R-biotypes showed no visible injuries. To minimize the variations due to circadian rhythm, the plants were harvested at the same time of the day (∼10 h after sunrise) for both the sampling times. The harvested leaves were finely ground with dry ice using a mortar and pestle and stored at −80 °C, and the finely powdered leaves were used for all subsequent analyses.

Metabolite Profiling by GC−MS. Low-molecular-weight polar metabolites in the tissues were identified and quantified using gas chromatography−mass-spectrometry (GC−MS). Polar metabolites were extracted from the ground tissues as described by Lisec et al.[26] and Suseela et al.,[15] with slight modifications. Briefly, about 100 mg of finely powdered leaf tissues was weighed into 1 mL of methanol and homogenized by sonication in an ice bath for 20 s at 50% amplitude, centrifuged at 12000*g*, and rapidly cooled on ice. The supernatant was transferred to precooled glass tubes, an equal volume of cold chloroform was added, and the solution was cooled at 4 °C. The metabolites were fractioned into polar and nonpolar phases with addition of 1 mL of cold water and then centrifuged at 671*g* for 1 min. About 1.5 mL of the aqueous−methanol phase was transferred to microfuge tubes. A subsample (150 μL) of this extract was transferred

DOI: 10.1021/acs.jafc.5b04223
J. Agric. Food Chem. 2015, 63, 9199−9209

into vials with glass inserts, 5 μL of 500 μg ml^{-1} ribitol (internal standard) in hexane and 5 μL of 2 mg ml^{-1} of d_{27}-myristic acid (retention time lock) in hexane were added to the vials, and then the samples were completely dried under a nitrogen stream. The dried samples were methoxylaminated at 60 °C with 20 μL of methoxylamine hydrochloride (20 mg mL^{-1}) in pyridine for 90 min followed by silylation of the metabolites with 90 μL of *N*-methyl-*N*-(trimethylsilyl)trifluoroacetamide (MSTFA) with 1% trimethylchlorosilane (TMCS) for 30 min at 40 °C. The derivatized metabolites were separated by gas chromatography (Agilent 7980, Agilent Technologies, Santa Clara, CA) on a J&W DB-5 ms column (30 m × 0.25 mm × 0.25 μm, Agilent Technologies) and analyzed using a transmission quadrupole mass detector (Agilent 5975 C series) with an electron ionization interface.[13] The initial oven temperature was maintained at 60 °C for 1 min, followed by temperature ramp at 10 °C/min to 300 °C, with a 7 min hold at 300 °C. Carrier gas (He) flow was maintained at a constant pressure of 76.53 kPa, and the injection port and the MS interphase were maintained at a constant temperature of 270 °C. The MS quadrupole temperature was maintained at 150 °C, and the MS source temperature was set at 260 °C. The electron multiplier was operated at a constant gain of 10 (EMV = 1478 V), and the scanning range was set at 50−600 amu, achieving 2.66 scans s^{-1}. Metabolite peaks were identified by comparing the absolute retention time and retention-time index of the sample with those of the in-house metabolomics library supplemented with the Fiehn Library (Agilent Technologies, Wilmington, DE, G1676AA).[27] Data deconvolution was performed using the Automatic Mass Spectral Deconvolution and Identification System (AMDIS v2.71, NIST) using the following parameters: Peak identification was limited to a minimum match factor of 70 relative to the retention index (RI) library and having an RI threshold window of 10 × 0.01(RI). A maximum match factor penalty of 30 was deducted from the final calculated net value in the case of RI mismatch. The peak abundance (integrated signal) was normalized with that of the ribitol (internal standard) abundance and expressed as a percentage of ribitol.

Phenylalanine Ammonia-Lyase (PAL) Assay. The PAL assay was carried out according to Shang et al.[28] with slight modifications. Briefly, 0.15 g of the ground leaves was homogenized in 1 mL of ice-cold sodium borate buffer (pH 8.3) by sonication, and the homogenates were immediately centrifuged (12000*g*, 5 min). The reaction mixtures consisting of the buffer and homogenates were preincubated at 40 °C for 5 min. The reaction was started by the addition of 50 mM L-phenylalanine. Controls (without L-phenylalanine) were prepared to determine the plant endogenous *trans*-cinnamic acid (*t*-CA) content. The reaction was terminated after 1 h with 5 N HCl and analyzed on HPLC−UV (LC 20-AT UFLC and Prominence SPD M20-A photodiode array, Shimadzu Scientific, Columbia, MD) by monitoring the abundance of *t*-CA at 290 nm. HPLC separation of *t*-CA was performed on a Kinetex XB-C18 column (100 mm × 4.60 mm × 2.6 μm, 100 Å, Phenomenex, Torrance, CA) at an isocratic flow rate of 0.7 mL min^{-1} using a solvent composition of 50:50 0.05% formic acid in water and methanol. The *t*-CA levels in the samples were calculated with respect to the calibration curve of the *t*-CA standard solution prepared in the same sodium borate buffer as that of the samples.

Glutathione Reductase and Thiobarbituric Acid Reactive Substance (TBARS) Assays. Glutathione reductase (GR) activity was determined on the basis of the oxidation of NADPH at 340 nm in the presence of oxidized glutathione disulfide (GSSG).[29] GR enzyme was extracted from the leaves by sonication with extraction buffer [0.1 M potassium phosphate (pH 7.6) and 2 mM EDTA] and then transferred into the assay mixture composed of 100 mM potassium phosphate buffer (pH 7.8), 0.5 M GSSG, and 0.2 M DTT. The assay was initiated with the addition of 0.2 M NADPH and incubated at 25 °C for 30 min. Endogenous levels of NADPH were determined with a blank (no NADPH addition). The GR activity was determined spectrophotometrically on the basis of the extinction coefficient of NADPH measured at 340 nm using a JASCO V-550 UV−vis spectrophotometer (eq S1).

Malondialdehyde (MDA) was quantified by a modified TBARS assay as reported by Hodges et al.[30] Briefly, about 0.1 g of ground tissue was weighed into 1 mL of extraction buffer (80:20 methanol/water solution) and sonicated three times for 20 s. A 250 μL volume of the extract was added to a final volume of 1 mL of assay mixture (50 mM NaOH, 25% (v/v) HCl, and 7.5 mM thiobarbituric acid (TBA)), and the reaction was started by incubating the assay mixture at 95 °C. After 30 min, the reaction was stopped by rapid cooling in ice for about 10 min. To account for interfering compounds, the absorbance was read at wavelengths of 440, 532, and 600 nm. False-positive absorbance (absorbance by non-MDA compounds) was corrected by incubating the extracts in a TBA-free assay solution. MDA equivalents were calculated as described by Hodges et al.[30] (eq S2).

Total Soluble Protein Quantification. Proteins were quantified with the bicinchoninic acid (BCA) protein assay kit according to the manufacture's recommended protocol (Pierce Chemical Co., Rockford, IL). Proteins were extracted from ground tissue into extraction buffer (20 mM phosphate buffer, pH 7.6) by sonication. The extract was diluted 10× with water, added to 400 μL of BCA working reagent (BCA-WR, 50:1 BCA reagent A/BCA reagent B), and made up to 1 mL using deionized (DI) water. The assay mix was incubated for 30 min at 37 °C and then rapidly cooled in ice for 5 min. The absorbance of all the samples was measured at 562 nm using a UV−vis spectrophotometer within 10 min of cooling. The concentrations of total soluble proteins (TSPs) were quantified using a protein concentration curve with bovine serum albumin as the standard protein.

Statistical Analysis. The relative concentrations of metabolites across the biotypes and treatments were analyzed by multivariate and univariate statistical analyses. To evaluate the main and interactive effects of the biotypes and herbicide treatments, we first analyzed the metabolomics data with permutational multivariate analysis of variance (PERMANOVA; Primer 7 PERMANOVA+, version 7.0.5, Primer-E Ltd., Plymouth, U.K.). Due to the non-normal distribution nature of metabolic data, PERMANOVA analysis is a more robust test than ANOVA/MANNOVA to identify statistical significance of the treatments.[31,32] Errors due to multiple comparisons were controlled using false discovery rates (FDR). The metabolomics data were autoscaled to satisfy the assumptions of normality and equal variance before multivariate analyses. Supervised partial least squares-discriminant analysis (PLS-DA) models were constructed using Metaboanalyst[33] and the Microsoft Excel add-in Multibase package (Numerical Dynamics, Japan) to test the significance of the effects of the biotype and herbicide treatments on the metabolite profiles, and the PLS-DA model was validated using permutation testing.[34] Hierarchical cluster analysis, using the Euclidean distance as a similarity measure, of the metabolite responses with respect to the treatments were visualized using heat maps. Univariate statistical analysis (ANOVA) was also performed to determine the statistical significance of the metabolite among the different treatment groups (biotypes and herbicide) followed by Tukey's HSD posthoc test. The statistical significances of the biochemical assay responses (concentrations of *t*-CA, NADPH, and MDA) were tested by two-way analysis of variance. Differences among individual means were tested using Tukey's HSD multiple comparison tests with $P_{value} < 0.05$ considered statistically significant. Statistical analyses were done using SAS (v9.2, SAS Institute, Cary, NC).

RESULTS AND DISCUSSION

GC−MS Metabolite Profiling. On the basis of the predefined deconvolution parameters (see the Materials and Methods), GC−MS analysis positively identified more than 60 metabolites across all samples on the basis of their mass-spectral fingerprints and retention-index matches (Table S1). PERMANOVA analysis confirmed that there was a significant interaction effect between biotype and herbicide treatment for both the time points of harvest (Table S2). From the total identified metabolite pool at 8 and 80 HAT, 49 and 52

DOI: 10.1021/acs.jafc.5b04223
J. Agric. Food Chem. 2015, 63, 9199−9209

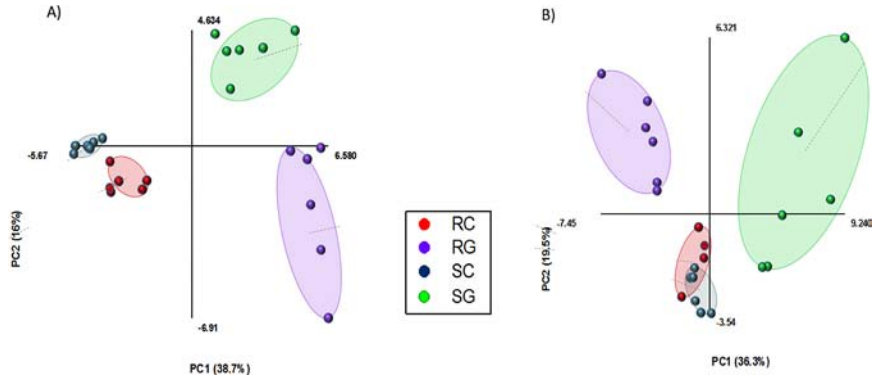

Figure 1. Partial least squares Discriminant Analysis (PLS-DA) score plot of first two principal components of the analysis of polar metabolites obtained from water- and glyphosate-treated S- and R-biotypes of *A. palmeri* at (A) 8 HAT and (B) 80 HAT. The permutation cross-validation of the PLS-DA model for 8 and 80 HAT had $P = 0.0005$ over 2000 iterations. The ellipses represent the 95% confidence regions.

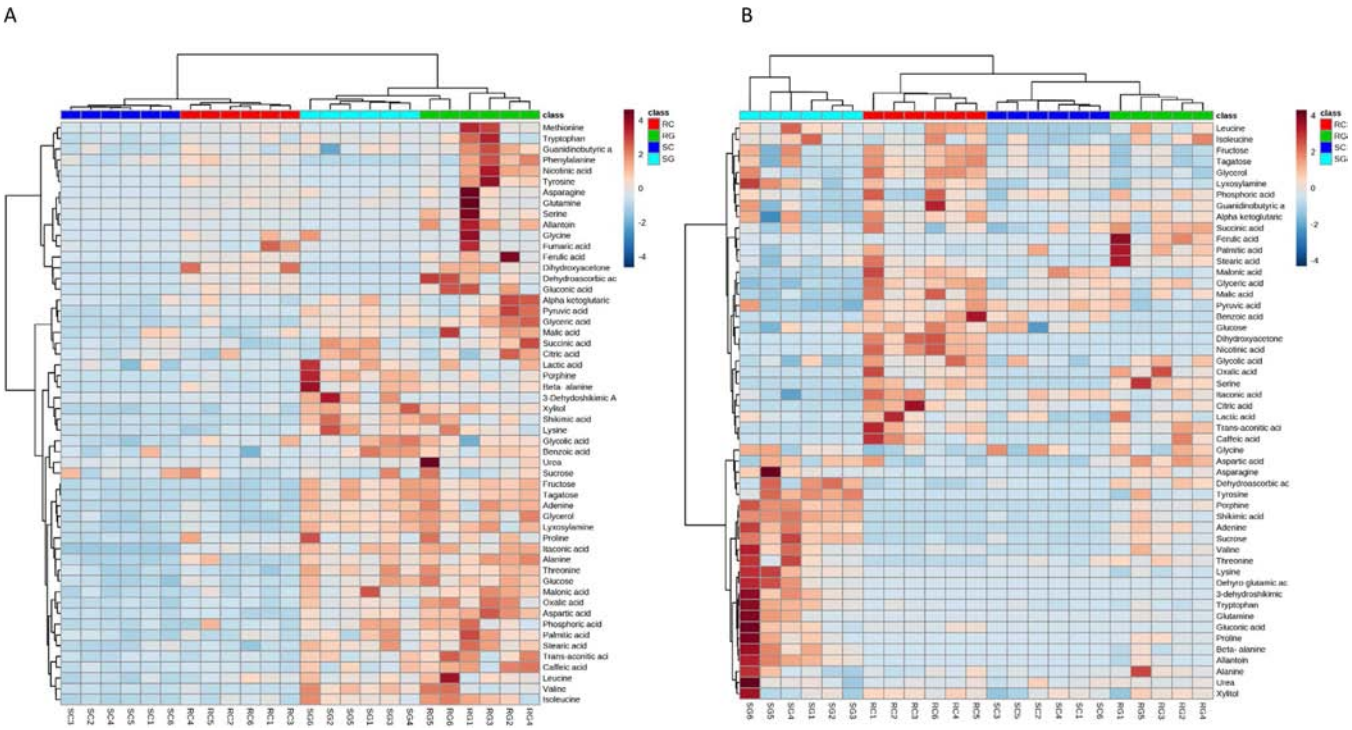

Figure 2. Heat map and two-way hierarchical clustering of polar metabolites in S- and R- biotypes of *A. palmeri* treated with water and glyphosate at (A) 8 HAT and (B) 80 HAT. The algorithm for heat map clustering was based on the Euclidean distance measure for similarity and the Ward linkage method for biotype clustering. ANOVA results comparing the means of each metabolite across treatment groups and the false discovery rate (FDR) for multiple testing corrections are given in Table S3. An enlarged dendrogram is given in Figure S1.

compounds were selected for further analysis that had a false discovery rate (FDR; percentage of false positives that are predicted to be significant) corrected *p*-values below 0.05 (Table S3). The robustness of the PLS-DA class discrimination was verified through permutation testing of separation distance on the basis of the ratio of the between-group sum of the squares and the within-group sum of the squares. The permutation cross-validation of the PLS-DA model for 8 and 80 HAT had $P = 0.0005$ over 2000 iterations, and the model goodness of fit was >0.85. PLS-DA revealed a clustering of the treatments for both the harvest times (Figure 1). At 8 HAT, the component 1 axis differentiated between the two treatments (water and glyphosate), while the PC-2 axis delineated the two biotypes (S and R) (Figure 1A). Interestingly, at 80 HAT, along the PC-1 axis, the glyphosate-treated R-biotype had a metabolic pool similar to that of the control R- and S-biotypes, indicating a potential recovery of the R-biotype from glyphosate toxicity (Figure 1B).

At 8 HAT, hierarchical clustering grouped the water control and glyphosate treatment into major clusters, indicating that, irrespective of their resistance level, the metabolisms of both biotypes were similarly influenced by glyphosate (Figure 2A, Figure S1A). Within the herbicide treatment clusters, the metabolic profile of the S-biotype was different from that of the R-biotype. At 8 HAT, the glyphosate treated R-biotypes had a higher abundance of phenylalanine, tyrosine, serine and nicotinic acid compared to the glyphosate treated S-biotype (Figure 2A, Table S3A). Also, the metabolite pools of nontreated S- and R-biotypes were more similar to each other compared to the metabolic responses between glyph-

DOI: 10.1021/acs.jafc.5b04223
J. Agric. Food Chem. 2015, 63, 9199−9209

osate-treated S- and R-biotypes (Figure 2A). At 24 HAT, the T4B1 absorbed 27% of the applied glyphosate and translocated 37% of the absorbed glyphosate out of the treated site, while the S-biotype absorbed 38% and translocated 40%.[11] Though less than 50% of the glyphosate was translocated out of the treated site, it was potent enough to induce metabolic perturbations in both biotypes within 8 HAT (Figure 2A). At 80 HAT, hierarchical clustering analysis grouped the glyphosate-treated S-biotype into a distinct cluster, while the glyphosate-treated R-biotype was more closely associated with the water-treated (control) S- and R-biotypes (Figure S1B). The metabolite pool of the glyphosate-treated R-biotype resembled that of the water-treated S-biotype rather than the water-treated R-biotype at 80 HAT (Figure 2B). The distinction of the glyphosate-treated S-biotype at 80 HAT from the rest of the treatments could be due to the continued glyphosate-induced disruption of the shikimate pathway, resulting in the differential abundance of several key metabolites such as shikimate, 3-dehydroshikimate, tyrosine, tryptophan, and asparagine (Figure 2B).

Shikimic acid accumulated in both the glyphosate-treated S- and R-biotypes in 8 HAT, indicating an initial, rapid, inhibition of EPSPS enzyme in both biotypes. A similar accumulation of shikimate following glyphosate treatment has been previously reported in T4B1.[11] Compared to that at 8 HAT, at 80 HAT the shikimate accumulation did not differ significantly in the R-biotype, while the shikimate concentration increased by 3-fold in the S-biotype (Figure 3). This continued accumulation of

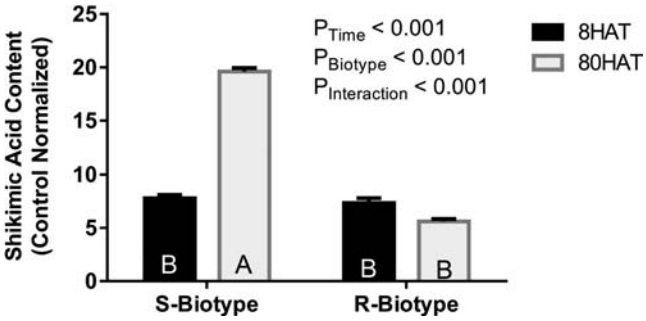

Figure 3. Shikimic acid abundance in glyphosate-treated *A. palmeri* during two harvest times. The data represent the mean ± SD of shikimic acid abundance in glyphosate-treated plants normalized with the abundance of shikimic acid in the water-treated control at respective harvest times. Bars with the same letters are not significantly different at 0.05% confidence (Tukey's HSD).

shikimic acid in the S-biotype could be due to the continued inhibition of EPSPS by glyphosate, and/or a loss of feedback control of the shikimate pathway. In plants, about 20% of the fixed carbon that flows through the shikimate pathway is regulated by the enzyme 3-deoxy-D-arabinoheptulosonate 7-phosphate (DAHP) synthase. Though no known inhibitor of plant DAHP synthase has been identified, arogenate is considered as a potential candidate for the allosteric inhibition of DAHP synthase.[35] As arogenate is synthesized downstream of shikimic acid, inhibition of EPSPS by glyphosate could result in decreased levels of arogenate, therefore impairing the allosteric regulation of DAHP synthase in the S-biotype, leading to continued accumulation of shikimic acid. Studies have reported an initial increase, followed by a subsequent decrease, in shikimate levels following exposure to sublethal doses of glyphosate in both glyphosate-susceptible and glyphosate-resistant plants.[36−38] The stable levels of shikimic acid at 80 HAT in the R-biotype could possibly be due to its conversion into downstream metabolites such as simple phenolic acid derivatives and/or loss of shikimic acid pathway inhibition due to the induction of expression of the multiple *EPSPS* gene copies, thereby diluting glyphosate effects on EPSPS.[39,40] The difference in translocation of glyphosate between T4B1 and the S-biotypes could also partly facilitate the observed reinstatement of cellular homeostasis. After 48 HAT, the glyphosate absorption in the T4B1 was 29%, while in the S-biotype, it was 50% of the applied glyphosate. Interestingly, though about 67% of the absorbed glyphosate in the T4B1 translocated out of the target site by 48 HAT,[11] it did not have an damaging effect on the plant metabolism at 80 HAT. Conversely, in the S-biotype, despite less than half of the absorbed glyphosate (46% of absorbed) being translocated out of the treated site,[11] plants continued to exhibit glyphosate toxicity. This shows that, though glyphosate was persistent in the R-biotype, glyphosate toxicity was mitigated, possibly through the increased *EPSPS* gene copies, complemented by a potential increased anti-oxidant machinery.

The inhibition of the shikimate pathway by glyphosate results in the disruption of aromatic amino acid biosynthesis. The aromatic amino acid concentrations in the control S- and R-biotypes were similar at both 8 and 80 HAT, indicating a lower inherent differences between the biotypes in the absence of herbicide-induced stress. However, after 80 HAT there were significant changes in the concentrations of the aromatic amino acids in both of the biotypes, where the glyphosate treated S-biotype had three times higher abundance of tryptophan and tyrosine (Figure 4). A similar observation of tyrosine accumulation after glyphosate application was reported in glyphosate-susceptible purple nutsedge.[41] In glyphosate-treated R-biotype, the concentration of phenylalanine increased by more than 7-fold, while the levels of tyrosine and tryptophan decreased at 80 HAT (Figure 4). However, phenylalanine increased similarly in the untreated S-biotype between 8 and 80 HAT. A few studies have reported the effect of these aromatic amino acids in reversing glyphosate toxicity,[42−44] although other studies have reported little or no effects of exogenous application of phenylalanine and tryptophan in reducing the toxicity of glyphosate.[45] The several-fold larger phenylalanine pool in the glyphosate-treated R-biotype than in the S-biotype at 80 HAT could serve as a significant pool for antioxidant phenylpropanoid metabolite synthesis in the R-biotype, which could partially mitigate the toxicity of glyphosate. Although the non-aromatic amino acids did not differ in the control S- and R-biotypes, the glyphosate-treated S-biotype had a higher pool of non-aromatic amino acids, possibly due to reduced protein synthesis or other amino acid utilization because of metabolic disruption caused by inhibition of the shikimate pathway. However, it should be noted that the interpretation of the physiology of plants based on pool sizes of pathway intermediates is difficult because pool size does not reflect pool flux.

Glyphosate has only one enzyme binding target in the plant, EPSPS. Blockage of the shikimate pathway at this site leads to many adverse secondary and tertiary effects on other pathways and processes. Most of the measured metabolite changes occur in the linked glycolysis pathway, oxidative pentose pathway, and tricarboxylic acid (TCA) cycle (Figure 5). In plants, the energy-producing stage of glycolysis is regulated by at least six known mechanisms.[46] The rate-limiting step of glycolysis, conversion

DOI: 10.1021/acs.jafc.5b04223
J. Agric. Food Chem. 2015, 63, 9199−9209

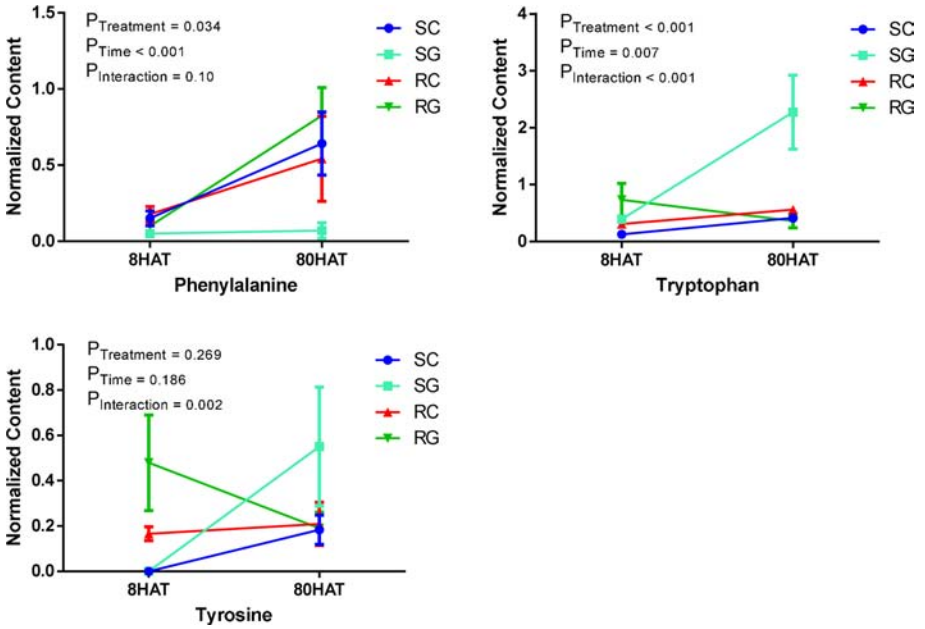

Figure 4. Comparisons of aromatic amino acids across water- and glyphosate-treated S- and R-biotypes of A. palmeri harvested at 8 and 80 HAT. The data represent the mean ± SD of the metabolites normalized to the total ion intensity of the internal standard (ribitol, 500 μg ml^{-1}). The mean ± SD was tested by two-way ANOVA with Tukey's HSD comparing across all treatments and biotypes at a confidence level of 0.05%. Tukey's comparison between the treatment means is given in Table S2.

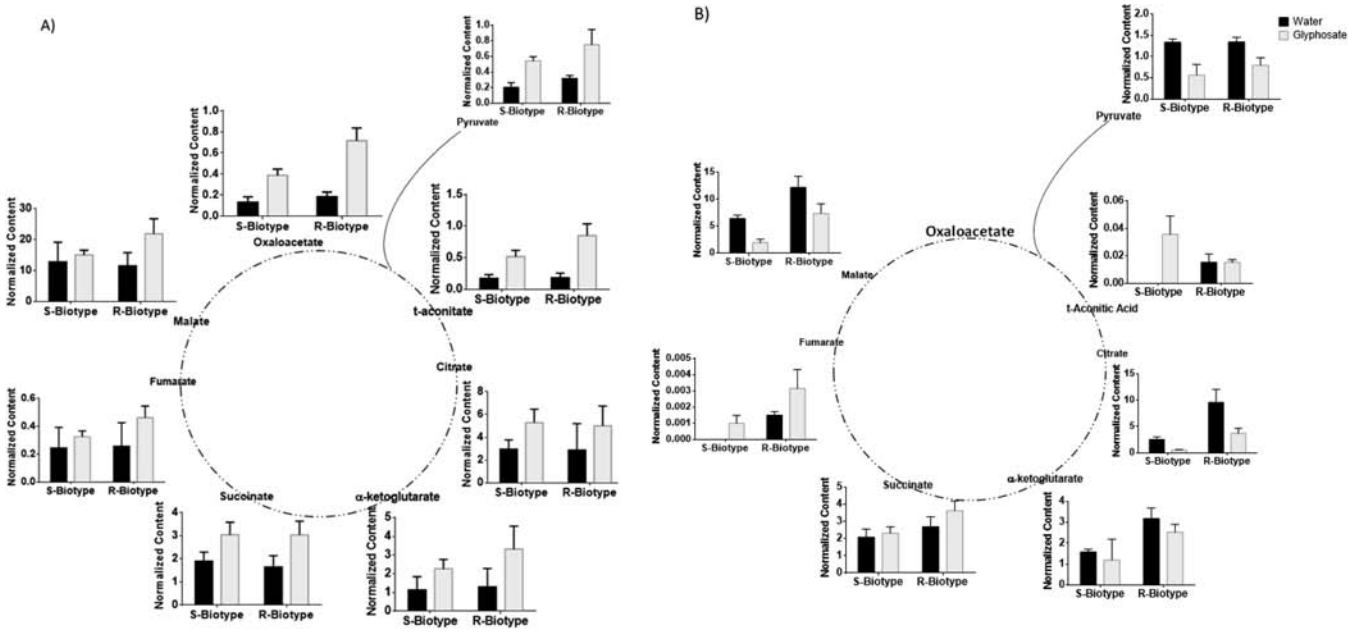

Figure 5. Tricarboxylic acid cycle metabolite pools in water- and glyphosate-treated S- and R-biotypes at (A) 8 HAT and (B) 80 HAT. The data represent the mean ± SD of the abundance of metabolites normalized to the total ion intensity of the internal standard (ribitol, 500 μg ml^{-1}). Tukey's comparison between the treatment means is given in Table S4.

of fructose-6-phosphate to fructose-1,6-bisphosphate by pyrophosphate-dependent phosphofructokinase (PPi-PFK), is activated by inorganic phosphates (Pi) and inhibited by phosphoenol pyruvate (PEP).[47] The ratio of Pi to PEP regulates the activity of PPPi-PFK. As glyphosate competes with PEP for binding to EPSPS, the glyphosate-sensitive biotype will have higher levels of underutilized PEP which could then inhibit the conversion of fructose-6-phosphate to fructose-1,6-bisphosphate. This block in the rate-limiting step of glycolysis could then lead to an overall accumulation of sugars due to impaired carbon metabolism.[48,49] This influence of glyphosate on carbohydrate metabolism is reflected in the accumulation of sugars in both the S- and R-biotypes within 8 HAT (Figure 6A). Sugar moves from sources (photosynthetically active tissues) to metabolically active sinks (e.g., meristems and young leaves), so inhibition of growth of the sinks results in sugar accumulation. Interestingly, at 80 HAT, the sugar levels in the glyphosate-treated S-biotype continued to accumulate, while that of the glyphosate-treated R-biotype was similar to

DOI: 10.1021/acs.jafc.5b04223
J. Agric. Food Chem. 2015, 63, 9199−9209

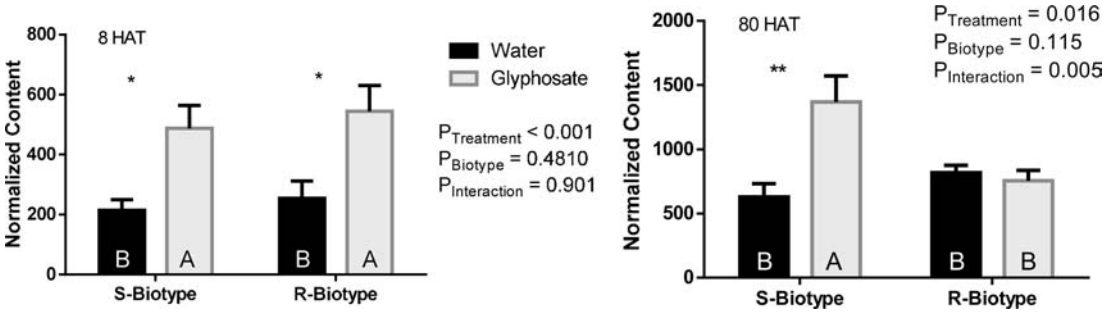

Figure 6. Total sugar metabolites in S- and R- biotypes of A. palmeri treated with glyphosate and water at (A, left) 8 HAT and (B, right) 80 HAT. The data represent the mean ± SD of the total sugar abundance normalized with respect to ribitol abundance (ribitol, 500 μg ml^{-1}). The mean ± SD was tested by two-way ANOVA with Tukey's HSD comparing across all treatments and biotypes at a confidence level of 0.05%. Bars with the same letters are not significantly different at 0.05% confidence.

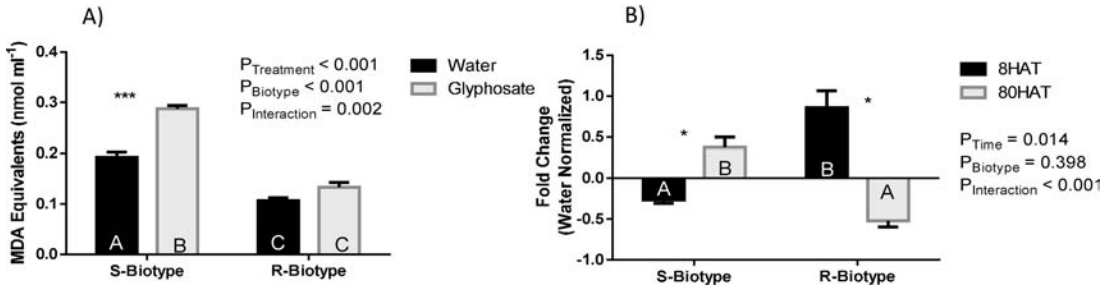

Figure 7. (A) TBARS assay quantifying malondialdehyde equivalents in the S- and R-biotypes of *A. palmeri* across the treatments at 80 HAT. (B) Glutathione reductase assay comparing the difference in NADPH levels in the glyphosate-treated S- and R-biotypes across 8 and 80 HAT. The data for the TBARS assay represent the mean ± SD of the assay, and the data for the GR assay represent the water normalized mean ± SD data of fold changes in NADPH levels. Bars with the same letters are not significantly different at 0.05% confidence.

that of the control biotypes (Figure 6B), indicating a recovery of the R-biotype.

The blockage of the shikimate pathway by glyphosate reverberated across other biochemical pathways and processes as evident by the fluxes of intermediates of the TCA cycle wherein all the major metabolites of the TCA cycle (pyruvic, *trans*-aconitic, citric, α-ketoglutaric, succinic, and malic acids) responded to glyphosate application (Table S4). At 8 HAT, a differential abundance in the concentrations of organic acids was observed in the glyphosate-treated S- and R-biotypes compared to the respective water control, with the glyphosate-treated biotypes exhibiting a substantial increase in concentrations of multiple organic acids (Figure 5A). However, at 80 HAT, in the glyphosate-treated S-biotype, except for succinate and α-ketoglutarate, all other metabolites of the TCA cycle responded to glyphosate application with a drastic reduction in citrate. In contrast, no significant perturbations of the TCA cycle were observed in the glyphosate-treated R-biotype except for the reduction in the levels of citric acid, similar to that of the glyphosate-treated S-biotype (Figure 5B). Overall, our results not only highlight the robustness of the metabolomics approach in identifying differential physiological responses of the S- and R-biotypes to glyphosate, but also identify metabolic-level differences between the R- and S-biotypes in the absence of herbicidal stress.

Biochemical Assays. The observed disruption of the oxidative pentose pathway and the energy-producing tricarboxylic acid cycle, following glyphosate application, could result in generation of reactive free radicals, which could then further initiate lipid peroxidation, resulting in the formation of the reactive compound malondialdehyde (MDA). Compared to the glyphosate-treated R-biotype, the glyphosate-treated S-biotype accumulated 49% higher MDA after 80 HAT (Figure 7A), indicating that higher levels of free radicals mediated lipid peroxidation occurs in the glyphosate-treated S-biotype. A similar observation of the deleterious effect of glyphosate on maize plants due to increased lipid peroxidation via MDA production was reported by Sergiev et al.[19] Thus, the death of the glyphosate-treated S-biotype could be partially accelerated by the complementary action of free radicals that result in observed lipid peroxidation.

Reduced levels of MDA accumulation in the R-biotype following glyphosate application (Figure 7A) could indicate an apparent increase in the activities of enzymes and secondary metabolites which can effectively quench the free radicals. Plants have a well-defined and extensive enzymatic and nonenzymatic antioxidant machinery to protect them from the free radicals generated during normal physiological metabolism.[50] In plants, the GR enzyme system serves as a major antioxidant defense. GR catalyzes the reduction of GSSG to glutathione (GSH), its antioxidant compound which neutralizes highly reactive ROS molecules. Increased GR activity results in increased production of GSH, enhancing the antioxidant potential. The reduction of GSSG to GSH is energy-dependent and utilizes NADPH as the energy supplier. Therefore, the GR activity is captured by monitoring the levels of NADPH[29] wherein a decrease/increase in NADPH levels indicates a proportional increase/decrease in GR activity. At 8 HAT, compared to the water-treated S-biotype, the glyphosate-treated S-biotype had a 26% decrease in NADPH levels (Figure 7B), thereby indicating higher GR activity than in the nontreated control. At 8 HAT, in the glyphosate-treated R-biotype, there was an 85% increase in NADPH levels, indicating lower GR activity in the glyphosate-treated R-biotype

DOI: 10.1021/acs.jafc.5b04223
J. Agric. Food Chem. 2015, 63, 9199−9209

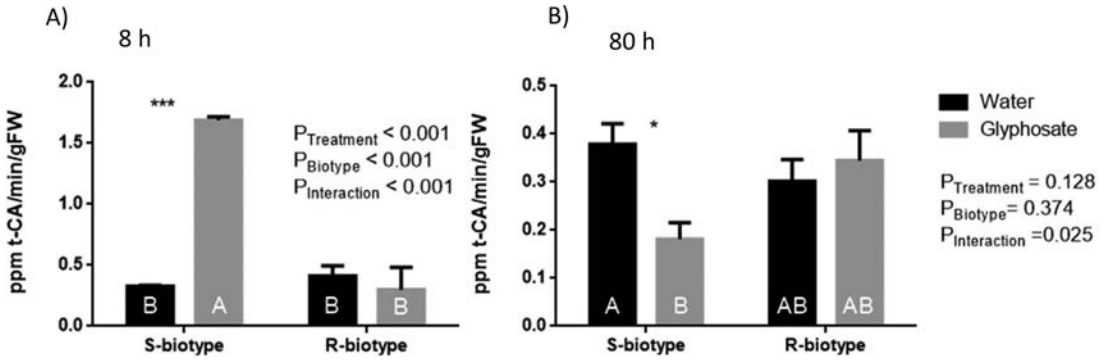

Figure 8. Phenylalanine ammonia-lyase (PAL) assay comparing the difference in activities of the PAL enzyme in the S- and R-biotypes of *A. plameri* across the treatments at (A) 8 HAT and (B) 80 HAT. The data represent the mean ± SD of the assays. Bars with the same letters are not significantly different at 0.05% confidence.

compared to its nontreated control (Figure 7B). However, at 80 HAT, compared to the water control R-biotype, there was a 51% reduction in the NADPH levels in the GR activity of the glyphosate-treated R-biotype, which potentially indicates higher GR activity in the glyphosate-treated R-biotype. Contrastingly, at 80 HAT, compared to those in the water-treated S-biotype, the NADPH levels increased 37% in the glyphosate-treated S-biotype, indicating a decrease in NADPH consumption. Lower GR activity (as indicated by higher NADPH levels) in the glyphosate-treated S-biotype at 80 HAT could indicate a decrease in synthesis of glutathione by GR, resulting in lower antioxidant potential despite higher levels of oxidative damage. Although it is possible that the lower utilization of NADPH in the S-biotype could also be due to the cessation of carbon fixation induced by the glyphosate toxicity, the concomitant higher accumulation of MDA in the glyphosate-treated S-biotype at 80 HAT (Figure 7A) indicates a lower GR activity (Figure 7B). The increased GR activity in the glyphosate-treated R-biotype at 80 HAT indicates a responsive but delayed GR-dependent antioxidant activity. Similar observations of the induction of plant stress response genes following glyphosate application was shown in *Festuca arundinacea* by Unver et al.[51] following miRNA and transcriptome analysis. Furthermore, transcriptome analysis of glyphosate-treated susceptible and resistant soybean plants (*Glycine max* (L.) Merr.) by Zhu et al.[52] had similar conclusions. Thus, the observed higher GR activity combined with the lower accumulation of MDA in glyphosate-treated R-biotypes indicates the existence of a robust free radical scavenging system in this biotype that could potentially complement the glyphosate resistance conferred by *EPSPS* gene copy amplification. Though less evident at 8HAT, at 80 HAT, compared to the S-biotyes, the R-biotypes exhibited 84% higher capacity to scavenge the 2,2-Diphenyl-2-picryl-hydrazyl (DPPH) free-radical (Method S2, Figure S5). This higher radical scavenging capacity of R-biotype is in agreement with the observed lower accumulation of MDA in the R-biotype (Figure 7A).

The phenylpropanoid pathway is a major secondary metabolic pathway that synthesizes a wide array of phenolic compounds (such as flavonoids and betalains) with radical scavenging capacity to reduce oxidative stress. As the rate-limiting step of this pathway is the conversion of phenylalanine to *t*-CA catalyzed by the PAL enzyme, the rate of formation of *t*-CA could partially reflect the antioxidant capacity of the plant. At 8 HAT, the extracted PAL activity was the same in the control groups for both biotypes and in the treated R-biotype (Figure 8A). The activity from the treated S-biotype was much higher at this time. However, at 80 HAT, the PAL activity was the same in all treatments except for reduced activity in the treated S-biotype (Figure 8B). This is in accordance with previous studies which observed rapid increases in PAL activity in glyphosate-treated plants that were transient, often peaking at about 24 HAT.[53,54] In this previous work, extracted PAL activity was temporarily enhanced by glyphosate treatment, while phenylpropanoid levels were decreased, suggesting that the PAL gene(s) is up-regulated by blockage of the shikimate pathway.

On the basis of the metabolite profiles of the S- and R-biotypes under both water and glyphosate treatment, two phenylpropanoid secondary metabolites, ferulic and caffeic acids, were identified. While ferulic acid was detected in the R-biotype in both the water control and glyphosate treatments at 8 HAT and only in the glyphosate treatment at 80 HAT, no ferulic acid was detected in the S-biotype in either water- or glyphosate-treated plants at both 8 and 80 HAT (Figure S2A). Similarly, at 8 HAT, caffeic acid was detected in both the control and glyphosate-treated S- and R-biotypes, but at 80 HAT, it was not detected in either the control or glyphosate-treated S-biotype, but was still present in the R-biotype in all treatments at all times. Interestingly, while the caffeic acid levels were elevated in the glyphosate treatment over the control at 8 HAT and not at 80 HAT, the level of caffeic acid in the control was much higher at 80 HAT than at 8 HAT (Figure S2B). This suggests that, due to the extra copies of the *EPSPS* gene in the R-biotype, there could be an increase in the levels of metabolites downstream of the shikimate pathway, including metabolites of the phenylpropanoid pathway. Further profiling of plant extracts using liquid chromatography tandem-mass spectrometry (LC-MS/MS) (Method S1) identified significantly higher abundance of certain phenylpropanoids, in R-biotype, particularly quinic acid conjugates of cinnamates (4-*O*-feruloylquinic acid (4-FQA) and 4-*O*-caffeoylquinic acid (4-CQA, crypto-chlorogenic acid)) (Figure S3, Figure S4). Compared to the water-treated S-biotype, the water-treated R-biotype had 2.5 and 4 fold higher abundance of 4-FQA and 4-CQA, respectively (Figure S4). This further supports our hypothesis that the R-biotype could possess an enhanced antioxidant capability which may play a complementary role in conferring resistance to glyphosate. The enhanced levels of certain phenylpropanoid compounds in the R-biotype may play a role in the different spectral reflectivities of the two *A. palmeri* biotypes.[56]

DOI: 10.1021/acs.jafc.5b04223
J. Agric. Food Chem. 2015, 63, 9199−9209

At 80 HAT, the control R-biotype contained 0.6 fold higher TSPs compared to the S-biotype, and the TSPs in both biotypes decreased at 80 HAT following glyphosate application. The R-biotype had about 35% reduction in protein levels as compared to the S-biotype (Figure 9). This decrease in protein

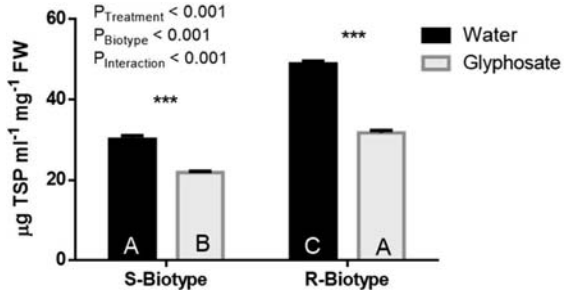

Figure 9. Bicinchoninic acid (BCA) assay for total soluble protein (TSP) quantification in water- and glyphosate-treated S- and R-biotypes of *A. palmeri* harvested at 80 HAT. The data represent the mean ± SD of the assay. Bars with the same letters are not significantly different at 0.05% confidence.

levels in the R-biotype could be attributed to the initial inhibition of the shikimate pathway as evident in the accumulation of shikimic acid at 8 HAT. The potential transient inhibition of the shikimate pathway could lead to protein catabolism to sustain growth, which might partly explain this observation. The reduced protein levels in the S-biotype could be attributed to the combined effect of catabolism and termination of protein synthesis.

Our results demonstrate the application of metabolomics as a complementary tool for further elucidating glyphosate resistance at the phenotypic level in *A. palmeri*. Metabolite profiling differentiated physiological differences between the S- and R-biotypes, both in the presence and in the absence of glyphosate treatment. Though both the S- and R-biotypes were exposed to identical environments under the two treatment conditions (water or glyphosate), the metabolite profile patterns of water-treated (control) plants within each biotype were not similar between the two harvest times. This could be attributed to the rapid fluxes of the measured metabolites that were altered in the intervening period between the two sampling time points. Importantly, the metabolic changes observed after glyphosate application capture the differences in response to glyphosate application by the two biotypes. The resistance to glyphosate, though primarily conferred by the multiple copies of the *EPSPS* gene in this resistant *A. palmeri* biotype, may be complemented by the antioxidative protective mechanisms. Considering the recent findings that *EPSPS* gene expression is not equal in all tissue types within a single individual of glyphosate-resistant *A. palmeri* biotypes,[21] the enhanced antioxidant potential might help to mitigate the secondary toxicity of glyphosate due to the production of free radicals in tissues with lower *EPSPS* copies. Also, the observed higher abundance of the anti-oxidant compounds derived from the phenylpropanoid pathway could potentially enhance the performance of this R-biotype under environmental stress.

■ ASSOCIATED CONTENT

Supporting Information

The Supporting Information is available free of charge on the ACS Publications website at DOI: 10.1021/acs.jafc.5b04223.

List of metabolites identified in water- and glyphosate-treated S- and R-biotypes of *A. palmeri*, statistical values for the metabolic responses to the treatments, the equations used to interpret the biochemical assays the LC-MS/MS spectra and relative abundance for phenolics and DPPH assay results (PDF)

■ AUTHOR INFORMATION

Corresponding Author

*Phone: 864-656-4453. E-mail: ntharay@clemson.edu.

Funding

Statistical approaches for this research were partly supported by NIH Grant 5P206M10344 received by P.G.

Notes

The authors declare no competing financial interest.

■ ACKNOWLEDGMENTS

We thank Vidya Suseela for helping with the metabolomics data interpretation, proof-reading, and giving valuable comments on presenting the manuscript in its current form. We also acknowledge William Molin for providing constructive comments on a previous version of this manuscript.

■ ABBREVIATIONS USED

EPSPS, 5-enolpyruvylshikimate-3-phosphate synthase; HAT, hours after treatment; RuBisCO, ribulose-1,5-bisphosphate carboxylase/oxygenase; 3-PGA, 3-phosphoglyceric acid; MDA, malondialdehyde; GR, glutathione reductase; GSSG, oxidized glutathione; GS, glutathione; PAL, phenylalanine ammonia-lyase; TSPs, total soluble proteins; TCA, tricarboxylic acid cycle; PEP, phosphoenolpyruvate; PPi-PFK, pyrophosphate-dependent phosphofructokinase; DAHP, 3-deoxy-D-arabino-heptulosonate 7-phosphate synthase; BCA, bicinchoninic acid; DPPH, 2,2-diphenyl-1-picrylhydrazyl; 4-FQA, 4-*O*-feruloyl-quinic acid; 4-CQA, caffeoylquinic acid

■ REFERENCES

(1) Duke, S. O.; Powles, S. B. Glyphosate: a once-in-a-century herbicide. *Pest Manage. Sci.* **2008**, *64*, 319−325.
(2) Dill, G. M. Glyphosate-resistant crops: history, status and future. *Pest Manage. Sci.* **2005**, *61*, 219−224.
(3) Duke, S. O.; Baerson, S. R.; Rimando, A. M. Herbicides: Glyphosate. In *Encyclopedia of Agrochemicals*; Plimmer, J. R., Gammon, D. W., Ragsdale, N. N., Eds.; John Wiley & Sons: New York, 2003.
(4) Sammons, R. D.; Gruys, K. J.; Anderson, K. S.; Johnson, K. A.; Sikorski, J. A. Reevaluating glyphosate as a transition-state inhibitor of EPSP synthase: Identification of an EPSP synthase-EPSP glyphosate ternary complex. *Biochemistry* **1995**, *34*, 6433−6440.
(5) Heap, I. The international survey of herbicide resistant weeds. http://www.weedscience.org (accessed May 11, 2015).
(6) Moore, J. W.; Murray, D. S.; Westerman, R. B. Palmer amaranth (*Amaranthus palmeri*) effects on the harvest and yield of grain sorghum (*Sorghum bicolor*). *Weed Technol.* **2004**, *18*, 23−29.
(7) Ward, S. M.; Webster, T. M.; Steckel, L. E. Palmer amaranth (*Amaranthus palmeri*): A review. *Weed Technol.* **2013**, *27*, 12−27.
(8) Délye, C. Unravelling the genetic bases of non-target-site-based resistance (NTSR) to herbicides: a major challenge for weed science in the forthcoming decade. *Pest Manage. Sci.* **2013**, *69*, 176−187.
(9) Délye, C.; Jasieniuk, M.; Le Corre, V. Deciphering the evolution of herbicide resistance in weeds. *Trends Genet.* **2013**, *29*, 649−658.
(10) Gaines, T. A.; Zhang, W.; Wang, D.; Bukun, B.; Chisholm, S. T.; Shaner, D. L.; Nissen, S. J.; Patzoldt, W. L.; Tranel, P. J.; Culpepper, A. S.; Grey, T. L.; Webster, T. M.; Vencill, W. K.; Sammons, R. D.; Jiang, J.; Preston, C.; Leach, J. E.; Westra, P. Gene amplification confers

glyphosate resistance in *Amaranthus palmeri*. *Proc. Natl. Acad. Sci. U. S. A.* **2010**, *107*, 1029−1034.
(11) Nandula, V. K.; Reddy, K. N.; Koger, C. H.; Poston, D. H.; Rimando, A. M.; Duke, S. O.; Bond, J. A.; Ribeiro, D. N. Multiple resistance to glyphosate and pyrithiobac in Palmer amaranth (*Amaranthus palmeri*) from Mississippi and response to flumiclorac. *Weed Sci.* **2012**, *60*, 179−188.
(12) Patti, G. J.; Yanes, O.; Siuzdak, G. Innovation: Metabolomics: the apogee of the omics trilogy. *Nat. Rev. Mol. Cell Biol.* **2012**, *13*, 263−269.
(13) Anderson, J. V. Emerging technologies: An opportunity for weed biology research. *Weed Sci.* **2008**, *56*, 281−282.
(14) Molinari, H. B. C.; Marur, C. J.; Daros, E.; de Campos, M. K. F.; de Carvalho, J. F. R. P.; Filho, J. C. B.; Pereira, L. F. P.; Vieira, L. G. E. Evaluation of the stress-inducible production of proline in transgenic sugarcane (*Saccharum* spp.): osmotic adjustment, chlorophyll fluorescence and oxidative stress. *Physiol. Plant.* **2007**, *130*, 218−229.
(15) Suseela, V.; Tharayil, N.; Xing, B.; Dukes, J. S. Warming and drought differentially influence the production and resorption of elemental and metabolic nitrogen pools in *Quercus rubra*. *Glob. Change Biol.* **2015**, doi: 10.1111/gcb.13033
(16) Tzin, V.; Galili, G. New insights into the shikimate and aromatic amino acids biosynthesis pathways in plants. *Mol. Plant* **2010**, *3*, 956−972.
(17) Servaites, J. C.; Tucci, M. A.; Geiger, D. R. Glyphosate effects on carbon assimilation, ribulose bisphosphate carboxylase activity, and metabolite levels in sugar beet leaves. *Plant Physiol.* **1987**, *85*, 370−374.
(18) de María, N.; de Felipe, M. R.; Fernández-Pascual, M. Alterations induced by glyphosate on lupin photosynthetic apparatus and nodule ultrastructure and some oxygen diffusion related proteins. *Plant Physiol. Biochem.* **2005**, *43*, 985−996.
(19) Sergiev, I. G.; Alexieva, V. S.; Ivanov, S. V.; Moskova, I. I.; Karanov, E. N. The phenylurea cytokinin 4PU-30 protects maize plants against glyphosate action. *Pestic. Biochem. Physiol.* **2006**, *85*, 139−146.
(20) Ahsan, N.; Lee, D.; Lee, K.; Alam, I.; Lee, S.; Bahk, J. D.; Lee, B. Glyphosate-induced oxidative stress in rice leaves revealed by proteomic approach. *Plant Physiol. Biochem.* **2008**, *46*, 1062−1070.
(21) Godar, A.; Koo, D.; Peterson, D.; Gill, B.; Jugulam, M. Stability of *EPSPS* gene copies in glyphosate-resistant Palmer amaranth (*Amaranthus palmeri*). *Proceedings of the Weed Science Society of America Annual Meeting*; Lawrence, KS, 2015; Vol. *220*.
(22) Pedersen, H. A.; Kudsk, P.; Fomsgaard, I. S. Metabolic Profiling of *Arabidopsis thaliana* reveals herbicide and allelochemical dependent alterations before they become apparent in plant growth. *J. Plant Growth Regul.* **2015**, *34*, 96−107.
(23) Trenkamp, S.; Eckes, P.; Busch, M.; Fernie, A. R. Temporally resolved GC-MS-based metabolic profiling of herbicide treated plants treated reveals that changes in polar primary metabolites alone can distinguish herbicides of differing mode of action. *Metabolomics* **2009**, *5*, 277−291.
(24) García-Villalba, R.; León, C.; Dinelli, G.; Segura-Carretero, A.; Fernández-Gutiérrez, A.; Garcia-Cañas, V.; Cifuentes, A. Comparative metabolomic study of transgenic versus conventional soybean using capillary electrophoresis-time-of-flight mass spectrometry. *J. Chromat. A* **2008**, *1195*, 164−173.
(25) Serra, A. A.; Couée, I.; Renault, D.; Gouesbet, G.; Sulmon, C. Metabolic profiling of *Lolium perenne* shows functional integration of metabolic responses to diverse subtoxic conditions of chemical stress. *J. Exp. Bot.* **2015**, *66*, 1801−1816.
(26) Lisec, J.; Schauer, N.; Kopka, J.; Willmitzer, L.; Fernie, A. R. Gas chromatography mass spectrometry-based metabolite profiling in plants. *Nat. Protoc.* **2006**, *1*, 387−396.
(27) Fiehn, O.; Wohlgemuth, G.; Scholz, M.; Kind, T.; Lee, D. Y.; Lu, Y.; Moon, S.; Nikolau, B. Quality control for plant metabolomics: reporting MSI-compliant studies. *Plant J.* **2008**, *53*, 691−704.
(28) Shang, Q. M.; Li, L.; Dong, C. J. Multiple tandem duplication of the phenylalanine ammonia-lyase genes in *Cucumis sativus* L. *Planta* **2012**, *236*, 1093−1105.
(29) Yannarelli, G. G.; Fernández-Alvarez, A. J.; Santa-Cruz, D. M.; Tomaro, M. L. Glutathione reductase activity and isoforms in leaves and roots of wheat plants subjected to cadmium stress. *Phytochemistry* **2007**, *68*, 505−512.
(30) Hodges, D. M.; DeLong, J. M.; Forney, C. F.; Prange, R. K. Improving the thiobarbituric acid-reactive-substances assay for estimating lipid peroxidation in plant tissues containing anthocyanin and other interfering compounds. *Planta* **1999**, *207*, 604−611.
(31) Anderson, M. J. A new method for non-parametric multivariate analysis of variance. *Austral Ecol.* **2001**, *26*, 32−46.
(32) Anderson, M. J. *Permutational Multivariate Analysis of Variance*; Department of Statistics, University of Auckland: Auckland, New Zealand, 2005.
(33) Xia, J.; Mandal, R.; Sinelnikov, I. V.; Broadhurst, D.; Wishart, D. S. MetaboAnalyst 2.0–a comprehensive server for metabolomic data analysis. *Nucleic Acids Res.* **2012**, *40*, W127−W133.
(34) Szymańska, E.; Saccenti, E.; Smilde, A. K.; Westerhuis, J. A. Double-check: validation of diagnostic statistics for PLS-DA models in metabolomics studies. *Metabolomics* **2012**, *8*, 3−16.
(35) Herrmann, K. M. The shikimate pathway as an entry to aromatic secondary metabolism. *Plant Physiol.* **1995**, *107*, 7−12.
(36) Steckel, L. E.; Main, C. L.; Ellis, A. T.; Mueller, T. C. Palmer amaranth (*Amaranthus palmeri*) in Tennessee has low level glyphosate resistance. *Weed Technol.* **2008**, *22*, 119−123.
(37) Mueller, T. C.; Massey, J. H.; Hayes, R. M.; Main, C. L.; Stewart, C. N. Shikimate accumulates in both glyphosate-sensitive and glyphosate-resistant horseweed (*Conyza canadensis* L. Cronq.). *J. Agric. Food Chem.* **2003**, *51*, 680−684.
(38) Becerril, J. M.; Duke, S. O.; Lydon, J. Glyphosate effects on shikimate pathway products in leaves and flowers of velvetleaf. *Phytochemistry* **1989**, *28*, 695−699.
(39) Weaver, L. M.; Herrmann, K. M. (1997). Dynamics of the shikimate pathway in plants. *Trends Plant Sci.* **1997**, *2*, 346−351.
(40) Görlach, J.; Raesecke, H. R.; Rentsch, D.; Regenass, M.; Roy, P.; Zala, M.; Keel, C.; Boller, T.; Amrhein, N.; Schmid, J. Temporally distinct accumulation of transcripts encoding enzymes of the prechorismate pathway in elicitor-treated, cultured tomato cells. *Proc. Natl. Acad. Sci. U. S. A.* **1995**, *92*, 3166−3170.
(41) Wang, C. Effect of glyphosate on aromatic amino acid metabolism in purple nutsedge (*Cyperus rotundus*). *Weed Technol.* **2001**, *15*, 628−635.
(42) Jaworski, E. G. Mode of action of N-phosphonomethylglycine. Inhibition of aromatic amino acid biosynthesis. *J. Agric. Food Chem.* **1972**, *20*, 1195−1198.
(43) Gresshoff, P. M. Growth inhibition by glyphosate and reversal of its action by phenylalanine and tyrosine. *Aust. J. Plant Physiol.* **1979**, *6*, 177−185.
(44) Imaoka, A.; Ueno, M.; Kihara, J.; Arase, S. Effect of glyphosate on tryptamine production and Sekiguchi lesion formation in rice infected with *Magnaporthe grisea*. *J. Gen. Plant Pathol.* **2008**, *74*, 109−116.
(45) Duke, S. O.; Hoagland, R. E. Effects of glyphosate on the metabolism of phenolic compounds: VII. Root-fed amino acids and glyphosate toxicity in soybean (*Glycine max*) seedlings. *Weed Sci.* **1981**, *29*, 297−302.
(46) Plaxton, W. C. The organization and regulation of plant glycolysis. *Annu. Rev. Plant Physiol. Plant Mol. Biol.* **1996**, *47*, 185−214.
(47) Smyth, D. A.; Wu, M.-X.; Black, C. C. Pyrophosphate and fructose 2,6-bisphosphate effects on glycolysis in pea seed extracts. *Plant Physiol.* **1984**, *76*, 316−320.
(48) Orcaray, L.; Zulet, A.; Zabalza, A.; Royuela, M. Impairment of carbon metabolism induced by the herbicide glyphosate. *J. Plant Physiol.* **2012**, *169*, 27−33.
(49) Colombo, S. L.; Andreo, C. S.; Chollet, R. The interaction of shikimic acid and protein phosphorylation with pep carboxylase from the C4 dicot *Amaranthus viridis*. *Phytochemistry* **1998**, *48*, 55−59.

DOI: 10.1021/acs.jafc.5b04223
J. Agric. Food Chem. 2015, 63, 9199−9209

(50) Gill, S. S.; Tuteja, N. Reactive oxygen species and antioxidant machinery in abiotic stress tolerance in crop plants. *Plant Physiol. Biochem.* **2010**, *48*, 909−930.
(51) Unver, T.; Bakar, M.; Shearman, R. C.; Budak, H. (2010). Genome-wide profiling and analysis of *Festuca arundinacea* miRNAs and transcriptomes in response to foliar glyphosate application. *Mol. Genet. Genomics* **2010**, *283*, 397−413.
(52) Zhu, J.; Patzoldt, W. L.; Shealy, R. T.; Vodkin, L. O.; Clough, S. J.; Tranel, P. J. Transcriptome response to glyphosate in sensitive and resistant soybean. *J. Agric. Food Chem.* **2008**, *56*, 6355−6363.
(53) Hoagland, R. E.; Duke, S. O.; Elmore, C. D. Effects of glyphosate on metabolism of phenolic compounds. III. Phenylalanine ammonia-lyase activity, free amino acids, soluble protein and hydroxyphenolic compounds in axes of dark-grown soybeans. *Physiol. Plant.* **1979**, *46*, 357−366.
(54) Duke, S. O.; Hoagland, R. E.; Elmore, C. D. Effects of glyphosate on metabolism of phenolic compounds. IV. Phenylalanine ammonia-lyase activity, free amino acids and soluble hydroxyphenolic compounds in axes of light-grown soybeans. *Physiol. Plant.* **1979**, *46*, 307−317.
(55) Lallemand, L. A.; Zubieta, C.; Lee, S. G.; Wang, Y.; Acajjaoui, S.; Timmins, J.; McSweeney, S.; Jez, J. M.; McCarthy, J. G.; McCarthy, A. A. A structural basis for the biosynthesis of the major chlorogenic acids found in coffee. *Plant Physiol.* **2012**, *160*, 249−260.
(56) Reddy, K. N.; Huang, Y.; Lee, M. A.; Nandula, V. K.; Fletcher, R. S.; Thomson, S. J.; Zhao, F. Glyphoste-resistant and glyphosate-susceptible Palmer amaranth (*Amaranthus palmeri* S. Wats.): hyperspectral reflectance properties of plant and potential classification. *Pest Manage. Sci.* **2014**, *70*, 1910−1917.

DOI: 10.1021/acs.jafc.5b04223
J. Agric. Food Chem. 2015, 63, 9199−9209